SOVIET PHYSICS
TECHNICAL PHYSICS

Volume 19 July 1974-June 1975

Herbert Lashinsky, Advisory Editor

American Institute of Physics Translations Advisory Board
Robert T. Beyer, Chairman
J. George Adashko, Freeman Dyson, Dwight Gray
Morton Hamermesh, David Harker, Howard A. Robinson

a translation of the journal
ЖУРНАЛ ТЕХНИЧЕСКОЙ ФИЗИКИ
Zhurnal Tekhnicheskoi Fiziki (Journal of Technical Physics) of the
Academy of Sciences of the USSR
Russian original Vol. 44, January–December 1974

Editorial Board
V.M. Tuchkevich, Editor
G.V. Skornyakov, Associate Editor
Zh.I. Alferov, V.V. Afrosimov, N.G. Basov
A.M. Bonch-Bruevich, S.E. Bresler, E.P. Velikhov
V.E. Golant, G.A. Grinberg, Yu.N. Denisyuk
V.M. Dukel'skii, Yu.A. Dunaev, B.P. Zakharchenya
N.A. Zlatin, N.I. Ionov, E.G. Komar (Deceased)
A.N. Oraevskii, A.M. Prokhorov, N.N. Tikhodeev

published by the American Institute of Physics

Soviet Physics—Technical Physics Vol. 19, No. 1, July 1974

(Russian original: Zh. Tekh. Fiz., Vol. 44, No. 1, pp. 1-240, January 1974)

THEORETICAL AND MATHEMATICAL PHYSICS

1 (3) Focusing of an astigmatic beam by a doublet and a symmetric triplet of quadrupole lenses . . . . V. I. Chetvertkov
3 (6) Round metal-optical waveguide filled with a two-layer dielectric . . . . V. A. Pruzhanovskii

PLASMA

9 (16) Excitation of Alfvén waves in decay instabilities . . . . A. G. Elfimov, F. M. Nekrasov
12 (22) Emission of waves from a plasma layer . . . . T. A. Davydova, A. A. Zhmudskii
16 (28) Stabilization of MHD instabilities by a high-frequency current in a straight system. . . . . V. P. Fedyakova
20 (34) Nonmonoenergetic relativistic electron beam in a bounded collisional plasma . . . . V. P. Grigor'ev, N. S. Shulaev
22 (38) Second-harmonic generation and emission in wave conversion at a plasma boundary. . . . . A. N. Kondratenko, V. G. Shaptala, V. M. Kuklin
25 (43) Conversion of an electromagnetic wave into an ion-acoustic wave in an inhomogeneous plasma . . . . A. N. Kondratenko, V. M. Kuklin
28 (48) Nonlinear plasma waves and ion-acoustic waves in an isotropic plasma . . . . V. Sh. Livadonov, S. M. Fainshtein
31 (53) Ionization discontinuity in large-amplitude striations . . . . A. V. Nedospasov, V. G. Petrov
35 (59) Experimental investigation of anode processes in a closed electron-drift accelerator . . . . I. V. Melikov
38 (65) Dynamics and emission of coaxial plasma shells in air . . . A. F. Aleksandrov, V. V. Perebeinos, A. T. Savichev, I. B. Timofeev
43 (73) Recombination in an expanding plasma . . . . Yu. A. Bykovskii, N. N. Degtyarenko, V. F. Elesin, V. E. Kondrashov, E. E. Lovetskii, A. N. Polyanichev, V. S. Fetisov
49 (83) Spatial characteristics and loss of plasma produced by an electron beam in a magnetic trap . . . . M. Yu. Bredikhin, A. I. Maslov, A. I. Skibenko, E. I. Skibenko, I. P. Fomin, V. B. Yuferov
53 (91) Microwave discharge in argon . . . . E. V. Belousov, A. S. Bryukhovetskii, A. V. Prokopov
57 (98) Electron energy distribution and electrical characteristics of the positive column in H_2 and $H_2 + Cl_2$ . . . . V. V. Zaitsev, A. I. Maksimov, V. I. Svettsov
60 (102) Effect of electron—atom collisions on electron motion in a gas diode . . . . V. I. Babanin, A. Ya. Énder
66 (113) Diagnostics of a laser-produced plasma by a scattering method using an electron-optical image converter . . . . . E. A. Burunov, G. M. Malyshev, G. T. Razdobarin, V. V. Semenov

ACCELERATORS

70 (119) Proton extraction from the 70-GeV accelerator for the Ludmila liquid-hydrogen chamber (extraction system S) . A. A. Aseev, A. I. Drozhdin, B. A. Zelenov, É. A. Merker, L. L. Moizhes, K. P. Myznikov, A. A. Roshchin, V. M. Tatarenko, M. A. Kholodenko, A. D. Artemov, L. N. Vaulin, V. I. Gordin, I. I. Kovalevskii, V. N. Rozhkov, M. M. Suvorov, A. S. Sudarushkin, V. I. Chuiko

HOLOGRAPHY

77 (131) Imaging properties of traveling intensity waves in the recording of dynamic three-dimensional holograms . . . . Yu. N. Denisyuk

PHYSICAL ELECTRONICS

81 (138) Extrapolation of the Langmuir S-curve to cesium pressures of 10-100 torr . . . . V. E. Dubinskii, S. Ya. Lebedev
84 (142) Effect of crystal structure on certain angular dependences of the ion—electron-emission yield . . . . B. A. Brusilovskii, V. A. Molchanov
88 (148) Perveance of a vacuum with a point cathode . . . . S. P. Bugaev, E. A. Litvinov, V. V. Lopatin, G. A. Mesyats

91 (153) Production of collimated beams of high-energy electrons . . . . V. I. Nemchenko

GENERAL

98 (164) Nonradiative electron transitions and thermal effects in laser-irradiated transparent dielectrics . . . . B. I. Makshantsev, A. A. Kovalev, R. K. Leonov, P. A. Yampol'skii
103 (173) Dielectric properties of foamed ceramics at millimeter wavelengths . . . . N. A. Irisova, G. V. Kozlov, V. E. Mandrusov, B. S. Cherepanov, I. M. Chernyshev
105 (177) Two-spin oscillator with optical orientation of electrons and nuclei . . . . R. A. Zhitnikov, V. V. Semenov
110 (185) Dynamic magnetic-resonance phenomena . . . . P. S. Kuts, V. S. Mel'nik

BRIEF COMMUNICATIONS

115 (193) Longitudinal oscillations in an ultrarelativistic electron plasma . . . . D. I. Dzhavakhishvili
116 (194) Contribution of multiphoton processes to the linear dielectric constant . . . . V. A. Bushuev, R. N. Kuz'min
117 (196) Effect of cathode emission on the threshold for striations . . . . N. A. Vorob'eva, Yu. M. Kagan, V. M. Milenin, A. Kh. Muradov
119 (197) Ionization oscillations in a plasma in the presence of ionizing radiation . . . . B. V. Vainer
121 (199) Plasma confinement in a time-increasing multipole magnetic field . . . . V. G. Padalka, N. S. Repalov
123 (201) Reflecting properties of an inhomogeneous anisotropic plasma layer . . . . V. A. Zhivulin, G. I. Makarov
124 (202) Current limiting by self magnetic field in a plasma accelerator . . . . A. G. Korsun
127 (206) Parametric plasma instabilities excited by the sudden application of an electric field . . . . A. B. Kitsenko, K. N. Stepanov
129 (208) Electron repulsion in a time-resolving electron-optical image converter . . . . M. M. Butslov, M. E. Gertsenshtein
131 (210) Aberrations in a straight ion-optical accelerator . . . . E. I. Gerasimov, A. I. Solnyshkov, G. V. Tarvid
134 (213) Effect of electron reflection on the voltage–current characteristics of a high-voltage, hollow-cathode, glow discharge . . . . Ya. Ya. Udris, V. A. Chernov, L. G. Guseva
136 (215) High-power nanosecond electron accelerator with inductive storage . . . . B. M. Koval'chuk, Yu. A. Kotov, G. A. Mesyats
138 (217) Ionization of a gas-discharge gap by fast electrons . . . . O. B. Evdokimov, A. P. Yalovets
140 (219) Ionization and recombination coefficients in a discharge excited by fast electrons . . . . Yu. I. Bychkov, Yu. D. Korolev, A. P. Khuzeev
142 (221) Peak current in a cold-cathode magnetron . . . . I. M. Vigdorchik, V. P. Timofeev
144 (224) Effect of selenium and sulfur on the work function of tungsten . . . . N. V. Volkov, Yu. K. Gus'kov, Z. N. Kononova, Yu. I. Kostikov
146 (225) Displacement of ion-current retardation curves in surface ionization in a strong field . . . . N. I. Ionov
148 (228) Investigation of the work function of a tungsten cathode after bombardment by inert-gas ions . . . . P. N. Chistyakov, R. A. Milovanova, V. V. Lytkin
150 (230) Switching characteristics of a discharge in water . . . . V. M. Kuleshov, S. L. Nedoseev, V. P. Smirnov, A. M. Spektor
152 (232) Reversibility of chalcogeneide materials in holography . . . S. B. Gurevich, N. N. Il'yashenko, B. T. Kolomiets, V. M. Lyubin, M. V. Sukharev
154 (234) Magnetoacoustic transducer based on the domain structure of a ferromagnetic material . . . . G. L. Gurevich, G. A. Vul'gal'ter
156 ERRATA

Soviet Physics – Technical Physics Vol. 19, No. 2, August 1974
(Russian Original: Zh. Tekh. Fiz., Vol. 44, No. 2, pp. 241-480, February 1974)

THEORETICAL AND MATHEMATICAL PHYSICS

157 (241) Calculation of permittivity of an inhomogeneous dielectric by a variational method . . . . . G. A. Ermakov, A. G. Fokin, T. D. Shermergor
161 (249) Calculation of bounds for the effective permittivity of an inhomogeneous dielectric . . . . . G. A. Ermakov, A. G. Fokin, T. D. Shermergor
166 (257) Resonance properties of a pulsating dielectric sphere . . . . . A. G. Nerukh, N. A. Khizhnyak
169 (263) Potential factors for an inhomogeneous ellipsoid . . . . . M. L. Levin, R. Z. Muratov
171 (267) Generation of Bernstein modes in a beam–plasma system . . . . . V. N. Fedorenko

PLASMA

175 (273) Excitation of electromagnetic ion cyclotron waves by fast ions . . . . . T. D. Kaladze, D. G. Lominadze, K. N. Stepanov
177 (277) Parametric instability of an electron beam in a magnetic field . . . . . A. I. Pasynok, N. S. Repalov
181 (284) Scattering by ion-acoustic waves in a rectangular waveguide . . . . . S. V. Troitskii
185 (291) Multimode parametric interactions in a plasma with low-frequency pumping . . . . . Yu. M. Sorokin, N. S. Stepanov
190 (300) Kinetic theory for wave reflection from a moving plasma . . . . . Yu. V. Bogomolov
193 (305) Scattering of high-frequency electromagnetic waves by ion-acoustic oscillations in a bounded plasma . . . . . V. G. Shaptala
197 (311) Electric field and plasma structure near a large charged body . . . . . L. A. Malyavin, A. M. Moskalenko
201 (318) Production of an ion beam by a magnetic system with opposed fields . . . . . V. B. Glasko, A. G. Sveshnikov, N. N. Semashko
206 (325) Structure of a perturbation near a highly charged body in a weakly ionized plasma . . . . . L. A. Malyavin, A. M. Moskalenko
211 (333) Electron energy distribution in the afterglow. I . . . . . A. B. Blagoev, Yu. M. Kagan, N. B. Kolokolov, R. I. Lyagushchenko
215 (339) Electron energy distribution in the afterflow. II . . . . . A. B. Blagoev, Yu. M. Kagan, N. B. Kolokolov, R. I. Lyagushchenko
220 (348) Radiation energy of a magnetoplasma compressor . . . . . V. I. Berkov, A. I. Morozov
224 (355) Physical properties of an electrodeless pulsed discharge in a gas-filled glass cell . . . . . Yu. I. Chutov, N. S. Baranchuk, M. R. Lozovich, V. G. Danilov
229 (364) Narrow-band decimeter radiation from lightning . . . . . E. L. Kosarev, Yu. G. Serezhkin

GENERAL

234 (372) Properties of underexpanded and overexpanded supersonic gas jets . . . . . A. V. Antsupov
239 (380) Gas-kinetic removal of neutral molecules from an ion beam . . . . . V. P. Ivanov
243 (387) Electron-microscope and x-ray study of thermionic emitters made from Mo–Pt alloys . . . . . B. B. Shishkin, R. S. Bakhtiyarov
251 (400) Analysis of the cathode spot in a vacuum arc . . . . . I. I. Beilis
257 (411) Emission processes at the cathode of an electric arc . . . . . I. I. Beilis
261 (419) Time dependence of ion currents produced through surface ionization. Ionization of Ba on the (111) face of iridium . . . . . É. Ya. Zandberg, E. V. Rut'kov, A. Ya. Tontegode
264 (424) Efficient ion source . . . . . D. Kh. Abdrashitova, V. G. Babaev, M. B. Guseva
267 (429) Measurement of statistical parameters of scattering particles in laminar flow by Doppler spectroscopy . . . . . A. P. Ivanov, A. Ya. Khairullina, A. P. Chaikovskii
271 (435) Condensation of a dense vapor flow . . . . . V. G. Dneprovskii, B. A. Osadin, N. V. Rusakov
275 (442) Effect of focusing conditions on the morphology of surface films produced with a laser . . . . . V. G. Dneprovskii, B. A. Osadin
278 (447) Thermophoresis and diffusophoresis of small, volatile aerosol particles . . . . . Yu. I. Yalamov, E. R. Shchukin

280 (451) Electron spectrometer for electric excitation of nuclei in a storage ring . . . . D. M. Nikolenko, S. G. Popov
284 (457) Strobe unit for measuring luminescence in the range 10^{-7}–$2 \cdot 10^{-10}$ sec . . . . V. A. Bonch-Bruevich, N. A. Tolstoi
287 (463) Optical characteristics of K-8 glass subject to radiation from a neodymium laser . . . . A. M. Bonch-Bruevich, Ya. A. Imas, V. S. Salyadinov, A. V. Shatilov

BRIEF COMMUNICATIONS

290 (468) Electron energy distribution in a high-frequency discharge in an axial magnetic field. . . . . S. D. Vagner, V. A. Virolainen, Yu. M. Kagan, T. A. Kalmykova
292 (470) Line shape of a quadrupole mass spectrometer . . . . G. I. Slobodenyuk
294 (472) Investigating prebreakdown fields in water by means of the Kerr effect. . . . . I. T. Ovchinnikov, K. V. Yanshin, É. V. Yanshin
296 (474) New method for obtaining probe characteristics. . . . . Yu. I. Osipov
299 (477) Condensation of an erosion plasma . . . . B. A. Osadin, N. V. Rusakov

Soviet Physics – Technical Physics Vol. 19, No. 3, September 1974

(Russian original: Zh. Tekh. Fiz., Vol. 44, No. 3, pp. 481-688 March 1974)

THEORETICAL AND MATHEMATICAL PHYSICS

301 (481) Energy resolution of quadrupole lenses for charge-particle beams . . . . V. S. Siksin
308 (491) Radiating discharges confined by walls . . . . A. F. Aleksandrov, I. S. Marshak, A. A. Rukhadze
315 (502) Nonlinear statistical theory of a condensate of plasmons. II. Stochastic heating of plasma ions by large-scale Langmuir turbulence . . . . F. Kh. Khakimov

PLASMA

319 (508) Surface waves in a magnetized plasma in a radio-frequency field . . . . E. E. Lovetskii, A. N. Starodub
323 (514) Magnetic field in a θ pinch with an axial conductor. . . . . . . Ya. F. Volkov, V. G. Dyatlov, N. I. Mitina
326 (519) Damping of ion-acoustic waves in a bounded plasma . . . . . A. N. Kondratenko, V. M. Kuklin,
329 (525) Forces in a Hall plasma accelerator . . . . O. N. Mironov
335 (536) Theory of the positive column in neon . . . . Yu. B. Golubovskii, Yu. M. Kagan, R. I. Lyagushchenko
340 (544) Similitude in Hall-current plasma accelerators. . . . . A. I. Morozov, I. V. Melikov
343 (549) Equilibrium flow in a Hall-current plasma accelerator. . . I. V. Melikov
347 (556) Focusing of a neutralized ion beam by a plasma-optics system. . . . . I. I. Demidenko, N. S. Lomino, A. I. Morozov, V. G. Padalka
351 (564) Fast electrons and x rays from nanosecond gas discharges at 0.1-760 torr. . . . . L. V. Tarasova, L. N. Khudyakova, T. V. Loiko, V. A. Tsukerman
354 (569) Electron energy distribution in helium, nitrogen, and their mixtures. . . . . K. D. Asvadurov, I. A. Vasil'eva, V. M. Torchinskii

QUANTUM ELECTRONICS

358 (575) Use of plasma accelerator for optical pumping of lasers. . N. P. Kozlov, Yu. S. Protasov
361 (580) Efficiency of light-beam conversion by dynamic three-dimensional phase holograms . . . . D. I. Stasel'ko, V. G. Sidorovich

ACCELERATORS

366 (588) Beam focusing in an accelerator with inductive energy storage . . . . V. A. Glukhikh, O. A. Gusev, E. G. Komar, V. S. Kuznetsov, M. P. Svin'in, R. P. Fidel'skaya
368 (591) High-current pulsed electron accelerator with an annular beam . . . . M. I. Avramenko, V. A. Glukhikh, O. A. Gusev, E. G. Komar, O. L. Komarov, V. S. Kuznetsov, A. S. Perlin, M. P. Svin'in

PHYSICAL ELECTRONICS

371 (596) Stability of field-emission beams in nanosecond discharges . . . . L. P. Babich
373 (599) Optimum dimensions of a coaxial thermionic converter . . V. V. Sinyavskii
378 (606) End current in a magnetron with a secondary-emission cathode . . . . G. G. Sominskii, S. A. Fridrikhov, O. Yu. Tsybin, A. P. Karizhskii
382 (612) Excitation collisions between magnesium ions and inert gas atoms. . . . . V. L. Ovchinnikov, O. B. Shpenik, I. P. Zapesochnyi
385 (617) Surface-ionization determination of the electron affinities of silver and gold . . . . E. Ya. Zandberg, A. G. Kamenev, V. I. Paleev
390 (625) Effect of ion microfields on emission of an arc cathode . . A. M. Dorodnov, V. B. Davydov, A. V. Kozyrev, Ya. A. Pomelov
394 (632) Simulation of ion scattering on diatomic molecules . . . . . M. L. Aleksandrov, N. S. Pliss, A. P. Shcherbakov

GENERAL

396 (635) Rate for evaporation of a liquid into vacuum . . . . A. P. Andreev, M. A. Gurevich

402 (644) Multiple reflection of light in a shock tube . . . . V. D. Mironov, V. I. Selyakov

BRIEF COMMUNICATIONS

405 (649) Nonlinear instability of a helicon packet in an anisotropic plasma. . . . . Ya. N. Istomin, V. I. Karpman
407 (651) Optimization of the paraxial asymptotic electric field in electron-optical systems. . . . . V. E. Ginzburg, V. N. Danilov
410 (655) Long-wave cyclotron instability in a plasma in an inhomogeneous magnetic field . . . . A. S. Kukushkin
412 (658) Transmission of a high-current relativistic beam through a gas . . . . Yu. V. Tkach, I. I. Magda, G. V. Skachek, S. S. Pushkarev, I. P. Panchenko
414 (660) Radar sounding of sea ice . . . . V. V. Bogorodskii, V. P. Tripol'nikov
416 (662) Two-section solenoid with internal "equally-loaded" section; power as a function of the length of the internal section . . . . G. S. Veisig, A. P. Doroshenko, P. P. Rybin
419 (666) Optical radiation from nanosecond discharges in dense gases. . . . . L. P. Babich
421 (668) Plasma density in a magnetoplasma compressor. . . . . . . A. K. Vinogradova, V. P. Vinogradov, A. I. Morozov, A. A. Sergeev
424 (671) Investigation of spatial distributions in a laser-produced plasma by Hα absorption. . . . . G. V. Ostrovskaya, N. A. Pobedonostseva
427 (674) Two-omegatron study of the pumping characteristics of an NÉM-300 magnetic-discharge pump for a mixture of gases . . . . M. K. Bulgakov, V. G. Rogozinskii
429 (677) Possible use of the schlieren method to measure characteristics of turbulence. V. G. Ivanov
432 (680) Titanium-pump system for hydrogen. . . . . K. G. Mirzoev, V. G. Rogozinskii, V. L. Ushkov
434 (682) Temperature dependence of trace diffusion coefficients of certain gases. . . . . A. É. Loiko, B. A. Ivakin, P. E. Suetin

Soviet Physics — Technical Physics Vol. 19, No. 4, October 1974

(Russian original: Zh. Tekh. Fiz., Vol. 44, No. 4, pp. 689-896, April 1974)

THEORETICAL AND MATHEMATICAL PHYSICS

435 (689) Charged-particle motion in a dipole magnetic field ..... L. G. Glikman

PLASMA

441 (698) Excitation of acoustic waves by ion-acoustic turbulence .. Kh. O. Abdulloev, F. Kh. Khakimov, V V. G. Makhan'kov
446 (706) Plasma acceleration in crossed electric and magnetic fields ..... V. I. Aref'ev
455 (723) Conversion of regular charge-density waves in an inhomogeneous plasma ..... S. S. Kalmykova, A. P. Tolstoluzhskii
459 (729) Role of collisions in plasma absorption of electromagnetic waves near the lower hybrid ..... B. V. Galaktionov, V. V. D'yachenko, M. M. Larionov, O. N. Shcherbinin
463 (735) Distributed systems for feedback control of a tokamak plasma ..... V. F. Gubarev, Yu. I. Samoilenko
468 (743) Plasma diffusion in the Tornado device ..... A. N. Kozyrev, B. P. Peregud
475 (754) Electron density in an argon afterglow ..... O. P. Bochkova, R. I. Lyagushchenko, É. A. Sukiasyan, Yu. A. Tolmachev
478 (759) Supersonic plasma jet from a high-power pulsed discharge ..... M. A. Sultanov
483 (766) Experimental investigation of microwave radiation produced by hypersonic flows ..... V. A. Lyutomskii, V. M. Polyakov, V. G. Testov

QUANTUM ELECTRONICS

486 (770) Parasitic amplitude modulation of a stabilized Nd^{3+}:YAG laser ..... N. N. Galaktionova, A. A. Mak, A. P. Khyuppenen
491 (778) Thermal effect of continuous laser radiation on optically transparent media ..... N. S. Bardina, A. I. Portnyagin, M. Yu. Sklyarov, A. A. Churin
495 (784) Quenching in the CF$_3$I photodissociation laser ..... G. A. Skorobogatov, V. M. Tret'yak, V. S. Komarov
499 (791) Energy input in electrical ionization lasers ..... Yu. I. Bychkov, Yu. D. Korolev, Yu. A. Kurbatov, G. A. Mesyats
503 (797) Pulsed neodymium-glass laser with periodic Q switching ..... T. A. Kuzovkova, E. V. Nilov, V. A. Rusov, I. N. Semenov, A. A. Chertkov
506 (803) Characteristics of the electrical ionization CO$_2$ laser ..... Yu. I. Bychkov, Yu. A. Kurbatov, V. V. Savin

ACCELERATORS

509 (808) Linear accelerator for beam injection into a slowly rising magnetic field ..... D. G. Borisov, A. I. Gryzlov, V. M. Levin, A. V. Ryabtsov

GENERAL

511 (812) Use of the distribution function to describe free molecular beams ..... I. G. Neudachin, B. T. Porodnov, P. E. Suetin
515 (818) Flow of low-density gases in a capillary grid ..... B. T. Porodnov, V. D. Akin'shin, V. I. Kichaev, S. F. Borisov, P. E. Suetin
519 (824) Transient molecular effusion characteristics ..... Yu. N. Lyubitov, V. Z. Belen'kii
523 (830) A transaxial lens ..... V. M. Kel'man, L. M. Nazarenko, E. M. Yakushev
526 (835) Differential electromagnetic characteristics at the interface between ice and water in the ocean ..... V. V. Bogorodskii, V. P. Tripol'nikov

BRIEF COMMUNICATIONS

529 (839) Evolution of monochromatic whistler and plasma-wave packets in a collisionless plasma ..... Ya. N. Istomin
531 (841) Diffraction of a plane electromagnetic wave by a conducting plane with a projection ..... A. A. Zilbergleit

533 (844) Reflection of electromagnetic waves by a moving plasma . V. I. Miroshnichenko
535 (848) A useful function in the thermodynamics of irreversible processes. . . . . A. V. Pamfilov, A. I. Lopushanskaya, L. B. Tsvetkova
538 (851) Effect of ion current on the measurement of the electron energy distribution function by the second-derivative method. . . . . V. A. Dovzhenko, A. P. Ershov, G. S. Solntsev
540 (854) Energy dependence of the focusing of ions by crystals . . . E. S. Mashkova, V. A. Molchanov, A. D. Pavlova
541 (855) Steady-state study of the temperature dependence of the mutual-diffusion coefficients of certain gases. . . . . N. D. Kosov, B. P. Solonitsyn
543 (857) Statistical characteristics of the turbulent wake behind a supersonic sphere . . . . V. G. Ivanov, G. I. Mishin, S. N. Palkin
546 (861) Gas focusing of a negative-ion beam . . . . M. D. Gabovich, A. P. Naida, I. M. Protsenko, L. S. Simonenko, I. A. Soloshenko
548 (863) Time characteristics of the near radiation field of the injection laser. . . . . Zh. I. Alferov, V. N. Deryagin, L. E. Marasin, Yu. V. Popov, E. L. Portnoi
549 (864) Frequency-doubling single-mode laser for picosecond pulses . . . . A. M. Bonch-Bruevich, A. M. Tkachuk, A. A. Fedorov
552 (868) Unidirectional cw oscillation in a solid state ring laser with a return mirror . . . . A. A. Mak, V. I. Ustyugov, V. A. Fromzel', M. M. Khaleev
554 (870) Measurement of plasma ion temperature by a thin probe with $T_i \gg T_e$. . . . . B. I. Kanaev, E. E. Yushmanov
556 (873) Effect of instrumental noise on a system with two spin oscillators using Cs^{133} and He^3. . . . . R. A. Zhitnikov, V. V. Semenov, P. A. Klyushkin
558 (875) Method for determining the absolute characteristics of CF_3I laser emission . . . . V. S. Komarov, V. G. Seleznev, G. A. Skorobogatov
561 (878) Electrostatic analyzer for wide beams. . . . . V. G. Kovalenko, B. V. Polenov
563 (881) Vacuum-UV and soft x-ray emission in a magnetoplasma compressor . . . . P. E. Kovrov, L. G. Tokarev
565 (883) Multiple recording and erasure of optical information in certain glassy chalcogenides . . . . V. V. Korsakov, V. I. Nalivaiko, V. G. Remesnik, V. G. Tsukerman
567 (886) Temperature dependence of the dielectric permittivity of single-crystal TiO_2 in the submillimeter range . . . . . A. A. Volkov, N. A. Irisova, G. V. Kozlov
569 (888) Low-voltage gun with a resonator for formation of electron bunches in a linear accelerator. . . . . V. A. Boiko, R. M. Voronkov, V. A. Danilichev
572 (891) Parametric excitation of surface waves in a spatially modulated electron beam. . . . . A. I. Pasynok, N. S. Repalov

Soviet Physics — Technical Physics Vol. 19, No. 5, November 1974

(Russian original: Zh. Tekh. Fiz., Vol. 44, No. 5, pp. 897-1120 May 1974)

575 (897) 250 years of the Academy of Sciences of the USSR

THEORETICAL AND MATHEMATICAL PHYSICS

581 (906) Two-dimensional diffraction on a system of straight segments (shields) . . . . G. A. Grinberg
586 (916) Conductivity of a medium with inhomogeneous inclusions in a magnetic field . . . . Yu. P. Emets
589 (922) Nonlinear polarizability of a gaseous medium in a longitudinal magnetic field . . . . V. A. Sokolov, L. M. Khayutin
592 (928) Theory of the cathode lens. III. Derivation of equations for composite cathode lenses . . . . V. M. Kel'man, A. A. Sapargaliev, E. M. Yakushev
597 (938) Theory of the cathode lens. IV. Aberrations of composite cathode lens . . . . V. M. Kel'man, A. A. Sapargaliev, E. M. Yakushev
600 (944) Variational analysis of thermal breakdown of a semiconductor irradiated by light . . . . V. L. Komolov
603 (950) Reflection of finite amplitude electromagnetic waves from a semiconductor plasma. . . . . Yu. F. Filippov
607 (956) Cerenkov instabilities of a relativistic beam in a periodic plasma-filled waveguide . . . . V. I. Kurilko, Yu. V. Tkach, V. A. Shendrik
612 (965) Local-potential study of the Bérnard problem in a homogeneous magnetic field. . . . . A. I. Lopushanskaya, V. N. Kapranov

PLASMA

615 (971) Linear theory for the low-frequency electromagnetic properties of an isotropic turbulent plasma. . . . . K. Komilov, F. Kh. Khakimov, V. N. Tsytovich
618 (977) Excitation of surface electromagnetic waves in a plasma cylinder surrounded by a hollow electron beam . . . . . . O. V. Dolzhenko, A. V. Zosimov, A. A. Rukhadze
622 (985) Launching and propagation of regular nonlinear waves in an anisotropic plasma-filled waveguide. . . . . V. I. Kurilko, A. P. Tols-toluzhskii, Ya. B. Fainberg
628 (995) Kinetic plasma instabilities excited by a monoenergetic beam . . . . A. I. Ranyuk, V. L. Sizonenko
630 (998) Quasilinear theory of beam-generated surface waves in a plasma . . . . V. I. Pakhomov, V. L. Sizonenko
635 (1006) Instabilities in a finite-β plasma with transverse current. I. . . . . A. I. Pyatak, V. L. Sizonenko
640 (1014) Instabilities in a finite-β plasma with transverse current. II . . . . A. I. Pyatak, V. L. Sizonenko
645 (1022) Charge-carrier density of the plasma produced in a Penning mixture by irradiation by uranium fission fragments and reactor radiation . . . . G. A. Batyrbekov, Yu. D. Kuznetsov, Zh. S. Takibaev
647 (1025) Expansion of a recombining plasma in vacuum. . . . . E. E. Lovetskii, A. N. Polyanichev, V. S. Fetisov
651 (1032) Investigation of ionization processes behind strong shock waves using an electrical conductivity probe . . . . V. A. Tishchenko, N. V. Khandurov, É. K. Chekalin
654 (1037) Theory of the low-voltage arc in a narrow gap. . . . . F. G. Baksht, A. A. Kostin, V. A. Nemchinskii
658 (1044) Continuous electron acceleration in a gas discharge . . . . G. D. Alkhazov

ACCELERATORS

660 (1047) Inductive energy storage in pulsed accelerators. . . . . . . V. A. Glukhikh, O. A. Gusev, E. G. Komar, M. P. Svin'in
662 (1051) Shaping of voltage pulses by discharging an inductive storage bank with a charged-particle beam. . . . . O. A. Gusev, E. G. Komar, V. B. Markov, E. M. Mellekh

GENERAL

664 (1055) Polarization of a cavity with a thermally deformed active element . . . . I. B. Vitrishchak, L. N. Soms, A. A. Tarasov

669 (1063) Gas cooling in transmission of high-power CO_2 laser radiation through the atmosphere . . . B. F. Gordiets, A. I. Osipov, R. V. Khokhlov
673 (1070) Nonlinear spherical aberrations and thermoelastic stresses in thermal self-focusing . . . A. A. Vigasin, Yu. A. Gorokhov, A. P. Sukhorukov, A. M. Khachatryan
676 (1076) Possible electrohydrodynamic effects in electrolytes . . . E. Z. Gak, É. Kh. Rokhinson, N. F. Bondarenko
678 (1080) Electron-scanning transformation of the potential distribution on an electrostatic target . . . V. L. Lentsman
680 (1084) Symmetric multielectrode tubular electrostatic lenses . . . L. G. Glikman, V. M. Kel'man, M. Sh. Nurmanov

BRIEF COMMUNICATIONS

683 (1088) Upper and lower limits on the capacitance of a plane capacitor . . . R. F. Fikhmanas, P. Sh. Fridberg
685 (1090) Impossibility of shielding against the rf radiation of a thermonuclear reactor with a cold-plasma sheath . . . A. S. Chikhachev
686 (1092) Absolute decay instability of low-frequency waves in an inhomogeneous plasma . . . A. D. Piliya, V. I. Fedorov
687 (1093) Effect of a high-frequency electric field on the energy loss of a charged particle in a medium . . . Zh. M. Diasamidze
689 (1095) Contraction of the positive column of a glow discharge due to the presence of negative ions . . . L. A. Mikhalev, L. N. Selin
691 (1097) Current-driven instability in a conducting fluid . . . A. M. Kovnatskii
692 (1099) Convection in a liquid dielectric in a longitudinal electric field . . . I. V. Ioffe, N. V. Kalinin
693 (1100) Infrared nitrogen laser using a transverse discharge . . . V. F. Tarasenko, Yu. I. Bychkov
694 (1101) Microwave maser with nonrelativistic electrons . . . A. S. Dement'ev, Yu. G. Pavlenko
696 (1104) Holography of raster objects . . . Sh. D. Kakichashvili
698 (1106) NÉM-1T magnetic-discharge pumps in the vacuum system of the I-100 linear accelerator . . . O. N. Krokhina, K. G. Mirzoev
700 (1108) Method for studying gas creep along a solid surface . . . B. M. Markeev
702 (1110) X-ray fluorescence of oxygen in H_2O . . . L. A. Smirnov
703 (1111) Dispersion of the dielectric constant of crystalline KH_2PO_4 near the "soft" mode frequency . . . V. V. Meriakri, Yu. M. Poplavko, E. F. Ushatkin
705 (1113) Formation of molecular ions in an alkali discharge . . . V. N. Paslen, A. M. Przhonskii
707 (1115) Current density of thermonic-field emission into a plasma at moderate fields . . . I. N. Ostretsov, V. A. Petrosov, A. A. Porotnikov, B. B. Rodnevich
709 (1117) Preservation of semiconductor field-emission cathodes . N. V. Egorov, G. N. Fursei, M. K. El'Nimr

Soviet Physics – Technical Physics Vol. 19, No. 6, December 1974

(Russian original: Zh. Tekh. Fiz., Vol. 44, No. 6, pp. 1121-1344, June 1974)

THEORETICAL AND MATHEMATICAL PHYSICS

711 (1121) The magnetostatic problem for thin closed shells...... I. P. Krasnov
713 (1125) Microwave propagation in a low-loss dielectric....... L. É. Rikenglaz
715 (1129) Maximum current of a beam with finite phase volume... G. I. Trubnikov, V. S. Kuznetsov

PLASMA

717 (1133) Symmetry of high-frequency plasma motions......... A. A. Zhmudskii, V. B. Taranov
719 (1137) Aperiodic instability in a plasma with external feedback........................... A. N. Igritskii
722 (1143) Magnetodrift waves in a finite-β plasma............ N. M. Ryzhov, V. L. Sizonenko, V. A. Suprunenko, E. A. Sukhomlin, Yu. V. Gutarev
726 (1151) Wave interaction in a thin plasma sheath............ A. V. Pashchenko, B. N. Rutkevich
732 (1161) Generation of drift waves by an rf field near the lower hybrid frequency......................... Yu. F. Baranov, D. G. Bulyginskii, M. I. Vil'dzhyunas, B. V. Galaktionov, N. V. Shustova
736 (1168) Coaxial plasma injector with programmed injection.... V. A. Burtsev, V. N. Litunovskii, M. P. Nadgornaya
741 (1176) Conversion of neutral hydrogen into protons in dense plasmas............................. T. A. Bazilevskaya, L. I. Krupnik, N. G. Shulika
745 (1183) Model for the low-voltage arc. I. Stationary solution... Yu. Yu. Abramov, G. G. Gladush
748 (1188) Model for the low-voltage arc. II. Stability......... Yu. Yu. Abramov, G. G. Gladush
751 (1193) Interferometer measurement of the neutral cesium distribution in a short low-voltage arc............ Yu. L. Serov, I. P. Yavor
755 (1200) Formation of a narrow gas jet in vacuum............ G. I. Dimov, V. Ya. Savkin
759 (1206) Electron-beam excited crossed-field discharge....... V. A. Saenko, M. M. Kasumov

ACCELERATORS

762 (1210) Extraction of synchrotron radiation from a cyclic electron accelerator with a strong magnetic field..... V. I. Kvochka, V. S. Panasyuk, V. F. Romanovskii, L. N. Samoilov, A. A. Sokolov, B. M. Stepanov, Yu. M. Tereshkin
767 (1218) Resonator with azimuthally varying end plates........ M. F. Vorogushin, V. I. Petrunin
770 (1222) Azimuthal and vertical motion in an accelerator with azimuthally varying electric field............... M. F. Vorogushin, V. I. Petrunin
773 (1228) Spatial and energy parameters of the relativistic electron beam of the Rius-5 accelerator........... A. T. Altyntsev, V. I. Koroteev

GENERAL

775 (1232) Kinetics of gasdynamic lasers. Effect of nozzle geometry on inversion........................ A. S. Biryukov, L. A. Shelepin
782 (1244) Photochemical waves in a medium with a branch-chain conversion mechanism....................... A. N. Oraevskii, V. P. Pimenov, V. A. Shcheglov
787 (1253) Direct and cascade four-photon parametric scattering of light in $LiIO_3$ crystals..................... S. M. Arakelyan, V. G. Tunkin, A. I. Kholodnykh, A. S. Chirkin
793 (1262) Vaporization and boiling of liquid metal in an exploding wire................................. M. M. Martynyuk
798 (1271) Approximate similarity relations in the electrical explosions of underwater conductors............ E. V. Krivitskii, V. K. Sholom
802 (1277) Breakdown caused by electron bombardment of the surface of an alloy electrode.................. N. V. Belan, G. I. Kostyuk, V. A. Pimkin
804 (1280) Emission characteristics of an explosive gallium cathode.............................. G. N. Fursei, V. M. Zhukov
808 (1287) Atomic recombination on a solid surface........... V. P. Pinchuk, A. N. Gorban', V. G. Kornich
811 (1292) Absorption of bismuth on tungsten. I. Steady-state processes.............................. M. A. Mittsev

815 (1298) Effects of cleaning on adsorption by germanium single crystals . . . . . Yu. I. Belyakov, M. P. Volkov, T. N. Kompaniets
817 (1302) Monte Carlo analysis of ion scattering in a mass spectrometer . . . . . M. L. Aleksandrov, L. N. Gall', N. S. Pliss
820 (1306) Behavior of molten salts in strong electric fields . . . . . A. Z. Éfendiev, O. M. Shabanov, S. M. Gadzhiev S. M. Tagirov
824 (1312) Shielding properties of superconducting shields . . . . . S. I. Bondarenko, S. S. Vinogradov, G. A. Gogadze, S. S. Perepelkin, V. I. Sheremet

BRIEF COMMUNICATIONS

829 (1321) Sign of the change in optical path length in a laser interferometer with feedback . . . . . I. M. Belousova, A. F. Zapryagaev
831 (1323) Spontaneous mode locking in a laser with a multifaceted active element . . . . . E. I. Kamenskii, V. V. Kozlov
833 (1326) Optical simulation of a radiator aperture with arbitrary amplitude–phase distribution . . . . . M. M. Butusov, Sh. V. Yurevichyus
835 (1328) Lasing properties of Yb^{3+} and Er^{3+} glass laser pumped by a laser . . . . . V. N. Kalinin, A. A. Mak, D. S. Prilezhaev, V. A. Fromzel'
837 (1331) Characteristics of diffraction gratings obtained by photoetching of semiconductor surfaces . . . . . L. V. Belyakov, D. N. Goryachev, M. N. Mizerov, E. L. Portnoi
839 (1333) Ion emission into vacuum from a discharge in crossed electric and magnetic fields . . . . . V. A. Nikitinskii, A. S. Zakharov
841 (1334) Angular aberration corrector in a cylindrical-mirror analyzer . . . . . V. V. Zashkvara, V. F. Tarasov
843 (1337) Resonant amplification of an image potential by an electromagnetic wave . . . . . Yu. I. Balkarei, É. M. Épshtein
845 (1339) Thermo-acoustic waves in conducting gases and liquids . P. A. Andreev

Soviet Physics – Technical Physics Vol. 19, No. 7, January 1975

(Russian original: Zh. Tekh. Fiz., Vol. 44, No. 7, pp. 1345-1568, July 1974)

THEORETICAL AND MATHEMATICAL PHYSICS

847 (1345) Hologram interferometry for vibration analysis (review) — V. S. Listovets, Yu. I. Ostrovskii
861 (1373) Stability of ball lightning — I. P. Stakhanov
865 (1380) Radiation from a charged particle moving close to an anisotropic dielectric — A. I. Plis, N. M. Safikhodzhaev
868 (1385) Estimate of the angular divergence in intense electron beams — V. S. Kuznetsov, Yu. P. Vakhrushin, O. L. Komarov, R. P. Fidel'skaya
871 (1389) Parametric instability of a spatially moderated electron beam in a magnetic field — N. S. Repalov, V. F. Tyrnov
874 (1395) Magnetohydrodynamic channel flow in a tapered magnetic field — S. A. Regirer
878 (1401) Nonstationary magnetohydrodynamic flow and wave propagation — M. Ya. Antimirov, Yu. Ya. Boguslavskii

PLASMA

880 (1405) Propagation and stability of large-amplitude ionization waves — M. S. Gorelik, L. D. Tsendin
883 (1410) Surface waves in periodic plasma systems — V. F. Dryakhlushin, Yu. A. Romanov
887 (1418) Solitary waves in anisotropic plasma waveguide — V. I. Kurilko, A. P. Tolstoluzhskii
891 (1424) Low pressure discharge with high-energy electrons — R. A. Demirkhanov, Yu. V. Kursanov, L. P. Skripal'
895 (1432) Stabilization of the major radius of toroidal pinch by a feedback system — V. V. Arsenin
898 (1437) High-frequency discharge in a mercury–helium mixture — S. D. Vagner, Yu. M. Kagan, A. I. Konstantinov, I. S. Niskonen
901 (1442) Effect of ionization and excitation on the penetration of an electromagnetic wave into a weakly ionized plasma — A. G. Boev, A. V. Prokopov
905 (1448) Optical investigation of a turbulent plasma — Ya. F. Volkov, V. G. Dyatlov, N. I. Mitina
909 (1455) Electron temperature in a high-frequency helium discharge — V. S. Voitsenya, A. Yu. Voloshko, V. G. Konovalov, S. I. Solodovchenko
911 (1458) Effect of molecular hydrogen on a cesium discharge. I — N. D. Morgulis, V. I. Klapchenko
914 (1463) Mass and energy analysis of ions in the cathode region of an anomalous glow discharge. II. Binary gas mixtures N_e+Ar and N_2+Ar — A. V. Bondarenko
919 (1472) Electromagnetic fields outside a synthesized plasma jet — E. V. Bogdanov, G. M. Mantrova, M. N. Yakovleva

ACCELERATORS

922 (1477) Efficiency of internal targets in the accelerator at the Institute of High-Energy Physics — V. I. Gridasov, K. P. Myznikov, V. N. Chepegin
926 (1484) Phase motion of particles in an accelerator with an azimuthally varying electric field — M. F. Vorogushin, V. I. Petrunin
930 (1490) Multiple-section linear electron accelerator with synchronized oscillators — V. F. Vikulov, V. A. Volodin, O. S. Milovanov
932 (1494) Control of output energy in linear electron accelerators — V. N. Golovin, N. P. Sobenin

QUANTUM ELECTRONICS

935 (1499) Crystal defects of heterostructures of AlAs-GaAs solid solutions and effect on the characteristics of injection lasers — L. V. Druzhinina, V. T. Bublik, L. M. Dolginov, P. G. Eliseev, M. P. Kerbelev, V. B. Osvenskii, I. Z. Pinsker, M. G. Shumskii
940 (1507) Determination of ionization potentials and electron affinities of certain elements by extrapolation — A. G. Kamenev, É. Ya. Zandberg, V. I. Paleev
942 (1511) Evaluation of charge distribution in a crossed-field device from ion bombardment of the cathode — V. I. Malyugin, G. G. Sominskii
946 (1517) Thermal conditions for a sandwich cold cathode — F. M. Benson, P. E. Troyan, Yu. B. Yankelevich

948 (1521)	Nanosecond x-ray pulses	G. A. Mesyats
952 (1528)	Superconducting magnetic shields	S. I. Bondarenko, V. I. Sheremet
956 (1534)	Effect of the adsorption rate on the diffusion of deuterium through nickel	Yu. I. Belyakov, Yu. I. Zvezdin, A. A. Kurdyumov, G. G. Nevdakha

BRIEF COMMUNICATIONS

959 (1539)	Ion-acoustic instability of a fully ionized ultrarelativistic plasma in an electric field	D. I. Dzhavakhishvili
961 (1541)	Correction of third-order angular aberration in a system with two electrostatic mirrors	V. V. Zashkvara
963 (1543)	Linear transient response of a fully ionized plasma in a pulsed electric field	V. V. Istomin, S. P. Sher, S. P. Dovgopol
965 (1545)	Capillary gravitational waves and the mechanogalvanic effect	E. D. Korlyakov
966 (1547)	Elimination of spherical aberration in an axial plasma lens	S. V. Lebedev, A. I. Morozov
967 (1548)	Achromatic plasma–lens system	A. I. Morozov, S. V. Lebedev
968 (1550)	Multiple-aperture ion source for electromagnetic mass separator	S. V. Lebedev
969 (1550)	Viscous momentum transport in a gaseous mixture	B. M. Markeev
971 (1553)	Atomic diffusion from a finite film over a solid surface	Yu. D. Kornyushkin
973 (1556)	Ion focusing of an electron beam in deep melting of a metal	M. D. Gabovich, V. P. Kovalenko, O. A. Metallov, O. K. Nazarenko, S. K. Pats'ora
975 (1557)	N_2O-N_2-He gasdynamic laser	Yu. I. Grin', V. G. Testov
976 (1559)	Scattering of He^+ ions by the core of the He atom	Z. Z. Latypov, A. A. Shaporenko
978 (1560)	Energy spectra of scattered particles in proton bombardment of a metal target	G. I. Zhabrev, V. A. Kurnaev, V. G. Tel'kovskii
980 (1562)	Mode coupling in a double-anode discharge	Yu. G. Zakharenko, V. E. Privalov

Soviet Physics—Technical Physics Vol. 19, No. 8, February 1975

(Russian original: Zh. Tekh. Fiz., Vol. 44, No. 8, pp. 1569-1808, August 1974)

THEORETICAL AND MATHEMATICAL PHYSICS

983	(1569)	Fundamentals of heat-pipe theory and design	M. M. Levitan, T. L. Perel'man
996	(1592)	Design of axisymmetric plasma lenses	A. I. Morozov, S. V. Lebedev
1001	(1601)	Acousto-electric waves in conducting media	P. A. Andreev
1005	(1608)	Equilibrium in a tokamak with noncircular cross section	L. E. Zakharov
1009	(1614)	Lagrange problem in magnetohydrodynamics	P. V. Zagorskii, Yu. P. Lun'kin
1012	(1619)	Liquid crystals in external fields	I. V. Ioffe
1016	(1625)	Effect of temperature-dependent conductivity on electromagnetic field, current, temperature, and impedance in a plane conductor. I	R. S. Kuznetskii
1020	(1633)	Parametric interaction of a charged particle beam with a periodic system	V. I. Koroza, E. S. Sukhovskii
1025	(1641)	Computer calculation of quasistationary pulsed magnetic fields	V. I. Yurchenko
1031	(1650)	Flux loss in the production of ultrastrong fields by rapid compression of conducting shells	V. I. Yurchenko
1034	(1656)	Stability of the diode	V. A. Buts

PLASMA

1038	(1662)	Low-frequency oscillations in counter-streaming high-current electron beams	A. P. Timoshenko, D. V. Iremashvili, Yu. K. Udovichenko
1042	(1669)	Cell for forming electron beams of arbitrary shape in a high-voltage gaseous discharge	I. V. Vagner, É. I. Bolgov, V. F. Grakun, V. L. Gokhfel'd, V. A. Kudlai
1046	(1675)	Scattering of an electron beam in a straight dc turbulent plasma	Yu. P. Golovanov, L. P. Zakatov, A. S. Kingsep, A. G. Plakhov
1050	(1682)	Effect of loss on electron avalanches in optical breakdown	V. I. Fisher
1053	(1687)	Power spectrum of potential fluctuations in a moving magnetoactive plasma	V. M. Kostin
1057	(1693)	Radiation emitted by charged particles trapped by plane electromagnetic waves	V. Ya. Davydovskii, A. S. Ukolov
1061	(1699)	Investigation of a plasma focus with a time-resolved laser interferometer	I. M. Zolototrubov, I. P. Skoblik, A. G. Tolstolutskii, V. I. Privezentsev
1063	(1703)	Plasma equilibrium and confinement in a poloidal heliotron configuration. I	V. G. Zykov, V. I. Karpukhin, Yu. F. Lonin, N. N. Podteregera, N. I. Rudnev, V. T. Tolok
1069	(1713)	Plasma equilibrium and confinement in a poloidal heliotron configuration. II	V. G. Zykov, V. I. Karpukhin, Yu. F. Lonin, N. N. Podteregera, N. I. Rudnev, A. I. Skibenko, V. T. Tolok, I. P. Fomin
1073	(1719)	Nonequilibrium ionization in the cathode region of a high-pressure arc	S. P. Reshenov

QUANTUM ELECTRONICS

1076	(1724)	Plasma dynamic lasers	S. A. Reshetnyak, L. A. Shelepin
1081	(1733)	Effect of plasma parameters on emission in an ion laser	I. E. Sakharov, V. V. Ermolin, S. V. Shatalin

ACCELERATORS

1085	(1740)	Self-excited waveguide buncher	N. M. Gavrilov, A. V. Nesterovich
1087	(1743)	Self-acceleration of an intense electron beam	I. A. Grishaev, A. N. Dedik, V. V. Zakutin, I. I. Magda, Yu. V. Tkach, A. M. Shenderovich

GENERAL

1090	(1749)	Secondary-electron energy in a resonance discharge in a three-electrode system	Yu. A. Kulikov, V. V. Ogienko, Yu. M. Trifonov
1093	(1753)	Microcells in cold cathodes	N. P. Kozlov, A. A. Lyapin, V. I. Khvesyuk
1096	(1758)	Evaporation rates of the system $ZrC + x\%W$ for the temperature range 2300-3000°K	N. M. Karnaukhova, V. A. Luknitskii, I. A. Maslov
1100	(1765)	Mass-spectrometer study of the ion composition of a glow discharge	N. P. Egorov, V. N. Komarov

1103 (1770) Energy losses of slow electrons reflected from molybdenum and tungsten single crystals — O. M. Artamonov, B. B. Bolotov, M. V. Kremkov

1105 (1774) Diffusion and solubility of helium in potassium chloride — A. Y. Kupryazhkin, P. V. Volobuev, P. E. Suetin

BRIEF COMMUNICATIONS

1108 (1779) Pulsed ion beams from a high-current plasma diode — B. A. Tskhadaya, A. A. Plyutto, K. V. Suladze

1110 (1781) Parallel-plate capacitor as a charged-particle spectrometer — Yu. D. Kornyushkin

1113 (1785) Energy exchange between electrons and molecular vibrational states in resonance collisions — A. Kh. Mnatsakanyan, G. V. Naidis

1116 (1788) Plasma decay instability in crossed fields — V. I. Farenik, V. V. Vlasov, A. M. Rozhkov, A. A. Kozharin

1118 (1790) Titanium adsorption on tungsten — Yu. K. Ustinov, S. V. Fedichev

1120 (1792) Effect of the radiation density on ion drift velocity in a cadmium–helium laser — G. N. Tolmachev, E. L. Latush, V. S. Mikhalevskii

1122 (1795) Dielectric strength of a vacuum gap with electrodes irradiated with He^+ and H^+ ions — A. P. Solodovnikov, Yu. M. Khirnyi

1123 (1796) Hydrodynamic stability of the Uragan stellarator — V. M. Zalkind, Yu. K. Kuznetsov, V. K. Pashnev, V. M. Tonkopryad

1126 (1799) Equations and boundary conditions for a three-dimensional quasistationary field — V. I. Yurchenko

1129 (1802) Steady-state operation of a surface-ionization thermionic converter — N. V. Volkov, Yu. K. Gus'kov, Yu. I. Kostikov, V. P. Pashchenko

1131 (1804) Transient thermionic-field emission from a point cathode — E. A. Litvinov, A. F. Shubin

Soviet Physics – Technical Physics Vol. 19, No. 9, March 1975

(Russian original: Zh. Tekh. Fiz., Vol. 44, No. 9, pp. 1809-2032, September 1974)

1133 (1809) Recent developments in surface ionization (review) É. Ya. Zandberg

PLASMA

1145 (1829) Transverse-current plasma instability D. G. Lominadze, V. L. Sizonenko
1150 (1839) Plasma instability due to an anisotropic electron distribution D. G. Lominadze, V. L. Sizonenko
1154 (1846) Stochastic acceleration of electrons in nanosecond discharges L. P. Babich
1157 (1852) Nonlinear interaction between a monochromatic ion-acoustic wave and a plasma V. P. Indykul
1160 (1857) High-frequency instabilities in an inhomogeneous, anisotropic finite-β plasma V. D. Egorenkov, A. I. Pyatak
1163 (1862) Modulation of microwaves by density fluctuations in a plasma L. A. Dushin, A. V. Serikov, A. I. Skibenko, E. V. Krivorukov, I. P. Fomin
1168 (1871) Measurement of plasma density distribution with a rectangular microwave cavity I. N. Moskalev
1171 (1877) Diffusion of quasistationary helical magnetic fields into the interior of cylindrical chambers. II V. F. Aleksin, S. S. Romanov

QUANTUM ELECTRONICS

1174 (1883) Solid-state laser with externally forced Q switching N. M. Galaktionova, A. A. Mak, A. P. Khyuppenen
1177 (1889) Aberrations in systems with plane and spherical detection apertures V. V. Izokh, A. V. Sergeev, I. Yu. Shmidov
1181 (1896) Correlation analysis of fine-structure images A. A. Kolesnikov, N. V. Lapteva

ACCELERATORS

1185 (1903) Coherent instability of a beam in a vacuum chamber with an irregular boundary E. S. Masunov
1188 (1909) Magnetic-field transport of a high-current electron beam A. V. Agafonov, V. S. Voronin, A. N. Lebedev, K. N. Pazin

ELECTRONICS

1193 (1917) Electron energy spectrum in a high-current vacuum diode S. P. Bugaev, V. I. Koshelev, M. N. Timofeev
1196 (1922) Multiphase, uniform, secondary-emission microwave discharge at a solid surface G. S. Luk'yanchikov
1200 (1929) Discharge in a cylindrical diode with surface ionization V. P. Osoka, A. V. Potarov
1205 (1938) Kinetic energy of ions produced by surface ionization. I. Distribution over the velocity components L. V. Sumin
1210 (1946) Dielectric strength of spark gaps following strong current pulses E. P. Bel'kov
1214 (1952) Electrical conductivity of a pseudoliquefied layer in an electric field V. V. Gal', V. I. Knov, K. A. Nikitin
1216 (1955) Multiple scattering of a focused beam of monoenergetic electrons G. N. Vyalov
1219 (1961) Double focusing in a system of 1/r electric and magnetic fields V. V. Zashkvara, V. N. Demin
1221 (1964) Numerical experiments on electron bombardment in crossed fields P. V. Romanov, A. S. Roshal'
1224 (1969) Effect of a high-current relativistic electron beam on a metal B. I. Dmitrenko, L. V. Leskov, G. P. Maksimov, S. L. Nedoseev, V. V. Savichev, V. P. Smirnov, A. M. Spektor

GENERAL

1226 (1973) Explosion driven magnetic generator with a matched inductive load L. S. Gerasimov
1231 (1981) Impurities and crystal dimensions in zone refining V. G. Glebovskii, B. M. Shipilevskii
1236 (1990) Hydrogen-ion mobility in a high-pressure unipolar corona A. G. Lyapin

1239 (1996)	Absolute-photometry determination of the rate constant of the gas-phase reaction of the radical compound C_3F_7 and $I(^2P_{3/2})$	G. A. Skorobogatov, V. S. Komarov, V. G. Seleznev
1242 (2002)	Optical methods for studying amplification of elastic surface waves in a stratified system	I. B. Yakovkin, D. V. Petrov, S. V. Bogdanov

BRIEF COMMUNICATIONS

1246 (2008)	Magnetohydrodynamic stability of a neutral current layer in a plasma	S. V. Bulanov
1248 (2011)	Radiation of electromagnetic waves by a modulated electron beam	S. G. Pankratov
1251 (2015)	Skin effect in a constant magnetic field	Z. K. Yankauskas, V. I. Chesonis, V. G. Skripnik
1253 (2017)	Graphical methods for constructing trajectories of small particles in electrostatic fields	N. I. Shtepa
1256 (2020)	Cumulative destruction of transparent dielectrics in repeated laser irradiation	L. D. Khazov, I. A. Fersman, V. Yu. Bortniker
1258 (2023)	Ion energy spectra and collective effects in a Penning ion source	V. I. Farenik, V. V. Vlasov, A. M. Rozhkov, A. A. Kozharin
1260 (2025)	Turbulent plasma heating and the Buneman instability	V. L. Sizonenko
1262 (2027)	Gas polymerization wave excited by monochromatic light	A. I. Plis, V. A. Shcheglov
1264 (2030)	Luminosity of a cylindrical spectrometer with a small off-axis source	V. V. Zashkvara

Soviet Physics—Technical Physics Vol. 19, No. 10, April 1975

(Russian original: Zh. Tekh. Fiz., Vol. 44, No. 10, pp. 2033-2240, October 1974)

THEORETICAL AND MATHEMATICAL PHYSICS

1267 (2033)	Heat transport problems with time-varying boundary conditions or moving boundaries (Stefan problem)	G. A. Grinberg
1273 (2043)	Stefan problem with motion of the phase-transition surface described by $y(\tau) = \sqrt{A\tau^2+B\tau+h^2}$	O. M. Chekmareva
1277 (2051)	Magnetic topography of toroidal systems	M. N. Skoblik, V. E. Ziser, A. V. Georgievskii, V. G. Peletminskaya
1281 (2058)	Rectangular conducting wedge in a moving electromagnetic field	I. D. Maergoiz, L. P. Nizhnik
1287 (2069)	Diffusion regime for electrostatic probes as a singular-perturbation problem	I. B. Chekmarev
1290 (2075)	Electromagnetic pulse radiated by a moving charged bunch in matter	N. A. Zvonnikov
1293 (2081)	State of a gas moving near a solid surface	S. P. Bakanov, B. M. Markeev

PLASMA

1295 (2085)	Drift instability in a weakly ionized plasma	S. V. Putvinskii, A. V. Timofeev
1300 (2095)	Nonlinear statistical theory for condensation of Langmuir plasmons. III. Energy flux for plasma turbulence	F. Kh. Khakimov, V. N. Tsytovich
1303 (2101)	Energy of charged particles accelerated by electromagnetic waves in a plasma with a spatially decreasing density	V. Ya. Davydovskii, A. S. Ukolov
1308 (2109)	Nonmonotonic potential distribution in the electrode region	A. I. Loshkarev
1312 (2116)	Nonlinear effects for the "kink" instability in an electron—ion ring	G. P. Berman
1317 (2126)	Instabilities in interpenetrating electron and ion beams	I. A. Soloshenko, L. P. Katsubo
1321 (2132)	Simplified model for the initial stage of exploding wire phenomena	N. N. Stolovich, V. G. Maksimov, N. S. Minitskaya
1329 (2146)	Electrical characteristics of underwater exploding wires	V. K. Sholom, E. V. Krivitskii, V. P. Litvinenko
1332 (2151)	Analytic model of the cesium arc	V. P. Pashchenko, V. L. Mironovich, I. P. Stakhanov
1337 (2159)	Thermionic emission properties of zirconium, hafnium, and titanium nitrides in cesium vapor	M. A. Eremeev, V. S. Neshpor, A. B. Novikov, E. M. Stefanovskaya, V. P. Fedorinov
1342 (2168)	Electron energy spectrum in high-energy nanosecond accelerators	V. V. Kremnev, G. A. Mesyats, V. P. Reznikov

ELECTRONICS

1345 (2174)	Shot noise in a thermionic cathode	A. F. Golubentsev, A. S. Shapovalov
1347 (2178)	Use of a field-emission microscope to measure the pressure of pump oil	V. Ya. Pliskovskii, M. S. Sukonnik, V. A. Shishkin
1352 (2186)	Emission parameters of a field-emission cathode	G. N. Freiberg
1355 (2192)	Composition of adsorbing and desorbing fluxes	Yu. A. Gel'man, V. I. Mikhailov, V. F. Vinogradov, Yu. N. Lyubitov
1359 (2198)	Radial distribution of density and potential in a glow discharge in CO_2 and water	A. I. Maksimov, V. F. Sokolov
1362 (2203)	High-frequency modulation of atomic beams for plasma diagnostics	P. A. Demchenko, L. I. Krupnik, K. A. Leontovich, E. S. Lyangner
1367 (2211)	Doppler profile of an atomic line to the differential excitation cross section	É. S. Parilis, V. Kh. Ferleger

GENERAL

1371 (2217)	Distortion of single turn solenoids in ultrahigh magnetic fields	G. A. Shneerson
1378 (2229)	Dependence of the basic parameters of $Al_xGa_{1-x}As$—GaAs solar converters on temperature and optical intensity	E. B. Vinogradova, M. B. Kagan, N. S. Koroleva, T. L. Lyubashevskaya, T. A. Nuller

1382 (2235) **Excitation of thermoelastic vibrations of a thin plate by a beam of fast charged particles** — **A. I. Kalinichenko, V. T. Lazurik-Él'tsufin**

Soviet Physics – Technical Physics Vol. 19, No. 11, May 1975

(Russian original: Zh. Tekh. Fiz., Vol. 44, No. 11, pp. 2241-2448, November 1974)

THEORETICAL AND MATHEMATICAL PHYSICS

1385 (2241)	Diffraction of electromagnetic waves by a dielectric wedge	A. A. Aleksandrova, N. A. Khizhnyak
1390 (2250)	Propagation of shock waves in inhomogeneous media	R. A. Glatman
1393 (2255)	Ponderomotive forces on a rotating conducting sphere in a time-varying inhomogeneous magnetic field	R. V. Lin'kov, Yu. M. Urman
1399 (2265)	Electromagnetic levitation of a liquid metal droplet with strong skin effect (surface shape and internal pressure)	A. N. Tverdokhlebov, A. L. Shuster
1403 (2272)	Fifth-order spherical aberration in focusing and correcting quadrupole–octupole systems	Ya. G. Lyubchik, T. Ya. Fishkova

PLASMA

1408 (2280)	Mechanism for plasma loss from a magnetic trap	V. I. Volosov
1412 (2286)	Measurement of ion density by the dispersion relation for an ion-beam plasma	M. D. Gabovich, L. P. Katsubo, I. A. Soloshenko
1414 (2290)	Axially symmetric neutralized electron beam	G. N. Vyalov, V. N. Evteev, Yu. M. Zolotaikin, K. N. Ul'yanov
1418 (2296)	Plasma synthesis by injection of an electron beam through an ion source	V. F. Virko, M. D. Gabovich, G. S. Kirichenko, O. K. Nazarenko
1421 (2302)	Measurement of plasma electron temperature with a sinusoidal probe potential	B. I. Kanaev, V. V. Piterskii, E. E. Yushmanov
1424 (2307)	Atomic density in the low-voltage arc in a cesium diode	F. G. Baksht, A. A. Kostin, Yu. L. Serov, I. P. Yavor
1426 (2311)	Free expansion of plasma jets	P. A. Demchenko, L. I. Krupnik, E. S. Lyangner
1429 (2317)	Laser-initiated vacuum discharge	V. P. Kovalenko, A. A. Makarevich, V. A. Rodichkin, A. M. Timonin
1432 (2322)	Effects due to streamer shape	É. D. Lozanskii, D. B. Pontekorvo
1434 (2326)	Electrical breakdown of vacuum gaps under superhigh voltage pulses	I. I. Kalyatskii, G. M. Kassirov, G. S. Smirnov
1436 (2329)	Volt–ampere characteristic of the low-voltage arc. I. Recombination model	P. P. Shcherbinin
1442 (2340)	Gasdynamic model of the spark discharge	Yu. K. Bobrov
1447 (2348)	Development of an inhibited glow discharge	Yu. A. Bystrov, S. A. Ivanov, Yu. F. Radchenko
1449 (2352)	Resistance and inductance of a gas arc	S. I. Barannik, S. B. Vasserman, A. N. Lukin
1454 (2360)	Electrical explosion of the metastable liquid phases of zinc, cadmium, and lead	M. M. Martynyuk, I. Karimkhodzhaev
1458 (2367)	Resistance and enthalpy of refractory exploding wires	M. M. Martynyuk, I. Karimkhodzhaev, V. I. Tsapkov

ELECTRONICS

1462 (2374)	Ion-optical system for shaping high-current ion beams	S. D. Grishin, V. F. Kuzovlev, R. V. Orlov, S. N. Ogorodnikov
1465 (2378)	Elimination of carbon impurities from platinum by heating in an oxygen atmosphere	L. P. Rekova, V. V. Mozgin, L. N. Zvyagintseva, V. N. Bondarenko, Ya. M. Fogel'
1468 (2383)	Radiation yield of ions in liquid dielectrics as a function of temperature and radiation energy	V. I. Ivanov, E. D. Kleshchenko, Yu. P. Sukhanovskii, V. V. Frolov
1471 (2388)	Steady-state electron density in photoionization of aerosol particles	G. V. Karachevtsev, A. A. Fridman

GENERAL

1474 (2393)	Surface evaporation of a solid transparent dielectric under the action of laser radiation	A. M. Bonch-Bruevich, Ya. A. Imas, A. A. Kovalev, P. S. Kondratenko, B. I. Makshantsev
1477 (2398)	Interaction of intense laser radiation with solid targets	L. V. Dubovoi, V. D. Dyatlov, V. I. Kryzhanovskii, A. A. Mak, R. N. Medvedev, A. N. Popytaev, V. A. Serebryakov, V. N. Sizov, A. D. Starikov

BRIEF COMMUNICATIONS

1480 (2404)	Laser compensation for thermal distortion in optical pumping	V. K. Zaitsev, V. A. Il'inskii, A. M. Marugin, V. M. Ovchinnikov
1482 (2405)	Theory of nonequilibrium shock waves	R. A. Glatman, I. V. Ioffe
1484 (2407)	Radio-frequency absorption in a plasma coinfined by rf plugs	K. S. Golovanivskii, V. D. Dougar-Jabon, L. A. Pokhmel'nykh
1486 (2410)	Motion of stable aerosol particles	O. A. Barsegyan, Yu. I. Yalamov
1488 (2412)	Motion of charged particles in a nonneutral plasma	E. N. Agafonova, L. I. Grechikhin
1490 (2414)	Initial stage of a high-current discharge in air	A. F. Aleksandrov, V. V. Perebeinos, A. T. Savichev, I. B. Timofeev
1492 (2416)	Electron energy distribution in a constricted, low-pressure hydrogen discharge	M. A. Abroyan, Yu. M. Kagan, N. B. Kolokolov, B. P. Lavrov
1494 (2417)	Spectral narrowing of a single-mode beam oscillator	V. A. Buts, V. I. Kurilko
1496 (2419)	Stabilization of two-stream instabilities	V. A. Buts
1498 (2421)	Acceleration of plasma electrons in strong electric fields	Z. A. Al'bikov, M. I. Ivanov, V. I. Kazacha, O. V. Kozlov, V. D. Rusanov, S. S. Sobolev,
1500 (2423)	Two modes of operation of an arc plasma source in an external magnetic field	A. G. Korsun, S. A. Meshcheryakov
1502 (2425)	Loss of neutralization for a stable neutralized ion beam	M. D. Gabovich
1504 (2428)	Analysis of magnetic deflection systems	O. M. Vovk, O. Ya. Popov
1505 (2430)	Nonlinear behavior of monochromatic surface waves excited by a beam	A. B. Kitsenko, I. M. Pankratov, K. N. Stepanov
1507 (2432)	Electron lifetimes in atmosphere at high pressure	V. N. Kapinos, Yu. A. Medvedev, N. N. Morozov, B. M. Stepanov
1508 (2433)	Low-frequency helical instability in a high-frequency electric field	V. S. Paverman, D. D. Tskhakaya
1510 (2436)	Method for optical modulation of an electron beam	V. I. Sotnikov
1512 (2438)	Liquid metal droplet with high surface tension in an axially-symmetric electromagnetic field (strong skin effect)	A. N. Tverdokhlebov, A. L. Shuster
1514 (2441)	Solution of the Stefan problem	A. M. Tsybin
1516 (2444)	Stigmatic sectored magnetic analyzer for a multiple-beam mass spectrometer	G. Kh. Chedzhemov

Soviet Physics – Technical Physics Vol. 19, No. 12, June 1975

(Russian original: Zh. Tekh. Fiz., Vol. 44, No. 12, pp. 2449-2692, December 1974)

THEORETICAL AND MATHEMATICAL PHYSICS

1519 (2449)	Rotation of Poynting vector for ultralow-frequency ion waves in an inhomogeneous plasma	Ya. L. Al'pert, R. N. Kaufman
1522 (2454)	Anomalous resistivity of a transverse plasma current at electron-cyclotron harmonics	V. I. Aref'ev, A. A. Chernov
1529 (2467)	Anomalous ion heating in a parametrically unstable plasma	I. S. Baikov, V. P. Silin
1534 (2476)	Transformation of nonlinear MHD waves	G. M. Zaslavskii, S. S. Moiseev, V. V. Mukhin
1538 (2483)	Two-stream flow in a thin plasma slab	A. V. Pashchenko, B. N. Rutkevich

PLASMA

1541 (2489)	Energy balance in Tokamaks in the "plateau–banana" transition	Yu. N. Dnestrovskii, D. P. Kostomarov
1543 (2493)	Anisotropic plasma heating near the lower hybrid frequency	V. M. Glagolev, V. V. Martynenko, Yu. V. Skosyrev
1547 (2500)	Interaction of a hollow electron beam with a plasma	N. M. Zemlyanskii, A. K. Berezin, Ya. B. Fainberg, L. I. Bolotin, S. S. Krivulya
1549 (2504)	Low-pressure self-maintained discharge with suppressed electron drift. I	V. K. Kalashnikov, Yu. V. Sanochkin
1554 (2512)	Low-pressure self-maintained discharge with suppressed electron drift. II	Yu. V. Sanochkin, V. K. Kalashnikov
1558 (2519)	Formation of a plasma focus in a plasma erosion accelerator. II. Energy characteristics of the dense plasma focus	N. P. Kozlov, L. V. Leskov, Yu. S. Protasov, V. I. Khvesyuk
1560 (2523)	Effect of rf ionization on a Hall-current plasma accelerator	I. I. Demidenko, N. S. Lomino, A. I. Morozov, V. G. Padalka
1564 (2529)	Analytic model for the arc regime and the thermionic converter	V. D. Bondarenko, A. I. Loshkarev
1569 (2537)	Dielectric breakdown of detonation products	V. L. Korol'kov, M. A. Mel'nikov, A. P. Tsyplenko
1571 (2539)	Anomalous high emission of a nonevaporating thermionic cathode in an arc	B. Ya. Moizhes, V. A. Nemchinskii
1577 (2548)	High-pressure hot-cathode arc without forced cooling	V. A. Nemchinskii
1579 (2551)	Hot probe measurements in a rarefied streaming plasma	E. M. Netsvetailov, L. V. Nosachev, V. V. Skvortsov
1584 (2559)	Wave excitation at half the gyrofrequency in counterstreaming electron beams	A. P. Timoshenko, D. V. Iremashvili, Yu. K. Udovichenko

QUANTUM ELECTRONICS

1587 (2563)	Mass spectrum of secondary ions ejected from the surface of a single crystal of gallium arsenide by argon ions	A. G. Koval', V. V. Bobkov, Yu. A. Klimovskii, S. S. Strel'chenko, V. V. Shubina, V. V. Lebedev, Ya. M. Fogel'
1590 (2568)	Coherent Compton effect in crystals	V. A. Bushuev, R. N. Kuz'min

GENERAL

1593 (2572)	Transformation of light beams by dynamic correctors using three-dimensional displacement phase holograms	V. G. Sidorovich, D. I. Stasel'ko
1598 (2580)	Electroluminescence spectra of the red luminescent diodes $p\text{-Al}_x\text{Ga}_{1-x}\text{As}-n\text{-Al}_y\text{Ga}_{1-y}\text{As}$ $(y > x)$	V. M. Busov, D. Z. Garbuzov, A. T. Gorelenok, D. S. Kop'ev

BRIEF COMMUNICATIONS

1601 (2585)	Gas temperature in the positive column of a medium-β helium discharge	Yu. M. Kagan, K. K. Paskalev
1604 (2588)	Temperature and electron density in the positive column of a medium-pressure helium discharge	Yu. M. Kagan, K. K. Paskalev
1606 (2591)	Direct current in a metal–selenium–metal structure bounded by an rf plasma	A. D. Andreev, S. I. Lubinskii
1608 (2594)	Measurement of transverse relaxation time T_2 of optically oriented He^4 with an oscillator magnetometer	N. A. Dovator, R. A. Zhitnikov, P. P. Kuleshov
1610 (2595)	Current-convective instability in a three-component plasma	E. Z. Meilikhov

1612 (2598) Effect of a magnetic field on spontaneous mode-locking in a He−Ne laser ($\Lambda = 0.63\ \mu$) — V. Yu. Petrun'kin, V. M. Nikolaev, O. I. Kotov, B. V. L'vov
1614 (2600) Exact solutions of the nonlinear electrodynamic equations — N. G. Puchkova, A. F. Kulish
1616 (2602) Streamer propagation after the voltage termination in a streamer chamber — N. S. Rudenko, V. I. Smetanin
1618 (2604) Electron-optical properties of postdeflection quadrupole lenses — T. Ya. Fishkova
1620 (2607) Frequency locking in a 3.39 μ laser — E. Yu. Andreeva, S. N. Gulyaev, D. K. Terekhin
1622 (2609) Efficiency of the scattering of "unstable" charged particles in quadrupole mass spectrometers — É. P. Sheretov, B. I. Kolotilin, M. P. Safonov
1625 (2613) Reflection of a high-current relativistic electron beam from a conducting surface — A. N. Didenko, A. I. Ryabchikov, V. A. Tuzov, Yu. P. Usov
1627 (2615) Thermal diffusion in a mixture of cesium vapor and helium — E. S. Bekmukhambetov, V. A. Donov
1629 (2617) Parametric excitation of helicon waves in a plasma by modulated radio frequency waves — V. S. Paverman, D. D. Tskhakaya
1631 (2620) Electrical strength of nitrogen and hydrogen at high pressures — É. A. Avilov, I. V. Belkin
1633 (2622) Coherent phase oscillations of electrons in a synchrotron — M. M. Nikitin
1635 (2623) Neutral particles from the interaction of laser radiation with a solid target — Yu. A. Bykovskii, N. M. Vasil'ev, I. D. Laptev, V. N. Nevolin
1636 (2625) Certain integral relations in the kinetic theory of gases — S. P. Bakanov
1639 (2629) Connection of magnetic lines of force in a neutral layer — A. T. Altyntsev, V. I. Krasov
1641 (2632) Correction to the paper "Resonant properties of a pulsating dielectric sphere" — A. G. Nerukh, N. A. Khizhnyak

ANNUAL INDEX

1643 Analytic subject index to volume 19
1664 Author index to volume 19

SUBJECT INDEX TO VOLUME 19

Papers are arranged in ascending page number order.

---

1. COMMUNICATION, EDUCATION, HISTORY, AND PHILOSOPHY

Correction to the paper "Resonant properties of a pulsating dielectric sphere" —A. G. Nerukh and N. A. Khizhnyak. 19(12), 1641 (Jun. 1975); CPM-7508X0515

2. MATHEMATICAL METHODS IN PHYSICS

Solution of the Stefan problem —A. M. Tsybin. 19(11), 1514–5 (May 1975); CPM-7506X1268

Monte Carlo analysis of ion scattering in a mass spectrometer —M. L. Aleksandrov, L. N. Gall', and N. S. Pliss. 19(6), 817–9 (Dec. 1974); CPM-7501X0817

3. CLASSICAL AND QUANTUM PHYSICS; MECHANICS AND FIELDS

3.50.– Classical electrodynamics and classical field theory

Resonance properties of a pulsating dielectric sphere —A. G. Nerukh and N. A. Khizhnyak. 19(2), 166–8 (Aug. 1974); CPM-7408X1430

Potential factors for an inhomogeneous ellipsoid —M. L. Levin and R. Z. Muratov. 19(2), 169–70 (Aug. 1974); CPM-7408X1433

Resonator with azimuthally varying end plates —M. F. Vorogushin and V. I. Petrunin. 19(6), 767–9 (Dec. 1974); CPM-7501X0767

Diffusion of quasistationary helical magnetic fields into the interior of cylindrical chambers. II. —V. F. Aleksin and S. S. Romanov. 19 (9), 1171–3 (Mar. 1975); CPM-7505X0593

Ponderomotive forces on a rotating conducting sphere in a time-varying inhomogeneous magnetic field —R. V. Lin'kov and Yu. M. Urman. 19(11), 1393–8 (May 1975); CPM-7506X1147

3.50.C Classical field theory

Charged-particle motion in a dipole magnetic field —L. G. Glikman. 19(4), 435–40 (Oct. 1974); CPM-7412X0219

Rectangular conducting wedge in a moving electromagnetic field —I. D. Maergoiz and L. P. Nizhnik. 19(10), 1281–6 (Apr. 1975); CPM-7506X0215

Exact solutions of the nonlinear electrodynamic equations —N. G. Puchkova and A. F. Kulish. 19(12), 1614–5 (Jun. 1975); CPM-7508X0488

Correction to the paper "Resonant properties of a pulsating dielectric sphere" —A. G. Nerukh and N. A. Khizhnyak. 19(12), 1641 (Jun. 1975); CPM-7508X0515

3.50.F Electrostatics and magnetostatics

The magnetostatic problem for thin closed shells —I. P. Krasnov. 19 (6), 711–2 (Dec. 1974); CPM-7501X0711

Computer calculation of quasistationary pulsed magnetic fields —V. I. Yurchenko. 19(8), 1025–30 (Feb. 1975); CPM-7504X1449

Flux loss in the production of ultrastrong fields by rapid compression of conducting shells —V. I. Yurchenko. 19(8), 1031–3 (Feb. 1975); CPM-7504X1455

Equations and boundary conditions for a three-dimensional quasistationary field —V. I. Yurchenko. 19(8), 1126–8 (Feb. 1975); CPM-7504X1550

Graphical methods for constructing trajectories of small particles in electrostatic fields —N. I. Shtepa. 19(9), 1253–5 (Mar. 1975); CPM-7505X0675

Magnetic topography of toroidal systems —M. N. Skoblik, V. E. Ziser, A. V. Georgievskii, and V. G. Peletminskaya. 19(10), 1277–80 (Apr. 1975); CPM-7506X0211

Electromagnetic levitation of a liquid metal droplet with strong skin effect (surface shape and internal pressure) —A. N. Tverdokhlebov and A. L. Shuster. 19(11), 1399–402 (May 1975); CPM-7506X1153

Liquid metal droplet with high surface tension in an axially-symmetric electromagnetic field (strong skin effect) —A. N. Tverdokhlebov and A. L. Shuster. 19(11), 1512–3 (May 1975); CPM-7506X1266

3.50.J Electromagnetic wave theory

Round metal–optical waveguide filled with a two-layer dielectric —V. A. Pruzhanovskii. 19(1), 3–8 (Jul. 1974); CPM-7407X1515

Diffraction of a plane electromagnetic wave by a conducting plane with a projection —A. A. Zilbergleit. 19(4), 531–2 (Oct. 1974); CPM-7412X0315

Two-dimensional diffraction on a system of straight segments (shields) —G. A. Grinberg. 19(5), 581–5 (Nov. 1974); CPM-7501X0375

Radiation from a charged particle moving close to an anisotropic dielectric —A. I. Plis and N. M. Safikhodzhaev. 19(7), 865–7 (Jan. 1975); CPM-7503X0753

Radiation emitted by charged particles trapped by plane electromagnetic waves —V. Ya. Davydovskii and A. S. Ukolov. 19 (8), 1057–60 (Feb. 1975); CPM-7504X1481

Radiation of electromagnetic waves by a modulated electron beam —S. G. Pankratov. 19(9), 1248–50 (Mar. 1975); CPM-7505X0670

Skin effect in a constant magnetic field —Z. K. Yankauskas, V. I. Chesonis, and V. G. Skripnik. 19(9), 1251–2 (Mar. 1975); CPM-7505X0673

Electromagnetic pulse radiated by a moving charged bunch in matter —N. A. Zvonnikov. 19(10), 1290–2 (Apr. 1975); CPM-7506X0224

Diffraction of electromagnetic waves by a dielectric wedge —A. A. Aleksandrova and N. A. Khizhnyak. 19(11), 1385–9 (May 1975); CPM-7506X1139

3.80.+ General theory of scattering

Microwave propagation in a low-loss dielectric —L. É. Rikenglaz. 19 (6), 713–4 (Dec. 1974); CPM-7501X0713

Diffraction of electromagnetic waves by a dielectric wedge —A. A. Aleksandrova and N. A. Khizhnyak. 19(11), 1385–9 (May 1975); CPM-7506X1139

5. STATISTICAL PHYSICS AND THERMODYNAMICS

5.60.– Transport processes, theory

Fundamentals of heat-pipe theory and design —M. M. Levitan and T. L. Perel'man. 19(8), 983–95 (Feb. 1975); CPM-7504X1407

Heat transport problems with time-varying boundary conditions or moving boundaries (Stefan problem) —G. A. Grinberg. 19(10), 1267–72 (Apr. 1975); CPM-7506X0201

Stefan problem with motion of the phase-transition surface described by $y(\tau)=\sqrt{A\tau^2+B\tau+h^2}$ —O. M. Chekmareva. 19(10), 1273–6 (Apr. 1975); CPM-7506X0207

5.90.+ Other topics in statistical physics and thermodynamics

A useful function in the thermodynamics of irreversible processes —A. V. Pamfilov, A. I. Lopushanskaya, and L. B. Tsvetkova. 19(4), 535–7 (Oct. 1974); CPM-7412X0319

Theory of nonequilibrium shock waves —R. A. Glatman and I. V. Ioffe. 19(11), 1482–3 (May 1975); CPM-7506X1236

Certain integral relations in the kinetic theory of gases —S. P. Bakanov. 19(12), 1636–8 (Jun. 1975); CPM-7508X0510

6. MEASUREMENT SCIENCE, GENERAL LABORATORY TECHNIQUES, AND INSTRUMENTATION SYSTEMS

Distributed systems for feedback control of a tokamak plasma —V. F. Gubarev and Yu. I. Samoilenko. 19(4), 463–7 (Oct. 1974); CPM-7412X0247

Effect of instrumental noise on a system with two spin oscillators using Cs^{133} and He^3 —R. A. Zhitnikov, V. V. Semenov, and P. A. Klyushkin. 19(4), 556–7 (Oct. 1974); CPM-7412X0340

Direct and cascade four-photon parametric scattering of light in $LiIO_3$ crystals —S. M. Arakelyan, V. G. Tunkin, A. I. Kholodnykh, and A. S. Chirkin. 19(6), 787–92 (Dec. 1974); CPM-7501X0787

7. SPECIFIC INSTRUMENTATION OF GENERAL USE IN PHYSICS

7.30.– Vacuum production and techniques

Two-omegatron study of the pumping characteristics of an NÉM-300 magnetic discharge pump for a mixture of gases —M. K. Bulgakov and V. G. Rogozinskii. 19(3), 427–8 (Sep. 1974); CPM-7412X1113

Titanium-pump system for hydrogen —K. G. Mirzoev, V. G. Rogozinskii, and V. L. Ushkov. 19(3), 432–3 (Sep. 1974); CPM-7412X1118

NÉM-1T magnetic-discharge pumps in the vacuum system of the 1–100 linear accelerator —O. N. Krokhina and K. G. Mirzoev. 19 (5), 698–9 (Nov. 1974); CPM-7501X0492

7.72.+ Particle beam production and handling, targets

Efficiency of internal targets in the accelerator at the Institute of High-Energy Physics —V. I. Gridasov, K. P. Myznikov, and V. N. Chepegin. 19(7), 922–5 (Jan. 1975); CPM-7503X0810

Multiple-aperture ion source for electromagnetic mass separator —S. V. Lebedev. 19(7), 968 (Jan. 1975); CPM-7503X0856

Cell for forming electron beams of arbitrary shape in a high-voltage gaseous discharge —I. V. Vagner, É. I. Bolgov, V. F. Grakun, V. L. Gokhfel'd, and V. A. Kudlai. 19(8), 1042–5 (Feb. 1975); CPM-7504X1466

Pulsed ion beams from a high-current plasma diode —B. A. Tskhadaya, A. A. Plyutto, and K. V. Suladze. 19(8), 1108–9 (Feb. 1975); CPM-7504X1532

Ion-optical system for shaping high-current ion beams —S. D. Grishin, V. F. Kuzovlev, R. V. Orlov, and S. N. Ogorodnikov. 19 (11), 1462–4 (May 1975); CPM-7506X1216

7.75.+ Mass spectrometers and mass spectrometry techniques

Line shape of a quadrupole mass spectrometer —G. I. Slobodenyuk. 19(2), 292–3 (Aug. 1974); CPM-7408X1556

Monte Carlo analysis of ion scattering in a mass spectrometer —M. L. Aleksandrov, L. N. Gall', and N. S. Pliss. 19(6), 817–9 (Dec. 1974); CPM-7501X0817

Multiple-aperture ion source for electromagnetic mass separator —S. V. Lebedev. 19(7), 968 (Jan. 1975); CPM-7503X0856

Double focusing in a system of $1/r$ electric and magnetic fields —V. V. Zashkvara and V. N. Demin. 19(9), 1219–20 (Mar. 1975); CPM-7505X0641

Stigmatic sectored magnetic analyzer for a multiple-beam mass spectrometer —G. Kh. Chedzhemov. 19(11), 1516–7 (May 1975); CPM-7506X1270

Efficiency of the scattering of "unstable" charged particles in quadrupole mass spectrometers —É. P. Sheretov, B. I. Kolotilin, and M. P. Safonov. 19(12), 1622–4 (Jun. 1975); CPM-7508X0496

7.90.+ Other topics in specialized instrumentation

Measurement of statistical parameters of scattering particles in laminar flow by Doppler spectroscopy —A. P. Ivanov, A. Ya. Khairullina, and A. P. Chaikovski. 19(2), 267–70 (Aug. 1974); CPM-7408X1531

Strobe unit for measuring luminescence in the range 10^{-7}–$2\cdot10^{-10}$ sec —V. A. Bonch-Bruevich and N. A. Tolstoi. 19(2), 284–6 (Aug. 1974); CPM-7408X1548

Sign of the change in optical path length in a laser interferometer with feedback —I. M. Belousova and A. F. Zapryagaev. 19(6), 829–30 (Dec. 1974); CPM-7501X0829

Hologram interferometry for vibration analysis —V. S. Listovets and Yu. I. Ostrovskii. 19(7), 847–60 (Jan. 1975); CPM-7503X0735

Fundamentals of heat-pipe theory and design —M. M. Levitan and T. L. Perel'man. 19(8), 983–95 (Feb. 1975); CPM-7504X1407

Use of a field-emission microscope to measure the pressure of pump oil —V. Ya. Pliskovskii, M. S. Sukonnik, and V. A. Shishkin. 19 (10), 1347–51 (Apr. 1975); CPM-7506X0281

Measurement of transverse relaxation time T_2 of optically oriented He^4 with an oscillator magnetometer–N. A. Dovator, R. A. Zhitnikov, and P. P. Kuleshov. 19(12), 1608–9 (Jun. 1975); CPM-7508X0482

28. NUCLEAR ENGINEERING AND NUCLEAR POWER STUDIES

Impossibility of shielding against the rf radiation of a thermonuclear reactor with a cold-plasma sheath —A. S. Chikhachev. 19(5), 685 (Nov. 1974); CPM-7501X0479

Energy balance in Tokamaks in the "plateau—banana" transition region —Yu. N. Dnestrovskii and D. P. Kostomarov. 19(12), 1541–2 (Jun. 1975); CPM-7508X0415

29. EXPERIMENTAL METHODS AND INSTRUMENTATION FOR ELEMENTARY-PARTICLE AND NUCLEAR PHYSICS

29.15.+ Electrostatic and linear particle accelerators

Multiple-section linear electron accelerator with synchronized oscillators —V. F. Vikulov, V. A. Volodin, and O. S. Milovanov. 19(7), 930–1 (Jan. 1975); CPM-7503X0818

Control of output energy in linear electron accelerators —V. N. Golovin and N. P. Sobenin. 19(7), 932–4 (Jan. 1975); CPM-7503X0820

Self-excited waveguide buncher —N. M. Gavrilov and A. V. Nesterovich. 19(8), 1085–6 (Feb. 1975); CPM-7504X1509

29.20.– Cyclic accelerators

Aberrations in a straight ion-optical accelerator —E. I. Gerasimov, A. I. Solnyshkov, and G. V. Tarvid. 19(1), 131–3 (Jul. 1974); CPM-7407X1643

High-power nanosecond electron accelerator with inductive storage —B. M. Koval'chuk, Yu. A. Kotov, and G. A. Mesyats. 19(1), 136–7 (Jul. 1974); CPM-7407X1648

Beam focusing in an accelerator with inductive energy storage —V. A. Glukhikh, O. A. Gusev, E. G. Komar, V. S. Kuznetsov, M. P. Svin'in, and R. P. Fidel'skaya. 19(3), 366–7 (Sep. 1974); CPM-7412X1052

High-current pulsed electron accelerator with an annular beam —M. I. Avramenko, V. A. Glukhikh, O. A. Gusev, E. G. Komar, O. L. Komarov, V. S. Kuznetsov, A. S. Perlin, and M. P. Svin'in. 19(3), 368–70 (Sep. 1974); CPM-7412X1054

Transmission of a high-current relativistic beam through a gas —Yu. V. Tkach, I. I. Magda, G. V. Skachek, S. S. Pushkarev, and I. P. Panchenko. 19(3), 412–3 (Sep. 1974); CPM-7412X1098

Linear accelerator for beam injection into a slowly rising magnetic field —D. G. Borisov, A. I. Gryzlov, V. M. Levin, and A. V. Ryabtsov. 19(4), 509–10 (Oct. 1974); CPM-7412X0293

Low-voltage gun with a resonator for formation of electron bunches in a linear accelerator —V. A. Boiko, R. M. Voronkov, and V. A. Danilichev. 19(4), 569–71 (Oct. 1974); CPM-7412X0353

Inductive energy storage in pulsed accelerators —V. A. Glukhikh, O. A. Gusev, E. G. Komar, and M. P. Svin'in. 19(5), 660–1 (Nov. 1974); CPM-7501X0454

Shaping of voltage pulses by discharging an inductive storage bank with a charged-particle beam —O. A. Gusev, E. G. Komar, V. B. Markov, and E. M. Mellekh. 19(5), 662–3 (Nov. 1974); CPM-7501X0456

Maximum current of a beam with finite phase volume —G. I. Trubnikov and V. S. Kuznetsov. 19(6), 715–6 (Dec. 1974); CPM-7501X0715

Extraction of synchroton radiation from a cyclic electron accelerator with a strong magnetic field —V. I. Kvochka, V. S. Panasyuk, V. F. Romanovskii, L. N. Samoilov, A. A. Sokolov, B. M. Stepanov, and Yu. M. Tereshkin. 19(6), 762–6 (Dec. 1974); CPM-7501X0762

Resonator with azimuthally varying end plates —M. F. Vorogushin and V. I. Petrunin. 19(6), 767–9 (Dec. 1974); CPM-7501X0767

Azimuthal and vertical motion in an accelerator with azimuthally varying electric field —M. F. Vorogushin and V. I. Petrunin. 19(6), 770–2 (Dec. 1974); CPM-7501X0770

Spatial and energy parameters of the relativistic electron beam of the Rius-5 accelerator —A. T. Altyntsev and V. I. Koroteev. 19(6), 773–4 (Dec. 1974); CPM-7501X0773

Phase motion of particles in an accelerator with an azimuthally varying electric field —M. F. Vorogushin and V. I. Petrunin. 19(7), 926–9 (Jan. 1975); CPM-7503X0814

29.20.D Storage rings

Coherent instability of a beam in a vacuum chamber with an irregular boundary —E. S. Masunov. 19(9), 1185–7 (Mar. 1975); CPM-7505X0607

29.20.L Synchrotrons

Coherent phase oscillations of electrons in a synchrotron —M. M. Nikitin. 19(12), 1633–4 (Jun. 1975); CPM-7508X0507

29.25.– Particle sources and targets, preparation and technology

Production of an ion beam by a magnetic system with opposed fields —V. B. Glasko, A. G. Sveshnikov, and N. N. Semashko. 19(2), 201–5 (Aug. 1974); CPM-7408X1465

Efficient ion source —D. Kh. Abdrashitova, V. G. Babaev, and M. B. Guseva. 19(2), 264–6 (Aug. 1974); CPM-7408X1528

Efficiency of internal targets in the accelerator at the Institute of High-Energy Physics —V. I. Gridasov, K. P. Myznikov, and V. N. Chepegin. 19(7), 922–5 (Jan. 1975); CPM-7503X0810

Energy spectra of scattered particles in proton bombardment of a metal target —G. I. Zhabrev, V. A. Kurnaev, and V. G. Tel'kovskii. 19(7), 978–9 (Jan. 1975); CPM-7503X0866

Ion energy spectra and collective effects in a Penning ion source —V. I. Farenik, V. V. Vlasov, A. M. Rozhkov, and A. A. Kozharin. 19 (9), 1258–9 (Mar. 1975); CPM-7505X0680

29.90.+ Other topics in high-energy and nuclear experimental methods and instrumentation

Proton extraction from the 70-GeV accelerator for the Ludmila liquid-hydrogen chamber (extraction system S) —A. A. Aseev, A. I. Drozhdin, B. A. Zelenov, É. A. Merker, L. L. Moizhes, K. P. Myznikov, A. A. Roshchin, V. M. Tatarenko, M. A. Kholodenko, A. D. Artemov, L. N. Vaulin, V. I. Gordin, I. I. Kovalevskii, V. N. Rozhkov, M. M. Suvorov, A. S. Sudarushkin, and V. I. Chuiko. 19 (1), 70–6 (Jul. 1974); CPM-7407X1582

Electron spectrometer for electric excitation of nuclei in a storage ring —D. M. Nikolenko and S. G. Popov. 19(2), 280–3 (Aug. 1974); CPM-7408X1544

NÉM-1T magnetic-discharge pumps in the vacuum system of the 1-100 linear accelerator —O. N. Krokhina and K. G. Mirzoev. 19 (5), 698–9 (Nov. 1974); CPM-7501X0492

Self-acceleration of an intense electron beam —I. A. Grishaev, A. N. Dedik, V. V. Zakutin, I. I. Magda, Yu. V. Tkach, and A. M. Shenderovich. 19(8), 1087–9 (Feb. 1975); CPM-7504X1511

Parallel-plate capacitor as a charged-particle spectrometer —Yu. D. Kornyushkin. 19(8), 1110–2 (Feb. 1975); CPM-7504X1534

Effects due to streamer shape —É. D. Lozanskii and D. B. Pontekorvo. 19(11), 1432–3 (May 1975); CPM-7506X1186

Streamer propagation after the voltage termination in a streamer chamber —N. S. Rudenko and V. I. Smetanin. 19(12), 1616–7 (Jun. 1975); CPM-7508X0490

32. ATOMIC AND MOLECULAR INTERACTIONS WITH RADIATION, SPECTROSCOPY

32.10.– Atomic spectroscopy

Dynamic magnetic-resonance phenomena —P. S. Kuts and V. S. Mel'nik. 19(1), 110–4 (Jul. 1974); CPM-7407X1622

Surface-ionization determination of the electron affinities of silver and gold —É. Ya. Zandberg, A. G. Kamenev, and V. I. Paleev. 19(3), 385–9 (Sep. 1974); CPM-7412X1071

Doppler profile of an atomic line to the differential excitation cross section —É. S. Parilis and V. Kh. Ferleger. 19(10), 1367–70 (Apr. 1975); CPM-7506X0301

32.20.– Molecular spectroscopy (measurement and phenomenology)

X-ray fluorescence of oxygen in H_2O —L. A. Smirnov. 19(5), 702 (Nov. 1974); CPM-7501X0496

Electromagnetic pulse radiated by a moving charged bunch in matter —N. A. Zvonnikov. 19(10), 1290–2 (Apr. 1975); CPM-7506X0224

33. MAGNETIC RESONANCES AND RELAXATION IN MOLECULES; NQR, MÖSSBAUER EFFECT

Dynamic magnetic-resonance phenomena —P. S. Kuts and V. S. Mel'nik. 19(1), 110–4 (Jul. 1974); CPM-7407X1622

34. ATOMIC AND MOLECULAR COLLISION PROCESSES AND INTERACTIONS

34.50.– Inelastic scattering of atoms and molecules

Conversion of neutral hydrogen into protons in dense plasmas —T. A. Bazilevskaya, L. I. Krupnik, and N. G. Shulika. 19(6), 741–4 (Dec. 1974); CPM-7501X0741

Energy spectra of scattered particles in proton bombardment of a metal target —G. I. Zhabrev, V. A. Kurnaev, and V. G. Tel'kovskii. 19(7), 978–9 (Jan. 1975); CPM-7503X0866

Doppler profile of an atomic line to the differential excitation cross section —É. S. Parilis and V. Kh. Ferleger. 19(10), 1367–70 (Apr. 1975); CPM-7506X0301

34.60.+ Charge transfer

Excitation collisions between magnesium ions and inert gas atoms —V. L. Ovchinnikov, O. B. Shpenik, and I. P. Zapesochnyi. 19(3), 382–4 (Sep. 1974); CPM-7412X1068

Simulation of ion scattering on diatomic molecules —M. L. Aleksandrov, N. S. Pliss, and A. P. Shcherbakov. 19(3), 394–5 (Sep. 1974); CPM-7412X1080

Formation of molecular ions in an alkali discharge —V. N. Paslen and A. M. Przhonskii. 19(5), 705–6 (Nov. 1974); CPM-7501X0499

Scattering of He^+ ions by the core of the He atom —Z. Z. Latypov and A. A. Shaporenko. 19(7), 976–7 (Jan. 1975); CPM-7503X0864

34.90.+ Other topics in atomic and molecular collision processes and interactions

Effect of electron-atom collisions on electron motion in a gas diode —V. I. Babanin and A. Ya. Énder. 19(1), 60–5 (Jul. 1974); CPM-7407X1572

Excitation collisions between magnesium ions and inert gas atoms —V. L. Ovchinnikov, O. B. Shpenik, and I. P. Zapesochnyi. 19(3), 382–4 (Sep. 1974); CPM-7412X1068

Simulation of ion scattering on diatomic molecules —M. L. Aleksandrov, N. S. Pliss, and A. P. Shcherbakov. 19(3), 394–5 (Sep. 1974); CPM-7412X1080

Flow of low-density gases in a capillary grid —B. T. Porodnov, V. D. Akin'shin, V. I. Kichaev, S. F. Borisov, and P. E. Suetin. 19(4), 515–8 (Oct. 1974); CPM-7412X0299

Energy exchange between electrons and molecular vibrational states in resonance collisions —A. Kh. Mnatsakanyan and G. V. Naidis. 19 (8), 1113–5 (Feb. 1975); CPM-7504X1537

35. EXPERIMENTALLY DERIVED INFORMATION ON ATOMS AND MOLECULES

Determination of ionization potentials and electron affinities of certain elements by extrapolation —A. G. Kamenev, É. Ya. Zandberg, and V. I. Paleev. 19(7), 940–1 (Jan. 1975); CPM-7503X0828

42. OPTICS

42.10.– Propagation and transmission in homogeneous media

Time characteristics of the near radiation field of the injection laser —Zh. I. Alferov, V. N. Deryagin, L. E. Marasin, Yu. V. Popov, and E. L. Portnoi. 19(4), 548 (Oct. 1974); CPM-7412X0332

Reflection of finite amplitude electromagnetic waves from a semiconductor plasma —Yu. F. Filippov. 19(5), 603–6 (Nov. 1974); CPM-7501X0397

Extraction of synchroton radiation from a cyclic electron accelerator with a strong magnetic field —V. I. Kvochka, V. S. Panasyuk, V. F. Romanovskii, L. N. Samoilov, A. A. Sokolov, B. M. Stepanov, and Yu. M. Tereshkin. 19(6), 762–6 (Dec. 1974); CPM-7501X0762

Diffraction of electromagnetic waves by a dielectric wedge —A. A. Aleksandrova and N. A. Khizhnyak. 19(11), 1385–9 (May 1975); CPM-7506X1139

Surface evaporation of a solid transparent dielectric under the action of laser radiation —A. M. Bonch-Bruevich, Ya. A. Imas, A. A. Kovalev, P. S. Kondratenko, and B. I. Makshantsev. 19(11), 1474–6 (May 1975); CPM-7506X1228

Laser compensation for thermal distortion in optical pumping —V. K. Zaitsev, V. A. Il'inskii, A. M. Marugin, and V. M. Ovchinnikov. 19(11), 1480–1 (May 1975); CPM-7506X1234

42.30.– Optical information, image formation and analysis

Nonlinear spherical aberrations and thermoelastic stresses in thermal self-focusing —A. A. Vigasin, Yu. A. Gorokhov, A. P. Sukhorukov, and A. M. Khachatryan. 19(5), 673–5 (Nov. 1974); CPM-7501X0467

Electron-scanning transformation of the potential distribution on an electrostatic target —V. L. Lentsman. 19(5), 678–9 (Nov. 1974); CPM-7501X0472

Optical simulation of a radiator aperture with arbitrary amplitude—phase distribution —M. M. Butusov and Sh. V. Yurevichyus. 19 (6), 833–4 (Dec. 1974); CPM-7501X0833

Correction of third-order angular aberration in a system with two electrostatic mirrors —V. V. Zashkvara. 19(7), 961–2 (Jan. 1975); CPM-7503X0849

Achromatic plasma-lens system —A. I. Morozov and S. V. Lebedev. 19(7), 967 (Jan. 1975); CPM-7503X0855

Aberrations in systems with plane and spherical detection apertures —V. V. Izokh, A. V. Sergeev, and I. Yu. Shmidov. 19(9), 1177–80 (Mar. 1975); CPM-7505X0599

Correlation analysis of fine-structure images —A. A. Kolesnikov and N. V. Lapteva. 19(9), 1181–4 (Mar. 1975); CPM-7505X0603

Fifth-order spherical aberration in focusing and correcting quadrupole—octupole systems —Ya. G. Lyubchik and T. Ya. Fishkova. 19 (11), 1403–7 (May 1975); CPM-7506X1157

42.40.– Holography

Imaging properties of traveling intensity waves in the recording of dynamic three-dimensional holograms —Yu. N. Denisyuk. 19(1), 77–80 (Jul. 1974); CPM-7407X1589

Reversibility of chalcogenide materials in holography —S. B. Gurevich, N. N. Il'yashenko, B. T. Kolomiets, V. M. Lyubin, and M. V. Sukharev. 19(1), 152–3 (Jul. 1974); CPM-7407X1664

Efficiency of light-beam conversion by dynamic three-dimensional phase holograms —D. I. Stasel'ko and V. G. Sidorovich. 19(3), 361–5 (Sep. 1974); CPM-7412X1047

Multiple recording and erasure of optical information in certain glassy chalcogenides —V. V. Korsakov, V. I. Nalivaiko, V. G. Remesnik, and V. G. Tsukerman. 19(4), 565–6 (Oct. 1974); CPM-7412X0349

Holography of raster objects —Sh. D. Kakichashvili. 19(5), 696–7 (Nov. 1974); CPM-7501X0490

Optical simulation of a radiator aperture with arbitrary amplitude—phase distribution —M. M. Butusov and Sh. V. Yurevichyus. 19 (6), 833–4 (Dec. 1974); CPM-7501X0833

Hologram interferometry for vibration analysis —V. S. Listovets and Yu. I. Ostrovskii. 19(7), 847–60 (Jan. 1975); CPM-7503X0735

Transformation of light beams by dynamic correctors using three-dimensional displacement phase holograms —V. G. Sidorovich and D. I. Stasel'ko. 19(12), 1593–7 (Jun. 1975); CPM-7508X0467

42.55.+ Masers

Microwave maser with nonrelativistic electrons —A. S. Dement'ev and Yu. G. Pavlenko. 19(5), 694–5 (Nov. 1974); CPM-7501X0488

42.60.– Lasers

Use of plasma accelerator for optical pumping of lasers —N. P. Kozlov and Yu. S. Protasov. 19(3), 358–60 (Sep. 1974); CPM-7412X1044

42.60.C Gas lasers

Ionization and recombination coefficients in a discharge excited by fast electrons —Yu. I. Bychkov, Yu. D. Korolev, and A. P. Khuzeev. 19(1), 140–1 (Jul. 1974); CPM-7407X1652

Quenching in the CF_3I photodissociation laser —G. A. Skorobogatov, V. M. Tret'yak, and V. S. Komarov. 19(4), 495–8 (Oct. 1974); CPM-7412X0279

Energy input in electrical ionization lasers —Yu. I. Bychkov, Yu. D. Korolev, Yu. A. Kurbatov, and G. A. Mesyats. 19(4), 499–502 (Oct. 1974); CPM-7412X0283

Characteristics of the electrical ionization CO_2 laser —Yu. I. Bychkov, Yu. A. Kurbatov, and V. V. Savin. 19(4), 506–8 (Oct. 1974); CPM-7412X0290

Method for determining the absolute characteristics of CF_3I laser emission —V. S. Komarov, V. G. Seleznev, and G. A. Skorobogatov. 19(4), 558–60 (Oct. 1974); CPM-7412X0342

Nonlinear polarizability of a gaseous medium in a longitudinal magnetic field —V. A. Sokolov and L. M. Khayutin. 19(5), 589–91 (Nov. 1974); CPM-7501X0383

Infrared nitrogen laser using a transverse discharge —V. F. Tarasenko and Yu. I. Bychkov. 19(5), 693 (Nov. 1974); CPM-7501X0487

Kinetics of gasdynamic lasers. Effect of nozzle geometry on inversion —A. S. Biryukov and L. A. Shelepin. 19(6), 775–81 (Dec. 1974); CPM-7501X0775

N_2O–N_2–He gasdynamic laser —Yu. I. Grin' and V. G. Testov. 19(7), 975 (Jan. 1975); CPM-7503X0863

Plasma dynamic lasers —S. A. Reshetnyak and L. A. Shelepin. 19(8), 1076–80 (Feb. 1975); CPM-7504X1500

Effect of plasma parameters on emission in an ion laser —I. E. Sakharov, V. V. Ermolin, and S. V. Shatalin. 19(8), 1081–4 (Feb. 1975); CPM-7504X1505

Effect of the radiation density on ion drift velocity in a cadmium-helium laser —G. N. Tolmachev, E. L. Latush, and V. S. Mikhalevskii. 19(8), 1120–1 (Feb. 1975); CPM-7504X1544

Absolute-photometry determination of the rate constant of the gas-phase reaction of the radical compound C_3F_7 and $I(^2P_{3/2})$ —G. A. Skorobogatov, V. S. Komarov, and V. G. Seleznev. 19(9), 1239–41 (Mar. 1975); CPM-7505X0661

Effect of a magnetic field on spontaneous mode-locking in a He—Ne laser ($\Lambda = 0.63\mu$) —V. Yu. Petrun'kin, V. M. Nikolaev, O. I. Kotov, and B. V. L'vov. 19(12), 1612–3 (Jun. 1975); CPM-7508X0486

42.60.G Solid lasers

Parasitic amplitude modulation of a stabilized Nd^{3+}:YAG laser —N. M. Galaktionova, A. A. Mak, and A. P. Khyuppenen. 19(4), 486–90 (Oct. 1974); CPM-7412X0270

Pulsed neodymium–glass laser with periodic Q switching —T. A. Kuzovkova, E. V. Nilov, V. A. Rusov, I. N. Semenov, and A. A. Chertkov. 19(4), 503–5 (Oct. 1974); CPM-7412X0287

Frequency–doubling single–mode laser for picosecond pulses —A. M. Bonch–Bruevich, A. M. Tkachuk, and A. A. Fedorov. 19(4), 549–51 (Oct. 1974); CPM-7412X0333

Unidirectional cw oscillation in a solid state ring laser with a return mirror —A. A. Mak, V. I. Ustyugov, V. A. Fromzel', and M. M. Khaleev. 19(4), 552–3 (Oct. 1974); CPM-7412X0336

Spontaneous mode locking in a laser with a multifaceted element —E. I. Kamenskii and V. V. Kozlov. 19(6), 831–2 (Dec. 1974); CPM-7501X0831

Lasing properties of Yb^{3+} and Er^{3+} glass laser pumped by a laser —V. N. Kalinin, A. A. Mak, D. S. Prilezhaev, and V. A. Fromzel'. 19 (6), 835–6 (Dec. 1974); CPM-7501X0835

Solid-state laser with externally forced *Q* switching —N. M. Galaktionova, A. A. Mak, and A. P. Khyuppenen. 19(9), 1174–6 (Mar. 1975); CPM-7505X0596

42.60.J Semiconductor lasers

Time characteristics of the near radiation field of the injection laser —Zh. I. Alferov, V. N. Deryagin, L. E. Marasin, Yu. V. Popov, and E. L. Portnoi. 19(4), 548 (Oct. 1974); CPM-7412X0332

42.60.L Laser resonators, cavities, and modulators

Parasitic amplitude modulation of a stabilized Nd^{3+}:YAG laser —N. M. Galaktionova, A. A. Mak, and A. P. Khyuppenen. 19(4), 486–90 (Oct. 1974); CPM-7412X0270

Polarization of a cavity with a thermally deformed active element —I. B. Vitrishchak, L. N. Soms, and A. A. Tarasov. 19(5), 664–8 (Nov. 1974); CPM-7501X0458

Sign of the change in optical path length in a laser interferometer with feedback —I. M. Belousova and A. F. Zapryagaev. 19(6), 829–30 (Dec. 1974); CPM-7501X0829

Spontaneous mode locking in a laser with a multifaceted element —E. I. Kamenskii and V. V. Kozlov. 19(6), 831–2 (Dec. 1974); CPM-7501X0831

Solid-state laser with externally forced *Q* switching —N. M. Galaktionova, A. A. Mak, and A. P. Khyuppenen. 19(9), 1174–6 (Mar. 1975); CPM-7505X0596

Effect of a magnetic field on spontaneous mode-locking in a He—Ne laser ($\Lambda=0.63\mu$) —V. Yu. Petrun'kin, V. M. Nikolaev, O. I. Kotov, and B. V. L'vov. 19(12), 1612–3 (Jun. 1975); CPM-7508X0486

42.60.N Laser beam interactions and properties

Nonradiative electron transitions and thermal effects in laser–irradiated transparent dielectrics —B. I. Makshantsev, A. A. Kovalev, R. K. Leonov, and P. A. Yampol'skii. 19(1), 98–102 (Jul. 1974); CPM-7407X1610

Optical characteristics of K–8 glass subject to radiation from a neodymium laser —A. M. Bonch–Bruevich, Ya. A. Imas, V. S. Salyadinov, and A. V. Shatilov. 19(2), 287–9 (Aug. 1974); CPM-7408X1551

Quenching in the CF$_3$I photodissociation laser —G. A. Skorobogatov, V. M. Tret'yak, and V. S. Komarov. 19(4), 495–8 (Oct. 1974); CPM-7412X0279

Gas cooling in transmission of high–power CO$_2$ laser radiation through the atmosphere —B. F. Gordiets, A. I. Osipov, and R. V. Khokhlov. 19(5), 669–72 (Nov. 1974); CPM-7501X0463

Nonlinear spherical aberrations and thermoelastic stresses in thermal self–focusing —A. A. Vigasin, Yu. A. Gorokhov, A. P. Sukhorukov, and A. M. Khachatryan. 19(5), 673–5 (Nov. 1974); CPM-7501X0467

Surface evaporation of a solid transparent dielectric under the action of laser radiation —A. M. Bonch-Bruevich, Ya. A. Imas, A. A. Kovalev, P. S. Kondratenko, and B. I. Makshantsev. 19(11), 1474–6 (May 1975); CPM-7506X1228

Interaction of intense laser radiation with solid targets —L. V. Dubovoi, V. D. Dyatlov, V. I. Kryzhanovskii, A. A. Mak, R. N. Medvedev, A. N. Popytaev, V. A. Serebryakov, V. N. Sizov, and A. D. Starikov. 19(11), 1477–9 (May 1975); CPM-7506X1231

Frequency locking in a 3.39μ laser —E. Yu. Andreeva, S. N. Gulyaev, and D. K. Terekhin. 19(12), 1620–1 (Jun. 1975); CPM-7508X0494

Neutral particles from the interaction of laser radiation with a solid target —Yu. A. Bykovskii, N. M. Vasil'ev, I. D. Laptev, and V. N. Nevolin. 19(12), 1635 (Jun. 1975); CPM-7508X0509

42.60.Q Laser beam applications

Effect of focusing conditions on the morphology of surface films produced with a laser —V. G. Dneprovskii and B. A. Osadin. 19 (2), 275–7 (Aug. 1974); CPM-7408X1539

Investigation of spatial distributions in a laser–produced plasma by Hα absorption —G. V. Ostrovskaya and N. A. Pobedonostseva. 19(3), 424–6 (Sep. 1974); CPM-7412X1110

Crystal defects of heterostructures of AlAs–GaAs solid solutions and effect on the characteristics of injection lasers —L. V. Druzhinina, V. T. Bublik, L. M. Dolginov, P. G. Eliseev, M. P. Kerbelev, V. B. Osvenskii, I. Z. Pinsker, and M. G. Shumskii. 19(7), 935–9 (Jan. 1975); CPM-7503X0823

Laser compensation for thermal distortion in optical pumping —V. K. Zaitsev, V. A. Il'inskii, A. M. Marugin, and V. M. Ovchinnikov. 19(11), 1480–1 (May 1975); CPM-7506X1234

42.65.– Nonlinear optics

Second–harmonic generation and emission in wave conversion at a plasma boundary —A. N. Kondratenko, V. G. Shaptala, and V. M. Kuklin. 19(1), 22–4 (Jul. 1974); CPM-7407X1534

Parasitic amplitude modulation of a stabilized Nd^{3+}:YAG laser —N. M. Galaktionova, A. A. Mak, and A. P. Khyuppenen. 19(4), 486–90 (Oct. 1974); CPM-7412X0270

Thermal effect of continuous laser radiation on optically transparent media —N. S. Bardina, A. I. Portnyagin, M. Yu. Sklyarov, and A. A. Churin. 19(4), 491–4 (Oct. 1974); CPM-7412X0275

Reflection of finite amplitude electromagnetic waves from a semiconductor plasma —Yu. F. Filippov. 19(5), 603–6 (Nov. 1974); CPM-7501X0397

Direct and cascade four–photon parametric scattering of light in LiIO$_3$ crystals —S. M. Arakelyan, V. G. Tunkin, A. I. Kholodnykh, and A. S. Chirkin. 19(6), 787–92 (Dec. 1974); CPM-7501X0787

Interaction of intense laser radiation with solid targets —L. V. Dubovoi, V. D. Dyatlov, V. I. Kryzhanovskii, A. A. Mak, R. N. Medvedev, A. N. Popytaev, V. A. Serebryakov, V. N. Sizov, and A. D. Starikov. 19(11), 1477–9 (May 1975); CPM-7506X1231

Transformation of light beams by dynamic correctors using three–dimensional displacement phase holograms —V. G. Sidorovich and D. I. Stasel'ko. 19(12), 1593–7 (Jun. 1975); CPM-7508X0467

Parametric excitation of helicon waves in a plasma by modulated radio frequency waves —V. S. Paverman and D. D. Tskhakya. 19 (12), 1629–30 (Jun. 1975); CPM-7508X0503

42.70.– Optical materials

Nonlinear spherical aberrations and thermoelastic stresses in thermal self–focusing —A. A. Vigasin, Yu. A. Gorokhov, A. P. Sukhorukov, and A. M. Khachatryan. 19(5), 673–5 (Nov. 1974); CPM-7501X0467

42.75.– Optical measurements and instrumentation

Effect of instrumental noise on a system with two spin oscillators using Cs^{133} and He^3 —R. A. Zhitnikov, V. V. Semenov, and P. A. Klyushkin. 19(4), 556–7 (Oct. 1974); CPM-7412X0340

Method for determining the absolute characteristics of CF$_3$I laser emission —V. S. Komarov, V. G. Seleznev, and G. A. Skorobogatov. 19(4), 558–60 (Oct. 1974); CPM-7412X0342

Extraction of synchroton radiation from a cyclic electron accelerator with a strong magnetic field —V. I. Kvochka, V. S. Panasyuk, V. F. Romanovskii, L. N. Samoilov, A. A. Sokolov, B. M. Stepanov, and Yu. M. Tereshkin. 19(6), 762–6 (Dec. 1974); CPM-7501X0762

42.78.– Optical lens and mirror systems

Focusing of an astigmatic beam by a doublet and a symmetric triplet of quadrupole lenses —V. I. Chetvertkov. 19(1), 1–2 (Jul. 1974); CPM-7407X1513

A transaxial lens —V. M. Kel'man, L. M. Nazarenko, and E. M. Yakushev. 19(4), 523–5 (Oct. 1974); CPM-7412X0307

42.80.– Optical devices, techniques, and applications

Round metal–optical waveguide filled with a two–layer dielectric —V. A. Pruzhanovskii. 19(1), 3–8 (Jul. 1974); CPM-7407X1515

Characteristics of diffraction gratings obtained by photoetching of semiconductor surfaces —L. V. Belyakov, D. N. Goryachev, M. N. Mizerov, and E. L. Portnoi. 19(6), 837–8 (Dec. 1974); CPM-7501X0837

42.90.+ Other topics in optics

Strobe unit for measuring luminescence in the range 10^{-7}–$2\cdot10^{-10}$ sec —V. A. Bonch–Bruevich and N. A. Tolstoi. 19(2), 284–6 (Aug. 1974); CPM-7408X1548

43. ACOUSTICS

Magnetoacoustic transducer based on the domain structure of a ferromagnetic material —G. L. Gurevich and G. A. Vul'gal'ter. 19 (1), 154–5 (Jul. 1974); CPM-7407X1666

Optical simulation of a radiator aperture with arbitrary amplitude—phase distribution —M. M. Butusov and Sh. V. Yurevichyus. 19 (6), 833–4 (Dec. 1974); CPM-7501X0833

Thermoacoustic waves in conducting gases and liquids —P. A. Andreev. 19(6), 845–6 (Dec. 1974); CPM-7501X0845

45. FLUID DYNAMICS

45.30.– Turbulence, convection, and heat transfer

Possible use of the schlieren method to measure characteristics of turbulence —V. G. Ivanov. 19(3), 429–31 (Sep. 1974); CPM-7412X1115

Statistical characteristics of the turbulent wake behind a supersonic sphere —V. G. Ivanov, G. I. Mishin, and S. N. Palkin. 19(4), 543–5 (Oct. 1974); CPM-7412X0327

Convection in a liquid dielectric in a longitudinal electric field —I. V. Ioffe and N. V. Kalinin. 19(5), 692 (Nov. 1974); CPM-7501X0486

45.40.– Compressible flows; shock and detonation phenomena

Properties of underexpanded and overexpanded supersonic gas jets —A. V. Antsupov. 19(2), 234–8 (Aug. 1974); CPM-7408X1498

Experimental investigation of microwave radiation produced by hypersonic flows —V. A. Lyutomskii, V. M. Polyakov, and V. G. Testov. 19(4), 483–5 (Oct. 1974); CPM-7412X0267

Statistical characteristics of the turbulent wake behind a supersonic sphere —V. G. Ivanov, G. I. Mishin, and S. N. Palkin. 19(4), 543–5 (Oct. 1974); CPM-7412X0327

Kinetics of gasdynamic lasers. Effect of nozzle geometry on inversion —A. S. Biryukov and L. A. Shelepin. 19(6), 775–81 (Dec. 1974); CPM-7501X0775

Propagation of shock waves in inhomogeneous media —R. A. Glatman. 19(11), 1390–2 (May 1975); CPM-7506X1144

Theory of nonequilibrium shock waves —R. A. Glatman and I. V. Ioffe. 19(11), 1482–3 (May 1975); CPM-7506X1236

45.45.– Rarefied gas dynamics

Condensation of a dense vapor flow —V. G. Dneprovskii, B. A. Osadin, and N. V. Rusakov. 19(2), 271–4 (Aug. 1974); CPM-7408X1535

Use of the distribution function to describe free molecular beams —I. G. Neudachin, B. T. Porodnov, and P. E. Suetin. 19(4), 511–4 (Oct. 1974); CPM-7412X0295

Flow of low–density gases in a capillary grid —B. T. Porodnov, V. D. Akin'shin, V. I. Kichaev, S. F. Borisov, and P. E. Suetin. 19(4), 515–8 (Oct. 1974); CPM-7412X0299

Composition of adsorbing and desorbing fluxes —Yu. A. Gel'man, V. I. Mikhailov, V. F. Vinogradov, and Yu. N. Lyubitov. 19(10), 1355–8 (Apr. 1975); CPM-7506X0289

45.50.– External flows, waves, instabilities, and cavitation

Properties of underexpanded and overexpanded supersonic gas jets —A. V. Antsupov. 19(2), 234–8 (Aug. 1974); CPM-7408X1498

Statistical characteristics of the turbulent wake behind a supersonic sphere —V. G. Ivanov, G. I. Mishin, and S. N. Palkin. 19(4), 543–5 (Oct. 1974); CPM-7412X0327

Local–potential study of the Bénard problem in a homogeneous magnetic field —A. I. Lopushanskaya and V. N. Kapranov. 19(5), 612–4 (Nov. 1974); CPM-7501X0406

Current–driven instability in a conducting fluid —A. M. Kovnatskii. 19(5), 691 (Nov. 1974); CPM-7501X0485

Formation of a narrow gas jet in vacuum —G. I. Dimov and V. Ya. Savkin. 19(6), 755–8 (Dec. 1974); CPM-7501X0755

Photochemical waves in a medium with a branch–chain conversion mechanism —A. N. Oraevskii, V. P. Pimenov, and V. A. Shcheglov. 19(6), 782–6 (Dec. 1974); CPM-7501X0782

Free expansion of plasma jets —P. A. Demchenko, L. I. Krupnik, and E. S. Lyangner. 19(11), 1426–8 (May 1975); CPM-7506X1180

45.55.+ Conducting fluids, magnetohydrodynamics, and electrohydrodynamics

Stabilization of MHD instabilities by a high–frequency current in a straight system —V. P. Fedyakova. 19(1), 16–9 (Jul. 1974); CPM-7407X1528

Radiating discharges confined by walls —A. F. Aleksandrov, I. S. Marshak, and A. A. Rukhadze. 19(3), 308–14 (Sep. 1974); CPM-7412X0994

Local–potential study of the Bénard problem in a homogeneous magnetic field —A. I. Lopushanskaya and V. N. Kapranov. 19(5), 612–4 (Nov. 1974); CPM-7501X0406

Possible electrohydrodynamic effects in electrolytes —E. Z. Gak, É. Kh. Rokhinson, and N. F. Bondarenko. 19(5), 676–7 (Nov. 1974); CPM-7501X0470

Current–driven instability in a conducting fluid —A. M. Kovnatskii. 19(5), 691 (Nov. 1974); CPM-7501X0485

Magnetohydrodynamic channel flow in a tapered magnetic field —S. A. Regirer. 19(7), 874–7 (Jan. 1975); CPM-7503X0762

Nonstationary magnetohydrodynamic flow and wave propagation —M. Ya. Antimirov and Yu. Ya. Boguslavskii. 19(7), 878–9 (Jan. 1975); CPM-7503X0766

45.65.– Nonhomogeneous flows

Measurement of statistical parameters of scattering particles in laminar flow by Doppler spectroscopy —A. P. Ivanov, A. Ya. Khairullina, and A. P. Chaikovski. 19(2), 267–70 (Aug. 1974); CPM-7408X1531

Condensation of a dense vapor flow —V. G. Dneprovskii, B. A. Osadin, and N. V. Rusakov. 19(2), 271–4 (Aug. 1974); CPM-7408X1535

Thermophoresis and diffusophoresis of small, volatile aerosol particles —Yu. I. Yalamov and E. R. Shchukin. 19(2), 278–9 (Aug. 1974); CPM-7408X1542

Motion of stable aerosol particles —O. A. Barsegyan and Yu. I. Yalamov. 19(11), 1486–7 (May 1975); CPM-7506X1240

45.80.+ Fluid-dynamic measurements and instrumentation

Measurement of statistical parameters of scattering particles in laminar flow by Doppler spectroscopy —A. P. Ivanov, A. Ya. Khairullina, and A. P. Chaikovski. 19(2), 267–70 (Aug. 1974); CPM-7408X1531

Possible use of the schlieren method to measure characteristics of turbulence —V. G. Ivanov. 19(3), 429–31 (Sep. 1974); CPM-7412X1115

Use of a field-emission microscope to measure the pressure of pump oil —V. Ya. Pliskovskii, M. S. Sukonnik, and V. A. Shishkin. 19 (10), 1347–51 (Apr. 1975); CPM-7506X0281

45.90.+ Other topics in fluid dynamics

Gas–kinetic removal of neutral molecules from an ion beam —V. P. Ivanov. 19(2), 239–42 (Aug. 1974); CPM-7408X1503

Measurement of statistical parameters of scattering particles in laminar flow by Doppler spectroscopy —A. P. Ivanov, A. Ya. Khairullina, and A. P. Chaikovski. 19(2), 267–70 (Aug. 1974); CPM-7408X1531

Radiating discharges confined by walls —A. F. Aleksandrov, I. S. Marshak, and A. A. Rukhadze. 19(3), 308–14 (Sep. 1974); CPM-7412X0994

Kinetics of gasdynamic lasers. Effect of nozzle geometry on inversion —A. S. Biryukov and L. A. Shelepin. 19(6), 775–81 (Dec. 1974); CPM-7501X0775

State of a gas moving near a solid surface —S. P. Bakanov and B. M. Markeev. 19(10), 1293–4 (Apr. 1975); CPM-7506X0227

51. THE PHYSICS OF FLUIDS

51.20.+ Viscosity and diffusion, experimental

Temperature dependence of trace diffusion coefficients of certain gases —A. É. Loiko, B. A. Ivakin, and P. E. Suetin. 19(3), 434 (Sep. 1974); CPM-7412X1120

Plasma diffusion in the Tornado device —A. N. Kozyrev and B. P. Peregud. 19(4), 468–74 (Oct. 1974); CPM-7412X0252

Steady-state study of the temperature dependence of the mutual–diffusion coefficients of certain gases —N. D. Kosov and B. P. Solonitsyn. 19(4), 541–2 (Oct. 1974); CPM-7412X0325

Thermal diffusion in a mixture of cesium vapor and helium —E. S. Bekmukhambetov and V. A. Donov. 19(12), 1627–8 (Jun. 1975); CPM-7508X0501

51.30.+ Thermal properties of gases

Gas cooling in transmission of high–power CO_2 laser radiation through the atmosphere —B. F. Gordiets, A. I. Osipov, and R. V. Khokhlov. 19(5), 669–72 (Nov. 1974); CPM-7501X0463

Gas temperature in the positive column of a medium-β helium discharge —Yu. M. Kagan and K. K. Paskalev. 19(12), 1601–3 (Jun. 1975); CPM-7508X0475

Temperature and electron density in the positive column of a medium-pressure helium discharge —Yu. M. Kagan and K. K. Paskalev. 19(12), 1604–5 (Jun. 1975); CPM-7508X0478

51.50.+ Electrical phenomena in gases

Extrapolation of the Langmuir S–curve to cesium pressures of 10–100 torr —V. E. Dubinskii and S. Ya. Lebedev. 19(1), 81–3 (Jul. 1974); CPM-7407X1593

Ionization of a gas–discharge gap by fast electrons —O. B. Evdokimov and A. P. Yalovets. 19(1), 138–9 (Jul. 1974); CPM-7407X1650

Production of an ion beam by a magnetic system with opposed fields —V. B. Glasko, A. G. Sveshnikov, and N. N. Semashko. 19(2), 201–5 (Aug. 1974); CPM-7408X1465

Physical properties of an electrodeless pulsed discharge in a gas–filled glass cell —Yu. I. Chutov, N. S. Baranchuk, M. R. Lozovich, and V. G. Danilov. 19(2), 224–8 (Aug. 1974); CPM-7408X1488

Fast electrons and x rays from nanosecond gas discharges at 0.1–760 torr —L. V. Tarasova, L. N. Khudyakova, T. V. Loiko, and V. A. Tsukerman. 19(3), 351–3 (Sep. 1974); CPM-7412X1037

Electron energy distribution in helium, nitrogen, and their mixtures —K. D. Asvadurov, I. A. Vasil'eva, and V. M. Torchinskii. 19(3), 354–7 (Sep. 1974); CPM-7412X1040

Stability of field–emission beams in nonsecond discharges —L. P. Babich. 19(3), 371–2 (Sep. 1974); CPM-7412X1057

Transmission of a high–current relativistic beam through a gas —Yu. V. Tkach, I. I. Magda, G. V. Skachek, S. S. Pushkarev, and I. P. Panchenko. 19(3), 412–3 (Sep. 1974); CPM-7412X1098

Optical radiation from nanosecond discharges in dense gases —L. P. Babich. 19(3), 419–20 (Sep. 1974); CPM-7412X1105

Nonlinear polarizability of a gaseous medium in a longitudinal magnetic field —V. A. Sokolov and L. M. Khayutin. 19(5), 589–91 (Nov. 1974); CPM-7501X0383

Stability of ball lightning —I. P. Stakhanov. 19(7), 861–4 (Jan. 1975); CPM-7503X0749

High–frequency discharge in a mercury—helium mixture —S. D. Vagner, Yu. M. Kagan, A. I. Konstantinov, and I. S. Niskonen. 19 (7), 898–900 (Jan. 1975); CPM-7503X0786

Effect of loss on electron avalanches in optical breakdown —V. I. Fisher. 19(8), 1050–2 (Feb. 1975); CPM-7504X1474

Dielectric strength of spark gaps following strong current pulses —E. P. Bel'kov. 19(9), 1210–3 (Mar. 1975); CPM-7505X0632

Effects due to streamer shape —É. D. Lozanskii and D. B. Pontekorvo. 19(11), 1432–3 (May 1975); CPM-7506X1186

Loss of neutralization for a stable neutralized ion beam —M. D. Gabovich. 19(11), 1502–3 (May 1975); CPM-7506X1256

Gas temperature in the positive column of a medium-β helium discharge —Yu. M. Kagan and K. K. Paskalev. 19(12), 1601–3 (Jun. 1975); CPM-7508X0475

Temperature and electron density in the positive column of a medium-pressure helium discharge —Yu. M. Kagan and K. K. Paskalev. 19(12), 1604–5 (Jun. 1975); CPM-7508X0478

Electrical strength of nitrogen and hyrodgen at high pressures —É. A. Avilov and N. V. Belkin. 19(12), 1631–2 (Jun. 1975); CPM-7508X0505

51.90.+ Other topics in the physics of fluids

Gas focusing of a negative–ion beam —M. D. Gabovich, A. P. Naida, I. M. Protsenko, L. S. Simonenko, and I. A. Soloshenko. 19(4), 546–7 (Oct. 1974); CPM-7412X0330

Photochemical waves in a medium with a branch–chain conversion mechanism —A. N. Oraevskii, V. P. Pimenov, and V. A. Shcheglov. 19(6), 782–6 (Dec. 1974); CPM-7501X0782

Thermoacoustic waves in conducting gases and liquids —P. A. Andreev. 19(6), 845–6 (Dec. 1974); CPM-7501X0845

Viscous momentum transport in a gaseous mixture —B. M. Markeev. 19(7), 969–70 (Jan. 1975); CPM-7503X0857

State of a gas moving near a solid surface —S. P. Bakanov and B. M. Markeev. 19(10), 1293–4 (Apr. 1975); CPM-7506X0227

Measurement of transverse relaxation time T_2 of optically oriented He^4 with an oscillator magnetometer–N. A. Dovator, R. A. Zhitnikov, and P. P. Kuleshov. 19(12), 1608–9 (Jun. 1975); CPM-7508X0482

52. THE PHYSICS OF PLASMAS AND ELECTRIC DISCHARGES

52.20.- Elementary processes in plasma

Expansion of a recombining plasma in vacuum —E. E. Lovetskii, A. N. Polyanichev, and V. S. Fetisov. 19(5), 647–50 (Nov. 1974); CPM-7501X0441

Effect of a high–frequency electric field on the energy loss of a charged particle in a medium —Zh. M. Diasamidze. 19(5), 687–8 (Nov. 1974); CPM-7501X0481

Conversion of neutral hydrogen into protons in dense plasmas —T. A. Bazilevskaya, L. I. Krupnik, and N. G. Shulika. 19(6), 741–4 (Dec. 1974); CPM-7501X0741

Acceleration of plasma electrons in strong electric fields —Z. A. Al'bikov, M. I. Ivanov, V. I. Kazacha, O. V. Kozlov, V. D. Rusanov, and S. S. Sobolev. 19(11), 1498–9 (May 1975); CPM-7506X1252

Loss of neutralization for a stable neutralized ion beam —M. D. Gabovich. 19(11), 1502–3 (May 1975); CPM-7506X1256

52.25.- Plasma basic properties

52.25.D Plasma kinetic equations

Recombination in an expanding plasma —Yu. A. Bykovskii, N. N. Degtyarenko, V. F. Elesin, V. E. Kondrashov, E. E. Lovetskii, A. N. Polyanichev, and V. S. Fetisov. 19(1), 43–8 (Jul. 1974); CPM-7407X1555

Microwave discharge in argon —E. V. Belousov, A. S. Bryukhovetskii, and A. V. Prokopov. 19(1), 53–6 (Jul. 1974); CPM-7407X1565

Symmetry of high–frequency plasma motions —A. A. Zhmudskii and V. B. Taranov. 19(6), 717–8 (Dec. 1974); CPM-7501X0717

Linear transient response of a fully ionized plasma in a pulsed electric field —V. V. Istomin, S. P. Sher, and S. P. Dovgopol. 19(7), 963–4 (Jan. 1975); CPM-7503X0851

Energy of charged particles accelerated by electromagnetic waves in a plasma with a spatially decreasing density —V. Ya. Davydovskii and A. S. Ukolov. 19(10), 1303–7 (Apr. 1975); CPM-7506X0237

Anisotropic plasma heating near the lower hybrid frequency —V. M. Glagolev, V. V. Martynenko, and Yu. V. Skosyrev. 19(12), 1543–6 (Jun. 1975); CPM-7508X0417

52.25.F Transport properties

Conductivity of a medium with inhomogeneous inclusions in a magnetic field —Yu. P. Emets. 19(5), 586–8 (Nov. 1974); CPM-7501X0380

Ion-acoustic instability of a fully ionized ultrarelativistic plasma in an electric field —D. I. Dzhavakhishvili. 19(7), 959–60 (Jan. 1975); CPM-7503X0847

Power spectrum of potential fluctuations in a moving magnetoactive plasma —V. M. Kostin. 19(8), 1053–6 (Feb. 1975); CPM-7504X1477

Measurement of ion density by the dispersion relation for an ion-beam plasma —M. D. Gabovich, L. P. Katsubo, and I. A. Soloshenko. 19(11), 1412–3 (May 1975); CPM-7506X1166

Anomalous resistivity of transverse plasma current at electron-cyclotron harmonics —V. I. Aref'ev and A. A. Chernov. 19(12), 1522–8 (Jun. 1975); CPM-7508X0396

52.25.G Fluctuation phenomena

Linear theory for the low-frequency electromagnetic properties of an isotropic turbulent plasma —K. Komilov, F. Kh. Khakimov, and V. N. Tsytovich. 19(5), 615–7 (Nov. 1974); CPM-7501X0409

52.25.K Thermodynamics of plasmas

Measurement of plasma electron temperature with a sinusoidal probe potential —B. I. Kanaev, V. V. Piterskii, and E. E. Yushmanov. 19 (11), 1421–3 (May 1975); CPM-7506X1175

52.25.M Dielectric properties

Dielectric breakdown of detonation products —V. L. Korol'kov, M. A. Mel'nikov, and A. P. Tsyplenko. 19(12), 1569–70 (Jun. 1975); CPM-7508X0443

52.25.P Emission, absorption, and scattering of radiation

Emission of waves from a plasma layer —T. A. Davydova and A. A. Zhmudskii. 19(1), 12–5 (Jul. 1974); CPM-7407X1524

Second-harmonic generation and emission in wave conversion at a plasma boundary —A. N. Kondratenko, V. G. Shaptala, and V. M. Kuklin. 19(1), 22–4 (Jul. 1974); CPM-7407X1534

Conversion of an electromagnetic wave into an ion-acoustic wave in an inhomogeneous plasma —A. N. Kondratenko and V. M. Kuklin. 19(1), 25–7 (Jul. 1974); CPM-7407X1537

Reflecting properties of an inhomogeneous anisotropic plasma layer —V. A. Zhivulin and G. I. Makarov. 19(1), 123 (Jul. 1974); CPM-7407X1635

Kinetic theory for wave reflection from a moving plasma —Yu. V. Bogomolov. 19(2), 190–2 (Aug. 1974); CPM-7408X1454

Scattering of high-frequency electromagnetic waves by ion-acoustic oscillations in a bounded plasma —V. G. Shaptala. 19(2), 193–6 (Aug. 1974); CPM-7408X1457

Role of collisions in plasma absorption of electromagnetic waves near the lower hybrid —B. V. Galaktionov, V. V. D'yachenko, M. M. Larionov, and O. N. Shcherbinin. 19(4), 459–62 (Oct. 1974); CPM-7412X0243

Experimental investigation of microwave radiation produced by hypersonic flows —V. A. Lyutomskii, V. M. Polyakov, and V. G. Testov. 19(4), 483–5 (Oct. 1974); CPM-7412X0267

Evolution of monochromatic whistler and plasma-wave packets in a collisionless plasma —Ya. N. Istomin. 19(4), 529–30 (Oct. 1974); CPM-7412X0313

Reflection of electromagnetic waves by a moving plasma —V. I. Miroshnichenko. 19(4), 533–4 (Oct. 1974); CPM-7412X0317

Reflection of finite amplitude electromagnetic waves from a semiconductor plasma —Yu. F. Filippov. 19(5), 603–6 (Nov. 1974); CPM-7501X0397

Impossibility of shielding against the rf radiation of a thermonuclear reactor with a cold-plasma sheath —A. S. Chikhachev. 19(5), 685 (Nov. 1974); CPM-7501X0479

Generation of drift waves by an rf field near the lower hybrid frequency —Yu. F. Baranov, D. G. Bulyginskii, M. I. Vil'dzhyunas, B. V. Galaktionov, and N. V. Shustova. 19(6), 732–5 (Dec. 1974); CPM-7501X0732

Electromagnetic fields outside a synthesized plasma jet —E. V. Bogdanov, G. M. Mantrova, and M. N. Yakovleva. 19(7), 919–21 (Jan. 1975); CPM-7503X0807

Radio-frequency absorption in a plasma confined by rf plugs —K. S. Golovanivskii, V. D. Dougar-Jabon, and L. A. Pokhmel'nykh. 19 (11), 1484–5 (May 1975); CPM-7506X1238

Rotation of Poynting vector for ultralow-frequency ion waves in an inhomogeneous plasma —Ya. L. Al'pert and R. N. Kaufman. 19 (12), 1519–21 (Jun. 1975); CPM-7508X0393

Anomalous ion heating in a parametrically unstable plasma —I. S. Baikov and V. P. Silin. 19(12), 1529–33 (Jun. 1975); CPM-7508X0403

52.30.+ Plasma flow; magnetohydrodynamics

Stability of field-emission beams in nonsecond discharges —L. P. Babich. 19(3), 371–2 (Sep. 1974); CPM-7412X1057

Plasma diffusion in the Tornado device —A. N. Kozyrev and B. P. Peregud. 19(4), 468–74 (Oct. 1974); CPM-7412X0252

Supersonic plasma jet from a high-power pulsed discharge —M. A. Sultanov. 19(4), 478–82 (Oct. 1974); CPM-7412X0262

Cerenkov instabilities of a relativistic beam in a periodic plasma-filled waveguide —V. I. Kurilko, Yu. V. Tkach, and V. A. Shendrik. 19 (5), 607–11 (Nov. 1974); CPM-7501X0401

Coaxial plasma injector with programmed injection —V. A. Burtsev, V. N. Litunovskii, and M. P. Nadgornaya. 19(6), 736–40 (Dec. 1974); CPM-7501X0736

Magnetohydrodynamic channel flow in a tapered magnetic field —S. A. Regirer. 19(7), 874–7 (Jan. 1975); CPM-7503X0762

Nonstationary magnetohydrodynamic flow and wave propagation —M. Ya. Antimirov and Yu. Ya. Boguslavskii. 19(7), 878–9 (Jan. 1975); CPM-7503X0766

Lagrange problem in magnetohydrodynamics —P. V. Zagorskii and Yu. P. Lun'kin. 19(8), 1009–11 (Feb. 1975); CPM-7504X1433

Magnetohydrodynamic stability of a neutral current layer in a plasma —S. V. Bulanov. 19(9), 1246–7 (Mar. 1975); CPM-7505X0668

Free expansion of plasma jets —P. A. Demchenko, L. I. Krupnik, and E. S. Lyangner. 19(11), 1426–8 (May 1975); CPM-7506X1180

Analysis of magnetic deflection systems —O. M. Vovk and O. Ya. Popov. 19(11), 1504 (May 1975); CPM-7506X1258

Two-stream flow in a thin plasma slab —A. V. Pashchenko and B. N. Rutkevich. 19(12), 1538–40 (Jun. 1975); CPM-7508X0412

Formation of a plasma focus in a plasma erosion accelerator. II. Energy characteristics of the dense plasma focus —N. P. Kozlov, L. V. Leskov, Yu. S. Protasov, and V. I. Khvesyuk. 19(12), 1558–9 (Jun. 1975); CPM-7508X0432

Hot probe measurements in a rarefied streaming plasma —E. M. Netsvetailov, L. V. Nosachev, and V. V. Skvortsov. 19(12), 1579–83 (Jun. 1975); CPM-7508X0453

52.35.– Waves, oscillations, and instabilities in plasma

Kinetic plasma instabilities excited by a monoenergetic beam —A. I. Ranyuk and V. L. Sizonenko. 19(5), 628–9 (Nov. 1974); CPM-7501X0422

Instabilities in a finite-β plasma with transverse current. I —A. I. Pyatak and V. L. Sizonenko. 19(5), 635–9 (Nov. 1974); CPM-7501X0429

Instabilities in a finite-β plasma with transverse current. II —A. I. Pyatak and V. L. Sizonenko. 19(5), 640–4 (Nov. 1974); CPM-7501X0434

Generation of drift waves by an rf field near the lower hybrid frequency —Yu. F. Baranov, D. G. Bulyginskii, M. I. Vil'dzhyunas, B. V. Galaktionov, and N. V. Shustova. 19(6), 732–5 (Dec. 1974); CPM-7501X0732

52.35.C Linear waves and oscillations

Excitation of Alfvén waves in decay instabilities —A. G. Elfimov and F. M. Nekrasov. 19(1), 9–11 (Jul. 1974); CPM-7407X1521

Emission of waves from a plasma layer —T. A. Davydova and A. A. Zhmudskii. 19(1), 12–5 (Jul. 1974); CPM-7407X1524

Stabilization of MHD instabilities by a high-frequency current in a straight system —V. P. Fedyakova. 19(1), 16–9 (Jul. 1974); CPM-7407X1528

Nonmonoenergetic relativistic electron beam in a bounded collisional plasma —V. P. Grigor'ev and N. S. Shulaev. 19(1), 20–1 (Jul. 1974); CPM-7407X1532

Conversion of an electromagnetic wave into an ion-acoustic wave in an inhomogeneous plasma —A. N. Kondratenko and V. M. Kuklin. 19(1), 25–7 (Jul. 1974); CPM-7407X1537

Nonlinear plasma waves and ion–acoustic waves in an isotropic plasma —V. Sh. Livadonov and S. M. Fainshtein. 19(1), 28–30 (Jul. 1974); CPM-7407X1540
Ionization discontinuity in large–amplitude striations —A. V. Nedospasov and V. G. Petrov. 19(1), 31–4 (Jul. 1974); CPM-7407X1543
Longitudinal oscillations in an ultrarelativistic electron plasma —D. I. Dzhavakhishvili. 19(1), 115 (Jul. 1974); CPM-7407X1627
Effect of cathode emission on the threshold for striations —N. A. Vorob'eva, Yu. M. Kagan, V. M. Milenin, and A. Kh. Muradov. 19(1), 117–8 (Jul. 1974); CPM-7407X1629
Ionization oscillations in a plasma in the presence of ionizing radiation —B. V. Vainer. 19(1), 119–20 (Jul. 1974); CPM-7407X1631
Parametric plasma instabilities excited by the sudden application of an electric field —A. B. Kitsenko and K. N. Stepanov. 19(1), 127–8 (Jul. 1974); CPM-7407X1639
Generation of Bernstein modes in beam–plasma system —V. N. Fedorenko. 19(2), 171–4 (Aug. 1974); CPM-7408X1435
Excitation of electromagnetic ion cyclotron waves by fast ions —T. D. Kaladze, D. G. Lominadze, and K. N. Stepanov. 19(2), 175–6 (Aug. 1974); CPM-7408X1439
Parametric instability of an electron beam in a magnetic field —A. I. Pasynok and N. S. Repalov. 19(2), 177–80 (Aug. 1974); CPM-7408X1441
Scattering by ion–acoustic waves in a rectangular waveguide —S. V. Troitskii. 19(2), 181–4 (Aug. 1974); CPM-7408X1445
Scattering of high–frequency electromagnetic waves by ion–acoustic oscillations in a bounded plasma —V. G. Shaptala. 19(2), 193–6 (Aug. 1974); CPM-7408X1457
Surface waves in a magnetized plasma in a radio–frequency field —E. E. Lovetskii and A. N. Starodub. 19(3), 319–22 (Sep. 1974); CPM-7412X1005
Damping of ion–acoustic waves in a bounded plasma —A. N. Kondratenko and V. M. Kuklin. 19(3), 326–8 (Sep. 1974); CPM-7412X1012
Nonlinear instability of a helicon packet in an anisotropic plasma —Ya. N. Istomin and V. I. Karpman. 19(3), 405–6 (Sep. 1974); CPM-7412X1091
Long–wave cyclotron instability in a plasma in an inhomogeneous magnetic field —A. S. Kukushkin. 19(3), 410–1 (Sep. 1974); CPM-7412X1096
Linear theory for the low–frequency electromagnetic properties of an isotropic turbulent plasma —K. Komilov, F. Kh. Khakimov, and V. N. Tsytovich. 19(5), 615–7 (Nov. 1974); CPM-7501X0409
Excitation of surface electromagnetic waves in a plasma cylinder surrounded by a hollow electron beam —O. V. Dolzhenko, A. V. Zosimov, and A. A. Rukhadze. 19(5), 618–21 (Nov. 1974); CPM-7501X0412
Quasilinear theory of beam–generated surface waves in a plasma —V. I. Pakhomov and V. L. Sizonenko. 19(5), 630–4 (Nov. 1974); CPM-7501X0424
Absolute decay instability of low–frequency waves in an inhomogeneous plasma —A. D. Piliya and V. I. Fedorov. 19(5), 686 (Nov. 1974); CPM-7501X0480
Current–driven instability in a conducting fluid —A. M. Kovnatskii. 19(5), 691 (Nov. 1974); CPM-7501X0485
Symmetry of high–frequency plasma motions —A. A. Zhmudskii and V. B. Taranov. 19(6), 717–8 (Dec. 1974); CPM-7501X0717
Magnetodrift waves in a finite–β plasma —N. M. Ryzhov, V. L. Sizonenko, V. A. Suprunenko, E. A. Sukhomlin, and Yu. V. Gutarev. 19(6), 722–5 (Dec. 1974); CPM-7501X0722
Nonstationary magnetohydrodynamic flow and wave propagation —M. Ya. Antimirov and Yu. Ya. Boguslavskii. 19(7), 878–9 (Jan. 1975); CPM-7503X0766
Surface waves in periodic plasma systems —V. F. Dryakhlushin and Yu. A. Romanov. 19(7), 883–6 (Jan. 1975); CPM-7503X0771
Solitary waves in anisotropic plasma waveguide —V. I. Kurilko and A. P. Tolstoluzhskii. 19(7), 887–90 (Jan. 1975); CPM-7503X0775
Low–frequency oscillations in counter–streaming high–current electron beams —A. F. Timoshenko, D. V. Iremashvili, and Yu. K. Udovichenko. 19(8), 1038–41 (Feb. 1975); CPM-7504X1462
Power spectrum of potential fluctuations in a moving magnetoactive plasma —V. M. Kostin. 19(8), 1053–6 (Feb. 1975); CPM-7504X1477
Stochastic acceleration of electrons in nanosecond discharges —L. P. Babich. 19(9), 1154–6 (Mar. 1975); CPM-7505X0576
Modulation of microwaves by density fluctuations in a plasma —L. A. Dushin, A. V. Serikov, A. I. Skibenko, E. V. Krivorukov, and I. P. Fomin. 19(9), 1163–7 (Mar. 1975); CPM-7505X0585
Wave excitation at half the gyrofrequency in counterstreaming electron beams —A. P. Timoshenko, D. V. Iremashvili, and Yu. K. Udovichenko. 19(12), 1584–6 (Jun. 1975); CPM-7508X0458

52.35.E Plasma instabilities

Parametric instability of a spatially moderated electron beam in a magnetic field —N. S. Repalov and V. F. Tyrnov. 19(7), 871–3 (Jan. 1975); CPM-7503X0759
Ion–acoustic instability of a fully ionized ultrarelativistic plasma in an electric field —D. I. Dzhavakhishvili. 19(7), 959–60 (Jan. 1975); CPM-7503X0847
Hydrodynamic stability of the Uragan stellarator —V. M. Zalkind, Yu. K. Kuznetsov, V. K. Pashnev, and V. M. Tonkopryad. 19(8), 1123–5 (Feb. 1975); CPM-7504X1547
Transverse-current plasma instability —D. G. Lominadze and V. L. Sizonenko. 19(9), 1145–9 (Mar. 1975); CPM-7505X0567
Plasma instability due to an anisotropic electron distribution —D. G. Lominadze and V. L. Sizonenko. 19(9), 1150–3 (Mar. 1975); CPM-7505X0572
High-frequency instabilities in an inhomogeneous, anisotropic finite-β plasma —V. D. Egorenkov and A. I. Pyatak. 19(9), 1160–2 (Mar. 1975); CPM-7505X0582
Magnetohydrodynamic stability of a neutral current layer in a plasma —S. V. Bulanov. 19(9), 1246–7 (Mar. 1975); CPM-7505X0668
Ion energy spectra and collective effects in a Penning ion source —V. I. Farenik, V. V. Vlasov, A. M. Rozhkov, and A. A. Kozharin. 19 (9), 1258–9 (Mar. 1975); CPM-7505X0680
Turbulent plasma heating and the Buneman instability —V. L. Sizonenko. 19(9), 1260–1 (Mar. 1975); CPM-7505X0682
Drift instability in a weakly ionized plasma —S. V. Putvinskii and A. V. Timofeev. 19(10), 1295–9 (Apr. 1975); CPM-7506X0229
Nonlinear effects for the "kink" instability in an electron-ion ring —G. P. Berman. 19(10), 1312–6 (Apr. 1975); CPM-7506X0246
Instabilities in interpenetrating electron and ion beams —I. A. Soloshenko and L. P. Katsubo. 19(10), 1317–20 (Apr. 1975); CPM-7506X0251
Mechanism for plasma loss from a magnetic trap —V. I. Volosov. 19 (11), 1408–11 (May 1975); CPM-7506X1162
Stabilization of two-stream instabilities —V. A. Buts. 19(11), 1496–7 (May 1975); CPM-7506X1250
Low-frequency helical instability in a high-frequency electric field —V. S. Paverman and D. D. Tskhakaya. 19(11), 1508–9 (May 1975); CPM-7506X1262
Anomalous resistivity of transverse plasma current at electron-cyclotron harmonics —V. I. Aref'ev and A. A. Chernov. 19(12), 1522–8 (Jun. 1975); CPM-7508X0396
Interaction of a hollow electron beam with a plasma —N. M. Zemlyanskii, A. K. Berezin, Ya. B. Fainberg, L. I. Bolotin, and S. S. Krivulya. 19(12), 1547–8 (Jun. 1975); CPM-7508X0421
Current-convective instability in a three-component plasma —E. Z. Meilikhov. 19(12), 1610–1 (Jun. 1975); CPM-7508X0484
Connection of magnetic lines of force in a neutral layer —A. T. Altyntsev and V. I. Krasov. 19(12), 1639–40 (Jun. 1975); CPM-7508X0513

52.35.G Nonlinear waves and nonlinear interactions

Excitation of Alfvén waves in decay instabilities —A. G. Elfimov and F. M. Nekrasov. 19(1), 9–11 (Jul. 1974); CPM-7407X1521
Emission of waves from a plasma layer —T. A. Davydova and A. A. Zhmudskii. 19(1), 12–5 (Jul. 1974); CPM-7407X1524
Stabilization of MHD instabilities by a high–frequency current in a straight system —V. P. Fedyakova. 19(1), 16–9 (Jul. 1974); CPM-7407X1528
Nonmonoenergetic relativistic electron beam in a bounded collisional plasma —V. P. Grigor'ev and N. S. Shulaev. 19(1), 20–1 (Jul. 1974); CPM-7407X1532
Conversion of an electromagnetic wave into an ion–acoustic wave in an inhomogeneous plasma —A. N. Kondratenko and V. M. Kuklin. 19(1), 25–7 (Jul. 1974); CPM-7407X1537
Nonlinear plasma waves and ion–acoustic waves in an isotropic plasma —V. Sh. Livadonov and S. M. Fainshtein. 19(1), 28–30 (Jul. 1974); CPM-7407X1540
Ionization discontinuity in large–amplitude striations —A. V. Nedospasov and V. G. Petrov. 19(1), 31–4 (Jul. 1974); CPM-7407X1543

Longitudinal oscillations in an ultrarelativistic electron plasma —D. I. Dzhavakhishvili. 19(1), 115 (Jul. 1974); CPM-7407X1627

Effect of cathode emission on the threshold for striations —N. A. Vorob'eva, Yu. M. Kagan, V. M. Milenin, and A. Kh. Muradov. 19(1), 117–8 (Jul. 1974); CPM-7407X1629

Ionization oscillations in a plasma in the presence of ionizing radiation —B. V. Vainer. 19(1), 119–20 (Jul. 1974); CPM-7407X1631

Parametric plasma instabilities excited by the sudden application of an electric field —A. B. Kitsenko and K. N. Stepanov. 19(1), 127–8 (Jul. 1974); CPM-7407X1639

Generation of Bernstein modes in beam–plasma system —V. N. Fedorenko. 19(2), 171–4 (Aug. 1974); CPM-7408X1435

Excitation of electromagnetic ion cyclotron waves by fast ions —T. D. Kaladze, D. G. Lominadze, and K. N. Stepanov. 19(2), 175–6 (Aug. 1974); CPM-7408X1439

Parametric instability of an electron beam in a magnetic field —A. I. Pasynok and N. S. Repalov. 19(2), 177–80 (Aug. 1974); CPM-7408X1441

Scattering by ion–acoustic waves in a rectangular waveguide —S. V. Troitskii. 19(2), 181–4 (Aug. 1974); CPM-7408X1445

Multimode parametric interactions in a plasma with low–frequency pumping —Yu. M. Sorokin and N. S. Stepanov. 19(2), 185–9 (Aug. 1974); CPM-7408X1449

Scattering of high–frequency electromagnetic waves by ion–acoustic oscillations in a bounded plasma —V. G. Shaptala. 19(2), 193–6 (Aug. 1974); CPM-7408X1457

Surface waves in a magnetized plasma in a radio–frequency field —E. E. Lovetskii and A. N. Starodub. 19(3), 319–22 (Sep. 1974); CPM-7412X1005

Damping of ion–acoustic waves in a bounded plasma —A. N. Kondratenko and V. M. Kuklin. 19(3), 326–8 (Sep. 1974); CPM-7412X1012

Nonlinear instability of a helicon packet in an anisotropic plasma —Ya. N. Istomin and V. I. Karpman. 19(3), 405–6 (Sep. 1974); CPM-7412X1091

Long–wave cyclotron instability in a plasma in an inhomogeneous magnetic field —A. S. Kukushkin. 19(3), 410–1 (Sep. 1974); CPM-7412X1096

Launching and propagation of regular nonlinear waves in an anisotropic plasma–filled waveguide —V. I. Kurilko, A. P. Tols–toluzhskii, and Ya. B. Fainberg. 19(5), 622–7 (Nov. 1974); CPM-7501X0416

Quasilinear theory of beam–generated surface waves in a plasma —V. I. Pakhomov and V. L. Sizonenko. 19(5), 630–4 (Nov. 1974); CPM-7501X0424

Absolute decay instability of low–frequency waves in an inhomogeneous plasma —A. D. Piliya and V. I. Fedorov. 19(5), 686 (Nov. 1974); CPM-7501X0480

Aperiodic instability in a plasma gap with external feedback —A. N. Igritskii. 19(6), 719–21 (Dec. 1974); CPM-7501X0719

Wave interaction in a thin plasma sheath —A. V. Pashchenko and B. N. Rutkevich. 19(6), 726–31 (Dec. 1974); CPM-7501X0726

Propagation and stability of large amplitude ionization waves —M. S. Gorelik and L. D. Tsendin. 19(7), 880–2 (Jan. 1975); CPM-7503X0768

Plasma decay instability in crossed fields —V. I. Farenik, V. V. Vlasov, A. M. Rozhkov, and A. A. Kozharin. 19(8), 1116–7 (Feb. 1975); CPM-7504X1540

Nonlinear interaction between a monochromatic ion-acoustic wave and a plasma —V. P. Indykul. 19(9), 1157–9 (Mar. 1975); CPM-7505X0579

Nonlinear statistical theory for condensation of Langmuir plasmons. III. Energy flux for plasma turbulence —F. Kh. Khakimov and V. N. Tsytovich. 19(10), 1300–2 (Apr. 1975); CPM-7506X0234

Nonlinear effects for the "kink" instability in an electron-ion ring —G. P. Berman. 19(10), 1312–6 (Apr. 1975); CPM-7506X0246

Motion of charged particles in a nonneutral plasma —E. N. Agafonova and L. I. Grechikhin. 19(11), 1488–9 (May 1975); CPM-7506X1242

Nonlinear behavior of monochromatic surface waves excited by a beam —A. B. Kitsenko, I. M. Pankratov, and K. N. Stepanov. 19 (11), 1505–6 (May 1975); CPM-7506X1259

Transformation of nonlinear MHD waves —G. M. Zaslavskii, S. S. Moiseev, and V. V. Mukhin. 19(12), 1534–7 (Jun. 1975); CPM-7508X0408

52.35.J Plasma turbulence

Nonlinear statistical theory of a condensate of plasmons. II. Stochastic heating of plasma ions by large–scale Langmuir turbulence —F. Kh. Khakimov. 19(3), 315–8 (Sep. 1974); CPM-7412X1001

Possible use of the schlieren method to measure characteristics of turbulence —V. G. Ivanov. 19(3), 429–31 (Sep. 1974); CPM-7412X1115

Excitation of acoustic waves by ion–acoustic turbulence —Kh. O. Abdulloev, F. Kh. Khakimov, and V. G. Makhan'kov. 19(4), 441–5 (Oct. 1974); CPM-7412X0225

Plasma acceleration in crossed electric and magnetic fields —V. I. Aref'ev. 19(4), 446–54 (Oct. 1974); CPM-7412X0230

Linear theory for the low–frequency electromagnetic properties of an isotropic turbulent plasma —K. Komilov, F. Kh. Khakimov, and V. N. Tsytovich. 19(5), 615–7 (Nov. 1974); CPM-7501X0409

Optical investigation of a turbulent plasma —Ya. F. Volkov, V. G. Dyatlov, and N. I. Mitina. 19(7), 905–8 (Jan. 1975); CPM-7503X0793

Turbulent plasma heating and the Buneman instability —V. L. Sizonenko. 19(9), 1260–1 (Mar. 1975); CPM-7505X0682

Nonlinear statistical theory for condensation of Langmuir plasmons. III. Energy flux for plasma turbulence —F. Kh. Khakimov and V. N. Tsytovich. 19(10), 1300–2 (Apr. 1975); CPM-7506X0234

Anomalous ion heating in a parametrically unstable plasma —I. S. Baikov and V. P. Silin. 19(12), 1529–33 (Jun. 1975); CPM-7508X0403

52.35.L Shock waves

Multiple reflection of light in a shock tube —V. D. Mironov and V. I. Selyakov. 19(3), 402–4 (Sep. 1974); CPM-7412X1088

Investigation of ionization processes behind strong shock waves using an electrical conductivity probe —V. A. Tishchenko, N. V. Khandurov, and É. K. Chekalin. 19(5), 651–3 (Nov. 1974); CPM-7501X0445

Propagation of shock waves in inhomogeneous media —R. A. Glatman. 19(11), 1390–2 (May 1975); CPM-7506X1144

52.40.– Plasma interactions

Pulsed ion beams from a high-current plasma diode —B. A. Tskhadaya, A. A. Plyutto, and K. V. Suladze. 19(8), 1108–9 (Feb. 1975); CPM-7504X1532

52.40.D Electromagnetic wave propagation in plasma

Effect of ionization and excitation on the penetration of an electromagnetic wave into a weakly ionized plasma —A. G. Boev and A. V. Prokopov. 19(7), 901–4 (Jan. 1975); CPM-7503X0789

Modulation of microwaves by density fluctuations in a plasma —L. A. Dushin, A. V. Serikov, A. I. Skibenko, E. V. Krivorukov, and I. P. Fomin. 19(9), 1163–7 (Mar. 1975); CPM-7505X0585

Energy of charged particles accelerated by electromagnetic waves in a plasma with a spatially decreasing density —V. Ya. Davydovskii and A. S. Ukolov. 19(10), 1303–7 (Apr. 1975); CPM-7506X0237

Parametric excitation of helicon waves in a plasma by modulated radio frequency waves —V. S. Paverman and D. D. Tskhakya. 19 (12), 1629–30 (Jun. 1975); CPM-7508X0503

52.40.F Antennas in plasma; plasma-filled wave guides

Surface waves in periodic plasma systems —V. F. Dryakhlushin and Yu. A. Romanov. 19(7), 883–6 (Jan. 1975); CPM-7503X0771

Solitary waves in anisotropic plasma waveguide —V. I. Kurilko and A. P. Tolstoluzhskii. 19(7), 887–90 (Jan. 1975); CPM-7503X0775

Electromagnetic fields outside a synthesized plasma jet —E. V. Bogdanov, G. M. Mantrova, and M. N. Yakovleva. 19(7), 919–21 (Jan. 1975); CPM-7503X0807

Electron lifetimes in atmosphere at high pressure —V. N. Kapinos, Yu. A. Medvedev, N. N. Morozov, and B. M. Stepanov. 19(11), 1507 (May 1975); CPM-7506X1261

52.40.H Solid-plasma interactions

Direct current in a metal—selenium—metal structure boundary by an rf plasma —A. D. Andreev and S. I. Lubinskii. 19(12), 1606–7 (Jun. 1975); CPM-7508X0480

52.40.K Sheaths

Surface waves in a magnetized plasma in a radio–frequency field —E. E. Lovetskii and A. N. Starodub. 19(3), 319–22 (Sep. 1974); CPM-7412X1005

Damping of ion–acoustic waves in a bounded plasma —A. N. Kondratenko and V. M. Kuklin. 19(3), 326–8 (Sep. 1974); CPM-7412X1012

Resonant amplification of an image potential by an electromagnetic wave —Yu. I. Balkarei and É. M. Épshtein. 19(6), 843–4 (Dec. 1974); CPM-7501X0843

Diffusion regime for electrostatic probes as singular-perturbation problem —I. B. Chekmarev. 19(10), 1287–9 (Apr. 1975); CPM-7506X0221

Nonmonotonic potential distribution in the electrode region —A. I. Loshkarev. 19(10), 1308–11 (Apr. 1975); CPM-7506X0242

Low-pressure self-maintained discharge with suppressed electron drift. I —V. K. Kalashnikov and Yu. V. Sanochkin. 19(12), 1549–53 (Jun. 1975); CPM-7508X0423

Low-pressure self-maintained discharge with suppressed electron drift. II —Yu. V. Sanochkin and V. K. Kalashnikov. 19(12), 1554–8 (Jun. 1975); CPM-7508X0428

52.40.M Beam interactions in plasma

Nonmonoenergetic relativistic electron beam in a bounded collisional plasma —V. P. Grigor'ev and N. S. Shulaev. 19(1), 20–1 (Jul. 1974); CPM-7407X1532

Spatial characteristics and loss of plasma produced by an electron beam in a magnetic trap —M. Yu. Bredikhin, A. I. Maslov, A. I. Skibenko, E. I. Skibenko, I. P. Fomin, and V. B. Yuferov. 19(1), 49–52 (Jul. 1974); CPM-7407X1561

Excitation of electromagnetic ion cyclotron waves by fast ions —T. D. Kaladze, D. G. Lominadze, and K. N. Stepanov. 19(2), 175–6 (Aug. 1974); CPM-7408X1439

Parametric instability of an electron beam in a magnetic field —A. I. Pasynok and N. S. Repalov. 19(2), 177–80 (Aug. 1974); CPM-7408X1441

Conversion of regular charge–density waves in a inhomogeneous plasma —S. S. Kalmykova and A. P. Tolstoluzhskii. 19(4), 455–8 (Oct. 1974); CPM-7412X0239

Excitation of surface electromagnetic waves in a plasma cylinder surrounded by a hollow electron beam —O. V. Dolzhenko, A. V. Zosimov, and A. A. Rukhadze. 19(5), 618–21 (Nov. 1974); CPM-7501X0412

Kinetic plasma instabilities excited by a monoenergetic beam —A. I. Ranyuk and V. L. Sizonenko. 19(5), 628–9 (Nov. 1974); CPM-7501X0422

Quasilinear theory of beam–generated surface waves in a plasma —V. I. Pakhomov and V. L. Sizonenko. 19(5), 630–4 (Nov. 1974); CPM-7501X0424

Electron–beam excited crossed–field discharge —V. A. Saenko and M. M. Kasumov. 19(6), 759–61 (Dec. 1974); CPM-7501X0759

Parametric instability of a spatially moderated electron beam in a magnetic field —N. S. Repalov and V. F. Tyrnov. 19(7), 871–3 (Jan. 1975); CPM-7503X0759

Design of axisymmetric plasma lenses —A. I. Morozov and S. V. Lebedev. 19(8), 996–1000 (Feb. 1975); CPM-7504X1420

Low-frequency oscillations in counter-streaming high-current electron beams —A. F. Timoshenko, D. V. Iremashvili, and Yu. K. Udovichenko. 19(8), 1038–41 (Feb. 1975); CPM-7504X1462

Scattering of an electron beam in a straight *dc* turbulent plasma —Yu. P. Golovanov, L. P. Zakatov, A. S. Kingsep, and A. G. Plakhov. 19(8), 1046–9 (Feb. 1975); CPM-7504X1470

Instabilities in interpenetrating electron and ion beams —I. A. Soloshenko and L. P. Katsubo. 19(10), 1317–20 (Apr. 1975); CPM-7506X0251

Measurement of ion density by the dispersion relation for an ion-beam plasma —M. D. Gabovich, L. P. Katsubo, and I. A. Soloshenko. 19(11), 1412–3 (May 1975); CPM-7506X1166

Rotation of Poynting vector for ultralow-frequency ion waves in an inhomogeneous plasma —Ya. L. Al'pert and R. N. Kaufman. 19 (12), 1519–21 (Jun. 1975); CPM-7508X0393

Interaction of a hollow electron beam with a plasma —N. M. Zemlyanskii, A. K. Berezin, Ya. B. Fainberg, L. I. Bolotin, and S. S. Krivulya. 19(12), 1547–8 (Jun. 1975); CPM-7508X0421

52.50.– Plasma production and heating

Distributed systems for feedback control of a tokamak plasma —V. F. Gubarev and Yu. I. Samoilenko. 19(4), 463–7 (Oct. 1974); CPM-7412X0247

52.50.D Plasma sources

Investigation of spatial distributions in a laser–produced plasma by Hα absorption —G. V. Ostrovskaya and N. A. Pobedonostseva. 19(3), 424–6 (Sep. 1974); CPM-7412X1110

Supersonic plasma jet from a high–power pulsed discharge —M. A. Sultanov. 19(4), 478–82 (Oct. 1974); CPM-7412X0262

Electron–beam excited crossed–field discharge —V. A. Saenko and M. M. Kasumov. 19(6), 759–61 (Dec. 1974); CPM-7501X0759

Low pressure discharge with high–energy electrons —R. A. Demirkhanov, Yu. V. Kursanov, and L. P. Skripal'. 19(7), 891–4 (Jan. 1975); CPM-7503X0779

Plasma synthesis by injection of an electron beam through an ion source —V. F. Virko, M. D. Gabovich, G. S. Kirichenko, and O. K. Nazarenko. 19(11), 1418–20 (May 1975); CPM-7506X1172

Two modes of operation of an arc plasma source in an external magnetic field —A. G. Korsun and S. A. Meshcheryakov. 19(11), 1500–1 (May 1975); CPM-7506X1254

52.50.G Plasma heating

Nonlinear statistical theory of a condensate of plasmons. II. Stochastic heating of plasma ions by large–scale Langmuir turbulence —F. Kh. Khakimov. 19(3), 315–8 (Sep. 1974); CPM-7412X1001

Expansion of a recombining plasma in vacuum —E. E. Lovetskii, A. N. Polyanichev, and V. S. Fetisov. 19(5), 647–50 (Nov. 1974); CPM-7501X0441

Spatial and energy parameters of the relativistic electron beam of the Rius–5 accelerator —A. T. Altyntsev and V. I. Koroteev. 19(6), 773–4 (Dec. 1974); CPM-7501X0773

Linear transient response of a fully ionized plasma in a pulsed electric field —V. V. Istomin, S. P. Sher, and S. P. Dovgopol. 19(7), 963–4 (Jan. 1975); CPM-7503X0851

Turbulent plasma heating and the Buneman instability —V. L. Sizonenko. 19(9), 1260–1 (Mar. 1975); CPM-7505X0682

Anisotropic plasma heating near the lower hybrid frequency —V. M. Glagolev, V. V. Martynenko, and Yu. V. Skosyrev. 19(12), 1543–6 (Jun. 1975); CPM-7508X0417

52.50.J Plasma production and heating by laser beams

Laser-initiated vacuum discharge —V. P. Kovalenko, A. A. Makarevich, V. A. Rodichkin, and A. M. Timonin. 19(11), 1429–31 (May 1975); CPM-7506X1183

52.55.– Plasma equilibrium and confinement

52.55.D General theory

Mechanism for plasma loss from a magnetic trap —V. I. Volosov. 19 (11), 1408–11 (May 1975); CPM-7506X1162

52.55.F Closed-confinement configurations

Magnetic field in a θ pinch with an axial conductor —Ya. F. Volkov, V. G. Dyatlov, and N. I. Mitina. 19(3), 323–5 (Sep. 1974); CPM-7412X1009

Stabilization of the major radius of toroidal pinch by a feedback system —V. V. Arsenin. 19(7), 895–7 (Jan. 1975); CPM-7503X0783

Optical investigation of a turbulent plasma —Ya. F. Volkov, V. G. Dyatlov, and N. I. Mitina. 19(7), 905–8 (Jan. 1975); CPM-7503X0793

Equilibrium in a tokamak with noncircular cross section —L. E. Zakharov. 19(8), 1005–8 (Feb. 1975); CPM-7504X1429

Plasma equilibrium and confinement in a poloidal heliotron configuration. I —V. G. Zykov, V. I. Karpukhin, Yu. F. Lonin, N. N. Podteregera, N. I. Rudnev, and V. T. Tolok. 19(8), 1063–8 (Feb. 1975); CPM-7504X1487

Plasma equilibrium and confinement in a poloidal heliotron configuration. II —V. G. Zykov, V. I. Karpukhin, Yu. F. Lonin, N. N. Podteregera, N. I. Rudnev, A. Y. Skibenko, V. T. Tolok, and I. P. Fomin. 19(8), 1069–72 (Feb. 1975); CPM-7504X1493

Hydrodynamic stability of the Uragan stellarator —V. M. Zalkind, Yu. K. Kuznetsov, V. K. Pashnev, and V. M. Tonkopryad. 19(8), 1123–5 (Feb. 1975); CPM-7504X1547

Energy balance in Tokamaks in the "plateau—banana" transition region —Yu. N. Dnestrovskii and D. P. Kostomarov. 19(12), 1541–2 (Jun. 1975); CPM-7508X0415

52.55.H Open-confinement configurations

Spatial characteristics and loss of plasma produced by an electron beam in a magnetic trap —M. Yu. Bredikhin, A. I. Maslov, A. I. Skibenko, E. I. Skibenko, I. P. Fomin, and V. B. Yuferov. 19(1), 49–52 (Jul. 1974); CPM-7407X1561

Plasma confinement in a time-increasing multipole magnetic field —V. G. Padalka and N. S. Repalov. 19(1), 121–2 (Jul. 1974); CPM-7407X1633

Magnetic field in a θ pinch with an axial conductor —Ya. F. Volkov, V. G. Dyatlov, and N. I. Mitina. 19(3), 323–5 (Sep. 1974); CPM-7412X1009

Radio-frequency absorption in a plasma confined by rf plugs —K. S. Golovanivskii, V. D. Dougar-Jabon, and L. A. Pokhmel'nykh. 19(11), 1484–5 (May 1975); CPM-7506X1238

52.55.J Confinement in fusion reactors

Magnetic topography of toroidal systems —M. N. Skoblik, V. E. Ziser, A. V. Georgievskii, and V. G. Peletminskaya. 19(10), 1277–80 (Apr. 1975); CPM-7506X0211

52.60.+ Relativistic plasma

Method for optical modulation of an electron beam —V. I. Sotnikov. 19(11), 1510–1 (May 1975); CPM-7506X1264

52.70.– Plasma diagnostic techniques and instrumentation

Electron lifetimes in atmosphere at high pressure —V. N. Kapinos, Yu. A. Medvedev, N. N. Morozov, and B. M. Stepanov. 19(11), 1507 (May 1975); CPM-7506X1261

52.70.D Electric and magnetic measurements

Charge-carrier density of the plasma produced in a Penning mixture by irradiation by uranium fission fragments and reactor radiation —G. A. Batyrbekov, Yu. D. Kuznetsov, and Zh. S. Takibaev. 19(5), 645–6 (Nov. 1974); CPM-7501X0439

Diffusion regime for electrostatic probes as singular-perturbation problem —I. B. Chekmarev. 19(10), 1287–9 (Apr. 1975); CPM-7506X0221

Measurement of plasma electron temperature with a sinusoidal probe potential —B. I. Kanaev, V. V. Piterskii, and E. E. Yushmanov. 19(11), 1421–3 (May 1975); CPM-7506X1175

Resistance and inductance of a gas arc —S. I. Barannik, S. B. Vasserman, and A. N. Lukin. 19(11), 1449–53 (May 1975); CPM-7506X1203

Acceleration of plasma electrons in strong electric fields —Z. A. Al'bikov, M. I. Ivanov, V. I. Kazacha, O. V. Kozlov, V. D. Rusanov, and S. S. Sobolev. 19(11), 1498–9 (May 1975); CPM-7506X1252

Hot probe measurements in a rarefied streaming plasma —E. M. Netsvetailov, L. V. Nosachev, and V. V. Skvortsov. 19(12), 1579–83 (Jun. 1975); CPM-7508X0453

Connection of magnetic lines of force in a neutral layer —A. T. Altyntsev and V. I. Krasov. 19(12), 1639–40 (Jun. 1975); CPM-7508X0513

52.70.G Radiofrequency and microwave measurements

Experimental investigation of microwave radiation produced by hypersonic flows —V. A. Lyutomskii, V. M. Polyakov, and V. G. Testov. 19(4), 483–5 (Oct. 1974); CPM-7412X0267

Investigation of ionization processes behind strong shock waves using an electrical conductivity probe —V. A. Tishchenko, N. V. Khandurov, and É. K. Chekalin. 19(5), 651–3 (Nov. 1974); CPM-7501X0445

Electromagnetic fields outside a synthesized plasma jet —E. V. Bogdanov, G. M. Mantrova, and M. N. Yakovleva. 19(7), 919–21 (Jan. 1975); CPM-7503X0807

Measurement of plasma density distribution with a rectangular microwave cavity —I. N. Moskalev. 19(9), 1168–70 (Mar. 1975); CPM-7505X0590

52.70.K Optical measurements

Diagnostics of a laser-produced plasma by a scattering method using an electron-optical image converter —E. A. Burunov, G. M. Malyshev, G. T. Razdobarin, and V. V. Semenov. 19(1), 66–9 (Jul. 1974); CPM-7407X1578

Multiple reflection of light in a shock tube —V. D. Mironov and V. I. Selyakov. 19(3), 402–4 (Sep. 1974); CPM-7412X1088

Optical radiation from nanosecond discharges in dense gases —L. P. Babich. 19(3), 419–20 (Sep. 1974); CPM-7412X1105

Investigation of spatial distributions in a laser-produced plasma by Hα absorption —G. V. Ostrovskaya and N. A. Pobedonostseva. 19(3), 424–6 (Sep. 1974); CPM-7412X1110

Vacuum-UV and soft x-ray emission in a magnetoplasma compressor —P. E. Kovrov and L. G. Tokarev. 19(4), 563–4 (Oct. 1974); CPM-7412X0347

Optical investigation of a turbulent plasma —Ya. F. Volkov, V. G. Dyatlov, and N. I. Mitina. 19(7), 905–8 (Jan. 1975); CPM-7503X0793

Electron temperature in a high-frequency helium discharge —V. S. Voitsenya, A. Yu. Voloshko, V. G. Konovalov, and S. I. Solodovchenko. 19(7), 909–10 (Jan. 1975); CPM-7503X0797

Investigation of a plasma focus with a time-resolved laser interferometer —I. M. Zolototrubov, I. P. Skoblik, A. G. Tolstolutskii, and V. I. Privezentsev. 19(8), 1061–2 (Feb. 1975); CPM-7504X1485

Atomic density in the low-voltage arc in a cesium diode —F. G. Baksht, A. A. Kostin, Yu. L. Serov, and I. P. Yavor. 19(11), 1424–5 (May 1975); CPM-7506X1178

Gasdynamic model of the spark discharge —Yu. K. Bobrov. 19(11), 1442–6 (May 1975); CPM-7506X1196

52.70.N Particle measurements

Production of collimated beams of high-energy electrons —V. I. Nemchenko. 19(1), 91–7 (Jul. 1974); CPM-7407X1603

Electron energy distribution in the afterglow. I —A. B. Blagoev, Yu. M. Kagan, N. B. Kolokolov, and R. I. Lyagushchenko. 19(2), 211–4 (Aug. 1974); CPM-7408X1475

Electron energy distribution in the afterglow. II —A. B. Blagoev, Yu. M. Kagan, N. B. Kolokolov, and R. I. Lyagushchenko. 19(2), 215–9 (Aug. 1974); CPM-7408X1479

Electron energy distribution in a high-freqeuncy discharge in an axial magnetic field —S. D. Vagner, V. A. Virolainen, Yu. M. Kagan, and T. A. Kalmykova. 19(2), 290–1 (Aug. 1974); CPM-7408X1554

New method for obtaining probe characteristics —Yu. I. Osipov. 19(2), 296–8 (Aug. 1974); CPM-7408X1560

Electron energy distribution in helium, nitrogen, and their mixtures —K. D. Asvadurov, I. A. Vasil'eva, and V. M. Torchinskii. 19(3), 354–7 (Sep. 1974); CPM-7412X1040

Effect of ion current on the measurement of the electron energy distribution function by the second-derivative method —V. A. Dovzhenko, A. P. Ershov, and G. S. Solntsev. 19(4), 538–9 (Oct. 1974); CPM-7412X0322

Measurement of plasma ion temperature by a thin probe with $T_i \gtrsim T_e$ —B. I. Kanaev and E. E. Yushmanov. 19(4), 554–5 (Oct. 1974); CPM-7412X0338

Charge-carrier density of the plasma produced in a Penning mixture by irradiation by uranium fission fragments and reactor radiation —G. A. Batyrbekov, Yu. D. Kuznetsov, and Zh. S. Takibaev. 19(5), 645–6 (Nov. 1974); CPM-7501X0439

Conversion of neutral hydrogen into protons in dense plasmas —T. A. Bazilevskaya, L. I. Krupnik, and N. G. Shulika. 19(6), 741–4 (Dec. 1974); CPM-7501X0741

Mass and energy analysis of ions in the cathode of an anomalous glow discharge. II. Binary gas mixtures Ne+Ar and N_2+Ar —A. V. Bondarenko. 19(7), 914–8 (Jan. 1975); CPM-7503X0802

High-frequency modulation of atomic beams for plasma diagnostics —P. A. Demchenko, L. I. Krupnik, K. A. Leontovich, and E. S. Lyangner. 19(10), 1362–6 (Apr. 1975); CPM-7506X0296

Measurement of ion density by the dispersion relation for an ion-beam plasma —M. D. Gabovich, L. P. Katsubo, and I. A. Soloshenko. 19(11), 1412–3 (May 1975); CPM-7506X1166

Free expansion of plasma jets —P. A. Demchenko, L. I. Krupnik, and E. S. Lyangner. 19(11), 1426–8 (May 1975); CPM-7506X1180

52.75.- Plasma devices and applications

Radiation energy of a magnetoplasma compressor —V. I. Berkov and A. I. Morozov. 19(2), 220–3 (Aug. 1974); CPM-7408X1484
Condensation of an erosion plasma —B. A. Osadin and N. V. Rusakov. 19(2), 299–300 (Aug. 1974); CPM-7408X1563
Focusing of a neutralized ion beam by a plasma-optics system —I. I. Demidenko, N. S. Lomino, A. I. Morozov, and V. G. Padalka. 19 (3), 347–50 (Sep. 1974); CPM-7412X1033
Plasma density in a magnetoplasma compressor —A. K. Vinogradova, V. P. Vinogradov, A. I. Morozov, and A. A. Sergeev. 19(3), 421–3 (Sep. 1974); CPM-7412X1107
Plasma diffusion in the Tornado device —A. N. Kozyrev and B. P. Peregud. 19(4), 468–74 (Oct. 1974); CPM-7412X0252

52.75.D Accelerators and propulsion

Experimental investigation of anode processes in a closed electron-drift accelerator —I. V. Melikov. 19(1), 35–7 (Jul. 1974); CPM-7407X1547
Current limiting by self magnetic field in a plasma accelerator —A. G. Korsun. 19(1), 124–6 (Jul. 1974); CPM-7407X1636
Forces in a Hall plasma accelerator —O. N. Mironov. 19(3), 329–34 (Sep. 1974); CPM-7412X1015
Similitude in Hall-current plasma accelerators —A. I. Morozov and I. V. Melikov. 19(3), 340–2 (Sep. 1974); CPM-7412X1026
Equilibrium flow in a Hall-current plasma accelerator —I. V. Melikov. 19(3), 343–6 (Sep. 1974); CPM-7412X1029
Use of plasma accelerator for optical pumping of lasers —N. P. Kozlov and Yu. S. Protasov. 19(3), 358–60 (Sep. 1974); CPM-7412X1044
Plasma acceleration in crossed electric and magnetic fields —V. I. Aref'ev. 19(4), 446–54 (Oct. 1974); CPM-7412X0230
Electron energy spectrum in high-energy nanosecond accelerators —V. V. Kremnev, G. A. Mesyats, and V. P. Reznikov. 19(10), 1342–4 (Apr. 1975); CPM-7506X0276
Formation of a plasma focus in a plasma erosion accelerator. II. Energy characteristics of the dense plasma focus —N. P. Kozlov, L. V. Leskov, Yu. S. Protasov, and V. I. Khvesyuk. 19(12), 1558–9 (Jun. 1975); CPM-7508X0432
Effect of rf ionization on Hall-current plasma accelerator —I. I. Demidenko, N. S. Lomino, A. I. Morozov, and V. G. Padalka. 19 (12), 1560–3 (Jun. 1975); CPM-7508X0434

52.75.F Magnetohydrodynamic generators and thermionic convertors

Optimum dimensions of a coaxial thermionic converter —V. V. Sinyavskii. 19(3), 373–7 (Sep. 1974); CPM-7412X1059
Vacuum-UV and soft x-ray emission in a magnetoplasma compressor —P. E. Kovrov and L. G. Tokarev. 19(4), 563–4 (Oct. 1974); CPM-7412X0347
Charge-carrier density of the plasma produced in a Penning mixture by irradiation by uranium fission fragments and reactor radiation —G. A. Batyrbekov, Yu. D. Kuznetsov, and Zh. S. Takibaev. 19 (5), 645–6 (Nov. 1974); CPM-7501X0439
Model for the low-voltage arc. I. Stationary solution —Yu. Yu. Abramov and G. G. Gladush. 19(6), 745–7 (Dec. 1974); CPM-7501X0745
Model for the low-voltage arc. II. Stability —Yu. Yu. Abramov and G. G. Gladush. 19(6), 748–50 (Dec. 1974); CPM-7501X0748
Interferometer measurement of the neutral cesium distribution in a short low-voltage arc —Yu. L. Serov and I. P. Yavor. 19(6), 751–4 (Dec. 1974); CPM-7501X0751
Effect of molecular hydrogen on a cesium discharge. I —N. D. Morgulis and V. I. Klapchenko. 19(7), 911–3 (Jan. 1975); CPM-7503X0799
Steady-state operation of a surface-ionization thermionic converter —N. V. Volkov, Yu. K. Gus'kov, Yu. I. Kostikov, and V. P. Pashchenko. 19(8), 1129–30 (Feb. 1975); CPM-7504X1553
Analytic model for the arc regime and the thermionic converter —V. D. Bondarenko and A. I. Loshkarev. 19(12), 1564–8 (Jun. 1975); CPM-7508X0438
Thermal diffusion in a mixture of cesium vapor and helium —E. S. Bekmukhambetov and V. A. Donov. 19(12), 1627–8 (Jun. 1975); CPM-7508X0501

52.80.- Electric discharges

Dynamics and emission of coaxial plasma shells in air —A. F. Aleksandrov, V. V. Perebeinos, A. T. Savichev, and I. B. Timofeev. 19(1), 38–42 (Jul. 1974); CPM-7407X1550
Microwave discharge in argon —E. V. Belousov, A. S. Bryukhovetskii, and A. V. Prokopov. 19(1), 53–6 (Jul. 1974); CPM-7407X1565
Effect of cathode emission on the threshold for striations —N. A. Vorob'eva, Yu. M. Kagan, V. M. Milenin, and A. Kh. Muradov. 19(1), 117–8 (Jul. 1974); CPM-7407X1629
Ionization of a gas-discharge gap by fast electrons —O. B. Evdokimov and A. P. Yalovets. 19(1), 138–9 (Jul. 1974); CPM-7407X1650
Ionization and recombination coefficients in a discharge excited by fast electrons —Yu. I. Bychkov, Yu. D. Korolev, and A. P. Khuzeev. 19(1), 140–1 (Jul. 1974); CPM-7407X1652
Switching characteristis of a discharge in water —V. M. Kuleshov, S. L. Nedoseev, V. P. Smirnov, and A. M. Spektor. 19(1), 150–1 (Jul. 1974); CPM-7407X1662
Production of an ion beam by a magnetic system with opposed fields —V. B. Glasko, A. G. Sveshnikov, and N. N. Semashko. 19(2), 201–5 (Aug. 1974); CPM-7408X1465
Physical properties of an electrodeless pulsed discharge in a gas-filled glass cell —Yu. I. Chutov, N. S. Baranchuk, M. R. Lozovich, and V. G. Danilov. 19(2), 224–8 (Aug. 1974); CPM-7408X1488
Efficient ion source —D. Kh. Abdrashitova, V. G. Babaev, and M. B. Guseva. 19(2), 264–6 (Aug. 1974); CPM-7408X1528
Electron energy distribution in a high-freqeuncy discharge in an axial magnetic field —S. D. Vagner, V. A. Virolainen, Yu. M. Kagan, and T. A. Kalmykova. 19(2), 290–1 (Aug. 1974); CPM-7408X1554
Radiating discharges confined by walls —A. F. Aleksandrov, I. S. Marshak, and A. A. Rukhadze. 19(3), 308–14 (Sep. 1974); CPM-7412X0994
Theory of the positive column in neon —Yu. B. Golobovskii, Yu. M. Kagan, and R. I. Lyagushchenko. 19(3), 335–9 (Sep. 1974); CPM-7412X1021
Fast electrons and x rays from nanosecond gas discharges at 0.1–760 torr —L. V. Tarasova, L. N. Khudyakova, T. V. Loiko, and V. A. Tsukerman. 19(3), 351–3 (Sep. 1974); CPM-7412X1037
Stability of field-emission beams in nonsecond discharges —L. P. Babich. 19(3), 371–2 (Sep. 1974); CPM-7412X1057
Optical radiation from nanosecond discharges in dense gases —L. P. Babich. 19(3), 419–20 (Sep. 1974); CPM-7412X1105
Current density of thermionic-field emission into a plasma at moderate fields —I. N. Ostretsov, V. A. Petrosov, A. A. Porotnikov, and B. B. Rodnevich. 19(5), 707–8 (Nov. 1974); CPM-7501X0501
Electron-beam excited crossed-field discharge —V. A. Saenko and M. M. Kasumov. 19(6), 759–61 (Dec. 1974); CPM-7501X0759
Emission characteristics of an explosive gallium cathode —G. N. Fursei and V. M. Zhukov. 19(6), 804–7 (Dec. 1974); CPM-7501X0804
Ion emission into vacuum from a discharge in crossed electric and magnetic fields —V. A. Nikitinskii and A. S. Zakharov. 19(6), 839–40 (Dec. 1974); CPM-7501X0839
Cell for forming electron beams of arbitrary shape in a high-voltage gaseous discharge —I. V. Vagner, É. I. Bolgov, V. F. Grakun, V. L. Gokhfel'd, and V. A. Kudlai. 19(8), 1042–5 (Feb. 1975); CPM-7504X1466
Discharge in a cylindrical diode with surface ionization —V. P. Osoka and A. V. Potarov. 19(9), 1200–4 (Mar. 1975); CPM-7505X0622

52.80.D Conductivity and discharges (low-field and Townsend)

Continuous electron acceleration in a gas discharge —G. D. Alkhazov. 19(5), 658–9 (Nov. 1974); CPM-7501X0452
Formation of molecular ions in an alkali discharge —V. N. Paslen and A. M. Przhonskii. 19(5), 705–6 (Nov. 1974); CPM-7501X0499
Coaxial plasma injector with programmed injection —V. A. Burtsev, V. N. Litunovskii, and M. P. Nadgornaya. 19(6), 736–40 (Dec. 1974); CPM-7501X0736
Breakdown caused by electron bombardment of the surface of an alloy electrode —N. V. Belan, G. I. Kostyuk, and V. A. Pimkin. 19(6), 802–3 (Dec. 1974); CPM-7501X0802
Low pressure discharge with high-energy electrons —R. A. Demirkhanov, Yu. V. Kursanov, and L. P. Skripal'. 19(7), 891–4 (Jan. 1975); CPM-7503X0779

Effect of ionization and excitation on the penetration of an electromagnetic wave into a weakly ionized plasma —A. G. Boev and A. V. Prokopov. 19(7), 901–4 (Jan. 1975); CPM-7503X0789

Effect of molecular hydrogen on a cesium discharge. I —N. D. Morgulis and V. I. Klapchenko. 19(7), 911–3 (Jan. 1975); CPM-7503X0799

Stochastic acceleration of electrons in nanosecond discharges —L. P. Babich. 19(9), 1154–6 (Mar. 1975); CPM-7505X0576

Volt—ampere characteristic of the low-voltage arc. I. Recombination model —P. P. Shcherbinin. 19(11), 1436–41 (May 1975); CPM-7506X1190

Initial stage of a high-current discharge in air —A. F. Aleksandrov, V. V. Perebeinos, A. T. Savichev, and I. B. Timofeev. 19(11), 1490–1 (May 1975); CPM-7506X1244

Low-pressure self-maintained discharge with suppressed electron drift. I —V. K. Kalashnikov and Yu. V. Sanochkin. 19(12), 1549–53 (Jun. 1975); CPM-7508X0423

Low-pressure self-maintained discharge with suppressed electron drift. II —Yu. V. Sanochkin and V. K. Kalashnikov. 19(12), 1554–8 (Jun. 1975); CPM-7508X0428

Gas temperature in the positive column of a medium-β helium discharge —Yu. M. Kagan and K. K. Paskalev. 19(12), 1601–3 (Jun. 1975); CPM-7508X0475

Temperature and electron density in the positive column of a medium-pressure helium discharge —Yu. M. Kagan and K. K. Paskalev. 19(12), 1604–5 (Jun. 1975); CPM-7508X0478

Electrical strength of nitrogen and hyrodgen at high pressures —É. A. Avilov and N. V. Belkin. 19(12), 1631–2 (Jun. 1975); CPM-7508X0505

52.80.H Glow; corona

Electron energy distribution and electrical characteristics of the positive column in H_2 and H_2+Cl_2 —V. V. Zaitsev, A. I. Maksimov, and V. I. Svettsov. 19(1), 57–9 (Jul. 1974); CPM-7407X1569

Production of collimated beams of high-energy electrons —V. I. Nemchenko. 19(1), 91–7 (Jul. 1974); CPM-7407X1603

Effect of electron reflection on the voltage-current characteristics of a high-voltage, hollow-cathode, glow discharge —Ya. Ya. Udris, V. A. Chernov, and L. G. Guseva. 19(1), 134–5 (Jul. 1974); CPM-7407X1646

Electron energy distribution in the afterglow. I —A. B. Blagoev, Yu. M. Kagan, N. B. Kolokolov, and R. I. Lyagushchenko. 19(2), 211–4 (Aug. 1974); CPM-7408X1475

Electron energy distribution in the afterglow. II —A. B. Blagoev, Yu. M. Kagan, N. B. Kolokolov, and R. I. Lyagushchenko. 19(2), 215–9 (Aug. 1974); CPM-7408X1479

Electron density in an argon afterglow —O. P. Bochkova, R. I. Lyagushchenko, É. A. Sukiasyan, and Yu. A. Tolmachev. 19(4), 475–7 (Oct. 1974); CPM-7412X0259

Contraction of the positive column of a glow discharge due to the presence of negative ions —L. A. Mikhalev and L. N. Selin. 19(5), 689–90 (Nov. 1974); CPM-7501X0483

Mass and energy analysis of ions in the cathode of an anomalous glow discharge. II. Binary gas mixtures Ne+Ar and N_2+Ar —A. V. Bondarenko. 19(7), 914–8 (Jan. 1975); CPM-7503X0802

Mode coupling in a double-anode discharge —Yu. G. Zakharenko and V. E. Privalov. 19(7), 980–2 (Jan. 1975); CPM-7503X0868

Mass-spectrometer study of the ion composition of a glow discharge —N. P. Egorov and V. N. Komarov. 19(8), 1100–2 (Feb. 1975); CPM-7504X1524

Radial distribution of density and potential in a glow discharge in CO_2 and water —A. I. Maksimov and V. F. Sokolov. 19(10), 1359–61 (Apr. 1975); CPM-7506X0293

Development of an inhibited glow discharge —Yu. A. Bystrov, S. A. Ivanov, and Yu. F. Radchenko. 19(11), 1447–8 (May 1975); CPM-7506X1201

52.80.M Arcs; sparks

Analysis of the cathode spot in a vacuum arc —I. I. Beilis. 19(2), 251–6 (Aug. 1974); CPM-7408X1515

Emission processes at the cathode of an electric arc —I. I. Beilis. 19 (2), 257–60 (Aug. 1974); CPM-7408X1521

Theory of the positive column in neon —Yu. B. Golobovskii, Yu. M. Kagan, and R. I. Lyagushchenko. 19(3), 335–9 (Sep. 1974); CPM-7412X1021

Electron energy distribution in helium, nitrogen, and their mixtures —K. D. Asvadurov, I. A. Vasil'eva, and V. M. Torchinskii. 19(3), 354–7 (Sep. 1974); CPM-7412X1040

Effects of ion microfields on emission of an arc cathode —A. M. Dorodnov, V. B. Davydov, A. V. Kozyrev, and Ya. A. Pomelov. 19(3), 390–3 (Sep. 1974); CPM-7412X1076

Theory of the low-voltage arc in a narrow gap —F. G. Baksht, A. A. Kostin, and V. A. Nemchinskii. 19(5), 654–7 (Nov. 1974); CPM-7501X0448

Model for the low-voltage arc. I. Stationary solution —Yu. Yu. Abramov and G. G. Gladush. 19(6), 745–7 (Dec. 1974); CPM-7501X0745

Model for the low-voltage arc. II. Stability —Yu. Yu. Abramov and G. G. Gladush. 19(6), 748–50 (Dec. 1974); CPM-7501X0748

Interferometer measurement of the neutral cesium distribution in a short low-voltage arc —Yu. L. Serov and I. P. Yavor. 19(6), 751–4 (Dec. 1974); CPM-7501X0751

Stability of ball lightning —I. P. Stakhanov. 19(7), 861–4 (Jan. 1975); CPM-7503X0749

Nonequilibrium ionization in the cathode region of a high-pressure arc —S. P. Reshenov. 19(8), 1073–5 (Feb. 1975); CPM-7504X1497

Nonmonotonic potential distribution in the electrode region —A. I. Loshkarev. 19(10), 1308–11 (Apr. 1975); CPM-7506X0242

Electrical characteristics of underwater exploding wires —V. K. Sholom, E. V. Krivitskii, and V. P. Litvinenko. 19(10), 1329–31 (Apr. 1975); CPM-7506X0263

Analytic model of the cesium arc —V. P. Pashchenko, V. L. Mironovich, and I. P. Stakhanov. 19(10), 1332–6 (Apr. 1975); CPM-7506X0266

Atomic density in the low-voltage arc in a cesium diode —F. G. Baksht, A. A. Kostin, Yu. L. Serov, and I. P. Yavor. 19(11), 1424–5 (May 1975); CPM-7506X1178

Volt—ampere characteristic of the low-voltage arc. I. Recombination model —P. P. Shcherbinin. 19(11), 1436–41 (May 1975); CPM-7506X1190

Gasdynamic model of the spark discharge —Yu. K. Bobrov. 19(11), 1442–6 (May 1975); CPM-7506X1196

Resistance and inductance of a gas arc —S. I. Barannik, S. B. Vasserman, and A. N. Lukin. 19(11), 1449–53 (May 1975); CPM-7506X1203

Electron energy distribution in a constricted, low-pressure hydrogen discharge —M. A. Abroyan, Yu. M. Kagan, N. B. Kolokolov, and B. P. Lavrov. 19(11), 1492–3 (May 1975); CPM-7506X1246

Two modes of operation of an arc plasma source in an external magnetic field —A. G. Korsun and S. A. Meshcheryakov. 19(11), 1500–1 (May 1975); CPM-7506X1254

Analytic model for the arc regime and the thermionic converter —V. D. Bondarenko and A. I. Loshkarev. 19(12), 1564–8 (Jun. 1975); CPM-7508X0438

Anomalous high emission of a nonevaporating thermionic cathode in an arc —B. Ya. Moizhes and V. A. Nemchinskii. 19(12), 1571–6 (Jun. 1975); CPM-7508X0445

High-pressure hot-cathode arc without forced cooling —V. A. Nemchinskii. 19(12), 1577–8 (Jun. 1975); CPM-7508X0451

52.80.P High-frequency discharge

High-frequency discharge in a mercury—helium mixture —S. D. Vagner, Yu. M. Kagan, A. I. Konstantinov, and I. S. Niskonen. 19 (7), 898–900 (Jan. 1975); CPM-7503X0786

Electron temperature in a high-frequency helium discharge —V. S. Voitsenya, A. Yu. Voloshko, V. G. Konovalov, and S. I. Solodovchenko. 19(7), 909–10 (Jan. 1975); CPM-7503X0797

Drift instability in a weakly ionized plasma —S. V. Putvinskii and A. V. Timofeev. 19(10), 1295–9 (Apr. 1975); CPM-7506X0229

Direct current in a metal—selenium—metal structure boundary by an rf plasma —A. D. Andreev and S. I. Lubinskii. 19(12), 1606–7 (Jun. 1975); CPM-7508X0480

52.80.Q Explosions

Nanosecond x-ray pulses —G. A. Mesyats. 19(7), 948–51 (Jan. 1975); CPM-7503X0836

Simplified model for the initial stage of exploding wire phenomena —N. N. Stolovich, V. G. Maksimov, and N. S. Minitskaya. 19(10), 1321–8 (Apr. 1975); CPM-7506X0255

Electrical characteristics of underwater exploding wires —V. K. Sholom, E. V. Krivitskii, and V. P. Litvinenko. 19(10), 1329–31 (Apr. 1975); CPM-7506X0263

Electron energy spectrum in high-energy nanosecond accelerators —V. V. Kremnev, G. A. Mesyats, and V. P. Reznikov. 19(10), 1342–4 (Apr. 1975); CPM-7506X0276

Electrical explosion of the metastable liquid phases of zinc, cadmium, and lead —M. M. Martynyuk and I. Karimkhodzhaev. 19(11), 1454–7 (May 1975); CPM-7506X1208

Resistance and enthalpy of refractory exploding wires —M. M. Martynyuk, I. Karimkhodzhaev, and V. I. Tsapkov. 19(11), 1458–61 (May 1975); CPM-7506X1212

Dielectric breakdown of detonation products —V. L. Korol'kov, M. A. Mel'nikov, and A. P. Tsyplenko. 19(12), 1569–70 (Jun. 1975); CPM-7508X0443

52.80.V Discharge in vacuum

Laser-initiated vacuum discharge —V. P. Kovalenko, A. A. Makarevich, V. A. Rodichkin, and A. M. Timonin. 19(11), 1429–31 (May 1975); CPM-7506X1183

Electrical breakdown of vacuum gaps under superhigh voltage pulses —I. I. Kalyatskii, G. M. Kassirov, and G. V. Smirnov. 19(11), 1434–5 (May 1975); CPM-7506X1188

52.90.+ Other topics in plasma physics and electric discharges

Electric field and plasma structure near a large charged body —L. A. Malyavin and A. M. Moskalenko. 19(2), 197–200 (Aug. 1974); CPM-7408X1461

Structure of a perturbation near a highly charged body in a weakly ionized plasma —L. A. Malyavin and A. M. Moskalenko. 19(2), 206–10 (Aug. 1974); CPM-7408X1470

Stability of ball lightning —I. P. Stakhanov. 19(7), 861–4 (Jan. 1975); CPM-7503X0749

61. STRUCTURE OF LIQUIDS AND SOLIDS; CRYSTALLOGRAPHY

61.80.- Radiation damage and other irradiation effects

Effect of crystal structure on certain angular dependence of the ion–electron–emission yield —B. A. Brusilovskii and V. A. Molchanov. 19(1), 84–7 (Jul. 1974); CPM-7407X1596

Investigation of the work function of a tungsten cathode after bombardment by inert–gas ions —P. N. Chistyakov, R. A. Milovanova, and V. V. Lytkin. 19(1), 148–9 (Jul. 1974); CPM-7407X1660

Energy dependence of the focusing of ions by crystals —E. S. Mashkova, V. A. Molchanov, and A. D. Pavlova. 19(4), 540 (Oct. 1974); CPM-7412X0324

Dielectric strength of a vacuum gap with electrodes irradiated with He^+ and H^+ ions —A. P. Solodovnikov and Yu. M. Khirnyi. 19 (8), 1122 (Feb. 1975); CPM-7504X1546

Effect of a high-current relativistic electron beam on a metal —B. I. Dmitrenko, L. V. Leskov, G. P. Maksimov, S. L. Nedoseev, V. V. Savichev, V. P. Smirnov, and A. M. Spektor. 19(9), 1224–5 (Mar. 1975); CPM-7505X0646

61.90.+ Other topics in structure of liquids and solids

Crystal defects of heterostructures of AlAs–GaAs solid solutions and effect on the characteristics of injection lasers —L. V. Druzhinina, V. T. Bublik, L. M. Dolginov, P. G. Eliseev, M. P. Kerbelev, V. B. Osvenskii, I. Z. Pinsker, and M. G. Shumskii. 19(7), 935–9 (Jan. 1975); CPM-7503X0823

Liquid crystals in external fields —I. V. Ioffe. 19(8), 1012–5 (Feb. 1975); CPM-7504X1436

Impurities and crystal dimensions in zone refining —V. G. Glebovskii and B. M. Shipilevskii. 19(9), 1231–5 (Mar. 1975); CPM-7505X0653

Coherent Compton effect in crystals —V. A. Bushuev and R. N. Kuz'min. 19(12), 1590–2 (Jun. 1975); CPM-7508X0464

62. MECHANICAL AND ACOUSTIC PROPERTIES OF CONDENSED MATTER

Optical characteristics of K–8 glass subject to radiation from a neodymium laser —A. M. Bonch–Bruevich, Ya. A. Imas, V. S. Salyadinov, and A. V. Shatilov. 19(2), 287–9 (Aug. 1974); CPM-7408X1551

Hologram interferometry for vibration analysis —V. S. Listovets and Yu. I. Ostrovskii. 19(7), 847–60 (Jan. 1975); CPM-7503X0735

Optical methods for studying amplification of elastic surface waves in a stratified system —I. B. Yakovkin, V. V. Petrov, and S. V. Bogdanov. 19(9), 1242–5 (Mar. 1975); CPM-7505X0664

Excitation of thermoelastic vibrations of a thin plate by a beam of fast charged particles —A. I. Kalinichenko and V. T. Lazurik-Él'tsufin. 19(10), 1382–3 (Apr. 1975); CPM-7506X0316

64. EQUATIONS OF STATE, PHASE EQUILIBRIA, AND PHASE TRANSITIONS

64.70.- Phase equilibria, phase transitions, and critical points

Condensation of a dense vapor flow —V. G. Dneprovskii, B. A. Osadin, and N. V. Rusakov. 19(2), 271–4 (Aug. 1974); CPM-7408X1535

Rate for evaporation of a liquid into vacuum —A. P. Andreev and M. A. Gurevich. 19(3), 396–401 (Sep. 1974); CPM-7412X1082

Vaporization and boiling of liquid metal in an exploding wire —M. M. Martynyuk. 19(6), 793–7 (Dec. 1974); CPM-7501X0793

Electrical explosion of the metastable liquid phases of zinc, cadmium, and lead —M. M. Martynyuk and I. Karimkhodzhaev. 19(11), 1454–7 (May 1975); CPM-7506X1208

65. THERMAL PROPERTIES OF CONDENSED MATTER

Thermal effect of continuous laser radiation on optically transparent media —N. S. Bardina, A. I. Portnyagin, M. Yu. Sklyarov, and A. A. Churin. 19(4), 491–4 (Oct. 1974); CPM-7412X0275

Variational analysis of thermal breakdown of a semiconductor irradiated by light —V. L. Komolov. 19(5), 600–2 (Nov. 1974); CPM-7501X0394

Vaporization and boiling of liquid metal in an exploding wire —M. M. Martynyuk. 19(6), 793–7 (Dec. 1974); CPM-7501X0793

Excitation of thermoelastic vibrations of a thin plate by a beam of fast charged particles —A. I. Kalinichenko and V. T. Lazurik-Él'tsufin. 19(10), 1382–3 (Apr. 1975); CPM-7506X0316

66. TRANSPORT PROPERTIES OF CONDENSED MATTER (NONELECTRONIC)

66.30.- Diffusion in solids

Behavior of molten salts in strong electric fields —A. Z. Éfendiev, O. M. Shabanov, S. M. Gadzhiev, and S. M. Tagirov. 19(6), 820–3 (Dec. 1974); CPM-7501X0820

Atomic diffusion from a finite film over a solid surface —Yu. D. Kornyushkin. 19(7), 971–2 (Jan. 1975); CPM-7503X0859

Diffusion and solubility of helium in potassium chloride —A. Ya. Kupryazhkin, P. V. Volobuev, and P. E. Suetin. 19(8), 1105–7 (Feb. 1975); CPM-7504X1529

66.90.+ Other topics in nonelectronic transport properties

Thermoacoustic waves in conducting gases and liquids —P. A. Andreev. 19(6), 845–6 (Dec. 1974); CPM-7501X0845

Thermal conditions for a sandwich cold cathode —F. M. Benson, P. E. Troyan, and Yu. B. Yankelevich. 19(7), 946–7 (Jan. 1975); CPM-7503X0834

Atomic diffusion from a finite film over a solid surface —Yu. D. Kornyushkin. 19(7), 971–2 (Jan. 1975); CPM-7503X0859

68. SURFACES AND INTERFACES; THIN FILMS AND WHISKERS

68.40.– Chemical reactions and surface treatment

Preservation of semiconductor field–emission cathodes —N. V. Egorov, G. N. Fursei, and M. K. El'Nimr. 19(5), 709 (Nov. 1974); CPM-7501X0503

Effects of cleaning on adsorption by germanium single crystals —Yu. I. Belyakov, M. P. Volkov, and T. N. Kompaniets. 19(6), 815–6 (Dec. 1974); CPM-7501X0815

Characteristics of diffraction gratings obtained by photoetching of semiconductor surfaces —L. V. Belyakov, D. N. Goryachev, M. N. Mizerov, and E. L. Portnoi. 19(6), 837–8 (Dec. 1974); CPM-7501X0837

68.90.+ Other topics in the structure and nonelectronic properties of surfaces and thin films

Method for studying gas creep along a solid surface —B. M. Markeev. 19(5), 700–1 (Nov. 1974); CPM-7501X0494

Atomic recombination on a solid surface —V. P. Pinchuk, A. N. Gorban', and V. G. Kornich. 19(6), 808–10 (Dec. 1974); CPM-7501X0808

Capillary gravitational waves and the mechanogalvanic effect —E. D. Korlyakov. 19(7), 965 (Jan. 1975); CPM-7503X0853

72. ELECTRONIC TRANSPORT IN CONDENSED MATTER

72.10.– Electronic conduction in metals and alloys

Behavior of molten salts in strong electric fields —A. Z. Éfendiev, O. M. Shabanov, S. M. Gadzhiev, and S. M. Tagirov. 19(6), 820–3 (Dec. 1974); CPM-7501X0820

Effect of temperature-dependent conductivity on electromagnetic field, current, temperature, and impedance in a plane conductor. I —R. S. Kuznetskii. 19(8), 1016–9 (Feb. 1975); CPM-7504X1440

Electrical conductivity of a pseudoliquefied layer in an electric field —V. V. Gal', V. I. Konov, and K. A. Nikitin. 19(9), 1214–5 (Mar. 1975); CPM-7505X0636

72.20.– Conductivity phenomena in semiconductors and insulators

Conductivity of a medium with inhomogeneous inclusions in a magnetic field —Yu. P. Emets. 19(5), 586–8 (Nov. 1974); CPM-7501X0380

Preservation of semiconductor field–emission cathodes —N. V. Egorov, G. N. Fursei, and M. K. El'Nimr. 19(5), 709 (Nov. 1974); CPM-7501X0503

Direct current in a metal—selenium—metal structure boundary by an rf plasma —A. D. Andreev and S. I. Lubinskii. 19(12), 1606–7 (Jun. 1975); CPM-7508X0480

72.90.+ Other topics in electronic transport in condensed matter

Acousto-electric waves in conducting media —P. A. Andreev. 19(8), 1001–4 (Feb. 1975); CPM-7504X1425

Rectangular conducting wedge in a moving electromagnetic field —I. D. Maergoiz and L. P. Nizhnik. 19(10), 1281–6 (Apr. 1975); CPM-7506X0215

Shot noise in a thermionic cathode —A. F. Golubentsev and A. S. Shapovalov. 19(10), 1345–6 (Apr. 1975); CPM-7506X0279

Dependence of the basic parameters of $Al_xGa_{1-x}As$—GaAs solar converters on temperature and optical intensity —E. B. Vinogradova, M. B. Kagan, N. S. Koroleva, T. L. Lyubashevskaya, and T. A. Nuller. 19(10), 1378–81 (Apr. 1975); CPM-7506X0312

73. ELECTRONIC STRUCTURE AND ELECTRICAL PROPERTIES OF SURFACES, INTERFACES, AND THIN FILMS

73.30.+ Surface double layers, Schottky barriers, and work functions

Effect of selenium and sulfur on the work function of tungsten —N. V. Volkov, Yu. K. Gus'kov, Z. N. Kononova, and Yu. I. Kostikov. 19(1), 144–5 (Jul. 1974); CPM-7407X1656

Investigation of the work function of a tungsten cathode after bombardment by inert–gas ions —P. N. Chistyakov, R. A. Milovanova, and V. V. Lytkin. 19(1), 148–9 (Jul. 1974); CPM-7407X1660

Resonant amplification of an image potential by an electromagnetic wave —Yu. I. Balkarei and É. M. Épshtein. 19(6), 843–4 (Dec. 1974); CPM-7501X0843

73.90.+ Other topics in electrical properties of surfaces, interfaces, and thin films

Displacement of ion–current retardation curves in surface ionization in a strong field —N. I. Ionov. 19(1), 146–7 (Jul. 1974); CPM-7407X1658

Capillary gravitational waves and the mechanogalvanic effect —E. D. Korlyakov. 19(7), 965 (Jan. 1975); CPM-7503X0853

Rectangular conducting wedge in a moving electromagnetic field —I. D. Maergoiz and L. P. Nizhnik. 19(10), 1281–6 (Apr. 1975); CPM-7506X0215

Direct current in a metal—selenium—metal structure boundary by an rf plasma —A. D. Andreev and S. I. Lubinskii. 19(12), 1606–7 (Jun. 1975); CPM-7508X0480

74. SUPERCONDUCTIVITY

Shielding properties of superconducting shields —S. I. Bondarenko, S. S. Vinogradov, G. A. Gogadze, S. S. Perepelkin, and V. I. Sheremet. 19(6), 824–8 (Dec. 1974); CPM-7501X0824

Superconducting magnetic shields —S. I. Bondarenko and V. I. Sheremet. 19(7), 952–5 (Jan. 1975); CPM-7503X0840

75. MAGNETIC PROPERTIES AND MATERIALS

Magnetoacoustic transducer based on the domain structure of a ferromagnetic material —G. L. Gurevich and G. A. Vul'gal'ter. 19 (1), 154–5 (Jul. 1974); CPM-7407X1666

Distortion of single-turn solenoids in ultrahigh magnetic fields —G. A. Shneerson. 19(10), 1371–7 (Apr. 1975); CPM-7506X0305

76. MAGNETIC RESONANCES AND RELAXATION IN CONDENSED MATTER; MÖSSBAUER EFFECT

Dynamic magnetic–resonance phenomena —P. S. Kuts and V. S. Mel'nik. 19(1), 110–4 (Jul. 1974); CPM-7407X1622

77. DIELECTRIC PROPERTIES AND MATERIALS

77.20.+ Permittivity

Dielectric properties of foamed ceramics at millimeter wavelengths —N. A. Irisova, G. V. Kozlov, V. E. Mandrusov, B. S. Cherepanov, and I. M. Chernyshev. 19(1), 103–4 (Jul. 1974); CPM-7407X1615

Contribution of multiphoton processes to the linear dielectric constant —V. A. Bushuev and R. N. Kuz'min. 19(1), 116 (Jul. 1974); CPM-7407X1628

Calculation of permittivity of an inhomogeneous dielectric by a variational method —G. A. Ermakov, A. G. Fokin, and T. D. Shermergor. 19(2), 157–60 (Aug. 1974); CPM-7408X1421

Calculation of bounds for the effective permittivity of an inhomogeneous dielectric —G. A. Ermakov, A. G. Fokin, and T. D. Shermergor. 19(2), 161–5 (Aug. 1974); CPM-7408X1425

Temperature dependence of the dielectric permittivity of single–crystal TiO$_2$ in the submillimeter range —A. A. Volkov, N. A. Irisova, and G. V. Kozlov. 19(4), 567–8 (Oct. 1974); CPM-7412X0351

Dispersion of the dielectric constant of crystalline KH$_2$PO$_4$ near the "soft" mode frequency —V. V. Meriakri, Yu. M. Poplavko, and E. F. Ushatkin. 19(5), 703–4 (Nov. 1974); CPM-7501X0497

77.90.+ Other topics in dielectric properties and materials

Investigating prebreakdown fields in water by means of the Kerr effect —I. T. Ovchinnikov, K. V. Yanshin, and É. V. Yanshin. 19(2), 294–5 (Aug. 1974); CPM-7408X1558

Nonlinear polarizability of a gaseous medium in a longitudinal magnetic field —V. A. Sokolov and L. M. Khayutin. 19(5), 589–91 (Nov. 1974); CPM-7501X0383

Effect of a high–frequency electric field on the energy loss of a charged particle in a medium —Zh. M. Diasamidze. 19(5), 687–8 (Nov. 1974); CPM-7501X0481

Convection in a liquid dielectric in a longitudinal electric field —I. V. Ioffe and N. V. Kalinin. 19(5), 692 (Nov. 1974); CPM-7501X0486

Dispersion of the dielectric constant of crystalline KH$_2$PO$_4$ near the "soft" mode frequency —V. V. Meriakri, Yu. M. Poplavko, and E. F. Ushatkin. 19(5), 703–4 (Nov. 1974); CPM-7501X0497

Microwave propagation in a low–loss dielectric —L. É. Rikenglaz. 19 (6), 713–4 (Dec. 1974); CPM-7501X0713

Liquid crystals in external fields —I. V. Ioffe. 19(8), 1012–5 (Feb. 1975); CPM-7504X1436

Radiation yield of ions in liquid dielectrics as a function of temperature and radiation energy —V. I. Ivanov, E. D. Kleshchenko, Yu. P. Sukhanovskii, and V. V. Frolov. 19(11), 1468–70 (May 1975); CPM-7506X1222

Dielectric breakdown of detonation products —V. L. Korol'kov, M. A. Mel'nikov, and A. P. Tsyplenko. 19(12), 1569–70 (Jun. 1975); CPM-7508X0443

78. OPTICAL PROPERTIES AND CONDENSED-MATTER SPECTROSCOPY AND OTHER INTERACTIONS OF MATTER WITH PARTICLES AND RADIATION

78.20.– Optical properties and materials

Dielectric properties of foamed ceramics at millimeter wavelengths —N. A. Irisova, G. V. Kozlov, V. E. Mandrusov, B. S. Cherepanov, and I. M. Chernyshev. 19(1), 103–4 (Jul. 1974); CPM-7407X1615

Optical characteristics of K–8 glass subject to radiation from a neodymium laser —A. M. Bonch–Bruevich, Ya. A. Imas, V. S. Salyadinov, and A. V. Shatilov. 19(2), 287–9 (Aug. 1974); CPM-7408X1551

Investigating prebreakdown fields in water by means of the Kerr effect —I. T. Ovchinnikov, K. V. Yanshin, and É. V. Yanshin. 19(2), 294–5 (Aug. 1974); CPM-7408X1558

78.70.– Other interactions of matter with particles and radiation

X–ray fluorescence of oxygen in H$_2$O —L. A. Smirnov. 19(5), 702 (Nov. 1974); CPM-7501X0496

Microwave propagation in a low–loss dielectric —L. É. Rikenglaz. 19 (6), 713–4 (Dec. 1974); CPM-7501X0713

Coherent Compton effect in crystals —V. A. Bushuev and R. N. Kuz'min. 19(12), 1590–2 (Jun. 1975); CPM-7508X0464

78.90.+ Other topics in optical properties of condensed matter

Strobe unit for measuring luminescence in the range 10^{-7}–$2\cdot10^{-10}$ sec —V. A. Bonch–Bruevich and N. A. Tolstoi. 19(2), 284–6 (Aug. 1974); CPM-7408X1548

Variational analysis of thermal breakdown of a semiconductor irradiated by light —V. L. Komolov. 19(5), 600–2 (Nov. 1974); CPM-7501X0394

Microwave maser with nonrelativistic electrons —A. S. Dement'ev and Yu. G. Pavlenko. 19(5), 694–5 (Nov. 1974); CPM-7501X0488

Lasing properties of Yb^{3+} and Er^{3+} glass laser pumped by a laser —V. N. Kalinin, A. A. Mak, D. S. Prilezhaev, and V. A. Fromzel'. 19 (6), 835–6 (Dec. 1974); CPM-7501X0835

Radiation from a charged particle moving close to an anisotropic dielectric —A. I. Plis and N. M. Safikhodzhaev. 19(7), 865–7 (Jan. 1975); CPM-7503X0753

Electroluminescence spectra of the red luminescent diodes p–Al$_x$Ga$_{1-x}$As—n–Al$_y$Ga$_{1-y}$As($y>x$) —V. M. Busov, D. Z. Garbuzov, A. T. Gorelenok, and D. S. Kop'ev. 19(12), 1598–600 (Jun. 1975); CPM-7508X0472

79. ELECTRON AND ION EMISSION BY LIQUIDS AND SOLIDS; IMPACT PHENOMENA

79.20.– Impact phenomena, including electron spectra and sputtering

Effect of crystal structure on certain angular dependence of the ion–electron–emission yield —B. A. Brusilovskii and V. A. Molchanov. 19(1), 84–7 (Jul. 1974); CPM-7407X1596

Nonradiative electron transitions and thermal effects in laser–irradiated transparent dielectrics —B. I. Makshantsev, A. A. Kovalev, R. K. Leonov, and P. A. Yampol'skii. 19(1), 98–102 (Jul. 1974); CPM-7407X1610

Optical characteristics of K–8 glass subject to radiation from a neodymium laser —A. M. Bonch–Bruevich, Ya. A. Imas, V. S. Salyadinov, and A. V. Shatilov. 19(2), 287–9 (Aug. 1974); CPM-7408X1551

Energy losses of slow electrons reflected from molybdenum and tungsten single crystals —O. M. Artamonov, B. B. Bolotov, and M. V. Kremkov. 19(8), 1103–4 (Feb. 1975); CPM-7504X1527

Dielectric strength of a vacuum gap with electrodes irradiated with He$^+$ and H$^+$ ions —A. P. Solodovnikov and Yu. M. Khirnyi. 19 (8), 1122 (Feb. 1975); CPM-7504X1546

Kinetic energy of ions produced by surface ionization. I. Distribution over the velocity components —L. V. Sumin. 19(9), 1205–9 (Mar. 1975); CPM-7505X0627

Cumulative destruction of transparent dielectrics in repeated laser irradiation —L. D. Khazov, I. A. Fersman, and V. Yu. Bortniker. 19(9), 1256–7 (Mar. 1975); CPM-7505X0678

Interaction of intense laser radiation with solid targets —L. V. Dubovoi, V. D. Dyatlov, V. I. Kryzhanovskii, A. A. Mak, R. N. Medvedev, A. N. Popytaev, V. A. Serebryakov, V. N. Sizov, and A. D. Starikov. 19(11), 1477–9 (May 1975); CPM-7506X1231

Mass spectrum of secondary ions ejected from the surface of a single crystal of gallium arsenide by argon ions —A. G. Koval', V. V. Bobkov, Yu. A. Klimovskii, S. S. Strel'chenko, V. V. Shubina, V. V. Lebedev, and Ya. M. Fogel'. 19(12), 1587–9 (Jun. 1975); CPM-7508X0461

Neutral particles from the interaction of laser radiation with a solid target —Yu. A. Bykovskii, N. M. Vasil'ev, I. D. Laptev, and V. N. Nevolin. 19(12), 1635 (Jun. 1975); CPM-7508X0509

79.40.+ Thermionic emission

Extrapolation of the Langmuir S–curve to cesium pressures of 10–100 torr —V. E. Dubinskii and S. Ya. Lebedev. 19(1), 81–3 (Jul. 1974); CPM-7407X1593

Electron–microscope and x–ray study of thermionic emitters made from Mo–Pt alloys —B. B. Shishkin and R. S. Bakhtiyarov. 19(2), 243–50 (Aug. 1974); CPM-7408X1507

Current density of thermionic–field emission into a plasma at moderate fields —I. N. Ostretsov, V. A. Petrosov, A. A. Porotnikov, and B. B. Rodnevich. 19(5), 707–8 (Nov. 1974); CPM-7501X0501

Transient thermionic–field emission from a point cathode —E. A. Litvinov and A. F. Shubin. 19(8), 1131–2 (Feb. 1975); CPM-7504X1555

Thermionic emission properties of zirconium, hafnium, and titanium nitrides in cesium vapor —M. A. Eremeev, V. S. Neshpor, A. B. Novikov, E. M. Stefanovskaya, and V. P. Fedorinov. 19(10), 1337–41 (Apr. 1975); CPM-7506X0271

Anomalous high emission of a nonevaporating thermionic cathode in an arc —B. Ya. Moizhes and V. A. Nemchinskii. 19(12), 1571–6 (Jun. 1975); CPM-7508X0445

79.70.+ Field emission and field ionization

Ion emission into vacuum from a discharge in crossed electric and magnetic fields —V. A. Nikitinskii and A. S. Zakharov. 19(6), 839–40 (Dec. 1974); CPM-7501X0839

Transient thermionic-field emission from a point cathode —E. A. Litvinov and A. F. Shubin. 19(8), 1131–2 (Feb. 1975); CPM-7504X1555

Recent developments in surface ionization (review) —É. Ya. Zandberg. 19(9), 1133–44 (Mar. 1975); CPM-7505X0555

Multiphase, uniform, secondary-emission microwave discharge at a solid surface —G. S. Luk'yanchikov. 19(9), 1196–9 (Mar. 1975); CPM-7505X0618

Emission parameters of a field-emission cathode —G. N. Freiberg. 19 (10), 1352–4 (Apr. 1975); CPM-7506X0286

79.90.+ Other topics in emission and impact phenomena in condensed matter

Time dependence of ion currents produced through surface ionization. Ionization of Ba on the (111) face of iridium —É. Ya. Zandberg, E. V. Rut'kov, and A. Ya. Tontegode. 19(2), 261–3 (Aug. 1974); CPM-7408X1525

Breakdown caused by electron bombardment of the surface of an alloy electrode —N. V. Belan, G. I. Kostyuk, and V. A. Pimkin. 19(6), 802–3 (Dec. 1974); CPM-7501X0802

Emission characteristics of an explosive gallium cathode —G. N. Fursei and V. M. Zhukov. 19(6), 804–7 (Dec. 1974); CPM-7501X0804

Atomic recombination on a solid surface —V. P. Pinchuk, A. N. Gorban', and V. G. Kornich. 19(6), 808–10 (Dec. 1974); CPM-7501X0808

Excitation of thermoelastic vibrations of a thin plate by a beam of fast charged particles —A. I. Kalinichenko and V. T. Lazurik-Él'tsufin. 19(10), 1382–3 (Apr. 1975); CPM-7506X0316

81. MATERIALS SCIENCE AND METALLURGY

81.20.– Methods of crystal growth and purification, including film deposition techniques

Effect of focusing conditions on the morphology of surface films produced with a laser —V. G. Dneprovskii and B. A. Osadin. 19 (2), 275–7 (Aug. 1974); CPM-7408X1539

Condensation of an erosion plasma —B. A. Osadin and N. V. Rusakov. 19(2), 299–300 (Aug. 1974); CPM-7408X1563

Impurities and crystal dimensions in zone refining —V. G. Glebovskii and B. M. Shipilevskii. 19(9), 1231–5 (Mar. 1975); CPM-7505X0653

81.35.– Vacuum metallurgy

Transient molecular effusion characteristics —Yu. N. Lyubitov and V. Z. Belen'kii. 19(4), 519–22 (Oct. 1974); CPM-7412X0303

Adsorption of bismuth on tungsten. I. Steady-state processes —M. A. Mittsev. 19(6), 811–4 (Dec. 1974); CPM-7501X0811

Evaporation rates of the system $ZrC+x\%W$ for the temperature range 2300-3000°K —N. M. Karnaukhova, V. A. Luknitskii, and I. A. Maslov. 19(8), 1096–9 (Feb. 1975); CPM-7504X1520

Composition of adsorbing and desorbing fluxes —Yu. A. Gel'man, V. I. Mikhailov, V. F. Vinogradov, and Yu. N. Lyubitov. 19(10), 1355–8 (Apr. 1975); CPM-7506X0289

Elimination of carbon impurities from platinum by heating in an oxygen atmosphere —L. P. Rekova, V. V. Mozgin, L. N. Zvyagintseva, V. N. Bondarenko, and Ya. M. Fogel'. 19(11), 1465–7 (May 1975); CPM-7506X1219

81.40.+ Ceramics and refractories

Dielectric properties of foamed ceramics at millimeter wavelengths —N. A. Irisova, G. V. Kozlov, V. E. Mandrusov, B. S. Cherepanov, and I. M. Chernyshev. 19(1), 103–4 (Jul. 1974); CPM-7407X1615

82. PHYSICAL CHEMISTRY

82.30.– Chemical reactions

Quenching in the CF_3I photodissociation laser —G. A. Skorobogatov, V. M. Tret'yak, and V. S. Komarov. 19(4), 495–8 (Oct. 1974); CPM-7412X0279

Formation of molecular ions in an alkali discharge —V. N. Paslen and A. M. Przhonskii. 19(5), 705–6 (Nov. 1974); CPM-7501X0499

Gas polymerization wave excited by monochromatic light —A. I. Plis and V. A. Shcheglov. 19(9), 1262–3 (Mar. 1975); CPM-7505X0684

82.50.– Photochemistry and radiation chemistry

Photochemical waves in a medium with a branch-chain conversion mechanism —A. N. Oraevskii, V. P. Pimenov, and V. A. Shcheglov. 19(6), 782–6 (Dec. 1974); CPM-7501X0782

Gas polymerization wave excited by monochromatic light —A. I. Plis and V. A. Shcheglov. 19(9), 1262–3 (Mar. 1975); CPM-7505X0684

Radiation yield of ions in liquid dielectrics as a function of temperature and radiation energy —V. I. Ivanov, E. D. Kleshchenko, Yu. P. Sukhanovskii, and V. V. Frolov. 19(11), 1468–70 (May 1975); CPM-7506X1222

Steady-state electron density in photoionizion of aerosol particles —G. V. Karachevtsev and A. A. Fridman. 19(11), 1471–3 (May 1975); CPM-7506X1225

82.65.– Surface processes

Transient molecular effusion characteristics —Yu. N. Lyubitov and V. Z. Belen'kii. 19(4), 519–22 (Oct. 1974); CPM-7412X0303

Method for studying gas creep along a solid surface —B. M. Markeev. 19(5), 700–1 (Nov. 1974); CPM-7501X0494

Atomic recombination on a solid surface —V. P. Pinchuk, A. N. Gorban', and V. G. Kornich. 19(6), 808–10 (Dec. 1974); CPM-7501X0808

Adsorption of bismuth on tungsten. I. Steady-state processes —M. A. Mittsev. 19(6), 811–4 (Dec. 1974); CPM-7501X0811

Effects of cleaning on adsorption by germanium single crystals —Yu. I. Belyakov, M. P. Volkov, and T. N. Kompaniets. 19(6), 815–6 (Dec. 1974); CPM-7501X0815

Effect of the adsorption rate on the diffusion of deuterium through nickel —Yu. I. Belyakov, Yu. I. Zvezdin, A. A. Kurdyumov, and G. G. Nevdakha. 19(7), 956–8 (Jan. 1975); CPM-7503X0844

Titanium adsorption on tungsten —Yu. K. Ustinov and S. V. Fedichev. 19(8), 1118–9 (Feb. 1975); CPM-7504X1542

Recent developments in surface ionization (review) —É. Ya. Zandberg. 19(9), 1133–44 (Mar. 1975); CPM-7505X0555

Surface evaporation of a solid transparent dielectric under the action of laser radiation —A. M. Bonch-Bruevich, Ya. A. Imas, A. A. Kovalev, P. S. Kondratenko, and B. I. Makshantsev. 19(11), 1474–6 (May 1975); CPM-7506X1228

82.80.– Chemical analysis and related physical methods of analysis

Line shape of a quadrupole mass spectrometer —G. I. Slobodenyuk. 19(2), 292–3 (Aug. 1974); CPM-7408X1556

Formation of molecular ions in an alkali discharge —V. N. Paslen and A. M. Przhonskii. 19(5), 705–6 (Nov. 1974); CPM-7501X0499

Mass spectrum of secondary ions ejected from the surface of a single crystal of gallium arsenide by argon ions —A. G. Koval', V. V. Bobkov, Yu. A. Klimovskii, S. S. Strel'chenko, V. V. Shubina, V. V. Lebedev, and Ya. M. Fogel'. 19(12), 1587–9 (Jun. 1975); CPM-7508X0461

Neutral particles from the interaction of laser radiation with a solid target —Yu. A. Bykovskii, N. M. Vasil'ev, I. D. Laptev, and V. N. Nevolin. 19(12), 1635 (Jun. 1975); CPM-7508X0509

82.90.+ Other topics in physical chemistry

Thermophoresis and diffusophoresis of small, volatile aerosol particles —Yu. I. Yalamov and E. R. Shchukin. 19(2), 278–9 (Aug. 1974); CPM-7408X1542

Possible electrohydrodynamic effects in electrolytes —E. Z. Gak, É. Kh. Rokhinson, and N. F. Bondarenko. 19(5), 676–7 (Nov. 1974); CPM-7501X0470

Vaporization and boiling of liquid metal in an exploding wire —M. M. Martynyuk. 19(6), 793–7 (Dec. 1974); CPM-7501X0793

Approximate similarity relations in the electrical explosions of underwater conductors —E. V. Krivitskii and V. K. Sholom. 19(6), 798–801 (Dec. 1974); CPM-7501X0798

Steady-state electron density in photoionizion of aerosol particles —G. V. Karachevtsev and A. A. Fridman. 19(11), 1471–3 (May 1975); CPM-7506X1225

84. ELECTROMAGNETIC TECHNOLOGY

84.30.– Electronic circuits

Nanosecond x-ray pulses —G. A. Mesyats. 19(7), 948–51 (Jan. 1975); CPM-7503X0836

Explosion driven magnetic generator with a matched inductive load —L. S. Gerasimov. 19(9), 1226–30 (Mar. 1975); CPM-7505X0648

84.40.– Antennas, transmission lines, and propagation

Round metal–optical waveguide filled with a two–layer dielectric —V. A. Pruzhanovskii. 19(1), 3–8 (Jul. 1974); CPM-7407X1515

Differential electromagnetic characteristics at the interface between ice and water in the ocean —V. V. Bogorodskii and V. P. Tripol'nikov. 19(4), 526–8 (Oct. 1974); CPM-7412X0310

Diffraction of a plane electromagnetic wave by a conducting plane with a projection —A. A. Zilbergleit. 19(4), 531–2 (Oct. 1974); CPM-7412X0315

Reflection of electromagnetic waves by a moving plasma —V. I. Miroshnichenko. 19(4), 533–4 (Oct. 1974); CPM-7412X0317

Two–dimensional diffraction on a system of straight segments (shields) —G. A. Grinberg. 19(5), 581–5 (Nov. 1974); CPM-7501X0375

Cerenkov instabilities of a relativistic beam in a periodic plasma–filled waveguide —V. I. Kurilko, Yu. V. Tkach, and V. A. Shendrik. 19 (5), 607–11 (Nov. 1974); CPM-7501X0401

Launching and propagation of regular nonlinear waves in an anisotropic plasma–filled waveguide —V. I. Kurilko, A. P. Tols–toluzhskii, and Ya. B. Fainberg. 19(5), 622–7 (Nov. 1974); CPM-7501X0416

Phase motion of particles in an accelerator with an azimuthally varying electric field —M. F. Vorogushin and V. I. Petrunin. 19(7), 926–9 (Jan. 1975); CPM-7503X0814

Parametric interaction of a charged particle beam with a periodic system —V. I. Koroza and E. S. Sukhovskii. 19(8), 1020–4 (Feb. 1975); CPM-7504X1444

84.60.– Direct energy conversion and energy storage

Inductive energy storage in pulsed accelerators —V. A. Glukhikh, O. A. Gusev, E. G. Komar, and M. P. Svin'in. 19(5), 660–1 (Nov. 1974); CPM-7501X0454

Shaping of voltage pulses by discharging an inductive storage bank with a charged–particle beam —O. A. Gusev, E. G. Komar, V. B. Markov, and E. M. Mellekh. 19(5), 662–3 (Nov. 1974); CPM-7501X0456

Explosion driven magnetic generator with a matched inductive load —L. S. Gerasimov. 19(9), 1226–30 (Mar. 1975); CPM-7505X0648

Dependence of the basic parameters of $Al_xGa_{1-x}As$—GaAs solar converters on temperature and optical intensity —E. B. Vinogradova, M. B. Kagan, N. S. Koroleva, T. L. Lyubashevskaya, and T. A. Nuller. 19(10), 1378–81 (Apr. 1975); CPM-7506X0312

84.70.+ High-current and high-voltage technology

Switching characteristis of a discharge in water —V. M. Kuleshov, S. L. Nedoseev, V. P. Smirnov, and A. M. Spektor. 19(1), 150–1 (Jul. 1974); CPM-7407X1662

Electron energy spectrum in a high-current vacuum diode —S. P. Bugaev, V. I. Koshelev, and M. N. Timofeev. 19(9), 1193–5 (Mar. 1975); CPM-7505X0615

Hydrogen-ion mobility in a high-pressure unipolar corona —A. G. Lyapin. 19(9), 1236–8 (Mar. 1975); CPM-7505X0658

84.80.– Particle beams and particle optics

Focusing of an astigmatic beam by a doublet and a symmetric triplet of quadrupole lenses —V. I. Chetvertkov. 19(1), 1–2 (Jul. 1974); CPM-7407X1513

Energy resolution of quadrupole lenses for charged–particle beams —V. S. Siksin. 19(3), 301–7 (Sep. 1974); CPM-7412X0987

Beam focusing in an accelerator with inductive energy storage —V. A. Glukhikh, O. A. Gusev, E. G. Komar, V. S. Kuznetsov, M. P. Svin'in, and R. P. Fidel'skaya. 19(3), 366–7 (Sep. 1974); CPM-7412X1052

Symmetric multielectrode tubular electrostatic lenses —L. G. Glikman, V. M. Kel'man, and M. Sh. Nurmanov. 19(5), 680–2 (Nov. 1974); CPM-7501X0474

Maximum current of a beam with finite phase volume —G. I. Trubnikov and V. S. Kuznetsov. 19(6), 715–6 (Dec. 1974); CPM-7501X0715

Azimuthal and vertical motion in an accelerator with azimuthally varying electric field —M. F. Vorogushin and V. I. Petrunin. 19(6), 770–2 (Dec. 1974); CPM-7501X0770

Angular aberration corrector in a cylindrical mirror analyzer —V. V. Zashkavara and V. F. Tarasov. 19(6), 841–2 (Dec. 1974); CPM-7501X0841

Radiation from a charged particle moving close to an anisotropic dielectric —A. I. Plis and N. M. Safikhodzhaev. 19(7), 865–7 (Jan. 1975); CPM-7503X0753

Spectral narrowing of a single-mode beam oscillator —V. A. Buts and V. I. Kurilko. 19(11), 1494–5 (May 1975); CPM-7506X1248

84.80.D Electron beams and electron optics

Parametric instability of an electron beam in a magnetic field —A. I. Pasynok and N. S. Repalov. 19(2), 177–80 (Aug. 1974); CPM-7408X1441

High–current pulsed electron accelerator with an annular beam —M. I. Avramenko, V. A. Glukhikh, O. A. Gusev, E. G. Komar, O. L. Komarov, V. S. Kuznetsov, A. S. Perlin, and M. P. Svin'in. 19(3), 368–70 (Sep. 1974); CPM-7412X1054

Transmission of a high–current relativistic beam through a gas —Yu. V. Tkach, I. I. Magda, G. V. Skachek, S. S. Pushkarev, and I. P. Panchenko. 19(3), 412–3 (Sep. 1974); CPM-7412X1098

Energy input in electrical ionization lasers —Yu. I. Bychkov, Yu. D. Korolev, Yu. A. Kurbatov, and G. A. Mesyats. 19(4), 499–502 (Oct. 1974); CPM-7412X0283

Characteristics of the electrical ionization CO_2 laser —Yu. I. Bychkov, Yu. A. Kurbatov, and V. V. Savin. 19(4), 506–8 (Oct. 1974); CPM-7412X0290

Electrostatic analyzer for wide beams —V. G. Kovalenko and B. V. Polenov. 19(4), 561–2 (Oct. 1974); CPM-7412X0345

Low–voltage gun with a resonator for formation of electron bunches in a linear accelerator —V. A. Boiko, R. M. Voronkov, and V. A. Danilichev. 19(4), 569–71 (Oct. 1974); CPM-7412X0353

Parametric excitation of surface waves in a spatially modulated electron beam —A. I. Pasynok and N. S. Repalov. 19(4), 572–3 (Oct. 1974); CPM-7412X0356

Theory of the cathode lens. III. Derivation of equations for composite cathode lenses —V. M. Kel'man, A. A. Sapargaliev, and E. M. Yakushev. 19(5), 592–6 (Nov. 1974); CPM-7501X0386

Theory of the cathode lens. IV. Aberrations of composite cathode lens —V. M. Kel'man, A. A. Sapargaliev, and E. M. Yakushev. 19(5), 597–9 (Nov. 1974); CPM-7501X0391

Cerenkov instabilities of a relativistic beam in a periodic plasma–filled waveguide —V. I. Kurilko, Yu. V. Tkach, and V. A. Shendrik. 19 (5), 607–11 (Nov. 1974); CPM-7501X0401

Electron–scanning transformation of the potential distribution on an electrostatic target —V. L. Lentsman. 19(5), 678–9 (Nov. 1974); CPM-7501X0472

Aperiodic instability in a plasma gap with external feedback —A. N. Igritskii. 19(6), 719–21 (Dec. 1974); CPM-7501X0719
Spatial and energy parameters of the relativistic electron beam of the Rius-5 accelerator —A. T. Altyntsev and V. I. Koroteev. 19(6), 773–4 (Dec. 1974); CPM-7501X0773
Estimate of the angular divergence in intense electron beams —V. S. Kuznetsov, Yu. P. Vakhrushin, O. L. Komarov, and R. P. Fidel'skaya. 19(7), 868–70 (Jan. 1975); CPM-7503X0756
Parametric instability of a spatially moderated electron beam in a magnetic field —N. S. Repalov and V. F. Tyrnov. 19(7), 871–3 (Jan. 1975); CPM-7503X0759
Control of output energy in linear electron accelerators —V. N. Golovin and N. P. Sobenin. 19(7), 932–4 (Jan. 1975); CPM-7503X0820
Ion focusing of an electron beam in deep melting of a metal —M. D. Gabovich, V. P. Kovalenko, O. A. Metallov, O. K. Nazarenko, and S. K. Pats'ora. 19(7), 973–4 (Jan. 1975); CPM-7503X0861
Stability of the diode —V. A. Buts. 19(8), 1034–7 (Feb. 1975); CPM-7504X1458
Self-excited waveguide buncher —N. M. Gavrilov and A. V. Nesterovich. 19(8), 1085–6 (Feb. 1975); CPM-7504X1509
Self-acceleration of an intense electron beam —I. A. Grishaev, A. N. Dedik, V. V. Zakutin, I. I. Magda, Yu. V. Tkach, and A. M. Shenderovich. 19(8), 1087–9 (Feb. 1975); CPM-7504X1511
Magnetic-field transport of a high-current electron beam —A. V. Agafonov, V. S. Voronin, A. N. Lebedev, and K. N. Pazin. 19(9), 1188–92 (Mar. 1975); CPM-7505X0610
Electron energy spectrum in a high-current vacuum diode —S. P. Bugaev, V. I. Koshelev, and M. N. Timofeev. 19(9), 1193–5 (Mar. 1975); CPM-7505X0615
Multiple scattering of a focused beam of monoenergetic electrons —G. N. Vyalov. 19(9), 1216–8 (Mar. 1975); CPM-7505X0638
Luminosity of a cylindrical spectrometer with a small off-axis source —V. V. Zashkvara. 19(9), 1264–5 (Mar. 1975); CPM-7505X0686
Fifth-order spherical aberration in focusing and correcting quadrupole—octupole systems —Ya. G. Lyubchik and T. Ya. Fishkova. 19 (11), 1403–7 (May 1975); CPM-7506X1157
Axially symmetric neutralized electron beam —G. N. Vyalov, V. N. Evteev, Yu. M. Zolotaikin, and K. N. Ul'yanov. 19(11), 1414–7 (May 1975); CPM-7506X1168
Stabilization of two-stream instabilities —V. A. Buts. 19(11), 1496–7 (May 1975); CPM-7506X1250
Method for optical modulation of an electron beam —V. I. Sotnikov. 19(11), 1510–1 (May 1975); CPM-7506X1264
Wave excitation at half the gyrofrequency in counterstreaming electron beams —A. P. Timoshenko, D. V. Iremashvili, and Yu. K. Udovichenko. 19(12), 1584–6 (Jun. 1975); CPM-7508X0458
Electron-optical properties of postdeflection quadrupole lenses —T. Ya. Fishkova. 19(12), 1618–9 (Jun. 1975); CPM-7508X0492
Reflection of a high-current relativistic electron beam from a conducting surface —A. N. Didenko, A. I. Ryabchikov, V. A. Tuzov, and Yu. P. Usov. 19(12), 1625–6 (Jun. 1975); CPM-7508X0499
Coherent phase oscillations of electrons in a synchrotron —M. M. Nikitin. 19(12), 1633–4 (Jun. 1975); CPM-7508X0507

84.80.G Ion beams and ion optics

Production of an ion beam by a magnetic system with opposed fields —V. B. Glasko, A. G. Sveshnikov, and N. N. Semashko. 19(2), 201–5 (Aug. 1974); CPM-7408X1465
Gas-kinetic removal of neutral molecules from an ion beam —V. P. Ivanov. 19(2), 239–42 (Aug. 1974); CPM-7408X1503
Focusing of a neutralized ion beam by a plasma-optics system —I. I. Demidenko, N. S. Lomino, A. I. Morozov, and V. G. Padalka. 19 (3), 347–50 (Sep. 1974); CPM-7412X1033
Energy dependence of the focusing of ions by crystals —E. S. Mashkova, V. A. Molchanova, and A. D. Pavlova. 19(4), 540 (Oct. 1974); CPM-7412X0324
Gas focusing of a negative-ion beam —M. D. Gabovich, A. P. Naida, I. M. Protsenko, L. S. Simonenko, and I. A. Soloshenko. 19(4), 546–7 (Oct. 1974); CPM-7412X0330
Electrostatic analyzer for wide beams —V. G. Kovalenko and B. V. Polenov. 19(4), 561–2 (Oct. 1974); CPM-7412X0345
Correction of third-order angular aberration in a system with two electrostatic mirrors —V. V. Zashkvara. 19(7), 961–2 (Jan. 1975); CPM-7503X0849
Elimination of spherical aberration in an axial plasma lens —S. V. Lebedev and A. I. Morozov. 19(7), 966 (Jan. 1975); CPM-7503X0854
Achromatic plasma-lens system —A. I. Morozov and S. V. Lebedev. 19(7), 967 (Jan. 1975); CPM-7503X0855
Multiple-aperture ion source for electromagnetic mass separator —S. V. Lebedev. 19(7), 968 (Jan. 1975); CPM-7503X0856
Parametric interaction of a charged particle beam with a periodic system —V. I. Koroza and E. S. Sukhovskii. 19(8), 1020–4 (Feb. 1975); CPM-7504X1444
Parallel-plate capacitor as a charged-particle spectrometer —Yu. D. Kornyushkin. 19(8), 1110–2 (Feb. 1975); CPM-7504X1534
Double focusing in a system of $1/r$ electric and magnetic fields —V. V. Zashkvara and V. N. Demin. 19(9), 1219–20 (Mar. 1975); CPM-7505X0641
Graphical methods for constructing trajectories of small particles in electrostatic fields —N. I. Shtepa. 19(9), 1253–5 (Mar. 1975); CPM-7505X0675
Plasma synthesis by injection of an electron beam through an ion source —V. F. Virko, M. D. Gabovich, G. S. Kirichenko, and O. K. Nazarenko. 19(11), 1418–20 (May 1975); CPM-7506X1172
Ion-optical system for shaping high-current ion beams —S. D. Grishin, V. F. Kuzovlev, R. V. Orlov, and S. N. Ogorodnikov. 19 (11), 1462–4 (May 1975); CPM-7506X1216
Loss of neutralization for a stable neutralized ion beam —M. D. Gabovich. 19(11), 1502–3 (May 1975); CPM-7506X1256
Stigmatic sectored magnetic analyzer for a multiple-beam mass spectrometer —G. Kh. Chedzhemov. 19(11), 1516–7 (May 1975); CPM-7506X1270

84.90.+ Other topics in electromagnetic technology

Two-spin oscillator with optical orientation of electrons and nuclei —R. A. Zhitnikov and V. V. Semenov. 19(1), 105–9 (Jul. 1974); CPM-7407X1617
Dynamic magnetic-resonance phenomena —P. S. Kuts and V. S. Mel'nik. 19(1), 110–4 (Jul. 1974); CPM-7407X1622
Shot noise in a thermionic cathode —A. F. Golubentsev and A. S. Shapovalov. 19(10), 1345–6 (Apr. 1975); CPM-7506X0279

85. ELECTRICAL AND MAGNETIC DEVICES

85.10.- Electron tubes

Effect of electron-atom collisions on electron motion in a gas diode —V. I. Babanin and A. Ya. Énder. 19(1), 60–5 (Jul. 1974); CPM-7407X1572
Perveance of a vacuum with a point cathode —S. P. Bugaev, E. A. Litvinov, V. V. Lopatin, and G. A. Mesyats. 19(1), 88–90 (Jul. 1974); CPM-7407X1600
Peak current in a cold-cathode magnetron —I. M. Vigdorchik and V. P. Timofeev. 19(1), 142–3 (Jul. 1974); CPM-7407X1654
End current in a magnetron with a secondary-emission cathode —G. G. Sominskii, S. A. Fridrikhov, O. Yu. Tsybin, and A. P. Karizhskii. 19(3), 378–81 (Sep. 1974); CPM-7412X1064
Electron-scanning transformation of the potential distribution on an electrostatic target —V. L. Lentsman. 19(5), 678–9 (Nov. 1974); CPM-7501X0472
Evaluation of charge distribution in a crossed-field device from ion bombardment of the cathode —V. I. Malyugin and G. G. Sominskii. 19(7), 942–5 (Jan. 1975); CPM-7503X0830
Stability of the diode —V. A. Buts. 19(8), 1034–7 (Feb. 1975); CPM-7504X1458
Secondary-electron energy in a resonance discharge in a three-electrode system —Yu. A. Kulikov, V. V. Ogienko, and Yu. M. Trifonov. 19(8), 1090–2 (Feb. 1975); CPM-7504X1514
Microcells in cold cathodes —N. P. Kozlov, A. A. Lyapin, and V. I. Khvesyuk. 19(8), 1093–5 (Feb. 1975); CPM-7504X1517
Numerical experiments on electron bombardment in crossed fields —P. V. Romanov and A. S. Roshal'. 19(9), 1221–3 (Mar. 1975); CPM-7505X0643

85.70.– Magnetic devices

Two–section solenoid with internal "equally–loaded" section; power as a function of the length of the internal section —G. S. Veisig, A. P. Doroshenko, and P. P. Rybin. **19**(3), 416–8 (Sep. 1974); CPM-7412X1102

Two–omegatron study of the pumping characteristics of an NÉM–300 magnetic discharge pump for a mixture of gases —M. K. Bulgakov and V. G. Rogozinskii. **19**(3), 427–8 (Sep. 1974); CPM-7412X1113

Shielding properties of superconducting shields —S. I. Bondarenko, S. S. Vinogradov, G. A. Gogadze, S. S. Perepelkin, and V. I. Sheremet. **19**(6), 824–8 (Dec. 1974); CPM-7501X0824

Distortion of single-turn solenoids in ultrahigh magnetic fields —G. A. Shneerson. **19**(10), 1371–7 (Apr. 1975); CPM-7506X0305

85.90.+ Other topics in electrical and magnetic devices

Electron repulsion in a time–resolving electron–optical image converter —M. M. Butslov and M. E. Gertsenshtein. **19**(1), 129–30 (Jul. 1974); CPM-7407X1641

Strobe unit for measuring luminescence in the range 10^{-7}–$2\cdot10^{-10}$ sec —V. A. Bonch–Bruevich and N. A. Tolstoi. **19**(2), 284–6 (Aug. 1974); CPM-7408X1548

Optimization of the paraxial asymptotic electric field in electron–optical systems —V. E. Ginzburg and V. N. Danilov. **19** (3), 407–9 (Sep. 1974); CPM-7412X1093

Upper and lower limits on the capacitance of a plane capacitor —R. F. Fikhmanas and P. Sh. Fridberg. **19**(5), 683–4 (Nov. 1974); CPM-7501X0477

Preservation of semiconductor field–emission cathodes —N. V. Egorov, G. N. Fursei, and M. K. El'Nimr. **19**(5), 709 (Nov. 1974); CPM-7501X0503

Vaporization and boiling of liquid metal in an exploding wire —M. M. Martynyuk. **19**(6), 793–7 (Dec. 1974); CPM-7501X0793

Approximate similarity relations in the electrical explosions of underwater conductors —E. V. Krivitskii and V. K. Sholom. **19**(6), 798–801 (Dec. 1974); CPM-7501X0798

Thermal conditions for a sandwich cold cathode —F. M. Benson, P. E. Troyan, and Yu. B. Yankelevich. **19**(7), 946–7 (Jan. 1975); CPM-7503X0834

Superconducting magnetic shields —S. I. Bondarenko and V. I. Sheremet. **19**(7), 952–5 (Jan. 1975); CPM-7503X0840

Electrical characteristics of underwater exploding wires —V. K. Sholom, E. V. Krivitskii, and V. P. Litvinenko. **19**(10), 1329–31 (Apr. 1975); CPM-7506X0263

91. GEOPHYSICS AND EARTH SCIENCES

Narrow–band decimeter radiation from lighting —E. L. Kosarev and Yu. G. Serezhkin. **19**(2), 229–33 (Aug. 1974); CPM-7408X1493

Radar sounding of sea ice —V. V. Bogorodskii and V. P. Tripol'nikov. **19**(3), 414–5 (Sep. 1974); CPM-7412X1100

Differential electromagnetic characteristics at the interface between ice and water in the ocean —V. V. Bogorodskii and V. P. Tripol'nikov. **19**(4), 526–8 (Oct. 1974); CPM-7412X0310

Evolution of monochromatic whistler and plasma–wave packets in a collisionless plasma —Ya. N. Istomin. **19**(4), 529–30 (Oct. 1974); CPM-7412X0313

Gas cooling in transmission of high–power CO_2 laser radiation through the atmosphere —B. F. Gordiets, A. I. Osipov, and R. V. Khokhlov. **19**(5), 669–72 (Nov. 1974); CPM-7501X0463

AUTHOR INDEX TO VOLUME 19

Papers are arranged in ascending page number order.

A

Abdrashitova, D. Kh.—Efficient ion source —D. Kh. Abdrashitova, V. G. Babaev, and M. B. Guseva. 19(2), 264–6 (Aug. 1974); CPM-7408X1528

Abdulloev, Kh. O.—Excitation of acoustic waves by ion-acoustic turbulence —Kh. O. Abdulloev, F. Kh. Khakimov, and V. G. Makhan'kov. 19(4), 441–5 (Oct. 1974); CPM-7412X0225

Abramov, Yu. Yu.—Model for the low-voltage arc. I. Stationary solution —Yu. Yu. Abramov and G. G. Gladush. 19(6), 745–7 (Dec. 1974); CPM-7501X0745

—Model for the low-voltage arc. II. Stability —Yu. Yu. Abramov and G. G. Gladush. 19(6), 748–50 (Dec. 1974); CPM-7501X0748

Abroyan, M. A.—Electron energy distribution in a constricted, low-pressure hydrogen discharge —M. A. Abroyan, Yu. M. Kagan, N. B. Kolokolov, and B. P. Lavrov. 19(11), 1492–3 (May 1975); CPM-7506X1246

Agafonov, A. V.—Magnetic-field transport of a high-current electron beam —A. V. Agafonov, V. S. Voronin, A. N. Lebedev, and K. N. Pazin. 19(9), 1188–92 (Mar. 1975); CPM-7505X0610

Agafonova, E. N.—Motion of charged particles in a nonneutral plasma —E. N. Agafonova and L. I. Grechikhin. 19(11), 1488–9 (May 1975); CPM-7506X1242

Akin'shin, V. D.—Flow of low-density gases in a capillary grid —B. T. Porodnov, V. D. Akin'shin, V. I. Kichaev, S. F. Borisov, and P. E. Suetin. 19(4), 515–8 (Oct. 1974); CPM-7412X0299

Al'bikov, Z. A.—Acceleration of plasma electrons in strong electric fields —Z. A. Al'bikov, M. I. Ivanov, V. I. Kazacha, O. V. Kozlov, V. D. Rusanov, and S. S. Sobolev. 19(11), 1498–9 (May 1975); CPM-7506X1252

Aleksandrov, A. F.—Dynamics and emission of coaxial plasma shells in air —A. F. Aleksandrov, V. V. Perebeinos, A. T. Savichev, and I. B. Timofeev. 19(1), 38–42 (Jul. 1974); CPM-7407X1550

—Radiating discharges confined by walls —A. F. Aleksandrov, I. S. Marshak, and A. A. Rukhadze. 19(3), 308–14 (Sep. 1974); CPM-7412X0994

—Initial stage of a high-current discharge in air —A. F. Aleksandrov, V. V. Perebeinos, A. T. Savichev, and I. B. Timofeev. 19(11), 1490–1 (May 1975); CPM-7506X1244

Aleksandrov, M. L.—Simulation of ion scattering on diatomic molecules —M. L. Aleksandrov, N. S. Pliss, and A. P. Shcherbakov. 19(3), 394–5 (Sep. 1974); CPM-7412X1080

—Monte Carlo analysis of ion scattering in a mass spectrometer —M. L. Aleksandrov, L. N. Gall', and N. S. Pliss. 19(6), 817–9 (Dec. 1974); CPM-7501X0817

Aleksandrova, A. A.—Diffraction of electromagnetic waves by a dielectric wedge —A. A. Aleksandrova and N. A. Khizhnyak. 19 (11), 1385–9 (May 1975); CPM-7506X1139

Aleksin, V. F.—Diffusion of quasistationary helical magnetic fields into the interior of cylindrical chambers. II. —V. F. Aleksin and S. S. Romanov. 19(9), 1171–3 (Mar. 1975); CPM-7505X0593

Alferov, Zh. I.—Time characteristics of the near radiation field of the injection laser —Zh. I. Alferov, V. N. Deryagin, L. E. Marasin, Yu. V. Popov, and E. L. Portnoi. 19(4), 548 (Oct. 1974); CPM-7412X0332

Alkhazov, G. D.—Continuous electron acceleration in a gas discharge —G. D. Alkhazov. 19(5), 658–9 (Nov. 1974); CPM-7501X0452

Al'pert, Ya. L.—Rotation of Poynting vector for ultralow-frequency ion waves in an inhomogeneous plasma —Ya. L. Al'pert and R. N. Kaufman. 19(12), 1519–21 (Jun. 1975); CPM-7508X0393

Altyntsev, A. T.—Spatial and energy parameters of the relativistic electron beam of the Rius-5 accelerator —A. T. Altyntsev and V. I. Koroteev. 19(6), 773–4 (Dec. 1974); CPM-7501X0773

—Connection of magnetic lines of force in a neutral layer —A. T. Altyntsev and V. I. Krasov. 19(12), 1639–40 (Jun. 1975); CPM-7508X0513

Andreev, A. D.—Direct current in a metal—selenium—metal structure boundary by an rf plasma —A. D. Andreev and S. I. Lubinskii. 19(12), 1606–7 (Jun. 1975); CPM-7508X0480

Andreev, A. P.—Rate for evaporation of a liquid into vacuum —A. P. Andreev and M. A. Gurevich. 19(3), 396–401 (Sep. 1974); CPM-7412X1082

Andreev, P. A.—Thermoacoustic waves in conducting gases and liquids —P. A. Andreev. 19(6), 845–6 (Dec. 1974); CPM-7501X0845

—Acousto-electric waves in conducting media —P. A. Andreev. 19 (8), 1001–4 (Feb. 1975); CPM-7504X1425

Andreeva, E. Yu.—Frequency locking in a 3.39μ laser —E. Yu. Andreeva, S. N. Gulyaev, and D. K. Terekhin. 19(12), 1620–1 (Jun. 1975); CPM-7508X0494

Antimirov, M. Ya.—Nonstationary magnetohydrodynamic flow and wave propagation —M. Ya. Antimirov and Yu. Ya. Boguslavskii. 19(7), 878–9 (Jan. 1975); CPM-7503X0766

Antsupov, A. V.—Properties of underexpanded and overexpanded supersonic gas jets —A. V. Antsupov. 19(2), 234–8 (Aug. 1974); CPM-7408X1498

Arakelyan, S. M.—Direct and cascade four-photon parametric scattering of light in $LiIO_3$ crystals —S. M. Arakelyan, V. G. Tunkin, A. I. Kholodnykh, and A. S. Chirkin. 19(6), 787–92 (Dec. 1974); CPM-7501X0787

Aref'ev, V. I.—Plasma acceleration in crossed electric and magnetic fields —V. I. Aref'ev. 19(4), 446–54 (Oct. 1974); CPM-7412X0230

—Anomalous resistivity of transverse plasma current at electron-cyclotron harmonics —V. I. Aref'ev and A. A. Chernov. 19(12), 1522–8 (Jun. 1975); CPM-7508X0396

Arsenin, V. V.—Stabilization of the major radius of toroidal pinch by a feedback system —V. V. Arsenin. 19(7), 895–7 (Jan. 1975); CPM-7503X0783

Artamonov, O. M.—Energy losses of slow electrons reflected from molybdenum and tungsten single crystals —O. M. Artamonov, B. B. Bolotov, and M. V. Kremkov. 19(8), 1103–4 (Feb. 1975); CPM-7504X1527

Artemov, A. D.—Proton extraction from the 70-GeV accelerator for the Ludmila liquid-hydrogen chamber (extraction system S) —A. A. Aseev, A. I. Drozhdin, B. A. Zelenov, É. A. Merker, L. L. Moizhes, K. P. Myznikov, A. A. Roshchin, V. M. Tatarenko, M. A. Kholodenko, A. D. Artemov, L. N. Vaulin, V. I. Gordin, I. I. Kovalevskii, V. N. Rozhkov, M. M. Suvorov, A. S. Sudarushkin, and V. I. Chuiko. 19(1), 70–6 (Jul. 1974); CPM-7407X1582

Aseev, A. A.—Proton extraction from the 70-GeV accelerator for the Ludmila liquid-hydrogen chamber (extraction system S) —A. A. Aseev, A. I. Drozhdin, B. A. Zelenov, É. A. Merker, L. L. Moizhes, K. P. Myznikov, A. A. Roshchin, V. M. Tatarenko, M. A. Kholodenko, A. D. Artemov, L. N. Vaulin, V. I. Gordin, I. I. Kovalevskii, V. N. Rozhkov, M. M. Suvorov, A. S. Sudarushkin, and V. I. Chuiko. 19(1), 70–6 (Jul. 1974); CPM-7407X1582

Asvadurov, K. D.—Electron energy distribution in helium, nitrogen, and their mixtures —K. D. Asvadurov, I. A. Vasil'eva, and V. M. Torchinskii. 19(3), 354–7 (Sep. 1974); CPM-7412X1040

Avilov, É. A.—Electrical strength of nitrogen and hyrodgen at high pressures —É. A. Avilov and N. V. Belkin. 19(12), 1631–2 (Jun. 1975); CPM-7508X0505

Avramenko, M. I.—High-current pulsed electron accelerator with an annular beam —M. I. Avramenko, V. A. Glukhikh, O. A. Gusev, E. G. Komar, O. L. Komarov, V. S. Kuznetsov, A. S. Perlin, and M. P. Svin'in. 19(3), 368–70 (Sep. 1974); CPM-7412X1054

B

Babaev, V. G.—Efficient ion source —D. Kh. Abdrashitova, V. G. Babaev, and M. B. Guseva. 19(2), 264–6 (Aug. 1974); CPM-7408X1528

Babanin, V. I.—Effect of electron-atom collisions on electron motion in a gas diode —V. I. Babanin and A. Ya. Énder. 19(1), 60–5 (Jul. 1974); CPM-7407X1572

Babich, L. P.—Stability of field-emission beams in nonsecond discharges —L. P. Babich. 19(3), 371–2 (Sep. 1974); CPM-7412X1057

—Optical radiation from nanosecond discharges in dense gases —L. P. Babich. 19(3), 419–20 (Sep. 1974); CPM-7412X1105

—Stochastic acceleration of electrons in nanosecond discharges —L. P. Babich. 19(9), 1154–6 (Mar. 1975); CPM-7505X0576

Baikov, I. S.—Anomalous ion heating in a parametrically unstable plasma —I. S. Baikov and V. P. Silin. 19(12), 1529–33 (Jun. 1975); CPM-7508X0403

Bakanov, S. P.—State of a gas moving near a solid surface —S. P. Bakanov and B. M. Markeev. 19(10), 1293–4 (Apr. 1975); CPM-7506X0227

—Certain integral relations in the kinetic theory of gases —S. P. Bakanov. 19(12), 1636–8 (Jun. 1975); CPM-7508X0510

Bakhtiyarov, R. S.—Electron-microscope and x-ray study of thermionic emitters made from Mo–Pt alloys —B. B. Shishkin and R. S. Bakhtiyarov. 19(2), 243–50 (Aug. 1974); CPM-7408X1507

Baksht, F. G.—Theory of the low-voltage arc in a narrow gap —F. G. Baksht, A. A. Kostin, and V. A. Nemchinskii. 19(5), 654–7 (Nov. 1974); CPM-7501X0448

—Atomic density in the low-voltage arc in a cesium diode —F. G. Baksht, A. A. Kostin, Yu. L. Serov, and I. P. Yavor. 19(11), 1424–5 (May 1975); CPM-7506X1178

Balkarei, Yu. I.—Resonant amplification of an image potential by an electromagnetic wave —Yu. I. Balkarei and É. M. É pshtein. 19(6), 843–4 (Dec. 1974); CPM-7501X0843

Baranchuk, N. S.—Physical properties of an electrodeless pulsed discharge in a gas-filled glass cell —Yu. I. Chutov, N. S. Baranchuk, M. R. Lozovich, and V. G. Danilov. 19(2), 224–8 (Aug. 1974); CPM-7408X1488

Barannik, S. I.—Resistance and inductance of a gas arc —S. I. Barannik, S. B. Vasserman, and A. N. Lukin. 19(11), 1449–53 (May 1975); CPM-7506X1203

Baranov, Yu. F.—Generation of drift waves by an rf field near the lower hybrid frequency —Yu. F. Baranov, D. G. Bulyginskii, M. I. Vil'dzhyunas, B. V. Galaktionov, and N. V. Shustova. 19(6), 732–5 (Dec. 1974); CPM-7501X0732

Bardina, N. S.—Thermal effect of continuous laser radiation on optically transparent media —N. S. Bardina, A. I. Portnyagin, M. Yu. Sklyarov, and A. A. Churin. 19(4), 491–4 (Oct. 1974); CPM-7412X0275

Barsegyan, O. A.—Motion of stable aerosol particles —O. A. Barsegyan and Yu. I. Yalamov. 19(11), 1486–7 (May 1975); CPM-7506X1240

Batyrbekov, G. A.—Charge-carrier density of the plasma produced in a Penning mixture by irradiation by uranium fission fragments and reactor radiation —G. A. Batyrbekov, Yu. D. Kuznetsov, and Zh. S. Takibaev. 19(5), 645–6 (Nov. 1974); CPM-7501X0439

Bazilevskaya, T. A.—Conversion of neutral hydrogen into protons in dense plasmas —T. A. Bazilevskaya, L. I. Krupnik, and N. G. Shulika. 19(6), 741–4 (Dec. 1974); CPM-7501X0741

Beilis, I. I.—Analysis of the cathode spot in a vacuum arc —I. I. Beilis. 19(2), 251–6 (Aug. 1974); CPM-7408X1515

—Emission processes at the cathode of an electric arc —I. I. Beilis. 19 (2), 257–60 (Aug. 1974); CPM-7408X1521

Bekmukhambetov, E. S.—Thermal diffusion in a mixture of cesium vapor and helium —E. S. Bekmukhambetov and V. A. Donov. 19 (12), 1627–8 (Jun. 1975); CPM-7508X0501

Belan, N. V.—Breakdown caused by electron bombardment of the surface of an alloy electrode —N. V. Belan, G. I. Kostyuk, and V. A. Pimkin. 19(6), 802–3 (Dec. 1974); CPM-7501X0802

Belen'kii, V. Z.—Transient molecular effusion characteristics —Yu. N. Lyubitov and V. Z. Belen'kii. 19(4), 519–22 (Oct. 1974); CPM-7412X0303

Belkin, N. V.—Electrical strength of nitrogen and hyrodgen at high pressures —É. A. Avilov and N. V. Belkin. 19(12), 1631–2 (Jun. 1975); CPM-7508X0505

Bel'kov, E. P.—Dielectric strength of spark gaps following strong current pulses —E. P. Bel'kov. 19(9), 1210–3 (Mar. 1975); CPM-7505X0632

Belousov, E. V.—Microwave discharge in argon —E. V. Belousov, A. S. Bryukhovetskii, and A. V. Prokopov. 19(1), 53–6 (Jul. 1974); CPM-7407X1565

Belousova, I. M.—Sign of the change in optical path length in a laser interferometer with feedback —I. M. Belousova and A. F. Zapryagaev. 19(6), 829–30 (Dec. 1974); CPM-7501X0829

Belyakov, L. V.—Characteristics of diffraction gratings obtained by photoetching of semiconductor surfaces —L. V. Belyakov, D. N. Goryachev, M. N. Mizerov, and E. L. Portnoi. 19(6), 837–8 (Dec. 1974); CPM-7501X0837

Belyakov, Yu. I.—Effects of cleaning on adsorption by germanium single crystals —Yu. I. Belyakov, M. P. Volkov, and T. N. Kompaniets. 19(6), 815–6 (Dec. 1974); CPM-7501X0815

—Effect of the adsorption rate on the diffusion of deuterium through nickel —Yu. I. Belyakov, Yu. I. Zvezdin, A. A. Kurdyumov, and G. G. Nevdakha. 19(7), 956–8 (Jan. 1975); CPM-7503X0844

Benson, F. M.—Thermal conditions for a sandwich cold cathode —F. M. Benson, P. E. Troyan, and Yu. B. Yankelevich. 19(7), 946–7 (Jan. 1975); CPM-7503X0834

Berezin, A. K.—Interaction of a hollow electron beam with a plasma —N. M. Zemlyanskii, A. K. Berezin, Ya. B. Fainberg, L. I. Bolotin, and S. S. Krivulya. 19(12), 1547–8 (Jun. 1975); CPM-7508X0421

Berkov, V. I.—Radiation energy of a magnetoplasma compressor —V. I. Berkov and A. I. Morozov. 19(2), 220–3 (Aug. 1974); CPM-7408X1484

Berman, G. P.—Nonlinear effects for the "kink" instability in an electron-ion ring —G. P. Berman. 19(10), 1312–6 (Apr. 1975); CPM-7506X0246

Biryukov, A. S.—Kinetics of gasdynamic lasers. Effect of nozzle geometry on inversion —A. S. Biryukov and L. A. Shelepin. 19(6), 775–81 (Dec. 1974); CPM-7501X0775

Blagoev, A. B.—Electron energy distribution in the afterglow. I —A. B. Blagoev, Yu. M. Kagan, N. B. Kolokolov, and R. I. Lyagushchenko. 19(2), 211–4 (Aug. 1974); CPM-7408X1475

—Electron energy distribution in the afterglow. II —A. B. Blagoev, Yu. M. Kagan, N. B. Kolokolov, and R. I. Lyagushchenko. 19(2), 215–9 (Aug. 1974); CPM-7408X1479

Bobkov, V. V.—Mass spectrum of secondary ions ejected from the surface of a single crystal of gallium arsenide by argon ions —A. G. Koval', V. V. Bobkov, Yu. A. Klimovskii, S. S. Strel'chenko, V. V. Shubina, V. V. Lebedev, and Ya. M. Fogel'. 19(12), 1587–9 (Jun. 1975); CPM-7508X0461

Bobrov, Yu. K.—Gasdynamic model of the spark discharge —Yu. K. Bobrov. 19(11), 1442–6 (May 1975); CPM-7506X1196

Bochkova, O. P.—Electron density in an argon afterglow —O. P. Bochkova, R. I. Lyagushchenko, É. A. Sukiasyan, and Yu. A. Tolmachev. 19(4), 475–7 (Oct. 1974); CPM-7412X0259

Boev, A. G.—Effect of ionization and excitation on the penetration of an electromagnetic wave into a weakly ionized plasma —A. G. Boev and A. V. Prokopov. 19(7), 901–4 (Jan. 1975); CPM-7503X0789

Bogdanov, E. V.—Electromagnetic fields outside a synthesized plasma jet —E. V. Bogdanov, G. M. Mantrova, and M. N. Yakovleva. 19(7), 919–21 (Jan. 1975); CPM-7503X0807

Bogdanov, S. V.—Optical methods for studying amplification of elastic surface waves in a stratified system —I. B. Yakovkin, V. V. Petrov, and S. V. Bogdanov. 19(9), 1242–5 (Mar. 1975); CPM-7505X0664

Bogomolov, Yu. V.—Kinetic theory for wave reflection from a moving plasma —Yu. V. Bogomolov. 19(2), 190–2 (Aug. 1974); CPM-7408X1454

Bogorodskii, V. V.—Radar sounding of sea ice —V. V. Bogorodskii and V. P. Tripol'nikov. 19(3), 414–5 (Sep. 1974); CPM-7412X1100

—Differential electromagnetic characteristics at the interface between ice and water in the ocean —V. V. Bogorodskii and V. P. Tripol'nikov. 19(4), 526–8 (Oct. 1974); CPM-7412X0310

Boguslavskii, Yu. Ya.—Nonstationary magnetohydrodynamic flow and wave propagation —M. Ya. Antimirov and Yu. Ya. Boguslavskii. 19(7), 878–9 (Jan. 1975); CPM-7503X0766

Boiko, V. A.—Low-voltage gun with a resonator for formation of electron bunches in a linear accelerator —V. A. Boiko, R. M. Voronkov, and V. A. Danilichev. 19(4), 569–71 (Oct. 1974); CPM-7412X0353

Bolgov, É. I.—Cell for forming electron beams of arbitrary shape in a high-voltage gaseous discharge —I. V. Vagner, É. I. Bolgov, V. F. Grakun, V. L. Gokhfel'd, and V. A. Kudlai. 19(8), 1042–5 (Feb. 1975); CPM-7504X1466

Bolotin, L. I.—Interaction of a hollow electron beam with a plasma —N. M. Zemlyanskii, A. K. Berezin, Ya. B. Fainberg, L. I. Bolotin, and S. S. Krivulya. 19(12), 1547–8 (Jun. 1975); CPM-7508X0421

Bolotov, B. B.—Energy losses of slow electrons reflected from molybdenum and tungsten single crystals —O. M. Artamonov, B. B. Bolotov, and M. V. Kremkov. 19(8), 1103–4 (Feb. 1975); CPM-7504X1527

Bonch-Bruevich, A. M.—Optical characteristics of K-8 glass subject to radiation from a neodymium laser —A. M. Bonch-Bruevich, Ya. A. Imas, V. S. Salyadinov, and A. V. Shatilov. 19(2), 287–9 (Aug. 1974); CPM-7408X1551

—Frequency-doubling single-mode laser for picosecond pulses —A. M. Bonch-Bruevich, A. M. Tkachuk, and A. A. Fedorov. 19(4), 549–51 (Oct. 1974); CPM-7412X0333

—Surface evaporation of a solid transparent dielectric under the action of laser radiation —A. M. Bonch-Bruevich, Ya. A. Imas, A. A. Kovalev, P. S. Kondratenko, and B. I. Makshantsev. 19(11), 1474–6 (May 1975); CPM-7506X1228

Bonch-Bruevich, V. A.—Strobe unit for measuring luminescence in the range 10^{-7}-$2\cdot10^{-10}$ sec —V. A. Bonch-Bruevich and N. A. Tolstoi. 19(2), 284–6 (Aug. 1974); CPM-7408X1548

Bondarenko, A. V.—Mass and energy analysis of ions in the cathode of an anomalous glow discharge. II. Binary gas mixtures Ne+Ar and N_2+Ar —A. V. Bondarenko. 19(7), 914–8 (Jan. 1975); CPM-7503X0802

Bondarenko, N. F.—Possible electrohydrodynamic effects in electrolytes —E. Z. Gak, É. Kh. Rokhinson, and N. F. Bondarenko. 19(5), 676–7 (Nov. 1974); CPM-7501X0470

Bondarenko, S. I.—Shielding properties of superconducting shields —S. I. Bondarenko, S. S. Vinogradov, G. A. Gogadze, S. S. Perepelkin, and V. I. Sheremet. 19(6), 824–8 (Dec. 1974); CPM-7501X0824

—Superconducting magnetic shields —S. I. Bondarenko and V. I. Sheremet. 19(7), 952–5 (Jan. 1975); CPM-7503X0840

Bondarenko, V. D.—Analytic model for the arc regime and the thermionic converter —V. D. Bondarenko and A. I. Loshkarev. 19 (12), 1564–8 (Jun. 1975); CPM-7508X0438

Bondarenko, V. N.—Elimination of carbon impurities from platinum by heating in an oxygen atmosphere —L. P. Rekova, V. V. Mozgin, L. N. Zvyagintseva, V. N. Bondarenko, and Ya. M. Fogel'. 19(11), 1465–7 (May 1975); CPM-7506X1219

Borisov, D. G.—Linear accelerator for beam injection into a slowly rising magnetic field —D. G. Borisov, A. I. Gryzlov, V. M. Levin, and A. V. Ryabtsov. 19(4), 509–10 (Oct. 1974); CPM-7412X0293

Borisov, S. F.—Flow of low-density gases in a capillary grid —B. T. Porodnov, V. D. Akin'shin, V. I. Kichaev, S. F. Borisov, and P. E. Suetin. 19(4), 515–8 (Oct. 1974); CPM-7412X0299

Bortniker, V. Yu.—Cumulative destruction of transparent dielectrics in repeated laser irradiation —L. D. Khazov, I. A. Fersman, and V. Yu. Bortniker. 19(9), 1256–7 (Mar. 1975); CPM-7505X0678

Bredikhin, M. Yu.—Spatial characteristics and loss of plasma produced by an electron beam in a magnetic trap —M. Yu. Bredikhin, A. I. Maslov, A. I. Skibenko, E. I. Skibenko, I. P. Fomin, and V. B. Yuferov. 19(1), 49–52 (Jul. 1974); CPM-7407X1561

Brusilovskii, B. A.—Effect of crystal structure on certain angular dependence of the ion-electron-emission yield —B. A. Brusilovskii and V. A. Molchanov. 19(1), 84–7 (Jul. 1974); CPM-7407X1596

Bryukhovetskii, A. S.—Microwave discharge in argon —E. V. Belousov, A. S. Bryukhovetskii, and A. V. Prokopov. 19(1), 53–6 (Jul. 1974); CPM-7407X1565

Bublik, V. T.—Crystal defects of heterostructures of AlAs–GaAs solid solutions and effect on the characteristics of injection lasers —L. V. Druzhinina, V. T. Bublik, L. M. Dolginov, P. G. Eliseev, M. P. Kerbelev, V. B. Osvenskii, I. Z. Pinsker, and M. G. Shumskii. 19(7), 935–9 (Jan. 1975); CPM-7503X0823

Bugaev, S. P.—Perveance of a vacuum with a point cathode —S. P. Bugaev, E. A. Litvinov, V. V. Lopatin, and G. A. Mesyats. 19(1), 88–90 (Jul. 1974); CPM-7407X1600

—Electron energy spectrum in a high-current vacuum diode —S. P. Bugaev, V. I. Koshelev, and M. N. Timofeev. 19(9), 1193–5 (Mar. 1975); CPM-7505X0615

Bulanov, S. V.—Magnetohydrodynamic stability of a neutral current layer in a plasma —S. V. Bulanov. 19(9), 1246–7 (Mar. 1975); CPM-7505X0668

Bulgakov, M. K.—Two-omegatron study of the pumping characteristics of an NÉM-300 magnetic discharge pump for a mixture of gases —M. K. Bulgakov and V. G. Rogozinskii. 19(3), 427–8 (Sep. 1974); CPM-7412X1113

Bulyginskii, D. G.—Generation of drift waves by an rf field near the lower hybrid frequency —Yu. F. Baranov, D. G. Bulyginskii, M. I. Vil'dzhyunas, B. V. Galaktionov, and N. V. Shustova. 19(6), 732–5 (Dec. 1974); CPM-7501X0732

Burtsev, V. A.—Coaxial plasma injector with programmed injection —V. A. Burtsev, V. N. Litunovskii, and M. P. Nadgornaya. 19(6), 736–40 (Dec. 1974); CPM-7501X0736

Burunov, E. A.—Diagnostics of a laser-produced plasma by a scattering method using an electron-optical image converter —E. A. Burunov, G. M. Malyshev, G. T. Razdobarin, and V. V. Semenov. 19(1), 66–9 (Jul. 1974); CPM-7407X1578

Bushuev, V. A.—Contribution of multiphoton processes to the linear dielectric constant —V. A. Bushuev and R. N. Kuz'min. 19(1), 116 (Jul. 1974); CPM-7407X1628

—Coherent Compton effect in crystals —V. A. Bushuev and R. N. Kuz'min. 19(12), 1590–2 (Jun. 1975); CPM-7508X0464

Busov, V. M.–Electroluminescence spectra of the red luminescent diodes p–$Al_xGa_{1-x}As$—n–$AlyGa_{1-y}As(y>x)$ —V. M. Busov, D. Z. Garbuzov, A. T. Gorelenok, and D. S. Kop'ev. 19(12), 1598–600 (Jun. 1975); CPM-7508X0472

Buts, V. A.—Stability of the diode —V. A. Buts. 19(8), 1034–7 (Feb. 1975); CPM-7504X1458

—Spectral narrowing of a single-mode beam oscillator —V. A. Buts and V. I. Kurilko. 19(11), 1494–5 (May 1975); CPM-7506X1248

—Stabilization of two-stream instabilities —V. A. Buts. 19(11), 1496–7 (May 1975); CPM-7506X1250

Butslov, M. M.—Electron repulsion in a time-resolving electron-optical image converter —M. M. Butslov and M. E. Gertsenshtein. 19(1), 129–30 (Jul. 1974); CPM-7407X1641

Butusov, M. M.—Optical simulation of a radiator aperture with arbitrary amplitude—phase distribution —M. M. Butusov and Sh. V. Yurevichyus. 19(6), 833–4 (Dec. 1974); CPM-7501X0833

Bychkov, Yu. I.—Ionization and recombination coefficients in a discharge excited by fast electrons —Yu. I. Bychkov, Yu. D. Korolev, and A. P. Khuzeev. 19(1), 140–1 (Jul. 1974); CPM-7407X1652

—Energy input in electrical ionization lasers —Yu. I. Bychkov, Yu. D. Korolev, Yu. A. Kurbatov, and G. A. Mesyats. 19(4), 499–502 (Oct. 1974); CPM-7412X0283

—Characteristics of the electrical ionization CO_2 laser —Yu. I. Bychkov, Yu. A. Kurbatov, and V. V. Savin. 19(4), 506–8 (Oct. 1974); CPM-7412X0290

—Infrared nitrogen laser using a transverse discharge —V. F. Tarasenko and Yu. I. Bychkov. 19(5), 693 (Nov. 1974); CPM-7501X0487

Bykovskii, Yu. A.—Recombination in an expanding plasma —Yu. A. Bykovskii, N. N. Degtyarenko, V. F. Elesin, V. E. Kondrashov, E. E. Lovetskii, A. N. Polyanichev, and V. S. Fetisov. 19(1), 43–8 (Jul. 1974); CPM-7407X1555

—Neutral particles from the interaction of laser radiation with a solid target —Yu. A. Bykovskii, N. M. Vasil'ev, I. D. Laptev, and V. N. Nevolin. 19(12), 1635 (Jun. 1975); CPM-7508X0509

Bystrov, Yu. A.—Development of an inhibited glow discharge —Yu. A. Bystrov, S. A. Ivanov, and Yu. F. Radchenko. 19(11), 1447–8 (May 1975); CPM-7506X1201

C

Chaikovski, A. P.—Measurement of statistical parameters of scattering particles in laminar flow by Doppler spectroscopy —A. P. Ivanov, A. Ya. Khairullina, and A. P. Chaikovski. 19(2), 267–70 (Aug. 1974); CPM-7408X1531

Chedzhemov, G. Kh.—Stigmatic sectored magnetic analyzer for a multiple-beam mass spectrometer —G. Kh. Chedzhemov. 19(11), 1516–7 (May 1975); CPM-7506X1270

Chekalin, É. K.—Investigation of ionization processes behind strong shock waves using an electrical conductivity probe —V. A. Tishchenko, N. V. Khandurov, and É. K. Chekalin. 19(5), 651–3 (Nov. 1974); CPM-7501X0445

Chekmarev, I. B.—Diffusion regime for electrostatic probes as singular-perturbation problem —I. B. Chekmarev. 19(10), 1287–9 (Apr. 1975); CPM-7506X0221

Chekmareva, O. M.—Stefan problem with motion of the phase-transition surface described by $y(\tau) = \sqrt{A\tau^2+B\tau+h^2}$ —O. M. Chekmareva. 19(10), 1273–6 (Apr. 1975); CPM-7506X0207

Chepegin, V. N.—Efficiency of internal targets in the accelerator at the Institute of High-Energy Physics —V. I. Gridasov, K. P. Myznikov, and V. N. Chepegin. 19(7), 922–5 (Jan. 1975); CPM-7503X0810

Cherepanov, B. S.—Dielectric properties of foamed ceramics at millimeter wavelengths —N. A. Irisova, G. V. Kozlov, V. E. Mandrusov, B. S. Cherepanov, and I. M. Chernyshev. 19(1), 103–4 (Jul. 1974); CPM-7407X1615

Chernov, A. A.—Anomalous resistivity of transverse plasma current at electron-cyclotron harmonics —V. I. Aref'ev and A. A. Chernov. 19(12), 1522–8 (Jun. 1975); CPM-7508X0396

Chernov, V. A.—Effect of electron reflection on the voltage–current characteristics of a high-voltage, hollow-cathode, glow discharge —Ya. Ya. Udris, V. A. Chernov, and L. G. Guseva. 19(1), 134–5 (Jul. 1974); CPM-7407X1646

Chernyshev, I. M.—Dielectric properties of foamed ceramics at millimeter wavelengths —N. A. Irisova, G. V. Kozlov, V. E. Mandrusov, B. S. Cherepanov, and I. M. Chernyshev. 19(1), 103–4 (Jul. 1974); CPM-7407X1615

Chertkov, A. A.—Pulsed neodymium–glass laser with periodic Q switching —T. A. Kuzovkova, E. V. Nilov, V. A. Rusov, I. N. Semenov, and A. A. Chertkov. 19(4), 503–5 (Oct. 1974); CPM-7412X0287

Chesonis, V. I.—Skin effect in a constant magnetic field —Z. K. Yankauskas, V. I. Chesonis, and V. G. Skripnik. 19(9), 1251–2 (Mar. 1975); CPM-7505X0673

Chetvertkov, V. I.—Focusing of an astigmatic beam by a doublet and a symmetric triplet of quadrupole lenses —V. I. Chetvertkov. 19 (1), 1–2 (Jul. 1974); CPM-7407X1513

Chikhachev, A. S.—Impossibility of shielding against the rf radiation of a thermonuclear reactor with a cold-plasma sheath —A. S. Chikhachev. 19(5), 685 (Nov. 1974); CPM-7501X0479

Chirkin, A. S.—Direct and cascade four-photon parametric scattering of light in $LiIO_3$ crystals —S. M. Arakelyan, V. G. Tunkin, A. I. Kholodnykh, and A. S. Chirkin. 19(6), 787–92 (Dec. 1974); CPM-7501X0787

Chistyakov, P. N.—Investigation of the work function of a tungsten cathode after bombardment by inert-gas ions —P. N. Chistyakov, R. A. Milovanova, and V. V. Lytkin. 19(1), 148–9 (Jul. 1974); CPM-7407X1660

Chuiko, V. I.—Proton extraction from the 70-GeV accelerator for the Ludmila liquid-hydrogen chamber (extraction system S) —A. A. Aseev, A. I. Drozhdin, B. A. Zelenov, É. A. Merker, L. L. Moizhes, K. P. Myznikov, A. A. Roshchin, V. M. Tatarenko, M. A. Kholodenko, A. D. Artemov, L. N. Vaulin, V. I. Gordin, I. I. Kovalevskii, V. N. Rozhkov, M. M. Suvorov, A. S. Sudarushkin, and V. I. Chuiko. 19(1), 70–6 (Jul. 1974); CPM-7407X1582

Churin, A. A.—Thermal effect of continuous laser radiation on optically transparent media —N. S. Bardina, A. I. Portnyagin, M. Yu. Sklyarov, and A. A. Churin. 19(4), 491–4 (Oct. 1974); CPM-7412X0275

Chutov, Yu. I.—Physical properties of an electrodeless pulsed discharge in a gas-filled glass cell —Yu. I. Chutov, N. S. Baranchuk, M. R. Lozovich, and V. G. Danilov. 19(2), 224–8 (Aug. 1974); CPM-7408X1488

D

Danilichev, V. A.—Low-voltage gun with a resonator for formation of electron bunches in a linear accelerator —V. A. Boiko, R. M. Voronkov, and V. A. Danilichev. 19(4), 569–71 (Oct. 1974); CPM-7412X0353

Danilov, V. G.—Physical properties of an electrodeless pulsed discharge in a gas-filled glass cell —Yu. I. Chutov, N. S. Baranchuk, M. R. Lozovich, and V. G. Danilov. 19(2), 224–8 (Aug. 1974); CPM-7408X1488

Danilov, V. N.—Optimization of the paraxial asymptotic electric field in electron-optical systems —V. E. Ginzburg and V. N. Danilov. 19(3), 407–9 (Sep. 1974); CPM-7412X1093

Davydov, V. B.—Effects of ion microfields on emission of an arc cathode —A. M. Dorodnov, V. B. Davydov, A. V. Kozyrev, and Ya. A. Pomelov. 19(3), 390–3 (Sep. 1974); CPM-7412X1076

Davydova, T. A.—Emission of waves from a plasma layer —T. A. Davydova and A. A. Zhmudskii. 19(1), 12–5 (Jul. 1974); CPM-7407X1524

Davydovskii, V. Ya.—Radiation emitted by charged particles trapped by plane electromagnetic waves —V. Ya. Davydovskii and A. S. Ukolov. 19(8), 1057–60 (Feb. 1975); CPM-7504X1481

—Energy of charged particles accelerated by electromagnetic waves in a plasma with a spatially decreasing density —V. Ya. Davydovskii and A. S. Ukolov. 19(10), 1303–7 (Apr. 1975); CPM-7506X0237

Dedik, A. N.—Self-acceleration of an intense electron beam —I. A. Grishaev, A. N. Dedik, V. V. Zakutin, I. I. Magda, Yu. V. Tkach, and A. M. Shenderovich. 19(8), 1087–9 (Feb. 1975); CPM-7504X1511

Degtyarenko, N. N.—Recombination in an expanding plasma —Yu. A. Bykovskii, N. N. Degtyarenko, V. F. Elesin, V. E. Kondrashov, E. E. Lovetskii, A. N. Polyanichev, and V. S. Fetisov. 19(1), 43–8 (Jul. 1974); CPM-7407X1555

Demchenko, P. A.—High-frequency modulation of atomic beams for plasma diagnostics —P. A. Demchenko, L. I. Krupnik, K. A. Leontovich, and E. S. Lyangner. 19(10), 1362–6 (Apr. 1975); CPM-7506X0296

—Free expansion of plasma jets —P. A. Demchenko, L. I. Krupnik, and E. S. Lyangner. 19(11), 1426–8 (May 1975); CPM-7506X1180

Dement'ev, A. S.—Microwave maser with nonrelativistic electrons —A. S. Dement'ev and Yu. G. Pavlenko. 19(5), 694–5 (Nov. 1974); CPM-7501X0488

Demidenko, I. I.—Focusing of a neutralized ion beam by a plasma-optics system —I. I. Demidenko, N. S. Lomino, A. I. Morozov, and V. G. Padalka. 19(3), 347–50 (Sep. 1974); CPM-7412X1033

—Effect of rf ionization on Hall-current plasma accelerator —I. I. Demidenko, N. S. Lomino, A. I. Morozov, and V. G. Padalka. 19 (12), 1560–3 (Jun. 1975); CPM-7508X0434

Demin, V. N.—Double focusing in a system of $1/r$ electric and magnetic fields —V. V. Zashkvara and V. N. Demin. 19(9), 1219–20 (Mar. 1975); CPM-7505X0641

Demirkhanov, R. A.—Low pressure discharge with high-energy electrons —R. A. Demirkhanov, Yu. V. Kursanov, and L. P. Skripal'. 19(7), 891–4 (Jan. 1975); CPM-7503X0779

Denisyuk, Yu. N.—Imaging properties of traveling intensity waves in the recording of dynamic three-dimensional holograms —Yu. N. Denisyuk. 19(1), 77–80 (Jul. 1974); CPM-7407X1589

Deryagin, V. N.—Time characteristics of the near radiation field of the injection laser —Zh. I. Alferov, V. N. Deryagin, L. E. Marasin, Yu. V. Popov, and E. L. Portnoi. 19(4), 548 (Oct. 1974); CPM-7412X0332

Diasamidze, Zh. M.—Effect of a high-frequency electric field on the energy loss of a charged particle in a medium —Zh. M. Diasamidze. 19(5), 687–8 (Nov. 1974); CPM-7501X0481

Didenko, A. N.—Reflection of a high-current relativistic electron beam from a conducting surface —A. N. Didenko, A. I. Ryabchikov, V. A. Tuzov, and Yu. P. Usov. 19(12), 1625–6 (Jun. 1975); CPM-7508X0499

Dimov, G. I.—Formation of a narrow gas jet in vacuum —G. I. Dimov and V. Ya. Savkin. 19(6), 755–8 (Dec. 1974); CPM-7501X0755

Dmitrenko, B. I.—Effect of a high-current relativistic electron beam on a metal —B. I. Dmitrenko, L. V. Leskov, G. P. Maksimov, S. L. Nedoseev, V. V. Savichev, V. P. Smirnov, and A. M. Spektor. 19(9), 1224–5 (Mar. 1975); CPM-7505X0646

Dneprovskii, V. G.—Condensation of a dense vapor flow —V. G. Dneprovskii, B. A. Osadin, and N. V. Rusakov. 19(2), 271–4 (Aug. 1974); CPM-7408X1535

—Effect of focusing conditions on the morphology of surface films produced with a laser —V. G. Dneprovskii and B. A. Osadin. 19 (2), 275–7 (Aug. 1974); CPM-7408X1539

Dnestrovskii, Yu. N.—Energy balance in Tokamaks in the "plateau—banana" transition region —Yu. N. Dnestrovskii and D. P. Kostomarov. 19(12), 1541–2 (Jun. 1975); CPM-7508X0415

Dolginov, L. M.—Crystal defects of heterostructures of AlAs–GaAs solid solutions and effect on the characteristics of injection lasers —L. V. Druzhinina, V. T. Bublik, L. M. Dolginov, P. G. Eliseev, M. P. Kerbelev, V. B. Osvenskii, I. Z. Pinsker, and M. G. Shumskii. 19(7), 935–9 (Jan. 1975); CPM-7503X0823

Dolzhenko, O. V.—Excitation of surface electromagnetic waves in a plasma cylinder surrounded by a hollow electron beam —O. V. Dolzhenko, A. V. Zosimov, and A. A. Rukhadze. 19(5), 618–21 (Nov. 1974); CPM-7501X0412

Donov, V. A.—Thermal diffusion in a mixture of cesium vapor and helium —E. S. Bekmukhambetov and V. A. Donov. 19(12), 1627–8 (Jun. 1975); CPM-7508X0501

Dorodnov, A. M.—Effects of ion microfields on emission of an arc cathode —A. M. Dorodnov, V. B. Davydov, A. V. Kozyrev, and Ya. A. Pomelov. 19(3), 390–3 (Sep. 1974); CPM-7412X1076

Doroshenko, A. P.—Two-section solenoid with internal "equally-loaded" section; power as a function of the length of the internal section —G. S. Veisig, A. P. Doroshenko, and P. P. Rybin. 19(3), 416–8 (Sep. 1974); CPM-7412X1102

Dougar-Jabon, V. D.—Radio-frequency absorption in a plasma confined by rf plugs —K. S. Golovanivskii, V. D. Dougar-Jabon, and L. A. Pokhmel'nykh. 19(11), 1484–5 (May 1975); CPM-7506X1238

Dovator, N. A.—Measurement of transverse relaxation time T_2 of optically oriented He^4 with an oscillator magnetometer —N. A. Dovator, R. A. Zhitnikov, and P. P. Kuleshov. 19(12), 1608–9 (Jun. 1975); CPM-7508X0482

Dovgopol, S. P.—Linear transient response of a fully ionized plasma in a pulsed electric field —V. V. Istomin, S. P. Sher, and S. P. Dovgopol. 19(7), 963–4 (Jan. 1975); CPM-7503X0851

Dovzhenko, V. A.—Effect of ion current on the measurement of the electron energy distribution function by the second-derivative method —V. A. Dovzhenko, A. P. Ershov, and G. S. Solntsev. 19 (4), 538–9 (Oct. 1974); CPM-7412X0322

Drozhdin, A. I.—Proton extraction from the 70-GeV accelerator for the Ludmila liquid-hydrogen chamber (extraction system S) —A. A. Aseev, A. I. Drozhdin, B. A. Zelenov, É. A. Merker, L. L. Moizhes, K. P. Myznikov, A. A. Roshchin, V. M. Tatarenko, M. A. Kholodenko, A. D. Artemov, L. N. Vaulin, V. I. Gordin, I. I. Kovalevskii, V. N. Rozhkov, M. M. Suvorov, A. S. Sudarushkin, and V. I. Chuiko. 19(1), 70–6 (Jul. 1974); CPM-7407X1582

Druzhinina, L. V.—Crystal defects of heterostructures of AlAs–GaAs solid solutions and effect on the characteristics of injection lasers —L. V. Druzhinina, V. T. Bublik, L. M. Dolginov, P. G. Eliseev, M. P. Kerbelev, V. B. Osvenskii, I. Z. Pinsker, and M. G. Shumskii. 19(7), 935–9 (Jan. 1975); CPM-7503X0823

Dryakhlushin, V. F.—Surface waves in periodic plasma systems —V. F. Dryakhlushin and Yu. A. Romanov. 19(7), 883–6 (Jan. 1975); CPM-7503X0771

Dubinskii, V. E.—Extrapolation of the Langmuir S-curve to cesium pressures of 10–100 torr —V. E. Dubinskii and S. Ya. Lebedev. 19 (1), 81–3 (Jul. 1974); CPM-7407X1593

Dubovoi, L. V.—Interaction of intense laser radiation with solid targets —L. V. Dubovoi, V. D. Dyatlov, V. I. Kryzhanovskii, A. A. Mak, R. N. Medvedev, A. N. Popytaev, V. A. Serebryakov, V. N. Sizov, and A. D. Starikov. 19(11), 1477–9 (May 1975); CPM-7506X1231

Dushin, L. A.—Modulation of microwaves by density fluctuations in a plasma —L. A. Dushin, A. V. Serikov, A. I. Skibenko, E. V. Krivorukov, and I. P. Fomin. 19(9), 1163–7 (Mar. 1975); CPM-7505X0585

D'yachenko, V. V.—Role of collisions in plasma absorption of electromagnetic waves near the lower hybrid —B. V. Galaktionov, V. V. D'yachenko, M. M. Larionov, and O. N. Shcherbinin. 19(4), 459–62 (Oct. 1974); CPM-7412X0243

Dyatlov, V. D.—Interaction of intense laser radiation with solid targets —L. V. Dubovoi, V. D. Dyatlov, V. I. Kryzhanovskii, A. A. Mak, R. N. Medvedev, A. N. Popytaev, V. A. Serebryakov, V. N. Sizov, and A. D. Starikov. 19(11), 1477–9 (May 1975); CPM-7506X1231

Dyatlov, V. G.—Magnetic field in a θ pinch with an axial conductor —Ya. F. Volkov, V. G. Dyatlov, and N. I. Mitina. 19(3), 323–5 (Sep. 1974); CPM-7412X1009

—Optical investigation of a turbulent plasma —Ya. F. Volkov, V. G. Dyatlov, and N. I. Mitina. 19(7), 905–8 (Jan. 1975); CPM-7503X0793

Dzhavakhishvili, D. I.—Longitudinal oscillations in an ultrarelativistic electron plasma —D. I. Dzhavakhishvili. 19(1), 115 (Jul. 1974); CPM-7407X1627

—Ion-acoustic instability of a fully ionized ultrarelativistic plasma in an electric field —D. I. Dzhavakhishvili. 19(7), 959–60 (Jan. 1975); CPM-7503X0847

E

Éfendiev, A. Z.—Behavior of molten salts in strong electric fields —A. Z. Éfendiev, O. M. Shabanov, S. M. Gadzhiev, and S. M. Tagirov. 19(6), 820–3 (Dec. 1974); CPM-7501X0820

Egorenkov, V. D.—High-frequency instabilities in an inhomogeneous, anisotropic finite-β plasma —V. D. Egorenkov and A. I. Pyatak. 19(9), 1160–2 (Mar. 1975); CPM-7505X0582

Egorov, N. P.—Mass-spectrometer study of the ion composition of a glow discharge —N. P. Egorov and V. N. Komarov. 19(8), 1100–2 (Feb. 1975); CPM-7504X1524

Egorov, N. V.—Preservation of semiconductor field-emission cathodes —N. V. Egorov, G. N. Fursei, and M. K. El'Nimr. 19(5), 709 (Nov. 1974); CPM-7501X0503

Elesin, V. F.—Recombination in an expanding plasma —Yu. A. Bykovskii, N. N. Degtyarenko, V. F. Elesin, V. E. Kondrashov, E. E. Lovetskii, A. N. Polyanichev, and V. S. Fetisov. 19(1), 43–8 (Jul. 1974); CPM-7407X1555

Elfimov, A. G.—Excitation of Alfvén waves in decay instabilities —A. G. Elfimov and F. M. Nekrasov. 19(1), 9–11 (Jul. 1974); CPM-7407X1521

Eliseev, P. G.—Crystal defects of heterostructures of AlAs–GaAs solid solutions and effect on the characteristics of injection lasers —L. V. Druzhinina, V. T. Bublik, L. M. Dolginov, P. G. Eliseev, M. P. Kerbelev, V. B. Osvenskii, I. Z. Pinsker, and M. G. Shumskii. 19(7), 935–9 (Jan. 1975); CPM-7503X0823

El'Nimr, M. K.—Preservation of semiconductor field-emission cathodes —N. V. Egorov, G. N. Fursei, and M. K. El'Nimr. 19(5), 709 (Nov. 1974); CPM-7501X0503

Emets, Yu. P.—Conductivity of a medium with inhomogeneous inclusions in a magnetic field —Yu. P. Emets. 19(5), 586–8 (Nov. 1974); CPM-7501X0380

Énder, A. Ya.—Effect of electron-atom collisions on electron motion in a gas diode —V. I. Babanin and A. Ya. Énder. 19(1), 60–5 (Jul. 1974); CPM-7407X1572

Épshtein, É. M.—Resonant amplification of an image potential by an electromagnetic wave —Yu. I. Balkarei and É. M. Épshtein. 19(6), 843–4 (Dec. 1974); CPM-7501X0843

Eremeev, M. A.—Thermionic emission properties of zirconium, hafnium, and titanium nitrides in cesium vapor —M. A. Eremeev, V. S. Neshpor, A. B. Novikov, E. M. Stefanovskaya, and V. P. Fedorinov. 19(10), 1337–41 (Apr. 1975); CPM-7506X0271

Ermakov, G. A.—Calculation of permittivity of an inhomogeneous dielectric by a variational method —G. A. Ermakov, A. G. Fokin, and T. D. Shermergor. 19(2), 157–60 (Aug. 1974); CPM-7408X1421

—Calculation of bounds for the effective permittivity of an inhomogeneous dielectric —G. A. Ermakov, A. G. Fokin, and T. D. Shermergor. 19(2), 161–5 (Aug. 1974); CPM-7408X1425

Ermolin, V. V.—Effect of plasma parameters on emission in an ion laser —I. E. Sakharov, V. V. Ermolin, and S. V. Shatalin. 19(8), 1081–4 (Feb. 1975); CPM-7504X1505

Ershov, A. P.—Effect of ion current on the measurement of the electron energy distribution function by the second-derivative method —V. A. Dovzhenko, A. P. Ershov, and G. S. Solntsev. 19 (4), 538–9 (Oct. 1974); CPM-7412X0322

Evdokimov, O. B.—Ionization of a gas-discharge gap by fast electrons —O. B. Evdokimov and A. P. Yalovets. 19(1), 138–9 (Jul. 1974); CPM-7407X1650

Evteev, V. N.—Axially symmetric neutralized electron beam —G. N. Vyalov, V. N. Evteev, Yu. M. Zolotaikin, and K. N. Ul'yanov. 19 (11), 1414–7 (May 1975); CPM-7506X1168

F

Fainberg, Ya. B.—Launching and propagation of regular nonlinear waves in an anisotropic plasma-filled waveguide —V. I. Kurilko, A. P. Tols-toluzhskii, and Ya. B. Fainberg. 19(5), 622–7 (Nov. 1974); CPM-7501X0416

—Interaction of a hollow electron beam with a plasma —N. M. Zemlyanskii, A. K. Berezin, Ya. B. Fainberg, L. I. Bolotin, and S. S. Krivulya. 19(12), 1547–8 (Jun. 1975); CPM-7508X0421

Fainshtein, S. M.—Nonlinear plasma waves and ion-acoustic waves in an isotropic plasma —V. Sh. Livadonov and S. M. Fainshtein. 19(1), 28–30 (Jul. 1974); CPM-7407X1540

Farenik, V. I.—Plasma decay instability in crossed fields —V. I. Farenik, V. V. Vlasov, A. M. Rozhkov, and A. A. Kozharin. 19(8), 1116–7 (Feb. 1975); CPM-7504X1540

—Ion energy spectra and collective effects in a Penning ion source —V. I. Farenik, V. V. Vlasov, A. M. Rozhkov, and A. A. Kozharin. 19(9), 1258–9 (Mar. 1975); CPM-7505X0680

Fedichev, S. V.—Titanium adsorption on tungsten —Yu. K. Ustinov and S. V. Fedichev. 19(8), 1118–9 (Feb. 1975); CPM-7504X1542

Fedorenko, V. N.—Generation of Bernstein modes in beam-plasma system —V. N. Fedorenko. 19(2), 171–4 (Aug. 1974); CPM-7408X1435

Fedorinov, V. P.—Thermionic emission properties of zirconium, hafnium, and titanium nitrides in cesium vapor —M. A. Eremeev, V. S. Neshpor, A. B. Novikov, E. M. Stefanovskaya, and V. P. Fedorinov. 19(10), 1337–41 (Apr. 1975); CPM-7506X0271

Fedorov, A. A.—Frequency-doubling single-mode laser for picosecond pulses —A. M. Bonch-Bruevich, A. M. Tkachuk, and A. A. Fedorov. 19(4), 549–51 (Oct. 1974); CPM-7412X0333

Fedorov, V. I.—Absolute decay instability of low-frequency waves in an inhomogeneous plasma —A. D. Piliya and V. I. Fedorov. 19(5), 686 (Nov. 1974); CPM-7501X0480

Fedyakova, V. P.—Stabilization of MHD instabilities by a high-frequency current in a straight system —V. P. Fedyakova. 19(1), 16–9 (Jul. 1974); CPM-7407X1528

Ferleger, V. Kh.—Doppler profile of an atomic line to the differential excitation cross section —É. S. Parilis and V. Kh. Ferleger. 19(10), 1367–70 (Apr. 1975); CPM-7506X0301

Fersman, I. A.—Cumulative destruction of transparent dielectrics in repeated laser irradiation —L. D. Khazov, I. A. Fersman, and V. Yu. Bortniker. 19(9), 1256–7 (Mar. 1975); CPM-7505X0678

Fetisov, V. S.—Recombination in an expanding plasma —Yu. A. Bykovskii, N. N. Degtyarenko, V. F. Elesin, V. E. Kondrashov, E. E. Lovetskii, A. N. Polyanichev, and V. S. Fetisov. 19(1), 43–8 (Jul. 1974); CPM-7407X1555

—Expansion of a recombining plasma in vacuum —E. E. Lovetskii, A. N. Polyanichev, and V. S. Fetisov. 19(5), 647–50 (Nov. 1974); CPM-7501X0441

Fidel'skaya, R. P.—Beam focusing in an accelerator with inductive energy storage —V. A. Glukhikh, O. A. Gusev, E. G. Komar, V. S. Kuznetsov, M. P. Svin'in, and R. P. Fidel'skaya. 19(3), 366–7 (Sep. 1974); CPM-7412X1052

—Estimate of the angular divergence in intense electron beams —V. S. Kuznetsov, Yu. P. Vakhrushin, O. L. Komarov, and R. P. Fidel'skaya. 19(7), 868–70 (Jan. 1975); CPM-7503X0756

Fikhmanas, R. F.—Upper and lower limits on the capacitance of a plane capacitor —R. F. Fikhmanas and P. Sh. Fridberg. 19(5), 683–4 (Nov. 1974); CPM-7501X0477

Filippov, Yu. F.—Reflection of finite amplitude electromagnetic waves from a semiconductor plasma —Yu. F. Filippov. 19(5), 603–6 (Nov. 1974); CPM-7501X0397

Fisher, V. I.—Effect of loss on electron avalanches in optical breakdown —V. I. Fisher. 19(8), 1050–2 (Feb. 1975); CPM-7504X1474

Fishkova, T. Ya.—Fifth-order spherical aberration in focusing and correcting quadrupole—octupole systems —Ya. G. Lyubchik and T. Ya. Fishkova. 19(11), 1403–7 (May 1975); CPM-7506X1157

—Electron-optical properties of postdeflection quadrupole lenses —T. Ya. Fishkova. 19(12), 1618–9 (Jun. 1975); CPM-7508X0492

Fogel', Ya. M.—Elimination of carbon impurities from platinum by heating in an oxygen atmosphere —L. P. Rekova, V. V. Mozgin, L. N. Zvyagintseva, V. N. Bondarenko, and Ya. M. Fogel'. 19(11), 1465–7 (May 1975); CPM-7506X1219

—Mass spectrum of secondary ions ejected from the surface of a single crystal of gallium arsenide by argon ions —A. G. Koval', V. V. Bobkov, Yu. A. Klimovskii, S. S. Strel'chenko, V. V. Shubina, V. V. Lebedev, and Ya. M. Fogel'. 19(12), 1587–9 (Jun. 1975); CPM-7508X0461

Fokin, A. G.—Calculation of permittivity of an inhomogeneous dielectric by a variational method —G. A. Ermakov, A. G. Fokin, and T. D. Shermergor. 19(2), 157–60 (Aug. 1974); CPM-7408X1421

—Calculation of bounds for the effective permittivity of an inhomogeneous dielectric —G. A. Ermakov, A. G. Fokin, and T. D. Shermergor. 19(2), 161–5 (Aug. 1974); CPM-7408X1425

Fomin, I. P.—Spatial characteristics and loss of plasma produced by an electron beam in a magnetic trap —M. Yu. Bredikhin, A. I. Maslov, A. I. Skibenko, E. I. Skibenko, I. P. Fomin, and V. B. Yuferov. 19(1), 49–52 (Jul. 1974); CPM-7407X1561

—Plasma equilibrium and confinement in a poloidal heliotron configuration. II —V. G. Zykov, V. I. Karpukhin, Yu. F. Lonin, N. N. Podteregera, N. I. Rudnev, A. Y. Skibenko, V. T. Tolok, and I. P. Fomin. 19(8), 1069–72 (Feb. 1975); CPM-7504X1493

—Modulation of microwaves by density fluctuations in a plasma —L. A. Dushin, A. V. Serikov, A. I. Skibenko, E. V. Krivorukov, and I. P. Fomin. 19(9), 1163–7 (Mar. 1975); CPM-7505X0585

Freiberg, G. N.—Emission parameters of a field-emission cathode —G. N. Freiberg. 19(10), 1352–4 (Apr. 1975); CPM-7506X0286

Fridberg, P. Sh.—Upper and lower limits on the capacitance of a plane capacitor —R. F. Fikhmanas and P. Sh. Fridberg. 19(5), 683–4 (Nov. 1974); CPM-7501X0477

Fridman, A. A.—Steady-state electron density in photoionizion of aerosol particles —G. V. Karachevtsev and A. A. Fridman. 19(11), 1471–3 (May 1975); CPM-7506X1225

Fridrikhov, S. A.—End current in a magnetron with a secondary-emission cathode —G. G. Sominskii, S. A. Fridrikhov, O. Yu. Tsybin, and A. P. Karizhskii. 19(3), 378–81 (Sep. 1974); CPM-7412X1064

Frolov, V. V.—Radiation yield of ions in liquid dielectrics as a function of temperature and radiation energy —V. I. Ivanov, E. D. Kleshchenko, Yu. P. Sukhanovskii, and V. V. Frolov. 19(11), 1468–70 (May 1975); CPM-7506X1222

Fromzel', V. A.—Unidirectional cw oscillation in a solid state ring laser with a return mirror —A. A. Mak, V. I. Ustyugov, V. A. Fromzel', and M. M. Khaleev. 19(4), 552–3 (Oct. 1974); CPM-7412X0336

—Lasing properties of Yb^{3+} and Er^{3+} glass laser pumped by a laser —V. N. Kalinin, A. A. Mak, D. S. Prilezhaev, and V. A. Fromzel'. 19(6), 835–6 (Dec. 1974); CPM-7501X0835

Fursei, G. N.—Preservation of semiconductor field-emission cathodes —N. V. Egorov, G. N. Fursei, and M. K. El'Nimr. 19(5), 709 (Nov. 1974); CPM-7501X0503

—Emission characteristics of an explosive gallium cathode —G. N. Fursei and V. M. Zhukov. 19(6), 804–7 (Dec. 1974); CPM-7501X0804

G

Gabovich, M. D.—Gas focusing of a negative-ion beam —M. D. Gabovich, A. P. Naida, I. M. Protsenko, L. S. Simonenko, and I. A. Soloshenko. 19(4), 546–7 (Oct. 1974); CPM-7412X0330

—Ion focusing of an electron beam in deep melting of a metal —M. D. Gabovich, V. P. Kovalenko, O. A. Metallov, O. K. Nazarenko, and S. K. Pats'ora. 19(7), 973–4 (Jan. 1975); CPM-7503X0861

—Measurement of ion density by the dispersion relation for an ion-beam plasma —M. D. Gabovich, L. P. Katsubo, and I. A. Soloshenko. 19(11), 1412–3 (May 1975); CPM-7506X1166

—Plasma synthesis by injection of an electron beam through an ion source —V. F. Virko, M. D. Gabovich, G. S. Kirichenko, and O. K. Nazarenko. 19(11), 1418–20 (May 1975); CPM-7506X1172

—Loss of neutralization for a stable neutralized ion beam —M. D. Gabovich. 19(11), 1502–3 (May 1975); CPM-7506X1256

Gadzhiev, S. M.—Behavior of molten salts in strong electric fields —A. Z. Éfendiev, O. M. Shabanov, S. M. Gadzhiev, and S. M. Tagirov. 19(6), 820–3 (Dec. 1974); CPM-7501X0820

Gak, E. Z.—Possible electrohydrodynamic effects in electrolytes —E. Z. Gak, É. Kh. Rokhinson, and N. F. Bondarenko. 19(5), 676–7 (Nov. 1974); CPM-7501X0470

Gal', V. V.—Electrical conductivity of a pseudoliquefied layer in an electric field —V. V. Gal', V. I. Konov, and K. A. Nikitin. 19(9), 1214–5 (Mar. 1975); CPM-7505X0636

Galaktionov, B. V.—Role of collisions in plasma absorption of electromagnetic waves near the lower hybrid —B. V. Galaktionov, V. V. D'yachenko, M. M. Larionov, and O. N. Shcherbinin. 19(4), 459–62 (Oct. 1974); CPM-7412X0243

—Generation of drift waves by an rf field near the lower hybrid frequency —Yu. F. Baranov, D. G. Bulyginskii, M. I. Vil'dzhyunas, B. V. Galaktionov, and N. V. Shustova. 19(6), 732–5 (Dec. 1974); CPM-7501X0732

Galaktionova, N. M.—Parasitic amplitude modulation of a stabilized Nd^{3+}:YAG laser —N. M. Galaktionova, A. A. Mak, and A. P. Khyuppenen. 19(4), 486–90 (Oct. 1974); CPM-7412X0270

—Solid-state laser with externally forced *Q* switching —N. M. Galaktionova, A. A. Mak, and A. P. Khyuppenen. 19(9), 1174–6 (Mar. 1975); CPM-7505X0596

Gall', L. N.—Monte Carlo analysis of ion scattering in a mass spectrometer —M. L. Aleksandrov, L. N. Gall', and N. S. Pliss. 19(6), 817–9 (Dec. 1974); CPM-7501X0817

Garbuzov, D. Z.–Electroluminescence spectra of the red luminescent diodes p–$Al_xGa_{1-x}As$—n–$AlyGa_{1-y}As(y>x)$ —V. M. Busov, D. Z. Garbuzov, A. T. Gorelenok, and D. S. Kop'ev. 19(12), 1598–600 (Jun. 1975); CPM-7508X0472

Gavrilov, N. M.—Self-excited waveguide buncher —N. M. Gavrilov and A. V. Nesterovich. 19(8), 1085–6 (Feb. 1975); CPM-7504X1509

Gel'man, Yu. A.—Composition of adsorbing and desorbing fluxes —Yu. A. Gel'man, V. I. Mikhailov, V. F. Vinogradov, and Yu. N. Lyubitov. 19(10), 1355–8 (Apr. 1975); CPM-7506X0289

Georgievskii, A. V.—Magnetic topography of toroidal systems —M. N. Skoblik, V. E. Ziser, A. V. Georgievskii, and V. G. Peletminskaya. 19(10), 1277–80 (Apr. 1975); CPM-7506X0211

Gerasimov, E. I.—Aberrations in a straight ion–optical accelerator —E. I. Gerasimov, A. I. Solnyshkov, and G. V. Tarvid. 19(1), 131–3 (Jul. 1974); CPM-7407X1643

Gerasimov, L. S.—Explosion driven magnetic generator with a matched inductive load —L. S. Gerasimov. 19(9), 1226–30 (Mar. 1975); CPM-7505X0648

Gertsenshtein, M. E.—Electron repulsion in a time–resolving electron–optical image converter —M. M. Butslov and M. E. Gertsenshtein. 19(1), 129–30 (Jul. 1974); CPM-7407X1641

Ginzburg, V. E.—Optimization of the paraxial asymptotic electric field in electron–optical systems —V. E. Ginzburg and V. N. Danilov. 19(3), 407–9 (Sep. 1974); CPM-7412X1093

Gladush, G. G.—Model for the low–voltage arc. I. Stationary solution —Yu. Yu. Abramov and G. G. Gladush. 19(6), 745–7 (Dec. 1974); CPM-7501X0745

—Model for the low–voltage arc. II. Stability —Yu. Yu. Abramov and G. G. Gladush. 19(6), 748–50 (Dec. 1974); CPM-7501X0748

Glagolev, V. M.—Anisotropic plasma heating near the lower hybrid frequency —V. M. Glagolev, V. V. Martynenko, and Yu. V. Skosyrev. 19(12), 1543–6 (Jun. 1975); CPM-7508X0417

Glasko, V. B.—Production of an ion beam by a magnetic system with opposed fields —V. B. Glasko, A. G. Sveshnikov, and N. N. Semashko. 19(2), 201–5 (Aug. 1974); CPM-7408X1465

Glatman, R. A.—Propagation of shock waves in inhomogeneous media —R. A. Glatman. 19(11), 1390–2 (May 1975); CPM-7506X1144

—Theory of nonequilibrium shock waves —R. A. Glatman and I. V. Ioffe. 19(11), 1482–3 (May 1975); CPM-7506X1236

Glebovskii, V. G.—Impurities and crystal dimensions in zone refining —V. G. Glebovskii and B. M. Shipilevskii. 19(9), 1231–5 (Mar. 1975); CPM-7505X0653

Glikman, L. G.—Charged–particle motion in a dipole magnetic field —L. G. Glikman. 19(4), 435–40 (Oct. 1974); CPM-7412X0219

—Symmetric multielectrode tubular electrostatic lenses —L. G. Glikman, V. M. Kel'man, and M. Sh. Nurmanov. 19(5), 680–2 (Nov. 1974); CPM-7501X0474

Glukhikh, V. A.—Beam focusing in an accelerator with inductive energy storage —V. A. Glukhikh, O. A. Gusev, E. G. Komar, V. S. Kuznetsov, M. P. Svin'in, and R. P. Fidel'skaya. 19(3), 366–7 (Sep. 1974); CPM-7412X1052

—High–current pulsed electron accelerator with an annular beam —M. I. Avramenko, V. A. Glukhikh, O. A. Gusev, E. G. Komar, O. L. Komarov, V. S. Kuznetsov, A. S. Perlin, and M. P. Svin'in. 19 (3), 368–70 (Sep. 1974); CPM-7412X1054

—Inductive energy storage in pulsed accelerators —V. A. Glukhikh, O. A. Gusev, E. G. Komar, and M. P. Svin'in. 19(5), 660–1 (Nov. 1974); CPM-7501X0454

Gogadze, G. A.—Shielding properties of superconducting shields —S. I. Bondarenko, S. S. Vinogradov, G. A. Gogadze, S. S. Perepelkin, and V. I. Sheremet. 19(6), 824–8 (Dec. 1974); CPM-7501X0824

Gokhfel'd, V. L.—Cell for forming electron beams of arbitrary shape in a high-voltage gaseous discharge —I. V. Vagner, É. I. Bolgov, V. F. Grakun, V. L. Gokhfel'd, and V. A. Kudlai. 19(8), 1042–5 (Feb. 1975); CPM-7504X1466

Golobovskii, Yu. B.—Theory of the positive column in neon —Yu. B. Golobovskii, Yu. M. Kagan, and R. I. Lyagushchenko. 19(3), 335–9 (Sep. 1974); CPM-7412X1021

Golovanivskii, K. S.—Radio-frequency absorption in a plasma confined by rf plugs —K. S. Golovanivskii, V. D. Dougar-Jabon, and L. A. Pokhmel'nykh. 19(11), 1484–5 (May 1975); CPM-7506X1238

Golovanov, Yu. P.—Scattering of an electron beam in a straight *dc* turbulent plasma —Yu. P. Golovanov, L. P. Zakatov, A. S. Kingsep, and A. G. Plakhov. 19(8), 1046–9 (Feb. 1975); CPM-7504X1470

Golovin, V. N.—Control of output energy in linear electron accelerators —V. N. Golovin and N. P. Sobenin. 19(7), 932–4 (Jan. 1975); CPM-7503X0820

Golubentsev, A. F.—Shot noise in a thermionic cathode —A. F. Golubentsev and A. S. Shapovalov. 19(10), 1345–6 (Apr. 1975); CPM-7506X0279

Gorban', A. N.—Atomic recombination on a solid surface —V. P. Pinchuk, A. N. Gorban', and V. G. Kornich. 19(6), 808–10 (Dec. 1974); CPM-7501X0808

Gordiets, B. F.—Gas cooling in transmission of high–power CO_2 laser radiation through the atmosphere —B. F. Gordiets, A. I. Osipov, and R. V. Khokhlov. 19(5), 669–72 (Nov. 1974); CPM-7501X0463

Gordin, V. I.—Proton extraction from the 70–GeV accelerator for the Ludmila liquid–hydrogen chamber (extraction system S) —A. A. Aseev, A. I. Drozhdin, B. A. Zelenov, É. A. Merker, L. L. Moizhes, K. P. Myznikov, A. A. Roshchin, V. M. Tatarenko, M. A. Kholodenko, A. D. Artemov, L. N. Vaulin, V. I. Gordin, I. I. Kovalevskii, V. N. Rozhkov, M. M. Suvorov, A. S. Sudarushkin, and V. I. Chuiko. 19(1), 70–6 (Jul. 1974); CPM-7407X1582

Gorelenok, A. T.—Electroluminescence spectra of the red luminescent diodes p–$Al_xGa_{1-x}As$—n–$AlyGa_{1-y}As(y>x)$ —V. M. Busov, D. Z. Garbuzov, A. T. Gorelenok, and D. S. Kop'ev. 19 (12), 1598–600 (Jun. 1975); CPM-7508X0472

Gorelik, M. S.—Propagation and stability of large amplitude ionization waves —M. S. Gorelik and L. D. Tsendin. 19(7), 880–2 (Jan. 1975); CPM-7503X0768

Gorokhov, Yu. A.—Nonlinear spherical aberrations and thermoelastic stresses in thermal self–focusing —A. A. Vigasin, Yu. A. Gorokhov, A. P. Sukhorukov, and A. M. Khachatryan. 19(5), 673–5 (Nov. 1974); CPM-7501X0467

Goryachev, D. N.—Characteristics of diffraction gratings obtained by photoetching of semiconductor surfaces —L. V. Belyakov, D. N. Goryachev, M. N. Mizerov, and E. L. Portnoi. 19(6), 837–8 (Dec. 1974); CPM-7501X0837

Grakun, V. F.—Cell for forming electron beams of arbitrary shape in a high-voltage gaseous discharge —I. V. Vagner, É. I. Bolgov, V. F. Grakun, V. L. Gokhfel'd, and V. A. Kudlai. 19(8), 1042–5 (Feb. 1975); CPM-7504X1466

Grechikhin, L. I.—Motion of charged particles in a nonneutral plasma —E. N. Agafonova and L. I. Grechikhin. 19(11), 1488–9 (May 1975); CPM-7506X1242

Gridasov, V. I.—Efficiency of internal targets in the accelerator at the Institute of High–Energy Physics —V. I. Gridasov, K. P. Myznikov, and V. N. Chepegin. 19(7), 922–5 (Jan. 1975); CPM-7503X0810

Grigor'ev, V. P.—Nonmonoenergetic relativistic electron beam in a bounded collisional plasma —V. P. Grigor'ev and N. S. Shulaev. 19(1), 20–1 (Jul. 1974); CPM-7407X1532

Grin', Yu. I.—N_2O–N_2–He gasdynamic laser —Yu. I. Grin' and V. G. Testov. 19(7), 975 (Jan. 1975); CPM-7503X0863

Grinberg, G. A.—Two–dimensional diffraction on a system of straight segments (shields) —G. A. Grinberg. 19(5), 581–5 (Nov. 1974); CPM-7501X0375

—Heat transport problems with time-varying boundary conditions or moving boundaries (Stefan problem) —G. A. Grinberg. 19(10), 1267–72 (Apr. 1975); CPM-7506X0201

Grishaev, I. A.—Self-acceleration of an intense electron beam —I. A. Grishaev, A. N. Dedik, V. V. Zakutin, I. I. Magda, Yu. V. Tkach, and A. M. Shenderovich. 19(8), 1087–9 (Feb. 1975); CPM-7504X1511

Grishin, S. D.—Ion-optical system for shaping high-current ion beams —S. D. Grishin, V. F. Kuzovlev, R. V. Orlov, and S. N. Ogorodnikov. 19(11), 1462–4 (May 1975); CPM-7506X1216

Gryzlov, A. I.—Linear accelerator for beam injection into a slowly rising magnetic field —D. G. Borisov, A. I. Gryzlov, V. M. Levin, and A. V. Ryabtsov. 19(4), 509–10 (Oct. 1974); CPM-7412X0293

Gubarev, V. F.—Distributed systems for feedback control of a tokamak plasma —V. F. Gubarev and Yu. I. Samoilenko. 19(4), 463–7 (Oct. 1974); CPM-7412X0247

Gulyaev, S. N.—Frequency locking in a 3.39μ laser —E. Yu. Andreeva, S. N. Gulyaev, and D. K. Terekhin. 19(12), 1620–1 (Jun. 1975); CPM-7508X0494

Gurevich, G. L.—Magnetoacoustic transducer based on the domain structure of a ferromagnetic material —G. L. Gurevich and G. A. Vul'gal'ter. 19(1), 154–5 (Jul. 1974); CPM-7407X1666

Gurevich, M. A.—Rate for evaporation of a liquid into vacuum —A. P. Andreev and M. A. Gurevich. 19(3), 396–401 (Sep. 1974); CPM-7412X1082

Gurevich, S. B.—Reversibility of chalcogenide materials in holography —S. B. Gurevich, N. N. Il'yashenko, B. T. Kolomiets, V. M. Lyubin, and M. V. Sukharev. 19(1), 152–3 (Jul. 1974); CPM-7407X1664

Gusev, O. A.—Beam focusing in an accelerator with inductive energy storage —V. A. Glukhikh, O. A. Gusev, E. G. Komar, V. S. Kuznetsov, M. P. Svin'in, and R. P. Fidel'skaya. 19(3), 366–7 (Sep. 1974); CPM-7412X1052

—High–current pulsed electron accelerator with an annular beam —M. I. Avramenko, V. A. Glukhikh, O. A. Gusev, E. G. Komar, O. L. Komarov, V. S. Kuznetsov, A. S. Perlin, and M. P. Svin'in. 19 (3), 368–70 (Sep. 1974); CPM-7412X1054

—Inductive energy storage in pulsed accelerators —V. A. Glukhikh, O. A. Gusev, E. G. Komar, and M. P. Svin'in. 19(5), 660–1 (Nov. 1974); CPM-7501X0454

—Shaping of voltage pulses by discharging an inductive storage bank with a charged-particle beam —O. A. Gusev, E. G. Komar, V. B. Markov, and E. M. Mellekh. 19(5), 662–3 (Nov. 1974); CPM-7501X0456

Guseva, L. G.—Effect of electron reflection on the voltage-current characteristics of a high-voltage, hollow-cathode, glow discharge —Ya. Ya. Udris, V. A. Chernov, and L. G. Guseva. 19(1), 134–5 (Jul. 1974); CPM-7407X1646

Guseva, M. B.—Efficient ion source —D. Kh. Abdrashitova, V. G. Babaev, and M. B. Guseva. 19(2), 264–6 (Aug. 1974); CPM-7408X1528

Gus'kov, Yu. K.—Effect of selenium and sulfur on the work function of tungsten —N. V. Volkov, Yu. K. Gus'kov, Z. N. Kononova, and Yu. I. Kostikov. 19(1), 144–5 (Jul. 1974); CPM-7407X1656

—Steady-state operation of a surface-ionization thermionic converter —N. V. Volkov, Yu. K. Gus'kov, Yu. I. Kostikov, and V. P. Pashchenko. 19(8), 1129–30 (Feb. 1975); CPM-7504X1553

Gutarev, Yu. V.—Magnetodrift waves in a finite-β plasma —N. M. Ryzhov, V. L. Sizonenko, V. A. Suprunenko, E. A. Sukhomlin, and Yu. V. Gutarev. 19(6), 722–5 (Dec. 1974); CPM-7501X0722

I

Igritskii, A. N.—Aperiodic instability in a plasma gap with external feedback —A. N. Igritskii. 19(6), 719–21 (Dec. 1974); CPM-7501X0719

Il'inskii, V. A.—Laser compensation for thermal distortion in optical pumping —V. K. Zaitsev, V. A. Il'inskii, A. M. Marugin, and V. M. Ovchinnikov. 19(11), 1480–1 (May 1975); CPM-7506X1234

Il'yashenko, N. N.—Reversibility of chalcogenide materials in holography —S. B. Gurevich, N. N. Il'yashenko, B. T. Kolomiets, V. M. Lyubin, and M. V. Sukharev. 19(1), 152–3 (Jul. 1974); CPM-7407X1664

Imas, Ya. A.—Optical characteristics of K-8 glass subject to radiation from a neodymium laser —A. M. Bonch-Bruevich, Ya. A. Imas, V. S. Salyadinov, and A. V. Shatilov. 19(2), 287–9 (Aug. 1974); CPM-7408X1551

—Surface evaporation of a solid transparent dielectric under the action of laser radiation —A. M. Bonch-Bruevich, Ya. A. Imas, A. A. Kovalev, P. S. Kondratenko, and B. I. Makshantsev. 19(11), 1474–6 (May 1975); CPM-7506X1228

Indykul, V. P.—Nonlinear interaction between a monochromatic ion-acoustic wave and a plasma —V. P. Indykul. 19(9), 1157–9 (Mar. 1975); CPM-7505X0579

Ioffe, I. V.—Convection in a liquid dielectric in a longitudinal electric field —I. V. Ioffe and N. V. Kalinin. 19(5), 692 (Nov. 1974); CPM-7501X0486

—Liquid crystals in external fields —I. V. Ioffe. 19(8), 1012–5 (Feb. 1975); CPM-7504X1436

—Theory of nonequilibrium shock waves —R. A. Glatman and I. V. Ioffe. 19(11), 1482–3 (May 1975); CPM-7506X1236

Ionov, N. I.—Displacement of ion-current retardation curves in surface ionization in a strong field —N. I. Ionov. 19(1), 146–7 (Jul. 1974); CPM-7407X1658

Iremashvili, D. V.—Low-frequency oscillations in counter-streaming high-current electron beams —A. F. Timoshenko, D. V. Iremashvili, and Yu. K. Udovichenko. 19(8), 1038–41 (Feb. 1975); CPM-7504X1462

—Wave excitation at half the gyrofrequency in counterstreaming electron beams —A. P. Timoshenko, D. V. Iremashvili, and Yu. K. Udovichenko. 19(12), 1584–6 (Jun. 1975); CPM-7508X0458

Irisova, N. A.—Dielectric properties of foamed ceramics at millimeter wavelengths —N. A. Irisova, G. V. Kozlov, V. E. Mandrusov, B. S. Cherepanov, and I. M. Chernyshev. 19(1), 103–4 (Jul. 1974); CPM-7407X1615

—Temperature dependence of the dielectric permittivity of single-crystal TiO_2 in the submillimeter range —A. A. Volkov, N. A. Irisova, and G. V. Kozlov. 19(4), 567–8 (Oct. 1974); CPM-7412X0351

Istomin, V. V.—Linear transient response of a fully ionized plasma in a pulsed electric field —V. V. Istomin, S. P. Sher, and S. P. Dovgopol. 19(7), 963–4 (Jan. 1975); CPM-7503X0851

Istomin, Ya. N.—Nonlinear instability of a helicon packet in an anisotropic plasma —Ya. N. Istomin and V. I. Karpman. 19(3), 405–6 (Sep. 1974); CPM-7412X1091

—Evolution of monochromatic whistler and plasma-wave packets in a collisionless plasma —Ya. N. Istomin. 19(4), 529–30 (Oct. 1974); CPM-7412X0313

Ivakin, B. A.—Temperature dependence of trace diffusion coefficients of certain gases —A. É. Loiko, B. A. Ivakin, and P. E. Suetin. 19 (3), 434 (Sep. 1974); CPM-7412X1120

Ivanov, A. P.—Measurement of statistical parameters of scattering particles in laminar flow by Doppler spectroscopy —A. P. Ivanov, A. Ya. Khairullina, and A. P. Chaikovski. 19(2), 267–70 (Aug. 1974); CPM-7408X1531

Ivanov, M. I.—Acceleration of plasma electrons in strong electric fields —Z. A. Al'bikov, M. I. Ivanov, V. I. Kazacha, O. V. Kozlov, V. D. Rusanov, and S. S. Sobolev. 19(11), 1498–9 (May 1975); CPM-7506X1252

Ivanov, S. A.—Development of an inhibited glow discharge —Yu. A. Bystrov, S. A. Ivanov, and Yu. F. Radchenko. 19(11), 1447–8 (May 1975); CPM-7506X1201

Ivanov, V. G.—Possible use of the schlieren method to measure characteristics of turbulence —V. G. Ivanov. 19(3), 429–31 (Sep. 1974); CPM-7412X1115

—Statistical characteristics of the turbulent wake behind a supersonic sphere —V. G. Ivanov, G. I. Mishin, and S. N. Palkin. 19(4), 543–5 (Oct. 1974); CPM-7412X0327

Ivanov, V. I.—Radiation yield of ions in liquid dielectrics as a function of temperature and radiation energy —V. I. Ivanov, E. D. Kleshchenko, Yu. P. Sukhanovskii, and V. V. Frolov. 19(11), 1468–70 (May 1975); CPM-7506X1222

Ivanov, V. P.—Gas-kinetic removal of neutral molecules from an ion beam —V. P. Ivanov. 19(2), 239–42 (Aug. 1974); CPM-7408X1503

Izokh, V. V.—Aberrations in systems with plane and spherical detection apertures —V. V. Izokh, A. V. Sergeev, and I. Yu. Shmidov. 19(9), 1177–80 (Mar. 1975); CPM-7505X0599

K

Kagan, M. B.—Dependence of the basic parameters of $Al_xGa_{1-x}As$—GaAs solar converters on temperature and optical intensity —E. B. Vinogradova, M. B. Kagan, N. S. Koroleva, T. L. Lyubashevskaya, and T. A. Nuller. 19(10), 1378–81 (Apr. 1975); CPM-7506X0312

Kagan, Yu. M.—Effect of cathode emission on the threshold for striations —N. A. Vorob'eva, Yu. M. Kagan, V. M. Milenin, and A. Kh. Muradov. 19(1), 117–8 (Jul. 1974); CPM-7407X1629

—Electron energy distribution in the afterglow. I —A. B. Blagoev, Yu. M. Kagan, N. B. Kolokolov, and R. I. Lyagushchenko. 19(2), 211–4 (Aug. 1974); CPM-7408X1475

—Electron energy distribution in the afterglow. II —A. B. Blagoev, Yu. M. Kagan, N. B. Kolokolov, and R. I. Lyagushchenko. 19(2), 215–9 (Aug. 1974); CPM-7408X1479

—Electron energy distribution in a high-freqeuncy discharge in an axial magnetic field —S. D. Vagner, V. A. Virolainen, Yu. M. Kagan, and T. A. Kalmykova. 19(2), 290–1 (Aug. 1974); CPM-7408X1554

—Theory of the positive column in neon —Yu. B. Golobovskii, Yu. M. Kagan, and R. I. Lyagushchenko. 19(3), 335–9 (Sep. 1974); CPM-7412X1021

—High-frequency discharge in a mercury—helium mixture —S. D. Vagner, Yu. M. Kagan, A. I. Konstantinov, and I. S. Niskonen. 19 (7), 898–900 (Jan. 1975); CPM-7503X0786

—Electron energy distribution in a constricted, low-pressure hydrogen discharge —M. A. Abroyan, Yu. M. Kagan, N. B. Kolokolov, and B. P. Lavrov. 19(11), 1492–3 (May 1975); CPM-7506X1246

—Gas temperature in the positive column of a medium-β helium discharge —Yu. M. Kagan and K. K. Paskalev. 19(12), 1601–3 (Jun. 1975); CPM-7508X0475

—Temperature and electron density in the positive column of a medium-pressure helium discharge —Yu. M. Kagan and K. K. Paskalev. 19(12), 1604–5 (Jun. 1975); CPM-7508X0478

Kakichashvili, Sh. D.—Holography of raster objects —Sh. D. Kakichashvili. 19(5), 696–7 (Nov. 1974); CPM-7501X0490

Kaladze, T. D.—Excitation of electromagnetic ion cyclotron waves by fast ions —T. D. Kaladze, D. G. Lominadze, and K. N. Stepanov. 19(2), 175–6 (Aug. 1974); CPM-7408X1439

Kalashnikov, V. K.—Low-pressure self-maintained discharge with suppressed electron drift. I —V. K. Kalashnikov and Yu. V. Sanochkin. 19(12), 1549–53 (Jun. 1975); CPM-7508X0423

—Low-pressure self-maintained discharge with suppressed electron drift. II —Yu. V. Sanochkin and V. K. Kalashnikov. **19**(12), 1554–8 (Jun. 1975); CPM-7508X0428

Kalinichenko, A. I.—Excitation of thermoelastic vibrations of a thin plate by a beam of fast charged particles —A. I. Kalinichenko and V. T. Lazurik-Él'tsufin. **19**(10), 1382–3 (Apr. 1975); CPM-7506X0316

Kalinin, N. V.—Convection in a liquid dielectric in a longitudinal electric field —I. V. Ioffe and N. V. Kalinin. **19**(5), 692 (Nov. 1974); CPM-7501X0486

Kalinin, V. N.—Lasing properties of Yb^{3+} and Er^{3+} glass laser pumped by a laser —V. N. Kalinin, A. A. Mak, D. S. Prilezhaev, and V. A. Fromzel'. **19**(6), 835–6 (Dec. 1974); CPM-7501X0835

Kalmykova, S. S.—Conversion of regular charge–density waves in a inhomogeneous plasma —S. S. Kalmykova and A. P. Tolstoluzhskii. **19**(4), 455–8 (Oct. 1974); CPM-7412X0239

Kalmykova, T. A.—Electron energy distribution in a high–freqeuncy discharge in an axial magnetic field —S. D. Vagner, V. A. Virolainen, Yu. M. Kagan, and T. A. Kalmykova. **19**(2), 290–1 (Aug. 1974); CPM-7408X1554

Kalyatskii, I. I.—Electrical breakdown of vacuum gaps under superhigh voltage pulses —I. I. Kalyatskii, G. M. Kassirov, and G. V. Smirnov. **19**(11), 1434–5 (May 1975); CPM-7506X1188

Kamenev, A. G.—Surface–ionization determination of the electron affinities of silver and gold —É. Ya. Zandberg, A. G. Kamenev, and V. I. Paleev. **19**(3), 385–9 (Sep. 1974); CPM-7412X1071

—Determination of ionization potentials and electron affinities of certain elements by extrapolation —A. G. Kamenev, É. Ya. Zandberg, and V. I. Paleev. **19**(7), 940–1 (Jan. 1975); CPM-7503X0828

Kamenskii, E. I.—Spontaneous mode locking in a laser with a multifaceted element —E. I. Kamenskii and V. V. Kozlov. **19**(6), 831–2 (Dec. 1974); CPM-7501X0831

Kanaev, B. I.—Measurement of plasma ion temperature by a thin probe with $T_i \gtrsim T_e$ —B. I. Kanaev and E. E. Yushmanov. **19**(4), 554–5 (Oct. 1974); CPM-7412X0338

—Measurement of plasma electron temperature with a sinusoidal probe potential —B. I. Kanaev, V. V. Piterskii, and E. E. Yushmanov. **19**(11), 1421–3 (May 1975); CPM-7506X1175

Kapinos, V. N.—Electron lifetimes in atmosphere at high pressure —V. N. Kapinos, Yu. A. Medvedev, N. N. Morozov, and B. M. Stepanov. **19**(11), 1507 (May 1975); CPM-7506X1261

Kapranov, V. N.—Local–potential study of the Bénard problem in a homogeneous magnetic field —A. I. Lopushanskaya and V. N. Kapranov. **19**(5), 612–4 (Nov. 1974); CPM-7501X0406

Karachevtsev, G. V.—Steady-state electron density in photoionizion of aerosol particles —G. V. Karachevtsev and A. A. Fridman. **19**(11), 1471–3 (May 1975); CPM-7506X1225

Karimkhodzhaev, I.—Electrical explosion of the metastable liquid phases of zinc, cadmium, and lead —M. M. Martynyuk and I. Karimkhodzhaev. **19**(11), 1454–7 (May 1975); CPM-7506X1208

—Resistance and enthalpy of refractory exploding wires —M. M. Martynyuk, I. Karimkhodzhaev, and V. I. Tsapkov. **19**(11), 1458–61 (May 1975); CPM-7506X1212

Karizhskii, A. P.—End current in a magnetron with a secondary–emission cathode —G. G. Sominskii, S. A. Fridrikhov, O. Yu. Tsybin, and A. P. Karizhskii. **19**(3), 378–81 (Sep. 1974); CPM-7412X1064

Karnaukhova, N. M.—Evaporation rates of the system ZrC+x%W for the temperature range 2300-3000°K —N. M. Karnaukhova, V. A. Luknitskii, and I. A. Maslov. **19**(8), 1096–9 (Feb. 1975); CPM-7504X1520

Karpman, V. I.—Nonlinear instability of a helicon packet in an anisotropic plasma —Ya. N. Istomin and V. I. Karpman. **19**(3), 405–6 (Sep. 1974); CPM-7412X1091

Karpukhin, V. I.—Plasma equilibrium and confinement in a poloidal heliotron configuration. I —V. G. Zykov, V. I. Karpukhin, Yu. F. Lonin, N. N. Podteregera, N. I. Rudnev, and V. T. Tolok. **19**(8), 1063–8 (Feb. 1975); CPM-7504X1487

—Plasma equilibrium and confinement in a poloidal heliotron configuration. II —V. G. Zykov, V. I. Karpukhin, Yu. F. Lonin, N. N. Podteregera, N. I. Rudnev, A. Y. Skibenko, V. T. Tolok, and I. P. Fomin. **19**(8), 1069–72 (Feb. 1975); CPM-7504X1493

Kassirov, G. M.—Electrical breakdown of vacuum gaps under superhigh voltage pulses —I. I. Kalyatskii, G. M. Kassirov, and G. V. Smirnov. **19**(11), 1434–5 (May 1975); CPM-7506X1188

Kasumov, M. M.—Electron–beam excited crossed–field discharge —V. A. Saenko and M. M. Kasumov. **19**(6), 759–61 (Dec. 1974); CPM-7501X0759

Katsubo, L. P.—Instabilities in interpenetrating electron and ion beams —I. A. Soloshenko and L. P. Katsubo. **19**(10), 1317–20 (Apr. 1975); CPM-7506X0251

—Measurement of ion density by the dispersion relation for an ion-beam plasma —M. D. Gabovich, L. P. Katsubo, and I. A. Soloshenko. **19**(11), 1412–3 (May 1975); CPM-7506X1166

Kaufman, R. N.—Rotation of Poynting vector for ultralow-frequency ion waves in an inhomogeneous plasma —Ya. L. Al'pert and R. N. Kaufman. **19**(12), 1519–21 (Jun. 1975); CPM-7508X0393

Kazacha, V. I.—Acceleration of plasma electrons in strong electric fields —Z. A. Al'bikov, M. I. Ivanov, V. I. Kazacha, O. V. Kozlov, V. D. Rusanov, and S. S. Sobolev. **19**(11), 1498–9 (May 1975); CPM-7506X1252

Kel'man, V. M.—A transaxial lens —V. M. Kel'man, L. M. Nazarenko, and E. M. Yakushev. **19**(4), 523–5 (Oct. 1974); CPM-7412X0307

—Theory of the cathode lens. III. Derivation of equations for composite cathode lenses —V. M. Kel'man, A. A. Sapargaliev, and E. M. Yakushev. **19**(5), 592–6 (Nov. 1974); CPM-7501X0386

—Theory of the cathode lens. IV. Aberrations of composite cathode lens —V. M. Kel'man, A. A. Sapargaliev, and E. M. Yakushev. **19**(5), 597–9 (Nov. 1974); CPM-7501X0391

—Symmetric multielectrode tubular electrostatic lenses —L. G. Glikman, V. M. Kel'man, and M. Sh. Nurmanov. **19**(5), 680–2 (Nov. 1974); CPM-7501X0474

Kerbelev, M. P.—Crystal defects of heterostructures of AlAs–GaAs solid solutions and effect on the characteristics of injection lasers —L. V. Druzhinina, V. T. Bublik, L. M. Dolginov, P. G. Eliseev, M. P. Kerbelev, V. B. Osvenskii, I. Z. Pinsker, and M. G. Shumskii. **19**(7), 935–9 (Jan. 1975); CPM-7503X0823

Khachatryan, A. M.—Nonlinear spherical aberrations and thermoelastic stresses in thermal self–focusing —A. A. Vigasin, Yu. A. Gorokhov, A. P. Sukhorukov, and A. M. Khachatryan. **19**(5), 673–5 (Nov. 1974); CPM-7501X0467

Khairullina, A. Ya.—Measurement of statistical parameters of scattering particles in laminar flow by Doppler spectroscopy —A. P. Ivanov, A. Ya. Khairullina, and A. P. Chaikovski. **19**(2), 267–70 (Aug. 1974); CPM-7408X1531

Khakimov, F. Kh.—Nonlinear statistical theory of a condensate of plasmons. II. Stochastic heating of plasma ions by large–scale Langmuir turbulence —F. Kh. Khakimov. **19**(3), 315–8 (Sep. 1974); CPM-7412X1001

—Excitation of acoustic waves by ion–acoustic turbulence —Kh. O. Abdulloev, F. Kh. Khakimov, and V. G. Makhan'kov. **19**(4), 441–5 (Oct. 1974); CPM-7412X0225

—Linear theory for the low–frequency electromagnetic properties of an isotropic turbulent plasma —K. Komilov, F. Kh. Khakimov, and V. N. Tsytovich. **19**(5), 615–7 (Nov. 1974); CPM-7501X0409

—Nonlinear statistical theory for condensation of Langmuir plasmons. III. Energy flux for plasma turbulence —F. Kh. Khakimov and V. N. Tsytovich. **19**(10), 1300–2 (Apr. 1975); CPM-7506X0234

Khaleev, M. M.—Unidirectional cw oscillation in a solid state ring laser with a return mirror —A. A. Mak, V. I. Ustyugov, V. A. Fromzel', and M. M. Khaleev. **19**(4), 552–3 (Oct. 1974); CPM-7412X0336

Khandurov, N. V.—Investigation of ionization processes behind strong shock waves using an electrical conductivity probe —V. A. Tishchenko, N. V. Khandurov, and É. K. Chekalin. **19**(5), 651–3 (Nov. 1974); CPM-7501X0445

Khayutin, L. M.—Nonlinear polarizability of a gaseous medium in a longitudinal magnetic field —V. A. Sokolov and L. M. Khayutin. **19**(5), 589–91 (Nov. 1974); CPM-7501X0383

Khazov, L. D.—Cumulative destruction of transparent dielectrics in repeated laser irradiation —L. D. Khazov, I. A. Fersman, and V. Yu. Bortniker. **19**(9), 1256–7 (Mar. 1975); CPM-7505X0678

Khirnyi, Yu. M.—Dielectric strength of a vacuum gap with electrodes irradiated with He^+ and H^+ ions —A. P. Solodovnikov and Yu. M. Khirnyi. **19**(8), 1122 (Feb. 1975); CPM-7504X1546

Khizhnyak, N. A.—Resonance properties of a pulsating dielectric sphere —A. G. Nerukh and N. A. Khizhnyak. **19**(2), 166–8 (Aug. 1974); CPM-7408X1430

—Diffraction of electromagnetic waves by a dielectric wedge —A. A. Aleksandrova and N. A. Khizhnyak. **19**(11), 1385–9 (May 1975); CPM-7506X1139

—Correction to the paper "Resonant properties of a pulsating dielectric sphere" —A. G. Nerukh and N. A. Khizhnyak. 19(12), 1641 (Jun. 1975); CPM-7508X0515

Khokhlov, R. V.—Gas cooling in transmission of high-power CO_2 laser radiation through the atmosphere —B. F. Gordiets, A. I. Osipov, and R. V. Khokhlov. 19(5), 669–72 (Nov. 1974); CPM-7501X0463

Kholodenko, M. A.—Proton extraction from the 70–GeV accelerator for the Ludmila liquid-hydrogen chamber (extraction system S) —A. A. Aseev, A. I. Drozhdin, B. A. Zelenov, É. A. Merker, L. L. Moizhes, K. P. Myznikov, A. A. Roshchin, V. M. Tatarenko, M. A. Kholodenko, A. D. Artemov, L. N. Vaulin, V. I. Gordin, I. I. Kovalevskii, V. N. Rozhkov, M. M. Suvorov, A. S. Sudarushkin, and V. I. Chuiko. 19(1), 70–6 (Jul. 1974); CPM-7407X1582

Kholodnykh, A. I.—Direct and cascade four-photon parametric scattering of light in $LiIO_3$ crystals —S. M. Arakelyan, V. G. Tunkin, A. I. Kholodnykh, and A. S. Chirkin. 19(6), 787–92 (Dec. 1974); CPM-7501X0787

Khudyakova, L. N.—Fast electrons and x rays from nanosecond gas discharges at 0.1–760 torr —L. V. Tarasova, L. N. Khudyakova, T. V. Loiko, and V. A. Tsukerman. 19(3), 351–3 (Sep. 1974); CPM-7412X1037

Khuzeev, A. P.—Ionization and recombination coefficients in a discharge excited by fast electrons —Yu. I. Bychkov, Yu. D. Korolev, and A. P. Khuzeev. 19(1), 140–1 (Jul. 1974); CPM-7407X1652

Khvesyuk, V. I.—Microcells in cold cathodes —N. P. Kozlov, A. A. Lyapin, and V. I. Khvesyuk. 19(8), 1093–5 (Feb. 1975); CPM-7504X1517

—Formation of a plasma focus in a plasma erosion accelerator. II. Energy characteristics of the dense plasma focus —N. P. Kozlov, L. V. Leskov, Yu. S. Protasov, and V. I. Khvesyuk. 19(12), 1558–9 (Jun. 1975); CPM-7508X0432

Khyuppenen, A. P.—Parasitic amplitude modulation of a stabilized Nd^{3+}:YAG laser —N. M. Galaktionova, A. A. Mak, and A. P. Khyuppenen. 19(4), 486–90 (Oct. 1974); CPM-7412X0270

—Solid-state laser with externally forced *Q* switching —N. M. Galaktionova, A. A. Mak, and A. P. Khyuppenen. 19(9), 1174–6 (Mar. 1975); CPM-7505X0596

Kichaev, V. I.—Flow of low-density gases in a capillary grid —B. T. Porodnov, V. D. Akin'shin, V. I. Kichaev, S. F. Borisov, and P. E. Suetin. 19(4), 515–8 (Oct. 1974); CPM-7412X0299

Kingsep, A. S.—Scattering of an electron beam in a straight *dc* turbulent plasma —Yu. P. Golovanov, L. P. Zakatov, A. S. Kingsep, and A. G. Plakhov. 19(8), 1046–9 (Feb. 1975); CPM-7504X1470

Kirichenko, G. S.—Plasma synthesis by injection of an electron beam through an ion source —V. F. Virko, M. D. Gabovich, G. S. Kirichenko, and O. K. Nazarenko. 19(11), 1418–20 (May 1975); CPM-7506X1172

Kitsenko, A. B.—Parametric plasma instabilities excited by the sudden application of an electric field —A. B. Kitsenko and K. N. Stepanov. 19(1), 127–8 (Jul. 1974); CPM-7407X1639

—Nonlinear behavior of monochromatic surface waves excited by a beam —A. B. Kitsenko, I. M. Pankratov, and K. N. Stepanov. 19 (11), 1505–6 (May 1975); CPM-7506X1259

Klapchenko, V. I.—Effect of molecular hydrogen on a cesium discharge. I —N. D. Morgulis and V. I. Klapchenko. 19(7), 911–3 (Jan. 1975); CPM-7503X0799

Kleshchenko, E. D.—Radiation yield of ions in liquid dielectrics as a function of temperature and radiation energy —V. I. Ivanov, E. D. Kleshchenko, Yu. P. Sukhanovskii, and V. V. Frolov. 19(11), 1468–70 (May 1975); CPM-7506X1222

Klimovskii, Yu. A.—Mass spectrum of secondary ions ejected from the surface of a single crystal of gallium arsenide by argon ions —A. G. Koval', V. V. Bobkov, Yu. A. Klimovskii, S. S. Strel'chenko, V. V. Shubina, V. V. Lebedev, and Ya. M. Fogel'. 19(12), 1587–9 (Jun. 1975); CPM-7508X0461

Klyushkin, P. A.—Effect of instrumental noise on a system with two spin oscillators using Cs^{133} and He^3 —R. A. Zhitnikov, V. V. Semenov, and P. A. Klyushkin. 19(4), 556–7 (Oct. 1974); CPM-7412X0340

Kolesnikov, A. A.—Correlation analysis of fine-structure images —A. A. Kolesnikov and N. V. Lapteva. 19(9), 1181–4 (Mar. 1975); CPM-7505X0603

Kolokolov, N. B.—Electron energy distribution in the afterglow. I —A. B. Blagoev, Yu. M. Kagan, N. B. Kolokolov, and R. I. Lyagushchenko. 19(2), 211–4 (Aug. 1974); CPM-7408X1475

—Electron energy distribution in the afterglow. II —A. B. Blagoev, Yu. M. Kagan, N. B. Kolokolov, and R. I. Lyagushchenko. 19(2), 215–9 (Aug. 1974); CPM-7408X1479

—Electron energy distribution in a constricted, low-pressure hydrogen discharge —M. A. Abroyan, Yu. M. Kagan, N. B. Kolokolov, and B. P. Lavrov. 19(11), 1492–3 (May 1975); CPM-7506X1246

Kolomiets, B. T.—Reversibility of chalcogenide materials in holography —S. B. Gurevich, N. N. Il'yashenko, B. T. Kolomiets, V. M. Lyubin, and M. V. Sukharev. 19(1), 152–3 (Jul. 1974); CPM-7407X1664

Kolotilin, B. I.—Efficiency of the scattering of "unstable" charged particles in quadrupole mass spectrometers —É. P. Sheretov, B. I. Kolotilin, and M. P. Safonov. 19(12), 1622–4 (Jun. 1975); CPM-7508X0496

Komar, E. G.—Beam focusing in an accelerator with inductive energy storage —V. A. Glukhikh, O. A. Gusev, E. G. Komar, V. S. Kuznetsov, M. P. Svin'in, and R. P. Fidel'skaya. 19(3), 366–7 (Sep. 1974); CPM-7412X1052

—High-current pulsed electron accelerator with an annular beam —M. I. Avramenko, V. A. Glukhikh, O. A. Gusev, E. G. Komar, O. L. Komarov, V. S. Kuznetsov, A. S. Perlin, and M. P. Svin'in. 19 (3), 368–70 (Sep. 1974); CPM-7412X1054

—Inductive energy storage in pulsed accelerators —V. A. Glukhikh, O. A. Gusev, E. G. Komar, and M. P. Svin'in. 19(5), 660–1 (Nov. 1974); CPM-7501X0454

—Shaping of voltage pulses by discharging an inductive storage bank with a charged-particle beam —O. A. Gusev, E. G. Komar, V. B. Markov, and E. M. Mellekh. 19(5), 662–3 (Nov. 1974); CPM-7501X0456

Komarov, O. L.—High-current pulsed electron accelerator with an annular beam —M. I. Avramenko, V. A. Glukhikh, O. A. Gusev, E. G. Komar, O. L. Komarov, V. S. Kuznetsov, A. S. Perlin, and M. P. Svin'in. 19(3), 368–70 (Sep. 1974); CPM-7412X1054

—Estimate of the angular divergence in intense electron beams —V. S. Kuznetsov, Yu. P. Vakhrushin, O. L. Komarov, and R. P. Fidel'skaya. 19(7), 868–70 (Jan. 1975); CPM-7503X0756

Komarov, V. N.—Mass-spectrometer study of the ion composition of a glow discharge —N. P. Egorov and V. N. Komarov. 19(8), 1100–2 (Feb. 1975); CPM-7504X1524

Komarov, V. S.—Quenching in the CF_3I photodissociation laser —G. A. Skorobogatov, V. M. Tret'yak, and V. S. Komarov. 19(4), 495–8 (Oct. 1974); CPM-7412X0279

—Method for determining the absolute characteristics of CF_3I laser emission —V. S. Komarov, V. G. Seleznev, and G. A. Skorobogatov. 19(4), 558–60 (Oct. 1974); CPM-7412X0342

—Absolute-photometry determination of the rate constant of the gas-phase reaction of the radical compound C_3F_7 and $I(^2P_{3/2})$ —G. A. Skorobogatov, V. S. Komarov, and V. G. Seleznev. 19(9), 1239–41 (Mar. 1975); CPM-7505X0661

Komilov, K.—Linear theory for the low-frequency electromagnetic properties of an isotropic turbulent plasma —K. Komilov, F. Kh. Khakimov, and V. N. Tsytovich. 19(5), 615–7 (Nov. 1974); CPM-7501X0409

Komolov, V. L.—Variational analysis of thermal breakdown of a semiconductor irradiated by light —V. L. Komolov. 19(5), 600–2 (Nov. 1974); CPM-7501X0394

Kompaniets, T. N.—Effects of cleaning on adsorption by germanium single crystals —Yu. I. Belyakov, M. P. Volkov, and T. N. Kompaniets. 19(6), 815–6 (Dec. 1974); CPM-7501X0815

Kondrashov, V. E.—Recombination in an expanding plasma —Yu. A. Bykovskii, N. N. Degtyarenko, V. F. Elesin, V. E. Kondrashov, E. E. Lovetskii, A. N. Polyanichev, and V. S. Fetisov. 19(1), 43–8 (Jul. 1974); CPM-7407X1555

Kondratenko, A. N.—Second-harmonic generation and emission in wave conversion at a plasma boundary —A. N. Kondratenko, V. G. Shaptala, and V. M. Kuklin. 19(1), 22–4 (Jul. 1974); CPM-7407X1534

—Conversion of an electromagnetic wave into an ion-acoustic wave in an inhomogeneous plasma —A. N. Kondratenko and V. M. Kuklin. 19(1), 25–7 (Jul. 1974); CPM-7407X1537

—Damping of ion-acoustic waves in a bounded plasma —A. N. Kondratenko and V. M. Kuklin. 19(3), 326–8 (Sep. 1974); CPM-7412X1012

Kondratenko, P. S.—Surface evaporation of a solid transparent dielectric under the action of laser radiation —A. M. Bonch-Bruevich, Ya. A. Imas, A. A. Kovalev, P. S. Kondratenko, and B. I. Makshantsev. 19(11), 1474–6 (May 1975); CPM-7506X1228

Kononova, Z. N.—Effect of selenium and sulfur on the work function of tungsten —N. V. Volkov, Yu. K. Gus'kov, Z. N. Kononova, and Yu. I. Kostikov. 19(1), 144–5 (Jul. 1974); CPM-7407X1656

Konov, V. I.—Electrical conductivity of a pseudoliquefied layer in an electric field —V. V. Gal', V. I. Konov, and K. A. Nikitin. 19(9), 1214–5 (Mar. 1975); CPM-7505X0636

Konovalov, V. G.—Electron temperature in a high-frequency helium discharge —V. S. Voitsenya, A. Yu. Voloshko, V. G. Konovalov, and S. I. Solodovchenko. 19(7), 909–10 (Jan. 1975); CPM-7503X0797

Konstantinov, A. I.—High-frequency discharge in a mercury—helium mixture —S. D. Vagner, Yu. M. Kagan, A. I. Konstantinov, and I. S. Niskonen. 19(7), 898–900 (Jan. 1975); CPM-7503X0786

Kop'ev, D. S.—Electroluminescence spectra of the red luminescnet diodes p–$Al_xGa_{1-x}As$—n–$AlyGa_{1-y}As(y>x)$ —V. M. Busov, D. Z. Garbuzov, A. T. Gorelenok, and D. S. Kop'ev. 19(12), 1598–600 (Jun. 1975); CPM-7508X0472

Korlyakov, E. D.—Capillary gravitational waves and the mechanogalvanic effect —E. D. Korlyakov. 19(7), 965 (Jan. 1975); CPM-7503X0853

Kornich, V. G.—Atomic recombination on a solid surface —V. P. Pinchuk, A. N. Gorban', and V. G. Kornich. 19(6), 808–10 (Dec. 1974); CPM-7501X0808

Kornyushkin, Yu. D.—Atomic diffusion from a finite film over a solid surface —Yu. D. Kornyushkin. 19(7), 971–2 (Jan. 1975); CPM-7503X0859

—Parallel-plate capacitor as a charged-particle spectrometer —Yu. D. Kornyushkin. 19(8), 1110–2 (Feb. 1975); CPM-7504X1534

Korolev, Yu. D.—Ionization and recombination coefficients in a discharge excited by fast electrons —Yu. I. Bychkov, Yu. D. Korolev, and A. P. Khuzeev. 19(1), 140–1 (Jul. 1974); CPM-7407X1652

—Energy input in electrical ionization lasers —Yu. I. Bychkov, Yu. D. Korolev, Yu. A. Kurbatov, and G. A. Mesyats. 19(4), 499–502 (Oct. 1974); CPM-7412X0283

Koroleva, N. S.—Dependence of the basic parameters of $Al_xGa_{1-x}As$—GaAs solar converters on temperature and optical intensity —E. B. Vinogradova, M. B. Kagan, N. S. Koroleva, T. L. Lyubashevskaya, and T. A. Nuller. 19(10), 1378–81 (Apr. 1975); CPM-7506X0312

Korol'kov, V. L.—Dielectric breakdown of detonation products —V. L. Korol'kov, M. A. Mel'nikov, and A. P. Tsyplenko. 19(12), 1569–70 (Jun. 1975); CPM-7508X0443

Koroteev, V. I.—Spatial and energy parameters of the relativistic electron beam of the Rius-5 accelerator —A. T. Altyntsev and V. I. Koroteev. 19(6), 773–4 (Dec. 1974); CPM-7501X0773

Koroza, V. I.—Parametric interaction of a charged particle beam with a periodic system —V. I. Koroza and E. S. Sukhovskii. 19(8), 1020–4 (Feb. 1975); CPM-7504X1444

Korsakov, V. V.—Multiple recording and erasure of optical information in certain glassy chalcogenides —V. V. Korsakov, V. I. Nalivaiko, V. G. Remesnik, and V. G. Tsukerman. 19(4), 565–6 (Oct. 1974); CPM-7412X0349

Korsun, A. G.—Current limiting by self magnetic field in a plasma accelerator —A. G. Korsun. 19(1), 124–6 (Jul. 1974); CPM-7407X1636

—Two modes of operation of an arc plasma source in an external magnetic field —A. G. Korsun and S. A. Meshcheryakov. 19(11), 1500–1 (May 1975); CPM-7506X1254

Kosarev, E. L.—Narrow-band decimeter radiation from lighting —E. L. Kosarev and Yu. G. Serezhkin. 19(2), 229–33 (Aug. 1974); CPM-7408X1493

Koshelev, V. I.—Electron energy spectrum in a high-current vacuum diode —S. P. Bugaev, V. I. Koshelev, and M. N. Timofeev. 19(9), 1193–5 (Mar. 1975); CPM-7505X0615

Kosov, N. D.—Steady-state study of the temperature dependence of the mutual-diffusion coefficients of certain gases —N. D. Kosov and B. P. Solonitsyn. 19(4), 541–2 (Oct. 1974); CPM-7412X0325

Kostikov, Yu. I.—Effect of selenium and sulfur on the work function of tungsten —N. V. Volkov, Yu. K. Gus'kov, Z. N. Kononova, and Yu. I. Kostikov. 19(1), 144–5 (Jul. 1974); CPM-7407X1656

—Steady-state operation of a surface-ionization thermionic converter —N. V. Volkov, Yu. K. Gus'kov, Yu. I. Kostikov, and V. P. Pashchenko. 19(8), 1129–30 (Feb. 1975); CPM-7504X1553

Kostin, A. A.—Theory of the low-voltage arc in a narrow gap —F. G. Baksht, A. A. Kostin, and V. A. Nemchinskii. 19(5), 654–7 (Nov. 1974); CPM-7501X0448

—Atomic density in the low-voltage arc in a cesium diode —F. G. Baksht, A. A. Kostin, Yu. L. Serov, and I. P. Yavor. 19(11), 1424–5 (May 1975); CPM-7506X1178

Kostin, V. M.—Power spectrum of potential fluctuations in a moving magnetoactive plasma —V. M. Kostin. 19(8), 1053–6 (Feb. 1975); CPM-7504X1477

Kostomarov, D. P.—Energy balance in Tokamaks in the "plateau—banana" transition region —Yu. N. Dnestrovskii and D. P. Kostomarov. 19(12), 1541–2 (Jun. 1975); CPM-7508X0415

Kostyuk, G. I.—Breakdown caused by electron bombardment of the surface of an alloy electrode —N. V. Belan, G. I. Kostyuk, and V. A. Pimkin. 19(6), 802–3 (Dec. 1974); CPM-7501X0802

Kotov, O. I.—Effect of a magnetic field on spontaneous mode-locking in a He—Ne laser $(\Lambda=0.63\mu)$ —V. Yu. Petrun'kin, V. M. Nikolaev, O. I. Kotov, and B. V. L'vov. 19(12), 1612–3 (Jun. 1975); CPM-7508X0486

Kotov, Yu. A.—High-power nanosecond electron accelerator with inductive storage —B. M. Koval'chuk, Yu. A. Kotov, and G. A. Mesyats. 19(1), 136–7 (Jul. 1974); CPM-7407X1648

Koval', A. G.—Mass spectrum of secondary ions ejected from the surface of a single crystal of gallium arsenide by argon ions —A. G. Koval', V. V. Bobkov, Yu. A. Klimovskii, S. S. Strel'chenko, V. V. Shubina, V. V. Lebedev, and Ya. M. Fogel'. 19(12), 1587–9 (Jun. 1975); CPM-7508X0461

Koval'chuk, B. M.—High-power nanosecond electron accelerator with inductive storage —B. M. Koval'chuk, Yu. A. Kotov, and G. A. Mesyats. 19(1), 136–7 (Jul. 1974); CPM-7407X1648

Kovalenko, V. G.—Electrostatic analyzer for wide beams —V. G. Kovalenko and B. V. Polenov. 19(4), 561–2 (Oct. 1974); CPM-7412X0345

Kovalenko, V. P.—Ion focusing of an electron beam in deep melting of a metal —M. D. Gabovich, V. P. Kovalenko, O. A. Metallov, O. K. Nazarenko, and S. K. Pats'ora. 19(7), 973–4 (Jan. 1975); CPM-7503X0861

—Laser-initiated vacuum discharge —V. P. Kovalenko, A. A. Makarevich, V. A. Rodichkin, and A. M. Timonin. 19(11), 1429–31 (May 1975); CPM-7506X1183

Kovalev, A. A.—Nonradiative electron transitions and thermal effects in laser-irradiated transparent dielectrics —B. I. Makshantsev, A. A. Kovalev, R. K. Leonov, and P. A. Yampol'skii. 19(1), 98–102 (Jul. 1974); CPM-7407X1610

—Surface evaporation of a solid transparent dielectric under the action of laser radiation —A. M. Bonch-Bruevich, Ya. A. Imas, A. A. Kovalev, P. S. Kondratenko, and B. I. Makshantsev. 19(11), 1474–6 (May 1975); CPM-7506X1228

Kovalevskii, I. I.—Proton extraction from the 70-GeV accelerator for the Ludmila liquid-hydrogen chamber (extraction system S) —A. A. Aseev, A. I. Drozhdin, B. A. Zelenov, É. A. Merker, L. L. Moizhes, K. P. Myznikov, A. A. Roshchin, V. M. Tatarenko, M. A. Kholodenko, A. D. Artemov, L. N. Vaulin, V. I. Gordin, I. I. Kovalevskii, V. N. Rozhkov, M. M. Suvorov, A. S. Sudarushkin, and V. I. Chuiko. 19(1), 70–6 (Jul. 1974); CPM-7407X1582

Kovnatskii, A. M.—Current-driven instability in a conducting fluid —A. M. Kovnatskii. 19(5), 691 (Nov. 1974); CPM-7501X0485

Kovrov, P. E.—Vacuum-UV and soft x-ray emission in a magnetoplasma compressor —P. E. Kovrov and L. G. Tokarev. 19 (4), 563–4 (Oct. 1974); CPM-7412X0347

Kozharin, A. A.—Plasma decay instability in crossed fields —V. I. Farenik, V. V. Vlasov, A. M. Rozhkov, and A. A. Kozharin. 19(8), 1116–7 (Feb. 1975); CPM-7504X1540

—Ion energy spectra and collective effects in a Penning ion source —V. I. Farenik, V. V. Vlasov, A. M. Rozhkov, and A. A. Kozharin. 19(9), 1258–9 (Mar. 1975); CPM-7505X0680

Kozlov, G. V.—Dielectric properties of foamed ceramics at millimeter wavelengths —N. A. Irisova, G. V. Kozlov, V. E. Mandrusov, B. S. Cherepanov, and I. M. Chernyshev. 19(1), 103–4 (Jul. 1974); CPM-7407X1615

—Temperature dependence of the dielectric permittivity of single-crystal TiO_2 in the submillimeter range —A. A. Volkov, N. A. Irisova, and G. V. Kozlov. 19(4), 567–8 (Oct. 1974); CPM-7412X0351

Kozlov, N. P.—Use of plasma accelerator for optical pumping of lasers —N. P. Kozlov and Yu. S. Protasov. 19(3), 358–60 (Sep. 1974); CPM-7412X1044

—Microcells in cold cathodes —N. P. Kozlov, A. A. Lyapin, and V. I. Khvesyuk. 19(8), 1093–5 (Feb. 1975); CPM-7504X1517

—Formation of a plasma focus in a plasma erosion accelerator. II. Energy characteristics of the dense plasma focus —N. P. Kozlov, L. V. Leskov, Yu. S. Protasov, and V. I. Khvesyuk. **19**(12), 1558–9 (Jun. 1975); CPM-7508X0432

Kozlov, O. V.—Acceleration of plasma electrons in strong electric fields —Z. A. Al'bikov, M. I. Ivanov, V. I. Kazacha, O. V. Kozlov, V. D. Rusanov, and S. S. Sobolev. **19**(11), 1498–9 (May 1975); CPM-7506X1252

Kozlov, V. V.—Spontaneous mode locking in a laser with a multifaceted element —E. I. Kamenskii and V. V. Kozlov. **19**(6), 831–2 (Dec. 1974); CPM-7501X0831

Kozyrev, A. N.—Plasma diffusion in the Tornado device —A. N. Kozyrev and B. P. Peregud. **19**(4), 468–74 (Oct. 1974); CPM-7412X0252

Kozyrev, A. V.—Effects of ion microfields on emission of an arc cathode —A. M. Dorodnov, V. B. Davydov, A. V. Kozyrev, and Ya. A. Pomelov. **19**(3), 390–3 (Sep. 1974); CPM-7412X1076

Krasnov, I. P.—The magnetostatic problem for thin closed shells —I. P. Krasnov. **19**(6), 711–2 (Dec. 1974); CPM-7501X0711

Krasov, V. I.—Connection of magnetic lines of force in a neutral layer —A. T. Altyntsev and V. I. Krasov. **19**(12), 1639–40 (Jun. 1975); CPM-7508X0513

Kremkov, M. V.—Energy losses of slow electrons reflected from molybdenum and tungsten single crystals —O. M. Artamonov, B. B. Bolotov, and M. V. Kremkov. **19**(8), 1103–4 (Feb. 1975); CPM-7504X1527

Kremnev, V. V.—Electron energy spectrum in high-energy nanosecond accelerators —V. V. Kremnev, G. A. Mesyats, and V. P. Reznikov. **19**(10), 1342–4 (Apr. 1975); CPM-7506X0276

Krivitskii, E. V.—Approximate similarity relations in the electrical explosions of underwater conductors —E. V. Krivitskii and V. K. Sholom. **19**(6), 798–801 (Dec. 1974); CPM-7501X0798

—Electrical characteristics of underwater exploding wires —V. K. Sholom, E. V. Krivitskii, and V. P. Litvinenko. **19**(10), 1329–31 (Apr. 1975); CPM-7506X0263

Krivorukov, E. V.—Modulation of microwaves by density fluctuations in a plasma —L. A. Dushin, A. V. Serikov, A. I. Skibenko, E. V. Krivorukov, and I. P. Fomin. **19**(9), 1163–7 (Mar. 1975); CPM-7505X0585

Krivulya, S. S.—Interaction of a hollow electron beam with a plasma —N. M. Zemlyanskii, A. K. Berezin, Ya. B. Fainberg, L. I. Bolotin, and S. S. Krivulya. **19**(12), 1547–8 (Jun. 1975); CPM-7508X0421

Krokhina, O. N.—NÉM-1T magnetic–discharge pumps in the vacuum system of the 1–100 linear accelerator —O. N. Krokhina and K. G. Mirzoev. **19**(5), 698–9 (Nov. 1974); CPM-7501X0492

Krupnik, L. I.—Conversion of neutral hydrogen into protons in dense plasmas —T. A. Bazilevskaya, L. I. Krupnik, and N. G. Shulika. **19**(6), 741–4 (Dec. 1974); CPM-7501X0741

—High-frequency modulation of atomic beams for plasma diagnostics —P. A. Demchenko, L. I. Krupnik, K. A. Leontovich, and E. S. Lyangner. **19**(10), 1362–6 (Apr. 1975); CPM-7506X0296

—Free expansion of plasma jets —P. A. Demchenko, L. I. Krupnik, and E. S. Lyangner. **19**(11), 1426–8 (May 1975); CPM-7506X1180

Kryzhanovskii, V. I.—Interaction of intense laser radiation with solid targets —L. V. Dubovoi, V. D. Dyatlov, V. I. Kryzhanovskii, A. A. Mak, R. N. Medvedev, A. N. Popytaev, V. A. Serebryakov, V. N. Sizov, and A. D. Starikov. **19**(11), 1477–9 (May 1975); CPM-7506X1231

Kudlai, V. A.—Cell for forming electron beams of arbitrary shape in a high-voltage gaseous discharge —I. V. Vagner, É. I. Bolgov, V. F. Grakun, V. L. Gokhfel'd, and V. A. Kudlai. **19**(8), 1042–5 (Feb. 1975); CPM-7504X1466

Kuklin, V. M.—Second–harmonic generation and emission in wave conversion at a plasma boundary —A. N. Kondratenko, V. G. Shaptala, and V. M. Kuklin. **19**(1), 22–4 (Jul. 1974); CPM-7407X1534

—Conversion of an electromagnetic wave into an ion–acoustic wave in an inhomogeneous plasma —A. N. Kondratenko and V. M. Kuklin. **19**(1), 25–7 (Jul. 1974); CPM-7407X1537

—Damping of ion–acoustic waves in a bounded plasma —A. N. Kondratenko and V. M. Kuklin. **19**(3), 326–8 (Sep. 1974); CPM-7412X1012

Kukushkin, A. S.—Long-wave cyclotron instability in a plasma in an inhomogeneous magnetic field —A. S. Kukushkin. **19**(3), 410–1 (Sep. 1974); CPM-7412X1096

Kuleshov, P. P.—Measurement of transverse relaxation time T_2 of optically oriented He^4 with an oscillator magnetometer —N. A. Dovator, R. A. Zhitnikov, and P. P. Kuleshov. **19**(12), 1608–9 (Jun. 1975); CPM-7508X0482

Kuleshov, V. M.—Switching characteristis of a discharge in water —V. M. Kuleshov, S. L. Nedoseev, V. P. Smirnov, and A. M. Spektor. **19**(1), 150–1 (Jul. 1974); CPM-7407X1662

Kulikov, Yu. A.—Secondary-electron energy in a resonance discharge in a three-electrode system —Yu. A. Kulikov, V. V. Ogienko, and Yu. M. Trifonov. **19**(8), 1090–2 (Feb. 1975); CPM-7504X1514

Kulish, A. F.—Exact solutions of the nonlinear electrodynamic equations —N. G. Puchkova and A. F. Kulish. **19**(12), 1614–5 (Jun. 1975); CPM-7508X0488

Kupryazhkin, A. Ya.—Diffusion and solubility of helium in potassium chloride —A. Ya. Kupryazhkin, P. V. Volobuev, and P. E. Suetin. **19**(8), 1105–7 (Feb. 1975); CPM-7504X1529

Kurbatov, Yu. A.—Energy input in electrical ionization lasers —Yu. I. Bychkov, Yu. D. Korolev, Yu. A. Kurbatov, and G. A. Mesyats. **19**(4), 499–502 (Oct. 1974); CPM-7412X0283

—Characteristics of the electrical ionization CO$_2$ laser —Yu. I. Bychkov, Yu. A. Kurbatov, and V. V. Savin. **19**(4), 506–8 (Oct. 1974); CPM-7412X0290

Kurdyumov, A. A.—Effect of the adsorption rate on the diffusion of deuterium through nickel —Yu. I. Belyakov, Yu. I. Zvezdin, A. A. Kurdyumov, and G. G. Nevdakha. **19**(7), 956–8 (Jan. 1975); CPM-7503X0844

Kurilko, V. I.—Cerenkov instabilities of a relativistic beam in a periodic plasma–filled waveguide —V. I. Kurilko, Yu. V. Tkach, and V. A. Shendrik. **19**(5), 607–11 (Nov. 1974); CPM-7501X0401

—Launching and propagation of regular nonlinear waves in an anisotropic plasma–filled waveguide —V. I. Kurilko, A. P. Tols–toluzhskii, and Ya. B. Fainberg. **19**(5), 622–7 (Nov. 1974); CPM-7501X0416

—Solitary waves in anisotropic plasma waveguide —V. I. Kurilko and A. P. Tolstoluzhskii. **19**(7), 887–90 (Jan. 1975); CPM-7503X0775

—Spectral narrowing of a single-mode beam oscillator —V. A. Buts and V. I. Kurilko. **19**(11), 1494–5 (May 1975); CPM-7506X1248

Kurnaev, V. A.—Energy spectra of scattered particles in proton bombardment of a metal target —G. I. Zhabrev, V. A. Kurnaev, and V. G. Tel'kovskii. **19**(7), 978–9 (Jan. 1975); CPM-7503X0866

Kursanov, Yu. V.—Low pressure discharge with high–energy electrons —R. A. Demirkhanov, Yu. V. Kursanov, and L. P. Skripal'. **19**(7), 891–4 (Jan. 1975); CPM-7503X0779

Kuts, P. S.—Dynamic magnetic–resonance phenomena —P. S. Kuts and V. S. Mel'nik. **19**(1), 110–4 (Jul. 1974); CPM-7407X1622

Kuz'min, R. N.—Contribution of multiphoton processes to the linear dielectric constant —V. A. Bushuev and R. N. Kuz'min. **19**(1), 116 (Jul. 1974); CPM-7407X1628

—Coherent Compton effect in crystals —V. A. Bushuev and R. N. Kuz'min. **19**(12), 1590–2 (Jun. 1975); CPM-7508X0464

Kuznetskii, R. S.—Effect of temperature-dependent conductivity on electromagnetic field, current, temperature, and impedance in a plane conductor. I —R. S. Kuznetskii. **19**(8), 1016–9 (Feb. 1975); CPM-7504X1440

Kuznetsov, V. S.—Beam focusing in an accelerator with inductive energy storage —V. A. Glukhikh, O. A. Gusev, E. G. Komar, V. S. Kuznetsov, M. P. Svin'in, and R. P. Fidel'skaya. **19**(3), 366–7 (Sep. 1974); CPM-7412X1052

—High–current pulsed electron accelerator with an annular beam —M. I. Avramenko, V. A. Glukhikh, O. A. Gusev, E. G. Komar, O. L. Komarov, V. S. Kuznetsov, A. S. Perlin, and M. P. Svin'in. **19**(3), 368–70 (Sep. 1974); CPM-7412X1054

—Maximum current of a beam with finite phase volume —G. I. Trubnikov and V. S. Kuznetsov. **19**(6), 715–6 (Dec. 1974); CPM-7501X0715

—Estimate of the angular divergence in intense electron beams —V. S. Kuznetsov, Yu. P. Vakhrushin, O. L. Komarov, and R. P. Fidel'skaya. **19**(7), 868–70 (Jan. 1975); CPM-7503X0756

Kuznetsov, Yu. D.—Charge–carrier density of the plasma produced in a Penning mixture by irradiation by uranium fission fragments and reactor radiation —G. A. Batyrbekov, Yu. D. Kuznetsov, and Zh. S. Takibaev. **19**(5), 645–6 (Nov. 1974); CPM-7501X0439

Kuznetsov, Yu. K.—Hydrodynamic stability of the Uragan stellarator —V. M. Zalkind, Yu. K. Kuznetsov, V. K. Pashnev, and V. M. Tonkopryad. **19**(8), 1123–5 (Feb. 1975); CPM-7504X1547

Kuzovkova, T. A.—Pulsed neodymium–glass laser with periodic Q switching —T. A. Kuzovkova, E. V. Nilov, V. A. Rusov, I. N. Semenov, and A. A. Chertkov. 19(4), 503–5 (Oct. 1974); CPM-7412X0287

Kuzovlev, V. F.—Ion-optical system for shaping high-current ion beams —S. D. Grishin, V. F. Kuzovlev, R. V. Orlov, and S. N. Ogorodnikov. 19(11), 1462–4 (May 1975); CPM-7506X1216

Kvochka, V. I.—Extraction of synchroton radiation from a cyclic electron accelerator with a strong magnetic field —V. I. Kvochka, V. S. Panasyuk, V. F. Romanovskii, L. N. Samoilov, A. A. Sokolov, B. M. Stepanov, and Yu. M. Tereshkin. 19(6), 762–6 (Dec. 1974); CPM-7501X0762

L

Laptev, I. D.—Neutral particles from the interaction of laser radiation with a solid target —Yu. A. Bykovskii, N. M. Vasil'ev, I. D. Laptev, and V. N. Nevolin. 19(12), 1635 (Jun. 1975); CPM-7508X0509

Lapteva, N. V.—Correlation analysis of fine-structure images —A. A. Kolesnikov and N. V. Lapteva. 19(9), 1181–4 (Mar. 1975); CPM-7505X0603

Larionov, M. M.—Role of collisions in plasma absorption of electromagnetic waves near the lower hybrid —B. V. Galaktionov, V. V. D'yachenko, M. M. Larionov, and O. N. Shcherbinin. 19(4), 459–62 (Oct. 1974); CPM-7412X0243

Latush, E. L.—Effect of the radiation density on ion drift velocity in a cadmium-helium laser —G. N. Tolmachev, E. L. Latush, and V. S. Mikhalevskii. 19(8), 1120–1 (Feb. 1975); CPM-7504X1544

Latypov, Z. Z.—Scattering of He$^+$ ions by the core of the He atom —Z. Z. Latypov and A. A. Shaporenko. 19(7), 976–7 (Jan. 1975); CPM-7503X0864

Lavrov, B. P.—Electron energy distribution in a constricted, low-pressure hydrogen discharge —M. A. Abroyan, Yu. M. Kagan, N. B. Kolokolov, and B. P. Lavrov. 19(11), 1492–3 (May 1975); CPM-7506X1246

Lazurik-Él'tsufin, V. T.—Excitation of thermoelastic vibrations of a thin plate by a beam of fast charged particles —A. I. Kalinichenko and V. T. Lazurik-Él'tsufin. 19(10), 1382–3 (Apr. 1975); CPM-7506X0316

Lebedev, A. N.—Magnetic-field transport of a high-current electron beam —A. V. Agafonov, V. S. Voronin, A. N. Lebedev, and K. N. Pazin. 19(9), 1188–92 (Mar. 1975); CPM-7505X0610

Lebedev, S. V.—Elimination of spherical aberration in an axial plasma lens —S. V. Lebedev and A. I. Morozov. 19(7), 966 (Jan. 1975); CPM-7503X0854

—Achromatic plasma–lens system —A. I. Morozov and S. V. Lebedev. 19(7), 967 (Jan. 1975); CPM-7503X0855

—Multiple–aperture ion source for electromagnetic mass separator —S. V. Lebedev. 19(7), 968 (Jan. 1975); CPM-7503X0856

—Design of axisymmetric plasma lenses —A. I. Morozov and S. V. Lebedev. 19(8), 996–1000 (Feb. 1975); CPM-7504X1420

Lebedev, S. Ya.—Extrapolation of the Langmuir S–curve to cesium pressures of 10–100 torr —V. E. Dubinskii and S. Ya. Lebedev. 19(1), 81–3 (Jul. 1974); CPM-7407X1593

Lebedev, V. V.—Mass spectrum of secondary ions ejected from the surface of a single crystal of gallium arsenide by argon ions —A. G. Koval', V. V. Bobkov, Yu. A. Klimovskii, S. S. Strel'chenko, V. V. Shubina, V. V. Lebedev, and Ya. M. Fogel'. 19(12), 1587–9 (Jun. 1975); CPM-7508X0461

Lentsman, V. L.—Electron–scanning transformation of the potential distribution on an electrostatic target —V. L. Lentsman. 19(5), 678–9 (Nov. 1974); CPM-7501X0472

Leonov, R. K.—Nonradiative electron transitions and thermal effects in laser–irradiated transparent dielectrics —B. I. Makshantsev, A. A. Kovalev, R. K. Leonov, and P. A. Yampol'skii. 19(1), 98–102 (Jul. 1974); CPM-7407X1610

Leontovich, K. A.—High-frequency modulation of atomic beams for plasma diagnostics —P. A. Demchenko, L. I. Krupnik, K. A. Leontovich, and E. S. Lyangner. 19(10), 1362–6 (Apr. 1975); CPM-7506X0296

Leskov, L. V.—Effect of a high-current relativistic electron beam on a metal —B. I. Dmitrenko, L. V. Leskov, G. P. Maksimov, S. L. Nedoseev, V. V. Savichev, V. P. Smirnov, and A. M. Spektor. 19(9), 1224–5 (Mar. 1975); CPM-7505X0646

—Formation of a plasma focus in a plasma erosion accelerator. II. Energy characteristics of the dense plasma focus —N. P. Kozlov, L. V. Leskov, Yu. S. Protasov, and V. I. Khvesyuk. 19(12), 1558–9 (Jun. 1975); CPM-7508X0432

Levin, M. L.—Potential factors for an inhomogeneous ellipsoid —M. L. Levin and R. Z. Muratov. 19(2), 169–70 (Aug. 1974); CPM-7408X1433

Levin, V. M.—Linear accelerator for beam injection into a slowly rising magnetic field —D. G. Borisov, A. I. Gryzlov, V. M. Levin, and A. V. Ryabtsov. 19(4), 509–10 (Oct. 1974); CPM-7412X0293

Levitan, M. M.—Fundamentals of heat-pipe theory and design —M. M. Levitan and T. L. Perel'man. 19(8), 983–95 (Feb. 1975); CPM-7504X1407

Lin'kov, R. V.—Ponderomotive forces on a rotating conducting sphere in a time-varying inhomogeneous magnetic field —R. V. Lin'kov and Yu. M. Urman. 19(11), 1393–8 (May 1975); CPM-7506X1147

Listovets, V. S.—Hologram interferometry for vibration analysis —V. S. Listovets and Yu. I. Ostrovskii. 19(7), 847–60 (Jan. 1975); CPM-7503X0735

Litunovskii, V. N.—Coaxial plasma injector with programmed injection —V. A. Burtsev, V. N. Litunovskii, and M. P. Nadgornaya. 19(6), 736–40 (Dec. 1974); CPM-7501X0736

Litvinenko, V. P.—Electrical characteristics of underwater exploding wires —V. K. Sholom, E. V. Krivitskii, and V. P. Litvinenko. 19(10), 1329–31 (Apr. 1975); CPM-7506X0263

Litvinov, E. A.—Perveance of a vacuum with a point cathode —S. P. Bugaev, E. A. Litvinov, V. V. Lopatin, and G. A. Mesyats. 19(1), 88–90 (Jul. 1974); CPM-7407X1600

—Transient thermionic-field emission from a point cathode —E. A. Litvinov and A. F. Shubin. 19(8), 1131–2 (Feb. 1975); CPM-7504X1555

Livadonov, V. Sh.—Nonlinear plasma waves and ion–acoustic waves in an isotropic plasma —V. Sh. Livadonov and S. M. Fainshtein. 19(1), 28–30 (Jul. 1974); CPM-7407X1540

Loiko, A. É.—Temperature dependence of trace diffusion coefficients of certain gases —A. É. Loiko, B. A. Ivakin, and P. E. Suetin. 19(3), 434 (Sep. 1974); CPM-7412X1120

Loiko, T. V.—Fast electrons and x rays from nanosecond gas discharges at 0.1–760 torr —L. V. Tarasova, L. N. Khudyakova, T. V. Loiko, and V. A. Tsukerman. 19(3), 351–3 (Sep. 1974); CPM-7412X1037

Lominadze, D. G.—Excitation of electromagnetic ion cyclotron waves by fast ions —T. D. Kaladze, D. G. Lominadze, and K. N. Stepanov. 19(2), 175–6 (Aug. 1974); CPM-7408X1439

—Transverse-current plasma instability —D. G. Lominadze and V. L. Sizonenko. 19(9), 1145–9 (Mar. 1975); CPM-7505X0567

—Plasma instability due to an anisotropic electron distribution —D. G. Lominadze and V. L. Sizonenko. 19(9), 1150–3 (Mar. 1975); CPM-7505X0572

Lomino, N. S.—Focusing of a neutralized ion beam by a plasma–optics system —I. I. Demidenko, N. S. Lomino, A. I. Morozov, and V. G. Padalka. 19(3), 347–50 (Sep. 1974); CPM-7412X1033

—Effect of rf ionization on Hall-current plasma accelerator —I. I. Demidenko, N. S. Lomino, A. I. Morozov, and V. G. Padalka. 19(12), 1560–3 (Jun. 1975); CPM-7508X0434

Lonin, Yu. F.—Plasma equilibrium and confinement in a poloidal heliotron configuration. I —V. G. Zykov, V. I. Karpukhin, Yu. F. Lonin, N. N. Podteregera, N. I. Rudnev, and V. T. Tolok. 19(8), 1063–8 (Feb. 1975); CPM-7504X1487

—Plasma equilibrium and confinement in a poloidal heliotron configuration. II —V. G. Zykov, V. I. Karpukhin, Yu. F. Lonin, N. N. Podteregera, N. I. Rudnev, A. Y. Skibenko, V. T. Tolok, and I. P. Fomin. 19(8), 1069–72 (Feb. 1975); CPM-7504X1493

Lopatin, V. V.—Perveance of a vacuum with a point cathode —S. P. Bugaev, E. A. Litvinov, V. V. Lopatin, and G. A. Mesyats. 19(1), 88–90 (Jul. 1974); CPM-7407X1600

Lopushanskaya, A. I.—A useful function in the thermodynamics of irreversible processes —A. V. Pamfilov, A. I. Lopushanskaya, and L. B. Tsvetkova. 19(4), 535–7 (Oct. 1974); CPM-7412X0319

—Local–potential study of the Bénard problem in a homogeneous magnetic field —A. I. Lopushanskaya and V. N. Kapranov. 19(5), 612–4 (Nov. 1974); CPM-7501X0406

Loshkarev, A. I.—Nonmonotonic potential distribution in the electrode region —A. I. Loshkarev. 19(10), 1308–11 (Apr. 1975); CPM-7506X0242

—Analytic model for the arc regime and the thermionic converter —V. D. Bondarenko and A. I. Loshkarev. 19(12), 1564–8 (Jun. 1975); CPM-7508X0438

Lovetskii, E. E.—Recombination in an expanding plasma —Yu. A. Bykovskii, N. N. Degtyarenko, V. F. Elesin, V. E. Kondrashov, E. E. Lovetskii, A. N. Polyanichev, and V. S. Fetisov. 19(1), 43–8 (Jul. 1974); CPM-7407X1555
—Surface waves in a magnetized plasma in a radio-frequency field —E. E. Lovetskii and A. N. Starodub. 19(3), 319–22 (Sep. 1974); CPM-7412X1005
—Expansion of a recombining plasma in vacuum —E. E. Lovetskii, A. N. Polyanichev, and V. S. Fetisov. 19(5), 647–50 (Nov. 1974); CPM-7501X0441
Lozanskii, É. D.—Effects due to streamer shape —É. D. Lozanskii and D. B. Pontekorvo. 19(11), 1432–3 (May 1975); CPM-7506X1186
Lozovich, M. R.—Physical properties of an electrodeless pulsed discharge in a gas-filled glass cell —Yu. I. Chutov, N. S. Baranchuk, M. R. Lozovich, and V. G. Danilov. 19(2), 224–8 (Aug. 1974); CPM-7408X1488
Lubinskii, S. I.—Direct current in a metal—selenium—metal structure boundary by an rf plasma —A. D. Andreev and S. I. Lubinskii. 19(12), 1606–7 (Jun. 1975); CPM-7508X0480
Lukin, A. N.—Resistance and inductance of a gas arc —S. I. Barannik, S. B. Vasserman, and A. N. Lukin. 19(11), 1449–53 (May 1975); CPM-7506X1203
Luknitskii, V. A.—Evaporation rates of the system $ZrC+x\%W$ for the temperature range 2300-3000°K —N. M. Karnaukhova, V. A. Luknitskii, and I. A. Maslov. 19(8), 1096–9 (Feb. 1975); CPM-7504X1520
Luk'yanchikov, G. S.—Multiphase, uniform, secondary-emission microwave discharge at a solid surface —G. S. Luk'yanchikov. 19 (9), 1196–9 (Mar. 1975); CPM-7505X0618
Lun'kin, Yu. P.—Lagrange problem in magnetohydrodynamics —P. V. Zagorskii and Yu. P. Lun'kin. 19(8), 1009–11 (Feb. 1975); CPM-7504X1433
L'vov, B. V.—Effect of a magnetic field on spontaneous mode-locking in a He—Ne laser $(\Lambda=0.63\mu)$ —V. Yu. Petrun'kin, V. M. Nikolaev, O. I. Kotov, and B. V. L'vov. 19(12), 1612–3 (Jun. 1975); CPM-7508X0486
Lyagushchenko, R. I.—Electron energy distribution in the afterglow. I —A. B. Blagoev, Yu. M. Kagan, N. B. Kolokolov, and R. I. Lyagushchenko. 19(2), 211–4 (Aug. 1974); CPM-7408X1475
—Electron energy distribution in the afterglow. II —A. B. Blagoev, Yu. M. Kagan, N. B. Kolokolov, and R. I. Lyagushchenko. 19(2), 215–9 (Aug. 1974); CPM-7408X1479
—Theory of the positive column in neon —Yu. B. Golobovskii, Yu. M. Kagan, and R. I. Lyagushchenko. 19(3), 335–9 (Sep. 1974); CPM-7412X1021
—Electron density in an argon afterglow —O. P. Bochkova, R. I. Lyagushchenko, É. A. Sukiasyan, and Yu. A. Tolmachev. 19(4), 475–7 (Oct. 1974); CPM-7412X0259
Lyangner, E. S.—High-frequency modulation of atomic beams for plasma diagnostics —P. A. Demchenko, L. I. Krupnik, K. A. Leontovich, and E. S. Lyangner. 19(10), 1362–6 (Apr. 1975); CPM-7506X0296
—Free expansion of plasma jets —P. A. Demchenko, L. I. Krupnik, and E. S. Lyangner. 19(11), 1426–8 (May 1975); CPM-7506X1180
Lyapin, A. A.—Microcells in cold cathodes —N. P. Kozlov, A. A. Lyapin, and V. I. Khvesyuk. 19(8), 1093–5 (Feb. 1975); CPM-7504X1517
Lyapin, A. G.—Hydrogen-ion mobility in a high-pressure unipolar corona —A. G. Lyapin. 19(9), 1236–8 (Mar. 1975); CPM-7505X0658
Lytkin, V. V.—Investigation of the work function of a tungsten cathode after bombardment by inert-gas ions —P. N. Chistyakov, R. A. Milovanova, and V. V. Lytkin. 19(1), 148–9 (Jul. 1974); CPM-7407X1660
Lyubashevskaya, T. L.—Dependence of the basic parameters of $Al_xGa_{1-x}As$—GaAs solar converters on temperature and optical intensity —E. B. Vinogradova, M. B. Kagan, N. S. Koroleva, T. L. Lyubashevskaya, and T. A. Nuller. 19(10), 1378–81 (Apr. 1975); CPM-7506X0312
Lyubchik, Ya. G.—Fifth-order spherical aberration in focusing and correcting quadrupole—octupole systems —Ya. G. Lyubchik and T. Ya. Fishkova. 19(11), 1403–7 (May 1975); CPM-7506X1157
Lyubin, V. M.—Reversibility of chalcogenide materials in holography —S. B. Gurevich, N. N. Il'yashenko, B. T. Kolomiets, V. M. Lyubin, and M. V. Sukharev. 19(1), 152–3 (Jul. 1974); CPM-7407X1664
Lyubitov, Yu. N.—Transient molecular effusion characteristics —Yu. N. Lyubitov and V. Z. Belen'kii. 19(4), 519–22 (Oct. 1974); CPM-7412X0303
—Composition of adsorbing and desorbing fluxes —Yu. A. Gel'man, V. I. Mikhailov, V. F. Vinogradov, and Yu. N. Lyubitov. 19(10), 1355–8 (Apr. 1975); CPM-7506X0289
Lyutomskii, V. A.—Experimental investigation of microwave radiation produced by hypersonic flows —V. A. Lyutomskii, V. M. Polyakov, and V. G. Testov. 19(4), 483–5 (Oct. 1974); CPM-7412X0267

M

Maergoiz, I. D.—Rectangular conducting wedge in a moving electromagnetic field —I. D. Maergoiz and L. P. Nizhnik. 19(10), 1281–6 (Apr. 1975); CPM-7506X0215
Magda, I. I.—Transmission of a high-current relativistic beam through a gas —Yu. V. Tkach, I. I. Magda, G. V. Skachek, S. S. Pushkarev, and I. P. Panchenko. 19(3), 412–3 (Sep. 1974); CPM-7412X1098
—Self-acceleration of an intense electron beam —I. A. Grishaev, A. N. Dedik, V. V. Zakutin, I. I. Magda, Yu. V. Tkach, and A. M. Shenderovich. 19(8), 1087–9 (Feb. 1975); CPM-7504X1511
Mak, A. A.—Parasitic amplitude modulation of a stabilized Nd^{3+}:YAG laser —N. M. Galaktionova, A. A. Mak, and A. P. Khyuppenen. 19(4), 486–90 (Oct. 1974); CPM-7412X0270
—Unidirectional cw oscillation in a solid state ring laser with a return mirror —A. A. Mak, V. I. Ustyugov, V. A. Fromzel', and M. M. Khaleev. 19(4), 552–3 (Oct. 1974); CPM-7412X0336
—Lasing properties of Yb^{3+} and Er^{3+} glass laser pumped by a laser —V. N. Kalinin, A. A. Mak, D. S. Prilezhaev, and V. A. Fromzel'. 19(6), 835–6 (Dec. 1974); CPM-7501X0835
—Solid-state laser with externally forced *Q* switching —N. M. Galaktionova, A. A. Mak, and A. P. Khyuppenen. 19(9), 1174–6 (Mar. 1975); CPM-7505X0596
—Interaction of intense laser radiation with solid targets —L. V. Dubovoi, V. D. Dyatlov, V. I. Kryzhanovskii, A. A. Mak, R. N. Medvedev, A. N. Popytaev, V. A. Serebryakov, V. N. Sizov, and A. D. Starikov. 19(11), 1477–9 (May 1975); CPM-7506X1231
Makarevich, A. A.—Laser-initiated vacuum discharge —V. P. Kovalenko, A. A. Makarevich, V. A. Rodichkin, and A. M. Timonin. 19(11), 1429–31 (May 1975); CPM-7506X1183
Makarov, G. I.—Reflecting properties of an inhomogeneous anisotropic plasma layer —V. A. Zhivulin and G. I. Makarov. 19 (1), 123 (Jul. 1974); CPM-7407X1635
Makhan'kov, V. G.—Excitation of acoustic waves by ion-acoustic turbulence —Kh. O. Abdulloev, F. Kh. Khakimov, and V. G. Makhan'kov. 19(4), 441–5 (Oct. 1974); CPM-7412X0225
Makshantsev, B. I.—Nonradiative electron transitions and thermal effects in laser-irradiated transparent dielectrics —B. I. Makshantsev, A. A. Kovalev, R. K. Leonov, and P. A. Yampol'skii. 19(1), 98–102 (Jul. 1974); CPM-7407X1610
—Surface evaporation of a solid transparent dielectric under the action of laser radiation —A. M. Bonch-Bruevich, Ya. A. Imas, A. A. Kovalev, P. S. Kondratenko, and B. I. Makshantsev. 19(11), 1474–6 (May 1975); CPM-7506X1228
Maksimov, A. I.—Electron energy distribution and electrical characteristics of the positive column in H_2 and H_2+Cl_2 —V. V. Zaitsev, A. I. Maksimov, and V. I. Svettsov. 19(1), 57–9 (Jul. 1974); CPM-7407X1569
—Radial distribution of density and potential in a glow discharge in CO_2 and water —A. I. Maksimov and V. F. Sokolov. 19(10), 1359–61 (Apr. 1975); CPM-7506X0293
Maksimov, G. P.—Effect of a high-current relativistic electron beam on a metal —B. I. Dmitrenko, L. V. Leskov, G. P. Maksimov, S. L. Nedoseev, V. V. Savichev, V. P. Smirnov, and A. M. Spektor. 19(9), 1224–5 (Mar. 1975); CPM-7505X0646
Maksimov, V. G.—Simplified model for the initial stage of exploding wire phenomena —N. N. Stolovich, V. G. Maksimov, and N. S. Minitskaya. 19(10), 1321–8 (Apr. 1975); CPM-7506X0255
Malyavin, L. A.—Electric field and plasma structure near a large charged body —L. A. Malyavin and A. M. Moskalenko. 19(2), 197–200 (Aug. 1974); CPM-7408X1461
—Structure of a perturbation near a highly charged body in a weakly ionized plasma —L. A. Malyavin and A. M. Moskalenko. 19(2), 206–10 (Aug. 1974); CPM-7408X1470

Malyshev, G. M.—Diagnostics of a laser-produced plasma by a scattering method using an electron-optical image converter —E. A. Burunov, G. M. Malyshev, G. T. Razdobarin, and V. V. Semenov. 19(1), 66–9 (Jul. 1974); CPM-7407X1578

Malyugin, V. I.—Evaluation of charge distribution in a crossed-field device from ion bombardment of the cathode —V. I. Malyugin and G. G. Sominskii. 19(7), 942–5 (Jan. 1975); CPM-7503X0830

Mandrusov, V. E.—Dielectric properties of foamed ceramics at millimeter wavelengths —N. A. Irisova, G. V. Kozlov, V. E. Mandrusov, B. S. Cherepanov, and I. M. Chernyshev. 19(1), 103–4 (Jul. 1974); CPM-7407X1615

Mantrova, G. M.—Electromagnetic fields outside a synthesized plasma jet —E. V. Bogdanov, G. M. Mantrova, and M. N. Yakovleva. 19(7), 919–21 (Jan. 1975); CPM-7503X0807

Marasin, L. E.—Time characteristics of the near radiation field of the injection laser —Zh. I. Alferov, V. N. Deryagin, L. E. Marasin, Yu. V. Popov, and E. L. Portnoi. 19(4), 548 (Oct. 1974); CPM-7412X0332

Markeev, B. M.—Method for studying gas creep along a solid surface —B. M. Markeev. 19(5), 700–1 (Nov. 1974); CPM-7501X0494

—Viscous momentum transport in a gaseous mixture —B. M. Markeev. 19(7), 969–70 (Jan. 1975); CPM-7503X0857

—State of a gas moving near a solid surface —S. P. Bakanov and B. M. Markeev. 19(10), 1293–4 (Apr. 1975); CPM-7506X0227

Markov, V. B.—Shaping of voltage pulses by discharging an inductive storage bank with a charged-particle beam —O. A. Gusev, E. G. Komar, V. B. Markov, and E. M. Mellekh. 19(5), 662–3 (Nov. 1974); CPM-7501X0456

Marshak, I. S.—Radiating discharges confined by walls —A. F. Aleksandrov, I. S. Marshak, and A. A. Rukhadze. 19(3), 308–14 (Sep. 1974); CPM-7412X0994

Martynenko, V. V.—Anisotropic plasma heating near the lower hybrid frequency —V. M. Glagolev, V. V. Martynenko, and Yu. V. Skosyrev. 19(12), 1543–6 (Jun. 1975); CPM-7508X0417

Martynyuk, M. M.—Vaporization and boiling of liquid metal in an exploding wire —M. M. Martynyuk. 19(6), 793–7 (Dec. 1974); CPM-7501X0793

—Electrical explosion of the metastable liquid phases of zinc, cadmium, and lead —M. M. Martynyuk and I. Karimkhodzhaev. 19(11), 1454–7 (May 1975); CPM-7506X1208

—Resistance and enthalpy of refractory exploding wires —M. M. Martynyuk, I. Karimkhodzhaev, and V. I. Tsapkov. 19(11), 1458–61 (May 1975); CPM-7506X1212

Marugin, A. M.—Laser compensation for thermal distortion in optical pumping —V. K. Zaitsev, V. A. Il'inskii, A. M. Marugin, and V. M. Ovchinnikov. 19(11), 1480–1 (May 1975); CPM-7506X1234

Mashkova, E. S.—Energy dependence of the focusing of ions by crystals —E. S. Mashkova, V. A. Molchanov, and A. D. Pavlova. 19(4), 540 (Oct. 1974); CPM-7412X0324

Maslov, A. I.—Spatial characteristics and loss of plasma produced by an electron beam in a magnetic trap —M. Yu. Bredikhin, A. I. Maslov, A. I. Skibenko, E. I. Skibenko, I. P. Fomin, and V. B. Yuferov. 19(1), 49–52 (Jul. 1974); CPM-7407X1561

Maslov, I. A.—Evaporation rates of the system ZrC+x%W for the temperature range 2300-3000°K —N. M. Karnaukhova, V. A. Luknitskii, and I. A. Maslov. 19(8), 1096–9 (Feb. 1975); CPM-7504X1520

Masunov, E. S.—Coherent instability of a beam in a vacuum chamber with an irregular boundary —E. S. Masunov. 19(9), 1185–7 (Mar. 1975); CPM-7505X0607

Medvedev, R. N.—Interaction of intense laser radiation with solid targets —L. V. Dubovoi, V. D. Dyatlov, V. I. Kryzhanovskii, A. A. Mak, R. N. Medvedev, A. N. Popytaev, V. A. Serebryakov, V. N. Sizov, and A. D. Starikov. 19(11), 1477–9 (May 1975); CPM-7506X1231

Medvedev, Yu. A.—Electron lifetimes in atmosphere at high pressure —V. N. Kapinos, Yu. A. Medvedev, N. N. Morozov, and B. M. Stepanov. 19(11), 1507 (May 1975); CPM-7506X1261

Meilikhov, E. Z.—Current-convective instability in a three-component plasma —E. Z. Meilikhov. 19(12), 1610–1 (Jun. 1975); CPM-7508X0484

Melikov, I. V.—Experimental investigation of anode processes in a closed electron-drift accelerator —I. V. Melikov. 19(1), 35–7 (Jul. 1974); CPM-7407X1547

—Similitude in Hall-current plasma accelerators —A. I. Morozov and I. V. Melikov. 19(3), 340–2 (Sep. 1974); CPM-7412X1026

—Equilibrium flow in a Hall-current plasma accelerator —I. V. Melikov. 19(3), 343–6 (Sep. 1974); CPM-7412X1029

Mellekh, E. M.—Shaping of voltage pulses by discharging an inductive storage bank with a charged-particle beam —O. A. Gusev, E. G. Komar, V. B. Markov, and E. M. Mellekh. 19(5), 662–3 (Nov. 1974); CPM-7501X0456

Mel'nik, V. S.—Dynamic magnetic-resonance phenomena —P. S. Kuts and V. S. Mel'nik. 19(1), 110–4 (Jul. 1974); CPM-7407X1622

Mel'nikov, M. A.—Dielectric breakdown of detonation products —V. L. Korol'kov, M. A. Mel'nikov, and A. P. Tsyplenko. 19(12), 1569–70 (Jun. 1975); CPM-7508X0443

Meriakri, V. V.—Dispersion of the dielectric constant of crystalline KH_2PO_4 near the "soft" mode frequency —V. V. Meriakri, Yu. M. Poplavko, and E. F. Ushatkin. 19(5), 703–4 (Nov. 1974); CPM-7501X0497

Merker, É. A.—Proton extraction from the 70-GeV accelerator for the Ludmila liquid-hydrogen chamber (extraction system S) —A. A. Aseev, A. I. Drozhdin, B. A. Zelenov, É. A. Merker, L. L. Moizhes, K. P. Myznikov, A. A. Roshchin, V. M. Tatarenko, M. A. Kholodenko, A. D. Artemov, L. N. Vaulin, V. I. Gordin, I. I. Kovalevskii, V. N. Rozhkov, M. M. Suvorov, A. S. Sudarushkin, and V. I. Chuiko. 19(1), 70–6 (Jul. 1974); CPM-7407X1582

Meshcheryakov, S. A.—Two modes of operation of an arc plasma source in an external magnetic field —A. G. Korsun and S. A. Meshcheryakov. 19(11), 1500–1 (May 1975); CPM-7506X1254

Mesyats, G. A.—Perveance of a vacuum with a point cathode —S. P. Bugaev, E. A. Litvinov, V. V. Lopatin, and G. A. Mesyats. 19(1), 88–90 (Jul. 1974); CPM-7407X1600

—High-power nanosecond electron accelerator with inductive storage —B. M. Koval'chuk, Yu. A. Kotov, and G. A. Mesyats. 19(1), 136–7 (Jul. 1974); CPM-7407X1648

—Energy input in electrical ionization lasers —Yu. I. Bychkov, Yu. D. Korolev, Yu. A. Kurbatov, and G. A. Mesyats. 19(4), 499–502 (Oct. 1974); CPM-7412X0283

—Nanosecond x-ray pulses —G. A. Mesyats. 19(7), 948–51 (Jan. 1975); CPM-7503X0836

—Electron energy spectrum in high-energy nanosecond accelerators —V. V. Kremnev, G. A. Mesyats, and V. P. Reznikov. 19(10), 1342–4 (Apr. 1975); CPM-7506X0276

Metallov, O. A.—Ion focusing of an electron beam in deep melting of a metal —M. D. Gabovich, V. P. Kovalenko, O. A. Metallov, O. K. Nazarenko, and S. K. Pats'ora. 19(7), 973–4 (Jan. 1975); CPM-7503X0861

Mikhailov, V. I.—Composition of adsorbing and desorbing fluxes —Yu. A. Gel'man, V. I. Mikhailov, V. F. Vinogradov, and Yu. N. Lyubitov. 19(10), 1355–8 (Apr. 1975); CPM-7506X0289

Mikhalev, L. A.—Contraction of the positive column of a glow discharge due to the presence of negative ions —L. A. Mikhalev and L. N. Selin. 19(5), 689–90 (Nov. 1974); CPM-7501X0483

Mikhalevskii, V. S.—Effect of the radiation density on ion drift velocity in a cadmium-helium laser —G. N. Tolmachev, E. L. Latush, and V. S. Mikhalevskii. 19(8), 1120–1 (Feb. 1975); CPM-7504X1544

Milenin, V. M.—Effect of cathode emission on the threshold for striations —N. A. Vorob'eva, Yu. M. Kagan, V. M. Milenin, and A. Kh. Muradov. 19(1), 117–8 (Jul. 1974); CPM-7407X1629

Milovanov, O. S.—Multiple-section linear electron accelerator with synchronized oscillators —V. F. Vikulov, V. A. Volodin, and O. S. Milovanov. 19(7), 930–1 (Jan. 1975); CPM-7503X0818

Milovanova, R. A.—Investigation of the work function of a tungsten cathode after bombardment by inert-gas ions —P. N. Chistyakov, R. A. Milovanova, and V. V. Lytkin. 19(1), 148–9 (Jul. 1974); CPM-7407X1660

Minitskaya, N. S.—Simplified model for the initial stage of exploding wire phenomena —N. N. Stolovich, V. G. Maksimov, and N. S. Minitskaya. 19(10), 1321–8 (Apr. 1975); CPM-7506X0255

Mironov, O. N.—Forces in a Hall plasma accelerator —O. N. Mironov. 19(3), 329–34 (Sep. 1974); CPM-7412X1015

Mironov, V. D.—Multiple reflection of light in a shock tube —V. D. Mironov and V. I. Selyakov. 19(3), 402–4 (Sep. 1974); CPM-7412X1088

Mironovich, V. L.—Analytic model of the cesium arc —V. P. Pashchenko, V. L. Mironovich, and I. P. Stakhanov. 19(10), 1332–6 (Apr. 1975); CPM-7506X0266

Miroshnichenko, V. I.—Reflection of electromagnetic waves by a moving plasma —V. I. Miroshnichenko. 19(4), 533–4 (Oct. 1974); CPM-7412X0317

Mirzoev, K. G.—Titanium–pump system for hydrogen —K. G. Mirzoev, V. G. Rogozinskii, and V. L. Ushkov. 19(3), 432–3 (Sep. 1974); CPM-7412X1118

—NÉM–1T magnetic–discharge pumps in the vacuum system of the 1–100 linear accelerator —O. N. Krokhina and K. G. Mirzoev. 19 (5), 698–9 (Nov. 1974); CPM-7501X0492

Mishin, G. I.—Statistical characteristics of the turbulent wake behind a supersonic sphere —V. G. Ivanov, G. I. Mishin, and S. N. Palkin. 19(4), 543–5 (Oct. 1974); CPM-7412X0327

Mitina, N. I.—Magnetic field in a θ pinch with an axial conductor —Ya. F. Volkov, V. G. Dyatlov, and N. I. Mitina. 19(3), 323–5 (Sep. 1974); CPM-7412X1009

—Optical investigation of a turbulent plasma —Ya. F. Volkov, V. G. Dyatlov, and N. I. Mitina. 19(7), 905–8 (Jan. 1975); CPM-7503X0793

Mittsev, M. A.—Adsorption of bismuth on tungsten. I. Steady–state processes —M. A. Mittsev. 19(6), 811–4 (Dec. 1974); CPM-7501X0811

Mizerov, M. N.—Characteristics of diffraction gratings obtained by photoetching of semiconductor surfaces —L. V. Belyakov, D. N. Goryachev, M. N. Mizerov, and E. L. Portnoi. 19(6), 837–8 (Dec. 1974); CPM-7501X0837

Mnatsakanyan, A. Kh.—Energy exchange between electrons and molecular vibrational states in resonance collisions —A. Kh. Mnatsakanyan and G. V. Naidis. 19(8), 1113–5 (Feb. 1975); CPM-7504X1537

Moiseev, S. S.—Transformation of nonlinear MHD waves —G. M. Zaslavskii, S. S. Moiseev, and V. V. Mukhin. 19(12), 1534–7 (Jun. 1975); CPM-7508X0408

Moizhes, B. Ya.—Anomalous high emission of a nonevaporating thermionic cathode in an arc —B. Ya. Moizhes and V. A. Nemchinskii. 19(12), 1571–6 (Jun. 1975); CPM-7508X0445

Moizhes, L. L.—Proton extraction from the 70–GeV accelerator for the Ludmila liquid–hydrogen chamber (extraction system S) —A. A. Aseev, A. I. Drozhdin, B. A. Zelenov, É. A. Merker, L. L. Moizhes, K. P. Myznikov, A. A. Roshchin, V. M. Tatarenko, M. A. Kholodenko, A. D. Artemov, L. N. Vaulin, V. I. Gordin, I. I. Kovalevskii, V. N. Rozhkov, M. M. Suvorov, A. S. Sudarushkin, and V. I. Chuiko. 19(1), 70–6 (Jul. 1974); CPM-7407X1582

Molchanov, V. A.—Effect of crystal structure on certain angular dependence of the ion–electron–emission yield —B. A. Brusilovskii and V. A. Molchanov. 19(1), 84–7 (Jul. 1974); CPM-7407X1596

—Energy dependence of the focusing of ions by crystals —E. S. Mashkova, V. A. Molchanov, and A. D. Pavlova. 19(4), 540 (Oct. 1974); CPM-7412X0324

Morgulis, N. D.—Effect of molecular hydrogen on a cesium discharge. I —N. D. Morgulis and V. I. Klapchenko. 19(7), 911–3 (Jan. 1975); CPM-7503X0799

Morozov, A. I.—Radiation energy of a magnetoplasma compressor —V. I. Berkov and A. I. Morozov. 19(2), 220–3 (Aug. 1974); CPM-7408X1484

—Similitude in Hall–current plasma accelerators —A. I. Morozov and I. V. Melikov. 19(3), 340–2 (Sep. 1974); CPM-7412X1026

—Focusing of a neutralized ion beam by a plasma–optics system —I. I. Demidenko, N. S. Lomino, A. I. Morozov, and V. G. Padalka. 19(3), 347–50 (Sep. 1974); CPM-7412X1033

—Plasma density in a magnetoplasma compressor —A. K. Vinogradova, V. P. Vinogradov, A. I. Morozov, and A. A. Sergeev. 19(3), 421–3 (Sep. 1974); CPM-7412X1107

—Elimination of spherical aberration in an axial plasma lens —S. V. Lebedev and A. I. Morozov. 19(7), 966 (Jan. 1975); CPM-7503X0854

—Achromatic plasma–lens system —A. I. Morozov and S. V. Lebedev. 19(7), 967 (Jan. 1975); CPM-7503X0855

—Design of axisymmetric plasma lenses —A. I. Morozov and S. V. Lebedev. 19(8), 996–1000 (Feb. 1975); CPM-7504X1420

—Effect of rf ionization on Hall–current plasma accelerator —I. I. Demidenko, N. S. Lomino, A. I. Morozov, and V. G. Padalka. 19 (12), 1560–3 (Jun. 1975); CPM-7508X0434

Morozov, N. N.—Electron lifetimes in atmosphere at high pressure —V. N. Kapinos, Yu. A. Medvedev, N. N. Morozov, and B. M. Stepanov. 19(11), 1507 (May 1975); CPM-7506X1261

Moskalenko, A. M.—Electric field and plasma structure near a large charged body —L. A. Malyavin and A. M. Moskalenko. 19(2), 197–200 (Aug. 1974); CPM-7408X1461

—Structure of a perturbation near a highly charged body in a weakly ionized plasma —L. A. Malyavin and A. M. Moskalenko. 19(2), 206–10 (Aug. 1974); CPM-7408X1470

Moskalev, I. N.—Measurement of plasma density distribution with a rectangular microwave cavity —I. N. Moskalev. 19(9), 1168–70 (Mar. 1975); CPM-7505X0590

Mozgin, V. V.—Elimination of carbon impurities from platinum by heating in an oxygen atmosphere —L. P. Rekova, V. V. Mozgin, L. N. Zvyagintseva, V. N. Bondarenko, and Ya. M. Fogel'. 19(11), 1465–7 (May 1975); CPM-7506X1219

Mukhin, V. V.—Transformation of nonlinear MHD waves —G. M. Zaslavskii, S. S. Moiseev, and V. V. Mukhin. 19(12), 1534–7 (Jun. 1975); CPM-7508X0408

Muradov, A. Kh.—Effect of cathode emission on the threshold for striations —N. A. Vorob'eva, Yu. M. Kagan, V. M. Milenin, and A. Kh. Muradov. 19(1), 117–8 (Jul. 1974); CPM-7407X1629

Muratov, R. Z.—Potential factors for an inhomogeneous ellipsoid —M. L. Levin and R. Z. Muratov. 19(2), 169–70 (Aug. 1974); CPM-7408X1433

Myznikov, K. P.—Proton extraction from the 70–GeV accelerator for the Ludmila liquid–hydrogen chamber (extraction system S) —A. A. Aseev, A. I. Drozhdin, B. A. Zelenov, É. A. Merker, L. L. Moizhes, K. P. Myznikov, A. A. Roshchin, V. M. Tatarenko, M. A. Kholodenko, A. D. Artemov, L. N. Vaulin, V. I. Gordin, I. I. Kovalevskii, V. N. Rozhkov, M. M. Suvorov, A. S. Sudarushkin, and V. I. Chuiko. 19(1), 70–6 (Jul. 1974); CPM-7407X1582

—Efficiency of internal targets in the accelerator at the Institute of High–Energy Physics —V. I. Gridasov, K. P. Myznikov, and V. N. Chepegin. 19(7), 922–5 (Jan. 1975); CPM-7503X0810

N

Nadgornaya, M. P.—Coaxial plasma injector with programmed injection —V. A. Burtsev, V. N. Litunovskii, and M. P. Nadgornaya. 19(6), 736–40 (Dec. 1974); CPM-7501X0736

Naida, A. P.—Gas focusing of a negative–ion beam —M. D. Gabovich, A. P. Naida, I. M. Protsenko, L. S. Simonenko, and I. A. Soloshenko. 19(4), 546–7 (Oct. 1974); CPM-7412X0330

Naidis, G. V.—Energy exchange between electrons and molecular vibrational states in resonance collisions —A. Kh. Mnatsakanyan and G. V. Naidis. 19(8), 1113–5 (Feb. 1975); CPM-7504X1537

Nalivaiko, V. I.—Multiple recording and erasure of optical information in certain glassy chalcogenides —V. V. Korsakov, V. I. Nalivaiko, V. G. Remesnik, and V. G. Tsukerman. 19(4), 565–6 (Oct. 1974); CPM-7412X0349

Nazarenko, L. M.—A transaxial lens —V. M. Kel'man, L. M. Nazarenko, and E. M. Yakushev. 19(4), 523–5 (Oct. 1974); CPM-7412X0307

Nazarenko, O. K.—Ion focusing of an electron beam in deep melting of a metal —M. D. Gabovich, V. P. Kovalenko, O. A. Metallov, O. K. Nazarenko, and S. K. Pats'ora. 19(7), 973–4 (Jan. 1975); CPM-7503X0861

—Plasma synthesis by injection of an electron beam through an ion source —V. F. Virko, M. D. Gabovich, G. S. Kirichenko, and O. K. Nazarenko. 19(11), 1418–20 (May 1975); CPM-7506X1172

Nedoseev, S. L.—Switching characteristics of a discharge in water —V. M. Kuleshov, S. L. Nedoseev, V. P. Smirnov, and A. M. Spektor. 19(1), 150–1 (Jul. 1974); CPM-7407X1662

—Effect of a high–current relativistic electron beam on a metal —B. I. Dmitrenko, L. V. Leskov, G. P. Maksimov, S. L. Nedoseev, V. V. Savichev, V. P. Smirnov, and A. M. Spektor. 19(9), 1224–5 (Mar. 1975); CPM-7505X0646

Nedospasov, A. V.—Ionization discontinuity in large–amplitude striations —A. V. Nedospasov and V. G. Petrov. 19(1), 31–4 (Jul. 1974); CPM-7407X1543

Nekrasov, F. M.—Excitation of Alfvén waves in decay instabilities —A. G. Elfimov and F. M. Nekrasov. 19(1), 9–11 (Jul. 1974); CPM-7407X1521

Nemchenko, V. I.—Production of collimated beams of high–energy electrons —V. I. Nemchenko. 19(1), 91–7 (Jul. 1974); CPM-7407X1603

Nemchinskii, V. A.—Theory of the low–voltage arc in a narrow gap —F. G. Baksht, A. A. Kostin, and V. A. Nemchinskii. 19(5), 654–7 (Nov. 1974); CPM-7501X0448

—Anomalous high emission of a nonevaporating thermionic cathode in an arc —B. Ya. Moizhes and V. A. Nemchinskii. 19(12), 1571–6 (Jun. 1975); CPM-7508X0445

—High–pressure hot–cathode arc without forced cooling —V. A. Nemchinskii. 19(12), 1577–8 (Jun. 1975); CPM-7508X0451

Nerukh, A. G.—Resonance properties of a pulsating dielectric sphere —A. G. Nerukh and N. A. Khizhnyak. 19(2), 166–8 (Aug. 1974); CPM-7408X1430

—Correction to the paper "Resonant properties of a pulsating dielectric sphere" —A. G. Nerukh and N. A. Khizhnyak. 19(12), 1641 (Jun. 1975); CPM-7508X0515

Neshpor, V. S.—Thermionic emission properties of zirconium, hafnium, and titanium nitrides in cesium vapor —M. A. Eremeev, V. S. Neshpor, A. B. Novikov, E. M. Stefanovskaya, and V. P. Fedorinov. 19(10), 1337–41 (Apr. 1975); CPM-7506X0271

Nesterovich, A. V.—Self-excited waveguide buncher —N. M. Gavrilov and A. V. Nesterovich. 19(8), 1085–6 (Feb. 1975); CPM-7504X1509

Netsvetailov, E. M.—Hot probe measurements in a rarefied streaming plasma —E. M. Netsvetailov, L. V. Nosachev, and V. V. Skvortsov. 19(12), 1579–83 (Jun. 1975); CPM-7508X0453

Neudachin, I. G.—Use of the distribution function to describe free molecular beams —I. G. Neudachin, B. T. Porodnov, and P. E. Suetin. 19(4), 511–4 (Oct. 1974); CPM-7412X0295

Nevdakha, G. G.—Effect of the adsorption rate on the diffusion of deuterium through nickel —Yu. I. Belyakov, Yu. I. Zvezdin, A. A. Kurdyumov, and G. G. Nevdakha. 19(7), 956–8 (Jan. 1975); CPM-7503X0844

Nevolin, V. N.—Neutral particles from the interaction of laser radiation with a solid target —Yu. A. Bykovskii, N. M. Vasil'ev, I. D. Laptev, and V. N. Nevolin. 19(12), 1635 (Jun. 1975); CPM-7508X0509

Nikitin, K. A.—Electrical conductivity of a pseudoliquefied layer in an electric field —V. V. Gal', V. I. Konov, and K. A. Nikitin. 19 (9), 1214–5 (Mar. 1975); CPM-7505X0636

Nikitin, M. M.—Coherent phase oscillations of electrons in a synchrotron —M. M. Nikitin. 19(12), 1633–4 (Jun. 1975); CPM-7508X0507

Nikitinskii, V. A.—Ion emission into vacuum from a discharge in crossed electric and magnetic fields —V. A. Nikitinskii and A. S. Zakharov. 19(6), 839–40 (Dec. 1974); CPM-7501X0839

Nikolaev, V. M.—Effect of a magnetic field on spontaneous mode-locking in a He—Ne laser ($\Lambda=0.63\mu$) —V. Yu. Petrun'kin, V. M. Nikolaev, O. I. Kotov, and B. V. L'vov. 19(12), 1612–3 (Jun. 1975); CPM-7508X0486

Nikolenko, D. M.—Electron spectrometer for electric excitation of nuclei in a storage ring —D. M. Nikolenko and S. G. Popov. 19 (2), 280–3 (Aug. 1974); CPM-7408X1544

Nilov, E. V.—Pulsed neodymium-glass laser with periodic Q switching —T. A. Kuzovkova, E. V. Nilov, V. A. Rusov, I. N. Semenov, and A. A. Chertkov. 19(4), 503–5 (Oct. 1974); CPM-7412X0287

Niskonen, I. S.—High-frequency discharge in a mercury—helium mixture —S. D. Vagner, Yu. M. Kagan, A. I. Konstantinov, and I. S. Niskonen. 19(7), 898–900 (Jan. 1975); CPM-7503X0786

Nizhnik, L. P.—Rectangular conducting wedge in a moving electromagnetic field —I. D. Maergoiz and L. P. Nizhnik. 19(10), 1281–6 (Apr. 1975); CPM-7506X0215

Nosachev, L. V.—Hot probe measurements in a rarefied streaming plasma —E. M. Netsvetailov, L. V. Nosachev, and V. V. Skvortsov. 19(12), 1579–83 (Jun. 1975); CPM-7508X0453

Novikov, A. B.—Thermionic emission properties of zirconium, hafnium, and titanium nitrides in cesium vapor —M. A. Eremeev, V. S. Neshpor, A. B. Novikov, E. M. Stefanovskaya, and V. P. Fedorinov. 19(10), 1337–41 (Apr. 1975); CPM-7506X0271

Nuller, T. A.—Dependence of the basic parameters of $Al_xGa_{1-x}As$—GaAs solar converters on temperature and optical intensity —E. B. Vinogradova, M. B. Kagan, N. S. Koroleva, T. L. Lyubashevskaya, and T. A. Nuller. 19(10), 1378–81 (Apr. 1975); CPM-7506X0312

Nurmanov, M. Sh.—Symmetric multielectrode tubular electrostatic lenses —L. G. Glikman, V. M. Kel'man, and M. Sh. Nurmanov. 19(5), 680–2 (Nov. 1974); CPM-7501X0474

O

Ogienko, V. V.—Secondary-electron energy in a resonance discharge in a three-electrode system —Yu. A. Kulikov, V. V. Ogienko, and Yu. M. Trifonov. 19(8), 1090–2 (Feb. 1975); CPM-7504X1514

Ogorodnikov, S. N.—Ion-optical system for shaping high-current ion beams —S. D. Grishin, V. F. Kuzovlev, R. V. Orlov, and S. N. Ogorodnikov. 19(11), 1462–4 (May 1975); CPM-7506X1216

Oraevskii, A. N.—Photochemical waves in a medium with a branch-chain conversion mechanism —A. N. Oraevskii, V. P. Pimenov, and V. A. Shcheglov. 19(6), 782–6 (Dec. 1974); CPM-7501X0782

Orlov, R. V.—Ion-optical system for shaping high-current ion beams —S. D. Grishin, V. F. Kuzovlev, R. V. Orlov, and S. N. Ogorodnikov. 19(11), 1462–4 (May 1975); CPM-7506X1216

Osadin, B. A.—Condensation of a dense vapor flow —V. G. Dneprovskii, B. A. Osadin, and N. V. Rusakov. 19(2), 271–4 (Aug. 1974); CPM-7408X1535

—Effect of focusing conditions on the morphology of surface films produced with a laser —V. G. Dneprovskii and B. A. Osadin. 19 (2), 275–7 (Aug. 1974); CPM-7408X1539

—Condensation of an erosion plasma —B. A. Osadin and N. V. Rusakov. 19(2), 299–300 (Aug. 1974); CPM-7408X1563

Osipov, A. I.—Gas cooling in transmission of high-power CO_2 laser radiation through the atmosphere —B. F. Gordiets, A. I. Osipov, and R. V. Khokhlov. 19(5), 669–72 (Nov. 1974); CPM-7501X0463

Osipov, Yu. I.—New method for obtaining probe characteristics —Yu. I. Osipov. 19(2), 296–8 (Aug. 1974); CPM-7408X1560

Osoka, V. P.—Discharge in a cylindrical diode with surface ionization —V. P. Osoka and A. V. Potarov. 19(9), 1200–4 (Mar. 1975); CPM-7505X0622

Ostretsov, I. N.—Current density of thermionic-field emission into a plasma at moderate fields —I. N. Ostretsov, V. A. Petrosov, A. A. Porotnikov, and B. B. Rodnevich. 19(5), 707–8 (Nov. 1974); CPM-7501X0501

Ostrovskaya, G. V.—Investigation of spatial distributions in a laser-produced plasma by $H\alpha$ absorption —G. V. Ostrovskaya and N. A. Pobedonostseva. 19(3), 424–6 (Sep. 1974); CPM-7412X1110

Ostrovskii, Yu. I.—Hologram interferometry for vibration analysis —V. S. Listovets and Yu. I. Ostrovskii. 19(7), 847–60 (Jan. 1975); CPM-7503X0735

Osvenskii, V. B.—Crystal defects of heterostructures of AlAs–GaAs solid solutions and effect on the characteristics of injection lasers —L. V. Druzhinina, V. T. Bublik, L. M. Dolginov, P. G. Eliseev, M. P. Kerbelev, V. B. Osvenskii, I. Z. Pinsker, and M. G. Shumskii. 19(7), 935–9 (Jan. 1975); CPM-7503X0823

Ovchinnikov, I. T.—Investigating prebreakdown fields in water by means of the Kerr effect —I. T. Ovchinnikov, K. V. Yanshin, and É. V. Yanshin. 19(2), 294–5 (Aug. 1974); CPM-7408X1558

Ovchinnikov, V. L.—Excitation collisions between magnesium ions and inert gas atoms —V. L. Ovchinnikov, O. B. Shpenik, and I. P. Zapesochnyi. 19(3), 382–4 (Sep. 1974); CPM-7412X1068

Ovchinnikov, V. M.—Laser compensation for thermal distortion in optical pumping —V. K. Zaitsev, V. A. Il'inskii, A. M. Marugin, and V. M. Ovchinnikov. 19(11), 1480–1 (May 1975); CPM-7506X1234

P

Padalka, V. G.—Plasma confinement in a time-increasing multipole magnetic field —V. G. Padalka and N. S. Repalov. 19(1), 121–2 (Jul. 1974); CPM-7407X1633

—Focusing of a neutralized ion beam by a plasma-optics system —I. I. Demidenko, N. S. Lomino, A. I. Morozov, and V. G. Padalka. 19(3), 347–50 (Sep. 1974); CPM-7412X1033

—Effect of rf ionization on Hall-current plasma accelerator —I. I. Demidenko, N. S. Lomino, A. I. Morozov, and V. G. Padalka. 19 (12), 1560–3 (Jun. 1975); CPM-7508X0434

Pakhomov, V. I.—Quasilinear theory of beam-generated surface waves in a plasma —V. I. Pakhomov and V. L. Sizonenko. 19(5), 630–4 (Nov. 1974); CPM-7501X0424

Paleev, V. I.—Surface-ionization determination of the electron affinities of silver and gold —É. Ya. Zandberg, A. G. Kamenev, and V. I. Paleev. 19(3), 385–9 (Sep. 1974); CPM-7412X1071

—Determination of ionization potentials and electron affinities of certain elements by extrapolation —A. G. Kamenev, É. Ya. Zandberg, and V. I. Paleev. 19(7), 940–1 (Jan. 1975); CPM-7503X0828

Palkin, S. N.—Statistical characteristics of the turbulent wake behind a supersonic sphere —V. G. Ivanov, G. I. Mishin, and S. N. Palkin. 19(4), 543–5 (Oct. 1974); CPM-7412X0327

Pamfilov, A. V.—A useful function in the thermodynamics of irreversible processes —A. V. Pamfilov, A. I. Lopushanskaya, and L. B. Tsvetkova. 19(4), 535–7 (Oct. 1974); CPM-7412X0319

Panasyuk, V. S.—Extraction of synchroton radiation from a cyclic electron accelerator with a strong magnetic field —V. I. Kvochka, V. S. Panasyuk, V. F. Romanovskii, L. N. Samoilov, A. A. Sokolov, B. M. Stepanov, and Yu. M. Tereshkin. 19(6), 762–6 (Dec. 1974); CPM-7501X0762

Panchenko, I. P.—Transmission of a high–current relativistic beam through a gas —Yu. V. Tkach, I. I. Magda, G. V. Skachek, S. S. Pushkarev, and I. P. Panchenko. **19**(3), 412–3 (Sep. 1974); CPM-7412X1098

Pankratov, I. M.—Nonlinear behavior of monochromatic surface waves excited by a beam —A. B. Kitsenko, I. M. Pankratov, and K. N. Stepanov. **19**(11), 1505–6 (May 1975); CPM-7506X1259

Pankratov, S. G.—Radiation of electromagnetic waves by a modulated electron beam —S. G. Pankratov. **19**(9), 1248–50 (Mar. 1975); CPM-7505X0670

Parilis, É. S.—Doppler profile of an atomic line to the differential excitation cross section —É. S. Parilis and V. Kh. Ferleger. **19**(10), 1367–70 (Apr. 1975); CPM-7506X0301

Pashchenko, A. V.—Wave interaction in a thin plasma sheath —A. V. Pashchenko and B. N. Rutkevich. **19**(6), 726–31 (Dec. 1974); CPM-7501X0726

—Two-stream flow in a thin plasma slab —A. V. Pashchenko and B. N. Rutkevich. **19**(12), 1538–40 (Jun. 1975); CPM-7508X0412

Pashchenko, V. P.—Steady-state operation of a surface-ionization thermionic converter —N. V. Volkov, Yu. K. Gus'kov, Yu. I. Kostikov, and V. P. Pashchenko. **19**(8), 1129–30 (Feb. 1975); CPM-7504X1553

—Analytic model of the cesium arc —V. P. Pashchenko, V. L. Mironovich, and I. P. Stakhanov. **19**(10), 1332–6 (Apr. 1975); CPM-7506X0266

Pashnev, V. K.—Hydrodynamic stability of the Uragan stellarator —V. M. Zalkind, Yu. K. Kuznetsov, V. K. Pashnev, and V. M. Tonkopryad. **19**(8), 1123–5 (Feb. 1975); CPM-7504X1547

Paskalev, K. K.—Gas temperature in the positive column of a medium-β helium discharge —Yu. M. Kagan and K. K. Paskalev. **19**(12), 1601–3 (Jun. 1975); CPM-7508X0475

—Temperature and electron density in the positive column of a medium-pressure helium discharge —Yu. M. Kagan and K. K. Paskalev. **19**(12), 1604–5 (Jun. 1975); CPM-7508X0478

Paslen, V. N.—Formation of molecular ions in an alkali discharge —V. N. Paslen and A. M. Przhonskii. **19**(5), 705–6 (Nov. 1974); CPM-7501X0499

Pasynok, A. I.—Parametric instability of an electron beam in a magnetic field —A. I. Pasynok and N. S. Repalov. **19**(2), 177–80 (Aug. 1974); CPM-7408X1441

—Parametric excitation of surface waves in a spatially modulated electron beam —A. I. Pasynok and N. S. Repalov. **19**(4), 572–3 (Oct. 1974); CPM-7412X0356

Pats'ora, S. K.—Ion focusing of an electron beam in deep melting of a metal —M. D. Gabovich, V. P. Kovalenko, O. A. Metallov, O. K. Nazarenko, and S. K. Pats'ora. **19**(7), 973–4 (Jan. 1975); CPM-7503X0861

Paverman, V. S.—Low-frequency helical instability in a high-frequency electric field —V. S. Paverman and D. D. Tskhakaya. **19**(11), 1508–9 (May 1975); CPM-7506X1262

—Parametric excitation of helicon waves in a plasma by modulated radio frequency waves —V. S. Paverman and D. D. Tskhakya. **19** (12), 1629–30 (Jun. 1975); CPM-7508X0503

Pavlenko, Yu. G.—Microwave maser with nonrelativistic electrons —A. S. Dement'ev and Yu. G. Pavlenko. **19**(5), 694–5 (Nov. 1974); CPM-7501X0488

Pavlova, A. D.—Energy dependence of the focusing of ions by crystals —E. S. Mashkova, V. A. Molchanov, and A. D. Pavlova. **19**(4), 540 (Oct. 1974); CPM-7412X0324

Pazin, K. N.—Magnetic-field transport of a high-current electron beam —A. V. Agafonov, V. S. Voronin, A. N. Lebedev, and K. N. Pazin. **19**(9), 1188–92 (Mar. 1975); CPM-7505X0610

Peletminskaya, V. G.—Magnetic topography of toroidal systems —M. N. Skoblik, V. E. Ziser, A. V. Georgievskii, and V. G. Peletminskaya. **19**(10), 1277–80 (Apr. 1975); CPM-7506X0211

Perebeinos, V. V.—Dynamics and emission of coaxial plasma shells in air —A. F. Aleksandrov, V. V. Perebeinos, A. T. Savichev, and I. B. Timofeev. **19**(1), 38–42 (Jul. 1974); CPM-7407X1550

—Initial stage of a high-current discharge in air —A. F. Aleksandrov, V. V. Perebeinos, A. T. Savichev, and I. B. Timofeev. **19**(11), 1490–1 (May 1975); CPM-7506X1244

Peregud, B. P.—Plasma diffusion in the Tornado device —A. N. Kozyrev and B. P. Peregud. **19**(4), 468–74 (Oct. 1974); CPM-7412X0252

Perel'man, T. L.—Fundamentals of heat-pipe theory and design —M. M. Levitan and T. L. Perel'man. **19**(8), 983–95 (Feb. 1975); CPM-7504X1407

Perepelkin, S. S.—Shielding properties of superconducting shields —S. I. Bondarenko, S. S. Vinogradov, G. A. Gogadze, S. S. Perepelkin, and V. I. Sheremet. **19**(6), 824–8 (Dec. 1974); CPM-7501X0824

Perlin, A. S.—High–current pulsed electron accelerator with an annular beam —M. I. Avramenko, V. A. Glukhikh, O. A. Gusev, E. G. Komar, O. L. Komarov, V. S. Kuznetsov, A. S. Perlin, and M. P. Svin'in. **19**(3), 368–70 (Sep. 1974); CPM-7412X1054

Petrosov, V. A.—Current density of thermionic–field emission into a plasma at moderate fields —I. N. Ostretsov, V. A. Petrosov, A. A. Porotnikov, and B. B. Rodnevich. **19**(5), 707–8 (Nov. 1974); CPM-7501X0501

Petrov, V. G.—Ionization discontinuity in large–amplitude striations —A. V. Nedospasov and V. G. Petrov. **19**(1), 31–4 (Jul. 1974); CPM-7407X1543

Petrov, V. V.—Optical methods for studying amplification of elastic surface waves in a stratified system —I. B. Yakovkin, V. V. Petrov, and S. V. Bogdanov. **19**(9), 1242–5 (Mar. 1975); CPM-7505X0664

Petrunin, V. I.—Resonator with azimuthally varying end plates —M. F. Vorogushin and V. I. Petrunin. **19**(6), 767–9 (Dec. 1974); CPM-7501X0767

—Azimuthal and vertical motion in an accelerator with azimuthally varying electric field —M. F. Vorogushin and V. I. Petrunin. **19**(6), 770–2 (Dec. 1974); CPM-7501X0770

—Phase motion of particles in an accelerator with an azimuthally varying electric field —M. F. Vorogushin and V. I. Petrunin. **19**(7), 926–9 (Jan. 1975); CPM-7503X0814

Petrun'kin, V. Yu.—Effect of a magnetic field on spontaneous mode-locking in a He—Ne laser ($\Lambda=0.63\mu$) —V. Yu. Petrun'kin, V. M. Nikolaev, O. I. Kotov, and B. V. L'vov. **19**(12), 1612–3 (Jun. 1975); CPM-7508X0486

Piliya, A. D.—Absolute decay instability of low–frequency waves in an inhomogeneous plasma —A. D. Piliya and V. I. Fedorov. **19**(5), 686 (Nov. 1974); CPM-7501X0480

Pimenov, V. P.—Photochemical waves in a medium with a branch–chain conversion mechanism —A. N. Oraevskii, V. P. Pimenov, and V. A. Shcheglov. **19**(6), 782–6 (Dec. 1974); CPM-7501X0782

Pimkin, V. A.—Breakdown caused by electron bombardment of the surface of an alloy electrode —N. V. Belan, G. I. Kostyuk, and V. A. Pimkin. **19**(6), 802–3 (Dec. 1974); CPM-7501X0802

Pinchuk, V. P.—Atomic recombination on a solid surface —V. P. Pinchuk, A. N. Gorban', and V. G. Kornich. **19**(6), 808–10 (Dec. 1974); CPM-7501X0808

Pinsker, I. Z.—Crystal defects of heterostructures of AlAs–GaAs solid solutions and effect on the characteristics of injection lasers —L. V. Druzhinina, V. T. Bublik, L. M. Dolginov, P. G. Eliseev, M. P. Kerbelev, V. B. Osvenskii, I. Z. Pinsker, and M. G. Shumskii. **19**(7), 935–9 (Jan. 1975); CPM-7503X0823

Piterskii, V. V.—Measurement of plasma electron temperature with a sinusoidal probe potential —B. I. Kanaev, V. V. Piterskii, and E. E. Yushmanov. **19**(11), 1421–3 (May 1975); CPM-7506X1175

Plakhov, A. G.—Scattering of an electron beam in a straight *dc* turbulent plasma —Yu. P. Golovanov, L. P. Zakatov, A. S. Kingsep, and A. G. Plakhov. **19**(8), 1046–9 (Feb. 1975); CPM-7504X1470

Plis, A. I.—Radiation from a charged particle moving close to an anisotropic dielectric —A. I. Plis and N. M. Safikhodzhaev. **19**(7), 865–7 (Jan. 1975); CPM-7503X0753

—Gas polymerization wave excited by monochromatic light —A. I. Plis and V. A. Shcheglov. **19**(9), 1262–3 (Mar. 1975); CPM-7505X0684

Pliskovskii, V. Ya.—Use of a field-emission microscope to measure the pressure of pump oil —V. Ya. Pliskovskii, M. S. Sukonnik, and V. A. Shishkin. **19**(10), 1347–51 (Apr. 1975); CPM-7506X0281

Pliss, N. S.—Simulation of ion scattering on diatomic molecules —M. L. Aleksandrov, N. S. Pliss, and A. P. Shcherbakov. **19**(3), 394–5 (Sep. 1974); CPM-7412X1080

—Monte Carlo analysis of ion scattering in a mass spectrometer —M. L. Aleksandrov, L. N. Gall', and N. S. Pliss. **19**(6), 817–9 (Dec. 1974); CPM-7501X0817

Plyutto, A. A.—Pulsed ion beams from a high-current plasma diode —B. A. Tskhadaya, A. A. Plyutto, and K. V. Suladze. **19**(8), 1108–9 (Feb. 1975); CPM-7504X1532

Pobedonostseva, N. A.—Investigation of spatial distributions in a laser–produced plasma by Hα absorption —G. V. Ostrovskaya and N. A. Pobedonostseva. **19**(3), 424–6 (Sep. 1974); CPM-7412X1110

Podteregera, N. N.—Plasma equilibrium and confinement in a poloidal heliotron configuration. I —V. G. Zykov, V. I. Karpukhin, Yu. F. Lonin, N. N. Podteregera, N. I. Rudnev, and V. T. Tolok. 19(8), 1063–8 (Feb. 1975); CPM-7504X1487
—Plasma equilibrium and confinement in a poloidal heliotron configuration. II —V. G. Zykov, V. I. Karpukhin, Yu. F. Lonin, N. N. Podteregera, N. I. Rudnev, A. Y. Skibenko, V. T. Tolok, and I. P. Fomin. 19(8), 1069–72 (Feb. 1975); CPM-7504X1493
Pokhmel'nykh, L. A.—Radio-frequency absorption in a plasma confined by rf plugs —K. S. Golovanivskii, V. D. Dougar-Jabon, and L. A. Pokhmel'nykh. 19(11), 1484–5 (May 1975); CPM-7506X1238
Polenov, B. V.—Electrostatic analyzer for wide beams —V. G. Kovalenko and B. V. Polenov. 19(4), 561–2 (Oct. 1974); CPM-7412X0345
Polyakov, V. M.—Experimental investigation of microwave radiation produced by hypersonic flows —V. A. Lyutomskii, V. M. Polyakov, and V. G. Testov. 19(4), 483–5 (Oct. 1974); CPM-7412X0267
Polyanichev, A. N.—Recombination in an expanding plasma —Yu. A. Bykovskii, N. N. Degtyarenko, V. F. Elesin, V. E. Kondrashov, E. E. Lovetskii, A. N. Polyanichev, and V. S. Fetisov. 19(1), 43–8 (Jul. 1974); CPM-7407X1555
—Expansion of a recombining plasma in vacuum —E. E. Lovetskii, A. N. Polyanichev, and V. S. Fetisov. 19(5), 647–50 (Nov. 1974); CPM-7501X0441
Pomelov, Ya. A.—Effects of ion microfields on emission of an arc cathode —A. M. Dorodnov, V. B. Davydov, A. V. Kozyrev, and Ya. A. Pomelov. 19(3), 390–3 (Sep. 1974); CPM-7412X1076
Pontekorvo, D. B.—Effects due to streamer shape —É. D. Lozanskii and D. B. Pontekorvo. 19(11), 1432–3 (May 1975); CPM-7506X1186
Poplavko, Yu. M.—Dispersion of the dielectric constant of crystalline KH_2PO_4 near the "soft" mode frequency —V. V. Meriakri, Yu. M. Poplavko, and E. F. Ushatkin. 19(5), 703–4 (Nov. 1974); CPM-7501X0497
Popov, O. Ya.—Analysis of magnetic deflection systems —O. M. Vovk and O. Ya. Popov. 19(11), 1504 (May 1975); CPM-7506X1258
Popov, S. G.—Electron spectrometer for electric excitation of nuclei in a storage ring —D. M. Nikolenko and S. G. Popov. 19(2), 280–3 (Aug. 1974); CPM-7408X1544
Popov, Yu. V.—Time characteristics of the near radiation field of the injection laser —Zh. I. Alferov, V. N. Deryagin, L. E. Marasin, Yu. V. Popov, and E. L. Portnoi. 19(4), 548 (Oct. 1974); CPM-7412X0332
Popytaev, A. N.—Interaction of intense laser radiation with solid targets —L. V. Dubovoi, V. D. Dyatlov, V. I. Kryzhanovskii, A. A. Mak, R. N. Medvedev, A. N. Popytaev, V. A. Serebryakov, V. N. Sizov, and A. D. Starikov. 19(11), 1477–9 (May 1975); CPM-7506X1231
Porodnov, B. T.—Use of the distribution function to describe free molecular beams —I. G. Neudachin, B. T. Porodnov, and P. E. Suetin. 19(4), 511–4 (Oct. 1974); CPM-7412X0295
—Flow of low-density gases in a capillary grid —B. T. Porodnov, V. D. Akin'shin, V. I. Kichaev, S. F. Borisov, and P. E. Suetin. 19(4), 515–8 (Oct. 1974); CPM-7412X0299
Porotnikov, A. A.—Current density of thermionic-field emission into a plasma at moderate fields —I. N. Ostretsov, V. A. Petrosov, A. A. Porotnikov, and B. B. Rodnevich. 19(5), 707–8 (Nov. 1974); CPM-7501X0501
Portnoi, E. L.—Time characteristics of the near radiation field of the injection laser —Zh. I. Alferov, V. N. Deryagin, L. E. Marasin, Yu. V. Popov, and E. L. Portnoi. 19(4), 548 (Oct. 1974); CPM-7412X0332
—Characteristics of diffraction gratings obtained by photoetching of semiconductor surfaces —L. V. Belyakov, D. N. Goryachev, M. N. Mizerov, and E. L. Portnoi. 19(6), 837–8 (Dec. 1974); CPM-7501X0837
Portnyagin, A. I.—Thermal effect of continuous laser radiation on optically transparent media —N. S. Bardina, A. I. Portnyagin, M. Yu. Sklyarov, and A. A. Churin. 19(4), 491–4 (Oct. 1974); CPM-7412X0275
Potarov, A. V.—Discharge in a cylindrical diode with surface ionization —V. P. Osoka and A. V. Potarov. 19(9), 1200–4 (Mar. 1975); CPM-7505X0622
Prilezhaev, D. S.—Lasing properties of Yb^{3+} and Er^{3+} glass laser pumped by a laser —V. N. Kalinin, A. A. Mak, D. S. Prilezhaev, and V. A. Fromzel'. 19(6), 835–6 (Dec. 1974); CPM-7501X0835
Privalov, V. E.—Mode coupling in a double-anode discharge —Yu. G. Zakharenko and V. E. Privalov. 19(7), 980–2 (Jan. 1975); CPM-7503X0868
Privezentsev, V. I.—Investigation of a plasma focus with a time-resolved laser interferometer —I. M. Zolototrubov, I. P. Skoblik, A. G. Tolstolutskii, and V. I. Privezentsev. 19(8), 1061–2 (Feb. 1975); CPM-7504X1485
Prokopov, A. V.—Microwave discharge in argon —E. V. Belousov, A. S. Bryukhovetskii, and A. V. Prokopov. 19(1), 53–6 (Jul. 1974); CPM-7407X1565
—Effect of ionization and excitation on the penetration of an electromagnetic wave into a weakly ionized plasma —A. G. Boev and A. V. Prokopov. 19(7), 901–4 (Jan. 1975); CPM-7503X0789
Protasov, Yu. S.—Use of plasma accelerator for optical pumping of lasers —N. P. Kozlov and Yu. S. Protasov. 19(3), 358–60 (Sep. 1974); CPM-7412X1044
—Formation of a plasma focus in a plasma erosion accelerator. II. Energy characteristics of the dense plasma focus —N. P. Kozlov, L. V. Leskov, Yu. S. Protasov, and V. I. Khvesyuk. 19(12), 1558–9 (Jun. 1975); CPM-7508X0432
Protsenko, I. M.—Gas focusing of a negative-ion beam —M. D. Gabovich, A. P. Naida, I. M. Protsenko, L. S. Simonenko, and I. A. Soloshenko. 19(4), 546–7 (Oct. 1974); CPM-7412X0330
Pruzhanovskii, V. A.—Round metal-optical waveguide filled with a two-layer dielectric —V. A. Pruzhanovskii. 19(1), 3–8 (Jul. 1974); CPM-7407X1515
Przhonskii, A. M.—Formation of molecular ions in an alkali discharge —V. N. Paslen and A. M. Przhonskii. 19(5), 705–6 (Nov. 1974); CPM-7501X0499
Puchkova, N. G.—Exact solutions of the nonlinear electrodynamic equations —N. G. Puchkova and A. F. Kulish. 19(12), 1614–5 (Jun. 1975); CPM-7508X0488
Pushkarev, S. S.—Transmission of a high-current relativistic beam through a gas —Yu. V. Tkach, I. I. Magda, G. V. Skachek, S. S. Pushkarev, and I. P. Panchenko. 19(3), 412–3 (Sep. 1974); CPM-7412X1098
Putvinskii, S. V.—Drift instability in a weakly ionized plasma —S. V. Putvinskii and A. V. Timofeev. 19(10), 1295–9 (Apr. 1975); CPM-7506X0229
Pyatak, A. I.—Instabilities in a finite-β plasma with transverse current. I —A. I. Pyatak and V. L. Sizonenko. 19(5), 635–9 (Nov. 1974); CPM-7501X0429
—Instabilities in a finite-β plasma with transverse current. II —A. I. Pyatak and V. L. Sizonenko. 19(5), 640–4 (Nov. 1974); CPM-7501X0434
—High-frequency instabilities in an inhomogeneous, anisotropic finite-β plasma —V. D. Egorenkov and A. I. Pyatak. 19(9), 1160–2 (Mar. 1975); CPM-7505X0582

R

Radchenko, Yu. F.—Development of an inhibited glow discharge —Yu. A. Bystrov, S. A. Ivanov, and Yu. F. Radchenko. 19(11), 1447–8 (May 1975); CPM-7506X1201
Ranyuk, A. I.—Kinetic plasma instabilities excited by a monoenergetic beam —A. I. Ranyuk and V. L. Sizonenko. 19(5), 628–9 (Nov. 1974); CPM-7501X0422
Razdobarin, G. T.—Diagnostics of a laser-produced plasma by a scattering method using an electron-optical image converter —E. A. Burunov, G. M. Malyshev, G. T. Razdobarin, and V. V. Semenov. 19(1), 66–9 (Jul. 1974); CPM-7407X1578
Regirer, S. A.—Magnetohydrodynamic channel flow in a tapered magnetic field —S. A. Regirer. 19(7), 874–7 (Jan. 1975); CPM-7503X0762
Rekova, L. P.—Elimination of carbon impurities from platinum by heating in an oxygen atmosphere —L. P. Rekova, V. V. Mozgin, L. N. Zvyagintseva, V. N. Bondarenko, and Ya. M. Fogel'. 19(11), 1465–7 (May 1975); CPM-7506X1219
Remesnik, V. G.—Multiple recording and erasure of optical information in certain glassy chalcogenides —V. V. Korsakov, V. I. Nalivaiko, V. G. Remesnik, and V. G. Tsukerman. 19(4), 565–6 (Oct. 1974); CPM-7412X0349
Repalov, N. S.—Plasma confinement in a time-increasing multipole magnetic field —V. G. Padalka and N. S. Repalov. 19(1), 121–2 (Jul. 1974); CPM-7407X1633

—Parametric instability of an electron beam in a magnetic field —A. I. Pasynok and N. S. Repalov. 19(2), 177–80 (Aug. 1974); CPM-7408X1441

—Parametric excitation of surface waves in a spatially modulated electron beam —A. I. Pasynok and N. S. Repalov. 19(4), 572–3 (Oct. 1974); CPM-7412X0356

—Parametric instability of a spatially moderated electron beam in a magnetic field —N. S. Repalov and V. F. Tyrnov. 19(7), 871–3 (Jan. 1975); CPM-7503X0759

Reshenov, S. P.—Nonequilibrium ionization in the cathode region of a high-pressure arc —S. P. Reshenov. 19(8), 1073–5 (Feb. 1975); CPM-7504X1497

Reshetnyak, S. A.—Plasma dynamic lasers —S. A. Reshetnyak and L. A. Shelepin. 19(8), 1076–80 (Feb. 1975); CPM-7504X1500

Reznikov, V. P.—Electron energy spectrum in high-energy nanosecond accelerators —V. V. Kremnev, G. A. Mesyats, and V. P. Reznikov. 19(10), 1342–4 (Apr. 1975); CPM-7506X0276

Rikenglaz, L. É.—Microwave propagation in a low-loss dielectric —L. É. Rikenglaz. 19(6), 713–4 (Dec. 1974); CPM-7501X0713

Rodichkin, V. A.—Laser-initiated vacuum discharge —V. P. Kovalenko, A. A. Makarevich, V. A. Rodichkin, and A. M. Timonin. 19(11), 1429–31 (May 1975); CPM-7506X1183

Rodnevich, B. B.—Current density of thermionic–field emission into a plasma at moderate fields —I. N. Ostretsov, V. A. Petrosov, A. A. Porotnikov, and B. B. Rodnevich. 19(5), 707–8 (Nov. 1974); CPM-7501X0501

Rogozinskii, V. G.—Two-omegatron study of the pumping characteristics of an NÉM-300 magnetic discharge pump for a mixture of gases —M. K. Bulgakov and V. G. Rogozinskii. 19(3), 427–8 (Sep. 1974); CPM-7412X1113

—Titanium-pump system for hydrogen —K. G. Mirzoev, V. G. Rogozinskii, and V. L. Ushkov. 19(3), 432–3 (Sep. 1974); CPM-7412X1118

Rokhinson, É. Kh.—Possible electrohydrodynamic effects in electrolytes —E. Z. Gak, É. Kh. Rokhinson, and N. F. Bondarenko. 19(5), 676–7 (Nov. 1974); CPM-7501X0470

Romanov, P. V.—Numerical experiments on electron bombardment in crossed fields —P. V. Romanov and A. S. Roshal'. 19(9), 1221–3 (Mar. 1975); CPM-7505X0643

Romanov, S. S.—Diffusion of quasistationary helical magnetic fields into the interior of cylindrical chambers. II. —V. F. Aleksin and S. S. Romanov. 19(9), 1171–3 (Mar. 1975); CPM-7505X0593

Romanov, Yu. A.—Surface waves in periodic plasma systems —V. F. Dryakhlushin and Yu. A. Romanov. 19(7), 883–6 (Jan. 1975); CPM-7503X0771

Romanovskii, V. F.—Extraction of synchroton radiation from a cyclic electron accelerator with a strong magnetic field —V. I. Kvochka, V. S. Panasyuk, V. F. Romanovskii, L. N. Samoilov, A. A. Sokolov, B. M. Stepanov, and Yu. M. Tereshkin. 19(6), 762–6 (Dec. 1974); CPM-7501X0762

Roshal', A. S.—Numerical experiments on electron bombardment in crossed fields —P. V. Romanov and A. S. Roshal'. 19(9), 1221–3 (Mar. 1975); CPM-7505X0643

Roshchin, A. A.—Proton extraction from the 70-GeV accelerator for the Ludmila liquid-hydrogen chamber (extraction system S) —A. A. Aseev, A. I. Drozhdin, B. A. Zelenov, É. A. Merker, L. L. Moizhes, K. P. Myznikov, A. A. Roshchin, V. M. Tatarenko, M. A. Kholodenko, A. D. Artemov, L. N. Vaulin, V. I. Gordin, I. I. Kovalevskii, V. N. Rozhkov, M. M. Suvorov, A. S. Sudarushkin, and V. I. Chuiko. 19(1), 70–6 (Jul. 1974); CPM-7407X1582

Rozhkov, A. M.—Plasma decay instability in crossed fields —V. I. Farenik, V. V. Vlasov, A. M. Rozhkov, and A. A. Kozharin. 19(8), 1116–7 (Feb. 1975); CPM-7504X1540

—Ion energy spectra and collective effects in a Penning ion source —V. I. Farenik, V. V. Vlasov, A. M. Rozhkov, and A. A. Kozharin. 19(9), 1258–9 (Mar. 1975); CPM-7505X0680

Rozhkov, V. N.—Proton extraction from the 70-GeV accelerator for the Ludmila liquid-hydrogen chamber (extraction system S) —A. A. Aseev, A. I. Drozhdin, B. A. Zelenov, É. A. Merker, L. L. Moizhes, K. P. Myznikov, A. A. Roshchin, V. M. Tatarenko, M. A. Kholodenko, A. D. Artemov, L. N. Vaulin, V. I. Gordin, I. I. Kovalevskii, V. N. Rozhkov, M. M. Suvorov, A. S. Sudarushkin, and V. I. Chuiko. 19(1), 70–6 (Jul. 1974); CPM-7407X1582

Rudenko, N. S.—Streamer propagation after the voltage termination in a streamer chamber —N. S. Rudenko and V. I. Smetanin. 19 (12), 1616–7 (Jun. 1975); CPM-7508X0490

Rudnev, N. I.—Plasma equilibrium and confinement in a poloidal heliotron configuration. I —V. G. Zykov, V. I. Karpukhin, Yu. F. Lonin, N. N. Podteregera, N. I. Rudnev, and V. T. Tolok. 19(8), 1063–8 (Feb. 1975); CPM-7504X1487

—Plasma equilibrium and confinement in a poloidal heliotron configuration. II —V. G. Zykov, V. I. Karpukhin, Yu. F. Lonin, N. N. Podteregera, N. I. Rudnev, A. Y. Skibenko, V. T. Tolok, and I. P. Fomin. 19(8), 1069–72 (Feb. 1975); CPM-7504X1493

Rukhadze, A. A.—Radiating discharges confined by walls —A. F. Aleksandrov, I. S. Marshak, and A. A. Rukhadze. 19(3), 308–14 (Sep. 1974); CPM-7412X0994

—Excitation of surface electromagnetic waves in a plasma cylinder surrounded by a hollow electron beam —O. V. Dolzhenko, A. V. Zosimov, and A. A. Rukhadze. 19(5), 618–21 (Nov. 1974); CPM-7501X0412

Rusakov, N. V.—Condensation of a dense vapor flow —V. G. Dneprovskii, B. A. Osadin, and N. V. Rusakov. 19(2), 271–4 (Aug. 1974); CPM-7408X1535

—Condensation of an erosion plasma —B. A. Osadin and N. V. Rusakov. 19(2), 299–300 (Aug. 1974); CPM-7408X1563

Rusanov, V. D.—Acceleration of plasma electrons in strong electric fields —Z. A. Al'bikov, M. I. Ivanov, V. I. Kazacha, O. V. Kozlov, V. D. Rusanov, and S. S. Sobolev. 19(11), 1498–9 (May 1975); CPM-7506X1252

Rusov, V. A.—Pulsed neodymium–glass laser with periodic Q switching —T. A. Kuzovkova, E. V. Nilov, V. A. Rusov, I. N. Semenov, and A. A. Chertkov. 19(4), 503–5 (Oct. 1974); CPM-7412X0287

Rutkevich, B. N.—Wave interaction in a thin plasma sheath —A. V. Pashchenko and B. N. Rutkevich. 19(6), 726–31 (Dec. 1974); CPM-7501X0726

—Two-stream flow in a thin plasma slab —A. V. Pashchenko and B. N. Rutkevich. 19(12), 1538–40 (Jun. 1975); CPM-7508X0412

Rut'kov, E. V.—Time dependence of ion currents produced through surface ionization. Ionization of Ba on the (111) face of iridium —É. Ya. Zandberg, E. V. Rut'kov, and A. Ya. Tontegode. 19(2), 261–3 (Aug. 1974); CPM-7408X1525

Ryabchikov, A. I.—Reflection of a high-current relativistic electron beam from a conducting surface —A. N. Didenko, A. I. Ryabchikov, V. A. Tuzov, and Yu. P. Usov. 19(12), 1625–6 (Jun. 1975); CPM-7508X0499

Ryabtsov, A. V.—Linear accelerator for beam injection into a slowly rising magnetic field —D. G. Borisov, A. I. Gryzlov, V. M. Levin, and A. V. Ryabtsov. 19(4), 509–10 (Oct. 1974); CPM-7412X0293

Rybin, P. P.—Two-section solenoid with internal "equally-loaded" section; power as a function of the length of the internal section —G. S. Veisig, A. P. Doroshenko, and P. P. Rybin. 19(3), 416–8 (Sep. 1974); CPM-7412X1102

Ryzhov, Ń. M.—Magnetodrift waves in a finite-β plasma —Ń. M. Ryzhov, V. L. Sizonenko, V. A. Suprunenko, E. A. Sukhomlin, and Yu. V. Gutarev. 19(6), 722–5 (Dec. 1974); CPM-7501X0722

S

Saenko, V. A.—Electron-beam excited crossed-field discharge —V. A. Saenko and M. M. Kasumov. 19(6), 759–61 (Dec. 1974); CPM-7501X0759

Safikhodzhaev, N. M.—Radiation from a charged particle moving close to an anisotropic dielectric —A. I. Plis and N. M. Safikhodzhaev. 19(7), 865–7 (Jan. 1975); CPM-7503X0753

Safonov, M. P.—Efficiency of the scattering of "unstable" charged particles in quadrupole mass spectrometers —É. P. Sheretov, B. I. Kolotilin, and M. P. Safonov. 19(12), 1622–4 (Jun. 1975); CPM-7508X0496

Sakharov, I. E.—Effect of plasma parameters on emission in an ion laser —I. E. Sakharov, V. V. Ermolin, and S. V. Shatalin. 19(8), 1081–4 (Feb. 1975); CPM-7504X1505

Salyadinov, V. S.—Optical characteristics of K-8 glass subject to radiation from a neodymium laser —A. M. Bonch-Bruevich, Ya. A. Imas, V. S. Salyadinov, and A. V. Shatilov. 19(2), 287–9 (Aug. 1974); CPM-7408X1551

Samoilenko, Yu. I.—Distributed systems for feedback control of a tokamak plasma —V. F. Gubarev and Yu. I. Samoilenko. 19(4), 463–7 (Oct. 1974); CPM-7412X0247

Samoilov, L. N.—Extraction of synchroton radiation from a cyclic electron accelerator with a strong magnetic field —V. I. Kvochka, V. S. Panasyuk, V. F. Romanovskii, L. N. Samoilov, A. A. Sokolov, B. M. Stepanov, and Yu. M. Tereshkin. 19(6), 762–6 (Dec. 1974); CPM-7501X0762

Sanochkin, Yu. V.—Low-pressure self-maintained discharge with suppressed electron drift. I —V. K. Kalashnikov and Yu. V. Sanochkin. 19(12), 1549–53 (Jun. 1975); CPM-7508X0423
—Low-pressure self-maintained discharge with suppressed electron drift. II —Yu. V. Sanochkin and V. K. Kalashnikov. 19(12), 1554–8 (Jun. 1975); CPM-7508X0428
Sapargaliev, A. A.—Theory of the cathode lens. III. Derivation of equations for composite cathode lenses —V. M. Kel'man, A. A. Sapargaliev, and E. M. Yakushev. 19(5), 592–6 (Nov. 1974); CPM-7501X0386
—Theory of the cathode lens. IV. Aberrations of composite cathode lens —V. M. Kel'man, A. A. Sapargaliev, and E. M. Yakushev. 19 (5), 597–9 (Nov. 1974); CPM-7501X0391
Savichev, A. T.—Dynamics and emission of coaxial plasma shells in air —A. F. Aleksandrov, V. V. Perebeinos, A. T. Savichev, and I. B. Timofeev. 19(1), 38–42 (Jul. 1974); CPM-7407X1550
—Initial stage of a high-current discharge in air —A. F. Aleksandrov, V. V. Perebeinos, A. T. Savichev, and I. B. Timofeev. 19(11), 1490–1 (May 1975); CPM-7506X1244
Savichev, V. V.—Effect of a high-current relativistic electron beam on a metal —B. I. Dmitrenko, L. V. Leskov, G. P. Maksimov, S. L. Nedoseev, V. V. Savichev, V. P. Smirnov, and A. M. Spektor. 19 (9), 1224–5 (Mar. 1975); CPM-7505X0646
Savin, V. V.—Characteristics of the electrical ionization CO$_2$ laser —Yu. I. Bychkov, Yu. A. Kurbatov, and V. V. Savin. 19(4), 506–8 (Oct. 1974); CPM-7412X0290
Savkin, V. Ya.—Formation of a narrow gas jet in vacuum —G. I. Dimov and V. Ya. Savkin. 19(6), 755–8 (Dec. 1974); CPM-7501X0755
Seleznev, V. G.—Method for determining the absolute characteristics of CF$_3$I laser emission —V. S. Komarov, V. G. Seleznev, and G. A. Skorobogatov. 19(4), 558–60 (Oct. 1974); CPM-7412X0342
—Absolute-photometry determination of the rate constant of the gas-phase reaction of the radical compound C$_3$F$_7$ and I(^{2}P$_{3/2}$) —G. A. Skorobogatov, V. S. Komarov, and V. G. Seleznev. 19(9), 1239–41 (Mar. 1975); CPM-7505X0661
Selin, L. N.—Contraction of the positive column of a glow discharge due to the presence of negative ions —L. A. Mikhalev and L. N. Selin. 19(5), 689–90 (Nov. 1974); CPM-7501X0483
Selyakov, V. I.—Multiple reflection of light in a shock tube —V. D. Mironov and V. I. Selyakov. 19(3), 402–4 (Sep. 1974); CPM-7412X1088
Semashko, N. N.—Production of an ion beam by a magnetic system with opposed fields —V. B. Glasko, A. G. Sveshnikov, and N. N. Semashko. 19(2), 201–5 (Aug. 1974); CPM-7408X1465
Semenov, I. N.—Pulsed neodymium–glass laser with periodic Q switching —T. A. Kuzovkova, E. V. Nilov, V. A. Rusov, I. N. Semenov, and A. A. Chertkov. 19(4), 503–5 (Oct. 1974); CPM-7412X0287
Semenov, V. V.—Diagnostics of a laser–produced plasma by a scattering method using an electron–optical image converter —E. A. Burunov, G. M. Malyshev, G. T. Razdobarin, and V. V. Semenov. 19(1), 66–9 (Jul. 1974); CPM-7407X1578
—Two–spin oscillator with optical orientation of electrons and nuclei —R. A. Zhitnikov and V. V. Semenov. 19(1), 105–9 (Jul. 1974); CPM-7407X1617
—Effect of instrumental noise on a system with two spin oscillators using Cs^{133} and He^3 —R. A. Zhitnikov, V. V. Semenov, and P. A. Klyushkin. 19(4), 556–7 (Oct. 1974); CPM-7412X0340
Serebryakov, V. A.—Interaction of intense laser radiation with solid targets —L. V. Dubovoi, V. D. Dyatlov, V. I. Kryzhanovskii, A. A. Mak, R. N. Medvedev, A. N. Popytaev, V. A. Serebryakov, V. N. Sizov, and A. D. Starikov. 19(11), 1477–9 (May 1975); CPM-7506X1231
Serezhkin, Yu. G.—Narrow–band decimeter radiation from lighting —E. L. Kosarev and Yu. G. Serezhkin. 19(2), 229–33 (Aug. 1974); CPM-7408X1493
Sergeev, A. A.—Plasma density in a magnetoplasma compressor —A. K. Vinogradova, V. P. Vinogradov, A. I. Morozov, and A. A. Sergeev. 19(3), 421–3 (Sep. 1974); CPM-7412X1107
Sergeev, A. V.—Aberrations in systems with plane and spherical detection apertures —V. V. Izokh, A. V. Sergeev, and I. Yu. Shmidov. 19(9), 1177–80 (Mar. 1975); CPM-7505X0599
Serikov, A. V.—Modulation of microwaves by density fluctuations in a plasma —L. A. Dushin, A. V. Serikov, A. I. Skibenko, E. V. Krivorukov, and I. P. Fomin. 19(9), 1163–7 (Mar. 1975); CPM-7505X0585
Serov, Yu. L.—Interferometer measurement of the neutral cesium distribution in a short low–voltage arc —Yu. L. Serov and I. P. Yavor. 19(6), 751–4 (Dec. 1974); CPM-7501X0751
—Atomic density in the low-voltage arc in a cesium diode —F. G. Baksht, A. A. Kostin, Yu. L. Serov, and I. P. Yavor. 19(11), 1424–5 (May 1975); CPM-7506X1178
Shabanov, O. M.—Behavior of molten salts in strong electric fields —A. Z. Éfendiev, O. M. Shabanov, S. M. Gadzhiev, and S. M. Tagirov. 19(6), 820–3 (Dec. 1974); CPM-7501X0820
Shaporenko, A. A.—Scattering of He$^+$ ions by the core of the He atom —Z. Z. Latypov and A. A. Shaporenko. 19(7), 976–7 (Jan. 1975); CPM-7503X0864
Shapovalov, A. S.—Shot noise in a thermionic cathode —A. F. Golubentsev and A. S. Shapovalov. 19(10), 1345–6 (Apr. 1975); CPM-7506X0279
Shaptala, V. G.—Second–harmonic generation and emission in wave conversion at a plasma boundary —A. N. Kondratenko, V. G. Shaptala, and V. M. Kuklin. 19(1), 22–4 (Jul. 1974); CPM-7407X1534
—Scattering of high–frequency electromagnetic waves by ion–acoustic oscillations in a bounded plasma —V. G. Shaptala. 19(2), 193–6 (Aug. 1974); CPM-7408X1457
Shatalin, S. V.—Effect of plasma parameters on emission in an ion laser —I. E. Sakharov, V. V. Ermolin, and S. V. Shatalin. 19(8), 1081–4 (Feb. 1975); CPM-7504X1505
Shatilov, A. V.—Optical characteristics of K–8 glass subject to radiation from a neodymium laser —A. M. Bonch–Bruevich, Ya. A. Imas, V. S. Salyadinov, and A. V. Shatilov. 19(2), 287–9 (Aug. 1974); CPM-7408X1551
Shcheglov, V. A.—Photochemical waves in a medium with a branch–chain conversion mechanism —A. N. Oraevskii, V. P. Pimenov, and V. A. Shcheglov. 19(6), 782–6 (Dec. 1974); CPM-7501X0782
—Gas polymerization wave excited by monochromatic light —A. I. Plis and V. A. Shcheglov. 19(9), 1262–3 (Mar. 1975); CPM-7505X0684
Shcherbakov, A. P.—Simulation of ion scattering on diatomic molecules —M. L. Aleksandrov, N. S. Pliss, and A. P. Shcherbakov. 19(3), 394–5 (Sep. 1974); CPM-7412X1080
Shcherbinin, O. N.—Role of collisions in plasma absorption of electromagnetic waves near the lower hybrid —B. V. Galaktionov, V. V. D'yachenko, M. M. Larionov, and O. N. Shcherbinin. 19(4), 459–62 (Oct. 1974); CPM-7412X0243
Shcherbinin, P. P.—Volt—ampere characteristic of the low-voltage arc. I. Recombination model —P. P. Shcherbinin. 19(11), 1436–41 (May 1975); CPM-7506X1190
Shchukin, E. R.—Thermophoresis and diffusophoresis of small, volatile aerosol particles —Yu. I. Yalamov and E. R. Shchukin. 19 (2), 278–9 (Aug. 1974); CPM-7408X1542
Shelepin, L. A.—Kinetics of gasdynamic lasers. Effect of nozzle geometry on inversion —A. S. Biryukov and L. A. Shelepin. 19(6), 775–81 (Dec. 1974); CPM-7501X0775
—Plasma dynamic lasers —S. A. Reshetnyak and L. A. Shelepin. 19 (8), 1076–80 (Feb. 1975); CPM-7504X1500
Shenderovich, A. M.—Self-acceleration of an intense electron beam —I. A. Grishaev, A. N. Dedik, V. V. Zakutin, I. I. Magda, Yu. V. Tkach, and A. M. Shenderovich. 19(8), 1087–9 (Feb. 1975); CPM-7504X1511
Shendrik, V. A.—Cerenkov instabilities of a relativistic beam in a periodic plasma–filled waveguide —V. I. Kurilko, Yu. V. Tkach, and V. A. Shendrik. 19(5), 607–11 (Nov. 1974); CPM-7501X0401
Sher, S. P.—Linear transient response of a fully ionized plasma in a pulsed electric field —V. V. Istomin, S. P. Sher, and S. P. Dovgopol. 19(7), 963–4 (Jan. 1975); CPM-7503X0851
Sheremet, V. I.—Shielding properties of superconducting shields —S. I. Bondarenko, S. S. Vinogradov, G. A. Gogadze, S. S. Perepelkin, and V. I. Sheremet. 19(6), 824–8 (Dec. 1974); CPM-7501X0824
—Superconducting magnetic shields —S. I. Bondarenko and V. I. Sheremet. 19(7), 952–5 (Jan. 1975); CPM-7503X0840
Sheretov, É. P.—Efficiency of the scattering of "unstable" charged particles in quadrupole mass spectrometers —É. P. Sheretov, B. I. Kolotilin, and M. P. Safonov. 19(12), 1622–4 (Jun. 1975); CPM-7508X0496
Shermergor, T. D.—Calculation of permittivity of an inhomogeneous dielectric by a variational method —G. A. Ermakov, A. G. Fokin, and T. D. Shermergor. 19(2), 157–60 (Aug. 1974); CPM-7408X1421

—Calculation of bounds for the effective permittivity of an inhomogeneous dielectric —G. A. Ermakov, A. G. Fokin, and T. D. Shermergor. 19(2), 161–5 (Aug. 1974); CPM-7408X1425

Shipilevskii, B. M.—Impurities and crystal dimensions in zone refining —V. G. Glebovskii and B. M. Shipilevskii. 19(9), 1231–5 (Mar. 1975); CPM-7505X0653

Shishkin, B. B.—Electron–microscope and x–ray study of thermionic emitters made from Mo–Pt alloys —B. B. Shishkin and R. S. Bakhtiyarov. 19(2), 243–50 (Aug. 1974); CPM-7408X1507

Shishkin, V. A.—Use of a field-emission microscope to measure the pressure of pump oil —V. Ya. Pliskovskii, M. S. Sukonnik, and V. A. Shishkin. 19(10), 1347–51 (Apr. 1975); CPM-7506X0281

Shmidov, I. Yu.—Aberrations in systems with plane and spherical detection apertures —V. V. Izokh, A. V. Sergeev, and I. Yu. Shmidov. 19(9), 1177–80 (Mar. 1975); CPM-7505X0599

Shneerson, G. A.—Distortion of single-turn solenoids in ultrahigh magnetic fields —G. A. Shneerson. 19(10), 1371–7 (Apr. 1975); CPM-7506X0305

Sholom, V. K.—Approximate similarity relations in the electrical explosions of underwater conductors —E. V. Krivitskii and V. K. Sholom. 19(6), 798–801 (Dec. 1974); CPM-7501X0798

—Electrical characteristics of underwater exploding wires —V. K. Sholom, E. V. Krivitskii, and V. P. Litvinenko. 19(10), 1329–31 (Apr. 1975); CPM-7506X0263

Shpenik, O. B.—Excitation collisions between magnesium ions and inert gas atoms —V. L. Ovchinnikov, O. B. Shpenik, and I. P. Zapesochnyi. 19(3), 382–4 (Sep. 1974); CPM-7412X1068

Shtepa, N. I.—Graphical methods for constructing trajectories of small particles in electrostatic fields —N. I. Shtepa. 19(9), 1253–5 (Mar. 1975); CPM-7505X0675

Shubin, A. F.—Transient thermionic-field emission from a point cathode —E. A. Litvinov and A. F. Shubin. 19(8), 1131–2 (Feb. 1975); CPM-7504X1555

Shubina, V. V.—Mass spectrum of secondary ions ejected from the surface of a single crystal of gallium arsenide by argon ions —A. G. Koval', V. V. Bobkov, Yu. A. Klimovskii, S. S. Strel'chenko, V. V. Shubina, V. V. Lebedev, and Ya. M. Fogel'. 19(12), 1587–9 (Jun. 1975); CPM-7508X0461

Shulaev, N. S.—Nonmonoenergetic relativistic electron beam in a bounded collisional plasma —V. P. Grigor'ev and N. S. Shulaev. 19(1), 20–1 (Jul. 1974); CPM-7407X1532

Shulika, N. G.—Conversion of neutral hydrogen into protons in dense plasmas —T. A. Bazilevskaya, L. I. Krupnik, and N. G. Shulika. 19(6), 741–4 (Dec. 1974); CPM-7501X0741

Shumskii, M. G.—Crystal defects of heterostructures of AlAs–GaAs solid solutions and effect on the characteristics of injection lasers —L. V. Druzhinina, V. T. Bublik, L. M. Dolginov, P. G. Eliseev, M. P. Kerbelev, V. B. Osvenskii, I. Z. Pinsker, and M. G. Shumskii. 19(7), 935–9 (Jan. 1975); CPM-7503X0823

Shuster, A. L.—Electromagnetic levitation of a liquid metal droplet with strong skin effect (surface shape and internal pressure) —A. N. Tverdokhlebov and A. L. Shuster. 19(11), 1399–402 (May 1975); CPM-7506X1153

—Liquid metal droplet with high surface tension in an axially-symmetric electromagnetic field (strong skin effect) —A. N. Tverdokhlebov and A. L. Shuster. 19(11), 1512–3 (May 1975); CPM-7506X1266

Shustova, N. V.—Generation of drift waves by an rf field near the lower hybrid frequency —Yu. F. Baranov, D. G. Bulyginskii, M. I. Vil'dzhyunas, B. V. Galaktionov, and N. V. Shustova. 19(6), 732–5 (Dec. 1974); CPM-7501X0732

Sidorovich, V. G.—Efficiency of light–beam conversion by dynamic three–dimensional phase holograms —D. I. Stasel'ko and V. G. Sidorovich. 19(3), 361–5 (Sep. 1974); CPM-7412X1047

—Transformation of light beams by dynamic correctors using three-dimensional displacement phase holograms —V. G. Sidorovich and D. I. Stasel'ko. 19(12), 1593–7 (Jun. 1975); CPM-7508X0467

Siksin, V. S.—Energy resolution of quadrupole lenses for charged–particle beams —V. S. Siksin. 19(3), 301–7 (Sep. 1974); CPM-7412X0987

Silin, V. P.—Anomalous ion heating in a parametrically unstable plasma —I. S. Baikov and V. P. Silin. 19(12), 1529–33 (Jun. 1975); CPM-7508X0403

Simonenko, L. S.—Gas focusing of a negative–ion beam —M. D. Gabovich, A. P. Naida, I. M. Protsenko, L. S. Simonenko, and I. A. Soloshenko. 19(4), 546–7 (Oct. 1974); CPM-7412X0330

Sinyavskii, V. V.—Optimum dimensions of a coaxial thermionic converter —V. V. Sinyavskii. 19(3), 373–7 (Sep. 1974); CPM-7412X1059

Sizonenko, V. L.—Kinetic plasma instabilities excited by a monoenergetic beam —A. I. Ranyuk and V. L. Sizonenko. 19(5), 628–9 (Nov. 1974); CPM-7501X0422

—Quasilinear theory of beam–generated surface waves in a plasma —V. I. Pakhomov and V. L. Sizonenko. 19(5), 630–4 (Nov. 1974); CPM-7501X0424

—Instabilities in a finite-β plasma with transverse current. I —A. I. Pyatak and V. L. Sizonenko. 19(5), 635–9 (Nov. 1974); CPM-7501X0429

—Instabilities in a finite-β plasma with transverse current. II —A. I. Pyatak and V. L. Sizonenko. 19(5), 640–4 (Nov. 1974); CPM-7501X0434

—Magnetodrift waves in a finite-β plasma —N. M. Ryzhov, V. L. Sizonenko, V. A. Suprunenko, E. A. Sukhomlin, and Yu. V. Gutarev. 19(6), 722–5 (Dec. 1974); CPM-7501X0722

—Transverse-current plasma instability —D. G. Lominadze and V. L. Sizonenko. 19(9), 1145–9 (Mar. 1975); CPM-7505X0567

—Plasma instability due to an anisotropic electron distribution —D. G. Lominadze and V. L. Sizonenko. 19(9), 1150–3 (Mar. 1975); CPM-7505X0572

—Turbulent plasma heating and the Buneman instability —V. L. Sizonenko. 19(9), 1260–1 (Mar. 1975); CPM-7505X0682

Sizov, V. N.—Interaction of intense laser radiation with solid targets —L. V. Dubovoi, V. D. Dyatlov, V. I. Kryzhanovskii, A. A. Mak, R. N. Medvedev, A. N. Popytaev, V. A. Serebryakov, V. N. Sizov, and A. D. Starikov. 19(11), 1477–9 (May 1975); CPM-7506X1231

Skachek, G. V.—Transmission of a high–current relativistic beam through a gas —Yu. V. Tkach, I. I. Magda, G. V. Skachek, S. S. Pushkarev, and I. P. Panchenko. 19(3), 412–3 (Sep. 1974); CPM-7412X1098

Skibenko, A. I.—Spatial characteristics and loss of plasma produced by an electron beam in a magnetic trap —M. Yu. Bredikhin, A. I. Maslov, A. I. Skibenko, E. I. Skibenko, I. P. Fomin, and V. B. Yuferov. 19(1), 49–52 (Jul. 1974); CPM-7407X1561

—Modulation of microwaves by density fluctuations in a plasma —L. A. Dushin, A. V. Serikov, A. I. Skibenko, E. V. Krivorukov, and I. P. Fomin. 19(9), 1163–7 (Mar. 1975); CPM-7505X0585

Skibenko, A. Y.—Plasma equilibrium and confinement in a poloidal heliotron configuration. II —V. G. Zykov, V. I. Karpukhin, Yu. F. Lonin, N. N. Podteregera, N. I. Rudnev, A. Y. Skibenko, V. T. Tolok, and I. P. Fomin. 19(8), 1069–72 (Feb. 1975); CPM-7504X1493

Skibenko, E. I.—Spatial characteristics and loss of plasma produced by an electron beam in a magnetic trap —M. Yu. Bredikhin, A. I. Maslov, A. I. Skibenko, E. I. Skibenko, I. P. Fomin, and V. B. Yuferov. 19(1), 49–52 (Jul. 1974); CPM-7407X1561

Sklyarov, M. Yu.—Thermal effect of continuous laser radiation on optically transparent media —N. S. Bardina, A. I. Portnyagin, M. Yu. Sklyarov, and A. A. Churin. 19(4), 491–4 (Oct. 1974); CPM-7412X0275

Skoblik, I. P.—Investigation of a plasma focus with a time-resolved laser interferometer —I. M. Zolototrubov, I. P. Skoblik, A. G. Tolstolutskii, and V. I. Privezentsev. 19(8), 1061–2 (Feb. 1975); CPM-7504X1485

Skoblik, M. N.—Magnetic topography of toroidal systems —M. N. Skoblik, V. E. Ziser, A. V. Georgievskii, and V. G. Peletminskaya. 19(10), 1277–80 (Apr. 1975); CPM-7506X0211

Skorobogatov, G. A.—Quenching in the CF_3I photodissociation laser —G. A. Skorobogatov, V. M. Tret'yak, and V. S. Komarov. 19(4), 495–8 (Oct. 1974); CPM-7412X0279

—Method for determining the absolute characteristics of CF_3I laser emission —V. S. Komarov, V. G. Seleznev, and G. A. Skorobogatov. 19(4), 558–60 (Oct. 1974); CPM-7412X0342

—Absolute-photometry determination of the rate constant of the gas-phase reaction of the radical compound C_3F_7 and $I(^2P_{3/2})$ —G. A. Skorobogatov, V. S. Komarov, and V. G. Seleznev. 19(9), 1239–41 (Mar. 1975); CPM-7505X0661

Skosyrev, Yu. V.—Anisotropic plasma heating near the lower hybrid frequency —V. M. Glagolev, V. V. Martynenko, and Yu. V. Skosyrev. 19(12), 1543–6 (Jun. 1975); CPM-7508X0417

Skripal', L. P.—Low pressure discharge with high–energy electrons —R. A. Demirkhanov, Yu. V. Kursanov, and L. P. Skripal'. 19(7), 891–4 (Jan. 1975); CPM-7503X0779

Skripnik, V. G.—Skin effect in a constant magnetic field —Z. K. Yankauskas, V. I. Chesonis, and V. G. Skripnik. 19(9), 1251–2 (Mar. 1975); CPM-7505X0673

Skvortsov, V. V.—Hot probe measurements in a rarefied streaming plasma —E. M. Netsvetailov, L. V. Nosachev, and V. V. Skvortsov. 19(12), 1579–83 (Jun. 1975); CPM-7508X0453

Slobodenyuk, G. I.—Line shape of a quadrupole mass spectrometer —G. I. Slobodenyuk. 19(2), 292–3 (Aug. 1974); CPM-7408X1556

Smetanin, V. I.—Streamer propagation after the voltage termination in a streamer chamber —N. S. Rudenko and V. I. Smetanin. 19 (12), 1616–7 (Jun. 1975); CPM-7508X0490

Smirnov, G. V.—Electrical breakdown of vacuum gaps under superhigh voltage pulses —I. I. Kalyatskii, G. M. Kassirov, and G. V. Smirnov. 19(11), 1434–5 (May 1975); CPM-7506X1188

Smirnov, L. A.—X-ray fluorescence of oxygen in H_2O —L. A. Smirnov. 19(5), 702 (Nov. 1974); CPM-7501X0496

Smirnov, V. P.—Switching characteristis of a discharge in water —V. M. Kuleshov, S. L. Nedoseev, V. P. Smirnov, and A. M. Spektor. 19(1), 150–1 (Jul. 1974); CPM-7407X1662

—Effect of a high-current relativistic electron beam on a metal —B. I. Dmitrenko, L. V. Leskov, G. P. Maksimov, S. L. Nedoseev, V. V. Savichev, V. P. Smirnov, and A. M. Spektor. 19(9), 1224–5 (Mar. 1975); CPM-7505X0646

Sobenin, N. P.—Control of output energy in linear electron accelerators —V. N. Golovin and N. P. Sobenin. 19(7), 932–4 (Jan. 1975); CPM-7503X0820

Sobolev, S. S.—Acceleration of plasma electrons in strong electric fields —Z. A. Al'bikov, M. I. Ivanov, V. I. Kazacha, O. V. Kozlov, V. D. Rusanov, and S. S. Sobolev. 19(11), 1498–9 (May 1975); CPM-7506X1252

Sokolov, A. A.—Extraction of synchroton radiation from a cyclic electron accelerator with a strong magnetic field —V. I. Kvochka, V. S. Panasyuk, V. F. Romanovskii, L. N. Samoilov, A. A. Sokolov, B. M. Stepanov, and Yu. M. Tereshkin. 19(6), 762–6 (Dec. 1974); CPM-7501X0762

Sokolov, V. A.—Nonlinear polarizability of a gaseous medium in a longitudinal magnetic field —V. A. Sokolov and L. M. Khayutin. 19(5), 589–91 (Nov. 1974); CPM-7501X0383

Sokolov, V. F.—Radial distribution of density and potential in a glow discharge in CO_2 and water —A. I. Maksimov and V. F. Sokolov. 19(10), 1359–61 (Apr. 1975); CPM-7506X0293

Solntsev, G. S.—Effect of ion current on the measurement of the electron energy distribution function by the second-derivative method —V. A. Dovzhenko, A. P. Ershov, and G. S. Solntsev. 19 (4), 538–9 (Oct. 1974); CPM-7412X0322

Solnyshkov, A. I.—Aberrations in a straight ion-optical accelerator —E. I. Gerasimov, A. I. Solnyshkov, and G. V. Tarvid. 19(1), 131–3 (Jul. 1974); CPM-7407X1643

Solodovchenko, S. I.—Electron temperature in a high-frequency helium discharge —V. S. Voitsenya, A. Yu. Voloshko, V. G. Konovalov, and S. I. Solodovchenko. 19(7), 909–10 (Jan. 1975); CPM-7503X0797

Solodovnikov, A. P.—Dielectric strength of a vacuum gap with electrodes irradiated with He^+ and H^+ ions —A. P. Solodovnikov and Yu. M. Khirnyi. 19(8), 1122 (Feb. 1975); CPM-7504X1546

Solonitsyn, B. P.—Steady-state study of the temperature dependence of the mutual-diffusion coefficients of certain gases —N. D. Kosov and B. P. Solonitsyn. 19(4), 541–2 (Oct. 1974); CPM-7412X0325

Soloshenko, I. A.—Gas focusing of a negative-ion beam —M. D. Gabovich, A. P. Naida, I. M. Protsenko, L. S. Simonenko, and I. A. Soloshenko. 19(4), 546–7 (Oct. 1974); CPM-7412X0330

—Instabilities in interpenetrating electron and ion beams —I. A. Soloshenko and L. P. Katsubo. 19(10), 1317–20 (Apr. 1975); CPM-7506X0251

—Measurement of ion density by the dispersion relation for an ion-beam plasma —M. D. Gabovich, L. P. Katsubo, and I. A. Soloshenko. 19(11), 1412–3 (May 1975); CPM-7506X1166

Sominskii, G. G.—End current in a magnetron with a secondary-emission cathode —G. G. Sominskii, S. A. Fridrikhov, O. Yu. Tsybin, and A. P. Karizhskii. 19(3), 378–81 (Sep. 1974); CPM-7412X1064

—Evaluation of charge distribution in a crossed-field device from ion bombardment of the cathode —V. I. Malyugin and G. G. Sominskii. 19(7), 942–5 (Jan. 1975); CPM-7503X0830

Soms, L. N.—Polarization of a cavity with a thermally deformed active element —I. B. Vitrishchak, L. N. Soms, and A. A. Tarasov. 19(5), 664–8 (Nov. 1974); CPM-7501X0458

Sorokin, Yu. M.—Multimode parametric interactions in a plasma with low-frequency pumping —Yu. M. Sorokin and N. S. Stepanov. 19(2), 185–9 (Aug. 1974); CPM-7408X1449

Sotnikov, V. I.—Method for optical modulation of an electron beam —V. I. Sotnikov. 19(11), 1510–1 (May 1975); CPM-7506X1264

Spektor, A. M.—Switching characteristis of a discharge in water —V. M. Kuleshov, S. L. Nedoseev, V. P. Smirnov, and A. M. Spektor. 19(1), 150–1 (Jul. 1974); CPM-7407X1662

—Effect of a high-current relativistic electron beam on a metal —B. I. Dmitrenko, L. V. Leskov, G. P. Maksimov, S. L. Nedoseev, V. V. Savichev, V. P. Smirnov, and A. M. Spektor. 19(9), 1224–5 (Mar. 1975); CPM-7505X0646

Stakhanov, I. P.—Stability of ball lightning —I. P. Stakhanov. 19(7), 861–4 (Jan. 1975); CPM-7503X0749

—Analytic model of the cesium arc —V. P. Pashchenko, V. L. Mironovich, and I. P. Stakhanov. 19(10), 1332–6 (Apr. 1975); CPM-7506X0266

Starikov, A. D.—Interaction of intense laser radiation with solid targets —L. V. Dubovoi, V. D. Dyatlov, V. I. Kryzhanovskii, A. A. Mak, R. N. Medvedev, A. N. Popytaev, V. A. Serebryakov, V. N. Sizov, and A. D. Starikov. 19(11), 1477–9 (May 1975); CPM-7506X1231

Starodub, A. N.—Surface waves in a magnetized plasma in a radio-frequency field —E. E. Lovetskii and A. N. Starodub. 19(3), 319–22 (Sep. 1974); CPM-7412X1005

Stasel'ko, D. I.—Efficiency of light-beam conversion by dynamic three-dimensional phase holograms —D. I. Stasel'ko and V. G. Sidorovich. 19(3), 361–5 (Sep. 1974); CPM-7412X1047

—Transformation of light beams by dynamic correctors using three-dimensional displacement phase holograms —V. G. Sidorovich and D. I. Stasel'ko. 19(12), 1593–7 (Jun. 1975); CPM-7508X0467

Stefanovskaya, E. M.—Thermionic emission properties of zirconium, hafnium, and titanium nitrides in cesium vapor —M. A. Eremeev, V. S. Neshpor, A. B. Novikov, E. M. Stefanovskaya, and V. P. Fedorinov. 19(10), 1337–41 (Apr. 1975); CPM-7506X0271

Stepanov, B. M.—Extraction of synchroton radiation from a cyclic electron accelerator with a strong magnetic field —V. I. Kvochka, V. S. Panasyuk, V. F. Romanovskii, L. N. Samoilov, A. A. Sokolov, B. M. Stepanov, and Yu. M. Tereshkin. 19(6), 762–6 (Dec. 1974); CPM-7501X0762

—Electron lifetimes in atmosphere at high pressure —V. N. Kapinos, Yu. A. Medvedev, N. N. Morozov, and B. M. Stepanov. 19(11), 1507 (May 1975); CPM-7506X1261

Stepanov, K. N.—Parametric plasma instabilities excited by the sudden application of an electric field —A. B. Kitsenko and K. N. Stepanov. 19(1), 127–8 (Jul. 1974); CPM-7407X1639

—Excitation of electromagnetic ion cyclotron waves by fast ions —T. D. Kaladze, D. G. Lominadze, and K. N. Stepanov. 19(2), 175–6 (Aug. 1974); CPM-7408X1439

—Nonlinear behavior of monochromatic surface waves excited by a beam —A. B. Kitsenko, I. M. Pankratov, and K. N. Stepanov. 19 (11), 1505–6 (May 1975); CPM-7506X1259

Stepanov, N. S.—Multimode parametric interactions in a plasma with low-frequency pumping —Yu. M. Sorokin and N. S. Stepanov. 19 (2), 185–9 (Aug. 1974); CPM-7408X1449

Stolovich, N. N.—Simplified model for the initial stage of exploding wire phenomena —N. N. Stolovich, V. G. Maksimov, and N. S. Minitskaya. 19(10), 1321–8 (Apr. 1975); CPM-7506X0255

Strel'chenko, S. S.—Mass spectrum of secondary ions ejected from the surface of a single crystal of gallium arsenide by argon ions —A. G. Koval', V. V. Bobkov, Yu. A. Klimovskii, S. S. Strel'chenko, V. V. Shubina, V. V. Lebedev, and Ya. M. Fogel'. 19(12), 1587–9 (Jun. 1975); CPM-7508X0461

Sudarushkin, A. S.—Proton extraction from the 70-GeV accelerator for the Ludmila liquid-hydrogen chamber (extraction system S) —A. A. Aseev, A. I. Drozhdin, B. A. Zelenov, É. A. Merker, L. L. Moizhes, K. P. Myznikov, A. A. Roshchin, V. M. Tatarenko, M. A. Kholodenko, A. D. Artemov, L. N. Vaulin, V. I. Gordin, I. I. Kovalevskii, V. N. Rozhkov, M. M. Suvorov, A. S. Sudarushkin, and V. I. Chuiko. 19(1), 70–6 (Jul. 1974); CPM-7407X1582

Suetin, P. E.—Temperature dependence of trace diffusion coefficients of certain gases —A. É. Loiko, B. A. Ivakin, and P. E. Suetin. 19 (3), 434 (Sep. 1974); CPM-7412X1120

—Use of the distribution function to describe free molecular beams —I. G. Neudachin, B. T. Porodnov, and P. E. Suetin. 19(4), 511–4 (Oct. 1974); CPM-7412X0295

—Flow of low-density gases in a capillary grid —B. T. Porodnov, V. D. Akin'shin, V. I. Kichaev, S. F. Borisov, and P. E. Suetin. 19(4), 515–8 (Oct. 1974); CPM-7412X0299

—Diffusion and solubility of helium in potassium chloride —A. Ya. Kupryazhkin, P. V. Volobuev, and P. E. Suetin. 19(8), 1105–7 (Feb. 1975); CPM-7504X1529

Sukhanovskii, Yu. P.—Radiation yield of ions in liquid dielectrics as a function of temperature and radiation energy —V. I. Ivanov, E. D. Kleshchenko, Yu. P. Sukhanovskii, and V. V. Frolov. 19(11), 1468–70 (May 1975); CPM-7506X1222

Sukharev, M. V.—Reversibility of chalcogenide materials in holography —S. B. Gurevich, N. N. Il'yashenko, B. T. Kolomiets, V. M. Lyubin, and M. V. Sukharev. 19(1), 152–3 (Jul. 1974); CPM-7407X1664

Sukhomlin, E. A.—Magnetodrift waves in a finite-β plasma —Ň. M. Ryzhov, V. L. Sizonenko, V. A. Suprunenko, E. A. Sukhomlin, and Yu. V. Gutarev. 19(6), 722–5 (Dec. 1974); CPM-7501X0722

Sukhorukov, A. P.—Nonlinear spherical aberrations and thermoelastic stresses in thermal self-focusing —A. A. Vigasin, Yu. A. Gorokhov, A. P. Sukhorukov, and A. M. Khachatryan. 19(5), 673–5 (Nov. 1974); CPM-7501X0467

Sukhovskii, E. S.—Parametric interaction of a charged particle beam with a periodic system —V. I. Koroza and E. S. Sukhovskii. 19(8), 1020–4 (Feb. 1975); CPM-7504X1444

Sukiasyan, É. A.—Electron density in an argon afterglow —O. P. Bochkova, R. I. Lyagushchenko, É. A. Sukiasyan, and Yu. A. Tolmachev. 19(4), 475–7 (Oct. 1974); CPM-7412X0259

Sukonnik, M. S.—Use of a field-emission microscope to measure the pressure of pump oil —V. Ya. Pliskovskii, M. S. Sukonnik, and V. A. Shishkin. 19(10), 1347–51 (Apr. 1975); CPM-7506X0281

Suladze, K. V.—Pulsed ion beams from a high-current plasma diode —B. A. Tskhadaya, A. A. Plyutto, and K. V. Suladze. 19(8), 1108–9 (Feb. 1975); CPM-7504X1532

Sultanov, M. A.—Supersonic plasma jet from a high-power pulsed discharge —M. A. Sultanov. 19(4), 478–82 (Oct. 1974); CPM-7412X0262

Sumin, L. V.—Kinetic energy of ions produced by surface ionization. I. Distribution over the velocity components —L. V. Sumin. 19(9), 1205–9 (Mar. 1975); CPM-7505X0627

Suprunenko, V. A.—Magnetodrift waves in a finite-β plasma —Ň. M. Ryzhov, V. L. Sizonenko, V. A. Suprunenko, E. A. Sukhomlin, and Yu. V. Gutarev. 19(6), 722–5 (Dec. 1974); CPM-7501X0722

Suvorov, M. M.—Proton extraction from the 70-GeV accelerator for the Ludmila liquid-hydrogen chamber (extraction system S) —A. A. Aseev, A. I. Drozhdin, B. A. Zelenov, É. A. Merker, L. L. Moizhes, K. P. Myznikov, A. A. Roshchin, V. M. Tatarenko, M. A. Kholodenko, A. D. Artemov, L. N. Vaulin, V. I. Gordin, I. I. Kovalevskii, V. N. Rozhkov, M. M. Suvorov, A. S. Sudarushkin, and V. I. Chuiko. 19(1), 70–6 (Jul. 1974); CPM-7407X1582

Sveshnikov, A. G.—Production of an ion beam by a magnetic system with opposed fields —V. B. Glasko, A. G. Sveshnikov, and N. N. Semashko. 19(2), 201–5 (Aug. 1974); CPM-7408X1465

Svettsov, V. I.—Electron energy distribution and electrical characteristics of the positive column in H_2 and H_2+Cl_2 —V. V. Zaitsev, A. I. Maksimov, and V. I. Svettsov. 19(1), 57–9 (Jul. 1974); CPM-7407X1569

Svin'in, M. P.—Beam focusing in an accelerator with inductive energy storage —V. A. Glukhikh, O. A. Gusev, E. G. Komar, V. S. Kuznetsov, M. P. Svin'in, and R. P. Fidel'skaya. 19(3), 366–7 (Sep. 1974); CPM-7412X1052

—High-current pulsed electron accelerator with an annular beam —M. I. Avramenko, V. A. Glukhikh, O. A. Gusev, E. G. Komar, O. L. Komarov, V. S. Kuznetsov, A. S. Perlin, and M. P. Svin'in. 19 (3), 368–70 (Sep. 1974); CPM-7412X1054

—Inductive energy storage in pulsed accelerators —V. A. Glukhikh, O. A. Gusev, E. G. Komar, and M. P. Svin'in. 19(5), 660–1 (Nov. 1974); CPM-7501X0454

T

Tagirov, S. M.—Behavior of molten salts in strong electric fields —A. Z. Éfendiev, O. M. Shabanov, S. M. Gadzhiev, and S. M. Tagirov. 19(6), 820–3 (Dec. 1974); CPM-7501X0820

Takibaev, Zh. S.—Charge-carrier density of the plasma produced in a Penning mixture by irradiation by uranium fission fragments and reactor radiation —G. A. Batyrbekov, Yu. D. Kuznetsov, and Zh. S. Takibaev. 19(5), 645–6 (Nov. 1974); CPM-7501X0439

Taranov, V. B.—Symmetry of high-frequency plasma motions —A. A. Zhmudskii and V. B. Taranov. 19(6), 717–8 (Dec. 1974); CPM-7501X0717

Tarasenko, V. F.—Infrared nitrogen laser using a transverse discharge —V. F. Tarasenko and Yu. I. Bychkov. 19(5), 693 (Nov. 1974); CPM-7501X0487

Tarasov, A. A.—Polarization of a cavity with a thermally deformed active element —I. B. Vitrishchak, L. N. Soms, and A. A. Tarasov. 19(5), 664–8 (Nov. 1974); CPM-7501X0458

Tarasov, V. F.—Angular aberration corrector in a cylindrical mirror analyzer —V. V. Zashkavara and V. F. Tarasov. 19(6), 841–2 (Dec. 1974); CPM-7501X0841

Tarasova, L. V.—Fast electrons and x rays from nanosecond gas discharges at 0.1–760 torr —L. V. Tarasova, L. N. Khudyakova, T. V. Loiko, and V. A. Tsukerman. 19(3), 351–3 (Sep. 1974); CPM-7412X1037

Tarvid, G. V.—Aberrations in a straight ion-optical accelerator —E. I. Gerasimov, A. I. Solnyshkov, and G. V. Tarvid. 19(1), 131–3 (Jul. 1974); CPM-7407X1643

Tatarenko, V. M.—Proton extraction from the 70-GeV accelerator for the Ludmila liquid-hydrogen chamber (extraction system S) —A. A. Aseev, A. I. Drozhdin, B. A. Zelenov, É. A. Merker, L. L. Moizhes, K. P. Myznikov, A. A. Roshchin, V. M. Tatarenko, M. A. Kholodenko, A. D. Artemov, L. N. Vaulin, V. I. Gordin, I. I. Kovalevskii, V. N. Rozhkov, M. M. Suvorov, A. S. Sudarushkin, and V. I. Chuiko. 19(1), 70–6 (Jul. 1974); CPM-7407X1582

Tel'kovskii, V. G.—Energy spectra of scattered particles in proton bombardment of a metal target —G. I. Zhabrev, V. A. Kurnaev, and V. G. Tel'kovskii. 19(7), 978–9 (Jan. 1975); CPM-7503X0866

Terekhin, D. K.—Frequency locking in a 3.39μ laser —E. Yu. Andreeva, S. N. Gulyaev, and D. K. Terekhin. 19(12), 1620–1 (Jun. 1975); CPM-7508X0494

Tereshkin, Yu. M.—Extraction of synchroton radiation from a cyclic electron accelerator with a strong magnetic field —V. I. Kvochka, V. S. Panasyuk, V. F. Romanovskii, L. N. Samoilov, A. A. Sokolov, B. M. Stepanov, and Yu. M. Tereshkin. 19(6), 762–6 (Dec. 1974); CPM-7501X0762

Testov, V. G.—Experimental investigation of microwave radiation produced by hypersonic flows —V. A. Lyutomskii, V. M. Polyakov, and V. G. Testov. 19(4), 483–5 (Oct. 1974); CPM-7412X0267

—N_2O-N_2-He gasdynamic laser —Yu. I. Grin' and V. G. Testov. 19 (7), 975 (Jan. 1975); CPM-7503X0863

Timofeev, A. V.—Drift instability in a weakly ionized plasma —S. V. Putvinskii and A. V. Timofeev. 19(10), 1295–9 (Apr. 1975); CPM-7506X0229

Timofeev, I. B.—Dynamics and emission of coaxial plasma shells in air —A. F. Aleksandrov, V. V. Perebeinos, A. T. Savichev, and I. B. Timofeev. 19(1), 38–42 (Jul. 1974); CPM-7407X1550

—Initial stage of a high-current discharge in air —A. F. Aleksandrov, V. V. Perebeinos, A. T. Savichev, and I. B. Timofeev. 19(11), 1490–1 (May 1975); CPM-7506X1244

Timofeev, M. N.—Electron energy spectrum in a high-current vacuum diode —S. P. Bugaev, V. I. Koshelev, and M. N. Timofeev. 19(9), 1193–5 (Mar. 1975); CPM-7505X0615

Timofeev, V. P.—Peak current in a cold-cathode magnetron —I. M. Vigdorchik and V. P. Timofeev. 19(1), 142–3 (Jul. 1974); CPM-7407X1654

Timonin, A. M.—Laser-initiated vacuum discharge —V. P. Kovalenko, A. A. Makarevich, V. A. Rodichkin, and A. M. Timonin. 19(11), 1429–31 (May 1975); CPM-7506X1183

Timoshenko, A. F.—Low-frequency oscillations in counter-streaming high-current electron beams —A. F. Timoshenko, D. V. Iremashvili, and Yu. K. Udovichenko. 19(8), 1038–41 (Feb. 1975); CPM-7504X1462

Timoshenko, A. P.—Wave excitation at half the gyrofrequency in counterstreaming electron beams —A. P. Timoshenko, D. V. Iremashvili, and Yu. K. Udovichenko. 19(12), 1584–6 (Jun. 1975); CPM-7508X0458

Tishchenko, V. A.—Investigation of ionization processes behind strong shock waves using an electrical conductivity probe —V. A. Tishchenko, N. V. Khandurov, and É. K. Chekalin. 19(5), 651–3 (Nov. 1974); CPM-7501X0445

Tkach, Yu. V.—Transmission of a high-current relativistic beam through a gas —Yu. V. Tkach, I. I. Magda, G. V. Skachek, S. S. Pushkarev, and I. P. Panchenko. 19(3), 412–3 (Sep. 1974); CPM-7412X1098

—Cerenkov instabilities of a relativistic beam in a periodic plasma-filled waveguide —V. I. Kurilko, Yu. V. Tkach, and V. A. Shendrik. 19(5), 607–11 (Nov. 1974); CPM-7501X0401

—Self-acceleration of an intense electron beam —I. A. Grishaev, A. N. Dedik, V. V. Zakutin, I. I. Magda, Yu. V. Tkach, and A. M. Shenderovich. 19(8), 1087–9 (Feb. 1975); CPM-7504X1511

Tkachuk, A. M.—Frequency-doubling single-mode laser for picosecond pulses —A. M. Bonch-Bruevich, A. M. Tkachuk, and A. A. Fedorov. 19(4), 549–51 (Oct. 1974); CPM-7412X0333

Tokarev, L. G.—Vacuum-UV and soft x-ray emission in a magnetoplasma compressor —P. E. Kovrov and L. G. Tokarev. 19 (4), 563–4 (Oct. 1974); CPM-7412X0347

Tolmachev, G. N.—Effect of the radiation density on ion drift velocity in a cadmium-helium laser —G. N. Tolmachev, E. L. Latush, and V. S. Mikhalevskii. 19(8), 1120–1 (Feb. 1975); CPM-7504X1544

Tolmachev, Yu. A.—Electron density in an argon afterglow —O. P. Bochkova, R. I. Lyagushchenko, É. A. Sukiasyan, and Yu. A. Tolmachev. 19(4), 475–7 (Oct. 1974); CPM-7412X0259

Tolok, V. T.—Plasma equilibrium and confinement in a poloidal heliotron configuration. I —V. G. Zykov, V. I. Karpukhin, Yu. F. Lonin, N. N. Podteregera, I. N. Rudnev, and V. T. Tolok. 19(8), 1063–8 (Feb. 1975); CPM-7504X1487

—Plasma equilibrium and confinement in a poloidal heliotron configuration. II —V. G. Zykov, V. I. Karpukhin, Yu. F. Lonin, N. N. Podteregera, I. N. Rudnev, A. Y. Skibenko, V. T. Tolok, and I. P. Fomin. 19(8), 1069–72 (Feb. 1975); CPM-7504X1493

Tolstoi, N. A.—Strobe unit for measuring luminescence in the range 10^{-7}–$2\cdot10^{-10}$ sec —V. A. Bonch-Bruevich and N. A. Tolstoi. 19(2), 284–6 (Aug. 1974); CPM-7408X1548

Tolstolutskii, A. G.—Investigation of a plasma focus with a time-resolved laser interferometer —I. M. Zolototrubov, I. P. Skoblik, A. G. Tolstolutskii, and V. I. Privezentsev. 19(8), 1061–2 (Feb. 1975); CPM-7504X1485

Tolstoluzhskii, A. P.—Conversion of regular charge-density waves in a inhomogeneous plasma —S. S. Kalmykova and A. P. Tolstoluzhskii. 19(4), 455–8 (Oct. 1974); CPM-7412X0239

—Launching and propagation of regular nonlinear waves in an anisotropic plasma-filled waveguide —V. I. Kurilko, A. P. Tols-toluzhskii, and Ya. B. Fainberg. 19(5), 622–7 (Nov. 1974); CPM-7501X0416

—Solitary waves in anisotropic plasma waveguide —V. I. Kurilko and A. P. Tolstoluzhskii. 19(7), 887–90 (Jan. 1975); CPM-7503X0775

Tonkopryad, V. M.—Hydrodynamic stability of the Uragan stellarator —V. M. Zalkind, Yu. K. Kuznetsov, V. K. Pashnev, and V. M. Tonkopryad. 19(8), 1123–5 (Feb. 1975); CPM-7504X1547

Tontegode, A. Ya.—Time dependence of ion currents produced through surface ionization. Ionization of Ba on the (111) face of iridium —É. Ya. Zandberg, E. V. Rut'kov, and A. Ya. Tontegode. 19(2), 261–3 (Aug. 1974); CPM-7408X1525

Torchinskii, V. M.—Electron energy distribution in helium, nitrogen, and their mixtures —K. D. Asvadurov, I. A. Vasil'eva, and V. M. Torchinskii. 19(3), 354–7 (Sep. 1974); CPM-7412X1040

Tret'yak, V. M.—Quenching in the CF_3I photodissociation laser —G. A. Skorobogatov, V. M. Tret'yak, and V. S. Komarov. 19(4), 495–8 (Oct. 1974); CPM-7412X0279

Trifonov, Yu. M.—Secondary-electron energy in a resonance discharge in a three-electrode system —Yu. A. Kulikov, V. V. Ogienko, and Yu. M. Trifonov. 19(8), 1090–2 (Feb. 1975); CPM-7504X1514

Tripol'nikov, V. P.—Radar sounding of sea ice —V. V. Bogorodskii and V. P. Tripol'nikov. 19(3), 414–5 (Sep. 1974); CPM-7412X1100

—Differential electromagnetic characteristics at the interface between ice and water in the ocean —V. V. Bogorodskii and V. P. Tripol'nikov. 19(4), 526–8 (Oct. 1974); CPM-7412X0310

Troitskii, S. V.—Scattering by ion-acoustic waves in a rectangular waveguide —S. V. Troitskii. 19(2), 181–4 (Aug. 1974); CPM-7408X1445

Troyan, P. E.—Thermal conditions for a sandwich cold cathode —F. M. Benson, P. E. Troyan, and Yu. B. Yankelevich. 19(7), 946–7 (Jan. 1975); CPM-7503X0834

Trubnikov, G. I.—Maximum current of a beam with finite phase volume —G. I. Trubnikov and V. S. Kuznetsov. 19(6), 715–6 (Dec. 1974); CPM-7501X0715

Tsapkov, V. I.—Resistance and enthalpy of refractory exploding wires —M. M. Martynyuk, I. Karimkhodzhaev, and V. I. Tsapkov. 19(11), 1458–61 (May 1975); CPM-7506X1212

Tsendin, L. D.—Propagation and stability of large amplitude ionization waves —M. S. Gorelik and L. D. Tsendin. 19(7), 880–2 (Jan. 1975); CPM-7503X0768

Tskhadaya, B. A.—Pulsed ion beams from a high-current plasma diode —B. A. Tskhadaya, A. A. Plyutto, and K. V. Suladze. 19(8), 1108–9 (Feb. 1975); CPM-7504X1532

Tskhakaya, D. D.—Low-frequency helical instability in a high-frequency electric field —V. S. Paverman and D. D. Tskhakaya. 19(11), 1508–9 (May 1975); CPM-7506X1262

Tskhakya, D. D.—Parametric excitation of helicon waves in a plasma by modulated radio frequency waves —V. S. Paverman and D. D. Tskhakya. 19(12), 1629–30 (Jun. 1975); CPM-7508X0503

Tsukerman, V. A.—Fast electrons and x rays from nanosecond gas discharges at 0.1–760 torr —L. V. Tarasova, L. N. Khudyakova, T. V. Loiko, and V. A. Tsukerman. 19(3), 351–3 (Sep. 1974); CPM-7412X1037

Tsukerman, V. G.—Multiple recording and erasure of optical information in certain glassy chalcogenides —V. V. Korsakov, V. I. Nalivaiko, V. G. Remesnik, and V. G. Tsukerman. 19(4), 565–6 (Oct. 1974); CPM-7412X0349

Tsvetkova, L. B.—A useful function in the thermodynamics of irreversible processes —A. V. Pamfilov, A. I. Lopushanskaya, and L. B. Tsvetkova. 19(4), 535–7 (Oct. 1974); CPM-7412X0319

Tsybin, A. M.—Solution of the Stefan problem —A. M. Tsybin. 19 (11), 1514–5 (May 1975); CPM-7506X1268

Tsybin, O. Yu.—End current in a magnetron with a secondary-emission cathode —G. G. Sominskii, S. A. Fridrikhov, O. Yu. Tsybin, and A. P. Karizhskii. 19(3), 378–81 (Sep. 1974); CPM-7412X1064

Tsyplenko, A. P.—Dielectric breakdown of detonation products —V. L. Korol'kov, M. A. Mel'nikov, and A. P. Tsyplenko. 19(12), 1569–70 (Jun. 1975); CPM-7508X0443

Tsytovich, V. N.—Linear theory for the low-frequency electromagnetic properties of an isotropic turbulent plasma —K. Komilov, F. Kh. Khakimov, and V. N. Tsytovich. 19(5), 615–7 (Nov. 1974); CPM-7501X0409

—Nonlinear statistical theory for condensation of Langmuir plasmons. III. Energy flux for plasma turbulence —F. Kh. Khakimov and V. N. Tsytovich. 19(10), 1300–2 (Apr. 1975); CPM-7506X0234

Tunkin, V. G.—Direct and cascade four-photon parametric scattering of light in $LiIO_3$ crystals —S. M. Arakelyan, V. G. Tunkin, A. I. Kholodnykh, and A. S. Chirkin. 19(6), 787–92 (Dec. 1974); CPM-7501X0787

Tuzov, V. A.—Reflection of a high-current relativistic electron beam from a conducting surface —A. N. Didenko, A. I. Ryabchikov, V. A. Tuzov, and Yu. P. Usov. 19(12), 1625–6 (Jun. 1975); CPM-7508X0499

Tverdokhlebov, A. N.—Electromagnetic levitation of a liquid metal droplet with strong skin effect (surface shape and internal pressure) —A. N. Tverdokhlebov and A. L. Shuster. 19(11), 1399–402 (May 1975); CPM-7506X1153

—Liquid metal droplet with high surface tension in an axially-symmetric electromagnetic field (strong skin effect) —A. N. Tverdokhlebov and A. L. Shuster. 19(11), 1512–3 (May 1975); CPM-7506X1266

Tyrnov, V. F.—Parametric instability of a spatially moderated electron beam in a magnetic field —N. S. Repalov and V. F. Tyrnov. 19(7), 871–3 (Jan. 1975); CPM-7503X0759

U

Udovichenko, Yu. K.—Low-frequency oscillations in counter-streaming high-current electron beams —A. F. Timoshenko, D. V. Iremashvili, and Yu. K. Udovichenko. 19(8), 1038–41 (Feb. 1975); CPM-7504X1462

—Wave excitation at half the gyrofrequency in counterstreaming electron beams —A. P. Timoshenko, D. V. Iremashvili, and Yu. K. Udovichenko. 19(12), 1584–6 (Jun. 1975); CPM-7508X0458

Udris, Ya. Ya.—Effect of electron reflection on the voltage-current characteristics of a high-voltage, hollow-cathode, glow discharge —Ya. Ya. Udris, V. A. Chernov, and L. G. Guseva. 19(1), 134–5 (Jul. 1974); CPM-7407X1646

Ukolov, A. S.—Radiation emitted by charged particles trapped by plane electromagnetic waves —V. Ya. Davydovskii and A. S. Ukolov. 19(8), 1057–60 (Feb. 1975); CPM-7504X1481

—Energy of charged particles accelerated by electromagnetic waves in a plasma with a spatially decreasing density —V. Ya. Davydovskii and A. S. Ukolov. 19(10), 1303–7 (Apr. 1975); CPM-7506X0237

Ul'yanov, K. N.—Axially symmetric neutralized electron beam —G. N. Vyalov, V. N. Evteev, Yu. M. Zolotaikin, and K. N. Ul'yanov. 19(11), 1414–7 (May 1975); CPM-7506X1168

Urman, Yu. M.—Ponderomotive forces on a rotating conducting sphere in a time-varying inhomogeneous magnetic field —R. V. Lin'kov and Yu. M. Urman. 19(11), 1393–8 (May 1975); CPM-7506X1147

Ushatkin, E. F.—Dispersion of the dielectric constant of crystalline KH_2PO_4 near the "soft" mode frequency —V. V. Meriakri, Yu. M. Poplavko, and E. F. Ushatkin. 19(5), 703–4 (Nov. 1974); CPM-7501X0497

Ushkov, V. L.—Titanium-pump system for hydrogen —K. G. Mirzoev, V. G. Rogozinskii, and V. L. Ushkov. 19(3), 432–3 (Sep. 1974); CPM-7412X1118

Usov, Yu. P.—Reflection of a high-current relativistic electron beam from a conducting surface —A. N. Didenko, A. I. Ryabchikov, V. A. Tuzov, and Yu. P. Usov. 19(12), 1625–6 (Jun. 1975); CPM-7508X0499

Ustinov, Yu. K.—Titanium adsorption on tungsten —Yu. K. Ustinov and S. V. Fedichev. 19(8), 1118–9 (Feb. 1975); CPM-7504X1542

Ustyugov, V. I.—Unidirectional cw oscillation in a solid state ring laser with a return mirror —A. A. Mak, V. I. Ustyugov, V. A. Fromzel', and M. M. Khaleev. 19(4), 552–3 (Oct. 1974); CPM-7412X0336

V

Vagner, I. V.—Cell for forming electron beams of arbitrary shape in a high-voltage gaseous discharge —I. V. Vagner, É. I. Bolgov, V. F. Grakun, V. L. Gokhfel'd, and V. A. Kudlai. 19(8), 1042–5 (Feb. 1975); CPM-7504X1466

Vagner, S. D.—Electron energy distribution in a high-freqeuncy discharge in an axial magnetic field —S. D. Vagner, V. A. Virolainen, Yu. M. Kagan, and T. A. Kalmykova. 19(2), 290–1 (Aug. 1974); CPM-7408X1554

—High-frequency discharge in a mercury—helium mixture —S. D. Vagner, Yu. M. Kagan, A. I. Konstantinov, and I. S. Niskonen. 19 (7), 898–900 (Jan. 1975); CPM-7503X0786

Vainer, B. V.—Ionization oscillations in a plasma in the presence of ionizing radiation —B. V. Vainer. 19(1), 119–20 (Jul. 1974); CPM-7407X1631

Vakhrushin, Yu. P.—Estimate of the angular divergence in intense electron beams —V. S. Kuznetsov, Yu. P. Vakhrushin, O. L. Komarov, and R. P. Fidel'skaya. 19(7), 868–70 (Jan. 1975); CPM-7503X0756

Vasil'ev, N. M.—Neutral particles from the interaction of laser radiation with a solid target —Yu. A. Bykovskii, N. M. Vasil'ev, I. D. Laptev, and V. N. Nevolin. 19(12), 1635 (Jun. 1975); CPM-7508X0509

Vasil'eva, I. A.—Electron energy distribution in helium, nitrogen, and their mixtures —K. D. Asvadurov, I. A. Vasil'eva, and V. M. Torchinskii. 19(3), 354–7 (Sep. 1974); CPM-7412X1040

Vasserman, S. B.—Resistance and inductance of a gas arc —S. I. Barannik, S. B. Vasserman, and A. N. Lukin. 19(11), 1449–53 (May 1975); CPM-7506X1203

Vaulin, L. N.—Proton extraction from the 70-GeV accelerator for the Ludmila liquid-hydrogen chamber (extraction system S) —A. A. Aseev, A. I. Drozhdin, B. A. Zelenov, É. A. Merker, L. L. Moizhes, K. P. Myznikov, A. A. Roshchin, V. M. Tatarenko, M. A. Kholodenko, A. D. Artemov, L. N. Vaulin, V. I. Gordin, I. I. Kovalevskii, V. N. Rozhkov, M. M. Suvorov, A. S. Sudarushkin, and V. I. Chuiko. 19(1), 70–6 (Jul. 1974); CPM-7407X1582

Veisig, G. S.—Two-section solenoid with internal "equally-loaded" section; power as a function of the length of the internal section — G. S. Veisig, A. P. Doroshenko, and P. P. Rybin. 19(3), 416–8 (Sep. 1974); CPM-7412X1102

Vigasin, A. A.—Nonlinear spherical aberrations and thermoelastic stresses in thermal self-focusing —A. A. Vigasin, Yu. A. Gorokhov, A. P. Sukhorukov, and A. M. Khachatryan. 19(5), 673–5 (Nov. 1974); CPM-7501X0467

Vigdorchik, I. M.—Peak current in a cold-cathode magnetron —I. M. Vigdorchik and V. P. Timofeev. 19(1), 142–3 (Jul. 1974); CPM-7407X1654

Vikulov, V. F.—Multiple-section linear electron accelerator with synchronized oscillators —V. F. Vikulov, V. A. Volodin, and O. S. Milovanov. 19(7), 930–1 (Jan. 1975); CPM-7503X0818

Vil'dzhyunas, M. I.—Generation of drift waves by an rf field near the lower hybrid frequency —Yu. F. Baranov, D. G. Bulyginskii, M. I. Vil'dzhyunas, B. V. Galaktionov, and N. V. Shustova. 19(6), 732–5 (Dec. 1974); CPM-7501X0732

Vinogradov, S. S.—Shielding properties of superconducting shields — S. I. Bondarenko, S. S. Vinogradov, G. A. Gogadze, S. S. Perepelkin, and V. I. Sheremet. 19(6), 824–8 (Dec. 1974); CPM-7501X0824

Vinogradov, V. F.—Composition of adsorbing and desorbing fluxes — Yu. A. Gel'man, V. I. Mikhailov, V. F. Vinogradov, and Yu. N. Lyubitov. 19(10), 1355–8 (Apr. 1975); CPM-7506X0289

Vinogradov, V. P.—Plasma density in a magnetoplasma compressor —A. K. Vinogradova, V. P. Vinogradov, A. I. Morozov, and A. A. Sergeev. 19(3), 421–3 (Sep. 1974); CPM-7412X1107

Vinogradova, A. K.—Plasma density in a magnetoplasma compressor —A. K. Vinogradova, V. P. Vinogradov, A. I. Morozov, and A. A. Sergeev. 19(3), 421–3 (Sep. 1974); CPM-7412X1107

Vinogradova, E. B.—Dependence of the basic parameters of $Al_xGa_{1-x}As$—GaAs solar converters on temperature and optical intensity —E. B. Vinogradova, M. B. Kagan, N. S. Koroleva, T. L. Lyubashevskaya, and T. A. Nuller. 19(10), 1378–81 (Apr. 1975); CPM-7506X0312

Virko, V. F.—Plasma synthesis by injection of an electron beam through an ion source —V. F. Virko, M. D. Gabovich, G. S. Kirichenko, and O. K. Nazarenko. 19(11), 1418–20 (May 1975); CPM-7506X1172

Virolainen, V. A.—Electron energy distribution in a high-freqeuncy discharge in an axial magnetic field —S. D. Vagner, V. A. Virolainen, Yu. M. Kagan, and T. A. Kalmykova. 19(2), 290–1 (Aug. 1974); CPM-7408X1554

Vitrishchak, I. B.—Polarization of a cavity with a thermally deformed active element —I. B. Vitrishchak, L. N. Soms, and A. A. Tarasov. 19(5), 664–8 (Nov. 1974); CPM-7501X0458

Vlasov, V. V.—Plasma decay instability in crossed fields —V. I. Farenik, V. V. Vlasov, A. M. Rozhkov, and A. A. Kozharin. 19(8), 1116–7 (Feb. 1975); CPM-7504X1540

—Ion energy spectra and collective effects in a Penning ion source — V. I. Farenik, V. V. Vlasov, A. M. Rozhkov, and A. A. Kozharin. 19(9), 1258–9 (Mar. 1975); CPM-7505X0680

Voitsenya, V. S.—Electron temperature in a high-frequency helium discharge —V. S. Voitsenya, A. Yu. Voloshko, V. G. Konovalov, and S. I. Solodovchenko. 19(7), 909–10 (Jan. 1975); CPM-7503X0797

Volkov, A. A.—Temperature dependence of the dielectric permittivity of single-crystal TiO_2 in the submillimeter range —A. A. Volkov, N. A. Irisova, and G. V. Kozlov. 19(4), 567–8 (Oct. 1974); CPM-7412X0351

Volkov, M. P.—Effects of cleaning on adsorption by germanium single crystals —Yu. I. Belyakov, M. P. Volkov, and T. N. Kompaniets. 19(6), 815–6 (Dec. 1974); CPM-7501X0815

Volkov, N. V.—Effect of selenium and sulfur on the work function of tungsten —N. V. Volkov, Yu. K. Gus'kov, Z. N. Kononova, and Yu. I. Kostikov. 19(1), 144–5 (Jul. 1974); CPM-7407X1656

—Steady-state operation of a surface-ionization thermionic converter —N. V. Volkov, Yu. K. Gus'kov, Yu. I. Kostikov, and V. P. Pashchenko. 19(8), 1129–30 (Feb. 1975); CPM-7504X1553

Volkov, Ya. F.—Magnetic field in a θ pinch with an axial conductor —Ya. F. Volkov, V. G. Dyatlov, and N. I. Mitina. 19(3), 323–5 (Sep. 1974); CPM-7412X1009

—Optical investigation of a turbulent plasma —Ya. F. Volkov, V. G. Dyatlov, and N. I. Mitina. 19(7), 905–8 (Jan. 1975); CPM-7503X0793

Volobuev, P. V.—Diffusion and solubility of helium in potassium chloride —A. Ya. Kupryazhkin, P. V. Volobuev, and P. E. Suetin. 19(8), 1105–7 (Feb. 1975); CPM-7504X1529

Volodin, V. A.—Multiple-section linear electron accelerator with synchronized oscillators —V. F. Vikulov, V. A. Volodin, and O. S. Milovanov. 19(7), 930–1 (Jan. 1975); CPM-7503X0818

Voloshko, A. Yu.—Electron temperature in a high-frequency helium discharge —V. S. Voitsenya, A. Yu. Voloshko, V. G. Konovalov, and S. I. Solodovchenko. 19(7), 909–10 (Jan. 1975); CPM-7503X0797

Volosov, V. I.—Mechanism for plasma loss from a magnetic trap — V. I. Volosov. 19(11), 1408–11 (May 1975); CPM-7506X1162

Vorob'eva, N. A.—Effect of cathode emission on the threshold for striations —N. A. Vorob'eva, Yu. M. Kagan, V. M. Milenin, and A. Kh. Muradov. 19(1), 117–8 (Jul. 1974); CPM-7407X1629

Vorogushin, M. F.—Resonator with azimuthally varying end plates —M. F. Vorogushin and V. I. Petrunin. 19(6), 767–9 (Dec. 1974); CPM-7501X0767

—Azimuthal and vertical motion in an accelerator with azimuthally varying electric field —M. F. Vorogushin and V. I. Petrunin. 19(6), 770–2 (Dec. 1974); CPM-7501X0770

—Phase motion of particles in an accelerator with an azimuthally varying electric field —M. F. Vorogushin and V. I. Petrunin. 19(7), 926–9 (Jan. 1975); CPM-7503X0814

Voronin, V. S.—Magnetic-field transport of a high-current electron beam —A. V. Agafonov, V. S. Voronin, A. N. Lebedev, and K. N. Pazin. 19(9), 1188–92 (Mar. 1975); CPM-7505X0610

Voronkov, R. M.—Low-voltage gun with a resonator for formation of electron bunches in a linear accelerator —V. A. Boiko, R. M. Voronkov, and V. A. Danilichev. 19(4), 569–71 (Oct. 1974); CPM-7412X0353

Vovk, O. M.—Analysis of magnetic deflection systems —O. M. Vovk and O. Ya. Popov. 19(11), 1504 (May 1975); CPM-7506X1258

Vul'gal'ter, G. A.—Magnetoacoustic transducer based on the domain structure of a ferromagnetic material —G. L. Gurevich and G. A. Vul'gal'ter. 19(1), 154–5 (Jul. 1974); CPM-7407X1666

Vyalov, G. N.—Multiple scattering of a focused beam of monoenergetic electrons —G. N. Vyalov. 19(9), 1216–8 (Mar. 1975); CPM-7505X0638

—Axially symmetric neutralized electron beam —G. N. Vyalov, V. N. Evteev, Yu. M. Zolotaikin, and K. N. Ul'yanov. 19(11), 1414–7 (May 1975); CPM-7506X1168

Y

Yakovkin, I. B.—Optical methods for studying amplification of elastic surface waves in a stratified system —I. B. Yakovkin, V. V. Petrov, and S. V. Bogdanov. 19(9), 1242–5 (Mar. 1975); CPM-7505X0664

Yakovleva, M. N.—Electromagnetic fields outside a synthesized plasma jet —E. V. Bogdanov, G. M. Mantrova, and M. N. Yakovleva. 19(7), 919–21 (Jan. 1975); CPM-7503X0807

Yakushev, E. M.—A transaxial lens —V. M. Kel'man, L. M. Nazarenko, and E. M. Yakushev. 19(4), 523–5 (Oct. 1974); CPM-7412X0307

—Theory of the cathode lens. III. Derivation of equations for composite cathode lenses —V. M. Kel'man, A. A. Sapargaliev, and E. M. Yakushev. 19(5), 592–6 (Nov. 1974); CPM-7501X0386

—Theory of the cathode lens. IV. Aberrations of composite cathode lens —V. M. Kel'man, A. A. Sapargaliev, and E. M. Yakushev. 19(5), 597–9 (Nov. 1974); CPM-7501X0391

Yalamov, Yu. I.—Thermophoresis and diffusophoresis of small, volatile aerosol particles —Yu. I. Yalamov and E. R. Shchukin. 19(2), 278–9 (Aug. 1974); CPM-7408X1542

—Motion of stable aerosol particles —O. A. Barsegyan and Yu. I. Yalamov. 19(11), 1486–7 (May 1975); CPM-7506X1240

Yalovets, A. P.—Ionization of a gas-discharge gap by fast electrons —O. B. Evdokimov and A. P. Yalovets. 19(1), 138–9 (Jul. 1974); CPM-7407X1650

Yampol'skii, P. A.—Nonradiative electron transitions and thermal effects in laser-irradiated transparent dielectrics —B. I. Makshantsev, A. A. Kovalev, R. K. Leonov, and P. A. Yampol'skii. 19(1), 98–102 (Jul. 1974); CPM-7407X1610

Yankauskas, Z. K.—Skin effect in a constant magnetic field —Z. K. Yankauskas, V. I. Chesonis, and V. G. Skripnik. 19(9), 1251–2 (Mar. 1975); CPM-7505X0673

Yankelevich, Yu. B.—Thermal conditions for a sandwich cold cathode —F. M. Benson, P. E. Troyan, and Yu. B. Yankelevich. 19(7), 946–7 (Jan. 1975); CPM-7503X0834

Yanshin, É. V.—Investigating prebreakdown fields in water by means of the Kerr effect —I. T. Ovchinnikov, K. V. Yanshin, and É. V. Yanshin. 19(2), 294–5 (Aug. 1974); CPM-7408X1558

Yanshin, K. V.—Investigating prebreakdown fields in water by means of the Kerr effect —I. T. Ovchinnikov, K. V. Yanshin, and É. V. Yanshin. 19(2), 294–5 (Aug. 1974); CPM-7408X1558

Yavor, I. P.—Interferometer measurement of the neutral cesium distribution in a short low-voltage arc —Yu. L. Serov and I. P. Yavor. 19(6), 751–4 (Dec. 1974); CPM-7501X0751

—Atomic density in the low-voltage arc in a cesium diode —F. G. Baksht, A. A. Kostin, Yu. L. Serov, and I. P. Yavor. 19(11), 1424–5 (May 1975); CPM-7506X1178

Yuferov, V. B.—Spatial characteristics and loss of plasma produced by an electron beam in a magnetic trap —M. Yu. Bredikhin, A. I. Maslov, A. I. Skibenko, E. I. Skibenko, I. P. Fomin, and V. B. Yuferov. 19(1), 49–52 (Jul. 1974); CPM-7407X1561

Yurchenko, V. I.—Computer calculation of quasistationary pulsed magnetic fields —V. I. Yurchenko. 19(8), 1025–30 (Feb. 1975); CPM-7504X1449

—Flux loss in the production of ultrastrong fields by rapid compression of conducting shells —V. I. Yurchenko. 19(8), 1031–3 (Feb. 1975); CPM-7504X1455

—Equations and boundary conditions for a three-dimensional quasistationary field —V. I. Yurchenko. 19(8), 1126–8 (Feb. 1975); CPM-7504X1550

Yurevichyus, Sh. V.—Optical simulation of a radiator aperture with arbitrary amplitude–phase distribution —M. M. Butusov and Sh. V. Yurevichyus. 19(6), 833–4 (Dec. 1974); CPM-7501X0833

Yushmanov, E. E.—Measurement of plasma ion temperature by a thin probe with $T_i \gtrsim T_e$ —B. I. Kanaev and E. E. Yushmanov. 19(4), 554–5 (Oct. 1974); CPM-7412X0338

—Measurement of plasma electron temperature with a sinusoidal probe potential —B. I. Kanaev, V. V. Piterskii, and E. E. Yushmanov. 19(11), 1421–3 (May 1975); CPM-7506X1175

Z

Zagorskii, P. V.—Lagrange problem in magnetohydrodynamics —P. V. Zagorskii and Yu. P. Lun'kin. 19(8), 1009–11 (Feb. 1975); CPM-7504X1433

Zaitsev, V. K.—Laser compensation for thermal distortion in optical pumping —V. K. Zaitsev, V. A. Il'inskii, A. M. Marugin, and V. M. Ovchinnikov. 19(11), 1480–1 (May 1975); CPM-7506X1234

Zaitsev, V. V.—Electron energy distribution and electrical characteristics of the positive column in H_2 and H_2+Cl_2 —V. V. Zaitsev, A. I. Maksimov, and V. I. Svettsov. 19(1), 57–9 (Jul. 1974); CPM-7407X1569

Zakatov, L. P.—Scattering of an electron beam in a straight *dc* turbulent plasma —Yu. P. Golovanov, L. P. Zakatov, A. S. Kingsep, and A. G. Plakhov. 19(8), 1046–9 (Feb. 1975); CPM-7504X1470

Zakharenko, Yu. G.—Mode coupling in a double-anode discharge —Yu. G. Zakharenko and V. E. Privalov. 19(7), 980–2 (Jan. 1975); CPM-7503X0868

Zakharov, A. S.—Ion emission into vacuum from a discharge in crossed electric and magnetic fields —V. A. Nikitinskii and A. S. Zakharov. 19(6), 839–40 (Dec. 1974); CPM-7501X0839

Zakharov, L. E.—Equilibrium in a tokamak with noncircular cross section —L. E. Zakharov. 19(8), 1005–8 (Feb. 1975); CPM-7504X1429

Zakutin, V. V.—Self-acceleration of an intense electron beam —I. A. Grishaev, A. N. Dedik, V. V. Zakutin, I. I. Magda, Yu. V. Tkach, and A. M. Shenderovich. 19(8), 1087–9 (Feb. 1975); CPM-7504X1511

Zalkind, V. M.—Hydrodynamic stability of the Uragan stellarator —V. M. Zalkind, Yu. K. Kuznetsov, V. K. Pashnev, and V. M. Tonkopryad. 19(8), 1123–5 (Feb. 1975); CPM-7504X1547

Zandberg, É. Ya.—Time dependence of ion currents produced through surface ionization. Ionization of Ba on the (111) face of iridium —É. Ya. Zandberg, E. V. Rut'kov, and A. Ya. Tontegode. 19(2), 261–3 (Aug. 1974); CPM-7408X1525

—Surface-ionization determination of the electron affinities of silver and gold —É. Ya. Zandberg, A. G. Kamenev, and V. I. Paleev. 19(3), 385–9 (Sep. 1974); CPM-7412X1071

—Determination of ionization potentials and electron affinities of certain elements by extrapolation —A. G. Kamenev, É. Ya. Zandberg, and V. I. Paleev. 19(7), 940–1 (Jan. 1975); CPM-7503X0828

—Recent developments in surface ionization (review) —É. Ya. Zandberg. 19(9), 1133–44 (Mar. 1975); CPM-7505X0555

Zapesochnyi, I. P.—Excitation collisions between magnesium ions and inert gas atoms —V. L. Ovchinnikov, O. B. Shpenik, and I. P. Zapesochnyi. 19(3), 382–4 (Sep. 1974); CPM-7412X1068

Zapryagaev, A. F.—Sign of the change in optical path length in a laser interferometer with feedback —I. M. Belousova and A. F. Zapryagaev. 19(6), 829–30 (Dec. 1974); CPM-7501X0829

Zashkavara, V. V.—Angular aberration corrector in a cylindrical mirror analyzer —V. V. Zashkavara and V. F. Tarasov. 19(6), 841–2 (Dec. 1974); CPM-7501X0841

Zashkvara, V. V.—Correction of third-order angular aberration in a system with two electrostatic mirrors —V. V. Zashkvara. **19**(7), 961–2 (Jan. 1975); CPM-7503X0849
—Double focusing in a system of $1/r$ electric and magnetic fields —V. V. Zashkvara and V. N. Demin. **19**(9), 1219–20 (Mar. 1975); CPM-7505X0641
—Luminosity of a cylindrical spectrometer with a small off-axis source —V. V. Zashkvara. **19**(9), 1264–5 (Mar. 1975); CPM-7505X0686
Zaslavskii, G. M.—Transformation of nonlinear MHD waves —G. M. Zaslavskii, S. S. Moiseev, and V. V. Mukhin. **19**(12), 1534–7 (Jun. 1975); CPM-7508X0408
Zelenov, B. A.—Proton extraction from the 70–GeV accelerator for the Ludmila liquid-hydrogen chamber (extraction system S) —A. A. Aseev, A. I. Drozhdin, B. A. Zelenov, É. A. Merker, L. L. Moizhes, K. P. Myznikov, A. A. Roshchin, V. M. Tatarenko, M. A. Kholodenko, A. D. Artemov, L. N. Vaulin, V. I. Gordin, I. I. Kovalevskii, V. N. Rozhkov, M. M. Suvorov, A. S. Sudarushkin, and V. I. Chuiko. **19**(1), 70–6 (Jul. 1974); CPM-7407X1582
Zemlyanskii, N. M.—Interaction of a hollow electron beam with a plasma —N. M. Zemlyanskii, A. K. Berezin, Ya. B. Fainberg, L. I. Bolotin, and S. S. Krivulya. **19**(12), 1547–8 (Jun. 1975); CPM-7508X0421
Zhabrev, G. I.—Energy spectra of scattered particles in proton bombardment of a metal target —G. I. Zhabrev, V. A. Kurnaev, and V. G. Tel'kovskii. **19**(7), 978–9 (Jan. 1975); CPM-7503X0866
Zhitnikov, R. A.—Two-spin oscillator with optical orientation of electrons and nuclei —R. A. Zhitnikov and V. V. Semenov. **19**(1), 105–9 (Jul. 1974); CPM-7407X1617
—Effect of instrumental noise on a system with two spin oscillators using Cs^{133} and He^3 —R. A. Zhitnikov, V. V. Semenov, and P. A. Klyushkin. **19**(4), 556–7 (Oct. 1974); CPM-7412X0340
—Measurement of transverse relaxation time T_2 of optically oriented He^4 with an oscillator magnetometer —N. A. Dovator, R. A. Zhitnikov, and P. P. Kuleshov. **19**(12), 1608–9 (Jun. 1975); CPM-7508X0482
Zhivulin, V. A.—Reflecting properties of an inhomogeneous anisotropic plasma layer —V. A. Zhivulin and G. I. Makarov. **19**(1), 123 (Jul. 1974); CPM-7407X1635
Zhmudskii, A. A.—Emission of waves from a plasma layer —T. A. Davydova and A. A. Zhmudskii. **19**(1), 12–5 (Jul. 1974); CPM-7407X1524
—Symmetry of high-frequency plasma motions —A. A. Zhmudskii and V. B. Taranov. **19**(6), 717–8 (Dec. 1974); CPM-7501X0717
Zhukov, V. M.—Emission characteristics of an explosive gallium cathode —G. N. Fursei and V. M. Zhukov. **19**(6), 804–7 (Dec. 1974); CPM-7501X0804
Zilbergleit, A. A.—Diffraction of a plane electromagnetic wave by a conducting plane with a projection —A. A. Zilbergleit. **19**(4), 531–2 (Oct. 1974); CPM-7412X0315
Ziser, V. E.—Magnetic topography of toroidal systems —M. N. Skoblik, V. E. Ziser, A. V. Georgievskii, and V. G. Peletminskaya. **19**(10), 1277–80 (Apr. 1975); CPM-7506X0211
Zolotaikin, Yu. M.—Axially symmetric neutralized electron beam —G. N. Vyalov, V. N. Evteev, Yu. M. Zolotaikin, and K. N. Ul'yanov. **19**(11), 1414–7 (May 1975); CPM-7506X1168
Zolototrubov, I. M.—Investigation of a plasma focus with a time-resolved laser interferometer —I. M. Zolototrubov, I. P. Skoblik, A. G. Tolstolutskii, and V. I. Privezentsev. **19**(8), 1061–2 (Feb. 1975); CPM-7504X1485
Zosimov, A. V.—Excitation of surface electromagnetic waves in a plasma cylinder surrounded by a hollow electron beam —O. V. Dolzhenko, A. V. Zosimov, and A. A. Rukhadze. **19**(5), 618–21 (Nov. 1974); CPM-7501X0412
Zvezdin, Yu. I.—Effect of the adsorption rate on the diffusion of deuterium through nickel —Yu. I. Belyakov, Yu. I. Zvezdin, A. A. Kurdyumov, and G. G. Nevdakha. **19**(7), 956–8 (Jan. 1975); CPM-7503X0844
Zvonnikov, N. A.—Electromagnetic pulse radiated by a moving charged bunch in matter —N. A. Zvonnikov. **19**(10), 1290–2 (Apr. 1975); CPM-7506X0224
Zvyagintseva, L. N.—Elimination of carbon impurities from platinum by heating in an oxygen atmosphere —L. P. Rekova, V. V. Mozgin, L. N. Zvyagintseva, V. N. Bondarenko, and Ya. M. Fogel'. **19**(11), 1465–7 (May 1975); CPM-7506X1219
Zykov, V. G.—Plasma equilibrium and confinement in a poloidal heliotron configuration. I —V. G. Zykov, V. I. Karpukhin, Yu. F. Lonin, N. N. Podteregera, N. I. Rudnev, and V. T. Tolok. **19**(8), 1063–8 (Feb. 1975); CPM-7504X1487
—Plasma equilibrium and confinement in a poloidal heliotron configuration. II —V. G. Zykov, V. I. Karpukhin, Yu. F. Lonin, N. N. Podteregera, N. I. Rudnev, A. Y. Skibenko, V. T. Tolok, and I. P. Fomin. **19**(8), 1069–72 (Feb. 1975); CPM-7504X1493

This index is based on the 1975 *Physics and Astronomy Classification Scheme* developed by AIP. It is not a translation. It was produced by computer-aided photocomposition directly from the magnetic tapes of the AIP's Current Physics Information System. Suggestions for improvements as well as other comments are welcome and should be addressed to the Editor.

This index includes microfilm reel and frame numbers for the convenience of those wishing to find articles in *Current Physics Microform* (CPM), the monthly microfilm edition of the complete set of journals of the American Institute of Physics. These numbers are given in the form **CPM-7201A0321**, where 72 refers to the year, 01 denotes the month (January in this example), A the cartridge, and 0321 the frame.

Focusing of an astigmatic beam by a doublet and a symmetric triplet of quadrupole lenses

V. I. Chetvertkov
D. V. Efremov NIIEFA, Leningrad

(Submitted April 6, 1973)
Zh. Tekh. Fiz., 44, 3-5 (January 1974)

Using a matrix method analytic expressions are obtained in the semithin-lens approximation for the optical parameters and gradients necessary to focus astigmatic beams for given lens geometries and object and image positions.

The solution of the inverse problem of particle optics – finding the magnitudes of the focusing fields and the optical parameters of the lenses for given beam requirements and configurations and known geometry – can facilitate the synthesis of optical systems.

We consider the solution of this problem for a doublet and a symmetric triplet for astigmatic beams with a small space charge as the matching of objects and images. We use the semithin approximation for quadrupole lenses.[1,2] The solution of this problem is known only for a doublet.[3] Figure 1 shows particle trajectories in perpendicular planes in a symmetric triplet. Trajectories in a doublet are constructed in similar fashion. Letters with subscripts and superscripts are used in Fig. 1 and in the test. Subscripts 1 and 2 refer to the corresponding gradient and superscripts denote the number of primes. Equivalent thin lenses with optical strengths g_m^n pass through the centers of the poles with the effective length L_m; d is the distance between centers of neighboring poles; a^n is the distance from the object to the entrance and b^n from the image to the exit. Without loss of generality Fig. 1 is drawn for $b'' < 0$, a^n, $b' > 0$.

We use a matrix method to describe the optics. The relation between a^n and b^n is given by[1]

$$b^n(A_{21}^n a^n + A_{22}^n) + (A_{11}^n a^n + A_{12}^n) = 0. \tag{1}$$

$$A^n = \begin{pmatrix} A_{11}^n & A_{12}^n \\ A_{21}^n & A_{22}^n \end{pmatrix}$$

is the transfer matrix between entrance and exit.

We introduce the notation

$$x_m^n = g_m^n d,\ A_m^n = \begin{pmatrix} 1 & 0 \\ -\frac{1}{d} x_m^n & 1 \end{pmatrix},\ A_d = \begin{pmatrix} 1 & d \\ 0 & 1 \end{pmatrix}.$$

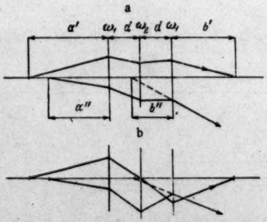

Fig. 1. Trajectories in a symmetrical triplet. $a' = 1$, $a'' = 0.75$, $b' = 0.784$, $b'' = -0.507$, $d = 0.4$, $L_1 = 0.2$, $L_2 = 0.4$ (dimensions in meters). a) Weak solution ($y_1 = 0.366$, $y_2 = 0.619$, $\omega_1 = 0.625$, $\omega_2 = 0.835$); b) strong solution ($y_1 = 0.730$, $y_2 = 1.245$, $\omega_1 = 0.919$, $\omega_2 = 1.294$).

In the semithin approximation

$$x_m^n = \begin{cases} \frac{d}{L_m}\omega_m \sin\omega_m & \text{for}\quad n = m, \\ -\frac{x_m^m}{1-\delta_m x_m^m} & \text{for}\quad n \neq m, \end{cases} \tag{2}$$

where $\delta_m = L_m/3d$.

We find the matrices for a doublet

$$A^n = A_2^n A_d A_1^n = \begin{pmatrix} (1 - x_1^n) & d \\ -\frac{1}{d}[(1 - x_1^n)x_2^n + x_1^n]; & (1 - x_2^n) \end{pmatrix} \tag{3}$$

and a symmetric triplet

$$A^n = A_1^n A_d A_2^n A_d A_1^n$$

$$= \begin{pmatrix} [(1 - x_1^n)(1 - x_2^n) - x_1^n]; & d(2 - x_2^n) \\ -\frac{1}{d}(1 - x_1^n)[(1 - x_1^n)x_2^n + 2x_1^n]; & A_{11}^n \end{pmatrix}. \tag{4}$$

Clearly $|A^n| = 1$. Using (1), (2), (3), or (4) for two values of n we obtain two equations for x_1' and x_2''. These equations can be written in compact form:

$$\sum_{p=0}^{N} h_{s,p} \cdot (x_1')^{N-p} = 0, \tag{5}$$

$$x_2'' = \frac{\sum\limits_{p=0}^{\frac{N}{2}} h_{q,p}(x_1')^{\frac{N}{2}-p}}{\sum\limits_{p=0}^{\frac{N}{2}} h_{q+1,p}(x_1')^{\frac{N}{2}-p}}, \tag{6}$$

where

$$h_{s,p} = \sum_{\nu=\nu_1}^{\nu_2} \sum_{\mu=1}^{2} (-1)^{\mu} h_{\mu,p-\nu} h_{s-\mu,\nu}.$$

$\nu_1 = p - \nu_2$, $\nu_2 = p$ for $p \leq 1$, $\nu_2 = (N/2)$ for $p > 1$.

For a doublet $N = 2$, $h_{10} = \beta'$, $h_{11} = -(\eta' - 1)$, $h_{20} = -(1 - \delta_2 h_{10})$, $h_{21} = (\alpha' + \delta_2 h_{11})$, $h_{30} = (\beta'' - \delta_1 h_{31})$, $h_{31} = (\eta'' - 1)$, $h_{40} = (1 - \delta_1 h_{41})$, $h_{41} = \alpha''$; for a symmetric triplet $N = 4$, $h_{10} = -2$, $h_{11} = 2(\theta' - 1)$, $h_{12} = -(2\eta' - \theta')$, $h_{20} = (1 - 2\delta_2)$, $h_{21} = -(\theta' - \delta_2 h_{11})$, $h_{22} = (\eta' + \delta_2 h_{12})$, $h_{30} = 2 - \delta_1[2(\theta'' - 1) - \delta_1 h_{32}]$, $h_{31} = 2[(\theta'' - 1) - \delta_1 h_{32}]$, $h_{32} = (2\eta'' - \theta'')$, $h_{40} = 1 - \delta_1(\theta'' - \delta_1\eta'')$, $h_{41} = (\theta'' - 2\delta_1\eta'')$, $h_{42} = \eta''$, where

$$\alpha^n = \left(1 + \frac{d}{a^n}\right),\ \beta^n = \left(1 + \frac{d}{b^n}\right),\ \eta^n = \alpha^n\beta^n,\ \theta^n = (\alpha^n + \beta^n).$$

Equation (5) is solved analytically. The value of x_2''

is found by substituting x_1' into (6). It is possible to take $q = 1$ or 3. From its meaning $x_m^m > 0$, and therefore of all possible solutions of (5) and (6) we retain only those which give positive pairs x_1' and x_2''. The solutions corresponding to maximum x_m^m are called "strong".[2] Using the values found for x_1' and x_2'' we compute x_1'' and x_2' and then g_m^n. Using x_m^n we determine the matrix A^n from (3) or (4). The optical parameters of the lenses are found. To calculate the gradients we must determine ω_m. We use (2) for $n = m$ in the form

$$y_m = \omega_m \sin \omega_m, \quad y_m = \frac{L_m}{d} x_m^m. \tag{7}$$

Making a Taylor's expansion of the function ω_m defined implicitly by (7), limiting ourselves to a few terms, and simplifying the coefficients we obtain

$$\omega_m \approx \sqrt{y_m}\left\{1 + \frac{y_m}{12}\left[1 + \frac{y_m}{4}\sum_{l=0}^{2}\left(\frac{y_m}{3}\right)^l\right]\right\}. \tag{8}$$

The relative error in computing ω_m from (8) is

$$\frac{\Delta\omega_m}{\omega_m} < 2 \cdot 10^{-4}\,(5 \cdot 10^{-3}) \text{ for } y_m < 0.85\,(1.25).$$

The values found for ω_m can be improved by Newton's method

$$\omega_m^{i+1} = \omega_m^i + \frac{y_m - \omega_m^i \sin \omega_m^i}{\sin \omega_m^i + \omega_m^i \cos \omega_m^i},$$

where i is the number of the approximation.

We determine the gradients from the known values of ω_m. For example, for magnetic lenses[3]

$$G_m = \left(\frac{\omega_m}{L_m}\right)^2 (BR),$$

where G_m is the gradient in T/m, BR is the magnetic rigidity of the particles in Tm, and L_m is in m.

A numerical example for a symmetric triplet is shown in Fig. 1. The relations obtained offer an effective method of calculating the focusing of astigmatic beams in ray optics and give a first approximation to envelope optics.

---

[1] S. Ya. Yavor, Focusing of Charged Particles by Quadrupole Lenses [in Russian], Atomizdat, Moscow (1968).

[2] V. I. Kotov and V. V. Miller, Focusing and Mass Separation of High-Energy Particles [in Russian], Atomizdat, Moscow (1969).

[3] V. V. Miller, Prib. Tekh. Eksp., 4, 23 (1964).

Round metal-optical waveguide filled with a two-layer dielectric

V. A. Pruzhanovskii

(Submitted July 24, 1972; resubmitted February 14, 1973)
Zh. Tekh. Fiz., 44, 6-15 (January 1974)

The theoretical section of this paper deals with the application of the characteristic equation for a three-layer coaxial structure to a round metal-optical waveguide filled with a two-layer dielectric, and also to an open two-layer dielectric waveguide with finite sheath thickness. An approximate solution based on the use of an asymptotic expansion of Bessel functions is obtained. Results of a numerical calculation are given. The second part of the article is devoted to an experimental investigation of this waveguide. Both single-mode and multimode designs, obtained by chemical silvering of a two-layer glass fiber, are considered. A procedure is described for measuring the fiber parameters and a method is given for silvering. Measurement results are cited and show that when the sheath is thick the silvering of the outer surface of the fiber decreases the attenuation of the waves propagating in the core. At the same time, silvering a fiber with a thin sheath increases this attenuation. Certain waveguide properties observed in the present study are discussed and practical applications of such a waveguide are discussed.

INTRODUCTION

Earlier articles[1,2] have dealt with coaxial and circular metal-optical waveguides. The present paper is devoted to a round waveguide filled with a two-layer dielectric in which the refractive index of the outer layer is somewhat lower than that of the inner one.

The use of a metallic shield to decrease the losses in a two-layer planar dielectric light pipe is discussed in ref. 3. Round metallic waveguides filled with a two-layer dielectric are investigated at microwave frequencies in refs. 4-7. The metal is regarded as a medium of infinite conductivity, and the problem is solved with zero boundary conditions. This method cannot be used at optical frequencies, where the metal must be regarded as a dielectric with a complex permittivity $\overset{*}{\varepsilon} = \varepsilon - i(4\pi\sigma/\omega)$ and it is necessary to solve the characteristic equation for a three-layer structure.

Such an equation has been solved in refs. 8 and 9. The method used in the first of these references, however, is not suitable for the determination of the damping introduced by the outer absorbing coating. The successive-approximation method developed in the second references calls for the use of a computer.

In contrast, the purpose of the theoretical part of the present paper is to obtain equations for the damping in an open and metallized two-layer fiber in explicit form.

The experimental section is devoted to the influence of metallization on the damping of the light flux and on its polarization in a two-layer glass fiber. There seem to be no other papers published on this question.

THEORY

Characteristic equation. The waveguide construction is shown in Fig. 1. It consists of a dielectric core I of radius ρ and refractive index n_1, of a dielectric sheath II with outer radius R and refractive index n_2 ($n_2 < n_1$), and of an outer metallic cover III. The outside radius of this cover should be regarded as infinite in view of the small skin depth in the metal. For the sake of comparison, we consider later the case in which medium III is free space or air.

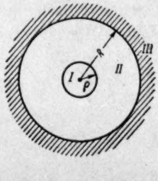

Fig. 1. Construction of the waveguide.

We turn to the previously derived[2] characteristic equation (1) for a three-layer coaxial waveguide (changing the index numbers of the media, in accord with Fig. 1). Of the solutions of this equation we are interested primarily in those corresponding to waves propagating in the core and attenuating in the sheath. Such solutions correspond to values of χ_2 lying near the imaginary axis in the complex plane, and to values χ_1 located near the real axis.

If the sheath is thick enough, $|\chi_2|R \gg 1$ so that we can apply the asymptotic Hankel expansion[10] to the functions $J_n(\chi_2R)$ and $N_n(\chi_2R)$. Substituting it in the indicated equation and neglecting terms of higher order than $\exp[-2|\chi_2|R]$, we represent this equation in the form

$$\left[\frac{J_n'(\chi_1\rho)}{J_n(\chi_1\rho)}\right]^2\frac{\varepsilon_1\mu_1\chi_2^2}{\varepsilon_2\mu_2\chi_1^2}-\frac{J_n'(\chi_1\rho)}{J_n(\chi_1\rho)}\frac{H_n^{(1)\prime}(\chi_2\rho)}{H_n^{(1)}(\chi_2\rho)}\frac{\chi_2}{\chi_1}\left(\frac{\varepsilon_1}{\varepsilon_2}+\frac{\mu_1}{\mu_2}\right)+\left[\frac{H_n^{(1)\prime}(\chi_2\rho)}{H_n^{(1)}(\chi_2\rho)}\right]^2$$
$$-\frac{\Gamma^2k_0^2n^2}{\chi_1^4\chi_2^2\rho^2}\left(1-\frac{\varepsilon_1\mu_1}{\varepsilon_2\mu_2}\right)^2+(-1)^n\frac{i8e^{i2\chi_2R}}{\pi\chi_2\rho qS_n^2(i2\chi_2R)\,[H_n^{(1)}(\chi_2\rho)]^2}$$
$$\times\left\{-\frac{J_n'(\chi_1\rho)}{J_n(\chi_1\rho)}\left(\gamma_*+\frac{i\alpha_*\psi}{2}\right)-\frac{\xi\pi^2\chi_2^2\rho R}{4}+\frac{H_n^{(1)\prime}(\chi_2\rho)}{H_n^{(1)}(\chi_2\rho)}(i\psi+\beta)\right\}=0, \quad (1)$$

where $S_n(z) = 1 + (4n^2-1)/4iz + \ldots$ is the series in the Hankel expansion,[10]

$$\alpha_*=\frac{\chi_2}{\chi_1}\left(\frac{\varepsilon_1}{\varepsilon_2}+\frac{\mu_1}{\mu_2}\right),\quad \gamma_*=\frac{H_n^{(1)\prime}(\chi_3R)}{H_n^{(1)}(\chi_3R)}\frac{\chi_2^2}{\chi_1\chi_3}\left(\frac{\varepsilon_1\varepsilon_3}{\varepsilon_2^2}+\frac{\mu_1\mu_3}{\mu_2^2}\right),$$
$$u\approx -i/2\chi_2R,\quad q=1+\zeta-i\beta+u(2-i\beta+u),$$
$$\psi=2(1+u)-qS_n(i2\chi_2R)\,S_n(-i2\chi_2R),$$

and the remaining notation is the same as in ref. 2.

The last term of this equation is small, since it contains the factor $\exp(-2|\chi_2|R)$. The remaining four terms coincide with the characteristic equation for a two-layer dielectric waveguide.[11] It is noteworthy that both the radius R and the parameters of the medium III enter only in the last term. The small value of this term corresponds to a small perturbation introduced by medium III into the structure of the waves propagating in dielectrics I and II.

Approximation solution. The characteristic equation (1) has complex coefficients with small imaginary parts. Its roots should therefore lie near the real roots of the real part of this equation. Since the latter, owing to the insignificance of the fifth term, coincide with the characteristic equation for a two-layer dielectric waveguide, we can use the approximate solution methods developed for the latter[12,13] and determine the real part of the root Re χ_1.

For example, for an He_{11} wave, we can use the approximation[13]

$$\operatorname{Re}\chi_1 \approx \frac{3\pi(1+\sqrt{2})\sqrt{\varepsilon_1-\varepsilon_2}}{\lambda\left\{1+\left[4+\left(\frac{2\pi\rho}{\lambda}\right)^4(\varepsilon_1-\varepsilon_2)^2\right]^{1/4}\right\}}. \tag{2}$$

For $J_n'(\chi_1\rho)/J_n(\chi_1\rho)$ and $H_n^{(1)'}(\chi_2\rho)/H_n^{(1)}(\chi_2\rho)$ we use an asymptotic expansion analogous to Eq. (16) of ref. 2 (the arguments of these functions for the practically realizable constructions of two-layer glass fibers[14] never drop below 0.9):

$$\frac{J_n'(z_1)}{J_n(z_1)} \approx f(y_{nm}-|z_1|), \tag{3}$$

$$\frac{H_n^{(1)'}(z_2)}{H_n^{(1)}(z_2)} \approx i\left(1+\frac{ig}{2z_2}\right). \tag{4}$$

Here, y_{nm} is the m-th zero of the derivative $J_n'(z)$, in the vicinity of which there are located the roots of (1) corresponding to the modes HE_{nm} and EH_{nm} (or H_{0m} and E_{0m} if n = 0), f and g are correction coefficients determined for $z_{10} = \operatorname{Re}(\chi_1)\rho$ and $z_{20} = i|\chi_{20}|\rho = (i\rho)[|k_1|^2 - |k_2|^2 - (\operatorname{Re}\chi_1)^2]^{1/2}$ by substituting the coresponding numerical values of the functions in (3) and (4).

We write the roots of Eq. (1) in the form $\chi_1 = |\chi_1|e^{i\varphi_1}$ and $\chi_2 = i|\chi_2|e^{i\varphi_2}$. If medium III is a metal, then we can write $\chi_1 \approx |\chi_1|$, $\chi_2 \approx i|\chi_2|$, $\dot{\varepsilon}_1 \approx \varepsilon_1$, $\dot{\varepsilon}_2 \approx \varepsilon_2$, and $\alpha_* \approx i|\alpha_*|$, since φ_1, φ_2, Δ_1, and Δ_2 are much smaller than the arguments of the complex quantities β, γ_*, and ζ. If the medium III is a dielectric (say, air), we can neglect this term completely.

Separating the imaginary part of Eq. (1) and solving it, we find

$$\varphi_1 = \frac{\Sigma + \operatorname{Im}\Omega}{\Delta}, \tag{5}$$

where we use the notation

$$\sum = \frac{f^2\varkappa^2\nu(2\tau-\Delta)}{\theta^2} + f\varkappa\left(|\alpha_*|\tau - \frac{\varepsilon_1\nu\Delta}{\varepsilon_2|\theta|}\right) + \frac{g\tau\nu}{|\chi_2|\rho} + \frac{\Gamma^2|k_2|^2n^2(1-\upsilon)^2}{|\chi_2|^2\rho^2|\chi_1|^4}\left(\frac{\upsilon\Delta}{1-\upsilon} + \frac{2\tau\theta^2}{1-\theta^2}\right), \tag{6}$$

$$\Delta = 2f^2\varkappa^2\upsilon\left(\frac{y_{nm}}{\varkappa\theta^2} - 1\right) + f|\alpha_*|(\nu y_{nm} - \varkappa\theta^2) - \frac{g\nu\theta^2}{|\chi_2|\rho} + \frac{2\Gamma^2|k_2|^2n^2(2+\theta^2)(1-\upsilon)^2}{|\chi_1|^4|\chi_2|^2\rho^2}, \tag{7}$$

$$\Omega = \frac{i2\pi e^{i2\chi_2R}}{\chi_2\rho q[S_n(i2\chi_2R)]^2[K_n(-i\chi_2\rho)]^2} \times\left\{\frac{J_n'(\chi_1\rho)}{J_n(\chi_1\rho)}\left(\gamma_* + \frac{i\alpha_*\psi}{2}\right) + \frac{\xi\pi^2\chi_2^2\rho R}{4} - \frac{H_n^{(1)'}(\chi_2\rho)}{H_n^{(1)}(\chi_2\rho)}(i\psi+\beta)\right\}. \tag{8}$$

$K_n(-i\chi_2\rho)$ is the MacDonald function, and

$$\varkappa = y_{nm} - |\chi_1|\rho,\ \Delta = \operatorname{tg}\Delta_1 - \operatorname{tg}\Delta_2,$$

$$\dot{\varepsilon}_1 = \varepsilon_1(1 - i\operatorname{tg}\Delta_1),\ \dot{\varepsilon}_2 = \varepsilon_2(1 - i\operatorname{tg}\Delta_2),$$

$$\theta = i\left|\frac{\chi_1}{\chi_2}\right|,\ \nu = 1 + (g/2|\chi_2|\rho),\ \upsilon = \varepsilon_1\mu_1/\varepsilon_2\mu_2.$$

The first term in this expression characterizes the damping of the light flux in the core material, the second introduces a correction for the field distribution and for the differences between the losses in the core and in the sheath. Both terms taken together determine the damping in a dielectric waveguide in the two-layer approximation, i.e., at R = ∞.

Substituting (5) in the equation $\Gamma = (k_1^2 - \chi_1^2)^{1/2}$ and isolating its imaginary part, we determine the damping constant (in decibels per unit length of the waveguide)

$$\gamma = \frac{8.6858}{\sqrt{|k_1|^2 - |\chi_1|^2}}\left(\frac{|k_1|^2\operatorname{tg}\Delta_1}{2} + \frac{|\chi_1|^2\Sigma}{\Delta} + \frac{|\chi_1|^2\operatorname{Im}\Omega}{\Delta}\right).$$

The last term in (9) corresponds to the damping introduced by the medium III. For $R \gg \rho$, the value is negligibly small. For a comparative estimate when $\varkappa \ll 1$ we neglect the first two terms of the numerator of (8), the quantities $|u| \ll 1$ and $|\zeta| \ll |\beta|$, and use the approximation $\psi \approx 1 + i\beta$. We then have for a metallic medium

$$\operatorname{Im}\Omega \approx \frac{2\pi\nu|\beta|\varphi_\beta e^{-2|\chi_2|R}}{|\chi_2|\rho(1-|\beta|)^2[K_n(|\chi_2|\rho)]^2}, \tag{10}$$

where φ_ρ is the argument of the complex quantity $\beta = -i|\beta|e^{i\varphi_\beta}$.

If medium III is a dielectric, the largest value in (8) is that of the argument of the complex quantity $e^{i2\chi_2R}$, and

$$\operatorname{Im}\Omega \approx -\frac{4\pi\nu R(\theta^2\varphi_1 + \tau)e^{-2|\chi_2|R}}{\rho(1+|\beta|)[K_n(|\chi_2|\rho)]^2}. \tag{11}$$

Results of numerical calculations. We present the results of numerical calculations for a silver-coated two-layer glass fiber with the following parameters: $\rho = 2.175\ \mu$, $R = 31.1\ \mu$, $n_1 = 1.516$, $n_2 = 1.5025$, tan $\Delta_1 = 6.135\cdot10^{-9}$ (or 400 dB/km) and tan $\Delta_2 = 1.541\cdot10^{-8}$ (or 1000 dB/km). The optical constants of silver $\varepsilon_{Ag} = -16.39$ and $\sigma_{Ag} = 1.273\cdot10^{14}$ (cgs esu) at $\lambda = 0.6328\ \mu$ are determined by linear interpolation between their values at $\lambda = 0.6$ and $0.65\ \mu$, given in ref. 15. The critical parameter of such a fiber is $(2\pi\rho/\lambda)(n_1^2 - n_2^2)^{1/2} = 4.34$; there can exist in this waveguide seven modes propagating in the core and attenuating in the sheath: HE_{11}, H_{01}, E_{01}, HE_{21}, HE_{12}, HE_{31}, and EH_{12}. The attenuation of the HE_{11} wave, calculated from Eqs. (5)-(9), is 426.6 dB/km, of which 25.6 dB/km are due to the second term of (9) and only $3.62\cdot10^{-37}$ dB/km to the third.

The H_{02} mode in such a waveguide has the smallest value of $|\chi_2|$ of all the symmetrical magnetic waves propagating in the sheath, and should therefore have the smallest attenuation. Since $\rho/R \ll 1$ for the design considered by us, this attenuation can be defined as the attenuation of the H_{01} mode in a round metal-optical waveguide filled with one dielectric II [i.e., using Eq. (3) of ref. 1]. It amounts to 1095.5 dB/km, of which 95.5 dB/km is due to the influence of metallic coating III.

If the sheath II of the described fiber is glass having the same loss as the core, i.e., if tan $\Delta_2 = 6.135\cdot10^{-9}$), then the second term of (9) decreases by 1.077 dB/km, so that the total attenuation of the HE_{11} wave is 402.077 dB/km. The damping of the H_{02} mode then decreases to 495.5 dB/km, of which 95.5 dB/km is brought about, as before, by the metallic medium III.

Comparing these results, we can verify at the same time that the metal-optical waveguide filled with a two-layer dielectric operating in the fundamental mode has a much lower attenuation than one filled with dielectric II alone (for the same cross section).

It is of interest to compare the results with the case of an open glass fiber in air. In this case the third term of (9) decreases to $-0.91 \cdot 10^{-39}$ dB/km (at $\tan \Delta_2 = 1.541 \cdot 10^{-8}$).

Thus in both cases, when medium III is metal or air, we obtain so small a value for the attenuation due to this medium that it can be neglected. But then we have no explanation for the experimentally observed 10-15% decrease of the attenuation in a two-layer glass fiber with a thick sheath, after the latter is coated with silver. To understand this phenomenon it is obviously necessary to consider the scattering of the light by the microstructure of the fiber.

EXPERIMENT

Measurement of fiber parameters and fiber metallization. The waveguide is fabricated from two-layer glass fibers of two types, single-mode and multimode.

The core of the single-mode fiber is made of K-3 glass with refractive index 1.5163 and attenuation 0.4 dB/m, while the sheath is made of K-8 glass with refractive index 1.51 and attenuation 1 dB/m. The outer diameter of the fiber is 62.2 m, and the core diameter is 4.35 μ. After preparation of the fiber, the refractive index of its sheath is measured by an immersion method and turns out to be 1.5025. The refractive index of the core remains unchanged at 1.516. It is measured in an experiment in which two fibers of the given type are joined.

To this end, different immersion liquids are placed in the gap (150 μ long) between the fiber end surfaces to be joined, and we plot the dependence of the light-flux transmission coefficient on their refractive indices. This dependence reveals two distinct maxima. The first, smaller in magnitude, corresponds to equality of the refractive indices of the liquid and of the sheath, while the second, larger maximum corresponds to equality of the refractive indices of the liquid and of the core.

In similar fashion we measure the parameters of the multimode fiber: $R = 10.3\ \mu$, $\rho = 9.3\ \mu$, and $\dot{n}_2 = 1.62$.

Chemical silvering of the fiber is affected by the procedure described in ref. 1, in a glass burette 75 cm long. Two thin diaphragms with openings in their centers and with notches on the edges to permit escape of air are placed in the burette.

TABLE 1

	Focal length of objective, mm				
	23.2	13.9	8.2	6.2	2.8
Diameter of caustic neck, μ	38.4	20.8	7.36	4.6	3.3
Beam divergence angle	4°25′	8°10′	23°30′	40°42′	38°

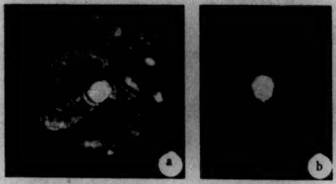

Fig. 2. Planar (a) and conical (b) ends of fibers, obtained by overheating them by passage of electric current through the silver coating.

The quality of the obtained coating is estimated from the value of its running resistance to direct current. For the single-mode fiber, after double silvering the resistance is 5 Ω/cm, while for the multimode fiber the value is 34 Ω/cm.

When the current flowing in the coating exceeds 180-200 mA, the single-mode fiber overheats, and the greatest overheating occurs in the glass dielectric, after which the silver film breaks. The cuts produced in this manner have a rather regular shape. Figure 2 shows photographs of planar and conical cuts (the latter are obtained by slightly stretching the fiber along the axis during the overheating).

To prevent oxidation of the silver coating, it is coated on the outside by asphalt–bitumen lacquer. This increases the fiber diameter, but also increases its strength.

In our experiments, we have investigated fibers with silvered sections that reached 1.4 m in length.

Description of apparatus. The method used by us to measure the damping of the light in the fiber is typical of most investigations on this subject.[16,17] The experimental arrangement is shown in Fig. 3. The light source is a helium–neon laser 1 ($\lambda = 0.6328\ \mu$), the light beam of which is focused on the entrance end of the fiber with the aid of a microobjective 2. The output-power level of the laser is monitored by an FD-1 photodiode placed at the rear mirror.

To eliminate the waves propagating in the sheath the open section of the waveguide is passed through an immersion trap 3. The latter is a glass plate with a drop of immersion liquid having the same refractive index as the sheath.

The exit end of the fiber is placed in front of the objective of microscope 4 with oil immersion. The refractive index of the latter is equal to the refractive index of the core. This choice decreases the scattering of the light flux by the random cleavages and roughnesses of the exit end. In addition, the improved matching of the exit end decreases the reflected backward wave.

Using the eyepiece of the microscope 4, it is possible to observe the structure of the field in the exit section of the waveguide, or to photograph it with the aid of a microphoto attachment. The output flux can be measured by attaching the housing of an FÉU-51 photomultiplier to this eyepiece.

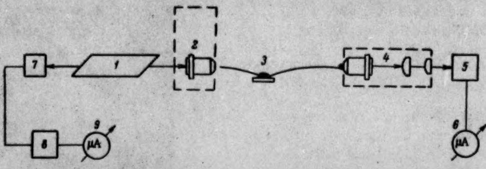

Fig. 3. Experimental arrangement. 1) Laser; 2) excitation source; 3) immersion trap; 4) exit microscope; 5) photomultipliers; 6, 9) microammeters; 7) photodiode; 8) emitter follower.

In the excitation source 2 we use not only an individual microobjective, but a complete reflected-light microscope (MIM-7) from which the illuminator is removed and a laser is placed on the same side as the illuminator. The optical system for excitation of this type was proposed earlier in ref. 16. Using the microscope eyepiece, it is possible to observe simultaneously the entrance end of the fiber and the light beam focused on it. It is easy to align the two accurately, by moving the fiber with the micrometric screws of the object stage of the microscope.

In addition, an arrangement of this type makes it possible to investigate the backward wave produced in the fiber by scattering from its inhomogeneities and by reflection from the mismatched exit end. The polarization of this wave is usually different from the polarization of the direct wave. Therefore, by introducing the analyzer of microscope 2, it is possible to extinguish the image of the direct wave and to observe only the backward wave through the eyepiece.

We present in conclusion Table 1, which lists the values of the neck diameter of the laser-beam caustic and its beam divergence in the focal planes of the various microobjectives. These data are essential in choosing the objective for the excitation of a wave of definite type in the fiber. They are both obtained with the MIM-7 microscope by measuring the diameter of the laser beam reflected from the surface of a glass plate.

Results of the experiment. The investigated fiber, strictly speaking, is not single-mode, since seven modes can exist in it (it would be more correct to call it a "few-mode" fiber). However, when such a fiber is excited by a light beam with a divergence angle 3-4°, only one mode, HE_{11}, is produced in it and propagates at an angle 3°25' to the fiber axis.

Figure 4a shows a photograph of the field distribution in the exit end of an uncoated single-mode fiber, obtained with the excitation described above, while Fig. 4b shows an similar photograph of the same fiber, but coated with silver on the outside. The bright round spot in the center of each of these photographs corresponds to the HE_{11} mode.

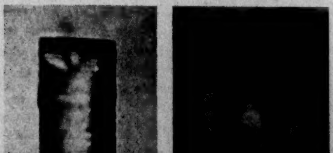

Fig. 4. Light flux at the exit of a single-mode fiber. a) In uncoated construction; b) in metallized construction.

The polarization of the light flux at the exit of the fiber is investigated with the aid of the rotating analyzer of microscope 4 and a compensating quartz wedge. Just as in ref. 17, the results reveal the simultaneous existence at the exit of HE_{11} mode components with plane and elliptic polarizations, and of a depolarized component. The intensity of the latter, however, decreases rapidly with increasing fiber length. In shorter fibers, the higher modes, having different polarizations, come into play, especially the modes propagating in the outer dielectric sheath.

In the present work we noted, in addition, that the character of the polarization of the exit light flux depends on the bends in the single-mode fiber. In practically any section of the latter it is possible to select a bend radius such that the output radiation has either only plane or only elliptic polarization (we have in mind a fiber of sufficient length). This phenomenon is equally well observed in open and metallized single-mode fibers.

This distinguishes the single-mode fiber from the multimode fiber, since the light flux of the latter is completely depolarized. As to the metallized multimode fiber with thin sheath, the number of its output modes is decreased as a result of mode selection by attenuation caused by the presence of the metal. Consequently, the output radiation contains in addition to the depolarized component also components with elliptic and plane polarization.

Figure 5a shows a photograph of the structure of the field in the exit section of a silvered multimode fiber, while Fig. 5b shows a photograph of the same field with the analyzer turned on. The grainy character of this structure is clearly seen on both photographs.

The attenuation of the light flux in the fiber before and after silvering is measured on the same samples by

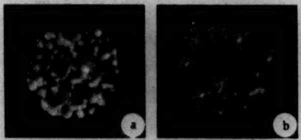

Fig. 5. Light flux at exit from silvered multimode fiber. a) With the analyzer of microscope 4 turned off; b) with the analyzer turned on.

TABLE 2. Attenuation of Light Flux in Fiber (in dB/m)

	Number of sample				
	1	2	3	4	5
Before silvering	1.33	1.9	1.85	2.91	2.91
After silvering	1.16	1.3	1.82	2.76	2.52

cutting off individual sections and determining the resultant changes of the output signal (at equal excitation conditions). To exclude the effect of a random cleaved surface on the exit end, the measurements are repeated on several cuts separated by 0.5-1 mm. The results of these measurements, averaged over 5-10 closely located cuts, are given in Table 2.

The obtained values of the attenuation exceed somewhat the calculated ones (for the HE_{11} mode). This is obviously due to the imperfect technology of fiber preparation, wherein the number of inhomogeneities in the fiber is greatly increased. In addition, a role is played by the presence of additional "waveguide scattering" of the light flux by the roughnesses of the boundaries.[18]

For a more exact determination of the difference between the attenuation in the fiber before and after silvering, we use also a differential method. We measure first the light flux at the exit from a fiber with a silvered section 1.4 m long. The silver film is then removed with nitric acid within several seconds, and the change of the output signal is recorded.

The measurements are performed on two samples of a single-mode fiber. For the first of them we obtain a 5.5% decrease of the output signal within 30 seconds after pouring the acid into the cell with the fiber, and another 16% decrease during the subsequent 3.5 minutes. When converted into running attenuation in the metallized section, this amounts to 0.18 and 0.48 dB/m, respectively. For the second sample, we obtain a 7% decrease of the signal within the first 30 seconds and another 4% after the next 30 seconds (0.21 and 0.13 dB/m). The initial increments are obviously due to the removal of the silver film, while those succeeding them (in time) are due to the damage of the glass fiber by the acid, which absorbs the metallic impurities and leaves, therefore, pores and cracks.

The attenuation in a multimode fiber is measured only by cutting off the measured sections (approximately 10 cm long). It is observed there that the attenuation is increased by silvering from 5-7 to 16-20 dB/m.

Comparing the obtained data, we can easily note a significant difference between the single-mode and multimode fibers. Whereas silvering the former reduces the attenuation by 10-15%, silvering the latter, to the contrary, increases the attenuation.

This is obviously due to the difference in the thickness of the sheath. In a single-mode fiber with a thick sheath, the loss introduced by the metal is smaller than the fraction of the scattered light reflected by the specularly reflecting metallic layer and returns to the HE_{11} wave via mode transformation by the inhomogeneities (in an uncoated fiber, this energy is radiated to the outside within the limits of the critical angle on the sheath–air interface and by scattering from the inhomogeneities of this interface). In a multimode fiber with a thin sheath, the losses caused by the metal exceed the energy returned by the metal, so that the attenuation is larger.

The observed decrease of the attenuation upon metallization of a fiber with a thick sheath is, of course, also of practical importance. As is well known, an uncoated single-mode fiber with an attenuation of 16 dB/km has been produced,[18] as well as a multimode fiber[19] with attenuation 2 dB/km. It is quite probable that owing to the lower losses to the absorption, the silvering of such a fiber would result in an even larger decrease of the attenuation than is observed in our case. This would be of great importance, since the already attained attenuations are close to the limits imposed by Rayleigh scattering in glass and by the "waveguide scattering" from the roughnesses of the boundaries.[18,20]

Of course, the designs investigated here do not exhaust all the possible variants of round metal-optical waveguides with two-layer dielectrics. To decrease the Rayleigh scattering in the core it is possible, for example, to replace it by a metallized quartz or glass capillary filled with liquid. It is reported in ref. 21 that glass capillaries filled with hexachlorbutadiene have been produced and have an attenuation of 6 dB/km. One can hope that the silvering of such capillaries will also decrease their attenuation.

The metallization of a dielectric waveguide transforms it into a covered metallic waveguide, one of the most significant advantages of which is the absence of spurious emission. In addition, metallization makes possible a certain decrease in the dielectric-sheath thickness without increasing the waveguide attenuation, so that the number of channels per unit cross section area of the cable can be increased.

CONCLUSION

We have shown that the designs considered here combine successfully the useful properties of dielectric and metallic waveguides. On the one hand, if the sheath is thick enough, the scattering of the light by the inhomogeneities of the metal–glass interface is greatly decreased; on the other hand, the presence of the metallic layer eliminates spurious emission from the fiber and decreases the attenuation.

The properties described above enable us to use the considered waveguide in optical-signal transmission systems and in optoelectronics.

---

[1] V. A. Pruzhanovskii, Zh. Tekh. Fiz., 38, 1035 (1968); 41, 2088 (1971) [Sov. Phys.–Tech. Phys., 13, 784 (1968); 16, 1654 (1972)].

[2] V. A. Pruzhanovskii, Zh. Tekh. Fiz., 40, 1161 (1970); 41, 1559 (1971) [Sov. Phys.–Tech. Phys., 15, 897 (1970); 16, 1230 (1972)].

[3] V. B. Belyanskii and N. A. Semenov, Otchet (Report), All-Union Extension Institute for Electric Communication (1968).

[4] H. Buchholz, Ann. Phys., 43, 313 (1943).

[5] R. D. Teasdale and Th. J. Higgins, Proc. Nat. Electr. Conf., Chicago, 5, 427 (1948).

[6] G. G. Bruck and E. R. Wicher, J. Appl. Phys., 18, 766 (1947).

[7] P. J. B. Clarricoats, Proc. IEEE, 108, pt. C, 170 (1961).
[8] A. W. Snyder, Proc. IEEE, 59, 6, 757 (1972).
[9] Yu. N. Kazantsev, Radiotekh. Elektron., 14, 1165 (1969).
[10] E. Jahnke, F. Emde, and F. Loesch, Special Functions [Russian translation], Nauka (1964).
[11] B. Z. Katsenelenbaum, Zh. Tekh. Phys., 19, 1182 (1949).
[12] A. W. Snyder, IEEE Trans. M. T. Tech., MIT-17, 1130 (1969).
[13] D. Gloge, Appl. Opt., 10, 2252 (1971).
[14] N. A. Valyus and A. S. Belanov, Radio Electronics of the Optical Band, Collected works, All-Union Extension Machine-Building Institute, 5 (1967).
[15] L. G. Schulz, J. Opt. Soc. Am., 44, 347 (1954).
[16] E. Snitzer and H. Osterberg, J. Opt. Soc. Am., 51, 499 (1961).
[17] L. G. Cohen, Bell Syst. Tech. J., 50, 23 (1971).
[18] D. B. Keck and A. R. Tynes, Appl. Opt., 11, 1502 (1972).
[19] R. D. Maurer, Electronics, 45, 30 (1972); Electronics Australia, 35, 10 (1973).
[20] F. P. Kapron, D. B. Keck, and R. D. Maurer, Appl. Phys. Lett., 17, 423 (1970).
[21] W. A. Gambling, D. N. Payne, and H. Matsumura, Opt. Commun., 6, 317 (1972).

Excitation of Alfvén waves in decay instabilities

A. G. Elfimov and F. M. Nekrasov

(Submitted January 17, 1973)
Zh. Tekh. Fiz., 44, 16–21 (January 1974)

The evolution of the wave numbers is studied for Alfvén waves transverse to a constant magnetic field. These waves are excited by the decay instability of a standing magnetoacoustic wave. It is shown that finite conductivity stabilizes the spectrum. The time required to establish a stationary spectrum is determined and the profile of the spectrum is found. Criteria are obtained for the stability of the Alfvén wave as a function of the plasma parameters and the amplitude of the pump wave. It is shown that there is no transfer of energy through the spectrum for a traveling pump wave.

The system of equations that describes the stability of characteristic magnetohydrodynamic oscillations of a plasma in the field of a pump wave has the form (see, for example, ref. 1)

$$\frac{d^2X^{\alpha}_{m}}{dt^2}+\Omega^2_{m,\alpha}X^{\alpha}_{m}=h_0\sum_{\alpha',m'}U^{\alpha\alpha'}_{mm'}X^{\alpha'}_{m'}, \tag{1}$$

where the $\Omega_{m,\alpha}$ are the characteristic frequencies of the linear oscillations of the plasma. The field of the pump wave is assumed to be weak, and its coordinate–time dependence is given by

$$\mathbf{H}^{(0)}(x,\ t)=h_0\sum_{m,n}\mathbf{A}_{m,n}\exp i(mk_0x+n\Omega_0t), \tag{2}$$

where k_0 and Ω_0 are related by the linear dispersion relation; h_0 is a dimensionless small parameter, and the matrix elements $U^{\alpha\alpha'}_{mm'}$ are periodic functions of the time, with period $2\pi\Omega_0^{-1}$. The dependence of the perturbations on the coordinate $\varkappa$ is represented, as usual, in the form

$$X^{\alpha}(x;\ t)=\sum_m X^{\alpha}_m(t)\exp i\varkappa_m x, \tag{3}$$

where $\varkappa_m = \varkappa + mk_0$. The indices of the Fourier transform with respect to the coordinates y and z are omitted. Throughout this paper, in discussing a spectral distribution we have in mind the distribution associated with the x coordinate.

A typical decay instability consists of the excitation of two normal modes $X^{\alpha_1}_{m_1}$ and $X^{\alpha_2}_{m_2}$, for which the so-called decay conditions are satisfied; these relate the characteristic frequencies and wave vectors of these modes to the corresponding characteristics of the pump wave.[2] The instability is excited by the transfer of energy from the pump wave to these oscillations.

A different situation obtains when the frequencies $\Omega_{m\alpha}$ do not depend or depend weakly on the subscript m (there is no dispersion or the dispersion is weak in the direction of the inhomogeneity of the pump wave). In this case, the decay condition for the frequencies

$$|\Omega_0|=|\Omega_{m,\alpha_1}|+|\Omega_{m,\alpha_2}| \tag{4}$$

is satisfied for all m_1 and m_2. There are now not two, but infinitely many spatial harmonics characterized by α_1 and α_2. One has the problem of the time behavior of the m spectrum of unstable amplitudes and the dependence of this behavior on the initial conditions.

We have considered this problem for Alfvén waves in a plasma in the presence of a magnetoacoustic pump wave. In papers[3–5] on the excitation of Alfvén waves by magnetoacoustic waves with which we are acquainted, the behavior of the spectrum has not been investigated.

The problem is solved using the equations of magnetohydrodynamics:

$$\left.\begin{aligned}\rho\left\{\frac{\partial V}{\partial t}+(\mathbf{V}\nabla)\mathbf{V}\right\}&=-\operatorname{grad}\left(P+\frac{\mathbf{H}^2}{8\pi}\right)+\frac{1}{4\pi}(\mathbf{H}\nabla)\mathbf{H},\\ \frac{\partial\rho}{\partial t}+\operatorname{div}\rho\mathbf{V}&=0;\quad P=P_0\left(\frac{\rho}{\rho_0}\right)^{\gamma},\\ \frac{\partial\mathbf{H}}{\partial t}&=\operatorname{curl}[\mathbf{VH}]+\frac{c^2}{4\pi\sigma}\nabla^2\mathbf{H}.\end{aligned}\right\} \tag{5}$$

The notation is customary. Effects associated with dissipation are assumed to be weak and are taken into account in the same way as in ref. 1 only in the investigation of the perturbations. The small parameter h_0 is the ratio of the amplitude of the field of the magnetoacoustic wave to H_0, the constant magnetic field. The problem is solved in the linear approximation in this parameter.

In the stationary state $[\partial/(\partial y) = \partial/(\partial z) = 0]$, the field and plasma are described by the relations

$$\left.\begin{aligned}H_z^{(0)}(x;\ t)&=H_0(1+h_0\cos k_0x\sin\Omega_0t),\\ v_x^{(0)}(x;\ t)&=-\frac{\Omega_0}{k_0}h_0\sin k_0x\cos\Omega_0t\\ \rho^{(0)}(x;\ t)&=\rho_0(1+h_0\cos k_0x\sin\Omega_0t),\\ P^{(0)}(x;\ t)&=P_0(1+\gamma h_0\cos k_0x\sin\Omega_0t),\\ \Omega_0^2=k_0^2(c_s^2+c_A^2);\ c_A^2&=\frac{H_0^2}{4\pi\rho_0};\quad c_s^2=\gamma\frac{P_0}{\rho_0}.\end{aligned}\right\} \tag{6}$$

In solving the perturbation problem we assume $\partial/\partial y = 0$. This simplifies the solution since it allows separation of the Alfvén branch from the magnetoacoustic branch. The equation that describes the Alfvén wave reduces to the equation for the y component of the velocity perturbation:

$$\begin{aligned}\frac{\partial^2v_y}{\partial t^2}+k_z^2c_A^2v_y&=-\frac{c^2}{4\pi\sigma}\left(k_z^2-\frac{\partial^2}{\partial x^2}\right)\frac{\partial v_y}{\partial t}\\ &+h_0\left[\frac{\Omega_0}{k_0}\sin k_0x\left(2\cos\Omega_0t\frac{\partial^2v_y}{\partial x\partial t}-\Omega_0\sin\Omega_0t\frac{\partial v_y}{\partial x}\right.\right.\\ &\left.\left.-\cos k_0x\left(k_z^2c_A^2\sin\Omega_0tv_y-\Omega_0\cos\Omega_0t\frac{\partial v_y}{\partial t}\right)\right)\right].\end{aligned} \tag{7}$$

The smallness of the dissipative effects assumed in this paper corresponds to the condition

$$h_0^2\ll\frac{c^2}{4\pi\sigma\Omega_0l^2_{\min}}\ll1, \tag{8}$$

where $l_{\min}$ is the minimum spatial scale of the problem.

Representing the solution in the form (3), we can reduce Eq. (7) to a system like (1) with frequency $\Omega^2_{m\alpha} = k_z^2 C_A^2$, which does not depend on m. However, it is more convenient to solve Eq. (7) directly and then to expand the solution in plane waves which are eigenfunctions for planar geometry.

The solution of Eq. (7) is based on Bogolyubov's idea of multiple time scales.[6] The method of solving the problem adopted here, which uses this idea, is described, for example, in ref. 7 and the literature cited there. To solve the problem we expand the desired function and the time derivatives in powers of the small parameter:

$$v_y = v_y^{(0)} + h_0 v_y^{(1)} + \ldots; \quad \frac{\partial}{\partial t} = \frac{\partial}{\partial t_0} + h_0 \frac{\partial}{\partial t_1} + \ldots; \tag{9}$$

where $t_0 \equiv t$, $t_1 \equiv h_0 t$, etc., substitute these expansions into the equation, and equate terms of equal powers of h_0. An important requirement is that there be no secular terms in the solution.

Let us first investigate Eq. (7) with zero dissipation. Our method leads to the following equations: The zeroth approximation is

$$\frac{\partial^2 v_y^{(0)}}{\partial t_0^2} + \frac{\Omega_0^2}{4} v_y^{(0)} = 0. \tag{10}$$

The first approximation is

$$\frac{\partial^2 v_y^{(1)}}{\partial t_0^2} + \frac{\Omega_0^2}{4} v_y^{(1)} + 2\frac{\partial^2 v_y^{(0)}}{\partial t_0 \partial t_1} = \frac{\Omega_0}{k_0} \sin k_0 x v_y^{(0)}$$
$$\times \left(2 \cos \Omega_0 t_0 \frac{\partial^2 v_y^{(0)}}{\partial x \partial t_0} - \Omega_0 \sin \Omega_0 t_0 \frac{\partial v_y^{(0)}}{\partial x}\right)$$
$$- \cos k_0 x \left(\frac{\Omega_0^2}{4} \sin \Omega_0 t_0 v_y^{(0)} - \Omega_0 \cos \Omega_0 t_0 \frac{\partial v_y^{(0)}}{\partial t_0}\right). \tag{11}$$

For simplicity, in Eqs. (10) and (11) we have used the condition of exact resonance $\Omega_0 = 2|k_z c_A|$. Substituting the solution

$$v_y^{(0)} = A(x;\ t_1) \cos \frac{1}{2} \Omega_0 t_0 + B(x;\ t_1) \sin \frac{1}{2} \Omega_0 t_0 \tag{12}$$

of Eq. (10) into Eq. (11) and using the condition that there are no secular terms in $v_y^{(1)}$ [vanishing of the coefficients of $\sin(1/2)\Omega_0 t_0$ and $\cos(1/2)\Omega_0 t_0$], we obtain

$$\frac{\partial A}{\partial t_1} = -\frac{\Omega_0}{8} \cos k_0 x A, \tag{13}$$

$$\frac{\partial B}{\partial t_1} = \frac{\Omega_0}{8} \cos k_0 x B, \tag{14}$$

$$\frac{\partial^2 v_y^{(1)}}{\partial t_0^2} + \frac{\Omega_0^2}{4} v_y^{(1)} = \Omega_0^2 \Big[\cos \frac{3}{2} \Omega_0 t_0 \Big(\frac{1}{k_0} \frac{\partial B}{\partial x} \sin k_0 x + \frac{3}{8} B \cos k_0 x\Big)$$
$$- \sin \frac{3}{2} \Omega_0 t_0 \Big(\frac{1}{k_0} \frac{\partial A}{\partial x} \sin k_0 x + \frac{3}{8} A \cos k_0 x\Big)\Big]. \tag{15}$$

The complete dependence $v_y^{(1)}$ on the slow time t_1 is determined by the equations of the higher approximation. Its determination goes beyond the limits determined by the accuracy of the present paper. Since the first approximation is a small correction to the solution of the zeroth approximation, we shall restrict ourselves in what follows to studying the dependence of the zeroth approximation on the slow time. Thus,

$$v_y \simeq v_y^{(0)} = A(x) \exp\Big(-\frac{h_0}{8} \Omega_0 t \cos k_0 x\Big) \cos \frac{1}{2} \Omega_0 t$$
$$+ B(x) \exp\Big(\frac{1}{8} h_0 \Omega_0 t \cos k_0 x\Big) \sin \frac{1}{2} \Omega_0 t. \tag{16}$$

The form of the functions A and B is determined by the initial and boundary conditions for v_y. It follows from (16) that the initial profile of the perturbation is strongly distorted with the course of time. A characteristic feature is the formation of peaks at the points $k_0 x = \pm n\pi$, with a height that increases with the time, the width being a decreasing function.

To describe the behavior of the perturbation in terms of spectral characteristics we must represent the solution (16) in the form

$$\left.\begin{aligned} v_y^{(0)} &= \sum_{s=-\infty}^{\infty} u_s \exp isk_0 x, \\ u_s &= \sum_n I_n\Big(\frac{h_0}{8} \Omega_0 t\Big)\Big[(-1)^n A_{s-n} \cos \frac{1}{2} \Omega_0 t + B_{s-n} \sin \frac{1}{2} \Omega_0 t\Big], \end{aligned}\right\} \tag{17}$$

where the I_n are modified Bessel functions and A_m and B_m are the Fourier coefficients of the expansions of the functions A(x) and B(x). To be specific, in deriving (17) we assume that the boundary conditions require periodicity of the solution with period $L = 2\pi/k_0$. An important characteristic associated with the spectral energy density is $|u_s|^2$ (averaging is performed over the period of the Alfvén oscillations). This quantity is

$$\overline{|u_s|^2} = \frac{1}{2} \sum_{n,n'} I_n\Big(\frac{1}{8} h_0 \Omega_0 t\Big) I_{n'}\Big(\frac{1}{8} h_0 \Omega_0 t\Big)$$
$$\times [(-1)^{n+n'} A_{s-n} A^*_{s-n'} + B_{s-n} B^*_{s-n'}]. \tag{18}$$

Bearing in mind that the main contribution in the sum in (18) is determined by the region $|n|, |n'| \lessdot (1/8) h_0 \Omega_0 t$, and also remembering that the asymptotic behavior of the modified Bessel functions depends weakly on the index, we can write Eq. (18) as

$$\overline{|u_s|^2} \simeq \frac{1}{2} I_0^2\Big(h_0 \frac{\Omega_0 t}{8}\Big) \sum_{m,\, m'=s-N}^{s+N} [(-1)^{m+m'} A_m A^*_{m'} + B_m B^*_{m'}], \tag{19}$$

where N is the integral part of $h_0 \Omega_0 t/8$. Thus, if a narrow spectrum of oscillations is excited at the initial time in the region $|m| \sim m_0$, the spectrum broadens with time. The width of the spectrum Δm_0 is determined roughly by the condition

$$\Delta m_0 \sim \frac{1}{8} h_0 \Omega_0 t. \tag{20}$$

But if the initial spectrum is broad, the spectral density of the energy will be determined in the course of time by an ever broader section of the spectrum of initial perturbations. The time dependence of the width of the spectrum (20) can also be found from the general form of the solution. It is sufficient to represent $\exp[(h_0 \Omega_0 t/8) \cos k_0 x]$ as a series and then the time of excitation of the harmonic m is determined approximately by

$$\frac{1}{m!}\Big(\frac{h_0 \Omega_0 t}{8}\Big)^m \sim 1. \tag{21}$$

From (17) one can determine the variation of the mean square of the velocity perturbation v_y^2 in the case of a random distribution of the phases of the initial perturbation:

$$\overline{v_y^2}=\sum_s\overline{|u_s|^2}=\frac{1}{2}I_0\left(\frac{h_0\Omega_0t}{4}\right)\sum_m(|A_m|^2+|B_m|^2). \tag{22}$$

It is to be expected that when allowance is made for the finite conductivity, the broadening of the spectrum due to the excitation of ever higher modes will be restricted. With dissipation Eqs. (14) and (15) are replaced by

$$\left.\begin{aligned}\frac{\partial A}{\partial t_1}+\frac{\Omega_0}{8}\cos k_0xA+\frac{c^2}{8\pi\sigma h_0}\left(k_z^2A-\frac{\partial^2A}{\partial x^2}\right)=0,\\ \frac{\partial B}{\partial t_1}-\frac{\Omega_0}{8}\cos k_0xB+\frac{c^2}{8\pi\sigma h_0}\left(k_z^2B-\frac{\partial^2B}{\partial x^2}\right)=0.\end{aligned}\right\} \tag{23}$$

It is easy to show that a solution of these equations satisfying the previously mentioned periodicity condition in the x coordinate has the form

$$\left.\begin{aligned}A=\sum_{m=0}^{\infty}\Big\{A_m^{(1)}\exp(-\alpha_m\Omega_0t)\,ce_{2m}\left(\frac{k_0x}{2};\ q\right)\\ +A_m^{(2)}\exp(-\beta_m\Omega_0t)\,se_{2m+2}\left(\frac{k_0x}{2};\ q\right)\Big\},\\ B=\sum_{m=0}^{\infty}\Big\{B_m^{(1)}\exp(-\alpha_m\Omega_0t)\,ce_{2m}\left(\frac{k_0x}{2};\ -q\right)\\ +B_m^{(2)}\exp(-\beta_m\Omega_0t)\,se_{2m+2}\left(\frac{k_0x}{2};\ -q\right)\Big\},\end{aligned}\right| \tag{24}$$

where $q = 2\pi\sigma\Omega_0h_0(k_0c)^{-2}$.

In Eq. (24), ce_{2m} and se_{2m+2} are Mathieu functions,[8] and the constants $A_m^{(1,2)}$ and $B_m^{(1,2)}$ are determined by the initial conditions. The characteristic exponents α_m and β_m are related to the eigenvalues $\alpha_{2m}(q)$ and $b_{2m+2}(q)$ of the functions $ce_{2m}(k_0x/2;\ q)$ and $se_{2m+2}(k_0x/2;\ q)$ by

$$\alpha_m=\frac{k_0^2c^2}{32\pi\sigma\Omega_0}\left(a_{2m}+1+\frac{c_s^2}{c_A^2}\right);\ \ \beta_m=\frac{k_0^2c^2}{32\pi\sigma\Omega_0}\left(b_{2m+2}+1+\frac{c_s^2}{c_A^2}\right). \tag{25}$$

In Eq. (25) we have used the resonance condition $4k_z^2c_A^2=k_0^2(c_A^2+c_s^2)$. For fixed q, the eigenvalues a_{2m} and b_{2m+2} form an infinite uniformly increasing sequence $a_0 < b_2 < a_2 < b_4 < \ldots$, and $a_0 \leq 0$ for all $|q|$, while b_2 changes sign in the region of $|q| \sim 8$. More detailed data can be obtained from the monograph in ref. 8. The asymptotic behavior of the solution (24) will be determined by the smallest eigenvalue. If the initial and boundary conditions are such that $A_0^{(1)}$ or $B_0^{(1)}$ in the expansion (24) are nonzero, a_0 is the eigenvalue. In this case, the instability condition is

$$a_0+1+\frac{c_s^2}{c_A^2}<0. \tag{26}$$

Taking account of the dependence $a_0(q)$ (see Appendix 2 in ref. 8, in which the data are rounded off with accuracy 10%) for $c_s^2/c_A^2 \ll 1$, we obtain

$$h_0>\frac{3k_0^2c^2}{4\pi\sigma\Omega_0}. \tag{27}$$

But if the initial and boundary conditions are such that $A_0^{(1)} = 0$ and $B_0^{(1)} = 0$ in the expansion (24) and $A_0^{(2)}$ or $B_0^{(2)}$ are nonvanishing, the asymptotic behavior will be determined by b_2 and the instability condition analogous to (27) has the form

$$h_0>\frac{27}{2}\frac{k_0^2c^2}{4\pi\sigma\Omega_0}. \tag{28}$$

An exact analysis of the transient processes described by Eq. (24) for arbitrarily specified initial conditions is fairly complicated. However, the asymptotic form of the perturbation will be described either by the function $ce_0(k_0x/2;\pm q)$ or $se_2(k_0x/2;\pm q)$. The time required to reach the asymptotic regime t_a is determined in these two cases by the conditions

$$\left.\begin{aligned}\left|t_a\frac{k_0^2c^2}{32\pi\sigma}\left[a_0(q)+1+\frac{c_s^2}{c_A^2}\right]\right|\sim 1,\\ \left|t_a\frac{k_0^2c^2}{32\pi\sigma}\left[b_2(q)+1+\frac{c_s^2}{c_A^2}\right]\right|\sim 1.\end{aligned}\right\} \tag{29}$$

Thus, allowance for dissipation leads, in contrast to (15), to a stationary form of the perturbation. The functions ce_0 and se_2 are also characterized by the presence of peaks, but their width remains finite in contrast to the function $(1/8h_0\Omega_0t\,\cos k_0x)$, for which the width of the peaks decreases with the time.

Comparing the two solutions (15) and (24) we obtain the following picture for the development of longwave perturbations. As long as dissipation is weak, energy is transferred to the shortwave part of the spectrum, the amplitudes increasing at the same time. With the excitation of high harmonics, for which damping is important, the profile of the spectrum begins to be stabilized and after the passage of time determined by Eq. (29) a stationary spectral profile is established.

It should be noted that the transfer of energy through the spectrum does not occur in the presence of a traveling wave above.

The general solution without dissipation has the form

$$A=\cos k_0x\left[\varphi_1(x)\exp\left(-\frac{1}{8}h_0\Omega_0t\right)+\varphi_2(x)\exp\left(\frac{1}{8}h_0\Omega_0t\right)\right],$$

$$B=(1-\sin k_0x)\,\varphi_2(x)\exp\left(\frac{1}{8}h_0\Omega_0t\right)$$

$$-(1+\sin k_0x)\,\varphi_1(x)\exp\left(-\frac{1}{8}h_0\Omega_0t\right).$$

The energy transfer to the shortwave part of the spectrum considered for an Alfvén wave can also occur for ion-acoustic waves when $c_s^2/c_A^2 \lessdot h_0$. This effect can play an appreciable role in the rf heating of a plasma.

---

[1] A. G. Elfimov and F. M. Nekrasov, Nucl. Fusion, 12, 201 (1972).
[2] V. N. Oraevskii, Nucl. Fusion, 4, 263 (1964).
[3] V. F. Aleksin and V. D. Khodusov, Ukr. Fiz. Zh., 16, 603 (1971).
[4] G. Vahala and D. Montgomery, Phys. Fluids, 14, 1137 (1971).
[5] J. A. Lehane and F. J. Paoloni, Plasma Phys., 14, 461 (1972).
[6] N. Bogolyubov, Zh. Eksp. Teor. Fiz., 16, 691 (1946).
[7] D. McCune, G. Sandri, and E. Frieman, Problems in the Kinetic Theory of Gases [Russian translation], Mir, Moscow (1965).
[8] N. W. McLachlan, Theory and Application of Mathieu Functions, Clarendon Press, Oxford (1947).

Emission of waves from a plasma layer

T. A. Davydova and A. A. Zhmudskii

T. G. Shevchenko Kiev State University

(Submitted February 2, 1973)
Zh. Tekh. Fiz., 44, 22-27 (January 1974)

Frequency spectra are given for waves emitted from a plane plasma layer at a finite temperature in the absence of an external magnetic field. As a result of the energy loss by radiation the frequencies are complex and this means that the waves are damped in the layer. This damping must be taken into account together with the other loss mechanisms in any study of the propagation and interaction of waves in bounded plasma systems.

1. INTRODUCTION

It is well known that the fact that a plasma is bounded leads to a series of specific properties connected with the propagation of waves: discrete frequency spectrum for the natural modes of the system and the possibility of surface waves.

It is also important that bounded plasma systems can produce oscillations with a finite lifetime, so that in addition to a real frequency spectrum there is also a spectrum with complex values of ω. This is because a bounded system, in contrast to an unbounded one, can lose energy by radiation. The oscillations which correspond to the radiated modes are damped in time and this increases the effective wave dissipation in the system.

Radiated modes were first found by Dawson and Oberman[1,2] for a plasma cylinder in a strong magnetic field. The general conditions for the existence of radiated modes were derived in refs. 3 and 4 for bounded plasma systems and the radiation mechanism was related to the Cerenkov effect. For radiation into a vacuum it is essential that the projection of the phase velocity of the wave on the plasma–vacuum surface exceed the velocity of light in vacuum ($\omega/k_{\parallel} > c$, where $k_{\parallel}$ is the projection of the wave vector onto the plasma–vacuum boundary).

In the present paper we derive the spectra of TE and TM waves emitted from a plane plasma layer of finite temperature in the absence of an external magnetic field. The radiation from a layer of cold plasma with $(\omega_p/c)a \gg 1$ (ω_p is the electron plasma frequency and a is the layer width) has been considered in ref. 5. We consider the radiation by studying the nonlinear wave interaction in the plasma layer.

2. STATEMENT OF THE PROBLEM

In order to investigate the high-frequency spectrum of oscillations in a plane isotropic plasma layer we make use of the usual system of linearized hydrodynamic equations for the electrons and consider the ions to be fixed (see, for example, ref. 6):

$$\left.\begin{aligned} n_0\frac{\partial \mathbf{v}}{\partial t}+\frac{en_0}{m}\mathbf{E}+s^2\nabla n&=0,\\ \frac{\partial n}{\partial t}+\operatorname{div} n_0\mathbf{v}&=0,\\ \frac{\partial \mathbf{H}}{\partial t}+c\operatorname{curl}\mathbf{E}&=0,\\ \frac{\partial \mathbf{E}}{\partial t}-c\operatorname{curl}\mathbf{H}-4\pi en_0\mathbf{v}&=0.\end{aligned}\right\}\qquad(1)$$

Here, $s = [\gamma(T/m)]^{1/2}$ is the velocity of sound and n_0 is the equilibrium plasma density. The remaining notation is standard.

We take the x axis to be perpendicular to the plasma layer and assume that the plasma is bounded by the planes $x = -a, a$. The system (1) must be supplemented by the boundary conditions at the plasma–vacuum boundary and at infinity. We assume that at the plasma–vacuum boundary the electrons undergo perfect reflection. In addition, the tangential components of the electric and magnetic fields are continuous at this boundary. At infinity we impose the condition that there be no incoming waves.

We further assume that the waves propagate in the x, y plane, i.e., $k_z = 0$. Since the system is linear and homogeneous in y, the variation of the disturbance with time and with the coordinate y can be taken in the form $\exp\{-i\omega t + ik_y y\}$.

The system (1) can then be reduced to the three equations

$$\frac{d^2\Psi_i}{dx^2}+\left(\frac{\omega^2-\omega_{pe}^2}{c_i^2}-k_y^2\right)\Psi_i=0,$$

$$\Psi_1=E_z,\ \Psi_2=H_z,\ \Psi_3=n,\ c_1=c_2=c,\ c_3=s.\qquad(2)$$

The other variables can be expressed in terms of E_z and H_z as follows:

$$v_z=-\frac{i}{\omega}\frac{e}{m}E_z,\ H_x=\frac{k_yc}{\omega}E_z,\ H_y=-\frac{ic}{\omega}\frac{\partial E_z}{\partial x},\qquad(3)$$

$$\left.\begin{aligned} v_x&=-i\frac{e}{m}\frac{ck_y}{\omega^2-\omega_{pe}^2}H_z-i\frac{s^2}{n^0}\frac{\omega}{\omega^2-\omega_{pe}^2}\frac{\partial n}{\partial x},\\ v_y&=-\frac{e}{m}\frac{c}{\omega^2-\omega_{pe}^2}\frac{\partial H_z}{\partial x}+\frac{s^2}{n_0}\frac{k_y\omega}{\omega^2-\omega_{pe}^2}n,\\ E_x&=-\frac{\omega ck_y}{\omega^2-\omega_{pe}^2}H_z+\frac{4\pi es^2}{\omega^2-\omega_{pe}^2}\frac{\partial n}{\partial x},\\ E_y&=-i\frac{c\omega}{\omega^2-\omega_{pe}^2}\frac{\partial H_z}{\partial x}+i\frac{4\pi es^2k_y}{\omega^2-\omega_{pe}^2}n.\end{aligned}\right\}\qquad(4)$$

The relation between the longitudinal and transverse oscillations is established through the boundary conditions. In a plane plasma layer there can be independent propagation of TE waves, in which the electric field vector is perpendicular to the plane of incidence, and TM waves, in which the magnetic field vector is perpendicular to this plane.

The problem can be stated as follows: For given k_y, given temperature and plasma density, find the spectrum of values of ω for which the solutions of (2) satisfy the boundary conditions.

3. EMISSION OF TE WAVES FROM A PLASMA LAYER

We start with the simple case of the emission of TE waves from a plasma layer. Inside the layer the waves are described by the equation

$$\frac{d^2E_z}{dx^2} + \left(\frac{\omega^2 - \omega_{pe}^2}{c^2} - k_y^2\right)E_z = 0 \tag{5}$$

and by the boundary continuity conditions

$$\{E_z\}_{x=\pm a} = 0, \quad \left\{\frac{d}{dx}E_z\right\}_{x=\pm a} = 0.$$

The waves in vacuum are described by (5) with $\omega_{pe} = 0$.

We introduce the following notation:

$$k^2 \equiv \frac{\omega^2 - \omega_{pe}^2}{c^2} - k_y^2, \quad \varkappa^2 \equiv \frac{\omega^2}{c^2} - k_y^2. \tag{6}$$

In accordance with the radiation condition at infinity we assume that in the vacuum where $x < -a$ the solution varies as $\sim \exp\{-i\varkappa x\}$ and that when $x > a$ the solution goes as $\sim \exp\{i\varkappa x\}$, where we take $\mathrm{Re}\,\varkappa > 0$. It can easily be shown that the solutions of (5) which satisfy the boundary conditions can be divided into those which are even and those which are odd with respect to the x coordinate.

For even solutions of E_z the spectrum of allowed values for ω can be found with the help of (6) from the dispersion equation

$$\operatorname{tg} ka = -\frac{i\varkappa}{k}. \tag{7}$$

For odd solutions of E_z the dispersion equation takes the form

$$\operatorname{tg} ka = -\frac{ik}{\varkappa}. \tag{8}$$

Equations (7) and (8) do not have purely real or imaginary solutions for ω. They are most easily solved in terms of the unknown ka. Using (6), we write (7) and (8) in the form

$$\operatorname{tg} ka = -i\sqrt{1 + \frac{\alpha_0^2}{(ka)^2}}, \tag{9}$$

$$\operatorname{tg} ka = -\frac{i}{\sqrt{1 + \frac{\alpha_0^2}{(ka)^2}}}, \tag{10}$$

where $\alpha_0^2 = (\omega_{pe}^2 a^2)/c^2$.

We put $ka = k_r + ik_i$. The solutions (9) and (10) satisfy $k_r > 0$, $k_i < 0$. These solutions can easily be found graphically. Numerical calculations give the variation of k_r and $|k_i|$ with α_0 shown in Fig. 1 for (9) and in Fig. 2 for (10). The asymptotic values of k_r and k_i for $\alpha_0 \gg 1$ can easily be obtained from (9) and (10).

It follows from (9) that when $\alpha_0 \gg |ka|$, $\cot ka \approx 0$, and so $ka \approx (\nu + 1/2)\pi$. In a similar way from (10) we get $ka \approx \nu\pi$. The correction terms can be found by successive approximations. Thus we obtain

$$\left.\begin{aligned} &k_r + ik_i \approx \left(\nu + \tfrac{1}{2}\right)\pi - \frac{\left(\nu + \frac{1}{2}\right)\pi}{\alpha_0^2} - i\,\frac{\left(\nu + \frac{1}{2}\right)\pi}{\alpha_0}, \\ &\nu = 0, 1, 2, \ldots, \ \alpha_0 \gg \left(\nu + \tfrac{1}{2}\right)\pi \end{aligned}\right\} \tag{11}$$

for even solutions,

$$\left.\begin{aligned} &k_r + ik_i \approx \nu\pi - \frac{\nu\pi}{\alpha_0^2} - i\,\frac{\nu\pi}{\alpha_0}, \\ &\nu = 1, 2, \ldots, \ \alpha_0 \gg \nu\pi \end{aligned}\right\} \tag{12}$$

for odd solutions.

It is easy to find the values of ω from (6). When $\alpha_0 \gg \nu\pi$ we get

$$\left.\begin{aligned} &\mathrm{Re}\,\omega_\nu \approx \sqrt{\omega_p^2 + k_y^2c^2 + k_r^2\frac{c^2}{a^2}}, \\ &\mathrm{Im}\,\omega_\nu \approx -\frac{k_r^2c^2}{\alpha_0 a^2}\frac{1}{\mathrm{Re}\,\omega_\nu}, \quad \nu = 0, 1, 2, 3, \ldots \end{aligned}\right\} \tag{13}$$

where k_r is given by (11) or (12).

As expected, the damping disappears in an unbounded plasma when $\alpha_0 \to \infty$ and the frequency spectrum becomes continuous. The value of $\mathrm{Re}\,ka$ corresponding to the highest mode is closer to the appropriate asymptote. This is connected with the fact that the wavelength decreases for high k values and for the highest mode ν the approximation to an unbounded plasma is more closely satisfied.

4. EMISSION OF TM WAVES FROM A PLASMA LAYER

We first consider a cold plasma ($\beta^2 = s^2/c^2 = 0$). For TM waves we have the equation

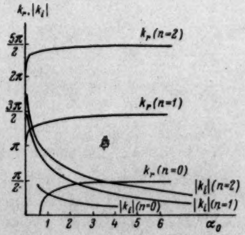

Fig. 1. Spectrum of values of ka for symmetric TE modes.

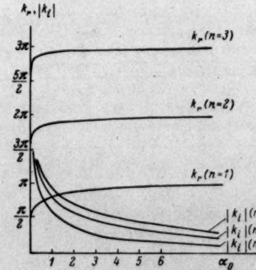

Fig. 2. Spectrum of values of ka for antisymmetric TE modes.

$$\frac{d^2H_z}{dx^2}+\left(\frac{\omega^2-\omega_{pe}^2}{c^2}-k_y^2\right)H_z=0$$

(for the vacuum $\omega_{pe} = 0$).

The tangential components of the fields E_y and H_z, i.e., H_z and $(1/\varepsilon)(dH_z/dx)$, are continuous at the plasma–vacuum boundary. Thus, for the even (symmetric) solutions of H_z we get the dispersion equation

$$\operatorname{tg} ka=-\frac{i\varkappa}{k}\varepsilon, \tag{14}$$

and for the odd (antisymmetric) solution

$$\operatorname{ctg} ka=\frac{i\varkappa}{k}\varepsilon. \tag{15}$$

Here, as before, k^2 and $\varkappa^2$ are defined by (6) and $\varepsilon = 1 - (\omega_{pe}^2/\omega^2)$. It follows from (6) that ε can be represented in the form

$$\varepsilon=\frac{k^2+k_y^2}{\varkappa^2+k_y^2}.$$

The solutions of (14) and (15) now depend not only on the parameter α_0, but also on k_y. In the two limiting cases $k_y^2 \gg \operatorname{Re}\varkappa^2$ and $k_y^2 \ll \operatorname{Re}\varkappa^2$ the roots of (14) and (15) are close to those already found (see Figs. 1 and 2) except that in the second case the roots for the symmetric and antisymmetric modes are interchanged. In the wide layer approximation $\alpha_0 \gg 1$, the dispersion of symmetric TM waves emitted from the plasma can be found from (13) and the following asymptotic equations:

$$ka\approx\nu\pi-\frac{\nu\pi}{\alpha_0}\left(1+\frac{k_y^2a^2}{\nu^2\pi^2}\right)\left(\frac{1}{\alpha_0}+i\right),\quad \text{if}\quad k_y^2\gg\operatorname{Re}\varkappa^2$$

$$ka\approx\left(\nu+\frac{1}{2}\right)\pi-\frac{\left(\nu+\frac{1}{2}\right)\pi}{\alpha_0}\left(1+\frac{\alpha_0^2}{k_y^2a^2}\right)\left(\frac{1}{\alpha_0}+i\right),$$

$$\text{if}\quad k_y^2\ll\operatorname{Re}\varkappa^2\ . \tag{16}$$

In order to find the dispersion of the antisymmetric mode we must put $\nu \to \nu + 1/2$ in (16).

When $\varepsilon < 0$, Eqs. (14) and (15) have purely imaginary roots $ka = ik_1$ corresponding to surface waves; the frequency of these is real and for $k_ya \gg 1$ we have

$$\omega^2=\frac{\omega_p^2}{2}\left(1-\frac{1}{4}\frac{\omega_p^2}{c^2k_y^2}\right).$$

We now consider the emission of TM waves from a plasma layer at a finite temperature. It can be shown that the solutions of the system (2) under the given boundary conditions split into two groups. In one group H_z is an even function of x and n is odd (we call these symmetric solutions) and in the other group H_z and n have the opposite parity (antisymmetric solutions). For the symmetric solutions the dispersion equation has the form

$$\frac{ik\operatorname{tg} ka}{\varepsilon}+i\varkappa=k_y^2\left(1-\frac{1}{\varepsilon}\right)\frac{\operatorname{tg} k_1a}{k_1}, \tag{17}$$

and for the antisymmetric solutions

$$\frac{k\operatorname{ctg} ka}{\varepsilon}-i\varkappa=k_y^2\left(1-\frac{1}{\varepsilon}\right)\frac{\operatorname{ctg} k_1a}{k_1}, \tag{18}$$

where $k_\parallel = [(\omega^2/c^2)(\varepsilon/\beta^2) - k_y^2]^{1/2}$ is the projection of the vector of the plasma oscillations along the layer.

When $k_y^2 < \omega^2/c^2$, surface waves are possible and the frequencies of these when $ka \gg (\omega_p a)/c$ are approximately equal to

$$\omega\approx\frac{\omega_p}{\sqrt{2}}\sqrt{1+\frac{k_yv_{Te}\sqrt{2}}{\omega_{pe}}}.$$

In addition, when $\omega \approx \omega_{pe}$, there is a discrete real spectrum of longitudinal plasma oscillations. This spectrum has been derived in ref. 7, for example, in the quasistatic approximation.

We are interested here, however, in the modes emitted from a system for which $k_y^2 < \operatorname{Re}(\omega^2/c^2)$ and $\operatorname{Re}k$, $\operatorname{Re}\varkappa$, $\operatorname{Re}k_\parallel > 0$. Then $\operatorname{Re}\varepsilon > 0$.

Since $|k_\parallel| \gg |k_\perp|$, we can consider two cases: $|ka| \ll 1$, $|k_\parallel a| \sim 1$ and $|ka| \sim 1$, $|k_\parallel a| \gg 1$.

Let us consider the first case.

Equation (17) takes the form

$$i\varkappa=\frac{k_y^2\left(1-\frac{1}{\varepsilon}\right)\operatorname{tg} k_1a}{k_1}, \tag{19}$$

and (18) becomes

$$\frac{1}{\varepsilon}-i\varkappa a=\frac{ak_y^2\left(1-\frac{1}{\varepsilon}\right)\operatorname{ctg} k_1a}{k_1}. \tag{20}$$

Since $|k_y| \ll |k_\parallel|$, we can solve (19) and (20) by the method of successive approximations and thus obtain for the symmetric mode

$$k_1a\approx\left(\nu+\frac{1}{2}\right)\pi-\frac{ik_y^2a^2}{\left(\nu+\frac{1}{2}\right)\pi\varkappa a}\left\{\frac{\frac{\omega_p^2a^2}{c^2}}{\left[\left(\nu+\frac{1}{2}\right)^2\pi^2+k_y^2a^2\right]\beta^2}\right\}, \tag{21}$$

where $\varkappa^2 = (k_\parallel^2 + k_y^2)\beta^2 + (\omega_p^2/c^2) - k_y^2$, $|\varepsilon| \lessdot 1$, $\nu = 0, 1, 2, \ldots$, and for the antisymmetric mode we have

$$k_1a\approx\nu\pi-\frac{k_y^2a^2}{\nu\pi}\left[\frac{\alpha_0^2}{\left(\frac{\nu^2\pi^2}{a^2}+k_y^2\right)a^2\beta^2+\alpha_0^2}\right]$$

$$\times\left(1+i\varkappa a\frac{\left(\frac{\nu^2\pi^2}{a^2}+k_y^2\right)a^2\beta^2}{\left(\frac{\nu^2\pi^2}{a^2}+k_y^2\right)a^2\beta^2+\alpha_0^2}\right),\quad \nu=1,\ 2,\ \ldots. \tag{22}$$

The spectrum of ω values can then easily be found from

$$\omega^2=\omega_p^2+(k_1^2+k_y^2)s^2, \tag{23}$$

and since $k_\parallel$ is complex, ω has a small negative imaginary part, which corresponds to radiation damping of the waves.

In the second case, where $ka \gg 1$, it turns out that $k_{II}r_D \sim 1$ if $a \sim \omega_p/c$ and the resonance terms connnected with the longitudinal oscillations are smeared out as a result of Landau damping, which is not described by the original hydrodynamic equations. Thus when $|ka| \gg 1$, we can neglect the right sides of (17) and (18). The ω spectrum of the emitted modes coincides with that found above for transverse TM waves in the cold plasma approximation. Thus in bounded plasma systems it is possible to have wave damping caused by the emission of fast waves ($v_{ph} > c$). This damping must be taken into account together with that produced by collisions and Landau damping when considering the propagation and nonlinear interaction of waves.

In conclusion we wish to thank V. N. Oraevskii for his interest in this work and for useful discussion.

---

[1] J. Dawson and C. Oberman, Phys. Fluids, 2, 103 (1959).

[2] G. Bekefi, Radiation Processes in Plasmas, Wiley, New York (1966).

[3] G. Schmidt and G. Halpem, Phys. Rev., 131, 217 (1963).

[4] G. Schmidt, Phys. Fluids, 7, 915 (1964).

[5] A. A. Zhmudskii and V. N. Oraevskii, Papers from the Third All-Union Conference of Plasma Theory [in Russian], Kiev (1971), p. 62.

[6] V. L. Ginzburg, The Propagation of Electromagnetic Waves in a Plasma, Addison-Wesley, New York (1964).

[7] D. D. Ryutov, Thesis, P. N. Lebedev Institute of Physics, Academy of Sciences of the USSR, Moscow (1965).

Stabilization of MHD instabilities by a high-frequency current in a straight system

V. P. Fedyakova

(Submitted March 26, 1973; resubmitted June 12, 1973)
Zh. Tekh. Fiz., 44, 28-33 (January 1974)

We describe an experimental study of the stabilizing action of a hf current which passes through an unstable (Kruskal–Shafranov) plasma with a quasistationary current in a straight system. The amplitude of the hf current needed to stabilize the plasma is smaller than that derived from the theory of dynamic stabilization and the range of stabilization for longitudinal field values is broader. The more effective stabilization is connected with the production of turbulence by the hf current in the plasma skin layer and the creation of a positive gas-kinetic pressure gradient inside the plasma.

The present paper presents the results of an experimental investigation into the possibilities of using a hf current to stabilize MHD instabilities in a plasma in a straight system. The value of the modulation coefficient required to stabilize the Kruskal–Shafranov instability $\eta = I_{\sim m}/I_{-} \simeq 0.3$ ($I_{\sim m}$ and I_{-} are the amplitudes of the hf and quasistationary currents respectively) is smaller than the value $\eta \gg 1$, which has previously been accepted in MHD stabilization theory. The more effective stabilization in the present case can be explained by the presence of a high-temperature cylindrical shell characterized by anomalous conductivity at the surface of the unstable plasma.

1. OBSERVATION OF THE INSTABILITY

The experiment has been carried out on the Omega device described in refs. 1 and 2. A plasma with a quasistationary current I_{-} = 3-10 kA and lifetime of about 280 μsec is created by a discharge between electrodes at a pressure of $p_0 = 10^{-2}$-10^{-3} mm Hg. The discharge takes place in a quartz tube $2a$ = 10 cm in diameter with a distance of L = 90 cm between the electrodes. Measurements with a streak camera and double electric probes show that the plasma is not in contact with the walls, that the density increases towards the axis, and that the boundary of the plasma is limited by the apertures in the end plates (diameter $2a$ = 4 cm). The temperature of the discharge is 10 eV. The experimental evidence all suggests that the plasma has a helical deformation caused by the fact that the Kruskal–Shafranov condition

$$q = \frac{2\pi a}{L}\frac{H_z}{H_\theta} > m \qquad (1)$$

is not satisfied. Here, m is the azimuthal mode number and takes on the integral values 1, 2, 3,... When condition (1) is not satisfied, a perturbation deforms the plasma, which assumes a helical shape with pitch which is greater than or equal to the pitch of the helical field line; all this has been observed in the experiment. The expression for the growth rate of an instability which produces a change in shape of the plasma has been obtained by Leontovich and Shafranov:[3]

$$\gamma^2 = \left|\frac{K_1(k_i a)}{K_0(k_i a)}\right| \frac{1}{4\pi a\rho}\left[-\frac{H_\theta^2 K_0(k_i a)}{a K_1(k_i a)} + k_i H_z^2 \pm \frac{H_\theta H_z}{a}\right], \qquad (2)$$

where K_1 and K_0 are modified Bessel functions, the k_i are the mode wave numbers, and ρ is the plasma density. The nature of the instability is determined experimentally as follows. First, for two values of the current approximate estimates are made of the instability growth rate from oscillograms of the time change in dH_θ at the beginning of the discharge ($t \simeq 0$). For I_{-} = 7 kA, $H_z = 0$, $\gamma \simeq 10^6$ sec^{-1}; for I_{-} = 10 kA and H_z = 1 kOe, $\gamma \simeq 2\cdot10^{-6}$ sec^{-1}. These measured values of γ agree to within ~50% with those calculated from (2). Second, the streak photographs show that the plasma is curved in the axial direction and that the wavelength is equal to the distance between the electrodes. Third, magnetic probes, oriented along azimuth and axis, measure the fluctuations in the magnetic field $\partial H_\theta/dt$ and $\partial H_z/dt$ and their distribution with radius, azimuth, and axial distance. The magnetic field oscillation has two branches: One at a frequency of 200 kHz and another, which modulates the first, at a frequency 30-50 kHz. Simultaneous measurements are made by magnetic probes of the distribution in amplitudes of both modes along the radius of the chamber. The maximum of the 200 kHz mode occurs in the central region; that for the low-frequency mode is near the walls. In the axial direction, the pitch of the helix is equal to the distance between the electrodes. If the position of the endplate limiters is changed, there are changes in the pitch of the oscillations, the frequency, and the spatial amplitude. A comparison of the oscillations of $\partial H_\theta/\partial t$ measured by magnetic probes placed in azimuth around the chamber shows that the plasma rotates at a frequency of 200 kHz. The oscillations in the magnetic field correlate with those in the signal (nT) measured by the double probes near the wall and in the center of the chamber. For 150 μsec the plasma undergoes quasiharmonic oscillations at 200 kHz, periodically touching the walls at a frequency of 30-50 kHz, and the growth rate is given by (2).

The oscillogram of $\partial H_\theta/\partial t$ is used to construct the relationship between the 200-kHz oscillations in the magnetic field and the value of H_z. Figure 1 shows the results for two values of the quasistationary current I_{-} = 4.8 and 8 kA. As the field H_z increases, the amplitude decreases and reaches a minimum for $q = (2\pi a/L)(H_z/H_\theta) > 1$, i.e., when the Kruskal–Shafranov conditions are satisfied. (In practice it is sufficient to suppress the m = 1 mode to eliminate any severe MHD instability.)

It is clear that the helical instability in this experiment with a quasistationary current arises because the Kruskal–Shafranov criterion is not satisfied.

2. SUPPRESSION OF THE INSTABILITY

A quasiharmonic current from a hf generator is used to stabilize the instabilities just described. When the generator is connected across the discharge gap, the overall current $I = I_{-} + I_{\sim}$, where $I_{\sim} = I_{\sim m}\cos\omega t$ is the varying current at a frequency of $\omega = 10^7$ sec^{-1}. Magnetic probes were used to measure the total magnetic field H_θ +

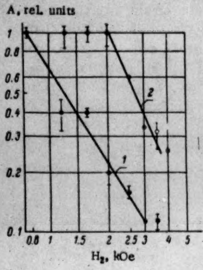

Fig. 1. Variation in the amplitude of the oscillations with the longitudinal magnetic field. 1) $I_- = 4.8$ kA; 2) $I_- = 8$ kA.

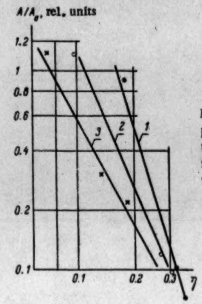

Fig. 3. Variation of the relative amplitude of oscillations in dH_θ/dt with the modul[illegible]on coefficient $\eta = I_{\sim m}/I_-$ for ξ = [illegible] Values of I_- in kA: 1) 3; 2) 5; 3) 7.5.

H_φ, where H_φ is the field of the hf current. The streak photographs and oscillograms of the signal from a photomultiplier directed at a point r = 3.5 cm from the axis of the chamber show that when a hf current $I_{\sim m} = 1$ kA passes through the plasma deformed by a quasistationary current of $I_- = 5$ kA, the plasma becomes linear and the radial oscillations disappear. Measurements by the magnetic probes show that there are no 200-kHz oscillations in the magnetic field of the plasma $\partial H_\theta/dt$.

A series of oscillograms of $\partial H_\theta/\partial t$ shows that the greater the amplitude of the quasiharmonic current, the smaller the oscillation amplitude for a fixed value of $I_- = 5.5$ kA. Similar observations suggest that the suppression of the plasma oscillations is a continuous process. In order to represent the degree of suppression graphically as a function of the discharge parameters, we introduce the following notation. The relative oscillation amplitude A/A_0 is defined as the ratio of the $\partial H_\theta/\partial t$ in a plasma stabilized by the hf current to the amplitude in a plasma with a quasistationary current alone. The modulation coefficient is the ratio of the amplitudes of the hf and quasistationary currents $\eta = I_{\sim m}/I_-$. The ratio of the longitudinal magnetic field to the field of the quasistationary current is denoted by the parameter $\xi = H_z/H_\theta$. The curves $A/A_0 = f(\xi)$, constructed from oscillograms of $\partial H_\theta/\partial t$ (in the time interval 30 μsec < t < 150 μsec) as shown in Fig. 2 indicate that there is a rapid change in the degree of suppression with the longitudinal magnetic field H_z as long as this field is smaller than that produced by the current itself. For $\xi = H_z/H_\theta > 1$-1.5, the relative oscillation amplitude is independent of H_z. The variation of relative oscillation amplitude with the modulation coefficient is shown in Fig. 3 for the case $\xi = 1.5$. As η increases, A/A_0 decreases earlier in a discharge with a higher current; final suppression of the instability (i.e., by a factor of 10 in amplitude) requires a modulation coefficient which is independent of the quasistationary current ($\eta \simeq 0.3$ when $\xi = 1.5$ and is slightly reduced with increase in ξ; η = 0 for ξ = 6). The values of the modulation coefficient required to reduce the amplitude by 10 times are shown in Fig. 4 as a function of ξ for $I_- = 3$, 5, and 7.5 kA. The points indicate the experimental values. The sharp increase in the required value of η for ξ < 1 suggests a change in the suppression mechanism. When $H_z = 0$, it is impossible to get hf stabilization even for the minimum quasistationary current of 3 kA. Stabilization here, if it is at all possible, requires η > 0.8. This might be due to the fact that when $H_z = 0$ the hf current goes to the walls of the chamber and does not create the necessary conditions for stabilization to occur. If only the hf current passes through the discharge channel, then over the whole range of values $0.2 < H_\varphi/H_\theta < 6$, no large-scale instabilities are observed despite the fact that the Kruskal–Shafranov criterion is not satisfied.

When $H_z = 0$, the hf current travels along the chamber walls forming a current cylinder with a skin-layer thickness δ and diameter approximately equal to 2*a* =

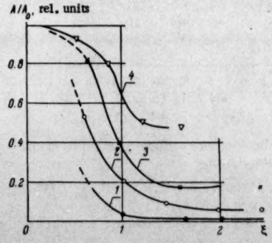

Fig. 2. Variation in the relative amplitude of the oscillations dH_θ/dt of the plasma with $\xi = H_z/H_\theta$ in the presence of a hf current $I_{\sim m} = 1.34$ kA. Values of I_- in kA: 1) 3; 2) 5; 3) 8; 4) 10.

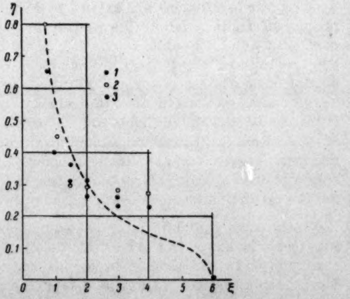

Fig. 4. Variation with $\xi = H_z/H_\theta$ of the modulation coefficient $\eta = I_{\sim m}/I_-$ required to suppress the oscillations in dH_θ/dt by a factor of 10. Values of I_- in kA: 1) 3; 2) 5; 3) 8.

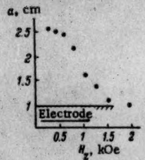

Fig. 5. Variation in the radius of a hf plasma with longitudinal magnetic field. $I_{\sim m}$ = 1.34 kA.

2A − δ. As H_z increases, the diameter of the skin cylinder decreases to that of the electrodes (for $I_{\sim m} = 1.34$ kA according to Fig. 5) when $H_z > H_{z\,cr} = H_\varphi L/2\pi a$. It is possible that in a longitudinal field $H_z < H_{z\,cr}$, the hf discharge is unstable and the widening of the discharge to the walls implies the absence of lf oscillations. When H_z exceeds $H_{z\,cr}$, the hf plasma becomes stable and has the same diameter as the electrodes. We can therefore suggest that the stabilizing action of the hf current on an unstable plasma is more effective when the hf discharge does not touch the walls and has a diameter close to that of the quasistationary plasma.

It is impossible to explain the experimental observations in terms of the dynamic stabilization theory because the values of the modulation coefficient are much smaller and the stability region is much wider than that given by the theories, e.g., refs. 4-7.

The gas-kinetic pressure of the plasma is measured by a diamagnetic probe for deformed and stabilized plasma. The amplitude of the pulse proportional to the pressure is an order of magnitude greater in the second case than in the first (for times $t \leq 30\ \mu$sec, when the cold impurities from the chamber walls have not yet interfered with the measurements). The greatest value of the diamagnetic signal occurs when only the hf current passes through the discharge gap. Spectral diagnostics and measurements with a double electric probe show that the electron temperature in a discharge with a hf current alone ($T_e \simeq 60$ eV) is much higher than with a quasistationary current even when the latter is hf stabilized. The hf field H_φ inside the plasma is concentrated in a skin layer, as in the case in which there is no constant current. It has been shown[8] that when an hf current passes through a skin layer in the discharge gap in the Omega apparatus, ion-acoustic oscillations are excited in the skin layer, the plasma conductivity falls by several orders of magnitude compared with the Coulomb value ($\sigma_{\exp} \simeq 10^{14}$ sec^{-1}, $\sigma_{\mathrm{Coul}} \simeq 10^{16}$ sec^{-1} for $I_{\sim m} = 1$ kA) and there is effective heating of the plasma to $(nT_e) \simeq 2 \cdot 10^{16}$ eV/cm^3 for $n = 2 \cdot 10^{14}$ cm^{-3}. Measurements of the density distribution of the particles with the double probes show that when a hf current passes through a quasistationary discharge, the maximum density occurs in the skin layer. This is probably explained by the preferential heating and ionization of the plasma in this layer.

Since stabilization is accompanied by heating in the skin layer the suggestion arises that the dissipation of electromagnetic wave energy in the skin region might produce a stable system. This idea is related physically to the production of a positive gas-kinetic pressure gradient inside the plasma when a hf current passes through the skin layer. The value of (nT) is a maximum in the current layer and falls to a minimum on the axis; this distribution might be important in the interpretation of the stability. The stabilizing effect of a hollow plasma configuration which does not touch the walls was noted by Tuck[9] back in 1958, when he showed that the stability is connected with the fact that the Suydam conditions

$$\frac{8\pi}{H_z^2}\left(\frac{dp}{dr}\right)+\frac{r}{4}\left(\frac{1}{\mu}\frac{d\mu}{dr}\right)^2>0,\quad \mu=\frac{H_\theta}{rH_z} \tag{3}$$

are satisfied in this case.

In the present experiment the stabilization condition can be estimated approximately as

$$\rho a\gamma^2 < \mathrm{grad}\,(nT). \tag{4}$$

The left side gives the force which deforms the plasma and which has a growth rate (2) (ρ is the plasma density). If grad (nT) inside the plasma is positive, condition (4) is satisfied when

$$\eta > 0.6\xi^{-1}\left|\frac{K_1(k_ia)}{K_0(k_ia)}\right|\left[-\frac{K_0(k_ia)}{K_1(k_ia)}+k_ia\pm\xi\right]. \tag{5}$$

For this to be true, it is necessary that the temperature in the moving plasma should not be able to equalize during the deformation time, i.e.,

$$\gamma > \tau^{-1}. \tag{6}$$

Condition (5) is always satisfied in the present experiment and condition (6), which is indicated graphically in Fig. 5 by the shaded line, coincides with the experimental points in view of the assumptions we have made. Other facts may be enlisted to explain the stabilizing effect of the hf current (for example, the change in the plasma conductivity tensor in the region affected by the hf electric field). However, despite the fact that there is no complete theory of hf stabilization, the experiment shows that the hf current does have a stabilizing effect by producing turbulence in the skin layer.

This work, first, proves the importance of using a hollow-configuration hf current for producing a stable MHD plasma. Secondly, the results have shown that the stabilization of a Kruskal−Shafranov unstable plasma with a quasistationary current requires a hf current with an amplitude some three or more times smaller than that of the quasistationary current, the exact value depending on the longitudinal magnetic field; this assumes that the plasma does not touch the chamber walls and that there is a positive gas-kinetic pressure gradient inside the plasma. Thirdly, the presence of a hf current in a plasma means that it is possible to work with H_z fields smaller than those required by the Kruskal−Shafranov criterion.

In conclusion, the author wishes to thank L. V. Dubovoi for useful discussion.

---

[1] A. B. Andrezen, V. P. Gordienko, L. V. Dubovoi, I. M. Roife, and S. P. Yakovlev, Zh. Tekh. Fiz., 36, 294 (1966) [Sov. Phys.−Tech. Phys., 11, 213 (1966)].

[2] V. P. Gordienko, L. V. Dubovoi, and I. M. Roife, Plasma Phys., 10, 449 (1968).

[3] M. A. Leontovich and V. D. Shafranov, Plasma Physics and the Problem

of Controlled Nuclear Reactions [in Russian], Vol. 1, Atomizdat, Moscow (1958), p. 207.

[4] S. M. Osovets, Zh. Eksp. Teor. Fiz., 39, 311 (1960) [Sov. Phys.–JETP, 12, 221 (1961)].

[5] N. A. Bobyrev and O. I. Fedyanin, Zh. Tekh. Fiz., 33, 1187 (1963) [Sov. Phys.–Tech. Phys., 8, 887 (1964)].

[6] M. A. Vasilevskii, I. M. Roife, and E. V. Seredenko, Zh. Eksp. Teor. Fiz., 60, 1621 (1971) [Sov. Phys.–JETP, 33, 877 (1971)].

[7] M. G. Nikulin, Zh. Tekh. Fiz., 39, 2144 (1969) [Sov. Phys.–Tech. Phys., 14, 1618 (1970)].

[8] L. V. Dubovoi and V. P. Fedyakova, Zh. Eksp. Teor. Fiz., 58, 1168 (1970) [Sov. Phys.–JETP, 31, 627 (1970)].

[9] J. Tuck, Second International Conference on Peaceful Uses of Atomic Energy, Geneva (1958), p. 1860.

Nonmonoenergetic relativistic electron beam in a bounded collisional plasma

V. P. Grigor'ev and N. S. Shulaev

Scientific Research Institute of Nuclear Physics, Electronics,
and Automation, Kirov Tomsk Polytechnic Institute
(Submitted April 11, 1973; resubmitted June 26, 1973)
Zh. Tekh. Fiz., 44, 34-37 (January 1974)

The interaction between a low-density relativistic electron beam and a spatially bounded magnetoactive plasma is analyzed. The longitudinal electromagnetic waves excited by the nonmonoenergetic beam are examined allowing for collisions between plasma electrons and heavy particles (neutral molecules or ions); the maximum growth rates are computed as functions of the system parameters. It is shown that an energy spread in the beam electrons results in a stabilization of hydrodynamic instability and the appearance of threshold currents.

A number of papers[1-5] are devoted to the theoretical study of the interaction between a relativistic electron beam and a bounded plasma. Despite the fact that these studies avoid a number of idealizations and bring the statement of the problem close to the experimental conditions, they do not allow for one essential factor: collisions between plasma electrons and heavy particles. As shown in refs. 6 and 7, allowance for collisions and the associated energy dissipation of the electromagnetic waves excited by a monoenergectic beam in an unbounded isotropic plasma results in changes in the interaction picture.

In the present study we investigate the interaction between a bounded nonmonoenergetic beam of relativistic electrons and a dissipative magnetoactive plasma. It is assumed that the uniform beam and plasma completely fill a waveguide of radius R (with ideally conducting walls) and that the system is subject to an external longitudinal magnetic field ($B_0 \parallel z$), with $B_0^2 \gg 8\pi n_b mc^2\gamma_0$, where $\gamma_0 = (1 - v_0^2/c^2)^{-1/2}$, n_b, v_0 are respectively the density and average directed velocity of the electron beam, and n_p is the density of the plasma electrons, $n_p \gg n_b$.

With these assumptions, if we give the perturbations as functions of the coordinates and time in the form $\Phi(r, \varphi, z, t) = \Phi(r)\exp\{i[k_z z + l\varphi - \omega t]\}$, we obtain the following dispersion equation to describe the electrostatic oscillations in the system:

$$1 - \frac{\omega_p^2}{\omega(\omega + i\nu)} - \int \frac{\omega_b^2\gamma^{-3}}{(\omega - k_z v)^2} F_0(\gamma)\, d\gamma + \frac{k_\perp^2}{k_z^2} \times\left[1 - \frac{\omega + i\nu}{\omega}\frac{\omega_p^2}{(\omega + i\nu)^2 - \Omega^2} - \int \frac{\omega_b^2\gamma F_0(\gamma)\, d\gamma}{\gamma^2(\omega - k_z v)^2 - \Omega^2}\right] = 0, \quad (1)$$

where ω_b and ω_p are respectively the plasma frequency of the beam and plasma electrons; $\Omega = eB_0/(mc)$; ν is the effective collision frequency between plasma electrons and heavy particles; $k_\perp = \mu_{s,l}/R$; $\mu_{s,l}$ is the s-th root of a l-th order Bessel function; and $F_0(\gamma)$ is the energy distribution function of the beam electrons in the unperturbed state.

An analysis of (1) indicates that the following waves can be excited in the system: plasma-waveguide waves corresponding to the characteristic spectrum of plasma oscillations in the waveguide,

$$\omega_{1,2}^2 = \frac{1}{2}(\omega_p^2 + \Omega^2) \pm \left[\frac{1}{4}(\omega_p^2 + \Omega^2)^2 - \frac{k_z^2}{k_z^2 + k_\perp^2}\omega_p^2\Omega^2\right]^{1/2}, \quad (2)$$

space-charge waves $\omega \approx k_z v$, and electron-cyclotron waves $\omega \approx k_z v \pm \Omega/\gamma$. The interaction between beam and plasma is strongest in the region of synchronism of the plasma-waveguide waves and the space-charge waves (Cerenkov instability) and the electron-cyclotron waves (cyclotron instability). Below we will consider separately the excitation of Cerenkov and cyclotron instabilities for $\nu/\omega \ll 1$ by an electron beam with an equilibrium distribution of the form

$$F_0(\gamma) = \frac{\Delta\gamma}{\pi}\frac{1}{(\gamma - \gamma_0)^2 + \Delta\gamma^2}, \quad (3)$$

where $\Delta\gamma$ is the longitudinal energy spread and $\xi = \Delta\gamma/\gamma_0 \ll 1$.

1. With synchronism between the plasma-waveguide waves and the space-charge waves the solution of dispersion equation (1) can be written in the form $\omega = k_z v_0 + \delta = \omega_0 + \delta$, $\delta/\omega_0 \ll 1$, where ω_0 is one of the roots of (2). For a dense plasma ($n_b \ll n_p$), limiting ourselves to linear terms in ξ, we obtain the following equation for determining the correction δ from Eqs. (1) and (3):

$$A\frac{\delta}{\omega_0} + \frac{k_\perp^2}{k_z^2}\frac{\omega_b^2\gamma_0}{\Omega^2} + iB - \frac{\omega_b^2}{\gamma_0^3}\frac{(1 + 3i\xi)}{\left(\delta + i\frac{\xi\omega_0}{\gamma_0^2\beta_0^2}\right)^2} = 0, \quad (4)$$

where

$$A = 2\left[\frac{\omega_p^2}{\omega_0^2} + \frac{k_\perp^2}{k_z^2}\frac{\omega_p^2\omega_0^2}{(\omega_0^2 - \Omega^2)^2}\right],$$

$$B = \frac{\nu}{\omega_0}\left[\frac{A}{2} + \frac{k_\perp^2}{k_z^2}\frac{\omega_p^2\Omega^2}{(\omega_0^2 - \Omega^2)^2}\right], \quad \beta_0 = \frac{v_0}{c}.$$

It can be shown from (4) that the maximum growth rate corresponds to the smallest transverse wave number $k_\perp = \mu_{1,0}/R = 2.4/R$ and that electrostatic waves are excited at a frequency $\omega^2 \approx \omega_0^2 \approx \omega_p^2$. Examination of the other branch that results from the solution of (2), $\omega_0^2 \approx \Omega^2$ for $k_z^2 \gg k_\perp^2$, shows that the instability is not excited at this frequency.

We consider the case of a dense plasma and high-energy beams; then

$$2\left(\frac{\nu\gamma_0}{2\omega_p}\right)^{2/3}\frac{\omega_p}{\omega_b} \gg 1, \quad (5)$$

and the solution of (4) corresponding to the unstable branch with maximum growth rate can be written in the form

$$\tilde{\delta} = \frac{\omega_b}{(2\gamma_0^3 B_{\min})^{1/3}}\left[-1 + i\left(1 - \xi\left[\frac{3}{2} + \frac{\omega_p B_{\min}^{1/3}}{\beta_0^2\gamma_0^{1/3}\omega_b}\right]\right)\right], \quad (6)$$

where

$$B_{\min}=\frac{\nu}{\omega_p}\left[1+\frac{\mu_{1,0}^2}{R^2}\frac{\beta_0^2c^2}{\omega_p^2}\right].$$

It follows from (6) that with increasing plasma resistance resulting from collisions between plasma electrons and heavy particles the growth rate for the Cerenkov instability decreases $\sim\nu^{-1/2}$. A low energy spread of the beam electrons also results in a weakening of the interaction between beam and plasma and a reduction in the growth rate.

It can be seen from (6) that for a nonmonoenergetic beam there is a threshold current value below which the Cerenkov instability does not arise:

$$I_{\mathrm{cr}}=\frac{mR^2c}{2e\beta_0^3}\frac{\omega_p^2B_{\min}}{\gamma_0(1-3\xi)}\xi^2. \tag{7}$$

The threshold current increases with the collision frequency $\sim\nu$ and for constant ξ it decreases with increasing beam energy $\sim\gamma_0^{-1}$.

In the opposite case of a less dense plasma in which the inverse of inequality (5) holds, the growth rate for the Cerenkov instability can be written in the form

$$\left.\begin{aligned}\operatorname{Im}\delta&=\left(\frac{\omega_p\omega_b^2}{A_{\min}\gamma_0^3}\right)^{1/3}\frac{(\sqrt{3}-\xi)}{2}-\frac{B_{\min}}{3A_{\min}}\omega_p-\frac{2\omega_p\xi}{3\beta_0^2\gamma_0^2},\\ A_{\min}&=2\left[1+\left(\frac{\mu_{1,0}}{R}\right)^2\frac{\beta_0^2c^2}{\omega_p^2}\right]\end{aligned}\right\} \tag{8}$$

and, as expected, depends only weakly on the collision frequency. Setting $\nu/\omega_p=\xi=0$ in (8), we obtain an expression which coincides with the Cerenkov-instability growth rate in a collisionless plasma.[3]

2. In the region of synchronism between plasma-waveguide waves and electron-cyclotron waves ($\omega\approx k_zv_0\pm\Omega/\gamma_0$), if we represent the solution in the form $\omega=\omega_0+\delta$, ($\delta/\omega_0\ll1$) and allow for the fact that $\omega_b^2/(\gamma_0\Omega^2)\ll1$, we obtain the following equation for the correction $\delta(\delta\ll\Omega/\gamma_0)$:

$$\frac{\delta}{\omega_0}+i\frac{B}{A}\mp\frac{k_\perp^2\omega_b^2}{2k_z^2\Omega\left(\delta+i\xi\frac{\Omega}{\gamma_0}\right)}=0, \tag{9}$$

where the minus sign refers to the fast electron-cyclotron wave and the plus sign to the slow wave.

We can readily show on the basis of (2) and (9) that for a dense plasma ($\omega_p^2\gg\Omega^2$), the instability is excited primarily at large transverse wave numbers $k_\perp$ and frequency $\omega_0\approx\omega_p$. Moreover, the solution of (9) indicates that the slow electron-cyclotron wave has the maximum growth rate:

$$\operatorname{Im}\delta=-\frac{1}{2}\left(\xi\frac{\Omega}{\gamma_0}+\nu\right)+\left[\frac{1}{4}\left(\xi\frac{\Omega}{\gamma_0}+\nu\right)^2+\frac{\omega_b^2\omega_p}{2\Omega}-\xi\frac{\Omega}{\gamma_0}\nu\right]^{1/2}. \tag{10}$$

The threshold current for the instability under consideration can be written in the form

$$I_{\mathrm{cr}}=\frac{mR^2c\beta_0}{2e}\frac{\Omega^2\nu}{\omega_p}\frac{\xi}{\gamma_0}. \tag{11}$$

It can be seen that the threshold current increases in proportion to the spread in energy ξ and the collision frequency ν.

A comparison of the threshold currents for the Cerenkov instability (7) and the cyclotron instability (11) indicates that when

$$\xi\left[1+\left(\frac{2.4}{R}\right)^2\frac{\beta_0^2c^2}{\omega_p^2}\right]\omega_p^2<\beta_0^4\Omega^2 \tag{12}$$

the Cerenkov instability arises. When the opposite of inequality (12) holds, the cyclotron instability is excited.

In conclusion we note that these results are obtained without allowing for collisions between beam electrons and plasma particles; for relativistic beams we will have $\nu_b/\delta\ll\nu/\omega_0$, where ν_b is the collision frequency for beam electrons and plasma particles.

The authors wish to thank A. N. Didenko for his interest.

---

[1] L. S. Bogdankevich and A. A. Rukhadze, Usp. Fiz. Nauk, 103, 609 (1971) [Sov. Phys.–Usp., 14, 163 (1971)].

[2] L. S. Bogdankevich, A. A. Rukhadze, and V. P. Tarakanov, Zh. Tekh. Fiz., 42, 900 (1972) [Sov. Phys.–Tech. Phys., 17, 715 (1972)].

[3] L. S. Bogdankevich and A. A. Rukhadze, Zh. Eksp. Teor. Fiz., 62, 233 (1972); Zh. Eksp. Teor. Fiz., 63, 899 (1972) [Sov. Phys.–JETP, 35, 126 (1972); 36, 473 (1973)].

[4] L. S. Bogdankevich, O. V. Dolzhenko, and A. A. Rukhadze, Radiotekh. Elektron., 17, 1646 (1972).

[5] V. K. Grishin and A. A. Kolomenskii, Zh. Tekh. Fiz., 42, 2604 (1972) [Sov. Phys.–Tech. Phys., 17, 2022 (1973)].

[6] E. A. Kornilov, S. A. Nekrashevich, Ya. B. Fainberg, and N. A. Shokhovtsov, ZhETF Pis. Red., 11, 284 (1970) [JETP Lett., 11, 185 (1970)].

[7] L. I. Rudakov, V. P. Smirnov, and A. M. Spektor, ZhETF Pis. Red., 15, 540 (1972) [JETP Lett., 15, 382 (1972)].

Second-harmonic generation and emission in wave conversion at a plasma boundary

A. N. Kondratenko, V. G. Shaptala, and V. M. Kuklin
A. M. Gor'kii Khar'kov State University
(Submitted January 8, 1973)
Zh. Tekh. Fiz., 44, 38-42 (January 1974)

The amplitude of the second harmonic emitted from a plasma layer is found for the case in which an electromagnetic wave incident from vacuum excites a longitudinal wave in the plasma. The intensity of the second harmonic at twice the plasma frequency is found as a function of the plasma width, the intensity of the (constant) magnetic field, and the angle of incidence of the wave at the fundamental frequency.

According to the theory of linear conversion of electromagnetic waves at a plasma–vacuum boundary, the field which arises in a plasma when an electromagnetic wave is incident at its boundary increases sharply when longitudinal waves are excited.[1-6] In a plasma layer field amplification is also possible in the case of a spatial resonance. Under these conditions the nonlinear plasma properties can turn out to be important.

In this work we use the approximation of a specified field[7] to analyze the generation and emission of electromagnetic waves at twice the plasma frequency (the second harmonic) by a plane layer of isotropic, magnetized plasma when this plasma is irradiated (from vacuum) by a wave whose electric vector is parallel to the incidence plane (p polarization) and whose frequency is approximately equal to the plasma frequency.

We assume the plasma to be homogeneous with sharp boundaries, and we neglect the changes in the equilibrium density in temperature, caused by the high-frequency field of the incident wave.

Alanakyan[8] has treated the excitation of the second harmonic of an electromagnetic wave in reflection of this wave from the sharp boundary of an isotropic plasma for the case in which the frequency of the incident wave is very different from the plasma frequency.

In the approximation of a slight nonlinearity $[(eE)\cdot(m\omega c)^{-1} \ll 1]$ the excitation of the second harmonic in the plasma is described by the nonlinear wave equation

$$\operatorname{curl}\operatorname{curl}\mathbf{E}_2 + \frac{\varepsilon(2\omega)}{c^2}\frac{\partial^2\mathbf{E}_2}{\partial t^2} = -\frac{4\pi}{c^2}\frac{\partial\mathbf{j}}{\partial t}, \tag{1}$$

where $\mathbf{j}$ is the part of the second-harmonic current which is quadratic in the field of the linear approximation.

Assuming the spatial dispersion to be small (the condition $qv_e \ll \omega$, where v_e is the electron thermal velocity, is always satisfied for propagating waves in a plasma), and assuming the ions to be immobile, we find the following from the equations of the quasihydrodynamic approximation:

$$\left.\begin{gathered}\mathbf{j} = -e\left(n_0\mathbf{v}^{(2)} + \frac{1}{2}n_1\mathbf{v}_1\right),\\ n_1 = -\frac{en_0}{m\omega^2}\nabla\mathbf{E}_1,\quad \mathbf{v}_1 = -\frac{ie}{m\omega}\mathbf{E}_1,\\ \mathbf{v}_2 = -\frac{i}{4\omega}\left\{(\mathbf{v}_1\nabla)\mathbf{v}_1 + \frac{e}{mc}[\mathbf{v}_1\mathbf{H}_1]\right\}.\end{gathered}\right\} \tag{2}$$

The notation is standard.

Using (2), we can convert Eq. (1) to

$$\operatorname{curl}\operatorname{curl}\mathbf{E}_2 + \frac{\varepsilon(2\omega)}{c^2}\frac{\partial^2\mathbf{E}_2}{\partial t^2} = \frac{e\Omega_e^2}{2m\omega^2c^2}\{[\mathbf{E}_1[\nabla\mathbf{E}_1]] + 3\mathbf{E}_1(\nabla\mathbf{E}_1)\}, \tag{3}$$

where Ω_e is the electron plasma frequency.

Equation (3) must be supplemented with boundary conditions for the fields at the plasma–vacuum boundary:[9]

$$\{\mathbf{E}_{2\tau}\} = 0,\quad [\mathbf{n}\{\mathbf{H}_{2\tau}\}] = \frac{4\pi}{c}\mathbf{j}^s, \tag{4}$$

where $\{\mathbf{E}_{2\tau}\}$ and $\{\mathbf{H}_{2\tau}\}$ are the discontinuities in the tangential components of the field at the boundary, $\mathbf{j}^S$ is the surface-current density, and $\mathbf{n}$ is a unit vector normal to the boundary, directed into the plasma.

ISOTROPIC PLASMA

We first consider a plane-parallel layer of isotropic plasma filling the region $0 < z < a$. The incident wave is

$$\left.\begin{gathered}\mathcal{E} = \mathbf{E}_0 e^{i(\mathbf{kr}-\omega t)},\quad \mathcal{E} = (\mathcal{E}_x, 0, \mathcal{E}_y),\\ \mathbf{k} = (k\sin\theta, 0, k\cos\theta),\quad k = \frac{\omega}{c},\quad |\Omega_e^2 - \omega^2| \ll \Omega_e^2,\end{gathered}\right\} \tag{5}$$

where θ is the angle of incidence.

Transverse and longitudinal waves are excited in the layer:

$$\begin{gathered}\mathbf{E}_1 = (\mathbf{L}_+e^{iqz} + \mathbf{L}_-e^{-iqz} + \mathbf{P}_+e^{i\varkappa_1 z} + \mathbf{P}_-e^{-i\varkappa_1 z})\,e^{i(k_x x-\omega t)},\\ q = k\left[\frac{2\varepsilon(\omega)}{3\beta^2} - \sin^2\theta\right]^{1/2},\quad \varkappa_1 = k[\varepsilon(\omega) - \sin^2\theta]^{1/2},\\ \varepsilon(\omega) = 1 - \frac{\Omega_e^2}{\omega^2} + i\frac{\nu}{\omega};\quad \beta = \frac{v_e}{c},\quad \omega > \Omega_e,\end{gathered} \tag{6}$$

where ν is the electron collision frequency.

The amplitudes of the waves are found in the linear approximation from the fields and the vanishing of the normal component of the hydrodynamic electron velocity at the plasma boundary. Using $\varepsilon(\omega) \ll 1$ and $q \gg \varkappa_1$, k, we find

$$\left.\begin{gathered}P_{\pm z} = \pm\frac{E_0qk_x\cos\theta}{\Delta_1\varkappa_1^2}\left[1 \pm e^{\mp i\varkappa_1 a}\left(i\frac{\varkappa_1 q}{k_x^2}\sin qa \mp \cos qa\right)\right],\\ L_{\pm z} = \mp\frac{E_0q^2\cos\theta}{\Delta_1\varkappa_1 k_x}(1 - e^{\mp iqa}),\\ \Delta_1 = -\frac{2q}{\varkappa_1}(1 - \cos qa\cos\varkappa_1 a) - \frac{q^2}{k_x^2}\sin qa\sin\varkappa_1 a.\end{gathered}\right\} \tag{7}$$

Solving Eq. (3), we find the field of the second harmonic in the plasma to be

$$\mathbf{E}_2 = \left(\mathbf{P}_{+2}e^{i\varkappa_2 z} + \mathbf{P}_{-2}e^{-i\varkappa_2 z} + \sum_j \mathbf{B}_j e^{i\xi_j z}\right)e^{2i(k_x x-\omega t)}, \tag{8}$$

where $\mathbf{P}_{\pm 2}$ are the amplitudes of the natural waves, $\varkappa_2 = 2k[\varepsilon(2\omega) - \sin^2\theta]^{1/2}$, and ξ_j and $\mathbf{B}_j$ are the transverse components of the wave vectors and the amplitudes of the induced waves; for brevity we omit the explicit expressions.

The electromagnetic waves at frequency $\omega \sim 2\Omega_e$ which are emitted by the plasma into vacuum propagate parallel to the reflected and transmitted signals at the fundamental frequency:

$$\mathscr{E}_2' = \mathbf{R}_2 e^{2i(\mathbf{k}'\mathbf{r} - \omega t)}, \quad \mathscr{E}_2'' = \mathbf{T}_2 e^{2i(\mathbf{k}\mathbf{r} - \omega t)},$$
$$\mathbf{k}' = (k_x,\ 0,\ -k_z). \tag{9}$$

In our case boundary condition (4) becomes

$$\{E_{2x}\} = 0, \quad \{H_{2y}\} = -i\frac{2\pi e}{c\omega} n_0 v_{1x} v_{1z}|_{z=0} = 0. \tag{10}$$

We thus find the amplitudes of the second harmonic in vacuum to be

$$T_2 = \frac{e^{-2ik_z a}}{\Delta_2}[D(\cos\theta \cos \varkappa_2 a - ig \sin \varkappa_2 a)$$
$$- C(i\cos\theta \sin \varkappa_2 a - g\cos \varkappa_2 a) + gA - B\cos\theta],$$
$$R_2 = \frac{1}{\Delta_2}[B(\cos\theta\cos \varkappa_2 a - ig\sin \varkappa_2 a)$$
$$+ A(i\cos\theta \sin \varkappa_2 a - g\cos \varkappa_2 a) + gC - D\cos\theta],$$
$$C = \frac{ieE_0^2 k_x}{4mk^2\varepsilon(2\omega)c^2}\Big[(P_{+z}e^{i\varkappa_1 a}$$
$$+ P_{-z}e^{-i\varkappa_1 a})(3L_{+z}e^{iqa} - L_{-z}e^{-iqa})$$
$$+ \frac{3}{2}(L_{+z}^2 e^{2iqa} + L_{-z}^2 e^{-2iqa}) + 3L_{+z}L_{-z}\Big],$$
$$D = \frac{-ieE_0^2\varkappa_1\varkappa_2}{4mc^2 k_x k^2\varepsilon(2\omega)}(P_{+z}e^{i\varkappa_1 a} - P_{-z}e^{-i\varkappa_1 a})(L_{+z}e^{iqa} + L_{-z}e^{-iqa}),$$
$$\Delta_2 = i\cos^2\theta \sin \varkappa_2 a - 2g\cos\theta\cos \varkappa_2 a + ig^2 \sin \varkappa_2 a,$$
$$g = \frac{\varkappa_2}{2k\varepsilon(2\omega)}, \quad C|_{a=0} = A, \quad D|_{a=0} = B. \tag{11}$$

Let us analyze these equations for certain particular cases. We assume that to a first approximation the longitudinal wave which is excited propagates in the plasma $[\varepsilon(\omega) > 0]$, while the transverse wave propagates in a "skin," except for angles of incidence in the interval satisfying $0 < \theta < \arcsin[\varepsilon(2\omega)]^{1/2}$.

If the transverse dimensions of the layer are large in comparison with the wavelength of the longitudinal wave and in comparison with the skin depth for the transverse wave, we can use the approximation for a semiinfinite plasma. Here we have $T_2 = 0$ and

$$R_2 = \frac{ieE_0^2 \sin\theta\cos^2\theta[(4\varepsilon(\omega) - \sin^2\theta)^{1/2}(0.75 - \sin^2\theta)^{1/2} - 3\sin^2\theta]}{2mc\Omega_e[\varepsilon(\omega) - \sin^2\theta][(0.75 - \sin^2\theta)^{1/2} + 0.75\cos\theta]}. \tag{12}$$

This equation has two maxima: a sharp maximum at angles of incidence $\theta \approx \arcsin[\varepsilon(\omega)]^{1/2}$ and a weaker maximum at $\theta \approx \arcsin[\varepsilon(2\omega)]^{1/2}$; these maxima are due to total internal reflection of the waves of the first and second harmonics from the plasma boundary.

The relative energy flux carried into vacuum by the second harmonic is

$$W = \frac{|R_2|^2}{E_0^2} = \left(\frac{eE_0}{mc\Omega_e}\right)^2 F(\theta). \tag{13}$$

Figure 1 shows the function $F(\theta)$ for $|\varepsilon| = 0.1$ and $\nu/\omega = 0.01$.

If the plasma layer is much thinner than the skin depth for the transverse wave ($|\varkappa a| \ll 1$), the radiation at frequency $2\Omega_e$ becomes symmetric on the two sides of the layer and becomes about $(\varkappa a)^{-2}$ times more intense than that from a semiinfinite plasma:

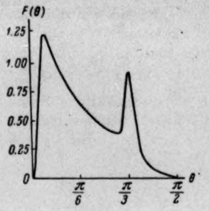

Fig. 1

$$R_2 = T_2 = \frac{8eE_0^2(1 - \cos qa)\cos\theta\sin^3\theta}{3mc\Omega_e(\varkappa a)^2 \sin qa[\varepsilon(\omega) - \sin^2\theta]}. \tag{14}$$

As sin qa decreases the amplitude of the second harmonic in vacuum increases, but at $\sin qa \ll k_x/q$ (corresponding to spatial resonance) Eq. (14) cannot be used; for $qa = (2n + 1)\pi$, where n = 1, 2, 3, . . . , we replace this equation by

$$R_2 = T_2 = \frac{eE_0^2 qa \sin 2\theta}{3m\Omega_e c(\varkappa a)^2}. \tag{15}$$

It follows from Eqs. (12)-(14) that at $\theta = 0$ the radiation at frequency $\omega \sim 2\Omega_e$ vanishes, because in the case of normal incidence a transverse wave at twice the fundamental frequency is not excited in the plasma.

MAGNETIZED PLASMA

We turn now to a plasma layer in a strong, fixed external magnetic field (for which $\omega_e \gg \Omega_e$, where ω_e is the electron gyrofrequency) perpendicular to the plasma boundaries.

In this case a p-polarized wave at frequency $\omega \sim \Omega_e$ incident obliquely excites two quasilongitudinal waves in the plasma:

$$\mathbf{E}_1 = (\mathbf{L}_+ e^{iqz} + \mathbf{L}_- e^{-iqz} + \mathbf{S}_+ e^{i\varkappa_1' z} + \mathbf{S}_- e^{-i\varkappa_1' z}),$$
$$S_{\pm z} = \pm\frac{E_0 q k_x \cos\theta}{\varepsilon^2(\omega)\varkappa_1'^2\Delta_3}\Big[1$$
$$\pm e^{\mp ik_z a}\left(i\frac{\varepsilon(\omega)\varkappa_1' q}{k_x^2}\sin qa \mp \cos qa\right)\Big],$$
$$L_{\pm z} = \mp\frac{E_0 q^2\cos\theta}{\varepsilon(\omega)k_x\varkappa_1'\Delta_3}(1 - e^{\mp iqa}),$$
$$\Delta_3 = -\frac{2q}{\varepsilon(\omega)\varkappa_1'}(1 - \cos qa\cos \varkappa_1' a) - \frac{q^2}{k_x^2}\sin qa \sin \varkappa_1' a,$$
$$\varkappa_1' = k\left[1 - \frac{\sin^2\theta}{\varepsilon(\omega)}\right]^{1/2}. \tag{16}$$

We find the nonlinear wave equation for this case from Eq. (3), taking into account the circumstance that the electrons move in one dimension (along $\mathbf{H}_0$), and taking into account the quasilongitudinal nature of the waves excited in the plasma at frequency $\omega \sim \Omega_e$:

$$\mathrm{curl\ curl}\ \mathbf{E}_2 + \frac{\hat{\varepsilon}(2\omega)}{c^2}\frac{\partial^2\mathbf{E}_2}{\partial t^2} = \frac{3e}{2mc^2}E_{1z}\frac{\partial E_{1z}}{\partial z}\mathbf{h}. \tag{17}$$

Here $\mathbf{h} = \mathbf{H}_0/H_0$, and the nonvanishing components $\varepsilon_{ik}(2\omega)$ are $\varepsilon_{11} = \varepsilon_{22} = 1$, $\varepsilon_{33} = \varepsilon(2\omega)$.

The field of the second harmonic excited in the plasma is

$$\mathbf{E}_2 = \left(\mathbf{S}_{+2}e^{i\varkappa_2' z} + \mathbf{S}_{-2}e^{-i\varkappa_2' z} + \sum_j \mathbf{A}_j e^{i\psi_j z}\right)e^{2i(k_x x - \omega t)}, \tag{18}$$

where $S_{\pm 2}$ are the amplitudes of the natural waves excited in the plasma at the second-harmonic frequency, ψ_j and A_j are the normal components of the wave vectors and the amplitudes of the induced waves, and $\varkappa_2' = \varkappa_1'(2\omega)$.

From the boundary conditions, which are the same as those for an isotropic plasma, (10), we find the amplitudes of the waves emitted by the layer at $\omega \approx 2\Omega_e$ into vacuum:

$$\left.\begin{gathered}
T_2 = \frac{1}{\Delta_4}\left[\frac{\varkappa_2'}{2k} A - C\left(i \sin \varkappa_2' a \cos\theta - \frac{\varkappa_2'}{2k} \cos \varkappa_2' a\right)\right] e^{-2ik_z a},\\
R_2 = \frac{1}{\Delta_4}\left[\frac{\varkappa_2'}{2k} C - A\left(i \sin \varkappa_2' a \cos\theta - \frac{\varkappa_2'}{2k} \cos \varkappa_2' a\right)\right],\\
C = -\frac{iek_x E_0^2}{2m\Omega_e^2}[L_{+z}^2 e^{2iqa} - L_{-z}^2 e^{-2iqa}\\
+ 2(S_{+z} e^{i\varkappa_1' a} + S_{-z} e^{-i\varkappa_1' a})(L_{+z} e^{iqa} + L_{-z} e^{-iqa})],\\
\Delta_4 = i \cos^2\theta \sin \varkappa_2' a - \frac{\varkappa_2'}{k} \cos\theta \cos \varkappa_2' a + i \frac{\varkappa_2'^2}{4k^2} \sin \varkappa_2' a,\\
A = C|_{a=0}.
\end{gathered}\right\} \quad (19)$$

We turn now to certain limiting cases.

For a semiinfinite plasma ($|qa|$, $|\varkappa_1' a|$, $|\varkappa_2' a| \gg 1$), we find from (19)

$$R_2 = \frac{i3e \cos^2\theta \sin^3\theta E_0^2}{m\Omega_e c\varepsilon(\omega)\sqrt{\varepsilon(2\omega)}}\Big\{[\varepsilon(\omega) - \sin^2\theta]\left[\frac{\sqrt{3}}{2}\cos\theta + \left(\frac{3}{4} - \sin^2\theta\right)^{1/2}\right]\Big\}^{-1}. \quad (20)$$

It follows from this equation that the amplitude of the second-harmonic wave emitted into vacuum at a frequency $\omega \approx 2\Omega_e$ is higher for a magnetized plasma than for an isotropic plasma, by a factor of about $1/\varepsilon(\omega) \gg 1$.

The emission of the second harmonic from a thin ($|\varkappa_1' a| \ll 1$) plasma layer is symmetric and more intense than that from a semiinfinite plasma, by a factor of $\sim |\varkappa_1' a|^{-2}$:

$$T_2 = R_2 = \frac{3ie \cos\theta \sin^3\theta E_0^2}{m\Omega_e c\varepsilon(\omega)(\varkappa_1' a)^2[\varepsilon(\omega) - \sin^2\theta]}.$$

Since $\varepsilon(\omega)|\varkappa_1' a|^2 \approx |\varkappa_1 a|^2$, the application of a strong magnetic field to a thin layer of isotropic plasma does not lead to an increase in the waves emitted at $\omega \approx 2\Omega_e$, in contrast with the case of a semiinfinite plasma.

---

[1] G. B. Field, Astrophys. J., 124, 555 (1956).

[2] D. A. Tidman, Phys. Rev., 117, 366 (1960).

[3] V. P. Silin and E. P. Fetisov, Zh. Eksp. Teor. Fiz., 41, 159 (1961) [Sov. Phys.—JETP, 14, 115 (1962)].

[4] Ts. D. Loladze and I. L. Tsintsadze, Radiofizika, 7, 374 (1964).

[5] A. M. Fedorchenko, Ukr. Fiz. Zh., 13, 1032 (1968).

[6] A. N. Kondratenko and I. N. Onishchenko, Zh. Tekh. Fiz., 38, 1397 (1968) [Sov. Phys.—Tech. Phys., 13, 1143 (1969)].

[7] N. Bloembergen, Nonlinear Optics, Benjamin, New York (1965).

[8] Yu. R. Alanakyan, Zh. Tekh. Fiz., 35, 1552 (1965) [Sov. Phys.—Tech. Phys., 10, 1202 (1966)].

[9] V. P. Silin and A. A. Rukhadze, Electromagnetic Properties of Plasma and Plasma-Like Media [in Russian], Atomizdat, Moscow (1961).

Conversion of an electromagnetic wave into an ion-acoustic wave in an inhomogeneous plasma

A. N. Kondratenko and V. M. Kuklin

A. M. Gor'kii Khar'kov State University

(Submitted February 19, 1973)
Zh. Tekh. Fiz., 44, 43-47 (January 1974)

An electromagnetic wave incident on an inhomogeneous, highly nonisothermal plasma is analyzed. The electric vector of the wave lies in the plane of incidence. The plasma density variation is linear. If the inhomogeneity is pronounced, so that the limiting ion plasma frequency found from the condition $\Omega_i(a) = \omega$ is in the skin layer, an ion-acoustic wave can be excited in the plasma. An equation is derived for the field of the ion-acoustic wave and solved in the asymptotic regions. The ion-acoustic wave is excited near the point $\Omega_i(a) = \omega$, where its amplitude becomes very large; it propagates into the plasma with an amplitude which decays like $\omega \ll \Omega_i(x)$ in inverse proportion to the density. If the skin depth for the electromagnetic wave satisfies $\delta \ll a$, the amplitude of the ion-acoustic wave is exponentially small.

1. The conversion of electromagnetic waves into ion-acoustic waves, and vice versa, at the sharp boundary of a highly nonisothermal plasma is analyzed in ref. 1. However, plasmas have sharp boundaries only in a solid. In a gaseous plasma there is always a transition region, which cannot be narrower than the Debye length. Since the wavelength of an ion-acoustic wave can be comparable to the Debye length, it is clearly of interest to analyze the conversion of low-frequency waves at the boundary of an inhomogeneous plasma.

We consider a semiinfinite, highly nonisothermal plasma ($T_e \gg T_i$) filling the region $x > 0$. Over the interval $0 < x < b$ the plasma is inhomogeneous, and its unperturbed density varies from zero to $n_0(b) \equiv n_0$. For $x \geq b$ the density is constant at n_0. An electromagnetic wave is incident on the plasma at an angle Θ; the electric vector of this wave lies in the plane of incidence, and the frequency of the wave is $\omega < \Omega_i(b)$, where $\Omega_i(b)$ is the limiting ion-plasma frequency. The z axis lies in the plane of incidence of the wave and the incident wave has the components

$$E_x = \alpha H,\ E_z = -\sqrt{1-\alpha^2}\, H,\ H \equiv H_y = e^{i\psi}, \tag{1}$$

where

$$\psi = (\alpha k z + k x\sqrt{1-\alpha^2} - \omega t),\ \alpha = \sin\theta,\ k = \frac{\omega}{c}.$$

In an inhomogeneous plasma the amplitude of the transverse wave decays exponentially[2] away from the point $x = x_0$, determined from the condition $\omega = \Omega_e(x_0) \cdot (\cos\theta)^{-1}$. Accordingly, the wave essentially cannot reach the point of the ion-plasma resonance, at which conditions are suitable for the excitation of an ion-acoustic wave, in a slightly inhomogeneous plasma. We assume the plasma to be highly inhomogeneous, in the sense that the transverse field penetrates a depth $\delta \sim c/\Omega_e(a) \sim a$ into the plasma, where a is found from the condition $\omega = \Omega_i(a)$. If $b \sim a$ the characteristic dimensions of the inhomogeneity are of the order of the skin depth.

Under these conditions we can neglect the singularity of the transverse field and wave conversion at the electron-plasma resonance. Our purpose is to determine the field in the region in which the ion-acoustic wave can propagate.

Writing the functional dependences on the time and z of all plasma properties associated with the waves as $\exp i(k\alpha z - \omega t)$, we find the following system of equations for the field in the plasma from the linearized Maxwell equations and the equations of two-fluid hydrodynamics:

$$\frac{d^2}{dx^2}H + \frac{dH}{dx}\,\frac{\beta_T^2\alpha^2\varepsilon_i \frac{d}{dx}\ln n_0(x) - \frac{d}{dx}\varepsilon}{\varepsilon - \alpha^2\beta_T^2\varepsilon_i} + k^2(\varepsilon - \alpha^2)H = \alpha\beta_T^2\frac{d}{dx}(\varepsilon_i E_x)\,\frac{\varepsilon\frac{d}{dx}\ln n_0 - \frac{d\varepsilon}{dx}}{\varepsilon - \alpha^2\beta_T^2\varepsilon_i}, \tag{2}$$

$$\frac{v_T^2}{\omega^2}\frac{d^2}{dx^2}(\varepsilon_i E_x) + \frac{v_T^2}{\omega^2}\frac{d}{dx}(\varepsilon_i E_x)\,\frac{\alpha^2\beta_T^2\frac{d\varepsilon_i}{dx} - \varepsilon\frac{d}{dx}\ln n_0(x)}{\varepsilon - \beta_T^2\alpha^2\varepsilon_i} + (\varepsilon - \alpha^2\beta_T^2\varepsilon_i)E_x = \alpha(1 - \beta_T^2\varepsilon_i)H + \frac{\alpha\frac{v_T^2}{\omega^2}\frac{d\varepsilon_i}{dx} - \varepsilon_i\frac{d}{dx}\ln n_0(x)}{\varepsilon - \alpha^2\beta_T^2\varepsilon_i}\,\frac{dH}{dx}, \tag{3}$$

$$ikE_z = (\varepsilon - \alpha^2\beta_T^2\varepsilon_i)^{-1}\left[\alpha\beta_T^2\frac{d}{dx}(\varepsilon_i E_x) - \frac{dH}{dx}\right], \tag{4}$$

where $\beta_T = v_T/c$, v_T is the electron thermal velocity, m_e and m_i are the electron and ion masses. We assume the inhomogeneity of the plasma to be linear in the transition layer:

$$\varepsilon_i = 1 - \frac{\Omega_i^2(b)\,x}{\omega(\omega + i\nu)\,b},\quad \varepsilon = \varepsilon_i - \frac{\Omega_e^2(b)\,x}{\omega^2 b},$$

where $\Omega_e(b)$ is the limiting plasma frequency and ν is the effective ion-collision frequency. When the motion of ions can be neglected system (2)-(4) reduces to a system analyzed previously.[2]

The hydrodynamic velocity of the plasma electrons can be determined from

$$\mathbf{v}_e = -\frac{i}{4\pi e\omega n_0(x)}\left\{\varepsilon_i\mathbf{E} - \frac{i}{k}\operatorname{curl}\mathbf{H}\right\}. \tag{5}$$

2. Since system (2)-(4) is complicated we make several simplifying assumptions. We neglect the terms which take account of the effect of the electron thermal motion on the transverse field in the plasma in Eqs. (2) and (4). We also neglect terms proportional to β_T^2 on the right side of Eq. (3) and in the coefficients in this equation. We assume that the dimension of the inhomogeneous region is much larger than the wavelength of the ion-acoustic wave in the plasma. We also neglect the terms proportional to $d/(dx)\ln n_0(x)$. Now system (2)-(4) splits into two equations for the transverse field,

$$\frac{d^2}{dx^2}H - \frac{d}{dx}\ln\varepsilon\,\frac{dH}{dx} + k^2(\varepsilon - \alpha^2)H = 0, \tag{6}$$

$$ikE_z = \frac{1}{\varepsilon}\frac{dH}{dx}, \tag{7}$$

and an equation for the longitudinal field,

$$\frac{d^2}{dx^2}(\varepsilon_i E_x) + \frac{\omega^2}{v_T^2}\varepsilon E_x = \alpha \frac{\omega^2}{v_T^2} H. \tag{8}$$

If we neglect the first term on the left side of Eq. (8), we find the familiar relation between the components of the electromagnetic field in the plasma:

$$E_x = \frac{\alpha}{\varepsilon} H. \tag{9}$$

Taking account of this term increases the degree of the equation, leading to the appearance of a new (ion-acoustic) wave in the region in which it can exist (Re $\varepsilon_i \leq 0$).

Longitudinal electron waves are localized in the region $1 \gg \varepsilon > 0$. Outside this region, on the left or right, the x component of the electric field must have the form of (9). Accordingly, Eq. (9) is a sort of boundary condition on Eq. (8) in the high-frequency region for $|\varepsilon| \gg 1$.

In the present case of longitudinal ion-acoustic waves the situation is slightly different: The ion-acoustic wave appears where Re $\varepsilon_i \leq 0$, so Eq. (9) can be used as a boundary condition only for the region Re $\varepsilon_i > 0$, where the amplitude of the longitudinal wave must fall off quite rapidly away from the point Re $\varepsilon_i = 0$. For negative values of Re ε_i the ion-acoustic wave also appears where a transverse wave cannot exist, because it is exponentially damped. Since there are two independent constants in the solution of Eq. (8), a second boundary condition is required. This condition must give the amplitude of the longitudinal wave in terms of the amplitude of the transverse wave in the region in which both exist (Re $\varepsilon_i \approx 0$). We adopt as this condition the requirement that as the transition region vanishes ($b \to 0$) the solution of Eq. (8) must go over to the solution for a plasma with a sharp boundary, (1). Analytically, this requirement in an inhomogeneous plasma is equivalent to the equation

$$v_{ex}(a) \approx 0, \tag{10}$$

where a is specified by the condition Re $\varepsilon_i(a) = 0$.

In the equation for the ion-acoustic wave, (8), the transverse field appears as a perturbing force which must be found by solving Eqs. (6) and (7) with boundary conditions expressing the continuity of the tangential components of the electromagnetic field at the boundaries. Since $|\varepsilon| \gg \alpha^2$ in the region of interest, and since the dimensions of the region $|\varepsilon| \sim \alpha^2$ are small, we can neglect the quantity α^2 in Eq. (6).

We find the following equations for the longitudinal component of the transverse field: In the region of inhomogeneous plasma[3]

$$E_x^{\mathrm{trI}}(x) = \frac{\alpha}{\varepsilon} H^{\mathrm{I}}(x) = \alpha C \{ I_{1/3}[\gamma u_i^3(x)] - Q I_{-1/3}[\gamma u_i^3(x)] \}, \tag{11}$$

where

$$C = 2\mu \frac{\left(\frac{\gamma}{2}\right)^{2/3} \Gamma\left(\frac{1}{3}\right)}{Q} \left\{ i \left(\frac{\gamma}{2}\right)^{1/3} \frac{\Gamma\left(\frac{1}{3}\right)}{\Gamma\left(\frac{2}{3}\right)} \frac{\mu}{Q} - \sqrt{1-\alpha^2} \right\}^{-1},$$

$$Q = \frac{I_{-1/3}[\gamma u_i^3(b)] + I_{1/3}[\gamma u_i^3(b)]}{I_{1/3}[\gamma u_i^3(b)] + I_{-1/3}[\gamma u_i^3(b)]},$$

$$\gamma = \frac{2}{3}\varkappa\beta_T, \quad \mu = \sqrt{\frac{m_e}{m_i}}, \quad u_i(x) = \frac{\Omega_i(x)}{\omega}, \quad \varkappa = \frac{\omega^3 b}{\Omega_i^3(b)\, v_s},$$

v_s is the sound velocity in the plasma and $\Gamma(x)$ is the gamma function.

In the region of the homogeneous plasma

$$E_x^{\mathrm{trII}}(x) = \frac{\alpha}{\varepsilon(b)} H^{\mathrm{II}}(x) = -\frac{\sqrt{3}}{\pi\gamma u_i^3(b)} \frac{\alpha C e^{-\frac{\Omega_i(b)}{v_s}(x-b)}}{I_{1/3}[\gamma u_i^3(b)] + I_{-1/3}[\gamma u_i^3(b)]}. \tag{12}$$

3. Equation (8) is conveniently written as

$$\frac{d^2}{dp^2}F + \varkappa^2\left(1 + \frac{1}{p}\right)F = \varkappa^2 E_x^{\mathrm{tr}}(p), \tag{13}$$

where $p = -\varepsilon_i$, $F \equiv \varepsilon_i E_x$.

The solution of Eq. (13) in the inhomogeneous region is

$$F^{\mathrm{I}}(p) = A_1 F_1(p) + A_2 F_2(p)$$
$$+ \pi\varkappa^2 \left[-F_1(p) \int_\infty^p E_x^{\mathrm{tr}}(p') F_2(p')\, dp' + F_2(p) \int_\infty^p E_x^{\mathrm{tr}}(p') F_1(p')\, dp' \right], \tag{14}$$

where $F_1(p)$ and $F_2(p)$ are the solutions of the homogeneous equation; these solutions are Whittaker functions of imaginary argument.[4]

For convenience, rather than treating the Whittaker functions we analyze the asymptotic representation[5] of the solution of Eq. (13) for Re $\varepsilon_i < 0$ and in the neighborhood Re $\varepsilon_i \approx 0$:

$$F_1 = \sqrt{p}\, H_1^{(1)}\left(\varkappa \int \left(1 + \frac{1}{p}\right)^{1/2} dp\right),$$
$$F_2 = \sqrt{p}\, H_1^{(2)}\left(\varkappa \int \left(1 + \frac{1}{p}\right)^{1/2} dp\right), \tag{15}$$

where $H_1^{(1,2)}$ are the Hankel functions of the first and second kinds. Here F_2 increases rapidly at Re $\varepsilon_i < 0$ and $|\varkappa \int (1 + 1/p)^{1/2} dp| \gg 1$, i.e., where conditions are not suitable for the ion-acoustic wave and where there must be no increasing solution. We therefore set A_2 equal to zero. As given in (15), $F_1(p)$ satisfies Eq. (13) when the following relations hold:

$$|p| \ll 1 \text{ and } p \gg 1, \quad \varkappa p \gg 1.$$

The case $p \gg 1$, $\varkappa p \ll 1$, corresponding to a plasma with a sharp boundary at large $|\varepsilon_i(b)|$, is of no particular interest.

The solution of Eq. (8) in the region of a homogeneous plasma is

$$F(x) = A_3 e^{iq(x-b)} + \varepsilon_i(b) E_x^{\mathrm{trII}}(x), \tag{16}$$

where $A_3/\varepsilon_i(b)$ is the ion-acoustic amplitude and

$$q = \frac{\Omega_i(b)}{v_s\sqrt{-\varepsilon_i(b)}}.$$

is the wave vector of the ion-acoustic wave.

The last term in Eq. (16), like the term in brackets in Eq. (14), describes the field of the transverse wave.

Using Eq. (10) and the continuity conditions on the field at the x = b boundary, we find the constants to be

$$A_1 = \frac{\alpha C\,\{I_{2/3}(\gamma) - Q I_{-2/3}(\gamma)\}}{\mu^2\sqrt{-\varepsilon_i(a)}\,H_1^{(1)}(2\varkappa\sqrt{-\varepsilon_i(a)})}, \tag{17}$$

$$A_3 = A_1\sqrt{-\varepsilon_i(b)}\,H_1^{(1)}\left(\varkappa\int\left(1+\frac{1}{p}\right)^{1/2}dp\right)\Big|_{p=-\varepsilon_i(b)}. \tag{18}$$

In determining A_3 we have neglected the x component of the transverse wave, because its amplitude is of order of m_e/m_i in comparison with the amplitude of the natural waves (the ion-acoustic waves). In the transition the amplitude of the ion-acoustic wave is

$$E_x^{l\,\mathrm{I}}(x) = \frac{\alpha C\,\{I_{2/3}(\gamma) - Q I_{-2/3}(\gamma)\}}{\mu^2\sqrt{-\varepsilon_i(a)}\,H_1^{(1)}(2\varkappa\sqrt{-\varepsilon_i(a)})}$$

$$\times\ \frac{H_1^{(1)}\left(\varkappa\int\left(1+\frac{1}{p}\right)^{1/2}dp\right)}{\sqrt{p}}\Bigg|_{p=-\varepsilon_i(x)}. \tag{19}$$

For the case b → ∞, i.e., when there is no "plateau" in the function $n_0(x)$, we set Q = 1 in Eq. (19) and write $\varkappa$ as

$$\varkappa = \frac{\omega}{v_s}\left(\frac{dp}{dx}\right)^{-1}.$$

In the region of homogeneous plasma (for finite values of b), we have

$$E_x^{l\,\mathrm{II}}(x) = E_x^{l\,\mathrm{I}}(b)\,e^{iq(x-b)}. \tag{20}$$

Since the amplitude of the electron field in the longitudinal wave, E_x^e, turns out to be approximately m_i/m_e times larger than the amplitude of the longitudinal component of the transverse field, E_x^{tr}, we are confronted with the question of the validity of our simplifications in Eqs. (2) and (4).

We can neglect the longitudinal field in Eqs. (2) and (4) if

$$\left|\frac{dH}{dx}\right| \gg \alpha\beta_T^2\left|\frac{d}{dx}(\varepsilon_i E_x^l)\right|.$$

This inequality reduces to

$$\left|\sqrt{-\varepsilon_i(a)}\right| \gg \alpha^2\beta_T, \tag{21}$$

which holds over a broad range of parameter values.

4. We now turn to certain particular cases.

a) If the frequency of the wave incident on the plasma is approximately equal to the limiting ion-plasma frequency, $\omega \approx \Omega_i(b)$, so that $|\mathrm{Re}\ \varepsilon_i(b)| \ll 1$, the amplitude of the field in the region of homogeneous plasma becomes the same as that in a plasma with a sharp boundary (1), when the transition layer is thin, and we have $(\omega_b/v_s)\sqrt{-\varepsilon_i(b)} \ll 1$:

$$E_x^l(x) = -\frac{2\alpha}{\sqrt{1-\alpha^2} - i\mu}\,\frac{e^{iq(x-b)}}{\varepsilon_i(b)}. \tag{22}$$

In the opposite case of a thick transition layer, with $2\varkappa\sqrt{-\varepsilon_i(b)} \gg 1$ and $b \lessdot c/[\Omega_l(b)]$, we find

$$E_x^l(x) = -\frac{2\alpha}{\sqrt{1-\alpha^2} - i\mu}$$

$$\times\sqrt{\frac{2}{\varkappa\pi}}\,\frac{\exp\left(\frac{i\omega b}{v_s}\sqrt{-\varepsilon_i(b)} - \frac{3\pi i}{4} + iq(x-b)\right)}{\sqrt{-\varepsilon_i(a)}\,H_1^{(1)}(2\varkappa\sqrt{-\varepsilon_i(a)})\,[-\varepsilon_i(b)]^{3/4}}. \tag{23}$$

When $|(\omega_b/v_s)\sqrt{-\varepsilon_i(a)}| \ll 1$ this equation simplifies:

$$E_x^l(x) = \frac{2\alpha}{\sqrt{1-\alpha^2} - i\mu}\sqrt{2\pi\varkappa}\,\frac{\exp\left(\frac{i\omega b}{v_s}\sqrt{-\varepsilon_i(b)} - \frac{3\pi i}{4} + iq(x-b)\right)}{[-\varepsilon_i(b)]^{3/4}}.$$

In the case $b \gg c/[\Omega_e(b)]$ $(\gamma \gg 1)$, the amplitude of the ion-acoustic wave is proportional to $\exp(-3/2\gamma)$, since the transverse wave cannot penetrate into the ion-resonance region.

b) If ω is small in comparison with $\Omega_i(x)$, Eq. (19) represents a traveling wave in the region $|\varepsilon_i(x)| \gg 1$, $|\varkappa\varepsilon_i(x)| \approx \omega x/b \gg 1$; the amplitude of this wave is inversely proportional to the plasma density:

$$E_x^l(x) = \frac{\alpha C\,\{I_{2/3}(\gamma) - Q I_{-2/3}(\gamma)\}}{\mu^2\sqrt{-\varepsilon_i(a)}\,H_1^{(1)}(2\varkappa\sqrt{-\varepsilon_i(a)})}\sqrt{\frac{2}{\varkappa\pi}}\,\frac{\omega^2}{\Omega_i^2(x)}\,e^{i\frac{\omega}{v_s}x - \frac{3\pi i}{4}}.$$

It follows that when the transverse field penetrates into the ion-resonance region we have $b \lessdot c/[\Omega_e(b)]$ and, if $(2\omega_a/v_s)\sqrt{-\varepsilon_i(a)} \ll 1$,

$$|E_x^l(x)| = \left|\frac{2\alpha}{\sqrt{1-\alpha^2} - i\mu}\right|\sqrt{2\pi\varkappa}\,\frac{\omega^2}{\Omega_i^2(x)}. \tag{24}$$

This value differs from the field amplitude in a plasma with a sharp boundary by the factor $\sqrt{2\pi\varkappa}$.

Knowing the amplitude of the ion-acoustic wave, it is also a simple matter to find the transformation coefficient, defined as the ratio of the flux density of the ion-acoustic wave to that of the electromagnetic wave.

---

[1] A. N. Kondratenko and I. N. Onishchenko, Zh. Tekh. Fiz., 38, 1397 (1968); 40, 384 (1970) [Sov. Phys. – Tech. Phys., 13, 1143 (1969)].

[2] V. L. Ginzburg, Propagation of Electromagnetic Waves in Plasma, Addison-Wesley, New York.

[3] H. B. Dwight, Tables of Integrals and Other Mathematical Data, Macmillan, New York (1961).

[4] E. T. Whittaker and G. N. Watson, A Course of Modern Analysis, Part 2, Cambridge Univ. Press, New York (1958).

[5] A. Erdélyi, Asymptotic Expansions, Dover, New York (1956).

Nonlinear plasma waves and ion-acoustic waves in an isotropic plasma

V. Sh. Livadonov and S. M. Fainshtein

Zhdanov Gor'kii Polytechnic Institute

(Submitted February 27, 1973; resubmitted May 28, 1973)
Zh. Tekh. Fiz., 44, 48-52 (January 1974)

Nonlinear longitudinal (plasma and ion-acoustic) waves in an isotropic plasma are investigated. An asymptotic method is used to derive truncated equations for the wave amplitude and phase. Particular solutions allowing for attenuation due to collisions and scattering by random inhomogeneities are analyzed; the nature of the stationary envelopes is clarified. Estimates are given for a plasma in a semiconductor like InSb. The hydrodynamic approximation is used.

Nonlinear waves in media with cubic nonlinearities have been investigated in detail (see, e.g., refs. 1-3). In both isotropic and anisotropic plasmas, self-focusing and self-compression of wave packets resulting from the nonlinear dependence of the permittivity ε_{nl} on the square of the electric field (electrostriction, heating, ionization, etc.) have been considered,[4-6] i.e., the cubic nonlinearity of the initial nonlinear wave equation has, in effect, been taken into account. In this paper we use the example of longitudinal (plasma and ion-acoustic) waves in an isotropic plasma to show that in analyzing interaction effects (and, similarly, self-focusing effects) in an isotropic plasma, it is also necessary to take account of the quadratic nonlinearity; in the second approximation in the small parameter of the problem this yields a contribution to ε_{nl} comparable with the cubic term. An asymptotic method is used to make a systematic analysis of the effects of dispersion, both linear (the term with $d^2\omega/dk^2$, ω and k being the frequency and wave number of the wave) and nonlinear, the nonlinear term being associated with a nonresonant process ($\omega + \omega \rightarrow 2\omega - \omega \rightarrow \omega$, see refs. 1 and 7). We utilize the hydrodynamic equations, i.e., we do not consider kinetic effects like Landau damping; this approach is valid if the velocity of the plasma waves is much greater than the electron thermal velocity and if $T \gg T_i$ for the ion-acoustic waves (T_i and T being the ion and electron temperatures).[8] We derive truncated equations for the complex electric field amplitudes and investigate various particular cases:[1] stationary envelopes and self-compression of the wave packet. We also allow for weak absorption due to particle collisions and scattering by random inhomogeneities in the equilibrium density. Estimates are given for a semiconductor plasma. It is shown that the results can be used for plasma diagnostics and also for obtaining pulsed signals from a longitudinal field.

1. NONLINEAR PLASMA WAVES

Plasma waves in a hot isotropic isothermal[2] plasma are described by the one-dimensional hydrodynamic equations for the electrons[3] and the Poisson equation for the electric field:

$$\frac{\partial E}{\partial x} = 4\pi e\rho,$$

$$\frac{\partial v}{\partial t} - \frac{e}{m}E + \frac{v_T^2}{N_0}\frac{\partial \rho}{\partial x} = -\mu\left(v\frac{\partial v}{\partial x} - \frac{v_T^2}{N_0^2}\rho\frac{\partial \rho}{\partial x}\right) - \mu^2\frac{v_T^2}{N_0^3}\rho^2\frac{\partial \rho}{\partial x},$$

$$\frac{\partial \rho}{\partial t} + N_0\frac{\partial v}{\partial x} = -\mu\frac{\partial(\rho v)}{\partial x}, \tag{1}$$

where E, v, and ρ are the deviations of the electric field, velocity, and density from the corresponding equilibrium values 0, 0, N_0, $v^2_T = \varkappa_0 T/m$ ($\varkappa_0$ is Boltzmann's constant). In the second equation in (1), the term associated with the pressure $v^2_T(\partial\rho/\partial x)/N_0 + \rho$ is expanded in a series including cubic terms. The parameter μ is introduced to denote the fact that the right side is small. We introduce the dimensionless quantities

$$\rho_{dl} = \rho/N_0,\ v_{dl} = \frac{v}{v_T},\ E_{dl} = \frac{eE}{m\omega_0 v_T};\ \left(\omega_0^2 = \frac{4\pi N_0 e^2}{m}\right),\ x_{dl} = x\frac{\omega_0}{v_T},$$
$$t_{dl} = t\omega_0,\ |\rho_{dl}|_{\max} \sim |v_{dl}|_{\max} \sim |E_{dl}|_{\max} \sim \mu \ll 1,\ 1 \gg \frac{kv_T}{\omega_0} \gg \mu.$$

The subscripts dl are omitted below. Using the asymptotic method,[1,7] we obtain a truncated second-approximation equation in μ for the complex amplitude of the electric field of the wave:

$$\frac{\partial a}{\partial t} + \frac{k}{\omega}\frac{\partial a}{\partial x} + \frac{i}{2}\frac{1}{\omega^3}\frac{\partial^2 a}{\partial x^2} = i\alpha a^2 a^*,$$

$$\omega^2 \doteq k^2 + 1\ (k \ll 1),\quad k \equiv k_{dl} = \frac{kv_T}{\omega_0},\ \omega \equiv \omega_{dl} = \frac{\omega}{\omega_0},$$

$$\alpha = -\frac{4}{3}\omega^3 k^2 - \frac{2}{3}\omega k^2 - \frac{1}{6}k^4\omega \simeq -\frac{8}{3}k^2\omega. \tag{2}$$

In deriving (2) we have allowed for both cubic and quadratic nonlinearities in (1); moreover, the right side of (2) incorporates terms with nonlinear dispersion associated with the process $\omega + \omega \rightarrow 2\omega - \omega \rightarrow \omega$.

We consider various particular cases: 1) the first approximation in μ allowing for small wave absorption, this being related either to ordinary collisions [in the second equation of (1) the term $\nu_{\text{eff}}v$] or to scattering of the average field by random inhomogeneities of the density N_0 equal to δN (see refs. 10 and 11). In both cases an additional term is introduced on the right side of (2): $\nu_\delta a$, where $\nu_{dl} = \nu_{\text{eff}}/2\omega_0$ for the case of collisions between electrons and other particles (ν_{eff} being the effective electron collision frequency) and[11] $\nu_\delta \simeq \langle(\delta N/N_0)^2\rangle\, l_0/k$ (where $l_0 = L/r_D$; L is the scale of the inhomogeneity and r_D is the Debye radius) for the case of scattering of the average field $\langle E\rangle$ by random inhomogeneities δN. The solution of (2) to order μ^2 can be readily obtained in the coordinates

$$\xi = t - \frac{x}{v_{gr}};\ A = F(\xi)e^{-\frac{\nu}{v_{gr}}x};\ \delta \equiv \frac{\varphi'_t}{\omega} = \int\frac{\alpha(A^2)'_t}{v_{gr}}dx + \Phi(\xi),$$

where A and φ are the real amplitude and phase of the wave, δ is the frequency deviation, and v_{gr} is the group velocity of the wave. In particular, for cosinusoidal modulation at the boundary x = 0: $A(0, t) = A_0 \cos \Omega t$ and $\delta(0, t) = 0$ the solution is of the form

$$\left.\begin{aligned} A &= A_0 l^{-\frac{\nu}{v_{gr}}x} \cos\left(t - \frac{x}{v_{gr}}\right)\Omega; \quad \nu \equiv \nu_{dl}. \\ \delta &= \delta_0\left[l^{-\frac{2\nu}{v_{gr}}x} - 1\right] \sin 2\Omega\left(t - \frac{x}{v_{gr}}\right), \end{aligned}\right\} \qquad (3)$$

where $\delta_0 = \alpha\Omega A_0^2/(2\nu)$. It is evident from (3) that as x increases the amplitude A decreases exponentially and that the frequency deviation tends to δ_0 as $x \to \infty$. This is readily understood, because as the amplitude decreases (i.e., decreasing nonlinearity), the change in wave phase becomes small and independent of the amplitude. Let us estimate δ_0 for the plasma in an InSb semiconductor: $I = 77°K$, $N \simeq 10^{17}$ cm^{-3}, $\nu_{eff} \simeq 5 \cdot 10^{11}$ sec^{-1}. If we specify a field of $\simeq 200$ V/cm at the boundary $x = 0$, at a distance $L \simeq 0.1$ mm we have $A \simeq 0.5$ mV/cm, and $\delta_0 \simeq 7\%$, where we have assumed that $\Omega/\omega_0 \simeq 0.1$ ($\omega_0 \simeq 10^{14}$ sec^{-1}). Thus, the change in amplitude and frequency deviation can be used to draw conclusions regarding the density of plasma electrons and the collision frequency ν_{eff}.

2) A general analysis of the envelopes, i.e., in which the solution depends on the single coordinate $\eta = t - (x/u)$ (u being the velocity of the envelope), is given in ref. 12. For our case the phase pictures in the (A, A'_η) plane are shown in Figs. 1 and 2, corresponding to solitons or cnoidal waves. Let us consider self-compression of a one-dimensional wave plasma field. Linearizing Eq. (2) for the real amplitudes and phases of the wave near the unperturbed values A_0 and φ_0 and seeking the solution in the form $e^{i\Omega t - iKx}$, we obtain

$$\Omega = Kv_{gr}\left[1 \pm \sqrt{\frac{v_{gr}^2 \varkappa^2 K^2}{4\omega^2} + \alpha\varkappa A_0^2}\right], \qquad (4)$$

where $\varkappa = \beta\omega/v_{gr}^2$ is the dispersion parameter of the plasma wave; $\beta = d^2\omega/(dk^2) \simeq 1/\omega^3$. Since $\alpha\varkappa < 0$, when

$$|\alpha\varkappa A_0^2| > v_{gr}^2 \frac{\varkappa^2 K}{4\omega^2} \qquad (5)$$

the plasma packet is unstable with respect to self-compression.4) We should note that our treatment of self-action in an isothermal plasma is valid if the power absorbed per unit volume

$$Q \simeq \frac{(mN_0 v_\sim^2 \nu_{eff})}{2} \qquad (6)$$

(where $v_\sim$ is the electron velocity in the field of the wave) is sufficiently small, i.e., at a sufficiently large field amplitude A_0 it is necessary to operate in a pulsed mode.

2. NONLINEAR ION-ACOUSTIC WAVES

Consider a strongly nonisothermal plasma ($T \gg T_i$, and for simplicity $T_i \simeq 0$), in which case, in the quasihydrodynamic approximation, the initial system has the form3

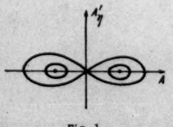

Fig. 1

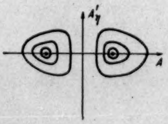

Fig. 2

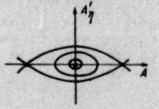

Fig. 3

$$\left.\begin{aligned} &E + \frac{\partial\varphi}{\partial x} = 0, \\ &\frac{\partial E}{\partial x} + \frac{\omega_{0i}^2}{v_{ia}^2}\varphi + \omega_{0i}^2\frac{M}{eN_0}\rho = \omega_{0i}^2\frac{M}{e}\left[\mu\frac{1}{2}\left(\frac{e\varphi}{\varkappa_0 T}\right)^2 - \mu^3\frac{1}{6}\left(\frac{e\varphi}{\varkappa_0 T}\right)^3\right], \\ &\frac{\partial v}{\partial t} + \frac{e}{M}E = -\mu v\frac{\partial v}{\partial x}, \\ &\frac{\partial\rho}{\partial t} + N_0\frac{\partial v}{\partial x} = -\mu\frac{\partial}{\partial x}(\rho v), \end{aligned}\right\} \qquad (7)$$

where E, φ, ρ, v are the deviations of the electric field, potential, density, and ion velocity from the equilibrium values 0, 0, N_0, 0; e/M is the specific charge of the ion; $\omega_{0i}^2 = 4\pi e^2 N_0/M$, $v_{ia} = (\varkappa_0 T/M)^{1/2}$ is the velocity of the ion-acoustic wave, and the parameter μ is introduced to denote the fact that the right sides of (7) are small. In the second equation in (7), we have expanded the function

$$n = N_0 \exp\left(-\frac{e\varphi}{\varkappa_0 T}\right)$$

in a series up to the cubic term (N_0 being the electron density). We introduce the dimensionless variables

$$\rho_{dl} = \frac{\rho}{N_0}, \quad v_{dl} = \frac{v}{v_{ia}}, \quad E_{dl} = \frac{eE}{\omega_{0i} M v_{ia}}, \quad \varphi_{dl} = \frac{e\varphi}{Mv_{ia}^2}, \quad x_{dl} = x\frac{\omega_{0i}}{v_{ia}},$$

$$t_{dl} = t\omega_{0i}; \quad |\rho_{dl}|_{max} \sim |v_{dl}|_{max} \sim |\varphi_{dl}|_{max} \sim |E_{dl}|_{max} \sim \mu \ll 1.$$

Below, the subscript dl is omitted. Using calculations similar to those in Sec. 1, we obtain the truncated equation for the complex potential of the ion-acoustic wave:

$$\left.\begin{aligned} &\frac{\partial a}{\partial t} + \frac{\omega^3}{k^3}\frac{\partial a}{\partial x} - \frac{i}{2}\frac{3\omega^5}{k^4}\frac{\partial^2 a}{\partial x^2} = i\alpha a^2 a^*, \\ &\alpha = -\frac{5}{4}\frac{k^2}{\omega^3} - \frac{3}{4}\frac{k^2}{\omega^5} - \frac{1}{12}\frac{\omega^3}{k^6} + \frac{1}{2\omega k^2} + \frac{1}{4}\frac{\omega^3}{k^4}, \end{aligned}\right\} \qquad (8)$$

where ω and k are related by the dispersion equation5)

$$\omega = \frac{k}{(1 + k^2)^{1/2}}, \quad \omega \equiv \omega_{dl} = \frac{\omega}{\omega_{0i}}, \quad k \equiv k_{dl} = \frac{kv_{ia}}{\omega_{0i}}.$$

Since the parameter $\alpha\varkappa > 0$ ($\varkappa = \beta\omega/v_{gr}^2$, $v_{gr} = \omega^3/k^3$, $\beta = -3\,\omega^5/k^4$) (see Sec. 1), self-compression of a one-dimensional packet of an ion-acoustic wave does not occur. Since $\alpha < 0$ for spatial beams, however, the self-focusing effect should be observed.6 Figure 3 shows phase pictures for a particular class of solutions (stationary waves), i.e., in a nonisothermal plasma it is possible to have shock waves of the envelopes and periodic nonsinusoidal waves. When there is weak absorption (the term νa), the solution is analogous to that given in Sec. 1. Estimates for a laboratory plasma show that it is possible to determine the plasma parameters from the wave absorption and from measurements of the frequency deviation.

The authors are indebted to A. G. Litvak and L. A. Ostrovskii for discussion.

---

[1] The form of the second-approximation equations is the same as in ref. 1, which offers an investigation of general problems without reference to specific systems. In the present paper, therefore, we focus on the specific plasma features of the problems in question.

[2] The conditions under which temperature variations can be neglected are given below.

[3] We consider high-frequency processes, in which the ion motion can be neglected. Moreover, we are not allowing for the force associated with the hf potential, this being valid if $k^2v_T^2/\omega_0^2 \gg m/M$ (where M is the ion mass).[4] In a weak field, we can also disregard resonant scattering by ions.[9]

[4] A similar situation is true of the spatial problem (self-focusing).

[5] We should note that the wave frequency should be ~1, where the dispersion is fairly large and the Landau attenuation for $T \gg T_i$ can be disregarded.

[1] A. V. Gaponov, L. A. Ostrovskii, and M. I. Rabinovich, Izv. Vuz. Radiofizika, 51, 1189 (1966).
[2] B. B. Kadomtsev and V. I. Karpman, Usp. Fiz. Nauk, 103, 193 (1971) [Sov. Phys. – Usp., 14, 40 (1971)].
[3] V. I. Karpman, Nonlinear Waves in Dispersing Media [in Russian], Izd. Nauka, Moscow (1973).
[4] A. G. Litvak, Candidate's Dissertation, Gor'kii State University (1967); Three Lectures on Nonlinear Wave Phenomena in Plasmas [in Russian], Izd. LGU (1972).
[5] A. G. Litvak, Izv. Vuz. Radiofizika, 9, 629 (1966).
[6] A. G. Litvak and V. I. Talanov, Izv. Vuz. Radiofizika, 10, 539 (1968).
[7] M. I. Rabinovich, Dokl. Akad. Nauk SSSR, 171, 1253 (1970).
[8] V. L. Ginzburg, Propagation of Electromagnetic Waves in a Plasma [in Russian], Izd. Nauka, Moscow (1970).
[9] V. N. Tsytovich, Theory of Turbulent Plasmas [in Russian], Izd. Atomizdat, Moscow (1971).
[10] V. V. Tamoikin and S. M. Fainshtein, Zh. Eksp. Teor. Fiz., 63, 213 (1972) [Sov. Phys. – JETP, 36, 112 (1973)].
[11] V. V. Tamoikin and S. M. Fainshtein, Zh. Eksp. Teor. Fiz., 64, 507 (1973).
[12] L. A. Ostrovskii, in: Nonlinear Optics [in Russian], Izd. Nauka, Sib. Ot., Novosibirsk (1968).
[13] V. I. Bespalov, A. G. Litvak, and V. I. Talanov, in: Nonlinear Optics [in Russian], Izd. Nauka, Sib. Ot., Novosibirsk (1968).

Ionization discontinuity in large-amplitude striations

A. V. Nedospasov and V. G. Petrov

Institute of High Temperatures, Academy of Sciences of the USSR, Moscow

(Submitted May 14, 1973)
Zh. Tekh. Fiz., 44, 53-58 (January 1974)

The potential discontinuity in large-amplitude striations in the positive column in an inert gas is investigated. With energy balance throughout the striation taken into account, a common solution is found for the electron kinetic equation, the continuity equation, and the equation of motion for ions. The potential profile and the electron distribution are found.

INTRODUCTION

Under certain conditions the plasma in the positive column in a discharge becomes unstable, and inhomogeneities arise transverse to the current, caused by an inhomogeneity of the ionization: striations.[1] Near the threshold for their appearance, these striations are of harmonic nature and their amplitude is given by the equations of the quasi-linear theory.[2-5] With a further change in the discharge parameters, leading to a more pronounced instability, the striations become ionization discontinuities: At the head of a striation there is a narrow zone in which a strong electric field separates plasma regions differing by an order of magnitude or more in density.[6] There is a region of gas excitation and ionization associated with this zone. Similar strong-field zones can arise in semiconductors, leading to the generation of microwaves (the Gunn effect).[7]

The hydrodynamic description leads to a satisfactory explanation for low-amplitude waves and the dispersion relations of the striations. However, this description is inapplicable for phenomena in a region in which the plasma parameters change abruptly. In several recent experimental papers a pronounced deformation has been observed in the electron distribution, and groups of fast electrons have been found in this zone.[8-10]

In the present work we find the structure of the discontinuity at the boundary between two striations from a common solution of the kinetic equation for the electron distribution function, the continuity equation, the equation of motion for ions, and the overall balance equations for the energy, ionization, and recombination within a striation. We assume the discharge to be diffusive.

EQUATION FOR THE ELECTRONS

The zone in which the potential is discontinuous in striations is usually quite narrow, and the distribution function changes only slightly as a function of the radius,[10] so we treat the problem in the one-dimensional approximation. The plasma density is small in comparison with the gas density, so that Coulomb scattering of electrons is negligible in comparison with scattering of electrons by atoms. However, the plasma density is high enough so that the plasma is quasineutral (the Debye length is much shorter than the width of the discontinuity).

We consider striations in inert gases in which elastic collisions of electrons with atoms predominate. If the frequency of these collisions is high, and the relative increase in the electron energy over a mean free path is small, the distribution function is approximately spherically symmetric. In this case we neglect the energy loss in elastic collisions in comparison with the energy acquired in the electric field and we neglect energy transfer between electrons.

Under these assumptions the symmetric and antisymmetric parts of the distribution function, f_0 and f_1, satisfy[11]

$$\frac{v}{3}\frac{\partial f_1}{\partial x}+\frac{e}{3mv^2}\frac{d\varphi}{dx}\frac{\partial(v^2 f_1)}{\partial v}=-\frac{f_0}{\tau_D}+St_{1,2}, \tag{1}$$

$$v\frac{\partial f_0}{\partial x}+\frac{e}{m}\frac{d\varphi}{dx}\frac{\partial f_0}{\partial v}+\frac{v}{\lambda_s}f_1=0, \tag{2}$$

where $St_{1,2}$ are the collision terms describing excitation and ionization; these terms are of order $(v/\lambda_c)f_0$, and $(v/\lambda_n)f_0$, respectively. Here, $\lambda_s(v)$, $\lambda_c(v)$, and $\lambda_n(v)$ are the mean free paths of an electron between elastic, excitation, and ionization collisions with gas atoms, and $\tau_D(v)$ is the characteristic time for the diffusive loss of charged particles to the wall. The radial profile of the plasma density, as in a homogeneous column, is given approximately by the Bessel function[12]

$$J_0\left(\mu\frac{r}{R}\right);\ \mu\approx 2.4.$$

We write the equations in the coordinate system moving with the striations toward the cathode. The positive direction of the Ox axis is the direction in which the electrons move.

The ratio f_0/τ_D is given by

$$\frac{f_0}{\tau_D\frac{v}{3}\frac{\partial f_1}{\partial x}}\sim\frac{f_0}{\tau_D\frac{\lambda_s v}{3}\frac{f_0}{s^2}}\sim\frac{D_a\mu^2 S^2}{D_e R^2}\ll 1,$$

where D_e and D_a are the coefficients for ambipolar diffusion and for electron diffusion, R is the radius of the discharge tube, and S is the characteristic dimension for changes in the distribution function; S is equal in order of magnitude to the width of the discontinuous region.

In the striation in front of the potential drop the loss of charged particles to the wall is much more rapid than ionization, but to the right of the potential drop, toward the anode, the rate of inelastic collisions increases. Kinetic equations (1) and (2) are analyzed in that part of the discontinuity in which excitation and ionization can still be neglected.

Nastoyashchii[13] solved system (1), (2) with vanishing right sides.

The boundary conditions for system (1), (2) on the cathode side of the discontinuous zone can be determined from the experimental data. The electric field is known to be weak over most of the striation, and the electron energy is approximately constant. We take the reference point to be the point at which the electron energy begins to increase.

The symmetric part of the distribution function is assumed to be Maxwellian; the non-Maxwellian part at electron energies higher than the first excitation level, where there are relatively few electrons, has no significant effect on the electron density or the potential profile. The asymmetric part of the distribution function on the cathode side of the discontinuous zone is found from (2).

We write the boundary conditions as $\varphi = 0$, and $d\varphi/dx = d\varphi/dx|_0$:

$$f_0 = A\exp\left\{-\frac{mv^2}{2T}\right\},\quad f_1 = \frac{\lambda_s}{l}A\exp\left\{-\frac{mv^2}{2T}\right\}$$

at x = 0. Here

$$A = \frac{n_1}{\left(\frac{2T\pi}{m}\right)^{3/2}},\quad \frac{1}{l} = \frac{e\left.\frac{d\varphi}{dx}\right|_0}{T} - \frac{1}{n_1}\left.\frac{dn}{dx}\right|_0,\quad n_1 = n(0)$$

(the quantity λ_s/l represents the directionality of the electron motion at x = 0).

The solution of Eqs. (1) and (2) under these boundary conditions is, for $\varepsilon = (mv^2)/2 - e\varphi > 0$,

$$f_0 = A\left[1 - \frac{\varepsilon\lambda_s(\varepsilon)}{l}\int\limits_0^x \frac{dx}{(\varepsilon + e\varphi)\lambda_s(\varepsilon + e\varphi)}\right]\exp\left\{-\frac{\varepsilon}{T}\right\}, \tag{3}$$

$$f_1 = A\frac{\varepsilon\lambda_s(\varepsilon)}{(\varepsilon + e\varphi)l}\exp\left\{-\frac{\varepsilon}{T}\right\}. \tag{4}$$

and the solution for $\varepsilon < 0$ is $f_0 = f_1 = 0$. (Here ε in the integrand is assumed an independent variable.)

The mean energy of the primary electrons moving away from the cathode increases; an estimate of the stepwise-ionization time τ_n yields the inequality $V_{st}\tau_n > l$ (V_{st} is the striation velocity). The ionization thus occurs primarily beyond the potential drop. Ionization events maintain a high density of slow secondary electrons on the anode side of this drop. These electrons from the cathode side are retarded by the potential drop and the density of these electrons can be determined from the Boltzmann equation

$$n = n_2\exp\left\{-\frac{e(\varphi_2 - \varphi)}{T}\right\}, \tag{5}$$

where n_2 and φ_2 are the maximum electron density and the potential drop.

Integrating Eq. (3) over v we can find the fast-electron density as a function of the electric potential: $n_f = 4\pi\int\limits_0^\infty v^2 f_0 dv$. The total electron density in the discontinuous zone is given [in terms of the dimensionless variables $z = x/l$ and $u(z) = (e\varphi)/T$] by

$$n = \frac{2n_1}{\sqrt{\pi}}\int\limits_0^\infty\left[1 - \frac{\varepsilon}{T}\lambda_s\left(\frac{\varepsilon}{T}\right)\int\limits_0^z \frac{dz}{\left(\frac{\varepsilon}{T} + u\right)\lambda_s\left(\frac{\varepsilon}{T} + u\right)}\right]$$
$$\times\sqrt{\frac{\varepsilon}{T} + u}\exp\left\{-\frac{\varepsilon}{T}\right\}d\frac{\varepsilon}{T} + n_2\exp\left\{-\frac{e\varphi_2}{T} + u\right\}. \tag{6}$$

IONIZATION–RECOMBINATION BALANCE WITHIN A STRIATION. EQUATION FOR THE IONS

The relation between the potential drop and the maximum electron density can be determined approximately from the known experimental data and from the assumption that the potential drop incorporates essentially the entire voltage difference over a striation.

Assuming that all the ions produced in a striation recombine at the wall within the given striation, we find the following equation from the energy-balance equation:

$$i\varphi_2 = K2\pi R\int\limits_0^{l_{st}}\left.\frac{\partial n}{\partial r}\right|_R dx \approx \mu\pi K D_a\int\limits_0^{l_{st}} n_0 dx \approx \mu\pi K D_a\frac{n_2}{2}l_{st}\,. \tag{7}$$

Here, K is the ionization expenditure, i.e., the average energy expended on the production of a single electron–ion pair; l_{st} is the length of the striation; and $i = (8\pi^2)\cdot e/3\int\limits_0^R r\left(\int\limits_0^\infty v^3 f_1 dv\right)dr$ is the total current.

The ionization expenditures can be found from experimental data on the positive column by comparing the average power evolved per unit length of the column with the current density of ions to the wall. The ionization expenditure is usually a few times the binding energy of the electron in the given atom.

The system of equations for the potential is closed by adding an equation for the ions; this is found by substituting the directed ion velocity $v_i = -b_i(d\varphi)/(dx) + V_{st}$ (where b_i is the ion mobility) into the continuity equation. Using the dimensionless variables z and u(z), we can write this equation as

$$\frac{d^2u}{dz^2} = -\frac{1}{n}\frac{dn}{dz}\left(\frac{du}{dz} - \frac{V_{st}l}{b_i T}\right) + \frac{D_a e}{b_i T}\frac{\mu^2 l^2}{R^2}. \tag{8}$$

SOLUTION FOR ARGON

System (6)–(8) simplifies considerably for argon, for which the mean free path satisfies[14] $\lambda_s \sim 1/v^2$ over the energy range 0.5–13 eV.

Here, Eq. (3) becomes

$$f_0 = A(1 - z)\exp\left\{-\frac{\varepsilon}{T}\right\};\quad \varepsilon > 0. \tag{9}$$

The dispersion in the distribution function does not change with increasing potential, so we can write

$$D_a = \frac{b_i}{e}\frac{\int\lambda_s v^3 f_0 dv}{\int\lambda_s v^2\frac{\partial f_0}{\partial v}dv} = \frac{b_i}{e}T.$$

We can write (6) and (8) as a single, relatively simple equation for the potential:

$$\frac{d^2u}{dz^2}=\left(\frac{du}{dz}-\frac{V_{st}\,l}{D_a}\right)$$

$$\times\frac{-\sqrt{u}+\left[(1-z)\frac{du}{dz}-1\right]I(z)+\frac{n_2}{n_1}\frac{2}{\sqrt{\pi}}\frac{du}{dz}\exp\left\{-\frac{e\varphi_2}{T}+u\right\}}{(1-z)\left[\sqrt{u}+I(z)\right]+\frac{n_2}{n_1}\frac{2}{\sqrt{\pi}}\exp\left\{-\frac{e\varphi_2}{T}+u\right\}}+\frac{\mu^2l^2}{R^2}, \quad (10)$$

where

$$I(z)=\int_0^\infty\frac{e^{-y}dy}{\sqrt{y+u(z)}}.$$

This solution is described by a monotonically increasing curve with an inflection point near the point at which the density of fast electrons, arriving from the left, becomes comparable to the density of slow electrons, arriving from the right. The electric field (du/dz) becomes so strong that the last term in (10) becomes inconsequential on the right of this point, especially since it is partially offset by ionization. The solution consists of two parts: In the left-hand region, where the charged-particle density is essentially the same as the primary-electron density, the electric field increases. Here we can neglect the terms in (1) corresponding to excitation and ionization.

In the right-hand region, where the slow-electron density is predominant, the electric field is weaker; here the solution is meaningful as long as this field is strong enough that we can neglect the ionization term in the potential equation. As we mentioned above, the ionization of excited atoms is shifted to the right from the point at which these excited atoms are produced, by a distance of about l.

To determine the average electron energy in the region in which the electric field decays, we must analyze the vanishing of fast electrons in inelastic collisions. It is difficult to solve the kinetic equation simultaneously taking into account the inhomogeneity of the electric field and inelastic collisions. However, we can estimate a characteristic length for the decay of the fast-electron density under the assumption that there is no electric field.

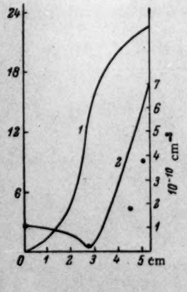

Fig. 1. Potential (1) and electron density (2) as functions of x. The points are the experimental values[10] of n_e.

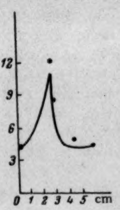

Fig. 2. Average electron energy as a function of x. The points are experimental.[10]

In this case we find the following equation for primary electrons from Eqs. (1) and (2):

$$\lambda_s\frac{\partial^2 f_0}{\partial x^2}=\frac{3}{\lambda_H}f_0;\quad\frac{1}{\lambda_H}=\frac{1}{\lambda_c}+\frac{1}{\lambda_n}.$$

Its solution can be written as follows, with the boundary condition $f_0 = f(v)$ at $x = x_0$:

$$f_0=f(v)\exp\left\{-(x-x_0)\sqrt{\frac{3}{\lambda_s\lambda_H}}\right\}.$$

We can approximate the boundary function by solution (9) at the field maximum.

COMPARISON WITH EXPERIMENT

We compare our results with the experimental data of ref. 10, found from measurements of the distribution function in large-amplitude striations in inert gases.

We select the case of argon at a pressure of 0.25 torr; the radius of the discharge tube is 3 cm, and the current is 0.4 A. Under these conditions the measured thickness of the discontinuous zone is 3 cm, and all the approximations used above are satisfied. With the measured electron density of $\sim 10^{10}$ cm^{-3} ahead of the potential drop, and with the measured electron temperature of 2.4 eV, the mean free path for elastic collisions is ~ 0.1 cm; the energy-relaxation lengths of electrons for collisions between electrons and for collisions between electrons and neutrals are higher than 10 cm.

The ionization expenditure is found from the data of ref. 15, where simultaneous measurements are made of the electron density, the electron temperature, and the average electric field in a tube 1 cm in radius with a current of 0.3 A.

At an argon pressure of 0.75 torr and at the value of the product pR given in ref. 10 (0.75 cm · torr) the ionization expenditure is 170 eV, i.e., approximately 11 times the ionization energy. The striation length, which appears in Eq. (7), can be set equal to four times the tube diameter; this is a valid assumption for the initial conditions in a large number of experiments on striations in argon. The

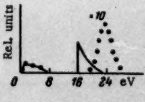

Fig. 3. Comparison of experimental (points) and calculated (solid curve) electron distribution functions.

potential profile calculated from Eqs. (10) and (7) is shown in Fig. 1. The distributions of the density and of the average electron energy are compared with the experimental points in Figs. 1 and 2. Figure 3 shows the calculated and experimental distribution functions near the maximum average energy. The electron densities on the two sides of the potential drop differ by a factor of 25, according to the measurements of ref. 10; our calculations yield $n_2/n_1 \approx 60$.

The agreement with the experimental density drop is satisfactory, especially since the measurements of the electron density in ref. 10 are not very accurate.

In the case of a strong electric field the shape of the electron distribution is a strong function of the longitudinal coordinate. Under these conditions we find a satisfactory agreement between the measured and the calculated distribution functions.

In conclusion the authors thank A. F. Nastoyashchii for useful comments and Yu. L. Igitkhanov and V. D. Khait for discussion.

---

[1] A. V. Nedospasov, Usp. Fiz. Nauk, 94, 439 (1968) [Sov. Phys. – Usp., 11, 174 (1968)].

[2] A. V. Nedospasov and Yu. B. Ponomarenko, Proc. Sixth Int. Conf. on Ionization Phenomena in Gases, Vol. 2, Paris (1963), p. 223.

[3] Yu. B. Ponomarenko, Prikl. Matem. Mekh., 28, 688 (1964).

[4] A. V. Nedospasov and Yu. B. Ponomarenko, Zh. Eksp. Teor. Fiz., 46, 926 (1964) [Sov. Phys. – JETP, 19, 631 (1964)].

[5] A. A. Vedenov and Yu. B. Ponomarenko, Zh. Eksp. Teor. Fiz., 46, 2247 (1964)[Sov. Phys. – JETP, 19, 1518 (1965)].

[6] B. N. Klyarfel'd, Zh. Eksp. Teor. Fiz., 22, 66 (1952)

[7] A. F. Volkov and Sh. M. Kogan, Usp. Fiz. Nauk, 96, 633 (1968) [Sov. Phys. – Usp., 11, 881 (1969)].

[8] S. W. Rayment and N. D. Twiddy, Nature, 216, 674 (1967).

[9] Yu. M. Kagan, N. B. Kolokolov, T. A. Krylova, and V. M. Milenin, Zh. Tekh. Fiz., 41, 120 (1971) [Sov. Phys. – Tech. Phys., 16, 88 (1971)].

[10] K. F. Bessonova, O. N. Oreshak, E. P. Ostapchenko, and V. A. Stepanov, Zh. Tekh. Fiz., 41, 979 (1971) [Sov. Phys. – Tech. Phys., 16, 770 (1971)].

[11] V. L. Ginzburg and A. V. Gurevich, Usp. Fiz. Nauk, 70, 201 (1960) [Sov. Phys. – Usp., 3, 115 (1960)].

[12] A. B. Stewart, J. Appl. Phys., 27, 911 (1956).

[13] A. F. Nastoyashchii, At. Energ., 25, 308 (1968).

[14] V. L. Granovskii, Electric Currents in Gases [in Russian], Gostekhizdat, Moscow (1952).

[15] B. N. Klyarfel'd (Klarfeld), J. Phys. (USSR), 5, 155 (1941).

Experimental investigation of anode processes in a closed electron-drift accelerator

I. V. Melikov

(Submitted March 7, 1973)
Zh. Tekh. Fiz., 44, 59-64 (January 1974)

The discharge regions adjacent to the anode surface in a closed electron-drift plasma accelerator (ACED) are studied. Electrons from the accelerator channel pass through the anode apertures entering into the internal cavity; these electrons cause primary ionization of the working gas (xenon) fed through the anode. Probe methods are used to determine the plasma parameters near the apertures in the anode (T_e = 5-13 eV and $N_e \approx 10^{10}$-10^{11} cm^{-3}) and the dependence of the parameters on the accelerator voltage and gas flowrate. The neutral gas pressure in the anode cavity is measured (~1 mm Hg) as a function of gas flowrate and mode of operation.

INTRODUCTION

References 1 and 2 report on experimental investigations of one-lens plasma accelerators with closed electron drift and an extended acceleration zone. The basic emphasis in these studies is on general characteristics of the accelerator, measurement of the physical plasma parameters in the channel, and the effect of the magnetic field configurations on the operation. When there is an extended ionization zone resulting in a broadening of the ion energy spectrum at the accelerator output,[1] it is also of interest to investigate both the ionization zone itself in the channel and the processes that occur in direct proximity to it, namely inside the anode through which the working substance is fed to the accelerator channel. The state of the working gas at the anode defines the initial conditions for subsequent development of ionization and acceleration processes in the channel. The present paper presents results of an experimental investigation of anode processes.

EXPERIMENTAL ARRANGEMENT AND PROCEDURE

Figure 1a shows a diagram of the accelerator model. Unlike the models used in refs. 1 and 2, the magnetic system has one magnetization coil. Moreover, the external insulator of the coaxial channel is provided by a tube of transparent quartz glass and windows are cut into the housing of the magnetic circuit. This makes it possible to observe and photograph the discharge both in the neighborhood of the anode and in part of the accelerator channel. The inner channel wall is also made of quartz.

Two types of anode are investigated: a "plane" anode and a "box-shaped" anode. The former is a stainless-steel plate 1.5 mm thick with 20 holes 2 mm in diameter for the gas to escape (holes of this size are chosen from considerations of optimum visual observation of the discharge in the regions adjacent to the anode). The working gas is fed into the cavity formed by the anode and an end-on insulator blocking the channel. Two tubes that support the anode and provide the current feed are also used for the leads of the probe circuits, these being mounted in the region beyond the anode over holes on the side that the gas is fed from, 3 mm from the anode surface. The probes are single cylindrical probes (tungsten wire 0.35 mm in diameter and 8 mm long); plane probes (tantalum, 4 × 4 mm) are also used.

The second type of anode is a hollow toroidal box similar to that used in refs. 1 and 2, with holes 0.5 mm in diameter for the gas to escape into the channel. The lateral surface of the anode has a quartz-glass window, and a single plane probe is mounted inside the anode over one of the gas-feed holes. In a number of experiments one of the anode tubes is used to measure gas pressure in the anode cavity (relative to the pressure in a vacuum chamber) using a U-tube manometer filled with PÉS-1 polyethylsiloxane fluid (specific gravity 0.87 g/cm^3).

NATURE OF DISCHARGE IN REGIONS ADJACENT TO THE ANODE

The use of transparent quartz as an insulation material for the outer channel wall, and the design features of the anodes make it possible to observe and photograph the discharge in both the anode region on the side of the accelerator channel and within the anode. Figure 2a shows a photograph of the discharge with one plane-anode version. In the photograph the anode is horizontal and the plasma flow is from top to bottom. The central core of the magnetic circuit can be seen through the transparent inner wall of the channel.

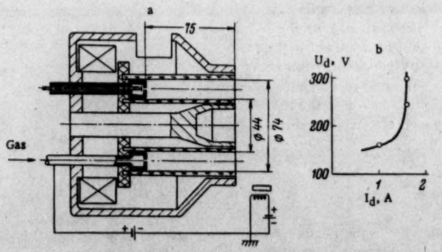

Fig. 1. a) Diagram of the accelerator model; b) volt–ampere characteristic of the discharge (xenon, $\dot{m}$ = 1.3 mg/sec).

Fig. 2. Nature of discharge in accelerator with "plane" (a) and "box-shaped" (b) anodes.

Analysis of the resultant patterns shows that the discharge in the region adjacent to the anode is localized in the vicinity of the holes, with bright plasma "flares" propagating in the channel parallel to the axis over a distance on the order of 2-5 mm (depending on the mode of operation) for a characteristic hole diameter of 2 mm. It is also evident that similar plasma emission in the region of the holes is observed inside the anode cavity on the side from which the gas is fed. The plasma "flares" are a bright blue-white and are clearly distinguished against the general reddish background of the plasma in the anode zone. (The color spectrum of the discharge is reproduced well when color slides are taken.)

With the box-shaped anode the discharge is similar (Fig. 2b). The photograph reveals plasma flares that flow into the accelerator channel through the holes. In this anode the holes are much smaller in diameter (0.5 mm as opposed to 2 mm), so that the plasma emission in the neighborhood of the holes is less pronounced than in the former case; nonetheless it can be seen fairly clearly through the window in the lateral surface of the anode. (The effect is less pronounced in the photographs because of the great difference in plasma emission intensity inside the anode and in the accelerator channel.)

On the basis of visual observation of the discharge in the anode regions we can assume that high-energy electrons penetrate from the channel into the anode through the holes, and electron-impact ionization of the working substance begins in the cavity of the anode itself and in the holes, i.e., to some degree we have a "hollow-anode" effect. The enhanced ionization probability also stems from the higher density of neutrals in these regions as compared to the initial segment of the accelerator channel. Thus, the gas that enters the zone of influence of the accelerating electric field from the anode is partially ionized.

MEASUREMENTS INSIDE THE ANODE

We use probe measurements and measurements of the gas pressure in the cavity of the box-shaped anode to obtain estimates of the plasma parameters inside the anode. The volt–ampere characteristics of both the plane and cylindrical probes have the customary form with pronounced ion-current saturation. By processing the ion branch and the initial segment of the electron branch of the characteristics,[3,4] we are able to evaluate the temperature of the electrons that penetrate into the anode cavity,

$$\frac{kT_e}{e}=\frac{1}{\dfrac{d\ln(I_\Sigma-I_{i0})}{dU}},$$

and also the charged-particle density in the region of the holes inside the anode at a distance of 3 mm from its inner surface:

$$I_{i0}=\frac{I_\Sigma}{2}en_eS\sqrt{\frac{kT_e}{M}},$$

where I_Σ is the total current on the probe, I_{i0} is the saturation ion current at the floating potential, S is the working area of the probe, M is the ion mass, e is the charge of the electron, T_e is the electron temperature, and n_e is the electron density. Plasma neutrality, $n_e \simeq n_i$ is assumed to hold.

Figure 3a shows T_e and n_e as functions of the voltage U_p for a plane anode, while Fig. 3b shows the same for a box-shaped anode with a xenon flowrate of 1.3 mg/sec. The experimental points on the curves correspond to typical modes of operation of the accelerator as noted on the volt–ampere characteristic (Fig. 1b). As U_p increases the electron temperature has a pronounced tendency to increase from 5-7 eV when the accelerator operates on the shallow segment of the characteristic (incomplete-ionization mode) to 10-13 eV at elevated discharge voltages (in a mode close to that of complete ionization). In the latter case, the dependence of T_e on U_p becomes saturated with further increases in U_p.

The charged-particle density in the anode cavity in the vicinity of the holes also increases with U_p, the characteristic density value being $n_e \simeq 10^{11}$ cm^{-3} for a plane and $n_e \simeq 10^{10}$ cm^{-3} for a box-shaped anode. This difference in n_e can be explained by the smaller hole diameter in the latter case. Figure 3c shows T_e and n_e inside the box-shaped anode as functions of the gas flowrate through the accelerator at U_p = 240 V. In the range 0.8-2.5 mg/sec an increase in the neutral gas flowrate leads to some electron cooling and to a stronger change in density in the region of the holes inside the anode.

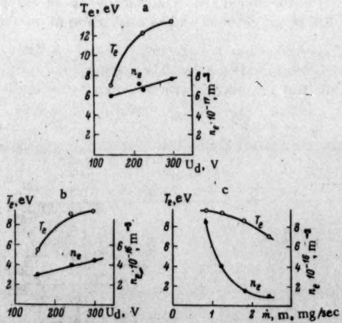

Fig. 3. Variation in electron temperature T_e and density n_e in the vicinity of the holes inside the anode: a) plane anode, xenon, $\dot{m}$ = 1.3 mg/sec; b) box-shaped anode, xenon, $\dot{m}$ = 1.3 mg/sec; c) box-shaped anode, U_d = 240 V.

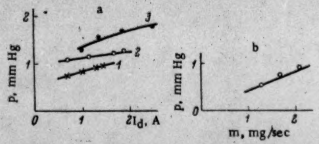

Fig. 4. Variation in gas pressure inside the cavity of box-shaped anode: a) during operation of accelerator; b) with cold gas blow-through; ṁ values, mg/sec: 1) 1.3 (xenon); 2) 1.7; 3) 2.

In view of the observed electron penetration from the accelerator channel through the holes in the anode into the inner cavity it is of interest to evaluate the gas pressure in the anode at which ionization occurs.

Figure 4 shows the change in gas pressure as measured by a U-tube manometer in a box-shaped anode for several xenon flowrates as a function of the discharge current at various points of the accelerator volt—ampere characteristic; the figure also shows the neutral gas pressure as a function of flowrate for cold flow-through of the anode (in the absence of a discharge). Despite the relatively low accuracy of this method of measurement, it is entirely possible to determine the gas-pressure level in the anode in question (1-1.5 mm Hg) and to investigate the way in which it depends on the accelerator's mode of operation.

Thermocouple measurements of the temperature of the front surface of the anode show that in the stationary mode customary for these tests ($\dot{m}$ = 1.3 mg/sec, I_d = 1.6 A) the anode temperature is T_a = 450°C and that it remains virtually constant with increasing voltage once the discharge-current saturation mode has been reached. Assuming that the gas temperature can rise to values of the order of T_a over the dwell time of the gas in the anode cavity (the mean free path at the above pressures being 0.1 mm), we can estimate the neutral-particle density in the anode; it turns out to be $\sim 10^{16}$ cm^{-3}.

DISCUSSION

Our experimental investigation of intraanode processes in an ACED has shown that penetration of high-energy electrons from the accelerator channel into the anode cavity causes initial ionization of the working gas inside the anode and the holes prior to the arrival of the gas in the accelerator zone.

The resultant estimates for the electron temperature inside the anode in the vicinity of the holes for various accelerator modes, T_e = 5-13 eV, coincide with the characteristic value T_e = 10 eV in the accelerator channel.[1] It has been noted, moreover, that the electron temperature increases within these limits with increasing discharge voltage in going from the mode in which the accelerator operates on the shallow section of the volt—ampere characteristic to a mode which is close to one of complete ionization. Further increases in U_d result in saturation of the dependence of T_e on U_d. Since the electrons that penetrate into the anode and the electrons near the side of the accelerator channel are obviously at the same temperature, the measured values of T_e to some extent characterize the level of this parameter in the channel. It is probable that in the accelerator channel the behavior of the electron temperature as a function of discharge voltage is similar to that given above.

The charged-particle density inside the anode at 3 mm from its surface (as evaluated by probe measurements) is 10^{10}–10^{11} cm^{-3}, depending on the hole diameter, which, for a characteristic pressure in the anode cavity of 1 mm Hg, corresponds to a relatively insignificant degree of plasma ionization, 10^{-6}–10^{-5}. Because the measurements are performed at the boundary of the region of virtual plasma emission inside the anode, and because the probability of ionization in the holes themselves is fairly large, we expect that the degree of ionization of the working gas entering the channel will be substantially greater than these values.

The authors wishes to thank A. I. Morozov for proposing the topic and V. V. Fishgoit for valuable comments.

---

[1] A. I. Morozov, Yu. V. Esipchuk, G. N. Tilinin, A. V. Trofimov, Yu. A. Sharov, and G. Ya. Shchepkin, Zh. Tekh. Fiz., 42, 54 (1972) [Sov. Phys. — Tech. Phys., 17, 38 (1972)].

[2] A. I. Morozov, Yu. V. Esipchuk, A. M. Kapulkin, V. A. Nevrovskii, and V. A. Smirnov, Zh. Tekh. Fiz., 42, 612 (1972) [Sov. Phys. — Tech. Phys., 17, 482 (1972)].

[3] V. D. Rusanov, Advanced Plasma Diagnostics [in Russian], Gosizdat, Moscow (1962).

[4] F. Chen, Electrical Probes, in: R. Huddlestone and S. Leonard (eds.), Plasma Diagnostics [Russian translation], Izd. Mir, Moscow (1967).

Dynamics and emission of coaxial plasma shells in air

A. F. Aleksandrov, V. V. Perebeinos, A. T. Savichev, and I. B. Timofeev

M. V. Lomonosov Moscow State University

(Submitted January 20, 1973)
Zh. Tekh. Fiz., 44, 65-72 (January 1974)

An experimental study has been made of the dynamics and radiation of high-current pulsed discharges (at currents up to ~300 kA) with return currents up to 100 cm long. These return currents are produced by the electrical explosion of many wires arranged along the generatrices of a cylinder in air. A study has been made of the dynamics of contracting, expanding, and steady-state plasma shells. In none of the experiments do individual discharge channels formed by the explosion of each wire coalesce into a single current shell. The characteristic dimensions and temperatures and the radiation emitted in various spectral ranges have been determined. Such discharges convert electrical energy into radiation efficiently.

1. INTRODUCTION

We have previously[1] pointed out the possibility that cylindrical plasma shells could be produced by the simultaneous explosion of many wires in air at atmospheric pressure, and we have described the basic characteristic of such shells for system of the Triax type,[2,3] i.e., for systems in which the shell has a certain steady-state radius corresponding to the magnetic field profile inside and outside the shell. This profile is achieved[3] when a current I_0, equal to half the discharge current $2I_0 = I_d$, flows inside the shell. The study of such discharges is of much practical as well as purely scientific interest: These discharges seem to be more promising than linear pinches for producing high-intensity radiation sources, because of their better stability and because of their larger emitting surfaces. Moving plasma shells (i.e., shells which expand or diverge and contract or converge) can turn out to be more convenient, particularly in the case in which discharges are ignited in an active medium. Moving shells are more convenient, in particular, because a diverging plasma shell must be more stable than a steady-state shell since there are no force instabilities. Experimentally, a converging pinch corresponds to a current distribution in a discharge for which $I_0 = 0$, while a diverging pinch corresponds to $I_0 = I_d$.

In this note we report on an experimental study of all three types of discharges: steady-state, converging, and diverging.

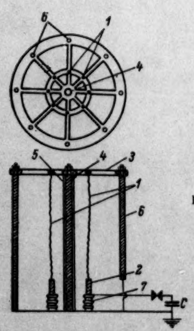

Fig. 1. Two views of the discharge chamber.

2. EXPERIMENTAL APPARATUS AND PROCEDURE

These discharges are produced with devices like that shown schematically in Fig. 1. The wires 1 which are to be exploded are mounted on cylindrical high-voltage electrode 2, which is 80 mm in diameter. The upper electrode 3 can be connected to the "ground" of the capacitor bank by inner copper rod 4, which is enclosed by insulating tube 5, and by eight external metal rods 6 arranged in a circle. The high-voltage electrode is mounted on insulators 7.

In studying steady-state cylindrical shells,[1] we use both inner and outer conductors. To study converging shells we removed the inner rod, and, finally, to study a diverging cylindrical shell we remove the outer conductors.

Under our experimental conditions the length of the discharge gap is varied from 20 to 100 cm.

The chamber is connected to the discharge circuit of a Foton apparatus, described in detail in ref. 4. This apparatus consists of a standard current-pulse generator. The total circuit capacitance is ~500 μF, and the period of the discharge current can be varied from 80 to ~110 μsec, depending on the experimental conditions. The maximum working voltage is 30 kV.

We have studied the typical shape and dimensions of the discharge channel with an SFR-2M ultrahigh-speed camera, recorded the voltage—current characteristics, and studied the overall yield, time behavior, and spectral composition of the discharge radiation. In the current measurements we use two Rogowski loops, one of which goes around the high-voltage electrode and measures the difference current $I_d - I_0$; the second goes around the inner rod and measures the axial discharge current I_0.

The nature and absolute yield of the radiation are studied by the methods described in detail in refs. 4 and 5.

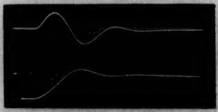

Fig. 2. Typical oscillogram of the axial current I_0 and the voltage across the discharge cap for a steady-state discharge 100 cm long and for a voltage U_0 = 300 kV on the capacitor bank.

3. GENERAL PICTURE OF THE DISCHARGE IN AIR

Breakdown of the discharge gap is initiated by the explosion of eight aluminum wires arranged along generatrices of a cylinder. The energy stored in the capacitor bank is varied, depending on the experimental conditions, from ~22 kJ ($C = 432\ \mu F$, $U_0 = 10$ kV) to 225 kJ ($C \simeq 500\ \mu F$, $U_0 = 30$ kV).

Figure 2 shows a typical oscillogram of the axial current I_0 and the voltage across the discharge gap for an initial bank voltage of 30 kV and for a discharge gap 100 cm long. We see that the discharge, as in the case of a linear pinch,[4] is approximately periodic with a long decay. The length of the first half-cycle of the discharge current is ~50 μsec under these conditions, and the discharge current I_d reaches 310 kA.

Figure 3 shows typical streak photographs of the discharges for the diverging and converging cases. Figure 4 shows a typical streak photograph of a steady-state discharge (a) and enlarged photographs of the discharge at certain stages; from these photographs we clearly see the interaction of the shock waves and the current channels. We also see that all eight of the wires explode essentially simultaneously and that there is a subsequent uniform growth of all the plasma channels.

Over the first 35-40 μsec of the discharges of the Triax type (Fig. 4), all the plasma channels lie at the same radius (the radius at which the wires are attached); then the channels move slowly outward, apparently because the inner return current is higher than the external return

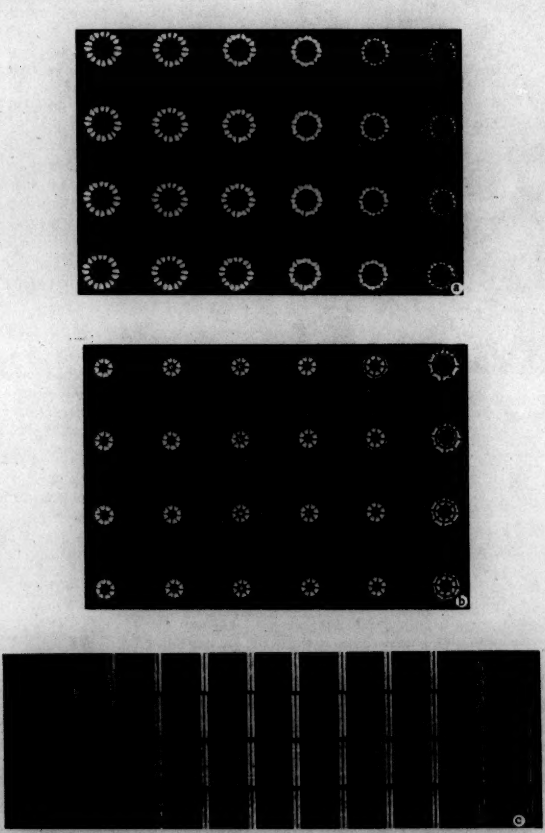

Fig. 3. Typical streak photographs of diverging (a) and converging (b, from the end; and c, from the side) discharges. The discharge length l = 40 cm, the discharge voltage U_0 = 20 kV, and the frames are 1 μsec apart.

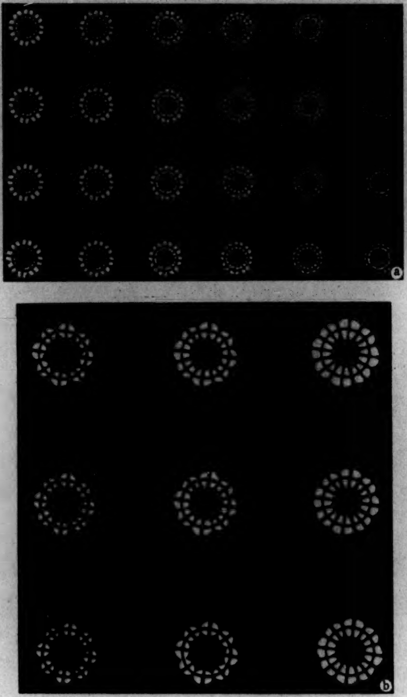

Fig. 4. a) Typical streak photograph of a steady-state discharge, with l = 40 cm and U_0 = 15 kV; b) enlarged photographs of the discharge at 8 and 16 μsec.

current.

In the formation of a converging plasma shell under the influence of the self magnetic fields, the individual discharge channels must move toward the axis of the discharge chamber (as in the skin effect in a discharge in a gas). This motion is observed experimentally, as can be seen from the streak photograph taken from the end of the discharge (Fig. 3b). At first, while the current is low, the discharge is in a steady state; then the channels begin to move toward the center. Near the current maximum the channels reach a velocity of $\sim 10^5$ cm/sec. In the later stages of the discharge, the channels move outward, apparently because of the excess air pressure at the axis, which arises as a result of the collision of shock waves moving toward the center of the chamber.

In the expanding discharge the magnetic field of the axial current causes the discharge channels to diverge (Fig. 3a) from the chamber axis. Under our experimental conditions, the discharge channels interact with each other weakly at this stage.

An extremely curious and important feature of these discharges is that the plasma channels formed by the explosions of the individual wires do not coalesce into a common emitting shell under any experimental conditions, even though an individual channel in free expansion would grow to a radius sufficient to significantly overlap neighboring channels. Furthermore, the plasmoids vigorously oppose the formation of a continuous current shell, undergoing a pronounced deformation. This situation is particularly evident on the streak photographs taken from the end (Fig. 4b) and the streak photographs taken from the side of the converging discharge (Fig. 3c). These photographs show that when different current channels touch, they continue to expand in the radial direction but stop expanding in the azimuthal direction (along the ring electrode); thereafter there is a regularly shaped, linear (along the radius) nonemitting zone between channels, having a width on the order of a few millimeters. The dynamics of a collision between different channels is interesting. On these photographs we clearly see cylindrical shock waves surrounding the discharge channels. After about 10 μsec, the shock waves collide, and the shock front becomes deformed. The collision of the shock waves does not, however, intensify the emission in the region between the channels, as might be expected; on the contrary, the shock wave is "squeezed out" of the collision region. After about 15 μsec, the boundary between channels becomes a dark, nonemitting region, while this boundary continues to emit quite intensely in regions in which the shock wave can propagate "freely."

4. DYNAMICS OF DISCHARGES WITH A RETURN CURRENT

We now discuss the dynamics of discharge with a return current for the case of discharges 20 cm long. Figure 5 shows the velocity of the axis of the discharge channel, v, as a function of the voltage on the capacitor bank for discharges of various types. These functional dependences are obtained by analyzing the streak photographs.

We see from these photographs that the velocity is a linear function of the voltage for the converging and diverging discharges, but for the steady-state discharge the channel velocity is essentially zero for all bank voltages.

Let us follow the development of a single discharge channel. Figure 6 shows the expansion velocity of the thermal zone of a channel as a function of the voltage on the capacitor bank. We see that as this voltage is increased the expansion velocity of the channel increases; for discharges of the Triax type the expansion velocity of the current zone changes slightly. This functional dependence is strongest for the diverging discharge because in this case the development of the current zones is a better approximation to free motion.

We turn now to the stability of the discharges with return currents. A careful study of the streak photographs of the various types of discharges during essentially the entire first cycle of the discharge current shows that the lateral surface of a discharge remains essentially smooth, without any visible large-scale shape distor-

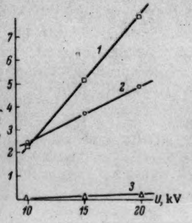

Fig. 5. Velocity of the discharge channel, v, as a function of the initial voltage. Here l = 20 cm. 1) Diverging; 2) converging; 3) steady-state discharges.

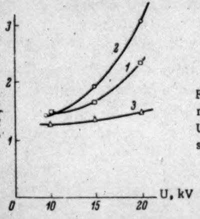

Fig. 6. Expansion velocity of the thermal zone of a channel as a function of U_0. 1) Diverging; 2) converging; 3) steady-state discharges.

tions. The discharge surface displays only a fine-scale ripple; the modulation depth of the lateral surface remains essentially constant throughout the main phase of the process (the first cycle of the discharge current).

5. RADIATION AND ENERGY CHARACTERISTICS

Time sweeps of the discharge spectrum reveal that the discharge emits like an absolute blackbody nearly throughout the first half-cycle of the discharge; this radiation is similar to that of the linear discharge studied in ref. 4. Most of the energy is emitted during this time interval. By the end of the first half-cycle the intensity of the continuous spectrum has fallen off sharply, and the spectrum is a complicated line spectrum.

We determine the brightness temperature of the discharges from the continuous radiation from the central region of the discharge channel. Figure 7 shows the brightness temperature obtained in this manner as a function of the voltage U_0 for various types of discharges; these curves correspond to the first current maximum. We see that the converging discharge is slightly hotter than the steady-state and diverging discharges, under otherwise equal conditions. The discharge temperature increases with increasing U_0, varying over the range ~1.4-2 eV as U_0 is varied from 10 to 20 kV.

Let us consider the energy characteristics for the steady-state discharge. From the voltage–current characteristics we can easily calculate the energy fed to the system over the first half-cycle, Q. For the cases l = 20 cm, U_0 = 20 kV and l = 100 cm, U_0 = 30 kV the values of Q are ~25 and 65 kJ, respectively, i.e., about 30% of the energy stored in the capacitor bank. Figure 8 shows, for these cases, the energy W radiated in various spectral intervals $\Delta\lambda$: over the entire spectral range, $0 < \lambda < \infty$ ($\Delta\lambda_1$); in the transparency band of air, 1860 Å $< \lambda < \infty$ ($\Delta\lambda_2$); and in the ultraviolet, 2200 Å $< \lambda <$ 2700 Å ($\Delta\lambda_3$). The maximum temperatures for these cases are ~2 and 1.5 eV. For this calculation we assume the discharge to have a strictly cylindrical outer surface throughout the entire processes, with a constant temperature equal to the brightness temperature of a discharge channel. It follows from these curves that about 8 and 15 kJ are radiated in these two cases in the transparency band of air during the first half-cycle of the current, i.e., about 30% and 40% of the energy supplied to the discharge, Q. In the ultraviolet region the radiated energy is about 2.5-3 kJ in both cases.

6. DISCUSSION OF RESULTS

We turn first to the circumstance that the plasma channels do not coalesce. In ref. 1 we advanced a hypothesis regarding the nature of this phenomenon, which we can summarize as follows: Because of the sharp density gradients at the boundaries of the shock wave and the thermal zone, a diffusive separation of charges should occur there, and double space-charge shells should form.[6] The interaction of these space charges should cause the shock waves to be "squeezed out" when their fronts collide obliquely, and it should cause a mutual repulsion of the thermal (current) channels. Since the zone between the shock wave and the current channels is transparent for the radiation, this zone is not heated or ionized even after the collision of the current channels; it therefore continues to appear as a nonemitting region on the streak photographs. Some simple calculations support this hypothesis. A potential difference arises over the distance on the order of several mean free paths λ, given in order of magnitude by $\varkappa T/e$. Then we easily find the deviation from quasineutrality δn in this zone, and we find a space charge $q \simeq e\delta n = e(\varkappa T/4\pi e^2\lambda^2)$.

The space-charge double shell can be thought of as a dipole with a dipole moment $q\lambda$, and the interaction of

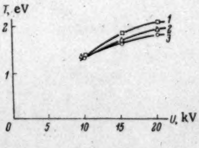

Fig. 7. Brightness temperature at the discharge-current maximum as a function of U_0. 1) Diverging; 2) converging; 3) steady-state discharges.

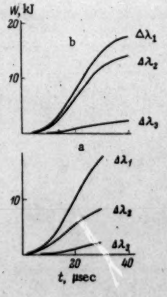

Fig. 8. Energy W emitted in various spectral intervals $\Delta\lambda$ as a function of the time ($\Delta\lambda_1$ = 0-∞, $\Delta\lambda_2$ = 1860 Å-∞, $\Delta\lambda_3$ = 2200-2700 Å). a) l = 20 cm, U_0 = 20 kV; b) l = 100 cm, U_0 = 30 kV.

the boundaries of the current zones can be treated as the interaction of these dipoles. Then the repulsive force between the zone boundaries is on the order of $F = 6q^2\lambda^2/r^4$, where r is the interaction distance. The streak photographs give us a value on the order of 1 mm for r (the thickness of the nonemitting zone between channels). Now expressing λ by the standard equation for the electron mean free path in a completely ionized plasma, and assuming $T \simeq 10^4$ °K and $N \simeq 5 \cdot 10^{18}$ cm^{-3} (ref. 4), we find the interaction force (per unit area) F to be on the order of a few thousand atmospheres. This value is far higher than the hydrodynamic pressure in the thermal zone, which does not exceed a hundred atmospheres. It would clearly be difficult to argue that there are other factors of a hydrodynamic nature which would lead to forces comparable to these electrostatic forces.

The difference between the temperatures in the different types of discharges has an obvious explanation: It is due to the temperature increase resulting from the interaction of different channels. In particular, the increase in the thermal energy during the collapse of the contracting discharge must be on the order of $Mv^2/2$, where M is the mass of the air entrained in the discharge and v is the shell velocity. Estimates show that under our experimental conditions this value is on the order of 0.5 eV, in satisfactory agreement with experiment (Fig. 7).

With regard to a theoretical calculation of the discharge parameters, we note the following: First, no theory exists for cylindrical coaxial discharges at present, and we know of no methods for numerically analyzing two-dimensional problems of magnetic radiative hydrodynamics. Second, during the early stages of the discharges it would be more meaningful to speak of the development of individual linear discharges. However, at the discharge currents in our experiments ($I \leq 300$ kA) the current through a single wire is so low that the lower limit on the applicability of the self-similar theory lies beyond the first half-cycle of the discharge.[4] Naturally, a self-similar calculation here will give temperatures and dimensions for the discharges which are greatly different from the experimental values.

Furthermore, the relative stability of these discharges in comparison with linear discharges[4] apparently shows that, for both vacuum return discharges and atmospheric discharges, the growth rates of the force instabilities are greatly reduced.

Finally, it follows from the data in Sec. 5 on the conversion of the energy supplied to the discharge, Q, into radiated energy $W(\Delta\lambda_2)$ that these discharges have approximately the same conversion coefficients as linear discharges.

The authors thank A. A. Rukhadze, V. S. Komel'kov, and F. A. Nikolaev for discussion of these results.

---

[1] A. F. Aleksandrov, V. V. Perebeinos, A. T. Savichev, and I. B Timofeev, Radiotekh. Elektron., 18, No. 11 (1973).

[2] O. A. Anderson, H. P. Furth, and J. M. Stone, and R. E. Wright, Phys. Fluids, 1, 489 (1958).

[3] L. A. Artsimovich, Controlled Thermonuclear Reactions [in Russian], GIFML, Moscow (1961).

[4] A. F. Aleksandrov, V. V. Zosimov, S. P. Kurdyumov, Yu. P. Popov, A. A. Rukhadze, and I. B. Timofeev, Zh. Eksp. Teor. Fiz., 61, 1841 (1971) [Sov. Phys.—JETP, 34, 979 (1972)].

[5] A. F. Aleksandrov, V. V. Zosimov, A. A. Rukhadze, V. I. Savoskin, and I. B. Timofeev, Preprint No. 72, P. N. Lebedev Physics Institute, Academy of Sciences of the USSR (1971).

[6] Ya. B. Zel'dovich and Yu. P. Raizer, Physics of Shock Waves and High-Temperature Hydrodynamic Phenomena [in Russian], Izd. Nauka, Moscow (1966).

[7] A. A. Rukhadze and S. A. Triger, Zh. Eksp. Teor. Fiz., 56, 1029 (1969) [Sov. Phys.—JETP, 29, 553 (1969)].

Recombination in an expanding plasma

Yu. A. Bykovskii, N. N. Degtyarenko, V. F. Elesin, V. E. Kondrashov, E. E. Lovetskii,
A. N. Polyanichev, and V. S. Fetisov
Moscow Engineering Physics Institute

(Submitted February 6, 1973; resubmitted May 21, 1973)
Zh. Tekh. Fiz., 44, 73-82 (January 1974)

The problem expansion of a spherically symmetric plasma into vacuum is solved on the basis of the equations of hydrodynamics, taking account of recombination and ionization. A numerical solution is given for the expansion of a highly ionized hydrogen plasma. In addition to the rarefaction wave, a "recombination" wave propagates into the plasma. There is a significant "quenching" of the degree of ionization if the initial plasma radius is of the order of the characteristic recombination length. When the initial plasma dimensions are large, recombination during the expansion is essentially complete. The problem of recombination in an expanding carbon plasma is also solved on the basis of the hydrodynamic equations averaged over the volume. The densities of ions X(Z) having various charges Z are found as functions of the time. The asymptotic values of X(Z) are found as a function of the initial plasma dimensions. Ions of a given charge Z can be produced efficiently if the initial plasma dimension is of the order of the characteristic recombination length for ions with charge Z.

INTRODUCTION

A large number of experiments have recently been reported on the expansion of plasmas into vacuum. The basic thrust has been to study the expansion of the plasma produced when a laser pulse strikes the surface of a solid target.[1-3] It has been shown[4] that recombination processes tending to change the charge spectrum of the ions play an important role in the expansion of a laser plasma.

The plasma expands under the influence of pressure and electrical forces. The electrical forces turn out to be important over distances of the order of the Debye length into the plasma from its interface with the vacuum,[5] so electric fields do not affect the motion of most of the material in large plasmas and can thus be neglected.

Recombination in an expanding plasma is studied in refs. 6-8, where certain restrictions are imposed on the gas dynamics of the expansion.

Below, the kinetics of recombination in a freely expanding plasma is analyzed in detail. The system of gas-dynamic equations taking account of inelastic processes is solved. It is shown that the yield of ions having a certain charge Z is a function of the ratio between the initial plasma dimension R_0 and the characteristic recombination length for these ions: At $R_0 \lesssim l_Z$, there is an efficient production of ions with charge less than Z. It is shown that a "recombination wave" propagates along with the rarefaction wave into the interior of a plasma which is initially unperturbed and at ionization equilibrium. Numerical results are reported for hydrogen and carbon plasmas.

STATEMENT OF THE PROBLEM AND BASIC EQUATIONS

We consider a spherically symmetric plasma consisting of neutrals, electrons, and ions of various charges. In writing the equations describing the expansion of the plasma into vacuum, taking account of ionization and recombination, we assume that the velocities of the various parts of the expanding plasma are the same, since the characteristic time required for equalization of the velocities is of the order of the momentum-relaxation times, which are small in comparison with the characteristic times for inelastic processes. We neglect the thermal conductivity. The electron thermal conductivity is negligible if the characteristic length l is large, specifically, if

$$l \gg \frac{6\sqrt{2}\,\pi^{3/2}}{L}\sqrt{\frac{M}{m}}\,(nr_D^3)\,r_D. \qquad (1)$$

Here, L is the Coulomb logarithm, M/m is the ratio of the ion and electron masses, n is the plasma density, and r_D is the Debye length. The ion thermal conductivity is smaller than the electron conductivity by a factor of $\sqrt{m/M}$ and is thus negligible. Below we assume that condition (1) holds. We assume that all the heavy components of the plasma are at the same temperature, but the electron temperature can be different. In fact, the ratio of the characteristic time for three-body recombination (which involves the liberation of energy in an electron gas) to the relaxation time for the electron and ion temperatures is

$$\frac{\tau_{\mathrm{rec}}}{\tau_{ei}} \sim \frac{(4\pi)^2 L}{3}\,\frac{m}{M}\,(nr_D^3)^2. \qquad (2)$$

If ratio (2) is small, the difference between the electron and ion temperatures can be large.

In finding the continuity equations for the various plasma components we take account of

$$A_{Z+1} + e \rightarrow A_Z + h\nu,$$

$$A_{Z+1} + 2e \rightleftarrows A_Z + e + h\nu,$$

where A_Z is an ion of charge Z.

We consider two types of recombination: three-body recombination with an electron as the third particle, and radiative recombination. The energy liberated in the electron capture in three-body recombination appears partially as heat and partially as radiation.[6] Assuming the plasma to be optically thin (estimates of the parameters used in the calculation are given in ref. 9), we assume that this radiation, like the radiation which arises in radiative recombination, is emitted from the gas.

We then find the following initial system of equations:

$$\left.\begin{aligned}
&\frac{\partial n_e}{\partial t}+\frac{1}{r^2}\frac{\partial}{\partial r}(r^2un_e)=A_e(n_Z,\ n_e,\ \Theta,\ T),\\
&\frac{\partial n_Z}{\partial t}+\frac{1}{r^2}\frac{\partial}{\partial r}(r^2un_Z)=A_Z(n_Z,\ n_e,\ \Theta,\ T),\\
&\frac{\partial u}{\partial t}+u\frac{\partial u}{\partial r}=-\left(M\sum_{Z=0}^{Z_m}n_Z\right)^{-1}\frac{\partial P}{\partial r},\\
&\frac{\partial P_e}{\partial t}+u\frac{\partial P_e}{\partial r}+\frac{5}{3}\frac{P_e}{r^2}\frac{\partial}{\partial r}(ur^2)=\frac{2}{3}Q_e,\\
&\frac{\partial P_i}{\partial t}+u\frac{\partial P_i}{\partial r}+\frac{5}{3}\frac{P_i}{r^2}\frac{\partial}{\partial r}(ur^2)=\frac{2}{3}Q_i.
\end{aligned}\right\} \qquad (3)$$

The first two equations in system (3) are the continuity equations for electrons and ions, respectively. The third equation is the equation of motion for a unit volume of the plasma. The last two equations describe the changes in the electron and ion pressures. The quantities A_e, A_Z, Q_e, and Q_i are given by

$$\left.\begin{aligned}
&A_e=n_e\sum_{Z=0}^{Z_m-1}\{n_Z\Gamma_1(Z)-n_{Z+1}\Gamma_2(Z+1)\},\\
&A_Z=n_e\{n_{Z+1}\Gamma_2(Z+1)+n_{Z-1}\Gamma_1(Z-1)\\
&\qquad -n_Z[\Gamma_1(Z)+\Gamma_2(Z)]\},\\
&Q_e=-(\Theta-T)n_e\sum_{Z=0}^{Z_m}n_Z\Gamma_5(Z)+n_e\sum_{Z=0}^{Z_m}n_Z\{\Gamma_4(Z)E_Z^*\\
&\qquad -I(Z)\Gamma_1(Z)-\frac{3}{2}\Theta\Gamma_3(Z)\},\\
&Q_i=(\Theta-T)n_e\sum_{Z=0}^{Z_m}n_Z\Gamma_5(Z).
\end{aligned}\right\} \qquad (4)$$

Here, Θ is the electron temperature, T is the temperature of the heavy particles, I(Z) is the ionization potential of an ion of charge Z [I(0) is the ionization potential of the neutrals], Z_m is the maximum ion charge, and $\Gamma_2 = \Gamma_3 + \Gamma_4$, where Γ_1, Γ_3, and Γ_4 are the coefficients for ionization, radiative recombination, and three-body recombination, respectively. The ionization coefficient is determined from the principle of detailed balance of the ionization and recombination:

$$\Gamma_1=2\left(\frac{2\pi mk}{h^2}\right)^{3/2}\frac{\Theta^{3/2}}{n_e}e^{-\frac{I(Z)}{\Theta}}\Gamma_2(Z+1). \qquad (5)$$

For Γ_3 we use[9]

$$\Gamma_3=2\cdot 10^{-13}\frac{Z^2}{\sqrt{\Theta}}\ . \qquad (6)$$

where θ is in electron volts. For Γ_4 we use[10]

$$\Gamma_4(Z)=\frac{4\pi\sqrt{2\pi}}{9}\frac{Z^3e^{10}}{\sqrt{m}\Theta^{9/2}}n_e. \qquad (7)$$

This equation gives a good approximation to the recombination coefficient at temperatures low in comparison with the ionization potential [$\Theta \ll I(Z)$]*. For example, at $\Theta \sim 10$ eV a carbon plasma consists primarily of high-charge ions (Z = 4), for which condition (*) is satisfied well. There are only a few singly charged ions, for which (7) predicts recombination coefficients which are too high, so the use of (7) at the beginning of the expansion does not lead to a large error. As the plasma expands, the number of singly charged ions increases, but the temperature decreases, so that we can continue to use (7) throughout the expansion stage. The coefficient Γ_5, which represents the relaxation rate of the electron and ion temperatures, is given by

$$\Gamma_5(Z)=\frac{8\sqrt{2\pi}}{3}\frac{\sqrt{m}}{M}e^4L\frac{Z^2}{\Theta^{3/2}}. \qquad (8)$$

Finally, E^*_Z is the energy liberated in the electron gas in a single three-body recombination event:[6]

$$E_Z^*=\begin{cases}6\cdot 10^4 I(Z-1)n_e^{1/6}\Theta^{1/12}, & E_Z^*>\Theta,\\ \Theta & ,\ E_Z^*<\Theta,\\ I(Z-1) & ,\ E_Z^*>I(Z-1).\end{cases}$$

An energy $I(Z-1) - E^*_Z$ is carried away from the plasma as radiation.

We now transform to Lagrange coordinates and introduce dimensionless quantities. We specify the dimensionless time to be $\tau = t/t_0$,

$$t_0=\frac{10^{27}T_0^{9/2}}{8.75n_a^2}$$

is the three-body recombination time, and T_0 and n_a are the initial temperature and density of the heavy particles. The dimensionless coordinate is

$$X=\frac{r}{l_0},$$

where $l_0 = t_0\sqrt{T_0/M}$ is the characteristic recombination length for a singly charged ion.

We convert the temperature, density, and velocity to dimensionless variables by dividing by T_0, n_a and $\sqrt{T_0/M}$, respectively; the result is the following system of equations in terms of dimensionless quantities, which we solve numerically:

$$\left.\begin{aligned}
&\frac{\partial n_a}{\partial\tau}+\frac{n_a}{\rho_0}\left(\frac{X}{R}\right)^2\frac{\partial u}{\partial R}\sum_{Z=0}^{Z_m}n_Z+\frac{2n_au}{X}=A_a,\\
&\frac{\partial u}{\partial\tau}=-\left(\frac{X}{R}\right)^2\frac{\partial P}{\partial R}\frac{1}{\rho_0},\\
&\frac{\partial P_m}{\partial\tau}+\frac{5}{3}P_m\left(\frac{X}{R}\right)^2\frac{\partial u}{\partial R}\sum_{Z=0}^{Z_m}\frac{n_Z}{\rho_0}+\frac{10}{3}\frac{P_mu}{X}=Q_m,\\
&\frac{\partial X}{\partial\tau}=u(R;t),
\end{aligned}\right\} \qquad (9)$$

$$(a=e,\ 0\leqslant Z\leqslant Z_m;\quad m=e,\ i).$$

Here, R is the Lagrange coordinate and $\rho_0 = \sum_{Z=0}^{Z_m} n_Z$ (r; t = 0).

We choose the difference scheme approximating system (9) in the following form:

$$\frac{u_j^{n+1}-u_j^n}{\Delta\tau}=-\left(\frac{X_j^n}{R_j}\right)^2\frac{P_{j+1/2}^n-P_{j-1/2}^n}{\Delta R}\frac{1}{\rho_0},$$

$$\frac{n_{j+1/2}^{n+1}(a)-n_{j+1/2}^n(a)}{\Delta\tau}=A_{j+1/2}^n(a)$$

$$-n_{j+1/2}^n\left\{\left(\frac{X_j^{n+1}}{R_j}\right)^2\frac{1}{\rho_0}\frac{u_{j+1}^{n+1}-u_j^{n+1}}{\Delta R}\right.$$

$$\left.\times\sum_{Z=0}^{Z_m}n_{j+1/2}^n(Z)+2\frac{u_{j+1}^{n+1}+u_j^{n+1}}{X_{j+1}^{n+1}+X_j^{n+1}}\right\},$$

$$\frac{P_{j+1/2}^{n+1}(m)-P_{j+1/2}^n(m)}{\Delta\tau}=Q_{j+1/2}^n(m)$$

$$-\frac{5}{3}P_{j+1/2}^n(m)\left\{\left(\frac{X_j^{n+1}}{R_j}\right)^2\frac{u_{j+1}^{n+1}-u_j^n}{\Delta R}\right.\quad\times$$

$$\times \frac{1}{\rho_0}\sum_{Z=0}^{Z_m} n^n_{j+1/2}(Z) + 2\frac{u^{n+1}_{j+1} + u^{n+1}_j}{X^{n+1}_{j+1} + X^{n+1}_j}\Bigg\},$$

$$X^{n+1}_j = X^n_j + u^{n+1}_j \Delta t. \qquad (10)$$

The condition for the stability for system (10) is found in the standard manner (by the Fourier-series method) to be

$$\Delta t < \sqrt{\frac{3}{5}}\left(\frac{R}{X}\right)^2 \frac{\rho_0 \Delta R}{\left(P\sum_{Z=0}^{Z_m} n_Z\right)^{1/2}}. \qquad (11)$$

Condition (11) results from a dispersion analysis of system (10). The terms due to collisions are discarded. However, in a numerical calculation the step chosen on the basis of condition (11) turns out to be too large, causing a rapid loss of accuracy. For example, the quantities A(α) in the continuity equations can be large, while the changes in n(α) over a time step must be small. The step chosen on the basis of condition (11) is not always satisfactory here. We have therefore worked out the following procedure for choosing a step: First we choose the step so that the changes in all quantities over the time step are small. Then we use condition (11) and, finally, choose the step which is the smaller of the two. We note that the step is determined from (11) in the later stage of the expansion, when inelastic processes have been essentially "frozen."

The accuracy of the numerical calculations is checked on the basis of conservation of the total energy:

$$4\pi\int_0^{R(t)} r^2 dr\left\{\sum_{Z=0}^{Z_m}\frac{u^2 n_Z}{2} + \frac{3}{2}(P_e + P_i)\right\} - 4\pi\int_0^t dt'\int_0^{R(t')} r^2 dr\,(Q_e + Q_i), \qquad (12)$$

where R(t) is the plasma radius at time t. We also calculate the total number of heavy particles, which must also be conserved. Finally, the quasineutrality of the expanding plasma must not be violated in the calculation. We note that in all calculation runs these quantities are conserved quite well.

To conclude this section we state the boundary conditions and write the equations used to calculate the initial ionization state of the plasma at specified values of the temperature and the heavy-particle density.

The boundary conditions for system (10) are

$$u^n_{j=0} = 0, \quad P^n_{J+1/2} = 0, \quad n^n_{J+1/2} = 0.$$

The first condition reflects the circumstance that the plasma velocity vanishes at the center of the plasma. The last two conditions correspond to conditions at the free boundary.

We assume that the plasma is initially in ionizational equilibrium; this is a legitimate assumption since the time required for the establishment of an ionization equilibrium is only a few nanoseconds,[9] which is shorter than the laser pulses used in the experiments of refs. 1-4 (50-100 nsec). It follows from the condition for ionization equilibrium that the right side of the first equation in (3) vanishes initially, so that

$$\sum_{Z=0}^{Z_m}\{n_Z\Gamma_1(Z) - n_{Z+1}\Gamma_2(Z+1)\}\big|_{t=0} = 0, \qquad (13)$$

which, along with the neutrality condition, makes it possible to calculate the initial ionization state on the basis of equations derived from Eq. (13):

$$\left.\begin{aligned} n_Z &= n_0\prod_{k=1}^{k=Z}\frac{\Gamma_1(k-1)}{\Gamma_2(k)};\quad n_0 = n_a\left[1 + \sum_{k=1}^{k=Z_m}\prod_{i=1}^{k}\frac{\Gamma_1(i-1)}{\Gamma_2(i)}\right]^{-1},\\ n_e&\left[1 + \sum_{k=1}^{Z_m}\prod_{i=1}^{i=k}\frac{\Gamma_1(i-1)}{\Gamma_2(i)}\right] = \sum_{k=1}^{Z_m} k\prod_{i=1}^{i=k}\frac{\Gamma_1(i-1)}{\Gamma_2(i)}\,n_a.\end{aligned}\right\} \qquad (14)$$

Calculations on the basis of Eqs. (14) are carried out on a computer.

EXPANSION OF A HYDROGEN PLASMA

In this section we describe a numerical solution of the system of difference equations (10) for a hydrogen plasma. The plasma is assumed to have an initial radius of R_0.

The densities of all particles, the temperature, and the pressure are assumed to be homogeneous along the radius. The initial plasma temperature chosen for the calculation is T_0 = 9 eV. The number of heavy particles per unit volume is chosen to be $n_a = 10^{19}\ \text{cm}^{-3}$. The initial charged-particle density, calculated from Eq. (14), is $n_e = 0.994 n_a$. Accordingly, we begin with a highly ionized plasma. The results reported here correspond to runs differing in the initial radius R_0. In the first run we use $R_0 = 10 l_0$, and in the second we use $R_0 = l_0$; we find the solutions for these two cases to differ qualitatively. The most important result is that in the case of the expansion of the smaller sphere there is an appreciable "quenching" of the degree of ionization. Increasing the radius by a factor of 10 results in a nearly complete recombination (Fig. 1). Figures 2 and 3 show the space–time distributions of the plasma parameters. During the expansion a spherical rarefaction wave propagates from the vacuum boundary toward the center of the plasma at a nearly constant velocity. We note that in the case of an adiabatic expansion the velocity in the rarefaction wave

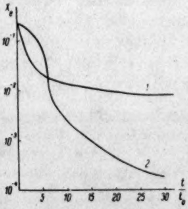

Fig. 1. Degree of ionization as a function of the time. 1) $R_0 = l_0$; 2) $R_0 = 10 l_0$.

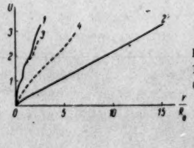

Fig. 2. Radial profile of the velocity. 1,2) $R_0 = l_0$; 3,4) $R_0 = 10 l_0$; t: 1) $0.57 t_0$; 2) $4.78 t_0$; 3) $5.38 t_0$; 4) $17.8 t_0$.

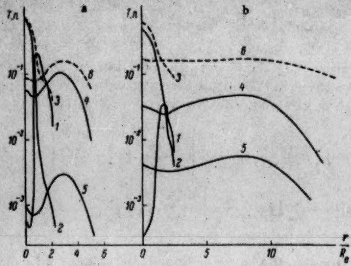

Fig. 3. Radial profiles of the temperature and densities at various times. a: $R_0 = 10 l_0$; $t = 5.38 t_0$ [1) $n_{Z=0}/n_a$; 2) $n_{Z=1}/n_a$; 3) T/T_0]; $t = 17.8 t_0$ [4) $10^2(n_{Z=0}/n_a)$; 5) $10^2(n_{Z=1}/n_a)$; 6) $10^2(T/T_0)$]. b: $R_0 = l_0$; $t = 0.57 t_0$ [1) $n_{Z=0}/n_a$, 2) $n_{Z=1}/n_a$, 3) T/T_0]; $t = 4.5 t_0$ [4) $10^2(n_{Z=0}/n_a)$, 5) $10^2(n_{Z=1}/n_a)$, 6) $10^2(T/T_0)$].

is an essentially linear function of the radius until the rarefaction reaches the center of the plasma; the linear functional dependence at the periphery of the plasma is retained at all values of t. We see from Fig. 2 that this functional dependence becomes nonlinear during the expansion of a recombining plasma; the asymptotic boundary velocity is larger for the plasma with the smaller initial radius. The calculated results show that this difference is due to the large relative loss (per particle) to radiation in the case of the plasma with the larger radius.

During the gas-dynamic expansion the local ionizational equilibrium is disrupted. A "recombination wave" propagates into the plasma behind the rarefaction front. The propagation velocity of this wave is lower than that of the rarefaction wave and decreases toward the center. Obviously, the characteristic delay time of the recombination after the rarefaction must be on the order of the time for disruption of the local ionizational equilibrium, which is a function of the rate of change of the gas-dynamic quantities (Θ and n). Figure 3 (curves 1) shows the boundary of the recombination wave; at this time the rarefaction wave has already reached the center. Behind the rarefaction front the ionization energy is efficiently converted into radiation and thermal energy, liberated in three-body recombination in the electron gas. The result is a bending of the curves showing the electron temperature behind the recombination front (curves 3). The density of neutrals ahead of the recombination front is reduced slightly because of the rarefaction, and it increases sharply (by two or three orders of magnitude) at the front. Behind the front the neutral density falls off because of expansion. In the later stages of the expansion the minima in the densities and temperature in the central region can be attributed to the conditions governing the reflection of the rarefaction wave from the center.

EXPANSION OF A CARBON PLASMA WITH SPECIFIED VELOCITY, DENSITY, AND TEMPERATURE PROFILES

We turn now to the expansion of a plasma containing ions of various charges. We use the procedure suggested by Mattioli,[8] by which we can convert the system of partial differential equations in (3) to a system of ordinary differential equations. We assume the temperatures and densities of the charged particles to be distributed uniformly along the radius. We write the velocity and density of the heavy particles as functions of the coordinate in the following manner:

$$\left.\begin{aligned} u(r;\, t) &= \dot{R}\xi, \\ \sum_{Z=0}^{Z_m} n_Z &= n_a\left[\frac{R_0}{R(t)}\right]^3 e^{-\xi^2}, \end{aligned}\right\} \qquad (15)$$

where $\xi = r/R(t)$, and R(t) is the instantaneous radius of the plasma–vacuum boundary.

Integrating system (3) over the plasma volume, and using (15), we find a system of ordinary differential equations for the temperatures, the charged-particle densities X_e and X_Z, and the radius R(t):

$$\frac{dX_e}{d\tau} = \bar{A}_e;\quad \frac{dX_Z}{d\tau} = \bar{A}_Z,$$

$$\frac{d^2R}{d\tau^2} = \frac{T + X_e\Theta}{R}\gamma_6^2,$$

$$\frac{3}{2}\frac{d(\Theta X_e)}{d\tau} + 3\frac{\Theta X_e}{R}\frac{dR}{d\tau} = \bar{Q}_e,$$

$$\frac{3}{2}\frac{dT}{d\tau} + 3\frac{T}{R}\frac{dR}{d\tau} = \bar{Q}_i.$$

Here we have used

$$\bar{A}_e = \frac{X_e}{R^3}\sum_{Z=0}^{Z_m}\{X_Z\bar{\Gamma}_1(Z) - X_{Z+1}\bar{\Gamma}_2(Z+1)\},$$

$$\bar{A}_Z = \frac{X_e}{R^3}\{[X_{Z+1}\bar{\Gamma}_2(Z+1) + X_{Z-1}\bar{\Gamma}_1(Z-1)]$$

$$- X_Z[\bar{\Gamma}_2(Z) + \bar{\Gamma}_1(Z)]\},$$

$$\bar{Q}_e = -\bar{Q}_i + \frac{X_e}{R^3}\sum_{Z=0}^{Z_m}\{\bar{E}_Z\bar{\Gamma}_4(Z) - I(Z)\bar{\Gamma}_1(Z) - \frac{3}{2}\Theta\bar{\Gamma}_3(Z)\},$$

$$\bar{Q}_i = (\Theta - T)\frac{X_e}{R^3}\sum_{Z=0}^{Z_m} X_Z\bar{\Gamma}_5(Z).$$

The transformed quantities are

$$\bar{\Gamma}_1 = \gamma_1\frac{Z^3}{\Theta_3}e^{-\frac{I(Z)}{\Theta}},\quad \bar{\Gamma}_2 = \bar{\Gamma}_3 + \bar{\Gamma}_4,$$

$$\bar{\Gamma}_3 = \gamma_3\frac{Z^2}{\Theta^{1/2}},\quad \bar{\Gamma}_4 = \gamma_4\frac{Z^3}{\Theta^{9/2}}\frac{X_e}{R^3},$$

$$\bar{\Gamma}_5 = \gamma_5\frac{Z^2}{\Theta^{3/2}},$$

$$\bar{E}_Z = \begin{cases} \gamma_6 I_{Z-1}\dfrac{X_e^{1/6}\Theta^{1/12}}{R^{1/2}}, & \bar{E}_Z > \Theta, \\ \Theta, & \bar{E}_Z < \Theta, \\ I(Z-1), & \bar{E}_Z > I(Z-1). \end{cases}$$

In system (9) we have introduced the dimensionless time $\tau = t/\tau_0$, where $\tau = R_0\sqrt{M/T_0}$ is the characteristic expansion time. The coefficients γ are the ratios of τ_0 to the characteristic times for the corresponding processes at t = 0:

$$\gamma_1 = 2^{-3/2}\frac{\tau_0}{\tau_1},\quad \gamma_3 = 2^{-3/2}\frac{\tau_0}{\tau_3},\quad \gamma_4 = 3^{-3/2}\frac{\tau_0}{\tau_4},\quad \gamma_5 = 2^{-3/2}\frac{\tau_0}{\tau_4}.$$

We also have $\gamma_6 = a\, n_a{}^{1/6}\Theta_0{}^{1/12}$, where $a = 6\cdot 10^{-4}$. The initial ionization state of the plasma is determined

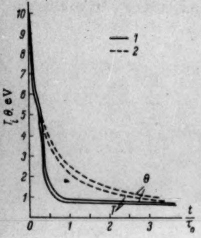

Fig. 4. Electron and ion temperatures as functions of the time. 1) $R_0 = 10^{-2}$, 2) $5 \cdot 10^{-2}$ cm.

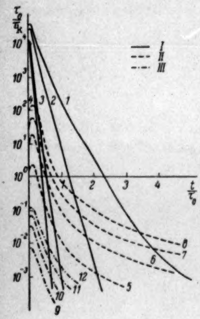

Fig. 5. Characteristic frequencies of inelastic processes. I) Ionization; II) three-body recombination; III) radiative recombination. 1) Z = 0; 2,5,9) 1; 3,6,10) 2; 4,7,11) 3; 8,12) 4.

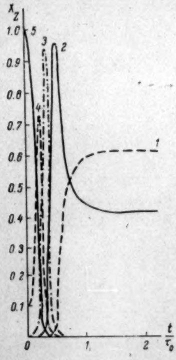

Fig. 6. Densities X_Z of ions of various charges as functions of the time. 1-5) Z = 0, 1, 2, 3, 4, respectively.

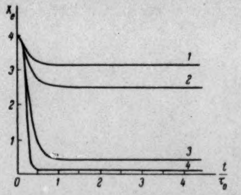

Fig. 7. Degree of ionization of the plasma, X_e, as a function of the time for various values of the ratio R_0/l_0. For all the calculations the recombination length of singly charged ions is $l_0 \approx 3.3 \cdot 10^{-2}$ cm. The initial plasma radius R_0 is: 1) $\sim 10^{-3}$; 2) $\sim 10^{-2}$; 3) $\sim 5 \cdot 10^{-2}$; 4) $\sim 10^{-1}$.

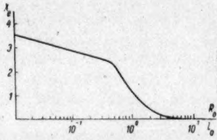

Fig. 8. Asymptotic value of X_e as a function of the initial plasma dimension.

from Eqs. (14) for a carbon plasma with $\Theta_0 = 10$ eV and $n_a = 10^{19}$ cm^{-3}. This plasma turns out to consist primarily of ions with Z = 4. The initial boundary velocity is assumed to be zero. We have carried out several calculation runs, varying the initial plasma dimensions. During the expansion the electron and ion temperatures fall off. For the plasma having the smaller initial radius, the temperature falls off smoothly as a function of the time (Fig. 4). For the plasma with the larger initial radius, recombinational heating and radiation are more important; there are kinks in curves 3 and 4 because of the pronounced deviation from adiabaticity. The difference between the electron and ion temperatures for given values of Θ_0 and n_a turns out to be small, because ratio (2) is large in comparison with unity. We see from Fig. (5) that the characteristic ionization frequency (curve 1) falls off as a function of the time—more rapidly, the larger Z. This decrease is a result of the exponential functional dependence of the ionization frequency on $I(Z)/\Theta$.

The rate of three-body recombination (which is the most probable type of recombination under these conditions) is a power function of the density and temperature, and for ions of different charges this rate falls off in approximately the same manner. During the initial stage of the expansion there is some increase in the recombination probability because of the temperature drop. The density decrease is not influential in this stage. The recombination probability subsequently falls off because of the density decrease. Because of the different rates at which the probabilities for recombination and ionization decrease, the ionization equilibrium is disrupted at different times for ions of different charges, e.g., the intersection of curves 1 and 3 shifts toward earlier times with increasing Z. Figure 6 illustrates the recombination kinetics during the expansion. During the inertial stage of the expansion, the ion density is "quenched." For this version of the calculation it is primarily singly charged ions and neutrals which are left.

Figure 7 shows the degree of ionization of the plasma as a function of the time for various initial radii. We see that the "quenching" occurs over a time $\tau_0 \sim R_0 \sqrt{M/T_0}$ (the characteristic expansion time). At $t > \tau_0$ the role of recombination becomes inconsequential. As the initial radius is reduced, the ultimate degree of ionization increases: For $R_0 = 3.5 l_0$ it is about 0.1, while for $R_0 = 0.35 l_0$ it is 2.5. Interestingly, the ultimate degree of ionization has a functional dependence on the initial radius such that X_e falls off rapidly as a function of R_0 near the characteristic recombination length l_0 (Fig. 8). For $R_0 > l_0$ the degree of ionization is small in comparison with unity; for $R_0 < l_0$ the final degree of ionization can exceed unity. This situa-

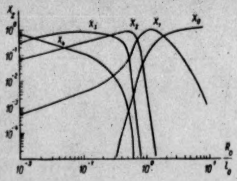

Fig. 9. Final densities as functions of R_0/l_0.

tion is clearly evident from Fig. 9, which shows the final densities of the ions of various charges as functions of R_0.

The yield of, e.g., doubly charged ions from the plasma can be increased by using an initial plasma radius of the order of $0.1l_0$; this radius evidently corresponds to the recombination length for doubly charged ions: The ratio of the recombination lengths of ions of different charges, according to (7), is

$$\frac{l_0(Z_1)}{l_0(Z_2)} \sim \left(\frac{Z_2}{Z_1}\right)^3,$$

and the efficient production of ions having a large charge would require a small initial plasma radius.

---

[1] N. G. Basov, O. N. Krokhin, and G. V. Sklizkov, Quantum Radiophysics. Proceedings of the P. N. Lebedev Physics Institute, Academy of Sciences of the USSR [in Russian], Vol. 52 (1970), p. 171; Zh. Eksp. Teor. Fiz., 54, 1073 (1968) [Sov. Phys. – JETP, 27, 575 (1968)].

[2] N. G. Basov, V. A. Boiko, Yu. P. Voinov, É. Ya. Kononov, S. L. Mandel'shtam, and G. V. Sklizkov, ZhETF Pis. Red., 5, 177 (1967) [JETP Lett., 5, 141 (1967)]; 6, 849 (1967) [JETP Lett., 6, 291 (1967)].

[3] O. B. Anan'in, Yu. A. Bykovskii, N. N. Degtyarenko, Yu. P. Kozyrev, S. M. Sil'nov, and B. Yu. Sharkov, ZhETF Pis. Red., 16, 543 (1972) [JETP Lett., 16, 384 (1972)].

[4] Yu. A. Bykovskii, N. N. Degtyarenko, V. F. Elesin, Yu. P. Kozyrev, and S. M. Sil'nov, Zh. Eksp. Teor. Fiz., 60, 1306 (1971) [Sov. Phys. – JETP, 33, 706 (1971)].

[5] S. I. Braginskii, Reviews of Plasma Physics, Vol. 3, Consultants Bureau, New York (1967).

[6] N. M. Kuznetsov and Yu. P. Raizer, Prikl. Mekh. Tekh. Fiz., No. 4, 10 (1965).

[7] Yu. V. Afanas'ev and V. B. Rozanov, Zh. Eksp. Teor. Fiz., 62, 247 (1972) [Sov. Phys. – JETP, 35, 133 (1972)].

[8] M. Mattioli, Plasma Physics, 13, 19 (1971).

[9] Ya. B. Zel'dovich and Yu. P. Raizer, Physics of Shock Waves and High Temperature Hydrodynamic Phenomena, Academic Press, New York (1966).

[10] A. V. Gurevich and L. P. Pitaevskii, Zh. Eksp. Teor. Fiz., 46, 1281 (1964) [Sov. Phys. – JETP, 19, 870 (1964)].

Spatial characteristics and loss of plasma produced by an electron beam in a magnetic trap

M. Yu. Bredikhin, A. I. Maslov, A. I. Skibenko, E. I. Skibenko, I. P. Fomin, and V. B. Yuferov

Physicotechnical Institute,
Academy of Sciences of the Ukrainian SSR, Khar'kov

(Submitted April 20, 1973)
Zh. Tekh. Fiz., 44, 83-90 (January 1974)

An experimental study has been made of the spatial characteristics of the plasma produced by the interaction of a high-current electron beam with a dense gas target in the center of a magnetic mirror. The average plasma dimensions and the radial profile of the density in the transverse cross section have been determined by probing the plasma at λ = 4 and 8 mm. These measurements yield the radial dimensions of the plasma column, the spatial profile of the plasma density, the total number of particles per unit length of the trap, and the degree of ionization of the plasma. It is concluded on the basis of these results that the most important mechanism for plasma loss from the trap during the active period of the discharge is loss of plasma in the mirror.

We have previously studied[1,2] the production and heating of plasmas at densities 10^{14}–10^{15} cm^{-3} in the interaction of a high-current electron beam with a dense gas target at the center of an open magnetic trap. We feel it worthwhile to determine the spatial distribution of this plasma for various discharge conditions; this information yields the maximum dimension of the plasma column, the total number of particles in the trap, and the degree of ionization of the plasma. This information can also furnish information on the production and heating of the dense plasma and can be used to evaluate the plasma loss across and along the magnetic field.

The experiments are carried out on the VGL-2 device.[1] The average plasma dimensions and the radial profile of the density in a cross section are determined by microwave probing at λ = 4 and 8 mm. During the active period of the discharge the plasma is usually opaque at these wavelengths. We therefore study the spatial characteristics of the plasma on the basis of the phase shift of the reflected signals or by measuring the phase shift of the reflected wave at one wavelength and determining the maximum density from the cutoff at other wavelengths. In several experiments a fixed double electrostatic probe is used to check the transverse dimensions.

Writing the radial profile of the density as

$$N(r)=N_{\max}\left[1-\left(\frac{r}{r_{\max}}\right)^{\gamma}\right] \qquad (1)$$

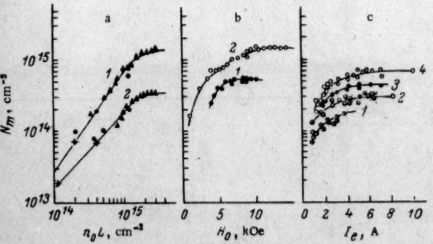

Fig. 1. Maximum plasma density as a function of: a) the neutral-gas density; b) the magnetic field; and c) the electron-beam current. a: H_0 = 5 kOe. 1) E_e = 30; 2) 15 keV. b: E_e = 30 keV. 1) $n_0L = 5 \cdot 10^{14}$; 2) $1 \cdot 10^{15}$ cm^{-2}. c: H_0 = 5 kOe, $n_0L = 8 \cdot 10^{14}$ cm^{-2}. 1) E_e = 9; 2) 15; 3) 22.5; 4) 30 keV.

and assuming that the phase of the reflected wave at a given time carries information about the position of the critical density for the given wavelength, we can write the maximum plasma radius, $r_{\max}$, and the exponent γ as

$$\left.\begin{aligned} r_{\max}&=r_1(1-S_1)^{-\frac{\lg r_1 r_2}{\lg\frac{1-S_1}{1-S_2}}}=\frac{r_1}{(1-S_1)^{1/\gamma}},\\ \gamma&=\lg\frac{1-S_2}{1-S_1}\lg\frac{r_1}{r_2}=\frac{\lg\frac{1-S_2}{1-S_1}}{\lg\frac{r_2}{r_1}},\end{aligned}\right\} \qquad (2)$$

where $S_{1,2} = N(r_{1,2})/N_{\max}$, $r_{1,2}$ are the radii of the reflecting layer for λ_1 and λ_2, respectively, and $N_{\max}$ is the maximum plasma density. The values of r_1 and r_2 are found from the phase of the reflected wave:[2]

$$\varphi=2\frac{\omega}{c}\int\limits_0^r\sqrt{1-\frac{N(r)}{N_{\text{cr}}}}\,dr-\frac{\pi}{2}. \qquad (3)$$

Since the outer boundary of the plasma is not determined in these experiments, we assume an axisymmetric distribution with a maximum at the axis and measure the phase shift from the time at which the critical density decays at the axis; in the transition layer, function (1) is extrapolated as a piecewise-linear function. Then,

$$r_{1,2}=\frac{3}{8}\lambda m_{1,2}, \qquad (4)$$

where $m_{1,2} = \varphi_{1,2}/\pi$ is the number of periods in the phase of the reflected signal corresponding to the motion of the reflecting layer from the axis to $r_{1,2}$.

If we can assume the function $N = f(r)$ to be fixed over a certain time interval, we can determine r_1 and r_2 from the phase shift of one reflected wave at different times. This method has been used previously.[3] Instead of using the average density, however, we use the known maximum density and simplify the calculation by means of this assumption regarding the radial distribution. In this case $N(r_1) = N(r_2)$ in Eq. (2), corresponding to the position of the reflecting layer for one wavelength at different times, for which the maximum densities are also different.

We have studied the spatial characteristics of the plasma produced by the electron beam at a beam energy $E_e \le 30$ keV, a beam current $I_e \le 20$ A, and an injection time ~ 400 μsec. Microwave horns are placed in the annular slit at the center of the mirror system ($R = H_{ml}/H_0 = 1.5$), as in ref. 1, and the phases of waves at $\lambda = 4$ and 8 mm reflected and transmitted by the plasma are measured. Maximum densities above $7 \cdot 10^{13}$ cm^{-3} are determined from the double-probe current as calibrated on the basis of the results of microwave and particle measurements. Figure 1 shows typical functional dependences of the maximum plasma density in the discharge on the discharge parameters.

Analyzing the oscillograms of the reflected microwave signals at $\lambda = 4$ and 8 mm in accordance with Eq. (4), we find the radius of the plasma column for several values of the density as a function of various discharge parameters: the neutral-gas density, the magnetic field at the center of the trap, and the energy and current of the electron beam interacting with the plasma (Figs. 2, 3). On the basis of these experimental functional dependences and Eqs. (1) and (2) we find the analogous functional dependences for the maximum plasma radius (shown in the same figures). The results are as follows.

1. The transverse dimension of the plasma column increases with increasing neutral-gas density; the rate of increase is faster for the layers having the lower plasma densities. The maximum plasma radius increases with increasing neutral-gas density only up to $n_0L \le 2 \cdot 10^{15}$ cm^{-2} and is 10-15 times larger than the beam radius.

2. As the magnetic field at the center of the trap is increased ($H_0 > 1.5$ kOe), the radii of plasma layers at the same density decrease. As the density is raised, the decrease in the transverse dimensions becomes less apparent, i.e., stronger magnetic fields are required to achieve the same contraction of the plasma column.

3. Examination of the behavior of the transverse plasma dimensions for various electron-beam currents reveals that when the current is reduced from 10-12 to 2 A, the value of r changes slightly. With a further decrease in I_e the plasma column contrasts rapidly. This behavior is a result of the conditions governing the formation of the dense plasma.[1] Increasing the beam energy leads to an increase in the radial dimensions over the entire range of neutral-gas densities. The values of r_{max} found at the two wavelengths for a given time and found from a single wavelength at different times are very nearly equal (curves 3 and 4 in Fig. 2).

From the experimental data in Figs. 2-4 and from Eqs. (1) and (2) we find the spatial profiles of the plasma density in a radial cross section of the plasma column (Figs. 4 and 5); the results agree with the results of the probe measurements (curve 4 in Fig. 5). We find that at low neutral-gas densities ($n_0L < 10^{14}$ cm^{-2}) the profile is described approximately by a quadratic parabola. As the neutral-gas density is increased, the region in which the plasma is most dense contracts, becoming only 1.5-2 times as large as the region filled by the electron beam. The density gradients dN/dr increase at high neutral-gas densities and decrease at low densities. At small values of n_0L the density gradients vary smoothly.

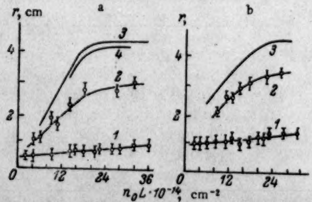

Fig. 2. Transverse dimensions of the plasma column as a function of the neutral-gas density for various plasma densities. t = 300 μsec. a) E_e = 15; b) 22.5 keV. 1) $N \ge 7 \cdot 10^{13}$; 2) $\ge 1.8 \cdot 10^{13}$; 3, 4) 0 cm^{-3}.

In weak magnetic fields ($H_0 \le 3$ kOe) the profile $N = f(r)$ is approximately uniform (curves 1-3 in Fig. 5), with a large density gradient near the trap wall. In stronger fields ($H_0 > 4$ kOe) the profile becomes a decaying profile with a large density gradient over the entire radius. At these field values the efficiency of plasma heating increases.[2] The relation between the shape of the profile and the heating efficiency can be explained on the basis of a hybrid resonance,[4] because with a gently sloping density profile (curve 4 in Fig. 5) the conditions in the layers having large radial dimensions are such that the frequencies of the waves excited in the plasma correspond to the frequency of the upper hybrid [$\overline{\omega} = \Omega(r)$]. In the case of a uniform or approximately uniform density profile this resonance condition is not satisfied, since the magnetic field is homogeneous within 5% over the plasma radius.

From the radial profiles of the plasma density we can evaluate the total number of plasma particles per unit length of the trap:

$$N_{\text{totl}} = \int_s N(S)\, dS(r). \tag{5}$$

Substituting Eq. (1) for N(r) into Eq. (5) and setting $dS = 2\pi r dr$, we find

$$N_{\text{totl}} = \pi N_{\max} r_{\max}^2 \frac{\gamma}{\gamma + 2}. \tag{6}$$

Figures 6 and 7 show the total number of particles per unit length of the trap as a function of the discharge parameters. We see that as the gas density increases, the total number of plasma particles increases over the entire range of densities n_0L, up to $3 \cdot 10^{15}$ cm^{-2} at a beam energy of 30 keV. At lower energies the increase in N_{totl} is

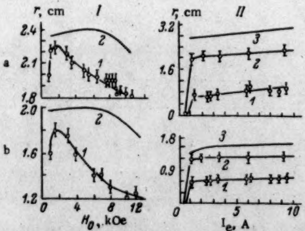

Fig. 3. Transverse dimensions of the plasma column as a function of the magnetic field (I) and of the current of the electron beam injected into the trap (II). I: 1) $N = 7 \cdot 10^{13}$; 2) 0 cm^{-3}. II: 1) $\ge 7 \cdot 10^{13}$; 2) $\ge 1.8 \cdot 10^{13}$; 3) 0 cm^{-3}. a) t = 300; b) 500 μsec.

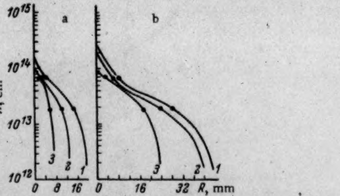

Fig. 4. Spatial profile of the plasma density for various neutral-gas densities at various times. a) $n_0L = 8 \cdot 10^{14}$; b) $1.35 \cdot 10^{15}$ cm^{-2}. 1) t = 300; 2) 400; 3) 500 μsec. E_e = 15 keV.

cut off at only $n_0L \simeq 2 \cdot 10^{15}$ cm^{-2}, apparently because the ionization coefficient of the plasma is less than unity for a given energy input into the discharge at values $n_0L > 2 \cdot 10^{15}$ cm^{-2}. Increasing the beam energy leads to an increase in the total number of particles and leads to complete ionization of the plasma. By measuring the total number of plasma particles and the radial profile of the neutral-gas density in the same cross section of the trap before the electron beam is injected we can determine the average charge of the argon ions in the discharge, since the time characteristic of ionization and the production of a dense plasma is shorter than the characteristic transit times of slow atoms across the moving gaseous target. Using the function[5] $n_0 = f(r)$ we can determine the total number of neutral particles per unit length of the trap through numerical integration. The average ion charge $\overline{Z}$ is defined as the ratio of the total number of plasma electrons to the total number of neutral particles under the condition $N_i = n_0$. Our calculations show that $\overline{Z}$ varies from 1.2 to 3.5 for a neutral-gas density of $n_0L = 8.4 \cdot 10^{14}$ cm^{-2} as the electron beam energy is raised from 15 to 30 keV. The observed values $\overline{Z} > 1$ are due to multiple ionization of argon atoms.

It follows from the function $N_{totl} = f(H_0)$ that in weak magnetic fields the total number of particles increases markedly with increasing field. At $H_0 > 3$ kOe the total number of particles per unit length varies only slightly in the central part of the trap. As the beam current is increased, this number increases, implying an increase in the value of Z for the plasma particles; this increase can in turn be attributed to an increase in the efficiency of the plasma heating with increasing electron-beam power (or current) since N_{totl} is a nonlinear function of $W_e = I_eE_e$.

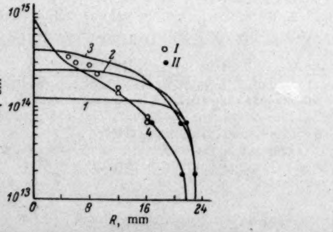

Fig. 5. Spatial profile of the plasma density for various magnetic fields at the center of the trap. 1) H_0 = 1; 2) 2; 3) 4; 4) ≥ 10 kOe. I) Experimental points obtained with a calibrated double electrostatic probe; II) obtained from microwave measurements.

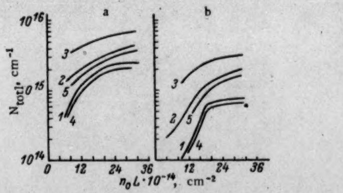

Fig. 6. Total number of particles per unit length of the trap as a function of the neutral-gas density. a) t = 300; b) 500 μsec. 1, 4) E_e = 15; 2, 5) 22.5; 3) 30 keV. 1, 2) Obtained at two wavelengths; 3-5) at a single wavelength.

On the basis of the data on the total number of particles in the trap we can write a balance equation for the particles in the trap during the active period of the discharge:

$$\frac{dN}{di} = \langle \sigma_e v_e \rangle n_0 N_e - \alpha_R N_e N_i - D_\perp \nabla^2 N_e - D_\parallel \nabla^2 N_e, \tag{7}$$

where n_0 is the neutral-gas density, N_e and N_i are the electron and ion densities, α_R is the recombination coefficient, and $D_\perp$ and $D_\parallel$ are the effective diffusion coefficients.

The total rate of particle loss from the trap, calculated from Figs. 3, 4, and 7, taking account of the transverse cross section of the plasma, is $(dN)/(dt) = 2 \cdot 10^{18}$ cm$^{-3} \cdot$ sec^{-1}. The first term on the right side of Eq. (7) gives the increase in the number of particles in the trap due to ionization of new gas supplied to the discharge; in the case of complete ionization of the gas, this term can be defined as

$$\langle \sigma_e v_e \rangle n_0 N_e = \frac{dn_0}{dt} = \eta q, \tag{8}$$

where q is the total amount of gas fed to the entrance of the collimating device which collimates the gas flow, and η is its gas efficiency, which has been determined previously[6] for various flow rates q. The other terms in Eq. (7) give the particle loss due to recombination and diffusion across and along the magnetic field. The effects of the individual terms in Eq. (7) are examined in the case

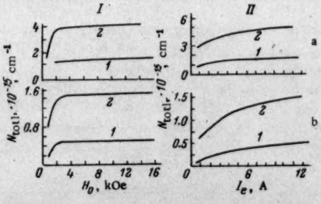

Fig. 7. Total number of particles per unit length of the trap as a function of the magnetic field (I) and of the electron-beam current (II). 1) E_e = 22.5; 2) 30 keV. a) t = 300; b) 500 μsec.

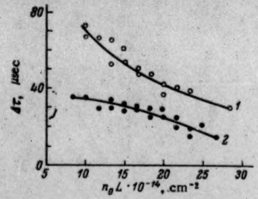

Fig. 8. Time required for the plasma to flow between the center of the trap and the mirror as a function of the neutral-gas density. 1) E_e = 15; 2) 30 keV.

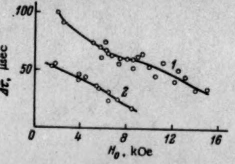

Fig. 9. Time required for the plasma to flow between the center of the trap and the mirror as a function of the magnetic field. 1) E_e = 15; 2) 30 keV.

of efficient heating of the plasma electrons,[2] e.g., with $E_e = 30$ keV, $n_0L = 8 \cdot 10^{14}$ cm^{-2}, $H_0 = 12$ kOe, $q = 22.6$ cm^3/sec, and $\eta = 0.1$. Here the plasma density is $4 \cdot 10^{14}$ cm^{-3}, its electron temperature is 1 keV, the average ion energy is ~ 90-100 eV, and the rate of ionization of the particles is $\eta q \approx 6 \cdot 10^{19}$ cm^{-3} · sec^{-1}. The recombination loss can be neglected since we have $\alpha_R N_e N_i = 4 \cdot 10^{11}$ cm^{-3} sec^{-1} at these plasma parameters.

The transverse-diffusion coefficient can be evaluated from the change in the radial density profile after the plasma is produced: We find $D_\perp = r^2/4t \simeq 2 \cdot 10^2$ cm^2/sec at 300 μsec after injection. Calculating the radial density gradient from Figs. 4 and 5 or from the radial profile of the plasma density, we find the loss due to diffusion across the magnetic field to be

$$\Delta\Gamma_\perp = D_\perp \nabla^2 N = D_\perp \frac{1}{r}\frac{\partial}{\partial r}\left(r\frac{\partial N}{\partial r}\right). \tag{9}$$

Using Eq. (1) for N in Eq. (9) and differentiating, we find

$$\Delta\Gamma_\perp = -D_\perp \frac{\gamma^2 N_{\max}}{r^{\gamma}_{\max}} r^{\gamma-2}. \tag{10}$$

For a parabolic density profile ($\gamma = 2$) we find $\Delta\Gamma_\perp = 4.7 \cdot 10^{16}$ cm^{-3} · sec^{-1}, and for a profile like that shown by curve 4 in Fig. 5 ($\gamma = 0.274$) we find $\Delta\Gamma_\perp$ $1.2 \cdot 10^{16}$ cm^{-3} · sec^{-1}.

The loss due to the flow of plasma to the mirror is evaluated from

$$\Delta\Gamma_\parallel = \frac{\bar{N} v S}{V}, \tag{11}$$

where $\bar{N}$ is the average plasma density beyond the mirror, v and S are the velocity and cross section of the plasma flow beyond the mirror, and V is the trap volume. To determine the longitudinal velocity component of the plasma moving along the magnetic field, we use a dual microwave interferometer which simultaneously measures the densities at the center of the trap and beyond the mirror. Figures 8 and 9 show the time required for a plasma with $N \geq 7 \cdot 10^{13}$ cm^{-3} to flow between the center of the system and the mirror (a distance of 30 cm) as a function of the neutral-gas density and the magnetic field. It follows from these figures that the plasma velocity varies from $3 \cdot 10^5$ to $2 \cdot 10^6$ cm/sec for the various discharge parameters. The increase in the longitudinal velocity with increasing magnetic field shows that in this beam–plasma discharge there is an increase in the longitudinal component of the energy of the plasma particles as well as in the transverse component,[2] i.e., the mechanisms of both transverse and longitudinal particle acceleration are operating. The increase in $v_\parallel$ with increasing neutral-gas density (or plasma density) is apparently due to an increase in the gas-kinetic pressure of the plasma at constant values of the magnetic field and the electron-beam power.

Taking account of the quantities in Eq. (11), we find that the loss due to the escape of plasma to the mirror is of the order of the total loss.

Accordingly, these measurements have revealed the radial dimensions of the plasma column, the spatial profile of the plasma density, and the total number of particles in the trap. From these results we conclude that the loss of plasma in the mirror is responsible for the total loss of plasma from the trap during the active period of the discharge.

---

[1] M. Yu. Bredikhin, A. M. Il'chenko, A. I. Maslov, A. I. Skibenko, E. I. Skibenko, and V. B. Yuferov, Ukr. Fiz. Zh., 14, 1167 (1969); At. Energ., 29, 276 (1970).

[2] M. Yu. Bredikhin, A. I. Maslov, A. I. Skibenko, E. I. Skibenko, and V. B. Yuferov, Zh. Tekh. Fiz., 41, 694 (1971) [Sov. Phys. – Tech. Phys., 16, 544 (1971)]; Ukr. Fiz. Zh., 16, 1180 (1971).

[3] A. I. Anisimov, N. I. Vinogradov, and V. E. Golant, in: Plasma Diagnostics (ed. B. P. Konstantinov) [in Russian], Gosatomizdat, Moscow (1963), p. 95.

[4] J. Preinhaelter, Plasma Phys., 10, 713 (1968).

[5] V. B. Yuferov, E. I. Skibenko, Yu. V. Kholod, A. M. Il'chenko, M. Yu. Bredikhin and A. I. Maslov, Zh. Tekh. Fiz., 41, (1971).

[6] V. B. Yuferov, E. I. Skibenko, A. M. Il'chenko, M. Yu. Bredikhin, and A. I. Maslov, Prib. Tekh. Eksp., 1, 183 (1971).

[7] V. B. Yuferov, E. I. Skibenko, A. M. Il'chenko, M. Yu. Bredikhin, and A. I. Maslov, Prib. Tekh. Eksp., 1, 183 (1971).

Microwave discharge in argon

E. V. Belousov, A. S. Bryukhovetskii, and A. V. Prokopov

Institute of Radiophysics and Electronics, Ukrainian Academy of Sciences, Khar'kov

(Submitted March 19, 1973)
Zh. Tekh. Fiz., 44, 91-97 (January 1974)

By simultaneously solving the Boltzmann kinetic equation and the energy balance equation we obtain the electron energy distribution function, the electron temperature, and other parameters of a microwave-discharge plasma in the skin layer. The kinetic equation takes account of the influence of the magnetic field, electron–electron collisions, and elastic and inelastic collisions. The experimental values of the electron density and gas temperature in a discharge excited in argon by a 3-cm band source are used for the numerical calculations. The results are compared with the experimental data.

INTRODUCTION

In connection with possible important practical applications,[1-4] interest has recently increased in gas discharges excited by rapidly alternating electromagnetic fields. This type of discharge is being investigated experimentally. The theory of a stationary microwave gas discharge is not well developed; there are essentially no kinetic analyses of this type of discharge, apart from refs. 5 and 6, in which the influence of elastic and inelastic collisions on the electron energy distribution function has been investigated. An analysis of the experimental data shows that it is also necessary to take electron–electron collisions into account since a stationary microwave discharge is characterized by a density N_e which exceeds the critical densities by one or two orders of magnitude; it is also of highly nonequilibrium character.[4] It is therefore of interest to examine the kinetics of processes occurring in a microwave discharge, taking account of the electromagnetic field and electron–electron, elastic, and inelastic collisions. The foregoing processes are taken into account in refs. 7 and 8 in the positive column of a dc discharge.

The present study is an attempt at a theoretical and experimental investigation of processes in a low-temperature microwave discharge using as an example the excitation of a discharge in argon by a 3-cm source.

KINETIC EQUATION

The kinetic equation for the isotropic part of the electron velocity distribution function $f_0(v)$ in a low-temperature plasma excited by a rapidly alternating field of frequency ω can be written in the form

$$\frac{1}{2v^2}\frac{\partial}{\partial v}\left\{v^2 P(v)\frac{\partial f_0}{\partial v}+v^3 P_1(v) f_0\right\}=(h_x+h_i)\nu_c f_0, \tag{1}$$

where

$$P_1(v)=2A_1(f_{00})+\delta\nu_m, \tag{2}$$

$$P(v)=2A_2(f_{00})+\frac{e^2E^2}{3m^2}\frac{\nu_m}{\nu_m^2+\omega^2}+\frac{kT_g}{m}\delta\nu_m. \tag{3}$$

Here, $A_1(f_{00})$ and $A_2(f_{00})$ describe the electron–electron interaction,[7,9] with the distribution function replaced by its first iteration, i.e., by the Maxwellian distribution; ν_m is the frequency of momentum-transfer elastic collisions; ν_c is the total collision frequency; h_x and h_i are the excitation and ionization efficiencies, respectively; T_g is the gas temperature; E is the electric field in the plasma. The remaining notation is standard. The electron–electron collisions depend on the electron density N_e and the temperature T_{1e} in the first iteration. To find these parameters in the general case it is necessary to solve the ionization and energy balance equations[9] for the function $f_0(v)$ defined by Eq. (1).

Following Kagan and Lyagushchenko,[7] we disregard the interaction with excited atoms, assuming their density to be small. Neglect of diffusion also imposes a lower bound on the permissible pressure values.[7,10]

There are no exact methods for solving Eq. (1). The inelastic collisions are usually taken into account with the aid of asymptotic methods.[5-7] In the case of the positive column of a dc discharge the WKB asymptotic form of the distribution function has been investigated in detail in refs. 7 and 8. The asymptotic distribution function used in these papers imposes a limitation on the electric-field amplitude. This limitation is dictated by the approximate method of determining the turning point, a knowledge of which is essential for an asymptotic representation of the distribution function in the inelastic interaction region.

In a dc discharge this limitation is of little importance in most cases; however, a microwave discharge is characterized by much higher values of the electric field.[11] We therefore propose in the present paper an asymptotic representation of the distribution function, such that the turning point coincides with the excitation threshold. We solve the kinetic equation in the following manner. We represent f_0 in the form

$$f_0=\varphi\Phi, \tag{4}$$

where

$$\varphi(v)=\exp\left\{-\int_0^v\frac{P_1(v)}{P_1(v)}v\,dv\right\}\equiv e^{-F(v)} \tag{5}$$

is the integral of Eq. (1) with zero right-hand side. By substituting (4) in (1) we obtain the following equation for Φ:

$$\frac{d^2\Phi}{d\xi^2}-Q(\xi)\Phi=0, \tag{6}$$

where $Q(\xi) = 2v^2(\xi)\varphi(\xi)h(\xi)\nu_c(\xi)q(\xi)$; $h = h_x + h_i$, and the new independent variable is defined by the relation

$$d\xi=\frac{dv}{v^2\varphi(v)P(v)}\equiv\frac{dv}{q(v)}. \tag{7}$$

It is easy to verify that replacement of the function to be found transforms the kinetic equation to the self-conjugate form; replacement of the independent variable (7) leads to the second canonical form, an equation of the wave type. Since $h(v) \equiv 0$ when $v < v_x$, where v_x corresponds to the excitation threshold, the quantity Q vanishes at all finite values $v \geq v_x$ only at the point ξ_x corresponding to $v = v_x$. It is known from the experimental data that $h\nu_c \sim v - v_x$ near threshold, so that the asymptotic form of the solution of (6) takes the following form:

$$\begin{aligned} \Phi &= C_1 + C_2 \int_0^v \frac{e^{F(v)}}{v^2 P(v)}\, dv \quad \text{if } v \leqslant v_x, \\ \Phi &= A \left[\frac{L}{Q^{1/2}}\right]^{1/2} K_{1/3}(L) \quad \text{if } v \geqslant v_x. \end{aligned} \tag{8}$$

Here,

$$L = \int_{v_x}^{v} \sqrt{\frac{2h\nu_e}{P(v)}}\, dv;$$

$K_{1/3}(L)$ is the MacDonald function. The integration constants C_1 and C_2 can be expressed in terms of the constant A by using the continuity conditions for the distribution function and its derivatives at the point $v = v_x$.

If we choose the independent variable to be the energy $u = mv^2/2$, we can obtain the electron energy distribution function $g_0(u)u^{1/2}$:

$$g_0(u)\, u^{1/2} = \begin{cases} A u^{1/2} e^{-F(u)} \left[1 - \frac{B}{2u_x} \int_u^{u_x} \left(\frac{u_x}{u}\right)^{3/2} \frac{P(u_x)}{P(u)} e^{F(u) - F(u_x)} du \right] & \text{if } u \leqslant u_x, \\ A u_x^{\frac{1}{2}} e^{-\frac{1}{2}[F(u) + F(u_x)]} \dfrac{\left(\frac{L}{Q^{1/2}}\right)^{1/2} K_{1/3}(L)}{\left[\left(\frac{L}{Q^{1/2}}\right)^{1/2} K_{1/3}(L)\right]_{u=u_x}} & \text{if } u \geqslant u_x. \end{cases} \tag{9}$$

The constant B is defined by the expression

$$B = u_x \frac{P_1(u_x)}{P(u_x)} - 1 + 2u_x \left\{\frac{\partial}{\partial u} \ln \left[\left(\frac{L}{Q^{1/2}}\right)^{1/2} K_{1/3}(L)\right]\right\}_{u=u_x},$$

and the quantity A is determined from the normalization condition

$$N_e = \int_0^\infty g_0(u)\, u^{1/2} du.$$

ENERGY BALANCE EQUATION AND FIELD IN PLASMA

As noted above, the density N_e and the temperature T_{1e}, which enter in the expression (9) for the distribution function, should be determined in the general case by simultaneously solving the ionization and energy balance equations. Under conditions typical of a nonequilibrium microwave discharge, the ionization and recombination processes proceed in many steps and are closely related to the kinetics of population of the atoms over the excited states.[12] On the other hand, the simultaneous determination of the electron energy distributions in the free and bound states is a very complicated problem; thus, instead of solving the ionization balance equation we use here the experimental values of N_e and determine the remaining unknown parameter T_{1e} from the energy balance equation.

In the energy balance equation we take account of the energy acquired by the electron from the electromagnetic field and the energy lost in elastic and inelastic collisions. The inelastic losses are due mainly to transitions to the first excited level.[12] The influence of collisions of the second kind will be neglected. The energy lost in direct ionization, according to our estimates, turns out to be negligibly small, while the losses due to stepwise ionization from the first excited state are of the order of several per cent of the total loss, and are therefore also disregarded here.

The energy balance equation is

$$\delta \int_0^\infty \nu_m u^{1/2} (u - u_g) g_0(u)\, du + \int_{u_x}^\infty h_x \nu_e u^{3/2} g_0(u)\, du = \int_0^\infty g_0(u) \frac{\partial}{\partial u} (\nu_{eE} u^{3/2})\, du. \tag{10}$$

We have used the notation

$$\nu_{eE} = 8.79 \cdot 10^{14} \frac{E^2}{u_{1e}\omega^2} \frac{\nu_m}{1 + \frac{\nu_m^2}{\omega^2}}, \tag{11}$$

$u_{1e} = 3kT_{1e}/2$, $u_g = 3kT_g/2$ (eV), and E is in V/cm.

In the case of argon we approximate the excitation cross section by Fabrikant's equation, which is given in ref. 13:

$$h_x \nu_e = 4 \cdot 10^8 p_0 u^{1/2} (u - 11.6) \exp\left\{1 - \frac{u - 11.6}{2.1}\right\}. \tag{12}$$

Here p_0 is the reduced gas pressure (in mm Hg).

Equation (10) and expression (9) for the distribution function contain the field in the plasma E. Strictly speaking, this field should be obtained by solving Maxwell's equations jointly with the equation for the distribution function. This is a very complicated independent problem, and we therefore consider in the present paper the behavior of the plasma parameters in a layer with dimensions smaller than those of the skin depth. The field in the plasma will be calculated from the equation for the case in which a plane wave of amplitude E_0 is incident on a half-space with homogeneous complex dielectric con- ε (ref. 14):

$$E = \frac{2E_0}{1 + \sqrt{\varepsilon}}, \tag{13}$$

where ε is determined by the relation

$$\varepsilon = 1 - \frac{4\pi e^2 N_e}{m(\omega^2 + \nu_{\text{eff}}^2)} \left\{K_e + i \frac{\nu_{\text{eff}}}{\omega} K_e\right\}. \tag{14}$$

Here, ν_{eff} is the effective frequency of the collision of the electrons with the neutrals, calculated for the first iteration of the distribution function.

RESULTS OF NUMERICAL CALCULATION AND COMPARISON WITH EXPERIMENT

The solution of the balance equation (10) and the de-

TABLE 1

	Manometer pressure p, mm Hg			
	6	14.5	20	80
p_0 (mm Hg)	3.6	8.34	11.5	41
E (V/cm)	69.4	47.3	43	41.7
T_{1e}(eV)	1.42	1.276	1.24	1.182
Λ (cm)	0.09	0.061	0.056	0.059

termination of the distribution function (9) have been carried out with a computer for the values $E_0 = 200$ V/cm and $\omega = 5.88 \cdot 10^{10}$ sec^{-1} in the pressure range 6-80 mm Hg. The electron densities N_e needed for the calculation are determined experimentally by microwave measurements of the plasma, using an arrangement described in detail in ref. 15; the dependence of the gas temperature T_g on the pressure is estimated with the aid of a tungsten thermocouple. The microwave discharge is ignited in a quartz tube with inner diameter 3 mm, placed perpendicularly to the broad walls of a standard 3-cm band waveguide. The power generated by the magnetron ensures a field $E_0 \sim 200$ V/cm in the waveguide. Table 1 lists the dependence of the reduced pressure p_0, of the field E in the plasma, of the temperature T_{1e} of the first iteration of the distribution function, and of the depth Λ of the skin layer on the manometer pressure p.

The ratio of the calculated distribution function to the Maxwellian function at the same values of the electron density and temperature is shown for different pressures in Fig. 1. As expected, in the energy region beyond the excitation threshold (marked by the arrow in Fig. 1), the calculated distribution function differs markedly from a Maxwellian.1) The decrease of the high-energy part of the distribution function in comparison with the Maxwellian function, as in the case of a dc discharge,[7,8] is due to the inelastic collisions. It is of interest to note that at high energies the variation of the distribution function as a function of the electron temperature and density is much stronger than that of the Maxwellian function corresponding to the same parameters. Thus, for example, in the region $u \sim 14$ eV, when T_{1e} changes from 1.2 to 1.43 eV (p changes from 80 to 6 mm Hg), the distribution function (9) increases by three orders of magnitude. For a Maxwellian distribution function, this increase amounts to only one order of magnitude.

The losses to elastic and inelastic collisions for the considered microwave discharge are illustrated in Fig. 2, which shows the relative fractions of energy lost by the electrons to excitation, Δ_x, and to heating of the gas, Δ_y. The figure shows for comparison the distribution of the losses in a dc discharge as taken from ref. 16. The effective field for the microwave discharge is defined in the usual manner

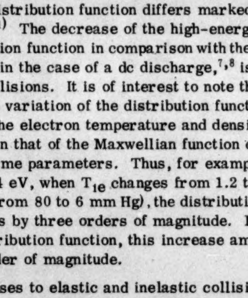

Fig. 1. Ratio of the obtained distribution function to the Maxwellian function vs the energy at different values of the reduced pressure. p_0, mm Hg: 1) 41; 2) 11.5; 3) 8.34; 4) 3.6.

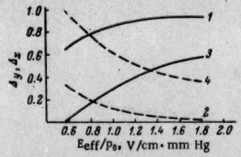

Fig. 2. Distribution of electron losses as a function of E_{eff}/p_0. 1, 2) Δ_x and Δ_y according to our calculations; 3, 4) Δ_x and Δ_y according to the data of ref. 16.

$$E_{\text{eff}} = \frac{E}{\sqrt{2}}\left(1 + \frac{\omega^2}{\nu_{\text{eff}}^2}\right)^{-1/2}.$$

The excess of inelastic losses over the elastic losses points to a less effective heating of the gas by the microwave field than in a dc discharge.

The calculated values of the electron temperature $T_e = (2/3)\langle u_e \rangle$, where $\langle u_e \rangle$ is the average energy, are shown in Fig. 3 as functions of the manometer pressure. The same figure shows the dependences of the electron density and of the electron gas, obtained experimentally and used in the calculations. The points show the experimental values of the electron temperature T_e as recalculated from the effective collision frequency measured by the microwave method. As follows from Fig. 3, the values $T_e \sim 1$-2 eV greatly exceed the value of T_g, which does not exceed 0.04-0.05 eV.

The right-hand side of Eq. (10) is the power W absorbed per unit volume in the skin layer of the microwave-discharge plasma. The absorbed power averaged over the cross section of the discharge tube is determined by experiment. For a qualitative comparison with experiment we define the averaged value of W as follows:

$$\tilde{W} = \frac{S}{S_0} W,$$

where S is the area of a ring of thickness equal to half the skin-layer depth, and S_0 is the area of the tube cross section.

Curves of W and $\tilde{W}$ versus the pressure are shown in Fig. 4. The points in this figure show the values of the specific absorbed power measured by a calorimetric method.

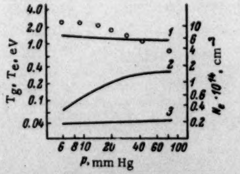

Fig. 3. Calculated dependence of the electron temperature T_e (curve 1) and experimental dependences of the electron density N_e (curve 2), of the gas temperature T_g (curve 3), and of the electron temperature T_e (points) on the pressure.

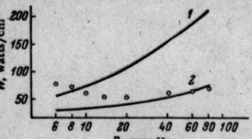

Fig. 4. Dependence of the power absorbed per cm³ of plasma on the manometer pressure. 1) W; 2) $\widetilde{W}$; the points show experimental values.

We call attention to the fact that at low pressures the experimental values of both the specific absorbed power (Fig. 4) and of the electron temperature (3) are higher than the corresponding calculated values. This discrepancy can apparently not be attributed to purely collisional absorption.[17-19]

At high pressures, the discrepancy in the experimental data in Fig. 4 is probably due to failure to take into account the spatial redistribution of the field inside the discharge gap and to neglect of the inhomogeneity of the electron density over its cross section.

CONCLUSIONS

1. By solving the Boltzmann kinetic equation including the electromagnetic field, the electron–electron, elastic, and inelastic collisions, we have obtained the electron energy distribution function in a microwave discharge; this distribution differs substantially from the Maxwellian distribution in the inelastic-interaction region.

2. A numerical solution has been obtained for the energy balance equation, using the obtained distribution function, and graphs have been constructed for the theoretical dependences of the electron temperature, of the elastic and inelastic losses, and of the power absorbed per unit plasma volume on the pressure.

3. The method discussed in the present paper makes it possible to determine by calculation important parameters of the plasma of a microwave discharge from known values of the electron density and the gas pressure.

The authors thank F. G. Bass and Yu. G. Gurevich for a discussion of the results and for useful remarks.

---

[1] At energies u < 9 eV, the calculated function exceeds the Maxwellian function by 1-4%, depending on the pressure p.

[1]P. L. Kapitsa, Zh. Eksp. Teor. Fiz., 57, 1801 (1969); 58, 377 (1970) [Sov. Phys. – JETP, 30, 973 (1970); 31, 199 (1970)].

[2]V. E. Golant and A. D. Piliya, Usp. Fiz. Nauk, 104, 413 (1972) [Sov. Phys. – Usp., 14, 413 (1973).

[3]A. M. Bass and H. P. Broida (eds.), Formation and Trapping of Free Radicals, Academic Press (1960).

[4]A. Ya. Usikov, I. D. Truten', A. P. Motornenko, and E. V. Belousov, Ukr. Fiz. Zh., 16, 705 (1971).

[5]V. E. Golant, Zh. Tekh. Fiz., 28, 755 (1957) [Sov. Phys. – Tech. Phys., 3, 703 (1958)].

[6]L. M. Kovrizhnykh, Zh. Eksp. Teor. Fiz., 37, 490 (1959) [Sov. Phys. – JETP, 10, 347 (1960)].

[7]Yu. M. Kagan and R. I. Lyagushchenko, Zh. Tekh. Fiz., 31, 445 (1961)[Sov. Phys. – Tech. Phys., 6, 321 (1961)]; 35, 821 (1964).

[8]Yu. M. Kagan, R. I. Lyagushchenko, and A. D. Khakhaev, Opt. Spektrosk., 14, 598 (1963); 15, 13 (1963).

[9]V. L. Ginzburg and A. V. Gurevich, Usp. Fiz. Nauk, 70, 201 (1960) [Sov. Phys. – Usp., 3, 115 (1960)].

[10]F. G. Bass and Yu. G. Gurevich, Usp. Fiz. Nauk, 103, 447 (1971) [Sov. Phys. – Usp., 14, 113 (1971)].

[11]A. I. Maksimov, Zh. Tekh. Fiz., 36, 1768 (1966) [Sov. Phys. – Tech. Phys., 11, 1316 (1967)].

[12]L. M. Biberman, V. S. Vorob'ev, and I. T. Yakubov, Usp. Fiz. Nauk, 107, 353 (1972) [Sov. Phys. – Usp., 15, 375 (1973)].

[13]W. Flugge, Ann. Phys., 18, 251 (1956).

[14]Ch. Wharton, in: Plasma Diagnostic Techniques, R. H. Huddlestone and S. L. Leonard (eds.), Academic Press (1965).

[15]E. V. Belousov and A. P. Motornenko, Zh. Tekh. Fiz., 41, 944 (1971) [Sov Phys. – Tech. Phys., 16, 743 (1971)].

[16]V. L. Granovskii, Electric Current in Gas, II [in Russian], Nauka, Moscow (1971).

[17]A. U. Trivelpiece, in: Engineering Problems of Magnetohydrodynamics [Russian translation], Mir (1965), p. 416.

[18]V. E. Golant, M. V. Krivosheev, and V. I. Fedorov, Zh. Tekh. Fiz., 40, 382 (1970) [Sov. Phys. – Tech. Phys., 15, 282 (1970)].

[19]N. Ts. Gerasimov, Dissertation, Moscow State Univ. (1972).

Electron energy distribution and electrical characteristics of the positive column in H_2 and $H_2 + Cl_2$

V. V. Zaitsev, A. I. Maksimov, and V. I. Svettsov
Ivanov Chemical Engineering Institute

(Submitted March 26, 1973; resubmitted May 28, 1973)
Zh. Tekh. Fiz., 44, 98-101 (January 1974)

The spatial variation of the electron energy distribution, the plasma potential, and of the floating potential in a striated glow discharge in hydrogen and in a hydrogen–chlorine mixture is studied experimentally at a pressure of 0.258 mm Hg and a current of 15 mA in a tube 26 mm in diameter and 50 cm long. It is shown that the fraction of high-energy electrons in the distribution function increases at a chlorine concentration of 0.01-0.1%. The radial variation of the floating potential and the plasma potential points to the possible existence of negative ions in the presence of chlorine.

The speed of processes in low-pressure discharge plasmas is in large measure determined by collisions of fast electrons. Thus, kinetic calculations require a knowledge of the electron energy distribution over the entire discharge volume. The distribution function has been investigated by many authors in inert[1–5] and molecular[6–9] gases.

It has been shown[10–12] that the degree of certain diatomic gases in a low-pressure discharge increases in the presence of small amounts of impurities which, as a rule, have a higher electron capture cross section; this leads to the production of negative ions. It seems that one mechanism by which impurities affect the plasma is the deformation of the electron energy distribution function, which changes the rate of dissociation of molecules under the action of electron impacts. In the present work we study the effect of chlorine impurities on the electron energy distribution in a striated positive column in a glow discharge in hydrogen. The investigations pertain to a discharge tube 26 mm in diameter and 500 mm long, at a current of 15 mA, and a pressure of 0.26 mm Hg. The linear gas flow velocity through the tube is several centimeters per second. The hydrogen is purified with the aid of a titanium generator[13] and is dried by cooling to liquid-nitrogen temperature. The chlorine is produced by thermal decomposition[14] of $CuCl_2$.

The electron energy distribution has been plotted by the method proposed by M. Druyvesteyn[15] using the experimental arrangement described in refs. 16 and 17. The plasma potential is found by equating to zero the second derivative of the probe current.[18–20]

The measurements are performed with 0.08-cm platinum probes with uninsulated tips 3 mm long which can be moved along the discharge tube axis and radius. The axial and radial positions of the probes can be measured to within ± 0.5 mm and ± 0.05 mm, respectively.

Before the measurements the discharge tube is processed for 3-4 h in pure hydrogen and then evacuated to a pressure of 10^{-5} mm Hg. To clean the probe a current five to six times the normal operating current (i.e., 250-300 mA) is drawn through the probe during processing.

The distribution function is normalized to unity using the expression

$$\int_0^\infty \sqrt{u}\,\frac{d^2i}{du^2}\,du = 1, \tag{1}$$

where u is the probe potential with respect to plasma.

The electron density is calculated from the probe current i_g and plasma potential

$$n_e = \frac{i_g}{e}\,\frac{4}{S}\,\frac{1}{\sqrt{\frac{2e}{m}}}\,\frac{\int_0^\infty \sqrt{u}\,\frac{d^2i}{du^2}\,du}{\int_0^\infty u\,\frac{d^2i}{du^2}\,du}. \tag{2}$$

Here, S is the probe area, and e and m are the electron charge and mass, respectively. Numerical calculations with expressions (1) and (2) have been carried out on a Promin'-2 computer.

RESULTS

We have investigated the effect of chlorine concentration in hydrogen on the electron energy distribution function. Typical results are shown in Figs. 1-3. In all measurements the distribution function has, in addition to the main peak at about 1 eV, a second peak at 10-15 eV.

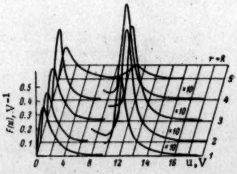

Fig. 1. Radial variation of electron energy distribution function in the positive column of a glow discharge. x/L = 0.1, where x is the distance from the cathode end of the striation, and L is the length of the striation. r: 1) 0; 2) 2; 3) 5; 4) 8; 5) 11.

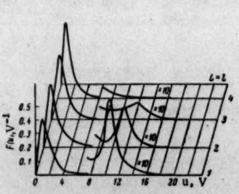

Fig. 2. Variation of electron energy distribution function for different locations of probe in a striation. *l*: 1) 0; 2) 4; 3) 8; 4) 11.

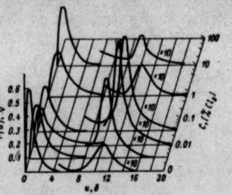

Fig. 3. Effect of electronegative impurity on the distribution function for r/R = 0.1 and x/L = 0.1.

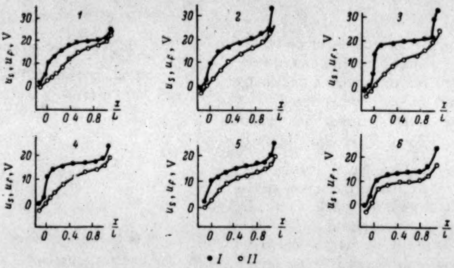

Fig. 4. Longitudinal variation of potential. 1) Plasma potential, u_s; II) floating potential, u_f; 1) H_2; Cl_2: 2) 0.004%; 3) 0.01%; 4) 0.04%; 5) 0.7%; 6) 10%.

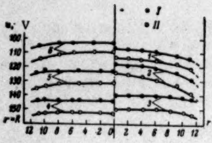

Fig. 5. Radial variation of potential. I) Plasma potential, u_s; II) floating potential, u_f; 1) H_2; Cl_2: 2) 0.004%; 3) 0.01%; 4) 0.04%; 5) 0.07%; 6) 10%.

In the direction from the axis towards the tube walls, the distribution function is enhanced by fast electrons from the second peak (Fig. 1, H_2 + 0.04% Cl_2) (see ref. 21). Along any given striation the peak decreases in the direction towards the discharge tail. The second peak disappears entirely in the tail of a striation (Fig. 2, H_2 + 0.04% Cl_2).

The data in Fig. 3 indicate that the addition of chlorine has a marked effect on the distribution function even at energies beyond the dissociation threshold of hydrogen molecules. This mechanism should thus appreciably affect the rate of dissociation of hydrogen molecules under the action of electron impacts and also the yield of hydrogen atoms.

The available data are insufficient for a detailed interpretation of the changes in the distribution function. Clearly, chlorine molecules, which cause rapid volume annihilation of electrons in the course of dissociative capture, change the charge balance conditions and the conditions of striation formation. The axial variation of the potential with impurity content is not gradual. The most rapid potential change at the beginning of a striation is observed at about 0.01% Cl_2 (Fig. 4). The variations of the longitudinal field and the electron energy distribution function are obviously closely related.

At the same time, the electron capture cross section and the ionization potential of Cl_2[22] have maxima near the first and second peaks respectively of the distribution function. It is thus reasonable to expect that the process of electron capture should reduce the first group in the distribution function, while the quite strong ionization of Cl_2 in high chlorine concentrations attenuates the second peak. Our measurements prove that the rate of electron capture is quite high at a chlorine concentration of about 0.01%. Figure 5 shows the radial distribution of potential for different Cl_2 concentrations. At about 0.01% Cl_2, the radial distribution is practically flat, indicating a high relative density of negative ions.[23]

---

[1] N. B. Kolokolov, Diss. LGU (1971).

[2] D. Herrmann, A. Rutscher, and S. Pfau, Beit. Plasmaphys., B11, 75 (1971).

[3] D. Herrmann, Beit. Plasmaphys., B11, 84 (1972).

[4] K. F. Bessonov, S. N. Oreshak, A. F. Stepanov, and V. A. Stepanov, Zh. Tekh. Fiz., 40, 1900 (1970) [Sov. Phys. – Tech. Phys., 15, 1481 (1971)].

[5] Yu. M. Kagan and V. M. Milenin, Zh. Tekh. Fiz., 35, 1907 (1965) [Sov. Phys. – Tech. Phys., 10, 1470 (1966)].

[6] N. D. Twiddy, Proc. Roy. Soc., 262, 379 (1961).

[7] M. Z. Novgorodov, A. P. Sviridov, and N. N. Sobolev, ZhETF Pis. Red., 8, 341 (1968) [JETP Lett., 8, 211 (1968)].

[8] Yu. I. Ivanov, L. S. Polak, and D. I. Slovetskii, Khim. Vys. Energ., 5, 312 (1971).

[9] Yu. I. Kagan and N. K. Mitrofanov, Zh. Tekh. Fiz., 41, 2065 (1971) [Sov. Phys. – Tech. Phys., 16, 1636 (1972)].

[10] R. A. Young, R. L. Sharpless, and R. Stringham, J. Chem. Phys., 40, 117 (1964).

[11] A. M. Bass and H. P. Broida (eds.), Formation and Trapping of Free Radicals, Academic Press (1960).

[18] V. M. Milenin, Zh. Tekh. Fiz., 41, 831 (1971) [Sov. Phys. – Tech. Phys., 16, 654 (1971)].
[19] A. I. Lukovnikov and M. Z. Novgorodov, Zh. Tekh. Fiz., 41, 2433 (1971) [Sov. Phys. – Tech. Phys., 16, 1931 (1972)].
[20] D. Herrmann, S. Pfau, and H. Kagel, Beit. Plasmaphys., B12, 1 (1972).
[21] R. L. F. Boyd and F. D. A. Boylett, Proc. Roy. Soc., A296, 233 (1967).
[22] S. C. Brown, Elementary Processes in Gas Discharges, Wiley, New York (1961).
[23] J. B. Thompson, Proc. Roy. Soc., A282, 503 (1961).
[12] F. MacTaggart, Plasmochemical Reactions in Electrical Discharges [Russian translation], Atomizdat, Moscow (1972).
[13] W. Espe and A. Hex, Feinwertechnik, 69, 489 (1963).
[14] F. P. Hubermann, J. Mol. Spectrosc., 20, 29 (1966).
[15] M. Druyvesteyn, Zs. Phys., 64, 781 (1930).
[16] V. V. Zaitsev, A. I. Maksimov, and V. I. Svettsov, Proc. of the Ivanovsk Chemical Engineering Institute, 14, 37 (1971).
[17] V. V. Zaitsev, A. I. Maksimov, and V. I. Svettsov, Zh. Tekh. Fiz., 42, 1894 (1972) [Sov. Phys.–Tech. Phys., 17, 1517 (1973)].

Effect of electron–atom collisions on electron motion in a gas diode

V. I. Babanin and A. Ya. Énder

Ioffe Physicotechnical Institute,
Academy of Sciences of the USSR, Moscow

(Submitted April 9, 1973)
Zh. Tekh. Fiz., 44, 102-112 (January 1974)

The kinetic equation for the electron distribution function in the gap of a plane gas diode is solved with elastic scattering of electrons by atoms. Specific calculations are made under the following assumptions: 1) The electric field is constant over the gap; 2) the scattering cross section is inversely proportional to electron velocity. The electron density and flux are computed in addition to the distribution function. The effect of various boundary conditions at the cathode on the parameters in question is considered. At low Knudsen numbers the diffusion approximation is valid and Knudsen-layer effects are demonstrated near the boundary. Study of the current as a function of the initial electron velocity at the cathode shows that the reflection onto the cathode is strongest when the initial electron energy is of the order of the energy acquired in the electric field in crossing the gap. For thermionic emission from the cathode a good approximate boundary condition is provided by an isotropic monoenergetic distribution with a velocity modulus that is equal to the mean-square velocity of the initial Maxwellian distribution.

The behavior of electrons in the gap of a gas diode is determined by the nature of the electric field and by collision processes. At modest voltages, for which excitation and ionization processes can be neglected, it is necessary to take account of elastic scattering of electrons by atoms. Reference 1 gives numerical estimates for the effect of electron scattering on the volt–ampere characteristic and the potential distribution over the diode gap for Knudsen numbers on the order of unity, using the Monte Carlo method. Reference 2 uses a kinetic equation to investigate the effect of electron scattering on the current passing through the diode when there is a plasma in the gap and the potential jumps are concentrated in narrow regions near the electrodes. In this case no electric field is present in the basic part of the gap in which scattering occurs.

In the present paper we solve the kinetic equation for the electron distribution function in the diode with an electric field in the gap, over a wide range of Knudsen numbers. The solution of the kinetic problem is necessary to compute the volt–ampere characteristics of the diode. In addition, a knowledge of the electron distribution function near the anode is needed to compute the ignition potential in the diode. In the region of low Knudsen numbers we consider the transition to the diffusion approximation and compare the results obtained in this approximation with the exact solutions. This procedure makes it possible to evaluate the effect of Knudsen boundary layers on the diode characteristics.

Consider a plane horizontal diode with transverse electrode dimensions that greatly exceed the electrode spacing d. We direct the x axis from the cathode to the anode and take the cathode to be the origin of the x coordinate and the potential $\Phi(x)$. The electron distribution function $f(x, \mathbf{v})$ depends on x and the velocity $\mathbf{v}$ with its components v_x, v_y, v_z. Since energy transfer in elastic collisions between electrons and atoms is small (of the order of the electron–atom mass ratio), we can neglect energy losses in collision events. In this approximation a collision only affects the direction of the electron velocity, and the kinetic equation can be written in the form

$$v_x \frac{\partial f(x, \mathbf{v})}{\partial x} + \frac{e}{m} \frac{d\Phi(x)}{dx} \frac{\partial f(x, \mathbf{v})}{\partial v_x} = \frac{f^*(x, v) - f(x, \mathbf{v})}{\tau(v)},$$

$$f^*(x, v) = \frac{1}{4\pi} \int\limits_{(4\pi)} f(x, \mathbf{v})\, d\Omega. \qquad (1)$$

Here, we use the model of the collision integral in which the term describing the approach to a given point of phase volume is proportional to the velocity of the distribution function as averaged over direction. In (1), e is the charge and m is the mass of the electron, $\tau(v) = [n_a \Sigma(v) v]^{-1}$ is the time between collisions, n_a is the density of atoms, and $\Sigma(v)$ is the total scattering cross section, which depends on the modulus of v. If the differential cross section is independent of the scattering angle, Eq. (1) is exact. The boundary conditions at the electrodes are

$$f(0, \mathbf{v})|_{v_x>0} = f_0(\mathbf{v}); \quad f(d, \mathbf{v})|_{v_x<0} = f_d(\mathbf{v}). \qquad (2)$$

Equation (1) with boundary conditions (2) can be formally integrated (see, e.g., ref. 3, where a similar procedure is carried out for a kinetic equation describing ion motion allowing for resonant charge transfer on atoms). If we limit ourselves to a monotonic potential distribution ($d\Phi/dx > 0$), after integration[1)] we have

$$f(x, \mathbf{v}) = \begin{cases} f_0[u(0), v_y, v_z]\, Z(0, x) + \int\limits_0^x J Z(x', x) \frac{dx'}{u(x')}; \\ \qquad \sqrt{\frac{2e\Phi(x)}{m}} < v_x < v, \\ \int\limits_\eta^x J Z(x', x) \frac{dx'}{u(x')} + \Bigl[f_d[-u(d), v_y, v_z]\, Z(\eta, d) \\ \quad + \int\limits_\eta^d J Z(\eta, x') \frac{dx'}{u(x')} \Bigr] Z(\eta, x); \quad 0 < v_x < \sqrt{\frac{2e\Phi(x)}{m}}, \\ f_d[-u(d), v_y, v_z]\, Z(x, d) + \int\limits_x^d J Z(x, x') \frac{dx'}{u(x')}; \\ \qquad -v < v_x < 0, \end{cases} \qquad (3)$$

$$J \equiv J[x', v(x')] = \tau^{-1}[v(x')]\, f^*[x', v(x')], \qquad (4)$$

$$Z(x_1, x_2) = \exp\left\{ -\int\limits_{x_1}^{x_2} \frac{dx''}{\tau[v(x'')]\, u(x'')} \right\}. \qquad (5)$$

Here,

$$u(x') = |v_x'| = \sqrt{v_x^2 - \frac{2e}{m}[\Phi(x) - \Phi(x')]}$$

is the absolute value of the x component of the velocity, and

$$v(x')=\sqrt{u(x)^2+v_y^2+v_z^2}$$

is the modulus of the electron velocity at x if at x the corresponding values are $|v_x|$ and v and the electron traverses a path between x' and x without collisions. Expressions (4) and (5) have a simple physical meaning: $jdx'dv'_x$ yields the electron flux resulting from collisions in an element of phase space $dx'dv'_x$ (the remaining coordinates being omitted as inessential). The fraction Z(x, x') of this flux [or Z(x,x'), depending on the direction of motion] reaches the point x and makes a contribution

$$JZ(x',\ x)\frac{dx'}{u(x')}$$

to the distribution function. Thus, the integral terms in (3) are the contributions to the distribution function from electrons that have experienced collisions in the gap prior to arriving at point x. The terms outside the integrand describe particles that have arrived at the point in question from the electrodes without collisions. In writing *f*(x, v) in the interval

$$0<v_x<\sqrt{\frac{2e\Phi(x)}{m}}$$

we allow for two possible types of electron trajectories: The first term corresponds to particles that move between the points x' and x (x' < x) with velocity projection $v'_x > 0$, while the second corresponds to particles on reverse trajectories, i.e., those which move from x' (x' > x) to the return point η with $v'_x < 0$ and then from η to x with $v'_x > 0$. The point η is determined from the condition $u(\eta) = 0$.

If we neglect energy losses in collisions, the total electron energy is conserved:

$$W=\frac{mv^2}{2}-e\Phi(x)=\text{const.}$$

Consequently, contributions to the distribution function at x for the given value of the modulus of v, i.e., the total energy W, can only come from those electrons which have the same total energy at other points. In other words, electrons with different total energies move independently of one another in the gap. If, therefore, we change from v to W in (3)-(5), i.e., if we assume that

$$v\equiv v(x,\ W)=\sqrt{\frac{2}{m}[W+e\Phi(x)]}, \qquad (7)$$

and introduce the distribution function

$$f(x,\ W,\ \vartheta,\ \varphi)=f[x,\ v(x,\ W),\ \vartheta,\ \varphi]\frac{v(x,\ W)}{m}$$

with respect to the energy W and angles ϑ and φ of a spherical coordinate system whose polar axis is directed along x, the variable W becomes a parameter of the equation. The equation itself describes the motion in the gap of electrons emitted by the cathode with kinetic energy W and by the anode with corresponding energy $W + e\Phi_d$ (Φ_d being the anode potential). Integrating both parts of the equation for *f*(x, W, ϑ, φ) over the angles and changing the order of integration on the right side, we can obtain an integral equation for the distribution function

$$\varphi(x,\ W)=4\pi f^*[x,\ v(x,\ W)]\frac{v(x,\ W)}{m}$$

over the energy W:

$$\varphi(x,\ W)=\varphi_0(x,\ W)\theta(W)+\varphi_d(x,\ W)\theta[W+e\Phi(x)] + \int\limits_{\eta(W)\theta(-W)}^{d} K(x,\ x',\ W)\varphi(x',\ W)\,dx'. \qquad (8)$$

Here, η(W) is determined from the condition

$$v(\eta,\ W)=0,\quad \theta(x)=\begin{cases}1, & x>0,\\ 0, & x<0,\end{cases}$$

$$K(x,\ x',\ W)=\frac{v(x',\ W)^{-1}}{2\tau(x',\ W)} \times \begin{cases} \displaystyle\int\limits_{\sqrt{\frac{2e}{m}[\Phi(x)-\Phi(x')]}}^{v(x,\ W)} Z(x',\ x)\frac{dv_x}{u(x')} + \int\limits_{\sqrt{\frac{2e}{m}[\Phi(x)-\Phi(x')]}}^{\sqrt{\frac{2e}{m}\Phi(x)}} Z(\eta,\ x')Z(\eta,\ x)\frac{dv_x}{u(x')}, & x'<x,\\ \displaystyle\int\limits_{-v(x,\ W)}^{0} Z(x,\ x')\frac{dv_x}{u(x')} + \int\limits_{0}^{\sqrt{\frac{2e}{m}\Phi(x)}} \cdot Z(\eta,\ x')Z(\eta,\ x)\frac{dv_x}{u(x')}; & x'>x,\end{cases} \qquad (9)$$

$$\left.\begin{aligned} \varphi_0(x,\ W)&=\frac{1}{m}\int\limits_0^{2\pi} d\varphi \int\limits_{\sqrt{\frac{2e}{m}\Phi(x)}}^{v(x,\ W)} f_0\Bigg[\sqrt{\frac{2W}{m}},\\ &\qquad \arccos\left[\frac{u(0)}{v(0,\ W)}\right],\ \varphi\Bigg] Z(0,\ x)\,dv_x,\\ \varphi_d(x,\ W)&=\frac{1}{m}\int\limits_0^{2\pi} d\varphi\Bigg\{\int\limits_{-v(x,\ W)}^{0} f_d\Bigg[\sqrt{\frac{2(W+e\Phi_d)}{m}},\\ &\qquad \arccos\left(\frac{-u(d)}{v(d,\ W)}\right),\ \varphi\Bigg] Z(x,\ d)\,dv_x\\ &\qquad + \int\limits_0^{\min\left[v(x,\ W),\ \sqrt{\frac{2e}{m}\Phi(x)}\right]} f_d\Bigg[\sqrt{\frac{2(W+e\Phi_d)}{m}},\\ &\qquad \arccos\left(\frac{-u(d)}{v(d,\ W)}\right),\ \varphi\Bigg] Z(\eta,\ d)Z(\eta,\ x)\,dv_x\Bigg\}. \end{aligned}\right\} \qquad (10)$$

In (9)-(10), $\tau(x,\ W) \equiv \tau[v(x,\ W)]$ and $Z(x_1,\ x_2)$ is determined from Eq. (5) with $\tau[v(x'')]$ replaced by $\tau(x'',\ W)$. The equations in (10) contain boundary functions (2) in the spherical coordinate system. Once $\varphi(x,\ W)$ is known we can readily compute the distribution function *f*(x, W, ϑ, φ) and the current density F(x, W) of electrons with a given energy W. The latter is determined by the right side of (8) with dv_x in (9) and (10) replaced by $v_x dv_x$. The total density n and flux ν at x are obtained by integrating $\varphi(x, W)$ and $F(x, W)$ with respect to the energy W.

We limit ourselves to the case in which the anode does not emit electrons and in which electrons which reach the electrodes are completely absorbed. In this case $f_d(v) = 0$, and $f_0(v)$ characterizes an external source at the cathode.[2] The boundary conditions on the cathode that we consider will be of three different types: a) a beam with fixed velocity v_0 directed along the normal to the cathode; b) an isotropic distribution with velocity modulus v_0; and c) a Maxwellian distribution with cathode temperature T.

The boundary functions $f_0(v)$ for $v_x > 0$, as normalized to the flux ν_0 in the x direction, have the following form, respectively:

$$\text{a)}\quad f_0=\frac{\nu_0}{2\pi v_0^3}\delta(v-v_0)\,\delta(1-\cos\vartheta),$$

$$\text{b)}\quad f_0=\frac{\nu_0}{\pi v_0^3}\delta(v-v_0),$$

$$\text{c)}\quad f_0=\frac{2\alpha^2\nu_0}{\pi}\exp(-\alpha v^2),\quad \alpha=\frac{m}{2kT}.$$

In cases a and b, the total energy $W_0 = (mv_0^2)/2$ is fixed and $\varphi_0(x, W)$ [and consequently, $\varphi(x, W)$ as well] is proportional to $\delta(W - W_0)$. Setting $\varphi_d = 0$ in (8) and integrating with respect to W, we obtain the following equation for $n(x, W_0)$, the density of monoenergetic electrons emitted by the cathode:

$$n(x,\ W_0)=n_0(x,\ W_0)+\int\limits_0^d K(x,\ x',\ W_0)\,n(x',\ W_0)\,dx'. \tag{11}$$

Here, $n_0(x, W_0)$ is the coefficient for $\delta(W - W_0)$ in (10) for $\varphi_0(x, W)$. Expressions for the distribution function $\chi(x, W_0, \vartheta, \varphi)$ over the angles and flux $\nu(x, W_0)$ of monoenergetic electrons in terms of $n(x, W_0)$ can be obtained similarly from the expressions for $f(x, W, \vartheta, \varphi)$ and $F(x, W)$. The solution of the problem for boundary condition c is found as the superposition of the solutions obtained for case b with various v_0 values, each solution being taken with weight $W_0/(kT)^2 \exp(-W_0/kT)$. For example, the density is

$$n(x)=\int\limits_0^\infty \frac{W_0}{(kT)^2}\exp\left(-\frac{W_0}{kT}\right)n(x,\ W_0)\,dW_0. \tag{12}$$

We use the resultant equations to calculate the boundary conditions of the form a, b, and c with the following assumptions: 1) τ = const, i.e., $\sum \sim 1/v$, and 2) the electric field E = const. These assumptions make the problem more specific and result in simplifications in the kernel of integral equation (8). The first assumption holds approximately for helium atoms;[4] the second holds at low current densities, where space-charge effects are unimportant. This assumption can also be used in analyzing deviations from the 3/2 law associated with scattering.

Let us consider the solution of (11) in greater detail. In changing to dimensionless variables, the basic parameter of the problem is isolated:

$$N=\frac{2d}{v_d\tau},\quad v_d=\sqrt{\frac{2e\Phi_d}{m}}=\sqrt{\frac{2e\,|E|\,d}{m}}.$$

For $e\Phi_d \gg W_0$ the parameter N is roughly equal to the inverse of the Knudsen number. (In the other limiting case, $e\Phi_d \ll W_0$, the function of the inverse Knudsen number is provided by the quantity $d/v_0\tau = v_dN/2v_0$.) In dimensionless variables (11) assumes the form

$$y(u)=y_0(u)+\int\limits_0^1 K(u,\ u')\,y(u')\,du', \tag{13}$$

$$K(u,\ u')=\frac{Nu'}{2\sqrt{u'^2+u_0^2}}\begin{cases}\displaystyle\int\limits_{\sqrt{u^2-u'^2}}^{\sqrt{u^2+u_0^2}}\exp[-N(\rho-\rho')]\frac{d\rho}{\rho'} \\ \displaystyle+\int\limits_{\sqrt{u^2-u'^2}}^{\infty}\exp[-N(\rho+\rho')]\frac{d\rho}{\rho'}, & u>u', \\ \displaystyle\int\limits_{-\sqrt{u^2+u_0^2}}^{\infty}\exp[-N(\rho'+\rho)]\frac{d\rho}{\rho'}, & u<u'.\end{cases} \tag{14}$$

Here

$$u=\sqrt{\frac{x}{d}}=\frac{\sqrt{\frac{2e}{m}\Phi(x)}}{v_d},\quad u_0=\frac{v_0}{v_d},$$

$$\rho=\frac{v_x}{v_d},\quad \rho'=\sqrt{\rho^2-(u^2-u'^2)}.$$

The density is measured in units of $n_0 = \nu_0/v_d$.

Substituting the boundary distribution functions into (10) we obtain the following for the term outside the integrand in (13):

$$y_0(u)=\begin{cases}\dfrac{1}{\sqrt{u^2+u_0^2}}\exp\left[-N\left(\sqrt{u^2+u_0^2}-u_0\right)\right] & \text{for case a)}, \\ \dfrac{2}{u_0^2}\displaystyle\int\limits_0^{u_0}\frac{\exp\left[-N\left(\sqrt{u^2+\rho_0^2}-\rho_0\right)\right]\rho_0\,d\rho_0}{\sqrt{u^2+\rho_0^2}} & \text{for case b)},\end{cases} \tag{15}$$

We also write out the expression for the dimensionless flux $i = \nu/\nu_0$:

$$i(u)=i_0(u)+\int\limits_0^1 K_1(u,\ u')\,y(u')\,du'. \tag{16}$$

Here the kernel $K_1(u, u')$ is determined from (14) with $d\rho$ replaced by $\rho\,d\rho$, and

$$i_0(u)=\begin{cases}\exp\left[-N\left(\sqrt{u^2+u_0^2}-u_0\right)\right] & \text{for case a}, \\ \dfrac{2}{u_0^2}\displaystyle\int\limits_0^{u_0}\exp\left[-N\left(\sqrt{u^2+\rho_0^2}-\rho_0\right)\right]\rho_0\,d\rho_0 & \text{for case b}.\end{cases} \tag{17}$$

When the number of collisions is large ($N \gg 1$), the expression for the flux at a distance from the boundaries can be simplified. In this case the principal term in (16) is the integral term, and the kernel has a sharp peak for $u = u'$. Expanding $y(u')$ in a Taylor series in the neighborhood of u and limiting ourselves to the first two terms in the expansion, we obtain the diffusion equation

$$i=\frac{1}{3N}y(u)-2\frac{u^2+u_0^2}{3N}\frac{dy}{d(u^2)}, \tag{18}$$

whose solution, allowing for the fact that the flux is con-

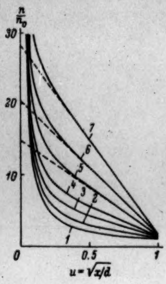

Fig. 1. Density distributions over the gap for u = 0. N: 1) 0; 2) 1; 3) 2; 4) 3; 5) 5; 6) 7; 7) 10.

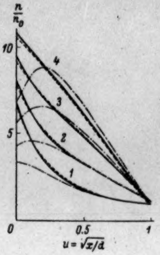

Fig. 2. Density distributions over the gap for $u_0 = u_m = 0.3$: boundary conditions a are represented by the dot–dash lines, conditions b by the dashed lines, and c by the solid lines; N: 1) 0; 2) 2; 3) 5; 4) 10.

stant over the gap, has the form $y(u) = 3Ny[1 + C(u^2 + u_0^2)^{1/2}]$, C being an arbitrary constant. This solution is a monotonic function of u, which is linear for $u_0 = 0$. We can similarly obtain the diffusion equation in the general case of an arbitrary dependence of the cross section on the energy and an arbitrary potential distribution. In dimensional variables, this has the form

$$\nu = U\,|E|\,n - D\frac{dn}{dx}. \tag{19}$$

Here

$$U = \frac{e\tau(x,\ W_0)}{3m} \text{ and } D = \frac{v^2(x,\ W_0)\,\tau(x,\ W_0)}{3}$$

are the local mobility and diffusion coefficients. Equation (19) has also been obtained in ref. 5 for a mean free path that is independent of velocity.

To obtain a numerical solution, Eq. (13) is reduced to a system of algebraic equations.[6] Assume that u_m, m = 0, 1, . . ., n, are points which break down the interval $0 \leq u \leq 1$ into n equal parts. Then the system of equations for determining the approximate values of the density y_m at the points $\tilde{u}_m = (u_{m-1} + u_m)/2$ has the form

$$\begin{gathered} y_m = y_{0m} + \sum_{p=1}^{n} A_{mp} y_p; \\ A_{mp} = \int\limits_{u_{p-1}}^{u_p} K(\tilde{u}_m,\ u')\,du';\quad m = 1,\ 2,\ \ldots\ n. \end{gathered} \tag{20}$$

The matrix elements A_{mp} are double integrals over fairly complex regions in the u', ρ plane, the integrand having a singularity at u' = u, ρ = 0 in the diagonal elements. After making the change of variables $t = N(\rho \pm \rho')$, $z = N\rho$ (the sign of ρ' being the same as the corresponding sign in the argument of the exponent of the integrand), we can integrate analytically with respect to the variable z; as a result we obtain

$$A_{mp} = I_{m,\,p-1} - I_{mp} + J_{mp} + \begin{cases} E_{mp} - E_{m,\,p-1}; & p < m, \\ 2 - E_{m,\,p-1} - E_{mp}; & p = m, \\ E_{m,\,p-1} - E_{m,\,p}; & p > m. \end{cases} \tag{21}$$

Here

$$E_{mp} = \exp(-|a_{mp}|),\ \ I_{mp} = a_{mp}[Ei(-|a_{mp}|) - Ei(-b_{mp})];$$
$$a_{mp} = N\left(\sqrt{\tilde{u}_m^2 + u_0^2} - \sqrt{u_p^2 + u_0^2}\right),\ \ b_{mp} = N(\tilde{u}_m + u_p);$$

Ei(x) is an integral exponent;

$$J_{mp} = N\int\limits_{u_{p-1}}^{u_p} \frac{(t - \tilde{u}_m)\exp[-N(t + \tilde{u}_m)]}{\sqrt{t^2 + u_0^2} + \sqrt{\tilde{u}_m^2 + u_0^2}}\,dt.$$

After computing the matrix elements, Eq. (20) is solved by successive approximations. We investigate the accuracy of the computations by varying the number of segments n and by checking the constancy of the flux at various points of the gap. The final data are obtained for n = 20. The error in the results for N = 10 and $u_0 \ll 1$ does not exceed 5% and decreases rapidly with decreasing number of collisions.

Let us now consider the computational results. Figures 1-4 show the density distribution over the gap for various N values (indicated on the figures). Figure 1 refers to zero initial electron velocity at the cathode. It is evident that an increase in the number of collisions leads to accumulation of electrons in the gap and to an increase in density. The curves N = 5, 7, 10 are linear at a distance from the boundaries, this corresponding (in the coordinates $\sqrt{x/d}$) to the diffusion approximation. The dashed lines give the results of solving (18) for a density in the center of the gap and a flux taken from the corresponding solutions of the kinetic equation. The solutions of the diffusion equation thus obtained and those of the kinetic equation coincide at a distance from the boundaries. In the Knudsen layer near the cathode, however, the solutions diverge (the effects of the Knudsen anode layer are not apparent in the coordinates used).

It is interesting to compare the density distributions over the gap for various conditions of type a) and b) with nonzero velocities u_0 (dot–dash and dashed curves in Figs. 2-4). The decrease in density near the cathode in case a as compared to b is associated with the fact that in the former case there are no particles emitted by the cathode at velocities directed along the electrodes. This leads to the appearance of characteristic maxima on the corresponding curves. The separation of the maxima from the cathode with increasing initial velocity is associated with the increase in the free path of the electrons. In the diffusion region, there is a tendency for curves re-

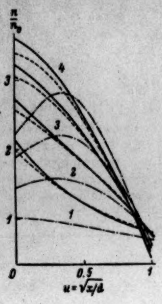

Fig. 3. Density distributions over the gap for $u_0 = u_m = 1$. N: 1) 0; 2) 2; 3) 5; 4) 10.

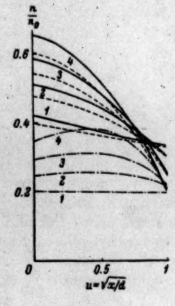

Fig. 4. Density distributions over the gap for $u_0 = u_m = 5$. N: 1) 0; 2) 2; 3) 5; 4) 10.

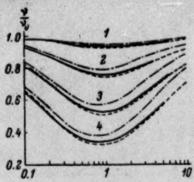

Fig. 5. Flux as a function of u_0 for cases a and b and of u_m for case c: N: 1) 0.5; 2) 2; 3) 5; 4) 10.

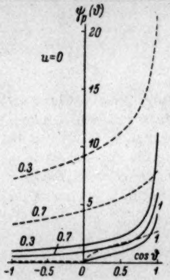

Fig. 6. Distribution functions of scattered electrons with respect to the angle ϑ for $u_0 = 0$: solid curves) N = 2; dashed curves) N = 10; the parameter on the curves represents the distance from the cathode $u = (x/d)^{1/2}$.

ferring to different boundary conditions to converge. The discrepancies here are associated with the unequal effect of the Knudsen anode layer on the electron flux with different boundary conditions.

The flux as a function of the initial velocity u_0 for various N for cases a (dot–dash curves) and b (dashed curves) is shown in Fig. 5. The strongest reflection of electrons from the volume onto the cathode occurs for $u_0 \approx 1$, i.e., for initial electron energy values on the order of the energy acquired in the electric field in passing through the gap. In the limiting cases of small and large initial velocities u_0, the reflection effect attenuates and $i \to 1$. Indeed, for $u_0 = 0$, only those electrons that are scattered in a direction that is strictly perpendicular to the cathode surface can reach the cathode, but the proportion of these electrons is infinitesimal. The increase in the flux as $u_0 \to \infty$ is asociated with the increase in free path, i.e., with the specific assumption regarding the way in which the electron scattering cross section depends on the velocity.

Figures 6 and 7 show distribution functions of monoenergetic electrons with respect to the angle ϑ at various points of the gap ϑ: $\Psi(\vartheta) = (1/n_0)\int_0^{2\pi} \chi(x, W_0, \vartheta, \varphi)d\varphi$ (the parameter shown on the curves is $u = \sqrt{x/d}$). Figure 6 ($u_0 = 0$) and 7a (case a, $u_0 = 0.5$) show the distribution functions $\psi_p(\vartheta)$ of scattered particles. The primary beam, attenuated by collisions, yields a contribution to the distribution function only for $\vartheta = 0$ in these cases, i.e., $\Psi_0(\vartheta) = y_0\,\delta(1-\cos\vartheta)$, and is not shown in the figures. Figure 7b (case b, $u_0 = 0.5$) shows the total distribution function. The solid curves refer to N = 2, while the dashed curves refer to N = 10. For $u_0 \neq 0$ the distribution functions have typical discontinuities at values of the angle $\vartheta = \vartheta_0$ given by the expression

$$\cos\vartheta_0 = \frac{u}{\sqrt{u_0^2 + u^2}} = \frac{e\Phi(x)}{\sqrt{W_0 + e\Phi(x)}},$$

which are particularly pronounced at low collision numbers. The discontinuities are associated with the effect of the boundary. In the case of a beam (Fig. 7a), the sharp decrease in the number of electrons in the interval $0 < \vartheta < \vartheta_0$ is to be explained by the fact that there is no contribution to the distribution function from electrons that have executed reverse trajectories, because of the presence of the electron-absorbing cathode. For an isotropic source at the cathode (Fig. 7b), the presence in the interval $0 < \vartheta < \vartheta_0$ of electrons that leave the cathode without collisions compensates for the effect of absorption of scattered electrons by the cathode and results in an increased number of electrons for these angle values. For large N there are discontinuities only in immediate proximity to the boundary. In the diffusion region, the distribution function depends weakly on the angle and is quasiisotropic.

In conclusion, we consider certain results for thermionic emission from the cathode [boundary conditions of type c]. Using the results obtained for case b and Eq. (12), we compute the density distributions over the gap for various values of $kT/e\Phi_d$. Similar calculations have also been performed for the electron flux. Comparison of the flux as a function of $kT/e\Phi_d$ for case c and of the flux as a function of u_0 for case b shows that the results virtually coincide in both cases if

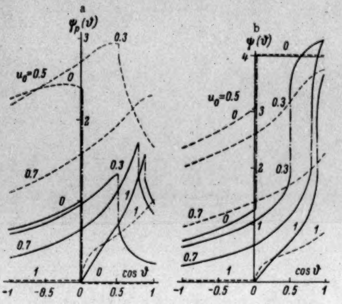

Fig. 7. Electron distribution functions with respect to the angle ϑ for cases a) and b) and with $u_0 = 0.5$.

$$u_0=\sqrt{\frac{3kT}{2e\Phi_d}}.$$

This result is illustrated in Fig. 5, in which the solid curves show the flux as a function of $u_m = \sqrt{v_m/v_d}$, where $v_m = \sqrt{3kT/m}$ is the root-mean-square velocity of the Maxwellian distribution. The greatest discrepancy in the region of the maxima of the curves does not exceed 5%.

Figures 2-4 give a comparison of the concentration distributions over the gap for boundary conditions b (dashed curves) and c (solid curves) for $u_0 = u_m$. It can be seen that there is good agreement here as well, particularly when the initial velocities are not large. The results are associated with the properties of the weighting function with which integration was performed in (12): The basic contribution to the density and flux in case c comes from electrons whose initial energy is on the order of the mean thermal energy of the Maxwellian distribution. As the cathode temperature increases, the weighting-function maximum is spread out, and this results in more pronounced discrepancies in the behavior of the density in cases b and c. These discrepancies are most pronounced near the cathode, but even here the maximum deviation in the curves (for $u_0 = 5$ and N = 10) does not exceed 10%.

Thus, in solving the kinetic equations for electrons with thermionic emission at the cathode we can replace the complex Maxwellian distribution by a simpler monoenergetic isotropic distribution with velocity modulus equal to the root-mean-square velocity as determined by the cathode temperature.

[1)] Similar equations for the case $f_d = 0$ are given in ref. 2.

[2)] Equation (8) can also be used for elastic reflection at the anode. In this case $f_d(v)$ is expressed in terms of the desired distribution function at the anode for $v_x > 0$ from the reflection condition.

[1] Ch. M. Goldstein, Intern. Conf. on Thermionic Electrical Power Generation, London, September (1965).
[2] É. L. Nagaev, Zh. Tekh. Fiz., 34, 745 (1964) [Sov. Phys. – Tech. Phys., 9, 569 (1964)].
[3] Yu. M. Kagan and V. I. Perel', Dokl. Akad. Nauk SSSR, 108, 222 (1956) [Sov. Phys. – Dokl., 1, 289 (1956)].
[4] D. R. Bates (ed.), Atomic and Molecular Processes, Academic Press (1962).
[5] G. Hertz, Zs. Phys., 32, 298 (1925).
[6] N. M. Krylov and N. N. Bogolyubov, Dokl. Akad. Nauk SSSR, Ser. A, 12, 283 (1929).

Diagnostics of a laser-produced plasma by a scattering method using an electron-optical image converter

E. A. Burunov, G. M. Malyshev, G. T. Razdobarin, and V. V. Semenov

A. F. Ioffe Physicotechnical Institute,
Academy of Sciences of the USSR, Leningrad

(Submitted March 22, 1973)
Zh. Tekh. Fiz., 44, 113-118 (January 1974)

A scattering method is used to study a spark in air at atmospheric pressure at times from 1.5 to 60 μsec after the spark is initiated. Radial profiles of the electron density are obtained in a single laser pulse by means of an electron-optical image converter. There is a high electron density in the plasma at distances out to 2 mm from the center of the spark. The dimensions of this region fall off as a function of the time and the density at the center of the spark falls off from $2\cdot10^{18}$ to $3\cdot10^{16}$ cm^{-3}.

We have used a scattering method to study the plasma of a laser spark in air previously, determining the electron temperature and density at the center of the laser spark from the collective-scattering spectrum[1] and determining the radial profile of the electron density.[2] In those experiments we have determined the laser parameters at a single time after the initiation of the spark.

In the present work we have used an electron-optical image converter to obtain radial density distributions in a laser spark at various times. We have studied a laser spark in air at atmospheric pressure at times from 1.5 to 60 μsec after the initiation of the spark.

The image converter makes it possible to obtain the radial profile of the electron density during a single laser pulse. It is therefore possible to avoid errors associated with changes in the parameters of the laser spark from pulse to pulse. It is also possible to obtain certain additional information and to carry out the experiments more rapidly.

EXPERIMENTAL APPARATUS

Figure 1 shows the experimental apparatus used in this study of the plasma of a laser spark by a scattering method involving detection of the radiation by an image converter.

The laser spark arises at the focal point of lens L_1(F = 3 cm), at which the radiation from ruby laser P_1, with an energy of about 1 J, is focused. The radiation from probing laser P_2, P_3 is focused by lens L_2(F = 20 cm) and passes through the spark, intersecting its axis at an angle of 90°. The laser producing the spark and the probing laser are synchronized,[3] by a total-internal reflection prism (R_1).

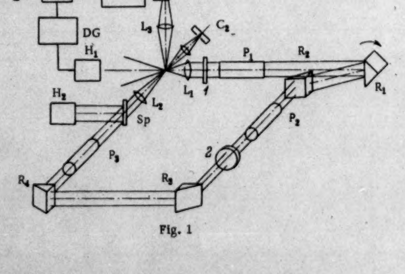

Fig. 1

The scattered radiation is detected at an angle of 90° with respect to the plane passing through the axes of the two lasers. Lens L_3(F = 10 cm) and rotating prism R_5 project the image of the scattering volume on a 1:1 scale onto the entrance slit of monochromator M in such a manner that different parts of the spark in the path of the probing beam are projected onto different vertical points of the slit. The image of the exit slit of the monochromator is focused by lens L_4(F = 9.8 cm) onto the photocathode of an electron-optical image converter (IC). The image obtained on the screen of the converter is photographed by camera C_1.

In addition to photographing the image on the image converter screen, we record oscillograms of both laser pulses, to monitor the laser energy and to determine the delay of the probe laser with respect to the laser producing the spark.

We also record shadow photographs of the spark at the same times, in order to determine the spark dimensions.

Spurious scattered radiation is suppressed by irises placed along the laser path, and the laser spark is enclosed in a light-tight housing. These measures reduce the spurious scattered radiation to a level of less than a few percent of the radiation scattered by the plasma or the air.

A DM-1 diffraction monochromator with a linear dispersion of 22 Å/mm and a relative aperture of 1:10 is used. The widths of the entrance and exit slits of the monochromator are 0.25 and 0.3 mm, respectively, and the slits are 10 mm high.

The radiation is detected by a UMI-93 electron-optical converter operating in the slave mode. The sweep direction is perpendicular to the height of the slit image. The sweep time is 10 μsec. The sweep is triggered by photocell H_1, which receives some of the light from the laser producing the spark. The trigger time is selected by delay generator DG for studying various phases of the spark. The gain of the image converter is set at a value (approximately 30) which provides a sufficient range of measurable radiation intensities at the scattering-signal level in our experiments. The resolution of the converter is at least 10 lines/mm.

The overall spatial resolution along the probing beam is about 0.2 mm. The number of resolvable elements along the laser beam is about 50. The resolution along the observation line is governed by the diameter of the probing laser beam, which is 0.3 mm. The resolution in the third direction is governed by the width of the entrance slit of the monochromator (0.25 mm).

The overall spatial resolution of the system for detecting the scattered radiation is thus about 0.02 mm^3 (0.2 × 0.3 × 0.25).

EXPERIMENTAL PROCEDURE

Figure 2a shows one of the photographs obtained from the screen of the image converter. This photograph shows a time sweep of the radiation passing through the monochromator and striking the photocathode of the image converter. The time axis here is directed from top to bottom. The horizontal axis corresponds to various points along the height of the monochromator slit.

During the early stages of the spark there is spurious scattered radiation from the laser producing the spark. This radiation has the same pulse length as the laser radiation (~ 30 nsec) and the same wavelength (λ = 6943 Å). The monochromator is tuned to this wavelength. The spurious scattered radiation therefore passes through the monochromator, strikes the photocathode of the image converter, and produces a bright band (the horizontal band at the top of the photograph) on the converter screen. The length of this band corresponds to the height of the monochromator slit.

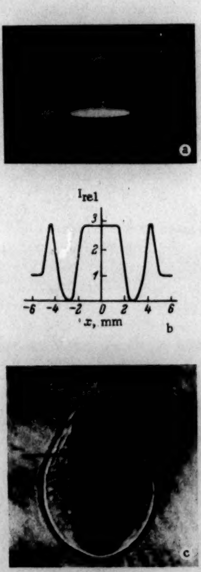

Fig. 2

The broadening of the band due to its displacement on the converter screen is small because of the comparatively low sweep rate; accordingly, the width of this band corresponds approximately to the width of the monochromator slit.

Part of the radiation in the continuous spectrum of the spark itself in the region λ = 6943 Å and within the spectral width of the monochromator slit also passes through the monochromator. This radiation is emitted from the entire volume of the laser spark selected by the entrance slit of the monochromator, and is integrated along the line of sight.

As time elapses, the dimension of the spark along the monochromator slit increases, while the radiation intensity decays. On the time-sweep photograph, accordingly, the light from the spark appears first at the center of the upper horizontal band and expands downward. The resolving time of this sweep is about 300 nsec.

When the probe laser operates, the radiation scattered by the plasma of the spark and by the gas is emitted from only a small volume along the laser beam. The direction of the probing beam penetrating the spark is shown on the shadow photograph in Fig. 2c.

The scattered radiation lies in a narrow spectral region near λ = 6943 Å (its spectral width is much narrower than that of the slit). It passes through the monochromator and forms a bright band on the converter screen (the lower part of the photograph).

The intensity distribution along the bright band corresponds to that of the scattered radiation along the laser beam penetrating the spark. This distribution, obtained with a microphotometer, is shown$^{1)}$ in Fig. 2b. Here, the intensity unit is that of the radiation scattered by air unperturbed by the laser spark.

On both the photograph and in Fig. 2b the intensity profile is radial with good spatial resolution and requires no further Abel analysis. The resolving time here is governed only by the length of the laser pulse and is about 30 nsec.

Figures 2a and 2b show that there is scattered radiation from the central region of a spark. This radiation corresponds to scattering by the plasma with intensity proportional to the electron density. About 2 mm from the center of the spark the electron density falls off, and the intensity of the scattered radiation decays rapidly. We see that the gas density reaches a maximum at the shock front and then falls to the density of the unperturbed gas (air at atmospheric pressure).

Since the cross section for scattering by air is known, we can determine the absolute electron density by comparing the intensities of the radiation scattered by air and by the plasma.

Accordingly, the photograph of the converter screen yields, with good temporal and spatial resolution, the radial profile of the electron density in the plasma, the absolute densities, the radial profile of the gas density, the spark radiation as a function of the time, etc.

The data in Fig. 2 are obtained by probing the spark 2.7 μsec after it is initiated. Figure 3 shows the corre-

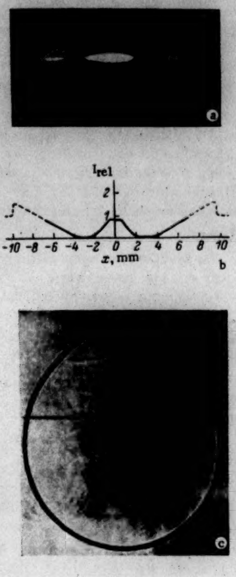

Fig. 3

sponding data for a different time (9.5 μsec). Here the sweep begins later, and the initial stages of the spark are not observed. The shock front has already gone beyond the height of the slit. Its position in Fig. 3b is shown by the dashed curves. The amount of radiation scattered from the central part of the spark in this case is approximately one third that of the preceding case. The electron densities differ by the same factor.

The errors involved in the determination of the absolute electron density consist primarily of the error in the measurement of the relative intensities of the radiation scattered by the plasma and the air and the error in the value of the collective-scattering cross section. In these calculations we assume this cross section to be half the Thomson cross section. The total error in the determination of the absolute electron density is estimated to be about 20%.

The relative electron densities for a given radial distribution are determined much more accurately.

RESULTS AND DISCUSSION

Figure 4 shows radial profiles of the intensity of the scattered radiation at four times, from 2.7 to 50 μsec. Here, as in Figs. 2b and 3b, the intensity unit is the intensity of Rayleigh scattering by unperturbed air. Initially, while the plasma is dense, the radiation scattered by it is several times more intense than Rayleigh scattering by unperturbed air. By 50 μsec the electron density has fallen off markedly, and the radiation scattered by the plasma falls to less than one third the intensity of Rayleigh scattering. We see from the intensity profile for 2.7 μsec that the gas density at the shock front is roughly three times the density of the unperturbed gas. The velocity of the shock front at this time can be determined from a series of shadow photographs taken in succession; it turns out to be 2.5 times the sound velocity in the unperturbed gas. These gas densities and front velocities agree well with shock-wave theory.[4] We therefore adopt the theoretical value for the temperature at the shock front – about 600°K under the present conditions. In a shock wave at this temperature and this density there would be no appreciable dissociation or ionization, so we find more support for the Rayleigh scattering mechanism in the shock wave.

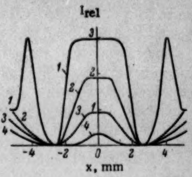

Fig. 4. Radial profiles of the intensity of the scattered radiation. t, μsec: 1) 2.7; 2) 6.5; 3) 9.5; 4) 50.

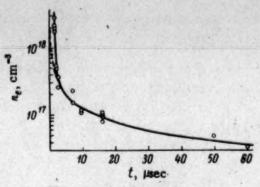

Fig. 5. Electron density at the center of the laser-spark plasma as a function of the time.

Figure 5 shows the change in the electron density as a function of the time for the center of the laser spark. The curve is drawn through the experimental points obtained for various sparks produced by beams with energies from 1 to 1.5 J. We see that from 1.5 to 60 μsec the electron density falls off by about two orders of magnitude. The density changes most rapidly during the first 3 μsec. Subsequently, from 3 to 60 μsec, the electron density decay is slower. Over this time interval the density decay is described by $n_e \sim t^{-0.7}$. This functional dependence, shown by the dashed curve in Fig. 5, merges with the experimental curve from 3 to 60 μsec. The more rapid density decay during the first 3 μsec can be attributed to the high recombination rate. The density decay at the center of the spark after 3 μsec can occur as a result of either recombination or radial expansion of the plasma. If the density decay is due primarily to expansion, as in the case of a laser spark in hydrogen during certain time intervals,[5] the increase in the specific volume as a function of the time under our conditions would be proportional to $t^{+0.7}$. This result agrees with strong-explosion theories.[2)] If, on the other hand, there is appreciable recombination, the increase in the specific volume at the center of the spark should be slower than $t^{+0.7}$.

The electron density in peripheral regions of the spark can be determined as a function of the time from the radial

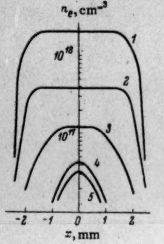

Fig. 6. Radial profiles of the electron density in the plasma of a laser spark. t, μsec: 1) 1.5; 2) 2.7; 3) 9.5; 4) 50; 6) 60.

profiles of the density at various times, from 1.5 to 60 μsec, after the appearance of a spark (Fig. 6). We see from this figure that the profiles are homogeneous at 1.5 and 2.7 μsec. The only important reduction in the electron density occurs in the boundary layer of the plasma in a region less than 1 mm wide. As time elapses, the electron density of the plasma falls off everywhere. The density decays most rapidly in the boundary layer of the plasma.

As a result there is spreading of the boundary layer. The boundary itself, despite the radial expansion, moves toward the center. This result is evidence of rapid recombination at the plasma boundary.

[1)] There is some nonuniformity in the illumination of the slit along its height, because of the slight misalignment of the slit with respect to the probing beam; this misalignment is difficult to avoid. This nonuniformity is taken into account in the analysis of the results.

[2)] According to strong-explosion theory[6] the specific volume is $v = 1/n_e \sim t^{6/5\gamma}$; if the ratio of specific heats $\gamma = C_p/C_v = 5/3$, we have $v \sim t^{0.72}$.

[1] G. M. Malyshev, G. T. Razdobarin, and V. V. Semenov, Zh. Tekh. Fiz., 42, 1429 (1972) [Sov. Phys.—Tech. Phys., 17, 1137 (1973)].

[2] G. M. Malyshev, G. T. Razdobarin, and V. V. Semenov, Plasma Diagnostics [in Russian] (in press).

[3] T. P. Evtushenko, G. M. Malyshev, G. V. Ostrovskaya, V. V. Semenov, and T. Ya. Chelidze, Zh. Tekh. Fiz., 36, 1115 (1966) [Sov. Phys.—Tech. Phys., 11, 818 (1966)].

[4] F. A. Baum, K. P. Stanyukovich, and B. I. Shekhter, Physcis of Explosions [in Russian], GIFML, Moscow (1959), p. 189.

[5] M. M. Litvak and D. F. Edward, Appl. Phys., 37, 4462 (1966).

[6] L. I. Sedov, Similarity and Dimensionality Methods in Mechanics [in Russian], Izd. Nauka, Moscow (1965), p. 241.

Accelerators

Proton extraction from the 70-GeV accelerator for the Ludmila liquid-hydrogen chamber (extraction system S)

A. A. Aseev, A. I. Drozhdin, B. A. Zelenov, É. A. Merker, L. L. Moizhes, K. P. Myznikov, A. A. Roshchin, V. M. Tatarenko, M. A. Kholodenko, A. D. Artemov, L. N. Vaulin, V. I. Gordin, I. I. Kovalevskii, V. N. Rozhkov, M. M. Suvorov, A. S. Sudarushkin, and V. I. Chuiko

Institute of High-Energy Physics, Serpukhov
Efremov Scientific-Research Institute of Electronics, Physics, and Automation, Leningrad

(Submitted April 4, 1973)
Zh. Tekh. Fiz., 44, 119-130 (January 1974)

Extraction of the proton beam from the 70-GeV accelerator of the Institute of High-Energy Physics for the Ludmila liquid-hydrogen chamber is described. The features of the beam extraction and transport systems, the design parameters, the tolerances, and the characteristics of the apparatus are discussed. The method used to align the system is discussed. The results of the alignment of the system are reported.

1. THE EXTRACTION SCHEME

To obtain the separated beams of secondary particles used in experiments with the Ludmila liquid-hydrogen chamber, the overall scheme[1] for extracting protons from the 70-GeV accelerator includes a provision for fast extraction in the S direction. According to the operating conditions of the radio-frequency (rf) separator, the extraction should last no more than 5 μsec, i.e., the beam must be extracted during one orbit or less. The operating conditions of the rf separator impose extremely rigid requirements on the characteristics of the beam focused on the external target and on the stability of these characteristics from cycle to cycle. The beam at the outer target must be no more than 1.5 mm in the vertical direction and 2 mm in the horizontal direction, with an angular divergence no larger than ± 2.5 mrad. The instability in the beam position must be better than ± 0.2 mm.

The basic principles used in the design of the fast-extraction system S and the beam-focusing system are described in ref. 2. Figure 1 shows the scheme for extracting the beam from the accelerator chamber. The apparatus used previously to extract protons in the direction of the Mirabel' chamber[3] (extraction system A) is used in this scheme. The fast extraction is achieved with pulsed magnet PM 16, in linear gap 16. Here, the field increases and decays during the time between the passages of successive bunches of the accelerated beam. The pulsed magnet deflects the beam into the gap of movable septum magnet DM 24. This magnet is inserted into the working part of the accelerator before the extraction section, being located at the inner edge of the accelerated beam. In this manner the deflection angle required in the pulsed magnet can be minimized. Magnet DM 24 deflects the beam into the gap of septum magnet DM 26; the field strength in the latter magnet determines whether the beam is extracted from the accelerator into linear gap 28 or 30. In these gaps, outside the vacuum chamber, are deflecting magnets DM 28 and DM 30, which deflect the extracted beam either toward the Mirabel' bubble chamber (extraction system A) or toward the Ludmila bubble chamber (extraction system S). This system provides rapid extraction of protons with an efficiency near 100% over the energy range 30-75 GeV. The system operates three times in each acceleration cycle; the extraction can be in different directions or in the same direction. In each extraction from 1 to 30 bunches of the accelerated beam can be extracted. The extraction time can be adjusted correspondingly from 15 nsec to 5 μsec. The energy level can also be varied from extraction to extraction.

The system for extracting the beam toward the Mirabel' chamber was put into operation in February 1972; it is described in detail elsewhere.[3,4] Below we summarize the work on extraction toward the Ludmila chamber; this extraction system was put into operation in October 1972.

2. FOCUSING SYSTEM

Figure 2 shows the arrangement of the elements of the system for transporting the extracted beam to the ex-

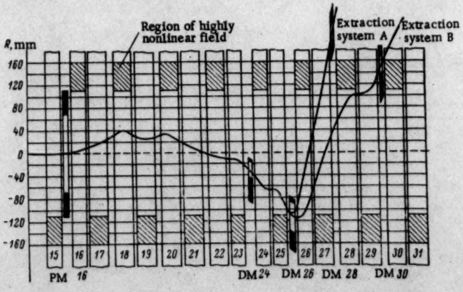

Fig. 1. Scheme for fast extraction of protons from the accelerator.

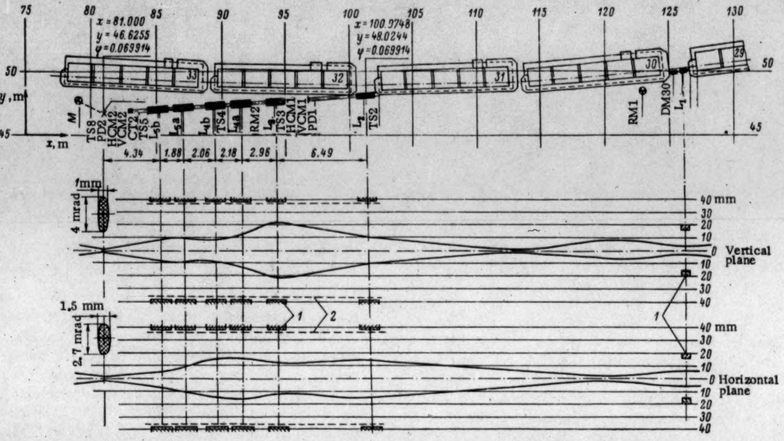

Fig. 2. Arrangement of the apparatus in the region in which the beam is transported to the external target. TS) Television screen; CT) current transformer; PD) position detector; RM) radiation monitor; M) target monitor; HCM) horizontal correcting magnet; VCM) vertical correcting magnet; 1) lens aperture; 2) aperture of vacuum chamber.

ternal target, which is 45 m away from the extraction point. More than 20 m of the trajectory of the extracted beam is in the fringing field of units 30 and 31. A quadrupole focusing lens L_1 is located in linear gap 30 in front of deflecting magnet DM 30 to compensate for the strong defocusing effect of the fringing field in the horizontal direction. Immediately after the extraction into "free space," in linear gap 32, is lens L_2, which prevents an extreme increase in the beam dimensions at the entrance to the triplet lens L_3, L_4, L_5.

The design of the optical system takes into account the actual characteristic of the accelerated beam as determined experimentally.[5] The design emittance in both planes is taken to be π mm · mrad. Since very rigid requirements are imposed on the beam focusing, careful account is taken of the accelerator magnetic field, the characteristics of the fringing field of the main magnet, and the actual characteristics of the magnets and lenses in the transport system. The extraction trajectory is completely outside regions with highly nonlinear magnetic fields. In calculation related to the motion within the working region of the accelerator (± 10 cm from the central orbit) the magnetic field is specified on the basis of the results of the magnetic measurements. The nonlinear terms of up to the fifth order, inclusively, in the expansion of the magnetic field are taken into account. The equations of motion are integrated numerically on a BÉSM-6 computer. The motion of the extracted beam in regions more than 10 cm radially away from the central orbit is calculated on the basis of a program in which the magnetic field is specified on the basis of a map plotted with an error no worse than ± 0.5% (ref. 6).

The parameters of the focusing system are chosen to minimize the dimensions of the beam envelope in both planes and thus to minimize the effects of the nonlinearities in the lenses and magnets. Figure 3 shows the beam dimension at the entrance to lens L_2 as a function of the gradient in lens L_1. A gradient of 65 T/m is chosen; this value minimizes the horizontal dimension of the beam at the entrance to lens L_2. The gradients in lenses L_2–L_5 are calculated on a computer by a program which allows the initial phase ellipse of the beam to be transformed in such a manner ellipse of the beam to be transformed in such a manner that a crossover with specified dimensions in both planes is achieved at the external target. The numerical values of the matrix elements for the transport along the extraction trajectory within the accelerator and in the fringing-field region are also calculated on a computer. Figure 4 shows the gradients in lenses L_2–L_4 as functions of the dimensions of the beam at the external target. The design dimensions are 1 mm (vertical) and 1.5 mm (horizontal) chosen on the basis of the beam spreading at the target due to instabilities in the magnet and lens currents and due to nonlinearities. For this case Fig. 2 shows the envelopes of the beam in both planes, the beam dimensions, and the angular divergence at the external target corresponding to an initial emittance of π mm · mrad.

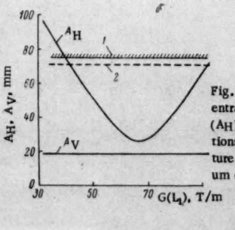

Fig. 3. Dimensions of the beam at the entrance to lens L_2 in the horizontal (A_H) and vertical (A_V) planes as functions of the gradient in lens L_1. 1) Aperture of lens L_2; 2) aperture of the vacuum chamber.

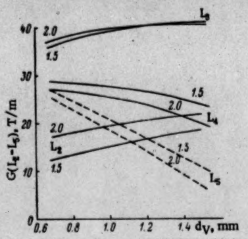

Fig. 4. Gradients in lenses L_2-L_4 for various horizontal (d_H) and vertical (d_V) dimensions of the beam at the external target. Here the parameter is d_H, in millimeters.

Since the transport system is long, methods have been worked out for correcting the direction and position of the extracted beam. In the horizontal plane the beam is guided by magnet DM 26 to the center of the exit window, in front of linear gap 30. After passing through lens L_1 the beam enters magnet DM 30, which deflects it to the center of correcting magnet HCM1. This magnet brings the beam into exact coincidence with the optical axis of the triplet lens. In the vertical plane the beam is guided along the center of the exit window by means of a local distortion of the vertical orbit of the circulating beam in the extraction region. Figure 5 shows the shape of the local distortions produced by two pairs of polar correcting windings of the main magnet of the accelerator. The distortion produced by windings 27 and 33 is intended to correct the extraction coordinate. That produced by windings 24 and 30 is intended to correct the vertical angle of the beam extraction. Through an appropriate choice of the currents in the two pairs of windings the beam can be guided exactly to the center of the exit window, at an extraction angle bringing the beam to the center of the triplet lens. If necessary, the beam axis can be brought into coincidence with the triplet axis by means of vertical corrector VC1. The pair of correcting magnets HCM2 and VCM2 in front of the external target regulates the point and angle at which the extracted beam is incident on the target, in such a manner that the secondary particles formed by the beam are guided exactly along the channel axis in the rf separator.

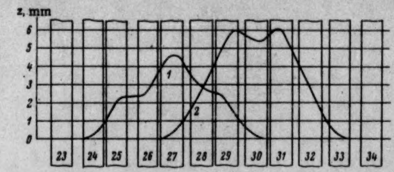

Fig. 5. Shape of the local distortions in the vertical orbit caused by polar windings 24 and 30 (curve 1) and 27 and 33 (curve 2).

3. BASIC CHARACTERISTICS OF THE APPARATUS

Table 1 shows the characteristics of the magnets and lenses in extraction system S. The pulsed magnet is a C-shaped ferrite magnet consisting of 10 sections. The single-turn winding is made from flat conductors. Each section is connected to a separate pulse generator. The field in a section of the magnet is excited by discharging an artificial storage line charged to 80 kV. The rise time of the current in the magnet is less than 150 nsec. The pulse length can be varied from 15 nsec to 5 μsec. Septum magnets DM 24 and DM 26 are of basically the same design, differing in the aperture dimensions. Their C-shaped cores are made from transformer iron. The single-turn windings of the magnets have an external conductor which is a thin partition (or septum), 3 mm thick for DM 24 and 5 mm thick for DM 26. Magnet DM 24 is movable. In each acceleration cycle it is inserted into the working region of the accelerator by a hydraulic system, which moves it 100 mm in 0.3 sec. The error of the positioning of the magnet in its working position is ± 0.5 mm. The pulsed magnet and the septum magnets were constructed at CERN and are described in detail elsewhere.[7,8] The other magnets and lenses have been developed in the Scientific-Research Institute for Electrophysical Apparatus. Deflection magnet DM 30, of type SP 143, is a C-shaped magnet with an aperture 40 mm wide and 32 mm high. It is constructed from stacks of iron-alloy plates 3 mm thick. Since the magnet is in the immediate vicinity of the accelerator, measures are taken to reduce its fringing field outside the gap. For this purpose a high-permeability partition is placed at the edge of the gap. This magnet will be used in the future in the slow-extraction

TABLE 1

Unit	Designation	Type	Length (iron), mm	Aperture mm		Maximum value		Working value*		Temporal stability of field, %	Spatial homogeneity at maximum field, %
				horizontal	vertical	field, T	gradient, T/m	field, T	gradient, T/m		
	DM 16										
Pulsed magnet	DM 24	—	3000	140	100	0.1	—	0.093	—	± 3.0	± 3.0
Deflecting magnet	DM 26	—	1500	35	30	1.0	—	0.56	—	± 0.1	± 0.1
		—	3000	60	30	1.4	—	0.496	—	± 0.1	± 0.1
	DM 30	SP 143	580	40	32	1.8	—	0.636	—	± 0.1	± 0.2
Correcting magnet	HCM 1	SP 147	500	80	58	1.8	—	—	—	± 0.1	± 0.5
	HCM 2	SP 147	500	80	58	1.8	—	—	—	± 0.1	± 0.5
	VCM 1	SP 148	500	58	80	1.8	—	—	—	± 0.1	± 0.5
	VCM 2	SP 148	500	58	80	1.8	—	—	—	± 0.1	± 0.5
Quadrupole lens	L_1	3K70	700	ø 30		—	100	—	66.6	± 0.1	± 0.5
	L_2	7.5K150A	1500	ø 75		—	40	—	15.0	± 0.1	± 0.5
	L_3	7.5K150A	1500	ø 75		—	40	—	39.1	± 0.1	± 0.5
	L_{4a}, L_{4b}	7.5K150A	1500	ø 75		—	40	—	27.4	± 0.1	± 0.5
	L_{5a}, L_{5b}	7.5K150A	1500	ø 75		—	40	—	21.0	± 0.1	± 0.5

*For a momentum of 70 GeV/c.

TABLE 2

Lens type	G_0, T/m	$k=3$		$k=4$		$k=5$		$k=6$		$k=10$	
		γ_3, %	φ_{03}, deg	γ_4, %	φ_{04}, deg	γ_5, %	φ_{05}, deg	γ_6, %	φ_{06}, deg	γ_{10}, %	φ_{010}, deg
3K70	50	0.09	47	0.43	126	0.06	0	0.69	10	0.64	187
	95	0.77	92	0.43	109	0.07	304	0.18	45	0.49	184
7.5K150A	20	0.04	176	0.12	302	0.02	67	0.39	343	0.06	219
	40	0.18	120	0.18	309	0.04	60	0.23	208	0.05	215

system, so its power supply shapes trapezoidal current pulses, at amplitudes up to 2 kA and with flat parts up to 1 sec long. The flat parts of the current pulses are regulated within ± 0.1%.

The transport system includes quadrupole lenses of two types. For the preliminary focusing, lens L_1 is a 3K70 lens with an aperture 30 mm in diameter. The other six lenses, of type 7.5K150A, have apertures 75 mm in diameter. All the correcting magnets are the same type and have apertures 58× 80 mm in size. The lenses and magnets of the transport system are pulsed. They are made from stacks of iron-alloy plate 0.5 mm thick. The power supplies feeding the magnets and lenses produce unipolar sinusoidal current pulses with amplitudes up to 5 kA and a half-period of about 10 msec. The amplitudes of these current pulses are regulated within ± 0.1%. Lens L_1, like magnet DM 30, will be used in the future in the slow-extraction system, so the corresponding power supplies are similar.

We have carefully studied the magnetic characteristics of each element. The magnetic-measurement program includes measurement of the gradient G_0 at the center of the lens, at its axis, as a function of the excitation current. It also involves measurement of the effective length of the lens, $L_{\mathrm{eff}} = (1/G_0)\int_{-\infty}^{\infty}(dB/dx)_{x=y=0}dz$. In the 7.5K150A lenses, the value of L_{eff} falls off by less than 1% when G_0 is changed from 6 to 40 T/m. The deviations in the values of L_{eff} from sample to sample are less than ± 0.2%. The induction components of the magnetic field of the lens can be written in terms of polar coordinates (r, φ) as the harmonic series

$$B_r = -\sum_{k=1}^{\infty} A_k r^{k-1} \sin(k\varphi + \varphi_{0k}), \tag{1}$$

$$B_\varphi = -\sum_{k=1}^{\infty} A_k r^{k-1} \cos(k\varphi + \varphi_{0k}), \tag{2}$$

where k is the index of the harmonic and φ_{0k} is the initial phase of harmonic k. We measure the relative integrated amplitudes of the harmonic components

$$\gamma_k = \frac{\int_{-\infty}^{\infty} A_k dz}{\int_{-\infty}^{\infty} A_2 dz} a^{k-2}$$

at aperture radius a. The error in the γ_k measurements for the fundamental harmonics is ± 0.01%. Typical measured values of γ_k and φ_{0k} for the two types of lenses are shown in Table 2.

Figure 6 illustrates the results of the measurements with curves of the relative deviation of the integral gradient along the transverse axes x and y for a 7.5K150A lens; these curves are plotted from the results of the harmonic analysis:

$$\frac{\Delta\int G_x dz}{\int G_x dz} = \frac{\int_{-\infty}^{\infty}\left(\frac{dB_y}{dx}\right)_{x,y} dz - \int_{-\infty}^{\infty}\left(\frac{dB_y}{dx}\right)_{x=y=0} dz}{\int_{-\infty}^{\infty}\left(\frac{dB_y}{dx}\right)_{x=y=0} dz}, \tag{3}$$

$$\frac{\Delta\int G_y dz}{\int G_y dz} = \frac{\int_{-\infty}^{\infty}\left(\frac{dB_x}{dy}\right)_{x,y} dz - \int_{-\infty}^{\infty}\left(\frac{dB_x}{dy}\right)_{x=y=0} dz}{\int_{-\infty}^{\infty}\left(\frac{dB_x}{dy}\right)_{x=y=0} dz}. \tag{4}$$

We measure the displacement of the longitudinal magnetic axis of the lens from the geometric axis in two transverse cross sections; the error of these measurements is ± 0.02 mm. We find that the displacement does not exceed ± 0.1 mm in either cross section.

For the correcting magnets we measure the magnetization curves, the effective length along the field, and the

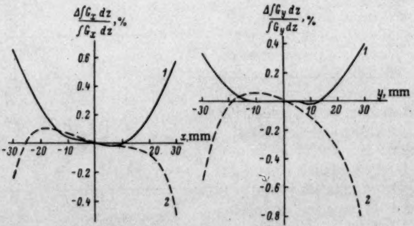

Fig. 6. Relative deviations of the integral gradient for a 7.5K150A lens at 20 T/m (curve 1) and 40 T/m (curve 2).

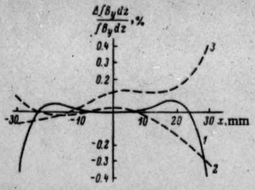

Fig. 7. Relative deviation of the integral field for an SP 147 magnet, measured in the median plane (curve 1), in the plane y = +15 mm (curve 2), and in the plane y = −15 mm (curve 3) at an induction of 1.8 T.

relative deviation of the integral field along the length of the magnet. Figure 7 shows typical curves of the relative deviation in the integral field for an SP 147 magnet, measured along the x axis in different vertical planes at an induction of 1.8 T. We see that the deviations do not exceed ± 0.5% in the working region.

Figure 2 shows the layout of the apparatus along the trajectory of the extracted beam. All the magnets and lenses have separately adjustable mounts. The correcting magnets and five triplet lenses are on a common mount for ease in adjustment. The external target, on a separate mount, can be moved accurately in the horizontal and vertical directions by remote control. The target is on a ring mount with a horizontal rotation axis. The removable ring is fitted with six holders, which can hold various targets for producing secondary particles, television screens for monitoring the beam, sets of foils for activation, and other measurement devices. The target is mounted in a junction in the vacuum line between correcting magnet HCM2 and the secondary-particle duct. Calculations have shown that a degradation of the vacuum along the extraction trajectory, even in a limited region, strongly affects the dimensions and emittance of the beam which is focused on the target. Accordingly, a forevacuum as high as 10^{-1} torr is maintained along the entire trajectory, beginning from the point at which the beam leaves the accelerator. The evacuated ion duct is made of stainless-steel tubing.

Television screens are mounted at the entrance to the extracting magnets, at characteristic points in the transport system, and on the external target for monitoring the beam. A PTU-103M industrial television system is used for remote monotoring of these screens. In this manner it is possible to monitor the dimensions, shape, and position of the extracted beam. The screens are moved into their working positions by electric drives. The metallic substrate is less than 0.3 mm thick so that it is possible to monitor on the basis of three screens simultaneously. More accurate operational control of the beam position is achieved with magnetic position sensors mounted at the entrance to the triplet and in front of the target. The beam intensity is measured with current transformers at the exit from the accelerator and in front of the target; there is also a reference current transformer in the accelerator ring. These detectors can measure the intensity in each bunch of the accelerated beam which is to be extracted, so it is possible to determine the extraction efficiency and the beam loss in the transport system. A Cerenkov detector which measures the particle flux from the target is used to monitor the adjustment of the channel and the efficiency of the interaction of the beam with the external target. The charge of the electrons ejected from the target bombarded by the proton beam is also measured. For this purpose the target is insulated from its holder; the resistance of the insulation is better than 10^9 Ω. Radiation monitors are mounted near narrow regions along the extraction trajectory to detect loss resulting from deviations from the normal extracting and focusing conditions. These monitors, which use scintillation detectors, generate signals proportional to the total loss. When the signal exceeds a specified level, a warning system is activated, and further operation of the fast-extraction system is blocked.

Operation of the extraction system is synchronized with the acceleration cycle by the B and T series of accelerator pulses.[9] The common B pulse, which corresponds within $\pm 5 \cdot 10^{-4}$ to the specified magnetic field, is selected in order to achieve the necessary accuracy in the synchronization of the fast-extraction system, the beam-transport system, the rf separator, and the Ludmila chamber. Time is measured with respect to this pulse by means of the T series of pulses, within $\pm 10^{-4}$. With the prevailing instability in the rate of increase of the magnetic field in the accelerator from cycle to cycle, this synchronization method makes it possible to select an extraction energy reproducible within less than $\pm 10^{-3}$.

4. ALIGNMENT OF THE SYSTEM

The lenses in the focusing system are arranged in accordance with the results of magnetic measurements. Samples with slight nonlinearities are used for lenses L_3 and L_4. Since the beam envelope reaches its maximum value in these lenses, nonlinear components of the field in these lenses have the greatest effect on the focusing. The effect of the field nonlinearities in the lenses on the characteristics of the beam focused on the external target is calculated on a BÉSM-6 computer. The system of the general equations of motion for protons having a specified momentum in the magnetic field is integrated over the effective length of the lens. The field in each lens is specified on the basis of the measurements through Eqs. (1) and (2). Figure 8 shows how the beam characteristics

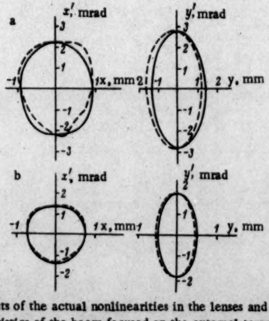

Fig. 8. Effects of the actual nonlinearities in the lenses and magnets on the characteristics of the beam focused on the external target at emittances of 2π mm • mrad (a) and π mm • mrad (b).

TABLE 3

Unit	Instability factor	Magnitude of instability, %	Increase in beam dimension (divergence)					
			in lenses*		at target			
			ΔA_r	ΔA_z	Δr	Δz	$\Delta r'$	$\Delta z'$
			mm		mm		mrad	
Accelerator	Change in emittance	100	14.80	17.06	0.64	0.38	1.08	1.80
	Change in energy	±0.1	±3.16	±0.01	±0.06	±0.00	±0.34	±0.00
	Instability of beam Δr (with an energy change)	±0.5mm	±4.68	±0.01	±0.17	±0.00	±0.38	±0.00
PM 16	Current instability	±3.0	±2.13	—	±0.07	—	±0.17	—
DM24		±0.1	±0.32	—	±0.01	—	±0.02	—
DM26		±0.1	±0.20	—	±0.02	—	±0.01	—
DM30		±0.1	±0.16	—	0.00	—	±0.01	—
L_1	Current instability	±0.1	0.01	0.01	0.00	0.00	0.00	0.00
L_2		±0.1	0.04	0.02	0.00	0.00	0.00	0.00
L_3		±0.1	0.02	—	0.01	0.01	0.01	0.01
L_4		±0.1	—	—	0.03	0.00	0.02	0.00
L_5		±0.1	—	—	0.00	0.00	0.01	0.00

*At the maximum of the envelope of the beam in the transport system.

at the external target are distorted by nonlinearities for two initial emittances of the accelerated beam. We see that with the selected lens arrangement the effect of these nonlinearities on the beam with an emittance of π mm · mrad is negligible. At an emittance 2π mm · rad the distortions are more significant, but even in this case the spreading of the beam at the target does not exceed ± 0.1 mm.

The magnetic field in the gap is specified by a map to evaluate the effect of inhomogeneities of the magnetic field in the correcting magnets. We find that inhomogeneities below 1-2% have no significant effect on the beam characteristics at the crossover.

Instability of the beam characteristics in the accelerator and instability of the power supplies for the lenses and the magnets affect the stability of the dimensions and position of the beam at the target. Table 3 summarizes the values of the possible changes in the beam characteristics at the target and in the beam size at the maximum envelope resulting from various instability factors.

The magnitudes of the current instabilities in the magnets and the lenses are based on the results of the alignment. Computer calculations are carried out to determine the beam spreading at the target corresponding to a change in the current at each element. For the instability values given in Table 3 the beam spreading at the target in the horizontal and vertical directions is negligible. The instability in the position of the beam at the target is also small, less than ± 0.1 mm.

Instability in the operation of the accelerator is more important. The most dangerous instability is an increase in the emittance of the accelerated beam. At one time the accelerator of the Institute of High-Energy Physics suffered from an anomalous beam spreading at the end of acceleration due to the nonlinear resonances $3Q_z = 29$, $2Q_z + Q_r = 29$, and $3Q_r = 29$. Modifications were made to achieve conditions more favorable for beam extraction and focusing:[5] During the entire acceleration cycle the working point on the diagram of synchrotron-oscillation frequencies is held in a region free of resonances. The beam is accelerated at the central radius, and the appropriate behavior of the currents in the polar windings correcting the magnetic-field gradient was found for this beam position. These measures reduce the emittance of the accelerated beam to π mm · mrad. The stability of the emittance in prolonged operation of the accelerator is also improved.

The radial position of the accelerated beam is stabilized by a feedback system using a position sensor in linear gap 15. In prolonged operation the instability of the radial position of the accelerated beam is less than ± 0.5 mm. The scatter in the energy values from cycle to cycle, governed by the error in the synchronization of the extraction time with the selected magnetic field in the accelerator, is less than ± 0.1%.

The geometric axis of the transport channel is brought into vertical coincidence with the median plane of unit 29 and with the axis of the secondary-particle channel. The centers of the lenses, magnets, television screens, position sensors, and external target are within 0.2 mm of this axis. The adjustments are made with respect to the aligned extraction trajectory. Because of the alignment of the fast-extraction system and the transport channel it is found that the extraction trajectory and the beam trajectory in the fringing field coincide with the design trajectory all the way to the external target. The center of the extracted beam is brought accurately into coincidence with the center of lens L_1 by magnet DM 26. The accuracy of this alignment is checked by changing the current in lens L_1: When the beam is correctly aligned with respect to the lens axis, a change in this current does not displace the beam on screen TS2. The beam displacement from the calculated trajectory does not exceed 3 mm over the entire trajectory, even without the additional correction; the correcting elements easily eliminated this error.

As the working conditions we select the calculated version of the focusing which leads to a beam having a horizontal dimension of 1.5 mm and a vertical dimension of 1 mm at the target. The calculated lens currents are achieved within $\pm 5 \cdot 10^{-4}$. Figure 9 shows the distribution of the beam intensity at the external target in both planes, obtained by the method of foil activation. For these measurements we use 10 × 10 mm stacks of aluminum foil 0.1 mm thick. The foil is irradiated over 100 cycles by the corresponding extracted bunches of the ac-

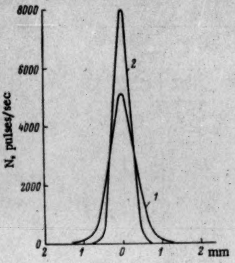

Fig. 9. Intensity distribution of the beam focused on the external target in the horizontal (curve 1) and vertical (curve 2) planes at an energy of 70 GeV.

celerated beam; then the activity induced in each of the foils is measured. The instability in the position of the beam center at the external target does not exceed ± 0.2 mm.

The beam dimensions at intermediate points in the transport system, determined with the television screens, agree well with the beam envelope shown in Fig. 2. At the optimum alignment of the system the extraction efficiency, defined as the ratio of the number of particles in the extracted bunches to the number of particles in the same bunches 150 μsec before extraction, is 97-98%. The beam is extracted from the accelerator chamber essentially without loss. In the magnets and lenses of the transport system there is much free space to spare, so the beam also passes through this system without loss. This is verified by the indications of the loss monitors mounted at all the narrow regions in the extraction trajectory, at the entrance to lens L_1, and in the transport system. When the system is aligned correctly, these monitors detect no beam loss. However, when the extraction efficiency falls off a few per cent, the point at which the loss occurs can be readily detected by these monitors.

Particles with energies from 30 to 70 GeV have been extracted and focused onto the external target. The results agree well with the calculations. The beam parameters at the external target satisfy the requirements imposed for operation of the rf separator.

In conclusion the authors thank all their colleagues who participated in the planning, construction, and alignment of the apparatus and who helped ensure the success of this work.

---

[1] K. P. Myznikov, Yu. M. Sapunov, V. M. Tatarenko, Yu. S. Fedotov, and A. M. Frolov, Preprint 68-57, Institute of High-Energy Physics, Serpukhov (1968).

[2] K. P. Myznikov, V. M. Tatarenko, and Yu. S. Fedotov, Preprint 70-79, Institute of High-Energy Physics, Serpukhov (1970).

[3] V. V. Komarov, O. V. Kurnaev, É. A. Merker, L. L. Moizhes, K. P. Miznikov, V. A. Sychev, V. M. Tatarenko, V. G. Tishin, Yu. S. Fedotov, P. Bossart, A. Ispert, I. Kamber, B. Kuiper, J. Kuppers, J. Leroux, A. Messina, S. Milner, J. Neuthal, P. Ribboni, H. Riege, H. Rossi, F. Fabiani, and Kh. Daikaizen, Preprint 72-98, Institute of High-Energy Physics, Serpukhov (1972).

[4] A. A. Aseev, A. G. Afonin, A. Boll, G. Davis, A. I. Drozhdin, B. Langezet, J. Mogen, L. L. Moizhes, K. P. Myznikov, G. Pflüm, V. M. Tatarenko, N. M. Tarakanov, and V. Volker, Preprint 72-50, Institute of High-Energy Physics, Serpukhov (1972).

[5] V. I. Gridasov, K. P. Myznikov, and V. N. Chepegin, Preprint 70-90, Institute of High-Energy Physics, Serpukhov (1970); At. Energ., 32, 1(1972).

[6] Yu. S. Glukhov, I. Ya. Korol'kov, I. K. Kuznetsov, V. F. Kuz'min, and A. A. Lednev, Preprint 67-44K, Institute of High-Energy Physics, Serpukhov (1967).

[7] E. Frick, B. Kuiper, A. Messina, and H. Riege, CERN PS (FES) 72-3, Fourth International Conference on Magnet Technology, Brookhaven, 1972.

[8] H. Van Breugel, R. Cuénot, S. Hérin, and B. Kuiper, CERN PS (FES) 72-4 Fourth International Conference on Magnet Technology, Brookhaven, 1972.

[9] A. I. Vagin, V. F. Kuz'min, K. P. Myznikov, and V. E. Pisarevskii, Preprint 68-26K, Institute of High-Energy Physics, Serpukhov (1968).

Holography

Imaging properties of traveling intensity waves in the recording of dynamic three-dimensional holograms

Yu. N. Denisyuk

(Submitted July 3, 1973)
Zh. Tekh. Fiz., 44, 131-137 (January 1974)

The properties of traveling intensity waves produced by the interference of radiation at different frequencies are investigated. It is shown that a spatial material model of a traveling wave formed by the addition of object radiation and a reference wave is analogous to a hologram in that it has the property of transforming the reference wave into the object-scattered radiation wave. The only difference is that the dynamic traveling wave model reproduces not only the amplitude, phase, and spectral composition, but also the frequency shift of the object wave relative to the reference wave. In this case, moreover, the spectral composition of the radiation corresponding to the pseudoscopic image is distorted by the Doppler effect. A theory is formulated for the effect on the basis of a solution of the wave equation in the first perturbation approximation and on the assumption that the detecting wave does not affect the structure of the hologram. A detailed analysis of the mechanism of the effect is also given in the special example of the interference of two plane waves at different frequencies. The effect can be used for the design of radiation converters as well as in real-time data-processing devices.

It has been shown[1-3] that a three-dimensional material model of a standing wave produced in the space around an object by the addition of the incident and scattered radiation is a kind of optical equivalent of that object, i.e., such a model has the capacity to affect the radiation in the same way as the object. We show in the present work that the effect is not restricted to the special case in which standing wave patterns are recorded and that imaging properties are inherent in any intensity waves, including traveling waves such as those produced in the recording of a moving object, where the wavelength of the scattered radiation is shifted relative to that of the incident radiation due to the Doppler effect.

We first investigate as a special example the singular features of the interference of two waves of different frequencies. We assume that two waves characterized by different values of the wave vector k and the frequency intersect in space.

The wave functions for these waves can be described by the expressions

$$\Psi_1(r, t) = a_1 e^{i(\mathbf{k}_1\mathbf{r} - \omega_1 t + \varphi_1)}, \tag{1}$$

$$\Psi_2(r, t) = a_2 e^{i(\mathbf{k}_2\mathbf{r} - \omega_2 t + \varphi_2)}. \tag{2}$$

The total intensity field of the waves is found by adding Ψ_1 and Ψ_2 and multiplying the result by the complex conjugate. We have

$$J(r) = a_1^2 + a_2^2 + 2a_1 a_2 \cos[\varkappa\mathbf{r} - \Omega t + (\varphi_1 - \varphi_2)], \tag{3}$$

where

$$\begin{gathered} \varkappa = \mathbf{k}_1 - \mathbf{k}_2, \\ \Omega = \omega_1 - \omega_2. \end{gathered} \tag{4}$$

Equation (3) is analogous in form to Eqs. (1) and (2) and also describes a plane traveling wave; in the given case, however, this wave is an intensity wave. We determine its propagation velocity by setting the argument of the cosine equal to a constant and then taking the derivative of the projection of the radius vector r by the wave vector $\varkappa$ for the intensity wave:

$$v = \frac{1}{|\varkappa|}\frac{d\varkappa\mathbf{r}}{dt} = \frac{\Omega}{|\varkappa|}. \tag{5}$$

We find the spatial period of the intensity wave Λ by means of an expression analogous to the relation between the wavelength λ and wave number k:

$$\Lambda = \frac{2\pi}{|\varkappa|}. \tag{6}$$

For the special case in which the interfering waves propagate in approximately opposite directions and their wavelengths differ only slightly Eqs. (5) and (6) describe a structure very similar to an ordinary standing wave. In this case,

$$v \approx \frac{\Omega}{2k}, \quad \Lambda \approx \frac{\lambda}{2}. \tag{7}$$

Inasmuch as $k = \omega/c$ and $\Omega \ll \omega$, we have $v \ll c$.

Consequently, the spatial period of the given intensity wave, as in the ordinary standing wave, is approximately equal to half the wavelength of the incident radiation. The only difference is that the given structure moves through space at a speed proportional to the frequency difference between the interfering waves.

Assume that a traveling intensity wave is recorded in a photosensitive medium, whose time constant τ satisfies the following conditions: It is greater than the period T of the light wave, so that the material medium does not reproduce intensity oscillations occurring at the optical frequency:

$$\tau > T = \frac{2\pi}{\omega}. \tag{8}$$

We assume in addition that the time constant τ is much smaller than the oscillation period of the intensity wave in its motion as a unit:

$$\tau \ll t = \frac{\Lambda}{v}. \tag{9}$$

Substituting the values of Λ and v from (5) and (6) into

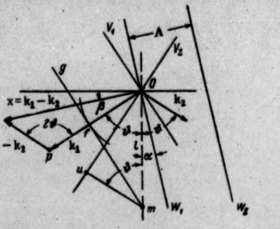

Fig. 1. Interaction of radiation with a material model of a traveling plane intensity wave. V_1, V_2) Interfering plane waves; k_1, k_2) wave vectors of V_1 and V_2; W_1, W_2) frontal surfaces of the traveling plane intensity wave; $\varkappa$) wave vector of W; Λ) spatial period of W.

(9), we obtain the foregoing condition in the form

$$\tau \ll \frac{2\pi}{\omega_1 - \omega_2}. \tag{10}$$

It is readily perceived that when conditions (8) and (10) are satisfied a traveling material harmonic occurs in the photosensitive medium, modeling the intensity distribution described by Eq. (3). Thus, in accordance with condition (8) the medium does not reproduce high-frequency intensity oscillations, so that the operation of multiplication of the wave function by its complex conjugate can be used in the calculation of the actual intensity. On the other hand, the intensity variations corresponding to wave propagation will be reproduced on account of condition (10).

We now analyze the interaction of radiation with the aforementioned harmonic in the first perturbation approximation, neglecting secondary scattering effects and the attenuation of the incident wave in its propagation through the volume of the hologram. We assume for simplicity that light is reflected only by antinode surfaces, i.e., we represent the harmonic as a set of parallel mirrors separated by a distance Λ and moving at a speed v [see Eqs. (5) and (6)]. The schematic arrangement of these mirrors (which we refer to hereinafter as "isophase") is given in Fig. 1. Here $\mathbf{k}_1$ and $\mathbf{k}_2$ are the wave vectors of the interfering plane waves V1 and V2, and W_1 is the intensity wave front surface, which after recording is converted into one of the isophase mirrors. This surface is perpendicular to its "wave vector" $\varkappa = \mathbf{k}_1 - \mathbf{k}_2$. Unlike the case of an ordinary standing wave, as the figure indicates, the surface W_1 does not coincide with Om, the bisector of the angle formed by the vectors $\mathbf{k}_1$ and $\mathbf{k}_2$. The direction of motion of the wave W_1 determines the vector $\varkappa$; the wave moves either in the direction of $\varkappa$ or in the opposite direction. The sign of the motion can be determined on the following basis. If $|\mathbf{k}_1| > |\mathbf{k}_2|$, the value of $\Omega = \omega_1 - \omega_2$ is positive, whereupon in accordance with (3) W_1 moves in the direction indicated by the vector $\varkappa$. If $|\mathbf{k}_1| < |\mathbf{k}_2|$, the sign of Ω changes, and the wave moves in the opposite direction. As is evident from the figure, this rule is in fact equivalent to saying that the intensity wave moves in the general direction of motion of the field wave characterized by the larger absolute value of the wave vector $\mathbf{k}$.

It may appear at first glance that the given system of isophasal mirrors does not have the attributes of a hologram, i.e., that it is incapable of transforming one of its formative waves into the other. Indeed, since the mirror surface W_1 is not the bisector of the angle formed by $\mathbf{k}_1$ and $\mathbf{k}_2$, a wave traveling in the direction of $\mathbf{k}_2$, according to the conventional laws of specular reflection, cannot be transformed into a wave traveling in the direction of $\mathbf{k}_1$. Also, it is readily noted that the distance Λ, Eq. (6), between the planes of the adjacent mirrors does not satisfy the Bragg condition, and this fact would seem to reaffirm the impossibility of the wave V_2 being transformed into V_1 or vice versa.

A more detailed analysis shows, however, that all of these effects are only apparent. When radiation is reflected from a moving mirror, Snell's law is violated, the angle of incidence being no longer equal to the angle of reflection. It turns out that the change of the reflection angle in the given situation is such as to ensure the possibility of mutual transformation of the waves V_2 and V_1. We now examine the latter effect in closer detail.

Suppose that one of the waves, say V_2, forming the moving isophasal mirror W_1 is incident on that mirror. We show that the motion of the mirror causes the wave V_2 to encounter the surface of the mirror along the bisector Om of the angle formed by the vectors $\mathbf{k}_1$ and $\mathbf{k}_2$. We are required to prove that the wave front, which intersects the mirror at the point O at the initial time $t = 0$, intersects an arbitrary point m of the bisector Om at precisely the time $t_1 = t_2$ when the moving isophasal mirror W_1 passes across it.

The latter condition is formally equivalent to requiring that the propagation times of the wave fronts W_1 and V_2 be equal up to the point m. Writing $Om = l$, and denoting the corresponding times by t_1 and t_2, we write this condition as follows (see Fig. 1):

$$t_1 = \frac{l \cos\vartheta}{c}, \tag{11}$$

$$t_2 = \frac{l \sin\alpha}{v}. \tag{12}$$

We find the angle α describing the deviation from the specular reflection law. From the triangle tpO we find

$$\sin\beta = \frac{k_2}{\varkappa} \sin 2\vartheta. \tag{13}$$

Then, taking account of (13), we write the following expression for sin α:

$$\sin\alpha = \cos(\beta + \vartheta) = \frac{\cos\vartheta \left\{\sqrt{\varkappa^2 - k_2^2 \sin^2 2\vartheta} - 2k_2 \sin^2\vartheta\right\}}{\varkappa}. \tag{14}$$

We use the triangle Otp to determine the value of $\varkappa^2$:

$$\varkappa^2 = k_1^2 + k_2^2 - 2k_1k_2 \cos 2\vartheta. \tag{15}$$

Substituting (15) into (14), we obtain

$$\sin\alpha = \frac{\cos\vartheta \left\{\sqrt{k_1^2 + k_2^2 - 2k_1k_2 \cos 2\vartheta - k_2^2 \sin^2 2\vartheta} - 2k_2 \sin^2\vartheta\right\}}{\varkappa}. \tag{16}$$

It can be shown that the expression under the square root in (16) reduces to the form

$$(k_1+k_2-2k_2\cos^2\vartheta)^2.$$

With this fact in mind we obtain

$$\sin\alpha=\frac{(k_1-k_2)\cos\vartheta}{x}. \tag{17}$$

Substituting the value of sin α from (17) along with the value of v into (12) with allowance for (15), we readily verify that $t_1 = t_2$ and that, therefore, the wave fronts W_1 and V_2 occur simultaneously at the point m. Inasmuch as the choice of the position of m on the bisector Om is entirely arbitrary, it is obvious that all other points of the bisector are points of impingement of the fronts V_2 and W_1. Under these conditions the wave reflected by the isophase mirror W_1 is very easily constructed by the Huygens principle (see Fig. 1). The wave V_2 is tangent to the mirror W_1 at the point O at the initial time t = 0. At that time a spherical wave emanates from the point O. In the time that it takes for the wave V_2 to reach the point m of the mirror the spherical wave emanating from the point O traverses the path um. Drawing the tangent to the spherical wave surface from the point m, we find the reflected wave V_2'. Consider the triangles Ofm and Oum. Inasmuch as their legs Of and um are equal and they share a common hypotenuse, they are congruent. It follows, therefore, that the angle fOm is equal to v and that the reflected wave V_2 moves in the direction of the vector k_2', i.e., is transformed into the second wave participating in the formation of the set of moving isophasal mirrors.

It can be shown by analogous constructions that the motion of the mirror W_1 being opposite to that of the wave with the smaller wave vector upon reflection the latter acquires a frequency shift such that the reflected wave reproduces not only the direction, but also the frequency of the second interfering component. To complete the proof it is also required to show that the Bragg condition is also satisfied. However, we shall not carry out the laborious constructions needed for this proof; we proceed instead to the more formal investigation of the general case in which a traveling intensity wave is formed by the interference of a reference wave with a complex in general, arbitrary, radiation wave scattered by an object.

Let the wave functions of the incident radiation and the radiation scattered by the object be given by the expressions

$$\Psi_r(rt)=\psi_r(r)e^{i\omega_r t} \tag{18}$$

$$\Psi_0(rt)=\psi_0(r)e^{i\omega_0 t}. \tag{19}$$

The intensity distribution function for the field surrounding the object is determined by adding (17) and (19) and multiplying the result by the complex conjugate. We also assume that under the action of the field the dielectric constant ε of the medium acquires an increment $\delta\varepsilon$ proportional to the perturbing intensity:

$$\varepsilon=\varepsilon_0+\delta\varepsilon, \tag{20}$$

where

$$\delta\varepsilon=\Psi_r\Psi_r^*+\Psi_0\Psi_0^*+\Psi_0\Psi_r^*+\Psi_r\Psi_0^*. \tag{21}$$

We introduce the following notation for the third and fourth terms of (21):

$$\Psi_0\Psi_r^*=G, \tag{22}$$

$$\Psi_2\Psi_r^*=G^*. \tag{23}$$

Multiplying (22) by Ψ_r, we readily verify that the third term coincides with the point multiplication operator transforming the reference wave into the radiation wave scattered by the object.

We consider the interaction described by expression (21) between the radiation and the material model of traveling intensity waves. In this case, since we are not so much concerned with the actual properties of the hologram itself as with the properties of the optical field forming it, we disregard the effect of the detecting wave on the structure of the hologram, assuming instead that the recording and reconstruction processes are independent. With all of the foregoing in mind we assume that the reference-wave radiation Ψ_r (18) is incident on a three-dimensional medium whose dielectric constant is described by (21). In accordance with our stated assumptions the wave function Ψ_r must obey the wave equation

$$\left(\nabla^2-\frac{\varepsilon_0}{c^2}\frac{d^2}{dt^2}\right)\Psi_r=0, \tag{24}$$

where ε_0 is the distribution function for the dielectric constant prior to recording of the intensity waves.

Under the action of the intensity wave the dielectric constant acquires the increment $\delta\varepsilon$ (21). It is clear that the wave function experiences a corresponding change. We represent the resultant wave function as the wave function Ψ_r of the unperturbed problem plus a small addition due to the presence of $\delta\varepsilon$:

$$\Psi=\Psi_r+\Psi_f. \tag{25}$$

The perturbed part of the wave function is the required wave function for the radiation reconstructed by the hologram. Substituting the value of ε from (21) and the value of Ψ from (25), neglecting second-order small terms, taking account of (24), and differentiating Ψ_r twice with respect to time, we obtain

$$\left(\nabla^2-\frac{\varepsilon_0}{c^2}\frac{d^2}{dt^2}\right)\Psi_f=-\frac{\delta\varepsilon}{c}\omega_r^2\Psi_r. \tag{26}$$

The solution of the inhomogeneous equation (26) has the following well-known form:

$$\Psi_f=-\frac{\omega_r^2}{4\pi c}\int\limits_{V\left(t-\frac{r}{c}\right)}\frac{\delta\varepsilon\Psi_r}{r}\,dV. \tag{27}$$

Here the index V(t − r/c) attached to the integral signifies that the integration is carried out over the volume V of the hologram and that the integrand, accordingly, is evaluated with a delay to account for the propagation time of the light to the point of observation. As in the case of recording of a standing wave, the third term of (21) is responsible for the formation of the image. Accordingly, replacing $\delta\varepsilon$ in (27) by the value of G from (22), we obtain

$$\Psi_f = -\frac{\omega_r^2 a_r^2}{4\pi c} \int\limits_{r\left(t-\frac{r}{c}\right)} \frac{\Psi_0}{2}\, dV, \tag{28}$$

where a_r is the amplitude of the reference wave.

Substituting into (28) the value of Ψ_0 from (19) with its time factor omitted, we rewrite this expression in the form

$$\Psi_f = -\frac{\omega_r^2 a_r^2}{4\pi c} e^{i\omega_0 t} \int\limits_V \frac{\psi_0(r)\, e^{ik_0 r}}{r}\, dV. \tag{29}$$

Expressions with similar integrals have been interpreted previously[1,3] as wave functions generated by the wave function in the integrand. Using this interpretation, we conclude that the wave function for the radiation reconstructed by the model of traveling intensity waves coincides with the wave function for the object-scattered radiation, correct to the effects indicated in refs. 1 and 3.

It is interesting to note that the behavior of the pseudoscopic image in the case analyzed here differs significantly from that encountered in the recording of standing waves. Thus, suppose that a counterwave Ψ_r' opposing the reference wave Ψ_r involved in the formation of the hologram is incident on the model of traveling intensity waves. Modifying expression (18), we write the wave function for this counterwave as follows:

$$\Psi_r' = \psi_r^*(r)\, e^{i\omega t}. \tag{30}$$

Replacing Ψ_r in (27) by the value of Ψ_r' from (30) and replacing $\delta\varepsilon$ by the value of G^* from (23) [the fourth term of (21) corresponds to the pseudoscopic image], we find the wave function for the radiation reflected by the model in this case:

$$\Psi_f' = -\frac{\omega_r^2 a_r^2}{4\pi c} e^{i(2\omega_r - \omega_0)t} \int\limits_V \frac{\Psi_0^*(r)\, e^{i(2k_r - k_0)r}\, dV}{r}. \tag{31}$$

It follows from (31) that the pseudoscopic image in the given case has a frequency shift due to the Doppler effect and is therefore somewhat distorted, because the integrand of (31) has a different form from the corresponding Kirchhoff equation.

We have thus shown that a spatial pattern of traveling intensity waves also has the potential capability for reconstruction of the wave field of an object. Moreover, in addition to other parameters of the wave field, the frequency shift of the spatial wave relative to the reference wave is also reproduced, indicating that the imaging properties of the spatial pattern of traveling intensity waves have an even more general character than the corresponding properties of a standing wave pattern. Also typical from this point of view is the fact that the pseudoscopic image in the case of traveling waves tends to break down while the true image is simultaneously preserved, i.e., the optical properties of the traveling wave model tend to approximate even closely the optical properties of the object, which, of course, does not form any pseudoscopic images.

The effect be exhibited directly in the majority of cases in the form represented here; when the medium reacts to the light at the instant of its inception, the detecting wave itself influences the structure of the traveling wave model, and this fact is disregarded in the present analysis. It is to be expected, however, that this and other related possible effects will affect only the details of the process without changing its basic properties.

The imaging of the properties of an object by a pattern of traveling intensity waves can be used for the design of diverse radiation converters in situations, among others, where it is required to vary the wavelength. It should also find applications in real-time data-processing devices, in particular for the formation of optical images in the recording of objects by means of acoustic and rf electromagnetic waves.

---

[1] Yu. N. Denisyuk, Dokl. Akad. Nauk SSSR, 144, 1275 (1962).
[2] Yu. N. Denisyuk, Opt. Spektrosk., 15, 522 (1963).
[3] Yu. N. Denisyuk, Opt. Spektrosk., 18, 276 (1965).

Physical electronics

Extrapolation of the Langmuir S-curve to cesium pressures of 10-100 torr

V. E. Dubinskii and S. Ya. Lebedev

(Submitted February 15, 1973)
Zh. Tekh. Fiz., 44, 138-141 (January 1974)

The thermionic current is plotted as a function of the temperature for titanium, niobium, tantalum, molybdenum, tungsten, nickel, rhenium, carbon, and type 1Kh18N9T steel in cesium vapor at pressures from 10^{-6} to 10-100 torr by an extrapolation of experimental data.

The thermionic current cannot be studied experimentally as a function of the sample temperature (the Langmuir S curve cannot be recorded) at cesium vapor pressures above 10^{-3} torr because a discharge occurs in the experimental apparatus. We have therefore extrapolated the experimental results reported previously[1] to cesium vapor pressures of 10-100 torr. The curves were calculated in 1963 and used for working purposes, but the pressures in the data on most of these elements and on type 1Kh18N9T (Soviet designation) stainless steel are now three orders of magnitude lower.[2] The extrapolation is carried out for those parts of the curves corresponding to the lowest surface coverage by cesium at the minimum work function.

EXTRAPOLATION METHOD

We illustrate the extrapolation method for titanium. Figure 1a shows the experimental and extrapolated values of log (j/T^2) as functions of the reciprocal temperature (1000/T) superimposed on a grid of lines of constant work function (φ = 1.42–3.95 V). Also in this figure are lines of constant work function plotted as log μ_a (the ordinate) vs 1000/T (the abscissa); here, j is the current density and μ_a is the atomic flux $(\mathrm{cm}^{-2}\cdot\mathrm{sec}^{-1})$.

The values of log μ_a are related to the pressure p (torr) and the temperature of the cesium vapor T (°K) by the familiar relation

$$\lg \mu_a = \lg p - \frac{1}{2}\lg T_a + 21.4843, \tag{1}$$

and the values of log p as a function of the temperature are taken from ref. 3:

$$\lg p = 10.5460 - 1.00 T_a - \frac{4500}{T_a} \tag{2}$$

for temperatures T_a below the melting point of cesium (302°K) or

$$\lg p = 11.0531 - 1.35 \lg T_a - \frac{4041}{T_a} \tag{3}$$

for $T_a > 302$°K.

Accordingly, by substituting log p from (2) and (3) into (1), we find log μ_a as a function of the temperature alone:

$$\lg \mu_a = 32.0303 - 1.5 \lg T_a - \frac{4150}{T_a} \quad (T_a < 302\,^\circ\mathrm{K}),$$

$$\lg \mu_a = 32.5374 - 1.85 \lg T_a - \frac{4041}{T_a} \quad (T_a > 302\,^\circ\mathrm{K}).$$

The lines of constant work function plotted in the coordinates $10^3/T$ and $\log(j/T^2)$ by the "total-current method" are straight lines $[\log(j/T^2) = \log A_0 - 2.30(e\varphi)/(kT)$, where $A_0 = 120\ \mathrm{A/cm^2\cdot deg\,K}]$. Clearly, this representation of the lines of constant work function as straight lines in terms of the coordinates 1000/T and log j (ref. 4) is frequently not correct.

The quantity log μ_a can be written as a function of the pressure. Such functions are shown in the upper part of the figure; the ordinate at the right shows log μ_a, and that at the left shows the pressure.

The S-curves are curves for constant values of the vapor temperature, the vapor pressure, and the flux μ_a. The intersections of each experimental curve with the series of lines of constant work function are displaced, at the same values on the abscissa, to the lines log μ_a = const(T_a) = const (p). According to Langmuir's "surface-phase" postulate, the values of log μ_a for a constant work function lie approximately on a straight line.[4,5] The lines of constant work function are drawn through these displaced experimental points in such a way that the slopes and spacings vary smoothly. Then these lines intersect the horizontal lines log μ_a = n, where n = 14, 15, 16, ..., 22.

In this manner the range of μ_a and, correspondingly, the pressure are increased (from $\mu_a = 10^{14}$ to $\mu_a = 10^{22}$ $\mathrm{cm}^{-2}\cdot\mathrm{sec}^{-1}$ and p = $0.54\cdot10^{-6}$–91 torr).

Then the opposite displacement is carried out: The intersections of the lines log μ_a = n with lines of constant work function are displaced (with the same abscissa) to the corresponding lines of constant work function in the coordinates 1000/T and log j/T^2. The resulting points, which correspond to the same value of μ_a, are joined by a curve. For low coverages this curve (dashed curve) is continued to the line for the work function of the element without cesium,[6] like the curves for tungsten in ref. 4.

Figure 1, b-i, shows the extrapolated curves for niobium, tantalum, molybdenum, tungsten, carbon, nickel, rhenium, and type 1Kh18N9T stainless steel.

To assist in the use of these curves we note that log j is found from data plotted from

$$\lg j = \lg \frac{j}{T^2} - 2\lg\left(\frac{1000}{T}\right) + 6.$$

These extrapolated curves differ from those reported in refs. 2-4 for the respective elements, apparently because of discrepancies in the original experimental data.

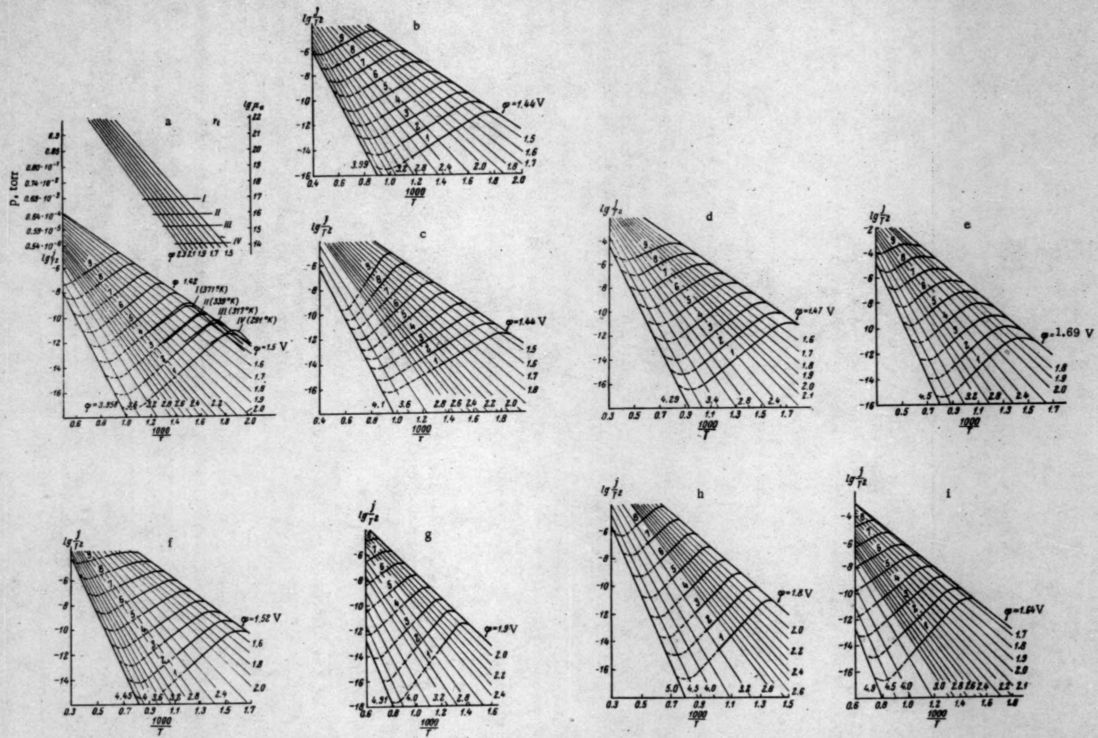

Fig. 1. The quantity j/T^2 as a function of the reciprocal cathode temperature for titanium (a) for various cesium vapor temperatures (T_a), and for niobium (b), tantalum (c), molybdenum (d), tungsten (e), carbon (f), nickel (g), rhenium (h), and type 1Kh18N9T stainless steel (i). T_a, °K: 1) 290; 2) 313; 3) 340; 4) 375; 5) 419; 6) 472; 7) 542; 8) 642; 9) 778 and 772 (Ti, Ta, W). n: 1) 14; 2) 15; 3) 16; 3) 17; 5) 18; 6) 19; 7) 20; 8) 21; 9) 22. In Part a, curves I-IV are experimental.

---

[1] S. Ya. Lebedev and Yu. Ya. Stavisskii, Izv. Akad. Nauk SSSR, Ser. Fiz., 28, 1499 (1964).

[2] R. G. Wilson, J. Appl. Phys., 37, 3161 (1966); 37, 4125 (1966).

[3] J. B. Taylor and J. Langmuir, Phys. Rev., 51, 753 (1937).

[4] R. L. Aamodt, L. J. Brown, and B. D. Nichols, J. Appl. Phys., 33, 2080 (1962).

[5] J. B. Taylor and J. Langmuir, Phys. Rev., 44, 423 (1933).

[6] V. S. Fomenko, Emission Properties of the Elements and Chemical Compounds [in Russian], Izd. Akad. Nauk UkrSSR, Kiev (1961).

Effect of crystal structure on certain angular dependences of the ion–electron-emission yield

B. A. Brusilovskii and V. A. Molchanov

M. V. Lomonosov Moscow State University

(Submitted December 15, 1972; resubmitted June 18, 1973)
Zh. Tekh. Fiz., 44, 142-147 (January 1974)

An experimental study is made of the angular dependences of the ion–electron-emission yield of a metal single crystal as the ion beam is displaced along crystallographic planes with different atomic-packing densities. The targets are molybdenum and copper crystals. These are bombarded by 30-keV argon ions. Under these conditions, when the ion beam moves along a plane with a high atomic density the half-width of the minimum corresponding to a close-packed crystallographic direction assumes its minimum value. The width of the maximum, measured at a fixed emission yield, assumes its maximum value under these conditions. The results are discussed qualitatively on the basis of the theory for crystal transparency.

When a solid surface is bombarded by intermediate-energy ions, intense electron emission is observed.[1] When the target is a single crystal, the angular dependences of the ion–electron-emission yield γ are nonmonotonic. In particular, study of the electron emission from the (100) face of a copper crystal shows a correlation between the minima of the angular dependences with directions in which the crystal lattice is most transparent. The shape, depth, and width of these minima yield information about the influence of the ordered atomic arrangement on electron emission from the crystal. These quantities have been studied as functions of the nature and energy of the incident ions, the distance between the atoms in the given crystallographic direction, the target temperature, etc.[1-6] However, the information which has been obtained on these properties as functions of the incidence angle of the ions and the azimuthal angle does not provide an adequate basis for reaching a complete understanding of the effect of the ordered structure on the emission. Study of the shape, depth, and width of the minima as functions of various factors can therefore yield information useful for reaching an understanding of the mechanism for electron emission in ion bombardment.

We report here on an experimental study of the shape and width of the minima corresponding to close-packed directions as functions of the azimuthal angle and the angle at which the ions are incident on the target.

The measurements are carried out by the standard procedure described elsewhere.[4] Singly charged 30-keV argon ions are used at a current density of ~ 2 mA/cm². The targets are the (110) and (111) faces of a molybdenum crystal and the (110) face of a copper crystal. The target can be rotated around two orthogonal axes. One axis lies in the plane of the target surface. The angular position around this axis, φ, is measured from the normal to the surface. The other axis is normal to the surface. The angular position around it, β, is measured from the ⟨112⟩ direction. The angles φ and β are measured within 1°.

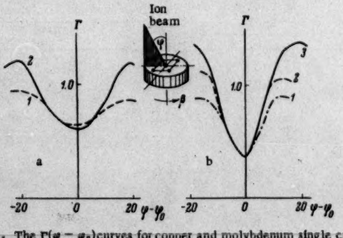

Fig. 1. The $\Gamma(\varphi - \varphi_0)$curves for copper and molybdenum single crystals.

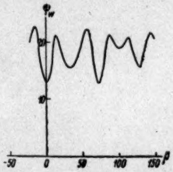

Fig. 2. The $\phi_W(\beta)$ curve for the <110> minimum of a copper crystal.

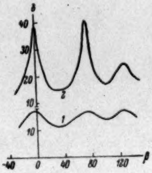

Fig. 3. The $\delta(\beta)$ curve for the <110> minimum of a copper crystal.

The ion–electron-emission yield γ is measured as a function of the angle at which the ions are incident on the target, φ, for a fixed angle β, or γ is measured as a function of β at fixed φ. The total increase in the yield γ for a metal crystal observed with an increase in the angle of incidence is known to be of approximately the same nature as the increase in the corresponding yield for a polycrystalline material, γ_p. Accordingly, to eliminate the influence of this common increase in a comparison of the yields, we compare values of the reduced yield Γ, defined by

$$\Gamma = \frac{\gamma}{\gamma_p}.$$

The value of γ_p is taken from ref. 7.

We turn first to the curves obtained at a fixed azimuthal angle β. Figure 1 shows parts of the $\Gamma(\varphi)$ curves corresponding to the ⟨111⟩ directions of a molybdenum crystal (Fig. 1a) and the ⟨110⟩ directions of a copper crystal (Fig. 1b). Here, the ordinate shows $(\varphi - \varphi_0)$ (φ_0 is the angle at which the incidence direction of the ions coincides

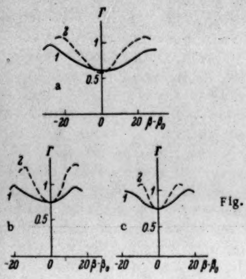

Fig. 4. The $\Gamma(\beta-\beta_0)$ curve for a molybdenum crystal.

with the corresponding crystallographic directions). Curves 1 and 2 in Fig. 1a are obtained by rotating the crystal around the ⟨110⟩ and ⟨123⟩ axes, and curves 1-3 in Fig. 1b are obtained by rotating it around the ⟨111⟩, ⟨100⟩ and ⟨115⟩ axes. We select these axes because the beam moves along planes differing in packing density. We see from this figure that for a given crystallographic direction the values of β, i.e., obtained by rotating the target around various axes, are approximately the same only at small values of $|\varphi-\varphi_0|$. It also follows from this figure that the minima observed as the beam moves along a close-packed plane have smaller depths and half-widths than the minima observed when the beam moves along a plane with a low density of atoms. The width measured at some arbitrarily chosen value Γ = const, on the other hand, is larger for the minimum obtained with the beam moving along a close-packed plane.

Figure 2 shows, as a function of the azimuthal angle β, the half-width of the ⟨110⟩ minimum of a copper crystal. We see that the half-width is a nonmonotonic function of β. The curve displays minima at β = 0, 35, 70, 100, and 126°. It follows from a stereographic projection of the (110) face that at these angles the plane of incidence of the beam (the plane passing through the beam and the normal to the surface) coincides with the (111), (110), (111), (113), and (100), planes respectively. The deepest minima are those at 0 and 70°. It follows from the data in this figure that

$$\psi_w(0)\simeq\psi_w(70)<\psi_w(35)<\psi_w(126)<\psi_w(100).$$

Figure 3 shows the functional dependence of the angle β of the widths of the minima, δ, measured at certain fixed values Γ = const. We see that the width of a minimum at Γ = const represents the rate of increase of the ion–electron-emission yield with increasing φ. Curves 1 and 2 in this figure are obtained for two arbitrarily chosen values of Γ: 0.65 for the first and 0.8 for the second. In both cases there are maxima on the curves corresponding to coincidence of the incidence direction with the (111) and (100) close-packed planes. The maximum corresponding to the (111) plane is higher than that corresponding to the (100) plane and increases with the value of Γ at which the $\delta(\beta)$ curve is recorded.

We turn now to the $\Gamma(\beta)$ curves for a fixed angle φ for the molybdenum (110) and (111) faces. Figure 4 shows parts of the $\Gamma(\beta-\beta_0)$ curves corresponding to the ⟨111⟩ (Fig. 4a) close-packed direction, the ⟨110⟩ direction (Fig. 4b), and the ⟨113⟩ direction (Fig. 4c). In these figures β_0 is the angle at which the beam direction coincides with the crystallographic direction in question. Curves 1 in Fig. 4 are obtained at incidence angles φ of 35, 35, and 31.5°K, respectively, while curves 2 are obtained at 70, 60, and 65°. In each figure the values of Γ for curves 1 and 2 are approximately equal only at angles $(\beta-\beta_0)$ less than 3-4°; at all other angles, Γ is lower for curves 1, i.e., for the lower value of φ. The half-widths of the minima on the $\Gamma(\beta-\beta_0)$ curves for the lower values of φ are larger by a factor of 1.5-1.7 than the half-widths of the corresponding minima at the large value of φ. Accordingly, the shape and half-width of the minima corresponding to a given direction are functions of the angle of incidence φ.

Let us compare the shape and half-width of a minimum corresponding to a certain crystallographic direction for the case in which the target is rotated around the normal to the surface (φ = const) with the shape and half-width of the same minimum when the target is rotated around some axis in the target plane (β = const). Figure 5 shows $\Gamma(\beta-\beta_0)$ and $\Gamma(\varphi-\varphi_0)$ curves corresponding to the low-index ⟨111⟩ (Fig. 5a) and ⟨100⟩ (Fig. 5b) axes. Curves 1 are obtained by rotating the copper crystal around the normal to the surface, while curves 2 are obtained by rotating around the ⟨110⟩ axis (Fig. 5a) or the ⟨100⟩ axis (Fig. 5b), both of which are in the plane of the target surface. In both cases the half-widths of the minima observed in the rotation around β are larger than those of the minima observed in the rotation around φ. It follows from these results that the shape and width of the minima on the $\Gamma(\varphi-\varphi_0)$ curves obtained at a fixed value of β are functions of this angle, while the shape and width of the minima on the $\Gamma(\beta-\beta_0)$ curves recorded at fixed φ are functions of φ.

We turn now to a qualitative discussion of these results. The minima corresponding to close-packed directions are formed because the surface atom shadows all atoms lying below it along the given direction.[8,9] If the beam is incident along a close-packed direction, an increase in the angle between the beam direction and the crystallographic direction under consideration, ψ_S, allows the interior atoms to emerge from the shadow and leads to an increase in Γ. For the $\Gamma(\varphi)$ curves the angle ψ_S would be $\varphi-\varphi_0$. As the beam is moved along a plane with a low packing density, ψ_S continues to increase with increasing ψ_S until all the atoms emerge from the shadow. As the beam is moved along a close-packed plane, there can apparently be situations in which atoms of lower layers, without completely emerging from the shadow of one atom, enter the shadow of a different atom, belonging to a neighboring row, at some angle ψ_S. As a result, the rate at which Γ increases with increasing ψ_S is lower than that

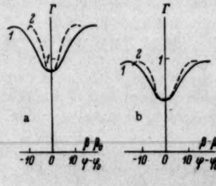

Fig. 5. The $\Gamma(\beta-\beta_0)$ and $\Gamma(\varphi-\varphi_0)$ curves for a copper crystal.

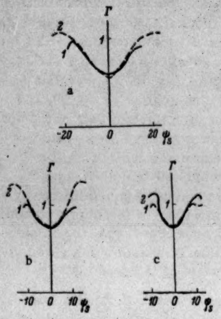

Fig. 6. The $\Gamma(\psi_s)$ curve for a molybdenum crystal.

in the case in which the beam moves along a plane with a low atomic density. With a further increase in ψ_s, the shadows of the atoms in the upper rows can begin to overlap, leading to further shadowing of the interior atoms. On the closest-packed planes, the shadow may become so pronounced at some value ψ_s that a further change in ψ_s has little effect on the effectiveness of the shadow, and the value of Γ should change a little. With a further increase in ψ_s the incidence direction of the beam approaches another close-packed direction, and Γ begins to decrease. Obviously, the higher the density of the atomic packing in the planes, the more pronounced the shadowing can become. It thus follows that the rate of increase of the $\Gamma(\psi_s)$ curve with increasing ψ_s depends on the plane along which the beam is moving, i.e., on the angle β. As a result, the width of the minimum, δ, is also a function of β; the functional dependence $\delta(\beta)$ must have a maximum where the incidence direction of the beam is parallel to a close-packed plane, and the maxima corresponding to the more closely packed planes must be larger. It is precisely this type of functional dependence $\delta(\beta)$ which is observed experimentally (Fig. 3). It also follows that the maximum value of $\Gamma_{\max}$, reached when the beam moves along a close-packed plane, is smaller than the maximum reached during motion along a loosely packed plane. This circumstance could lead to a decrease in the half-width of the minimum on the $\Gamma(\varphi-\varphi_0)$ curve obtained when the target is rotated around the axis perpendicular to a close-packed plane. According to our experiments (Fig. 2) the minima on the $\psi_W(\beta)$ curve are in fact observed when the beam moves along a close-packed plane. Since the atomic density in the planes in an fcc crystal falls off in the order (111), (100), (110), (113), the depth and half-width of the minima should apparently also fall off in the same order. However, this order is not completely reproduced experimentally. For example, the half-width of the minimum at β = 35° is larger than that of the minimum at β = 0, i.e., larger than the half-width of the minimum corresponding to the closest-packed plane; and the minimum at β = 35° is deeper than that of β = 126°. Accordingly, the appearance of a minimum at β = 35° may be partially or completely due to the overlap of neighboring minima, rather than to the effect of the ordered arrangement of atoms in the planes. The same can apparently be said regarding the minimum at β = 100°.

We turn now to Fig. 4, from which we see that the shape and half-width of the minima on the $\Gamma(\beta-\beta_0)$ curves corresponding to close-packed directions and a certain fixed value of φ differ from those obtained for the same direction but a different fixed value of φ. One possible cause of this behavior could be a functional dependence of ψ_s on β and φ. On the other hand, as in the case of the $\Gamma(\varphi)$ curves, this difference could be due to the effect of the ordered arrangement of atoms in planes forming the given direction. Here, however, account must be taken of the circumstance that, in contrast with rotation around φ, the angle between the plane along which the beam moves and some close-packed plane is not constant during the rotation around β; this circumstance can affect the shape and half-width of the minimum under consideration. It follows from the geometry of the problem that the angle between the incidence direction and the crystallographic direction, ψ_s, can be written as

$$\cos\psi_s = \cos\varphi\cos\varphi_1 + \sin\varphi\sin\varphi_1\cos(\beta-\beta_0),$$

where φ_1 is the angle between the given crystallographic direction and the normal to the target surface, and $\beta-\beta_0$ is the angle formed by the plane containing the normal to the target surface and the given direction with the plane of incidence of the beam. The $\Gamma(\beta-\beta_0)$ curves shown in Fig. 4 are converted into $\Gamma(\psi_s)$ curves on the basis of this equation; the results are shown in Fig. 6. Here the shapes of the minima obtained at different values of φ and small values of ψ_s agree well, i.e., the difference between the shapes of these minima on the $\Gamma(\beta-\beta_0)$ curves at small $\beta-\beta_0$ can in fact be attributed to a functional dependence of ψ_s on φ, φ_1 and β. At larger values of ψ_s, however, there is a difference between the shapes of minima 1 and 2 on the $\Gamma(\psi_s)$ curves. As in the case of the $\Gamma(\varphi)$ curves, this difference is apparently due to a sensitivity of the emission to the ordered arrangement of atoms in the planes; in certain cases it could also be due to an overlap of the given minimum with the minimum corresponding to the neighboring crystallographic direction. As in the previous case, the differences between the shapes and half-widths of the minima observed when the target is rotated around the axis perpendicular to the plane of the target surface and the corresponding properties of the minima corresponding to the same directions but observed when the target is rotated around an axis lying in this plane can apparently be attributed to a functional dependence of the half-width of the minimum on the angles φ, φ_1, and β and to the sensitivity of the emission to the ordered arrangement of atoms in the close-packed planes (Fig. 5).

We have thus shown that the $\psi_W(\beta)$ and $\delta(\beta)$ curves are nonmonotonic and that the shapes and half-widths of the minima on the $\Gamma(\varphi-\varphi_0)$ and $\Gamma(\beta-\beta_0)$ curves are functions of the angles β and φ, respectively. The experimental results have been discussed qualitatively on the basis of existing ideas regarding the mechanism for ion–electron emission.

In conclusion the authors thank A. V. Smirnov for assistance in this work and Z. K. Zolina for help in orienting the single crystals.

---

[1] D. Medved and G. E. Strausser, Adv. in Electronics and Electron Phys., 21, 101 (1965).

[2] E. S. Mashkova and V. A. Molchanov, Fiz. Tverd. Tela, 6, 3704 (1964) [Sov. Phys. – Solid State, 6, 2967 (1965)].

[3] H. Sommerfeldt, E. S. Masckova, and V. A. Molchanov, Rad. Eff., 9, 267 (1971).

[4] B. A. Brusilovsky and V. A. Molchanov, Rad. Eff., 8, 71 (1971).

[5] Yu. V. Martynenko, Fiz. Tverd. Tela, 8, 637 (1966) [Sov. Phys. – Solid State, 8, 515 (1966)].

[6] H. Sommerfeldt, E. S. Mashkova, and V. A. Molchanov, Fiz. Tverd. Tela, 13, 819 (1971) [Sov. Phys. – Solid State, 13, 676 (1971)].

[7] I. N. Evdokimov, E. S. Masckova, V. A. Molchanov, and D. D. Odintsov, Phys. Status Solidi, 19, 401 (1967).

[8] D. D. Odintsov, Fiz. Tverd. Tela, 5, 1114 (1963) [Sov. Phys. – Solid State, 5, 813 (1963)].

[9] G. V. Martynenko, Phys. Status Solidi, 15, 767 (1966).

Perveance of a vacuum with a point cathode

S. P. Bugaev, E. A. Litvinov, V. V. Lopatin, and G. A. Mesyats
Institute of Atmospheric Optics, Siberian Branch,
Academy of Sciences of the USSR, Tomsk

(Submitted July 17, 1972)
Zh. Tekh. Fiz., 44, 148-152 (January 1974)

The voltage–current characteristics have been obtained for vacuum diodes with point cathodes operating under conditions of explosive electron emission. A difference is found between the oscillograms of the electron current at small (~50 kV) and large (~300 kV) amplitudes of the voltage pulses. The electron current is shown to be space-charge-limited. The electron current is using the x radiation produced by stopping the beam in a metal foil. There is a difference at low and high voltages: At low voltages the current-density distribution over the beam cross section is Gaussian; at high voltages the beam has an annular cross section.

Point cathodes operating under conditions of explosive emission of electrons are frequently used in the diodes of nanosecond pulsed electron accelerators and x-ray apparatus.[1] The appearance of the discharge current in the evacuated gap of such a diode during electrical breakdown coincides with the appearance of a plasmoid at the cathode (a cathode burst[2]), which expands at $v = 2 \cdot 10^6$ cm/sec. The current through the diode under these conditions is limited by the space charge ("3/2" law).[1,3]

We report here on a study of the current-carrying capability of a diode with a point cathode; the electron-beam has also been studied. The diode has a single-point cathode and a plane anode, separated by a vacuum gap of width d. When a voltage pulse is applied to the cathode, the plasma of the cathode burst appears (Fig. 1). The experiments are carried out under conditions such that the burst appears for times not exceeding 10^{-9} sec.

The perveance $p = iu^{-3/2}$ is found as a function of the ratio $vt/(d - vt)$ (where i is the current and u is the voltage drop across the diode) with $5 \cdot 10^{-12}$ cm $\leq d \leq 6 \cdot 10^{-1}$ cm and at voltages $10^4 \leq u_0 \leq 1.6 \cdot 10^5$ V in refs. 1,3. The experimental points are shown in Fig. 1. Examination of this figure shows that the current through the diode is limited by the space charge of electrons in the gap.

When the electric field at the point is higher than the fields in refs. 1,3, the current behavior is different. Figure 2 shows oscillograms of the diode voltage and current, x-ray patterns of the electron beam at the anode and histograms of the beam density for a given point at 75 and 300 kV. In the first case the current pulse is triangular, in the second it is trapezoidal with a sharp rising part. The perveance p for high values of u is shown in Fig. 1. The beam structure is studied by detecting the bremsstrahlung from the anode, which is a disk of tantalum foil 150 μ thick; a piece of photographic film is pressed tightly against the back side of the foil. The beam structure also changes with increasing u, becoming annular with a central core.

To calculate p we must solve the nonlinear partial differential equations describing the motion of the charged particles, taking into account the space charge of these particles. This is a very difficult task. Ivey[4] described certain approximate methods used to calculate the electric current through complex diodes. The most versatile method is that of Matricon and Trouve,[5] which is based on the total capacitances of different configuration. In these calculations the specific capacitances are equated. We write the solution of the Poisson equation, taking account of the space charge and the nonvanishing field at the cathode for the case of a plane diode:

$$\left(\frac{4\pi j}{\sqrt{2\frac{e}{m}}}\right)^2 d^2 - \frac{E^3 d}{3} + \frac{uE^2}{3} - \frac{4u^{3/2}}{9}\left(\frac{4\pi j}{\sqrt{2\frac{e}{m}}}\right) = 0. \qquad (1)$$

If the current density j is set equal to zero, Eq. (1) corresponds to the electrostatic case without space charge: $E = -u/d$. If $E = 0$, the cathode is completely shielded by space charge: $j = (\sqrt{2(e/m)}/9\pi)(u^{3/2}/d^2)$. Intermediate cases are described by Eq. (1). If we find the field for an arbitrary configuration and equate it to the field of a plane capacitor, we can find the effective gap width d_{eff}; substituting this into the "3/2" equation for the planar diode, we find the current density. A similar approach has been used by Dyke and Trolan[6] in a study of the effect of space charge on field emission. The total current can be found by integrating over the emitting surface. For this case the distribution of the potential φ can be written as[7]

$$\left.\begin{aligned} &\varphi = \frac{u}{(d - vt)^{\nu}}\left[r^{\nu} - (vt)^{2\nu+1} r^{-\nu-1}\right] P_{\nu}(\cos\theta), \\ &0 \leqslant \nu \leqslant 1, \quad P_{\nu}(\cos\alpha) = 0, \quad \alpha > \frac{\pi}{2}, \end{aligned}\right\} \qquad (2)$$

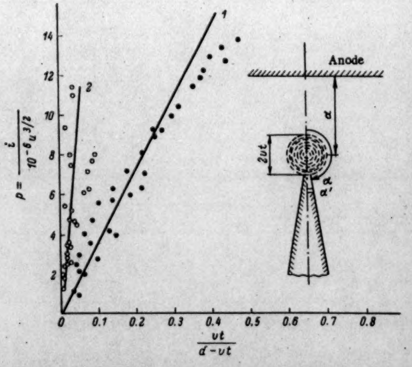

Fig. 1. Perveance of a diode with a point cathode as a function of the normalized time vt/(d − vt). Here v is the plasma-expansion velocity, d is the width of the gap, and t is the time. The voltage u is: 1) ≤ 50, 2) ≥ 200 kV.

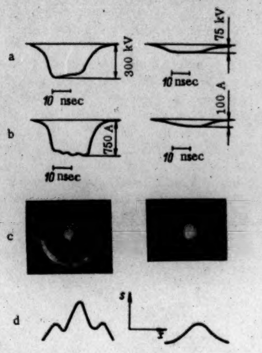

Fig. 2. a) Oscillograms of the voltage across a diode with a point cathode; b) current oscillograms; c) x-ray patterns of the electron beam; d) histograms of the current density.

where $P_\nu(x)$ is a Legendre function and r and θ are spherical coordinates; then

$$d_{\text{eff}}^{-1} = \left(\frac{vt}{d-vt}\right)^{\nu} (vt)^{-1} (2\nu+1) P_\nu(\cos\theta)$$

and

$$i = 2.33 \cdot 10^{-6} u^{3/2} \left(\frac{vt}{d-vt}\right)^{2\nu} (2\nu+1)^2 \int d\Omega p_\nu^2(\cos\theta). \qquad (3)$$

Since it is ussually true that $\alpha \simeq 160°\text{-}170°$, we find[8] $\nu \simeq 0.5$. The integration in (3) can be carried out over the solid angle subtended by the anode at the center of the cathode burst ($\Omega \simeq 2\pi$) or over the entire free surface of the plasma [$\Omega \simeq 2\pi(1-\cos\alpha)$]. There is an uncertainty here because we do not know the relative number of electrons that reach the collector. If we set the coefficient in (3) equal to the arithmetic mean of the numbers obtained in the specified integration range, we find

$$i = 37 \cdot 10^{-6} u^{3/2} \frac{vt}{d-vt}. \qquad (4)$$

Line 1 in Fig. 1 shows the perveance p as a function of the ratio vt/(d − vt) according to (4). Experimental points from ref. 3 are also shown; we believe the agreement is good.

We attribute the faster increase in the diode current at high voltages to the appearance of plasma from the lateral surface of the point, resulting from the explosion of microscopic protuberances there. To estimate the distance r_1 from the end of the point at which these explosions can occur, we use (2), finding, for $r_1 \gg vt$,

$$r_1 = \frac{2u^2\beta^2}{(d-vt)E^2\pi^2(1+\cos\alpha)}. \qquad (5)$$

where E is the local field at the lateral surface, and β is the amplification of the electric field, which takes into account the presence of microscopic roughness. For the plasma to appear during the rise time of the pulse, $t_r \simeq 5$ nsec, we would have to have[9] $E \approx 10^8$ V/cm. In the experiments described above, the pertinent values are u = 300 kV, d = 1 cm, $\alpha \simeq 165°$, and $r_1 \simeq 0.1$ cm, so we find $\beta \simeq 50$. Since $r_1 \gg vt$ (in our case, $vt \simeq 10^{-2}$ cm), the result would be an increase in the electron current more rapid than that in ref. 3. This effect has been erroneously attributed to an increase in the expansion velocity of the plasma burst, v. To estimate the perveance, we use the method of equating specific capacitances, described above. For $r_1 \gg vt$,

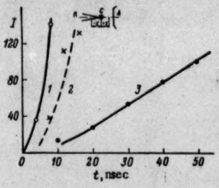

Fig. 3. Increase in the glow intensity I as a function of the elapsed time following the application of the voltage pulse. r, mm: 1) 0; 2) −0.5; 3) +0.5.

$$p = \left\{37\frac{vt}{d-vt} + 3\frac{r_1\left[\operatorname{tg}(\pi-\alpha') + \frac{vt}{r_1}\right]}{[1+\cos(\pi-\alpha')](d-vt)}\right\} \cdot 10^{-6}. \qquad (6)$$

The first term in (6) corresponds to emission from the cathode burst formed during the explosion of the end of the point, and the second corresponds to emission from the lateral surface when the plasma forms there as a result of the explosion of microscopic protuberances. Estimates for, e.g., $t = 1.2 \cdot 10^{-8}$ sec, d = 1.25 cm, and $u = 2.4 \cdot 10^5$ V lead to an experimental perveance of $\sim 3 \cdot 10^{-6}$ perv, while the theoretical value, determined from Eq. (6), is $\sim 4 \cdot 10^{-6}$ perv. Accordingly, the rapid current increase at the leading edge of the pulse (Fig. 2) can be attributed to explosive emission from the plasma formed at the lateral surface of the emitter. This conclusion is supported by the glow observed at the lateral surface of a point cathode during the first few nanoseconds after the application of the voltage pulse. A narrow optical slit was used in ref. 11 to time the appearance of the glow at certain distances from the end of the tip (Fig. 3); the results found there show that the area of the lateral surface covered by the glow increases with increase amplitude of the voltage across the diode. This effect cannot be attributed to expansion of the plasma, for the glow in the gap appears much later than that at the lateral surface of the tip.

At large values of u the concept of a perveance is slightly arbitrary, since the "3/2" law does not hold, because the area of the lateral surface over which the plasma can appear is a function of the voltage u.

We turn now to the reason for the annular structure of the electron beam. Electrons emitted from the lateral surface move in an electric field E and a magnetic field H, due to the current flowing through the emitter. This situation can be thought of approximately as roughly similar to the motion of a charged particle in orthogonal E and B fields. The circular magnetic field of the current deflects the electrons toward the cathode. The electron trajectories for a similar case were calculated in ref. 12; they turn out to be such that the beam can acquire a hollow structure. The effect is small if $(e\mu_0 H/m)t \ll 1$, where t is the transit time[13] and

$$\varphi = \frac{\left(\frac{e}{m}\right) j^2}{\varepsilon_0^2} \frac{t^4}{8}.$$

Setting $H \simeq 2i/4\pi y$ and $y \simeq r_1 \sin(\pi - \alpha')$, we find

$$t \ll \frac{2\pi r_1 \sin(\pi - \alpha') m}{e\mu_0} \left[\frac{ej}{6\varepsilon_0 m r_1 \sin(\pi - \alpha')} \right]^{1/3}. \tag{7}$$

Equation (7) is written in units of the International System. The current density j can be calculated on the basis of the effective gap width d_{eff}. Estimates for the experiments mentioned above yield $i \ll 10^3$ A, completely consistent with the observed behavior. Finally, the axial maximum of the current density in the electron beam can be attributed to the combined effects of the self magnetic field of the beam and of the ions entrained by the beam. The pinching of an electron beam during capture of ions from a plasma was described in refs. 14. This effect is usually accompanied by an anomalous acceleration of ions toward the anode[14] and occurs primarily in the axial part of the beam.

---

[1] G. A. Mesyats and D. I. Proskurovskii, ZhETF Pis., 13, 7 (1971) [JETP Lett., 13, 4 (1971)].

[2] G. A. Mesyats, S. P. Bugaev (Bougaev), and D. I. Proskurovskii (Proskourovsky), Discharges and Electrical Insulation in Vacuum, Proceedings of the Third International Symposium, Paris (1968), p. 218.

[3] G. A. Mesyats, G. P. Bazhenov, R. B. Baksht, E. A. Litvinov, D. I. Proskurovskii (Proskourovsky), V. P. Rotshtein (Rotstein), and S. P. Vavilov, Discharges and Electrical Insulation in Vacuum. Proceedings of the Third International Symposium, Waterloo, Ontario (1970), p. 121.

[4] H. F. Ivey, Advances in Electronics and Electron Physics, Vol. 1 (1954), p. 137; Problemy Sovremennoi Fiziki, No. 6, 5 (1956).

[5] M. Matricon and S. Trouve, L'Onde Electr., 30, 510 (1950).

[6] W. P. Dyke and I. K. Trolan, Phys. Rev., 89, 799 (1953).

[7] W. R. Smythe, Static and Dynamic Electricity, McGraw-Hill, New York (1950).

[8] E. Jahnke, F. Emde, and F. Lösche, Tables of Higher Functions, McGraw-Hill, New York (1960).

[9] G. K. Kartsev, G. A. Mesyats, D. I. Proskurovskii, V. P. Rotshtein, and G. N. Fursei, Dokl. Akad. Nauk SSSR, 192, 309 (1970) [Sov. Phys.-Dokl., 15, 475 (1970)].

[10] V. M. Logunov, A. G. Ponomarenko, and L. P. Fominskii, Preprint 43-71, Institute of Nuclear Physics, Siberian Branch, Academy of Sciences of the USSR, Novosibirsk (1971).

[11] R. B. Baksht, M. N. Urbazaev, and S. P. Vavilov, Izv. VUZ. Fiz. (in press).

[12] W. H. McNeill and I. R. Uglum, IEEE Trans. Nucl. Sci., NS-16, 3 (1969).

[13] P. L. Kirstein, G. Kino, and W. Waters, Space-Charge Flow, McGraw-Hill, New York (1967).

[14] E. D. Korop and A. A. Plyutto, Zh. Tekh. Fiz., 40, 12 (1970).

Production of collimated beams of high-energy electrons

V. I. Nemchenko

(Submitted January 14, 1972; resubmitted February 12, 1973)
Zh. Tekh. Fiz., 44, 153-163 (January 1974)

A study has been made of the properties of an extended, hindered discharge between plane electrodes at low pressure (0.26-0.047 torr) at voltages up to 15-20 kV. When the mean free paths of the charged particles are comparable to the characteristic dimension of the bounding insulator and interelectrode distance, the primary mechanism leading to an increase in the resistance of the hindered discharge and contraction at the axis is radial diffusion of charged particles from the active zone of the discharge. When the pressure is reduced to a critical value, and when the potential drop is increased to a critical value, the current is cut-off because of transverse loss. These critical values are functions of the diameter of the quartz insulator and the distance between electrodes. An arrangement of this kind can be used to produce collimated beams of high-energy electrons because of the high resistance of the discharge, the large potential drop (up to 15-20 kV), the high axial density, the high current density at the cathode spot, and the fact that most of the electrons are under essentially collisionless conditions.

Electron-beam diagnostics of flowing gases and plasmas is increasing in importance because of the accuracy and versatility of the method. The electron beams are usually produced by standard three-electrode guns with a hot cathode and magnetic or electrostatic beam focusing. This method suffers from the disadvantage that an independent vacuum system is required to produce a high vacuum $5 \cdot 10^{-5}$-10^{-6} mm in the beam region and in the aperture sections used for extracting the beam into the working chamber. This unnecessary complication of the apparatus reduces the usefulness of the beam for diagnostic purposes.

Plasma electron sources exploiting the properties of glow discharges may turn out to be useful for operation in evacuated aerodynamic tubes operating continuously in the slip and transient regimes. Methods for using plasma sources to produce electron beams have been developed rapidly in recent years. In particular, the plasma of a glow discharge between a hemispherical cathode and a plane anode at a pressure of 2-$5 \cdot 10^{-2}$ torr has been used to produce an electron beam and focus it onto a target.[1] In a slightly different arrangement, a glow discharge in an electrical-discharge tube with a lateral anode and magnetic focusing of electrons onto the target has been used at the same pressures.[1]

In several instances a discharge with a hollow cathode in the working chamber has been used to produce electron beams in welding and smelting.[2-5] It has been found that at certain pressures and voltages a discharge with a high ohmic resistance arises in the hollow cathode and an electron beam is emitted from the cathode. The beam can be highly focused because its space charge is neutralized by the ions. It is difficult to use an electron gun to study highly inhomogeneous jet flows or the flows which occur in hypersonic flow around a model because several discharge modes exist.

Dubinina and Ibadov[6] have described a hollow spherical cathode of a special design which can produce electrons with a high exit compression. A glow discharge is excited in the cathode cavity by an rf discharge. At an air pressure of the order of 1 torr the electron energy is about 0.2-0.3 keV. A disadvantage of the closed plasma electron source described above is the low electron energy – 2-3 keV at gas pressures from 5 to 0.02 torr; this energy is clearly too low for diagnostics of gas flows in the slip regime. Use of an electron gun for diagnostic purposes in gas dynamics is described, in particular, in ref. 7; unfortunately, no information is given there regarding the operating principle or design of the gun.

Examination of the basic properties of a glow discharge and the principles for producing collimated beams reveals that use of the cathode part of the discharge, at small interelectrode separations and low pressures (a "hindered" glow discharge[8,9]) holds some promise for producing a discharge with a high ohmic resistance and a high electron energy in a closed volume. Another way to produce a discharge with a high ohmic resistance would be to use the extended discharge which arises when the transverse dimensions of the discharge gas are limited.[8-10] Some study has been made of the effect of insulating limiting surfaces on the properties of discharges at high pressures (4-10 torr) in a large positive column.

In both cases the voltage across the discharge gap must be raised (above that required for an unlimited discharge) to compensate for the reduced cathode emission resulting from the reduction in the number of particles bombarding the cathode. A variety of factors lead to the loss of active particles. An extended discharge with a large positive column is essentially useless for producing high-energy electron beams. On the other hand, a hindered glow discharge cannot provide high discharge current densities because of the limited power level of the system; thus, this type of discharge cannot produce a sufficiently intense collimated electron beam. In the cathode part of the discharge the electrons, whose energy is governed by the cathode fall, undergo few collisions and escape along nearly linear trajectories normal to the surfaces of the electrodes. On the basis of these arguments we conclude that the most promising system for producing collimated beams of high-energy electrons is an extended hindered discharge in the cathode fall and in the adjacent part of the negative glow. The negative glow is important for producing a stable discharge.

We report here on an experimental study of a hindered glow discharge between plane electrodes in quartz tubes of various shapes and diameters at voltage drops up to 20 kV and at pressures from 0.26 to 0.047 torr. We describe the properties of the extended hindered glow discharge which develops under these conditions and certain properties of the collimated electron beam.

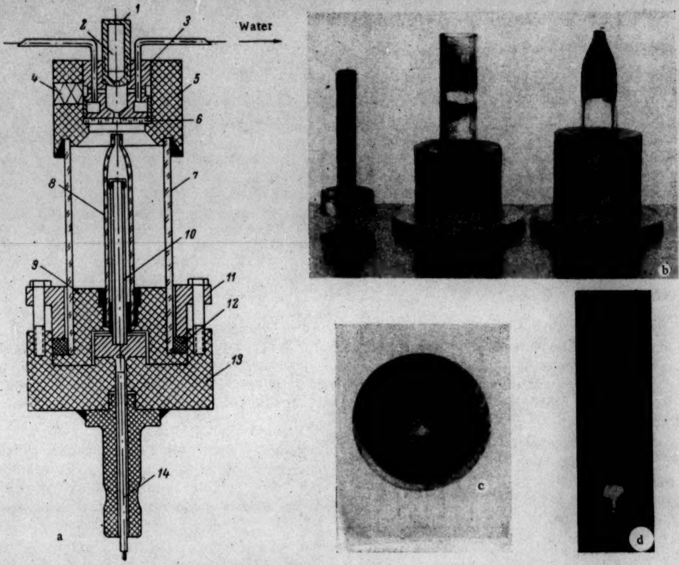

Fig. 1. Construction and certain characteristics of the discharge device. a) Construction of the discharge gap; b) cathodes with a flat end (1), a cylindrical quartz insulator (2), and a constricted quartz insulator (3); 3) surface of the end of the cathode, displaying erosion tracks; d) cathode region of the extended hindered discharge [1) Cathode; 2) quartz insulator; 3) contracted discharge column; 4) anode unit; 5) electron beam in working chamber].

Figure 1a shows the discharge gap used in these experiments. The cathode and anode units are connected by a glass mount 7. Stainless-steel anode 3 has an aperture 1.8 mm in diameter at its center and a cooling-water jacket. Limiting diaphragm 2 and quartz capillary 1 are screwed into the anode to increase the resistance of the gap between the cathode and the walls of the working chamber which is at the anode potential. The anode has a special recess and an aperture for communication between the inner volume of the discharge gap and the working chamber of the vacuum tube, through shielding metal grid 4. The cathode unit consists of the main body 13, high-voltage vacuum lead 14, insulating base 9, quartz insulator 8 (either 2 or 3 in Fig. 1b), and the cathode proper 10. The cathode with the flat end is made from stainless steel, clad in a quartz tube (1 in Fig. 1b). The cathode is 7 mm in diameter.

Power is supplied to the discharge gap from a supply with an NOM-2 transformer and a voltage doubler with D-1008 diodes. The primary circuit is regulated by a ferroresonant regulator. The output voltage is regulated by an autotransformer in the primary circuit. The discharge gap is connected through a ballast resistance of 1-3 kΩ in a positive-ground circuit.

The geometric parameters of the discharge gap which primarily determine the properties of the discharge in the specified pressure range are the interelectrode distance l and the diameter of the discharge tube, d. The interelectrode distance is chosen so that a small part of the negative glow is retained over the entire pressure range. At large values of the cathode fall V_k the product pL, which governs the size of the Faraday dark space at various pressures p, is a weak function of V_k. Under these conditions the data of ref. 8 can be used to estimate the appropriate electrode separation, which is then adjusted experimentally. In these experiments this distance is fixed at 25 mm. In connection with the diameter of the discharge tube, we note that the effect of limiting insulating surfaces on the characteristics of discharges has been described in the literature[8-10] for pressures on the order of 4-10 torr and at small voltage drops. Under these conditions the ratio E/p is comparatively small, and the mean free paths of the particles are small in comparison with the characteristic gap dimensions. However, collimated beams of high-energy electrons are more readily produced at large values of E/p [> 5-10 kV/(cm · torr)] and when the mean free paths of the particles are comparable to the characteristic gap dimensions. There is essentially no information on this case in the literature, so we have carried out special experiments to choose an appropriate diameter for the gas-discharge tube. All the results on the discharge characteristics are obtained by the standard glow-discharge techniques, involving processing of the electrodes at low pressures to the point at which the metal is sputtered.

Figure 2a shows the voltage–current characteristics of unlimited discharges in the evacuated chamber at pres-

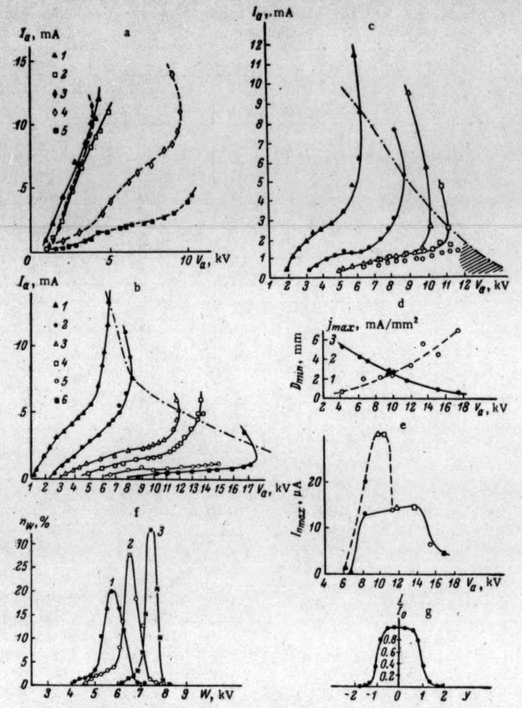

Fig. 2. Certain characteristics of the discharge as functions of the pressure for various configurations of the discharge gap. a: 1) Voltage–current characteristics of an unlimited discharge in the working chamber at a pressure of 0.21 torr; 2) the same, at 0.15 torr; 3-5) voltage–current characteristics of discharges at a pressure of 0.15 torr in cylindrical quartz insulators of various diameters [d, mm: 3) 33; 4) 14.5; 5) 10.2]. b: Voltage–current characteristics of discharges in cylindrical quartz insulators for various pressures in the working chamber. 1) p = 0.26 torr; 2) 0.15; 3) 0.105; 4) 0.084; 5) 0.068; 6) 0.057. c: Voltage–current characteristics of discharges in constricted quartz insulators at various pressures (the notation is the same as in Fig. 2b). d: Maximum current density (dashed curve) and minimum diameter of the cathode spot (solid curve) as functions of the voltage drop. e: Maximum electron-beam current for discharges in cylindrical insulators (solid curve) and in constricted insulators (dashed curve) as a function of V_a at various pressures (the same as in Fig. 2b). f: Electron energy distributions. 1) V_k = 6.0 kV; 2) 6.7; 3) 7.7 (p = 0.15 torr). g: Current distribution along a diameter of the electron beam for $V_a \approx$ 8 kV, p = 0.15 torr, and I_a = 7 mA.

sures of 0.21 torr (1) and 0.15 torr (2), along with those for discharges in cylindrical quartz tubes of various diameters at 0.15 torr. We see that the use of an insulating surface to limit the size of the discharge gap reduces the discharge current at a given voltage drop across the gap. As the supply voltage is raised to a certain limit, there is a transition from an increasing voltage–current characteristic to a decreasing one.$^{1)}$ As the tube diameter is reduced, the transition region shifts toward higher voltages, i.e., the discharge resistance increases. The change in the sign of the derivative of the characteristic can be attributed to two factors. First, the uncooled cathode is warmed because the intensity at which it is bombarded increases with increasing particle energy; this behavior is also observed in an unlimited discharge (1 and 2 in Fig. 2a). Second, there is a change in the pressure in the gap when the temperature increases and when cathode material is sputtered (and the evacuation rate is limited). The pressure change can be seen by comparing the characteristics for limited and unlimited discharges (1-3 in Fig. 2a). The characteristic for a limited discharge at the maximum tube diameter, at which the role of the insulating surface

TABLE 1. Ratio of the Mean Free Paths of Various Charged Particles and Neutral Molecules to the Diameter of the Discharge Tube

p, torr	d, mm					
	33			14.6		
	1	2	3	1	2	3
260	$1.41 \cdot 10^{-2}$	$7.1 \cdot 10^{-3}$	$6.1 \cdot 10^{-2}$	$3.19 \cdot 10^{-2}$	$1.6 \cdot 10^{-2}$	$1.37 \cdot 10^{-1}$
210	$1.7 \cdot 10^{-2}$	$8.8 \cdot 10^{-3}$	$7.5 \cdot 10^{-2}$	$3.85 \cdot 10^{-2}$	$1.99 \cdot 10^{-2}$	$1.7 \cdot 10^{-1}$
150	$2.39 \cdot 10^{-2}$	$1.23 \cdot 10^{-3}$	$1.05 \cdot 10^{-1}$	$5.33 \cdot 10^{-2}$	$2.78 \cdot 10^{-2}$	$2.36 \cdot 10^{-1}$
105	$3.4 \cdot 10^{-2}$	$1.76 \cdot 10^{-2}$	$1.5 \cdot 10^{-1}$	$7.66 \cdot 10^{-2}$	$3.98 \cdot 10^{-2}$	$3.38 \cdot 10^{-1}$
84	$4.25 \cdot 10^{-2}$	$2.2 \cdot 10^{-2}$	$1.86 \cdot 10^{-1}$	$9.57 \cdot 10^{-2}$	$4.96 \cdot 10^{-2}$	$4.23 \cdot 10^{-1}$
68	$5.24 \cdot 10^{-2}$	$2.72 \cdot 10^{-2}$	$2.32 \cdot 10^{-1}$	$1.19 \cdot 10^{-1}$	$6.15 \cdot 10^{-2}$	$5.23 \cdot 10^{-1}$
57	$6.25 \cdot 10^{-2}$	$3.24 \cdot 10^{-2}$	$2.76 \cdot 10^{-1}$	$1.41 \cdot 10^{-1}$	$7.33 \cdot 10^{-2}$	$6.24 \cdot 10^{-1}$
47	$7.5 \cdot 10^{-2}$	$3.94 \cdot 10^{-2}$	$3.34 \cdot 10^{-1}$	$1.70 \cdot 10^{-1}$	$8.9 \cdot 10^{-1}$	$7.54 \cdot 10^{-1}$

p, torr	d, mm					
	10.2			2		
	1	2	3	1	2	3
260	$4.62 \cdot 10^{-2}$	$2.33 \cdot 10^{-2}$	$1.98 \cdot 10^{-1}$	$2.33 \cdot 10^{-1}$	$1.16 \cdot 10^{-1}$	1.0
210	$5.6 \cdot 10^{-2}$	$2.9 \cdot 10^{-2}$	$2.45 \cdot 10^{-1}$	$2.81 \cdot 10^{-1}$	$1.45 \cdot 10^{-1}$	1.23
150	$7.75 \cdot 10^{-2}$	$4.04 \cdot 10^{-2}$	$3.43 \cdot 10^{-1}$	$3.9 \cdot 10^{-1}$	$2.03 \cdot 10^{-1}$	1.72
105	$1.11 \cdot 10^{-1}$	$5.8 \cdot 10^{-2}$	$4.91 \cdot 10^{-1}$	$5.6 \cdot 10^{-1}$	$2.9 \cdot 10^{-1}$	2.47
84	$1.4 \cdot 10^{-1}$	$7.22 \cdot 10^{-1}$	$6.13 \cdot 10^{-1}$	$7.0 \cdot 10^{-1}$	$3.62 \cdot 10^{-1}$	3.09
68	$1.73 \cdot 10^{-1}$	$8.9 \cdot 10^{-2}$	$7.56 \cdot 10^{-1}$	$8.65 \cdot 10^{-1}$	$4.5 \cdot 10^{-1}$	3.82
57	$2.05 \cdot 10^{-1}$	$1.1 \cdot 10^{-1}$	$9.0 \cdot 10^{-1}$	1.03	$5.35 \cdot 10^{-1}$	4.55
47	$2.45 \cdot 10^{-1}$	$1.29 \cdot 10^{-1}$	1.07	1.24	$6.5 \cdot 10^{-1}$	5.5

in shaping the discharge is slight, and at low voltage drops (characteristic 3), coincides with that for an unlimited discharge at the same pressure (2); then, as the current and the voltage drop increase, there is a transition to the characteristic of the unlimited discharge at a higher pressure (1). In this apparatus an increase in the supply voltage thus increases the pressure.

Accordingly, steady-state characteristics can be obtained only if the supply voltage is held for a period of time at each higher value before the corresponding experimental point is recorded. During this period the values of p, V_a, I_a, and I_n reach a steady-state. If, instead, the supply voltage is increased rapidly, the discharge can jump irreversibly to the descending branch of the characteristic. Figure 2b shows discharge characteristics for various pressures in the working chamber for discharges in cylindrical quartz tubes having an inside diameter of 11.2 mm. Reducing the pressure in the chamber reduces the discharge current at a fixed voltage drop and shifts the extremum on the voltage – current characteristic toward higher voltages.

The experimental results (expecially the discharge characteristics for various tube diameters but at fixed values of l, p, and V_a) show the dominant role of diffusion, which leads to a rapid transverse loss of charged particles, in shaping the discharge.

A quantitative theory for transverse loss has been worked out for high pressures and low values of the ratio, E/p, for which the mean free paths of the particles are much smaller than the characteristic gap dimensions, and the particle energy distribution is Maxwellian or approximately so.[8,11] When E/p is large, the drift velocity of the charged particles is much higher than the thermal velocity, the mean free paths of the particles are comparable to the characteristic dimensions of the discharge, and the particle energies and energy distributions are non-Maxwellian and (generally) unknown. No reliable recommendations have been offered for calculating the transverse loss due to diffusion under such conditions.

From the results in Figs. 2a and 2b we see that under these experimental conditions the field E reaches nearly 10 kV/cm and that E/p can reach 140 kV/(cm · torr). At these values of E/p the mechanism governing the transverse loss would apparently be the scattering of particles in collisions and the resulting escape of charged particles from the active zone of the discharge. Ambipolar diffusion would apparently be important for low-energy particles.

Table 1 shows the ratios of the mean free paths of various charged particles and neutral molecules to the diameter of the discharge tube.

To evaluate the mean free paths with respect to ion–molecule collisions we use data on the drift velocity in strong electric fields.[11] The mean free path of nitrogen molecules is evaluated from viscosity measurements at 500°K (ref. 11).

For electron–molecule collisions at high energies we use the reduced mean free path found[11] for electrons from the absorption coefficient of electrons in the given gas.[12] The degree of ionization of the gas is assumed low.

Comparison of the data in this table with the experimental results in Figs. 2a and 2b reveals that the effective current reduction in a discharge limited by insulating surfaces is caused by the same factors which cause the increase in the mean free paths of the charged particles in comparison with the characteristic dimension of the discharge gap. There is a relative decrease in the current when the tube diameter or gas pressure is reduced or when the particle energy is increased.

The transverse loss due to charged-particle diffusion depletes primarily the peripheral regions of the discharge, leading to the formation of an active discharge zone at the tube axis, to a narrowing of the negative glow, and to a contraction of the cathode spot (see, e.g., Figs. 1c and 1d). The spot diameter can be determined for various voltage drops and working-chamber pressures from the erosion tracks on the cathode surface (Fig. 1c). Figure 2d shows the minimum spot diameter as a function of the maximum voltage drop for various pressures. A narrowing of the negative glow and a contraction of the cathode spot have been observed in hindered discharges at higher pressures and lower voltage drops previously,[9,10] but under those conditions the effects are not as pronounced. At low working-chamber pressures and at large voltage drops the spot can narrow to a diameter of 0.8 mm, and a further increase in the voltage drop (beyond a certain critical value) or a further pressure reduction cuts off the current (for a given tube diameter).

The concentration of the discharge in the axial region and the contraction of the cathode spot which occur when the voltage drop is increased or the pressure reduced are accompanied by an increase in the current density at the cathode spot (Fig. 2d); this increase causes a local heating of the cathode and intensifies the formation of a central discharge zone.

Since the trajectories of most of the electrons in the cathode fall are essentially linear and normal to the cathode surface, any cross-section of the electron beam not too far from the cathode is a projection of the cathode spot in a hindered discharge (Fig. 1d). Accordingly, the intensity of the collimated electron beam emerging from the anode aperture is governed by the current density at the cathode spot. We in fact observe an increase in the beam current (measured with a Faraday cup in the working chamber 120 mm from the exit limiter; Figs. 2d and 2e) when the current density increases.

The negative glow plays an important role in shaping and stabilizing an extended hindered discharge: It furnishes photons, ions, and (at large V_a) x rays which induce electron emission from the cathode. We therefore study how a constriction in the insulating surface near the negative glow affects the discharge characteristics. In these experiments we use a quartz insulator of simple shape (3 in Fig. 1b). The voltage–current characteristics of a discharge in a discharge tube with a constricted insulator lie considerably below those for a discharge in a cylindrical insulator at high pressures (Figs. 2c and 3). At low pressures, the characteristics rise in the region of large voltage drops because of the supply of insulator material directly in the discharge zone. For the same reason, the transition from a discharge with an ascending characteristic to one with a descending characteristic occurs at a lower voltage than in the case of a cylindrical insulator. A distinctive feature of discharges in a constricted tube is the earlier cutoff of the current at high voltages and low gas pressures. In the hatched region in Fig. 2c a steady-state glow discharge with an ascending characteristic cannot exist.

Timofeeva[13] and Granovskii[14] observed a current cutoff in a constricted low-pressure tube operating under conditions corresponding to high-current arc discharges; they have offered an interpretation for this effect and suggested several practical applications. However, this effect has apparently not been observed previously in extended, hindered glow discharges. In this latter case the nature of the cutoff is slightly different. The mean free paths of the charged particles are comparable to or much larger than the diameter of the constricted part of the tube (Table 1). The concentration of the discharge at the axis becomes even more pronounced, and the cathode spot is very small (~ 0.5 mm at 10 kV and p = 0.084 torr); with a further increase in V_a or decrease in p the charged-particle density in the active zone turns out to be insufficient for the maintenance of a stable discharge, so that the current is cutoff. At pressures below 0.080–0.09 torr an increase in V_a is not accompanied by an immediate current cutoff; instead there is initially an unstable pulsating discharge. With a further increase in V_a the pulsation frequency decreases, and finally, at some $V_{a\,cr}$, the current is cutoff.

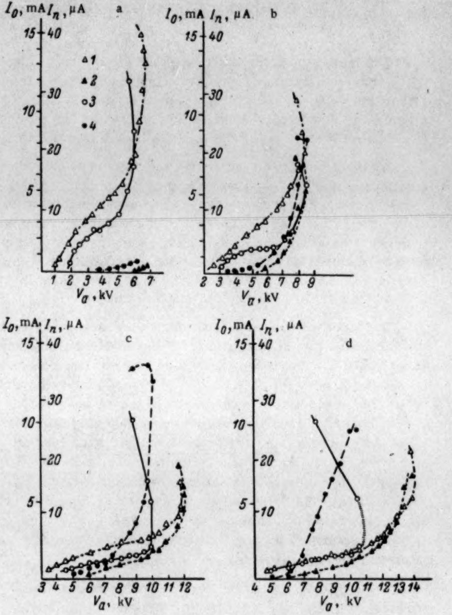

Fig. 3. Comparative characteristics of the discharges and electron-beam currents for discharges in cylindrical insulators and in constricted insulators, for various pressures in the working chamber. p, torr: a) 0.25; b) 0.15; c) 0.105; d) 0.084. 1, 3) Discharge current; 2, 4) beam current; 1, 2) cylindrical tube; 3, 4) constricted tube.

The apparent explanation is that at breakdown, which occurs at $V_{br} > V_{st}$ and at gas pressure and temperature p_{br} and T_{br}, some material is supplied from the cathode to the gap, the density increases, and V_a falls. As the evacuation continues, the pressure is reduced slightly, the density is also reduced, the gas temperature exceeds T_{br}, and V_a increases, approaching its steady-state value. In addition, the cathode spot expands, the transverse loss increases, and the current is cut off; then the process is repeated.

The increase in the discharge-current density caused by the tube constriction leads to an increase in the intensity of the collimated electron beam (Fig. 2e), to a level higher than that in a cylindrical tube; however, the electron beam fills a smaller volume and its energy is lower.

Figure 3 compares the characteristics of hindered discharges in cylindrical tubes with those in constricted tubes; shown here are the voltage–current characteristics of the discharges and the current of the collimated electron beam as a function of the voltage drop across the gap for various pressures in the working chamber. The beam current is measured with a Faraday cup while the beam is limited by a metal limiter 0.8 mm in diameter.

The electron emission increases with increasing voltage for both types of insulators. This result can be attributed to the concentration of the discharge at the axis as a result of diffusive loss and to the increased absorption and scattering of electrons in the gas because of their increased energy; e.g., at energies above 800 eV fewer than 1% of the electrons are scattered through angles larger than 1° (ref. 11). As the electrons increase in energy the scattering characteristic becomes even narrower.¹⁾ The combination of insulator, anode exit aperture, and limiter, with a small cathode spot and at high electron energies, acts as a natural filter for slower electrons, which are scattered through large angles.

We study the electron energy distribution over the working ranges of p and V_a by the retardation method. The apparatus for retarding the electrons is placed in the working chamber of the vacuum tube, where it is mounted on a three-coordinate manipulator. The error in the readings of two of the coordinates is on the order of 0.05 mm. The electrons enter this apparatus some 120-125 mm away from the point at which they leave the source. Replaceable limiters with apertures from 2 to 0.05 mm are used at the entrance to the retarding apparatus for studying the current distribution in the spot. The working cavity in this apparatus is evacuated to $2\text{-}5 \cdot 10^{-5}$ torr through flexible tubing. Figure 2f shows an illustrative energy distribution for a working-chamber pressure on the order of 0.15 torr and for various voltage drops. As the voltage drop across the gap is increased, the beam becomes more nearly monoenergetic. The averaging interval in the electron energy distribution is 0.25 keV. The electrons observed at relatively low energies results from the slowing of electrons in collisions with gas molecules between the electron source and the energy analyzer. In a hindered discharge the average electron energy is approximately equal to the voltage drop across the gap. Figure 2g shows the current distribution over the spot for the same working-chamber pressure. Under all conditions the beam divergence is less than 1°.

This description of the electron characteristics would be incomplete without mention of the difference between the characteristics corresponding to insulators of different shape at the transition from an ascending voltage–current characteristic to a descending one: While the electron-beam current continues to increase at the beginning of the descending branch when the cylindrical insulator is used, it falls off in the case of the constricted tube. This behavior can be attributed to marked heating of the constriction (to white heat), which is accompanied by the appearance of many thermal electrons and ions, which in turn disrupt the mechanism outlined above.

On the basis of these results regarding the cutoff of the hindered-discharge current at large ratios of the charged-particle mean free paths to the diameter of the quartz discharge tube and on the basis of studies[8,10] of the limitation of a discharge by insulating surfaces, we can recommend the use of a narrow insulating channel, along with systems of limiters and metal injection needles, for extracting the electron beam into the working chamber. In particular, a quartz capillary (1 in Fig. 1a) with an inside diameter of 1.2 mm led to a 40-50% increase in the breakdown voltage in the outer part of the working chamber under the specified experimental conditions. The source described here is used successfully to visualize tenuous gas flows.

RESULTS

1. Limiting the cathode region of a hindered glow discharge with insulating surfaces sharply reduces the current because of transverse diffusive loss, increases the discharge resistance, and requires an increase of 20-25 kV in the voltage supplied to the discharge gap, when the mean free paths for the charged particles are comparable to the characteristic dimensions of the insulating surfaces.

2. The current reduction due to transverse loss occurs primarily in the periphery of the discharge, causing the cathode spot to contract to a very small size (as small as 0.8 mm) at high voltage drops and at low pressures.

3. At low pressures and high voltages, effective limitation of the discharge, especially in the negative glow, leads to a cutoff of the current and ends the operation of the source.

4. When the discharge is significantly concentrated near the axis of the discharge tube, the current density at the cathode spot is high, the pressure is low, and the voltage drop is high, the apparatus described here is a source of high-energy collimated electrons with a narrow energy spread.

In conclusion the author thanks B. I. Zaslavskii for his continued interest.

---

1) Here and below we use the customary terminology in describing the characteristics, but the coordinate axes are interchanged for convenience in interpreting the current characteristics of the channeled-electron beam.

---

[1] R. B. Belser and A. P. Youmans, 33, 1109 (1962)

[2] H. L. L. Van Paassen and E. C. Mully, Proc. IEEE, 52, 316 (1964).

[3] E. C. Mully and J. Litton, Jr., in: Electron- and Ion-Beam Technology [Russian translation], Izd. Metallurgiya, Moscow (1968).

[4] I. D. Hernqvist, RCA Rev., 21, 170 (1960).

[5] L. M. Lidsky, S. D. Rothleader, D. J. Rose, and S. Yoshikawa, Appl. Phys., 33, 2490 (1962).

[6] E. I. Dubinina and S. Ibadov, Izv. Akad. Nauk SSSR, Ser. Fiz., 32, 1262 (1968).

[7] V. V. Volchkov and A. V. Ivanov, Izv. Akad. Nauk SSSR, Mekhan. Zhid. Gaza, No. 3, 160 (1969).

[8] A. von Engel, Ionized Gases, Oxford Univ. Press, London (1965).

[9] A. E. Aizentson and N. G. Kashnikov, Zh. Tekh. Fiz., 36, 2051 (1966) [Sov. Phys. – Tech. Phys., 11, 1525 (1967)].

[10] T. N. Lakomkina and V. F. Kholmogorskii, Elektron. Tekh., Ser. 3, Gaz. Prib., No. 3 (19), 11 (1970).

[11] E. W. McDaniel, Collision Phenomena in Ionized Gases, Wiley, New York (1964).

[12] W. H. J. Childs, Physical Constants, Halsted Press (Wiley), New York (1972).

[13] G. G. Timofeeva, Elektron. Tekh., Ser. 3. Gaz. Prib., No. 3 (19), 41 (1970).

[14] V. L. Granovskii, Electric Currents in Gases [in Russian], Vol. 1, Izd. Nauka, Moscow (1971).

General

Nonradiative electron transitions and thermal effects in laser-irradiated transparent dielectrics

B. I. Makshantsev, A. A. Kovalev, R. K. Leonov, and P. A. Yampol'skii

(Submitted October 30, 1972; resubmitted June 29, 1973)
Zh. Tekh. Fiz., 44, 164-172 (January 1974)

We discuss the heating of a cluster of impurity centers in a transparent dielectric irradiated by a laser pulse, taking account of the temperature dependence of the nonradiative electron transitions in the centers. It is assumed that the centers absorb the laser light. It is shown that the temperature in such a cluster is a nontrivial function of the number of impurity particles and the intensity of the laser radiation. An explanation is offered for the experimental size of the photocurrent induced by laser radiation in crystalline quartz, and its dependence on the radiation intensity.

Among the mechanisms for the fracture of transparent solid dielectrics by giant laser pulses the one which has received the greatest recognition is electric breakdown in the field of the light wave.[1-3] It has been shown experimentally[3,4] that no electron avalanche is generated by ruby laser radiation with an intensity lower than threshold by more than an order of magnitude, but a substantial photocurrent is observed. At the present time the production of free electrons by laser radiation is explained by multiphoton ionization,[4,5] but estimates show that the number of electrons formed during the irradiation time $\tau \approx 4 \cdot 10^{-8}$ sec should be substantially smaller than the experimentally observed value.

The probability of multiphoton ionization per unit time, w, is given by[5]

$$w = \omega\left(\frac{\omega_0}{\omega}\right)^{3/2} \exp\left[2E\left(\frac{\omega_0}{\omega}+1\right)-\frac{\omega_0}{\omega}\right]\left(\frac{I}{I'}\right)^{E\left(\frac{\omega_0}{\omega}+1\right)}. \qquad (1)$$

Here ω is the frequency of the photon, $\hbar\omega_0$ is the ionization potential, the symbol E(. . .) denotes the integral part of a number, and $I' = 2mc_0\omega^2\hbar\omega_0/\pi e^2$, where m is the mass of an electron, c_0 is the velocity of light, and e is the electron charge. Using Eq. (1) for crystalline quartz,[4] where $\hbar\omega \approx 7$ eV, irradiated by light from a ruby laser with intensity $I = 2 \cdot 10^8$ W/cm² we find the number of free electrons $N_e = Nw\tau = 2 \cdot 10^7$ cm^{-3}, which is significantly smaller than the experimental value[4] $Ne \approx 10^{11}$ cm^{-3}. Here, $N \approx 5 \cdot 10^{22}$ cm^{-3} is the bound electron density under the assumption that oxygen atoms are ionized.[3]

Since experiment shows that the dependence of the photocurrent on intensity is strongly nonlinear, it is impossible to account for the photoconductivity by ionization of other traps. Estimates of the size of the photocurrent made by using the theory of multiphoton ionization for equidistant intermediate levels[4] are not satisfactory since these levels are not found experimentally.

Thus, in spite of the importance of the question of the size of the photocurrent which precedes optical fracture and apparently is closely related to it, existing theory does not give a satisfactory explanation of the size of the photocurrent produced in transparent dielectrics by laser radiation.

It is also necessary to take account of the fact that the experimentally observed threshold values[1-3] of the radiation intensity at which the fracture of transparent dielectrics begins are smaller than the theoretical values calculated by the theory of light breakdown by more than two orders of magnitude.[1,2] In addition, at least for a ruby laser, fracture by multiphoton ionization should be observed before the theoretical threshold for breakdown.

On the basis of the above considerations it is clear it is of great interest to consider another model of the interaction of laser radiation with transparent dielectrics.

In ref. 6 local heating of a dielectric is considered a consequence of nonradiative electron transitions in impurity centers absorbing laser radiation. It is known[7,8] that impurities tend to form clusters 100-1000 Å in diameter in semiconductors and dielectrics. Therefore it is of interest, from the point of view of the problem of optical fracture of transparent dielectrics, to investigate the heating of such a cluster in exposure to laser radiation, taking account of the temperature dependence of the probability of a nonradiative electron transition of impurity centers. By an impurity center we mean an impurity particle with its immediate surroundings.

DERIVATION OF THE FUNDAMENTAL EQUATION

We assume that the clusters are spherical. In addition we assume that the density of the clusters is so small that their interaction can be neglected. We consider a cluster of radius $R = n^{1/3}r_0$. Here, n is the number of centers in the cluster and $2r_0$ is the distance between neighboring centers. The number n is assumed to be such that $2RK_\omega \ll 1$, where $K_\omega = \sigma n/(4\pi R^3/3)$, and σ is the cross section for the absorption of laser radiation by a single center. For the two-level model of an absorbing center

$$\frac{dP}{dt} = -\left[\frac{2\sigma(T)I}{\varepsilon}+\nu(T)\right]P+\frac{\sigma(T)I}{\varepsilon}, \qquad (2)$$

where P is the probability of finding a center in the excited state, ε is the energy of a photon, and $\nu(T)$ is the probability of a nonradiative electron transition in a center, depending of the time t, and, generally, on the position of the center in the cluster. The quantity $\nu(T)$ is ordinarily given by an Arrhenius relation of the form $\nu(T) = A\exp[-W/k(T+T_0)]$, where we take the initial temperature T_0 as the zero temperature reading, and A and W are constants. In Eq. (2) the intensity of the laser radiation is assumed to be so large that spontaneous radiative transitions can be neglected. By assuming the mean free path of a phonon to be appreciably smaller than the size of a cluster we can write the heat-conduction equation for the temperature T as

$$\frac{\partial T}{\partial t}=\operatorname{div}\,[\varkappa f(r)+\varkappa'(1-f(r))]\operatorname{grad}T+F(t,\ T)f(r). \tag{3}$$

In Eq. (3) $\varkappa = \lambda(T)/c\rho$ is the diffusivity, where $\lambda(T)$, c, and ρ are respectively the thermal conductivity, the specific heat, and the density of the material in the cluster, and $\varkappa'$ is the diffusivity of the material outside the cluster. We assume that c, ρ and c', ρ' are independent of temperature. The function $f(r) = 1$ if $|\mathbf{r}| = r \leq R$, and $f(r) = 0$ if $r > R$. The function $F(t, T) = \varepsilon\nu(T)P(t, T)/(4\pi r_0^3 c\rho/3)$. We note that the time τ the laser radiation acts on the material is omitted in Eqs. (2) and (3). This can be done since we are interested in the temperature inside a cluster, and this temperature is established in a time much shorter than τ.

To investigate the characteristics of Eqs. (2) and (3) it is necessary[9] to investigate the solution of these equations as a function of the parameters entering them under stationary conditions. We find the equation for the temperature $\bar{T}$ at the center of a cluster. Taking account of the boundary conditions, from Eq. (3) for the steady-state case we have

$$\left.\begin{aligned}\int\limits_0^{T(r)}\varkappa\,dT&=\chi(r),\\ \int\limits_0^{T(r=R)}\varkappa'\,dT&=\frac{1}{R}\int\limits_0^R Fr'^2\,dr',\end{aligned}\right\} \tag{4}$$

where $\chi(r) = -\int\limits_0^r Fr'(1 - r'/r)dr' + \int\limits_0^R Fr'(1 - r'/r)\,dr' + \int\limits_0^{T(r=R)} \varkappa dT$. The first equation in (4) gives $R(r) = \varphi(\chi(r))$, and the second gives $T(r = R)$. We consider the case in which $F(T(r))$ is a slowly varying function up to a value of r close to R. Then, writing F(T) in the form $F(\bar{T}) + F[T(r)] - F(\bar{T})$, where $F[T(r)] - F(\bar{T})$ is a small correction, the expression for $\chi(r)$ can also be written as a main term plus a small correction $\chi = \chi_0(r) + \chi_1(r)$. Then,

$$\chi_0=\frac{F(\bar{T})}{6}(R^2-r^2)+\int\limits_0^{T(r=R)}\varkappa\,dT$$

and

$$\chi_1=-\int\limits_0^r[F(T(r'))-F(\bar{T})]\left(1-\frac{r}{r'}\right)r'dr'$$

$$+\int\limits_0^R[F(T(r'))-F(\bar{T})]\left[1-\frac{r'}{R}+\frac{\varkappa(r=R)}{\varkappa'(r=R)}\frac{r'}{R}\right]r'dr'.$$

If

$$\langle\chi_0\rangle\gg\langle|\chi_1|\rangle\ \text{and}\ \langle\varphi(\chi_0)\rangle\gg\left\langle\left|\frac{\partial\varphi}{\partial\chi_0}\chi_1\right|\right\rangle, \tag{5}$$

where the symbol $\langle\ldots\rangle$ denotes averaging over the volume of a cluster, $T(r) = \varphi[\chi_0(r)]$, and Eqs. (4) for determining the temperature take the form

$$\left.\begin{aligned}\int\limits_0^{T(r)}\varkappa\,dT&=\chi_0(\bar{T},\ r)&&(r\leqslant R),\\ \int\limits_0^{T(r=R)}\varkappa'\,dT&=\frac{1}{3}F(\bar{T})R^2&&(r>R).\end{aligned}\right\} \tag{6}$$

Determining $T(r) = \varphi(r, \bar{T})$ from (6) and setting $r = 0$ we obtain the equation for $\bar{T}$

$$\bar{T}=\varphi(r=0,\ \bar{T}). \tag{7}$$

We note that Eq. (7) is valid only when (5) is satisfied.

In our work we consider crystals in which, according to theory, the diffusivity is inversely proportional to $T_0 + T$ for sufficiently high temperature,[7] i.e.,

$$\varkappa(T)=\frac{\varkappa_0}{1+\frac{T}{T_0}}\ \text{and}\ \varkappa'=\frac{\varkappa_0'}{1+\frac{T}{T_0}}.$$

However, this relation is valid only up to the temperature at which the portion of the crystal under consideration melts. This temperature can be estimated in the following way. The order of magnitude of the characteristic time of a phase transition can be found from

$$\tau_m\simeq\tau_0\exp\left[\frac{U}{k(T+T_0)}\right],$$

where $1/\tau_0$ is the frequency of the atomic vibrations controlled by the bond which is broken as a result of the melting of the material,[10] $U = 0.5 + 0.7$ D, and D is the binding energy of the atoms involved. If τ is the time the laser radiation acts on the material, the maximum temperature of the crystal before it melts is estimated from the condition $\tau \sim \tau_m$. Hence

$$T\simeq\frac{\frac{U}{k}}{\ln\frac{\tau}{\tau_0}}-T_0\simeq\frac{\frac{U}{k}}{\ln\frac{\tau}{\tau_0}}\,\frac{\frac{U}{k}}{\ln\frac{\tau}{\tau_0}}\gg T_0.$$

Thus the relation $\varkappa = \varkappa_0/(1 + T/T_0)$ and $\varkappa' = \varkappa_0'/(1 + T/T_0)$ will hold only for $T \nless (U/k)/\ln(\tau/\tau_0)$. For example, for crystalline quartz in which the Si–O bond is broken, with $\tau_0 \approx 10^{-4}$ sec and $U \approx 3$ eV, we obtain $T \nless 2500°$ for $\tau = 4 \cdot 10^{-8}$ sec.

When the temperature established in the cluster is so high that $\langle T\rangle \gg (U/k)/\ln(\tau/\tau_0)$, the whole cluster and an appreciable region around it will be in the molten state. In the molten material the diffusivity is assumed to be independent of temperature and equal to $\varkappa_m$ inside the cluster and $\varkappa_m'$ outside it. Then, since $\langle T\rangle \gg (U/k)/\ln(\tau/\tau_0)$ Eqs. (6) and (7) are used, as before, to find the temperature inside the cluster, but we must set $\varkappa = \varkappa_m$ inside the cluster and $\varkappa = \varkappa_m'$ outside it. At fusion all the parameters appearing in F(T) are assumed constant. In particular, the distance between centers $2r_0$ can be considered constant since the viscosity of the liquid is high at the temperatures of interest.

Taking account of the above, from Eqs. (6) we have

$$T(r)=T_0\left\{\exp\left[\psi(\bar{T})\left(1-\frac{\frac{r^2}{R^2}}{\frac{2\varkappa_0}{\varkappa_0'+1}}\right)\right]-1\right\}\ \text{for}\ T\ll\frac{\frac{U}{k}}{\ln\frac{\tau}{\tau_0}} \tag{8}$$

and

$$T(r) = T_0 \frac{\varkappa_0}{\varkappa_m} \frac{\frac{2\varkappa_m}{\varkappa'_m + 1}}{\frac{2\varkappa_0}{\varkappa'_0 + 1}} \psi(\bar{T}) \left(1 - \frac{\frac{r^2}{R^2}}{\frac{2\varkappa_m}{\varkappa'_m + 1}}\right) \text{ for } T \gg \frac{\frac{U}{k}}{\ln \frac{\tau}{\tau_0}},$$

where $\Psi(\bar{\bar{T}}) = F(\bar{\bar{T}}) R^2 (2\varkappa_0/\varkappa'_0 + 1)/6\varkappa_0 T_0$.

Introducing the dimensionless temperature $\Theta = \alpha \bar{\bar{T}}$, where $\alpha = W\ kT_0^2$, taking account of the fact that $R = n^{1/3} r_0$, and using Eqs. (2) and (8), we transform Eq. (7) to the form

$$\Theta = \Phi(\Theta), \tag{9}$$

where

$$\Phi(\Theta) = \Theta_0 [\exp \psi(\Theta) - 1] \text{ for } \Theta \leqslant \frac{\frac{\alpha U}{k}}{\ln \frac{\tau}{\tau_0}}$$

and

$$\Phi(\Theta) = \Theta_0 \frac{\varkappa_0}{\varkappa_m} \frac{\frac{2\varkappa_m}{\varkappa'_m + 1}}{\frac{2\varkappa_0}{\varkappa'_0 + 1}} \psi(\Theta) \text{ for } \Theta \gg \frac{\frac{\alpha U}{k}}{\ln \frac{\tau}{\tau_0}}.$$

Here

$$\psi(\Theta) = \frac{1}{e\Theta_0} \left(\frac{n}{n_0}\right)^{2/3} \frac{I}{I'} \frac{\exp\left[\frac{\Theta\Theta_0}{(\Theta + \Theta_0)}\right]}{\frac{I}{I'} + \exp\left[\frac{\Theta\Theta_0}{(\Theta + \Theta_0)}\right]},$$

$\Theta_0 = \alpha T_0$, $e = 2.718\ldots$, $I' = I_0 \sigma(\Theta)/\sigma_0$, $I_0 = \varepsilon \nu_0 / 2\sigma_0$ and $\sigma_0 = \sigma(T + T_0 = 0°K)$, where $\nu_0 = A \exp(-W/kT_0)$, and

$$n_0 = \left[\frac{16\pi c p \varkappa_0 r_0}{e \varepsilon \alpha \nu_0 (1 + 2\varkappa_0/\varkappa'_0)}\right]^{3/2}.$$

INVESTIGATION OF THE FUNDAMENTAL EQUATION

We investigate the characteristics of the solution of Eq. (9) as a function of the parameters. For given transparent dielectrics and impurity centers the only variable parameter in Eq. (9) is n, the number of centers in a cluster. For certain values of n the temperature Θ as a function of intensity can experience a jump at $I = I_{cr}(n)$. This is shown in Fig. 1 where the solution of Eq. (9) is plotted for three values of the intensity $I_1 < I_2 = I_{cr} < I_3$ for n close to $n_0 (n > n_0)$. If I approaches $I_{cr} (I < I_{cr})$, i.e., if curve 1 approaches curve 2, the solution Θ_1 approaches1) the solution $\Theta_2 = \Theta_{cr}$. If $I > I_{cr}$ and $I \to I_{cr}$, no matter how close curves 2 and 3 are to each other, the solution Θ_3 does not approach Θ_{cr}. To find I_{cr} as a function of n and the other parameters it is necessary, as is clear from Fig. 1, to find Θ_{cr} and I_{cr} from the equations

$$\Theta_{cr} = \Phi(\Theta_{cr}, I_{cr}),$$

$$1 = \frac{\partial}{\partial \Theta_{cr}} \Phi(\Theta_{cr}, I_{cr}).$$

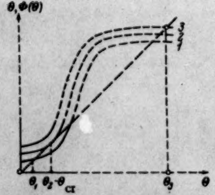

Fig. 1. Solution of Eq. (9) for three values of the intensity $I_1 < I_2 = I_{cr} < I_3$ for $n \approx n_0 (n > n_0)$. The open curves are plotted on an arbitrary scale.

We consider the usual situation $\Psi(\Theta_{cr}, T_{cr}) \ll 1$, $\Theta_{cr} \ll \Theta_0$, and $\sigma(\Theta) \approx \sigma_0$ for $\Theta \nless \Theta_{cr}$. Taking account of the form of the function $\Phi(\Theta)$ for small values of Θ for the above set of equations we have

$$\left.\begin{aligned} \Theta_{cr} &= \frac{I_{cr}}{eI_0} \left(\frac{n}{n_0}\right)^{2/3} \frac{\exp \Theta_{cr}}{\frac{I_{cr}}{I_0} + \exp \Theta_{cr}}, \\ 1 &= \frac{1}{e} \left(\frac{I_{cr}}{I_0}\right)^2 \left(\frac{n}{n_0}\right)^{2/3} \frac{\exp \Theta_{cr}}{\left[\frac{I_{cr}}{I_0} + \exp \Theta_{cr}\right]^2}. \end{aligned}\right\} \tag{10}$$

We note that (5) is satisfied at $\Theta = \Theta_{cr}$. This follows the first equation in (8) and the relations $\Psi(\Theta)_{cr}, I_{cr}) \ll 1$, and $\sigma(\Theta) = \text{const}$. Analysis of Eq. (10) shows that when the conditions mentioned above are satisfied $\Theta = \Theta(I)$ determined from Eq. (9) behaves as follows:

If $n < n_0$, $\Theta = \Theta(I)$ increases continuously with increasing intensity and approaches a limiting value smaller than unity. Thus, clusters containing a number of particles $n < n_0$ are not of interest since such clusters will always exhibit a low temperature.

If $n_0 \leq n < n'_0$, where $n'_0 = n_0 (4/e)^{3/2}$, $\Theta = \Theta(I)$ is an increasing function having a jump at $I = I_{cr}(n)$ and approaching a limiting value as $I \to \infty$.

For $n - n_0 \ll n_0$ $I_{cr}(n) \approx (3eI_0/2)/\ln(n/n_0)$, and

$$\Theta_{cr}(n) \simeq 1 - \frac{2}{3} \ln \frac{n}{n_0}. \tag{11}$$

$$\text{for } \sqrt{1 - n/n'_0} \ll 1 \quad I_{cr}(n) \simeq e^2 I_0 \left(1 + \frac{4}{3} \frac{(n'_0 - n)}{n'_0}\right) \text{ and}$$

$$\Theta_{cr}(n) \simeq 2\left(1 - \sqrt{\frac{2}{3} \frac{n'_0 - n}{n'_0}}\right). \tag{12}$$

Since it follows from (11) and (12) that $I \leq \Theta_{cr} \leq 2$, the inequality $\Psi(\Theta_{cr}, I_{cr}) = \Theta_{cr}/\Theta_0 \ll 1$ assumed above is satisfied. Ordinarily $T \approx 300°K$ and $W \sim 1000\ \text{cm}^{-1}$, and therefore $\Theta_0 = W/kT_0 \sim 4$. The assumption that the cross section for the absorption of monochromatic light $\sigma(\Theta)$ is constant for $\Theta \sim \Theta_{cr}$ is also well substantiated. For example in the harmonic approximation[11]

$$\sigma(\Theta) = \frac{\sigma_0}{1 - \xi} \exp\left(-\frac{2\xi y^2}{1 - \xi}\right) I_{l-0}\left(\frac{2y^2}{1 - \xi}\right). \tag{13}$$

Here, σ_0 is the cross section for the absorption of a photon at absolute zero,

$$\xi = \exp\left(-\frac{\hbar\omega_{vib}}{W} \frac{\Theta_0^2}{\Theta + \Theta_0}\right),$$

where $\omega_{vib} \sim 500\text{-}1000\ \text{cm}^{-1}$ is the frequency of vibrational motion inside an impurity center, $y \leq 1$, and $I_{l=0}[2y^2/(1-\xi)]$ is the zero-order Bessel function of imaginary argument. Since $\hbar\omega_{vib} \sim W$, for $\Theta \sim \Theta_{cr} \ll \Theta_0$, $\xi \ll 1$, and $\sigma(\Theta) \approx \sigma_0$.

The jump in the temperature Θ is a maximum when $n = n_0(I_{cr} = \infty)$ and is equal to

$$\Theta - \Theta_{cr} \simeq \Theta \simeq \frac{\varkappa_0}{\varkappa_m} \frac{\frac{2\varkappa_m}{\varkappa'_m + 1}}{\frac{2\varkappa_0}{\varkappa'_0 + 1}} e^{\Theta_0 - 1}.$$

An n increases the temperature jump decreases and vanishes at $n = n'$. Finally for $n \geq n'_0$ $\Theta = \Theta(I)$ is a continuously increasing function of the intensity, approaching a maximum. The inequality (5) is satisfied also at high temperatures ($\Theta_0 \nless \Theta$).

Thus it is clear that for a sufficiently high radiation intensity a high temperature is reached only in cluster with $n > n_0$. We estimate the temperature $\overline{T} = \Theta/\alpha$ for crystalline quartz when n the number of particles in a cluster is close to n_0 and the intensity $I = I_{cr}(n) + 0$. It will be seen that $\overline{T} \gg (U/k)/\ln(\tau/\tau_0)$. Therefore, using Eq. (9) for this case and setting $\varkappa_0 = \varkappa'_0$, $\varkappa_m = \varkappa'_m$, $\Theta_0 = 3.8$, $e^{\Theta_0}\Gamma/I \approx (2/3)e^{\Theta_0 - 1}[\sigma_0/\sigma(\Theta)]\ln(n/n_0) = 0.75$, and $T_0 = 300$°K and using the fact that $\varkappa_0/\varkappa_m = 6.7$ and $\Theta \gg \Theta_0$ for quartz we obtain[2)] $T = T_0(\varkappa_0/\varkappa_m)\Psi(\varkappa_0) \approx 6 \cdot 10^3$°K.

We determine the values of I, I_0, Γ, and n corresponding to this temperature. For $\nu_0 = 10^9$ sec^{-1}, $\varepsilon = 1.78$ eV, $\sigma_0 = 10^{-17}$ cm^2, and $\sigma(T = 6 \cdot 10^3$°K$) = 4.3 \cdot 10^{-17}$ cm^2 (since at high temperatures according to Eq. (13) $\sigma(\Theta) = \sigma_0 e^{2y^2} \cdot (4\pi y^2 \alpha \hbar\omega_{vib}/k\Theta)^{-1/2}$ we have $I_0 = 1.4 \cdot 10^7$ W/cm^2, $\Gamma = 3.3 \cdot 10^6$ W/cm^2, and $I = e^{\Theta_0}\Gamma/0.75 = 2 \cdot 10^8$ W/cm^2. By setting $c\rho\varkappa_0 \approx 2 \cdot 10^{-2}$ cal/cm sec deg and $r_0 = 10^7$ cm we obtain $n \sim n_0 = 1.7 \cdot 10^6$. For the parameters chosen all the conditions assumed above are satisfied. In particular for the time to establish a steady-state temperature in a cluster we have the inequality

$$\frac{R^2}{4\varkappa_0} = \frac{n^{2/3} r_0^2}{4\varkappa_0} < \tau_{st} < \frac{R^2}{4\varkappa_m}.$$

Consequently $\tau_{st} \ll \tau$, since $10^{-9} < \tau_{st} < 6 \cdot 10^{-9}$ sec, and $\tau = 4 \cdot 10^{-8}$ sec.

PHOTOCONDUCTIVITY

Free electrons appear in clusters at high temperatures as a result of thermal ionization. The electron density $n_e(r)$ can be estimated by the Saha equation

$$\frac{n_e^2}{N} = 6 \cdot 10^{21} T_{eV}^{3/2} \exp\left(-\frac{J}{kT(r)}\right), \tag{14}$$

which holds qualitatively in the case under consideration. In Eq. (14) N is the particle density of the host material, and $J = \hbar\omega$ is its ionization potential, which is assumed not to decrease. T_{eV} is the temperature in electron volts. Equation (14) assumes the equality of the statistical weights of an ion and a neutral particle. Using (14) and (9) and the fact that

$$\frac{\frac{r^2}{R^2}}{\frac{2\varkappa_m}{\varkappa'_m + 1}} \ll 1 \text{ and } \frac{J}{2\left(\frac{2\varkappa_m}{\varkappa'_m + 1}\right)kT} \geqslant 1,$$

we have for the electron density averaged over the volume of a cluster

$$\langle n_e \rangle = \frac{3\pi}{2}\sqrt{15N} \cdot 10^{10} T_{eV}^{3/4}\left(2\frac{\varkappa_m}{\varkappa'_m} + 1\right)\frac{\exp\left(-\frac{J}{2kT}\right)}{\left(\frac{J}{2kT} + \frac{3}{4}\right)^{3/2}}.$$

Substituting into this expression the values of I, ν_0, σ_0, n_0, etc. chosen above, we obtain $\langle n_e \rangle \approx 10^{19}$ cm^{-3}. Thus heating produces an appreciable local density of free electrons in a cluster. If among the impurity clusters with $n > n_0$ there are mainly clusters with $n \approx n_0$, it follows from the above that the appearance of free electrons in clusters as a result of laser radiation will have a threshold. As will be seen later, it follows from this that the appearance of photoconductivity also has a threshold.

It is interesting to note that such clusters are favorable for the beginning of the development of an electron avalanche in the focal volume.

It appears that this is a possible explanation of the previously noted divergence of the experimental and theoretical values of the intensity of laser radiation at which breakdown occurs.

We note that in Eqs. (3) and (4) the heating of the material as a result of the interaction with the lattice of free electrons accelerated in the field of a light wave should have been taken into account. For intensities $I = 2\text{-}5 \cdot 10^8$ W/cm^2 which interest us, the field of the laser radiation still does not lead to the development of an electron avalanche.[3]

We now consider the question of the size of the photocurrent produced by laser radiation in a transparent dielectric placed in a static electric field. Simple estimates show that the number of electrons leaving a heated clusters of impurity centers during the time of irradiation and taking part in photoconductivity is negligible small. However, because of the high electron density in a cluster an appreciable number of radiative recombinations occur, and this leads to the production of ultraviolet photons with energies higher than the ionization potential of the dielectric. These photons will produce ionization more or less uniformly over the focal volume and create free charge carriers. The density of ultraviolet photons produced per unit time can be estimated from the expression[10] $z = 4 \cdot 10^{23} N\sigma^0_{\omega_0} J^2_{eV} T_{eV}(r) \exp[-J/kT(r)]$ sec^{-1} cm^{-3}, where $\sigma^0_{\omega_0}$ is the cross section for the absorption of a photon of energy equal to the ionization potential in the ground state. Consequently the density of electrons taking part in photoconductivity is $N_e = N_c \langle z \rangle 4\pi r_0^3 \tau/3$, where N is the average density of the impurity centers. Using the second equation in (8) we have

$$N_e = 4 \cdot 10^{24} N N_c r_0^3 \left(\frac{\frac{2\varkappa_m}{\varkappa'_m + 1}}{\frac{J}{kT} + 1}\right)^{3/2} \sigma^0_{\omega_0} J^2_{eV} T_{eV} \tau \exp\left(-\frac{J}{kT}\right). \tag{15}$$

Here, the dependence of N_e on the intensity is given in

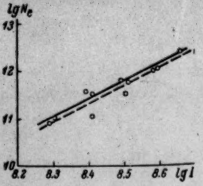

Fig. 2. Density of photoelectrons as a function of the intensity of laser radiation for crystalline quartz. Solid curve is experimental;[4] open curve is theoretical, obtained from Eq. (15).

terms of the temperature $\overline{T}$ by Eq. (9). In particular for crystalline quartz for an intensity $I = 2 \cdot 10^8$ W/cm^2 and values of the parameters chosen earlier, and assuming a density $N_c \sim 10^{14}$ cm^{-3} we obtain $N_e \approx 10^{11}$ cm^{-3}, which agrees with experiment.[4] Thus with the proposed model the theory offers an order of magnitude explanation of the experimental values of N_e for sufficiently low values of the intensity I. Moreover N_e as a function of I found from Eq. (15) by using the same values of the parameters for crystalline quartz is not in bad agreement with the experimental curve (Fig. 2).

CONCLUSION

We have considered a model of the interaction of laser radiation with transparent crystalline dielectrics based on the assumption that a small fraction of the impurity centers, which are good absorbers of laser radiation, are located in clusters. Under the action of radiation the clusters are heated as a result of nonradiative electron transitions in the impurity centers; the probability of the transformation of adsorbed energy into heat is assumed to depend exponentially on the temperature.

It is shown that if n, the number of the impurity centers in a cluster, is less than a certain value n_0 the temperature in the cluster is low (< 400°K) for any intensity of the incident radiation. If $n > n_0$ the cluster temperature $T \sim 10^4$°K for a certain intensity of the laser radiation. For clusters satisfying the condition $n_0 < n < (4/e)^{3/2} n_0$ the steady-state temperature $\overline{T}$ as a function of the intensity experiences a jump at $I = I_{cr}$. An expression has been obtained for the number of conduction electrons produced by a laser pulse in a transparent dielectric. This relation yields an explanation of the experimental size of the photocurrent and its dependence on the intensity of the laser radiation in crystalline quartz. The proposed model is based on the mechanism of the generation of free electrons by ultraviolet photons produced by radiative recombination in strongly heated clusters.

If most of the clusters in the dielectric contain a number of centers close enough to n_0, the dependence of the photopeak on intensity will experience a jump at $I = I_{cr}$ just as the temperature does.

For a sufficiently high intensity of the incident radiation strongly heated clusters can serve as centers from which an electron avalanche will propagate over the whole focal volume.

The discussion presented for transparent crystals can be applied to noncrystalline transparent dielectrics without any fundamental changes by assuming that the latter contain sufficiently large regions of crystallization containing the impurity centers we have considered. A similar assumption enables us to understand why the experimentally determined thresholds for the fracture of crystalline quartz and glass are nearly the same in spite of the great difference in their strength characteristics.

---

1) For the intensity I_1 shown in Fig. 1 Eq. (9) has three roots. The physical situation is described by the smallest root.

2) We choose the parameters such that later we can explain the experimental data on photoconductivity induced in crystalline quartz by laser radiation.

[1] G. M. Zverev, T. N. Mikhailova, V. A. Pashkov, and N. M. Solov'eva, Zh. Eksp. Teor. Fiz., 53, 1849 (1967) [Sov. Phys. – JETP, 26, 1053 (1968)].
[2] P. M. Mednis and V. M. Fain, Zh. Eksp. Teor. Fiz., 62, 812 (1972) [Sov. Phys. – JETP, 35, 429 (1972)].
[3] B. S. Sharma and K. E. Rieckhoff, Canad. J. Phys., 48, 1178 (1970).
[4] B. S. Sharma and K. E. Rieckhoff, Canad. J. Phys., 45, 3781 (1967).
[5] L. V. Keldysh, Zh. Eksp. Teor. Fiz., 47, 1945 (1964) [Sov. Phys. – JETP, 20, 1307 (1965)].
[6] B. I. Makshantsev, R. K. Leonov, and P. A. Yampol'skii, ZhETF Pis. Red., 14, 175 (1971) [JETP Lett., 14, 115 (1971)].
[7] J. M. Ziman, Electrons and Phonons, Clarendon Press, Oxford (1960).
[8] V. M. Gavrilko, K. F. Kashkurov, G. V. Kleshchev, and G. M. Safronov, Izv. AN SSSR Ser. Neorgan. Mater., 6, 421 (1970).
[9] D. A. Frank-Kamenetskii, Diffusion and Heat Transfer in Chemical Kinetics [in Russian], Nauka, Moscow (1967).
[10] Ya. B. Zel'dovich and Yu. P. Raizer, Physics of Shock Waves and High-Temperature Hydrodynamic Phenomena [in Russian], Fizmatgiz, Moscow (1963).
[11] J. J. Markham, Rev. Mod. Phys., 31, 956 (1959).

Dielectric properties of foamed ceramics at millimeter wavelengths

N. A. Irisova, G. V. Kozlov, V. E. Mandrusov, B. S. Cherepanov, and I. M. Chernyshev

P. N. Lebedev Physics Institute,
Academy of Sciences of the USSR, Moscow

(Submitted April 17, 1973)
Zh. Tekh. Fiz., 44, 173-176 (January 1974)

A study is made of the dielectric properties of porous ceramic materials at millimeter wavelengths. The transmission is found to drop sharply at certain frequencies (when the wavelength is about twice the mean diameter of the pores in the material). The more uniform the porosity of the material, the steeper the slope of the transmission curve. At large wavelengths the investigated materials are transparent and do not change their refractive properties. Porous ceramic materials show promise as filters for electromagnetic radiation.

Foamed ceramics are transparent at microwave frequencies and have a low value of dielectric constant. These new porous ceramic materials have already found successful application in a number of decimeter and centimeter devices, e.g., as fillers for loaded resonators and measuring lines operating under high-temperature conditions.

A study of the properties of foamed ceramics in the millimeter range is necessary in order to assess their possibilities at shorter wavelengths.

We have measured the refractive index and absorption in the millimeter range of a number of porous glazed ceramics with different chemical compositions, specific gravities, and characteristic pore diameter. The results are compared with data at 3 cm (see ref. 1).

The refractive index in the millimeter range is measured on a quasioptical setup (Rozhdestvenskii interferometer scheme).[2] One-dimensional ruled elements with a period much less than the radiation wavelength[3] serve as power dividers and polarizers in the interferometer. The coefficient of absorption is measured with an apparatus similar to that described in ref. 4. The measured variation of the transmission with wavelength for four samples is shown in Fig. 1. It can be seen that at λ = 3 mm the transmittance of all samples is greater than 80%, although for samples 3 and 4 it falls to 0.1% when the wavelength decreases to 1.5 mm. The transmission of samples 1 and 2 also falls off sharply but at shorter wavelengths. We cite in Table 1 the measured values of the refractive index n and the loss tangent tan δ of the investigated materials for λ = 3 cm and λ = 3 mm. It can be seen from these figures that the refractive index has no dispersion in the wavelength range from 3 cm to 3 mm. The increase in tan δ is probably due to the long-wave "tails" of the lattice absorption lines. The sharp drop in the transmission of the samples in the region 2.5–1 mm cannot be accounted for in this manner, however, since the measured transmission curves of solid samples having the same chemical composition as the investigated foamed samples have no sharp changes in this region.

TABLE 1

Sample No.	λ = 3 mm			λ = 3 cm	
	n	n^2	tg δ · 10^4	ε	tg δ · 10^4
1	1.30	1.69	20	1.70	3.0
2	1.16	1.35	30	1.36	10.0
3	1.20	1.44	25	1.44	2.0
4	1.26	1.59	27	1.60	2.8

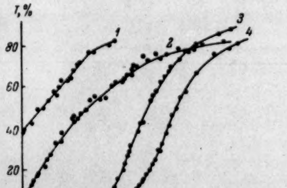

Fig. 1. Plots of transmission T versus wavelength λ for various porous samples.

The sharp change in the transmission of the foamed samples may be due to scattering of the incident radiation by the pores within the samples. To check this possibility an experiment has been set up to detect the scattered radiation. The experimental arrangement is shown schematically in Fig. 2. The radiation[5] from a monochromatic BWO is converted, with the aid of a horn-lens antenna and a ruled element,[3] into a plane linearly polarized wave which falls upon the sample (the latter is located behind the aperture of a diaphgram). The radiation receiver (an OAP-4) is mounted on a rotatable rod whose axis of rotation passes through the investigated sample. By scannning the receiver in angle it is possible to measure the radiation power transmitted through the sample along the optical axis of the system and also the power scattered at various angles. In these experiments the receiver is used without the lens. Its receiving area is 6 mm in diameter. The rotatable rod is 300 mm long and the resulting angular resolution is 1°. The results of the measurements are recorded on a two-coordinate pen recorder. The angle of rotation of the rod φ is recorded along the X axis of the recorder and the signal from the receiver along the Y axis. Traces obtained at λ = 3.1 and 2.0 mm are shown

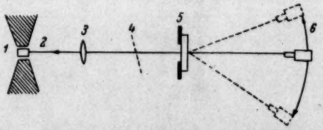

Fig. 2. Schematic diagram of apparatus for detecting scattering of millimeter radiation by sample. 1) Generator (backward wave tube); 2) horn; 3) lens; 4) polarizer; 5) diaphgram with investigated sample; 6) receiver.

in Fig. 3. It can be seen that radiation at $\lambda = 3.1$ mm drops about 20% from the initial intensity when it passes through the sample and that it retains its narrow-beam character. At $\lambda = 2.0$ mm the radiation intensity recorded by the receiver at $\varphi = 0$ is only 3.5% of its initial intensity. A randomly serrated scattering curve is observed, however, at angles of observation different from zero. As the investigated materials consist of a ceramic matrix within which spheroidal bubbles of air randomly distributed, it is clear that the porous structure of the material is responsible for the scattering of the electromagnetic radiation.

With a view to relating the wavelength of the scattered radiation to the characteristic parameters of the porous materials, the diameters of the pores are measured under the microscope and histograms plotted of pore density versus pore diameter. The resulting smoothed out distributions are shown in Fig. 4. A comparison of Figs. 4 and 1 yield the relationship between the shape of the pore size distribution curves and the frequency variation of the transmission of the corresponding samples, namely, the transmission curve is the less steep the larger the spread in the pore distribution. The scattering is almost complete when the wavelength is about twice the pore diameter. This situation is illustrated in Fig. 5.

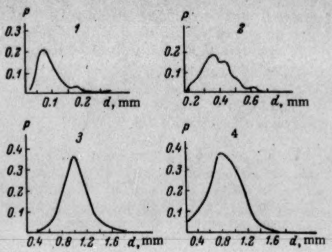

Fig. 4. Distribution of pores with respect to size for four samples 1-4.

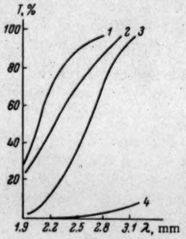

Fig. 5. Transmission curves for porous samples of same composition and thickness for different values of mean pore diameter 1) 0.64; 2) 0.8; 3) 1.07; 4) 1.43 mm.

CONCLUSIONS

Our millimeter wavelength investigation of porous ceramic materials has shown that at certain frequencies (radiation wavelength about twice the mean pore diameter) the transmission of the material drops sharply. The more uniform the porosity, the steeper the slope of the transmission curve. At long wavelengths foamed ceramics are transparent and do not change their refractive properties.

It appears that porous ceramic materials have potential use as cut-off filters for electromagnetic radiation.

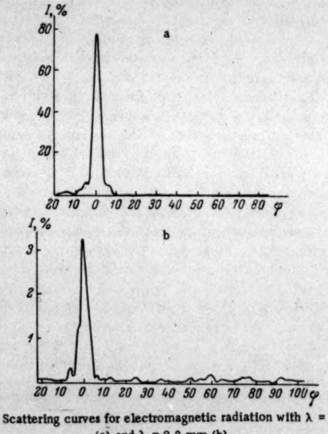

Fig. 3. Scattering curves for electromagnetic radiation with $\lambda = 3.1$ mm (a) and $\lambda = 2.0$ mm (b).

---

[1] Z. A. Nosova, V. V. Khresina, L. K. Sovetova, and B. S. Cherepanov, Tr. Nauch. Issled. Inst. Stroikeramika, 27, 251 (1967).

[2] G. V. Kozlov, Prib. Tekh. Eksp., 4, 152 (1971).

[3] N. A. Irisova, Vestn. AN SSSR, 10, 63 (1968).

[4] E. M. Dianov, N. A. Irisova, and A. M. Prokhorov, Prib. Tekh. Eksp., 4, 140 (1965).

[5] M. B. Golant, Z. T. Alekseenko, Z. S. Korotkova, L. A. Lunkina, A. A. Negirev, O. P. Petrova, T. B. Rebrova, and V. S. Savel'ev, Prib. Tekh. Eksp., 3, 231 (1969).

[6] Positive Decision of VNIIGPÉ No. 1755793/26 of January 5, 1973, in respect of Author's Specification of N. A. Irisova, G. V. Kozlov, V. E. Mandrusov, B. S. Cherepanov, and I. M. Chernyshev entitled "A Filter for Electromagnetic Radiation".

Two-spin oscillator with optical orientation of electrons and nuclei

R. A. Zhitnikov and V. V. Semenov
M. I. Kalinin Polytechnic Institute, Leningrad
(Submitted June 7, 1973)
Zh. Tekh. Fiz., 44, 177-184 (January 1974)

A system of two spin oscillators with optical pumping of Cs^{133} and He^3 atoms located in a single absorption cell is described. The Cs^{133} spin oscillator is used to automatically stabilize a magnetic field. The application of the system of two spin oscillators in magnetometry and inertial sensing is studied experimentally and theoretically.

INTRODUCTION

Optically pumped spin oscillators have found wide application in quantum magnetometry;[1-4] quantum gyroscopes[5] based on this principle are also being studied. In these applications the optically pumped spin oscillator has many important advantages: signal-to-noise ratio independent of the field, continuous operation, high accuracy and stability, absence of a null shift, etc. However, the spin oscillators presently used in magnetometry operate on only one isotope and at a single frequency. Quantum gyroscopes use systems of two spin oscillators operating simultaneously on two isotopes of mercury: Hg^{199} and Hg^{201}. The frequencies of these two oscillators differ approximately by a factor of 3, which makes it possible, to a large extent, to take account of the magnetic field variations that give spurious deviations in the gyroscope readout.

It is of considerable interest to develop a system of two spin oscillators with optical pumping of two different elements in a single cell; one a nuclear paramagnetic material and the other an electronic paramagnetic material. This would make it possible to obtain two different (by two or three orders of magnitude) resonant frequencies in a strictly identical magnetic field, and to eliminate the effect of field gradients. In quantum magnetometry this would eliminate several errors due to frequency shifts which exist in contemporary quantum magnetometers. In quantum gyroscopes the use of electron paramagnetic resonance makes it possible to develop a system to effectively stabilize a magnetic field, as opposed to merely indicating its variation as is now the case.[6] Then the nuclear spin oscillator signal in a stabilized magnetic field contains the gyroscopic information about the angle and angular rate.

The present paper describes the design and investigation of a system of two spin oscillators with optical pumping, one of which operates at the magnetic resonance frequency of Cs^{133} [ν (Hz) = 3.5 · 10^5 H (Oe)], and the other at the NMR frequency of He^3 [ν(Hz) = 3.2 · 10^3 H (Oe)]. The signal from the Cs^{133} spin oscillator is used to stabilize the magnetic field, and the He^3 spin oscillator allows one to determine the field stability. This system encounters certain difficulties, since it is necessary to ensure a high degree of optical orientation of the Cs^{133} atoms in the presence of a gas discharge in the He^3 buffer gas, and nuclear orientation of the He^3 nuclei in the presence of a paramagnetic impurity in the form of atomic cesium. On the basis of this investigation we can evaluate experimentally and theoretically the feasibility of using the two-spin oscillator system in magnetometry and inertial sensing.

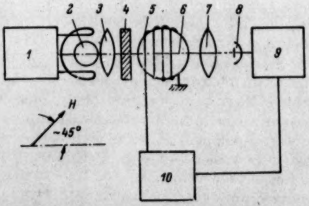

Fig. 1. Block diagram of the optically pumped spin oscillator. 1) Lamp power supply; 2) spectral lamp; 3 and 7) condenser lenses; 4) circular polarizer; 5) radio-frequency coil; 6) absorption cell; 8) photodetector; 9) amplifier; 10) phase shifter.

BASIC PROPERTIES OF SPIN OSCILLATORS WITH OPTICAL PUMPING OF Cs^{133} AND He^3 ATOMS

A block diagram of the optically pumped spin oscillator is shown in Fig. 1. Optical orientation of atoms of the working material is accomplished by circularly polarized radiation supplied by a spectral pumping lamp and a circular polarizer. At resonance the light to the photodetector is modulated at the Larmor frequency ω_0 (ref. 7). The ac voltage from the photodetector output is amplified, passed through a phase shifter, and applied to the radiofrequency coil. The system oscillates at the frequency ω_0 if the gain of the feedback loop is unity, and the total phase shift in the closed loop is zero. Both the Cs^{133} and He^3 spin oscillators operate in this manner. However, each of these oscillator systems has its own inherent characteristics related to the optical pumping process.

In the Cs^{133} spin oscillator the magnetic resonance line of the optically oriented atoms is an envelope of a set of Zeeman components, usually unresolved under the experimental conditions. With a change of the light intensity, cell temperature, and orientation of the optical system relative to the magnetic field the relative intensities of these components change, which causes a shift of the resonance line center and of the oscillation frequency.[8] In low magnetic fields additional frequency shifts occur due to higher harmonics of the transverse component of the magnetization vector. This is discussed in ref. 1, where the following expression is given for the frequency of a spin oscillator with zero phase shift in the feedback loop:

$$\omega = \omega_0\left(1 + \frac{1}{\omega_0^2\tau_2^2}\right)^{1/2}, \tag{1}$$

where τ_2 is the transverse relaxation time, which takes account of the effect of the pumping light. Then the maximum amplitude of the optical pumping signal S_x obtains at the frequency

$$\omega=\omega_0\left(1-\frac{1}{\omega_0^2\tau_2^2}\right)^{1/2}. \tag{2}$$

These frequency shifts severely limit the accuracy of magnetometers based on the Cs^{133} spin oscillator, particularly in measurements of weak magnetic fields where the Q factor of the cesium resonance line is small. The He^3 spin oscillator has several merits as compared to the cesium oscillator, of which the most notable are the absence of thermal dependence of the resonant frequency and the absence of shifts with changes in the light intensity. This is due to the fact that the pumping light does not interact directly with the ground state atoms, whose orientation is established by exchange collisions with metastable states.[9] However, such exchange collisions result in a resonant frequency shift $\Delta\nu$ and a change in the resonance linewidth L of the oriented He^3 atoms. The following expressions for $\Delta\nu$ and L are given in ref. 10, derived using the density matrix formalism:

$$\Delta\nu=\frac{2\omega_e\tau(2+7\omega_e^2\tau^2)}{3\pi T(1+\omega_e^2\tau^2)(1+16\omega_e^2\tau^2)}, \tag{3}$$

$$L=\frac{1}{\pi T}\left[1-\frac{5}{9(1+16\omega_e^2\tau^2)}-\frac{4}{9(1+\omega_e^2\tau^2)}\right], \tag{4}$$

where τ and T are the lifetimes of the metastable and ground states with respect to exchange; $\omega_e = -2\mu_B H$; and μ_B is the Bohr magneton. It follows from Eqs. (3) and (4) that $\Delta\nu$ and L decrease with decreasing magnetic field. Theory predicts,[11] and experiments have verified,[12] that significant signal intensities are attained in He^3 in magnetic fields below 10 mOe. These considerations indicate that it is feasible to use the He^3 spin oscillation in weak magnetic fields; in addition to strong signals, smaller frequency shifts are to be expected.

Let us now consider the properties of a system of two-spin oscillators using optically oriented Cs^{133} and He^3 nuclei in a single absorption cell. The introduction into the cell of cesium atoms with vapor pressure of the order of 10^{-5} torr shows essentially no effect on the optical pumping of He^3 at room temperature, since the partial pressure of impurities at which a noticeable decrease of the relaxation time of the metastable state occurs is 10^{-4} torr (ref. 9). Moreover, the presence of cesium in the discharge absorption cell appears to be helpful, since it acts as a getter of the impurities that are released by the walls of the cell during operation.[13] However, the presence of the high-frequency discharge in the cell, which is needed for the formation of the metastable helium atoms, can significantly reduce the degree of orientation of the Cs^{133} atoms due to electron collisions, which decrease the relaxation time; this leads to lower intensities of the resonance signals and to line broadening. This situation creates considerable difficulties in the construction of a system of two spin oscillators with simultaneous optical orientation of He^3 and Cs^{133} in the same cell; nevertheless, we have succeeded in building such a system, in which the Cs^{133} spin oscillator is used to stabilize the magnetic field by means of a phase-lock loop (refs. 14 and 15). The signals from the cesium atoms in the discharge are strong enough for this stabilization.

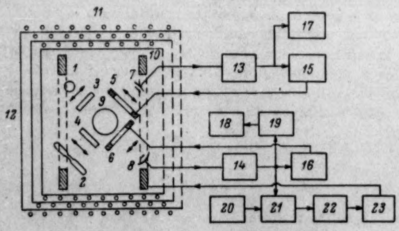

Fig. 2. Block diagram of the experimental arrangement.

EXPERIMENTAL ARRANGEMENT

The experimental arrangement is shown in Fig. 2. To reduce the magnetic field and its inhomogeneities, the entire optical circuit (the spectral pumping lamps 1 and 2; the circular polarizers 3 and 4; the absorption cell 9; and the photodetectors 7 and 8) is placed in a triple cylindrical magnetic shield 12. The outside shield is made of electric steel, and the two inner shields are of permalloy-79 (the inner cylinder is 380 mm in diameter, 500 mm long, and has a wall thickness of 1 mm). Each shield is equipped with a demagnetizing coil 11, fed with current of up to 10 A at standard line frequency. The required magnetic field, whose relative inhomogeneity within the volume of the absorption cell is $2 \cdot 10^{-3}$, is established at the center of the shield by Helmholtz coils 10. The spin oscillators,, which include, in addition to the optical circuits, the amplifiers 13 and 14 (U-2-6) and phase shifters 15 and 16, operate on the cell filled with He^3 at a pressure of 1 torr and Cs^{133} vapor. The pumping lamp of the He^3 spin oscillator is filled with He^4 at a pressure of 7 torr. Both the lamp and the cell are excited by a capacitive electrodeless discharge from a high-frequency (40 MHz) source. In the Cs^{133} spin oscillator the spectral pumping lamp, in which an inductive discharge is excited, is filled with argon at a pressure of 1 torr, and contains cesium vapor. The axes of the radio-frequency coils 5 and 6 are orthogonal to prevent inductive coupling. The oscillation frequencies are determined with the frequency meters 17 and 18 (Ch-3-32); the frequency of the Cs^{133} spin oscillator is measured using a frequency divider 19 (1:1000), which makes the measurements more accurate.

The magnetic field is stabilized by the cesium spin oscillator and a feedback loop, which contains a balanced phase detector 21, a quartz generator 20 (G3-44), an adjustment element 22, and a magnetic field control unit 23. The adjustment element is a proportional integrating filter,[14] which allows us to improve the dynamic characteristics of the magnetic field stabilization system. The phase detector output is an error voltage proportional to the phase difference between the signals from the spin oscillator (the sensor of the magnetic field variations) and from the reference quartz oscillator G3-44. The control voltage from the proportional integrating filter is converted into a current, which produces a correction of the magnetic field in the Helmholtz coils. The accuracy with which the magnetic noise is suppressed in this system can be determined from the coefficient W, which is the ratio of the fluctuations in the spin oscillator frequency caused by this noise with the magnetic field stabilization loop closed and open. As follows from ref. 16, the coefficient W is given by

$$W=\xi\left\{\frac{1+\frac{\Delta^2}{16}\xi^2}{1+\left[(\Delta_1+1)^2-\frac{\Delta}{2}\right]\xi^2+\frac{\Delta^2}{16}\xi^4}\right\}^{1/2}. \qquad (5)$$

Here, we have used the notation

$$\Delta=\frac{8}{\pi}\Omega T_1;\quad \Delta_1=\frac{2}{\pi}\Omega T_2;\quad \xi=\frac{\pi f}{2\Omega},$$

where Ω is the locking band; f is the frequency of the disturbance; T_1 and T_2 are the characteristic time constants of the proportional integrating filter, which in our case are 10 and 11 msec, respectively.

A light filter is used in the He^3 spin generator in front of the photodetector, which effectively attenuates the scattered signal from the optically oriented Cs^{133} atoms. The scattered signal from He^3 is the noise level, and does not affect the operation of the Cs^{133} spin generator and the stabilization scheme.

EXPERIMENTAL RESULTS

The system of two spin oscillators operates in a range of magnetic fields from 4 to 100 mOe. The low value of the magnetic field is limited by the bandwidth of the amplifier of the He^3 feedback loop and by the low Q factor of the magnetic resonance line of the optically oriented Cs^{133} atoms. The upper limit is determined by saturation of the shield material by the stray magnetic field produced by the Helmholtz coils. The residual magnetic field of the shield after high-temperature backing in a hydrogen atmosphere and subsequent demagnetization does not exceed 10 gamma along the cylinder axis. The static shielding factor is 5000. The calculated value of this factor, obtained from the equations of ref. 17, is 8300. The discrepancy between these values is due particularly to the less than ideal shape of the shield (the length should be much larger than the diameter), and to the seams and apertures required in the construction process.

The dynamic shielding factor is evaluated experimentally by comparing the mean-square frequency fluctuations of two spin oscillators with optical pumping of Cs^{133} atoms, one of which operates in the laboratory magnetic field outside the shield, and the other in the magnetic field established inside the shield. The fluctuations of the laboratory magnetic field in a 1 Hz band are attenuated by the shield by a factor of about 100, which is close to the calculated value for the dynamic shielding factor of 130. The maximum amplitude of the magnetic field fluctuations inside the shield does not exceed 0.5 gamma in one second.

The principal characteristic of the operation of the Cs^{133} spin oscillator is the presence of a weak high-frequency discharge in the cell, which not only lowers the intensity of the observed signals but also leads to a frequency shift. The magnitude of this shift varies inversely with the magnetic field and discharge intensity. The phase-frequency characteristics of the cesium spin oscillator, operating in a 15 mOe magnetic field, are shown in Fig. 3 for different discharge intensities. The numbers in brackets indicate the relative discharge intensities measured by the voltage at the electrodes of the absorption cell. The decrease in the slope of the characteristic is related to a broadening of the magnetic resonance line of the optically oriented cesium atoms. At the same time, we observe the shielding of the radio field by the plasma, which partially decreases the radio-frequency line broadening.

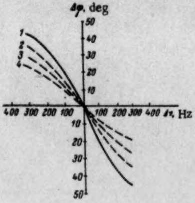

Fig. 3. Phase-frequency characteristics of the spin oscillator with optical pumping of Cs^{133} atoms for different discharge intensities. The discharge intensity is given in relative units. 1) Without discharge; 2) {10}; 3) {20}; 4) {30}.

The low helium pressure (~ 1 torr) causes a small diffusion time τ_{el} of the oriented Cs^{133} atoms to the cell walls. We use a Pyrex cell of volume 50 cm^3, for which τ_d is 3 msec. This relatively short diffusion time, combined with the unresolved hyperfine structure and the radio-frequency and optical broadening, results in a rather broad width of the cesium signal S_x: 1100 Hz for very weak discharges in the cell. The signal-to-noise ratio is about 150 in the 200 kHz bandwidth of the U-2-6 amplifier. The observed signal from Cs^{133} under these conditions is large enough to effectively stabilize the magnetic field inside the shield by means of the phase-lock loop described above. The system also ensures smooth tuning of the magnetic field within the locking range (2 mOe) by tuning the G3-44 reference oscillator. The proportional integrating filter makes it possible to obtain a capture range which in magnitude is close to the locking range. In the stabilization regime the mean-square frequency fluctuation of the cesium spin oscillator does not exceed 0.005 Hz over several seconds, and is determined primarily by the instability of the quartz oscillator. This frequency fluctuation corresponds to a variation in the magnetic field of less than 0.002 gamma.

The stabilization of the magnetic field makes it possible to measure accurately several characteristics of the magnetic resonance of optically oriented He^3 atoms. We obtain a good agreement between the experimental values for $\Delta\nu$ and L and those given by Eqs. (3) and (4). Figure

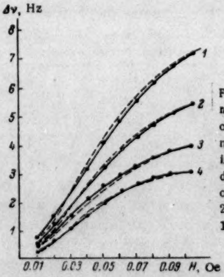

Fig. 4. Dependence of the magnetic resonance linewidth of the optically oriented He^3 ground state atoms on the magnetic field for different discharge intensities in the absorption cell. The dashed curves represent the behavior obtained from Eq. (4). 1) T = 60 msec; 2) T = 80 msec; 3) T = 110 msec; 4) T = 140 msec.

4 shows the behavior of L as a function of the magnetic field obtained at different discharge intensities in the absorption cell. The value of $\Delta\nu$ is determined experimentally by measuring the frequency shift of the He^3 spin oscillator when the cell discharge intensity and the magnetic field are changed. This shift is observed to decrease with decreasing magnetic field and discharge intensity in agreement with Eq. (3), which points out the dominant role of the metastability exchange in the frequency shift of the He^3 spin oscillator.

The spin oscillator with optical pumping of He^3 atoms operates with the magnetic field stabilization loop both closed and open. With the stabilization loop open, the recorded frequency fluctuations of the He^3 and Cs^{133} spin oscillators are completely correlated. These fluctuations are monitored by two Ch3-32 frequency meters with counting accuracy of $\sim 10^{-5}$ Hz of the He^3 frequency and $\sim 10^{-3}$ Hz of the Cs^{133} frequency. Stable operation of the field stabilization system is obtained in a magnetic field of 10 mOe, in which the Q factor of the magnetic resonance line of the optically oriented Cs^{133} atoms is not too low (~ 3). The short-term stability of the He^3 spin generator over a 30 sec interval is better than $5 \cdot 10^{-5}$ Hz with a signal-to-noise ratio of 20 in a 200 kHz bandwidth of the U-2-6 amplifier. A broadening of the He^3 spin generator line is observed with time (the linewidth reaches $5 \cdot 10^{-4}$ Hz ofter one hour of operation), which evidently is caused by electrical noise related to the instability of the supply voltages, changes of the discharge intensities in the pumping lamps and the cell, etc.

To verify this assumption we have calculated theoretically the effect of line noise on the operation of the spin oscillator, and have derived expressions for the linewidth $\Delta\omega$ based on spectral correlation analysis:[18]

$$\Delta\omega = \frac{\pi(n+1)}{\Gamma\left(\frac{1}{n+1}\right)}\left[\frac{A_\varphi}{(4Q\tau_2)^2\,\Gamma(n+2)\sin\frac{\pi}{2}(n+1)}\right]^{\frac{1}{n+1}}, \quad 0<n<1, \qquad (6)$$

$$\Delta\omega = \frac{1}{2Q\tau_2}\left[\frac{2A_\varphi \pi t^{n-1}}{\Gamma(n)\sin\frac{\pi(n-1)}{2}}\right]^{1/2}, \quad 1<n\leqslant 2, \qquad (7)$$

$$\Delta\omega = \frac{1}{2Q}\left\{2A_\varphi\left[\frac{\pi t^{n-1}}{\tau_2^2\Gamma(n)\sin\frac{\pi(n-1)}{2}} - 2\Gamma(3-n)\,t^{n-3}\sin\frac{\pi(n-2)}{2}\right]\right\}^{1/2}, \qquad (8)$$
$$2\leqslant n<3,$$

where $Q = 1/2\omega_0\tau_2$ is the Q factor of the magnetic resonance line; A_φ is a constant characterizing the noise intensity; n is a coefficient which indicates the degree of increase in the line noise at low frequencies; Γ is the gamma function, dependent on n; and t is the observation time satisfying the condition

$$\frac{4}{A_\varphi} > t > \left(\frac{\omega_0^2\tau_2^4}{A_\varphi}\right)^{1/3}. \qquad (9)$$

It is evident from Eqs. (7) and (8) that for $n > 1$ the spin oscillator frequency will drift with time. To evaluate $\Delta\omega$, it is necessary to know the constant A_φ and n, whose measurement entails considerable experimental difficulties. However, it is possible to compute $\Delta\omega$ for the case of line noise related to flicker noise in the semiconductor photodetector. From data in the literature, A_φ can be taken to be of the order of 10^{-9} sec. Then, setting $n = 2$ and substituting the experimental values into Eq. (8), we obtain the following values for the linewidths of the He^3 and Cs^{133} spin oscillators after one hour of operation in a 10 mOe magnetic field: $\sim 10^{-4}$ Hz for He^3 (with T = 30 msec); and ~ 1 Hz for Cs^{133}. Such a large value of $\Delta\omega$ for the cesium spin oscillator is due to a low value of the Q factor of the resonance line, which indicates the necessity of operating in a higher magnetic field. In the case of the He^3 spin oscillator, increasing the magnetic field is undesirable since it results in decreased signal intensity due to a loss of coherence between the ground and metastable states.[11]

CONCLUSION

This work has resulted in the construction of a system of two simultaneously operating spin oscillators with optical pumping of Cs^{133} and He^3 atoms located in the same absorption cell. We have studied the properties of the system in a magnetic field stabilized by a phase-lock on the Cs^{133} spin oscillator. The presently attained short-term frequency stability of the spin oscillators ($5 \cdot 10^{-5}$ Hz in the He^3 and $5 \cdot 10^{-3}$ Hz in Cs^{133}) allows us to reach certain conclusions concerning the potential application of this system in quantum magnetometry and inertial sensing. The long-term stability problem of an optically pumped spin oscillator requires further attention. The experiment shows, and the calculations verify, that the long-term stability of a spin oscillator is limited by nonstationary line noise, which leads to increasing $\Delta\omega$ with time. The study of the noise characteristics of the basic elements of a spin oscillator, i.e., the photodetectors, absorption cells, and pumping lamps, is of considerable importance. The investigation of the noise characteristics of these elements helps in the selection of their optimum operating conditions and in reducing the increase of $\Delta\omega$. As follows from Eqs. (7) and (8), $\Delta\omega$ is inversely proportional to the Q factor of the magnetic resonance line of the optically oriented atoms in the working medium. With decreasing magnetic field the Q factor of the Cs^{133} line decreases and that of the He^3 line increases, which leads to different values for the optimum magnetic field in which the maximum long-term stability is achieved, and in which the smallest frequency shifts of the spin oscillators are obtained with these elements. The nature of these shifts is different in He^3 and Cs^{133}, and thus the error incurred in the measurement of a magnetic field, when this system is used in quantum magnetometry, can be determined. The combination magnetometer with two spin oscillators, He^3 and Cs^{133}, can also be used for simultaneous measurement of the magnetic field with high accuracy (with the He^3 signal) and of the fluctuations of this field with high sensitivity (with the Cs^{133} signal) at the same point in space.

In quantum inertial sensing the system of two spin oscillators with optical pumping of He^3 and Cs^{133} atoms makes it possible to construct a simple, quite sensitive device having all the known qualities of quantum gyroscopes. Under the conditions of the magnetic field stabilized by the automatic control of the Cs^{133} spin oscillator frequency, the angular rotation rate measured by the He^3 spin oscillator frequency will be underestimated by only 1%.

In conclusion we note that in the above system of two spin oscillators with a single absorption cell it is possible to use in place of Cs^{133} also elements such as Rb^{85} and Rb^{87}, and obviously also He^4. The use of the latter in this system would be of considerable interest due to its high gyromagnetic ratio and thermal independence. Operation with these elements would broaden the investigation, and would facilitate the selection of the optimum combination of the nuclear the electron paramagnetic substances for systems with two spin oscillators.

---

[1] A. L. Bloom, Appl. Opt., 61, 1 (1962).

[2] M. I. Usher, W. E. Stuart, and S. H. Hall, J. Sci. Instrum., 41, 544 (1964).

[3] T. Kubo, Japan. J. Appl. Phys., 9, 12 (1970).

[4] L. D. Schearer, F. D. Colegrove, and G. K. Walters, Rev. Sci. Instrum., 34, 1363 (1963).

[5] I. Klass, Aviation Week, 88, 7 (1963).

[6] I. H. Simpson, Astronaut. and Aeronaut., 2, 42 (1964).

[7] H. G. Dehmelt, Phys. Rev., 105, 1487 (1957).

[8] S. Ando, Japan. J. Appl. Phys., 4, 793 (1965).

[9] F. D. Colegrove, L. D. Schearer, and G. K. Walters, Phys. Rev., 132, 2561 (1963).

[10] J. Dupont-Roc, Compt. Rend. Acad. Sci., 273, 1 (1971).

[11] R. B. Partridge and G. W. Series, Proc. Phys. Soc., 88, 983 (1966).

[12] A. Donszelmann, Physica, 56, 138 (1971).

[13] R. A. Zhitnikov and I. A. Kravtsov, Zh. Tekh. Fiz., 40, 2131 (1970) [Sov. Phys. – Tech. Phys., 15, 1662 (1971)].

[14] V. V. Shakhgil'dyan and A. A. Lyakhovkin, Phase Lock Loops [in Russian], Svyaz', Moscow (1966).

[15] R. G. Skrynnikov and A. P. Naumov, Geofiz. Apparat., No. 49, Nedra, Leningrad (1972).

[16] M. V. Kapranov, Radiotekh. Elektron., 1, 192 (1958).

[17] A. Thomas, IEEE Trans. El. Compat. U.E.M.C., 10, No. 1, 142 (1968).

[18] R. A. Zhitnikov, P. A. Klyushkin, V. V. Semenov, and G. V. Fomin, Zh. Tekh. Fiz., 43, 1965 (1973) [Sov. Phys. – Tech. Phys., 18, 1238 (1974)].

Dynamic magnetic-resonance phenomena

P. S. Kuts and V. S. Mel'nik

Uzhgorod State University

(Submitted March 26, 1973)
Zh. Tekh. Fiz., 44, 185-192 (January 1974)

Dynamic effects are studied in a magnetized gyromagnetic medium that interacts in resonant fashion with a weak magnetic field with transverse polarization; the precession frequency of the magnetic moments varies harmonically in a field of arbitrary amplitude and frequency. Argand diagrams are used to study dynamic hysteresis effects and periodic pulsed amplification of the transverse polarization field by the medium. A microwave-range method using a ferrite is used for an experimental check of the calculation. Physical interpretations of the dynamic phenomena are given.

INTRODUCTION

The problem we consider is closely associated both with resonance gyromagnetic (in particular, ferrite) devices (with variable magnetization) and with the problem of undistorted reproduction of magnetic-resonance signals. The analysis of a number of such devices is based on the notion that the change in the magnetizing field is adiabatic; however, a precise analysis capable of giving the conditions and optimum modes of operation is possible only if a dynamic analysis of the magnetic moments of the working medium is used.

A systematic study of the effect of variable magnetization on the parameters of ferromagnetic resonance has been undertaken earlier by Fabrikov. He obtained an expression[1] which describes dynamic effects in ferrites. We should also note Anderson's study[2] in the field of nuclear magnetic resonance. From the point of view of the spectral analysis of magnetic resonance, the utility of these results is obvious, but the study of the magnetization in time encounters serious difficulties, these being associated with the necessity of summing weakly convergent infinite series. Attempts to make an approximation of the problem that is linear in the magnetizing field (see, e.g., refs. 3, 4) do not solve the problem. We should also note that a theoretical investigation of the effect of rapid linear passage of the resonance region on the shape of the nuclear induction signals was made earlier by Jacobsohn and Wangsness,[5] subject to the condition that the magnetic system is in equilibrium at the beginning of each passage.

In this paper we study dynamic phenomena in magnetic resonance when a gyromagnetic system is harmonically magnetized by a field of arbitrary amplitude and frequency. The state of the medium at the beginning of each period need not be in equilibrium and can be determined by the prehistory.

THEORY

A gyrotropic medium that interacts with a magnetic field can be described by the Landau–Lifshitz equation[6] with a dissipative term in the Bloch–Wangsness form:[4,7]

$$\dot{\mathbf{M}} = -\mu_0 |\gamma| [\mathbf{MH}] + \mathbf{R}, \tag{1}$$

where

$$\mathbf{R} = \frac{\mathbf{e}_1}{T_2}\left(\frac{\chi_{st}}{\mu_0} H_x - M_x\right) + \frac{\mathbf{e}_2}{T_2}\left(\frac{\chi_{st}}{\mu_0} H_y - M_y\right) + \frac{\mathbf{e}_3}{T_1}(M_0 - M_z),$$

where **M** is the magnetization of the medium; **H** is the magnetic field; μ_0 is the permeability of vacuum; $|\gamma|$ is the absolute value of the gyromagnetic ratio; T_1 and T_2 are the longitudinal and transverse relaxation times; χ_{st} is the static susceptibility; M_0 is the equilibrium magnetization in a constant field H_0; and $\mathbf{e}_1$, $\mathbf{e}_2$, $\mathbf{e}_3$, are unit vectors of the rectangular coordinate system x, y, z, respectively. The magnetic field $\mathbf{H} = \mathbf{e}_3[H_0 + h_m(t)] + \mathbf{h}(t)$, which acts inside the medium, will be assumed to be homogeneous. Assume that the variable term in the magnetizing component varies harmonically, $h_m(t) = h_{0m} \cos \Omega t$, and that the weak exciting field is represented in complex form, $\mathbf{h}(t) = \mathbf{h} \exp(i\omega t)$, $\mathbf{h} = \mathbf{e}_1 h_x + \mathbf{e}_2 h_y$, $|\mathbf{h}| \ll H_0, h_{0m}$.

Equation (1) can be solved by successive approximations in the amplitude of the field h(t). Writing the desired solution in the form $\mathbf{M} = \mathbf{M}_0 + \mathbf{m} \exp(i\omega t)$, where $|\mathbf{m}| \ll |\mathbf{M}_0|$, we find that in the steady-state mode $M_x = m_x$, $M_y = m_y$, and $M_z = M_0$, where

$$m_x = im_y. \tag{2}$$

If we replace the transverse components of **h** and **m** by the linear combinations $h_+ = h_x + ih_y$, $m_+ = m_x + im_y$, in a first approximation in the resonant region we have

$$m_+ = \left(\frac{\chi_{st}}{\mu_0} - i\frac{M_0}{\Delta H}\right) \sum_{k,l=-\infty}^{+\infty} (-1)^l \frac{J_{k-l}(q) J_k(q)}{1 + iX_k} \exp(il\Omega t) h_+, \tag{3}$$

where $\Delta H = (\mu_0 |\gamma| T_2)^{-1}$ is the half-width of the resonance curve; $X_k = T_2(\omega - \omega_0 + k\Omega)$, $\omega_0 = \mu_0 |\gamma| H_0$ is the resonant frequency; $q = \mu_0 |\gamma| h_{0m} \Omega^{-1}$ is the modulation index; and $J_k(q)$ is a Bessel function of the first kind. For narrowband media with a large equilibrium magnetization M_0, for which the term χ_{st}/μ_0 can be disregarded, Eq. (3) becomes the familiar Fabrikov expression[1] if the spectrum of the transverse magnetic field contains the one frequency ω.

Expression (2) indicates that the forced oscillations of the transverse magnetization constitute clockwise rotation of the end of the vector **m** about the positive direction of the z axis, which has circular polarization. It is obvious that the oscillation amplitude depends on the nature and direction of the polarization of the exciting field, its proximity to the resonant state, and the parameters of the variable magnetization, namely, the modulation depth and frequency.

We should note that when there is no resonance detuning, $\omega - \omega_0 = 0$, the series in (3) become the sums that

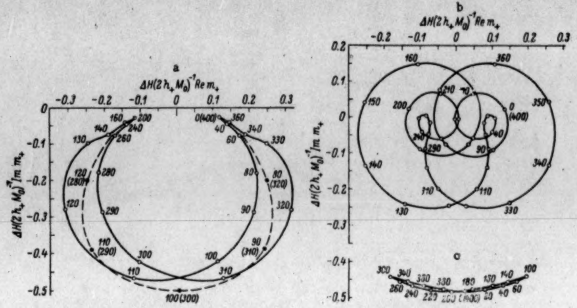

Fig. 1. Argand diagrams for the magnetization $m_+(t)$ with detuning $\omega - \omega_0 = 0$ and various values of the frequencies Ω and amplitudes h_{0m}: a) $\Omega = 0.1T_2^{-1}$, $h_{0m} = 4\Delta H$; b) $\Omega = T_2^{-1}$, $h_{0m} = 9\Delta H$; c) $\Omega = 10T_2^{-1}$, $h_{0m} = 4\Delta H$; the dashed curve is the adiabatic curve ($\Omega \to 0$) for $h_{0m} = 4\Delta H$.

are obtained in ref. 8. For arbitrary detuning, however, this transformation cannot be performed, and hence it becomes necessary to compute them. For this purpose we employed a computer for a broad range of parameters of the problem:

$$\Omega T_2, \ \ (\omega - \omega_0)\, T_2, \text{ and } h_{0m}(\Delta H)^{-1}, \tag{4}$$

which represent the frequency of the modulating field Ω, the detuning $\omega - \omega_0$, and the amplitude h_{0m} respectively, as normalized to the half-width of the resonant absorption curve ΔH.

The time dependence of the transverse magnetization amplitude $m_+(t)$ is given in the form of Argand diagrams,[9] which require that we separate the real and imaginary parts $\mathrm{Re}\, m_+$ and $\mathrm{Im}\, m_+$ in (3). For the separation to be unambiguous we assume, without loss of generality, that the exciting magnetic field is oriented along the x axis, i.e., $h = h_x$. Figure 1 gives the most typical curves as applied to narrow-band gyromagnetic media. The numbers next to the curves denote the time in units of $2\pi \cdot (400\ \Omega)^{-1}$. The dashed curve corresponds to the adiabatic approximation, in which Ω is determined by the instantaneous value of the magnetizing field. Evidently the shape of the dynamic curves differs markedly from the adiabatic curve; on the dashed curve the points referring to different half-periods of the magnetizing field coincide, while on the solid curves they do not. This means that at finite Ω values the amplitude $m_+(t)$ is not a single-valued function of the variable magnetizing field $h_m(t)$, and this is a characteristic feature of hysteresis. We will call this dynamic resonance. Figures 1a and 1c give a quantitative characterization of the delay in $m_+(t)$ relative to its adiabatic values.

At magnetization frequencies comparable to the inverse relaxation time ($\Omega \sim T_2^{-1}$) and at amplitudes h_{0m} that exceed the half-width of the resonance absorption curve ΔH, dynamic hysteresis is accompanied by spiral magnetization oscillations, which, in certain time intervals, go into the upper half-plane of the complex $m_+(t)$, where $\mathrm{Im}\, m_+ > 0$, and, as we will see, the medium is characterized by negative absorption (amplification) of energy of the weak magnetic field $\mathbf{h}(t)$. The number and intensity of the amplification pulses are determined by the parameters of the variable magnetizing field and depend on the amount of resonant detuning. The motion of the magnetization $m_+(t)$ in this case is illustrated by Fig. 1b; evidently, negative-absorption pulses arise after resonance and attenuate rapidly with increasing distance from resonance.

If the medium in question is a small ferrite specimen in a rectangular waveguide, the transmission factor for an electromagnetic wave through this electrodynamical system, in accordance with ref. 10, can be written in the form

$$T = \frac{P}{P_0} = (1 + A\, \mathrm{Im}\, m_+)^2 + (A\, \mathrm{Re}\, m_+)^2, \tag{5}$$

where

$$A = \frac{\lambda_W v}{2\pi ab}\left(\frac{2\pi}{\lambda_W}\sin\frac{\pi}{a}x_0 + \frac{\pi}{a}\cos\frac{\pi}{a}x_0\right)^2 \frac{\mu_0}{2h_+},$$

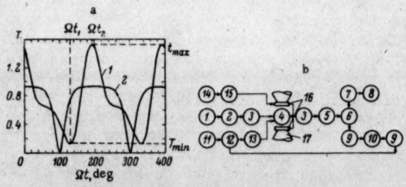

Fig. 2. a) Transmission factor as a function of time for an amplitude $h_{0m} = 4\Delta H$, detuning $\omega - \omega_0 = 0$, and frequencies Ω: 1) T_2^{-1}; 2) $\to 0$; b) block diagram of experimental apparatus: 1) klystron; 2) attenuator; 3) ferrite isolators; 4) working section; 5) microwave detector; 6) coaxial switch; 7) averaging device; 8) recorder; 9) broad-band amplifiers; 10) broad-band oscilloscope; 11) broad-band generator; 12) power amplifier; 13) magnetization-current measuring device; 14) field detuning unit; 15) detuning-current measuring device; 16) detuning coil; 17) constant magnet.

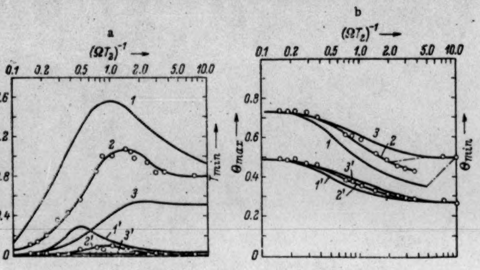

Fig. 3. Amplitude (a) and phase (b) of extrema of transmission factors as a function Ω for $\omega - \omega_0 = 0$: amplitudes h_{0m}: 1, 1') 4ΔH; 2, 2') 2ΔH; 3, 3') ΔH; the experimental points are plotted on the corresponding theoretical curves. Here and in Fig. 4, 1, 2, and 3 refer to the maximum while 1', 2', and 3' refer to the minimum.

and P and P_0 are the transmitted and incident radiation powers; λ_w is the wavelength in the waveguide; v is the volume of the specimen; a and b are the dimensions of the broad and narrow walls of the waveguide; and x_0 is the distance from the narrow wall to the specimen. The coefficient A is independent of the magnetic properties of the specimen being determined by the parameters of the experimental device.

We should note that m_+ appears in (5) as a quantity that is constant in time. Obviously, the substitution of (3), where $m_+ = m_+(t)$, into (5) will be correct if $m_+(t)$ is a slowly varying function of time with respect to the field of frequency ω. This holds in our case if we assume that $\Omega \ll \omega$. Figure 2a shows a typical T = T(t) curve as computed for $A = 2.8 \cdot 10^{-4} (\mu_0/h_+)$; the axes give the values of T_{min}, T_{max}, and the phases Ωt_1, Ωt_2 of the extrema. Curve 2 in the same figure shows the adiabatic relationship. We have investigated the behavior of the extrema of the transmission factor as a function of the parameters of the variable magnetizing field and the detuning. The results are shown in Figs. 3 and 4, where $\Theta_{min} = (\Omega t_1/400)$ and $\Theta_{max} = (\Omega t_2/400)$ are the dimensionless phases of the extrema.

EXPERIMENT

In our investigations, we employ the system shown in Fig. 2b. The gyromagnetic medium is provided by a sphere of yttrium ferrite garnet 0.97 mm in diameter, magnetized to saturation. The specimen with its magnetizing coil is placed inside a segment of rectangular waveguide with a cross section of 23 × 10 mm at the point of circular polarization of the microwave magnetic field. The H_{10} mode is excited in the waveguide; the wavelength in free space is 31 mm. The width of the resonance curve is $2\Delta H = 1.08$, and the saturation magnetization is $M_0 = 1750$ G.

The exciting field is provided by a klystron, whose power level ensures that the crystal detector operates in the square-law mode. The variable magnetizing field is created by a broad-band generator together with a power amplifier. The current in the coil that modulates the field is measured by a VTVM on the basis of the voltage drop across a resistor soldered into the central conductor of the coaxial feed cable. The magnetic saturation of the medium is not disturbed in the process of magnetization. Detuning of the constant magnetizing field from resonance is provided by a stabilized current source; the detuning current is measured with a milliammeter.

We employ the "open-pass" method of recording the ferromagnetic resonance with respect to two channels: The constant component of the transmission factor is measured by a plotter, while the variable component, after amplification, is recorded by a two-beam broad-band oscilloscope, one of whose inputs is fed a voltage that functions as a reference voltage in phase measurements. The electrical lengths of the signal and reference circuits are the same, and the phase shift between the reference voltage and the current in the coil with the specimen, resulting from the reactive nature of the magnetization circuits, is taken into account. We measure the amplitudes and phases of the extrema of the transmission factor T(t), as shown in Fig. 2a. The results are shown by the points in Figs. 3 and 4. The relative errors in the amplitude measurements are 6%; for the phase measurements they are 7%.

RESULTS AND DISCUSSION

As can be seen from Figs. 3 and 4, the theoretical results are in satisfactory agreement with the experimental data. The curves reflect quantitatively the dynamics of the absorption by the medium of the energy of a magnetic field of frequency ω in a specific electrodynamic system (waveguide with ferrite), and make it possible to analyze the above phenomena.

To consider the delay in the response of the medium to the variable magnetizing field in relatively pure form, let us consider the case of zero detuning ($\omega - \omega_0 = 0$) and low field amplitudes, e.g., $h_{0m} = \Delta H$ (Fig. 3). In the low-frequency region, where $\Omega \ll T_2^{-1}$ (the relaxation time T_2 will be assumed to be constant), the parameters of the extrema of the transmission factor are close to their adiabatic values. As Ω rises, the phases of the extrema increase monotonically, tending asymptotically to the values

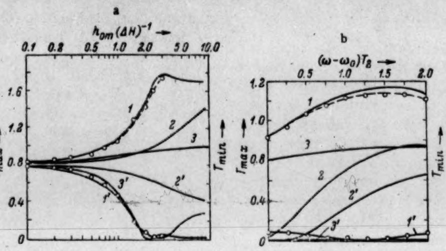

Fig. 4. Extremum values of transmission factor as a function of amplitude h_{0m} for $\omega-\omega_0 = 2T_2^{-1}$ (a) and as a function of the detuning $\omega-\omega_0$ for $h_{0m} = 2\Delta H$ (b). Frequency Ω: 1) T_2^{-1}; 2) $10T_2^{-1}$; 3) $0.1T_2^{-1}$.

of $3\pi/2$ for the maximum and π for the minimum (Fig. 3b). The swing in the oscillations of the transmission factor ($T_{max} - T_{min}$) drops off beginning with frequencies $\Omega \sim T_2^{-1}$ and tends to zero in the region of large Ω (Fig. 3a).

It is clear that when magnetic resonance is harmonically traversed by a field of arbitrary frequency and low amplitude ($h_{0m} \leq \Delta H$), there is a delay in the phase of the absorption signal relative to the initial value corresponding to adiabatic variation of the field. The limiting delay corresponds to the region of infinitely large Ω and amounts to $\pi/2$. The amplitude of the resonance signal at transmission frequencies comparable to the inverse relaxation time drops, tending to zero for $\Omega \gg T_2^{-1}$.

We should note that for large magnetizing-field amplitudes, $h_{0m} > \Delta H$, the delay in the resonance curve is similar to the case considered above (Fig. 3), but it is accompanied by substantial distortion in the line shape in the region $\Omega \gtrsim T_2^{-1}$, in particular, by attenuating post-resonance oscillations (see, e.g., Fig. 2a).

Figure 4a clearly illustrates the resonance-signal intensity as a function of the amplitude h_{0m} when there is detuning ($\omega-\omega_0 = 2T_2^{-1}$). It can be seen that for all h_{0m} the intensity of the variable component of the absorption for $\Omega = T_2^{-1}$ is always greater than at other frequencies.

Another important dynamic effect is periodic pulse amplification by the magnetized medium of the energy of the transverse polarization field. Let us determine the conditions for this effect to arise. It can be seen from Fig. 3b that for transmission amplitudes $h_{0m} > \Delta H$ the phase–frequency response of the transmission-factor maximum has a discontinuity; the discontinuity point is determined by the value of Ω (as before, T_2 will be assumed to be constant) and depends on the amplitude h_{0m}. Exact values of the parameter $(\Omega T_2)^{-1}$ at which the discontinuities occur were not found computationally, but the regions in which they are located are noted in Fig. 3b by the dot–dash line. The nature of the phase discontinuity is as follows. At some frequency Ω, in addition to the typical adiabatic maximum in the transmission factor whose phase is π, a new dynamic maximum appears, whose value increases with Ω. The instant at which the dynamic maximum exceeds the adiabatic one corresponds to the discontinuity point, since the phase of the maximum that appears will differ. At low magnetizing-field amplitudes the adiabatic maximum goes over smoothly into the dynamic one with increasing Ω, and there is no phase discontinuity.

The dynamic maximum in the transmission factor T ensures that there is amplification ($T_{max} > 1$) (for adequate magnetization depth) in the frequency region $\Omega \sim T_2^{-1}$ (Fig. 3a). The threshold value of the magnetizing field is determined both by Ω and by the resonance detuning. It can be seen from Figs. 3a and 4 that for $\Omega = T_2^{-1}$ and $\omega-\omega_0 = 0$ pulse amplification appears beginning with $h_{0m} = 2\Delta H$, while for $\omega-\omega_0 = 2T_2^{-1}$ and the same frequency it appears beginning with $h_{0m} = 0.8\,\Delta H$. Obviously, the pulse power gain is numerically equal to T_{max}. The way in which it depends on the parameters of the problem is illustrated by the same figure. The repetition frequency of the amplification pulses exceeds the frequency of the magnetizing field by a factor of 2 if the detuning $\omega-\omega_0 = 0$, and is equal to it if $\omega-\omega_0 \geq \mu_0|\gamma|\Delta H$. We should also note that at large longitudinal field amplitudes ($h_{0m} \gg \Delta H$) a packet consisting of several pulses that exceed the level $T = 1$ usually arises after resonance; the pulse intensity decreases rapidly with increasing distance from resonance.

It can be seen from the above that the delay in the response of the medium to a variable magnetizing field is determined by the parameter T_2, which constitutes the memory of earlier precession states of some of the magnetic moments. If a precession state is affected by the field $h_m(t)$ in a slowly varying fashion ($\Omega \ll T_2^{-1}$), the magnetic polarization of the medium is determined by the instantaneous value of this field. Otherwise, the prehistory of the medium affects its behavior. In the particular case of large frequencies in which $\Omega \gg T_2^{-1}$, over a period $2\pi/\Omega$ the magnetization differs very little from its initial value (at $t = 0$) and is determined primarily by resonance detuning (Fig. 1c).

The spiral magnetization oscillations (Fig. 1b) which arise after resonance and, under certain conditions result in amplification of the field of frequency ω, are interpreted by Jacobsohn and Wangsness.[5] Here the oscillations are regarded as beats, which arise from the superposition of the attenuating free intrinsic precession of the magnetization and the forced precession resulting from the variable field that acts instantaneously. What remains, therefore, is to explain the radiation mechanism.

In the resonant state, a system of magnetic moments effectively absorbs the energy of a transverse polarization field. When it departs rapidly from resonance into the weak-absorption region, e.g., as a result of changes in the magnetizing field, the system "remembers" its previous state over a time T_2 and hence the energy stored in resonance can be transmitted to the radiation field when there is a certain phase relationship between the field and the magnetization. By simple operations on the quantity $m_v = m_+ \exp(i\omega t)$ we can see that if the field $\mathbf{h}(t)$ has resonant polarization (clockwise in this case), $\mathrm{Re}\, m_+$ is the magnetization component that oscillates in phase with the field, while $\mathrm{Im}\, m_+$ leads it by an angle $\pi/2$. The theory of magnetic resonance (see, e.g., ref. 11) tells us that if $\mathrm{Im}\ m_+ < 0$ a system of magnetic moments absorbs the energy of a field of frequency ω, while if $\mathrm{Im}\, m_+ > 0$ it radiates. As can be seen from Fig. 1b, the radiation conditions ($\mathrm{Im}\, m_+ > 0$) are established in a pulsed fashion as a result of the beats. Since the curve on the Argand diagram is the trajectory of motion of the end of the vector $\mathbf{m}(t)$ in the coordinate system that rotates with frequency ω, while the field $\mathbf{h}$ is oriented along the $\mathrm{Re}\, m_+$ axis, a phase shift $0 < \varphi < \pi$ between the magnetization and the field corresponds to radiation, while a shift $\pi < \varphi < 2\pi$ corresponds to absorption. Obviously, radiation resulting in pulse amplification of the field of frequency ω is coherent, and a gyromagnetic medium is not in an inverted state in this case, since $M_z \approx M_0$.

CONCLUSIONS

In this paper we have given an analysis of effects resulting from the magnetization dynamics of a gyromagnetic medium: resonance hysteresis and the associated pulse periodic amplification of the transverse polarization field. The solution of the problem is given in the form of Argand diagrams, which illustrate the motion of the magnetization in the coordinate system that rotates with frequency ω. The quantities $\mathrm{Re}\, m_+$ and $\mathrm{Im}\, m_+$ make it possible to determine the real and imaginary parts of the magnetic susceptibility of the medium relative to the field of frequency ω at any instant of time. Computer calculations are given in units of the static parameters of the medium and can be applied to any magnetic material (nuclear paramagnetics, e.g., allowing for the sign of γ).

The waveguide-ferrite arrangement used in the experiments is intended to check the theoretical results. However, these results can also be applied to other electrodynamic systems containing gyromagnetic media (e.g., resonators).

Obviously, dynamic effects have a marked influence on the operation of devices based on magnetic resonance in a variable-magnetization mode. The results of this study can also be useful here. Moreover, the possibility of creating new devices that utilize the dynamic phenomena we have described is not ruled out.

The authors thank V. L. Strizhevskii for his interest.

---

[1] V. A. Fabrikov, Radiotekh. Elektron., 6, 1707 (1961).

[2] W. Anderson, in: NMR and EPR Spectroscopy [Russian translation], Izd. Mir, Moscow (1964).

[3] K. Halbach, Helv. Phys. Acta, 27, 259 (1954).

[4] I. A. Deryugin, P. S. Kuts, and V. L. Strizhevskii, Radiotekhnika, 22, 81 (1967).

[5] B. A. Jacobsohn and R. K. Wangsness, Phys. Rev., 73, 942 (1948).

[6] L. Landau and E. Lifshitz, Phys. Zs. Sowjetunion, 8, 153 (1935).

[7] A. L. Mikaélyan, Theory and Application of Ferrites at Microwave Frequencies [in Russian], Gosénergoizdat, Moscow–Leningrad (1963).

[8] A. M. Zaezdnoi (ed.), Tables and Formulas of Sums of Trigonometric Series of the Form $\sum_{n=1}^{\infty} [J_n(r)/(n^2 + a^2)]_{\sin}^{\cos} nx$ and $\sum_{n=1}^{\infty} [nJ_n(r)/(n^2 + a^2]_{\sin}^{\cos} nx$ [in Russian], Izd. LÉTI, Leningrad (1961).

[9] D. Demco and R. Baican, Studia Univ. Babes-Bolyai, Ser. Math.-Phys., 14, 87 (1969).

[10] A. V. Kislyakovskii and V. S. Vuntesmeri, Izv. Vuzov SSSR, Radiotekhnika, 9, 665 (1966).

[11] A. Loesche, Nuclear Induction [Russian translation], IL, Moscow (1963).

Longitudinal oscillations in an ultrarelativistic electron plasma

D. I. Dzhavakhishvili

Tbilisi State University

(Submitted March 20, 1973; resubmitted June 8, 1973)
Zh. Tekh. Fiz., 44, 193-194 (January 1974)

An investigation is made of longitudinal oscillations excited by a low-density beam of cold electrons in an ultrarelativistic electron plasma with thermal velocities of the order of the velocity of light. The growth rate is found and compared with the case of a nonrelativistic electron plasma.

It is well known[1,2] that both longitudinal and transverse oscillations at high frequencies ($\omega \gg kc$ or $\omega \gtrsim kc$, where ω is the frequency and k is the wave number) can propagate in an ultrarelativistic electron plasma containing particles with thermal energies appreciably higher than their rest energies ($T_0 \gg mc^2$, where T_0 is the temperature in energy units and m is the rest mass of an electron). These waves are not damped[2] since their phase velocity is greater than the velocity of light. In addition there are weakly damped longitudinal electromagnetic oscillations[2] with $V_f = \omega/k \lesssim c$.

It is also obvious that the passage of a beam of nonrelativistic electrons with velocities $u \ll c$ through such a plasma cannot lead to an instability of the high-frequency oscillations referred to above. The shortwave branch ($\omega \ll kc$) of the longitudinal and transverse oscillations cannot exist because of the strong shielding of the waves in the plasma.[2] We show, however, that it is possible to excite longitudinal oscillations with a frequency lower than kc in a hot electron plasma by a cold electron beam ($T_1 \ll mc^2$, where T_1 is the temperature of the beam electrons) having a beam velocity $u \ll c$ and a small spread in thermal velocities [$\omega - \mathbf{ku} \gg kv_1$, where $v_1 = (T_1/m)^{1/2}$ is the thermal velocity of the beam particles].

By using the expression for the longitudinal dielectric constant of an electron plasma[1] we obtain the dispersion relation for the beam–plasma system within the limits indicated above:

$$1+\frac{\omega_0^2}{\lambda k^2c^2}\left[1+\frac{i\pi\omega}{2kc}\right]-\frac{\alpha\omega_0^2}{(\omega-\mathbf{ku})^2}=0, \tag{1}$$

where $\omega_0 = (4\pi e^2 n_0/m)^{1/2}$ is the plasma frequency of the electrons, $\alpha = n_1/n_2$ is the ratio of the electron density in the beam to that of the plasma ($\alpha \ll 1$), and $\lambda = T_0/(mc^2)$ is a dimensionless number ($\lambda \gg 1$).

By discarding the small imaginary part of (1) we find the spectrum of the oscillations excited by the beam

$$\omega=\mathbf{ku}-\frac{\alpha^{1/2}\omega_0}{\left(1+\frac{1}{k^2d_0^2}\right)^{1/2}}, \tag{2}$$

where

$$d_0=\left(\frac{T_0}{4\pi e^2 n_0}\right)^{1/2}$$

is the Debye length of the plasma electrons.

It is clear that (2) is an unstable solution since the phase velocity of the wave becomes smaller than the beam velocity. An instability of this type is discussed in ref. 3, for example.

The growth rate of the oscillations determined by Eq. (2) is given by

$$\gamma=\frac{\pi}{4}\frac{\alpha^{1/2}\lambda^{1/2}}{(1+k^2d_0^2)^{3/2}}\left\{\mathbf{ku}-\frac{kc\alpha^{1/2}\lambda^{1/2}}{(1+k^2d_0^2)^{1/2}}\right\}. \tag{3}$$

Instabilities can arise only when $u > u_{cr}$, where

$$u_{cr}=\frac{\alpha^{1/2}\lambda^{1/2}}{\cos\theta}\frac{c}{(1+k^2d_0^2)^{1/2}}, \tag{4}$$

and θ is the angle between **k** and **u**.

In contrast with ref. 3, where the small parameter α ($\alpha \ll 1$) is arbitrary, in the present case it is necessary to restrict α by the condition

$$\alpha<\left(\frac{u}{c}\right)^{1/2}\frac{1+k^2d_0^2}{\lambda}. \tag{5}$$

For longwave oscillations ($kd_0 \ll 1$)

$$u_{cr}\approx\frac{\alpha^{1/2}\lambda^{1/2}}{\cos\theta}c,\quad \gamma\approx\frac{\pi}{4}\alpha^{1/2}\lambda^{1/2}ku\cos\theta \tag{6}$$

and it is clear that the critical value of the beam velocity is appreciably larger than the result given in ref. 3, and γ is larger by $\lambda^{1/2}$ for the same value of α.

It follows from (3) and (4) that for short waves ($kd_0 \gg 1$)

$$u_{cr}\approx\frac{\alpha^{1/2}\omega_0}{k\cos\theta},\quad \gamma\approx\frac{\pi}{4}\frac{\alpha^{1/2}u\omega_0\cos\theta}{ck^2d_0^2}. \tag{7}$$

It is clear that u_{cr} is now of the same order of magnitude as in ref. 3, but γ is much smaller for a fixed α.

It is easy to see that if the beam of electrons passing through the hot electron plasma with the velocity $u \ll c$ was ultrarelativistic ($T_1 \gg mc^2$), the electromagnetic oscillations with $\omega \ll kc$ would be screened.

Finally it should be noted that the instability discussed above does not occur for transverse waves.

The author is indebted to N. L. Tsintsadze for helpful discussion.

---

[1] V. P. Silin and A. A. Rukhadze, Electromagnetic Properties of Plasma and Plasma-Like Media [in Russian], Gosatomizdat, Moscow (1961).

[2] V. P. Silin, Zh. Eksp. Teor. Fiz., 38, 1577 (1960) [Sov. Phys.–JETP, 11, 1136 (1960)].

[3] A. B. Mikhailovskii, The Theory of Plasma Instabilities, Vol. 1, Consultants Bureau, New York (1973).

Contribution of multiphoton processes to the linear dielectric constant

V. A. Bushuev and R. N. Kuz'min

M. V. Lomonosov Moscow State University

(Submitted June 12, 1973)
Zh. Tekh. Fiz., 44, 194-196 (January 1974)

Multiphoton corrections to the linear dielectric constant are given; these derive from linear spontaneous inelastic scattering processes described by quadratic and cubic polarizability of the medium. The results of calculations of Raman susceptibility show that the greatest contribution to the imaginary part of the linear dielectric constant is due to Compton scattering on weakly bound electrons in the x-ray band.

In calculating the linear dielectric constant $\varepsilon(\omega \mathbf{k})$ one usually uses first-order perturbation theory. However, Raman parametric, Compton, and other modes of inelastic scattering (IS) can obviously lead to additional attenuation (damping) of the incident wave, and make a contribution to the imaginary part ε''; in accordance with the Kramers–Kronig relation, there must also be a contribution to the real part ε', which determines the refractive index.[1]

In this paper we show that for moderately intense incident waves (pumping) one can introduce an increment to the dielectric constant $\Delta\varepsilon_{IS}(\omega \mathbf{k})$, which acts like an ordinary linear dielectric constant, but whose imaginary part describes the attenuation of the pump due to nondissipative inelastic scattering processes in a solid angle of 4π sr. For simplicity we will confine ourselves to considering multiphoton corrections due only to linear (with respect to pumping intensity) inelastic scattering.

Inelastic scattering can be described phenomenologically by means of the imaginary part of a nonlinear increment to the dielectric constant $\Delta\hat{\varepsilon}_s \equiv \Delta\hat{\varepsilon}(\omega_s \mathbf{k}_s)$, an expression for which is given in ref. 2. Here, ω_s and $\mathbf{k}_s$ are the frequency and wave vector of the wave scattered in the frequency range $d\omega_s$ and the solid angle range $d\Omega_s$. In general, both the quadratic and cubic polarizability of the medium make a contribution to $\Delta\varepsilon_s \sim |E|^2$, where E is the amplitude of the plane monochromatic pumping wave. In a material system both virtual (parametric scattering), and real [Raman[1)]] transitions occur.[3,4]

The nonlinear polarization at the pumping frequency ω is $\Delta\hat{\varepsilon}(\omega \mathbf{k})\mathbf{E}$, where $\Delta\varepsilon$ is easily obtained from the results given in ref. 2 by analogy with $\Delta\varepsilon_s$. It is important to note that $\Delta\varepsilon$ is proportional to the intensity $|E_s|^2$, but in spontaneous inelastic scattering, when the number of scattered photons is much smaller than unity, we can replace $|E_s|^2$ by $2\pi\hbar\omega_s/(n_s V)$, where V is the normalization volume, and n_s is the refractive index calculated using the unperturbed dielectric constant, $\varepsilon^{(0)}(\omega_s \mathbf{k}_s)$. Hence it follows that the overall polarization is proportional to the first power of the pumping field. If the incremental dielectric constant is to have the meaning of a correction to the usual linear dielectric constant, it is necessary to average $\Delta\varepsilon$ over all possible values and directions $\mathbf{k}_s$ and polarizations $\mathbf{e}_s$.

Thus, introducing the next order in perturbation theory leads to an additional polarizability of the medium, which defines its nonlinearity and the intensity of the vacuum fluctuations. In this case, the effective absorption factor of the fundamental wave is

$$\left.\begin{aligned} \mu = \mu^{(0)} + \mu_{IS} = \frac{\omega\varepsilon''}{cn}, \quad \varepsilon = \varepsilon^{(0)} + \Delta\varepsilon_{IS} \\ \Delta\varepsilon_{IS} = \sum_{\mathbf{e}_s} \int (\mathbf{e}\Delta\hat{\varepsilon}\mathbf{e})\, g_s d\omega_s d\Omega_s, \end{aligned}\right\} \qquad (1)$$

where $g_s = V\omega_s^2 n_s^3/(2\pi c)^3$ is the mode density of a single polarization at a frequency ω_s, and for simplicity the medium is assumed to be isotropic and weakly absorbing. The corresponding integrated corss section of inelastic scattering in calculations on a single unit cell is μ_{IS}/n_0, where n_0 is the density of the number of cells.

In the optical band, as a rule $\mu_{IS} \ll \mu^{(0)}$. Thus, according to refs. 5 and 6, due to parametric and Raman scattering processes $\mu_{IS} \sim 10^{-6}$-10^{-7} cm^{-1}. When the pumping frequency is increased in the x-ray band it is easy to show, using the method of calculating solid-state Raman susceptibility developed, for example, in refs. 3 and 7, that the most effective of the inelastic scattering processes is Compton scattering by free and weakly bound electrons.[2)] In the random phase approximation we have

$$(\mathbf{e}\Delta\varepsilon\mathbf{e})'' = -\left(\frac{eq}{m\omega\omega_s}\right)^2 (\mathbf{e}\mathbf{e}_s)^2 |E_s|^2 \operatorname{Im} \frac{1}{\varepsilon^{(0)}(\Omega \mathbf{q})},$$

where $\Omega \equiv \omega - \omega_s$, $\mathbf{q} \equiv \mathbf{k} - \mathbf{k}_s$, and it follows from relations (1) that in like materials the fraction of the absorption due to the Compton effect (more effectively, as is well known, for fairly high q) and the photoelectric effect, described by the dielectric constant $\varepsilon^{(0)''}$, may be of the same order. Thus, in beryllium $\mu^{(0)} \sim \mu_{IS} \sim 0.3$ cm^{-1} in the case of an unpolarized pump at ~ 0.8 Å.

In conclusion we note that the formalism described above is easily generalized to the case of the propagation of x rays in ideal crystals, where the effect of inelastic scattering leads to a certain renormalization of the coefficients of the dynamic theory. A microscopic description of this effect is given in ref. 9.

The authors thank D. N. Klyshko for useful discussion.

[1)] Compton scattering and Brillouin scattering, which are better known in x-ray optics as thermal diffusion scattering, also apply.

[2)] A possible exception is the not yet completely explained anomalously high inelastic scattering cross section of x rays by F centers, observed in ref. 8.

[1] L. D. Landau and E. M. Lifshitz, Quantum Mechanics, Addison-Wesley (1958).
[2] D. N. Klyshko, V. F. Kutsov, A. N. Penin, and B. F. Polkovniko, Zh. Eksp. Teor. Fiz., 62, 1846 (1972).
[3] N. Bloembergen, Nonlinear Optics, Benjamin (1965).
[4] V. M. Fain, Quantum Radiophysics, Vol. 1, Photons and Nonlinear Media [in Russian], Sovetskoe Radio, Moscow (1972).
[5] D. N. Klyshko, Zh. Eksp. Teor. Fiz., 55, 1006 (1968) [Sov. Phys. – JETP, 28, 522 (1969)].
[6] I. L. Fabelinskii, Molecular Scattering of Light [in Russian], Nauka, Moscow (1965).
[7] A. Pine, Phys. Rev., 139, A902 (1965).
[8] N. G. Alexandropoulos, Phys. Rev., B1, 4115 (1970); B3, 2670 (1971).
[9] A. M. Afansev and Yu. Kagan, Acta Crystallogr., A24, 163 (1968).

Effect of cathode emission on the threshold for striations

N. A. Vorob'eva, Yu. M. Kagan, V. M. Milenin, and A. Kh. Muradov

A. A. Zhdanov Leningrad State University

(Submitted June 13, 1973)
Zh. Tekh. Fiz., 44, 196-197 (January 1974)

Experimental results showing the influence of cathode emission on the threshold for striations in a helium discharge are reported. Striations of two types can arise, depending on whether the cathode operates in the saturation regime.

Existing theories for striations[1-3] describe the conditions under which the plasma becomes unstable, i.e., they furnish a basis for calculating the threshold for the appearance of striations. In these theories the plasma is assumed to be unbounded, and the threshold current is taken to be the current at which the growth rate of the perturbation, a rate which is governed only by conditions within the plasma, becomes positive. It is assumed that the electrode regions cannot affect the appearance of striations.

Actually, however, in discharge tubes of finite length the threshold currents for the existence of striations can be functions of the length of the tube and the feedback. In several cases striations can be induced by oscillations in the plasma (cathode oscillations, oscillations of the anode fall, etc.).

We report here a study of the threshold for the existence of striations as a function of the cathode emission current. In experiments with a discharge tube 2.8 cm in diameter and 70 cm long, with a tungsten-wire cathode, in helium at pressures from 0.3 to 0.8 torr, we find the threshold discharge currents, i.e., those at which striations arise, for various cathode emission currents.

Figure 1 shows the thresholds for several cathode emission currents. It should be noted that the lowering of the threshold for the appearance of striations which occurs when the cathode emission current is reduced is due to the appearance of striations of a second type, having parameters different from those of the oscillations which arise at high emission currents (when the cathode is in the saturation regime). The striations of this second type have a frequency twice that of the striations of the first type over the same length. Another distinctive feature of these striations is that their amplitude falls off appreciably from the cathode toward the anode (striations of the first type decay toward the cathode).

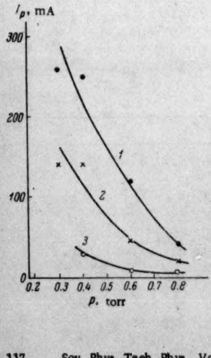

Fig. 1. Lower threshold for the existence of striations as a function of the pressure for various levels of cathode emission (for various cathode heater currents). Heater current I, A: 1) 6.8; 2) 6.3; 3) 5.6.

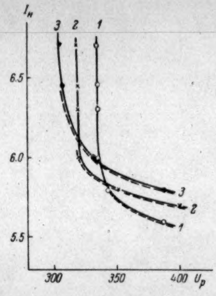

Fig. 2. Voltage drop across the discharge tube as a function of the cathode emission. These experiments are carried out in helium at a pressure of 0.6 torr (the dashed curves show the region in which striations exist). Discharge current I, mA: 1) 10; 2) 20; 3) 50.

We thus find the following picture for the appearance of striations as the cathode emission current is varied.

1. At heater currents at which the cathode is in the saturation regime, striations of the first type arise at a frequency from 5 to 11 kHz (varying with the pressure) and a length of 8-9 cm. The amplitude of these striations falls off toward the cathode.

2. As the cathode emission current is reduced, the striations arise at lower discharge currents, and their frequency varies from 10 to 25 kHz, again varying with the pressure. The amplitude of these striations falls off toward the anode. Increasing the discharge current while holding the heater current constant leads to the appearance of striations of the first type, which can displace the striations of the second type at a sufficiently high current.

Figure 2 shows the potential difference between the electrodes of the discharge tube as a function of the cathode heater current for fixed discharge currents. The points at which striations of the second type appear and the regions over which they exist are indicated. The striations appear at the bend in the characteristics, even though the parameters of the positive column are the same for the entire curve.

Accordingly, calculations of the lower threshold for instabilities in discharges of finite length must take into account the conditions prevailing near the cathode as well as the properties of the plasma which are functions of i, p, and R.

---

[1] A. V. Nedospasov, Usp. Fiz. Nauk, 94, 439 (1968) [Sov. Phys. – Usp., 11, 174 (1968)].
[2] L. Pekarek, Usp. Fiz. Nauk, 94, 463 (1968) [Sov. Phys. – Usp., 11, 188 (1968)].
[3] L. D. Tsendin, Zh. Tekh. Fiz., 40, 1600 (1970) [Sov. Phys. – Tech. Phys., 15, 1245 (1971)].

Ionization oscillations in a plasma in the presence of ionizing radiation

B. V. Vainer

Rostov-on-Don State University

(Submitted April 9, 1973; resubmitted June 18, 1973)
Zh. Tekh. Fiz., 44, 197-199 (January 1974)

It is shown that the presence of ionizing radiation in a plasma can cause an instability. Expressions are obtained for the frequency and growth rate of the ionization oscillations.

We consider the self-consistent problem of oscillations of a plane-parallel layer of plasma in which electrons and positive ions move towards the walls as a result of ambipolar diffusion and in which there is a counterflow from the walls into the volume of the plasma of neutral particles resulting from the recombination of electrons and ions on the walls. Ionization can occur within the volume of the plasma through electron impact and the action of radiation.

The equations describing the time variation of the number densities of the particles can be written

$$\frac{\partial n}{\partial t} = D\Delta n - \beta n n_e - In, \tag{1}$$

$$\frac{\partial n_{i,e}}{\partial t} = -\operatorname{div}(\mathbf{v}_{i,e} n_{i,e}) + \beta n n_{i,e} + In, \tag{2}$$

$$\mathbf{v}_{i,e} = b_{i,e}\left(\mathbf{E} - \frac{T_{i,e}}{e}\frac{\nabla n_{i,e}}{n_{i,e}}\right), \tag{3}$$

$$n_i = n_e. \tag{4}$$

In these equations n, n_i, and n_e denote the number densities of neutrals, positive ions, and electrons respectively; D is the coefficient of diffusion of the neutrals; E is the self-consistent electric field; b_e and b_i are the mobilities of the electrons and the positive ions; the term $\beta n n_e$ characterizes the ionization of neutrals by electron impact; and the term In characterizes the ionization of neutrals by radiation.

The plasma is assumed to be significantly nonisothermal, i.e., the temperature of neutrals and ions T_i is assumed to be far below the electron temperature T_e.

In this problem the processes of ambipolar diffusion and diffusion of neutral atoms take place in a dense host neutral gas which does not participate in the formation of ions.

The boundary condition for system (1)-(4) has the form

$$n_i(x = \pm l) = 0, \tag{5}$$

where $2l$ is the thickness of the plasma layer.

The radiation is assumed to be weak, i.e.,

$$I \ll \beta n_i.$$

In the zeroth approximation the stationary solution is

$$n_i^{(0)} = A_i \cos \varkappa x, \tag{6}$$

where

$$\varkappa^2 = \frac{\beta n}{b_i T_e}$$

(n = const to within terms of order T_i/T_e).

Taking terms of the next order into account and utilizing condition (5), we find

$$\varkappa l = \frac{\pi}{2} - \frac{I}{\beta A_i}. \tag{7}$$

Let us now investigate the stability of this system. We seek the solution of Eqs. (1)-(4) in the form

$$n_j(x, t) = n_{0j}(x) + \delta n_j(x, t),$$

where $n_{0j}(x)$ is the stationary solution and δn_j is a harmonic perturbation.

Linearizing system (1)-(4) with respect to small perturbations, we obtain the following equations for the ion and neutral-particle density perturbations

$$-i\omega\delta n_i = b_i T_e \frac{d^2\delta n_i}{dx^2} + \beta n \delta n_i + \beta n_i \delta n + I\delta n, \tag{8}$$

$$-i\omega\delta n = D\frac{d^2\delta n}{dx^2} - \beta n \delta n_i - \beta n_i \delta n - I\delta n. \tag{9}$$

We consider slow oscillations, i.e.,

$$D\varkappa^2, \quad I \ll \omega \ll \beta n \tag{10}$$

and seek the solution of (8)-(9) in the form of an expansion in the small parameter $\omega/\beta n$. We have

$$\delta n_i^{(0)} = d_i \cos \varkappa x,$$

and from (9)

$$\delta n^{(0)} = \frac{\beta n d_i \cos \varkappa x}{i\omega - D\varkappa^2 - I}\left(1 + \frac{\beta A_i \cos \varkappa x}{i\omega - D\varkappa^2 - I}\right). \tag{11}$$

The equation for the first correction to the zeroth approximation has the form

$$\begin{aligned} \frac{d^2\delta n_i^{(1)}}{dx^2} + \varkappa^2\delta n_i^{(1)} = &- \frac{i\omega d_i \cos \varkappa x}{b_i T_e} \\ &- \frac{I}{b_i T_e}\frac{\beta n d_i \cos \varkappa x}{i\omega - D\varkappa^2 - I}\left(1 + \frac{\beta A_i \cos \varkappa x}{i\omega - D\varkappa^2 - I}\right) \\ &- \frac{\beta A_i}{b_i T_e}\frac{\beta n d_i \cos^2 \varkappa x}{i\omega - D\varkappa^2 - I}\left(1 + \frac{\beta A_i \cos \varkappa x}{i\omega - D\varkappa^2 - I}\right). \end{aligned} \tag{12}$$

Solving (12) by variation of parameters and utilizing boundary condition (5) gives the dispersion relation in the form

$$\cos \varkappa l + \frac{1}{\varkappa^2} \int_0^{\pi/2} f(\omega, \tau) \cos \tau d\tau = 0, \tag{13}$$

where $f(\omega, \tau)$ is the right side of Eq. (12).

Using (7), we find the frequency ω' and the growth rate ω''

$$\left.\begin{aligned} \omega' &= \left(\frac{8}{3\pi}\right)^{1/3} \beta (nA_i)^{1/3}, \\ \omega'' &= -\frac{D\varkappa^2}{2} + \frac{n\dot{I}}{\pi A_i}. \end{aligned}\right\} \tag{14}$$

The perturbation will be unstable when

$$I > \frac{\pi A_i D\varkappa^2}{2n}. \tag{15}$$

It should be noted that this instability criterion does not contradict (10), since

$$\frac{n_i}{n} \ll 1.$$

We have thus shown that the presence of ionizing radiation in a weakly ionized plasma may result in an ionization instability. It should also be observed that this instability can appear in a plasma with a different geometry cylindrical.

In conclusion I should like to thank Prof. L. S. Marochnik and the participants in his seminar for their interest.

---

[1] Yu. R. Alanakyan and Yu. M. Aivazyan, Zh. Eksp. Teor. Fiz., 59, 1032 (1970) [Sov. Phys.—JETP, 32, 561 (1971)].

[2] Yu. R. Alanakyan and Yu. M. Alivazyan, Zh. Tekh. Fiz., 42, 738 (1972) [Sov. Phys. —Tech. Phys., 17, 581 (1972)].

[3] Yu. R. Alanakyan and B. V. Vainer, Zh. Tekh. Fiz., 43, 698 (1973) [Sov. Phys.—Tech. Phys., 43, 441 (1973)].

Plasma confinement in a time-increasing multipole magnetic field

V. G. Padalka and N. S. Repalov

Physicotechnical Institute,
Academy of Sciences of the Ukrainian SSR, Khar'kov

(Submitted October 5, 1972)
Zh. Tekh. Fiz., 44, 199-201 (January 1974)

The motion of plasma particles in a multipole-type magnetic trap is studied when the current producing the magnetic field configuration increases in time. The trajectories of the particles are established and it is shown that the plasma is confined in a narrow region near the separatrix.

Multipole magnetic traps[1] have been intensively studied in recent years. The interest in this magnetic confinement system stems from the fact that the plasma in a multipole magnetic field is stable up to a certain critical magnetic surface. In the magnetohydrodynamic limit this surface is given by the condition[1]

$$\frac{\partial}{\partial\psi}\oint\frac{dl}{H}=0$$

and, in the case of finite ion orbits, by[2]

$$\frac{\partial}{\partial\psi}\oint dl=0\,.$$

As a rule, the current in the rings of a closed multipole trap is induction-excited and the system is filled with plasma by external injection of a plasma jet from a pulsed plasma gun. The mean energy of hydrogen ions captured by the trap[3,4] is 50–100 eV.

The change in the intensity of the multipole magnetic field during the plasma containment time must be taken into account when interpreting the experimental results. The induced electric field E_z, along the axis of the multipole system, leads to drift of the plasma particles along the normals to the magnetic surfaces, the direction of the drift determined by the sign of the time derivative of the current in the current-carrying rings. The plasma density distribution accordingly varies during the containment cycle, and as will be shown below, when the current in the conductors increases the plasma drifts toward the separatrix irrespective of whether the plasma is located inside or outside the separatrix. The plasma is then confined in a region near the separatrix and is also heated.

We consider the motion of charged particles in a nonstationary multipole magnetic field, restricting the discussion to a linear infinite field of quadrupole configuration. Such a field is produced by two linear parallel currents flowing in the same direction. The vector potential of the magnetic field has a single component A_z, directed along the axis of the multipole. In polar coordinates centered on the axis of symmetry of the system A_z can be expressed in the form

$$A_z(r,\varphi,t)=\frac{I(t)}{c}\ln\left[\frac{(r^2+a^2)^2-4ra^2r^2\sin^2\varphi}{a^4}\right], \tag{1}$$

where r is the radial distance, φ the polar angle, $2a$ is the distance between the axes of the current-carrying conductors, and I(t) is the current in the conductor.

The magnetic field produced by the currents has only φ and r components:

$$\left.\begin{aligned}H_\varphi&=-\frac{4Irr^2+a^2\cos2\varphi}{ca^4\quad\psi(r,\varphi)},\\ H_r&=-\frac{4Ir}{ca^4}\frac{a^2\sin2\varphi}{\psi(r,\varphi)},\end{aligned}\right\} \tag{2}$$

where

$$\psi(r,\varphi)=\frac{r^4+2a^2r^2\cos2\varphi+1}{a^4}.$$

It is evident that the equation $\psi(r, \varphi)$ = const defines the magnetic surface of the multipole field.

If the particle Lagrangian

$$L=\frac{m}{2}(\dot r^2+r^2\dot\varphi^2+\dot z^2)+\frac{e}{c}\dot zA_z \tag{3}$$

is independent of the coordinate z and time, during the motion of the particle in such a field the axial component of the generalized momentum is conserved:

$$P_z=m\dot z+\frac{e}{c}A_z \tag{4}$$

as is the kinetic energy:

$$W=\frac{m}{2}(\dot r^2+r^2\dot\varphi^2+\dot z^2). \tag{5}$$

The allowed region for the motion of the particles can be established with the aid of these integrals of motion. It is evident that this region lies between the magnetic surfaces

$$\psi_{1,2}=\left(\frac{r_0^2}{a^2}-1\right)\exp(\pm2\rho_L). \tag{6}$$

Here

$$\rho_L=\frac{mv_0c^2}{2eI}$$

is the effective Larmor radius of the particle, v_0 is its velocity, and r_0 the coordinate of the intersection of the self magnetic surface of the particle with the plane containing the currents. Accordingly, for an adiabatic change of magnetic field ($\omega_H \gg 1/T$, where T is the characteristic time of the change of the magnetic field) one would naturally expect the particles to be displaced along with their confining magnetic surfaces (6).

A detailed picture of the motion of the plasma particles in a nonstationary magnetic field can be obtained by integrating the equations of motion. After averaging over a cyclotron rotation and neglecting drift due to magnetic field gradient, the equations of motion can be written in

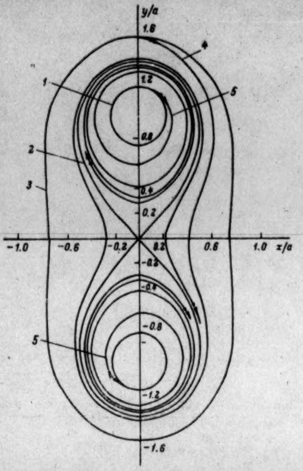

Fig. 1. Topology of magnetic surfaces and trajectories of guiding centers of particles in a multipole magnetic field increasing with time. Magnetic surfaces: 1) $\psi = 0.1936\,(r_0 = 1.2)$; 2) $\psi = 1\,(r_0 = \sqrt{2})$; 3) $\psi = 2.434\,(r_0 = 1.6)$; 4 and 5 denote trajectories of guiding centers of particles ($v_\parallel = 0.1$ cm/sec, T = 10 A/sec).

the form

$$\left.\begin{aligned} \frac{dr}{dt} &= \frac{v_\parallel H_r}{H} + c\frac{EH_\varphi}{H^2}, \\ \frac{d\varphi}{dt} &= \frac{1}{r}\frac{v_\parallel H_\varphi}{H} + \frac{c}{r}\frac{EH_r}{H^2}, \end{aligned}\right\} \tag{7}$$

where

$$H = (H_\varphi^2 + H_r^2)^{1/2}, \quad E = -\frac{1}{c}\frac{\partial A_r}{\partial t}, \quad v_\parallel = \frac{(\mathbf{v}\cdot\mathbf{H})}{H}.$$

Equations (7) are integrated on a digital computer for the case of a linearly varying current. Typical particle trajectories in a magnetic field increasing with time are shown in Fig. 1. It can be seen that irrespective of whether the particle is initially located inside or outside the separatrix ($\psi = 1$), it drifts towards the separatrix as the magnetic field increases.

Thus, a plasma in a time-increasing multipole magnetic field is localized near the separatrix, where it is adiabatically heated and its density increases.

In conclusion we thank O. E. Lysenko and V. I. Panchenko for carrying out the computer calculations.

---

[1] T. Ohkawa and D. W. Kerst, Phys. Rev. Lett., 7, 41 (1961).

[2] I. I. Demidenko, N. S. Lomino, V. G. Padalka, and N. S. Repalov, Zh. Tekh. Fiz., 41, 917 (1971) [Sov. Phy.—Tech. Phys., 16, 723 (1971)].

[3] R. A. Dory, D. W. Kerst, D. M. Meade, W. E. Wilson, and C. W. Erickson, Phys. Fluids, 9, 997 (1966).

[4] V. P. Goncharenko, I. I. Demidenko, N. S. Lomino, and V. G. Padalka, Zh. Tekh. Fiz., 40, 1206 (1970) [Sov. Phys.—Tech. Phys., 15, 932 (1970)].

Reflecting properties of an inhomogeneous anisotropic plasma layer

V. A. Zhivulin and G. I. Makarov

A. A. Zhdanov Leningrad State University

(Submitted May 30, 1973)
Zh. Tekh. Fiz., 44, 201-202 (January 1974)

The transmission of a TM electromagnetic wave through an inhomogeneous layer of a cold plasma with electron polarization in a constant homogeneous magnetic field is analyzed. The layer is unbounded and homogeneous along the y and z axes but has a finite thickness $2x_0$ and is inhomogeneous along the x axis. The electric vector of the incident wave lies in the xz plane. The diagonal component of the relative dielectric permittivity tensor $\varepsilon'_{xx}(x)$ for the plasma has (in the absence of losses) an n-th order zero (n = 2, 4, 6. . .) at the point x = 0. If there are no losses and the constant magnetic field is directed along the y axis, the TM wave is completely shielded by the layer. The shielding effect is not observed for other directions of the magnetic field.

The effect described below has been discussed earlier in ref. 1. That paper considers the transmission of a TM electromagnetic wave through a thin inhomogeneous layer of a cold isotropic plasma with electron polarization. The layer is located in vacuum. It is unbounded and homogeneous along the y and z axes but has a finite thickness $2x_0$ and is inhomogeneous in the x direction. The electron density varies as

$$N(x)=n_0\left[1-(-1)^n\left(\frac{x}{x_0}\right)^n\right] \quad |x|\leqslant x_0,\ n=2,\ 3,\ 4\ldots . \tag{1}$$

According to the results of ref. 1, a TM wave (with electric vector in the xz plane) will not pass through the layer in the absence of any loss mechanism if its frequency ω is equal to the critical value, i.e., the plasma frequency at the point x = 0.

It is of interest to consider the effect of a constant homogeneous magnetic field and this is the subject of the present paper [we take even values of the parameter n in (1) and neglect the effect of the ions]. We consider three particular cases, in which $Y = Y_x$, $Y = Y_y$, or $Y = Y_z$ ($Y = \omega_H/\omega$, where ω_H is the electron gyro-frequency). It is further assumed that the wave is incident from $x < -x_0$, that the electric vector lies in the xz plane, and that the component of the relative dielectric permittivity tensor for the plasma $\varepsilon'_{xx}(x)$ has (in the absence of losses) an n-th order zero at the origin:

$$\varepsilon'_{xx}(x)=0. \tag{2}$$

The problem can be solved by the method of successive approximations (such as has been used, for example, in the study of surface waves in plasma layers[2,3]). The boundary conditions are that the tangential components of the electromagnetic field must be continuous at $x = \pm x_0$. In order to avoid ambiguities (pole in the integrand) we first allow for collisional losses. The effective collision frequency is taken to be constant throughout the layer. The losses are then neglected (the appropriate transition is made in the approximate solution). It then turns out that a TM wave does not penetrate into the region x > 0. However, if $Y = Y_x$ or $Y = Y_z$, then waves of both polarizations occur in the field which penetrates through the layer since a TE wave is excited in the plasma and this passes through the plane x = 0 and there in turn generates a TM wave. If, on the other hand, $Y = Y_y$, the TE wave is not excited by the TM wave and the latter is completely shielded for all angles of incidence (including normal incidence).

The present authors have derived approximate equations (whose accuracy can be determined) for the reflection and transmission coefficients and also for the electromagnetic field components inside the layer (with $Y = Y_x$, $Y = Y_y$, or $Y = Y_z$). They are rather cumbersome and are therefore not given here.

It should be noted in conclusion that in the absence of losses the field inside the layer is a nonanalytical function of x for both the anisotropic and isotropic[1] cases. In particular, the normal component of the electric field becomes infinite at the origin.

Thus the layer we have considered does not allow the transmission of a TM wave if $Y = Y_y$ when condition (2) is satisfied. The shielding effect is not observed for other directions of the constant magnetic field. We have checked this result for $Y = Y_x$ and $Y = Y_z$ and it can anyway easily be seen from what has been said above that the picture is not changed in the intermediate cases (the TM wave will be excited by a TE wave in the region x > 0).

These results can be of interest in a number of practical situations connected with the interaction of an electromagnetic wave with plasmas in which it is important to know the behavior of the field inside the plasma.

---

[1] I. G. Kondrat'ev and M. A. Miller, Izv. VUZ., Radiofizika, 11, 885 (1968).
[2] K. N. Stepanov, Zh. Tekh. Fiz., 35, 1002 (1965) [Sov. Phys. – Tech. Phys., 10, 773 (1965)].
[3] K. N. Stepanov, Zh. Tekh. Fiz., 35, 1349 (1965) [Sov. Phys. – Tech. Phys., 10, 1048 (1966).

Current limiting by self magnetic field in a plasma accelerator

A. G. Korsun

(Submitted December 21, 1972)
Zh. Tekh. Fiz., 44, 202-206 (January 1974)

A study is made of the stationary flow in a coaxial accelerator in which plasma is supplied from the end face of the central electrode. If the discharge current is large a plasma jet is formed in the interelectrode space as a result of the pinch effect. The jet is compressed with increasing current strength and detaches from the outer electrode at a certain limiting current.

We consider the axially symmetric stationary flow of plasma in a high current coaxial accelerator with zero external magnetic field.[1] A completely ionized plasma is supplied to the discharge from the end of the central electrode. The mass flow rate of the accelerated material is G. At large currents I the radial electromagnetic forces compress the flow (pinch effect) and a jet with profile r = R(x) (Fig. 1) is formed in the space between the electrodes. We assume that the transverse componets of flow velocity and current density are much smaller tha the axial values ($v \ll u$, $j_r \ll j_x$), that the jet is long ($R' = \partial R/\partial x \ll 1$), and that the electron and ion temperatures are constant over the cross section [$T_e = T_e(x)$, $T_i = T_i(x)$]. The latter condition holds in the linear pinch.[2-4]

The plasma flow is described by the equations for a continuous medium,[5] which have the following dimensionless form:

$$\left.\begin{aligned}
&\frac{1}{A^2} n(\mathbf{v}\nabla)\mathbf{v} = 2\mathbf{j}\times\mathbf{B} - \frac{1}{2}\nabla p \quad p = nT \quad T = T_e + T_i,\\
&\frac{3}{2}\nabla(p\mathbf{v}) + p\nabla\mathbf{v} = \frac{8}{R_m}\frac{j^2}{\sigma} + \xi\left(\frac{3}{2} j_x \frac{\partial T_e}{\partial x} - T_e \mathbf{j}\frac{\nabla n}{n}\right),\\
&\frac{3}{2}\nabla(p_i\mathbf{v}) + p_i\nabla\mathbf{v} = Q_\Delta = \frac{12\Pi}{R_m}\frac{n^2}{\sigma}(T_e - T_i),\\
&\nabla(n\mathbf{v}) = 0 \quad \mathbf{j} = \frac{1}{2}\nabla\times\mathbf{B} \quad \sigma = T_e^{3/2} \quad T_e = \theta T,\\
&\frac{\partial}{\partial r}\left(\frac{j_x}{\sigma}\right) = \frac{\partial}{\partial x}\left(\frac{j_r}{\sigma}\right) + \frac{1}{2} R_m\left[B\left(\frac{\partial u}{\partial x} + \frac{\partial v}{\partial r}\right) + u\frac{\partial B}{\partial x} + v\frac{\partial B}{\partial r}\right]\\
&- \frac{1}{4}\xi R_m\left[\frac{B}{n^2}\left(\frac{\partial n}{\partial r}\frac{\partial B}{\partial x} - \frac{\partial n}{\partial x}\frac{\partial rB}{r\partial r}\right) + \frac{2B}{rn}\frac{\partial B}{\partial x} + \frac{1}{2n}\frac{\partial T_e}{\partial x}\frac{\partial n}{\partial r}\right].
\end{aligned}\right\} \qquad (1)$$

The dimensional equations are reduced to dimensionless form with the aid of the following scaling: for the linear dimensions and the velocities – the jet radius R_0 and flow velocity U_0 in the initial cross section; the plasma density n, the temperatures T, T_e, T_i, the magnetic induction B, the current density j, and the conductivity σ are respectively scaled in terms of

$$n_0 = \frac{G}{m_i \pi R_0^2 U_0}, \quad T_0 = \frac{\mu I^2 m_i U_0}{8\pi G}, \quad B_0 = \frac{\mu I}{2\pi R_0},$$

$$j_0 = \frac{I}{\pi R_0^2}, \quad \sigma_0 = \sigma^0 T_0^{3/2}.$$

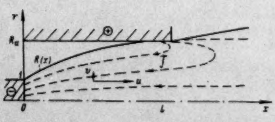

Fig. 1

Here, μ is the permeability, m_i the ions mass, and σ^0 the constant of proportionality in the expression for $\sigma(T_e)$.

Similarity criteria are the Alfvén number A, the exchange parameter ξ (see ref. 6), the magnetic Reynolds number R_m, and the "linear ion"[3] or dimensionless flow rate Π

$$A^2 = \frac{\mu I^2}{4\pi G U_0}, \quad \xi = \frac{m_i I}{eG}, \quad R_m = \mu\sigma_0 U_0 R_0,$$

$$\Pi = \frac{\mu e^2 G}{4\pi m_i^2 U_0} = \frac{A^2}{\xi^2}.$$

If the outer electrode is the anode the exchange parameter $\xi < 0$; for the opposite polarity, $\xi > 0$.

The boundary conditions for the dimensionaless quantities have the following form: at r = Rn = 0, R = 1/R; at r = 0, B = 0; at x = 0, u = 1. It will be shown below that the solution is self-similar when $R' \ll 1$. At x = 0 the solution must satisfy special conditions on n, T, v, j. The conditions on the electromagnetic quantities as the cathode and the anode have little effect on how the parameters in a long jet are distributed because $R_{ma} < 1$ near the cathode and perturbations decay in a distance of the order of unity; near the anode $R_{ma} > 1$ so that perturbations are removed by the flow and decay on route to the cathode in a distance of order R_a/R_{ma} (see Fig. 1).[7]

In order to simplify Eqs. (1) and obtain analytic expressions we utilize a series expansion in the small parameter R'. We note the following three points. First, since all the terms on the right side of the last of Eqs. (1) are of order R' or higher, it follows that in the zeroth approximation j_x/σ is constant over the cross section (as in the linear pinch[2]) but varies along the length of the flow due to the expansion of the jet. Second, because of the weak expansion of the jet, the compressive radial electromagnetic forces are balanced by the pressure in the jet to terms of order R'^2. Accordingly, as in the linear pinch, the following relationship holds:[2,8]

$$T_p \frac{G}{m_i \bar{U}_p} = \frac{\mu I^2}{8\pi}, \qquad (2)$$

where $T_p = T_0 T$ and $\bar{U}_p = U_0 \bar{u}$ are the dimensional temperature and the dimensional mean flow velocity, and T and $\bar{u}$ are the corresponding dimensionless quantities. Third, the requirement of radial equilibrium implies that the force accelerating the flow can be expressed

$$f_x = 2j_r B - \frac{1}{2}\frac{\partial p}{\partial x} = \frac{1}{r^2}\int_0^r \frac{\partial p}{\partial r} r\,dr$$

and, if $p = (1/R^2)\varphi(r/R)$, it follows that

$$f_x = p\frac{R'}{R} = nT\frac{R'}{R}.$$

Consequently, from the equation of motion

$$\frac{1}{A^2}n\left(u\frac{\partial u}{\partial x} + v\frac{\partial u}{\partial r}\right) = f_x$$

for T = T (x) and u (0, r) = 1, we find that the velocity u is constant over the cross section; utilizing (2), we have

$$u = 1 + A^2 \ln R.$$

Thus, the solution of Eqs. (1) in the zeroth approximation has the simple form

$$B = \frac{r}{R^2}, \quad j_x = \frac{1}{R^2}, \quad j_r = j_x\frac{R}{r}R', \quad p = nT = \frac{2}{R^2}\left(1 - \frac{r^2}{R^2}\right),$$
$$T = u = 1 + A^2 \ln R, \quad v = u\frac{r}{R}R'. \tag{3}$$

Despite the fact that the axial electromagnetic force primarily accelerates the peripheral layers of the flow ($j_r B \sim r^2$), while the main mass is concentrated near the axis ($n \sim 1 - r^2/R^2$), the axial velocity is constant over the cross section in the first approximation. Formally, this is a consequence of $p = (1/R^2)\varphi(r/R)$. Actually, the constancy of u comes about because the forces acting on the ions[10] (the electric field, the "electron wind", $-\nabla p_i$, thermal forces) are distributed over the cross section in such a manner that the net force f_x is proportional to n. If $\xi < 0$, the ions are accelerated against the electric field by the "electron wind", the thermal force, and the force $-\nabla p_i$. If $\xi > 0$, the electric field accelerates and the "electron wind" decelerates the ion flow.

If ion heating by electrons is insignificant (the thermal Q_Δ is small), the ions simply cool down as the jet expands:

$$\frac{T_i}{T_i(0)} = (R^2 u)^{-2/3}.$$

If $T_i(0) \ll T_e(0)$, then $T_i \ll T_e = T$, i.e., $\theta = 1$ everywhere. If the term Q_Δ is large, then $T_i = T_e$ i.e., $\theta = 1/2$.

For θ = const the energy equation in conjunction with (3) yields the jet profile

$$x = \frac{1}{8}R_m(1 - \theta\xi)\,\theta^{3/2}\left[(1 + A^2 \ln R)^{5/2}R^2 - 1\right]. \tag{4}$$

The first-order (in R') corrections to the solution for B, j_x, and p have the form:

$$B_1 = -\frac{1}{8}R_m A^2\sigma\frac{r}{R}\left[y + \xi(1-\theta)\frac{R^2}{r^2}y\ln y\right]R', \quad y = 1 - \frac{r^2}{R^2},$$
$$j_{x1} = \frac{1}{8}R_m A^2\sigma\left[1 - 2y + \xi(1-\theta)(\ln y - 1)\right]\frac{R'}{R},$$
$$p_1 = \frac{1}{8}R_m A^2\sigma\left[\frac{1}{4}y(2-3y) + \xi(1-\theta)\left(y\ln y - \frac{1}{2}y - \frac{1}{2}\int_0^y\frac{\ln t}{1-t}\,dt\right)\right].$$

It follows from (4) that increasing I at constant G compresses the jet. The appearance of limiting currents in a high-current accelerator can be described on this basis. If the current is less than the limiting value, the plasma stream touches a certain part of the anode through which the entire current flows. As the current increases toward the limiting value, the jet is compressed and the touched part decreases. The current is then concentrated either at the end of a cylindrically shaped anode or near the critical cross section of an anode shaped as a Laval nozzle.

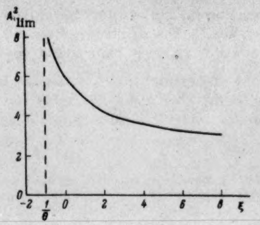

Fig. 2. Variation of limiting value of A^2 with ξ. L = 8, R_a = 2, R^0_m = 0.02; θ = 1.

For a current greater than the limiting value the plasma flow detaches from the anode and a gap with a small plasma concentration appears between the jet and the anode. This leads to an increase in voltage in the near-anode region.[11]

If $u_a \gg 1$, i.e., $A^2 \ln R_a \gg 1$, using $\sigma_0 = (m_i U_0^2/2)^{3/2}A^3$ we obtain the following expression for the limiting value of A^2

$$A^8_{\lim} = \frac{8L}{(1-\theta\xi)\,\theta^{3/2}R^0_m R_a^2(\ln R_a)^{5/2}}, \quad R^0_m = \sigma^0\left(\frac{m_i U_0^2}{2}\right)^{3/2}U_0 R_0, \tag{5}$$

or in dimensional form,

$$\frac{I^8_{\lim}}{G^4}\left(1 - \theta\frac{m_i I_{\lim}}{eG}\right)\left(\frac{m_i}{2}\right)^{3/2}\mu\sigma^0\left(\frac{\mu}{4\pi}\right)^4 = \frac{8L_D}{R^2_{aD}(\ln R_{aD}/R_0)^{5/2}\theta^{3/2}},$$

where L_D and R_{aD} denote the dimensional length and radius of the anode.

The limiting current is independent of U_0 and weakly dependent on R_0. The variation of $A^2_{\lim}$ with ξ is shown in Fig. 2 and with anode dimensions in Fig. 3.

The flow velocity, being dependent only on $A^2 \ln R_a$, reaches its maximum value at limiting currents in an accelerator of given geometry. As can be seen from (5) the increase in flow velocity is due to the increase in the

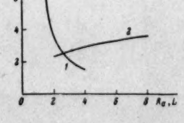

Fig. 3. Variation of limiting value of A^2 with anode dimensions. R^0_m = 0.02, θ = 1, ξ = −4; 1 $A^2_{\lim}$ versus R_a for L = 8; 2 $A^2_{\lim}$ versus L for R_a = 2.

length of the accelerator or in the conductivity due to plasma turbulence.[12] The efficiency of the collisional mechanism of acceleration is improved in both cases.

The author wishes to thank K. V. Leskov for his constant interest in the work and for valuable remarks, and A. I. Morozov for a useful discussion on the results.

---

[1] A. A. Porotnikov, in: Plasma Accelerators [in Russian], Izd. Mashinostroenie, Moscow (1973).

[2] A. Schlüter, Zs. Naturforsh., 5a, 72 (1950).

[3] S. I. Braginskii, in: Plasma Physics and the Problem of Controlled Thermonuclear Reactions [in Russian], Izd. AN SSSR, Moscow (1958), Vol. 1.

[4] S. I. Braginskii and V. D. Shafranov, in: Plasma Physcis and the Problem of Controlled Thermonuclear Reactions [in Russian], Izd. AN SSSR, Moscow (1958). Vol. 2.

[5] S. I. Braginskii, in: Reviews of Plasma Physics, Vol. 1 Consultants Bureau, New York (1965).

[6] A. I. Morozov and L. S. Solov'ev, Dokl. Akad Nauk SSSR, 164, 80 (1965) [Sov. Phys.—Dokl., 10, 834 (1966)].

[7] A. G. Korsun and A. L. Levin, PMTF, No. 3, 20 (1970).

[8] W. H. Bennett, Phys. Rev., 45, 890 (1934).

[9] H. Maecker, Zs. Phys., 141, 198 (1955).

[10] A. I. Morozov, E. V. Artyushkov, L. S. Solov'ev, and Shubin, in: Low-Temperature Plasma [in Russian]. Izd. Mir, Moscow (1967).

[11] A. M. Bishaev and A. G. Korsun, in: Topics in the Physics of Low-Temperature Plasma [in Russian], Izd. Nauka i Tekhnika, Minsk (1970).

[12] E. K. Zavoiskii and L. I. Rudakov, Plasma Physics (Collective Processes in Plasmas and Turbulent Heating) [in Russian], Izd. Znanie, Moscow (1967).

2

Parametric plasma instabilities excited by the sudden application of an electric field

A. B. Kitsenko and K. N. Stepanov
Technical Physics Institute,
Academy of Sciences of the Ukrainian SSR, Khar'kov
(Submitted April 14, 1973)
Zh. Tekh. Fiz., 44, 206-208 (January 1974)

The present work considers the parametric instability in a plasma which occurs on the sudden application of an external electric field $\mathbf{E}(t) = \mathbf{E}_0 \sin \omega_0 t$. The unperturbed distribution function for particles of species α is a doubly periodic function of time with periods $2\pi/\omega_0$ and $2\pi/\omega_\alpha$ (ω_α is the cyclotron frequency for particles of species α). A dispersion equation is obtained for oscillations at a frequency and growth rate much smaller than the pump frequency ω_0. The equation is analyzed for the case of a cold plasma in which the oscillatory velocity of the electrons in the field E is greater than the thermal velocity. It is shown that parametric instabilities are most strongly developed under the resonance conditions $\omega_\pm \approx k_z\bar{u}^{(\alpha)} + m_0\omega_0 + r_0\omega_{Be}$ ($m_0, r_0 = 0, \pm1, \pm2, \ldots$. $\bar{u}^{(\alpha)}$ is the average electron drift speed along the magnetic field and $\omega_\pm$ are the natural frequencies of the longitudinal electron oscillations in the plasma).

In this work we consider the parametric instability in a plasma with an external magnetic field which occurs in the sudden application of an external varying electric field $\mathbf{E}(t) = \mathbf{E}_0 \sin \omega_0 t$. Parametric instability in a plasma is usually considered under conditions in which the field E(t) is applied slowly (adiabatically) at $t = t_0 \to -\infty$. "Sudden" application of the field means that the time taken to establish the field in the region where the instability develops is much smaller than the period of the pump field $2\pi/\omega_0$. It is then possible to get new parametric effects which produce plasma instabilities connected with cyclotron rotation of the particles under the action of the field **E** in the direction perpendicular to the magnetic field $\mathbf{B}_0$ and with the drift of the electrons relative to the ions, parallel to $\mathbf{B}_0$, at some average velocity under the action of the field component E_z parallel to $\mathbf{B}_0$.

A particle with charge e_α and mass m_α, with zero velocity at $t = 0$, will for $t > 0$ move with a velocity $\mathbf{u}^{(\alpha)}(t) = \mathbf{u}_E^{(\alpha)}(t) + \mathbf{u}_B^{(\alpha)}(t)$, where

$$\left.\begin{aligned} u_{Ex,y}^{(\alpha)}(t) &= \frac{e_\alpha}{m_\alpha(\omega_{B\alpha}^2-\omega_0^2)}\left(E_{0x,y}\omega_0\cos\omega_0 t \pm E_{0y,x}\omega_{B\alpha}\sin\omega_0 t\right),\\ u_{Bx,y}^{(\alpha)}(t) &= -u_{Ex,y}^{(\alpha)}(0)\cos\omega_{B\alpha}t \mp u_{Ey,x}^{(\alpha)}(0)\sin\omega_{B\alpha}t,\\ u_{Ez}^{(\alpha)}(t) &= -\bar{u}^{(\alpha)}\cos\omega_0 t,\quad u_{Bz}^{(\alpha)} = \bar{u}^{(\alpha)} \equiv \frac{e_\alpha E_{0z}}{m_\alpha\omega_0}. \end{aligned}\right\} \qquad (1)$$

For adiabatic application of the field $\mathbf{E}(t)$, $\mathbf{u}^{(\alpha)} = \mathbf{u}_E^{(\alpha)}$.

If the plasma particles have a Maxwellian velocity distribution at $t = 0$, the distribution function for $t > 0$ is

$$f_\alpha(\mathbf{v}, t) = \frac{n_{0\alpha}}{(2\pi)^{3/2} v_{T\alpha}^3}\exp\left\{-\frac{[\mathbf{v}-\mathbf{u}^{(\alpha)}(t)]^2}{2v_{T\alpha}^2}\right\}\left(v_{T\alpha} = \sqrt{\frac{T_\alpha}{m_\alpha}}\right). \qquad (2)$$

This distribution is nonstationary (it is a double periodic function of time with periods $2\pi/\omega_0$ and $2\pi/\omega_{B\alpha}$), and therefore various parametric effects are produced. The oscillatory variation in (2) with period $2\pi/\omega_{B\alpha}$ means that the sudden application of the field **E** leads to much richer possibilities in the appearance of resonance effects.

Using the Fourier–Laplace transform we can easily obtain the following equation to describe small oscillations in the plasma:

$$\varphi(\omega) + \sum_{\alpha=e,i}\ \sum_{s,m,l,r=-\infty}^{\infty} J_{s+m}(a_E^{(\alpha)})\, J_m(a_E^{(\alpha)}) \times J_{l+r}(a_B^{(\alpha)})\, J_r(a_B^{(\alpha)})\, e^{-i(s\delta_\alpha+s\pi+l\mu_\alpha)},$$

$$\delta\varepsilon_\alpha(\omega - k_z\bar{u}^{(\alpha)} + m\omega_0 + r\omega_{B\alpha})\,\varphi(\omega - s\omega_0 - l\omega_{B\alpha}) = Q(\omega), \qquad (3)$$

where

$$a_E^{(\alpha)} = \frac{|e_\alpha|}{m_\alpha}\left[\left(\frac{k_z E_{0z}}{\omega_0^2} + \frac{\mathbf{k}_\perp \mathbf{E}_{0\perp}}{\omega_0^2-\omega_{B\alpha}^2}\right)^2 + \frac{\omega_{B\alpha}^2[\mathbf{k}\mathbf{E}_0]_z^2}{\omega_0^2(\omega_0^2-\omega_{B\alpha}^2)^2}\right]^{1/2},$$

$$\operatorname{ctg}\delta_\alpha = \frac{\omega_0}{\omega_{B\alpha}}\left(\frac{k_z E_{0z}}{\omega_0^2} + \frac{\mathbf{k}_\perp\mathbf{E}_{0\perp}}{\omega_0^2-\omega_{B\alpha}^2}\right)\frac{\omega_0^2-\omega_{B\alpha}^2}{[\mathbf{k}\mathbf{E}_0]_z},$$

$$a_B^{(\alpha)} = \frac{1}{\omega_{B\alpha}}\left[k_x u_{Ex}^{(\alpha)}(0) + k_y u_{Ey}^{(\alpha)}(0)\right],$$

$$\mu_\alpha = \operatorname{arc\,tg}\frac{k_y}{k_x} - \operatorname{arc\,tg}\frac{u_{Ex}^{(\alpha)}(0)}{u_{Ey}^{(\alpha)}(0)},$$

$\delta\varepsilon_\alpha(\omega)$ is the contribution of particles of species α to the longitudinal dielectric permittivity of the plasma, $J_n(x)$ is the Bessel function, $\varphi(\omega) = \iint_0^\infty \varphi(\mathbf{r}, t)\exp(i\omega t - i\mathbf{k}\mathbf{r})\,d\omega\,d\mathbf{r}$, $\varphi(\mathbf{r}, t)$ is the potential and $Q(\omega)$ is a quantity proportional to the Fourier transform of the initial perturbation in the distribution function.

For the electron oscillations ($\delta\varepsilon_i \approx 0$), we can easily obtain the dispersion equation $1 + \delta\varepsilon_e(\omega) = 0$ from (3). This equation is identical with the dispersion equation for $\mathbf{E} = 0$, i.e., the high-frequency electron oscillations have the same frequencies as those with $E = 0$ to within an accuracy to the harmonics of the pumping and electron cyclotron frequencies.

We consider the low-frequency oscillations ($\omega_{Bi} \ll |\omega| \ll \omega_0, \omega_{pe}, \omega_{Be}$). In this case the dispersion equation has the form

$$1 + \delta\varepsilon_i(\omega) \sum_{m,r=-\infty}^{\infty} J_m^2(a_E^{(e)})\, J_r^2(a_B^{(e)}) \times [1 + \delta\varepsilon_e(\omega - k_z\bar{u}^{(e)} + m\omega_0 + r\omega_{Be})]^{-1} = 0. \qquad (4)$$

In a strong pumping field when $u^{(e)} \gg v_{Te}$, we can make use of the hydrodynamic expressions $\delta\varepsilon_i \approx -\omega_{pi}^2/\omega^2$ and $\delta\varepsilon_e = -\omega_{pe}^2\cos^2\theta/\omega^2 - \omega_{pe}^2\sin^2\theta/(\omega^2-\omega_{Be}^2)$, where θ is the angle between the wave vector **k** and $\mathbf{B}_0$.

Remembering that $|\omega| \ll \omega_0, \omega_{pe}, \omega_{Be}$, we find from (4) that $\omega = \pm\omega_1$, where

$$\omega_1^2=\omega_{pi}^2\Big[1-J_0^2(a_B^{(e)\prime})J_0^2(a_B^{(e)\prime})-2J_0^2(a_B^{(e)\prime})J_1^2(a_B^{(e)\prime})$$

$$-\sum_{m,r}{}' J_r^2(a_B^{(e)\prime})J_m^2(a_B^{(e)\prime})\frac{\delta\varepsilon_e(m\omega_0+r\omega_{Be}-k_z\bar{u}^{(e)})}{1+\delta\varepsilon_e(m\omega_0+r\omega_{Be}-k_z\bar{u}^{(e)})}\Big]. \qquad (6)$$

The summation here over m and r is from $-\infty$ to ∞ except for $m = 0$ and $r = 0$ and also $m = 0$ and $r = \pm 1$.

Under the resonance condition $m_0\omega_0 + r_0\omega_{Be} - k_z\bar{u}^{(e)} \approx \omega_\pm$, where $\omega_\pm$ are the frequencies of longitudinal electron oscillations in the magnetic field with $\mathbf{E} = 0$,

$$\omega_\pm^2=\frac{1}{2}(\omega_{pe}^2+\omega_{Be}^2)\pm\frac{1}{2}[(\omega_{pe}^2+\omega_{Be}^2)^2-4\omega_{pe}^2\omega_{Be}^2\cos^2\theta]^{1/2},$$

the frequency ω is defined by the expression

$$\omega^2=\frac{1}{2}(\omega_1^2+\delta^2)\pm\frac{1}{2}[(\omega_1^2-\delta^2)^2-4\delta\gamma_0^3]^{1/2}, \qquad (7)$$

where

$$\left.\begin{aligned}\delta&=m_0\omega_0+r_0\omega_{Be}-k_z\bar{u}^{(e)}-\omega_\pm,\\ \gamma_0&=\left[\frac{2\omega_{pi}^2J_{m_0}^2(a_B^{(e)\prime})J_{r_0}^2(a_B^{(e)\prime})}{\delta\varepsilon_e'(\omega_\pm)}\right]^{1/3},\\ \delta\varepsilon_e'(\omega)&=\frac{2\omega_{pe}^2\cos^2\theta}{\omega^3}+\frac{2\omega\omega_{pe}^2\sin^2\theta}{(\omega^2-\omega_{Be}^2)^2},\end{aligned}\right\} \qquad (8)$$

and the quantity ω_1^2 is given by (6) with $m \neq m_0$ and $r \neq r_0$.

Equations (6) and (7) are a generalization of the results for parametric[2] and Buneman[3] instabilities of a plasma in a magnetic field for the case of sudden application of $\mathbf{E}(t)$.

If $\omega_0 \sim \omega_{pe} \sim \omega_{Be}$, the maximum value of the growth rate $\gamma_{max} \sim \gamma_0 \sim \omega_{pe}(m_e/m_i)^{1/3}$ is of the same order of magnitude as for adiabatic application of the field $\mathbf{E}$. The extra sources of instability, in addition to those considered in refs. 1 and 2, are connected with the appearance of a drift of electrons relative to the ions along B_0 with an average velocity $\bar{u}^{(e)}$ when $E_{0z} \neq 0$ and with electron oscillations at a frequency ω_{Be} when $E_{0x,y} \neq 0$. The presence of the electron oscillations means that it is possible to produce parametric excitation if the pumping frequency lies in the range $\min(\omega_{pe}, \omega_{Be}) < \omega_0 < \max(\omega_{pe}, \omega_{Be})$ with $\omega_0 > (\omega_{pe}^2 + \omega_{Be}^2)^{1/2}$. In particular, at low frequencies ($\omega_0 \gg \omega_{pe} > \omega_{Be}$) when $\omega_+ \approx r_0\omega_{Be}$ we get the following expression for the growth rate:

$$\gamma_{max}\approx\omega_{pe}\left[\left(\frac{m_e}{m_i}\right)J_0^2(a_B^{(e)\prime})J_{r0}^2(a_B^{(e)\prime})\right]^{1/3}\left(a_B^{(e)\prime}\sim\frac{\omega_{Be}}{\omega_0}a_B^{(e)\prime}\ll a_B^{(e)\prime}\right). \qquad (9)$$

We note in conclusion that the effects considered here, caused by the initial kick given to the particles by the application of the field $\mathbf{E}$, should also occur in the intermediate case when the time of the transient effects is of the order of the pump period $2\pi/\omega_0$.

---

[1] V. P. Silin, Usp. Fiz. Nauk, 108, 625 (1972) [Sov. Phys.–Usp., 15, 742 (1973)]; A Survey of Phenomena in Ionized Gases, International Atomic Energy Authority, Vienna (1968), p. 205.

[2] Yu. M. Aliev, V. P. Silin and H. Watson, Zh. Eksp. Teor. Fiz., 50, 943 (1966) [Sov. Phys.–JETP, 23, 626 (1966)].

[3] A. B. Mikhailovskii, The Theory of Plasma Instabilities, Vol. 1, Consultants Bureau, New York (1973).

Electron repulsion in a time-resolving electron-optical image converter

M. M. Butslov and M. E. Gertsenshtein

(Submitted April 2, 1973)
Zh. Tekh. Fiz., 44, 208-210 (January 1974)

In principle, pulsed time resolving electron-optical image converters can achieve a time resolution of 10^{-14} sec in the case of a faint light signal. Distortions of the transit time from the photocathode to the deflecting system caused by electrostatic repulsion of electrons are evaluated. Comparatively strong signals, corresponding to 10^3 electrons in a pulse of minimum length, are acceptable.

In principle, pulsed electron-optical image converters can achieve a time resolution of 10^{-14} sec for visible light.[1,2] However, there has been no previous analysis of the role of the signal intensity; we consider this question here.

Electrons in a beam formed by a short light pulse are repelled by electrostatic forces; some of the electrons are accelerated while others are retarded, and the net result is that the pulse entering the deflecting system can be spread out. We speak in terms of electrostatic repulsion, rather than the role of the space charge, although these effects are essentially the same. The term "space charge" is usually used in physical electronics in analyzing intense electron beams, either steady-state or with a steady-state component, and usually in the theory of the plane diode.[3,4] In this situation the entire volume near the cathode is filled with electrons. In a pulsed image converter the situation is radically different: A short light pulse of length τ_1 generates a thin "disk," which moves from the cathode to the deflecting system. This disk fills a volume one-millionth that of the diode, so that the equations derived for the diode are not applicable; accordingly, to avoid confusion we will not use the term space charge. The thickness of this disk is always much smaller than its other dimensions. The time required to traverse the entrance stage, from the photocathode to the deflecting system, τ_0, is of the order of 10^{-8} sec and can in principle be reduced to 10^{-9} sec. The disk thickness, according to the equations for uniformly accelerated motion, is proportional to $(\tau_1/\tau_0)^2$ at the photocathode and (τ_1/τ_0) at the deflecting system. Accordingly, the thickness of the disk at the photocathode in the case of a light pulse $\tau_1 \sim 10^{-12}$ sec long is only one-millionth of the distance across the gap, and the thickness at the deflecting system is one-thousandth of this distance.

Repulsion increases the transverse and longitudinal dimensions of the disk; here we will be concerned only with the longitudinal repulsion, which reduces the time resolution of the entrance cascade.

We assume that the motion of the disk is known when there is no electrostatic repulsion, and we assume that there are no magnetic focusing fields. The longitudinal electric field of the disk outside the disk and at its boundary is

$$E' = 2\pi\sigma, \quad \sigma = \frac{eN}{\pi R_\perp^2}, \quad E' = \frac{2eN}{R_\perp^2}, \tag{1}$$

where σ is the surface charge density, N is the number of photoelectrons in the bunch, and $R_\perp$ is the disk radius.

The equations of motion for electrons are

$$\frac{dv}{dt} = \frac{e}{m} E_0 + \frac{e}{m} E'(r, t). \tag{2}$$

Multiplying by v and integrating we find

$$\begin{gathered} v^2 = \frac{2e}{m} U + \frac{2e}{m} \int E'(r, t)\, dr + v_T^2, \\ v_T^2 = \frac{2e}{m} \Delta M_T, \end{gathered} \tag{3}$$

where the integral is evaluated along the electron trajectory, and U is the potential of the accelerating and focusing field. Equation (3) also includes a term describing the energy spread of the photoelectrons. The correction to the velocity is

$$\frac{\delta v}{v} = \frac{1}{2} \left\{ \frac{1}{U_0} \int E'\, dr + \frac{\Delta U_T}{U_0} \right\}, \tag{4}$$

where U_0 is the potential difference between the cathode and the deflecting system.

Using (1), we find the following equation for the disk boundary:

$$\frac{\delta v}{v} = \frac{1}{2} \left\{ \frac{2eN}{U_0} \int \frac{dr}{R_\perp^2(r)} + \frac{\Delta U_T}{U_0} \right\}. \tag{5}$$

All quantities in Eq. (5) are known. As is evident from the derivation, Eq. (5) holds as long as the thickness of the disk is much less than its radius.

In the case of a charge density which is uniform with respect to thickness in the disk, the field varies linearly, so there will be a factor of $1/\sqrt{3}$ involved in calculating the rms velocities.

Our problem is to find the intensity at which the role of repulsion and the role of the energy spread become comparable. The time spread is

$$\frac{\delta\tau}{\tau_0} = -\frac{\delta v}{v}, \quad \frac{\delta\tau}{\tau_0} = \frac{2}{\sqrt{3}} \frac{eN}{U_0} \int \frac{dr}{R_1^2} \simeq \frac{\Delta U_T}{U_0} = 2 \cdot 10^{-5}. \tag{6}$$

Strictly speaking, the equation for $\delta\tau$ is only an approximation; the difference in the transit time is a function of the rate of increase of the velocity. Accordingly, all equations below are approximate.

We consider the simplest and least favorable case, that of transit from a homogeneous field between the photocathode and the deflecting system without focusing; then we can write

$$\begin{gathered} R_\perp = \text{const}, \quad U_0 = Ex_0, \\ \frac{\delta\tau}{\tau_0} = \frac{2}{\sqrt{3}} \frac{eN}{U_0} \int \frac{dr}{R_\perp^2} \cong \frac{eN}{E_0 R_\perp^2}, \quad \delta\tau \sim \tau_1. \end{gathered} \tag{7}$$

With $\tau_0 \sim 10^{-9}$ sec, we have, according to Eq. (6), a tolerable value of $\delta\tau \cong 2 \cdot 10^{-14}$ sec. Assuming $E_0 = 200$ statvolts/cm = 60 kV/cm and $R_1 = 100\,\mu = 10^{-2}$ cm, we find

$$N < \frac{2 \cdot 10^{-5} E_0 R_{\perp}^{2}}{e} \simeq 10^{3} \text{ electrons},$$

i.e., satisfactory intensities; the statistical error in the amplitude is less than 10%. The spot radius must be such that the image of the spot on the screen shifts by at least a spot diameter over the resolution time. Since the spot diameter is a function of many factors, we will use the more customary language of the current density. Equation (7) can be rewritten as

$$\frac{\pi}{\sqrt{3}} \frac{eN}{\delta\tau_1 \pi R_{\perp}^{2}} \sim \frac{E_0}{\tau_0}, \quad \frac{\pi}{\sqrt{3}} j = \frac{E_0}{\tau_0},$$
$$n = \frac{N}{\pi\tau_1 R_{\perp}^{2}}, \quad j = en, \tag{8}$$

where n is the number of electrons from a unit area per second. Assuming $E_0 = 200$ statvolts/cm and $\tau_0 \simeq 10^{-9}$ sec, we find $n \sim 0.2 \cdot 10^{19}$ electrons/(mm^2 · sec) and $j \simeq 0.3$ A/mm^2.

Accordingly, at these intensities, a single pulse $\tau_1 \sim 10^{-14}$ sec long spreads out very little as a result of electrostatic repulsion of electrons. What will happen to a more complex signal? If the length of this complex signal is such that the thickness of the electron disk is less than its diameter, all the equations above for the field remain valid. We construct some imaginary planes corresponding to a time interval τ_1; the distances between these planes increase only because of the electrons between them. Accordingly, the estimates above for the resolution also hold in the case of complex signals. However, when resolution is not the only consideration and times must be measured, the permissible intensities will be lower. Concrete estimates can be obtained from velocity equation (5).

It is important to note that these calculations hold only for paraxial beams in the axisymmetric electron-optical systems currently in use. A fundamental feature of such systems is chromatic aberration,[3] which limits the time resolution;[2] the limitation becomes more severe, the higher the photon energy. Accordingly, in time-resolving image converters it would be desirable to design a special, nonaxisymmetric electron-optics system with compensation for chromatic aberration. These questions lie outside the scope of this note.

---

[1] M. M. Butslov, Usp. Nauch. Fotograf., 6, 76 (1959).

[2] E. K. Zavoiskii and S. D. Fanchenko, Dokl. Akad. Nauk SSSR, 100, 661 (1959).

[3] A. A. Zhigarev, Electron Optics and Electron-Beam Devices [in Russian], Izd. Vysshaya Shkola, Moscow (1972).

[4] J. R. Pierce, Theory and Design of Electron Beams, Van Nostrand, Princeton, New Jersey (1949).

Aberrations in a straight ion-optical accelerator

E. I. Gerasimov, A. I. Solnyshkov, and G. V. Tarvid

D. V. Efremov Scientific-Research Institute of Electrophysical Apparatus

(Submitted April 9, 1973)
Zh. Tekh. Fiz., 44, 210-213 (January 1974)

A 150-keV ion-optical accelerator with an ion current of 3 mA is investigated. The beam-parameter is investigated. The beam-parameter measurement system enables us to obtain data on the current-density distribution over the beam radius and phase diagrams in transverse planes in the different regimes of accelerator operation. The causes of distortion in the phase-volume configuration and the change in the current-density distribution in the beam cross section are investigated. The action of nonlinear focusing forces, which leads to a considerable increase in the effective phase volume, is shown to be a decisive factor. It is also possible to form beams with current-density distribution close to equilibrium, using focusing elements with strong spherical aberration.

Recently, in connection with the development of powerful proton linear accelerators, serious consideration has been given to the quality of the ion beam both from the ion source and also at the exit of the straight accelerator used as the injector for the linear accelerator. In order to refine the beam parameters, formation of a charged-particle beam from the plasma in the ion source has been studied.[1] The causes of distortion of the configuration of the transverse phase volume of the ion beam in the accelerating and transporting channels have been investigated. In particular, it has been shown[2] that one of the causes of the increase in effective phase volume is the action of nonlinear Coulomb forces.

In the present study it is experimentally shown that the presence of nonlinear focusing forces in the ion-optical accelerator system strongly distorts the phase-volume configuration and reduces the mean phase density in the beam at the accelerator exit. Investigations have been carried out on an accelerator with proton energies up to 150 keV with a duoplasmatron ion source.[3] To measure the beam characteristics, we use an iris method; the selected part of the beam is observed on a quartz screen. The measurement system enables us to obtain data on the current-density distribution over the beam cross section, the projection of the transverse phase volume onto the xx' plane, and the cross section of the transverse phase volume intersected by the plane $y = y' = 0$, where x, y, and z are Cartesian coordinates, $x' = (dx)/(dz)$, $y' = (dy)/(dz)$, z is the longitudinal coordinate (along the beam axis). For a beam with axial symmetry, with which we are concerned in the accelerator, the distribution function can be represented in coordinates of RR' and $t = R\Theta'$ (R, R' and t are the radius, and the relative radial and azimuthal velocities). Conversion to a cylindrical coordinate system enables us to consider independently the motion of particles with constant angular momentum (Rt = const), where the Liouville theorem holds for each section cut by the plane Rt = const.

The scheme of the ion-optical accelerator system and the potential distribution between the electrodes are given in Fig. 1a. For the measurement of the beam parameters at the accelerator exit it is noted that the nature of the particle distribution over transverse angles (which corresponds to distribution in the plane R = const)

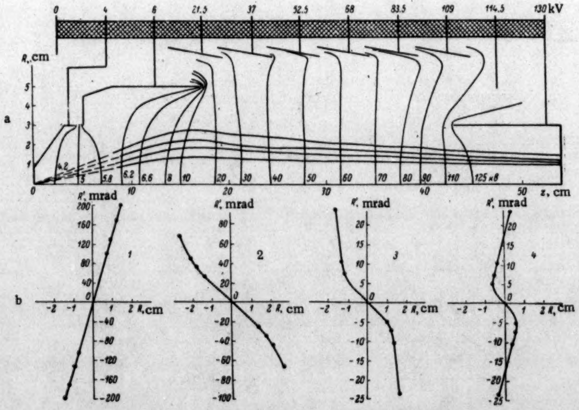

Fig. 1. a) Diagram of ion-optical accelerator system, potential distribution between electrodes, and particle trajectories; b) phase diagrams in RR' plane for different cross sections along the beam path: z, cm: 1) 7.5; 2) 20; 3) 46; 4) 126.

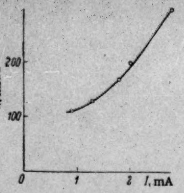

Fig. 2. Dependence of variation in beam divergence angle beyond the extraction electrode on the beam current.

is essentially independent of the geometry of the ion-selection region in the ion source. The geometry of the ion-selection region, which determines the initial beam parameters, is varied over wide limits. Conical and cylindrical expanders are examined, and grids are located on the expander and on the extraction electrode; however, no qualitative change in the nature of the distribution at the accelerator exit is observed.

Therefore, the principal cause determining the observable nature of the distribution can be assumed to be the aberration in the initial part of the ion-optical system, where the transverse dimension of the beam is comparable with the optical-electrode dimensions (Fig. 1a). In the ion source we can select an operational regime with a comparatively low potential at the extraction electrode; owing to the variation in ion density in the penetrating plasma and variation of its form, with increasing arc current there is an almost linear increase in current and divergence angle in the beam beyond the extraction electrode (Fig. 2). Operating in this regime we can vary the beam diameter in the focusing-electrode region. The effect of this parameter on the particle distribution over transverse coordinates and velocities at the accelerator exit can be seen from Fig. 3, which shows how the cross section of the transverse phase volume varies (in coordinates R, R'); also shown is the current-density distribution with increasing arc current, the potentials at the electrodes of the ion-optical system being held constant. From Fig. 3 we see that with increasing beam diameter the boundary of the phase-volume cross section bends and therefore the phase-volume projection increases. There is also a variation in the nature of the current-density distribution over the beam cross section. Figure 4 shows how the phase diagrams and the current-density distribution vary with potential on the focusing electrode. With increasing optical force of the lens (with decreasing potential) the longitudinal spherical aberration decreases. Thus, we can in principle select an operational regime for which the distortion in the phase-volume configuration is a minimum.

From an analysis of phase diagrams and curves of the current-density distribution we see that the existence of nonlinear focusing forces leads to a redistribution of

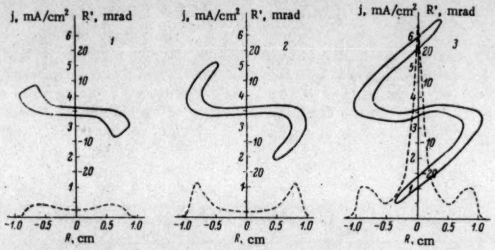

Fig. 3. Cross section of transverse phase volume intersected by the plane Rt = 0 and current-density distribution along the radius for different beam currents. I, mA: 1) 1; 2) 2; 3) 3.

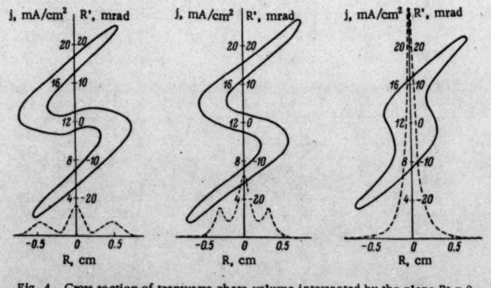

Fig. 4. Cross section of transverse phase volume intersected by the plane Rt = 0 and current-density distribution along the beam radius for different focusing-electrode potentials.

phase density in the charged-particle beam along the acceleration channel and in the transporting channel. This effect enables us to shape the beam at a given location with current-density distribution over the cross section close to equilibrium, which is of great importance in accelerators used, for example, as neutron generators; in this case it is very important to irradiate uniformly the physical target because of the large thermal loads.

The observed nature of the phase-density distribution in the beam is qualitatively independent of the current over a wide range (from 0.1 to 3 mA). This indicates that in the beams being investigated the redistribution of the phase density due to nonlinear Coulomb forces is not a decisive factor; it enables us to neglect the action of space charge, and to investigate particle dynamics in the accelerator by geometric optics under the assumption that we have a point source of particles. The trajectory is constructed on a T-61 trajectory tracer. The results of such constructions and also the phase diagrams in the RR' plane are given in Fig. 1. From these diagrams (Fig. 1b) we see that the phase-volume configuration is distorted because of the nonlinear focusing forces in the ion-optical system, which leads to an increase in the "effective" phase volume.

Coulomb forces have a large effect in injectors of modern linear accelerators,[5] designed for obtaining ion beams with currents of the order of hundreds of milliamperes. Because of the nonlinearity of these forces there is also an increase in the effective phase volume. As a rule, in these accelerators the beam occupies the entire volume inside the accelerating and shaping electrodes; therefore in such a beam, as a result of the presence of aberrations, a large distortion of the phase-volume configuration is possible.

In the present case it has been shown how great these distortions are in an accelerator for comparatively weak currents, where we can neglect the action of Coulomb forces. In high-current accelerators, it is necessary to take account of both factors determining the particle dynamics over the entire accelerating and transporting channels.

---

[1] Th. Slyuters, Proc. of the 1972 Proton Linear Conf., October 10-13, Los Alamos (1972), p. 283.

[2] V. S. Kuznetsov, Zh. Tekh. Fiz., 37, 932 (1967); 38, 274 (1968); 40, 2099 (1970) [Sov. Phys.–Tech. Phys., 12, 670 (1967); 13, 198 (1968); 15, 1635 (1971)].

[3] A. V. Andreev, I. Ya. Barit, L. T. Duev, Yu. B. Evdokimov, N. F. Ivanov, L. N. Katsaurov, A. N. Kuznetsov, I. M. Pronman, A. I. Solnyshkov, G. V. Tarvid, S. G. Tsepakin, and K. V. Yakshin, Prib. Tekh. Eksp., No. 5, 262 (1972).

[4] N. F. Ivanov, Yu. P. Sivkov, and A. I. Solnyshkov, Prib. Tekh. Eksp., No. 5, 30 (1965).

[5] V. S. Kuznetsov and A. I. Solnyshkov, Transactions of the All-Union Conference on Charged-Particle Accelerators (1968), p. 337.

Effect of electron reflection on the voltage—current characteristics of a high-voltage, hollow-cathode, glow discharge

Ya. Ya. Udris, V. A. Chernov, and L. G. Guseva

(Submitted December 26, 1972)
Zh. Tekh. Fiz. 44, 213-215 (January 1974)

The ability of a high-voltage, hollow-cathode glow discharge to produce a focused beam of fast electrons, combined with a high discharge stability up to high power levels, is used to produce cold-cathode electron beams at power levels up to tens of kilowatts and higher.[1]

Many workers have emphasized the part played by electrons reflected from the anode in maintaining the high-voltage glow discharge. For example, in ref. 2 the interaction of electrons reflected from the anode with the walls of the discharge tube, and the secondary electrons thereby produced have been advanced as the main mechanism by which the discharge is maintained. According to theoretical results given in ref. 3, where the electron regeneration factors[1)] for the most probable processes are calculated, the regeneration coefficient for reflected electrons is found to be approximately twice that for primary electrons.

Taking into account the fact that in the electron beams of a glow discharge the whole electron flux emitted by the cathode is derived from outside the gas-discharge gap, the part played by the electrons reflected from the anode is reduced to a minimum. Hence, it is possible to estimate the effect of electron reflection on the discharge current. With this aim in mind we plot voltage—current characteristics of the high-voltage gaps of two configurations: A and B. In the first of these the emission of electrons from the anode cavity is cut off, and the flux as a whole is directed to the anode; in the second the electron beam is produced outside the discharge space. Configuration A consists of a plane anode and cathode, placed parallel to one another inside a cylindrical glass tube; the diameter of the electrodes is 100 mm. In configuration B there is a circular opening in the anode, through which the beam is introduced. To focus the electrons in the plane of the output opening, the surface of the cathode, which also has a diameter of 100 mm, is made in the form of a concave sphere of radius of curvature 120 mm. In both cases the cathode material is a low-carbon steel, and the working gas is helium. The pressure is chosen so that the region of the cathode full of potential fills only a small part of the anode cavity over the whole measurement range. Before plotting the characteristics the surface of the cathode is cleaned by a glow discharge.

Particular consideration is given to the fact that in configuration B for the chosen diameter of the opening, the beam electrons do not hit the walls of the anode. Calculations made with the aim of estimating the fraction of electrons incident on the anode due to scattering by helium atoms show that not less than 95% of the beam emerges beyond the limits of the discharge. Measurements of the heat dissipated at the anode confirm this figure. Consequently, in the anode cavity of configuration B there is essentially no ionization by reflected electrons.

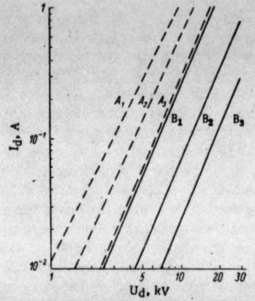

Fig. 1. Voltage—current characteristics of a high-voltage, hollow-cathode glow discharge for two configurations of the gas-discharge gap A and B. The working gas is helium, and the pressure p, torr is: A_1) 0.6; B_1) 0.7; A_2, B_2) 0.4; A_3, B_3) 0.3.

The results of the measurements are shown in Fig. 1. The voltage—current characteristics are described by power functions of the form $I_d = f(p)\,U_d^m$, where I_d and U_d are the current and voltage of the discharge, and $f(p)$ is a function of the pressure p. Plotted on a log—log scale, they are represented by straight lines with a slope m ≃ 2.5 for both configurations. The dashed lines pertain to configuration A, and the solid lines to configuration B. The slope of the characteristics over the chosen range is almost independent of the pressure, which is the parameter of the set of curves shown in Fig. 1.

The elimination of reflected electrons from the discharge space of configuration B causes the B characteristics for the same pressure to lie to the right of the A characteristics. The attaiment of the same discharge current in the B configuration requires a greater relative intensity of such processes as volume ionization by the primary electron flux and ion—electron emission from the cathode than in the A configuration. The reason that the characteristics lie more to the right is that for a given pressure an increase in the voltage leads to an increase in the energy of the ions and neutrals which bombard the cathode, and, consequently, leads to an increase in the ion—electron emission factor. On the other hand, for a fixed discharge voltage, an increase in the pressure leads to an increase in the density of the gas atoms, and hence to an increase in the ions produced by the primary beam. An increase in the pressure therefore, in effect, compensates for the absence of ionization by reflected electrons. How intense the latter is can be seen, for example, from the fact that to maintain a current of 0.3 A in the B configuration one must either increase the voltage from 8.5 to 30 kV, or increase the pressure from 0.3 to 0.75 torr, i.e., by a factor of 2.5.

At the same time, the fact that a high-voltage glow discharge maintains high stability under conditions when there is no reflection of electrons from the anode shows that the process of electron reflection is certainly not necessary for this form of discharge to exist. In the gas-discharge technique a method has been proposed for using known experimental data and behavior to calculate discharge gaps which are similar in configuration but differ in geometrical dimensions. It is also used in relation to gas-discharge electron beams. However, it follows from the results obtained here that when the characteristics of a gap with plane-parallel electrodes are used, without the electrons being removed outside the limits of the discharge space, it is necessary to make a considerable correction when estimating the pressure. Thus, if the beam as a whole is removed from the discharge region, the working pressure will be many times higher than for a similar closed gap.

We can summarize the above results as follows.

1. The results confirm that in a configuration in which the entire electron beam strikes the anode, electron reflection plays an important part in maintaining the high-voltage glow discharge. From the point of view of forming charged particles, necessary to ensure emission from the cathode, the reflected electrons give an effect equivalent to a severalfold increase in the pressure in the discharge space. However, the high-voltage glow discharge does not depend for its existence on electron reflection from the anode.

2. Identical (i.e., with the same slope) voltage–current characteristics have been obtained, for different pressures, for a high-voltage glow discharge with a hollow anode for a discharge gap with solid plane-parallel electrodes and a configuration with an anode which has an opening which enables the electron beam to pass outside the discharge.

3. When making estimates of configurations in which the electron beam is extracted, using experimental data which pertain to the high-voltage discharge in closed plane-parallel configurations, it is necessary to take into account that when the beam is extracted from the discharge space the working pressure should be considerably higher than in a closed gap with similar geometric ratios.

---

1)By the regeneration factor we mean the number of electrons which are reproduced from the cathode of the glow discharge due to processes in the volume and at the electrodes due to an initially emitted electron.

---

[1] Ya. Ya. Udris, L. G. Guseva, and V. A. Chernov, Zh. Tekh. Fiz., 36, 1140 (1966) [Sov. Phys.–Tech. Phys., 11, 840 (1966)]; R. A. Dugdale, J. Mater. Sci., No. 1, 160 (1969); J. H. Holliday and G. G. Isaacs, J. Sci. and Tech., 38, 15 (1971).

[2] G. W. McClure, Phys. Rev., 124, 969 (1961).

[3] L. G. Guseva, Izv. Akad. Nauk SSSR, Ser. Fiz., 28, 141 (1964).

High-power nanosecond electron accelerator with inductive storage

B. M. Koval'chuk, Yu. A. Kotov, and G. A. Mesyats

Atmospheric Optics Institute,
Academy of Sciences of the USSR, Tomsk

(Submitted June 7, 1973)
Zh. Tekh. Fiz., 44, 215-217 (January 1974)

An electron accelerator has been developed in which the primary energy storage is the capacity of a Marks generator (300 kV, $12 \cdot 10^{-3}$ pF). The Marks generator discharges into the inductive energy storage through several parallel copper wires 50 μ in diameter, the inductive storage being the self-inductance of the generator. The wires explode at current maximum. The energy stored in the inductor is transferred to a diode with a multifront cathode. The accelerator yields an electron beam with an electron energy of 600 keV, a current of 5.2 kA, and pulse about 100 nsec long.

High-power nanosecond electron accelerators usually contain two capacitative energy storage units: slow storage and "fast" storage. The first is either a bank of capacitors with a pulse transformer or a Marks generator, while the second takes the form of coaxial lines or strip lines (see ref. 1). The specific energy stored in the capacitative bank is usually 0.01 to 0.1 J/cm^3, and therefore generators of this type with energy up to 10^6 J have dimensions of up to several tens of meters. The largest accelerator dimension is usually determined by the fast reservoir, since the electrical strength of the capacitors used in the slow storage is usually much greater than the insulation strength in the fast storage. The immediate task is then to make the fast storage.

Inductive storage can store energy more efficiently by two or three orders of magnitude. The accelerator voltage pulse is obtained by discharging the capacitor through the inductive storage, and interrupting the current at the instant it reaches the required value (Fig. 1). For example, if the current breaker resistance increases linearly with time, $R_b = at$, and for a load resistance $R_l \gg (L/C_1)^{1/2}$, the breaker terminals show a voltage pulse of length $t_p = (L/a)^{1/2}$ and amplitude

$$U_M = 2U_0 \sqrt{aC_1},$$

where U_0 is the initial voltage on the capacitor. Therefore, to obtain large pulse amplitude and short duration one must increase the rate of growth of the current breaker resistance. Using an exploding wire breaker one obtains the largest rate of growth of resistance with a large number of parallel fine wires (see ref. 2). Assuming that the wire conductance falls off during the progress of the wave of evaporation, at zero time we have

$$\left(\frac{dR_b}{dt}\right)_{t=0} = \frac{16\rho l v}{\pi n d^3},$$

where ρ is the specific resistance; n, *l*, and d are the number of wires, and their length and diameter; and v is the speed of the evaporation wave.

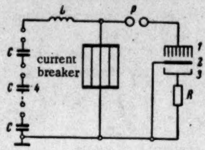

Fig. 1. Circuit of electron accelerator. 1) Multipoint cathode; 2) metal foil anode; 3) Faraday cup; 4) Marks generator, with pulse capacitance $C_1 = C/n$, where n is the number of stages; R is the current measurement shunt.

We have made up an accelerator in which the slow storage is a Marks generator with five stages, with total voltage 350 kV and pulse capacitance $C_1 = 12 \cdot 10^3$ pF. The current breaker is five copper wires 50 μ in diameter. The diode of the accelerator has a multipoint cathode, a foil anode to generate electrons, and a Faraday cup. The inductive storage (L = 6.1 μH) is the self-inductance of the Marks generator discharge circuit. After 0.6 μsec, at a current of 11 kA, the wires explode, the voltage on the inductor L increases, the discharge gap p fires, and a pulse of accelerating voltage is applied to the diode. The electron current pulse has an amplitude of 5.2 kA, the maximum electron energy is 600 keV, and the pulse length is ~100 nsec (Fig. 2).

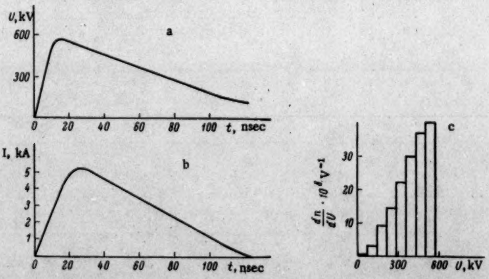

Fig. 2. a) Voltage between the cathode 1 and the anode 2; b) current of electrons in the Faraday cup; c) electron energy spectrum.

The electron energy spectrum is determined from the voltage and current oscillograms, assuming that the electron energy at any time is equal to the voltage difference between the anode and cathode. In this case

$$\frac{dn}{dU}=\frac{i(U)}{e}\frac{dt}{dU},$$

where i(U) is the diode current as a function of the diode voltage, e is the electron charge, and dt/dU is the time derivative of the diode voltage.

Thus, using a current breaker with several fine parallel wires, we have been able to shorten the pulse length by an order of magnitude and to increase the pulse amplitude by almost a factor of 2. The fraction of energy transferred from the capacitor bank to the electron beam is about 20%.

---

[1] G. A. Mesyats, A. S. Nasibov, and V. V. Kremnev, The Formation of Nanosecond High-Voltage Pulses [in Russian], Izd. Energiya, Moscow (1971).

[2] Yu. A. Kotov, N. G. Kolganov, and V. S. Sedoi, in: High-Power Nanosecond Pulse Sources for Electron Accelerators [in Russian], Izd. Nauka, Novosibirsk (1973).

Ionization of a gas-discharge gap by fast electrons

O. B. Evdokimov and A. P. Yalovets

Scientific Research Institute of Electronic Introscopy,
Tomsk Polytechnic Institute
(Submitted February 17, 1973)
Zh. Tekh. Fiz., 44, 217-219 (January 1974)

The distribution of the energy lost in ionization by electrons with initial energies of 0.1-0.5 MeV in the presence of an external accelerating electric field below 2.8 kV/atm · cm is presented. The distribution of the energy lost by the primary electrons when the losses by ionization are much smaller than the increase in energy due to the field is considered.

The ionization of gas-discharge gaps by fast electrons, as shown in refs. 1, 2, etc., enables one to subject the volume discharge to high gas pressure and thereby increase the power of gas switches,[1] and the specific energy emission of electroionization lasers.[2]

The electric field in the gas acts on the electron beam passing through the gas, in particular on the output of bremsstrahlung,[3] and on the ionization distribution produced by it. In turn, the ionization distribution has an effect on the field configuration in the gap, on the electric field strength, and hence on the operation of the corresponding devices. For example, for the operation of an electroionization laser a uniform field in the gap is the most suitable; in practice this can only occur when the ionization produced by the beam is uniform over the volume. To increase the efficiency of the beam, irradiation from the cathode by electrons whose mean free path is close to the value of the interelectrode distance is the optimum.

In this paper we describe results of calculations on the spatial distribution of the energy lost in nitrogen by electrons D with initial energies T_0 from 0.1 to 0.5 MeV in the presence of an electric field.

Because of the smallness of the paths of the secondary particles over this energy range, the distributions of the energy lost and absorbed are practically identical, so the distribution of the energy lost through the energy of formation of an ion pair gives the ionization distribution.

The results of the calculations are valid not only for nitrogen, but for other gases also, in which the effective order number is close to 7 (for example, CO_2 and air). The calculations are made in the continuous slowing approximation by the section model method. It is well known[4] that the continuous slowing approximation is adequate for calculating the distribution of the lost energy (with the exception of depths close to the mean free path, where there are few particles), and the gap model method[5] enables one to describe the transfer of fast electrons in this approximation. In other words, the theoretical approach to this problem is in no way inferior in accuracy to the experimental approach, since the electron interaction cross section for the above-mentioned energies is well known.

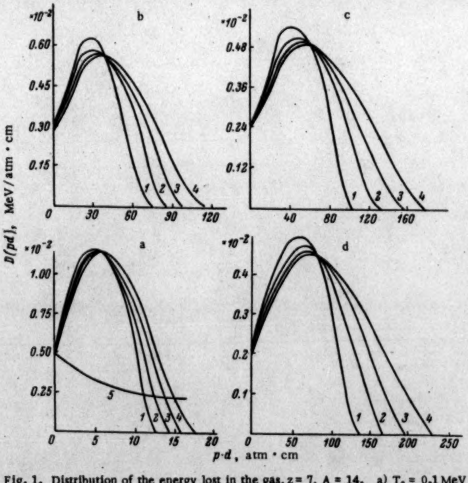

Fig. 1. Distribution of the energy lost in the gas, z = 7, A = 14. a) T_0 = 0.1 MeV for fields eE/p, keV/atm · cm: 1) 0, 2) 0.965, 3) 1.75, 4) 2.82, 5) 30 (nonscattering medium); b) T_0 = 0.3 MeV; eE/p, keV/atm · cm: 1) 0, 2) 0.774, 3) 1.29, 4) 1.8; c) T_0 = 0.4 MeV; eE/p, keV/atm · cm: 1) 0, 2) 774, 3) 1.29, 4) 1.8; d) T_0 = 0.5 MeV; eE/p, keV/atm · cm: 1) 0, 2) 0.7, 3) 0.9, 4) 1.61.

In a previous paper[6] using the section model method we have solved the problem of the transport of fast electrons in a material in the presence of an electric field. The method enables us to calculate the trajectory differential flux I(x, T, cos θ) at a depth x, which is expressed in terms of the energy differential flux φ(x, T, cos θ) by the equation $I = \varphi B$, where $B = B(T)$ are the specific energy losses. In the present work we have calculated the distribution of the energy lost by the electrons D(x) in terms of I(x, T, cos θ) using the following equation:

$$D(x) = 2\pi \int_0^{T_0} dT \int_{-1}^{1} d\cos\theta\, |1 - eEB^{-1}(T)\cos\theta|^{-1}\, I(x,\ T,\ \cos\theta), \tag{1}$$

where T is the kinetic energy of an electron, θ is the angle between the x axis and the direction of the electron momentum, and eE is the force on an electron from the field side.

Figure 1 shows the results of numerical calculations in accelerating fields (irradiation from the cathode side) for different values of eE/p for a single incident electron. It follows from the figure that for fields up to eE/p = 2.8 keV/atm · cm the ionization distribution remains very nonuniform, and only in the region of the extremum is the distribution practically uniform. As E is increased, the value of the electron mean free path increases and also the energy retained by the electron in the gas, for example, the area under the curve of the energy lost for $T_0 = 0.5$ MeV for eE/p = 1.61 keV/atm · cm is greater than that for eE = 0 by a factor of 1.44. This of course only holds in the small-time region, so long as there has been no considerable redistribution of the field.

For high field strengths, when eE > B, the main part of the electrons will be in the accelerating field and will travel along the field. However, not all electrons will behave in this way, since some of them will be scattered at large angles and will find themselves in a retarding electric field. The limiting case occurs when the scattering can be neglected and the energy of the electrons T as a function of the depth is given by the nonlinear equation

$$\frac{dT}{dx} = eE - B(T), \tag{2}$$

then D(x) = B[T(x)]. Curve 5 of Fig. 1a gives the distribution of lost energy obtained in this way for eE/p = 30 keV/atm · cm.

Hence, in a uniform field the lost energy distribution as E increases changes from the curves shown in the figure into D(x) = B[T(x)].

The specific ionization ψ, produced by a beam with a current density j A/cm^2 in a gas at a pressure of p atm, can be calculated in terms of D from the equation ψ (ion pairs · cm^{-3} · sec^{-1}) = $jDe^{-1}\varepsilon^{-1}$, where ε is the mean energy of ion pair formation.

The authors thank G. P. Mesyats for suggesting the problem and for useful discussion, and V. V. Kremnev for fruitful comments.

---

[1] B. M. Koval'chuk, V. V. Kremnev, and G. A. Mesyats, Dokl. Akad. Nauk, SSSR, 191, 76 (1970) [Sov. Phys. – Dokl., 15, 267 (1970)].

[2] G. N. Basov, É. M. Belenov, V. A. Danilychev and A. F. Suchkov, Kvant. Elektron, 3, 121 (1971) [Sov. J. Quant. Eletron., 1, 306 (1971)].

[3] L. P. Babich, Zh. Tekh. Fiz., 27, 1617 (1972).

[4] L. V. Spencer, Phys. Rev., 98, 1597 (1955).

[5] A. A. Vorob'ev, O. B. Evdokimov, and B. A. Kononov, in: High-Dose Dosimetry (in Russian), FAN (1966), p. 216; Izv. TPI, 143, 70 (1966); O. B. Evdokimov, Izv. Vuzov, Fizika, No. 1, 17 (1973).

[6] O. B. Evdokimov and A. P. Yalovets, Izv. Vuzov, Fizika, No. 10, 32 (1973).

Ionization and recombination coefficients in a discharge excited by fast electrons

Yu. I. Bychkov, Yu. D. Korolev, and A. P. Khuzeev

Institute of Atmospheric Optics, Siberian Branch,
Academy of Sciences of the USSR

(Submitted November 27, 1972)
Zh. Tekh. Fiz., 44, 219-221 (January 1974)

The development of gas discharge initiated by a short beam of fast electrons is analyzed. Using current oscillograms it is possible to find the ionization and recombination coefficients; these coefficients have been measured in the range of electric fields of interest for ionization lasers.

Gas discharges excited by beams of fast electrons are used for noninductive switching of large current pulses[1,2] and for pumping a new class of lasers called electro-ionization lasers.[3-6] Gas lasers are usually filled with mixtures of CO, N_2, and He in various proportions for which ionization and recombination coefficients are not available; moreover, data on recombination are contradictory even for pure gases.[7] This situation presents serious difficulties, not only in quantitative calculations of discharge parameters, but also in qualitative interpretation of the observed processes. In this note we suggest a method of measuring the ionization and recombination coefficients and present the results obtained in the range of electric fields important for gas lasers.

In these experiments the discharge is started by injecting a nanosecond beam of electrons into a gap in parallel with which there is a capacitance C charged to a voltage U_0. Thus, the initial electron density n_0 in the discharge gap depends on the beam current. The discharge development depends on the condition prevailing in the gap;[8] however, a typical form for high densities $n_0 > 10^{12}$ cm^{-3} is fast settling of the cathode fall[2,4] whose value is a small fraction of the voltage U_0 applied to the gap. The current density j depends on the electron density in the positive column n:

$$j = env_-. \tag{1}$$

Here, e is the electron charge, and v_- is the drift velocity.

If the capacitance C is large enough so that $U(t) = U_0 =$ const during the growth of the discharge, the electron density can be easily found from carrier balance in the positive column:

$$\frac{dn}{dt} = (\alpha - \eta) v_- n - \beta n^2, \tag{2}$$

where α is the first Townsend coefficient, η is the sticking probability, and β is the recombination coefficient.

The solution of (2) has the form

$$n = n_{st} \frac{e^{(\alpha-\eta)v_- t}}{e^{(\alpha-\eta)v_- t} - 1 + \frac{n_{st}}{n_0}}. \tag{3}$$

The steady-state electron density n_{st} is found from the condition $dn/(dt) = 0$,

$$n_{st} = \frac{(\alpha - \eta) v_-}{\beta}. \tag{4}$$

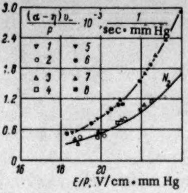

Fig. 1. The function $(\alpha - \eta)v_-/p$ for nitrogen and $CO_2 : N_2 = 1:1$ mixture; p = 4.8 (1), 3.4 (2), 2.4 (3), and 1 (4) atm (nitrogen); 4.5 (5), 3.3 (6), 1.9 (7), and 1 (8) atm (mixture).

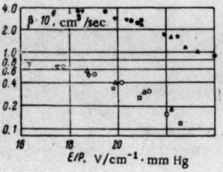

Fig. 2. The function $\beta = \beta(E/p)$ for the same pressures as in Fig. 1.

Equations (3) and (1) describe the oscillograms of current flowing through the gap. By measuring the values of n_{st} and n_0 from the oscillograms it is possible, from the best fit between the theoretical and experimental curves, to determine $(\alpha - \eta)v_-$ and hence, from (4), β.

The validity of this approach has been carefully checked for nitrogen for which α and v_- are known. Figure 1 shows the function

$$\frac{(\alpha - \eta) v_-}{p} = f\left(\frac{E}{p}\right)$$

plotted from the data of ref. 8, and experimental points obtained by the method described above. The figure also shows the variation of the ionization coefficient for the mixture $CO : N_2 = 1:1$. It is evident that the ionization coefficient in nitrogen in the mixture is higher than in pure nitrogen. This is due to the fact that for equal values of E/p the ionization coefficient of pure CO_2 is higher even if the breakdown voltages of both gases are approximately equal. The ionization coefficient of the mixture decreases more rapidly with decreasing E/p, which is probably due to sticking to CO_2 molecules.

Figure 2 shows the functions $\beta = \beta(E/p)$. The value $\beta \sim 10^{-6}$ cm^3/sec indicates that dissociative electron–ion recombination takes place in the discharge.

The authors thank G. A. Mesyats for proposing the topic and for discussion.

---

[1] B. M. Koval'chuk, V. V. Kremnev, and G. A. Mesyats, Dokl. Akad. Nauk SSSR, 191, 76 (1970) [Sov. Phys.—Dokl., 15, 267 (1970)].

[2] B. M. Koval'chuk, V. V. Kremnev, G. A. Mesyats, and Yu. F. Potalitsyn, Prikl. Mekh. Tekh. Fiz., 6 (1971).

[3] N. G. Basov, É. M. Belenov, V. A. Danilychev, and A. F. Suchkov, Kvantovaya Elektron., 3, 121 (1971) [Sov. J. Quant. Electron., 1, 306 (1971)].

[4] N. G. Basov, É. M. Belenov, V. A. Danilychev, O. N. Kerimov, I. B. Kovsh, and A. F. Suchkov, ZhETF Pis. Red., 14, 421 (1971) [JETP Lett., 14, 285 (1971)].

[5] C. A. Fenstermacher, W. T. Leland, M. J. Mutter, J. P. Rink, and K. Boyer, Seventh Intern. Quantum Electronics Conf., Montreal, May, 1972.

[6] G. A. Mesyats, Yu. I. Bychkov, V. V. Kremnev, Yu. D. Korolev, Yu. A. Kurbatov, and V. V. Savin, Preprint IOA CO AN SSSR, No. 3 (1972).

[7] I. MacDaniel, Collision Processes in Ionized Gases [Russian translation], Izd. Mir, Moscow (1967).

[8] V. L. Granovskii, Electrical Current in Gases [in Russian], Izd. Nauka, Moscow (1971).

Peak current in a cold-cathode magnetron

I. M. Vigdorchik and V. P. Timofeev

Institute of Radio Physics and Electronics,
Academy of Sciences of the Ukrainian SSR, Khar'kov

(Submitted February 19, 1973)
Zh. Tekh. Fiz., 44, 221-223 (January 1974)

The voltage–current characteristics of magnetron diodes with cold secondary emission platinum cathodes are analyzed. It is shown that the anode current is proportional to the Langmuir current. The coefficient of proportionality, which is independent of the geometric parameters of the diodes, is obtained and is approximately equal to 0.08. This relation can be used to calculate the peak anode current in cold-cathode magnetron devices.

The important part played by the secondary-emission properties of the cathode of magnetrons has led to attempts to construct devices which operate entirely with secondary electrons.[1–3] To do this, magnetrons have been constructed (see, for example, ref. 3), which have keep-alive electrodes at the ends of the main (uncooled) cathode; these provide the initial current. Sometimes the main cathode heater is turned off after intense oscillation has started. These designs lead to problems of the thermal balance of the device, which have not so far been solved.

One of the solutions of this problem is to design a magnetron in which the main cathode is cooled (for example, with water), and is made of a material which has a secondary emission coefficient in the cold state $\delta > 1$. A small initial current is produced by a heated cathode, remote from the magnetron interaction space, and placed at the end of the main cathode. This not only avoids electron bombardment of the heated emitter, increasing the useful life or the device, but also provides smooth control of the current injected into the interaction space; under certain conditions the magnetrons can be amplitude modulated.

A study of the effect of the secondary emission coefficient of the material of the main cathode on the operation of magnetron devices, the nature of the voltage–current characteristics, and the value of the oscillatory power gives the following main results. We have been able to establish a relation between the maximum secondary emission coefficient of the cold cathode and the output parameters of the magnetron oscillator. It is found that the voltage–current characteristics of magnetron devices with secondary emission cold cathodes have sharp peaks. An increase in the anode voltage U_a leads to an increase in the anode current up to a certain maximum value I_{am}, followed by a sharp decrease in current to very small values, of the order of the initial thermionic emission current, for values of U_a greater than the critical value.[5] The geometric position of the points of maximum current for different magnetic field intensities H forms the maximum current boundary (MCB). Both in magnetron oscillators and in diodes the maximum current boundary is close to a straight line. The slope and positions of this line depend on the secondary emission coefficient of the material of the main cathode. When the maximum secondary emission coefficient δ_m is increased, the value of I_{am} also increases, and the maximum current boundary shifts towards currents

$$I_{am} = \text{const}\,(\delta_m - 1). \tag{1}$$

When investigating the characteristics of pulsed magnetrons with a cold cathode it is found[6] that I_{am} depends linearly on the product EH (E is the electric field in the anode–cathode gap), and the effect of the geometric parameters of the magnetron device on the maximum anode currents is also considered.[7,8]

The purpose of the present investigation is to study the dependence of the maximum current boundary on the external fields (U_a, H) and the geometric parameters of the tube, and also to investigate the divergence from linear behavior of the maximum current in the case of a magnetron diode with a side thermionic cathode and a cold main cathode of a pure metal, namely, platinum ($\varepsilon_m \approx 1.8$).

Along the axis of a copper anode we place a cathode coated with platinum foil (thickness 0.05 mm) which is cooled with water. At the end of the anode block we place an L-type thermionic cathode. The magnetron diodes are supplied from a pulsed modulator. The anode voltage pulse length is 0.5 μsec, and the pulse frequency is 200 Hz. Inside the sealed-off device a vacuum of the order of 10^{-7} mm is maintained with the help of a getter pump.

A typical curve of the anode current of the pulsed magnetron diode against the anode voltage is shown in Figs. 1 and 2. As can be seen from the figures, the maximum current boundary (the dashed curve) is close to a straight line, as has been previously noted.[5,7]

To determine the functional dependence of the maximum current on the anode voltage the results of the measurements are processed using the method of least squares,[9] and we also draw a graph of I_{am} against U_a on a logarithmic scale (Fig. 3). It can be seen that the maximum anode current of the diode for a given magnetic field is proportional to $U_a^{3/2}$ (the deviation from this relation is less than 5% and may be due to experimental errors):

$$I_{am} = \text{const}\,U_a^{3/2}. \tag{2}$$

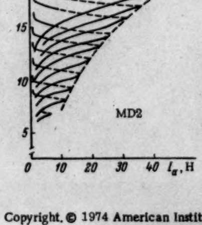

Fig. 1. Voltage–current characteristic of a magnetron diode with a cold main cathode of platinum (D_a = 4.9 mm, and D_k = 2.8 mm). The magnetic field varies from 3660 to 5500 Oe.

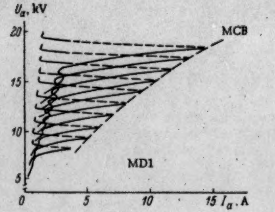

Fig. 2. Voltage–current characteristic of a magnetron diode with a cold main cathode of platinum (D_a = 4 mm, and D_k = 1.65 mm). The magnetic field varies from 3660 to 5670 Oe.

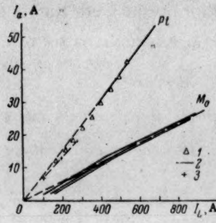

Fig. 4. Maximum anode current against the Langmuir current in magnetron diodes with a cold cathode of platinum and molybdenum. 1) Our data; 2) data from ref. 5; 3) data from ref. 7.

The results obtained can be given a clear physical meaning by relating the value of the limiting current to the Langmuir current, the characteristic parameter of the conventional diode operating under space-charge limited conditions. In fact, when considering the kinematic model of a magnetron diode, for example in ref. 10, it is shown that under space-charge conditions when $H/H_{cr} \rightarrow 1$ (H_{cr} is the critical magnetic field for given U_a), the anode current in a cylindrical magnetron diode under static conditions has a value of approximately $0.08 I_L$, where I_L is the Langmuir current

$$I_L = \frac{14.6 \cdot 10^{-6} U_a^{3/2}}{\frac{D_a}{2\beta^2}} l_a \tag{3}$$

(l_a is the anode length, and β^2 is a function of the ratio of the anode diameter D_a and the cathode diameter D_k).

In magnetron devices with a cold secondary-emission cathode the point of maximum anode current corresponds to operation of the tube with $H/H_{cr} \rightarrow 1$.

By comparing the above considerations and the data of previous investigations [Eqs. (1) and (3)] with the results obtained given by Eq. (2), we can state that the maximum anode current in magnetron diodes with a cold cathode is proportional to the Langmuir current:

$$I_{am} = k(\delta_m - 1) I_L. \tag{4}$$

For comparison we consider the behavior of the curves $I_{am} = f(I_L)$ constructed using the data in refs. 5 and 7, in which pulsed magnetron diodes with cold secondary-emission cathodes of pure metal are investigated. As can be seen from Fig. 4, the maximum current boundaries corresponding to tubes with different geometries lie close to two straight lines, the slope of which is determined by the value of the secondary emission coefficient of the material of the main cathode. The departure from linear behavior in percentage terms on average does not exceed the overall measurement error. The same figure shows the position of the maximum current boundary of one of the magnetron diodes of our geometry with a cold cathode of platinum, and also using the data given in ref. 7. The value of k in all three cases is approximately 0.08.

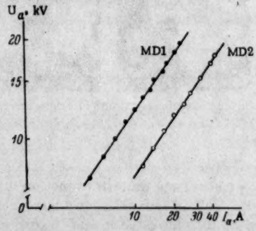

Fig. 3. Maximum current in a logarithmic system of coordinates.

According to preliminary data the relation given by Eq. (4) is also obtained for an anode current close to the maximum, the value of k in this case being less and also not constant, becoming a function of the ratio H/H_{cr}. The physical interpretation of this phenomenon, in our opinion, is that the value of the diffusion flow of electrons to the anode is mainly determined by the magnetic field, i.e., the ratio H/H_{cr}.

The results which have been obtained here enable us to carry out practical calculations of the maximum anode current I_{am} in a magnetron with a cold cathode, if we choose the material of the cathode δ_m and the mode of operation of the device U_a. The error involved according to our data on average is not greater than 10%.

Equation (4) obtained above should be useful in the construction of magnetron oscillators.

---

[1] J. B. Fisk, H. D. Hagstrum, and P. L. Hartman, Bell Syst. Tech. J., 25, 167 (1946).

[2] S. Ya. Braude and I. E. Ostrovskii, Izv. Akad. Nauk SSSR, 10, 65 (1946).

[3] G. B. Collins, Microwave Magnetrons, McGraw-Hill (1948).

[4] I. M. Vigdorchik, Author's Certificate No. 324937M, class HOIj 25/50, 8 Aug. 1947; I. M. Vigdorchik and M. S. Yanovskii, Author's Certificate No. 323837M, class HOZ c 1/00, 1 Dec. 1948.

[5] R. Jepsen and M. Muller, J. Appl. Phys., 22, 1196 (1951).

[6] J. R. Vaughan, in: Crossed Field Microwave Devices, E. Okress (ed.), Academic Press (1961).

[7] G. G. Sominskii and S. A. Fridrikhov, VRE, Elektronika, No. 3, 81 (1963).

[8] G. G. Sominskii, D. Terekhnin, and S. A. Fridrikhov, VRE, Elektronika, No. 10, 99 (1964).

[9] P. F. Fil'chakov, Numerical and Graphical Methods in Applied Mathematics (in Russian), Naukova Dumka, Kiev (1970).

[10] S. Ya. Braude, Zh. Eksp. Teor. Fiz., 5, 621 (1935); G. A. Grinberg, Selected Problems in the Mathematical Theory of Electrical and Magnetic Phenomena (in Russian), Akad. Nauk SSSR, Moscow–Leningrad (1948).

Effect of selenium and sulfur on the work function of tungsten

N. V. Volkov, Yu. K. Gus'kov, Z. N. Kononova, and Yu. I. Kostikov

(Submitted April 23, 1973)
Zh. Tekh. Fiz., 44, 224-225 (January 1974)

The effect of selenium and sulfur on the work function of tungsten has been studied. For sulfur a thermionic-emission method based on the total current as a function of the sulfur vapor pressure and the cathode temperature is used. For selenium, a field-emission microscope is used at selenium flux densities of 10^{10}-10^{16} atoms/cm^2 and at tip temperatures of 300-1700°K.

Adsorption of electronegative elements, e.g., oxygen and the halogens, on a tungsten surface significantly increases the work function (see e.g., refs. 1, 2). The only element of the oxygen group which has been used in detailed studies of the effect on the work functions of tungsten and other refractory metals is oxygen. There is definite interest in how other elements of this group (sulfur, selenium, and tellurium) affect the work function of refractory metals. The results of such experiments can be useful for studying the characteristics of thermionic converters.

We report here measurements of the work function of tungsten on which selenium and sulfur are adsorbed. The measurements are carried out with especially pure (99.997%) selenium and sulfur; before being placed in the experimental apparatus, these elements are redistilled in a high oil-free vacuum.

The work function of polycrystalline tungsten is studied in sulfur vapor by a thermionic-emission method on the basis of the total current; these experiments are carried out in a diode with working and protective anodes over the temperature range 1900-2400°K and at sulfur vapor pressures from 10^{-3} to 10^{-1} torr. The vacuum under the working conditions is of the order of 10^{-8} torr. An electric discharge (oil-free) pump is used for the vacuum. The work function measured for the tungsten before the sulfur is injected into the apparatus is 4.5 eV. Figure 1 shows the work function of tungsten as a function of the cathode temperature for various sulfur vapor pressures. We see that the work function of polycrystalline tungsten increases appreciably in sulfur vapor, to 5.3 eV (by 0.8 eV). The sensitivity of our apparatus is not adequate for measuring work functions above 5.3 eV, so we can not determine the ultimate change in the work function. Figure 1 also shows the change in the work function of polycrystalline tungsten at three oxygen pressures, according to the results of Batzies[3] and Greaves and Stickney.[4] A point which seems to deserve some attention is that the change in the tungsten work function corresponding to a change in the sulfur vapor pressure by half an order of magnitude is the same as that observed (at the same cathode temperature) when the oxygen vapor pressure is changed by 1.5 orders of magnitude (over the measured range).

We have studied the effect of selenium on the work function of tungsten in a field-emission microscope at selenium flux densities of 10^{10}-10^{16} atoms/(cm^2 · sec) and at tungsten-tip temperatures of 300-1700°K.

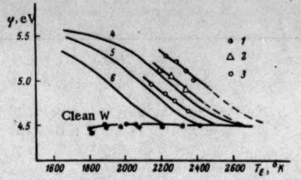

Fig. 1. Work function of tungsten in sulfur vapor as a function of the substrate temperature. Pressure p, torr: 1) 10^{-1}; 2) $5 \cdot 10^{-2}$; 3) 10^{-2}; 4) $1.4 \cdot 10^{-5}$; 5) $5 \cdot 10^{-7}$; 6) 10^{-8} (in an oxygen atmosphere).

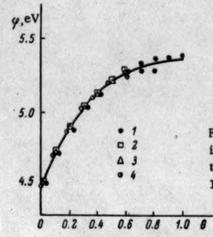

Fig. 2. Work function of tungsten during deposition of selenium for various tip temperatures. T_e, °K: 1) 300; 2) 1065; 3) 1225; 4) 1275.

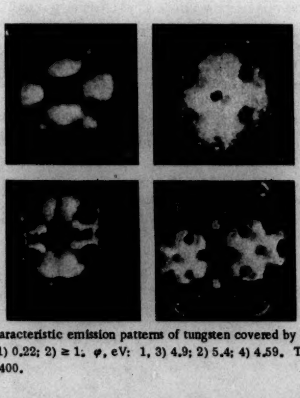

Fig. 3. Characteristic emission patterns of tungsten covered by a selenium film. θ: 1) 0.22; 2) ≥ 1. φ, eV: 1, 3) 4.9; 2) 5.4; 4) 4.59. T_e, °K: 1,2) 300; 3,4) 1400.

The experimental apparatus is evacuated and processed with a discharge pump. The working vacuum is 10^{-9} torr. Figure 2 shows the work function of tungsten found as a function of the selenium coverage. We see that the work function increases significantly as selenium is adsorbed. With a monolayer coverage the work function is increased by 0.9 eV, to 5.4 eV. Figure 3 shows how selenium is adsorbed on various tungsten faces. There is a predominant adsorption near the {112} faces. At coverages greater than a monolayer, small crystals form, but these crystals do not significantly change the work function of the tungsten tip. Selective adsorption of selenium leads to the appearance of large formations or large crystals near {112} faces at tip temperatures in the range 1400-1700°K. These formations reduce the work function of the tungsten tip to 3.8-3.9 eV; this effect is sensitive to the electric field intensity. When the tip is heated, the large crystalline formations vanish and the work function is restored to the value corresponding to the given degree of coverage.

---

[1] R. Gomer and J. K. Hulm, J. Chem. Phys., 27, 1363 (1957).

[2] C. W. Jonett and B. J. Hopkins, Surf. Sci., 22, 392 (1970).

[3] P. Batzies, Second International Conference on TEPG, Stresa, Italy, 1968.

[4] W. Greaves and R. E. Stickney, Surf. Sci., 11, 395 (1968).

Displacement of ion-current retardation curves in surface ionization in a strong field

N. I. Ionov
A. F. Ioffe Physicotechnical Institute,
Academy of Sciences of the USSR, Leningrad
(Submitted July 4, 1973)
Zh. Tekh Fiz., 44, 225-227 (January 1974)

In weak fields which accelerate ions the discontinuity on the retardation curves corresponds to the contact potential difference of the homogeneous emitter and collector, U_0. In surface ionization in a strong electric field which accelerates ions the quantity $U_0 = (V - \varphi') + (k/e)T\ln(\alpha/A)$ determined from the retardation curves is equal to the difference between the ionization potential of the particles ionized on the emitter surface, V, and the collector work function φ' and is also a function of the degree of ionization α (T is the emitter temperature, A is the pre-exponential factor in the Langmuir–Saha equation, k is the Boltzmann constant, and e is the ion charge). This equation can be used to determine the values of V from the experimental quantities U_0.

The retardation curves for the current of positive ions formed by surface ionization in a strong accelerating electric field are analyzed in ref. 1, but there is an error: The surface potential for ions at the collector is taken into account incorrectly. This error is repeated in ref. 2. In the present note we analyze the problem again, eliminating the error.

Figure 1 shows schematically the potential curve for an ion A^+ at the emitter surface with an external field $\mathcal{E} = 0$ (curve 1), for the case in which the ionization potential of the atom, V, is higher than the work function of the surface, φ. In the region $x > x_{cr}$ (where x_{cr} is the critical charge-exchange distance) the electronic interaction in the system of the adsorbed atom and the absorbent is cut off. In the region $x < x_{cr}$, the interaction between the adsorbed atom and the surface is primarily the chemical binding force; in the region $x > x_{cr}$ it is predominantly the electrostatic force of the polarization interaction. For ions in this latter case the predominant force is the Coulomb force of the mirror image. An external field $\mathcal{E}$ which accelerates ions (curve 2) and the surface field form a potential barrier (curve 3) which peaks at point x_0.

The behavior of the potential energy of ions at the surface of the collector is analogous, but the forces are in the opposite directions.

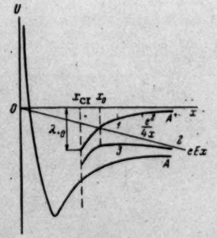

Fig. 1

The external field accelerating ions from the emitter is usually produced by an intermediate grid at a potential of $-U_g$ with respect to the collector. We denote by $\mathcal{E}_c$ the external field at the emitter surface which compensates the surface field throughout the region from $x = \infty$ to x_{cr}, and we consider the motion of ions from the emitter to the collector through the accelerating grid in two cases: 1) $\mathcal{E} < \mathcal{E}_c$ and 2) $\mathcal{E} > \mathcal{E}_c$.

1. $\mathcal{E} < \mathcal{E}_c$. Ions from the emitter surface pass above the potential barrier at x_0 with thermal velocities and move thereafter in the accelerating field between the emitter and the grid. The kinetic energy of the directional motion of the ions during passage through the grid is given by the following equation, which takes account of the contact potential difference:

$$E_1 = e\left(U_g - \mathcal{E}x_0 - \frac{e}{4x_0}\right) - \Delta(x_0) + e(\varphi_g - \varphi)$$

$$= e(U_g - \sqrt{e\mathcal{E}} + \varphi_g - \varphi) - \Delta(x_0). \quad (1)$$

Here, the term $\Delta(x_0)$ takes account of a possible deviation of the potential of the polarization forces from the Coulomb potential.[1,2]

The energy lost by an ion in the retarding field between the grid and the peak x_0' of the potential barrier at the collector (quantities referring to the collector are primed) is

$$E_2 = e(U_g - U - \sqrt{e\mathcal{E}'} + \varphi_g - \varphi') - \Delta(x_0'), \quad (2)$$

where U is the negative potential of the collector with respect to the emitter (supplied by an external source).

Above the barrier at x_0' the kinetic energy E_k of the directed motion of ions is

$$E_c = E_1 - E_2 = e(U + \varphi' - \varphi - \sqrt{e\mathcal{E}} + \sqrt{e\mathcal{E}'}) - \Delta(x_0) + \Delta(x_0'). \quad (3)$$

In an analysis of the ions on the basis of their initial energy the drift component of the energy is $E_k = 0$, so we find from (3),

$$eU_0 = e(\varphi - \varphi' + \sqrt{e\mathcal{E}} - \sqrt{e\mathcal{E}'}) + \Delta(x_0) - \Delta(x_0'). \quad (4)$$

If $\mathcal{E}$ and $\mathcal{E}'$ are relatively small (corresponding to ionization in a weak field), the quantity U_0 is equal to the contact potential difference between the emitter and the collector $U_0 = \varphi - \varphi'$. The same is true (within the difference between the correction terms Δ) when the emitter and collector form a plane capacitor in the center of which there is a plane grid.

Experiments on ionization in a strong field are usually carried out in an apparatus which is approximately a spherical capacitor, with a tip-shaped emitter. In this case $\mathscr{E}'$ and $\Delta(x_0')$ are negligibly small and Eq. (4) becomes

$$eU_0 = e(\varphi - \varphi' + \sqrt{e\mathscr{E}}) + \Delta(x_0). \tag{5}$$

When the initial ion velocities obey a Maxwell distribution, and the surfaces of the emitter and collector are homogeneous in terms of work function, the point with potential U_0 on the voltage–current curves $\log i = f(U)$ corresponds to the intersection of the two linear regions of the retardation curves (the ion-retardation region and the ion-saturation region). In the case of a constant flux of atoms (which undergo ionization) to the emitter surface, the quantity U_0 is related to the degree of ionization α, given by[1]

$$\alpha = A \exp \frac{1}{kT}\left[e(\varphi - V + \sqrt{e\mathscr{E}}) + \Delta(x_0)\right], \tag{6}$$

where T is the emitter temperature and A is the preexponential factor. The quantity α is a strong function of $\mathscr{E}$. Substituting $e\sqrt{e\mathscr{E}} + \Delta(x_0)$ from (6) into (5), we find

$$eU_0 = e(V - \varphi') + kT \ln \frac{\alpha}{A}. \tag{7}$$

If we choose the value of $\mathscr{E}$ in (6) so that $\alpha = A$, the second term in (7) vanishes at any T.

2. $\mathscr{E} > \mathscr{E}_c$. In this case $x_0 = x_{cr}$ and $e^2/4x_{cr} + \Delta(x_{cr}) = \lambda_{+0}$; the right side of this last equation is the work done against polarization forces over the entire range of these forces between x_c and $x = \infty$. Now, E_1 is not given by Eq. (1) but by

$$E_1 = e(U_c - \mathscr{E}x_{cr} + \varphi_g - \varphi) - \lambda_{+0}. \tag{8}$$

The value of E_2 for a spherical capacitor is again given by (2), where account must be taken of the conditions $e\sqrt{e\mathscr{E}'} \simeq 0$ and $\Delta(x_0') \simeq 0$. The equation analogous to (5) for eU_0 is

$$eU_0 = e(\varphi - \varphi' + \mathscr{E}x_{cr}) + \lambda_{+0}. \tag{9}$$

The degree of ionization $\mathscr{E} > \mathscr{E}_c$ is given by[1]

$$\alpha = A \exp \frac{1}{kT}\left[e(\varphi - V + \mathscr{E}x_{cr}) + \lambda_{+0}\right]. \tag{10}$$

Substituting $e\mathscr{E}x_{cr} + \lambda_{+0}$ from (10) into (9), we again find Eq. (7) for U_0.

Equation (7) differs from the equations obtained previously in the following: 1) There is no term λ'_{+0} (refs. 1,2) or $e^2/4x$ (ref. 3) in it; 2) Equation (7) takes into account the functional dependence of U_0 on α; 3) it holds for both small and large $\mathscr{E}_c$ and is not a function of the behavior of the surface potential at $x > x_{cr}$.

We assume above that the work functions φ and φ' are homogeneous over the emitter and collector surfaces. If the surfaces are inhomogeneous, the plot of the ion distribution as the function $\log i = f(U)$ will be nonlinear at small initial ion energies, and the distribution itself will be wider along the U axis. This question requires further analysis.

Equation (7) can be used in an experimental determination of the ionization potentials of particles being ionized, V, from the displacement of the retardation curves. If the retardation curves for ions of two different materials are measured under the same conditions, the relative displacement of these curves will be

$$e(U_{01} - U_{02}) = e(V_1 - V_2) + kT\left(\ln \frac{\alpha_1}{A_1} - \ln \frac{\alpha_2}{A_2}\right). \tag{11}$$

According to Eqs. (6) and (10), the value of α for ionization by a field is a very strong function of $\mathscr{E}$ in the region in which there is a change in the sign of the arguments of the exponential functions; this functional dependence is stronger, the smaller T. Accordingly, it is not difficult to experimentally choose $\mathscr{E}_1$ and $\mathscr{E}_2$ for which the second term in (11) is negligibly small. Then, knowing one of the values V, we can calculate the other from Eq. (11).

The displacement of the retardation curves for argon ions has been measured by Muller with $\mathscr{E}_1 = 1.3 \cdot 10^8$ V/cm and $\mathscr{E}_2 = 1.7 \cdot 10^8$ V/cm; it is $\Delta U_0 = U_{02} - U_{01} = 1.2$ V. A calculation from Eq. (5) yields a value only half as large: $\Delta U_0 = 0.6$ V. For inert gases ($V > 10$ V), the field desorbing the ions apparently satisfies $\mathscr{E} > \mathscr{E}_c$, so Eq. (9) should be used to evaluate this quantity.[2] The same equation can be used to evaluate x_{cr}, which we find (neglecting the functional dependence of λ_{+0} on $\mathscr{E}$) to be $x_{cr} = (\Delta U_0)/(\Delta\mathscr{E})$. According to the data given above for argon, we would have $x_{cr} = 3$ Å.

We note in conclusion that if the particles are ionized in the volume by the tunneling of an electron through the potential barrier of the particles which is "skewed" by the field (autoionization), the spatial position of the autoionization zone can be determined from the experimental retardation curves.

---

[1] N. I. Ionov, Zh. Tekh. Fiz., 39, 721 (1969) [Sov. Phys.–Tech. Phys., 14, 542 (1969)].

[2] É. Ya Zandberg and N. I. Ionov,, Surface Ionization [in Russian], Izd. Nauka, Moscow (1969).

[3] E. W. Müller, Adv. Electronics Electron Phys., 13, 83 (1960).

Investigation of the work function of a tungsten cathode after bombardment by inert-gas ions

P. N. Chistyakov, R. A. Milovanova, and V. V. Lytkin

Moscow Engineering Physics Institute

(Submitted March 26, 1973)
Zh. Tekh. Fiz., 44, 228-230 (January 1974)

It is found that the work function of a polycrystalline tungsten cathode is reduced by 0.2-0.25 eV after treatment by a high-current glow discharge in an inert gas (argon) in comparison with the standard value of φ obtained when the treatment is carried out in vacuum. A similar reduction in φ has been found earlier for a molybdenum cathode. The experimental results are explained by the variation in structure of the cathode surface and penetration of inert-gas ions of comparatively low energy (up to 250 eV) into the tungsten crystal lattice.

In earlier studies[1] the values for the work function φ obtained by the photoelectric method were compared for a polycrystalline molybdenum cathode after the following forms of treatment and purification: 1) ion bombardment in a high-current glow discharge, in an inert gas, with a pressure of units and tens of torr; 2) high-temperature heating due to the electron bombardment.

The values for φ obtained in the first case are 0.15-0.2 eV lower than in the second case, which is explained by the change in surface structure and the introduction of inert-gas ions (neon) into the molybdenum crystal lattice during the glow discharge.

Values of φ are obtained in ref. 2 for nickel, titanium, and the (001) and (110) faces of molybdenum after treatment of the cathodes by ion bombardment in a glow discharge with high current density. These values of φ are also considerably less (by 0.06-0.4 eV) than values attained in studies of other authors, where only vacuum treatment and purification of the cathode surfaces were used.

Oman and Dillon[3] have measured the work function of the (111) face of niobium using the photoelectric method. For well-annealed surfaces the work function is 4.66 eV. As a result of bombardment by argon ions, at energy 500 eV, current density 0.1 mA/cm^2, and times of 10 min and above, the work function is reduced to 4.09 eV.

Thus the effect of a reduction in the work function of a surface resulting from bombardment of inert-gas ions has been established for various metals.

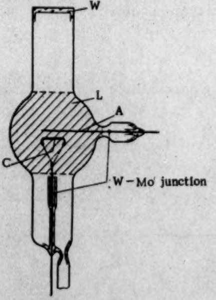

Fig. 1

The present study is a continuation of investigations carried out earlier in the laboratory of Moscow Engineering Physics Institute on the work functions of clean metal surfaces after their treatment by a high-current glow discharge in inert gases, and has been carried out for tungsten.

Tungsten, like molybdenum, is a metal for which the work function obtained in vacuum is known with good accuracy. In particular, the values of φ usually obtained for polycrystalline samples by the method of thermionic emission are in the range 4.5-4.6 eV, with the mean values being in the range 4.52-4.54 eV.

The values of φ are determined using devices of two kinds. In the first kind the principal treatment and purification of the cathodes are by a high-current glow discharge in an inert gas (argon) in a sealed-off device. The experiment with the second type of device is carried out entirely in a vacuum apparatus. The principal forms of treatment and purification of the cathode are both direct annealing in vacuum and also treatment by a high-current glow discharge in an inert gas.

Figure 1 shows the first kind of device with a plane cathode 20 mm in diameter and 0.05 mm thick. The cathode, the holders, and the principal rod, to which they are fastened, are made of tungsten. The anode is a tungsten rod 0.8 mm in diameter. To measure the spectral characteristic of the photocurrent, we direct ultraviolet light through the quartz window W onto the cathode surface.

The treatment of the device at the vacuum station consists of heating the entire device up to 400°C with a vacuum better than 10^{-5} torr, then annealing the cathode with a high-frequency current up to 1500-1700°C, first at a vacuum of order 10^{-6} torr, and after a 4-6 h annealing, the vacuum at the maximum temperature was $4-9 \cdot 10^{-7}$ torr. Next, the devices are filled with argon at pressure 4-7 torr, and the cathodes are treated with a high-current glow discharge with mean current 100-150 mA ($j = 15-25$ mA/cm^2) for 2-3 h. The argon in the system varies by a factor of 2-3 as required. During this treatment the tungsten is intensely sputtered and is deposited on the walls of the bulb of the device (layer L, Fig. 1). The normal cathode drop U_d falls in proportion to the purification of the cathode by ion bombardment in a glow discharge from 170-180 to 112-115 V. Next, the devices are sealed off from the vacuum station at an argon pressure of 12 torr.

The treatment of the cathodes by a glow discharge with mean current density 40-50 mA/cm^2 is continued in the sealed-off devices until stable and reproducible values of U_d are established; at an argon pressure of 12 torr this is 113 ± 1 V for 12 identical devices.

In addition to control of the purity of the cathode surface and gas based on the magnitude of U_d, which allows us to determine the presence of adsorbed atoms of noninert gases on the cathode surface, there is also control of the cathode surface based on post-discharge (exoelectron) emission.[4] This method allows us to determine the presence on the metal surfaces of thin films or local inclusions of dielectrics and semiconductors. Measurements show that the currents do not exceed 10^{-19} A and the decreases in time that are characteristic for post-discharge emission are not observed. Thus, there is no post-discharge emission, and the measured background current, fixed in time, can be attributed to cosmic radiation and terrestrial radioactive sources. This current has repeatedly been measured in our laboratory.

After the treatment the tungsten-cathode surface can be assumed to be atomically pure based both on the agreement among the quantities U_d for all 12 devices and on the absence of post-discharge emission.

Next, the spectral characteristics of the tungsten-cathode photocurrents are measured. A DMR-4 monochromator and a DVS-25 hydrogen lamp are used. The photocurrent in the gas medium is measured, just as in the entire series of studies beginning with ref. 1, by a statistical method of pulsed breakdown based on the mean statistical delays of the gas breakdown.

Processing the spectral characteristics according to the Fowler–Dubridge method gives an average value of the work function for 12 devices for a polycrystalline tungsten surface after ion bombardment in a high-current glow discharge in argon of 4.42 ± 0.02 eV. This value of φ is obtained for cathodes made from two samples of tungsten ribbon with impurity content no greater than 0.03%.

In the second type of device the cathode is made in the form of a tungsten strip 3 mm wide, with the length of the plane working part equal to 10 mm and the thickness 0.05 mm; direct heating by a current up to high temperatures and treatment by a high-current glow discharge in an inert gas are both allowed. The device is heated with pumping at the vacuum station up to 400°C with a system residual pressure no higher than 10^{-5} torr; then, for 15 h the cathode is annealed by a current up to a temperature 2500°C with a vacuum of order[1)] 10^{-7} torr. The device is then filled with spectroscopically pure argon and it is further purified using a titanium and molybdenum purifier. The value of φ measured after high-temperature heating of the cathode is 4.62 eV; then the argon is pumped, the cathode is again annealed up to a temperature of 2000°C for a vacuum of $2 \cdot 10^{-7}$ torr (in the same experimental device in which the Ti and Mo getters were evaporated, the vacuum was considerably greater), after which argon is admitted and the value $\varphi = 4.6$ eV is measured. This result, attained without treating the tungsten cathode with a high-current glow discharge, has been repeated several times.

Treatment of the cathode by a glow discharge in argon at a pressure of 12 torr with a current density of 18 mA/cm^2 for 2 h does not noticeably change φ; however, increasing the current density to 24 mA/cm^2 ($I = 150$ mA) and treatment of the cathode for 1 h reduces φ to 4.4 eV, and for a current density $j = 32$ mA/cm^2 ($I = 200$ mA) after 5 min of treatment, φ is decreased to 4.35 eV.

The reduction in tungsten-cathode work function that is found can be explained by the change in structure of its surface and introduction of argon ion into the tungsten crystal lattice. The latter effect is usually investigated at higher ion energies; for example, Collingon and Leck[5] noted that with bombardment of tungsten by 1-keV argon ions, the mean depth of ion penetration into the metal is 5 Å. In our experiment the cathode potential drop in the glow discharge is 180-250 V for a peak value of the current density of 70-100 mA/cm^2. In this case for a cathode temperature of about 1300°C the gas near the cathode is strongly evacuated and a certain fraction of the ions are incident on the cathode with an energy close to the total energy: 180-250 eV. As is shown by the results of this experiment, a fraction of the argon ions are introduced into the tungsten crystal lattice even at the energies being considered here.

[1)] The post-discharge emission is practically absent for all stages of the latter cathode treatment.

---

[1] P. N. Chistyakov and R. A. Milovanova, Zh. Tekh. Fiz., 31, 746 (1961); 42, 2161 (1972) Sov. Phys.–Tech. Phys., 6, 538 (1961); 17, 1707 (1973)].

[2] R. A. Milovanova and P. N. Chistyakov, Zh. Tekh. Fiz., 33, 356 (1963); Proc. Seventh International Conference on Phenoména in Ionized Gases, Vol. 1, Belgrade (1965), p. 216; Physical Electronics, Proc. Moscow Engineering Physics Institute (MIFI), No. 3 (1966), p. 44.

[3] R. Oman and J. Dillon, Surf. Sci., 2, 227 (1964).

[4] P. N. Chistyakov, Zh. Tekh. Fiz., 33, 1395 (1963)[Sov. Phys.–Tech. Phys., 8, 1037 (1964)].

[5] J. Collingon and J. Leck, Trans. Eighth Nat. Vac. Symp., Second Int. Congress, Vol. 1 (1962), p. 275; Sorption Processes in a Vacuum [in Russian], Atomizdat, Moscow (1966), p. 18.

Switching characteristics of a discharge in water

V. M. Kuleshov, S. L. Nedoseev, V. P. Smirnov, and A. M. Spektor

(Submitted March 5, 1973)
Zh. Tekh. Fiz., 44, 230-232 (January 1974)

The switching characteristics of discharge gaps are studied in water as a function of the characteristic impedance of the shaping line ρ_s over the range 2.5-30 Ω. A line with an electrical length of 50 nsec is charged to $\nless$ 120 kV. Most of the experiments are carried out at fields up to 10^6 V/cm. The minimum rise time, $\tau_r \simeq$ 7 nsec, and the maximum rate of current increase, $I/\tau_r \simeq 10^{12}$ A/sec, are detected with ρ = 13 Ω. Up to 50% of the energy stored in the line is absorbed in the switch during a pulse. The operation remains qualitatively the same with a voltage of 400 kV on a line with ρ = 15 Ω.

The very good insulating properties of pure distilled water, which have been demonstrated on several occasions,[1,2] have been exploited in the design of high-power miniature shaping lines. Switches in which the breakdown occurs in water would be obvious candidates for use as switches with water lines. The possibility of using such switches was first raised in ref. 3. The present lack of a theory describing breakdown in water with high input-power levels complicates the practical use of water switches. Little experimental information has been reported. Alkhimov et al.[4] report the existence of a gaseous sheath around the streamer propagating from the anode toward the cathode. We can evidently expect similarities between the characteristics of water and gas switches at high gas pressures. It is difficult to obtain fast current rises, with $dI/(dt) \sim 10^{13}$ A/sec, with single-channel gas switches, so multichannel switches must be used for switching low-resistance shaping lines with water insulation. We report here a study of the pulse shape as a function of the characteristic impedance of the line being switched, carried out in order to choose the appropriate number of channels.

We have studied the characteristics of self-breakdown switches in water using shaping lines with an electrical length of τ_e = 50 nsec and characteristic impedances from 2.5 to 30 Ω. A line consisting of two strips 700 × 70 × 2 mm in size is placed in a distilled-water bath (the resistivity of the water is 200-400 kΩ · cm). The line is charged to 70-120 kV in $T \leq 0.5$ μsec. The maximum charging current at the time at which the line switch operates is below 1 kA. The radius of the hemispherical electrodes of the switch is 0.8 cm and the gap between the electrodes is varied from 1 to 1.5 mm. The charging voltage and pulse shape are monitored by a resistive divider with a resolving time of 2-3 nsec located at the open end of the line. The resistance of the divider is much higher than the characteristic impedance of the line. Most of the measurements are carried out with ρ = 2.5, 13, and 30 Ω.

The breakdown occurs at a field $\sim 10^6$ V/cm. The breakdown can be arranged to occur at the peak of the charging voltage or after it by adjusting the gap. Accordingly, the overvoltage on the switch can be adjusted. Figure 1 shows typical oscillograms of the voltage pulses. From these U(t) curves we can distinguish two stages in the development of the breakdown. In the first stage, the voltage increases rapidly to 0.5-0.8 of the peak pulse amplitude. In the second stage the voltage increases slowly, nearly to the peak value. From the circumstance that the current increase in the first stage is governed by both the inductance of the breakdown channel, L, and its resistance, R, we find $L < 10^{-8}$ H. Assuming that there is only a single breakdown channel and that its radius is a weak function of the time,[5] we can assume $dL/dt \nless 0$. Then, from the oscillograms in Fig. 1 we can easily determine R(t), the energy dissipated in the switch Q, and the efficiency of the switch switching a single shaping line with a stored energy W:

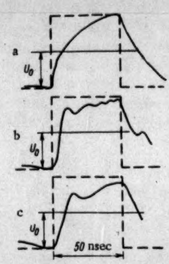

Fig. 1. Shape of the voltage pulse at the end of the open line. ρ, Ω: a) 2.5; b) 13; c) 30. Here U_0 is the charging voltage.

$$\eta_1 = \frac{W - Q}{W}.$$

We note that the value of Q/W for a double shaping line is half as large if $R(t)/\rho \ll 1$ at $t = \tau_e$. The values of τ_r, η, and I/τ_r obtained from Fig. 1 are shown in Table 1. Figure 2 shows the function R(t) for the same conditions.

The overvoltage strongly influences the pulse shape, as is evident from Fig. 3. In the "undervoltage" regime (Fig. 3b), the channel resistance oscillates rapidly, and at times the current in the channel vanishes; it reappears after a second breakdown. This behavior implies that the

TABLE 1

ρ_{ie}, Ω	U_{cha}, kV	τ_0, nsec	η_1, %	I/τ_0, A/sec
2.5	70	33	50	$5 \cdot 10^{11}$
13	100	7	50	10^{12}
30	100	12	50	$1.2 \cdot 10^{11}$
DFL, $\rho = 15$ Ω	400	22	$\eta_2 = 75\%$	$1.2 \cdot 10^{12}$

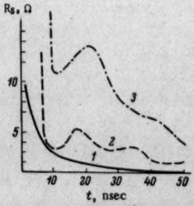

Fig. 2. Resistance of the breakdown channel of the switch as a function of the time. ρ, Ω: 1) 2.5; 2) 13; 3) 30.

pulse shape is a strong function of the electric field. In several experiments we have connected an additional line with an electrical length $\tau = 0.1\tau_e$ and with $\rho = 0.1\rho_e$ in parallel with the switch to improve the rising edge and shape of the pulse. Presumably the rising edge would improve with an increase in the energy fed to the channel in the first stage of the operation. However, this improvement turns out to be negligible, as can be seen by comparing Figs. 3b and 3c. This type of operation is unsuitable because the energy stored in the auxiliary line is approximately equal to that stored in the main line.

The scatter in the breakdown times of the switch, $\Delta\tau$, is a function of the overvoltage. If the breakdown occurs at the voltage equal to the peak of the charging voltage, $\Delta\tau$ is usually of the order of 50 nsec. Reducing this spread is an important consideration for multichannel switches in water, so we have carried out experiments with trigatron ignition in an attempt to reduce $\Delta\tau$. In these experiments the ignition pulse has a rise time of 1-2 nsec, a length of 40 nsec, and a power of up to $5 \cdot 10^7$ W. As expected, the rise time and shape of the pulse are essentially unaffected, but $\Delta\tau$ is approximately halved.

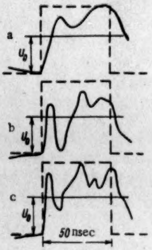

Fig. 3. Shape of the voltage pulses in a 30 Ω line. a) Breakdown with increasing voltage on the switch; b) breakdown with decreasing voltage on the switch; c) breakdown of a switch connected to a correcting line.

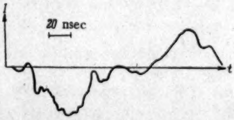

Fig. 4. Shape of the current pulse from the short-circuited double shaping line. $\rho = 15\ \Omega$, $U_0 = 400$ kV.

The characteristics of the water switch with spherical electrodes are qualitatively the same when voltage pulses at amplitudes up to 400 kV are switched. Figure 4 shows an oscillogram of the current in a short-circuited strip-type double shaping line of the Neptun accelerator with $\tau = 40$ nsec and $\rho = 15\ \Omega$ at U = 400 kV. Under these conditions we find $I/\tau_r \simeq 1.2 \cdot 10^{12}$ A/sec and $\eta_2 \simeq 75\%$, in satisfactory agreement with the data in the accompanying table for $\rho = 13\ \Omega$. The value of $\tau_r \simeq 20$ nsec can be reduced to ~ 10 nsec by increasing the overvoltage. However, this type of operation is energetically unfavorable. Since the transmitted power per unit length of the channel is $E(U/\rho)$ (where E is the electric field in the gap), we can expect to reduce the relative loss in the switching of high-power lines.

When Rogowski electrodes 70 mm in diameter are used in the switch, the discharge develops from a single point on the anode along several channels, according to the erosion tracks on the electrodes.

We note in conclusion that in our experiments on the switching of a line with $\emptyset = 70\ \Omega$ the use of multichannel water switches improves the rising edge of the pulse.

The authors thank E. K. Zavoiskii and K. I. Tarakanov for their support of this work and G. P. Maksimov for assistance in constructing the experimental apparatus.

---

[1] V. M. Lagunov, Dissertation [in Russian], IYaF SO AN SSSR, Novosibirsk (1969).

[2] O. P. Pecherskii, A. M. Sidoruk, V. D. Tarasov, and V. A. Tsukerman, Dokl. Akad. Nauk SSSR, 192, 1266 (1970) [Sov. Phys. – Dokl., 15, 594 (1970)].

[3] G. A. Mesyats and G. A. Vorob'ev, Izv. VUZ. Fiz., No. 3, 21 (1962).

[4] A. P. Alkhimov, V. V. Vorob'ev, V. F. Klimkin, A. G. Ponomarenko, and R. I. Soloukhin, Dokl. Akad. Nauk SSSR, 194, 1052 (1970) [Sov. Phys. – Dokl., 15, 959 (1971)].

[5] S. I. Braginskii, Zh. Eksp. Teor. Fiz., 34, 1548 (1958) [Sov. Phys. – JETP, 7, 1068 (1958)].

Reversibility of chalcogenide materials in holography

S. B. Gurevich, N. N. Il'yashenko, B. T. Kolomiets, V. M. Lyubin, and M. V. Sukharev

A. F. Ioffe Physicotechnical Institute,
Academy of Sciences of the USSR, Leningrad

(Submitted June 1, 1973)
Zh. Tekh. Fiz., 44, 232-234 (January 1974)

The reversibility of glassy chalcogenide semiconducting films is studied on the basis of the relative transmission and the diffraction efficiency. The amplitude contrast is unaffected by cyclic heat treatment, which erases the recorded information, while the diffraction efficiency falls off rapidly after the first cycle. The extent of this decrease is largely a function of the film composition. It is concluded that these films, made from the appropriate materials, can be used as reversible media in holography.

An important property of glassy chalcogenide semiconductors (GCS) as media for holography is their reversibility, i.e., information can be recorded, read out, and erased repeatedly.[1-5] The conclusion that these materials are reversible is reached through a study of the change in the relative transmission of a laser beam by films of these materials before and after erasure.[1-5] Of importance for holography is not only the amplitude recording, which results from a change in transmission, but also the phase recording, which results from a change in the path difference for light rays; in the case of the GCS, there is a change in the refractive index of the material. The basic parameter of this amplitude–phase recording is chosen to be the diffraction efficiency of the holograms stored in GCS films.

We report here a joint study of the reversibility of GCS films on the basis of their relative transmission and diffraction efficiency. We use GCS films of the As–Se and As–Se–I systems obtained by deposition in vacuum on silicate glass substrates. The experiments involve a repeated recording and erasure of spots, produced by irradiating the material with an unmodulated laser beam, and they involve recording and erasing holograms (two-beam diffraction gratings). The relative transmission τ/τ_0 and the diffraction efficiency η are recorded as functions of the exposure time t. The recording and readout are achieved with an LG-36 He–Ne laser (λ = 6328 Å). In erasure the sample is placed in a thermostat and held for 10 min at a temperature from 150 to 190°C, depending on the composition of the material. After the recorded diffraction grating is erased, the residual diffraction efficiency is measured, and a new diffraction grating is recorded in the same place. In addition, analogous spots and holograms are periodically recorded in previously unexposed regions.

The experiments show that the behavior of the blackening curve as a function of the time is not affected, within the experimental error (± 10%), after erasure–recording cycles, but the diffraction efficiency falls off rapidly after the first erasure, remaining approximately constant thereafter.

Figure 1 shows illustrative plots of the relative transmission τ/τ_0 (curve 1) and the relative diffraction efficiency η/η_0 (curve 2) against the number of erasure–recording cycles N for GCS films of the As–Se–I system. The change in the relative transmission is measured after each erasure cycle, after a 10-min irradiation of the film with an unmodulated laser beam at an intensity of about 3 mW/mm^2. Here, relative diffraction efficiency means the ratio of the maximum achievable diffraction efficiency after the N-th erasure–recording cycle, η, to the maximum achievable efficiency η_0 before the first heat treatment (before the first erasure).

Since the maximum diffraction efficiency falls off severalfold after the first erasure, while the amplitude contrast is unchanged, we can suggest that it is the phase component of the recorded holograms which undergoes the greatest change after the first heat treatment; the amplitude component remains unchanged.

This behavior should apparently be interpreted on the basis of a change in the polymer structure of the GCS films caused by laser radiation, observed in ref. 4. The initial structure of fresh GCS films is evidently unstable and quite different from that of films which have been subjected to heat treatment. The change in the structure of the material during the heat treatment leads to changes in the refractive index of the films, but causes essentially no change in the absorption properties.

Another important observation is that the extent to which the diffraction efficiency is changed by the first erasure is a function of the film composition. Figure 2 shows the relative diffraction efficiency η/η_0 as a function of the number of erasure–recording cycles N for As$_2$Se$_3$ films (curve 1) as well as for films of the As–Se and As–Se–I

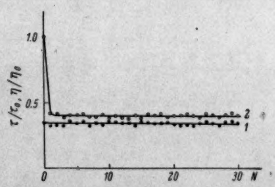

Fig. 1. Relative transmission τ/τ_0 (curve 1) and relative diffraction efficiency η/η_0 (curve 2) as functions of the number of erasure–recording cycles N for GCS films of the As–Se–I system.

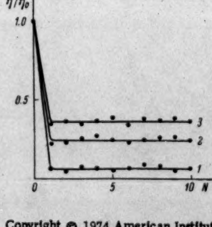

Fig. 2. Relative diffraction efficiency η/η_0 as a function of the number of erasure–recording cycles N for As$_2$Se$_3$ films (curve 1) and for films of the As–Se system (curve 2) and the As–Se–I system (curve 3).

systems (curves 2 and 3, respectively). The decrease in the diffraction efficiency is most pronounced (to 0.06) for the As_2Se_3 films and least pronounced (to 0.36) for the films of the As–Se–I system.

In none of the GCS films which we have studied do we observe a significant difference between regions of the films which had been exposed repeatedly and which had not been exposed at all.

Measurements carried out after the erasure of the holograms show that the residual diffraction efficiency is at least two orders of magnitude lower than that obtained as a result of the subsequent recording.

From these results we can draw the following conclusions:

1. The first heat-treatment cycle, which erases the information, changes the polymer structure of the GCS films in such a manner that the absorption properties are completely restored, while the refractive index is not completely restored. Subsequent erasure cycles do not change the structure of the material, so these properties remain constant after succeeding heat-treatment cycles.

2. The reversible properties of the GCS films are strongly dependent on the film composition; with an appropriate choice of material, a very small change in the diffraction efficiency after the first erasure can be achieved.

3. Since the values of the diffraction efficiency of holograms recorded on the GCS films remain approximately constant during successive erasure–recording cycles, we can think of the first heat-treatment cycle as one in which the GCS material is "formed." Obviously, GCS films can be used as reversible media for recording holograms.

---

[1] S. A. Keneman, Appl. Phys. Lett., 19, 205 (1971).

[2] J. S. Berkes, S. W. Ing, and W. J. Hillegas, J. Appl. Phys., 42, 4908 (1971).

[3] S. B. Gurevich, N. N. Il'yashenko, B. T. Kolomiets, V. M. Lyubin, V. I. Nalivaiko, Yu. E. Nesterikhin, V. G. Tsukerman, and D. F. Chernykh, Report to the First All-Union Conference on Holography, Tbilisi, 1972.

[4] S. B. Gurevich, N. N. Il'yashenko, B. T. Kolomiets, V. M. Lyubin, D. F. Chernykh, and V. P. Shilo, Zh. Tekh. Fiz., 43, 217 (1973) [Sov. Phys. – Tech. Phys., 18, 142 (1973)].

[5] S. B. Gurevich, N. N. Il'yashenko, B. T. Kolomiets, V. M. Lyubin, V. I. Nalivaiko, and V. G. Tsukerman, in: Optical Methods of Treating Information [in Russian] (in press).

Magnetoacoustic transducer based on the domain structure of a ferromagnetic material

G. L. Gurevich and G. A. Vul'gal'ter

(Submitted February 28, 1973; resubmitted June 28, 1973)
Zh. Tekh. Fiz., 44, 234-236 (January 1974)

The generation of an acoustic wave which propagates in the plane of a ferrite film divided into band domains is considered. The requirements needed for high efficiency in such a magnetoacoustic transducer are given.

To achieve efficient conversion of electromagnetic energy into acoustic energy it is necessary that the source of sound be modulated in space with a scale of the order of the wavelength of the acoustic wave. This modulation can be carried out artificially, but one can also use the inherent modulation of the properties of the solid. It is of particular interest to use the domain structure of a ferromagnetic material for this purpose.

A transducer which uses the domain structure of a film of permalloy and which excites a volume wave perpendicular to the plane of the film is considered in ref. 1. The efficiency of this transducer is extremely small.

In this paper we consider efficient generation of phonons when a wave is excited which propagates in the plane of a ferrite film which is divided into domains; the requirements on the film parameters are given. Acoustic oscillations in a thin film are easily transformed into surface acoustic waves. Thus, we consider a ferrite film of thickness L with 180-degree band domains, the walls of which are parallel to the yz plane (the z axis is in the direction of the normal to the film), deposited on a metal substrate. The dimensions of the film in the x and y directions are L_x and L_y. A metal film is deposited on top of the ferrite film, joined at $y = L_y$ with the metal substrate, so that a current-carrying loop is formed; this produces a magnetic field parallel to the x axis in the ferrite film.

We assume that the ratio of the size of a domain D to the thickness of the domain wall δ is much greater than unity, while $L \ll L_x, L_y$.

We also assume that the axis of easy magnetization is perpendicular to the plane of the film, and that the equilibrium magnetic moments $\mathbf{M}_0$ in neighboring domains are respectively parallel or antiparallel to the z axis. We assume the end of the wall x = 0 to be free. The other end of the film $x = L_x$ is loaded with a matched load, for example, it can be in contact with a medium with acoustic impedance equal to the acoustic impedance of the film.1)

A current $Je^{i\omega t}$ passes through the current-carrying loop. Since $L_x, L_y \gg L$, this current produces a uniform magnetic field $h_x e^{i\omega t} = 4\pi J/(cL_x)e^{i\omega t}$ in the ferrite film.

The high-frequency field will excite magnetization oscillations which, by virtue of magnetostriction, give rise to acoustic waves which propagate along the x axis. Since the external field is essentially uniform in the film, and the wavelength of the acoustic oscillation is of the order of $D \gg \delta$, we can neglect exchange interaction and consider the domain wall as a geometric boundary.[2] We assume that the material is isotropic in its elastic properties and neglect the acoustic attenuation. Assuming that all the quantities depend only on the x coordinate, it is easy to obtain linearized equations for the deviation of the magnetization from the equilibrium value $\mathbf{m} = \mathbf{M} - \mathbf{M}_0$, and the elastic displacement vector **u** (see ref. 3). Then, the only nonvanishing component which is excited is u_z, which satisfies the equation

$$\rho \frac{\partial^2 u_z}{\partial t^2} - c_{44} \frac{\partial^2 u_z}{\partial x^2} = \frac{B_2}{M_0^2} \frac{\partial}{\partial x} (m_x M_0(x)), \tag{1}$$

where B_2 is the magnetostriction constant, c_{44} is the elastic constant, ρ is the ferrite density, and $M_0(x) = \pm M_0$ depending on whether the magnetic moment of the domain is parallel or antiparallel to the z axis.

Neglecting the reverse action of the acoustic waves on the magnetization oscillations, m_x is found from the Landau–Lifshitz equation and has the form[4]

$$m_x = \chi_{xx} h_x = \frac{1}{\beta} \frac{\omega_0^2 + i\omega\Delta\omega}{\omega_0^2 - \omega^2 + 2i\omega\Delta\omega} h_x. \tag{2}$$

Here β is the anisotropy constant, $\omega_0 = \gamma\beta M_0$ is the ferromagnetic resonance frequency (γ is the gyromagnetic ratio), and Δω is the half-width of the ferromagnetic resonance line.

Since $M_0(x)$ oscillates with period 2D, u_z will be excited efficiently if the condition $\omega = nv(\pi/8)$ is satisfied, where n = 1, 2, 3..., and $v = \sqrt{c_{44}/\rho}$ is the velocity of sound in the ferromagnetic material.

Consider the excitation of the first harmonic $u_z(x > L_x, t) = A \exp[i\omega t - i(\omega/v_1)x]$, where v_1 is the velocity of sound in the medium in contact with the film.

The solution of Eq. (1) with the boundary conditions $[(\partial u_z/\partial x)(0, t) = 0$, continuity of $u_z(x, t)$ and $c_{44}(\partial u_z/\partial x) \cdot (x, t)$ for $x = L_x]$ yields A. We find that the acoustic flux power for $x > L_x$ is $W_a = (1/2)R_2 J^2$, and

$$R_a = \frac{64}{c^2} c_{44} \frac{\omega^2}{v} \left(\frac{B_2}{M_0 c_{44}}\right)^2 L L_y |\chi_{xx}|^2. \tag{3}$$

The Joule power loss in the ferrite can be represented in the form

$$W = -\int \overline{\left(\mathbf{m}, \frac{\partial \mathbf{h}}{\partial t}\right)} dV - \frac{1}{2} R J^2$$

(the wavy bar denotes averaging over the period of the oscillations), where

$$R = -\frac{16}{c^2} \pi^2 \omega \frac{L L_y}{L_x} \operatorname{Im} \chi_{xx}, \tag{4}$$

In addition, the portion of the power W_p dissipated in the current-conducting plates and the reactive element, which it is necessary to connect to the above system to compensate its inherent reactance, is

$$W_p = \frac{\omega |\mathscr{L}|}{2c^2 Q} J^2,$$

where

$$\mathscr{L} = 4\pi \frac{LL_y}{L_x}(1 + 4\pi Re\chi_{xx})$$

is the inductance of the system, and Q is the Q factor of the reactive elements.

Note that L and D are connected by the relation[5] $D = (\alpha\beta)^{1/4}(L)^{1/2}$ (α is the exchange interaction constant).

The condition for the transducer to be efficient is $W_a \gg W, W_p$, whence it follows that

$$\frac{W_a}{W} = \frac{4}{\pi} Nc_{44}\left(\frac{B_2}{M_0c_{44}}\right)^2 \frac{|\chi_{xx}|^2}{-\mathrm{Im}\,\chi_{xx}} \gg 1, \tag{5}$$

$$\frac{W_a}{W_p} = 16Nc_{44}\left(\frac{B_2}{M_0c_{44}}\right)^2 \frac{|\chi_{xx}|^2}{|1 + 4\pi\,\mathrm{Re}\,\chi_{xx}|} \gg \frac{1}{Q}, \tag{6}$$

where $N = L_x/D$ is the number of domains in the length of the transducer.

In very thin films a state of uniform magnetization is energetically more suitable, since this leads to the existence of a domain of minimum dimensions in a film of given material. In this case we must distinguish two cases:[6] If $\beta < 4\pi$, the minimum dimensions of the domain $D_{\min} \simeq \pi\sqrt{3\alpha/\beta}$, and if $\beta > 4\pi$, then $D_{\min} \simeq \sqrt{\alpha\beta/4}$. It is clear that a necessary condition for constructing a transducer which operates at a given frequency ω is the condition $D = v(\pi/\omega) > D_{\min}$, which gives

$$\left.\begin{aligned} &\sqrt{\frac{\alpha}{\beta}} < \frac{v}{\omega\sqrt{3}}, \quad \beta < 4\pi, \\ &\sqrt{\alpha\beta} < 4\pi\frac{v}{\omega}, \quad \beta > 4\pi. \end{aligned}\right\} \tag{7}$$

For yttrium iron garnet $c_{44} = 7.64 \cdot 10^{11}$ dynes/cm^2, $v = 3.84 \cdot 10^5$ cm/sec, $B_2 = 6.96 \cdot 10^6$ ergs/cm^3, $M_0 = 139$ G, $\alpha = 3.73 \cdot 10^{-11}$ cm^2, $\beta = 2K_1/M_0^2 = 0.65$, $\gamma = 1.76 \cdot 10^7$ Oe^{-1} · sec^{-1}, and $\Delta\omega/\omega_0 \sim 10^{-3}$ (ref. 7), so that at a frequency of 1 GHz for N = 50 we obtain $W_a/W \simeq 5$, $W_a/W_p \simeq 0.07$.

Hence, for values of Q that can be achieved in practice (Q ~ 100) conditions (5) and (6) are satisfied. If we assume that $L_y = 10L$, then $R_a \simeq 0.12\Omega$. The input impedance with a compensating reactance connected in parallel with the transducer is $(\omega L^2)/R_a \simeq 25\Omega$. Since the working frequency in our example is far from the ferromagnetic resonance ($\omega \simeq 4\omega_0$), the bandwidth of the transducer is not determined by the narrow ferromagnetic resonance line, but by the number of domains N (the order of magnitude of the relative bandwidth is 1/N).

The above estimates indicate that a transducer based on domains should be quite efficient. To increase the operating frequency it is obviously necessary to choose a material with a magnetostriction constant B_2 greater than that of yttrium iron garnet, and a higher resonance frequency.

In conclusion we note the possibility of controlling the working frequency of the transducer. The application of a constant external field perpendicular to the surface of the film leads to a change in the period of the domain structure, and it can be easily shown that the relative change in the period is determined by the parameter $[H_0/(\beta M_0)]^2$, where H_0 is the applied field. Since the working frequency is inversely proportional to the period of the domain structure, the application of an external field leads to a change in the working frequency.

[1)] In particular, this medium can be the ferrite film itself of thickness L, on the surface of which is deposited a current-carrying metal film.

[1] M. H. Seavey, Jr., Proc. IEEE, 52, 1387 (1965).
[2] I. A. Gilinskii, Zh. Eksp. Teor. Fiz., 61, 1996 (1971) [Sov. Phys.–JETP, 34, 1064 (1972)].
[3] W. P. Mason (ed.), Physical Acoustics, Vol. 3, Academic Press (1966).
[4] A. G. Gurevich, Microwave Ferrites [in Russian], GIFML, Moscow (1960).
[5] L. D. Landau and E. M. Lifshitz, Electrodynamics of Continuous Media, Pergamon Press (1960).
[6] R. V. Telesnin (ed.), Thin Ferromagnetic Films [in Russian], Mir, Moscow, (1964).
[7] W. P. Mason (ed.), Physical Acoustics, Vol. 4, Academic Press (1966).

ERRATA

Corrections to the March 1974 Issue (Vol. 18, No. 9)

Page	Column	Line	Printed as:	Should read:
1218	II	12 from bottom	$\omega_p = (4\pi e^2/m)^{1/2}$	$\omega_p = (4\pi N_e e^2/m)^{1/2}$
1219	I	8 from top	$\beta = 6\cdot 10^{-22}\ldots$	$\beta \simeq 6\cdot 10^{-27}\ldots$
1220	I	Eq. (4.3)	$N_y > N_e = \frac{R}{(R-1)}\frac{g_b}{g_a}\frac{K_{b,a}}{q_a}\left(1+\frac{\nu_a}{\nu_b}\right)$	$N_y > N_e = \frac{R}{(R-1)}\frac{g_b}{g_a}\frac{K_{b,a}}{q_a}\left(1+\frac{\nu_a}{\nu_u}\right)$
1220	II	Eq. (4.4)	$I_{b,a} = \frac{N_y - N_e}{N_y\left(\frac{N_y+K_{b,a}}{g_b}\right.}Q$	$I_{ba} = \frac{N_y - N_e}{N_y\left(N_y+\frac{K_{b,a}}{q_b}\right)}Q$
1221	I	17 from bottom	2'p and 3'p; $q_a/q_b \equiv q_2/q_3 = 1/4$	2^1P and 3^1P; $q_a/q_b \equiv q_2/q_3 \simeq 2.5$
1221	I	9 from bottom	$2\cdot 20^{-7}$ cm^3/sec	$2\cdot 10^{-7}$ cm^3/sec
1221	I	5 from bottom	$N_e \approx 10^{18}$ cm^{-3}	$N_c \approx 10^{18}$ cm^{-3}
1221	II	3 from top	$\nu_a \approx 6\cdot 10^2$ sec^{-1}	$\nu_a = 6\cdot 10^{-1}$ sec^{-1}
1222	II	Eq. (4)	$U(x, y) = -\frac{\exp(-jkL)}{-j\lambda L}\ldots$	$U(x, y) = \frac{\exp(-jkL)}{-j\lambda L}\ldots$

Calculation of permittivity of an inhomogeneous dielectric by a variational method

G. A. Ermakov, A. G. Fokin, and T. D. Shermergor

(Submitted May 14, 1973)
Zh. Tekh. Fiz., 44, 241-248 (February 1974)

A variational method is presented for calculating the effective permittivity of an inhomogeneous dielectric, ε^*. It is shown that this method can be used to construct an exact expression for ε^* representing an expansion in terms of multiple-point correlation functions of all orders. The lowest approximation of the method corresponds to the singular approximation of the renormalization method, based on the theory of random functions. In the second part the variational principle is used to bracket the values of ε^*. With this in mind the approximation which assumes the field is uniform within each phase (the UPF approximation) is applied and the conditions under which the UPF approximation agrees with the singular approximation are analyzed. Expressions are obtained for the effective constants in the UPF approximation when it does not agree with the singular approximation.

Among the various approximation methods used to calculate the effective permittivities of inhomogeneous dielectrics the ones which have gained the most acceptance are the variational method first proposed by Hashin and Shtrikman,[1] the renormalization method based on the theory of random functions,[2] the self-consistent method,[3] and the structure regularization approximation[4] in which the actual structure is replaced by an idealized strictly periodic structure. Each of these methods has its advantages and disadvantages. The variational method generally leads to exact upper and lower bounds for the effective permittivity ε^*_{ij}, but these are far apart. With the renormalization method an exact expression for the effective permittivity can be constructed formally but a direct calculation cannot be carried through since it requires taking account of multiple-point correlation functions of all orders. This difficulty is commonly avoided by limiting the calculation to the lower approximations of the method,[2] or to the singular approximation[5] which takes account only of the singular components of the second derivatives of the Green's function. In this approximation the renormalization method leads to upper and lower values of the effective permittivity, but the question of whether they form bounds is difficult to resolve without energy arguments. The self-consistent method is convenient because of its simplicity. Ordinarily it leads to an approximate value lying within the Hashin–Shtrikman bracket. The disadvantage of the method is that it does not take account of the interaction of the components, so that it is not suitable for describing matrix mixtures. The advantage of the structure regularization method is that it does not require the assumption of small concentrations or small differences of the permittivities of the components, but replacing a disordered structure by an idealized regular one introduces a certain error.

The availability of a large number of approximation formulas for calculating effective permittivities of various structures poses the problem of choosing the appropriate theoretical formula for describing an actual system. Because of the large variety of real structures an experimental test of various theoretical formulas involves extensive study. In this connection it is of interest to compare various methods in order to find the possibilities of their further development or to determine the limits within which a given method is not only valid a priori, but also leads to the smallest error. We analyze the variational and the renormalization methods from this point of view. It is shown first that the variational method gives a formal rigorous solution of the problem, and as in the renormalization method, the calculation of the effective permittivity in explicit form reduces to the evaluation of multiple integrals containing multiple-point correlation functions of all orders.

In the second part the approximation in which the field is uniform in each phase (the UPF approximation) is discussed and the conditions under which this approximation is equivalent to the singular approximation are analyzed.

1. FORMAL CONSTRUCTION OF THE EFFECTIVE PERMITTIVITY USING A VARIATIONAL METHOD

We consider an inhomogeneous dielectric whose permittivity tensor ε_{ij} is a random function of coordinates, and a homogeneous dielectric (comparison body) with the same size and shape with the permittivity ε^c_{ij}. This approach permits the introduction of the polarization vector $\tau_i = D_i - \varepsilon^c_{ij}E_j$, where D and E are respectively the electric displacement and the electric field in the inhomogeneous dielectric.

We denote the average values of quantities by angle brackets, the deviations of quantities from their values in the comparison body by primes, and central random values by double primes:

$$\varepsilon'_{ij} = \varepsilon_{ij} - \varepsilon^c_{ij}, \quad \tau''_i = \tau_i - \langle\tau_i\rangle. \tag{1.1}$$

We limit our discussion to ergodic fields for which statistical averaging over an ensemble agrees with volume averaging. We average over a volume whose linear dimensions are very much larger than the spatial scale of correlations, but small as compared with distances over which the regular part of the functions changes significantly. Then according to the variational principle formulated for this problem by Hashin and Shtrikman[1] the functional

$$U = \frac{1}{2}\int \left(\varepsilon^c_{ij}\langle E_i\rangle\langle E_j\rangle - \tau_i p_{ij}\tau_j + \tau''_i E''_i + 2\tau_i\langle E_i\rangle\right) d\mathbf{r}, \tag{1.2}$$

will be stationary for fields which satisfy

$$E_i = p_{ij}\tau_j, \quad p_{ij}\varepsilon'_{jk} \equiv \delta_{ik} \tag{1.3}$$

with the subsidiary and boundary conditions

$$\nabla_i\left(\varepsilon^c_{ij}E''_j + \tau''_i\right) = 0, \quad \varphi''|_S = 0, \quad \mathbf{E} = -\nabla\varphi. \tag{1.4}$$

The stationary value of the functional (1.2) is an absolute minimum when $\varepsilon^c_{ij} - \varepsilon_{ij} \geq 0$, and an absolute maximum otherwise. Here, the matrix inequality is understood in the sense of the positive semidefinite character of the quadratic form.

We determine the Green's function G of the regular operation L^c by the equation

$$L^cG = -\delta(\mathbf{r}),\quad L^c \equiv \nabla_i \varepsilon^c_{ij} \nabla_j. \tag{1.5}$$

Then using the first equation in (1.4) we obtain

$$E''_i = G_{,ij} * \tau''_j \equiv Q_{ij}\tau''_j. \tag{1.6}$$

Here, the subscripts after the comma denote differentiation with respect to the corresponding coordinates, the asterisk denotes convolution, and Q_{ij} is an integral operator whose kernel is $G_{,ij}$.

Substituting the value of $\mathbf{E}''$ determined from (1.6) into Eq. (1.2) we obtain a functional specified by the noncentral random functions τ. By varying this functional with respect to τ we find its stationary value and the functions for which it is stationary:

$$U_0 = \frac{1}{2}\int (\varepsilon^c\langle\mathbf{E}\rangle + \langle\tau\rangle)\langle\mathbf{E}\rangle\, d\mathbf{r} \equiv \frac{1}{2}\int \varepsilon^*\langle\mathbf{E}\rangle^2 d\mathbf{r}, \tag{1.7}$$

$$\tau = (p - Q)^{-1}[\langle\mathbf{E}\rangle - Q\langle\tau\rangle]. \tag{1.8}$$

From now on we use matrix notation and drop the subscripts on vectors and tensors.

Averaging Eq. (1.8) and expressing $\langle\tau\rangle$ and τ'' in terms of $\langle\mathbf{E}\rangle$ we find from Eqs. (1.6)-(1.8), after some transformations,

$$\mathbf{E} = (I - Q\varepsilon')^{-1}\langle(I - Q\varepsilon')^{-1}\rangle^{-1}\langle\mathbf{E}\rangle, \tag{1.9}$$

$$\varepsilon^* = \langle\varepsilon(I - Q\varepsilon')^{-1}\rangle\langle(I - Q\varepsilon')^{-1}\rangle^{-1}. \tag{1.10}$$

In obtaining Eqs. (1.7)-(1.10) we use the fact that the integral operator Q is symmetric, i.e., it satisfies the functional equation $(\varphi, QF) = (Q\varphi, f)$.

We express the second derivative of the Green's function as the sum of singular and regular components

$$\left.\begin{aligned} &G_{,ij} = G^s_{,ij} + G^f_{,ij},\quad \int G^s_{,ij}\varphi\, d\mathbf{r} \equiv \varphi(0)g_{ij},\quad g_{ij} \equiv \int_{V_0} G_{,ij}\, d\mathbf{r},\\ &\int G^f_{,ij}\varphi\, dr \equiv \int_{V_0} G_{,ij}[\varphi - \varphi(0)]\, d\mathbf{r} + \int_{V-V_0} G_{,ij}\varphi\, d\mathbf{r}, \end{aligned}\right\} \tag{1.11}$$

where $\varphi(\mathbf{r})$ is an arbitrary, finite, twice differentiable function, and the volume element V_0 includes the origin. Since $G_{,ij}$ is a homogeneous generalized function of degree −3 the integral g_{ij} depends only on the shape of the volume element $V_0 \subset V$, and not on its size.[6]

From the equations given above it is clear that the partition of $G_{,ij}$ and, consequently, the partition of the integral operator Q_{ij}, into singular and regular components is not unique but depends on the shape of the surface of the element V_0. The question of the choice of shape of this element is discussed in the second section of this paper.

Since $G^s_{,ij} = g_{ij}\delta(\mathbf{r})$, the integral operator Q^s_{ij} degenerates into a constant tensor g_{ij}, whereas Q^f_{ij} remains an integral operator.

We introduce the operators[7]

$$R \equiv (I - Q^f l)^{-1}\langle(I - Q^f l)^{-1}\rangle^{-1} = \lim_{n\to\infty} R_n,$$

$$R_n \equiv \sum_{k=0}^{n} (Hl)^k,$$

$$H \equiv (I - M)Q^f,\quad M\varphi \equiv \langle\varphi\rangle,$$

$$l \equiv \varepsilon'(I - g\varepsilon')^{-1} = (p - g)^{-1} \tag{1.12}$$

and use the representation that follows from the definitions (1.11) and (1.12):

$$\left.\begin{aligned} I - Q\varepsilon' &= (I - Q^f l)(I - g\varepsilon'),\\ (I - Q\varepsilon')^{-1} &= (I - g\varepsilon')^{-1}R\langle(I - Q^f l)^{-1}\rangle,\\ \langle(I - Q\varepsilon')^{-1}\rangle^{-1} &= \langle(I - Q^f l)^{-1}\rangle^{-1}\langle(I - g\varepsilon')^{-1}R\rangle^{-1}. \end{aligned}\right\} \tag{1.13}$$

Then, substituting Eq. (1.13) into (1.9) we find

$$\mathbf{E} = A\langle\mathbf{E}\rangle,\quad A \equiv (I - g\varepsilon')^{-1}R\langle(I - g\varepsilon')^{-1}R\rangle^{-1}. \tag{1.14}$$

Hence, replacing R by R_n we obtain

$$\mathbf{E} = \lim A_n\langle\mathbf{E}\rangle,\quad A_n \equiv (I - g\varepsilon')R_n\langle(I - g\varepsilon')^{-1}R_n\rangle^{-1}. \tag{1.15}$$

Limiting ourselves to the n-th approximation in powers of the random operator Hl, we find approximate values of the total field and the effective permittivity:

$$\mathbf{E}^{(n)} = A_n\langle\mathbf{E}\rangle,\quad \varepsilon^{(n)} = \langle\varepsilon A_n\rangle. \tag{1.16}$$

Equation (1.16) together with (1.12) and (1.15) for all n agrees with the solutions obtained by the renormalization method.[7] Thus the description of inhomogeneous media by variational principles is equivalent to the description by the renormalization method.

In the limiting case n → ∞ the approximate solutions (1.16) for the field $\mathbf{E}^{(n)}$ and the effective permittivity $\varepsilon^{(n)}$ go over into the exact solution (1.14). The other limiting case n = 0 gives the singular approximation of the variational method. Setting n = 0 in Eq. (1.16) and using (1.6) we find

$$\mathbf{E}^{(0)} = (I - g\varepsilon')^{-1}\langle(I - g\varepsilon')^{-1}\rangle^{-1}\langle\mathbf{E}\rangle, \tag{1.17}$$

$$\varepsilon^{(0)} = \langle\varepsilon(I - g\varepsilon')^{-1}\rangle\langle(I - g\varepsilon')^{-1}\rangle^{-1}. \tag{1.18}$$

These same equations can also be obtained by using the singular approximation of the renormalization method.

Substitution of the explicit expression for A_n into Eq. (1.16) for the effective permittivity yields a cumbersome expression. To simplify it we consider the case in which the fields $\langle\tau\rangle$ and $\langle\mathbf{E}\rangle$ are uniform. Then the operator Q_{ij} degenerates into the constant tensor

$$Q_{ij}\langle\tau_j\rangle = G_{,ij} * \langle\tau_j\rangle = g_{ij}\langle\tau_j\rangle, \tag{1.19}$$

and Eq. (1.8) is replaced by

$$\tau = (p - Q)^{-1}[\langle\mathbf{E}\rangle - g\langle\tau\rangle]. \tag{1.20}$$

We average this expression and express $\langle\tau\rangle$ and τ'' in terms of $\langle\mathbf{E}\rangle$. Then, using (1.7) we find

$$\varepsilon^* = \varepsilon^c + [g + \langle(p - Q)^{-1}\rangle^{-1}]^{-1} I. \tag{1.21}$$

We introduce the notation

$$p^* = (\varepsilon^* - \varepsilon^c)^{-1},\quad l^* = (p^* - g)^{-1}. \tag{1.22}$$

Then using the last of Eqs. (1.12) and (1.13), Eq. (1.21) can be written in the form

$$l^* = \lim_{n\to\infty} l^{(n)},\quad l^{(n)} = \langle lY^{(n)}\rangle,\quad Y^{(n)} = \sum_{k=0}^{n}(Q^f l)^k. \tag{1.23}$$

Here, $Y^{(n)}$ is a constant tensor. The equation obtained, together with (1.22), determines both the exact and the approximate values of the effective permittivity. We emphasize that in (1.23) the expansion is carried out with the regular parts of the second derivatives of the Green's function.

In the singular approximation (n = 0) we find $l^{(0)} = \langle l\rangle$ which is equivalent to (1.18).

For uniform average fields $\langle E\rangle$ and $\langle \tau\rangle$ the expression for the total field E is also simplified. Using (1.19) we find

$$\mathbf{E} = (I - g\varepsilon')^{-1} Y^{(\infty)} (I - g\varepsilon^{*\prime})\langle \mathbf{E}\rangle, \quad \varepsilon^{*\prime} \equiv \varepsilon^* - \varepsilon^0. \tag{1.24}$$

By using (1.22) this equation can be written in a somewhat different form:

$$\mathbf{E} = \lim_{n\to\infty} \mathbf{E}^{(n)}, \quad \mathbf{E}^{(n)} = plY^{(n)}(p^{(n)}l^{(n)})^{-1}\langle \mathbf{E}\rangle, \quad p^{(n)} \equiv (\varepsilon^{(n)} - \varepsilon^0)^{-1}. \tag{1.25}$$

The singular approximation (1.17) is obtained from this for n = 0.

2. THE UPF APPROXIMATION

The singular approximation involves only the local field, i.e., the total field at a given point is determined only by its average value and the random component of the permittivity. Another procedure is possible, based only on the assumption of the uniformity of the field within each phase (the UPF approximation). It will be shown later that in this approximation, first applied by Hashin and Shtrikman, the field in a given phase is generally determined not only by the average field and the random component of the permittivity in that phase, but also by the values in all other phases.

We discuss the UPF approximation for a multiphase mixture of isotropic components. We define phase averaging by using the scalar indicator function f_α which is equal to unity if the given point belongs to the phase under consideration, and zero otherwise. The average value of the indicator function and the dependence of the structure function on it are given by

$$\begin{gathered}\langle f_\alpha\rangle = v_\alpha, \quad x_{\alpha\beta}(\mathbf{r}) \equiv \langle f_\alpha(\mathbf{r}_0) f_\beta(\mathbf{r}_0 + \mathbf{r})\rangle = v_\alpha v_\beta + B_{\alpha\beta}\varphi_{\alpha\beta}(\mathbf{r}),\\ B_{\alpha\beta} = B_{\beta\alpha} = v_\alpha(\delta_{\alpha\beta} - v_\beta), \quad \varphi_{\alpha\beta}(0) = 1.\end{gathered} \tag{2.1}$$

The components of the correlation indicator function $\varphi_{\alpha\beta}$ are related by

$$\varphi_{\alpha\alpha} = \sum_\beta v_\beta \varphi_{\alpha\beta}, \tag{2.2}$$

which follows from summing the second of Eqs. (2.1) over β. Hence for a two-phase mixture $\varphi_{11} = \varphi_{22} = \varphi_{12} = \varphi$. However, for a multiphase mixture the various components can be described by different functions $\varphi_{\alpha\beta}$, reflecting different ordering of the phases. We denote the phase averaging operator by M_α. Then we find from Eq. (1.6)

$$\left.\begin{gathered}M_\alpha E''_i(\mathbf{r}) = \frac{1}{v_\alpha}\langle E''_i(\mathbf{r}) f_\alpha(\mathbf{r})\rangle = \frac{1}{v_\alpha}\int G_{,ij}(\mathbf{r}) K_{\alpha j}(\mathbf{r})\,d\mathbf{r},\\ K_{\alpha j}(\mathbf{r}) \equiv \langle f_\alpha(\mathbf{r}_0)\tau''_j(\mathbf{r}_0 + \mathbf{r})\rangle.\end{gathered}\right\} \tag{2.3}$$

We now assume that the field $\tau''_j(\mathbf{r})$ is uniform within each phase:

$$\tau''_j(\mathbf{r}) = \sum_\beta^n f_\beta(\mathbf{r})\tau''_{\beta j}. \tag{2.4}$$

Substituting (2.4) into (2.3) we find

$$K_{\alpha j}(\mathbf{r}) = \sum_\beta^n \tau''_{\beta j} x_{\alpha\beta}(\mathbf{r}), \tag{2.5}$$

which, after substitution into the first equation in (2.3), gives

$$E''_{\alpha i} \equiv M_\alpha E''_i = \sum_\beta^n C^{\alpha\beta}_{ij}\tau''_{\beta j}, \quad C^{\alpha\beta}_{ij} = \frac{1}{v_\alpha}\int G_{,ij}(\mathbf{r}) x_{\alpha\beta}(\mathbf{r})\,d\mathbf{r}. \tag{2.6}$$

It follows from Eqs. (2.6) and (1.5) that the coefficients $C^{\alpha\beta}_{ij}$ have the following properties:

$$v_\alpha C^{\alpha\beta}_{ij} = v_\beta C^{\beta\alpha}_{ij}, \quad \varepsilon^0_{ij} C^{\alpha\beta}_{ij} = -\delta_{\alpha\beta}. \tag{2.7}$$

Substituting the explicit value of $x_{\alpha\beta}$ into the second equation in (2.6) we find

$$\left.\begin{gathered}C^{\alpha\beta}_{ij} = q^{\alpha\alpha}_{ij}\delta_{\alpha\beta} + v_\beta(g_{ij}\Theta_{\alpha\beta} - q^{\alpha\beta}_{ij}),\\ q^{\alpha\beta}_{ij} = \int G_{,ij}(\mathbf{r})\varphi_{\alpha\beta}(\mathbf{r})\,d\mathbf{r},\end{gathered}\right\} \tag{2.8}$$

where the tensor g_{ij} is given by (1.11) and all the elements of the matrix $\{\Theta_{\alpha\beta}\}$ are unity.

Thus in the UPF approximation the quantity $E''_{\alpha i}$ is determined not only by the value of $\tau''_{\alpha j}$ in that phase, but also by its values in all the other phases. In the singular approximation, on the other hand, correlation relations between phases are ignored. By replacing $G_{,ij}$ by $G^s_{,ij}$ in the second of Eqs. (2.8) we obtain

$$q^{\alpha\beta s}_{ij} = g_{ij}\Theta_{\alpha\beta}, \quad C^{\alpha\beta s}_{ij} = g_{ij}\delta_{\alpha\beta}, \quad E''^s_{\alpha i} = g_{ij}\tau''_{\alpha j}. \tag{2.9}$$

On the other hand the last equation in (2.9) is obtained directly from (1.6) by multiplying it on the left by the operator M_α and replacing $G_{,ij}$ by $G^s_{,ij}$.

Since the UPF approximation brackets the value of the effective permittivity, it follows from (2.8) that the singular approximation gives a bracket only when $q^{\alpha\beta}_{ij} \equiv g_{ij}\Theta_{\alpha\beta}$. Using the singular approximation for $q^{\alpha\beta}_{ij} \neq g_{ij}\Theta_{\alpha\beta}$ would significantly distort the form of the functional (1.2) and therefore would destroy its extremum character. Thus, using the relation

$$E''_{\alpha i} = q^{\alpha\alpha}_{ij}\tau''_{\alpha j} - \sum_\beta^n v_\beta q^{\alpha\beta}_{ij}\tau''_{\beta j}, \tag{2.10}$$

which holds in the UPF approximation, the third term of the functional (1.2) determining the nonlocal relations between D_i and E_i takes the form

$$\langle \tau''_i E''_i\rangle = \sum_\alpha^n v_\alpha \tau''_{\alpha i} q^{\alpha\alpha}_{ij}\tau''_{j\alpha} - \sum_\alpha\sum_\beta v_\alpha v_\beta \tau''_{\alpha i} q^{\alpha\beta}_{ij}\tau''_{\beta j}, \tag{2.11}$$

whereas in the singular approximation (2.11) is replaced by

$$\langle \tau''_i E''^s_i\rangle = \sum_\alpha^n v_\alpha \tau''_{\alpha i} g_{ij}\tau''_{\alpha j}, \tag{2.12}$$

which shows, as already noted, that in this approximation correlation relations between phases are not taken into account.

Thus the UPF approximation always gives bounds, while the singular approximation does so only when $q^{\alpha\beta}_{ij} = g_{ij}\Theta_{\alpha\beta}$. We show that the sufficient condition for the agreement of the two approximations is

$$\varphi_{\alpha\beta}(\mathbf{r}) = \Phi_{\alpha\beta}(\rho), \quad \rho^2 \equiv a_{ik}x_i x_k, \tag{2.13}$$

where a_{ik} is a certain symmetric constant tensor and $\Phi_{\alpha\beta}(\rho)$ is any function compatible with the usual conditions imposed on the coordinate dependence of the correlation functions.[8] To do this we perform the integration in the second of Eqs. (2.8). We extend the integration over the individual layers ($\rho_{n-1}, \rho_n = \rho_{n-1} + \Delta\rho$) with a common center of similitude. Then the function $\varphi_{\alpha\beta}(\mathbf{r})$ is changed only in the direction normal to the surface of the layer. Therefore, assuming that $\Delta\rho$ is sufficiently small and applying the theorem of the mean we obtain

$$q_{ij}^{\alpha\beta} = g_{ij}^{\alpha\beta}(0)\,\varphi_{\alpha\beta}(0) + \sum_{n=1}^{\infty} \varphi_{\alpha\beta}(n)\,[g_{ij}(n) - g_{ij}(n-1)], \tag{2.14}$$

where $\varphi_{\alpha\beta}(n)$ is the value of the function $\varphi_{\alpha\beta}(\mathbf{r})$ in the n-th layer, $g_{ij}(n)$ is the function defined by Eq. (1.11), calculated by integrating over the outer surface of the corresponding layer. Taking account of the fact that the tensor g_{ij} depends only on the shape of the volume of integration V_0 and not on its size we find that $g_{ij}(n) = g_{ij}(n-1)$ for any n, and hence $q_{ij}^{\alpha\beta} = g_{ij}(0)\Theta_{\alpha\beta} \equiv g_{ij}\Theta_{\alpha\beta}$. This shows the agreement of the two approximations when $\varphi_{\alpha\beta}(\mathbf{r})$ satisfies (2.13). It also follows that if $\varphi_{\alpha\beta}(\mathbf{r})$ is described by (2.13) the shape of the element of volume of integration in Eq. (1.11) is given by the shape of the characteristic surface $a_{ik}x_i x_k$ = const.

As an example of a relation of the type (2.13) we cite correlation functions of the form

$$\ln \varphi_{\alpha\beta} = -b_{\alpha\beta}\rho^m, \quad m = 1,\ 2, \tag{2.15}$$

used to describe textured multiphase systems assumed to have identical phase interactions. Here the factors $b_{\alpha\beta}$ take account of the difference in scales of correlation between different phases.

The approximation which assumes a uniform field within each phase agrees with the singular approximation, i.e., $q_{ij}^{\alpha\beta} = q_{ij}\Theta^{\alpha\beta}$ if $\varphi_{\alpha\beta} = \varphi\Theta_{\alpha\beta}$ and therefore $q_{ij}^{\alpha\beta} = q_{ij}\Theta_{\alpha\beta}$ for the structures under consideration. This follows from (1.5), (2.7), and (2.8). Structures for which $\varphi_{\alpha\beta} = \varphi\Theta_{\alpha\beta}$ include two-phase composite materials with isotropic components, single-phase and two-phase nontextured polycrystalline aggregates, and certain types of textured polycrystalline aggregates.

If the structure under investigation is such that the correlation function $\varphi_{\alpha\beta}$ is different for different phases, the calculation of the effective permittivity is complicated. We present a calculation for this case. Substituting Eq. (2.10) into the functional (1.2) and using (2.2) and (2.8) we find that it has an extremum for fields satisfying

$$\tau_{\alpha i} = \sum_{\beta} (X^{-1})_{ij}^{\alpha\beta}\, v_\beta \langle E_j \rangle, \tag{2.16}$$

$$X_{ij}^{\alpha\beta} \equiv v_\alpha [(p_{ij}^{\alpha} - q_{ij}^{\alpha\alpha})\,\delta_{\alpha\beta} + v_\beta q_{ij}^{\alpha\beta}].$$

Here, the quantities p_{ij} are given by (1.3). Averaging (2.16) and substituting it into (1.7) we find

$$\varepsilon_{ij}^{*} = \varepsilon_{ij}^{c} + \sum_{\alpha}\sum_{\beta} v_\alpha v_\beta (X^{-1})_{ij}^{\alpha\beta}. \tag{2.17}$$

It is easy to see that for $q_{ij}^{\alpha\beta} = q_{ij}\Theta_{\alpha\beta}$, i.e., when the UPF approximation degenerates into the singular approximation, Eq. (1.18) for the effective permittivity follows from Eqs. (2.16) and (2.18).

The generalization of the variational method we have proposed enables us, in principle, to find the exact value for ε_{ij}^{*}, since the necessary information on the structure of the inhomogeneous material is contained in the multiple-point moment functions of the permittivity. However, the same difficulties arise as in the renormalization method, namely the insufficiency of the information on the relations of the multiple-point correlation functions to the structure function and the mathematical difficulties involved in evaluating integrals of high multiplicity. At the present time these difficulties are overcome in the renormalization method by using the singular approximation, and in the variational method by the UPF approximation. We emphasize that in the formulation of the variational method Hashin and Shtrikman considered only those media for which the UPF and the singular approximations agree.

From what was shown in the first part of this paper on the equivalence of the two methods it follows that both can be used to calculate complex structures, but in this case either the singular approximation or the UPF approximation must be used in its most general form.

The width of the bracket for ε_{ij}^{*} is critically dependent on a proper choice of the permittivity of the comparison body. Thus choosing successively $\varepsilon^c = \varepsilon_1$ and $\varepsilon^c = \varepsilon_2$ for a two-phase composite consisting of isotropic phases we obtain the Hashin–Shtrikman bracket. Other combinations of ε_α and v_α can also be chosen as ε^c. The problem of the optimum choice of ε_{ij}^{c} for various inhomogeneous dielectrics is discussed in the following paper.

---

[1] Z. Hashin and S. Shtrikman, Phys. Rev., 130, 129 (1963).

[2] A. G. Fokin and T. D. Shermergor, Zh. Tekh. Fiz., 39, 1308 (1969) [Sov. Phys. – Tech. Phys., 14, 984 (1970)].

[3] V. I. Odelevskii, Zh. Tekh. Fiz., 21, 667 (1951).

[4] G. A. Van Fo Fy, The Theory of Reinforced Materials [in Russian], Naukova Dumka, Kiev (1971).

[5] A. G. Fokin, Zh. Tekh. Fiz., 41, 1073 (1971) [Sov. Phys. – Tech. Phys., 16, 849 (1971)].

[6] I. M. Gel'fand and G. E. Shilov, Generalized Functions and Operations on Them [in Russian], Fizmatgiz, Moscow (1959).

[7] A. G. Fokin, Zh. Tekh. Fiz., 43, 71 (1973) [Sov. Phys. – Tech. Phys., 18, 44 (1973)].

[8] A. S. Monin and A. M. Yaglom, Statistical Hydromechanics [in Russian], Nauka, Moscow (1965), part 1.

Calculation of bounds for the effective permittivity of an inhomogeneous dielectric

G. A. Ermakov, A. G. Fokin, and T. D. Shermergor

(Submitted June 7, 1973)
Zh. Tekh. Fiz., 44, 249-256 (February 1974)

Using a variational method the bounds for effective permittivities are calculated by optimizing the properties of a comparison body. It is shown that for a number of structures this method brackets the permittivity values more closely than the Hashin–Shtrikman method. The calculation is performed for a nontextured N-component mixture of isotropic phases, a nontextured N-phase polycrystalline aggregate, and a filamentary composite. Working formulas are obtained for the case of a very inhomogeneous phase consisting of either a multilayer cylinder or a multilayer sphere.

A comparison of the variational and the renormalization methods for calculating the permittivity of microscopically inhomogeneous dielectrics shows that for a number of structures the approximation which assumes the field is uniform within a given phase (the UPF approximation), applied for the first time in the variational method, and the singular approximation developed initially in the renormalization method lead to the same results.[1] Thus the bounds for the effective permittivity ε^* of such structures can be calculated from singular-approximation equations expressing ε^* in terms of the permittivity ε^c of a comparison body, and ε^c can be determined by the variational method.

We discuss three very simple cases: a composite of isotropic phases, a multiphase polycrystalline aggregate, and monodirectional anisotropic filaments in an isotropic matrix. The corresponding values of the effective permittivity are

$$\varepsilon^* = \left[\sum_{\alpha=1}^{N} v_\alpha (\varepsilon_\alpha + 2\varepsilon^c)^{-1}\right]^{-1} - 2\varepsilon^c \tag{1}$$

for a nontextured N-component mixture of isotropic phases,

$$\varepsilon^* = 3\left(\sum_{\alpha=1}^{N} v_\alpha \Delta^\alpha_{ii}\right)^{-1} - 2\varepsilon^c, \quad \Delta^\alpha_{ik}(\varepsilon^\alpha_{kj} + 2\varepsilon^c_{kj}) \equiv \delta_{ij} \tag{2}$$

for a nontextured N-phase polycrystalline aggregate, and

$$\begin{aligned} \varepsilon^*_{11} = \varepsilon^*_{22} = 2\{v_f[(\varepsilon^f_{11} + \varepsilon^c_{11})^{-1} + (\varepsilon^f_{22} + \varepsilon^c_{11})^{-1}] \\ + 2v_m(\varepsilon_m + \varepsilon^c_{11})^{-1}\}^{-1} - \varepsilon^c_{11}, \\ \varepsilon^*_{33} = v_f\varepsilon^f_{33} + v_m\varepsilon_m \end{aligned} \tag{3}$$

for a composite consisting of filaments of orthorhombic symmetry in an isotropic matrix, with both the filaments and one of the axes of second order oriented along the x_3 axis. Here Greek letters denote the number of the phase, v_α is the volume fraction of phase α, ε^s_{ij} is the effective permittivity in the singular approximation, and the indices f, m, and c denote quantities referring to a filament, the matrix, and the comparison body, respectively.

Equations (1)-(3) determine the effective values of the permittivity of multiphase structures with an irregular spatial distribution of phases. It is assumed that each of the phases is homogeneous. In addition, many composite materials have very inhomogeneous phases. Typical examples are fiberglass-reinforced plastics in which reinforcement is provided by hollow glass fibers or coated fibers. But even in polycrystalline aggregates and composites with inert fillers the properties of a phase within a grain can vary due to the increase of defects in regions near boundaries and the resulting nonuniform distribution of impurity atoms. This inhomogeneity should be taken into account if the thickness of the boundary layer separating the grains of an inhomogeneous material is comparable with the average size of a grain of the inhomogeneity.

The approximate value of the effective permittivity of such complex systems can be calculated as before by using Eqs. (1)-(3), but now the permittivity of a given phase must take account of the inhomogeneity. It should be emphasized that the effective characteristics of a phase can be calculated in the usual way when the average fields are uniform. The corresponding equations for a composite sphere and a composite cylinder, structures most frequently used to produce composite materials, are given in the Appendix.

CHOICE OF PERMITTIVITY TENSOR OF COMPARISON BODY. GENERAL PROCEDURE

Equations (1)-(3) will bracket the values of effective permittivities if the upper and lower values of the permittivity of the comparison body ε^c_+ and ε^c_- have been found correctly. It follows from the results of refs. 2 and 3 that the optimum choice of the tensors ε^c_+ and ε^c_- is based on the solution of the inequalities

$$M \leqslant 0, \ N \leqslant 0, \tag{4}$$

where the quadratic forms M and N are defined by the relations

$$\left.\begin{aligned} M \equiv \langle \xi\varepsilon'\xi \rangle, \ N \equiv \langle \eta\gamma'\eta \rangle, \ \xi \equiv \mathbf{E} - \mathbf{E}_0, \\ \eta \equiv \varepsilon^c\xi, \ \varepsilon' = \varepsilon - \varepsilon^c, \ \gamma' = \gamma - \gamma^c, \ \gamma\varepsilon = \gamma^c\varepsilon^c = I. \end{aligned}\right\} \tag{5}$$

Below we use matrix notation, $\mathbf{E}_0$ is the random electric field in the UPF approximation, and $\mathbf{E}$ is a certain piecewise-continuous trial field whose potential at the outer boundary of the body satisfies the condition

$$\varphi - \varphi_0|_S = 0, \ \mathbf{E} \equiv \nabla\varphi_0. \tag{6}$$

It is easy to see that the inequalities (4) are satisfied if

$$\varepsilon' \leqslant 0, \ \gamma' \leqslant 0, \tag{7}$$

from which

$$\varepsilon^c_+ - \varepsilon \geqslant 0, \ \varepsilon - \varepsilon^c_- \geqslant 0. \tag{8}$$

Here, the subscripts + and − denote quantities referring to the upper and lower bounds respectively, and the inequalities are understood in the sense of the positive semidefinite nature of the corresponding quadratic forms.

The inequalities (8) were proposed by Hashin and

Shtrikman.[4] The corresponding bracket for effective permittivities will not be optimum since these inequalities are defined for an arbitrary system of vectors, while the inequalities (4) are defined for a system of vectors satisfying the equations

$$\langle\xi\rangle=\langle\eta\rangle=0, \tag{9}$$

which follow from Eq. (6) after integrating over the surface and using the gradient theorem.[5]

The possibility of narrowing the Hashin–Shtrikman bracket follows from the fact that imposing the subsidiary constraints (9) on the families of quadratic forms M and N compresses the spectrum of eigenvalues of these families (or leaves it unchanged in the degenerate case). Therefore the maximum eigenvalues of these families, determined by the equations

$$\langle\xi(\varepsilon-\varepsilon^c)\xi\rangle=0,\ \langle\eta(\gamma-\gamma^c)\eta\rangle=0, \tag{10}$$

are either decreased or remain unchanged. Consequently, taking account of the subsidiary constraints can narrow the bracket in comparison with the Hashin–Shtrikman bracket.

The electric field of a multiphase polycrystalline aggregate in the UPF approximation is given by

$$\left.\begin{aligned}&\mathbf{E}^\alpha=(I-F^\alpha)^{-1}\Big[\sum_\alpha v_\alpha\int\psi_\alpha(I-F^\alpha)^{-1}\,d\Omega\Big]^{-1}\langle\mathbf{E}\rangle,\\&\mathbf{E}=\mathbf{E}^\alpha(\Omega),\ F^\alpha=F^\alpha(\Omega)=\sum_\beta\int C^{\alpha\beta}(\Omega,\ \Omega_0)\,\varepsilon'^\beta(\Omega_0)\,d\Omega_0,\end{aligned}\right\} \tag{11}$$

where $C^{\alpha\beta}(\Omega, \Omega_0)$ is a certain constant tensor introduced in ref. 1, $\psi_\alpha(\Omega)$ is the texture function of phase α, the indices α and β indicate the number of the phase, and the solid angle Ω determines the orientation of the crystallographic axes. It follows from Eq. (11) that the vector $\mathbf{E}^\alpha(\Omega)$ can be written as the product of a certain tensor, constant for a given phase and chosen orientation of its crystallographic axes, and a constant vector. Therefore the vectors ξ and η can be written in the form

$$\xi^\alpha(\Omega)=H^\alpha(\Omega)\,\xi_*,\ \eta^\alpha(\Omega)=H^\alpha(\Omega)\,\eta_*. \tag{12}$$

Here, $H^\alpha(\Omega)$ is a certain arbitrary tensor, constant for a given phase α and orientation Ω of its crystallographic axes; the symmetry and orientation of the principal axes of the tensor $H^\alpha(\Omega)$ will be determined by the tensor $F^\alpha(\Omega)$, and ξ_* and η_* are arbitrary vectors.

It follows from (12) and (9) that the tensor H^α must satisfy

$$\sum_\alpha v_\alpha\int H^\alpha(\Omega)\,\Psi_\alpha(\Omega)\,d\Omega=0. \tag{13}$$

N-PHASE COMPOSITE

We consider a mixture of N isotropic components. In this case $\Psi_\alpha = (4\pi)^{-1}$, $\varepsilon'_{ij} = \varepsilon'\delta_{ij}$. Then by taking account of Eq. (12) the first of Eqs. (10) gives

$$\sum_\alpha v_\alpha H^\alpha_{i\alpha}H^\alpha_{j\alpha}\varepsilon'_\alpha=0,\ \varepsilon'_\alpha=\varepsilon_\alpha-\varepsilon^c. \tag{14}$$

An analogous equation can be obtained for γ^c. Taking account of the independence of the components H_{ij} and condition (13) it is easy to see that Eqs. (13) and (14) are equivalent to

$$\sum_{\alpha=1}^{N}\rho_\alpha^2 b_\alpha=0,\ \sum_{\alpha=1}^{N}\rho_\alpha=0,\ \rho_\alpha\equiv v_\alpha h_\alpha,\ b_\alpha\equiv\frac{\varepsilon_\alpha-\varepsilon^c}{v_\alpha}, \tag{15}$$

where h_α is an arbitrary scalar, constant within one phase.

By the elimination of ρ_N Eq. (15) can be reduced to the equation for a family of quadratic forms

$$\sum_{\alpha,\beta=1}^{N-1}\rho_\alpha(A_{\alpha\beta}-\varepsilon^c B_{\alpha\beta})\rho_\beta=0, \tag{16}$$

$$A_{\alpha\beta}\equiv\frac{\varepsilon_\alpha}{v_\alpha}\delta_{\alpha\beta}+\frac{\varepsilon_N}{v_N}\theta_{\alpha\beta},\ B_{\alpha\beta}\equiv\frac{1}{v_\alpha}\delta_{\alpha\beta}+\frac{1}{v_N}\theta_{\alpha\beta}, \tag{17}$$

where all the elements of the matrix Θ are unity. Reducing the matrices (17) to triangular form by the Gaussian algorithm[6] we find the secular equation for the eigenvalues ε^c of the family of forms (16)

$$\prod_{\beta=1}^{N}(\varepsilon_\beta-\varepsilon^c)\sum_{\alpha=1}^{N}v_\alpha(\varepsilon_\alpha-\varepsilon^c)^{-1}=0. \tag{18}$$

A similar equation can be obtained for γ^c

$$\prod_{\beta=1}^{N}(\gamma_\beta-\gamma^c)\sum_{\alpha=1}^{N}v_\alpha(\gamma_\alpha-\gamma^c)^{-1}=0. \tag{19}$$

In Eq. (18) all of the ε_α are different. Therefore it determines the eigenvalues ε^c, the largest of which will be smaller than the smallest value found in accord with the first of inequalities (8). Thus taking account of the subsidiary condition (9) decreases the value of ε^c_+ and lowers the upper bound for the effective permittivity.

The same considerations show that the largest of the values of γ^c found from Eq. (19) will be smaller than the smallest value γ^c_- found in accord with the second of the inequalities (8), and consequently the lower bound for ε^* determined by using the permittivity of the comparison body $\varepsilon^c = 1/\gamma^c$ will be larger than that found by using the second of inequalities (8). Thus it has been shown that Eqs. (18) and (19) narrow the Hashin–Shtrikman bracket.

Equations (1), (18), and (19) can be used to bracket ε^* since the singular and the UPF approximations agree for a nontextured mixture of N isotropic components.[1,7]

For a two-phase mixture we find from (18)

$$\varepsilon^c_+=v_1\varepsilon_2+v_2\varepsilon_1=\varepsilon_1\varepsilon_2\langle\varepsilon^{-1}\rangle. \tag{20}$$

Similarly, from Eq. (19) we find ε^c_- determining the lower bound

$$\varepsilon^c_-=(v_1\gamma_2+v_2\gamma_1)^{-1}=\varepsilon_1\varepsilon_2\langle\varepsilon\rangle^{-1}. \tag{21}$$

Equations (20) and (21) agree with those obtained in ref. 2. If $\varepsilon_2 > \varepsilon_1$ they reduce to the inequalities

$$\varepsilon_1<\varepsilon^c_-<\varepsilon^c_+<\varepsilon_2, \tag{22}$$

whereas the Hashin–Shtrikman bracket is determined by $\varepsilon^c_+ = \varepsilon_2$, $\varepsilon^c_- = \varepsilon_1$.

The width of the bracket calculated by Eqs. (1), (20), and (21) is compared with that of the Hashin–Shtrikman bracket in Fig. 1, where ε^+, ε^- and ε^+_{HS}, ε^-_{HS} are plotted

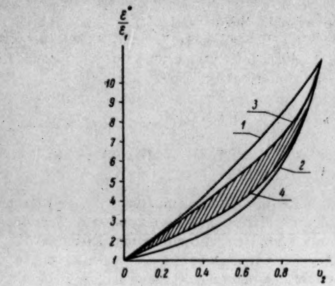

Fig. 1. Bounds for the effective permittivity of a two-component nontextured mixture. 1) $\varepsilon^{+}_{HS}/\varepsilon_1$, 2) $\varepsilon^{-}_{HS}/\varepsilon_1$, 3) $\varepsilon^{+}/\varepsilon_1$, 4) $\varepsilon^{-}/\varepsilon_1$.

as functions of the concentration for $(\varepsilon_2 - \varepsilon_1)/\varepsilon_1 = 10$. It is clear from the figure that the improved bracket can be significantly narrower than the Hashin–Shtrikman bracket (ε^{-}_{HS}, ε^{+}_{HS}).

If the spatial distribution of components is such that the singular and the UPF approximations do not agree, as occurs, for example, for different ordering of the phases of a multicomponent composite, ε^* can be calculated as before by using Eqs. (18) and (19), since they are derived in the more general UPF approximation, but expressing the effective permittivity in terms of ε^c requires replacing (1) by the equation derived in the UPF approximation,[1]

$$\left.\begin{aligned} &\varepsilon^*_{ij} = \varepsilon^c_{ij} + \sum_{\alpha,\beta} v_\alpha v_\beta (X^{-1})^{\alpha\beta}_{ij},\ X^{\alpha\beta}_{ij} = v_\alpha[(p^\alpha_{ij} - q^{\alpha\alpha}_{ij})\delta_{\alpha\beta} + v_\beta q^{\alpha\beta}_{ij}],\\ &p^\alpha_{ij}(\varepsilon^\alpha_{jk} - \varepsilon^c_{jk}) \equiv \delta_{ik},\ q^{\alpha\beta}_{ij} = \int G_{,ij}(\mathbf{r})\varphi^{\alpha\beta}(\mathbf{r})\,d\mathbf{r},\ \varepsilon^c_{ij} = \varepsilon^c\delta_{ij}. \end{aligned}\right\} \quad (23)$$

Here, $G_{,ij}$ is the second derivative of the Green's function of the operator $\varepsilon^c\nabla^2$, and $\varphi^{\alpha\beta}$ is the correlation indicator function.

MULTIPHASE POLYCRYSTALLINE AGGREGATE

We turn now to a discussion of a nontextured multiphase polycrystalline aggregate. In this case the UPF approximation degenerates into the singular. Accordingly we have

$$\left.\begin{aligned} &C^{\alpha\beta}_{ij}(\Omega,\ \Omega_0) = C\delta_{ij}\delta_{\alpha\beta}\delta(\Omega - \Omega_0),\\ &F^\alpha_{ij}(\Omega) = C\varepsilon'^\alpha_{ij}(\Omega),\ C = -\frac{1}{3\varepsilon^c},\ \psi_\alpha = \frac{1}{4\pi}. \end{aligned}\right\} \quad (24)$$

It follows from this that the tensor H^β can be written in the form

$$H^\beta_{ij}(\Omega) = \alpha^\beta_{im}\alpha^\beta_{jm}H^\beta_m. \quad (25)$$

Here the H^β_m are the principal values of the tensor H^β, and the α_{im} are the direction cosines of the principal axes with respect to the laboratory coordinate system.

We now substitute Eq. (25) into (12), and (12) into (10), and use the fact that for an aggregate, averaging is performed over both the phases and the orientations of the crystallographic axes. Then Eq. (10) and condition (13) take the form

$$\left.\begin{aligned} &\sum_\alpha^N\sum_m^3 v_\alpha(H^\alpha_m)^2(\varepsilon^\alpha_m - \varepsilon^c) = 0,\ \sum_\alpha^N\sum_m^3 v_\alpha(H^\alpha_m)^2(\gamma^\alpha_m - \gamma^c) = 0,\\ &\sum_\alpha^N\sum_m^3 v_\alpha H^\alpha_m = 0, \end{aligned}\right\} \quad (26)$$

where the ε^α_m are the principal values of the tensor ε^α, and ε^c is a scalar, since for a quasitropic dielectric the permittivity tensor of the comparison body is also taken to be isotropic.

Comparing Eqs. (26) and (15) we find that the problem of calculating ε^c for an N-phase polycrystalline aggregate reduces to the calculation of ε^c for a 3N-phase composite consisting of isotropic phases. Hence it follows that the solution of Eq. (26) is given by equations analogous to (18) and (19):

$$\prod_{\alpha=1}^N\prod_m^3(\varepsilon^\alpha_m - \varepsilon^c)\sum_\beta^N\sum_n^3 v_\beta(\varepsilon^\beta_n - \varepsilon^c)^{-1} = 0, \quad (27)$$

$$\prod_{\alpha=1}^N\prod_m^3(\gamma^\alpha_m - \gamma^c)\sum_\beta^N\sum_n^3 v_\beta(\gamma^\beta_n - \gamma^c)^{-1} = 0. \quad (28)$$

Equations (27) and (28) are equations of the (3N − 1)-th degree for ε^c and γ^c. The maximum root of Eq. (27) determines ε^c_+, and the maximum root of Eq. (28) gives ε^c_-. Substituting these values of ε^c_+ and ε^c_- into Eq. (2) we obtain the upper and lower bounds for ε^* (ε^+ and ε^-). It is clear that if all the ε^α_n are different the bracket determined this way will be narrower than the Hashin–Shtrikman bracket.

For a single-phase polycrystalline aggregate we find from Eq. (27) that ε^c is given by

$$\left.\begin{aligned} &(\varepsilon^c)^2 - 2\varepsilon^c\langle\varepsilon\rangle + \varepsilon_1\varepsilon_2\varepsilon_3\langle\varepsilon^{-1}\rangle = 0,\\ &\langle\varepsilon\rangle = \frac{1}{3}(\varepsilon_1 + \varepsilon_2 + \varepsilon_3),\ \langle\varepsilon^{-1}\rangle = \frac{1}{3}\left(\frac{1}{\varepsilon_1} + \frac{1}{\varepsilon_2} + \frac{1}{\varepsilon_3}\right). \end{aligned}\right\} \quad (29)$$

The larger of the two roots ε^c of Eq. (29) must be chosen for determining the upper bound. Therefore

$$\varepsilon^c_+ = \max\varepsilon^c = \langle\varepsilon\rangle + (\langle\varepsilon\rangle^2 - \varepsilon_1\varepsilon_2\varepsilon_3\langle\varepsilon^{-1}\rangle)^{1/2}. \quad (30)$$

Similarly from Eq. (28) we find the value of ε^c_- determining the lower bound as the value of the reciprocal of the larger of the roots γ^c.

$$(\varepsilon^c_-)^{-1} = \max\gamma^c = \langle\varepsilon^{-1}\rangle + [\langle\varepsilon^{-1}\rangle^2 - (\varepsilon_1\varepsilon_2\varepsilon_3)^{-1}\langle\varepsilon\rangle]^{1/2}. \quad (31)$$

FILAMENTARY DIELECTRIC

In conclusion we discuss filaments of orthorhombic symmetry oriented along the x_3 axis. One of the axes of second order is parallel to the filament axes, and the other two are oriented arbitrarily. In this case Eq. (25) can be written for the tensor H with the direction cosines α_{ij} determining rotation about the axis of a filament. Substituting Eq. (25) into (12), and (12) into (10), and averaging we obtain a set of equations for ε^c and γ^c:

$$\left.\begin{aligned} &\sum_{\alpha,\,n=1}^2 v_\alpha(H^\alpha_n)^2(\varepsilon^\alpha_n - \varepsilon^c_1) = 0,\\ &\sum_{\alpha,\,n=1}^2 v_\alpha(H^\alpha_n)^2(\gamma^\alpha_n - \gamma^c_1) = 0,\ \sum_{\alpha,\,n=1}^2 v_\alpha H^\alpha_n = 0, \end{aligned}\right\} \quad (32)$$

$$\sum_{\alpha=1}^2 v_\alpha(H^\alpha_3)^2(\varepsilon^\alpha_3 - \varepsilon^c_3) = 0,\ \sum_{\alpha=1}^2 v_\alpha(H^\alpha_3)^2(\gamma^\alpha_3 - \gamma^c_3) = 0,\ \sum_{\alpha=1}^2 v_\alpha H^\alpha_3 = 0. \quad (33)$$

Equation (32) determines the components of the tensors ε^c and γ^c of the comparison body in the plane transverse to the filaments, and Eq. (33) in the direction of the filaments.

Equations (32) and (33) can be put in the form

$$\left.\begin{aligned} v_f \sum_{n=1}^{2} (\varepsilon_n^f - \varepsilon_1^c)^{-1} + 2v_m (\varepsilon_m - \varepsilon_1^c)^{-1} = 0, \\ \varepsilon_{3+}^c = v_f \varepsilon_m + v_m \varepsilon_3^f. \end{aligned}\right\} \quad (34)$$

Analogous equations hold for γ^c

$$\left.\begin{aligned} v_f \sum_{n=1}^{2} (\gamma_n^f - \gamma_1^c)^{-1} + 2v_m (\gamma_m - \gamma_1^c)^{-1} = 0, \\ \frac{1}{\varepsilon_{-3}^c} = \frac{v_f}{\varepsilon_m} + \frac{v_m}{\varepsilon_3^f}. \end{aligned}\right\} \quad (35)$$

Here ε_{1+}^c is equal to the larger of the roots of the quadratic equation (34), and $1/\varepsilon_-^c$ is the larger of the roots of the quadratic equation (35) for γ_1^c. Substituting ε_+^c and ε_-^c into Eq. (3) we obtain the required bracket for $\varepsilon_1{}^* = \varepsilon_2{}^*$. It is clear from Eq. (3) that the third principal value of the effective tensor ε^* is computed exactly.

The variational method discussed above brackets the value of the effective permittivity; greater accuracy evidently requires details of the interactions of the components. The arithmetic mean can be taken as an approximate value of ε^* within the bracket if the interactions of the components are identical; for matrix mixtures the upper bound can be taken if the matrix has a permittivity $\varepsilon_2 > \varepsilon_1$, and the lower bound otherwise. Obviously in special cases when none of the components are simply connected but their interactions are different, the geometric mean of the permittivities ε^+ and ε^- or their reciprocals could be used.

We emphasize that in spite of a certain arbitrariness in the choice of ε^* within the calculated bounds, this procedure leads to better results than the self-consistent method does. In a number of cases the self-consistent method leads to a value of ε^* lying outside our calculated bounds. We show this. The expressions for the self-consistent solution are obtained by setting $\varepsilon^c = \varepsilon^* \equiv \varepsilon^{sc}$. Then the familiar equations of the singular approximation (1)-(3) can be written in the form

$$\langle (\varepsilon - \varepsilon^*)[I - g(\varepsilon - \varepsilon^*)]^{-1} \rangle = 0, \quad (36)$$

where matrix notation has been used, ε is a random tensor, and g is a constant tensor determining the singular part of the second derivatives of the Green's function.[1,2]

Limiting ourselves to a consideration of a two-phase mixture of isotropic components and taking account of the fact that the self-consistent solution always lies within the Voigt–Royce bracket

$$\langle \varepsilon^{-1} \rangle^{-1} \leqslant \varepsilon^{sc} \leqslant \langle \varepsilon \rangle. \quad (37)$$

In addition we note that the effective tensor ε^s is a monotonically increasing function of ε^c. Therefore by using Eq. (1) we can carry out the following mappings of the manifolds ε^c on ε^s:

$$\left.\begin{aligned} \varepsilon^c = [\varepsilon_1, \varepsilon_2] \to \varepsilon^s = [\varepsilon_{HS}^-, \varepsilon_{HS}^+], \\ \varepsilon^c = [\langle \varepsilon^{-1} \rangle^{-1}, \langle \varepsilon \rangle] \to \varepsilon^s = [\varepsilon_0^-, \varepsilon_0^+], \\ \varepsilon^c = \varepsilon^{sc} \to \varepsilon^s \equiv \varepsilon^{sc} \subset [\varepsilon_0^-, \varepsilon_0^+], \\ \varepsilon^c = [\varepsilon_-^c, \varepsilon_+^c] \to \varepsilon^s = [\varepsilon^-, \varepsilon^+]. \end{aligned}\right\} \quad (38)$$

Using the definitions (20) and (21) of the quantities ε_-^c and ε_+^c it is easy to show that

$$\left.\begin{aligned} \varepsilon_-^c < \varepsilon_+^c < \langle \varepsilon^{-1} \rangle^{-1}, \left(0 \leqslant v_1 < \frac{\sqrt{\varepsilon_1}}{\sqrt{\varepsilon_1} + \sqrt{\varepsilon_2}}\right), \\ \langle \varepsilon \rangle < \varepsilon_-^c < \varepsilon_+^c, \left(\frac{\sqrt{\varepsilon_2}}{\sqrt{\varepsilon_1} + \sqrt{\varepsilon_2}} < v_1 \leqslant 1\right). \end{aligned}\right\} \quad (39)$$

Under these conditions $\varepsilon^{sc} \subset [\langle \varepsilon^{-1} \rangle^{-1}, \langle \varepsilon \rangle] \not\subset [\varepsilon_-^c, \varepsilon_+^c]$, and therefore $\varepsilon^{sc} \subset [\varepsilon_0^-, \varepsilon_0^+] \not\subset [\varepsilon^-, \varepsilon^+]$. Thus the self-consistent solution can fall outside the improved bounds calculated by the variational method.

APPENDIX

EFFECTIVE PERMITTIVITY OF A MULTILAYER SPHERE AND CYLINDER

We calculate the effective permittivity of a multilayer dielectric sphere consisting of isotropic layers. Suppose such a sphere is situated in a uniform external field of intensity $\mathbf{E}_0$. Then choosing the origin at the center of the sphere we have for the potential in the α-th layer

$$\varphi_\alpha = -A_\alpha \mathbf{E}_0 \mathbf{r} \left(1 - \frac{C_\alpha}{r^3}\right), \ \alpha = 1, \ldots, N. \quad (A.1)$$

The constants A_α and C_α are found from the condition of continuity of the potential and the normal component of the electric displacement at the interface between the layers. This leads to the following recurrence relations:

$$A_\alpha = A_{\alpha+1} \frac{C_{\alpha+1} - r_\alpha^3}{C_\alpha - r_\alpha^3}, \ C_{\alpha+1} = r_\alpha^3 \frac{(2d_\alpha + 1) C_\alpha + (d_\alpha - 1) r_\alpha^3}{2(d_\alpha - 1) C_\alpha + (d_\alpha + 2) r_\alpha^3}, \quad (A.2)$$

where $d_\alpha = \varepsilon_\alpha \varepsilon_{\alpha+1}^{-1}$, and r_α is the radius of the α-th layer. There must be added the relations $C_1 = 0$ and $A_{N+1} = 1$, which follow from the uniformity of the field in the central spherical layer and the requirement that the field at infinity be $\mathbf{E}_0$.

From Eq. (A.1) we find the average value of the electric displacement and the electric field intensity of a multilayer dielectric sphere:

$$\langle \mathbf{D} \rangle = \sum_{\alpha=1}^{N} v_\alpha \varepsilon_\alpha A_\alpha \mathbf{E}_0, \quad \langle \mathbf{E} \rangle = \sum_{\alpha=1}^{N} v_\alpha A_\alpha \mathbf{E}_0. \quad (A.3)$$

Hence the effective permittivity is

$$\varepsilon^* = \frac{\sum_{\alpha=1}^{N} v_\alpha \varepsilon_\alpha A_\alpha}{\sum_{\alpha=1}^{N} v_\alpha A_\alpha}. \quad (A.4)$$

In the special case of a two-layer sphere we find from this

$$\varepsilon^* = \varepsilon_2 \frac{\varepsilon_1 (1 + 2n) + 2\varepsilon_2 (1 - n)}{\varepsilon_1 (1 - n) + \varepsilon_2 (2 + n)}, \quad n \equiv \frac{r_1^3}{r_2^3}. \quad (A.5)$$

The effective permittivity of a multilayer cylinder is calculated in a similar way. The potential in the α-th layer of a dielectric cylinder is given by

$$\varphi_\alpha = -A_\alpha \mathbf{E}_0 \mathbf{r} \left(1 - \frac{C_\alpha}{r^2}\right). \quad (A.6)$$

The recurrence relations between the constants now take the form

$$\left.\begin{aligned} A_\alpha = A_{\alpha+1} \frac{C_{\alpha+1} - r_\alpha^2}{C_\alpha - r_\alpha^2}, \quad A_{N+1} = 1, \\ C_{\alpha+1} = r_\alpha^2 \frac{(d_\alpha + 1) C_\alpha + (d_\alpha - 1) r_\alpha^2}{(d_\alpha - 1) C_\alpha + (d_\alpha + 1) r_\alpha^2}, \quad C_1 = 0, \end{aligned}\right\} \quad (A.7)$$

and the effective permittivity will as before be given by (A.4).

In the special case of a two-layer cylinder we find

$$\varepsilon^* = \varepsilon_2 \frac{\varepsilon_1(1+m)+\varepsilon_2(1-m)}{\varepsilon_1(1-m)+\varepsilon_2(1+m)}, \quad m \equiv \frac{r_1^2}{r_2^2}. \qquad \text{(A.8)}$$

---

[1] G. A. Ermakov, A. G. Fokin, and T. D. Shermergor, Zh. Tekh. Fiz., 44, 241 (1974) [Sov. Phys. – Tech. Phys., 19, 157 (1974)].

[2] A. G. Fokin, Zh. Tekh. Fiz., 43, 71 (1973) [Sov. Phys. – Tech. Phys., 18, 44 (1973)].

[3] R. Hill, Prog. Appl. Mech., The Prager Anniversary Volume, New York–London (1963), p. 99.

[4] Z. Hashin and S. Shtrikman, Phys. Rev., 130, 129 (1963).

[5] G. Korn and T. Korn, Mathematical Handbook for Scientists and Engineers, McGraw-Hill, New York (1961).

[6] F. R. Gantmakher, Theory of Matrices [in Russian], Nauka, Moscow (1967).

[7] A. G. Fokin, Zh. Tekh. Fiz., 41, 1073 (1971) [Sov. Phys. – Tech. Phys., 16, 849 (1971)].

Resonance properties of a pulsating dielectric sphere

A. G. Nerukh and N. A. Khizhnyak
A. M. Gor'kii Khar'kov State University

(Submitted May 3, 1973)
Zh. Tekh. Fiz., 44, 257-262 (February 1974)

Maxwell's equations in integral form are derived in the first approximation in v/c for a moving inhomogeneous medium allowing for the effect of the motion of the medium on the boundary conditions. A constitutive equation is derived for a dielectric with "quasielastic" molecules and an internal velocity field v(r, t); this equation differs from the Minkowski equations by a term accounting for the inhomogeneity induced in the density of the medium by the motion of the latter. The internal field of a small dielectric sphere of variable radius is determined as an example. It is shown that the internal field is amplified for a harmonic time variation of the radius, corresponding to exchange of energy between the electric field and the moving medium.

1. The solution of electrodynamic problems in moving media depends on the nature of the motion of the medium. For uniform steady motion (the velocity field being described by a constant vector v = const) it is most logical to go over to a comoving reference frame.[1,2] This is the approach used in a study of the propagation of generalized plane waves in a moving isotropic medium.[3]

The electrodynamics of an accelerating medium [for which the uniform velocity field is described by a vector **v**(t) which depends only on the time] can be formulated in general terms by going over to a local coordinate system,[4] although specific problems are treated in the approximation $v/c \ll 1$. Also investigated in ref. 4 is wave propagation in an unbounded uniformly accelerated medium and in a rotating medium. Petrov[5] uses the Maxwell's equations in covariant notation and transforms from a noninertial to an inertial frame to solve the problem of the scattering of a field by a uniformly translating and rotating impedance cylinder. A single comoving reference frame can be introduced in all of these cases.

The latter procedure is impossible in the case of arbitrary nonuniform motion of a medium [**v** = **v**(**r**, t)]. It is possible to analyze some situations,[6,7] such as the nonuniform, tangential, and stationary motion of layers of a medium relative to one another [$\mathbf{v} = \{v_x(z), 0, 0\}$], by using the equations for a uniformly moving medium at each point and considering the entire problem in the laboratory frame.

It is essential to note that the authors of all the foregoing investigations have been compelled to limit the solution of specific problems to the approximation $v/c \ll 1$, an assumption that is justified by the conditions actually encountered in practice.

It is practical to approach the solution of electrodynamic problems in arbitrarily moving media [**v** = **v**(**r**, t)] using the first-order approximation in v/c at the outset. Then the problem can be investigated in the laboratory frame and Maxwell's equations used for the medium at rest, but with the appropriate constitutive equations and boundary conditions.

In the present paper we derive a constitutive equation for a class of dielectrics and solve the problem of the scattering of an electromagnetic wave by a small dielectric sphere of variable radius. We solve the problem by the method of integral equations.[8,9]

2. In the derivation of the constitutive relations we use Maxwell's equations in the form[2,10]

$$\left.\begin{aligned} \operatorname{curl}\mathbf{E} &= -\frac{1}{c}\frac{\partial\mathbf{B}}{\partial t}, \quad \operatorname{div}\mathbf{B}=0,\\ \operatorname{curl}\mathbf{B} &= \frac{1}{c}\frac{\partial\mathbf{D}}{\partial t}, \quad \operatorname{div}\mathbf{D}=0, \end{aligned}\right\} \tag{1}$$

where the medium is characterized by a single electric induction vector D, expressed in terms of the electric (**P**) and magnetic (**M**) polarizations of the medium as follows:

$$\frac{\partial\mathbf{D}}{\partial t}=\frac{\partial\mathbf{E}}{\partial t}+4\pi\left(\frac{\partial\mathbf{P}}{\partial t}+c\operatorname{curl}\mathbf{M}\right). \tag{2}$$

We confine the analysis to a nonmagnetic ($\mu = 1$) dielectric that is nondispersive in the rest state and is composed of "quasielastic molecules," where an irrotational velocity field $\mathbf{v} = c\boldsymbol{\beta}(\mathbf{r}, t)$ is given in the dielectric. We determine the polarization of the medium by averaging the molecular electric moment **p** and magnetic moment **m**. A molecule moving with a velocity **v** has moments $\mathbf{p} = \mathbf{p}_0$ and $\mathbf{m} = [\mathbf{p}_0(\mathbf{v}/c)]$, where $\mathbf{p}_0$ is the dipole moment in the rest state. If the fields **E** and **B** are given in the laboratory frame, then $\mathbf{p}_0 = \alpha(\mathbf{E} + [(\mathbf{v}/c)\mathbf{B}])$, where α is the polarizability of the molecule. Consequently,

$$\mathbf{p}=\alpha\left(\mathbf{E}+\left[\frac{\mathbf{v}}{c}\mathbf{B}\right]\right), \quad \mathbf{m}=\alpha\left[\mathbf{E}\frac{\mathbf{v}}{c}\right]. \tag{3}$$

Averaging (3) by means of the distribution function, we find

$$\left.\begin{aligned} \mathbf{P} &= \alpha n\mathbf{E}+\alpha\frac{1}{c}[\mathbf{qB}],\\ \mathbf{M} &= \alpha\frac{1}{c}[\mathbf{Eq}], \end{aligned}\right\} \tag{4}$$

where $n = \int f\,d\mathbf{v}$ and $\mathbf{q} = \int \mathbf{v}f\,d\mathbf{v}$ are the density and flux of particles of the medium. Assuming that the perturbation of the distribution function f_1 due to the impressed force $\mathbf{F} = c\dot{\boldsymbol{\beta}}$ is small and solving the kinetic equation, we obtain

$$f_1=-c\frac{\partial f_0}{\partial\mathbf{v}}\int_{-\infty}^{t}\dot{\boldsymbol{\beta}}(t', \mathbf{v}, \mathbf{r}-\mathbf{v}(t-t'))\,dt'. \tag{5}$$

We adopt $f_0 = n_0\delta(\mathbf{v})$ as the equilibrium function, calculate n and **q**, substitute the result into (4), and find the following expressions for the polarization moments in terms of the fields:

$$\left.\begin{aligned}\mathbf{P}&=\alpha n_0\left(\mathbf{E}-c\mathbf{E}\int_{-\infty}^{t}\nabla\boldsymbol{\beta}\,dt'+[\boldsymbol{\beta}\mathbf{B}]\right),\\ \mathbf{M}&=\alpha n_0[\mathbf{E}\boldsymbol{\beta}].\end{aligned}\right\} \tag{6}$$

Then the constitutive equation (2) as a function of the fields assumes the form

$$\frac{\partial\mathbf{D}}{\partial t}=\varepsilon\frac{\partial\mathbf{E}}{\partial t}+(\varepsilon-1)\frac{\partial}{\partial t}\left(-c\mathbf{E}\int_{-\infty}^{t}\nabla\boldsymbol{\beta}\,dt'+[\boldsymbol{\beta}\mathbf{B}]\right)+c(\varepsilon-1)\,\mathrm{curl}\,[\mathbf{E}\boldsymbol{\beta}], \tag{7}$$

where $\varepsilon = 1 + 4\pi\alpha n_0$ is the static dielectric constant of the medium.

It will be advantageous below to represent relation (7) in the form D(**E**). Expressing B in terms of **E** by means of Eqs. (1), we have

$$\mathbf{D}=\varepsilon\mathbf{E}-c(\varepsilon-1)\mathbf{E}\int_{-\infty}^{t}\nabla\boldsymbol{\beta}\,dt'-c(\varepsilon-1)\left[\boldsymbol{\beta}\int_{-\infty}^{t}\mathrm{curl}\,\mathbf{E}\,dt'\right]+c(\varepsilon-1)\int_{-\infty}^{t}\mathrm{curl}\,[\mathbf{E}\boldsymbol{\beta}]\,dt'. \tag{8}$$

Equation (8) differs from the familiar Minkowski equations by the presence of the second term on the right-hand side; this term vanishes for an incompressible medium.

3. Before undertaking the solution of the problem of electromagnetic wave scattering by bodies with moving boundaries we take account of the singularities induced in the integral equations by the use of Maxwell's equations in the form (1) and the constitutive equation in the form (8). According to the method of Green's functions,[8,9] the integral equations corresponding to the system (1) have the form

$$\left.\begin{aligned}\mathbf{E}&=\mathbf{E}_0'+\frac{1}{4\pi}\left(\mathrm{grad\,div}-\frac{1}{c^2}\frac{\partial^2}{\partial t^2}\right)\\ &\times\frac{\partial^2}{\partial t^2}\int_{-\infty}^{\infty}dt'\int_{V(t')}\frac{\tau-\frac{1}{c}R}{R}h\left(\tau-\frac{1}{c}R\right)(\mathbf{D}-\mathbf{E})\,d\mathbf{r}',\\ \mathbf{B}&=\mathbf{B}_0'+\frac{1}{4\pi c}\,\mathrm{curl}\,\frac{\partial^3}{\partial t^3}\\ &\times\int_{-\infty}^{\infty}dt'\int_{V(t')}\frac{\tau-\frac{1}{c}R}{R}h\left(\tau-\frac{1}{c}R\right)(\mathbf{D}-\mathbf{E})\,d\mathbf{r}',\end{aligned}\right\} \tag{9}$$

where $\tau = t - t'$, $R = |\mathbf{r}-\mathbf{r}'|$, h(t) is the Heaviside function, and $\mathbf{E}_0'$ and $\mathbf{B}_0'$ are the incident fields corresponding to the medium at rest. Inasmuch as **E** suffers a discontinuity at the boundary and D includes the spatial derivatives of **E**, the differentiation operators must be taken outside the integral sign in order to remove the singularities of the integrand. It is necessary in this case to regard the velocity as a continuous function, as indicated by Pauli.[1] Carrying out the required transformations we obtain the final expression for the integral equation:

$$\begin{aligned}\mathbf{E}&=\mathbf{E}_0+\frac{\varepsilon-1}{4\pi}\left(\mathrm{grad\,div}-\frac{1}{c^2}\frac{\partial^2}{\partial t^2}\right)\frac{\partial^2}{\partial t^2}\\ &\times\int_{-\infty}^{\infty}dt'\int_{V(t')}\frac{\tau-\frac{1}{c}R}{R}h\left(\tau-\frac{1}{c}R\right)\\ &\times\left\{\mathbf{E}-c\mathbf{E}\int_{-\infty}^{t'}\nabla\boldsymbol{\beta}\,dt''-c\left[\mathrm{curl}\,\boldsymbol{\beta}\int_{-\infty}^{t'}\mathbf{E}\,dt''\right]\right.\\ &\left.-c\nabla\boldsymbol{\beta}\int_{-\infty}^{t'}\mathbf{E}\,dt''+2c\left(\int_{-\infty}^{t'}\mathbf{E}\,dt''\nabla\right)\boldsymbol{\beta}\right\}d\mathbf{r}'-\frac{\varepsilon-1}{4\pi}\left(\mathrm{grad\,div}-\frac{1}{c^2}\frac{\partial^2}{\partial t^2}\right)\\ &\times\mathrm{grad}\,\frac{\partial^2}{\partial t^2}\int_{-\infty}^{\infty}dt'\int_{V(t')}\frac{\tau-\frac{1}{c}R}{R}hc\boldsymbol{\beta}\int_{-\infty}^{t'}\mathbf{E}\,dt''\,d\mathbf{r}'\\ &+\frac{\varepsilon-1}{4\pi c}\,\mathrm{curl}\,\frac{\partial^4}{\partial t^4}\int_{-\infty}^{\infty}dt'\int_{V(t')}\frac{\tau-\frac{1}{c}R}{R}\\ &\times h\left\{\left[\boldsymbol{\beta}\int_{-\infty}^{t'}\mathbf{E}\,dt''\right]+\int_{-\infty}^{t'}[\boldsymbol{\beta}\mathbf{E}]\,dt''\right\}d\mathbf{r}'.\end{aligned} \tag{10}$$

The magnetic field is determined from the second relation (9) by spatial integration. By solving Eq. (10) we find the field inside the scattering body.

The integral equation is greatly simplified in the quasistatic case. Thus, if s, the dimension of the body, is much smaller than the characteristic inhomogeneity scale of the field λ, we can neglect the delay inside the body, and we can also neglect the time derivatives in the zeroth approximation in s/λ. Equation (10) assumes the form

$$\begin{aligned}\mathbf{E}&=\mathbf{E}_0+\frac{\varepsilon-1}{4\pi}\,\mathrm{grad\,div}\int_{V(t)}\frac{d\mathbf{r}'}{R}\left\{\mathbf{E}+c\int_{-\infty}^{t}\left(-\mathbf{E}\nabla\tilde{\boldsymbol{\beta}}+[\tilde{\mathbf{E}}\,\mathrm{curl}\,\boldsymbol{\beta}]\right.\right.\\ &\left.\left.+2(\tilde{\mathbf{E}}\nabla)\boldsymbol{\beta}-\tilde{\mathbf{E}}\nabla\boldsymbol{\beta}\right)dt'\right\}-\frac{\varepsilon-1}{4\pi}\,\mathrm{grad\,div\,grad}\int_{V(t)}\frac{d\mathbf{r}'}{R}c\boldsymbol{\beta}\int_{-\infty}^{t}\mathbf{E}\,dt'\end{aligned} \tag{11}$$

Here, the variables with a tilde are to be integrated over t'.

4. As an example we now consider the scattering of a wave by a sphere with a time-varying radius. The strain vector for the elastic sphere can be written with good accuracy[11] in the form $\boldsymbol{\xi} = \xi(t)\mathbf{r}$. The velocity of the medium in this case becomes $\mathbf{v} = \dot{\xi}\mathbf{r}$. Inserting this value into (11) and assuming the field to be uniform inside the sphere, we obtain

$$\mathbf{E}=\mathbf{E}_0-\frac{\varepsilon-1}{3}(1-3\xi(t))\mathbf{E}+\frac{4}{3}(\varepsilon-1)\dot{\xi}(t)\int_{-\infty}^{t}\mathbf{E}\,dt'. \tag{12}$$

The solution of the latter equation has the form

$$\begin{aligned}\mathbf{E}&=\left[\frac{\varepsilon+2}{3}-(\varepsilon-1)\xi(t)\right]^{-1}\mathbf{E}_0\\ &+\frac{4}{3}(\varepsilon-1)\dot{\xi}(t)\left[\frac{\varepsilon+2}{3}-(\varepsilon-1)\xi(t)\right]^{-7/3}\\ &\times\left\{A\mathbf{E}_0+\int_0^{t}\left[\frac{\varepsilon+2}{3}-(\varepsilon-1)\xi(t')\right]^{1/3}\mathbf{E}_0\,dt'\right\},\end{aligned} \tag{13}$$

where the constant A is evaluated from the initial conditions.

We analyze expression (13) for a variation of the sphere radius according to the law $\xi = \xi_0 \sin(\Omega t + \varphi)$. Rewriting the first term in the form

$$\frac{3}{\varepsilon - 3(\varepsilon - 1)\xi(t) + 2}\mathbf{E}_0,$$

we see that it is analogous to the expressions for the internal field of a sphere at rest with an effective dielectric constant $\varepsilon_{\mathrm{eff}} = \varepsilon - 3(\varepsilon - 1)\xi(t)$. The disparity between $\varepsilon_{\mathrm{eff}}$ and ε is caused by the strain-induced inhomogeneity of the material of the sphere.

The second term differs qualitatively from the first term on account of the presence of the integral. Suppose that the strain of the sphere is small ($\xi_0 < 1$) and that the incident field is $\sim e^{i\omega t}$. Clearly, the integrand can be expanded in a series in ξ_0 for a qualitative analysis of the integral. We write the first two terms of the integrated series simultaneously with the factor in front of the braces in (13):

$$\frac{4}{3}(\varepsilon - 1)\xi_0\Omega\cos(\Omega t + \varphi)\left[\frac{\varepsilon + 2}{3} - (\varepsilon - 1)\xi_0 \sin(\Omega t + \varphi)\right]^{-7/3}$$
$$\times\left(\frac{\varepsilon+2}{3}\right)^{1/3}\left\{\frac{e^{i\omega t} - 1}{i\omega}\right.$$
$$-\frac{\varepsilon - 1}{\varepsilon + 2}\xi_0\cos\varphi\left(\frac{i\omega\sin\Omega t - \Omega\cos\Omega t}{\Omega^2 - \omega^2}e^{i\omega t} + \frac{\Omega}{\Omega^2 - \omega^2}\right)$$
$$\left.-\frac{\varepsilon - 1}{\varepsilon + 2}\xi_0\sin\varphi\left(\frac{\Omega\sin\Omega t + i\omega\cos\Omega t}{\Omega^2 - \omega^2}e^{i\omega t} - \frac{i\omega}{\Omega^2 - \omega^2}\right)\right\}. \quad (14)$$

We investigate the resonance case ($\omega \to \Omega$). Passing to the limit in relation (14), we find that the internal field grows as $\sim \Omega t e^{i\psi} \cos(\Omega t + \varphi)$. It also turns out to grow for pulsation of the sphere in a constant field ($\omega = 0$). Since the excited alternating field has the frequency Ω in this case, the resonance condition is always satisfied. The initial phase angle φ is inconsequential here.

It is important in this connection to consider the linear expansion and compression of the sphere ($\mathbf{v} = \xi_0 t\mathbf{r}$) in a constant field $\mathbf{E}_0$. The internal field is

$$\mathbf{E} = \mathbf{E}_0\left(\frac{\varepsilon + 2}{3}\right)^{4/3}\left[\frac{\varepsilon + 2}{3} - \xi_0(\varepsilon - 1)t\right]^{-4/3}, \quad (15)$$

where $\xi_0 = 0$ for $t < 0$ and has a value $\pm\xi_0$ for $t \geq 0$ for expansion and compression, respectively. As we see from (15), the internal field grows in expansion and decays in compression of the sphere, and the two processes are asymmetrical; the growth during expansion is more rapid than the decay during compression. Obviously, this asymmetry also accounts for the growth of the field for a harmonic variation of the sphere radius.

5. The amplification of the field under definite conditions is due to energy exchange between the mechanical motion of the medium and the electromagnetic field. We now show that this feature is also confirmed by an analysis of the energy conservation principle.

The Poynting theorem[12,13] for a stationary nonuniformly moving medium [$\mathbf{v} = \mathbf{v}(\mathbf{r})$] with the density variation ignored has the form

$$-\sigma\mathbf{E}\mathbf{E}_{\mathrm{imp}} = \frac{c}{4\pi}\operatorname{div}[\mathbf{E}\mathbf{H}] + \sigma E^2 + \left(\rho\mathbf{v} + \frac{\sigma\mu}{c}[\mathbf{v}\mathbf{H}]\right)\mathbf{E} + \frac{\partial W}{\partial t}, \quad (16)$$

where σ is the conductivity of the medium, ρ is the density of charges, and W is the electromagnetic energy density, which is defined as

$$W = \frac{1}{8\pi}(\mathbf{E}\mathbf{D}' + \mathbf{B}\mathbf{H}) = \frac{1}{8\pi}\left(\mu H^2 + \varepsilon E^2 - 2\frac{\varepsilon\mu - 1}{c^2}\mathbf{v}[\mathbf{E}\mathbf{H}]\right), \quad (17)$$

where

$$\mathbf{D}' = \varepsilon\mathbf{E} + \frac{\varepsilon\mu - 1}{c}[\mathbf{v}\mathbf{H}].$$

In the absence of impressed field sources ($\mathbf{E}_{\mathrm{imp}} = 0$) expression (16) describes the energy transfer between the medium and the field. The case of a conducting medium has been investigated by Zel'dovich,[14] who found the conditions under which the field is amplified in scattering by a rotating conducting cylinder.

In the case of a nonconducting medium we consider the previous example of a sphere in a constant field with a linearly varying radius. We have from (16)

$$\frac{\partial W}{\partial t} = -\frac{c}{4\pi}\operatorname{div}[\mathbf{E}\mathbf{H}]. \quad (18)$$

Inasmuch as

$$\mathbf{H} = \mathbf{B} + \frac{\varepsilon - 1}{c}[\mathbf{v}\mathbf{E}],$$

we approximately determine the magnetic field induced inside the sphere by the motion of the medium. To do so we substitute the unperturbed field $\mathbf{E}_0$ into the second relation (9) and obtain as a result

$$\mathbf{B} = -\frac{5}{3}\frac{\varepsilon - 1}{c}[\mathbf{v}\mathbf{E}_0]. \quad (19)$$

The expression for the variation of the energy density then acquires the form

$$\frac{\partial W}{\partial t} = \frac{\varepsilon - 1}{3\pi}\xi_0 E_0^2. \quad (20)$$

It is evident from the latter that the field energy will grow or diminish, depending on the direction of motion ($\pm\xi_0$).

---

[1] W. Pauli, Theory of Relativity, Pergamon, London–New York (1958).

[2] I. E. Tamm, Principles of the Theory of Electricity [in Russian], Izd. Nauka, Moscow (1966).

[3] M. Aalund and G. Johansen, J. Appl. Phys., 42, 2669 (1971).

[4] T. C. Mo, J. Math. Phys., 11, 2589 (1970); Radio Sci., 6, 673 (1971).

[5] B. M. Petrov, Radiotekh. Elektron., 17, 1799 (1972).

[6] V. G. Gavrilenko, G. A. Lupanov, and N. S. Stepanov, Izv. VUZ. Radiofiz., 15, 183 (1972).

[7] G. A. Lupanov, Izv. VUZ. Radiofiz., 15, 1139 (1972).

[8] N. A. Khizhnyak, Zh. Tekh. Fiz., 28, 1592 (1958) [Sov. Phys. – Tech. Phys., 3, 1466 (1958)].

[9] A. G. Nerukh and N. A. Khizhnyak, Zh. Tekh. Fiz., 43, 1113 (1973) [Sov. Phys. – Tech. Phys., 18, 711 (1973)].

[10] V. P. Silin and A. A. Rukhadze, Electromagnetic Properties of Plasmas and Plasma-like Media [in Russian], Gosatomizdat, Moscow (1961).

[11] P. M. Morse and H. Feshbach, Methods of Theoretical Physics, Vol. 2, McGraw-Hill, New York (1953).

[12] R. T. Compton and C. T. Tai, IEEE Trans. Antennas and Propagation, AP-12, 238 (1964).

[13] I. A. Deryugin and V. I. Vorontsov, Izv. VUZ. Radiofiz., 9, 1155 (1966).

[14] Ya. B. Zel'dovich, ZhETF Pis. Red., 14, 270 (1971) [JETP Lett., 14, 180 (1971)]; Zh. Eksp. Teor. Fiz., 62, 2076 (1972).

Potential factors for an inhomogeneous ellipsoid

M. L. Levin and R. Z. Muratov

(Submitted August 15, 1973)
Zh. Tekh. Fiz., 44, 263-266 (February 1974)

Recursion relations are obtained for internal and external potential factors of an inhomogeneous triaxial ellipsoid; these are expressed in terms of tabulated demagnetization coefficients. The degeneration of an ellipsoid into a spheroid and into a sphere is considered.

The long-standing problem of the field or an inhomogeneous ellipsoid has now emerged from the classical framework of the Newton–Lyapunov treatment, where it was of minor importance and therefore not treated in handbooks and treatises on potential theory. Recently the solution of this problem has become pressing, for example, in the investigation of the dynamics of dense bunches of charged particles,[1,2] and for the construction of an approximate theory of diffraction by small bodies.[3,4]

In the new applications of the problem of the potential of an inhomogeneous body, the inhomogeneity itself is not described in ellipsoidal coordinates, but in ordinary Cartesian coordinates. Therefore the key to the problem is finding the potential of the sources with a power distribution law inside the body. For ellipsoidal bodies the general method of solving this problem was indicated in the 19th century by Ferrers[5] and Dyson.[6] The final closed equations for the source potential with normalized density

$$\rho(x, y, z) = \left(\frac{x}{a}\right)^{\alpha}\left(\frac{y}{b}\right)^{\beta}\left(\frac{z}{c}\right)^{\gamma} \tag{1}$$

(a, b, and c are the ellipsoid semiaxes; α, β, and γ are nonnegative integers) are constructed in ref. 7. Thus, when all the exponents are even ($\alpha = 2\lambda$, $\beta = 2\mu$, $\gamma = 2\nu$), the equation for the potential inside the ellipsoid is of the form

$$\Phi_{2\lambda, 2\mu, 2\nu} = \frac{8\pi}{4^{\sigma}}(2\lambda)!\,(2\mu)!\,(2\nu)! \times \sum_{i=0}^{\sigma}\sum_{j=0}^{\sigma-i}\sum_{k=0}^{\sigma-i-j}\frac{S_{ijk}}{(\sigma-i-j-k)!}x^{2i}y^{2j}z^{2k}\Gamma_{ijk}^{(\lambda,\mu,\nu)}, \tag{2}$$

where

$$\Gamma_{ijk}^{(\lambda,\mu,\nu)} = \sum_{l=0}^{\lambda}\sum_{m=0}^{\mu}\sum_{n=0}^{\nu}\frac{S_{lmn}}{(\lambda-l)!\,(\mu-m)!\,(\nu-n)!}a^{2l}b^{2m}c^{2n}M_{i+l,\,j+m,\,k+n}. \tag{3}$$

Here

$$\left.\begin{gathered}\sigma = \lambda+\mu+\nu+1,\\ S_{lmn} = \frac{(-2)^{l+m+n}}{(2l)!\,(2m)!\,(2n)!},\\ M_{lmn} = (2l-1)!!\,(2m-1)!!\,(2n-1)!!\\ \times\frac{abc}{2}\int_0^{\infty}\frac{du}{(a^2+u)^l(b^2+u)^m(c^2+u)^n\Delta},\\ \Delta^2 = (a^2+u)(b^2+u)(c^2+u).\end{gathered}\right\} \tag{4}$$

We will call the quantities M_{lmn} the internal potential factors of the ellipsoid. We will call the sum $l + m + n$ characterizing the dimensionality of the factor its weight. In particular, the factors of unit weight M_{100}, M_{010}, and M_{001} are the ordinary depolarization coefficients (the demagnetization factors), for which detailed tables exist.[8-10]

The potential outside the ellipsoid (see ref. 11) is described by equations of the form (2) and (3), in which the factors M_{lmn} are replaced by functions of the observation point. These functions (we will call them external potential factors) are obtained from Eq. (4) by replacing the lower limit by the ellipsoidal coordinate of the observation point:

$$\mathcal{M}_{lmn}(\xi) = (2l-1)!!\,(2m-1)!!\,(2n-1)!! \times\frac{abc}{2}\int_{\xi}^{\infty}\frac{du}{(a^2+u)^l(b^2+u)^m(c^2+u)^n\Delta}, \tag{5}$$

where $\xi > 0$ is the maximum root of the equation

$$\frac{x^2}{a^2+\xi}+\frac{y^2}{b^2+\xi}+\frac{z^2}{c^2+\xi} = 1. \tag{6}$$

(Below, we will call the ellipsoid described by Eq. (6) the coordinate ellipsoid.)

To actually use expressions of the type (2) and (3) and similar equations for the potentials outside the ellipsoid we must know the values of the internal and external factors. In this work we introduce recursion relations, which allow us to express all the potential factors in terms of the tabulated demagnetization coefficients M_{100}, M_{010}, and M_{001}.

1. INTERNAL FACTORS OF THE ELLIPSOID

As is known, the demagnetization coefficients of the ellipsoid are interconnected by the relations

$$M_{100}+M_{010}+M_{001} = 1, \tag{7}$$

$$a^2M_{100}+b^2M_{010}+c^2M_{001} = M_{000}. \tag{8}$$

For factors with weight 2 the definition (4) implies the equations

$$\left.\begin{aligned}(a^2-b^2)M_{110} &= M_{010}-M_{100},\\ (b^2-c^2)M_{011} &= M_{001}-M_{010},\\ (c^2-a^2)M_{101} &= M_{100}-M_{001}.\end{aligned}\right\} \tag{9}$$

To derive the general recursion relations we use the fact that the initial definition (4) can be rewritten in the form[7]

$$M_{lmn} = (\hat\partial_a)^l(\hat\partial_b)^m(\hat\partial_c)^n M_{000}, \tag{10}$$

where we have introduced the operator

$$\hat\partial_a = -\frac{\partial}{\partial a}\left(\frac{\dots}{a}\right) = \frac{1}{a^2}-\frac{1}{a}\frac{\partial}{\partial a}. \tag{11}$$

Applying the operator $(\hat\partial_a)^l(\hat\partial_b)^m(\hat\partial_c)^n$ to (7) and (8), we obtain the relations

$$M_{l+1,m,n}+M_{l,m+1,n}+M_{l,m,n+1} = \frac{(2l-1)!!\,(2m-1)!!\,(2n-1)!!}{a^{2l}b^{2m}c^{2n}}, \tag{12}$$

$$a^2M_{l+1,m,n}+b^2M_{l,m+1,n}+c^2M_{l,m,n+1} = (2l+2m+2n+1)M_{lmn}. \tag{13}$$

Application of this same operator to (9) yields the recursion relations

$$\left.\begin{aligned} M_{l+1,m+1,n} &= -\frac{(2m+1)M_{l+1,m,n}-(2l+1)M_{l,m+1,n}}{a^2-b^2}, \\ M_{l,m+1,n+1} &= -\frac{(2n+1)M_{l,m+1,n}-(2m+1)M_{l,m,n+1}}{b^2-c^2}, \\ M_{l+1,m,n+1} &= -\frac{(2l+1)M_{l,m,n+1}-(2n+1)M_{l+1,m,n}}{c^2-a^2}. \end{aligned}\right\} \quad (14)$$

It is clear that these relations do not apply for factors of the form M_{100}, for which two or three indices are equal to zero. Such factors must be transformed beforehand, using (12).

Thus, an arbitrary internal factor of the ellipsoid can be finally expressed in terms of the demagnetization coefficients.

We now consider the degenerate case, in which the ellipsoid is transformed into a spheroid ($a = b \neq c$). Evidently, we have

$$M_{lmn} = M_{mln} \quad (15)$$

and

$$\frac{M_{l+1,m,n}}{2l+1} = \frac{M_{l,m+1,n}}{2m+1}. \quad (16)$$

From Eqs.(12), (13), and (16) it follows that

$$\begin{aligned} &2\frac{l+m+1}{2l+1}(a^2-c^2)M_{l+1,m,n} \\ &= -\frac{(2l-1)!!\,(2m-1)!!\,(2n-1)!!}{a^{2(l+m)}c^{2(n-1)}} + (2l+2m+2n+1)M_{lmn}, \end{aligned} \quad (17)$$

$$\begin{aligned} (a^2-c^2)M_{l,m,n+1} &= \frac{(2l-1)!!\,(2m-1)!!\,(2n-1)!!}{a^{2(l+m-1)}c^{2n}} \\ &\quad -(2l+2m+2n+1)M_{lmn}. \end{aligned} \quad (18)$$

Equations (15), (17), and (18) allow us to express the factors M_{lmn} in terms of an arbitrary demagnetization coefficient of the spheroid $M = M_{001}$.

For a sphere ($a = b = c$), using (12) and (13) we immediately obtain the general equation

$$M_{lmn} = \frac{(2l-1)!!\,(2m-1)!!\,(2n-1)!!}{2(l+m+n)+1}a^{-2(l+m+n-1)}. \quad (19)$$

2. EXTERNAL FACTORS OF THE ELLIPSOID

From the definition (5) of the external factors $\mathcal{M}_{lmn}$ it is clear that an equivalent definition (10) holds for them:

$$\mathcal{M}_{lmn}(\xi) = (\hat{\partial}_a)^l(\hat{\partial}_b)^m(\hat{\partial}_c)^n\mathcal{M}_{000}(\xi).$$

The relations (7) and (8) for factors with unit weight are replaced, as can be easily verified, by

$$\mathcal{M}_{100}+\mathcal{M}_{010}+\mathcal{M}_{001} = \frac{abc}{\sqrt{(a^2+\xi)(b^2+\xi)(c^2+\xi)}},$$

$$a^2\mathcal{M}_{100}+b^2\mathcal{M}_{010}+c^2\mathcal{M}_{001} = \mathcal{M}_{000} - \frac{abc}{\sqrt{(a^2+\xi)(b^2+\xi)(c^2+\xi)}}\xi.$$

Therefore, the external factors are not given by (12) and (13) but by the relations

$$\mathcal{M}_{l+1,m,n}+\mathcal{M}_{l,m+1,n}+\mathcal{M}_{l,m,n+1} = \frac{(2l-1)!!\,(2m-1)!!\,(2n-1)!!\,abc}{(a^2+\xi)^{l+1/2}(b^2+\xi)^{m+1/2}(c^2+\xi)^{n+1/2}}, \quad (20)$$

$$\begin{aligned} &a^2\mathcal{M}_{l+1,m,n}+b^2\mathcal{M}_{l,m+1,n}+c^2\mathcal{M}_{l,m,n+1} \\ &= (2l+2m+2n+1)\mathcal{M}_{lmn} - \frac{(2l-1)!!\,(2m-1)!!\,(2n-1)!!\,abc}{(a^2+\xi)^{l+1/2}(b^2+\xi)^{m+1/2}(c^2+\xi)^{n+1/2}}\xi. \end{aligned} \quad (21)$$

Multiplying (20) by ξ and combining with (21), we rewrite (21) in the more compact form

$$\begin{aligned} &(a^2+\xi)\mathcal{M}_{l+1,m,n}+(b^2+\xi)\mathcal{M}_{l,m+1,n}+(c^2+\xi)\mathcal{M}_{l,m,n+1} \\ &\qquad = (2l+2m+2n+1)\mathcal{M}_{lmn}. \end{aligned} \quad (22)$$

Then, the form of (9) is preserved for the external factors. Hence, the recursion relations (14) also hold for $\mathcal{M}_{lmn}(\xi)$. Together with (20) and (22) these allow us to express the arbitrary external factor $\mathcal{M}_{lmn}(\xi)$ in terms of factors of unit weight $\mathcal{M}_{100}(\xi)$, $\mathcal{M}_{010}(\xi)$, and $\mathcal{M}_{001}(\xi)$. Although the latter are not tabulated, they are, however, very simply connected with the demagnetization coefficients of the ellipsoid. This is a general relation, and holds between the external and internal factors of an ellipsoid in general.

It is established in an elementary way. Actually if in the integral (5) we make the substitution

$$u = u' + \xi,$$

then

$$\mathcal{M}_{lmn}(\xi) = \frac{abc}{a'b'c'}M'_{lmn}, \quad (23)$$

where

$$a' = \sqrt{a^2+\xi}, \quad b' = \sqrt{b^2+\xi}, \quad c' = \sqrt{c^2+\xi},$$

and M'_{lmn} is the internal factor of an ellipsoid with semiaxes a', b', and c', i.e., a coordinate ellipsoid.

Thus, for all l, m, and n the ratio $\mathcal{M}_{lmn}/M'_{lmn}$ is equal to the ratio of the volume of the principal ellipsoid to the volume of the coordinate ellipsoid. Now it is clear that Eqs. (20) and (22) and the recursion relations for $\mathcal{M}_{lmn}(\xi)$ are essentially equivalent to Eqs. (12)-(14), written for the internal factors of the coordinate ellipsoid.

We will not write out the equations referring to the degenerate case of a spheroid, and we present only an expression for the external factor of a sphere:

$$\mathcal{M}_{lmn}(\xi) = \frac{(2l-1)!!\,(2m-1)!!\,(2n-1)!!}{2l+2m+2n+1}\frac{a^3}{r^{2(l+m+n)+1}}. \quad (24)$$

---

[1] O. E. Lysenko and N. A. Khizhnyak, Structure of the Space-Charge Field of an Ellipsoidal Bunch of Charged Particles [in Russian], Izd. FTI AN UkrSSR, Khar'kov (1970).

[2] F. J. Sacherer, IEEE Trans., NS-18, 1105 (1971).

[3] M. L. Levin and R. Z. Muratov, Zh. Tekh. Fiz., 38, 1623 (1968) [Sov. Phys. – Tech. Phys., 13, 1318 (1969)].

[4] O. E. Lysenko and N. A. Khizhnyak, Zh. Tekh. Fiz., 40, 475 (1970) [Sov. Phys. – Tech. Phys., 15, 366 (1970)].

[5] N. M. Ferrers, Quart. J. Pure and Appl. Math., 14, 1 (1877).

[6] F. W. Dyson, Quart. J. Pure and Appl. Math., 25, 259 (1891).

[7] M. L. Levin and R. Z. Muratov, Astrophys. J., 166, 441 (1971).

[8] J. A. Osborn, Phys. Rev., 67, 351 (1945).

[9] E. C. Stoner, Phil. Mag., Series 7, 36, 803 (1945).

[10] V. N. Beloozerov and R. Z. Muratov, Radiotekh. Elektron., 17, 902 (1972).

[11] R. Z. Muratov, Tr. Radiotekh. Inst., No. 11 (Teor. i Tekh. UsKor.), 212 (1972).

Generation of Bernstein modes in a beam–plasma system

V. N. Fedorenko

A. F. Ioffe Physicotechnical Institute, Academy of Sciences of the USSR, Leningrad

(Submitted April 4, 1973; resubmitted July 24, 1973)
Zh. Tekh. Fiz., 44, 267-272 (February 1973)

The correlation of fluctuating electric fields associated with Bernstein modes in a beam–plasma system is analyzed. The criteria for the kinetic instability of Bernstein modes are analyzed. Certain experimental results are interpreted.

1. STATEMENT OF THE PROBLEM

The excitation of Bernstein modes in a beam–plasma system has been discussed frequently in the literature in attempts to explain experiments on the anomalously intense electromagnetic radiation of a magnetoactive plasma at harmonics of the electron gyrofrequency.[1–7] The complexity of the dispersion relations and of the description of nonlinear effects for Bernstein modes has forced various workers to find instability criteria[3] or to calculate the polarization loss of fast electrons at harmonics of the electron gyrofrequency when there is no instability.[4] The incompleteness of the description in either approach is obvious; the problem requires further analysis.

We restrict the analysis below to the statistical properties of superthermal electric fields due to excitation of Bernstein modes in the beam–plasma system. We interpret certain experimental results[5–8] on this basis. The calculation is carried out by the "random-force" method[9] or the method of "dressed test particles;"[1] we actually calculate the superthermal increment in the electric field caused by a low-intensity beam of fast electrons in the plasma. The plasma is assumed to be infinite and homogeneous.

2. CORRELATION OF ELECTRIC FIELDS IN THE BEAM REGION

According to the method of dressed test particles the motion of electrons in a plasma in an external magnetic field is described by specifying their trajectories: $\mathbf{x}^s(t) = x_0^s + R_H^s \mathrm{Sin}(\omega_H t + \alpha_0^s)$; $y^s(t) = y_0^s + R_H^s \mathrm{Cos}(\omega_H t + \alpha_0^s)$; $z^s(t) = z_0^s + v_\parallel^s t$. The quantities x_0^s, y_0^s, z_0^s, α_0^s, $v_\parallel$, and $R_H^s = v_\perp^s/\omega_H^s$ are random quantities; an averaging will subsequently be carried out over them. Also, $\omega_H = eH/(mc)$ is the electron gyrofrequency, $v_\parallel^s$ and $v_\perp^s$ are the velocity components of electron s, and R_H^s is the electron Larmor radius. The plasma in which the test charge is moving is characterized by a dielectric tensor $\varepsilon_{ij}(\mathbf{k}, \omega)$. The Fourier component of the polarization electric field produced by this charge is[1,10]

$$\mathbf{E}^s(\mathbf{k}, \omega) = \frac{4\pi i\mathbf{k}}{k^2\varepsilon(\mathbf{k}, \omega)}\rho^s(\mathbf{k}, \omega). \tag{1}$$

Here, $\rho^s(\mathbf{k}, \omega) = e\int_{-\infty}^{\infty} \exp[-i\omega t + i\mathbf{k}\mathbf{r}^s(t)]dt$ is the Fourier component of the test-charge density, and $\varepsilon(\mathbf{k}, \omega) = [k_i\varepsilon_{ij}(\mathbf{k}, \omega)k_j]/k^2$ is the longitudinal dielectric constant of the plasma, which governs the dispersion of the electrostatic oscillations.[1,10] Calculating $\rho^s(\mathbf{k}, \omega)$ and using (1), we can write an equation for the autocorrelation function of the electric fields of the test charges in the $(\mathbf{k}, \omega)$ representation: $\langle E_\alpha(\mathbf{k}_1, \omega_1)E_\beta^*(\mathbf{k}_2, \varphi_2)\rangle$ (ref. 1). Since we are interested in only the superthermal increment to the electric fields within the plasma which is caused by the low-intensity electron beam in the plasma, we consider only the beam particles as test particles. Furthermore, we neglect the finite size of the beam region, i.e., we actually analyze the situation within this region. Carrying out the necessary averaging in $\langle E_\alpha(\mathbf{k}_1, \omega_1)E_\beta^*(\mathbf{k}_2, \omega_2)\rangle$ and transforming to the $(\mathbf{r}, t)$ representation, we find

$$\langle E_\alpha E_\beta^*\rangle = \frac{2}{\pi}N_1e^2\int\frac{f_1(\mathbf{v})\,d^3v}{|v_\parallel|}\sum_{m=-\infty}^{\infty}\int d^3k\,d\omega \times \frac{e^{i\omega\Delta t - i\mathbf{k}\Delta\mathbf{r}}k_\alpha k_\beta J_m^2(k_\perp R_H)\,\delta\left(k_\parallel - \frac{\omega - m\omega_H}{v_\parallel}\right)}{k^4|\varepsilon(\mathbf{k}, \omega)|^2}. \tag{2}$$

Here, N_1 is the density of beam particles; $f_1(\mathbf{v})$ is the distribution function of these particles, which satisfies $\int f_1(\mathbf{v})d^3v = 1$; $J_m(x)$ is the Bessel function. Since the system is homogeneous and in the steady state, the correlation function in the $(\mathbf{r}, t)$ representation, $\langle E_\alpha E_\beta^*\rangle$, is a function of only $|\Delta t| = |t_1 - t_2|$ and $|\Delta\mathbf{r}| = |\mathbf{r}_1 - \mathbf{r}_2|$.

In the case of slightly damped plasma waves in an equilibrium, magnetoactive, collisionless plasma, $\mathrm{Re}\,\varepsilon_0$ and $\mathrm{Im}\,\varepsilon_0$ are given by[1–4,11]

$$\mathrm{Re}\,\varepsilon_0(\mathbf{k}, \omega) = 1 - 2\left(\frac{\omega_p}{\omega_H}\right)^2\sum_{l=1}^{\infty}I_l(\lambda)\frac{e^{-\lambda}}{\lambda}\frac{l^2}{\left[\left(\frac{\omega}{\omega_H}\right)^2 - l^2\right]}, \tag{3}$$

$$\mathrm{Im}\,\varepsilon_0(\mathbf{k}, \omega) = \sqrt{\pi}\left(\frac{\omega_p}{\omega_H}\right)^2\alpha_0\sum_{l=-\infty}^{\infty}I_l(\lambda)\frac{e^{-\lambda}}{\lambda}e^{-\alpha_l^2}, \tag{4}$$

where $\lambda = (k_\perp r_H)^2$; $r_H = v_0/\omega_H$; $v_0 = \sqrt{T/m}$; and $\alpha_l = |(\omega - l\omega_H)/\sqrt{2}v_0k_\parallel|$.

The condition for small damping is $\alpha_l^2 \gg 1$; this condition can evidently be satisfied by choosing sufficiently small $k_\parallel$. It can be shown that a sufficient criterion is[3] $|k_\parallel| \ll k_\perp$. According to (2), the value of $k_\parallel$ is given by the "radiation condition" $k_\parallel = (\omega - m\omega_H)/v_\parallel$. If $\omega \approx m\omega_H$, the condition $(\alpha_l^m)^2 \gg 1$, which must hold for all l, is most sensitive to the term with $m = l$ in (4). For this term we must have $v_\parallel^2/(2v_0^2) \gg 1$. This result shows that only fast (superthermal) electrons can generate slightly damped Bernstein modes.

In an actual calculation on the basis of Eq. (2), taking Eqs. (3) and (4) into account, comparatively simple and graphic equations can be found only in the case $\omega_p^2 < \omega_H^2$, in which all branches of the Bernstein-mode dispersion curves are near and above each harmonic n of the gyrofrequency: $\Delta\omega_n(k_\perp) \equiv \omega_n(k_\perp) - n\omega_H \ll \omega_H$ (refs. 1-3, 11). In this case we need retain in Eq. (3) only the one term with $l = n$. Furthermore, if $[v_\parallel/\sqrt{2}v_0]^2 \gg 1$, but $[v_\parallel\Delta\omega_n(k_\perp)/(\sqrt{2}v_0\omega_H]^2 \lessdot 1$, we need retain only the one term with $l = m = n$ in Eqs. (2) and (4). We then find

$$\langle E_\alpha E_\beta^*\rangle = 4N_1 e^2 \int \frac{f_1(\mathbf{v})\, d^3v}{\eta(v_\parallel)\,|v_\parallel|} \sum_{n=1}^{\infty} \int d\mathbf{k}_\perp dk_\parallel \frac{k_\alpha k_\beta}{k^4} J_n^2(k_\perp R_H)\, \Delta\omega_n(k_\perp)$$

$$\times e^{i\omega_n(k_\perp)\Delta t - |\gamma_n(k_\perp)\Delta t| - i\mathbf{k}\Delta\mathbf{r}} \delta\left(k_\parallel - \frac{\Delta\omega_n(k_\perp)}{v_\parallel}\right), \qquad (5)$$

where

$$\left.\begin{aligned} &\Delta\omega_n(k_\perp) = n\omega_H \left(\frac{\omega_p}{\omega_H}\right)^2 I_n(\lambda)\frac{e^{-\lambda}}{\lambda}; \quad \gamma_n(k_\perp) = \eta(v_\parallel)\,\Delta\omega_n(k_\perp); \\ &\eta(v_\parallel) = \frac{\sqrt{\pi}}{2}\left|\frac{v_\parallel}{v_0}\right| \exp\left(-\frac{v_\parallel^2}{2v_0^2}\right) \ll 1; \quad d\mathbf{k}_\perp \equiv k_\perp dk_\perp d\Phi. \end{aligned}\right\} \qquad (6)$$

The summation is carried out over all the Bernstein modes.

We turn to an analysis of Eq. (5). a) Since $k_\parallel = [\Delta\omega_n(k_\perp)]/v_\parallel < \omega_H/v_\parallel$, and since typically[11,12] $k_\perp \sim r_H^{-1}$, we have $k_\parallel/k_\perp < v_0/v_\parallel \ll 1$. Accordingly, the autocorrelation function for the field components E_α and E_β along H is small in comparison with that of the normal components.

b) The spatial-correlation radius is given, according to (5), by $|\Delta r_\perp| \sim k^{-1} \sim R_H$; $|\Delta z| \sim k_\parallel^{-1} > k_\perp^{-1}\ (v_\parallel/v_0) \sim R_H(v_\parallel/v_0) \gg R_H$. The explanation for this result is that the test particles are completely uncorrelated, and the correlation radius for the electric fields in the plane perpendicular to H is governed by the Larmor radii of the individual particles, R_H. The correlation radius along H turns out to be much larger than R_H, because in this approximation the particles move without collisions along H, retaining their "initial phases."

c) The purely temporal ($\Delta r = 0$) correlation of the fields is governed, according to Eqs. (5) and (6), by the ranges of the frequency $\omega_n(k_\perp)$ in the integrals over $dk_\perp$ and by the relative weights of the terms in the summation over n. A numerical calculation shows that in the case under consideration here ($\omega_H^2 > \omega_p^2$) the term with n = 1 is important; the second term is an order of magnitude lower; etc. This behavior is in accordance with the circumstance that the "passband" $\Delta\omega_n(k_\perp)$ in the integrand becomes rapidly narrower with increasing harmonic index in the case $\omega_p^2 < \omega_H^2$ (refs. 1-4, 11). The correlation time $\Delta t \sim 1/[\Delta\omega_n(k_\perp)]$ turns out to be equal to several periods of the electron gyration, since $\Delta\omega_n(k_\perp) < \omega_H$. In the case $\omega_p^2 > \omega_H^2$ the passband is $\Delta\omega_n(k_\perp) \sim \omega_H$, and correlation time $\Delta t \sim 1/\omega_H$ turns out to be shorter than in the case $\omega_p^2 < \omega_H^2$).

d) Up to this point we have neglected the collisional damping of Bernstein modes. As a result we find the small factor $\eta(v_\parallel)$ in the denominator in (5), which comes from $\mathrm{Im}\,\varepsilon_0(\mathbf{k}, \omega_n(\mathbf{k}))$. At sufficiently large values of $v_\parallel$ the Bernstein modes are "radiated by the test particles" at very small angles with respect to the normal to the magnetic field: $k_\parallel/k_\perp \ll 1$. Accordingly, we have $\alpha_\xi^2 \gg 1$ in $\mathrm{Im}\,\varepsilon_0(\mathbf{k}, \omega)$, so the collisionless-damping factor becomes smaller than the collisional factor. The collisional damping of Bernstein modes has not been studied adequately. Works which have appeared on this question[12] do not furnish a basis for calculating the corresponding damping factor. As a rough estimate we can set $\gamma_{st} \sim \nu_{ei}$, where ν_{ei} is the effective frequency of electron–ion collisions, although this estimate could be too high in the case $\omega_p^2 < \omega_H^2$. According to (5), the maximum value of $\sqrt{\langle E^2\rangle}$ is governed by the minimum possible value of $\eta(v_\parallel^*)$, which in turn is found from the condition $\gamma_n(k_\perp) = \eta(v_\parallel^*) \times \Delta\omega_n(k_\perp) \geqslant \nu_{ei}$. This condition determines the optimum values of $v_\parallel^*$.

e) We have also neglected the contribution of the beam distribution function $f_1(\mathbf{v})$ to $\mathrm{Im}\,\varepsilon(\mathbf{k}, \omega)$. Within the framework of the method of dressed test particles we must require $|\mathrm{Im}\,\varepsilon_1(\mathbf{k}, \omega) < |\mathrm{Im}\,\varepsilon_0(\mathbf{k}, \omega)|$, in order to avoid a possible instability. As is shown in Sec. 4 below, this condition can be formulated approximately as $N_1/N_0 < \exp[-v_\parallel^2/2v_0^2]$.

On the basis of this analysis we can determine conditions under which the nonthermal increment to the electric fields due to the excitation of Bernstein modes reaches its maximum value, and we can estimate some values. For example, choosing $N_0 = 10^{13}$ cm^{-3}, we find $\omega_p = 2\cdot 10^{11}$ sec^{-1}. Then choosing $\omega_H = 1.5\,\omega_p = 3\cdot 10^{11}$ sec^{-1}, T = 1 eV, and $v_0 = 4\cdot 10^7$ cm/sec, we find, according to paragraph d), $\nu_{ei} \sim 5\cdot 10^8$ sec^{-1} and $\eta_{\min}(v_\parallel^*) = 2\cdot 10^{-3}$, which correspond to $v_\parallel^* = 4v_0 = 16\cdot 10^7$ cm/sec and $N_{1\max} \sim 10^{-3}N_0 \sim 10^{10}$ cm^{-3}. For these parameter values we have $\langle E^2\rangle_{\max} \sim 10^{-3}$ Oe/cm^3 and $\sqrt{\langle E^2\rangle} \approx 3\cdot 10^{-2}$ Oe$^{1/2}\cdot$cm$^{-3/2} \approx$ 10/V cm. The strength of the thermal fields, evaluated from the equation for an isotropic plasma,[1,9] $\langle E^2\rangle/N_0T \sim (2\pi N_0 L_d^3)^{-1}$, turns out to be on the same order of magnitude.

3. ACCOUNT OF THE FINITE TRANSVERSE DIMENSIONS OF THE BEAM. FIELD CORRELATION FAR FROM THE BEAM

Again we assume the plasma to be infinite and homogeneous, characterizing it by $\varepsilon_0(\mathbf{k}, \omega)$. In this statement of the problem we can take account of the finite size of the beam region in the direction transverse to H and analyze the correlation of the electric fields due to Bernstein modes outside the region in which these modes are generated. As a result we find an equation for $\langle E_\alpha E_\beta^*\rangle$ in the $(\mathbf{r}, t)$ representation which is analogous to Eq. (5), but in which the integrand in the integral over $d\mathbf{k}_\perp$ is multiplied by the function

$$F_n(\mathbf{r}_\perp, \mathbf{k}_\perp) = \frac{a^2}{2\pi} \int d\Delta\mathbf{k}_\perp \frac{J_1(a|\Delta\mathbf{k}_\perp|)}{a|\Delta\mathbf{k}_\perp|} e^{-\mathbf{r}_\perp\Delta\mathbf{k}_\perp}$$

$$\times \left\{1 - i\mathbf{k}_\perp\cdot\Delta\mathbf{k}_\perp \frac{dg_n(k_\perp^2)}{dk_\perp^2}[g_n(k_\perp^2)\,\eta(v_\parallel)]^{-1}\right\}^{-1}, \qquad (7)$$

where a is the radius of the cylindrical beam, $\mathbf{k}_\perp = (1/2)(\mathbf{k}_{1\perp} + \mathbf{k}_{2\perp})$; $\Delta\mathbf{k}_\perp = \mathbf{k}_{1\perp} - \mathbf{k}_{2\perp}$; $g_n(k_\perp^2) = I_n(\lambda)e^{-\lambda}\lambda^{-1}$; $\lambda = k_\perp^2 r_H^2$. Since $|\mathbf{k}_{1\perp}| \sim |\mathbf{k}_{2\perp}| \sim r_H^{-1}$ and since we effectively have $|\Delta\mathbf{k}_\perp| \sim a^{-1}$, where we are assuming $a \gg r_H$, we find $|\Delta\mathbf{k}_\perp/\mathbf{k}_\perp| \sim r_H/a \ll 1$. As $a \to \infty$ we find $F_n(\mathbf{r}_\perp, \mathbf{k}_\perp) \to 1$, and we again find Eq. (5).

The correlation function $\langle E_\alpha E_\beta^*\rangle$ taking $F_n(\mathbf{r}_\perp, \mathbf{k})$ into account is a function of Δt, $\Delta\mathbf{r}$, and $\mathbf{r}_\perp$, the distance from the beam axis. The factor for the propagation of Bernstein modes away from the beam axis takes $F_n(\mathbf{r}_\perp, \mathbf{k}_\perp)$ into account. We see from the structure of $F_n(\mathbf{r}_\perp, \mathbf{k}_\perp)$ that the quantity

$$L_d^{(n)r}(k_\perp) = \left|k_\perp - \frac{dg_n(k_\perp^2)}{dk_\perp^2}[g_n(k_\perp^2)\,\eta(v_\parallel)]^{-1}\right|$$

serves as the damping length for Bernstein mode n with specified $k_\perp$. This quantity is equal to that calculated from the familiar equation:[10] $L_d(k) = v_g(k)/\gamma(k) = \partial\omega(k)/\partial k\gamma^{-1}(k)$, where $\omega(k)$ and $\gamma(k)$ must be written in accordance with Eq. (6). Bernstein modes are observed outside the beam if $L_d^{(n)}(k_\perp) \gg a$, but this condition cannot be satisfied at all wavelengths. As is evident from the dispersion curves,[1-3] there are regions of $k_\perp$ in which $\partial\omega/(\partial k_\perp) \approx 0$. We restrict the discussion here to the particular case for which Eq. (5) is derived. According to paragraph c of Sec. 2, only the harmonic with n = 1 is important in this equation. The dispersion curves for the first Bernstein mode show that the low group velocities are found at $k_\perp r_H \ll 1$; over a broader part of the passband, on the other hand, where $k_\perp \sim r_H^{-1}$, we have $v_g \sim v_0$, with $\partial\omega^{(1)}(k_\perp^2)/(\partial k_\perp^2) < 0$, corresponding formally to a "negative group velocity."[1] Accordingly, the condition $L_d^{(1)}(k_\perp) \gg a$ can be satisfied for nearly all wavelengths. For example, with $v_0 = 4 \cdot 10^7$ cm/sec and $H = 10^3$ G we find $r_H \simeq 10^{-3}$ cm, while with $\eta(v_\parallel) \simeq 10^{-3}$ we find $L_d^{(1)} \sim$ 1 cm. Let us examine the behavior of $\langle E_\alpha E_\beta^*\rangle$ outside the beam: $r_\perp \gg a$ (for $L_d^{(1)} \gg a$). We evaluate $F_1(\mathbf{r}_\perp, \mathbf{k}_\perp)$ and use the result for the integration in (5) over Φ in the integral over $d\mathbf{k}_\perp = k_\perp dk_\perp d\Phi$. Here the k_x axis in $\mathbf{k}_\perp$ space is directed along $\mathbf{r}_\perp$, while we have $k_y \parallel \mathbf{r}_\perp$. We find

$$\langle E_x E_x^*\rangle \sim \left(\frac{a}{r}\right)\exp\left[-\frac{r_\perp}{L_d^{(1)}(k_\perp)}\right];$$

$$\langle E_y E_x^*\rangle \sim \left(\frac{a}{r}\right)^2\exp\left[-\frac{r_\perp}{L_d^{(1)}(k_\perp)}\right];$$

$$\langle E_y E_y^*\rangle \sim \left(\frac{a}{r}\right)^3\exp\left[-\frac{r_\perp}{L_d^{(1)}(k_\perp)}\right].$$

There is an interesting feature in the space–time correlation of the fields in the case $r_\perp \gg a$, $L_d^{(1)} \gg a$. It turns out that, since $[\partial\omega^{(1)}(k_\perp^2)]\,(\partial k_\perp^2) < 0$, an important role in the integral over $d\Phi$ is played by angles $\Phi \approx \pi$, i.e., $\mathbf{k}_\perp$ is antiparallel to $\mathbf{r}_\perp$. If we choose $\Delta \mathbf{r}_\perp \parallel \mathbf{r}_\perp$ we find that the factor $\exp[i\omega^{(1)}(k_\perp)\Delta t + k_\perp \Delta r_\perp]$ in Eq. (5) characterizes a wave process in which the phase surfaces move in the direction opposite $\Delta\mathbf{r}_\perp$, i.e., toward the beam axis.

4. KINETIC INSTABILITIES OF THE BEAM IN A PLASMA WITH RESPECT TO EXCITATION OF BERNSTEIN MODES

Tataronis and Crawford[3] analyzed hydrodynamic instabilities of a system consisting of a Maxwellian plasma and a "cold" beam, $f_1(\mathbf{v}) = 1/2\pi v_\perp^*)\,[\delta(v_\parallel - v_\parallel^*)\,\delta(v_\perp - v_\perp^*)]$, in the frequency intervals between harmonics of the electron gyrofrequency. The hydrodynamic stage in the beam relaxation is rapidly replaced by a kinetic stage,[13] so it is interesting (particularly in the case of steady-state injection) to study the development of instabilities at harmonics of the gyrofrequency for a beam having a thermal spread. We therefore write $f_1(\mathbf{v})$ as

$$f_1(\mathbf{v}) = \alpha\,\frac{\exp\left[-\left(\frac{v_\parallel - v_\parallel^*}{\Delta v_\parallel}\right)^2 - \left(\frac{v_\perp - v_\perp}{\Delta v_\perp}\right)^2\right]}{2\pi^2\xi\Delta v_\parallel \Delta v_\perp^2}, \tag{8}$$

where $\alpha = N_1/N_0 \ll 1$; $\xi = v_\perp^*/\Delta v_\perp \gg 1$; $v_\parallel^*/\Delta v_\parallel \gg 1$; $v_\parallel^*/v_\perp^* \gg 1$; and $\int f_1(\mathbf{v})d^3v = \alpha$.

Beams like that described approximately by $f_1(\mathbf{v})$ in (8) have been produced experimentally.[5-8] To calculate $\mathrm{Im}\,\varepsilon_1(\mathbf{k}, \omega)$ with $f_1(\mathbf{v})$ and to compare it with $\mathrm{Im}\,\varepsilon_0(\mathbf{k}, \omega)$, we use the standard equations,[1-3,10,11] finding

$$\mathrm{Im}\,\varepsilon_1(\mathbf{k}, \omega) = \frac{2\sqrt{\pi}\,\omega_p^2\alpha}{k^2|k_\parallel|(\Delta v_\parallel)^3}\sum_{l=-\infty}^{\infty} e^{-\left(\frac{\omega - l\omega_H - k_\parallel v_\parallel^*}{k_\parallel \Delta v_\parallel}\right)^2} \times J_l^2\left(\frac{k_\perp v_\perp^*}{\omega_H}\right)(\omega - l\omega_H - k_\parallel v_\parallel^*). \tag{9}$$

In deriving (9) we assumed $k_\perp \Delta v_\perp \ll \omega_H$. Since $k_\perp \sim r_H^{-1}$ for Bernstein modes, this condition implies $\Delta v_\perp \ll v_0$. Since there is a magnetic field, the case $\Delta v_\parallel \gg \Delta v_\perp$ is possible.

Comparison of Eqs. (9) and (4) shows that for the harmonic with $\omega(k_\perp) \simeq l\,\omega_H$ the values of $k_\parallel = [\omega(k_\perp) - l\,\omega_H]/v_\parallel$ found from the "radiation condition" cause an exponentially weak damping of waves in a Maxwellian plasma, $\mathrm{Im}\,\varepsilon_0 \sim \exp[-v_\parallel^2/(2v_0^2)] \ll 1$ [see Eq. (6)], but the corresponding exponential function in $\mathrm{Im}\,\varepsilon_1$ is not small:

$$\exp\left[-\left(\frac{\omega - l\omega_H}{k_\parallel \Delta v_\parallel} - \frac{v_\parallel^*}{\Delta v_\parallel}\right)^2\right] = \exp\left[-\left(\frac{v_\parallel - v_\parallel^*}{\Delta v_\parallel}\right)^2\right] \leqslant 1.$$

Accordingly, to satisfy the condition $|\mathrm{Im}\,\varepsilon_1| < |\mathrm{Im}\,\varepsilon_0|$ we can write the approximate criterion $\alpha = N_1/N_0 < \exp[-v_\parallel^2/(2v_0^2)]$. The sign of $\mathrm{Im}\,\varepsilon_1$ is governed by the quantities in the brackets in (9) and can be either positive or negative. When $|\mathrm{Im}\,\varepsilon_1| > |\mathrm{Im}\,\varepsilon_0|$, an instability develops in the region $\mathrm{Im}\,\varepsilon_1 < 0$. Stone and Auer[4] have calculated the rate at which fast electrons are lost due to excitation of Bernstein modes by the method of dressed test particles. Comparison of this theory with experiment[7] shows that it is necessary to postulate a group of particles with $v_\perp^* \sim 4v_0$ and $\alpha \sim 0.1$ in the plasma in order to explain the observed intensity of the radiation at the harmonics and to explain the observed spectral characteristics (under the assumption of a 100% transformation of Bernstein modes into electromagnetic waves). However, an instability should develop under these conditions, since we have $\exp[-v_\parallel^2/(2v_0^2)] \sim 10^{-3}$. Apparently an instability with respect to the excitation of Bernstein modes develops in all experiments carried out to observe radiation at harmonics, so it becomes a theoretical problem to explain the intensity of this radiation.

Idehara et al.[6] measured the intensity of the radiation at the harmonics as a function of the path length traveled by the beam in the plasma during steady-state injection, z. In the region z < z* they observe a rapid increase in the intensity; at z = z* they observe saturation and then a comparatively slower decay. Equation (9) yields a qualitative explanation for this behavior. This behavior reflects primarily the course of the beam relaxation due to excitation of numerous branches of waves, even when the situation is clearly not one-dimensional ($\omega_p > \omega_H$). The theoretical relaxation models of ref. 14 therefore cannot be used, but we can assume that the relaxation consists of an increase in the values $\Delta v_\parallel$ and $\Delta v_\perp$ in (8) with increasing z (unfortunately, the corresponding experimental data are not given in ref. 6). The factor governing the amplitude of Bernstein modes, which is proportional to $\mathrm{Im}\,\varepsilon_1(\mathbf{k}, \omega)$ according to (9), behaves in the following manner: For $z < z^*(\Delta v_\parallel < \Delta v_\parallel^*)$ the minimum arguments of the exponential functions in (9) are larger than unity, but the increase in $\Delta v_\parallel$ with increasing z leads to a rapid increase in the factor and to its saturation at $z = z^*$ and $\Delta v_\parallel = \Delta v_\parallel^*$, at which point the minimum arguments are again on the order of unity. With a further increase in

$\Delta v_{\parallel}$ and $\Delta v_{\perp}$, there is a slower (power-law) decrease in the factor.

We note that the approximate criterion for kinetic instability of the beam with respect to the excitation of Bernstein modes which we found above, $N_1/N_0 > \exp[-v_{\parallel}^2/(2v_0^2)]$, is not affected by the relation between ω_p and ω_H. This situation is characteristic of a hydrodynamic instability, which has been predicted[3] only for $\omega_p^2 > \omega_H^2$. Incidentally, in certain experiments[8] the instability at the harmonics develops even with $\omega_p^2 < \omega_H^2$.

In conclusion the author thanks A. S. Grebinskii, A. Z. Dolginov, A. D. Piliya, V. I. Federov, and D. G. Yakovlev for several discussions of this work.

---

[1] G. Bekefi, Radiation Processes in a Plasma, Wiley, New York (1967).

[2] F. W. Crawford, Nuclear Fusion, 5, 73 (1965).

[3] J. A. Tataronis and F. W. Crawford, J. Plasma. Phys., 4, 231 (1970).

[4] P. M. Stone and P. L. Auer, Phys. Rev., 138, A695 (1965).

[5] T. Idehara, K. Ohkubo, and S. Tanaka, J. Phys. Soc. Japan, 27, 187 (1969).

[6] T. Idehara, K. Ohkubo, and S. Tanaka, J. Phys. Soc. Japan, 30, 1169 (1971).

[7] C. D. Lustig, Phys. Rev., 139, A63 (1965).

[8] G. Bekefi and E. B. Hooper, Appl. Phys. Lett., 4, 135 (1964).

[9] A. G. Sitenko, Electromagnetic Fluctuations in a Plasma [in Russian], Izd. KhGU, Khar'kov (1965).

[10] V. L. Ginzburg and A. A. Rukhadze, Waves in a Magnetoactive Plasma [in Russian], Izd. Nauka, Moscow (1970).

[11] A. B. Mikhailovskii, Theory of Plasma Instabilities, Vol. 1, Consultants Bureau, New York (1973).

[12] A. E. Krupina, Izv. VUZ. Radiofiz., 13, 849 (1970); 15, 517 (1972).

[13] V. N. Tsytovich, Theory of a Turbulent Plasma [in Russian], Atomizdat, Moscow (1971).

[14] Ya. B. Fainberg and V. D. Shapiro, Zh. Eksp. Teor. Fiz., 47, 1389 (1964) [Sov. Phys. – JETP, 20, 937 (1965)].

Plasma

Excitation of electromagnetic ion cyclotron waves by fast ions

T. D. Kaladze, D. G. Lominadze, and K. N. Stepanov

(Submitted May 16, 1973)
Zh. Tekh. Fiz., 44, 273-276 (February 1974)

The growth rate is computed for ion cyclotron waves that propagate across the magnetic field in a deuterium plasma. The waves are excited by a low-density beam of fast ions that result from fusion reactions.

The presence of fast monoenergetic ions (products of fusion reactions) leads to various plasma instabilities.[1-8] In a low-pressure plasma the largest growth rates correspond to electrostatic plasma oscillations[2] and fast magnetoacoustic waves[8] propagating nearly at right angles to the magnetic field. The electrostatic oscillations considered in ref. 2 are excited only when $\beta \leqslant 10^{-3}$. The fast magnetoacoustic waves considered in ref. 8 are not an isolated branch at $\beta \geqslant 0.1$ but represent segments of the ion cyclotron modes.[9,10]

In the present paper we use the analysis of ion cyclotron modes of ref. 10 to investigate excitation of these modes by fast monoenergetic ions. We show that the growth rate for these modes is of the same order as those considered in refs. 2 and 8:

$$\gamma = \eta\left(\frac{n_0'}{n_0}\right)^{1/3}\omega_{Bi}, \tag{1}$$

where n_0' and n_0 are the densities of the fast and cold ions, respectively.

The dispersion relation for extraordinary waves propagating at right angles to the magnetic field is

$$(\varepsilon_1+\delta\varepsilon_1)N^2-(\varepsilon_1+\delta\varepsilon_1)(\varepsilon_1'+\delta\varepsilon_1')+(\varepsilon_2+\delta\varepsilon_2)^2=0, \tag{2}$$

where $N = kc/\omega$ is the refractive index. In the absence of the fast ions the components of the permittivity tensor ε_i are

$$\varepsilon_1=-\frac{\omega_{pi}^2}{\omega}\sum_{n=-\infty}^{\infty}\frac{a_1}{\omega-n\omega_{Bi}},$$

$$\varepsilon_1'=-\frac{\omega_{pi}^2}{\omega}\sum_{n=-\infty}^{\infty}\frac{a_1'}{\omega-n\omega_{Bi}},$$

$$\varepsilon_2=-\frac{\omega_{pe}^2}{\omega\omega_{Be}}-\frac{\omega_{pi}^2}{\omega}\sum_{n=-\infty}^{\infty}\frac{a_2}{\omega-n\omega_{Bi}},$$

where

$$a_1=\frac{n^2}{x^2}e^{-x^2}I_n(x^2),$$

$$a_1'=\left[\frac{n^2}{x^2}I_n(x^2)+2x^2(I_n(x^2)-I_n'(x^2))\right]e^{-x^2},$$

$$a_2=n\left[I_n'(x^2)-I_n(x^2)\right]e^{-x^2},$$

$x = k\rho_i$, $\rho_i = v_{Ti}/\omega_{Bi}$ is the ion Larmor radius for the thermal velocity $v_{Ti} = (T_i/m_i)^{1/2}$, $I_n(x^2)$ is the modified Bessel function and I_n' is the derivative.

The contribution of the fast monoenergetic ions to the components of the permittivity tensor is determined by the relations

$$\delta\varepsilon_1=\frac{\omega_p'^2}{k^2v_0^2}-\frac{\omega_p'^2}{\omega_B'}\sum_{n=-\infty}^{\infty}\frac{b_1}{\omega-n\omega_B'},$$

$$\delta\varepsilon_1'=-\frac{\omega_p'^2}{\omega_B'}\sum_{n=-\infty}^{\infty}\frac{b_1'}{\omega-n\omega_B'}-\delta\varepsilon_1,$$

$$\delta\varepsilon_2=-\frac{\omega_p'^2}{\omega_B'}\sum_{n=-\infty}^{\infty}\frac{b_2}{\omega-n\omega_B'},$$

where

$$b_1=\frac{4}{A^2}\frac{\omega}{\omega_B'}J_{2n}(A),$$

$$b_1'=\frac{1}{A}\frac{\omega_B'}{2\omega}\left\{A\left[J_{2(n-1)}(A)+J_{2(n+1)}(A)\right]\right.$$

$$\left.+\int_0^A\left[J_{2(n-1)}(y)+J_{2(n+1)}(y)\right]dy\right\},$$

$$b_2=\frac{2}{A}J_{2n}'(A),\quad A=\left(\frac{2kv_0}{\omega_B'}\right),$$

J_{2n} is the Bessel function, $\omega'_p = (4\pi z'e^2n_0'/m')^{1/2}$ is the plasma frequency of the fast ions, $\omega'_B = z'eB_0/(m'c)$ is the cyclotron frequency of the fast ions, and v_0 is the velocity (we ignore the thermal energy spread $\sim T_i$ of the fast ions compared with $m'v_0^2/2$).

In the zeroth approximation ($n'_0 \to 0$), the dispersion relation (2) has solutions $\omega = \omega^{(j)}(k)$, where $(j-1)\omega_{Bi} < \omega^{(j)} < j\omega_{Bi}$ ($j = 1, 2 \ldots$), corresponding to cyclotron waves in the plasma (see refs. 9 and 10) and solutions corresponding to cyclotron oscillations of the fast ions: $\omega = n\omega'_B$. An instability arises when $n'_0 \ll n_0$ in the intersection region of these curves $k \approx k_0$, where $\omega^{(j)}(k_0) = n\omega'_B$.

Setting $\omega = \omega^{(j)}(k) + \Delta\omega$, where $\Delta\omega \ll \omega_{Bi}$ from (2) we have

$$\Delta\omega=-\frac{1}{2}(\omega^{(j)}-n\omega_B')\pm\frac{1}{2}\left[(\omega^{(j)}-n\omega_B')^2-4\gamma_m^2\right]^{1/2}, \tag{3}$$

where

$$\gamma_m^2=-\frac{\omega_p'^2}{\omega_B'}\left.\frac{\left[(N^2+\varepsilon_1-\varepsilon_1')b_1-\varepsilon_1b_1'+2\varepsilon_2b_2\right]}{\frac{d}{d\omega}(\varepsilon_1N^2-\varepsilon_1\varepsilon_1'+\varepsilon_2^2)}\right|_{\omega=\omega^{(j)}} \tag{4}$$

An instability occurs for $\gamma_m^2 > 0$ if $|\omega^{(j)} - n\omega'_B| < 2\gamma_m$. The maximum value of the growth rate γ_m is of the same order as (1). For a low-pressure plasma ($\beta \ll 1$), Eq. (4) goes over into the expression obtained in ref. 8 when $k\rho_i \ll 1$.

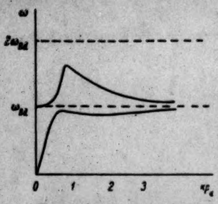

Fig. 1. Frequencies $\omega^{(j)}(k)$ (j = 1, 2) as a function of $k\rho_d$ for a deuterium plasma with β_i = 0.1 in the absence of fast ions.

For a deuterium plasma (i = d), the spectra in the absence of fast ions are shown in Fig. 1 for β = 0.1 (more detailed curves for $\omega^{(j)}(k)$ are shown in ref. 10). In the presence of fast tritium ions, these spectra are changed as shown in Fig. 2.

Using the results of the numerical calculations of ref. 10, one can show that for $\beta \geqslant 1$ an intersection of the branches $\omega = \omega^{(j)}(k)$ and $\omega = \omega_{Bt} = (2/3)\,\omega_{Bd}$ is possible for only the first cyclotron branch of the oscillations of a deuterium plasma ($0 < \omega^{(1)}(k) < \omega_{Bd}$), which corresponds in the longwave limit ($k\rho_i \ll 1$) to a magnetoacoustic wave with frequency $\omega(k) = kv_A$, where $v_A = c\omega_{Bi}/\omega_{pi}$. For $\beta \leq 0.1$, an "interaction" of the cyclotron branch $\omega = n\omega_{Bd}$ occurs for both the first branch $\omega = \omega^{(j)}(k)$ and for the branches with higher numbers $j \geq 2$. For $j \geq 2$, the frequency $\omega^{(j)}(k)$ intersects the frequency $n\omega'_B$ at two values x_0.

TABLE 1

j	β	$x_0 = k_0\rho_i$	A	η
1	0.1	0.2	10	0.21
	1	0.4	16	0.20
	10	0.5	16	0.19
2	0.1	0.4	12	0.22
		1.5	42	0.02
3	0.1	0.8	28	0.51
		1.2	33	0.07
4	0.1	0.9	23	0.26
		3.6	105	0.02
5	0.1	1.3	39	0.23
		2.3	70	0.05
6	0.1	1.4	41	0.27
		5.6	167	0.02

TABLE 2

j	β	$x_0 = k_0\rho_i$	A	η
2	0.1	0.4	12	0.31
		1.5	23	0.07
3	0.1	0.8	13	0.44
		1.2	20	0.15
6	0.1	1.4	19	0.66
		5.6	85	0.08

In Table 1 we give the results of a calculation of the growth rate for the first six branches excited by fast tritium ions. It is assumed that $v_{Td} = 0.1v_0$. Table 1 contains the calculated values of the coefficient η, which occurs in Eq. (1) for the growth rate, and also the values of the parameter $x_0 = k_0\rho_i$ at which the branches intersect and the corresponding values of A. Similar results for fast He³ ions are shown in Table 2. In this case $\omega'_B = \omega_{BHe^3} = (4/3)\omega_{Bd}$ $v_{Td} = 0.1v_0$. The results given in Tables 1 and 2 confirm the estimate (1) (the value of η varies for the first branches in the range $0.1 \leqslant \eta \leqslant 1$).

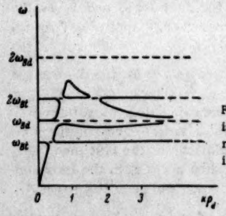

Fig. 2. Dependence of the characteristic frequencies of a deuterium plasma in the presence of a group of fast ions at low density.

---

[1] Ya. I. Kolesnichenko and V. N. Oraevskii, At. Energ., 23, 289 (1967).

[2] L. V. Korablev, Zh. Eksp. Teor. Fiz., 53, 1600 (1967) [Sov. Phys. – JETP, 26, 922 (1968)].

[3] L. V. Korablev and L. I. Rudakov, Zh. Eksp. Teor. Fiz., 54, 818 (1968) [Sov. Phys. – JETP, 27, 439 (1968)].

[4] V. S. Belikov, Ya. I. Kolesnichenko, and V. N. Oraevskii, Zh. Eksp. Teor. Fiz., 55, 2210 (1968) [Sov. Phys. – JETP, 28, 1172 (1969)].

[5] Ya. I. Kolesnichenko, Ukr. Fiz. Zh., 14, 1070 (1969).

[6] V. S. Belikov, Ya. I. Kolesnichenko, and V. N. Oraevskii, Ukr. Fiz. Zh., 14, 1242 (1969).

[7] V. S. Belikov, Ya. I. (Ja. J.) Kolesnichenko, and V. N. Oraevskii (Oraevskiy), Plasma Physics and Controlled Nuclear Fusion Research, Vienna IAEA, Vol. III (1971), p. 411.

[8] A. B. Mikhailovskii, in: Reviews of Plasma Physics, Vol. 6 [in Russian], Atomizdat, Moscow (1972).

[9] A. B. Kitsenko and K. N. Stepanov, Nucl. Fusion, 4, 272 (1964).

[10] T. D. Kaladze, D. G. Lominadze, and K. N. Stepanov, Zh. Tekh. Fiz., 42, 243 (1972) [Sov. Phys. – Tech. Phys., 17, 196 (1972)].

Parametric instability of an electron beam in a magnetic field

A. I. Pasynok and N. S. Repalov

Physicotechnical Institute, Academy of Sciences of the Ukrainian SSR, Khar'kov

(Submitted April 13, 1973)
Zh. Tekh. Fiz., 44, 277-283 (February 1974)

A linear theory is developed for the oscillations of an electron beam in a spatially periodic electrostatic field in a presence of a homogeneous magnetic field. In contrast to the case $H_0 \to \infty$, there are additional resonance regions due to the intersection of branches of the dispersion diagram. The conditions under which such resonances occur are studied; expressions are obtained for the maximum growth rates in these resonance regions; the dependence of the growth rate on the period of the modulating field and on the magnitude of the magnetic field are found.

The parametric instability characteristic of an electron beam moving in an external modulating electrostatic field can have important practical applications. The large controllable growth rate[1] and the possibility of frequency tuning and control of the bandwidth[2] make the use of such an arrangement as a microwave amplifier or generator very promising. In the higher resonance regions ($k_0U_0 = n\omega_0$, $n = 3, 4 \ldots$) the interaction between the characteristic oscillations of the beam and the external modulating field leads to effective exchange of energy between the spectral components of the beam oscillations, in which case it is possible to get amplification at a multiplied frequency.[3]

Although the nonlinear theory predicts a suppression of the instability,[4] this occurs at a fairly large amplitude of the electric field of the wave. Therefore, the effect of resonance amplification of space-charge waves of a beam by an external electrostatic field can be used for collective acceleration of charged particles. A high-current electron beam is the basis of a device that is to realize such acceleration. Bearing in mind that the effect of the electric field of the wave approaches the effect of the focusing magnetic field $[(a\omega_0/c) \to \omega_H/\omega_0]$ with increasing beam density, we conclude that the motion of the particles at right angles to the magnetic field can have a significant influence. In addition, the study of the parametric instability in a finite magnetic field is also of interest from another point of view: Under these conditions there exist resonance regimes due to an additional (not present in the case $\omega_H/\omega_0 \to \infty$) branch of characteristic oscillations of the beam. In some cases (for example, when one uses a cold cathode) such resonances are more accessible to experimental investigation than the plasma resonances.[5]

ELECTRIC FIELD IN A MODULATED CYLINDRICAL BEAM

Restricting our study to the linear stage of the instability, we consider the propagation of a weak signal along an electron beam of radius a moving in a perfectly conducting waveguide. The beam is modulated by an electrostatic field $E_M = E_0 \sin k_0 z$ and focused by a homogeneous magnetic field H_0 directed along the axis of the system. The hydrodynamic parameters of the beam in a steady state are given by[2]

$$U_{st} = U_0(1 - \xi\cos k_0 z), \quad n_{st} = n_0(1 + \xi\cos k_0 z),$$

where $\xi = (e\varphi_0)/2mU_0^2$ and φ_0 is the potential of the modulating field. Being interested primarily in slow waves ($U_{ph} \ll c$) and assuming, therefore, that the perturbations are electrostatic, $\mathbf{E} = -\nabla\varphi$, we write the original system of equations in the form

$$\Delta\varphi = -4\pi e n, \quad \frac{\partial n}{\partial t} + \operatorname{div} n\mathbf{U} = 0, \quad m\frac{d\mathbf{U}}{dt} = -e\nabla\varphi + \frac{e}{c}\mathbf{U}\times\mathbf{H}. \tag{1}$$

Since the deviations of all quantities from their values in the steady state are assumed to be small, we linearize the continuity equation and the equation of motion. Then for axisymmetric perturbations ($\partial/(\partial\varphi) = 0$) that depend on the time as $e^{i\omega t}$, we obtain

$$\begin{gathered} i\omega n_1 + n_{st}(z)\left(\frac{\partial U_{1r}}{\partial r} + \frac{U_{1r}}{r} + \frac{\partial U_{1z}}{\partial z}\right) + U_{st}(z)\frac{\partial n_1}{\partial z} \\ -(n_1U_0 - n_0U_1)\frac{\partial U_{st}(z)}{\partial z} = 0, \\ i\omega U_{1r} + U_{st}(z)\frac{\partial U_{1r}}{\partial z} = -\frac{e}{m}\frac{\partial\varphi_1}{\partial r} + \omega_H U_{1\varphi}, \\ i\omega U_{1\varphi} + U_{st}(z)\frac{\partial U_{1\varphi}}{\partial z} = -\omega_H U_{1r}, \\ i\omega U_{1z} + U_{st}(z)\frac{\partial U_{1z}}{\partial z} + \xi k_0 U_0 U_{1z}\sin k_0 z = -\frac{e}{m}\frac{\partial\varphi_1}{\partial z}, \end{gathered} \tag{2}$$

where the subscript 1 is appended to the deviations of the corresponding quantities from their values in the steady state.

Making a Fourier transformation with respect to the z coordinate in the original system of equations, we find that the Poisson equation becomes

$$\frac{1}{r}\frac{\partial}{\partial r}r\frac{\partial}{\partial r}\varphi(k, r) - k^2\varphi(k, r) = -4\pi e\mathbf{n}(k, r), \tag{3}$$

and the equation of motion and the continuity equation form an infinite chain of algebraic equations that can be written symbolically as

$$\left.\begin{gathered} n\left(\frac{1}{r} + \frac{\partial}{\partial r}\right)\hat{D}\mathbf{U}_r + \hat{M}\mathbf{n} - n_0\hat{N}\mathbf{U}_z = 0, \\ \hat{K}\mathbf{U}_r = -\frac{e}{m}\frac{\partial\varphi}{\partial r} + \omega_H\mathbf{U}_\varphi, \\ \hat{K}\mathbf{U}_\varphi = -\omega_H\mathbf{U}_r, \\ \hat{M}\mathbf{U}_z = \frac{e}{m}\hat{L}\varphi. \end{gathered}\right\} \tag{4}$$

Here, $\mathbf{U}_\alpha$, $\mathbf{n}$, and φ are column vectors of infinite dimension in the wave-number space ($k \pm mk_0$, $m = 0, 1, 2 \ldots$) and the subscript 1 has been omitted. The elements of the matrices $\hat{D}$, $\hat{M}$, $\hat{N}$, $\hat{K}$, and $\hat{L}$ are

$$\left.\begin{gathered} D_{mn} = \frac{\xi}{2}\delta_{m-1n} + \delta_{mn} + \frac{\xi}{2}\delta_{m+1n}, \\ M_{mn} = \lambda_m\delta_{m-1n} + \gamma_m\delta_{mn} + \lambda_m\delta_{m+1n}, \\ N_{mn} = \frac{\lambda_m}{U_0}\delta_{m-1n} + ik_m\delta_{mn} + \frac{\lambda_m}{U_0}\delta_{m+1n}, \\ K_{mn} = \lambda_{m-1}\delta_{m-1n} + \gamma_m\delta_{mn} + \lambda_{m+1}\delta_{m+1n}, \\ L_{mn} = ik_m\delta_{mn}, \end{gathered}\right\} \tag{5}$$

where $\gamma_m = i(\omega - (k \pm mk_0)U_0)$; $\lambda_m = i(\xi/2)(k \pm mk_0)U_0$;

$k_m = k \pm mk_0$. Multiplying the last three equations in (4) by the corresponding inverse matrices, we find the vectors

$$\begin{gathered} \mathbf{U}_r = -\frac{e}{m}\hat{K}^{-1}\frac{\partial\varphi}{\partial r} + \omega_H\hat{K}^{-1}\mathbf{U}_\varphi, \\ \mathbf{U}_\varphi = -\omega_H\hat{K}^{-1}\mathbf{U}_r, \\ \mathbf{U}_z = \frac{e}{m}\hat{M}^{-1}\hat{L}\varphi. \end{gathered} \tag{6}$$

The relations in (6) together with the first equation of (4) can be used to express the perturbation of the beam density in terms of the wave potential:

$$\mathbf{n} = \frac{e}{m}n_0\left[\hat{M}^{-1}\hat{N}\hat{M}^{-1}\hat{L} + \frac{1}{r}\frac{\partial}{\partial r}\left(r\frac{\partial}{\partial r}\right)\hat{M}^{-1}\hat{D}\hat{F}^{-1}\hat{K}^{-1}\right]\varphi, \tag{7}$$

where $\hat{F} = \hat{e} + \omega_H^2(\hat{K}^{-1})^2$ and $\hat{e}$ is the identity matrix in the k space.

Substitution of $\mathbf{n}$ from (7) into Eq. (3) leads to the final equation, which describes the propagation of a weak signal along an electron beam focused by a homogeneous longitudinal magnetic field of arbitrary magnitude:

$$\frac{1}{r}\frac{\partial}{\partial r}\left(r\frac{\partial}{\partial r}\right)\varphi - k^2\varphi = -\omega_0^2\hat{Q}\varphi, \tag{8}$$

where $\hat{Q}$ is the linear operator in the square brackets of Eq. (7).

The inverse matrices in $\hat{Q}$ can be represented as series in powers of ξ. One can show that if all the diagonal elements of the inverse matrices obtained in this manner are nonvanishing then the series converges uniformly. In the expansion of the inverse matrices we now omit all terms except the diagonal terms and terms linear in ξ; then Eq. (8) becomes

$$\begin{aligned} &\varepsilon_1\frac{1}{r}\frac{\partial}{\partial r}r\frac{\partial\varphi(k, r)}{\partial r} - k^2\varepsilon_3\varphi(k, r) \\ &= \frac{\xi}{2}\left(a_{-1} + b_{-1}\frac{1}{r}\frac{\partial}{\partial r}r\frac{\partial}{\partial r}\right)\varphi(k - k_0, r) \\ &+ \frac{\xi}{2}\left(a_{+1} + b_{+1}\frac{1}{r}\frac{\partial}{\partial r}r\frac{\partial}{\partial r}\right)\varphi(k + k_0, r), \end{aligned} \tag{9}$$

where a_{-1} and a_{+1} are defined by

$$a_{-1} = \frac{k(k - k_0)\,\omega_0^2\varkappa(k, k - k_0)}{(\omega - kU_0)[\omega - (k - k_0)U_0]}, \quad a_{+1} = \frac{k(k + k_0)\,\omega_0^2\varkappa(k, k + k_0)}{(\omega - kU_0)[\omega - (k + k_0)U_0]}, \tag{10}$$

and ε_1 and ε_3 are the corresponding components of the permittivity tensor of the beam in the hydrodynamic approximation:

$$\varepsilon_1(k, \omega) = 1 - \frac{\omega_0^2}{(\omega - kU_0)^2 - \omega_H^2}, \quad \varepsilon_3(k, \omega) = 1 - \frac{\omega_0^2}{(\omega - kU_0)^2}, \tag{11}$$

and the coefficients b_{-1} and b_{+1} are given by

$$\begin{aligned} b_{\pm1} = 1 - \varepsilon_1(k, \omega) - \frac{(k \pm k_0)U_0}{\omega - kU_0} \\ \times (1 - \varepsilon_1(k \pm k_0, \omega))\left[1 + \frac{\omega_H^2}{\omega_0^2}(1 - \varepsilon_1(k, \omega))\right] \\ - \frac{(k \pm k_0)U_0}{\omega - (k \pm k_0)U_0}(1 - \varepsilon_1(k, \omega))\left[1 + \frac{\omega_H^2}{\omega_0^2}(1 - \varepsilon_1(k \pm k_0, \omega))\right]. \end{aligned} \tag{12}$$

RESONANCE CONDITIONS AND FIELDS IN AN ELECTRON BEAM THAT COMPLETELY FILLS A WAVEGUIDE

If the beam completely fills the cross section of a waveguide, we can write the solution of the chain of equations which is finite at the axis and vanishes at the conducting walls ($r = a$) in the form

$$\varphi(k, r) = \sum_n A_n(k)\,J_0\left(\sigma_n\frac{r}{a}\right). \tag{13}$$

We restrict ourselves to studying interactions in which only three waves – two characteristic waves and a modulating wave – participate.[2] When the solution (13) is substituted into the system (9) we assume that only the coefficients A_k and A_{k+k_0} are nonvanishing. We obtain a system of algebraic equations for these coefficients for the lowest mode ($n = 1$):

$$\left.\begin{aligned} D_k(\omega)A_k + \frac{\xi}{2}\left(a_{+1}(k) - \frac{\sigma_{01}^2}{a^2}b_{+1}(k)\right)A_{k+k_0} = 0, \\ \frac{\xi}{2}\left(a_{-1}(k + k_0) - \frac{\sigma_{01}^2}{a^2}b_{-1}(k + k_0)\right)A_k + D_{k+k_0}(\omega)A_{k+k_0} = 0, \end{aligned}\right\} \tag{14}$$

where $D_k(\omega) = (\sigma_{01}^2/a^2)\varepsilon_1(k, \omega) + k^2\varepsilon_3(k, \omega)$.

Equating the determinant of (14) to zero we find the dispersion relation

$$\begin{aligned} D_k(\omega)D_{k+k_0}(\omega) = \frac{\xi^2}{4}\left[a_{+1}(k) - \frac{\sigma_{01}^2}{a^2}b_{+1}(k)\right] \\ \times\left[a_{-1}(k + k_0) - \frac{\sigma_{01}^2}{a^2}b_{-1}(k + k_0)\right]. \end{aligned} \tag{15}$$

To terms of order ξ, the amplitudes of the spectral components of the field are, from (14),

$$A_k = \frac{1}{D_k(\omega)}, \quad A_{k+k_0} = \frac{\xi}{2}\,\frac{a_{-1}(k + k_0) - \frac{\sigma_{01}^2}{a^2}b_{-1}(k + k_0)}{D_k(\omega)\,D_{k+k_0}(\omega)}. \tag{16}$$

Since ξ is small, A_k and A_{k+k_0} can be commensurable only under resonance conditions, for which $D_k(\omega)$ and $D_{k+k_0}(\omega)$ vanish simultaneously. In this case, the solutions of the dispersion relation $\omega(k)$ become complex, and a state with constant wave amplitude becomes unstable. The maximum growth rate at exact resonance can be found by analogy with ref. 2;

$$\gamma_{\max} = \frac{\xi}{2}\,\frac{\left[a_{+1}(k) - \frac{\sigma_{01}^2}{a^2}b_{+1}(k)\right]^{1/2}\left[a_{-1}(k + k_0) - \frac{\sigma_{01}^2}{a^2}b_{-1}(k + k_0)\right]^{1/2}}{[D'_\omega(k, \omega)\,D'_\omega(k + k_0, \omega)]^{1/2}}. \tag{17}$$

Calculations show that the numerator of (17) is always positive at resonance; therefore there the instability arises only when the frequency derivatives of $D_k(\omega)$ and $D_{k+k_0}(\omega)$ have opposite signs. The physical meaning of this condition can be elucidated on the basis of the following arguments: The internal energy of the electromagnetic field of waves with wave-vector projections onto the z axis equal to k and $k + k_0$ is

$$W_k \sim \frac{A_k^2}{8\pi}\frac{\partial}{\partial\omega}(\omega D_k(\omega)), \quad W_{k+k_0} \sim \frac{A_{k+k_0}^2}{8\pi}\frac{\partial}{\partial\omega}(\omega D_{k+k_0}(\omega)). \tag{18}$$

Suppose that the beam–field system is conservative, i.e., we have broken the energy channel linking the waves to the external source which is realized through the modulating wave. It is obvious that all changes in such a system preserve both the energy and the wave number. Comparison of these conditions shows[6-8] the system is unstable if one of the excited waves is a negative-energy wave ($\omega D'_\omega(k, \omega) < 0$). This is the case when

$$D'_\omega(k, \omega) D'_\omega(k+k_0, \omega) < 0. \tag{19}$$

To establish the conditions under which there is parametric instability in the beam, i.e., the inequality (19) is satisfied, we find the solution of Eq. (15) as $\xi \to 0$. Setting $D_k(\omega) = 0$, we find

$$\omega'^2_{1,2} = \frac{1}{2}(\omega_0^2 + \omega_H^2) \pm \frac{1}{2}\sqrt{(\omega_0^2 + \omega_H^2)^2 - 4\omega_0^2\omega_H^2 \frac{k^2}{k^2 + \frac{\sigma_{01}^2}{a^2}}}. \tag{20}$$

The condition $D_{k+k_0}(\omega) = 0$ leads to the similar dependence

$$\omega''^2_{1,2} = \frac{1}{2}(\omega_0^2 + \omega_H^2) \pm \frac{1}{2}\sqrt{(\omega_0^2 + \omega_H^2)^2 - 4\omega_0^2\omega_H^2 \frac{(k+k_0)^2}{(k+k_0)^2 + \frac{\sigma_{01}^2}{a^2}}}. \tag{21}$$

Using the relation $\tan\theta = (k_\perp/k) = (\sigma_{01}/ak)$, we see that Eqs. (20) and (21) describe the dispersion of longitudinal waves propagating in a cold electron plasma at an angle θ to the magnetic field. It is not difficult to show that there are three types of resonance conditions that lead to a parametric instability. Let us first consider the case of a strong magnetic field ($\omega_H > \omega_0$). In this case, there is a plasma–plasma resonance if the branches of the dispersion diagram that tend asymptotically to ω_0 as $k \to \infty$ intersect. The resonance region is determined by the inequality

$$\omega_0 < k_0 U_0 \leqslant 2\omega_0. \tag{22}$$

If $k_0 U_0$ is greater than twice the plasma frequency, the dispersion curves cannot intersect, and there is no resonance. But if $k_0 U_0$ approaches ω_0, the system enters the region of basic resonance; although this is stronger than the parametric resonance, it leads to a stationary modulation of the beam, i.e., one in which the potential of the perturbation grows in space but does not depend on the time. The plasma–plasma resonance with broadest band occurs when $k_0 U_0 \simeq 2\omega_0$. In this case, there is amplification in the frequency band:

$$\frac{1}{O\left(\frac{U_T^2}{U_0^2}\right)} > \omega > \omega_{\min}(\xi). \tag{23}$$

The instability band is bounded from above in frequency by the thermal motion of the beam particles[1] and from below by the amplitude of the modulating field. The maximum growth rate in this region is

$$\gamma_{\max} = \frac{3}{4}\xi\omega_0 = \frac{1}{2}\frac{ek_0\varphi_0}{mU_0}. \tag{24}$$

Cyclotron–cyclotron resonance occurs when the cyclotron branches of the dispersion diagram intersect. This resonance occurs when

$$\omega_H + (\omega_0^2 + \omega_H^2)^{1/2} > k_0 U_0 \geqslant 2\omega_H \tag{25}$$

and is the one with the broadest band near the lower boundary. The region of frequencies in which there is signal amplification because of cyclotron–cyclotron resonance is also determined by an inequality like (23). It should be pointed out that the calculation of the growth rate near the lower boundary of the resonance on the basis of Eq. (17) is incorrect because the basic assumption in the derivation of Eq. (9) – that the diagonal elements of the matrices $\hat{F}^{-1}$ and $\hat{K}^{-1}$ vanish – no longer holds, and the procedure for expanding the inverse matrices in powers of ξ leads to divergent series for $k \gg k_\perp$.

The third kind of instability that occurs in an electron beam with a finite focusing magnetic field is due to a cyclotron–plasma resonance; this occurs when

$$\omega_0 + (\omega_0^2 + \omega_H^2)^{1/2} > k_0 U_0 > \omega_H. \tag{26}$$

An instability occurs in the frequency interval (23) when

$$k_0 U_0 \to \omega_H + \omega_0. \tag{27}$$

The maximum growth rate can be calculated, and is

$$\gamma = \frac{3}{4}\omega_0 \frac{\sigma U_0}{\sqrt{\omega_0^2 + \omega_H^2}}. \tag{28}$$

In weak magnetic fields ($\omega_H < \omega_0$), the region of the plasma–plasma resonance is determined by (25), of the cyclotron–cyclotron resonance by (22), and of the cyclotron–plasma resonance by (26). In this case, the maximum growth rate for the cyclotron resonance is

$$\gamma = \frac{3}{4}\omega_H \frac{\sigma U_0}{\sqrt{\omega_0^2 + \omega_H^2}}. \tag{29}$$

DISPERSION PROPERTIES OF A MODULATED ELECTRON BEAM

We investigate the dispersion properties of a modulated electron beam in a homogeneous magnetic field. To do this, assuming $\xi \neq 0$ we solve Eq. (15) in the neighborhood of each of the above resonances, i.e., near the point of intersection of the corresponding dispersion curves. A typical dependence of the signal frequency on the projection of the wave vector on the z axis is shown in Fig. 1. In the frequency interval $\omega_{\min} < \omega < \omega_{\max}$ the solution of the dispersion relation $\omega(k)$ becomes complex, i.e., the beam is unstable against the excitation of waves in the given frequency interval. The width of the instability region $\omega_{\max} - \omega_{\min}$ for fixed ω_H/ω_0 and g_0 is proportional to ξ, the modulation depth of the beam. The maximum growth rate for any resonance condition depends on both the magnitude of the magnetic field and the period of the modulating field $r\lambda/k_0$. In particular, for the plasma–cyclotron resonance, $\gamma_{\max}$ is shown as a function of g_0 in Fig. 2. It can be seen from Fig. 2 that $\gamma_{\max}$ reaches its greatest value near the upper boundary (26). If g_0 increases further, the growth rate decreases rapidly and at $g_0 = g_{0\max}$ the beam becomes stable. An increase of the focusing field decreases the growth rate of the cyclotron–

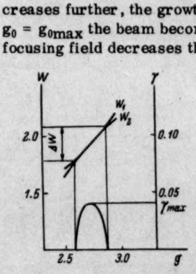

Fig. 1. Dependence of the signal frequency on the projection of the wave vector onto the z axis under resonance conditions [$W = \omega/\omega_0$, $g = (k_z U_0)/\omega_0$].

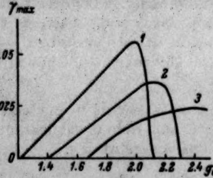

Fig. 2. Maximum growth rate as a function of the period of the modulating field. H: 1) 1.0; 2) 1.25; 3) 1.5; $H = \omega_H/\omega_0$.

plasma instability on the one hand, and displaces the upper boundary of the resonance to larger g_0. In the case of plasma–plasma resonance, an increase in H_0 is accompanied by an increase in γ_{max}, which tends to its limiting value (24).

A large series of calculations made for different values of g_0 enables us to determine the instability region for these resonances (at a constant magnetic field). In Fig. 3 we show the boundaries of these regions and the region corresponding to stable solutions of the dispersion relation (15). It can be seen that the width of the amplification band varies with the period of the modulating field: As long as $g_0 < g_{0,\mathrm{lim}}$, which corresponds to the upper boundary of the instability, a narrow band of frequencies can be amplified in the beam with growth rate $\gamma < \gamma_{\mathrm{lim}}$, and with increasing g_0 the range of amplified frequencies becomes larger and amplification can occur with growth rate of the order of γ_{lim}.

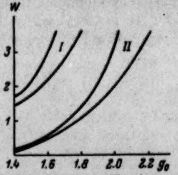

Fig. 3. Regions of instability of a modulated beam under the conditions for the existence of plasma–plasma (I) and plasma–cyclotron (II) resonance (H_0 = const).

---

[1] N. S. Repalov and V. F. Tyrnov, Zh. Tekh. Fiz., 42, 905 (1972) [Sov. Phys. – Tech. Phys., 17, 719 (1972)].

[2] A. I. Pasynok and N. S. Repalov, Zh. Tekh. Fiz., 42, 2452 (1972) [Sov. Phys. – Tech. Phys., 17, 1913 (1973)].

[3] N. S. Repalov and N. A. Khizhnyak, Zh. Tekh. Fiz., 40, 2065 (1970) [Sov. Phys. – Tech. Phys., 15, 1608 (1971)].

[4] N. S. Repalov and N. A. Khizhnyak, Zh. Tekh. Fiz., 36, 219 (1966) [Sov. Phys. – Tech. Phys., 11, 162 (1966)].

[5] G. G. Aseev, G. G. Kuznetsova, N. S. Repalov, and N. A. Khizhnyak, Zh. Tekh. Fiz., 42, 2264 (1972) [Sov. Phys. – Tech. Phys., 17, 1777 (1973)].

[6] V. M. Dikasov, L. I. Rudakov, and L. D. Pyutov, Zh. Eksp. Teor. Fiz., 48, 913 (1965) [Sov. Phys. – JETP, 21, 608 (1965)].

[7] V. N. Tsytovich, Nonlinear Effects in Plasma, Plenum, New York (1970).

[8] G. Bekefi, Radiation Processes in Plasmas, Wiley, New York (1966).

Scattering by ion-acoustic waves in a rectangular waveguide

S. V. Troitskii

A. M. Gor'kii Khar'kov State University

(Submitted April 19, 1973)
Zh. Tekh. Fiz., 44, 284-290 (February 1974)

An analytical expression is obtained for the scattering cross section for the fundamental mode in a rectangular waveguide containing a plasma in which there is a directed drift of the electrons with respect to the ions. Using linear theory, we study scattering conditions close to threshold, where the fluctuation level in the plasma is anomalously large. An experiment is described which involves scattering by ion-acoustic oscillations in a helium positive column located in a rectangular waveguide.

INTRODUCTION

Incoherent scattering of electromagnetic waves is one of the most reliable of present-day methods for noncontact plasma diagnostics. It has found extensive application both in studies of the upper ionized layers of the atmosphere and in laboratory plasma diagnostics (for example, by means of lasers).

In both cases, however, it is usually assumed that the wavelength of the probing signal is considerably smaller than the dimensions of the plasma; this assumption allows us to neglect boundary effects and serves as the basis for a comparison of experimental results with the theory for incoherent scattering of waves in an unbounded plasma.

However, there is considerable interest in the case in which the wavelength of the probing signal, λ_0, is comparable with the dimension l of the plasma. Successful realization of the incoherent scattering method in this case demands a theory which describes incoherent scattering in bounded plasma volumes; a comparison of experimental and theoretical data when $\lambda_0 \sim l$ is possible only with a systematic consideration of boundary effects.

Some of the first results of an analytic study of incoherent scattering in a bounded plasma appear in refs. 1-3. The present paper describes an experiment on scattering of microwaves by fluctuations in the plasma of the positive column of a glow discharge in a rectangular waveguide. Earlier results[2,3] are generalized to the case of a nonequilibrium plasma with a directed drift of electrons with respect to ions in order to compare the experimental data with theory.

EFFECT OF DIRECTED ELECTRON DRIFT ON SCATTERING IN A WAVEGUIDE

We consider a rectangular waveguide completely filled by a homogeneous electron–ion plasma that is not in equilibrium. The dielectric tensor of the plasma (including electron drift with a velocity u with respect to stationary ions) is determined in the nonrelativistic case $u \ll c$ (neglecting spatial dispersion) by the following expression:[4]

$$\varepsilon_{ij}(\omega, \mathbf{k}) = \varepsilon(\omega)\delta_{ij} - \frac{\omega_p^2}{\omega'^2}\left[\frac{\omega'}{\omega^2}(k_i u_j + u_i k_j) + k^2\frac{u_i u_j}{\omega^2}\right], \tag{1}$$

where

$$\left.\begin{aligned} \varepsilon(\omega) = 1 - \frac{\omega_p^2}{\omega^2} - \frac{\omega_{pi}^2}{\omega^2}, \quad \omega' = \omega - \mathbf{ku}, \\ \omega_p^2 = \frac{4\pi e^2 N}{m_e}, \quad \omega_{pi}^2 = \frac{4\pi e^2 N}{m_i}, \end{aligned}\right\} \tag{2}$$

e and m_e are the charge and mass of the electron, m_i is the mass of the ion, and N is the equilibrium plasma density.

A plasma with the tensor (1) is not isotropic for any direction of the velocity **u**. However, it is evident that the deviation from isotropy in (1) in the nonrelativistic case $u \ll c$ for fast waves with a phase velocity $v_p > c$ is determined by small terms of order

$$\frac{ku}{\omega} \ll 1. \tag{3}$$

Therefore when (3) is satisfied, it is inexpedient to solve the problem of wave propagation in a waveguide filled by a medium with the tensor (1); neglecting the small terms in (1), we describe the plasma in the waveguide by the dielectric constant

$$\varepsilon_{ij}(\omega) = \delta_{ij}\varepsilon(\omega).$$

We point out that despite the possibility of neglecting the quite small effect of drift velocity on wave propagation (in analogy to the neglect of the effect of spatial dispersion on electromagnetic wave propagation), consideration of drift velocity, like consideration of spatial dispersion, is necessary in principle for the calculation of the correlation functions which determine the incoherent scattering cross sections; in the linear theory it is precisely this consideration which determines the structure of the scattering cross section and the effectiveness of wave scattering by plasma fluctuations.[5]

Thus the inequality (3) gives a condition for which the problem of scattering in a waveguide containing a nonequilibrium plasma can be solved as before[2,3] and the analytic expressions for the scattering cross section in the case of equilibrium (**u** = 0) and nonequilibrium (**u** ≠ 0) plasmas agree formally, with the one difference that in the latter case (**u** ≠ 0) the correlation function for the electron density must be calculated with the electron drift included.

Limiting the discussion to scattering of the fundamental mode (with frequency ω_0) and excitation of the H_{m0} mode (with frequency ω), and following ref. 2, we write the differential scattering cross section as

$$\frac{d\sigma^{\alpha}_{H_{10}\to H_{m0}}}{d\omega} = \frac{\dfrac{16\pi^5 r_e^2\omega}{\omega_0}}{ab\,|k_z|\,k_{z0}}\left\{\langle\delta n^2\rangle_{q_-^{\alpha}\Delta\omega}(1+\delta_{m1}) + \langle\delta n^2\rangle_{q_+^{\alpha}\Delta\omega}\right\}. \tag{4}$$

In contrast to ref. 2, we shall understand by the quantities $\langle\delta n^2\rangle_{q_\pm^{\alpha}\Delta\omega}$ the spectral distributions of the correlation functions for electron density calculated with electron drift included. For a nonequilibrium (but stable) plasma, the assumptions made earlier[1-3] regarding the smallness of the correlation radius in comparison with the scattering plasma volume remain valid and we use the expression for the electron density correlation function in an unbounded plasma:[5,6]

$$\langle \delta n^2 \rangle_{q\Delta\omega} = \frac{2q^2}{(2\pi)^4 e^2 |\varepsilon_l|^2}$$
$$\times \left\{ |1 + 4\pi\varkappa_l^i|^2 \frac{T_e}{\Delta\omega - \mathbf{qu}}\, \mathrm{Im}\, \varkappa_l' + |4\pi\varkappa_l'|^2 \frac{T_i}{\Delta\omega}\, \mathrm{Im}\, \varkappa_l^i \right\}, \tag{5}$$

where

$$\left.\begin{aligned} &\varepsilon_l = 1 + 4\pi(\varkappa_l' + \varkappa_l^i),\\ &\varkappa_l' = \frac{1}{4\pi r_d^2 q^2}\left\{1 - \varphi(z') + i\sqrt{\pi}\, z' e^{-z'^2}\right\},\\ &\varkappa_l^i = \frac{t}{4\pi r_d^2 q^2}\left\{1 - \varphi(z_i) + i\sqrt{\pi}\, z_i e^{-z_i^2}\right\},\\ &z' = \sqrt{\frac{m_e}{2T_e}}\,\frac{(\Delta\omega - \mathbf{qu})}{q}, \quad z_i = \sqrt{\frac{m_i}{2T_i}}\,\frac{\Delta\omega}{q}, \quad \Delta\omega = \omega - \omega_0,\\ &t = \frac{T_e}{T_i}, \quad r_d^2 = \frac{T_e}{4\pi e^2 N}, \quad \varphi(z) = 2ze^{-z^2}\int_0^z e^{x^2}dx. \end{aligned}\right\} \tag{6}$$

Here, T_e and T_i are respectively the electron and ion temperatures in energy units, and the index α takes on the values (±) with $\alpha = (+)$ corresponding to forward scattering and $\alpha = (-)$ to backscattering.

With substitution of (6) in Eqs. (4) and (5), the quantity q for the change in the wave vector during scattering in the waveguide takes on a discrete set of values as a function of the number m which arises because of the wave scattering $\mathbf{q} \to \mathbf{q}_\pm^\alpha$,

$$\left.\begin{aligned} &\mathbf{q}_\pm^\alpha = \mathbf{e}_x \frac{(m \pm 1)\pi}{a} + \mathbf{e}_z q_z^\alpha, \quad q_z^\alpha = \alpha k_z - k_{z0},\\ &k_{z0} = \sqrt{\frac{\omega_0^2}{c^2}\varepsilon(\omega_0) - \frac{\pi^2}{a^2}}, \quad k_z = \sqrt{\frac{\omega^2}{c^2}\varepsilon(\omega) - \left(\frac{m\pi}{a}\right)^2}, \end{aligned}\right\} \tag{7}$$

a and b are the transverse dimensions of the waveguide; $\mathbf{e}_x$ and $\mathbf{e}_z$ are unit vectors along the corresponding axes.

For small frequency variations, $q\sqrt{T_e/m_e} \ll \Delta\omega \ll q\sqrt{T_i/m_i}$, $z' \ll 1$, $z_i \gg 1$, the correlation function (5) can be written

$$\langle \delta n^2 \rangle_{q\Delta\omega} = \sqrt{\frac{\pi}{8M}}\,\frac{\pi N R(q)\, q V_s}{(2\pi)^4 (1 + r_d^2 q^2)^3}\,\frac{\delta(\Delta\omega - \omega_s) + \delta(\Delta\omega + \omega_s)}{|\gamma(\mathbf{q}, \Delta\omega)|}, \tag{8}$$

where

$$\left.\begin{aligned} &\gamma(\mathbf{q}, \Delta\omega) = \sqrt{\frac{\pi}{8M}}\left[\frac{qV_s}{(1 + r_d^2 q^2)^2}\left(1 + \sqrt{Mt^3}\, e^{-\frac{t/2}{1 + r_d^2 q^2}}\right) - \frac{\frac{\Delta\omega \mathbf{qu}}{qV_s}}{1 + r_d^2 q^2}\right],\\ &R(q) = 1 + \frac{\pi t^3}{2(1 + r_d^2 q^2)}\, e^{-\frac{t}{1 + r_d^2 q^2}} + \sqrt{Mt}\, e^{-\frac{t/2}{1 + r_d^2 q^2}},\\ &M = \frac{m_i}{m_e}, \quad V_s^2 = \frac{T_e}{m_i}, \quad \omega_s = \frac{qV_s}{\sqrt{1 + r_d^2 q^2}}. \end{aligned}\right\} \tag{9}$$

Equating the damping $\gamma(\mathbf{q}, \Delta\omega)$ to zero[5] we can determine the boundary between damped and growing ion-acoustic oscillations with frequencies $\pm\omega_s$. The fact that the correlation functions approach infinity when $\gamma(\mathbf{q}, \Delta\omega) \to 0$ is analogous to the anomalously high level of fluctuation in matter near the liquid–gas phase transition, and within the limits of linear theory Eqs. (4) and (8) describe a significant increase in the scattering cross section for electromagnetic waves in a rectangular waveguide filled with a plasma when $\gamma(\mathbf{q}, \Delta\omega) \to 0$, which corresponds to the well-known phenomenon of critical opalescence.

Let the drift velocity be $\mathbf{u} \parallel Oz$, i.e., coincide with the direction of propagation of an incident wave in the waveguide. In this case, the expressions for the forward-scattering cross sections agree with the corresponding expressions in the case of a waveguide containing an equilibrium plasma[2] since for small changes in frequency $\Delta\omega$, $q_z^+ \approx 0$ and $\mathbf{q}^+\mathbf{u} = q_z^+ u \approx 0$. We shall therefore only consider back-scattering in the following and omit the index α everywhere.

For back-scattering, the product $\mathbf{q}_\pm \mathbf{u}$ is always negative and $\gamma(\mathbf{q}, \Delta\omega)$ can go to zero only when $\Delta\omega = -\omega_s$. For $\Delta\omega = \omega_s$, $\gamma(\mathbf{q}, \omega_s)$ does not go to zero, the ion-acoustic oscillations experience strong damping, and the scattering cross section is smaller than for $\Delta\omega = -\omega_s$.

In the following, we limit ourselves to $H_{10} \to H_{10}$ scattering (m = 1). For practical purposes, the integrated scattering cross sections, which are

$$\sigma = \int_{-\infty}^{\infty} \frac{d\sigma_{H_{10} \to H_{10}}}{d\omega}\, d\omega.$$

are of interest.

Substituting Eq. (8) into Eq. (4), we obtain the results of integration of the scattering cross section with the help of $\delta(\Delta\omega - \omega_s)(\sigma_+)$ or of $\delta(\Delta\omega + \omega_s)(\sigma_-)$ in the form

$$\sigma_\pm = \frac{\pi^3 N r_e^2 V_s}{ab\omega_0 k_{z0}}\sqrt{\frac{\pi}{8M}}\,\{2f^\pm(q_-) + f^\pm(q_+)\}, \tag{10}$$

where

$$\left.\begin{aligned} &f^\pm(q) = \frac{q\omega^\pm R(q)}{(1 + r_d^2 q^2)^3\, |k_z^\pm \gamma^\pm(q)|},\\ &\omega^\pm = \omega_0 \pm \omega_s, \quad k_z^\pm = k_z(\omega^\pm), \quad \gamma^\pm(q) = \gamma(q, \pm\omega_s). \end{aligned}\right\} \tag{11}$$

In order to study the scattering cross section σ_- near the critical mode ($\gamma^-(q) = 0$) for negative detuning, we write $\gamma^-(q)$ in the long-wave region $r_d^2 q^2 \ll 1$ as a series in powers of $r_d^2 q^2$

$$\gamma^-(q) = q\sqrt{\frac{\pi}{8M}}\left\{\left(V_0 - \frac{|q_z|u}{q}\right)\right.$$
$$\left. - r_d^2 q^2\left[2V_0 - \frac{V_s}{2}\sqrt{Mt^3}\, e^{-t/2} - \frac{3}{2}\,\frac{|q_z|u}{q}\right] + \ldots\right\}, \tag{12}$$

where

$$V_0 = V_s(1 + \sqrt{Mt^3}\, e^{-t/2}). \tag{13}$$

In particular, since $|q_{z-}| = q_-$, we consider the case $u = V_0$. In this case, for $\Delta\omega = -\omega_s$ the damping constant can be represented as

$$\gamma^-(q_-) \cong \sqrt{\frac{\pi}{8M}}\, r_d^2 q_-^3 V_1, \tag{14}$$

where

$$V_1 = \frac{V_s}{2}\left[\sqrt{Mt^3}\,(t - 1)\, e^{-t/2} - 1\right]. \tag{15}$$

Since only nongrowing ion-acoustic oscillations are considered in the scattering, $\gamma^{-}(q_{-})$ must be positive and the condition $\gamma^{-}(q_{-}) = 0$ (or $V_1 = 0$) gives a critical ratio t_c for the temperatures, which can be determined from (see ref. 7 also)

$$t_c^{3/2}e^{-t_c/2}(t_c-1)=\frac{1}{\sqrt{M}}. \qquad (16)$$

When $u = V_0$ and $r_d^2q^2 \ll 1$, from Eq. (12) we have

$$\gamma^{-}(q_{+})\cong\sqrt{\frac{\pi}{8M}}\,q_{+}V_0\left(1-\frac{|q_{r+}|}{q_{+}}\right). \qquad (17)$$

In the region of ion sound

$$\frac{1}{r_d^2q^2}=\frac{\omega_{pi}^2}{\omega_s^2}-1,$$

and taking account of Eqs. (14), (17), and (11), when $t_c \gtrsim t \gg 1$ and $R(q) \cong 1$ we obtain from Eq. (10)

$$\sigma_{-}\cong\frac{\pi^2Nr_e^2}{ab\omega_0k_{z0}}\left\{2\,\frac{V_s}{V_1}\,\frac{\omega_{-}^{-}}{|k_z(\omega_{-}^{-})|}\left(\frac{\omega_{pi}^2}{\omega_s^2}-1\right)+\frac{V_s}{V_0}\,\frac{\omega_{+}^{-}}{|k_z(\omega_{+}^{-})|\left(1-\frac{|q_{r+}|}{q_{+}}\right)}\right\}, \qquad (18)$$

where $\omega_{\pm}^{-} = \omega^{-}(q_{\pm})$.

For small $\Delta\omega \ll \omega_0$, one can make the approximation $\omega_{\pm}^{-} \approx \omega_0$, $|k_z(\omega_{\pm}^{-})| \approx k_{z0}$, so that

$$\sigma_{-}\cong\frac{\pi^2Nr_e^2}{abk_{z0}^2}\left\{2\,\frac{V_s}{V_1}\left(\frac{\omega_{pi}^2}{\omega_s^2}-1\right)+\frac{V_s}{V_0\left(1-\frac{|q_r|}{q_{+}}\right)}\right\}. \qquad (19)$$

EXPERIMENT AND DISCUSSION OF RESULTS

The device shown in Fig. 1 is used for the experimental study of incoherent scattering in a waveguide. A study has been made of back-scattering of the fundamental wave in a standard rectangular waveguide for the three-centimeter range (cross section 10 × 23 mm). The helium plasma in the positive column of a glow discharge with gas pressures of 0.06-10 mm Hg and discharge currents of 2-150 mA is located in the waveguide. By means of a ferrite Y coupler (see Fig. 1), the reflected signal (including that scattered by plasma fluctuations) of the fundamental H_{10} mode is directed to a P5-10 high-sensitivity superheterodyne receiver with a threshold sensitivity of $7\cdot10^{-17}$ W. At the receiver input there is a resonator with a 10 MHz passband which is tuned to the frequency of the device and which blanks out the scale signal at the receiver. Power measurements are made in a narrow passband of the receiver having a width of 1 MHz at 50% power level.

Power scattered by fluctuations for a given detuning from the central frequency f_0 of the oscillator is determined from the difference between the total power measured by the receiver during probing of the plasma and the sum of the intrinsic radiation of the plasma and the power reaching the receiver with no plasma present in the waveguide. The power meter PM provides an indication of the level of continuous power from the probing-signal generator. This same arrangement (Fig. 1) without the oscillator can also be used for studies of intrinsic plasma radiation. In comparison with the experimental scattering arrangement used in ref. 8 and also in comparison with experiments on the scattering of laser light where the scattered energy is distributed in all directions and only an insignificant portion of the scattered signal reaches the receiver, the scattered energy is propagated in only two directions in this waveguide scheme: forward and backward, with the back-scattering cross section greater than the cross section for forward scattering as shown by calculation (see, for example, ref. 2).

Introduction of the glass vessel PV into the waveguide is accomplished by means of the separable sections SC, which are cut into two halves so that the lines of high-frequency conductivity currents do not pass through the plane of the cut. To reduce reflections, the vessel is closed off with half-wave conical transition sections. The thin-walled glass vessel, rectangular in cross section and 70-110 mm long, is fabricated by means of a special massive rectangular bronze mold which is heated to 500°C by heating elements during molding and which produces a vessel with external dimensions of 9.8 × 22.8 mm. The wire anode of the vessel is within the waveguide and along its axis, and the cylindrical cold cathode is removed from the waveguide by means of a tube 9 mm in diameter; this ensures insignificant perturbation of the wave field by the electrodes of the discharge vessel.

Measurements are made of integrated back-scattering cross sections multiplied by the magnitude of the entire plasma volume in the waveguide. Measurements are made for various detuning values $\Delta f = f - f_0$ from the central frequency of the oscillator spectrum starting with Δf ± 10 MHz.

Waveguide methods are used for determining the fundamental parameters of the plasma.[9] The electron density

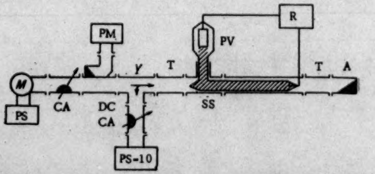

Fig. 1. Experimental arrangement. M) Oscillator; PS) power supply; CA) calibrated attenuator; DC) directional coupler; PM) power meter; Y) Y coupler, T) transition section; SS) separable section; PV) plasma vessel; A) absorber; R) rectifier.

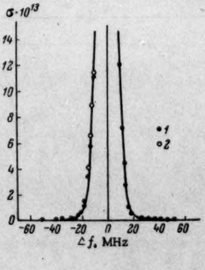

Fig. 2. Back-scattering cross section as a function of detuning Δf. He, $N = 6\cdot10^{10}$ cm^{-3}, $T_r = 5\cdot10^{4}$ K, λ_0 = 3.2 cm; 1) measurements; 2) points calculated from Eq. (19) for $\omega_s \leq \omega_{pi}$.

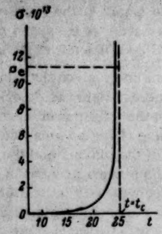

Fig. 3. The relation $\sigma_-(t)$ calculated from Eq. (19). He, $\Delta f = -10$ MHz, σ_e is the measured scattering cross section.

$\overline{N}_V$ averaged over the volume is determined from the measured phase shift and damping of the waves introduced by the plasma; the effective electron radiation temperature T_r is determined from measured thermal radiation power and the plasma absorption coefficient on the basis of the waveguide form of the Kirchhoff law. For example, in a helium discharge tube containing helium at p = 9 mm Hg, I_p = 70 mA, $\overline{N}_V = 6 \cdot 10^{10}$ cm^{-3}, and $T_r = 5 \cdot 10^4$°K.

In all cases, we observe a linear dependence of scattered energy on probing-signal power, which reaches 10 W in the continuous mode. The dependence of scattered power on plasma electron density is also observed to be linear.

Over the entire discharge current range of 10-150 mA the values of the measured scattering cross sections are considerably greater than those corresponding to scattering by fluctuations in an equilibrium plasma[2]. Figure 2 gives typical curves for the dependence of back-scattering cross sections on the detuning Δf in a rectangular waveguide containing a plasma (discharge tube length L = 100 mm). The experimental and theoretical data are in satisfactory agreement for comparatively small negative detuning $\Delta f = \omega_s/2\pi \lessapprox 15$ MHz. This is obviously evidence that we are dealing with scattering by ion-acoustic oscillations in a highly nonisothermal plasma under nearly critical conditions. For positive detuning, however, we have not obtained experimentally the significant reduction in scattering cross section predicted by theory in comparison with scattering for negative detuning.

Actually, the linear dependence of the scattered signal power (or σ_-) on $1/\omega_s^2$ is typical. It is easy to see such a dependence in Eq. (19) if we neglect the second term in comparison with the first for large $t \gg 1$ and $V_1 \to 0$. As has been shown,[8] one can determine the plasma density N approximately (and also the ratio V_s/V_1) from the slope of the line $\sigma_-(1/\omega_s^2)$ plotted from the experimental data (see Fig. 2).

Figure 3 shows the dependence of the scattering cross section σ_- on the parameter t of a nonisothermal plasma calculated from Eq. (19) for $\Delta f = -10$ MHz. As is evident, the value of the critical ratio t of the temperatures for a helium plasma is approximately 24.9. A comparison of the experimentally measured scattering cross section σ_e at the same detuning with the curve in Fig. 3 makes it possible to judge how nonisothermal the plasma is (in our case, $t \simeq 24.4$).

We note in conclusion that plasma inhomogeneity can have a significant effect on scattering by fluctuations; consideration of this effect and the effect of the bounded geometry on the spectral composition of the correlation functions in analytic studies of incoherent scattering should lead to a more complete agreement of experimental and theoretical results.

---

[1] I. A. Akhiezer, Zh. Tekh. Fiz., 33, 935 (1963) [Sov. Phys. – Tech. Phys., 8, 699 (1964)].
[2] I. P. Yakimenko and S. V. Troitskii, Izv. VUZ. Radiofiz., 11, 1309 (1968).
[3] I. P. Yakimenko, Zh. Tekh. Fiz., 39, 2163 (1969) [Sov. Phys. – Tech. Phys., 14, 1632 (1970)].
[4] A. A. Rukhadze, Zh. Tekh. Fiz., 32, 669 (1962) [Sov. Phys. – Tech. Phys., 7, 488 (1962)].
[5] A. I. Akhiezer, I. A. Akhiezer, R. V. Polovin, A. G. Sitenko, and K. N. Stepanov, Collective Oscillations in Plasma [in Russian], Atomizdat, Moscow (1964).
[6] A. G. Sitenko, Electromagnetic Fluctuations in Plasma [in Russian], Izd. Khar'kov. Univ., Khar'kov (1965).
[7] S. Ichimaru, Ann. Phys., 20, 78 (1962).
[8] V. Arunasalam and S. C. Brown, Phys. Rev., 140A, 471 (1965).
[9] V. E. Golant, Ultrahigh-Frequency Methods for Plasma Investigations [in Russian], Izd. Nauka, Moscow (1968).

Multimode parametric interactions in a plasma with low-frequency pumping

Yu. M. Sorokin and N. S. Stepanov
N. I. Lobachevskii Gor'kii State University

(Submitted April 20, 1973)
Zh. Tekh. Fiz., 44, 291-299 (February 1974)

Multimode processes are analyzed in an isotropic, collisionless electron plasma whose density varies as a function of position and time under the influence of a low-frequency pumping wave. The spectrum of the high-frequency perturbation is assumed to be broad (on the scale of the pumping frequency) and smooth, so that the problem can be reduced to one of analyzing a single first-order partial differential equation for a complex amplitude. In this system, the perturbation spectrum can periodically shift upward or downward and undergo deformation, and the total wave energy can change. Synchronization of the pump with the high-frequency signal causes a monotonic shift of the spectrum upward (or downward), a simultaneous compression (or expansion) of the spectrum, and an increase (or decrease) in the total wave energy, depending on the particular phase relations. Both the boundary-value problem and the initial-value problem are solved.

1. An extensive literature has recently developed on the parametric interaction of waves in nonlinear dispersive media, particularly plasmas (see, e.g., refs. 1-9). The analysis of such processes generally reduces to an analysis of a system of truncated equations for waves which satisfy synchronism conditions. As sufficiently high-frequency photons merge and decay in slightly nonlinear dispersive media, the number of such waves turns out to be extremely limited, and in practice the process can be described completely on the basis of a three-wave interaction or a four-wave interaction. However, if the decay processes in a certain part of the spectrum involve photons of significantly lower frequencies, this model becomes inadequate, because the synchronous-interaction band, including that for systems with an appreciable dispersion, can include combination spectra of higher orders. For example, in a plasma with low-frequency pumping even in the case of a slight nonlinearity, the number of waves which interact effectively can increase significantly; this has been shown, in particular, by experiments on parametric regeneration in waveguide systems with long electron beams.[10] More recently, the excitation of a broad spectrum of combination harmonics has been observed[11] directly in a plasma column in the interaction of high-frequency electromagnetic waves with ion-acoustic waves; dynamic spectra of this interaction have been recorded.

Accordingly, there is much theoretical and practical interest in multimode processes in which the number of interacting harmonics is not specified beforehand and can, in principle, be infinite. It becomes a much more complicated matter to analyze a slightly dispersive nonlinear system when a large number of harmonics are taken into account, and finding a solution for a perturbation with an arbitrary spectrum is difficult. For this reason, analyses of such processes[12-15] have been based on at least two simplifying assumptions: The perturbation in the parameters of the medium by any of the interacting waves is small, and the dispersion of the system is neglected in the frequency range studied; outside this range the spectrum is arbitrarily cut off where necessary. The weak-nonlinearity approximation makes it possible to write the desired solution as an expansion in terms of a set of waves satisfying the dispersion relation of the unperturbed medium; neglecting the dispersion implies a constant frequency detuning for any of the elementary decay processes within the spectra range considered. However, in contrast with optical processes, the first of these assumptions can be easily violated in the case of microwave processes in a plasma when the pumping is strong or when the density of an electron beam is modulated. The second assumption becomes difficult to justify if combination harmonics of higher order are taken into account. Furthermore, for boundary perturbations (or initial perturbations, depending on the type of problem) including many spectral components, analysis of the solutions derived in refs. 12-15 becomes difficult, since the amplitude of each wave at a given spatial point is expressed in terms of the amplitudes specified at the boundaries of the medium for all waves. For this reason, the solutions have been analyzed in these papers for boundary conditions containing only two harmonics. An important consideration for further development of this problem, however, is the general conclusion[12-15] that the spectrum for the process expands and smooths considerably during the course of the specified interaction. Exploitation of this circumstance leads to important simplifications in the problems of parametric systems with low-frequency pumping (the restrictions mentioned above are also relaxed). Solutions having a broad but smooth spectrum are analyzed, in which case the amplitudes of the parametrically coupled harmonics are approximately equal, and the interactions among these harmonics can be described by means of purely differential equations, rather than differential—difference equations.

An approach of this kind was suggested previously for systems having periodically varying boundary conditions: a resonator with a vibrating wall[16] and a long line with a varying capacitive load.[17] Depending on the propagation time of the waves in the line (or resonator) and on the phase relations among the signal harmonics, a periodic or monotonic shift of the spectrum of the initial perturbation upward or downward, with a simultaneous expansion or compression of this spectrum and with a change in the total signal energy, becomes possible.[1)]

Below we use a similar method to study the parametric interaction of high-frequency waves in a density-modulated electron plasma in a homogeneous, nondispersive dielectric ($\varepsilon = \text{const}$, $\mu = 1$). This model can be thought of as an approximation to a semiconducting medium, or it can be associated with the presence of slow-wave systems in practical devices. We analyze the features of the transformation of the spectrum and energy of the waves in such a system, and we determine the conditions for the appearance of accumulative effects, both for a broad-band perturbation specified at the boundary of the medium and for the initial-value problem.

2. For brevity we restrict the analysis to the one-dimensional case. The basic features of the multimode interactions in this system are best analyzed on the basis of the highly simplified model of a cold, isotropic, collisionless plasma; in this case the propagation of transverse electromagnetic waves is described by the following linearized equations in the specified-field approximation and for a strong longitudinal (pump) wave:

$$\frac{\partial^2 A}{\partial z^2}-\frac{\varepsilon}{c^2}\frac{\partial^2 A}{\partial t^2}=\frac{\varepsilon}{c^2}\omega_{p0}^2[1+p\cos(\Omega t-Kz)]A. \tag{1}$$

This equation is written for the transverse component of the magnetic vector potential A (H = curl A, E = − (1/c) · ∂A/∂t); here $\omega_{p0} = [4\pi e^2 N_0/(m\varepsilon)]^{1/2}$ is the plasma frequency, e, m, and N_0 are the charge, mass, and unperturbed density of the electrons, and c is the speed of light.[2]

We turn first to the boundary-value problem. We assume that a broad-band perturbation with a uniformly spaced frequency spectrum $\omega_l = \Omega l$ is specified in the plasma at z = 0. The amplitudes of the spectral components, $a_l(0)$, are slowly varying functions of index l. This formulation of the problem could correspond, e.g., to the operation of a source at the plasma boundary which generates a periodic train of narrow pulses with period T = $2\pi/\Omega$ equal to the pumping period. Furthermore, as follows from the arguments in Sec. 1 and the experimental results of ref. 11, this boundary-value problem can be used to analyze the evolution of high-frequency decay processes in a plasma at large distances from the boundary, even when the approximations adopted in refs. 12-15 do not hold. It is also possible to reach certain general conclusions regarding the nature of the transformation of the signal spectrum and energy; these conclusions, in particular, supplement the results of refs. 12-15 in their range of applicability.

On this basis we seek a solution of Eq. (1) in the form

$$A(z,\ t)=\sum_{l\geqslant 1} a_l(z)\exp i(\Omega lt-k_l z+\delta l), \tag{2}$$

where the phase shift δ = const between adjacent harmonics evidently determines the position of the pulses exciting the system with respect to the pump wave, and the complex amplitude $a_l(z)$ is a slowly varying function of its argument z and its index l:

$$\frac{\partial a_l}{\partial z}\ll k_l a_l, \tag{3a}$$

$$|a_{l+1}-a_l|\ll a_l. \tag{3b}$$

Substituting (2) into (1), using condition (3a), and isolating from the resulting summation the terms which are harmonic in t at the same frequency [or, equivalently, averaging over t with a weight factor (− iΩlt)], we find the following equation for the complex amplitude a_l:

$$2k_l\frac{da_l}{dz}-i\gamma_l a_l-i\frac{\varepsilon p}{2c^2}\omega_{p0}^2\{a_{l-1}\exp i[(k_l-k_{l-1}-K)z-\delta] + a_{l+1}\exp i[(k_l-k_{l+1}+K)z+\delta]\}=0, \tag{4}$$

where $\gamma_l = k_l^2-(\varepsilon/c^2)(\omega_l^2-\omega_{p0}^2)$.

Solving differential–difference equation (4) for the general case is difficult, but under condition (3b) and under the assumption $l \gg 1$ we can treat the complex amplitudes a_l as continuous and smooth functions of argument l, setting

$$a_{l\pm 1}=a_l\pm\frac{\partial a_l}{\partial l}. \tag{5}$$

Furthermore, this multimode interaction can be important only in the case of a weak dispersion, so we can introduce the frequency detuning χ_l as follows:

$$k_l-k_{l-1}-K=\chi_l-\frac{1}{2}\frac{\partial\chi_l}{\partial l},\ k_{l+1}-k_l-K=\chi_l+\frac{1}{2}\frac{\partial\chi_l}{\partial l}. \tag{6}$$

Neglecting second-order terms in the spirit of inequalities (3a) and (3b), we find, after substituting (5) and (6) into (4), a first-order differential equation for $a_l(z)$:

$$2k_l\frac{\partial a_l}{\partial z}-\frac{\varepsilon p}{c^2}\omega_{p0}^2\exp\left(-\frac{i}{2}\frac{\partial\chi_l}{\partial l}z\right)\sin(\chi_l z-\delta)\frac{\partial a_l}{\partial l}-i\Psi_l(z)a_l=0, \tag{7}$$

where

$$\Psi_l(z)=\gamma_l+\frac{\varepsilon p}{c^2}\omega_{p0}^2\exp\left(-\frac{i}{2}\frac{\partial\chi_l}{\partial l}z\right)\cos(\chi_l z-\delta).$$

The solution of Eq. (7) satisfying the boundary condition $a_l(0) = a_{l_0}$ can be found by the method of characteristics,

$$a_l(z)=a_{l_0}\exp\left\{\frac{i}{2}\int\limits_{\xi(z,\ l)=\xi(0,\ l_0)}\Psi_l(z)k_l^{-1}dz\right\}, \tag{8}$$

if we know the integral $\xi(z, l)$ of the characteristic equation

$$\frac{\varepsilon p}{c^2}\omega_{p0}^2\exp\left(-\frac{i}{2}\frac{\partial\chi_l}{\partial l}z\right)\sin(\chi_l z-\delta)\,dz=-2k_l\,dl. \tag{9}$$

We emphasize that the form of the dispersion relation for wave system (2) has not, generally speaking, been specified (we have simply imposed the condition $\partial\chi_l/\partial l \ll \chi_l$). As shown below, this circumstance allows us to simplify Eq. (9) and to express its integral $\xi(z, l)$ in terms of elementary functions.

3. Multimode solution (8) found in Sec. 2 must obviously satisfy condition (3a) for any z, so we find the following inequalities:

$$\varepsilon\omega_{p0}^2 p\ll c^2k_l^2, \tag{10a}$$

$$|\gamma_l|\ll k_l^2. \tag{10b}$$

The first of these inequalities defines the spectral range in which a solution of this type holds, and the second serves essentially as a dispersion relation for wave system (2) used here. We see from (10b) that such a system can be constructed unambiguously in a certain (quite narrow) range, so we can ultimately choose this system at our convenience. From the physical point of view it seems natural to first analyze a set of waves satisfying the dispersion relation of a homogeneous plasma with a density $N_0(\gamma_l = 0)$. According to (2), this approach corresponds to the ordinary procedure of expanding the field in terms of waves of the unperturbed system. However, here the spectrum of wave numbers k_l (and thus the detuning χ_l) is not uniformly spaced, so it becomes difficult to analyze solution (8) [because of the need to integrate characteristic equation (9)].

Accordingly, for convenience in analyzing the resulting solution it is best to choose a system of waves with a uniform spacing of wave numbers k_l. The simplest system of this type is obviously a set of waves satisfying the dispersion relation of a retarding dielectric medium:

$$k_l^2 = \frac{\varepsilon}{c^2}\Omega^2 l^2. \tag{11}$$

The weak dispersion of real system (1) is taken into account in the phase factors in (8).

This set of waves satisfies requirement (10b) if

$$\varepsilon\omega_{p0}^2 \ll c^2 k_l^2, \tag{12}$$

i.e., in the high-frequency part of the spectrum; under these conditions inequality (10a) is automatically satisfied also.

According to (11) we have $\chi_l = \chi = (\sqrt{\varepsilon}/c)\Omega - K =$ const here and characteristic equation (9) can be integrated easily. For the characteristic passing through the point $l = l_0$ at $z = 0$, we find

$$l^2 = l_0^2 - \sigma_\sim[\cos\delta - \cos(\chi z - \delta)], \tag{13}$$

where $\sigma_\sim = (\sqrt{\varepsilon}/c)[\omega_{p0}^2 p/(\Omega\chi)]$. We see from (8) that the amplitudes of the harmonics $|a_l(z)|$ for wave system (11) remain constant along characteristics (13); only their phases change. Accordingly, with $\chi \neq 0$ in this system there is a shift of boundary-perturbation spectrum a_{l0} upward and downward which is periodic in z (with a period of $2\pi/\chi$). The modulation depth

$$l = \frac{1}{2}(l_{\max} - l_{\min}) = \frac{1}{2}\left|\sqrt{l_0^2 + \sigma_\sim(1 - \cos\delta)} - \sqrt{l_0^2 - \sigma_\sim(1 + \cos\delta)}\right|$$

turns out to be different for different characteristics.$^{3)}$ This wave-type shift occurs with respect to the average level

$$l = \frac{1}{2}(l_{\max} + l_{\min}) = \frac{1}{2}\left(\sqrt{l_0^2 + \sigma_\sim(1 - \cos\delta)} + \sqrt{l_0^2 - \sigma_\sim(1 + \cos\delta)}\right),$$

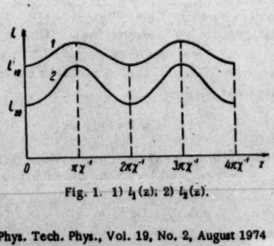

Fig. 1. 1) $l_1(z)$; 2) $l_2(z)$.

which is generally different from l_0. Thus the boundary-perturbation spectrum can either increase or decrease on the average, depending on the phase relations in the system. If, e.g., $\delta = 0$, and if the phase velocity of the pump wave satisfies $\Omega/K > (\sqrt{\varepsilon}/c)^{-1}$ $(\sigma_\sim < 0)$, there are no components at frequencies lower than at $z = 0$ at any $z \neq 0$. Figure 1 shows function (13) for this case, for two values of l_0.

We also see from these equations that there is a deformation of the spectrum as well as a shift and that this deformation is also periodic in z. Let us consider two arbitrary characteristics along which $l = l_1(z)$ and $l = l_2(z)$, where $l_1(0) = l_{10}$ and $l_1(0) = l_{20}$ (Fig. 1). We use the notation $\Delta l = l_1 - l_2$, $\Delta\sigma = l_1^2 - l_2^2$, where the functions $l_1(z)$ and $l_2(z)$ are evaluated at the same value of z, including $z = 0$: $\Delta l(0) = \Delta l_0$, $\Delta\sigma(0) = \Delta\sigma_0$. Then, by virtue of (13) we can write

$$\Delta\sigma = \Delta\sigma_0; \tag{14}$$

i.e., the square integral $\Delta\sigma$ remains constant along the characteristics. Equation (14) can be rewritten as

$$(l_1 + l_2)\Delta l = (l_{10} + l_{20})\Delta l_0, \tag{15}$$

from which we see that when the spectrum is shifted upward it broadens, and when it is shifted downward it contracts.

There is an analogous time transformation of the spectrum of broadband signals in a transmission line loaded by a periodically varying capacitance[17] if the propagation time of the waves in the line is not equal to a multiple of the period in the variation of the capacitance. The conclusion regarding periodic transformation of a high-frequency spectrum with nonvanishing detuning has been given previously,[14,15] but our approach gives a more complete picture of this process.

It is interesting to analyze the features of this spectral transformation in the case of "synchronism," in which case the phase velocities of the high-frequency transverse waves in (11) coincide with that of the longitudinal low-frequency wave:

$$c^2K^2 = \varepsilon\Omega^2. \tag{16}$$

Here $\chi \to 0$, and Eq. (13) can be rewritten as

$$l^2 = l_0^2 + \frac{\sqrt{\varepsilon}}{c}\frac{\omega_{p0}^2}{\Omega}\sin\delta z, \tag{17}$$

from which we see that the transformation of the spectrum is of an accumulative nature. For example, if $0 < \delta < \pi$, there is a monotonic upward shift of the spectrum and a simultaneous contraction, according to (15), while with $\pi < \delta < 2\pi$ there is a downward shift of the spectrum and a simultaneous expansion (Fig. 2). In the latter case the range of values of z over which this solution is valid is limited by inequality (12).

These conclusions agree, in particular, with the results of refs. 13-15, where it is noted that there can be a predominant transformation of the spectrum of decay processes in the case of zero tuning, toward higher or lower frequencies, depending on the sign of the difference between the coefficients of the nonlinear interaction for adjacent harmonics. The nature of the deformation of the spectrum was not studied.

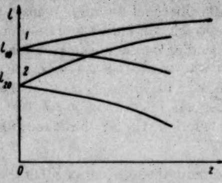

Fig. 2. 1) $l_1(z)$; 2) $l_2(z)$.

We note that a process of this type can also occur (as a function of the time) for the transmission line with a variable capacitive load[17] mentioned above, if the propagation time of the wave in the line is a multiple of the period of the changes in the capacitance. This condition obviously corresponds physically to the satisfaction of synchronism conditions (11), (16) with respect to the coordinate z. For the case of an ideal plane resonator with a vibrating boundary the monotonic upward shift of the spectrum is accompanied by an expansion, and the downward shift is accompanied by contraction, as shown in ref. 16.

4. The energy characteristic of this multimode process is evidently the time average of the energy flux density $\bar{S}$ in a specified cross section z = const. Since $a_l(z)$ is a slowly varying amplitude of the spectral component of vector potential **A**, the amplitudes of the corresponding components of the vectors **E** and **H** are approximately equal to $\omega_l c^{-1} a_l$ and $k_l a_l$, so that for a signal filling a spectral band Δl_0 at z = 0 we can write

$$\bar{S}=\frac{1}{4\pi\Delta t}\int\limits_{\Delta t} dt' \iint\limits_{\Delta l(\xi=\mathrm{const})} \omega_l k_{l'} a_l a_{l'}^*$$

$$\times \exp i[(\omega_l-\omega_{l'})t'-(k_l-k_{l'})z]\,dl\,dl'. \tag{18}$$

Since the solution of type (2) found above is periodic in t, the averaging interval Δt can be taken equal to Δt = T = 2π/Ω. Substituting dispersion relation (11) for the selected wave system into (18), we find

$$\bar{S}=\frac{\Omega^2\sqrt{\varepsilon}}{8\pi^2 c}\iint\limits_{\Delta l(\xi=\mathrm{const})} dl\,dl'\,a_{l'}^* a_l l' l$$

$$\times \exp i\left[\Omega\frac{\sqrt{\varepsilon}}{c}(l'-l)z\right]\int\limits_{-\pi}^{\pi}\exp i(l-l')\zeta\,d\zeta. \tag{19}$$

In evaluating the integral over ζ we must remember that the variable l is treated above as continuous only under the condition $l \gg 1$. Strictly speaking, l only takes on integer values, and in the exponential function in the integral over ζ the difference $l-l'$ cannot be less than unity. It is easy to see, however, that the variable l can again be assumed to be continuous here if the limits on the integration over ζ are extended to infinity. As a result we find from (19)

$$\bar{S}=\frac{\Omega^2\sqrt{\varepsilon}}{4\pi c}\int\limits_{\Delta l(\xi=\mathrm{const})}|a_l|^2 l^2\,dl$$

or, according to the mean-value theorem,

$$\bar{S}=\frac{\Omega^2\sqrt{\varepsilon}}{4\pi c}\Delta l\,(|a_l|^2 l^2)_{\xi=\xi_*} \tag{20}$$

along some characteristic ξ_*, which intersects the z = 0 boundary within the interval Δl_0. Substituting (15) into (20), we find the following energy relation for multimode interactions in systems of type (1):

$$\frac{\bar{S}(l_1+l_2)}{l_*^2}=\frac{\bar{S}_0(l_{10}+l_{20})}{l_{*0}^2}. \tag{21}$$

Accordingly, in this system an increase (or decrease) in the average frequency of the multimode process is accompanied by a simultaneous increase (decrease) in the waves and a simultaneous contraction (expansion) of their spectrum. It must be emphasized that Eq. (21) remains valid, not only for the entire broad-band signal, but also for any finite spectral interval Δl, of this signal, considered along the corresponding characteristics.

We also see from (21) that the energy transformations in a system having a large number of waves is generally a function of the perturbation spectrum specified at the boundary, since the nature of this spectrum determines the choice of characteristic ξ_* within interval Δl and thus the values of l_* and l_{*0} in (21). As spectral interval Δl is contracted this functional dependence becomes weaker and weaker, and in the limit $\Delta l/l \to 0$ we find

$$\frac{\bar{S}}{l}=\frac{\bar{S}_0}{l_0}, \tag{22}$$

which, by virtue of the periodicity of system (1), is essentially the familiar adiabatic variant for quasiharmonic wave packets in slightly inhomogeneous and slightly nonsteady-state dispersive media.[8,18] Accordingly, Eq. (21) can be thought of in a certain sense as a generalization of this invariant to the case of multimode (i.e., significantly nonharmonic) processes in systems of type (1) with periodically varying parameters.

5. As mentioned above, an equation like (8) for the wave set (11) is the solution of the boundary-value problem formulated here only under condition (12), i.e., in the high-frequency part of the spectrum. It should be noted, however, that with certain reasonable limitations on the spectral width of the unknown solution characteristic system (9) can be integrated in terms of elementary functions even for smaller values of ω_l, k_l. Let us analyze this possibility.

Before we choose a concrete wave system, the only limitations on the validity of solution (8) are inequalities (10a) and (10b). On the other hand, the circumstance that (9) can be integrated in terms of elementary functions becomes obvious when the spectrum of wave numbers k_l is spaced uniformly. We assume that within some band ($\Delta l \gg 1$) we have a set of waves satisfying these requirements. We write the dispersion relation of the desired system of waves as

$$k_l^2-\frac{\varepsilon}{c^2}(\Omega^2 l^2-\omega_{p0}^2)=\gamma_l,$$

where γ_l is some set of values (both positive and negative) which can be determined from the condition $k_l - k_{l-1} = \Delta =$ const and which satisfy inequality (10b).

It is easy to see that condition Δ = const leads to the following equation for γ_l:

$$\gamma_l = \frac{\varepsilon\omega_{p0}^2}{c^2}\left(1 - \frac{l^2}{l_s^2}\right), \tag{23}$$

where l_s is some fixed number for a given spectral band; this number should be chosen within interval Δl. Then, using (10a), we find from inequality (10b)

$$\frac{|l^2 - l_s^2|}{l_s^2} \leqslant p, \tag{24}$$

which, along with (10a), specifies the conditions for the applicability of solution (8) for the specified wave system.

This wave system satisfies the dispersion relation

$$k_l^2 = \frac{\varepsilon}{c^2}\Omega^2 l^2\left(1 - \frac{\omega_{p0}^2}{\Omega^2 l_s^2}\right), \tag{25}$$

which obviously corresponds to a piecewise-linear approximation of the dispersion curve of a homogeneous plasma with a density N_0 near frequency $\omega_s = \Omega l_s$.

We see from (25) that we should substitute into (8) and (9) the following:

$$\chi_l = \chi = \frac{\sqrt{\varepsilon}}{c}\Omega\left(1 - \frac{\omega_{p0}^2}{\Omega^2 l_s^2}\right) - Kl; \tag{26}$$

Using (23) we can then analyze solution (8) in detail, as in Secs. 3 and 4. Omitting the details, we note that for small modulation indices p this approach allows us to analyze the solution of system (1) at frequencies near the plasma frequency. However, the dispersion becomes important here, and the spectral width of the signal whose transformation can be treated by this method becomes narrower, in accordance with (24). For sufficiently high-frequency waves [see (12)] we can set $l_s \to \infty$; then we find the same results as in Secs. 3 and 4.

6. The initial-value problem can be treated in the same way. If, at t = 0, we specify in an unbounded system a perturbation which is periodic with respect to z and has a period $2\pi/K$, we can seek the solution of original equation (1) in the form

$$A(z, t) = \sum_{l \geqslant 1} a_l(t) \exp i(\omega_l t - Klz + \delta l). \tag{27}$$

Under the conditions

$$\frac{\partial a_l}{\partial t} \ll \omega_l a_l, \quad \frac{\partial a_l}{\partial l} \ll a_l, \quad \frac{\partial \vartheta_l}{\partial l} \ll \vartheta_l, \tag{28}$$

where ϑ_l is introduced on the basis of

$$\omega_{l+1} - \omega_l - \Omega = \vartheta_l + \frac{1}{2}\frac{\partial \vartheta_l}{\partial l}, \quad \omega_l - \omega_{l-1} - \Omega = \vartheta_l - \frac{1}{2}\frac{\partial \vartheta_l}{\partial l},$$

we find

$$2\omega_l \frac{\partial a_l}{\partial t} + \omega_{p0}^2 p \exp\left(\frac{i}{2}\frac{\partial \vartheta_l}{\partial l} t\right)\sin(\vartheta_l t + \delta)\frac{\partial a_l}{\partial l} - i\Phi_l(t) a_l = 0, \tag{29}$$

which is analogous to (7). Here

$$\Phi_l(t) = \frac{c^2}{\varepsilon}\gamma_l + \omega_{p0}^2 p \exp\left(\frac{i}{2}\frac{\partial \vartheta_l}{\partial l} t\right)\cos(\vartheta_l t + \delta).$$

Equation (29) can be solved by the method of characteristics, used in Sec. 2 for Eq. (7). The subsequent analysis does not differ from that of Secs. 3 and 4. For example, for wave systems satisfying the dispersion relation $\omega_l^2 = c^2/\varepsilon K^2 l^2$, with $\omega_l^2 \gg \omega_{p0}^2$ and $\vartheta = (c/\sqrt{\varepsilon})K - \Omega \neq 0$, we find a wave-type time shift of the spectrum of the initial perturbation with a period of $2\pi/\theta$. With $\Omega/K = c/\sqrt{\varepsilon}$, we find a monotonic upward or downward shift of the spectrum, depending on a phase of δ. The upward shift of the spectrum is accompanied by a contraction of the spectrum and an increase in the wave energy (in this case the energy density averaged over the period $L = 2\pi/K$), according to (14), (15), and (21). When the spectrum is shifted downward, it expands, and the energy density of the waves decreases.

As in the case of the boundary-value problem, the existence of cumulative effects at $\Omega/K = c/\sqrt{\varepsilon}$ corresponds to a parametric instability of this system with respect to the specified periodic perturbation.

---

1) There is a certain methodological analogy with refs. 14 and 15, where, in particular, the coefficients of the nonlinear interaction of excited combination harmonics were assumed to be weak functions of the harmonic indices; however, this assumption is not related to the approximation proposed above, which takes account of the spectral shape of the process under consideration.

2) Three-frequency processes for such a system are analyzed in ref. 3, where it is also shown that this approximation becomes invalid even at $|p| \ll 1$, if the group velocity of the electromagnetic waves approaches the phase velocity of the pump Ω/k.

3) The quadratic deviation $|\delta \sim| = (l_{max}^2 - l_{min}^2)/2$ is independent of the index l_0.

---

[1] V. N. Oraevskii and R. Z. Sagdeev, Zh. Tekh. Fiz., 32, 1291 (1962) [Sov. Phys. – Tech. Phys., 7, 955 (1963)].

[2] L. A. Ostrovskii and N. S. Stepanov, Zh. Eksp. Teor. Fiz., 45, 1473 (1963) [Sov. Phys. – JETP, 18, 1018 (1964)].

[3] N. S. Stepanov, Izv. VUZ. Radiofiz., 6, 461 (1963).

[4] V. P. Silin, Zh. Eksp. Teor. Fiz., 48, 1679 (1965) [Sov. Phys. – JETP, 21, 1127 (1965)].

[5] S. A. Akhmanov and R. V. Kokhlov, Problems of Nonlinear Optics [in Russian], Izd. Akad. Nauk SSSR, Moscow (1964).

[6] S. A. Akhmanov and R. V. Khokhlov, Usp. Fiz. Nauk, 88, 439 (1966) [Sov. Phys. – Usp., 9, 210 (1966)].

[7] M. M. Sushchik, V. M. Fortus, and G. I. Freidman, Izv. VUZ. Radiofiz., 13, 631 (1970).

[8] L. A. Ostrovskii and N. S. Stepanov, Izv. VUZ. Radiofiz., 14, 489 (1971).

[9] V. P. Silin, Usp. Fiz. Nauk, 108, 625 (1972) [Sov. Phys. – Usp., 15, 742 (1973)].

[10] S. A. Akhmanov, S. D. Gvozdover, A. S. Gorshkov, and V. G. Dmitriev, Zh. Tekh. Fiz., 33, 90 (1963) [Sov. Phys. – Tech. Phys., 8, 61 (1963)].

[11] V. D. Fedorchenko, V. I. Muratov, and B. N. Rutkevich, Nucl. Fusion, 8, 37 (1968).

[12] P. A. Sturrock, Proc. Roy. Soc., 242A, 1230 (1957); in: Microwaves in Plasmas [Russian translation], IL, Moscow (1961).

[13] I. S. Danilkin, Zh. Tekh. Fiz., 36, 266 (1966) [Sov. Phys. – Tech. Phys., 11, 193 (1966)].

[14] A. S. Bakai, Zh. Eksp. Teor. Fiz., 55, 266 (1968) [Sov. Phys. – JETP, 28, 140 (1969)].

[15] A. S. Bakai, Nucl. Fusion, 10, 53 (1970).

[16] V. N. Krasil'nikov and A. M. Pankratov, in: Problems of Wave Diffraction and Propagation [in Russian], No. 8, Izd. LGU (1968), p. 59.

[17] N. S. Stepanov, Radiotekh. Elektron., 15, 1885 (1970).

[18] N. S. Stepanov, Zh. Eksp. Teor. Fiz., 53, 2186 (1967) [Sov. Phys. – JETP, 26, 1234 (1968)].

Kinetic theory for wave reflection from a moving plasma

Yu. V. Bogomolov

Radiotechnical Institute, Academy of Sciences of the USSR, Moscow

(Submitted June 11, 1973)
Zh. Tekh. Fiz., 44, 300-304 (February 1974)

The reflection of a plane electromagnetic wave at normal incidence on a moving plasma half-space is analyzed. The plasma is in a fixed magnetic field parallel to the plasma boundary. The spatial dispersion is assumed to be weak and the plasma boundary is specified by assuming diffuse reflection of electrons. The surface impedance is calculated for the ordinary wave and the extraordinary wave.

The interaction of electromagnetic radiation with a moving plasma is of interest in a variety of problems: the acceleration and diagnostics of plasmoids, amplification of radiowaves, and plasma containment by electromagnetic pressure. In practice this interaction is frequently realized in a slow-wave structure. To elucidate the main physical features of the problem, we consider a more abstract problem and assume that the electromagnetic field has the form of a plane wave and that the phase velocity of this wave is reduced by means of a dielectric. This model has been used for both isotropic plasmas[1] and a magnetoactive plasma.[2-5] In the latter case the magnetic field is perpendicular to the boundary.

In the present paper the problem is formulated as follows. We consider a half-space $x > 0$ filled with plasma. A constant magnetic field H_0, which is homogeneous within the plasma, is directed along the z axis parallel to the plasma boundary. The plasma boundary is simulated by the condition of diffuse reflection of electrons. We ignore the motion of the ions and collisions. It is assumed that the thermal motion of the electrons is weak and it is treated as a perturbation. The system of coordinates x, y, z is rigidly attached to the plasma. The plasma moves with velocity **V** parallel to the x axis. The entire space is filled with a dielectric of permittivity ε and magnetic permeability equal to unity in the laboratory frame. It is assumed that the dispersion of the dielectric is unimportant. Assume that a plane electromagnetic wave of arbitrary polarization is incident normally on the plasma. This wave can be split into two normal modes: $\mathbf{E} \parallel H_0$ (ordinary wave) and $\mathbf{E} \perp H_0$ (extraordinary wave). We wish to calculate the surface impedance for the two modes. Knowing the impedance, we can calculate the coefficients of reflection and absorption. We shall restrict ourselves to the case in which the phase velocity of the wave is greater than the plasma velocity.

Ordinary wave. It is simplest to solve the problem in the coordinate system attached to the plasma. In this system the dielectric moves along the x axis with velocity $V = \beta c$. We describe the plasma by a system of equations consisting of Maxwell's equations and a transport equation with self-consistent field for the electrons. We represent the electron distribution function in the form $f_0 + f$, where f_0 is the unperturbed (Maxwellian) distribution function and f is the correction associated with the wave. In a magnetic field parallel to the surface the electrons can be split into two groups. Some execute a periodic motion, knowing nothing of the surface. The penetration of a field into a plasma consisting of only such electrons has been considered (in the absence of a dielectric) by Dnestrovskii and Kostomarov.[6] Other electrons are constantly colliding with the boundary, being scattered diffusely on it. The condition of diffuse reflection takes the form $f = 0$ at the boundary.

The solution of the linearized transport equation

$$-i\omega f + v\cos\delta\frac{\partial f}{\partial x} + \omega_H\frac{\partial f}{\partial \delta} = \frac{e}{m}\frac{\partial f_0}{\partial v_z}E_z \tag{1}$$

for the diffuse boundary has the form

$$f(x,\delta) = \frac{e}{m\omega_H}\frac{\partial f_0}{\partial v_z}\left[(e^{-2\pi\mu}-1)^{-1}\eta(x-x_0)\int\limits_{\delta}^{\delta+2\pi} + \eta(x_0-x)\right] \times e^{\mu(\delta-\delta')}E_z(x')\,d\delta', \tag{2}$$

Here, v and δ are polar coordinates in the velocity space; $\omega_H = eH_0/mc$ is the electron gyrofrequency; $\mu = i\omega/\omega_H$; δ_0 is the angle at which an electron leaves the wall; $\eta(\zeta)$ is the step function, equal to zero for $\zeta < 0$ and unity for $\zeta > 0$. Further, x_0, δ_0, x' are defined by

$$\left.\begin{aligned} x_0 &= \frac{v}{\omega_H}(\sin\delta + 1), \\ \delta_0 &= \arcsin\left(\sin\delta - \frac{x\omega_H}{v}\right), \\ x' &= x + \frac{v}{\omega_H}(\sin\delta' - \sin\delta). \end{aligned}\right\} \tag{3}$$

The function f_0 has the form

$$f_0 = N\left(\frac{m}{2\pi T}\right)^{3/2}\exp\left[-\frac{m}{2T}(v^2 + v_z^2)\right], \tag{4}$$

where N is the number of electrons in 1 cm^3 and T is the temperature in energy units. The time factor $\exp(-i\omega t)$ is omitted throughout.

In the ordinary wave, only the components E_z, D_z, H_y, B_y, j_z are nonvanishing. Maxwell's equations are

$$\left.\begin{aligned} \frac{dH_y}{dx} &= -ikD_z + \frac{4\pi}{c}j_z, \\ \frac{dE_z}{dx} &= -ikB_y, \end{aligned}\right\} \tag{5}$$

where $k = \omega/c$. These equations must be augmented by the material equations, which (in the case of a moving dielectric) take the form of Minkowski's relations[7]

$$D_z = \varepsilon a E_z + bH_y, \quad B_y = aH_y + bE_z, \tag{6}$$

where

$$a = \frac{1-\beta^2}{1-\varepsilon\beta^2}, \quad b = \frac{\beta(\varepsilon-1)}{1-\varepsilon\beta^2}.$$

Substituting (6) into (5) and eliminating H_y, we find

$$\frac{d^2E_z}{dx^2}+2ikb\frac{dE_z}{dx}+k^2(\varepsilon a^2-b^2)E_z=-\frac{4\pi ika}{c}j_z. \tag{7}$$

Note that the term with the first derivative arises solely because of the motion of the dielectric. The current j_z is related to f by

$$j_z=-e\int_0^\infty v\,dv\int_{-\pi/2}^{3\pi/2}d\delta\int_{-\infty}^{\infty}v_z f\,dv_z. \tag{8}$$

The given range of variation of the angle δ is obvious for a particle colliding with the boundary. For a cold plasma, $j_z=-(\omega_0^2/4\pi i\omega)E_z$, where $\omega_0=\sqrt{4\pi e^2N/m}$ is the plasma frequency. In this case, the plasma can be described by the permittivity $\varepsilon_0=1-\omega_0^2/\omega^2$.

We introduce an operator $I_z(E_z)$, which vanishes for a cold plasma:

$$I_z(E_z)=-\frac{\omega_0^2}{c^2}E_z-\frac{4\pi i\omega}{c^2}j_z. \tag{9}$$

Then Eq. (7) becomes

$$\frac{d^2E_z}{dx^2}+2ikb\frac{dE_z}{dx}+k^2\left(\varepsilon a^2-b^2-\frac{a\omega_0^2}{\omega^2}\right)E_z=aI_z(E_z). \tag{10}$$

For the space outside the plasma,

$$\frac{d^2E_z}{dx^2}+2ikb\frac{dE_z}{dx}+k^2(\varepsilon a^2-b^2)E_z=0. \tag{11}$$

We seek a solution of Eqs. (10)-(11) in the form

$$E_z=E_{z0}+u_z, \tag{12}$$

where E_{z0} corresponds to a cold plasma, and u_z characterizes the thermal motion. We consider the case of weak spatial dispersion

$$\frac{kv}{\omega_H}\ll 1. \tag{13}$$

If inequality (13) holds, u_z can be regarded as a perturbation:

$$u_z\ll E_{z0}. \tag{14}$$

For E_{z0} in the "subluminous" case $(1-\varepsilon\beta^2>0)$ we have the well-known expressions (the incident wave has amplitude unity)

$$E_{z0}(x)=\begin{cases}\dfrac{2\sqrt{\varepsilon}}{\sqrt{\varepsilon}+M}\exp(ih_1x)\ (x>0),\\ \exp\left(ik\dfrac{\sqrt{\varepsilon}+\beta}{1+\sqrt{\varepsilon}\beta}x\right)+\dfrac{\sqrt{\varepsilon}-M}{\sqrt{\varepsilon}+M}\exp(-ih^{\text{refl}}x)\ (x<0),\end{cases} \tag{15}$$

where

$$M=\sqrt{\varepsilon-\frac{\omega_0^2}{\omega^2 a}},\ h_1=-kb+kaM,\ h^{\text{refl}}=k\frac{\sqrt{\varepsilon}-\beta}{1-\sqrt{\varepsilon}\beta}.$$

Substituting (12) into (10)-(11) and taking into account (14), we obtain equations for the function $u_z(x)$:

$$u_z''+2ikbu_z'+k^2\left(\varepsilon a^2-b^2-\frac{a\omega_0^2}{\omega^2}\right)u_z=aI_z(E_{z0})\ (x>0), \tag{16}$$

$$u_z''+2ikbu_z'+k^2(\varepsilon a^2-b^2)u_z=0\ (x<0). \tag{17}$$

We solve Eq. (16) by variation of constants, remembering that the solution is bounded at $x=\infty$; we take account of the radiation condition in the solution of (17). On the boundary $x=0$ we require continuity of u_z and du_z/dx. For $u_z(x)$ outside the plasma we obtain the expression

$$u_z(x)=B\exp(-ih^{\text{refl}}x), \tag{18}$$

where

$$\left.\begin{aligned}B&=\frac{a}{i(h_1+h^{\text{refl}})}\int_0^\infty e^{-ih_2s}I_z(E_{z0}(s))\,ds,\\ h_2&=-kb-kaM.\end{aligned}\right\} \tag{19}$$

We write down the expression for B in more detail. For this case, we must first take account of Eqs. (2), (8), (9), and (15) and integrate with respect to v_z. We then introduce a new variable δ_0 in place of s in the part of (19) that corresponds to collisions of electrons with the boundary. The relationship between δ_0 and s is

$$s=(v/\omega_H)(\sin\delta-\sin\delta_0). \tag{20}$$

In the remaining part of (19) we can integrate with respect to s directly. Remembering this and making some simple identity transformations, we find

$$B=-\frac{2a\sqrt{\varepsilon}\omega_0^2}{c^2(\sqrt{\varepsilon}+M)(h_1+h^{\text{refl}})(h_1-h_2)}W, \tag{21}$$

where

$$\begin{aligned}W={}&1+\frac{\mu m}{2\pi T}(e^{-2\pi\mu}-1)^{-1}\\ &\times\int_0^\infty v\exp\left[i\frac{v}{\omega_H}(h_1-h_2)\right]dv\int_0^{2\pi}d\delta\int_\delta^{\delta+2\pi}\Phi\,d\delta'\\ &-\frac{i\mu m(h_1-h_2)}{2\pi\omega_HT}\int_0^\infty v^2dv\int_{-\pi/2}^{\pi/2}\cos\delta_0\\ &\times\exp\left[-i\frac{v}{\omega_H}(h_1-h_2)\sin\delta_0\right]d\delta_0\int_{\delta_0}^{\pi-\delta_0}d\delta\int_{\delta_0}^{\delta}\Phi\,d\delta',\end{aligned} \tag{22}$$

$$\Phi=\exp\left[-\frac{mv^2}{2T}+\mu(\delta-\delta')+i\frac{v}{\omega_H}(h_1\sin\delta'-h_2\sin\delta)\right]. \tag{23}$$

We define the impedance Z by

$$Z\equiv R+iX=-\frac{E_z(0)}{H_y(0)}. \tag{24}$$

The most interesting case is the one in which the wave is a skin wave (M purely imaginary). Using (6), (5), (12), and (18), we find

$$Z=\frac{1}{M}\left(1-\frac{i\omega_0^2}{2a\omega^2M^2}\operatorname{Im}W\right). \tag{25}$$

Expanding W in a series in h_1v/ω_H and h_2v/ω_H (k, h_1, h_2 are of the same order), we find

$$\operatorname{Im}W=a|M|\left(\frac{2T}{\pi mc^2}\right)^{1/2}\left(1+\frac{\cos^2\pi\Omega}{4\Omega^2-1}\right), \tag{26}$$

where $\Omega=\omega/\omega_H$. Hence,

$$Z=\left(\frac{T}{2\pi mc^2}\right)^{1/2}\frac{a\omega_0^2}{\omega_0^2-\varepsilon a\omega^2}\left(1+\frac{\cos^2\pi\Omega}{4\Omega^2-1}\right)-i\left(\frac{\omega_0^2}{\omega^2a}-\varepsilon\right)^{-1/2}. \tag{27}$$

The complex reflection coefficient r is related to the impedance by

$$r=\frac{\sqrt{\varepsilon}Z-1}{\sqrt{\varepsilon}Z+1}. \tag{28}$$

The absorption coefficient A, which is defined by

$$A=1-|r|^2, \tag{29}$$

is

$$A=2a\left(\frac{2\varepsilon T}{\pi mc^2}\right)^{1/2}\left(1+\frac{\cos^2\pi\Omega}{4\Omega^2-1}\right). \tag{30}$$

Thus, the thermal motion of the electrons leads to absorption of the electromagnetic wave. The absorption has a surface character and is due to the fact that the electric field of the wave performs work on an electron that collides with the boundary. The absorption is of the order of the ratio of the mean electron thermal velocity to the velocity of light. If ε = 1, then a = 1 and Eq. (30) goes over into the well-known expression.[8,9]

Extraordinary wave. If an extraordinary wave is incident on the plasma a longitudinal field E_x arises. With regard to this component of the field, we shall also assume that perturbation theory applies. Omitting the intermediate calculations, we write down the impedance $Z = E_y(0)/H_z(0)$ for "subluminous" motion of the plasma and skinning of the wave:

$$Z=\left(\frac{T}{2\pi mc^2}\right)^{1/2}\frac{a\omega^2\omega_0^2F}{\omega_0^2(\varepsilon\omega^2-\omega_0^2)-\varepsilon a\omega^2[\varepsilon(\omega^2-\omega_H^2)-\omega_0^2]}$$
$$-i\left(\frac{\omega_0^2}{\omega^2a}\frac{\omega_0^2-\varepsilon\omega^2}{\omega_0^2-\varepsilon(\omega^2-\omega_H^2)}-\varepsilon\right)^{-1/2}, \tag{31}$$

where

$$F=\frac{1}{\varepsilon(\Omega^2-1)-\Omega_0^2}\left\{2\varepsilon^2+\frac{(\Omega_0^2-\varepsilon\Omega^2)^2}{\Omega^2}+\frac{3\cos^2\pi\Omega}{(1-4\Omega^2)(9-4\Omega^2)}\right.$$
$$\left.\times\left[6\varepsilon^2+8\varepsilon(\varepsilon\Omega^2-\Omega_0^2)+\left(4-\frac{3}{\Omega^2}\right)(\varepsilon\Omega^2-\Omega_0^2)^2\right]\right\}, \tag{32}$$

$$\Omega_0=\omega_0/\omega_H.$$

The radicand in the imaginary part of the impedance is positive (skin wave). The absorption coefficient is

$$A=2a\left(\frac{2\varepsilon T}{\pi mc^2}\right)^{1/2}\frac{\omega^2F}{\omega_0^2-\varepsilon\omega^2}. \tag{33}$$

As for the ordinary wave, the absorption is proportional to $\sqrt{T}$. If ε = 1, Eq. (33) goes over into the well-known expression.[10]

The above expressions have been written down in the coordinate system attached to the plasma. The absorption coefficient in the laboratory frame is

$$A_{\text{lab}}=\left(\frac{1+\sqrt{\varepsilon}\beta}{1-\sqrt{\varepsilon}\beta}\right)^2A. \tag{34}$$

I should like to thank M. L. Levin for discussion.

---

[1] M. A. Lampert, Phys. Rev., 102, 299 (1956).

[2] Ya. B. Fainberg and V. M. Tkalich, Zh. Tekh. Fiz., 29, 491 (1959) [Sov. Phys. – Tech. Phys., 4, 438 (1959)].

[3] V. I. Kurilko, Zh. Tekh. Fiz., 31, 71 (1961) [Sov. Phys. – Tech. Phys., 6, 50 (1961)].

[4] V. I. Kurilko and V. I. Miroshnichenko, Zh. Tekh. Fiz., 32, 803 (1962) [Sov. Phys. – Tech. Phys., 7, 588 (1963).

[5] V. I. Miroshnichenko, Izv. Vyssh. Ucheb. Zaved. Radiofiz., 9, 666 (1966).

[6] Yu. N. Dnestrovskii and D. P. Kostomarov, Zh. Eksp. Teor. Fiz., 39, 845 (1960) [Sov. Phys. – JETP, 12, 587 (1961)].

[7] L. D. Landau and E. M. Lifshitz, Electrodynamics of Continuous Media, Pergamon Press, Oxford (1960).

[8] É. A. Kaner and Yu. A. Belov, Izv. Vyssh. Ucheb. Zaved. Radiofiz., 5, 47 (1962).

[9] Yu. V. Bogomolov, Izv. Vyssh. Ucheb. Zaved. Radiofiz., 14, 1168 (1971).

[10] Yu. V. Bogomolov, Zh. Tekh. Fiz., 42, 281 (1972) [Sov. Phys. – Tech. Phys., 17, 224 (1972)].

Scattering of high-frequency electromagnetic waves by ion-acoustic oscillations in a bounded plasma

V. G. Shaptala

A. M. Gor'kii Khar'kov State University

(Submitted April 9, 1973)
Zh. Tekh. Fiz., 42, 305-310 (February 1974)

The scattering of a high-frequency electromagnetic wave by regular ion-acoustic oscillations is studied in a plane homogeneous plasma with and without a fixed magnetic field parallel to the plasma boundary. The problem is treated in the hydrodynamic approximation and the nonlinearity is assumed to be weak. Expressions are found for the electromagnetic waves emitted into the vacuum at frequencies $\Omega_n = \Omega + n\omega$ (Ω is the frequency of the electromagnetic wave and ω is the frequency of the ion-acoustic wave, $n = \pm 1, \pm 2, \ldots$) for the case of total internal reflection and for transparency. It is shown that the amplitude of the scattered wave increases as the frequency of the probing signal approaches the plasma frequency.

1. The scattering of high-frequency electromagnetic waves by low-frequency fluctuations of a stable and turbulent plasma has been studied and is used for plasma diagnostics.[1,2] However, under certain conditions, for example when beams of charged particles pass through a plasma, regular low-frequency oscillations are excited in the plasma with an amplitude that exceeds appreciably the amplitudes of the fluctuating fields. If high-frequency probing of such a plasma is used, radiation is emitted at combination frequencies and this reflects the dynamics of the interaction between the regular high- and low-frequency waves.

Study of the characteristics of the scattered waves can yield additional information on the processes that take place in the plasma and on its parameters. In the present paper we consider the scattering of high-frequency electromagnetic waves by regular ion-acoustic oscillations of a plane plasma with and without a fixed magnetic field. General questions and special cases involving the nonlinear interaction of waves in a bounded plasma have been investigated in refs. 3-6.

2. We consider a plane-parallel layer $0 < x < 2d$ of homogeneous nonisothermal plasma ($T_e \gg T_i$, where T_α is the temperature of the plasma particles) in which there propagates an ion-acoustic wave $\varphi \propto \exp[i(q_z z - \omega t)]$, where φ is the electric potential. Assume that a high-frequency plane wave is incident on the boundary $x = 0$ from the vacuum side:

$$\mathbf{E}_0^v = \mathscr{E} e^{i(\mathbf{kr} - \Omega t)}, \quad k = \frac{\Omega}{c}, \quad \Omega \gg \omega. \tag{1}$$

The nonlinear interaction of the low- and high-frequency waves gives rise to electromagnetic oscillations at the combination frequencies $E_n \propto \exp[i(\xi_{nx}x + k_{n\tau}r_\tau - \Omega_n t)]$, and these are radiated into the vacuum:

$$\mathbf{E}_n^v = e^{i(\mathbf{k}_{n\tau}\mathbf{r}_\tau - \Omega_n t)} \begin{cases} \mathscr{E}_n \exp(-ik_{nx}x), \\ \mathscr{E}_n' \exp(ik_{nx}x), \end{cases} \tag{2}$$

where $k_{n\tau} = k_\tau + nq_z$, $k_{nx} = (k_n^2 - k_{n\tau}^2)^{1/2}$, $k_n = \Omega_n/c$, $\Omega_n = \Omega + n\omega$, $n = \pm 1, \pm 2, \ldots$; $\mathscr{E}_n$ and $\mathscr{E}_n'$ are the amplitudes of the scattered waves reflected from the boundary of the plasma and transmitted through the layer that we wish to determine. We assume that the plasma is fairly broad for the high-frequency wave and that its boundaries are sharp, i.e., $2d\,|\xi_{nx}| \gg 1$, $l\,|\xi_{nx}| \ll 1$, where l is the width of the transition region of inhomogeneous plasma.

In the approximation of weak nonlinearity

$$\left(\frac{e\varphi}{m_e v_{Te}^2},\ \frac{eE_n}{m_e \Omega_n c} \ll 1\right)$$

the interaction between the low- and high-frequency waves is described by a system of coupled nonlinear wave equations augmented by the nonlinear boundary conditions for the fields at the plasma–vacuum interface.[5,6]

In the case of total internal reflection of the high-frequency waves from the layer and also when they propagate in the plasma with appreciable phase difference ($\Delta = \xi_{nx} - \xi_{n-1x} - q_x \sim \xi_{nx}$) the change in the amplitudes of the interacting waves can be ignored (prescribed-field approximation).

In the resonance case ($\Delta \gg \xi_{nx}$) one can only find the boundary values of the amplitudes of the high-frequency waves in this approximation and for $x > 1/\xi_{nx}$, $1/q_x$ one must take account of the x dependence of the amplitudes of the interacting waves:

$$\begin{gathered} \varphi = b_1(x) e^{iq_x x} + b_2(x) e^{-iq_x x}, \\ E_n = A_n^+(x) e^{i\xi_{nx} x} + A_n^-(x) e^{-i\xi_{nx} x}. \end{gathered} \tag{3}$$

If we ignore the high-frequency waves reflected from the second boundary of the layer (this is valid if the reflection coefficients are small, $R_n \ll 1$), from the nonlinear wave equations (see, for example, refs. 3-4) we obtain the following system of dynamical equations,

$$\left.\begin{aligned} 2i\frac{\partial b_1}{\partial x} &= V_{bA} \sum_n A_n A_{n-1}^* e^{i\Delta_1(n,\, n-1)x}, \\ 2i\frac{\partial b_2}{\partial x} &= -V_{bA} \sum_n A_n A_{n-1}^* e^{i\Delta_2(n,\, n-1)x}, \\ 2i\frac{\partial A_n}{\partial x} &= V_{AA}\left[b_1 A_{n-1} e^{i\Delta_1(n-1,\, n)x} + b_2 A_{n-1} e^{i\Delta_2(n-1,\, n)x}\right. \\ &\quad \left. + b_1^* A_{n+1} e^{i\Delta_1(n+1,\, n)x} + b_2^* A_{n+1} e^{i\Delta_2(n+1,\, n)x}\right], \end{aligned}\right\} \tag{4}$$

where $\Delta_{1,2}(n, n-1) = \xi_{nx} - \xi_{n-1x} \pm q_x$, and V_{bA} and V_{AA} are the wave-coupling coefficients, whose weak dependence on n can be ignored. The solution of the system of equations (4), which is found in ref. 7, is

$$\left.\begin{aligned} A_n(x) &= \sum_{m=-\infty}^{\infty} A_m(0)\, i^{n-m} e^{i(n-m)\beta} J_{n-m}(V_{AA}|B(x)|), \\ b_{1,2}(x) &= b_{1,2}(0) \\ &\pm \frac{V_{bA}}{2\Delta_{1,2}(n,\, n-1)}\left[1-e^{i\Delta_{1,2}(n,\,n-1)x}\right]\sum_n A_n(0)A^*_{n-1}(0), \\ B(x) &= \int_0^x \left[b_1(x)e^{i\Delta_2(n-1,\,n)x}+b_2(x)e^{i\Delta_1(n-1,\,n)x}\right]dx, \end{aligned}\right\} \quad (5)$$

where $\beta = \arg B$ and J_n is a Bessel function.

We shall consider the scattering of high-frequency waves by ion-acoustic oscillations of a plasma layer in two cases.

3. Assume that a symmetric ion-acoustic wave is excited in an isotropic plasma:

$$\varphi = \cos q_x(x-d)\, e^{i(q_z z-\omega t)}. \quad (6)$$

If $\omega \ll \omega_{pi}$, then $q_x \approx \pi/d$ and $q_z = (q_s^2 - q_x^2)^{1/2}$, where $q_s = \omega/v_s$ is the wave number of the ion acoustic wave, $v_s = [\gamma(T_e/m_i)]^{1/2}$, γ is the adiabatic exponent, and $\omega_{p\alpha} = (4\pi e^2 n_0/m_\alpha)^{1/2}$ is the plasma frequency.

Assume that the probing high-frequency wave is incident at normal incidence on the boundary $x = 0$ and that its electric field is at right angles to the plane of propagation of the ion acoustic wave ($\mathcal{E}_{0y} = \mathcal{E}_0$). The scattered waves have the same polarization ($E_{ny} = E_n$) and are radiated into the vacuum at the angles $\theta_n = \operatorname{arc\,tg}(nq_z)/k_n$.

The system of nonlinear wave equations that describes the interaction of the ion-acoustic and electromagnetic high-frequency waves in the hydrodynamic approximation ($\xi_n u \ll \Omega_n$, $qu \gg \omega$) has the form

$$\left.\begin{aligned} \Delta\mathbf{E}_n + \xi_n^2\mathbf{E}_n &= \frac{e\omega_{pe}^2}{2m_e u^2 c^2}(\varphi\mathbf{E}_{n-1}+\varphi^*\mathbf{E}_{n+1}), \\ \Delta(\Delta\varphi + q_s^2\varphi) &= -\frac{eq_s^2}{2m_e\Omega^2}\sum_n(\xi_n-\xi_{n-1})^2\mathbf{E}_n\mathbf{E}^*_{n-1}, \end{aligned}\right\} \quad (7)$$

where $u = [\gamma(T_e/m_e)]^{1/2}$, $\xi_n^2 = k_n^2(1-\omega_{pe}^2/\Omega_n^2) = k_n^2\varepsilon_n$.

We ignore collisions and the motion of the ions in the field of the high-frequency waves.

The fields of the interacting waves satisfy the following boundary conditions at the plasma–vacuum interface:

$$\left.\begin{aligned} (E_n^p - E_n^v)\big|_{x=0,\,2d} = 0,\ \left(\frac{\partial E_n^p}{\partial x}-\frac{\partial E_n^v}{\partial x}\right)\Big|_{x=0,\,2d} &= 0 \\ v_{\omega x}\big|_{x=0,\,2d} = 0,\ (\varphi^p-\varphi^v)\big|_{x=0,\,2d} &= 0, \\ \left(\frac{\omega_{pi}^2}{\omega^2}\frac{\partial\varphi^p}{\partial x}+\frac{\partial\varphi^v}{\partial x}\right)\Big|_{x=0,\,2d}& \\ = -\frac{i\, e\omega_{pe}^2 q_x^2}{2m_e\omega^2\Omega^2 q_s^2}\sum_n \Delta_1(n,\, n-1)\,\mathbf{E}_n\mathbf{E}^*_{n-1}\big|_{x=0,\,2d}&. \end{aligned}\right\} \quad (8)$$

Let us consider first the generation of scattered waves when they undergo total internal reflection from the plasma ($\xi_{nx}^2 < 0$). Ignoring the change in the amplitudes of the interacting waves, we obtain the following equation for the wave amplitudes at the combination frequencies from Eqs. (7) and the boundary conditions (8):

$$\mathcal{E}_n = E_n(0) = -\frac{e\varphi_0\omega_{pe}^2}{2m_e u^2c^2(k_{nx}+\xi_{nx})}\left[\frac{\xi_{nx}+\xi_{n-1x}}{(\xi_{nx}+\xi_{n-1x})^2-q_x^2}E_{n-1}(0) + \frac{\xi_{nx}+\xi_{n+1x}}{(\xi_{nx}+\xi_{n+1x})^2-q_x^2}E_{n+1}(0)\right], \quad (9)$$

where

$$\xi_{nx}^2 \approx \xi^2 + 2n\frac{\Omega\omega}{c^2} - (nq_z)^2.$$

The interaction of the waves becomes stronger if the high-frequency signal is cut off, i.e., if $\Omega \lessapprox \omega_{pe}$, so that $\xi^2 \ll (nq_z)^2$. In this case when $q_s d \gg \pi$, $q_x \ll q_z$ it follows from Eq. (8) that

$$\mathcal{E}_n = 2\mathcal{E}_0\left(-\operatorname{sg} n\,\frac{e\varphi_0}{2m_e u^2}\frac{k}{q_z}\right)^{|n|}\prod_{j=1}^{|n|}\frac{1}{2j-1}, \quad (10)$$

where

$$\operatorname{sg} n = \begin{cases} -1 & n<0, \\ 1 & n>0. \end{cases}$$

If $q_s d \approx \pi$, so that $q_z^2 \ll q_s^2$, $\omega\Omega/c^2$, the amplitudes of the waves scattered into the vacuum are

$$\mathcal{E}_n = 2\mu\mathcal{E}_0\left(\frac{e\varphi_0 k^2}{m_e u^2 q_s^2}\sqrt{\frac{\omega}{2\Omega}}\right)^{|n|}\prod_{j=1}^{|n|}\sqrt{j}+\sqrt{j-1}, \quad (11)$$

where

$$\mu = \begin{cases} 1 & n>0, \\ i^{|n|} & n<0. \end{cases}$$

For an arbitrary polarization of the probing wave with respect to the plane of propagation of the ion acoustic wave, and also if its front is not strictly parallel to the boundary of the plasma, electron plasma waves are excited in the plasma when $\Omega \approx \omega_{pe}$ at the frequencies Ω_n: $E_n^l \propto \exp(i\xi_{nx}^l x)$, $\xi_{nx}^l = (\Omega_n/u)(\varepsilon_n)^{1/2}$. If $\xi_{nx}^l \gg nq_z$, i.e., the electron plasma waves propagate at almost right angles to the plasma boundary, the emission into the vacuum is determined by the electromagnetic waves $E_n \propto \exp(i\xi_{nx}x)$, and (10) and (11) remain valid.

If the frequency of the probing signal satisfies $\Omega > \omega_{pe}$, so that the scattered waves propagate in the plasma ($\xi_{nx}^2 > 0$, $R_n \ll 1$) with small phase difference [$\Delta(n, n-1) \approx q_x \ll \xi_{nx}$], their amplitudes change with the coordinate x in accordance with (5). In this case, the coupling coefficients and the boundary values of the high-frequency waves are given by

$$\left.\begin{aligned} V_{AA} = \frac{e\omega_{pe}^2}{2m_e u^2c^2\xi},\quad V_{bA} &= -\frac{e\omega^2}{m_e v_s^2\Omega^2 q_x}\left[1+\frac{q_z^2u^2(q^2-q_s^2)}{\omega^2q^2}\right], \\ A_n(0) &= \mathcal{E}_0\left(-\frac{e\varphi_0\omega_{pe}^2}{8m_e u^2\Omega^2}\right)^{|n|} \end{aligned}\right\} \quad (12)$$

Substituting these equations into (5) we find from the boundary conditions (8) the amplitudes of the scattered waves transmitted through the layer into the vacuum:

$$\mathcal{E}'_n = \frac{2\xi_{nx}}{\xi_{nx} + k_{nx}} e^{i2d(\xi_{nx} - k_{nx})} \sum_{m=-\infty}^{\infty} A_m(0)\, i^{n-m} J_{n-m}(\chi d), \tag{13}$$

where

$$\chi = \frac{e\varphi_0}{8m_e u^2}\left(\frac{e\mathcal{E}_0}{m_e v_e \Omega}\right)^2 \xi.$$

If $\chi d < 1$, and the frequency of the probing wave is sufficiently high that $\xi_{nx} \approx k_{nx}$, the expression (12) simplifies to

$$\mathcal{E}'_n \approx A_n(0)\, J_0(\chi d) + i\,(A_{n+1} + A_{n-1})\, J_1(\chi d). \tag{14}$$

4. We now consider a symmetric ion-acoustic wave (5) propagating in a layer of magnetoactive plasma ($H_0 \| z$). In the frequency range $\omega \ll \omega_{Hi} \ll \omega_{pi}$, the components of the wave vector of the ion acoustic wave are

$$q_x \approx \frac{\pi}{d}, \quad q_z = \left(\frac{\omega^2}{\omega_{Hi}^2} q_x^2 + q_s^2\right)^{1/2},$$

where $\omega_{H\alpha} = (e_\alpha H_0)/(m_\alpha c)$ is the cyclotron frequency of the plasma particles. Suppose the high-frequency probing wave is incident normally on the boundary $x = 0$. We restrict ourselves to the case in which the scattered waves propagate almost at right angles to the external magnetic field, i.e., $\xi_n, \varkappa_n \gg n q_z$, where $\xi_n = k_n(\varepsilon_n)^{1/2}$,

$$\varkappa_n = k_n \left[\frac{(\Omega_n^2 - \omega_{pe}^2)^2 - \omega_{He}^2 \Omega_n^2}{\Omega_n^2 (\Omega_n^2 - \omega_{He}^2 - \omega_{pe}^2)}\right]^{1/2}$$

are the wave numbers of the ordinary and the extraordinary wave for transverse propagation. In this case, the coupling between the ordinary and the extraordinary high-frequency waves can be ignored, i.e., a probing wave with electric field parallel or perpendicular to the external constant magnetic field will excite scattered waves of the same polarization.

The nonlinear equations for the interacting waves in the hydrodynamic approximation ($\varkappa_n u$, $\xi_n u \ll \Omega_n$, $q_z u \gg \omega$, $q_x u \ll \omega_{He}$) are

$$\left.\begin{aligned} &\frac{\partial^2 \varphi}{\partial x^2} - \frac{\omega_{Hi}^2}{\omega^2}(q_z^2 - q_s^2)\,\varphi = -\frac{2\pi e n_0 \omega_{Hi}}{u^2 \omega_{pi}^2} \sum_n \mathbf{v}_n \mathbf{v}^*_{n-1}, \\ &\operatorname{curl}\operatorname{curl} \mathbf{E}_n - \varepsilon_n k_n^2 \mathbf{E}_n = -\frac{2\pi e n_0 \Omega_n}{c^2 \omega}(\mathbf{v}_{n-1} \nabla \mathbf{v}_\omega + \mathbf{v}_{n+1} \nabla \mathbf{v}^*_\omega), \end{aligned}\right\} \tag{15}$$

where

$$\left.\begin{aligned} &\mathbf{v}_n = -\frac{ie\Omega_n}{m_e(\Omega_n^2 - \omega_{He}^2)}\left(\mathbf{E}_n - \frac{\omega_{He}^2}{\Omega_n^2}\mathbf{h}(\mathbf{h}\mathbf{E}_n) + i\frac{\omega_{He}}{\Omega_n}\mathbf{h} \times \mathbf{E}\right), \\ &\mathbf{v}_\omega = \frac{e\omega(\omega^2 \mathbf{q} + i\omega_{He}\mathbf{h} \times \mathbf{q} - \omega_{He}^2 q_z \mathbf{h})}{m_e[\omega^2(\omega_{He}^2 - \omega^2 + q^2u^2) - \omega_{He}^2 q_z^2 u^2]}, \quad \mathbf{h} = \frac{\mathbf{H}_0}{H_0}. \end{aligned}\right\} \tag{16}$$

The boundary conditions satisfied by the fields of the ion-acoustic and high-frequency waves on the plasma–vacuum interface are

$$\begin{gathered} (\varphi^p - \varphi^v)|_{x=0,2d} = 0, \\ \left(\frac{\omega_{pi}^2}{\omega_{Hi}^2}\frac{\partial \varphi^p}{\partial x} - \frac{\partial \varphi^v}{\partial x}\right)\Big|_{x=0,2d} = -\frac{2\pi e n_0}{\omega \Omega}\sum_n (v_{nx} \nabla v^*_{n-1} + v^*_{n-1x} \nabla \mathbf{v}_n)|_{x=0,2d}, \\ (\mathbf{E}^p_{n\tau} - \mathbf{E}^v_{n\tau})|_{x=0,2d} = 0, \\ (\varepsilon_{11} E^p_{nx} + \varepsilon_{12} E^p_{ny} - E^v_{nx})|_{x=0,2d} = \frac{2\pi e n_0}{\Omega_n \omega}(v_{n-1x} \nabla \mathbf{v}_\omega + v_{n+1x} \nabla \mathbf{v}^*_\omega)|_{x=0,2d}. \end{gathered} \tag{17}$$

If longitudinal high-frequency waves are excited, we use the additional boundary condition $v_{nx}|_{x=0,2d} = 0$.

Let us consider the generation of scattered waves when they undergo total internal reflection from the plasma ($\xi_{nx}^2, \varkappa_{nx}^2 < 0$). If the electric field of the probing wave is parallel to the external constant magnetic field, the amplitudes of the waves radiated into the vacuum are

$$\mathcal{E}_n = \frac{2k_{nx}}{k_{nx} + \xi_{nx}} \mathcal{E}_0 \left[-\frac{e\varphi_0 \omega_{pe}^2}{4m_e u^2 c^2 \xi(k + \xi)}\right]^{|n|}. \tag{18}$$

If extraordinary high-frequency waves are excited in the plasma, the radiation at the combination frequencies into the vacuum is amplified when the frequency of the probing signal approaches the hybrid frequency, i.e., $\Omega \gtrsim (\omega_{He}^2 + \omega_{pe}^2)^{1/2} - \omega_g$,

$$\mathcal{E}_n \approx i2\sqrt{2}\,\frac{\omega_g \sqrt{\omega_g(\Omega - \omega_g)}}{\omega_{He}\omega_{pe}}\left[-\frac{\sqrt{2}\, e\varphi_0 (\omega_g^2 + \omega_{He}^2)\,\omega_{pe} k}{16 m_e u^2 \omega_g^2 \sqrt{\omega_g(\Omega - \omega_g)}\, q_x}\right]^{|n|} \frac{\mathcal{E}_0}{n!}. \tag{19}$$

If high-frequency waves propagate in the plasma and are weakly reflected from the plasma–vacuum interface ($R_n \ll 1$ for $\Omega_n \gg \omega_{pe}$ for ordinary waves and for $\Omega_n \approx \omega_{pe}$ for extraordinary waves) there is a resonant interaction between the high-frequency wave and the ion-acoustic wave [$\Delta_{1,2}(n, n-1) \approx \pm q_x \ll u_{nx}$], which changes their amplitudes in accordance with (4). For ordinary waves, the coupling coefficient V_{AA} and the boundary values of the scattered waves, $A_n(0)$, are the same as for an isotropic plasma. The coupling coefficient V_{bA} is

$$V_{bA} = -\frac{e\omega_{He}\omega_{Hi}}{2m_e q_x u^2 \Omega^2}. \tag{20}$$

For extraordinary high-frequency waves the coupling coefficients and boundary values of the amplitudes are

$$V^e_{AA} = \frac{e\omega_{pe}^2 q_z^2}{m_e u^2 \omega_{He} \varkappa}, \quad V^e_{bA} = \frac{e\omega_g^2}{m_i \omega \Omega}, \tag{21}$$

$$\left.\begin{aligned} &A^e_n(0) = \mathcal{E}_0\left[\frac{e\varphi_0}{8m_e u^2}F(\Omega)\right]^{|n|}\left(\frac{\Omega^2 - \omega_{He}^2}{\Omega^2 - \omega_g^2}\right)^{1/2}, \\ &F(\Omega) = \frac{\omega_{pe}^2[\Omega^4 - \Omega^2(3\omega_{He}^2 + \omega_{pe}^2) + \omega_{He}^2\omega_{pe}^2]}{\Omega^2(\Omega^2 - \omega_g^2)^2}. \end{aligned}\right\} \tag{22}$$

From the boundary conditions (17) we find the amplitudes of scattered waves transmitted through the layer into the vacuum. For ordinary waves

$$\mathcal{E}'_n = \frac{2\xi_{nx}}{\xi_{nx} + k_{nx}} e^{i2d(\xi_{nx} - k_{nx})} \sum_{m=-\infty}^{\infty} A_m(0)\, i^{n-m} J_{n-m}(\chi d), \tag{23}$$

where

$$\chi = \frac{1}{8}\left(\frac{e\mathcal{E}_0}{m_e \Omega u}\right)^2 \frac{e\varphi_0 \omega_{pe}^4 \omega_{He} \omega_{Hi}}{m_e u^2 \Omega^4 u^2 q_x^2}\,\xi.$$

For extraordinary waves

$$\mathcal{E}_n'^e = -\frac{\varkappa_{nx}}{k_{nx}+\varkappa_{nx}} e^{i2(\varkappa k_x - k_x)d} \sum_{k=0}^{|n|} \sum_{m=-\infty}^{\infty} \times \left(i \frac{e\varphi_0 \omega_{pi}}{4m_e u c \omega_{He}} \right)^{|n|-k} A_m(0)\, J_{k-m}(\chi^e d), \qquad (24)$$

where

$$\chi^e = \frac{1}{2}\left(\frac{e\mathcal{E}_0}{m_e u \Omega}\right) \frac{e\varphi_0 q_z \Omega \omega_{pi} (\omega_{pe}^2 + \omega_{He}^2) q_e}{m_e u^2 \varkappa \omega \omega_{He}^4} F(\Omega).$$

If χ^d, $\chi^{ed} < 1$ and $\varkappa_{nx}$, $\xi_{nx} \simeq k_{nx}$, the expressions (23) and (24) simplify and reduce to the form (14).

I wish to thank A. S. Bakai and A. N. Kondratenko for suggesting the topic and for helpful discussion.

---

[1] A. G. Sitenko, Electromagnetic Fluctuations in a Plasma, New York (1967).

[2] V. E. Golant, Microwave Plasma Diagnostics [in Russian], Nauka, Moscow (1968).

[3] N. N. Bloembergen, Nonlinear Optics, Benjamin, New York (1965).

[4] K. S. Karplyuk, L. I. Kolesnichenko, and V. N. Oraevskii, Preprint 69.3, IF Akad. Nauk SSSR, Kiev (1969).

[5] Yu. A. Alanakyan, Zh. Tekh. Fiz., 35, 1552 (1965) [Sov. Phys. – Tech. Phys., 6, 1202 (1966)].

[6] A. N. Kondratenko and V. G. Shaptala, Ukr. Fiz. Zh., 14, 1092 (1969).

[7] A. S. Bakai, Nucl. Fusion, 10, 53 (1970).

Electric field and plasma structure near a large charged body

L. A. Malyavin and A. M. Moskalenko

Institute of Terrestrial Magnetism, the Ionosphere, and Radio Propagation,
Academy of Sciences of the USSR, Moscow

(Submitted April 10, 1973; resubmitted August 16, 1973)
Zh. Tekh. Fiz., 44, 311-317 (February 1974)

The perturbations of a weakly ionized plasma in the neighborhood of a charged spherical body are discussed. The dimensions of the body are assumed to be large in comparison with the Debye radius of the unperturbed plasma. The distribution of the electric potential and the electron and ion densities are determined for various potentials on the body. The intensity of the electric field is determined. The total electron and ion currents to the surface of the body are calculated.

INTRODUCTION

The study of the electric field and the charged-particle density distribution in the neighborhood of a body in a weakly ionized plasma is of considerable interest in problems connected with the direct measurement of electric fields from a high-altitude, constant-level, drifting balloon. Much the same problem arises also in the probe measurements widely used in plasmas. The theoretical study of this subject is therefore the concern of a considerable amount of work (for example, see ref. 1 and the references therein).

However, because of the mathematical difficulties encountered in reaching a solution, the complete equation system is solved numerically in most papers. One can point out refs. 2 and 3, in which the problem of a large spherical body is solved by separation of the perturbed zone in its neighborhood into a double layer and a neutral region.

In the present paper, this separation for a large sphere is carried out more rigorously and greater attention is devoted to a study of the limiting cases of high and low potential on the body.

FORMULATION OF THE PROBLEM

We consider a completely absorbing, spherical body in a weakly ionized plasma. We assume the dimension of the body R_0 is much greater than the Debye radius of the unperturbed plasma D,

$$R_0 \gg D,\ D=\left(\frac{T_e}{4\pi e^2 N_0}\right)^{1/2}.$$

Here, T_e is the electron temperature in energy units, e is the charge on the ions (the electron charge is $-e$), and N_0 is the unperturbed electron (and ion) density.

The mean free path of plasma particles is assumed to be much smaller than the characteristic dimensions of the problem.

The electron density N_e, the ion density N_i, and the electric potential φ are determined by the steady-state continuity equations and the Poisson equation:

$$\left.\begin{aligned} &\operatorname{div}\mathbf{j}_e=0,\quad \operatorname{div}\mathbf{j}_i=0,\\ &\Delta\varphi=-4\pi e(N_i-N_e). \end{aligned}\right\} \qquad (1)$$

Here, j_e and j_i are the electron and ion current densities, which are[4]

$$\mathbf{j}_e=-D_e\nabla N_e+\frac{\sigma_e}{e}\nabla\varphi,$$

$$\mathbf{j}_i=-D_i\nabla N_i-\frac{\sigma_i}{e}\nabla\varphi,$$

where D_e, D_i and σ_e, σ_i are respectively the diffusion and conductivity coefficients for electrons and ions. In the case of a weakly ionized plasma these are connected by the Einstein relations:

$$\sigma_e=\frac{e^2N_e}{T_e}D_e,\quad \sigma_i=\frac{e^2N_i}{T_i}D_i.$$

Here, T_i is the ion temperature in energy units.

We take into account the spherical symmetry of the problem and convert to the dimensionless variables

$$\xi=\frac{r}{R_0},\ n_e=\frac{N_e}{N_0},\ n_i=\frac{N_i}{N_0},\ \varphi^*=\frac{e\varphi}{T_e},$$
$$I_e^*=\frac{I_e}{I_{e0}},\ I_i^*=\frac{I_i}{I_{i0}};\ I_{e0}=4\pi R_0N_0D_e,\ I_{i0}=4\pi R_0N_0D_i,$$

where r is the distance from the center of the sphere, and I_e and I_i are the total electron and ion currents at the surface of the body.

After a single integration, Eq. (1) takes the form[5]

$$\left.\begin{aligned} &\frac{dn_e}{d\xi}-n_e\frac{d\varphi^*}{d\xi}=\frac{I_e^*}{\xi^2},\\ &\frac{dn_i}{d\xi}+\beta n_i\frac{d\varphi^*}{d\xi}=\frac{I_i^*}{\xi^2},\\ &\varepsilon\frac{1}{\xi^2}\frac{d}{d\xi}\left(\xi^2\frac{d\varphi^*}{d\xi}\right)=n_e-n_i;\ \beta=\frac{T_e}{T_i}=O(1),\ \ \varepsilon=\left(\frac{D}{R_0}\right)^2\ll 1, \end{aligned}\right\} \qquad (2)$$

where O is a symbol for order of magnitude. The boundary conditions are: $\varphi^*=\varphi_0^*$, $n_e=n_i=0$ for $\xi=1$, and $\varphi^*=0$, $n_e=n_i=1$ for $\xi\to\infty$.

We assume for definiteness that the body is charged positively ($\varphi_0^*>0$) so that the attracted particles are electrons and the repelled particles are ions.

NEUTRAL REGION

Setting $n_e(\xi)=n_i(\xi)=n_q(\xi)$, $\varphi^*(\xi)=\varphi_q^*(\xi)$, and solving Eqs. (2), we obtain for the neutral region

$$\left.\begin{aligned} &n_q(\xi)=1-\frac{A}{\xi},\\ &\varphi_q^*(\xi)=B\ln\left(1-\frac{A}{\xi}\right). \end{aligned}\right\} \qquad (3)$$

Here and in the following we have

$$A = \frac{\beta I_e^* + I_i^*}{1+\beta}, \quad B = -\frac{I_e^* - I_i^*}{\beta I_e^* + I_i^*}.$$

The boundary conditions at infinity are taken into account in Eqs. (3).

The neutral solution (3) is the zeroth approximation to the asymptotic expansion of the perturbation solution of the system (2) in the form of a series in powers of the perturbation parameter ε. More precisely, if we seek a solution of the system (2) in the form

$$n_e = n_e^{(0)} + \varepsilon n_e^{(1)} + \ldots, \tag{4}$$

etc., then $n_e^{(0)} = n_i^{(0)} = n_q$, $\varphi^{*(0)} = \varphi_q^*$.

Near the point $\xi = \xi_{cr} \equiv A$, the solution of system (2) in the form of a series in powers of ε can be represented in the following manner:

$$\left.\begin{aligned}
n_e &= \left(1 - \frac{A}{\xi}\right)\left[1 + \varepsilon \frac{Q_e}{(\xi - A)^3} + \cdots\right],\\
n_i &= \left(1 - \frac{A}{\xi}\right)\left[1 + \varepsilon \frac{Q_i}{(\xi - A)^3} + \cdots\right],\\
\varphi^* &= B \ln\left(1 - \frac{A}{\xi}\right)\left[1 + \varepsilon \frac{P}{(\xi - A)^3 \ln\left(1 - \frac{A}{\xi}\right)} + \cdots\right];\\
Q_e &= \frac{AB}{(1+\beta)}\left(-1 + \frac{\beta B}{2}\right), \quad Q_i = \frac{\beta AB}{(1+\beta)}\left(1 + \frac{B}{2}\right),\\
P &= \frac{A}{3(1+\beta)}\left[-2 - (1-\beta)B + 0.5\beta B^2\right].
\end{aligned}\right\} \tag{5}$$

The pertubation solution (5) has a singularity at the critical point $\xi_{cr} \equiv A$, where the assumption about the smallness of the perturbation breaks down and the solution loses meaning. The solution (5) has a singularity of the form ε/x^3, where x is the distance from the critical point. Consequently, the region in which Eq. (5) is invalid is a neighborhood of the point ξ_{cr} of the order of $\varepsilon^{1/3}$.

DOUBLE LAYER

We introduce new independent and dependent variables

$$x = \frac{\xi - A}{\varepsilon^{1/3}}, \quad H_e = \frac{n_e}{\varepsilon^{1/3}}, \quad H_i = \frac{n_i}{\varepsilon^{1/3}},$$

which are of the order of unity in a neighborhood of the point $\xi_{cr} \equiv A$ of the order[6] of $\varepsilon^{1/3}$.

In the new variables, the system (2) becomes

$$\left.\begin{aligned}
\frac{dH_e}{dx} - H_e \frac{d\varphi^*}{dx} &= \frac{I_e^*}{(A + \varepsilon^{1/3}x)^2},\\
\frac{dH_i}{dx} + \beta H_i \frac{d\varphi^*}{dx} &= \frac{I_i^*}{(A + \varepsilon^{1/3}x)^2},\\
\frac{d^2\varphi^*}{dx^2} + \frac{2\varepsilon^{1/3}}{A + \varepsilon^{1/3}x}\frac{d\varphi^*}{dx} &= H_e - H_i.
\end{aligned}\right\} \tag{6}$$

The form of the equation system (6) suggests the following form for the inner expansions:

$$H_e = H_e^{(0)} + \varepsilon^{1/3} H_e^{(1)} + \ldots, \text{ etc.}$$

We substitute these expressions in Eqs. (6). We then obtain a system of equations for the functions $H_e^{(0)}$, $H_i^{(0)}$, and $\varphi^{*(0)}$. For convenience, we transform to the variable $t = x + (A-1)/\varepsilon^{1/3} = (\xi - 1)/\varepsilon^{1/3}$. We then have

$$\left.\begin{aligned}
\frac{dH_e}{dt} - H_e \frac{d\varphi^*}{dt} &= \frac{I_e^*}{A^2},\\
\frac{dH_i}{dt} + \beta H_i \frac{d\varphi^*}{dt} &= \frac{I_i^*}{A^2},\\
\frac{d^2\varphi^*}{dt^2} &= H_e - H_i.
\end{aligned}\right\} \tag{7}$$

For brevity, we omit the index (0) here and in the following.

The inner boundary conditions for the system (7) remain as before ($\varphi^* = \varphi_0^*$, $H_e = H_i = 0$, when $t = 0$). As outer boundary conditions, we require that when $x = 1$ the solution of equation system (7) be equal to the leading terms of the inner expansion of the neutral solution. We than obtain $\varphi^* = \varphi_1^* \equiv B\ln(\varepsilon^{1/3}/A)$, $H_e = H_i = 1/A$ when $t = t_1 \equiv 1 + (A-1)/\varepsilon^{1/3}$.

Solutions for the first two equations in (7) including the boundary conditions when $t = t_1$ are

$$\left.\begin{aligned}
H_e(t) &= \frac{1}{A} e^{(\varphi^* - \varphi_1^*)} - \frac{I_e^*}{A^2} e^{\varphi^*} \int_t^{t_1} e^{-\varphi^*(t')} dt',\\
H_i(t) &= \frac{1}{A} e^{-\beta(\varphi^* - \varphi_1^*)} - \frac{I_i^*}{A^2} e^{-\beta\varphi^*} \int_t^{t_1} e^{\beta\varphi^*(t')} dt'.
\end{aligned}\right\} \tag{8}$$

Using the boundary conditions for the particle densities at the surface of the body, we obtain a system of two transcendental equations for the determination of I_e^* and I_i^*:

$$\left.\begin{aligned}
e^{-\varphi_1^*} - \frac{I_e^*}{A} \int_0^{t_1} e^{-\varphi^*(t)} dt &= 0,\\
e^{\beta\varphi_1^*} - \frac{I_i^*}{A} \int_0^{t_1} e^{\beta\varphi^*(t)} dt &= 0.
\end{aligned}\right\} \tag{9}$$

LOW AND HIGH POTENTIAL ON THE BODY

For low values of the potential on the body, $\varphi_0^* \ll 1$, the potential will also be low everywhere in its neighborhood, i.e., $\varphi^* \ll 1$. Then the exponentials in Eqs. (9) can be expanded in powers of φ^* and limited to linear terms; the electron current I_e^* and the ion current I_i^* then can be represented by

$$I_e^* = 1 + \delta, \quad I_i^* = 1 - \gamma,$$

where $\delta \ll 1$ and $\gamma \ll 1$. In the linear approximation relative to δ and γ we have

$$A = 1 + \frac{\beta\delta - \gamma}{1+\beta}, \quad \varphi_1^* = -\frac{\delta + \gamma}{1+\beta} \ln \varepsilon^{1/3}, \quad t_1 = 1 + \frac{\beta\delta - \gamma}{(1+\beta)\varepsilon^{1/3}}. \tag{10}$$

Substituting these expressions in Eqs. (9) and equating terms with $\varepsilon^{-1/3}$ and $\ln\varepsilon^{1/3}$ to zero, we obtain

$$\beta\delta = \gamma, \quad \varphi_1^* = \int_0^{t_1} \varphi^*(t)\, dt. \tag{11}$$

In this case, $A = t_1 = 1$. Remembering the monotonicity of the function φ^*, we have from the second of Eqs. (11)

$$\varphi_1^* = \varphi^*(t) = \varphi_0^* \tag{12}$$

for $0 \leq t \leq 1$.

Thus for φ_0^*, the field potential at the external boundary of the double layer is φ_0^*, i.e., in a linear approximation relative to φ^*, a double layer does not exist around a spherical absorbing body.

From the second equation in (10) and the first equations in (11) and (12), we obtain

$$I_e^* = 1 + \frac{\varphi_0^*}{\ln \frac{1}{\varepsilon^{1/3}}},\ , I_i^* = 1 - \frac{\beta\varphi_0^*}{\ln \frac{1}{\varepsilon^{1/3}}}.$$

For the neutral region $\xi \geq 1 + \varepsilon^{1/3}$, we have in accordance with Eqs. (3)

$$n_q = 1 - \frac{1}{\xi},\ \varphi_q^* = \frac{\varphi_0^*}{\ln \varepsilon^{1/3}} \ln\left(1 - \frac{1}{\xi}\right), \tag{13}$$

with the first expression for particle density valid for $\xi \geq 1$.

Note that the boundary conditions $n_i = n_e = 0$ for particle densities at the surface of the absorbing body indicate that the plasma in the neighborhood of such a body is stripped of charged particles, which is particularly apparent from the first equation in (13). This leads to an increase in the thickness of the double layer in comparison with the case of a low-density plasma. In fact, when $\varepsilon \to 0$, the thickness of the double layer is $l \sim \varepsilon^{1/3} \gg l_1 \sim \varepsilon^{1/2}$, where l_1 is the thickness of the double layer around a large body in a low-density plasma.[7]

For high potentials on the body, $\varphi_0^* \gg 1$, the ion current at the body is close to zero,

$$A = \frac{\beta}{1+\beta} I_e^*,\ B = -\frac{1}{\beta}.$$

The ion distribution in the double layer is described by the Boltzmann equation

$$H_i(t) = \frac{1}{A} e^{-\beta(\varphi^* - \varphi_1^*)},$$

which follows from the second equation in (8) when $I_i^* = 0$.

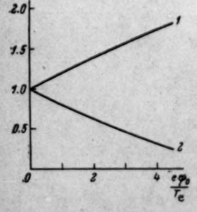

Fig. 1. Dependence of total electron current I_e^* (attracted particles) and total ion current I_i^* (repelled particles) on the potential of the body for $R_0/D = 100$ and $\beta = 1$. 1) I_e/I_{e_0}; 2) I_i/I_{i_0}.

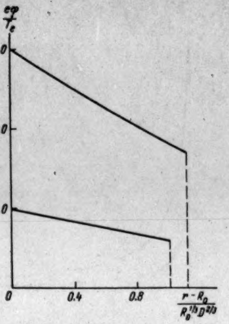

Fig. 2. Variation of the potential field in the double layer around the surface of a large body ($R_0/D = 100$) for $\beta = 1$ and various values φ_0^*.

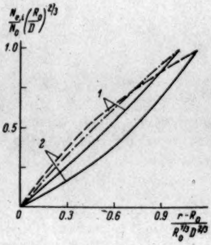

Fig. 3. Density of electrons (attracted particles) and of ions (repelled particles) in the double layer around the surface of a large body ($R_0/D = 100$) for $\beta = 1$ and various values of φ_0^*: 1) 1; 2) 3.

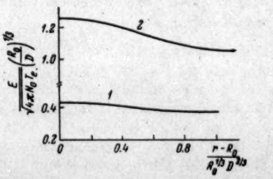

Fig. 4. Variation of electric field in the double layer around the surface of a large body ($R_0/D = 100$) for $\beta = 1$ and various values of φ_0^* φ_0^*: 1) 1; 2) 3.

We estimate the electron current at the body. For $\varphi_0^* \gg 1$, the potential of the field in the double layer is sharply reduced from the value φ_0^* at the surface of the body to some other value φ_1^*. Assuming that for $0 \leq t \leq t_1$

$$\varphi^*(t) = \varphi_0^* - \frac{\varphi_0^* - \varphi_1^*}{t_1} t,$$

and substituting this function in the first equation in (9), we obtain

$$I_e^* = \frac{1+\beta}{\beta} + O(\varepsilon^{1/3}\varphi_0^*).$$

Furthermore,

$$A = 1 + O(\varepsilon^{1/3}\varphi_0^*),\ \ \varphi_1^* = \frac{1}{\beta} \ln \frac{1}{\varepsilon^{1/3}},\ \ t_1 = O(\varphi_0^*).$$

It then follows that the thickness of the double layer, which is proportional to t_1, increases as φ_0^* increases.

Note that we assume here the thickness of the double layer is small in comparison with the dimension of the body, i.e., $l = \varepsilon^{1/3} t_1 \ll 1$. This is valid only when there is

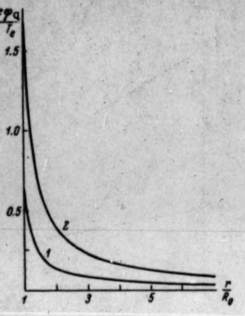

Fig. 5. Variation of potential in neutral region in the neighborhood of a body ($R_0/D = 100$) for $\beta = 1$ and various values of φ_0^*. φ_0^*: 1) 1; 2) 3.

a limit on the magnitude of the potential on the body:

$$\varphi_0^* \ll \frac{1}{\varepsilon^{1/3}} = \left(\frac{R_0}{D}\right)^{2/3}.$$

RESULTS OF CALCULATIONS

Equation (7), including the conditions (9), is solved numerically by linearization[8] for arbitrary values of the potential φ_0^* on the body. Results of the calculations for $R_0/D = 100$ and $\beta = T_e/T_i = 1$ are shown in Figs. 1-5.

Figure 1 shows the dependence of the electron currents I_e^* (attracted particles) and of the ion current I_i^* (repelled particles) on the potential $\varphi_0^* = e\varphi_0/T_e$ of the body. The curves in Fig. 1 are in good agreement with corresponding curves published previously.[1,3,9]

Using the resultant value of I_e^* and I_i^*, we find that the quantities $Q_e \ll 1$ and $|Q_i| \ll 1$ when $\varphi_0^* < 4$. Consequently, the second term in the square brackets in Eqs. (5) makes only a small correction to the neutral solution for these values of φ_0^* and for $\xi \geq A + \varepsilon^{1/3}$. Thus the neutral solution (3) is valid for $A + {}^{1/3} \leq \xi \leq \infty$, and for $1 \leq \xi \leq A + \varepsilon^{1/3}$ the double-layer solution, which is determined by the equation system (7), where the same assumption was made, is valid.

Figure 2 shows the behavior of the potential $\varphi^* = e\varphi/T_e$ in the double layer around the surface of the body for $\varphi_0^* = 1$ and 3.

The distribution of electron density $H_e = (N_e/N_0) \cdot (R_0/D)^{2/3}$ and of ion density $H_i = (N_i/N_0)(R_0/D)^{2/3}$ in the double layer is shown in Fig. 3 for various potentials on the body.

The variation of electric field $E^* = -d\varphi^*/dt = [E/(4\pi N_0 T_e)^{1/2}](R_0/D)^{1/3}$, where $E = -d\varphi/dr$ in the double layer as a function of distance from the surface of the body, is shown in Fig. 4 for $\varphi_0^* = 1$ and 3. For $\varphi_0^* \gg 1$, the electric field at the surface of the body itself is $E_0^* = 2$.

Using the values obtained for the electron current I_e^* and the ion current I_i^* at the surface of the body, we now determine from Eqs. (3) the particle distribution and the behavior of the electric potential in the neutral region. We finally find that for $\varphi_0^* = 1$ and 3 the curve for n_q practically merges with the curve for $\varphi_0^* = 0$, i.e., particle distribution in the neutral region is almost independent of the potential on the body.

Figure 5 shows the dependence of the electric potential $\varphi_q^* = e\varphi_q/T_e$ on distance for $\varphi_0^* = 1$ and 3.

We note in conclusion that this analysis is made under the assumption the mean free paths l_e for electrons and l_i for ions are much smaller than the thickness of the double layer around the surface of the body, i.e.,

$$l_e \ll R_0^{1/3} D^{2/3}, \quad l_i \ll R_0^{1/3} D^{2/3}.$$

The authors are grateful to A. V. Gurevich for discussion and to I. A. Zhulin for his interest.

---

[1] A. A. Yastrebov, Zh. Tekh. Fiz., 32, 809, 1143 (1972) [Sov. Phys. – Tech. Phys., 17, 637 (1972)].
[2] C. H. Su and S. H. Lam, Phys. Fluids, 6, 1479 (1963).
[3] I. M. Cohen, Phys. Fluids, 6, 1492 (1963).
[4] A. V. Gurevich and E. E. Tsedilina, Usp. Fiz. Nauk, 91, 609 (1967) [Sov. Phys. – Usp., 10, 214 (1967)].
[5] L. A. Malyavin and A. M. Moskalenko, Zh. Tekh. Fiz., 43, 722 (1973) [Sov. Phys. – Tech. Phys., 18, 456 (1973)].
[6] M. Van Dyke, Perturbation Methods in Fluid Mechanics [Russian translation], Izd. Mir, Moscow (1967).
[7] A. V. Gurevich, Geomagn. i Aeronomiya, 3, 1021 (1963).
[8] R. Bellman and R. Kalaba, Quasilinearization and Nonlinear Boundary-Value Problems [Russian translation], Izd. Mir, Moscow (1968).
[9] J. Redbill, Raket. Tekh. Kosmonavtika, 7, 56 (1966).

Production of an ion beam by a magnetic system with opposed fields

V. B. Glasko, A. G. Sveshnikov, and N. N. Semashko

M. V. Lomonosov Moscow State University

(Submitted March 27, 1973; resubmitted August 20, 1973)
Zh. Tekh. Fiz., 44, 318-324 (February 1974)

The effect of variation of parameters of the magnetic system and injection parameters on the production of a beam is analyzed. The investigation is carried out for a system with opposed magnetic fields. The parameters are varied close to their values to ensure "optimum" beam-focusing conditions.

1. In many situations it is necessary to produce focused beams of intermediate-energy ions (10-100 keV) at high currents (tens of amperes). Gas-discharge ion sources with large ion-emitting surfaces are one method of obtaining such beams. The efficiency of this device is determined primarily by the magnetic system, which must provide an arc discharge with the required configuration (since the plasma serves as the ion emitter) and must focus the ion beam (large cross section).

The problem of designing magnetic systems to ensure focusing of a charged-particle beam is usually solved either empirically or by an approximate calculation of the motion of the paraxial beam.[1-4] In the general formulation the problem of determining the magnetic field that will produce a charged-particle beam with given properties is a typical synthesis problem, and is characterized by an instability of the solution against small variations of the "input information" (the given properties of the beam).

We have considered earlier[3] the problem of designing an axially symmetric magnetic field in the region $0 < z < z_{ex}$ and the conditions for injection of beam particles into the $z = 0$ plane, for which, at the exit from the system in the $z = z_{ex}$ plane, the charge-particle beam satisfies definite focusing requirements. We assume that the ion beam consists of separate noninteracting rays whose trajectories depend on the injection conditions. If the magnetic field and the injection conditions can be specified by a finite number of parameters $(p_1, \ldots, p_N)$, the problem of determining the magnetic field and the injection conditions for which the formulated beam has the required properties reduces to the problem of the "quasioptimization" of a certain positive functional $\Phi(p_1, \ldots, p_N)$, whose minimum corresponds to the "optimum" properties of the beam that is formed.

Besides determining the "optimum" conditions of beam focusing there is considerable interest in analyzing the effect on the production of a beam of the variation of parameters of the magnetic system and the injection conditions. This question is considered in the present work for the case of a system with opposed magnetic fields.

2. The magnetic field is produced by a system of four current-carrying coils (Fig. 1). The two central coils (I) with currents flowing in opposition form the principal field (H_I); the external current-carrying coils (II) are magnetic lenses (H_{II}).

This system is intended for a high-current ion source. Near the median surface of the field ($z = 0$) an arc discharge is ignited along radial lines of force, forming a plasma ring. The side surfaces of this ring serve as the ion emitter. Ions are extracted from the plasma across the magnetic lines of force by a strong electric field and are accelerated along the longitudinal (z) axis.

The magnetic field is determined by specifying the longitudinal component of the field H_z as a function of $F(z)$ for a certain value of radial coordinate $\bar{r}$:

$$H_z(r, z) \equiv F(z) = H_I(z) + \alpha H_{II}(z - z_{II}), \tag{1}$$

where the functions $H_I(z)$ and $H_{II}(z)$ approximate the given values of the longitudinal component H_z for the specified radius $\bar{r}$ of the actual magnetic system consisting of two pairs of coils.

The parameter α determines the ratio of the currents in the first and second pairs of coils, and z_{II} is the position of the coils (II) with respect to the $z = 0$ plane. Specifying the magnetic field in the form (I) enables us to represent the magnetic-field components H_z and H_r in the following form over the entire region of motion of the particles:

$$\left.\begin{aligned} H_z &= \sum_{n=1}^{N} d_n \frac{I_0(k_n r)}{I_0(k_n \bar{r})} \sin k_n z, \\ H_r &= -\sum_{n=1}^{N} d_n \frac{I_1(k_n r)}{I_0(k_n \bar{r})} \cos k_n z, \end{aligned}\right\} \tag{2}$$

where $k_n = (n\pi)/L$, d_n is the Fourier coefficient for the field $H_z(\bar{r}, z)$, and L is the period.

Because of the axial symmetry, the vector potential of the magnetic field has the form $\mathbf{A} = \{0, A_\varphi(r, z), 0\}$, and the generalized azimuthal momentum p_φ is a first integral of the equations of motion; $p_\varphi = rv_\varphi + rA_\varphi(r, z) = \text{const}$. Since the magnetic field satisfies the condition $A_\varphi(r, 0) = A_\varphi(r, z_{ex}) = 0$, the particles that emerge from the system (for $z > z_{ex}$) will not have an azimuthal velocity component: $v_\varphi(r, z_{ex}) = 0$ if the injection condition is satisfied: $v_\varphi(r, 0) = 0$. The latter condition is a constraint on the position of the ion-emitting surface in the magnetic field.

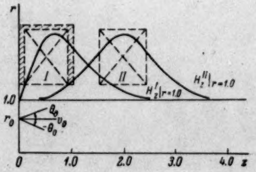

Fig. 1. Diagram of magnetic system. $H_z = 0$ for $z = 6$.

We consider a beam consisting of separate beams of charged particles of specified energy E_0 (total velocity v_0), which are formed under specified initial conditions in the median plane of the field ($z = 0$), radius r_0, and angular spread $\delta\theta_0$ in the (r, z) plane. Thus, the injection parameters $p_1 = r_0$, $p_2 = \theta_0$, $p_3 = v_0$.

The motion of charged particles in the field (2) is investigated by numerical integration of the exact equations of motion.[2] The system is solved in dimensionless (dl) quantities in terms of dimensional (d) quantities as follows:

$$r_{\mathrm{dl}} = \frac{r_{\mathrm{d}}}{R_0},\quad v_{\mathrm{dl}} = \frac{v_{\mathrm{d}}}{v_0},\quad h_{\mathrm{dl}} = \frac{H_{\mathrm{d}}}{H_0},\quad \tau = \omega_{H_0} t. \tag{3}$$

The dimensional constants are related by the condition

$$\frac{eH_0}{mc} = \frac{v_0}{R_0}, \tag{4}$$

i.e., the similitude parameter of the system

$$\chi = \frac{H_0 R_0}{A v_0} = 1.1 \cdot 10^4 \frac{1}{A}\ [\mathrm{G/cm}]. \tag{5}$$

Here, A is the atomic mass unit ($A = 1$ for H_1^+ ions).

Hence, taking R_0, a linear dimension of the system (e.g., the inner radius of the coil) as an independent parameter, we can analyze the system by variation of the parameters that characterize the magnetic field (H_0) and its geometry (K), for various initial conditions of the particle motion (r_0, θ_0). Variation of the parameter H_0 is equivalent to variation of the particle velocity v_0 ($H_0 \sim 1/v_0$) and variation of the parameter K is equivalent to variation of the geometry ($K \equiv \pi R_0/L$); L/R_0 is the ratio between the longitudinal and transverse dimensions of the system.

The particles are injected into the $z = 0$ plane and the trajectories are calculated up to $z_{ex} = 5.9$, where the field H_z is taken equal to zero. The limiting injection radius r_0 is determined by the construction of the ion source, and lies in the range $0.1 < r_0 < 0.8$. The initial velocity v_0 varies from 0.508 to 6.0. The initial ray angle θ_0 for each injection radius is varied in the (r, z) plane from −5° to + 5°; the central ray ($\theta_0 = 0$) is parallel to the z axis.

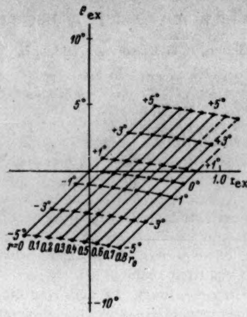

Fig. 2. Phase diagram of beam in exit plane of system ($z_{ex} = 5.9$). Initial conditions: $z = 0$; $0 \le r_{0i} \le 0.8$; $-5° \le \theta_0 \le +5°$; $v_0 = 6.0$.

Results of a numerical integration of the equations of motion are given in Figs. 2 and 5 in the form of phase diagrams of the beams, i.e., the coordinates and angles (r_{ex}, $dr/dz \sim \theta_{ex}$) of the rays in the exit plane ($z = z_{ex}$) are indicated as functions of the initial conditions r_0, θ_0, and v_0. Only the half of the total beam injected into the positive half-plane ($z = 0$, $r > 0$) is represented. Points on the r_{ex}, θ_{ex} diagram in the upper half-plane ($\theta_{ex} > 0$) correspond to diverging rays; those in the lower half-plane ($\theta_{ex} < 0$) correspond to rays that converge to the axis. Points located in the right half-space of the diagram ($r_{ex} > 0$) correspond to rays that do not intersect the z axis, and those in the left half-space ($r_{ex} < 0$) correspond to rays that intersect the z axis in the magnetic-field region ($z < z_{ex}$).

As an illustration Fig. 3 gives the behavior of the rays

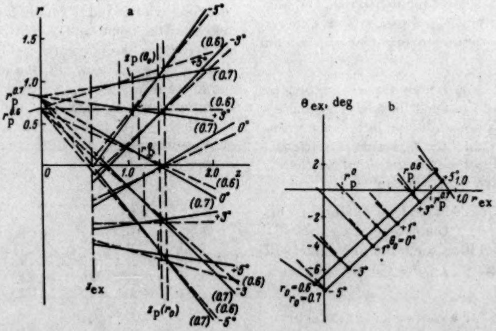

Fig. 3. Trajectories of rays of two beams outside the magnetic field (a) and the corresponding phase diagram in the exit plane $z_{ex} = 5.4$ (b). Initial conditions: $z = 0$, $r_0 = 0.6$ and 0.7, $-5° \le \theta_0 \le +5°$, $v_0 = 3.0$.

outside the magnetic field ($z > z_{ex} = 5.9$), for two beams injected with $z = 0$, $r_0 = 0.6$ and 0.7, $\theta_0 = \pm 5°$ and the corresponding phase diagram (r_{ex}, θ_{ex}) in the z_{ex} plane.

In the absence of beam aberrations the phase lines corresponding to the rays r_{0i} = const are rectilinear and parallel. In this case all the rays of the beam intersect in a single plane $z = z_p(r_{0i})$ at radii $r = r_p(r_{0i})$. The coordinate $r_p(r_{0i})$ is determined by the intersection point corresponding to a line on the phase plane with the abscissa axis. The value of $z_p(r_{0i})$ can be determined from the obvious relation

$$z_p = z_{ex} + (r_p - r_{ex}) \operatorname{ctg} \theta_{ex}. \tag{6}$$

Similarly, the coordinate $r_p(\theta_{0i})$ is determined from the intersection point of the corresponding phase line θ_{0i} = const with the abscissa axis, and the value of $z_p(\theta_{0i})$ from Eq. (6). The deflection of the phase lines r_{0i} = const confirms the existence of aberrations in the initially converging beam and blurring of the focal ring r_p, and violation of the parallelism of the lines characterizes the displacement of the focal plane $r_p(r_{0i})$. The deflection and nonparallelism of the phase lines θ_{0i} = const confirm the existence of aberrations in the initially parallel beam.

In the case being considered (a characteristic example is represented in Fig. 3) the phase lines r_{0i} = const are straight lines but are not parallel. This result indicates the intersection of the rays r_{0i} = const θ_0 = var at definite radii $r_p(r_{0i})$ with formation of a ring in different planes $z_p(r_{0i})$. The deflection and nonparallelism of the phase lines θ_0 = const, r_0 = var also indicate that the rays intersect at different radii $r_p(\theta_{0i})$ in the $z_p(\theta_{0i})$ planes, whose coordinates z_p increase in proportion to the decrease in the initial radius r_{0i}.

Along ray trajectories with specific initial parameters (r_0, θ_0) we can construct a beam distribution over the radius in transverse planes (z = const) under the following assumptions: In the $z = 0$ plane several tubular beams are injected, for which the radius r_0 is much greater than the initial width δr_0 (thus they can be compared with an element of a ribbon beam); the entire beam is confined within the initial angle $\theta_0 = \pm 5°$; the current density distribution as a function of the initial angle of divergence θ_0 is assumed linear. Summing the beams with different initial injection radii we can determine the configuration of the composite beam (Fig. 4).

3. From an analysis of the trajectories of the rays comprising the ion beam, we can draw certain conclusions.

a. For small initial particle velocities ($v_0 < 3$) the ray trajectories intersect the longitudinal z axis in the region of the magnetic field ($z < 5.9$). This corresponds to a short-focus magnetic system, and the initial conditions (r_0, θ_0) have a strong effect on the exit parameters (r_{ex}, θ_{ex}). It is not possible in practice to produce a beam of particles for further transport with a wide range of initial conditions r_0, θ_0.

b. In proportion to the increase of initial velocity v_0($v_0 > 3$) the beam from the refocused source becomes diverging (Fig. 5). Intersection of the central ray ($\theta_0 = 0$) with the z axis is eliminated with increasing v_0, thereby increasing the focal length of the system. A region of large values of v_0($v_0 \simeq 6$) is convenient for transport of the beam for large distances (scale of tens of transverse dimensions of the beam). The initial conditions do not strongly affect the beam configuration. In practice, beams with various injection radii r_0 are superimposed on each other, and their intensities are summed (Fig. 4). This allows us to use as an ion-emitting surface the entire central part of the median surface of the magnetic field ($z = 0$, $0 < r_0 < 0.8$).

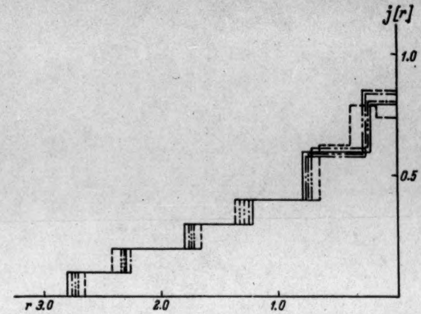

Fig. 4. Beam distribution over radius in $z = 30$ plane for emission of five beams. Initial conditions: $z = 0$; $r_0 = 0.3, 0.4, 0.5, 0.6, 0.7$; $-5° \leq \theta_0 \leq +5°$, $v_0 = 6.0$.

c. The configuration (divergence) of the beam proves to be, as expected, most strongly affected by the initial angular spread of the beam $\delta\theta_0$. A reduction in spread from $\theta_0 = \pm 5°$ to $\theta_0 = \pm 3°$ changes significantly the configuration of the ion beam and its transverse dimensions (Figs. 2, 3, and 5).

d. For production of hydrogen-ion beams containing the two components H_1^+ and H_2^+ there should be no noticeable separation of ions according to mass. This can be concluded from a comparison of the data, e.g., for $v_0 = 4.2$, corresponding to H_1^+ ions, and $v_0 = 6.0$, corresponding to H_2^+ ions.

e. A definite correction to the exit parameters of the beams can be made using a single magnetic lens (the coils

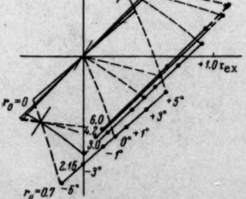

Fig. 5. Phase diagram of beam in exit plane ($z_{ex} = 5.9$) for various velocities. v_0: 2.15, 3.0, 4.2, 6.0 Initial conditions: $z = 0$, $0 \leq r_0 \leq 0.7$, $-5° \leq \theta_0 \leq +5°$.

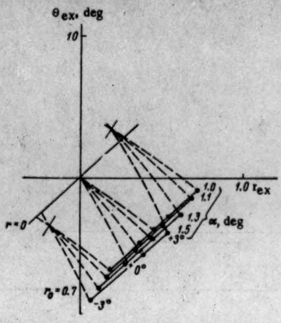

Fig. 6. Phase diagram of beam in exit plane $z_{ex} = 5.9$ with variation of parameter α (current in lens II). The position of the lens $z_l = 2$. Only the phase lines corresponding to rays $r_0 = 0.7$ are plotted.

II). As is to be expected in favorable cases, when $v_0 > 3$ for lens fields comparable in magnitude with the principal fields the exit beam can be finely adjusted without varying the principal field (Fig. 6). This is convenient since it does not lead to a change in the operation regime of the ion source. The position of the lens with respect to the median surface (z_l) does not play a significant role in the production of the beam (Fig. 7) and can be compensated by the magnitude of the lens field.

f. Analysis of the r_{ex}, θ_{ex} phase diagrams shows that the effect of a variation of parameters of the magnetic system on the production of the exit beam can be estimated approximately using elementary relations of geometrical optics. Actually, the beam aberrations are small and do not play a decisive role in the production of the beam. Only an insignificant nonparallelism is observed in the phase lines r_{0i} = const and the observed deflection in the lines θ_{0i} = const is small (Fig. 2). This indicates that the radius of the focal ring (r_f) and the position of the focal plane (z_f) are functions of the initial radius r_0 (Fig. 3).

4. The effect of the second parameter of the system $k = \pi/(L/R_0)$ characterizing the distance between the coils (or the maxima of the field on the z axis) is investigated in a model magnetic field, which is expressed by a single harmonic of the field (2):

$$\left.\begin{aligned} h_r &= I_1(kr)\cos kz,\\ h_z &= -I_0(kr)\sin kz.\end{aligned}\right\} \qquad (7)$$

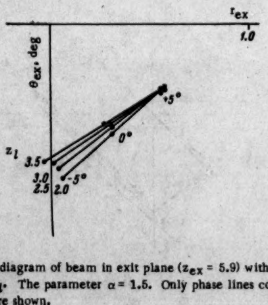

Fig. 7. Phase diagram of beam in exit plane ($z_{ex} = 5.9$) with variation of lens position z_l. The parameter $\alpha = 1.5$. Only phase lines corresponding to rays $r_0 = 0.7$ are shown.

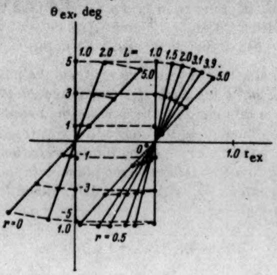

Fig. 8. Phase diagram of beam in exit plane ($z_{ex} = L$) for variation of geometrical parameter of system L/R_0.

This allows us to analyze comparatively simply the relative effect of the geometrical parameter of the system on the configuration of the exit particle beam for various injection conditions (r_0, θ_0) and initial velocities v_0.

In the field model that we have assumed the distance between the coils, where $h_z|_{r=0} = 1$, proves to be equal to L/R_0 (in dimensionless units). The exit plane, in which the coordinates and angles r_{ex}, θ_{ex} are calculated, is found at a distance L/R_0 from the median surface $z_{ex} = L$. The equations of motion are integrated for $0 < z < L$, $0 < r < R_0$. The injection parameters remain as previously. The geometrical parameter L/R_0 varies from 1 to 5: from a system "compressed" along the z axis to a "stretched" system. For comparison we note that in the first case the magnetic system corresponds approximately to the parameter $L/R_0 \approx 2$.

The calculated results are represented in Fig. 8 in the form of a phase diagram in the position of the exit points (r_{ex}, θ_{ex}) in the "exit" plane ($z_{ex} = L/R_0$) as a function of the initial conditions (r_0, θ_0) for initial velocity $v_0 = 0.508$. Calculations have also been carried out for other values of the velocity v_0. The qualitative picture remains unchanged.

Analysis of the phase diagrams of the beam shows that for variation of parameter L/R_0 there is a definite change in the optical force of the magnetic system. In proportion to the increase in parameter L/R_0 (expansion of the system) the optical force increases somewhat (the focal length decreases). In the large this fact leads to the fact that for expansion of the system with the other parameters remaining fixed, we require a decrease in the magnetic field H_0 (or velocity v_0) to obtain a similar beam configuration. A change in the geometrical factor within certain limits does not change the qualitative nature of the production of an ion beam.

---

[1] V. M. Kel'man and S. Ya. Yavor, Electron Optics [in Russian], Izd. Nauka, Moscow (1963).

[2] J. R. Pierce, Theory and Design of Electron Beams, Van Nostrand (1954).

[3] V. B. Glasko, A. G. Sveshnikov, and N. N. Semashko, Zh. Tekh. Fiz., 40, 270 (1970) [Sov. Phys. – Tech. Phys., 15, 196 (1970)].

[4] A. G. Sveshnikov, V. M. Volosov, V. B. Glasko, and N. N. Semashko, Zh. Tekh. Fiz., 37, 2137 (1967) [Sov. Phys.–Tech. Phys., 12, 1573 (1968)].

Structure of a perturbation near a highly charged body in a weakly ionized plasma

L. A. Malyavin and A. M. Moskalenko

Institute of Terrestrial Magnetism, Ionosphere, and Radiowave Propagation,
Academy of Sciences of the USSR, Moscow

(Submitted April 10, 1973; resubmitted August 16, 1973)
Zh. Tekh. Fiz., 44, 325-332 (February 1974)

Perturbations caused by a spherical body with a high potential in weakly ionized plasma are discussed. The cases in which the body is much larger and much smaller than the Debye radius of the unperturbed plasma are analyzed in detail. The distributions of electric potential, electron density, and ion density near the body have been determined. Total particle fluxes to the body surface are calculated.

FORMULATION OF THE PROBLEM

Large body. Consider a spherical body in a weakly ionized plasma. Assume that the body is totally absorbing, i.e., all electrons are absorbed and ions neutralized on reaching the body surface. Let the surface of the body be at the potential φ_0.

The mean free path of the plasma particles is assumed to be much smaller than the characteristic dimensions of the problem.

The electron density N_e, the ion density N_i, and the electric potential φ are described by the steady-state macroscopic equations of continuity and by the Poisson equation:

$$\left.\begin{aligned} &\operatorname{div}\mathbf{j}_e=0, \quad \operatorname{div}\mathbf{j}_i=0,\\ &\Delta\varphi=-4\pi e(N_i-N_e). \end{aligned}\right\} \tag{1}$$

Here e is the ion charge (the electron charge is $-e$), and $\mathbf{j}_e$ and $\mathbf{j}_i$ are the electron and ion flux densities, given by[1]

$$\mathbf{j}_e=-D_e\nabla N_e+\frac{\sigma_e}{e}\nabla\varphi,$$

$$\mathbf{j}_i=-D_i\nabla N_i-\frac{\sigma_i}{e}\nabla\varphi,$$

where D_e, D_i and σ_e, σ_i are respectively the diffusion and conductivity for electrons and ions. In case of a weakly ionized plasma these are related by the Einstein equation:

$$\sigma_e=\frac{e^2N_e}{T_e}D_e, \quad \sigma_i=\frac{e^2N_i}{T_i}D_i.$$

Here T_e and T_i are the electron and ion temperature in energy units.

To be definite, assume that the body is positively charged ($\varphi_0 > 0$) so that electrons are attracted and ions repulsed.

Let us first consider a large body, i.e., a body whose radius R_0 is much greater than the Debye radius of the unperturbed plasma D:

$$R_0\gg D, \quad D=\left(\frac{T_e}{4\pi e^2N_0}\right)^{1/2},$$

where N_0 is the unperturbed electron (and ion) density.

In a former work[2] the present authors proved that for

$$\varphi_0\ll\frac{T_e}{e}\left(\frac{R_0}{D}\right)^{3/2}$$

the charge of the body is screened in a thin double layer near its surface. The layer thickness is $\sim R_0^{1/3}D^{2/3}$. The thickness of this layer increases with the body potential.

Consider now the case of very high body potentials, when

$$\varphi_0\gg\frac{T_e}{e}\left(\frac{R_0}{D}\right)^{3/2}.$$

With such potentials, the perturbed domain near the body consists of region of neutrality, the double layer, the space charge region, and a diffusion layer. The variation of the relative electron density N_e/N_0 and ion density N_i/N_0 is shown in Fig. 1, in which r denotes the distance from the sphere center.

In the equations of neutrality and the double layer, the absorbing layer is a sphere of radius R_c, where R_c is the radius of the space charge region. We introduce the dimensionless variables

$$\xi=\frac{r}{R_c}, \quad n_e=\frac{N_e}{N_0}, \quad n_i=\frac{N_i}{N_0}, \quad \varphi^*=\frac{e\varphi}{T_e};$$

$$I_{ee}^*=\frac{I_e}{I_{e0}}\xi_0, \quad I_{e0}=4\pi R_0N_0D_e, \quad \xi_0=\frac{R_0}{R_c},$$

where I_e is the total electron flux to the surface of the body.

After one integration, (1) becomes

$$\left.\begin{aligned} &\frac{dn_e}{d\xi}-n_e\frac{d\varphi^*}{d\xi}=\frac{I_{ee}^*}{\xi^2},\\ &\frac{dn_i}{d\xi}+\beta n_i\frac{d\varphi^*}{d\xi}=0,\\ &\varepsilon\Delta\varphi^*=n_e-n_i; \quad \varepsilon=\left(\frac{D}{R_c}\right)^2\ll1, \quad \beta=\frac{T_e}{T_i}=O(1). \end{aligned}\right\} \tag{2}$$

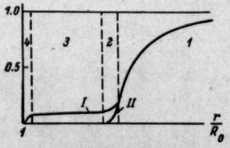

Fig. 1. Variation of the density of electrons (attracted particles) N_e and ions (repulsed particles) N_i in the vicinity of a highly charged body. 1) Neutral domain; 2) double layer; 3) space-charge region; 4) diffusion layer; I) N_e/N_0; II) N_i/N_0.

This takes account of the fact that at high positive potentials of the body, the ion flux to the surface $I_i = 0$. The boundary conditions are $\varphi^* = \varphi_0$, $n_e = n_i = 0$ for $\xi = \xi_0$, and $\varphi^* = 0$, $n_e = n_i = 1$ for $\xi \to \infty$.

Following ref. 2, let us consider the neutral region and the double layer.

Neutral region. In this region ($A + \varepsilon^{1/3} \le \xi < \infty$) we have

$$n_2(\xi) = 1 - \frac{A}{\xi}, \quad \varphi_2^*(\xi) = B \ln\left(1 - \frac{A}{\xi}\right),$$

where

$$A = \frac{\beta}{1+\beta} I_{ec}^*, \quad B = -\frac{1}{\beta}.$$

The particle density and the electric field potential obey the Boltzmann equation

$$n_2(\xi) = \exp\left[-\beta\varphi_2^*(\xi)\right],$$

as follows from the second equation in the system (2).

Double layer ($1 \le \xi \le A + \varepsilon^{1/3}$). Let us introduce the new independent and dependent variables

$$x = \frac{\xi - A}{\varepsilon^{1/3}}, \quad H_e = \frac{n_e}{\varepsilon^{1/3}}, \quad H_i = \frac{n_i}{\varepsilon^{1/3}},$$

which in the neighborhood of the critical point $\xi_{cr} = A$ of the order $\varepsilon^{1/3}$ have the order of unity.

To within terms of the order $\varepsilon^{1/3}$ and using the new variables, (2) becomes

$$\left.\begin{aligned} &\frac{dH_e}{dx} - H_e \frac{d\varphi^*}{dx} = \frac{I_{ec}^*}{A^2}, \\ &\frac{dH_i}{dx} + \beta H_i \frac{d\varphi^*}{dx} = 0, \\ &\frac{d^2\varphi^*}{dx^2} = H_e - H_i. \end{aligned}\right\} \qquad (3)$$

For the sake of convenience, let us put $t = x + (A - 1)/\varepsilon^{1/3} = (\xi - 1)/\varepsilon^{1/3}$. Then, in place of (3) we have

$$\left.\begin{aligned} &\frac{dH_e}{dt} - H_e \frac{d\varphi^*}{dt} = \frac{I_{ec}^*}{A^2}, \\ &\frac{dH_i}{dt} + \beta H_i \frac{d\varphi^*}{dt} = 0, \\ &\frac{d^2\varphi^*}{dt^2} = H_e - H_i. \end{aligned}\right\} \qquad (3a)$$

The boundary conditions for (3a) are

$$\varphi^* = \varphi_1^* \equiv B \ln(\varepsilon^{1/3}/A), \; H_e = H_i = 1/A \; \text{for} \; t = t_1 \equiv 1 + (A-1)/\varepsilon^{1/3};$$

$$\varphi^* = \varphi_2^* \gg 1 \; \text{for} \; t = 0.$$

Here φ_2^* is the potential at the inner boundary of the double layer. The case $\varphi_2^* \gg 1$ has been discussed in detail in ref. 2. In particular, the expression derived for I_{ec}^* is

$$I_{ec}^* = \frac{1+\beta}{\beta}.$$

Note that this result derives essentially from the condition A = 1.

As before, the ion distribution in the double layer is described by the Boltzmann equation

$$H_i(t) = \frac{1}{A} e^{-\beta(\varphi^* - \varphi_1^*)}.$$

When $\varphi_2^* \gg 1$, the electric field $E_0^* = -d\varphi^*/dt(0)$ is equal to

$$E_0^* = -C,$$

where C is a constant of the order of unity. If $\beta = 1$ and $R_0/D = 100$, the constant C = 2 (see ref. 2).

Space-charge region ($\xi \le 1$). In the space-charge region we have to solve the system (2). Also, if $\xi < 1$, the field potential φ^* is of the order of φ_0^* and thus $\varphi^* \gg 1$. The density of ions (repulsed particles) n_i at $\varphi^* \gg 1$ is exponentially small and can be neglected. The electron density n_e in the double layer is of the order $\varepsilon^{1/3}$ and decreases in the space-charge region.

Thus, in the space-charge region the system (2) becomes

$$\left.\begin{aligned} &\varepsilon^{1/3} \frac{dH_e}{d\xi} - \varepsilon^{1/3} H_e \frac{d\varphi^*}{d\xi} = \frac{I_{ec}^*}{\xi^2}, \\ &\varepsilon^{2/3} \Delta\varphi^* = H_e. \end{aligned}\right\} \qquad (4)$$

By introducing the new variable

$$\Phi = \varepsilon^{1/3}\varphi^* = \frac{e\varphi}{T_e}\left(\frac{D}{R_0}\right)^{1/3},$$

the system (4) is changed to

$$\left.\begin{aligned} &\varepsilon^{1/3} \frac{dH_e}{d\xi} - H_e \frac{d\Phi}{d\xi} = \frac{I_{ec}^*}{\xi^2}, \\ &\varepsilon^{1/3} \Delta\Phi = H_e. \end{aligned}\right\} \qquad (4a)$$

In the first equation a small parameter stands in front of a higher derivative. Thus, except for a thin diffusion layer near the body surface, the system (4a) is everywhere equal to

$$\begin{aligned} &-H_e \frac{d\Phi}{d\xi} = \frac{I_{ec}^*}{\xi^2}, \\ &\varepsilon^{1/3} \Delta\Phi = H_e. \end{aligned} \qquad (5)$$

For $\xi = \xi_0$ the field potential on the surface of the body is φ_0, i.e.,

$$\Phi(\xi_0) = \Phi_0 \equiv \frac{e\varphi_0}{T_e}\left(\frac{D}{R_0}\right)^{1/3}. \qquad (6a)$$

On the exterior boundary of the space-charge region at $\xi = 1$, the field potential is of the order T_e/e, so that

$$\Phi|_{\xi \to 1} \to 0. \qquad (6b)$$

Equating the derivatives of the field potential on the exterior boundary of the space-charge region and on the interior boundary of the double layer, we have

$$\frac{d\Phi}{d\xi}(1) = -C. \qquad (6c)$$

The boundary conditions (6a)-(6c) completely describe the solution of the system (5) and the radius of the space-charge region.

The system (5) can be solved as follows. H_e is found from the first equation and substituted into the second. After changing the variables $\xi = 1/\eta$, we have

$$\Phi(\xi) = \left(\frac{2}{3}\frac{I^*_{ee}}{\varepsilon^{1/3}}\right)^{1/3} F_1(\xi),\ F_1(\xi) = \int\limits_{\xi}^{1} \frac{dt}{t^2}\sqrt{1+g-t^3},\ g = \frac{3\varepsilon^{1/3}C^2}{2I^*_{ee}}. \qquad (7)$$

Expression (7) has been derived taking account of the boundary conditions (6b) and (6c). The boundary condition (6a)

$$\Phi(\xi_0) = \Phi_0$$

determines ξ_0, i.e., the radius of the space-charge region:

$$R_c = \frac{R_0}{\xi_0}.$$

The function $F_1(\xi)$ can be expressed in terms of elliptic integrals. However, in calculating the asymptotics for $\xi \ll 1$ or $\xi \to 1$, and in tabulating the function $F_1(\xi)$, it is more convenient to represent the function as an integral (see ref. 7).

If $\xi \ll 1$ we have

$$F_1(\xi) = \frac{1}{\xi}, \quad \Phi(\xi) = \left(\frac{2}{3}\frac{I^*_{ee}}{\varepsilon^{1/3}}\right)^{1/3}\frac{1}{\xi}.$$

Thus, for very large R_c/r ratios, i.e., for very high body potentials when $\varphi_0^{1/2} \gg (T_e/e^{1/2})(R_0/D)^{1/2}$, the space charge near the body does not play a significant role and decreases according to the Coulomb law

$$\varphi = \varphi_0 \frac{R_0}{r}.$$

In this case we have

$$R_c = 1.10 R_0 \left(\frac{\beta}{1+\beta}\right)^{1/2} \left(\frac{e\varphi_0}{T_e}\frac{D}{R_0}\right)^{1/2}. \qquad (8)$$

Thus, for very high body potentials the radius of the space-charge region increases with φ_0 in proportion to $\varphi_0^{1/2}$.

If $\xi \to 1$, we have

$$F_1(\xi) = \sqrt{g}\,(1-\xi), \quad \Phi(\xi) = C(1-\xi).$$

Whence, for relatively low body potentials

$$\varphi_0^* \equiv \frac{e\varphi_0}{T_e}\left(\frac{D}{R_0}\right)^{2/3} \ll 1,$$

the thickness of the space-charge region is small in comparison with the radius of the body. In this case the space-charge region forms a thin charged layer near the surface of the body; this case has been discussed in ref. 2. The dependence of the radius R_c on the body potential φ_0 for $\beta = 1$ and $R_0/D = 100$ is shown in Table 1.

TABLE 1

$\varphi_0^{(*)}$	R_c/R_0	$\varphi_0^{(*)}$	R_c/R_0	$\varphi_0^{(*)}$	R_c/R_0	$\varphi_0^{(*)}$	R_c/R_0	$\varphi_0^{(*)}$	R_c/R_0
0.00	1.00	0.8	1.21	6	1.79	30	3.03	150	5.91
0.02	1.01	1.0	1.24	7	1.87	35	3.22	200	6.72
0.05	1.02	1.4	1.31	8	1.94	40	3.39	250	7.44
0.10	1.04	1.7	1.35	9	2.01	45	3.55	300	8.08
0.15	1.06	2.0	1.39	10	2.07	50	3.70	350	8.68
0.20	1.07	2.5	1.45	12	2.20	55	3.85	400	9.24
0.25	1.09	3.0	1.51	14	2.31	60	3.99	500	10.25
0.30	1.10	3.5	1.56	16	2.42	70	4.25	600	11.17
0.40	1.12	4.0	1.61	18	2.52	80	4.50	700	12.01
0.50	1.15	4.5	1.66	20	2.61	90	4.73	800	12.80
0.60	1.17	5.0	1.70	25	2.83	100	4.95	900	13.54

Figure 2 shows the variation of the potential in the space-charge region, as given by expressions (7), for $\beta = 1$, $R_0/D = 100$, and for different values of φ_0^*.

Let us substitute expression (7) for the potential $\Phi(\xi)$ into the first equation of the system (5). Thus,

$$H_e(\xi) = \sqrt{\frac{3I^*_{ee}\varepsilon^{1/3}}{2}}\frac{1}{\sqrt{1+g-\xi^3}}.$$

Considering this expression, we have for $r = R_c$

$$\frac{N_e}{N_0} = \frac{1+\beta}{\beta C}\frac{R_0}{R_c}\left(\frac{D}{R_0}\right)^{1/3}.$$

If $\varphi_0^{1/2} \gg (T_e/e)^{1/2}(R_0/D)^{1/2}$, then near the body (at the exterior boundary of the diffusion layer) we obtain

$$\frac{N_e}{N_0} = 1.10\left(\frac{1+\beta}{\beta}\right)^{3/2}\left(\frac{DT_e}{R_0 e\varphi_0}\right)^{1/2}.$$

The variation of electron density in the space-charge region is shown in Fig. 2 for $\beta = 1$, $R_0/D = 100$, and for different values of φ_0^*.

Diffusion layer. In the diffusion layer the electron density is given by the first equation of the system (4a). This equation can be replaced by the approximate expression of ref. 3:

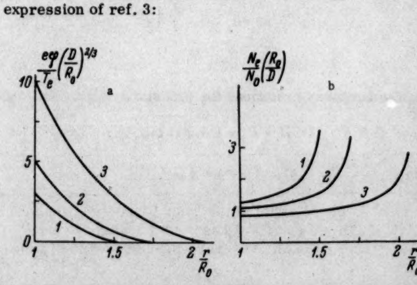

Fig. 2. Variation of the potential (a) and electron (attracted particles) density (b) in the space-charge region for R/D = 100, β = 1, and different φ_0^*: 1) 3; 2) 5; 3) 10.

$$\varepsilon^{1/3}\frac{dH_e}{d\xi}-H_e\frac{d\Phi}{d\xi}(\xi_0)=\frac{\Gamma^*_{ee}}{\xi_0^2}. \tag{9}$$

The corresponding internal variable is $z=(\xi-\xi_0)/\varepsilon^{1/3}$, and Eq. (9) can be reduced to

$$\frac{dH_e}{dz}+H_e\left|\frac{d\Phi}{d\xi}(\xi_0)\right|=\frac{\Gamma^*_{ee}}{\xi_0^2}.$$

The solution of this equation which satisfies the boundary condition $H_e(z=0)=0$ is

$$H_e(z)=\frac{\Gamma^*_{ee}}{\xi_0^2}\left|\frac{d\Phi}{d\xi}(\xi_0)\right|^{-1}\left[1-\exp\left\{-\left|\frac{d\Phi}{d\xi}(\xi_0)\right|z\right\}\right].$$

The uniformly valid ($\xi_0 \le \xi \le 1$) first-order approximation has the form

$$H_e(\xi)=\frac{\Gamma^*_{ee}}{\xi^2}\left|\frac{d\Phi}{d\xi}(\xi)\right|^{-1}-\frac{\Gamma^*_{ee}}{\xi_0^2}\left|\frac{d\Phi}{d\xi}(\xi_0)\right|^{-1}$$
$$\times\exp\left\{-\left|\frac{d\Phi}{d\xi}(\xi_0)\right|\frac{(\xi-\xi_0)}{\varepsilon^{1/3}}\right\}+o(1). \tag{10}$$

From (10) it follows that the diffusion layer thickness l_d is

$$l_d=R_e\varepsilon^{1/3}\left|\frac{d\Phi}{d\xi}(\xi_0)\right|^{-1}.$$

Whence, for $e\varphi_0/T_e \ll (R_0/D)^{2/3}$, we have $l_d \sim R_0^{1/3}D^{2/3}$, as expected. For $(e\varphi_0/T_e)^{1/2} \gg (R_0/D)^{1/2}$, when the field near the body is a Coulomb field, $l_d = R_0(T_e/e\varphi_0)$. In this case the thickness of the diffusion layer is much smaller the Debye radius D.

Particle flux. The total flux of particles to the surface of the body is given by

$$I_e=\Gamma^*_{ee}I_{e0}\frac{1}{\xi_0}=\frac{1+\beta}{\beta}4\pi R_e N_0 D_e. \tag{11}$$

If $\varphi_0^*(D/R_0)^{2/3} \to 0$, the ratio $R_c/R_0 \to 1$, and the flux I_e is equal to $[(1+\beta)/\beta]I_{e0}$, as should be. As is obvious from (8) and (11), at very high body potentials $(e\varphi_0/T_e)^{1/2} \gg (R_0/D)^{1/2}$, we have

$$I_e=1.10I_{e0}\left(\frac{1+\beta}{\beta}\right)^{3/4}\left(\frac{e\varphi_0}{T_e}\frac{D}{R_0}\right)^{1/2}. \tag{12}$$

Thus, when $\varphi_0 \to \infty$, the particle flux increases in proportion to $\varphi_0^{1/2}$.

The variation of the flux I_e/I_{e0} with $\varphi_0^*(D/R_0)^{2/3}$ is shown in Fig. 3 for $\beta = 1$ and $R_0/D = 100$.

Small body ($R_0 \ll D$). For very high body potentials φ_0 the dimensions of the highly perturbed domain (the space-charge region) are much greater than the Debye radius. It can be thus expected that the variation of the field is similar to the case of a large body. The space-charge region (8) is then given by

$$R_c=1.10D\left(\frac{\beta}{1+\beta}\right)^{1/4}\left(\frac{e\varphi_0}{T_e}\frac{R_0}{D}\right)^{1/2}.$$

The condition $R_c \gg D$ is satisfied when

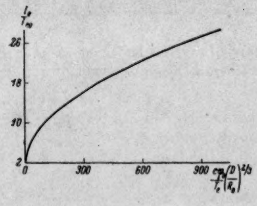

Fig. 3. Total flux of electrons (attracted particles) as a function of body potential φ_0 for $R_0/D = 100$ and $\beta = 1$.

$$\left(\frac{e\varphi_0}{T_e}\right)^{1/2} \gg \left(\frac{D}{R_0}\right)^{1/2}. \tag{13}$$

The electron flux I_e is in this case described by expression (12).

If

$$\frac{e\varphi_0}{T_e} \ll \frac{D}{R_0}, \tag{14}$$

but since as before $e\varphi_0/T_e \gg 1$, the electron flux is[4]

$$\frac{I_e}{I_{e0}}=\frac{e\varphi_0}{T_e}. \tag{15}$$

The dependence of the flux I_e on the potential of a small body is shown in Fig. 4 for $\beta = 1$. Obviously, for very high potentials $e\varphi_0/T_e \sim D/R_0$, only the asymptotic behavior of the function I_e/I_{e0} is known exactly under the conditions (14) and (13). However, the expressions (15) and (12) fit together so that the complete curve can be plotted approximately.

It should be noted in conclusion that throughout this work the mean free paths of the electrons and ions have been assumed to be much smaller than any of the characteristic dimensions of the problem. As the structure of the perturbed domain in the neighborhood of a highly charged body is almost unaffected by the diffusion layer, the above considerations concerning a large body (excepting perhaps the diffusion layer) are valid when the mean free paths of the electrons l_e and ions l_i are much smaller than the thickness of the double layer, the smallest of the remaining dimensions. Thus, as in ref. 2, the analysis has been carried out under the assumption that

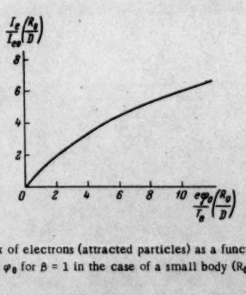

Fig. 4. Total flux of electrons (attracted particles) as a function of body potential φ_0 for $\beta = 1$ in the case of a small body ($R_0 \ll D$).

$$l_e \ll R_0^{1/2} D^{1/2}, \quad l_i \ll R_0^{1/2} D^{1/2}.$$

In the case of a small body, the mean free paths have been assumed negligible in comparison with the dimension of the body.

The authors thank A. V. Gurevich for discussion and I. A. Zhulin for his interest.

---

[1] A. V. Gurevich and E. E. Tsedilina, Usp. Fiz. Nauk, 91, 609 (1967) [Sov. Phys. – Usp., 10, 214 (1967)].

[2] L. A. Malyavin and A. M. Moskalenko, Zh. Tekh. Fiz., 44, 311 (1974) [Sov. Phys. – Tech. Phys., 19, 197 (1974)].

[3] J. Cole, Perturbation Methods in Applied Mathematics, Ginn-Blaisdell, New York (1968).

[4] L. A. Malyavin and A. M. Moskalenko, Zh. Tekh. Fiz., 43, 722 (1973) [Sov. Phys. – Tech. Phys., 18, 456 (1973)].

Electron energy distribution in the afterglow. I

A. B. Blagoev, Yu. M. Kagan, N. B. Kolokolov and R. I. Lyagushchenko

A. A. Zhdanov Leningrad State University

(Submitted July 2, 1973)
Zh. Tekh. Fiz., 44, 333-338 (February 1974)

The electron energy distribution function in the afterglow is usually assumed to be a Maxwellian. However, one might expect a considerable departure from this distribution for fast electrons. In the present paper we describe a method for the experimental determination of the electron energy distribution and the densities of charged particles and metastable atoms in the afterglow. The results of measurements in helium carried out in a tube 2.7 in diameter at pressures of 1 and 2 torr and currents of 0.45 and 1.8 A are presented. The high-energy part of the distribution function exhibits effects due to metastables.

1. During the last few years a number of papers have reported investigations of the afterglow in the positive column. Investigations of the afterglow yield information on the deionization time, which is of practical importance. In addition, it is possible, under afterglow conditions, to study reactions in which heavy particles (ion and metastable atoms) participate.

The estimate of the decay of electron excitation and ionization in these papers is usually made starting from traditional considerations, using the idea of an electron temperature T_e and a Maxwellian electron energy distribution. However, under afterglow conditions we might expect a considerable departure of the distribution from a Maxwellian for the fast electrons. We consider the processes in a decaying plasma in more detail. For values of the gas pressure p and the tube radius R which are reasonably large ($pR \gg 1$ torr · cm) the plasma deionization process can be divided into two stages. During the first stage there is a rapid cooling of the electrons to a temperature of the order of the temperature of the atoms T_a. The cooling process takes place in a time of the order of $\tau_a \simeq 1/(\delta \nu_a)$, where δ is the fractional energy dissipated in collisions, and ν_a is the electron–atom collision frequency. During the time τ_a the density of the electrons and metastable atoms does not change to any great extent. During the second stage recombination of the charged particles and excitation of the metastable atoms occur. These processes take a much longer time than τ_a. During this stage most of the electrons lie in the energy range from zero to several tens of electron volts. Since electron–electron interactions for electrons with these energies are strong, a Maxwellian distribution is established in this energy range with a certain temperature T_e. The value of T_e may be much greater than T_a, since a number of processes take place in the plasma which lead to the appearance of fast electrons and, as a consequence, to heating of the electron gas. The number of Maxwellian electrons with energies $\varepsilon \gg kT_e$ is very small, so the presence of sources of fast electrons in this energy range can lead to a considerable departure of the distribution function from a Maxwellian; the number of electrons in this range may be much larger than for a Maxwellian distribution characterized by the temperature of the slow electrons T_e.

Processes which give rise to fast electrons include the following.

1. Collisions of the second kind between electrons and metastable atoms.

2. Collisional–radiative recombination.

3. The formation of an atomic ion when two metastable atoms collide.

4. The formation of a molecular ion when two metastable atoms collide.

The role of these processes has been discussed in ref. 1.

The fast electrons which arise in the plasma can dissipate their energy in several ways: a) by interaction with slow plasma electrons; b) by collisions with gas atoms and ions; c) by recombination at the walls of the tube and in the volume. Competition between a, b, and c leads to a situation in which ε_{eff}, the effective energy introduced by the fast electrons into the electron system, is not equal to the initial energy ε; depending on the conditions this quantity can assume any value from zero to the initial energy. The quantity ε_{eff} determines the degree of heating of the slow electrons. To calculate it, it is necessary to know the distribution function of the fast electrons, that is, the distribution function for $\varepsilon \gg kT$. The distribution of the fast electrons is also of independent interest, for example, for estimating the contribution of excitation processes by electron collisions in the afterglow.

A problem similar to that being considered here is considered in ref. 1. However, no measurements were made of the distribution function of the fast electrons, and the theoretical discussion contains errors which make the results obtained in a number of cases not only quantitatively but also qualitatively incorrect. Hence, the problem in this investigation is to measure and calculate the form of the distribution function under afterglow conditions.

2. The measurements are carried out in the afterglow of a periodic discharge in helium at pressures of 1 and 2 torr and currents of 0.45 and 1.8 A. A block diagram of the experimental apparatus is shown in Fig. 1. Voltage pulses with $\tau_1 = 20$ μsec and repetition frequency 2 kHz are applied to the electrodes of the discharge tube. We use a tube 35 cm long with internal diameter of 2.7 cm with cooled electrodes; at the axis, in the central part, there are two cylindrical probes with the following dimensions: length $l_1 = 1.4$; $l_2 = 1.5$ cm, radius $r_1 = 5 \cdot 10^{-3}$, and $r_2 = 3 \cdot 10^{-3}$ cm. The grounded anode of the discharge tube is used as the reference electrode in the probe measurements.

The following afterglow parameters are determined experimentally: the electron energy distribution function, the charged-particle density, and the density of metastable atoms in the 2^3S_1 state. We consider the measurements in detail below.

In our previous paper[2] we have described a pulsed method of measuring the distribution function in a plasma with periodically varying parameters. The measurements in the afterglow use an arrangement based on the switching of the probe current. The basic idea of the method is as follows. An alternating signal of the form

$$\Delta V = A(1 + \cos\omega_1 t)\sin\omega_2 t \tag{1}$$

is introduced into the probe circuit together with a constant bias.

In our investigation $f_1 = \omega_1/2\pi = 400$ Hz, $f_2 = \omega_2/2\pi = 100$ kHz. The probe circuit is opened and closed only during the measurement time. Then, the amplitude of the signal of frequency ω_1, to which the selective circuit is tuned, will contain as the main term a quantity proportional to the second derivative of the probe current with respect to the probe potential at the time t:

$$i_{\omega_1} = \frac{\tau}{T}\left[\frac{A^2}{2}i''(V, t_0) + \frac{7}{64}A^4 i^{\mathrm{IV}}(V, t_0) + \ldots\right]\cos\omega_1 t, \tag{2}$$

where τ is the time at which the switch circuit is closed. The switching frequency of the circuit is $f = 1/T$, where T is the period between discharge current pulses. By varying V for fixed t_0, we can find i″ as a function of V and t_0 for given t_0. By making measurements for different t_0, we obtain i″ (V, t_0) at different afterglow times. The electron energy distribution function is related to i″ (V, t_0) by the well-known Dryuvesteyn relation.[3]

To obtain the absolute values of the distribution function we calibrate the measuring circuit.[4] For the shape of differentiating signal mentioned above the relation between the distribution function and the quantities measured in the experiment is as follows:

$$nf(\varepsilon) = 8.42 \cdot 10^{11}\frac{\sqrt{V}}{A^2 S}\frac{x}{x_k} i_{\omega_1 k}. \tag{3}$$

Here, $nf(\varepsilon)$ is the electron energy distribution function in $\mathrm{eV^{-1}\,cm^{-3}}$, V is the retarding potential of the probe in volts, A is half the peak value of the modulating voltage in volts, S is the area of the probe in $\mathrm{cm^2}$, $i_{\omega 1k}$ is the amplitude of the calibrating current in amperes, x_k is the deflection of the automatic recorder when the calibrating current flows through the probe circuit, and x is the deflection of the recorder in the measurements. The number of particles in the energy range of interest is found by graphical integration of Eq. (3) in the appropriate energy range.

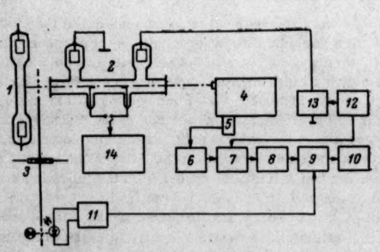

Fig. 1. Block diagram of the experimental apparatus. 1) Additional tube used for optical measurements; 2) discharge tube; 3) modulator disk; 4) monochromator; 5) photomultiplier; 6) emitter follower; 7) electronic switch; 8) narrow-band amplifier; 9) synchronous detector; 10) recording instrument; 11) reference voltage generator; 12) master generator; 13) discharge power supply; 14) pulsed circuit for probe measurements.

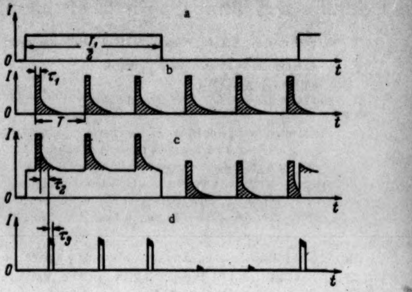

Fig. 2. Illustrating the optical method of measurement. a) Light flux from tube 1 after the modulator; b) light flux from tube 2; c) total light flux entering the monochromator; d) form of the signal at the input of the narrow-band amplifier. The time relations in this figure are arbitrary.

Obtaining the distribution function in the afterglow is known to be a difficult problem. Since the main group of electrons in the decaying plasma has a Maxwellian distribution with mean energy ≈ 0.1 eV, the small oscillations of the space potential (0.1 V) present in our experiments do not enable us to determine the true behavior of the second derivative of the probe current over the range of plasma potentials. Consequently, we cannot measure the space potential from the position of the characteristic points on the curve i″ (V, t_0) or obtain the electron density by integrating the experimental curve of i″ (V, t_0). For this reason we use the following method to determine the charged-particle density. At the afterglow time of interest we find the saturation ion current on an oscilloscope. The temperature of the distribution (in °K) is found from the retarding potentials of the probe, equal to 0.4-0.6 V, from the equation

$$T_e = \frac{11600}{\frac{d\ln i''(V, t_0)}{dV}}. \tag{4}$$

For these electron energies the distribution function is a Maxwellian due to the large part played by Coulomb interactions, while the curve of i″(V) in this region is not distorted by oscillations of the space potential. In the measurement of T_e the value of A is 0.05 V.

From the known temperature T_e and the measured ion saturation current density j, we can find the electron density n from the equation

$$n(T_e + T_a) = 2 \cdot 10^{12}\frac{r}{\lambda_+}\sqrt{MT_a}\, j \ln\frac{l}{r x_0}, \tag{5}$$

where T_a is the temperature of the atoms (in °K), λ_+ is the mean free path of the ions (in cm), M is the atomic weight, j is the ion saturation current density (in mA/cm^2), and l is the probe length.

The quantity $x_0 = (1 + u)(1 + 0.05\,u)$, where

$$u = 2.3\cdot 10^{-2}\left(\frac{V_1^3\lambda_+}{j^2M}\right)^{1/3}\frac{1}{r}.$$

Here, V is the probe potential with respect to the plasma potential. Equation (5) differs from that given in ref. 5 in that the atomic temperature is taken into account on the left side. This is necessary in the afterglow, since the temperatures T_e and T_a are quantities of the same order. The use of probe theory at medium pressures to determine the electron density is due to the fact that the mean free path of the ions for charge exchange is several times smaller than the dimensions of the probe sheath. In calculations using Eqs. (3) and (5) it is necessary to know the space potential V_s. This quantity is found from the potential of a floating probe V_f using the following equation:[4]

$$V_s - V_f = \frac{T_e}{11600}\ln\left(0.7\sqrt{\frac{M}{m}}\,\frac{S}{S_1}\right), \tag{6}$$

where m is the electron mass, M is the mass of the atom, S is the probe area, S_1 is the area on the layer, and T_e is the electron temperature (in °K).

The use of Eq. (6) is justified, since the sheath radius is small at these potentials. Since the mean energy in the afterglow is low, the value of $V_f - V_s$ in helium can be calculated with an accuracy better than 0.2 V from the equation

$$V_f - V_s = 3.5\cdot 10^{-4}T_e. \tag{7}$$

3. To measure the density of metastable atoms in the 2^3S_1 state in the afterglow, we use the radiation absorption method employing two tubes (Fig. 1). Using this method we measure the intensity of the radiation from tube 1 which passes through the absorbing tube 2. This quantity, however, may be considerably smaller than the intensity of the radiation of tube 2. Hence, in measurements of this type it is important for the recording system to record only the signal from tube 1. To solve this problem we use an alternating-current recording circuit employing synchronous detection. A characteristic of this circuit is the fact that it enables measurements to be made at any instant of time of interest under periodically recurrent discharge conditions. The principle of operation of the circuit is illustrated in Figs. 1 and 2.

In tube 1, of radius 1 cm and containing helium at a pressure of 1 torr, a dc discharge is ignited (i = 150 mA). The radiation from this tube passes successively through the modulator 3 and the tube 2, and together with the natural radiation of tube 2 is incident on the entrance slit of the monochromator 4. The time behavior of this flux is shown in Fig. 2c. The signal from the output of the photomultiplier 5 is fed to an emitter follower 6, and then to an electronic switch 7. The electronic switch is opened at a frequency equal to the frequency at which the tube 2 strikes. The length of the opening pulse τ_3 and its delay τ_2 with respect to the discharge pulse are controlled. The value of the delay is determined by the phase of the afterglow in which the measurements are made. The form of the signal at the output of the electronic switch is shown in Fig. 2d. This signal is applied to a narrow-band amplifier 8 and then to the synchronous detector 9. The narrow-band amplifier is tuned to the modulation frequency of the light flux of tube 1, and is equal to 600 Hz. The reference voltage of the synchronous detector of the same frequency operates the unit 11, consisting of a photodiode and an amplifier. In the signal applied to the input of the narrow-band amplifier the amplitude of the harmonic at the modulation frequency is proportional to the light flux of tube 1 only. Consequently, the measuring voltmeter 10 records the light flux from tube 1 at the chosen instant of afterglow.

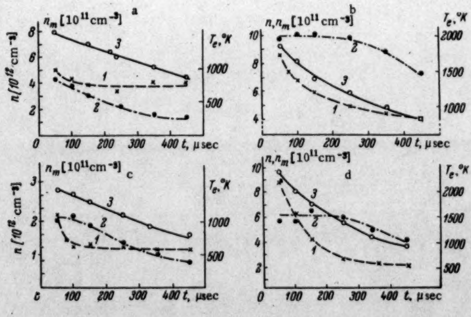

Fig. 3. Variation of electron temperature (1), electron density (2), and density of metastable atoms in the 2^3S_1 state (3) in the afterglow. a) Pulse current 1.8 A, pressure torr; b) current pulse 0.45 A, pressure 2 torr; c) pulse current 1.8 A, pressure 1 torr; d) pulse current 0.45 A, pressure 1 torr.

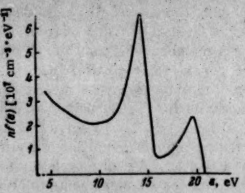

Fig. 4. Typical form of the electron energy distribution function in the afterglow. Helium pressure 1.5 torr, pulse current 0.45 A. The measurement is made 50 μsec after the discharge pulse ceases.

We measure the relative absorption of the 3889 Å triplet line of helium. At the pressures and currents which we use the radiation and absorption profiles of each of the triplet lines can be assumed to be of Doppler form,[6] and the absorption in tube 1 is not taken into account. The temperature of the atoms of the radiating and absorbing tube is taken to be 400°K. It can be shown that a change in the atom temperature of 100°K leads to an error in determining the density of the metastable atoms of less than 10%.

The results obtained for the electron temperature, the charged-particle density, and the density of the metastable atoms are shown in Fig. 3. A typical experimental distribution function in the afterglow is shown in Fig. 4. Note the maxima in the region of 15 and 20 eV. These characteristics are due, respectively, to reactions in which two metastable atoms participate, and collisions of the second kind between electrons and metastable atoms.

The results of systematic measurements of the distribution function, a discussion of the experimental material, and theoretical calculations of the distribution function are given in the second part of this paper.

---

[1] J. C. Ingraham and S. C. Brown, Phys. Rev., 138A, 1015 (1965).

[2] A. B. Blagoev, B. Kolokolov, and V. M. Milenin, Zh. Tekh. Fiz., 42, 1701 (1972) [Sov. Phys. – Tech. Phys., 17, 1359 (1972)].

[3] Yu. M. Kagan and V. I. Perel, Usp. Fiz. Nauk, 81, 409 (1963) [Sov. Phys. – Usp., 6, 767 (1964)].

[4] Yu. M. Kagan and N. K. Mitrofanov, Zh. Tekh. Fiz., 41, 2065 (1971) [Sov. Phys. – Tech. Phys., 16, 1636 (1972)].

[5] V. M. Zakharova, Yu. M. Kagan, K. S. Mustafin and V. I. Perel, Zh. Tekh. Fiz., 30, 442, (1960) [Sov. Phys. – Tech. Phys., 5, 411 (1960)].

[6] D. A. Myshkis and I. Ya. Fugol, Trudy FTINT, No. 1, 204 (1968).

Electron energy distribution in the afterglow. II

A. B. Blagoev, Yu. M. Kagan, N. B. Kolokolov and R. I. Lyagushchenko

A. A. Zhdanov Leningrad State University

(Submitted July 2, 1973)
Zh. Tekh. Fiz., 44, 339-347 (February 1974)

The results of probe measurements on the distribution function in the afterglow of a helium plasma at pressures of 1 and 2 torr and currents of 0.45 and 1.8 A are presented. The distribution function in the energy range 4-20 eV has a complex nonmonotonic form. The number of electrons in this energy range is many orders of magnitude greater than in a Maxwellian distribution with the temperature of the slow electrons T_e. These characteristics are due to the production of fast electrons in reactions in which metastable atoms participate. The results of the experiment are compared with theoretical calculations of the distribution function in the afterglow. The agreement is satisfactory. Absolute measurements of the distribution function of the fast electrons and a comparison with theoretical calculation enable us to determine the constants and cross sections of the elementary processes. The following values are obtained: the cross section $\sigma_1 \approx 0.6 \cdot 10^{-16}$ cm^2 for collisions of the second kind $He(2^3S_1) + e \rightarrow He(1^1S_0) + e$, the constant $\beta_2 \approx 10^{-9}$ cm$^3 \cdot$ sec^{-1} for the reaction $He(2^3S_1) + He(2^3S_1) \rightarrow He_2^+ + e$, and the constant $\beta_3 \approx 2 \cdot 10^{-9}$ cm$^3 \cdot$ sec^{-1} for the reaction $He(2^3S_1) + He(2^3S_1) \rightarrow He^+ + He + e$.

1. In the preceding paper[1] we describe a method of investigating the electron energy distribution in the afterglow of the positive column and give results of measurements in a helium plasma at pressures of 1 and 2 torr and currents of 0.45 and 1.8 A.

Systematic measurements of the distribution function in absolute units for different stages of the afterglow are shown in Figs. 1 and 2. Figure 3 shows the change in the number of electrons with time for different energy ranges. It can be seen from Fig. 1 that the distribution function in the energy range 4-20 eV has a complex nonmonotonic form. The number of electrons in this energy range is many orders of magnitude greater than in a Maxwellian distribution at the temperature of the slow electrons T_e, and the decrease with time of the number of fast electrons is comparatively slow. These characteristics can be explained by assuming that fast electrons are produced as a result of a number of reactions in which metastable atoms participate. Thus, the presence of a maximum in the energy range around 20 eV can be due to the reaction

$$He(2^3S_1) + e \rightarrow He(1^1S_0) + e. \qquad (1)$$

In this reaction electrons are created in an energy range of the order of several kT_e in the region of 19.8 eV. The maximum in the energy range around 15 eV can be due to the reaction

$$He(2^3S_1) + He(2^3S_1) \rightarrow He_2^+ + e. \qquad (2)$$

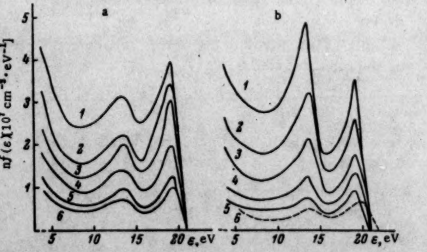

Fig. 1. Form of the distribution function in the afterglow. t, μsec: 1) 50; 2) 100; 3) 150; 4) 250; 5) 350; 6) 450; p = 2 torr, i, A: a) 1.8; b) 0.45.

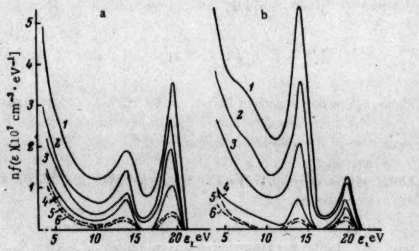

Fig. 2. Form of the distribution function in the afterglow. The notation is the same as in Fig. 1; p = 1 torr.

In this reaction electrons are produced[2] with energies of about 15 eV. The continuous energy spectrum in the range 4-12 eV occurs as a result of the reaction

$$He(2^3S_1) + He(2^3S_1) \rightarrow He^+ + He + e. \qquad (3)$$

From the data in ref. 2, in this reaction electrons may be produced over a wide energy range from zero to 14.5 eV.

In collisional–radiative recombination the mean increment in energy of the electron is about 0.35 eV, so the effect of recombination on the shape of the distribution in the energy range 4-20 eV should not be very great. However, this process can lead to heating of the slow electrons.

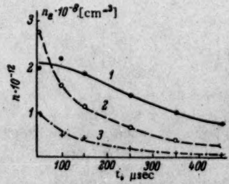

Fig. 3. The variation of the number of electrons with time for different energy ranges. 1) Total number of electrons n; 2) number of electrons n_ε with energies ε = 16 eV, i = 1.8 A, p = 1 torr.

All these reactions also occur in a steady discharge, but their effect is masked by the high electron flux in the high energy range of velocity space due to heating of the electrons in the electric field. These reactions can play a role in the region outside the steady discharge where there is no electric field. Such conditions obtain in the experiment described in ref. 3.

2. We now give a theoretical analysis of the electron energy distribution in the afterglow. The distribution function of the fast electrons $f_0(\varepsilon)$ can be obtained from the following considerations. If the characteristic times of variation of electron and metastable atom densities is much greater than the relaxation time of the electron energy, the problem can be regarded as quasistationary, and we can omit the derivative with respect to time in the kinetic equation. Then, if fast-electron sources are present, the kinetic equation for the distribution function $f_0(\varepsilon)$ in the energy range $\varepsilon \gg kT_e$ can be written in the form

$$\sqrt{\frac{2m}{\varepsilon}}\frac{d}{d\varepsilon}\varepsilon j_\varepsilon+\left(\frac{1}{\tau}+\nu^*\right)f_0-R(\varepsilon)=0. \qquad (4)$$

Here, j_ε is the electron flux density through the surface of energy ε in velocity space due to elastic collisions with atoms and interelectron interaction, τ is the lifetime of the electrons with ε, ν^* is the frequency of inelastic collisions with atoms, and $R(\varepsilon)$ is the density of the sources of fast electrons.

Using the usual expressions for the electron–electron and electron–atom collision operators,[4] we obtain the following expression for j_ε:

$$j_\varepsilon=-\sqrt{\frac{\varepsilon}{2m}}\left[\nu_e(\varepsilon)\left(kT_e\frac{df_0}{d\varepsilon}+f_0\right)\delta\nu_a(\varepsilon)\left(kT_a\frac{df_0}{d\varepsilon}+f_0\right)\right]. \qquad (5)$$

Here, $\nu_e(\varepsilon) = 2\sqrt{2}\pi e^4 Ln/\sqrt{m}\varepsilon^{3/2}$ is the electron–electron collision frequency, L is the Coulomb logarithm, $\nu_a(\varepsilon)$ is the frequency of elastic collision with atoms, and $\delta = 2m/M$ is the fractional energy dissipated per collision.

In problems of the relaxation of fast electrons with $\varepsilon \gg kT_e$, kT_a, terms with $(df_0)/(d\varepsilon)$ in Eq. (5) can be neglected.[5] The physical meaning of this approximation is that the fast electrons which arise due to the action of sources are mainly slowed down by collisions with slow electrons and atoms.

Using Eq. (5) we write Eq. (4) in the form

$$\frac{1}{\sqrt{\varepsilon}}\frac{d}{d\varepsilon}\left[\varepsilon^{\frac{3}{2}}(\nu_e+\delta\nu_a)f_0\right]-\left(\frac{1}{\tau}+\nu^*\right)f_0+R=0. \qquad (6)$$

The solution of Eq. (6) is the function

$$f_0=\frac{1}{\varepsilon^{3/2}(\nu_e+\delta\nu_a)}\int_\varepsilon^\infty R(\varepsilon')\exp\left[-\int_\varepsilon^{\varepsilon'}\frac{(1+\nu^*\tau)\,d\varepsilon}{\varepsilon\tau(\nu_e+\delta\nu_a)}\right]\sqrt{\varepsilon'}\,d\varepsilon'. \qquad (7)$$

The form of function (7) depends on the value of the parameter $(1 + \nu^*\tau)/[(\nu_e + \delta\nu_a)\tau]$ for a given value of the energy ε. When this parameter is much smaller than unity, i.e., the "absorption" time of a fast electron $\tau/(1 + \nu^*\tau)$ is much greater than the "retardation" time $1/(\nu_e + \delta\nu_a)$,

$$f_0\simeq\frac{1}{\varepsilon^{3/2}(\nu_e+\delta\nu_a)}\int_\varepsilon^\infty R(\varepsilon')\sqrt{\varepsilon'}\,d\varepsilon'. \qquad (8)$$

For a single-energy source $R = I\delta(\varepsilon - \varepsilon_0)$ in this case we obtain a step distribution

$$f_0=\begin{cases}\dfrac{I}{\varepsilon^{3/2}(\nu_e+\delta\nu_a)} & \text{for } \varepsilon<\varepsilon_0,\\ 0 & \text{for } \varepsilon>\varepsilon_0.\end{cases} \qquad (9)$$

In the opposite limiting case $(1 + \nu^*\tau)/[(\nu_e + \delta\nu_a)\tau] \gg 1$ the exponent in Eq. (7) has a sharp maximum when $\varepsilon' = \varepsilon$, so that $R(\varepsilon')\sqrt{\varepsilon'}$ can be removed from under the integral when $\varepsilon' = \varepsilon$ and

$$\int_\varepsilon^{\varepsilon'}\frac{(1+\nu^*\tau)}{\varepsilon\tau(\nu_e+\delta\nu_a)}\frac{d\varepsilon}{\varepsilon}\simeq\frac{1+\nu^*\tau}{\varepsilon\tau(\nu_e+\delta\nu_a)}(\varepsilon'-\varepsilon),$$

when

$$f_0\simeq\frac{R(\varepsilon)\tau(\varepsilon)}{1+\nu^*\tau}. \qquad (10)$$

The form of the distribution in this case is determined to a large extent by the form of the source. For a single-energy source a single-energy distribution is obtained.

It follows from the results obtained in ref. 2 that the distribution has a form similar to (10) for any value of the parameter $(1+\nu^*\tau)/[(\nu_e+\delta\nu_a)\tau \gg 1$. This is due to the fact that the differential operators of electron–electron collisions and of elastic collisions of electrons with atoms are written in the relaxation time approximation, which is inadmissible.

The electron lifetime τ is determined by recombinations in the volume, and diffusion to the walls of the tube. The potential difference between the walls and the center of the tube, which arises when there is ambipolar diffusion of the slow electron, has a value of the order of several $(kT_e)/e$. For this reason we assume that the electrons with energies $\varepsilon \gg kT$ drift to the walls under free diffusion conditions. If we assume that the reflection coefficient of the fast electrons at the walls is zero, the diffusion time $\tau_D = r^2/[5.8D(\varepsilon)]$, where r is the radius of the tube, and $D(\varepsilon) = 2\varepsilon/(3m\nu_a)$ is the free diffusion coefficient. For the inert gases the value of τ_D for $pr \leqslant 10$ torr · cm turns out to be very much smaller than the volume recombination time, so that we assume below that $\tau = \tau_D$.

In the case of helium the source density can be represented in the form

$$R(\varepsilon)=R_1(\varepsilon)+R_2(\varepsilon)+R_3(\varepsilon),$$

where R_1, R_2, and R_3 are the source densities due to processes (1), (2), and (3). For process (1) we have

$$R_1(\varepsilon)=\frac{g_a}{g_m}\frac{nn_m}{n_a}\nu^*(\varepsilon)\left(\frac{m}{2\pi kT_e}\right)^{3/2}\exp\left(-\frac{\varepsilon-\varepsilon_1}{kT_e}\right), \qquad (11)$$

where n_m and n_a are the densities of metastable and normal atoms, ε_1 is the excitation energy of the metastable atoms, and g_a and g_m are statistical weights. In writing Eq. (11) we assume that the slow electrons have a Maxwellian distribution, and we use the relation between the cross sections of collisions of the first and second kinds. For R_2 and R_3 we use the expression given in ref. 2,

$$R_2 = \frac{\beta_2 n_m^2}{g(\varepsilon_2)} \delta(\varepsilon - \varepsilon_2), \qquad (12)$$

$$R_3 = \frac{(2m)^{3/2} \beta_3 n_m^2}{\pi^2 \varepsilon_3^3} (\varepsilon_3 - \varepsilon)^{3/2} \Theta(\varepsilon_3 - \varepsilon), \qquad (13)$$

where $\varepsilon_2 = 15$ eV, $\varepsilon_3 = 14.5$ eV, β_2 and β_3 are the rate constants of the reactions (2) and (3), $\Theta(x) = 1$ (for $x \geq 0$) and 0 (for $x < 0$), and $g(\varepsilon) = 4\pi\sqrt{2\varepsilon}/m^{3/2}$ is the density of states of an electron with energy ε.

The collision frequency ν_a in the energy region $\varepsilon \geq 4$ eV for helium can be assumed constant, and is given by[6]

$$\nu_a = 2.3 \cdot 10^9 p. \qquad (14)$$

Substituting Eqs. (11), (12), (13), and (14) in Eq. (7) we can obtain the final form of the distribution for helium. Expression (11) for $\varepsilon - \varepsilon_1 \gg kT_e$ is exponentially small, so that the distribution function turns out to be practically zero everywhere for $\varepsilon > \varepsilon_1$, with the exception of a small region of the order of kT_e. Since $\nu^*(\varepsilon) = 0$ for $\varepsilon \leq \varepsilon_1$, the quantity $R_1(\varepsilon)$ has a sharp maximum in the region $\varepsilon - \varepsilon_1 \approx kT_e$. Hence, the contribution of inelastic collisions to the exponent can be estimated by means of the parameter

$$a^2 = \frac{\nu^*(\varepsilon_1 + kT_e)}{\nu_e(\varepsilon_1) + \delta\nu_a(\varepsilon_1)} \frac{kT_e}{\varepsilon_1}.$$

The factor $(kT_e)/\varepsilon_1$ has the physical meaning of the fractional energy an electron of energy $\varepsilon \simeq \varepsilon_1 + kT_e$ must lose to leave the inelastic collision region. For helium with $kT_e \lessdot 0.2$ eV, $a^2 \leq 10^{-2}$, so that in all the subsequent equations we assume $\nu^* = 0$.

Taking these factors into account, we can write the following expression for the electron energy distribution in the helium plasma:

$$\begin{aligned} nf(\varepsilon) = g(\varepsilon) f_0 = {} & \frac{16}{\pi} \left(\frac{\varepsilon_1}{\varepsilon_3}\right)^3 \frac{\beta_3 n_m^2}{\varepsilon_3 \nu_e(\varepsilon_1)} \frac{\sqrt{x}}{1 + \gamma x^{3/2}} \\ & \times \int_x^{x_3} (x_3 - x')^{3/2} \exp\left(-k^2 \int_x^{x'} \frac{x^{3/2} dx}{1 + \gamma x^{3/2}}\right) \sqrt{x'} dx' \\ & + \frac{\beta_2 n_m^2 \Theta(x_2 - x)}{\nu_e(\varepsilon_1) \varepsilon_1} \frac{\sqrt{x}}{1 + \gamma x^{3/2}} \exp\left(-k^2 \int_x^{x_2} \frac{x^{3/2} dx}{1 + \gamma x^{3/2}}\right) \\ & + \frac{\beta_1 n n_m}{\nu_e(\varepsilon_1) \varepsilon_1} \frac{\Theta(1 - x) \cdot \sqrt{x}}{1 + \gamma x^{3/2}} \exp\left(-k^2 \int_x^1 \frac{x^{3/2} dx}{1 + \gamma x^{3/2}}\right). \end{aligned} \qquad (15)$$

Here,

$$x = \frac{\varepsilon}{\varepsilon_1}, \; x_2 = \frac{\varepsilon_2}{\varepsilon_1}, \; x_3 = \frac{\varepsilon_3}{\varepsilon_1}, \; k^2 = \frac{5.8 \cdot D(\varepsilon_1)}{r^2 \cdot \nu_e(\varepsilon_1)}, \; \gamma = \frac{\delta\nu_a}{\nu_e(\varepsilon_1)},$$

and β_1, β_2, β_3 are the rate constants of the processes (1), (2), and (3).

All of the above considerations pertain to electrons with $\varepsilon \gg kT_e$. The electron distribution function ($\varepsilon \lessdot kT$) will be a Maxwellian with temperature T_e, which in general will not be equal to the temperature of the atoms T_a. The Maxwell distribution for slow electrons will be established due to interelectron interaction, which is very strong for energies $\varepsilon \simeq 0.01$-0.1 eV.

The temperature of the slow electrons T_e is determined by the following energy balance equations:

$$euEn + E_{\mathrm{eff}} - H = 0. \qquad (16)$$

Here, H is the reduction in the energy of the electron gas in unit volume and in unit time due to collisions between slow electrons and atoms, and E_{eff} is the similar increment in energy due to the production of fast electrons; the term euEn takes account of the possible heating of the electrons by the residual electric field. The quantity H is given by the usual expression

$$H = \delta\nu_{\mathrm{eff}}(T_e) \frac{3}{2} k (T_e - T_a) n. \qquad (17)$$

For helium, the transport cross section is independent of the energy in the low-energy range. In this case we have

$$\nu_{\mathrm{eff}}(T_e) = \frac{4}{3} \sqrt{\frac{8kT_e}{\pi m}} \frac{1}{\lambda}, \quad u = \frac{8eE\lambda}{3\pi m} \left(\frac{8kT_e}{\pi m}\right)^{-1/2},$$

and $\lambda = 1/17p$ is the mean free path of an electron.[7]

The quantity E_{eff} is equal to the energy transferred by the fast electrons to the slow electrons. The value of E_{eff}, due to processes (1), (2), and (3), is

$$E_{\mathrm{eff}} = \int_0^\infty \varepsilon S_e(f_0) g(\varepsilon) d\varepsilon. \qquad (18)$$

Here,

$$S_e(f_0) = -\sqrt{\frac{2m}{\varepsilon}} \frac{d}{d\varepsilon} \left(\nu_e \sqrt{\frac{\varepsilon^3}{2m}} f_0\right) \qquad (19)$$

is the interelectron collision operator for $\varepsilon \gg kT_e$, and f_0 is the distribution function of the fast electrons given by Eq. (7). Since $kT_e \ll \varepsilon_1, \varepsilon_2, \varepsilon_3$, the lower limit of integration in Eq. (18) is zero. Substituting Eqs. (7) and (19) in Eq. (18), integrating by parts, and changing the order of integration, we obtain the following general expression for E_{eff}:

$$E_{\mathrm{eff}} = \int_0^\infty d\varepsilon' R(\varepsilon') g(\varepsilon') \int_0^{\varepsilon'} \frac{\nu_e}{\nu_e + \delta\nu_a} \exp\left[-\int_\varepsilon^{\varepsilon'} \frac{d\varepsilon}{\varepsilon(\nu_e + \delta\nu_a)\tau}\right]. \qquad (20)$$

It is easy to understand the physical meaning of Eq. (20) by noting that the quantity

$$\varepsilon_{\mathrm{eff}}(\varepsilon') = \int_0^{\varepsilon'} \frac{\nu_e}{\nu_e + \delta\nu_a} \exp\left[-\int_\varepsilon^{\varepsilon'} \frac{d\varepsilon}{\varepsilon(\nu_e + \delta\nu_a)\tau}\right] d\varepsilon \qquad (21)$$

can be interpreted as an effective energy introduced by the fast electrons with initial energies ε' into the system of slow electrons. For $(\nu_e + \delta\nu_a)\tau \gg 1$, we have

$$\varepsilon_{\text{eff}} = \int_0^{\varepsilon'} \frac{\nu_e}{\nu_e + \delta\nu_a}\, d\varepsilon. \qquad (22)$$

If $\nu_e\tau \gg 1$, $\nu_e \gg \delta\nu_a$ we have

$$\varepsilon_{\text{eff}} \simeq \varepsilon'. \qquad (23)$$

For $(\nu_e + \delta\nu_a)\tau \ll 1$ the exponential in Eq. (21) has a sharp peak for $\varepsilon = \varepsilon'$, which enabled us to carry out the integration in general form. In this case we obtain

$$\varepsilon_{\text{eff}} \simeq \nu_e\tau\varepsilon'. \qquad (24)$$

The physical meaning of Eqs. (22)-(24) is obvious.

If we substitute in Eq. (20) the expression for $R(\varepsilon)$ in the form of the sum $R = R_1 + R_2 + R_3$, where R_1, R_2, and R_3 are defined by Eqs. (11), (12) and (13), then E_{eff} splits into three terms $E_{\text{eff}}(1)$, $E_{\text{eff}}(2)$, and $E_{\text{eff}}(3)$. We will confine ourselves to writing expressions for these quantities for the case in which

$$\frac{k^2}{1+\gamma} = \frac{1}{(\nu_e + \delta\nu_a)\tau}\bigg|_{\varepsilon=\varepsilon_1} \gg 1,$$

since it is this situation which occurs under the experimental conditions. Taking Eqs. (24), (11), and (12) into account we obtain

$$E_{\text{eff}}(1) = \frac{\varepsilon_1\beta_1 n n_m}{k^2}, \qquad (25)$$

$$E_{\text{eff}}(2) = \frac{\varepsilon_2\beta_2 n_m^2}{k^2 x_2^{5/4}}. \qquad (26)$$

In the expression

$$E_{\text{eff}}(3) = \int_0^{\varepsilon_3} R_3(\varepsilon')\, g(\varepsilon')\, \varepsilon_{\text{eff}}(\varepsilon')\, d\varepsilon' \qquad (27)$$

one must not substitute ε_{eff} from Eq. (24) since the conditions under which Eq. (24) can be used may not apply when ε' is only several times less than ε_3, because $\nu_e\tau \sim 1/\varepsilon'^{5/2}$. For an approximate estimate of $E_{\text{eff}}(3)$ we divide the region of integration into two regions $0 < \varepsilon' \le \varepsilon_0$ and $\varepsilon_0 < \varepsilon' < \varepsilon_3$, where ε_0 is defined by the condition $\nu_e(\varepsilon_0)\tau(\varepsilon_0) = 1$. When $\varepsilon' < \varepsilon_0$ we put $\varepsilon_{\text{eff}} \simeq \varepsilon'$, and the contribution to the integral from the region $\varepsilon' > \varepsilon_0$, where ε_{eff} falls sharply, can be neglected. We then obtain from Eq. (27)

$$E_{\text{eff}}(3) = \beta_3 n_m^2 \frac{32}{\pi}\varepsilon_3 \int_0^{\sqrt{\frac{\varepsilon_0}{\varepsilon_3}}} t^4(1-t^2)^{3/2}\, dt \equiv \beta_3 n_m^2 \Delta\varepsilon_3. \qquad (28)$$

An expression for the integral in Eq. (28) is derived, for example, in ref. 8. The quantity $\Delta\varepsilon_3$ has the meaning of the mean energy introduced by an electron produced by process (3) into the system of slow electrons.

In expression (16) it is also necessary to take account of the contribution of the collisional–radiative recombination process. The fast electron produced in the collisional–radiative recombination process[9] has a mean energy $\varepsilon = 0.35$ eV. For these energies $\nu_e \gg \delta\nu_a$, $\nu_e\tau \gg 1$, and, consequently, we can assume that the energy ε_4 is completely transferred to the slow electrons. Then we have

$$E_{\text{eff}}(4) = \varepsilon_4\beta_4(n)\, n^2, \qquad (29)$$

where $\beta_4(n)$ is the recombination rate constant. Substituting Eqs. (17), (25), (26), (28), and (29) in Eq. (16) we obtain an expression which gives the value of the electron temperature:

$$\delta\nu_{\text{eff}}(T_e)\frac{3}{2}k(T_e - T_a) = \frac{\Delta\varepsilon_3\beta_3 n_m^2}{n} + \frac{\varepsilon_2\beta_2 n_m^2}{k^2 x_2^{5/4} n} + \frac{\varepsilon_1\beta_1 n_m}{k^2} + \varepsilon_4\beta_4 n. \qquad (30)$$

Heating of the slow electrons in the afterglow has been discussed previously.[2,10,11] Expression (13) differs from the corresponding expressions in refs. 10 and 11 in that it takes account of the fact that not all the energy of the fast electrons which originate in the plasma is transferred to the slow electrons. For example, for processes (1) and (2) the fraction of the energy transferred to the slow electrons under our experimental conditions is small. As regards ref. 2, our expression (13) for $E_{\text{eff}}(2)$ is close to the expression obtained in ref. 2, but the expressions for $E_{\text{eff}}(1)$ and $E_{\text{eff}}(3)$ differ considerably. It should be noted that process (3) makes a considerable contribution to the heating.

3. We now discuss the results. As can be seen from Eq. (15), the nature of the distribution function in the region of fast electrons depends on the rate constants β_1, β_2, β_3 of the reactions (1), (2), and (3). The values of these constants cannot be regarded as well established. For example, for the constant β_1 the data given in the literature differ by an order of magnitude.[12-14] There is as yet no single opinion as regards which of the reactions in which two metastable atoms participate – (2) or (3) – takes preference in the plasma of the afterglow, and in the experiments which we made we measured the overall coefficient $\beta_2 + \beta_3$ of these reactions.

It is possible, by comparing results of the calculations of the distribution function with the experimental curves, to obtain values of these constants. Thus, the number of electrons in the energy range 16-20 eV is determined by reaction (1). Substituting in expression (15) the experimentally obtained values of the overall electron density and the density of the metastable atoms, and integrating it over this energy range, we obtain a quantity which depends only on the coefficient β_1. Comparing this number of fast electrons with the experimental value, we find the value of β_1. The value of β_1 found in this way varies from $1.9 \cdot 10^{-9}$ to $0.6 \cdot 10^{-9}$ cm$^3 \cdot$ sec^{-1}, depending on the conditions.

Taking into account the change in electron temperature we obtain a value $\sigma_1 = 0.6 \cdot 10^{-16}$ cm^2 for the cross section for collisions of the second kind, which is constant to within 20%. This result is in good agreement with the results obtained in ref. 13.

To determine the constant β_2 we can use the following considerations. As can be seen from Eq. (10) for small values of the parameter $(\nu_e + \delta\nu_a)\tau$ the distribution func-

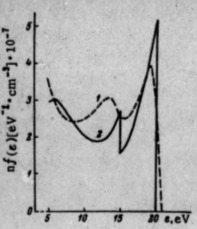

Fig. 4. Comparison between the experimental distribution function (1) and the theoretical distribution function (2). i = 1.8 A, p = 2 torr, t = 50 μsec.

tion is proportional to the source density R(ε). Hence, when the parameter $(\nu_e + \delta\nu_a)\tau/_{\varepsilon=\varepsilon_2} \simeq 0.01$, we can assume that the number of electrons in the energy range 10–16 eV is due to the process (2), since the source density of the process (3) is small for these energies. By choosing the appropriate experimental conditions we find $\beta_2 \simeq 10^{-9}\ \mathrm{cm}^3 \cdot \mathrm{sec}^{-1}$.

By proceeding in the same way we can find the value of the constant β_3. Its value is found to be $2 \cdot 10^{-9}\ \mathrm{cm}^3 \cdot \mathrm{sec}^{-1}$. The overall value $\beta_2 + \beta_3 \simeq 3 \cdot 10^{-9}\ \mathrm{cm}^3 \cdot \mathrm{sec}^{-1}$ is in fairly good agreement with the value of $2 \cdot 10^{-9}\ \mathrm{cm}^3 \cdot \mathrm{sec}^{-1}$ given in the literature.[15]

Figure 4 shows the distribution functions calculated theoretically and measured experimentally. In the calculations we use values of the electron density and the density of metastable atoms used in the first part of this paper,[1] and also the values of the rate constants of reactions (1), (2), and (3) which we obtain. As can be seen, the theoretical and experimental curves agree satisfactorily. The slight differences may be due to the comparatively large amplitude of the differentiating signal when measuring the distribution function. The part played by this effect in distorting the shape of the experimental curve can be seen from Fig. 2. Curves 1–4 are obtained with an amplitude of the differentiating signal A = 0.7 V, while curves 5–6 are obtained with an amplitude A = 1 V. The broadening of the curves as A is increased is very noticeable. In Fig. 1 all the curves are obtained with A = 0.7 V. An exception is curve 6 of Fig. 1b, for which A = 1 V. We carry out control measurements with different amplitudes of differentiating signals A = 0.5–1.1 V. As the amplitude is increased the shape of the curve changes somewhat, but the electron density determined in the energy range 5 eV from the different curves differs by no more than 10%. Hence, to obtain β_1, β_2, β_3 we use integration of the distribution function in this energy range.

TABLE 1. Comparison of the Values of the Electron Temperature (°K) Calculated from Eq. (30), with the Measured Values

p, torr	i = 1.8 A				i = 0.46 A			
	t = 50 μsec		t = 450 μsec		t = 50 μsec		t = 450 μsec	
	theory	experiment	theory	experiment	theory	experiment	theory	experiment
1	900	1100	740	570	1810	2150	530	530
2	880	1000	770	750	1750	1750	740	850

We now analyze the results obtained from the measurements of electron temperature. Table 1 compares values of T_e, °K, calculated from Eq. (30), with the measured values. Taking into account the possible experimental error, which is about 15%, and the approximate nature of the calculations, the agreement is quite satisfactory. The calculation shows that for large values of the parameter k^2 it is process (3) of processes (1)–(4) which makes the main contribution to the heating of the electrons. The comparatively high values of the electron temperature in the initial stages of the afterglow for i = 0.45 A is due to the presence of a residual electric field $E/p \simeq 0.07\ \mathrm{V/cm \cdot torr}$.

The following main conclusions can be drawn.

1. The number of fast electrons in the afterglow is relatively large (about 10^8–$10^9\ \mathrm{cm}^{-3}$), and many orders of magnitude greater than for a Maxwell distribution with temperature $T_e \simeq 300$–2000°K. It is necessary to bear this fact in mind when estimating the excitation processes in the afterglow.

2. Absolute measurements of the distribution function of the fast electrons are a convenient method of determining the constants of elementary processes. In particular, this method enables the constants of processes (2) and (3) to be found separately.

It should be emphasized that when determining the constants β_2 and β_3 separately, we used the data from ref. 2 on the spectrum of electrons formed in these reactions. The form of this spectrum has not yet been finally established. If it changes, the values of the constants β_2 and β_3 may also change. On the other hand, the value of $\beta_2 + \beta_3$ which we have found depends only slightly on the shape of this spectrum.

---

[1] A. B. Blagoev, Yu. M. Kagan, N. B. Kolokolov, and R. I. Lyagushchenko, Zh. Tekh. Fiz., 44, 333 (1974) [Sov. Phys. – Tech. Phys., 19, 211 (1974)].
[2] J. C. Ingraham and S. C. Brown, Phys. Rev., 138A, 1015 (1965).
[3] A. N. Soldatov and N. A. Prilezhaeva, Izv. Vuz. Fizika, No. 11, 51 (1971).
[4] V. L. Ginzburg and A. V. Gurevich, Usp. Fiz. Nauk, 70, 201 (1960) [Sov. Phys. – Usp., 3, 115 (1960)].
[5] R. I. Lyagushchenko, Zh. Eksp. Teor. Fiz., 63, 1706 (1972) [Sov. Phys. – JETP, 36, 901 (1973)].
[6] H. Massey and E. Burhop, Electronic and Ionic Impact Phenomena, Oxford Univ. Press (1952).
[7] G. N. Gerasimov, R. I. Lyagushchenko, and G. P. Startsev, Opt. Spektrosk., 30, 606 (1971).
[8] I. I. Ryzhik and I. S. Gradshtein, Tables of Integrals, Series, Sums, and Products [in Russian], Gostekhizdat, Moscow – Leningrad (1951).
[9] A. V. Gurevich and L. P. Pitaevskii, Zh. Eksp. Teor. Fiz., 46, 281 (1964) [Sov. Phys. – JETP, 19, 870 (1964)]; M. A. Guzinov, I. B. Zherardo, and L. G. Verden, Phys. Rev., 149, 91 (1966).
[10] J. Polman and P. C. Drop, J. Appl. Phys., 43, 1577 (1972).
[11] I. Ya. Fugol, Doctorate Dissertation, FTINT, Khar'kov (1971).
[12] R. Mosburg, Phys. Rev., 152, 166 (1966).
[13] E. E. Ferguson and M. Schluter, Planet. Space Sci., 9, 701 (1966).
[14] I. Ya. Fugol, D. N. Grigorashchenko, and D. A. Myshkis, Zh. Eksp. Teor. Fiz., 60, 659 (1971) [Sov. Phys. – JETP, 33, 358 (1971)].
[15] A. V. Phelps and J. Molmar, Phys. Rev., 89, 1202 (1953).

Radiation energy of a magnetoplasma compressor

V. I. Berkov and A. I. Morozov

(Submitted April 17, 1973)
Zh. Tekh. Fiz., 44, 348-353 (February 1974)

The spectral and spatial energy densities of a magnetoplasma compressor are studied. Most of the radiated energy is in the vacuum-UV region. The radiation energy is a strong function of the voltage to which the bank is charged and the gas pressure.

One of the most important considerations in plasma experiments is the energy balance. The energy balance established for an actual system can be used to evaluate the operating efficiency of the system and to monitor the accuracy of measurements. In a magnetoplasma compressor,[1-3] the energy stored in the capacitor bank is converted into the kinetic energy of the particles, radiated energy, energy evolved at the electrodes, and energy liberated as a result of Joule heating in the supply cables.

We report here on a bolometer study of the radiated energy in the discharge volume of a magnetoplasma compressor.

THE MK-10 MAGNETOPLASMA COMPRESSOR

The experiments are carried out on the apparatus whose electrode unit is shown in Fig. 1. This unit consists of a conical cathode, 12 anode rods, an insulator, and eight thermal valves. The electrodes are made of copper, and the insulator is alundum. Gas is injected from the eight thermal valves for 250 μsec. The anode rods are arranged in a circle 220 mm in diameter. The cathode is 120 mm in diameter. The schematic circuit of the compressor consists of the capacitor bank for the discharge, the valve bank, the dc power supplies which charge the band, the system which produces the ignition pulse, and the blocking system. The apparatus is fed from a capacitor bank with C = 2400 μF and U = 5 kV. The discharge current and voltage are functions of the pressure and nature of the working gas (hydrogen or air). At low pressures (P ≤ 0.3 torr) the discharge is aperiodic. For hydrogen the current is aperiodic even at moderate pressures (P ~ 1 torr). The maximum discharge current for operation in air is 350 kA, and that in hydrogen is 250 kA. The half-period of the discharge is 65 μsec. The total circuit inductance is 200 cm. The experiments are carried our under various operating conditions of the MK-10 (during injection of the working gas from the valves and with a preliminary filling of the vacuum chamber, and at various bank voltages). Various filters (gaseous, quartz, and glass) are used to study the spectral distribution of the energy.

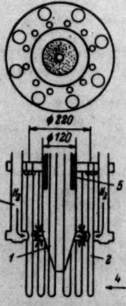

Fig. 1. Electrode unit of the MK-10. 1) Cathode; 2) anode rods; 3) eight thermal valves; 4) direction in which the spectrum is recorded; 5) insulator.

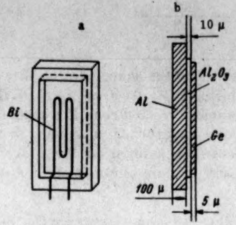

Fig. 2. The bolometer detectors.

BOLOMETER DESIGN AND MEASUREMENT CIRCUIT

The bismuth bolometer is made of aluminum foil d = 35 μ thick with an oxide layer d_2 = 5 μ thick. The thermistor on the surface of the oxide film of the bismuth bolometer consists of an alloy of 99.4% Bi and 0.6% Pb. As a control, some of the measurements are made with a germanium bolometer with a uniformly deposited germanium film. Figure 2 shows the construction of the bolometer detectors. The schematic circuits for the measurements with the bolometers are shown in Figs. 3 and 4; these circuits are dc voltage dividers. Here R_A is an auxiliary resistance used to detect the voltage across the bolometer. The circuit parameters must satisfy the relation $\Delta R_b/(R_b + R_A) \ll 1$. When there is a constant current through the bolometer, the energy fed to the plate is related to quantities which can be measured directly by

$$W = mc\frac{\Delta V_b}{a V_b}\frac{1}{\kappa}, \tag{1}$$

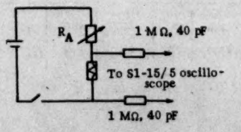

Fig. 3. Power circuit for the bismuth bolometer.

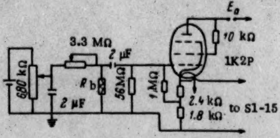

Fig. 4. Circuit of the power supply and cathode follower for the germanium bolometer.

where W is the energy, m is the mass of the aluminum substrate, c is the heat capacity of Al, α is the temperature coefficient, ΔV_b is the detected change in the bolometer voltage, V_b is the bias voltage, and $\varkappa$ is the absorptance. To detect small changes ΔV_b corresponding to emission in the visible part of the spectrum, we use an S1-15/5 oscilloscope with a differential input. The noise level is considerably reduced when a voltage is applied to the bolometer. The bolometer and oscilloscope are at a floating potential; experience has shown that this arrangement reduces the interference in comparison with the arrangement in which the bolometer and oscilloscope are connected to the discharge chamber (to ground, or to a terminal of the discharge circuit).

Figure 5 shows a typical bolometer signal.

ABSORPTANCE OF THE BOLOMETER AND ITS CALIBRATION

As shown below, the radiative loss in a magnetoplasma compressor is due primarily to radiation in the vacuum-UV part of the spectrum. The absorptance for this radiation for various materials, including aluminum, is high.[4,5] Accordingly, the absorptance is essentially the same for blackened and unblackened bolometers. However, the question of the absorptance of an unblackened bolometer becomes important for energy measurements in the visible or near-UV region. All the measurements reported here are carried out with a blackened bolometer. The bismuth bolometer is blackened by sputtering a thin platinum wire in vacuum. The operation of the blackened bolometer is checked by comparing known signals, produced during the detection of the radiative energy from a flash bulb before and after blackening.

Since the detecting surface of the high-resistance germanium bolometer is thick (100 μ), it turns out to be sufficient to blacken the bolometer with ordinary lampblack. The blackening increases the bolometer signal corresponding to the flashbulb by a factor of 6.8, indicating an absorptance of 15% for the unblackened bolometer. The blackening does not affect the bolometer characteristics, since the blackening process itself is monitored by measuring the energy radiated by the flashbulb.

The absolute calibration of the bolometer is carried out on an IKT-1M apparatus, designed for measuring pulsed light energy. As a result of all the measurements, we find a sensitivity of 6.1 V/J · cm² for a germanium bolometer 1 cm in diameter. The error in the calibration of the bolometer is less than 15%; it consists of the error in the operation of the IKT-1M (10%) and the errors in reading the signals. Repeated measurement of the radiative energy of the compressor under the same conditions reveals a scatter in the values of this energy from discharge to discharge; in certain cases this scatter reaches 40%, but it is generally within 20%. These measurements therefore have errors less than 35%.

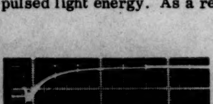

Fig. 5. Typical bolometer signal.

INSERTION OF THE BOLOMETER INTO THE VACUUM CHAMBER

Figure 6 gives a general idea of the layout of the measurement circuit. The vertical grooves in the flange of the MK-10 make photography possible at five points along the radius above the compressor axis and at five points below the axis. The collimating tube, with a special adapter for the vacuum gasket, is moved along the radius in 1 cm steps. In a qualitative experimental test to ensure that there is no significant absorption of radiation from the focal region by the residual gas in the vacuum chamber, we carry out special measurements along the longitudinal axis of the compressor, through a diverter in the cathode while injecting hydrogen from eight thermal valves. During the injection of the working gas (hydrogen) from the valves, the residual pressure in the chamber is 10^{-5} torr. At this pressure the radiation is not absorbed over 60 cm, especially since most of the energy is carried by ionized impurity atoms. A preliminary filling of the discharge region with hydrogen from the distributing ring of valves also has no effect on the absorption.

Although there is a time of 250 μsec between ignition pulses in the discharge circuit of the valve bank and the discharge circuit of the main bank, so gas can fill the interelectrode region, the gas cannot reach the cathode cavity through which the observation is carried out, since the distributing ring is behind the diverter (the aperture in the cathode) and there are no reflecting surfaces in front on it. However, during the discharge some of the ions are deflected from the cathode region to the diverter because of the high pressure at the focus of the discharge. Since the cathode aperture and the bolometer are quite far apart (60 cm), most of these ions recombine at the cathode and

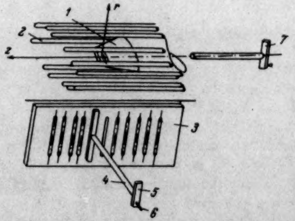

Fig. 6. Experimental arrangement. 1) Cathode; 2) anode rods; 3) flange; 4) collimator; 5) vacuum-sealed bolometer holder; 6) leadout plug (to oscilloscope); 7) bolometer position for observation along the longitudinal axis.

return to the cavity as neutrals. In this case the absorption is not resonant and is even weaker. It is primarily heavy impurity ions which are drawn from the cathode film into the diverter.

Since the plasma jet in the MK-10 has a strongly expressed directed velocity, the detection direction is chosen either along the flow direction or perpendicular to it to prevent charged and neutral particles from reaching the bolometer. In addition, we use a magnetic filter with a field of H = 80 Oe to prevent the return of the ions.

The level of radiated energy corresponding to the admission of H_2 is compared with that corresponding to a preliminary H_2 pressure in the vacuum chamber of 0.2 torr. The oscillograms of the current and voltage under these circumstances are most similar. This comparison shows that the bolometer detects 22% more energy in the case of hydrogen admission than in the case of a preliminary filling. This result is indirect evidence that the residual H_2 in the path to the bolometer absorbs some of the radiation. We do not observe an effect of the magnetic filter beyong the scatter in values for the individual discharges. In view of the detection directions selected, the existence of the gas filter, and the removal of the bolometer to a remote point we can conclude that the bolometer detects the energy of the electromagnetic radiation.

MEASUREMENTS OF THE ENERGY OF THE ELECTROMAGNETIC RADIATION

Both the MK-10 itself and the discharge occurring in it are cylindrically symmetric, so when a suitable arrangement is used for inserting the bolometer into the vacuum chamber, measurements can be carried out at various cross sections and at various radial positions. Then, after an Abel inversion, we find results showing how much electromagnetic energy $W_1(r, z)$ is evolved at a given radius from 1 cm^3 in various cross sections. In the Abel inversion it is assumed that no radiation is absorbed in the plasma. For the central zone of the discharge for operation with either air or hydrogen, this condition is not satisfied completely, so the height of the peak in the resulting $W_1(r, z)$ distributions can be slightly low. However, we expect that this difference is not very pronounced, since a large part of the energy from the central zone is due to doubly charged OIII and NIII ions and triply charged OIV and NIV ions, for which the absorption is slighter than for OII and NII ions because of the small dimensions of the zone (D ≤ 1 cm).

In preliminary measurements through glass and quartz filters it is found that most of the radiated energy is evolved in the vacuum-UV part of the spectrum. For the compression zone we construct functional dependences of the radiated energy W_c on the voltage to which the discharge bank is charged, under the assumption of a point source. The radiation is detected from a zone D = 3 cm in diameter through a tube 2 cm in diameter at the position r = 0, z = 3 (Fig. 6). These functional dependences are shown in Fig. 7 for working-gas (air) pressures of $P_1 = 0.2$, $P_2 = 1$, and $P_3 = 3$ torr and for a hydrogen pressure of P = 0.2 torr. The rapid increase in W_c with increasing bank voltage is interesting. In a discharge with P = 1 torr (air), a 1-kV increase in the bank voltage increases the radiated energy by a factor of 2.4. This result shows that the function $W_c(U)$ increases more rapidly than the third power of the voltage but more slowly than the fourth power. An analogous increase in the energy of the short-wave radiation is detected through foils in measurements with a photomultiplier. The radiated energy from the compression zone can be described as a cubic function of the bank voltage for working-gas (air) pressures of P = 0.2 and 3 torr:

$$W_c = 10U^3,$$

where W_c is in joules and U is in kilovolts.

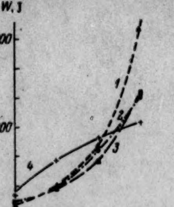

Fig. 7. Energy radiated from the compression zone as a function of the bank voltage. P_{air}, torr: 1) 0.2; 2) 1; 3) 3. p_{H_2} = 0.2 torr.

Figure 8 shows the total radiated energy of the pressure as a function of the voltage for working-gas (air) pressures of $P_1 = 0.2$ (curve 1), $P_2 = 1$ (2), and $P_3 = 5$ torr (3). The total radiated energy is detected by a bolometer mounted on an observation window of the compressor in such a manner that radiation from the entire discharge volume can strike it. The total radiated energy increases rapidly with increasing bank voltage and with decreasing hydrogen pressure; the same is true of the radiated energy of an air plasma. For working gases of air and hydrogen at P = 0.1 torr, the function $W_0(u)$ can be described by

$$W_0^{air} \approx 240U^3,$$

$$W_0^{hyd} \approx 390U^3.$$

At P = 1 torr for both gases the total radiated energy is a cubic function of the bank voltage:

$$W_0 \simeq 34U^3.$$

The radiated energy for a hydrogen plasma is higher than that in the case of an air plasma at low pressures because of the impurities in the hydrogen plasma and its higher temperature.

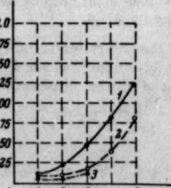

Fig. 8. Total energy radiated by the compressor as a function of the bank voltage. P_{air}, torr: 1) 0.2; 2) 1; 3) 5.

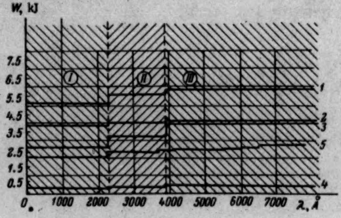

Fig. 9. Total radiated energy in various spectral ranges: I) W_{vac}; II) $W_{vac} + W_{nr-UV}$; III) $W_{vac} + W_{nr-UV} + W_{vis}$. For III, the values of U(kV) and P (torr), respectively, are: 1) 5, 0.1; 2) 5, 1; 3) 4, 0.1; 4) 1, 0.1; 5) 3, 0.1.

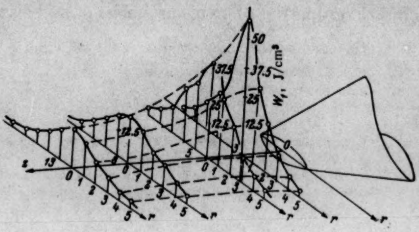

Fig. 10. Distribution of the radiated-energy density for the case of pulsed injection of hydrogen.

We also carry out bolometer measurements of the radiated energy integrated over the volume of the MK-10 in the visible and near-UV parts of the spectrum. The visible region is singled out by a glass filter, while the visible and near-UV are singled out by a quartz filter. The filters are placed in front of the bolometer, at its vacuum connection to the discharge chamber. Detection of the spectral lines on a DFS-13 apparatus shows that the quartz filter which we use transmits radiation up to 2300 Å. The radiative energies of the air plasma for three spectral regions ($\lambda \approx$ 0-2300, 2300-3800, and 3800-7000 Å) and for various operating conditions of the compressor are shown by the stepped lines in Fig. 9. The ratio W_{vis}/W_0 varied from 2% to 27% over the various operating conditions of the compressor in both air and hydrogen. Lower values of this ratio are found for lower working pressures in the range studied (0.1-5 torr).

We turn now to the spatial distribution of the density of the total radiated energy W_1 (joules per cubic centimeter) along the longitudinal axis and along the radius for the case of pulsed injection of hydrogen (U = 5 kV). In this case the discharge has the best spectral purity. The hydrogen pressure in the interelectrode gap before the beginning of the discharge, with an injection time of $\tau = 250$ μsec, is $\leqslant 1$ torr. The residual pressure in the chamber is $5 \cdot 10^{-5}$ torr. Under these conditions, according to spectral studies with a DFS-6 spectrograph (the vacuum region), the emission lines of ions from the compression zone (MK-10) correspond to the ions CIV, CIII, OIII, SiIV, SiIII, etc. All these elements are impurities, and the plasma is optically thin for the emission lines of these ions. Figure 10 shows the $W_1(r, z)$ distribution obtained by an Abel inversion of the experimental data. The density of the radiated energy at the maximum is $W_1(r = 0, z = 3) = 58$ J/cm³. The half-width of the $W_1(r)$ distribution for z = 3 cm is 2.5 cm. Summation of the energy over the discharge zone ($0 \leq z \leq 13$ cm) yields 8200 J, or about 50% of the energy supplied to the discharge. Local measurements of the radiated energy are also carried out for other conditions. We find that the height of the peaks in the $W_1(r)$ distributions decreases while the half-widths increase with increasing working-gas pressure.

All our measurements of the energy of the electromagnetic radiation, both in the vacuum region and in the visible and near-UV regions, show that W is a strong function of the voltage on the discharge bank and of the working-gas pressure. The total energy radiated by the plasma in the MK-10 compressor (for a bank energy of 30 kJ) is 30%-50% of the energy supplied to the discharge, $\int iudt$, depending on the discharge conditions.

In conclusion the authors thank P. E. Kovrov, Yu. S. Maksimov, L. G. Tokarev, and D. A. Shcheglov for assistance in this work.

---

[1] A. I. Morozov, Zh. Tekh. Fiz., 37, 2147 (1967) [Sov. Phys. – Tech. Phys., 12, 1580 (1968)].

[2] Marshall and I. Henius, Plasma Physics and Controlled Nuclear Fusion Research, Vol. 2, Culham (1965), p. 449.

[3] J. K. Boyce, Usp. Fiz. Nauk, 30, 245 (1946).

[4] V. D. Kirillov, Zh. Tekh. Fiz., 30, 320 (1960) [Sov. Phys. – Tech. Phys., 5, 295 (1960)].

Physical properties of an electrodeless pulsed discharge in a gas-filled glass cell

Yu. I. Chutov, N. S. Baranchuk, M. R. Lozovich, and V. G. Danilov

T. G. Shevchenko Kiev State University

(Submitted January 11, 1973)
Zh. Tekh. Fiz., 44, 355-363 (February 1974)

An experimental study has been made of an electrodeless discharge excited by a sinusoidal 50-kHz voltage in a plane glass cell filled with argon, neon, xenon, or a mixture of these gases at a pressures 1-50 torr. The potentials at which this discharge is ignited and quenched have been measured. The charge transferred to the external circuit over a half-period of the supply voltage has been measured. The results are used in an analysis of the bistable nature of this discharge which is of interest in connection with the development of ac plasma display devices. The description of the bistable nature of the discharge on the basis of the deposited charge is not complete; in particular, this description does not explain the change in the discharge diameter which is observed experimentally in the bistable region.

INTRODUCTION

An intense effort is currently being devoted to the development of ac plasma display devices[1-7] whose parameters are governed by the physical properties of an electrodeless pulsating discharge. According to ref. 8 a discharge of this type is an ac discharge, whose basic parameters change considerably over a half-period of the supply voltage. In the limiting case, the pulsed discharge can be thought of as a periodic train of short pulsed discharges.

A property of pulsed electrodeless discharges which is important for use in plasma display devices is the bistable nature of the operation. By definition, a pulsed discharge is bistable over a certain range of the applied alternating voltage (the bistable range) if it is capable of maintaining one of two different initial states for an infinitely long time in this range; in one state there is a discharge, while in the other there is not.

Several workers[1-7] believe that the bistable nature of this discharge results from an additional electric field which is produced in the gas by charges deposited on the dielectric walls during the breakdown. This opinion is based on the results of a study of a low-frequency electrodeless discharge.[9-11]

However, the results of refs. 9-11 may not be applicable to plasma display devices because of the qualitative difference between low-frequency discharges and the discharge in a display device, which occurs at a frequency of ~ 150 kHz. The difference results from the fact that the characteristic time for the deposition of charge on the dielectric walls is equal roughly to the transit time of the ions through the gas-filled gap (~ 10^{-4} sec), which is much longer than the time interval between two successive discharges in plasma display devices. In low-frequency discharges, we find the opposite situation. Since this time interval is short, the plasma produced during a brief pulsed discharge in a plasma display device may not have vanished completely by the beginning of the succeeding pulsed discharge. Accordingly, ionized, excited, and metastable atoms can exist in the gas-filled volume of the display device before the succeeding breakdown; these atoms would facilitate this succeeding breakdown and thereby influence the bistable nature of the discharge.

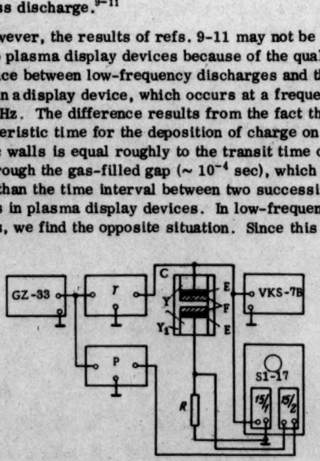

Fig. 1. Block diagram of the experimental apparatus.

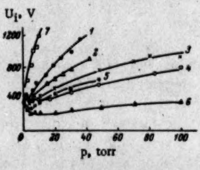

Fig. 2. Potential at which the discharge is ignited in a cell without the additional glass pieces, U_i, as a function of the gas pressure p. 1) Xe; 2) 50% Ne + 50% Xe; 3) 85% Ne + 15% Xe; 4) 95% Ne + 5% Xe; 5) Ar; 6) Ne; 7) air.

Accordingly, several mechanisms leading to a bistable nature can operate in plasma display devices. To determine the relative importance of these mechanisms it is necessary to study the physical properties of pulsating electrodeless discharges at high frequencies. The basic purpose of the work described below is to determine the role of deposited electric charge in the mechanism responsible for the bistable nature of such a discharge.

EXPERIMENTAL PROCEDURE

The experiments are carried out on the apparatus shown in Fig. 1. The electrodeless pulsed discharge is excited in cell C, which consists of two glass cylinders Y with flat ends F (50 mm in diameter), sealed in a third cylinder Y_1 in such a way that the flat ends F are parallel. Each of the flat glass pieces F is 5 mm thick, and they are 5 mm apart. Circular metal electrodes E, with diameter slightly less than 50 mm, are pressed tightly against the outside of glass pieces F. In several of the experiments additional glass pieces 5 mm thick with diameter equal to that of electrode E are inserted between electrodes E and pieces F. The cell is processed by standard vacuum techniques; after it is evacuated to ~ 10^{-5} torr it is filled with the appropriate gas. In these experiments we use argon, neon, "pure" xenon, and mixtures of these gases. The gas pressure in the cell is varied over the range 1-50 torr, so that the parameters of the experimental cell are equivalent to those of the cell of a plasma display device as follows from the appropriate similarity law.

The experiments are carried out with a sinusoidal voltage at a frequency of 50 kHz. The regulated voltage source is a standard GZ-33 generator; the output voltage is fed through step-up resonance autotransformer T (with an output resistance of ~ 100 kΩ) and through a small resistance of R ~ 300 Ω to electrodes E. The voltage beyond the autotransformer is measured by a VKS-7B voltmeter and the shape is monitored on an S1-17 oscilloscope.

The ignition potential U_i and the quenching potential U_q are measured for the electrodeless pulsed discharge in the cell; the current pulses produced in the external circuit of cell C during the breakdown are also measured. The ignition and quenching of the discharge are determined visually on the basis of the associated glow and are also determined from the appearance and vanishing of the current pulses. In several of the experiments we measure the ignition potentials between nickel electrodes directly in the gas; these electrodes are 5 mm apart. Significantly, no appreciable shape distortion of the supply voltage is observed during breakdown in any of the cases studied. The current pulses flowing in the external circuit of the cell are inferred from the voltage pulses across a resistance of R = 300 Ω. These voltage pulses are fed to one input of an S1-15/2 differential amplifier in the S1-17 oscilloscope. A sinusoidal voltage is fed through phase shifter P to the other input of this amplifier and used to balance the sinusoidal voltage produced across resistance R by the capacitive current.

EXPERIMENTAL RESULTS

Figure 2 shows the ignition potential of the electrodeless discharge, U_i, as a function of the gas pressure p for various conditions. These functional relations are obtained in cell C without the additional glass pieces, under conditions such that the discharge glow covers nearly the entire inner surface of flat glass pieces F during breakdown (Fig. 1). The functional relations between the quenching potential U_q and p are similar.

We see from Fig. 2 that the functional dependence of U_i on p display minima characteristic of Paschen curves.

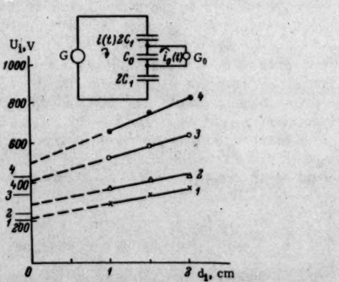

Fig. 3. Ignition potential of a discharge in argon, U_i, as a function of the thickness of the glass plates d_1 for various pressures. p, torr: 1) 5; 2) 10; 3) 30; 4) 50. The equivalent circuit of the discharge cell is shown at the top.

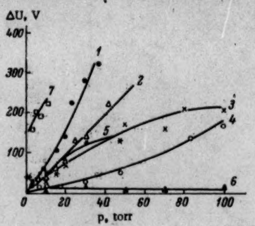

Fig. 4. Bistable range of the discharge ΔU, as a function of the gas pressure p. The notation is the same as in Fig. 2.

However, it should be noted that the quantities U_i and U_q are functions not only of the nature and pressure of the gas filling the cell, but also of the total thickness d_1 of the glass pieces F, since part of the sinusoidal voltage applied across electrodes E is applied across these glass pieces. That this is true can be seen from Fig. 3, which shows illustrative functional dependences of U_i on d_1 for various argon pressures. Similar functional relations are obtained for the other gases. We see from Fig. 3 that the functional dependence of U_i on d_1 is described by straight lines; extrapolation of these lines to the ordinate axis yields the "true" ignition potentials of the electrodeless discharge, $U_{i.0}$. In similar fashion we can determine the "true" quenching potentials for the discharge.

The markers on the ordinate axis in this figure show the ignition potentials for discharges in argon between nickel electrodes measured under the conditions corresponding to lines 1-4. We see from Fig. 3 that these potentials differ negligibly from the "true" ignition potentials $U_{i.0}$; furthermore, they are essentially equal to the breakdown potentials for argon in a homogeneous, fixed electric field, as reported in, e.g., ref. 12.

From the measured values of U_i and U_q we calculate the bistable range $\Delta U = U_i - U_q$. Figure 4 shows the resulting functional dependence of ΔU on the gas pressure. Comparison of Figs. 4 and 2 shows that there is a correlation between ΔU and U_i: As U_i increases, so does ΔU. We see from Fig. 4 that the maximum value of ΔU is found in Xe (curve 1), while the discharge in Ne has essentially no bistable range (curve 6).

The current pulses in the external circuit of the cell during the breakdown are approximately triangular with a half-width of about 3 μsec, much shorter than the half-period of the supply voltage, i.e., this discharge is a pulsating discharge. We should add that when the cell is filled with neon current pulses cannot be detected.

Numerical integration of the current pulses reveals the charge transferred in the external circuit of the cell during a single breakdown, ΔQ. We find ΔQ as a function of various parameters. Figure 4 shows ΔQ as a function of the sinusoidal voltage U applied to electrodes E, for argon with three thicknesses d_1 of the flat glass pieces F. The arrows on the abscissa in Fig. 5a show the quenching potentials for this discharge; the corresponding breakdown potentials for the discharge are shown by arrows near the lines. The "true" ignition potentials and quenching potentials for the discharge ($U_{i.0}$ and $U_{q.0}$), determined from the functional dependence of U_i and U_q on d_1, are 400

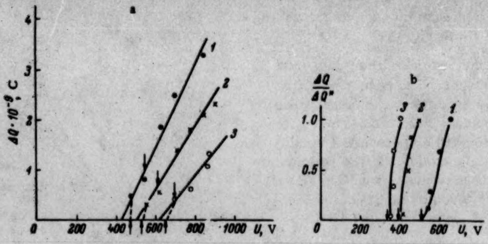

Fig. 5. a: Charge transferred in the external circuit during a single pulse, ΔQ, as a function of the amplitude of the applied voltage, U, for various thicknesses of the flat glass pieces d_1. Argon, 30 torr. d_1, cm: 1) 1; 2) 1.5; 3) 2.0. b: Behavior of the quantity ΔQ/ΔQ* in the bistable region of the discharge. Argon. p, torr: 1) 50; 2) 30; 3) 10.

and 300 V, respectively, for the conditions of Fig. 5a.

We see from Fig. 5a that the functional dependence of ΔQ on U is described by a straight line; the slopes of lines 1-3 are 11.4, 7.7, and 4.3 pF, respectively.

The functional dependences of ΔQ on U are measured at various argon pressures over the range 1-50 torr in the cell; the results are essentially the same as those in Fig. 5a over the entire range of the applied sinusoidal voltage, except in the bistable region.

Figure 5b shows examples of the behavior of ΔQ, in relative units, in the bistable region; we see that as U decreases in this region there is a sharp decrease in ΔQ (ΔQ* is the amount of charge transferred in the external circuit at the ignition potential). We also note a simultaneous decrease in the cross-sectional area of the discharge: The discharge contracts toward its center. We also note that near the ignition potentials shown by arrows in Fig. 5b the values of ΔQ are much smaller than ΔQ*.

It is interesting to examine the relation between the length of the bistable range ΔU and the charge ΔQ*; functional dependences of ΔQ* on ΔU are shown in Fig. 6 for the same cell without the additional glass pieces (d_1 = 1 cm). There is no information for neon in this figure because the corresponding values of ΔQ and ΔQ* are extremely small.

Figure 7 shows the functional dependence of ΔQ* on ΔU obtained in an argon-filled cell at various values of d_1. We see from Figs. 6 and 7 that the functional dependences of ΔQ* on ΔU are described by straight lines, whose slopes are functions of d_1 and of the nature of the gas filling the cell. Table 1 shows the slopes of the lines, $d\Delta Q^*/(d\Delta U)$, calculated from the data in Figs. 6 and 7. The changes in ΔU (and thus ΔQ*) along the lines in Figs. 6 and 7 were caused by changing the pressure p of the gas filling the cell (Fig. 4).

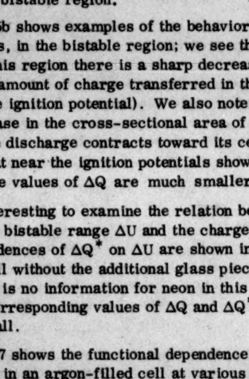

Fig. 6. Charge transferred in the external circuit of the cell during a single pulse at the ignition potential, ΔQ*, as a function of the length of the bistable range ΔU. The notation is the same as in Fig. 2.

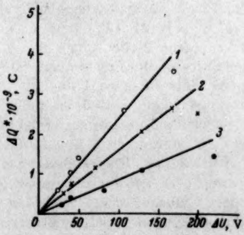

Fig. 7. Functional dependence of ΔQ* on ΔU in an argon filled cell for various glass thicknesses. d_1, cm: 1) 1.0; 2) 1.5; 3) 2.0.

DISCUSSION OF RESULTS

The equivalent circuit of the electrodeless discharge according to refs. 5 and 9 is shown at the top in Fig. 3, where C_0 is the capacitance of the capacitor corresponding to the gas-filled gap of the cell of width d_0; $2C_1$ is the capacitance of the capacitor formed by the inner surface of the glass and electrode E; G is an ideal supply-voltage generator; and G_0 is the generator representing the charging of the inner glass surfaces by the discharge current. Special measurements show that under these experimental conditions $C_0 = 4.25$ pF and $C_1 = 17.2/n$ pF, where n is the total number of glass pieces of thickness d_1 separating electrodes E from the discharge gap. According to the equivalent circuit, we have

$$U_0=\frac{C_1}{C_1+C_0}U=\frac{1}{1+\frac{d_1}{\varepsilon d_0}}U, \qquad (1)$$

where U and U_0 are the alternating voltages applied to electrodes E and to the gas-filled gap, respectively.

A discharge occurs in the cell when U_0 reaches $U_{i.0}$; according to (1), U_i is described as a function of d_1 by

TABLE 1

Gas	$\frac{2C_1^2}{C_1+C_0}$, pF	$\frac{\partial\Delta Q^*}{\partial\Delta U}$, pF	Ratio	Note
Xe	11.5	8.0	1.45	Line *1*, Fig. 7
50% Ne+50% Xe	11.5	10.0	1.15	Line *2*, Fig. 7
85% Ne+15% Xe	11.5	8.7	1.32	Line *3*, Fig. 7
95% Ne+5% Xe	11.5	14.5	0.80	Line *4*, Fig. 7
Ar	11.5	23.0	0.50	Line *5*, Fig. 7
Ar	6.8	16.6	0.40	Line *2*, Fig. 8
Ar	4.5	10.0	0.45	Line *3*, Fig. 8

$$U_i = U_{i,0} + \frac{d_1}{\varepsilon d_0} U_{i,0}. \tag{2}$$

The data in Fig. 3 satisfy Eq. (2). The values of ε calculated from the slopes of lines 1-4 in this figure are 5.8, 6.8, 6.6, and 6.2, respectively, close to the value obtained from a comparison of C_0 and C_1: $\varepsilon \sim 4$. On the basis of this result and the circumstance that there is no distortion of the applied voltage during the breakdown we conclude that the equivalent circuit in Fig. 3 is applicable under the present experimental conditions.

Since the functional dependence of U_i on the gas pressure p is described by Paschen curves, and since the values of $U_{i.0}$ are approximately equal to the breakdown potentials in a homogeneous, fixed electric field, we can assume that the mechanism for the gas breakdown in this discharge is approximately the same as that in a fixed electric field. Accordingly, in choosing gases or mixtures thereof for achieving a desired ignition potential for a pulsating electrodeless discharge we can, in a first approximation, use the results found in a study of breakdown in fixed electric fields.

Using the equivalent circuit in Fig. 3 we can write the following equations for the behavior of the voltage drop across the dielectric layers of the cell (ΔU_1) and across the gas-filled cavity (ΔU_0) during the time τ as currents $i_0(t)$ and $i(t)$ flow:

$$\Delta U_1(\tau) = \frac{1}{C_1}\int_0^\tau i(t)\,dt, \tag{3}$$

$$\Delta U_0(\tau) = \frac{1}{C_0}\int_0^\tau i(t)\,dt - \frac{1}{C_0}\int_0^\tau i_0(t)\,dt. \tag{4}$$

Since generator G is ideal, we can write, for any τ,

(5)

then using (4) we find

$$-\Delta U_0(\tau) = \frac{1}{C_1}\int_0^\tau i(t)\,dt. \tag{6}$$

On the other hand, if the charging of the inner glass surfaces is responsible for the bistable nature of the discharge, we can write, by analogy with refs. 3 and 4,

$$-\Delta U_0\left(\frac{T}{2}\right) = 2(U_0 - U_{q,0}), \tag{7}$$

where U_0 is the maximum (over a half-period) value of the external voltage applied to the inner gas-filled cavity of the cell, $U_{q.0}$ is the "true" quenching potential of the discharge in the inner cavity of the cell, and $\Delta U_0(T/2)$ is the change in the voltage drop in the gas-filled cell over the half-period of the supply voltage, T/2, which results from the charging. For a sinusoidal applied voltage, U_0 would be the peak value.

From Eqs. (1), (6), and (7) we find the charge transferred in the external circuit of the cell during half-period T/2, ΔQ, as a function of the peak value U of the sinusoidal voltage applied to electrodes E:

$$\Delta Q\left(\frac{T}{2}\right) = \int_0^{\frac{T}{2}} i(t)\,dt = \frac{2C_1^2}{C_1+C_0}U - 2C_1U_{q.0}. \tag{8}$$

Graphically, Eq. (8) is a straight line intersecting the U axis at a value U^* related to the "true" quenching potential $U_{q.0}$ by

$$U_{q.0} = \frac{C_1}{C_1+C_0}U^*. \tag{9}$$

The slope of line (8) is governed by the cell parameters, and its intersection with the abscissa, according to (9), is a function of both the cell parameters and the properties of the gas filling the inner cavity of the cell.

Table 2 shows the parameters $[\partial\Delta Q/(\partial U), U^*]$ for the lines in Fig. 5, the values of $U_{q.0}$ calculated from Eq. (9), and the values of the parameter $2C_1^2/(C_1 + C_0)$ for these experimental conditions. We see from this table that the slope of the lines in Fig. 5 is described well by Eq. (8) and that the values of $u_{q.0}$ calculated for various d_1 are essentially equal to the "true" quenching potential determined previously, equal to 300 V in this case. On the basis of this correspondence we can claim that at sufficiently high values of the applied voltage the discharge is cut off in each half-period by the deposited electric charge.

The deviation from the linear function (8) found in the bistable region (Fig. 5) means that the diameter of the discharge in this region (and thus the value of C_1) is not constant. This change in the discharge diameter probably occurs for the same reasons as that in a normal glow discharge.[13]

We turn now to data on the length of the range over which the discharge is bistable, ΔU, shown in Figs. 6 and 7. If the factor governing the bistable nature is the electric field of the deposited charge,[1-7] the discharge will be bistable if the voltage drop across the inner cavity of the cell, U_0, satisfies

$$U_{i,0} - \frac{1}{2}\Delta U_0 \leqslant U_0 \leqslant U_{i,0}, \tag{10}$$

TABLE 2

d_1, cm	$\frac{\partial\Delta Q}{\partial U}$, pF	$\frac{2C_1^2}{C_1+C_0}$, pF	U^*, V	U_{q0}, V
1.0	11.4	11.5	430	290
1.5	7.7	6.8	510	310
2.0	4.3	4.5	630	320

where ΔU_0 is the change in U_0 resulting from the deposition of charge ΔQ_0 over a single half-period at a voltage approximately equal to the quenching potential. From (1), (10), (7), and (8) we find an equation for ΔU:

$$\Delta U = \frac{1}{2}\frac{C_1 + C_0}{C_1}\Delta U_0 = \frac{C_1 + C_0}{2C_1^2}\int_0^{\frac{T}{2}} i(t)\,dt = \frac{C_1 + C_0}{2C_1^2}\Delta Q_0\left(\frac{T}{2}\right). \quad (11)$$

However, we can assume that ΔQ_0 and ΔQ^* are related by $\Delta Q_0 = k\Delta Q^*$, where k is an arbitrary number. Then Eq. (11) becomes

$$\Delta U = \frac{C_1 + C_0}{2C_1^2} k\Delta Q^*\left(\frac{T}{2}\right). \quad (12)$$

It follows from these arguments that confirmation of Eq. (11) or (12) could be taken as evidence that the discharge is bistable because of the electric field of the deposited charge.

Under the present experimental conditions it is more convenient to test Eq. (12), because of the change in the discharge diameter in the bistable region. As mentioned above, the functional dependence of ΔQ^* on ΔU is linear (Figs. 6 and 7). Accordingly, the discharge studied here obeys Eq. (12), and the value of k in this equation is constant for each gas or for each mixture. Further confirmation of Eq. (12) comes from the circumstance that the discharge in a cell filled with pure neon is not bistable and that there is extremely little deposited charge.

The values of k and of all the other parameters required to calculate k are shown in Table 2. We see from this table that $k > 1$ in several cases; when this is so, the charge deposited per unit area of the glass surface near the quenching potential must be larger by a factor of k than the corresponding amount of charge deposited at the ignition potential in order to explain the observed range of bistable behavior. However, according to ref. 5 a stable pulsating discharge cannot exist under this condition if the role of the current pulses is simply one of forming the deposited charge.

Accordingly, the description of the bistable behavior of the discharge on the basis of deposited charge is not complete. In particular, this description does not explain the change in the discharge diameter in the bistable region. Further research is required to determine the complete picture of the phenomena occurring in a pulsating electrodeless discharge at a high frequency.

CONCLUSION

This experimental study of a pulsating electrodeless discharge resulting from the application of a sinusoidal supply voltage at 50 kHz to a glass cell filled with argon, neon, xenon, or a mixture of these gases has revealed the following behavior.

1. The discharge occurs in the cell at levels of the sinusoidal voltage approximately equal to the breakdown potential in a homogeneous, fixed electric field. We can therefore assume that the mechanism for the gas breakdown in this discharge is approximately that for breakdown in a fixed electric field.

2. When the discharge is in the bistable region and the applied voltage is changed, a significant change occurs in the discharge diameter.

3. The description of the properties of the discharge in the bistable region on the basis of the effect of the electric field of the deposited charge is not complete.

In conclusion the authors thank N. D. Morgulis for his interest in this work, and Yu. N. Posypaiko and S. I. Demidenko for assistance in the experiments.

---

[1] H. G. Slottow, IEEE Conf. Rec. Conf. Display Devices, New York (1970), p. 57.

[2] D. L. Bitzer and H. G. Slottow, Proceedings of the Fall Joint Computer Conference, San Francisco (1966), p. 541.

[3] R. L. Johnson, D. L. Bitzer, and H. G. Slottow, IEEE Trans. Electron. Devices, ED-18, No. 9, 642 (1971).

[4] H. G. Slottow and W. D. Petty, IEEE Trans. Electron. Devices, ED-18, No. 9, 650 (1971).

[5] W. D. Petty and H. G. Slottow, IEEE Trans. Electron. Devices, ED-18, No. 9, 654 (1971).

[6] H. J. Hoehn and R. A. Martel, IEEE Trans. Electron. Devices, ED-18, No. 9, 654 (1971).

[7] L. F. Weber, IEEE Trans. Electron. Devices, ED-18, No. 9, 664 (1971).

[8] N. A. Kaptsov and N. A. Popov, Zh. Eksp. Teor. Fiz., 27, 97 (1954); 30, 68 (1956) [Sov. Phys. – JETP, 3, 147 (1956)].

[9] J. M. El Bakkal and L. B. Loeb, J. Appl. Phys., 33, 1567 (1962).

[10] W. L. Harries and A. von Engel, Proc. Phys. Soc., B64, 916 (1951).

[11] A. B. Dmitriev, Zh. Tekh. Fiz., 33, 1104 (1963); 34, 1494 (1964) [Sov. Phys. – Tech. Phys., 8, 823 (1964); 9, 1155 (1965)].

[12] J. M. Meek and J. D. Craggs, Electrical Breakdown of Gases, Oxford Univ. Press, London (1953).

[13] N. A. Kaptsov, Electrical Phenomena in Gases and Vacuum [in Russian], GITTL, Moscow (1947), p. 444.

Narrow-band decimeter radiation from lightning

E. L. Kosarev and Yu. G. Serezhkin

Institute of Physical Problems,
Academy of Sciences of the USSR, Moscow

(Submitted May 28, 1973)
Zh. Tekh. Fiz., 44, 364-371 (February 1974)

Observations of narrow-band decimeter radiation from lightning are reported. The radiation power can reach 10^{-9}-10^{-8} W at the input of a spectrum analyzer and this corresponds to a spectral flux density of more than 10^{-12}-10^{-11} W/m^2 · Hz at a distance of 1 km from the lightning. In the range of time intervals 30-200 msec, the number of cases in which the radiation lasts longer than a time T is proportional to $1/T^2$. The maximum observed duration is 0.17 sec. The narrow-band radiation always occurs after streak lightning and the average delay time is 0.25 sec; the most probable delay time is 0.15 sec. The possible sources of the radiation and the connection between this radiation and ball lightning are discussed.

INTRODUCTION

In 1967 the present authors started a number of experiments designed to test the Kapitsa hypothesis regarding the electromagnetic nature of ball lightning[1] and showed[2-4] that streak lightning gives rise to microwave radiation with a continuous spectrum. The power is almost independent of frequency in the range $300 < f < 3000$ MHz and is of the order of 10^{-14} W/m^2, at a distance of the order of 1 km from the lightning.

The spectrum differs from the $1/f^2$ law, which holds for the longer wavelengths and which is obtained as a result of the spectral decomposition of the field produced by a lightning current pulse of the order of 10^{-4}-10^{-3} sec. This difference, and the presence of extended pulses of microwave radiation (up to 10^2 sec) even after the main phase of the discharge, indicate that the radiation is caused by plasma processes in an ionized discharge channel of streak lightning with a lifetime[5] of 0.1-1 sec.

The spectral measurements in refs. 2-4 were made by means of microwave receivers tuned to separate discrete frequencies and therefore the results really refer to the continuous radiation spectrum, which has the character of noise. However, it was found when the radiation was recorded simultaneously on various frequencies that the microwave radiation was sometimes different from noise (which is characterized by an identical time variation on the different frequencies).

From the point of view of the Kapitsa hypothesis it is particularly interesting to observe the coherent narrow-band radiation. For this purpose we have used decimeter range spectrum analyzers with a sweep time of less than 10^{-3} sec to record all the microwave radiation independently of its time of appearance. These instruments were in fact employed in the 1967 measurements. However, their low sensitivity ($\sim 10^{-9}$ W at the input) and their poor recording system (visual observation from a CRO screen) mean that the narrow-band radiation could not be observed reliably and so no discussion of this aspect of the work was given in the published papers.[2-4] A detailed study of the narrow-band structure became possible only after considerable improvement of the apparatus.

APPARATUS AND EXPERIMENTAL METHOD

A block diagram of the present experimental apparatus is given in Fig. 1. In order to increase the sensitivity of the spectrum analyzer, the input stage uses a traveling-wave tube with a gain of 25 dB and a noise figure of 10 dB. The I.F. amplifier is a U2-5 unit with bandwidth of 5 MHz at 100 MHz.

The spectrum analyzer works in the central part of the decimeter region. The choice of this range is dictated by the fact that the 1967 observations show that the narrow-band radiation is concentrated in this region. The sensitivity of the analyzer is better than 10^{-12} W for long monochromatic signals and 10^{-11} W for signals with length of the order of 10^{-5} sec. The sensitivity is determined by means of signals from radar units and by a standard generator technique involving comparison with a P5 measuring receiver and a D4 attenuator.

The heterodyne stage uses a backward wave tube, which is frequency-modulated by a 4 kHz sine wave. The same sinsusoidal voltage is employed as the line sweep on the television-type display. The received signals modulate the brightness on the screen. Thus the horizontal motion on the screen corresponds to the frequency sweep of the analyzer. The total sweep time is 125 μsec. Both the forward and reverse sweep of the spot across the screen are used for display.

There are no filters in the input to the analyzer to distinguish between the upper and lower sidebands of the received signal. The ambiguity is eliminated as follows. Monochromatic radiation in the 200 MHz band would, under the modulation conditions described here, be observed at two places on the screen and the frequency f could be determined uniquely. If a signal appears at only one place on the screen, it is possible to determine the sign in the

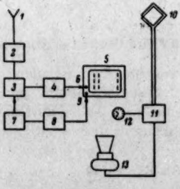

Fig. 1. Block diagram of the spectrum analyzer. 1) Wide-band disk-cone antenna; 2) input traveling wave tube amplifier; 3) heterodyne stage with backward wave oscillator and mixer; 4) I.F. amplifier; 5) video display; 6) input to video amplifier; 7) sweep oscillator for backward wave tube; 8) low-frequency phase shifter; 9) input to line sweep amplifier; 10) loop antenna; 11) circuit for controlling clock flash and triggering camera; 12) clock; 13) automatic camera.

equation $f = f_h + f_{if}$ (f_h is the heterodyne frequency). However, it is not possible to reliably identify short signals (T ≲ 1 msec) in different parts of the screen and so the ambiguity cannot be completely eliminated.

The signals on the screen are recorded by an automatic RFK-5 camera in the following way. The camera operates with a normally open shutter. The brightness on the screen is adjusted so that in the absence of signals the film is not fogged in a time of the order of 1 min. The time scan of the received signals during this period is achieved by means of a continuous frame sweep 20 msec long corresponding to a velocity of 65 cm/sec on the film.

During a lightning discharge, the low-frequency electromagnetic radiation (2-60 kHz) is received on the loop antenna and after a delay of about 20 msec switches on the film movement mechanism. In order to get more or less constant film speed and to ensure continuous exposure, the grab mechanism, which usually controls the start–stop motion of the film, and the sectoral shutter, which periodically cuts off the light, are removed from the camera. The vertical film movement at 30 cm/sec is achieved by means of a toothed traction wheel. The radiation is recorded for about 1 sec after each lightning discharge.

In this way, two time sweeps are used simultaneously: a fast sweep (frame sweep on the television indicator) and a slow sweep (mechanical movement of the film). This double system permits time resolution of the short pulses of radiation and recording of the long-duration radiation over an extended period. However, there is one basic disadvantage: an uncertainty in the measurement of the pulse length over the range 0-30 msec. For pulses of longer duration, in which we are mainly interested, the uncertainty can be neglected.

The lightning signals were recorded during the summer of 1972 in the Lenin Hills, Moscow. The method is as follows. When a storm approaches to within a distance of 10-15 km the system is switched on automatically or manually. In addition to the spectrum analyzer and recorder, the system also includes a 100 MHz receiver for recording the storm intensity on a pen chart and a tape recorder for the thunder so that the distance to the lightning can be determined. The various recordings are aligned by means of time marks. The spectrum analyzer uses the same disk–cone antenna as in the previous experiments;[2-4] this is designed to detect radiation with the electric field polarized vertically. The operation and sensitivity of the analyzer are monitored before and during the storms by means of signals from radar installations.

The maximum time for continuous automatic recording is 1.5 hours. If another storm approaches the station, the system is again switched on automatically or manually and the measurements continue until the storm is ended.

OBSERVATIONAL RESULTS

Measurements with the total system have been carried out during eight storms from July 8 to September 26, 1972. The best signals were recorded during the storm of the night 24-25 August; this was the first storm after a heat wave which lasted almost two months in Moscow.

Figure 2 shows an example of a recording of the lightning on August 24 at 23^{h}54'32" (the distance to the lightning is 6-8 km). The radiation pulse is about 10 msec long and has a continuous spectrum over the given range with a maximum at the higher frequencies. The two vertical lines to the left at the bottom, formed by a succession of dots, are the radar signals. The lines on the right are the same signals observed at the image frequency. Continuous-spectrum radiation similar to that shown in Fig. 2 has been studied in detail in our previous papers.[2-4]

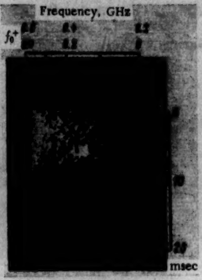

Fig. 2. A pulse of wide-band radiation from lightning. Discharge August 24, 1972, 23^{h}54'32". The three vertical lines formed by a series of dots are radar signals.

At the peak of this storm, from 21^{h}30' to 22^h, radiation with a discrete spectrum is observed clearly during the initial stages. An example of this non-noise radiation is given in Fig. 3 (21^{h}57'58", distance about 5 km). The same radar signals as in Fig. 2 can be seen in the upper part of the picture (which is obtained by exposure on a stationary film). The narrow-band radiation, which is clearly seen in the middle of the picture, appears some 40 msec after the lightning discharge.

This radiation consists of two intense pulses, each about 5 msec long,$^{1)}$ followed by a series of weaker pulses 20-30 msec long, which cannot be seen on the print but are discernible on the film. It is clear from the photograph that the radiation differs from normal radar signals both in length and in frequency.

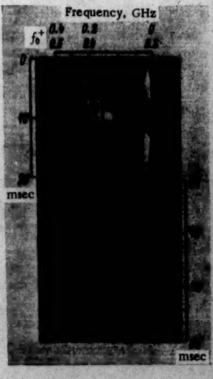

Fig. 3. Narrow-band radiation from lightning. Discharge August 24, 1972. 21^{h}57'58".

The observed discrete-spectrum radiation is not a result of direct low-frequency induction in the measuring apparatus, since such induced signals could not have a frequency exactly equal to the line-sweep frequency of the display unit. The connection between the observed radiation and lightning is further proved by the fact that no case of such radiation has been observed during control measurements in the autumn after the end of the storm season.[2)] Thus the narrow-band microwave pulses are in fact emitted during discharges of streak lightning.

Discrete-spectrum radiation has been observed 39 times during the storm of August 24, 1972. The results of a statistical analysis of the radiation parameters are given below. A rough estimate of the power is made by comparison with the radar signals and the continuous-spectrum radiation and gives a value of 10^{-9}-10^{-8} W. In order to determine the spectral density of the radiation it is necessary to know the bandwith. The actual value of this bandwidth was not measured but it seems to be considerably narrower than that of the radar signals. Thus, only the lower limit of the spectral density for the discrete-spectrum radiation can be given; it is 10^{-12}-10^{-11} W/m^2 · Hz at a distance of 1 km from the lightning. This value is at least two orders of magnitude greater than the density for the continuous-spectrum radiation as measured in our earlier work.[2-4]

The frequencies of all the discrete-frequency radiation are different from the radar frequencies f_1 and f_2. Figure 4 shows the frequency distribution averaged over each 10 MHz interval. Owing to the comparatively small number of observations (N = 39) and to the possible errors in the measurement of the short-duration radiation, Fig. 4 conveys only the important feature of the distribution, which is the presence of two groups: a more intense one on the left and a less intense one on the right.

The observed frequency distribution is in qualitative agreement with the results of preliminary measurements made in Armenia during 1967 with apparatus having a smaller resolving power. Since the observing conditions and the apparatus were quite different in 1967 and 1972, the similarity of the observed frequency distribution is strong evidence that the narrow-band radiation is in fact connected with lightning and not with induced voltages or equipment effects.

We now turn to the time characteristics of the narrow-band radiation. Figure 5 gives the accumulative distribution of the number of cases n when the radiation lasts for a time $\Delta t > T$ and the corresponding probability P = n/N. The observed distribution is closely approximated by the expression

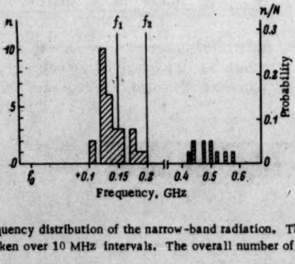

Fig. 4. Frequency distribution of the narrow-band radiation. The average has been taken over 10 MHz intervals. The overall number of observations is 39.

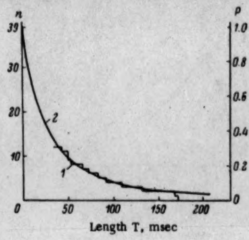

Fig. 5. Distribution in duration of the narrow-band radiation. The abscissa shows the duration T and the ordinate gives the number of pulses with a duration greater than T. 1) Observed distribution; 2) approximating expression (1) with τ = 50 msec.

$$P(\Delta t > T) = \frac{2}{\tau}\int_{T}^{\infty}\frac{d(\Delta t)}{\left(1+\frac{\Delta t}{\tau}\right)^{3}} = \frac{1}{\left(1+\frac{T}{\tau}\right)^{2}}, \qquad (1)$$

in which the parameter τ is equal to the average duration of the narrow-band radiation pulses:

$$\langle\Delta t\rangle = \frac{2}{\tau}\int_{0}^{\infty}\frac{\Delta t\, d(dt)}{\left(1+\frac{\Delta t}{\tau}\right)^{3}} = \tau.$$

The best agreement with the observations is obtained with τ = 50 msec. We may point out that the maximum length of the observed narrow-band radiation is 170 msec and this is an order of magnitude greater than the corresponding figure for the wide-band radiation observed in refs. 3 and 4 (10 msec).

Another characteristic of the narrow-band radiation is that it occurs with a considerable delay after the beginning of the streak lightning discharge. Figure 6 gives the cumulative distribution of the number of pulses n with a time of appearance $t > t_0$. The observed distribution of n = NP can be well approximated by a gamma distribution, for which

$$P(t > t_0) = \frac{\frac{\alpha}{\Gamma(\alpha)}}{\tau_0}\int_{t_0}^{\infty}\left(\frac{\alpha t}{\tau_0}\right)^{\alpha-1}\exp\left(-\frac{\alpha t}{\tau_0}\right)dt. \qquad (2)$$

The parameter τ_0 in this expression, equal to the average delay of the narrow-band radiation

$$\langle t\rangle = \frac{\frac{\alpha}{\Gamma(\alpha)}}{\tau_0}\int_{0}^{\infty} t\left(\frac{\alpha t}{\tau_0}\right)^{\alpha-1}\exp\left(-\frac{\alpha t}{\tau_0}\right)dt = \tau_0,$$

and the parameter α are determined by making the best fit between (2) and the observed results; these parameters turn out to be given by τ_0 = 0.25 sec and α = 2.56. Figure 6 also gives the density corresponding to the gamma dis-

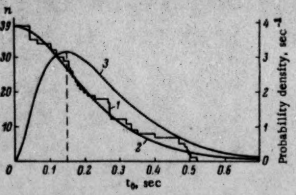

Fig. 6. Distribution of the time delay of the narrow-band radiation after the beginning of the streak lightning discharge. 1) Observed distribution of the number of pulses with a time of appearance greater than t; 2) gamma distribution approximation (2) with $\tau_0 = 0.25$ sec and $\alpha = 2.56$; 3) density of the approximating gamma distribution.

tribution (curve 3). It can be seen that the most probable delay is equal to about 0.15 sec. The maximum observed delay is 0.52 sec.

The most interesting feature of the narrow-band radiation is that it is subjected to a periodic amplitude modulation with a period of 2-5 msec. Figure 7 shows a recording of radiation lasting for 170 msec. This is the longest case of narrow-band radiation that we have observed. The periodic amplitude modulation is quite clear, especially in the central part of the recording. It should be noted that such obvious modulation is not observed on all occasions but only with the long-duration radiation. In the majority of cases, only a few pulses are seen (Fig. 3, for example).

POSSIBLE SOURCES OF THE NARROW-BAND RADIATION

Since the narrow-band radiation lasts for quite a long time (50 msec on average, with not less than 5% of cases having length greater than 150 msec), and appears with a considerable time delay after the start of the streak lightning discharge (average 0.25 sec, most probable value 0.15 sec), we can draw the following definite conclusion: The source of the radiation is the ionized channel of the streak lightning. The times in fact correspond to the lifetime of the channel as determined both by optical measurements of the overall duration of the lightning flash and by electrical measurements of the interpulse currents. The relevant data are given in Uman.[5]

For the less intense group of narrow-band radiation in the upper part of the range (Fig. 4) we can define a more definite source. It seems that about half the signals in this group arise as a result of scattering of the continuous radiation from a broadcast station by the ionized channel. In the absence of any storm, no signals are observed in this range. But sometimes (independently of any storm), we observe an intense broadcast signal which is continuous in time and has a frequency which corresponds to that of the narrow-band signals of the lightning radiation in this range.

The amplitude of the scattered field depends on both the parameters of the lightning channel (that is, mainly on the maximum electron density and the variation of density with radius) and on the relative positions of the transmitter, channel, and receiver. In view of the approximate nature of our power measurements, we cannot compare our observations with even the simplest theory of microwave scattering by a lightning channel.[6] If the accuracy of the measurements is increased, this observation of scattered radiation could become an effective method of studying lightning channels.

As regards the more intense group of radiation in Fig. 4, it is very probable that the primary source of radiation is the streak lightning channel itself since in this region we do not observe any signals which are not related to the lightning. A comparison of the narrow-band radiation spectra obtained in 1967 and 1972 leads to the same conclusion.

If this conclusion is accepted, we can propose the following mechanism for the generation of the radiation. A ionized discharge channel from streak lightning with a diameter of the order of 10 cm, an electron density of 10^{16}-10^{18} cm^{-3}, and a temperature of 10,000-30,000° can be represented as a waveguide for all waves up to plasma wavelength (which here corresponds to the submillimeter zone). Since strong electric fields (up to 10,000-20,000 V/m) are observed during storms and also high directive electron fluxes, the electron distribution function is doubtless very far from an equilibrium one. Under these conditions, amplifications of the magnetic bremsstrahlung and Cerenkov radiation of the discharge electrons are possible in the magnetic field of the lightning at wavelengths corresponding to transverse plasma resonances; such effects have been observed with radiowave scattering at meteor trails and in experiments with a laboratory plasma.[7,8] The amplitude modulation could arise as a result of mode competition as in lasers and through interference of the coherent radiation from different parts of the diffusion expanding channel.

CONCLUSION

We have discovered a hitherto unknown long-duration narrow-band microwave radiation from lightning. The maximum observed length is 0.17 sec. The radiation appears some 0.1-0.4 sec after the leader stage of the lightning discharge and is emitted by the ionized discharge channel.

The data are insufficient to be able to state definitely that this radiation is the cause of the ball lightning discussed by Kapitsa. Although the frequency and length of

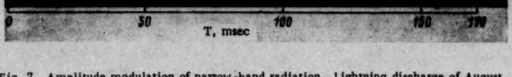

Fig. 7. Amplitude modulation of narrow-band radiation. Lightning discharge of August 24, 1972, $21^h54'42"$; length of the radiation pulse is 170 msec.

the radiation pulse correspond to the value in Kapitsa's hypothesis, the intensity is inadequate to support the prolonged existence of ball lightning. It is possible that the narrow-band radiation has a higher intensity in the direct vicinity of its point of origin, i.e., the ionized channel.

It would therefore be of particular interest to measure the radiation close to the lightning itself. Such measurements could be made by the stimulated lightning method developed by Newman.[9]

The effect that we have observed – discrete lines in the microwave spectrum of lightning – is of interest not only in the electromagnetic hypothesis of ball lightning but also from the point of view of plasma physics. It is desirable that it should be studied by other laboratories.

The authors thank P. L. Kapitsa for his continuous interest in this work and for his support, and L. A. Vainshtein and Yu. N. Khlopov for valuable discussions.

---

1) Because of the uncertainty in measuring the length of short pulses it is possible that the length here is determined by the fast scale and is therefore equal to 2 msec.

2) One pulse similar to that shown in Fig. 3 was recorded during the control measurements on October 12, 1972 but its frequency is identical with that of the radar station f_1.

---

[1] F. L. Kapitsa, "The nature of ball lightning", Dokl. Akad. Nauk SSSR, 101, 245 (1955).

[2] E. L. Kosarev, A. B. Vaganov, B. S. Zakirov, L. B. Luganskii, É. A. Narusbek, and V. N. Camosyuk, Zh. Tekh. Fiz., 38, 1831 (1968) [Sov. Phys. – Tech. Phys., 13, 1477 (1969)].

[3] E. L. Kosarev, V. G. Zatsepin, and A. V. Mitrofanov, Zh. Tekh. Fiz., 41, 315 (1971) [Sov. Phys. – Tech. Phys., 16, 237 (1971)].

[4] E. L. Kosarev, V. G. Zatsepin (Zatzepin), and A. V. Mitrofanov, J. Geophys. Res., 75, 7524 (1970).

[5] M. A. Uman, Lightning, McGraw-Hill, New York (1969).

[6] G. A. Dawson, J. Geophys. Res., 77, 4518 (1972).

[7] E. I. Fialko, Radar Methods of Studying Meteors [in Russian], Sovetskoe Radio, Moscow (1961).

[8] K. J. Parbhakar and B. C. Gregory, Can. J. Phys., 49, 2578 (1971).

[9] M. M. Newman, J. R. Stahman, J. D. Robb, E. A. Lewis, S. G. Martin, and S. V. Zinn, J. Geophys. Res., 72, 4761 (1967).

General

Properties of underexpanded and overexpanded supersonic gas jets

A. V. Antsupov

(Submitted April 9, 1973)
Zh. Tekh. Fiz., 44, 372-379 (February 1974)

An experimental study is made of the conditions governing the regular reflection of a shock in underexpanded and overexpanded supersonic gas jets. Simple empirical equations are proposed for several structural properties of the flow of a single supersonic jet and of the jet emerging from a four-nozzle arrangement. The empirical behavior is used to develop a simple engineering method for calculating the jet structure.

Axisymmetric supersonic jets have an extremely wide variety of practical applications in various fields of modern technology. The recent intensification of interest in problems associated with the use of supersonic jets has stimulated several papers on jet flows and related questions (see, e.g., refs. 1-4). Despite the important progress which has been achieved, certain questions have received little study. There are serious difficulties involved in working out a method to calculate the properties over the entire flow field of a supersonic jet because the flow is generally three-dimensional, with regions of supersonic and subsonic velocities and shocks. The theoretical solutions available (found by the method of net points and characteristics) can be used in calculations for supersonic jets in the absence of subsonic internal regions;[5,6] when such subsonic internal regions exist the calculations can be carried out only in the initial gas-dynamic region (the first "barrel").[7,8] In practice, however, most jets have subsonic internal regions. Furthermore, since the viscosity is neglected, the range of validity of the numerical calculations based on the idealized model is not clear. The experiments which have been reported do not explain the structure of the jet in several ranges of the governing parameters which are of industrial interest. The flow immediately beyond the nozzle exit has been studied in detail, but several problems of practical interest require knowledge of the properties farther downstream along the jet. We report here an experimental study of the physical picture of the flow and of the properties describing the structure of the entire flow field of a single underexpanded or overexpanded supersonic jet and of a jet from a four-nozzle arrangement. The experiments were carried out with jets from nozzles having the properties shown in Table 1, for various ratios of the static pressure at the nozzle exit, p_a, to the pressure in the surrounding medium, p_s (i.e., for various values of index giving the deviation from the "nominal pressure conditions," $n = p_a/p_s$) from the value corresponding to separated flow in the nozzle to 15.

The Reynolds number, determined from properties at the nozzle exit and the diameter of the nozzle exit, d_a, is $(1-5) \cdot 10^6$.

Notation. p) Pressure; M) Mach number; $\varkappa$) polytropic index; n) index giving the deviation from "nominal pressure conditions;" θ) the vertex half-angle of the conical nozzle; i) number of nozzles in the arrangement. Subscripts: 0) Drag; a) exit cross section of the nozzle; s) surrounding medium; m) axis of the jet; bo) boundary of the jet; so) cross-section farthest downstream at which the sound velocity is reached at the jet axis. Linear dimensions are expressed in diameters of the nozzle exit and are written with an overhead bar. Here $\bar{p}'_0 = (p'_0 - p_s)/p_s$ is the relative overpressure. A prime denotes the value of a parameter behind the normal shock in the supersonic flow. The values of the parameters in the supersonic flow are determined from the indications of a Pitot tube and from shadow photographs of the supersonic jet. On the basis of the changes in the basic gas-dynamic parameters (the total and static pressures and the velocity), the flow field is arbitrarily divided into three regions in this study of the supersonic jet: the gas-dynamic, transition, and basic regions.[9] Figure 1 shows the flow scheme of the supersonic jet along with the basic geometric characteristics, from which we can determine the positions of the basic parts of the jet, construct its approximate contour, and determine the periodicity of the changes in the parameters in the gas-dynamic region. In this region, which begins at the nozzle exit, the gas-dynamic parameters vary over the transverse cross sections of the jet and vary periodically along the jet axis. The total pressure behind the normal shock at the minima increases with distance from the nozzle exit (Fig. 1). The maximum of the total-pressure (velocity) profile in the transverse cross section of the jet moves periodically along the radius with distance from the nozzle exit (from the periphery of the jet toward its axis and back). We can assume by convention that the gas-dynamic region is bounded by the cross

TABLE 1. Parameters of Supersonic Nozzles

Nozzle No.	M_a	d_a	θ_a, deg	$\varkappa_a$	i	Nozzle No.	M_a	d_a	θ_a, deg	$\varkappa_a$	i
1	1	14.6	0	1.4	1	*11*	3.00	15.20	12	1.4	1
2	1.4	9.70	5	1.4	1	*12*	2.99	15.00	24	1.4	1
3	1.57	10.15	5	1.4	1	*13*	3.19	10.00	18	1.4	1
4	1.98	15.00	6	1.4	1	*14*	4.08	15.25	12	1.4	1
5	1.98	15.00	12	1.4	1	*15*	5.05	10.06	12	1.4	1
6	1.98	15.00	18	1.4	1	*16*	2.43	18.60	12	1.14	1
7	1.98	15.00	24	1.4	1	*17*	2.65	12.00	12	1.4	4
8	2.65	20.50	12	1.4	1	*18*	3.35	12.00	12	1.4	4
9	3.07	15.20	0	1.4	1	*19*	2.10	15.00	0	1.4	1
10	3.01	15.30	6	1.4	1						

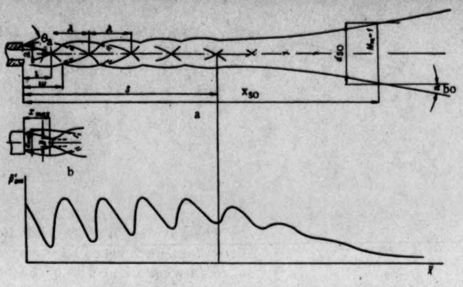

Fig. 1. Flow scheme of a single supersonic jet with regular (a) and irregular (b) reflection of the shock. Here D is the diameter of the central shock; d_{max} is the maximum diameter of the first "barrel" of the jet; S is the gas-dynamic region of the jet; x_{so} is the supersonic core of the jet.

section in which the pressure at a minimum of the jet axis, $\bar{p}_{0m}$, reaches a maximum (Fig. 1). The position of this cross section with respect to the end of the nozzle is given by the empirical equation

$$S = l + 4\lambda.$$

The periodic changes in the gas-dynamic parameters are caused by the shocks in this region. In the transition region the variations in the gas-dynamic parameters along the axis and radius become small; there is no clearly defined periodic structure, and the static pressure becomes equal to the atmospheric pressure, but supersonic flow is maintained in the central region. In the basic region the turbulent mixing of the jet and the surrounding medium reaches the axis; the velocity profile has a maximum at the jet axis and becomes approximately the same as that of self-similar flow. Three regimes of flow from the nozzle at supercritical pressure drops can be distinguished on the basis of the ratio p_a to p_s: the overexpanded regime ($n < 1$), the "nominal regime" ($n = 1$) and the underexpanded regime ($n > 1$). The qualitative differences between the jets corresponding to these three regimes are evident near the nozzle exit in the "initial gas-dynamic region," sometimes called the "first barrel." In this region the shocks develop fully. In all three regimes there can be a regular reflection of the incident shock (Fig. 1). In the case of irregular reflection, the incident shock is reflected from the axis, and a central shock (Mach disk) is formed; behind this disk the flow is subsonic, separated from the supersonic flow by a contact surface (Fig. 1b). In a jet emerging from a profiled nozzle with a uniform velocity field at the nozzle exit, there is a range of values of n near $n = 1$ in the "nominal" regime for all nozzles with $M_a \geq 1$ in which there is flow with regular reflection of an incident shock. In jets from conical nozzles the range n in which there is flow with regular reflection increases with increasing M_a and decreases with increasing vertex half-angle of the nozzle. Figure 2 shows our experimental results and those from refs. 1 and 10 on the range of n over which there can be regular reflection in an air jet (the internal region); here n is plotted as a function of the vertex half-angle of the nozzle θ_a and M_a. It follows from these results that for each value of M_a and for constant $\varkappa_a$ there is a limiting vertex half-angle θ_*, above which there is no regular reflection of the shock in the jet. On the basis of experimental results for an air jet from a conical nozzle, the following equation is proposed for the limiting vertex half-angle of the nozzle as a function of M_a:

$$\theta_* = \operatorname{arc\,tg}(0.22\sqrt{M_a - 1}).$$

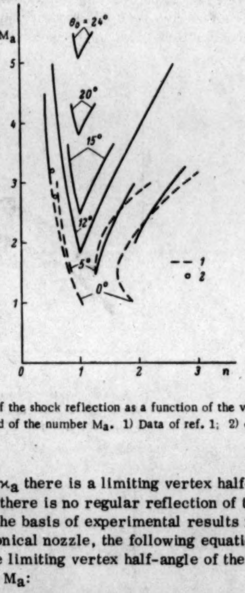

Fig. 2. Nature of the shock reflection as a function of the vertex half-angle of the nozzle and of the number M_a. 1) Data of ref. 1; 2) data of ref. 10 for $\theta_a = 0°$.

This functional dependence is shown in Fig. 3. In air jets from convergent nozzles ($M_a = 1$) with a subsonic region calculated from the Vitoshinskii equation, there is regular shock reflection up to $n = 1.94$.

The gas-dynamic region can be characterized by the following geometric parameters: l, the position of the point at which the incident shock is reflected; w, the length of the initial gas-dynamic region (the first barrel); λ, the wavelength of the periodic structure (the distance between

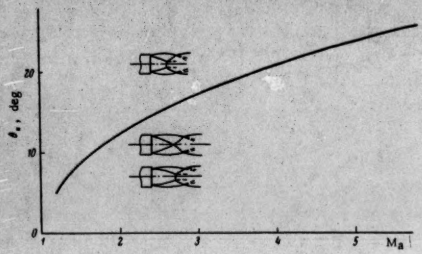

Fig. 3. Limiting vertex half-angle of the nozzle as a function of M_a for $\varkappa_a = 1.4$.

adjacent shock-reflection points); and the position and radius of the maximum cross section in the first barrel. The values of l, w, and λ for jets from conical nozzles with vertex half-angles $\theta_a < \theta_*$ and with $M_a \geq 1.5$ are essentially not functions of θ_a in the underexpanded regime and are self-similar in terms of the composite quantity $[\varkappa_a(M_a^2 - 1)]^{1/2}$. The quantities $\bar{l}/[\varkappa_a(M_a^2-1)]^{1/2}$ and $\bar{w}/[\varkappa_a(M_a^2-1)]^{1/2}$ are piecewise-linear functions of n in this underexpansion regime ($n \geq 1$):

$$\tilde{l} = \frac{\bar{l}}{\sqrt{\varkappa_a(M_a^2-1)}} = \frac{n}{1.20+0.30n},$$

$$\tilde{w} = \frac{\bar{w}}{\sqrt{\varkappa_a(M_a^2-1)}} = \frac{n}{0.80+0.25n}.$$

The wavelength of the periodic structure corresponds to the distance between adjacent maxima or minima of the curve showing the profile of the total pressure behind the normal shock, $\bar{p}'_{0m}$, along the jet axis (Fig. 1). The quantity $\bar{\lambda}/[\varkappa_a(M_a^2-1)]^{1/2}$ can be described by the following empirical equation as a function of n for regimes in which the periodic structure is observed:

$$\tilde{\lambda} = \frac{\bar{\lambda}}{\sqrt{\varkappa_a(M_a^2-1)}} = 1.05\sqrt{n} - 0.1.$$

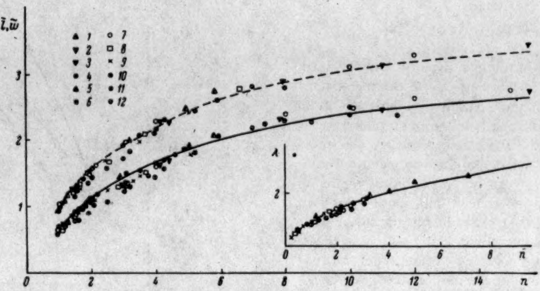

Fig. 4. The quantities $\tilde{w}$ (solid curve), $\tilde{l}$ (dashed curve), and $\tilde{\lambda}$ as functions of n. M_a: 1) 1.57; 2, 3) 1.98; 4) 2.65; 5) 3.07; 6) 3.01; 7) 3.00; 8) 4.08; 9) 5.05; 10) 2.43; 11) 2.65; 12) 3.35. θ_a, deg: 1) 5; 2, 6) 6; 3, 4, 7-12) 12; 5) 0. $\varkappa_a$: 1-9, 11, 12) 1.4; 10) 1.14. i: 1-10) 11; 12) 4.

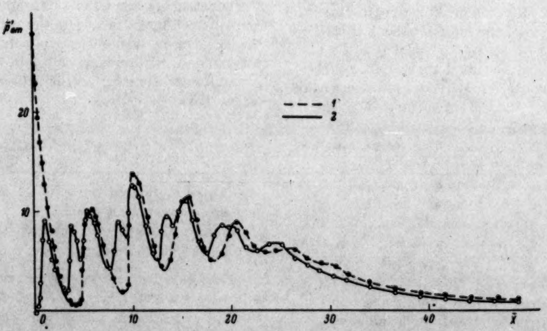

Fig. 5. Change in the relative total pressure behind the normal shock p'_{0m}, along the jet axis ($M_a = 2.65$, $n = 3$, $\varkappa_a = 1.4$). 1) Single jet; 2) composite jet.

The coefficients in the equations for the parameters l, w, and λ are determined by the method of least squares. Figure 4 shows the proposed functional dependences along with experimental data. This figure shows points corresponding to a hot-gas jet (alcohol–oxygen) with $\varkappa_a = 1.14$, found by Blagosklonov. In addition to studying a single supersonic jet, we studied the parameters of a composite air jet from a four-nozzle arrangement. Analysis of the photographs of the composite jet and of the pressure measurements by the Pitot tube along the axis of the composite jet shows that beyond the initial gas-dynamic region the composite jet has a repeating structure of shocks similar to the structure of a single jet of equivalent flow rate, having the same parameter values as the composite jet at the nozzle exit. The experimental values of l, w, and λ for the composite air jet from a four-nozzle arrangement are also shown in Fig. 4. In analyzing the experimental results we determine the diameter of the equivalent nozzle from

$$d_a^{\text{equ}} = \sqrt{i d_a}.$$

Comparison of the experimental results for single and composite jets shows that the values of l, w, and λ of the composite jet are described by equations which hold for the single jet which is equivalent in terms of flow rate.

Figure 5 compares the profiles of the relative total overpressure behind a normal shock along the axis of a single jet and along that of the equivalent composite jet. It follows from Fig. 5 that the pressure varies periodically along the axis of the composite jet over a distance of λ. There are surges in the pressure $\bar{p}'_{0m}$ for the composite jet not found in the single equivalent jet; these surges are also repeated at the same wavelength as that of the periodic structure. These surges result from the interaction of the additional shocks in the composite jet; in turn, the additional shocks result from the interference of the shocks of the composite jets in the initial gas-dynamic region. The structure of the initial gas-dynamic region of a composite jet is described in ref. 11. The basic maxima of the profile of the pressure $\bar{p}'_{0m}$ along the axis of the composite jet agree in magnitude and position with those in the equivalent single jet. The maximum pressures $\bar{p}'_{0m}$ at these additional peaks correspond to the positions of the minima of the pressure profile along the axis of the equivalent single jet. The numerical values of the minima of the $\bar{p}'_{0m}$ profile along the axis in a single jet are much smaller than those in the case of the composite jet, so that the amplitude of the variations in the pressure $\bar{p}'_{0m}$ at the axis of the single jet is higher than that in the composite jet. It follows from measurements of the pressure field in various meridional planes in the gas-dynamic region of the composite jet that the composite jet is cross-shaped in the gas-dynamic region in cross sections normal to the jet axis; correspondingly, there is an important difference between the profile of the gas-dynamic parameters in different planes.

In jets from nozzles with $\theta_a > \theta_*$, the values of the parameters l and w decrease with increasing θ_a, and the periodic wave structure is disrupted, so that the value of λ cannot be determined. This result is based on shadow and Töpler photographs of the jets and the measurements of the pressure by the Pitot tube along the jet axis. We propose the following empirical equations for l and w for $\theta_a > \theta_*$:

$$l = \frac{n}{1.20 + 0.30n}[1 - \operatorname{tg}(\theta_a - \theta_*)]\sqrt{\varkappa_a(M_a^2 - 1)},$$

$$\bar{w} = \frac{n}{0.80 + 0.25n}[1 - 1.2\operatorname{tg}(\theta_a - \theta_*)]\sqrt{\varkappa_a(M_a^2 - 1)}.$$

The diameter of the maximum cross section of the jet in the initial gas-dynamic region increases with increasing θ_a but is really not a function of M_a. We propose the following empirical equation for the diameter of the maximum cross section in a jet of cold air:

$$d_{\max} = (1 + 0.57\theta_a)n^{0.6}.$$

This functional dependence has been checked experimentally up to n = 40. As $\varkappa_a$ is reduced, the jet diameter increases.

The distance from the nozzle exit to a given maximum cross section of the jet is (0.8–1)l. In the case of irregular shock reflection there is an additional characteristic: the central shock. The diameter of the central shock is a strong function of the vertex half-angle of the nozzle and of n. Figure 6 shows the diameter of the central shock as a function of n for various values of the parameter θ_a. For jets from conical nozzles with θ_a = 12° in the underex-

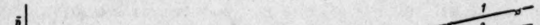

Fig. 6. Diameter of the central shock as a function of n; the parameter is θ_a. M_a = 2, $\varkappa_a$ = 1.4, θ_a, deg: 1) 24; 2) 0; 3) 18; 4) 6; 5) 12.

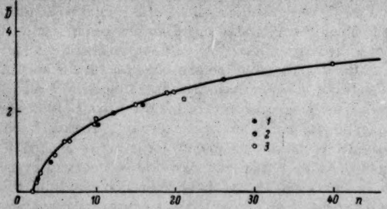

Fig. 7. Diameter of the central shock as a function of n for an air jet ($\varkappa_a$ = 1.4) from a convergent nozzle. 1) Experimental data of ref. 13; 2) of ref. 1; 3) M_a = 1. $\varkappa_a$ = 1.4, i = 1.

panded regime we propose the following empirical equation for the diameter of the central shock:

$$\bar{D}=\frac{0.65}{M_a}(n-0.55M_a)^{0.62}.$$

This equation is determined from studies of a cold air jet ($\varkappa_a$ = 1.4) in the range M_a = 1.5-5. Some of the results found by Blagosklonov for hot jets ($\varkappa_a$ = 1.14) agree with this equation. At $\theta_a \neq 12°$ the experimental results diverge from this empirical equation. For jets of cold air from a convergent nozzle the diameter of the central shock is described well by

$$\bar{D}=\lg n^{5/2}-\frac{3}{4}.$$

This functional dependence has been checked experimentally up to n = 40 and is shown along with the experimental data in Fig. 7.

The maximum diameter of succeeding barrels of the jet remains essentially constant over the gas-dynamic part of the jet. In the transition region the angle between the boundary and the axis increases, becoming constant in the basic region. From the experimental data we find the tangent of this angle in the basic region to be tan α_{bo} = 0.18, in agreement with the results of refs. 9 and 19. According to the experimental results, the angle between the boundary and the axis of the jet becomes constant at the end of the supersonic core of the jet, whose length is given by the empirical equation

$$\bar{X}_{so}=(4.4n+3+\beta)\exp 0.11\varkappa_a M_a^2.$$

This functional dependence holds up to n = 7. In jets with regular reflection, the value of the parameter β changes from 0 to 3 as a function of the shock intensities and the acoustic feedback.[12,14] When there is a central shock in the jet the value is β = 0. The diameter at the end of the supersonic core of the jet is found in terms of parameters at the nozzle exit on the basis of the equation expressing conservation of angular momentum along the jet:

$$\bar{d}_{so}=2.72\sqrt{nM_a^2+\frac{n-1}{\varkappa_a}}.$$

In the basic region of the composite jet the dimensionless velocity profiles agree with those of a single jet and can thus be described by the Schlichting "3/2 law."[12] The length of the supersonic core in the composite jet is essentially the same as that of the supersonic core in the equivalent single jet. Accordingly, calculations for the basic region of a composite jet can be carried out completely by the methods proposed for a single jet.

---

[1] E. S. Love, C. E. Grigsby, L. P. Lee, and M. J. Woodling, NASA Tech. Rep. R-6, 292 (1959).

[2] V. S. Avduevskii, A. V. Ivanov, I. M. Karpman, V. D. Traskovskii, and M. Ya. Yudelovich, Izv. Akad. Nauk SSSR, Mekhan. Zhidk. i Gaza, No. 3, 63 (1970).

[3] G.I. Averenkova, É. A. Ashratov, and T. G. Volkonskaya, Scientific Report No. 100-3A (380), MGU VTs (1969).

[4] G. F. Glotov, V. A. Zhokhov, F. A. Kukanov, N. I. Kukanova, and A. I. Soinov, Study of Flows with Gas Jets. Reviews. Translations, Abstracts [in Russian], No. 290, BNTI TsAGI (1969), p. 303.

[5] M. Ya. Ivanov, A. N. Kraiko, and N. V. Mikhailov, Zh. Vychislit. Matem. Matem. Fiz., 12, 441 (1972).

[6] M. Ya. Ivanov and A. I. Kraiko, Zh. Vychislit. Matem. Matem. Fiz., 12, 805 (1972).

[7] É. A. Ashratov, Izv. Akad. Nauk SSSR, Mekhan. Zhidk. Gaza, No. 1, 158 (1966).

[8] G. I. Averenkova, É. A. Ashratov, T. G. Volkonskaya, Yu. N. D'yakonov, N. I. Egorova, D. A. Mel'nikov, G. S. Roslyakov, and V. I. Uskov, Tr. VTs MGU, Part 1 (1970); Part 2 (1971).

[9] G. N. Abramovich (editor), Study of Turbulent Jets of Air, Plasma, and Real Gases [in Russian], Izd. Mashinostroenie, Moscow (1967).

[10] D. A. Mel'nikov, Izv. Akad. Nauk SSSR, OTN Mekhanika i Mashinostroenie, No. 3, 24 (1962).

[11] I. P. Ginzburg, V. D. Prikhod'ko, and A. M. Sizov, Scientific Notes of Leningrad State University. Gas Dynamics and Heat Transfer [in Russian], Collection No. 2 (1970), p. 55.

[12] D. R. Glass, Raketnaya Tekhnika i Kosmonavtika, 6, 82 (1968).

[13] C. E. Peters and W. I. Phares, AIAA Paper No. 70-229, 9 (1970).

[14] I. W. Shirie and I. G. Seubold, AIAA J., 5, 2062 (1967).

Gas-kinetic removal of neutral molecules from an ion beam

V. P. Ivanov

Scientific-Research Institute of Applied Mathematics and Cybernetics,
N. I. Lobachevskii Gor'kii State University

(Submitted February 17, 1973; resubmitted May 18, 1973)
Zh. Tekh. Fiz., 44, 380-386 (February 1974)

Impurity molecules are removed from ion beams by transverse gas flows produced by nozzles, capillary screens, etc. The high-velocity ions of the beam pass unhindered through the gas flow, but neutral molecules in the beam, moving at thermal velocities, collide with the molecules of the flow and are removed from the beam. It is difficult to carry out exact calculations for this complicated system. Below we propose an approximate method for calculating the required properties of the gas flow and evaluate the secondary contamination of the beam by the molecules from the gas flow.

1. INITIAL EQUATIONS

Impurity neutral molecules are removed from ion beams by transverse gas flows produced by nozzles, capillary screens, etc.[1] In real systems for gas-kinetic purification the density of the transverse gas flow is much higher than that of the neutral gas in the ion beam, so we can apparently neglect the influence of the beam on the flow and assume that the secondary contamination of the beam by the molecules of the gas flow is a consequence of the thermal motion of these molecules. Between the emitter and the absorber the transverse gas flow is randomized as a result of collisons between molecules of this flow. In the present paper we analyze the case in which the diameter of the ion beam is much larger than the mean free path of the molecules in the transverse flow and in which the gas in the flow is approximately in equilibrium.

A rigorous calculation of the gas flows between the emitter and the absorber requires the use of high-speed computers, even in the simplest case of one-dimensional flows.[2] Below, the randomized flow is analyzed approximately; it is regarded as the result of the relaxation of a spatially homogeneous gas from an initial state described by the velocity distribution function of the emitted molecules. The results of this analysis agree satisfactorily with the available exact data.[2] The contamination of the ion beam by molecules of the transverse flow is evaluated in terms of the number of molecules incident from a spatially homogeneous randomized flow on a specular reflection area at velocities lying within a specified solid angle around the normal to the area. This area is equal to the cross-sectional area of the ion beam and is parallel to the macroscopic velocity of the transverse gas flow.

The following simplified model for a real system for a gas-kinetic purification (a "gas gate") is the best approximation to these assumptions. We assume that the gas flows from an emitting strip I to a completely absorbing strip II of width ε between specularly reflecting side walls III, in which there are circular apertures S_1 and S_2 for the beam (Fig. 1). We assume these apertures to be small and to have a negligible effect on the state of the gas in the flow. To find the macroscopic velocity v and $\bar{\nu}$, the average thermal velocity of the molecules in the randomized flow from the probability-density distribution for the velocities of the molecules scattered by the emitter, we assume that the state of the randomized gas in the flow does not differ greatly from that immediately after randomization in an unbounded space, if the state of the spatially homogeneous gas is initially described by the velocity distribution function for the emitted molecules. In this case we can write

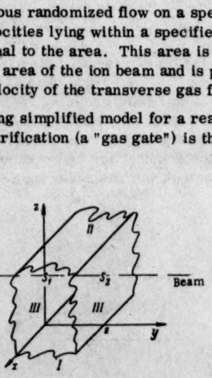

Fig. 1

$$v = \bar{\nu}_{0x}, \tag{1.1}$$

$$v^2 + \overline{\nu^2} = \overline{\nu_0^2}. \tag{1.2}$$

Here, ν_0 is the random velocity of a molecule scattered by the emitter. When the molecular velocities obey a Maxwellian distribution, the average thermal velocity of the molecules $\bar{\nu}$ is related to the mean square velocity $\overline{\nu^2}$ by

$$\overline{\nu^2} = 1.176\bar{\nu}^2. \tag{1.3}$$

The density of the gas flow n or the density of molecules in the flow N, which are related by

$$n = vN, \tag{1.4}$$

is chosen so that the density of molecules in the beam is reduced by a factor of α. If we assume that molecules are removed from the beam as a result of a single collision with molecules from the flow, and if we neglect the possibility that these molecules are returned to the beam as a result of subsequent collisions, we conclude that the probability for the molecules of the beam to traverse the gas flow is inversely proportional to the attenuation:

$$\exp\left(-\frac{\varepsilon}{\lambda}\right) = \frac{1}{\alpha}, \tag{1.5}$$

where λ is the mean free path of the beam molecules with respect to the molecules of the gas flow.

This mean free path is given by

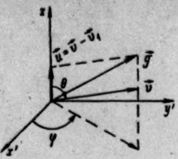

Fig. 2

$$\lambda = \int_0^\infty \frac{\nu_1}{\omega(\nu_1)} f(\nu_1)\, d\nu_1, \tag{1.6}$$

where ν_1 is the velocity of the beam molecule, $\omega(\nu_1)$ is the frequency at which beam molecules moving at ν_1 collide with molecules of the gas flow, $f(\nu_1)\,d\nu_1$ is the relative number of beam molecules having velocities in the interval $(\nu_1, \nu_1 + d\nu_1)$, and $f(\nu_1)$ is the probability-density distribution of the absolute velocities of the beam molecules.

The frequency at which a beam molecule moving at $\boldsymbol{\nu}_1$ collides with molecules of the flow moving at velocities $\mathbf{v} + \boldsymbol{\nu}$ is

$$d\omega = \pi (r + r_1)^2 |\mathbf{v} + \boldsymbol{\nu} - \boldsymbol{\nu}_1|\, dN = \sigma g dN. \tag{1.7}$$

Here, dN, the number of molecules of the gas flow with velocities between $\boldsymbol{\nu}$ and $\boldsymbol{\nu} + d\boldsymbol{\nu}$, is given by

$$dN = \frac{\beta^3 N}{\pi^{3/2}} \nu^2 e^{-\beta^2 \nu^2} \sin\theta\, d\theta\, d\varphi\, d\nu, \tag{1.8}$$

for an equilibrium gas, where $1/\beta = \bar{v}/1.128$, θ and φ are the polar and azimuthal angles giving the orientation of velocity $\boldsymbol{\nu}$ in the coordinate system x', y', z' moving with the gas (Fig. 2).

Using the notation $u = v - \nu_1$ and directing the z' axis along u, we can write

$$g = \sqrt{(u + \nu\cos\theta)^2 + \nu^2 \sin^2\theta} = \sqrt{u^2 + 2u\nu\cos\theta + \nu^2}. \tag{1.9}$$

Substituting Eqs. (1.9) and (1.8) into (1.7), integrating over φ, θ, ν, and treating the molecules in the thermal-velocity range as hard spheres with σ = const, we find

$$\omega = \frac{\sigma N}{\beta}\left[\frac{e^{-\beta^2 u^2}}{\sqrt{\pi}} + \operatorname{erf}(\beta u)\left(\beta u + \frac{1}{2\beta u}\right)\right], \tag{1.10}$$

$$\beta = \frac{2}{\sqrt{\pi}\,\bar{v}}, \quad \operatorname{erf}(x) = \frac{2}{\sqrt{\pi}} \int_0^x e^{-t^2} dt.$$

Since $\nu_1 \perp v$ and $u = |v - \nu_1|$, we have $u = (v^2 + \nu_1^2)^{1/2}$ (Fig. 3). Finally

$$\omega(\nu_1) = \frac{\sigma N}{\beta}\left[\frac{e^{-\beta^2 (v^2 + \nu_1^2)}}{\sqrt{\pi}} + \operatorname{erf}\left(\beta\sqrt{v^2 + \nu_1^2}\right)\left(\beta\sqrt{v^2 + \nu_1^2} + \frac{1}{2\beta\sqrt{v^2 + \nu_1^2}}\right)\right]. \tag{1.11}$$

As mentioned above, the transverse gas flow which removes neutral molecules from the beam is a source of secondary contamination of the beam. According to our assumptions, any molecule of the gas flow which intersects cross-section S_2 (Fig. 1) within a specified solid angle $\Delta\Omega$ around the normal to S_2 enters the beam.[1)] The flux density of molecules converted from the flow to the beam per unit time is

$$n_1 = n' p. \tag{1.12}$$

Here n', the number of molecules of the flow intersecting unit cross section S_2 in the equilibrium gas, is

$$n' = \frac{\bar{v} N}{4}, \tag{1.13}$$

and p, the probability that the velocity of a molecule intersecting cross section S_2 lies within solid angle $\Delta\Omega$, is, according to Eq. (2.5) of ref. 3,

$$p = \frac{\Delta\Omega \exp(-1.27 v^2/\bar{v}^2)}{\pi}. \tag{1.14}$$

It follows from these equations that as the thickness of the transverse gas flow is increased but the total gas flow rate is held constant there is a reduction of the secondary contamination of the ion beam by molecules of the gas flow without any change in the filtering properties of the flow.

We see from Eq. (1.5) that $\varepsilon/\lambda = \ln\alpha$, i.e., the mean free path of the beam molecules with respect to molecules of the gas flow, λ, is proportional to the thickness of the flow, ε ($\lambda \sim \varepsilon$). From Eq. (1.11), we find λN = const. Substituting $N \sim 1/\lambda \sim 1/\varepsilon$ into Eqs. (1.13) and (1.12), we see that the number of molecules of the gas flow which enter the beam, n_1, is inversely proportional to the beam thickness ε ($n_1 \sim 1/\varepsilon$). The total gas flow rate in the flow is proportional to εn; substituting in $n \sim N \sim 1/\varepsilon$, ~~we see~~ that the total flow rate is not a function of ε.

2. CALCULATED RESULTS

We calculate the density of a transverse argon flow 20 cm thick at which the flux density of neutral hydrogen in the ion beam, 20 cm in diameter, falls off by a factor of α = 400, from an initial value of $5.74 \cdot 10^{16}$ cm^{-2} · sec^{-1} to $1.43 \cdot 10^{14}$ cm^{-2} · sec^{-1}. We evaluate the secondary contamination of the beam by argon molecules under the condition $\Delta\Omega = 0.34 \cdot 10^{-2}$ sr (argon molecules which intersect cross section S_2 and enter circle S_3, 25 cm in diameter and 380 cm from S_2, enter the beam; Fig. 1). To be definite we assume that the argon molecules move away from the emitter surface and that the hydrogen molecules move along the beam with velocities obeying a Maxwellian dis-

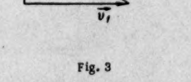

Fig. 3

tribution, with an average velocity corresponding to room temperature:

$$f(v_1)\,dv_1 = \frac{4\beta_1^3}{\sqrt{\pi}} v_1^2 \exp(-\beta_1^2 v_1^2) \qquad (2.1)$$

$$\beta_1 = \frac{1.128}{\bar{v}_1},$$

where $\bar{\nu}_1 = 17.7 \cdot 10^4$ cm/sec, $r_1 = 1.35 \cdot 10^{-8}$ cm, $\bar{\nu}_0 = 3.8 \cdot 10^4$ cm/sec, and $r = 1.7 \cdot 10^{-8}$ cm. The initial density of hydrogen in the beam $N_1 = n_1/\bar{\nu}_1 = 3.24 \cdot 10^{11}$ cm^{-3}; under equilibrium conditions a pressure of 10^{-5} torr corresponds to this density.

We analyze the operation of the gas gate for the following cases of the emission of argon molecules:

1) Emission in a cosinusoidal distribution.

2) Emission by means of a screen consisting of relatively short circular capillaries having a diameter-to-length ratio of $d/l = 0.115$.

3) Emission by means of a screen consisting of long capillaries with $d/l = 0.02$.

4) Normal emission, for which the velocities of the emitted molecules are parallel and normal to the emitter surface.

For the required degree of purification, the transverse flux of argon must be such that the mean free path of the hydrogen molecules among the argon molecules is, in correspondence with Eq. (1.5),

$$\lambda = \frac{\varepsilon}{\ln a} = 3.33 \text{ cm}. \qquad (2.2)$$

1. In the case of emission in a cosinusoidal distribution, the molecules have a Maxwellian distribution in the velocity half-space $\nu_{0z} > 0$, so we find $\nu_{0z}/\bar{\nu}_0 = 0.5$.

According to equations (1.1)-(1.3) the velocities of the ordered and thermal motion of the molecules of the flow are

$$v = 0.5\bar{v}_0 = 1.9 \cdot 10^4 \text{ cm/sec},$$

$$\bar{v} = 0.89\bar{v}_0 = 3.4 \cdot 10^4 \text{ cm/sec}, \; \frac{v}{\bar{v}} = 0.56. \qquad (2.3)$$

These values agree satisfactorily with those calculated on a BÉSM-6 computer for a one-dimensional gas flow. Those calculations show that in the case of a cosinusoidal emission distribution and with Kn = 0.125 the gas halfway between the planes is described approximately by a Maxwell distribution with $v = 0.3\bar{\nu}_0$, $v/\bar{\nu} = 0.52$ (ref. 2).

Using v, $\bar{\nu} \ll \bar{\nu}_1$, we find from Eqs. (1.6) and (1.11) that[2)]

$$\lambda N \approx \frac{1}{\pi(r + r_1)^2} = \frac{1}{\sigma} = 3.43 \cdot 10^{14} \text{ cm}^{-2}. \qquad (2.4)$$

Substituting the value of λ (2.2) into (2.4), we find the desired argon density in the transverse flow to be

$$N = 1.03 \cdot 10^{14} \text{ cm}^{-3}.$$

At equilibrium at room temperature this density would correspond to a pressure of $2.9 \cdot 10^{-3}$ torr. The flux density of the argon is, according to Eq. (1.4),

$$n = vN = 1.96 \cdot 10^{18} \text{ cm}^{-2} \cdot \text{sec}^{-1}.$$

According to Eqs. (1.12)-(1.14) the flux density of the argon in the ion beam beyond the gas gate is

$$n_1 = 6.3 \cdot 10^{14} \text{ cm}^{-2} \cdot \text{sec}^{-1}.$$

2. For the case in which the emitter is a capillary screen consisting of relatively short capillaries, we can use the directional pattern (shown in Fig. 2 of ref. 4) of the free-molecular flow of gas out of a tube with $d/l = 0.115$ and a numerical integration to find $\bar{\nu}_{0z}/\bar{\nu}_0 = 0.62$. Repeating the calculations above, we find the velocity of the ordered motion of the argon flow and the mean thermal velocity of the molecules in this flow after the randomization of the flow to be, respectively,

$$v = 0.62\bar{v}_0 = 2.35 \cdot 10^4 \text{ cm/sec}, \bar{v} = 0.82\bar{v}_0 = 3.12 \cdot 10^4 \text{ cm/sec}.$$

The density of the argon flow from the surface of the capillary screen is

$$n = 2.4 \cdot 10^{18} \text{ cm}^{-2} \cdot \text{sec}^{-1}.$$

The density of the argon flow in the ion beam beyond the capillary screen is

$$n_1 = 4.2 \cdot 10^{14} \text{ cm}^{-2} \cdot \text{sec}^{-1}.$$

To determine the dimensions of the capillaries which provide free-molecular gas flow, we assume that the gas is approximately in equilibrium in the volume from which the gas flows through the screen. If we neglect the oppositely directed flow of gas which is incident on the capillaries from the region between the emitter and the absorber, we can determine the gas density in the volume from

$$N_2 = \frac{4n}{kp_1\bar{v}_0}, \qquad (2.5)$$

where $\bar{\nu}_0$ is the mean thermal velocity of the gas molecules in the volume, k is the transmission of the screen, p_1 is the probability for transit of the gas molecules through the capillaries, and n is the density of the transverse gas flow. For capillaries having $d/l = 0.115$, we would have $p_1 = 0.128$ (ref. 5). Assuming k = 0.5, we find $N_2 = 4.0 \cdot 10^{15}$ cm^{-3}. The corresponding pressure is $1.1 \cdot 10^{-1}$ torr, and the mean free path of the gas molecules is about 0.5 mm. If the capillaries are shorter than 0.25 mm (and have diameters smaller than 0.029 mm), we conclude that the gas flow through the capillaries is approximately free-molecular flow.

3. We now assume the screen to consist of long capillaries, with $d/l = 0.02$. From the directional pattern in Fig. 2 of ref. 4, we estimate $\bar{\nu}_{0z}/\bar{\nu}_0 = 0.72$. Now the desired reduction of the amount of neutral hydrogen in the beam is achieved at an argon flux density of

$$n = 2.8 \cdot 10^{18}\ \mathrm{cm}^{-2} \cdot \mathrm{sec}^{-1}.$$

The flux density of argon in the beam beyond the gas gate is

$$n_1 = 2.4 \cdot 10^{14}\ \mathrm{cm}^{-2} \cdot \mathrm{sec}^{-1}.$$

The probability for transit of molecules through a tube with $d/l = 0.02$ is $p_1 = 0.0258$ (ref. 5). According to Eq. (2.5), the density of argon in the volume from which the argon flows through the screen must be

$$N_2 = 2.3 \cdot 10^{16}\ \mathrm{cm}^{-3}.$$

The corresponding pressure is $7 \cdot 10^{-1}$ torr, and the mean free path of the argon molecules is 0.085 mm. Accordingly, for approximately free-molecular flow of argon through the capillaries, the length and diameter of the capillaries must satisfy the conditions $l < 0.042$, $d < 0.00084$ mm.

4. We turn now to the case of normal emission. In this case the ordered and mean thermal velocities in the randomized argon flow are, respectively,

$$v = \bar{v}_0 = 3.8 \cdot 10^4\ \mathrm{cm/sec},$$
$$\bar{v} = 0.39\bar{v}_0 = 1.5 \cdot 10^4\ \mathrm{cm/sec}.$$

The argon flux density is

$$n = 3.9 \cdot 10^{18}\ \mathrm{cm}^{-2} \cdot \mathrm{sec}^{-1}.$$

The argon flux density in the beam is

$$n_1 = 0.8 \cdot 10^{12}\ \mathrm{cm}^{-2} \cdot \mathrm{sec}^{-1}.$$

Accordingly, when a capillary screen is used the contamination of the ion beam by argon molecules is slightly less than in the least favorable case of emission in a cosinusoidal distribution. For example, when a screen consisting of relatively short capillaries, with $d/l = 0.115$, is used, the contamination is reduced by a factor of 1.5, and when long capillaries ($d/l = 0.02$) are used, the contamination is reduced by a factor of 2.6. The directionality of the emission is highest in the case of free-molecular gas flow through capillaries; here relatively long capillaries must be very fine ($d \approx 0.0008$ mm for $d/l = 0.002$).

In the hypothetical case of normal emission the contamination of the beam by argon is reduced by a factor of more than 10^{-3}.

Let us check the original assumptions we have used in the calculation for a case of practical interest, that of a screen consisting of relatively short capillaries. The energy of the thermal motion of all the argon molecules in a unit volume is $m\bar{v}^2N/2 = 3.9\ \mathrm{ergs/cm^3}$, and the kinetic energy of the hydrogen molecules in a unit volume of the beam is

$$\frac{m_1\overline{v_1^2}N_1}{2} = 2.0 \cdot 10^{-3}\ \mathrm{erg/cm^3}.$$

Since the thermal energy of all the argon molecules in the beam–flow interaction region is much higher than the total kinetic energy of the hydrogen molecules in the same region, we can apparently neglect the perturbing influence of the beam on the flow. The mean free path of the argon molecules in the flow is about 1.9 cm (at equilibrium). The transverse dimension of the beam is much larger than the mean free path of the molecules in the gas flow, so we would expect a significant randomization of the argon in a large part of the interaction region.

In the case of a screen consisting of capillaries with $d/l = 0.115$ and $d < 0.03$ mm, a reduction of the number of neutral hydrogen molecules in the ion beam by a factor of 400 requires an argon pressure of $1.1 \cdot 10^{-1}$ torr in the volume from which the argon enters the screen. In this case the ion beam is contaminated with argon, whose flux density in the beam is $4.2 \cdot 10^{14}\ \mathrm{cm}^{-2} \cdot \mathrm{sec}^{-1}$ higher than the residual flux density of hydrogen in the beam, which is $1.4 \cdot 10^{14}\ \mathrm{cm}^{-2} \cdot \mathrm{sec}^{-1}$ (by assumption, the initial hydrogen pressure in the beam was 10^{-5} torr).

In conclusion the author thanks I. N. Golovin for suggesting the problem and for useful discussions.

---

1)Because of collisions, some of these molecules return to the flow, and the actual contamination of the beam is generally smaller than that found from this estimate.

2)This equation holds for any of the emission cases considered here.

[1] M. N. Kogan, Dynamics of a Low-Density Gas [in Russian], Izd. Nauka, Moscow (1967).

[2] F. G. Cheremisin, Izd. Akad. Nauk SSSR, Mekhan. Zhidk. i Gaza, No. 2 (1972).

[3] V. P. Ivanov and Yu. I. Neimark, Izd. Akad. Nauk SSSR, Mekhan. Zhidk. i Gaza, No. 4 (1967).

[4] A. I. Naumov, Zh. Tekh. Fiz., 33, 127 (1963) [Sov. Phys. – Tech. Phys., 8, 88 (1963).

[5] D. N. Davis, J. Appl. Phys., 31, 1169 (1960).

Electron-microscope and x-ray study of thermionic emitters made from Mo–Pt alloys

B. B. Shishkin and R. S. Bakhtiyarov

M. V. Lomonosov Moscow State University

(Submitted November 9, 1972; resubmitted February 13, 1973)
Zh. Tekh. Fiz., 44, 387-399 (February 1974)

Emitters of alloys of Mo with Pt (having 1, 5, 10, and 15 wt.% Pt) have been studied in an emission electron microscope, a scanning electron microscope, and an x-ray microanalyzer. The formation of a film of the low-melting component (Pt) on the surface of the alloy with 1% Pt was studied in the emission electron microscope. As this film forms the local work function displays hysteresis in its functional dependence on the temperature. The Pt emerges onto the surface of the alloy along grain boundaries and at structural defects. The studies with the scanning electron microscope and the x-ray microanalyzer show that the Pt films are not monolayers. Histograms showing the distribution of the surface area of the alloy with respect to work function have been constructed on the basis of the electron emission microscopy. Current hypotheses regarding the mechanism for the emission of these alloys are discussed. An equation is derived for the thermionic current from an emitting surface for which the work function is inhomogeneous. An equation is derived for the thermionic-emission current of a metal whose conduction band has a complicated structure. Within the framework of the Sommerfeld model of the metal this equation is the same as the ordinary Richardson–Dushman equation.

INTRODUCTION

The search for thermionic emitters with specified properties has stimulated much work on binary and ternary alloys. Over the 10-year history of the study of alloys as thermionic emitters various hypotheses have guided the search for suitable emitters: the film hypothesis of Dyubua,[1–4] the spot-field hypothesis of Matskevich,[5] and Samsonov's hypothesis[6] of the relation of the thermionic emission of an alloy with its electronic energy spectrum.

The basic experimental results on the emission of binary and ternary alloys have been reviewed by Matskevich.[5] Among the papers published since this review, note should be taken of those dealing with experiments on the emission of various faces of alloy single crystals.[7–9]

The first two hypotheses can be tested by a joint electron-microscope and x-ray study (Sec. 1) of thermionic emitters.[10] In the present experiments, described below, the alloys are studied in an emission electron microscope, a scanning electron microscope, and an x-ray microanalyzer. The complexities involved in an analysis of the third hypothesis are discussed in Sec. 3 and in the conclusion.

1. EXPERIMENTAL RESULTS

The Mo–Pt alloy specimens are prepared in an MIFI-9 arc furnace on a water-cooled copper hearth in purified argon. The ingots are first cut into disks 7 mm in diameter and then ground and electropolished. We prepared and studied four alloys: alloy A, Mo + 1 wt.% Pt; alloy B, Mo + 5 wt.% Pt; alloy C, Mo + 10 wt.% Pt; and alloy D, Mo + 15 wt.% Pt.

Study of the alloys in the emission electron microscope. These experiments are carried out in a small, high-vacuum emission electron microscope with a magnetic immersion objective which we have designed and constructed. The apparatus is described in detail elsewhere.[11–13] Four specimens of alloys A-D and specimens of polycrystalline W and Mo are mounted simultaneously on the frame of the specimen holder. A Pt grid of known dimensions is mounted on one of the specimens for determination of the image magnification. The W and Mo specimens are used as test specimens for measuring the work function φ and its functional dependence on the temperature, $\varphi(T)$.

The pressure in the microscope is less than 10^{-7} torr in the experiments; the range of image magnifications is from ×50 to ×350. The collector system can be used to measure local emission currents with a resolution of 1.4 μ. In several of the experiments a chart recorder is connected to the output of a U-1-6 amplifying electrometer to record the contrast distribution curves.

The specimen temperature is determined by a pyrometer. In experiments carried out to find the temperature coefficient of the work function, we have constructed a calibration of the specimen temperature against the heating power. The temperature is determined with a tungsten/tungsten–rhenium thermocouple.

Typical emission photomicrographs of the alloys are shown in Fig. 1. Larger grains or "crystallites" are visible on the surfaces of alloys having relatively little platinum (A and B). On the surfaces of the grains themselves we see dark spots: platinum-enriched regions and interaxial regions of dendrites formed during the crystallization.

The images of alloy D (Fig. 1b) are radically different. The photomicrographs of this alloy reveal a clearly defined dendrite structure. The images in the emission micrographs of alloy C display a structure similar to that of alloy D.

To measure the effective local work function of the large grains (like those found on alloy A) it is sufficient to measure the emission current, the specimen temperature, and the magnification.[14] The current density at the specimen is

$$j(x, y)=\frac{I(xM, yM)}{S_0}M^2, \tag{1}$$

where I(xM, yM) is the current in the plane of the screen, M is the magnification, and S_0 is the area of the aperture in the screen.

We treat the complex emission patterns of type D, displaying the fine structure of the emission centers, in the following manner. First, we do not scan the electron beam[14] to obtain continuous contrast curves; instead we measure the local current at N points in the image plane. The current density calculated from Eq. (1) is substituted into the equation

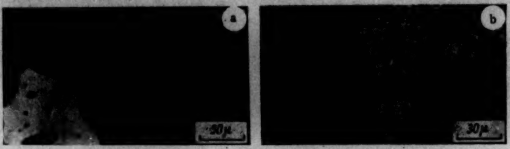

Fig. 1. Typical photomicrographs in the emission electron microscope. a) Alloy B; alloy D.

$$j_{(x,y)} = A'T^2 e^{-\frac{\overline{e\varphi}(x,y)}{kT}}. \tag{2}$$

In contrast with the Richardson–Dushman equation, here $\overline{e\varphi}(x, y)$ is the average of the work function over the region S_0/M^2 and $A' = A_0(1-R)\, f[\bar{\varphi}_\Sigma(x, y)]$, where $f[\bar{\varphi}_\Sigma(x, y)]$ is a functional of the generalized spot field.[14] If we set $A' = 120.4$ A/(cm^2 · deg^2), we can easily find $\overline{\varphi(x, y)}$ from the values of j(x, y) and M measured in the emission microscope. We call the work function calculated in this manner the "effective local work function," $\bar{\varphi}(x, y) = \varphi_{\text{loc}}$. To determine the emissivity of the entire emitter we carry out N measurements of φ_{loc}. The entire "spectrum" of work functions can be represented in the following manner. First, we find the maximum emission contrast $R = \varphi_{\max} - \varphi_{\min}$. Then we choose a method for partitioning the interval R into subintervals Δ. If the N measurement points are chosen at random, according to ref. 15, the interval R should be partitioned into subintervals

$$\Delta(\varphi) = \frac{R}{1 + 3.3 \log N}. \tag{3}$$

Accordingly, the magnitude of the subinterval $\Delta(\varphi)$ is a function of the number of measurements N, and for large values of N the subinterval $\Delta(\varphi)$ can be made arbitrarily small. Knowing $\Delta(\varphi)$, we can partition interval R into subintervals

$$m = \frac{R}{\Delta(\varphi)}. \tag{4}$$

In turn, the total number of measurements N is partitioned into subgroups N_i such that

$$\sum_{i=1}^{m} N_i = N. \tag{5}$$

Knowing R, N, and N_i we can construct a histogram of the density function of φ_{loc} over the surface of the cathode under study:

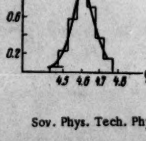

Fig. 2. Histogram of the density of the work function over the surface of a cathode of alloy D.

$$\mu(\varphi) = \frac{1}{N} \frac{N_i}{\Delta(\varphi)}. \tag{6}$$

When N is chosen satisfactorily$^{1)}$ we can assume that $N_i \sim dS$, and that $N \sim S$, the surface area of the cathode. Physically, the meaning of the function $\mu(\varphi)$ is the same as that of the function

$$\beta(\varphi) = \frac{1}{S} \frac{dS}{d\varphi}, \tag{7}$$

introduced in the analysis by Bulyginskii and Dobretsov.[17] Figure 2 shows a typical histogram of the density function of φ_{loc} for alloy D. This curve can be approximated by a Gaussian function over the interval ($\varphi_{\min} = 4.45$ V, $\varphi_{\max} = 4.75$ V):

$$\beta(\varphi) = 5.8 \exp[-96(\varphi - 4.62)^2]. \tag{8}$$

A knowledge of the function $\beta(\varphi)$ is frequently a sufficient basis for calculating the relations between the local emission parameters of a cathode and the integral parameters.[18]

Figure 3 shows the measured local work functions of the specimens studied over a broad temperature range; it is important to note that all the specimens are studied under identical vacuum conditions.

For tungsten and molybdenum we obtain values of the temperature coefficient of the work function which are slightly too high because of the relatively poor vacuum (10^{-7} torr).

For Mo–Pt emitters the temperature coefficient of the work function is higher. For alloy B $d\varphi/dT \sim 9 \cdot 10^{-4}$ V/deg, for alloy C, $6 \cdot 10^{-4}$ V/deg, and for alloy D, $1 \cdot 10^{-3}$ V/deg.

It should be noted that there are serious difficulties involved in measuring the local emission as a function of

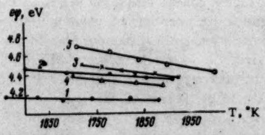

Fig. 3. The work φ_{loc} as a function of the temperature. 1) Mo; 2) W; 3) alloy B; 4) alloy C; 5) alloy D. These results correspond to the situation after the first heating at T > 2100°K.

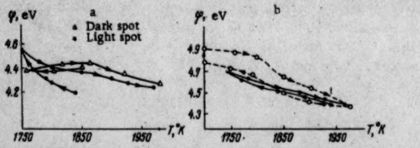

Fig. 4. The work function φ_{loc} as a function of the temperature for alloy A. a: Functional dependences obtained after 10 min. Filled points – grain with a low work function; triangles – high work function. b: Functional dependences for a grain with a high work function. Filled points – functional dependence obtained after 10 min; circles – after 40 min.

the temperature or time for a small cathode, because of the possible displacement of the image with respect to the collector system. We therefore carry out a more detailed study of alloy A, which has large regions of homogeneous emission. Figure 4 shows the work functions measured for two grains after alloy A is heated briefly at T > 2100°K (Fig. 4a).

The arrows show the direction in which the temperature is changed. A curve is recorded over an average of 10 min. For a grain with a low work function (curve 1), the work function increases sharply from 4.2 to 4.55 V as the temperature is reduced from 1840 to 1750°K. Interestingly, when the temperature is raised to its original value, the work function turns out to be 0.2 V higher. A further increase in the temperature reduces the work function. These drops in the emission with temperature changes are not observed for a grain with a high work function (curve 2).

We then record analogous curves for a single grain, varying the time (Fig. 4b). Curve 3 is recorded over 10 min; the overall behavior is the same as that of curve 2. Curve 4 is recorded over 40 min; over this time we again observe the "hysteresis forms" in the functional dependence of the work function on the temperature.

This type of change in φ_{loc} involving hysteresis is typical of film systems. In a subsequent series of experiments with alloy A we attempt to find suitable temperatures and times for visualizing migrational surface processes.

Figure 5 shows thermionic-emission photomicrographs characterizing one such process. Figure 5a shows the emitter surface immediately after the high-temperature heating. Let us consider the entire process for the case of a poorly emitting grain (which appears dark on the image), extended in the vertical direction (arrow 1). The entire area at the left emits homogeneously, except for grain boundaries and other structural defects.

Figure 5b shows the same region at a lower temperature. At the left of the reference grain we clearly see a grain which is essentially indistinguishable in Fig. 5a (where only the boundaries of this grain are visible). The arrows on the image show the positions at which the diffusing element is emerging. As expected, these positions correspond to grain boundaries and structural defects. The new grain, which becomes visible after the temperature is reduced, begins to emit less intensely than the first grain. We also observe contrast within the grain. In Fig. 5c this grain is covered by an optimum film, and the contrast within the grain disappears. In this last figure we see yet another grain, which emits like the reference grain. As the temperature is raised, the image in Fig. 5a can be restored, and the entire process can be repeated.

It is evident from these photomicrographs that the emission of alloy A is governed by the selective adsorption of individual faces, being a function of the relation between the rates of diffusion and desorption of the elements of the alloy. The conditions prevailing in the preliminary treatment of the specimen strongly affect the entire process. We believe that it is precisely because of this circumstance that migrational processes were not visible previously in alloys with small amounts of the low-melting component.

It is important to note that the adsorption and migrational processes of the low-melting component continue quite rapidly and, in the case of alloy A, are accompanied by the appearance of a hysteresis loop in the functional dependence of the local work function on the temperature for those grains on which these processes occur (Fig. 4).

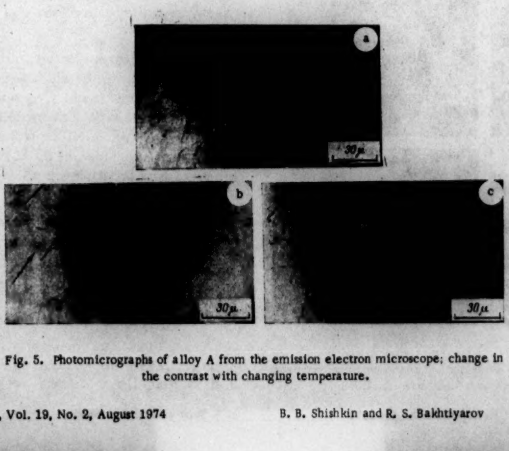

Fig. 5. Photomicrographs of alloy A from the emission electron microscope; change in the contrast with changing temperature.

Study of the alloys in the scanning electron microscope. These experiments are carried out in a JEOL apparatus.[2)] We are concerned primarily with alloy A.

To show that the image contrast in Fig. 5 changes because of adsorption and migration of the low-melting component (Pt) we exploit the circumstance that the secondary-electron-emission yield of platinum, σ_{Pt}, is higher than that of molybdenum, σ_{Mo} (ref. 19). We obtain images of the alloys in the scanning electron microscope after various types of heat treatment in the emission electron microscope.

The image contrast in the scanning electron microscope is produced by the microrelief and variations over the surface in the secondary-emission yield.[20] The images of alloys A-D obtained in the scanning microscope correlate well with the emission and optical photomicrographs. Figure 6 shows a series of photomicrographs of alloy A. The grain boundaries are bright, and the depressions on the surfaces of the grains turn out to be voids; only the edges of these voids are covered by a thin platinum film. The molybdenum base can be inspected within the voids at high magnification.

Study of the alloys in the x-ray microanalyzer. These experiments are carried out in a Cameca x-ray microanalyzer. We record the characteristic x radiation corresponding to the Lα line of platinum. We record curves showing the surface density of platinum after various types of heat treatment. Figure 7 shows the Pt distribution over the surfaces of alloys A and D after these alloys were held at T ≤ 1800°K. For alloy A the Pt content in the surface layer is much higher than that in the interior (Fig. 7a). A more complicated pattern is observed for alloy D (Fig. 7b). Here regions having the same platinum content as in the interior alternate with regions of a high platinum content (roughly twice that in the interior) on the surface.

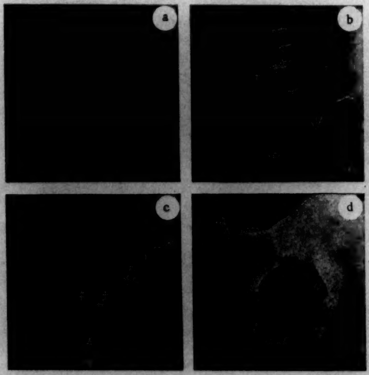

Fig. 6. Photomicrographs of the same region of alloy A obtained in the scanning electron microscope at various magnifications.

Intense evaporation of platinum begins at temperatures above 1900-2000°K. Figure 7b shows the platinum distribution for alloy B after it is held at T > 2000°K: The average Pt content falls to ~ 3%.

2. DYNAMICS OF THE EMISSION OF Mo–Pt ALLOYS

Here we compare our results with those hypotheses regarding the mechanism for the thermionic emission of alloys mentioned in the introduction.

Film hypothesis. The results described in Sec. 1 for alloy A, containing a small amount of platinum in molybdenum, confirm directly the role of a film mechanism in the thermionic emission of the alloy. It is important to emphasize that in a discussion of the results found in a study of only certain emission processes there is a possible ambiguity in the interpretation.

This ambiguity results from the interaction of the specimens with the residual gas in the emission electron microscope (we recall that the pressure in our apparatus was $p \sim 10^{-7}$ torr). Accordingly, in an attempt to distinguish the role of the specimen itself in its emission, we also carry out a multifaceted electron-microscope study of specimens of the alloys as well as test specimens of W and Mo. On the basis of the study of alloy A in the scanning microscope (Fig. 6) and in the x-ray microanalyzer (Fig. 7) we can assert that there are temperature ranges and heating times which result in the formation of a platinum film over the surface of alloy A.

Accordingly, the electron emission of alloy A is governed by both the emitter itself (i.e., by diffusion of platinum to the surface, migration of platinum, and desorption) and the interaction of the emitter with the residual gas in the apparatus. Each of these processes is a strong function of the temperature and is characterized by a certain heat of adsorption (or desorption) or diffusion (or migration) coefficient; together, they lead to a functional dependence of φ_{loc} on the temperature which displays hysteresis (Fig. 4). Separate study of these processes requires further refinement of the procedure for the experiments in the emission microscope: improving the vacuum in the apparatus, measuring the partial pressures of the residual gases, and carrying out various types of prototype experiments.

The experiments in the emission microscope show that platinum moves to the surface particularly rapidly along grain boundaries and at structural defects. As a result, each grain of the alloy is inhomogeneous with respect to emission. A more or less complicated distribution of φ_{loc} over the surface of the alloy is ultimately established after the heat treatment in the emission microscope (see, e.g., Fig. 2).

The fact that the Pt films can be observed in the scanning microscope and the x-ray microanalyzer as well as in the emission microscope shows that these films are not monolayers; on the contrary, they are rather thick. The appearance of these films on the surface of the alloy is accompanied by an increase in φ_{loc} (Fig. 4).

On the basis of our observation of surface processes in the emission microscope and measurement of the $\beta(\varphi)$ distributions (Figs. 1 and 2) we can also discuss the sec-

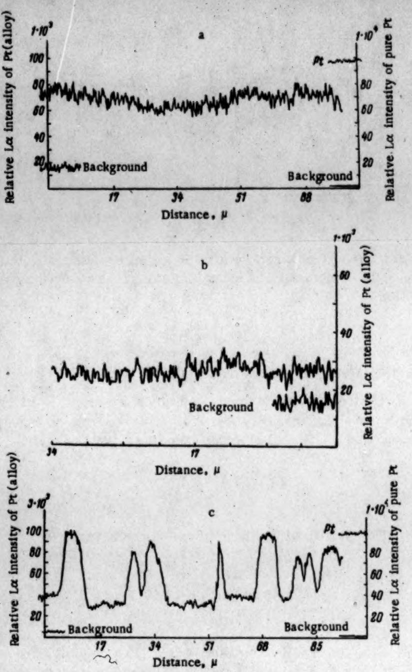

Fig. 7. Distribution of Pt over the surfaces of the alloys. a) Alloy A; b) alloy D; c) alloy B after heating.

ond hypothesis for the emission mechanism of binary alloys.

Hypothesis of spot fields. If the $\beta(\varphi)$ curves have been obtained, they can be used to relate the local emission of a specimen to the integrated emission.

We assume that there are m types of emission centers over the surface of a specimen. The total area occupied by centers of type i is assumed to be S_i. Then we have $\sum_{i=1} S_i = S$, where S is the total surface area of the emitter.

We assume that the values of $\varphi_{i\min}$ and $\varphi_{i\max}$ are known for each type of emission center. However, each type of center can be characterized by a function $\beta i(\varphi)$. If the emission centers emit independently, we can calculate the density of the emission current from spots of type i:

$$j_i = \int_{\varphi_{i\min}}^{\varphi_{i\max}} A_i T^2 \exp\left(-\frac{e\varphi}{kT}\right)\beta_i(\varphi)\,d\varphi. \tag{9}$$

We find the total current emitted by the entire surface to be

$$I = \sum_{i=1}^{m} S_i j_i. \tag{10}$$

Using Eq. (10) we can easily find (under the assumption of independently emitting spots) the work function of a spotty emitter averaged over the electron current:

$$\varphi^e = -\frac{kT}{e}\ln\frac{\sum_{i=1}^{m} S_i \int_{\varphi_{i\min}}^{\varphi_{i\max}} A_i \exp\left(-\frac{e\varphi}{kT}\right)\beta_i(\varphi)\,d\varphi}{AS}. \tag{11}$$

In deriving Eq. (11) we have formally divided the entire emitting surface into m types of spots. This division should of couse be carried out in correspondence with those physicochemical processes which occur on the surface of a complicated emitter. In other words, it is desirable to find criteria for sorting the spots. Such criteria can be based on physical processes which occur on the surface of a binary alloy. On the surface there are spots of the following types:

1. Various faces of the grains of the alloys components.

2. Various faces of the grains of various structural phases of the alloy.

3. Faces of grains covered by residual gas films, which give a set of values of φ_i which are functions of T, p (the pressure), and the residual gas composition.

4. Faces covered by films of material which have diffused from within the emitter; again the values of φ_i are functions of T.

5. Various types of chemical compounds which are essentially always present on the surface (particularly, carbides and oxides).

This list could of course be extended. In the experiments carried out in the emission microscope it is not always possible (particularly for complicated structures of type D) to specify (Fig. 1b) the type of spot corresponding to a given part of the surface. We therefore do not characterize a complicated cathode by a set of functions $\beta_i(\varphi)$ but by a single function $\beta(\varphi)$ (Fig. 2). In this case we can calculate $\tilde{\varphi}^e$ from an equation like (11):

$$\varphi^e = -\frac{kT}{e}\ln\frac{\int_{\varphi_{\min}}^{\varphi_{\max}} A_\varphi \exp\left(-\frac{e\varphi}{kT}\right)\beta(\varphi)\,d\varphi}{SA}. \tag{12}$$

Knowing $\beta(\varphi)$ and assuming $A_\varphi = A = \text{const}$ we can calculate any average work function of the emitter (i.e., an average over the surface, an average over the electron or ion current, an average photoelectronic work function, etc.).[11,18]

Equations (10) and (11) also contain possible nonmonotonic functional dependences of the thermionic-emission current of the binary alloy on the alloy composition.

Unfortunately, we have nothing to compare the calculations with, because we do not have results from a study of the integrated emission of specimens of Mo–Pt alloys.

We emphasize that Eq. (11) is derived under the assumption that the emission of the various spots is independent. The situation is much more complicated if the interaction of spots is taken into account. The extremely interesting effects which arise in this case are responsible for the fine structure of the anomalous Schottky effect. We propose to discuss these questions in a separate paper.

In concluding this section we support the assertion[21] that the experimental procedure must be carefully thought out (and described in detail in the corresponding papers!) in each specific study of the integrated work function of a complicated specimen, $\overline{\varphi}$.

3. POSSIBLE RELATION BETWEEN THE THERMIONIC EMISSION OF METALS AND ALLOYS AND THE COMPLICATED STRUCTURE OF THE CONDUCTION BANDS

The density distribution of electronic states in the conduction band, $\rho(\varepsilon)$, has now been calculated theoretically and determined experimentally for several metals and alloys. It is well known that knowledge of these functions yields information about the energy distribution of electrons in the conduction band,

$$f(\varepsilon)=\rho(\varepsilon)\frac{1}{\exp\left[\frac{\varepsilon-\varepsilon_F}{kT}\right]+1}, \tag{13}$$

where ε is the electron energy (measured from the bottom of the conduction band of the metal) and ε_F is the Fermi energy. If the function $f(\varepsilon)$ is known for a given metal or alloy, most of the characteristics of a metal governed by conduction electrons can be calculated automatically.[22,23]

An experimental method for determining $\rho(\varepsilon)$ over a broad energy range – the Spicer photoemission method[24] – has been used in experimental studies of Cu and Ag (ref. 25), W (ref. 26), Mo (ref. 27), Pt (ref. 28), and several other specimens. In particular, a peak has been found in $\rho(\varepsilon)$ immediately adjacent to the Fermi level in the conduction band of Mo (ref. 27) (Fig. 8). This peak is due to d electrons of molybdenum and naturally is manifest in experimental studies of any of the optical properties of this metal (the spectral coefficients, the quantum yield of photoelectrons, and their distribution functions).

The results of experiments on the thermo-photoemulsion of Mo and the Mo–BaO system carried out in our laboratory find a natural explanation in terms of this peak.[29] It is hoped that the thermionic-emission effects are related, to the complicated structure of the conduction bands of real metals and alloys. The Samsonov hypothesis[6] follows directly from this idea but ignores the fundamental difficulties involved here.[30]

In a formal discussion we can analyze the thermionic emission of a real material on the basis of this scheme. From the $\rho(\varepsilon)$ distribution found from quantum-mechanical calculations[31] at T = 0°K or found experimentally and from the Fermi function we can find,[3] according to (13), the distribution function $f(\varepsilon)$.

We assume that the work function of the specimen, φ, is known (from either theory or experiment). Then those

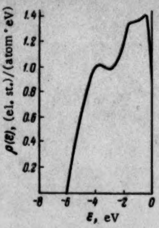

Fig. 8. Density of states in the conduction band of Mo, according to the experimental results of ref. 27.

electrons whose kinetic energies $\varepsilon_\perp$ (associated with the velocity component normal to the surface) satisfy the condition

$$\varepsilon_\perp \geqslant \varepsilon_F + e\varphi \tag{14}$$

participate in the thermionic emission.

The relative number of such electrons is given by the yield function $T(\varepsilon)$ (refs. 24, 29). If we assume an isotropic distribution of electron velocities, we can write

$$T(\varepsilon)=\left(\frac{1}{2}-\sqrt{\frac{\varepsilon_F+e\varphi}{\varepsilon}}\right). \tag{15}$$

The density of emitted thermionic electrons is

$$n=\int_0^\infty f(E)\,T(E)\,dE, \tag{16}$$

where the energy E is measured from the vacuum level. Finally, we find the thermionic-emission current density by the standard method:

$$j=en\bar{v}, \tag{17}$$

where $\bar{v}$ is the most probable velocity of the emitted electrons.

Using the expression for $\rho(\varepsilon)$ found on the basis of the Sommerfeld model of a metal,[22] we find

$$j=\frac{4\pi mek^2}{h^3}T^2\Psi\left[\frac{E}{kT},\ \frac{\varepsilon_F+e\varphi}{kT}\right]\exp\left(-\frac{e\varphi}{kT}\right)=A_0\Psi T^2\exp\left(-\frac{e\varphi}{kT}\right), \tag{18}$$

i.e., the ordinary Richardson–Dushman equation. The complicated functional Ψ in (18) is approximately equal to unity, but always slightly smaller.

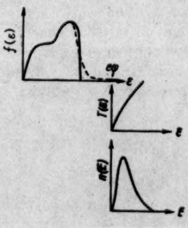

Fig. 9. Scheme for calculating the thermionic emission current of molybdenum.

The scheme for the numerical calculation of j for Mo on the basis of the actual $\rho(\varepsilon)$ distribution is clear from Fig. 9. Similar schemes can be easily worked out for Pt, W, and other metals, for which $\rho(\varepsilon)$ and φ are known.

Using the formal scheme described above for analyzing thermionic emission, we can also find the hysteresis forms of the functional dependence of the thermionic emission current on the temperature and thus find the effective values of φ_{loc} measured in our experiments (Figs. 3 and 4). Exact calculations cannot be carried out at present because the functions $\varepsilon_F(T)$ and $\varphi(T)$ are not known.

According to this scheme for analyzing the thermionic emission of metals and alloys having a conduction band complicated in structure, the thermionic-emission current density is given by

$$j = A[\rho]T^n \exp\left[-\frac{e\varphi}{kT}\right], \tag{19}$$

where A is governed by the density of electronic states in the conduction band of the emitter; the exponent n can be either larger or smaller than 2, depending on $\rho(\varepsilon)$ and $T(\varepsilon)$.

CONCLUSION

The results of this joint electron-microscope and x-ray study of emitters of Mo–Pt alloys cannot be explained on the basis of any single model for the emission of an alloy.

We have reported the first observation of the formation of films of the low-melting component (Pt) on the surface of a binary Mo–Pt alloy having a small amount of Pt (1%). Our experimental results show that these films, which lead to an increase in the value of φ_{loc}, are not monolayers. The frequent attempts which have been made to explain the results of a study of the integrated emission of alloys on the basis of the model of an electrical double layer (this model is convenient for explaining the "arrangement" of atoms on any ideal, usually single-crystal, surface) are not satisfactory for the case of Mo–Pt alloys. Furthermore, there is a basis for assuming that this double-layer model is also unsuitable for alloys of other compositions.

On the basis of this experimental study of the spottiness of emitters of these alloys, we can relate the local thermionic-emission properties to the integrated properties, which are usually measured in practice. On the basis of Eqs. (11) and (12) for $\bar{\varphi}^e$ derived here, it is clear that we can expect a complicated, nonmonotonic functional dependence of $\bar{\varphi}^e$ on the alloy composition [through $\beta_i(\varphi)$ and $\beta(\varphi)$]. The situation which arises in an attempt to relate the integrated and the local emission properties of an emitter is considerably more complicated when the fine structure of the anomalous Schottky effect is taken into account.[18]

We believe that many aspects of the phenomenon of thermionic emission (not only the emission of binary alloys) can be explained on the basis of the scheme analyzed above [(13)–(18)].

In this formal scheme (and we again emphasize that it is only a formal scheme) the thermionic emission current density is governed by, first, the state of the specimen surface [by the quantity $e\varphi$ which appears in the exponential function in $e\varphi$] and, second, the internal electronic structure of the specimen (the electronic-state density is related to the value of the constant A_0).

Our scheme for analyzing the phenomenon of thermionic emission is completely consistent with the current quantum-mechanical theory of this phenomenon.[32]

Our scheme for analyzing this phenomenon contradicts the classical thermodynamic description,[33] according to which A_0 is a universal constant for all thermionic emitters, governed by the zero of the entropy.

This contradiction, which is a fundamental question regarding the mechanism for this phenomenon, has already generated some discussion[6,30] but unfortunately has not yet been resolved.

---

1) The usual test of the suitability of the choice is the agreement of the histograms for N_1 and N_2 measurements, where $N_2 > N_1$ (ref. 16). In ref. 16, $\Delta(\varphi)$ is chosen to be the error in the measurement of φ_{loc}. It follows from our experiments that $\Delta(\varphi)$ must be chosen to be of the order of or at least no smaller than the error in the method used to measure φ. This error is governed by the operating stability of the apparatus (the constancy of M, the stability of the gun which heats the specimen, etc.) and is generally much smaller than the error in the measurement.

2) The authors thank R. S. Gvozdover for assistance in the experiments in the JEOL scanning electron microscope.

3) After multiplication of the functions appearing in (13), the resulting curve must be renormalized.

---

[1] B. Ch. Dyubua, A. I. Pekarev, B. N. Popov, and M. A. Tylkina, Radiotekh. Elektron., 7, 1568 (1962).

[2] B. Ch. Dyubua, O. K. Kultashev, and L. V. Gorshkova, Fiz. Tverd. Tela, 8, 1105 (1966) [Sov. Phys. – Solid State, 8, 882 (1966)].

[3] B. Ch. Dyubua and O. K. Kultashev, Fiz. Met. Metalloved., 21, 396 (1966).

[4] B. Ch. Dyubua and L. A. Ermolaev, Surface Phenomena in Melts and in the Solid Phases Appearing in Them [in Russian], Kabardino-Balkarskoe Kinzhn. Izd., Nal'chik (1965), p. 429.

[5] T. L. Matskevich, Zh. Tekh. Fiz., 38, 401 (1968) [Sov. Phys. – Tech. Phys., 13, 295 (1968)].

[6] G. V. Samsonov, Yu. B. Paderno, and V. S. Fomenko, Zh. Tekh. Fiz., 36, 1435 (1966) [Sov. Phys. – Tech. Phys., 11, 1070 (1967)].

[7] N. B. Smirnova, B. G. Smirnov, S. M. Mikhailov, and S. P. Sytaya, Fiz. Tverd. Tela, 11, 962 (1969) [Sov. Phys. – Solid State, 11, 784 (1969)].

[8] N. B. Smirnova, B. G. Smirnov, S. M. Mikhailov, and G. N. Shuppe, Fiz. Tverd. Tela, 12, 1277 (1970) [Sov. Phys. – Solid State, 12, 1001 (1970)].

[9] E. M. Savitskii, L. N. Litvak, and I. V. Burov, Zh. Tekh. Fiz., 41, 2431 (1971) [Sov. Phys. – Tech. Phys., 16, 1929 (1972)].

[10] R. S. Bakhtiyarov and B. B. Shishkin, Zh. Tekh. Fiz., 42, 2229 (1972) [Sov. Phys. – Tech. Phys., 17, 1752 (1973)].

[11] I. Buribaev, Dissertation [in Russian], MGU (1971).

[12] B. B. Shishkin, G. V. Spivak, V. G. Dyukov (Djukov), R. S. Bakhtiyarov (Bachtijarov), and I. Buribaev, Proceedings of the Seventh International Congress on ECEM, Grenoble, 1970.

[13] I. Buribaev, R. S. Bakhtiyarov, V. G. Dyukov, G. V. Spivak, and B. B. Shishkin, Izv. Akad. Nauk SSSR, Ser. Fiz., 34, 1513 (1970).

[14] G. V. Spivak and B. B. Shishkin, Radiotekh. Elektron., 11, 1826 (1966).

[15] E. S. Venttsel', Theory of Probability [in Russian], Izd. Nauka, Moscow (1964).

[16] B. B. Shishkin, V. M. Pumpurs, and G. V. Spivak, Izv. Akad. Nauk SSSR, Ser. Fiz., 7, 1169 (1968).

[17] D. G. Bulyginskii and L. N. Dobretsov, Zh. Tekh. Fiz., 26, 977 (1956) [Sov. Phys. – Tech. Phys., 1, 957 (1956)].

[18] R. S. Bakhtiyarov, Author's abstract, Dissertation [in Russian], MGU (1973).

[19] I. M. Bronshtein and B. S. Fraiman, Secondary Electron Emission [in Russian], Izd. Nauka, Moscow (1969).

[20] G. V. Spivak, G. V. Saparin, and M. V. Bykov, Usp. Fiz. Nauk, 99, 635 (1969) [Sov. Phys. – Usp., 12, 756 (1970)].

[21] M. Green (ed.), Solid State Surface Science, Dekker, New York (1970), Ch. 4.

[22] H. Bethe and A. Sommerfeld, Electronic Theory of Metals [Russian translation], ONTI, Moscow (1938).

[23] I. M. Lifshits, M. Ya. Azbel', and M. I. Kaganov, Electronic Theory of Metals [in Russian], Izd. Nauka, Moscow (1971).

[24] W. E. Spicer, Proceedings of the International Colloquium on "Optical Properties and Electronic Structure of Metals and Alloys," Paris, September 1965, p. 246.

[25] C. N. Berglund and W. E. Spicer, Phys. Rev., 136, A1044 (1964).

[26] C. R. Zeisse, Proceedings of the International Conference on "Electronic Density of States," Nat. Bur. Std., Gaithersburg, Md., November 1969.

[27] K. A. Kress and G. J. Lapeyre, Proceedings of the International Conference on "Electronic Density of States," Nat. Bur. Std., Gaithersburg, Md., November 1969.

[28] S. F. Lin, D. T. Pierce, and W. E. Spicer, Phys. Rev., B4, 326 (1971).

[29] B. B. Shishkin and I. Buribaev, Radiotekh. Elektron., (in press); I. Buribaev, Author's abstract, Dissertation [in Russian], MGU (1971).

[30] L. N. Dobretsov and T. L. Matskevich, Zh. Tekh. Fiz., 36, 1449 (1966) [Sov. Phys. – Tech. Phys., 11, 1081 (1967)].

[31] L. F. Mattheis, Phys. Rev., 139, A1893 (1965).

[32] A. M. Brodskii and Yu. Ya. Gurevich, Theory of Electron Emission from Metals [in Russian], Izd. Nauka, Moscow (1973); A. M. Brodskii and Yu. Ya. Gurevich, Zh. Eksp. Teor. Fiz., 54, 213 (1968) [Sov. Phys. – JETP, 27, 114 (1968)]; Semicond.; A. M. Brodskii (Brodscij) and Yu. Ya. (Yu. Ja.) Gurevich, Phys. Status Solidi, 40, 139 (1970).

[33] O. W. Richardson, Emission of Electricity from Hot Bodies, London (1916); H. Tetrode, Ann. Phys., 38, 434 (1912); O. Sackur, Ann. Phys., 40, 67 (1913); S. Dushman, Phys. Rev., 21, 623 (1923).

Analysis of the cathode spot in a vacuum arc

I. I. Beilis

Institute of High Temperatures,
Academy of Sciences of the USSR, Moscow

(Submitted August 4, 1972; resubmitted June 26, 1973)
Zh. Tekh. Fiz., 44, 400–410 (February 1974)

A complete system of equations is given for the cathode region of a vacuum arc. Long-lived cathode spots are considered. The effect of the total spot current on the degree of ionization, the cathode temperature, the electric field, the current density, the electron temperature, the charged-particle density, and the rate of removal of vapor from the cathode region is determined. The effects of the thermophysical and emission constants of the cathode material and changes in the cathode potential drop and the mass flow rate of material from the cathode are also found. The role of multiply charged ions and excited atoms in the ion current in the cathode region is also studied.

At the present time the literature does not contain a theory for the cathode spot of an arc discharge. Detailed analyses of existing attempts to explain the cathode processes in the electric arc have been given by Rakhovskii[1] and by Kesaev.[2] As a rule, such attempts are unsatisfactory in a number of ways. For example, the theoretical model contains a free parameter, with the result that the system of equations is not closed. Moreover, the theoretical models used by various authors are concerned with processes occurring in the solid and at its surface (heat conduction, emission of electrons from the cathode) whereas the processes taking place in the cathode region (motion of the charge carriers, rate of generation and loss, heating of the cathode gas) are usually ignored. The attempt of Kozlov and Khvesyuk[3] to fill this gap is unsuccessful since their results contradict the hypotheses on which their paper is based. In a recent paper, Kulyapin[4] concerns himself solely with the thermophysical and emission processes at the cathode without relating them to the parameters of the plasma.

A physical and mathematical model free from the above defects is developed in refs. 5 and 6 on the basis of an analysis of the elementary processes occurring in the cathode region of a vacuum arc. In the range of parameters considered in ref. 6 the cathode plasma, in which the electric field is relatively small ($E_{\text{plasma}} \leqslant 10^3$ V/cm), is separated from the cathode by a collisionless sheath, across which almost all the cathode potential drop occurs. Plasma ions are accelerated in this collisionless sheath and impinge upon the cathode, heating it through conversion of their kinetic and potential energy. The potential distribution and electric field in the collisionless sheath are determined by the positive space charge of ions arriving from the plasma. The electric field arising in this sheath facilitates emission of electrons from the cathode and communicates energy to charged particles moving in this sheath. Emitted electrons, which are accelerated by the positive space-charge field, carry energy to the cathode plasma. This energy is dissipated in the cathode plasma in ionization and heating of the plasma. Ionization occurs both through collisions with fast electrons and through thermal ionization. The resulting ions diffuse toward the cathode surface at a rate determined by resonance charge exchange.

In this model the parameters taken to be prescribed are: the total current at the spot I, the cathode voltage drop u_c, the mass rate of erosion of cathode material G_{er}, and the physical constants of the cathode material. The quantities subject to determination are: the current density i_0, the fraction of the current density carried by electrons $s = i_e/i_0$, the cathode temperature T_C, the heavy-particle temperature T, the electron temperature T_e, the degree of ionization α, the macroscopic rate of removal of electrode material from the cathode region u, the plasma density, and the electric field E at the cathode surface.

In this paper we present a detailed analysis of the solution of the system of equations of refs. 5 and 6 over a wide range of values of I, and we also determine how the parameters of the cathode spot vary with the thermophysical constants, the work function, the cathode voltage drop, and the amount of material eroded from the cathode. We also examine the steady-state regime of the discharge at the cathode.

THE SYSTEM OF EQUATIONS

For convenience we list the complete system of equations describing the processes in the cathode region of a vacuum arc.[5,6] The equation for the ion flux is

$$\left.\begin{aligned} \Gamma_i &= -(1+\theta) D_{ia}\frac{dn_i}{dx} + n_i u + \alpha D_{ia}\psi, \\ D_{ia} &= \frac{0.4 \cdot V_{iT}}{(n_a + n_i)\sigma_{ai}}, \quad \theta = \frac{T_e}{T}, \\ \psi &= \frac{1}{kT}\left[\frac{dP}{dx} - n_i\frac{d(kT_e)}{dx} - (n_a + n_i)\frac{d(kT)}{dx}\right], \quad \alpha = \frac{n_i}{n_a + n_i}. \end{aligned}\right\} \tag{1}$$

The ion equation of continuity is

$$\frac{d\Gamma_i}{dx} = \sigma_i n_a N_{e0} \exp\left[-\int_0^x (n_a\sigma_i + 2n_i\sigma_{\text{cr}})\,dx\right] + \beta n_0^2 n_i\left[1 - \left(\frac{n_i}{n_0}\right)^2\right]. \tag{2}$$

The boundary conditions are

$$D_{ia}\frac{dn_i}{dx}\Big|_{x=0} = \frac{1}{2} n_a v_{iT}; \quad n_i|_{x=\infty} = n_0; \quad n_a = P/kT - (1+\theta) n_i.$$

The energy balance equation for the plasma electrons is

$$\begin{aligned} s(eu_e + 2kT_{\text{C}}) - (1 - s + \alpha\zeta) u_i = 3kT_e(1 + \alpha\zeta) \\ + Q^{**} + (1 - s) kT_e\left(\frac{m_i T_e}{m_e T}\right)^{1/2} e^{-\frac{eu_e}{kT_e}}, \end{aligned} \tag{3}$$

where

$$Q^{**} = \frac{1}{i_0}\int_0^l \frac{3m_e}{m_i}\frac{n_i}{\tau_{ie}}(T_{\text{e}} - T)\,dx; \quad \zeta = \frac{e G_{\text{er}}}{m_i I}.$$

Equation (3) allows for heating of the plasma electrons by an energetic beam of electrons accelerated in the cathode drop region and for cooling through the process of ionization, through energy transfer to heavy particles in elastic collisions, and through the reverse flow of plasma electrons in the tail of the Maxwellian distribution with an energy in excess of eu_c.

The energy equation for the heavy component is

$$\frac{5}{2}k(n_a+n_i)u\frac{dT}{dx}=-\frac{d}{dx}\left(-\lambda_a\frac{dT}{dx}+\mu_{ai}J_i\right)+\frac{3m_e}{m_i}\frac{n_i}{\tau_{ie}}k(T_e-T),$$
$$\mu_{ai}=0.17n_akT/n_i,\ J_i=\Gamma_i-n_iu. \tag{4}$$

with boundary conditions: $T|_{x=0}=T_c$, $(\lambda_a dT/dx)_{x=\infty}=q_{iT}$.

Let us estimate the contribution of the term Q^{**} in (3). We integrate (4) to obtain

$$\frac{5}{2}k(T_e-T_c)u(n_i+n_a)=-(q^l_{i+a}-q^w_{i+a})+\int\limits_0^l\frac{3m_ek(T_e-T)n_i}{m_i\tau_{ie}}dx. \tag{5}$$

Taking the expression of Gogosov et al.[7] for the heat flux to the wall q^w_{i+a}, and assuming that the heat flux at the external boundary of the region of relaxation $q^l_{i+a}=0$, it is easy to show that $i_0Q^{**}=(5kT/2)(1+7T_c/5T_e)eu(n_i+n_a)$. The role of Q^{**} in Eq. (3) can be estimated, for example, in terms of its ratio to the first term on the right side of this equation. It is readily seen that if $(1+\alpha\xi)\cdot\theta/5eG_{er}>1$, then the term Q^{**}, which describes the energy transferred by the electrons to the heavy particles, can be neglected in Eq. (3). On the basis of this condition the term Q^{**} will not be taken into account in (3) in the specific calculations given below for the investigated range of variation of the current I.

Let us now consider the role of the terms in (4). For convenience, utilizing $(n_i+n_a)u=G_{er}i_0/Im_i$, we rewrite (4) in the following form:

$$\frac{d}{dx}\left(-\lambda_a\frac{dT}{dx}+\mu_{ai}J_i+\frac{5}{2}kT\frac{G_{er}i_0}{Im_i}\right)=\frac{3m_e}{m_i}\frac{n_i}{\tau_{ei}}k(T_e-T). \tag{6}$$

In determining the temperature T of the heavy particles from Eq. (6) all the terms of this equation must, generally speaking, be taken into account.

However, a detailed examination [by comparing the individual terms in (6)] of the region in which the electron and heavy-particle temperatures become equal has shown that the length of this region can be much greater than, much smaller than, or comparable with the relaxation region, depending on the charged-particle density. In the first and second cases, without solving Eq. (6) one can write T = const in the relaxation region; this constant is equal, respectively, to T_c or T_e. For example, for $n_i\sim 10^{18}$ cm^{-3} and with no density gradient ($J_i=0$), Eq. (6) acquires the form $d[-\lambda_a(dT/dx)]/dx=0$, from which it follows that $T=\text{const}=T_c$. When the relaxation region and the region in which the temperatures equalize are comparable, the heavy-particle temperature in the Debye sheath will not be a constant.

For the range of parameters investigated below it is not possible to make an unequivocal estimate of the heavy-particle temperature T. Accordingly, we shall solve our system of equations for $T=T_c$; however, to find the effect of a variation in the absolute value of T, the case $T=T_e$ is also considered.

Let us now consider the equations describing the processes taking place within the solid and at its surface.[1)]

The electron current i_e in the collisionless sheath adjacent the cathode is determined from the equation

$$si_0=\frac{4e\pi m_ekT_c}{h^3}\int\limits_{-\infty}^{\infty}\frac{\ln\left[1+\exp\left(-\frac{\varepsilon}{kT_c}\right)\right]d\varepsilon}{\exp\left[\frac{6.85\cdot 10^7(\varphi-\varepsilon)^{3/2}\theta(\tilde{y})}{E}\right]}-\frac{e}{4}n_iv_{eT}e^{-\frac{eu_c}{kT_e}}. \tag{7}$$

The first term on the right side of Eq. (7) determines the emission current allowing for the action of the positive space-charge field on the electrons; the electron energy distribution ε in the conduction band at the corresponding cathode temperature is described by Fermi–Dirac statistics. The second term on the right gives the number of electrons from the plasma with energies greater than eu_c.

In the calculations the following expression[8] is used for $\theta(\tilde{y})$:

$$\theta(\tilde{y})=1-\tilde{y}^2\left[1+0.85\sin\left(\frac{1-\tilde{y}}{2}\right)\right].$$

The system of equations is solved below for the so-called long-lived spots. The elementary processes taking place in such spots can be regarded as steady-state, while the unsteady burning of the discharge can be ascribed solely to the establishment of the thermal process in the bulk of the electrode. Accordingly, the lifetime of the cathode spot will vary from 10^{-4} to 1 sec. Energy balance at the cathode gives:

$$0.24\left[(1-s)u_{\text{eff}}i_0+\frac{e}{4}n_iv_{eT}e^{-eu_c/kT_e}(2kT_e+\varphi-3.62\cdot 10^{-4}\sqrt{E})\right]$$
$$=2\lambda_T\sqrt{\frac{i_0}{I}}(T_c-300)\left[\frac{2}{\pi}\operatorname{arc\,tg}\sqrt{\frac{4\pi a i_0 t}{I}}\right]^{-1}+\left(\lambda_e+\frac{2kT_c}{m_i}\right)G_{er}\frac{i_0}{I}$$
$$+1.4\cdot 10^{-12}T_c^4, \tag{8}$$
$$(1-s)u_{\text{eff}}=(1-s)(u_c+u_i)-\varphi+3.62\cdot 10^{-4}\sqrt{E}. \tag{8a}$$

Allowance is made in (8) and (8a) for heating of the cathode through conversion of the potential and kinetic energy of ions and of electrons from the tail of the Maxwellian distribution bombarding the cathode. The heat flux into the electrode is calculated on the assumption that the current in the cathode spot is distributed according to a Gaussian law and that the electrode itself, in comparison with the effective size of the source of heat, is a semiinfinite body. The cathode is cooled through the evaporation and removal of material from the cathode region (G_{er}, experimentally[1] determinable) and through losses to radiation according to the Stefan–Boltzmann law. The cathode is also cooled as a result of emission of electrons. The energy carried away from the cathode by the electrons is taken to be the work function φ reduced[10] by the Schottky effect ($T_c\sim$ 3600–4000°K). The electric field is determined from the equation

TABLE A

	i_0, A/cm²	T_C, °K	w_e, eV	α_∞	s	f_w
First method	$5\cdot10^4$	3720	1.22	0.11	0.456	0.7
Second method	$5.63\cdot10^4$	3737	1.33	0.1	0.464	1

$$E^2 = 7.57\cdot10^5 (u_c)^{1/2} i_0 \Big[(1-s)(1.845\cdot10^3 A_i)^{1/2} - s - \Big(\frac{2e}{m_e}\Big)^{1/2} \frac{en_i}{2i_0}\frac{kT_e}{u_c^{1/2}}\big(1-e^{-eu_c/kT_e}\big)\Big]. \tag{9}$$

Equation (9) is essentially the Mackeown equation including the effect of space charge of the electrons moving from the plasma to the cathode. In the collisionless sheath the plasma electrons are assumed to follow a Boltzmann distribution ($u_c \sim 15$ eV, $w_e \sim 1$ eV). This term can be neglected if $w_e/(w_i e u_c)^{1/2} \ll 2.7\cdot10^3$.

The degree of ionization α in the equilibrium region is determined from the Saha equation

$$3.8\cdot10^{-10}\frac{10^{A_s - B_s/T_k}}{(w_k w_i)^{1/2}} = \frac{1-\alpha}{\alpha^2}(w_e)^{3/2} e^{-3u_i/2w_e}. \tag{10}$$

When Eqs. (1) and (2) are written in dimensionless form (below) we see that if

$$\frac{(1+\theta)D_{ia}}{\beta n_0^2 l_i^2} \ll 1, \tag{11}$$

the ion density gradient occurs mainly at a distance from the cathode equal to the ion mean free path l_i. The ion density does not vary with increasing distance from the cathode above this value and is equal to the equilibrium value. In this case the flux of ions to the cathode can be determined in two ways. Assuming that the hydrodynamic relation holds up to the wall (x = 0), by solving the system of equations (1)–(10), we can determine the ion flux from the boundary condition of Eq. (2), which depends on the density at the wall n_w. The other method is as follows. Without considering the processes occurring in a distance of one mean free path, we regard the ion density as constant and equal to the equilibrium value up to the wall. Since the ion distribution function is a Maxwellian[6] it follows that the ion flux is given by $n_0 v_{iT}/4$, and Eqs. (1) and (2) in the general system can be dropped.

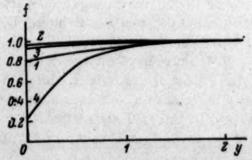

Fig. 1. Ion density distribution in the cathode plasma f as a function of distance y.

TABLE 1

Number appended to curves of Fig. 1	n_0, cm⁻³	D_{ia}, cm²/sec	i_s, A/cm²	θ
1	10^{20}	1	10^5	10
2	10^{19}	10, 0.1	10^4	3
3	10^{19}	0.1	10^6	10
4	10^{19}	0.1	10^5	10

The system of equations for a copper cathode was solved by these two methods for a current of 200 A. The results of the calculations are shown in Table A. Here, $f_w = n_w/n_0$. The results given by the two methods agree and the ion density at the wall as determined by the first method is close to the equilibrium value. Accordingly, system (1)–(10) is simplified when (11) is satisfied.

Before discussing the solution of the system of equations let us estimate the influence of excited atoms and multiply charged ions in the relaxation region and consider Eqs. (1) and (2) in more detail allowing for the excitation process.

The presence of excited atoms in the cathode region can result in stepwise ionization and thus constitutes an additional source of ions. It can also reduce the energy of the plasma electrons when the excited atoms move to the cathode or pass through the outer boundary of the relaxation region. The energy flux carried away to the cathode by the excited atoms, of density n^*, we estimate, for example, from the expression $(n^* v_{iT} u^*/4)$ (the energy flux through the outer boundary of the relaxation region will be still smaller since $v_{iT} \gg u$). Comparing this expression with the first term on the right side of (3) gives $[2w_e(1+\alpha\xi)/(1-s)u^*]\,n_0/n^* \sim n_0/n^*$. The energy carried away by excited atoms thus becomes significant only when n^* is close to n_0. On the assumption that the excited atoms obey a Boltzmann distribution ($w_e \sim 1$ eV, $n_a \sim 10^{20}$ cm⁻³),

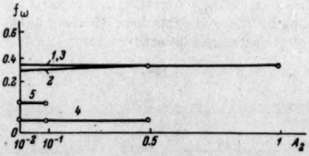

Fig. 2. Variation of ion density at wall f_w with density of excited atoms A_2 at θ = 10.

TABLE 2

Number appended to curves of Fig. 2	n, cm⁻³	D_{ia}, cm²/sec	f_w A/cm²
1	10^{20}	0.1	10^5
2	10^{19}	0.1	10^6
3	10^{19}	10	10^4
4	10^{19}	0.1	10^4
5	10^{19}	0.01	10^6

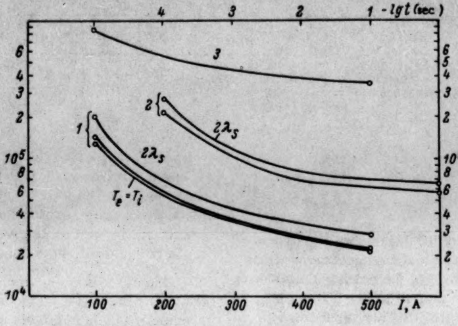

Fig. 3. Variation of current density i_0 with total current I (curves 1) and with discharge duration (curves 2). Curve 3 shows the variation of the electric field E (V/cm) with total current.

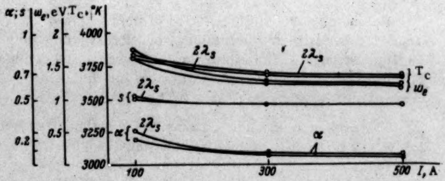

Fig. 4. Variation with the total current I of degree of ionization α, current fraction carried by electrons s, electron energy w_e, and cathode temperature T_c.

the quantity n* can be estimated from $n^*/n_a \sim \exp(-u^*/w_e) \sim 10^{-2}$. It follows, taking $\alpha \sim 0.1$ (see the Table 1), that $n_0/n^* \gg 1$. We note that as a rule it is mainly ion lines that are observed in experimental studies of cathode spots on copper.

With the aim of determining how the quantities n*; D_{ia}; i_e; T_e; n_0 affect the nonequilibrium region we write equations like (1) and (3) in dimensionless form, remembering that electrons leave the beam through excitation of neutrals, stepwise ionization, direct ionization, and by scattering by charged particles. Ions are generated as a result of stepwise and direct ionization:

$$\frac{d^2f}{dy^2} = A_1[(1+\theta)(1-f) - A_2]\exp\left\{-\left[(1+\theta)(1-f) + \frac{f\sigma_k}{\sigma_i+\sigma^*} - A_2\left(1-\frac{\sigma_i^*}{\sigma_i+\sigma^*}\right)\right]By\right\} - A_2A_3\exp\left\{-\left[(1+\theta)(1-f) + \frac{f\sigma_k}{\sigma_i+\sigma^*} - A_2\left(1-\frac{\sigma_i^*}{\sigma_i+\sigma^*}\right)\right]By\right\} + A_4\frac{df}{dy} - f(1-f^2). \tag{12}$$

The boundary conditions are $df/dy/_{y=0} = A_5 f_w$, $df/dy|_{y=\infty} = 0$, where $A_1 = \sigma_i i_e/e\beta n_0^2$, $f = n_i/n_0$, $A_3 = i_e\sigma_i^*/e\beta n_0^2$, $B = (\delta_i + \sigma^*)(D_{ia}/\beta)^{1/2}$, $A_4 = i_0 G_{er}/\mathrm{Im}\, n_0^2(\beta D_{ia})^{1/2}$, $A_5 = v_{iT}/2n_0(\beta D_{ia})^{1/2}$, $y = (\beta n_0^2/D_{ia})^{1/2}x$. The value T_e is chosen to make the degree of ionization unity at infinity. The remaining parameters are prescribed in the following ranges: $i_e = 10^4$–10^6 A/cm², $D_{ia} = 0.01$–10 cm²/sec, $n_0 = 10^{18}$–10^{20} cm^{-3}, $A_2 = n^*/n_0 = 10^{-2}$–1. The results of calculations based on Eq. (12) are shown in part in Figs. 1 and 2 and in Tables 1 and 2. These results show that the ion density distribution at the cathode is not greatly affected by the direct and stepwise ionization. This indicates the relatively small role played by the beam in the ionization process and the dominant role of thermal ionization. The ion density at the wall f_w begins to depart significantly from the equilibrium value only at relatively large T_e ($\theta = 10$) and small D_{ia}. The diffusion coefficient has a significant effect when $D_{ia} \le 0.1$. Reducing D_{ia} from 0.1 to 0.01 cm²/sec reduces the degree of ionization at the wall f_w (at y = 0) from 0.55 to 0.25. An estimate of the effect of the rate of flow of vapor from the cathode region on the ion density distribution by eliminating the corresponding term ($A_4 = 0$) in Eq. (12) shows that this effect can be neglected in the investigated range of parameters.

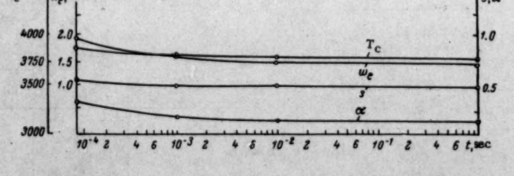

Fig. 5. Effect of discharge lifetime on degree of ionization α, current fraction carried by electrons s, electron energy w_e, and cathode temperature T_c.

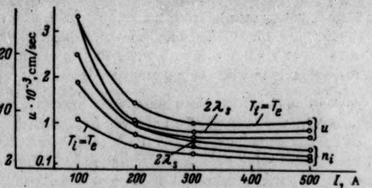

Fig. 6. Variation of ion density n_i and macroscopic rate of flow of vapor u with current strength I.

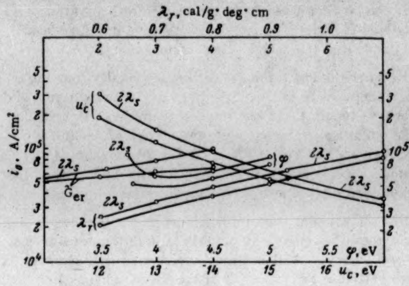

Fig. 8 Effect on current i_0 of varying the work function φ, the thermal conductivity λ_T, the heat of evaporation λ_s, and the mass flow rate G_{er} of cathode material.

Finally, let us determine the effect of multiply charged ions on the ion current and the energy of the electrons in the cathode region. The presence of multiply charged ions in the electrode regions is noted in refs. 11 and 12. We estimate the contribution of such ions in terms of the equilibrium value in the charged-particle balance for an arc discharge in copper, assuming that the charged particles are produced in the form of singly (n_i), doubly (n_{2i}), and triply (n_{3i}) charged ions. The degree of ionization $\alpha = n_e/(n_a + n_e)$, where $n_e = n_i + 2n_{2i} + 3n_{3i}$ by virtue of quasineutrality. Assuming also constancy of pressure, we determine the total density $n_n = P/kT = \theta n_e + n_i + n_{2i} + n_{3i} + n_a$. The densities of ions of all forms can be obtained from the following relationships: $n_e n_i/n_a = A_1^0$, $n_e n_{2i}/n_i = A_2^0$; $n_e n_{3i}/n_{2i} = A_3^0$, A_1^0, A_2^0, A_3^0 are equilibrium constants, dependent on the electron energy w_e. The heating of the plasma electrons we determine for simplicity by assuming that the beam electrons dissipate their energy solely on ionization and that the electron gas is cooled via the electron current through the outer boundary of the relaxation region.

Under these assumptions, when $T \sim 4000$°K, $s = 0.5$, $n_n \sim 10^{20}$ cm^{-3} we find that the various densities are $n_i \approx 1.1 \cdot 10^{19}$ cm^{-3}, $n_{2i} \approx 1.65 \cdot 10^{18}$ cm^{-3}, $n_{3i} \approx 1.4 \cdot 10^{14}$ cm^{-3}, $n_e \approx 1.4 \cdot 10^{19}$ cm^{-3}, and $w_e \approx 3.3$ eV. A calculation carried out under these assumptions for the case of singly charged ions alone gives $w_e \approx 3.64$ eV. Thus, the presence of multiply charged ions has little effect on the electron energy and on the ion current ($n_i \approx n_e$).

DISCUSSION OF SOLUTIONS

Equations (1)-(10) are solved for the cathode region of an arc discharge on copper subject to (11) and the conditions $T_e = T_i \neq T_c$ and $T_i = T_c \neq T_e$ for currents in the range from 100 to 500 A and for various times of burning of the discharge. The room-temperature values of the thermophysical constants are used in all the calculations. Deviations of these constants from these values will, however, be analyzed in detail. Figure 3 shows plots of current density i_0 versus the total current I for a stationary spot (curves 1) and plots of i_0 versus discharge duration for I = 200 A (curves 2). The results of solving the equations pertain to the condition $T_i = T_c$. The curve corresponding to $T_i = T_e$ is shown for comparison; here and below the legend $T_i = T_e$ will be appended to such curves. In like manner, curves to which the legend $2\lambda_s$ is appended correspond to solving the system of equations for a heat of evaporation λ_s equal to twice the room-temperature value. It can be seen from Fig. 3 that the current density i_0 in a discharge with lifetime of 10^{-3} sec and longer is close to the value of i_0 in the steady-state regime. Varying the total current I from 100 to 500 A varies the steady-state current density from $1.4 \cdot 10^5$ to $2 \cdot 10^4$ A/cm^2, i_0 varying very slightly with ion temperature.

It is interesting to note that an analysis of the areas of cathode spots on copper, measured using an SFR-1 high-speed photorecorder with a special optical attachment in the time loop regime,[9] shows that the current density in stationary and almost stationary spots varies from $3 \cdot 10^4$ to 10^5 A/cm^2 for current variations from 200 to 300 A. This current is distributed over a group of spots. As the distance between individual spots within this group is much smaller than the diameter of the spots, the group can be regarded in the calculations as constituting a single cathode spot.

Figure 4 shows the variation with total current I of the degree of ionization α, the fraction of the current carried by electrons s, the electron energy w_e, and the cathode temperature T_c. It can be seen that these quantities vary but little with I; their mean values are: $T_c \sim 3800$°K, $s \sim 0.5$, $\alpha \sim 0.1$, $w_e \sim 1$ eV. Figure 5 shows these quantities vary with the lifetime of the cathode spot

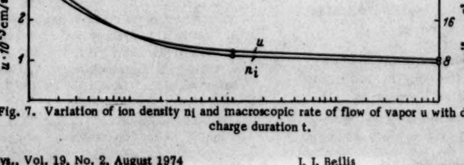

Fig. 7. Variation of ion density n_i and macroscopic rate of flow of vapor u with discharge duration t.

t. It can be concluded from the curves of Fig. 5 that α, s, w_e, and T_c scarcely vary with time and can thus be determined from the steady-state expressions.

Figures 6 and 7 show how the ion density and the macroscopic rate of flow of vapor vary with current I and discharge length t. It can be seen from these figures that these quantities vary but slighlty and are of order respectively, $n_i \sim 2 \cdot 10^{18}$-10^{19} cm^{-3}, $u \sim 10^3$ cm/sec. Conditions $u \ll v_{iT}$ and (11), allowing for the data on the other parameters cited above, are thus satisfied.

At the present time information on the thermophysical properties of electrode materials at high temperatures is very sparse.[13] Calculations are accordingly carried out to estimate the influence of the thermophysical parameters and also the effect of inaccuracy in measurements of the work function, the cathode drop, and the flow rate of electrode material on the current density in the cathode spot i_0. These calculations show (Fig. 8) that inaccuracy in measurements of these quantities introduces an error approximately equal to that obtained in the experimental determination of the current density. The rest of the parameters of the spot are also not affected greatly.

The results contained in Fig. 8 are of special interest when it is remembered that the view hitherto expressed in the literature is that it is the thermophysical parameters and the emission constants that have the decisive influence on the processes in the cathode spot. It would appear that this conclusion has been reached on the basis of an analysis of individual equations, which, as a rule, have not been solved simultaneously. The results of solving the system of equations simultaneously show that, despite variation of the thermophysical and emission constants, the processes in the cathode spot adjust themselves in such a manner that the current density and the other parameters of the spot do not vary significantly.

An analysis of the system of equations for copper shows that the main loss of energy at the cathode is due to thermal conduction. The emission of electrons from the cathode is mainly determined by the thermionic mechanism together with the Schottky effect. Solving the system of equations with this mechanism of emission gives results for all parameters of the discharge that are close to the values cited above. For example, the difference between the current density for I = 200 A is as follows: $5.63 \cdot 10^4$ and $5.7 \cdot 10^4$ A/cm^2; for I = 300 A the difference is $3.57 \cdot 10^4$ and $3.63 \cdot 10^4$ A/cm^2. Ionization and removal of energy due to the electron current at the outer boundary of the relaxation region are the main processes responsible for the loss of energy in the cathode plasma. The removal of vapor from the cathode region has no effect on the ion current, although it must be taken into account in the energy balance of the cathode plasma. The parameter values and the physical processes in the cathode spot vary very slightly with total current and discharge conditions. Preliminary studies of the system of equations for tungsten have shown, however, that the solution may depend significantly on the vapor pressure.

In conclusion we note the following. An expression has been obtained by Kesaev[2] for estimating the minimum current density i_{0m} in a cathode spot on a massive cathode. An estimate of i_{0m} for a cellular current gives $i_{0m} \approx 3 \cdot 10^7$ A/cm^2 and for $I \approx 200$ A $i_{0m} \approx 5 \cdot 10^5$ A/cm^2. This result differs substantially from the results of our calculations (Fig. 3). This discrepancy may be explained by the use in ref. 2 of a value of s ($s \approx 0.95$) that is much too high in comparison with the results on Fig. 4.

It would appear that the assumptions used in Kesaev's calculation by the method of signatures on thin films do not reflect the phenomena taking place in a real cathode spot for the following reason. Calculations of the temperature fields[14] for a wide range of current densities show that the dimensions of the melting zone do not greatly exceed (by less than a factor of 2) the dimensions of the zone heated to the boiling point. As it is precisely in the latter zone that intense evaporation and electron emission take place, it follows that assuming the cathode spot to be a point source of heat may lead to erroneous results. For this reason, evidently, the use of the melting point T_{melt} in Eq. (45.4) of ref. 2 is also erroneous, since the width of the signature δ, determined with a certain error, may in fact characterize an isotherm with a temperature greater than T_{melt}. Increasing the temperature in Eq. (45.4) by a factor of 2 increases the fraction of the current carried by ions by a factor of 2 for δ = const.

Finally, with very thin films ($d \sim 0.025\,\mu$) the energy removed by thermal conduction may be negligible in comparison with the energy expended in removing material from the cathode region. This can be seen by comparing the energy flux falling upon a film cathode $(1-s)I(u_c + u_i - \varphi)$ with the energy flux removed from the cathode region (the requisite numerical values of the quantities appearing in the equations may be taken from ref. 2). The fluxes become comparable when s = 0.8, while[2] for s = 0.95 the energy flux from the cathode begins to exceed the incoming energy flux.

The author wishes to thank G. A. Lyubimov for discussion.

---

1) The equations given here also allow for processes occurring in the cathode plasma.

---

[1] V. I. Rakhovskii, Physical Principles of the Switching of Electric Current in a Vacuum [in Russian], Izd. Nauka, Moscow (1970).
[2] I. G. Kesaev, Cathode Processes of the Electric Arc [in Russian], Izd. Nauka, Moscow (1968).
[3] V. P. Kozlov and V. I. Khvesyuk, Zh. Tekh. Fiz., 41, 2135 (1971); 41, 2142 (1971) [Sov. Phys.—Tech. Phys., 16, 1691; 16, 1697 (1972)].
[4] V. M. Kulyapin, Zh. Tekh. Fiz., 41, 381 (1971) [Sov. Phys.—Tech. Phys., 16, 287 (1971)].
[5] I. I. Beilis, and V. I. Rakhovskii, Teplofiz. Vys. Temp., 7, 620 (1969).
[6] I. I. Beilis, G. A. Lyubimov, and V. I. Rakhovskii, Dokl. Akad. Nauk SSSR, 203, 71 (1972) [Sov. Phys.—Dokl., 17, 225 (1972)].
[7] V. V. Gogosov, V. A. Polyanskii, I. P. Semenova, and A. E. Yakubenko, Mekhan. Zhidk. Gaza, No. 2, 31 (1969).
[8] I. I. Beilis, Teplofiz. Vys. Temp., 9, 184 (1971).
[9] N. M. Zykova, Candidates's Dissertation [in Russian], Institute of Physics, Siberian Branch, Academy of Sciences of the USSR, Krasnoyarsk (1968).
[10] T. H. Lee, J. Appl. Phys., 49, 453 (1960).
[11] W. D. Davis and H. C. Miller, J. Appl. Phys., 40, 2212 (1969).
[12] A. A. Plyutto, V. N. Ryzhkov, and A. G. Kapin, Zh. Eksp. Teor. Fiz., 47, 494 (1964) [Sov. Phys.—JETP, 20, 328 (1965)].
[13] V. É. Peletskii, D. L. Timrot, and V. Yu. Voskresenskii, High-Temperature Investigations of the Thermal and Electrical Conductivities of Solids [in Russian], Izd. Énergiya, Moscow (1971).
[14] I. I. Beilis, G. V. Levchenko, V. S. Potokin, V. I. Rakhovskii, and N. N. Rykalin, Fiz. Khim. Obrabotki Materialov, No. 3, 19 (1967).

Emission processes at the cathode of an electric arc

I. I. Beilis
Institute of High Temperatures,
Academy of Sciences of the USSR, Moscow

(Submitted January 26, 1973; resubmitted July 26, 1973)
Zh. Tekh. Fiz., 44, 411-418 (February 1974)

The energy distribution of the electrons emitted from the cathode of an arc is calculated as a function of electric field and cathode temperature. Certain conclusions are reached concerning the emission mechanism in cathode spots for copper. In long-lived and slowly moving spots electrons are emitted by the thermionic mechanism with the Schottky effect. Contemporary experimental data on the current density for rapidly moving spots cannot be explained on the basis of thermionic-field (T−F) emission. The cooling and heating of the cathode as a result of electron emission (the Nottingham effect) are discussed. The presence of a minimum value of work function for which a long-lived spot can exist on a copper cathode is noted. An estimate is given for the effect of any inaccuracy in the calculation of the electric field.

The basic assumption in most theories of the electric arc is that emission processes at the cathode are responsible for the charge carriers in the cathode region.[1,2] The primary difference between theories lies in the preference given to one or other of the emission mechanisms: thermionic emission, field emission, or thermionic-field (T−F) emission. The physics of each of these electron-emission mechanisms and the derivation of appropriate relations are given in detail in refs. 3-6. Accordingly, we shall not analyze the familiar relationships here but shall only make a preliminary study of specific relationships used to describe the processes occurring at the cathode.

We shall not specify any particular type of emission and shall assume for generality that electrons can be emitted by the cathode from any energy level in the conduction band. The electron energy distribution in ε_n in the metal is described by Fermi−Dirac statistics and the probability that an electron will tunnel from the metal through the potential barrier at the metal−vacuum boundary is characterized by the transmission coefficient.[3-5]

In this case, as shown in refs. 3-5, the emission current density can be calculated from the relationship

$$i_e = e \int\limits_{-\infty}^{+\infty} N_e(\varepsilon,\ T_k)\, D(\varepsilon,\ E)\, d\varepsilon. \tag{1}$$

Applying Fermi−Dirac statistics for the electron flux falling on unit area of the barrier, N_e, we have

$$N_e(\varepsilon,\ T_k) = \frac{4e\pi m_e kT_k}{h^3} \ln\left[1 + \exp\left(-\frac{\varepsilon}{kT_k}\right)\right], \tag{2}$$

where e is the electron charge, $\varepsilon = \varepsilon_n - \varepsilon_0$, ε_0 is the Fermi level, T_k is the cathode temperature, E is the electric field, m_e is the electron mass, and k is Boltzmann's constant.

Let us consider the transmission coefficient D. The theory considered in refs. 3-5 holds for the one-dimensional case and is based on the free-electron model. This model gives several different expressions for D depending on additional assumptions used in the derivation.[5,8] As noted in refs. 4 and 6, the results of calculating D via these expressions differ by a factor of 2. On the basis of the generalized WKB method Kemble[7] obtains an expression for D which differs from those mentioned above in that it describes the emission process by one relation both for tunneling electrons and for electrons above the barrier. However, as correctly noted by Itskovich,[6] it is precisely near the summit of the barrier, the features of which were taken into account by Kemble, that the potential distribution used by Kemble is invalid. Accordingly, any refinement in the calculation of D within the framework of the free-electron model that does not allow for an arbitrary dispersion law, as noted by Itskovich,[6] cannot increase the accuracy of results deriving from this model.

In this connection a theory of electron emission has been constructed by Itskovich[6] for the case of an arbitrary dispersion law. The results obtained by Itskovich show that allowing for the law of dispersion in the theory of electron emission leads to the familiar relations obtained earlier[3-5] but with a slightly increased value of the work function φ. Thus, allowing for a complex dispersion law is equivalent to making a certain correction to the value of the work function φ. As noted in refs. 6, 9, and 10 this correction has a noticeable effect only for the noble metals and depends on the topology of the Fermi surface. Accordingly, in the case of copper under arc conditions there is no need to allow for the effect of a complex dispersion law.

An original attempt to construct a theory of emission free from the essentially classical approach of refs. 3-6 (e.g., the existence of a potential barrier at the metal−vacuum boundary, the free-electron model) was made by Brodskii and Gurevich.[11] The use of the threshold approximation developed by these authors depends on the existence of a small parameter connected with the relatively small range of energies of emitted electrons, the concepts of the theory of potential scattering lying at the basis of the proposed model. A clear explanation is given in ref. 11 of the processes of electron emission at large transmission coefficients ($D \sim 1$) on the basis of a comparison of the wavelength of emitted electrons with the thickness of the potential barrier. It turns out that the emission process in this case does not depend on the shape of the potential barrier and that the expression for D is dictated solely by classical model concepts. Accordingly, varying the specific form of this expression cannot have a decisive effect on the results of emission calculations.

Unfortunately, no final relationships are obtained in ref. 11 by means of which the process of T−F emission, considered below, can be calculated. Accordingly, in performing our emission calculations, we may utilize Eq. (1), which has been experimentally confirmed by Andreev[12] (in the ranges of E and T_k considered below), while the specific form of the expression for D may be chosen solely from considerations of convenience in the ensuing calculations.

On the basis of the above we shall analyze the emission processes on the cathode utilizing the simplest and most frequently employed expression for the transmission coefficient first proposed by Bethe and Sommerfeld:[5]

$$D(\varepsilon, E) = \exp\left[-\frac{6.85 \cdot 10^7 (\varphi - \varepsilon)^{3/2} \theta(\tilde{y})}{E}\right], \tag{3}$$

where $\tilde{y} = (e^3E)^{1/2}/|\varepsilon|$ and $\theta(\tilde{y})$ is the Nordheim function.

An expression for $\theta(\tilde{y})$ in analytic form is obtained in ref. 13:

$$\theta(\tilde{y}) = 1 - \tilde{y}^2\left\{1 + \mu \sin\left[\frac{1-\tilde{y}}{2}\right]\right\},$$

where μ is a variable coefficient. Choosing the expression for the transmission coefficient in the Bethe–Sommerfeld form is also convenient in that it permits comparison of our results with the results of similar calculations by Dolan and Dyke,[14] where D has the form (3) but which were carried out for a different range of parameters.

Thus, utilizing (1), (2), and (3), the expression for the emission current density has the form

$$i_e = \frac{4e\pi m_e kT_k}{h^3} \int\limits_{-\infty}^{+\infty} \frac{\ln\left[1 + \exp\left(-\frac{\varepsilon}{kT_k}\right)\right] d\varepsilon}{\exp\left[\frac{6.85 \cdot 10^7 (\varphi - \varepsilon)^{3/2} \theta(\tilde{y})}{E}\right]}. \tag{4}$$

The emission process described by (4) can have the character of thermionic emission, field emission, or T−F emission depending on the ratio of the cathode temperature T_k and the electric field E. It is known[4] that the existence of a specific mechanism of emission is determined by the corresponding distribution in energy of the emitted electrons. In a qualitative study of the effect of varying T_k and E it is thus of considerable interest to establish how the energy distribution of the emitted electrons varies as a function of the two variables T_k and E. Such a study was made by Dolan and Dyke.[14] The calculations carried out by these authors pertain, however, to a very narrow range of variation of T_k and E and do not give a complete description of the quantities of interest in the range of values of E and T_k characteristic of arc discharges.[2]

In this connection we cite below the results of calculations carried out over a wider range of variation of the parameters. The method of calculation is similar to that of Dolan and Dyke[14] but differs in that the results are not presented in relative units, but in the form of plots of $i_e(\varepsilon)$, the dependence of the emission current density on the energy of the electrons in the metal. This also makes it possible to estimate the emission current density as a function of the specific values of E and T_k.

An expression for the emission current density $i_e(\varepsilon)$ as a function of electron energy ε is readily obtained from (1) on inserting (2) and (3) in the form

$$i_e(\varepsilon) = \frac{4e\pi m_e kT_k}{h^3} \frac{\ln\left[1 + \exp\left(-\frac{\varepsilon}{kT_k}\right)\right]}{\exp\left[\frac{6.85 \cdot 10^7 (\varphi - \varepsilon)^{3/2} \theta(\tilde{y})}{E}\right]}. \tag{5}$$

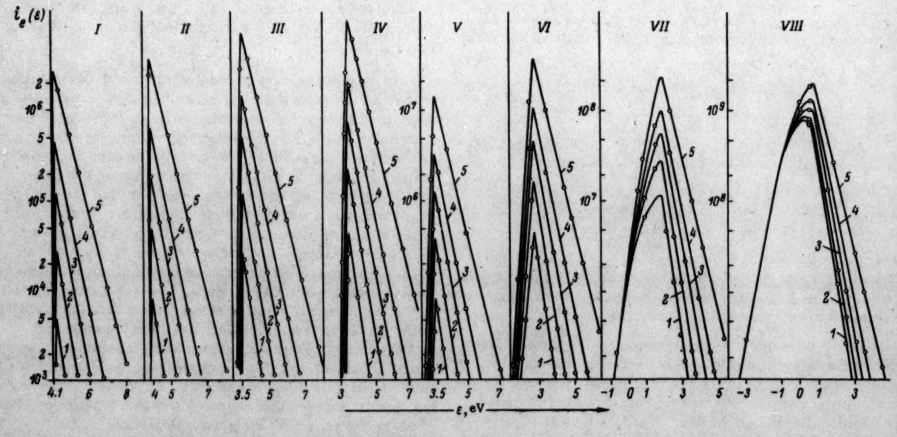

Fig. 1. Emission current density $i_e(\varepsilon)$ versus energy of emitted electrons (φ = 4.5 eV) for various values of the electric field and cathode temperature. The emission density (A/cm²) is plotted along the ordinate axis; the energy of emitted electrons (in eV taken from the Fermi level ε = 0) is plotted along the abscissa axis. Curves I-VIII correspond to the following values of the electric field (V/cm): $10^6, 2\cdot10^6, 5\cdot10^6, 7\cdot10^6, 10^7, 2\cdot10^7, 5\cdot10^7, 10^8$; these values of the electric field correspond to the following values of φ_S(eV): 4.12, 3.96, 3.65, 3.5, 3.3, 2.8, 1.81, 0.7. Curves 1-5 correspond to the following cathode temperatures: 3500, 4000, 4500, 5000, 6000°K.

Expression (5) is essentially the product $N_e(\varepsilon, T_k)D(\varepsilon, E)$ and so represents the distribution in energy of the flux of electrons that have leaked through the potential barrier with a probability $D(\varepsilon, E)$. The calculations are carried out in the ranges $T_k = 3500$–6000°K, $E = 10^6$–10^8 V/cm for $\varphi = 4.5$ eV. The results are presented in Fig. 1 in the form of a series of curves. For each curve I–VIII the caption cites the respective electric field and the work function φ_S, where $\varphi_S = \varphi - (e^3E)^{1/2}$ is the work function as reduced by the Schottky effect. The quantity $i_e(\varepsilon)$ is plotted along the ordinate axis and ε along the abscissa axis, where $\varepsilon = 0$ denotes the position of the Fermi level.

It is evident from Fig. 1 that increasing the electric field shifts the curves into a region of negative values of ε, indicating the increasing role of field emission. With increasing cathode temperature the number of electrons excited to higher levels increases, with the result that the T–F character of the emission becomes more clearly expressed. These features quite clearly demonstrate the transition from the one type of emission to the other and confirm the previous results.[14] A characteristic of the curves of Fig. 1 is that the position of the maximum of each of the curves corresponds to an electron energy equal to φ_S. An exception is the case $E = 10^8$ V/cm and $T_k \leqslant 5000$°K, which is displaced towards smaller energy values.

For fields $E \leqslant 10^7$ V/cm the number of emitted electrons with energy less than φ_S is negligible for any cathode temperature in the investigated range of variation of E and T_k. Even when $E \sim 5 \cdot 10^6$ V/cm and $T_k \sim 4000$°K the emission current density can reach a value of 10^5 A/cm^2. An interesting and very evident fact that can be seen from the curves of Fig. 1 is that the Nottingham effect, i.e., heating of the cathode through the emission of electrons with energy less than the energy at the Fermi level, begins to manifest itself when $E \sim 5 \cdot 10^7$ V/cm and becomes significant when $E \sim 10^8$ V/cm. It thus turns out that the Nottingham effect shows up in the investigated range of temperatures only when the height of the potential barrier is small ($\varphi \sim 0.7$ eV, Fig. 1). The emission current density can then exceed 10^9 A/cm^2.

On the whole one can conclude from an analysis of the curves of Fig. 1 that the Nottingham effect, which manifests itself only under conditions characteristic of the prebreakdown and spark stages of the discharge[15] ($E \sim 10^8$ V/cm; $i_e \sim 10^8$–10^9 A/cm^2), will play a negligible role in the thermal balance for the cathodes of an arc discharge[1,2] ($d\dot{J}/dt < 10^7$ A/sec). At the same time, in calculating the effect of cooling of the cathode through the emission of excited electrons one can assume that the electrons carry away from the cathode an energy of about φ_S when $E \leqslant 2 \cdot 10^7$ V/cm (Fig. 1). The contribution of tunneling electrons to the total emission flux, as follows from the figure, is probably not large.

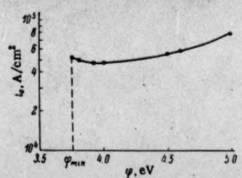

Fig. 2. Variation of current density in cathode spot with work function of cathode material. φ_{min} is the minimum work function of a copper cathode for which stationary existence of spot is possible.

The results obtained above can be used directly to study the parameters of the cathode region of the arc. In refs. 16 and 17 a study is made of a system of equations describing[2] the long-lived ($t \leqslant 10^{-4}$ sec) spots on a copper cathode and incorporating Eq. (4), and the dominance of thermal emission of electrons from the cathode was pointed out. Considering the range of values of E and T_k obtained when solving this system of equations (for completeness the results of the calculations of ref. 16 are presented in Table 1) it is not hard to see that this conclusion follows from a consideration of the results presented in Fig. 1 and described above. Table 1 also lists the values of the degree of ionization α, the electron energy w_e, the densities of charged and neutral particles, n_i and n_a respectively, in the cathode plasma, and the current density i_0 and the fraction of the current carried by electrons s obtained through solving the system of equations of ref. 16. Evidently the values of these parameters calculated allowing for Eq. (4) almost coincide with the values calculated allowing for the thermionic mechanism of electron emission with the Schottky correction.

The presence of the thermionic mechanism of emission in cathode spots indicates that the only effect of the electric field at the cathode is to change the effective value of the work function by an amount $\Delta\varphi = (e^3E)^{1/2}$ due to the Schottky effect. Thus, for example, doubling the field E changes $\Delta\varphi$ by a factor of $\sqrt{2}$. The resulting change of i_0, the most important parameter characterizing the cathode

TABLE 1

I, A	α	s	T_k°, K	w_e, eV	$E \cdot 10^{-6}$, V/cm	$i_0 \cdot 10^{-4}$, A/cm^2	$n_i \cdot 10^{-19}$, cm^{-3}	$(n_i + n_a) \cdot 10^{-19}$, cm^{-3}
Emission in accordance with Eq. (4)								
100	0.189	0.5	3816	1.6	8.44	14.2	14.5	76.5
200	0.098	0.464	3737	1.33	5.51	5.63	6.2	62.9
300	0.072	0.454	3689	1.23	4.43	3.57	4.0	55.6
500	0.052	0.446	3641	1.14	3.51	2.21	2.55	49
Thermionic emission allowing for the Schottky effect								
100	0.161	0.493	3883	1.56	8.48	14.1		
200	0.089	0.462	3781	1.317	5.55	5.7		
300	0.066	0.452	3730	1.22	4.47	3.63		
500	0.049	0.446	3670	1.14	3.53	2.24		

TABLE 2

	Temperature (T, °C)				
	i_0, A/cm^2				
t, sec	10^4	10^5	10^6	$5\cdot10^6$	10^7
1	304	926	3486	—	9276
10^{-3}	255	916	3010	6794	—
10^{-5}	—	—	2557	—	—
10^{-6}	23	223	1704	5286	8080

spot, is insignificant, as follows from the curve of $i_0(\varphi)$ of ref. 16 (Fig. 2). An analysis of the curve of Fig. 2 shows that the possible inaccuracy in the determination of E connected with the use of the Mackeown equation[18] will not introduce any appreciable error into the determination of the current density in long-lived spots.

A very interesting result is the minimum value of the work function for which the solution of the system of equations of ref. 16 still exists; for copper this minimum value is $\varphi_{\min} \sim 3.75$ eV (Fig. 2). Below this value, i.e., for $\varphi < \varphi_{\min}$, the solution of the system becomes unstable. A detailed study of this system of equations has shown that the absence of a solution (with acceptable accuracy) for $\varphi < \varphi_{\min}$ is not only due to the processes taking place at the surface of the solid (emission of electrons and variation of thermal regime of cathode due to variation of emission cooling effects), but also to the cathode plasma. Thus, it turns out that as φ is reduced the temperature required to achieve the previous emission current density is decreased significantly (for $\varphi = 4.5$ eV $T_k = 3737$°K, for $\varphi = 4.0$ eV $T_k = 3314$°K); as a result, the density of the particles (including charged particles) in the cathode plasma is also reduced. When φ is equal to $\varphi_{\min}$, the ion current falls to a value at which the corresponding heat flux is insufficient to heat the cathode to the temperature required to obtain the corresponding emission current from the cathode. In this case the system of equations for the cathode region will have no solution.

The presence of a regime (characterized by the minimum value of the work function $\varphi_{\min}$) in which long-lived cathode spots can exist in arcs with an evaporating cathode and also the relatively weak variation of the current density in the cathode spot with work function (greater than $\varphi_{\min}$) indicate that this type of discharge is regulated mainly by the thermal regime, which adjusts itself during the burning of the arc in the cathode spot.

The position is quite different for rapidly moving ($v \sim 10^3$ cm/sec) cathode spots. The lifetime of such spots[1] $t \sim 10^{-6}$–10^{-5} sec. In such a short time the cathode region in the spot can be heated to temperatures at which T−F emission is possible only if the current density i_0 is sufficiently large. Table 2 shows the spot temperatures for various individual values of i_0 (top row) and times t calculated through the equation of ref. 16 for a stationary source of heat and ignoring the erosion of cathode material for copper (current strength $\tilde{J} = 10$ A, $s = 0.5$, cathode fall $u_c = 15$ V). It can be seen from the table that significant heating of the cathode in rapidly moving spots can occur when $i_0 > 10^6$ A/cm^2. Remembering that it is possible that $\tilde{J} < 10a$, $s > 0.5$ in such spots and that the velocity is in fact not zero, it follows that we must have[1] $i_0 \gg 10^6$ A/cm^2. The hitherto experimentally measured values of i_0 in arc spots correspond to $i_0 \leqslant 10^6$ A/cm^2. Furthermore, the measurements of Golub' et al.[19] show that in fast spots, i_0 may be $\sim 10^4$–10^5 A/cm^2. It is also pointed out by these authors that the previously obtained values of i_0 in fast spots may be too high through the use of recording apparatus with a low light sensitivity (in the case of the optical method of measurement).

Such a low current density cannot, of course, be explained on the basis of T−F emission (Fig. 1) or on the basis of pure field emission. In the latter case[1] one would require $i_0 > 10^7$ A/cm^2. It can thus be concluded from the present calculations (Fig. 1, Table 2) that contemporary experimental data on the current density for short-lived, rapidly moving spots are not described by the traditional ideas of existing emission mechanisms (which permit calculation of the mean electron emission current), and that the thermal processes determining the mean temperature of the cathode in the spot are not significant as far as the maintaining of this type of discharge is concerned.

---

[1] I. G. Kesaev, The Cathode Processes of the Electric Arc [in Russian], Izd. Nauka, Moscow (1968).

[2] V. I. Rakhovskii, The Physical Principles of the Switching of Electric Current in a Vacuum [in Russian], Izd. Nauka, Moscow (1970).

[3] L. N. Dobretsov and M. V. Gomoyunova, Emission Electronics [in Russian], Izd. Nauka, Moscow (1966).

[4] M. I. Elinson and G. F. Vasil'ev, Field Emission [in Russian], Fizmatgiz, Moscow (1958).

[5] H. Bethe and A. Sommerfeld, The Electronic Theory of Metals [Russian translation], ONTI, Moscow (1938).

[6] F. I. Itskovich, Candidate's Dissertation [in Russian], Khar'kov (1967).

[7] E. C. Kemble, The Fundamental Principles of Quantum Mechanics, McGraw-Hill (1937), p. 4.

[8] L. W. Nordheim, Proc. Roy. Soc. (London), A, 121, 626 (1928).

[9] F. I. Itskovich, Summaries of Reports presented at 14th All-Union Conf. on Emission Electronics [in Russian], Tashkent (1970), p. 30.

[10] F. I. Itskovich, Zh. Eksp. Teor. Fiz., 50, 1425 (1966) [Sov. Phys.—JETP, 23, 945 (1966)]; 52, 6 (1967).

[11] A. M. Brodskii and Yu. Ya. Gurevich, Izv. AN SSSR, Ser. Fiz., 33, 388 (1969).

[12] I. S. Andreev, Zh. Tekh. Fiz., 22, 1428 (1952).

[13] I. I. Beilis, Teplofiz. Vys. Temp., 9, 184 (1971).

[14] W. W. Dolan and W. P. Dyke, Phys. Rev., 95, 327 (1954).

[15] G. A. Mesyats, 10th Intern. Conf. on Phenomena in Ionized Gases, Oxford (1971), p. 333.

[16] I. I. Beilis, Zh. Tekh. Fiz., 44, 2400 (1974) [Sov. Phys.—Tech. Phys., 19, 000 (1974)].

[17] I. I. Beilis, in: Electrical Contacts [in Russian], Sixth All-Union Conf., Moscow (1972), p. 104.

[18] I. I. Beilis, G. A. Lyubimov, and V. I. Rakhovskii, Dokl. Akad. Nauk SSSR, 188, 552 (1969) [Sov. Phys.—Dokl., 14, 897 (1970)].

[19] V. N. Golub', V. V. Kantsel', and V. I. Rakhovskii, in: Electrical Contacts [in Russian], Sixth All-Union Conf., Moscow (1972), pp. 59, 129.

Time dependence of ion currents produced through surface ionization. Ionization of Ba on the (111) face of iridium

É. Ya. Zandberg, E. V. Rut'kov, and A. Ya. Tontegode

A. F. Ioffe Physicotechnical Institute, Leningrad

(Submitted June 18, 1973)
Zh. Tekh. Fiz., 44, 419-423 (February 1974)

The time required to establish the steady-state current (i.e., the equilibrium coverage of the emitter with atoms of the material being ionized) subsequent to a change of temperature of the emitter is studied for a constant flux of particles. A connection is found between the required expectation time and the heats of evaporation of atoms and ions from the surface of the emitter, the emitter temperature, and the amount by which it is changed. It is shown that for large heats of evaporation of particles from the emitter the temperature dependence of the ion currents and of the neutral flux from the surface significantly distorts the time dependence of these quantities. The results are illustrated by the ionization of Ba on the (111) face of iridium. The heats of evaporation of atoms and Ba$^+$ ions from the (111) face of Ir are determined and the manner in which the atomic and ionic lifetimes vary with temperature is established.

The temperature dependence I(T) of ion currents produced by ionization on the surface of a solid of a constant flux of particles yields information on many physicochemical characteristics of the interaction of the particles with the solid.[1]

It has been observed[2,3] in studies on the ionization of alkali metal atoms that at low emitter temperatures the time to establish the steady-state current subsequent to a change of temperature is very much greater than the time to establish the temperature. For slow time dependences of the currents one records the transient currents corresponding to arbitrarily chosen expectation times.[3] In principle the time dependence of the currents introduces an error into the measured threshold temperature for ionization of easily ionized elements, the most important ionization characteristic of such elements.[3,1]

It follows from ref. 4 that the time variation of the ion currents can be observed in many cases of surface ionization, and the higher the temperature the greater the heat of evaporation of particles from the surface. Ignoring the time dependence of the currents can result in an incorrect determination of those characteristics found from the temperature dependence of currents from surface ionization. Accordingly, the dependence of the ion currents on time and temperature in surface ionization of constant fluxes of particles is a topic worthy of attention.

TIME DEPENDENCE OF ION CURRENTS

The variation of the ion currents with time subsequent to a change in the emitter temperature T is considered by Tontegode and Yusifov.[4]

With a rapid change of T from T_1 to T_2 the equilibrium coverage of the emitter by adsorbed particles for T_1 (which is assumed not to have time to change during the rapid cooling from T_1 to T_2) becomes a nonequilibrium value for the new temperature T_2; with the passage of time it approaches the new equilibrium value. The variation of the coverage with time causes the current to vary.

Assume that a constant flux ν of neutrals impinges upon the emitter and let the equilibrium coverage at T_1 be N_1 and the equilibrium coverage at the lower temperature T_2 be N_2. For simplicity we assume an instantaneous transition from T_1 to T_2. The time variation of the surface coverage N subsequent to switching to T_2 is described by the familiar equation[1]

$$\frac{dN}{dt}+W(T_2)\,N=\nu, \tag{1}$$

where $W(T_2)$, the probability that an ionized particle will be evaporated from the emitter at T_2, is given by

$$W(T_2)=C\exp\left[-\frac{l_+}{kT_2}\right]+D\exp\left[-\frac{l_0}{kT_2}\right]. \tag{2}$$

It is assumed here that the sticking coefficient of the particles to the emitter is unity and that the experiments are conducted under conditions such that the flux of particles does not affect the work function of the emitter for all T. Under these conditions l_0 and l_+ can be regarded as independent of the coverage in the range from N_1 to N_2.

Integrating (1) subject to the boundary condition N = N_1 at t = 0 gives

$$\ln\left(\frac{\nu-N_1W(T_2)}{\nu-N(t)\,W(T_2)}\right)=tW(T_2). \tag{3}$$

It can be seen from (3) that the transition from the steady-state coverage $N_1 = \nu/W(T_1)$ at T_1 to the greater steady-state coverage $N_2 = \nu/W(T_2)$ at T_2 occurs in a time $t = \infty$. Accordingly, let us estimate the time required to reach a coverage close to the equilibrium value N_2. We represent this coverage by $N = \gamma N_2$ (where $\gamma \lesssim 1$) and denote the time required to reach it by t^*. We find from (3)

$$\ln\left[\frac{1-\frac{W(T_2)}{W(T_1)}}{1-\gamma}\right]=t^*W(T_2)$$

$$t^*=\frac{\ln\left[\frac{1}{1-\gamma}\left(1-\frac{W(T_2)}{W(T_1)}\right)\right]}{W(T_2)}. \tag{4}$$

Equation (4) shows that for given l_0 and l_+ and a prescribed value of γ, the time t^* depends significantly on the temperature T_2: The higher the temperatures T_1, T_2 and the smaller the difference between them, the smaller the value of t^*. For given values of T_2 and $T_1 - T_2$ the time t^* will be greater for ionization of materials with greater l_0 and l_+. It also follows from (4) that t^* does not depend on the density of the flux of particles impinging upon the emitter.

Using Eq. (4) we can determine the time t^* required to achieve a coverage which approaches the equilibrium coverage with a given degree of approximation. Accordingly, (4) determines the conditions for obtaining both ion currents with a given degree of approximation to equilibrium and also fluxes of neutrals if the coefficient of ionization $\beta \ll 1$. In the particular cases of $\beta \approx 1$ (easily ionized elements, $W = C \exp[-l_0/kT]$) and $\beta \approx 0$ (desorbed flux of neutrals $W = D \exp[-l_0/kT]$) Eq. (4) simplifies.

Figure 1 shows plots of $t^*(l_+)$ calculated from (4) for ionization of easily ionized elements for various temperatures and the same difference $T_1 - T_2 = 100$°K for $\gamma = 0.9$ and $C = 10^{13}$ sec^{-1}. The dashed line in Fig. 1 corresponds to $t^* = 100$ sec. It can be seen that this expectation time is insufficient to achieve $\gamma = 0.9$ at low T and large l_+; the temperatures at which a time dependence of the currents should be observed increase with increasing l_+. Figure 1 also explains why the currents depend on time only in the region of low threshold temperatures for alkali metals ($l_+ = 2.0$-2.5 eV).

IONIZATION OF Ba ON THE (111) FACE OF IRIDIUM

In this case the ionization potential $\varphi \simeq 5.8$ V (Zandberg and Tontegode[5]) and V = 5.21 volts, so that the condition $e(\varphi - V) \gg kT$ is satisfied and the current should be independent of T at temperatures above threshold. However, as the heat of evaporation of the Ba$^+$ ions must be greater than that of atomic ions of the alkali metals due to the covalent interaction between the s electron of the Ba$^+$ ion and the metal,[6] one can expect a strong time dependence of the currents, which will affect the form of I(T).

We have experimentally measured I(T) for a current of Ba$^+$ ions produced by surface ionization of the (111) face of Ir for a constant flux of Ba atoms and have measured the heat of evaporation of Ba$^+$ ions from this face.

The metal mass spectrometer arrangement described in ref. 7 is used in the measurements; the vacuum system is augmented by a liquid-nitrogen-cooled titanium pump. The pressure of the residual gas under working conditions is $\sim 3 \cdot 10^{-9}$ torr and is distributed over the main components in the following manner: $P_{He} \cong 2.4 \cdot 10^{-9}$ torr, $P_{H_2} \cong 5 \cdot 10^{-10}$ torr, $\bar{P}_{CO} \cong 6 \cdot 10^{-11}$ torr.

The (111) face is brought out to the surface of an iridium ribbon of purity 99.96% by the method described in ref. 5. The ribbon temperature is measured with an optical micropyrometer. The work function of the face is determined from Richardson plots and is 5.78 ± 0.05 V. Barium atoms are supplied to the face from a Knudsen effusion cell filled with metallic barium purity 99.9%. The impurities in the barium are Sr and Mg.

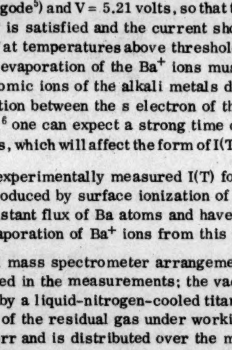

Fig. 1. Expectation time required to achieve a coverage with $\gamma = 0.9$ versus ion heat of evaporation l_+. The various curves correspond to different temperatures T_1, T_2, but with the same (100°) difference $T_1 - T_2$. Temperatures $T_1 - T_2$ (°K): 1) 2000-1900; 2) 1800-1700; 3) 1600-1500; 4) 1400-1300; 5) 1200-1100; 6) 1000-900; 7) 800-700.

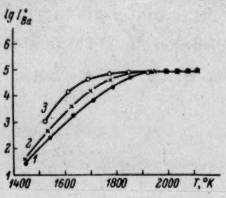

Fig. 2. Experimentally obtained variation of current of Ba$^+$ ions with temperature for ionization of Ba atoms on (111) face of Ir. Different curves correspond to different expectation times: 1) 30; 2) 240; 3) 600 sec. The current is expressed in the usual units.

Figure 2 shows plots of I(T) obtained by reducing the temperature of the iridium in 100° steps for various values of the expectation time at each temperature. At high temperatures the current does not depend on T, as should be the case when $e(\varphi - V) \gg kT$. However, at high temperatures (1950°K) the time dependence of the currents starts to distort the temperature dependence I(T), the more so the smaller the expectation time. At small expectation times the region T < 1950°K may easily be taken to be the threshold region of ionization. This would, however, be a spurious threshold region. This result can be seen from a comparison of the curves of Fig. 2, obtained for various expectation times, and the determinations of the work function for thermionic electrons from the total current (this is possible for T ≥ 1600°K; no reduction of $\varphi_{tot\,T}$ at low T is observed). The threshold region of ionization temperatures is not achieved at the Ba flux density used in the experiments.

The time dependence of the current of Ba$^+$ ions at T ~ 1900°K indicates that the heat of evaporation of Ba$^+$ ions from the (111) face of iridium is large. It follows from Fig. 1 that l_+ must be greater than 5 eV.

We determine the heat of evaporation of Ba$^+$ ions from the (111) face of Ir by two methods: by the method of constant coverage[4] and by the beam modulation technique.[8] In both cases the range of variation of T is 1940-1700°K.

From ref. 4 the ion heat of evaporation is

$$l_+ = \frac{\ln \frac{I_1}{I_2}}{\frac{1}{k}\left(\frac{1}{T_2} - \frac{1}{T_1}\right)}. \qquad (5)$$

where I_1 is the steady-state current at the initial temperature T_1 and I_2 is the nonsteady-state initial current at the final temperature T_2, and the ion lifetime

$$\tau_+(T_1) = \frac{I_2 t}{I_1 \ln\left(\frac{1 - \frac{I_2}{I_1}}{1 - \frac{I_3}{I_1}}\right)}, \qquad (6)$$

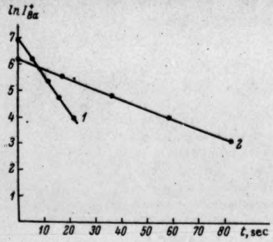

Fig. 3. Variation of current of Ba$^+$ ions with time after interruption of incident flux of Ba atoms. Temperature T (°K): 1) 1910; 2) 1840. The current is expressed in the usual units.

where I_3 is the total current at $T = T_2$ a time t after the temperature is switched to $T = T_2$.

Thirty determinations of l_+ are made for various combinations of T_1 and T_2 in the cited temperature range; we find $l_+ = (5.18 \pm 0.08)$ eV, where the error is the mean-square error. Application of the Schottky cycle gives

$$l_0 = (5.75 \pm 0.09)\ \text{eV}.$$

When determining $\tau_+(T_1)$ from (6) we take different T_2 for each prescribed T_1 and also vary I_3 and the corresponding expectation time t.

At T = 1925°K the ionic lifetime $\tau_+ = (18 \pm 2)$ sec and at T = 1880°K it has increased to $\tau_+ = (36 \pm 3)$ sec. Knowing $\tau_+(T_1)$ and l_+ and the equation $\tau_+ = \tau_{+0} \exp[l_+/kT]$, it is an easy matter to determine the quantity $\tau_{+0} = (5 \pm 3) \cdot 10^{-13}$ sec.

Knowing l_+, l_0, φ, and τ_+ we can find $\tau_0 = \tau_{00} \exp \cdot [l_0/kT]$, the lifetime on the surface of uncharged particles (Ba ions), using the expression[1] for the degree of surface ionization

$$\alpha(T) = \frac{W_+(T)}{W_0(T)} = \frac{Q_+}{Q_0} \exp\left(\frac{\varphi - V}{kT}\right); \tag{7}$$

in this expression Q_+/Q_0 is the ratio of the partition functions of the ion and atom states at temperature T. For various T we find $W_0(T)$ and $\tau_{00} = (10 \pm 8) \cdot 10^{-13}$ sec.

The quantities C and D in (2) are also determined: $C = (2 \pm 1) \cdot 10^{12}\ \text{sec}^{-1}$ and $D = (10 \pm 8) \cdot 10^{11}\ \text{sec}^{-1}$.

By interrupting the flux of the Ba atoms to the Ir surface at fixed temperatures graphs of I(t) are obtained for various T and graphs of $\ln I = f(t)$ constructed (Fig. 3). The quantity $W_+(T)$ is determined from the slopes of the graphs. The results are

$$l_+ = (5.17 \pm 0.10)\ \text{eV},$$
$$l_0 = (5.74 \pm 0.11)\ \text{eV},$$
$$\tau_{+0} = (2.0 \pm 0.3) \cdot 10^{-13}\ \text{sec}.$$

These values agree well with the values obtained by us by the continuous coverage method.[4]

The authors are indebted to N. I. Ionov for discussion.

---

[1] É. Ya. Zandberg and N. I. Ionov, Surface Ionization [in Russian], Izd. Nauka, Moscow (1969).

[2] N. I. Ionov, Zh. Tekh. Fiz., 26, 2200 (1956) [Sov. Phys. – Tech. Phys., 1, 2134 (1957)].

[3] É. Ya. Zandberg, Zh. Tekh. Fiz., 27, 2583 (1957) [Sov. Phys. – Tech. Phys., 2, 2399 (1957)].

[4] A. Ya. Tontegode and F. K. Yusifov, Zh. Tekh. Fiz., 41, 1717 (1971) [Sov. Phys. – Tech. Phys., 16, 1353 (1972)].

[5] É. Ya. Zandberg and A. Ya. Tontegode, Fiz. Tverd. Tela, 12, 1124 (1970) [Sov. Phys. – Solid State, 12, 878 (1970)].

[6] M. D. Scheer and J. Fine, J. Chem. Phys., 38, 307 (1963).

[7] É. Ya. Zandberg and A. Ya. Tontegode, Zh. Tekh. Fiz., 35, 149 (1965).

[8] S. V. Starodubtsev, ZhETF, 19, 215 (1949).

Efficient ion source

D. Kh. Abdrashitova, V. G. Babaev, and M. B. Guseva

M. V. Lomonosov Moscow State University

(Submitted October 25, 1972)
Zh. Tekh. Fiz., 44, 424-428 (February 1974)

A universal plasma ion source is described which can generate both gas ions and metal ions with an output of 1.5 mA at a discharge current below 300 mA and an extraction voltage of 4 kV. The ion source makes use of a hot-cathode Penning discharge. The metal vapor atmosphere with pressures $p \sim 10^{-3}$ torr is obtained by cathode sputtering. The plasma density in the source is increased by a magnetic trap for electrons in the region of the cathode and by electron-optical contraction of the plasma in an inhomogeneous magnetic field generated by superposition of magnetic fields, namely an external magnetic field and the field of the cathode helix. The source unit makes it possible to obtain a discharge in metal vapors in self-sputtering operation at pressures $p \leq 10^{-3}$ torr in the area of the exit opening in place of the pressure $P \geq 10^{-2}$ torr of ref. 1. Ions are emitted from the large surface of the plasma inside the discharge chamber. The outflow of neutral gas is limited by the small opening in the extraction electrode, which is an integral part of the discharge chamber.

INTRODUCTION

An ion source, which can generate ions of an inert gas or of metals, has been developed for research work on the formation of thin films. As with most other ion sources of this type, a hot-cathode discharge is employed. The efficiency of the source is increased by using a Penning discharge. The atmosphere of metal vapor is created by cathode sputtering. Among the possible ways of approaching the problem, there is one which uses the features of the Penning discharge and the features of a sputtered electrode at a negative potential: The sample is in the form of a cylinder which is surrounded by the cathode helix (Figure 1a).

This version of the hot-cathode Penning discharge has the following features.

1. When a homogeneous external magnetic field equal and opposite to the field generated by the cathode helix is applied, a magnetic trap is generated inside the sample electrode (Fig. 2). The result is trapping of electrons in this region; this creates a high degree of ionization inside the sample, where the vapor pressure of the sputtered material is highest.

2. The geometry of the sample electrode increases the efficiency with which the material is used because most of the non-ionized atoms hit the opposite wall of the sample.

3. The outflow of ions from the cylindrical sample causes a longitudinal potential gradient in the sample region and, hence, a gradient in the electron velocity parallel to the axis.[2] Under certain conditions these electron velocities can exceed the random velocities of the electrons. Thus, conditions are obtained for the electron-optical contraction of the plasma in an inhomogeneous magnetic field[3,4] so that the plasma density on the axis is greater than under similar conditions in conventional ion sources of this type (Figure 3). It is possible to obtain ion-output currents (neon and copper) of about 1.5 mA at an extraction voltage of 4 kV and at reduced discharge currents ($J_a \leq 300$ mA rather than $J_a = 1$ A) and external fields of 180 Oe (in place of 500 Oe in similar units).

4. Stable operation of the cathode is guaranteed by the high pressure maintained in the cathode region.

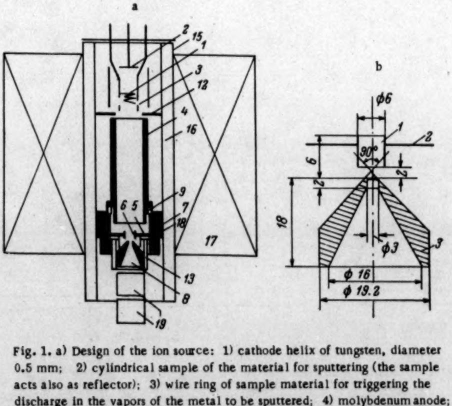

Fig. 1. a) Design of the ion source: 1) cathode helix of tungsten, diameter 0.5 mm; 2) cylindrical sample of the material for sputtering (the sample acts also as reflector); 3) wire ring of sample material for triggering the discharge in the vapors of the metal to be sputtered; 4) molybdenum anode; 5) second ion reflector with focusing cylinder mounted in the reflectors; 6) focusing cylinder; 7) shield; 8) extracting electrode, which is also the first electrode of an einzel lens. b) Extracting electrode: 1) focusing cylinder; 2) reflector of the source; 3) extractor.

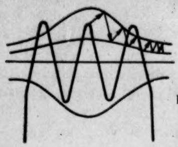

Fig. 2. Magnetic trap in the region of the cathode.

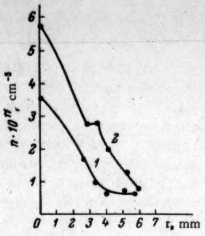

Fig. 3. Radial distribution of the plasma density in the plane of the exit opening of the discharge chamber. 1) Conventional ion source with electron oscillations in magnetic field; 2) ion source shown in Fig. 1a.

DESIGN OF THE SOURCE

The main components of the plasma chamber are shown in Fig. 1a. The other components (7, 12) of the discharge chamber are provided to keep insulators 9, 13, and 14 from becoming coated by metal vapors.

Double-wall cylinder 15 is the housing of the source. Nonmagnetic stainless steel is the main material of which the unit is fabricated. The insulators are made of aluminum oxide. The magnetic coil 17 is outside the housing.

The power supply is shown in Fig. 4. The source requires a power of 100-200 W under various conditions. The dissipated power is carried away by the cooling water, which circulates in chamber 16 between the walls of the housing.

This design provides reliable operation. The coatings on the surface of the insulators are insignificant: The leakage resistance of the insulators is 500 MΩ at 500 V after 25 hours operation of the source.

CHARACTERISTICS OF OPERATION

In this section we describe source parameters which distinguish the source from that of ref. 1, in which a hot-cathode Penning discharge is also used. In addition, we list data characteristic of the extraction system.

Figure 5 shows the dependence of the discharge current I_a on the external magnetic field (V_a = const). The subscript 1 refers to the conventional ion source of ref. 1, in which a Penning discharge is used (the potential V_s of the sample is equal to the potential V_a of the anode); subscript 2 refers to the version under consideration ($V_s \leq V_{cathode}$). Curves 1 and 2 are obtained with free operation of the cathode (the current drawn from the cathode is limited by the space charge; $I_a \cong I^-$). Curve 2a corresponds to application of a load to the cathode ($I^- \cong I^+$). I^- denotes the electron component, and I^+, the ion component of the discharge current.

1. The minimum voltage required to maintain the discharge is, in the conventional source, 20-25 V ($V_s = V_a$); in the present version the minimum voltage is 50 V ($V_s < 0$).

2. When the external magnetic field H_{ext} = 100 Oe (H_{ext} = 100 Oe = $-H_c$), a minimum of I_a is observed on curve 2, whereas the discharge is cut off on curve 1 (I_a = 0).

3. With H_{ext} = 180 Oe, curve 1 is characterized by saturation of the discharge current J_a, whereas a sharp maximum appears on curve 2. In this case, $I_{a_2} > I_{a_1}$.

4. When the external field is increased further curve 2 tends asymptotically to curve 1.

5. When a load is applied to the cathode (curve 2a), the difference in the characteristics $I_a = f(H)$ disappears: The discharge current reaches its maximum at H_{ext} = 180 Oe and remains constant thereafter, like the current I_{a_1}.

The behavior of this system can be explained as follows: When $H_{ext} = -H_k$, the magnetic mirror which is formed in the cathode area (Fig. 2) prevents the electrons from escaping into the discharge gap. The discharge is interrupted when $V_s = V_a$ (curve 1). The potential gradient inside the negative sample electrode ($V_s \leq V_k$) reduces the reflection of the magnetic mirror, which becomes transparent for a certain group of electrons, i.e., the discharge is ignited ($I_{a\,min} \neq 0$, curves 2 and 2a).

The maximum on curve 2 at H_{ext} = 180 Oe seems to be related to electron-optical plasma contraction. In pro-

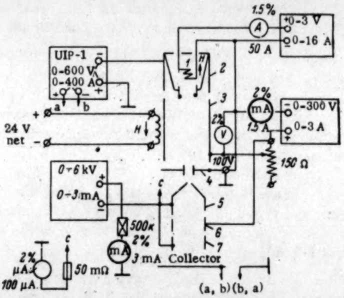

Fig. 4. Block diagram of the power supply.

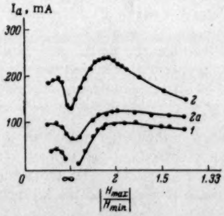

Fig. 5. Dependence of the discharge current on the external magnetic field. 1) Conventional ion source I_{heater} = 16 A, V_a = 25 V; 2) proposed ion source, free operation of the cathode, I_{heater} = 16 A, V_a = 50 V; 3) proposed ion source, cathode operated with a load, I_{heater} = 13 A, and V_a = 118 V.

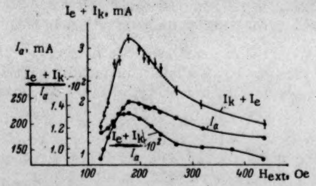

Fig. 6. Output ion current and plasma contraction as functions of the external magnetic field. $V_a = 56$ V and $V_e = 5250$ V.

portion to the increase in the external magnetic field ($H_{ext} >$ 180 Oe), the electron-optical effect decreases due to a reduction of the degree of magnetic field inhomogeneity; curve 2 approaches curve 1.

When the voltage applied to the discharge increases due to increasing cathode-voltage drops due to the load, the ratio of directed velocity to random velocities of the electrons is shifted in favor of the random velocities. This reduces the electron-optical contraction, in full agreement with Figure 5 (curve 2a).

Similarly, the external magnetic field influences the ion-output current from the source, i.e., the current $I_k + I_e$ (I_k denotes the ion current passing through the extractor to a Faraday cylinder, and I_e denotes the ion current fraction which ends on the extractor). The curve $(I_k + I_e)/I_a = f(H)$ (Fig. 6) has its maximum at 180 Oe ($H_{max}/H_{min} = 2.25$), which means that the maximum plasma contraction occurs under these conditions.

The ions are extracted from the source with a voltage of 4-5 kV. The maximum current flow seems to correspond to the crossover position in the extractor opening. At an extraction voltage of 4 kV the maximum current in the system is obtained under the following conditions in a neon atmosphere: $I_a = 180$ mA, $H_{ext} = 180$ Oe, and $V_a = 56$ V. The transmitted current is 71%, and the ion current in the beam is $I_k^+ = 1$ mA. At $V_{extr} = 5$ kV the maximum current flow is 65% and is observed at $I_a = 300$ mA, $H_{ext} = 180$ Oe, and $V_a = 56$ V. The current in the ion beam is 1.5 mA.

With this design of the extraction system (Fig. 1b), the amount of gas leaking from the discharge chamber is given by the dimensions of the opening in the extractor.

The width of the energy spectrum is given by the voltage applied to the discharge as in the case of the usual Penning ion source. The width of the energy spectrum is independent of the potential on the sample electrode and independent of the potential of the extractor, which should be checked in the modification of the extraction system considered.

The ion beam is then formed with the aid of an einzel lens with center electrode at the anode potential of the discharge chamber (Fig. 1a). The geometric parameters of the einzel lens are derived on the following basis. The length of the cylinder of the first electrode is chosen so that the crossover of the beam (object) is located outside the field of the lens. Furthermore, in order to obtain an ion beam which is parallel at the output, the focus of the ion-optical system is shifted along with the crossover of the beam (extractor opening). The aperture of the beam is determined from the retardation curve on a plane electrode situated at a distance of 10 cm from the lens. Then, the effect of the space charge is taken into account. Good parallelism of the ion current behind the lens is established, i.e., the ion-optical system works in a manner close to that calculated.

Our source is operated in a neon atmosphere or in a copper vapor atmosphere. In the latter case, the discharge is initiated in neon and afterwards transferred into a copper-vapor atmosphere by ion sputtering of the copper sample. The addition of neon to the discharge is then stopped. One must bear in mind that difficulties can be encountered when a metal sample is sputtered under the conditions existing in the discharge chamber of the ion source. For example, when the sample is irradiated with a flux of ions of an inert gas (energy of the ions about 600 eV), the sample is coated with a film which is hard to remove by sputtering. At low temperatures, this film is a polymer film which develops in the interaction of the ion current and the vapors of the diffusion-pump oil adsorbed on the sample surface. At high temperatures (up to the melting point of the sample), the film consists of metal. These films are formed on the substrate when the substrate surface is irradiated with ions of an inert gas, provided that metal vapors are present in the chamber even at low partial pressures $p \geq 10^{-9}$ torr.

The copper sample is sputtered in the following manner. First, the discharge is ignited in neon ($I_a = 280$ mA and $V_a = 56$ V). Copper ring 3 ($V_{ring} = -500$ V) is heated by ion bombardment to a temperature at which an intensive evaporation takes place. The supply of neon is thereafter interrupted. The discharge current increases to $I_a = 500$ mA at $V_a = 20$ V and the discharge continues to burn in copper vapors. The cathode sputtering of the cylindrical copper sample around the anode is initiated by applying a negative voltage. Ring 3 rapidly evaporates and cathode sputtering of the sample (self-sputtering) is the only mechanism maintaining the atmosphere of copper vapors in the discharge chamber. A copper-ion current of 1.5 mA is obtained at $I_a = 500$ mA, $H_{ext} = 180$ Oe, and $V_{extr} = 4$ kV.

Ions of various metals can be obtained in this fashion. The thermal conditions in the discharge chamber must evidently be controlled in certain cases. When copper ions are generated, the plasma chamber is operated with no constraints, i.e., it is not heated or cooled.

---

[1] W. L. Rautenbach, Nucl. Instr. and Meth., 9, 199 (1966).

[2] D. Kh. Abdrashitova and M. B. Guseva, Moscow State University [in Russian] (in press).

[3] G. V. Spivak and E. L. Stolyarova, Zh. Tekh. Fiz., 18 (1948).

[4] G. V. Spivak and L. I. Golik, Zh. Tekh. Fiz., 19, 839 (1949).

Measurement of statistical parameters of scattering particles in laminar flow by Doppler spectroscopy

A. P. Ivanov, A. Ya. Khairullina, and A. P. Chaikovskii

Physics Institute, Academy of Sciences of the Belorussian SSR, Minsk

(Submitted February 19, 1973)
Zh. Tekh. Fiz., 44, 429-434 (February 1974)

The possibility solving the inverse problem for scattering of coherent radiation in moving media is discussed. Equations are obtained that relate the spectral dependence of fluctuations in the intensity of scattered radiation to the velocity and size distributions of the particles. The problem is easily inverted for scattering in laminar flow when an external field acts on the particles. Experimental results are presented.

The problem of a noncontact measurement of the characteristics of dispersed media is important in science and engineering. In the present paper we investigate the optical field of scattered radiation in moving media and use the results to develop a method of measuring the size and velocity distributions of particles in the dispersed material. The essence of the method is measurement of the Doppler-frequency spectrum of the optical field $S(\omega)$ resulting from scattering by the moving particles. If the particle sizes ρ and speeds v are connected by a simple analytical relationship, the particle size distribution $n(\rho)$ and speed distribution $n(\mathbf{v})$ can be recovered from $S(\omega)$. Conditions favorable for the application of this method can be created artificially in certain cases and often occur naturally in actual flow of a liquid or a gas. For example, a simple relationship between particle size and velocity holds for steady fall of particles in a liquid or gaseous medium, in the settling of particles from a laminar flow under the action of gravity, and in the motion of charged particles in an electric field. A more complex situation occurs in a turbulent flow (see ref. 2). We have conducted detailed investigations of cases of scattering of radiation by particles moving in a laminar flow of liquid or gas, and fall in a medium at rest.

1. THE SPECTRAL FUNCTION $S(\omega)$

The calculation of the spectral function $S(\omega)$ for the fluctuations in the intensity of radiation experiencing single scattering in a volume V and combined with a reference signal, as is usual when investigating a Doppler frequency spectrum, is carried out under the following assumptions.

a) The field of nonuniformities in the scattering volume V is stationary and homogeneous. The particles do not leave the photometric volume V during the time required to correlate the intensity fluctuations at the observation point, and the particle velocities do not change.

b) The density of the scattering particles is small, i.e., the particles are not interacting with each other.

c) Multiple scattering does not occur.

d) The scattered and reference signals are coherent.

The photodetecting surface is much smaller than the coherence area of the scattered radiation, and the angle between the fronts of the scattered and reference radiation is small.

The intensity of the total optical field of the scattered radiation and the reference beam at time t is[2]

$$\begin{aligned} I(t) = |E(t)|^2 = a_0^2 + \sum_i a_i^2 \Theta_i(t) \\ + 2a_0 \sum_i a_i \Theta_i(t) \cos\{\varphi + \varphi_i + \mathbf{k}\mathbf{r}_i(t)\} \\ + \sum_{i \neq j}\sum a_i a_j \Theta_i(t)\,\Theta_j(t) \exp[i\mathbf{k}\{\mathbf{r}_i(t) - \mathbf{r}_j(t)\} + i(\varphi_i - \varphi_j)], \end{aligned} \tag{1}$$

where $\Theta_i(t) = I$ if the i-th particle is in the volume, and 0 if the i-th particle is not in the volume; a_0, φ_0 are the amplitude and phase of the field of reference radiation; a_i, φ_i are the amplitude and phase of the scattered radiation; $\mathbf{r}_i(t)$ is the radius vector of the location of the i-th scattering particle; and $\mathbf{k} = \mathbf{k}_s - \mathbf{k}_0$; $\mathbf{k}_0$, $\mathbf{k}_s$ are the wave number vectors of the incident and scattered radiation.

In contrast to ref. 2 we consider the case in which the motion of the scattering particle depends on its parameters.

Then the expression for the autocorrelation function will have the form

$$\begin{aligned} K(\tau) = \langle I(t)\, I(t+\tau)\rangle - \langle I(t)\rangle^2 \\ = [\overline{a_i^4} - (\overline{a_i^2})^2]\langle N\rangle + (\overline{a_i^2})^2(\langle N^2\rangle - \langle N\rangle^2) + 2a_0^2 \langle \sum_i a_i^2 \Theta_i(t) \cos[\mathbf{k}\Delta\mathbf{r}]\rangle \\ + \langle \sum_m \sum_n a_m^2 a_n^2 \Theta_m(t)\,\Theta_n(t) \exp i\mathbf{k}(\Delta\mathbf{r}_m - \Delta\mathbf{r}_n)\rangle - \overline{a_i^4}\langle N\rangle. \end{aligned} \tag{2}$$

The bar denotes averaging over the particles in the volume V, and the brackets denote averaging over the observation time $T \gg \tau$. According to assumption a) the probability of displacement of the i-th particle by $\Delta\mathbf{r}$ in time τ is

$$P(\Delta\mathbf{r}_i \mid \tau) = \delta(\Delta\mathbf{r}_i - \mathbf{v}_i\tau), \tag{3}$$

where $\mathbf{v}_i$ is the velocity of the i-th particle.

We assume that the scattering particles are spherical, so that $a_i^2 = a_i^2(\rho_i, \mathbf{k})$, where ρ_i is the radius of the i-th particle. We denote the multivariate distribution of the probabilities $v_i^k = \mathbf{v}_i(\mathbf{k}/k)$. Substituting Eq. (3) into Eq. (2), we obtain

$$\begin{aligned} K(\tau) = [\overline{a_i^4} - (\overline{a_i^2})^2]\langle N\rangle + (\overline{a_i^2})^2(\langle N^2\rangle - \langle N^2\rangle) \\ + 2a_0^2\langle N\rangle \int_{-\infty}^{\infty} P(v^k, \rho)\, a^2(\rho, \mathbf{k}) \cos[\mathbf{k}\mathbf{v}\tau]\, dv^k d\rho \\ + \langle N\rangle^2 \iint_{-\infty}^{\infty} P(v_m^k \rho_m v_n^k \rho_n)\, a_m^2 a_n^2 \\ \times \exp\{i\mathbf{k}(\mathbf{v}_m - \mathbf{v}_n)\tau\}\, dv_m^k dv_n^k d\rho_m d\rho_n - \overline{a_i^4}\langle N\rangle. \end{aligned} \tag{4}$$

The spectral function for the fluctuations of intensity of scattered radiation is

$$S(\omega)=\frac{1}{2\pi}\int_{-\infty}^{\infty}e^{i\omega\tau}K(\tau)\,d\tau=[\overline{a_i^4}-(\overline{a_i^2})^2]\langle N\rangle$$

$$+(\overline{a_i^2})[\langle N^2\rangle-\langle N\rangle^2]\delta(\omega)$$

$$+\iiiint n(v_m^k\rho_m v_n^k\rho_n)\,a_m^2a_n^2\delta[\omega-(v_m^k-v_n^k)]\,dv_m^k dv_n^k d\rho_m d\rho_n$$

$$-\overline{a_i^4}\langle N\rangle\delta(\omega)]$$

$$+a_0^2\int\int_{-\infty}^{\infty}n(v^k,\ \rho)\,a^2(\rho,\ \mathbf{k})[\delta(\omega-\mathbf{kv})+\delta(\omega+\mathbf{kv})]\,dv^k d\rho. \qquad (5)$$

The first group of terms on the right side of Eq. (5) results from fluctuations of intensity of radiation scattered by individual particles, and from fluctuations in the number of particles in volume V. The second term describes the Doppler frequency shift for the radiation scattered by two particles moving with relative velocity $\mathbf{v}_{mn} = \mathbf{v}_m - \mathbf{v}_n$. The third term gives the Doppler frequency shift for scattering by a particle moving with velocity $\mathbf{v}$ in the laboratory coordinate system. If the intensity of scattered radiation is much less than that of the reference signal, the spectral function becomes

$$S(\omega)=\frac{a_0^2}{k}\left[\int_{-\infty}^{\infty}a^2(\rho,\ \mathbf{k})\,n(v_1^k,\ \rho)\,d\rho+\int_{-\infty}^{\infty}a^2(\rho,\ \mathbf{k})\,n(v_2^k,\ \rho)\,d\rho\right], \qquad (6)$$

where $v_1^k = \omega/k$, $v_2^k = -\omega/k$.

In almost all cases the velocity vectors for all the scattering particles lie within a cone with apex angle $\gamma < \pi$. Therefore we can choose the vector **k** to satisfy one of the following conditions:

$$\left.\begin{array}{l}1)\ n(v_i^k,\ \rho)=0\ \text{for}\ \mathbf{kv}_i<0\\ \text{or}\ 2)\ n(v_i^k,\ \rho)=0\ \text{for}\ \mathbf{kv}_i>0.\end{array}\right\} \qquad (7)$$

Then only one term remains in Eq. (6). Since

$$P(v^k,\ \rho)=P(v^k)\,P(\rho\,|\,v^k)=P(\rho)\,P(v^k\,|\,\rho), \qquad (8)$$

we obtain the following equation for the particle size distribution function:

$$S[|kv^k|]=\frac{a_0^2}{k_0^2}\frac{BdQd\Omega}{k\Delta S}V\int\mu(\rho,\ \mathbf{k})\,n(\rho)\,P(v^k\,|\,\rho)\,d\rho, \qquad (9)$$

where B and dQ are the brightness and the solid angle of the radiation incident on the photometric volume V; $\Delta\Omega$ and ΔS are the reception angle and the working area of the photocathode, normal to the incident radiation; $\mu(\rho, \mathbf{k})$ is the scattering index normalized in the usual way, $(1/k_0^2)\cdot\int\mu(\rho, \mathbf{k})\,d\omega = \alpha$ (α is the particle scattering cross section); and a_0^2 is the reference radiation intensity.

It follows from Eq. (9) that the contribution to the spectral function at frequency ω is from radiation scattered by particles with velocity a_0^2.

Making use of Eqs. (7) and (8), we can also write Eq. (6) in the form

$$S(|kv^k|)=\frac{a_0^2}{k_0^2}\frac{BdQ\Delta\Omega}{\Delta Sk}Vn(v^k)\int\mu(\rho,\ \mathbf{k})\,P(\rho\,|\,v^k)\,d\rho. \qquad (10)$$

Equations (9) and (10) are equations for the functions $n(\rho)$ and $n(v^k)$, and can be solved if the experimental conditions allow determination of the functions $P(v^k/\rho)$ and $P(\rho/v^k)$.

Relations (9) and (10) are greatly simplified if there is a unique relation between ρ and v^k.

We assume that there is scattering of coherent radiation by particles moving in a laminar stream with velocity $\mathbf{v}_i = \mathbf{v}_0 + \mathbf{W}_i$, where $\mathbf{v}_0$ is the velocity of the medium, $\mathbf{W}_i$ is the relative velocity of the i-th particle, σ_0 = const is the medium density, and σ_i = const is the particle density. Gravity acts on the particles in addition to the hydrodynamic forces. In the region of applicability of the Stokes equation[2] we have

$$\mathbf{W}_i=\frac{2}{9}\frac{\Delta\sigma}{\eta}\rho_i^2\mathbf{g}. \qquad (11)$$

Here $\Delta\sigma = \sigma_i - \sigma_0$, η is the viscosity of the medium, and $\mathbf{g}$ is the gravitational acceleration.

Relations (9) and (10) take the following simple form:

$$n(v^k)=\frac{\Delta Sk_0^2kS\,[|kv^k|]}{a_0^2BdQ\Delta\Omega V\mu\left[\mathbf{k},\ \rho=\sqrt{\frac{9}{2}\eta\frac{(v^k-v_0^k)}{\Delta\sigma g}}\right]}, \qquad (12)$$

$$n(\rho)=\frac{4}{9}\frac{k_0^2\Delta Sk}{a_0^2BdQ\Delta\Omega V}\frac{\Delta\sigma g^k\rho}{\mu(\mathbf{k},\ \rho)}S\left[\left|\mathbf{k}\left(\mathbf{v}_0+\frac{2}{9}\frac{\Delta\sigma}{\eta}\rho^2\mathbf{g}\right)\right|\right]. \qquad (13)$$

Relations (12) and (13) allow us to determine $n(v^k)$ and $n(\rho)$ from the experimentally obtained function $S(\omega)$. The frequency spectrum is usually measured in relative units. To determine $n(v^k)$ or $n(\rho)$ in absolute units it is sufficient, for example, to measure the transmission for radiation propagating straight through the photometric volume.

We note that the problem of calculating $n(v^k)$ and $n(\rho)$ is correctly posed in the case considered, in distinction from other problems of this kind, e.g., the small angle method (ref. 3) and the spectral transparency method (ref. 4).

We now determine the limits of applicability of this method. 1. As formulated above the method is suitable only for laminar flows in the region of application of the Stokes equation (refs. 1, 5).

2. The limit of resolution of two close fractions is given by the resolution of the spectral analyzer and can be calculated from the inequality

$$\frac{\Delta f}{f}<\frac{\Delta\omega}{\omega}=\frac{\mathbf{k}(\mathbf{v}_2-\mathbf{v}_1)}{\mathbf{k}\left(\mathbf{v}_0+\frac{\mathbf{w}_1+\mathbf{w}_2}{2}\right)}=\frac{\frac{4}{9}\frac{\Delta\rho\sigma_0}{\eta}\mathbf{kg}}{\mathbf{k}\left(\mathbf{v}_0+\frac{2}{9}\frac{\Delta\sigma\rho}{\eta}(\rho_1^2+\rho_2^2)\,\mathbf{g}\right)}, \qquad (14)$$

where $\Delta f/f$ is the relative resolution of the spectral instrument, $\rho_0 = (\rho_1 + \rho_2)/2$, and $\Delta\rho = \rho_2 - \rho_1$.

2. EXPERIMENT

The method described above has been used to measure the sizes of scattering particles passing through the photometric volume at different times in precipitation

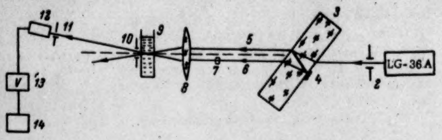

Fig. 1. Experimental arrangement. 1) LG-36A gas laser; 2, 10, 11) diaphragms; 3) plane-parallel slab; 4) reflecting coating; 5,. 6) primary and reference rays; 7) neutral filter; 8) lens; 9) medium; 12) type FÉU-79 photomultiplier; 13) amplifier; 14) FSP-80 spectral analyzer.

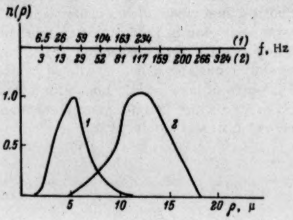

Fig. 3. Particle size distribution function n(ρ). 1) Corundum; 2) glass.

of the particles in a fluid at rest ($v_0 = 0$). The experimental conditions satisfy all the conditions enumerated in Sec. 1. The experimental arrangement is illustrated in Fig. 1. A special feature is the method for forming the reference signal, which is obtained by double reflection of the incident radiation from the plane-parallel slab 3, which has a small optical wedge angle. In this case the primary and reference rays are parallel. The rays are focused by the single lens 8. This optical system gives very simple compliance with the condition (c) of Part 1. Adjustment of the system simply means locating the medium at the focus of lens 8. An FSP-80 spectral analyzer is used to perform parallel analysis of the random signal with the aid of 38 filters spanning the range 2 Hz to 20 kHz.

A thin cell 9, filled with distilled water, is positioned at the focus of lens 8. The scattering particles are introduced into the cell in small samples. To determine the effect on the measured results of perturbation of the medium upon the addition of the scattering particles, of oscillations of the fluid and of convective motion (i.e., the instrumental background), we perform an experiment with latex particles ($\rho = 0.09\ \mu$, $\Delta\sigma = 0.06\ \text{g/cm}^3$), which in fact follow the motion of the medium completely. Figure 2a shows the spectral function for the latex particles. The spectral broadening due to Brownian motion for the given experimental geometry is $\Delta f < 1$ Hz (ref. 6), which is much less than the bandwidth of the analyzer filters, and introduces essentially no distortion into the shape of the function $S(f)$ under investigation.

The test specimens we use are particles of corundum ($\Delta\sigma = 3\ \text{g/cm}^3$) and glass ($\Delta\sigma = 1.5\ \text{g/cm}^3$). The size distribution is shown in Fig. 3. At the top of the figure is the frequency scale corresponding to a specific particle radius. Because of their different rates of fall, some time after the particles are introduced into the medium we see a vertical particle size stratification, which changes with time. Therefore, particles ranging from coarse to very fine traverse the photometric volume and the maximum in the measured spectral function is displaced towards low frequency (Fig. 4). The experimentally obtained range of variation of frequency f (Fig. 4) agrees with that calculated (Fig. 3). During the experiment data obtained from measurements of $S(f)$ are compared with results of measurements under the microscope of samples taken from the scattering volume immediately following measurement of $S(f)$. The results coincide within a tolerance given by the transmission bandwidth of the analyzer filters.

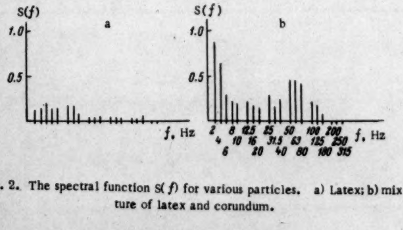

Fig. 2. The spectral function $S(f)$ for various particles. a) Latex; b) mixture of latex and corundum.

The sensitivity of this method is a matter of practical interest. Figure 2b shows the spectral function $S(f)$ for the case of a two-component disperse medium, consisting of a combination of particles of latex and corundum. The intensity of the radiation scattered by the latex is approximately an order of magnitude greater than that from the corundum, but the appearance of the corundum particles in the volume V is easily recorded.

Thus, when applicable, this method enables one to establish the particle velocity and size distribution functions. It is simple, both from the viewpoint of technical implementation and as regards mathematical reduction of the results of direct measurement. It is especially useful for recording the appearance in the scattering volume of particles which differ in density or size from particles previously occupying the volume.

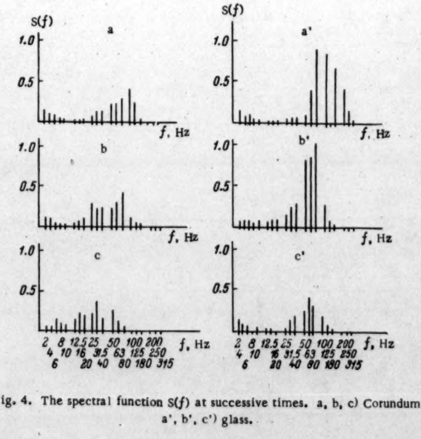

Fig. 4. The spectral function $S(f)$ at successive times. a, b, c) Corundum; a', b', c') glass.

The method described allows analysis of the microstructure and the velocity field of a dispersed phase with good time and space resolution, and, when allied with the cross-correlation method of ref. 7, allows measurement of the parameters of large-scale nonuniformities, thus providing a large volume of information concerning processes occurring in streams of liquid or gas.

---

[1] S. Sou, Hydrodynamics of Multiphase Systems [Russian translation], Izd. Mir, Moscow (1971).

[2] P. J. Bourke, J. Phys. A: Gen. Phys., 3, 216 (1970).

[3] K. S. Shifrin and I. B. Kolmakov, Izv. AN SSSR, Ser. Fiz. Atmos. Okeana, No. 12, 1271 (1967).

[4] K. S. Shifrin and A. Ya. Perel'man, Opt. Spektrosk., 15, 4, 5, 6 (1964); 20, No. 1 (1966).

[5] A. Fort'e, Mechanics of Suspensions [Russian translation], Izd. Mir, Moscow (1971).

[6] R. Pecora, J. Chem. Phys., 40, 1604 (1964).

[7] N. F. Derevyanko and A. N. Trokhan, Zh. Prikl. Mekh. Tekh. Fiz., No. 4, 52 (1969).

Condensation of a dense vapor flow

V. G. Dneprovskii, B. A. Osadin, and N. V. Rusakov

(Submitted December 12, 1972; resubmitted April 12, 1973)
Zh. Tekh. Fiz., 44, 435-441 (February 1974)

The distinctive features of the conditions prevailing during the condensation of a dense vapor flow produced in pulsed evaporation by means of highly intense heat sources (lasers, exploding wires, and plasma guns) are analyzed. Equations describing the nonequilibrium layer immediately adjacent to the condensation surface are derived for the case in which some of the molecules are elastically reflected from the condensation surface and for the case of diffuse reflection. It is shown that, in contrast with the conditions for condensation in free-molecular vapor flow, the properties of this nonequilibrium layer in this case are strong functions of the condensation coefficient. For example, in the case of elastic reflection with a condensation coefficient $\alpha \leq 0.85$ the condensation occurs from a flow which has been nearly stopped. The conditions under which the derived equations are applicable are discussed. It is shown that they can be used to solve transient problems.

There are a number of recent papers which deal with the use of intense heat sources (lasers, exploding wires, and plasma guns) to produce thin films.[1–4] The vapor (or plasma) flow toward the condensation surface (a substrate or wall) in experiments of this type is distinguished by high velocities (frequently much higher than the thermal velocities) and high densities, so that such a flow is usually treated as a gas-dynamic flow, in contrast with the free-molecular flows which were previously used to deposit thin films in vacuum.[5]

Under molecular-flow conditions, with the mean free path larger than the distance from the evaporator to the substrate, the circumstance that the condensation coefficient is not equal to unity has essentially no influence on the condensation process. For a dense flow, on the other hand, this circumstance should, in general, change the flow conditions (the external problem) and change the condensation conditions and the temperature field in the condensation device (the internal problem).

A distinctive feature of the external problem of the condensation of a dense vapor flow is that it is necessary to analyze the nonequilibrium vapor sheath immediately adjacent to the substrate. This sheath results from both evaporation and the circumstance that the condensation coefficient is different from unity.

In this work we analyze the conditions prevailing near the surface at which a dense vapor flow condenses.

We assume that a vapor flow is incident from the left on a vertical substrate. The vapor is a monatomic ideal gas having the following properties at infinity, i.e., at the outlet from the evaporator: density n_∞, temperature T_∞ (mass density ρ_∞ and pressure p_∞), and flow velocity v_∞. We assume that at infinity the flow has an equilibrium distribution function in the coordinate system fixed in the flow:

$$f_\infty = n_\infty \left(\frac{m}{2\pi k T_\infty}\right)^{3/2} \exp\left\{-\frac{m}{2kT_\infty}\left[(v_x+v_\infty)^2+v_y^2+v_z^2\right]\right\}. \quad (1)$$

The x axis is directed toward the oncoming flow, and v_∞ is the magnitude of the flow velocity.

In a nonequilibrium sheath with thickness of the order of the mean free path at the wall, there are two oppositely directed flows; the distribution function at the wall is then written as the sum

$$f_0 = f_- + f_+, \quad (2)$$

where f_- describes the particles incident on the wall ($v_x \leq 0$) and f_+ describes the reflected particles ($v_x \geq 0$). The actual forms of f_- and f_+ are functions of the conditions prevailing at the condensation surface (elastic reflection of atoms which have not condensed, diffuse reflection, reevaporation, etc.). If these functions are specified, e.g., Maxwellian distributions, the problem which remains is simply one of determining the parameters of these distributions.

A similar approach to the kinetics of the nonequilibrium sheath which arises during evaporation in vacuum has been developed by Romanov and Pustovalov.[6] In the case of evaporation the use of the distribution function at infinity as given in (1) requires certain additional reservations,[7] while in our case condition (1) is simply a specified condition.

We treat the steady-state problem, i.e., we first assume that the temperature of the condensation surface does not change during condensation and that reevaporation does not occur. Second, we assume that the transient gas-dynamic pressure which arises as the oncoming flow collides with the wall has decayed and produced a steady-state flow. The criterion for the absence of reevaporation is given below. With regard to the assumption of a gas-dynamic steady-state, we note that, e.g., under the experimental conditions of ref. 4, the transient flow pattern is observed for only a few microseconds, so that even when the condensation continues for only tens of microseconds the assumption of a steady-state is in accordance with the actual nature of the process.

CONDITIONS AT THE WALL FOR ELASTIC REFLECTION

In the case in which some of the particles are elastically reflected we can approximate f_- as an equilibrium function (n_0, T_0, v_0) with a clipped positive tail, and we can approximate f_+ as the mirror-reflected distribution with ordinates smaller than those of f. In other words,

$$f_- = a_- \exp\left\{-\frac{m}{2kT_0}\left[(v_x+v_0)^2+v_y^2+v_z^2\right]\right\}, \quad v_x \leqslant 0, \quad (3)$$

$$f_+ = a_+ \exp\left\{-\frac{m}{2kT_0}\left[(v_x-v_0)^2+v_y^2+v_z^2\right]\right\}, \quad v_x \geqslant 0, \quad (4)$$

where v_0 is the magnitude of the "velocity" of the forward and reverse flows.

Normalizing f_0 to the particle density at the wall, n_0, and using the condition for the elastic reflection of uncondensed particles in one of the three equivalent forms

$$\left.\begin{aligned} M&=M_-+M_+=\alpha M_-,\\ P&=P_-+P_+=(2-\alpha)P_-,\\ W&=W_-+W_+=\alpha W_-, \end{aligned}\right\} \tag{5}$$

we find the following equations for the normalization factors:

$$a_-=\frac{2}{2-\alpha}\frac{n_0}{(\sqrt{\pi}v_{T0})^3[1+\operatorname{erf}(z)]}, \tag{6}$$

$$a_+=\frac{2(1-\alpha)}{2-\alpha}\frac{n_0}{(\sqrt{\pi}v_{T0})^3[1+\operatorname{erf}(z)]}. \tag{7}$$

In (5), M₋, P₋, and W₋ are the mass, momentum, and energy fluxes associated with distribution function f_- (toward the substrate); M₊, P₊, and W₊ are the mass, momentum, and energy fluxes associated with distribution function f_+ (from the substrate); and M, P, and W are the resultant fluxes to the substrate. Explicitly,

$$\left.\begin{aligned} M_-&=\int_{-\infty}^{0}\int_{-\infty}^{\infty}\int_{-\infty}^{\infty} f_- m v_x^2\,dv_x\,dv_y\,dv_z,\\ P_-&=\int_{-\infty}^{0}\int_{-\infty}^{\infty}\int_{-\infty}^{\infty} f_- m v_x^2\,dv_x\,dv_y\,dv_z,\\ W_-&=\int_{-\infty}^{0}\int_{-\infty}^{\infty}\int_{-\infty}^{\infty} f_- \frac{m}{2}(v_x^2+v_y^2+v_z^2)\,v_x\,dv_x\,dv_y\,dv_z. \end{aligned}\right\} \tag{8}$$

In Eqs. (6) and (7) we have used

$$v_{T0}=\sqrt{\frac{2kT_0}{m}},\quad z=\frac{v_0}{v_{T_0}},\quad \operatorname{erf}(z)=\frac{2}{\sqrt{\pi}}\int_0^z \exp(-\xi^2)\,d\xi.$$

In the steady-state the values of M, P, and W are constant along the flow so that, with absolute values in mind, we can write these quantities as

$$\left.\begin{aligned} M&=mn_\infty v_\infty=\rho_\infty v_\infty,\\ P&=n_\infty kT_\infty+mn_\infty v_\infty^2=p_\infty+\rho_\infty v_\infty^2,\\ W&=\frac{5}{2}n_\infty kT_\infty v_\infty+\frac{m}{2}n_\infty v_\infty^3=\rho_\infty v_\infty\left(\frac{5}{2}\frac{p_\infty}{\rho_\infty}+\frac{v_\infty^2}{2}\right), \end{aligned}\right\} \tag{9}$$

i.e., equate the corresponding gas-dynamic fluxes.[8,9] On the other hand, calculating the kinetic moments in (8), we find

$$\left.\begin{aligned} &M=\frac{\alpha}{2-\alpha}n_0 m v_0 f_M(z);\quad f_M(z)=z+\frac{1}{\sqrt{\pi}}\frac{\exp(-z^2)}{1+\operatorname{erf}(z)};\\ &P=n_0 m v_{T0}^2 f_P(z);\quad f_P(z)=z^2+\frac{1}{2}+\frac{1}{\sqrt{\pi}}\frac{z\exp(-z^2)}{1+\operatorname{erf}(z)};\\ &W=\frac{\alpha}{2-\alpha}n_0\frac{m}{2}v_{T0}^3 f_W(z);\\ &f_W(z)=z^3+\frac{5}{2}z+\frac{1}{\sqrt{\pi}}\frac{(z^2+2)\exp(-z^2)}{1+\operatorname{erf}(z)}. \end{aligned}\right\} \tag{10}$$

By solving system (10) we can determine the properties n₀, T₀, v₀ of the nonequilibrium sheath, which are to be understood as the parameters of the nonequilibrium distribution function at the wall, f_0, for the specified gas-dynamic fluxes at the outlet from the evaporator (M, P, W) and for the specified condensation coefficient α. From (10) we find an equation for z:

$$F(z)=\frac{f_M f_W}{f_P^2}=2\left(\frac{2-\alpha}{\alpha}\right)^2\frac{MW}{P^2}. \tag{11}$$

Here, F(z) is a monotonically decreasing function, which tends toward unity as z → ∞ (Fig. 1). In this connection, the specification of M, P, and W means that not all possible values of α are allowed, but only those for which

$$1\geqslant\alpha\geqslant\alpha_{\min}=\frac{2}{1+\sqrt{\frac{P^2}{2MW}F(0)}}. \tag{12}$$

It is easy to see the physical meaning of this result: With $\alpha<\alpha_{\min}$ the inverse effect of the substrate on the evaporator becomes so strong that it changes the fluxes M, P, and W; the perturbation of the flow which results from the collision with the wall is propagated back to the evaporator.

CONDITIONS AT THE WALL FOR DIFFUSE REFLECTION

We again assume that the reverse particle flow arises only because α is different from unity, but we assume that the velocity distribution of the reflected particles is governed by the surface temperature T_n, which is assumed low ($T_n \ll T_0$) and relatively constant during the condensation. In other words, we write the distribution function at the wall in form (2) where

$$f_-=a_-\exp\left\{-\frac{m}{2kT_0}[(v_x+v_0)^2+v_y^2+v_z^2]\right\},\quad v_x\leqslant 0, \tag{13}$$

$$f_+=a_+\exp\left\{-\frac{m}{2kT_n}(v_x^2+v_y^2+v_z^2)\right\},\quad v_x\geqslant 0. \tag{14}$$

As before, normalizing f_0 to n₀ and using the same mass-reflection condition, we find

$$a_-=\frac{2n_0}{(\sqrt{\pi}v_{T0})^3}\frac{1}{[1+\operatorname{erf}(z)][1+\sqrt{\pi}(1-\alpha)yz]+(1-\alpha)y\exp(-z^2)}, \tag{15}$$

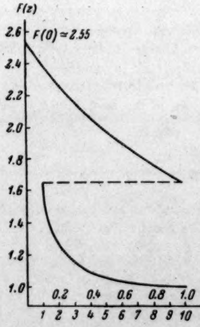

Fig. 1

$$a_+ = \frac{2(1-\alpha)n_0}{(\sqrt{\pi}v_{T0})^3}\frac{\sqrt{\pi}\,z\,[1+\mathrm{erf}(z)] + \exp(-z^2)}{[1+\mathrm{erf}(z)][1+\sqrt{\pi}(1-\alpha)yz] + (1-\alpha)y\exp(-z^2)}y^4, \tag{16}$$

where $y = v_{T0}/v_{Tn}$, $v_{Tn} = (2kT_n/m)^{1/2}$.

We again write

$$M = M_- + M_+ = \alpha M^- \tag{17}$$

and assume since T_n is low that

$$P = P_-,\quad W = W_-. \tag{18}$$

Then after calculating the kinetic moments in (8) we find

$$\left.\begin{aligned} M &= \alpha n_0 m v_{T0}\frac{f_M(z)}{f(y,z)},\\ P &= n_0 m v_{T0}^2\frac{f_P(z)}{f(y,z)},\\ W &= n_0\frac{m}{2}v_{T0}^3\frac{f_W(z)}{f(y,z)}, \end{aligned}\right\} \tag{19}$$

where f_M, f_P, and f_W are again given by Eqs. (10); M, P, and W are given by Eqs. (9); and

$$f(y,z) = 1 + \sqrt{\pi}(1-\alpha)yz + (1-\alpha)y\frac{\exp(-z^2)}{1+\mathrm{erf}(z)}. \tag{20}$$

By solving system (19) we can determine the properties of the nonequilibrium sheath, n_0, T_0, and v_0, which are to be understood as the parameters of the nonequilibrium distribution function at the wall, f_0, for the specified gas-dynamic fluxes at the outlet from the evaporator (M, P, and W), the condensation coefficient α, and the temperature of the condensation surface, T_n. From (19) we find an equation for F(z):

$$F(z) = \frac{f_M f_W}{f_P^2} = \frac{2}{\alpha}\frac{MW}{P^2}. \tag{21}$$

From this equation we find, for specified values of M, P, and W,

$$1 \geqslant \alpha \geqslant \alpha_{\min} = \frac{2MW}{P^2}\frac{1}{F(0)}. \tag{22}$$

Equation (22) predicts smaller "allowed" values of the condensation coefficient than does Eq. (12), in accordance with the lesser effect of the substrate on the evaporator in the case of diffuse reflection.

We now turn to a numerical example. We assume that the parameters of the flow at the outlet from the evaporator are $n_\infty = 10^{16}$ cm^{-3}, $T_\infty = 5 \cdot 10^3$ °K, and $v_\infty = 5 \cdot 10^5$ cm/sec. We assume that the vapor is a monatomic ideal gas with an atomic weight $\mu = 32$ (the atomic weight of sulfur), and we assume that the substrate surface is at $T_n = 500$°K. Table 1 shows the characteristics of the nonequilibrium sheath: the conditions at the wall for the case of elastic reflection (the upper two rows) and for the case of diffuse reflection (the remaining rows). It follows from this table that if the condensation coefficient is even slightly different from unity in the case of elastic reflection there will be a significant slowing of the flow in front of the wall (with $\alpha = 0.85$ the condensation occurs from a flow which has been slowed essentially completely). In the case of diffuse reflection the flow is slowed less (and smaller values α are "allowed"), but there is a much higher density in the nonequilibrium sheath.

TABLE 1

α	z	$n_0 \cdot 10^{-16}$, cm^{-3}	$T_0 \cdot 10^{-3}$, °K	$v_0 \cdot 10^{-5}$, cm/sec
0.90	0.90	1.90	18.6	2.80
0.85	0.42	2.52	24.6	1.50
0.90	2.00	3.24	8.9	4.28
0.80	1.50	6.12	10.4	3.46
0.70	1.01	9.95	12.4	2.53
0.50	0.22	23.0	14.0	0.68

This example is obviously purely illustrative since we have neglected the actual state of the material.

CONDITION FOR NO REEVAPORATION

The inverse evaporation from the substrate is governed by the temperature of the surface on which the condensation occurs. In the moving coordinate system ($x' = x + v_k t$) when the condensation occurs on a homogeneous substrate (the thermal constants of the substrate and the condensate are the same), the heat-conduction problem can be written

$$\left.\begin{aligned} &\frac{\partial T}{\partial t} = a^2\frac{\partial^2 T}{\partial x'^2} - v_k\frac{\partial T}{\partial x'},\quad x' \geqslant 0,\\ &\left.\frac{\partial T}{\partial x'}\right|_{x'=0} = -\frac{Q}{k},\quad T(x',0) = T_0, \end{aligned}\right\} \tag{23}$$

where $v_k = M/\gamma$ is the condensation rate, $Q = W + (\lambda - c_p T)$ is the heat flux, λ is the heat of evaporation, c_p is the specific heat of the condensate at constant pressure, k is the thermal conducitivity, a^2 is the thermal diffusivity, T_0 is the initial substrate temperature, and the x axis is directed into the substrate. Neglecting the enthalpy of the condensate in comparison with W, we can simplify the boundary condition in (23) ($Q = W + \lambda M$), and using the method of integral transforms we can find the following solution for this problem:[9]

$$T(x',t) = T_0 + \frac{aQ}{k}\exp\left(\frac{v_k}{2a^2}x'\right)\int_0^t\left\{\frac{1}{\sqrt{\pi\tau}}\exp\left[-\left(\frac{v_k^2}{4a^2}\tau + \frac{x'^2}{4a^2\tau}\right)\right] + \frac{v_k}{2a}\exp\left(-\frac{v_k}{2a^2}x'\right)\mathrm{erfc}\left(\frac{x'}{2a\sqrt{\tau}} - \frac{v_k}{2a}\sqrt{\tau}\right)\right\}d\tau, \tag{24}$$

where erfc(z) = 1 − erf(z). We then find the surface temperature to be

$$T(0,t) = T_0 + \frac{aQ}{k}\int_0^t\left[\frac{1}{\sqrt{\pi\tau}}\exp\left(-\frac{v_k^2}{4a^2}\tau\right) + \frac{v_k}{2a}\mathrm{erfc}\left(-\frac{v_k}{2a}\sqrt{\tau}\right)\right]d\tau. \tag{25}$$

Introducing the unit of time $t^* = 4a^2/v_k^2$ and the unit of temperature $T^* = aQ\sqrt{t^*}/\sqrt{\pi}k)$, we can rewrite (25) as

$$u = \int_0^\theta\left[\frac{\exp(-\xi)}{\sqrt{\xi}} + \sqrt{\pi}\,\mathrm{erfc}(-\sqrt{\xi})\right]d\xi, \tag{26}$$

where

$$u = \frac{T - T_0}{T^*}\ \text{and}\ \theta = \frac{t}{t^*}.$$

For $\theta \ll 1$, the condition which corresponds physically to the initial stage of the process or to a condensation rate which is small in comparison with the velocity at which the thermal wave moves into the substrate, we can rewrite (26) as

$$u = 2\sqrt{\theta} + \sqrt{\pi}\theta, \qquad (27)$$

which differs only by the second term from the familiar solution for the case without condensation.

The condition of no evaporation can evidently be written[10]

$$M \gg \sqrt{\frac{\mu}{2\pi R T_n}}\, P(T_n), \qquad (28)$$

where R is the universal gas constant, $P(T_n)$ is the saturation vapor pressure of the given material, and $T_n \equiv T(0, t)$. With specified M and W we can use this condition to determine the maximum duration of steady-state condensation over which we can neglect reevaporation.

Numerical calculations show that for the condensation of sulfur on sulfur ($n_\infty = 10^{16}$ cm^{-3}, $T_\infty = 5 \cdot 10^5$, and $v_\infty = 5 \cdot 10^5$ cm/sec^{-1}, as before), reevaporation must be taken into account after only $t > t_p \simeq 6 \cdot 10^{-6}$ sec, while for condensation of copper on copper, with the same properties of the vapor flow, reevaporation can be neglected for a time $t = t_p \simeq 0.3$ sec.

We have analyzed the conditions prevailing at the wall in the condensation of a dense vapor flow, making significant use of the assumption of a steady-state. Turning briefly to the transient stage in the collision of the flow with the substrate, we note that the transient flow which results can be divided into two parts: a nonequilibrium kinetic part having a side on the order of the mean free path l, directly adjacent to the wall; and a gas-dynamic part (with possible rapid changes in the properties). If the characteristic time for changes in the properties in the nonequilibrium region is $\tau \sim l/v \ll t_y$, where t_y is the characteristic time for the establishment of a steady-state flow, we can use Eqs. (2)-(4) or (2), (13), and (14) above as boundary conditions for the kinetic region and use Eqs. (10) or (19) as boundary conditions for the gas-dynamic region.

In conclusion we turn to the errors associated with the approximation of the nonequilibrium distributions by a sum of Maxwellian distributions.

Obviously, any distribution with one or several clearly defined peaks can be approximated as the sum of one or more Maxwellian distributions [as was done in (2)], whose most probable velocities coincide with the peaks and whose "temperatures" give the widths of these peaks. When the distributions are normalized in the same manner, the areas under the curves representing the real and approximate distributions will be equal, and the error due to the approximation can be expressed in terms of the difference between the ordinates of the two curves. For each concrete value of v_x this error can be large; the parameters of the Maxwellian distributions describe only the general features of the situation.

When there are only two peaks – a main peak corresponding to most of the particles, at equilibrium, and an additional peak giving the deviation from equilibrium – we can estimate the errors by using the kinetic equation with a relaxation term. For the problems considered here (in the steady-state, with no fields), this term is

$$v_x \frac{\partial f}{\partial x} = -\frac{f - f_e}{\tau} \qquad (29)$$

where f_e is the equilibrium distribution function and τ is the relaxation time. Finding the ratio f/f_e from (29), we can treat the quantity

$$\delta \sim \frac{\tau}{l}\left(v_x \frac{\Delta f}{f_e}\right) \qquad (30)$$

as the relative error in the determination of the parameters of the main peak. Here l represents the dimension of the nonequilibrium sheath, over which the value of $f = f(v_x)$ changes by Δf. The distribution f_e as well as τ and l are governed by the particles corresponding to the main peak.

It follows from (30) that the errors in the approximation decrease with decreasing amplitude of the auxiliary peak and with decreasing separation of this peak from the ordinate axis. For example, for the case of elastic reflection the quantity δ reduces simply to the ratio of the normalization factors a_+ and a_-, becoming equal to $\sim(1 - \alpha)$. Accordingly, at sufficiently large condensation coefficients, Eqs. (2)-(4) turn out to be a good approximation. In the case of diffuse reflection it follows from (15) and (16) that Δf increases, and the values of v_x for the additional peak decrease. The errors remain approximately the same.

---

[1] H. M. Smith and A. F. Turner, Appl. Opt., 4, 147 (1965).

[2] P. D. Zavitsanos and W. E. Sauer, J. Electrochem. Soc., 115, 109 (1968).

[3] L. N. Aleksandrov, E. I. Dagman, V. I. Zelevinskaya, V. I. Petrosjan, and P. A. Skripkina, Thin Solid Films, Vol. 5, (1970), p. 1.

[4] B. A. Osadin and V. N. Rusakov, Zh. Tekh. Fiz., 44, 477 (1974) [Sov. Phys. – Tech. Phys., 19, 299 (1974)].

[5] L. Holland, Vacuum Deposition of Thin Films, Wiley, New York (1956).

[6] G. S. Romanov and V. K. Pustovalov, Izv. AN SSSR, Ser. Fiz. Mat., No. 4, 84 (1967).

[7] S. I. Anisimov, Ya. A. Imas, G. S. Romanov, and Yu. V. Khodyko, Effect of Intense Radiation on Metals [in Russian], Izd. Nauka, Moscow (1970).

[8] Ya. B. Zel'dovich and Yu. P. Raizer, Physics of Shock Waves and High-Temperature Hydrodynamic Phenomena [in Russian], Izd. Nauka, Moscow (1966).

[9] Tables of Integral Transforms (Handbook of the Mathematical Library) [in Russian], Vol. 1, Izd. Nauka, Moscow (1969).

[10] W. Heinze, Introduction to Vacuum Technology [Russian translation], Vol. 1, Gosenergoizdat, Moscow (1960).

Effect of focusing conditions on the morphology of surface films produced with a laser

V. G. Dneprovskii and B. A. Osadin

(Submitted December 12, 1972; resubmitted May 26, 1973)
Zh. Tekh. Fiz., 44, 442-446 (February 1974)

Experiments on the vacuum deposition of thin films by means of a neodymium-glass laser operating in the free-run mode are reported. An optimum situation, corresponding to the minimum number of macroscopic film defects (drops, breaks, and punctures), is achieved by defocusing the beam. This situation is shown to correspond to the formation of a shallow hole (whose depth h is much smaller than its transverse dimensions) at the target. For Cu and Si with a total energy of about 150 J per pulse a radiation flux density of $q_0 \sim 10^6$ W/cm² corresponds to the optimum conditions.

Many papers have recently appeared on the use of lasers to deposit thin films in vacuum.[1-12] Interest in this method stems from the several advantages of causing evaporation with laser radiation: the minimization of the contamination of the deposited films, the possibility of achieving a high vapor-deposition rate (~ 10^6 Å/sec or higher), the possibility of evaporating refractory materials, the possibility of retaining the stoichiometry of complicated substances, the possibility of working with radioactive substances, etc. On the other hand, exploitation of these advantages is seriously hindered by the inhomogeneity of the products resulting from the destruction of a material by laser radiation: In addition to the vapor phase there are drops and even solid macroscopic particles.

In this note we describe the optimum conditions for the vacuum deposition of thin films by a laser (corresponding to the minimum number of macroscopic film defects) by defocusing the laser radiation. We have studied two materials (Cu and Si).

The experiments are carried out in an evacuated chamber at a pressure of (1-2) · 10^{-5} torr. A neodymium-glass laser (PGLS-4 glass) is used in the free-running mode. The wavelength is 1.06 μ, the pulse length is 1.6-1.8 msec, and the pulse energy can be varied up to 200 J. The relative error in the measurement of the pulse energy is about 15%. The laser radiation enters the vacuum chamber through a glass window and is focused by a lens (f = 160 mm) on the ground surface of the target (the material to be evaporated). The surface plane of the target makes an angle of 45° with the beam direction. The destruction products settle on a 45 × 60 mm glass substrate held parallel to the sample surface about 30 mm away.

The flux density is changed by changing the lens–target separation; we use $l = f$, $1.025f$, $1.050f$, $1.075f$, $1.100f$, and $1.125f$. With $l = f$ the diameter of the light spot is 500 μ. The laser beam is defocused intentionally by moving the lens away from the target; otherwise, the radiation would be focused on the target as the hole is deepened. As a rule, we study thin films produced by a single laser pulse (pulse energy of 145-160 J).

EXPERIMENTAL RESULTS

At lens–target separations of $l = f$, $1.025f$, $1.050f$, and $1.075f$ we obtain Cu and Si films differing markedly in quality (i.e., in terms of the presence of macroscopic defects). With $l = 1.100f$ and $l = 1.125f$ we detect no trace of the condensate on the substrate, either by weighing or under a microscope. We also note that sulfur (whose thermal conductivity is much poorer than that of Cu or Si) flies apart in pieces when subjected to laser radiation under analogous conditions; large individual formations can be detected by the unaided eye on the substrate along the films.

Typical experimental results for Cu and Si are shown in Table 1: d, the diameter of the laser beam at the target surface in the case of normal incidence; W, the energy of the coherent radiation reaching the target; q, the energy flux density of the coherent radiation at the target surface; d_{min}, d_{max}, and h, the minimum dimensions of the hole on the target surface and the depth of the hole, respectively; Δm, the mass loss of the target per pulse; Δm_c, the mass of condensate deposited on the substrate per pulse; and σ, the total area of the film covered by macroscopic defects (drops, breaks, and punctures), in relative units ($\sigma = Nd^2$, where N is the number of defects per unit area and d is the average defect dimension).

Figure 1 shows photographs of Cu and Si films at a magnification of × 92, along with the corresponding shapes of the holes formed by the laser radiation at the target (in a cross section along d_{max}) and photographs of the holes (×8), corresponding to the most extreme defocusing used in these experiments at which film formation was detected ($l = 1.075f$).

DISCUSSION OF RESULTS

1. It follows from the photographs of the films (Fig. 1) that there is an obvious correspondence between the

TABLE 1

l	d, mm	W, J		$q \cdot 10^{-6}$, W/cm²		d_{min}, mm		d_{max}, mm		h, mm		Δm, mg		Δm_c, mg		σ	
		Cu	Si	Cu	Si	Cu	Si	Cu	Si	Cu	Si	Cu	Si	Cu	Si	Cu	Si
	$f = 0.50$	$f = 123$	$f = 117$	$f = 25.4$	$f = 24.3$	$f = 1.10$	$f = 1.40$	$f = 1.45$	$f = 1.85$	$f = 7.0$	$f = 5.5$	$f = 51.1$	$f = 13.6$	$f = 2.7$	$f = 3.1$	$f = 4.7 \cdot 10^{-1}$	$f = 6.2 \cdot 10^{-1}$
$1.025f$	1.11	123	107	5.1	4.6	1.15	1.70	1.50	2.30	6.5	4.0	48.2	8.7	6.5	4.0	$4.0 \cdot 10^{-2}$	$2.0 \cdot 10^{-2}$
$1.050f$	1.72	114	123	2.0	2.1	2.00	2.45	2.40	3.10	2.5	2.0	29.9	7.5	2.5	2.0	$1.3 \cdot 10^{-2}$	$0.5 \cdot 10^{-2}$
$1.075f$	2.34	112	113	1.1	1.1	2.34	2.90	2.80	3.75	0.6	0.5	9.6	5.6	0.6	0.5	$3.0 \cdot 10^{-4}$	$3.6 \cdot 10^{-4}$

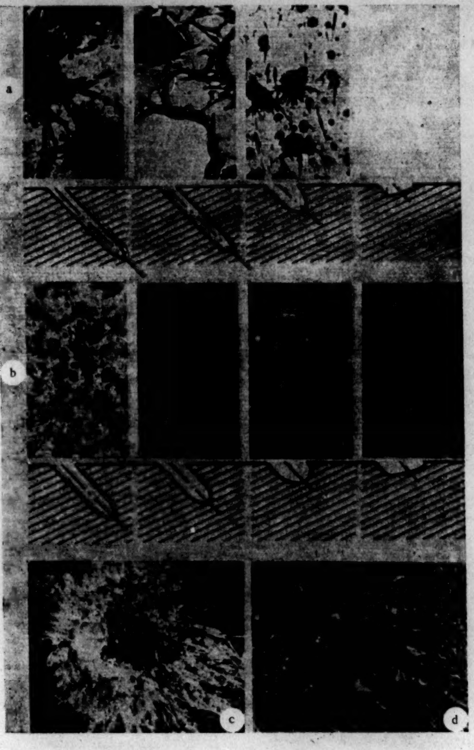

Fig. 1. a) Photographs of Cu films (×92) and shapes of the holes left by the laser radiation on a copper target (×8). The lens–target separation increases from left to right: $l = f$, $1.025f$, $1.050f$, $1.075f$; b) the same, for Si; c) photograph of the hole on a copper target with $1 = 1.075f$; d) the same for Si.

film quality and the shape of the hole formed by the laser radiation in the target. Over the range of radiation flux densities used here, $q = (1\text{-}25) \cdot 10^6$ W/cm^2, an increase in q leads to a deepening of the hole and an increase in the number of macroscopic defects in the film, primarily drops. This result is simple to explain on the basis of current ideas on the mechanism for the formation of apertures by laser radiation.[13] The vapor formed at the bottom of the hole by the direct effect of the radiation condenses partially on the walls of the hole, causing them to melt; at the same time, the high pressure forces the liquid film into a gas-dynamic flow issuing from the hole. Accordingly, a deep hole operates like a directional source of destruction products, consisting largely of the liquid phase. According to estimates based on the energy balance, the relative amount of the liquid phase in the destruction products of Cu with $l = f$, $1.025f$, and $1.050f$ is at least 70–80%; for Si, because of the lower thermal conductivity, higher melting point, and higher viscosity of the liquid phase, this relative amount is slightly less.

The sputtering effect is apparently also affected by the gas absorbed and dissolved in the target material[9] and by the peak nature of the laser pulse.[14]

2. In our case the optimum lens–target separation should be assumed to be $l = l_0 = 1.075f$ (Fig. 1, Table 1). Relatively small holes ($h \ll d_{\min}$) correspond to this separation. On the basis of these measurements it is difficult to draw any reliable conclusions regarding the relative amount of liquid phase in the destruction products for the case $l = l_0$, but photographs of the holes (Fig. 1c and d) show that in the case of a shallow hole the liquid phase is not entrained by the vapor flow and simply "spatters" out of the hole, ending up on the target surface. Evidence that the vapor phase is predominant in the latter case comes from the film quality and the energy balance.

3. Accordingly, the optimum conditions (corresponding to the fewest number of macroscopic defects in the films produced by laser evaporation) in this setup are those for which the laser radiation forms a shallow hole

at the target (the depth of the hole is much less than its transverse dimensions). The energy flux density corresponding to these conditions is $q = q_0 \approx 10^6$ W/cm^2. Obviously, we have not exhausted the possibilities for optimizing the conditions; in particular, a lens having a longer focal length might be useful. However, under our conditions, a reduction of the energy flux density from q_0 by a factor of only 1.5 leads to both the disappearance of the film and the disappearance of the hole from the target (the laser radiation leaves only a slightly fused trace). This latter result is apparently due to the circumstance that the coefficient for the reflection of the radiation from the target surface is a strong function of the state of the surface and of the value of q (ref. 13). Increasing the energy flux density to a value only twice q_0 leads to a sharp degradation of the film quality.

4. It is worthwhile to compare the experimental value of q_0 with the theoretical estimate of the flux density corresponding to the beginning of evaporation, derived in ref. 13. We adopt the following equation for evaluating the flux density which leads to a significant evaporation of material, q^*:

$$q^* = \frac{T^* \sqrt{\pi c_l \varkappa_e}}{2\sqrt{t_0}},$$

where $T^* = (\lambda A)/10R$ is the characteristic temperature, λ is the heat of evaporation, A is the atomic weight, R is the universal gas constant, c_l is the specific heat of the lattice per unit volume, and $\varkappa_e$ is the electronic thermal conductivity. This equation yields $q^*_{Cu} = 3 \cdot 10^5$ W/cm^2 and $q^*_{Si} = 1.5 \cdot 10^5$ W/cm^2.

Because of the known arbitrariness in the specification of T^*, corresponding to the beginning of significant evaporation, we calculate q_0 within the framework of the theory of thermal conductivity, using data on the saturation vapor pressure of Cu and Si (ref. 15). If we define the time which elapses from the beginning of the effect of the thermal pulse to the beginning of significant evaporation, t^*, in terms of the temperature $T(t^*)$, at which we have

$$q_v = \lambda \dot{m} [T(t^*)] = 0.5q,$$

where q_v is the heat loss due to evaporation, $\dot{m}$ is the evaporation rate, and q is the radiation flux density of the target surface, we can show that with $t_0 \sim 10^{-3}$ sec and $q \geq 10^6$ W/cm^2 we would have $t^* \ll t_0$.

Accordingly, for a free-running laser and for the radiation flux densities used in our experiments, the evaporation can be assumed quasisteady-state, and q_0 can be evaluated from the simple equation (we asssume a rectangular laser pulse)

$$q_0 = \frac{\gamma \lambda h}{t_0},$$

where γ is the density of the target material, h = (0.1-0.2)d, and d is the diameter of the laser beam at the target surface.

For the values of h_{Cu} and h_{Si} taken from Table 1, this equation yields $q_0Cu = 1.6 \cdot 10^6$ W/cm^2 and $q_{0Si} = 10 \cdot 10^6$ W/cm^2.

More accurate estimates would require taking account of the reflection of the radiation from the target surface and the discontinuous nature of this radiation.

---

[1] H. M. Smith and A. F. Turner, Appl. Opt., 4, 147 (1965).

[2] K. Y. Nichols, Brit. Commun. and Electron., 12, 368 (1965).

[3] H. Schwarz and H. A. Tourtellotte, J. Vac. Sc. Tech., 3, 307 (1966).

[4] V. P. Zakharov, A. N. Pilyankevich, and V. N. Chuguev, Elektron. Tekh., Ser. 6, Mikroelektronika, No. 4, 67 (1967).

[5] I. A. R. Samson, I. P. Padur, and A. Sharma, J. Opt. Soc. Amer., 57, 966 (1967).

[6] G. Groh, J. Appl. Phys., 39, 1805 (1968).

[7] P. D. Zavitsanos and W. E. Sauer, J. Electrochem. Soc., 115, 109 (1968).

[8] G. Hass and J. B. Ramsay, Appl. Opt., 8, 1115 (1969).

[9] H. Schwarz and H. A. Tourtellotte, J. Vac. Sci. Technol., 6, 373 (1969).

[10] V. S. Ban and D. A. Kramer, J. Mater. Sci., 5, 978 (1970).

[11] V. N. Markovskii and R. A. Taipov, Use of Lasers for Producing Thin-Film Microcircuits [in Russian], Izd. LDNTP, Leningrad (1968).

[12] K. L. Chopra, Thin Film Phenomena, McGraw-Hill, New York (1969).

[13] S. I. Anisimov, Ya. A. Imas, G. S. Romanov, and Yu. V. Khodyko, Effect of Intense Radiation on Metals [in Russian], Izd. Nauka, Moscow (1970).

[14] N. N. Rykalin and A. A. Uglov, FKhOM, No. 2, 30 (1970).

[15] W. Heinz, Introduction to Vacuum Technology [Russian translation], Vol. 1, GÉI, Moscow (1960).

Thermophoresis and diffusophoresis of small, volatile aerosol particles

Yu. I. Yalamov and E. R. Shchukin

Institute of Physical Chemistry, Moscow

(Submitted February 8, 1973; resubmitted July 9, 1973)
Zh. Tekh. Fiz., 44, 447-450 (February 1974)

The thermophoresis and diffusophoresis of small, volatile particles, i.e., particles on whose surfaces there can be appreciable condensation and evaporation of the drop material, are analyzed in the steady-state approximation. The contribution of the volatility to the force equation is shown to be directly proportional to the reciprocal of the Knudsen number; this contribution is negligibly small.

INTRODUCTION

A theory has been derived for the thermophoresis and diffusophoresis of small, nonvolatile aerosol particles[1-5] ($Kn = \lambda/R > 1$). Here, "volatile aerosol particles" are those on whose surfaces the aerosol material can condense and evaporate; in certain cases, e.g., water droplets in air, these processes can be important.

Since the volatility strongly influences the motion of moderately large and large volatile particles,[4,6-14] it is worthwhile also to analyze the motion of small volatile particles; we take up this problem below in the steady-state approximation.

CALCULATION OF THE FORCE AND VELOCITY OF THERMODIFFUSOPHORESIS

We consider a small spherical particle of radius R ($Kn = \lambda/R > 1$) suspended in a binary gaseous mixture with mean free path λ, an inhomogeneous distribution of the temperature T, and a density n_{10}. One component of the mixture (in our case the first component, n_1) consists of molecules of the same material as the drop. The temperature and density gradients of the gaseous mixture are small enough so that we can use the distribution function for the gas molecules in the first approximation in the temperature and density gradients.

We analyze the particle motion in a coordinate system fixed at the center of mass of the mixture.

As the particle moves it experiences a thermodiffusophoretic force $\mathbf{F}_{TD}$ due to the temperature and density gradients, and it experiences the drag of the medium, $\mathbf{F}_u$. The total force, equal to the sum of $\mathbf{F}_{TD}$ and $\mathbf{F}_u$, is found in the kinetic theory of gases by integrating the momentum flux of the molecules incident on the drop over the surface of the drop:[1-5,15]

$$\mathbf{F} = -\sum_i \int ds \sum_{\mp} \int d\mathbf{v}_i \mathbf{v}_i \mathbf{v}_i m_i f_i^{\mp}, \tag{1}$$

where $f_i^{\mp}$ are the distribution functions of the incident (−) and reflected (+) molecules, and m_i and $\mathbf{v}_i$ are the mass and velocity of molecules of species i.

Taking account of the smallness of the influence of a particle on the distribution of molecules in the surrounding gas,[1-5,15] for simplicity we adopt a volume distribution function for the incident molecules in the approximation based on the first two Sonine polynomials:[16]

$$f_i = n_i \left(\frac{m_i}{2\pi kT}\right)^{3/2} \exp\left(-\frac{m_i v_i^2}{2kT}\right)\left\{1 - \frac{m_i}{kT}\mathbf{v}_i\mathbf{u} - \left[(-1)^{i-1}\frac{d_0\rho_1\rho_2}{\rho n_i m_i^{1/2}} + d_{(-1)^{i-1}} S^1_{3/2}\left(\frac{m_i}{2kT}v_i^2\right)\right]\sqrt{\frac{m_i}{2kT}}\,\mathbf{v}_i \nabla n_{10} - \left[(-1)^{i-1}\frac{a_0\rho_1\rho_2}{\rho n_i m_i^{1/2}} + a_{(-1)^{i-1}} S^1_{3/2}\left(\frac{m_i}{2kT}v_i^2\right)\right]\sqrt{\frac{m_i}{2kT}}\,\mathbf{v}_i \nabla \ln T\right\}. \tag{2}$$

In Eq. (2), T is the temperature of the gas surrounding the particle; n_i is the number density of molecules of species i (per unit volume); $\rho_i = m_i n_i$; $\rho = \rho_1 + \rho_2$, $n = n_1 + n_2$; $n_{10} = n_1/n$; $S^1_{3/2}$ is the Sonine polynomial;[16] a_0, d_0, $a_{(-1)^{i-1}}$ and $d_{(-1)^{i-1}}$ are quantities which are functions of the nature of the interaction of the molecules and the thermodynamic properties of the medium, which are expressed in terms of the coefficients a_{ik} calculated in ref. 16; k is the Boltzmann constant.

Assuming that some of the molecules of the second species are reflected diffusely and some undergo specular reflection with a tangential-momentum accommodation coefficient q_2 (refs. 1-5), we seek the distribution function at the surface of the particle, f_2^+, in the following form:

$$f_2^+ = q_2 f_{2w}^0 + (1 - q_2) f_2^- [\mathbf{v}_2 - 2\mathbf{n}_r(\mathbf{n}_r\mathbf{v}_2)], \tag{3}$$

where f_{2w}^0 is a local Maxwellian distribution and $\mathbf{n}_r$ is the unit vector along the outward normal.

In the equation for the distribution function for molecules of the first species escaping from the surface of the particle we have taken account of the circumstance that the relative number of molecules which are evaporated from the surface of the drop material in a diffuse distribution is proportional to the coefficient α_m and that the relative number of incident molecules which undergo specular reflection is proportional to $(1-\alpha_m)$ (refs. 16, 17, 19):

$$f_1^+ = \alpha_m n_{1s} \exp\left(\frac{2V_1 l}{RkT_s}\right) \exp\left\{\frac{-m_1 v_1^2}{2kT_s}\right\} \left(\frac{m_1}{2\pi kT_s}\right)^{3/2} + (1 - \alpha_m) f_1^- [\mathbf{v}_1 - 2\mathbf{n}_r(\mathbf{n}_r\mathbf{v}_1)], \tag{4}$$

where α_m is the mass accommodation coefficient,[16,19] T_s is the temperature at the given point on the particle surface, n_{1s} is the saturation vapor density of the drop material above the plane of the surface at T_s, V_1 is the volume per molecule in the solid or liquid phase of the aerosol particle, and l is the surface tension.

Solving Eq. (5) (which follows) for the temperature distribution in the interior of the particle, T_k, and using the system of boundary conditions (6), (7), we find the distributions of the quantities T_{w2}, n_{w2}, and $T_s = T_k|_{r=R}$ by introducing the energy accommodation coefficient γ_2 and taking account of the difference between T_{w2} and T_s:

$$\Delta T_k = 0, \tag{5}$$

$$(\mathbf{N}_2\mathbf{n}_r) = 0, \tag{6}$$

$$\mathbf{n}_r(\mathbf{E}_2 + \mathbf{E}_1 + L m_1 \mathbf{N}_1) = -\varkappa_k(\mathbf{n}_r \nabla T_k)|_{r=R}, \tag{7}$$

where

$$\mathbf{N}_i=\int d\mathbf{v}_i\mathbf{v}_i f_i;\quad \mathbf{E}_i=\int d\mathbf{v}_i\mathbf{v}_i\frac{m_i v_i^2}{2}f_i, \tag{8}$$

n_r is the unit vector along the outward normal, $\varkappa_k$ is the thermal conductivity of the particle material, L is the latent heat of evaporation at $T = T_S$ (refs. 1, 6, 17, 18), and T_{W2} and n_{W2} are the distributions over the particle surface of the temperature and density of reflected molecules of the second species.

Condition (6) takes account of the fact that molecules of the second species do not penetrate the surface of the particle, while condition (7) expresses conservation of the energy flux across this surface. This energy flux consists of terms proportional to the temperature and density gradients, which appear in the expression for $(E_1 + E_2)$; account is taken of the heat of the phase transition at the given point, Lm_1N_1.

Substituting the values found for T_{W2}, T_S, and n_{W2} into Eqs. (3) and (4), and integrating (1), we find the total force to be

$$\mathbf{F}=\mathbf{F}_{TD}+\mathbf{F}_u, \tag{9}$$

where

$$\begin{aligned}\mathbf{F}_{TD}=&-\frac{4}{3}\sqrt{\pi}R^2kT\left\{\frac{2d_0\rho_1\rho_2}{\rho}\left[\frac{(1+\delta_{11})}{\sqrt{m_1}}-\frac{(1+\delta_{21})}{\sqrt{m_2}}\right]-[d_1n_1(1+\delta_{12})\right.\\&\left.+d_{-1}n_2(1+\delta_{22})]+\Theta_{11}R\right\}n\nabla n_{10}\\&-\frac{4}{3}\sqrt{\pi}R^2kT\left\{\frac{2a_0\rho_1\rho_2}{\rho}\left[\frac{(1+\beta_{11})}{\sqrt{m_1}}-\frac{(1+\beta_{21})}{\sqrt{m_2}}\right]\right.\\&\left.-[a_1(1+\beta_{12})+a_{-1}(1+\beta_{22})]-\Theta_{22}R\right\}\nabla\ln T.\end{aligned} \tag{10}$$

In (10) we use

$$\delta_{11}=\alpha_m\frac{\pi}{8}\frac{kn_2}{\varkappa_k}\sqrt{\frac{2kT}{\pi m_1}}\left[\frac{5}{2}+\frac{Lm_1}{kT}\right]pR, \tag{11}$$

$$\delta_{12}=\alpha_m\frac{5}{16}\pi\frac{kn_2}{\varkappa_k}\sqrt{\frac{2kT}{\pi m_1}}\,pR, \tag{12}$$

$$\beta_{11}=\delta_{11};\ \beta_{12}=\delta_{12};\ \beta_{21}=\delta_{21};\ \beta_{22}=\delta_{22}, \tag{13}$$

$$\left.\begin{aligned}\delta_{21}=&\sqrt{\frac{T_{w2}}{T}}\frac{\pi}{8}\delta_2+\delta_2(1-\gamma_2)\frac{\pi}{64}\sqrt{\frac{T}{T_{w2}}}\\&+\frac{\pi}{8}\gamma_2\delta_2\frac{kn_2}{\varkappa_k}\sqrt{\frac{2kT}{\pi m_2}}\left(\frac{5}{4}-\frac{T_s}{T}\right)pR,\end{aligned}\right\} \tag{14}$$

$$\delta_{22}=\frac{5}{32}\pi\delta_2(1-\gamma_2)\sqrt{\frac{T_{w2}}{T}}+\frac{5}{16}\pi\gamma_2\delta_2\frac{kn_2}{\varkappa_k}\sqrt{\frac{2kT}{\pi m_2}}\,pR, \tag{15}$$

$$\Theta_{11}=\left[(1-\alpha_m)-(1-\delta_2)-\sqrt{\frac{T_{w2}}{T}}\delta_2\right], \tag{16}$$

$$\Theta_{22}=\frac{n_2}{2}\gamma_2\delta_2\sqrt{\frac{T_{w2}}{T}};\quad \Theta_{33}=\frac{5}{4}+\frac{Lm_1}{2kT} \tag{17}$$

$$\left.\begin{aligned}p=&\left\{\frac{\delta_2\gamma_2}{2}\sqrt{\frac{T_{w2}}{T}}+\alpha_m T_s\frac{n_{1s}}{n_2}\right.\\&\left.\times\exp\left(\frac{2V_1l}{RkT_s}\right)\left[\frac{d\ln n_{1s}}{dT_s}-\frac{2V_1l}{RkT_s^2}+\frac{1}{T_s}\right]\right\}.\end{aligned}\right\} \tag{18}$$

The viscous force is

$$\begin{aligned}\mathbf{F}_u=&-\frac{8}{3}\sqrt{2\pi kT}R^2\left\{n_2\sqrt{m_2}\left[1+\frac{\pi}{8}\sqrt{\frac{T_{w2}}{T}}\delta_2\right.\right.\\&\left.+\frac{\pi}{64}\delta_2(1-\gamma_2)\sqrt{\frac{T}{T_{w2}}}+\frac{\pi}{8}\gamma_2\delta_2\frac{n_2k}{\varkappa_k}\sqrt{\frac{2T}{\pi m_2}}\,pR\left(\frac{5}{4}-\frac{T_s}{T}\right)\right]\\&\left.+n_1\sqrt{m_1}\left[1+\frac{\pi}{8}\alpha_m\Theta_{33}\frac{kn_2}{\varkappa_k}\sqrt{\frac{2kT}{\pi m_1}}\,pR\right]\right\}\mathbf{u}.\end{aligned} \tag{19}$$

In Eqs. (10)-(19), a_0, d_0, and $a_{\pm1}$, $d_{\pm1}$ are constants governed by the masses of the gas molecules, m_1 and m_2, and the nature of the interaction between them: they are expressed in terms of the coefficients a_{ik} calculated in ref. 16. Also, $\bar{T}$, $\bar{T}_S$, and $\bar{T}_{W2}$ are the average temperatures of the medium, the aerosol particle, and the molecules of the second species reflected from the surface of the particle; n_1 and n_2 are the average number densities (per unit volume) of molecules of the first and second species; $n = n_1 + n_2$; $n_{10} = n_1/n$; and $(dn_{1S})/(d\bar{T}_S)$ is the derivative of the saturation vapor density above the plane of the surface with respect to the temperature at $\bar{T}_S$. The particle velocity can be found by setting Eq. (9) equal to zero.

The average temperature of the drop surface, $\bar{T}_S$, and that of the reflected molecules of the second species, $\bar{T}_{W2}$, are found from Eqs. (20) and (21):

$$\begin{aligned}&\gamma_2\delta_2n_2\sqrt{\frac{T}{m_2}}k[T_s-T]+\alpha_m\frac{k}{\sqrt{m_1}}\left[n_{1s}(T_s)T_s^{3/2}\exp\left(\frac{2V_1l}{RkT_s}\right)-n_1T^{3/2}\right]\\&+\alpha_m\frac{L\sqrt{m_1}}{2}\left[n_{1s}(T_s)\exp\left(\frac{2V_1l}{RkT_s}\right)T_s^{1/2}-n_1T^{1/2}\right]=0,\end{aligned} \tag{20}$$

$$T_{w2}=\gamma_2T_s+(1-\gamma_2)T. \tag{21}$$

DISCUSSION OF RESULTS

We have derived equations for the thermodiffusophoretic force and the drag force of the medium, taking account of the effects of volatility.

At a vanishing temperature gradient these equations become the equations for pure diffusophoresis of volatile particles, and with $n_1 = 0$, $a_0 = 0$, and $a_1 = 0$ they become the equations for the thermophoresis of volatile particles.

We see from Eqs. (10)-(19) that the contribution of the volatility effects to the force equations is proportional to R/λ. Numerical estimates, on the other hand, show that the contribution of volatility effects for substances of practical interest is less than 1%, and in an estimate of the forces exerted on volatile particles we can use the equations found above for nonvolatile particles, setting $q_1 = 0$.

---

[1] B. V. Deryagin and S. P. Bakanov, Dokl. Akad. Nauk SSSR, 117, 959 (1957).

[2] B. V. Deryagin and S. P. Bakanov, Kolloidn. Zh., 21, 377 (1959).

[3] L. Waldmann, Z. Naturforsch., 14a, 589 (1959).

[4] Yu. I. Yalamov, Doctoral Dissertation [in Russian], IFKh Akad. Nauk SSSR, Moscow (1968).

[5] Yu. I. Yalamov and E. Shchukin, Izv. Akad. Nauk SSSR, Mekhn. Zhidk. i Gaza, No. 3, 186 (1972).

[6] Yu. I. Yalamov and E. R. Shchukin, Zh. Fiz. Khim., 45, 2421 (1971).

[7] B. V. Deryagin and Yu. I. Yalamov, Dokl. Akad. Nauk SSSR, 174, 1048 (1967) [Sov. Phys. – Dokl. 12, 587 (1969)].

[8] B. V. Deryagin and Yu. I. Yalamov, Dokl. Akad. Nauk SSSR, 175, 59(1967) [Sov. Phys. – Dokl., 12, 694 (1968)].

[9] B. V. Deryagin and Yu. I. Yalamov, Zh. Tekh. Fiz., 38, 556 (1968) [Sov. Phys. – Tech. Phys., 13, 412 (1968)].

[10] B. V. Deryagin, Yu. I. Yalamov, and V. S. Galoyan, Kolloidn. Zh., 33, 509 (1971).

[11] B. V. Deryagin, Yu. I. Yalamov, and V. S. Galoyan, Dokl. Akad. Nauk SSSR, 201, 127 (1971).

[12] Yu. I. Yalamov, B. V. Deryagin, and V. S. Galoyan, J. Coll. and Interf. Sci., 32, 793 (1971).

[13] B. V. Deryagin, Yu. I. Yalamov, and A. I. Storozhilova, J. Coll. and Interf. Sci., 22, 117 (1971).

[14] B. V. Deryagin, A. I. Storozhilova, G. I. Shcherbina, and B. A. Obukhov, Dokl. Akad. Nauk SSSR, 201, 651 (1971).

[15] J. R. Brock, J. Coll. and Interf. Sci., 25, 392 (1967).

[16] S. Chapmann and T. G. Cowling, Mathematical Theory of Non-Uniform Gases, Cambridge (1952).

[17] N. A. Fuks, Evaporation and Growth of Drops in a Gaseous Medium [in Russian], Izd. Akad. Nauk SSSR, Moscow (1958).

[18] K. Huang, Statistical Mechanics, Wiley, New York–London–Sydney (1963).

[19] P. N. Shankar, J. Fluid Mech., 40, 385 (1970).

Electron spectrometer for electric excitation of nuclei in a storage ring

D. M. Nikolenko and S. G. Popov

(Submitted September 18, 1972; resubmitted April 12, 1973)
Zh. Tekh. Fiz., 44, 451-456 (February 1974)

A magnetic electron spectrometer with 180° focusing and a wide energy range is described. The spectrometer uses wire spark chambers. The instrument is used for experiments on electric excitation of nuclei in a storage ring and has been calibrated at the VÉP-1 storage ring. The resolution (half-width of the peak for elastically scattered electrons) is 160 keV for a 40-MeV beam. Certain other experiments which can be carried out with a storage ring with an internal target are discussed.

Considerable progress has been recently made in the study of the properties of atomic nuclei by means of electron scattering. The interest in such experimental methods is based on the fact that the interaction of electrons with nuclei is amenable to an accurate theoretical description and on the fact that electron scattering offers far more possibilities than photonuclear reactions.[2] Exact experiments have been made possible by the development of linear accelerators, which provide strong particle beams with a relatively low energy spread. The development of electron storage devices also opens up new possibilities in this field.[3-5] Because of radiation damping the energy spread of the electron beam in a storage ring is small ($\sim 10^{-4}$ in existing devices) and is not affected by the introduction of a very thin target. Nevertheless, the "effective thickness" (the product of target thickness and the number of times an electron crosses it) can be as high as 0.2 radiation length units.[3]

A very thin target, for example consisting of a stream of gas or vapor, makes it possible to reconstruct the kinematics of scattering processes involving secondary low-energy particles and heavy particles. The recoil nucleus can be regarded as such a secondary particle. Kinematic considerations[6] indicate that for a fixed electron scattering angle the recoil nuclei are emitted in the same direction both in pure elastic scattering and in scattering involving the emission of bremsstrahlung γ photons (to within $\sim 1/\gamma$, where γ is the relativistic factor and the energy of the recoil nucleus is neglected). Recoil nuclei, excited in inelastic scattering, move at an angle φ to this direction. The angle can be found from

$$\operatorname{tg}\varphi = \frac{p - p'}{2p}\operatorname{ctg}\frac{\theta}{2},$$

where θ is the angle of the scattered electron, p and p' are the electron momenta before and after scattering. Using the anticoincidence mode with "elastic" recoil nuclei, or the coincidence mode with "inelastic" nuclei, it is possible to eliminate the bremsstrahlung background in inelastic scattering (see refs. 2, 7, 8).

The operating conditions of electron storage rings allow the application of wire spark chambers as detectors. This makes it possible to build a multichannel instrument with high energy resolution capable of analyzing a wide range of energies at one time. Simultaneous detection of electrons over a wide range of energies increases the rate of statistical data acquisition and facilitates the determination of relative cross sections. Thus, it is not desirable to use double focusing spectrometers, conventionally used in linear accelerators, as they only cover a narrow energy range.[8,9]

The magnetic electron spectrometer described below is intended for use in experiments on electric excitation of nuclei. The spectrometer is equipped with two wire spark chambers and the energy range $E_{max}/E_{min} \simeq 2$.

The magnetic field of the spectrometer is uniform. The two spark chambers are positioned along one line in the field. Since the field of the main magnet along the part of the electron trajectory ending at the entrance to the first chamber is compensated (by the compensating magnet 3 in Fig. 1) so that electrons of any energy crossing this path can suffer only a parallel displacement, the electrons cross the first spark chamber in the direction they have when leaving the target. The radius of an electron in the field of the main magnet is given by $R = R_0/\cos\alpha$, where $R_0 = (x_1 + x_2 + L)/2$, x_1 and x_2 are coordinates of the electron in the first and second chamber, respectively, L is the distance between the origins of the x_1 and x_2 coordinates (Fig. 1), and α is the angle between the direction of motion of an electron through the first chamber and the normal to the plane of the wire electrode of the chamber (entrance angle into the first chamber). This angle is determined from the coordinate x_1 assuming a point target and calculating the parallel displacement for any specific electron energy.

The stray fields of the main and compensating magnets provide edge focusing of electrons in a direction normal to the magnet pole plane. The electrons are focused primarily by the compensating magnet when leaving its field and entering the field of the main magnet. The focal

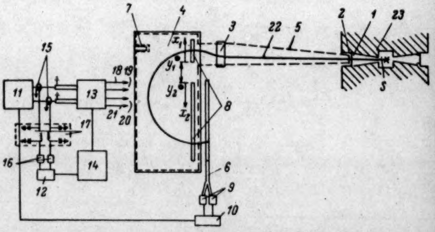

Fig. 1. Experimental arrangement: 1) VÉP-1 ton; 2) spectrometer entrance window; 3) compensating magnet pole; 4) main magnet pole; 5) active region of spark chambers; 6) scintillation counter; 7) NMR detector socket; 8) spark chambers; 9) photomultiplier; 10) fast coincidence circuit; 11) high-voltage pulse generator; 12) slow coincidence circuit; 13) ferrite memory cube; 14) sampling and punching circuit; 15) ferrite pickups; 16) discriminators; 17) integrating circuits; 18, 19) multicore cables for application of high-voltage pulses to the spark chambers; 20, 21) bunched conductors of spark-chamber ground wires; 22) electron trajectory; 23) cross section of VÉP-1 storage ring magnets.

length is estimated as ~ 1 m for particles of maximum energy. Since the spectrometer chamber measures two electron coordinates (x and y, y being the coordinate normal to the magnet pole plane), it is possible to determine the focal length experimentally. The obtained result agrees with the estimate. Knowing y_1 and y_2 for the electron allows us, if necessary, to take account of the transverse electron-momentum component in calculating the electron energy.

The spectrometer design has been described in ref. 4 and is similar in many details to that described in ref. 10. The following two changes have been made: To reduce the error in entrance angle determination caused by multiple scattering, the entrance foil of the spectrometer has been brought out to the storage ring foil, and the compensating magnet has been made with parallel poles of 30 × 200 mm with a 20 mm gap between them. The wire chambers have a glass textolite frame. The grounded wires for determining the electron flight coordinates x_1, x_2 are wound with a 0.5 mm pitch. The high-voltage electrode wires, which determine the y_1, y_2 coordinates, are parallel to the grounded wires and have a 1 mm pitch. The electrode gap is 7 mm. The spark chambers are filled with helium at atmospheric pressure with an admixture of 2% ethyl alcohol. The high-voltage pulse applied to the spark chamber has an exponential shape (time constant of 1.6 μsec) and an amplitude of 5.5 kV. The second chamber is separated from the first by a light shield. The apertures of the entrance and exit chambers are respectively 26 × 155 and 38 × 450 mm. The maximum electron radius in the main magnet field is limited by the construction and by the size of the useful magnetic-field region and is about 30 cm. Thus, $R_{\max}/R_{\min} \simeq 2$ (L = 130 mm).

The spectrometer has been tested on the VÉP-1 storage[1] ring with an electron beam energy of 40 MeV. The targets are a chemically pure aluminum foil and a shaped stream of water vapor at a pressure of about 10^{-4} torr striking a liquid-nitrogen trap. The second case corresponds to the so-called hyperfine target (see ref. 3). The spectrometer has been located so that the first chamber is approximately one meter from the target. The solid angle of the spectrometer is then approximately $2 \cdot 10^{-3}$ sr.

The VÉP-1 and spectrometer magnet coils, connected in series, are supplied from a single motor generator. The coil current is electronically stabilized. The magnetic fields are monitored by a nuclear magnetic resonance apparatus.

Figure 1 shows a block diagram of the experiment. An electron scattered in the target passes through the magnetic system of the spectrometer and is detected by the scintillation counter 6; to reduce false triggering by noise, the counter has two photomultipliers 9 connected to a fast coincidence circuit 10. The counter triggers the high-voltage pulse generator 11, which feeds the spark chambers. The sampling (ferrite memory cube 13) and tape-punching system 14 operates only when both spark chambers 8 fire simultaneously. The information is fed to a digital computer.

Firing of the spark chamber is indicated by pulses taken from the secondary winding of a ferrite-core transformer 15, whose primary carries the high-voltage pulses. Pulses from the secondary windings are shown in Fig. 2 (top waveform). The left- and right-hand photographs were taken before and after chamber firing respectively. The pulse in Fig. 2a is due to current charging the chamber capacitance when the high-voltage pulse is applied. The first pulse in Fig. 2a' is due to the same cause while the second is produced by the current surge during chamber breakdown. The time T between these two pulses corresponds to the breakdown development in the chamber. The bottom waveforms in Fig. 2 show the same pulses after passing the integrating circuit (17 in Fig. 1); it is seen that after chamber firing the pulse has a much higher amplitude and can be easily identified in the discriminator (16 in Fig. 1).

It should be noted that when the chamber is triggered by light produced in breakdown of the second chamber (this effect has been discussed in ref. 10), T is much longer than when breakdown is initiated by a particle (see Table 1). This feature can be exploited in systems using many chambers in which the use of light shields is undesirable.

The spectrometer resolution is affected by the following factors: spatial resolution of the chamber, displacement of the electron from its ideal trajectory as a result of multiple scattering in the chamber gas, uncertainty of the entrance angle to the first chamber, fluctuation of ionization loss in the VÉP-1 and spectrometer foils and in the chamber gas, and inhomogeneity of the main magnet field.

These effects have been estimated as follows.

1. The spatial resolution of the chambers has been measured and found to be equal to $(\Delta x^2)^{1/2} = 0.30$. The contribution to the spectrometer resolution is

$$\frac{\Delta E}{E} = \left(\frac{\overline{\Delta x^2}}{2R^2}\right)^{1/2},$$

where R is the radius of particle trajectory in the magnetic field.

2. If the electron displacement due to multiple scattering in gas is calculated from the simplified dependence of the mean-square angle $\overline{\theta^2}$ on the path traveled in gas:

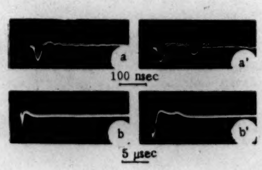

Fig. 2

TABLE 1. Time of Breakdown Development in Spark Chamber (in nsec)

	U, kV			
	6.6	6.0	5.5	5.0
Particle initiated	70	80	120	170
Light initiated	20	170	250	400

$\overline{\theta^2} = k(l/E^2)$ (where l is the length of the path), then taking into account 180° scattering we have

$$\frac{\Delta E}{E} = \frac{1}{E}\left(k\frac{\pi R^3}{8}\right)^{1/2}.$$

3. The energy error due to the uncertainty of the entrance angle to the first chamber is $(\Delta E)/E = \tan\alpha(\overline{\Delta\alpha^2})^{1/2}$. The error in the angle α results from multiple scattering in the foils and gas in front of the first chamber, which is due to the fact that the extended target does not allow full compensation of the stray fields.

Table 2 shows the individual contributions of the various factors in the spectrometer resolution (σ is the mean-square deviation) for an electron energy 40 MeV and R = 28 cm; the table also lists the energy spread of the storage ring beam and the overall resolution of the experiment.

Figure 3 shows peaks for elastically scattered electrons. The two bottom curves have been obtained with the compensating magnet switched off. The entrance angles α at the first chamber are in this case considerable (14° on the average). Curve c has been plotted assuming that the distance between the flight coordinates in the spark chamber is equal to the diameter of trajectory of particles in a magnetic field. Curve b shows the spectrum of the same electrons corrected for the entrance angle approximately calculated from the entrance coordinate at the first chamber. The topmost curve has been obtained with the compensating magnet in operation. The experimental curve is in this case asymmetric. The resolution determined from the left-hand drop of the curve is in good agreement with the calculated resolution (Table 2).

TABLE 2

Factor	σ, keV
Entrance angle error	10
Spatial resolution of chambers	30
Displacement of electrons because of multiple scattering	40
Fluctuation of ionization loss	5
Nonuniformity of main magnet field	5
Spectrometer resolution	50
Energy spread of storage ring beam	30
Overall resolution	60

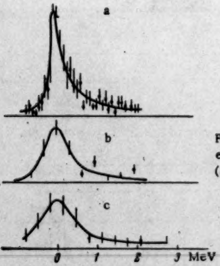

Fig. 3. Peaks of elastically scattered electrons: σ = 65(a), 200 (b), and 500 (c) keV; Al^{27}, 40 MeV, 128°.

The asymmetry of the peak is significantly affected by the loss of energy of electrons passing through the wires of the first chamber. Thus, with 0.1 mm bronze wires, 26% of all electrons pass through one wire and lose a total of 180 keV. Figure 4 shows electron peaks obtained with 0.1 bronze wires (1) and 0.03 nichrome wires (2) in the first chamber. To facilitate comparison different scales are used so that the peak heights are the same. The left sides of the peaks practically coincide. The right side of the peak is lower with thin wires than with the thicker ones. The half-widths are 160 and 200 keV respectively. A water vapor target (2) gives a peak due to electrons elastically scattered by hydrogen.

As is evident from Table 2, the contribution of the energy spread of the storage ring beam into the overall resolution is not dominant. Moreover, if the beam energy is increased up to some limit (approximately 100 MeV), there is even an absolute decrease in energy spread. For example, for a VÉP-1 beam of 100 MeV and 30 sec lifetime,[11] σ = 15 keV. Thus, there are good reasons for improving the spectrometer resolution.

One of the possible ways to improve resolution is to reduce the effect of multiple scattering on the path between the two chambers. This can be achieved by gas filling only a small volume of the spectrometer between the two chambers. Since it is important that the material traversed by electrons be as thin as possible, particularly in the first chamber, a thin lavsan film is indicated. The construction can be facilitated by using argon at a low pressure in the chambers.[12] As indicated above, the resolution is proportional to $R^{3/2}$ with respect to electron displacement by multiple scattering, and to $1/R$ with respect to spatial resolution of the chambers. If the first effect is eliminated, the radius of electron trajectory in the magnetic field can be increased so that the contribution of spatial resolution of the chambers into the overall spectrometer resolution is minimized.

The authors thank V. A. Kabannik and A. P. Chabanov for help with the experiments, V. A. Semenychev for building the spark chambers, and all laboratory workers who contributed to this work. The authors also are indebted to A. P. Onuchin for useful comments.

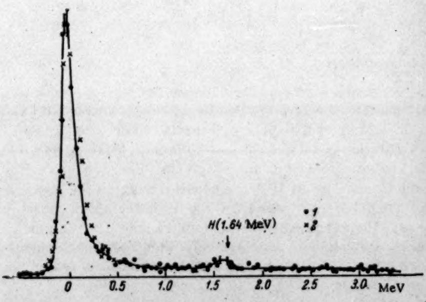

Fig. 4. Electron peaks obtained with 0.1 mm bronze wires (1) and 0.03 mm nichrome wires (2) in the first chamber: 1) Al^{27}, 40 MeV, 52°, $\Gamma_{1/2}$ = 200 keV; 2) O^{16} (H_2O), 40.5 MeV, 90°, $\Gamma_{1/2}$ = 160 keV.

---

[1] G. I. Budker, E. A. Kushnirenko, A. A. Naumov, A. P. Onuchin, S. G. Popov, V. A. Sidorov, A. N. Skrinskii, and G. M. Tumaikin, At. Energ., 19, 498 (1965).

[2] Proc. of the Intern. Conf. on Electromagnetic Interactions at Low and Moderate Energies, Vol. 3, Moscow (1967).

[3] G. I. Budker, A. P. Onuchin, S. G. Popov, and G. M. Tumaikin, Yad. Fiz., 6, 775 (1967).

[4] V. G. Zelevinskii, D. M. Nikolenko, S. G. Popov, and G. M. Tumaikin, Izv. Akad. Nauk SSSR, Ser. Fiz., 23, 686 (1969).

[5] S. T. Belaev (Belajev), G. I. Budker, and S. G. Popov, High-Energy Physics and Nuclear Structure Conference, Plenum Press, New York–London (1970), p. 606.

[6] L. I. Schiff, Phys. Rev., 87, 750 (1952).

[7] D. B. Isabelle and G. B. Bishop, Nucl. Phys., 45, 309 (1963).

[8] F. Gudden, G. Fricke, H. G. Clerc, and P. Brix, Z. Physik, 181, 453 (1954).

[9] K. Iton, M. Oyamada, and Y. Torizuka, Phys. Rev., C., 2, 2181 (1970).

[10] P. I. Golubnichii (Golubnichiy), L. M. Kurdadze, D. M. Nikolenko, A. P. Onuchin, S. G. Popov, and V. A. Sidorov, Nucl. Instr. and Meth., 67, 22 (1969); P. I. Golubnichii, L. M. Kurdadze, D. M. Nikolenko, A. P. Onuchin, S. G. Popov, and V. A. Sudorov, Preprint Inst. Nucl. Phys., Novosibirsk (1968).

[11] V. L. Auslender, É. I. Zinin, G. N. Kulipanov, S. I. Mishenev, C. G. Popov, A. N. Skrinskii, G. M. Tumaikin, and Yu. M. Shatunov, At. Energ., 22, 200 (1967).

[12] I. Fisher, Proc. of the Intern. Conf. on Electromagnetic Interactions at Low and Moderate Energies, Vol. 4, Moscow (1967), p. 179.

Strobe unit for measuring luminescence in the range 10^{-7}-$2 \cdot 10^{-10}$ sec

V. A. Bonch-Bruevich and N. A. Tolstoi

(Submitted May 18, 1973)
Zh. Tekh. Fiz., 44, 457-462 (February 1974)

A method of measuring luminescence relaxation times τ in the range 10^{-7}-$2 \cdot 10^{-10}$ sec is described. The time scale of the investigated signals is linearly transformed by means of a sampling oscilloscope, and subsequent measurement of τ is performed with a low-frequency unit. Storage methods are used in the low-frequency part of the device to improve the signal-to-noise ratio.

The value of information on the kinetics of induced physical phenomena (photoconductivity, luminescence, populations of energy levels, and so on) is well known. The increasing interest in such phenomena has given rise to a demand for a technique for investigating transient processes that is capable of extension to ever-increasing ranges of the measured parameters, especially the relaxation time τ. One important requirement is that the technique be convenient and simple.

The taumeter technique[1] is one of the simplest and most effective ways[1)] of measuring τ. Proposed in 1947 (initially for the range 10^{-1}-10^{-5} sec), this technique has been developed greatly over the last 25 years. In particular, instruments have been built utilizing a mechanical light modulator[2] (10^{-1}-10^{-7} sec), an electrooptical light modulator[2] (10^{-5}-10^{-8} sec), the IS-3 flash lamp[3] ($5 \cdot 10^{-6}$-$2 \cdot 10^{-8}$ sec), etc. Such embodiments of the taumeter technique have been the basis of many investigations on the kinetics of induced phenomena.

The main feature and advantage of the taumeter technique is that the values of τ accessible to correct measurement can be one and a half orders smaller than the times characterizing the intrinsic time delay of the apparatus used (rise time of exciting pulses, photomultiplier, and oscilloscope delay). This important property is directly connected with the "functional balance" or "null" character of the taumeter method of measurement. The analog nature of the taumeter method, in which the investigated relaxation process induced by an exciting pulse is swept on an oscilloscope screen by the process induced in an analog RC circuit by the same exciting pulse, in effect eliminates the delay introduced by the measuring apparatus. Apparatus delay does not introduce errors into the measurements but only reduces the sensitivity of the method. Since the initial sensitivity is extremely high (we have in mind the sensitivity of the method under conditions when the delay is negligible compared with τ), the real sensitivity remains satisfactory, even when the delay is 30-40 times greater than the delay of the process under investigation.

A second important property conferred by the analog nature of the method is that the shape of the exciting pulse plays a comparatively small role: The pulse need not be rectangular. It is sufficient that the pulse have at least one steep edge, which, as is well known, is a characteristic of flash lamps. The essence of the matter is that the differential (kinetic) equation of an exponentially relaxing process and the differential equation of an electrical RC circuit are formally identical. When RC = τ an RC integrating circuit distorts any exciting pulse in the same manner as the investigated object, so that the taumeter loop on the oscilloscope screen degenerates into a straight line for any shape of exciting pulse.

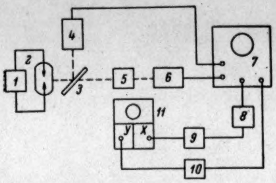

Fig. 1. Block diagram of strobing ultrataumeter. 1) Flash lamp power supply; 2) flash lamp; 3) beam-splitting plate; 4) X-channel photomultiplier; 5) investigated object; 6) Y-channel photomultiplier; 7) S1-39 sampling oscilloscope; 8) taumeter measuring circuit; 9) X-channel storage device; 10) Y-channel storage device; 11) S1-19 oscilloscope.

The present paper describes an ultrataumeter utilizing standard elements, in which effective use is made of the above features.

A block diagram of the ultrataumeter is shown in Fig. 1. The main component is a two-channel S1-39 sampling oscilloscope with a 0.7 GHz response which is used to expand the time scale. Luminescence is excited in the investigated object by a DKSSh-120 xenon flash lamp operating in a regime of high-voltage periodic self-breakdown. By suitably choosing the parameters of the discharge circuit of the lamp (discharge capacitance about 50 pF) the length of the leading edge of the radiation pulse can be reduced to 3 nsec. The length of the trailing edge is an order of magnitude longer. The repetition frequency of the pulses (1-2 kHz) is set by the supply voltage (10-15 kV). A beam-splitting plate forms two light beams. One of these beams excites the luminescence of the sample, located in the "main" Y channel of the taumeter. The other beam is used to produce an analog signal in the sweep (X) channel. The required regions in the lamp emission spectrum and in the luminescence spectrum of the sample are selected by glass light filters. Two photomultipliers of the same type serve as light receivers. The signals from the photomultipliers of the two channels are fed to the inputs of the S1-39 sampling oscilloscope. The envelopes of the peaks of the low-frequency pulses removed from the S1-39 outputs constitute the time-transformed main and sweep signals. The main Y signal is then fed to a storage device and then to the Y input of an S1-19 oscilloscope. The sweep (X) signal passes through a calibrated RC circuit with variable R and C (the measuring circuit of the taumeter) to a storage device and then to the X input of the S1-19 oscilloscope, in which the sweep unit is replaced by a preamplifier identical to the preamplifier of the Y channel. The screen of the S1-19, on which the envelope of the Y signal is swept by the envelope of the X signal, is used to monitor the straightening out of the taumeter loop. The storage devices are RC integrating circuits with variable time constants and cathode followers at the inputs.

The two channels of the device as a whole are balanced (by adjusting optical distances, cable lengths, photomultiplier power supplies, time constants of storage devices in both channels) until, at an RC of the taumeter circuit equal to zero and both photomultiplier cathodes illuminated by the same light pulse, a straight line is obtained in place of a loop on the screen of the S1-19.

Thus, the main and the sweep signals are functionally balanced after transformation (slowing down) of their time scale by many orders of magnitude, for example, from the nanosecond to the millisecond region. At the same time the storage devices greatly enhance the signal-to-noise ratio.

The oscillograms of Figs. 2 and 3 illustrate the features and the possibilities of the method. The role played by the storage devices is seen clearly. In principle, the storage devices degrade the time resolution of the method; however, the improvement in the signal-to-noise ratio is so large that the time resolution actually improves when they are used. The optimum value of the time constant of the storage devices is different under different measurement conditions but can be set up without difficulty.

In a measurement of τ (equal to 4 nsec) of an alcohol solution of rhodamine C (Fig. 2d) the time resolution of the method with FÉU-28 photomultipliers is better than ± 1 nsec. Indeed, as Figs. 2e and f show, insertion into the taumeter circuit of RC values of 5 or 3 nsec results in the appearance of distinct loops. Figures 2h and i show that τ can be measured by the described method in signals with a signal-to-noise ratio of the order of unity. We note that the time resolution of the method is mainly determined by the transient response of the FÉU-28, which is by no means the optimum photoreceiver for time measurements.

The time resolution is considerably enhanced by using FÉU-30 photomultipliers. For example, in a measurement of the $\tau = 6.4$ nsec of an alcohol solution of 4-methylamino-N-methylphthalimide[4] (Fig. 3a), distinct loops are observed for a taumeter imbalance of 0.2 nsec (Fig. 3b, c). The time resolution here is now determined by the delay of all the components of the setup and is estimated as ± 0.1 nsec.

We note that different true time delays in the X and Y channels, which should not be confused with different response times of the channels, also result in the formation of loops on the oscilloscope screen. Figure 3e shows such a loop, obtained by increasing the path of the light in the Y channel of an initially balanced system by 30 cm, which

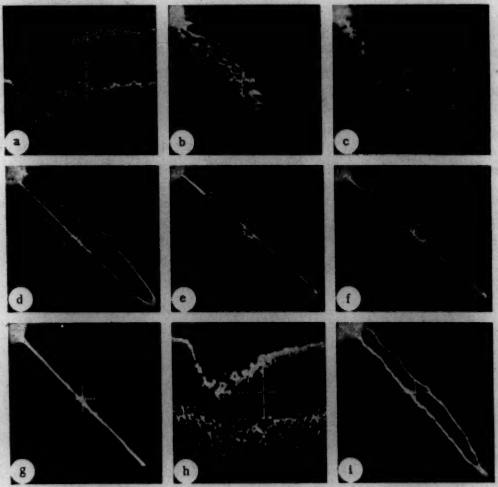

Fig. 2. Oscillograms illustrating operation of strobing ultrataumeter with FÉU-28 photomultipliers. a) Signals in X and Y channels of balanced device observed on screen of S1-19 sampling oscilloscope (scales: 20 nsec/div along horizontal, 200 mV/div along vertical); b) line observed on S1-19 screen on sweeping signals of oscillogram (a) one with the other (storage devices off); c) loop from sample with τ = 4 nsec (storage devices off); d) same as c, but with storage devices on; e) loop overcompensated, 5 nsec introduced; f) loop undercompensated, 3 nsec introduced; g) loop compensated, 4 nsec introduced; h) form of signals on screen of S1-19 for large noise level in sample luminescence signal with τ = 4 nsec (lower beam), scales: 20 nsec/div along horizontal, 20 mV/div for lower and 100 mV/div for upper signal along vertical; i) loop obtained from oscillogram h.

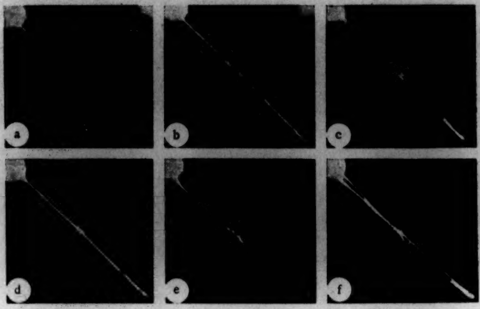

Fig. 3. Oscillograms illustrating operation of strobing ultrataumeter with FÉU-30 photomultipliers. a) Loop from sample with $\tau = 6.4$ nsec; b) undercompensated loop, 6.2 nsec introduced; c) overcompensated loop, 6.6 nsec introduced; d) compensated loop, 6.4 nsec introduced; e) loop resulting from 1 nsec optical delay in Y channel; f) an attempt to straighten the loop of oscillogram (e) by introducing RC into the X channel.

corresponds to 1 nsec. Such a loop can no longer be straightened out by introducing an RC in the X channel (Fig. 3f). A delay of 1 nsec can thus be clearly distinguished by the described method.

As an illustrative example of the quality of the measurements of the τ of fast luminophors that can be attained, we show in Fig. 4 the temperature dependence of the luminescence time constant of a Decalin solution of 3-monomethylamino-N-methylphthalimide. Parallel measurements of the luminescence efficiency η made by E. N. Viktorova, who kindly presented us with the investigated solution, give excellent coincidence of the form of the curves $\tau(T)$ and $\eta(T)$. (Figure 4 gives a rough idea of the photometric sensitivity of the method. The curve was obtained with a light flux of about 10^{16}-10^{17} photons/sec falling upon the cathode of the photomultiplier.)

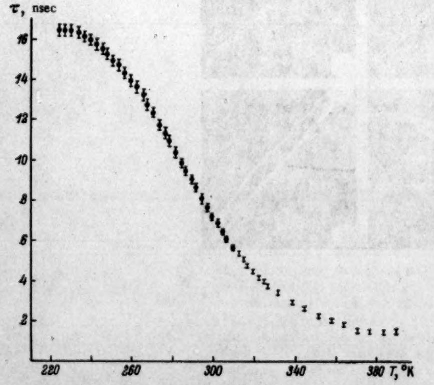

Fig. 4. Temperature dependence of luminescence time constant of Decalin solution of 3-monomethylamino-N-methylphthalimide.

Thus, the time range within the scope of the proposed method covers, to a considerable extent, the range in which phase fluorometers operate.[5] Besides simplicity and cheapness, the strobing taumeter possesses yet another promising feature: Being based on pulsed excitation it can, in principle, be used with high-power exciting sources, e.g., a laser operating in the periodic pulsed mode. This opens up at least two interesting possibilities. Firstly, investigations can be conducted in the nonlinear region, i.e., under conditions when τ depends on the intensity of the exciting radiation. Secondly, investigations can be conducted under conditions when the luminescence is extremely weak, e.g., under conditions of spectral expansion or in local investigations through a microscope. The latter is likely to be of considerable interest in connection with biological applications.

We note in conclusion that the lower time limit of the strobing ultrataumeter ($2 \cdot 10^{-10}$ sec) is probably not the ultimate. The method can probably be extended to times in the range 10^{-10}-10^{-11} sec by using faster flash lamps and better photomultipliers.

---

1) We shall concern ourselves here only with optical signals and an exponential relaxation described by a single value of τ. This covers the case of a nonexponential process approximated by an effective value of τ.

---

[1] N. A. Tolstoi and P. P. Feofilov, Usp. Fiz. Nauk, 16, 44 (1950).
[2] N. A. Tolstoi, N. N. Tkachuk, and A. M. Tkachuk, Izv. AN SSSR, Ser. Fiz., 21, 4 (1957).
[3] N. A. Tolstoi and A. M. Tkachuk, Opt. Spektrosk., 15, 698 (1962).
[4] I. I. Reznikova, ZhOKh, 5, 1260 (1969).
[5] A. M. Bonch-Bruevich, V. A. Molchanov, I. V. Karazin, and V. L. Shirokov, Prib. Tekh. Eksp., 2, 53 (1958).
[6] V. A. Bonch-Bruevich, in: Flash Photometry [in Russian], Izd. Mashinostroenie, Leningrad (1973).

Optical characteristics of K-8 glass subject to radiation from a neodymium laser

A. M. Bonch-Bruevich, Ya. A. Imas, V. S. Salyadinov, and A. V. Shatilov

(Submitted August 23, 1973)
Zh. Tekh. Fiz., 44, 463-467 (February 1974)

The change in the bulk refractive index (Δn) of K-8 optical glass is measured while the glass is exposed to pulses from a free-running neodymium laser. The observed Δn values correspond to temperature variations of several tens of degrees at radiation fluxes which are close to the threshold for the optical breakdown of K-8 glass. The value of the absorption coefficient corresponds to the tabulated value. A possible mechanism for optical breakdown is discussed.

PROBLEM AND EXPERIMENTAL TECHNIQUE

Interferometry is used in ref. 1 to investigate the change in the refractive index (Δn) in bulk K-8 glass which has been placed into the focal plane of a lens in application of radiation from a free-running neodymium laser. Since there is no correlation between the change in the refractive index and the time-dependent structure of the laser radiation, it is concluded that the destruction of the K-8 glass takes place by a thermoelastic mechanism. Estimates of the absorption coefficient (k) are based upon calculations of the temperature of the glass volume irradiated and result in $k = 0.02\ \mathrm{cm}^{-1}$, which is higher by approximately one order of magnitude than the usual residual absorption coefficient of K-8 glass. The discrepancy can be explained by the assumption that k depends on the temperature and that it increases during the laser pulse. The value $k = 0.02\ \mathrm{cm}^{-1}$, which is obtained in experiments, must be considered an integrated characteristic averaged over the entire laser pulse. If this assumption is correct, the dependence of the temperature of the irradiated sample area on the radiation flux density must be nonlinear.

In the present work we wish to determine the nonlinear component of the refractive index. As in ref. 1, we use a Michelson interferometer to measure Δn (Fig. 1). A sample 1 of optical K-8 glass is inserted into one arm of the interferometer and irradiated with the pulses from a free-running neodymium-glass laser 2 (pulse length τ = 400 μsec). The laser is provided with a telescope-type resonator and operator under conditions close to single-mode-operation (divergence of the radiation $\Theta = 3 \cdot 10^{-4}$ rad). The radiation is focused with an optical system 3, which is composed of a cylindrical lens (f = 2320 mm) and a spherical lens (f = 280 mm) located 100 mm behind the cylindrical lens. The beam has a cross section of 0.12 × 5 mm in the focal plane of the optical system. A specially selected diaphragm 4, which is inserted behind optical system 3, provides a uniform distribution of the light flux along the focal line. The focal line is parallel to the axis of the interferometer. As a consequence, the sensitivity of the arrangement to changes in the refractive index is increased considerably. Variations in the refractive index are determined by means of the following expression:

$$\Delta n = \frac{\lambda \Delta S}{2ld}, \tag{1}$$

where l denotes the size of the optical inhomogeneity, d denotes the distance between the bands of the interference pattern, ΔS denotes the shift of a band, and λ denotes the wavelength of the illuminating radiation source. In order to eliminate from our considerations the Δn fraction related to striction, the interference pattern is photographed 0.01–0.2 sec after the radiation pulse of the neodymium-glass laser. We use a single-mode ruby laser 5 operating with single giant pulses as the illuminating source. The radiation of this laser is polarized so that the electric vector is in the plane passing through the focal line and the optical axis of laser 2 (yz plane). The Q factor is modulated with a passive shutter of KS-19 glass. The ruby laser pulse can be delayed with respect to the initiation of the radiation pulse by 100 μsec to 0.5 sec.

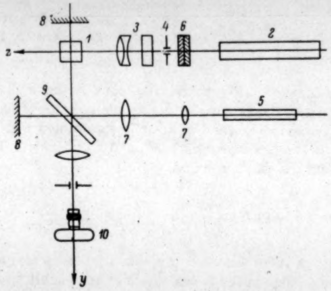

Fig. 1. Experimental arrangement. 1) K-8 glass sample; 2) neodymium-glass laser; 3) focusing system; 4) diaphragm; 5) ruby laser; 6) neutral attenuating filters; 7) Galilean telescope (×70 magnification); 8) mirrors of the Michelson interferometer; 9) dividing plate; 10) camera.

RESULTS AND THEIR DISCUSSION

Figure 2 shows interference patterns of optical inhomogeneities which develop at various times after the start of the pulse from the neodymium laser. The results of the quantitative evaluation of the interference patterns are indicated in Fig. 3. The interference patterns are obtained at $Q = 13.4\ \mathrm{kJ/cm^2}$ in the focal area, which is approximately one half the threshold value. The threshold at which the bulk of the glass is destroyed is about 25-30 $\mathrm{kJ/cm^2}$. It is noteworthy that when the interference pattern spreads in the course of time, the area under the Δn(x) curve is approximately constant, which means that there is a linear relation between Δn and the temperature. This conclusion agrees with the results of the calculation given below and makes it possible to determine the change in the refractive index and the temperature by the time at which the laser pulse terminates. For example, for $Q = 13.4\ \mathrm{kJ/cm^2}$, the maximum variation of the refractive index referred to the end of the laser pulse is $\Delta n = 1.4 \cdot 10^{-4}$.

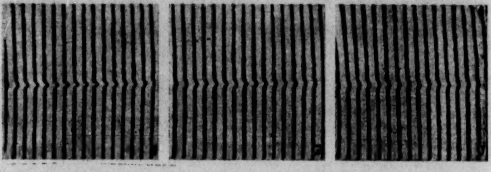

Fig. 2. Interference patterns of optical inhomogeneities at various times after the beginning of the pulse from the neodymium laser. τ_d denotes the time by which the ruby laser pulse is delayed relative to the beginning of the pulse from the neodymium laser. 2:1 scale. τ_d(msec): 1) 45; 2) 110; 3) 200; Q = 13.4 kJ/cm².

The changes of the refractive index in the heated layer consist of two components, i.e., a purely temperature-dependent component, which is usually associated with the shift of the main absorption band, and a component associated with the thermal stress:

$$\Delta n=\left(\frac{\partial n}{\partial T}\right)_\sigma \Delta T+\left(\frac{\partial n}{\partial \sigma_\parallel}\right)_T \sigma_\parallel+\left(\frac{\partial n}{\partial \sigma_\perp}\right)_T \sigma_{\perp\perp}+\left(\frac{\partial n}{\partial \sigma_{\perp\perp}}\right)_T \sigma_{\perp\perp}. \quad (2)$$

The notation is as follows: $\sigma_\parallel$ and $\sigma_\perp$ denote thermoelastic stresses, which in the yz plane are parallel and perpendicular to the vector of ruby-laser radiation, respectively; and $\sigma_{\perp\perp}$ denotes stresses perpendicular to the yz plane. Under the assumption that the entire irradiated layer is uniformly heated to a temperature T, we obtain the following expressions[2] for $\sigma_\parallel$ and $\sigma_\perp$:

$$\left.\begin{aligned}\sigma_\parallel&=-\frac{E}{1-\mu}\Delta\varepsilon_\parallel,\\ \sigma_\perp&=-\frac{E}{1-\mu}\Delta\varepsilon_\perp,\end{aligned}\right\} \quad (3)$$

where E and μ denote the elastic moduli; and $\Delta\varepsilon_\parallel$ and $\Delta\varepsilon_\perp$ denote deformations in directions parallel and perpendicular to the z axis, respectively. Obviously,

$$\Delta\varepsilon_\parallel=\Delta\varepsilon_\perp=\alpha(T-\bar{T}),$$

where α denotes the thermal expansion coefficient of the glass; $\bar{T}$ denotes the average temperature of the sample, which in the case under consideration can be replaced by the sample temperature T_0 outside the heated layer. The stress $\sigma_{\perp\perp}$ develops because the sample is compressed by an amount close to its thermal deformation $\Delta\varepsilon = \alpha\Delta T$, contrary to the case in which the heated layer fills the entire cross section area of the sample in the yz plane and, hence, the sample can freely expand in the direction of the temperature gradient (see, e.g., ref. 3). The corresponding stress is

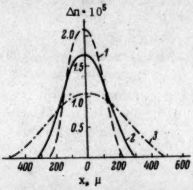

Fig. 3. Refractive index variation (Δn) of the bulk of the glass at various times after the beginning of the pulse from the neodymium laser. τ_d = (msec): 1) 45; 2) 110; 3) 200; Q* = 13.4 kJ/cm².

$$\sigma_{\perp\perp}=-E\Delta\varepsilon+\mu(\sigma_\parallel+\sigma_\perp), \quad (4)$$

where the second component accounts for the stresses acting in the yz plane. Since

$$\left(\frac{\partial n}{\partial T}\right)_\sigma\equiv\beta=2.2\cdot10^{-6}\ \text{deg}^{-1}$$

(the values of the constants were taken from refs. 4 and 5 for K-8 glass) and

$$\left(\frac{\partial n}{\partial \sigma_\parallel}\right)_T\equiv C_1=-0.5\cdot10^{-7}\ \text{cm}^2/\text{kg}\ ,$$

$$\left(\frac{\partial n}{\partial \sigma_{\perp\perp}}\right)_T=\left(\frac{\partial n}{\partial \sigma_\perp}\right)_T\neq C_2=-3.2\cdot10^{-7}\ \text{cm}^2/\text{kg}\ ,$$

we obtain finally an expression for Δn:

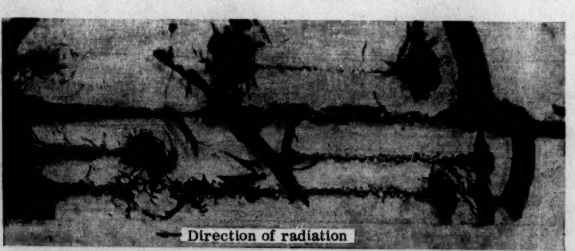

Fig. 4. Microphotographs of needle-like areas in which the K-8 glass sample is destroyed. ×40. Q* = 30 kJ/cm².

$$\Delta n = \Delta T\left[\beta + (C_1 + (2+\mu)C_2)\frac{aE}{1-\mu}\right]. \qquad (5)$$

With the above experimental value $\Delta n = 1.4 \cdot 10^{-4}$, we obtain $\Delta T = 20°C$ and, when we use the self-evident expression

$$k = \frac{\rho C \Delta T}{Q}, \qquad (6)$$

where $\rho C = 2$ kJ/cm^3·deg denotes the specific heat per unit volume of the K-8 glass, we obtain $k = 3 \cdot 10^{-3}$ cm^{-1}, which, within the error limits of the experiment and the calculations, corresponds to the calculated coefficient of residual absorption.

Under the conditions of our experiments, this k value is almost constant at least up to $Q = (0.7\text{-}0.9)Q^*$ (Q^* denotes the threshold of the energy density). Thus, it appears that the k value of ref. 1 may be too large. We note that so small ΔT values which are observed in the peak of the free-running laser at $Q \leq Q^*$ rule out the assumption that the K-8 glass is destroyed by a thermal effect. The destruction which occurs in the glass when the threshold Q^* is exceeded by 15% (Fig. 4) is in its form close to the destruction resulting from strictional self-focusing. The destruction develops when a nanosecond pulse is effective. Characteristic thin filaments develop in both cases. The appearance of these filaments may be related to the fact that the wave front of the beam is broken into areas which are self-focusing. Self-focusing increases the flux density inside individual filaments so that optical breakdown occurs.[6]

---

[1] N. G. Basov, O. N. Krokhin, N. V. Morachevskii, and G. V. Sklizkov, FIAN, Preprint No. 102.

[2] A. D. Kovalenko, Principles of Thermoelasticity [in Russian], Kiev (1970).

[3] A. A. Mak, V. M. Mit'kin, L. N. Soms, A. I. Stepanov, and O. S. Shchavelev, OMP, No. 9, 42 (1971).

[4] All-Union State Standard 13659-68, Uncolored Optical Glass, Physicochemical Properties and Parameters [in Russian].

[5] E. E. Berezina, OMP, No. 2, 38 (1970).

[6] A. V. Shatilov, G. P. Gusev, and G. D. Dvornikov, OMP, No. 4, 18 (1972).

Electron energy distribution in a high-frequency discharge in an axial magnetic field

S. D. Vagner, V. A. Virolainen, Yu. M. Kagan, and T. A. Kalmykova
Karelian State Pedagogical Institute, Petrozavodsk

(Submitted July 18, 1973)
Zh. Tekh. Fiz., 44, 468-469 (February 1974)

The second-derivative method is used to measure the electron energy distribution functions in a high-frequency helium discharge. The functions are used to calculate the ionization rate. When an axial magnetic field is applied the ionization rate increases sharply from the axis of the tube towards the walls. This effect is due to a change in the radial electron energy distribution caused by the magnetic field.

In this note we consider the effect of a magnetic field on the electron energy distribution in a high-frequency helium discharge. The measurements are based on the second-derivative method[1] and are performed in a 32 mm diameter discharge tube at a current of 160 mA and helium pressures of 0.05 and 0.2 torr. The frequency of the exciting field is 25 MHz. The distance between the external ring electrodes is 35 and 20 cm. The high-frequency current is measured by means of photoelectric devices set up next to the tube electrodes. Cylindrical probes 0.2 and 0.06 mm in diameter and 3 and 5 mm long are sealed into the central part of the tube. The 0.06 mm probe can be moved radially. The probes are perpendicular to the magnetic field.[2] Two identical, symmetrically positioned, antiprobes are placed near the probes on the walls. In contrast to ref. 1, one of the antiprobes is used as the reference electrode and is held at a constant potential relative to the plasma during the measurements. For the purposes of calculation the plasma potential is taken as the value at which the second derivative of the probe current passes through zero.

Figure 1 gives distribution functions for three positions of the movable probe. When a magnetic field is applied the fraction of fast electrons in the center of the tube is decreased sharply; however, there is very little change at the periphery. It is noted that the radial distribution of the total electron density is approximation by a Bessel function. Similar results are obtained at a pressure of 0.2 torr with an interelectrode distance of 35 cm.

The measured distribution functions are used to calculate the number of ionization events per electron per unit time z(r). The following equation is used:

$$z(r)=\frac{\sqrt{\frac{2e}{m}}\int\limits_{V_i}^{\infty} Q_i(V)\sqrt{V}F(r,V)\,dV}{\int\limits_0^{\infty} F(rV)\,dV}, \qquad (1)$$

TABLE 1

H, Oe	r/R	$n\cdot 10^{-9}$, cm^{-3}	$z\cdot 10^{-4}$, sec^{-1}	$z_1\cdot 10^{-4}$, sec^{-1}	$z_T\cdot 10^{-4}$, sec^{-1}
0	0	3.6	3.0	3.6	2.4
	0.4	2.2	3.2		
	0.8	1.1	4.4		
420	0	5.9	0.16	0.84	1.1
	0.4	4.0	0.50		
	0.8	1.9	2.3		

where F(r, V) is the measured distribution function, $Q_i(V)$ and V_i are the ionization cross section and ionization potential, and e and m are the charge and mass of an electron. The cross section for direct ionization $Q_i(V)$ is taken from ref. 3. Since the distribution function with the field present depends on the distance from the axis r, the quantity z is a function of r, in contrast to the Schottky theory, where it is assumed to be constant.

An estimate of the importance of stepwise ionization[1] made on the basis of the population of resonance and metastable levels measured by the reabsorption method[5] has shown that this process leads to an ionization rate at least an order of magnitude smaller than that for direct ionization.

Knowing z(r) and the radial variation of the total density n(r) we can determine the average ionization rate over the cross section from the equation

$$z_1=\frac{\int\limits_R^0 z(r)\,n(r)\,r\,dr}{\int\limits_0^R n(r)\,r\,dr}, \qquad (2)$$

where R is the tube radius.

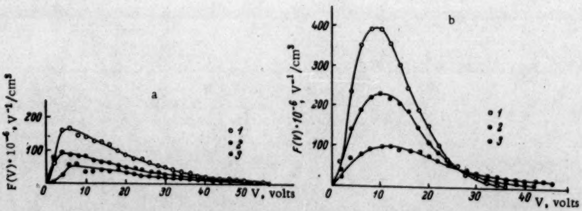

Fig. 1. Electron energy distribution functions at various distances from the axis of the discharge tube. p = 0.05 torr, L = 20 cm. Values of r/R: 1) 0; 2) 0.4; 3) 0.8. H in oersteds: a) 0; b) 420.

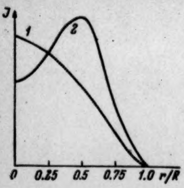

Fig. 2. Radial distribution of the relative radiation intensity. λ = 5016 Å. Values of H in oersteds: 1) 0; 2) 420.

An average ionization rate z_2 can also be determined from the value of the ion current density to the wall j if we assume that the recombination of charged particles occurs at the walls of the tube; we use the equation

$$z_2 = \frac{Rj}{e\int\limits_0^R n(r)\,r\,dr}. \tag{3}$$

Values for z_1 and z_2 are given in Table 1 and are in close agreement under all conditions. Evidently, z is essentially constant in the absence of a magnetic field over the whole of the cross section. With the magnetic field, z increases sharply with r. Although the value of z near the axis drops markedly when the magnetic field is applied, the value near the periphery changes very little. The measured radial distribution of radiation intensity of certain spectral lines confirms qualitatively the radial variation of the distribution functions (Fig. 2). The change in the electron distribution function with radius must be taken into account in any calculation of the average ionization rate over a cross section.

The relation between the radial variation in the electron distribution function in a magnetic field and the so-called anomalous diffusion in a high-frequency discharge[6] requires special examination.

---

[1] S. D. Vagner, V. A. Virolainen, and Yu. M. Kagan, Zh. Tekh. Fiz., 39, 669 (1969) [Sov. Phys. – Tech. Phys., 14, 502 (1969)].

[2] Yu. M. Kagan and V. I. Perel', Zh. Tekh. Fiz., 38, 1663 (1968) [Sov. Phys. – Tech. Phys., 13, 1348 (1969)].

[3] S. C. Brown, Elementary Processes in Gas Discharges, Wiley, New York (1961).

[4] V. F. Bratsev and V. I. Ochkur, Zh. Eksp. Teor. Fiz., 52, 955 (1967) [Sov. Phys. – JETP, 25, 631 (1967)].

[5] S. É. Frish and O. P. Bochkova, Vest. LGU, No. 16, 40 (1961).

[6] S. D. Vagner, N. A. Krylov, and B. V. Shlyaev, Zh. Eksp. Teor. Fiz., 57, 1543 (1969) [Sov. Phys. – JETP, 30, 834 (1970)].

Line shape of a quadrupole mass spectrometer

G. I. Slobodenyuk

(Submitted January 15, 1973; resubmitted June 20, 1973)
Zh. Tekh. Fiz., 44, 470-472 (February 1974)

The shape and intensity of a line in the mass spectrum of a quadrupole mass spectrometer have been studied as functions of the energy of the ions injected into the analyzer, V_{acc}, and as functions of the ratio of the voltages in the analyzer, $U/V = \lambda$. A criterion for evaluating the overall quality of the detector is proposed and a simple method is described for determining the resolving power of the spectrometer.

This experimental study has been carried out because of the importance of the characteristics of a quadrupole mass spectrometer, the difficulties involved in an exact analytic description of them, and the absence of information on this question in the literature (there are only a few fragmentary reports[1-4]).

The experiments are carried out on the KM-2 apparatus, which is part of the KM-4 gas analyzer.[5] The lines of molecular oxygen $^{16}O_2^+$ (M = 32 amu) and the xenon isotope $^{134}Xe^+$, which are isolated in the mass spectrum, are monitored. These lines appear in the mass spectrum when air and pure xenon, respectively, are injected at a pressure of $(3\text{-}4) \cdot 10^{-6}$ torr into the working chamber of the gas analyzer, evacuated beforehand to a pressure of 2 10^{-7} torr. The signal is recorded at the minimum scanning rate in the KM-2 (0.15 amu/sec) and at the maximum feed rate for the chart of an ÉPP-09MZ recording potentiometer. All the information with which we are concerned here is shown in Figs. 1 and 2: the variations in the shape and intensity of a line in the mass spectrum of the KM-2 corresponding to a change in the energy of the ions injected into the analyzer (V_{acc}, V) and a change in the ratio of the analyzer voltages (λ, arbitrary units), respectively. These figures show two series of recordings of the molecular oxygen line correspondihg to the specified operating conditions of the quadrupole mass spectrometer. The quantitative changes in the line intensities can be determined on the basis of the line amplitudes and the scaling factors indicated in the figures.

We can reach certain conclusions on the basis of these figures. 1) As V_{acc} is reduced and λ increased, the corresponding increase in the absolute resolution of the quadrupole mass spectrometer at the 50% level is accompanied by an extremely nonuniform decrease in the line intensity. Initially, this decrease is not very pronounced (see the first nine peaks at the left in Fig. 1 and the first 11 peaks in Fig. 2), but then the decrease becomes important, amounting to a factor of tens or hundreds. 2) In both cases, as the resolution increases the line changes from a dome shape (in agreement with the results of ref. 3) to a bell shape with large tails. It is found in observation of the change in the line shape at various pressures in the detector of the spectrometer that these tails are due not only to the factors discussed in ref. 4, but also, and significantly, to scattering of " unstable"[1,4] ions by the residual gas molecules at the end of the analyzer. This scattering helps the ions reach the ion detector. 3) There is a characteristic distortion of the peak shape (indicated by the arrows in Figs. 1 and 2) caused by distortions of the analyzer field and leading to a parasitic peak broadening. All these variations in the shape and intensity of the $^{16}O_2^+$ peak are reproduced in the behavior of the $^{134}Xe^+$ peak.

Comparing the results, we conclude that there is an optimum adjustment for the resolution of the spectrometer, i.e., for minimizing possible changes in sensitivity. The method consists essentially of simultaneously changing two quantities, V_{acc} and λ, in accordance with an equation which can be derived in an elementary manner from the equations for the absolute resolution, which follow from the theory of quadrupole mass spectrometers: $U_{acc} = 0.089(Mf^2L^2/A^{2/3})(1-\lambda/0.16784)$, where M is the ion mass

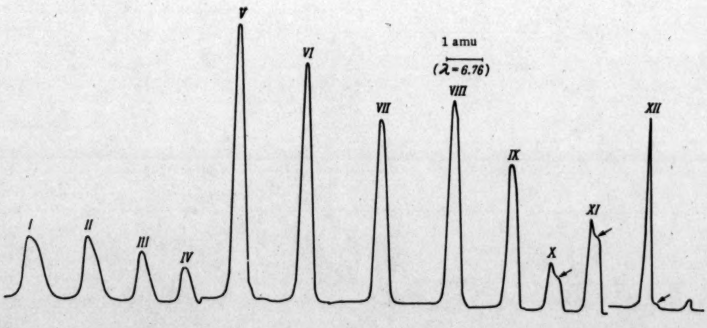

Fig. 1. Amplitude and shape of the $^{16}O_2^+$ pulse as functions of the electric potential accelerating the ions upon their injection into the analyzer (U_{acc}) ($P_\varepsilon = 3.6 \cdot 10^{-6}$ torr). The arrows show characteristic distortions. $\lambda = 6.76$. Ordinate scale, U_{acc}(V): I) 1:1, 40; II) 1:1, 30; III) 1:1, 20; IV) 1:1, 14; V) 1:0.134, 14; VI) 1:0.134, 13; VII) 1:0.134, 11.5; VIII) 1:0.122, 11; IX) 1:0.122, 10; X) 1:0.122, 9; XI) 1:0.05, 8.5; XII) 1:0.015, 8; XIII) 1:0.0058, 7.

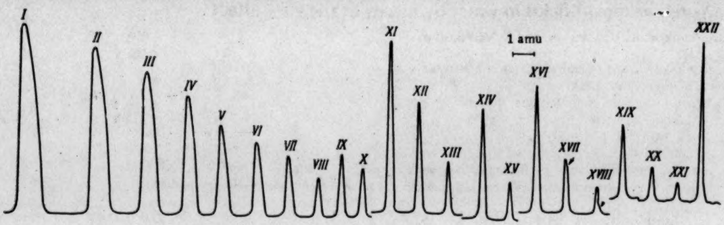

Fig. 2. Amplitude and shape of the $^{16}O_2^+$ pulse as functions of the ratio $\lambda = U/V$ ($P_\varepsilon = 3.6 \cdot 10^{-6}$ torr, $U_{acc} = 9.87$). The arrows show characteristic distortions. I) 1:1, 1; II) 1:1, 2; III) 1:1, 3; IV) 1:1, 4; V) 1:1, 5; VI) 1:1, 5.5; VII) 1:1, 6; VIII) 1:1, 6.76; IX) 1:1.57, 6.76; X) 1:1.57, 7; XI) 1:0.46, 7.5; XII) 1:0.46, 7.5; XIII) 1:0.46, 8.0; XIV) 1 :0.2, 8.0; XV) 1:0.2, 8.5; XVI) 1:0.06, 8.5; XVII) 1:0.06, 9.0; XVIII) 1:0.06, 9.5; XIX) 1:0.023, 9.5; XX) 1:0.023, 10; XXI) 1:0.023, 10.5; XXII) 1:0.0004, 11.00. (The $^{14}N_2^+$ peak.)

(amu), f is the frequency (megahertz) of the rf voltage in the analyzer, L is the length of the analyzer (centimeters), and A is the ratio of the peak amplitude to the signal level at which the resolution is required.

A second conclusion is that we can evaluate the nature and, sometimes, the magnitude of the imperfections in the field configuration in the analyzer on the basis of the characteristic distortions which these imperfections cause in the peak shape. Furthermore, the minimum value of U_{acc} at which it is still possible to obtain the mass-spectrum signal if the relation given above between U_{acc} and λ is satisfied is an objective measure of the imperfections of the analyzer and the ion source. This minimum value can thus serve as a criterion for evaluating the production quality of the detector in a quadrupole mass spectrometer or as a criterion for the cleanliness of the field-shaping electrodes; contamination of these electrodes also distorts the field configuration in the analyzer and the ion source.

When the KM-2 is adjusted in the optimum manner, stable operation is possible with the following set of basic parameters: At an absolute resolution of 0.5 amu at the 50% level at a mass of 219 amu and at a recording rate of 0.4 amu/sec, a sensitivity of $2 \cdot 10^{-12}$ torr nitrogen equivalent is obtained. The dynamic range of the apparatus is[4] $2.6 \cdot 10^5$, and the isotopic sensitivity is 10^4 at 18 and 19 amu. The maximum working pressure in the detector is $1.5 \cdot 10^{-4}$ torr.

In the course of our experiments we have found and successfully used a simple method for achieving an operational relative quantitative evaluation of the signal discrimination of the quadrupole mass analyzer in the mass range being analyzed. This method consists essentially of recording the mass spectrum at a low resolution, with a low signal discrimination and an approximately unit signal-suppression factor. Then, with the apparatus operating normally, the spectrum is recorded at the required resolution. The changes in the intensity ratios for lines of different masses in the two spectra yield the (normalized) desired functional dependence of the discrimination (or suppression) factor on the mass number in the mass range being analyzed. To determine the mass discrimination in the KM-2, we record the spectra of singly, doubly, and triply charged xenon at relative mass resolutions of 70 and 500 at a mass of 134 amu. The ratios of the peak intensities $^{132}Xe^{+++}$:$^{132}Xe^{++}$:$^{132}Xe^{+}$ are 1:4.8:13.4 in the first case and 1:1.44:0.3 in the second. From these ratios we find the discrimination factors at masses of 44, 66, and 132 amu, referred to the signal at 44 amu, to be 1:0.3:0.022.

---

[1] W. Paul, H. Reinhard, and U. Zahn, Zs. Phys., 152, 143 (1958).

[2] P. H. Dawson, J. Vac. Sci. and Technol., 9, 487 (1972).

[3] G. I. Slobodenyuk, Zh. Tekh. Fiz., 37, 1535 (1967) [Sov. Phys. – Tech. Phys., 12, 1117 (1968)].

[4] G. I. Slobodenyuk, Zh. Tekh. Fiz., 41, 1016 (1971) [Sov. Phys. – Tech. Phys., 16, 798 (1971)].

[5] G. I. Slobodenyuk, in: The Electronics Industry [in Russian], No. 2 (1972), p. 82.

Investigating prebreakdown fields in water by means of the Kerr effect

I. T. Ovchinnikov, K. V. Yanshin, and É. V. Yanshin

Institute of Automation and Electrometry, Siberian Branch,
Academy of Sciences of the USSR
Siberian Scientific-Research Power Institute, Novosibirsk

(Submitted February 21, 1973)
Zh. Tekh. Fiz., 44, 472-474 (February 1974)

The electric field distribution in the gap formed by extended electrodes is investigated in fields of 1.3 MV/cm. Space charge, which can distort the field in the gap, is not formed for 200 nsec (measurement error of 0.3%).

The electric field distribution in the discharge gap is of considerable importance in the theory of breakdown and in the development of methods of controlling electrical discharges indielectrics. From this point of view water is of interest because it is a good example of a polar liquid; in addition, it finds many applications in high-voltage electrical devices, such as pulsed energy storage units, switches, etc.

We have studied the field distribution in a Kerr cell formed by cylindrical brass electrodes (diameter 1 cm, length 5 cm, and gap 0.2 cm), filled with distilled water.[1)]

The light from an ISSh-400 flash tube is passed through a collimating device, a filter, a piece of polaroid P_1, to the cell, and is analyzed by means of the polaroid P_2. The transmitted light is recorded by sweeping the slit of a "Kanal" high-speed electrooptical photorecorder.[1]

The light intensity incident on the photocathode of the recorder is

$$I = I_0 \sin^2 \pi B l E^2,$$

where $B \sim 10^{-11}$ cm/V^2 is the Kerr constant of water,[2] and l is the optical path length in the field E. As the voltage across the cell electrodes is increased, alternate illumination and darkening of the gap occurs and a series of alternate dark and bright bands are recorded on the photosweep. If the field across the observed volume is uniform, the bands will be straight lines perpendicular to the time axis of the chronogram. Any deviation of the field from uniformity will give rise to a corresponding bending of the bands.

On the part of the chronogram (see Fig. 1) corresponding to the flat part of the pulse ($50 < t < 200$ nsec) there are four pairs of straight bands, i.e., the field in the gap is uniform. The appearance of these bands is due to the small change in the voltage across the cell. In our case, for a pulse amplitude U = 265 kV and a corresponding field $E \sim 1.3$ MV/cm, a change in the field of 0.3% gives rise to the appearance of a single additional band.

The limited resolution time, determined mainly by the slit width, enables us to record only the first pair of bands on the leading edge of the pulse ($0 < t < 50$ nsec). During this time the total number is approximately 75 pairs. The interval between the dark and bright bands for the first pair is approximately 5 nsec, and 0.1 nsec for the last pair.

The symmetric broadening of the dark bands at the

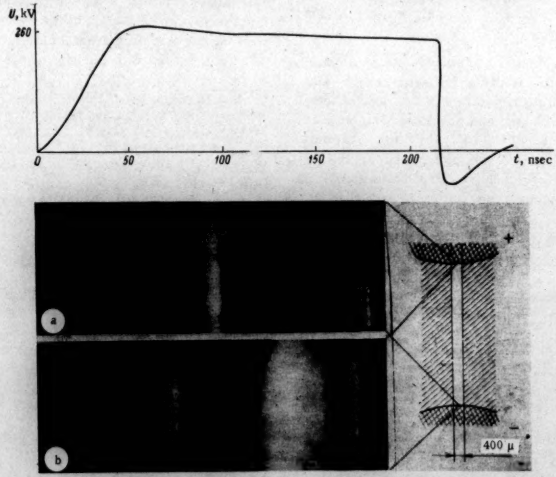

Fig. 1. Slit sweeps of the light modulated by the Kerr cell, combined with an oscillogram of the applied pulse. a) Polaroids crossed; b) polaroids uncrossed. The position of the slit with respect to the cell electrodes is shown on the right.

edges is due to current overload of the electrooptical converter. This can be seen by comparing the photosweeps, where, when the orientation of a polaroid is changed, the bands corresponding to the same voltage change their direction of curvature, while the bright bands are always convex.

Hence, from the photosweeps obtained it follows that for a field of E ~ 1.3 MV/cm the field in the gap remains uniform to at least 0.3% for 200 nsec. This shows, in particular, the untenability of the hypothesis which explains the "polarity effect" (the predominant development of the discharge from the anode in water when pulses of length $\leq 10^{-6}$ sec act) as due to the formation of a space charge, resulting from the emission of electrons from the cathode into the interelectrode gap, which increases the field in the region of the anode[3-5] by more than a factor of 1.5. Hence additional difficulties arise in explaining the electric breakdown of water from the point of view of ionization theory.

The authors thank Yu. N. Vershinin for suggesting the problem and for his interest.

---

1) The parameters of the cell and of the high-voltage pulse are chosen to provide a field ≥ 1 MV/cm in the gap; at the same time breakdown is controlled by limiting the pulse length.

[1] B. A. Baryshev, L. V. Gyavgyanen, L. M. Diamant, A. M. Iskol'dskii, L. L. Krasnogolovyi, and Yu. E. Nesterikhin, Avtometriya, No. 6, 53 (1971).

[2] N. A. Zlatin, Physics of Fast Processes, Vol. 1 [in Russian], Mir, Moscow (1971).

[3] G. I. Skanavi, Physics of Dielectrics, High-Field Region [in Russian], GIFML, Moscow (1958).

[4] I. Adamchevskii, Electrical Conductivity of Liquid Dielectrics [in Russian], Énergiya, Leningrad (1972).

[5] I. S. Stekol'nikov and V. Ya. Ushakov, Zh. Tekh. Fiz., 35, 1962 (1965).

New method for obtaining probe characteristics

Yu. I. Osipov

P. N. Lebedev Physics Institute
Academy of Sciences of the USSR, Moscow
(Submitted December 8, 1972)
Zh. Tekh. Fiz., 44, 474-477 (February 1974)

A new method is proposed for obtaining probe characteristics. This method avoids the difficulties which arise in studying plasmas with high particle densities and high energy densities.

1. In the usual method of obtaining the probe characteristic (Fig. 1a), an external (adjustable) voltage source is connected between the probe and a reference electrode.[1] The power of this source must exceed the power evolved in the external probe circuit in the flow of the saturation electron current I_{e0}, which is proportional to the probe area and the electron density n_e. For example, in the plasma of an Ar^+ laser we have $n_e \sim 10^{13}$–10^{14} cm^{-3}, and for a probe 1 mm long and 0.1 mm in diameter the current I_p can reach 1.0 A or more. Estimates show that in this case the power capacity of an external voltage source suitable for the measurements is hundreds or thousands of watts. Serious technical difficulties arise in designing such voltage sources. Sometimes a charged high-capacitance capacitor bank is used, and the probe characteristic is recorded point by point (with each point corresponding to a certain bank voltage). This method, which requires much time, can be used if the plasma is stable enough over the time required to obtain the entire characteristic.

In this note we propose a new pulsed method for obtaining probe characteristics; we have used this method successfully to study the plasma in a cw Ar^+ laser. The method is based on the circumstance that the probe current is a function only of the probe potential with respect to the plasma; in other words, the shape of the probe characteristic is not a function of the parameters of the external part of the probe circuit and is governed solely by processes which occur in the plasma itself and at the electrodes. This statement is true if the time required to record the characteristic, τ, is short in comparison with any characteristic time for changes in the plasma properties, τ_1, but large in comparison with the time required for a redistribution of the ions in the sheath, τ_2. This latter time is approximately equal to the ratio of the Debye length λ_D to the ion thermal velocity v_+, and for the plasma of an Ar^+ laser it is $(10^{-3}\ \mathrm{cm})/(10^5\ \mathrm{cm/sec}) = 10^{-8}$ sec.

If an RC circuit is connected between the probe and the reference electrode (e.g., the anode) (Fig. 1b), the situation is equivalent to that which would obtain if we connect to the RC circuit an emf $U_f = V_f - V_a$ (Fig. 1a). A transient process begins in the circuit: A current I_p flows and charges capacitance C. The voltage between the probe and the anode, U(t), which is equal to the sum of the voltage across the capacitance, $U_C(t)$, and that across the resistance, $U_R(t)$, increases from some initial value $U_{ini} = V_{ini} - V_a$ to $U_f = V_f - V_a$ ($U_{ini} = RI_{ini}$). The probe potential assumes all values from V_{ini} to the floating potential V_f. (If R = 0, we have $V_{ini} = V_a$; if $R \to \infty$, we have $V_{ini} \to V_f$; Fig. 1a.)

If the voltage $U_R(t) = RI_p(t)$ is fed to the Y plates of an oscilloscope and the voltage $U(t) = U_C(t) + U_R(t)$ to the X plates, the electron branch of the probe characteristic is produced on the oscilloscope screen. The values of R and C only govern the recording time and the initial potential V_{ini} from which the recording of the electron branch of the characteristic begins.

If the cathode is used as a reference electrode, the ion branch of the probe characteristic is obtained in a completely analogous manner. In this case the probe potential assumes all values from $\sim V_k$ to V_f. The RC circuit can be replaced by an RL or an RCL circuit.

This method has the following advantages: 1) There is no external voltage source in the probe circuit; 2) it is extremely simple; 3) the parameters of the external circuit are independent of the electron density and other plasma properties; 4) this arrangement can be used to study a variety of steady-state, transient, and pulsed

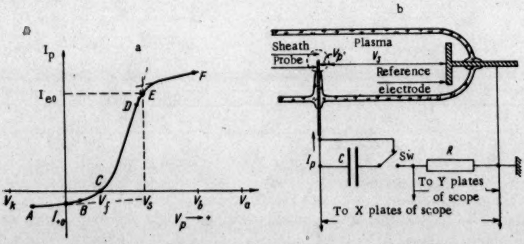

Fig. 1. a) Typical probe (voltage–current) characteristic. V_k is the cathode potential, V_f is the floating potential, V_s is the space potential, V_b is the breakdown potential at the probe, V_a is the anode potential, I_p is the probe current, and I_{e0} and I_{f0} are the electron and ion saturation currents, respectively; b) schematic diagram of the new method for obtaining a single-probe characteristic.

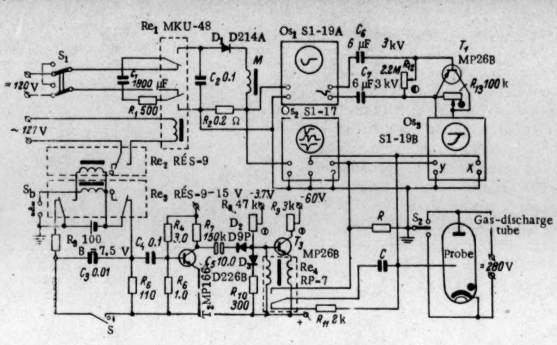

Fig. 2. Schematic diagram of the electronics.

plasmas, because the recording time can be easily adjusted over a broad range by changing the values of R and C. This method thus simplifies and extends the range of applicability of the probe method. It is only necessary to satisfy two conditions, which are standard for the single-probe method: 1) There must be a suitable reference electrode; 2) the recording time τ must satisfy the condition $\tau_2 \ll \tau \ll \tau_1$ stated above.

2. Another difficulty arises from the circumstance that in plasmas with a high energy density and a high particle density (in this case I_{e0} is also high) there is the danger that the probe will be destroyed. Estimates for an Ar^+ laser (energy density of 200-700 W/cm^3) show that the probe cannot be left in the plasma safely at the floating potential for more than 0.1 sec, and the time over which the characteristic is recorded cannot exceed 1 msec. It is therefore necessary to use a moving probe[2] and a pulsed method to record the characteristic. In our setup a "jumping" probe is thrust directly upward by an electromagnet (M) for 20-40 msec. It penetrates a specified distance into the plasma and hovers at its uppermost point for 200-500 μsec while the probe characteristic is recorded. Then it falls freely back to its initial position in ~ 80 msec. The maximum probe displacement during the measurement (account is taken of the elastic impact with the ring, which limits its motion) does not exceed 0.1 mm. The probe remains in the discharge plasma for about 35 msec. Figure 2 shows the complete circuit for controlling and synchronizing the probe motion and recording the probe characteristics. When the button switch (S_b) is pushed (the cable release for a camera is used), capacitance C_1 (1800 μF), charged to 120 V, discharges through the electromagnet (M), in which the ring with the probe and contacts (K) are held in a quartz tube. When the probe reaches its uppermost position and closes the contacts, a small capacitance C_3 (previously charged by battery B) discharges completely through resistance R_5. This arrangement prevents arcing between contacts K when they subsequently are opened. The voltage pulse across resistance R_5 triggers a blocking generator, whose transformer is the winding of relay RP-7, which closes the RC circuit. When this method is used to actuate relay RP-7, the delay between the closing of the contacts (K) and the closing of the RC circuit does not exceed 0.5 msec. The probe characteristic is recorded by an oscilloscope (Os_3: an S1-19B oscilloscope with two BPU-1 units). The current $I_p(t)$ and the potential U(t) are recorded, along with the magnet (M) current, by oscilloscope Os_2 (S1-17). Since the RC circuit is open as the probe is rising, and capacitance C is shorted, the U(t) behavior gives the radial profile of the floating potential. To eliminate a perturbing effect on the plasma by the field of magnet M, and to turn this magnet off before the recording of the probe characteristic is begun, we use a diode (D_1) and adjust the relative positions of magnet M and the ring with the probe. This adjustment is monitored on oscilloscope Os_2. Oscilloscope Os_1 (S1-19) is used as a pulse generator and to indicate the time over which the beam of oscilloscope Os_3 is intensified. The beam is intensified by a pulsed shunting of variable resistance R_{13} by a transistor (T_1); this resistance regulates the beam brightness of the S1-19 oscilloscope. In this manner we can adjust the beam brightness from zero to maximum and thus work at shorter recording times. Oscilloscopes Os_1 and Os_2 are

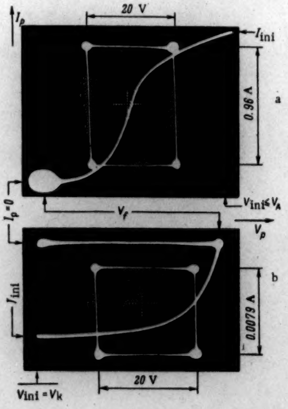

Fig. 3. Oscillograms of the probe characteristic obtained by this method. a) Electron branch; b) ion branch. The horizontal line at the top shows the change in the floating potential as the probe moves through the plasma. The scale rectangles are produced by briefly feeding calibrated periodic rectangular voltages from two generators to both pairs of oscilloscope plates (while the probe is rising).

triggered by the leading edge of the current pulse in magnet M. Switch S_2 is used to switch from the mode in which the electron branch of the characteristic is recorded to that in which the ion branch is recorded. Relays Re_1, Re_2, and Re_3 are used because it is necessary to hold part of the circuit at the floating potential during the measurement and to avoid a double grounding. As an example, Fig. 3 shows oscillograms of both branches of the probe characteristic, obtained with this apparatus in the plasma of an Ar^+ laser. The construction of the probe unit and the results of measurements in the plasma of an Ar^+ laser will be published separately.

In conclusion the author thanks N. N. Sobolev, V. F. Kitaeva, and A. A. Sapronov for their interest; the author is indebted to A. L. Shelekhov and V. P. Ageev for their participation in this work.

---

[1] O. V. Kozlov, Electric Probes in a Plasma [in Russian], Atomizdat, Moscow (1969); Yu. M. Kagan and V. I. Perel', Usp. Fiz. Nauk, 81, 409(1963) [Sov. Phys. – Usp., 6, 767 (1964)]; L. Schott, in: Plasma Diagnostics (ed. W. Lochte-Holtgreven), Interscience, New York (1968).

[2] Collection: Measurement of Transient Temperatures and Heat Fluxes [Russian translation], Izd. Mir, Moscow (1966), p. 92.

Condensation of an erosion plasma

B. A. Osadin and N. V. Rusakov

(Submitted December 12, 1972)
Zh. Tekh. Fiz., 44, 477-478 (February 1974)

The experimental use of a plasma gun as a pulsed evaporator for depositing thin films in vacuum is reported. The condensation rate is found to be 10^6-10^8 Å/sec, or five to six orders of magnitude higher than the condensation rate obtained with standard methods for obtaining thin films. Under certain conditions a brightly glowing plasma sheath is observed directly in front of the condensation surface. This sheath results from the difference of the condensation coefficient from unity. Other unusual features of the physical conditions for the condensation of an erosion plasma are reported.

1. Over the last two decades there has been an intense study of devices that generate pulsed plasma flows, particularly generators of an erosion plasma, i.e., the plasma produced in a vacuum discharge as a result of the destruction of the electrodes or of dielectric inserts.[1] Various applications have been found for erosion-plasma generators (in spectroscopy, in physical studies of cool plasmas, propulsion, etc.), but there has been essentially no use of these generators in applications associated with condensation of erosion-plasma streams. We believe that the study of this condensation can be very worthwhile both for studying the physics of the condensation process and in techniques for producing thin films, which are widely used in modern electronics.[2]

2. We have carried out an experimental study of the condensation of sulfur vapor produced with a plasma gun whose design and basic characteristics are described elsewhere.[3] The only changes in the experimental apparatus are in the method used to initiate the discharge, which is initiated by a high-voltage pulse (~ 40 kV) and the subsequent discharge of an auxiliary capacitor (2 μF, 500 V) in the electrode material (molybdenum) and in the material of the auxiliary insulator (alundum), chosen in order to reduce the corresponding impurity levels in the plasma.

The condensation occurs on flat substrate plates (glass or copper) at various distances from gun and at various angles with respect to its axis.

In addition to carrying out the measurements which are standard for plasma guns (recording oscillograms of the discharge currents, measuring the sulfur expenditure per discharge as a function of the voltage on the capacitor bank, and taking streak photographs of the plasma glow), we use traps 25 mm in diameter and 40 mm long, made of stainless steel foil, to study the angular distribution of the mass emission (Fig. 1). We study the sulfur films produced on a substrate in one or several discharges under an MIM-7 microscope; we determine the thickness of these films by weighing them and with an MII-4 interferometer.

3. In our experiments the condensation conditions are markedly different from the ordinary condensation conditions for the case in which thin films are deposited in vacuum by means of various types of evaporators.[4,5] In our experiments we are dealing with the condensation of a gas-dynamic flow, in which the mean free path of the vapor particles is less than or much less than the distance from gun (evaporator) to the substrate ($\lambda \ll d$). The density of sulfur atoms in the incident flow is 10^{14}-10^{16} cm^{-3}, depending on the discharge energy and the distance d, and the deposition rate of the condensate is 10^6-10^8 Å/sec, i.e., five or six orders of magnitude higher than the typical deposition rates achieved with steady-state evaporators. The flow velocities of (4-7) · 10^5 cm/sec and the high ethalpy of the plasma produce heat fluxes of 10^4-10^5 W/cm^2 to the substrate, so that during the condensation various layers of the condensate are at quite different temperatures, and these temperatures vary as a function of the time. At a heat flux larger than or roughly equal to 3 · 10^5 W/cm^2 we observe reevaporation of the condensate and even destruction of the copper substrate.

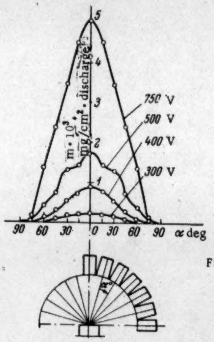

Fig. 1. Angular distribution of the mass emission. C = 280 μF.

4. With d ≤ 10 cm, a brightly glowing plasma "cushion" is observed near the substrate surface (Fig. 2). The formation of this plasma can be attributed to the reverse flow of vapor from the substrate, which results from incomplete condensation or reevaporation from the substrate. Calculations of the thermal conditions and comparison of the streak photographs for the glass and copper substrates show that the presence of elastically or diffusely reflected particles can be assumed primarily responsible for the formation of the plasma cushion. Photometry of the streak photographs reveals that the brightest part of the cushion is about 0.3-0.4 mm from the substrate, (~ λ). Accordingly, in these experiments the erosion plasma condenses from a plasma sheath at (2-4) · 10^4 °K directly adjacent to the substrate. Here again there is a difference from the condensation conditions in ordinary methods for producing thin films in vacuum.

5. We produce sulfur films ranging in thickness from several hundred to several thousand angstroms (the thickness increment varies from tens to hundreds of angstroms per discharge). Measurements of the film thickness reveal that films quite uniform with respect to thickness can be produced at a moderate discharge energy (W < 35 J),

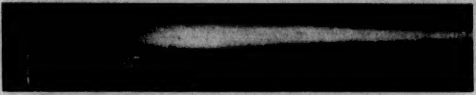

Fig. 2. Streak photograph of the plasma glow at the substrate (the vertical scale is 5:1, while the horizontal scale is 5 mm = 1 μsec).

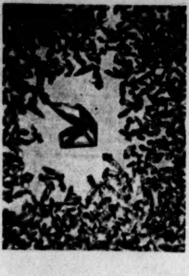

Fig. 3. Photograph of part of the film after it was held for 48 h in air (×600).

in good agreement with Fig. 1. Inspection of the films immediately after their production under a microscope at ×600 reveals no defects or foreign inclusions. After the films are held for 60 h in air, they crystallize (Fig. 3). First, individual crystals form at inhomogeneities of the substrate; then the crystallization spreads over the entire surface. The large crystals break up into smaller crystals, and the film becomes polycrystalline. Relative thin films retain their initial appearance relatively longer.

---

[1] L. Ya. Min'ko, Production and Study of Pulsed Plasma Flows [in Russian], Izd. Nauka i Tekhnika, Minsk (1970).

[2] V. G. Dneprovskii, B. A. Osadin, N. V. Rusakov, and G. L. Shapovalov, Elektron. Tekh. Mikroelektronika, 3, 79 (1972).

[3] A. M. Andrianov, A. I. Zemskov, V. V. Prut, and V. A. Khrabrov, Zh. Tekh. Fiz., 39, 433 (1969) [Sov. Phys. – Tech. Phys., 14, 318 (1969)].

[4] L. Holland, Vacuum Deposition of Thin Films, Wiley, New York (1956).

[5] K. L. Chopra, Thin Film Phenomena, McGraw-Hill, New York (1969).

Theoretical and mathematical physics

Energy resolution of quadrupole lenses for charged-particle beams

V. S. Siksin

(Submitted May 3, 1973; resubmitted July 16, 1973)
Zh. Tekh. Fiz., 44, 481-490 (March 1974)

The energy resolution of a system consisting of a 90° deflecting magnet and a doublet of quadrupole lenses is found for arbitrary values of the field parameters of the individual lenses of the doublet. In three-dimensional (k_1, k_2, F) space the energy resolution function F(k_1, k_2) is represented by a surface. Cross sections of this energy resolution surface made by planes perpendicular to the plane of its base (k_1, k_2) which pass through the origin form a family of characteristic curves with maxima. The values of the energy resolution are the same at these maxima, being equal to the energy resolution of the beam produced by the deflecting magnet alone. It is established that the necessary and sufficient condition for the preservation and reproduction of a chosen energy resolution curve of the beam, and thus the preservation and reproduction of the value of the energy resolution for a change in the field parameters k_1 and k_2 of the individual lenses of the doublet, is the preservation of a constant value of k_1/k_2 equal to 1.02, 2.05, and 0.51, and cases "c" and "d" have been determined. The value of the energy resolution of a beam of protons in the regions of transition from a virtual to a real image of the object (beam crossover) for various values of k_1/k_2 does not depend on C, the distance from the exit lens of the doublet to the crossover plane, at which the energy resolution is determined. For k_1/k_2 equal to 1.02, 2.05, and 0.51, various distances C, and cases c and d differences are found in the effect of variations of the parameters k_1 and k_2 on the energy resolution. The energy resolution curves are compared for these cases. The values of the parameters $k_{1\max}$ and $k_{2\max}$ corresponding to the beat value of the energy resolution are determined. The widths of these curves are found.

INTRODUCTION

The general considerations for energy resolution of a beam of charged particles in a system consisting of a 90° deflecting magnet and a doublet of quadrupole lenses are given in ref. 1. Those principles are applicable to nonrelativistic and relativistic particles. These principles are illustrated in ref. 1 for the case of identical values of the field parameters of the individual lenses of the doublet of quadrupole lenses. In the present note we discuss the energy resolution of a beam of charged particles by a 90° deflecting magnet and a doublet of quadrupole lenses for arbitrary values of the field parameters k_1 and k_2 of the individual lenses of the doublet.

PRINCIPLES OF THE ENERGY RESOLUTION OF A BEAM OF CHARGED PARTICLES FOR ARBITRARY VALUES OF THE FIELD PARAMETERS OF THE INDIVIDUAL LENSES OF A DOUBLET OF QUADRUPOLE LENSES

We consider the transmission of a beam of charged particles through a system consisting of a 90° deflecting magnet and a doublet of quadrupole lenses. The energy resolution in the plane perpendicular to the axis of the beam and at a distance C from the last lens of the doublet is given by[1]

$$F=\pm\frac{\Delta E}{E}=\frac{2\Delta x}{\left(2r_0+\frac{B}{X}-\frac{C}{X}\right)}\quad\text{for}\quad\frac{B}{X}\geqslant\frac{C}{X},\qquad(1a)$$

$$F=\pm\frac{\Delta E}{E}=\frac{2\Delta x}{\left(2r_0+\frac{C}{X}-\frac{B}{X}\right)}\quad\text{for}\quad\frac{B}{X}<\frac{C}{X},\qquad(1b)$$

where $\Delta x = \pm\ 0.05$ cm is the deviation of the beam from the axis a distance C from the right-hand edge of the last lens of the doublet, and all the terms of the sum in the denominators of (1a) and (1b) are measured in centimeters. The quantity B is the distance from the right-hand edge of the exit lens of the doublet to the image of the object, the beam crossover, located at the focus of the magnetic analyzer. The quantity X is the magnification of the doublet of quadrupole lenses. The quantity $2r_0$ is twice the radius of deflection of the beam in the analyzing magnet. Equation (1a) holds if $B/X \geq C/X$. This condition corresponds to the formation of a virtual or a real image of the object (beam crossover) and to finding a real image either in the plane in which the energy resolution of the beam is determined, or in planes to the right of it in the direction of the beam axis. Equation (1b) holds if $B/X < C/X$. In this case a real image of the object is formed; the beam crossover lies between the right-hand edge of the exit lens and the plane in which the energy resolution is determined. All the quantities B, C, and X are positive. Equations (1a) and (1b) are applicable to nonrelativistic and relativistic particles.

There are two ways of arranging the individual lenses of the doublet. In the first case "c" in the plane in which the proton momenta are dispersed the beam diverges in the first lens of the doublet and converges in the second. In the second case "d" in the same plane of dispersion of the magnet the beam converges in the first lens and diverges in the second. We denote the field parameters of the first lens of the doublet by k_1 and the second by k_2. The ion-optical quantities B_c, B_d, X_c, X_d, B_c/X_c, B_d/X_d, C/X_c, and C/X_d, and the energy resolution of the beam F have been calculated by computer using the equations given in ref. 1. From these calculations the function F(k_1, k_2) is found. Each of the equations (1a) and (1b) relating the quantities F, k_1, and k_2 is the equation of a surface. The function F(k_1, k_2) calculated for cases c and d and distances C = 100 and 800 cm is shown in Figs. 1a, 2a, 1b, and 2b. The function F(k_1, k_2) has also been calculated for cases c and d and distances C = 200, 314, 506, and 700 cm. For each distance C it is represented by a complicated surface in three-dimensional F, k_1, k_2 space. Cross sections of this surface of energy resolutions made by planes perpendicular to its base (k_1, k_2) and passing through the origin form characteristic curves with maxima. The energy resolution of the beam is the same at these maxima, being equal to the energy resolution of the beam produced by the deflecting magnet alone (10^{-3}).

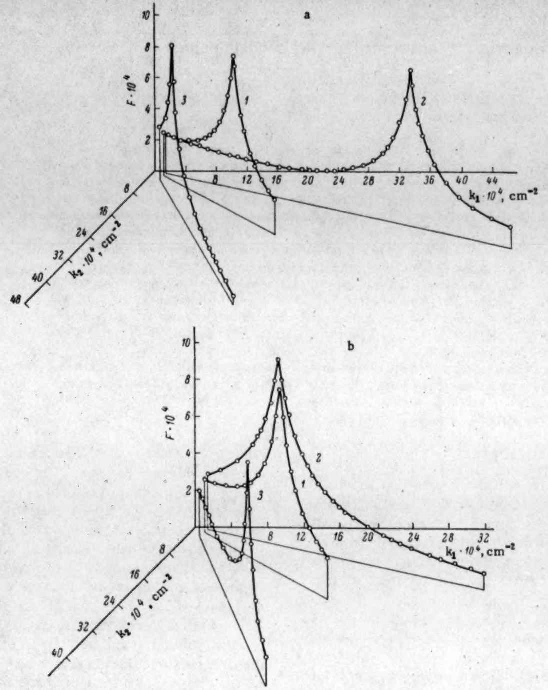

Fig. 1. Energy resolution surfaces of a beam of protons for lens arrangement c (a) and d (b). Distance C = 100 cm. Curves 1, 2, and 3 correspond to k_1/k_2 equal to 1.02, 205, and 0.51 respectively.

In these figures, curve 1 corresponds to essentially identical values of the field parameters $k_1 \approx k_2$ ($k_1/k_2 = 1.02$). Curve 2 corresponds to the ratio $k_1/k_2 = 2.05$, and curve 3 holds for $k_1/k_2 = 0.51$. Segments of the energy resolution curves of the beam 4-14 correspond to values of k_1/k_2 equal to 1.2, 0.87, 0.75, 0.83, 0.9, 0.92, 1.09, 1.11, 1.14, 1.33, and 1.45. The figures also show the projections of the energy resolution curves on the (k_1, k_2) plane. It is clear from Figs. 1 and 2 that the energy resolution surfaces are different for cases c and d. In case d the values of the parameters $k_{1\,\max}$ and $k_{2\,\max}$ corresponding to the maxima of the various energy resolution curves 1, 2, 3 lie closer to one another than in case c. In addition, when the lenses of the doublet are interchanged curves 2 and 3 are reversed.

If, in an attempt to focus the beam, the field parameters k_1 and k_2 of the individual lenses are changed separately and the ratio k_1/k_2 is not kept constant, there will be a jump from one energy resolution curve to another with irregular changes in the energy resolution of the beam. Consequently, an examination of the energy resolution surfaces leads to an important condition: the theorem on the preservation and reproduction of the value of the energy resolution of the beam in focusing by a doublet of quadrupole lenses.

A necessary and sufficient condition for keeping a given energy resolution curve and thus keeping a given energy resolution with changes in the field parameters k_1 and k_2 is that the ratio k_1/k_2 must be kept constant.

COMPARISON OF ENERGY RESOLUTION CURVES CALCULATED FOR CERTAIN VALUES OF k_1/k_2 AND VARIOUS DISTANCES C

Figures 3 and 4 show curves 1, 2, and 3 previously represented in three-dimensional F, k_1, k_2 space. As in the case of identical values of the field parameters $k_1 \approx k_2$, these curves show that there are only two possibilities for obtaining high energy resolution of a beam of protons. One way is to operate the doublet of quadrupole lenses in the weak defocusing regime, i.e., on the left-hand slopes of the curves. The second way is to operate in the strong focusing regime, i.e., on right-hand slopes of the curves.

Table 1 shows some calculated values of the energy resolutions for C = 800 cm.

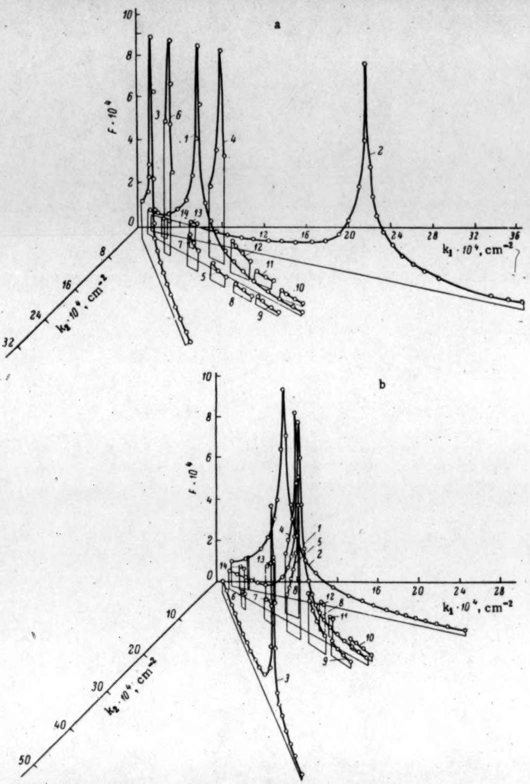

Fig. 2. Energy resolution surfaces of a beam of protons for case c(a) and for case d (b). Distance C = 800 cm. Curves 1, 2, and 3 are calculated for k_1/k_2 equal to 1.02, 2.05, and 0.51. Fragments of curves 4-14 were obtained for k_1/k_2 equal to 1.02, 0.87, 0.75, 0.83, 0.9, 0.92, 1.02, 1.11, 1.14, 1.33, and 1.45.

TABLE 1. Comparison of Energy Resolutions of a Beam of Protons

Case	$k_1 \cdot 10^4$, cm^{-2}	k_1/k_2	$F \cdot 10^4$
c	1.86	0.51	2.05
c	1.86	1.02	1.04
c	1.86	2.05	0.829
c	23.6	2.05	1.98
c	23.6	1.02	0.2
c	60	2.05	0.082
c	23.6	0.51	0.086
d	1.86	0.51	0.655
d	1.86	1.02	0.909
d	1.86	2.05	1.12
d	24.6	0.51	0.333
d	24.6	1.02	0.306
d	24.6	2.05	0.303
d	29.5	0.51	0.13
d	29.5	2.05	0.202

Table 2 gives values of the field parameters of the first lens of the doublet $k_{1\max}^{(1)}$, $k_{1\max}^{(2)}$, and $k_{1\max}^{(3)}$ obtained from curves 1, 2, and 3 of Figs. 3a and 4a and similar curves for distances C = 200, 314, 506, and 700 cm and corresponding curves for case c, in which the last lens of the doublet is a converging lens. The superscripts (1), (2), and (3) refer to the energy resolution curves with k_1/k_2 equal to 1.02, 2.05, and 0.51 respectively. These values of the field parameters correspond to the maximum value of the energy resolution of a beam of charged particles (10^{-3}), which depends only on the dispersion of the magnet. The values of $\Delta k_1^{(1)}$, $\Delta k_1^{(2)}$, and $\Delta k_1^{(3)}$ listed in Table 3 are the widths at half-maximum of curves 1, 2, and 3. These widths characterize the slopes of the energy resolution curves. The ratios of these widths to the values of the field parameter of the first lens corresponding

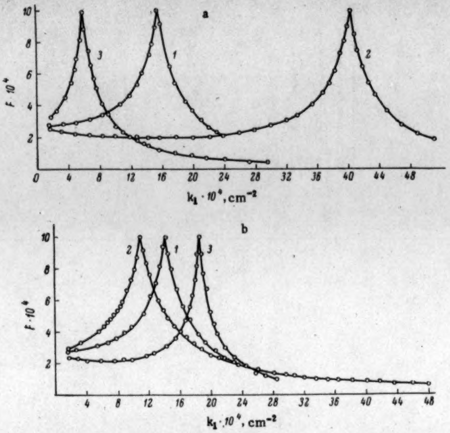

Fig. 3. Comparison of curves showing the energy resolutions of a beam of protons as a function of k_1 for case c (a), case d (b), and C = 100 cm. Curves 1, 2, and 3 correspond to k_1/k_2 equal to 1.02, 2.05, and 0.51.

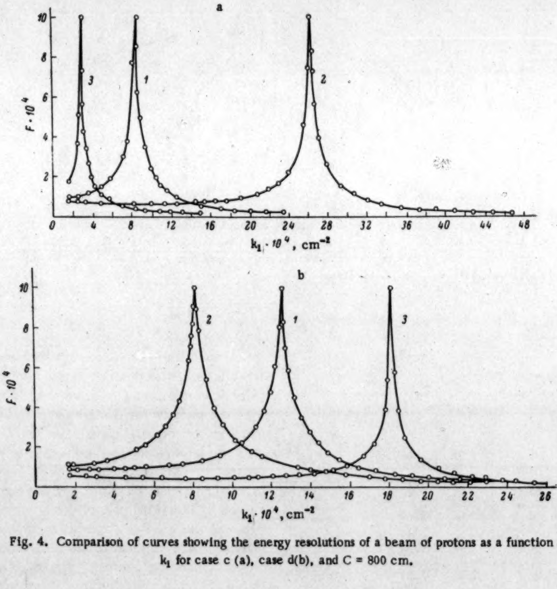

Fig. 4. Comparison of curves showing the energy resolutions of a beam of protons as a function of k_1 for case c (a), case d(b), and C = 800 cm.

TABLE 2. Comparison of Energy Resolution Curves in Case c

Distance C, cm	$k_{1\,max}^{(1)}\cdot 10^{-4}$, cm^{-2}	$k_{1\,max}^{(2)}\cdot 10^{-4}$, cm^{-2}	$k_{1\,max}^{(3)}\cdot 10^{-4}$, cm^{-2}	$\Delta k_1^{(1)}\cdot 10^{-4}$, cm^{-2}	$\Delta k_1^{(2)}\cdot 10^{-4}$, cm^{-2}	$\Delta k_1^{(3)}\cdot 10^{-4}$, cm^{-2}	$\frac{\Delta k_1^{(1)}}{k_{1\,max}^{(1)}}$, rel. units	$\frac{\Delta k_1^{(2)}}{k_{1\,max}^{(2)}}$, rel. units	$\frac{\Delta k_1^{(3)}}{k_{1\,max}^{(3)}}$, rel. units
100	15.6	40.4	6	5.8	6	3.6	0.37	0.15	0.6
200	11.8	32.8	4.3	3.4	3.8	2	0.29	0.12	0.46
314	10.25	29.8	3.7	2.4	2.8	1.36	0.23	0.094	0.37
506	9.15	27.8	3.2	1.7	1.8	0.8	0.18	0.06	0.25
700	8.64	26.6	3	1.3	1.5	0.7	0.15	0.056	0.23
800	8.5	26.3	2.9	1.12	1.12	0.42	0.13	0.043	0.14

TABLE 3. Comparison of Energy Resolution Curves in Case d

Distance C, cm	$k_{1\,max}^{(1)}\cdot 10^{-4}$, cm^{-2}	$k_{1\,max}^{(2)}\cdot 10^{4}$, cm^{-2}	$k_{1\,max}^{(3)}\cdot 10^{4}$, cm^{-2}	$\Delta k_1^{(1)}\cdot 10^{4}$, cm^{-2}	$\Delta k_1^{(2)}\cdot 10^{4}$, cm^{-2}	$\Delta k_1^{(3)}\cdot 10^{4}$, cm^{-2}	$\frac{\Delta k_1^{(1)}}{k_{1\,max}^{(1)}}$, rel. units	$\frac{\Delta k_1^{(2)}}{k_{1\,max}^{(2)}}$, rel. units	$\frac{\Delta k_1^{(3)}}{k_{1\,max}^{(3)}}$, rel. units
100	14.2	11	18.6	6	7	3.1	0.42	0.64	0.17
200	13.4	9.65	18.4	3.4	4.1	1.7	0.26	0.42	0.092
314	12.9	9	18.3	2.5	3	1.1	0.2	0.33	0.06
506	12.75	8.5	18.25	1.7	1.9	0.8	0.13	0.22	0.044
700	12.6	8.2	18.2	1.2	1.5	0.55	0.096	0.18	0.03
800	12.6	8.1	18.15	1.05	1.3	0.45	0.083	0.16	0.025

to the maximum value of the energy resolution characterize the effect of variations of the field parameters of the lenses k_1 and k_2 on the energy resolution. It can be seen from curves 1, 2, and 3 and the data of Table 2 that for variations of the field parameters close to the values $k_{1\,max}^{(1)}$, $k_{1\,max}^{(2)}$, and $k_{1\,max}^{(3)}$, the transition into the region of higher energy resolutions depends on the value of k_1/k_2. The same variations of the field parameters of the lenses give a very much larger reduction in the value of the energy resolution for large values of the ratio of the field parameters.

Table 3 lists the values of the field parameters of the first lens of the doublet $k_{1\,max}^{(1)}$, $k_{1\,max}^{(2)}$, $k_{1\,max}^{(3)}$, and $\Delta k_1^{(1)}$, $\Delta k_1^{(2)}$, $\Delta k_1^{(3)}$, obtained from curves 1, 2, and 3 of Figs. 3b and 4b and similar curves for C = 200, 314, 506, and 700 cm, and case d curves for the same values of the ratio of the field parameters. In this case F diminishes for variations of the parameters k_1 and k_2 about the values $k_{1\,max}$ and $k_{2\,max}$. This decrease is even greater for $k_1/k_2 = 0.51$. The energy resolution F depends on the field parameter k_2 of the exit lens of the doublet in the same way as it does on k_1. The only difference is in the scale of the abscissa axis. The values of F corresponding to given values of k_2 can be obtained from curves 1, 2, 3 of the same figures.

The values of the parameters $k_{1\,max}^{(1)}$, $k_{2\,max}^{(2)}$, and $k_{max}^{(3)}$, corresponding to the maximum value of the energy resolution, the widths of the energy resolution curves $\Delta k_2^{(1)}$, $\Delta k_2^{(2)}$, and $\Delta k_2^{(3)}$, and the ratios $\Delta k_2^{(1)}/k_{2\,max}^{(1)}$, $\Delta k_2^{(2)}/k_{2\,max}^{(2)}$, and $\Delta k_2^{(3)}/k_{2\,max}^{(3)}$ can also be found from curves 1, 2, and 3. These curves and Tables 2 and 3 show that a change in the distance C from the exit lens of the doublet to the place where the energy resolution is determined changes the values of $k_{1\,max}^{(1)}$, $k_{1\,max}^{(2)}$, and $k_{1\,max}^{(3)}$. As C is increased $k_{1\,max}$ and $k_{2\,max}$ are decreased, and the maxima of the energy resolution curves are shifted into the region of lower values of the field parameters. This shift is very much larger in case c. The widths of the energy resolution curves $\Delta k_1^{(1)}$, $\Delta k_1^{(2)}$, $\Delta k_1^{(3)}$, and $\Delta k_2^{(1)}$, $\Delta k_2^{(2)}$, $\Delta k_2^{(3)}$ decrease as the distance C is increased, and the energy resolution is diminished.

THE CHANGE IN THE ENERGY RESOLUTION OF A BEAM OF PROTONS WITH THE FIELD PARAMETERS k_1 AND k_2, THE RATIO k_1/k_2, AND THE DISTANCE C

The energy resolution of a beam of protons as a function of the field parameters of the lenses of the doublet k_1 and k_2 is given in ref. 1 for identical values of the field parameters and various distances C. Here, we consider arbitrary values of these parameters. Figures 5 and 6 show energy resolution curves calculated for the object (crossover of the proton beam) at the focus of the magnetic analyzer. The ratio of the parameters of each of these curves[15] is constant. For the curves of Figs 5 and 6 k_1/k_2 = 0.51 and 2.05 respectively. The energy resolution curves for the proton beam shown in Fig. 5 (1, 3, 5, 7, 9, and 11) correspond to case c with C = 100, 200, 314, 506, 700, and 800 cm. Curves 2, 4, 6, 8, 10, 12 (Fig. 5b) are calculated for case d and the same values of C. The curves shown in Fig. 6 are calculated for cases c and d and the same distances C.

These energy resolution curves are clearly symmetric, and exhibit maxima. The energy resolution at the maximum is the same for all distances C and is equal to the energy resolution of the beam due to the dispersion of the magnet alone. The values of the field parameters $k_{1\,max}$ and $k_{2\,max}$ corresponding to the largest value of the energy resolution depend strongly on whether the last lens of the doublet is converging or diverging in the plane of dispersion of the magnet.

The values of the parameters $k_{1\,max}$ and $k_{2\,max}$ also depend on the ratio k_1/k_2. The energy resolution curves are nonuniformly shifted into the region of smaller values of k_1 and k_2 when the target is moved away from the lens doublet, i.e., when the distance C is increased. The energy resolution of a beam of charged particles improves as the distance C is increased. Figure 5 shows that for

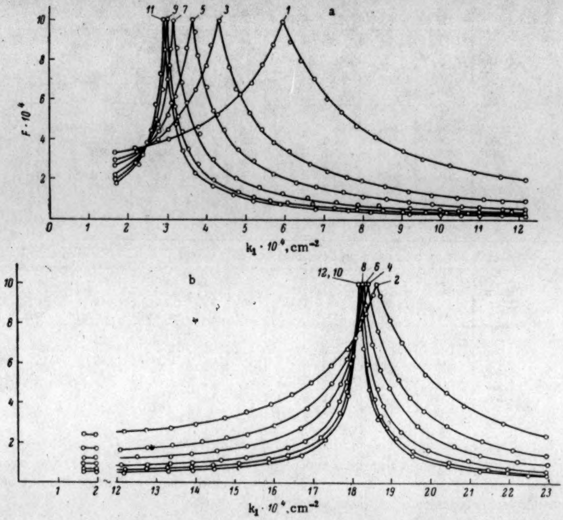

Fig. 5. Comparison of energy resolution for a beam of protons: a) in case c; b) in case d for distances C equal to 100, 200, 314, 506, 700, and 800 cm, and $k_1/k_2 = 0.51$.

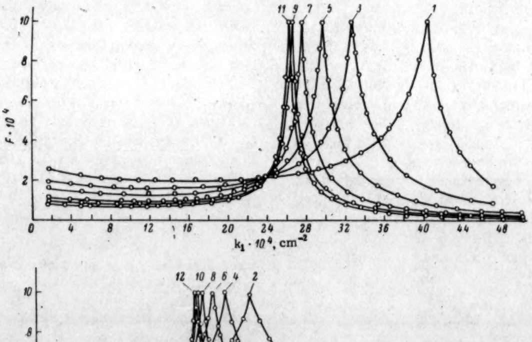

Fig. 6. Comparison of energy resolution curves for a beam of protons: a) in case c; b) in case d for distances C equal to 100, 200, 314, 506, 700, and 800 cm, and $k_1/k_2 = 2.05$.

$k_1 = 2.46 \cdot 10^{-4}$ cm^{-2} (case c) and $k_1 = 1.81 \cdot 10^{-3}$ cm^{-2} (case d) the energy resolution curves intersect at points corresponding to the regions of transition from a virtual to a real image of the object, the crossover of the beam. The values of the energy resolutions of the beam for these values of the field parameters are $3.63 \cdot 10^{-4}$ and $7.44 \cdot 10^{-4}$ respectively and remain unchanged for various values of C in the 100-800 cm range.

The energy resolution curves shown in Fig. 6 for $k_1 = 2.39 \cdot 10^{-4}$ cm^{-2} (case d) also intersect at points corresponding to regions of transition from a virtual to a real image of the object (the beam crossover) and the values of the energy resolution are $2.12 \cdot 10^{-4}$ and $5.06 \cdot 10^{-4}$ respectively and do not depend on the distance C.

RESULTS AND DISCUSSION

1. The general principles derived analytically[1] for the energy resolution of a beam of charged particles by a system consisting of a 90° deflecting magnet and a doublet of quadrupole lenses have been illustrated for arbitrary values of the field parameters of the doublet lenses.

2. For arbitrary values of the field parameters of the individual lenses of the doublet k_1 and k_2 the energy resolution function $F(k_1, k_2)$ is represented by a surface in three-dimensional F, k_1, k_2 space. Cross sections of this energy resolution surface made by planes perpendicular to the plane of its base (k_1, k_2) and passing through the origin form a family of characteristic curves with maxima. The values of the energy resolutions at all these maxima are the same and equal to the value of the energy resolution of the beam produced by the deflecting magnet alone.

3. The necessary and sufficient condition for the preservation and reproduction of a chosen energy resolution curve for the beam and, thus, the preservation and reproduction of the value of the energy resolution for a change of the field parameters k_1 and k_2 of the individual lenses of the doublet is the preservation of a constant value of k_1/k_2.

4. The differences in the energy resolutions of the beam for $k_1/k_2 = 1.02$, 2.05, and 0.51 and cases c and d have been determined.

5. The value of the energy resolution of a beam of protons in the transition regions from a virtual to a real image of the object (the beam crossover) for various values of k_1/k_2 does not depend on the value of C, the distance from the exit lens of the doublet to the beam crossover plane, where the energy resolution is determined.

6. For $k_1/k_2 = 1.02$, 2.05, and 0.51, various distances C, and cases c and d differences were found in the effect of variations of k_1 and k_2 on the energy resolution of the beam. The energy resolution curves have been compared in these cases. The values of $k_{1\,\max}$ and $k_{2\,\max}$ corresponding to the largest value of the energy resolution were determined. The widths of the curves have been found.

---

[1] V. S. Siksin, Zh. Tekh. Fiz., 43, 1818 (1973) [Sov. Phys.—Tech. Phys., 18, 1153 (1974)].

Radiating discharges confined by walls

A. F. Aleksandrov, I. S. Marshak, and A. A. Rukhadze
M. V. Lomonosov Moscow State University

(Submitted June 22, 1973
Zh. Tekh. Fiz., 44, 491-501 (March 1974)

The possibility of deriving a systematic magnetohydrodynamic theory for pulsed xenon tubes is analyzed. At temperatures high enough so that the emission of the discharge approaches that of an absolute blackbody and the energy loss at the walls is negligible it is possible to find an exact solution for the problem of the equilibrium and stability of radiating discharges confined by walls on the basis of the radiative magnetohydrodynamic model. The results agree with experimental data and available numerical calculations.

1. INTRODUCTION

The equilibrium and stability of high-current discharges in a dense plasma under conditions of intense radiative heat transfer have been studied theoretically and experimentally[1-6] in connection with the design of high-intensity pulsed light sources. The emitter must have properties corresponding to a brightness temperature of 3-5 eV in order to provide a maximum radiation in the spectral range near 2000 Å. At these high temperatures it is extremely undesirable to allow contact between the discharge channel and the walls of the vessel. Therefore, the discharge current in such sources must be high enough to provide magnetic confinement of the plasma in a limited volume by means of the self current (the pinch effect). However, such a discharge confined at equilibrium by the magnetic field of a current turns out to be unstable with respect to the development of strong instabilities. The conversion coefficient for the radiation, i.e., the ratio of the radiated energy to that stored in the system, is approximately the same as in ordinary pulsed gas-discharge tubes.[7,8] Accordingly, in those cases in which the spectral range of interest lies in the visible region, the most efficient sources would apparently be relatively low-current discharges in a dense plasma having a brightness temperature of 1-2 eV. Examples of such sources are ordinary pulsed xenon tubes. Here the term "low-current discharge" means that the discharge current is not high enough to lead to the pinch effect; under these conditions the plasma is confined in equilibrium by the walls of the discharge tube. Under these conditions strong instabilities cannot be tolerated, so in this sense we can speak of a discharge stabilized by the walls of the discharge chamber (stabilization of this type is clearly displayed in the xenon pumping tubes mentioned above).

Much effort has been devoted to theoretical calculations of the physical properties of such wall-confined discharges.[8-12] In most of this work,[8-11] however, either the plasma is assumed to be completely optically transparent or empirical corrections are introduced for the optical grayness of the discharge.[8,10] Clearly, this model of the discharge is valid only at low current densities, low temperatures, and low plasma densities; furthermore, it cannot yield the spectral distribution of the radiation. Accordingly, an approximate numerical calculation has been carried out[12] for the properties of the gas-discharge plasma in pulsed radiation sources. The results of this calculation agree with experimental results,[13,14] even though the temperature is actually assumed to be radially homogeneous in ref. 12. This homogeneity seems unlikely in the transparency region of the plasma; it requires a special study.

Analysis shows, however, that at high temperatures, $T \geqslant 1.5$ eV, there are broad ranges of the external discharge properties (the specific power supplied to the discharge, W; the discharge current density j_0; and the initial pressure in the tube, p_0) for which the discharge radiates like an absolute blackbody and over which a rigorous analytic calculation is possible.

In the present work we report the results of such a calculation, analyze the range of applicability of the derived equations, and compare the results with the results of ref. 12 and with experiment.

2. INITIAL ASSUMPTIONS AND BASIC EQUATIONS

We consider a discharge confined by walls in which the temperature is 1.5-2.0 eV and in which the initial pressure ranges from some tenths of an atmosphere to several atmospheres (typical conditions in pulsed xenon tubes). Under these conditions, as follows from data reported elsewhere,[8,10,12] the gas in the discharge channel can be assumed to be completely ionized. Furthermore, for a typical discharge-tube diameter of the order of 1 cm, the radiation of the discharge at such high temperatures and plasma densities differs only slightly from that of an absolute blackbody, as has been shown by calculations[12] and experiments.[9,14] Under these conditions we can use the approximation of radiative heat transfer, i.e., neglect electronic heat transfer in comparison with radiative transfer.

In accordance with the definition in the introduction we require two conditions: First, we require that the magnetic pressure of the discharge current be small in comparison with the kinetic pressure of the plasma,

$$\frac{B^2}{8\pi} \ll p; \tag{2.1}$$

Second, we require that the pressure in the discharge be constant,

$$p = (1+z)n\varkappa T = p_w = \text{const}, \tag{2.2}$$

where p_w is the pressure at the wall of the discharge tube, z is the average ion charge, $\varkappa$ is the Boltzmann constant, and n is the charged-particle density in the plasma.

Under these assumptions it is a straightforward matter to write the complete system of equations used to study any transient phenomena in this discharge. This system of equations is similar to the usual system of MHD equations with radiative heat transfer. They follow from the system of equations introduced in ref. 2, in which we incorporate conditions (2.1) and (2.2) (we will not write these equations out explicitly here).

We restrict the analysis to the case of an equilibrium, steady-state [d/(dt) = 0, v = 0] discharge, for which we can write this system of equations as

$$\left.\begin{aligned} &\operatorname{curl}\mathbf{B}=\frac{4\pi}{c}\sigma\mathbf{E};\\ &\operatorname{div}\left\{\frac{c^2}{16\pi^2}\frac{1}{\sigma}[\operatorname{curl}\mathbf{B}\times\mathbf{B}]-\chi\operatorname{grad}T\right\}=0,\\ &p=(1+z)n\varkappa T=p_w=\text{const},\end{aligned}\right\}\qquad(2.3)$$

where

$$\sigma=\alpha T^n,\quad \chi=\beta\frac{T^m}{p^k}\qquad(2.4)$$

are the conductivity and radiation thermal diffusivity of the plasma. The values of m and k, which govern the functional dependence of the radiation diffusivity on the temperature and pressure, are themselves governed by the mechanism by which light is absorbed in the plasma (below we refine these values for specific cases). Under conditions of complete ionization, the value of n is a weak function of the nature of the material This functional dependence varies strongly as a function of the degree of ionization of the plasma.

Finally, to close the problem, we require a symmetric temperature profile over the cross section of the discharge, and we specify the energy balance in the discharge under the assumption that the energy which appears as Joule heat is partially carried away from the plasma surface as blackbody radiation and partially expended in heating and evaporating the surfaces confining the discharge:

$$-\int_V\sigma E^2d\mathbf{r}+S\delta T^4(a)+SQ_w=0.\qquad(2.5)$$

Here V and S are the volume and surface area of the plasma, T(*a*) is the temperature at the boundary of this volume, and Q_W is the specific rate at which heat is evolved at the tube walls, a function of the actual wall temperature T_W. It is shown elsewhere[12] that at temperatures of 1-2 eV we can write

$$\left.\begin{aligned} &T_w\approx 0.8T(a),\\ &Q_w(T_w)\simeq 0.125Q_w(T(a))\\ &=\frac{0.125n}{\sqrt{2\pi M_i}}(\varkappa T(a))^{3/2}\left\{\frac{1}{2}\ln\frac{M_i}{m}+4+\frac{E_i}{\varkappa T(a)}\right\},\end{aligned}\right\}\qquad(2.6)$$

where M_i is the ion mass and E_i is the ionization energy of an atom in the plasma. Comparison of the loss due to radiation and the loss at the walls shows that it is important to take Q_W into account over broad ranges of plasma pressures and temperatures. However, at initial tube pressures which are not too high and at high temperatures T(*a*), we can neglect Q_W. For example, with p_0 = 300 torr, a typical initial pressure in a xenon discharge, and with T = 2 eV, the loss at the walls is about 20% of the radiation loss.[15]

3. EQUILIBRIUM OF A PLANE DISCHARGE

We consider a plane plasma layer which is inhomogeneous (bounded) along the x axis and to which is applied a homogeneous, fixed electric field $\mathbf{E}_0$ = const along the z axis (there is no skinning of the field in the plasma because of its low conductivity). This case corresponds to some extent to pulsed tubes with a rectangular cross section[16] and, partially, to "hollow" pulsed tubes with a thin plasma layer between external and internal cylindrical shells.[17] Here the magnetic field obviously lies along the y axis and vanishes at the axis.

System (2.3) can be solved exactly if χ(T) and σ(T) are functions of the plasma temperature alone. This condition is in fact satisfied for this discharge, because of the condition p = const. Accordingly, in the most general case, we set

$$\chi=\beta_0T^m,\quad \sigma=\alpha T^n.\qquad(3.1)$$

Then, we find an equation for T from Eqs. (2.3):

$$\frac{d}{dx}T^m\frac{dT}{dx}+T^n\delta=0,\quad \delta=\frac{\alpha}{\beta}E_0^2=\text{const},\qquad(3.2)$$

which is to be solved with the boundary conditions

$$T|_{x=0}=T(0)\quad \left.\frac{dT}{dx}\right|_{x=0}=0.\qquad(3.3)$$

This equation can be easily integrated by means of the variable substitution u = (1/2)[dT/(dx)]²; when the odd parity of the derivative dT/dx is taken into account, this equation yields the temperature distribution in quadratures:

$$\int_T^{T(0)}\frac{dT}{F[T,T(0)]}=|x|,\qquad(3.4)$$

where

$$F[T,T(0)]=T(0)^{-m}\left\{\frac{2\delta T(0)^{n+m+1}}{n+m+1}\left[1-\left(\frac{T}{T(0)}\right)^{m+n+1}\right]\right\}^{1/2}.\qquad(3.5)$$

Knowing T(x), we can easily find the density distribution ρ(x) and the magnetic field distribution B(x) from Eqs. (2.3). In particular, we find

$$\rho(x)=\frac{np_w}{(1+z)\varkappa T(x)}.\qquad(3.6)$$

Equations (3.5) and (3.6) determine the equilibrium of the discharge at a given temperature at the discharge axis, T(0), determined from the energy balance. From (2.5) we then find

$$-2\int_0^a\sigma E^2dx+2\delta T^4(0)=0,\qquad(3.7)$$

where $2a$ is the thickness of the discharge. We have neglected processes involving energy absorption by the walls of the discharge tube in this equation, in correspondence with the estimates above, and also in view of the known[8,16-20] high-energy efficiency of pulsed xenon tubes as radiation sources (the efficiency reaches 60-85% over the spectral range 1800-450 nm, in terms of the electrical energy dissipated in the tubes).

From (3.7) and

$$\int_{T(a)}^{T(0)} \frac{dT}{F[T,\ T(0)]} = a \qquad (3.8)$$

we determine T(0) and T(a), thereby completely solving the problem for the equilibrium of a wall-confined discharge in a dense, optically opaque plasma.

The general equations derived here, which govern the equilibrium characteristics of the discharge, can be simplified in two limiting cases: a) when the thickness a is so small that the temperature is nearly homogeneous over the plasma cross section, i.e., in the case T(0) ≃ T(a); b) when a is large and T(0) ≫ T(a). Let us consider these limiting cases in more detail.

Case a. When the discharge thickness a is so small that T(0) ≃ T(a), we can use (3.4) and expand in terms of the small deviation from the maximum temperature, finding

$$\left.\begin{aligned} T(x) &= T(0)\left[1 - \frac{x^2}{x_T^2}\right], \\ x_T^2 &= \frac{2}{\delta}\, T(0)^{m-n+1} = \frac{2\beta_0}{\alpha E_0^2}\, T(0)^{m-n+1}. \end{aligned}\right\} \qquad (3.9)$$

On the other hand, from the thermal-balance equation, (3.7), we find

$$a = \frac{\delta T(0)^{n-4}}{\alpha E^2}\left[1 - \frac{(4-n)\,a^2}{x_T^2}\right]. \qquad (3.10)$$

It is easy to see that Eqs. (3.9) and (3.10) hold only if $a^2 \ll x_T^2$ or, equivalently,

$$E > \frac{\delta T(0)^{\frac{7-n-m}{2}}}{\sqrt{2a\beta}}. \qquad (3.11)$$

We now incorporate the relation $\chi = (16/3)\hat{\sigma} l_p T(0)^3 = \beta_0 T(0)^m$ and require satisfaction of the obvious condition for the applicability of the approximation of radiative heat transfer: $2a > l_p$. Then we find

$$E > \frac{4\sqrt{2}}{\sqrt{3}}\, \frac{\delta T(0)^{\frac{7-n-m}{2}}}{\sqrt{a\beta}}. \qquad (3.12)$$

If condition (3.11) is not satisfied, the plasma temperature in the discharge cannot be assumed to be only slightly inhomogeneous, and we instead have case b. If inequality (3.12) is not satisfied, we have a situation corresponding to the conversion of the discharge from opaque to transparent. Accordingly, case a holds in an optically dense plasma over a quite narrow range of plasma properties, given by the inequalities

$$\frac{8}{\sqrt{3}} > \frac{E\sqrt{2a\beta}}{\delta T(0)^{\frac{7-n-m}{2}}} > 1. \qquad (3.13)$$

Case b. We now consider the opposite case, in which T(0) > T(a) and in which the plasma temperature varies significantly over the discharge thickness. In this case, working from Eq. (3.4) and introducing $t = [T/T(0)]^{(m-n+1)/2}$, we find

$$T(0)^{\frac{m-n+1}{2}} = \frac{a\sqrt{2\delta(m+n+1)}}{B\left(1 - \frac{n}{m+n+1},\ \frac{1}{2}\right)}, \qquad (3.14)$$

where

$$B(p,\ q) = \int_0^1 t^{p-1}(1-t)^{q-1}\,dt = \frac{\Gamma(p)\,\Gamma(q)}{\Gamma(p+q)}. \qquad (3.15)$$

On the other hand, from energy-balance equation (3.7) we find

$$\hat{\sigma} T^4(0) = \alpha E^2 \int_{T(a)}^{T(0)} \frac{T^n(x)\,dT}{F[T,\ T(0)]} \simeq \alpha E^2 \int_0^{T(0)} \frac{T^n dT}{F[T,\ T(0)]}. \qquad (3.16)$$

Now carrying out the integration by the method described above, and using (3.14), we finally find the desired quantity T(0), which is a characteristic of the radiation of the discharge:

$$\hat{\sigma} T(a)^4 = E_0 \sqrt{\frac{2\alpha\beta T(0)^{n+m+1}}{n+m+1}}. \qquad (3.17)$$

Here T(0) is given by (3.14).

Finally, we write the voltage–current characteristic of the discharge. It is easy to see that the total current per unit width of the discharge is

$$I_0 = 2\int_0^a j_0\,dx = 2\int_0^a \sigma E_0\,dx = 2\alpha E_0 \int_{T(a)}^{T(0)} \frac{T^n dT}{F[T,\ T(0)]} \qquad (3.18)$$

Now, using (3.4) and (3.7) we find

$$I_0 = \frac{2\hat{\sigma} T^4(a)}{E_0}, \quad \int_{T(a)}^{T(0)} \frac{dT}{F[T,\ T(0)]} = a. \qquad (3.19)$$

Equations (3.18) and (3.19) completely determine the voltage–current characteristic of the discharge, $I_0(E)$. (This characteristic can be written out explicitly for limiting cases a and b considered above.)

In case a, using Eq. (3.10) we find

$$I_0 = 2aE_0T^n(0) = 2aE_0\left(\frac{\alpha a E_0^2}{\delta}\right)^{\frac{n}{4-n}} \sim E^{\frac{4+n}{4-n}}. \tag{3.20}$$

In case b, we find from Eqs. (3.14) and (3.17)

$$I_0 = 2\sqrt{\frac{2\alpha\beta T(0)^{n+m+1}}{n+m+1}} = \sqrt{\frac{8\alpha\beta}{n+m+1}} \times \left\{\frac{a\sqrt{2\frac{\alpha}{\beta}E_0^2(n+m+1)}}{B\left(\frac{m+1}{n+m+1}, \frac{1}{2}\right)}\right\}^{\frac{m+n+1}{m-n+1}} \sim E^{\frac{m+n+1}{m-n+1}}. \tag{3.21}$$

Finally, it should be kept in mind that the total discharge current is bounded from above by inequality (2.1), which leads to the condition

$$I_0 < c\sqrt{\frac{2p_w}{\pi}}. \tag{3.22}$$

Only if this condition is satisfied are all the equations derived above valid. It is easy to see that (3.22) gives an upper limit on the discharge field E for a given discharge width. This limitation must be taken into account along with (3.13).

4. EQUILIBRIUM OF A CYLINDRICAL DISCHARGE

Let us consider the case in which the plasma is cylindrical, an assumption corresponding to the situation in an ordinary tubular pulsed xenon tube – a common situation in practice. As in the case of a plane discharge, we can reduce system (2.3) to an equation for T:

$$\frac{1}{r}\frac{d}{dr}rT^m\frac{dT}{dr} + T^n\delta = 0, \tag{4.1}$$

where δ is given by Eq. (3.2). The boundary conditions are analogous to (3.3). We restrict the analysis to the case in which the temperature varies only slightly over the discharge – the case of most practical interest. Then we easily find

$$T(r) = T(0)\left[1 - \frac{r^2}{r_T^2}\right], \quad r_T = \frac{4}{\delta}T(0)^{m-n+1} = \frac{4\beta}{\alpha E^2}T(0)^{m-n+1}. \tag{4.2}$$

The temperature at the discharge axis, T(0), is calculated from the energy-balance equation in the discharge. Assuming as before that the discharge radiates as an absolute blackbody, we can write this equation as

$$\delta T^4(0)\left[1 - \frac{4a^2}{r_T^2}\right] = \frac{\alpha E^2 a}{2}T^n(0)\left[1 - \frac{na^2}{2r_T^2}\right], \tag{4.3}$$

where *a* is the radius of the discharge tube. Hence we can write, approximately,

$$T(0) = \left(\frac{\alpha E^2 a}{2\delta}\right)^{1/(4-n)}. \tag{4.4}$$

From the condition for the homogeneity of the temperature ($a \ll r_T^2$) and the condition for the applicability of the approximation of radiative heat transfer ($a > l_p$), we find restrictions on the electric field in the discharge [cf. (3.13)]:

$$\sqrt{\frac{32}{3}} > \frac{E\sqrt{\alpha\beta}}{\delta T(0)^{(7-m-n)/2}} = \xi(E, T(0)) > 1. \tag{4.5}$$

From the condition under which we can neglect the magnetic pressure we find a restriction on the total discharge current:

$$I < ca\sqrt{2\pi p_w}. \tag{4.6}$$

Finally, the voltage–current characteristic of the discharge is

$$I = 2\pi\int_0^a jr\,dr = \pi a^2\alpha\left(\frac{\alpha a}{2\delta}\right)^{n/(4-n)}E^{(4+n)/(4-n)}. \tag{4.7}$$

We note that here the current is of the ordinary dimensionality, in contrast with the currents in (3.20) and (3.22).

5. STABILITY OF A WALL-CONFINED DISCHARGE

In these discharges the magnetic field of the current is negligibly weak, so there are no strong instabilities such as constrictions and kinks, which are typical of high-current self-constricted discharges and are consequences of the inequality of the magnetic and MHD pressures.[1,2] The only dangerous instability could be the superheating instability,[3] because in a completely ionized plasma there can be no current-contraction mechanisms (there can be no shunting of the glow discharge, accompanied by an abrupt current increase), which are characteristic of a weakly ionized plasma in which the gas temperature is significantly inhomogeneous over the cross section of the discharge tube.[21] To analyze the possible growth of this instability we start from the equation

$$\rho T\left[\frac{\partial s}{\partial t} + (\mathbf{v}\nabla)s\right] = \sigma E^2 - \operatorname{div}\chi\nabla T, \tag{5.1}$$

where s is the entropy per unit mass of the plasma. In the case of an ideal, completely ionized plasma we have

$$s = \frac{(1+z)\varkappa}{M_i}\ln\frac{T^{3/2}}{\rho}. \tag{5.2}$$

If

$$\frac{c^2}{4\pi\sigma a^2} \gg \omega \sim \frac{j^2}{\sigma p_w}, \tag{5.3}$$

and there is no skinning of the field in the plasma, whether the superheating instability occurs depends on the slope of the function

$$\varphi(T) = \frac{T\chi(T)}{\sigma(T)}. \tag{5.4}$$

As shown previously,[22] the discharge displays the superheating instability if $\varphi'(T) < 0$, but this instability cannot develop if $\varphi'(T) > 0$. If

$$\omega \sim \frac{j^2}{\sigma p_w} \gg \frac{v_s}{a}, \tag{5.5}$$

the plasma density does not manage to change during the growth of the instability; we can write [cf. (2.4)] $\sigma \sim T^n$ and $\chi \sim T^{m-k}$ for the conductivity and the radiation thermal diffusivity in this case. As a result we find

$$\varphi(T) \sim T^{m-k-n+1}. \tag{5.6}$$

The condition for the onset of the instability is

$$m-k-n+1<0. \tag{5.7}$$

If the inequality opposite to (5.5) holds, we have $\sigma \sim T^n$ and $\chi \sim T^m$, and the necessary condition for the onset of the superheating instability is

$$m-n+1<0. \tag{5.8}$$

Finally, according to (5.1), the growth rate for the superheating instability, under conditions such that this instability can occur, is determined by the characteristic time for Joule heating (or supercooling) of the plasma and is given in order of magnitude by

$$\operatorname{Im}\omega \simeq \frac{j^2}{\sigma p_w}. \tag{5.9}$$

It is important to note that conditions (5.7) and (5.8) are necessary but not sufficient conditions. For the development of the superheating instability, another necessary condition is

$$\sigma E^2 \geqslant \frac{\varkappa T}{r_T^2}, \tag{5.10}$$

where r_T is the scale of the inhomogeneity of the plasma temperature in the equilibrium (or quasiequilibrium) state of the discharge.

6. DISCUSSION OF RESULTS

These results are of a completely general nature and hold for discharges in arbitrary optically opaque media. Let us apply them to the case of a discharge in xenon at initial pressure of $p_0 \lessapprox 1$ atm and at $T \simeq 1.5$-2 eV. At these pressures and temperatures we have $z = 1$, and the conductivity and thermal diffusivity of the xenon are described by

$$\sigma = aT^{3/2}, \quad n = \frac{3}{2}, \quad a = 4\cdot 10^7,$$
$$\chi = \beta_0 T^{13/2}, \quad m = \frac{13}{2}, \quad \beta_0 = \frac{2.5\cdot 10^{-8}}{p_w^2}, \quad k = 2. \tag{6.1}$$

Here we have used the ordinary expression for the conductivity of a completely ionized plasma for σ, while for the radiation thermal diffusivity we have used the expression given by the Kramers-Unsöld approximation for photoionization absorption by xenon atoms.[23]

We first note that $m-n+1 = 6 > 0$ and $m-n-k+1 = 4 > 0$. Accordingly, a discharge in xenon under conditions such that the xenon is optically opaque is stable with respect to perturbations of the superheating type.

The Rosseland mean free path for light in xenon under these conditions is

$$l_p = \beta_1 T^{7/2}, \quad \beta_1 = \frac{3}{16}\frac{\beta}{\delta}. \tag{6.2}$$

At $p_0 \simeq 0.5$ atm $\simeq 0.5\cdot 10^5$ dyn/cm² and with $T \simeq 10^4$ °K we find $l_p \simeq 0.5$ cm, $\sigma_0 \simeq 4\cdot 10^{13}$ sec⁻¹, and $\chi \simeq 1.6\cdot 10^7$ erg/(cm · g · cm) [sic].

According to (4.5), with $T(0) \simeq 10^4$ °K a discharge in xenon will be nearly homogeneous with respect to the temperature if the field E_0 lies in the range

$$250\,\text{V/cm} \simeq 0.8\ \text{cgs esu} > E_0 > 0.25\ \text{cgs esu} \simeq 70\ \text{V/cm}. \tag{6.3}$$

In strong fields, the condition for optical opacity of the plasma is not satisfied, while in weak fields the condition for homogeneity of the temperature is not satisfied. We assume $E \simeq 100$ V/cm $\simeq 1/3$ cgs esu; then from (3.14) we find the discharge width to be

$$2a = 0.3\ \text{cm}. \tag{6.4}$$

The radiation of the plasma under these conditions is similar to that of a blackbody at $T_0 = 1$ eV, and the voltage–current characteristic, according to (4.7), is

$$j_0 = 1.1\cdot 10^{14} E_0^{11/4}. \tag{6.5}$$

For a comparison of this theoretical characteristic with experimental data it is convenient to rewrite the characteristic as

$$\sigma = 0.39 j^{7/11}. \tag{6.6}$$

For pulsed krypton and xenon tubes having inside diameters from 0.2 to 1.4 cm, a cold gas pressure of ~0.15 atm, and electric fields from 15 to 150 V/cm, it has been found experimentally[8] that σ can be described satisfactorily as a function of j by

$$\sigma = 4.66 j^{1/2}, \tag{6.7}$$

which also turns out to be approximately valid for a much broader range of electric fields (up to 6000 V/cm) and for much broader ranges of the other parameters.

In ref. 24 for xenon tubes of approximately the same diameters, at cold pressures of 0.25-1 atm and at current densities of 0.4-10 kA/cm^2, it is found that σ is described accurately as a function of j by the empirical equation

$$\sigma = 0.885 j^{1/2}. \tag{6.8}$$

The following empirical equation is found in ref. 25 for xenon tubes with inside diameters from 0.5 to 1.8 mm, at a cold pressure of about 0.5 atm:

$$\sigma = A j^{1/2}. \tag{6.9}$$

Here A increases from 0.2 to 0.56 with increasing diameter and increasing rise time of the current.

Finally, a study[26] of xenon tubes with inside diameters of 0.7 and 1.6 cm and cold pressures of 0.5-0.8 atm at current densities of 0.3-3 kA/cm^2 reveals that empirical equation (6.8) is satisfied extremely well; for a cold pressure of 0.15 atm, an analogous equation is found, in which the coefficient of $j^{1/2}$ is about 1.15. Some increase in σ with decreasing pressure has been observed in several cases (see, e.g., ref. 8), and we can assume that the increase in A noted in ref. 25 with increasing diameter and increasing current rise time is a consequence of the escape of some of the gas from the working part of the tube into the cold regions near the electrodes and to a corresponding reduction of the gas density between the electrodes (the volumes near the electrodes are minimized in ref. 26, and no functional dependence of σ on the diameter is detected).

Functional dependence (6.8) is also verified in ref. 27 over broader ranges of the parameters. The differences among empirical relations (6.7)-(6.9) are seen from Fig. 1 to be slight, possibly within the corresponding experimental errors, for the current-density range studied in detail. Theoretical curve 4 in this figure, plotted from (6.6), lies quite close to all the experimental curves, implying a satisfactory agreement between theory and experiment in terms of the voltage−current characteristic.

Returning to Eq. (6.5), we find, with E = 1/3 cgs esu, we have $j_0 \simeq 3300$ A/cm^2, a result which is consistent with inequality (4.8).

At fields weaker than the lower limit in (6.3), the plasma temperature becomes very inhomogeneous in the discharge, and the efficiency of the source must fall off appreciably, again in agreement with experiment.[8] For example, with E = 30 V/cm, we find (p_0 = 1 atm) $T(0) \simeq 1$ eV from (3.14) and $T(a)$ = 6400°K from (3.17). Figure 2 shows the temperature in the discharge as a function of the current density, calculated theoretically from Eq. (4.4); also shown here is the result of a numerical calculation[12] and experimental results.[28-30] We see that there is a satisfactory agreement at high current densities, $j_0 \gg 5$ kA/cm^2. Under these conditions the discharge parameters are such that all the simplifications used in this paper are valid. At lower current densities the discrepancy between the theoretical and experimental results increases; nevertheless, our simple analytic relations still yield correct estimates of the basic discharge parameters.

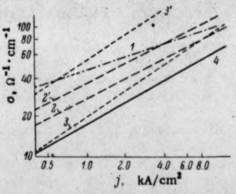

Fig. 1. Voltage−current characteristics of tubular flash lamps. 1-3) Experimental curves. 1) Ref. 8; 2) ref. 26, 400-600 torr; 2') ref. 26, 100 torr; 3) ref. 25, small a and t; 3') ref. 25, large a and t; 4) theoretical voltage−current characteristic from (6.6).

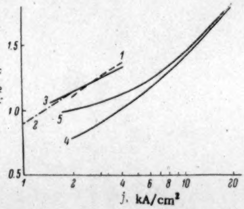

Fig. 2. Temperature as a function of the current density. 1) Ref. 28; 2) ref. 29; 3) ref. 30; 4) theoretical curve, from (4.4); 5) results of a numerical calculation.[12]

---

[1] A. F. Aleksandrov and A. A. Rukhadze, Usp. Fiz. Nauk, 105, 784 (1971); 102 (1974).

[2] A. A. Rukhadze and S. A. Triger, Zh. Prikl. Mekhan. Tekh. Fiz., No. 3, 11 (1968); Preprint No. 168, P. N. Lebedev Physics Institute (1968).

[3] A. A. Rukhadze and S. A. Triger, Preprint No. 26, P. N. Lebedev Physics Institute (1969).

[4] A. F. Aleksandrov, E. P. Kaminskaya, and A. A. Rukhadze, Zh. Prikl. Mekhan. Tekh. Fiz., No. 1, 33 (1971).

[5] A. F. Aleksandrov, V. V. Zosimov, S. P. Kurdyumov, Yu. P. Popov, A. A. Rukhadze, and I. B. Timofeev, Zh. Eksp. Teor. Fiz., 61, 1841 (1971) [Sov. Phys.−JETP, 34, 979 (1972)].

[6] A. F. Aleksandrov, N. V. Zosimov, A. A. Rukhadze, V. I. Savoskii, and I. B. Timofeev, Preprint No. 72, P. N. Lebedev Physics Institute (1971).

[7] A. D. Klementov, G. V. Mikhailov, F. A. Nikolaev, V. B. Rozanov, and Yu. P. Sviridenkov, Teplofiz. Vys. Temp., 8, 736 (1970).

[8] I. S. Marshak, Pulsed Light Sources [in Russian], Gosenergoizdat, Moscow−Leningrad (1963).

[9] I. C. Moden, Proceedings of the Eight International Congress of High-Speed Photography, Stockholm, 1968, p. 23.

[10] A. A. Bakeev and R. E. Rovinskii, Teplofiz. Vys. Temp., 8, 1121 (1970).

[11] A. T. Rakhimov and V. D. Pis'mennyi, Dokl. Akad. Nauk SSSR, 196, 812 (1971) [Sov. Phys.−Dokl., 16, 102 (1971)].

[12] A. A. Shcherbakov, Zh. Prikl. Spektrosk., 15, 610 (1971).

[13] V. I. Bulykov, A. S. Doinikov, and V. G. Ignat'ev, Svetotekhnika, 10, 21 (1967).

[14] L. I. Gavrilova, A. S. Doinikov, V. G. Ignat'ev, and V. E. Mnuskin, in: Pulsed Photometry [in Russian], Izd. Mashinostroenie, Leningrad (1969).

[15] A. A. Bakeev, T. I. Narozhnaya, R. E. Rovinskii, and N. N. Cheburkin, Radiotekh. Elektron., 14, 1231 (1969).

[16] Yu. G. Anikiev, R. G. Vdovchenko, M. E. Zhabotinskii, and I. S. Marshak, Opt. Spektrosk., 32, 392 (1972).

[17] V. P. Kirsanov and S. V. Troshkin, Svetotekhnika, No. 1 (1967).

[18] L. I. Gavrilova, A. S. Doinikov, S. G. Zhigach, and M. K. Molchanova, Svetotekhnika, No. 5, 14 (1971).

[19] A. S. Doinikov, E. A. Eremin, Yu. A. Kalinin, and V. K. Pakhomov, in:

Pulsed Photometry [in Russian], No. 2, Izd. Mashinostroenie, Leningrad (1972).

[20] S. I. Andreev and V. E. Gavrilov, Opt. Spektrosk., 26, 121 (1969).

[21] V. N. Vasil'eva, I. A. Grishina, Yu. K. Zemtsov, V. D. Pis'mennyi, and A. T. Rakhimov, Abstracts of reports, Third All-Union Conference on the Physics of Low-Temperature Plasmas [in Russian], Izd. MGU, Moscow (1967), p. 314.

[22] V. D. Pis'mennyi (Pismenny) and A. T. Rakhimov, Phys. Lett., 33a, 17 (1970).

[23] Ya. B. Zel'dovich and Yu. P. Raizer, Physics of Waves and High-Temperature Hydrodynamic Phenomena [in Russian], Izd. Nauka, Moscow (1966).

[24] J. H. Goncz, J. Appl. Phys., 36, 742 (1965).

[25] S. I. Andreev and V. E. Gavrilov, Zh. Tekh. Fiz., 38, 1697 (1968) [Sov. Phys.—Tech. Phys., 13, 1376 (1969)].

[26] A. A. Bakeev and R. E. Rovinskii, Teplofiz. Vys. Temp., 8, 207 (1970).

[27] I. V. Demenik, V. E. Mnuskin, B. V. Skvortsov, and V. B. Fedorov, Zh. Tekh. Fiz., 38, 1092 (1968) [Sov. Phys.—Tech. Phys., 13, 829 (1968)].

[28] S. I. Andreev and V. E. Gavrilov, Zh. Tekh. Fiz., 40, 1300 (1970) [Sov. Phys.—Tech. Phys., 15, 1002 (1970)].

[29] L. I. Gavrilova, A. S. Doinikov, and V. G. Ignat'ev, Zh. Prikl. Spektrosk., 12, 537 (1970).

[30] A. A. Bakeev, R. E. Rovinskii, and I. P. Shirokova, Opt. Spektrosk., 27, 215 (1969).

Nonlinear statistical theory of a condensate of plasmons.
II. Stochastic heating of plasma ions by large-scale Langmuir turbulence

F. Kh. Khakimov
V. I. Lenin Tadzhik State University, Dushanbe

(Submitted May 14, 1973; resubmitted September 7, 1973)
Zh. Tekh. Fiz., 44, 502-507 (March 1974)

The heating of ions due to low-frequency waves generated by a Langmuir turbulence is evaluated. The calculations are carried out under the assumption that the ion motion is one-dimensional (the ions are "magnetized").

INTRODUCTION

Low-frequency waves are known to be excited in a plasma with plasma turbulence;[1,2] when these waves interact with the plasma particles, the latter are heated. Khakimov and Tsytovich[3] analyzed the stochastic heating of electrons due to low-frequency waves generated by plasma turbulence. These authors found the spectra of a strong turbulence of low-frequency pulsations excited by plasma turbulence. In the present paper we analyze the stochastic heating of ions under the same conditions. As in ref. 3, we assume the ion motion to be one-dimensional; we assume a strong magnetic field ($\omega_{Hi} \gg \omega_{pi}$), but consider the case $v_{li} < \omega/k < v_{Te}$ and $v_{li} < v_{Ti}$, since $\omega < kv_{Ti} < k_1 v_{Ti}$, i.e., $k < k_1$, where k_1 is the wave number of the plasma waves.

The results show that the ion heating rate differs by a factor v_{Ti}/v_{Te} from the electron heating rate.

1. LINEAR THEORY OF THE MODULATION INSTABILITY

A nonlinear theory for the absorption of plasma waves is derived in ref. 3; in particular, an analysis is made of the profound change in the electromagnetic properties of a plasma at low frequencies under the influence of high-frequency turbulence. Our purpose here is to find the analytic form of the low-frequency dielectric constant of the plasma, which is a linear function of the spectral energy of the turbulence, W_{k_1,ω_1}:

$$W = \int W_{k_1,\omega_1} dk_1 d\omega_1. \tag{1}$$

Here, W is the total energy of the condensate.

To find the form of the dielectric constant we use the equation $\operatorname{div} E = 4\pi e n$ and the quasilinear equation for the distribution function, which takes account of the effect of high-frequency waves:

$$-i(\omega - kv) f^{R(1)i}_{k,\omega} = -\frac{e}{m_i} E^R_{k,\omega} \frac{\partial \Phi^i}{\partial v} + \frac{\partial}{\partial v} D_1 \frac{\partial \Phi^i}{\partial v}. \tag{2}$$

Here Φ^i is the ion distribution function for the basic turbulent state,

$$D_1 = i(\omega - kv) n^{(1)}_k \left(\frac{e}{m_i}\right)^2 \frac{\omega^2_{pi}}{n_0} \int \frac{I_{k_1,\omega_1} dk_1 d\omega_1}{\bar{\varepsilon}(k - k_1,\ \omega - \omega_1)\, \omega_1 (\omega_1 - \omega)^3} \tag{3}$$

is the diffusion coefficient, and I_{k_1,ω_1} is the correlation function for the high-frequency fluctuations.

In our case, $kv_{li} < \omega < kv_{Ti}$, for one-dimensional plasma turbulence

$$\omega_{k_1} = \omega_{pe} + \frac{3}{2} \frac{k_1 v^2_{Te}}{\omega_{pe}}$$

we have

$$\varepsilon^i(k,\ \omega) = 1 + \frac{\dfrac{\omega^2_{pi}}{k^2 v^2_{Ti}}}{1 + \dfrac{n_0}{v^2_{Ti}} d_1}, \tag{4}$$

where

$$d_1 = \left(\frac{e}{m_i}\right)^2 \frac{\omega^2_{pi}}{n_0} \int \frac{I_{k_1,\omega_1} dk_1 d\omega_1}{\bar{\varepsilon}(k - k_1,\ \omega - \omega_1)\, \omega_1 (\omega_1 - \omega)^3}. \tag{5}$$

For $kv_{li} < \omega < kv_{Te}$ we have $d_1 \approx 3k^2 v^2_{Te} W / 4n_0^2 m_e \omega^2$; then

$$\varepsilon^e(k,\ \omega) = 1 + \frac{\dfrac{\omega^2_{pe}}{k^2 v^2_{Te}}}{1 + \dfrac{3W}{4n_0 T_e} \dfrac{k^2 v^2_{Te}}{\omega^2}}. \tag{6}$$

Using (4) and (6) under the conditions $\varepsilon^e(k, \omega)$, $\varepsilon^i(k, \omega) \gg 1$, we find the dispersion relation

$$\omega^2 = -k^2 v^2_{\sim} \frac{1 + \left(\dfrac{m_e}{m_i}\right)^{1/2}}{1 + \dfrac{T_i}{T_e}}. \tag{7}$$

Here $v^2_{\sim} = 3W/4n_0 m_e$. When $\omega > kv_{\sim}(T_e/T_i)^{1/2}(m_e/m_i)^{1/4}$ we have

$$\omega^2 = -k^2 v^2_{\sim} \frac{T_e}{T_e + T_i}. \tag{8}$$

Equation (8) shows an aperiodic buildup of the waves:

$$\omega = \pm ikv_{\sim}\left(1 + \frac{T_i}{T_e}\right)^{-1/2}. \tag{9}$$

In the opposite limiting case $\omega < kv_{\sim}(T_e/T_i)^{1/2}[m_e \cdot (m_i)^{-1}]^{1/4}$,

$$\omega^2 = -k^2v_{\sim}^2\left(1 + \sqrt{\frac{m_e}{m_i}}\right). \tag{10}$$

2. EQUATION FOR THE AVERAGED DISTRIBUTION FUNCTION

Following the calculation procedure of ref. 3, and neglecting the smallness of the phase velocities of the low-frequency waves ($\omega/k \ll \omega_L/k_L$, where ω_L and k_L are the frequency and wave number of the plasma waves), we find an equation for Φ which takes account of the average effect of both the high-frequency and low-frequency waves:

$$\frac{\partial\Phi}{\partial t} + v\frac{\partial\Phi}{\partial z} = I_1 + I_2, \tag{11}$$

where

$$I_1 = -\frac{e}{m_i}\left\langle E^R \frac{\partial f^{R(1)}}{\partial v}\right\rangle_l = -\frac{e}{m_i}\frac{\partial}{\partial v}\int \left\langle E^R_{k',\omega'} f^{R(1)}_{k,\omega}\right\rangle_l dk\,dk'\,d\omega\,d\omega', \tag{12}$$

$$\begin{aligned} I_2 &= -\frac{e}{m_i}\left\langle E^{T(1)} \frac{\partial f^{T(1)}}{\partial v}\right\rangle_{h,l} \\ &= -\frac{e}{m_i}\frac{\partial}{\partial v}\int \left\langle E^{T(1)}_{k_1'',\omega_1''} f^{T(1)}_{k_1',\omega_1'}\right\rangle_{h,l} dk_1'\,dk_1''\,d\omega_1'\,d\omega_1'', \end{aligned} \tag{13}$$

and "h" and "l" denote averages over high and low frequencies.

The first quasilinear integral I_1 takes account of the correlation of low-frequency fluctuations, while I_2 takes account of the effect of high-frequency fields on the low-frequency fields and vice versa.

To determine I_1 we must know the exact form of distribution function $f^{R(1)}_{k,\omega}$.

However, we note that the correction to the ion distribution function due to the high-frequency fields turns out to be smaller than the electron correction, so that the ion distribution function is

$$f^{R(1)}_{k,\omega} = -i\frac{e}{m_i}\frac{E^R_{k,\omega}}{\omega - kv}\frac{\partial\Phi}{\partial v}. \tag{14}$$

Substituting this quantity into (12) we find

$$\begin{aligned} I_1 &= i\left(\frac{e}{m_i}\right)^2\frac{\partial}{\partial v}\int \frac{\left\langle E^R_{k,\omega}E^R_{k',\omega'}\right\rangle l}{\omega - kv}\frac{\partial\Phi}{\partial v}\,dk\,dk'\,d\omega\,d\omega' \\ &= 4\pi i\left(\frac{e}{m_i}\right)^2\frac{\partial}{\partial v}\int \frac{w_{k,\omega}}{\omega - kv}\frac{\partial\Phi}{\partial v}\,dk\,d\omega \\ &= \frac{4\pi^2e^2}{m_i^2}\frac{\partial}{\partial v}\int w_{k,\omega}\delta(\omega - kv)\frac{\partial\Phi}{\partial v}\,dk\,d\omega. \end{aligned} \tag{15}$$

The second quasilinear collison integral I_2 can be determined by using the expression for the linear part of $f^{T\,(1)}_{k,\omega}$ (ref. 4). Then we find

$$\begin{aligned} I_2 &= i\left(\frac{e}{m_i}\right)^2\frac{\partial}{\partial v}\int \frac{\left\langle E^{T(1)}_{k_1'',\omega_1''}E^{T(1)}_{k_1',\omega_1'}\right\rangle}{\omega_1' - k_1'v}\frac{\partial\Phi}{\partial v}\,dk_1'\,dk_1''\,d\omega_1'\,d\omega_1'' \\ &= i\left(\frac{e}{m_i}\right)^2\frac{\partial}{\partial v}\int \frac{\left|E^{T(1)}_{k_1',\omega_1'}\right|^2}{\omega_1' - k_1'v}\frac{\partial\Phi}{\partial v}\delta(k_1' + k_1'')\,\delta(\omega_1' + \omega_1'')\,dk_1'\,dk_1''\,d\omega_1'\,d\omega_1'' \\ &= i\left(\frac{e}{m_i}\right)^2\frac{\partial}{\partial v}\int \frac{\left|E^{T(1)}_{k_1',\omega_1'}\right|^2}{\omega_1' - k_1'v}\frac{\partial\Phi}{\partial v}\,dk_1'\,d\omega_1' \\ &= -\pi\left(\frac{e}{m_i}\right)^2\frac{\partial}{\partial v}\int \delta(\omega_1' - k_1'v)\frac{\partial\Phi}{\partial v}\left|E^{T(1)}_{k_1',\omega_1'}\right|^2 dk_1'\,d\omega_1'. \end{aligned} \tag{16}$$

On the other hand, it is known that[3]

$$\left|E^{T(1)}_{k_1,\omega_1}\right|^2 = \frac{\omega_{pi}^6}{n_0^3 m_i}\frac{1 + 2\xi}{(1 + \xi)^2}I_{k_1,\omega_1}\int \frac{w_{k',\omega'}\,dk'\,d\omega'}{\left|\bar{\varepsilon}(k_1 - k', \omega_1 - \omega')\right|^2}\frac{\left|C_{k',\omega'}\right|^2}{(\omega_1 - \omega')^4}, \tag{17}$$

where

$$\xi = \frac{n_0 m_i}{T_e + T_i}d_2, \quad d_2 = \left(\frac{e}{m_i}\right)^2\frac{\omega_{pi}^2}{n_0}\int \frac{I_{k_1,\omega_1}\,dk_1\,d\omega_1}{\bar{\varepsilon}(k - k_1, \omega - \omega_1)\,\omega_1^2(\omega_1 - \omega)^2}. \tag{18}$$

Using these results, we can compare I_1 and I_2. Using (17) and carrying out the corresponding lengthy but straightforward calculations, we find that I_2 differs by a factor of $(W/nT)(kv_{Te}/\omega)^2(m_e/m_i)^2$ from I_1 in our case. From the condition that the spectral distribution $w_{k,\omega}$ reach a maximum at $\omega/(kv_{Te}) \sim 1$ we find

$$\frac{I_2}{I_1} \sim \frac{W}{nT}\left(\frac{m_e}{m_i}\right)^2 \ll 1.$$

Accordingly, from Eq. (15) we can determine the ion heating rate if we know $w_{k,\omega}$.

3. EQUATION FOR THE CORRELATION FUNCTION FOR LOW-FREQUENCY FLUCTUATIONS

To determine the specific form of $w_{k,\omega}$, which takes account of the nonlinear response of the plasma to a low-frequency perturbation, we must first find $f^{R(2)}_{k,\omega}$, which is a quadratic function of E^R:

$$\begin{aligned} f^{R(2)}_{k,\omega} &= -i\left(\frac{e}{m_i}\right)\frac{1}{\omega - kv}\frac{\partial}{\partial v}\int \left(E^R_{k_1,\omega_1}f^{R(1)}_{k_2,\omega_2} - \left\langle E^R_{k_1,\omega_1}f^{R(1)}_{k_2,\omega_2}\right\rangle\right) \\ &\quad \times \delta(k - k_1 - k_2)\,\delta(\omega - \omega_1 - \omega_2)\,dk_1\,dk_2\,d\omega_1\,d\omega_2 \\ &\quad + \frac{an^{(2)}_{k,\omega}}{\omega - kv}\frac{\partial}{\partial v}(\omega - kv)\frac{\partial\varphi}{\partial v}, \end{aligned} \tag{19}$$

where

$$a = \frac{d_1}{1 + \xi}, \quad d_1 = \left(\frac{e}{m_i}\right)^2\frac{\omega_{pi}^2}{n_0}\int \frac{I_{k_1,\omega_1}\,dk_1\,d\omega_1}{\bar{\varepsilon}(k - k_1, \omega - \omega_1)\,\omega_1(\omega_1 - \omega)^3}. \tag{20}$$

Using the equation $E^R_{k,\omega} = (4\pi ie/k)(n^e_{k,\omega} - n^i_{k,\omega})$ and Eq. (19), after lengthy but straighforward calculations analogous to those of ref. 3, we find an equation for the correlation functions of the low-frequency waves:

$$v_\lambda = v_{\lambda e} + v_{\lambda i},$$

where $v_{\lambda e}$ is the electron correlation function described by Eq. (30) of ref. 3, and

$$v_{\lambda i} = \int\limits_0^\lambda \frac{d\lambda_1}{\lambda_1^4} \int\limits_\lambda^{\lambda_1} \frac{\lambda_1 - \lambda_2}{\lambda_2^4 (\lambda - \lambda_1)(\lambda - \lambda_2)} v_{\lambda_1, k_1} v_{\lambda_2, k_2} d\lambda_2 \tag{21}$$

is the equation for the ion correlation function, where

$$\lambda_i = \frac{\omega}{kv_{Ti}}, \quad \lambda_0^2 = \frac{3W}{4n_0 T_e}, \quad v_{\lambda, k} = \frac{\omega_{pi}^2}{2\pi n_0 m_i v_{Ti}^2} w_{k, \omega}.$$

Let us consider the case $\omega/k < v_{Ti}$ and $\omega_1/k_1 > v_{Ti}$, i.e., the case in which ions interact with electrons with large phase velocities, $\omega/k \gg v_{Te}$. Using the form of the correlation function for the electrons, $v_{\lambda e} \simeq \lambda_e^4/\lambda_0^4$, we seek a solution of Eq. (21) in the form

$$v_{\lambda_i} \simeq \left(\frac{m_e}{m_i}\right)^4 \frac{\lambda_i^4}{\lambda_0^8} = \text{const.} \tag{22}$$

In this case we find $v_{\lambda i} \gg v_{\lambda e}$.

Multiplying Eq. (1) by $(mv^2/2)$, integrating over all velocities, and using the solution of Eq. (21), we find the particle heating rate to be

$$\begin{aligned} \frac{d(n_0 T_i)}{dt} &= \frac{\omega_{pi}^2}{n_0} \int w_{k,\omega} v \delta(\omega - kv) \frac{\partial \Phi^i}{\partial v} dk d\omega dv \\ &\simeq n_0 T_i k_{\max} v_{Ti} \lambda_{i\max} \approx n_0 T_i k_{\max} v_{Te} \frac{v_{Ti}}{v_{Te}}. \end{aligned} \tag{23}$$

Using[3]

$$\frac{k_{\max} v_{Te}}{\omega_{pe}} = \left(\frac{W}{nT_e}\right)^{1/2} \xi',$$

where $\xi' = \sqrt{(m_e/m_i)(T_i/T_e)}$, we find the following estimate for the ion heating rate:

$$\frac{1}{nT_i} \frac{d}{dt}(nT_i) = \frac{v_{Ti}}{v_{Te}} \xi' \left(\frac{W}{nT_e}\right)^{1/2} \omega_{pe}. \tag{24}$$

in other words, the ion heating rate is v_{Ti}/v_{Te} times the electron heating rate.

4. EFFECT OF MODULATED WAVES WITH LOW PHASE VELOCITIES ON THE LINEAR PROPERTIES OF THE CONDENSATE

We turn now to the question of how the linear properties of the condensate are affected by the excitation of modulated waves with $\omega < kv_{Ti}$. In analyzing the linear properties of a condensate of plasmons, we take account only of the response $f^T_{k,\omega}$, which is linear in $E^1_{k,\omega}$. We must first find an equation for the correlation function of the high-frequency fluctuations:

$$\langle E^T_{k,\omega} E^T_{k',\omega'} \rangle_h = I_{k,\omega} \delta(k + k') \delta(\omega + \omega'), \tag{25}$$

where

$$I_{k,\omega} = -\frac{4\pi ie}{k} \int \langle E^T_{k',\omega'} f^T_{k,\omega} \rangle dk' d\omega' dv. \tag{26}$$

Now we expand all the quantities $E^T_{k,\omega}$ and $f^T_{k,\omega}$ in series in E^R and retain only the linear terms:

$$E^T_{k,\omega} = E^{T(0)}_{k,\omega} + E^{T(1)}_{k,\omega}, \quad f^T_{k,\omega} = f^{T(0)}_{k,\omega} + f^{T(1)}_{k,\omega}, \tag{27}$$

where "(0)" and "(1)" designate the ground turbulent state and the deviation from it.

Using the following equation[4] for $f^{T(0)}_{k,\omega}$,

$$f^{T(0)}_{k,\omega} = -i \frac{e}{m_i} \frac{E^{T(0)}_{k,\omega}}{\omega - kv} \frac{\partial \Phi^i}{\partial v}, \tag{28}$$

and substituting it into (20), we find

$$\varepsilon_{k,\omega} I_{k,\omega} = 0, \tag{29}$$

where

$$\varepsilon_{k,\omega} = 1 + \frac{\omega_{pi}^2}{n_0 k} \int \frac{1}{\omega - kv} \frac{\partial \Phi^i}{\partial v} dv \approx 1 + \frac{\omega_{pi}^2}{k^2 v_{Ti}^2}$$

is the ordinary linear dielectric constant.

However, in (28) we have taken account only of the linear functional dependence; we have neglected the effect of low-frequency modulated waves.

We now take into account the effects of low-frequency modulated waves:

$$\begin{aligned} \delta f^{T(0)}_{k,\omega} = &-i\left(\frac{e}{m_i}\right) \frac{1}{\omega - kv} \frac{\partial}{\partial v} \int \left(E^{T(1)}_{k_1,\omega_1} f^{R(1)}_{k_2,\omega_2} + E^R_{k_2,\omega_2} f^{T(1)}_{k_1,\omega_1}\right) \\ &\times \delta(k - k_1 - k_2) \delta(\omega - \omega_1 - \omega_2) dk_1 dk_2 d\omega_1 d\omega_2 \end{aligned} \tag{30}$$

and

$$\begin{aligned} f^{T(1)}_{k,\omega} = &-i \frac{e}{m_i} \frac{E^{T(1)}_{k,\omega}}{\omega - kv} \frac{\partial \Phi}{\partial v} - i \frac{e}{m_i} \frac{1}{\omega - kv} \frac{\partial}{\partial v} \int \left(E^{T(0)}_{k_1,\omega_1} f^{R(1)}_{k_2,\omega_2} + E^R_{k_1,\omega_1} f^{T(0)}_{k_2,\omega_2}\right) \\ &\times \delta(k - k_1 - k_2) \delta(\omega - \omega_1 - \omega_2) dk_1 dk_2 d\omega_1 d\omega_2 \end{aligned}$$

or

$$\delta f^{T(0)}_{k,\omega} = -\frac{4\pi e^2}{m_i^2} \frac{1}{\omega - kv} \frac{\partial}{\partial v} \int \frac{w_{k_1,\omega_1} dk_1 d\omega_1}{\omega - \omega_1 - (k - k_1) v} \frac{\partial f^{T(0)}_{k,\omega}}{\partial v} -$$

$$-\left(\frac{e}{m_i}\right)^2\frac{1}{\omega-kv}\frac{\partial}{\partial v}\int\frac{1}{\omega-\omega_1-(k-k_1)v}\frac{\partial}{\partial v}\left\langle E^R_{k_1,\omega_1}E^{T(0)}_{k_2,\omega_2}f^{R(1)}_{k_3,\omega_3}\right\rangle_l$$
$$\times\,\delta(k-k_1-k_2-k_3)\,\delta(\omega-\omega_1-\omega_2-\omega_3)\,dk_1dk_2dk_3d\omega_1d\omega_2d\omega_3$$
$$-\,i\left(\frac{e}{m_i}\right)\frac{1}{\omega-kv}\frac{\partial}{\partial v}\int\left\langle E^{(T(1)}_{k,\omega}\left(f^{R(1)}_{k_2,\omega_2}-i\frac{e}{m_i}\frac{E^R_{k_2,\omega_2}}{\omega_1-k_1v}\frac{\partial\Phi}{\partial v}\right)\right\rangle_l$$
$$\times\,\delta(k-k_1-k_2)\,\delta(\omega-\omega_1-\omega_2)\,dk_1dk_2d\omega_1d\omega_2, \qquad (32)$$

where w_{k_1,ω_1} is the correlation function for low-frequency waves, introduced in the equation

$$\langle E^R_{k,\omega}E^R_{k',\omega'}\rangle_l = 4\pi w_{k,\omega}\delta(k+k')\delta(\omega+\omega'). \qquad (33)$$

Now substituting (32) into (26) and setting $E^T_{k,\omega} = E^{T(0)}_{k,\omega}$, we find the corrections to the linear part of the dielectric constant due to the effect of modulated waves. The correction due to the first two terms in (32) is small because $W/nT \ll 1$, as in ref. 3.

The basic change comes from the third term in (32), which makes the following contribution to the right side of (26):

$$-\frac{4\pi e^2}{m_i^2k}\int\frac{dv}{\omega-kv}\left\langle\!\left\langle E^{T(0)}_{k',\omega'}E^{T(1)}_{k_1-k',\,\omega_1'-\omega'}\right\rangle_h\frac{\partial}{\partial v}\left(f^{R(1)}_{k_2,\omega_2}-i\frac{e}{m_i}\frac{E^R_{k_2,\omega_2}}{\omega_1-k_1v}\frac{\partial\Phi}{\partial v}\right)\right\rangle_l$$
$$\times\,\delta(k-k_2-k_1'+k')\,\delta(\omega-\omega_2-\omega_1'+\omega')\,dk_1dk_2dk'd\omega'd\omega_1d\omega_2. \qquad (34)$$

Neglecting the second term because of the large quantity $\omega-\omega_2$, using the value $\langle E^{T(0)}_{k',\omega'}E^{T(1)}_{k_1'-k',\omega_1'-\omega'}\rangle_h$ from ref. 3, and assuming $f^{R(1)}_{k,\omega}$ to be a linear function of E^R, we find the following equation from (26) for the correction to the dielectric constant which takes account of the modulated waves:

$$\varepsilon^R_{k,\omega}=\frac{\omega^2_{pi}}{n_0^3m_i}\int|C_{k',\omega'}|^2\frac{w_{k',\omega'}dk'd\omega'}{\tilde{\varepsilon}(k-k',\,\omega-\omega')}, \qquad (35)$$

where

$$C_{k',\omega'}=\int\frac{1}{\omega'-k'v}\frac{\partial\Phi^i}{\partial v}dv. \qquad (36)$$

We see from Eq. (35) that the absorption of plasma waves is due to only the imaginary part of $1/\tilde{\varepsilon}(k-k',\,\omega-\omega')$. As in the case of electrons, when we neglect the nonlinear correction to $\tilde{\varepsilon}$, we find that the damping of the condensate is due to a wave resonance of the condensate plasmons and modulation waves.

5. DISCUSSION OF RESULTS

The results found here can be compared with the heating of plasma ions observed experimentally under beam−plasma interaction conditions in Q machines.[5] According to ref. 5, we have a ratio $T_i/T_e \simeq 0.1$-0.25 at various electron temperatures. Calculations based on the equation

$$\frac{T_e}{T_i}=(\omega_{pe}t)^2\frac{W}{nT_e}\left(\frac{m_e}{m_i}\right)\xi'^2 \qquad (37)$$

for a turbulence energy level[5] of $W/(nT_e) = 10^{-2}$-10^{-3}, for the value $\xi' \simeq 10^{-4}$, and under the assumption $t = L/v_{Ti}$, (where L is the length of the apparatus) lead to

$$\frac{T_i}{T_e}\simeq 0.2.$$

We see that the theoretical result agrees satisfactorily with experiment.

In conclusion the author thanks V. N. Tsytovich for interest in this work and for discussion of these results.

---

[1] A. A. Vedenov and L. I. Rudakov, Dokl. Akad. Nauk SSSR, 159, 767 (1964) [Sov. Phys.−Dokl., 9, 1073 (1965)].

[2] A. Gailitis, Izv. AN LatvSSR, Ser. Fiz.−Tekh. Nauk, 4, 13 (1965).

[3] F. Kh. Khakimov and V. N. Tsytovich, Zh. Eksp. Teor. Fiz., 64, 1261 (1973).

[4] V. N. Tsytovich, Theory of a Turbulent Plasma [in Russian], Atomizdat, Moscow (1971).

[5] V. T. Astrelin, N. S. Buchel'nikova, and A. M. Kudryavtsev, Zh. Tekh. Fiz., 40, 1185 (1970) [Sov. Phys.− Tech. Phys., 15, 915 (1970)].

Plasma

Surface waves in a magnetized plasma in a radio-frequency field

E. E. Lovetskii and A. N. Starodub

Moscow Engineering-Physics Institute

(Submitted February 8, 1973)
Zh. Tekh. Fiz., 44, 508-513 (March 1974)

The effect of an external radio-frequency electric field (rf field) on the surface waves of a magnetized plasma is analyzed. A strong rf field can lead to stabilization or to a change in the growth region. The parametric excitation of low-frequency surface waves by an rf field is analyzed.

When a plasma is confined by an external magnetic field, surface waves can exist and grow at the plasma–vacuum boundary.[1,2] The basic mechanism for the growth of these waves is charge convection in the field of the wave; this phenomenon is very important in low-frequency waves, i.e., frequencies below the ion plasma frequency. It has been shown that crossing of the magnetic lines of force does not always effectively stabilize surface waves. For this reason we turn to an analysis of the possibility of suppressing surface-wave instabilities by an rf electric field. Electron oscillations in an rf field lead to spatial dispersion, which is one of the mechanisms by which an rf field affects plasma waves. Fainberg and Shapiro[3] analyzed the effect of an rf field on plasma drift waves with wavelengths small in comparison with the characteristic scale of the inhomogeneity; they found that a strong rf field stabilizes oscillations with $\omega \gg k_z v_{Te}$ and changes the instability region for frequencies $\omega \ll k_z v_{Te}$. The effect of an rf field on the low-frequency surface-wave spectra is similar.

It is known that an rf field can parametrically excite surface waves in a plasma.[4,5] Below we focus on the resonant interaction of an rf field with surface waves. We find that under these conditions surface waves can grow rapidly, with growth rates exceeding the ion plasma frequency.

1. We consider electrostatic surface waves of a plasma at its interface with a vacuum. The plane boundary is perpendicular to the x axis. The plasma is in a fixed, homogeneous magnetic field **B** and an rf electric field $\mathbf{E}(t) = \mathbf{E}_0 \sin \omega_0 t$, both of which are parallel to the plasma boundary, along the z axis. We assume that in the region of the smeared-out boundary the plasma is slightly inhomogeneous, i.e., that the Larmor radii of the particles are small in comparison with the characteristic dimension of the plasma inhomogeneity, L. For a slightly inhomogeneous plasma we can use the standard procedure of solving the kinetic equations and obtain the Poisson equation in the following form for the Fourier coefficients of the electric potential:

$$\Delta\Phi_s = \sum_{n,\,p=-\infty}^{\infty} \int dk_x e^{ik_x x} \Phi_p(k_x) M(k_x,\ x,\ \omega_n) J_{n-s}(\mu) J_{n-p}(\mu), \quad (1)$$

where the kernel $M(k_x, x, \omega_n)$ differs from that found in ref. 6 by the replacement $\omega \to \omega_n = \omega + n\omega_0$, $J_p(\mu)$ is the Bessel function with argument $\mu = k_z E_0/\omega_0^2\,(e_i/M + e/m)$, and the electric potential is written in the form $\Phi = \sum_{s=-\infty}^{\infty} \Phi_s \cdot e^{-i(\omega + s\omega_0)t}$. A summation over the different types of particles is also carried out in Eq. (1).

The wavelength of the surface waves is large in comparison with the characteristic scale of the inhomogeneity and even larger in comparison with the Larmor radii of the particles. Under these conditions, integrodifferential equation (1) reduces to a second-order differential equation for Φ_s.

According to the standard procedure for obtaining the dispersion relation for surface waves, we should substitute the solutions of the Poisson equation in the homogeneous regions on the two sides of the boundary into the boundary conditions. We find the boundary conditions on the potential by integrating the Poisson equation along x in the inhomogeneous region. The dispersion relation is found by setting the following determinant equal to zero:

$$\left| \delta_{np} - \frac{\Delta\varepsilon_{in}}{1+\Delta\varepsilon_{in}} \sum_q \frac{\Delta\varepsilon_{eq}}{1+\Delta\varepsilon_{eq}} J_{p-q}(\mu) J_{n-q}(\mu) \right| = 0, \quad (2)$$

where

$$\Delta\varepsilon_n = \frac{1}{2(\varkappa + k_0)} \frac{\omega_L^2}{\Omega^2} \left\{ \varkappa + \left(\varkappa + 2k_y \frac{\Omega}{\omega_n}\right) J_+\left(\frac{\omega_n}{|k_z| v_T}\right) \right.$$
$$\left. - \omega_n \left[\frac{\varkappa + k_y}{\omega_n - \Omega} J_+\left(\frac{\omega_n - \Omega}{|k_z| v_T}\right) + \frac{\varkappa - k_y}{\omega_n + \Omega} J_+\left(\frac{\omega_n + \Omega}{|k_z| v_T}\right) \right] \right\},$$
$$J_+(x) = x e^{-x^2/2} \int_{i\infty}^{x} d\tau e^{\tau^2/2}, \quad \omega_L^2 = \frac{4\pi N e^2}{m}, \quad \Omega = \frac{eB}{mc},$$

and $k_0^2 = k_y^2 + k_z^2$. The quantity $\varkappa$, which represents the reciprocal of the wavelength in the homogeneous region, is defined by

$$\left| \delta_{np} - \frac{\Delta\sigma_{in}}{1+\Delta\sigma_{in}} \sum_q \frac{\Delta\sigma_{eq}}{1+\Delta\sigma_{eq}} J_{p-q}(\mu) J_{n-q}(\mu) \right| = 0, \quad (3)$$

where

$$\Delta\sigma_n = \frac{\omega_L^2}{v_T^2(\varkappa^2 - k_0^2)} \left[J_+\left(\frac{\omega_n}{|k_z| v_T}\right) - 1 \right]$$
$$+ \frac{\varkappa^2 - k_y^2}{\varkappa^2 - k_0^2} \frac{\omega_L^2}{\Omega^2} \left[J_+\left(\frac{\omega_n}{|k_z| v_T}\right) - \frac{\omega_n}{\omega_n - \Omega} J_+\left(\frac{\omega_n - \Omega}{|k_z| v_T}\right) - \frac{\omega_n}{\omega_n + \Omega} J_+\left(\frac{\omega_n + \Omega}{|k_z| v_T}\right) \right].$$

Solving system (2), (3), we can analyze the surface waves of a magnetized plasma in an rf field. If we assume $\omega_0 \gg \omega_{Li}, \Omega_i$, we can simplify system (2), (3), finding

$$\left. \begin{aligned} 1 - \frac{\Delta\varepsilon_{i0}}{1+\Delta\varepsilon_{i0}} \sum_n \frac{\Delta\varepsilon_{en} J_n^2}{1+\Delta\varepsilon_{en}} = 0, \\ 1 - \frac{\Delta\sigma_{i0}}{1+\Delta\sigma_{i0}} \sum_n \frac{\Delta\sigma_{en} J_n^2}{1+\Delta\sigma_{en}} = 0. \end{aligned} \right\} \quad (4)$$

We will analyze this system of equations for two frequency ranges of the surface waves. When $\omega \lessgtr \omega_{Li}$, surface waves of the magnetized plasma can grow in the absence of an external rf field. We therefore turn to the stabilizing effect of the rf field for such waves. Furthermore, surface waves can be parametrically excited by an external rf field. We consider the parametric effect of an rf field on high-frequency surface waves ($\omega \gg \omega_{Li}$) which are stable in the absence of an rf field.

2. The analysis of the stabilizing effect of the rf field on the low-frequency surface waves ($\omega \lesssim \omega_{Li}$) is simplified considerably if the frequency of the rf field is higher than that used in deriving Eqs. (4): $\omega_0 \gg \omega_{Li}^2/\Omega_i, k_z v_{Te} \cdot (\omega_{Li}/\Omega_i)$. This situation corresponds primarily to the case of a dense plasma, with $\omega_{Li} \gg \Omega_i$. In a low-density plasma, we require $\omega_0 \gg k_z V_{Te}$. Furthermore, the plasma densities are limited from above by the condition $\omega_{Le} \ll \Omega_e$. Then we are left with only the n = 0 terms in the sums of Eqs. (4).

We begin the analysis of Eqs. (4) simplified in this manner with the case in which the electron thermal velocity is large in comparison with the plane velocity of the waves, i.e., when $\omega \ll k_z v_{Te}$. In this frequency range, growing ion-acoustic surface waves can exist in the absence of an rf field.[1,2] The rf field modifies the wave spectra slightly and the conditions under which the waves exist.

In a dense plasma, $\omega_{Li} \gg \Omega_i$, surface ion-acoustic waves can exist only in the nonisothermal case $T_e \gg T_i$ at a frequency $\omega \lesssim \Omega_i$ under the condition $k_y > k_z \gg k_y \cdot (m/M)^{1/2}$. The presence of an rf field can change this latter condition: If the field is so strong that $1-J_0^2 \simeq 1$, this condition becomes $k_z \gg k_y\,(\omega_{Le}/\Omega_e)$. The spectrum of surface ion-acoustic waves in the presence of an rf field is

$$\left.\begin{aligned}\omega^2 &= \frac{1}{2}\{k_0^2 v_s^2 + \Omega_i^2 + \omega_{Li}^2(1-J_0^2)\\ &\pm \sqrt{[k_0^2 v_s^2 + \Omega_i^2 + \omega_{Li}^2(1-J_0^2)]^2 - 4k_0^2 v_s^2 \Omega_i^2}\},\\ \gamma &= \sqrt{\frac{\pi}{2}}\frac{\omega^2}{|k_z| v_{Te}}\frac{\Omega_i^2-\omega^2}{k_0^2 v_s^2 \Omega_i^2 - \omega^4}\left\{k_0^2 v_s^2 - \frac{\omega^2}{2}\left[1 + \frac{\omega_{Li}^2}{\omega^2-\Omega_i^2}(1-J_0^2)\right.\right.\end{aligned}\right\} \quad (5)$$

where $v_s^2 = T_e/M$. It follows from (5) that an external rf field does not stabilize surface ion-acoustic waves, but it can significantly change the shape of the spectrum. In particular, under the condition $\omega_{Li}^2(1-J_0^2) \gg \Omega_i^2$, we can write (5) as

$$\omega^2 = \frac{k_0^2 v_s^2 \Omega_i^2}{k_0^2 v_s^2 + \omega_{Li}^2(1-J_0^2)}, \quad \gamma = \sqrt{\frac{\pi}{8}}\frac{\omega^2}{|k_z| v_{Te}}\frac{k_0^2 v_s^2(\Omega_i^2-\omega^2)}{k_0^2 v_s^2 \Omega_i^2 - \omega^4}. \qquad (6)$$

In a low-density plasma with $\omega_{Li} \ll \Omega_i$, growing surface ion-acoustic waves can also exist. The frequency of these waves is low in comparison with the ion gyrofrequency and is given by

$$\omega = -\frac{k_y \omega_{Li}^2}{|k_y| \Omega_i \left[1 + \left(1 + \frac{\omega_{Li}^2}{k_y^2 v_s^2}\right)^{1/2}\right]}, \quad \gamma = \sqrt{\frac{\pi}{2}}\frac{\omega^2}{|k_z| v_{Te}} J_0^2. \qquad (7)$$

These waves can exist under the conditions

$$k_y \frac{\omega_{Li}}{\Omega_i} \gg k_z \gg \frac{k_y \omega_{Li}^2}{|k_y| v_{Te} \Omega_i \left[1 + \left(1 + \frac{\omega_{Li}^2}{k_y^2 v_s^2}\right)^{1/2}\right]} \text{ and } \frac{T_i}{T_e} \ll \frac{\Omega_i^2}{\omega_{Li}^2}.$$

The first of these conditions holds for $k_y v_{Te} \gg \omega_{Li}$; it follows from the second condition that the waves can occur even in an isothermal plasma. The growth rate of the waves falls off with increasing rf fields.

We turn now to the range of wave frequencies which are considerably higher than the ion gyrofrequency but which still satisfy $\omega \lesssim \omega_{Li}$. Surface waves exist in this frequency range in a highly nonisothermal plasma under the condition $T_i/T_e \ll \Omega_i^2/\omega_{Li}^2$; their spectrum can be conveniently found for the two limiting cases $k_y v_s \gg \omega_{Li}$ and $k_y v_s \ll \omega_{Li}$.

If $k_y v_s \gg \omega_{Li}$, we have

$$\omega^2 = \frac{\omega_{Li}^2}{2}\left[1 - \frac{a(a+1)}{a^2+1} J_0^2\right], \qquad (8)$$

where

$$a = \sqrt{\frac{\pi}{8}}\frac{k_y}{|k_y|}\frac{\omega_{Li}^2}{|k_z| v_{Te} \Omega_i}.$$

An increase in the amplitude of the rf field reduces the growth rate of the waves in (8).

If $k_y v_s \ll \omega_{Li}$, the surface-wave spectrum has the following form:

$$\omega^2 = \omega_{Li}^2 \frac{1 + b(1-J_0^2)}{1+b}, \quad \gamma \sqrt{\frac{\pi}{8}}\frac{\omega_{Li}^2}{|k_z| v_{Te}}\frac{bJ_0^2}{(1+b)^2}, \qquad (9)$$

where

$$b = \frac{\pi}{2}\frac{k_y^2}{k_z^2}\frac{\omega_{Le}^2}{\Omega_e^2}.$$

An increase in the amplitude of the rf field can lead to a stabilization of waves (9), as in the case of spectrum (8).

We turn now to surface waves in the case in which the electron thermal velocity is lower than the phase velocity of the waves, i.e., $\omega \gg k_z v_{Te}$. The frequency of these waves must be small in comparison with the ion gyrofrequency.

We first assume a dense plasma: $\omega_{Li} \gg \Omega_i$. If $\varkappa = |k_y|$, and if $\alpha \gg \Omega_i^2/(k_y^2 v_s^2)$, where

$$\alpha = \frac{k_y}{|k_z|}\left(\frac{m}{M}\right)^{1/2},$$

the dispersion relation becomes

$$\omega^3 - \omega\frac{\omega_{Li}^2}{2}(1-J_0^2) - \frac{k_y}{|k_y|} k_z^2 v_{Te}^2 \Omega_i = 0, \qquad (10)$$

from which we see that unstable solutions are possible only when the electron thermal motion is taken into account, for which case the condition

$$12\sqrt{3}\, k_z^2 v_{Te}^2 \Omega_i \gg \omega_{Li}^2 \mu^3 \qquad (11)$$

must hold.

The maximum growth rate of the waves is of order $(k_z^2 v_{Te}^2 \Omega_i)^{1/3}$. If the condition opposite to (11) holds, the plasma is stable because of the influence of the rf field. The critical amplitude of the rf field – above which these waves do not grow – is

$$\frac{m\omega_0^2}{ek_z\omega_{Li}}\left(12\sqrt{3}k_z^2v_{Te}^2\Omega_i\right)^{1/3}.$$

If α is much smaller than $[\Omega_i/(k_yv_s)]^2$ but still large, we have the following surface-wave spectrum:

$$\omega^2=-i\frac{\alpha k_z^2v_{Te}^2}{1+\alpha^2\frac{\omega_{Li}^2}{\Omega_i^2}(1-J_0^2)}. \tag{12}$$

It follows from this expression that the waves become stabilized by the external rf field under the condition $\alpha(\omega_{Li}^2/\Omega_i^2)(1-J_0^2) \gtrsim 1$, i.e., when the field amplitude reaches

$$E_0\sim\frac{m\omega_0^2\Omega_i}{ek_z\omega_{Li}}\left(\frac{2}{\alpha}\right)^{1/2}.$$

For a low-density plasma, $\omega_{Li} \ll \Omega_i$, we consider two possibilities: First, if $\varkappa = |k_y|$, i.e., if $\alpha \gg \Omega_i\omega_{Li}/(k_y^2v_s^2)$, the dispersion relation is

$$\omega^3-\frac{\omega}{4}\frac{\omega_{Li}^4}{\Omega_i^2}(1-J_0^2)-\frac{1}{2\Omega_i}k_z^2v_{Te}^2\omega_{Li}^2=0. \tag{13}$$

This equation has a solution corresponding to growth under the condition $12\sqrt{6}k_z^2v_{Te}^2 > (\omega_{Li}^4/\Omega_i^2)\mu^3$. The maximum growth rate of the waves in this case turns out to be on the order of $(k_z^2v_{Te}^2\omega_{Li}^2/\Omega_i)^{1/3}$. The waves are stabilized when the rf field exceeds an ampltitude

$$\frac{m\omega_0^2}{ek_z}\left(12\sqrt{6}\frac{k_z^2v_{Te}^2\Omega_i^2}{\omega_{Li}^4}\right)^{1/3}.$$

Second, if $\alpha \ll \omega_{Li}\Omega_i(k_y^2v_s^2)$ but $\alpha \gg \Omega_i/\omega_{Li}$, the plasma is unstable with respect to the excitation of surface waves having the spectrum

$$\omega^2=-i\frac{\omega_{Li}}{\Omega_i}\frac{\alpha k_z^2v_{Te}^2}{1+\alpha^2\frac{\omega_{Li}^2}{\Omega_i^2}(1-J_0^2)}. \tag{14}$$

If the amplitude of the external rf field reaches the order of $m\omega_0^2/(ek_z)(\Omega_i/\alpha\omega_{Li})^{1/2}$, the waves in (14) are stabilized, since a condition for their existence, $\omega \gg k_zv_{Te}$ is violated.

3. We turn now to the question of a parametric excitation of surface waves in a magnetized plasma by an external rf field. In the absence of an external field, there is a parametric buildup[4] of surface waves in a cold plasma at the resonance frequency $\omega_{Le}/\sqrt{2}$. In a magnetized plasma, with $\Omega_e^2 \gg \omega_{Le}^2$, we can determine the resonant frequency $\omega_r = (\omega_{Li}^2/\Omega_i)(k_y/k_0+\varkappa)$ from the first equation in (4). As the external frequency ω_0 or its harmonic $n\omega_0$ approaches the resonant frequency, the n-th term in dispersion relation (4) increases in magnitude and can become much higher than the other terms of the series, with the possible exception of the zeroth term. Here the dispersion relation simplifies considerably, since only the zeroth and n-th terms are retained in the sum.

We first consider surface waves having a frequency $\omega \gg \omega_{Li}, \Omega_i$. For such frequencies it follows from the second equation in (4) that

$$\varkappa^2=k_0^2+\frac{\omega_{Li}^2}{v_s^2}\left[1-J_+\left(\frac{\omega}{|k_z|v_{Te}}\right)\right]. \tag{15}$$

The corresponding dispersion relation can be written

$$\omega^3-n\omega_0\xi_n\omega^2+\frac{\varkappa}{k_y}\Omega_i\omega_r^2J_n^2=0, \tag{16}$$

where the detuning is $\xi_n = (\omega_r/n\omega_0)-1$. Among the solutions of this equation are those corresponding to the most intense, aperiodic growth. Let us consider the case in which $\varkappa$ is not a function of ω; this is true at freqeuncies $\omega \ll k_zv_{Te}$ if $\varkappa = (k_0^2+\omega_{Li}^2/v_s^2)^{1/2}$ and at frequencies $\omega \gg k_zv_{Te}$ if $\varkappa = |k_y|$, if $k_y \gg k_z(\omega_{Le}/\omega)$. We find two spectra from Eq. (16), depending on the magnitude of the detuning. At a slight detuning, $(n\omega_0\xi_n)^3 \ll (\varkappa/k_y)\Omega_i\omega_r^2J_n^2$, we have a cubic spectrum,

$$\omega^3=-\frac{\varkappa}{k_y}\Omega_i\omega_r^2J_n^2, \tag{17}$$

while if the opposite condition holds we have a spectrum

$$\omega=\frac{\varkappa\Omega_i\omega_r^2J_n^2}{k_yn\omega_0\xi_n}. \tag{18}$$

It is crucial for the growth of waves (18) that the signs of k_y and ξ_n be opposite.

Furthermore, there is a possible immediate parametric buildup of two surface waves. We illustrate this situation with the example of waves at frequency $\omega \ll \omega_{Li}, \Omega_i, k_zv_{Te}$ in a dense plasma $\omega_{Li} \gg \Omega_i$. If the frequency of the external field satisfies $\omega_0 \gg k_zv_{Te}(\omega_{Li}/\Omega_i)$ the quantity $\varkappa$ satisfies

$$\varkappa^2=k_0^2+\frac{\Omega_i^2}{v_s^2}\left(1+i\sqrt{\frac{\pi}{2}}\frac{\omega}{|k_z|v_{Te}}\right)\left[1+\frac{\omega_{Li}^2}{\Omega_i^2}(1-J_0^2)\right]. \tag{19}$$

Under these conditions the dispersion relation splits into two factors, one of which corresponds to ion-acoustic surface waves, discussed above, and the other of which can be written as

$$1-i\sqrt{\frac{\pi}{2}}\frac{\omega_rJ_0^2}{|k_z|v_{Te}}-\frac{\omega_rJ_n^2}{\omega-n\omega_0\xi_n}=0. \tag{20}$$

We find the frequency

$$\omega=n\omega_0\xi_n+\omega_rJ_n^2 \tag{21}$$

and the growth factor

$$\gamma=\sqrt{\frac{\pi}{2}}\frac{\omega_r^2}{|k_z|v_{Te}}\left[J_0^2J_n^2-\frac{(1+J_n^2)(\xi_n+J_n^2)}{2\varkappa(\varkappa+k_0)}\right] \tag{22}$$

for the surface waves which are excited by the rf field at the same time as waves corresponding to the resonant frequency. Equations (21) and (22) contain only the real part of $\varkappa$.

The authors thank Yu. M. Aliev and O. M. Gradov for discussion.

---

[1] E. E. Lovetskii and V. P. Silakov, Zh. Tekh. Fiz., 39, 1709 (1969) [Sov. Phys.—Tech. Phys., 14, 1283 (1970)].

[2] E. E. Lovetskii and A. N. Starodub, Zh. Tekh. Fiz., 42, 2010 (1972) [Sov. Phys.—Tech. Phys., 17, 1612 (1973)].

[3] Ya. B. Fainberg and V. D. Shapiro, Zh. Eksp. Teor. Fiz., 52, 293 (1967) [Sov. Phys.—JETP, 25, 189 (1967)].

[4] Yu. M. Aliev and É. Ferlengi, Zh. Eksp. Teor. Fiz., 57, 1623 (1969) [Sov. Phys.—JETP, 30, 877 (1970)].

[5] Yu. M. Aliev, O. M. Gradov, and A. Yu. Kirii, Zh. Eksp. Teor, Fiz., 63, 112 (1972) [Sov. Phys.—JETP, 36, 59 (1973)].

[6] I. S. Baikov and A. A. Rukhadze, Zh. Tekh. Fiz., 35, 1913 (1965) [Sov. Phys.— Tech. Phys., 10, 1477 (1966)].

Magnetic field in a θ pinch with an axial conductor

Ya. F. Volkov, V. G. Dyatlov, and N. I. Mitina
Physicotechnical Institute,
Academy of Sciences of the Ukrainian SSR, Khar'kov

(Submitted April 13, 1973; resubmitted August 3, 1973)
Zh. Tekh. Fiz., 44, 514-518 (March 1974)

For the presence near the axis of a θ pinch of a magnetic flux, of an inverse external flux, magnetic lines of force near the axis of an azimuthal plasma current form a system of closed concentric lines. With the application of an azimuthal magnetic field the lines of force form toroidal magnetic surfaces whose major axis is the axis of the θ-pinch system. The aim of the present work is to experimentally investigate the principal parameters formed in the discharge of closed magnetic configurations. The basic investigation method is probe magnetic measurements. Using the Maxwell equation curl $H = (4\pi/c)j$, we obtain the topography of the azimuthal plasma current. To analyze the structure of the magnetic field we numerically integrate the equation of magnetic lines of force $dr/B_r = dz/B_z = r d\varphi/B_\varphi$, where B_r, Bz, and B_φ are the magnetic-field components, the z axis is the axis of the θ-pinch system. In a θ-pinch system with an applied azimuthal field there exist Tokamak-type toroidal magnetic configurations. The magnetic-surface cross sections are extended along the axis of the system. The characteristic dimensions of the cross sections are of the order of the major radius of the surfaces. This facilitates obtaining a sufficient margin of stability, which in the experiment is $q \approx 6$. The system has mean minimum B of the order of several tens of percent and shear of about $S \approx 0.4$. The time of existence of the given configuration is determined by the period of the discharge ($T = 30 = 30$ μsec) and is about 7 μsec.

With a reverse flux near the axis of a θ pinch, the magnetic lines of force near the axis of an azimuthal plasma current form a system of closed concentric lines, with centers on the current axis. If an azimuthal magnetic field is applied to such a θ pinch, the lines of force become helical lines which lie on toroidal surfaces, the major axis being the axis of the θ-pinch system. Such a magnetic configuration is topologically similar to Tokamak configurations. The azimuthal plasma current of the θ pinch corresponds to the main plasma current in the Tokamak, and the azimuthal field corresponds to the toroidal field.

A toroidal magnetic field produced by a quasistationary current through a rod along the axis of the θ-pinch system was first used to stabilize a discharge.[1] Similar systems have been subsequently studied from the point of view of plasma confinement.[2-4]

In the production of a Tokamak-type magnetic configuration the ratio between the magnetic field of the induced current and the primary θ-pinch current is highly important. The magnitude of the plasma current should be such that inside the plasma ring the total magnetic flux due to the θ pinch and the current should be in the direction opposite to that of the external flux. This is possible only with an initial reverse flux. For this purpose we use an initial external reverse field[2] or a specially constructed current-carrying rod[4] in which the current through helical windings located on the rod surface produces the necessary magnetic-field component. In the system being studied here the necessary ratio of magnetic fields is obtained as a result of the reverse magnetic flux maintained inside the plasma ring by the preceding half-period of the discharge.[5]

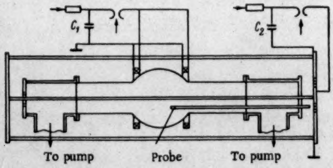

Fig. 1. Schematic diagram of apparatus. $C_1 = 60$ μF is the capacitor bank supplying the coils of the B_z field; $C_2 = 3000$ μF is the capacitor bank supplying the rod.

The aim of the present work is to investigate experimentally the parameters of a θ pinch with an applied azimuthal magnetic field, when the system is used as a closed magnetic configuration.

APPARATUS AND METHODS

The investigations are carried out on the apparatus shown in Fig. 1. This is a θ pinch with period $T = 30$ μsec and magnetic field $B_{z0} = 12$ kG. The quasistationary ($T = 600$ μsec) current in the rod $I_z = 6 \cdot 10^4$ A. The diameter of the glass discharge chamber is $D = 22$ cm. The working gas is helium at $p = (5\text{-}8) \cdot 10^{-3}$ mm Hg. The mean plasma density is 10^{14}-10^{15} cm^{-3}.

The principal measurements make use of magnetic probes. The probe consists of two search coils 3.5 mm in diameter, oriented in mutually perpendicular planes so that one of them records the axial component and the other, the radial or azimuthal component of the magnetic field as a function of orientation (cylindrical coordinate system). The coils are insulated from the plasma by a 5-mm diam. glass tube. The probe can be moved along the axis and along the radius.

Using the magnetic measurements we calculated the topography of plasma currents using Maxwell's equation with small displacement current:

$$\text{curl } \mathbf{H} = \frac{4\pi}{c} \mathbf{j}.$$

For systems in which the principal part of the magnetic flux is caused by plasma currents, the introduction of a probe unavoidably causes a disturbance in the current structure, which affects the accuracy of the method.

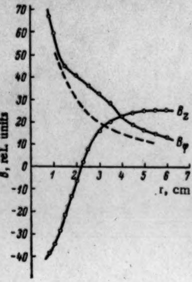

Fig. 2. Distribution of axial B_z and azimuthal B_φ components of magnetic field along radius in central plane of system (z = 0). Dashed curve) the function $B \sim 1/r$ ($B_{z_0} = 12$ kG, $I_z = 6 \cdot 10^4$ A, $p_0 = 6 \cdot 10^{-3}$ mm Hg, t = 2.7 μsec after origin of the vacuum B_z field).

Under the most favorable conditions, we are able to distinguish the separate details of the distribution of currents with characteristic dimension equal to the probe dimension.[6] Estimates show that the mean free path does not exceed the dimensions of the plasma structure. This gives us confidence that the distortions introduced by the probe are not so large as to cause significant variations in the current structure.

The errors in the magnetic-field measurement are below 15%, and the error in numerical methods is less than 1%.

RESULTS

We determine the axial, radial, and azimuthal magnetic-field components as functions of coordinates and time, assuming axial symmetry of the fields.

The results confirm the existence, inside the plasma ring, of sizable trapped fields, the lifetime of which is 5-7 μsec. The radial distribution of the axial field differs principally from the vacuum field. There is also some increase in azimuthal component in the cross section of the plasma ring (Fig. 2).

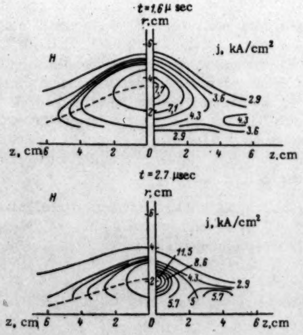

Fig. 3. Cross sections of magnetic surfaces (left) and lines of equal current density (right). $B_{z_0} = 12$ kG, $I_z = 6 \cdot 10^4$ A, $P_0 = 6 \cdot 10^{-3}$ mm Hg.

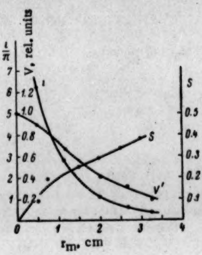

Fig. 4. Dependence of twist angle of lines of force i of specific volume V' and shear S on mean radius of cross section of magnetic surface. $B_{z_0} = 12$ kG, $I_z = 6 \cdot 10^4$ A, $p_0 = 6 \cdot 10^{-3}$ mm Hg.

Knowing the experimental dependences of the magnetic-field components of the coordinates, we can analyze the magnetic-field structure, using the equation of the magnetic lines of force:

$$\frac{dr}{B_r} = \frac{dz}{B_z} = \frac{r d\varphi}{B_\varphi},$$

where the z axis is the axis of the θ pinch. The first two terms give an equation for the cross sections of the magnetic surfaces. Results of numerical integration of this equation are shown in Fig. 3. The cross sections of magnetic surfaces near the magnetic axis ($B_z = B_r = 0$) are nearly elliptical. With increasing distance from the axis they become extended along the z axis so that the cross sections of the peripheral surfaces become larger, like segments of circles with secant parallel to the z axis. The numerical analysis carried out on the behavior of the lines of force on the magnetic surface indicates that it is possible to estimate values of the rotational transform, of the lines of force i, shear S, and specific volume V'. The results are shown in Fig. 4. Near the last closed surface the rotational transform $i \approx 0.3\pi$, which corresponds to a stability margin $q = 2\pi/i \approx 6$. Near the magnetic axis we have $q < 1$.

Variation of the rotational transform confirms the presence of shear. Near the axis the shear is equal to zero; it reaches a maximum value of S = 0.4 at the boundary surface.

The specific volume V' is a maximum on the magnetic axis and decreases as the magnetic surface approaches the boundary surface. This indicates the existence of minimum B or a so-called magnetic well near the axis. The well reaches values 80 ± 45%. We note that in the given case minimum B occurs only on the average. On external sections of the magnetic surfaces an "antiwell" exists.

An important characteristic of the discharge is the magnitude and distribution of the plasma current. Figure 3 shows lines of equal current density. The values of current density are obtained from the magnetic measurements. The current axis is displaced inward with respect to the magnetic axis. The total azimuthal current reaches a value of 50 kA.

We should note the splitting of the lines of equal current density and the appearance of two additional current axes, symmetric with respect to the central plane. These axes lie in regions where $B_z = 0$. It is possible for the minimum-B condition to be satisfied here; this contributes toward the confinement of the plasma in this region.

The noncircular shape of the cross sections of the magnetic surfaces is worth noting. In this case the satisfaction of the stability criterion[7,8] is facilitated. This allows us to attain sizable plasma currents for comparatively small stabilizing fields. In our case a current of order 50 kA is reached with a stabilizing B_φ field of the order of the current field ($\sim$10 kG).

We note that in the absence of a toroidal field the plasma current in the investigated regime is less than 10-15 kA. It lasts for 1-1.5 μsec. Considerable fluctuations in current are observed, which indicates the presence of an instability.

DISCUSSION

Thus, closed magnetic surfaces exist in a θ pinch with an applied azimuthal field.

The experimentally observed lifetime of the closed configuration is about 7 μsec and is evidently limited by the discharge period (compression phase lasts for $T/4 = 7.5$ μsec). The plasma confinement time in systems with an axial current-carrying rod[2-4] is 20-30 μsec and is limited either by the instability caused by plasma rotation or by the decrease in stability margin during the discharge. In our case the maximum possible confinement time is limited by the diffusion time of the magnetic field, which for typical discharge parameters[9] ($T_e \approx 1$ keV) is of the order of several hundredths of a microsecond.

Increasing the discharge period without considerable changes in the other parameters probably can considerably increase the lifetime of a given magnetic configuration. This makes it possible to study sufficiently rapid processes, such as plasma heating, development of instabilities; etc. in closed magnetic systems.

During the discharge the major and minor radii of the toroidal surfaces are compressed. The most rapid changes occur in the first 1-1.5 μsec; afterwards, the dimensions remain essentially constant. The existence inside the plasma ring of a reverse magnetic flux makes it possible for a certain equilibrium configuration of the ring to be attained.

With a sufficiently rapid decrease in cross-sectional area of the plasma ring the magnetic flux through the cross section is maintained, which leads to a deviation in distribution of the toroidal field B_φ from the $B_\varphi \sim 1/r$ law (Fig. 2). Poloidal surface currents with density of order 1 kA/cm² are observed.

The existence of a difference between the toroidal magnetic field inside the plasma and outside it affects the equilibrium and stability of the plasma,[10] since it changes the balance of pressure, and creates additional shear on the surface. Furthermore, if the surface currents are not parallel to **B**, then the ponderomotive force $F_\varphi = (j_z B_r - j_r B_z)(1/c)$ causes the plasma to rotate, which can lead to instabilities.

Based on the method of production (plasma current) the magnetic configuration being investigated is similar to Tokamaks, but based on its parameters (shear, magnetic well, shape of cross section) it is close to Spherators.

CONCLUSIONS

1. In a θ-pinch system with an applied azimuthal magnetic field there exist Tokamak-type closed magnetic configurations.

2. The cross sections of the magnetic surfaces are extended along the axis of the system. The characteristic dimensions of the cross sections are of the order of the major radius of the surfaces.

3. The system has mean minimum B of the order of several tens of percent and shear $S \approx 0.4$.

4. It is possible to use the θ-pinch system with an applied azimuthal field to study rapid processes (instability, turbulence) for toroidal plasma confinement.

The authors thank V. P. Sebko and V. I. Tyup for useful discussion.

---

[1] Ya. F. Volkov, V. T. Tolok, and K. D. Sinel'nikov, Zh. Tekh. Fiz., 32, 811 (1962) [Sov. Phys. – Tech. Phys., 7, 593 (1963)].
[2] A. C. Kolb, M. P. Young, and E. A. McLean, LASL, Report LA-3770, p. G 5-1 (1967).
[3] S. Yoshikawa, LASL, Report LA-3770, p. G 6-1 (1967).
[4] L. Janicke, P. Noll, and J. Schlüter, Bull. Am. Phys. Soc., Ser. II, 13, 1551 (1968).
[5] T. A. El-Khalafaway, Ya. F. Volkov, A. Youssef, and L. El-Hak, Proc. Ninth Intern. Conf. on Phenomena in Ionized Gases, Bucharest (1969), 3. 1. 8. 3, p. 211.
[6] I. H. Malmberg, Rev. Sci. Instr., 35, 1622 (1964).
[7] L. S. Solov'ev, ZhETF Pis. Red., 16, 420 (1972) [JETP Lett., 16, 298 (1972)].
[8] L. A. Artsimovich and V. D. Shafranov, ZhETF Pis. Red., 15, 72 (1972) [JETP Lett., 15, 51 (1972)].
[9] Ya. P. Volkov, V. G. Dyatlov, and N. I. Mitina, in: Interaction of Charged Particles with a Plasma [in Russian], Kiev (1967), p. 139.
[10] J. H. Misguich and C. Mercier, Plasma Phys., 14, 418 (1972).

Damping of ion-acoustic waves in a bounded plasma

A. N. Kondratenko and V. M. Kuklin

A. M. Gor'kii Khar'kov State University

(Submitted April 6, 1973; resubmitted September 3, 1973)
Zh. Tekh. Fiz., 44, 519-524 (March 1974)

The propagation of surface and volume ion-acoustic waves along the axis of a cylindrical plasma waveguide in a constant magnetic field is considered. The problem is solved in the linear hydrodynamic approximation. The dispersion equations are investigated; phase and group velocities and damping factors for the waves are determined. The damping factors contain a term collisional–dissipative term as a resonance associated with the presence of an inhomogeneous transition layer. It is shown that the properties of volume ion-acoustic waves in an unbounded plasma can be different from those in a waveguide of small radius.

DISPERSION EQUATION

Surface ion-acoustic waves in a strongly nonisothermal ($T_e \gg T_i$) plasma layer with a sharp boundary have been investigated.[1,2] In experiments, however, one often has to deal with cylindrical plasma waveguides rather than plasma layers. In addition, a sharp boundary is usually not realized with a gaseous plasma and there is a finite transition layer of inhomogeneous plasma where one should expect absorption of wave energy because of resonance effects.[3-6] In this paper we study the propagation of low-frequency waves ($\omega \ll \Omega_i$, where Ω_i is the ion plasma frequency) in a cylindrical waveguide filled with an inhomogeneous highly nonisothermal plasma.

The plasma is in a fixed magnetic field H_0 oriented along the z axis of the plasma column. We consider symmetric waves for which $\partial/(\partial\varphi) = 0$. We choose the dependence of perturbed quantities on the coordinate z and time in the form $\exp i(k_3 z - \omega t)$. The unperturbed density of singly charged ions and of electrons is assumed to be constant and equal to n_0 in the radial interval $0 \le r \le R_1$, and to decrease monotonically to zero for $R_n < r \le R_2$.

Since the phase velocity of these low-frequency waves is much smaller than the thermal velocity of plasma electrons, v_T, the magnetic field of the wave can be neglected. From the linearized Maxwell equations and the hydrodynamic equations we obtain a system of two equations for the electric field of the ion-acoustic wave:

$$\frac{dE_z}{dr} = ik_3 E_r, \tag{1}$$

$$E_z = \frac{-i}{k_3 g(r) r} \frac{d}{dr}(r\varepsilon_1 E_r), \tag{2}$$

where

$$g(r) = -\varepsilon_3 - \frac{\Omega_e^2(r)}{k_3^2 v_T^2}, \quad \varepsilon_1 = 1 - \frac{\Omega_i^2(r)}{\omega(\omega + i\nu) - \omega_i^2}, \quad \varepsilon_3 = 1 - \frac{\Omega_i^2(r)}{\omega(\omega + i\nu)},$$

$$\Omega_{i,e}^2 = \frac{4\pi e^2 n}{m_{i,e}}, \quad \omega_i = \frac{eH_0}{m_i c},$$

ν is the effective ion collision frequency (it is assumed $\nu \ll \omega$) and $m_{i,e}$ is respectively the ion or electron mass.

Eliminating E_z from Eqs. (1) and (2), we obtain an equation for the determination of the component E_r:

$$\varepsilon_1 \frac{d}{dr}\left[\frac{1}{g(r) r} \frac{d}{dr}(rF)\right] + k_3^2 F = 0, \tag{3}$$

where $F = \varepsilon_1 E_r$.

The system (1)-(3) holds for $c \to \infty$, or, more rigorously, $c \gg \omega R_1$, ω/k_3, where c is the velocity of light.

Solving (2) and (3) in the homogeneous plasma region $r < R_1$, we obtain the following expression for the components of the field:

$$E_r = C_0 I_1(\varkappa r), \tag{4}$$

$$E_z = iC_0 \frac{k_3}{\varkappa} I_0(\varkappa r), \tag{5}$$

where

$$\varkappa^2 = \frac{\varepsilon_{30}}{\varepsilon_{10}}\left(k_3^2 + \frac{\Omega_{e0}^2}{v_T^2 \varepsilon_{30}}\right), \tag{6}$$

$I_n(x)$ is the Bessel function of imaginary argument; ε_{10}, ε_{30}, and Ω_{e0} are the values of the corresponding quantities in the homogeneous plasma region; C_0 is a constant.

Setting the wave amplitude at the vacuum boundary equal to unity, we obtain for the region $r > R_2$

$$E_r = K_1(k_3 r), \tag{7}$$

$$E_z = -iK_0(k_3 r), \tag{8}$$

where $K_n(x)$ is the MacDonald function.

In the transition region $R_1 < r < R_2$ (assuming it to be small,

$$|\varkappa(R_2 - R_1)| \ll 1, \quad k_3(R_2 - R_1) \ll 1, \tag{9}$$

the solution of the system (2), (3) can be represented by a series in powers of the small parameter (9). Limiting the series to the first two terms of the expansion, we obtain

$$F(r) = \frac{A}{r}\int_{R_1}^{r} g(r')r'dr'\left[1 - k_3^2\int_{R_1}^{r'} \frac{dr''}{\varepsilon_1(r'')r''}\int_{R_1}^{r''} g(\rho)\rho d\rho - \ldots\right]$$
$$+ \frac{B}{r}\left[1 - k_3^2\int_{R_1}^{r} g(r')r'dr'\int_{R_1}^{r'} \frac{dr''}{\varepsilon_1(r'')r''} - \ldots\right], \tag{10}$$

$$iE_z(r) = \frac{A}{k_3}\left[1 - k_3^2\int_{R_1}^{r} \frac{dr'}{\varepsilon(r')r'}\int_{R_1}^{r'} g(r'')r''dr'' - \ldots\right]$$
$$- Bk_3\int_{R_1}^{r} \frac{dr'}{\varepsilon_1(r')r'} - \ldots. \tag{11}$$

The constants A and B are determined from the continuity of the fields at the interface with the homogeneous plasma:

$$A = -\frac{k_3^2}{\varkappa} C_0 I_0(\varkappa R_1), \tag{12}$$

$$B = R_1 \varepsilon_{10} C_0 I_1(\varkappa R_1). \tag{13}$$

Continuity of the fields at the vacuum boundaries make it possible to obtain the dispersion equation

$$A\left\{-\int_{R_1}^{R_2} g(r)\, r\, dr \left[1 - k_3^2 \int_{R_1}^{r} \frac{dr'}{\varepsilon_1(r')\, r'} \int_{R_1}^{r'} g(r'')\, r'' dr''\right] + \frac{R_2 K_1(k_3 R_2)}{k_3 K_0(k_3 R_2)}\left[1 - k_3^2 \int_{R_1}^{R_2} \frac{dr}{\varepsilon_1(r)\, r} \int_{R_1}^{r} g(r')\, r' dr'\right]\right\}$$
$$- B\left[1 - k_3^2 \int_{R_1}^{R_2} g(r)\, r\, dr \int_{R_1}^{r} \frac{dr'}{\varepsilon_1(r')\, r'} + \frac{k_3 R_2 K_1(k_3 R_2)}{K_0(k_3 R_2)} \int_{R_1}^{R_2} \frac{dr}{\varepsilon_1(r)\, r}\right] = 0. \tag{14}$$

Neglecting small terms proportional to (9) and considering only the contribution of the resonance portion of the last integral in Eq. (14), we write it in the form

$$f(k_3 R_2) + \varkappa R_1 \varepsilon_{10} \frac{I_1(\varkappa R_1)}{I_0(\varkappa R_1)} = -\frac{\pi i r^*}{R_1} f^2(k_3 R_2), \tag{15}$$

where

$$r^* = -\frac{R_1}{r} \left.\frac{\omega^2 - \omega_i^2}{\frac{d\Omega_i^2(r)}{dr}}\right|_{r=R_0}, \quad f(z) = z\frac{K_1(z)}{K_0(z)},$$

and R_0 is determined from the condition Re $\varepsilon_1(R_0) = 0$.

SURFACE WAVES

Neglecting dissipative effects (particle collisions and absorption of wave energy in the resonance layer), the dispersion equation (15), which describes the propagation of surface waves ($\varkappa^2 > 0$) in a plasma waveguide with sharp boundaries ($R_1 = R_2 = R$), takes the form

$$-\varepsilon_{10} \frac{\varkappa}{k_3} \frac{I_1(\varkappa R)}{I_0(\varkappa R)} = \frac{K_1(k_3 R)}{K_0(k_3 R)}. \tag{16}$$

Letting the phase velocity of the wave go to zero ($k_3 \to \infty$), we find an upper bound for the frequency:

$$\omega_{\text{ub}} = \sqrt{\frac{\Omega_{i0}^2 + \omega_i^2}{2}}. \tag{17}$$

In the limit of large waveguide radius, the wave is a surface wave and it is easily shown that the frequency falls in the range $\omega_i < \omega < \omega_{\text{ub}}$.

We consider a number of special cases.

a) In a semiinfinite plasma, the dispersion equation (16) takes the form

$$k_3^2 = \frac{\Omega_{i0}^2 \varepsilon_{10}}{v_s^2 (1 - \varepsilon_{10}\varepsilon_{30})}, \tag{18}$$

where $v_s = \sqrt{T_e/m_i}$ is the ion-acoustic velocity.

If the frequency of the wave is much smaller than the ion plasma frequency, $\omega \ll \Omega_{i0}$, the dependence of ω on k_3 is the same as for acoustic waves in a unbounded plasma:

$$\omega = k_3 v_s. \tag{19}$$

In addition, $\varkappa \ll k_3$, and the wave penetrates far into the plasma. When the frequency approaches the limiting values, k_3 and $\varkappa$ increase rapidly, the wave is confined to the boundary of the plasma, and the phase velocity goes to zero.

Letting $k_3 \to k_3' = k_3 + i\delta$, $\delta \ll k_3$, from Eq. (15) we obtain the damping factor for a wave in a semiinfinite medium:

$$\frac{\delta}{k_3} = \frac{\nu\omega(1 - \varepsilon_{10})}{(\omega^2 - \omega_i^2)\, \varepsilon_{10}(1 - \varepsilon_{10}\varepsilon_{30})} + \pi \frac{r^*}{r_d^2} \sqrt{\frac{\varepsilon_{10}}{(1 - \varepsilon_{10}\varepsilon_{30})^3}}, \tag{20}$$

where $r_d = \Omega_{e0}/v_T$.

The second term in Eq. (20) is responsible for resonance damping of the wave in the transition region of the plane. If the frequency ω approaches the frequency bound ω_{ub}, Eq. (20) is inapplicable, the damping factor rises rapidly, and the wave is highly damped.

The phase velocity and group velocity for a weakly damped wave are

$$v_{\text{ph}} = v_s \frac{\omega}{\Omega_{i0}} \sqrt{\frac{1 - \varepsilon_{10}\varepsilon_{30}}{\varepsilon_{10}}}, \tag{21}$$

$$v_{\text{gr}} = 2\frac{v_s \sqrt{\varepsilon_{10}(1 - \varepsilon_{10}\varepsilon_{30})^3}}{\Omega_{i0}\left(\frac{\partial\varepsilon_{10}}{\partial\omega} + \varepsilon_{10}^2 \frac{\partial\varepsilon_{30}}{\partial\omega}\right)}. \tag{22}$$

b) If the depth of penetration into the plasma is much greater than the waveguide radius,

$$\varkappa R \ll 1, \tag{23}$$

the dispersion equation (16) becomes

$$-\varepsilon_{30}\varkappa^2 R^2 = 2f(k_3 R). \tag{24}$$

Since $f(x) \gtrsim 1$ for all $x = k_3 R$ with the exception of a small neighborhood near $x = 0$, where $f(x)$ decreases as $1/\ln x$, $|\varepsilon_{30}| \gg 1$ is a condition for expanding Eq. (24).

Solving Eq. (24) with respect to frequency, we find

$$\omega = \frac{\Omega_{i0} k_3 R r_d}{\sqrt{R^2 + 2r_d^2 f(k_3 R)}}. \tag{25}$$

It is easy to see that $k_3 r_d \ll 1$ follows from the condition $\omega \ll \Omega_{i0}$. Thus $f r_d^2 \ll R^2$ and the dispersion equation for a narrow plasma waveguide is the same as that for acoustic waves in an unbounded plasma [Eq. (19)].

The damping factor is given by

$$\frac{\delta}{k_3} = \frac{\nu}{2\omega} + \frac{\pi r^* r_d^2 f^2(k_3 R)}{R^3}. \tag{26}$$

It then follows that damping of a wave in a narrow cylindrical waveguide is always small if $\nu \ll \omega$, $r_d \ll R$.

The phase and group velocities of the wave differ very little from the ion-acoustic velocity v_s in a unbounded plasma.

c) These results obtained can be generalized to the case of a narrow inhomogeneous cylinder in which the plasma density varies monotonically along the radius. For this case (23) is written

$$\left| k_3^2 \int_0^R \frac{dr}{\varepsilon_1(r) r} \int_0^R g(r') r' dr' \right|^{1/2} \ll 1. \tag{27}$$

The dispersion equation (15) is inapplicable and one should use Eq. (14), setting $R_1 = 0$, $R_2 = R$, and $B = 0$. As in the preceding case, the relationship $\omega(k_3)$ has the form (19). The damping factor is determined from Eq. (26), where all quantities are replaced by their average values

$$\bar{y} = \frac{2}{R^2} \int_0^R y(r) r dr. \tag{28}$$

As before, the damping of the wave is small, and the phase and group velocities are of the same order as v_s.

In the last two cases the constant magnetic field $H_0 < (\omega c m_i / e)$ has no effect on the propagation of the ion-acoustic waves. When the inequality is reversed, surface low-frequency waves are not excited in a plasma.

VOLUME WAVES

If $\varkappa^2 < 0$, as in Eq. (6), the fields in the plasma are expressed by oscillating Bessel functions of the first kind and represent volume waves. For large waveguide radii, the volume low-frequency waves do not differ from ordinary ion-acoustic waves in an unbounded plasma and their properties do not depend on boundary effects. For small radii, however, the properties of ion-acoustic waves in bounded and unbounded plasma can be quite different.

The dispersion equation for ion-acoustic waves in a plasma waveguide, including resonance absorption effects, has the following form ($R_2 - R_1 \ll R_1 = R$):

$$-\varepsilon_{10} q R \frac{J_1(qR)}{J_0(qR)} + f(k_3 R) = -\pi i \frac{r^*}{R} f^2(k_3 R), \tag{29}$$

where

$$q = i\varkappa = \left[-\frac{\varepsilon_{30}}{\varepsilon_{10}} \left(k_3^2 - \frac{\Omega_{i0}^2}{v_T^2 \varepsilon_{30}} \right) \right]^{1/2}.$$

The left side of Eq. (29) defines $k_3(\omega)$. It can be defined with satisfactory accuracy in the following manner. Within the limits of a monotonic variation of $k_3(\omega)$, we let k_3 go to zero. Then $f \to 0$ and $qR \approx \lambda_{p1}$, where λ_{p1} is a root of the first-order Bessel function. If $k_3 \to \infty$, then $f \to \infty$ and $qR \approx \lambda_{p0}$, where λ_{p0} is a root of the zero-order Bessel function. It is reasonable to assume that

$$q \approx \frac{\lambda_p}{R}, \tag{30}$$

where λ_p falls between λ_{p0} and λ_{p1}. We then determine $k_3(\omega)$ from

$$k_3^2 = -\frac{1}{\varepsilon_{30}} \left(\frac{1}{r_d^2} + \varepsilon_{10} \frac{\lambda_p^2}{R^2} \right). \tag{31}$$

Using Eq. (31) we determine the frequency region in which volume ion-acoustic waves can be excited. In the case of a strong magnetic field $\omega_i > \Omega_{i0}$, two frequency ranges are possible: $0 < \omega < \Omega_{i0}$ and $\omega_i < \omega < \omega_1$, where

$$\omega_1 = \left[\omega_i^2 + \Omega_{i0}^2 \left(1 + \frac{R^2}{r_d^2 \lambda_p^2} \right)^{-1} \right]^{1/2}. \tag{32}$$

In the second range, the signs of the phase and group velocities are different. If $\omega_i < \Omega_{i0}$, the frequency region is also represented by two ranges: $0 < \omega < \omega_i$ and $\omega \in (\omega_1, \Omega_{i0})$. In the second range for this case, anomalous dispersion is also observed when $\omega_1 > \Omega_{i0}$.

For large waveguide radii the last term in Eq. (31) is small and $k_3(\omega)$ is similar to the dispersion law in an unbounded plasma. In some cases, however, both terms on the right in Eq. (31) can be of the same order of magnitude.

Assuming that the damping is small, we obtain the damping factor of the wave from Eq. (29):

$$\frac{\delta}{k_3} \approx \frac{\nu}{4} \left[\frac{\lambda_p^2 r_d^2}{R^2 + \varepsilon_{10} \lambda_p^2 r_d^2} \frac{d\varepsilon_{10}}{d\omega} - \frac{1}{\varepsilon_{30}} \frac{d\varepsilon_{30}}{d\omega} \right] - \frac{\pi r^* J_0^2(\varkappa R) K_1^2(k_3 R)}{R \varepsilon_{30} K_0^2(k_3 R)}. \tag{33}$$

As in the case of surface waves, the second term in Eq. (33) represents resonance absorption of wave energy in the homogeneous plasma layer. As is clear from the expression given above, resonance damping is inversely proportional to waveguide radius and vanishes in a semi-infinite plasma. For small waveguide radii one expects a strong increase in resonance damping. We also give the group velocity of the wave:

$$v_{gr} = \frac{-2}{k_3} \left[\frac{1}{\varepsilon_{30}} \frac{d\varepsilon_{30}}{d\omega} + \frac{\lambda_p^2}{\varepsilon_{30} R^2 k_3^2} \frac{d\varepsilon_{10}}{d\omega} \right]^{-1}. \tag{34}$$

For a fixed wave vector k_3, the time decrement $\mathrm{Im}\,\omega = \gamma$ is easily determined for the case of weak damping ($\gamma \ll \omega$) from the following expression:

$$\gamma = v_{gr} \delta. \tag{35}$$

---

[1] A. N. Kondratenko, Yadernyi Sintez, 5, 267 (1965).

[2] A. N. Kondratenko, Zh. Tekh. Fiz., 36, 1943 (1966) [Sov. Phys.—Tech. Phys., 11, 1448 (1967)].

[3] V. L. Ginzburg, Propagation of Electromagnetic Waves in Plasma, Gordon and Breach.

[4] V. V. Gil'denburg, Zh. Eksp. Teor. Fiz., 45, 1978 (1963) [Sov. Phys.—JETP, 18, 1359 (1964)].

[5] Yu. A. Romanov, Zh. Eksp. Teor. Fiz., 47, 2119 (1964) [Sov. Phys.—JETP, 20, 1355 (1965)].

[6] K. N. Stepanov, Zh. Tekh. Fiz., 35, 1002 (1965) [Sov. Phys.—Tech. Phys., 10, 773 (1965)].

Forces in a Hall plasma accelerator

O. N. Mironov

(Submitted July 9, 1973)
Zh. Tekh. Fiz., 44, 525-535 (March 1974)

The forces in a stationary Hall plasma accelerator are calculated. Analytic expressions are obtained for the average flow parameters at the accelerator exit and the forces as functions of dimensionless parameters characterizing the flow and plasma acceleration in the accelerator channel. The results are of interest in the evaluation of accelerator characteristics and in the analysis of plasma flow in the channel.

Plasma acceleration under stationary conditions can be accomplished in various ways. For example, if an external magnetic field coaxial with the electrodes is superimposed on an electric discharge in a plasma of low or medium density (10^{12}–10^{15} cm^{-3}) which is heated between coaxial electrodes, the rate of plasma emission and the accelerator efficiency can be increased significantly.[1-3] In the literature, such accelerators have been called magnetoplasmodynamic accelerators[2,3] or Hall accelerators.[1,4] In these accelerators, in the MHD approximation plasma acceleration occurs mainly through the effect of the electromagnetic Ampere force $j_\theta = b_r$. The appearance of an Ampere force is associated with the creation of a Hall current with density j_θ due to closed electron drift in the crossed electromagnetic fields. In contrast to the arrangement discussed in ref. 5, plasma flow along the channel in this acceleration scheme is a three-component flow. Therefore, the analysis and calculation of the forces which act in the various directions and which determine flow structure are of particular interest. In addition, such an analysis is important from the viewpoint of evaluating the capabilities of Hall accelerators. The present paper is concerned with these equations.

1. FORMULATION OF THE PROBLEM

We consider steady-state flow of a neutral plasma in an axisymmetric channel, a diagram of which is shown in Fig. 1. Let the working material be fed into the accelerator channel through the central electrode, which is the cathode. We assume this material is ionized near the cathode so that plasma in the channel is propagated from the cathode in the form of a jet in which the degree of ionization is constant. We choose a general system for electric current flow in the channel and calculate the forces under the following assumptions.

1. The plasma is nonviscous and thermally nonconducting.

2. The working material is singly ionized.

3. The plasma is ionized to a high degree so that we need not consider slippage of ions relative to neutrals.

4. The plasma approximation is valid, i.e., the ion and electron densities are equal in all flow regions.

The time-averaged plasma behavior is treated, i.e., time variations of the parameters in the equations are neglected.

6. The plasma flow is axisymmetric.

In accelerators with this arrangement, the Hall parameter for the electrons is usually greater than or equal to unity, and the Hall parameter for ions is much less than unity. To achieve this condition a magnetic field is created which satisfies the condition

$$R_{iL} > R_s \gg R_{eL},$$

where R_{iL} and R_{eL} are the Larmor radii for ions and electrons respectively and R_s is the characteristic transverse dimension of the channel. Under these assumptions we can write the following conservation laws for steady-state plasma flow:[6]

$$\left.\begin{aligned} &\operatorname{div}\rho\mathbf{v} = 0, \quad \rho(\mathbf{v}\nabla)\mathbf{v} = -\nabla p + \mathbf{j}\times\mathbf{B}, \\ &\rho(\mathbf{v}\nabla)\left(h + \frac{\mathbf{v}^2}{2}\right) = \mathbf{j}\cdot\mathbf{E}, \quad \operatorname{div}\mathbf{j} = 0. \end{aligned}\right\} \tag{1.1}$$

In order to obtain a closed system of equations we add to Eq. (1.1) a generalized Ohm's law of the form

$$\mathbf{j} = \sigma\left(\mathbf{E} + \mathbf{v}\times\mathbf{B} - \frac{\mathbf{j}\times\mathbf{B}}{n_e e} + \frac{\nabla p_e}{n_e e}\right), \tag{1.2}$$

where ion slip is neglected, and Maxwell's equations for the electromagnetic field:

$$\operatorname{curl}\mathbf{B} = \mu\mathbf{j}, \ \operatorname{div}\mathbf{B} = 0, \operatorname{curl}\mathbf{E} = 0. \tag{1.3}$$

The connection between the thermodynamic variables h (enthalpy), p, and ρ and the dependence of the transfer coefficients on these same variables is assumed to be known. Conventional notation is used in Eqs. (1.1), (1.2), and (1.3).

We introduce a cylindrical coordinate system (r, θ, x) with origin coinciding with the center of the end surface of the cathode. Let the initial distributions of all quantities be given and the basic variables have the following components:

$$\mathbf{v}\{v,\ w,\ u\},\ \ \mathbf{j}\{-j_r,\ -j_\theta,\ -j_x\},\ \mathbf{B}\{b_r,\ -b_\theta,\ b_x\}.$$

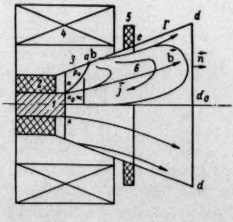

Fig. 1. Diagram of the accelerator. 1) Cathode; 2, 5) insulators; 3) anode; 4) solenoid; 6) region of current flow and plasma acceleration.

The equation of motion in component form for a steady-state axisymmetric flow can be written

$$\left.\begin{aligned} \rho\mathbf{v}\cdot\nabla(vr)-\rho(v^2+w^2) &= -r\frac{\partial p}{\partial r}-j_\theta b_x-j_x b_\theta, \\ \rho\mathbf{v}\cdot\nabla(wr) &= j_r b_x - j_x b_r, \\ \rho\mathbf{v}\cdot\nabla(u) &= -\frac{\partial p}{\partial x}+j_r b_\theta + j_\theta b_r. \end{aligned}\right\} \quad (1.4)$$

We consider the surface Γ (Fig. 1), which encompases the entire volume where electromagnetic forces act on the plasma and which is represented in a meridian plane passing through the accelerator axis by the contour $k_0 k a b e d d_0 k_0$. The following boundary conditions and initial conditions must be satisfied at the boundaries of this contour:

$$\left.\begin{aligned} &\mathbf{j}\cdot\mathbf{n}=0 \text{ on } ka,\ bed,\ dd_0. \\ &\mathbf{v}\cdot\mathbf{n}=0 \text{ on } ka,\ abed. \\ &p=p_{\mathrm{H}} \text{ on } edde. \\ &-\int_{A_{kk}}\rho\mathbf{v}\cdot\mathbf{n}\,dA=\int_{A_{dd}}\rho\mathbf{v}\cdot\mathbf{n}\,dA=G, \\ &\int_{A_{kk}}\mathbf{j}\cdot\mathbf{n}\,dA=-\int_{S_{ab}}\mathbf{j}\cdot\mathbf{n}\,dS=J_{\mathrm{d}}. \end{aligned}\right\} \quad (1.5)$$

Here, **n** is the outward normal from the surface Γ, A is the area of the cross section of the channel, S is the area of the surface Γ corresponding to the contour segment $k_0 k a b d d_0 k_0$, G is the flow rate of the working material, and J_d is the total discharge current.

Equation (1.4) and the boundary conditions (1.5) make it possible to calculate the change in plasma momentum and angular momentum due to the electromagnetic forces. We integrate the x component of the equation of motion over the volume in which the discharge current interacts with the external magnetic field with dV = dAdx, $dA = \pi dr^2$. Using the vector identity $\rho\mathbf{v}\cdot\nabla(u) = \operatorname{div}\rho u\mathbf{v} - u\operatorname{div}\rho\mathbf{v}$, the continuity equation $\operatorname{div}\rho\mathbf{v} = 0$, and Gauss's theorem, we obtain

$$\oiint_{\Gamma}\rho u\mathbf{v}\cdot\mathbf{n}\,dA=-\oiint_{\Gamma}p\mathbf{n}\cdot\mathbf{e}_x\,dA+\int_0^x\int_A(j_r b_\theta+j_\theta b_r)\,dA\,dx. \quad (1.6)$$

The plasma momentum in the section dd under boundary conditions (1.5) is according to Eq. (1.6) determined by the expression

$$\int_{A_{dd}}\rho u^2 dA=\int_{A_{kk}}(\rho u^2+p)\,dA-\int_{A_{ee}}p_{\mathrm{H}}\,dA +\int_0^{L_0}p_R\left(\frac{dA}{dx}\right)dx+\int_V(j_r b_\theta+j_\theta b_r)\,dV, \quad (1.7)$$

where L_0 is the accelerator length from cathode to exit section and p_R is the pressure at the channel boundary. The first term on the right in Eq. (1.7) corresponds to the initial plasma momentum and pressure in the initial section, the second term to the counterpressure of the surrounding gas, the third term of the plasma pressure on the channel wall (outside the contour boundary k*a* the pressure is assumed constant), and the last term to the electromagnetic forces applied to the solenoid ($\int_V j_\theta b_r dV$) and to the current-carrying circuit ($\int_V j_r b_\theta dV$). Ordinarily the initial plasma momentum and the counterpressure of the surrounding gas can be neglected. Actually, the ratio of initial momentum to final momentum in order of magnitude for the case of effective plasma acceleration is

$$\frac{\int_{A_{kk}}\rho u^2 dA}{\int_{A_{dd}}\rho u^2 dA}\sim\frac{u(x=0)}{u(x=L_d)}\simeq 0.05-0.01.$$

Here, L_d is the distance along the x axis from the cathode to the section in which the interaction of discharge current and plasma flow with the external magnetic field can be assumed complete. The force resulting from counterpressure of the surrounding gas can be neglected if the pressure p_H satisfies the condition

$$\frac{\int_{A_{ee}}p_{\mathrm{H}}\,dA}{\int_{A_{dd}}\rho u^2 dA}\sim\frac{p_{\mathrm{H}}A_{ee}}{Gu(x=L_d)}\ll 1.$$

This condition is satisfied in most cases.

The pressure in the initial section can be eliminated from Eq. (1.7) if the equation for plasma equilibrium in the radial direction is used. We assume that v = w = 0 at the cathode. Then if the plasma flow in the initial section is irrotational, i.e., $\partial v/\partial x = \partial u/\partial r$, and the profile of the axial flow velocity is uniform in the radial direction, the inertial terms are essentially zero. Integrating the remaining terms in the first equation of the system (1.4) over the area of the transverse section of the channel ($dA = \pi dr^2$), we obtain

$$\int_{A_{kk}}p\,dA=p_* A_{kk}-\frac{1}{2}\int_{A_{kk}}(j_\theta b_x+j_x b_\theta)\,r\,dA. \quad (1.8)$$

In Eq. (1.8), p_* is the pressure in the channel outside the boundaries of the current region (Fig. 1). When the pressure in the section dd is approximately equal to p_H the reactive force acting on the accelerator will be numerically equal to the plasma momentum in the section dd. In view of these estimates and Eq. (1.8) we can write

$$F=\int_{A_{dd}}\rho u^2 dA=F_B+F_c+F_a, \quad (1.9)$$

$$F_B=\int_V j_\theta b_r\,dA\,dx-\frac{1}{2}\int_{A_{kk}}j_\theta b_x r\,dA, \quad (1.10)$$

$$F_c=\int_V j_r b_\theta\,dA\,dx-\frac{1}{2}\int_{A_{kk}}j_x b_\theta r\,dA, \quad (1.11)$$

$$F_a=p_* A_{kk}+\int_0^L p_R\frac{dA}{dx}\,dx. \quad (1.12)$$

Here, F_B is the force which arises because of interaction of the discharge current with the external magnetic field and which is applied to the solenoid and to the accelerator cathode; F_c is the force which arises because of the interaction between the discharge current and the self-magnetic field and which is applied to the current-carrying circuit and to the cathode; F_a is the aerodynamic component of the reaction force resulting from plasma pressure on the channel walls. It is clear that the aerodynamic component of the reaction force can be neglected when there are strong electromagnetic fields. An expression for the angular momentum can be obtained if the second equation in the system (1.4) is integrated over the interaction volume for the electromagnetic forces. Actually, using the vector equality $\rho \mathbf{v} \cdot \nabla(wr) = \operatorname{div}(\rho \mathbf{v} \cdot wr) - wr \operatorname{div} \rho \mathbf{v}$, the relation $\operatorname{div} \rho \mathbf{v} = 0$, the boundary condition $\mathbf{v} \cdot \mathbf{n} = 0$ on the lateral surface of the region of integration, and Gauss's theorem, in a manner similar to that used above, we obtain

$$\int_{A_{dd}} \rho u w r\,dA = \int_{A_{kk}} \rho u w r\,dA + \int_A \int_0^x (j_r b_x - j_x b_r)\,dA\,dx. \qquad (1.13)$$

The integral relation (1.13) determines the angular momentum of the plasma in the section dd; for a given radial dependence of w it can be used to calculate the angular velocity and moment of inertia of the plasma in that section.

Experiments[7] indicate that the plasma rotates as a unit, i.e., $w = \omega r$. Substituting $w = \omega r$ in Eq. (1.13) and converting to averaged parameters

$$\int_A \rho u \omega r\,dA \simeq \rho u \omega \int_A r^2\,dA$$

for $\omega(x = 0) = 0$, $G = \rho u \pi R^2$ we have

$$\omega_d = \frac{2\int_A \int_0^x (j_r b_x - j_x b_r)\,dA\,dx}{G R_d^2}. \qquad (1.14)$$

In Eq. (1.14), R_d and ω_d are the radius of the jet and the angular velocity of the plasma in the section dd, G is the flow rate of the working material through a cross section of the channel. The quantity $GR_d^2/2$ is the moment of inertia of the plasma.

When $F_a \ll F_B$, by converting to averaged flow parameters, $\int_{A_{dd}} \rho u^2\,dA = uG$, we have the following relation for the average plasma velocity in section dd:

$$u_d = \frac{F_a + F_c}{G}. \qquad (1.15)$$

2. CALCULATION OF ELECTROMAGNETIC FORCES

We now calculate the integrals for the electromagnetic forces. The force F_c has been calculated previously[8,9] for an axisymmetric discharge assuming the absence of bunching. It is proportional to the square of the total discharge current. In calculating the integrals in Eqs. (1.10) and (1.14) we note that Ohm's law neglecting ion slip can be written as

$$\mathbf{j} = \frac{\sigma(\alpha)}{\alpha n_0 e}\left(n_e e\mathbf{E} + \frac{e}{m_i}\alpha \mathbf{g} \times \mathbf{B} - \mathbf{j} \times \mathbf{B} + \nabla p_e\right). \qquad (2.1)$$

Here, $\mathbf{g} = \rho \mathbf{v}$ is the mass flow vector, α is the degree of ionization, m_i is the mass, and n_0 is the total number of particles per unit volume. We now vectorially multiply the current density determined from Ohm's law in the form (2.1) by the field induction $\mathbf{b}$ and write the resultant expression in component form. For the axisymmetric case ($\partial/\partial\theta = 0$), using the vector relation $(\mathbf{j} \times \mathbf{B}) \times \mathbf{b} = (\mathbf{j} \cdot \mathbf{b}) \cdot \mathbf{B} - (\mathbf{B} \cdot \mathbf{b}) \cdot \mathbf{j}$, and for $\mathbf{b}_i \perp \mathbf{b}$, $\mathbf{j}\{-j_r, -j_\theta, -j_x\}$, $\mathbf{g}\{g_r, g_\theta, g_x\}$, $\mathbf{b}\{b_r, 0, b_x\}$, we obtain

$$j_\theta b_r = \beta_r\left[\frac{e\alpha}{m_i}(g_r b_x - g_x b_r) + (j_r b_x - j_x b_r)\right], \qquad (2.2)$$

$$j_\theta b_x = -\beta_x\left[\frac{e\alpha}{m_i}(g_r b_x - g_x b_r) + (j_r b_x - j_x b_r)\right], \qquad (2.3)$$

$$(\mathbf{j} \times \mathbf{b})_\theta = j_r b_x - j_x b_r. \qquad (2.4)$$

Here, $\beta_x = \sigma(\alpha) b_x/(\alpha n_0 e)$ is the Hall parameter calculated for the axial component of the field; $\beta_r = \sigma(\alpha) b_r/(\alpha n_0 e)$ is the Hall parameter calculated for the radial component of the field. The field intensity $\mathbf{E}$ does not appear in Eqs. (2.2) and (2.3) because $(\mathbf{E} \times \mathbf{b})_r = (\mathbf{E} \times \mathbf{b})_x = 0$. Using the equations

$$\begin{gathered}\frac{\partial \Psi}{\partial r} = g_x r, \quad \frac{\partial \Psi}{\partial x} = -g_r r, \quad \frac{\partial J}{\partial r} = j_x r, \\ \frac{\partial J}{\partial x} = -r j_r, \quad \frac{\partial \Phi}{\partial r} = r b_x, \quad \frac{\partial \Phi}{\partial x} = -r b_r,\end{gathered} \qquad (2.5)$$

we introduce functions for the mass flow, electric current, and magnetic field, where

$$\Psi = \int_0^r g_x r\,dr, \quad J = \int_0^r j_x r\,dr, \quad \Phi = \int_0^r b_x r\,dr. \qquad (2.6)$$

In this case, the equations for the conservation of mass and charge and for continuity of magnetic lines of force ($\operatorname{div} \mathbf{b} = 0$) are satisfied automatically. We replace the quantities g_x, g_r, j_x, j_r, b_x, b_r in Eqs. (2.2), (2.3) and (2.4) by the corresponding derivatives of current functions in Eqs. (2.5). Because of the relation

$$\frac{\partial}{\partial x}\left(f \frac{\partial \varphi}{\partial z}\right) = f \frac{\partial^2 \varphi}{\partial x \partial z} + \frac{\partial f}{\partial x}\frac{\partial \varphi}{\partial z}$$

after simple transformations we have

$$\left.\begin{gathered} j_\theta b_r = -\beta_x(\alpha)\frac{b_r}{b_x}\frac{1}{r^2}\left\{\frac{e\alpha}{m_i}\left[\frac{\partial}{\partial x}\left(\Psi \frac{\partial \Phi}{\partial r}\right) - \frac{\partial}{\partial r}\left(\Psi \frac{\partial \Phi}{\partial x}\right)\right]\right. \\ \left. + \frac{\partial}{\partial x}\left(J \frac{\partial \Phi}{\partial r}\right) - \frac{\partial}{\partial r}\left(J \frac{\partial \Phi}{\partial x}\right)\right\}, \\ j_\theta b_x = -\frac{b_x}{b_r} j_\theta b_r, \\ (\mathbf{j} \times \mathbf{b})_\theta = -\frac{1}{r^2}\left[\frac{\partial}{\partial x}\left(J \frac{\partial \Phi}{\partial r}\right) - \frac{\partial}{\partial r}\left(J \frac{\partial \Phi}{\partial x}\right)\right]. \end{gathered}\right\} \qquad (2.7)$$

The equations (2.7) make it possible to calculate the integrals $\int_V j_\theta b_x r\,dA\,dx$ and $\int_V (\mathbf{j} \times \mathbf{b})_\theta r\,dA\,dx$. Indeed, if we take the Hall parameter outside the integral sign in the integral $\int_V j_\theta b_x r\,dA\,dx$ using the theorem of the mean, by the use of Green's equation (plane analogy of Gauss's theorem) we have

$$\int_V j_\theta b_x r\,dA\,dx = -2\pi \langle \beta_x \rangle \oint \left(\frac{e\alpha}{m_i}\Psi + J\right) d\Phi, \qquad (2.8)$$

$$\int_V (\mathbf{j} \times \mathbf{b})_\theta r\,dA\,dx = 2\pi \oint J\,d\Phi. \qquad (2.9)$$

The integration is carried out along the closed contour $k_0kabdd_0k_0$, which encloses the region where the discharge current and the plasma flow interact with the external magnetic field.

To calculate the volume integral of the axial component of the electromagnetic force it is necessary to know the dependence of the quantity b_r/b_x on the variables x and r; this quantity characterizes the slope of the magnetic lines of force relative to the channel axis. We assume the magnetic field induced by the Hall currents is small in comparison with the external field. Then the ratio b_r/b_x for the external magnetic field can be determined by expanding b_r and b_x in powers of r with respect to the induction of the magnetic field on the axis $b_0(x)$. For a typical channel radius $R_s \ll R_c$ (R_c is the internal radius of the solenoid), the expansions of b_r and b_x can be limited to the first term, so that

$$\frac{b_r}{b_x}=-\frac{r}{2R_s}\frac{d\ln b_0^0}{dx^0}=\frac{r}{2R_s}\varkappa. \tag{2.10}$$

Here, $b_0^0 = b_0(x)/b_s$, $x^0 = x/R_s$, where b_s is a typical value of the external magnetic field induction in the channel (for example, at the cathode) and $b_0(x)$ is the magnetic induction on the channel axis.

Calculated dependences on $z^0 = z/a_1$ for the quantities b_0^0 and $\varkappa$ are shown in Fig. 2 for several versions of solenoids with the constant current density ordinarily used in accelerator testing. It is clear from Fig. 2 that the quantity $\varkappa$ first rises rapidly from 0 to its maximum value and then either remains constant or decreases slowly as z^0 increases. We substitute b_r/b_x from Eq. (2.10) into Eq. (2.2) for $(\mathbf{j} \times \mathbf{b})_x$ and take the quantity $\beta_x\varkappa$ outside the integral sign in $\int_V j_\theta b_r dV$ using the theorem of the mean. This can be done if β_x does not change markedly in the volume of the accelerator channel. By analogy with what has been done before, we obtain

$$\int_V j_\theta b_r dA\,dx=\frac{\pi\beta_x(\alpha)\varkappa}{R_s}\oint\left(\frac{e\alpha}{m_i}\Psi+J\right)d\Phi. \tag{2.11}$$

We compute the contour integrals in Eqs. (2.8), (2.9), and (2.11). Let the distribution of j_x, g_x, and b_x be uniform in the initial section, i.e., at the cathode. To simplify the calculations, we assume that the distributions of b_x and g_x are uniform in the section dd. In addition, we assume that the short-circuit region at the anode is small, i.e., the points a and b of the contour $k_0kabdd_0k_0$ are close to each other. This last condition makes it possible to disregard the drop in discharge current along the axial coordinate in the anode short-circuit region in calculating a contour integral. The contour integral $\oint[(e\alpha/m_i)\Psi + J)]d\Phi$ over the contour $k_0kabdd_0k_0$ can be written

$$\oint\left(\frac{e\alpha}{m_i}\Psi+J\right)d\Phi=\int_k^a\left(\frac{e\alpha}{m_i}\Psi+J\right)d\Phi+\int_b^d\left(\frac{e\alpha}{m_i}\Psi+J\right)d\Phi$$
$$-\int_{d_0}^d\left(\frac{e\alpha}{m_i}\Psi+J\right)\frac{\partial\Phi}{\partial r}dr+\int_{k_0}^k\left(\frac{e\alpha}{m_i}\Psi+J\right)\frac{\partial\Phi}{\partial r}dr. \tag{2.12}$$

Here, the sections kk and dd are assumed to be plane so that $d\Phi = (\partial\Phi/\partial r)dr$, and the integrals along the segments ab and d_0k_0 are zero because $d\Phi = 0$. Because the quantities Ψ and J remain constant on the segments ka and bd of the contour, with J = 0 on the segment bd, the first and second integrals in (2.12) will be

$$\int_k^a\left(\frac{e\alpha}{m_i}\Psi+J\right)d\Phi=\left(\frac{e\alpha}{m_i}\Psi_0+J_0\right)(\Phi_a-\Phi_k), \tag{2.13}$$

$$\int_b^d\left(\frac{e\alpha}{m_i}\Psi+J\right)d\Phi=\frac{e\alpha}{m_i}\Psi_0(\Phi_d-\Phi_a). \tag{2.14}$$

Here, $\Psi_0 = \int_0^R g_x r dr = G/2\pi$, $J_0 = \int_0^R j_x r dr = J_p/2\pi$, R is the boundary of the plasma jet or of the channel, $\Phi_a = \int_0^{R_a} b_x r dr$, $\Phi_k = \int_0^{R_k} b_x r dr$, $\Phi_d = \int_0^{R_d} b_x r dr$ are the magnetic field fluxes through the area of a section of the channel or of the plasma jet at the corresponding points a, k, and d on the contour. By definition, $\partial\Phi/(\partial r) = b_x r$, $\Psi = \int_0^r g_x r dr$, $\Phi = \int_0^r b_x r dr$. Then the third and fourth integrals for uniform radial distribution of g_x, j_x, and b_x and for the boundary condition $\mathbf{j}\cdot\mathbf{n} = 0$ on dd will be

$$\int_{d_0}^d\left(\frac{e\alpha}{m_i}\Psi+J\right)\frac{\partial\Phi}{\partial r}dr=\frac{e\alpha}{m_i}\Psi_0\frac{\Phi_d}{2}, \tag{2.15}$$

$$\int_{k_0}^k\left(\frac{e\alpha}{m_i}\Psi+J\right)\frac{\partial\Phi}{\partial r}dr=\left(\frac{e\alpha}{m_i}\Psi_0+J_0\right)\frac{\Phi_k}{2}. \tag{2.16}$$

In the distributions of g_x and b_x in the section dd of the plasma jet, the value of the integral on the left side of Eq. (2.15) will differ from Eq. (2.15) only by a factor of order unity. For example, in the case of a jet profile $g_x = g_0[1 - (r/R)^{3/2}]$ (g_0 is the value of the mass flow on the axis), the factor is 1.36.

Summing the calculated integrals in Eq. (2.12), after simple transformations we obtain

$$\oint\left(\frac{e\alpha}{m_i}\Psi+J\right)d\Phi=J_0\Phi_k\left(1+\frac{\alpha}{\xi}\right)\left\{\frac{\Phi_a}{\Phi_k}\left[1+\frac{\alpha}{\alpha+\xi}\left(\frac{c}{2}\frac{\Phi_d}{\Phi_a}-1\right)\right]-\frac{1}{2}\right\}. \tag{2.17}$$

Here, c is a factor of order unity, which takes account of the nonuniform distribition of g_x in the section dd, and $\xi = m_i J0/e\psi_0$ is an exchange parameter. The exchange parameter was first introduced in ref. 10 and characterizes

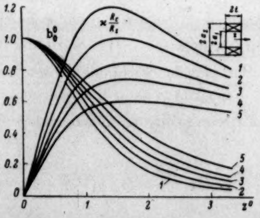

Fig. 2. Axial distribution of the quantity $b_0^0(x)$ and of the parameter $\varkappa$ for solenoids with constant current density. δ: 1) 1.4; 2) 1.9; 3) 2.5; 4) 3.0; 5) 4.0. γ = 0.6, $\delta = a_2/a_1$, $\gamma = t/a_1$, $z^0 = z/a_1$.

the ratio between the Hall electric field and the induction electric field **v** × **b**.

It should be noted that the limitations under which the contour integral (2.12) is calculated are not fundamental; for a given cathode shape, given distributions of g_x, j_x, and b_x at the beginning of the channel, known distributions of g_x and b_x in section dd of the plasma jet, and a known reduction of discharge current in the segment *ab* of the contour, the integrals on the right side of Eq. (2.12) can be calculated easily.

The axial force accelerating the plasma and acting on the solenoid can be written with the use of Eq. (2.17):

$$\int\limits_V j_\theta b_r dA\,dx = \frac{\langle \beta_x(a)\rangle \varkappa}{2R_s} J_d \Phi_k \left(1+\frac{a}{\xi}\right)\left\{\frac{\Phi_a}{\Phi_k}\left[1+\frac{a}{a+\xi}\left(\frac{c}{2}\frac{\Phi_d}{\Phi_a}-1\right)\right]-\frac{1}{2}\right\}. \tag{2.18}$$

The angular momentum relative to the x axis, or the torque which acts to twist the plasma, can be found from Eq. (2.9):

$$\int\limits_V (j_r b_x - j_x b_r)\, r\, dA\,dx = J_d \Phi_k \left(\frac{\Phi_a}{\Phi_k}-\frac{1}{2}\right). \tag{2.19}$$

Consequently, the angular velocity of the plasma in the section dd will be given by

$$\omega_d = \frac{2J_d \Phi_k \left(\frac{\Phi_a}{\Phi_k}-\frac{1}{2}\right)}{G R_d^2}.$$

Note that for $\Phi_k = b_k(R_k^2/2)$, the angular velocity of the plasma is proportional to the parameter $J_d b_k/G$. This dependence has been observed experimentally.[11]

To compute the integral determining the plasma pressure force on the cathode in Eq. (1.10) we use the representation of $j_\theta b_x$ in the form (2.7). We then have

$$\int\limits_A j_\theta b_x r\, dA = 2\pi \langle \beta_x(a)\rangle \left\{ \int\limits_0^R \frac{\partial}{\partial x}\left[\left(\frac{ea}{m_i}\Psi + J\right)\frac{\partial \Phi}{\partial r}\right] dr - \int\limits_0^R \frac{\partial}{\partial r}\left[\left(\frac{ea}{m_i}\Psi + J\right)\frac{\partial \Phi}{\partial x}\right] dr \right\}. \tag{2.20}$$

With the help of the rule for differentiation of an integral with respect to a parameter, we obtain

$$\int\limits_A j_\theta b_x r\, dA = 2\pi \langle \beta_x\rangle \left\{ \frac{d}{dx}\int\limits_0^R \left(\frac{ea}{m_i}\Psi + J\right)\frac{\partial \Phi}{\partial r}\, dr - 2\left(\frac{ea}{m_i}\Psi_0 + J_0\right)\left[\frac{d\Phi(r=R)}{dx}\right]_{x=0} \right\}.$$

Because of the conservation of Ψ and J within the boundaries of the plasma jet for uniform distribution of g_x, j_x, and b_x along the cathode radius, using (2.16) derived above we have

$$\int\limits_A j_\theta b_x r\, dA = -\frac{3}{2}\frac{\langle \beta_x\rangle}{R_s} J_d \Phi_k \left(1+\frac{a}{\xi}\right)\left[\frac{d\Phi^0}{dx^0}\right]_{x=0}. \tag{2.21}$$

Here, $\Phi^0 = \Phi/\Phi_k$, $\Phi = \int\limits_0^{R(x)} b_x r\,dr$, $x^0 = x/R_s$.

Near the cathode one can assume the magnitude of the magnetic field induction to be independent of radius, i.e., $\Phi_k = b_k(R_k^2/2)$. Equations (2.18) and (2.21) then make it possible to write the component of the force resulting from the interaction between the discharge current and the external magnetic field in the form

$$F_s = \frac{\langle \beta_x\rangle \varkappa}{4} J_d b_k R_k \left(1+\frac{a}{\xi}\right) f\left(\frac{\Phi_a}{\Phi_k},\ \frac{\Phi_d}{\Phi_a},\ \xi,\ a,\ \left[\frac{d\Phi^0}{dx^0}\right]_{x=0}\right). \tag{2.22}$$

Here, the function *f* is defined by

$$f = \frac{\Phi_a}{\Phi_k}\left[1+\frac{a}{a+\xi}\left(\frac{c}{2}\frac{\Phi_d}{\Phi_a}-1\right)\right]-\frac{1}{2}+\frac{3}{2}\frac{1}{\varkappa}\left[\frac{d\Phi^0}{dx^0}\right]_{x=0}. \tag{2.23}$$

According to Eq. (1.5), the average velocity of the plasma in the section dd when $F_c \ll F_B$ will be

$$u = \frac{\langle \beta_x\rangle \varkappa}{4}\frac{J_p b_k R_k}{G}\left(1+\frac{a}{\xi}\right) f. \tag{2.24}$$

3. ANALYSIS OF THE RESULTS

It is clear from Eqs. (2.8), (2.9), and (2.11) that the dimensionless parameters $\langle B_x\rangle$, $\varkappa$, α, $\xi = m_i J/(e\psi)$ determine the nature of the plasma flow in the channel. For example, the dimensionless parameter $\varkappa$ for the shape of the magnetic field defines the ratio between the axial force accelerating the plasma and the radial force leading to its compression. The complex parameter $\langle \beta_x\rangle \varkappa (1 + \alpha/\xi)$ defines the ratio between axial and torsional plasma forces. From the viewpoint of efficient plasma acceleration in the axial direction it is necessary to ensure a parameter value $\langle \beta_x\rangle \varkappa \gg 1$ with an increase in the value of the parameter $\varkappa$ being advisable. An increase in the Hall parameter will lead to simultaneous increase in the axial and compressive plasma forces. The parameters α and ξ in these accelerators are interrelated so that for sufficiently complete ionization of the plasma it is necessary to ensure that $\xi \geq 1$.

In addition, Eqs. (2.8), (2.9), and (2.11) indicate that the magnitudes of all the forces and moments which result from the interaction between the discharge current and the external magnetic field depend significantly on the shape of the magnetic field in the channel. For example, if the magnetic lines of force are closed from cathode to anode the values of the forces and moments will be zero because the equality $d\Phi = 0$ is satisfied.

As is clear from Eqs. (2.21) and (2.23), the plasma pressure force on the cathode will be determined completely if the axial dependence of the radius of the plasma jet boundary and of the quantity b_x is known. When the boundary of the plasma jet coincides with a magnetic line of force the pressure on the cathode will be zero. If $d\Phi^0/(dx^0) > 0$, the pressure on the cathode is positive because of plasma compression toward the axis, i.e., an increased pressure is created at the cathode relative to the pressure p_* outside the jet. If $d\Phi^0/dx^0 < 0$, the pressure at the cathode is negative relative to $p_* A_{kk}$. In that case, a region of reduced pressure relative to the pressure p_* is created at the cathode. Note that by definition $\Phi = \int\limits_0^R b_x r\,dr = b_x(R^2/2)$, where the dependence of b_x on x is usually known. The dependence on x of the radius R of the boundary of the plasma jet is not known precisely and is determined by the laws for plasma diffusion in electromagnetic fields.

Now let $d\Phi^0/dx^0 = 0$ and assume that $\Phi_d = \Phi_a$, $\alpha = c \simeq 1$. In addition, we assume the quantity 0.5 in Eq. (2.23) can be neglected in comparison with Φ_a/Φ_k. In this case, the expression for F_B is simplified significantly and is determined only by the reaction acting on the solenoid,

$$F_B \simeq \frac{\langle\beta_x\rangle\varkappa}{4} J_d b_k R_k \frac{\Phi_a}{\Phi_k}\left(1+\frac{\alpha}{2\xi}\right). \tag{3.1}$$

It is clear from Eq. (3.1) that the reaction force on the solenoid, which arises through the imposition of an external magnetic field on the discharge, is directly proportional to the quantity $J_d b_k R_k$, which has the dimensionality of a force multiplied by a number of dimensionless parameters. These dimensionless parameters, $\langle\beta_x\rangle$, α, $\varkappa$, ξ, and Φ_a/Φ_k, are similarity parameters because when they are the same for two different accelerator models the quantities F_B, u_d, and ω_d will be identical for $F_c < F_B$ and the equality of $J_d b_k R_k$.

Physically, the quantity $J_d b_k R_k$ is the force which acts on a linear current-carrying conductor of length R_k in a magnetic field of induction b_k perpendicular to the current. The factor $(1 + \alpha/2\xi)$ takes account of motion of the conductor in the magnetic field in the direction of the electric current through the quantity ξ. The shape parameter $\varkappa$ for the magnetic field determines the actual magnitude of the magnetic field induction, $\varkappa b_k$, with which the Hall current interacts. From the viewpoint of a current-carrying conductor, this parameter characterizes the slope of the magnetic induction vector relative to the axis of the current-carrying conductor in the direction of current flow. The parameter Φ_a/Φ_k characterizes the spatial structure of the discharge. The Hall parameter determines the degree of transformation of discharge current into Hall current, or the true current which must be transmitted along a linear conductor in order to simulate the force acting on the plasma.

In almost all experiments with accelerators, the magnitude of the Hall parameter is known inexactly. Here it is assumed constant in the derivation of the equations for the electromagnetic forces. This assumption is valid in two cases, which are also realized in practice in the operation of Hall accelerators. First, this occurs when the current flow in the accelerator follows the circuit proposed in ref. 3. In this case, current transport across magnetic lines of force occurs outside the accelerator in a gas cloud within which $n_e \simeq$ const, $T_e \simeq$ const, $\varkappa =$ const, and $b_x \simeq$ const. Second, the Hall parameter can be considered to be constant and equal to some effective value when oscillations of the electric field in the plasma are present.[12] Usually oscillations in electron density are a source of oscillations in the electric field intensity. An analysis of Ohm's law was given[13] including fluctuations in electron density and it was shown that the effective value of the Hall parameter remains constant over a broad range of variation of the "ordinary" value of the Hall parameter and is determined by the relative magnitude of the density fluctuations. Note that the first case is realized when the atom density in the surrounding space is comparable to the particle density in the plasma flow; the second case is realized in a high vacuum. In the general case, the magnitude of the Hall parameter can be determined and its role in the acceleration process explained only through a comparison of theoretical and experimental relations and by direct measurements.

It should be pointed out in conclusion that the region of applicability for the relations obtained here corresponds to plasma acceleration in the channel of a Hall accelerator with $\xi \geq 1$, $\langle\beta_x\rangle > 1$, $R_{iL} > R_a \gg R_{eL}$, and $R_c \gg R_k$.

The author thanks A. I. Morozov and I. P. Nekrasov for valuable discussions.

---

[1] W. Grossman, Jr., R. V. Hess, and N. A. Hassan, AIAA, J., 3, 1034 (1965).

[2] S. Bennett, R. R. John, G. Enos, and A. Tuchman, AIAA Paper 66-239.

[3] G. Kruelle, AIAA Paper 67-672.

[4] Jan Rosciszewski, Phys. Fluids, 10, 1095 (1967).

[5] A. I. Morozov, Yu. V. Esipchuk, G. N. Tilinin, A. V. Trofimov, Yu. A. Sharov, and G. Ya. Shchepkin, Zh. Tekh. Fiz., 42, 54 (1972) [Sov. Phys.—Tech. Phys., 17, 38 (1972)].

[6] S. I. Braginskii, "Transport Phenomena in Plasma," Reviews of Plasma Physics, Vol. 1, Consultants Bureau, New York (1965).

[7] U. Kogelschatz, AIAA J., 8, 150 (1970).

[8] Von H. Maecker, Zs. Physik, 141, 198 (1065).

[9] R. R. John, S. Bennett, and J. F. Connors, Astronautica Acta, 11, 97 (1065).

[10] A. I. Morozov and L. S. Solov'ev, Dokl. Akad. Nauk SSSR, 164, 80 (1965) [Sov. Phys.—Dokl., 10, 834 (1966)].

[11] Plasma Accelerators, 125 [in Russian], Izd. Mashinostroenie, Moscow (1973).

[12] G. C. Janes and R. S. Lowder, Phys. Fluids, 9, 1115 (1966).

[13] J. F. Louis, Phys. Fluids, 10, 2062 (1967).

Theory of the positive column in neon

Yu. B. Golobovskii, Yu. M. Kagan, and R. I. Lyagushchenko

A. A. Zhdanov Leningrad State University

(Submitted July 16, 1973)
Zh. Tekh. Fiz., 44, 536-543 (March 1974)

A theory is developed for a stationary positive column in a neon discharge at pressures of tens and hundreds of torr; the analysis includes the non-Maxwellian nature of the fast-electron distribution function, stepwise ionization, the emission of resonance radiation, volume recombination, and heating of the atomic gas. The theory is compared with experimental results.

1. The development of a theory for the positive column at pressures of tens and hundreds of torr has been discussed recently.[1-4] Such a theory must take account of the actual form of the electron energy distribution function. This function is determined from the kinetic equation with elastic and inelastic collisions between electrons and atoms and interelectron interactions.[9] By means of this distribution function one can determine the total number of ionization events per unit volume per unit time. In this case, stepwise ionization from low metastable and resonance levels plays a fundamental role. If the emission of resonance radiation is neglected, the total number of ionization events is equal to the total number of inelastic collisions, which can be determined directly from the kinetic equation.[6] A theory of the positive column has been developed using such an approximation.[1-4] One can write a closed system of equations for determination of the electron density n, the electron temperature T_e, and the longitudinal field E. Further development of the theory includes nonuniform heating of the gas,[6-8] emission of resonance radiation,[9] and the effect of recombination.[10]

An attempt is made here to construct a theory for the positive column in a neon discharge including simultaneous consideration of nonuniform heating, resonance radiation emission, and volume recombination.

2. The basic equations are[1]

$$\left.\begin{aligned}&\frac{1}{\rho}\frac{d}{d\rho}\left\{\rho b_p\left[u_e\frac{dn}{d\rho}+\frac{1}{2}n\frac{du_e}{d\rho}\right]\right\}+Z-\Gamma=0,\\&n(R)=0\quad\left.\frac{dn}{d\rho}\right|_{\rho=0}=0;\end{aligned}\right\}\tag{1}$$

$$\left.\begin{aligned}&\frac{1}{\rho}\frac{d}{d\rho}\left[\rho\varkappa\frac{d\Theta}{d\rho}\right]+jE=0,\\&\Theta(R)=\Theta_R\quad\left.\frac{d\Theta}{d\rho}\right|_{\rho=0}=0;\end{aligned}\right\}\tag{2}$$

$$i=2\pi\int_0^R j(\rho)\rho d\rho,\tag{3}$$

$$u_e=0.27\sqrt{\frac{M}{m}}E\lambda,\tag{4}$$

$$p=Nk\Theta.\tag{5}$$

Here $j = eEb_en$ is the current density; $u_e = (kT_e)/e$; the thermal conductivity coefficient for neon is assumed to be $\varkappa = C\sqrt{\Theta}$, where[11] C = 265 (erg/sec) (cm/deg$^{3/2}$); $b_p = B\sqrt{\Theta}/p$, where[12] $B = 8.7\cdot10^4$; $b_e = A(\sqrt{\Theta}/\sqrt{p})(1/\sqrt{E})$, where[13] $A = 5.9\cdot10^4$; $\Gamma = \gamma n^2$ is the number of recombination events (per unit volume per unit time). It is assumed that $\gamma = \gamma_0\sqrt{300/T_e}$, where[14] $\gamma_0 = 1.75\cdot10^{-7}\ \mathrm{cm^3\cdot sec^{-1}}$.

We assume in Eq. (4), as earlier,[1] that the main energy loss for the electrons occurs through elastic collisions with gas atoms.

3. We determine the number of ionization events Z under the assumption that stepwise ionization occurs from the $2p^53s$ level in neon. It is therefore necessary to solve a system of balance equations for the population of all four $2p^53s$ levels. This leads to extremely cumbersome expressions and requires a knowledge of a large number of cross sections for the transitions between these levels. These cross sections are not known exactly. However, the known data for these cross sections[15] show that they are very large, which leads to strong mixing in the $^3P_{0,1,2}$ system. One can therefore assume that the atoms in $^3P_{0,1,2}$ levels are distributed in accordance with statistical weights. This makes it possible to regard the $^3P_{0,1,2}$ system as a single effective ^3P level. In constructing the balance equations for the ^3P and $^1P_1$ levels, we consider the following processes.

a. Excitation from the ground state. The number of excitation events in the effective ^3P level is determined under the assumption that the number of excitation events of the $^3P_0$, $^3P_1$, $^3P_2$, and $^1P_1$ levels goes like the statistical weights and the total number of excitation events in all four levels coincides with the total number of inelastic collisions α. Then the total number of excitation events of the effective ^3P level is $3\alpha/4$.

The basis for this assumption is the fact that the cross sections for direct excitation of the $^3P_0$, $^3P_1$, and $^3P_2$ levels calculated from tables[16] in an energy region of a few volts in the neighborhood of the excitation threshold are proportional to the statistical weights. This condition is less well satisfied for the $^1P_1$ level; however, the contribution from excitation of this level to the total excitation of all four levels is relatively small.

b. Radiative decay of the $^3P_1$ level. Radiative decay of the $^3P_1$ level is characterized by a decay probability. According to Holstein[17] we have

$$A_{\mathrm{eff}}=0.2\sqrt{\frac{\lambda}{R}}A,$$

for the dispersion tail of the line, where A is the probability of spontaneous transition. The probability for radiative decay of the effective ^3P level considering the proportionality to statistical weights for the populations of the $^3P_{0,1,2}$ levels is $(1/3)A_{\mathrm{eff}}$.

c. Transitions between ^3P and $^1P_1$ levels. The probability of a transition from level k to level m of the $2p^53s$ system through a $2p^53p$ level is nW_{km},

where

$$W_{km}=\sum_{i=1}^{10}\langle v\sigma\rangle_{ki}\frac{A_{im}}{\sum_{k=1}^{4}A_{ik}}. \tag{6}$$

The subscript i numbers the levels in the $2p^5 3p$ system, and the subscripts k and m, levels in the $2p^5 3s$ system. In all cases, numbering is in the order of increasing level energy. A_{im} is the probability of the radiative transition i → m. The product of rate by the cross section for the appropriate process averaged over a Maxwellian distribution is determined with the help of tables.[16]

The probability of transition from the effective ^3P level to the $^1P_1$ level through a $2p^5 3p$ level is nW_Y, where

$$W_Y=\frac{1}{\sum_{k=1}^{3}g_k}\sum_{k=1}^{3}g_k W_{kY}. \tag{7}$$

The probability of transition from the $^1P_1$ level to the effective ^3P level through a $2p^5 3p$ level is nW'_Y, where

$$W'_Y=\sum_{m=1}^{3}W_{Ym}. \tag{8}$$

A calculation for T_e = 30,000°K yields $W_Y = 0.87 \cdot 10^{-7}$ and $W'_Y = 3.1 \cdot 10^{-7}$.

Direct transitions between the $^3P_{0,1,2}$ and $^1P_1$ levels may also occur, but the cross sections for these transitions are not known. If it is assumed the cross sections for these transitions are no larger than the cross sections between $^3P_{0,1,2}$ levels, consideration of these transitions does not qualitatively change the particle balance in the $^3P_{0,1,2}$ system.

d. Stepwise ionization. We introduce $nW_{\Sigma\infty}$, the total probability of ionization from the ^3P level, where

$$W_{\Sigma\infty}=\sum_{k=1}^{3}\frac{g_k}{\sum_{k=1}^{3}g_k}\langle v\sigma\rangle_{k\infty}. \tag{9}$$

Using the material above, the equations of balance for the atomic densities N_Σ and N_Y in the ^3P and $^1P_1$ levels are written in the form

$$\frac{3}{4}\alpha+N_Y nW'_Y=N_\Sigma\left[nW_Y+nW_{\Sigma\infty}+\frac{g_2}{\sum_{k=1}^{3}g_k}A_{\text{eff}}\right], \tag{10}$$

$$\frac{1}{4}\alpha+N_\Sigma nW_Y=N_Y[nW'_Y+A_Y]. \tag{11}$$

In Eq. (11) we neglect breakdown of the fourth level because of ionization.

The number Z of ionization events is equal to $N_\Sigma nW_{\Sigma\infty} + N_Y nW_{Y\infty}$. Substituting N_Σ and N_Y from Eqs. (10) and (11), we obtain

$$Z=\alpha\frac{nW_{\Sigma\infty}\left(\frac{W_Y}{W'_Y}+\frac{3}{4}\frac{A_Y}{nW_Y}\right)}{A_Y+\left(\frac{A_Y}{nW_Y}+\frac{W'_Y}{W_Y}\right)\left(nW_{\Sigma\infty}+A_2\frac{g_2}{\sum_{i=1}^{3}g_i}\right)}. \tag{12}$$

Obvious limiting cases follow from Eq. (12).

When A_Y and $A_2 \to 0$ (neglect of resonance radiation emission), $Z = \alpha$.

When A_Y and $A_2 \to \infty$ (very high emission of resonance radiation), we have

$$Z=\frac{3}{4}\alpha\frac{nW_{\Sigma\infty}}{nW_Y+A_2\frac{g_2}{\sum_{i=1}^{3}g_i}}.$$

The quantities $\langle v\sigma\rangle_{k\infty}$ in Eq. (9) are calculated with the help of earlier results[18] using effective principal quantum numbers.

The results can be approximated by

$$nW_{\Sigma\infty}=225\tilde{n}u_e^3, \tag{13}$$

where $\tilde{n} = n \cdot 10^{-11}$ and u_e is in volts.

In this case, the calculation takes account only of direct ionization from the ^3P level. Associative ionization can also occur where there is excitation of levels separated from the ionization energy by an amount[19] less than, or equal to, 0.6 eV.

If we consider the limiting case, in which all excited atoms in this band are ionized, then the quantity $\sigma_{k\infty}$ in Eq. (9) should be understood to mean the sum of the cross sections for ionization and excitation of the corresponding levels. The calculation can be performed using tables of cross sections.[16] We then obtain

$$nW_{\Sigma\infty}=455\tilde{n}u_e^3, \tag{14}$$

where u_e is in volts.

The true value of $nW_{\Sigma\infty}$ lies between the values given by Eqs. (13) and (14). It is necessary to know the cross section for associative ionization, which is poorly known for neon. We therefore use the lower limit of the quantity given by Eq. (13).

The total number α of inelastic collisions is obtained from the expression[6]

$$\alpha=\frac{4\chi}{\sqrt{\pi}}n\nu_{ee}(u_e)(1+\gamma u_1^3)\exp\left[-\frac{u_1^2}{4}+\frac{u_1}{4\gamma}-\frac{1}{2\gamma}\left(1+\frac{1}{4\gamma}\right)\ln(1+2\gamma u_1)\right], \tag{15}$$

where $\nu_{ee}(u_e)$ and $\nu_{ea}(u_e)$ are the frequencies of interelectron and elastic electron–atom collisions at an energy $\varepsilon = eu_e$; $\gamma = (m/M)(\nu_{ea}/\nu_{ee})$; $u_1 = eV_1/kT_e$, where V_1 is the first excitation potential; χ is a function depending slightly on plasma parameters; we assume χ = 0.5 in the calculations.

In accordance with Eq. (12), the final expression for Z then is

$$Z=Z_1\alpha, \tag{16}$$

$$Z_1=225\tilde{n}u_e^3\frac{3.58+19.25\frac{1}{\tilde{n}\sqrt{R}}\exp\frac{2}{u_e}}{4.8\cdot 10^5\frac{1}{\sqrt{R}}+\left(3.58+\frac{25.7}{\tilde{n}\sqrt{R}}\exp\frac{2}{u_e}\right)\left(0.8\cdot 10^4\frac{1}{\sqrt{R}}+225\tilde{n}u_e^3\right)}; \tag{17}$$

u_e is in volts.

4. We turn to a solution of the system (1)-(5) by successive approximations. In Eq. (2), we introduce $x = \rho/R$ and $\tau = (\Theta/\Theta_0)^{3/2}$ and approximate the dependence of current density on ρ by a Bessel function, setting $j = j_0 J_0(2.4x)$. Then from Eq. (3) we have

$$j=\frac{i}{0.43\pi R^2}. \qquad (18)$$

The solution of Eq. (2) takes the form

$$\tau=\frac{1}{h}+\frac{h-1}{h}J_0(2.4x), \qquad (19)$$

where

$$h=\left(\frac{\Theta_0}{\Theta_R}\right)^{3/2}=1+\frac{0.19}{C}\frac{iE}{\Theta_R^{3/2}}. \qquad (20)$$

Using the expressions for current density, electron mobility, and Eq. (18), we obtain

$$n_0=\frac{1}{0.43\pi R^2 A}\frac{ip}{R^2\sqrt{E\Theta_0}}. \qquad (21)$$

Introducing the variables $x = \rho/R$ and $\omega = (n/n_0)\sqrt{\Theta/\Theta_0}$ in Eq. (1), we obtain

$$\frac{1}{x}\frac{d}{dx}\left[x\tau^{1/3}\frac{d\omega}{dx}\right]+\frac{(Z-\Gamma)R^2}{b_p(0)\,u_e(0)\,n_0}=0, \qquad (22)$$

$$\omega(0)=1,\ \frac{d\omega}{dx}\Big|_{x=0}=0,\ \ \omega(1)=0. \qquad (23)$$

Expressing n_0, $u_e(0)$, and Θ_0 through i/R, pR, Θ_R, and R by means of Eqs. (4), (5), and (21), we obtain an equation for ω in terms of the parameter ER. For given external parameters, the magnitude of ER is determined by the boundary conditions (23). The equation is solved numerically. The solution yields a profile of ω and a value of ER.

It should be noted that in the numerical integration of Eq. (22) with the initial conditions (23), the behavior of the function ω depends strongly on the parameter ER. In the numerical integration it is therefore necessary to vary the value of ER with a high degree of accuracy. This feature is illustrated in Fig. 1.

Using the function ω, one can find an expression for n_0 in the next approximation from Eq. (3) by calculating the integral $\int_0^1 \omega x dx$. The pressure p with the discharge on appears in the theory. The pressure p_0 with no discharge is usually measured experimentally. The relation between p and p_0 depends on the configuration of the discharge tube. If the cold volumes are small, this relation has the form

$$p=p_0\frac{\Theta_R}{3\Theta_k}\left[1+\sqrt{\frac{\Theta_0}{\Theta_R}}+\frac{\Theta_0}{\Theta_R}\right], \qquad (24)$$

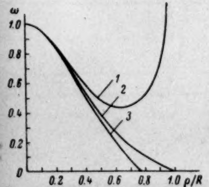

Fig. 1. Solution of Eq. (22) as a function of the parameter ER. pR = 96 torr · cm; i/R = 41.6 mA/cm; ER, V: 1) 34.2; 2) 34.268; 3) 34.3.

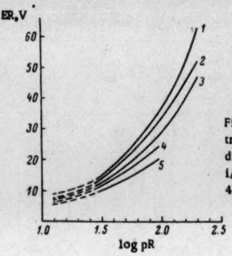

Fig. 2. Dependence of reduced electric field ER(V) on pressure pR with discharge on. Here and in Figs. 3-6, i/R, mA/cm: 1) 4.16; 2) 8.4; 3) 21; 4) 41.6; 5) 84.

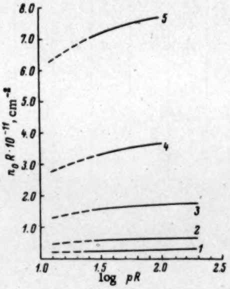

Fig. 3. Dependence of electron density $n_0R\cdot10^{-11}$ (cm^{-2}) on pressure pR with discharge on.

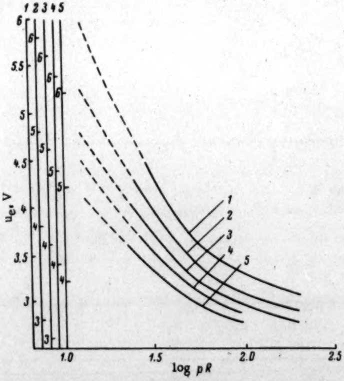

Fig. 4. Dependence of electron temperature u_e(V) on pressure pR with discharge on. Each curve has its own scale on the ordinate.

TABLE 1. Values of Positive Column Parameters Measured Experimentally[21] (I), Calculated by Old Theory[8] (II), and Calculated by New Theory (III)

		$p_0R = 36$						
		i/R						
		4.16	8.4	21	41.6	84	167	333
ER, V	I	15.5	15.3	13.3	11.0	9.0	7.93	6.5
	II	13.6	13.6	13.5	12.4	9.94	9.0	6.5
	III	18.25	17.5	16.75	16.05	15.0	13.65	12.0
n_0R $\times 10^{-11}$, cm^{-2}	I	0.31	0.60	1.74	3.82	6.35	12.4	20.3
	II	0.28	0.60	1.5	3.5	7.4	16.6	40.7
	III	0.251	0.514	1.42	3.05	6.67	14.3	31.4
u_e, V	II	3.04	3.02	2.99	2.89	2.42	2.12	1.63
	III	3.66	3.56	3.53	3.56	3.57	3.54	3.44
Θ_0, °K	III	361	372	403	446	525	656	871
pR, torr · cm	III	42.7	43.3	45.9	47.7	52.1	58.8	68.6
Z_1	III	0.0304	0.0462	0.0723	0.096	0.127	0.172	0.236

		$p_0R = 60$						
		i/R						
		4.16	8.4	21	41.6	84	167	333
ER, V	I	27.0	25.2	22.8	17.7	12.6	10.2	7.95
	II	21.6	21.0	20.4	19.2	15.9	12.6	9.0
	III	27.55	26.6	25.4	24.2	22.6	20.6	18.1
n_0R $\times 10^{-11}$, cm^{-2}	I	0.39	0.73	1.91	6.45	12.3	—	—
	II	0.29	0.63	1.60	3.60	7.90	21.0	44.4
	III	0.270	0.585	1.595	3.40	7.30	15.6	33.5
u_e, V	II	2.74	2.76	2.76	2.74	2.52	2.20	1.40
	III	3.35	3.30	3.32	3.37	3.43	3.44	3.33
Θ_0, °K	III	368	383	426	487	590	756	1020
pR, torr · cm	III	71.7	73.3	77.6	83.8	94.0	109	131
Z_1	III	0.0264	0.0408	0.0651	0.0882	0.120	0.165	0.228

		$p_0R = 96$						
		i/R						
		4.16	8.4	21	41.6	84	167	333
ER, V	I	39.4	36	30.7	26.4	15.4	11.5	9.6
	II	30.7	30.7	28.6	26	23.1	18.2	13.5
	III	40.9	39.45	37.45	35.5	33.0	30.05	27.2
n_0R $\times 10^{-11}$, cm^{-2}	I	0.45	0.84	2.5	5.2	19.5	—	—
	II	0.31	0.65	1.7	3.74	8.1	22.7	48.3
	III	0.275	0.604	1.63	3.46	7.42	15.8	34.5
u_e, V	II	2.46	2.45	2.45	2.42	2.36	2.20	2.03
	III	3.14	3.11	3.16	3.24	3.32	3.35	3.36
Θ_0, °K	III	376	400	458	550	675	882	1210
pR, torr · cm	III	116	119	129	143	165	197	245
Z_1	III	0.0238	0.0373	0.0604	0.0827	0.114	0.159	0.231

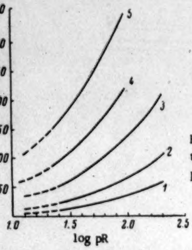

Fig. 5. Dependence of neutral gas temperature $\theta_0 - \theta_R$(°K) on pressure pR with discharge on.

for a cylindrical tube, where Θ_k is the temperature in the absence of a discharge.

In the derivation of this equation the Bessel function is approximated by a parabola.

Calculated results for ER, n_0R, u_e, and Θ_0 as functions of pR and i/R are shown in Figs. 2-5. The function ω is shown in Fig. 6.

A comparison is made in Table 1 of values for ER and n_0R which have been determined experimentally,[21] calculated from a theory not including emission of resonance radiation and recombination,[8] and calculated from the present theory. Consideration of resonance radiation emission and recombination significantly increases the value of the field and of the electron temperature. From Table 1, where the quantity Z_1 [see Eq. (16)] is also presented, it is clear that the role of emission is extremely important, especially at low currents.

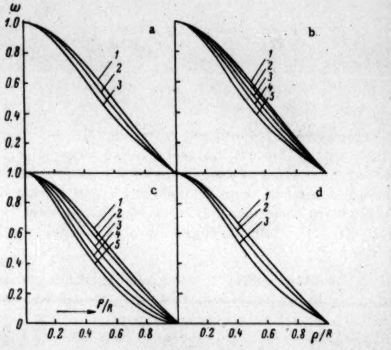

Fig. 6. Radial decrease in the function ω, pR, torr · cm: a) 36; b) 60; c) 96; d) 200.

TABLE 2. Check of Similarity Rules for Positive Column Parameters (pR = 60 torr · cm; i/R = 41.6 mA/cm)

	R, cm			
	1.2	2.8	9	36
ER	15.05	15.15	15.30	15.50
n_0R	10.66	10.62	10.55	10.47
u_e	2.95	2.96	3.01	3.05
Θ_0	443	445	446	447

The calculated values at low currents are in good agreement with experimental values. The agreement gets worse as the current increases. It should be noted that in the region i/R ≈ 40 an abrupt transition of the discharge into a contracted state occurs which is accompanied by the appearance of striations. The steady-state theory is not applicable under these conditions.

In addition to i/R, pR, and Θ_R, the quantity Z also clearly depends on $\sqrt{R}$, which may lead to a breakdown of the similarity rules.[20] In practice, however, the deviations from the similarity rules are small, as is clear from Table 2.

A number of the assumptions made in the calculation of the quantity Z_1 makes it possible to assume that the quantity Z is determined with a severalfold accuracy. Such variations in the quantity Z lead to variations of 10-20% in the values of the parameters ER, n_0R, and u_e.

In addition, the theory contains a number of assumptions such as neglect of the contribution of inelastic collisions to the energy balance and inaccuracies in the values used for elementary process cross sections.

The divergence between experimental and theoretical values up to the discontinuity is also in the range of 10-20%.

---

[1] Yu. B. Golubovskii, (Ju. B. Golubosvskij), Yu. (Ju.) M. Kagan, R. I. Lyagushchenko (Ljagustschenko), and P. Michel, Beitr. Plasmaphys., 8, 423 (1968).

[2] K. Wojaczek, Beitr. Plasmaphys., 6, 211 (1966).

[3] Yu. B. Golubovskii (Ju. B. Golubovskij), Yu. (Ju.) M. Kagan, and R. I. Lyagushchenko (Ljagustschenko), Beitr. Plasmaphys., 10, 427 (1970).

[4] Yu. B. Golubovskii, Yu. M. Kagan, and R. I. Lyagushchenko, Zh. Tekh. Fiz., 38, 1934 (1968) [Sov. Phys.–Tech. Phys., 13, 1553 (1969)].

[5] Yu. M. Kagan and R. I. Lyagushchenko, Zh. Tekh. Fiz., 31, 445 (1961); 34, 1873 (1964) [Sov. Phys.–Tech. Phys., 6, 321 (1961); 9, 1445 (1965)].

[6] Yu. M. Kagan and R. I. Lyagushchenko, Opt. Spektrosk., 17, 168 (1964).

[7] K. Wojazek, Beitr. Plasmaphys., 7, 149 (1967); 8, 109 (1968).

[8] Yu. B. Golubovskii (Ju. B. Golubovskij), Yu. (Ju.) M. Kagan, R. I. Lyagushchenko (Ljagustschenko), and P. Michel, Beitr. Plasmaphys., 10, 265 (1970).

[9] Yu. M. Kagan, R. I. Lyagushchenko, and N. Khristov, Zh. Tekh. Fiz., 41, 2053 (1971) [Sov. Phys.–Tech. Phys., 16, 1627 (1972)].

[10] K. Wojaczek, Beitr. Plasmaphys., 9, 243 (1969).

[11] S. Chapman and T. Cowling, Mathematical Theory of Nonuniform Gases, Cambridge Univ. Press (1952).

[12] S. Brown, Elementary Processes in Gas Discharges, Wiley, New York (1961).

[13] Yu. B. Golubovskii and R. I. Lyagushchenko, Zh. Tekh. Fiz., 41, 2454 (1971) [Sov. Phys.–Tech. Phys., 16, 1947 (1972)].

[14] I. Philbrick, F. J. Mehr, and M. A. Biondi, Phys. Rev., 181, 271 (1969).

[15] A. V. Phelps, Phys. Rev., 114, 1011 (1969).

[16] L. A. Vainshtein and L. A. Minaeva, ZhPS, 9, 60 (1968).

[17] I. Holstein, Phys. Rev., 72, 1212 (1947).

[18] V. F. Brattsev and V. I. Ochkur, Astron. Zh., 42, 1034 (1965) [Sov. Astron., 9, 794 (1966)].

[19] B. M. Smirnov, Atomic Collisions and Elementary Processes in Plasma [in Russian], Atomizdat, Moscow (1968).

[20] S. Pfau, A. Rutscher, and K. Wojaczek, Beitr. Plasmaphys., 9, 333 (1969).

[21] Yu. B. Golubovskii (Ju. B. Golubovskij), Yu. (Ju.) M. Kagan, R. I. Lyagushchenko (Ljagustschenko), and P. Michel, Beitr. Plasmaphys., 8, 445 (1969).

Similitude in Hall-current plasma accelerators

A. I. Morozov and I. V. Melikov

(Submitted July 9, 1973)
Zh. Tekh. Fiz., 44, 544-548 (March 1974)

The various ionization regimes ("point," "drift," and "compact-jet") in a Hall-current plasma accelerator are discussed. For the case of drift ionization, which is the most efficient in terms of the energy expended in ionization and ion loss to the wall for the channel, an equation is found for the ionization length in terms of the flow parameters. This equation gives the efficiency of the accelerator for various working media. The ion dynamics in a Hall-current plasma in the case in which ionization occurs is treated in the kinetic approximation. The solution is shown to depend on two similarity criteria–analogs of the Froude and Knudsen numbers. The ionization length is found as a function of these criteria.

Experiments have shown that in Hall-current plasma accelerators, in which electron drift is suppressed and in which there is an extended acceleration zone, the working medium can be either a gas[1,2] or a metal.[3] The differences in behavior which are encountered in operation with various working media can be attributed primarily to the ionization process, whose course depends on the specific conditions. For example, if the working medium is supplied to the accelerator channel from some volume (anode) through an aperture, the frequent result is "point ionization,"[4] in which each aperture in the anode acts like a point plasma source. Under the influence of the supercritical pressure drop, the plasma expands from such a source in the channel at an angle of ~ 180°, leading to a significant loss of ions to the wall. On the other hand, volume ionization of the working medium can occur in a "compact jet," i.e., in a gas jet issuing from apertures in the anode. Such a jet can be followed well by probes in measurements of both the ion current and the potential profile. A distinguishing feature of a jet is the production of a pronounced gradient of the pressure (or of $E_\perp$), which also leads to the rapid loss of ions at the channel wall. These two ionization regimes occur particularly frequently in the case of operation with an easily ionizable substance.

There is another ionization regime, in principle the optimum regime, that of "drift" ionization, which arises in comparatively strong magnetic and electric fields. The ions which are produced are subjected to the axial electric field $E_\parallel$ due to the magnetization of the electrons. Again in this case there is component $E_\perp$, but since the ionization occurs over the entire width of the channel the pressure gradients are vanishingly small. The drift-ionization regime occurs in a Hall-current accelerator in the region in which the ion current reaches its maximum; the secondary ionization of neutrals reflected from the wall obviously also is of a drift nature. It is this ionization regime with which we are concerned in the analysis below.

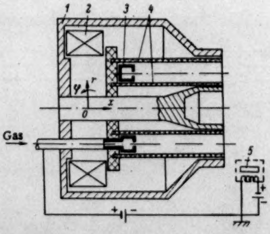

Fig. 1. The accelerator. 1) Magnetic circuit; 2) magnetization coil; 3) anode; 4) insulators; 5) neutralizer cathode.

1. Let us consider in more detail the ionization parameters in a Hall-current accelerator (Fig. 1). The criterion determining the efficiency of the accelerator operation with various working media (instead of considering the interaction of the ion flow with the channel wall) is taken to be the characteristic length of the channel over which the ionization of the working medium is essentially complete: λ_n. Assuming in a first approximation that this ionization length λ_n is shorter than the characteristic dimension of the inhomogeneity of the flow (e.g., the channel length L), we can assume

$$\lambda_n = \frac{v_a}{\beta n_e}. \tag{1}$$

Here, v_a is the characteristic velocity of the neutrals, n_e is the electron density averaged over the ionization length, and $\beta(T_e, A) \equiv \langle \sigma v_e \rangle_n$ is the ionization coefficient, which is a function of the electron temperature T_e and the nature of the working medium A (see, e.g., ref. 5). On the other hand, ions of mass M moving a distance λ_n in an electric field E acquire a velocity

$$v_i = \langle v \rangle = \frac{1}{n_i}\int_0^\infty v f(x, v)\, dv = \frac{1}{\chi}\left(\frac{2eE\lambda_n}{M}\right)^{1/2}. \tag{2}$$

Here $f(x, v)$ is the ion velocity distribution, and $\chi \sim 1$ is a dimensionless constant. Comparing Eqs. (1) and (2) we conclude that

$$\lambda_n = \frac{1}{\chi^2}\frac{2eEv_a^2}{M\beta^2 n_e^2 v_i^2}.$$

Also, taking account of the plasma-quasineutrality condition $n_e \simeq n_i$, and using

$$n_i v_i = q_i \simeq q_0 \quad \text{for} \quad x \simeq \lambda_n,$$

where q_i and q_0 are the flux of ions and the total heavy-particle flux at the entrance to the channel, we find

$$\lambda_n = \frac{1}{\chi^2}\frac{2eEv_a^2}{M\beta^2 q_0^2}. \tag{3}$$

We have thus derived an equation for a criterion of the operating efficiency. This criterion takes account of the nature of the working medium (M, β), the intensity of the flow (q_0, v_a), and the electrical parameters of the accelerator. We can now show that Hall-current accelerators operating with any working medium are similar in terms of efficiency if the condition λ_n = idem is satisfied, where λ_n is given by Eq. (3).

2. For a more detailed analysis of the processes occurring in a Hall-current accelerator we consider the dynamics of the ion flow in the accelerator channel, taking account of ionization and the consumption of neutral atoms. Since collisions between ions and other particles are negligibly rare, and since the ion Larmor radius is much longer than the length of channel, in describing the dynamics of the ion component we must use a kinetic equation in which collisions can be neglected but in which ionization must be taken into account.[6] As a first approximation we formulate the problem in the following manner.

The ion motion is steady-state and one-dimensional in a known longitudinal electric field E(x), and the quasineutrality condition $n_e \simeq n_i = \int_0^\infty f(v)dv$ is satisfied. We neglect the interaction of ions with the wall and the effect of the magnetic field on the ion trajectories. The profile of the electron temperature, $T_e(x)$, and the characteristic ion temperature T_i are known.

The motion of the neutrals before their ionization by electrons is also one-dimensional and collisionless (free-molecular flow). The atomic temperature T_a is known.

The (single-step) ionization of the atoms occurs by electron impact.

The flows of ions, q_{i0}, and atoms, q_{a0}, in the initial cross section of the channel are specified, and the particle velocities are described by one-sided Maxwell distributions with temperatures T_i and T_a, respectively.[7] The flows of ions and atoms are homogeneous over the cross section of the channel.

In this formulation of the problem the behavior of the ions and atoms is described by

$$\left.\begin{aligned} v\frac{\partial f(x,\,v)}{\partial x}+\frac{e}{M}E(x)\frac{\partial f(x,\,v)}{\partial v}&=\beta(x)\,n_e(x)\,g(x,\,v),\\ v\frac{dg(x,\,v)}{dx}&=-\beta(x)\,n_e(x)\,g(x,\,v)\end{aligned}\right\}\tag{4}$$

with the following boundary conditions at x = 0:

$$\left.\begin{aligned} f(0,\,v)&=\frac{Mq_{i0}}{kT_i}\exp\left(-\frac{Mv^2}{2kT_i}\right)\cdot\\ g(0,\,v)&=\frac{Mq_{a0}}{kT_a}\exp\left(-\frac{Mv^2}{2kT_a}\right)\cdot \end{aligned}\; v\geqslant 0, \quad f(0,\,v)=g(0,\,v)=0,\;\; v<0.\right\}\tag{5}$$

Here $f(x,v)$ and $g(x,v)$ are the ion and atom velocity distributions, and $\beta(x) = \beta(T_e, A)$ is the coefficient of electron-impact ionization of the atoms.[5] Knowing $f(0,v)$ and $g(0,v)$ we can determine the densities and average velocities of the ions and atoms at the entrance to the channel:

$$n_{i0}=\int_0^\infty f(0,\,v)\,dv=q_{i0}\left(\frac{\pi M}{2kT_i}\right)^{1/2},\quad v_{i0}=\left(\frac{2kT_i}{\pi M}\right)^{1/2},$$

$$n_{a0}=\int_0^\infty g(0,\,v)\,dv=q_{a0}\left(\frac{\pi M}{2kT_a}\right)^{1/2},\quad v_{a0}=\left(\frac{2kT_a}{\pi M}\right)^{1/2},\tag{6}$$

where $q_0 = q_{i0} + q_{a0}$, $n_0 = n_{i0} + n_{a0}$.

In addition, the particle flow at the entrance can be characterized by the velocity

$$v_0^*=\frac{q_0}{n_0}=\gamma v_{a0},$$

where

$$\gamma=1+\alpha_0\left(\frac{1}{\theta}-1\right),\quad \alpha_0=\frac{n_{i0}}{n_{i0}+n_{a0}},\quad \theta=\left(\frac{T_a}{T_i}\right)^{1/2}.\tag{7}$$

At the typical values $T_i/T_a \geqslant 10$ and with $\alpha_0 = 0.01$-0.1 this coefficient is $\gamma = 1.02$-1.2.

To convert to dimensionless variables we use the flow parameters at the entrance to the channel, n_0, v_0^*, β_0, and $E_0 = \varepsilon_0 U_p/L$, along with the channel length L:

$$\left.\begin{aligned} x'=\frac{x}{L},\;\; v'=\frac{v}{v_0^*},\;\; f'=\frac{f}{\frac{n_0}{v_0^*}},\;\; g'=\frac{g}{\frac{n_0}{v_0^*}},\;\; \varepsilon=\frac{EL}{\varepsilon_0 U_p},\\ n_i'=\frac{n_i}{n_0},\;\; n_a'=\frac{n_a}{n_0},\;\; \beta'=\frac{\beta}{\beta_0}\;\;\cdot\end{aligned}\right\}\tag{8}$$

We can now write Eqs. (4) and boundary conditions (5) as follows (below we omit the primes from the dimensionless quantities):

$$\left.\begin{aligned} v\frac{\partial f(x,\,v)}{\partial x}+\frac{1}{\xi}\varepsilon(x)\frac{\partial f(x,\,v)}{\partial v}&=\frac{1}{\zeta}\beta(x)\,n_e(x)\,g(x,\,v),\\ v\frac{dg(x,\,v)}{dx}&=-\frac{1}{\zeta}\beta(x)\,n_e(x)\,g(x,\,v),\end{aligned}\right\}\tag{9}$$

$$\left.\begin{aligned} f(0,\,v)&=\frac{2}{\pi}\alpha_0\gamma\theta\exp\left(-\frac{\gamma^2\theta^2}{\pi}v^2\right)\cdot\\ g(0,\,v)&=\frac{2}{\pi}(1-\alpha_0)\,\gamma\exp\left(-\frac{\gamma^2}{\pi}v^2\right), \end{aligned}\; v\geqslant 0, \quad f(0,\,v)=g(0,\,v)=0,\;\; v<0.\right\}\tag{10}$$

Here $\varepsilon(x)$ is the shape coefficient of the electric field.

We see that our problem contains two dimensionless similarity parameters:[8] an analog of the Froude number,

$$\xi=\frac{Mv_0^{*2}}{e\varepsilon_0 U_p}\tag{11}$$

and an analog of the Knudsen number,

$$\zeta=\frac{v_0^*}{\beta_0 n_0 L};\tag{12}$$

We also have the parameters α_0, γ, and θ, defined by (7).

3. The results of the solution of system (9), (10) are given in detail and analyzed in the following paper (ref. 9). Here we note that by specifying the parameter ζ by

$$\zeta=\frac{v_0^{*2}}{\beta_0 q_0 L}$$

and constructing the combination of similarity criteria

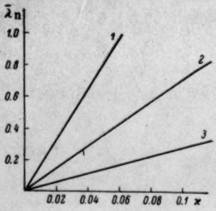

Fig. 2. Ionization length as a function of the complex similarity parameter. q_i: 1) 0.9; 2) 0.7; 3) 0.3.

$$\varkappa = \frac{\zeta^2}{\xi} = \frac{eE_0 v_0^{*2}}{M\beta_0^2 a_0^2 L}, \tag{13}$$

where $E_0 = \varepsilon_0(U_p/L)$, we can find a relation between Eq. (3) for the ionization length λ_n and similarity parameter $\varkappa$ in (13):

$$\bar{\lambda}_n = \frac{\lambda_n}{L} \sim \varkappa \tag{14}$$

Accordingly, we can assert that the relative ionization length $\bar{\lambda}_n$ is actually (within a constant factor which is a function of the structure of the flow and the ionization dynamics) the similarity criterion for the processes in a Hall-current accelerator.

Calculations[9] support this functional dependence. Figure 2 shows λ_n as a function of $\varkappa$ for three cases: When the ion flow over a length λ_n reaches 0.9, 0.7, and 0.3 of the total heavy-particle flow. [For these calculations it was assumed that $E(x) = E_0 = \text{const}$]. If we adopt the channel length corresponding to the first of these three cases, $\bar{\lambda}_n^{0.9}$, as the characteristic length of the ionization zone in the accelerator, we can approximate the functional dependence found by

$$\bar{\lambda}_n^{0.9} \simeq 5\pi\varkappa. \tag{15}$$

In conclusion the authors thank V. A. Abramov and V. V. Fishgoit for useful discussions.

---

[1] A. I. Morozov, Yu. V. Esipchuk, G. N. Tilinin, A. V. Trofimov, Yu. A. Sharov, and G. Ya. Shchepkin, Zh. Tekh. Fiz., 42, 54 (1972) [Sov. Phys.—Tech. Phys., 17, 38 (1972)].

[2] G. S. Janes and J. Dotson, Proceedings of the Fifth Symposium on the Engineering Aspects of MHD, MIT Press (1964), p. 135.

[3] C. O. Brown and E. A. Pinsley, AIAA J., 3, 853 (1965).

[4] I. V. Melikov, Zh. Tekh. Fiz., 44, 59 (1974) [Sov. Phys.—Tech. Phys., 19, 35 (1974)].

[5] L. M. Biberman, A. Kh. Mnatsakanyan, and I. T. Yakubov, Usp. Fiz. Nauk, 102, 431 (1970) [Sov. Phys.—Usp., 13, 728 (1971)].

[6] Plasma Accelerators [in Russian], Izd. Mashinostroenie, Moscow (1972).

[7] V. L. Granovskii, Electric Currents in Gases. Steady-State Currents [in Russian], Izd. Nauka, Moscow (1971).

[8] M. N. Kogan, Dynamics of a Low-Density Gas [in Russian], Izd. Nauka, Moscow (1967).

[9] I. V. Melikov, Zh. Tekh. Fiz., 44, 549 (1974) [Sov. Phys.—Tech. Phys., 19, 343 (1974)].

Equilibrium flow in a Hall-current plasma accelerator

I. V. Melikov

(Submitted July 9, 1973)
Zh. Tekh. Fiz., 44, 549-553 (March 1974)

The dynamical problem of the ion flow in the channel of a Hall-current plasma accelerator is solved for the case in which ionization and "consumption" of neutrals are taken into account. The profile of the ion distribution function and of its moments along the channel are determined on a computer. The effect of external parameters (the electric field, the flow rate of the working medium, the initial degree of ionization, etc.) on the length of the ionization zone is analyzed. The characteristic operating regions of such an accelerator are determined for various working media and for conditions under which the accelerator has an acceptable efficiency.

1. The following system of equations describing the dynamics of ions and atoms in the channel of a Hall-current plasma accelerator, in which electron drift is suppressed and in which there is an extended acceleration zone, is derived in dimensionless form in ref. 1:

$$\left.\begin{aligned} v\frac{\partial f(x,v)}{\partial x}+\frac{1}{\xi}\varepsilon(x)\frac{\partial f(x,v)}{\partial v}&=\frac{1}{\zeta}\beta(x)n_e(x)g(x,v),\\ v\frac{dg(x,v)}{dx}&=-\frac{1}{\zeta}\beta(x)n_e(x)g(x,v)\,.\end{aligned}\right\}\qquad(1)$$

The corresponding boundary conditions at x = 0 are

$$\left.\begin{aligned} f(0,v)&=\frac{2}{\pi}\alpha_0\gamma\theta\exp\left(-\frac{\gamma^2\theta^2}{\pi}v^2\right)\\ g(0,v)&=\frac{2}{\pi}(1-\alpha_0)\gamma\exp\left(-\frac{\gamma^2}{\pi}v^2\right)\end{aligned}\quad v\geqslant 0,\right.$$
$$f(0,v)=g(0,v)=0,\ v<0.\qquad(2)$$

Here, $f(x, v)$ and g(x, v) are the ion and atom velocity distributions, $\beta(x) = \beta(T_e, A)$ is the ionization coefficient,

$n_e \simeq n_i = \int_0^\infty f(x, v)dv$,

$$\xi=\frac{Mv_0^{*2}}{e\varepsilon_0U_p},\quad \zeta=\frac{v_0^*}{\beta_0n_0L},\qquad(3)$$

$$\left.\begin{aligned}\alpha_0=\frac{n_{i0}}{n_0},\ n_0=n_{i0}+n_{a0},\ \gamma=1+\alpha_0\left(\frac{1}{\theta}-1\right),\\ \theta=\left(\frac{T_a}{T_i}\right)^{1/2},\ v_0^*=\frac{q_0}{n_0}=\gamma v_{a0}.\end{aligned}\right\}\qquad(4)$$

Here, the subscript "0" denotes the characteristic value of a parameter at the entrance to the channel. The accelerator anode lies at the cross section x = 0, and the working medium is supplied in this cross section. The medium is assumed to be distributed homogeneously over the channel cross section.

To solve this problem we must know the functions E(x) and T_e(x). The electron dynamics in a Hall-current accelerator is not governed by collisional processes. It has been shown[2] that the anomalously high plasma conductivity across the magnetic field is due to electron drift in the crossed fields H_r and E_φ; these fields arise because of instabilities which build up in the accelerator. As a result, we do not at present have an acceptable method for calculating E(x) or T_e(x). However, following Morozov,[3] we can take these functional dependences directly from experiment in analyzing models for Hall-current accelerators. We find that in many of the most interesting cases the functional dependence $E_x(x)/H_r(x) \simeq$ const holds. Furthermore, since the behavior of E(x) and T_e(x) can be complicated, we simplify the calculations by seeking the solution over a short distance x_{k-1}-x_k, over which the functions E(x), T_e(x), and β(x) can be assumed to be linear. Moreover, since the quantity $n_e \simeq n_i$ which appears in Eq. (1) is governed by the unknown distribution function $f(x, v)$, the latter can be found within a specified error (0.01 in the calculated results shown below) by carrying out iterations with respect to n_i.

Under these assumptions, the equation for $f(x, v)$ can be solved by the method of characteristics,[4] while that for g(x, v) can be solved by direct integration.

We find

$$f_k(v)=\mu(v)f_{k-1}(v_0)+\frac{\xi}{\zeta}\int_{\mu(v)v_0}^{v}\frac{\beta(x')n_i(x')}{\varepsilon(x')}g(x',v')\,dv',\qquad(5)$$

$$g_k(v)=g_{k-1}(v)\exp\left(-\frac{1}{\zeta v}\int_{x_{k-1}}^{x_k}\beta(x)n_i(x)\,dx\right).\qquad(6)$$

Here,

$$\mu(v)=\begin{cases}1 \text{ for } v\geqslant\bar{v}\\ 0 \text{ for } v<\bar{v}\end{cases}\quad \bar{v}=\left(\frac{2}{\xi}\int_{x_{k-1}}^{x_k}\varepsilon(x)\,dx\right)^{1/2},\quad v_0^2=v^2-\bar{v}^2.\qquad(7)$$

The coordinate x' is found from the condition

$$v^2=v'^2+\frac{2}{\xi}\int_{x'}^{x_k}\varepsilon(x)\,dx.$$

For the case of a linear function ε(x) we have

$$x'=\frac{\delta x}{\delta\varepsilon}\left\{\varepsilon_k-\left[\varepsilon_{k-1}^2+\frac{\delta\varepsilon}{\delta x}\xi(v^2-v'^2)\right]^{1/2}\right\},\qquad(8)$$

where $\delta x = x_k - x_{k-1}$ and $\delta\varepsilon = \varepsilon_k - \varepsilon_{k-1}$.

The ion and atom velocity distribution functions are calculated on a computer. From the functions $f(x, v)$ and g(x, v) found this way we determine the first few moments of the distribution functions: the densities n(x), the fluxes q(x), the average directed velocities ⟨v⟩, and the momen-

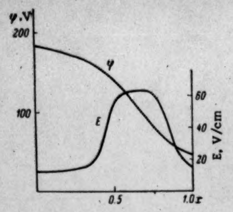

Fig. 1. Characteristic profiles of the potential and the electric fields in the accelerator channel.

tum flux of the particles r(x), defined by

$$\left.\begin{array}{l} n(x)=\int\limits_0^\infty f(x,\,v)\,dv;\quad q(x)=\int\limits_0^\infty vf(x,\,v)\,dv; \\ \langle v\rangle=\frac{q(x)}{n(x)};\quad r(x)=\int\limits_0^\infty v^2f(x,\,v)\,dv. \end{array}\right\} \tag{9}$$

2. We turn now to the specific functions E(x) and $T_e(x)$ adopted in this problem and to the method for calculating the ionization coefficient. It follows from criterial functional dependence (3) and solution (5) that the ion distribution function is a function of the electric field, in particular, of the value of the field at the entrance to the channel, E_0. Accordingly, in our first series of calculations we determine the effect of the electric field in the channel and of other flow parameters on the dynamics of the ion flow and the length of the ionization zone. For this case the calculations are carried out as a function of the ratio of the similarity criteria ξ and ζ for a homogeneous electric field over the channel length, $E(x) = E_0 = \text{const}$.

In a second series of calculations we adopt the behavior of E(x) and of the potential $\varphi(x)$ characteristic for this type of accelerator (Fig. 1).

Lacking more accurate experimental data, we adopt an electron temperature of $T_e(x) = 10$ eV = const for these rough calculations. The electron temperature is in fact observed to be on this order of magnitude over broad ranges of parameter values in Hall-current accelerators operating with various working media.[3]

The primary mechanism for the ionization of atoms in such an accelerator is ionization by drifting electrons.[1] We therefore use the procedure of ref. 5 to calculate the ionization coefficient. We take only single-step ionization into account, and we assume an equilibrium energy distribution for the electrons. Table 1 shows the calculated ionization coefficients β for $T_e = 10$ eV for several gaseous and metallic substances.

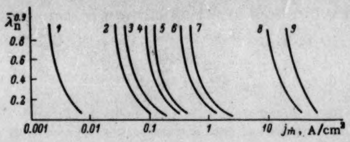

Fig. 2. Working regions of the Hall-current accelerator for various working substances. $E_0 = 15$ V/cm, $T_e = 10$ eV. 1) Cs; 2) Mg; 3) Xe; 4) Li; 5) Kr; 6) Ar; 7) N; 8) H; 9) He.

While the value of β for metals is essentially constant over the electron-temperature range $T_e = 5$–15 eV, that for the gases varies by a factor of 4–6 over this range. Accordingly, if the calculated results are to be a good approximation to the actual situation, it is important to accurately determine T_e experimentally in the various specific systems.

In calculating the ion and atom distribution functions we divide the channel length into 100 equal segments. The characteristic step in the velocity integration is $h_v = 0.3$.

3. We begin the discussion of results with an analysis of the effects of various factors on the ionization efficiency in a Hall-current accelerator. A criterial functional dependence of the ionization length λ_n (defined in terms of the relative ion flux q_i) on the complex similarity parameter is derived in ref. 1:

$$\bar{\lambda}_n=\frac{\lambda_n}{L}=a\varkappa;\quad \varkappa=\frac{\zeta^2}{\xi}=\frac{eE_0v_0^{*2}}{M\beta_0^2q_0^2L}. \tag{10}$$

On the basis of this functional dependence we can draw certain conclusions regarding the operation of a Hall-current accelerator with various working media. Below we choose as the characteristic length of the ionization zone the distance over which the relative ion flux reaches $q_i = 0.9$, $\bar{\lambda}_n^{0.9}$. Figure 2 shows $\bar{\lambda}_n^{0.9}$ as a function of the mass flow rate, expressed in current units, for several possible working media. Here, the characteristic parameters are $E_0 = 15$ V/cm, $T_e = 10$ eV, $T_a = 600$°K, L = 4 cm, and $\alpha_0 = 0.01$ (calculations show that a change in the ion temperature from $T_i \simeq T_a$ to $T_i \simeq 1$ eV because of the strong electric field and rapid ionization has essentially no effect on the integral flow charac-

TABLE 1

	Element								
	H	He	Li	N	Mg	Ar	Kr	Xe	Cs
β, cm²·sec⁻¹	$2.1\cdot10^{-8}$	$2.6\cdot10^{-9}$	$3.7\cdot10^{-7}$	$3.3\cdot10^{-8}$	$3.3\cdot10^{-7}$	$1.6\cdot10^{-8}$	$2.5\cdot10^{-8}$	$4\cdot10^{-8}$	$8.5\cdot10^{-7}$

teristics).

On the basis of these results we can determine the ranges of electrical parameters of the accelerators and the ranges of application for various working media. For example, we see that for an acceptable accelerator efficiency the ion current density in the channel must be above certain critical values: ~0.1 A/cm^2 for xenon and ~1 A/cm^2 for argon and nitrogen. The discharge currents differ by an order of magnitude. There is no upper limit on the current density in this formulation of the problem, since estimates show that collisions between ions are negligible, and resonant charge exchange of ions with atoms becomes appreciable as the flow of the substance is increased in a progressively narrowing part of the channel, having a dimension comparable to the length of the ionization zone, over which the potential drop is slight.

It follows from (10) that the length of the ionization zone is governed largely by the strength of the electric field in this part of the channel and by the temperature (velocity) of the neutral atoms. A reduction of either of these parameters tends to increase the rate of ionizing collisions because of the increase in the particle density (or lifetime) in the ionization zone. Figure 3 shows the ionization length $\bar{\lambda}_n^{0.9}$ as a function of the flow rate of the substance (xenon) for several characteristic values of E_0 and T_a. While T_a (and v_a) is strongly influenced by the method used to supply the working media and by heat evolution in and near the anode, the electric field intensity (within a coefficient which is a function of T_e) is in several cases governed by the geometry of the magnetic field, H_r, as was mentioned above. Accordingly, if the electric field is to be weak in the ionization zone, the magnetic field H_r in the channel must fall off from the end of the channel toward the anode. This conclusion is in qualitative agreement with experimental results,[6] according to which a magnetic field decreasing in the opposite direction leads to a slight increase in the ion current over the channel length, and "ionizational oscillations" are built up over the entire volume of the accelerator channel.

In the calculations we also studied the effect of the initial degree of ionization α_0 on the flow parameters.

Figure 4 shows $\bar{\lambda}_n^{0.9}$ as a function of the flow rate of the working medium for initial values of $\alpha_0 = 0.1$, 0.01, and 0.001. We see that at flow rates providing a comparatively narrow ionization zone, $\bar{\lambda}_n^{0.9} < 0.3$, the effect of α_0 in this range is slight, and there is essentially no effect at $\alpha_0 < 0.001$. Accordingly, the development of a discharge in the accelerator channel does not require any type of powerful preionizer.

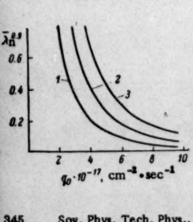

Fig. 3. Effects of the electric field and the atom temperature on the ionization length. Xe, T_a = 600°K; E_0, V/cm; 1) 7.5; 2) 15; 3) 25; E_0 = 7.5 V/cm; T_a^0 K: 1) 600; 2) 1200; 3) 2000.

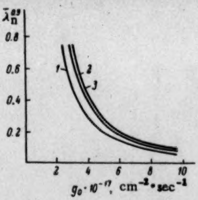

Fig. 4. Effect of the initial degree of ionization α_0: 1) 0.1; 2) 0.01; 3) 0.001.

4. As an example we consider the results calculated for equilibrium flow in a Hall-current accelerator having the E(x) and φ(x) distributions typical of this type of accelerator (Fig. 1). The basic initial data are as follows: a working medium of xenon, T_e = 10 eV, T_a = 600°K, T_i = 6000°K, $\alpha_0 = 0.01$, and L = 4 cm. Figure 5 shows the changes over the channel length in the ion velocity distribution, the ion flux q_i, the ion density n_i, and the quantity $\eta_v = R^2/2\dot{m}I_i(\varphi_a - \varphi_k)$, which gives the scatter in the ion velocities at the exit from the accelerator due to the extended ionization zone. Here R is the ion momentum, $\dot{m}$ is the mass flow rate of the medium, I_i is the ion current at the exit, φ_a is the plasma potential near the anode, and φ_k is the plasma potential at the end of the channel ($\varphi_a - \varphi_k$ = 140 V).

It is interesting to note the behavior of the ion flux, which qualitatively reproduces that of the measured ion current in the ionization zone after the entire cross section of the channel is filled with a working substance.[7,8] The subsequent reduction of the ion current which occurs under real conditions is attributed to the escape of ions to the wall, neglected in our calculation model.

It also follows from the calculated results that the maximum charged-particle density increases with increasing flow flux and shifts toward the anode. At comparatively low flow rates a region is observed near the anode which is depleted of charged particles, because the effect of the electric field on the ions is not balanced by the production of ions in ionization events.

Among the other results we note the behavior of the parameter η_v as a function of the total flux (Fig. 5d). This parameter is the limiting efficiency of a certain idealized model of an accelerator in which only the expenditure on ionization is taken into account. On the basis of these results, we can assert, e.g., that at flow rates of a gaseous working substance lower than $2 \cdot 10^{17}$ cm^{-2} · sec^{-1} an acceleration efficiency higher than 0.5-0.6 cannot be achieved in real accelerators.

Calculation of the flow dynamics of neutrals in a Hall-current accelerator has shown that low-velocity particles are "consumed" most rapidly in ionization, so that (under our assumptions regarding the nature of the flow, i.e., that it is collisionless, free-molecular flow) the atomic velocity averaged over the distribution function increases by a factor of about 2-3 by the end of the channel.

5. Accordingly, these calculations for equilibrium flow in a Hall-current accelerator have yielded a concrete criterial dependence of the length of the ionization zone on the complex similarity parameter, which incorporates the nature of the working medium, its flow rate,

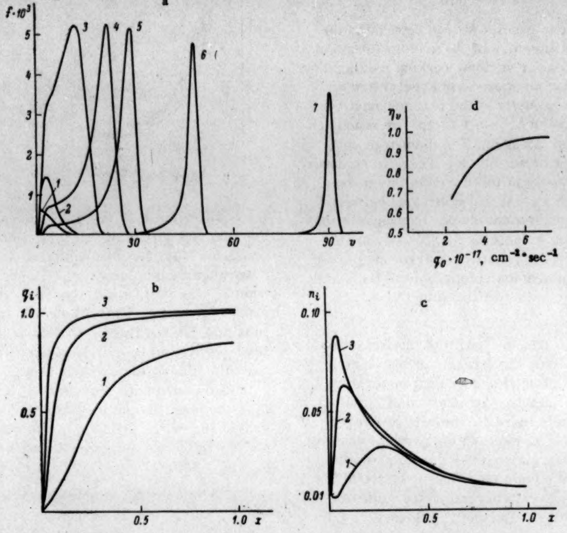

Fig. 5. Changes in the basic parameters of the ion flow in the accelerator channel. Xe, T_e = 10 eV, $T_a = 600°K$, $T_i = 6000°K$, $\alpha_0 = 0.01$, $L = 4$ cm, and φ and E(x) from Fig. 1. a: $q_0 = 4.8 \cdot 10^{17}$ cm^{-2}·sec^{-1}: 1) x = 0; 2) 0.01; 3) 0.1; 4) 0.2; 5) 0.3; 6) 0.5; 7) 1.0. b,c: 1) $q_0 = 2.4 \cdot 10^{17}$ cm^{-2}·sec^{-1}; 2) $4.8 \cdot 10^{17}$; 3) $7.2 \cdot 10^{17}$. d: $\varphi_a - \varphi_k = 140$ V.

the rate at which the neutral component is supplied, the channel length, and characteristic electrical and ionizational parameters in the anode region of the channel. This criterial dependence has been used to estimate the possible ranges of electrical parameters in Hall-current accelerators using various working media.

We have studied the effect of the magnitude and behavior of the electric field and of the initial degree of ionization on the dimensions of the ionization zone. We find that for efficiency of the ionization and acceleration the radial magnetic field must have a positive gradient in the direction from the anode toward the end of the channel. This conclusion agrees qualitatively with experimental results. The efficiency of an ideal accelerator was found as a function of the flow rate of the working medium with an account of the expenditure on ionization. This analysis gives us a more complete picture of equilibrium flow in a Hall-current accelerator.

In conclusion the author thanks A. I. Morozov for suggesting the topic and for constant interest in this work, and V. V. Fishgoit for discussion of the calculated results.

---

[1] A. I. Morozov and L. V. Melikov, Zh. Tekh. Fiz., 44, 544 (1974) [Sov. Phys.–Tech. Phys., 19, 340 (1974)].

[2] A. I. Morozov, Yu. V. Esipchuk, A. M. Kapulkin, V. A. Nevrovskii, and V. A. Smirnov, Zh. Tekh. Fiz., 43, 972 (1973) [Sov. Phys.–Tech. Phys., 18, 615 (1973)].

[3] A. I. Morozov, in: Plasma Accelerators [in Russian], Izd. Mashinostroenie, Moscow (1973), p. 85.

[4] V. V. Stepanov, Course in Differential Equations [in Russian], Gostekhizdat, Moscow–Leningrad (1950).

[5] L. M. Biberman, A. Kh. Mnatsakanyan, I. T. Yakubov, Usp. Fiz. Nauk, 102, 431 (1970) [Sov. Phys.–Usp., 13, 728 (1971)].

[6] A. I. Morozov, Yu. V. Esipchuk, A. M. Kapulkin, V. A. Nevrovskii, and A. V. Smirnov, Zh. Tekh. Fiz., 42, 612 (1972) [Sov. Phys.–Tech. Phys., 17, 482 (1972)].

[7] Yu. V. Esipchuk, in: Plasma Accelerators [in Russian], Izd. Mashinostroenie, Moscow (1973), p. 75.

[8] A. I. Morozov, Yu. V. Esipchuk, G. N. Tilinin, A. V. Trofimov, Yu. A. Sharov, and G. Ya. Shchepkin, Zh. Tekh. Fiz., 42, 54 (1972) [Sov. Phys.–Tech. Phys., 17, 38 (1972)].

Focusing of a neutralized ion beam by a plasma-optics system

I. I. Demidenko, N. S. Lomino, A. I. Morozov, and V. G. Padalka

Physicotechnical Institute,
Academy of Sciences of the Ukrainian SSR, Khar'kov

(Submitted July 30, 1973)
Zh. Tekh. Fiz., 44, 556-563 (March 1974)

The focusing of a neutralized beam of hydrogen ions by a plasma lens is studied. An axisymmetric plasma-optics system with closed electron drift focuses a plasma flow effectively and can be used as an element in a plasma–injector system.

Considerable effort is currently being devoted to the study and development of plasma lenses because of their possible use in several important applications: plasma accelerators, high-current mass separators, etc. It is therefore useful to examine questions related to the collimation and focusing of high-current ion beams whose space charge is neutralized by electrons.

The corpuscular optics of low-current ion beams neglects the space-charge field on the beam and the electrostatic interaction between individual ions.[1] These simplifications are possible at low beam densities; in this case the space charge is negligible and the electric scalar potential satisfies the Laplace equation:

$$\Delta\Phi = 0. \tag{1}$$

These restrictions are not necessary for high-current ion beams whose space charge is neutralized, if appropriate conditions are arranged for penetration of the electric field into the low-density plasma. The basic factor opposing this penetration is the high electron mobility. The equation of motion of the electronic component of a plasma in the simplified hydrodynamic approximation is

$$mn_e \frac{d\mathbf{v}_e}{dt} = -\nabla p_e - en_e\left(\mathbf{E} + \frac{1}{c}[\mathbf{v}_e\mathbf{H}]\right) + \frac{en_e}{\sigma}\mathbf{j}, \tag{2}$$

where σ is the beam conductivity, $\mathbf{j}$ is the beam current density, and n_e is the electron density in the beam, which is equal to the ion density n_i in a neutral medium.

We use the following assumptions:

1. The random energy of the electrons is small in comparison with the potential difference in the system: $W_e \ll e\varphi$.

2. The current density in the beam is low enough to satisfy the condition $\mathbf{j} \ll \sigma\mathbf{E}$.

3. The directed electron velocities are lower than or of the order of the ion velocities: $v_e \lesssim v_i$.

Under these conditions the equation of motion for the electrons becomes

$$\mathbf{E} + \frac{1}{c}[\mathbf{v}_e\mathbf{H}] = 0. \tag{3}$$

It follows that an electric field can exist in a low-density plasma only if there is a magnetic field and if there is electronic drift; the electric field is perpendicular to both $\mathbf{H}$, and $\mathbf{v}_e$. Accordingly, the magnetic lines of force must lie along electric equipotentials. This conclusion holds when the electron pressure is negligible. More rigorously, we state that it is the "thermalized potential"

$$\Phi^*(\psi) = \Phi - \frac{kT_e(\psi)}{e}\ln\frac{n}{n_0} \tag{4}$$

which is conserved along a magnetic line of force. Here $T_e(\psi)$ is the electron temperature and n_0 is the normalization density. As $T_e \to 0$ or $\ln(n/n_0) \to 0$, a magnetic line of force is, in a first approximation, an equipotential:

$$\Phi = \Phi(\psi). \tag{5}$$

Morozov[2] has shown that axisymmetric electromagnetic systems in which the electric and magnetic fields do not have azimuthal components and in which the electron drift is in the azimuthal direction and is closed can be used to focus plasma or neutralized ion beams. These systems have been called "plasma-optics systems." We note that the use of plasma optics largely eases the restriction on the magnitude of the beam space charge. Furthermore, simple means can be used to correct aberrations in plasma-optics systems. Finally, in several cases such systems have a considerably higher refractive power than vacuum magnetic systems or electrostatic systems. These features of plasma lenses are related to the redistribution of the electric field within the lens and to the replacement of Laplace equation (1) by the condition that the magnetic lines of force be equipotentials, condition (5).

Let us consider an extremely simple focusing system – a thin ring carrying a current I, i.e., an ordinary magnetic lens – and let us assume that this ring has been charged to a potential φ. The focal length of such a lens for the transmission of a weak, unneutralized ion beam is (in the thin-lens approximation)

$$\frac{1}{F} = \frac{3\pi^3}{16}\frac{e^2}{M_i c^4}\frac{1}{W_i}\frac{I^2}{R} + \frac{3\pi}{128R}\left(\frac{e\varphi}{W_i}\right)^2. \tag{6}$$

In the particular cases $I \neq 0$, $\varphi = 0$ and $I = 0$, $\varphi \neq 0$ we find magnetic and electrostatic lenses, respectively. The focal length of the magnetic lens is given by

$$\text{a)}\quad \frac{1}{f_H} = \frac{3\pi^3}{16}\frac{e^2}{M_i c^4}\frac{1}{W_i}\frac{I^2}{R} \quad\text{or}\quad f_H = 1.8\cdot 10^5\frac{M_i W_i R}{I^2}$$

where M_i is in atomic units, W_i is in electron volts, and I is in amperes. In this case we have ion-momentum focusing. The focal length of the electrostatic lens is given by

$$\text{b)}\quad \frac{1}{f_E} = \frac{3\pi}{128R}\left(\frac{e\varphi}{W_i}\right)^2, \quad f_E = 13.6\left(\frac{W_i}{e\varphi}\right)^2 R;$$

in this case we have ion-energy focusing.

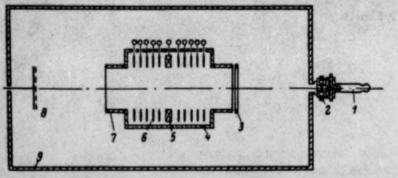

Fig. 1. The experimental apparatus. 1) Ion source; 2) electrostatic lens; 3) electronic compensator; 4) magnetic shield; 5) magnet coil; 6) disks; 7) fitting; 8) probe; 9) housing of vacuum chamber.

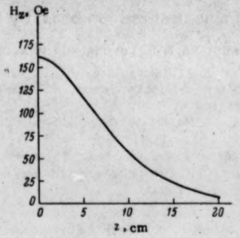

Fig. 2. Profile of the magnetic field along the axis of the plasma lens.

When a dense, neutralized ion beam with current I and a potential φ passes through such a lens the electric field is altered to the form $\Phi = \Phi(\psi)$, where $\psi = rA_\varphi$ is the magnetic flux function and A_φ is a component of the magnetic vector potential $\mathbf{A} = \mathbf{A}(0, A_\varphi, 0)$. The focal length of such a plasma lens is calculated in ref. 3 under the assumption of the simple functional dependence $\Phi = k\psi$:

$$\frac{1}{f}=\frac{1}{f_H}+\frac{2}{R}\left(\frac{e\varphi}{W_i}\right), \quad f=\frac{R}{2}\left(\frac{W_i}{e\varphi}\right)\frac{1}{1+\alpha}, \tag{7}$$

where $\alpha = 2.8 \cdot 10^{-6}[I^2(M_i\varphi)]$ (I is in amperes, M_i is in atomic units, and φ is in volts). In a real situation we have $\alpha \ll 1$.

The differences among these three cases become more apparent when we write the equations relating f, f_H, and f_E:

$$\frac{f}{f_H}=\frac{\alpha}{1+\alpha}, \quad \frac{f}{f_E}=3.68 \cdot 10^{-2}\frac{e\varphi}{W_i}\frac{1}{1+\alpha}. \tag{8}$$

For the specific case of the injection of a beam of hydrogen ions ($M_i = 1$) at 5 keV and for a lens having the properties $T = 3 \cdot 10^3$ A, R = 10 cm, and $\varphi = 1$ kV, we have $f \cong 25$ cm, $f_H = 10^3$ cm, $f_E = 3.4 \cdot 10^3$ cm, i.e., under these conditions the plasma lens has a refractive power two orders of magnitude better than that of an electrostatic lens or magnetic lens.

Experimental studies of plasma lenses and neutralized beams of helium and argon ions support the results of these calculations.[4]

The plasma lens which we have studied is an element of a quasisteady-state plasma injector; we calibrate and study the operation of this system with a neutralized beam of hydrogen ions.

EXPERIMENTAL APPARATUS

The experimental apparatus is shown in Fig. 1. The beam of hydrogen ions is produced by an rf ion source with an immersion lens; the beam energy is 4-8 keV, and the output current of the source can reach 200 μA. The ion source is connected to an evacuated chamber ~ 1 m^3 in volume, within which the plasma lens is mounted. The housing of the chamber is made of nonmagnetic steel in order to reduce magnetic distortions. The plasma lens has an inside diameter of 20 cm; in the median plane of the lens there is a multilayer magnet coil in a copper shield insulated from the winding. The magnet coil is fed a constant current from a storage battery; Fig. 2 shows the profile of the magnetic field of the lens along the axis of the system. Coaxial with the coil is a system of 10 copper disks; these disks, which are insulated from the shield of the magnet coil and from each other, are designed for the desired potential distribution in the focusing plasma. The entire plasma-optics system is enclosed in a shield of soft magnetic steel in order to suppress stray magnetic fields and to satisfy the thin-lens conditions. The voltage is fed to the shield of the magnet coil and to the disks from a bank of series-connected capacitors. The potential profile is symmetric with respect to the median plane of the lens, and the potential falls off linearly from the median plane to the edges of the system.

A ring-shaped electron emitter, coaxial with the entrance limiter of the lens, is used to compensate for the space charge of the beam.

The converging ion beam from the lens is analyzed by a multilayer, multichannel probe, which consists of a set of concentric copper rings 5 mm wide and 5 mm apart. The probe is coaxial with the lens and the source; the ion current is measured with each of the rings in succession.

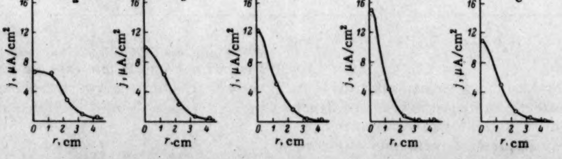

Fig. 3. Radial distributions of the ion current density at various distances from the median plane of the lens. z, cm: a) 33; b) 38; c) 48; d) 58; e) 68. The beam energy is $W_i = 6$ keV, and $\varphi = 1$ kV.

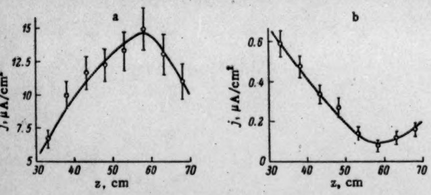

Fig. 4. Axial distribution of the ion current density at two radial positions. r: a) 0; b) 4.25 cm.

The probe can be moved along the axis of the system; the distance between the median plane of the lens and the point of the beam crossover near the exit limiter of the ion source is held constant at ~ 62 cm.

The working vacuum is ~ $5 \cdot 10^{-6}$ torr.

MEASUREMENTS OF THE FOCAL LENGTH OF THE PLASMA LENS

The lens causes a well-defined focusing of the beam only when the electric and magnetic fields are superimposed. The beam can be observed visually if the residual gas pressure in the chamber is increased to ~ $5 \cdot 10^{-5}$ torr because the excitation of the neutral gas is sufficient for visual observation. The diverging ion beam leaving the ion source and entering the plasma lens is converted into a converging beam after it leaves the plasma lens. This effect vanishes when the magnetic field of the lens is turned off ($I = 0$) or when the voltage is removed from the lens ($\varphi = 0$). In these cases the emission caused by the beam leaving the lens is similar to that in the case of a lens turned off completely ($I = 0$, $\varphi = 0$). This behavior is qualitative evidence that the refractive power of the plasma lens is much higher than that of an electrostatic or magnetic lens at the same levels of the current and potential.

To determine the position of the focal point of the ion beam we use the multilayer probe to study the radial distributions of the ion current density at various distances from the median plane of the plasma lens; the results are shown in Fig. 3. As the multilayer probe (collector) is moved along the axis, the radial distribution of the ion current density narrows, and there is a simultaneous increase in the current density at the axis. Beyond the plane of the focus, the radial distribution begins to broaden, and there is a simultaneous decrease in the current density at the axis. Figure 4 shows results found in measurements of the axial change in the current density at the axis of the system and at a radius of r = 4.25 cm. We see that in the image plane the current density at the axis reaches a maximum, while the current density at an appreciable distance from the axis reaches a minimum. Under these experimental conditions the distance from the median plane of the lens to the crossover point of the beam near the exit limiter of the ion source is roughly equal to the distance from the median plane to the current-density extremum at the axis of the system; hence we expect the half-width of the radial distribution of the current density in the focal region to be approximately equal to the beam diameter near the crossover point of the ion source. In fact, we find the half-width of the radial distribution of the current density near the focus to be ~ 20 mm, which is comparable with the diameter of the beam crossover at the exit from the ion source (~ 16 mm). However, the observed halo of the ion beam near the focus is evidence of spherical aberration in the system; this aberration could be eliminated by providing the appropriate potential distribution over the disks of the plasma lens.

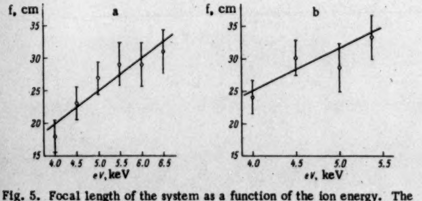

Fig. 5. Focal length of the system as a function of the ion energy. The lens potential φ is: a) 1; b) 0.8 kV.

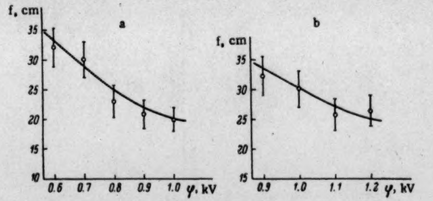

Fig. 6. Focal length of the system as a function of the lens potential. The ion energy is: a) 4; b) 6 keV.

We calculate the focal length of the plasma lens from the thin-lens equation,

$$\frac{1}{f}=\frac{1}{a}+\frac{1}{b}, \tag{9}$$

where a is the distance from the beam crossover at the exit from the ion source to the median plane of the plasma lens and b is the distance from the median plane of the lens to the image plane. Since the value of a is held constant in these experiments, we can calculate f simply by determining the distance b. We carry out these measurements with a magnetic field of ~ 150 Oe at the center of the magnet coil, an ion-beam current of 80 μA entering

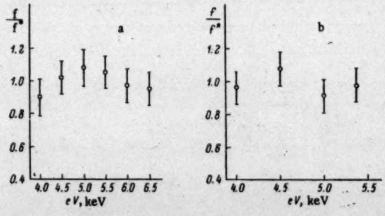

Fig. 7. Ratio of the experimental focal length of the system, f, to the calculated value, f^*, as a function of the ion energy. The lens potential φ is: a) 1; b) 0.8 kV.

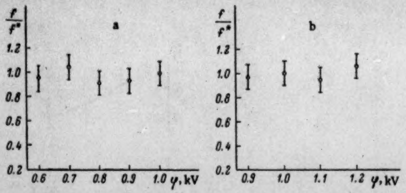

Fig. 8. Ratio of the experimental focal length f to the calculated length f^* as a function of the lens potential. The ion energy is a) 4; b) 6 keV.

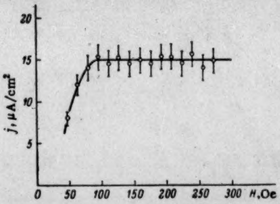

Fig. 10. Ion current density at the axis of the system in the focal region as a function of the magnetic field. W_i = 6 keV, φ = 1 kV, I_i = 120 μA.

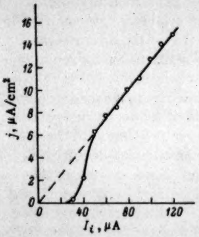

Fig. 9. Ion current density at the axis of the system in the focal region as a function of the beam current entering the lens. W_i = 6 keV, φ = 1 kV.

the lens, and various beam-ion energies and lens potentials.

We find that the focal length of the plasma-optics system varies in proportion to the energy of the beam ions at a fixed lens potential (Fig. 5), and it varies inversely with the lens potential at a fixed beam energy (Fig. 6). These results are in accordance with theoretical function (7).

We compare the values found for the focal length of the plasma lens in this manner (f) with the values calculated from Eq. (7) (f^*) for various beam energies and lens potentials. The results (Figs. 7 and 8) show that the experimental focal lengths agree within an error of less than 10% with the theoretical values found for a thin plasma lens.

DISRUPTION OF FOCUSING

The focusing of the neutralized ion beam by the plasma lens can be disrupted at a sufficiently high density of the plasma causing the focusing, at which the Debye shielding radius becomes comparable to the dimension of the magnetic ring. We study this disruption of focusing by measuring the current density at the axis of the system near the focus as a function of the current of ions entering the plasma lens. We find (Fig. 9) that the current density at the focus is a linear function of the ion current entering the lens over the current range 50-120 μA, i.e., the focusing effect of the plasma lens under these conditions is not a function of the ion beam current. However, at currents of ~ 40-50 μA we find a rapid drop in the ion current density at the axis near the focus, due to disruption of the focusing properties of the plasma lens.

The Debye shielding radius is given by

$$\lambda_D = \left(\frac{kT_e}{4\pi n_i e^2}\right)^{1/2}, \tag{10}$$

where $n_i = I_i/ev_i\pi R^2$ and $v_i = [2(W_i - e\varphi)/M_i]^{1/2}$; assuming $kT_e = 0.2$ eV, $M_i = 1.67 \cdot 10^{-24}$ g, $I_i = 40$ μA, $W_i = 5$ keV, and $\varphi = 1$ kV, we find $\lambda_D = 0.35$ R. In other words, at a beam current $I_i = 40$ μA the Debye shielding radius becomes comparable to the radius of the focusing system.

The focusing can also be disrupted when the magnetic field is reduced below a critical level. We see from Fig. 10 that the ion current density in the focal region is not a function of the magnetic field at fields H > 100 Oe. However, when the magnetic field is reduced to H < 100 Oe, we observe a rapid drop in the ion current density at the axis of the system in the focal region: evidence of the disruption of the focusing properties of the plasma lens.

These experiments have thus demonstrated plasma focusing in a system with closed electron drift. A plasma-optics system, whose refractive power is much higher than that of ordinary magnetic and electrostatic lenses, and for which there is no serious restriction on the ion beam current, can be used as an element in a plasma-injection system and for many other applications.

---

[1] V. M. Kel'man and S. Ya. Yavor, Electron Optics [in Russian], Izd. Akad. Nauk SSSR, Moscow–Leningrad (1963).

[2] A. I. Morozov, Dokl. Akad. Nauk SSSR, 163, 1363 (1965) [Sov. Phys.–Dokl. 10, 775 (1966)].

[3] S. V. Lebedev and A. I. Morozov, Zh. Tekh. Fiz., 36, 960 (1966) [Sov. Phys.–Tech. Phys., 11, 707 (1966)].

[4] V. V. Zhukov, A. I. Morozov, and G. Ya. Shchepkin, ZhETF Pis. Red., 9, 24 (1969) [JETP Lett., 9, 14 (1969)].

Fast electrons and x rays from nanosecond gas discharges at 0.1-760 torr

L. V. Tarasova, L. N. Khudyakova, T. V. Loiko, and V. A. Tsukerman

(Submitted April 10, 1973)
Zh. Tekh. Fiz., 44, 564-568 (March 1974)

The electron and x-ray pulses from nanosecond discharges are studied in various gases at pressures 0.1-760 torr. The pulse length at half-height does not exceed 1.5 nsec. A study by the method of attenuation curves shows that the effective energy of the x radiation is 9-15 keV; the effective energy beyond a copper filter 8-12 mm thick is 130-200 keV. The maximum x-ray dose is 0.1-10 mR/pulse, depending on the nature of the gas in the immediate vicinity of the anode. A group of fast electrons is detected having an energy higher than the applied voltage (which is of the order of hundreds of keV). These electrons are accelerated near the cathode of the discharge.

X rays are produced in discharges in gases;[1-7] the x-ray energies are 4-40 keV in air and helium at pressures up to 760 torr, implying the presence of fast electrons in gas discharges at comparatively high pressures. The appearance of fast electrons can be attributed to conditions in the discharge gap such that the energy lost due to elastic and inelastic collisions is less than the energy acquired by electrons as a result of their acceleration in an electric field. Attempts have been made[6-9] to establish a theoretical explanation for these runaway electrons.

The papers cited above contain no information about fast electrons capable of escaping from the discharge chamber. In the work reported here, an outgrowth of that reported in refs. 4 and 5, we have discovered additional effects, which imply that the radiation of nanosecond gas discharges has a complex composition. Under conditions similar to those of refs. 4 and 5 we detect [along with soft x rays (9-15 keV)] fast electrons, which escape through the anode and through the chamber window.

Below we report a study of the characteristics of the electronic and x-ray pulses produced in nanosecond discharges in various gases.

The experiments are carried out in a steel chamber with a plastic insulator. The chamber is filled with one of several gases: air, deuterium, helium, argon, or xenon. The pressure is varied over the range 10^{-2}-760 torr. The chamber is evacuated by rotating or oil-diffusion pumps. The cathodes are polished tungsten-alloy rods 12-14 mm in diameter having a hemispherical working surface with a curvature radius of r = 3-7 mm. In some of the experiments we notch the working surface in order to intensify the electric field at the resulting irregularities. A cutting tool is used to make notches 0.5 mm thick at 1-mm steps in two perpendicular directions. The anode is an aluminum foil 8-15 μ thick. The interelectrode distance d is 10-15 mm. The chamber window, behind the anode, is made of a thin polyethylene terephthalate film (5-10 μ).

In all the experiments the high voltage is produced by a high-voltage pulse transformer, in whose secondary circuit a high-pressure switch is connected in series with the chamber. A similar arrangement has been proposed by Belkin and described in refs. 10 and 11. The discharge capacitance, formed by the generator housing and the housing of the high-pressure switch, is about 40 pF, and the resistance shunting the discharge chamber is 200 Ω.

The high-pressure switch, which sharpens the front of the voltage pulse, is similar to the devices described in ref. 12. This switch is filled with hydrogen to an overpressure of ~ 50 atm. The voltage pulse reaches a height U_g of 160-180 kV, governed by the breakdown voltage of the switch. The rise time of the pulse does not exceed 1 nsec.

The x-radiation is detected by KID-2 and DK-02 dosimeters, thermoluminescent glass, and x-ray film. Electrons escaping from the chamber are detected by a Faraday cup and x-ray film. The time characteristics are studied by means of 14ÉLU10 electron x-ray multipliers having a resolution of ~ 1.2 nsec at the front; these multipliers were developed by Andreev and Guseva at the All-Union Scientific-Research Institute of Opticophysical Instruments and are described in ref. 13. The results which we find in measurements of the pulse characteristics by various methods are in satisfactory agreement.

In order of decreasing number of fast electrons detected beyond the chamber window, the gases we have studied are: helium, deuterium, air, argon, and xenon. The functional dependence of the electron yield on the pressure can vary; under constant experimental conditions ($U_g \simeq$ 160 kV, d = 15 mm, and polished cathode having r = 3 mm), the number of fast electrons observed in the case of helium increases as the pressure is raised from 100 to 760 torr, while the number observed for the case of argon decreases.

Figure 1 shows the number of electrons as a function of the pressure for discharges in air at a generator working voltage of 176 kV. The voltage drop across the chamber electrodes, measured from the oscillograms, is 100 kV at atmospheric pressure. The electron yield is determined by means of a Faraday cup. Here and in the figures which follow, each point on a curve represents the average of 30-50 measurements. Curve 1 corresponds to a filter of 5 mg/cm² (a transmitted-electron energy above 40 keV, while curve 2 corresponds to a filter of 53 mg/cm² (above 160 keV). We see that among the electrons escaping from the chamber there is a group having a relatively high energy; the relative number of electrons in this group is a function of the pressure.

We study the time characteristics of the radiation from the discharges and the penetrating power of this ra-

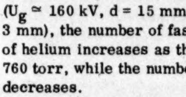

Fig. 1. Number of electrons detected outside the chamber window as a function of the pressure for discharges in air. d = 15 mm, smooth electrode, r = 6 mm.

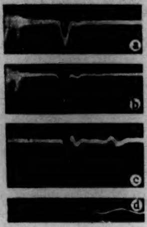

Fig. 2. Oscillograms of electron pulses (a, c) and x-ray pulses (b). a) Discharge in air, d = 15 mm, p = 760 torr, U_g = 170 kV; b) helium, d = 10 mm, p = 22 torr, U_g = 150 kV; c) helium, d = 10 mm, p = 22 torr, U_g = 150 kV; d) time marker, f = 100 MHz.

diation in most detail for two situations: discharges in air at atmospheric pressure with a smooth cathode, with electrodes 15 mm apart, and under conditions corresponding to the maximum electron yield; helium discharges at a pressure of 22 torr, with notched cathode, and with electrodes 10 mm apart. Figure 2 shows typical oscillograms of the x radiation and electrons, detected by the 14ÉLU10 multiplier and the Faraday cup. The pulse length at half-height does not exceed 1.5 nsec. The differences between the lengths and shapes of the electron pulses detected with the Faraday cup and the 14ÉLU10 multiplier result from the different resolving times of these detectors.

We can get a rough idea about the energetic inhomogeneity of the radiation by plotting attenuation curves based on the attenuation in metal filters.[14] Figure 3 shows the number of electrons escaping from the discharge chamber and detected by the Faraday cup as a function of the thickness of the aluminum filter for discharges in helium (Fig. 3a) and air (Fig. 3b). The attenuation curves are recorded under approximately identical experimental conditions, except that the switches (sharpeners) are different. The differences observed in the behavior of these curves can apparently be attributed to variations in the rise time of the voltage pulses.

Attenuation curves for electrons in the strong-filtration region (120-180 mg/cm^2) are recorded by means of the 14ÉLU10. When the voltage across the discharge gap is 100-120 kV, an appreciable number of electrons pass through a filter 170-180 mg/cm^2 thick; according to the estimates in refs. 15 and 16 (which are clearly on the conservative side), these electrons had energies of 340-360 keV. These energies are much higher than the measured voltage.

Figure 4 shows attenuation curves of the x radiation corresponding to the same discharge conditions as the electron curves. These measurements are made with the KID-2 dosimeter. The maximum x-ray dose for discharges in air at atmospheric pressure is 10^{-1} mR per pulse, while that for discharges in helium at 22 torr is 10 mR per pulse. The experimental data in Figs. 3 and 4 correspond to broad electron and x-ray beams, so we can draw definite conclusions about the energy only for the high-energy part of the spectrum. The energy of the x rays which pass through a copper filter 8-12 mm thick is 130-200 keV. Accordingly, the x-ray attenuation curves, like the electron curves, imply the existence of fast electrons in nanosecond-range discharges.

In general, the shapes of the electron and x-ray attenuation curves indicate that the fast electrons in the discharges do not all have the same energy. Curves 5 and 6 in Fig. 3b are typical monoenergetic electrons. The spectrum for helium has a large number of electrons at 200-270 keV; the number of electrons corresponding to 340 keV and above is two or three orders of magnitude lower. For discharges in air the spectrum is shifted toward higher energies (Fig. 3b).

The effective x-ray energy, determined from the half-attenuation thickness during photography of an aluminum wedge through 2 mm of beryllium, is 9-15 keV.

The fast electrons undergo relatively little scattering in the gas discharge, so it is possible to obtain a magnified image of the emitting centers on the cathode by placing a piece of film against the back of the anode. The degree of magnification corresponds to the geometry of the discharge gap. Figure 5 shows an image of this type for a notched cathode obtained in a discharge in helium at p = 22 torr. This photograph is taken through a filter of 43.5 mg/cm^2, so the image is formed by electrons at energies above 170 keV. These photographs verify that fast electrons are produced near the cathode.

Several workers studying discharges in vacuum and

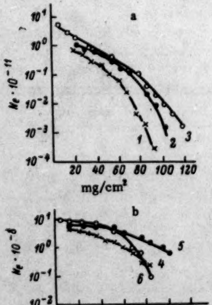

Fig. 3. Attenuation curves for the electrons detected near the chamber window. a: Discharges in helium, p = 22 torr, d = 10 mm. 1) U_g = 140 kV; 2) U_g = 180 kV; 3) U_g = 170 kV. b: Discharges in air, p = 760 torr, d = 15 mm. 4) U_g = 140 kV; 5) U_g = 180 kV; 6) U_g = 170 kV.

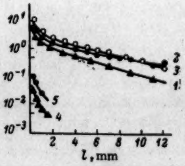

Fig. 4. Attenuation curves of the x radiation near the chamber window for discharges in helium (1-3) and air (4,5).

Fig. 5. Image of the beam of fast electrons beyond the anode.

in gases at low pressures (see, e.g., refs. 17-23) have detected a hard component of the x radiation and electrons at energies above the applied voltage. Our experimental results show that this "superhard" radiation can be obtained even at relatively high pressures under certain conditions. This effect can be attributed to the statistical acceleration of part of the beam of field-emitted electrons by turbulent pulsations excited near the cathode by this beam.[24]

It should be noted that the existence of these fast electrons, having energies above the voltage applied to the discharge gap, is responsible for an incorrect determination of the integrated x-ray dose in refs. 4 and 5. When a filter 7 mg/cm^2 thick is used, much of the film blackening is due to these fast electrons.

RESULTS

1. In nanosecond-range discharges in gases at pressures up to 760 torr there exists a group of fast electrons, having energies exceeding the applied voltage (hundreds of keV).

2. The maximum x-ray dose beyond the chamber window is ~ 10 mR/pulse for discharges in helium at 22 torr and ~ 0.1 mR/pulse for discharges in air at 760 torr.

3. The maximum number of electrons escaping from the chamber window is ~ 10^{12} per pulse for helium and ~ 10^9 per pulse for air.

---

[1] S. Frankel, V. Higland, T. Sloan, O. Van Dyck, and W. Wales, Nucl. Inst. Meth., 44, 345 (1966).

[2] Yu. L. Stankevich and V. G. Kalinin, Dokl. Akad. Nauk SSSR, 177, 72 (1967) [Sov. Phys.—Dokl., 12, 1042 (1968)].

[3] R. C. Noggle, E. P. Krider, and J. R. Wayland, J. Appl. Phys., 39, 4746 (1968).

[4] L. V. Tarasova and L. N. Khudyakova, Third International Symposium, Paris (1968).

[5] L. V. Tarasova and L. N. Khudyakova, Zh. Tekh. Fiz., 39, 1530 (1969) [Sov. Phys.—Tech. Phys., 14, 1148 (1970)].

[6] V. V. Kremnev and Yu. A. Kurbatov, Zh. Tekh. Fiz., 42, 795 (1972) [Sov. Phys.—Tech. Phys., 17, 626 (1972)].

[7] G. A. Mesyats, Yu. I. Bychkov, and V. V. Kremnev, Usp. Fiz. Nauk, 107, 201 (1972) [Sov. Phys.—Usp., 15, 282 (1972)].

[8] Yu. L. Stankevich, Zh. Tekh. Fiz., 40, 1476 (1970) [Sov. Phys.—Tech. Phys., 15, 1138 (1971)].

[9] L. P. Babich and Yu. L. Stankevich, Zh. Tekh. Fiz., 42, 1674 (1972) [Sov. Phys.—Tech. Phys., 17, 1333 (1973)].

[10] N. V. Belkin, N. I. Komyak, E. A. Peliks, and V. A. Tsukerman, Prib. Tekh. Eksp., No. 2, 194 (1972).

[11] N. I. Komyak and E. A. Peliks, Defektoskopiya, No. 3, 127 (1971).

[12] É. A. Abilov, N. V. Belkin, A. V. Dudin, A. P. Zykov, M. A. Kanunov, and A. A. Razin, Prib. Tekh. Eksp., No. 1 (1973).

[13] L. I. Andreeva and B. M. Stepanov, Prib. Tekh. Eksp., No. 5, 199 (1962).

[14] K. Siegbahn (editor), Beta- and Gamma-Ray Spectroscopy, Interscience, New York (1955).

[15] S. V. Starodubtsev and A. M. Romanov, Passage of Charged Particles through Matter [in Russian], Izd. Akad. Nauk UzbSSR, Tashkent (1962).

[16] K. K. Aglintsev, Dosimetry of Ionizing Radiation [in Russian], GITTL, Moscow (1957).

[17] S. K. Händel, Brit. J. Appl. Phys., 14, 181 (1963).

[18] L. N. Khudyakova, E. K. Gutnikova, and L. V. Tarasova, Zh. Tekh. Fiz., 34, 2044 (1964) [Sov. Phys.—Tech. Phys., 9, 1572 (1965)].

[19] N. G. Pavlovskaya and T. V. Kudryavtseva, Prib. Tekh. Eksp., No. 2, 198 (1972).

[20] N. G. Pavlovskaya, T. V. Kudryavtseva, N. A. Dron', G. N. Sloeva, and A. V. Tsvetkov, Prib. Tekh. Eksp., 1, 26 (1973).

[21] L. A. Artsimovich, A. M. Andrianov, E. I. Dobrokhotov, S. Yu. Luk'yanov, I. M. Podgornyi, V. I. Sinitsyn, and N. V. Filippov, At. Energ., 1, 84 (1956).

[22] S. Yu. Luk'yanov and I. M. Podgornyi, At. Energ., 1, 97 (1956).

[23] N. G. Koval'skii, I. M. Podgornyi, and S. Khvashchevskii, Zh. Eksp. Teor. Fiz., 35, 940 (1958) [Sov. Phys.—JETP, 8, 656 (1959)].

[24] L. P. Babich, Zh. Tekh. Fiz. (in press).

Electron energy distribution in helium, nitrogen, and their mixtures

K. D. Asvadurov, I. A. Vasil'eva, and V. M. Torchinskii
Institute of High Temperatures,
Academy of Sciences of the USSR, Moscow

(Submitted December 19, 1972; resubmitted July 23, 1973)
Zh. Tekh. Fiz., 44, 569-574 (March 1974)

The electron energy distribution has been measured in helium, nitrogen, and mixtures of helium and nitrogen at pressures of 0.5-3 torr, currents of 0.1-0.5 A, and nitrogen contents from 0.5 to 50%. In mixtures with a nitrogen content below 5% the distribution function is close to that in helium. As the nitrogen content is increased the distribution function is at first broadened and the average and most probable values of the electron energy increase; when the nitrogen content of the mixture reaches 30-50% the distribution approaches that in nitrogen and the average electron energy decreases. In discussing the errors of the procedure for finding the energy distribution function particular attention is paid to the determination of the plasma potential. The most important contribution to the difference between the potential zero and the maximum of the second derivative of the probe current comes from the deterioration of the relation between the probe—plasma resistance and the resistance of the probe circuit at the plasma potential. An argument is given for determining the plasma potential from the zero of the second derivative.

The electron energy distribution function has been investigated in the positive column of an arc in helium, nitrogen, and mixtures of these gases at pressures from 0.5 to 3 torr, currents from 0.1 to 0.5 A, and nitrogen admixtures from 0.5 to 50%. The tubes use indirectly heated cathodes and hollow cylindrical anodes with inner diameters of 22 and 30 mm. Cylindrical tungsten probes 50 to 100 μ in diameter and 4 mm long are located at the axis. The filament power is supplied by batteries, and the anode and probe circuit power by regulated power supplies.

The electron energy distribution function $f(\varepsilon)$ is determined from the second derivative of the probe current by superposing the modulated potential

$$v_1(t)=a(1+M\cos\omega t)\sin\Omega t, \tag{1}$$

on the probe potential; $\omega = 1$ kHz, $\Omega = 80$ kHz, $a = 0.5$ V, $M = 8$.

Oscillations and plasma noise in the probe circuit are displayed on an oscilloscope by connecting a 12 Ω noninductive resistor between the probe and the input to a selective amplifier. The ratio of the useful signal plasma to the plasma noise current in the probe circuit is greater than 10. No measurements are performed in the presence of significant electrical oscillations. Stationary striations are also monitored. Although the positive column looked uniform, a high-contrast photograph showed a regular nonuniformity. Poorly defined stationary striations are photographed in helium and in helium–nitrogen mixtures. The discharge in nitrogen is uniform.

Sicha and Rezacova[1] have shown that in striations of sufficiently small amplitude, in which there is no secondary maximum on the distribution function in the fast electron region, the distribution function remains constant along the column. We have also taken some distribution functions along a poorly defined striation. No hump is observed in the fast electron region; the distribution function remains essentially constant along a striation, i.e., the results characterize the positive column as a whole rather than individual points within a striation. The error in the determination of the distribution function is made up of the error in determining the second derivative and the error in determining the plasma potential. We first estimate the error in determining the second derivative. The instrumental error in isolating a harmonic of frequency ω is determined mainly by the error of the recording instrument and does not exceed 2%. In order to find how much a harmonic of frequency ω affects the second derivative the current must be decomposed into its spectrum, as in refs. 2 and 3 for the second-harmonic method. If the plasma is nonstationary, the potential varies according to $b\cos\omega' t$, where ω' is not a multiple of ω, and the distribution function is a periodic function of the time with frequency ω' the current component at frequency ω can be written in the form

$$i_\omega=\frac{a^2}{2}i_0''+\frac{a^2b}{4}i_1''+\left(\frac{7}{64}a^4+\frac{a^2b^2}{8}\right)i_0^{\mathrm{IV}}+\ldots, \tag{2}$$

where i_0 and i_1 are the zeroth and the first approximation terms, and i_ω is determined not only by the second, but also by higher derivatives of the current. In these experiments $a/b \geq 10$, and the contribution of higher harmonics is less than 3%. Thus the total error in determining the second derivative is less than 5%.

In obtaining electron distribution functions from curves of the second derivatives some authors[4–8] take the plasma potential to be the potential at which the second derivative passes through zero; others[9–11] assume that the plasma potential is equal to the potential at which the second derivative is a maximum.

For an ideal probe characteristic the potential at the maximum of the second derivative would agree with the space potential. Usually the characteristic and its derivatives are distorted. Distortion arises because of the decrease in the electron density near the probe. This effect has been studied in refs. 12 and 13. Also, as the probe potential approaches that of the plasma, the relation between the resistance of the probe sheath R_{sh} and the sum of the other resistances in the probe circuit deteriorates. The probe circuit includes the resistance of the plasma gap between the outer edge of the probe sheath and the reference electrode Rd_{pl}, and also the resistance of the electric circuit elements R_{ci}. R_{ci} can be different for direct and alternating currents ($R_{ci=}$ and $R_{ci\sim}$).

If V is the dc voltage in the probe circuit and ε_{pl} is the potential difference in the arc between the probe and the reference electrode, for an ideal probe characteristic

$$V-\varepsilon_{pl}=V_{sh} \tag{3}$$

while in the actual case

$$V-\varepsilon_{\mathrm{pl}}=V_{\mathrm{sh}}+i(R_{\mathrm{pl}}+R_{\mathrm{ci}\,-}). \qquad (4)$$

For negative probe potentials which do not exceed the absolute magnitude of the floating potential the probe current is opposite in sign to the potential applied to the sheath; hence, for an actual characteristic $|V - \varepsilon_{pl}| < |V_{sh}|$. This inequality is strengthened as the plasma potential is approached, but in constructing the probe characteristic it is assumed that Eq. (3) holds. This leads to an apparent decrease in the probe current and its derivatives close to the plasma potential. The range of potentials ΔV_1 in which the distortion occurs for direct current can be found by first estimating the decrease in probe current

$$\frac{i_{\mathrm{id}}}{i_{\mathrm{act}}}=\frac{R_{\mathrm{sh}}+R_{\mathrm{pl}}+R_{\mathrm{ci}\,-}}{R_{\mathrm{sh}}}. \qquad (5)$$

In order to find ΔV_1 by using (5) it is necessary to specify the current as a function of the potential for a known electron distribution function.

In finding the second derivative of the probe current by (2) it is assumed that the whole variable signal of amplitude *a* is applied across the probe sheath. As a matter of fact, as the plasma potential is approached an increasingly larger part of the potential drop is across the resistance $R_{pl} + R_{ci\,\sim}$, and this leads to a decrease in the amplitude of the harmonic, and consequently to an apparent decrease of the second derivative in the following ratio:

$$\frac{i''_{\mathrm{id}}}{i''_{\mathrm{act}}}=\left(\frac{R_{\mathrm{sh}}+R_{\mathrm{pl}}+R_{\mathrm{ci}\,\sim}}{R_{\mathrm{sh}}}\right)^2. \qquad (6)$$

For a known distribution function the range of potentials ΔV_2 in which the value of the second derivative is distorted can be found by using (6).

All the distortions described make the potential at which the second derivative is a maximum more negative with respect to the plasma potential. We now estimate the region of distortion of the probe characteristic close to the plasma potential under the experimental conditions described here.

According to refs. 12 and 13 the electron drain decreases the electron density and the current to a 50 μ diameter probe close to the plasma potential by 4-5%, which corresponds to a value of ΔV_3 of less than 0.2 V for a Maxwellian distribution.

In estimating the effect of the probe circuit we take $R_{ci=} = 100\,\Omega$, $R_{ci\,\sim} = 120\,\Omega$; R_{pl} and R_{sh} vary from 130 Ω and 2.7 kΩ for helium at a pressure of 0.5 torr and a current of 0.5 to 1 kΩ and 7.4 kΩ for nitrogen at 1 torr and 0.2 A. We note that the distance between the probe and the reference electrode has only a small effect on the value of R_{pl} since the largest part of this resistance comes from the part of the plasma with a small transverse cross section adjoining the probe sheath.

An estimate using (5) and (6) for a Maxwellian distribution and the experimental average energies $\bar{\varepsilon}$ gives $\Delta V_1 = 0.5$ V and $\Delta V_2 = 1.0$ V in helium at a pressure of 0.5 torr and a current of 0.5 A; in nitrogen at a pressure of 1 torr and a current of 0.2 A $\Delta V_1 = 0.3$ V and $\Delta V_2 = 0.5$ V; in a mixture of helium and nitrogen (5%) at a pressure of 0.5 torr and a current of 0.5 A $\Delta V_1 = 0.8$ V and $\Delta V_1 = 1.7$ V. A comparison of the values shows that the drain leads to the smallest distortion of the probe characteristic. The greatest distortion gives rise to an apparent decrease in the second derivative according to (6). These conclusions hold independently of the form of the electron distribution function.

The region of distortion of the second derivative due to the effects described above can be obtained from the summation $\Delta V = \Delta V_1 + \Delta V_2 + \Delta V_3$. ΔV agrees with the experimental value of the difference between the positions of the maximum and the zero of the second derivative for a distribution of the form

$$f(\varepsilon)=\sqrt{\varepsilon}\,\exp(\alpha\varepsilon)^n \text{ and } 1<n<2. \qquad (7)$$

This is the basis for assuming that the space potential is the potential at which the second derivative is zero.

The zero potential can be determined to an accuracy of 0.5 V. If the distribution function is written in the form (7) the error is given by

$$\delta\left\{f(U)\right\}=\frac{1}{2}\frac{\Delta U}{U}+n\alpha^n U^{n+1}\Delta U.$$

An estimate for n = 2 shows that an uncertainty of ~ 0.5 V in the plasma potential leads to an error of less than 10% in the distribution function.

Thus the total error in measuring the distribution function in our experiments is less than 15%. The inaccuracy in determining the space potential significantly affects the determination of the distribution function, and therefore in refs. 14 and 15 there were attempts to find the space potential independently of the probe characteristics method. To do this the transmission of characteristic low-frequency noise and plasma oscillations to the probe is investigated. It seems to us that this method does not furnish more information than the stationary probe characteristic and its derivatives as long as oscillations with frequencies substantially lower than the plasma frequency are observed.[16] The conclusions of ref. 16 are

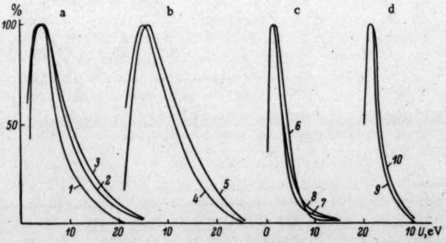

Fig. 1. Effect of current (i) and tube diameter (d_T) on the shape of the electron distribution in helium and nitrogen. a) Helium, p = 0.5 torr: 1) i = 100 mA, d_T = 3 cm, $\bar{\varepsilon}$ = 6.4 eV; 2) i = 300 mA, d_T = 3 cm, $\bar{\varepsilon}$ = 7.5 eV; 3) i = 550 mA, d_T = 3 cm, $\bar{\varepsilon}$ = 7.9 eV; b) helium, p = 0.5 torr: 4) i = 200 mA, d_T = 2.2 cm, $\bar{\varepsilon}$ = 7.9 eV; 5) i = 400 mA, d_T = 2.2 cm, $\bar{\varepsilon}$ = 9.5 eV; c) nitrogen, i = 200 mA: 6) p = 0.9 torr, d_T = 2.2 cm, $\bar{\varepsilon}$ = 3.3 eV; 7) p = 1 torr, d_T = 3 cm, $\bar{\varepsilon}$ = 2.9 eV; 8) p = 2 torr, d_T = 3 cm, $\bar{\varepsilon}$ = 3.2 eV; d) nitrogen, p = 3 torr: 9) i = 200 mA, d_T = 3 cm, $\bar{\varepsilon}$ = 2.9 eV; 10) i = 500 mA, d_T = 3 cm, $\bar{\varepsilon}$ = 3.2 eV.

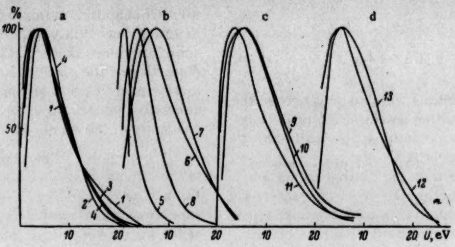

Fig. 2. Distribution functions in mixtures of helium and nitrogen. a: 1) helium, p = 0.5 torr, i = 500 mA, d_T = 3 cm, $\bar{\varepsilon}$ = 7.9 eV; 2) the same + 0.5% nitrogen; 3) the same + 1% nitrogen; 4) the same + 5% nitrogen. b: 5) nitrogen, p = 1 torr, i = 500 mA, d_T = 3 cm, $\bar{\varepsilon}$ = 3.3 eV; 6) helium, p = 0.5 torr, i = 200 mA, d_T = 2.2 cm, $\bar{\varepsilon}$ = 7.9 eV. 7) the same + 10% nitrogen, $\bar{\varepsilon}$ = 9.8 eV; 8) the same + 30% nitrogen, $\bar{\varepsilon}$ = 5.9 eV. c: 9) helium, p = 1 torr, i = 200 mA, d_T = 2.2 cm, $\bar{\varepsilon}$ = 10 eV; 10) the same + 10% nitrogen, $\bar{\varepsilon}$ = 9 eV; 11) the same + 50% nitrogen, $\bar{\varepsilon}$ = 8.2 eV. d: 12) helium, p = 0.5 torr, i = 400 mA, d_T = 2.2 cm, $\bar{\varepsilon}$ = 9.5 eV; 13) the same + 20% nitrogen, $\bar{\varepsilon}$ = 8.8 eV.

confirmed by experiments.[17]

Figure 1 shows the energy distribution curves for electrons in helium and nitrogen for various currents, pressures, and tube diameters. As the current increases and the tube radius decreases the curves are displaced toward higher energies with an increase in the average energy and the relative content of faster electrons. A change in pressure has little effect on the distribution function in nitrogen. These experimental curves agree with published distribution functions in helium[18] and nitrogen.[5] A comparison of $f(\varepsilon)$ in helium and nitrogen shows the depletion of the distribution function in the region just above the most probable energy which characterizes a molecular gas. Figure 2 shows mixtures with various percentage contents of nitrogen. Additions of nitrogen not exceeding 5% (Fig. 2a) have little effect on the distribution function independently of the tube diameter, pressure, or current. A larger amount of nitrogen (Fig. 2, b, c and d) produces a sharp change in the electron distribution function. A comparison of curve 6 with 7 and 12 with 13 shows that the distribution functions can be broader in mixtures with 10–20% nitrogen than in helium. A still larger nitrogen content (30% for curve 8 and 50% for curve 11) narrows the distribution function and changes its shape toward that characteristic of pure nitrogen (curve 5). The energy distribution function for electrons in mixtures is different from that in helium as a result of many processes, the most important of which are the following.

First, there are inelastic collisions of electrons with nitrogen molecules. Secondly, the gas is more easily ionized since the ionization potential of nitrogen is substantially lower than that of helium. Ionization can occur as the result of collisions of excited helium atoms with nitrogen molecules. For small admixtures of nitrogen (up to 5%) these effects apparently nearly compensate one another, which accounts for the weak dependence of the distribution function and the average energy on the nitrogen content. The broadening of the distribution function and the increase in $\bar{\varepsilon}$ for 10–20% admixtures of nitrogen may be a result of easier ionization. The addition of still more nitrogen so diminishes the role of helium in the mixture that the distribution function takes on the characteristic nitrogen shape, and the average energy decreases.

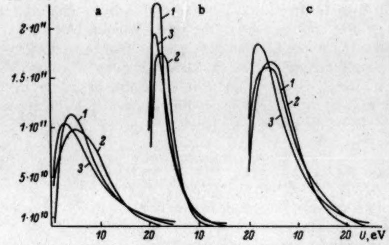

Fig. 3. Comparison of experimental distributions (1) with Druyvesteyn (2) and Maxwellian (3) distributions. a) Helium, p = 0.5 torr, i = 300 mA, $\bar{\varepsilon}$ = 7.4 eV; b) nitrogen, p = 1 torr, i = 500 mA, $\bar{\varepsilon}$ = 3.3 eV; c) mixture of He, p = 0. 5 torr + 5% N_2, i = 500 mA, $\bar{\varepsilon}$ = 6.6 eV.

In all the cases investigated the electron distribution function differs from a Maxwellian. Nevertheless it is convenient to use the Maxwellian distribution in calculations of the kinetics of plasma processes, and sometimes this is possible. This is shown in Fig. 3, where experimental distribution functions obtained under certain conditions are plotted together with Druyvesteyn and Maxwellian functions normalized at the average energy and the electron density obtained from the experimental distribution functions.

It is clear that the experimental curve is closer to a Maxwellian in helium (Fig. 3a) than in nitrogen and mixtures (Figs. 3b, c). However, in the 8–25 eV energy range for all cases of helium and helium–nitrogen mixtures, and in the 3–15 eV range for nitrogen, the divergence does not exceed the error in measuring the distribution function.

---

[1] M. Sicha and V. Rezacova, Czech. J. Phys., B21, 794 (1971).

[2] Yu. M. Kagan, V. M. Milenin, N. K. Mitrofanov, and V. A. Smirnov, Zh. Tekh. Fiz., 39, 1985 (1969) [Sov. Phys.−Tech. Phys., 14, 1497 (1970)].

[3] K. F. Bessonova, O. N. Oreshak, A. F. Stepanov, and V. A. Stepanov, Zh. Tekh. Fiz., 41, 100 (1971) [Sov. Phys.−Tech. Phys., 16, 72 (1971)].

[4] A. Kilvington, R. P. Jones, and J. D. Swift, J. Sci. Inst., 44, 517 (1967).

[5] M. Z. Novgorodov, A. G. Sviridov, and N. N. Sobolev, ZhETF Pis. Red., 8, 341 (1968) [JETP Lett., 8, 211 (1968)].

[6] Yu. A. Ivanov, L. S. Polak, and D. I. Slovetskii, Teplofiz. Vys. Temp., 9, 1151 (1971).

[7] Yu. M. Kagan, N. B. Kolokolov, T. A. Krylova, and V. M. Milenim, Zh. Tekh. Fiz., 41, 120 (1971) [Sov. Phys.−Tech. Phys., 16, 88 (1971)].

[8] C. J. Chen, J. Wu, F. Wu, and D. Shaw, Bull. Amer. Phys. Soc.; 16, 1286 (1971).

[9] N. A. Vorob'eva, Yu. M. Kagan, and V. M. Milenin, Zh. Tekh. Fiz. 33, 571 (1963) [Sov. Phys.−Tech. Phys., 8, 423 (1963)].

[10] O. N. Oreshak, A. F. Stepanov, and V. A. Stepanov, Zh. Tekh. Fiz., 41, 126 (1971) [Sov. Phys.−Tech. Phys., 16, 93 (1971)].

[11] Yu. M. Kagan and N. K. Mitrofanov, Zh. Tekh. Fiz., 41, 2065 (1971) [Sov. Phys.−Tech. Phys., 16, 1636 (1972)].

[12] R. Huddlestone and S. Leonard (eds.) Plasma Diagnostic Techniques, Academic Press, New York (1965), Chap. 4.

[13] A. I. Lukovnikov and M. Z. Novogorodov, Krat. Soobshch. po Fiz., FIAN, 1, 27 (1971).

[14] A. A. Zaitsev, M. Ya. Vasil'eva, and V. N. Mnev, Zh. Eksp. Teor. Fiz., 36, 1590 (1959) [Sov. Phys.−JETP, 9, 391 (1959)].

[15] V. M. Milenin, Zh. Tekh. Fiz., 41, 831 (1971) [Sov. Phys.−Tech. Phys., 16, 654 (1971)].

[16] K. D. Asvadurov, I. A. Vasil'eva, and V. M. Torchinskii, Zh. Tekh. Fiz., 42, 207 (1972) [Sov. Phys.−Tech. Phys., 17, 166 (1972)].

[17] S. L. F. Richards, G. J. Lloyd, and R. P. Jones, J. Phys. D; Appl. Phys., 6, 695 (1973).

[18] Yu. M. Kagan, in: Spectroscopy of a Gas Discharge Plasma, S. É. Frish editor, [in Russian], Nauka, Leningrad (1970).

Use of plasma accelerator for optical pumping of lasers

N. P. Kozlov and Yu. S. Protasov

N. É. Bauman Moscow Technical College

(Submitted February 12, 1973; resubmitted August 6, 1973)
Zh. Tekh. Fiz., 44, 575-579 (March 1974)

On the basis of a study of the radiation properties of a dense plasma focus and an analysis of the requirements that must be met by a light source for exciting organic dye solutions it is shown that pulsed plasma accelerators of the erosion type can, in principle, be used for the optical pumping of organic dye lasers. A laser has been designed for pumping by the plasma focus of a pulsed accelerator operating in a vacuum of ~ 10^{-6} torr; the working medium and a protective liquid filter are pumped through the active zone of the laser. The lasing properties of a laser with the dye rhodamine 6G are studied. Methods for increasing the efficiency of the laser are discussed.

A distinctive feature of pulsed plasma accelerators of the erosion type is the possibility of regulating the spectral composition of the radiation over a broad range through the choice of an appropriate working medium: a metal, a dielectric, a combination, etc. Furthermore, the self-focusing of the plasma jet in the accelerator in the compression mode and the high radiation energy can be exploited to excite a population inversion in the active media of essentially all types of laser: solid-state, gas, organic-dye, etc. Study of the temporal characteristics of the plasma emission and of the discharge dynamics[1-3] shows that it may be possible to obtained focused light bursts having the required length, front curvature, pulse shape, and magnitude and spectral distribution.[4]

One way to increase the power of a laser is to increase the power of the pumping source. As a rule, this approach causes the peak of the source radiation to shift toward shorter wavelengths (in our case, to the vacuum-UV, at wavelengths shorter than 1000 Å). Accordingly, the most promising materials for pumping by powerful sources of incoherent light are those in which the absorption bands are broad in the visible and UV ranges. Organic dyes are such materials.[5]

Organic dye lasers are currently the only type of lasers whose radiation frequency can be tuned over a broad spectral range (several hundred angstroms) either by changing the parameters of the solution or resonator or by inserting a wavelength selector (e.g., a diffraction grating) into the resonator. With the appropriate dye it is possible to achieve intense coherent radiation at nearly any wavelength between 3400 and 11,750 Å.

It has been found experimentally and theoretically[6,7] that in the case of pumping in the visible range by flashlamps or harmonics of a ruby or neodymium-glass laser the lower threshold for lasing of the more suitable dyes is four or five times higher than that for ruby, so high-intensity sources are required for laser action. Furthermore, since the molecules in organic dyes are in an excited singlet state, there can be a radiationless transition to a lower triplet state in addition to the transition to the ground state. Accordingly, an effort should be made to reach the lasing threshold before the number of molecules in the triplet state becomes large. For such a pumping source the light pulse must have a steep front.

Plasma light sources have an essentially unlimited maximum deexcitation energy, and the freedom to regulate the temporal and spectral characteristics of the discharge makes them the most promising source for achieving high energy and power levels in dye lasers.

Noteworthy among the working materials having comparatively low lasing thresholds are the oxazoles, coumarins, and rhodamines.[7]

Extrapolation of the functional dependence of the lasing energy on the energy input[7] reveals the lasing threshold for rhodamine 6G, which is ~ 17 J. The source which we have studied has a high deexcitable energy and can be used to achieve lasing without a reduction of the steepness of the light-pulse front (4-6 μsec). Since much of the radiation energy falls at wavelengths shorter than 2700 Å, where rhodamine 6G undergoes photodecomposition, protective filters must be used to cut off this part of the plasma radiation.

ORGANIC DYE LASER

A plasma focus exists as a stable plasma formation, localized in space and over the discharge time, only for ambient pressures below ~ 10^{-4} torr, so that serious difficulties arise in the construction of such a laser. If the laser lead is removed from the evacuated volume, it cannot be placed close to the illuminator, so there is a severe loss in the efficiency at which light energy is transferred from the focus to the laser head. Placing the head in vacuum with the accelerator, on the other hand, also requires some optimization, since even slight contact with a plasma jet would lead to the destruction of the resonator mirrors. Nor is it possible to "tie" the discharge to the metal frame of the illuminator or to metal parts of the head, for they would be destroyed. Accordingly, the selection of a highly efficient illuminator and the optimum layout largely govern the efficiency of the laser.

As mentioned above, heating of the dye leads to a spatial stratification of the active medium and the lasing level is lowered sharply; since the characteristic for thermal stabilization of the dye is long, the active medium must be pumped through the cavity of a cuvette. The UV component of the radiation from the focus leads to the photodecomposition of rhodamine 6G even before the lasing threshold is reached, so filters (usually liquid) must be used to absorb the light at wavelengths shorter than 2700 Å. This hard component of the radiation leads to intense erosion of the illuminator, which therefore must be coated with a diffusely reflecting protective material (e.g., silicon dioxide). Several experiments have shown[7] that stable lasing characteristics can be achieved only by pumping

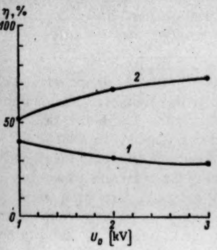

Fig. 1. Efficiency of an elliptical reflector. 1) The $\eta(U_0)$ functional dependence in integrated light; 2) that in the transmission region of quartz.

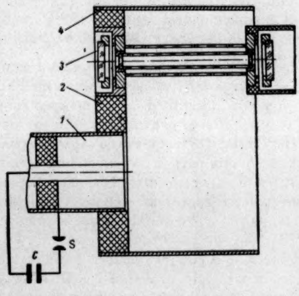

Fig. 2. Arrangement of the organic dye laser. 1) M2-K accelerator; 2) insulating bushing; 3) laser head; 4) reflector.

the protective filter. A four-channel contact with the atmosphere is therefore necessary, and the experiment is significantly complicated; the tubes through which the materials are pumped must be as small as possible, withstand a vacuum of ~ 10^{-6} torr, and be transparent, so that a check can be made to ensure that there are no air bubbles in either cavity of the cuvette.

In our experiments we study various possible arrangements of the laser and reflector, made from polished duralumin and having various shapes; a combination of spherical and elliptical half-cylinders, an ellipse, and a cone.

We evaluate the efficiency of the illuminator in the following manner: The reflector is originally held on a dielectric bushing 30 mm thick, pressed against the outer electrode of the accelerator. At the first focus of the illuminator is a compressed plasma zone; at the second, at the position of the cuvette, a hollow cylinder having the same diameter as the cuvette is placed. Two Chromel–Copel thermocouples are fused to the thin-walled cylinder, which is a blackbody, and the thermal emf is detected by an M254 instrument. In this manner, the integrated radiation flux transferred from the plasma focus to the cuvettes is determined, and the efficiency of the illuminator is calculated as the ratio of the energy received by the blackbody to the radiation energy of the focus. The best illuminator among those we have studied is the elliptical reflector, which permits the closest packing of the cuvette and the accelerator without loss of contact with the plasma. Figure 1 (curve 1) shows the efficiency determined in this manner for an elliptical illuminator with a major semiaxis of 240 mm and a minor semiaxis of 210 mm, as a function of the initial voltage on the capacitor bank. It should be kept in mind here that the absorption coefficient of aluminum is approximately unity[8] at wavelengths shorter than 2000 Å, so it is better to determine the efficiency in the transmission region of quartz (2320 Å) (curve 2 in Fig. 1). According to these results, the efficiency of the elliptical mirror reaches ~ 70%. The $\eta(U_0)$ function must have an extremum, since an increase in U_0 leads to an improvement in the focusing of the plasma jet and to a shift of the radiation maximum of the system toward shorter wavelengths and an increase in the relative amount of energy absorbed by the reflector. Taking these circumstances into account, we conclude that the difference between the behavior of curves 1 and 2 for U_0 = 1 and 2 kV is plausible.

The resonator of the laser is formed by external plane mirrors having dielectric coatings with reflection coefficients of 99 and 60%. The mirrors are mounted in metal holders, with which it is possible to adjust the mirrors with respect to the ends of the cuvette and the entire head. At the dead end of the cuvette a supporting metal cup is mounted in a dielectric flange between the accelerator and the reflector. The cup, used for protection against the plasma, is made from ebonite and is in immediate contact with the measuring elements of the system. The head is made rigid by means of two thin pins connecting the cups. The diameter of the outer quartz tube is 10 mm, its length is 30 mm, and the diameter of the inner tube is 3 mm.

Figure 2 shows the laser. The laser head is attached rigidly in a bushing connecting the accelerator and the illuminator. The extensions of the tube for pumping the dye and the filter pass through the bushing at one end; at the other end they emerge from the reflector and, after passing through special connectors, are mounted on the vertical flange of the vacuum chamber.

LASING PROPERTIES OF A RHODAMINE 6G LASER

We have studied the lasing properties of this laser, in which the working medium is a solution of rhodamine 6G in dehydrated alcohol at a concentration of ~ $1.5 \cdot 10^{-4}$ M. The filter protecting the working medium from photodecomposition is a 4% solution of sodium acetate. It should be noted that our purpose in these experiments is not to optimize the laser by choosing the best dye concentration, resonator parameter, cuvette volume, etc.; we choose these parameters to be approximately the same as the optimum parameters for a rhodamine 6G laser with flash pumping.[6]

It was shown previously[7] that the lasing energy is quite sensitive not only to the Q of the resonator, but

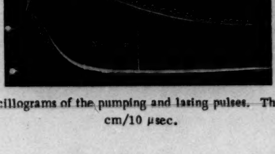

Fig. 3. Oscillograms of the pumping and lasing pulses. The scale is 1 cm/10 μsec.

also to the purity of the dye and of the other materials and items in contact with the solutions; thus, before we fill the system with the dye and the filter we wash the cuvettes, the hoses, and the connectors with ordinary alcohol and then dehydrated alcohol.

In the experiment the dye is pumped through the active zone after each discharge, and the filter is pumped through after three or four discharges, since the lasing energy falls off by a factor of nearly 2 at the second pumping pulse. Since part of the dye in the leadout tubes is subjected to the UV radiation of the plasma, we replace all the dye in the circulation volume.

The light source is an M2-K coaxial accelerator,[1] which operates with a copper plasma with $U_0 = 3$ kV, since we have shown previously that the emission spectrum of a copper plasma has intense regions of continuum at 3500-5500 Å, corresponding to the absorption bands of rhodamine 6G.

The system we use to detect the lasing allows us to determine the absolute value of the lasing energy and its time dependence.

The protective cup of the external mirror of the head is held against the screen of a calibrated F-1 photocell and a metallic bolometer, whose output signals are amplified by a preamplifier and sent to the input of an S1-16 oscilloscope. The photocell housing and the electromagnetic shield are designed to prevent optical contact with the plasma. At the same time we use a DMR-4 monochromator and an FÉU-12A photomultiplier to detect the plasma emission at 5900 ± 3 Å through an aperture in the reflector. We also detect the discharge current and the integrated (over the spectrum) radiation of the pumping pulse by means of photomultipliers.

Figure 3 shows oscillograms of the pumping and lasing pulses for $U_0 = 3$ kV. We see that the lasing pulse has a shape reminiscent of that of the pumping pulse. The pumping intensity is several times higher than the threshold level, so the lasing occurs with an essentially negligible delay. The length of the lasing pulse is ~ 14 μsec. The lasing energy, determined by integrating the signal, is ~ 0.22 J, while the lasing power is 0.15 MW. When the pumping pulse is repeated, the lasing energy falls by a factor of 2.5, and at the third pumping pulse we detect only a slight lasing peak, due to the appearance of a radial temperature gradient in the cuvette, a temperature stratification of the active medium, and the partial photodecomposition of this medium; these results agree with results found with flash pumping.[8] The temperature-relaxation time is 4-5 min. Accordingly, the energy content is 0.35 J/cm^3, which is not the limiting value[7] and which shows that it may be possible to significantly increase the lasing energy.

The divergence of the radiation in the unoptimized system, governed by essentially the geometric dimensions of the cuvette alone, is $\sim 2 \cdot 10^{-3}$ rad. The lasing efficiency in our case is ~ 0.11% and corresponds to a laser with flash pumping. It should be noted that this efficiency can be increased: first, by choosing the optimum concentration of the active medium, the optimum reflection coefficients of the resonator mirrors, the optimum resonator Q, and the optimum cuvette volume; second, by increasing the steepness of the front of the pumping signal, by using the optimum distribution of radiation energy in the spectrum of the plasma focus, and by increasing the pumping energy (it has been shown[7] that the lasimg energy is a linear function of the energy supplied to the discharge).

The advantages of a plasma focus as a pumping source are displayed most fully when the active media used have absorption bands in the UV part of the spectrum; one such medium is a solution of paraterphenyl in cyclohexane and in standard[9] POPOP, since the radiation maximum of the focus is nearer this part of the spectrum. The possibility of controlling the spectral distribution of the deexcited energy through the appropriate choice of working media makes this source more suitable than ordinary straight pinches[10] for the design of powerful lasers. The use of a plasma focus as a pumping source in a dye laser makes it possible, in principle, to design a laser which operates in the vacuum-UV part of the spectrum (up to 1200 Å): an extremely important feature.

In conclusion the authors thank A. N. Rubinov for advice and assistance in constructing the laser.

---

[1] N. P. Kozlov, L. V. Leskov, Yu. S. Protasov, and V. I. Khvesyuk, Zh. Tekh. Fiz., 43, 740 (1973) [Sov. Phys.—Tech. Phys., 18, 466 (1973)].

[2] N. A. Kozlov and Yu. S. Protasov, Teplofiz. Vys. Temp., 10, No. 6 (1972).

[3] V. A. Alekseev, A. Ya. Balagurov, N. P. Kozlov, L. V. Leskov, Yu. S. Protasov, and V. I. Khvesyk, Report to the Sixth All-Union Conference on Nonlinear Optics, Minsk, 1972.

[4] N. P. Kozlov, L. V. Leskov, Yu. S. Protasov, and V. I. Khvesyuk, Teplofiz. Vys. Temp., 11, No. 1 (1973).

[5] A. P. Ivanov, Opt. Spektrosk., 8, No. 2 (1960).

[6] B. I. Stepanov and A. N. Rubinov, Usp. Fiz. Nauk, 95, 45 (1968) [Sov. Phys.—Usp., 11, 304 (1968)].

[7] M. Bass, T. Deich, and M. Veber, Usp. Fiz. Nauk, 105 (1971).

[8] A. V. Sokolov, Optical Properties of Metals [in Russian], Fizmatgiz, Moscow (1961).

[9] G. A. Abakumov, A. P. Simonov, V. V. Fadeev, L. A. Kharitonov, and R. V. Khokhlov, ZhETF Pis. Red., 9, 15 (1966) [JETP Lett., 9, 9 (1969)].

[10] I. V. Antonov, S. A. Mikhnov, V. S. Prokudin, A. N. Rubinov, B. I. Stepanov, and B. V. Skvortsov, Zh. Prikl. Spektrosk., 14, No. 1 (1971).

Efficiency of light-beam conversion by dynamic three-dimensional phase holograms

D. I. Stasel'ko and V. G. Sidorovich

(Submitted August 23, 1973)
Zh. Tekh. Fiz., 44, 580-587 (March 1974)

The efficiency with which energy is transferred between waves propagating in dynamic phase holograms is analyzed. Under certain conditions, the energy of one of the beams incident on the hologram can be almost completely transferred to the other beam, regardless of the initial ratio of beam intensities.

There has been a great deal of interest in the properties of holograms recorded in media whose optical properties can be changed reversibly by incident light. Such holograms are frequently called "dynamic," since they are capable of reacting to spatial and temporal changes in the parameters of the incident beam during recording. Most of the reported work on dynamic holography has involved phase gratings in media whose refractive indices vary in proportion to the intensity of the optical field. The conversion of the incident beams into beams of higher diffraction orders has been treated as the basic result of the effect of a dynamic hologram.[1-4] Considerably less attention has been paid to the redistribution of energy between the objective and reference beams. This topic is treated in ref. 5, in connection with a study of the mechanism for the formation of three-dimensional phase diffraction gratings in lithium niobate crystals. On the basis of the theory worked out by Kogelnik and their own experimental data, Staebler and Amodei[5] conclude that the energy exchange between the object and reference beams observed in the recording of holograms in these crystals occurs because the holographic phase grating is displaced by approximately one fourth of a period with respect to the sinusoidal interference pattern which forms this grating.

However, this energy exchange between the object and reference beams in the recording of dynamic holograms can be of much independent importance, especially if it is found possible to transfer a considerable amount of energy to one of the original beams. It follows from general considerations that the energy transfer between light beams should be most efficient in three-dimensional phase holograms, but no theory is presently available for such holograms. Below we attempt to partially bridge this gap by analyzing the recording of simple dynamic phase holograms in various media. We proceed by analyzing the steady-state system of truncated nonlinear coupled equations for the amplitudes of the waves propagating in the hologram. Effects of the three-dimensional nature of the dynamic phase gratings are taken into account, as is the displacement of the gratings with respect to the interference patterns which form them. We find that under certain conditions energy can be transferred from one of the beams incident on the hologram to the other, regardless of the initial intensity ratio of these beams. This property of dynamic holograms presents us with an opportunity to effectively control the spatial and temporal characteristics of light beams by means of considerably less intense beams, and it furnishes a basis for solving one of the most important problems of dynamic holography: that of correcting nonstationary wave fronts in real time.

To derive the coupled equation for the amplitudes of the propagating waves we begin by analyzing the nonlinear wave equation. We assume that two plane monochromatic waves at the same frequency ω are incident on the surface of the medium in which the hologram is formed; we assume that the waves are polarized normally with respect to the incidence plane. Then the amplitude of the electric field vector, E(x, z), satisfies the equation

$$\nabla^2 E(x, z) + k_0^2 \varepsilon [E(x, z)] E(x, z) = 0, \tag{1}$$

where $k_0 = \omega/c$ is the wave number of the light incident on the hologram, $\varepsilon[E(x, z)]$ is the dielectric constant of the medium, the XOZ plane is the incidence plane of the wave, the X and Y axes are along the boundary of the hologram, and the Z axis is normal to it. For the assumed wave polarization and orientation of axes we have $E_x = E_z = 0$ and $E_y = E$. In specifying the boundary conditions we start by assuming that two plane waves with amplitudes $C_1(0)$ and $C_{-1}(0)$ are incident on the hologram at angles of $\pm\theta$ with respect to the normal (Fig. 1). Also assuming that the hologram has an approximately unit dielectric constant and that the relative changes in ε caused by the light are small, we write $\varepsilon(E)$ as

$$\varepsilon(E) = 1 + \Delta\varepsilon(E), \tag{2}$$

where $\Delta\varepsilon(E) \ll 1$. The first of these latter assumptions is not crucial; we adopt it only so that we can neglect reflection and refraction of light at the boundaries of the hologram. The second assumption is more fundamental; it allows us to write the solution of Eq. (1) in the form

$$E(x, z) = e^{ik_z z} U(x, z), \tag{3}$$

where U(x, z) is a slowly varying function of z and where $k_z = k_0 \cos\theta$.

Substituting Eq. (3) into Eq. (1), cancelling out the exponential terms, and discarding the second derivatives of U with respect to z, we find a truncated equation for U:

$$2ik_z \frac{\partial U}{\partial z} + \frac{\partial^2 U}{\partial x^2} + k_z^2 U + k_0^2 \Delta\varepsilon(E) U = 0. \tag{4}$$

Exploiting the periodicity of the conditions at the boundary of the hologram, we write U(x, z) as

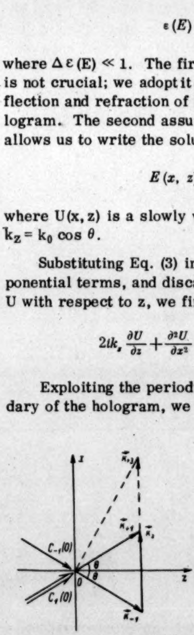

Fig. 1. Vector diagram of waves propagating in a dynamic hologram system.

$$U(x,\ z)=\sum_{n=-\infty}^{\infty} C_n(z)\,e^{ink_x x}. \tag{5}$$

Substituting (5) into (4) we find

$$2ik_z\frac{\partial}{\partial z}\sum_{n=-\infty}^{\infty} C_n(z)\,e^{ink_x x}+k_z^2\sum_{n=-\infty}^{\infty} C_n(z)(1-n^2)\,e^{ink_x x}$$
$$+k_0^2\Delta\varepsilon(E)\sum_{n=-\infty}^{\infty} C_n(z)\,e^{ink_x x}=0. \tag{6}$$

To proceed further in this analysis we must specify a concrete functional dependence of $\Delta\varepsilon$ on E. Here we consider the cases in which

$$\Delta\varepsilon=\alpha\,|E|^2 \tag{7}$$

and

$$\Delta\varepsilon=\beta\frac{\partial |E|^2}{\partial x}. \tag{8}$$

Equation (7) gives an approximate description of the functional dependence of the dielectric constant of a nonlinear medium on the amplitude of the light field in dynamic holograms recorded in absorbing liquids, while Eq. (8) corresponds to a recording in a crystal like lithium niobate: With a sinusoidal intensity distribution in the interference pattern this reaction of the medium corresponds to the observed displacement of the grating by one fourth of the period with respect to this pattern. [The plus sign on the right side of Eq. (8) corresponds to the case in which $\beta > 0$ and in which the C axis of the crystal lies along the X axis.] Since the phase gratings in nonlinear media obeying Eq. (7) coincide in position with the interference pattern which forms them, we call such gratings "undisplaced gratings."

Substituting Eqs. (7) and (8) into Eq. (6), using Eqs. (3) and (5) for E(x, z) and U(x, z), cancelling out the factor of $2ik_z$, and equating to zero the sums of the coefficients of terms having identical exponential factors, we find systems of coupled differential equations for the two cases:

$$\frac{dC_n}{dz}-\frac{i}{2}(1-n^2)\,k_x\,\mathrm{tg}\,\theta C_n$$
$$=\frac{i}{2}\alpha\frac{k_0^2}{k_z}\sum_{l+m-k=n} C_lC_mC_k^*\ (n=\pm 1,\ \pm 3\ldots) \tag{9}$$

for the case of undisplaced phase gratings;

$$\frac{dC_n}{dz}-\frac{i}{2}(1-n^2)\,k_x\,\mathrm{tg}\,\theta C_n=-\frac{\beta}{2}\frac{k^2}{k_z}k_x\sum_{l+m-k=n}(m-k)\,C_lC_mC_k^*$$
$$(n=\pm 1,\ \pm 3\ldots) \tag{10}$$

for the case of displaced gratings. Introducing the notation

$$B_n=\frac{1}{2}(1-n^2)\,k_x\,\mathrm{tg}\,\theta=\frac{1-n^2}{2}\frac{2\pi}{\lambda}\frac{\sin^2\theta}{\cos\theta}, \tag{11}$$

$$f_n(z)=\begin{cases}\dfrac{i}{2}\alpha\dfrac{k^2}{k_z}\displaystyle\sum_{l+m-k=n} C_lC_mC_k^* & \text{for undisplaced gratings}\\ -\dfrac{\beta}{2}\dfrac{k^2}{k_z}k_x\displaystyle\sum_{l+m-k=n}(m-k)\,C_lC_mC_k^* & \text{for displaced gratings,}\end{cases} \tag{12}$$

and multiplying the equations in systems (9) and (10) by the corresponding interference factors e^{-iB_nz}, we convert them to "total-differential" form, so that we can now write the equations for $C_n(z)$ in integral form:

$$C_n(z)=e^{iB_nz}\left[\int_0^z f_n(z')\,e^{-iB_nz'}\,dz'+C_n(0)\right]. \tag{13}$$

It follows from Eqs. (13) that the nature of the light propagation in the hologram is strongly influenced by the ratio between the rates of change of the functions $f_n(z')$ and e^{-iB_nz} in the integrand. The first of these functions describes the scattering of the amplitudes of the interacting waves into a wave of a given order by the thin layer of the hologram with coordinate z'; the second takes into account the phase difference which arises when the amplitudes of the light scattered by different thin layers are combined. We have n = ± 1 for the incident beams, so that the exponential term is equal to unity, regardless of the geometry of the recording; this circumstance corresponds to satisfaction of the Bragg condition for these waves. For waves of higher order ($n \neq \pm 1$) we have $B_n \neq 0$, and the radiation scattered by different thin layers is not in phase. When the rates of change of the wave amplitudes due to scattering by the hologram are small by comparison with the oscillation rates of the functions e^{-iB_nz}, we can neglect integrals like (13) for the amplitudes of the higher-order waves and retain in systems (9) and (10) only the terms corresponding to the several lowest orders of diffraction. Furthermore, in correspondence with a case of practical importance, we assume that the waves incident on the hologram differ markedly in amplitude, e.g., that $|C_{-1}(0)| \ll |C_1(0)|$.

Under these assumptions we can retain three coupled equations, for n = ± 1 and n = 3, in each of systems (9) and (10):

$$\frac{dC_1}{dz}=iA\,[2C_3C_{-1}C_1^*+(|C_1|^2+2|C_{-1}|^2+2|C_3|^2)\,C_1], \tag{14a}$$

$$\frac{dC_{-1}}{dz}=iA\,[C_1C_1C_3^*+(|C_{-1}|^2+2|C_1|^2+2|C_3|^2)\,C_{-1}], \tag*{14b)}$$

$$\frac{dC_3}{dz}-iB_3C_3=iA\,[C_1C_1C_{-1}^*+(|C_3|^2+2|C_1|^2+2|C_{-1}|^2)\,C_3] \tag{14c}$$

for the case corresponding to Eq. (7); and

$$\frac{dC_1}{dz}=-\gamma\,|C_{-1}|^2C_1+\gamma\,|C_3|^2C_1, \tag{15a}$$

$$\frac{dC_{-1}}{dz}=\gamma\,|C_1|^2C_{-1}+\gamma C_1^2C_3^*, \tag{15b}$$

$$\frac{dC_3}{dz}-iB_3C_3=-\gamma C_1^2C_{-1}^*+\gamma\,|C_1|^2C_3 \tag{15c}$$

for the case corresponding to Eq. (8). Here

$$A=\frac{\alpha}{2}\frac{k^2}{k_z},\quad \gamma=\beta\frac{k^2}{k_z}k_x. \tag{15d}$$

Substituting $C_i = \bar{C}_i\exp\left(-i2Az\sum_i |C_i|^2\right)$ into (14), we find the following system of equations for $\bar{C}_i(z)$:

$$\frac{d\bar{C}_1}{dz}+iA\,|\bar{C}_1|^2\bar{C}_1=2iA\bar{C}_3\bar{C}_{-1}\bar{C}_1^*, \tag{16a}$$

$$\frac{d\bar{C}_{-1}}{dz}+iA\,|\bar{C}_{-1}|^2\bar{C}_{-1}=iA\bar{C}_1\bar{C}_1\bar{C}_3^*, \tag{16b}$$

$$\frac{d\bar{C}_3}{dz}+iA\left(|\bar{C}_3|^2-\frac{B_3}{A}\right)\bar{C}_3=iA\bar{C}_1\bar{C}_1\bar{C}_{-1}^*. \tag{16c}$$

[In deriving (16) we have exploited the circumstance that the sum $\sum_i |C_i(z)|^2 = \text{const} = \sum_i |C_i(0)|^2$ is an integral of system (14).]

The terms with quadratic amplitudes on the left side of (16) cause a difference between the phase velocities of plane waves because of their self-interaction, as can be seen by setting the right sides of Eqs. (16) equal to zero. Energy exchange between the waves is described by the terms on the right sides of Eqs. (16). Let us consider the general features of this process as light propagates into the interior of the hologram. Near the surface of the hologram we can neglect the third term on the left side of Eq. (16c) by virtue of the smallness of $\overline{C}_3$. Determining $\overline{C}_3(z)$ from (13), and substituting the result into Eqs. (16a) and (16b), we find that the increment in the amplitude of the weaker wave is in phase with the amplitude $\overline{C}_{-1}(0)$, while the increment in the amplitude of the stronger wave is shifted by π radians with respect to the initial amplitude $\overline{C}_1(0)$. This result corresponds to the intensification of the weaker wave $\overline{C}_{-1}$ at the expense of the stronger wave $\overline{C}_1$. In turn, as we see from Eq. (16c), an increase in $\overline{C}_{-1}$ increases the rate at which $\overline{C}_3$ increases. It is not difficult to show that in a thin layer near the surface of a hologram the amplitudes of both waves increase exponentially, with an argument of $A|C_1(0)|^2 z$. As we move away from the surface of the hologram the influence of the discarded term in Eq. (16c) becomes significant; as a result, the increments in the amplitudes of the interacting waves become increasingly out of phase with respect to the amplitudes themselves. With $z_0' \sim \pi/B_3$ this displacement is 180°, and energy begins to be returned from the amplified waves to the stronger wave. In the case of a low conversion efficiency, with $|\overline{C}_{-1}(z)|$ and $|C_3(z)| \ll |\overline{C}_1(z)|$, the subsequent energy exchange between waves is oscillatory, with a spatial period of $2z_0'$. Accordingly, in undisplaced dynamic gratings there exists an effective amplification length for weak beams, governed by z_0'. Substituting the value of B_3 from (11) into the equation for z_0', and using $\Lambda = \lambda/2\sin\theta$ (which relates the period of the interference patterns, Λ, to the wavelength and the angle between the beams), we find that holograms having a thickness equal to the effective amplification depth z_0' satisfy the condition $z_0' < \Lambda^2/\lambda$; such holograms can be treated as thin holograms.[6] It is therefore natural to expect that the efficiency with which light beams are converted by means of undisplaced dynamic phase gratings should not exceed about 30%, which corresponds to the limiting diffraction efficiency of thin phase holograms.[6] It is clear from this discussion that attempts to raise the efficiency of dynamic holograms of this type by resorting to a recording of a more three-dimensional nature (by increasing the angle between the beams) are counterproductive, since the result is a decrease in z_0'. At large values of θ the beams in such holograms will propagate essentially without energy transfer.

We turn now to an analysis of system (15), which describes the propagation of waves in displaced dynamic three-dimensional holograms. The most important difference between these equations and relations (16) (for undisplaced gratings) is the appearance of the terms $-\gamma|C_{-1}|^2 C_1$ and $\gamma|C_1|^2 C_{-1}$, which provide energy transfer from one of the Bragg beams to the other without the participation of higher-order waves. We will show that under certain conditions this process plays a decisive role and is capable of leading to a complete energy transfer between Bragg beams.

Let us first evaluate the influence of the most intense higher order (n = 3). Assuming $|C_3(z)| \ll |C_{-1}(z)$ and $C_1(z) \simeq C_1(0)$, we find from Eq. (15b) that

$$C_{-1}(z) \simeq C_{-1}(0)\, e^{\gamma |C_1(0)^2| z}. \qquad (17)$$

Substituting this equation into the equation for $C_3(z)$, from (13) we find

$$C_3(z) = -e^{-\gamma |C_1(0)|^2 z} e^{iB_3 z} \gamma C_1^2(0)\, C_{-1}(0) \int_0^z e^{2\gamma |C_1(0)|^2 z'} e^{2-iB_3 z} dz'. \qquad (18)$$

The integral in (18) can be evaluated easily and we can evaluate the intensity ratio of the waves with n = 3 and n = − 1:

$$\frac{|C_3|^2}{|C_{-1}|^2} = \left(\frac{\gamma |C_1(0)|^2}{B_3}\right)^2. \qquad (19)$$

From (19) we find a condition for the suppression of waves of higher diffraction orders in a dynamic three-dimensional hologram:

$$\frac{\gamma |C_1(0)|^2}{B_3} = \frac{\Delta\varepsilon}{8\sin^2\theta} \ll 1. \qquad (20)$$

We see from Eq. (20) that, in contrast with the case of static three-dimensional holograms,[6] the degree to which higher-order beams are suppressed by dynamic three-dimensional holograms is not dependent on the thickness of the hologram. A numerical estimate of the ratio $|C_3|^2/|C_{-1}|^2$ on the basis of (19) shows that for angles θ of the order 1° and for $\Delta\varepsilon \simeq 10^{-5}$ this ratio is 10^{-5}. Accordingly, at $\theta \geq 1°$ the effect of the higher orders on the energy exchange between Bragg beams can be neglected, and the analysis can be restricted to the equations for the amplitudes of the original waves:

$$\frac{dC_1}{dz} = -\gamma |C_{-1}|^2 C_1, \qquad (21a)$$

$$\frac{dC_{-1}}{dz} = \gamma |C_1|^2 C_{-1}. \qquad (21b)$$

Rewriting system (21) in integral form,

$$C_1(z) = C_1(0)\, e^{-\gamma \int_0^z |C_{-1}(z)|^2 dz}, \qquad (22a)$$

$$C_{-1}(z) = C_{-1}(0)\, e^{\gamma \int_0^z |C_1(z)|^2 dz}, \qquad (22b)$$

we note that the integrals in the exponential functions of these equations are positive, nondecreasing quantities. It follows that energy transfer between Bragg waves is unidirectional, and when the hologram is thick enough the energy of one wave can be transferred completely to the other. Accordingly, dynamic three-dimensional phase holograms recorded in media with a displacement of the grating are capable of light-beam conversion with an efficiency of nearly 100%. The direction of the energy transfer is governed by the direction in which the grating is displaced with respect to the interference pattern: The peaks of $\varepsilon(E)$ must be displaced with respect to those of the interference pattern in the direction of the amplifying wave.

The explicit functional dependence of amplitudes C_{-1} and C_1 on z can be found in the following manner. Dividing Eq. (22b) by Eq. (22a) we find

$$\frac{C_{-1}(z)}{C_1(z)}=\frac{C_{-1}(0)}{C_1(0)}e^{\gamma\int_0^z(|C_1(z)|^2+|C_{-1}(z)|^2)dz} \tag{23}$$

Since the sum

$$|C_1(z)|^2+|C_{-1}(z)|^2=\mathrm{const}=|C_1(0)|^2+|C_{-1}(0)|^2 \tag{24}$$

is an integral of system (22), the integration in (23) yields

$$\frac{C_{-1}(z)}{C_1(z)}=\frac{C_{-1}(0)}{C_1(0)}e^{\gamma(|C_1(0)|^2+|C_{-1}(0)|^2)z}. \tag{25}$$

Converting from (25) to an equation for the intensities of the Bragg waves, $J_1(z) = |C_1(z)|^2$ and $J_{-1}(z) = |C_{-1}(z)|^2$, and taking the logarithms of both sides of the resulting equation, we find

$$\ln\frac{J_{-1}(z)}{J_1(z)}=\ln\frac{J_{-1}(0)}{J_1(0)}+2\gamma[J_{-1}(0)+J_1(0)]z. \tag{26}$$

This equation can be used to determine the intensity ratio of the waves at an arbitrary cross section of the hologram from the intensities of the incident waves specified at the boundary, $J_1(0)$ and $J_{-1}(0)$, and from the value of the parameter γ, a characteristic of the medium. The values of the intensities themselves can be easily found by means of integral (24). The family of equations (26) for different values of γ and for different intensities $J_1(0)$ and $J_{-1}(0)$ describes a set of straight lines whose ordinate intercepts are governed by the value of $\ln[J_{-1}(0)/J_1(0)]$ and whose slopes are governed by the value of $\gamma\,[J_1(0) + J_{-1}(0)]$. The linear nature of this expression shows that the necessary degree of energy transfer between the Bragg beams, governed by the ratio $J_{-1}(z)/J_1(z)$, can be attained, regardless of the initial intensity ratio of the waves incident on the hologram, $J_{-1}(0)/J_1(0)$. This relation affects only the depth at which this transfer is achieved.

Figure 2 shows the result of an illustrative calculation of $J_{-1}(z)$ and $J_1(z)$ from Eq. (26); the solid curves show the intensity of the waves propagating in the hologram, while the dashed curve shows the profile of the modulation depth of the dielectric constant over the thickness of the hologram, $\Delta\varepsilon(z) = 2(\Delta\varepsilon)'\sqrt{J_1(z)\,J_{-1}(z)}/J_1(0)$. For this calculation we assume the parameter $(\Delta\varepsilon)' = 2\beta k_x[J_1(0) + J_{-1}(0)]$, which governs the changes in the dielectric constant of the medium, is 10^{-5}; we also assume $J_{-1}(0)/J_1(0) = 10^{-8}$, $\lambda = 7\cdot10^{-5}$ cm, and $\theta = 0.2$ rad. The additional stage of the energy transfer, according to (17), is characterized by an exponential increase in C_{-1} and a corresponding exponential increase in the modulation depth of the hologram. Then, because of the decrease in the intensity of the stronger wave, the process slows down; at $C_{-1}(z_m) = C_1(z_m)$ the modulation depth reaches a maximum, and then it decreases as wave $C_1(z)$ is attenuated. In this example we find that the energy of this wave has essentially been converted to the originally weaker wave, C_{-1}, at a depth of about 25 cm.

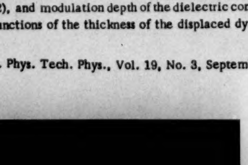

Fig. 2. Normalized intensities of the Bragg beams, $J_{-1}(z)/J_1(0)$ (1) and $J_1(z)/J_1(0)$ (2), and modulation depth of the dielectric constant of the medium, $\Delta\varepsilon$ (3), as functions of the thickness of the displaced dynamic hologram.

In concluding this analysis of dynamic holograms, we turn to an estimate of the amplification coefficients for weak beams in the exponential growth regions [with $C_{-1}(z) \ll C_1(z) \simeq C_1(0)$], in which, as was shown above, the amplitudes of the waves in the undisplaced and displaced gratings increase in proportion to $e^{A|C_1(0)|^2z}$ and $e^{\gamma|C_1|(0)|^2z}$, respectively. Using Eqs. (7), (8), and (15d) along with the approximation

$$\Delta n(|E|^2)\simeq\frac{\Delta\varepsilon(|E|^2)}{2n_0}\simeq\frac{\Delta\varepsilon(|E|^2)}{2},$$

we can convert the quantities $2A|C_1(0)|^2$ and $2\gamma|C_1(0)|^2$ (which represent the initial intensity amplifications of the waves) to the same form:

$$2A|C_1(0)|^2,\ 2\gamma|C_1(0)|^2=k_{\mathrm{am}}(0)=\frac{4\pi}{\lambda\cos\theta}\Delta n(|E_1|^2)_{z=0}, \tag{27}$$

where $\Delta n(|E_1|^2)_{z=0}$ are the characteristic changes in the refractive index of the medium under the influence of a light field of amplitude E_1. Substituting $\lambda = 7\cdot10^{-5}$ cm, $\cos\theta \simeq 1$, and the values $\Delta n(|E|^2) = 10^{-4}$–$10^{-5}$ (typical for dynamic holograms) into (27), we find that the initial amplification coefficients for dynamic holograms range from 2 to 20 cm^{-1}, some two or three orders of magnitude higher than those achievable in inversion media of solid-state coherent-radiation sources. Accordingly, by using a dynamic hologram as amplifier we can achieve a significant amplification of weak signals at comparatively small thicknesses of the amplifying layer.

Amplification of weak light beams is not the only possible application: The ability of displaced dynamic holograms to cause an essentially complete energy transfer between incident light beams, regardless of their initial intensity ratio, can be exploited to stabilize the propagation of light beams having a uniform distribution of the field over their cross section. Figure 3 shows an arrangement for this stabilization. The beam whose direction is to be stabilized is split into two parts by half-silvered mirror M. Most of the beam passes through the mirror and reaches the dynamic displaced hologram DDH (beam I), while the weaker beam (II) is expanded by telescope system T, with a Γ^x-fold increase, and sent to the DDH, at some angle with respect to the first beam. When the con-

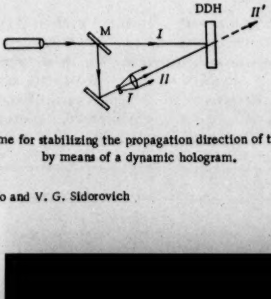

Fig. 3. Scheme for stabilizing the propagation direction of the light beam by means of a dynamic hologram.

ditions described above are satisfied, beam I can be converted into beam II', moving in the same direction as beam II; the change in the direction of beam I by an angle of α leads to a change (lower by a factor of Γ^x) in the angular deviation of converted beam II'.

In conclusion we should point out that these results can be generalized to the case in which the beams are polarized in the plane of incidence; this case is of interest in connection with the recording of holograms in lithium niobate crystals. In this case a description of the wave propagation in the hologram is more convenient in terms of the equation for the amplitude of the magnetic field vector, H (see also ref. 7). Calculations analogous to those above for the case of displaced dynamic holograms lead to a system of equations like (21), differing only in the replacement of the factor γ by $\gamma' - \gamma_e \cos^2 2\theta$, where γ_e may be quite different from γ (e.g., we would have $\gamma_e \gg \gamma$, in lithium niobate crystals[5]).

The authors thank Yu. N. Denisyuk for his assistance and for interest in this work and Yu. A. Anan'ev and S. G. Przhibel'skii for useful discussion of certain topics.

---

[1] H. J. Gerritsen, Appl. Phys. Lett., 10, 239 (1967).

[2] H. Eichler, G. Enterlein, J. Munschau, and H. Stahl, Z. Angew. Phys., 31, 1 (1971).

[3] B. I. Stepanov, E. V. Ivakin, and A. S. Rubanov, Dokl. Akad. Nauk SSSR, 196, 567 (1971) [Sov. Phys.–Dokl., 16, 46 (1971)].

[4] A. V. Gnatovskii, P. P. Pogoretskii, and M. S. Soskin, Ukr. Fiz. Zh., 17, 1564 (1972).

[5] D. L. Staebler and J. J. Amodei, J. Appl. Phys., 43, 1042 (1972).

[6] H. Kogelnik, Bell. Syst. Tech. J., 48, 2909 (1969).

[7] C. B. Burckhardt, JOSA, 56, 1502 (1966).

Beam focusing in an accelerator with inductive energy storage

V. A. Glukhikh, O. A. Gusev, E. G. Komar, V. S. Kuznetsov, M. P. Svin'in, and R. P. Fidel'skaya

D. V. Efremov Scientific-Research Institute
Institute of Electrophysical Apparatus, Leningrad

(Submitted August 15, 1973)
Zh. Tekh. Fiz., 44, 588-590 (March 1974)

Questions related to the maintenance and focusing of a beam in an accelerator having inductive energy storage are examined. Equations are derived and curves are plotted to determine beam and accelerator parameters such that the charged-particle beam is not cut off or defocused.

We are concerned here with certain general questions related to the maintenance and focusing of the beam in a pulsed accelerator. The charged-particle beam, which links the winding of a solenoid, produces a magnetic field which is used to focus the beam itself. Below we analyze the conditions under which the beam passing through the solenoid produces a magnetic field strong enough to conduct the beam through the solenoid.

The equation of the envelope for a magnetically confined beam (i.e., for the case in which the cathode is in a magnetic field B) is

$$\frac{d^2r}{dz^2}=\frac{I}{4\pi\varepsilon\sqrt{2\eta}\,U_0^{3/2}r}-\frac{\eta B^2r}{8U_0}\left(1-\frac{r_k^4}{r^4}\right). \quad (1)$$

Here, r is the beam radius, r_k is the beam radius at the cathode, I is the beam current, U_0 is the potential corresponding to the energy of the particles at the axis, ε is the permittivity of free space, and $\eta = e/m$ is the charge-to-mass ratio of the particles. Since we are interested in the case in which the currents are at nearly their limiting values, we consider the dip in the potential over the beam cross section. For this purpose we assume $U_0 = 0.5U$, where U is the potential of the electron chamber. We write B in terms of the solenoid current, which is equal to the beam current:

$$B=\mu NI. \quad (2)$$

Here, μ is the vacuum permeability, and N is the number of turns per meter.

Substituting (2) into (1), we find

$$\frac{d^2r}{dz^2}=\frac{I}{2\pi\varepsilon\sqrt{\eta}\,U^{3/2}r}-\frac{\eta\mu^2N^2I^2r}{4U}\left(1-\frac{r_k^4}{r^4}\right). \quad (3)$$

To find an approximate solution of Eq. (3) for small changes in the beam envelope we assume that $r - r_k = \Delta r \ll r_k$ over the length of the solenoid, l. Expanding the right side of Eq. (3) in a series, we find

$$\frac{d^2(\Delta r)}{dz^2}+K^2\Delta r=C_1, \quad (4)$$

where

$$C_1=\frac{I}{2\pi\varepsilon\sqrt{\eta}\,U^{3/2}r_k};\quad C_2=\frac{\eta\mu^2N^2I^2}{U};\quad K^2=C_2+\frac{C_1}{r_k}.$$

The solution of Eq. (4) for the initial conditions

$$\Delta r\big|_{z=0}=0,\quad \frac{d(\Delta r)}{dz}\bigg|_{z=0}=0$$

is

$$\Delta r=\frac{c_1}{K^2}(1-\cos Kz). \quad (5)$$

Specifying a definite value $\Delta r = (\Delta r)_{max}$, we can find the functional dependence of the minimum potential $V = V_{cr}$ at which the condition $\Delta r \le \Delta r_{max}$ is satisfied for a specified beam current I and solenoid length. Figure 1 shows an illustrative case for the following parameters: $\Delta r/r_k = 0.2$, $r_k = 0.1$ m, $l = 1$ m, and $N = 10^3$ turns/m.

The region above the curve $V_{cr} = V_{cr}(I_{cr})$ corresponds to the situation in which the beam is not defocused after passing through the solenoid.

However, the beam cannot pass through the solenoid at all values of I and V which satisfy the focusing conditions: The maximum beam current which can be drawn at an energy eV_{lim} is limited, being equal to[1]

$$I_{lim}=1.6\pi\varepsilon\sqrt{2\eta}\,U_{lim}^{3/2}\frac{1}{1+2\ln\frac{R}{r}}. \quad (6)$$

The current calculated from this equation corresponds to the situation in which $V_0 = 0.5V$ because of the dip in the potential over the beam cross section. Here, R is the tube radius. Figure 1 shows the functional dependence $V_{lim}(I_{lim})$. The cross-hatching shows the region which satisfies conditions (5) and (6).

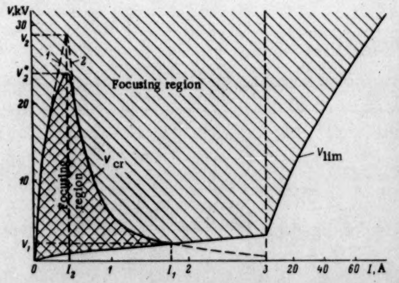

Fig. 1. Region in which a focused beam exists for r = 0.1 m, (Δr)/r = 0.2, l = 1 m, and N = 10^3 turns/m.

The intersection of the V_{cr} and V_{lim} curves gives the lower boundary of the region in which a focused beam exists. An analytic expression for the parameters of this point, V_1 and I_1, can be found from (5) and (6) by setting $I_{lim} = I_{cr}$:

$$V_1 = \frac{\left(1 + 2\ln\frac{R}{r_k}\right)^{1/3}}{2.12\pi\varepsilon\mu\eta r_k\left(\frac{\Delta r}{r_k}\right)^{1/3} N}, \tag{7}$$

$$I_1 = \frac{0.73}{\sqrt{\pi\varepsilon}\,\eta\left(1 + 2\ln\frac{R}{r}\right)^{1/4}(\mu r_k N)^{2/3}\left(\frac{\Delta r}{r_k}\right)^{3/4}}. \tag{8}$$

At the specified solenoid and beam parameters (Fig. 1) we have $I_1 = 1.64$ A and $V_1 = 2.2$ kV.

To find the (approximate) parameters of the second characteristic point (I_2, V_2), which governs the region in which a focused beam exists, we consider two extreme cases: 1) $K_z \ll \pi/2$; 2) $K_z \geq \pi/2$.

At low currents, with $K_z \ll \pi/2$, the quantity Δr is governed primarily by the Coulomb repulsive forces. Using Eq. (5), we can write, approximately,

$$\Delta r_{max} \simeq \frac{C_1 l^2}{2}. \tag{9}$$

Substituting in the value of C_1, we find

$$V_{cr} = \left[\frac{I l^2}{4\pi\varepsilon\sqrt{\eta}\, r_k^2\left(\frac{\Delta r_{max}}{r_k}\right)}\right]^{1/3} \tag{10}$$

(curve 1 in Fig. 1).

As the current is increased the focusing effect of the magnetic field becomes increasingly important, until a force equilibrium is reached, i.e., until $C_1 = C_2\Delta r_{max}$. Then $K^2 \simeq C_2$, and from (5) we find

$$\Delta r_{max} \simeq \frac{C_1}{C_2} \tag{11}$$

(curve 2 in Fig. 1). Substituting the values of C_1 and C_2, we find

$$V_{cr} = \frac{1}{\left[2\pi\varepsilon\eta^{2/3}(\mu N r_k)^2\left(\frac{\Delta r_{max}}{r_k}\right) I_{cr}\right]^2}. \tag{12}$$

To determine the intersection of branches 1 and 2, we equate Eqs. (10) and (12), finding

$$V_2 = \frac{l}{2\sqrt{2}\,\pi\varepsilon\eta\mu N r_k^4\left(\frac{\Delta r_{max}}{r_k}\right)}, \tag{13}$$

$$I_2 = \frac{1}{2^{1/4}(\pi\varepsilon l)^{1/2}\eta(\mu N)^{3/2} r_k\left(\frac{\Delta r_{max}}{r_k}\right)^{1/2}}. \tag{14}$$

For the example considered above (Fig. 1) we have $I_2 = 0.45$ A and $V_2 = 29$ kV. We note that this value of V_2 differs only slightly from the exact value of the maximum potential, $V_2^* = 24$ kV, calculated from Eq. (5).

The quantity V_2 represents the minimum potential at which the beam can pass through the solenoid over the entire current range, from zero to the limiting value [given by Eq. (6)]. This is an important situation for the case in which the solenoid is driven by a charged-particle beam. If, on the other hand, the solenoid is charged beforehand by means of a current source, and if the working beam current is higher than I_1 (which is usually the case), the minimum beam potential is governed by condition (6) alone.

---

[1] J. R. Pierce, Theory and Design of Electron Beams, Van Nostrand, Princeton, New Jersey (1949).

High-current pulsed electron accelerator with an annular beam

M. I. Avramenko, V. A. Glukhikh, O. A. Gusev, E. G. Komar,
O. L. Komarov, V. S. Kuznetsov, A. S. Perlin, and M. P. Svin'in

D. V. Efremov Scientific-Research Institute of Electrophysical Apparatus, Leningrad

(Submitted August 15, 1973)
Zh. Tekh. Fiz., 44, 591-595 (March 1974)

Certain questions related to the design and construction of a high-current pulsed accelerator with a pulse length of 10^{-4} sec, a beam current of $2 \cdot 10^{4}$ A, and an electron energy of 1 MeV are discussed. The pulsed accelerating voltage is produced by an electrical solenoid in which energy from an auxiliary power supply is stored with a high-speed current switch. It is shown that an annular thermionic cathode should be used to produce a beam having the specified parameters. The focusing and maintenance of the annular structure of the beam are achieved by means of the inhomogeneous magnetic field of the solenoid.

INTRODUCTION

Beam power levels of the order of 10^{12} W per pulse with pulse lengths of 10^{-8}-10^{-7} sec have been achieved in high-current electron accelerators. In certain cases, however, it is necessary to have pulsed electron beams with pulse lengths two to three orders of magnitude longer.

In this work we examine certain aspects of the design of a high-current pulsed accelerator with a pulse length of $\sim 10^{-4}$ sec, a beam current of $\sim 2 \cdot 10^{4}$ A, and an electron energy of ~ 1 MeV. We assume that the pulsed accelerating voltage is provided by an electrical solenoid in which energy from an auxuliary power supply is stored with a high-speed current switch.

A field-emission cathode cannot be used with high-voltage pulses with lengths of the order of 10^{-4} sec because of the mechanical destruction of the cathode and because the plasma which appears at the surface of the field-emission cathode and moves with a velocity of the order of 10^{6} cm/sec moves 100 cm in 100 msec. In other words, the plasma moves much farther than the distance between the electrodes; thus, the plasma short circuits the gap, cutting off the beam current.

It is essentially impossible to obtain directly a beam with an energy of $\varepsilon = 1$ MeV from a plasma source, since the dielectric strength of the emitter-accelerating electrode gap is too low. We therefore turn to a thermionic cathode with a large emission surface. Cathodes of this type can produce a current density of the order of 40-50 A/cm² at pulse lengths of $\sim 10^{-4}$ sec.

ELECTRON GUN

The shaping and transporting of high-current electron beams is complicated by the effect of the space charge, which limits the beam current.

We have considered two methods for shaping the electron beam: plasma and vacuum methods. The plasma method cannot be used in this case because the various instabilities which arise as the electron current flows through the plasma restrict the limiting (or critical) beam current. In particular, the growth time for the most dangerous instability, the beam-drift instability, is given by[2]

$$\tau = \left(\frac{\omega_{He}}{\omega_{Hi}}\right)^{1/3} \left(\frac{a^2}{2v^2}\right)^{1/3}, \tag{1}$$

where $\omega_{He} = eH/(mc)$, m and e are the electron mass and charge, H is the external magnetic field, $\omega_{Hi} = eH/(m_i c)$; m_i is the ion mass, a is the beam radius, and v is the velocity of the beam electrons. With the plasma and beam parameters under consideration here, the growth time for this instability is of order $\tau = 100$ nsec, much shorter than the current pulse.

Furthermore, at a power level of order 1 MW the acceleration region cannot be protected from the penetration of plasma from the drift region.

We therefore adopt the vacuum method for shaping the electron beam in the drift region. The limiting current of a nonneutral relativistic electron beam moving along the axis of a metal tube of radius R in the drift region is[2]

$$I_0 = \frac{17}{1 + 2\ln\frac{R}{r_0}} (\gamma^{2/3} - 1)^{3/2}\ [\text{kA}], \tag{2}$$

where r_0 is the beam radius and γ is the Lorentz factor.

Equation (2) states that when the beam completely fills the cross section of the tube ($R = r_0$) the limiting current at an energy of $\varepsilon = 1$ MeV is 19 kA. However, when we take account of the circumstance that the beam cannot be allowed to strike the walls of the drift tube, we conclude that the ratio R/r_0 should be no smaller than 2. In this case the limiting current is about 10 kA, lower than the desired value. Considerably higher currents can be achieved through the use of annular electron beams. The limiting current for an annular beam is

$$I = \frac{17 (\gamma^{2/3} - 1)^{3/2}}{1 + 2\ln\frac{R}{r_0}} \left(\frac{r_0}{a}\right) [\text{kA}], \tag{3}$$

where a is the thickness of the ring ($r_0 \gg a$).

We see from Eq. (3) that if we choose the ratio r_0/a to be 5, the limiting current is 50 kA, 2.5 times the desired value.

Accordingly, an annular electron beam at a current of ~ 20 kA can be stably transported in vacuum at a ratio $r_0/a = 5$. We choose the parameter of the annular gun to be as follows: an outer cathode radius of 22 cm, an inner radius of 17 cm, a cathode–anode separation of 8.3 cm, a maximum voltage of 1 MV, and a current density of 50 A/cm².

The maximum electric field at the anode is $|E|_{\max} = 160$ kV/cm.

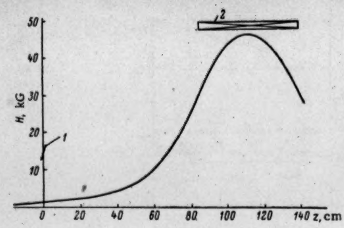

Fig. 1. Profile of the magnetic field at the solenoid axis. 1) Annular cathode; 2) solenoid.

BEAM-FORMING SYSTEM

An inhomogeneous magnetic field should be used to focus an intense annular electron beam; the cathode of the gun should also be in the magnetic field. We make this choice because the focusing system must, first, preserve the hollow structure of the beam at the selected ratio $r_0/a = 5$ and, second, provide a beam radius of 3 cm at the exit from the accelerator, i.e., the beam must be compressed by a factor of about 7. If the cathode is in a strong magnetic field the electrons will follow the magnetic lines of force and the shape of the beam boundary will be governed by the lines of force. The magnetic field required for this focusing method can be found from[3]

$$B=\frac{1}{2}\sqrt{\frac{I}{\frac{\pi\varepsilon_0}{\sqrt{2}}\left(\frac{e}{m_0}\right)^{1/2}\{U(1+\eta U)\}^{1/2}\Delta r r_k}}\ [\mathrm{T}], \qquad (4)$$

where I is the beam current, U is the beam potential, r_k is the beam radius at the cathode, Δr is the magnitude of the pulsations in the beam boundary, e and m_0 are the charge and rest mass of the electron, $\eta = e/(2m_0c^2)$, and ε_0 is the permittivity of free space.

Assuming that the pulsation amplitude must not exceed 3% of the width of the annular beam, from Eq. (4) we find that the magnetic field at the cathode must be about 1 kG. If a beam with an initial radius of $R_0 = 22$ cm is to be compressed to a radius of 3 cm, the magnetic field must be about 50 kG.

Figure 1 shows the profile of the magnetic field at the axis of the solenoid producing the accelerating voltage. We see from this figure that the cathode of the gun must be 86.5 cm from the center of the solenoid in order to satisfy the requirements imposed on the parameters of the annular beam. Then the necessary magnetic field of 1 kG is established near the cathode.

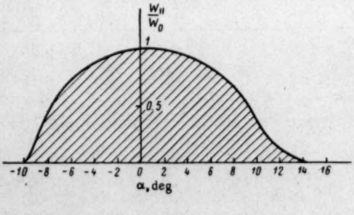

Fig. 2. The $W_{\parallel}/W_0(\alpha)$ functional dependence.

It is also necessary to take account of certain features of the motion of particles in strong and inhomogeneous magnetic fields. Particles moving in such fields can, under certain conditions, be reflected from regions in which the field is strong.[4] In our case we must not only suppress this reflection, but also any significant loss in the longitudinal energy of the particles, since the limiting current decreases with decreasing longitudinal velocity.

Reflection does not occur under the condition[4]

$$\sin\alpha_0 \leqslant \sqrt{\frac{H_0}{H_{\max}}}, \qquad (5)$$

where α_0 is the angle between the vector representing the total velocity of the particle and the magnetic field vector at $H = H_0$, and $H_{\max}$ is the maximum magnetic field.

It follows from (5) that with the specified values of the magnetic field at the cathode and at the center of the solenoid the beam is cut off if the initial inclination angle exceeds 9°. The inclination angle of the magnetic lines of force near the cathode varies from 13 to 17°, so the cathode surface must be moved through an angle of 15° with respect to the normal to the axis of the system in order to satisfy condition (5). In this case the initial inclination angle of the trajectory of the extreme electrons deviates by less than ± 2° from the inclination angle of the magnetic lines of force. We have carried out numerical calculations in order to evaluate the change in the longitudinal velocity of the particles in this case.

In our case the Coulomb forces have a slight effect in comparison with that of the external focusing magnetic field, and there are no accelerating electric fields, so the equations of motion become[5]

$$\left.\begin{aligned}\ddot{r} &= -\frac{e^2}{4\pi^2 m_0^2\gamma^2}\frac{\Psi-\Psi_k}{r}\left[2\pi B_z-\frac{\Psi-\Psi_k}{r^2}\right],\\ \ddot{z} &= -\frac{e^2}{4\pi^2 m_0^2\gamma^2}\frac{\Psi-\Psi_k}{r^2}\frac{\partial\Psi}{\partial z},\end{aligned}\right\} \qquad (6)$$

where e and m_0 are the charge and rest mass of the electron, γ is the Lorentz factor, Ψ is the magnetic flux, and B_z is the axial component of the magnetic field.

We have calculated the functional dependence $W_{\parallel}/W_0(\alpha)$, where W is the energy associated with the longitudinal motion at the exit from the accelerator and W_0 is the total energy.

Figure 2 shows the results of the numerical calculations. The inclination angle of the lines of force lies within ± 2° of the center of the cathode over the width of the cathode. It follows from Fig. 2 that this change in the initial inclination angle of the trajectories of extreme electrons with respect to the magnetic lines of force does not lead to any significant loss in longitudinal energy, so the limiting beam current is essentially unaffected.

Figure 3 shows a schematic diagram of the accelerator optics and the profile of the electron beam.

It follows from Fig. 3 that this optical scheme both preserves the hollow structure of the beam with a ratio

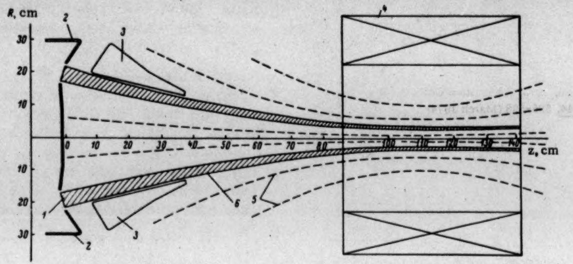

Fig. 3. Schematic of the accelerator and profile of the electron beam. 1) Annular cathode; 2) electrode near the cathode; 3) anode; 4) focusing solenoid; 5) magnetic lines of force; 6) profile of the annular beam.

$r_0/a = 5$ and produces a beam with the specified diameter at the exit from the accelerator. The pulsations in the boundary of the beam are smaller than 5%, essentially undistinguishable in this figure.

---

[1] M. V. Nezlin, Usp. Fiz. Nauk, 102, 105 (1970) [Sov. Phys.—Usp., 13, 608 (1971)].

[2] L. S. Bogdankevich, I. I. Zhelyazkov, and A. A. Rukhadze, Zh. Eksp. Teor. Fiz., 57, 315 (1969) [Sov. Phys.—JETP, 30, 174 (1970)].

[3] J. R. Pierce, Theory and Design of Electron Beams, Van Nostrand, Princeton, New Jersey (1949).

[4] D. J. Rose and J. Clark, Jr., Plasmas and Controlled Fusion, MIT Press, Cambridge, Mass. (1961).

[5] S. I. Molokovskii and A. D. Sushkov, Intense Electron and Ion Beams [in Russian], Izd. Energiya, Moscow (1972).

Physical electronics

Stability of field-emission beams in nanosecond discharges

L. P. Babich

(Submitted June 25, 1973; resubmitted October 15, 1973)
Zh. Tekh. Fiz., 44, 596-598 (March 1974)

The stability of the field-emission beams in a plasma is analyzed in the collisionless approximation. It is assumed that turbulent heating of the plasma can occur near the cathode in nanosecond vacuum and gas discharges; it is also assumed that a group of stochastically accelerated electrons, having an energy exceeding the applied voltage, can be produced.

There is currently considerable interest in nanosecond discharges in gas and in vacuum.[1,2] In such discharges, a system consisting of a field-emission beam and a plasma is established near a microscopic irregularity on the cathode; this system can be unstable. The appearance, in nanosecond discharges, of electrons with energies exceeding the applied voltage[3,4] can be due to the stochastic acceleration of electrons of the field-emission beam in the turbulence generated by the beam itself in the plasma near the cathode.

To study the stability of field-emission beams in the plasma near the cathode we use the dispersion relation in the collisionless approximation:[5]

$$\varepsilon^{l}(\omega, k)=1-\frac{4\pi e^{2}}{m}\left\{\int_{c}\frac{f_{0}(\mathbf{v})\,d\mathbf{v}}{(\omega-\mathbf{kv})^{2}}+\int_{c}\frac{f_{1}(\mathbf{v})\,d\mathbf{v}}{(\omega-\mathbf{kv})^{2}}\right\}=0, \qquad (1)$$

where the integration is carried out in accordance with the Landau contour[5] and the positive x axis is opposed to the external field **E**.

Assuming a Maxwellian distribution displaced by a velocity $\mathbf{v}_0$ for the plasma electrons and assuming that the distribution function for the field-emission beam satisfies[6]

$$\int_{-\infty}^{\infty} f_{1}(\mathbf{v})\,dv_{z}dv_{y}=\frac{4\pi m^{2}}{h^{3}}e^{-c}\exp\left(-\frac{mv_{x}^{2}-2eEx+2|\zeta|}{2d}\right)$$
$$\times\,\theta\left(eEx-|\zeta|-\frac{mv_{x}^{2}}{2}\right)\left(eEx-|\zeta|-\frac{mv_{x}^{2}}{2}\right),$$
$$\left(x^{2}\geqslant\frac{e^{2}}{4eE},\ v_{x}\geqslant\sqrt{\frac{2W_{e}}{m}}\right), \qquad (2)$$

we find the following dispersion relation from (1):

$$\varepsilon_{0}^{l}(\omega, k)-\frac{1}{d_{1}^{2}k^{2}}\left\{\int_{u_{1}}^{u_{2}}\frac{f(u)}{\left(u-\frac{\omega}{kv_{d}}\right)^{2}}+2\pi i\eta\left(\frac{\omega}{kv_{d}}\right)\frac{\partial f(u)}{\partial u}\bigg|_{\frac{\omega}{kv_{d}}}\right\}=0, \qquad (3)$$

where $\varepsilon_0^l(\omega, k)$ is the dielectric constant of the Maxwellian plasma,[7]

$$v_{d}=\sqrt{\frac{2d}{m}},\quad d_{1}^{2}=\frac{\pi\hbar^{3}\exp(c)}{\sqrt{2}\,m^{1.5}e^{2}},\quad u=\frac{v_{x}}{v_{d}},\quad u_{1}=\sqrt{\frac{eEx-|W_{e}|}{d}},$$

$$u_{2}=\sqrt{\frac{eEx-|\zeta|}{d}},\quad f(u)=(u_{2}^{2}-u^{2})\exp(u^{2}-u_{2}^{2})\,\theta(u_{2}^{2}-u^{2}).$$

Since $(\Delta u_{21})/u_2=(u_2-u_1)/u_2 \ll 1$, we find the following equation from (3) for unstable states ($\eta = 0$):

$$1+\frac{1}{d_{0}^{2}k^{2}}\left\{1+i\sqrt{\pi}\,\frac{\omega-kv_{0}}{kv_{Te}}\,W\left(\frac{\omega-kv_{0}}{kv_{Te}}\right)-\left(\frac{\omega_{p1}d_{0}k}{u_{2}v_{d}k-\omega}\right)^{2}\right\}=0, \qquad (4)$$

where W is the Cramp function[8] and where

$$\omega_{p1}^{2}=\frac{v_{d}^{2}}{2d_{1}^{2}u_{2}}\left[1-(1+2u_{2}\Delta u_{21})\exp(-2u_{2}\Delta u_{21})\right].$$

From Eq. (4) we can determine the frequencies and growth rates of the modes excited by the field-emission beam in the plasma.

When $|(\omega-kv_0)/kv_{Te}| \ll 1$ it follows from (4) that

$$1+\frac{1}{d_{0}^{2}k^{2}}\left(1+i\sqrt{\pi}\,\frac{\omega-kv_{0}}{kv_{Te}}\right)-\left(\frac{\omega_{p1}}{u_{2}v_{d}k-\omega}\right)^{2}=0. \qquad (5)$$

Assuming $\omega = u_2v_dk + \omega^{(1)}$ here, where $\operatorname{Re}\omega^{(1)} \equiv \omega_1$ and $\operatorname{Im}\omega^{(1)} \equiv \gamma$, we consider three different cases.

a) $|(\omega_1/k)| \ll |u_2v_d-v_0|$:

$$\begin{cases}\omega_{1}=\pm\omega_{p1}\left[\dfrac{1+d_{0}^{-2}k^{-2}+\sqrt{(1+d_{0}^{-2}k^{-2})^{2}+\pi d_{0}^{-4}k^{-4}v_{Te}^{-2}(u_{2}v_{d}-v_{0})^{2}}}{2(1+d_{0}^{-2}k^{-2})^{2}+2\pi d_{0}^{-4}k^{-4}v_{Te}^{-2}(u_{2}v_{d}-v_{0})^{2}}\right]^{1/2};\\[2ex] \gamma=-\sqrt{\dfrac{\pi}{2}}\,\omega_{p1}\dfrac{u_{2}v_{d}-v_{0}+\dfrac{\omega_{1}}{k}}{d_{0}^{2}k^{2}\omega_{1}v_{Te}\left[(1+d_{0}^{-2}k^{-2})^{2}+\pi d_{0}^{-4}k^{-4}v_{Te}^{-2}(u_{2}v_{d}-v_{0})^{2}\right]}.\end{cases} \qquad (6a)$$

b) With $1+d_0^{-2}k^{-2} \gg \sqrt{\pi}\,d_0^{-2}k^{-2}v_{Te}^{-1}(u_2v_d-v_0+\omega_1/k)$:

$$\begin{cases}\omega_{1}=\pm\omega_{p1}(1+d_{0}^{-2}k^{-2})^{-1/2};\\[1ex] \gamma=-\sqrt{\dfrac{\pi}{2}}\,\omega_{1}\dfrac{u_{2}v_{d}-v_{0}+\dfrac{\omega_{1}}{k}}{d_{0}^{2}k^{2}v_{Te}(1+d_{0}^{-2}k^{-2})}.\end{cases} \qquad (6b)$$

c) With condition a) and with the inequality opposite b):

$$\begin{cases}\omega_{1}=\pm\omega_{p1}d_{0}k\left[\dfrac{v_{Te}}{2\sqrt{\pi}(u_{2}v_{d}-v_{0})}\right]^{1/2};\\[1ex] \gamma=|\omega_{1}|.\end{cases} \qquad (6c)$$

The condition $|(\omega-kv_0)/kv_{Te}| \ll 1$ can be satisfied in a hot plasma which is essentially at the emitter surface; this case could arise, e.g., in explosive emission[9,10] in vacuum discharges.

When $|(\omega-kv_0)/kv_{Te}| \gg 1$, it follows from (4) that[7]

$$0=1-\frac{\omega_{p1}^{2}}{(\omega-u_{2}v_{d}k)^{2}}-\frac{\omega_{p0}^{2}}{(\omega-u_{2}v_{d}k)^{2}}, \qquad (7)$$

and the problem reduces to the analysis of the two-stream instability.

a) With $|\omega| \gg kv_0$, it follows from (7) that[7]

$$\begin{cases}\operatorname{Re}\omega=u_{2}v_{d}k;\\[1ex] \gamma=\omega_{p1}\left[\left(\dfrac{\omega_{p0}}{u_{2}v_{d}k}\right)^{2}-1\right]^{-1/2},\ \left(\dfrac{\omega_{p0}}{k}>u_{2}v_{d}\right).\end{cases} \qquad (8a)$$

if u_2v_dk is far from ω_{p0}, or

$$\begin{cases} \operatorname{Re}\omega = u_2v_dk - \frac{1}{2}\left(\frac{1}{2}\omega_{p1}^2\omega_{p0}\right)^{1/3}; \\ \gamma = \sqrt{\frac{3}{4}}\left(\frac{1}{2}\omega_{p1}^2\omega_{p0}\right)^{1/3}, \end{cases} \tag{8b}$$

if $u_2v_dk = \omega_{p0}$.

b) If $|\omega| \ll kv_0$, then

$$\begin{cases} \operatorname{Re}\omega = u_2v_dk; \\ \gamma = \omega_{p1}\left[\left(\frac{\omega_{p0}}{kv_0}\right)^2 - 1\right]^{-1/2}, \quad \left(\frac{\omega_{p0}}{k} > v_0\right). \end{cases} \tag{8c}$$

c) The cases $|\omega| \gg u_2v_dk$ and $|\omega| \ll u_2v_d$ reduce to cases a) and b), respectively, with the substitutions $u_2v_dk \rightleftharpoons kv_0$, $\omega_{p0} \rightleftharpoons \omega_{p1}$. The condition $|(\omega - kv_0)/kv_{Te}| \gg 1$ is satisfied if the boundary of the cold plasma is far from the emitter; this condition can be satisfied in gaseous discharges.

An instability in the field-emission electron beam can influence the characteristics of discharges. The beam can give up a large part of its energy in the gas-discharge plasma, thereby heating the plasma electrons. As these electrons are heated, nonlinear processes become more important,[11] and some of the electrons of the field-emission beam can be stochastically accelerated to high energies. This mechanism is apparently responsible for the experimental observation of electrons with energies exceeding the applied voltage in nanosecond vacuum and gaseous discharges.

---

[1] G. A. Mesyats, Yu. I. Bychkov, and V. V. Kremnev, Usp. Fiz. Nauk, 107, 201 (1972) [Sov. Phys.—Usp., 15, 282 (1972)].

[2] G. A. Mesyats, 10th International Conference on Phenomena in Ionized Gases, 1971, Invited Papers, p. 333, Oxford, England, September 13-18, 1971.

[3] N. G. Pavlovskaya and T. V. Kudryavtseva, Prib. Tekh. Eksp., No. 2, 198 (1972).

[4] L. P. Babich, L. V. Tarasova, and T. V. Loiko, Report to the Symposium on High-Current Plasma Emission Electronics, Tomsk, May, 1973.

[5] L. D. Landau, Zh. Eksp. Teor. Fiz., 16, 574 (1946).

[6] R. H. Good and E. W. Müller, Handbuch der Physik, 21, 176 (1956).

[7] A. B. Mikhailovskii, Theory of Plasma Instabilities, Vol. 1, Consultants Bureau, New York (1973).

[8] V. N. Faddeeva and N. M. Terent'ev, Tables of the Probability Integral of a Complex Argument [in Russian], Gostekhizdat, Moscow (1954).

[9] G. A. Mesyats and D. I. Proskurovskii, ZhETF Pis. Red., 13, 7 (1971) [JETP Lett., 13, 4 (1971)].

[10] G. I. Fursei, A. A. Antonov, and V. M. Zhukov, Vestn. LGU, 10, 75(1971).

[11] V. N. Tsytovich, Nonlinear Effects in Plasmas [in Russian], Izd. Nauka, Moscow (1967).

Optimum dimensions of a coaxial thermionic converter

V. V. Sinyavskii

(Submitted February 12, 1973)
Zh. Tekh. Fiz., 44, 599-605 (March 1974)

The condition for the maximum specific energy is used to obtain simple expressions for the optimum values of the relative length, diameter, and thickness of the emitter shell, of the collector, and of the collector insulation in a coaxial thermionic converter. The optimum values are given in terms of functional dependences on the appropriate similitude criteria. The results calculated from these equations agree with the results of the many-parameter optimization.

The optimum geometric parameters of a thermionic converter cell must be chosen before experimental assemblies are constructed. The most complete answer to this problem comes from the many-parameter optimization, e.g., ref. 1. However, cases are possible in which most of the parameters are known or specified on the basis of external considerations, so that only certain ones can be chosen arbitrarily. In these cases it is necessary to find relations that can be used to choose the free parameters of the optimization.

In this work we use the condition for maximum useful electrical power per unit volume to obtain simple expressions to determine the optimum values of such parameters as the length of the emitter, the diameter of the core, the thickness of the emitter shell, that of the collector, and that of the collector insulation in a coaxial thermionic converter cell.

TARGET FUNCTION

The target function for the optimization of individual parameters of a thermionic cell is taken to be the expression for the specific energy (the useful electrical power per unit volume) written in terms of the electrical and geometric characteristics of a section containing a single cell:[1)]

$$E=\frac{W}{V_{se}}, \qquad (1)$$

where W is the specific energy of the cell and

$$V_{se}=\frac{\sqrt{3}}{2}s^2t \qquad (2)$$

is the volume of the section. The radial and axial dimensions of the section can be determined from

$$s=2(r_0+\delta_E+\Delta_E), \qquad (3)$$

$$t\approx l_E+l_K, \qquad (4)$$

where

$$\Delta_E=L+\delta_C+\delta_I+\delta_{st}+\frac{\delta_t}{2}\cdot \qquad (5)$$

The following equation is derived for W in ref. 1:

$$W=2\pi r_E\left\{\int_0^{l_E} jv\,dz-\frac{r_E}{r_E\delta_E}\int_0^{l_E}\rho_E\left[\int_0^{z} j\,dz\right]^2dz-\frac{r_E}{r_C\delta_C}\int_0^{l_E}\rho_C\left[\int_z^{l_E} j\,dz\right]^2dz\right.$$

$$\left.-\frac{2\pi r_E\rho_K l_K}{S_K}\left[\int_0^{l_E} j\,dz\right]^2-\frac{r_I}{r_E\delta_I}\int_0^{l_E}\frac{\Delta V^2}{\rho_I}dz\right\}, \qquad (6)$$

where the first term in the brackets is the power generated at the electrodes, while the following terms are, respectively, the ohmic losses of electrical power in the emitter, the collector, and the connector and the loss due to current leakage through the collector insulation.

To obtain simple results we consider a simplified equation for E; this follows from (6) under the assumption that the distributions of current density j and the potential difference v are constant along the emitter and that ρ_E, ρ_C, ρ_I, and ΔV are homogeneous:

$$E=\frac{4\pi r_E l_E}{\sqrt{3}\,s^2t}jv\left(A-B_I\frac{r_I}{\delta_I}\right), \qquad (7)$$

where

$$A=1-l_E^2\frac{j}{v}\left(\frac{1}{3}\frac{\rho_E}{\delta_E}+\frac{1}{3}\frac{r_E\rho_C}{r_C\delta_C}+2\pi r_E\frac{l_K\rho_K}{S_K l_E}\right), \qquad (8)$$

$$B_I=\frac{\Delta V^2}{jvr_E\rho_I} \qquad (9)$$

are dimensionless parameters.

From the condition

$$\frac{\partial E}{\partial x_i}=0, \qquad (10)$$

where x_i is the parameter to be optimized, we can find equations for the optimum values of the emitter length l_E^{opt}, the core radius r_E^{opt} (or the emitter radius $r_E^{opt}=r_0^{opt}+\delta_E$), the thickness of the emitter part of the shell δ_E^{opt}, the collector thickness δ_C^{opt}, and the insulation thickness δ_I^{opt}.

To find x_i^{opt} we introduce into target function (7) an equation for the optimum connector cross section, S_K, which is a function of some of the parameters x_i which are to be optimized:

$$S_K^{opt}=2\pi r_E l_E l_K j\sqrt{\frac{\rho_K}{\lambda_K(T_E-T_C)\eta}}. \qquad (11)$$

Then we can rewrite Eq. (8) as

$$A=1-l_E^2\frac{j}{v}\left\{\frac{1}{3}\frac{\rho_E}{\delta_E}+\frac{1}{3}\frac{r_E\rho_C}{r_C\delta_C}+\frac{\sqrt{\rho_K\lambda_K(T_E-T_C)\eta}}{l_E^2j}\right\}. \qquad (12)$$

As a result of the introduction of S_K^{opt} into (7) in the optimization of any of the x_i, the connector cross section S_K takes on the optimum value in accordance with x_i^{opt}.

OPTIMUM VALUES OF THE PARAMETERS

In this section we derive equations for the optimum values of the parameters of a coaxial thermionic cell on the basis of condition (10). Since the leakage current is relatively low, $j_{leak} \ll j$, we neglect the power loss due to the leakage currents in the derivation of all the equations except that for δ_I^{opt}.

Optimum emitter length. The optimum value of the relative length of the emitter, $\tilde{l}_E = l_E/l_K$, is

$$l_E^3 - \frac{2}{3} l_E^2 + \frac{1}{4} B_l = 0, \tag{13}$$

where

$$B_l = \frac{12}{l_K^2 j} \frac{v - \sqrt{\rho_E \lambda_E (T_E - T_C)\eta}}{\frac{\rho_E}{\delta_E} + \frac{r_E}{r_C}\frac{\rho_C}{\delta_C}} \tag{14}$$

is a dimensionless parameter.

For all cases of practical interest (B > 2) the discriminant of the cubic equation is positive and we can write the solution of (13) in the form

$$l_E^{opt} = \frac{1}{2}\left(1 + \sqrt[3]{1 + B_l + \sqrt{B_l^2 - 2B_l}} + \sqrt[3]{1 + B_l - \sqrt{B_l^2 - 2Bl}}\right). \tag{15}$$

When $Bl \geq 10$ Eq. (15) reduces to

$$l_E^{opt} = 1 + \sqrt[3]{\frac{1}{4} B_l}. \tag{16}$$

Optimum emitter radius. For r_0^{opt}, and, correspondingly, r_E^{opt} we find the following equation from condition (10):

$$A\left(1 - \frac{4r_E}{s}\right) + l_E^2 \frac{j}{v}\left(\frac{r_E}{2\delta_E}\frac{\rho_E}{\delta_E}\frac{\rho_E^*}{\rho_0} + \frac{r_E}{r_C}\frac{\Delta_E}{r_C}\frac{\rho_C}{\delta_C}\right) = 0, \tag{17}$$

where A, r_E, r_C, and s are functions of r_0.

When $\rho_E^* \ll \rho_0$ and $\delta_E \ll r_0$ Eq. (17) becomes the simple equation

$$r_E^{opt} = \Delta_E, \tag{18}$$

or for the dimensionless emitter radius $\tilde{r}_E = r_E/s$ we find from (18)

$$\tilde{r}_E^{opt} = \frac{1}{4}. \tag{19}$$

Optimum emitter thickness. From condition (10) we find a cubic equation for the optimum relative thickness of the emitter shell, $\tilde{\delta}_E = \delta_E/l_E$, for the case of a nonconducting core. This equation is conveniently written in the form

$$\left(\tilde{\delta}_E + \frac{b}{3}\right)^3 + p\left(\tilde{\delta}_E + \frac{b}{3}\right) + q = 0, \tag{20}$$

where the dimensionless coefficients

$$\left.\begin{aligned} b &= \frac{r_0 - \Delta_E}{l_E} - 2B_E, \quad p = -\frac{b^2}{3} - 3B_E\frac{r_0}{l_E}, \\ q &= 2\left(\frac{b}{3}\right)^3 + bB_E\frac{r_0}{l_E} - B_E\frac{r_0}{l_E}\left(\frac{r_0 + \Delta_E}{l_E}\right) \end{aligned}\right\} \tag{21}$$

are functions of the dimensionless parameter

$$B_E = \frac{1}{3}\frac{l_E j \rho_E}{v - \frac{1}{3} l_E^2 j \frac{\rho_C}{\delta_C} - \sqrt{\lambda_E \rho_E (T_E - T_C)\eta}}. \tag{22}$$

The solution of Eq. (20) is governed by the sign of the discriminant

$$D = \left(\frac{p}{3}\right)^3 + \left(\frac{q}{2}\right)^2. \tag{23}$$

In the case of a nonconducting core we would usually have D < 0, so we will use trigonometric solution (20). Of the three real positive roots of (20) there is generally only a single positive root for typical parameter values; this root is given by

$$\left.\begin{aligned} \tilde{\delta}_E^{opt} &= 2\sqrt{-p/3}\cos\frac{\alpha}{3} - \frac{b}{3} \quad \text{for} \quad q < 0, \\ \delta_E^{opt} &= 2\sqrt{-p/3}\cos\left(\frac{\pi}{3} - \frac{\alpha}{3}\right) - \frac{b}{3} \quad \text{for} \quad q \geqslant 0, \end{aligned}\right. \tag{24}$$

where α is found from

$$\cos\alpha = \frac{|q|}{2\sqrt{-(p/3)^3}}.$$

The value of $\tilde{\delta}_E^{opt}$ is strongly influenced by the conductivity of the core, which can be taken into account through the effective resistivity of the emitter,

$$\rho_E^* = \frac{\rho_E}{1 + \frac{r_0}{2\delta_E}\frac{\rho_E}{\rho_0}}. \tag{25}$$

Using (25) we again find Eq. (20) from condition (10) for $\tilde{\delta}_E^{opt}$ for the case of a conducting core; however, the coefficients b, p, and q are

$$\left.\begin{aligned} b &= \frac{r_0 - \Delta_E}{l_E} - 2B_E + \frac{r_0}{l_E}\frac{\rho_E}{\rho_0}, \\ p &= -\frac{b^2}{3} - 3B_E\frac{r_0}{l_E} + \frac{r_0}{2l_E}\frac{\rho_E}{\rho_0}\left(2\frac{r_0 - \Delta_E}{l_E} - B_E + \frac{r_0}{2l_E}\frac{\rho_E}{\rho_0}\right), \\ q &= 2\left(\frac{b}{3}\right)^3 - \frac{b}{3}\left[-3B_E\frac{r_0}{l_E} + \frac{r_0}{2l_E}\frac{\rho_E}{\rho_0}\left(2\frac{r_0 - \Delta_E}{l_E} - B_E + \frac{r_0}{2l_E}\frac{\rho_E}{\rho_0}\right)\right] \\ &\quad - B_E\frac{r_0}{l_E}\frac{r_0 + \Delta_E}{l_E} - \frac{r_0}{2l_E}\frac{r_0 - \Delta_E}{l_E}\frac{\rho_E}{\rho_0}\left(B_E - \frac{r_0}{2l_E}\frac{\rho_E}{\rho_0}\right). \end{aligned}\right\} \tag{26}$$

Optimum collector thickness. For optimum relative collector thickness $\tilde{\delta}_C = \delta_C/l_E$ is given by the following expression from condition (10):

$$\tilde{\delta}_C^{opt} = \frac{\rho_C}{6A_C}\left\{1 + \sqrt{1 + \frac{12A_C}{\rho_C l_E}\left(r_E + L + \delta_I + \delta_{st} + \frac{\delta_f}{2}\right)}\right\}. \tag{27}$$

where

$$A_C=\frac{1}{jl_E}\left[4v-\sqrt{\rho_E\lambda_E(T_E-T_C)\eta}\right]-\frac{1}{3}\frac{\rho_E}{\delta_E}l_E. \tag{28}$$

Using

$$\frac{12A_C}{\rho_C l_E}\left(r_E+L+\delta_\mathrm{I}+\delta_\mathrm{st}+\frac{\delta_t}{2}\right)\gg 1,$$

we find

$$\tilde{\delta}_C^{\mathrm{opt}}=\sqrt{\frac{\rho_C l_E}{3A_C}\left(r_E+L+\delta_\mathrm{I}+\delta_\mathrm{st}+\frac{\delta_t}{2}\right)}\approx\sqrt{\frac{\rho_C l_E}{6A_C}s}. \tag{29}$$

If we take

$$\sqrt{\lambda_E\rho_E(T_E-T_C)\eta}\leqslant 0.1\ \mathrm{V},$$

i.e., more than an order of magnitude smaller than 4v, and simultaneously using

$$\frac{4v}{l_E j}\gg\frac{1}{3}l_E\frac{\rho_E}{\delta_E},$$

we conclude that we can write $\tilde{\delta}_\mathrm{C}^{\mathrm{opt}}$ as

$$\tilde{\delta}_C^{\mathrm{opt}}=\frac{1}{2}\sqrt{B_C}, \tag{30}$$

where

$$B_\mathrm{C}=\frac{1}{3}\frac{j}{v}\rho_C\left(r_E+L+\delta_\mathrm{I}+\delta_\mathrm{st}+\frac{\delta_t}{2}\right)\approx\frac{1}{6}\frac{j}{v}\rho_C s \tag{31}$$

is a dimensionless parameter.

OPTIMUM THICKNESS OF THE COLLECTOR INSULATION

The optimum relative thickness of the collector insulation $\tilde{\delta}_\mathrm{I}=\delta_\mathrm{I}/r_\mathrm{I}$ is given by the following equation from condition (10):

$$\tilde{\delta}_\mathrm{I}^{\mathrm{opt}}=\frac{3}{2}\frac{B_\mathrm{I}}{2A+B_\mathrm{I}}\left\{1+\sqrt{1+\frac{2}{9}\frac{2A+B_\mathrm{I}}{B_\mathrm{I}}\left(1+\frac{\delta_\mathrm{st}+\delta_t/2}{r_\mathrm{I}}\right)}\right\}, \tag{32}$$

where the dimensionless parameters A and B_I are given by (8) and (9).

For plausible values of ΔV and ρ_I and $B_\mathrm{I} < 10^{-2}$, we can simplify Eq. (32). If we assume A to be of the order of unity, so that $A/B_\mathrm{I} \gg 1$ and

$$\frac{2}{9}\frac{2A+B_\mathrm{I}}{B_\mathrm{I}}\left(1+\frac{\delta_\mathrm{st}+\delta_t/2}{r_\mathrm{I}}\right)\gg 1,$$

we can rewrite (32) as

$$\tilde{\delta}_\mathrm{I}^{\mathrm{opt}}=\frac{3}{4}\left\{\frac{B_\mathrm{I}}{A}+\frac{2}{3}\sqrt{\frac{B_\mathrm{I}}{A}\left(1+\frac{\delta_\mathrm{st}+\delta_t/2}{r_\mathrm{I}}\right)}\right\} \tag{33}$$

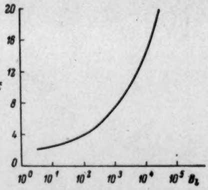

Fig. 1. Optimum relative emitter length $\tilde{l}_\mathrm{E} = l_\mathrm{E}/l_\mathrm{K}$ as a function of the dimensionless parameter B_l.

When $B_\mathrm{I}/A < 10^{-2}$ we can use the condition $[\delta_\mathrm{st} + (\delta_t/2)]/r_\mathrm{I} < 1$ to find a simpler expression for $\tilde{\delta}_\mathrm{I}^{\mathrm{opt}}$ from (33):

$$\tilde{\delta}_\mathrm{I}^{\mathrm{opt}}=\frac{1}{2}A_\mathrm{I}\sqrt{B_\mathrm{I}}, \tag{34}$$

where

$$A_\mathrm{I}=\sqrt{\frac{1}{A}\left(1+\frac{\delta_\mathrm{st}+\delta_t/2}{r_\mathrm{I}}\right)}\approx\sqrt{\frac{s}{2r_\mathrm{I}A}} \tag{35}$$

is a dimensionless coefficient approximately equal to unity.

DISCUSSION

Let us consider certain results of this determination of the optimum values of certain parameters of a thermionic cell and, in particular, the use of these equations.

The optimum relative emitter length $\tilde{l}_\mathrm{E}^{\mathrm{opt}} = l_\mathrm{E}^{\mathrm{opt}}/l_\mathrm{K}$ is governed by the dimensionless parameter B_l alone, which is proportional to the ratio of the useful potential difference to the voltage drop per unit length across the electrodes. Figure 1 shows the relation $\tilde{l}_\mathrm{E}(B_l)$ obtained from (15).

For w = 5 W/cm² and for typical values of the other cell parameters we have $l_\mathrm{E}^{\mathrm{opt}} \approx 3$ cm. As w increases, $l_\mathrm{E}^{\mathrm{opt}}$ decreases. The quantity $l_\mathrm{E}^{\mathrm{opt}}$ is independent of the cell radius and (at constant values of the electrode resistivities) of the other radial dimensions of the cell. Of the geometric parameters, that which has the greatest influence on $l_\mathrm{E}^{\mathrm{opt}}$ is connector length l_K. Figure 2 shows the relative emitter length $\tilde{l}_\mathrm{E}^{\mathrm{opt}}$ and its absolute length $l_\mathrm{E}^{\mathrm{opt}}$

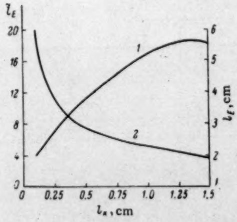

Fig. 2. Effect of the connector length l_K on $\tilde{l}_\mathrm{E}^{\mathrm{opt}}$: 1) l_E; 2) $\tilde{l}_\mathrm{E}$.

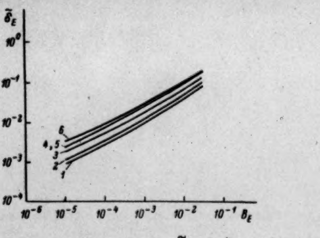

Fig. 3. Optimum relative emitter thickness $\tilde{\delta}_E = \delta_E/l_E$ as a function of the dimensionless parameter B_E. r_0/l_E: 1) 0.5; 2) 0.1; 3, 4) 0.25; 5,6) 0.5. Δ_E/l_E: 1, 2, 3, 5) 0.01; 4,6) 0.1.

as functions of l_K for a typical thermionic converter.

It should be noted that the result found for l_E^{opt} from (15) agrees with the results of the many-parameter optimization.

Equation (18) can be used to determine r_0^{opt} and thus r_E^{opt} (or r_E^{opt} directly); this latter radius corresponds to the maximum emitter surface area per unit volume:

$$F_{sp} = \frac{4\pi r_E l_E}{\sqrt{3}\, s^2 t};$$

condition (18) can be obtained from the condition $F_{sp} \to \max$.

We see from (19) that $\tilde{r}_E^{opt}$ is not explicitly a function of the axial dimensions of the cell, the specific energy, or the resistivities of the electrodes. However, there is an implicit functional dependence if δ_E, δ_C, and δ_I in (18) are assigned their optimum values in accordance with (24), (30), and (34). However, r_E^{opt} cannot always be chosen from (18); in choosing r_E it is necessary to take account of several restrictions associated with strength, criticality, techniques for constructing and assembling the devices, etc. These restrictions usually lead to values of r_E larger than given by (18). Accordingly, (18) and (19) can be recommended only for use in finding certain limiting values of r_E; the final choice of r_E must be based on the restrictions mentioned above.

The optimum relative thickness of the emitter shell, $\tilde{\delta}_E = \delta_E/l_E$, is governed, according to (24), by the dimensionless parameter B_C, which is proportional to the ratio of the voltage drop per unit length at the emitter to the useful potential difference of the cell. Figure 3 shows a typical functional dependence of $\tilde{\delta}_E^{opt}$ of B_E for the case of a nonconducting core.

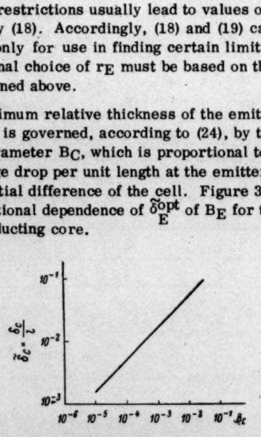

Fig. 4. Optimum relative collector thickness $\tilde{\delta}_C = \delta_C/l_E$ as a function of the dimensionless parameter B_C.

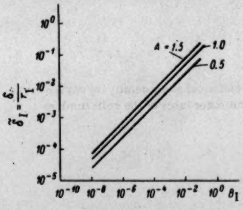

Fig. 5. Relative thickness of the collector insulation $\tilde{\delta}_I = \delta_I/r_I$ as a function of the dimensionless parameter B_I.

As the conductivity of the core is increased, δ_E^{opt} decreases in the limit $\delta_E^{opt} \to 0$, because, as the current flows through the conducting core, and δ_E is reduced, the volume of the section decreases slightly, so the useful electrical power per unit volume increases.

The optimum relative collector thickness $\tilde{\delta}_C^{opt} = \delta_C^{opt}/l_E$ is a function of the dimensionless parameter B_C alone; the functional dependence $\tilde{\delta}_C^{opt}(B_C)$ found from (30) is shown in Fig. 4.

The thickness of the collector insulation δ_I^{opt} in this formulation of the problem, in which δ_I is governed only by the leakage current through the insulation and the radial cell dimension s, is proportional to r_I and $\sqrt{B_I}$. The dimensionless insulation thickness $\tilde{\delta}_I = \delta_I/r_I$ is governed, according to (34), essentially by the dimensionless parameter B_I; physically, this parameter corresponds to the ratio of the leakage power density $w_{le} = j_{le}\Delta V$ at an insulation thickness equal to the emitter thickness, to the power density of the thermionic converter, w = jv. Figure 5 shows the $\tilde{\delta}_I^{opt}(B_I)$ functional dependence. With w = 5 W/cm², ΔV = 30-50 V, and $\rho_I = 10^7$-10^9 Ω·cm, the value of δ_I^{opt} does not exceed a few tens of microns. However, the final choice of δ_I^{opt} can also be influenced by such phenomena as thermal and dielectric breakdown of the insulation or the electrical transport of ions as well as by considerations related to the radiation strength of the insulation and the facility with which the collector assembly can be constructed. Accordingly, the appropriate corrections must be made to the value of δ_I^{opt} found from (34).

CONCLUSION

The equations derived above can be used to find the optimum values of such geometric parameters as the length of the cell, the thickness of the emitter, that of the collector, and that of the collector insulation. The results found for these parameters agree with the results of the many-parameter optimization of the cell,[1] so we can recommend Eqs. (16), (24), (31), and (34) above for determining the optimum geometry of the cell. When it is necessary to optimize several parameters, the latter can also be determined from these equations by the method of successive approximations. In certain cases the optimum values found for certain of the parameters must be corrected on the basis of additional restrictions and requirements.

---

[1] Notation: E) Specific energy (W/cm³); F_{1e}) specific surface area (cm²/cm³);

j) current density (A/cm^2); L) interelectrode gap (cm); l) length (cm); r) radius (cm); S) cross-sectional area (cm^2); s) radial dimension of section (cm); T) temperature (°C); t) axial dimension of section (cm); ΔV) potential difference between the collector and the mass (V); V_{se}) volume of section (cm^3); v) potential difference between the electrodes (V); W) electrical power (watts); w) electrical power density (W/cm^2); δ) thickness (cm); δ_t) distance between the outer tubes of the cells (cm); η) efficiency; λ) thermal conductivity [W/(cm · deg)]; ρ) resistivity (Ω · cm). Subscripts: E) emitter; C) collector; I) insulation; K) connector; 0) core; st) supporting tube.

---

[1] Yu. A. Broval'skii and V. V. Sinyavskii, Zh. Tekh. Fiz., 42, 1909 (1972) [Sov. Phys.—Tech. Phys., 17, 1530 (1973)].

End current in a magnetron with a secondary-emission cathode

G. G. Sominskii, S. A. Fridrikhov, O. Yu. Tsybin, and A. P. Karizhskii

M. I. Kalinin Leningrad Polytechnical Institute

(Submitted June 4, 1973)
Zh. Tekh. Fiz., 44, 606-611 (March 1974)

An experimental study has been made of the end current in a magnetron with a cold cathode. The volume in which the number of electrons is multiplied by the input microwave signal is determined. There is an azimuthal modulation of the space charge at the period of the slow-wave system. New data are reported on the radial profile of the end current.

In order to understand the operation of M-type devices, it is important to determine the conditions under which the space charge interacts with the rf field of the slow-wave system. It is customary to assume (see, e.g., refs. 1-3) that the general features of the operation of generators and amplifiers with crossed fields can be understood on the basis of an analysis of the interaction of electrons with only the fundamental spatial harmonic of the microwave field. In this case the mechanism for energy transfer by electrons to the microwaves becomes clear. However, several features of the operation of M-type devices cannot be explained on the basis of such a crude specification of the field of the slow-wave system. The azimuthal modulation of the electron and ion bombardment of the cathodes observed in refs. 4 and 5 apparently implies that inhomogeneities of the electric field of the slow-wave system influence the motion of space charge. Malyugin et al.[5] believe that the modulation of the ion current to the cathode must be due to the existence of azimuthal inhomogeneities of the electron cloud, which can observed in a study of the space-charge distribution.

It has been shown[6-8] that information about the space-charge distribution in crossed-field devices can be obtained by analyzing the characteristics of the end current (the flow of electrons parallel to the magnetic field). We report here a study of the distribution of the end current in a magnetron. We have also studied the interaction region by probing with an electron beam directed parallel to the magnetic field. We are primarily interested in the azimuthal inhomogeneities of the space charge under conditions corresponding to intense microwave oscillations.

2. EXPERIMENTAL PROCEDURE AND APPARATUS

The measurements are carried out in pulsed 10-cm magnetrons with cold secondary-emission cathodes of a CuBeAl alloy, triggered by a microwave signal from an auxiliary magnetron.[9] The magnetic field B, parallel to the axis of the device, is produced by two Helmholtz coils, between which the magnetron is placed. The inhomogeneity of the magnetic field in the working region is less than 2%. Pulses of anode voltage U_a, whose repetition frequency f and length τ can be varied over broad ranges, are fed to the cathode of the magnetron with respect to the grounded anode unit. Most of the measurements are carried out at pulse lengths $2 \le \tau \le 10\,\mu$sec. The experimental devices are continuously evacuated; the operating pressure does not exceed 10^{-6} torr.

Figure 1 shows the experimental device. The diameters of the anode 1 and cathode 2 are 16 and 6 mm, respectively. The anode unit is 20 mm high. The end shields usually used to prevent electrons from escaping along the magnetic field are replaced by grids 3 and 4. In the analysis of the end current electrons move from the interaction region to fluorescent shell 5, passing through grids 3, 6, and 7. Fine grid 7, held against the shield surface, is used to prevent the shield from being charged by the electron current. A slow-wave voltage U_{sw}, which can be used to cut off the end current, is applied between the cathode and grid 6, which is 3 mm from end grid 3. In the 3-mm gap between grids 6 and 7, electrons are accelerated by a voltage of U ~ 5-10 kV before they strike the shield. Since the value of eU is considerably higher than any possible initial energy of the electrons emitted from the working region of the magnetron, the glow of the fluorescent shield caused by the electron bombardment reflects the distribution of the end-current density in the plane perpendicular to the axis of the device.[6]

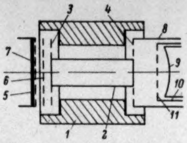

Fig. 1. The experimental magnetron. 1) Anode; 2) cathode; 3,4) end shields; 4,5) fluorescent shield; 6,7) grids; 8) cylinder of cathode mount; 9) cathode of electron gun; 10) guard electrode with grid 11.

To produce the electron beam used to probe the space charge, an electron gun is placed in cathode mount 8. The gun consists of a cathode 9 with an emitting end surface about 15 mm in diameter and a guard electrode 10 with grid 11. A negative bias voltage of $U_b = -400$ V, applied between cathode 9 and grid 11, cuts off the gun until pulse U_s, synchronized with the pulses of the magnetron anode voltage, is fed to the control electrode. The electrons emerging from the gun are accelerated by the pulsed voltage $U_p \sim 8$-16 kV applied between the control electrode and the cathode mount; these pass through grid 4 into the working region of the experimental device. The length of the probing-beam pulses, τ_{pr}, is shorter than τ.

The beam electrons which traverse the magnetron reach the shield if the voltage U_p is greater in magnitude than the retarding voltage U_r. In observation of the glow of the shield induced by the probing beam the end current of electrons from the space charge is cut off by a voltage of $U_r \simeq -2$-3 kV. Accordingly, under all the experimental conditions studied, the inequality $|U_p| > |U_r|$ is satisfied. Grids 3, 4, 6, and 11 have a transparency of 30%, while grid 7 has a transparency of 80%. Special measurements show that the use of grids 3 and 4 instead of solid elec-

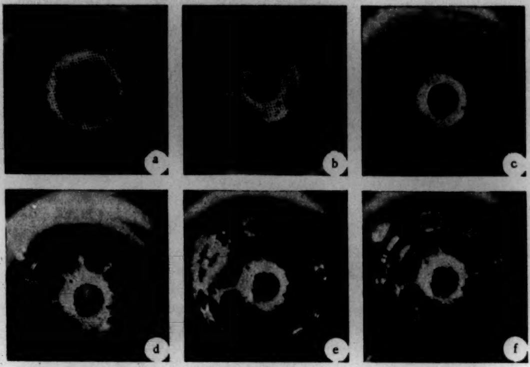

Fig. 2. Photographs of the images on the fluorescent shield in bombardment by the end current. $B = 0.12$ T. U_a, kV: a) 2.9; b) 4.7; c) 8.7; d) 10.9; e) 12.8; f) 13.1.

trodes has essentially no effect on the operation of the experimental device, whose basic characteristics (the voltage–current characteristic, the functional dependence of the rf output power on the anode voltage, and the spectrum of the rf power) do not differ appreciably from the characteristics of a magnetron with solid end shields.

3. EXPERIMENTAL RESULTS

The changes in the shape of the end-current distribution accompanying a change in the operating conditions of the experimental device are conveniently followed on photographs of the fluorescent shield taken at a constant magnetic field and at various values of the anode voltage. Figure 2 shows photographs taken with B = 0.12 T. Under the condition $U_a \leqslant 3$ kV (Fig. 2a) the shield glows near the anode, apparently because of the existence of space charge, which arises as a result of the secondary-emission multiplication of electrons at the anode surface under the influence of the input microwave signal P_{in}. As U_a is increased electron multiplication begins near the cathode. For example, when $U_a = 4.7$ kV (Fig. 2b), the cathode and anode regions are the brightest objects on the shield. A further increase in the anode voltage is accompanied by a fading of the glow at the anode. Over the range $7.0 \leqslant U_a \leqslant 9.5$ kV the only appreciably bright ring is that near the cathode (Fig. 2c). When U_a reaches 9.5 kV the anode current falls abruptly (Fig. 3), because electrons begin to interact effectively with oscillations of the slow-wave system.

The glow, which becomes appreciable in the region far from the cathode at $U_a > 9.5$ kV, results from the space charge of the electrons emitted by the cathode and moving toward the anode. The glow in the region far from the cathode is azimuthally inhomogeneous (Fig. 2d). As U_a is increased beyond 9.5 kV the anode current behaves nonmonotonically. On the voltage–current characteristic measured at B = 0.12 T we see three peaks, corresponding to different oscillation modes. As the anode voltage is varied over the range $9.5 \leqslant U_a \leqslant 13.1$ kV, there is no qualitative change in the shape of the image on the fluorescent shield; there is only a change in its intensity. Fixed bright features or "spokes" can be distinguished on the shield; the periodicity of their spatial pattern approximately reproduces that of the slow-wave system of the anode unit, which consists of eight resonators (Figs. 2d-2f). Similar changes are observed in the images corresponding to other values of the magnetic field over the entire range studied ($0.1 \leq B \leq 0.14$ T).

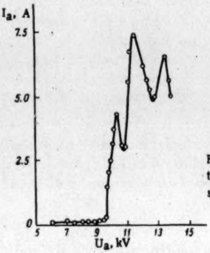

Fig. 3. Voltage–current characteristic of the experimental magnetron measured at a magnetic field of B = 0.12 T.

To obtain quantitative information about the end-current distribution we carry out a photometric study of photographs of the shield, using an MF-4 microphotometer. Figure 4 shows a typical functional dependence of the quantity I (the relative intensity of the light) on the azimuthal coordinate φ. Here, I is the ratio of the negative transparency at the cathode surface I'_k to the value of I' at the given point. In the recording of an $I = I(\varphi)$ curve the values of I were determined at points lying on circles of a given radius r. The characteristic in Fig. 4 is measured at B = 0.12 T, $U_a = 12.8$ kV, and r = 5.5 mm. Analysis of these $I = I(\varphi)$ curves shows that under conditions corresponding to intense microwave oscillations in the interaction region there is a deep azimuthal modulation of the end current, which apparently reflects inhomogeneities in the space charge. The space charge can be modulated by inhomogeneities of both the electrostatic and rf fields due to the "broken" nature of the anode (due to the gaps

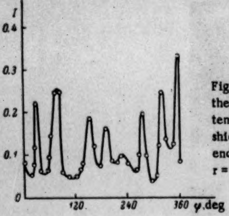

Fig. 4. The $I = I(\varphi)$ characteristic for the azimuthal distribution of the intensity of the glow on the fluorescent shield during its bombardment by the end current. B = 0.12 T, U_a = 12.8 kV, r = 5.5 mm.

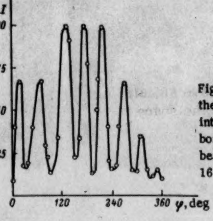

Fig. 6. The $I = I(\varphi)$ characteristic for the azimuthal distribution of the glow intensity on the fluorescent shield in bombardment by the probing electron beam. B = 0.1 T, U_a = 6 kV, U_p = 16 kV, r = 5.5 mm.

and layers of the slow-wave system). The role of these factors in the modulation cannot be evaluated in a study of the characteristics of the end current because the end current exists only when both U_a and the rf power are nonvanishing.

When we probe the magnetron with an electron beam we are also able to observe a modulation of the outer boundary of the beam, at the spatial period of the slow-wave system of the anode unit. Figure 5 shows a photograph of the fluorescent shield in bombardment by the electron beam, taken with B = 0.1 T, U_a = 6 kV, and U_p = 16 kV. When there is an input microwave signal azimuthal inhomogeneities are visible at the outer boundary; these disappear at $P_{in} = 0$. Figure 6 shows the $I = I(\varphi)$ curve obtained by microphotometry of the photograph in Fig. 5 at r = 5.5 mm.

The results obtained with electron probing show that there can be an azimuthal modulation of the space charge under the influence of the microwave field of the slow-wave system.

The data on the azimuthal distribution of the end current agree with information in the literature[5] on the modulation of the ion current to the cathode in an M-type amplifier and, we believe, show that azimuthal inhomogeneities are characteristic of the space charge in both generators and amplifiers with crossed fields operating at a high microwave level.

We record the $I = I(r)$ characteristics for the radial distribution of the glow intensity at fixed values of the coordinate φ. Figure 7 shows the $I = I(r)$ curves obtained near the maximum ($\varphi = 70°$) and the minimum ($\varphi = 120°$) of the $I = I(\varphi)$ curve measured at B = 0.12 T and U_a = 12.8 kV. We see that the light reaches its greatest intensity I_m at the hub of the electron cloud near the cathode. The smooth nature of the $I = I(r)$ curve near the cathode could be due to saturation of the fluorescent shield during bombardment by a dense electron current. As r is increased near the synchronization radius r_s the value of I falls abruptly to the value I_1, which varies slightly over the range $4.5 \leq r \leq 6$–6.5 mm. Near the anode the intensity reaches a maximum.

We can explain some features of these end-current characteristics on the basis of the motion of electrons in the interaction region of the experimental device. The radial component of the electric field causes the electron stream to drift around the axis. The motion of electrons to the anode in a magnetron occurs under the influence of the azimuthal component of the microwave field, which reaches a maximum near the central gap of the resonator. At low microwave amplitudes, the electrons, which are displaced toward the anode near one of the slits, continue to rotate around the cathode, and there is no significant change in their radial position until the neighboring gap is reached. There they are again displaced toward the anode. The process continues until the electrons reach the anode surface. As the microwave intensity is increased, a point is reached at which a large number of the electrons from the region between the boundary of the hub and the anode manage to reach the anode while they are moving near one gap. Under these conditions we would expect a deep modulation of the space charge above the boundary of the hub of the electron cloud.

The maximum of the end current on the $I = I(r)$ characteristics could be a consequence of the high space-charge density near the anode, due to either the existence of an additional emission source at the anode or the incidence on this region of some of the electrons which are not intercepted by the preceding layer.

Fig. 5. Photograph of the image on the fluorescent shield in bombardment by the probing electron beam. B = 0.1 T, U_a = 6 kV, r = 16 kV.

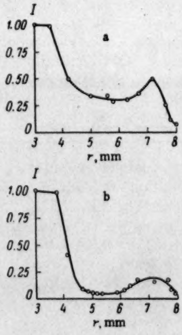

Fig. 7. The $I = I(r)$ characteristics for the radial distribution of the intensity of the glow on the fluorescent shield in bombardment by the end current. B = 0.12 T, U_a = 12.8 kV. a) φ = 70°; b) 120°.

On the basis of this analysis of the end-current characteristics of a cold-cathode magnetron we have thus determined the part of the working region in which secondary-emission multiplication of electrons occurs under the influence of the input microwave signal, we have detected an azimuthal modulation of the space charge at the spatial period of the slow-wave system, and we have obtained new information about the radial distribution of the end current, which can be attributed to the existence of a maximum in the space-charge density near the anode surface as well as near the cathode.

---

[1] G. B. Collins, Microwave Magnetrons, McGraw-Hill, New York (1948).

[2] E. Okress (ed.), Crossed Field Microwave Devices, Academic Press, New York (1962).

[3] S. I. Bychkov, Questions of the Theory and Practical Use of Magnetron Devices [in Russian], Izd. Sovet-skoe Radio, Moscow (1967).

[4] V. K. Rosnovskii, Elektron. Tekh., Ser. 1, Elektronika SVCH, No. 3, 163 (1969).

[5] V. I. Malyugin, G. G. Sominskii, and L. M. Gorshkova, Elektron. Tekh. Ser. 1, Elektronika SVCH, No. 7, 3 (1972).

[6] G. G. Sominskii, Zh. Tekh. Fiz., 35, 1782 (1965) [Sov. Phys.—Tech. Phys., 10, 1377 (1966)].

[7] G. G. Sominskii and S. F. Kirsanov, Physical Electronics, Works of the Leningrad Polytechnical Institute [in Russian], No. 277, Izd. Énergiya, Moscow—Leningrad (1967).

[8] G. G. Sominskii, Zh. Tekh. Fiz., 38, 663 (1968) [Sov. Phys.—Tech. Phys., 13, 497 (1968)].

[9] B. V. Kuteev and G. G. Sominskii, Zh. Tekh. Fiz., 42, 1761 (1972) [Sov. Phys.—Tech. Phys., 17, 1407 (1973)].

Excitation collisions between magnesium ions and inert gas atoms

V. L. Ovchinnikov, O. B. Shpenik, and I. P. Zapesochnyi

Problems Laboratory for the Physics of Electron Collisions,
Uzhgorod State University

(Submitted March 12, 1973; resubmitted July 10, 1973)
Zh. Tekh. Fiz., 44, 612-616 (March 1974)

Excitation processes are studied in collisions of Mg$^+$ ions with inert gas atoms over the energy range from threshold to 2500 eV and the spectral range 2200-6600 Å. The excitation processes in collisions of Mg$^+$ with He, Ar, Kr, and Xe atoms are different from those in collisions of Mg$^+$ with Ne atoms, because of the different natures of the partners. A "competition" between two energetically close inelastic channels of the reaction Mg$^+$–Ne leads to an oscillation of the total cross sections for excitation of the spectral lines.

There has been comparatively little previous study of excitation processes in ion–atom collisions. The work that has been carried out has been concerned primarily with excitation processes in collisions of alkali metal ions and inert gas ions with inert gas atoms,[1-4] of alkali metal ions with alkali metal atoms, and of alkali metal ions and alkali earth ions with cadmium atoms.[6] Valuable information has been obtained about the probabilities for the reactions to proceed through various channels and about the excitation of the interacting particles.

We report here on a study of excitation processes in low-energy collisions of Mg$^+$ ions with inert gas atoms. These experiments represent the beginning of a systematic study of the excitation of energy levels in collisions of alkali earth ions with He, Ne, Ar, Kr, Xe atoms in the energy range from threshold to 2.5 keV and over a broad spectral range.

The experiments are carried on by an optical method, through detection of the emission of the excited particles produced in the collisions. The experimental apparatus, which is like that described in ref. 6, consists of an ion source with an ion-optics system, a collision chamber with a gas-injection device, the spectral instrument, and a unit for photoelectric detection of the radiation.

The magnesium-ion source, which operates under conditions corresponding to a low-voltage discharge, and the ion-optics system, which includes a 127° cylindrical electrostatic selector and focusing lenses, provide a magnesium-ion current up to 1 μA in the collision chamber with a beam cross section of 1 × 3 mm over the energy range 50-2500 eV. The collision chamber is filled with spectrally pure inert gas from a special glass injection system. The pressure in the chamber is held constant by means of a precision needle valve and is measured by a thermocouple (LT-2) and vacuum gauges (LM-2) (the appropriate corrections are incorporated[7]). The radiation generated during the collisions is directed by a quartz optical system to the entrance slit of a monochromator (ZMR-3 or MDR-2), placed at a right angle with respect to the beam; the radiation is detected at the exit from this system by a photomultiplier (FÉU-18A or FÉU-79). The output signal from the photomultiplier is processed by narrow-band amplification and phase detection. The ion beam (or light flux) is modulated by feeding rectangular blanking pulses to one of the electrodes of the ion-optics system.

The absolute values of the excitation cross sections are determined by a photoelectric comparison of the intensity of the spectral lines excited in the ion–atom collisions with the intensities of reference He and Ne lines excited by electron impact. Account is taken of the spectral sensitivity of the entire detection system. The reference lines are λ 3448, λ 3889, λ 4713, λ 4922 Å He I and λ 3520, λ 5852 Å Ne I, whose effective electron-excitation cross sections have been measured repeatedly.[8,9] This simple method is convenient because it allows us to determine the excitation cross sections in collisions of Mg$^+$ ions with all partners with the same error: 60-80%.

The excitation functions and effective excitation cross sections of the spectral lines are measured under conditions ensuring single collisions: at gas pressures of $7 \cdot 10^{-3}$ torr and below in the collision chamber and at all values of the magnesium-ion beam current achievable. Measures were taken to suppress the production of secondary electrons at the point at which the radiation is detected.

The emission spectrum recorded in the optical range 2200-6600 Å in collisions of Mg$^+$ ions with He, Ar, Kr, and Xe atoms consists of the Mg I and Mg II lines alone. The spectrum for Mg$^+$–Ne collisions is more complicated: In addition to the Mg I and Mg II lines there are lines of neon atoms and ions (Ne I and Ne II). The most intense are the spectral lines of Mg II: the resonant doublet at λλ 2795, 2803 Å and the lines from the first excited S and F levels at λλ 2928, 2936 Å, and λ 4481 Å, respectively. The resonant line λ 2852 Å and the triplet lines λλ 5167, 5173, 5184 Å and λλ 3829, 3832, 3838 Å are excited in the Mg I spectrum. The Mg$^+$–Ne collisions reveal certain Ne I lines which are emitted in transitions between $2s^22p^53s$ and $2s^22p^53p$ electronic configurations: λλ 5852, 6143, 6402, 6506 Å. There are also Ne II lines: λ 3547 and λ 3237 Å.

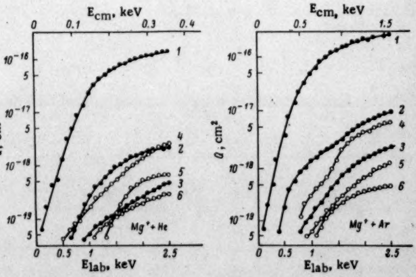

Fig. 1. Cross sections for the excitation of spectral lines in Mg$^+$ –He and Mg$^+$–Ar collisions as functions of the energy. 1) λλ 2795; 2803 Å Mg II; 2) λλ 2928, 2936 Å Mg II; 3) λ 4481 Å Mg II; 4) λ 2852 Å Mg I; 5) λλ 3829, 3832, 2828 Å Mg I; 6) λλ 5167, 5173, 5184 Å Mg I.

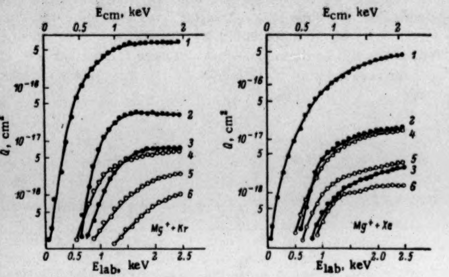

Fig. 2. Excitation cross sections for the spectral lines in Mg⁺−Kr and Mg⁺−Xe collisions as functions of the energy. 1) λλ 2795, 2803 Å Mg II; 2) λλ 2928, 2936 Å Mg II; 3) λ 4481 Å Mg II; 4) λ 2852 Å Mg I; 5) λλ 3829, 3832, 3838 Å Mg I; 6) λλ 5167, 5173, 5184 Å Mg I.

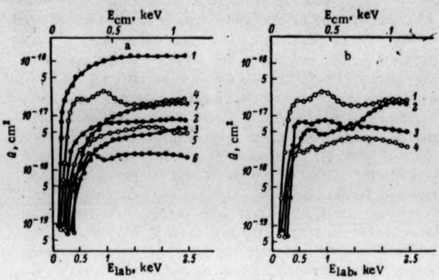

Fig. 3. Excitation cross sections for the spectral lines in Mg⁺−Ne collisions as a function of the energy. a: 1) λλ 2795, 2803 Å Mg II; 2) λλ 2928, 2936 Å Mg II; 3) λ 4481 Å Mg II; 4) λ 2852 Å Mg I; 5) λλ 2795/32/38 Å Mg I; 6) λ 6506 Å Ne I; 7) λ 3237 Å Ne II. b: 1) λ 2852 Å Mg I; 2) λ 5852 Å Ne, I; 3) photoexcitation cross section for the lines λ 6143, λ 6506, λ 6402 Å Ne I; 4) λλ 5167, 5173, 5184 Å Mg I.

We have studied the excitation functions and measured the effective excitation cross sections of all these spectral lines; the results are shown in Figs. 1-3. These results are obtained by averaging over the results of at least five separate measurements. The excitation functions for essentially all lines observed in Mg^+-He, Mg^+-Ar, Mg^+-Kr, and Mg^+-Xe collisions (Figs. 1 and 2) are monotonically increasing curves having indistinct experimental thresholds far above the kinematic thresholds (by a factor of from 2 to 30). There is a tendency for the excitation cross sections to increase from He to Ar, Kr, and Xe. For the Mg^+-Ne reaction there is a clearly defined threshold with a rapid increase in the cross sections near the threshold and a high efficiency for charge exchange of Mg^+ ions into excited states. Furthermore, the excitation curves for several of the lines display an oscillatory structure (Fig. 3).

It is difficult to analyze unambiguously these results, lacking information of any type about the levels of the quasimolecule formed by the Mg^+ ion and the inert gas atom during the collision. Nevertheless, a qualitative interpretation can be based on the ratios of the energy balances for the excitation of the particles in collision of these partners. This approach is equivalent to analyzing the position of the quasimolecule levels at infinite separation of the nuclei. We say that the "ground level" is that of the Mg^+A quasimolecule (where A represents an inert gas atom) and the "excited levels" are those of $Mg^{+*}A$, Mg^*A^+, Mg^+A^*, etc. Each of these symbols actually represents a group of levels corresponding to excitation to various states of the starred particle.

Since the $Mg^{+*}(3^2P_{1/2,\ 3/2})$ level is the lowest-lying level for any A, it must be excited most efficiently. It is therefore completely plausible to find the effective cross section for the resonant doublet Mg II (λλ 2795/2803 Å) to be the highest in all the gases. A gradual decrease in the energy of the Mg^*A^+ levels from He to Xe should lead to an increase in the excitation efficiency of the Mg I lines, in agreement with experiment. We can apparently attribute the absence from the emission spectrum (except for that corresponding to Mg^+-Ne collisions) of lines corresponding to the target atom to the circumstance that the Mg^+A^* levels accessible to study are the highest-lying of the excited levels of the quasimolecule, so their population is energetically the least favorable.[1)]

The monotonic nature of the excitation functions for Mg^+-He, Ar, Kr, and Xe collisions and the pronounced "retardation" of the experimental thresholds in comparison with the kinematic thresholds apparently indicate a "quasiadiabatic" nature of the interaction of these partners. Analysis of the results shows that most of the curves can be described between the threshold and 2-2.5 keV by[10]

$$Q(v) = K \exp - \frac{l \Delta E}{4\hbar v},$$

where K is a constant which is a function of the nature of the process, ħ is Planck's constant, l is the interaction radius of the particles for the "adiabatic parameter," ΔE is the energy defect of the process, and v is the velocity of the incident ion.

For example, for Mg^+-Xe collisions and for the λλ 2795, 2803 Å Mg II lines we have $\Delta El = 11.3$ eV · Å and $K = 10^{-14}$ cm²; for Mg^+-Ar, for the λλ 2928, 2936 Å lines we have $\Delta El = 14.4$ eV · Å and $K = 4.8 \cdot 10^{-16}$ cm²; and for Mg^+-He, for the λλ 5167, 5173, 5184 Å Mg I lines we have $\Delta El = 137$ eV · Å and $K = -1.3 \cdot 10^{-17}$ cm². We can assume that in this case the population of the excited levels near the threshold appears by means of tunnel transitions.[11] The pronounced discrepancy between the experimental and theoretical excitation thresholds is evidently due to the low probability for tunneling, as a consequence of which the excitation cross sections for levels near the threshold are vanishingly small, while the thresholds we have detected are governed by the sensitivity of the detection system. We see from Figs. 1-3 that the experimental excitation thresholds for all lines are governed by the energies at which the effective cross sections reach values of the order of (3-5) · 10^{-21} cm².

Excitation in collisions of Mg^+ ions with neon atoms is apparently due to a completely different interaction between the colliding particles. The clearly defined experimental thresholds and the rapid increase in intensity near the threshold indicate that in this case we are dealing with a Landau–Zener mechanism for population of the excited levels. This circumstance is also apparently responsible for the effective population of various excited levels: $Mg^{+*}Ne$, $Mg^{+}Ne^{*}$, and $Mg^{+}Ne^{+*}$, especially $Mg^{*}Ne^{+}$. The oscillatory structure of the excitation functions for certain lines (Fig. 3) could be a consequence of the interaction of energetically close excited levels of $Mg^{*}Ne^{+}$ and $Mg^{+}Ne^{*}$ (ref. 2). Such an interaction apparently occurs between the $Mg^{*}(3^1P_1)\,Ne^{+}$ level and the group of nearby $Mg^{+}Ne^{*}$ levels ($2p^5 3p\, ^3D_3$, $^3D_2{}^1$, D_2) and between the $Mg^{*}(4^3S_1)\,Ne^{+}$ and $Mg^{+}Ne^{*}$ ($2p^5 3p\, ^1S_0$) levels. The energy differences between the positions of these levels at infinity are 0.29–0.37 and 0.07 eV, respectively. This hypothesis is supported by the observation that the excitation functions for the spectral lines from these levels oscillate out of phase; their excitation cross sections are approximately equal (see Fig. 3b, curves 1 and 3 and curves 2 and 4). On the other hand, the spectral lines from energetically isolated levels do not exhibit such a structure (curves 1–3, 5, 7 in Fig. 3a).

We note in conclusion that the existence of two or more energetically close levels of a quasimolecule at infinite separation of the nuclei is not, however, a sufficient condition for the appearance of oscillations in the total cross sections, as can be seen from our results. For example, there are many such excited levels of the quasimolecules $Mg^{+}-He$, $Mg^{+}-Ar$, $Mg^{+}-Kr$, and $Mg^{+}-Xe$, but we do not observe oscillations of the corresponding excitation functions (Figs. 1 and 2). All this indicates the complexity of the mechanism for the interaction for heavy particles and again emphasizes the need for further experimental study of collisions with a wider variety of partners.

---

[1] We have not studied the most intense resonant lines of the inert gas atoms because of the limited spectral range.

[1] V. B. Matveev, S. V. Bobashev, and V. M. Dukel'skii, Zh. Eksp. Teor. Fiz., 57, 1534 (1969) [Sov. Phys. – JETP, 30, 829 (1970)].

[2] V. A. Ankudinov, S. V. Bobashev, and V. I. Perel', Zh. Eksp. Teor. Fiz., 60, 906 (1971) [Sov. Phys. – JETP, 33, 490 (1971)].

[3] S. S. Pop, I. Yu. Krivskii, I. P. Zapesochnyi, and M. V. Baletskaya, Zh. Eksp. Teor. Fiz., 59, 696 (1970) [Sov. Phys. – JETP, 32, 380 (1971)].

[4] N. H. Tolk, C. W. White, S. H. Dworetsky, and L. A. Farrow, Phys. Rev. Lett., 25, 1251 (1970).

[5] V. Aquilanti, G. Luiti, F. Vecchio-Cattivi, and G. G. Volpi, VII JCPEAC, Abstracts of Papers, Amsterdam (1971), p. 600.

[6] O. B. Shpenik, A. N. Zavilopulo, and I. P. Zapesochnyi, Zh. Eksp. Teor. Fiz., 62, 879 (1972) [Sov. Phys. – JETP, 35, 466 (1972)].

[7] A. I. Pipko, V. Ya. Pliskovskii, and E. A. Penchko, Design and Construction of Vacuum Systems [in Russian], Izd. Energiya, Moscow (1970).

[8] I. P. Zapesochnyi and P. V. Fel'tsan, Ukr. Fiz. Zh., 10, 1197 (1965).

[9] P. V. Fel'tsan, I. P. Zapesochnyi, and M. M. Povch, Ukr. Fiz. Zh., 11, 1222 (1966).

[10] H. S. W. Massey and E. H. S. Burhop, Electronic and Ionic Impact Phenomena, Oxford Univ. Press, London (1952).

[11] E. E. Nikitin and M. Ya. Ovchinnikova, Usp. Fiz. Nauk, 104, 379 (1971) [Sov. Phys. – Usp., 14, 394 (1972)].

Surface-ionization determination of the electron affinities of silver and gold

É. Ya. Zandberg, A. G. Kamenev,

and V. I. Paleev

A. F. Ioffe Physicotechnical Institute,
Academy of Sciences of the USSR, Leningrad

(Submitted July 9, 1973)
Zh. Tekh. Fiz., 44, 617-624 (March 1974)

A surface-ionization method is used to find the electron affinity S, based on a comparison of the temperature dependences of the thermionic and negative-ion currents from inhomogeneous emitters (absolute method). The sources of systematic error in the determination of S by this method, due to either assumptions incorporated in the method itself or secondary processes involving the formation of negative ions which accompany surface ionization, are discussed. The values of S for silver and gold determined by the absolute method are S(Ag) = 1.38 ± 0.10 V and S(Au) = 2.34 ± 0.10 V.

The photodetachment of electrons from negative ions (PD) has recently been used to determine the electron affinities of several elements: gold and platinum, from the threshold energy of the photons, and copper and silver, from an analysis of the energy spectra of the detached electrons.[1-3] The values found for S(Cu, Ag, Au) are significantly lower than the values found previously by surface-ionization (SI) methods.[4-6] The results are compared in Table 1.

In principle, the optical methods for determining S are more accurate than the SI methods. However, the discrepancies between the values of S determined by the PD and SI methods exceed the stated experimental errors. In an effort to explain these discrepancies, Hotop[2] has suggested that the thermodynamic equilibrium between the emitter and the adsorbed film of particles to be ionized (which is a necessary condition for the use of the SI methods) is in fact not established, that the method of determining the difference[4] $S_x - S_0$ is not valid in those cases in which the negative-ion currents are compared for elements differing markedly in chemical properties, and that the polycrystalline nature of the emitters used in the SI method plays an important role.

If the arguments of ref. 2 are valid, the SI methods used to determine the values of S for many elements are not suitable for this purpose. We have therefore analyzed the errors incorporated in the method by which S is determined by means of surface ionization, analyzed possible experimental errors, and carried out new measurements of S(Ag, Au) by an absolute SI method.

ANALYSIS OF THE ABSOLUTE METHOD FOR DETERMINING S WHEN POLYCRYSTALLINE EMITTERS ARE USED

The absolute method for determining S is based on a comparison of the temperature dependences of the thermionic and negative-ion currents from a given part of the emitting surface.[8]

According to the Saha–Langmuir equation, the negative-ion current in ionization of atoms on homogeneous metals under ordinary conditions $e(\varphi - S) \gg kT$ is[8]

$$I_n = \frac{1-R_-}{1-R_0} A_- s e \nu \exp\left[\frac{e(S - \varphi + \sqrt{e\mathcal{E}})}{kT}\right]; \qquad (1)$$

where R_- and R_0 are the reflection coefficients for negative ions and neutrals, respectively. at the potential barrier at the emitter surface; A_- is the ratio of statistical sums corresponding to negative-ion states, Q_-, to those corresponding to neutrals, Q_0; s is the emitting surface area; e is the ion charge; ν is the number of ionizable atoms per square centimeter of emitter surface area per second; T is the temperature; φ is the emitter work function; $\mathcal{E}$ is the electric field at the emitter surface; and k is the Boltzmann constant.

We assume that there is no question regarding the applicability of the Saha–Langmuir equation in determining the electron affinity S of atoms in the case in which the emitters are metallic: The values of S for several elements (Cl, Br, I, F, S, and H), including some chemically active elements, that have been found by SI methods agree with the more accurate values found by PD methods.[8] The applicability of SI methods in determinations of atomic ionization potentials V has been demonstrated: The values of V found by SI methods, even for rare-earth atoms, have been verified by spectroscopic determinations.[8] Finally, studies of the energy distribution of atomic ions yield direct information about the establishment of a thermal equilibrium between adsorbed atoms and metallic emitters.[7,8]

All the surface-ionization experiments which have been carried out show that the ratios $(1-R_+)/(1-R_0)$ and $(1-R_-)/(1-R_0)$ are approximately equal to unity and are independent of T. For the case of Ag and Au atoms on a tungsten surface it has been shown experimentally[9] that $R_0 = 0$. In principle, the coefficients R_+ and R_- must be smaller than R_0, because of the effects of image forces in the case of charged particles.[10] Accordingly, $R_- = 0$ for Ag and Au, so that Eq. (1) is simplified.

The thermionic current from a homogeneous emitter is given by the Richardson–Dushman equation:

$$I_e = A_0 T^2 (1 - \overline{R}_e) s \exp\left[\frac{-e(\varphi - \sqrt{e\mathcal{E}})}{kT}\right], \qquad (2)$$

where $A_0 = 120$ A/(cm^2 · deg^2) is a universal constant, and $\overline{R}_e$ is the coefficient for the reflection of thermionic electrons from the emitter surface averaged over the initial velocities. This reflection coefficient is a function of T.

When $R_- = R_0 = 0$, and in the approximation in which the values of $\overline{R}_e$ and the statistical-sum ratios A_- are independent of T, we find the equation usually used to determine S:

TABLE 1

No.	Element	S, V	Ref.	Measurement method
1	Cu	1.5±0.5	[4]	SI. Comparison of the negative-ion currents of two elements. The difference S(I) - S(Cu) is measured; it is assumed that S(I) = 3.07 V
2	Cu	1.78±0.16	[5]	SI. Comparison of the currents of positive and negative ions of two elements. The difference S(Cu) − S(Ag) is measured; it is assumed that S(Ag) = 1.90 ± 0.15 V
3	Cu	1.226±0.010	[1, 2]	PD. Determination from the electron energy spectrum
4	Ag	2.0±0.2	[4]	SI as in No. 1
5	Ag	1.90±0.15	[6]	SI. The negative-ion current is compared with the thermionic current
6	Ag	1.303±0.010	[1, 2]	PD. Determination from the electron energy spectrum
7	Au	2.8±0.1	[4]	SI as in No. 1
8	Au	2.3086±0.0007	[1, 3]	PD. Determination from the threshold photon energy

$$S = -\frac{k}{e}\frac{d}{d\left(\frac{1}{T}\right)}\left(\ln\frac{I_e}{I_n T^2}\right). \qquad (3)$$

However, the value A_- can be a function of T, since $Q_- = f(T)$ and $Q_0 = f(T)$. The only excited levels E of ions and atoms which are pertinent for surface ionization are those whose energies are comparable to kT, since the excitation source is simply the thermal energy of the emitter. The excited levels of neutrals and positive atomic ions are known accurately[11,12] and can always be taken into account (for Cu, Ag, and Au atoms there are no levels having energies near kT, and for these elements the values of Q_0 are independent of T). Whether levels having $E \approx kT$ exist for negative ions is usually not known. If they do exist, neglect of the functional dependence $Q_-(T)$ must lead to a measured value S' which is lower than the actual value S: Since $Q_-(T)$ increase with increasing T, we find from Eqs. (1) and (2) that

$$-\frac{k}{e}\frac{d}{d\left(\frac{1}{T}\right)}\ln\frac{I_e}{I_n T^2} = S - \Delta = S', \qquad (4)$$

where Δ is a positive quantity.

According to refs. 1-3, there are no excited levels near kT for the Au^- and Ag^- ions.

If the emitter is polycrystalline and consists of a set of areas s_i having work functions φ_i, we have the following equations under ordinary conditions $e(\varphi_{i\,\min} - S) \gg kT$, i.e., when the contact fields of the spots are compensated by the external field $\mathcal{E}$ at the emitter surface:

$$I_n = A_- e\nu \exp\left[\frac{e\left(S + \sqrt{e\mathcal{E}}\right)}{kT}\right]\sum_i s_i \exp\left(-\frac{e\varphi_i}{kT}\right), \qquad (5)$$

$$I_e = A_0 T^2 \exp\left[\frac{e\sqrt{e\mathcal{E}}}{kT}\right]\sum_i s_i\left(1 - \bar{R}_{ie}\right)\exp\left(-\frac{e\varphi_i}{kT}\right). \qquad (6)$$

It follows from Eqs. (5) and (6) that with $\bar{R}_{ie} = \bar{R}_e$ and $\bar{R}_e$ independent of T over the appropriate temperature range Eq. (3) can be used to determine S even in the case of polycrystalline emitters. Whether the conditions $\bar{R}_i = \bar{R}_e$ and $\bar{R}_e(T) = \text{const}$ hold can be determined by determining S from Eq. (3) for some element for which the value of S is well-known, e.g., for iodine.

In Eq. (3) it is assumed that the flux of ionizable particles, ν, is not affected by a change in the emitter temperature. If the vapor of the element contains molecules in addition to atoms, the condition $\nu(T) = \text{const}$ is not satisfied if the degree of molecular dissociation at the emitter is smaller than unity and is a significant function of the emitter temperature. In this case the electron affinities determined from Eq. (3) for elements whose vapor contains molecules are actually certain values S' lower than the actual values S.

Accordingly, even in the case of homogeneous and polycrystalline emitters, a determination of S by an absolute SI method can lead to values S' which are too low. Accordingly, if the SI method yields values S' > S, the fault lies not with assumptions incorporated in the SI method itself, but with systematic experimental errors. In an effort to ascertain these errors we have used an absolute SI method to determine S(Ag, Au).

DETERMINATION OF S(Ag, Au) BY AN ABSOLUTE SI METHOD

a. Apparatus. A metal spectrometer with a water-cooled ion-source chamber is used.[12] The resolution at half-height of the lines is ~ 150.

Figure 1 shows the arrangement of the ion source. The emitter is a polycrystalline wire 1 of W or Mo, 200 μ

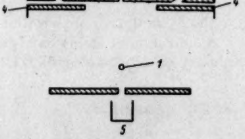

Fig. 1. Arrangement of the ion source and the thermionic-electron collectors.

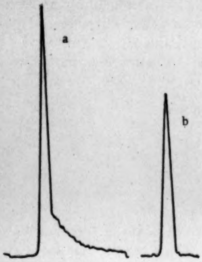

Fig. 2. Shape of the I$^-$ lines in ionization of KI on a tungsten wire. T, °K: a) 2450; b) 2150.

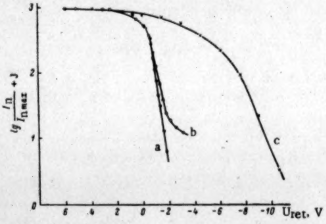

Fig. 3. Retardation curves for I$^-$ ions. a) Ions formed by SI(T = 2150°K); b) total flux of ions due to SI and conversion (T = 2450°K); c) conversion ions distinguished from the total current at T = 2450°K. The absolute values of the maximum conversion current constitute a few percent of the maximum total current.

in diameter. The wire is held in a fixed position with respect to the entrance slit of the mass analyzer at all temperatures by means of a weight system for suspending the wires and holding them under tension. The gold or silver is placed in molybdenum ampoules 3 with external heating jackets enclosed in heat shields. The atomic fluxes from the evaporators can be cut off by baffles 4.

The thermionic electrons are collected by collectors 5-7 (collector 7 can be placed in the position of one of the evaporators, while movable collector 6 can be removed). Electron collector 6 should be used to measure the values of I_e from the same part of the wire as that from which the ion current is drawn. However, simultaneous measurements of I_e at the three collectors (5-7) showed that the Richardson work function φ_R^* has the same value when any of these collectors is used. Operation of the evaporator does not affect the value of φ_R^* found through the use of any of these collectors. This result indicates that the wires have only a slight coverage of ionizable atoms at the flux densities used. Since the same values of φ_R^* are found when any of the three collectors is used, the grain size on the polycrystalline wires used is small in comparison with the size of the surface region from which the thermionic electrons are collected. This circumstance was not checked in previous measurements[6] of S(Ag) by an absolute method involving the use of thermionic collector 7 (Fig. 1).

The pressure of residual gas and vapor is ~ $5 \cdot 10^{-7}$ torr under working conditions.

The wire temperature is measured by an optical micropyrometer; account is taken of the light absorption in the glass port. The temperature of the tungsten wires is varied over the range 2450-2100°K, and that of the molybdenum wires is varied over the range 2200-1850°K.

The potential differences accelerating the ions and electrons are 800-1000 V, corresponding to fields $\mathscr{E} \approx 10^4$ V/cm at the wire surface. This field is sufficient to compensate for the contact fields of the spots and to produce a saturation current; these fields $\mathscr{E}$ are considerably weaker than those which would cause field emission.

The ion collector is an open-type ion-electron multiplier, operated in the circuit of ref. 13 and having a gain of ~ $1 \cdot 10^4$. The sensitivity of the collector of the mass analyzer in a measurement of the ion current is ~ $1 \cdot 10^{-17}$ A/div of the scale of the indicating device. A plane energy-analyzing grid is placed in front of the ion collector; this analyzer gives the ion distribution with respect to the normal component of the initial translational velocity (the ion retardation curves[8]).

b. Measurements of S of iodine. To test the assumptions used in the derivation of Eq. (3) and to determine the accuracy with which the values of S are determined by the absolute SI method we have studied iodine, for which approximately equal values have been found for the electron affinity in experiments by different methods: S(I) = 3.063 ± 0.003 V (ref. 14), S(I) = 3.076 ± 0.005 V (refs. 15, 16), and S (I) = 3.04 ± 0.05 V (ref. 17). Furthermore, iodine is used as a reference element in ref. 4 in the determinations of S(Cu, Ag, Au).

The I atoms are produced by placing the salt KI in ampoule 3 (Fig. 1), as in ref. 4; the molecules of this salt dissociate completely on clean W or Mo surfaces.[8] At the selected flux of molecules from the evaporator, ν, the values of φ_R^* do not change when any of the thermionic-electron collectors are used to measure I_e.

The I$^-$ lines recorded for various values of T of the tungsten and molybdenum wires show that at high T the lines have tails on the high-mass side. Figure 2 shows the shape of the I$^+$ lines at two temperatures, while Fig. 3 shows the retardation curves for the I$^-$ ions. Figures 2 and 3 show that the I$^-$ lines at high T are composite, i.e., they are formed not only by ions resulting from surface ionization, but also by ions resulting from the conversion

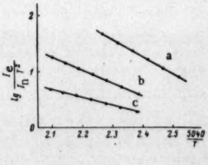

Fig. 4. The function log (I_e/I_nT^2) = f(5040/T) for I(a), Au(b), and Ag(c).

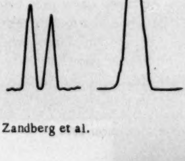

Fig. 5. Shape of the isotopic lines of Ag (a) and Au (b) at T = 2450°K.

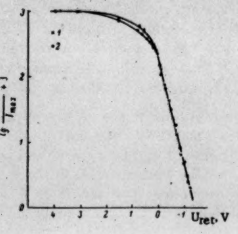

Fig. 6. Superimposed retardation curves for Ag^+ ions (1) and Ag^- ions (2) at T = 2200°K.

of positive I^+ ions into negative I^- ions at the emitter surface. The I^+ ions are produced during the ionization of I atoms in the volume between the emitter and accelerating electrode 2 (Fig. 1) by thermionic electrons which are accelerated by the field. The mechanism for the formation of conversion ions was discussed in ref. 18, and the distortions which they cause in the mass spectra of negative ions in the case of a surface-ionization ion source have been discussed in ref. 19. The results of this group of experiments show that the conversion-ion currents become appreciable at tungsten-wire temperatures $T \gtrsim 2250$°K and at molybdenum-wire temperatures $T \gtrsim 2050$°K. Accordingly, we have measured the values of S(I) at values of T for which there is essentially no conversion current. Operation at lower emitter temperatures also significantly reduces the I^- background current and thereby improves the accuracy with which S(I) is determined (the background current of I^- ions, measured when the flow of KI molecules is cut off, can be different when this flow is turned on, and the difference can increase with the emitter temperature).

Figure 4a shows a typical curve of the functional dependences

$$\lg\left(\frac{I_e}{I_n T^2}\right) = f\left(\frac{5040}{T}\right)$$

obtained for iodine. From many series of determinations of S(I) from such curves, using tungsten and molybdenum wires, we find S(I) = 3.08 ± 0.07 V, where the error is the rms error. From the good agreement of these values with those found[14-16] by PD methods we conclude that the systematic errors due to the use of polycrystalline emitters and the assumptions of the method do not exceed a few hundredths of a volt. The SI method has a larger random error than the PD method, primarily because of its greater sensitivity to the error in the determination of the emitter temperature.

c. Measurements of S(Ag, Au). Studies of the shape of the Ag^- and Au^- lines in the mass spectra at various emitter temperatures show that these lines do not contain conversion ions, nor are there measurable background Ag^- or Au^- currents. The reason lies in the circumstance that the vapor pressures of these elements are lower than that of I in a system with identical emitter temperatures. Figure 5 shows typical Ag^- and Au^- lines, while Fig. 6 shows the superposition of the retardation curves for the Ag^- and Ag^+ ions. The equal slopes of the linear regions of these retardation curves, which imply an identical ion temperature, and the approximate equality of this temperature to the emitter temperatures constitute evidence that the Ag^- ions, like the Ag^+ ions, are formed by surface ionization.

Typical functional dependences

$$\lg\left(\frac{I_e}{I_n T^2}\right) = f\left(\frac{5040}{T}\right)$$

for Ag and Au are shown in Fig. 4.

Repeated determinations of S(Ag, Au) on various W and Mo wires revealed S(Ag) = 1.38 ± 0.10 V and S(Au) = 2.34 ± 0.10 V, where the error is the rms error. These values agree well with those found by the PD methods (Table 1), but the errors are larger.

CONCLUSION

These measurements of S for I, Ag, and Au show that SI methods give the correct values of S for these elements, but special experiments must be carried out to determine the mechanism for the formation of the negative ions which are detected. Such determinations were carried out in ref. 7 but not in earlier experiments.[4,6]

If we make the natural assumption that in the comparison of the currents of Cu^-, Ag^-, and Au^- ions with the current of I^- ions in ref. 4 some of the I^- ions were of conversion origin, we find an explanation for the high values of S(Cu, Ag, Au) found in ref. 4 and the correct values of the differences S(Ag) − S(Au), etc. [The I^- conversion current contribution to the total I^- current leads to values S'(I) which are lower than the actual values S(I).] Accordingly, the errors in the differences S(I) − S(Ag, Au, Cu) are apparently not due to differences in the chemical properties of elements of groups I and VII, as was suggested in refs. 2 and 3.

Differences in the chemical properties of elements can play a role in the determination of S by methods in which the SI currents are compared only if these elements react with the emitter at a rate which is a function of the emitter temperature or if the atoms of these elements diffuse into the interior of the emitter and have different activation energies for diffusion. In such cases a change in T will change the resultant flux density of ionizable particles to the emitter surface. Reactions between the ionizable atoms on the emitter surface can be neglected because of the low surface coverage under these experimental conditions. Some information about the coverage of the emitter surface comes from the value of its work function; thus, in a determination of S it is desirable to monitor the work function, even though it does not appear in the equation from which S is determined.

These measurements of S(Ag) and S(Au) have shown, in complete agreement with the theory for surface ionization of atoms on polycrystalline emitters,[8] that the inhomogeneity of the emitter with respect to the work function due to its polycrystalline nature has essentially no effect on the measured values of S.

For small values of S all the SI methods require high densities of particle fluxes; in this case the secondary

TABLE 2

Element X	$S(Ag) - S(X)$, V	Ref.	$S(X)$, V
Si	0.06±0.02	[7]	1.24±0.02
Ge	0.16±0.03		1.14±0.03
Sn	0.14±0.06	[6]	1.16±0.06
Pb	0.25±0.08		1.05±0.08
Sb	0.40±0.07	[6]	0.90±0.07
Bi	0.14±0.06		1.16±0.06
Cu	0.12±0.06	[5]	1.18±0.06

processes affecting the measured values of S become more important. Surface-ionization methods can apparently be used at $S \ngtr 1$ V. In this case the method of a twofold comparison of the currents of positive ions[6] is less sensitive to experimental conditions than is the absolute method or the method in which the functional dependences of the negative-ion currents of two elements are compared.

In conclusion we list in Table 2 the differences S(Ag) − S(X) measured by the twofold comparison method[6] for the atoms of seven elements X (refs. 5-7) and the values of S(X) calculated on the basis of the value of S(Ag) = 1.30 ± 0.01 V from refs. 1, 2, rounded to the nearest hundredth of a volt.

The value S(Cu) = 1.18 ± 0.06 V agrees well with the value S(Cu) = 1.226 ± 0.010 V obtained by the PD method,[1,2] and the value S(Si) = 1.24 ± 0.02 V is approximately equal to the value determined for this quantity by the PD method in ref. 20. The values of S have not yet been determined by the PD method for the other methods in Table 2.

The authors thank N. I. Ionov for discussion.

---

[1] H. Hotop, R. A. Bennett, and W. C. Lineberger, Abstracts of Papers, 25th Annual Gaseous Electronics Converence, October 17-20, 1972. The University of Western Ontario, London, Ontario, Canada.

[2] H. Hotop, R. A. Bennett, and W. C. Lineberger, J. Chem. Phys., 58, 2373 (1973).

[3] H. Hotop and W. C. Lineberger, J. Chem. Phys., 58, 2379 (1973).

[4] I. N. Bakulina and N. I. Ionov, Dokl. Akad. Nauk SSSR, 155, 309 (1964) [Sov. Phys. – Dokl., 9, 217 (1964)].

[5] É. Ya. Zandberg, A. G. Kamenev, and V. I. Paleev, Zh. Tekh. Fiz., 41, 1057 (1971) [Sov. Phys. – Tech. Phys., 16, 832 (1971)].

[6] É. Ya. Zandberg and V. I. Paleev, Dokl. Akad. Nauk SSSR, 190, 562 (1970) [Sov. Phys. – Dokl., 15, 52 (1970)].

[7] É. Ya. Zandberg, A. G. Kamenev, and V. I. Paleev, Zh. Tekh. Fiz., 41, 1983 (1971) [Sov. Phys. – Tech. Phys., 16, 1567 (1972)].

[8] É. Ya. Zandberg and N. I. Ionov, Surface Ionization [in Russian], Izd. Nauka, Moscow (1969).

[9] A. Y. Cho and C. D. Hendricks, J. Appl. Phys., 40, 3339 (1969).

[10] J. B. Taylor and I. Zangmuir, Phys. Rev., 44, 423 (1933).

[11] C. E. Moore, "Atomic Energy Levels," Nat. Bur. Stand. (U. S.) Circ., 467, 1 (1949); 2 (1952); 3 (1958).

[12] É. Ya. Zandberg and V. I. Paleev, Zh. Tekh. Fiz., 34, 2048 (1964) [Sov. Phys. – Tech. Phys., 9, 1575 (1965)].

[13] B. A. Mamyrin and V. I. Paleev, Prib. Tekh. Eksp., No. 2, 200 (1969).

[14] R. St. Berry and C. W. Reimann, J. Chem. Phys., 38, 1540 (1963).

[15] L. Branscomb and J. Smith, J. Chem. Phys., 25, 598 (1956).

[16] B. Steiner, M. Seman, and L. Branscomb, J. Chem. Phys., 37, 1200 (1962).

[17] É. F. Chaikovskii, L. G. Mel'nik, and G. M. Pyatigorskii, Zh. Tekh. Fiz., 40, 225 (1970) [Sov. Phys. – Tech. Phys., 15, 163 (1970)].

[18] É. Ya. Zandberg, Zh. Tekh. Fiz., 25, 1386 (1955).

[19] É. Ya. Zandberg and V. I. Paleev, Zh. Tekh. Fiz., 42, 844 (1972) [Sov. Phys. – Tech. Phys., 17, 665 (1972)].

[20] D. Feldmann, Zs. Naturforsh., 26^a, 1100 (1971).

Effect of ion microfields on emission of an arc cathode

A. M. Dorodnov, V. B. Davydov, A. V. Kozyrev, and Ya. A. Pomelov
N. E. Bauman Moscow Technical College

(Submitted June 19, 1973)
Zh. Tekh. Fiz., 44, 625-631 (March 1974)

A refined model is proposed for the cathode fall on the basis of the individual-zone method. This refinement treats the effect of the microfields of individual ions on the emission characteristics of an arc cathode. Calculations using this model give the additional emission of electrons per individual ion as a function of the parameters of the cathode surface.

In explaining the experimental current densities of arc cathodes and in constructing theoretical models for such cathodes[1,2] it is usually assumed that the emission of electrons from the cathode obeys the Richardson–Schottky law and that the electric field at the cathode surface is given by the McKeown equation. However, study of thermionic tungsten cathodes at low pressures has shown[3,4] that under these conditions the emission is anomalous and does not satisfy the traditional model. A significantly anomalous emission has also been observed from graphite cathodes, even at atmospheric pressure.[5]

One promising approach to improving the classical emission equations in the presence of plasma is to take account of the microfields of individual ions.

In general, the field at the cathode calculated from the Poisson equation through the McKeown equation, E_k, cannot be used in the equations for thermionic, field, and thermionic-field emission, because this procedure only gives the average field: Because of the microfields of ions, the local field at the cathode, E, can differ considerably from E_k. Since the current density j_e in all the emission equations is an exponential function of the field, the contribution of stronger fields turns out to be larger, thereby increasing the emission current. This effect is particularly pronounced when $E \gg E_k$. Accordingly, the averaging must be carried out, not over the field, but over the current, and the nature of the change in the local field at the cathode must be taken into account.

Two basic methods have been proposed to solve this problem.

1. First, there is the statistical approach, first developed by Ecker and Müller.[6]

In this method, the ions in the cathode sheath are assumed to be stochastically independent and Markovian chains are used to calculate the probability density W(E) for the existence of a field E at a given point on the cathode. Then the emission equation is averaged over this probability density:

$$j_e = \int_0^\infty j(E)\, W(E)\, dE. \tag{1}$$

This approach has been applied to the Fowler–Nordheim law for field emission;[6] the result is a significant increase in the emission current (an order of magnitude).

Second, there is the method of individual zones. In this method, some "average" ion is chosen, and the additional charge emitted from the cathode in an individual zone during the transit of the ion through this zone, Q_e, is determined.

The choice of an "average ion" is equivalent to averaging the additional contribution from each ion to the cathode emission, $Q_e(\mathbf{v}, \mathbf{r})$, over the ion distribution function at the cathode surface, $f_i(\mathbf{v}, \mathbf{r})$:

$$\bar{Q}_e = \frac{1}{n_i} \int\limits_{(\mathbf{r})} \int\limits_{(\mathbf{v})} Q_e(\mathbf{v}, \mathbf{r})\, f_i(\mathbf{v}, \mathbf{r})\, d\mathbf{r}\, d\mathbf{v}. \tag{2}$$

In Eq. (2) the integration is carried out over μ space.

By assuming a monoenergetic ion flux through the cathode we can evaluate integral (2). In this case the ion distribution function is represented by a δ function, whose normalized form is

$$f_i = n_i \delta(\mathbf{v} - \mathbf{v}_i). \tag{3}$$

Here, $\mathbf{v}_i$ is the average ion velocity and n_i is the ion density.

Then the equation for $\bar{Q}_e$ is

$$\bar{Q}_e = \int\limits_{(\mathbf{r})} \int\limits_{(\mathbf{v})} Q_e(\mathbf{v}, \mathbf{r})\, n_i \delta(\mathbf{v} - \mathbf{v}_i)\, d\mathbf{r}\, d\mathbf{v} = Q(\mathbf{v}_i), \tag{4}$$

and the emission equation (e.g., for the case of a Richardson–Schottky law) becomes

$$j_e = j_{ep} + j_i \frac{Q_e}{e}. \tag{5}$$

The first term in Eq. (5) is given by the Richardson–Schottky emission equation,

$$j_{ep} = A T_k^2 \exp\left(-\frac{e\varphi_k - e\sqrt{eE_k}}{kT_k}\right), \tag{6}$$

and j_i is the ion current density at the cathode.

The method of individual zones was worked out by Kisliuk[7] and Bauer.[8] Kisliuk[7] solved the problem of electron emission due to tunneling, taking account of the effect of the field of an individual ion approaching the cathode. Kisliuk showed that the increase in the emission can become important only when the field near the cathode is strong, $E_k > 3 \cdot 10^7$ V/cm, e.g., in breakdown of a discharge gap.

Bauer reduced the problem to one of determining the lowering of the potential barrier at the metal–plasma interface due to the distortion caused by an ion approaching the cathode; then the additional electron emission is calculated on the basis of the law for thermionic-field emission. The results found show that at cathode temperatures

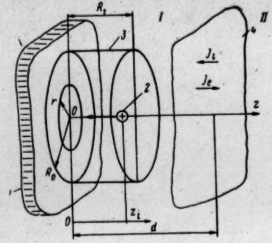

Fig. 1. Model for the individual zone of an ion. I) Collisionless zone; II) ionization zone; 1) cathode; 2) approaching ion; 3) individual zone; 4) boundary of the collisionless zone.

of T_k = 3000-3500°K and at fields near the cathode of $E_k = 0.5 \cdot 10^6 - 5 \cdot 10^7$ V/cm, up to four additional electrons can be emitted per ion approaching the cathode. It should be pointed out, however, that the model proposed by Bauer is imperfect. In analyzing the lowering of the potential barrier Bauer neglects the effect of the right-hand barrier formed by the ion (Fig. 2); it is of fundamental importance to take this effect into account when the ion is close to the cathode because this effect can influence the final results. It is precisely because of this circumstance that the choice of a distance for neutralization of the ion from the cathode surface is of fundamental importance in Bauer's calculations. Several simplifying assumptions introduced in the analyzis of the barrier shape[8] can also affect the calculated results.

In this work we use an improved model for the cathode region to develop the individual-zone method for the case of Richardson–Schottky emission. The following structure of the cathode sheath is proposed for taking account of the effects of the ion microfields on the emission (Fig. 1). Adjacent to the plane and smooth cathode surface is collisionless zone I of thickness d, containing a positive space charge; this zone produces an electric field at the cathode whose average value is E_k and which does not have a radial component. There is a potential drop U_k over the thickness of the collisionless zone. Ions of charge q and mass M formed in the necessary density in the quasineutral ionization zone (II) move toward the cathode; as they approach it, they are neutralized at the neutralization distance R_n. We adopt a cylindrical coordinate system (r, θ, z) with origin at the cathode surface. The z axis is normal to the cathode and passes through the center of the approaching ion, whose instantaneous distance from the surface is z_i.

Using the familiar image method we find the following shape for the barrier at the interface of the metal and the medium for this case:

$$U(z,\ r,\ z_i,\ E_k,\ q) = E_k z + \frac{e}{4z} + \frac{q}{\sqrt{(z_i - z)^2 + r^2}} - \frac{q}{\sqrt{(z_i + z)^2 + r^2}}. \tag{7}$$

In the asymptotic cases $z_i \to \infty$, $r \to \infty$, $z_i \to 0$, this barrier becomes the classical Schottky barrier,

$$U = E_k z + \frac{e}{4z}. \tag{8}$$

Figure 2 shows the shape of the potential barrier for various positions of the ion. We see from Fig. 2 that the lowering of the potential barrier is a function of the position of the ion: When the ion is close to the cathode the left-hand barrier is so low that the right-hand barrier begins to play the decisive role in the emission. In principle, Eq. (7) can be used to find the lowering of the potential barrier, ΔU, as a function of r, z_i, and E_k:

$$\Delta U(r,\ z_i,\ E_k,\ q) = \min_{z \geqslant 0} U(z,\ r,\ z_i,\ E_k,\ q). \tag{9}$$

From this functional dependence we can in turn determine the emission, taking account of the individual field of the ion,

$$j(r,\ z_i,\ E_k,\ q) = A T_k^2 \exp\left(-\frac{e\varphi_k}{kT_k}\right) \exp\left[\frac{e\Delta U(r,\ z_i,\ E_k,\ q)}{kT_k}\right] \tag{10}$$

and we can determine the additional electron current per ion at a fixed ion distance z_i,

$$I_e(z_i,\ E_k,\ q) = 2\pi \int_0^{R_0} [j(r,\ z_i,\ E_k,\ q) - j_{eP}]\, r\,dr. \tag{11}$$

Here, R_0 is the characteristic dimension of the individual zone (Fig. 1). The quantity R_0 is subject to a restriction which follows from the condition for the applicability of the individual-zone method:

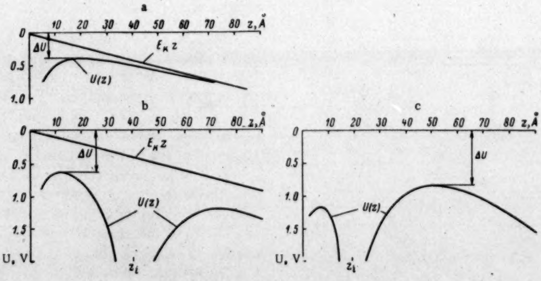

Fig. 2. Potential barriers at the cathode surface for various ion positions. $E_k = 10^6$ V/cm, β = 1, r = 0. a) $z_i \to \infty$ and $z_i = 0$; b) z_i = 40 Å; c) z_i = 19 Å.

$$R_0 \leqslant \min(d,\ \bar{n}_i^{-1/3}) \qquad (12)$$

The thickness of the space-charge zone is determined from the Langmuir–Boguslavskii equation,

$$d = \sqrt{\frac{\left(\frac{2q}{M}\right)^{1/2} U^{3/2}}{9\pi j_i}}, \qquad (13)$$

and the average ion density n_i is determined from the Poisson equation,

$$E_k = 4\pi q \int_0^d n_i dz = 4\pi \bar{n}_i dq. \qquad (14)$$

The electric field at the cathode surface, E_k, is related to the ion current density j_i by the McOwen equation:

$$E_k^2 = 16\pi\left(\frac{M}{2q}\right)^{1/2} U_k^{1/2} j_i. \qquad (15)$$

The relation describing the motion of the ion, $z_i = z_i(t)$, for the motion in the field of space charge near the cathode is, according to ref. 4,

$$z_i = d - \frac{\pi}{3}\frac{2q}{M} j_i t^3. \qquad (16)$$

Substituting this relation into Eq. (11) and integrating $I_e[z_i(t), E_k, q]$ over the time required for the ion to move from R_1 [R_1 must satisfy condition (12)] to R_n, we find that the additional charge emitted per ion within its individual zone is

$$Q_e = 2\pi \int_{t_1}^{t_2} dt \int_0^{R_0} \{j[r,\ z_i(t),\ E_k,\ q] - j_{eP}\} r dr, \qquad (17)$$

where $z_i(t_1) = R_1$ and $z_i(t_2) = R_n$.

We carry out calculations by this procedure in terms of the dimensionless variables

$$u = \frac{U}{\sqrt{eE_k}};\ \xi = \frac{z}{\frac{1}{2}\sqrt{\frac{e}{E_k}}};\ \nu_i = \frac{z_i}{\frac{1}{2}\sqrt{\frac{e}{E_k}}};\ \rho = \frac{r}{\frac{1}{2}\sqrt{\frac{e}{E_k}}};\ \mu = \frac{d}{\frac{1}{2}\sqrt{\frac{e}{E_k}}}, \qquad (18)$$

which we can use to eliminate E_k from (7):

$$u(\xi,\ \rho,\ \nu_i,\ \beta) = \frac{1}{2}\xi + \frac{1}{2\xi} + \frac{2\beta}{\sqrt{(\nu_i - \xi)^2 + \rho^2}} - \frac{2\beta}{\sqrt{(\nu_i + \xi)^2 + \rho^2}}. \qquad (19)$$

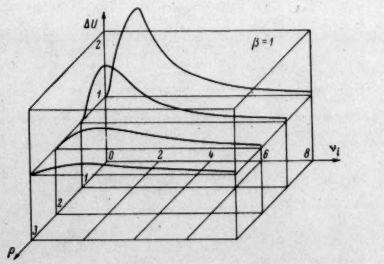

Fig. 3. The functional dependence $\Delta U = \Delta U(\rho,\ \nu_i,\ \beta)|_{\beta=1}$.

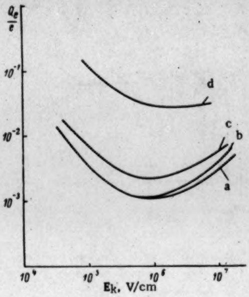

Fig. 4. Electron yield Q_e/e as a function of E_k at T_k = 3000°K. $\beta = 1$. a) $\rho_0 = 10$, $\rho_1 = 10$, $\rho_2 = 0$; b) $\rho_0 = 10$, $\rho_1 = 10$, $\rho_2 = \eta$; c) $\rho_0 = \mu$, $\rho_1 = \mu$, $\rho_2 = 0$, d) $\rho_0 = \mu$, $\rho_1 = \mu$, $\rho_2 = 0$.

Here, $\beta = q/e$. Then numerical methods are used to find the stationary points of the function $u(\xi,\ \rho,\ \nu_i,\ \beta)$ through the use of the condition $\partial u(\xi,\ \rho,\ \nu_i,\ \beta)/(\partial\xi) = 0$; then we find the minima and the value of expression (19) at the minima in the region $\xi > 0$ for fixed values of the parameters β, ρ, and ν_i. The result of this procedure for $\beta = 1$ (singly charged ions) is the function

$$\Delta u|_{\beta=1} \equiv \left.\frac{\Delta U}{\sqrt{eE_k}}\right|_{q=e} = \Delta u(\rho,\ \nu_i,\ \beta)|_{\beta=1}, \qquad (20)$$

shown in Fig. 3. The maximum value of the function $\Delta u(\rho,\ \nu_i,\ \beta)|_{\beta=1}$, equal to 2.39, is reached at $\rho = 0$ and at the value of ν_i corresponding to the ion position at which the left-hand and right-hand barriers are of the same height. Using (15) and (18), we can rewrite integral (17):

$$Q_e = \pi\left(\frac{M}{2\beta}\right)^{1/4}\left(\frac{e}{3}\right)^{3/4}\frac{U_k^{1/4}}{E_k^{11/4}} A T_k^2 \exp\left(-\frac{e\varphi_k}{kT_k}\right)\int_{\rho_2}^{\rho_1}\frac{d\nu_i}{(\mu - \nu_i)^{2/3}}$$
$$\times \int_0^{\rho_0}\left\{\exp\left[\frac{e\sqrt{eE_k}\,\Delta u(\rho,\ \nu_i,\ \beta)}{kT_k}\right] - \exp\left(\frac{e\sqrt{eE_k}}{kT_k}\right)\right\}\rho d\rho, \qquad (21)$$

where

$$\rho_0 = \frac{R_0}{\frac{1}{2}\sqrt{\frac{e}{E_k}}};\ \rho_1 = \frac{R_1}{\frac{1}{2}\sqrt{\frac{e}{E_k}}};\ \rho_2 = \frac{R_n}{\frac{1}{2}\sqrt{\frac{e}{E_k}}} = \eta.$$

Equation (21) was integrated numerically. Figures 4 and 5 show some of the calculated results, for $\beta = 1$, U_k = 5 V, φ_k = 4.5 V, M = 40 · 1.67 · 10^{-27} kg (argon), and for T_k and E_k over the ranges T_k = 2800–3500°K and E_k = 10^4–1.5 · 10^7 V/cm. For comparison, Fig. 5 shows curves plotted from Bauer's results.[8] As mentioned above, the lowering of the potential barrier Δu tends toward the classical Schottky correction (Δu → 1) as $\nu_i \to 0$. Comparison with the analogous case of Bauer ($\nu_i \to 0$, Δu → ∞) shows that the singularity at Δu as $\nu_i \to 0$ makes the result of the evaluation of integral (21) strongly dependent on the method used to truncate it. In ref. 8 the integral is truncated at the ion-neutralization distance R_n = 8.5 Å, so even a slight error in the choice of R_n (there is no reliable experimental information on R_n) can lead to a significant distortion

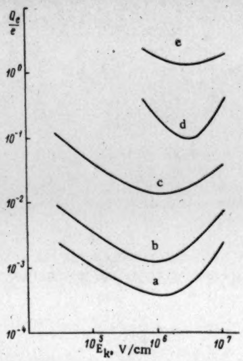

Fig. 5. Electron yield Q_e/e as a function of E_k for $\rho_0 = 10$, $\rho_1 = 10$, and $\rho_2 = 0$. T_k, °K: a) 2800; b) 3000; c) 3500. Curves d and e are plotted from Bauer's results[8] for 3000 and 3500°K, respectively, $\beta = 1$.

of the final results (curves d and e in Fig. 5). The elimination of the singularity in the lowering of the potential barrier Δu as $\nu_l \to 0$ in our model means that the calculated results are only weakly dependent on this neutralization distance. Accordingly, the integration to $\rho_2 = 0$ ($R_n = 0$) does not significantly affect the value of Q_e (curves a and b in Fig. 4). We note that this circumstance is not the consequence of any additional assumption, but the result of taking account of the effect of the right-hand barrier.

Variation of the radial dimension of the individual zone, ρ_0, has little effect on Q_e (curve c in Fig. 4), while variation of the axial dimension ρ_1 has a stronger effect (curve d in Fig. 4).

Using these results we can easily find an upper estimate on the electron yield Q_e/e per ion for the case in which multiply charged ions move toward the cathode. Using (19) and (21), we find

$$\Delta u(\rho, \nu_l, \beta) \leqslant \beta \Delta u(\rho, \nu_l, \beta)|_{\beta=1}, \tag{22}$$

$$\frac{Q_e}{e} \leqslant \frac{\beta^{10/3}}{e}[Q_e(E_{\text{eff}})|_{\beta=1} + j_{eP}(E_{\text{eff}})\pi R_0^2 \Delta t|_{q=e}] - j_{eP}(E_k)\pi R_0^2 \Delta t. \tag{23}$$

Here, $E_{\text{eff}} = \beta^2 E_k$, $\Delta t = t_2 - t_1$, and $\Delta t|_{q=e} = t_2|_{q=e} - t_1|_{q=e}$. The quantity $Q_e(E_{\text{eff}})_{\beta=1}$ is the value of expression (21) evaluated at $\beta = 1$ and E_{eff}, $j_{eP}(E_{\text{eff}})$, and $j_{eP}(E_k)$ are the values of expression (6) calculated for fields of E_{eff} and E_k, respectively, at the cathode.

The electron yield Q_e/e is a function of the motion of the ion in the individual zone. In the same manner we can find an upper estimate for all possible trajectories of singly charged ions:

$$\frac{Q_e}{e} < \frac{\pi R_0^2}{e} \Delta t [j_{eP}(E'_{\text{eff}}) - j_{eP}(E_k)], \tag{24}$$

where $E'_{\text{eff}} = 5.7E_k$, and the quantities $j_{eP}(E'_{\text{eff}})$ and $j_{eP}(E_k)$ are calculated as in the previous case.

We see from (23) and (24) that in order to explain the anomalous emission by the individual-zone method we must take account of effects which increase the time the ion spends in the individual zone (e.g., charge exchange, reflection of ions, etc.).

---

[1] W. Neumann, Beitr. Plasmaphys., 9, 499 (1969).

[2] B. A. Moizhes and V. A. Nemchinskii, Zh. Tekh. Fiz., 42, 1001 (1972) [Sov. Phys. – Tech. Phys., 17, 793 (1972)].

[3] A. M. Dorodnov, N. P. Kozlov, and Ya. A. Pomelov, Teplofiz. Vys. Temp., 9, 483 (1971).

[4] A. M. Dorodnov, in: Plasma Accelerators [in Russian], Izd. Mashinostroenie, Moscow (1973).

[5] Y. Murooka and K. R. Hearne, J. Appl. Phys., 43, 2656 (1972).

[6] G. Ecker and K. G. Müller, Z. Naturforsch., 14, 511 (1959).

[7] P. P. Kisliuk, J. Appl. Phys., 30, 51 (1959).

[8] A. Bauer, Beitr. Plasmaphys., 6, 281 (1966).

Simulation of ion scattering on diatomic molecules

M. L. Aleksandrov, N. S. Pliss, and A. P. Shcherbakov

Special Construction Bureau for Analytic Instrument Construction,
Academy of Sciences of the USSR, Leningrad

(Submitted April 26, 1973; resubmitted July 27, 1973
Zh. Tekh. Fiz., 44, 632-634 (March 1974)

A method is proposed for calculating the classical deflection function $\Theta(b)$, averaged over all molecular orientations, for the scattering of ions or atoms by diatomic molecules in the kiloelectron-volt range; a modified Firsov potential is used for the interatomic interaction. Analytic expressions approximating Ar^+-N_2 and U^+-N_2 are constructed for the Θ (b) pairs. The calculated functional dependence is recommended for use in statistical simulation of the scattering of ions by diatomic residual gas molecules in mass spectrometers.

INTRODUCTION

The method of statistical simulation is a versatile analytic tool for studying the scattering of ions by residual gas molecules in a mass spectrometer and is used in instrument design.[1] An important element in the method is simulation of the initial conditions for the ion motion after the scattering; it is convenient to use for this purpose the functional dependence $\Theta = \Theta(b)$, i.e., that of the center-of-mass scattering angle on the impact parameter b, which is assumed to be a random quantity with a distribution density

$$p(b)=\begin{cases} cb, & b\in(b_1, b_2),\\ 0, & b\overline{\in}(b_1, b_2),\end{cases}$$

where c is a normalization constant, and b_1 and b_2 are governed by the range of Θ which is most important in studying scattering in mass spectrometers: $0.017 < \Theta < 0.350$ rad.

We report here an attempt to determine the Θ(b) functional dependence for the scattering of ions by diatomic molecules over the energy range 4-16 keV. Classical mechanics can be used for these energies and angles. The effect of inelastic energy loss on the angular distribution of scattered particles is neglected because it is small in comparison with the ion energy.

CALCULATION OF THE ANGLE THROUGH WHICH IONS ARE SCATTERED BY DIATOMIC MOLECULES

Scattering of ions in this energy range is governed by short-range repulsive forces. Following ref. 2, to describe this interaction we can use a modified Firsov potential, written in the atomic system of units (in which we have $\hbar = m_e = e^2 = 1$):

$$V(r)=\frac{Z_1Z_2}{r}\chi(r), \tag{1}$$

where Z_1 and Z_2 are the charges of the atomic nuclei, and

$$\chi(r)=\left[a\exp\left(-\frac{\alpha}{A}r\right)+b\exp\left(-\frac{\beta}{A}r\right)\right]^2$$

is the shielding function, where $a = 0.7111$, $b = 0.2889$, $\alpha = 0.1750$, $\beta = 1.6625$, and $A = 0.8853/(Z_1^{1/2} + Z_2^{1/2})^{2/3}$.

A feature of the scattering of ions by residual gas molecules like N_2 and O_2 is the anisotropy of their interaction with the diatomic molecules. To describe this interaction we use a two-center representation of the potential, i.e., we write the potential for the interaction with a molecule of species AB as

$$\tilde{V}(r)=V(r_{AC})+V(r_{BC}),$$

where r is the distance between the ion of species C and the center of gravity of the AB molecule, r_{AC} and r_{BC} are the interatomic distances, and V(r) is the potential given by Eq. (1).

In small-angle scattering of particles by a spherically symmetric potential the function Θ(b) is described approximately by[3]

$$\Theta(b)=\frac{\Delta p}{p}=-\frac{b}{E}\int_b^\infty\frac{dV}{dr}\frac{dr}{\sqrt{r^2-b^2}}=-\frac{b}{E}P(b), \tag{2}$$

where E is the energy of the relative motion, Δp is the transverse momentum, and p is the momentum of the particle after the scattering.

For the two-center potential $\tilde{V}(r)$ and for scattering through small angles we assume, in accordance with ref. 4, that the momentum Δp, which governs the deflection angle of the particle, is equal to the sum of the momenta obtained in the interaction of the ion with each atom of the molecule on an essentially rectilinear trajectory. Since the relative velocity of the colliding particles is high we can assume that the molecular orientation remains the same throughout the collision. This orientation is specified by the direction of the axis of the diatomic molecule by means of the polar angle ψ (the polar axis is chosen to be the direction along the relative velocity) and by the azimuthal angle φ.

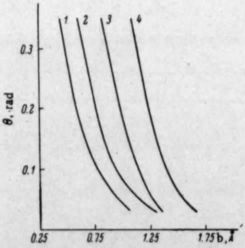

Fig. 1. The functions Θ (b). 1) Ar^+-Si, 12 keV (ref. 2); 2) Ar^+-N_2, 12 keV; 3) U^+-Si, 16 keV (ref. 2); 4) U^+-N_2, 16 keV.

Then using Eq. (7) from ref. 4, we find the following expression for Θ for a fixed orientation of the molecule:

$$\Theta(b, \Psi, \varphi) = \frac{1}{E}[b_1^2 P^2(b_1) + b_2^2 P^2(b_2)$$

$$+ 2(b^2 - r_0^2 \sin^2\Psi) P(b_1) P(b_2)]^{1/2} = \frac{\Phi(b, \Psi, \varphi)}{E}.$$

Here, $b_i^2 = b^2 + 2(-1)^i b r_0 \sin\Psi \sin\varphi + r_0^2 \sin^2\Psi$ $(i = 1, 2)$, $2r_0$ is the internuclear distance in the molecule, b is the impact parameter, measured from the center of gravity of the molecule, and $P(b_i)$ is found from the integral in (2), where potential (1) is used as V(r).

Assuming the distribution of the unit vector which specifies the orientation of the molecule to be homogeneous over a sphere of unit radius, we can find the scattering angle averaged over all possible molecular orientations:

$$\Theta(b) = \frac{1}{4\pi E} \int_0^\pi \sin\Psi d\Psi \int_0^{2\pi} \Phi(b, \Psi, \varphi)\, d\varphi. \quad (3)$$

Since the potential used here is universal, Eq. (3) can be used for a computer calculation of the classical deflection function Θ(b) for any system of a monatomic ion and diatomic molecule or atom and diatomic molecule for various energies E.

EXAMPLE

As an example we calculate the functions Θ(b) for the Ar^+-N_2 pair (curve 2 in Fig. 1, for an ion energy of 12 keV) and the U^+-N_2 pair (curve 4, for an ion energy of 16 keV) for Θ in the range from 0.017 to 0.350 rad. Shown for comparison in this figure are the deflection functions obtained on the basis of the calculations of Nikulin[2] for a single-center modified Firsov potential for the same ions (curve 1 for Ar^+ and curve 3 for U^+). These curves are plotted for the same energies, but the target is an Si atom, which has the same mass as the N_2 molecule, and the nuclear charge of this atom is equal to the total charge of the nitrogen nucleus.

We see from this figure that account of the two centers leads to stronger scatter at a given impact parameter and thus to an increase in the total scattering cross section.

It should be noted that this method for calculating the scattering of ions by diatomic molecules can also be used for scattering involving a single-center potential; for this purpose the internuclear distance $2r_0$ should be set equal to zero. The results found in this case agree within 8% with the results of ref. 2; the discrepancy is maximal for large angles, due to the approximate nature of Eq. (2), but it essentially vanishes at small angles.

To simulate the initial conditions for the motion of the ion after the scattering it is necessary to know the analytic function Θ(b), which makes it possible to calculate the scattering angle for any random value of b. Using an expansion in terms of Laguerre functions to approximate these curves, and restricting the expansion to the second order, we find the following analytic expressions:

$$\Theta = \frac{1}{E} e^{-4.3b}(102.2 - 38.7b + 11.7b^2)$$

for the Ur^+-N_2;

$$\Theta = \frac{1}{E} e^{-3.2b}(20.1 - 15.1b + 5.3b^2)$$

for the Ar^+-N_2.

In these equations the impact parameter b is given in angstroms, the energy of the relative motion, E, is given in kiloelectron volts, and the angle Θ is given in radians. The error of this approximation does not exceed 3%.

CONCLUSIONS

A method has been proposed for a computer calculation of the classical deflection function Θ(b) in the kiloelectron-volt energy range for any pair consisting of a monatomic ion and diatomic molecule or atom and diatomic molecule.

The analytic approximations obtained for the function Θ(b) for certain pairs are convenient for simulating scattering of ions by residual gas molecules in mass spectrometers over the entire energy range considered.

---

[1] Abstracts of Reports, Fifth All-Union Conference on the Physics of Electronic and Atomic Collisions, Uzhgorod (1972), p. 223.

[2] V. K. Nikulin, Zh. Tekh. Fiz., 41, 33 (1971) [Sov. Phys. – Tech. Phys., 16, 21 (1971)].

[3] L. D. Landau and E. M. Lifshitz, Mechanics, Addison-Wesley, Reading, Mass. (1960).

[4] V. B. Leonas, Usp. Fiz. Nauk, 107, 29 (1972) [Sov. Phys. – Usp., 15, 266 (1972)].

Rate for evaporation of a liquid into vacuum

A. P. Andreev and M. A. Gurevich
M. I. Kalinin Leningrad Polytechnical Institute

(Submitted March 28, 1973; resubmitted June 28, 1973)
Zh. Tekh. Fiz., 44, 635-643 (March 1974)

A method is described for determining the evaporation coefficient of a liquid, and experimental results are reported. Photography and a thermocouple technique are used to measure the diameter and temperature, respectively, of drops of methanol, ethanol, and n-propanol evaporated into vacuum. A residual gas pressure of about $5 \cdot 10^{-3}$ torr is maintained in the chamber by condensing the vapor on the walls of the vessel by means of liquid nitrogen. Heat is supplied to the drop by radiation. In each experiment the temperature and rate of decrease in the diameter of a drop remain approximately constant (the drop diameter changes from 2 to 1 mm). The temperature ranges studied are from −96 to −56°C for methanol, from −86 to −36°C for ethanol, and from −65 to −13°C for n-propanol. The evaporation coefficient is calculated from the measured temperature and evaporation rate by means of the Knudsen–Hertz–Langmuir equation. At the lowest temperatures the evaporation coefficients for the alcohols, α, are found to be about an order of magnitude higher than the values given in the literature for higher temperatures. The evaporation rate increases with increasing temperature for all three alcohols, but the evaporation coefficient decreases. Over these temperature ranges the evaporation coefficients decrease from 0.4 to 0.2 for methanol, from 0.6 to 0.15 for ethanol, and from 0.5 to 0.1 for n-propanol. Empirical equations are found for the temperature dependence of the evaporation coefficient for these alcohols:

$$\alpha = A \exp\left[-\frac{(T-T_{\mathrm{me}})^3}{C}\right] + B.$$

Here, T_{me} is the melting point of the corresponding alcohol, and A, B, and C are constants for each alcohol. This equation describes the results found in the present work as well as experimental data reported elsewhere.

INTRODUCTION

To the best of our knowledge, there is no generally accepted method for calculating the evaporation coefficient of a liquid as a function of the temperature, and the experimental data available for most substances cover only a narrow temperature range.[1,2] Our purpose here is to measure the evaporation coefficients of three alcohols at comparatively low temperatures and to use the results, along with data in the literature, to draw conclusions about the functional dependence of the evaporation coefficient on temperature.

The evaporation rate is usually calculated from the Knudsen–Hertz–Langmuir equation

$$i = \frac{\alpha v_{\mathrm{av}}}{4}(c_s - c_0) \tag{1}$$

or if the vapor can be treated as an ideal gas, from

$$i = \alpha \sqrt{\frac{M}{2\pi R T_s}}(P_s - P_0). \tag{2}$$

Here, i is the mass flux of vapor from a unit area of the evaporation surface, α is the evaporation coefficient, v_{av} is the average thermal velocity of the vapor molecules, c_s and P_s are respectively the density and pressure of the saturated vapor at the surface temperature, c_0 and P_0 are the density and pressure of the vapor at a distance on the order of a mean free path from the evaporation surface, T_s is the absolute temperature of the evaporation surface, M is the molecular weight of the substance, and R is the universal gas constant.

These equations are best thought of as defining the concept of the "evaporation coefficient."

As a rule, the evaporation coefficient of the liquid is determined by measuring the evaporation rate, the temperature of the evaporation surface, and the vapor pressure near it. Either this vapor is held constant by continuous evacuation of the working chamber or its gradual increase is taken into account; here the equation for α incorporates the difference between two pressures, P_s and P_0, which are approximately equal. The measured values of P_0 are generally somewhat uncertain, especially when low pressures ($1 \cdot 10^{-3}$–$5 \cdot 10^{-1}$ torr) must be measured. Reliable measurements of P_0 are not required if $P_0 \ll P_s$,

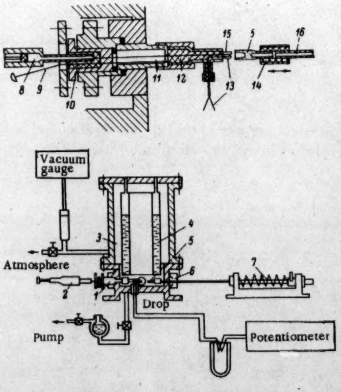

Fig. 1. The experimental apparatus. 1) Inlet device; 2) syringe; 3) chamber; 4) liquid-nitrogen vessel; 5) glass cap; 6) Wilson seal; 7) release; 8) syringe reservoir; 9) pin; 10) plug; 11) intermediate chamber; 12) Teflon bushing; 13) thermocouple; 14) Teflon coupling; 15) glass arm; 16) shaft.

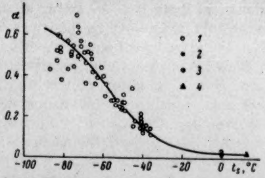

Fig. 3. Evaporation coefficient of ethanol as a function of the temperature. 1) This work; 2) ref. 9; 3) ref. 11; 4) ref. 10.

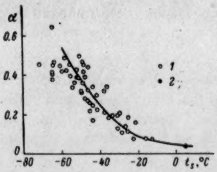

Fig. 4. Evaporation coefficient of n-propanol as a function of the temperature. 1) This work; 2) ref. 9.

Over a time not exceeding 10% of the total evaporation time, the drop cools to a certain temperature governed by the illumination and the properties of the liquid; for the rest of the time (until the drop diameter falls to almost half its initial value), its temperature varies only slightly, by 2-3°C. This change in surface temperature can lead to a change of 15-25% in the evaporation rate of these alcohols, according to Eq. (2). Within approximately the same error the functional dependence of the drop diameter on the time is linear.

The decrease in the diameter of a spherical drop is related to the mass flux from a unit area of the surface, i, by

$$i=\frac{1}{\pi\delta^2}\frac{dm}{d\tau}=\frac{1}{2}\rho_s\frac{d\delta}{d\tau}. \qquad (5)$$

Here, m is the mass of the drop, δ is its diameter, ρ_s is the liquid density, and τ is the time.

From the $T_s \equiv T_s(\tau)$ curves we distinguish a region over which the temperature does not change by more than 2-3°C; averaging over this region, we assign it the value of $\Delta\delta/(\Delta\tau) \approx \overline{[d\delta/(d\tau)]}$ obtained for the same time interval.

The evaporation coefficient is calculated from an equation found by substituting Eq. (5) into Eq. (2):

$$\alpha=\frac{\rho_s\frac{d\delta}{d\tau}}{2\sqrt{\frac{M}{2\pi RT_s}}P_s\left(1-\frac{P_0}{P_s}\right)}. \qquad (6)$$

In our case $P_0 \ll P_s$.

The liquid density ρ_s and the saturation vapor pressure P_s are taken from refs. 3-5. Where information is not available on the working temperatures we determine the density by a linear extrapolation and we determine P_s through an extrapolation by the Cox–Antoine method. (The P_s extrapolation is carried out at −67 to −96°C for methanol and from −43 to −65°C for n-propanol; the values of P_s for ethanol are known over the entire temperature range).

The resulting evaporation coefficients are shown in Figs. 2-4, along with the values of α for these alcohols which we have found in the literature.

The results found from measurements of the evaporation rate and calculation of the evaporation coefficient are tabulated at the end of this paper.

CHECK OF THE RELIABILITY OF THE EXPERIMENT

Judging from the reviews in refs. 2, 6, and 8, we conclude that two fundamental errors are the most dangerous in a measurement of the evaporation coefficient. One is a discrepancy between the measured temperature and the surface temperature.

In our experiments much of the heat is supplied to the drop along the leads of the thermocouple, which absorbs radiation from the lamp. It could be argued that the indications of the thermocouple depend on the position of the junction within the drop (on the immersion depth L) and on the heat flux passing through the thermocouple.

We assume that in the experimental functional dependence $d\delta/(d\tau) = F(T)$

$$T=T_s+\Phi\left[\left(\frac{Q}{Q_\Sigma}\right)_1,\ \left(\frac{L}{r}\right)_1\right].$$

Here, r is the drop radius, L/r is the relative immersion depth of the junction of the thermocouple in the drop, and Q/Q_Σ is the relative energy supplied through the thermocouple.

Let us change Q/Q_Σ abruptly. (For this purpose we insert the end of a copper wire 0.35 mm in diameter into the drop; the wire is held at a certain distance from the thermocouple. At the given radiation densities the result would be a severalfold change in the evaporation rate and a simultaneous change in the detector temperature T.) Now we have

$$\frac{d\alpha}{d\tau}=F(T)=F\left\{T_s+\Phi\left[\left(\frac{Q}{Q_\Sigma}\right)_2,\ \left(\frac{L}{r}\right)_1\right]\right\}.$$

It turns out that for any T

$$F\left\{T_s+\Phi\left[\left(\frac{Q}{Q_\Sigma}\right)_1,\ \left(\frac{L}{r}\right)_1\right]\right\}=F\left\{T_s+\Phi\left[\left(\frac{Q}{Q_\Sigma}\right)_2,\ \left(\frac{L}{r}\right)_1\right]\right\}.$$

It should be noted that the equality of evaporation rates necessarily implies the equality of the surface-evaporation temperatures T_s. Hence,

$$\Phi\left[\left(\frac{Q}{Q_\Sigma}\right)_1,\ \left(\frac{L}{r}\right)_1\right]=\Phi\left[\left(\frac{Q}{Q_\Sigma}\right)_2,\ \left(\frac{L}{r}\right)_1\right];$$

i.e., the error in the temperature measurement is not a function of the relative heat flux through the thermocouple.

In an analogous manner we show that the error in the temperature measurement is not a function of the depth to which the junction of the thermocouple is immersed in the liquid. The results are shown in Fig. 5. Since it would but this condition would at first glance seem impossible to satisfy, since superheating by even a few degrees can cause boiling.

However, the condition $P_0 \ll P_s$ can be satisfied for several liquids at a relatively low temperature, and boiling can be prevented if the liquid is evaporated as drops. Let us consider the pressure acting on the surface of a spherical drop in evaporation into vacuum, P_Σ:

$$P_\Sigma = P_e + P_\sigma = P_s\frac{\alpha}{2} + \frac{2\sigma}{r}. \qquad (3)$$

Here, P_e is the "reactive" pressure due to the evaporation (its relationship to P_s is demonstrated, e.g., in ref. 2), P_σ is the Laplace pressure, σ is the surface tension of the liquid, and r is the drop radius.

Boiling will evidently not occur if

$$P_s < P_\Sigma = \frac{2\sigma}{r\left(1 - \frac{\alpha}{2}\right)}. \qquad (4)$$

For example, a drop of ethanol 1 mm in radius must evaporate into vacuum without boiling at $t_s < -40°C$, corresponding to a saturation vapor pressure of $P_s \approx 0.4$ torr.

Condition (4) is of course not a necessary condition; it is also necessary to take account of the size of the vaporization centers. In our experiments we do not observe boiling even at P_s slightly higher than P_Σ.

EXPERIMENTAL APPARATUS AND PROCEDURE

The experimental apparatus is shown in Fig. 1.

Chamber 3, 4.5 liters in volume, is evacuated by a mechanical pump through a liquid-nitrogen trap to a residual pressure no higher than $5 \cdot 10^{-3}$ torr (the pressure is measured by a thermocouple vacuum gauge). Then isolating glass 5 is pressed against the end of inlet device 1.

Liquid drops with an initial diameter of about 2 mm are formed in the volume (0.15 cm^3) isolated by glass cap 5 and the end of Teflon bushing 12. In this volume there is a glass arm 15, mounted on the end of the bushing to which the junction of thermocouple 13 is attached. A syringe needle 2 is inserted through an axial aperture in the bushing, and the piston forces the liquid onto the arm (the end of the arm is 0.5-0.7 mm in diameter).

The rotation axis of plug 10, with two Teflon gaskets, is 2.5 mm away from the axis of bushing 12. Accordingly, by removing the syringe needle from the axial aperture and rotating the plug through 180°, it is possible to insert pin 9 in place of the needle. In this manner, the volume containing the drop is completely isolated.

The cap is linked through Teflon coupling 14 with shaft 16, which transmits the force to advance or withdraw the cap from spring-loaded release 7. After the cap is withdrawn, drops begin to evaporate; a low pressure is maintained in the chamber through the condensation of the liquid vapor on the walls of vessel 4, previously filled with liquid nitrogen. However, there must be no air at atmospheric pressure in the volume isolated by the cap, for this air could increase the pressure of uncondensed gas in the chamber by an order of magnitude. Degradation of the vacuum is avoided by evacuating intermediate chamber 11 through the axial aperture of the bushing after each loading of the syringe. To prevent liquid in syringe reservoir 8 from being withdrawn, the needle of the syringe is inserted into the rear of the bushing. After the evacuation is completed, and the cap is pressed into place, the syringe needle is removed from the bushing, and a small amount of emerging liquid saturates the intermediate chamber; atmospheric air does not penetrate into the chamber because plug 10 isolates it from the atmosphere.

During the evaporation the changes in the drop size are detected by photography in transmitted light. The drop temperature is measured by a Chromel–Alumel thermocouple with a lead diameter of 0.1 mm which is inserted into the drop; the temperature is recorded on an ÉPP-09 potentiometric recorder. The measurements of the drop temperature and size are synchronized by shorting the input to the potentiometer during the recording of each frame; this procedure produces time markers.

The energy required to evacuate the drop is supplied by radiation from the motion-picture projection lamp which is also used for the photography. The radiation density can be altered by varying the current through the lamp; for high radiation densities a short-focus lens is used inside the vacuum chamber. The total range of radiation densities is (0.25-200) $\cdot 10^{-2}$ W/cm^2.

The experimental results are used to construct functional dependences of the diameter of the observed projection of the drop on the time. (During the adjustment of the system the drop is suspended so that its maximum and minimum diameters lie in the observed plane throughout the evaporation.)

EXPERIMENTAL RESULTS

We have studied the evaporation of drops of methanol, ethanol, and n-propanol. We use analytically pure liquids, except that in several cases we use rectified ethanol and incorporate the appropriate correction.

Since the drop is initially at a temperature at which condition (4) does not hold, the cap is not withdrawn abruptly, but in two stages. First, the compression force is reduced, the vapor escapes into the vacuum chamber, and the drop rapidly cools, evaporating. After 1-2 sec, the drop has cooled to a point at which condition (4) is satisfied, and the cap is withdrawn completely.

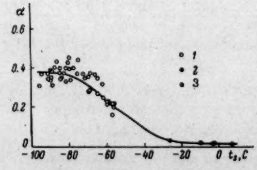

Fig. 2. Evaporation coefficient of methanol as a function of the temperature. 1) This work; 2) refs. 9, 12; 3) ref. 12.

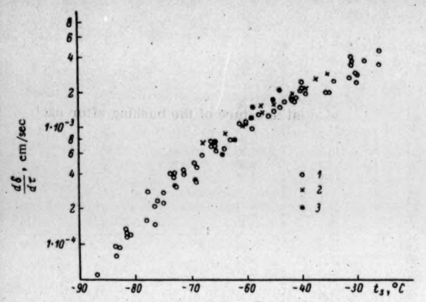

Fig. 5. Diagram used to check for a systematic error in the temperature measurement. Measured rates of change of the diameter of an ethanol drop: 1) basic series of measurements (the junction of the thermocouple is in the upper part of the drop); 2) series in which a copper wire is inserted; 3) series in which the thermocouple junction is in the lower part of the drop.

be difficult to assume that the systematic error in the temperature measurement, Φ, is actually not a function of these factors, we conclude that this error is smaller than the measurement error; thus, the experimental dependence is the dependence on the actual temperature of the drop surface:

$$\frac{d\delta}{d\tau}=F(T_s).$$

Intense mixing apparently prevents any important inhomogeneity of the temperature field in the drop; we have observed on several occasions that dust particles reaching the drop move rapidly.

The second dangerous possibility of error arises because the effect of the diffusive resistance to vapor transport and thus of inverse condensation is frequently neglected. Under quasisteady-state conditions the rate of the phase transition itself is actually equal to the rate at which vapor is withdrawn through a layer of a foreign gas. According to the scheme described by Fuks,[6] molecules are exchanged without hindrance between the surface of the drop and a sphere of radius (r + Δ), while in vacuum (Δ is a length on the order of the mean free path), and far from the drop surface, Fick's law operates.

TABLE 1

	A	*B*	*C*
Methanol	0.36 (1 ± 0.13)	0.017	$1.1\cdot10^5$
Ethanol	0.65 (1 ± 0.12)	0.020	$2.5\cdot10^5$
n-Propanol	0.96 (1 ± 0.21)	0.035	$4.2\cdot10^5$

Since the vapor pressure at the absorbing surface under our experimental conditions is much lower than the saturation vapor pressure in the temperature range studied, we find, in the approximation of spherical symmetry,

$$I=\frac{I_{\text{vac}}}{1+\xi};\;\xi=\frac{v_{\text{av}}\alpha r^2}{4D}\left(\frac{1}{r+\Delta}-\frac{1}{b}\right). \tag{7}$$

Here I is the mass flux of vapor from the drop surface, I_{vac} is the mass flux of vapor into absolute vacuum, b is the radius of the absorption sphere, and D is the diffusion coefficient. Obviously, the measured evaporation rate will be closer to the evaporation rate into vacuum, the lower ξ is in comparison with unity.

In planning the experiments we estimate the values of ξ, calculating the diffusion coefficient and the mean free path (used instead of Δ) from the equations for the hard-sphere model. We assume the evaporation coefficient to be equal to unity, and we neglect 1/b in comparison with 1/(r + Δ) (these simplifications can only lead to values of ξ which are too high). Estimates show that under these experimental conditions ξ < 0.10.

Evidence that the diffusive resistance is negligible comes from the circumstance that the measured evaporation rates of the drop do not exceed 5% of the rates which can be achieved by diffusion under the corresponding conditions. Incidentally, in all these estimates we neglect the Stefan flux from the evaporation surface, which would

TABLE 2. Evaporation Rate and Evaporation Coefficient of Methanol

Temperature $-t_s$, °C	Evaporation rate $(d\delta/d\tau)\cdot10^{-4}$, cm/sec	Evaporation coefficient α	Temperature $-t_s$, °C	Evaporation rate $(d\delta/d\tau)\cdot10^{-4}$, cm/sec	Evaporation coefficient α
96	0.64	0.30	78	7.00	0.40
95	0.90	0.37	76	8.10	0.37
92	1.37	0.37	75	10.1	0.44
91	1.29	0.35	73	10.9	0.37
91	1.40	0.34	72	11.7	0.35
91	1.62	0.39	70	11.3	0.28
90	1.67	0.35	70	13.9	0.36
89	1.80	0.38	69	13.0	0.29
89	1.54	0.31	69	16.9	0.38
88	2.30	0.41	66	21.0	0.37
87	2.69	0.43	65	18.3	0.27
86	2.88	0.38	65	23.6	0.35
85	2.70	0.35	62	28.8	0.32
85	3.35	0.40	62	23.5	0.25
84	3.00	0.35	60	27.3	0.23
83	3.71	0.37	60	25.0	0.21
82	3.50	0.33	59	28.7	0.23
82	4.40	0.40	57	33.6	0.22
81	5.53	0.43	57	24.5	0.16
80	5.50	0.34	57	35.1	0.22
80	6.20	0.46	56	33.4	0.20
80	5.30	0.40			

TABLE 3. Evaporation Rate and Evaporation Coefficient of Ethanol

Temperature $-t_s$, °C	Evaporation rate $(d\delta/d\tau)\cdot 10^{-4}$, cm/sec	Evaporation coefficient α	Temperature $-t_s$, °C	Evaporation rate $(d\delta/d\tau)\cdot 10^{-4}$, cm/sec	Evaporation coefficient α
87	0.53	0.43	64	6.62	0.36
84	0.94	0.53	63	8.00	0.39
83	0.88	0.48	61	11.2	0.44
83	0.93	0.60	60	11.7	0.40
82	1.33	0.60	59	10.0	0.30
82	1.22	0.54	58	13.7	0.36
82	1.15	0.52	56	13.1	0.28
81	1.17	0.38	55	14.6	0.28
78	1.56	0.44	54	15.5	0.26
78	2.00	0.57	53	17.5	0.28
77	2.04	0.51	52	18.0	0.25
77	1.43	0.50	51	18.0	0.24
76	2.31	0.52	51	19.0	0.24
75	2.71	0.55	50	22.5	0.27
75	2.20	0.45	50	26.0	0.31
74	4.00	0.70	50	23.0	0.27
73	3.75	0.62	49	21.0	0.23
73	4.00	0.64	46	31.0	0.34
73	4.00	0.64	45	21.0	0.15
73	3.16	0.50	44	26.8	0.18
73	3.08	0.50	41	28.0	0.15
71	4.32	0.57	41	37.0	0.19
71	4.05	0.55	41	43.0	0.22
69	5.00	0.51	41	40.0	0.20
69	3.45	0.36	40	31.5	0.15
69	4.62	0.46	40	30.0	0.14
68	5.85	0.52	40	26.0	0.12
66	7.60	0.55	39	40.0	0.16
66	7.02	0.51	36	49.0	0.14
66	7.15	0.50	36	37.5	0.11
66	6.32	0.42			

TABLE 4. Evaporation Rate and Evaporation Coefficient of n-Propanol

Temperature $-t_s$, °C	Evaporation rate $(d\delta/d\tau)\cdot 10^{-4}$, cm/sec	Evaporation coefficient α	Temperature $-t_s$, °C	Evaporation rate $(d\delta/d\tau)\cdot 10^{-4}$, cm/sec	Evaporation coefficient α
65	1.30	0.41	48	10.0	0.39
65	1.38	0.42	47	12.8	0.44
65	1.25	0.38	46	9.66	0.33
65	2.18	0.65	46	8.00	0.27
65	1.60	0.45	46	8.55	0.26
64	1.80	0.47	46	7.24	0.22
61	2.40	0.45	44	6.40	0.17
60	2.57	0.42	44	13.1	0.35
59	3.50	0.49	44	9.70	0.25
58	3.50	0.43	42	10.7	0.23
56	4.10	0.40	42	14.3	0.30
56	4.60	0.46	38	23.5	0.32
54	4.00	0.34	38	15.8	0.22
54	4.55	0.38	37	28.6	0.34
54	2.00	0.17	35	17.6	0.19
54	4.80	0.37	34	21.8	0.20
53	5.40	0.39	31	30.0	0.20
52	6.40	0.43	31	20.0	0.13
51	5.41	0.33	30	36.6	0.21
51	8.50	0.50	29	20.7	0.11
50	6.16	0.32	27	30.8	0.14
50	6.40	0.32	26	28.7	0.12
50	9.60	0.47	25	47.7	0.19
49	10.0	0.46	23	23.0	0.074
49	9.25	0.42	21	55.7	0.157
49	8.00	0.37	16	43.4	0.078
48	7.00	0.28	13	55.6	0.076

evidently lead to an underestimate of the rate at which vapor is removed.

To check our estimate of the effects of the diffusive resistance we carry out a series of experiments involving the evaporation of ethanol drops at a much higher pressure of uncondensed gas: $P_g = (1.5\text{–}3.7)\cdot 10^{-1}$ torr. Under these conditions we have $\Delta \approx l \ll r$, and Eq. (7) reduces to

$$I = \frac{I_{\text{vac}}}{1 + \frac{r v_{\text{av}} \alpha}{4D}} = \frac{I_{\text{vac}}}{1 + \frac{v_{\text{av.}} \alpha \, (\overline{rP_g})}{4\,(DP_g)}}. \tag{8}$$

We calculate the value of DP_g from the standard gas-kinetic equation,[7] and we determine the time average of rP_g from experiment. Since the radius r decreases as time elapses, while P_g increases because of inleakage, the product rP_g varies little as a function of the time.

From the values α calculated from the results of the basic series of experiments, we can calculate the value of I_{vac} on the basis of the observed rate I. The satisfactory agreement (within the experimental error) of the results calculated from Eq. (8) with the experimental results carried out in the kinetic region verifies that this equation can be used to calculate the evaporation rate under conditions representing a transition stage between the kinetic and diffusive regimes. Unfortunately, we were not able to compare the equations given in ref. 6, since they all reduce to form (8) under our experimental conditions.

GENERALIZATION OF THE EXPERIMENTAL RESULTS

We have selected empirical equations which satisfactorily describe (see Figs. 2-4) the evaporation rate as a function of the temperature T_s for the three alcohols:

$$\alpha = A \exp\left[-\frac{(T_s - T_{me})^3}{C}\right] + B. \qquad (9)$$

Here T_{me} is the melting point of the alcohol. The values of A, B, and C (constant for each alcohol) are shown in Table 1. The confidence interval is calculated for a confidence level of 0.68.

This equation describes our results and the other experimental results available in the literature.

The functional dependence of the evaporation coefficient on the temperature described by Tables 2-4 does not agree with theoretical predictions with which we are familiar.[1,8] Apparently, the nature of the functional dependence of the evaporation coefficient on the temperature can be explained on the basis of associations of molecules in both in the liquid and vapor.

The authors thank graduate students V. K. Popov, V. E. Loshkarev, and B. I. Izrailev for participation in various stages of this work.

---

[1] R. F. Strickland-Constable, Kinetics and Mechanism of Crystallization, Academic Press, New York (1968).

[2] P. Paul, J. ARS, 32, 1321 (1962).

[3] J. Timmermans, Physico-chemical constants of pure organic compounds, Amsterdam (1950).

[4] C. von Drucker, E. Jimeno and W. Kangro, Zs. Physik. Chem., 90, 513 (1915).

[5] International Critical Tables, Vol. 3, McGraw-Hill, New York (1928).

[6] N. A. Fuks, Evaporation and Growth of Drops in a Gaseous Medium [in Russian], Izd. Akad. Nauk SSSR, Moscow (1958).

[7] R. C. Reid and T. K. Sherwood, The Properties of Gases and Liquids, McGraw-Hill, New York (1966).

[8] O. Knacke and I. N. Stranski, "The mechanism of evaporation," in: Progress in Metal Physics, Vol. 6, B. Chalmers and R. King (eds.), Pergamon Press, New York (1956), p. 181.

[9] M. Baranaev, Zh. Fiz. Khim., 13, 1635 (1939).

[10] H. Bucka, Zs. Physik. Chem., 195, 260 (1950).

[11] L. von Bongdandy, H. C. Kleist, and O. Knacke, Zs. Electrochem., 59, 460 (1955).

[12] L. I. Delaney, R. W. Houston, and L. C. Eagleton, Chem. Eng. Sci., 19, 105 (1964).

Multiple reflection of light in a shock tube

V. D. Mironov and V. I. Selyakov
Moscow Engineering-Physics Institute

(Submitted March 21, 1973; resubmitted August 6, 1973)
Zh. Tekh. Fiz., 44, 644-648 (March 1974)

A method is proposed for distinguishing the emission from a hot gas from multiply reflected light in a shock tube; the method is based on the measurement of the intensity of the multiply reflected light before the shock wave arrives in the field of view of the detector.

The emission method is one of the most versatile and widespread diagnostic tools for shock-tube experiments. When this method is used in the visible or IR regions the experimenter is confronted with a peculiar phenomenon: Before the incident shock wave arrives in the field of view of the detector the detector records a monotonically increasing emission signal whose level can be a significant fraction of the total intensity. This effect has been attributed to multiple reflection of light at the walls of the shock tube.[1-3] When the shock tube passes through the field of vision of the optical system the sum of the direct emission (the useful signal) and the multiply reflected light is recorded. This multiple reflection not only interferes with measurements of absolute emission intensities, but also distorts the functional dependence of the emission intensity on the time and thus ultimately leads to errors in the measurement of relaxation times.[1] Instrumental methods for eliminating multiple reflection have not always been successful, especially in shock tubes with narrow cross section.

In principle, it is possible to calculate the contribution of multiple reflection to the measured intensity. This calculation requires knowledge of the reflection characteristic of the walls of the shock tube as well as the magnitude of the reflection coefficient. These properties are strongly influenced by the magnitude and shape of the microscopic surface irregularities, the material, the method used to deposit the protective coating, etc. The use of standard samples to determine the reflection properties can thus lead to large errors; on the other hand, it is generally impossible to measure the reflection properties of the experimental apparatus under operating conditions.

We note, however, that the multiply reflected light observed before the arrival of the shock waves carries information about the reflection of light at the walls of the shock tube, so it may be possible to determine the multiple-reflection contribution to the detected emission of the gas volume behind the shock front (ordinarily called the "piston") by measuring the intensity of the multiply reflected light before the arrival of the shock wave. This method is based on the assumption of similarity in the distribution of the emission intensity with respect to the cross sections of the piston. In particular, for tubes having a circular cross section the intensity of the emission of a unit volume can be written as $I(\xi, r) = I(\xi)\varphi(r)$, where ξ is the coordinate along the tube axis; the origin of this coordinate is at the shock front, and the coordinate is measured opposite the flow. Also, $\varphi(r)$ is the radial distribution, which is not a function of ξ. We also assume that the conditions governing the light reflection are constant along the tube channel.

We denote by $i^{\omega}(x)$ the intensity of multiply reflected light detected before the arrival of the shock wave; here x is the position of the shock front with respect to the optical axis of the detector (Fig. 1). As the piston passes into the field of view of the optical device a total intensity $J(\xi)$ is recorded; this intensity consists of the actual (desired) intensity $J^{act}(\xi)$ and the intensity of multiply reflected light, which we denote in this case by $i^e(\xi)$. The time coordinate of the oscillogram is converted to the linear coordinate used here through the use of the known velocity of the shock wave, $x = U_s t$. Times before the arrival of the shock wave are assigned negative values.

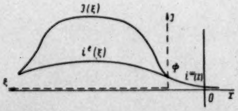

Fig. 1. Intensity of emission from the piston and that of multiply reflected light in the fixed (laboratory) coordinate system (x, J) and in the moving coordinate system (ξ, J) fixed at the shock front Φ. The motion is from left to right. The optical axis of the detector is at x = 0.

CASE OF A PISTON WHICH IS HOMOGENEOUS WITH RESPECT TO ITS LENGTH

Let us consider the case in which $J(\xi) = \text{const}$. Assume that a piston of length l is arranged as shown in Fig. 2. The contribution to the multiple reflection of light (detected by the detector along with the direct emission) from the part of the piston to the left of the axis is assumed to be the multiple reflection of light from the entire piston at $x = 0$, minus the contribution of the rear of the piston $\xi > x_0$. This latter contribution is in turn assumed to be given by the negative value of the multiple reflection of light, again of the entire piston at $x = x_0 - l$, etc. The contribution of the right-hand side of the piston is taken into account similarly. As a result we find

$$i^e(\xi)|_{\xi=x_0} = 2\sum_{n=0}^{\infty} i^{\omega}(-nl) - \sum_{n=0}^{\infty} i^{\omega}(x_0-(n+1)l) - \sum_{n=0}^{\infty} i^{\omega}(-x_0-nl). \tag{1}$$

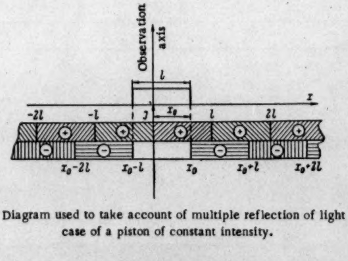

Fig. 2. Diagram used to take account of multiple reflection of light in the case of a piston of constant intensity.

In writing the last term in Eq. (1) we have taken account of the symmetry of the reflection properties of the channel walls with respect to the optical axis.

Using Eq. (1) and the measured intensity of the "early" emission i^{ω} as a function of the distance of the shock front from the optical axis, x, we calculate the intensity of the multiple reflection of light for any position of the piston with respect to the detector. Since i^{ω} falls off quite rapidly with increasing x, it is sufficient to retain only the first few terms in the summation in Eq. (1).

PISTON WHICH IS INHOMOGENEOUS WITH RESPECT TO ITS LENGTH

Since the magnitude of the multiple reflection of light is a linear function of the actual emission intensity of the piston, in analyzing multiple reflection in the channel of the shock tube we can introduce the transfer coefficient k(x), defined as the ratio of the detected intensity of multiple reflection of light of an infinitesimally thin layer, whose position with respect to the optical axis is given by the coordinate x, to the actual emission intensity of this layer:

$$k(x)=\lim_{\Delta\xi\to 0}\frac{i^{\omega}(x)}{J_{\text{act}}(x)\,\Delta\xi(x)}. \tag{2}$$

This transfer coefficient automatically takes account of the geometric conditions of detection; for a given experimental apparatus the geometry is a function of x alone, so that no additional information is required about the nature of the reflection or the magnitude of the reflection coefficient. The transfer coefficient has the symmetry property

$$k(x)=k(-x).$$

Using the transfer coefficient we can describe multiple reflection by the following equations: For the case in which the piston has not reached the observation zone, and the coordinate of the optical axis in the moving system is x < 0,

$$i^{\omega}(x)=\int_0^l k(x-\xi)\{J(\xi)-i^e(\xi)\}\,d\xi \tag{3}$$

for the case in which the piston is at the optical axis, $l \geq x \geq 0$,

$$i^e(x)=\int_0^l k(x-\xi)\{J(\xi)-i^e(\xi)\}\,d\xi, \tag{4}$$

where $J = J^{\text{act}} + i^e$ is the detected intensity.

Equations (3) and (4) constitute a system of Fredholm equations of the first and second kinds with unknown functions i^e and k. Since the kernels and the free terms are bounded and continuous, we can use the trapezoidal equation to replace integral equations (3) and (4) by the system of algebraic equations

$$i^{\omega}(x_p)=\sum_{q=1}^{N}k(x_p-x_q)\{J(x_q)-i^e(x_q)\}\,\Delta x, \tag{5}$$

$$i^e(x_r)=\sum_{q=1}^{N}k(x_r-x_q)\{J(x_q)-i^e(x_q)\}\,\Delta x, \tag{6}$$

where $\Delta x = l/N$; p = 1, 2, ..., ∞; r, q = 1, 2, ..., N; $x_p < 0$; and x_q, $x_r > 0$. We also assume that the transfer coefficient is essentially constant over the piston length l at a certain distance L. In this case we can write the intensity of the multiple reflection of light as

$$i^{\omega}(-L)=k(-L)\int_0^l \{J(\xi)-i^e(\xi)\}\,d\xi.$$

We can use this assumption to limit the number of equations in (5).

We solve system (5), (6) by the method of successive approximations, specifying a trial function $i_0^e(x)$. When values of the trial function $i_0^e(x)$ at the points $x = x_q$ are substituted in, Eq. (5) converts into a system of linear equations in the transfer coefficients. The determinant of this system is diagonal and nonvanishing. Solving system (5) we find the first approximation for the values of transfer coefficient $k_1(x)$. Then we substitute the values found for $k_1(x)$ into system (6) and find the first approximation for the intensity of the multiply reflected light within the piston, i_1^e. We again substitute this value into system (5), find the next approximation for the values of the transfer coefficient, etc.

It can be shown that the values found for $k_s(x)$ and $i_s^e(x)$ by the method of successive approximations reduce to certain limiting functions $\bar{k}(x)$ and $\bar{i^e}(x)$ which are the solutions of system (5), (6) if

$$\frac{J_{\max}^{\text{act}}\Delta x}{J_{\min}^{\text{act}}\Delta x}\,\frac{\sum_q k_q\Delta x}{1-\sum_q k_q\Delta x}<1, \tag{7}$$

where $J_{\max}^{\text{act}}$ and $J_{\min}^{\text{act}}$ are the maximum and minimum values of the actual intensity of the piston emission found from the trapezoid equation in writing system (5)-(6).

We note that, when criterion (7) holds, the solution of (5), (6) is unique and is a continuous function of the initial conditions.

As a rule, the value of $J_{\max}^{\text{act}}\Delta x$ is relatively independent of the choice of partition, while $J_{\min}^{\text{act}}\Delta x$ is strongly dependent on this choice. Accordingly, the partition must be quite coarse in order for criterion (7) to hold. Estimates of the error involved in replacing the system of integral equations by the system of algebraic equations[4,5] show that for partitions satisfying criterion (7) the error associated with this replacement remains completely satisfactory. Accordingly, the error involved in separating the measured radiation intensity into the actual intensity and the intensity of multiply reflected light is governed primarily by the errors in the measurement of $J_{\text{act}}^{\min}$.

Using Eqs. (5) and (6) we can show that the errors are related by

$$\max|\Delta i^e|<\frac{J_{\text{act}}^{\max}\Delta x}{J_{\text{act}}^{\min}\Delta x}\left\{1-\left(1+\frac{J_{\max}^{\text{act}}\Delta x}{J_{\min}^{\text{act}}\Delta x}\right)\sum_q k_q\Delta x\right\}^{-1}\max|\Delta i^{\omega}|. \tag{8}$$

Inequality (8) gives a mathematically rigorous estimate of the maximum possible error in the determination of i^e. When we take into account the actual relationship between the intensity of multiply reflected light and the transfer coefficients, we can show

$$|\Delta i^{e}| \sim \frac{J_{\max}^{\text{act}}\Delta x}{J_{\min}^{\text{act}}\Delta x}|\Delta i^{\omega}|. \tag{9}$$

Using these estimates, we can determine the error involved in distinguishing the actual intensity from the measured intensity, provided that we know the experimental error in the intensity of multiply reflected light measured before the arrival of the shock wave. In the case of relative measurements, there are basically two factors which contribute to the error in the determination of i^{ω}: noise in the light detector and the error in the recording. When there is a good signal-to-noise ratio, the error in the determination of i^{ω} can be greatly reduced by separately recording the intensity of the multiply reflected light before the arrival of the shock wave, using an amplification providing the largest possible reflection of the indicating device.

We have used this method to determine the contribution of multiple reflection of light to the emission in a study of the vibrational relaxation of carbon monoxide heated in an incident shock wave. Concrete calculations show that the left side of (7) turns out to be approximately equal to unity when the partition used provides the necessary accuracy in the replacement of the integral equations by algebraic equations. Accordingly, the convergence rate of the successive approximations is a strong function of the choice of the initial approximation i_0^e. It turns out that the best initial approximation is the function $i_0^e(\xi)$, constructed in the approximation of a constant-intensity piston. This initial approximation will evidently be convenient in other cases also. Figure 3 shows an oscillogram of the radiation in the fundamental band of CO at $\lambda = 4.7\ \mu$, obtained in a shock tube 57 mm in diameter. On this oscillogram we see the emission detected before the arrival of the shock wave (region I). The time at which the shock wave arrives is recorded by a piezoelectric transducer at the optical axis of the detection system. The "0" shows the initial approximation i_0^e, found under the assumption of a piston of constant intensity. In this case the third approximation of the intensity of multiply reflected light turns out to lie between the first and second and is not shown in this figure.

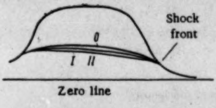

Fig. 3. Diagram used to determine the contribution of multiple reflection of light to the emission intensity.

CONCLUSION

These results demonstrate the applicability of this method, based on a measurement of the intensity of multiply reflected light before the arrival of the shock wave, for determining the contribution of multiply reflected light to the detected emission of the gas behind a shock front. When this method is used, it is a simple matter to evaluate the intensity of the multiply reflected light when the change in the radiation intensity over the length of the piston can be neglected. For an accurate account of the contribution of multiply reflected light, the method of successive approximations must be used to solve system (5)-(6). In the first case the calculations are elementary. This algorithm for an accurate determination of the contribution of multiply reflected light to the measured intensity can be easily adapted for computer calculations.

In conclusion the authors thank E. P. Fetisov and A. I. Lukovnikov for useful comments and for discussion of this work.

---

[1] T. A. Brabbs, J. Chem. Phys., 49, 1433 (1968).

[2] W. C. Hooker and R. C. Millikan, J. Chem. Phys., 38, 214 (1963).

[3] A. Ya. Vinokurov, E. M. Kudryavtsev, V. D. Mironov, and E. S. Tekhov, Proceedings of the Third All-Union Symposium on Combustion and Explosions [in Russian], Izd. Nauka, Moscow (1972), p. 690.

[4] L. Ya. Tslaf, Variational Calculus and Integral Equations [in Russian], Izd. Nauka, Moscow (1970).

[5] S. G. Mikhlin, Lectures on Linear Integral Equations [in Russian], Fizmatgiz, Moscow (1959).

Brief communications

Nonlinear instability of a helicon packet in an anisotropic plasma

Ya. N. Istomin and V. I. Karpman

Institute of Terrestrial Magnetism, the Ionosphere,
and Radio-Wave Propagation,
Academy of Sciences of the USSR, Moscow

(Submitted July 9, 1973)
Zh. Tekh. Fiz., 44, 649-651 (March 1974)

The instability region of a nonlinear quasimonochromatic packet of helicons ("whistlers") in a plasma with a loss cone is wider than that predicted by linear theory.

As is shown in ref. 1, the evolution of a quasimonochromatic wave packet of whistlers propagating parallel to the magnetic field in a collisionless plasma is described in the adiabatic approximation by

$$\frac{\partial h}{\partial t} - aF(h)\frac{\partial h}{\partial z} = 0, \tag{1}$$

where $h = B/B_0$ is the ratio of the slowly varying magnetic field of the wave, B, to the constant external field B_0, and the function F(h) is governed by the interaction of the wave with resonant particles (having velocities sufficiently close to the resonant velocity $v_R = (\omega - \omega_c)/k$, where ω is the wave frequency, ω_c is the gyrofrequency, and k is the wave number). Instead of writing the general expression for F(h) found in ref. 1 [for our purposes the most important feature of this function is that $F(h) > 0$], we turn to a more detailed examination of the constant a, whose sign determines the evolution of the packet:[1]

$$a = \frac{64}{3\pi^2}\gamma_L\tau_m W_T^{1/2}\frac{\int\limits_0^\infty f_0'(W)\,W^{5/2}dW}{\int\limits_0^\infty f_0'(W)\,W^3 dW}. \tag{2}$$

Here,

$$\gamma_L = \frac{\pi^2\omega_p^2\omega}{k^2c^2}\left(1 - \frac{\omega}{\omega_c}\right)\int\limits_0^\infty f_0'(W)\,W^3 dW \tag{3}$$

is the growth rate of the wave in the linear approximation, where

$$f_0'(W) = \left(\frac{\partial f}{\partial u} + \frac{\omega_c}{kW}\frac{\partial f}{\partial W}\right)_{u=v_R}, \tag{4}$$

$f(u, W)$ is the distribution function unperturbed by the wave, u is the longitudinal component of the particle velocity, W is its transverse component, and τ_m is the characteristic nonlinear oscillation period of the longitudinal velocity u about its resonant value v_R: $\tau_m = (k\omega_c h_m W_T)^{-1/2}$, where h_m is the maximum relative amplitude in the packet, and W_T is the average transverse thermal velocity of the electrons.

It follows from Eq. (1) that the evolution of a packet having a length considerably exceeding $v_R\tau_m$ (the criterion for the adiabatic approximation) proceeds in such a way that the maximum packet amplitude does not change (h_m = const), while its spatial width increases if $a > 0$ or decreases if $a < 0$. The constancy of the maximum packet amplitude corresponds to a familiar feature of the quasilinear theory of monochromatic waves: The amplitude of a plane wave no longer changes when the distribution function in the resonant region becomes ergodic.[1)]

In connection with the question of whether the packet spreads or contracts as a function of the sign of a, we note that this effect is due to the difference between the average motion of resonant particles in the field of the packet and in an incident plane wave. The spreading of the packet is actually a manifestation, in the nonlinear "quasiergodic" stage, of the effect of the instability, while a reduction in the packet width corresponds to resonant cyclotron damping.

We see from Eq. (2) that if the ratio of the integrals on the right side is positive, the sign of a is the same as the sign of the growth rate in the linear approximation, γ_L, i.e., the packet is unstable (or stable) in a plasma which is unstable (or stable) in the linear approximation. This situation is realized, e.g., in an anisotropic plasma having a bi-Maxwellian distribution (i.e., having difference longitudinal and transverse temperatures), so that the instability condition for such a plasma found in the linear approximation in ref. 3 also holds for nonlinear packets.

Here we show that there can be cases in which the region of the nonlinear instability is generally broader than in the linear approximation. As a simple example we consider a plasma with a loss cone, which has an unperturbed distribution function of the form

$$f(u, W) = n\left[\Gamma(j+1)\,\pi^{3/2}W_T^{2j+2}u_T\right]^{-1}W^{2j}\exp\left(-\frac{u^2}{u_T^2} - \frac{W^2}{W_T^2}\right). \tag{5}$$

Substituting (5) into (4) and (2), we find

$$a = \frac{64}{3\pi^2}\gamma_L\tau_m\frac{\Gamma\left(j+\frac{3}{4}\right)\left[j/\left(j+\frac{3}{4}\right)-\beta\right]}{\Gamma(j+1)\left[j/(j+1)-\beta\right]}, \tag{6}$$

where

$$\beta = 1 - \frac{W_T}{u_T}\left(1 - \frac{\omega}{\omega_c}\right). \tag{7}$$

The instability condition in the linear approximation ($\gamma_L > 0$) is

$$\frac{\omega}{\omega_c} < \rho_L \equiv \left(1 - \frac{u_T}{W_T}\right) + \frac{u_T}{W_T}\frac{j}{j+1}. \tag{8}$$

The condition for a nonlinear instability ($a > 0$), on the other hand, is seen from (6) to correspond to a broader range:

$$\frac{\omega}{\omega_c} < \rho_{NL} \equiv \left(1 - \frac{u_T}{W_T}\right) + \frac{u_T}{W_T}\frac{j}{j + \frac{3}{4}}. \tag{9}$$

Accordingly, in the frequency range $\rho_L < \omega/\omega_c < \rho_{NL}$, which lies in the linear-stability region, the packet retains its nonlinear instability.

As another characteristic example we consider the distribution function

$$f(V^2, \alpha) = \text{const}\,\frac{\sin^{2j}\alpha}{E^n}, \tag{10}$$

which is frequently used to describe the "hot-electron" component in the magnetospheric plasma [$\alpha = \arctan W/u$ is the pitch angle and $E = m(u^2 + W^2)/2$ is the kinetic energy]. In this case we have

$$\rho_L = \frac{j(j+2)}{(j+1)(j+n+1)}; \quad \rho_{NL} = \frac{j\left(j + \frac{7}{4}\right)}{\left(j + \frac{3}{4}\right)(j+n+1)}$$

and, as above, $\rho_{NL} \geq \rho_L$; these parameters are equal at $j = 0$.

We note in conclusion that, despite the close analogy mentioned in the footnote between the nonlinear theory of the resonant interaction of a wave with particles for whistlers and plasmons, the nonlinear-instability region is broader than the linear region only for whistlers, since, as is evident from (2), this broadening is due to the additional integrals over the transverse velocities.

The authors thank D. R. Shklyar for useful discussion.

---

[1] The quasilinear theory of monochromatic waves for whistlers is very reminiscent in both form and results of the corresponding theory for monochromatic longitudinal waves in an isotropic plasma. For a more detailed discussion of this point the reader is referred to the literature cited in ref. 1. The adiabatic theory for the evolution of a quasimonochromatic packet of plasma waves, which also leads to Eq. (1), is discussed in ref. 2.

[1] Ya. N. Istomin and V. I. Karpman, Zh. Eksp. Teor. Fiz., 63, 131 (1972) [Sov. Phys. – JETP, 36, 69 (1973)].
[2] D. D. Ryutov and V. N. Khudik, Zh. Eksp. Teor. Fiz., 64, 1252 (1973).
[3] R. Z. Sagdeev and V. D. Shafranov, Zh. Eksp. Teor. Fiz., 39, 181 (1960) [Sov. Phys. – JETP, 12, 130 (1961)].

Optimization of the paraxial asymptotic electric field in electron-optical systems

V. E. Ginzburg and V. N. Danilov
Institute of Radio Engineering and Electronics,
Academy of Sciences of the USSR, Moscow

(Submitted February 17, 1973; resubmitted July 20, 1973)
Zh. Tekh. Fiz., 44, 651-655 (March 1974)

A simple and fairly accurate paraxial asymptotic form is developed for the electric field inside and outside a dense electron beam; this is used in the analysis of paraxial axisymmetric electron-optical systems. It is possible to treat a strong inhomogeneity current density in a cross section, marked aberrations, and the intersection of electron trajectories, taking account of space-charge forces.

The development of calculational techniques makes timely the problem of computer design of optimum electron-optical systems (EOS). Requirements imposed on the trajectories and the electrodes must be satisfied simultaneously. First, trajectories must produce the required beam. As a rule the trajectories of the beam electrons must be similar although in many cases, as in the use of electrostatic lenses to shape electron beams with a weak inhomogeneity of the current density over the cross section, intersections of trajectories are unavoidable because of aberrations. The electrodes in turn must be technically feasible and the interelectrode distances must satisfy electrical strength requirements. Since computer design involves calculating a large number of variations, the calculational technique on which it is based, besides being accurate, must use a short calculational time per variation.

At the present time the electrodes of an EOS are synthesized for given beam characteristics on the basis of paraxial expansions of the field and beam parameters in powers of the transverse coordinate.[1-4] Paraxial expansions assume that the current density is only slightly nonuniform over the cross section of the beam, and are special cases of asymptotic expansions in powers of a small geometric parameter ε, which characterizes the narrowness of the beam, and a parameter ν which characterizes the narrowness of the band occupied by the electrodes.[5]

$$\varphi=\sum \varepsilon^k \varphi_k(r,\ z),\ \psi=\sum \nu^k \psi_k(r,\ z). \tag{1}$$

Here φ is the electric potential inside the beam, ψ is the potential outside the beam, and r and z are cylindrical coordinates. The coefficients φ_k allow a non-power-law radial dependence corresponding to a strong nonuniformity of the current density. The parameter ν is generally much larger than ε since the band of definition of the external field is several times broader than the band occupied by beam. Generally speaking, the errors of the expansions are commensurate if the series for ψ contains more terms than the series for φ.

Synthesized electrodes generally turn out to be complex; in practice electrodes are constructed from cylindrical and conical surfaces. Computer simulations to analyze beam perturbations due to the simplification of electrode shapes are much more time consuming than synthesis. The present paper seeks the simplest asymptotic approximation permitting the synthesis and analysis of an axisymmetric EOS with adequate accuracy. The corresponding approximations for a plane-symmetric EOS are similar and will not be presented.

An estimate is made of the electric forces acting outside the cathode region of an electron gun,[6] including a triode,[7] in electrostatic lenses,[8] and in systems with electron retardation.[9] The forces determined by the fourth derivative of the potential on the U_z axis are commesurate with the forces due to the space charge ρ; outside the beam these forces exceed the forces corresponding to the expansions.

$$\varphi=U-\frac{1}{4}U''r^2+\frac{1}{64}U^{\mathrm{IV}}r^4+4\pi\int\limits_0^r\frac{dr}{r}\int\limits_0^r\rho r dr, \tag{2}$$

$$\psi=U-\frac{1}{4}U''r^2+\frac{1}{64}U^{\mathrm{IV}}r^4-\frac{1}{2304}U^{\mathrm{VI}}r^6+\Pi+B\ln\frac{r}{r_{\mathrm{B}}}, \tag{3}$$

$$B=2\frac{I_{\mathrm{B}}}{v},\ 2\pi\int\limits_0^r\rho r dr=\frac{I}{v},\ \Pi=\frac{2}{v}\int\limits_0^{r_{\mathrm{B}}}I\frac{dr}{r},\ v=\sqrt{\frac{2e}{m}U}.$$

Here the family of trajectories is given in parametric form $r = r(z, I_0)$. The parameter I_0 is equivalent to the parameter r_H, the radial coordinate of an electron with a given trajectory at the entrance to the system, and represents the current flowing in the system through a circle of radius r_H. The subscript B denotes quantities referring to the beam boundary. It is convenient to have the parameter I_0 change by the same amount from trajectory to trajectory. If the trajectories do not intersect, the trajectory parameter I_0 in any cross section of the beam corresponds to the current I flowing through a circle whose radius is equal to the radial coordinate of the electron. If there are intersections I_0 remains a trajectory parameter equivalent to r_H. For machine calculations it is convenient to number the trajectories, e.g., from 1 to 10, and to take account of the change in space-charge forces by the exchange of I_0 values between intersecting trajectories. Then I_0 and I will correspond. The following assumption is made to evaluate the integrals in Eqs. (2) and (3). In each cross section of an annulus whose inner and outer radii are determined by the radial coordinates of electrons with adjacent trajectories there is a uniformly distributed current equal to the difference in the values of I_0 for these trajectories.

Expansions (2) and (3) contain terms related both to the charges on the electrodes, including those induced by the beam, and to the space-charge density ρ. We limit ourselves to terms larger than or commesurate with the first approximation for the space charge potential. The ratios of the orders of magnitude of the forces, confirming the validity of approximations (2) and (3) for the systems named above, are shown in Fig. 1 for the case of a single electrostatic lens.[8] The transformation to dimensionless quantities normalized to unity for the EOS's named above separates out the small parameters in Eqs. (2) and (3): ε in front of r in (2), ν in front of r in (3), and ε^2 in front

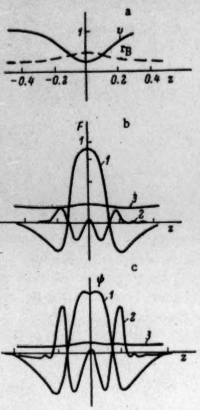

Fig. 1. Ratios of orders of magnitude of forces in an electrostatic lens shaping a beam with a perveance of 0.78 $\mu A/V^{3/2}$. a) Distribution of potential U along the axis of the lens and along the boundary trajectory of an electron r_B; b) forces F acting on a boundary electron of the beam determined by (1) the second derivative of the potential, (2) the fourth derivative, and (3) the space charge; c) contribution of these forces to the potential distribution outside the beam.

of ρ and I. Thus, in comparison with the asymptotic forms[5] the space charge terms are displaced to higher approximations. The modified paraxial equation for a family of electron trajectories $r(z, I_0)$, within the framework of the same asymptotic accuracy, has the form

$$2r''\left(U-\frac{r^2}{4}U''-G_1\right)(1+r'^2)^{-1}+r'\left(U'-\frac{1}{4}r^2U'''+G_2\right)+\frac{r}{2}U''-\frac{r^3}{16}U^{IV}+G_3=\frac{2I}{rv};\ r'=\frac{\partial r}{\partial z}. \quad (4)$$

The terms G_1, G_2, and G_3 describe the effect of the magnetic field

$$G_1=\frac{m}{e}\frac{v_\theta^2}{2},\ G_2=\frac{v_\theta}{c}H_r,\ G_3=\frac{v_\theta}{c}\left(H_z-\frac{mcv_\theta}{er}\right),$$
$$v_\theta=\frac{e}{mc}\left(A_\theta-A_{\theta k}\frac{r_k}{r}\right),\ A_\theta=\frac{r}{2}H-\frac{r^3}{16}H'',\ H_z=\frac{1}{r}\frac{\partial(rA_\theta)}{\partial r},$$
$$H_r=-\frac{\partial A_\theta}{\partial z}.$$

Here H is the intensity of the magnetic field, A_θ is the azimuthal component of the vector potential, v_θ is the azimuthal component of the electron velocity, e and m are the charge and mass of the electron, c is the velocity of light, and the subscript k denotes quantities referring to the cathode.

We present below the results obtained by this method. The synthesis of an axisymmetric electrostatic lens shaping a beam with a perveance of 0.78 $\mu A/V^{3/2}$ is shown in Fig. 2. For this case

$$U=U_0(0.233+0.767\ \mathrm{th}\ 20z^2).$$

The running time on an M-220 computer is 30 sec. The same lens is calculated by an analytical method on a BÉSM-6 computer. The trajectories in the two cases agree within the accuracy of the curves. The spatial distribution of the potential for these cases is shown in Fig. 3. In the region where the potential gradients are large the equipotentials coincide within the accuracy of the curves, but in drift tubes the behavior of the equipotentials is somewhat different. This difference can be explained simply.

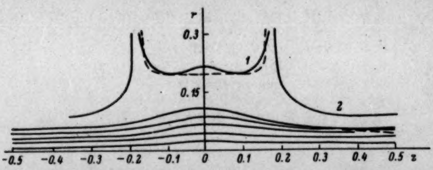

Fig. 2. Electrodes of an electrostatic lens, and electron trajectories. Open curves show a simplified electrode with zero potential, and the perturbed boundary trajectory, ψ: 1) 0; 2) $1U_0$.

If the potential on the axis is given by a polynomial of the sixth degree or less, expansions (2) and (3), neglecting space charge, yield an exact solution of Laplace's equation. Although the space charge forces are taken into account in the present problem they do not play a decisive role, as follows from Fig. 1. Near z = 0 the higher terms of the series for tanh $20z^2$ are small and as long as the series can be replaced by a sixth-degree polynomial Laplace's equation is solved exactly. In the drift tube region the higher terms of the series are important but there the potential gradients are small and therefore the trajectories through the whole lens are considered accurate over all.

Figure 2 shows that aberrations play an important role in the lens. They are still larger if the perveance is increased without decreasing the length of the lens. In principle the aberrations can be compensated by increasing the space-charge density of the beam from the axis to the boundary. Figure 4a shows the lens

$$\frac{U}{U_0}=0.44+0.56\ \mathrm{th}\ 16.7z^2-0.136e^{-23.4z^2},$$

shaping a beam with a perveance of 1.5 $\mu A/V^{3/2}$ and similar trajectories. The calculation was performed for 10 trajectories, five of which are shown in the figure. The current distribution over the cross section of the beam necessary for this is shown in Fig. 4b. Lenses with such a large nonuniformity of the current density cannot be synthesized by using an expansion in powers of the transverse coordinate.

To analyze the small perturbations in the potential on the axis we add the correction $\Delta(z)$ representing a su-

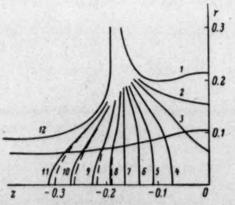

Fig. 3. Spatial distribution of potential for lens of Fig. 2. The solid curves are obtained by an analytic method using program KSI on a BÉSM-6 computer, and the open curves by our method. ψ: 1) 0, 2) 0.1, 3) 0.2, 4) 0.3, 5) 0.4, 6) 0.5, 7) 0.6, 8) 0.7, 9) 0.8, 10) 0.9, 11) 0.95, 12) $1U_0$.

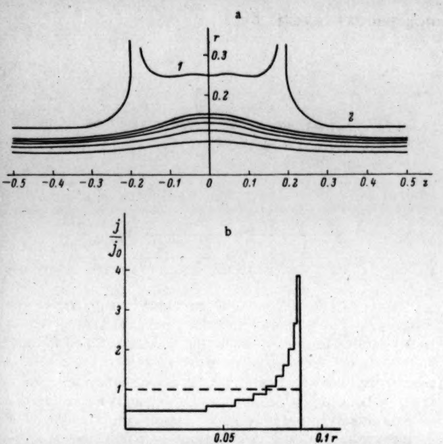

Fig. 4. a) Electrostatic lens shaping a beam with a perveance of 1.5 $\mu A/V^{3/2}$; ψ: 1) 0; 2) $1U_0$. b) Distribution of current density over the cross section of the beam entrance to a lens whose aberrations are compensated and through which the electron trajectories are similar.

perposition of functions e.g., $\Delta(z) = \sum_k A_k e^{\alpha k z^2}$. The coefficients in this expansion are chosen in such a way that the paraxial expansion of the harmonic field connected with this correction would lead to the given perturbation in the shape of the electrodes. To do this we specify 5-10 times as many points on the electrodes as there are coefficients to be determined and use the method of least squares to determine the coefficients A_k. This is a somewhat unusual application of the method of least squares since the analytic continuation of a function rather than the function itself is approximated.

By solving Eq. (4) and taking account of the field of the correction we find the perturbations of the trajectories. The perturbations of the trajectories arising from the perturbations of the space charge forces are hardly larger than the inaccuracies in plotting the graphs and can be ignored. Figure 2 shows the perturbation of the zero electrode to give it a more technological shape, and the perturbation of the boundary trajectory. For this case

$$\frac{U}{U_0} = 0.233 + 0.767\,\mathrm{th}\,20z^2 - 0.0388e^{-16z^2} + 0.0543e^{-28z^2} - 0.0307e^{-40z^2}.$$

The asymptotic form is generally valid outside the cathode region. In the immediate vicinity of the cathode the space charge forces are commensurate with the forces given by the second derivative of the potential, and taking account of higher derivatives gives a divergence. However, if the beam has a perveance of several units ($\mu A/V^{3/2}$) the forces given by higher approximations are small at distances from the cathode smaller than a quarter of its diameter. For a machine calculation the coefficient of the higher approximations, normally equal to unity but set equal to zero near the cathode, can vary smoothly from zero, corresponding to the model of a spherical diode, to unity for the asymptotic form. The determination of the zero electrode in the cathode region can be reduced to drawing a straight line from an edge point of the cathode at an angle of 67.5° with the boundary of the beam until it intersects the zero electrode given by (3). It should be noted that the model of a spherical diode is used in all the other methods of calculation in the cathode region.

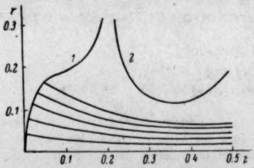

Fig. 5. Electrodes of a gun shaping a plane-symmetric beam, and the electron trajectories. ψ: 1) 0; 2) $1U_0$.

Figure 5 shows the results of the synthesis of a plane symmetric gun with a perveance per square of 1.8 $\mu A/V^{3/2}$

$$\frac{U}{U_0} = 0.92\,\mathrm{th}\,3.33x^{4/3}(1 + 1.6x + 3.32x^2).$$

The trajectories and perveance are in good agreement with numerical calculations.

Thus, the proposed procedure enables us to describe beams with a stronger transverse nonuniformity than is possible with the paraxial expansion,[2-4] and with intersecting trajectories. The solution of the external problem is so simplified that it appears possible to solve the analysis problem as a refinement of the synthesis problem. The solution of the external problem here does not require transforming to a curvilinear coordinate system and back; taking account of the contribution to the shape of the electrodes from the fourth and sixth derivatives of the axial potential does not require finding the extremely cumbersome higher expansions of the space-charge field. Aberrations are taken into account only through the presence of the term proportional to the fourth derivative of the axial potential. The expression for the external field does not contain the sources of nonuniformity arising in refs. 2-4 from representing the field in a nonharmonic coordinate system connected with the boundary trajectory which has a large curvature in the EOS considered.

In our opinion the asymptotic form described here is a necessary step away from classical electron optics; we go from the representation of the field in terms of the boundary trajectory of the beam to the representation of the beam trajectories in terms of the field parameters.

---

[1] J. P. Pierce, Theory and Design of Electron Beams, Van Nostrand, New York (1954).

[2] P. Kirstein, G. Kino, and W. Waters, Space-Charge Flow, McGraw-Hill, New York (1967).

[3] V. T. Ovcharov, Radiotekh. Elektron., 7, 1367 (1962); 12, 2156 (1967).

[4] V. T. Ovcharov and V. V. Penzyakov, Radiotekh. Elektron., 15, 1651, 1897 (1970).

[5] V. N. Danilov, Prikl. Mekh. Tekh. Fiz., No. 5, 3 (1968); Thesis, Institute of Radio Engineering and Electronics [in Russian] (1968).

[6] I. V. Nevskii and V. T. Ovcharov, Elektron. Tekh., Ser. 1, Electronics of Ultra-High Frequency 7, 62 (1969).

[7] N. S. Zinchenko, Zh. Tekh. Fiz., 38, 184 (1968) [Sov. Phys.—Tech. Phys., 13, 130 (1968)].

[8] O. A. Dokolin and P. V. Nevskii, Elektron. Tekh., Ser. 1, Electronics of Ultra-High Frequency, 11, 96 (1971).

[9] V. E. Ginzburg, Elektron. Tekh., Ser. 1, Electronics of Ultra-High Frequency 5, 61 (1971).

Long-wave cyclotron instability in a plasma in an inhomogeneous magnetic field

A. S. Kukushkin

(Submitted June 4, 1973)
Zh. Tekh. Fiz., 44, 655-658 (March 1974)

A differential equation is found for a long-wave-cyclotron instability in a plasma cylinder field. The eigenvalue problem for this equation with homogeneous boundary conditions is solved numerically. The inhomogeneity of the magnetic field reduces the growth rate.

INTRODUCTION

In a plasma with a nonequilibrium ion velocity distribution – a case typical of open confinement systems – ion instabilities can be excited at a frequency near the ion gyrofrequency or its harmonics. The linear theory for this instability in a plasma in a homogeneous magnetic field has been worked out in great detail (see, e.g., refs. 1, 2). In real systems, however, the field is always inhomogeneous. Since the instability is due to resonance effects (plasma waves and cyclotron rotation), the inhomogeneity of the field can be significant.

In most work on the cyclotron instability in an inhomogeneous magnetic field attention has been focused on the effect of an inhomogeneity along a line of force. However, in a plasma with the shape of a pancake (transverse dimension larger than the longitudinal dimension), the inhomogeneity across the magnetic field[19] is more important.

The exact integrodifferential equation for this case is rather complicated. However, for the long-wave case the ratio of the Larmor radius to the characteristic transverse dimension (23/957) becomes a small parameter. It can therefore be used for an expansion, as in ref. 3, and a second-order differential equation can be obtained. Below we derive the eigenvalue problem for this equation, with a homogeneous boundary condition at the surface of the plasma cylinder; we solve this problem numerically.

It turns out that even a pronounced inhomogeneity (an increment in the gyrofrequency which is much larger than the growth rate) does not provide complete stabilization; instead, it simply reduces the growth rate and changes the frequency of the long-wave instability.

OSCILLATION EQUATION

We consider a plasma cylinder of radius R_0 and homogeneous density in a magnetic field which is directed along the axis of the cylinder. We assume the magnetic lines of force to be straight, and that the functional dependence of the field on the radius $H_z = H_0[1-\rho(r/R_0)^2]$, where $\rho \ll 1$. We consider a perturbation in the electric potential like

$$\varphi = \psi(r)\, e^{-i\omega t + ikz + im\theta}$$

in the cylindrical coordinate system r, θ, z.

For simplicity we assume the electrons to be cold ($T_e = 0$). Then, using the method of ref. 3, and assuming $|(v_\perp/\omega_i)(d\psi/dr)| \ll 1$, we obtain the following equation for modes near the ion gyrofrequency, $\omega \approx \omega_i$:

$$\frac{1}{r}\frac{d}{dr}\left(r(1+A(r))\frac{d\psi}{dr}\right) - \frac{m^2}{r^2}(1-A(r))\psi - k^2\left(1-\frac{\omega_{0e}^2}{\omega^2}\right)\psi = 0, \quad (1)$$

where

$$A(r) = \frac{\omega_{0i}^2}{4\omega_i^2}\int_0^\infty v_\perp^3\, dv_\perp \int_{-\infty}^{\infty} dv_\parallel \frac{(\omega - kv_\parallel)\frac{1}{v_\perp}\frac{\partial f_0}{\partial v_\perp} + k\frac{\partial f_0}{\partial v_\parallel}}{\omega - \omega_j(r) - kv_\parallel}.$$

Here ω_j is the plasma frequency for particles of species j, ω_i is the ion gyrofrequency, and $f_0(v_\parallel, v_\perp)$ is the equilibrium ion distribution function. Since Eq. (1) holds only for long-wave modes, the effects of the nonmonotonic nature of the distribution of ions with respect to transverse velocity are inconsequential, and we can choose as f_0 an anisotropic Maxwell distribution with $T_\perp \gg T_\parallel$. To simplify the calculations we restrict the discussion to the case m = 0. Then Eq. (1) becomes

$$\frac{1}{r}\frac{d}{dr}\left(r(1+A(r))\frac{d\psi}{dr}\right) - k^2\left(1-\frac{\omega_{0e}^2}{\omega^2}\right)\psi = 0, \quad (2)$$

where

$$A(r) = \frac{\tau}{2}\frac{\omega_{0i}^2}{\omega_i^2}\left(1 + i\sqrt{\pi}\frac{\omega_i}{ku}\left(\frac{1}{\tau} + \frac{\omega-\omega_i(r)}{\omega_i}\right)W\left(\frac{\omega-\omega_i(r)}{\omega_i}\right)\right).$$

Here

$$\tau = \frac{T_\perp}{T_\parallel},\quad u = \sqrt{\frac{2T_\parallel}{m_i}},\quad \omega_i(r) = \omega_i\left(1-\rho\left(\frac{r}{R_0}\right)^2\right),$$

and

$$W(z) = e^{-z^2}\left(1 + \frac{2i}{\sqrt{\pi}}\int_0^z e^{t^2}dt\right)$$

is the probability integral of complex argument.

EIGENMODES

We supplement Eq. (2) with the boundary conditions

$$\psi(R_0) = 0,\ \psi(0) = 1 \quad (3)$$

and we seek the eigenvalues ω for this problem (the case Im $\omega > 0$ corresponds to an instability).

When $\rho = 0$ (a homogeneous field) and $|(\omega-\omega_i)/ku| \gg 1$ (a pronounced anisotropy of the temperatures) we can replace the function W(z) by its asymptotic representation $W(z) \approx (i/\sqrt{\pi})\,(1/z + 1/2z^3)$. Then the eigenfuntions of the problem are the Bessel functions $J_0(k[(1-\omega_{0e}^2/\omega^2)/(1+A)]^{1/2}r)$ and we find the following dispersion relation for ω:

$$\frac{k^2}{\mu^2}\left(1-\frac{\omega_{0e}^2}{\omega^2}\right) = -(1+A),$$

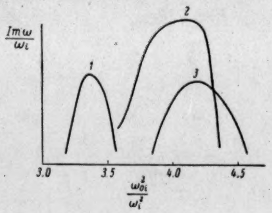

Fig. 1. Functional dependence of the growth rate on the plasma density in various fields. ρ: 1) 0.1; 2) 0; 3) −0.1.

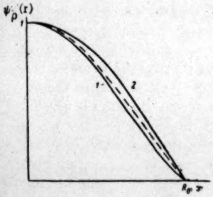

Fig. 2. Eigenfunctions $\psi_\rho(r)$ for various fields. The dashed curve shows the Bessel function $J_0(\mu r/R_0)$. ρ: 1) 0.1; 2) −0.1.

where μ is the first root of Bessel function $J_0(z)$. This equation (in different notation) is analyzed in ref. 4.

Here we consider the case $\rho \neq 0$. We cannot solve Eq. (2) analytically, so we are forced to find the eigenvalues ω for problem (2), (3) by a numerical method.

Figure 1 shows the functional dependence of the growth rates on the parameter ω_{0e}^2/ω_i^2 for the case

$$p \equiv \left(\frac{\mu}{R_0\omega_i}\right)^2 \frac{2T_\perp}{m_i} = 0.3, \; q \equiv \left(\frac{k}{\omega_i}\right)^2 \frac{2T_\perp}{m_i} = 0.1, \; \tau = 4 \cdot 10^3$$

and for various values of ρ. Here the real part of ω is approximately equal to the minimum value of the gyrofrequency in the plasma. This picture is qualitatively the same as that described by the results of ref. 5.

Figure 2 shows the eigenfunctions $\psi_\rho(r)$ for various values of ρ; we see that they are approximated by $\psi_0 \equiv J_0(\mu r/R_0)$. The quantity $1 + A(r)$ has no zeros at Im $r \geq 0$, Im $\omega \geq 0$, although these zeros move arbitrarily close to the real r axis as the parameter $\alpha = \sqrt{\tau/q}$ increases. However, in cases of practical interest, the value of α does not exceed the value $\alpha = 200$ assumed in our calculations.

Accordingly, the modes remain long-wave over plausible ranges of the parameters, even in an inhomogeneous field, so that the assumptions used in deriving Eq. (1) are valid and this formulation of the problem is internally consistent.

The good approximation of the eigenfunctions of problem (2), (3) by the Bessel functions, which are the basis functions for the expansion in ref. 5, confirms the validity of this expansion for long-wave perturbations.

We note that the transverse inhomogeneity of the field does not lead to complete stabilization; instead, it only causes a reduction in the growth rate for long-wave modes.

The author thanks V. V. Arsenin for suggesting this problem, and thanks Yu. N. Dnestrovskii for his interest.

---

[1] A. V. Timofeev and V. I. Pistunovich, in: Reviews of Plasma Physics, Vol. 5, Consultants Bureau, New York (1970).

[2] A. B. Mikhailovskii, Theory of Plasma Instabilities, Consultants Bureau, New York (1973).

[3] V. V. Arsenin and A. D. Selidovkin, Izv. VUZ. Radiofiz., 12, 1141 (1969).

[4] Yu. N. Dnestrovskii, D. N. Kostomarov, and V. I. Pistunovich, Yadernyi Sintez, 3, 30 (1963).

[5] A. S. Kukushkin, Zh. Tekh. Fiz., 43, 1416 (1973) [Sov. Phys.—Tech. Phys., 18, 899 (1974).

Transmission of a high-current relativistic beam through a gas

Yu. V. Tkach, I. I. Magda, G. V. Skachek,
S. S. Pushkarev, and I. P. Panchenko

Physicotechnical Institute, Academy of Sciences of the Ukrainian SSR, Khar'kov

(Submitted March 26, 1973; resubmitted July 2, 1973)
Zh. Tekh. Fiz., 44, 658-660 (March 1974)

The formation of the return current is studied experimentally in an electron accelerator at energies up to 1 MeV and at currents up to 50 kA. The results agree with a model which only takes account of elementary processes. The velocity of the ionization front is measured in various gases at pressures of $5\cdot 10^{-2}$-10 torr.

The transmission of high-current relativistic beams through a neutral gas is of interest in several problems (e.g., heating plasmas, powerful microwave and x-ray sources, pumping gas and solid-state lasers, etc.) in which processes of beam energy transport are important. We report here a study of the transmission through a gas of a pulsed electron beam at an energy of 1.0 MeV, a current up to 50 kA, and a pulse length of $3\cdot 10^{-8}$ sec. The beam is produced by a high-current accelerator, which uses a cylindrical double shaping line and distilled water as a dielectric.[1]

We study the transmission of such a beam through a gas-filled metal chamber 300 cm long and 11 cm in diameter. To determine the energy lost by the beam we carry out calorimetric measurements of the beam energy at the entrance and exit of the plasma chamber. The difference between the corresponding calorimeter readings gives the energy lost by the beam as it travels through the gas. Figure 1 illustrates the efficiency of energy transport by a high-current relativistic beam as a function of the gas pressure in the chamber. We see that the optimum conditions for passage of the beam obtain at 0.5-2 torr.

It has been shown previously[2,3] that the transmission of a high-current relativistic beam through a plasma under conditions such that the current rise time t_r is much shorter than the skin time $t_r \ll t_d = 4\pi\sigma r^2/c^2$ (here σ is the plasma conductivity, r is the beam radius, and c is the speed of light) leads to the production of a return current, which tends to cancel the self-magnetic field of the beam. Figure 1 apparently shows that at pressures below 0.2 torr the return current is not sufficient to balance the self-magnetic field of the beam because of the low plasma density; the electron Larmor radius becomes smaller than the beam radius, thereby blocking the beam. As the pressure is raised above 4 torr one of the mechanisms that degrades the beam transport is scattering of electrons of the return current by ions and gas atoms. These transport conditions were studied previously.[1] Measurements of beam transport through a gas show that at pressures of 0.5-2 torr an electron beam can transport up to 80% of the energy over a length of 300 cm. The fraction of the energy lost is apparently due to the escape to the chamber walls of electrons accelerated in radial fields, due to the incomplete neutralization of the beam charge and scattering of electrons by the anode foil and gas atoms. It is also necessary to take account of the energy carried to the walls by particles accelerated in fields excited in collective interactions of the relativistic beam with the plasma. At low pressures the formation time of the return current and, thus, the characteristic time for neutralization of the self-magnetic field of the beam, can become comparable to the length of the current pulse (Fig. 2a), and again there would be a reduction of the energy characteristic of the beam. The formation time for the return current during the transmission of a relativistic beam through the gas is determined experimentally. The formation time for the return current is determined as a function of the pressure from signals taken from shunts detecting the electron-beam current I_m and the current flowing through the walls of the plasma chamber, $I_{wa} = I_m - I_{ret}$. Figure 2a,b, shows oscillograms of I_{wa}, which illustrate the formation of the return current in helium at various pressures. The experimental values of the return current formation time in various gases are shown along with the theoretical values in Table 1. The return current formation time is determined from

$$\frac{1}{t_b}\exp\left(\frac{t_b - t_n}{t_i}\right) = \frac{80}{p}\,\frac{1}{t_i\,(t_i + t_n)}\,\frac{1}{\beta}\,, \tag{1}$$

where t_b is the formation time of the return current, t_i

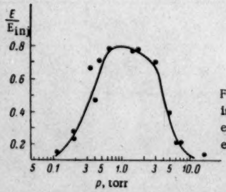

Fig. 1. Transport curve for a relativistic electron beam in air. The average beam current is 40 kA, and the energy is 0.6-0.7 MeV.

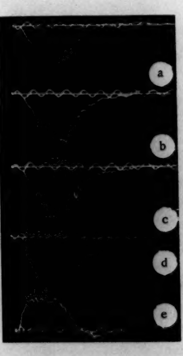

Fig. 2. Formation of the return current in helium. The beam current is 25 kA, and its energy is 0.8 MeV. The oscillograms shown here are proportional to the current flowing through the chamber wall, I_{wa}, for various gas pressures. p, torr: a) 10^{-1}; b) $1.7\cdot 10^{-1}$; c) $3.1\cdot 10^{-1}$; d) 1.3; e) beam-current pulse. The period of the time marker is 10^{-8} sec.

TABLE 1. Formation Time for the Return Current in Various Gases as a Function of the Pressure (electron energy of 0.8 MeV and current of 25 kA)

Gas	Pressure, torr				
	0.1	0.3	0.6	1.0	2.0
Hydrogen.	23.5	18.0	14.5	12.5	10.0
Helium	20.0	17.5	16.5	16.0	15.0
Neon	21.0	14.5	13.0	12.0	11.0
Argon	22.0	11.5	9.5	9.0	—
Air.	20.0	13.0	8.5	7.0	—
Air.	27.0 *	9.0 *	7.0 *	6.0 *	—

*Values of t_b calculated from Eq. (1).

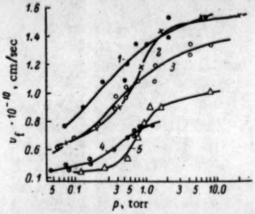

Fig. 3. Velocity of the ionization front as a function of the nature and pressure of the gas. Beam current of 25 kA and energy of 0.8 MeV. 1) Nitrogen; 2) argon; 3) hydrogen; 4) helium; 5) propane–butane mixture.

is the ionization time, t_n is the neutralization time, p is the gas pressure, and β is the velocity of the beam electrons.

This equation is derived under the approximation of a diffusion mechanism for the formation of the return current.[4] The agreement between the observed return current formation time and the theoretical time shows that elementary processes are predominant in the mechanism for the formation of plasma by the relativistic beam. A similar result was obtained in refs. 5-7.

An important characteristic of the transmission of a high-current relativistic beam through a gas is the velocity of the ionization front.[8] In our experiments we measure this velocity in the following manner: We place four loop-shaped pickups along the axis in the plasma chamber to detect the passage of the ionization front. The time intervals between the signals from the pickups are recorded on a six-trace oscilloscope with a time resolution better than $2 \cdot 10^{-10}$ sec; the velocity of the ionization front is calculated from these time intervals. The measured velocities of the ionization fronts in helium and nitrogen agree in order-of-magnitude with those calculated from the following equation:[9]

$$v_f = \sqrt{\frac{mc^3}{2\pi e j_0}}\, \nu_i \left(\gamma^{2/3} - 1\right)^{3/4}, \tag{2}$$

where $j_0 = env_0$ is the beam current density, ν_i is the ionization rate, γ is the relativistic factor, e is the electron charge, and m is the electron mass.

Figure 3 shows the measured velocities of the ionization front as a function of the pressure for various gases. We see that the front velocity does not exceed $1.6 \cdot 10^{10}$ cm/sec.

It was shown in refs. 9-11 that when a high-current relativistic beam is injected into a gas ions are captured and accelerated to a velocity $v_i = v_f$ in the potential well of depth $e\varphi \leqslant mc^2(\gamma - 1)$ at the ionization front. The efficiency of this mechanism is relatively low because the accelerated ions leave the potential well after they overtake the ionization front. Fainberg has proposed a method for increasing the efficiency of this acceleration through an increase in the velocity of the ionization front as it propagates through the plasma chamber. Under these conditions, the ions spend a considerable time in the accelerating field, so that the acceleration efficiency is increased. In our experiments we have studied the possibility of increasing the velocity of the ionization front by producing a pressure gradient along the chamber axis. Our measurements show that with a pressure changing from 0.2 torr at the front of the chamber to 1-2 torr at its end, the velocity of the ionization front increases by a factor of 1.4- 1.6, depending on the nature of the gas.

In conclusion the authors thank Ya. B. Fainberg for interest in this work, and E. A. Lemberg, N. P. Gadetskii, and V. D. Bondarenko for assistance in the experiments.

---

[1] Yu. V. Tkach, Ya. B. Fainberg, I. I. Magda, V. D. Shapiro, V. I. Shevchenko, A. I. Zykov, E. A. Lemberg, I. N. Mondrus, and N. P. Gadetskii, ZhETF Pis. Red., 7, 368 (1972) [JETP Lett., 7, 290 (1972)].

[2] A. A. Ivanov and L. I. Rudakov, Zh. Eksp. Teor. Fiz., 58, 1332 (1970) [Sov. Phys.-JETP, 31, 715 (1970)].

[3] W. H. Bennett and T. G. Roberts, Plasma Phys., 10, 381 (1968).

[4] D. A. McArthur and J. W. Poukey, Phys. Rev. Lett., 27, 1765 (1971).

[5] P. A. Miller, J. B. Gerardo, and J. W. Poukey, J. Appl. Phys., 43, 3001 (1972).

[6] P. A. Miller and J. B. Gerardo, J. Appl. Phys., 43, 3008 (1972).

[7] D. W. Swain, J. Appl. Phys., 43, 398 (1972).

[8] L. S. Levine, I. M. Vitkovitsky, and D. A. Hammer, J. Appl. Phys., 42, 1863 (1971).

[9] S. E. Rosinskii and A. A. Rukhadze, ZhETF Pis. Red., 11, 53 (1971).

[10] S. E. Graybill and L. R. Uglum, J. Appl. Phys., 41, 236 (1970).

[11] I. Runder, B. Ecker, and G. Ionas, Phys. Rev. Lett., 24, 2263 (1970).

Radar sounding of sea ice

V. V. Bogorodskii and V. P. Tripol'nikov
Arctic and Antarctic Scientific-Research Institute, Leningrad
(Submitted July 31, 1973)
Zh. Tekh. Fiz., 44, 660-662 (March 1974)

The possible use of active radar methods to measure the thickness of sea ice has been suggested. Methods are available for measuring the thicknesses of floating ice covers.[1] Technical aspects of this problem have been examined.[2-5]

In the present work we discuss the results of an experiment on the radar sounding of sea ice from an aircraft. For this experiment we use a pulsed locator with the following parameters: carrier frequency, 100 MHz; pulse length 50 nsec; antenna directivity 6 dB; a locator potential of 140 dB.

The experiments are carried out near the SP-21 drifting station on pack ice more than 3 m thick, which is many years old; on pack ice ranging from 2 to 3 m in thickness, which is two years old; and on young ice 1-1.5 m thick. The results demonstrate directly feasibility of remote measurements of the thickness of ice formations of this type. Figure 1a shows oscillograms of the radar sounding of pack ice from an aircraft flying at an altitude of 100 m at a speed of 150 km/h; these oscillograms are taken in succession at an exposure time of 0.5 sec. A feature of the reflected pulses received on board the aircraft is the short lifetime of their stable image. The lifetime proper is governed by the speed of the aircraft. The level of the reflected signals recorded during the flight is governed by the state of the reflecting surfaces and the physical properties of the medium (ice). The signal reflected from the top of the ice is subjected to fluctuations due to irregularities in the relief and to variations in the matching of the snow cover with the upper layers of the ice. The same factors, along with scattering and absorption in the ice – factors which vary during horizontal motion over the ice – cause fluctuations in the signals reflected from the lower boundary of the ice. It should also be noted that the nature of the fluctuations is affected by the size of the "spot" irradiated by the radar.

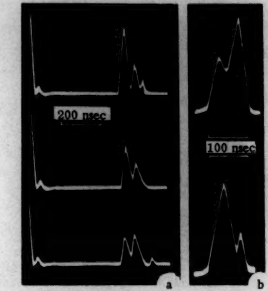

Fig. 1. Oscillograms obtained in the sounding of ice in the ocean. a) Pack ice with an average thickness of 5-6 m; b) superposition of the signals reflected from the top and bottom of young ice 1.5-1.7 m thick.

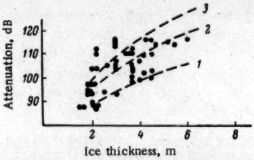

Fig. 2. Total attenuation of the signals reflected from the ice–water interface as a function of the ice thickness. 1) 1; 2) 3; 3) 5 dB/m.

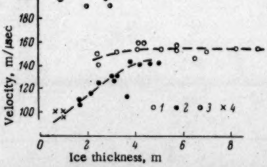

Fig. 3. Propagation velocity of the radar signal in the ice. 1) In pack ice without a snow cover; 2) for regions of pack ice covered by snow more than 0.5 m thick; 3) for pack ice with a porous texture; 4) in young ice 1-1.5 m thick at an air temperature of – 23 to – 25°C.

Signal fluctuations, although weaker, are found even in the sounding of fields of young ice, with level, almost smooth, surfaces. Measurements show that the total attenuation of signals reflected from the top of the ice varies from 90 to 120 dB when the aircraft is 100 m above packed ice. Of this fluctuation, the calculated geometric loss is 80 dB, and the (Fresnel) reflection loss is 10 dB for a dielectric constant of $\varepsilon' = 3.5$ for the ice. Accordingly, the loss due to scattering by the surface and the impedance mismatch of the media is 0-30 dB; for young ice, this latter loss is 0-10 dB. The total attenuation of the signals reflected from the bottom of the ice is on the same order of magnitude. The dashed curves in Fig. 2 show the calculated functional dependences of the total attenuation on the ice thickness at fixed values of the specific absorption in homogeneous ice with plane-parallel surfaces; the points show the experimental attenuations. This figure shows that the specific absorption does not exceed 1-5 dB/m in these experiments. Shown here is the entire range of signal amplitudes, without statistical characteristics. The fact that the signals shown in Fig. 1 are recorded at an exposure time of 0.5 sec and the fact that the aircraft moves 20 m during this time imply that it would be useful to use a statistical approach in analyzing the results. For this purpose it would be necessary to use a photodetection method with a short exposure time or to use some other rapid recording device.

There is another, extremely important, aspect of this problem: The thickness of the ice shown in Fig. 2 is calculated from the results of the sounding on the basis of the equation $h = v\tau/2$, where τ is the time interval between the reflected pulses and z is the propagation velocity of the signal in the ice.

The reliability of an interpretation of data from radar sounding of ice in the ocean is a function of the reliability of the signal-propagation velocity. The velocity of electromagnetic waves in ice in the ocean is governed by the relative amounts of liquid, solid, and gaseous phases (brine, crystalline ice, and air bubbles) in the ice. Accordingly, the propagation velocity of the radar signal can differ in ice formations of different ages and which were formed under different conditions. The velocity of vertical propagation of electromagnetic waves, averaged over the thickness, has been measured in regions of the ice fields along the flight path. These measurements show that the wave velocity in pack ice takes on different values over the same ice field. In regions devoid of a snow cover the propagation velocity averages 150 m/μsec (Fig. 3); in regions where the snow cover is more than 0.5 m thick, this velocity decreases with decreasing ice thickness. This fact can be explained by assuming that heat accumulates under snow-covered regions, so these regions are relatively rich in the liquid phase. Accordingly, the results of the radar sounding make the ice pack seem more homogeneous with respect to thickness than it actually is. Where the ice has a clearly defined porous structure, the propagation velocity is 190-200 m/μsec. The velocity of electromagnetic waves in young ice 1 m thick is 90-100 m/μsec at a stable air temperature of from −23 to −25°C. This velocity decrease is attributed to the greater salinity of young ice, since a high salinity is also a prerequisite for a relatively high content of liquid phase. The velocity of the radar signal in young ice is presumably governed significantly by the temperature conditions also. The velocity may be lower, the thinner the ice and the higher its temperature. Because of the fluctuations in the signal velocity in ice in the ocean, a correct interpretation of the results of radar mapping of the thickness requires a knowledge of the temperature conditions and a classification of the ice being probed.

---

[1] V. V. Bogorodskii, Physical Methods for Studying Glaciers [in Russian], Gidrometizdat, Leningrad (1968).

[2] V. V. Bogorodskii and V. P. Tripol'nikov, Problemy Arktiki i Antarktiki, No. 39, 135 (1972).

[3] M. I. Finkel'shtein, V. G. Glushnev, and A. N. Petrov, Fiz. Atmos. Okeana, 7, 1323 (1971).

[4] M. I. Finkel'shtein, Radiotekh. Elektron., 15, 2468 (1970).

[5] "Glacier sounding in polar regions," Reprint from Geographical J., 135, Part 4 (December, 1969).

Two-section solenoid with internal "equally-loaded" section; power as a function of the length of the internal section

G. S. Veisig, A.P. Doroshenko, and P. P. Rybin

Institute of Physics, Siberian Branch,
Academy of Sciences of the USSR, Krasnoyarsk

(Submitted July 3, 1973; resubmitted August 16, 1973)
Zh. Tekh. Fiz., 44, 662-666 (March 1974)

A two-section solenoid whose internal section is wound from a tape of varying width to provide the desired current density is analyzed. The turns of this internal section are not in mechanical contact with each other. The current-density distribution is specified in such a manner that the mechanical stress is the same, equal to the maximum tolerable, in all turns of the solenoid (except those of the external section). This distribution makes it possible to achieve strong magnetic fields. The outer radius of the internal section is shown to be a function of the length of this section; the functional dependence is found. The functional dependence of the power drawn by the entire solenoid on the length of the internal section is also found. There is a particular length of this section for which the power is a minimum. Upper and lower limits are found for this length.

The maximum solenoid field attainable with a material of limited strength is achieved by mechanically loading all the material of the solenoid to the maximum tolerable point[1] (we call such a solenoid an "equally loaded solenoid"). Since it is difficult to find the necessary current-density distribution j(r, z), we restrict the treatment below to a search for the values of j (r) which provide a uniform stress σ in the central plane of the solenoid, using the floating-turn model. In this case we have

$$\sigma = \frac{1}{10} H(r) j(r) r, \tag{1}$$

where H(r) is the magnetic field (in oersteds) at a point r between r_1 and r_2 [r_1 and r_2 are the inner and outer radii of the solenoid (in centimeters)], and σ and j(r) are given in dynes per square centimeter and amperes per square centimeter, respectively.

We approximate H(r) by

$$H(r) = \frac{4\pi\lambda}{10} \int_r^{r_2} j(r) \frac{k(r)}{\sqrt{k^2(r)+1}}\, dr, \tag{2}$$

where λ is the filling coefficient, and k(r) is equal to half the width of a layer of the solenoid winding divided by the radius of this layer. It should also be noted that Eq. (2) holds only for $k(r) \gg 1$. Then we can write Eq. (1) as

$$\sigma = r j(r) \frac{4\pi\lambda}{100} \int_r^{r_2} j(r) \frac{k(r)}{\sqrt{k^2(r)+1}}\, dr. \tag{3}$$

We are faced with the following problem: How do we vary j(r) in a real device in such a manner that it corresponds to Eq. (3) ? For this solenoid we adopt a wide tape of constant thickness, whose width 2b (r) we can vary at will. We note that b (r) = rk(r) and $j(r) = [j(r_1)k(r_1)r_1]/[rk(r)]$.

Substituting the latter expression into (3), we find an equation for k(r) as

$$k(r) = \frac{4\pi\lambda j^2(r_1) k^2(r_1) r_1^2}{100\sigma} \int_r^{r_2} \frac{dr}{r\sqrt{k^2(r)+1}}. \tag{4}$$

We then see that $k(r_2) = 0$. This result contradicts the condition $k(r) \gg 1$ and also leads to $j(r_2) = \infty$, which is meaningless. To avoid this difficulty, we assume the solenoid to be in an external field H_1 (i.e., we introduce an external section of the Bitter or Kolmov type; the structure of the latter is preferable, since it allows us to construct the solenoid from a single common tape).

Then Eq. (4) becomes

$$k(r) = \frac{j(r_1)\, k(r_1) r_1}{10\sigma} \left(\frac{4\pi\lambda j(r_1)\, k(r_1) r_1}{10} \int_r^{r_2} \frac{dr}{r\sqrt{k^2(r)+1}} + H_1 \right).$$

If we assume $\sigma = (1/10) r_1 j(r_1) H_0$ [$H_0 = H(r_1) + H_1$], we can rewrite the equation for k(r) as

$$k(r) = \frac{k(r_1)}{H_0} \left(\frac{4\pi\lambda\sigma k(r_1)}{H_0} \int_r^{r_2} \frac{dr}{r\sqrt{k^2(r)+1}} + H_1 \right). \tag{5}$$

Then we see that

$$k(r_2) = \frac{H_1}{H_0} k(r_1). \tag{6}$$

Differentiating the right and left sides of (5) with respect to r, we find a differential equation with separable variables[2] whose solution is

$$\ln\frac{r}{r_1} = \frac{H_0^2}{8\pi\sigma\lambda k^2(r_1)} \Big[k(r_1)\sqrt{k^2(r_1)+1} - k(r)\sqrt{k^2(r)+1} + \ln\frac{k(r_1)+\sqrt{k^2(r_1)+1}}{k(r)+\sqrt{k^2(r)+1}} \Big].$$

Then using (6) we find

$$\alpha = \left[\frac{k(r_1)+\sqrt{k^2(r_1)+1}}{hk(r_1)+\sqrt{h^2k^2(r_1)+1}} \right]^{\frac{\tau}{k^2(r_1)}} e^{\frac{\tau}{k^2(r_1)}\left[k(r_1)\sqrt{k^2(r_1)+1} - hk(r_1)\sqrt{h^2k^2(r_1)+1}\right]}, \tag{7}$$

where

$$\alpha = \frac{r^2}{r_1}, \quad h = \frac{H_1}{H_0}, \quad \tau = \frac{H_0^2}{8\pi\sigma\lambda}.$$

In Eq. (7), $k(r_1)$ and H_1 appear as independent variables. Analysis of their changes shows that α increases as $k(r_1)$ decreases, while α tends toward $\exp[(H_0^2 - H_1^2)/8\pi\sigma\lambda]$ as $k(r_1)$ becomes infinite. Similarly, α becomes infinite as H_1 tends toward zero, while α tends toward unity as H_1 tends toward H_0.

Let us consider the power drawn by the entire solenoid as a function of $k(r_1)$ and H_1. This power, W (watts), can be written as

$$W = \frac{400\pi\lambda\sigma^2 k^2(r_1)\rho}{H_0^2}\int_{r_1}^{r_2}\frac{dr}{k(r)} + \frac{H_1^2\rho}{G^2\lambda}r_2, \tag{8}$$

where ρ is the resistivity ($\Omega \cdot$ cm), G is the form factor of the external section,[3] and r_2 is both the external radius of the internal section and the internal radius of the external section.

In Eq. (8), as in Eq. (7), $k(r_1)$ and H_1 appear as independent variables. It is very important to ascertain the behavior of W as a function of $k(r_1)$ and H_1. For this purpose it is necessary to find the value of $k(r_1)$ at which W is a minimum, i.e., to find the best form factor for the entire solenoid.

We apply the mean-value theorem[4] to the integral in Eq. (8); then using Eq. (5) and performing some trivial transformations of Eq. (8), we find

$$W = wk(r_1)(r_2 - r_1) + Vr_2, \tag{9}$$

where

$$w = \frac{400\pi\sigma^2\lambda\rho}{H_0(H(\xi) + H_1)}\quad (r_1 \leqslant \xi \leqslant r_2),$$

$$V = \frac{H_1^2\rho}{G^2\lambda}.$$

Since $\lim_{k\to\infty}(k/\sqrt{k^2+1}) = 1$, we have $k(r_1) \sim \sqrt{k^2(r_1)+1}$ for $k(r_1) \gg 1$. Equation (7) can thus be rewritten as

$$\alpha = th^{-\frac{\tau}{k^2(r_1)}}, \tag{10}$$

where $t = \exp[(H_0^2 - H_1^2)/8\pi\sigma\lambda]$. Hence Eq. (9) becomes

$$W = r_1 wk(r_1)\left(th^{-\frac{\tau}{k^2(r_1)}} - 1\right) + r_1 Vth^{-\frac{\tau}{k^2(r_1)}}. \tag{11}$$

Analysis of Eq. (11) shows that $W = r_1 V$ at $H_1 = H_0$ (i.e., in this case only the external section draws power), and the power increases without bound as H_1 tends toward zero. This result again emphasizes the need for an additional section for our solenoid.

We now expand $h^{-\tau}/k^2(r_1)$ in a series in powers of $1/[k^2(r_1)]$:

$$h^{-\frac{\tau}{k^2(r_1)}} = \sum_{n=0}^{\infty}\frac{1}{n!}a^n\left(\frac{1}{k^2(r_1)}\right)^n,$$

where $a = \tau \ln h^{-1}$. Then Eq. (11) becomes

$$W(k(r_1)) = wr_1 k(r_1)(t-1) + r_1 Vt$$
$$+ r_1 wt\sum_{n=1}^{\infty}\frac{1}{n!}a^n\left(\frac{1}{k(r_1)}\right)^{2n-1} + r_1 Vt\sum_{n=1}^{\infty}\frac{1}{n!}a^n\left(\frac{1}{k(r_1)}\right)^{2n}.$$

Now it is easy to see that the function $W[k(r_1)]$ is analytic on the interval $(0, \infty)$, so it can be continued over the entire interval.[5]

TABLE 1

No.	H_0, kOe	σ, kg/mm^3	$k(r_1)$	α (common)	G
1	250	40	2.14	6	0.148
2	350	40	3	11.6	0.101
3	350	60	3	8.3	0.078
4	500	60	4.29	20.2	0.050
5	500	80	4.29	13.5	0.051
6	500	100	4.29	10.9	0.049
7	700	100	6	39	0.025
8	700	120	6	24.6	0.028

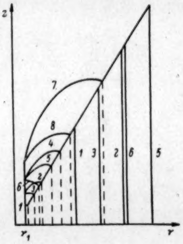

Fig. 1. Profiles of various solenoids (one fourth of a cross section is shown). The labels on the curves correspond to the boundaries between the internal and external sections; r_1 is the internal radius of the solenoids. The external sections are not shown for solenoids 4, 7, and 8 (because of their large size).

The first derivative of $W[k(r_1)]$ with respect to $k(r_1)$, $W'_{k(r_1)}[k(r_1)]$, is

$$W'(k(r_1)) = r_1 w(t-1) - r_1 wt\sum_{n=1}^{\infty}\frac{2n-1}{n!}a^n\left(\frac{1}{k(r_1)}\right)^{2n}$$
$$- r_1 Vt\sum_{n=1}^{\infty}\frac{2n}{n!}a^n\left(\frac{1}{k(r_1)}\right)^{2n+1}.$$

Then we see that $W'_{k(r_1)}(0) = -\infty$ and $W'_{k(r_1)}(\infty) = r_1 w(t-1)$, and the first derivative of $W[k(r_1)]$ with respect to $k(r_1)$ is everywhere positive on the interval $(0, \infty)$. It follows that the function $W[k(r_1)]$ has a minimum at the one point $k(r_1) = km$.

Since it is difficult to find km, we restrict the treatment here to a search for that interval (A, B) on which $W[k(r_1)]$ is close to the minimum, and near point A of which the function $W[k(r_1)]$ decreases (it increases at point B). We find the end points of this interval to be

$$A = \left(\frac{ta}{t-1}\right)^{1/3},$$

$$B = \frac{wA(th^{-\tau/A^2} - 1) + Vt(h^{-\tau/A^2} - 1)}{w(t-1)}.$$

Numerical evaluations of A, B, and $W[k(r_1)]$ show that the interval (A, B) lies between 2 and 6. Under these conditions, the solenoid is not too long, but the field is sufficiently homogeneous. If we turn our attention from the power to the form factor, we find that for fields no stronger than 700 kOe the form factor does not fall below 0.02, i.e., it remains high enough to allow us to proceed to engineering calculations.

Since all the calculations carried out analytically are approximate, of an accuracy inadequate for actual design, we have worked out a program for calculations on an M222 computer and carried out calculations for the following solenoids: a field of 250 kOe and a strength of 40 kg/mm^2; 350 kOe and strength of 40 and 60 kg/mm^2; 500 kOe and strengths of 60, 80, and 100 kg/mm^2; and 700 kOe and strengths of 100 and 120 kg/mm^2. We assume $k(r_2)$ to be equal to 1.5 [an assumption which always corresponds to the condition that $k(r_1)$ lie on the interval (A, B)], and we assume the external section to be a tape solenoid of trapezoidal cross section having $\alpha = 4.5$ (the ratio of the outer radius to the internal radius) and $k = 1.5$ ($G = 0.194$), mounted flush against the internal section. The field produced by the external section is $H_1 = 175$ kOe.

The calculated results are shown in Table 1, where, for convenience, the form factors are shown instead of the power.

Profiles of the solenoids are shown in Fig. 1.

---

[1] V. A. Ignatchenko and M. M. Karpenko, Zh. Tekh. Fiz., 38, 200 (1968) [Sov. Phys.—Tech. Phys., 13, 143 (1968)].

[2] I. G. Petrovskii, Lectures on the Theory of Ordinary Differential Equations [in Russian], Izd. Nauka, Moscow (1970).

[3] V. P. Karasik, Physics and Technology of Strong Magnetic Fields [in Russian], Izd. Nauka, Moscow (1964).

[4] V. I. Smirnov, Course in Higher Mathematics [in Russian], Vol. 1, Izd. Nauka, Moscow (1967).

[5] M. A. Evgrafov, Analytic Functions [in Russian], Izd. Nauka, Moscow (1968).

Optical radiation from nanosecond discharges in dense gases

L. P. Babich

(Submitted September 4, 1972)
Zh. Tekh. Fiz., 44, 666-667 (March 1974)

An equation is derived for the photon yield of the optical radiation in the discrete spectrum of nanosecond-range gas discharges. It is shown that the familiar Legler equation gives a yield which is an order of magnitude too high. The conditions under which this yield is proportional to the electron density are found. Under these conditions, the development of ionization in nanosecond-range gas discharges can be studied by an optical method.

The optical radiation in the discrete spectrum is an important source of information about the space-time development of gas discharges.[1-3]

Because of the recent interest in nanosecond gas discharges, we feel it worthwhile to determine the applicability to such discharges of the familiar results on the discrete-spectrum yield[1,2] and to evaluate the possibility of studying the characteristics of these discharges by an optical method.

In a dense gas the discrete-spectrum photon yield per ionization event, Q, is given by the following equation, which takes "quenching" into account:[2]

$$Q=Q_0\left(\frac{E}{p}\right)\left(1+\frac{p}{p_0}\right)^{-1}, \tag{1}$$

where $p_0 = (n_1\sigma_q v_{rel}\,\tau^*)^{-1}$ is a constant for a given gas, and $Q_0(E/p) = \langle\sigma_{ex}v_e\rangle/\langle\sigma_i v_e\rangle$ is a function which decreases with increasing E/p. Here, n_1 is the density of the gas particles (the value of n_g at p = 1 torr and t = 0°C, $v_{rel} = \sqrt{2}vT$ is the average relative velocity of the gas particles, v_e is the electron velocity, τ^* is the lifetime of the excited state, σ_{ex} and σ_i are the cross sections for excitation and ionization by electron impact, and σ_q is the "quenching" cross section.

Introducing the average rates

$$\nu_{ex}=n_1\langle\sigma_{ex}v_e\rangle,\ \nu_i=n_1\langle\sigma_i v_e\rangle,\ \nu_q=n_1\sigma_q v_{rel},\ \nu^*=\tau^{*-1},$$

we can write

$$\frac{dn^*}{dt}=p\nu_{ex}n_e-\nu^*n^*-p\nu_q n^* \tag{2}$$

for the rate at which excited atoms are generated in the given state per unit volume,

$$\frac{dn_e}{dt}=p\nu_i n_e \tag{3}$$

for the rate of impact generation of electrons, and

$$\frac{dn_{\mathrm{m}}}{dt}=\nu^*n^* \tag{4}$$

for the rate of spontaneous emission of photons. Here we have assumed n^*, $n_e \ll n_g$.

A joint solution of Eqs. (2)-(4) with $dn^*/(dt) = 0$ leads to Eq. (1). However, in nanosecond discharges the equilibrium between the generation and decay of excited states is disrupted, since the discharge duration satisfies $t \leqslant \tau^*$, $(p\nu_q)^{-1}$, and the derivative on the left side of Eq. (2) can turn out to be larger than the last two terms on the right side.

Solving Eqs. (2)-(4) jointly for $dn^*/(dt) \neq 0$, we find

$$n_{\mathrm{m}}(t)=\frac{p\nu_{ex}\nu^*}{\nu^*+p(\nu_i+\nu_q)}\,n_e(0)\left\{\frac{\exp(p\nu_i t)-1}{p\nu_i}+\frac{\exp[-(\nu^*+p\nu_q)t]-1}{\nu^*+p\nu_q}\right\}. \tag{5}$$

With $(\nu^*+p\nu_q)t \gg 1$, $p\nu_i t \gg 1$, $p\nu_i \ll \nu^*+p\nu_q$, we find Eq. (1) from Eq. (5).

If $p\nu_i t \gg 1$ and

$$(\nu^*+p\nu_q)t\ll 1 \tag{6}$$

or

$$\exp(p\nu_i t)\gg\frac{p\nu_i}{\nu^*+p\nu_q}, \tag{6a}$$

then

$$Q=\frac{n_{\mathrm{m}}}{n_e}=\frac{\nu_{ex}}{\nu_i}\frac{\nu^*}{\nu^*+p(\nu_i+\nu_q)}=Q_0\left(\frac{E}{p}\right)\left[1+\frac{p}{p_1\left(\frac{E}{p}\right)}\right]^{-1}, \tag{7}$$

where $p_1(E/p) = p_0(1+\nu_i/\nu_q)^{-1}$ is a function of E/p.

Accordingly, when (6) or (6a) holds the proportionality is conserved between the photon yield from a unit volume of a discharge and the electron density at the given instant.

If we neglect electron diffusion,[4] we have $\nu_i = (\alpha/p)v_-$, where α is the first Townsend coefficient and v is the electron drift velocity; then p_1 and conditions (6) and (6a) become

$$p_1=p_0\left(1+\frac{p_0\alpha v_-}{p\nu^*}\right)^{-1}, \tag{8}$$

$$\left(1+\frac{p}{p_0}\right)\nu^*t\ll 1, \tag{9}$$

$$\left(1+\frac{p}{p_0}\right)\nu^*\exp(\alpha v_- t)\gg\alpha v_-. \tag{9a}$$

TABLE 1

	p_0, torr [1,2]	$\frac{\alpha}{p}$, cm^{-1}·torr^{-1} [6]	v_-, cm/sec	ν^*, sec^{-1} [2]	p_1, torr	$\frac{Q(7)}{Q_0}$	$\frac{Q(1)}{Q_0}$
N_2	60	0.455	$2.94 \cdot 10^7$	$2.86 \cdot 10^7$ [7],	2.1	$2.7 \cdot 10^{-3}$	$7.3 \cdot 10^{-2}$
				$5.56 \cdot 10^7$	3.9	$5.1 \cdot 10^{-3}$	
H_2	20	0.785	$3.85 \cdot 10^7$	$\sim 10^8$	1.4	$1.9 \cdot 10^{-3}$	$2.6 \cdot 10^{-2}$

Table 1 shows values found for $Q(7)/Q_0$ in N_2 for the transition $C^3\Pi_u \rightarrow B^3\Pi_g$ (the second positive system) and in H_2 for transitions from $2^1\Pi_u$ (the Werner series) in nanosecond range discharges with $E/p = 100$ V/(cm · torr) and $p = 760$ torr. Also shown here are the values of $Q(1)/Q_0$ calculated from Eq. (1). For v_- we used the results of a linear extrapolation of the data of ref. 5 into the region of large E/p (Table 1).

We see that the use of the equation for the photon yield of photons per ionization event based on the condition of an equilibrium between the generation and decay of excited states leads to a yield in the case of nanosecond discharges which is more than an order of magnitude higher.

The constancy of the photon yield per ionization event for a given value of E/p in nanosecond-range discharges allows us to use an optical method for studying the development of ionization in such discharges.

---

[1] H. Raether, Electron Avalanches and Breakdown in Gases, Butterworth and Co., London.

[2] W. Legler, Zs. Phys., 173b, 169 (1963).

[3] H. Tholl, Zs. Naturforsch., 19a, 346, 704 (1964).

[4] L. Huxley, Austr. J. Phys., 21, 761 (1968).

[5] J. Frommhold, Zs. Phys., 160b, 554 (1960).

[6] J. M. Meek and J. D. Craggs, Electrical Breakdown of Gases, Oxford Univ. Press, London (1953).

[7] R. Imholf and F. Read, J. Phys. B. (Atom. Mol. Phys.), 4, 1063 (1971).

Plasma density in a magnetoplasma compressor

A. K. Vinogradova, V. P. Vinogradov, A. I. Morozov, and A. A. Sergeev

(Submitted August 15, 1973)
Zh. Tekh. Fiz., 44, 668-671 (March 1974)

The plasma density distribution is measured in the gap between the electrodes and at the focus in a magnetoplasma compressor by means of a Michelson interferometer with time resolution. The process is shown to be quasisteady-state; oscillations occur and are particularly intense when neutron emission is observed.

A magnetoplasma compressor is a coaxial system in which the plasma acceleration is accompanied by a radial contraction of the plasma.[1-4] We report here measurement of the plasma-density distribution in such a compressor having time resolution. The experimental results reported here have been obtained for the two compressors shown schematically in Fig. 1. The discharge is achieved in hydrogen at an initial pressure of 0.25-5 torr. Oscillograms of the voltage and the discharge current are shown in Fig. 2.

The plasma density is measured with a Michelson interferometer. The interference pattern is projected onto the slit of a camera operating in the streak mode. The slit is perpendicular to the axis of the compressor. When the interferometer and the camera are moved along the axis of the system, the radial distribution of the density can be measured in various cross sections along the z axis (Fig. 1). The light source is a modified He–Ne laser (LG-75), which can operate in either the continuous or pulsed modes. The maximum radiation density in the pulse, whose length is ~2 msec, is nearly the same (~25 mW) as in the continuous mode. The intensity of the laser light varies negligibly during the time which elapses during the events being studied. For a better use of the output power of the laser, the light beam is expanded by a cylindrical lens in the direction parallel to the camera slit. The interferograms are synchronized with oscillograms of the discharge current and voltage by means of a brief light flash from an IFK-20 lamp, which is triggered at the same time as the discharge. The resolving time, governed by the intensity of the illuminator and the sensitivity of the photographic film, is 0.5 μsec. The interferometer operates in either of two modes: In the first mode the mirrors are adjusted so that the interference field contains a large number of fringes (20-50), which are perpendicular to the slit of the streak camera. This mode is used primarily to obtain radial distribution of the plasma density. The second mode, in which there only one or two fringes, is used to obtain a clear picture of the density distribution (Fig. 3).

The fringe shift is measured on a Mir-12 microscope within 0.01 mm, corresponding to 0.05 of an interference fringe when the shift being measured is from 0.2 to two fringe widths. From the interferograms we select those which are most symmetric with respect to the axis, and we subject them to the Abel inversion. The radial distribution is averaged over several discharges for each cross section and for each time selected.

At a certain time on the interferograms we usually see an approximately identical shift of the fringes over the entire field of vision (8 cm). This shift is due to the appearance of low-density plasma between the external electrode and the chamber walls. In the analysis of the interferograms carried out to determine the plasma-density distribution near the axis of the instrument this fringe shift causes a small correction to the calculated plasma density and is usually subtracted as a background.

Interferograms are recorded inside the accelerating channel at three cross sections along the z axis; the density distributions are shown in Fig. 4. There is a general tendency for the density to increase with decreasing R and increasing z, in agreement with the assumed pattern of particle motion in the accelerating channel of a magnetoplasma compressor. Details of the distribution are still quite uncertain, and additional experiments are required for a more complete picture of the plasma flow. The dip in the density near the cathode evident from Fig. 4 can be attributed to a stronger magnetic field there,[2] which leads to a magnetization of the electrons, the appearance of a gradient in the electric field, and the acceleration of ions in this region. At the end of the cathode the magnetic field weakens, and the dip vanishes.

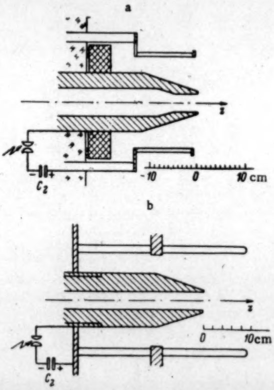

Fig. 1. Two versions of the compressor with rod anodes. a) MPK-1; b) MPK-2. The anode of MPK-1 is made from 28 rods; that of MPK-2 is made from 12 rods.

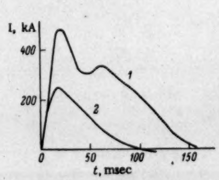

Fig. 2. Oscillograms of the discharge current. 1) MPK-1, U_0 = 3 kV, p_0 = 5 torr; 2) MPK-2, U_0 = 5 kV, p_0 = 0.25 torr.

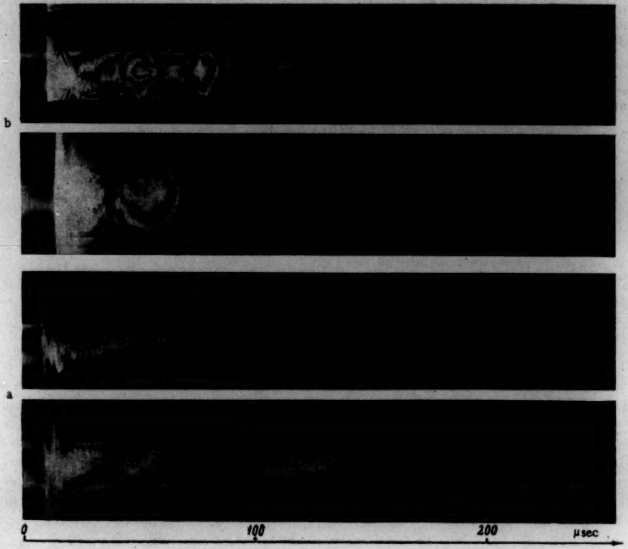

Fig. 3. Series of interferograms corresponding to the cross section z = 4 cm (1) and the cross section z = 10 cm (2) for the same (U_0 = 5 kV) initial voltage on the capacitor bank of the MPK-2, p_0, torr: a) 0.25; b) 2.

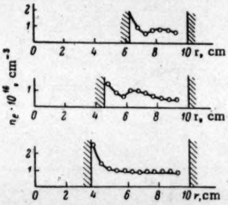

Fig. 4. Distribution of the plasma density in the accelerating channel of the MPK-1. p_0 = 5 torr, U_0 = 3 kV, t = 50 μsec. The electrodes are indicated by the hatching. z, cm: a) 10.5; b) 5.5; c) 2.5.

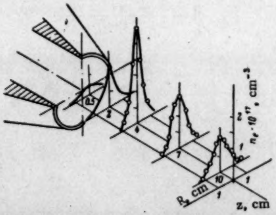

Fig. 5. Radial distribution of the plasma density in the compression zone of the MPK-2. p_0 = 0.25 torr U_0 = 5 kV, t = 40 μsec.

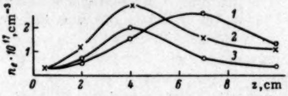

Fig. 6. Distribution of the plasma density along the axis of the MPK-2. U_0 = 5 kV, p_0 = 0.25 torr. t, μsec: 1) 30; 2) 40; 3) 60.

The radial distribution of the plasma density is shown in Fig. 5 for several cross sections beyond the end of the cathode (z > 0). While the average density in the gap is $\sim 10^{16}$ cm^{-3} (Fig. 4), it reaches a value of $\sim 4 \cdot 10^{17}$ cm^{-3} at the "focus," 4 cm from the end of the cathode. We see from Figs. 5 and 6 that the region of increased density has a radius of ~0.5 cm and a length of ~5 cm. Interestingly, the maximum density is a weak function of the initial gas pressure in the chamber. For example, as the initial pressure is increased from 0.25 to 2 torr, the maximum density at the z = 4 cm cross section does not change by more than a factor of 1.5-2. The plasma density at the compressor axis measured in discharges having different initial voltages on the capacitor bank (3, 4, and 5 kV) at times corresponding to a given discharge current turns out to be the same, within the spread in experimental values. This result is evidence for the quasisteady-state nature of the process i.e., it shows that the plasma properties in the compression zone are governed by the instantaneous value of the discharge current and are relatively weak functions of the time which has elapsed since the beginning of the discharge.

On almost all the interferograms we see that there are oscillations of the focus in the direction perpendicular to the axis of the compressor (radial oscillations), and there are periodic changes in the plasma density. Both types of oscillations are characterized by frequencies of 500 kHz and higher. As the initial gas density is increased, the oscillation amplitude decreases. At a very low initial voltage (3 kV), the frequency of the radial oscillations decreases (~ 200 kHz), while their amplitude increases significantly.

For several microseconds after the discharge current reaches its maximum the plasma oscillations at the focus are strongest and occur at the highest frequency. It is during this period that the focus is the source of neutron emission in operation with deuterium.[5]

In conclusion the authors thank P. E. Kovrov and L. G. Tokarev for assistance in the experiments.

---

[1] A. I. Morozov, P. E. Kovrov, and A. K. Vinogradova, ZhETF Pis. Red., 7, 257 (1968) [JETP Lett., 7, 199 (1968)].

[2] A. E. Prinn, B. W. Ricketts, N. Tsagas, and A. A. Newton, Fifth European Conference on Controlled Fusion and Plasma Physics, Contributed Papers, Vol. 1, Grenoble, France (1972).

[3] A. K. Vinogradova, P. E. Kovrov, A. I. Morozov, and L. G. Tokarev, Zh. Tekh. Fiz., 43, 2553 (1973) [Sov. Phys.—Tech. Phys., 18, 1604 (1974)].

[4] R. P. Vasil'eva, M. I. Pergament, and A. I. Yaroslavskii, Plasma Physics and Controlled Nuclear Fusion Research, Vol. 2, IAEA, Vienna (1969), p. 39.

[5] A. K. Vinogradova, V. P. Vinogradov, and A. I. Morozov, Zh. Tekh. Fiz., 43, 1637 (1973) [Sov. Phys.—Tech. Phys., 18, 1032 (1974)].

Investigation of spatial distributions in a laser-produced plasma by Hα absorption

G. V. Ostrovskaya and N. A. Pobedonostseva
A. F. Ioffe Physicotechnical Institute,
Academy of Sciences of the USSR

(Submitted July 16, 1973)
Zh. Tekh. Fiz., 44, 671-674 (March 1974)

In an earlier paper,[1] the parameters of a plasma produced by a laser in hydrogen were determined from the absorption of the Hα line. A laser spark in air was used as the continuum source. The operation of the two lasers (producing sparks in hydrogen and in air) is synchronized by one of the Q-switching prisms. The same prism is also used to obtain a time scan of the laser spark emission along the spectrograph slit. A homogeneous plasma is assumed in the first-order approximation. We then determine the average plasma parameters over the absorbing layer.

The present paper presents a detailed study of the spatial distribution of the parameters of a laser-produced plasma. The investigation is of interest both for the possibility of measuring plasma parameters by the absorption method and for developing a gasdynamic model of the expansion of the laser-produced plasma.

The apparatus described in ref. 1 is used to determine local plasma parameters. However, the time scan of the plasma emission is in the direction perpendicular to the spectrograph slit (Fig. 1a). The absorption spectrum obtained in this case corresponds to a particular time (the exposure time ≈ 60 nsec), while the spectral energy distribution determined from the height of the line corresponds to different regions of the plasma. An additional lens is also employed to image the air spark on the stop, after which the image is projected onto the spark in hydrogen. The stop allows us to observe the half-line from one side of the axis of symmetry of the spark during emission and to observe from the other side during absorption (Fig. 1b).

By taking these spectrograms at different distances from the axis, one can measure the values $\overline{kl}$ averaged over different cross sections (k is the absorption coefficient and l is the thickness of the illuminated layer). The radial distribution of the absorption coefficient can be obtained from $\overline{kl}$ by solving the Abel equation numerically using the Pierce method.[2] The radial distribution $k_{\lambda 0}(r/r_0)$ of the absorption coefficient at the center of the line is shown in Fig. 2 for a pressure of 3 atm. Measurements are performed at three times ($\tau = 0.8, 1.3, 1.7$ sec); however, in this figure, as in all the following figures, the experimental error is given only for the curves corresponding to $\tau = 0.8$ sec. As can be seen from the figure, the absorption coefficient is a maximum near the boundary of the illuminated zone and decreases towards the center of the plasma. As τ increases the distribution of the absorption coefficient becomes more uniform.

The values of $k_\lambda(r/r_0)$ are obtained for different distances from the center of the absorption line in similar fashion. This allows us to construct local profiles of the absorbed line. Figure 3 gives the local values of the linewidth Δλ. The local profiles of the absorbed line are used to determine the electron density N_e and the density of absorbing atoms N*; the atomic density N_0 is the normal state and the temperature T are calculated by assuming thermodynamic equilibrium.

The electron density is calculated from

$$N_e = 8 \cdot 10^{12} \left(\frac{\Delta\lambda}{\alpha_{1/2}}\right)^{3/2}, \tag{1}$$

where $\alpha_{1/2}$ is the half-width of the Stark profile calculated from Griem and Δλ is the experimental value of the absorption linewidth (in Å) measured at half-height.

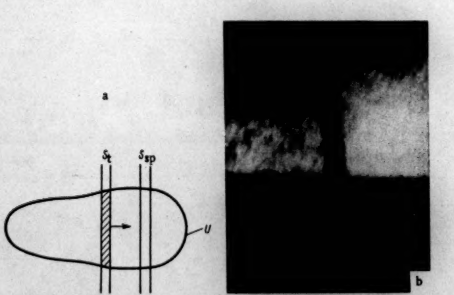

Fig. 1. (a) Arrangement for obtaining the spectrum with time and spatial resolution: U) image of the spark; S_t) time slit; S_{sp}) spectral slit; the shadowed region is cut off by the time slit and the arrow indicates the scanning direction. b) The upper portion shows the absorbed Hα line, the lower portion shows the emitted line.

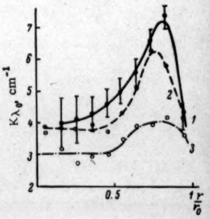

Fig. 2. Radial distribution of the absorption coefficient in the center of the Hα line. Here and in Figs. 3-6: τ in μsec: 1) 0.8; 2) 1.3; 3) 1.7.

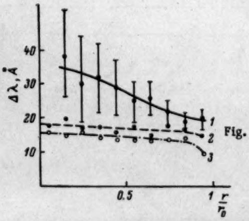

Fig. 3. Local values of the Hα linewidths.

TABLE 1. Parameters of the Laser Spark Plasma

	τ, μsec											
	0.8				1.3				1.7			
	I	II	III	IV	I	II	III	IV	I	II	III	IV
$k_{\lambda 0}$, cm^{-1}	7.4	4.0	5.0	5.0	6.3	3.8	4.5	4.5	4.1	3.0	3.4	3.6
Δλ, Å	38	20	27	26	18	15	17	18	16	10	14	14
$N_e \cdot 10^{-17}$, cm^{-3}	8.6	3.0	5.2	4.9	2.8	2.1	2.6	2.8	2.2	1.1	1.9	1.8
$N^* \cdot 10^{-15}$, cm^{-3}	1.8	1.0	1.3	1.3	1.0	0.6	0.7	0.7	0.50	0.40	0.42	0.44
$N_0 \cdot 10^{-17}$, cm^{-3}	10.0	0.8	2.7	1.8	7.0	1.5	3.7	2.9	7.7	1.7	3.2	2.8
T, deg	23000	17000	18800	18700	17000	14400	15700	16000	16000	12000	15100	15000

Note: (I) maximum value, (II) minimum, (III) average, (IV) integrated.

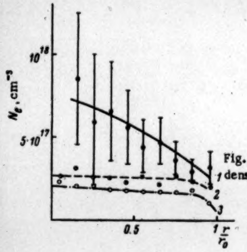

Fig. 4. Radial distribution of electron density.

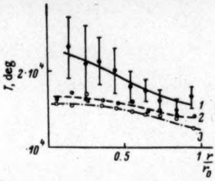

Fig. 6. Radial distribution of the temperature.

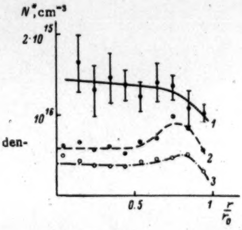

Fig. 5. Radial distribution of the density of absorbing atoms.

To determine N^*, N_0, and T we use the well-known equation relating $\int_0^\infty k_\nu d\nu$ to the density of absorbing atoms:

$$\int_0^\infty k_\nu d\nu = \frac{\pi e^2}{m_0 c} f_s N^* \left(1 - e^{-(\Delta E)/(kT)}\right), \tag{2}$$

and the Boltzmann and Saha equations. The radial distributions of N_e, N^*, and T calculated from these equations are shown in Figs. 4-6. It follows from these figures that within the limits of experimental error for N_e (≈30%), N^* (≈ 20%), and T (≈ 25%), the radial distribution of these quantities is fairly uniform.

The table gives the maximum, minimum, and average radial values of $k_{\lambda 0}$, Δλ, N_e, N^*, N_0 and T, and also the values of these parameters determined from the integrated (over the central cross section) profile of the Hα line (without using the Abel equation). Comparison of these data indicates that the plasma parameters determined from the absorption line profiles integrated over the cross section give a reasonable fit to the average radial values of these parameters.

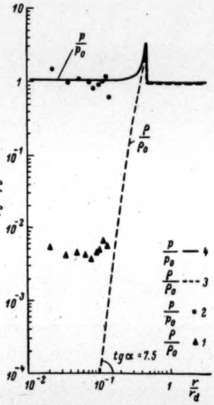

Fig. 7. Radial distribution of the density (1 is experimental and 2 theoretical) and the pressure (2 is experimental and 4 theoretical). The abscissa gives the distance from the center of the plasma with respect to the dynamic radius $r_d = (E_0/p_0)^{1/3}$ where E_0 is the energy released at the center (≈ 10^6 ergs).

The measured values of N_e, N_0, and T are used to calculate the radial density distribution of the gas $\rho = m_H (N_e + N_0)$ and the pressure $p = kT\,(2N_e + N_0)$. In Fig. 7, the radial distributions of ρ and p refer to the initial density ρ and pressure p_0 at time τ = 0.8 μsec. This figure also gives the radial distributions of ρ and p for a point explosion with a back pressure calculated according to Korobeinikov.[4] It is evident from the figure that the experimental values of the pressure give a good fit to the theoretical curve while the gas density distribution differs substantially from that given by point explosion theory.

Thus, in spite of the fact that point explosion theory gives a fairly good description of the propagation of a shock wave arising in the laser-produced breakdown of gases[5,6] and also of the density profile behind the shock front,[7] the theory does not provide an adequate description of the plasma parameters in the central regions, primarily because of the limited area of energy release during laser spark formation.

---

[1] T. P. Evtushenko, V. Kh. Mkrtchyan, and G. V. Ostrovskaya, Zh. Tekh. Fiz., 41, 2581 (1971) [Sov. Phys.—Tech. Phys., 16, 2049 (1972)].

[2] V. I. Pierce, in: Production and Investigation of High-Temperature Plasma, V. A. Fabricant (ed.) [Russian translation], IL, Moscow (1962), p. 221.

[3] H. R. Griem, Plasma Spectroscopy, McGraw-Hill, New York (1964).

[4] V. P. Korobeinikov, N. S. Mel'nikov, and E. V. Ryazanov, Point Explosion Theory [in Russian], Fizmatgiz, Moscow (1961).

[5] T. P. Evtushenko, G. M. Malyshev, G. V. Ostrovskaya, V. V. Semenov, and T. Ya. Chelidze, Zh. Tekh. Fiz., 36, 1115 (1966) [Sov. Phys.—Tech. Phys., 11, 818 (1966)].

[6] K. Büchl, K. Hohla, R. Wienecke, and S. Witkovski, Phys. Lett., 26A, 248 (1968).

[7] A. I. Alcock, E. Panarella, and S. A. Ramsden, in: Proc. Seventh Intern. Conf. on Phenomena in Ionized Gases, Belgrade (1965).

Two-omegatron study of the pumping characteristics of an NÉM-300 magnetic discharge pump for a mixture of gases

M. K. Bulgakov and V. G. Rogozinskii

(Submitted July 16, 1973)
Zh. Tekh. Fiz., 44, 674-767 (March 1974)

A two-omegatron method is used to study the pumping characteristics of an NÉM-300 magnetic-discharge pump as air and oxygen are admitted into the pump. The partial pumping rate of oxygen is shown to exceed that of nitrogen by a factor of 3-5. On the other hand, the pumping rate for a mixture of gases measured by a two-gauge method during the admission of air and oxygen is approximately equal to the calculated pumping rate for a given gas mixture. It follows from these results that measurement of the pumping rate by the two-omegatron method gives a more complete picture of the pumping process.

A qualitative picture of the pumping mechanism in a Penning cell, which is the pumping element in a magnetic-discharge pump, shows that the pumping of gases is affected by several factors, among which the composition of the gas being pumped and the pump memory are important. The effects of the components of the gas being pumped apparently are functions of their partial pressures and physical properties. These effects can be manifested in absorption of the gas being pumped on deposited titanium films and in the interaction of ions and gas with the cathode surface. For example, the presence of an argon impurity in the gas being pumped increases the rate at which titanium is sputtered and, thus, the rate at which the other gases are pumped.[1]

To study the pumping characteristics we use a system based on an ÉRA-300 apparatus, which consists of an NÉM-300 pump, in which one half of the electrode units have rectangular cells 20 × 40 mm in size while the other half have cells 20 × 60 mm in size,[2] and the measuring cap shown schematically in Fig. 1.

In the measurement procedure the complete spectrum of the gas mixture is recorded at each pressure by two IPDO-1 instruments, and the total pressure is measured by two VI-12 vacuum gauges. Before each measurement, a vacuum better than $3 \cdot 10^{-8}$ torr is established in the apparatus; the basic components of the residual gas spectrum under these conditions are H_2 (13.5%), N_2 + CO (67%), and Ar (6.%).

We study the pumping characteristics of the pump on the basis of a natural mixture of gases in air and on the basis of oxygen. Air flows into the pump through one of the leakage valves; the delay time between the pressure reading under the diaphgram and above the diaphgram in the range from $5 \cdot 10^{-8}$ to $5 \cdot 10^{-7}$ torr is 35-40 min, and at pressures above $5 \cdot 10^{-7}$ torr it is 15-20 min. The partial pressures and pumping rates are measured for the four basic components: H_2, CO + N_2, O_2, and Ar; account is taken of the sensitivity coefficient with respect to each gas. The pumping rate is calculated from

$$S_n = C\left(\frac{P_2}{P_1} - 1\right), \tag{1}$$

where C is the transmission of the diaphragm for the given gas, and P_1 and P_2 are the pressure below and above the diaphragm, respectively.

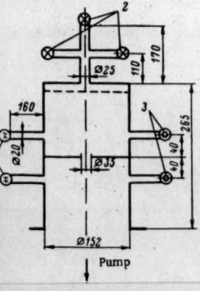

Fig. 1. The measuring cap. 1) RMO-4s pickup; 2) leakage valves for admitting the various gases; 3) IM-12 pickup.

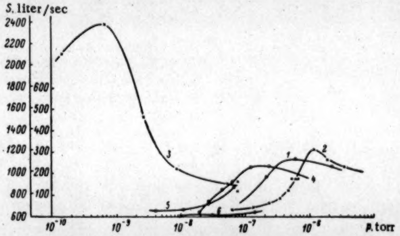

Fig. 2. Pumping rate as a function of the pressure during the admission of air. 1) Pumping rate calculated from the equation for a gaseous mixture; 2) pumping rate measured by the two-gauge method; 3) pumping rate for oxygen (scale of 600-2400 liter/sec); 4) pumping rate for nitrogen; 5) for hydrogen; 6) for argon.

We simultaneously measure the pumping rate for the gas mixture by the two-gauge method. For comparison, we calculate the pumping rate for a gaseous mixture from

$$S(\mathrm{cm}) = \frac{\sum_{i=1}^{n} s_i p_i \mu_i}{\sum_{i=1}^{n} r_i \mu_i \sum_{i=1}^{n} p_i}, \tag{2}$$

where s_i is the partial pumping rate of gas i, p_i is its partial pressure, μ_i is its molecular weight, and $r_i = p_i / \sum_{i=1}^{n} p_i$ is the relative pressure of the given gas in the mixture used in the measurement of the pumping rate. Using the procedure described above, we have carried out a series of measurements in which we supplied oxygen to one of the leakage valves. Figure 2 shows the pumping rates of the components as functions of the pressure in an air flow. We see from this figure that the pumping rate in terms of

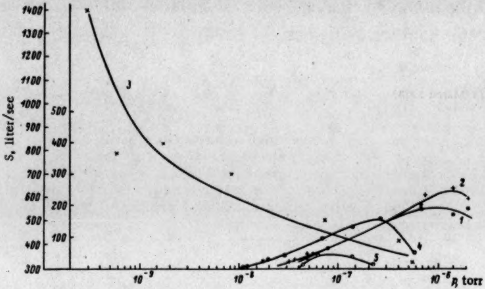

Fig. 3. Pumping rate as a function of the pressure for the admission of oxygen. 1) Pumping rate calculated from the equation for a gaseous mixture; 2) pumping rate measured by the two-gauge method; 3) pumping rate for oxygen (scale of 300-1400 liter/sec); 4) pumping rate for nitrogen; 5) for argon.

oxygen is much higher than that in terms of air. At pressures $3 \cdot 10^{-8}$-$5 \cdot 10^{-6}$ torr and at a pumping rate of 30-300 liter/sec in terms of air, the pumping rate in terms of oxygen is 2000-900 liter/sec at oxygen partial pressures in the range 10^{-10}-10^{-7} torr. The pumping rate calculated for the given mixture in accordance with Eq. (2) (curve 1) initially deviates slightly from the curve showing the pumping rate measured by the two-gauge method (curve 2), while in the range $8 \cdot 10^{-7}$-$3 \cdot 10^{-6}$ torr the two curves lie close together.

Figure 3 shows the pumping rates for the admission of oxygen. We see from these curves that the pumping rate in terms of oxygen is 1400-500 liter/sec over the pressure range $3 \cdot 10^{-10}$-10^{-7} torr. On the other hand, the pumping rate calculated on the basis of three components (O_2, N_2 + CO, Ar) is approximately equal to that measured by the two gauges in the pressure range $7 \cdot 10^{-8}$-$2 \cdot 10^{-6}$ torr.

The relative error in a measurement of the pumping rate is calculated from

$$\frac{\Delta s}{s} = \frac{2\frac{\Delta p_1}{p_1}}{1 - \frac{p_1}{p_2}}, \tag{3}$$

which is obtained from Eq. (1).

Including the relative error of about 10% of the IPDO-1 apparatus in calculating the pumping rates in terms of oxygen over the partial-pressure range from $3 \cdot 10^{-10}$ to $5 \cdot 10^{-7}$ torr, we find the relative error to be 20-25%.

It follows from the curves showing the partial pumping rates that the pumping rate in terms of oxygen for a mixture of oxygen and air is quite different from the pumping rate for nitrogen, especially at a low nitrogen partial pressure. When oxygen is admitted, its pumping rate is slightly lower than when air is admitted. These oxygen pumping rates with respect to the air pumping rates differ from the results reported in ref. 3, apparently because the pumping rate there was measured by a two-gauge method, in which no account was taken of the composition of the gas in the pump. It follows from Figs. 2 and 3 that the pumping rates calculated for a gas mixture are approximately equal to the values measured by the two-gauge method. Accordingly, the two-omegatron method gives a more complete picture of the nature of the pumping.

The high oxygen pumping rate can apparently be attributed to the high activity of oxygen in interactions with the titanium film.[4] It also follows from these results that the pumping of a gaseous mixture is affected by the mutual effects of all the components; this conclusion is based on the circumstance that the pumping rate for a gas mixture differs strongly from the pumping rates for such components as O_2, Ar, and H_2.

---

[1] B. D. Power, High Vacuum Pumping Equipment, Chapman, London (1966).

[2] V. G. Rogozinskii, V. V. Ryabov, and V. L. Ushkov, Preprint 70-89, Institute of High-Energy Physics, Serpukhov (1970).

[3] L. Malter and G. Mandoli, Residual Gases in Electron Tubes [Russian translation], Izd. Energiya, Moscow—Leningrad (1965).

[4] S. Dushman, Scientific Foundations of Vacuum Techniques, Wiley, New York (1962).

Possible use of the schlieren method to measure characteristics of turbulence

V. G. Ivanov
A. I. Ioffe Physicotechnical Institute, Academy of Sciences of the USSR, Leningrad

(Submitted July 9, 1973)
Zh. Tekh. Fiz., 43, 677-679 (March 1973)

Analytical expressions are derived which relate measured values of the correlation function and the one-dimensional spectrum of schlieren screen brightness fluctuations to the correlation function and the one-dimensional and energy spectra of refractive index fluctuations of a turbulent medium.

In investigations of turbulent flow of a liquid, gas, or plasma, increasing attention has been paid in recent years to optical methods which compare favorably with contact methods as regards good spatial resolution, absence of perturbation of the test medium, and the possibility of measurement in hot and high-speed gas flow.

However, optical methods of measuring turbulence characteristics have not as yet been widely applied because the output signal of the optical system (the screen brightness) has a complex functional dependence on the refractive index of the turbulent flow. It is therefore important to establish the relation between statistical characteristics of the refractive-index fluctuations and those of screen brightness.

Attempts to solve this problem for the most effective optical method, the schlieren method, have not led to satisfactory results. For example, the integrodifferential equation obtained in ref. 1 cannot be used to determine the statistical characteristics of refractive index fluctuations of a turbulent medium from measured values of the correlation function of the schlieren screen brightness since this equation does not relate these characteristics in explicit form. Again, analysis has shown that the final result obtained in ref. 2 is incorrect, while the expressions derived in ref. 3 are valid only for the case of a Gaussian distribution function for the correlation of refractive index fluctuations, a situation which is very dubious in turbulent flow (see ref. 4).

Let $n(\mathbf{x})$ be the fluctuating, statistically homogeneous field of the refractive index lying between $x_3 - l$ and $x_3 + l$ and extending to infinity in the other two directions. To within a dimensional constant, the schlieren screen brightness is related to the refractive index of a turbulent flow, with the knife-edge parallel to the flow, by the following expression:

$$C(x_1, x_2) = \int_{x_3-l}^{x_3+l} \frac{\partial}{\partial x_2} n(x_1, x_2, x_3)\, dx_3.$$

It can be seen from this expression that the refractive index field is reflected in that of the screen brightness by means of an integrodifferential operator belonging to the class of operators examined in ref. 5, viz.

$$C(\mathbf{x}) = \int K(\mathbf{s})\, n(\mathbf{x} + \mathbf{s})\, dV(\mathbf{s}), \tag{1}$$

where

$$K(\mathbf{s}) = \begin{cases} -\delta(s_1)\,\delta'(s_2) & \text{for} \quad s_3 \leqslant l, \\ 0 & \text{for} \quad s_3 > l, \end{cases}$$

δ is the delta function and δ' is the derivative of the delta function.

In what follows, where not explicitly stated, the integration is carried out over all space.

We denote by $E(\mathbf{k})$ and $T(\mathbf{k})$ the spectra of refractive index fluctuations and those of schlieren screen brightness, respectively.

Then, as follows from ref. 5, the original field spectrum is related to that of the image field as follows:

$$T(\mathbf{k}) = S(\mathbf{k})\, E(\mathbf{k}), \tag{2}$$

where

$$S(\mathbf{k}) = \frac{1}{(2\pi)^3} \int \psi(\tau) \exp(-i\mathbf{k}\tau)\, dV(\tau),$$

$$\psi(\tau) = \int K(\mathbf{s} + \tau)\, K(\mathbf{s})\, dV(\mathbf{s}).$$

Relation (2) permits an analogy to be drawn between optical measurement of turbulence parameters for which representation of the output signal in the form of Eq. (1) holds, and the passage of random signals through linear electrical circuits. For instance, the kernel $K(\mathbf{s})$ which determines the properties of the measuring system corresponds to the generalized response of a linear system to a unit pulse, while the function $S(\mathbf{k})$ is a generalization, to within a constant multiplier, of the square of the transfer function of the linear system. Thus, the function $S(\mathbf{k})$ shows how fluctuations of various frequencies (wave numbers) are transmitted by a linear measuring system.

We now calculate the functions $\psi(\tau)$ and $S(\mathbf{k})$ pertaining to the schlieren method:

$$\psi(\tau) = \int_{-l}^{l-|\tau_3|} ds_3 \iint_{-\infty}^{+\infty} \delta(s_1)\,\delta'(s_2)\,\delta(s_1 + \tau_1)\,\delta'(s_2 + \tau_2)\, ds_1 ds_2$$

$$= -(2l - |\tau_3|)\,\delta(\tau_1)\,\delta''(\tau_2) \quad \text{for} \quad |\tau_3| \leqslant 2l;$$

$$S(\mathbf{k}) = -\frac{1}{(2\pi)^3} \iint_{-\infty}^{+\infty} \int_{-2l}^{2l} (2l - |\tau_3|)\,\delta(\tau_1)\,\delta''(\tau_2)$$

$$\exp(-ik_1\tau_1 - ik_2\tau_2 - ik_3\tau_3)\, d\tau_1 d\tau_2 d\tau_3$$

$$= \frac{k_2^2 l^2}{2\pi^3} \left(\frac{\sin k_3 l}{k_3 l}\right)^2 \text{for } |\tau_3| \leqslant 2l.$$

In the expression obtained for $S(\mathbf{k})$ the factor $[\sin k_3 l/(k_3 l)]^2$ results from the light rays passing through an optical nonuniformity of width $2l$, while the factor k_2^2 represents the sensitivity of the schlieren method to the first derivative of the refractive index.

From Eq. (2) we have

$$T(\mathbf{k}) = \frac{k_2^2 l^2}{2\pi^3} \left(\frac{\sin k_3 l}{k_3 l}\right)^2 E(\mathbf{k}).$$

Taking the Fourier transform of T(k), we obtain an expression for the correlation function $\beta(\xi)$ for screen brightness fluctuations:

$$\beta(\xi)=\frac{l^2}{2\pi^3}\int k_3^2\left(\frac{\sin k_3 l}{k_3 l}\right)^2 E(\mathbf{k})\exp(i\mathbf{k}\xi)\,dV(\mathbf{k}).$$

If the width of the nonuniformity is much larger than any characteristic scale of the turbulence, the function $[\sin k_3 l/(k_3 l)]^2$ can be replaced by the delta function; then

$$\beta(\xi_1,\ \xi_2)=\frac{2l}{\pi^2}\int_0^\infty\int_0^\infty k_3^2 E\left(\sqrt{k_1^2+k_2^2}\right)\exp(ik_1\xi_1+ik_2\xi_2)\,dk_1dk_2.$$

We introduce the polar coordinates

$$k_1=k\cos\varphi,\quad k_2=k\sin\varphi,\quad dk_1dk_2=kdkd\varphi.$$

Then, the correlation function for screen brightness fluctuations measured along the x_1 axis is

$$\beta(\xi_1)=\frac{2l}{\pi^2}\int_0^\infty k^3E(k)\int_{-\pi}^{\pi}\sin^2\varphi\exp(ik\xi_1\cos\varphi)\,d\varphi dk=\frac{4l}{\pi\xi_1}\int_0^\infty k^2E(k)\,J_1(k\xi_1)\,dk. \tag{3}$$

Taking the Mellin transform of this expression we obtain the relation between the three-dimensional spectrum of refractive index fluctuations E(k) and the correlation function for screen brightness fluctuations $\beta(\xi_1)$:

$$kE(k)=\frac{\pi}{4l}\int_0^\infty \xi_1^2\beta(\xi_1)\,J_1(k\xi_1)\,d\xi_1. \tag{4}$$

Hinze[4] gives the following relation between the three-dimensional spectrum E(k), the energy spectrum $E_n(k)$, and the one-dimensional spectrum $E(k_1)$ as measured by means of instrumentation:

$$E_n(k)=4\pi k^2E(k),$$

$$E(k_1)=\int_{k_1}^\infty\frac{E_n(k)}{k}\,dk.$$

Then the expressions relating the correlation function for schlieren screen brightness fluctuations to the energy and one-dimensional spectra of refractive index fluctuations in a turbulent medium are as follows:

$$\left\{\begin{aligned}&\xi_1\beta(\xi_1)=\frac{l}{\pi^2}\int_0^\infty E_n(k)\,J_1(k\xi_1)\,dk, &(5)\\ &\frac{E_n(k)}{k}=\frac{\pi^2}{l}\int_0^\infty \xi_1^2\beta(\xi_1)\,J_1(k\xi_1)\,d\xi_1, &(6)\end{aligned}\right.$$

$$\left\{\begin{aligned}&\beta(\xi_1)=\frac{l}{\pi^2}\int_0^\infty k_1E(k_1)\,J_0(k_1\xi_1)\,dk_1, &(7)\\ &E(k_1)=\frac{\pi^2}{l}\int_0^\infty \xi_1\beta(\xi_1)\,J_0(k_1\xi_1)\,d\xi_1. &(8)\end{aligned}\right.$$

Thus, by means of Eqs. (4), (6), and (8) we can numerically integrate measured values of the correlation function for screen brightness fluctuations and obtain the three-dimensional, energy, and one-dimensional spectra of refractive index fluctuations.

We now consider the expression for the correlation function for fluctuations of a scalar field for the case of homogeneous and isotropic turbulence proposed by Tatarskii:[4]

$$R(r)=\frac{\gamma^2}{2^{\nu-1}\Gamma(\nu)}\left(\frac{r}{r_0}\right)^\nu K_\nu\left(\frac{r}{r_0}\right),$$

where K_ν is a modified Bessel function; Γ is the gamma function; γ is the mean square magnitude of the fluctuations; r_0 is the characteristic scale of the turbulence, and ν is a parameter determining the form of the correlation function.

Then the one-dimensional spectrum of refractive index fluctuations will be

$$E(k_1)=\frac{2\gamma^2}{\sqrt{\pi}}\frac{\Gamma\left(\nu+\frac{1}{2}\right)}{\Gamma(\nu)}\frac{r_0}{[1+(k_1r_0)^2]^{\nu+1/2}}. \tag{9}$$

Substituting Eq. (9) into Eq. (7), we obtain

$$\beta(\xi_1)=\frac{l}{\pi^{3/2}}\frac{\gamma^2}{\Gamma(\nu)\,2^{\nu-3/2}}\frac{1}{r_0}\left(\frac{\xi_1}{r_0}\right)^{\nu-1/2}K_{\nu-1/2}\left(\frac{\xi_1}{r_0}\right), \tag{10}$$

and therefore the one-dimensional spectrum of schlieren screen brightness fluctuations measured along the x_1 axis is

$$T(k_1)=\frac{2l}{\pi^3}\frac{\gamma^2}{[1+(k_1r_0)^2]^\nu}, \tag{11}$$

i.e., in the high frequency (or high wave number) region the one-dimensional spectrum of refractive index fluctuations is related to the schlieren output signal spectrum as follows:

$$E(k_1)\sim\frac{T(k_1)}{k_1}\ \text{for}\ k_1r_0\gg 1. \tag{12}$$

The integral scale of the refractive index fluctuations is related to the length scale r_0 by the expression

$$\Lambda_n=\sqrt{\pi}\,\frac{\Gamma\left(\nu+\frac{1}{2}\right)}{\Gamma(\nu)}r_0. \tag{13}$$

Thus, if the one-dimensional spectrum of refractive index fluctuations can be approximated by Eq. (9), we can use Eqs. (10)-(13) and the relations $\beta(\xi_1)$ and $T(k_1)$ resulting from statistical processing of the schlieren output signals to find analytical expressions for the correlation function, and the one-dimensional and energy spectra of refractive index fluctuations, and we can also determine the integral scale Λ_n.

Since the refractive index for gases is usually a linear function of the density, in investigations of turbulent gas flows by the schlieren method we can use the analytical expressions derived here and the statistical characteristics of schlieren screen brightness fluctuations to find the statistical characteristics of the density fluctuations.

In conclusion the author thanks G. I. Mishin and S. N. Palkin for useful discussions.

[1] Thompson and Taylor, RTK, 7, 250 (1969).
[2] W. Clay, L. Herriman, and R. Slattery, Phys. Fluids, 8, 1792 (1965).
[3] S. R. Stefanov, A. M. Trokhan, and Yu. D. Chashechkin, Zh. Prikl. Mekh. Tekh. Fiz., No. 5, 103 (1971).
[4] J. O. Hinze, Turbulence, McGraw-Hill, New York (1959).
[5] M. S. Uberoid and L. S. G. Kovasznay, Quart. Appl. Math., 10, 375 (1953).

Titanium-pump system for hydrogen

K. G. Mirzoev, V. G. Rogozinskii, and V. L. Ushkov

(Submitted July 16, 1973)
Zh. Tekh. Fiz., 44, 680-682 (March 1974)

A study is reported of a vacuum system used to pump 1000-1500 cm^3 · atm/h of hydrogen in continuous flow through the ion source of the injector of an I-100 linear proton accelerator. The vacuum system consists of two NÉM-1T pumps and a getter pump, whose pumping rate is 10^4 liter/sec at $1 \cdot 10^{-6}$ torr. The system operates stably at a flow rate of up to 500 cm^3 · atm/h and at pressure below $1 \cdot 10^{-5}$ torr. In pulsed supply of hydrogen through the source at a rate of 0.125 Hz, the pumping is achieved by two NÉM-1T pumps at an average pressure of $1.6 \cdot 10^{-6}$ torr. Information obtained from extensive use of the NÉM-1T pumps to pump hydrogen in the pulsed mode is reported.

The injector[1] of the I-100 linear proton accelerator initially operated with a continuous hydrogen flow of 1000-1500 cm^3 · atm/h through the ion source with a chamber pressure of $1\text{-}2 \cdot 10^{-5}$ torr, maintained by two high-vacuum oil-vapor VA-8-4 pumps with venetian-blind liquid-nitrogen traps. The penetration of oil vapor and its decomposition products into the chamber of the injector and into the resonator of the linear accelerator led to frequent high-voltage breakdowns, reducing the reliability of accelerator operation.

To study the possibility of oil-free pumping of the injector, we have studied a pumping system consisting of a titanium getter pump and two NÉM-1T magnetic-discharge pumps. On the basis of a GIN-5 pump[2] we design and construct a pump without an ionizer, so that we are able to increase the number of titanium evaporators to eight. The getter pump has been tested to $1 \cdot 10^{-5}$ torr by VN-2MG and VA-05-4 pumps with a nitrogen trap. After the body of the pump is heated to 70-80°C, and after the evaporators are outgassed, a limiting vacuum of $(1\text{-}2) \cdot 10^{-7}$ torr is achieved after 7-8 h of operation of the two evaporators, each of which is heated by ~ 1900 W. During this period the VA-05-4 pump operates continuously. The pumping rate in terms of hydrogen, measured by the two-gauge method, is about 10^4 liter/sec over the pressure range $1 \cdot 10^{-6}\text{-}2 \cdot 10^{-5}$ torr. Figure 1 shows the behavior of the partial pressures of CH_4, CO_2, CO + N_2, H_2 and Ar, obtained with an IPDO-1 device while the valve of the VA-05-4 device is off and with operation of one evaporator at a heater power of 1900 W. During these measurements the total pressure varies from $2 \cdot 10^{-7}$ to $(3\text{-}5) \cdot 10^{-6}$ torr. We see that the partial pressures of CH_4 and CO_2 increase rapidly initially and then reach nearly equilibrium values. This behavior is apparently due to the establishment of an equilibrium between the production and oxidation of methane involving the production of CO_2, which is pumped by the deposited titanium film.

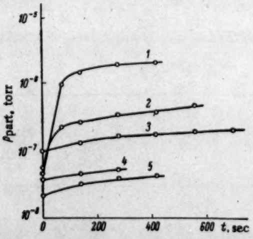

Fig. 1. Partial pressures of CH_4 (curve 1), CO_2 (2), H_2 (3), CO + N_2 (4), and Ar (5) during operation of the getter pump with one evaporator and a closed valve of the VA-05-4 device.

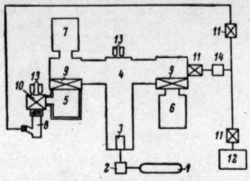

Fig. 2. Vacuum system of the injector. 1) Hydrogen tank; 2) injection system and buret; 3) ion source; 4) accelerating tube and chamber of injector; 5) getter pump; 6) NÉM-1T No. 1; 7) NÉM-1T No. 2; 8) VA-05-4 oil-vapor pump; 9) DU-500 valve; 10) DU-160 valve; 11) DU-85 valve; 12) VN-7MG pump; 13) LM-2 and LT-2 gauges; 14) DU-85 ion trap.

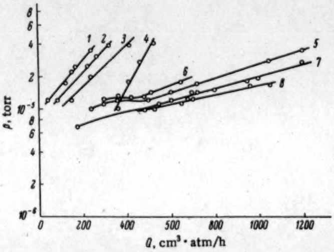

Fig. 3. Pressure in the injector as a function of the hydrogen flow rate with operation of one and two NÉM-1T pumps and getter-pump evaporators at various levels of heating power.$^{1-3}$ One NÉM-1T and one evaporator. W, watts: 1) 1530; 2) 1800; 3) 2000. 4, 5) One NÉM-1T and two evaporators. W, watts: 4) 1800; 5) 2200. 6-8) Two NÉM-1T's and two evaporators. W, watts: 6) 2000; 7) 2200; 8) 2400.

The pumping characteristics of the injector with the titanium pumps are studied on the apparatus shown schematically in Fig. 2. A preliminary evacuation to $1 \cdot 10^{-5}$ torr is achieved by VN-7MG and VA-05-4 pumps with a liquid-nitrogen trap. The hydrogen flow through the ion source is measured by a buret method, and the pressure is measured by an LM-2 ionization gauge in terms of the nitrogen equivalent. During the evacuation of the hydrogen two evaporators operate simultaneously with a heating power of 14-15 W per square centimeter of the initial surface of the evaporator. Under these conditions the chamber pressure does not exceed $(1\text{-}2) \cdot 10^{-5}$ torr, and the getter pump works for ~ 200 h before it is necessary to change evaporators. The results of tests of this pumping system are shown in Fig. 3. In operation of this system for 150 h at pressures above $1.5 \cdot 10^{-5}$ torr, pressure variations of $(2-6) \cdot 10^{-5}$ torr with a period of 3-5 min, lasting from 10 min to 3 h, are observed because of the argon instability. These variations arise and vanish either spontaneously or upon a change in the hydrogen flow rate. Accordingly, this pumping system can operate stably at pressures below $1 \cdot 10^{-5}$ torr, so that it is possible to evacuate a hydrogen flow of 500 $cm^3 \cdot atm/h$.

We have also designed and constructed an ion source with pulsed hydrogen injection[3] at a rate corresponding to the operating cycle of the accelerator; the hydrogen flow in the pulse is the same as for continuous flow, while the average hydrogen flow is 20-40 $cm^3 \cdot atm/h$. Under these conditions, two NÉM-1T magnetic-discharge pumps can be used for evacuation. The arrangement of the system is like that shown in Fig. 2; NÉM-1T No. 2 (7) replaces getter pump (5), while a TMN-200 turbomolecular pump replaces the VA-05-4 (8). This system has been used successfully for about five years.

The average pressure in the chamber during operation of the source, measured by an LM-2 gauge, is $\sim 1.6 \cdot 10^{-6}$ torr. The NÉM-1T pumps operate in continuous cycles of 1000-2000 h with stops for 150-200 h. Both pumps have operated more than $2 \cdot 10^4$ h before replacement, cleaning, and reassembly.

From the measured average volume of the craters in the cathodes of the pumps we determine the titanium flow rate and estimate the average efficiency of the titanium sputtering: 0.05-0.1 atom/ion.

An estimate of the saturation of the cathodes with hydrogen yields 0.02 atoms of H_2 per Ti atom, and the amount of H_2 absorbed by the Ti film is estimated to be 5% of the total amount of evacuated H_2. It follows that hydrogen is pumped primarily by the cathodes of the pumps, and, as is mentioned in ref. 4, as a result of the penetration of ions and diffusion of hydrogen into the titanium. Inspection of the cathode plates of the pumps shows that there are no cracks, deformations, or damaged regions on their surfaces, which would be characteristics of hydrogen saturation of the surface layer of titanium. The cathode plates may end up in this state because hydrogen manages to diffuse into the interior of the plate during the time between pulses in the case of pulsed injection, so it does not saturate the surface layer. As is shown in ref. 5, the coefficient for the penetration of hydrogen ions into titanium is reduced when the surface layer of titanium is saturated with hydrogen; then, after a pause, this coefficient resumes its original value.

The authors thank V. A. Teplyakov for discussion of the results and A. S. Nazarov and M. V. Kuznetsov for designing and constructing the getter pump.

---

[1] M. A. Abroyan, V. P. Gerasimov, F. G. Zheleznikov, G. P. Zabolotskaya, N. F. Ivanov, A. V. Ivlev, V. L. Komarov, V. S. Kuznetsov, G. M. Latmanizova, I. M. Rolfe, and A. I. Solnyshkov, Proceedings of the International Conference on Accelerators, Dubna, 1963 [in Russian], Atomizdat, Moscow (1964).

[2] A. S. Nazarov, G. F. Ivanovskii, and M. V. Kuznetsov, Prib. Tekh. Eksp., No. 2, 102 (1966).

[3] N. N. Kutorga, V. A. Sevost'yanov, and V. A. Teplyakov, Proceedings of the Second All-Union Conference on Charged-Particle Accelerators [in Russian], Izd. Nauka, Moscow (1972), p. 88.

[4] J. H. Singleton, J. Vac. Sci. and Technol., 8, 275 (1971).

[5] E. S. Borovik, N. P. Katrich, and G. T. Nikolaev, in: Ultrahigh-Vacuum Physics and Technology [in Russian], Izd. Mashinostroenie, Leningrad (1968), p. 47.

Temperature dependence of trace diffusion coefficients of certain gases

A. É. Loiko, B. A. Ivakin, and P. E. Suetin
S. M. Kirov Ural Polytechnical Institute, Sverdlovsk

(Submitted May 21, 1973)
Zh. Tekh. Fiz., 44, 682-684 (March 1974)

The diffusion coefficients have been measured for 11 pairs of gases (He–D_2, H_2–Kr, Ar–Xe, Kr–Xe, H_2–CO_2, D_2–CO_2, He–CO_2, Ne–CO_2, Ar–CO_2, Kr–CO_2, and Xe–CO_2) as functions of the concentration over the temperature range 77-600°K.

There are several reasons for the interest in the trace diffusion coefficients of gases as functions of the temperature: First, the information currently available on the functional dependence on the concentration is clearly inadequate and is even partially contradictory. Second, measurements carried out with small gradients make it possible to study diffusion in "pure" form and to minimize the corrections due to the nonideal nature of the gases. Finally, the results found in measurements of the trace diffusion coefficients over a broad temperature range can provide a more accurate construction of the intermolecular potentials.

We have measured the trace diffusion coefficients for 11 pairs of gases. The experimental apparatus and procedure are described in detail elsewhere.[1–3] All the measurements are carried out at a concentration of 2.5% for the trace component. We estimate the experimental error to be ~0.9%.

The experimental diffusion coefficients for traces of the heavy and light components, converted to 1 atm in the standard manner, are shown in Tables 1 and 2. With a light-component trace the measurements are carried out at three temperatures: a low temperature, room temperature, and a high temperature. For the systems He–D_2, Ar–CO_2, and Kr–Xe, we find no functional dependence of the diffusion coefficient on the concentration within the experimental error.

Analysis of these results shows that the functional dependence of the diffusion coefficients on the concentration increases with increasing temperature and is responsible for a variation of 1-4% for all the pairs studied. The experimental results support the conclusions of the rigorous kinetic theory of low-density gases[4] regarding the weak functional dependence of the diffusion coefficients on the concentration.

The experimental results agree with the data of ref. 5 for systems of inert gases, within the experimental errors. For the He–CO_2 system there is a good agreement with the results of ref. 6. The functional dependence on the concentration for the He–CO_2 pair reported in ref. 7, however, is much stronger than that which follows from our results. We do not have information on the functional dependence of concentration for the other systems with which to compare our results.

TABLE 1. "Trace" Diffusion Coefficients ($D \cdot 10^4$, m^2/sec) of the Heavy Component at a Pressure of 760 torr

He–D_2		H_2–Kr		Ar–Xe		Kr–Xe		H_2–CO_2		D_2–CO_2		He–CO_2		Ne–CO_2		Ar–CO_2		Kr–CO_2		Xe–CO_2	
T, °K	D	T, °K	D	T, °K	D	T, °K	D	T, °K	D	T, °K	D	T, °K	D	T, °K	D	T, °K	D	T, °K	D	T, °K	D
77.2	0.131	128.3	0.150	128.0	0.0219	163.2	0.0238	174.4	0.238	174.4	0.174	173.2	0.249	176.1	0.1032	175.3	0.0554	173.2	0.0391	175.0	0.0311
132.5	0.324	163.5	0.236	163.4	0.0361	203.6	0.0366	203.0	0.314	203.2	0.231	203.2	0.323	201.2	0.131	203.4	0.0739	203.2	0.0543	203.4	0.0425
183.6	0.569	203.1	0.352	203.1	0.0541	243.4	0.0522	233.2	0.407	233.2	0.301	233.2	0.410	231.3	0.171	233.1	0.0968	233.2	0.0720	233.1	0.0564
233.4	0.851	243.4	0.488	243.4	0.0773	297.4	0.0758	263.2	0.509	263.2	0.376	263.2	0.506	263.2	0.217	263.2	0.123	263.2	0.0911	263.2	0.0723
295.3	1.29	295.7	0.706	290.3	0.107	402.1	0.137	291.5	0.612	293.8	0.467	294.6	0.600	296.6	0.271	296.0	0.156	293.2	0.112	291.7	0.0881
401.2	2.17	386.2	1.13	384.4	0.182	484.4	0.192	415.6	1.17	415.6	0.880	409.3	1.03	417.9	0.500	418.2	0.292	409.3	0.214	407.2	0.168
470.7	2.88	482.5	1.684	483.5	0.277	589.5	0.278	489.0	1.58	488.2	1.18	510.9	1.50	484.1	0.651	484.2	0.380	510.9	0.322	498.8	0.243
592.1	4.29	577.4	2.34	578.7	0.384	682.2	0.359	580.7	2.16	581.2	1.60	595.9	1.968	586.8	0.912	587.2	0.534	595.9	0.422	593.2	0.328
				673.7	0.502	767.6	0.435									670.8	0.669	662.9	0.504	674.4	0.408
				764.9	0.631											775.8	0.865	776.1	0.657	776.9	0.527

TABLE 2. "Trace" Diffusion Coefficients ($D \cdot 10^4$, m^2/sec) of the Light Component at a Pressure of 760 torr

H_2–Kr		Ar–Xe		H_2–CO_2		D_2–CO_2		He–CO_2		Ne–CO_2		Kr–CO_2		Xe–CO_2	
T, °K	D	T, °K	D	T, °K	D	T, °K	D	T, °K	D	T, °K	D	T, °K	D	T, °K	D
163.5	0.240	163.4	0.0359	174.4	0.242	174.4	0.176	173.2	0.251	176.1	0.1034	173.2	0.0395	175.0	0.0311
295.7	0.729	290.3	0.107	291.5	0.623	293.8	0.474	294.6	0.607	296.6	0.272	293.2	0.111	291.7	0.0883
482.5	1.746	764.9	0.640	489.0	1.59	488.2	1.19	595.9	2.023	586.8	0.916	595.9	0.417	593.2	0.332

---

[1] P. E. Suetin, A. É. Loiko, B. A. Kalinin, and Yu. F. Gerasimov, Inzh.-Fiz. Zh., 19, No. 5 (1970).

[2] P. E. Suetin, B. A. Kalinin, and A. É. Loiko, Zh. Tekh. Fiz., 40, 1735 (1970) [Sov. Phys.–Tech. Phys., 15, 1349 (1971)].

[3] A. É. Loiko, B. A. Ivakin, and P. E. Suetin, Zh. Tekh. Fiz., 43, 416 (1973) [Sov. Phys.–Tech. Phys., 18, 266 (1973)].

[4] J. O. Hirschfelder, C. F. Curtiss, and R. B. Bird, Molecular Theory of Gases and Liquids, Willey, New York (1954).

[5] R. J. J. Van Heiningen, J. P. Harpe, and J. M. Beenakker, Physica, 38, 1 (1968).

[6] K. R. Harris, T. N. Bell, and P. Dunlop, Can. J. Chem., 50, 1874 (1972).

[7] V. F. Vyshinskaya, N. D. Kosov, L. I. Kurlanov, and G. P. Martynova, in: Physics [in Russian], No. 5, Alma-Ata (1971), p. 78.

Theoretical and mathematical physics

Charged-particle motion in a dipole magnetic field

L. G. Glikman

(Submitted June 5, 1973)
Zh. Tekh. Fiz., 44, 689-697 (April 1974)

Simple relations are found which characterize the features of charged-particle motion in the field of a magnetic dipole. In particular, the conditions necessary for penetration of a particle to the center of the magnetic dipole are refined and conditions are determined which are sufficient for a magnetic dipole to act as a mirror that reflects incident particles.

Numerous papers have been devoted to the study of charged-particle motion in the field of a magnetic dipole and some of the results are given in monographs.[1,2] An exact solution of the equations of motion for a charged-particle in such a field can only be found for the case in which the particle trajectory lies the median (equatorial) plane, which is an antisymmetry plane for the magnetic field. A detailed study of particle motion under arbitrary initial conditions requires numerical integration of the appropriate system of differential equations. However, important results can also be obtained by a qualitative study. In particular, by making use of the conservation laws for energy and generalized azimuthal momentum the allowed and forbidden regions of particle motion can be determined.[1]

A method similar to that proposed in ref. 3 and later used in refs. 4 and 5 is employed here for consideration of the features of particle motion. By means of this method one can study qualitatively some new features of charged-particle motion in the field of a magnetic dipole.

The Hamilton–Jacobi equation for this problem, written in the spherical coordinate system r, θ, ψ with its origin at the point which the magnetic dipole is located is

$$\left(\frac{\partial S}{\partial r}\right)^2+\frac{1}{r^2}\left(\frac{\partial S}{\partial \vartheta}\right)^2+\left(\frac{\frac{\partial S}{\partial \psi}}{r\sin\vartheta}-\frac{eM}{c}\frac{\sin\vartheta}{r^2}\right)^2=\frac{m^2v^2}{1-\frac{v^2}{c^2}}. \qquad (1)$$

Here, S is the contracted action function; e, m, and v are respectively the charge, rest mass, and velocity of the particle; c is the velocity of light in vacuum; M is the absolute value of the dipole magnetic moment **M**. The coordinate system is oriented so that the vector **M** is antiparallel to the z axis of the Cartesian coordinate system x, y, z, which corresponds to the selected spherical coordinate system r, θ, ψ. For definiteness, the motion of a positively charged particle is considered. After introduction of the Störmer unit of length

$$a=\sqrt{\frac{eM}{mcv}\sqrt{1-\frac{v^2}{c^2}}}$$

and the function

$$F=\frac{S\sqrt{1-\frac{v^2}{c^2}}}{mva}$$

the Hamilton–Jacobi equation (1) takes the form

$$\rho^2P_\rho^2+P_\vartheta^2+\left(\frac{2\gamma}{\sin\vartheta}-\frac{\sin\vartheta}{\rho}\right)^2-\rho^2=0. \qquad (2)$$

Here

$$\rho=\frac{r}{a},\quad P_\rho=\frac{\partial F}{\partial\rho},\quad P_\vartheta=\frac{\partial F}{\partial\vartheta},$$

$$2\gamma=\frac{\partial F}{\partial\psi}=\rho^2\sin^2\vartheta\frac{d\psi}{dl}+\frac{\sin^2\vartheta}{\rho}=\mathrm{const}, \qquad (3)$$

l is the length of the path traversed by the particle, expressed in Störmer units.

From the system of Hamiltonian equations corresponding to Eq. (2), we obtain

$$\frac{dP_\rho^2}{d\rho}=-\frac{2P_\rho^2}{\rho}+\frac{2}{\rho}-\frac{4\gamma}{\rho^4}+\frac{2\sin^2\vartheta}{\rho^5}. \qquad (4)$$

From Eq. (4), which describes P_ρ^2 as a function of the two variables ρ and ϑ, we transform to differential inequalities characterizing P_ρ^2 as a function of the single variable ρ. We determine allowed values of the quantity $\sin^2\vartheta$, which appears on the right side of Eq. (4), by using the condition

$$\rho^2-\rho^2P_\rho^2-\left(\frac{2\gamma}{\sin\vartheta}-\frac{\sin\vartheta}{\rho}\right)^2\geqslant 0. \qquad (5)$$

which follows from Eq. (2).

This condition is satisfied if

$$f\leqslant\sin^2\vartheta\leqslant g, \qquad (6)$$

where f is the smaller, and g the larger, root of the quadratic equation in $\sin^2\vartheta$:

$$\sin^4\vartheta+\rho u\sin^2\vartheta+4\gamma^2\rho^2=0. \qquad (7)$$

Here,

$$u=\rho^3P_\rho^2-\rho^3-4\gamma. \qquad (8)$$

The solutions of Eq. (7) are of the form

$$f=\frac{\rho}{2}\left(-u-\sqrt{u^2-16\gamma^2}\right), \qquad (9)$$

$$g=\frac{\rho}{2}\left(-u+\sqrt{u^2-16\gamma^2}\right). \qquad (10)$$

The function u is not positive, as follows from Eq. (2):

$$-\rho P_\vartheta^2-\frac{4\gamma^2\rho}{\sin^2\vartheta}-\frac{\sin^2\vartheta}{\rho}\leqslant 0,$$

and therefore both roots of Eq. (7) are nonnegative.

The inequality

$$\frac{dP_\rho^2}{d\rho} \geqslant -\frac{2P_\rho^2}{\rho} + \frac{2}{\rho} - \frac{4\gamma}{\rho^4} + \frac{1}{\rho^4}\left(-u - \sqrt{u^2 - 16\gamma^2}\right), \tag{11}$$

follows from Eqs. (4), (6), and (9), and is transformed by using Eq. (8):

$$\rho \frac{du}{d\rho} \geqslant -\sqrt{u^2 - 16\gamma^2}. \tag{12}$$

From Eq. (12), we obtain

$$\frac{df}{d\rho} \geqslant 0. \tag{13}$$

Actually, because of the nonnegativity of f and the inequality (12),

$$\frac{df}{d\rho} = \frac{f}{\rho\sqrt{u^2 - 16\gamma^2}}\left(\sqrt{u^2 - 16\gamma^2} + \rho\frac{du}{d\rho}\right) \geqslant 0.$$

Considering the equation

$$fg = 4\gamma^2\rho^2 \tag{14}$$

and Eq. (13) we can write

$$\frac{d}{d\rho}\left(\frac{g}{\rho^2}\right) \leqslant 0. \tag{15}$$

We obtain additional inequalities characterizing the properties of the functions f and g by using Eqs. (4), (6), and (10):

$$\frac{dP_\rho^2}{d\rho} \leqslant -\frac{2P_\rho^2}{\rho} + \frac{2}{\rho} - \frac{4\gamma}{\rho^4} + \frac{1}{\rho^4}\left(-u + \sqrt{u^2 - 16\gamma^2}\right).$$

We then have

$$\rho \frac{du}{d\rho} \leqslant \sqrt{u^2 - 16\gamma^2}. \tag{16}$$

From Eqs. (10), (14), and (16), there follows

$$\frac{dg}{d\rho} \geqslant 0, \tag{17}$$

$$\frac{d}{d\rho}\left(\frac{f}{\rho^2}\right) \leqslant 0. \tag{18}$$

Relations which characterize the features of particle motion more precisely than (17) and (18) can be obtained for the case $g_0 > 1$ (the subscript zero indicates initial values of the variables). In this case, using Eq. (4) we write

$$\frac{dP_\rho^2}{d\rho} \leqslant -\frac{2P_\rho^2}{\rho} + \frac{2}{\rho} - \frac{4\gamma}{\rho^4} + \frac{2}{\rho^5}.$$

After simple transformations, we obtain

$$\frac{d}{d\rho}\left(\frac{u\rho + 1}{\rho^2}\right) \leqslant 0. \tag{19}$$

This inequality can also be written

$$\frac{d}{d\rho}\left(\frac{1 - f - g}{\rho^2}\right) \leqslant 0. \tag{20}$$

Using these inequalities we estimate the boundary of the allowed region for particle motion in that portion of the trajectory in which ρ varies monotonically (sign of P_ρ does not change). We consider separately the cases in which ρ is nonincreasing and where ρ is nondecreasing.

1. If ρ decreases monotonically it follows from (13), (15), (17), and (18) that for arbitrary initial conditions

$$f_0\frac{\rho^2}{\rho_0^2} \leqslant f \leqslant f_0, \tag{21}$$

$$g_0\frac{\rho^2}{\rho_0^2} \leqslant g \leqslant g_0. \tag{22}$$

If $g_0 > 1$, features of particle motion are characterized more precisely than the lower bound in (21) and the upper bound in (22) by the inequality following from Eq. (19):

$$\frac{u\rho + 1}{\rho^2} \geqslant \frac{u_0\rho_0 + 1}{\rho_0^2}. \tag{23}$$

From (23) we find a lower bound for f:

$$f \geqslant -\frac{\rho}{2}\left[u_0\frac{\rho}{\rho_0} + \frac{\rho}{\rho_0^2} - \frac{1}{\rho} + \sqrt{\left(u_0\frac{\rho}{\rho_0} + \frac{\rho}{\rho_0^2} - \frac{1}{\rho}\right)^2 - 16\gamma^2}\right], \tag{24}$$

The size of the region of allowed particle motion for $g_0 < 1$ is estimated in the following manner:

$$f_0\frac{\rho^2}{\rho_0^2} \leqslant \sin^2\vartheta(\rho) \leqslant g_0. \tag{25}$$

In this case, a charged-particle approaching the magnetic dipole does not pass through the equatorial plane. When $g_0 > 1$,

$$-\frac{\rho}{2}\left[u_0\frac{\rho}{\rho_0} + \frac{\rho}{\rho_0^2} - \frac{1}{\rho} + \sqrt{\left(u_0\frac{\rho}{\rho_0} + \frac{\rho}{\rho_0^2} - \frac{1}{\rho}\right)^2 - 16\gamma^2}\right] \leqslant \sin^2\vartheta(\rho) \leqslant 1. \tag{26}$$

We have estimated the magnitude of the region of allowed motion under the assumption that ρ decreases monotonically. Under the same assumption, we now find an estimate for the quantity P_ρ^2. From the definition of this quantity, it follows that

$$P_\rho^2 = \cos^2\alpha,$$

where α is the angle between the radius vector **r**, characterizing the particle position in space, and the particle vector velocity **v**. We use the bounds on P_ρ^2 later to investigate charged-particle motion in nonmonotonic variation of ρ along the trajectory.

When

$$\frac{\rho^2}{\rho_0^2} \geqslant \frac{f_0}{g_0} \tag{27}$$

it follows from (13) that

$$\rho^4 P_\rho^2 \leqslant \rho^4 + 4\gamma\rho - \frac{\rho^2}{\rho_0^2} g_0 - f_0. \tag{28}$$

If $\gamma = 0$, $f_0 = 0$ and (28) is valid for all values of ρ. When $\gamma > 0$ and

$$\frac{\rho^2}{\rho_0^2} \leqslant \frac{f_0}{g_0}, \tag{29}$$

the bound for P_ρ^2 reduces to the trivial quantity

$$P_\rho^2 \leqslant 1. \tag{30}$$

If γ is negative and ρ satisfies (29), we can use the bound

$$\rho^4 P_\rho^2 \leqslant 8\gamma\rho + \rho^4, \tag{31}$$

which holds for arbitrary values of ρ, but is less accurate than (28) under condition (27). The inequality (31) follows from the nonnegativity of the expressions under the square root sign in Eqs. (9) and (10).

The lower bound for P_ρ^2 will be different for $g_0 < 1$ and $g_0 > 1$. If $g_0 < 1$, we obtain from (17)

$$\rho^4 P_\rho^2 \geqslant \rho^4 + 4\gamma\rho - \frac{\rho^2}{\rho_0^2} f_0 - g_0. \tag{32}$$

When $g_0 > 1$, we obtain from (23)

$$\rho^4 P_\rho^2 \geqslant \rho^4 + 4\gamma\rho + \frac{\rho^2}{\rho_0^2}(1 - f_0 - g_0) - 1. \tag{33}$$

2. ρ increases monotonically. For arbitrary initial conditions, the limits for the functions f and g now have the form

$$f_0 \leqslant f \leqslant \frac{\rho^2}{\rho_0^2} f_0, \tag{34}$$

$$g_0 \leqslant g \leqslant \frac{\rho^2}{\rho_0^2} g_0. \tag{35}$$

When

$$\frac{\rho^2}{\rho_0^2} \geqslant \frac{1}{f_0} \tag{36}$$

the upper bound for the function f becomes the trivial one

$$f \leqslant 1. \tag{37}$$

If $g_0 > 1$ the features of the particle motion are described by the relation

$$\frac{u\rho + 1}{\rho^2} \leqslant \frac{u_0\rho_0 + 1}{\rho_0^2}. \tag{38}$$

more precisely than by the inequalities (34) and (35) giving an upper bound for f and a lower bound for g.

Using (38) we write the upper bound for f in this case as follows:

$$f \leqslant -\frac{\rho}{2}\left[u_0 \frac{\rho}{\rho_0} + \frac{\rho}{\rho_0^2} - \frac{1}{\rho} + \sqrt{\left(u_0 \frac{\rho}{\rho_0} + \frac{\rho}{\rho_0^2} - \frac{1}{\rho}\right)^2 - 16\gamma^2}\right]. \tag{39}$$

Using these relations we determine the inequalities which bound the dimensions of the allowed region for charged-particle motion. If $g_0 < 1$,

$$f_0 \leqslant \sin^2\vartheta(\rho) \leqslant \frac{\rho^2}{\rho_0^2} g_0. \tag{40}$$

The upper bound in (40) transforms to the trivial quantity

$$\sin^2\vartheta \leqslant 1 \tag{41}$$

for

$$\frac{\rho^2}{\rho_0^2} \geqslant \frac{1}{g_0}, \tag{42}$$

i.e., the trajectory of a particle can intersect the equatorial plane of the magnetic dipole only for $\rho \geq \rho_0/(g_0)^{1/2}$.

When $g_0 > 1$, we have

$$f_0 \leqslant \sin^2\vartheta(\rho) \leqslant 1. \tag{43}$$

The lower bound for the quantity P_ρ^2

$$\rho^4 P_\rho^2 \geqslant \rho^4 + 4\gamma\rho - \frac{\rho^2}{\rho_0^2} g_0 - f_0. \tag{44}$$

follows from (13).

If $g_0 < 1$, we find that for

$$\frac{\rho^2}{\rho_0^2} \leqslant \frac{g_0}{f_0} \tag{45}$$

$$\rho^4 P_\rho^2 \leqslant \rho^4 + 4\gamma\rho - \frac{\rho^2}{\rho_0^2} f_0 - g_0. \tag{46}$$

by using (17).

When $\gamma = 0$, (46) is valid for any value of ρ. When $\gamma > 0$ and

$$\frac{\rho^2}{\rho_0^2} \geqslant \frac{g_0}{f_0}, \tag{47}$$

we have the trivial bound (30). If $\gamma < 0$ and ρ satisfies (47), the relation (31) should be used for the upper bound of the quantity P_ρ^2. When $g_0 > 1$, we obtain from (19)

$$\rho^4 P_\rho^2 \leqslant \rho^4 + 4\gamma\rho + \frac{\rho^2}{\rho_0^2}(1 - f_0 - g_0) - 1. \tag{48}$$

The relations obtained above under the assumption that ρ varies monotonically in the portion of the trajectory under consideration can be used for the investigation of charged-particle trajectories in more complex cases. For example, we consider the motion of a charged particle in one of the most interesting cases from the standpoint of geophysical application, where

$$0 \leqslant \gamma < 1 \tag{49}$$

and the particle approaches the magnetic dipole. It is well known that satisfaction of the condition (49) is necessary in order that a charged particle coming fron infinity approach the center of the dipole. We shall determine below additional conditions which are necessary for particle penetration to the center of the dipole and we shall also determine conditions sufficient for the magnetic dipole to act as a mirror which reflects an incident particle when (49) is satisfied.

For further investigation we shall have to know the roots of

$$\rho^4 + 4\gamma\rho - \frac{\rho^2}{\rho_0^2} g_0 - f_0 = 0, \tag{50}$$

$$\rho^4 + 4\gamma\rho - \frac{\rho^2}{\rho_0^2} f_0 - g_0 = 0. \tag{51}$$

We factor the left sides of these equations. Then Eq. (50) takes the form

$$\left(\rho^2 + \frac{2|\gamma|}{\sqrt{f_0}}\rho - \sigma_\gamma \sqrt{f_0}\right)\left(\rho^2 - \frac{2|\gamma|}{\sqrt{f_0}}\rho + \sigma_\gamma \sqrt{f_0}\right) = 0, \tag{52}$$

where

$$\sigma_\gamma = \begin{cases} \frac{|\gamma|}{\gamma}, & \gamma \neq 0, \\ 1 & \gamma = 0, \end{cases}$$

and Eq. (51) is written in the following manner:

$$\left(\rho^2 + \frac{2|\gamma|}{\sqrt{g_0}}\rho - \sigma_\gamma \sqrt{g_0}\right)\left(\rho^2 - \frac{2|\gamma|}{\sqrt{g_0}}\rho + \sigma_\gamma \sqrt{g_0}\right) = 0. \tag{53}$$

The point on the trajectory at which P_ρ changes sign, i.e., where $\rho(l)$ reaches an extremum, will be called a deflection point. Values of the variables at the deflection point are indicated by the subscript "def". The inequality (28) indicates that for a particle approaching the dipole

$$\rho_{\text{def}} \geqslant \rho_k, \tag{54}$$

at the first deflection point, where ρ_k is the positive root of Eq. (50) closest to ρ_0 having a value less than ρ_0. Since (28) holds where ρ satisfies the inequality (27), the relation (54) is satisfied when

$$\rho_k \geqslant \rho_0 \sqrt{\frac{f_0}{g_0}}. \tag{55}$$

In determining the roots of Eq. (50), we use the fact that it can be written in the form (52). We write expressions for the roots for positive values of γ. If

$$\gamma^2 < f_0 \sqrt{f_0}, \tag{56}$$

Eq. (50) has a single positive root:

$$\rho_{11} = -\frac{\gamma}{\sqrt{f_0}} + \sqrt{\frac{\gamma^2}{f_0} + \sqrt{f_0}}. \tag{57}$$

When the condition

$$\gamma^2 > f_0 \sqrt{f_0} \tag{58}$$

is satisfied, Eq. (50) has the two positive roots in addition to ρ_{11}:

$$\rho_{12} = \frac{\gamma}{\sqrt{f_0}} - \sqrt{\frac{\gamma^2}{f_0} - \sqrt{f_0}}, \tag{59}$$

$$\rho_{13} = \frac{\gamma}{\sqrt{f_0}} + \sqrt{\frac{\gamma^2}{f_0} - \sqrt{f_0}}. \tag{60}$$

When the three roots of Eq. (50) exist, the values of ρ lie either in the interval $[\rho_{11}, \rho_{12}]$ or in the range $[\rho_{13}, \infty]$. In the first case, when

$$\rho_0 \in [\rho_{11}, \rho_{12}], \tag{61}$$

and (56) is satisfied so that Eq. (50) has a single positive root, the bound (54) takes the form

$$\rho_{\text{def}} \geqslant \rho_{11}. \tag{62}$$

However, it is easy to verify that the inequality (55) is not satisfied for $\rho_k = \rho_{11}$. Therefore, under the specified conditions the bound for ρ_{def} reduces to the trivial quantity

$$\rho_{\text{def}} \geqslant 0. \tag{63}$$

If (58) is satisfied and

$$\rho_0 \geqslant \rho_{13}, \tag{64}$$

the bound (54) takes the form

$$\rho_{\text{def}} \geqslant \rho_{13}. \tag{65}$$

Now the inequality (55) holds for $\rho_k = \rho_{13}$.

Thus the conditions (58) and (64) are sufficient for at least one point of deflection to exist on the trajectory of a particle approaching the magnetic dipole. We shall show that when (58) and (64) are satisfied, there will be only one deflection point on the particle trajectory. Using the bound (44) obtained above we write the inequality

$$\rho^4 P_\rho^2 \geqslant \rho^4 + 4\gamma\rho - \frac{\rho^2}{\rho_{\text{def}}^2} g_{\text{def}} - f_{\text{def}}, \tag{66}$$

which characterizes the trajectory of a particle after the point of deflection in a segment where $\rho(l)$ increases monotonically. The equal sign in (66) corresponds to the point of deflection. When $\rho = \rho_{\text{def}}$, therefore, the right side of this expression will be zero, i.e., $\rho = \rho_{\text{def}}$ is a root of

$$\rho^4 + 4\gamma\rho - \frac{\rho^2}{\rho_{\text{def}}^2} g_{\text{def}} - f_{\text{def}} = 0. \tag{67}$$

It is easy to verify that Eq. (67) has three positive roots and $\rho = \rho_{\text{def}}$ is the largest of these. The existence of three positive roots for Eq. (67) follows from the inequality

$$\gamma^2 > f_{\text{def}} \sqrt{f_{\text{def}}}. \tag{68}$$

The last expression can be proven by using relations (21) and (58). We write the positive roots of Eq. (67),

$$\rho_{21} = -\frac{\gamma}{\sqrt{f_{\text{def}}}} + \sqrt{\frac{\gamma^2}{f_{\text{def}}} + \sqrt{f_{\text{def}}}}, \tag{69}$$

$$\rho_{22} = \frac{\gamma}{\sqrt{f_{\text{def}}}} - \sqrt{\frac{\gamma^2}{f_{\text{def}}} - \sqrt{f_{\text{def}}}}, \tag{70}$$

$$\rho_{23} = \frac{\gamma}{\sqrt{f_{\text{def}}}} + \sqrt{\frac{\gamma^2}{f_{\text{def}}} - \sqrt{f_{\text{def}}}}, \tag{71}$$

where

$$\rho_{21} < \rho_{22} < \rho_{23}.$$

The fact that $\rho_{\text{def}} = \rho_{23}$ follows from the inequality

$$\rho_{\text{def}} \geqslant \rho_{13} > \rho_{22}. \tag{72}$$

The inequality $\rho_{\text{def}} \geq \rho_{13}$ is the relation (65) proven above. The inequality $\rho_{13} > \rho_{22}$ is easily proven if the relations (21) and (58) are used. What has been said above shows that the right side of (66) is positive for all $\rho > \rho_{\text{def}}$. Therefore $P_\rho^2 > 0$ for these values of ρ. Thus the conditions (58) and (64) are sufficient for the existence of one, and only one, deflection point on the trajectory of a particle in this case. When these conditions are satisfied, the magnetic dipole acts as a mirror reflecting particles incident on it. For penetration of a particle to the center of a magnetic dipole, it is necessary that condition (56), for which Eq. (50) has a single positive root, be satisfied in addition to (49), or that the conditions (58) and (61) hold.

It is easy to verify that the conditions found, which are sufficient for particle reflection by a magnetic dipole field, are equivalent to a limitation imposed on the value of the angle α_0 between the radius vector $\mathbf{r}_0$ corresponding to the particle position in space at the initial time and the initial vector velocity of the particle, $\mathbf{v}_0$. This limitation is given by

$$b^3 (b-2)^2 < \sin^2 \alpha_0 \leqslant (b^3 - 2)^2, \tag{73}$$

where

$$b = \frac{\gamma^{1/3}}{\rho_0}. \tag{74}$$

For particle penetration to the center of the magnetic dipole, it is necessary that we have either

$$\sin^2 \alpha_0 < b^3 (b-2)^2, \tag{75}$$

or the simultaneous satisfaction of the two inequalities

$$\sin^2 \alpha_0 > b^3 (b-2)^2, \tag{76}$$

$$\sin^2 \alpha_0 > (b^3 - 2)^2. \tag{77}$$

If

$$b < 1, \tag{78}$$

the upper bound in (73) is always satisfied and the inequality (77) cannot hold. Under the condition (78), therefore, a sufficient condition for particle reflection by a magnetic dipole field can be represented as

$$\sin^2 \alpha_0 > b^3 (b-2)^2, \tag{79}$$

and a necessary condition for particle penetration to the center of a magnetic dipole leads to (75).

We now determine an upper bound for ρ_{def}, assuming as before that condition (49) is satisfied and the charged particle approaches the magnetic dipole. This bound will differ depending on whether g_0 is greater or less than unity. We confine ourselves to obtaining a bound for ρ_{def} when $g_0 < 1$. Similar bounds, but in considerably more cumbersome form, can easily be determined for $g_0 > 1$.

Using (32), we find that

$$\rho_{\text{def}} \leqslant \rho_n, \tag{80}$$

where ρ_n is the positive root of Eq. (51) having a value closest to but less than ρ_0. In finding the roots of Eq. (51), we use its representation in the form (53). As in the solution of Eq. (50), we shall assume γ is positive. If

$$\gamma^2 < g_0 \sqrt{g_0}, \tag{81}$$

Eq. (51) has the single positive root

$$\rho_{31} = -\frac{\gamma}{\sqrt{g_0}} + \sqrt{\frac{\gamma^2}{g_0} + \sqrt{g_0}}. \tag{82}$$

Consequently $\rho_n = \rho_{31}$ when (81) is satisfied. When

$$\gamma^2 > g_0 \sqrt{g_0} \tag{83}$$

Eq. (51) has in addition to ρ_{31} the positive roots

$$\rho_{32} = \frac{\gamma}{\sqrt{g_0}} - \sqrt{\frac{\gamma^2}{g_0} - \sqrt{g_0}}, \tag{84}$$

$$\rho_{33} = \frac{\gamma}{\sqrt{g_0}} + \sqrt{\frac{\gamma^2}{g_0} - \sqrt{g_0}}. \tag{85}$$

When (83) is satisfied, $\rho_n = \rho_{31}$ if $\rho_0 \leq \rho_{32}$, and $\rho_n = \rho_{33}$ if $\rho_0 \geq \rho_{33}$.

Thus under condition (49) the minimum distance to which a charged-particle approaches the center of a magnetic dipole when there is monotonic variation of ρ will always be less than ρ_n. When the conditions found for particle reflection by a magnetic dipole field are satisfied, the double bound

$$\rho_k \leqslant \rho_{\text{def}} \leqslant \rho_n.$$

exists for ρ_{def}.

After reflection by the magnetic dipole field, the charged-particle in this case ($g_0 < 1$) will move in a region characterized by the inequality

$$f_0 \frac{\rho_k^2}{\rho_0^2} \leqslant \sin^2 \vartheta(\rho) \leqslant g_0 \frac{\rho^2}{\rho_k^2}. \tag{86}$$

---

[1] C. Störmer, The Polar Aurora, Clarendon Press, Oxford (1955).

[2] L. I. Dorman, V. S. Smirnov, and M. I. Tyasto, Cosmic Rays in the Magnetic Field of the Earth [in Russian], Izd. Nauka, Moscow (1971).

[3] L. G. Glikman, Zh. Tekh. Fiz., 42, 972 (1972) [Sov. Phys. – Tech. Phys., 17, 769 (1972)].

[4] L. G. Glikman, Zh. Tekh. Fiz., 42, 1182 (1972) [Sov. Phys. – Tech. Phys., 17, 940 (1972)].

[5] L. G. Glikman, Zh. Tekh. Fiz., 42, 1550 (1972) [Sov. Phys. – Tech. Phys., 17, 1243 (1973)].

Excitation of acoustic waves by ion-acoustic turbulence

Kh. O. Abdulloev, F. Kh. Khakimov, and V. G. Makhan'kov

(Submitted June 19, 1973)
Zh. Tekh. Fiz., 44, 698-705 (April 1974)

We consider unstable acoustic (a) waves with frequency $\omega \ll \nu_e, \nu_i$ in a dense, fully ionized plasma characterized by a high level of ion-acoustic (s) turbulence. The interaction is a decay interaction. When the level of the (s) turbulence u = W/n T exceeds a threshold value u_{thr}, unstable acoustic waves are excited in the region $\omega < \nu_e, \nu_i$. As a result s-wave energy is transferred to smaller k values. Under certain conditions this process can compete with energy transfer due to induce s-wave scattering on plasma ions. The instability growth rates and the threshold value are given.

1. INTRODUCTION

In connection with the large number of experiments which have been carried out on the turbulent heating of plasmas,[1,3] considerable interest is being given to the study of ion-acoustic (s) turbulence.[4,7]

It is well known that ion-acoustic waves have a nondecay spectrum,[4] i.e., it is impossible to satisfy both of the conditions

$$\left.\begin{array}{l}\omega_1+\omega_2=\omega_3,\\ \mathbf{k}_1+\mathbf{k}_2=\mathbf{k}_3\end{array}\right\} \tag{1.1}$$

simultaneously. Here, ω_1, ω_2, ω_3 and $\mathbf{k}_1$, $\mathbf{k}_2$, $\mathbf{k}_3$, are the frequencies and wave vectors of the interacting waves. As a result, the principal nonlinear effect leading to the establishment of the (s) turbulence spectrum is assumed to be the induced scattering of ion-acoustic waves on plasma particles.[4-6] On the other hand, the "forbiddenness" for decay in the acoustic part of the spectrum is comparatively small: $\Delta\omega_f \sim \omega_s k_i^2 d_e^2$ (d_e is the electron Debye radius).

By applying very trivial dimensional considerations we can draw the following conclusions: The nonlinear frequency shift due to turbulence at a frequency near ω_s can be roughly estimated as[7]

$$\Delta\omega_s \sim \omega_s \frac{W}{nT} \tag{1.2}$$

(here, W is the energy density of the turbulence in the region $\sim \omega_s$ and nT is the thermal energy density in the plasma) and the degree of "forbiddenness" for decay for the ion-acoustic (s) turbulence, as noted above, is

$$\Delta\omega_f \sim \omega_1 k_1^2 d_e^2, \tag{1.3}$$

where

$$k_1^2 d_e^2 \ll 1.$$

Comparing (1.2) and (1.3), we conclude qualitatively that the condition that must be satisfied for a decay interaction is

$$\Delta\omega_s > \Delta\omega_f$$

or in our case (see also ref. 7).

$$\frac{W}{nT} > k_1^2 d_e^2. \tag{1.4}$$

This kind of interaction must lead to an energy transfer from s waves down the spectrum to lower frequencies ω and wave numbers[7] k [in the acoustic part of the spectrum $\omega_s = kv_s$, $v_s = v_{Te}(m_e/m_i)^{1/2}$].

If we are interested in the excitation of acoustic waves by s turbulence we need consider only one low-frequency wave$^{1)}$ $\omega \ll \omega_1, \omega_2$, since $\omega_{1,2} \gg \nu_i$, and $\omega \ll \nu_i$, so that $k \ll k_1, k_2$. The energy change in each interaction event is negligible and the resultant energy transfer of the ion-acoustic waves is of a "relay" (differential) nature.

2. DISPERSION EQUATION FOR A HIGHLY COLLISIONAL PLASMA WITH FULLY DEVELOPED ION-ACOUSTIC TURBULENCE

The ion-acoustic branch in a nonisothermal plasma ($T_e \gg T_i$) goes over to the acoustic branch when $k_\nu \sim \nu_e/v_e$ (ν_e is the frequency of binary electron−electron and electron−ion collisions; ν_i is the ion−ion collision frequency; v_e and v_i are the thermal velocities of the electrons and ions respectively, $v_{e,i}^2 = T_{e,i}/m_{e,i}$). As a result, decay interactions of linear ion-acoustic (s) and acoustic (a) waves are forbidden by the conservation laws. If the ion-acoustic turbulence reaches a certain level [condition (1.4)], however, the broadening of the field correlation functions can lead to decay.[7] In order to study this effect, by analogy with ref. 8 we now obtain the dispersion equation for acoustic (a) waves in the presence of developed ion-acoustic turbulence.

Neglecting dissipative effects connected with Landau damping, we use the equations of collisionless hydrodynamics to describe the (s) waves

$$\frac{\partial n_e}{\partial t}+\operatorname{div} n_e\mathbf{v}_e=0,\quad \frac{\partial n_i}{\partial t}+\operatorname{div} n_i\mathbf{v}_i=0, \tag{2.1}$$

$$\frac{\partial \mathbf{v}_e}{\partial t}+(\mathbf{v}_e\nabla)\,\mathbf{v}_e=-\frac{T_e}{m_e n_e}\nabla n_e+\frac{e}{m_e}\mathbf{E}, \tag{2.2}$$

$$\frac{\partial \mathbf{v}_i}{\partial t}+(\mathbf{v}_i\nabla)\,\mathbf{v}_i=-\frac{e}{m_i}\mathbf{E}. \tag{2.3}$$

For low frequencies the equations have the form

$$\frac{\partial n_e}{\partial t}+\operatorname{div} n_e\mathbf{v}_e=0,\quad \frac{\partial n_i}{\partial t}+\operatorname{div} n_i\mathbf{v}_i=0, \tag{2.4}$$

$$n_e\left[\frac{\partial}{\partial t}+(\mathbf{v}_e\nabla)\right]v_{e,\alpha}=-\frac{1}{m_e}\frac{\partial n_eT_e}{\partial x_\alpha}+\frac{e}{m_e}n_eE_\alpha-\frac{1}{m_e}\frac{\partial \pi_{e\alpha\beta}}{\partial x_\beta}+\frac{R_{T\alpha}}{m_e}, \tag{2.5}$$

$$n_i\left[\frac{\partial}{\partial t}+(\mathbf{v}_i\nabla)\right]v_{i,\alpha}=-\frac{1}{m_i}\frac{\partial n_iT_i}{\partial x_\alpha}-\frac{1}{m_i}\frac{\partial \pi_{i\alpha\beta}}{\partial x_\beta}-\frac{e}{m_i}n_iE_\alpha-\frac{R_{T\alpha}}{m_i}, \tag{2.6}$$

$$n_e\frac{3}{2}\left[\frac{\partial}{\partial t}+(\mathbf{v}_e\nabla)\right]T_e+n_eT_e\frac{\partial \mathbf{v}_e}{\partial \mathbf{r}}=-\pi_{e\alpha\beta}\frac{\partial v_{e\alpha}}{\partial x_\beta}-\frac{\partial}{\partial \mathbf{r}}\mathbf{q}_e, \tag{2.7}$$

Expression (2.22) has been obtained under the assumption that the ion-acoustic wave packet has a spread $\Delta\omega$ in frequency and a spread $\Delta\mathbf{k}_1$ in angle. We denote the aperture angle (i.e. the divergence) of the s-wave packet by $\Delta\vartheta_0$. Using the conservation of energy in the decay and allowing for the nonlinear frequency shifts of the interacting waves we get

$$\delta\left(\omega-\frac{\mathbf{k}\mathbf{k}_1}{kk_1}\omega_a-\delta\omega_{\mathbf{k}_1}^{H}\right)=0 \quad \text{or} \quad 1-\cos\left(\widehat{kk_1}\right)\sim\frac{\vartheta_0^2}{2}\sim\left(\frac{k_1}{k}\right)\frac{W}{nT},$$

assuming that $\delta\omega_{\mathbf{k}_1}^{H}\sim\omega_{\mathbf{k}_1}W/nT$.

The change $\delta\Delta\omega_{\mathbf{k}\mathbf{k}_1}$ for a change of angles $\mathbf{k}_1$ is of order

$$\delta\Delta\omega_{\mathbf{k}\mathbf{k}_1}\approx\left(\frac{kv_s}{2}\right)\frac{k}{k_1}\frac{\Delta k_1}{k_1}+kv_s\Delta\vartheta_0. \tag{2.23}$$

Using (2.23), we can write (2.22) in the form[2)]

$$\begin{aligned}\omega'-i\gamma_{\mathbf{k}}^{s}={}&-i\frac{\pi}{2}\omega_a\cos^2\vartheta_0\frac{u}{\Delta\vartheta_0+\frac{k}{2k_1}\frac{\Delta k_1}{k_1}+au}\\&-i\pi\omega_a\cos\vartheta_0\sin^2\vartheta_0\frac{u}{\Delta\vartheta_0+\frac{k}{2k_1}\frac{\Delta k_1}{k_1}+au}\\&+i\frac{\pi}{2}\omega_a\cos^2\vartheta_0\sin^2\vartheta_0\frac{u}{\left(\Delta\vartheta_0+\frac{k}{2k_1}\frac{\Delta k_1}{k_1}+au\right)^2},\end{aligned} \tag{2.24}$$

where u = W/nT and W is the total energy density in the s-wave packet.

We noted above (see also ref. 10) that if $\delta(\Delta\omega_{\mathbf{k}\mathbf{k}_1})>\omega'$, there is kinetic instability with a growth rate which can be estimated as

$$\gamma_k'=\frac{\pi}{8}\omega_a\frac{W}{nT}\frac{\cos^2\vartheta_0\sin^2\vartheta_0}{\left(\Delta\vartheta_0+\frac{k}{2k_1}\frac{\Delta k_1}{k_1}+au\right)^2}. \tag{2.25}$$

From (2.24) we get the condition for the excitation of acoustic waves by ion-acoustic turbulence

$$\cos^2\vartheta_0\sin^2\vartheta_0>\left(\Delta\vartheta_0+\frac{k}{2k_1}\frac{\Delta k_1}{k_1}+au\right)(\cos^2\vartheta_0+2\cos\vartheta_0\sin^2\vartheta_0). \tag{2.26}$$

In order-of-magnitude terms

$$\sin^2\vartheta_0>\left(\Delta\vartheta_0+\frac{k}{2k_1}\frac{\Delta k_1}{k_1}+au\right)\left(1+2\frac{\sin^2\vartheta_0}{\cos\vartheta_0}\right). \tag{2.27}$$

There is no excitation if $\sin\vartheta_0=0$ or $\cos\vartheta_0=0$. The conditions for decay are $u>k_1^2d_e^2$ and $\vartheta_0^2\sim(k_1/k)u$. Therefore (2.27) can be rewritten as

$$u>u_\vartheta=\frac{k}{k_1}\left(\Delta\vartheta_0+\frac{k}{2k_1}\frac{\Delta k_1}{k_1}+au\right). \tag{2.28}$$

Remembering that $\gamma>(m_e/m_i)\nu_e$, we obtain the condition for which *a* waves can be excited:

$$\gamma_{\mathbf{k}}^{s}\sim\frac{\pi}{8}\omega_a\frac{u}{\left(\Delta\vartheta_0+\frac{k}{2k_1}\frac{\Delta k_1}{k_1}+au\right)^2}>\frac{m_e}{m_i}\nu_e$$

or

$$u>u_\nu=\frac{m_e}{m_i}\frac{\nu_e}{\omega_a}\frac{8}{\pi}\left(\Delta\vartheta_0+\frac{k}{2k_1}\frac{\Delta k_1}{k_1}+au\right)^2. \tag{2.29}$$

The instability threshold is determined by the greater of (2.28) and (2.29):

$$u_{\text{thr}}=\max\{u_\nu,\ u_\vartheta,\ k_1^2d_e^2\}. \tag{2.30}$$

The ratio of (2.28) to (2.29) when

$$\Delta\vartheta\gg\frac{k}{2k_1}\frac{\Delta k_1}{k_1}+au$$

is

$$\frac{u_\vartheta}{u_\nu}=\frac{k}{k_1}\frac{m_i}{m_e}\frac{\omega_a}{\nu_e}\frac{1}{\Delta\vartheta}. \tag{2.31}$$

If we neglect imaginary terms in (2.29), which is possible when $\omega'>\delta(\Delta\omega_{\mathbf{k}\mathbf{k}_1})$, (2.24) is replaced by

$$\begin{aligned}\omega'-i\gamma_{\mathbf{k}}^{s}={}&-\frac{\omega_a^2}{2}\cos^2\vartheta_0\frac{u}{\omega'-\Delta\omega_{\mathbf{k}\mathbf{k}_1}}-\frac{\omega_a^2u\cos\vartheta_0\sin^2\vartheta_0}{\omega'-\Delta\omega_{\mathbf{k}\mathbf{k}_1}}\\&-\frac{\omega_a^3}{2}\cos^2\vartheta_0\sin^2\vartheta_0\frac{u}{(\omega'-\Delta\omega_{\mathbf{k}\mathbf{k}_1})^2}.\end{aligned}$$

Thus, when $\omega'\gg\Delta\omega_{\mathbf{k}\mathbf{k}_1}$ we have

$$\begin{aligned}\omega'^2(\omega'-i\gamma_{\mathbf{k}}^{s})={}&-\omega'\frac{\omega_a^2}{2}\cos^2\vartheta_0u-\omega'u\omega_a^2\cos\vartheta_0\sin^2\vartheta_0\\&-u\frac{\omega_a^3}{2}\cos^2\vartheta_0\sin^2\vartheta_0,\end{aligned} \tag{2.32}$$

which for $\omega'>\gamma_{\mathbf{k}}^{s}$ describes the instability of the hydrodynamic type with a growth rate

$$\omega'=(-1)^{1/3}\omega_a^2\left[\frac{u}{2}\sin^2\vartheta_0\cos^2\vartheta_0\right]^{1/3}; \tag{2.33}$$

when $\omega'\ll\gamma_{\mathbf{k}}^{s}$ this gives rise to a dissipative instability

$$\omega'=\omega_a\left(\frac{\omega_a}{i\gamma_{\mathbf{k}}^{s}}\right)^{1/2}\left[\frac{u}{2}\cos^2\vartheta_0\sin^2\vartheta_0\right]^{1/2}. \tag{2.34}$$

The criteria for these instabilities are respectively[3)]

$$1>\sin^2\vartheta_0\cos^2\vartheta_0u_0>\max\left\{2(\Delta\vartheta)^3,\ \left(\frac{m_e}{m_i}\frac{\nu_e}{\omega_a}\right)^3\right\} \tag{2.35}$$

and

$$\left(\frac{m_e}{m_i}\right)^3\left(\frac{\nu_e}{\omega_a}\right)^3>\sin^2\vartheta_0\cos^2\vartheta_0u_0>(\Delta\vartheta)^3. \tag{2.36}$$

It is evident from (2.35) and (2.36) that these instabilities appear when $\Delta\vartheta\ll1$.

DISCUSSION

The above analysis shows that under certain conditions anisotropic ion-acoustic turbulence can be unstable against the excitation of acoustic waves. The growth rate of the instability can be estimated from (2.25) or

$$\gamma\leqslant\frac{\pi}{4}\omega_a\frac{u^2\frac{k_1}{k}}{\left(\Delta\vartheta_0+\frac{k}{2k_1}\frac{\Delta k_1}{k_1}+au\right)^2}\quad\text{for}\quad u<\frac{k}{k_1} \tag{3.1}$$

$$n_i \frac{3}{2}\left[\frac{\partial}{\partial t}+(\mathbf{v}_i\nabla)\right]T_i + n_i T_i \frac{\partial \mathbf{v}_i}{\partial \mathbf{r}} = -\pi_{i\alpha\beta}\frac{\partial v_{i\alpha}}{\partial x_\beta} - \frac{\partial}{\partial \mathbf{r}}\mathbf{q}_i, \qquad (2.8)$$

where

$$\mathbf{R}_T = -0.71 n_e \frac{\partial T_e}{\partial \mathbf{r}}, \quad \mathbf{q}_e = -3.16\frac{n_e T_e}{m_e \nu_e}\frac{\partial T_e}{\partial \mathbf{r}},$$

$$\mathbf{q}_i = -3.9\frac{n_i T_i}{m_i \nu_i}\frac{\partial T_i}{\partial \mathbf{r}}, \quad \pi_{e\alpha\beta} = -0.73\frac{n_e T_e}{\nu_e}W^e_{\alpha\beta},$$

$$\pi_{i\alpha\beta} = -0.96\frac{n_i T_i}{\nu_i}W^i_{\alpha\beta}, \quad W_{\alpha\beta} = \frac{\partial V_\alpha}{\partial x_\beta} + \frac{\partial V_\beta}{\partial x_\alpha} - \frac{2}{3}\delta_{\alpha\beta}\frac{\partial \mathbf{V}}{\partial \mathbf{r}}.$$

It should be noted that the following simplifications have been made in writing (2.4)-(2.8): 1) We are interested in the case $(m_e/m_i)\nu_e \ll \omega \ll kv_e, k^2v_e^2/\nu_e$ [this implies $\omega_a \gg (m_e/m_i)\,\nu_e$, i.e., the frequency of the "acoustic branch" is greater than the temperature equalization rate] so that quantities proportional to $\delta\nu = 3\,(m_e/m_i)\,\nu_e$ can be neglected; 2) we neglect the displacement current $(kv_e \ll \omega_{pe})$, putting $V_i^R = V_e^R$ or $U = V_e - V_i = 0$. We solve the system (2.1)-(2.8) by successive approximations, i.e., we expand all functions in series and retain only terms of second order or lower in the electric field. The system of equations taken to this degree of accuracy with $\omega \gg k^2v_e^2/\nu_e$ is greatly simplified. Equation (2.5) assumes the following form in the frequency range of interest:

$$n_0\frac{dV^{(2)}}{dt} + \frac{1.71}{m_e}n_0\frac{\partial T^{(2)}}{\partial x} + \frac{T_0}{m_e}\frac{\partial n^{(2)}}{\partial x} = \frac{T_0}{m_e n_0}n^{(1)}\frac{\partial n^{(1)}}{\partial x}, \qquad (2.9)$$

while the energy balance for the Fourier components is

$$T^{(2)} = -i\frac{m_e\nu_e}{3.16}\frac{1}{k}V_k^{(2)} - i\frac{m_e\nu_e}{3.16 n_0^2}\frac{1}{k^2}\int \omega_2 n_{k_1}^{(1)} n_{k_2}^{(1)} d\lambda, \qquad (2.10)$$

and for the case in which we are interested

$$V_{ke}^{(2)} = -\frac{1}{2}\frac{e^2}{T_e^2}\frac{\omega}{k}\int\left[1 - \frac{\omega_1}{\omega}\frac{(\mathbf{k}\mathbf{k}_1)}{k_1^2} - \frac{\omega_2}{\omega}\frac{(\mathbf{k}\mathbf{k}_2)}{k_2^2}\right]\frac{E_{k_1}^{(1)}E_{k_2}^{(1)}}{k_1k_2}d\lambda. \qquad (2.11)$$

In order to get (2.11), we make use of the fact that the contribution $(V_e\nabla)\,V_e$ is smaller than $(v_e/n_0)^2\,\tilde{n}_e\,(\nabla\tilde{n}_e)$ by an order of magnitude in $(v_e/v_s)^2 \sim (m_e/m_i)^{-1}$ if $\omega \ll kv_e$; thus the above term can be neglected.

Similar reasoning for the ion component of the plasma gives

$$V_{ik}^{(2)} = \frac{1}{3}\frac{kv_i^2}{\omega}\frac{1}{n_0^2}\int n_{ik_1}^{(1)}n_{ik_2}^{(1)}d\lambda + i\frac{0.71}{m_i}\frac{\nu_e}{k}\frac{1}{n_0^2}\int n_{ek_1}^{(1)}n_{ek_2}^{(1)}d\lambda$$
$$+ \frac{1}{2}\frac{kv_i^2}{\omega}\frac{1}{n_0^2}\int n_{ik_1}^{(1)}n_{ik_2}^{(1)}\left(\frac{\omega_2}{\omega}\frac{(\mathbf{k}\mathbf{k}_2)}{k_2^2} + \frac{\omega_1}{\omega}\frac{(\mathbf{k}\mathbf{k}_1)}{k_1^2}\right)d\lambda. \qquad (2.12)$$

Hence,

$$j_k^{(2)} = en_0\left(V_k^{(e)(2)} - V_k^{(i)(2)}\right) = \int S_1(k, k_1, k_2)E_{k_1}^{(1)}E_{k_2}^{(1)}d\lambda, \qquad (2.13)$$

$$d\lambda = \delta(k - k_1 - k_2)\,dk_1dk_2;$$

$$S_1(k, k_1, k_2) = S_{1e}(k, k_1, k_2) + S_{1i}(k, k_1, k_2).$$

After substitution of the values of S_{1e} and S_{1i} we see that $S_{1e} \gg S_{1i}$; therefore

$$S_1(k, k_1, k_2) = \frac{1}{2}\frac{n_0e^3}{T_{0e}^2}\frac{\omega}{kk_1k_2}\left[\frac{\omega_1}{\omega}\frac{(\mathbf{k}\mathbf{k}_1)}{kk_1} + \frac{\omega_2}{\omega}\frac{(\mathbf{k}\mathbf{k}_2)}{kk_2} - 1\right], \qquad (2.14)$$

where k corresponds to the low frequencies and k_1 and k_2 to the high frequencies which are of the order of the turbulence fluctuation frequencies.

From the system (2.1)-(2.3) we can easily find the components of the nonlinear current $S_2(k_1, k', k_2')$ defined by the functions $\tilde{V}_{k_{1e}}^{(1)}$ and $\tilde{V}_{k_{1i}}^{(1)}$ [see (2.13)]:

$$\tilde{V}_{k_1e}^{(1)} = \frac{e^2}{T_{0e}^2}\int E_{k_2'}^{(0)}E_{k'}^{R}\left[\frac{\omega'}{k_2'k'^2}\frac{(\mathbf{k}_1\mathbf{k}')}{k_1k'} + \frac{\omega_2'}{k_2'^2k'}\frac{(\mathbf{k}_1\mathbf{k}_2')}{k_1k_2'}\right]d\lambda_1'$$
$$- \frac{e^2}{T_{0e}^2}\int E_{k_2'}^{(0)}E_{k'}^{R}\frac{\omega_1}{k_2'k'k_1}d\lambda_1'. \qquad (2.15)$$

It is evident that the dissipation effects are negligible in the case we are considering, $\omega < k^2v_e^2/\nu_e$.

Correspondingly, for the ions

$$\tilde{V}_{k_1i}^{(1)} = \int\frac{(\mathbf{k}_2'\mathbf{k}')}{k_2'k'}\frac{k_1}{\omega_1}\tilde{V}_{k_2'e}^{(0)}V_{k',e}^{R}d\lambda_1'$$
$$= -\frac{e^2}{T_{0e}^2}\int\frac{(\mathbf{k}_2'\mathbf{k}')}{k_2'k'}\frac{\omega_2'}{k_2'^2}\frac{\omega'}{k'^2}\frac{k_1}{\omega_1}E_{k'}^{R}E_{k_2'}^{(0)}d\lambda_1'. \qquad (2.16)$$

The nonlinear current

$$j_{k_1}^{(1)} = -en_0\left(\tilde{V}_{k_1e}^{(1)} - \tilde{V}_{k_1i}^{(1)}\right) = \int S_2(k_1, k', k_2')E_{k_2'}^{(0)}E_{k'}^{R}d\lambda_1', \qquad (2.17)$$

where

$$S_2(k_1, k', k_2') = \frac{e^3n_0}{T_{0e}^2}\frac{1}{k_2'k'}\left[\frac{(\mathbf{k}_1\mathbf{k}')}{k_1k'}\frac{\omega'}{k'} + \frac{(\mathbf{k}_2'\mathbf{k}_1)}{k_2'k_1}\frac{\omega_2'}{k_2'} + \frac{(\mathbf{k}_2'\mathbf{k}')}{k_2'k'}\frac{\omega_2'\omega'}{k_2'k'}\frac{k_1}{\omega_1} - \frac{\omega_1}{k_1}\right]. \qquad (2.18)$$

The dispersion equation describing the excitation of acoustic waves by s waves has the form[8,10]

$$\omega' - i\gamma_{\mathbf{k}}^{s} = -\int\frac{w(\mathbf{k}, \mathbf{k}_1)\left(N_{\mathbf{k}_1}^{s} - N_{\mathbf{k}_1-\mathbf{k}}^{s}\right)}{\omega' - \Delta\omega_{\mathbf{k},\mathbf{k}_1} + i\delta}d\mathbf{k}_1. \qquad (2.19)$$

Here, ω' is the nonlinear correction term to the frequency of the acoustic waves

$$\omega' = \omega - \operatorname{Re}\omega_{\mathbf{k}}^{s}, \quad \Delta\omega_{\mathbf{k},\mathbf{k}_1} = \operatorname{Re}\left(\omega_{\mathbf{k}_1}^{s} - \omega_{\mathbf{k}} + \omega_{\mathbf{k}_1-\mathbf{k}}\right),$$

$\gamma_{\mathbf{k}}^{s}$ is the linear growth rate, $N_{\mathbf{k}_1}^{s}$ is the number of s-wave photons, $w(\mathbf{k}, \mathbf{k}_1)$ is usually the probability of the decay process; in this case it is proportional to the product of the nonlinear polarizabilities S_1 and S_2:

$$w(\mathbf{k}, \mathbf{k}_1) = \frac{2\left(\frac{n_0e^3}{T_{0e}^2}\right)^2\frac{\omega\omega_1}{k^2k_1^2}\left(\frac{\mathbf{k}\mathbf{k}_1}{kk_1}\right)^2}{\frac{\omega_{k_1}^{s}\partial\varepsilon}{\partial\omega}\Big|_{\omega-\Omega_{k_1}^{s}}\frac{\partial\varepsilon}{\partial\omega}\Big|_{\omega_{\mathbf{k}}}\frac{\partial\varepsilon}{\partial\omega}\Big|_{\Omega_{k_1}^{s}}}. \qquad (2.20)$$

After substituting (2.20) into (2.19), we get

$$\omega' - i\gamma_{\mathbf{k}}^{s} = -\frac{\omega_a^2}{2n_0T_e}\int\frac{k_1}{k}\left(\frac{\mathbf{k}_1\mathbf{k}}{k_1k}\right)^2\frac{\mathbf{k}\left(\frac{\partial W_{\mathbf{k}_1}}{\partial\mathbf{k}_1}\right)}{\omega' - \Delta\omega_{\mathbf{k}\mathbf{k}_1} + i\delta}d\mathbf{k}_1. \qquad (2.21)$$

The kinetic instability usually arises when $\Delta\omega_{\mathbf{k}\mathbf{k}_1} > \omega'$ and the integrand is proportional to $-i\pi\delta\,(\Delta\omega_{\mathbf{k}\mathbf{k}_1})$. Then, after integration by parts, Eq. (2.21) becomes

$$\omega' - i\gamma_{\mathbf{k}}^{s} = -i\frac{\pi}{2}\omega_a^2\int\frac{W_{\mathbf{k}_1}}{n_0T_e}d^3\mathbf{k}_1\left(\mathbf{k}\frac{\partial}{\partial\mathbf{k}_1}\right)\left(\frac{k_1}{k}\left(\frac{\mathbf{k}\mathbf{k}_1}{kk_1}\right)^2\delta\left(\omega - \left(\frac{\mathbf{k}\mathbf{k}_1}{kk_1}\right)\omega_a\right)\right)$$
$$= -i\frac{\pi}{2}\omega_a^2\int u_{\mathbf{k}_1}d^3\mathbf{k}_1\left[\left(\frac{\mathbf{k}\mathbf{k}_1}{kk_1}\right)^2\delta\left(\omega - \frac{\mathbf{k}\mathbf{k}_1}{kk_1}\omega_a\right) + 2\left(\frac{\mathbf{k}\mathbf{k}_1}{kk_1}\right)\left(1 - \left(\frac{\mathbf{k}\mathbf{k}_1}{kk_1}\right)^2\right)\right.$$
$$\left.\times\,\delta\left(\omega - \frac{\mathbf{k}\mathbf{k}_1}{kk_1}\omega_a\right) - \left(\frac{\mathbf{k}\mathbf{k}_1}{kk_1}\right)^2\omega_a\left(1 - \left(\frac{\mathbf{k}_1\mathbf{k}}{k_1k}\right)^2\right)\delta'\left(\omega - \frac{\mathbf{k}\mathbf{k}_1}{kk_1}\omega_a\right)\right]. \qquad (2.22)$$

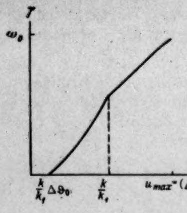

Fig. 1. Variation of the instability growth rate γ with u_0 for fixed values of the cone angle $\Delta\vartheta_0$ and the average wave number k_1 of the s waves.

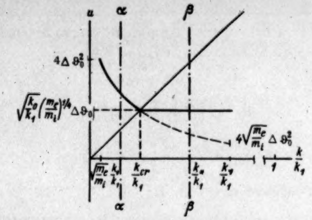

Fig. 2. Variation of the instability threshold for acoustic waves u_0 with the wave number k, where $k_{cr}=\Delta\vartheta_0(k_1k_\nu)^{1/2}(m_e/m)^{1/4}$.

and $\gamma \sim (\pi/4)\,\omega_a\,(u/\Delta\theta_0^2)$ with $u > k/k_1$. We use the fact that $\sin^2\vartheta_0 \sim \vartheta_0^2 \lessgtr (k_1/k)u$.

Remembering that γ must be less than ω_a, we obtain the upper limit on u as

$$u < u_{\max} = \Delta\vartheta_0^2, \tag{3.2}$$

Thus the quantity u can be neglected everwhere in the denominator in comparison with $\Delta\vartheta_0$. It follows from (3.2) that the smaller the cone angle of the s waves, the lower the energy at which there is a large change in dispersion in the acoustic region.

Figure 1 shows the relation between the instability growth rate γ and u_0 for fixed values of the cone angle $\Delta\vartheta_0$ and the average wave number k_1 of the s waves; Fig. 2 gives the variation in the instability threshold for acoustic waves u_0 with wave number k. In Fig. 3 we show the variation of u_0 with the cone angle $\Delta\vartheta_0$ of the s waves for fixed k.

If, on the other hand, the anisotropy of the s turbulence is small, $\Delta\vartheta_0 \to 1$, only the kinetic instability with $\gamma \ll \omega_a$ is possible.

It should be noted in conclusion that the instability we have considered leads to a transfer of the energy of the s waves from the collisionless wave-number region ($k > k_\nu$) to the region in which Coulomb collisions are important. This process can be considered as an additional mechanism for dissipation of the s-wave energy.

In the region of small wave numbers, but larger than k_ν, where, according to ref. 7, the main energy of the turbulence is concentrated, the dissipation of the s waves through ion–ion collisions[11] is characterized by

$$\gamma \sim 0.6\nu_i\frac{T_i}{T_e}, \tag{3.3}$$

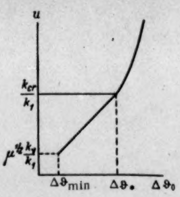

Fig. 3. Variation of the instability threshold for acoustic waves u_0 with the cone angle $\Delta\vartheta_0$ of the s waves for fixed k.

and the Landau damping of the electrons by

$$\gamma \sim \sqrt{\frac{\pi}{8}}\left(\frac{m_e}{m_i}\right)^{1/2}\omega_s. \tag{3.4}$$

Comparing (3.3) and (3.4), we find that when

$$k < k_\nu\left(\frac{T_e}{T_i}\right)^{1/2} \tag{3.5}$$

the damping of the s waves is determined entirely by collisions.

The dissipation of the s-wave energy by the instability we have considered can have a value as high as $\gamma \lessgtr \nu_i$, which not only exceeds (3.3) but also (3.4) if

$$k < k_\nu\left(\frac{T_e}{T_i}\right)^{3/2}. \tag{3.6}$$

Thus [for a sufficiently high level of s turbulence in the region (3.6)] the present process can determine the form of the ion-acoustic turbulence spectrum.

We take this opportunity to thank V. N. Tsytovich for discussion.

---

1) We study the stability of the s turbulence against the excitation of acoustic waves.

2) The resonance denominators in (2.24) contain the frequency spreading connected with the shift and broadening of the s-wave correlation functions.[7]

3) Here $\Delta\vartheta = \Delta\vartheta_0 + (k/k_1)(\Delta k_1/k_1)$.

[1] E. K. Zavoiskii and L. I. Rudakov, Plasma Physics (Collective Processes and Turbulent Heating) [in Russian], Znanie, Moscow (1967); Atom. Energ., 23, 417 (1967).

[2] S. M. Hamberger and L. S. Sharp, Proc. Fourth European Conf. on Plasma Physics and Contr. Fusion (Rome), 65, 64 (1970).

[3] S. M. Hamberger and M. Friedman, Phys. Rev. Lett., 21, 674 (1968); B. A. Demidov, N. I. Elagin and S. D. Fanchenko, Dokl. Akad. Nauk SSSR, 174, 327 (1960) [Sov. Phys. – Dokl., 12, 467 (1967)].

[4] B. B. Kadomtsev, Reviews of Plasma Physics, Vol. 4, Consultants Bureau New York (1966); B. B. Kadomtsev and V. I. Petviashvili, Zh. Eksp. Teor. Fiz., 43, 2234 (1962) [Sov. Phys. – JETP, 16, 1578 (1963)]; V. I. Petviashvili, Dokl. Akad. Nauk SSSR, 153, 1295 (1963) [Sov. Phys. – Dokl., 8, 1218 (1964)].

[5] I. A. Akhiezer, Zh. Eksp. Teor. Fiz., 47, 952, 2269 (1964) [Sov. Phys. – JETP, 20, 637, 1519 (1965)].

[6] L. I. Rudakov and V. N. Tsytovich, Plasma Phys., 13, 213 (1971); Preprint 28 of Lebedev Phys. Institute (1970).

[7] V. N. Tsytovich, Theory of Turbulent Plasma, Consultants Bureau, New York (1973), Chap. 4; V. N. Tsytovich, Plasma Phys., 13, 741 (1971).

[8] V. G. Makhan'kov and V. N. Tsytovich, Preprint of United Nuclear Research Institute, P9-3980, Dubna (1968); Zh. Tekh. Fiz., 40, 681 (1970) [Sov. Phys. – Tech. Phys., 15, 530 (1970)].

[9] S. I. Braginskii, Reviews of Plasma Physics, Vol. 1, Consultants Bureau New York (1965).

[10] V. N. Tsytovich, Zh. Tekh. Fiz., 39, 1756 (1969) [Sov. Phys. – Tech. Phys., 14, 1321 (1970)].

[11] E. E. Lovetskii and A. A. Rukhadze, Zh. Eksp. Teor. Fiz., 41, 1845 (1961) [Sov. Phys. – JETP, 14, 1312 (1962)].

Plasma acceleration in crossed electric and magnetic fields

V. I. Aref'ev

(Submitted January 10, 1973; resubmitted August 7, 1973)
Zh. Tekh. Fiz., 44, 706-722 (April 1974)

From an analysis of experiments on electromagnetic plasma acceleration in crossed E and H fields we conclude that the acceleration is unstable and turbulent in principle. A model of a plane accelerating current sheath is used to investigate the turbulence ion-acceleration mechanism. Quasilinear theory, which describes weakly turbulent processes in the plasma, is used to study the development of the most dangerous transverse (Hall) current-driven instabilities, which produce a large contribution to the anomalous resistance of the plasma and lead to turbulence acceleration. The anode and pulsed current sheaths are investigated with allowance for the self-consistent anomalous resistance. It is noted that there can be local amplification of the Hall current in the microscopic turbulence; at a high noise level this leads to local demagnetization of the electrons and breakaway of the drift current.

In a number of experimental papers[1-10] on electromagnetic plasma acceleration it has been noted that an important role is played by unstable, turbulence processes; these can determine the flow and runaway patterns of a plasma in crossed E and H fields. Theoretical examinations of these problems (see refs. 11-13, for example) have drawn attention to the fact that the process of plasma acceleration in crossed electric and magnetic fields is, in principle, unstable and turbulent at least because it is impossible in practice to avoid the excitation of the most dangerous low-frequency instabilities of the transverse (Hall) current, which have the maximum effect on the anomalous resistance of the plasma. Thus the problem necessarily arises of dealing with so-called "turbulence plasma acceleration,"[13] based on a systematic analysis of the anomalous processes such as have been fully described in the review of ref. 1.

The most important experimental results are as follows:

1) The existence of limiting acceleration regions (the "current crisis") above which the plasma flow in an accelerator becomes unstable and turbulent.

2) The development of intense low-frequency (coherent) and high-frequency (random) oscillations, which lead to the appearance of many anomalous effects.[1]

3) The partial or total breakdown of "accelerating current layers" (Fig. 1) as a result of the growth of unstable turbulence processes and a basic change in the acceleration conditions.

4) The generation of "fast particles" as a result of the turbulence processes.

Emphasizing the general nature of the anomalous effects 1-4, we can draw the important conclusion that the acceleration of a plasma in E and H fields is an unstable and turbulence process in principle. Thus the frequent and important problem of acceleration in (E, H) fields of an unstable turbulence plasma, which is one aspect of turbulence heating, must be considered entirely on the basis of collective processes. We now consider some of the problems connected with turbulence plasma acceleration.

1. THE MECHANISM OF TURBULENCE PARTICLE ACCELERATION IN (E, H) FIELDS

Although there is a wide variety of existing plasma accelerators, [stationary (Hall), pulsed, etc.][1] a common feature in their operation is the formation of an accelerating current sheath, shown schematically in Fig. 1, in which energy is transferred to the plasma from the electromagnetic field and transformed into kinetic energy of the charged particles. In Hall accelerators, for example, a highly nonuniform current sheath is produced next to the anode (Fig. 1a); this is often called the anode sheath. In pulsed systems (Fig. 1b), a pulsed current sheath is produced. Using the model of a plane accelerating current sheath enables us to classify accelerators according to the interaction time of the external electromagnetic fields: We have stationary pulsed and periodic types. With this model we can take account of the special features of the plasma acceleration process in E, H fields and clarify the details of the turbulence acceleration mechanism.

We make use of the equations for a weakly turbulent plasma and consider the balance of forces acting on the electrons and ions:

$$M\frac{d\mathbf{v}_i}{dt}=e\left(\mathbf{E}+\frac{1}{c}[\mathbf{v}_i\mathbf{H}]\right)+\mathbf{F}_{i,i}+\mathbf{F}^f_{i,i}+\mathbf{F}_{i,e}+\mathbf{F}^f_{i,e}; \qquad (1)$$

$$m\frac{d\mathbf{v}_e}{dt}=-e\left(\mathbf{E}+\frac{1}{c}[\mathbf{v}_e\mathbf{H}]\right)+\mathbf{F}_{e,e}+\mathbf{F}^f_{e,e}+\mathbf{F}_{e,i}+\mathbf{F}^f_{e,i}. \qquad (2)$$

Here, $\mathbf{F}_{i,j}$, $\mathbf{F}_{i,e}$, $\mathbf{F}_{e,e}$, $\mathbf{F}_{e,i}$ are the forces produced by binary collisions and $\mathbf{F}^f_{i,i}$, $\mathbf{F}^f_{i,e}$, $\mathbf{F}^f_{e,e}$, $\mathbf{F}^f_{e,i}$ are the collective friction forces, which appear either between different groups of ions (electrons) or between electrons and ions. In contrast to the forces based on binary collisions, the collective friction forces are generally unbalanced, i.e., the force can be greater on one of the interacting components than on the other. This is because part of the momentum and energy is carried away by unstable plasma oscillations. We can use (1) and (2) to derive the main features of the acceleration mechanism for ions in an unstable, turbulent plasma.

a. The ion–ion friction forces $\mathbf{F}_{i,i}$ and $\mathbf{F}^f_{i,i}$ can pro-

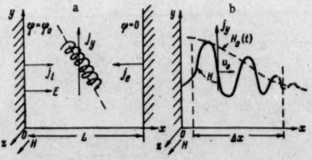

Fig. 1. Movement of a plasma particle in an "accelerating anode layer" (a) and in an pulsed current sheath (b).

duce acceleration only at the expense of ion energy. Examples are plasma currents with ion beams, thermodynamically nonequilibrium energy distributions of groups of similar ions produced by ionization, charge transfer and other processes, and the acceleration of an ensemble of ions of different masses. It should be noted that an energy transfer mechanism based on turbulence ion–ion friction is very effective, especially when it is remembered that the characteristic time for turbulence heating (acceleration) of ions $\tau^f_{i,i} < \tau_{i,i}$, which is of the order of magnitude of the growth time of ion–ion instabilities,[14] can be much less than the transit time of the plasma τ_0. Reference 13 considers several examples which show the effectiveness of this acceleration mechanism. The first of these is connected with the interaction in the accelerating current sheath of two types of ion: light ions and heavy ions with masses and densities equal to n_1, n_2, and M_1, M_2. If both pass across a sheath of identical potential difference (Fig. 1a), the light ions acquire a velocity which is $(M_2/M_1)^{1/2}$ times higher than that of the heavy ions. Under these conditions an ion beam instability is produced and this leads to equalization of the momentum in a time much smaller than the transit time. From the condition for energy and momentum balance between the two types of ion, we find that the limiting estimate of the energy of the heavy ions is $(M_2/M_1)^{1/2}$ times the applied potential difference. A similar situation is considered in ref. 15, where the development of a drift instability in a plasma containing impurity ions is accompanied by anomalous acceleration of the impurities in collective oscillations to very high energies, much greater than the energy of the main mass of ions; the theoretical calculation gives a satisfactory explanation of experiments carried out on Zeta.[16] Another mechanism considered in ref. 13 can appear when a "slow beam" of ions (electrons) is generated as a result of ionization or charge exchange in the accelerating current sheath; under certain conditions an ion–ion or electron–electron beam instability develops and this can lead to the rapid acceleration of a small group of ions to high energies. Estimates of the limiting energies of the fast ions in refs. 13 and 17 show the effectiveness of this mechanism.

b. Of particular interest are the acceleration mechanisms based on the electron–ion friction forces $\mathbf{F}_{i,e}$ and $\mathbf{F}^f_{i,e}$ which exist in a plasma through which a current is flowing. The collective electron–ion friction effect is then necessarily accompanied by the development of low-frequency current-driven instabilities and the appearance of anomalous resistance.[18,19] This acceleration process can also prove effective because the characteristic time for the transfer of momentum from electrons to ions in a turbulent plasma $\tau^f_{e,i}$, which is of the order of the growth time of the current-driven instabilities,[17] is comparatively small. Estimates of the limiting ion energies[13,17] confirm this conclusion. It should be noted, however, that if the turbulent forces acting on the electrons and ions are balanced, i.e., are equal in magnitude and opposite in sign, there can be no acceleration in the direction of the force $\mathbf{F}^f_{i,e}$, i.e., it is necessary that there be a lack of balance in order for this mechanism to be effective. Let us consider in more detail the acceleration effect connected with collective friction forces $\mathbf{F}^f_{e,e}$ and $\mathbf{F}^f_{e,i}$ acting only on the electron component. We thus assume complete imbalance when the momentum lost by the electrons in Cerenkov radiation is not transferred to the ions, but is carried away by turbulent fluctuations; from (2) we obtain the condition for the existence of an electric field in the plasma and can thus determine the electric force on **E**, which is the only one which produces acceleration of the ions:

$$\mathbf{E} = -\frac{1}{c}[\mathbf{v}_e\mathbf{H}] + \frac{1}{e}(\mathbf{F}^f_{e,e} + \mathbf{F}^f_{e,i}) - \frac{m}{e}\frac{d\mathbf{v}_e}{dt}. \tag{3}$$

It can thus be seen that the electric field accelerating the ions can be maintained, firstly by the external forces, i.e., the Lorentz force $-(e/c)\,[\mathbf{v}_e\mathbf{H}]$ (this effect is realized in all Hall accelerators; cf. the classification of acceleration mechanisms in a laminar plasma given in ref. 1); secondly, by the unbalanced forces of internal friction $\mathbf{F}^f_{e,e}$ and $\mathbf{F}^f_{e,i}$; thirdly, by the inertia force of the electrons (this effect is small in practice).

We consider first on the basis of (3) only one of the collective friction forces $\mathbf{F}^f_{e,e}$, $\mathbf{F}^f_{e,i}$, assuming that it is much greater than the others. It is easy to obtain a simple criterion for this condition: It is necessary that the effective frequency of electron scattering by the oscillations exceed the electron cyclotron frequency, $\nu_f > \omega_{He}$, the condition that the electrons should not be magnetized. It thus becomes obvious that the best approach to the turbulence plasma acceleration process is directly related to the most effective realization of the deacceleration process of electrons which actually acquire energy in a noninertial way from the external fields. A large number of experiments on the generation of fast particles are best explained by just this acceleration mechanism; this includes those in fast pinches[20,21] in paramagnetic pinches like Zeta,[16] in stationary[22] and pulsed[23,24] gas discharges, in high-current arcs,[25] and in the plasma focus.[26] For example, the experiments of Plyutto[27] on the generation of fast particles can be satisfactorily interpreted by internal friction forces $\mathbf{F}^f_{e,e}$ and $\mathbf{F}^f_{e,i}$. We may note in this connection that the collective force of electron–electron friction $\mathbf{F}^f_{e,e}$ is directly connected with the thermodynamically nonequilibrium energy distribution of the electrons (which is formed, for example, in a current-beam plasma, during ionization processes in a gas-discharge plasma, and so on). The physical importance of this force is directly related to the development of various beam-type instabilities, which lead to severe slowing down of electrons and transfer of energy to the self-consistent electric field [see (3)]. We may also note that the appearance of a large collective friction force $\mathbf{F}^f_{e,e}$ can lead not only to the formation of strong electric fields which accelerate the ions, but also to demagnetization of the electrons on waves with $\nu_f > \omega_{He}$. A nonsteady-state type of motion is then set up in the accelerating current sheath with changes in the acceleration conditions.

c. In the simplest case, if we exclude all collisions and neglect electron inertia, we can get an electric field, which, owing to the Hall effect in the plasma, is self-consistent with the movement of the charges:

$$\mathbf{E} = -\frac{1}{c}[\mathbf{v}_e\mathbf{H}]. \tag{4}$$

The conditions for this to exist are that there should be a transverse magnetic field and an electron drift motion. A basic requirement is that the ions which are accelerated by the electric field in the plasma should not be "magnetized". This reduces to the requirement that the ion Larmor radius should be much greater than either the size of the system of the characteristic scale size of the inhomogeneities in the electric field ($\rho_{Hi} \gg \Delta$)]. This is in essence, as has been noted in ref. 1, the direct method of accelerating ions in E, H fields, but the very realization of this process necessarily leads to various instabilities and the appearance of the turbulence acceleration mechanisms discussed above. If we use the well-known criterion for ion-acoustic or electron-acoustic instability $u > v_s$, where the velocity of the electrons

$$u=\left(\frac{c}{H}\right)\frac{\partial\varphi}{\partial x},$$

and $v_s = (T_e/M)^{1/2}$ is the velocity of ion sound, we can establish that the microscopic instabilities of the transverse current, which make the biggest contribution to the anomalous resistance of the plasma, exist in any current sheath smaller than the ion Larmor radius $\Delta < \rho_{Hi}$. Thus the question of laminar dissipationless acceleration is contradictory right from the start.

Considering the acceleration process of a plasma in E, H fields as unstable and turbulent from the very beginning, we now analyze this effect in two cases which are of practical interest: stationary (Fig. 1a) and pulsed (Fig. 1b) acceleration.

3. TURBULENCE ACCELERATION IN A STATIONARY HALL SHEATH

There are a number of publications (refs. 1-6, for example) devoted to the experimental study of unstable, turbulence processes in Hall type E, H accelerators. A particular property of these devices is the formation near the anode of a space-charge sheath (called the anode sheath), in which the ionization and electric field are concentrated. Ions are accelerated in this sheath and electrons drift across the magnetic field (Fig. 1a).

The development of high-frequency instabilities in the accelerating anode sheath, as has been noted in refs. 5 and 6, leads to turbulent heating of the plasma and an increase in the transverse mobility of the electrons. As a result, the electron current to the anode is increased. Other instabilities, observed in refs. 1-4, are low-frequency coherent oscillations in the form of a rotating azimuthal inhomogeneity in the electric field. The development of these oscillations brings about a basic change in the acceleration conditions. The accelerating current sheath transfers from the less stable dispersion branch to the more stable; the dissipationless acceleration condition becomes collisional and the stable laminar configuration becomes unstable and turbulent. The study of these processes is left to a special investigation and we limit ourselves here to an analysis of the high-frequency instabilities and microscopic turbulence. Using quasilinear theory[28] to describe a weakly turbulent plasma, we can establish the main microscopic effects resulting from transverse current-driven instabilities.

1. A common idea in the study of accelerating current sheaths is that introduced in ref. 1 of an accelerator from a given dispersion branch. Thus, for example, we can consider acceleration in the following branches: electron-acoustic, ion-acoustic, cyclotron, and so on with stationary acceleration, and magnetoacoustic, Alfvén, etc., for pulsed acceleration.

We will simplify the problem here and consider a plane model of the accelerating anode sheath. In the space between the anode, of potential φ_0, and the cathode, situated at a distance L away with zero potential, a space-charge sheath is formed close to the anode. We assume a constant ion current from the anode j_i directed along the x axis and a constant electron current from the cathode j_e. The ions are accelerated in the x direction by an electric field which is sufficiently strong so that the average ion Larmor radius is considerably greater than the distance between the anode and cathode. A constant magnetic field H is directed along the z axis and the electrons drift in the crossed fields in the y direction, forming a Hall current j_y. In order for there to be an x component of electron current, we must have collisions which produce a change in the electron momentum along the y direction (these collisions might in practice be ionizing or Coulomb collisions). In a collisionless plasma, the role of elastic collisions is played by collective scattering of electrons by the random oscillations excited by the Hall current-driven instabilities.

We consider the high-frequency Hall current-driven instabilities which can lead to turbulent heating of the plasma in the current layer and to the appearance of anomalous resistance. Following ref. 18, we note the following important physical fact. In our model, the ion generation process is reduced to a purely surface (electrode) effect, whereas in practice the generation and acceleration of ions in all experiments[1-6] take place simultaneously. As a result, the ions acquire an effective spread in velocities which may be related to the appearance of an effective ion temperature T_i, i.e., the ions must be considered as "hot", $T_i \simeq e\varphi_0$ from the start.

Making use of refs. 18 and 19, we quote without derivation the dispersion equation which describes the electrostatic instability of the transverse current in a collisionless plasma,

$$\begin{aligned}\varepsilon = 1 + \frac{1}{k^2 d_i^2}\left[1 + i\sqrt{\pi} z_i W(z_i)\right] \\ + \frac{1}{k^2 d_e^2}\sum_{n=-\infty}^{\infty} I_n e^{-\mu}\left[1 + i\sqrt{\pi}\frac{\tilde{\omega}}{k_z v_{T_e}} W\left(\frac{\tilde{\omega} - n\omega_{He}}{k_z v_{T_e}}\right)\right] = 0.\end{aligned} \tag{5}$$

Here

$$d_\alpha = \frac{v_{T_\alpha}}{\omega_{p_\alpha}},\quad v_{T_\alpha} = \left(\frac{2T_\alpha}{m_\alpha}\right)^{1/2},\quad \omega_{p_\alpha} = \left(\frac{4\pi n_\alpha e_\alpha^2}{m_\alpha}\right)^{1/2},\quad z_i = \frac{(\omega - \mathbf{k}\mathbf{v}_i)}{k v_{Ti}},$$

$$\tilde{\omega} = \omega - \mathbf{ku} - \mathbf{kv}_e,\quad \alpha = e,\ i;\quad \omega_{He} = \frac{eH}{mc};$$

m and M are the electron and ion masses respectively, $\mu = k_\perp^2 \rho_{He}^2/2$, $\rho_{He} = v_{Te}/\omega_{He}$, k_x, k_y, and k_z are the components of the wave vector **k**, ω is the oscillation frequency, $I_n(\mu)$ is the Bessel function, W is a Cramp function, u is the current velocity of the electrons along the y axis:

$$u = \frac{c}{H}\frac{\partial\varphi}{\partial x}, \tag{6}$$

v_i and v_e are the average ion and electron velocities along the x axis ($v_i = j_i/n_ie$, $v_e = j_e/n_ee$).

a. A study of (5) in the region $\omega_{Hi} \ll \omega \lessdot \omega_{He}$ for the case of high electron energy $T_e > T_i$ shows[18,19] that the most unstable perturbations are the "oblique" ones $(m/M)^{1/2} < k_z/k \ll 1$ with wavelengths of the order of the Larmor radius $k^{-1} \simeq \rho_{He}$ (ion-acoustic oscillations). For a Maxwellian electron velocity distribution, the frequency ω_k and growth rate γ_k of the most unstable oscillations are ($\gamma_k < \omega_k$).

$$\left.\begin{aligned} &\omega_k = \mathbf{kv}_i + kv_s\bar{a},\ \bar{a} = (1 + k_\perp^2\rho_{He}^2)^{-1/2},\ v_s = \left(\frac{T_e}{M}\right)^{1/2};\\ &\gamma_k = \frac{\sqrt{\pi}}{2}kv_s\bar{a}^3 z_e \exp\left(-\frac{z_e^2}{2}\right),\ z_e = \frac{(\mathbf{ku} + \mathbf{kv}_e - \omega_k)}{k_z v_{Te}}. \end{aligned}\right\} \quad (7)$$

The most unstable perturbations are those for which $k_z/k \lessdot u/v_{Te}$. The oscillations are unstable when $u > v_s$ and have a maximum growth rate of order $\omega_{e,i} = (\omega_{Hi}\omega_{He})^{1/2}$ (which is reached when $k_\perp^{-1} \simeq \rho_{He}$).

b. In the high-frequency region $\omega \simeq \omega_{He}$ for a plasma with hot ions $T_i > T_e$, an instability (Bernstein modes) is excited at harmonics of the electron cyclotron frequency[29] for high values of the current velocity $u \gtrdot v_{Te}$. In the particular case of purely transverse oscillations ($k_z \equiv 0$) near the n-th cyclotron harmonic, from (5) we have

$$\begin{gathered} \omega_k = +k(u^* - u),\ u^* = \frac{n\omega_{He}}{k}\left[1 + \frac{T_i}{T_e}I_n e^{-\mu}\right];\\ \gamma_k = \gamma_{\max}\left(\frac{u - u^*}{v_{Ti}}\right)\exp\left[-\frac{(u - u^*)^2}{2v_{Ti}^2}\right],\\ \gamma_{\max} = n\omega_{He}\frac{v_{Ti}}{u}\left[2\ln\left(\frac{u}{v_{Ti}}\frac{T_i}{T_e}\sqrt{\pi}\, I_n e^{-\mu}\right)\right]^{1/2}. \end{gathered} \quad (8)$$

The most unstable waves are those with $u - u^* \lessdot v_{Ti}$. The development of this instability, as is shown in ref. 29, produces a significant increase in the anomalous resistance of the plasma. This subject is currently being discussed in connection with collisionless shocks.

c. In the low-frequency region $\omega_{Hi} \ll \omega < \omega_{He}$ with $T_i > T_e$, a low-threshold instability of the electron-acoustic type[18] is excited; this can be considered as an instability at the zeroth cyclotron harmonic. The frequency ω_k and growth rate γ_k of the most unstable of the oblique perturbations $m/M \ll k_z/k \ll (m/M)^{1/2}$ of this type are

$$\left.\begin{aligned} &\omega_k = \mathbf{ku} + \mathbf{kv}_e + k_z\left(\frac{T_i}{m}\right)^{1/2}\bar{a},\ \bar{a} = (1 + k_\perp^2\rho_e^2)^{-1/2};\\ &\gamma_k = \frac{\sqrt{\pi}}{2}k_z\left(\frac{T_i}{m}\right)^{1/2}\bar{a}^3 z_i \exp\left[-\frac{z_i^2}{2}\right],\ z_i = \frac{\left[u - \frac{k_z}{k}\left(\frac{T_i}{m}\right)^{1/2}\right]}{v_{Ti}}. \end{aligned}\right\} \quad (9)$$

The unstable oscillations with $u > (k_z/k)(T_i/m)^{1/2}$, $\mathbf{ku} < 0$ have the maximum growth rate, of order $\sim \omega_{e,i}$. The development of microscopic turbulence in these forms can lead to turbulent plasma heating and the appearance of anomalous resistance. We will analyze the situation on the basis of quasilinear theory.

2. As an example showing the main features of the quasilinear relaxation of current-driven instabilities, we consider the development in the anode sheath of instabilities of the ion-acoustic type. In the drift approximation, the quasilinear equation which describes the turbulent heating and diffusion of electrons in (x, v_z) space as a result of Cerenkov radiation–absorption has the form[30]

$$\begin{aligned} &\frac{\partial f_e}{\partial t} + \frac{\partial}{\partial x}\left(\frac{j_e}{n_ee}f_e\right)\\ &= \sum_k\left(\frac{1}{v_z}\frac{\partial}{\partial v_z} - \frac{k_y}{\bar{\omega}_k\omega_{He}}\frac{\partial}{\partial x}\right)D_k\left(\frac{1}{v_z}\frac{\partial f_e}{\partial v_z} - \frac{k_y}{\bar{\omega}_k\omega_{He}}\frac{\partial f_e}{\partial x}\right), \end{aligned} \quad (10)$$

where

$$D_k(x, t) = \pi\frac{e^2}{m^2}|\varphi_k|^2\bar{\omega}_k^2\delta(\bar{\omega}_k - k_zv_z),$$

and the oscillation energy density W_k is given by $[W_k = (k^2|\varphi_k|^2/8\pi)\omega_k(\partial\varepsilon/\partial\omega_k)]$

$$\left(\frac{\partial}{\partial t} + \frac{\partial\omega_k}{\partial k_x}\frac{\partial}{\partial x}\right)\ln W_k = \pi\frac{\omega_k^2M}{k^2mn_e}\int\left(k_z\frac{\partial f_e}{\partial v_z} - \frac{k_y}{\omega_{He}}\frac{\partial f_e}{\partial x}\right)\delta(\bar{\omega} - k_zv_z)\,dv_z. \quad (11)$$

The study of the self-consistent system of equations (10) and (11) follows the pattern in ref. 30 for the case of turbulence effects at the front of a magnetoacoustic shock wave. We supplement (10) and (11) by the equations describing the motion of the ions in the anode sheath and the equation for the potential

$$\left.\begin{aligned} &j_i = en_iv_i,\ \frac{\partial}{\partial x}\left(\frac{Mv_i^2}{2} + e\varphi\right) = 0;\\ &\frac{\partial^2\varphi}{\partial x^2} = 4\pi e(n_e - n_i),\ n_e = \int f_e dv_z. \end{aligned}\right\} \quad (12)$$

We also use the approach of ref. 30 and replace the summation over k in (10) and (11) by a single term, which gives a small contribution to the diffusion coefficient D(k). Finally, we introduce the new variables

$$\xi = \frac{v_z^2}{2},\quad \eta = \frac{v_z^2}{2}\Big| + \frac{\omega_{He}}{\bar{k}_y}\int_0^x\left(\omega_k - \bar{k}_y\frac{c}{H}\frac{\partial\varphi}{\partial x'}\right)dx' = \frac{v_z^2}{2} - \frac{e}{m}(\varphi_i - \varphi_0),$$

and we obtain the following heat-wave type solution for the stationary case:

$$\left.\begin{gathered} f_e = f_{0e} + \left(\frac{\bar{k}_zj_i}{\omega_{\bar{k}}j_e}\right)\frac{\partial}{\partial\xi}(W_{\bar{k}} - W_0),\\ \mathrm{li}\left(\frac{W_{\bar{k}}}{W_0}\right) = \frac{1}{2}z_0(z_0 - z). \end{gathered}\right\} \quad (13)$$

Here li is the logarithmic integral, f_{0e} is the electron distribution function at $\varphi = 0$, $W_k = W_0$, W_0 is the energy of the thermal fluctuations,

$$z = \frac{\xi}{\sqrt{\eta}}\left(\frac{\pi\omega_k^2W_0e}{m\omega_{Hi}\bar{k}j_e}\right)^{-1/2},$$

z_0 is the initial self-similar coordinate, defined by the conditions $\varphi = 0$, $u = v_s$:

$$z_0 = \left(\frac{T_e\omega_{Hi}\bar{k}j_e}{\pi W_0e\omega_k^2}\right)^{1/2}.$$

It follows from this solution that the electron distribution function in velocity space has the form of a steep step with a width which increases monotonically with potential.

Thus the thermal energy of the electrons, defined as $nT_e = (1/2)\int mv_z^2 f_e dv_z$, increases monotonically from the cathode to the anode. The limiting electron energy is determined by the competition between turbulent heating and cooling by diffusion along the x axis; from (10) we find

$$T_e \lesssim \frac{m\omega_{He}\bar{\omega}_k \Delta x}{\bar{k}_y} \simeq e\varphi_0. \tag{14}$$

A similar analysis can be made of the nonlinear effects which appear on the development of instabilities at the electron cyclotron harmonics (8) and electron-acoustic modes (9). The principal macroscopic effect which arises in the development of these instabilities can be reduced to the appearance of a collective friction force

$$\mathbf{R}_f = \sum_k \gamma_k \frac{\mathbf{k}}{\omega_k} W_k. \tag{15}$$

Here, γ_k is the growth rate of the instabilities and W_k is the energy density of the oscillations.

It is well known[19,29] that an important question which arises in the study of instabilities of the types (8) and (9) is the identification of the nonlinear mechanism producing saturation of the oscillation energy. The relevant mechanism here is the electron nonlinearity. This means that the transfer of oscillation momentum to the electrons takes place by nonlinear processes. It is likely that in the saturation region of instabilities of types (8) and (9), the momentum lost by the ions in Cerenkov radiation of the oscillations is transmitted entirely to the electrons. Thus there will be a collective friction force $\mathbf{R}_{fe}$ (15) acting on the electrons and this will be equal in magnitude but opposite in sign to the force $\mathbf{R}_{fi}$ acting on the ions. We now consider cases where the energy level of the oscillations is close to the saturation value.

3. Let us determine the structure of the anode sheath (Fig. 1a) in two cases which are important in practice: a) when an ion-acoustic instability develops, i.e., in a plasma with $T_e > T_i$; b) when an instability develops at the electron cyclotron harmonics, i.e., in a plasma with $T_i > T_e$. In this way we are able to allow quantitatively for the main macroscopic effect of the turbulence – the self-consistent anomalous resistance – and to establish the principal qualitative effects of particle dynamics in a weakly turbulent plasma.

We approximate the electron and ion distribution functions, which have the form of steep steps in velocity space, by Maxwellian distributions with effective temperatures T_e and T_i. The problem then reduces to a system of hydrodynamic equations. We consider the first case.

a. Substituting the Maxwellian function for the electrons into the original system (10)-(12), integrating over velocities and summing over wave numbers, we obtain the following equations by analogy with ref. 30 after allowing for the resonance variation of the diffusion coefficient D_k with k discussed above:

$$j_i = en_i v_i, \quad \frac{d}{dx}\left(\frac{Mv_i^2}{2} + e\varphi\right) = 0, \quad \frac{d^2\varphi}{dx^2} = 4\pi e(n_e - n_i),$$

$$j_e = \frac{c}{H}\left[\frac{mn_e\nu c}{H}\frac{d\varphi}{dx}\right.$$
$$\left. + \sum_k k_y \frac{W_k}{\omega_k}\frac{\sqrt{\pi}}{2}\left(\frac{kv_e}{k_z v_{Te}}\right)\left(\frac{k_y c}{H}\frac{d\varphi}{dx} - \mathbf{kv}_i - \mathbf{kv}_e\right)\right],$$

$$v_i \frac{d\ln W_k}{dx} = \sqrt{\pi}\left(\frac{kv_e}{k_z v_{Te}}\right)\left(\frac{k_y c}{H}\frac{d\varphi}{dx} - \mathbf{kv}_i - \mathbf{kv}_e\right). \tag{16}$$

Here, ν is the frequency of elastic electron collisions unconnected with the turbulence effect. We note that we have to maximize with respect to wavelengths in (16), $\bar{k}_z/\bar{k} \leqslant u/v_{Te}$, $\bar{k}^{-1} \simeq \rho_{He}$, to get the values for which the growth rate (7) is a maximum. In addition to (16), which gives a correct qualitative account of the principal macroscopic effects of ion-acoustic turbulence, we introduce the boundary conditions

$$\varphi(0) = \varphi_0, \quad \varphi(L) = 0, \quad v_i(0) = v_0, \quad W_k(L) = W_0. \tag{17}$$

The integral of (16), which shows how the noise energy varies with potential, has the form

$$\ln\left(\frac{W_k}{W_0}\right) = 2\sqrt{\pi}\frac{\bar{k}_y}{\omega_{Hi}}\left(\frac{\bar{k}v_e}{k_z v_{Te}}\right)\left[\left(v_0^2 + \frac{2e\varphi_0}{M}\right)^{1/2} - \left(v_0^2 + \frac{2e}{M}(\varphi_0 - \varphi)\right)^{1/2}\right]$$
$$- \sqrt{\pi}\frac{\bar{k}v_e}{k_z v_{Te}}\bar{k}(L - x). \tag{18}$$

We make use of the neutrality condition in the sheath $n_e \simeq n_i$ (the criterion for this is that $\Delta x > (T_i/m)^{1/2}(1/\omega_{He})$ and get a single equation for the potential from (16):

$$j_e = \frac{mc^2\nu j_i}{eH^2\left[v_0^2 + \frac{2e}{M}(\varphi_0 - \varphi)\right]^{1/2}}\frac{d\varphi}{dx} + \frac{c}{2H}W_0\frac{d}{dx}\exp\left(\frac{\sqrt{\pi}\bar{k}v_e}{\left|\frac{c}{H}\frac{d\varphi}{dx}\right|}\right)$$
$$\times \left\{\frac{2\left[\left(v_0^2 + \frac{2e\varphi_0}{M}\right)^{1/2} - \left(v_0^2 + \frac{2e}{M}(\varphi_0 - \varphi)\right)^{1/2}\right]}{\omega_{Hi}} - (L - x)\right\}. \tag{19}$$

We have here maximized with respect to the most unstable oscillations. It can be seen from this equation that the role of binary collisions is important over the scale lengths of the inhomogeneities in the potential:

$$\Delta x \sim \frac{v_0}{\omega_{Hi}}\left(\frac{\nu}{\omega_{He}}\frac{j_i}{j_e}\right).$$

The role of turbulence dissipation appears in a nonlinear form through the exponential variation of the friction force with the current velocity and potential

$$R_f = \frac{d}{dx}W_{\bar{k}} = W_0\frac{d}{dx}\exp\left(\frac{\sqrt{\pi}\bar{k}v_e}{\left|\frac{c}{H}\frac{d\varphi}{dx}\right|}\right)$$
$$\times \left\{\frac{\left[\left(v_0^2 + \frac{2e\varphi_0}{M}\right)^{1/2} - \left(v_0^2 + \frac{2e}{M}(\varphi_0 - \varphi)\right)\right]^{1/2}}{\omega_{Hi}} - (L - x)\right\}. \tag{20}$$

It can be seen from this expression that the friction force decreases with increasing current velocity. As a result, the structure of the anode sheath is again of the steep step type (Fig. 2a) with a sharp change in potential near the cathode, i.e., in the region where there is an exponential growth in the noise energy from the thermal fluctuation level W_0 to some maximum value W_{max} determined by the nonlinear processes. From (19) we can estimate the integrated effect of the turbulent dissipation in the anode sheath. This dissipation occurs over a region of typical size:

$$\Delta x \simeq \frac{1}{4\sqrt{\pi}} \frac{v_0}{\omega_{Hi}} \ln\left(\frac{W_{\max}}{W_0}\right). \tag{21}$$

It has been noted in ref. 30, however, that local effects of the microscopic turbulence occurring over much smaller scales are also important. Physically, this is because the diffusion character of the quasilinear relaxation process implies that the Hall current, which is the cause of the instability, is pulled by the noise into the region in which the energy of the oscillations is small, i.e., towards the cathode. The general solution, which describes the potential over both the sloping and steep parts of the distribution, can be found from (19) by a method similar to that used for a shock wave in ref. 30:

$$\begin{aligned}\frac{1}{\omega_{Hi}}\left[\left(v_0^2+\frac{2e\varphi_0}{M}\right)^{1/2}-\left(v_0^2+\frac{2e}{M}(\varphi_0-\varphi)\right)^{1/2}-\omega_{Hi}(L-x)\right] \\ =\frac{2\sqrt{\pi}\,\bar{k}v_s}{\omega_{Hi}}\int_L^x dx'\left\{\ln\left[\frac{2Hj_e(L-x')}{cW_0}-\frac{2Hj_i\nu}{cW_0\omega_{He}\omega_{Hi}}\right.\right. \\ \left.\left.\times\left\{\left(v_0^2+\frac{2e\varphi_0}{M}\right)^{1/2}-\left(v_0^2+\frac{2e}{M}(\varphi_0-\varphi)\right)^{1/2}\right\}\right]\right\}^{-1}.\end{aligned} \tag{22}$$

The corresponding Hall current distribution is

$$\begin{aligned}j_y=en\frac{c}{H}\frac{d\varphi}{dx}=\frac{j_i}{\left(v_0^2+\frac{2e(\varphi_0-\varphi)}{M}\right)^{1/2}\ln\left(\frac{W_{\tilde{k}}}{W_0}\right)}\left[\left(v_0^2+\frac{2e\varphi_0}{M}\right)^{1/2}\right. \\ \left.-\left(v_0^2+\frac{2e}{M}(\varphi_0-\varphi)\right)^{1/2}-\omega_{He}(L-x)\right].\end{aligned} \tag{23}$$

Figure 2a shows the distribution of the principal quantities φ, W_k, and j_y in the anode sheath. A characteristic feature of the solution is the steep front in the potential, current, and noise level near the cathode. The typical scale of the inhomogeneity here is

$$\Delta x \simeq \frac{eW_{\tilde{k}}}{2j_e m\omega_{He}}, \tag{24}$$

i.e., it can be smaller than the Larmor radius when $\Delta x < \rho_{He}$. If this happens, then the local method of investigating the instabilities is no longer valid and it becomes impossible to consider the electrons as magnetized, $\nu_f > \omega_{He}$; we therefore assume that above some sufficiently high noise level $W_{\tilde{k}} > 2mj_i v_0 \nu/(e\omega_{Hi})$, the potential drop near the cathode becomes so sharp that there is local demagnetization of the electrons and a complex nonstationary system of motion is set up. We can use the solution we have obtained to find the value of the electron current (which is a free parameter in this problem) at which ion-acoustic turbulence is necessarily established:

$$j_e \simeq \frac{c}{2H}\frac{dW_{\tilde{k}}}{dx} \simeq \frac{cW_{\max}}{2H\Delta x} \simeq en\frac{2\sqrt{\pi}}{3}\left[\frac{T_e}{M\left(\frac{2e\varphi_0}{M}\right)^{1/2}}\right]\frac{1}{\ln\left(\frac{nT_e}{3W_0}\right)}. \tag{25}$$

Here we have estimated $W_{\max} \simeq nT_e/3$. The power scattered in turbulent heating of the plasma is equal to the work done by the electron current j_e in the electric field E and the power fed into acceleration of the ions is equal to the work done by the ion current in this electric field. We can compare these two powers: the useful power which goes to accelerating the ions, and the power which is used for turbulent heating of the electrons,

$$\frac{j_i E}{j_e E} \simeq \frac{3}{2\sqrt{\pi}}\left(\frac{2e\varphi_0}{T_e}\right)\ln\left(\frac{nT_e}{3W_0}\right). \tag{26}$$

It can be seen from these estimates that if the ion-acoustic instability is set up, a considerable fraction of the power fed to the accelerator is scattered in turbulent heating of the electrons.

b. We now consider the second case, in which macroscopic turbulence at the electron cyclotron harmonics occurs in the anode sheath [see (8)]. By analogy with the previous case, we write down the initial system of hydrodynamic equations describing the distribution of the principal parameters φ, W_k, and j_y in the anode sheath,

$$\left.\begin{aligned}j_i=en_iv_i,\quad \frac{d}{dx}\left(\frac{Mv_i^2}{2}+e\varphi\right)=0,\quad \frac{d^2\varphi}{dx^2}=4\pi e(n_e-n_i), \\ j_e=\frac{c}{H}\left[\frac{\nu n_e mc}{H}\frac{d\varphi}{dx}+\sum_k\gamma_k\frac{k}{\omega_k}W_k\right], \\ v_e\frac{d\ln W_k}{dx}=2\gamma_k, \\ \omega_k=k(u^*-u),\quad \gamma_k=\gamma_{\max}\left(\frac{u-u^*}{v_{Ti}}\right)\exp\left[-\frac{(u-u^*)^2}{2v_{Ti}^2}\right].\end{aligned}\right\} \tag{27}$$

The boundary conditions are the same as those in (17). The structure of the turbulent Hall sheath is studied as before. For example, the integral relating the noise energy to the potential is

$$\begin{aligned}\ln\left(\frac{W_{\tilde{k}}}{W_0}\right)=\frac{2\gamma_{\max}j_i}{v_{Ti}j_e}\left[\frac{\left(v_0^2+\frac{2e\varphi_0}{M}\right)^{1/2}-\left(v_0^2+\frac{2e}{M}(\varphi_0-\varphi)\right)^{1/2}}{\omega_{Hi}}\right. \\ \left.-\int_L^x\frac{u^*dx'}{\left[v_0^2+\frac{2e}{M}(\varphi_0-\varphi)\right]^{1/2}}\right].\end{aligned} \tag{28}$$

We now find the principal equation for the potential φ and the expression for the collective friction force R_f:

$$\begin{aligned}j_e=\nu n_e m\left(\frac{c}{H}\right)^2\frac{d\varphi}{dx} \\ +\frac{c}{H}\frac{\gamma_{\max}}{v_{Ti}}W_0\exp\left\{\frac{2\gamma_{\max}j_i}{v_{Ti}j_e\omega_{Hi}}\left[\left(v_0^2+\frac{2e\varphi_0}{M}\right)^{1/2}-\left(v_0^2+\frac{2e}{M}(\varphi_0-\varphi)\right)^{1/2}\right.\right. \\ \left.\left.-\omega_{Hi}\int_L^x\frac{u^*dx'}{\left[v_0^2+\frac{2e}{M}(\varphi_0-\varphi)\right]^{1/2}}\right]\right\},\end{aligned} \tag{29}$$

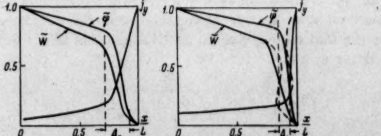

Fig. 2. Variation of the main parameters in the accelerating anode sheath; $\tilde{\varphi} = \varphi/\varphi_{\max}$, $\tilde{W} = W_{\tilde{k}}/W_{k,\max}$, $\tilde{j}_y = j_y/j_{y,\max}$ for the development of an ion-acoustic instability (a) and an electron cyclotron instability (b).

$$R_f = \frac{\gamma_{\max}}{v_{Ti}} W_k. \tag{30}$$

The first term in (29) gives the contribution to the current from the classical transverse mobility $b_{e\perp} = \nu/\omega_{He}^2(e/m)$, while the second term allows for the effect of turbulence on this mobility. Using the boundary conditions, we find the following solution from (27), (28), and (29):

$$\left.\begin{aligned} \ln\left|\frac{W_k f_e^*}{W_0\left(f_e^* + \frac{c}{H}\frac{\gamma_{\max}}{v_{Ti}}W_k\right)}\right| &= \frac{2\gamma_{\max}\omega_{He}}{v_{Ti}\nu}\left(\frac{f_e^*}{j_e}\right)(L-x), \\ j_y = en\frac{c}{H}\frac{d\varphi}{dx} &= enu^* + \frac{j_e v_{Ti}}{2\gamma_{\max}}\frac{d\ln W_k}{dx}, \end{aligned}\right\} \tag{31}$$

where

$$f_e^* = \frac{\nu}{\omega_{He}} en_0 u^* - j_e.$$

Figure 2b shows the x distribution of the main parameters φ, W_k, and j_y. The characteristic inhomogeneity scale over which the integrated effect of the turbulence is felt is equal to

$$\Delta x \simeq \frac{c}{\omega_{pe}}\left(\frac{m}{M}\right)^{1/2}\frac{1}{n'}\frac{\ln\left(\frac{W_{\max}}{W_0}\right)}{\left[2\ln\left(\frac{u}{v_{Ti}}\sqrt{\pi}\frac{T_i}{T_e}I_n e^{-\mu}\right)\right]^{1/2}} \quad (n' = 1,\ 2,\ 3,\ \ldots).$$

The power going into turbulent heating can be estimated as

$$(j_e E) \simeq \frac{c}{H}\frac{\gamma_{\max}}{v_{Ti}}W_{\max}E \simeq (j_i E)\frac{W_{\max}\ln\left(\frac{W_{\max}}{W_0}\right)}{mnv_0^2}\left(\frac{m}{M}\right)^{1/2}\left(\frac{H_0^2}{8\pi ne\varphi_0}\right)^{1/2}, \tag{32}$$

and forms a significant fraction of the useful power $(j_i E)$ going into the acceleration of the ions. We can also estimate the integrated value of the transverse electron mobility:

$$b'_{e\perp} = \frac{e}{m\omega_{He}}\left(\frac{mv_{Ai}j_e}{Mv_0 j_i}\right)\frac{1}{n'}\frac{\ln\left(\frac{W_{\max}}{W_0}\right)}{\left[2\ln\frac{u}{v_{Ti}}\frac{T_i}{T_e}\right]^{1/2}}.$$

It should be noted that the stationary solutions found above for the two types of instability in the anode sheath might not be realized in practice. This is because, as we saw earlier, the potential front near the cathode may become so steep that $\Delta x < \rho_{He}$. The electron drift may then be demagnetized and there can be a breakaway in the current j_y. This effect is analogous to the inversion of the ion flow at a shock front considered in ref. 30. It can be shown that with cyclotron oscillations this effect occurs earlier at a noise level of

$$\ln\left(\frac{W_{\max}}{W_0}\right) \simeq \left(\frac{\omega_{He}}{\nu}\frac{T_e}{2e\varphi_0}\right)\left(\frac{f_e^* 2n'}{j_e}\right)\left[2\ln\frac{u}{v_{Ti}}\frac{T_i}{T_e}\sqrt{\pi}I_n e^{-\mu}\right]^{1/2}. \tag{33}$$

In Fig. 2b, the flow inversion effect in the anode sheath is depicted by the dashed line. Thus, during turbulent acceleration in a stationary sheath there are two effects to be considered. Firstly, there can be severe energy dissipation in turbulent heating of the plasma at small-scale instabilities. Secondly, new effects can occur: local amplification of the Hall current, leading to demagnetization of the electron drift and inversion of the ion flow.

3. TURBULENCE ACCELERATION IN A PULSED CURRENT SHEATH

A pulsed current sheath (a model of which is shown in Fig. 1b) is characterized by strong perturbation of the magnetic field because the transfer of energy takes place at a rate close to the Alfvén velocity $v_{Ai} = H/(4\pi nM)^{1/2}$. For this reason a pulsed current sheath is often considered as a magnetoacoustic wave[17] propagating in the positive x direction with a velocity v_0 across the magnetic field (Oz). Thus the problem of acceleration in pulsed current sheaths is similar in many ways to that of collisionless dissipation in the front of a magnetoacoustic shock wave.[30] This approach is used in ref. 13 for an analysis of the turbulence processes involved in the generation of fast particles in many pulsed plasma devices.[20,21,16,22-27] We may also note that this problem is strongly connected with the turbulent heating of a plasma by nonlinear MHD waves.[7-10] One of the characteristic features of the dynamics of a pulsed current sheath is the excitation of intense MHD oscillations. This excitation can occur, for example, under the well-known "fast" acceleration conditions spontaneously as a result of growth of transverse current-driven instabilities. The excitation of MHD oscillations is accompanied by a change in the conditions of acceleration and leads to a rearrangement of the pulsed sheath owing to the fact that the acceleration transfers from a less stable to a more stable branch. In addition, this excitation also necessarily leads to the appearance of an electrostatic instability in the transverse current and turbulent heating of the ions.[7-10] Since these effects have had direct experimental confirmation (for example in the turbulent heating of ions by MHD waves[9,10] and in experiments on the generation of fast particles in pulsed plasma accelerators[23,24]), it is desirable to be able to describe them quantitatively.

We introduce a system of hydrodynamic equations which include the macroscopic effects of electron-acoustic (9) or cyclotron (8) instabilities and the principal Maxwell equations; these describe the dynamics of a plane pulsed current sheath when nonlinear MHD oscillations are excited:

$$\left.\begin{aligned} &\frac{\partial\rho}{\partial t} + \frac{\partial}{\partial x}(\rho v) = 0 \quad (\rho = nM), \\ &\frac{\partial}{\partial t}(\rho v) = -\frac{\partial}{\partial x}\left(\rho v^2 + \frac{H^2}{8\pi}\right), \\ &\frac{1}{c}\frac{\partial H}{\partial t} + \frac{\partial E_y}{\partial x} = 0, \\ &E_y = -\left(\frac{\partial}{\partial t} + v\frac{\partial}{\partial x}\right)\frac{mc}{4\pi ne^2}\frac{\partial H}{\partial x} + \frac{vH}{c} - \frac{1}{ne}R_{fy}, \\ &\left(\frac{\partial W_k}{\partial t} + \frac{\partial\omega_k}{\partial k_x}\frac{\partial W_k}{\partial x}\right) = 2\gamma_k W_k. \end{aligned}\right\} \tag{34}$$

We consider two cases for the frequency ω_k and growth rate γ_k; a) electron-acoustic instability (9); b) cyclotron instability (8). These give effects which are qualitatively similar but which are different in magnitude. The first equation in (34) is the law of conservation of mass, the second shows the conservation of momentum, the third is one of the Maxwell equations, the fourth is a statement of Ohm's law allowing for the electron inertia along y and the collective friction force, and the fifth is the noise equation.

We first neglect any energy dissipation and obtain equations which describe the nonlinear magnetoacoustic oscillations:

$$\left.\begin{aligned}\frac{\partial\rho}{\partial t}&=-\frac{\partial}{\partial x}(\rho v),\\ \frac{\partial(\rho v)}{\partial t}&=-\frac{\partial}{\partial x}\left(\rho v^2+\frac{H^2}{8\pi}\right),\\ \frac{\partial H}{\partial t}+\frac{\partial}{\partial x}(vH)-\frac{\partial}{\partial x}\left(\frac{\partial}{\partial t}+v\frac{\partial}{\partial x}\right)&\frac{mc^2}{4\pi ne^2}\frac{\partial H}{\partial x}=0.\end{aligned}\right\}\tag{35}$$

In the linear approximation we obtain a periodic solution for the magnetic field from (35):

$$H(x,t)=H_{0\sim}\cos(\Omega t-qt+\Psi).\tag{36}$$

The amplitude of the oscillations in the magnetic field $H_{0\sim}$ is independent of time. The frequency Ω of the magnetoacoustic oscillations is given by the dispersion relation

$$\frac{\Omega^2}{q^2}=\frac{H_0^2}{4\pi\rho_0}\frac{\frac{\omega_{pe}^2}{c^2}}{\left(q^2+\frac{\omega_{pe}^2}{c^2}\right)},\tag{37}$$

where q is the wave number. If friction is taken into account, the energy of the magnetoacoustic wave is dissipated and $H_{0\sim}(t)$ is reduced. If we know the attenuation, we can determine the rate of the turbulent heating of the ions.[10] Following the well-known Van der Pol method from the theory of nonlinear oscillations, we average the system (34) over the phase of the "fast" oscillations Ψ and get a system of truncated equations, which describe the change in amplitude of the magnetoacoustic wave.

a. We now assume that the amplitude of the wave is a slow function of time and we expand (34) in a series in the small parameters $v_\sim q/\Omega \ll 1$, $\gamma_{\max}/\Omega < 1$; allowing for dissipation due to electron-acoustic turbulence we find

$$\left.\begin{aligned}&\rho_\sim=\rho_0\frac{H_0H_\sim}{4\pi\rho_0}\left(\frac{q}{\Omega}\right)^2,\quad v_\sim=\frac{H_0H_\sim}{4\pi\rho_0}\left(\frac{q}{\Omega}\right)+\frac{H_\sim^2}{8\pi\rho_0}\left(\frac{q}{\Omega}\right),\\ &H_\sim=\left(\frac{aq}{\Omega}\right)^2\frac{\partial^2H_\sim}{\partial t^2}+\frac{q}{\Omega}v_\sim H_0+\frac{q}{\Omega}v_\sim H_\sim\\ &\qquad+\frac{\partial}{\partial t}\sum_{k_z}\left(\frac{qc}{2\Omega n_0e}\right)\frac{W_{\bar k}}{\left[|\mathbf{u}|-\frac{k_z}{\bar k}\left(\frac{T_i}{m}\right)^{1/2}\right]},\\ &\frac{\partial\ln W_k}{\partial t}=\sqrt{\pi}\,k_z\left(\frac{M}{m}\right)^{1/2}\left[|\mathbf{u}|-\frac{k_z}{\bar k}\left(\frac{T_i}{m}\right)^{1/2}\right],\end{aligned}\right\}\tag{38}$$

where

$$a=\frac{c}{\omega_{pe}},\quad |\mathbf{u}|=\frac{cq}{4\pi en_0\Omega}\frac{\partial}{\partial t}|H_\sim|,$$

We now maximize in terms of the wavelength of the most unstable oscillations, $\bar k_z(T_i/m)^{1/2}=\bar k|\mathbf{u}|$, $\bar k^{-1}=\rho_e$. As a result, we can replace the summation over k_z by a single term. Then averaging over the fast phase Ψ from (38) we have

$$\begin{aligned}\frac{\partial H_{0\sim}}{\partial t}&=\frac{16\Omega W_0}{H_{0\sim}(aq)^2}\int\limits_{\Psi_0}^{\pi/4}\frac{\sin\Psi\,d\psi\,\frac{d}{d\psi}\exp|\beta H_{0\sim}^2 2\sin\Psi\cos\Psi|}{\left\{\sin\Psi-\sin\Psi_0\left[1+\left(\frac{M}{m}\right)^{1/4}\right]\right\}}\\ &\simeq\frac{16\Omega W_0}{H_{0\sim}(aq)^2}\left\{\exp(\beta H_{0\sim}^2)-\left(\frac{m}{M}\right)^{1/4}\exp[\beta H_{0\sim}^2\sin 2\Psi_0]\right\}.\end{aligned}\tag{39}$$

We have used the notation

$$\beta=\sqrt{\pi}\,\frac{\omega_{ei}}{\Omega}(aq)^2\frac{M}{m8\pi n_0T_i},\quad \sin\Psi_0=\frac{4\pi en_0}{cqH_{0\sim}}v_{Ti}\left(\frac{m}{M}\right)^{1/4}.$$

The solution of (39) has the form

$$\exp(-\beta H_{0\sim}^2)+\frac{32W_0\beta}{(aq)^2}(\Omega t)+C=0.\tag{40}$$

Here C is a constant of integration which depends on the initial conditions, for example on the way the energy is introduced into the pulsed sheath by the magnetic piston. Using (40), we can estimate the characteristic size of the attenuation front Δx and the amount of attenuation $(\Omega\Delta t)$ of the nonlinear wave:

$$\left.\begin{aligned}\Delta x&\simeq\frac{4}{\pi q}\beta H_{\sim,\max}^2,\\ (\Delta t\Omega)&\simeq\frac{4}{\pi}\beta H_{\sim,\max}^2.\end{aligned}\right\}\tag{41}$$

Knowing the attenuation $(\Delta t\Omega)$, we can estimate the rate for the turbulent heating of the ions in the front $d(nT_i)/dt$ and the limiting energy of the ions $T_{i,\mathrm{lim}}$:

$$\left.\begin{aligned}\frac{d(nT_i)}{dt}&=\frac{H_{\sim,\max}^2}{8\pi}\Omega,\\ T_{i,\mathrm{lim}}&=2\left(\frac{M\omega_{e,i}}{m\Omega}\right)^{1/2}\frac{H_{\sim,\max}^2}{8\pi n_0}(aq).\end{aligned}\right\}\tag{42}$$

Thus the ions can be effectively heated as a result of the dissipation of the energy of the nonlinear magnetoacoustic wave. This effect is a well-known one in experiments[9,10] on plasma heating by magnetoacoustic waves. The electrons are heated either by nonlinear processes or by Coulomb collisions. The turbulent heating of the ions by magnetoacoustic waves (which are known to be excited in many pulsed accelerators[7,8]) can explain the observed generation of fast particles.

b. The development of cyclotron instabilities which produce a large increase in anomalous resistance is possible at comparatively large magnetic field amplitudes, i.e., $H_\sim > H_0(m/M)^{1/2}(u^*/v_{Ai})$. We can estimate the importance of this effect in the turbulent heating (acceleration) of ions. The initial equations in this case are written in the form

$$\left.\begin{aligned}H_\sim&=\left(\frac{aq}{\Omega}\right)^2\frac{\partial^2H_\sim}{\partial t^2}+\left(\frac{qv_{Ai}}{\Omega}\right)^2H_\sim+\frac{\partial}{\partial t}\frac{qc}{2\Omega n_0e}\frac{W_{\bar k\sim}}{|\mathbf{u}_\sim|-u^*},\\ \frac{\partial\ln W_{\bar k\sim}}{\partial t}&=2\gamma_{\max}\frac{|\mathbf{u}_\sim|-u^*}{v_{Ti}}.\end{aligned}\right\}\tag{43}$$

We use the notation

$$|\mathbf{u}_{\sim}|=\frac{cq}{4\pi e n_0\Omega}\left|\frac{\partial H_{\sim}}{\partial t}\right|.$$

Averaging over the fast phase Ψ, we obtain an equation for the amplitude of the magnetic field oscillations:

$$H(x,\ t)=H_{0\sim}(t)\cos(\Omega t-qx+\Psi), \tag{44}$$

$$\frac{\partial H_{0\sim}}{\partial t}=\frac{8\Omega W_0}{H_{0\sim}(aq)^2}\exp(\tilde{\beta}H_{0\sim}), \tag{45}$$

where

$$\tilde{\beta}=\frac{2\gamma_{\max}cq}{v_{T_i}4\pi e n_0\Omega}.$$

We can get the solution of the equation by the same method as for (40) and can then determine the characteristic size of the front Δx and the magnitude of the attenuation $(\Omega\Delta t)$:

$$\left.\begin{aligned}\Delta x&=\frac{4a}{\pi}\left(\frac{H_{\sim,\max}\gamma_{\max}}{H_0\Omega}\right)\left(\frac{MH_0^2}{m4\pi n_0T_i}\right)^{1/2},\\ \Delta t\Omega&\simeq\Delta xq.\end{aligned}\right\} \tag{46}$$

Using these expressions, we can find the rate of turbulent heating of ions and the limiting energy of the ions as

$$\left.\begin{aligned}\frac{d}{dt}(nT_i)&=\frac{H_{0\sim}^2}{8\pi}\Omega,\\ T_{i,\,\lim}&=\left(\frac{H_{\sim,\max}^2}{8\pi n_0}\right)\left(\frac{M}{m}\right)^{1/3}\left(\frac{4\sqrt{2}aq}{\pi}\frac{H_{\sim,\max}\gamma_{\max}}{H_0\Omega}\right)^{2/3}.\end{aligned}\right\} \tag{47}$$

It follows from a comparison of (42) and (47) that instabilities at the electron cyclotron harmonics lead to a more effective dissipation of the energy of a nonlinear magnetoacoustic wave and a stronger heating of the ions than do the electron-acoustic instabilities. The conductivity, estimated from (46) by the equation $\sigma_f\simeq(ne^2/m)\cdot(a^2q/\Omega\Delta x)$, is

$$\sigma_f\simeq\left(\frac{ne^2}{m\gamma_{\max}}\right)\frac{\pi qa}{4}\left(\frac{H_0}{H_{\sim,\max}}\right)\left(\frac{m4\pi n_0T_i}{MH_0^2}\right)^{1/2}.$$

Thus the propagation of a pulsed current sheath and the excitation of nonlinear MHD waves produce, as a result of microscopic turbulence, effective mechanisms for collective friction and lead to a severe dissipation of the MHD-wave energy and the turbulent heating (acceleration) of the ions.

---

[1] Collection: Plasma Accelerators [in Russian], L. A. Artsimovich (ed.), Mashinostroenie, Moscow (1973).

[2] G. S. Janes and A. Bratenahl, Bull. Am. Phys. Soc., Ser. 11, 6 (1961).

[3] A. Bratenahl, G. S. Janes, and A. Z. Kantrowitz, Bull. Am. Phys. Soc., Ser. 11, 6 (1961).

[4] E. G. Lary, K. C. Meyerland, Jr., and F. Salz, Bull. Am. Phys. Soc., Ser. 11, 7 (1962).

[5] V. I. Aref'ev and B. S. Borisov, in: Plasma Accelerators [in Russian], L. A. Artsimovich (ed.), Mashinostroenie, Moscow (1973), p. 142.

[6] G. S. Jeyes and J. Dotson, in: Applied Magnetohydrodynamics, [Russian translation], Izd. Mir, Moscow (1965), p. 235.

[7] M. V. Babykin, P. P. Gavrin, E. K. Zavoiskii, L. I. Rudakov, and V. A. Skoryupin, Zh. Eksp. Teor. Fiz., 43, 411 (1962) [Sov. Phys. – JETP, 16, 295 (1963)].

[8] A. A. Kalmykov, A. D. Timofeev, and B. A. Shevchuk, in; Plasma Accelerators [in Russian], L. A. Artsimovich (ed.), Mashinostroenie, Moscow (1973), p. 278; Papers from the Second All-Union Conf. on Plasma Accelerators [in Russian], Academy of Sciences of the USSR, Minsk (1973), p. 33.

[9] I. A. Kovan and A. M. Spektor, Zh. Eksp. Teor. Fiz., 53, 1278 (1967) [Sov. Phys. – JETP, 26, 747 (1968)].

[10] V. I. Aref'ev, I. A. Kovan, and L. I. Rudakov, ZhETF Pis. Ref., 7, 286 (1968) [JETP Lett., 7, 223 (1968)].

[11] V. I. Aref'ev. A. A. Kalmykov, and L. V. Leskov, Papers from the Second All-Union Conf. on Plasma Accelerators [in Russian], Academy of Sciences of the USSR, Minsk (1973), p. 241.

[12] V. I. Aref'ev and L. V. Leskov, Zh. Tekh. Fiz., 42, 2345 (1972) [Sov. Phys. – Tech. Phys., 17, 1829 (1973)].

[13] V. I. Aref'ev and L. V. Leskov, in: Plasma Accelerators [in Russian], L. A. Artsimovich (ed.), Mashinostroenie, Moscow (1973), p. 191.

[14] B. B. Kadomtsev, in: Plasma Physics and Problems of Controlled Thermonuclear Reactions, Vol. 4 [in Russian], Izd. AN SSSR, Moscow (1965), p. 364.

[15] V. I. Aref'ev, Zh. Eksp. Teor. Fiz., 57, 1387 (1968) [Sov. Phys. – JETP, 30, 751 (1970)].

[16] P. C. Thoneman, E. P. Butt, R. Carruthers, A. N. Dellis, D. W. Fry, A. Gibson, C. N. Harding, D. J. Lees, R. W. P. Mc Whirter, P. S. Pease, S. A. Ramsden, and S. Ward, Nature, 181, 217 (1958).

[17] V. I. Aref'ev and L. V. Leskov, Zh. Tekh. Fiz., 42, 2353 (1972) [Sov. Phys. – Tech. Phys., 17, 1833 (1973)].

[18] V. I. Aref'ev, Zh. Tekh. Fiz., 42, 1373 (1972) [Sov. Phys. – Tech. Phys., 17, 1095 (1973)].

[19] D. G. Lominadze, Zh. Eksp. Teor. Fiz., 63, 1300 (1972) [Sov. Phys. – JETP, 36, 686 (1973)].

[20] L. A. Artsimovich, A. M. Andrianov, E. I. Dobrokhotov, S. Yu. Luk'yanov, I. M. Podgornyi, V. I. Sinitsyn, and N. V. Filippov, Atom. Energ., 3, 76 (1956).

[21] L. A. Artsimovich, S. Yu. Luk'yanov, I. M. Podgornyi, and S. A. Chuvatin, Zh. Eksp. Teor., Fiz., 33, 3 (1957) [Sov. Phys. – JETP, 6, 1 (1958)].

[22] A. I. Morozov, in: Plasma Accelerators [in Russian], L. A. Artsimovich (ed.), Mashinostroenie, Moscow (1973), p. 5.

[23] A. A. Kalmykov, S. A. Trubchaninov, A. D. Timofeev, and B. A. Shevchuk, Zh. Tekh. Fiz., 34, 1005 (1954) [Sov. Phys. –Tech. Phys., 9, 779 (1964)].

[24] L. V. Leskov, A. A. Kalmykov, and M. I. Pergament, in: Plasma Accelerators [in Russian], L. A. Artsimovich (ed.), Mashinostroenie, Moscow (1973), p. 183.

[25] J. R. McNally, Jr., and M. R. Skidmore, J. Opt. Soc. Am., 47, 863 (1957).

[26] M. I. Pergament and A. I. Yaroslavskii, in: Plasma Accelerators [in Russian], L. A. Artsimovich (ed.), Mashinostroenie, Moscow (1973), p. 268; I. N. Burdonskii, R. P. Vasil'eva, A. I. Morozov, M. I. Pergament, and A. I. Yaroslavskii, in: Plasma Accelerators [in Russian], L. A. Artsimovich (ed.), Mashinostroenie, Moscow (1973), p. 244.

[27] A. A. Plyutto, V. N. Rytkov, and A. T. Kalin, Zh. Eksp. Teor. Fiz., 47, 494 (1964) [Sov. Phys. – JETP, 20, 328 (1965)].

[28] A. A. Vedenov, in: Reviews of Plasma Physics, Consultants Bureau, New York (1967).

[29] A. A. Galeev, D. G. Lominadze, A. D. Pataraya, R. Z. Sagdeev, and K. N. Stepanov, ZhETF Pis. Red., 15, 417 (1972) [JETP Lett., 15, 294 (1972)].

[30] V. I. Aref'ev, Zh. Tekh. Fiz., 43, 1881 (1973) [Sov. Phys. – Tech. Phys., 18, 1189 (1974)].

Conversion of regular charge-density waves in an inhomogeneous plasma

S. S. Kalmykova and A. P. Tolstoluzhskii

A. M. Gor'kii State University, Khar'kov

(Submitted February 12, 1973; resubmitted October 5, 1973
Zh. Tekh. Fiz., 44, 723-728 (April 1974)

The efficiency of conversion into an electromagnetic wave of a regular charge-density wave amplified by a monoenergetic beam is studied theoretically for an anisotropic plasma waveguide with inhomogeneous axial density. The dependence of the conversion coefficient on the degree of plasma inhomogeneity obtained through numerical calculations in a self-consistent approximation is compared with the corresponding results of an analytic study of a piecewise uniform density profile.

Collective interactions between a charged-particle beam and a plasma lead to an experimental increase in the amplitude of the field because of induced coherent Cerenkov radiation of the beam particles, which is amplified by the bunching caused by this radiation.[1,2] It is important to emphasize that the gain (growth rate) which characterizes the efficiency of this interaction is only positive for slow beam charge-density waves ($V_f < V_0$); fast charge-density waves ($V_f > V_0$) are damped with the same factor; however, the damping of transverse waves is not sensitive to beam density, but is determined by binary or collective collisions between plasma particles.

In many applications (astrophysics, plasma-beam heating, microwave generation, etc.), there is an interest in investigation of the efficiency for conversion of a charge-density wave amplified collective interaction into electromagnetic waves.[1)] Such conversion may occur in an inhomogeneous plasma in the neighborhood of a point at which the wave vectors of both waves coincide; the basis is the coherent transition radiation from the sequence of bunches formed by the field of a slow quasilongitudinal wave.[8-10]

Analytic study of this problem is made difficult by the lack of effective methods for solving differential equations with variable coefficients. In fact, the semiclassical approximation is not applicable in the region of greatest interest: the neighborhood of the conversion point, at which the wave number spectrum in the problem is degenerate. On the other hand, when this degeneracy is removed, because of dissipation for example, these waves prove to be weakly coupled so that the magnitude of the conversion effect becomes small.[2)] Those analytic solutions that can be obtained for certain special density profiles are not always realized experimentally (in an experiment, for example, it is impossible to achieve a linear density profile without encountering a contradiction with the requirement for a positive plasma density n_p). Under these conditions, there is interest in the use of a numerical experiment for studying the interconversion of waves in a nonequilibrium plasma. The present paper is devoted to this problem.

We consider the simplest model in which collective interaction of a monoenergetic electron beam with an inhomogeneous magnetized plasma is described by a self-consistent system of hydrodynamic equations of motion and continuity for the beam particles and by the Maxwell equations for the field. When the beam and plasma densities are uniform over a section of a circular cylindrical waveguide with conducting walls at the radius a located in a strong external magnetic field (ω_b^2, ω_p^2, $\omega \ll \omega_H^2$), the problem of finding the dependence on the longitudinal coordinate of the dimensionless amplitudes of the electric field and also on the variable components of density and velocity ($\tilde{N}$ and $\tilde{V}$) of a beam of regular (ω = const) axially symmetric oscillations reduces to a solution of the following system of differential equations:

$$\left.\begin{array}{c}
\varkappa\frac{d\mathcal{E}_\perp}{d\zeta}=(\beta_0^2\varepsilon-\varkappa^2)\mathcal{E}_z-i\mu\beta_z(\tilde{N}+\tilde{V});\quad \frac{d\tilde{V}}{d\zeta}=i\tilde{V}-\mathcal{E}_z;\\
\frac{d}{d\zeta}(\varepsilon\mathcal{E}_z)=-\varkappa\mathcal{E}_\perp-\mu\tilde{N};\quad \frac{d\tilde{N}}{d\zeta}=i(\tilde{N}-\tilde{V})+\mathcal{E}_z;\\
\varepsilon(\zeta)\equiv 1-\frac{\omega_p^2(\zeta)}{\omega^2(1+i\eta)};\quad \eta\equiv\frac{\nu}{\omega};\quad \beta_0\equiv\frac{V_0}{c};\\
\mu\equiv\frac{4\pi e^2 n_0}{m_0\gamma^3\omega^2};\quad \varkappa\equiv\frac{\lambda_n V_0}{\omega a};\quad \gamma\equiv(1-\beta_0^2)^{-1/2};\quad \zeta\equiv\frac{\omega z}{V_0},
\end{array}\right\} \tag{1}$$

where V_0 is the equilibrium beam velocity; ν is the collision frequency for plasma particles; $J_0(\lambda_n) = 0$; $\omega_p^2 = (4\pi e^2 n_p)/(m_0)$.

In the absence of plasma inhomogeneity [$d/d\zeta n_p(\zeta) = 0$), the system (1) has four independent plane-wave solutions for which the wave numbers are determined by the dispersion equation

$$\varkappa^2=\left[\varepsilon(\zeta)-\frac{\mu}{(1-k)^2}\right](\beta_0^2-k^2). \tag{2}$$

Two of these solutions, which vanish when the beam current goes to zero, we shall call the fast (1) and slow (2) quasilongitudinal waves (l). The other two solutions, which are characterized by finite values of the wave numbers when $V_0 \to 0$ and which remain finite in the absence of a beam,[8,9] are called the forward (3) and backward (4) transverse waves (t). Analytic expressions for the corresponding wave numbers are easily obtained in the limiting case of small beam currents ($\mu \ll 1$):

$$\left.\begin{array}{c}
k_{1,2}=1\mp\frac{\mu^{1/2}}{[\varepsilon(\zeta)+\varkappa^2\gamma^2]^{1/2}};\\
k_{3,4}=\pm\left[\beta_0^2-\frac{\varkappa^2/\varepsilon}{1-\frac{\mu}{\varepsilon\left(1\mp\sqrt{\beta_0^2-\frac{\varkappa^2}{\varepsilon}}\right)^2}}\right]^{1/2}.
\end{array}\right\} \tag{2a}$$

We estimate the conversion efficiency for an amplified slow charge-density wave (2) at a plasma density inhomogeneity. It is necessary to assign a plasma density profile. Most suitable for a numerical experiment is a profile such that the plasma density is constant at large distances from the inhomogeneity. For example, this condition is satisfied by the following dependence of plasma density on the coordinate ζ:

$$n_p(\zeta)=\frac{1}{2}[n_+ + n_- + (n_+ - n_-)\,\mathrm{th}\,\zeta|z], \tag{3}$$

where the density values $n_\pm$ for $\zeta \to \pm\infty$ are determined respectively by the requirement that the conversion point $\zeta = \zeta_*$ be located within the range of density values under consideration. The coordinate ζ_* of the conversion point is determined by the agreement of the quasiclassical wave numbers for the amplified slow wave (2) and the forward transverse wave (3); at this point the gain for a slow longitudinal wave goes to zero in the absence of dissipation ($\eta = 0$). Differentiating Eq. (2) with respect to ε and equating the coefficient of $dk/d\varepsilon$ to zero, we obtain

$$-k_*\left[\varepsilon_* - \frac{\mu}{(1-k_*)^2}\right] + \frac{\mu(\beta_0^2 - k_*^2)}{(k_*-1)^3} = 0, \tag{4}$$

which, together with Eq. (2), determines the value of ε at the conversion point (ε_*) and the corresponding wave number k_*. In the limiting case $\mu \ll 1$, $\beta_0^2 \ll 1$, and $\eta \to 0$, we obtain

$$\left.\begin{aligned} \varepsilon_* &= -\varkappa^2 + \left(\frac{\mu}{\varkappa^2}\right)^{1/3}; \\ k_* &= 1 + \left(\frac{\mu}{\varkappa^2}\right)^{1/3}. \end{aligned}\right. \tag{4a}$$

It is then clear that the conversion point is shifted from the point of beam synchronism with the transverse wave 3 ($\varepsilon + \varkappa^2 = 0$) into the region of lower plasma densities. In the self-consistent problem the region of maximum Cerenkov amplification ($\varepsilon + \varkappa^2 = 0$) and the region of maximum conversion (emission of a transverse wave) $\varepsilon + \varkappa^2 = (\mu/\varkappa^2)^{1/3}$ are separated in space. This makes it possible to distinguish the effects of Cerenkov and transition radiation by the beam particles, at least qualitatively. In the constrained problem, which corresponds to the case of low beam current, the region of maximum radiation intensity corresponds to the point of synchronism ($\varepsilon + \varkappa^2 = 0$, compare ref. 10) and the separation of Cerenkov and transition radiation is obviously difficult[3)] in the case ($\mu \to 0$).

The variation in plasma density chosen above makes it possible to provide with sufficient accuracy the conditions corresponding to the scattering of any of the characteristic waves of both uniform waveguides. In fact, at large distances from the inhomogeneity ($|\zeta| \gg z$), where the plasma density is constant, these waves are independent so that their field patterns can be identified in accordance with the solutions of Eq. (2) for the corresponding homogeneous plasma waveguide; by substituting the various roots of Eq. (2) into the relations between the field amplitudes

$$\left.\begin{aligned} &\tilde{V}_s = A_s\tilde{N}_s;\ (\mathcal{E}_\parallel)_s \equiv B_s\tilde{N}_s;\ (\mathcal{E}_\perp)_s \equiv C_s\tilde{N}_s;\ H_s = D_s\tilde{N}_s; \\ &A_s \equiv \frac{1-k_s}{k_s};\ B_s \equiv i\frac{(k_s-1)^2}{k_s};\ C_s \equiv -\frac{\varkappa(k_s-1)^2}{k_s^2-\beta_0^2};\ D_s \equiv \frac{\varkappa}{k_s}C_s, \end{aligned}\right\} \tag{5}$$

we obtain boundary conditions at infinity for a type s wave.

Solutions of physical interest must not yield a backward transverse wave (4) arriving at the inhomogeneity from $+\infty$. When $z \to \infty$, this solution must give a reflected wave of desired amplitude and also a forward transverse wave (3) and charge-density waves (1 and 2) with given amplitudes.[11] We assume below that $\tilde{N}_1^- = \tilde{N}_3^- = 0$, $\tilde{N}_2^- = 1$.

The numerical solution of the corresponding boundary value problem is difficult and we therefore use a reduction to the Cauchy problem[12] for the determination of the scattered fields; a solution of the original boundary value problem is sought in the form of a superposition of two solutions of the system (1) with initial conditions at $-\infty$, each of which corresponds to the existence at $-\infty$ of only one of the characteristic waves of the system. The ratio of the amplitudes of these waves is determined by the requirement that there be no wave coming from $+\infty$ in the general solution.

For example, let $N^{(l)}(\zeta)$ be the solution which transforms into an amplified wave of a left-handed waveguide and $N^{(t)}(\zeta)$ the solution which describes the scattering of backward transverse wave (4) of a right-handed waveguide, which also transforms into the same wave – the backward wave in the left-handed waveguide – for $\zeta \to -\infty$. The superposition $N = N^{(l)} + N^{(t)}$ yields the desired solution if the corresponding amplitudes of the supplementary waves $N^{(l)}(-\infty)$ and $N^{(t)}(-\infty)$ meet the condition for the incoming wave amplitudes going to zero when $\zeta \to +\infty$,

$$N_4(\zeta \to +\infty) \equiv T_{4\,2}^{(l)}N_2^{(l)}(-\infty) + T_{4\,4}^{(t)}N_4^{(t)}(-\infty) = 0, \tag{6}$$

where $T_{4\,2}^{(l)}$ and $T_{4\,4}^{(t)}$ are the conversion factors for the supplementary solutions "l" and "t".

Considering condition (6), the amplitude of a scattered type s wave and particularly the coefficient $T_{3\,2}$ for the conversion of a quasilongitudinal wave 2 into a quasitransverse wave 3 are determined uniquely by

$$\left.\begin{aligned} N_s(+\infty) &= N_s^{(l)} + N_s^{(t)} = \left[T_{s\,2}^{(l)} + T_{s\,4}^{(t)}\frac{T_{4\,2}^{(l)}}{T_{4\,2}^{(t)}}\right]N_2(-\infty); \\ N_3(+\infty) &= T_{3\,2}N_2(-\infty) = \left[T_{3\,2}^{(l)} - \frac{T_{3\,4}^{(t)}}{T_{4\,4}^{(t)}}T_{4\,2}^{(l)}\right]N_2(-\infty). \end{aligned}\right\} \tag{7}$$

Thus the problem of calculating the conversion of an amplified wave into other types of waves reduces to Fourier analysis of the supplementary solutions (l) and (t) in the region $\zeta \gg L$.

Numerical solutions of the supplementary problems "l" and "t" are obtained by the Runge–Kutta technique using an M-220 computer. For each fixed value of the parameters L, $n_\pm$, μ, η, and β_0^2, we calculate the fields (l, t), velocities $\tilde{V}^{(l,t)}$, and densities $\tilde{N}^{(l,t)}$ as functions

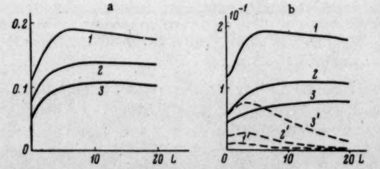

Fig. 1. Dependence on plasma density gradient for modulus of the coefficient T_{32} for conversion of an amplified wave into a transverse wave. a) $\eta = 10^{-7}$; $\mu = 10^{-2}$; $\beta = 0.2$; $\varepsilon_- = -2.25$; $\varkappa$: 1, 2) 0.8; 3) 1.0; ε_+: 1, 3) −0.16; 2) −0.10. b) $\varkappa$: 1, 1') 0.8; 2, 2') 1.0; 3, 3') 1.2; ε_-: 1, 2, 3) −3.0; 1', 2', 3') −0.16; ε_+: 1, 2, 3) −0.16; 1', 2', 3') 3.0.

of the coordinates, after which the conversion coefficients are determined from the solution of the algebraic equation system

$$\left.\begin{aligned}
\tilde{N}^{(l)}(\zeta) &= \sum_{s=1}^{4} T_{s2}^{(l)} \exp(ik_s\zeta)\, N_2^{(l)}(-\infty),\\
\tilde{V}^{(l)}(\zeta) &= \sum_{s=1}^{4} A_s T_{s2}^{(l)} \exp(ik_s\zeta)\, N_2^{(l)}(-\infty),\\
\mathcal{E}_{\parallel}^{(l)}(\zeta) &= \sum_{s=1}^{4} B_s T_{s2}^{(l)} \exp(ik_s\zeta)\, N_2^{(l)}(-\infty),\\
\mathcal{E}_{\perp}^{(l)}(\zeta) &= \sum_{s=1}^{4} C_s T_{s2}^{(l)} \exp(ik_s\zeta)\, N_2^{(l)}(-\infty);
\end{aligned}\right\} \quad (8a)$$

$$\left.\begin{aligned}
\tilde{N}^{(t)}(\zeta) &= \sum_{s=1}^{4} T_{s4}^{(t)} \exp(ik_s\zeta)\, N_4^{(t)}(-\infty),\\
\tilde{V}^{(t)}(\zeta) &= \sum_{s=1}^{4} A_s T_{s4}^{(t)} \exp(ik_s\zeta)\, N_4^{(t)}(-\infty),\\
\mathcal{E}_{\parallel}^{(t)}(\zeta) &= \sum_{s=1}^{4} B_s T_{s4}^{(t)} \exp(ik_s\zeta)\, N_4^{(t)}(-\infty),\\
\mathcal{E}_{\perp}^{(t)}(\zeta) &= \sum_{s=1}^{4} C_s T_{s4}^{(t)} \exp(ik_s\zeta)\, N_4^{(t)}(-\infty).
\end{aligned}\right\} \quad (8b)$$

As expected, the values of the conversion coefficients $T_{s2}^{(l)}$ and $T_{s4}^{(t)}$ are constant for $\zeta/L > 4$ within the error of the numerical calculations (10^{-3}). Substitution of the quantities $T_{s2}^{(l)}$ and $T_{s4}^{(t)}$ into Eq. (7) yields values of the desired conversion coefficient T_{32}.

Values of the modulus of the conversion coefficient computed in this way are shown in Fig. 1 as functions of the degree of plasma inhomogeneity. It is clear from the figure that in the general case the efficiency for conversion of an amplified wave into a transverse wave depends weakly on the magnitude of the plasma density gradient, remaining the same in order of magnitude both for discontinuously changing plasma density[4] and for relatively small gradient (L = 20). Physically, this effect can be explained by the fact that the number of coherently radiating bunches[2] increases as the gradient decreases, which compensates for the reduction of the losses from each bunch. The curves given in Fig. 1a also illustrate the conversion anisotropy (see ref. 9): the dependence of conversion efficiency not only on the value of the plasma density differential, but also on the sign of the corresponding gradient; the modulus of the conversion coefficient is greater for a decreasing density than for an increasing density.

To check the accuracy of the numerical experiment, the results are compared with the results of an analytic study of the problem for a discontinuously varying plasma density.[9] In this case an explicit expression for the desired conversion coefficient (L = 0) is easily obtained from the conditions for equality of the tangential components of the electric and magnetic fields and also of the beam density and velocity at the surface of discontinuity $\zeta = 0$

$$\left.\begin{aligned}
1 + T_{42}^{(-)} &= T_{32}^{(+)} + T_{12}^{(+)} + T_{22}^{(+)},\\
A_2^{(-)} + T_{42}^{(-)} A_4^{(-)} &= T_{32}^{(+)} A_3^{(+)} + T_{12}^{(+)} A_1^{(+)} + T_{22}^{(+)} A_2^{(+)},\\
C_2^{(-)} + T_{42}^{(-)} C_4^{(-)} &= T_{32}^{(+)} C_3^{(+)} + T_{12}^{(+)} C_1^{(+)} + T_{22}^{(+)} C_2^{(+)},\\
D_2^{(-)} + T_{42}^{(-)} D_4^{(-)} &= T_{32}^{(+)} D_3^{(+)} + T_{12}^{(+)} D_1^{(+)} + T_{22}^{(+)} D_2^{(+)},
\end{aligned}\right\} \quad (9)$$

where the coefficients A_s, B_s, C_s, and D_s are defined by Eqs. (5).

In the numerical experiment, as in a real experiment, the parameter μ is small ($\mu \lessdot 10^{-2}$); thus, we obtain the following analytic expression for T_{32} at L = 0:

$$T_{32}(L=0) = \frac{\mu\varkappa^2 R_+ (1+R_-)(S_- - S_+)}{(R_+ + R_-)(1-R_-)^2 (S_- + S_+)\,|\varepsilon_+|}, \qquad (10)$$

$\varkappa \equiv (\lambda_n V_0)/\omega a$, λ_n is the n-th root of the Bessel function $J_0(\lambda) = 0$;

$$R_\pm \equiv \left(\beta_0^2 + \frac{\varkappa^2}{|\varepsilon_\pm|}\right)^{1/2};\ S_\pm \equiv |\varepsilon_\pm| - \varkappa^2\gamma^2;$$

$$\varepsilon_\pm \equiv 1 - \frac{\omega_{p\pm}^2}{\omega(\omega + i\nu)};\ \omega_{p\pm}^2 \equiv \frac{4\pi e^2}{m_0} n_\pm;\ n_\pm \equiv n_p(\pm 0).$$

It is easy to see that the asymptotes to the curves given in Fig. 1 agree as expected with calculated results from Eq. (10) with an accuracy of the order of $\mu^{1/2}$. In the nonrelativistic case ($\beta_0^2 \ll 1$), this expression agrees with that given in ref. 10.

The main results of the numerical analysis can be formulated as follows.

1. The efficiency for conversion from an amplified longitudinal wave into a transverse wave for a varying density gradient depends weakly on the details of the density profile because of the increase in the number of coherently emitting bunches as the degree of plasma inhomogeneity decreases. The conversion rate in this case is considerably greater than for the case of a linear profile (compare ref. 10).

2. In order of magnitude, the modulus of the conversion coefficient is determined by its value for a discontinuous density profile given the same value for the plasma density differential and for its other geometrical parameters.

3. Numerical calculations and analytical studies demonstrate the existence of significant anisotropy in the dependence of conversion rate on the sign of the plasma density gradient, for which the anisotropy of transition radiation from beam particles provides a basis.

---

[1] Results for the conversion of the characteristic waves in an equilibrium plasma are presented in a monograph[3] and review papers;[4,5] this effect was first discussed in ref. 7 for nonequilibrium beam–plasma systems (see also refs. 8-10).

[2] Furthermore, dissipation changes qualitatively the behavior of both waves; the slow beam wave in the neighborhood of the conversion point grows with a gain proportional to the value of the resistive splitting $\Delta k_\parallel \sim (\nu/\omega)^{1/2} \times (n_b/n_p)^{1/2}$ and the quasitransverse wave is damped with the same factor.[10]

[3] The authors thank V. K. Yulpatov for pointing this out.

[4] For several values of $\varkappa$, the numerical calculations are carried out to L ≈ 50; in this case, the drop in the modulus of T_{32} remains linear with a slight slope ($\alpha \approx 0.15$).

---

[1] Ya. B. Fainberg, At. Energ., 11, 313 (1961).

[2] V. I. Kurilko, Dissertation, Khar'kov State University (1970); Dokl. Akad. Nauk SSSR, 208, No. 4 (1972).

[3] V. L. Ginzburg, Propagation of Electromagnetic Waves in Plasma [in Russian], Izd. Nauka, Moscow (1967).

[4] A. V. Timofeev, Usp. Fiz. Nauk, 102, 185 (1970) [Sov. Phys. – Usp., 13, 632 (1971)].

[5] V. E. Golant and A. D. Piliya, Usp. Fiz. Nauk, 104, 413 (1971) [Sov. Phys.– Usp., 14, 413 (1972)].

[6] N. S. Erokhin, V. I. Kurilko, M. B. Levin, M. G. Lyubarskii, N. G. Matsiborko, S. S. Moiseev, I. N. Onishchenko, A. P. Tolstoluzhskii, Ya. B.

Fainberg, V. D. Shapiro, and V. I. Shevchenko, Plasma Physics and Controlled Fusion [in Russian], Vol. 2, IAEA Press, Vienna (1971), p. 195.
[7] S. S. Kalmykova and V. I. Kurilko, Prikl. Matem. Makhan., 33, 638 (1969).
[8] S. S. Kalmykova, Dokl. Akad. Nauk SSSR, 208, No. 5, 1062 (1972) [Sov. Phys. – Dokl., 18, 149 (1973)].
[9] S. S. Kalmykova, Plasma Phys., 16, 132 (1974).
[10] S. S. Kalmykova, V. I. Kurilko, V. I. Kucherov, and A. P. Tolstoluzhskii, Zh. Eksp. Teor. Fiz., 64, 471 (1973) [Sov. Phys. – JETP, 37, 240 (1973)].
[11] H. A. Haus, Noise in Electronic Instruments [Russian translation], Izd. Energiya, Moscow-Leningrad (1964), p. 104.
[12] G. N. Lance, Numerical Methods for High-Speed Computers, Gordon and Breach (1960).

Role of collisions in plasma absorption of electromagnetic waves near the lower hybrid

B. V. Galaktionov, V. V. D'yachenko, M. M. Larionov, and O. N. Shcherbinin

A. F. Ioffe Physicotechnical Institute,
Academy of Sciences of the USSR, Leningrad

(Submitted July 16, 1973)
Zh. Tekh. Fiz., 44, 729-734 (April 1974)

An experiment on localization of rf power absorption in the FT-1 Tokamak device for a low-temperature discharge mode at frequencies close to the lower hybrid frequency is described. The role of collisional absorption of retarded electromagnetic waves is analyzed. Calculated results are given for the real and imaginary parts of the transverse index of refraction for $\nu/\omega = 0.01$. It is concluded that the efficiency of collisional absorption in the neighborhood of the lower hybrid frequency is high under the present experimental conditions.

Experiments on the interaction between high-frequency waves and the plasma in the FT-1 device at frequencies close to the lower hybrid frequency have been reported previously.[1] It was assumed that the absorption of rf power by the plasma was associated with the conversion of electromagnetic waves into slow, highly damped plasma waves.[2] Such a conversion should occur locally in plasma regions where the "hybrid resonance" condition is satisfied – the lower hybrid frequency is equal to the field frequency:

$$\omega = \omega_L = \left(\omega_{He}\omega_{Hi}\frac{\omega_p^2}{\omega^2_{He} + \omega_p^2}\right)^{1/2}. \tag{1}$$

Here, ω_L is the lower hybrid frequency, ω_p is the plasma frequency ω_{He} and ω_{Hi} are the electron and ion cyclotron frequencies.

However, collisional absorption of electromagnetic waves should also play an important role in a cool plasma. Experiments are described here for a low-temperature discharge mode, and the role of collisional absoption of slowed waves near the lower hybrid frequency is analyzed.

The FT-1 device is a Tokamak. The discharge chamber has a major radius of 62 cm, a minor radius of 20 cm, and a limiter radius of 17 cm. The toroidal magnetic field along the axis can reach 9 kOe. The discharge is excited in hydrogen at $2 \cdot 10^{-4}$ mm Hg. At comparatively low discharge currents, 0.5-5 kA, where complete ionization of the plasma is not achieved, the density depends on the current and varies from $0.5 \cdot 10^{12}$ to $7 \cdot 10^{12}$ cm^{-3}. In this mode the main mechanism for plasma energy loss is optical emission from neutrals and impurity ions. For this reason the electron temperature is "frozen" at a level of 3-4 eV. The intensity of light emission from the plasma is proportional to the absorbed power. By observing the variation in the luminous intensity from various plasma regions affected by an rf pulse one can determine the amount of absorbed rf power and the localization of the regions in which absorption occurs.[3]

Plasma luminosity is recorded with two photomultipliers fitted with periscopes which can be shifted vertically in diagnostic ports in the neighborhood of the plasma column. The light detectors record luminosity from narrow regions of the discharge along a chord parallel to the equatorial plane of the torus. The relative locations of the antennas and the optical detectors are shown in Fig. 2a. As is clear from the figure, it is possible to observe plasma luminosity distribution over a section of the discharge both at an antenna location and in sections separated from an antenna by 90 and 180° around the torus.

The rf oscillator is operated at 280 MHz and the power fed into a pulse is 8 kW for a period of 0.5 msec. Two stub antennas 18 cm long enclosed in a quartz shell are used to excite the waves and to pick up a signal transmitted through the plasma. The antennas are inserted from the upper side of the chamber and are located in the shadow of the limiter in sections separated by 90° along the torus; they are oriented along the stationary magnetic field. Because the antenna length is less than a quarter vacuum wavelength, the antennas excite a radio-frequency electric field with an effective longitudinal deceleration factor $N_z \approx 1.5$-2.0.

The experiments are carried out with a magnetic field of 5 kOe on the chamber axis. The mean plasma density over a cross section is determined by microwave interferometry in the 4-millimeter range. The density distribution over a cross section is determined by means of a double probe. A typical density distribution measured for a discharge current of 4 kA is shown in curve 1 of Fig. 1. The density varies slightly within the limits of the limiter and decreases by a factor of 2-3 at the wall of the discharge chamber in the shadow of the limiter. Because of toroidal nonuniformity of the longitudinal magnetic field, condition (1) for the conversion of waves with a frequency of 280 MHz can be satisfied at various points over the chamber cross section for plasma densities of $3 \cdot 10^{12}$ cm^{-3} and higher. Curve 2 in Fig. 1 shows the distribution of magnetic field over the chamber cross section and curve 3, the value of the "resonance" plasma densities corresponding to condition (1) for this magnetic field distribution. The points at which curves 1 and 3 intersect determine the regions of wave conversion in the equatorial section of the

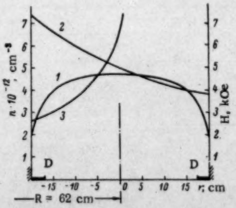

Fig. 1. 1) Plasma density distribution over discharge section; 2) magnetic field distribution; 3) values of "resonance" plasma densities for experimental conditions; D) diaphragm position.

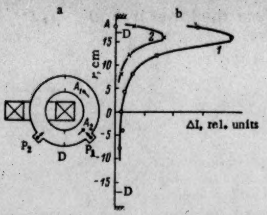

Fig. 2. a) Diagram of device: A_1, A_2) rf antennas; P_1, P_2) light detectors; b) distribution of additional luminosity over chamber cross section; radiator, A_1; $n = 2 \cdot 10^{12}$ cm^{-3}; 1) curve obtained from detector P_1, 2) curve obtained with detector P_2.

chamber. Within the plasma volume these regions form a closed surface which is asymmetric with respect to the discharge axis. As is well known, there is usually an opaque barrier between the plasma boundary and the conversion region, in which the electromagnetic waves are damped exponentially. However, the opaque barrier vanishes when the waves are decelerated along the magnetic field, and the hybrid resonance region becomes accessible to waves incident from outside.[4]

The measurements show that rf power is absorbed in the plasma under the present experimental conditions. During discharge the level of reflected power in the channel feeding the antenna does not exceed 20% of the operating power over a broad range of magnetic fields and plasma densities, while the reflection from the empty chamber is close to 100%. Transmission of a rf signal between the two antennas separated by 90° along the torus is observed only at very low densities ($n < 10^{11}$ cm^{-3}). At the same time, it turns out that the distribution of additional luminosity over the chamber volume due to the rf pulse depends significantly on plasma density. When $n \gtrsim 4 \cdot 10^{12}$ cm^{-3}, additional luminosity arises only in the immediate neighborhood of an antenna. When $n \approx 2 \cdot 10^{12}$ cm^{-3}, the increase in luminosity becomes noticeable at distances up to 1 m from the antenna along the length of the torus (Fig. 2b). A sharp drop in luminosity is observed moving away from an antenna across the magnetic field. When $n \lesssim 1 \cdot 10^{12}$ cm^{-3}, an increase in luminosity occurs over the entire volume of the chamber (Fig. 3). When $n \approx 5 \cdot 10^{11}$ cm^{-3}, the luminosity distribution both over a cross section and around the chamber is uniform. It should be remembered that linear conversion cannot occur when $n < 3 \cdot 10^{12}$ cm^{-3}. Obviously, the absorption of waves under these conditions is to be attributed to a collisional mechanism.

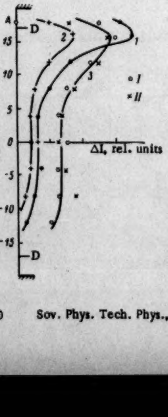

Fig. 3. 1) Light distribution curve obtained for detector P_1 with $n = 1 \cdot 10^{12}$ cm^{-3}; 2) the same for detector P_2; 3) $n = 5 \cdot 10^{11}$ cm^{-3} [(I)P_1; II) P_2].

In order to clarify the role of collisional damping of retarded electromagnetic waves we calculate the dependence of the real ($N_\perp$) and imaginary ($\varkappa$) parts of the index of refraction on plasma density for conditions resembling the experimental conditions. Terms associated with collisions of ions and electrons are taken into account in the dielectric tensor. In a coordinate system with its z axis along the magnetic field ($\omega_{Hi} \ll \omega \ll \omega_{He}$) we have

$$\hat{\varepsilon} = \begin{pmatrix} \varepsilon_1 & \varepsilon_2 & 0 \\ -\varepsilon_2 & \varepsilon_1 & 0 \\ 0 & 0 & \varepsilon_3 \end{pmatrix}, \tag{2}$$

where

$$\left.\begin{aligned} \varepsilon_1 &= 1 + \frac{\omega_p^2}{\omega_{He}^2} - \frac{\omega_{pi}^2}{\omega^2} - i\left(\frac{\omega_p^2}{\omega_{He}^2}\frac{\nu_e}{\omega} + \frac{\omega_{pi}^2}{\omega^2}\frac{\nu_i}{\omega}\right); \\ \varepsilon_2 &= 2\left(\frac{\omega_p^2}{\omega_{He}^2}\frac{\omega}{\omega_{He}}\frac{\nu_e}{\omega} - \frac{\omega_{pi}^2}{\omega^2}\frac{\omega_{Hi}}{\omega}\frac{\nu_i}{\omega}\right) + i\left(\frac{\omega_p^2}{\omega_{He}^2}\frac{\omega_{He}}{\omega} + \frac{\omega_{pi}^2}{\omega^2}\frac{\omega_{Hi}}{\omega}\right); \\ \varepsilon_3 &= 1 - \frac{\omega_p^2}{\omega^2}\left(1 + i\frac{\nu_e}{\omega}\right). \end{aligned}\right\} \tag{3}$$

The quantity $N_z = (k_z c)/\omega$, which characterizes the deceleration of a wave along the magnetic field, is taken as a parameter. It is assumed that the plasma parameters depend on a single coordinate perpendicular to the magnetic field. In this case, only the component of the wave vector parallel to this coordinate varies in wave propagation. The two solutions of the dispersion equation

$$(N_\perp - i\varkappa)^2 = \frac{B \pm \sqrt{B^2 - 4AC}}{2A} \tag{4}$$

determine the variation in the real and imaginary parts of the transverse index of refraction for propagation of E and H waves.[5] Here,

$$\left.\begin{aligned} A = \varepsilon_1;\ B &= \varepsilon_1^2 + \varepsilon_2^2 + \varepsilon_1\varepsilon_3 - (\varepsilon_1 + \varepsilon_3)N_z^2; \\ C &= \varepsilon_3(\varepsilon_1^2 + \varepsilon_2^2 - 2\varepsilon_1 N_z^2 + N_z^4). \end{aligned}\right\} \tag{5}$$

A calculation is performed for E waves in a hydrogen plasma in which the E_z component of the field is different

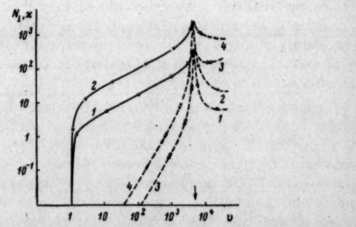

Fig. 4. Dispersion curves for $u = 2800$. 1) $N_\perp$ ($N_z = 2$); 2) $N_\perp$ ($N_z = 10$); 3) $\varkappa$($N_z = 2$); 4) $\varkappa$($N_z = 10$). Solid curves for $\nu_e = \nu_i = 0$, dashed curves for $\nu_e/\omega = \nu_i/\omega = 0.01$.

from zero. As has been shown,[5] the index of refraction for this mode has a singularity, where the condition (1) for lower hybrid resonance is satisfied.

The dependence of the real and imaginary parts of the transverse index of refraction on the parameter $v = \omega_p^2/\omega^2$, which is proportional to the plasma density, is shown in Fig. 4. Curves are given for two values of the longitudinal deceleration, $N_z = 2$ and $N_z = 10$. The value of the magnetic field determines the dimensionless parameter $u = \omega_{He}^2/\omega^2 = 2800$. For at 280 MHz the corresponding magnetic field is 5.3 kOe. The resonance density for these conditions is $5 \cdot 10^{12}$ cm^{-3}, and the critical density is 10^9 cm^{-3}. The dashed curves refer to $\nu_e/\omega = \nu_i/\omega = 0.01$. Values calculated for a collisionless plasma are represented by the solid lines. It is clear that even when $n = 10^{10}$-10^{11} cm^{-3} ($v = 10$-100), $N_\perp$ is of the order of 10. Note that at the antenna positions in this mode of operation the probe measurements yield density values of at least 4-$6 \cdot 10^{11}$ cm^{-3} ($v = 400$-600). Collisions begin to show an effect on the index of refraction only in the neighborhood of the conversion region (indicated in the figure by an arrow). It is also clear that when $n \gtrsim 10^{12}$ cm^{-3} and for the assumed collision frequencies, the absorption coeffficient $\varkappa$ can reach values of the order of unity. This means that the characteristic damping length $\delta = \lambda_0/(4\pi\varkappa)$, in which the power in an electromagnetic wave is reduced by a factor of e, is reduced to a few centimeters.

The relative roles of ion and electron collisions in wave damping is also determined by calculation. In this case the collision frequency of either electrons or ions with other particle species is alternately set to zero in the calculation. It turns out that when $\nu_e = \nu_i$ the contribution of ion collisions to the absorption coefficient is 60% in the given range of plasma parameters.

We now estimate the collision frequency typical of the plasma under these experimental conditions. The electron collision frequency is determined directly from measurements of the conductivity. Under these conditions, $\nu_e \approx 2 \cdot 10^{-6} n_e$. For $n_e = 5 \cdot 10^{12}$ cm^{-3}, we obtain $\nu_e = 10^7$ sec^{-1}. This value includes electron collisions with ions and with neutrals. Thus for the maximum values of plasma density realized in the experiment, $\nu_i/\omega \approx 0.01$. As far as the ions are concerned we find that the frequency of elastic and charge-exchange collisions of ions with neutral hydrogen falls within the range 10^5-10^6 sec^{-1} so that $10^{-4} < \nu_i/\omega < 10^{-3}$. It is clear from these estimates that in the low-temperature discharge mode studied here collision damping lengths from 10 cm to 1 m can be expected, depending on n_e. Electron collisions should play the main role in wave absorption. Furthermore, in the high-density case ($n > 3 \cdot 10^{12}$ cm^{-3}), where the hybrid resonance region appears in the plasma, collision damping is so large that the excited waves are absorbed near an antenna and do not reach regions where their conversion into plasma waves is possible.

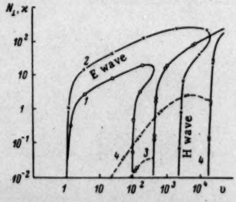

Fig. 5. Dispersion curves for u = 700. 1) $N_\perp$ ($N_z = 2$); 2) $N_\perp$ ($N_z = 10$); 3) $\varkappa$ ($N_z = 2$); 4) $\varkappa$ ($N_z = 10$). Solid curves are for $\nu_e = \nu_i = 0$, dashed curves for $\nu_e/\omega = \nu_i/\omega = 0.01$.

The dependence of $N_\perp$ and $\varkappa$ on plasma density is shown in Fig. 5 for low magnetic fields (u = 700); the lower hybrid resonance condition is not satisfied anywhere. It is clear that conversion of an E wave into an H wave occurs at a certain plasma density. The dispersion curves for both types of waves close on each other, forming a loop. For high densities the index of refraction becomes imaginary, i.e., a cutoff develops, even in the absence of collisions. The existence of collisions is responsible for a marked rise in the absorption coefficient of the waves near the cutoff. The damping lengths near the cutoff are of the same order of magnitude as in the previous case. This explains why good absorption of hf power over a broad range of magnetic fields is observed experimentally. The appearance of a transmitted signal during plasma decay when $n_e < 10^{11}$ cm^{-3} is obvious evidence for a rise in damping length to values of the order of the spacing between the antennas (1 m).

It is of interest to compare the magnitude of collisional absorption in the plasma and the chamber walls. We use the absorption coefficient for normal incidence of a plane wave on a metal surface, which is

$$\alpha = \frac{4}{c}\sqrt{\frac{\omega\mu}{8\pi\sigma}},$$

where σ is the conductivity of the metal and μ is the magnetic permeability. For stainless steel $\alpha \approx 3 \cdot 10^{-4}$ at these frequencies. The coefficient for absorption of a wave by a plane plasma layer of thickness l can be taken to be l/δ for a single passage of the wave. When the plasma is contained within a closed metal shell, high-frequency power will be absorbed in the plasma by collision after multiple reflections if $l/\delta > \alpha$. Under our experimental conditions, this relation is satisfied over the entire range of the parameters. It is clear, however, that the fraction of hf power lost to the chamber walls will increase in proportion to the rise in plasma temperature. Estimates show that in our case ($n = 2 \cdot 10^{12}$ cm^{-3}) the absorption in the walls is comparable to collision absorption in the plasma only when $\nu/\omega \approx 10^{-6}$, which corresponds to an electron temperature of approximately 1 keV for a hydrogen plasma.

The calculations thus show that for frequencies very different from the lower hybrid frequency even comparatively rare collisions lead to a large value for the absorption coefficient in plasma. This mechanism is connected with significant slowing down of the waves and does not have a critical dependence on the magnetic field. When a reflecting metal shell is present around the plasma, it can ensure good absorption of hf power at comparatively low collision frequencies also because of multiple reflection of electromagnetic waves from the chamber walls. The experimental results agree with the calculation.

The authors are grateful to V. E. Golant, A. D. Piliya, and V. I. Fedorov for valuable discussions.

---

[1] I. P. Gladkovskii, V. E. Golant, V. V. D'yachenko, M. M. Larionov, L. S. Levin, V. V. Rozhdestvenskii, V. A. Sadovaikov, and O. N. Shcherbinin, Zh. Tekh. Fiz., 43, 1632 (1973) [Sov. Phys. – Tech. Phys., 18, 1029(1974)].

[2] V. E. Golant and A. D. Piliya, Usp. Fiz. Nauk, 104, 413 (1971) [Sov. Phys. – Usp., 14, 413 (1972)].

[3] V. E. Golant, M. M. Larionov, L. S. Levin, L. P. Pakhomov, K. A. Podushnikova, V. V. Rozhdestvenskii, and G. A. Serebrenyi, Papers at Sixth European Conference on Plasma Physics and Controlled Thermonuclear Fusion, Moscow (1973).

[4] T. Stix, Theory of Plasma Waves, McGraw-Hill, New York (1962).

[5] V. E. Golant, Zh. Tekh. Fiz., 41, 2492 (1971) [Sov. Phys. – Tech. Phys., 16, 1980 (1972)].

Distributed systems for feedback control of a tokamak plasma

V. F. Gubarev and Yu. I. Samoilenko
Institute of Cybernetics,
Academy of Sciences of the Ukrainian SSR, Kiev
(Submitted June 26, 1973)
Zh. Tekh. Fiz., 44, 735-742 (April 1974)

Closed systems for feedback control of the equilibrium position of the plasma in a tokamak are described. The equilibrium is analyzed for an arbitrary distribution of the longitudinal current over the plasma cross-section for a large aspect ratio $a/R \ll 1$. The feedback control, a control shell, is introduced by means of the winding density function γ and the function W(p), which relates the magnetic flux incident on the shell, Φ_0, to the flux due to the current flowing in the winding Φ_1. The dynamical errors due to the nonideal nature of the frequency characteristic and the effect of the steel chamber are analyzed. This method can be used to analyze plasma equilibrium in a variety of feedback control systems. This method yields the requirements that must be satisfied by the feedback control system.

Experience has now been gained in the use of a special winding system with feedback controlled winding currents intended for use in maintaining the equilibrium of the toroidal plasma in a tokamak.[1] A feedback control system of this type has been used successfully in extending the time for which plasma is confined in equilibrium. However, this capability does not exhaust all the advantages of this new method for actively intervening in plasma processes.

Below we describe closed systems for feedback control of the equilibrium state of a plasma in a tokamak; we analyze the equilibrium of the plasma in the vacuum chamber, taking account of complicating factors (the effect of the steel chamber, the iron core, and the physical devices used for control), and analyze the requirements imposed on the control system.

We analyze the equilibrium under the assumption of "weak toroidicity" for large aspect ratio: $a/R_0 \ll 1$ (a and R_0 are respectively the minor and major radii of the plasma). Following ref. 2, we introduce a special coordinate system (r, θ, ω), which is related to the cylindrical coordinates (R, φ, z) based on the symmetry axis of the torus by

$$R=R_0+r\cos\omega,\ \varphi=\theta,\ z=r\sin\omega. \quad (1)$$

The components of the metric tensor introduced in ref. 3, which correspond to the coordinate system selected here, are used in carrying out differentiation and integration and in vector equations.

The equilibrium can be described for an arbitrary distribution of the longitudinal current over the cross-section of the plasma. In the first approximation in $\varepsilon = a/R_0$, if a plasma of circular cross-section is to be at equilibrium at the $R = R_0$, $z = 0$ axis, the magnetic field at the plasma surface ($r = a$) must be, according to ref. 2,

$$H_r=0,\ H_\theta=H_0\left(1-\frac{a}{R_0}\cos\omega\right),\ H_\omega=H_I\left[1+\frac{a}{R_0}\Lambda(a)\cos\omega\right]. \quad (2)$$

Here, H_0 is the longitudinal magnetic field on the axis, H_I is the longitudinal field in the plasma at the upper and lower parts of the plasma surface, and $\Lambda(a)$ is the asymmetry parameter of the poloidal field, which is a function of the distributions of the plasma pressure and the current density.

Satisfaction of (2) requires the application of an external magnetic field perpendicular to the plane of the torus. If this field, $H_\perp$, is constant the changes in the longitudinal plasma current, the radius a, and the parameter $\Lambda(a)$ will cause the plasma to move in the chamber during the discharge, at any time assuming a position such that condition (2) is satisfied. Accordingly, during the discharge control should be maintained by a perpendicular magnetic field on the basis of a specified program or automatically, by a feedback system; combined control is also possible. In this work we analyze the feedback control case; we analyze the dynamics of plasma formation in the quasistatic (equilibrium) approximation, in which the characteristic time for changes in the position of the plasma in the chamber is much longer than the period of the natural oscillations of the plasma for the spatial modes with m = 1, k = 0.

The task of the feedback-control system is to limit movements of the plasma in the vacuum chamber to a tolerable range during the discharge. One way to do this would be to construct a distributed feedback "enforcer", a control shell in the form of windings on the toroidal surface surrounding the plasma. Two-pole feedback controllers are connected to the windings.[4] If the winding consists of a large number of turns wound with in inhomogeneous density on the toroidal surface ($r = b$, $b > a$), the winding-density function $\gamma(\omega)$ can be used to introduce an equivalent surface current density at the control shell:

$$\mathbf{j}(p,\ \omega)=I(p)\,\gamma(\omega), \quad (3)$$

where I(p) is the Laplace transform of the winding current. Accordingly, the structure of the quasisteady-state magnetic field produced by the current in the winding is specified completely by the function $\gamma(\omega)$, which is a spatial characteristic of the enforcer (such feedback control systems are called distributed feedback controllers). Since the purpose of the feedback control system is to influence the plasma motion by means of a magnetic field perpendicular to the plane of the torus, the function $\gamma(\omega)$ must be

$$\gamma(\omega)=\{0,\ \gamma_\theta(\omega),\ 0\}.$$

Here, $\gamma_\theta(\omega)$ must be as good as possible an approximation of a cosinusoidal function of ω for the first harmonic. The presence of other, higher, harmonics can affect, the equilibrium shape of the plasma cross-section (especially for high gain coefficients).

The current in the winding is controlled by means of a two-pole controller which is a controllable source or controllable resistance with a power supply. We can consider the input to the controller to be the flux of the incident magnetic field, Φ_0. Correspondingly, the flux of the magnetic field of the winding current, Φ_1, can be treated as the output of the controller. Our problem is to synthesize a control function W(p) which establishes the required functional dependence between the input and the output:

$$\Phi_1(p) = -W(p)\,\Phi_0(p) \tag{4}$$

or

$$\Phi_0(t) = -\int_0^t f(t-\tau)\,\Phi_1(\tau)\,d\tau, \tag{5}$$

where

$$f(t) = \frac{1}{2\pi j}\int_{s-j\infty}^{s+j\infty}\frac{e^{pt}}{W(p)}\,dp;$$

here Φ_0(p) and Φ_1(p) are the Laplace transforms of the corresponding fluxes, and *f*(t) is the kernel of the inverse operator of the controller.

The condition for the feasibility of a controller using elements with lumped parameters is that W(p) be a proper, rational-fraction function with real coefficients. The minus sign means that the control magnetic field must be in the direction opposite the incident field. Accordingly, (4) corresponds to the boundary condition for a shell having a negative μ and a definite dispersion characteristic.

In these feedback-control systems the incident flux must be decoupled from that reflected from the shell, since the sensed and controlled fields exist at the same point in space. In this connection it is expedient to use a single winding, which is used simultaneously for the sensing and control functions. In this case the decoupling can be achieved in the electrical circuit of the controller by means of bridges. A controller of this design is convenient and is structurally analogous to the copper housing which performs the same functions in many tokamak devices. The controller can also be designed according to the classical principle. In this case two windings are required; they are decoupled either by means of an electrical circuit (e.g., a transformer circuit) or by virtue of their spatial arrangement. However, this structural solution can be cumbersome and may not provide a sufficient decoupling in the necessary frequency range. The magnetic field in the region between the plasma and the control shell and in the region outside the shell can be expressed in terms of the scalar potential H = grad φ, which satisfies the Laplace equation

$$\frac{\partial}{\partial x^i}\left(\sqrt{g}\,g^{ik}\frac{\partial\varphi}{\partial x^k}\right) = 0\ (x^1 = r,\ x^2 = \theta,\ x^3 = \omega,\ g = det\,\|g_{ik}\|), \tag{6}$$

where g^{ik} are the components of the metric tensor.

The scalar potential φ for the region between the plasma and the control shell can be written

$$\varphi = \varphi_0 + \varphi_1.$$

Here, φ_0 is the magnetic potential due to the longitudinal plasma current, and φ_1 is the potential associated with the external sources, including the controlling effect of the shell.

In a first approximation, with equilibrium condition (2) satisfied, we find

$$\left.\begin{aligned}\varphi_0 &= H_I a\omega + \frac{H_I^{-}a}{2R_0}\left(-r\ln\frac{8R_0}{r} + \frac{a^2}{r}\Lambda_1\right)\sin\omega,\\ \varphi_1 &= R_0H_0\theta + \frac{r}{2R_0}H_I a\left(\ln\frac{8R_0}{a} - 1 + \Lambda_1\right)\sin\omega,\\ \Lambda_1 &= \Lambda(a) + \frac{1}{2}.\end{aligned}\right\} \tag{7}$$

Similarly, we can write the magnetic potential outside the shell as

$$\varphi = \varphi_2 + \varphi_3.$$

Here φ_2 corresponds to the potential passing through the magnetic-field shell, and φ_3 corresponds to the external longitudinal field and the field reflected from the iron core. The effect of the iron core is taken into account in ref. 5. Using the result found there we write

$$\left.\begin{aligned}\varphi_2 &= H_I a\omega + \frac{H_I a}{2R_0}\left(-r\ln\frac{8R_0}{r} + \frac{C}{r}\right)\sin\omega,\\ \varphi_3 &= R_0H_0\theta + \frac{r}{2R_0}H_I a\psi\sin\omega,\\ \psi &= 4R_0^2\int_0^\infty x\left[I_0(xR_1)\,K_1(xR_0)\frac{K_0(xR_0)}{K_0(xR_1)}\right]dx,\end{aligned}\right\} \tag{8}$$

where R_1 is the radius of the cylindrical iron core.

For further manipulations we transform to the coordinate system (r_1, θ, ω_1), which is fixed in the control shell:

$$r \approx r_1 - \Delta\cos\omega_1,\quad \sin\omega \approx \sin\omega_1\left(1 - \frac{\Delta}{r_1}\cos\omega_1\right),$$

$$\omega \approx \omega_1 + \frac{\Delta}{r_1}\sin\omega_1,\quad \cos\omega \approx \cos\omega_1 + \frac{\Delta}{2r_1} - \frac{\Delta}{2r_1}\cos 2\omega_1,$$

where Δ is the displacement of the geometric axis of the control shell with respect to the axis of the plasma formation, and Δ/b is a small parameter. Since the shell is narrow, we can find the arbitrary constant C in (8) from the continuity condition for the normal component of the magnetic field at the surface $r_1 = b$.

$$\left(\frac{\partial\varphi_0}{\partial r_1} + \frac{\partial\varphi_1}{\partial r_1}\right)_{r_1=b} = \left(\frac{\partial\varphi_2}{\partial r_1} + \frac{\partial\varphi_3}{\partial r_1}\right)_{r_1=b}. \tag{9}$$

We find, to first-order

$$C = -b^2\left[\ln\frac{8R_0}{a} - 1 + \left(1 - \frac{a^2}{b^2}\right)\Lambda_1 - \psi\right]. \tag{10}$$

Now we must find the flux incident on the magnetic-field shell, Φ_1, and the flux of the magnetic field produced by the current in the shell, Φ_2. Then, using (5) we find the displacement of the plasma with respect to the control shell Δ.

Following ref. 6, we write the winding-density function $\gamma(\omega)$ in terms of the surface magnetization function $\Gamma(\omega)$ by means of

$$\left.\begin{aligned} &\gamma = \operatorname{rot}\Gamma, \quad \Gamma = \{\Gamma_b(\omega),\ 0,\ 0\}, \\ &\Gamma_b(\omega) = \sum_{m=1}^{\infty} \Gamma_m \sin m\omega. \end{aligned}\right\} \tag{11}$$

Then, to calculate the magnetic flux penetrating the shell, Φ, we use the equation[6]

$$\Phi = \iint_S \mathbf{B}\cdot\Gamma\, dS = \mu_0 \int_0^{2\pi}\int_0^{2\pi} \left(g_{\theta\theta}^{1/2} g_{\omega_1\omega_1}^{1/2} g^{-1} \frac{\partial\varphi}{\partial r_1}\right)_{r_1=b} \Gamma_b(\omega_1)\, d\omega_1 d\theta, \tag{12}$$

finding

$$\begin{aligned} \Phi_0 &= \mu_0 \int_0^{2\pi}\int_0^{2\pi} \left[g_{\theta\theta}^{1/2} g_{\omega_1\omega_1}^{1/2} g^{-1}\left(\frac{\partial\varphi_0}{\partial r_1} + \frac{\partial\varphi_3}{\partial r_1}\right)\right]_{r_1=b} \Gamma_b(\omega_1)\, d\omega_1 d\theta \\ &\approx -\pi^2\mu_0 abH_I\left[\ln\frac{8R_0}{b} - 1 + \frac{a^2}{b^2}\Lambda_1 + \frac{2R_0\Delta}{b^2} - \psi\right]\Gamma_1, \\ \Phi_1 &= \mu_0 \int_0^{2\pi}\int_0^{2\pi} \left[g_{\theta\theta}^{1/2} g_{\omega_1\omega_1}^{1/2} g^{-1}\left(\frac{\partial\varphi_1}{\partial r_1} - \frac{\partial\varphi_3}{\partial r_1}\right)\right]_{r_1=b} \Gamma_b(\omega_1)\, d\omega_1 d\theta \\ &\approx \pi^2\mu_0 abH_I\left[\ln\frac{8R_0}{a} - 1 + \Lambda_1 - \psi\right]\Gamma_1. \end{aligned} \tag{13}$$

Substituting (13) into (5), we find an expression for the displacement:

$$\begin{aligned} \Delta(t) = \frac{b^2}{2R_0}\Bigg[&\frac{1}{a(t)H_I(t)}\int_0^t f(t-\tau)\,a(\tau)\,H_I(\tau)\left(\ln\frac{8R_0}{a} - 1 + \Lambda_1 - \psi\right)d\tau \\ &- \left(\ln\frac{8R_0}{b} - 1 + \frac{a^2\Lambda_1}{b^2} - \psi\right)\Bigg]. \end{aligned} \tag{14}$$

We find the current in the conductor winding, I, from the condition giving the discontinuity in the tangential magnetic field components at the control shell; in our case this condition is[6]

$$I\Gamma_b = \varphi_-(b) - \varphi_+(b), \tag{15}$$

where $\varphi_+ = \varphi_2 + \varphi_3$, $\varphi_- = \varphi_0 + \varphi_1$.

Then, to a first approximation we can write

$$I = \frac{abH_I}{R_0\Gamma_1}\left(\ln\frac{8R_0}{a} - 1 + \Lambda_1 - \psi\right). \tag{16}$$

Accordingly, the current in the control shell is not a function of the control relation (in which the natural oscillations of the plasma are not taken into account), but is a function of the spatial characteristics of the winding alone. The current decreases as the winding is brought closer to the plasma and as the plasma is made more cosinusoidal.

For the case of stiff control W(p) = k, we find

$$\Delta = \frac{b^2}{2R_0}\left[\frac{1}{k}\left(\ln\frac{8R_0}{a} - 1 + \Lambda_1 - \psi\right) - \left(\ln\frac{8R_0}{b} - 1 + \frac{a^2}{b^2}\Lambda_1 - \psi\right)\right]. \tag{17}$$

With k = 1 and $\psi = 0$, this equation is the same as that derived by Shafranov for the case of an ideal liner:

$$\Delta = \frac{b^2}{2R_0}\left[\ln\frac{b}{a} + \left(1 - \frac{a^2}{b^2}\right)\Lambda_1\right].$$

The second expression in parentheses in (17) gives the position of the equivalent magnetic axis of the system, which is displaced in the chamber; the first expression in parentheses gives the displacement of the plasma from this magnetic axis. Using the coefficient k we can effectively control the plasma position from values $\Delta < 0$ all the way to the magnetic axis and for any values $\Delta > 0$ within the limits specified by the chamber. During discharge the plasma parameters can change, leading to changes in the parameter Λ_1 and the radius a. Accordingly, the plasma position is not fixed, even in case of an ideal regulator W(p) = k. If the plasma radius does not change (a = const), in the case k = b^2/a^2 the situation can be invariant with respect to other plasma parameters. Then the plasma position is governed by geometric factors alone, being independent of the plasma parameters:

$$\Delta = \frac{1}{2R_0}\left[a^2\left(\ln\frac{8R_0}{a} - 1 - \psi\right) - b^2\left(\ln\frac{8R_0}{b} - 1 - \psi\right)\right]. \tag{18}$$

In general, a second feedback loop should be formed making use of information on the plasma radius and perhaps other parameters of the plasma which are measured during the discharge.

Let us consider the control function contemporary control systems:

$$W(p) = k\frac{\tau p\,(Tp+1)}{(\tau p+1)(\theta p+1)}. \tag{19}$$

In (19) we neglect the nonideal nature of the differentiating unit of the controller.

Then we have

$$f(t) = \frac{1}{k}\left[\frac{\theta}{T}\,\delta(t) + \left(\frac{T-\theta}{T^2} - \frac{1}{\tau}\right)e^{-t/T} + \frac{1}{\tau}\right]. \tag{20}$$

Here $\delta(t)$ is the Dirac delta function, the time constants τ and θ determine the working frequency (τ = 1-5 sec, θ = 10^{-4}-$5\cdot10^{-4}$ sec), and T is the time constant of the differentiating unit.

Using asymptotic expansions to evaluate the integral in (14), we find the following approximate equation, which holds at times long after the beginning of the discharge:

$$\begin{aligned} \Delta(t) \approx \frac{b^2}{2R_0}\Bigg\{&\frac{1}{k}\Bigg[\Delta_0(t) + \frac{\theta - T}{aH_I}\frac{d}{dt}(aH_I\Delta_0) \\ &+ \frac{1}{\tau aH_I}\int_0^t a(\tau)\,H_I(\tau)\,\Delta_0(\tau)\,d\tau\Bigg] \\ &- \left(\ln\frac{8R_0}{b} - 1 + \frac{a^2}{b^2}\Lambda_1 - \psi\right)\Bigg\}, \end{aligned} \tag{21}$$

where

$$\Delta_0(t) = \ln\frac{8R_0}{a} - 1 + \Lambda_1 - \psi.$$

With this control function the displacements of the plasma caused by changes in its parameters are supplemented by a displacement due to the nonideal nature of the controller at low and high frequencies. From the second expression in brackets in this equation we can find the requirements which are imposed on the upper controller frequency: $T \ll \tau_1$, $\theta \ll \tau_1$, where τ_1 is the minimum characteristic time for changes in the plasma parameters and the current during the discharge. The integral term describes the plasma drift and is due to the steep drop in the controller characteristic at low frequencies. Hence, the condition $\tau_p/\tau \ll 1$, where τ_p is the plasma confinement time, must be satisfied. Accordingly, the requirements on the controller are determined from (20) in terms of the tolerable displacements and the nature of the changes in the plasma parameters.

In most experimental devices there is a steel chamber (a bellows) between the plasma and the control shell; this chamber affects (albeit slightly) the control dynamics of the equilibrium plasma position. To take this effect into account we consider the passage of the magnetic field through a thin cylindrical chamber ($h/c \ll 1$, where h is the thickness and c is the radius of the chamber) with conductivity σ. We find the penetration of the magnetic field through the chamber from the diffusion equation

$$\frac{\partial \mathbf{H}}{\partial t} = \nu_H \nabla^2 \mathbf{H}, \ \left(\nu_H = \frac{1}{\sigma\mu_0}\right). \qquad (22)$$

In the case under consideration here, the approximate solution for the Laplace transforms of the magnetic field components, $\widetilde{H}_r$ and $\widetilde{H}_\omega$, is

$$\left.\begin{aligned} H_r &= (D_1 e^{\gamma_1 x} + D_2 e^{\gamma_2 x}) \sin \omega, \\ H_\omega &= [(c\gamma_1 + 1) D_1 e^{\gamma_1 x} + (c\gamma_2 + 1) D_2 e^{\gamma_2 x}] \cos \omega. \end{aligned}\right\} \qquad (23)$$

Here,

$$\gamma_1 = \frac{1}{2c}(\sqrt{9 + 4c^2\sigma\mu_0 p} - 3); \ \gamma_2 = \frac{1}{2c}(\sqrt{9 + 4c^2\sigma\mu_0 p} + 3);$$

$$x = r - c; \ x/c \ll 1,$$

and D_1 and D_2 are arbitrary constants, to be determined from the boundary conditions.

The changes in the normal and tangential components of the magnetic field in the chamber are given by

$$\left.\begin{aligned} H_r|_0 - H_r|_h &= [(1 - e^{\gamma_1 h}) D_1 + (1 - e^{\gamma_2 h}) D_2] \sin \omega, \\ H_\omega|_0 - H_\omega|_h &= [(c\gamma_1 + 1)(1 - e^{\gamma_1 h}) D_1 \\ &+ (c\gamma_2 + 1)(1 - e^{\gamma_2 h}) D_2] \cos \omega. \end{aligned}\right\} \qquad (24)$$

It follows from (24) that the radial component of the magnetic field changes significantly during passage through the chamber when $\gamma_1 h$ or $\gamma_2 h$ is on the order of unity. This situation corresponds to a characteristic frequency of the order of 500 kHz for the changes in the magnetic field with $h = 10^{-3}$ m and $c = 0.2$ m. On the other hand, there is an appreciable change in the tangential component of the magnetic field when $\gamma_1^2 ch$ or $\gamma_2^2 ch$ is of order unity. In turn, the field changes at a corresponding frequency of the order of 4-5 kHz for the same chamber dimensions. Accordingly, in the frequency range over which we are examing the the equilibrium of the plasma configuration we can assume that the normal component of the magnetic field is continuous at the surface $r_1 = c$, while the tangential component has a discontinuity equal to some equivalent surface current. Accordingly, the effect of the chamber can be taken into account by means of an inertial shell between the plasma and the distributed controller. We therefore consider another shell, at $r_1 = c(a < c < b)$, having a transfer function $W_1(p)$ which relates the flux of the magnetic field incident on it, Φ_2, to the flux of the magnetic field of the intrinsic current in the shell, Φ_3:

$$\Phi_3(p) = -W_1(p)\Phi_2(p). \qquad (25)$$

Then, by analogy with the procedure used to determine the equilibrium position with a single shell, we write the magnetic potential φ as two terms (corresponding to the transmitted field and the field of the external sources) for each of three regions: that between the plasma and the first shell, that between the shells, and that outside the second shell. The arbitrary constants are determined from conditions (2) and (25) and the continuity condition for the normal components at the surfaces $r_1 = c$ and $r_1 = b$. The magnetic flux is calculated from (12) and (13). Then, using (5), we find an equation for the position of the plasma configuration in the chamber:

$$\Delta(t) = \frac{1}{2R_0}\left[b^2\Delta_1 F_1(t) + c^2 F_2(t) - a^2\Delta_1 - c^2\left(\ln\frac{8R_0}{c} - 1 - \psi\right)\right], \qquad (26)$$

where

$$F_1(t) = \frac{1}{a(t)H_I(t)}\int_0^t f_1(t-\tau)\,a(\tau)\,H_I(\tau)\,d\tau;$$

$$F_2(t) = \frac{1}{a(t)H_I(t)}\int_0^t f_2(t-\tau)\,a(\tau)\,H_I(\tau)\,\Delta_0(\tau)\,d\tau;$$

$$f_1(t) = \frac{1}{2\pi j}\int_{s-j\infty}^{s+j\infty} \frac{W_2(p) + W_1(p)W_2(p)}{W_1(p) + W_2(p)} e^{pt}\,dp;$$

$$f_2(t) = \frac{1}{2\pi j}\int_{s-j\infty}^{s+j\infty} \frac{1 + W_1(p)W_2(p)}{W_1(p) + W_2(p)} e^{pt}\,dp;$$

$$W_2(p) = \frac{c^2}{b^2}W(p); \ \Delta_1 = \frac{c^2}{b^2}\left(\ln\frac{8R_0}{c} - 1 - \psi\right) - \ln\frac{8R_0}{b} + 1 + \psi.$$

If we set $W_1(p) = 0$ or $W_2(p) = 0$, we find that Eq. (26) is the same as Eq. (14) above, for the displacement in the case of a single shell.

We can use Eq. (26) to analyze the equilibrium position of the plasma configuration, taking the chamber into account, even when there is feedback control system. Treating the chamber as an aperiodic differentiating unit in the automatic-regulation system, we find

$$W_1(p) = \frac{\tau_k p}{l(\tau_k p + 1)}. \qquad (27)$$

Here l ($l \sim 1$) is a dimensionless quantity, equal to the first coefficient in the Fourier expansion of the equivalent surface current in the chamber in terms of ω, and $\tau_k = L_k/R_k$ is the time constant of the chamber, equal to the self-induction L_k divided by the resistance R_k.

Analysis of (23) shows that τ_k is of the order of $(1.6-2.0)\cdot 10^{-4}$ sec for the chamber dimensions listed above. Taking (19) into account with T = 0, and using the asymptotic expansions to evaluate the integrals, we find

$$\Delta(t)\approx\frac{b^2}{2R_0}\left\{\Delta_1\frac{(k_1-1)\tau_k}{k_1 laH_I}\frac{d}{dt}(aH_I)+\frac{c^2}{b^2k_1}\left[\Delta_0(t)+\frac{1}{\tau aH_I}\int\limits_0^t a(\tau)H_I(\tau)\Delta_0(\tau)\,dt\right]+\frac{c^2}{b^2k_1}\left[\frac{(k_1^2-1)\tau_k}{k_1 l}+\theta\right]\frac{1}{aH_I}\frac{d}{dt}(\Delta_0 aH_I)-\left(\ln\frac{8R_0}{b}-1+\frac{a^2}{b^2}\Lambda_1-\psi\right)\right\}. \qquad (28)$$

Here $k_1=(c^2/b^2)k$; Δ_1 is given by (26); and $\Delta(t)$ is given in (21). We see from Eq. (28) that the effect of the steel chamber is an additional displacement which occurs during changes in the plasma parameters during the discharge. The quantity τ_k must satisfy $\tau_k \ll \tau_1$.

The method of this paper can be used to analyze various means and principles of systems for feedback control of the equilibrium position of the plasma in a tokamak and to take the effects of various factors and the surroundings into account.

We note in conclusion that the results of this theoretical work agree with experimental results obtained on the TO-1 device.

---

[1] L. I. Aretemenkov, I. N. Golovin, P. I. Kozlov, P. I. Melekov, N. N. Shvindt, V. K. Butenko, V. F. Gubarev, A. I. Kukhtenko, Yu. P. Ladikov-Roev, and Yu. I. Samoilenko, Plasma Physics and Controlled Nuclear Fusion Research, 1971, Vol. 1, IAEA, Vienna (1971), p. 359.

[2] V. D. Shafranov, in: Reviews of Plasma Physics, Vol. 2, Consultants Bureau, New York (1966).

[3] B. B. Kadomtsev, in: Reviews of Plasma Physics, Vol. 5, Consultants Bureau, New York (1970).

[4] V. K. Butenko, Yu. P. Ladikov-Roev, and Yu. I. Samoilenko, in: Cybernetics and Computer Technology [in Russian], No. 8, Izd. Nauka Dumka, Kiev (1971).

[5] V. F. Gubarev and Yu. G. Krivonos, in: Distributed Control of Processes in Complex Systems [in Russian], Izd. Inst. Kibernetiki, Kiev (1973).

[6] Yu. P. Ladikov, and Yu. I. Samoilenko, Zh. Tekh. Fiz., 42, 2062 (1972) [Sov. Phys. – Tech. Phys., 17, 1644 (1973)].

Plasma diffusion in the Tornado device

A. N. Kozyrev and B. P. Peregud

A. F. Ioffe Physicotechnical Institute,
Academy of Sciences of the USSR, Leningrad

(Submitted July 16, 1973)
Zh. Tekh. Fiz., 44, 743-753 (April 1974)

The results of a numerical calculation of classical diffusion of a fully ionized plasma in an axisymmetric model of the Tornado trap are reported and discussed. Comparison of the calculated results with experiment shows that the actual plasma decay is governed by classical or pseudoclassical diffusion. The ratio of the local Bohm and classical diffusion coefficients ($n \approx 10^{12}$ cm^{-3}, $T_e = 0.5$ eV) is in the range 3-30. The assumption of a classical diffusion mechanism leads to a satisfactory description of the plasma lifetime as a function of the particle density, the neutral pressure, the current, and the ratio of the helix currents, m.

The lifetimes of individual particles in the Tornado device are evaluated in refs. 1 and 2 in the drift approximation and for conditions under which drift is suppressed. These terms are at least two orders of magnitude higher than the plasma lifetimes measured in ref. 3. In this situation, a natural next step toward understanding the mechanism governing the plasma loss from the trap is to analyze collective effects, in particular, to analyze classical particle diffusion and determine the diffusive lifetime. The simple estimate of this time $\tau \cong L^2/D$ is unreliable for Tornado since the magnetic field in this trap, as in multipoles,[4] can vary from point to point by an order of magnitude. On the other hand, a rigorous formulation of the plasma-diffusion problem meets with the ncessity of having to solve a three-dimensional diffusion equation in a complicated magnetic field.

As a compromise, the actual Tornado trap is replaced by an axisymmetric model. The magnetic field in this model has closed magnetic surfaces throughout the volume, so that the problem can be reduced to one of solving a one-dimensional diffusion equation.[4] The equation is solved numerically, and the calculated results furnish a basis for a discussion of experimental data on plasma confinement[3] from the standpoint of classical transverse diffusion.

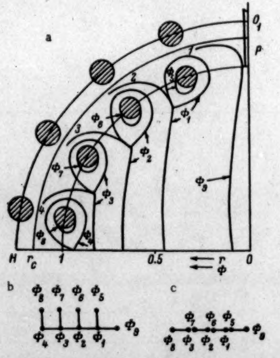
a
O_1
P
1
2
3
4
Φ_1
Φ_2
Φ_3
Φ_4
Φ_5
Φ_6
Φ_7
Φ_8
Φ_9
H
r_c
1
0.5
0
r
Φ
b
Φ_8 Φ_7 Φ_6 Φ_5
Φ_9
Φ_4 Φ_3 Φ_2 Φ_1
c
Φ_7 Φ_6 Φ_5
Φ_9
Φ_8 Φ_3 Φ_2 Φ_1

Fig. 1. a: One quadrant of the intersection of the trap with a plane passing through the symmetry axis, 00_1. Shaded circles) cut ends of the conductors; HO) radius lying in the equatorial plane of the trap; r_c) spherical separatrix; $\Phi_1 - \Phi_4$) separatrices passing through singularities of the poloidal field; $\Phi_5 - \Phi_8$) magnetic surfaces tangent to the conductors; Φ_9) outer magnetic surface. b: The magnetic-flux coordinate axis for the case in which the separatrices and the conductor surfaces do not have points in common. c: The magnetic-flux axis for the case in which the separatrices intersect the conductor surface. The axis is partitioned into segments, and the trap is partitioned into unconnected regions.

1. CALCULATION MODEL AND PROCEDURE

Figure 1 shows one-quadrant of a cross-section of the axisymmetric model of the Tornado device. Each helix of the trap is replaced by a set of k rings (equal to the number of turns of the helix) lying on the surface of the sphere in parallel planes. On the spheres, the rings are arranged at identical angular intervals and in such a manner that if a radius drawn from the common center of these spheres intersects a ring on the inner sphere, it also intersects a ring on the outer sphere. Furthermore, two semiinfinite, unclosed conductors P, lying on the symmetry axis of the system, 00_1, are used to simulate the linear crosspiece and the current conductors of the Tornado. The current is assumed to be the same in all the rings on the surface of the given sphere, while the ratio of the currents in the rings in different spheres, m, can be adjusted. It is also assumed that all the conductors are of finite thickness; in the calculations of the magnetic field and the lines of force, however, the current is assumed to be concentrated at the axes of the conductors.

The magnetic field of this current system has toroidal magnetic surfaces throughout the volume; the layers of these surfaces are separated by multiply connected separatrices (Fig. 1a). The position of each magnetic surface can be specified by the value of the magnetic flux Φ between this surface and the outer magnetic surface, Φ_9.

If the diffusion perpendicular to magnetic field **B** is governed by a local diffusion coefficient $D_1(r, B, t)$, the particle flux through magnetic surface Φ is

$$\Gamma(\Phi, t) = -2\pi \oint r D_1 \nabla_\perp n\, dl,$$

where n is the density and r is the distance from the symmetry axis of the system to element dl. The integration is carried out over a closed line of force of the field of the annular conductors, B_p, i.e., along the intersection of the magnetic surface with a plane (Fig. 1). Since the derivative of the density with respect to the normal to surface Φ, h is $\partial n/(\partial h) = -2\pi r B_p\, \partial n/(\partial \Phi)$, if the density at the magnetic surface is constant we can write

$$\Gamma(\Phi, t) = D(\Phi, t) \frac{\partial n}{\partial \Phi},$$

where

$$D(\Phi, t) \equiv (2\pi)^2 \oint r^2 B_p D_1 dl$$

is the surface diffusion coefficient.

Applying the continuity equation to a force tube of volume $dV = -U(\Phi)\, d\Phi$, where $U(\Phi) = \oint (dl/B_p)$, we find

$$U(\Phi)\frac{\partial n}{\partial t} = \frac{\partial}{\partial \Phi} D(\Phi,\ t)\frac{\partial n}{\partial \Phi}, \qquad (1)$$

the one-dimensional diffusion equation.[4]

The boundary conditions for Eq. (1) are the conditions $n = 0$ at the outer magnetic surface, Φ_9, and at the bounding magnetic surfaces, Φ_p(p = 5.8; Fig. 1a), which are tangent to the conductor surfaces. Figure 1 shows the magnetic surfaces for the case $k = 8$ (k is the number of rings on a single sphere). We see that, in addition to the outer separatrix the magnetic field has $k/2$ multiply connected separatrices passing through the null points of poloidal field B_p. Corresponding to these separtrices are the magnetic fluxes Φ_s(s = 1, 2, 3 and 4). At these values of Φ the magnetic-flux coordinate axis branches. Figure 1b illustrates the branching for the case $k = 8$. Here, the magnetic-flux axis, which begins at the outer magnetic surface Φ_9, branches at points Φ_s and ends at the magnetic surfaces Φ_p which are tangent to the conductors. At the branch points the continuity conditions for the particle density and flux must hold:

$$n_{ls}(\Phi_s,\ t) = n_{ms}(\Phi_s,\ t) = n_{ns}(\Phi_s,\ t);\ \Gamma_{ls} + \Gamma_{ms} + \Gamma_{ns} = 0,$$

where l, m, n run over the values corresponding to adjacent regions.

Accordingly, the problem of plasma diffusion in the trap is reduced to that of finding a common solution of a system of equations like (1), each of which describes diffusion in the gap of the magnetic-flux axis either between two neighboring branch points or between a branch point and a neighboring end point.

The local classical-diffusion coefficient of a magnetized plasma is known to be

$$D = \frac{\alpha + \beta n}{B^2};\ \alpha = \frac{m_e c^2}{e^2}\nu_{en}(T_i + ZT_e);\ \ \beta = \frac{m_e c^2 \nu_{ei}}{e^2 n}(T_i + ZT_e),$$

where T_e and T_i are the electron and ion temperatures, and ν_{ei} and ν_{en} are the rates at which electrons collide with ions and neutrals, respectively. Otherwise, the notation is standard. Below we assume that α and β are independent of magnetic flux Φ, i.e., we assume that the temperatures, the neutral density, the chemical composition, etc., are independent of the coordinates throughout the plasma.

After the equation for the diffusion coefficient is substituted into Eq. (1), the latter becomes

$$U(\Phi)\frac{\partial n}{\partial t} = \frac{\partial}{\partial \Phi}(1 + \lambda n) F(\Phi)\frac{\partial n}{\partial \Phi}, \qquad (2)$$

where

$$F(\Phi) = (2\pi)^2 \oint \frac{r^2 B_p}{B^2}\, dl.$$

Here, the density is given in arbitrary units n_0, the magnetic flux Φ is given in units of IR/c (I is the current in one of the inner rings and R is the radius of the inner sphere), and the time is given in units of $\vartheta_1 = I^2/\sigma c^2$. The single parameter, λ is the ratio of the rate at which electrons collide with ions at a density n_0 to the rate at which

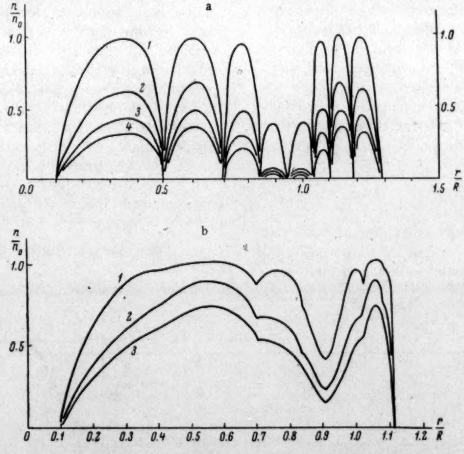

Fig. 2. a: Radial density distributions in the equatorial plane corresponding to various values of t/ϑ_2: 1) 0.05; 2) 0.40; 3) 0.80; 4) 1.25 (m = 0.7; the conductors are intersected by the separatrices $\Delta\Phi/\Phi_0 = -2$). b: Radial density distributions in the equatorial plane corresponding to various values of t/ϑ_2: 1) 0.05; 2) 0.30; 3) 0.60 (m = 0.7; between the sepratrices and the magnetic surfaces tangent to the conductors there is a magnetic-surface layer $\Delta\Phi/\Phi_0 = +3$).

electrons collide with neutrals: $\lambda = \nu^0_{el}/\nu_{en}$.

In two limiting cases – the case of a strongly ionized plasma, $\lambda n \gg 1$, and that of a weakly ionized plasma, $\lambda n \ll 1$, – we can incorporate all physical parameters (the density $\lambda n \gg \lambda$, the temperature, the current, etc.) into the time scale. (In the case $\lambda n \gg 1$ it is convenient to introduce the scale $\vartheta_2 = \vartheta_1/\lambda = I^2/\beta n_0 c^2$). Then the solution of Eq. (2) in these two cases is a function only of the arrangement of bounding surfaces and the nature of the functions, U(Φ), F(Φ), and F'(Φ).

The positions of the magnetic surfaces bounding the plasma are a function of the conductor diameter d. As this diameter is increased, the distance from the bounding surfaces to the inner separatrices, i.e., to the branch points of the magnetic-flux axis is reduced. If the conductor diamter is such that the separatrices are tangent to or intersect the conductors, system (2) can be broken up into individual segments (Fig. 1c).

The dimensionless functions U and F are independent of the current in the conductors and of the trap dimensions; they are governed completely by the field structure, i.e., by the arrangement of lines of force and the relative distribution of the magnetic field along these lines. In the present problem there are three parameters which govern the field structure: the number of rings on a sphere, k; the ratio of the radii of the spheres, μ; and the ratio of the currents in the rings in different spheres, m. Accordingly, the solution of system (2) is a function of the four parameters d, k, μ, and m.

System (2) with the initial condition n(Φ, 0) = 1 is solved on a computer by the method of finite differences; the values of U, F, and F' at the mesh points are determined by numerical integration along the lines of force. Because of the calculation times required we are not able to find solutions expressed as functional dependences of all four parameters, so we hold two of them (the number of rings and the ratio of the sphere radii) constant, at values approximately equal to the experimental values: k = 8 and μ = 1.25. Nevertheless, from the calculations which have been carried out we can draw certain conclusions regarding the behavior of the solution as a function of k and μ.

2. CALCULATED RESULTS

Most of the calculations have been carried out for the case of a fully ionized plasma. Figure 2 shows the radial density distributions in the equatorial plane of the trap,

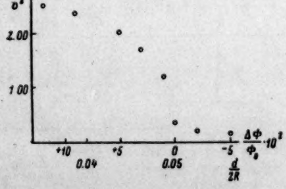

Fig. 3. Plasma lifetime as a function of the magnetic flux between the separatrix and the bounding magnetic surface.

TABLE 1. Relative Particle Loss at the Various Conductors and Through the Outer Magnetic Surface

	Conductor				
	1	2	3	4	outer surface
Flux gi (the separatrices intersect the conductor surface)	0.06	0.24	0.29	0.23	0.18
Flux gi (the separatrices do not intersect the conductor surfaces)	0.02	0.09	0.18	0.23	0.48

Note: see Fig. 1 for an explanation of the conductor designations.

n = n(r, t), obtained for various times from the solution of system (2), n(Φ, t), and from the calculated function Φ = Φ(r). The conductor diameters in Fig. 2a are such that the inner separatrices touch the conductor surfaces, and the trap volume is divided into four independent regions, at whose boundaries n = 0 is satisfied. In Fig. 2a the abscissas of the points with n = 0 are equal to the distances between the separatrices and the symmetry axis of the system in the equatorial plane. Because of the different diffusion lengths the plasma decay occurs at different rates in different gaps; the relative number of particles in the gap having the maximum diffusion length increases continuously in time, and the decay rate of the entire plasma approaches that of the plasma in this gap.

At smaller conductor diameters (Fig. 2b), i.e., when the conductors are "protected" by a layer of magnetic surfaces, the radial density distribution also has minima, but they are not as deep, and the depths fall off monotonically with increasing thickness of this layer.

Figure 3 shows the lifetime as a function of the conductor diameter, or, more precisely, as a function of the flux between the separatrices and the magnetic surfaces tangent to the conductors, ΔΦ. The flux is assumed to be negative if the separatrices intersect the conductor surfaces; it is assumed to vanish if the separatrices are tangent to the conductor surfaces; and it is assumed to be positive if the conductors are separated from the separatrices by a layer of magnetic surfaces. In our system, this is possible only if the conductor diameters are different, but the difference need not be great (no greater than 10%). The numbers below the abscissa show the relative conductor diameter of the ring nearest the equatorial plane of the trap.

We see that the lifetime is strongly influenced by the

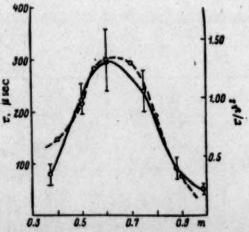

Fig. 4. Plasma lifetime as a function of the ratio of helix currents, m. Solid curve, left-hand scale) experimental;[3] dashed curve) calculated.

conductor diameter: It increases by about an order of magnitude as the diameter is reduced 25% from the value at which the separatrix is tangent to the conductor surface.

As the conductor diameter is reduced the particle loss decreases, as can be seen from Table 1, which shows the relative particle fluxes to the conductors and through the outer magnetic surface, $g_i = \Gamma_i/\Sigma\Gamma_i$.

The flux

$$\Gamma_i = \beta n_i F_i(\Phi) \frac{\Delta n_i}{\Delta\Phi_i}$$

is determined from the difference between the densities at the outer magnetic surface and the one adjacent to it, one step away from it on the flux mesh. When the corresponding separatrices intersect the conductor surfaces, most of the loss (82%) occurs at the conductors, and the loss of particles through the outer bounding magnetic surface is only 18%. Table 1 also shows the loss for the case of a minimum conductor diameter ($\Delta\Phi/\Phi_0 = +12$). In this case an appreciable loss occurs through the outer bounding magnetic surface (48%), while the loss at the conductors is 52%. These values remain essentially constant in time after the establishment of a diffusion density distribution.

Figure 4 shows the calculated plasma lifetime τ/ϑ_2 as a function of the current ratio m for a device with conductors tangent to the separatrices (dashed curve). In these calculations we take account of the functional dependence on m of the outer bounding magnetic surface: As the current ratio is reduced from the value at which a spherical separatrix exists in the two-helix device the separatrix in the model with rings becomes deformed and expands. At a certain value m_1 the separatrix begins to intersect the surface of the conductors on the outer sphere. As m is reduced further, other magnetic surfaces, under the separatrix, also begin to intersect the conductors. The outer bounding surface for the plasma in the case $m < m_1$ is a surface which is tangent to at least one conductor. Its position is determined by successive approximations, based on a check of the magnetic lines of force.

We see from Fig. 4 that as the current ratio is reduced the lifetime increases, reaching a maximum at m = 0.65, after which it decreases. We offer the following qualitative explanation for this behavior: At m = 0.9 the fields within the inner sphere and in the gap between the spheres are markedly different. For example with m = 0.9 for a device with k = 8 the field within the inner sphere is lower than that between the spheres[5] by a factor of 6–7. As the current ratio is reduced, i.e., as the current in the rings on the surface of the outer sphere is reduced, the field within the inner sphere increases, while that in the gap between the spheres decreases. When m = 0.65 the fields become equal, and the device becomes "uniformly stable" with respect to local diffusion loss. At this point the lifetime reaches a maximum. A further decrease leads to an expansion of the separatrix, which begins to intersect conductors on the outer sphere (see ref. 2, especially the figures there). The result is a decrease in the diffusion length. The field in the gap between spheres becomes weaker than that within the inner sphere, and the two factors reduce the lifetime.

On the basis of these functional dependences of the plasma lifetime on the current ratio and conductor diameter we can also draw certain conclusions regarding the lifetime as a function of the number of rings k and the ratio of the sphere radii, μ.

The lifetime $\tau \sim L^2H^2$ should apparently be a weak function of k, at least for devices with relatively thick conductors, since $H \sim k$, while the diffusion length $L \cong R/k$, where R is the radius of the device.

The functional dependence of the lifetime on μ should apparently be similar to that on the current ratio m. At μ = 1.25 and m = 0.9, the field within the inner sphere is weaker than that in the gap between the spheres. As μ, is increased, i.e., as the radius of the outer sphere is increased, these fields become equal, and eventually the field in the gap between the spheres becomes weaker than that within the inner sphere. There is some basis for assuming that the lifetime reaches a maximum when the fields are equal as in the case of the functional dependence on m.

It is interesting to determine the values of m and μ for which the device has both a spherical separatrix and a maximum lifetime with respect to classical diffusion. A spherical separatrix exists if m and μ satisfy[6] $m = \mu^{-1/2}$. Approximate equality of the fields within the inner sphere and in the gap between the spheres leads to[1,2] $8/(\mu - 1) = \pi k(1 - m/\mu)$. From these conditions we can find m and μ for a specified value of k. For example, of the devices with k = 8 the best is that with μ = 1.6 and m = 0.7. Accordingly, if the intention is to achieve longer diffusion times experimentally (usually, μ = 1.25 and m = 0.9), and if the radius of the inner sphere is specified, the outer radius should be increased.

3. COMPARISON OF THE CALCULATED RESULTS WITH EXPERIMENTAL DATA

Confinement experiments[3] have been carried out with two devices whose parameters are shown in Table 2. These devices differ in the dimensions, thickness, and currents of the conductors. In each case the device is filled with plasma through a discharge between an electrode inserted into the trap near one pole and a conductor of the inner helix near the other pole. During the plasma decay the density is determined by means of a microwave interferometer ($\lambda = 10.8$ mm, $n_{cr} = 10^{13}$ cm^{-3}). Functional dependences of the density and the time are found for various conditions and used to calculate the lifetime $\tau = d \ln n/dt$

TABLE 2.

	Variant	
	1	2
Number of helix turns, k	9	9
Radius of inner helix, R, cm	8	12.5
Ratio of the radii of the outer and inner helices $\mu = R_1/R$	1.25	1.25
Conductor radius r, cm	0.4	0.5
Relative conductor radius, r/R	0.05	0.04
Maxwell current in inner helix, I_{max}, kA	4.1	7.5
H_2 pressure before breakdown, torr	10^{-5}—10^{-3}	$1 \cdot 10^{-4}$

as a function of: 1) the initial H_2 pressure in the chamber, 2) the magnetic field (i.e., the current in the helices), and 3) the ratio of the currents in the helices (see ref. 3, especially the curves there and Figs. 4 and 5).

Considerably less information has been obtained about the electron and ion temperatures. The electron temperature is determined from the conductivity at the end of the active cycle and is of the order of 3-5 eV. Furthermore, during the plasma decay, more precisely, at the point at which the microwave signal is cutoff, probe measurements are carried out in trap No. 1. The electron temperature turns out to be $T_e = 1.5\text{-}1.2$ eV some 100-150 μsec after the end of the active cycle. In trap No. 2 the electron temperature is determined at the cutoff time from the relative intensity of the hydrogen Balmer lines. The temperature was found to be $T_e = 3$ eV. No reliable information has been obtained about the ion temperature T_i.

Most of the experiments carried out to determine the lifetime for various physical conditions are carried out at $n = 10^{12}$ cm^{-3} during the plasma decay. This density level is reached some 150-200 μsec after the end of the active cycle. Other plasma parameters (T_e, T_i, n_0) are not determined at these times, but we can estimate them on the basis of the available data.

An electron temperature of 1 eV is found by extrapolating the measured values for the time interval 100-150 μsec.

The density of neutrals, n_0, during the plasma decay is assumed to be equal to the density before breakdown (usually, $n_0 = 3 \cdot 10^{13}$ cm^{-3}). Because of the relatively large volume of the chamber and because the mean free path of the neutrals with respect to dissociation and ionization is considerably longer than the characteristic plasma dimensions under the conditions $T_e \leq 3\text{-}5$ eV and $n^+ \leq 10^{14}$ cm^{-3}, estimates show the relative density change is $\Delta n_0/n_0 \ll 1$.

An estimate of the ion temperature T_i can be found from the energy balance and by comparing the characteristic times for energy transfer from electrons to ions, τ_i, and from ions to the neutrals. With $T_e \cong T_i \cong 1$ eV we have[1]) $\tau_i \cong 7 \cdot 10^{-5}$ sec and $\tau_{tra} \cong 3 \cdot 10^{-6}$ sec. Accordingly, the plasma ions must be much cooler than the electrons, at a temperature approximately equal to that of the neutrals. For subsequent estimates we assume $T_i \cong 0.2$ eV.

Several assumptions are used in the derivation of the equations describing classical diffusion and in the calculations. We will now show that these assumptions are justified in the real plasma of ref. 3.

Estimates show that the inequality $\nu_{ei} > \nu_{en}$ is satisfied in the plasma; this inequality also follows from the shape of the decay curves, according to which the decay constant is a function of the density.

In the calculations the plasma is assumed to be magnetized, i.e., the assumption $\nu_{ei}\nu_{en}/\omega_e\omega_i \ll 1$ is used. This condition is satisfied if the current satisfies the inequality $10^2\ \mathrm{A} \ll \mathrm{I}$.

The equations describing classical diffusion are applicable if the conditions $l_\perp \gg \rho_i$ and $l_\perp \gg \rho_i(\nu_{ei}/\omega_e)(\lambda + T_e/T_i)$ are satisfied, where $l_\perp = |n/\nabla n|$ and ρ_i is the ion Larmor radius. The first condition is the more stringent since the factor $(\nu_{ei}/\omega_e)(1 + T_e/T_i)$ is considerably smaller than unity under the experimental conditions ($\nu_{ei} \cong 3 \cdot 10^6$ sec^{-1}, $\omega_e \cong 1 \cdot 10^{10}$ sec^{-1}, $T_e \cong 1$ and $T_i \cong 0.2$ eV). A lower estimate on the characteristic length for changes in the density, $l_\perp$, can be found from the radial density distribution in Fig. 2a. For the case of the least favorable density distribution, in which the modulation depth of the distribution is nearly 100% in the central region of the device, we have $l_\perp = R/k$, where k is the number of rings on a single sphere. In the central region of the device and in the gap between the spheres, the values of $l_\perp$ are 1 and 0.1 cm, respectively, while the ion Larmor radii are 0.1 and 0.01 cm. Accordingly, the inequality $l_\perp \gg \rho_i$ is satisfied in these regions, except near singularities of the poloidal field, where the opposite inequality $l_\perp < \rho_i$, in fact seems to hold. However, the volume over which this latter inequality holds is much smaller than the plasma volume; hence we can neglect the influence of the processes which occur in these less extensive regions on the decay mechanism for the plasma as a whole.

The principal distinction between the Tornado device and the model adopted for the calculations is that there are no magnetic surfaces in the actual device. Therefore, the density should be leveled off not only as a result of diffusion but also as a result of the motion of macroscopic plasma volumes along lines of force, in the direction opposite that of $\nabla_\parallel p$. The characteristic lifetimes in this case are of order $L[m_i/(T_e + T_i)^{1/2}]$, where L/R is the length over which the pressure falls to zero. The average length of the lines of force, L/R, is of order 10^3-10^4 in a device with infinitesimally thin conductors in the case m = 1 (i.e., when there is no separatrix).[2] In this case the characteristic times are of order 10^{-2}-10^{-1} sec (R = 10 cm) under the experimental conditions. In a device with conductors of finite thickness, the lines of force have a smaller average length, since they intersect the conductors. Nevertheless, the average length and the characteristic time are apparently of the same order of magnitude in this case, since the conductors are intersected repeatedly by given lines of force[5] belonging to the surface layer itself. The transit lifetimes found are much longer than the diffusion lifetimes, so the presence or absence of precise magnetic surfaces is not important; from this standpoint the behavior of the plasma in the model should be essentially the same as that in the device.

In the calculations it is also assumed that the density is the same over an entire magnetic surface and that the temperature and density ot the neutral are the same throughout the plasma. The first condition implies that the density does not vary appreciably over a single revolution of a line of force around a system. This is the case if at least one of the inequalities λ_i, $\lambda_e < l_\parallel$ is satisfied, where $l_\parallel = H/|\Delta_\parallel H|$ is the characteristic dimension of the inhomogeneities in the magnetic field and λ_e and λ_i are the electron and ion mean free paths. Under the experimental conditions these values are $\lambda_e \cong 10$ cm, $\lambda_i \cong 0.2$ cm, and $l_\parallel \cong 1$ cm. Furthermore, the adiabatic condition for the particle motion is not satisfied near the singularities of the poloidal field, i.e., $\rho_i|\nabla H|/H > 1$. Again the result is a tendency for the density to become constant along a line of force. The density of neutrals

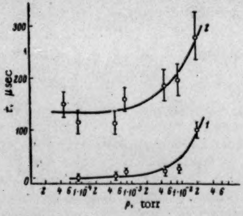

Fig. 5. Plasma lifetime as a function of the neutral pressure in trap No. 1. 1) H = 0; 2) H = H_{max} = 1300 Oe (this curve is from ref. 3).

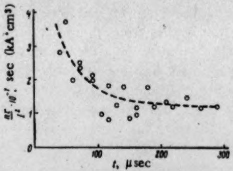

Fig. 6. The quantity $\tau_0 T_e^{1/2} = kn\tau / I^2$ as a function of the time elapsed since the end of the active cycle.

is apparently constant over the plasma volume, since the mean free path of the neutrals with respect to charge exchange and ionization is much longer than the characteristic dimensions of the plasma formation at $n = 10^{12}$ cm^{-3}. It follows that the ion and electron temperatures are also approximately constant over the plasma volume, if we assume that the energy loss of the ions is governed by charge exchange, and that the electrons lose energy as a result of collisions with ions.

Accordingly, the assumptions used in these calculations are justified and it is legitimate to compare the calculated and experimental results, even though the actual Tornado trap and its model differ radically in field structure.

The plasma lifetime is given by

$$\tau\,(\mathrm{sec}) = \vartheta_2\tau_0 = 4.5\cdot 10^7\tau_0 \frac{I^2\,(\mathrm{kA})\,T_e^{1/2}\,(\mathrm{eV})}{n\,(\mathrm{cm}^{-3})}, \tag{3}$$

where τ_0 is a dimensionless time, ϑ_r is the time scale, and I is the current in the inner helix. It follows from Eq. (3) that the lifetime is proportional to the square of the current, i.e., to the square of the field, and inversely proportional to the density. Experimentally the lifetime is found to be a quadratic function of the field and is found to increase with decreasing density (see the curves in ref. 3). The dimensionless time τ_0 is a function of the field structure and, in particular, of the ratio of the currents in the helices. Figure 4 shows the experimental and calculated functional dependences of the lifetime τ on the current ratio m. The calculated curve is normalized to the experimental curve at m = 0.6. These curves coincide within the experimental errors.

The only experimental curve which cannot be explained on the basis of transverse diffusion is that showing the lifetime as a function of the neutral pressure (Fig. 5). At $p \lessapprox 5\cdot 10^{-3}$ torr the lifetime is independent of the pressure, but as the pressure is increased from $5\cdot 10^{-3}$ to $2\cdot 10^{-2}$ torr it increases by a factor of about 2-3. In the case of transverse diffusion the behavior of the function $\tau(p)$ should be just the opposite, since an increase in the pressure would be accompanied by an increase in the rate of collisions, both because of an increase in the number of neutrals and because of a possible decrease in T_e. However, we note that the curves in Fig. 5 for H = 0 and H ≠ 0 begin to arise at approximately the same pressure. In the case H = 0 the lifetime increases because the plasma decay acquires a diffusion nature (at $p \cong 5\cdot 10^{-3}$ torr, we would have $\lambda_{in} \cong R$). It is natural to assume that even in the case H ≠ 0 longitudinal diffusion will begin to play a decisive role at $p > 5\cdot 10^{-3}$ torr. In particular, for devices in which the density distribution is deeply modulated (Fig. 2a), the appearance of an appreciable number of neutrals can alter the loss mechanism at the conductors, from a drift mechanism along the lines of force to a diffusion mechanism in the longitudinal direction. In turn, there is a decrease in the modulation depth of the density distribution, a decrease in the density gradients, and an increase in the lifetime. This effect is noticeable if the characteristic time for particle transport across the magnetic field is comparable to that for particle transport along the lines of force over a length of the order of the device radius. From the curves in Fig. 5 we find $\tau(H \neq 0, p < 5\cdot 10^{-3}$ torr$) \cong \tau(H = 0, p = 2\cdot 10^{-2})$, so it is physically plausible to conclude that an increase in the lifetime by a factor of 2-3 upon a pressure change from $5\cdot 10^{-3}$ to $2\cdot 10^{-2}$ torr is in fact cause by this mechanism. We thus conclude that there is a qualitative agreement between the calculated and experimental results.

A quantitative comparison of the results runs into certain difficulties: There is the familiar uncertainty regarding the magnitude of the electron temperature, and there is an uncertainty regarding the value of τ_0 for real helical devices. However, if we assume τ_0 to be the same as for models having the same relative conductor radius v/R, we find that the calculations yield lifetimes of $\tau = 5\cdot 10^{-3}$ and $7\cdot 10^{-4}$ sec for the larger and the smaller device respectively (I = 7.5, 4 kA; τ_0 = 2.5, 1.0), with m = 0.6, T_e = 1 eV, and $n = 1\cdot 10^{-2}$ cm^{-3}. The experimental lifetimes for the same conditions are $\tau = 8\cdot 10^{-4}$ and $3\cdot 10^{-4}$ sec, respectively, for the larger and smaller devices. Accordingly, we find extremely satisfactory agreement between the calculated and experimental values of τ.

If we assume that the assumption of a diffusion mechanism for the experimental plasma decay is now justified, we can determine the temperature as a function of the time and the parameter τ_0.

Figure 6 shows the quantity $\tau_0 T_e^{1/2} = n\tau/I^2$ as a function of the time for the smaller device, plotted from the experimental values of n, τ and I. The active cycle ends at time t = 0; at this time $T_e \cong$ 3-5 eV. One hundred microseconds after the end of the discharge $\tau_0 T_e^{1/2}$ has fallen by a factor of about 3, corresponding to a decrease in T_e to 0.3-0.5 eV. Over the next 200 μsec the changes in $\tau_0 T_e^{1/2}$ do not exceed 20-30%. If we assume T_e = 0.3-0.5 eV, we find τ_0 = 0.5-0.6.

A density level of 10^{12} cm^{-3} is generally reached experimentally 100-150 μsec after the end of the active cycle. If we assume that at this time T_e is not 1 eV, but, as follows from Fig. 6, smaller by a factor of 2-3, we find an even better agreement between the calculated and experimental results for τ (the calculated values are $\tau = 3 \cdot 10^{-3}$ and $4 \cdot 10^{-4}$ sec, and the experimental values are $\tau = 8 \cdot 10^{-4}$ and $3 \cdot 10^{-4}$ sec for the larger and smaller traps, respectively).

Accordingly, one result of these plasma-diffusion calculations is a justification for the argument that the plasma decay under the experimental conditions is governed either by neoclassical transverse diffusion or by so-called pseudoclassical diffusion.[7] During the plasma decay the conditions throughout the trap (except near the singularities) are such that the ratio of the local Bohm and classical diffusion coefficients is $D_B/D_c = eH(16\nu_{ei} m_s c)^{-1} > 1$. Accordingly, with $n \cong 10^{12}$ cm^{-3} and $T_e \cong 0.5$ eV, and at the maximum current, this ratio varies from 3 to 30 from point to point in the trap.

---

[1] The degree of dissociation of the hydrogen molecules is assumed to be nearly 100%.

---

[1] A. N. Kozyrev, B. P. Peregud, and Z. V. Fedichkina, Zh. Tekh. Fiz., 42, 2466 (1972) [Sov. Phys. – Tech. Phys., 17, 1923 (1973)].
[2] A. N. Kozyrev, V. M. Kuznetsov, B. P. Peregud, and Z. V. Fedichkina, Zh. Tekh. Fiz., 41, 2305 (1971) [Sov. Phys. – Tech. Phys., 16, 1830 (1972)].
[3] G. A. Galechyan and B. P. Peregud, Zh. Tekh. Fiz., 39, 1696 (1969) [Sov. Phys. – Tech. Phys., 14, 1272 (1970)]. Preprint, Physicotechnical Institute, 1969; G. A. Galechan, G. V. Vorb'ev (Vorobjev), and B. P. Peregud (Peregood), Third European Conference on Controlled Fusion and Plasma Physics, Utrecht, 1969.
[4] G. D. Hobbs and J. B. Taylor, Plasma Phys., 10, 207 (1968).
[5] A. N. Kozyrev and B. P. Peregud, Zh. Tekh. Fiz., 40, 950 (1970) [Sov. Phys. – Tech. Phys., 15, 734 (1970)].
[6] B. P. Peregud and A. A. Semenov, Zh. Tekh. Fiz., 41, 2297 (1971) [Sov. Phys. – Tech. Phys., 16, 1824 (1972)].
[7] S. Yoshikawa, Phys. Fluids, 13, 2300 (1970).

Electron density in an argon afterglow

O. P. Bochkova, R. I. Lyagushchenko, É. A. Sukiasyan, and Yu. A. Tolmachev

A. A. Zhdanov Leningrad University

(Submitted April 12, 1973)
Zh. Tekh. Fiz., 44, 754-758 (April 1974)

A probe-pulse method is used to measure the electron density in the afterglow of a dc discharge in argon at pressures of 0.3-2.5 mm Hg and currents of 30 and 50 mA. An approximate calculation is given for the time rate of change of the electron temperature and the electron density in the argon afterglow. The experimental results are compared with theory.

In the present paper, the electron density is determined in the early afterglow of a dc discharge in argon. The probe-pulse method described in ref. 1 is used to determine the electron density in the decaying plasma of a pulsed electric discharge in helium.

A voltage pulse of amplitude and length such that it does not produce ionization, either direct or stepwise, is applied to the electrodes of the discharge tube after termination of the discharge at some time during the afterglow. The current flowing through the gap during the pulse depends on the number of charged particles remaining in the volume at the given time.

The value of the electron density $\bar{n}_e$ averaged over the volume is related to the current I during the pulse by

$$\bar{n}_e = \frac{I}{e\bar{v}\pi R^2}, \tag{1}$$

where $\bar{v}$ is the electron drift velocity and R is the radius of the discharge tube. The electron drift velocity is a function of the ratio of the field voltage E to the gas pressure p. The experimental relation $\bar{v} = \bar{v}(E/p)$ is given in ref. 2 for argon.

A schematic diagram of the experimental arrangement is given in Fig. 1. The probe voltage pulse is supplied to the electrodes of the 35 mm diameter tube from the delay circuit of a G5-7A generator. The pulse current is measured on the oscilloscope using the voltage drop across the resistance R_2. The field voltage is also measured on the oscilloscope by using two probes placed on the tube axis with a separation of 11 cm.

The length of the probe pulse must be sufficient to establish a value of the electron density corresponding to E/p. This requirement is not very severe for argon: In the range of E/p values of interest the electron drift velocity varies slowly. On the other hand, the variation in electron density should be negligible during the probe pulse. We use a 10 μsec pulse.

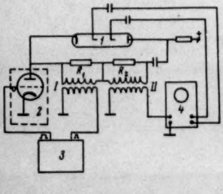

Fig. 1. Experimental arrangement. 1) Discharge tube; 2) circuit for termination of the discharge; 3) G5-7A generator; 4) S1-17 double-beam oscilloscope; I, II) transformers; R_1, R_2) resistances.

In the argon afterglow the electron temperature drops to the atomic temperature in a time of the order of milliseconds. The probe pulse is applied in a way that ensures that the electron temperature is determined by this field, and is of the order of 10,000°K.

According to ref. 3, the electron temperature in argon is related to E/p by

$$T_e = 3.65 \cdot 10^4 \sqrt{\frac{E}{p}} \tag{2}$$

where E is in V/cm and p in mm Hg.

In the experiment, E/p is of the order of 0.2 V/cm · mm Hg and $T_e = 16{,}300$°K.

The increase in electron temperature during the pulse should lead, on the one hand, to an increase in electron density due to ionization, and on the other, to a decrease in n_e due to the increasing rate of electron diffusion to the tube walls. The relative variation in electron density during the pulse is determined by

$$\frac{\Delta n_e}{n_e} = 1 - \exp\left(-\frac{1}{\tau_D} + z_0\right)\tau\,(\mathrm{pul}) = 1 - \exp\left\{-\frac{1}{\tau_D} + \sqrt{\frac{8kT_e}{\pi m}}\left[n_m q_{mi} \exp\left(-\frac{\varepsilon_i - \varepsilon_m}{kT_e}\right) + n_0 q_{0i} \exp\left(-\frac{\varepsilon_i}{kT_e}\right)\right]\right\}\tau_{\mathrm{pul}}, \tag{3}$$

where τ_D is the diffusion time for charged particles, z_0 is the number of ionization events produced by one electron per unit time, q_{mi} and q_{0i} are average cross sections for stepwise and direct ionization, ε_i is the ionization energy of a normal atom, ε_m is the excitation energy of a metastable atom, and n_m and n_0 are the densities of metastable and normal atoms.

Under our conditions $n_0 = 3.2 \cdot 10^{16}\ \mathrm{cm}^{-3}$, $n_m = 2 \cdot 10^{11}\ \mathrm{cm}^{-3}$, $T_e = 16{,}300$°K, $\tau_{\mathrm{pul}} = 10^{-5}$ sec, and $\tau_D = 3.1 \cdot 10^{-4}$ sec. Since $q_{0i} = 10^{-17}\ \mathrm{cm}^2$ and $q_{mi} = 10^{-15}\ \mathrm{cm}^2$, we find that $(\Delta n_e)/n_e \simeq 2\%$.

It can be seen that an increase in electron temperature during the pulse up to 16,300°K has a negligible effect on the electron density during the pulse.

The electron densities averaged over the volume are found experimentally at different times in the afterglow for pressures of 0.3, 0.55, 0.73, 1.0, and 2.5 mm Hg and currents of 30 and 50 mA for each pressure. Figure 2 gives experimental curves for the drop in electron density during the afterglow for three pressures and currents of 30 and 50 mA for each pressure. In this figure the electron densities in the discharge at p = 0.73 mm Hg and currents of 30 and 50 mA are measured using two probes.

The agreement between the values of the electron density in the discharge and in the early afterglow for the same pressure and current is satisfactory.

The curves for the drop in electron density are reproduced to within 5-10%. Systematic errors are the main cause of experimental error, which is of the order of 30-35%.

Under the experimental conditions the charged particles are lost as a result of ambipolar diffusion to the walls of the discharge tube; this is confirmed by the nature of the drop in electron density during the afterglow.

The diffusion time of particles to the walls is determined by $\tau_D = \Lambda^2/D_a$, where Λ is the characteristic diffusion length and D_a is the coefficient of ambipolar diffusion. Under our conditions $\Lambda^2 = 0.53\ \mathrm{cm}^2$. If we use the data of ref. 2 for the argon ion mobility, then

$$D_a = \frac{1220}{p} U_e, \tag{4}$$

where U_e is the electron temperature in volts.

Under our conditions $\tau_D = 0.53\ p/1220\ U_e$ ranges from 50-650 μsec in the discharge. Thus, when p = 0.73 mm Hg and i = 50 mA, $\tau_D = 160$ μsec in the discharge.

If the electron temperature does not decrease with time during the afterglow, assuming that the charged particles are lost only as a result of ambipolar diffusion, the drop in electron density during the afterglow must occur exponentially with a damping constant equal to τ_D. It can be seen from Fig. 3 that there is a slower drop in the electron density. This deviation is due to the fact that the electron temperature decreases with time during the afterglow and, consequently, the diffusion time increases.

We consider an approximate theoretical calculation for the time rate of change of the electron temperature and density after termination of the discharge for the given initial conditions.

The behavior of the electron density is determined by the electron energy balance equation, which can be written

$$\frac{d}{dt}\left(\frac{3}{2}kT_e\right) = e\bar{v}E - \delta_{\mathrm{eff}}\,\nu_{\mathrm{eff}}(T_e)\frac{3}{2}k(T_e - T_a), \tag{5}$$

where $\bar{v}$ is the electron drift velocity, E is the field voltage, $\nu_{\mathrm{eff}}(T_e)$ is the effective collision frequency dependent on the electron energy, $\delta_{\mathrm{eff}} = 2\ m/M$ is the energy lost by an electron in a collision with an atom, m and M are the electron and atomic masses, and T_a is the atomic temperature.

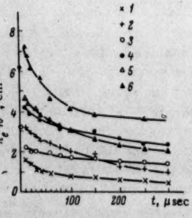

Fig. 2. Drop in electron density during the afterglow of an argon discharge. p in mm Hg: 1, 2) 0.55; 3, 4) 0.73; 5, 6) 2.5. i in mA: 1, 3, 5) 30; 2, 4, 6) 50.

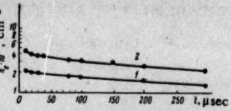

Fig. 3. Drop in electron density on a semilogarithmic scale for p = 0.73 mm Hg. i in mA: 1) 30; 2) 50.

The variation in electron temperature as a function of time during the alterglow can be obtained by solving Eq. (5) with E = 0.

To calculate the effective collision frequency as a function of the electron energy it is necessary to know the dependence of the transport cross section for electron scattering by argon atoms on the electron energy and to allow for the electron energy distribution

$$\nu_{\mathrm{eff}} = \frac{\langle q(\varepsilon)\, n_a v \varepsilon \rangle}{\frac{3}{2}kT_e},$$

where $q(\varepsilon)$ is the transport cross section for electron scattering by atoms, n_a is the atomic density, v is the electron velocity, and ε is the electron energy. In argon $q(\varepsilon)$ differs little from the total cross section for elastic scattering. Graphs of the experimental dependence of these cross sections on the electron energy are given in ref. 2, as is the dependence of the cross section P_c on $(V)^{1/2}$ in argon. The cross section P_c is related to the total elastic scattering cross section by $P_c = 3.53 \cdot 10^{16} q$. A good approximation of the dependence of P_c on V is given by

$$P_c = 35e^{-40V} + 6V.$$

The first term is significant only when V < 0.2 volts; therefore, the following simple approximation can be used:

$$P_c = 6V.$$

Solving Eq. (5) for E = 0, we obtain the following time dependence of the electron temperature during the afterglow:

$$U_e(t) = \frac{U_e(0)}{\left(6 \cdot 10^4 p U_e^{3/2}(0)\, t + 1\right)^{2/3}}, \tag{6}$$

where U_e is the electron temperature in volts and $U_e(0)$ is the electron temperature during the discharge.

Equation (6) is obtained by assuming that $U_e \gg U_a$, where U_a is the atomic temperature in volts.

When p = 0.73 mm Hg and i = 50 mA, $U_e(0) \approx 2$ V. 10 μsec after termination of the discharge, $U_e = 1.18$ V, which corresponds to 13,700°K; after 50 μsec, $U_e = 0.54$ V or $T_e = 6300$°K; after 200 μsec, $U_e = 0.245$ V or $T_e = 2800$°K. The electron temperature falls by a factor of e after ~ 15 μsec.

If the charged particles are lost during the afterglow as a result of ambipolar diffusion, the electron density varies with time as

$$n_e(t) = n_e(0)\exp\left(-\frac{1}{\Lambda^2}\int\limits_0^t D_a(t)\,dt\right)$$

or, according to (4),

$$n_e(t) = n_e(0)\exp\left(-\frac{1220}{\Lambda^2 p}\int\limits_0^t U_e(t)\,dt\right). \tag{7}$$

We substitute $U_e(t)$ into (7) according to (6) and after integrating we get

$$n_e(t) = n_e(0)\exp\left\{\frac{0.061}{\Lambda^2 p^2\sqrt{U_e(0)}}\left[(6\cdot 10^4 p U_e^{3/2}(0)\,t + 1)^{1/3} - 1\right]\right\}. \tag{8}$$

According to Eq. (8), the drop in electron density during the afterglow of a discharge in argon should occur more slowly than is observed in experiment. Thus, when p = 0.73 mm Hg, the electron density from 10 μsec after termination of the discharge to 300 μsec decreases in the experiment by factors of 1.95 and 1.57 for currents of 50 and 30 mA, respectively, but according to the calculation, n_e falls by a factor of 1.43 during this time.

The discrepancy can be explained both by the approximate nature of the theoretical premises and the possible distortion of the experimental results due to induction.

The authors thank S. É. Frish for discussion of the results.

---

[1] G. N. Gerasimov, R. I. Lyagushchenko, and G. P. Startsev, Opt. Spektrosk., 30, 606 (1971).

[2] S. C. Brown, Basic Data of Plasma Physics, MIT Press, Cambridge, Mass. (1959).

[3] Yu. B. Golubovskii (Golubowski), Yu. M. Kagan, and R. I. Lyagushchenko (Ljagustschenko), Plasma Physik, B10, 427 (1970).

Supersonic plasma jet from a high-power pulsed discharge

M. A. Sultanov

V. I. Lenin Tadzhik University, Dushanbe

(Submitted December 18, 1972)
Zh. Tekh. Fiz., 44, 759-765 (April 1974)

The structure of a single, spatially isolated plasma jet is investigated using a discharge chamber with a cylindrical aperture. A high-power pulsed discharge is used with different parameters for the electric discharge circuit and the diameter of the exit aperture. Under certain conditions (low capacitance and low voltage) a periodic flow of gas from the nozzle is observed in the plasma jet structure under conditions corresponding to a supercritical pressure drop for continuous flow. Different discharge conditions are investigated, the basic parameters of the jet are determined, and an analogy is shown with gasdynamic processes in air at atmospheric pressure.

The structure of the supersonic plasma jet (SPJ) has been investigated in a large number of papers. For example, the hydrodynamic nature of the flow of electrode jets into the discharge gap in a pulsed discharge was first pointed out in ref. 1, and the formation of dark spaces near the electrodes was first discussed in ref. 2. Other authors[3-6] point out the intermittent nature of the flow of electrode material and discuss the formation of the periodic structure.[7-9]

In our view, continuation of research in this direction is of interest to those studying shock-compressed plasma regions produced by the collision of two plasma[10-12] or laser[13-15] jets, those investigating the mechanism for erosion of different solids due to an SPJ,[16-18] and others. Moreover, the study of these jets is of independent interest and also provides additional information on the mechanism for the flow of the electrode material into a discharge.

Certain data given in the present paper indicate that the formation of plasma jets under supersonic conditions is of an intermittent nature. Moreover, there is an analogy between the processes that occur in the flow of a gas from a nozzle with a supercritical pressure drop in air at atmospheric pressure and those in the flow of the plasma jets of a high-power pulsed discharge from a discharge chamber with a cylindrical aperture in air at atmospheric pressure.

The SPJ is produced by the arrangement of electrodes and discharge chamber shown in Fig. 1. The arrangement produces jets with different energy densities and velocities, depending on the diameter of the discharge chamber and the parameters of the discharge circuit. In the present investigation we consider more than 40 regimes for producing plasma jets, varying the capacity of the bank of pulsed capacitors (the capacity ranges from 200-1200 μF in steps of 100 μF), the voltage (0.25-3 kV), and the diameter of the exhaust aperture (3.0-4.8 mm).

Typical time scans and frame photographs are shown in Fig. 2. The photographs are obtained on an SFR-2M streak camera with a scan rate of 1-25 $\cdot$ 10^3 m/sec and a framing rate of 1.25 $\cdot$ 10^5 frames/sec.

The photographs indicate that the plasma jet issuing from the aperture is axially inhomogeneous. Periodic variations in the brightness are evident (Fig. 2a), especially in the center of the pulse (the streak frame in Fig. 2c corresponds to the discharge conditions with continuous scan in Fig. 2a).

The periodic structure of the jet has been noted earlier in refs. 7 and 9, which show that it is due to the formation of compressive shocks. The detailed analysis of the jet structure undertaken in the present paper indicates that the jets exhibit all the basic characteristics of a continuous gas stream flowing from a nozzle with supersonic velocity with a supercritical pressure drop into a motionless medium. For comparison, a Schlieren photograph of the flow of air from a nozzle with a supercritical pressure drop taken from ref. 19 (there is a fourfold drop in pressure at the mouth of the nozzle) is shown in Fig. 2d.

The streak photographs indicate that near the washer surface there is a weakly luminous region similar to a dark cathode space.[1,2,8] It is characteristic that in our case a dark space is observed both for negative and positive polarity of the original electrode. Beyond the dark space there is a separate sharp boundary of an intensely luminous region. Moreover, some of the streak photographs show inclined bands whose formation is evidently due to oscillations in the density of the vapor issuing from the electrode. These oscillations, at a frequency of approximately 5 $\cdot$ 10^5 Hz, determine the fine time structure of the jet, whose formation is not considered in the present paper. Under certain conditions bands can be observed on the negatives not only in the intensity luminous region but also in the dark space. Consideration of these streak photographs indicates that at the boundary between

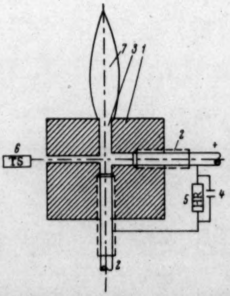

Fig. 1. Schematic diagram of the discharge chamber and the position of the electrodes for producing an individual, spatially separate supersonic jet. 1) Dielectric cube; 2) metallic electrodes; 3) cylindrical channel for ejection of the plasma flow; 4) bank of pulsed capacitors; 5) high-voltage rectifier; 6) triggering system; 7) free jet.

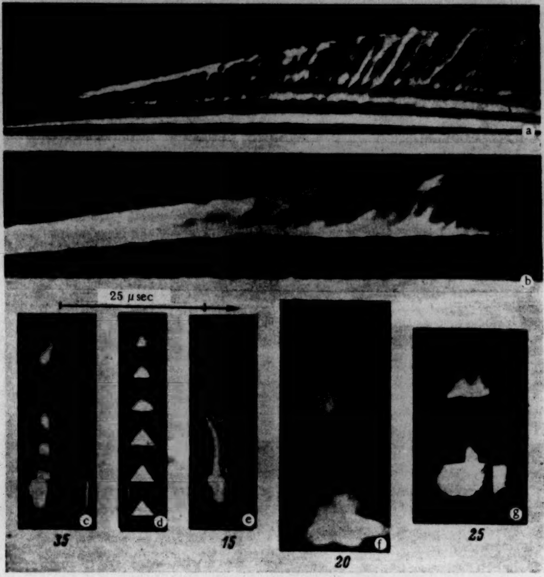

Fig. 2. Time scans (a, b), frames of high-speed film (c, e, f, g) of supersonic plasma jets, and a Schlieren photograph of gas flow from the nozzle under conditions of a supercritical pressure drop (d). Discharge circuit: C = 400 μF and U = 0.25 kV (a, c, e); C = 200 μF and U = 2 kV (b); C = 200 μF and U = 6 kV (f); C = 300 μF and U = 3 kV (g).

the dark and light spaces there is a break in the bands toward the side of smaller inclination. This indicates a shock-like decrease in the jet (vapor) velocity in this region. With more powerful discharge conditions (C = 300 μF and U = 2 kV) the vapor velocity in the dark space region is 6-7 km/sec and in the intensely luminous region it is 1.5-2 km/sec (Fig. 2b). In the present case, the period structure disappears, i.e., with a more powerful discharge the compressive jump moves away from the washer. The same pattern is observed in the frames of high-speed scanning for a discharge circuit with C = 200 μF and U = 6 kV (Fig. 2f) and C = 400 μF and U = 3 kV (Fig. 2g). With a stronger discharge the compression region moves comparatively far away, and the streak photographs record only one compressive jump.

A plasma jet structure similar to that described above is also observed in refs. 3 and 7 for an electrical discharge in a closed volume and a plasma flow from a small aperture. The authors show that the boundary between the dark and light spaces is a shock wave generated by a supersonic jet flow into a motionless medium. The supersonic flow of the vapor of the electrode material and the shock-like decrease in velocity in the jet of a pulsed discharge shows that the boundary between the regions of different intensity is a shock wave.

Shock waves are formed in jets flowing from nozzles when the pressure inside the nozzle is much greater than the pressure in the ambient atmosphere. When the pressure inside the nozzle declines, the shock wave should acquire a quasistationary structure. In the jets of a pulsed discharge, a similar structure is sometimes observed in the final stages of the pulses when the energy density at the electrodes, and consequently the vapor pressure in the zone damaged by the discharge, substantially changes their surfaces.

Thus, when vaporized material flows from an electrode with an insulating washer a jet structure is observed which is similar to that for the supersonic flow of a plasma from a nozzle. Extending the analogy, one can assume that region of contact between the discharge and the electrode surface has the properties of a reservoir in which the pressure exceeds the atmospheric pressure appreciably. The flow of the electrode material is similar to a supersonic plasma flow, and the jet is a supersonic plasma stream.

An extremely important feature is the fact that the jet structure does not exhibit random changes during the pulse, as is the case for discharges between open electrodes.[20] There is some a change of direction after a change in the discharge current. This means that the method chosen for localization of the discharge allows us to stabilize the formation and propagation of jets to a significant degree.

A structure similar to that shown in Figs. 2a and 2c should be observed when there is a pressure drop at the

TABLE 1. Basic Parameters of Supersonic Plasma Flows

Flow parameters	Capacity, µF										
	600			700			800				
	voltage, kV										
	1	2	3	1	2	3	0.25	0.5	1	2	3
Length of jet periodic structure, mm	17	25	27	19	27	30	8	14	17	21	26
Diameter of exhaust aperture, mm	4.0	4.0	4.0	3.5	3.5	4.5	3.5	3.5	3.5	3.5	4.5
Mach number M	3.4	4.9	5.2	5.5	7.7	6.5	2.0	3.3	3.7	4.7	4.5
Vapor velocity in jet, km/sec	4—5	5—6	8—10	5—7	7—8	5—6	4—5	6—8	8—10	8—9	5—6
Velocity of luminous front, m/sec	750	1050	1275	1125	1300	1125	500	650	720	1100	1250
Vapor pressure in discharge chamber, atm	21	48	55	38	75	52	9	22	91	46	44
T_2/T_1	2.4	4.0	4.3	4.7	8.3	6.2	1.1	2.4	2.8	3.5	3.5
P_2/P_1	13	70	30	34	66	47	50	12	15	25	22
ρ_2/ρ_1	5.6	7.3	7.6	7.7	8.7	8.3	2.0	5.5	6.0	5.2	7.0

mouth of the nozzle in the direction of decreasing pressure outside the nozzle; the pressure drop must exceed a certain critical value determined by the parameters of the gas in the nozzle and the medium. A supersonic velocity is observed in the flow in the free jet outside the nozzle. In the rarefaction region outside the nozzle the pressure drops to a value below that of the surrounding medium into which the jet flows. In the photographs, this zone is represented by the dark space at the sides of bands of increased brightness which are curvilinear compressive shocks. A good illustration is shown in Fig. 2e. A similar pattern is partially observed in the final stage of the pulse.

It should be noted that with a stronger discharge refractive lines in the background of the opaque plasma region (refraction lines) can be observed on the frames of high-speed film as the plasma jet flows from the aperture of the discharge chamber. A similar pattern is noted in ref. 21, in which a laser-produced jet from a carbon target is investigated using a shadowgraph method. The authors indicate that the angle of inclination of these lines can be used to estimate the plasma density gradient.

Curvilinear compressive shocks can also be observed in the middle of the pulse for more powerful discharges. This is especially clear in Fig. 2f. It can be seen from the photographs that in the center of the flow in the core of the jet and above, the dark space is bounded by a straight compressive shock. The conditions behind this compressive shock are similar to those at the nozzle mouth; thus, the pattern of the pressure flow determines the periodic structure of the jet. In the straight shock the velocity in the center becomes subsonic. In the outer part of the flow the velocity remains supersonic. As a result of the interaction between the jet core and the outer flow the velocity over the entire flow becomes supersonic.

A similar pattern is observed in an investigation of a laser-produced jet[22] using high-speed photography. The authors consider the formation of the compressive shock to be the result of the directed motion of the vapor flow from a crater in the target.

The fundamental relations of thermodynamics[23–25] indicate a sharp increase in temperature, density, and pressure in compressive shocks. This causes an increase in luminosity in the regions behind the compressive shock.

The quantitative parameters characterizing the properties of jets as continuous plasma flows can be obtained by using gasdynamics. One can easily determine the length of the periodic structure (the height of the dark electrode space) from time scans of plasma streams. If the length of the periodic structure is known, one can determine the pressure inside the aperture from which the jet issues, the Mach number in the region ahead of the compressive shock, and the increase in temperature, density, and pressure in this shock.

The periodic structure L is related to the pressure p_1 inside the nozzle by[25]

$$L = 0.89d\sqrt{\frac{p_1 - 1.9p_2}{p_2}}, \tag{1}$$

where d is the nozzle diameter and p_2 is the presure in the ambient medium.

An approximate value of the Mach number in the region ahead of the compressive shock can be obtained from

$$L = 1.3d\sqrt{M^2 - 1}. \tag{2}$$

The velocity of the vapor in the jet ahead of the compressive shock can be measured from time scans of the inclined bands whose appearance is evidently related to fluctuations in the vapor density.

Analysis of spectrograms taken with various values of the parameters in the discharge circuit indicates that the plasma largely consists of erosion products from the discharge chamber and the electrodes and of air components. Therefore, the plasma can be regarded as a diatomic gas and at a discharge temperature of the order of 10^{4}°K the value of γ can be set at ~ 1.25. If the Mach number is known, the temperature and pressure variations in the compressive shock can be determined from the Rankine–Hugoniot relations[23–25]

$$\left.\begin{aligned} \frac{p_2}{p_1} &= \frac{2\gamma}{\gamma+1}M^2 - \frac{\gamma+1}{\gamma-1}, \\ \frac{\rho_2}{\rho_1} &= \frac{(\gamma-1)M^2+2]}{(\gamma+1)M^2}, \\ \frac{T_2}{T_1} &= \frac{[2\gamma M^2-(\gamma-1)][(\gamma-1)M_1^2+2]}{(\gamma+1)^2M^2}. \end{aligned}\right\} \tag{3}$$

We note that the value of γ for the plasma is somewhat smaller than that for a monatomic gas due to the ionization and the emission. For our calculations, however, it is sufficient to obtain just a provisional value for γ since its magnitude does not have a strong effect on the estimates. Therefore, ref. 26 can be used to obtain a value of ~ 1.25.

The results of measurements under some of the discharge conditions considered in this paper are shown in Table 1, which also gives the vapor velocity in the jet, the recession velocity of the luminous front, and the vapor pressure inside the discharge chamber. All the data refer to the middle stage of the pulse, except for the recession velocity of the luminous front, whose value is determined at the onset of the discharge. Analysis of the table indicates that all the parameters of the plasma stream vary with the capacity and voltage of the discharge circuit. Approximately the same dependence applies to the diameter of the aperture. The maximum velocity of the vapor flow appears with increasing pressure in the aperture. In high-power discharges this pressure can be several hundred atmospheres.

It is evident from Fig. 2f that the leading edge of the jet has a relatively sharp boundary which moves from the mouth of the discharge chamber with a velocity that is several times smaller than the vapor velocity in the jet. Under the present conditions the velocity of the leading edge in the initial stage of the pulse is 500 m/sec; the vapor velocity in the jet is 5-6 km/sec.

A similar pattern was first observed in ref. 27 for a spark discharge through a capillary. It was established that a relatively slow-moving luminous front with a limited rate of propagation of the plasma of the shock wave moving from the mouth of the aperture in air also characterizes the initial stage of the pulse. However, the periodic structure was not observed.

A development of the luminous region similar to the one described in the present paper has also been observed in expansion of a spark discharge channel,[28] a discharge in a T-shaped tube,[29] in a high-voltage discharge with an annular electrode,[30],[31] etc. In these cases the rate of propagation of the luminous front is limited by the shock wave formed in the atmosphere surrounding the discharge due to the rapid release of energy in a small volume. It follows that the periodic structure cannot form in the jet sooner than the shock wave can move from the mouth of the aperture to a corresponding distance. The time interval necessary for formation of the complete jet structure is larger, the lower the velocity of the shock wave and the longer the wavelength of the periodic structure.

By analogy with ref. 27, the jet can be considered as a plasma piston produced and fed by the shock wave in the atmosphere. Since the jet emerging from the aperture has a periodic structure, the receding shock wave and the luminous front should interact successively with the compression and rarefaction waves of the jet. Since the rate of propagation of the shock wave is proportional to the square root of the downstream pressure, its velocity should not decrease when interacting with the rarefaction wave, and it should not increase in interacting with the compression wave.

Thus, the formation of supersonic plasma jets in a high-power pulsed discharge is a hydrodynamic detonation process. After the shock wave has moved a large distance from the mouth of the discharge chamber its structure begins to resemble the structure of a continuous gas stream flowing from a nozzle with a supercritical drop in pressure. The interaction between the quasistationary wave structure of the jet and the shock wave in air leads to a periodic variation of the rate of propagation of the luminous front above the jet core during the formation period. A supersonic flow is observed in the region in front of the first compression.

---

[1] S. L. Mandel'shtam, N. K. Sukhodrev, and V. P. Shabanskii, Proceedings of the 10th Conference on Spectroscopy [in Russian] (1958), Vol. 2, p. 148.

[2] E. I. Vorontsov, Proceedings of the 10th Conference on Spectroscopy [in Russian] (1958), Vol. 2, p. 154.

[3] L. I. Grechikhin and L. Ya. Min'ko, Zh. Tekh. Fiz., 32, 1072 (1963) [Sov. Phys. – Tech. Phys., 7, 784 (1963)].

[4] V. K. Semenov and L. A. Spektorov, Zh. Tekh. Fiz., 34, 853 (1964) [Sov. Phys. – Tech. Phys., 9, 651 (1964)].

[5] L. Ya. Min'ko, Generation and Investigation of Supersonic Plasma Flows [in Russian], M. A. El'yashevich (ed.), Nauka i Tekhnika, Minsk (1970).

[6] B. B. Davydov and L. Ya. Min'ko, Zh. Tekh. Fiz., 41, 73 (1971) [Sov. Phys. – Tech. Phys., 16, 53 (1971)].

[7] L. I. Grechikhin, L. Ya. Min'ko, and V. E. Plyuta, Opt. Spektrosk., 12, 120 (1962).

[8] M. A. Sultanov and L. I. Keselevskii, Zh. Prikl. Spektrosk., 1, 268 (1964).

[9] L. I. Grechikhin and L. Ya. Min'ko, Zh. Tekh. Fiz., 37, 1169 (1967) [Sov. Phys. – Tech. Phys., 12, 846 (1967)].

[10] M. A. Sultanov and L. I. Keselevskii, Teplofiz. Vys. Temp., No. 1, 40 (1966).

[11] M. A. Sultanov, Zh. Prikl. Spektrosk., 5, 375 (1966).

[12] M. A. Sultanov, Ninth Intern. Conf. on Phenomena in Ionized Gases, Contributed Papers, Bucharest (1969).

[13] N. G. Basov, V. A. Gribkov, O. N. Krokhin, and G. V. Sklizkov, Zh. Eksp. Teor. Fiz., 54, 1073 (1968) [Sov. Phys. – JETP, 27, 575 (1968)].

[14] V. A. Gribkov, O. N. Krokhin, V. Ya. Nikulin, G. V. Sklizkov, and M. A. Sultanov, Abstracts of the Second All-Union Conference on the Physics of the Interaction between Optical Radiation and a Condensed Medium [in Russian], Leningrad, 1972; Preprint, Fiz. Inst. Akad. Nauk SSSR, No. 41, p. 36.

[15] Yu. V. Afanas'ev, V. A. Gribkov, O. N. Krokhin, V. Ya. Nikulin, G. V. Sklizkov, and M. A. Sultanov, Preprint, Fiz. Inst. Akad. Nauk SSSR, No. 41, p. 36 (1973).

[16] M. A. Sultanov and L. I. Keselevskii, Teplofiz. Vys. Temp., No. 3, 375 (1966).

[17] M. A. Sultanov, Teplofiz. Vys. Temp., No. 5, 963 (1970); Prikl. Mekh. Tekh. Fiz., No. 3, 120 (1970).

[18] M. A. Sultanov and V. N. Narzullaev, Ninth Intern. Conf. on Phenomena in Ionized Gases, Bucharest (1969), p. 123.

[19] M. E. Deich, Engineering Gasdynamics [in Russian], Gosenergoizdat, Moscow (1961).

[20] L. I. Keselevskii and M. A. Sultanov, Prikl. Mekh. Tekh. Fiz., No. 4, 96 (1966).

[21] N. G. Basov, O. N. Krokhin, and G. V. Sklizkov, Tr. Fiz. Inst. Akad. Nauk SSSR, 52, 171 (1970).

[22] V. A. Batanov, V. A. Bogatyrev, N. K. Sukhodrev, and V. B. Fedorov, Zh. Eksp. Teor. Fiz., 64, 825 (1973).

[23] L. D. Landau and E. M. Lifshits, Mechanics of Continuous Media [in Russian], Gostekhizdat, Moscow (1954).

[24] Ya. B. Zel'dovich and Yu. P. Raizer, Physics of Shock Waves and High-Temperature Hydrodynamic Phenomena [in Russian], Fizmatgiz, Moscow (1966).

[25] Shih-i Pai, Fluid Dynamics of Jets, Van Nostrand, New York (1954).

[26] A. S. Predvoditelev (ed.), Tables of Thermodynamic Functions of Air, Akad. Nauk SSSR, Moscow (1957).

[27] A. A. Babushkin, Zh. Eksp. Teor. Fiz., 14, 184 (1944).

[28] I. S. Abramson, N. M. Gegechkori, S. I. Drabkina, and S. R. Mandel'shtam, Zh. Eksp. Teor. Fiz., 17, 862 (1947).

[29] V. S. Komel'kov, Yu. V. Skvortsov, and V. N. Tereshchenko, Zh. Eksp. Teor. Fiz., 33, 719 (1963).

[30] H. Morgenroth, H. Heb, K. Kishcel, R. Rademarcher, and K. Seliger, Ann. Phys., 8, 175 (1961).

[31] H. Heb, K. Kishcel, H. Morgenroth, R. Rademarcher, and K. Seliger, Ann. Phys., 8, 189 (1961).

Experimental investigation of microwave radiation produced by hypersonic flows

V. A. Lyutomskii, V. M. Polyakov, and V. G. Testov
Institute of Radio Engineering and Electronics,
Academy of Sciences of the USSR, Moscow

(Submitted May 29, 1973)
Zh. Tekh. Fiz., 44, 766-769 (April 1974)

The temperature of hypersonic flows is measured using their self-microwave radiation. Experimental results are given for the temperature and conductivity of hypersonic waves behind models moving through air with velocities of 4-4.6 km/sec and at an initial pressure of 40-100 torr. The dimensions of the ionization zone in argon are estimated from the measured microwave radiation of the shock wave.

When bodies move with hypersonic velocities through a rarefied gas a complex plasma structure forms around them; the plasma can be arbitrarily divided into the following regions: the ionization region, the shock wave, and the near and far wakes. Laboratory investigations of the microwave radiation from these regions can be carried out in shock tubes or ballistic devices. Consideration of their geometrical dimensions can help clarify the possibility of resolving these regions in space.

The characteristic dimension of the ionization region in the direction of the flow axis is of the order[1] of (Γd)/2, where d is the model (tube) diameter and Γ is the ratio of the characteristic values of radiative and convective transfer

$$\Gamma = \frac{\sigma u^5}{\rho_\infty c_p^4}. \qquad (1)$$

Here, σ is the Stefan–Boltzmann constant, u is the flow velocity, ρ is the flow density, c_p is the specific heat at constant pressure, and the subscript ∞ refers to the flow parameters at infinity.

It can be seen from Fig. 1 that at a pressure of 10 torr, a model diameter of ~ 1 cm, and velocities of ~ 5 km/sec the ionization region in air is approximately 10 cm in the ballistic device. In the shock tube, due to the large dimensions of the contact surface, significantly larger dimensions of this region can be obtained, and the use of argon significantly increases the ionization region.

In the ballistic device the stand-off distance of the shock from the surface of the moving body Δ_s can be taken as the characteristic dimension of the shock region. The following expression:[2]

$$\Delta_s = \frac{d}{3}\left(\frac{\rho_s}{\rho_\infty} - 1\right)^{-1}, \qquad (2)$$

indicates that this dimension is a fraction of the model diameter. For example, with a model of ~ 1 cm, Δ_s does not exceed several millimeters.

In the shock tube the dimensions of the contract surface of the shock-heated gas are several tens of centimeters for pressures of 5-20 torr and velocities[3] of 3-5 km/sec. The geometrical dimensions of the wake exceed those of all the other regions and are more than 1000 diameters of the moving body.[2]

If we assume that the resolution of the directional pattern of the antenna has a lower limit of the order of 1.5 λ, for microwave measurements in the centimeter and millimeter ranges both the ionization and the shock regions can be resolved in shock tubes, and the ionization region and the wake can be resolved in ballistic devices.

The intensity of radiation from the heated gas at frequency f, expressed in terms of the brightness temperature T_B, can be estimated from[4]

$$T_B = [1 - R(f)] \int_0^l T_r(x)\,\varkappa(x)\, e^{-\int_x^l \varkappa(x')\,dx'}\, dx, \qquad (3)$$

where T_r is the radiation temperature, R is the reflection coefficient with respect to the power at the boundary of the plasma structure (it is assumed that the boundary is fairly steep), $\varkappa$ is the absorption coefficient for the low-temperature plasma, and l is the thickness of the plasma layer.

If we assume that the plasma electrons have a Maxwellian velocity distribution and that the electron temperature is equal to the gas temperature, then the radiation temperature is equal to the gas temperature.

The temperature of the air in the wake can be determined from[5]

$$\frac{T}{T_\infty} = 1 + \frac{(\gamma - 1)\, c_x M_\infty^2}{\left[\frac{x}{d}(\gamma - 1)\, c_x + 1\right]}, \qquad (4)$$

where γ is the ratio of the specific heats at constant pressure and constant volume, and c_x is the drag coefficient.

The gas temperature in the shock region (between the shock front and the surface of the body) is determined from[3]

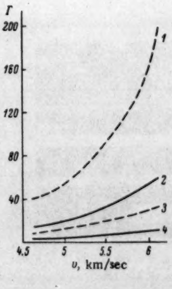

Fig. 1. p_∞ atm: 1, 2) 10^{-2}; 3, 4) $5 \cdot 10^{-2}$; 1, 3) Ar; 2, 4) air.

$$\frac{T}{T_\infty}=\frac{\left(\gamma M^2-\frac{\gamma-1}{2}\right)\left(\frac{\gamma-1}{2}M^2+1\right)}{\left(\frac{\gamma+1}{2}\right)^2 M^2}, \qquad (5)$$

where M is the Mach number.

The absorption and reflection coefficients are determined by the electron density N_e and the electron collision frequency ν.

Calculations indicate that with velocities of the order of 4.5 km/sec the brightness temperature of the shock region in air is about 4000°K. The brightness temperature of the wake can reach ~ 3500° for x/d ~ 20 and 1000°K for d/x ~ 1000. Modern sensitive microwave detectors have a noise temperature of $\delta T \sim 0.1°$ for a time constant $\tau =$ 1 sec. If we assume that measurements of the microwave of a hypersonic flow require a time constant of the order of tens of microseconds and that the sensitivity of the detector depends on the time constant as[4]

$$\delta T=\frac{T_D}{\sqrt{\tau\Delta f}}, \qquad (6)$$

then it becomes clear that a sensitivity of the order of 200° can be attained in the experiments. The calculations and experiments indicate that this sensitivity is sufficient to record microwave radiation from the appropriate regions of a hypersonic flow.

EXPERIMENTAL METHOD AND RESULTS

A ballistic device and a shock tube have been used to measure the characteristics of hypersonic flows.[6]

The self-microwave radiation and conductivity of the wake are measured in the ballistic device at hypersonic velocities of the model. The model is a copper-plated aluminum sphere 5.3 mm in diameter. The experiments are carried out in air at 20-160 torr and ~ 290°K in the pressure chamber. The model is fired from a light-gas gun with a velocity of 3000-4600 m/sec. A synchronization station which measures the velocity and photographs the model during flight is set up along the path of the model. The electron density and the effective frequency of collisions between electrons and neutrals are measured using two-resonator radiointerferometers ($\lambda_1 = 30$ and $\lambda_2 = 60$ cm). The low-frequency conductivity of the wake is measured directly by an electrodynamic method.[7]

The measured antenna temperature of the microwave radiation is related to the brightness temperature by

$$T_A=k\frac{S_W}{S_A}T_B, \qquad (7)$$

where K is the antenna loss, S_W/S_A is the ratio of the area of the wake in the minimum resolution area of the directional pattern to the area of the entire area. The wake dimensions are determined[8] from $d_W/d = 0.87\,(x/d)^{1/3}$. Measurements of a 2.4 cm wave indicate that at velocities of ~ 4 km/sec and a pressure of 40 torr, microwave radiation from the near-wake region is observed (Fig. 2a). With higher velocity and pressure (u = 4.6 km/sec and $p_\infty =$ 160 torr) a delay of the microwave signal is observed with respect to the flight of the model (Fig. 2b). In all likelihood, this is due to the formation of a supercritical plasma density in the wake directly behind the model and the resultant increase in reflection at the boundary. The duration of the microwave signal is determined by the nature of the drop in electron density and temperature along the wake. To estimate these characteristics we use data obtained from interferometer measurements of the conductivity. The measured values of the low-frequency conductivity and the effective collision frequency are used to determine the high-frequency conductivity of the wake:

$$\sigma=\sigma_{lf}\,\frac{1}{1+\frac{\omega^2}{\nu_{eff}^2}}, \qquad (8)$$

where σ_{lf} is related to the electron density and the collision frequency by $\sigma_{lf} = e^2N_e/(m\nu_{eff})$. The high-frequency conductivity thus obtained is used to calculate the absorption and reflection characteristics of the wake in the wavelength region under investigation.

Figure 3 gives theoretical and experimental profiles of the temperature along the wake. It is clear from the figure that they show satisfactory qualitative agreement.

The use of low model velocities and air prevents detection of the ionization region in the ballistic device. Therefore, microwave radiation from this region is measured in a shock tube with an argon atmosphere. The measurements are carried out at pressures of 5 to 10 torr and shock velocities of M ~ 6-7.5. Absorption, reflection, and electric probe current are measured simultaneously with the radiation. The measurements indicate that microwave radiation from the ionization region is observed for Mach numbers greater than 6.5, although it is true that the dimensions of the region are appreciably smaller than the calculated dimensions. In all likelihood, this is due to the

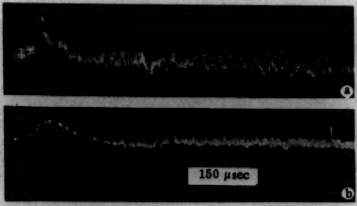

Fig. 2. Microwave radiation of the wake. a) u = 4.3 km/sec, p_∞ = 40 torr; b) u = 4.6 km/sec, p_∞ = 160 torr.

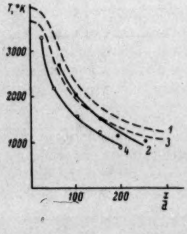

Fig. 3. Temperature distribution in the wake. 1, 2) M = 13.1, p_∞ = 160 torr; 3, 4) M = 12.3, p_∞ = 40 torr; 1, 3) theoretical curves.

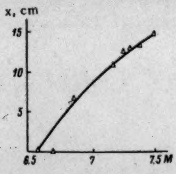

Fig. 4

low electron density at the beginning of the region. Figure 4 gives the dependence of the dimensions of the region ahead of the shock front, from which the microwave radiation is observed on the velocity of the incident shock. The very low absorption in this region (less than 0.1 dB) indicates the nonequilibrium nature of this radiation.

The preliminary results given here indicate that the self-microwave radiation can be used to measure the temperature in the wake and to estimate the variation in the dimensions of the ionization region as a region of the flow parameters.

In conclusion, the authors thank G. I. Mishin and S. N. Palkin for making it possible to carry out this investigation and for their support.

---

[1] Cohn, Raket. Tekh. Kosmonavt., No. 3, 142 (1967).

[2] J. J. Martin, Atmospheric Reentry, Prentice-Hall, Englewood Cliffs, New Jersey (1966).

[3] A. G. Gaydon and I. R. Hurle, The Shock Tube in High-Temperature Chemical Physics, Reinhold, New York (1963).

[4] A. E. Basharinov, L. T. Tuchkov, V. M. Polyakov, and N. I. Ananov, Measurement of Radiative Heat and Plasma Microwave Radiation [in Russian], Sov. Radio, Moscow (1968).

[5] Webb and Chromas, Raket. Tekh. Kosmonavt., No. 5, 33 (1965).

[6] V. G. Testov, Yu. S. Lobastov, and T. V. Bazhenova, Zh. Tekh. Fiz., 41, 1196 (1971) [Sov. Phys. – Tech. Phys., 16, 944 (1971)].

[7] V. N. Gadion, V. G. Ivanov, G. I. Mishin, and S. N. Palkin, Zh. Tekh. Fiz., 41, 350 (1971) [Sov. Phys. – Tech. Phys., 16, 262 (1971)].

[8] V. N. Gadion, V. G. Ivanov, G. I. Mishin, S. N. Palkin, and L. I. Skurin, Zh. Tekh. Fiz., 42, 1049 (1972) [Sov. Phys. – Tech. Phys., 17, 832 (1972)].

Quantum electronics

Parasitic amplitude modulation of a stabilized Nd $^{3+}$: YAG laser

N. M. Galaktionova, A. A. Mak, and A. P. Khyuppenen

(Submitted April 10, 1973)
Zh. Tekh. Fiz., 44, 770-777 (April 1974)

The dependence of the modulation and noise of a single-mode cw Nd^{3+}:YAG laser on pump-lamp current and loss modulation are investigated experimentally. The results are in good agreement with the solutions of the nonstationary rate equations. The modulation depth at which the continuous lasing mode turns into noise spiked lasing is determined. Stabilization of the laser parameters results in steady lasing with an amplitude-modulation spectral width less than 200 Hz at the 0.1 level; the ratio of noise power to radiation power is below 0.4% between 20 Hz and 600 kHz.

1. One of the most promising trends in the development of radiation sources of high spectral brightness is the reduction of the spectral width of solid state lasers and stabilization of the frequency. One important prerequisite for a successful solution of this problem is stabilization of the radiation power level, i.e., a low amplitude-noise level. One of the causes of random modulation of the intensity is the modulation of resonator loss. It has been shown in refs. 1-4 that such modulation can be caused by fluctuating and homogeneous pumping, by unstable cooling conditions, and by fluctuations of mirror position and the optical length of resonator due to changes in shape. Stabilization of resonator parameters, pumping, and cooling conditions result in a considerable reduction of the modulation in cw Nd^{3+}:YAG lasers.

The purpose of this work is an experimental investigation of the connection between resonator loss and pumping modulation and laser radiation noise, a quantitative estimate of the effect of active element cooling conditions on loss modulation, and the achievement of minimum parasitic modulation in a single-mode CW Nd^{3+}:YAG laser pumped by krypton arc lamps.

2. The dependence of the amplitude modulation on the loss and pump modulation can be found by solving the nonstationary rate equations in which the pump or loss appear as harmonic functions:

$$\gamma=\gamma_0(1+m_\gamma \sin \omega t), \tag{1}$$

$$W=W_0(1+m_{pp}\sin \omega t). \tag{2}$$

where γ is the loss rate; W is the pump rate (proportional to pump power); the subscript "0" denotes stationary values; and m_γ and m_{pp} are the loss and pump modulation indices respectively. Since balance equations and their solutions are well known,[4,5,8] we analyze the solutions. Note that the expressions given below are solutions of kinetic equations for a four-level system with a depleted lower active level and homogeneously broadened emission in the single-mode approximation. To a first approximation in perturbation theory, the solutions of nonstationary equations give expressions for the relative magnitude of the variable component of radiation intensity in the resonator:

$$\frac{U_i(t)}{U_0}=A_i m_i \sin(\omega t+\varphi_i), \tag{3}$$

where U_0 is the steady-state radiation density in the resonator (proportional to the radiation power P_0), the subscript "i" can denote either "γ" or "pp",

$$A_\gamma=\gamma_0\left[\frac{\omega^2+4\beta^2}{(\omega^2-\omega_p^2)^2+4\beta^2\omega^2}\right]^{1/2}, \tag{4}$$

$$\varphi_\gamma=\operatorname{arc\,tg}\left[\frac{\omega(\omega_p^2-\omega^2-4\beta^2)}{2\beta\omega_p^2}\right], \tag{5}$$

$$A_{pp}=\frac{2\beta\gamma_0}{[(\omega_p^2-\omega^2)^2+4\beta^2\omega^2]^{1/2}}, \tag{6}$$

$$\varphi_{pp}=\operatorname{arc\,tg}\left(-\frac{2\beta\omega}{\omega_p^2-\omega^2}\right), \tag{7}$$

$$\omega_p\simeq\sqrt{\frac{\gamma_0(n-1)}{\tau}}, \tag{8}$$

$$\gamma_0=\frac{\sigma c}{2L}, \tag{9}$$

$$\beta=\frac{n}{2\tau}, \tag{10}$$

β and ω_p are the damping constant and the circular frequency of the relaxation oscillations respectively ($\omega_p \gg 2\beta$), σ is the two-pass loss of the resonator, c is the velocity of light, L is the optical length of the resonator, n is the ratio of pump power to threshold power, τ is the lifetime of the excited state, and ω is the circular perturbation frequency.

The solutions have been obtained assuming that

$$U_i \ll U_0,\quad N_i \ll N_0,\quad m_\gamma \ll 1,\quad m_{pp} \ll 1,$$

where N_0 is the steady-state inverted population of the active level, and N_i is the variable component of population inversion.

The radiation power modulation indices are found from (3):

$$m_{P_i}=\frac{P_{a_i}}{P_0}=\frac{U_{a_i}}{U_0}=|A_i|\,m_i, \tag{11}$$

where P_{a_i} is the variable component of laser radiation power; the subscript "a" denotes the corresponding amplitude.

The factors A_i describe the outline of the resonance response of radiation power to small perturbations. The expressions for these factors for three different relationships between ω_p and ω are given below:

$$A_\gamma = \left| \begin{array}{ll} \dfrac{(\omega^2\tau^2+n^2)^{1/2}}{n-1} & \omega^2 \ll \omega_p^2, \quad (12) \\ \dfrac{\gamma_0}{2\beta} & \omega = \omega_p, \quad (13) \\ \dfrac{\gamma_0}{\omega} & \omega^2 \gg \omega_p^2; \quad (14) \end{array} \right.$$

$$A_{pp} = \left| \begin{array}{ll} \dfrac{n}{n-1} & \omega^2 \ll \omega_p^2, \quad (15) \\ \dfrac{\gamma_0}{\omega_p} & \omega = \omega_p, \quad (16) \\ \dfrac{2\beta\gamma_0}{\omega^2} & \omega^2 \gg \omega_p. \quad (17) \end{array} \right.$$

Expressions (12) and (15) indicate that equal loss and pump modulation result in equal radiation modulation, provided $\omega \ll \beta$. In all other cases, radiation modulation is much more affected by less modulation.

Let us estimate the allowable magnitude of m_l for a modulation index $m_p = 10^{-2}$ in the case of a laser with the following parameters: crystal length $l = 5$ cm, crystal diameter $d = 0.3$ cm, resonator length 60 cm, plane mirrors with transmission coefficients $T_1 = 0.05$ and $T_2 = 0.005$, passive crystal loss factor $\sigma_e = 0.005\ \text{cm}^{-1}$, $n = 2$, $\tau = 2 \cdot 10^{-4}$ sec, $\omega_p = 3 \cdot 10^5\ \text{sec}^{-1}$, $\gamma_0 = 1.7 \cdot 10^7\ \text{sec}^{-1}$, $\beta = 0.5 \cdot 10^4\ \text{sec}^{-1}$:

$$\omega^2 \ll 4\beta^2 \ll \omega_p^2, \quad m_\gamma = m_{pp} = 0.5 \cdot 10^{-2},$$
$$\omega = \omega_p, \quad m_\gamma = 6 \cdot 10^{-6}, \ m_{pp} = 1.8 \cdot 10^{-4},$$
$$\frac{\omega^2}{\omega_p^2} = 10, \quad m_\gamma = 6 \cdot 10^{-4}, \ m_{pp} = 6 \cdot 10^{-2}.$$

3. The laser used in the experiments is pumped by two high-pressure krypton lamps in a twin gold-plated elliptical illuminator. The lamp supply is stabilized and the voltage ripple factor is below $2 \cdot 10^{-4}$. The active element is cooled in a closed-loop system with a stabilized pump power supply. To reduce the effect of vibrations, the angle between the element and resonator axes is 15' and the element end faces are coated (R ~ 0.1%). The necessary resonator stiffness is provided by mounting the mirrors on heavy steel plates connected by Invar bars. To damp external vibrations, the entire experimental apparatus is placed on a heavy stiff plate cushioned with pieces of vacuum rubber pipe. Metal pipes are placed between the resonator mirrors and the end faces of the active element to prevent effects due to convective air currents.

The modulation is measured with the circuit shown in Fig. 1. The radiation is detected by an FÉU-62 photomultiplier whose photocurrent is kept constant; the signal across the photomultiplier load is 100 mV. The internal noise of the measuring system is measured by illuminating the photocathode with an incandescent bulb. The measured noise is 0.2 mV between 0.02 and 650 kHz. The alternating component of the photocurrent is amplified and applied to a spectrum analyzer. The spectrum analyzer is calibrated with a standard signal generator. The spectral density of the modulation index is determined from photographs. The radiation noise is analyzed by an ASChKh-1 spectrum analyzer at frequencies from 0.02 to 20 kHz and by an SCh-8 analyzer up to 650 kHz. The circuit makes it possible to measure the modulation index to $5 \cdot 10^{-5}$ at frequencies up to 20 kHz and to $3 \cdot 10^{-4}$ from 20 to 650 kHz. As in the case of radiation modulation measurement, the modulation of the pump lamp current is determined by measuring the voltage across a resistance connected in series with the lamp.

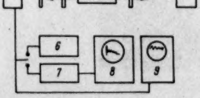

Fig. 1. Circuit for measuring amplitude modulation of laser radiation. 1) Active element; 2) resonator mirrors; 3) power meter; 4) radiation detector (FÉU-62 photomultiplier); 5) neutral filters; 6) dc voltmeter; 7) measuring amplifier; 8) spectrum analyzer (ASChKh-1 or SCh-8); 9) oscilloscope.

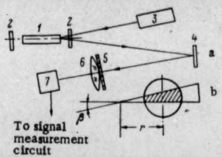

Fig. 2. a: Optical circuit for measuring the vibrations of the active element: 1) active element; 2) resonator mirrors; 3) gas laser; 4) rotating mirror; 5) mask; 6) lens; 7) FÉU-62 photomultiplier. b: Position of gas laser spot relative to the slit.

The noise conditions are strongly affected by vibrations of the active element caused by the perturbing effect of the cooling stream, the magnitude and nature of these vibrations depending on the rate of coolant flow. It has been found that one of the causes of radiation modulation is lateral bending of the active element and changes in the angular position of its axis.

The optical circuit shown in Fig. 2 has been used to estimate the active element vibrations. After reflection from the active element end face and rotating mirror 4, the radiation of a single-mode gas laser passes through slit 5 and is focused by lens 6 on the FÉU-62 photocathode. The slit is triangular with a small vertex angle. The position of the light spot (circle) relative to the slit is shown in Fig. 2b. Changes in the angular position of the element end face, which cause beam displacement along the slit, are determined from the variation of the photomultiplier output signal. The signal spectrum is analyzed with the aid of a spectrum analyzer as in the noise spectrum measurements. Assuming a constant and homogeneous power distribution in the gas laser beam, the vibration spectrum is determined by the spectral density of the alternating component $E(f)$ of the photomultiplier output signal:

$$\alpha(f) = \frac{E(f)}{E_0} \frac{r}{2D}, \quad (18)$$

where E_0 is the dc component of the signal, D is the distance between the element end face and slit, and r is the distance from the center of the light spot on the slit to the vertex of the triangular slit in the absence of vibrations.

In the presence of periodic vibrations, the vibration amplitude can be written

TABLE 1

f, Hz	$T = 1\%$									$T = 5\%$									$T = 8\%$		
	$n = 1.09$			$n = 1.33$			$n = 1.72$			$n = 1.05$			$n = 1.22$			$n = 1.62$			$n = 1.06$		
	$m_J(f)\cdot 10^4$	$m_p(f)\times 10^4$		$m_J(f)\cdot 10^4$	$m_p(f)\times 10^4$		$m_J(f)\cdot 10^4$	$m_p(f)\times 10^4$		$m_J(f)\cdot 10^4$	$m_p(f)\times 10^4$		$m_J(f)\cdot 10^4$	$m_p(f)\times 10^4$		$m_J(f)\cdot 10^4$	$m_p(f)\times 10^4$		$m_J(f)\cdot 10^4$	$m_p(f)\times 10^4$	
		Experiment	Theory		Experiment	Theory		Experiment	Theory		Experiment	Theory		Experiment	Theory		Experiment	Theory		Experiment	Theory
50	0.23	3.5	5.2	0.30	3.3	2.5	0.21	1.1	0.96	0.23	11.5	9.8	0.18	3.5	2.1	0.18	0.70	0.94	0.25	—	8.7
100	0.28	4.2	6.8	0.26	2.6	2.1	0.28	0.6	1.3	0.23	11.0	9.8	0.28	4.4	2.8	0.26	0.87	1.3	0.35	9.4	12
200	0.24	4.9	6.0	0.32	3.3	2.5	0.17	1.2	0.84	0.25	7.5	10.0	0.42	3.2	2.5	0.16	0.61	0.77	0.21	6.0	7.5
750	0.034	0.5	0.8	0.054	0.28	0.22	—	—	—	0.05	1.2	2.0	0.1	0.47	0.56	0.034	0.08	0.16	0.031	0.9	1.1
1500	0.015	0.12	0.36	0.027	0.08	0.11	—	—	—	0.028	0.4	1.1	0.03	0.18	0.18	0.017	0.07	0.08	0.01	0.27	0.35
2250	0.006	0.06	0.15	0.011	0.15	0.05	—	—	—	0.007	0.17	0.28	0.017	—	0.1	0.007	0.024	0.036	—	0.11	—

$$a = a_m(f)\,\Delta f, \tag{19}$$

where $\alpha_m(f)$ is the spectral vibration density at the vibration frequency, and Δf is the oscillation bandwidth

To excite relaxation oscillations of laser radiation intensity, the resonator is perturbed by increasing the rate of coolant flow. The frequencies of these oscillations are measured by ASChKh-1 and SCh-8 spectrum analyzers.

All experiments are carried out with the laser lasing in a single transverse mode, the TEM_{00} mode. The longitudinal mode spectrum consists of two to three groups of three to four modes each. The total spectrum width does not exceed 0.2 Å.

4. The experimental f_{ex} and the theoretical f_{th} [calculated from Eq. (8)] frequencies of relaxation oscillations are listed below:

n	1.1	1.3	1.5	2
f_{ex}, kHz	13.5	30	40	54
f_{th}, kHz	15	26	34	47

The spectral densities of modulation indices of radia-

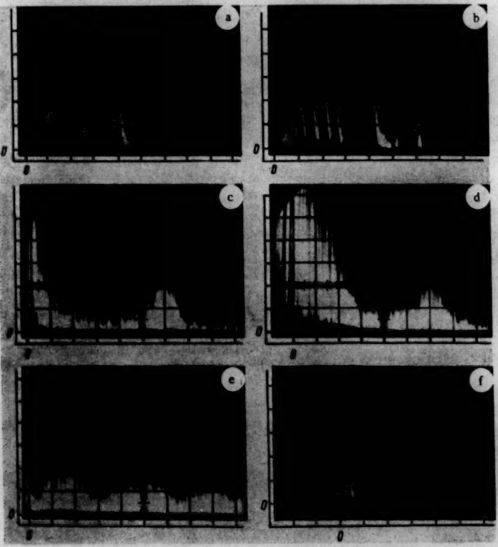

Fig. 3. Spectrograms: a, c, e, f) radiation noise spectra; b) lamp current modulation spectrum; d) active element vibration spectrum. Horizontal axis: 50 Hz (a, b, f), 500 Hz (c, d), and 2000 Hz (e) per division. Vertical axis: a, f) 6 μV/Hz (n = 1.3); b) 0.1 mA/Hz (J_0 = 19 A); c) 0.16 μV/Hz (n = 1.6, Re = 1.5 · 10^4); d) 0.14 · 10^{-8} Hz^{-1}; e) 0.24 μV/Hz (Re = 1.8 · 10^4).

TABLE 2

$Re \cdot 10^{-3}$	$n = 2.3$			$n = 1.52$			$n = 1.15$		
	$m_p(f) \cdot 10^5$		$m_\gamma(f) \cdot 10^6$	$m_p(f) \cdot 10^5$		$m_\gamma(f) \cdot 10^6$	$m_p(f) \cdot 10^5$		$m_\gamma(f) \cdot 10^6$
	Experiment	Theory		Experiment	Theory		Experiment	Theory	
8	—	0.11	0.32	0.25	—	0.32	0.54	0.8	0.32
11	0.19	—	0.54	0.41	0.43	0.54	0.95	1.4	0.54
15	0.28	—	0.8	0.51	0.64	0.8	4.3	2.2	0.8
18	0.72	—	2.2	2	1.7	2.2	—	5.7	2.2

tion $m_p(f)$ and pump lamp current $m_J(f)$ are listed in Table 1. The measurements are taken with exit mirror transmissions at parasitic modulation frequencies of the lamp current. Theoretical values of $m_p(f)$ are calculated assuming that pump power is proportional to the electric power $m_{pp}(f) = 2m_J(f)$. The characteristic modulation spectra of laser radiation and lamp current are shown in Fig. 3, a and b respectively.

The spectra in Fig. 3, c and d clearly show the connection between the modulation of radiation and vibrations of the active element. It has been found that as the coolant flow rate V increases, the element end face starts to vibrate at a low frequency which increases with increasing V. Still further increase of V causes the appearance of periodic oscillations of the end face at about 3 kHz, while the low-frequency random vibrations decay. The dependence of the maximum spectral density $\alpha(f)$ at frequencies up to 500 Hz and of the amplitude of periodic oscillations α of the element end face at 3000 Hz on the Reynolds number Re is shown in Fig. 4 [the solid portion of the $\alpha(Re)$ curve corresponds to experimental data]. In the laser radiation, the periodic component appears at lower Re numbers and is not accompanied by noise. The 3 kHz modulation increases with increasing Re, the frequency bandwidth increases, and the parasitic modulation spectrum becomes almost white (Fig. 3e). Radiation oscillograms indicate that the lasing becomes spiked. The measured frequency of the element end face is in good agreement with the calculated[11] natural frequency of transverse oscillations of the element:

$$f = \frac{b}{2\pi l^2}\sqrt{\frac{EI}{\rho S}}, \tag{20}$$

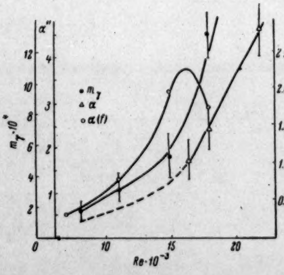

Fig. 4. Dependence of loss modulation index m_γ, angular amplitude of end face oscillations α at 3 kHz; and spectral density of chaotic vibrations $\alpha(f)$ at 20-500 Hz on the Reynolds number.

where E is the elastic modulus, I is the moment of inertia of the element cross-section, S is the cross-sectional area, ρ is the density, and b is a factor which depends on the element mounting. With rigidly mounted end faces b = 22.4, and f = 6.8 kHz, with freely supported end faces b = 9.87 and f = 3 kHz.

5. The experimental results show satisfactory agreement of the relaxation oscillation frequencies and the dependence of radiation power modulation on pump modulation with theoretical values (the spectral density of modulation indices is measured to within ~ 30%). The modulation of radiation caused by element vibrations can be explained by resonator loss modulation. Perturbations by coolant flow cause the active element simultaneously to change the angular position of its axis in the resonator (giving rise to a chaotic vibration spectrum) and to bend at the frequency of its natural transverse oscillations. Coating of the element end faces and removing them from the resonators explains the fact that variations of the angular position of the element do not affect the radiation modulation. At the same time, lateral bending of the rod distorts the resonator geometry, causing an equivalent mirror misalignment by the angle θ:

$$\theta = 2\alpha(\varkappa - 1), \tag{21}$$

where $\varkappa$ is the refractive index of the active element.

Variations of the Q factor of a spherical resonator caused by mirror misalignment are very difficult to determine analytically (in the experiment a spherical resonator derives from the fact that the weak thermal lens formed by the active element is left uncompensated). Thus, the experimental and theoretical data on the connection between laser radiation modulation and loss modulation caused by the perturbing effect of coolant flow have been compared in the following manner. With fixed Re we measure the spectral density of the radiation modulation index $m_p(f)$ at the frequency of transverse element oscillations for different values of n. The spectral density of the loss modulation index $m_\gamma(f)$ is then calculated from (12) at one value of n. This value of $m_\gamma(f)$ is then used to calculate $m_p(f)$ for other n values. The calculated and experimental results are listed in Table 2.

The loss modulation indices m_γ as a function of the Re number, calculated from the corresponding values of $m_\gamma(f)$ at f = 3 kHz, are shown in Fig. 4, where

$$m_\gamma = m_\gamma(f)\Delta f,$$

and Δf is the bandwidth of periodic oscillations of the active element.

At n = 1.15 and $m_\gamma \sim 10^3$, the radiation modulation at f = 3 kHz increases abruptly and spikes appear in the laser oscillations. The radiation modulation spectrum is continuous (Fig. 3e). The amplitude of equivalent angular oscillations of the resonator mirrors θ, corresponding to this value of m_γ, and calculated from Eq. (21) is about 5.5". Extrapolation of $\alpha \sim m_\gamma$ in the direction of small Re numbers indicates that for small n, radiation modulation can be considerable for angular mirror oscillations with an amplitude as small as ~ 0.4".

The noise spectrum of a stabilized laser does not exceed 200 Hz for pumping excesses as large as 1.3. No noise has been detected in this case in the frequency band from 500 Hz to 650 kHz. The noise power does not exceed 0.4% of generation power.

These results indicate that the solutions of nonstationary rate equations can be used in estimating the allowable loss and pumping modulation of a single-mode laser. The dependence of the radiation noise power on the noise of the krypton lamp current can be written as

$$P_{\mathrm{n}} = \frac{2P_0}{J_0} \int_{\omega} A_{\mathrm{pp}}(\omega)\, J(\omega)\, d\omega, \tag{22}$$

where J_0 and $J(\omega)$ are the steady-state value and spectral density of lamp current noise.

In the practically important case

$$P_{\mathrm{n}} = \frac{2P_0 J_{\mathrm{n}}}{J_0} \frac{n}{n-1}, \tag{23}$$

$m_p(f)$ at the frequency of transverse element oscillations for different values of n. The spectral density of the loss modulation index $m_\gamma(f)$ is then calculated from (12) at one value of n; This value of $m_\gamma(f)$ is then used to calculate $m_p(f)$ for other n values. The calculated and experimental results are listed in Table 2. where J_n is the effective value of the pumping lamp noise current.

The authors thank V. Popova, G. E. Novikov, and M. M. Khaleev for helping with the experiment, and V. I. Ustyugov for a discussion of the results.

---

[1] N. M. Galaktionova, V. F. Egorova, A. A. Mak, and B. M. Sedov, Abstracts of the Scientific Conference on Quantum Electronics [in Russian], Erevan (1967).

[2] N. M. Galaktionova, V. F. Egorova, and A. A. Mak, Opt. Spektrosk., 25, 305 (1968).

[3] G. N. Vinokurov, N. M. Galaktionova, V. F. Egorova, and A. A. Mak, ZhETF Pis. Red., 10, 367 (1969) [JETP Lett., 10, 232 (1969)].

[4] G. N. Vinokurov, N. M. Galaktionova, V. F. Egorova, A. A. Mak, B. M. Sedov, and Ya. I. Khanin, Zh. Eksp. Teor. Fiz., 60, 489 (1971) [Sov. Phys. – JETP, 33, 262 (1971)].

[5] H. G. Danielmeyer, J. Appl. Phys., 41, 4014 (1970).

[6] T. Kimura and K. Otsuka, J. Appl. Phys., 40, 5399 (1969).

[7] T. Kimura and K. Otsuka, IEEE J. Quant. Electron., QE-6, 764 (1970).

[8] R. Polloni and O. Srelto, IEEE J. Quant. Electron., QE-4, 481 (1968).

[9] G. D. Baldwin and I. T. Basil, IEEE J. Quant. Electron., QE-7, 179 (1971).

[10] W. Koechner, IEEE J. Quant. Electron., QE-8, 656 (1972).

[11] L. D. Landau and E. M. Lifshitz, Theory of Elasticity, Addison-Wesley (1959).

Thermal effect of continuous laser radiation on optically transparent media

N. S. Bardina, A. I. Portnyagin, M. Yu. Sklyarov, and A. A. Churin

M. V. Lomonosov Moscow State University

(Submitted April 17, 1973)
Zh. Tekh. Fiz., 44, 778-783 (April 1974)

The thermal effect of continous radiation from a YAG : Nd^{3+} laser on glassy media and single crystals is studied. Expressions are obtained for the distribution of temperature and thermoelastic stresses in the irradiated sample. Estimates are given for the absorbed power necessary to form melts in the media. The theory agrees with the experimental data obtained with samples made of tinted glasses and single crystals. It is proposed, that in the high-temperature region the thermal effect on glassy media is associated with a change in the macroscopic parameters; while in the case of single crystals, the effect is associated with a microscopic rearrangement.

The thermal effect of continuous laser radiation in weakly absorbing media is observable even at low power levels. Appearing initially as thermal stresses (focusing, defocusing) laser radiation at higher levels of absorbed power causes considerable stress and elastic deformation (induced double refraction), plastic deformation, mechanical failure, and phase transitions.

The nature of the induced thermal effects is essentially determined by the temperature distribution in the medium being irradiated. The temperature field established in the samples under the action of continuous laser radiation depends not only on the level of the incident radiation, but also on the relationship between the geometric dimensions of the cross-section of the laser beam and those of the sample. The clearest thermal effects are manifested in the region of the beam–medium interface. Surface and subsurface effects are the most pronounced in the interaction of continuous laser radiation with strongly absorbing media.

CALCULATION OF THE THERMAL EFFECT

The stationary temperature distribution in a cylindrical sample of radius R can be found from the solution of the homogeneous equation for heat conduction.[1] The source function for the case of a weakly absorbing medium is taken to be of the form

$$W=\begin{cases}\frac{P}{\pi La^2} & \text{for}\quad r\leqslant a,\\ 0 & \text{for}\quad R\geqslant r>a,\end{cases}$$

where a is the radius of the beam of incident radiation, P is the power absorbed in the sample, and L is the length of the sample.

We obtain the following expression for the temperature field:

$$T(r)=\begin{cases}-\frac{P}{4\pi La^2\varkappa}r^2+\Theta_1 & \text{for}\quad r\leqslant a,\\ \frac{P}{2\pi L\varkappa}\ln\frac{R}{r}+\Theta_2 & \text{for}\quad R\geqslant r>a,\end{cases}\tag{1}$$

where $\varkappa$ is the coefficient of thermal conductivity of the medium,

$$\Theta_1=T_0+\frac{P}{2\pi L\alpha R}+\frac{P}{4\pi L\varkappa}\left[2\ln\frac{R}{a}+1\right],$$

$$\Theta_2=T_0+\frac{P}{2\pi L\alpha R},$$

where α is the coefficient of heat transfer.

We note that Θ_2 is the temperature at the surface of the sample, while Θ_1 is the temperature established on the axis of the beam, T_0 is the temperature of the surrounding medium, and

$$\Theta_1-\Theta_2=\frac{P}{4\pi L\varkappa}\left[2\ln\frac{R}{a}+1\right].$$

It is clear that the temperature at the surface of the sample remains constant with decreasing laser beam radius. It is reasonable to expect this behavior, since the boundary conditions are not changed. However, the temperature at the beam axis increases as the beam radius is reduced (for P = const). The temperature difference between the center and the surface of the sample also increases (Fig. 1). The temperature difference between the center and the edge of the beam remains constant.

In order to obtain the distribution of thermoelastic stresses in the sample, we substitute the expressions obtained for the temperature distribution into the equation derived by Timoshenko.[2] After carrying out the integration, and making a correction to the component σ_z for the case of the "free" ends, for $r \leq a$ we get

$$\sigma_r(r)=-K\left[\frac{a^2}{R^2}+4\ln\frac{R}{a}-\frac{r^2}{a^2}\right],$$

$$\sigma_\varphi(r)=-K\left[\frac{a^2}{R^2}+4\ln\frac{R}{a}-\frac{3r^2}{a^2}\right],$$

$$\sigma_z(r)=-2K\left[\frac{a^2}{R^2}+4\ln\frac{R}{a}-\frac{2r^2}{a^2}\right];$$

and for $R \geq r > a$

$$\sigma_r(r)=-K\left[a^2\left(\frac{1}{R^2}-\frac{1}{r^2}\right)+4\ln\frac{R}{r}\right],$$

$$\sigma_\varphi(r)=-K\left[a^2\left(\frac{1}{R^2}+\frac{1}{r^2}\right)+4\ln\frac{R}{r}-4\right],$$

$$\sigma_z(r)=-2K\left[\frac{a^2}{R^2}-2+4\ln\frac{R}{r}\right],$$

$$K=\frac{\beta EP}{16\pi L\varkappa(1-\mu)},$$

where β is the coefficient of linear expansion of the medium, E is Young's modulus, and μ is the Poisson coefficient.

Figure 2 shows the calculated values of $\sigma_2(r)$, $\sigma_\varphi(r)$, and $\sigma_z(r)$ for samples of optical glass. A positive value corresponds to tension, and a negative value corresponds to compression. It is clear from these calculations that the internal stresses for samples made of optical glass can reach hundreds of kilograms per square centimeter.

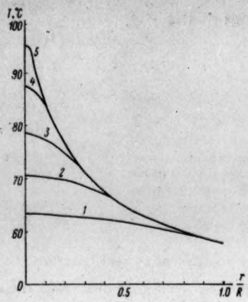

Fig. 1. The stationary temperature distribution in the sample for various values of beam radius a: 1) R; 2) 0.5R; 3) 0.25R; 4) 0.1R; 5) 0.05R.

Under telescopic compression of the laser beam stresses go as high $5 \cdot 10^3$-10^4 kg/cm^2, which is considerably higher than the experimental values of the tensile strengths of glass. The maximum values of σ_r, σ_φ, and σ_z occur at the point r = 0. Estimates of the temperature and stresses at the beam axis give the following results. For given values of R and a, stresses which are greater than the tensile strength of glass are reached at a power level which is larger than that necessary to attain the melting temperature T_1. For temperatures at the axis which are larger than T_1, the temperature distribution is given by the same equations (1), while the character of the stresses changes radically. We will assume that melting occurs for $r \leq b$. As a result, all stresses in this region vanish. Since the temperature difference between the axis of the beam and its boundary is small, the case of $b > a$ is the most common.

For this case, the stresses in the region $b \leq r \leq R$ are treated in the calculation as the stresses of a half cylinder with the given temperature difference between the walls:[3]

$$\sigma_r^* = -4K\left[\ln\frac{R}{r} + \frac{b^2}{R^2 - b^2}\left(1 - \frac{R^2}{r^2}\right)\ln\frac{R}{b}\right],$$

$$\sigma_\varphi^* = -4K\left[\ln\frac{R}{r} + \frac{b^2}{R^2 - b^2}\left(1 + \frac{R^2}{r^2}\right)\ln\frac{R}{b} - 1\right].$$

EXPERIMENTAL RESULTS

A YAG : Nd^{3+} laser, which has been previously described in the literature,[4] is used to supply the continuous radiation for the experimental studies. The glass samples are 3 mm thick and 10 mm in diameter. The coefficient of heat transfer α is $0.002\ \mathrm{W \cdot cm^{-2} \cdot deg^{-1}}$, while the coefficient of thermal conductivity of the glass $\varkappa$ is $7 \cdot 10^{-3}\ \mathrm{W \cdot cm^{-1} \cdot deg^{-1}}$.

The calculation of the temperature field enables one

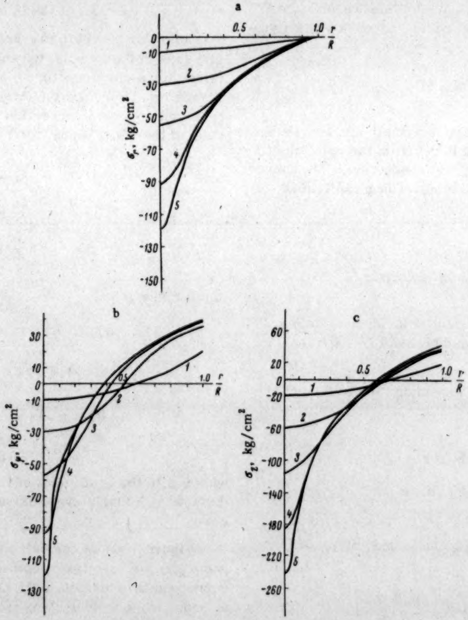

Fig. 2. The distribution of the stationary field of thermoelastic stresses in a sample as a function of a. a) radial; b) angular; c) along z.

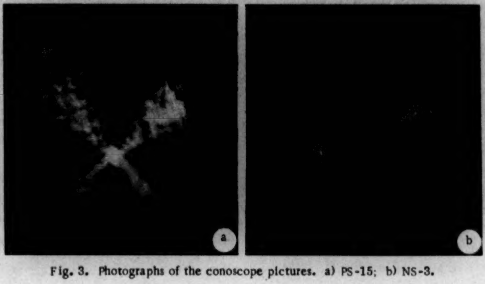

Fig. 3. Photographs of the conoscope pictures. a) PS-15; b) NS-3.

to estimate the value of the absorbed power P_1 necessary to form a melt in the sample at the axis of the laser beam.

Table 1 lists the calculated and experimental values of laser power needed to reach the melting point temperature at the beam axis. To within the accuracy achieved under our conditions (experimental error 30-40% calculation errors ~ 15%), the agreement between the experimental and calculated values can be considered satisfactory.

Measurements of the characteristics of the induced thermal lens are made in order to estimate the temperature distribution. Its parameters are determined by measuring the diameter of the radiation spot in the focal plane of a long-focus lens. In order to take account of the change in the dispersion of the laser radiation itself (in variation of the radiated power level), the measurements are made both with and without the sample. The dimensions of the radiation spot are measured photographically by using electron-optical conversion of its image on a ceramic screen on whose surface is deposited a measuring grid. In certain experiments, the radiation of a He–Ne laser operating in the TEM_{00} mode is used for test purposes. The experimental data are found to be in satisfactory agreement with the theoretical calculation.[5] A discrepancy is observed at high values of P. The reason for this disagreement evidently lies in the change in the parameters of the medium due to the increase in temperature.

The stress distribution is determined by means of induced double refraction. The test radiation of a He–Ne laser is used to observe the induced double refraction. The radiation is passed through classical conoscopes, within which are placed the samples under investigation. Totally reflecting (for $\lambda = 1.06\ \mu$) mirrors and deflecting plates are used to shield the camera from the primary radiation. The conoscope patterns which are obtained for the various samples made of optical glass filters with different amounts of absorption over a laser wavelength closely resemble each other in their essential features (Fig. 3). The stabilization time of the conoscope pictures is 1-2 sec. The relaxation of the conoscope picture takes 3-4 sec. The contrast of the pictures shows a considerable increase at higher power densities. No essential changes in the character of the picture occur, however. Complete relaxation of the induced double refraction takes place right up to melting and disintegration (observations are made on samples made of NS-2, NS-3, FS-7, PS-6, SZS-5, ZS-1, ZhS-16, and PS-15). The photographs are used to estimate the amount of induced double refraction, with the following result:

$$\Delta n_{x,y} = (0.3 \pm 0.1) \cdot 10^{-4}.$$

An investigation of the distribution of double refraction in the samples shows that it reaches its maximum value in the region of the beam–medium interface, rather than on the axis of the laser beam. Relaxation of the stresses

TABLE 1

Filter brand	$k\lambda$, mm^{-1}	Laser power, W		
		calculated		experimental
		$a = 1$ cm	$a = 0.1$ cm	$a = 0.1$ cm
NS-1	0.05	45	30	25
NS-2	0.12	20	13	9
NS-3	0.22	12.7	8.5	6
NS-6	0.17	16.5	10.3	7.5
NS-11	1.28	6.27	4.18	3
NS-18	1.75	6.15	4.1	2.5
NS-13	0.82	6.6	4.4	3
IKS-3	0.110	22.5	15.0	12
IKS-6	0.063	37.2	24.8	17
IKS-7	0.084	27.0	18.0	15

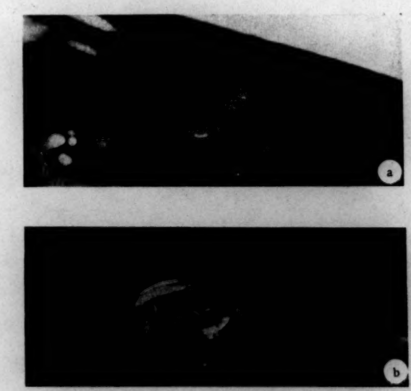

Fig. 4. Photographs of melts at the entrance surface of samples. a) PS-15 b) SZS-22.

in the material within the beam occurs when the softening temperature is reached.

Traces of melts appear at the entrance and exit surfaces of the sample. The form of the melts at both surfaces is the same, but depends essentially on the sample material, the absorbed power, and the focusing. The most common forms of the melts are shown in Fig. 4. The most characteristic form of the initial fissure is that of a circle concentric with the beam. Typical microfissures have a width of from 5 to 20 μ; the diameter of the circles is ~ 3 a. When inhomogeneities are present in the medium, the fissure splits and its shape diverges from that of a circle. Attempts to cut the sample near the fissure cause it to split along the cylindrical surface resting on the fissure.

We have also carried out all of the above-described calculations and experiments for single-crystals made of KDR, ADR, $LiNbO_3$, and others. The results are qualitatively similar to those described above for the case of optical glass. An essential difference does arise, however, in approximating the phase transition temperature. Melting in a single-crystal medium is a very sensitive effect, which depends on a number of factors. In the high temperature region, for glassy media there is a range of softening temperature and the associated changes in the macroscopic parameters of the medium. In crystals, the high temperature region with the presence of thermoelastic stresses is more likely to be associated with a rearrangement of the microscopic structure, rather than being directly related to the macroscopic characteristics.

---

[1] G. Karslou, and D. Eger, Thermal Conductivity of Solid Bodies [in Russian], Izd. Nauka, Moscow (1964), Chapter VII, 2.

[2] S. P. Timoshenko, Theory of Elasticity [in Russian], GITTL, Moscow–Leningrad (1937), Chapter II, Sec. 114.

[3] S. P. Timoshenko, Strength of Materials [in Russian], Izd. Nauka, Moscow (1965), Chapter VI, Sec. 44.

[4] A. I Portnyagin and A. A. Shokin, Prib. Tekh. Eksp., No. 5, 186 (1971).

[5] N S. Bardina, N. L. Pavlova, and A. I. Portnyagin, Proc. Second All-Union Conf. on Physics of the Effect of Optical Radiation on Condensed Media, Leningrad (1972).

Quenching in the CF_3I photodissociation laser

G. A. Skorobogatov, V. M. Tret'yak, and V. S. Komarov

A. A. Zhdanov Leningrad State University

(Submitted April 26, 1973)
Zh. Tekh. Fiz., 44, 784-790 (April 1974)

A model of the CF_3I laser is constructed in which allowance is made for fast reactions of the CF_3 radical; the latest data on the temperature dependences of the rate constants of the chemical reactions are used. The model gives reasonable agreement between the theoretical and experimental characteristics of the stimulated emission of the CF_3I laser over a wide range of pump rates and initial pressures.

1. FORMULATION OF THE PROBLEM

In 1964 Kasper and Pimentel[1,2] obtained laser action on the transition

$$I^1 + h\nu\,(0.942\text{ eV}) \rightarrow I^0 + 2h\nu\,(0.942\text{ eV}) \qquad (1)$$

with the photodissociative pumping mechanism

$$RI + h\nu_{\text{pump}} \rightarrow R + I^1, \qquad (2)$$

where I^1 denotes $I(^2P_{1/2})$, I^0 denotes $I(^2P_{3/2})$, and R denotes the radicals CF_3, C_2F_5, C_3F_7, CH_3, C_2H_5, C_3H_7, etc. However, even for CF_3I and C_3F_7I, the most efficient working materials in terms of power output, the total photon yield of stimulated emission per unit volume G_Σ does not exceed 5-10% of the maximum possible value, $G_{\Sigma\max}$ [see Eq. (64) in ref. 3].

The first mathematically correct treatment of chemical processes leading to quenching in the CF_3I laser is that of Zalesskii and Venediktov,[4] who use Pollack's[5] recombination mechanism for the accumulation of molecular iodine

$$I^l + I^m + M_i \xrightarrow{k_{3ilm}} I_2 + M_i \; (l,\, m=0,\, 1;\; i=1,\, 2) \;\; (3-i,\, l,\, m) \qquad (3)$$

supplemented by the reaction

$$I^1 + I_2 \xrightarrow{k_{21}} I^0 + I_2. \qquad (4)$$

[In (3) M_1 denotes I_2 and M_2 denotes CF_3I]. Zalesskii and Venediktov[4] obtained a certain correlation between the calculated and the experimental values of G_Σ and t_{qu}, the time at which stimulated emission is quenched, but only for weak pumping ($\varphi \leq 10^{20}$ photons/cm^2 · sec in the CF_3I absorption band) and for moderately high pressures ($[CF_3I]_0 \sim 100$ torr). Accordingly, Zalesskii and Moskalev[6] then considered a pyrolysis quenching mechanism in which the quenching is due to population of the lower laser level as a result of the pyrolysis of the working material:

$$CF_3I \rightarrow CF_3 + I^0.$$

In their paper[6] Zalesskii and Moskalev conclude that for trifluoromethane as working substance (unlike, for example, the more thermostable perfluorinated propyl iodide), pyrolysis is quite capable of quenching. We show in ref. 7, however, that if the calculations are not performed for fixed values of the pump power and initial pressure of the working gas, but for the entire experimentally accessible range of these parameters ($[CF_3I]_0$ from 8 to 800 torr, φ from $4 \cdot 10^{20}$ to $4 \cdot 10^{23}$ photons/cm^2 · sec), then the pyrolysis mechanism does not explain existing experimental data on the quenching time and energy output of the CF_3I laser.

Zalesskii[8] later constructed a kinetic model of the CF_3I laser which, for $[CF_3I]_0 = 100$ torr and $\varphi \simeq 4.5 \cdot 10^{21}$ photons/cm^2 · sec, gives good agreement between the experimental and theoretical values of t_{qu} and G_Σ. Nevertheless, there are good reasons for doubting the completeness of the model of ref. 8. First, even when $[CF_3I]_0 = 20$ torr and $\varphi \sim 4 \cdot 10^{21}$, as Zalesskii notes in ref. 8, satisfactory agreement between the calculated and experimental values of t_{qu} and G_Σ does not obtain. Second, the model of ref. 8 consists essentially of processes (1)-(4) used in ref. 4 supplemented by certain insignificant processes (this can be seen from Table 2 of ref. 8, for instance), whereas we had previously pointed out[7] that model (1)-(4) is incomplete as it only works at low pump powers ($\varphi \leq 10^{21}$ photons/cm^2 · sec) and not for all values of $[CF_3I]_0$.

Further, in ref. 8 Zalesskii estimates the rate constant k_{3200} from the boiling point of CF_3I and the resulting value used by him, $2.2 \cdot 10^{-32} \exp(855/T)$ cm^6/mole^2 · sec in the range 20-200°C, is three times greater than the true value, $(1.4 \pm 0.4) \cdot 10^{-33} \exp\,[(1600 \pm 400)/T]$, experimentally obtained[9] by flash photolysis. The high value of k_{3200} must unavoidably create an illusion of validity of model (1)-(4) at higher values of φ. This illusion is heightened by the use of a temperature-independent rate constant $k_{21} = 5 \cdot 10^{-12}$ cm^3/mole · sec (see ref. 10), whereas the true value of $k_{21} = 3.9 \cdot 10^{-14} \exp(1660/T)$ cm^3/mole · sec (ref. 11) is less than $5 \cdot 10^{-12}$ even at 350°K, being only $6 \cdot 10^{-13}$ at 600°K. [These remarks pertain not only to Zalesskii's paper,[8] but also to the papers by Filyukov and Karpov,[12] which are mathematically correct and very interesting, but in which the chemical ideas do not go beyond the model (1)-(4)].

On the other hand, our calculations[7] and the calculations of other investigators[4,8,12] are somewhat out of date. Thus, it is assumed in refs. 4, 12 that $k_{3i11} = k_{3i10} = k_{3i00}$, while in ref. 7 we take $k_{3i10} = k_{3i00}$, $k_{3i11} = 0$. Direct measurements[13,14] have shown, however, that within the limits of experimental error $k_{3i11} = k_{3i10} = 0$. Furthermore, and this is most important, we have previously shown[15,16] that the strong quenching of excited $I(^2P_{1/2})$ atoms at low pressures $[CF_3I]_0$ and at high pump powers cannot be explained by the formation of molecular iodine I_2 through any realistic mechanism, and that this quenching must be ascribed to some other particles. Indeed, Pimentel et al.[17] have recently determined, by flash photolysis, the rate constant of the process

$$I(^2P_{1/2}) + CF_3 \xrightarrow{k_{10}} I(^2P_{3/2}) + CF_3. \qquad (5)$$

At 298°K this quantity is $3.7 \cdot 10^{-12}$ cm^3/mole · sec. Increasing the temperature by a few hundred degrees results in an order of magnitude increase of k_{26}, and it is accordingly 100 times greater than k_{21} (see ref. 11). According to Pimentel et al.[17] the rate constants for the reactions

$$I(^2P_{3/2}) + CF_3 \xrightarrow{k_{60}} CF_3I, \tag{6}$$

$$CF_3 + CF_3 \xrightarrow{k_{700}} C_2F_6, \tag{7}$$

are also very large.

It would thus appear that the operation of the CF_3I laser is governed by reactions (5)-(7), especially at low pressures and high pump powers.

2. CHOICE OF RATE CONSTANTS

In accordance with the ideas of Sec. 1, the main processes occurring in the working volume of the CF_3I laser can be taken to be processes (1)-(7) and the reaction

$$CF_3 + I_2 \xrightarrow{\bar{k}_{900}} CF_3I + I(^2P_{3/2}), \tag{8}$$

the rate constant of which, from ref. 18, is $\bar{k}_{900} = 4.3 \times 10^{-12}$ cm^3/mole · sec. (In the present work we use the notation for the rate constants adopted in our previous papers.[3,7,15,16])

As mentioned in Sec. 1, experimental data[13,14] imply that $k_{3i11} = k_{3i10} = 0$. From ref. 19, $k_{3100} = 1.287 \times 10^{-33} \cdot (T/300)^{3/2} \exp(2676/T)$ cm^6/mole^2 · sec; from ref. 9, $k_{3200} = 1.4 \times 10^{-33} \cdot \exp(1600/T)$ cm^6/mole^2 · sec; and from ref. 11, $k_{21} = 3.9 \cdot 10^{-14} \exp \times (1660/T)$ cm^3/mole · sec. It remains to choose the rate constants for the reactions (6)-(7).

The values given by Pimentel et al.[17] cannot be regarded as completely correct. In mathematical terms, two algebraic equations are obtained in ref. 17 for the three unknowns, k_{26}, k_{60}, and $k_{7300}\,[Ar]_0$, where k_{7300} is the rate constant of the reaction

$$2CF_3 + Ar \rightarrow C_2F_6 + Ar \tag{9}$$

and $[Ar]_0 = 100$ torr. One equation is obtained from photolysis of CF_3I in a kinetic experiment and the second from an analysis of the composition of the final products of the photolysis of CF_3I. The authors of ref. 17, guiding themselves by the analogy with the reaction $Cl + CH_3 \rightarrow CH_3Cl$, take for k_{60} the value $6 \cdot 10^{-10}$ cm^3/mole · sec, after which calculations give for the other two unknowns $k_{26} = 3.65 \cdot 10^{-12}$, $k_{7300}\,[Ar]_0 = 9.8 \times 10^{-12}$ cm^3/mole · sec for 25°C and $k_{26} = 4.5 \cdot 10^{-12}$, $k_{7300}\,[Ar]_0 = 1.18 \cdot 10^{-11}$ for 60°C. A mathematical analysis shows, however, that for such a large value of $k_{60} = 6 \cdot 10^{-10}$ laser action in the CF_3I laser would not be quenched until the temperature of the working mixture reaches ~ 1500°K. The experimental data on the operation of the CF_3I laser accordingly imply that k_{60} is much smaller than $6 \cdot 10^{-10}$. The choice of a new value of k_{60} does not greatly influence the values of k_{26} calculated by Pimentel. Thus, for 25°C the value $k_{60} = 1.5 \cdot 10^{-10}$ corresponds to the value $k_{26} = 4.55 \cdot 10^{-12}$, and $k_{60} = 7.5 \cdot 10^{-11}$ corresponds to $k_{26} = 5.10 \cdot 10^{-12}$. Finally, according to our calculations in conjunction with the experimental results of Pimentel et al.,[17] we find that

$$k_{60} = 1.5 \cdot 10^{-11} \text{ corresponds to } k_{26} = 9.8 \cdot 10^{-11} \sqrt{\frac{T}{300}}\, e^{-581/T}, \tag{10a}$$

$$k_{60} = 2 \cdot 10^{-11} \text{ corresponds to } k_{26} = 7.2 \cdot 10^{-11} \sqrt{\frac{T}{300}}\, e^{-581/T}, \tag{10b}$$

$$k_{60} = 3.75 \cdot 10^{-11} \text{ corresponds to } k_{26} = 4.46 \cdot 10^{-11} \sqrt{\frac{T}{300}}\, e^{-581/T}. \tag{10c}$$

Turning now to the rate constant k_{700} we note that, strictly speaking, there are no experimental data for this quantity. The point is that all measurements of the recombination rate of CF_3 radicals have been made either in the presence of argon[17,20,21] or in the presence of perfluoroacetone,[22] so that the bimolecular constants given in refs. 17, 20-22 are sums

$$k_{700} + k_{7i00}[M_i], \tag{11}$$

where k_{7i00} is the rate constant for recombination of CF_3 radicals on a third body M_i:

$$2CF_3 + M_i \rightarrow C_2F_6 + M_i.$$

A study of the values of the sum (11) given by the various authors gives approximately k_{700} (293°K) = 10^{-11} cm^3/mole · sec; accordingly, in our calculations we use the value

$$k_{700} = 10^{-11} \sqrt{\frac{T}{300}} \quad \text{cm}^3\text{/mole} \cdot \text{sec}$$

Thus, in our model (1)-(8) we utilize the experimentally measured values of all rate constants except k_{60}. The value of k_{60} is found by comparing the characteristics of the CF_3I laser calculated from (1)-(8) with experiment.

3. KINETIC MODEL OF CF_3I LASER

Reactions (2)-(7) listed in Sec. 1, 2 coincide respectively with reactions (6), (10-ilm), (9-1), (9-6), (13-0), (14-00) of our previous paper,[3] while reaction (8) is the inverse of reaction (16-00) of ref. 3. The operation of the CF_3I laser will be described within the framework of the model of Sec. 1 of ref. 3, and we shall assume that the critical inversion is equal to zero (P = 0), $s_{00} = 0$ (see refs. 13, 1), and that the pump pulse $\varphi(t)$ is of the form

$$\varphi(t) = M\Theta(t), \tag{12}$$

where $\Theta(t)$ is the Heaviside function. The rectangular waveform (12) of the pump pulse is chosen so that the effect of the chemical processes on the output radiation pulse should be obscured as little as possible by the shape of the pumping pulse.

Under the stated assumptions, stimulated emission commences at t = 0 and its variation in time G(t), along with the variation in time of the concentrations of all the components, will be described by Eqs. (20)-(26) of ref. 3. In the case of model (1)-(8) these equations acquire the following form:

$$G(t) = \frac{2}{3}\gamma[RI] - \sum_{i=1,6} k_{2i}[M_i][I^1] + \frac{1}{3}[I^0]^2 \sum_{i=1,2} k_{3i00}[M_i]$$

$$+\frac{1}{3}k_{60}[I^0][R]-\frac{1}{3}\bar{k}_{900}[R][I_2], \qquad (13)$$

$$\frac{d[RI]}{dt}=-\gamma[RI]+k_{60}[I^0][R]+\bar{k}_{900}[R][I_2], \qquad (14)$$

$$\frac{d[J^1]}{dt}=\gamma[RI]-G(t)-\sum_{i=1,6}k_{2i}[I^1][M_i], \qquad (15)$$

$$\frac{d[I^0]}{dt}=G(t)+\sum_{i=1,6}k_{2i}[I^1][M_i]-[I^0]^2\sum_{i=1,2}k_{3i00}[M_i]$$
$$-k_{60}[I^0][R]+\bar{k}_{900}[R][I_2]. \qquad (16)$$

$$\frac{d[I_2]}{dt}=\frac{1}{2}[I^0]^2\sum_{i=1,2}k_{3i00}[M_i]-\bar{k}_{900}[R][I_2], \qquad (17)$$

$$\frac{d[R]}{dt}=\gamma[RI]-k_{60}[R][I^0]-k_{700}[R]^2-\bar{k}_{900}[R][I_2], \qquad (18)$$

where M_1, M_2, M_6 denote I_2, RI, and R respectively, R denotes CF_3, and

$$\gamma\equiv s_0 M \ (1/\text{sec}). \qquad (19)$$

Here, s_0 is the mean (over the absorption band) absorption cross section for CF_3I and M is the pump power in the CF_3I band, whence (19) immediately characterizes the pump rate in the chemical system.

The equation for $[C_2F_6]$ can be separated from Eqs. (13)-(18) and has not been written out. In Eqs. (13)-(18) all the constants k are explicit functions of temperature T. The time variation of T is described with the aid of the approximation of Section 2 of ref. 3; accordingly, from Eq. (45) of ref. 3 for the model (1)-(8) considered here

$$T(t)=T_0+\frac{K}{C_{RI}}(1-e^{-\gamma t})=293+4883(1-e^{-\gamma t}), \qquad (20)$$

where C_{RI} = 16.9 cal/deg · mole is the molar specific heat of CF_3I, and K = 82,500 cal = 3.58 eV is the heat input to the system for absorption of a single pump photon in (2).

Numerical integration of Eqs. (13)-(18) is carried out on a BÉSM-6 high-speed digital computer. The calculations are performed for the three variants of model (1)-(8) corresponding to cases (10a), (10b), and (10c) with temperature dependence (20), and also for two variants of model (1)-(4) with the values of k_{3i00} and k_{21} specified in Sec. 2 and with temperature dependence (20) in the one variant and a temperature dependence T(t) = const = T_0 in the other. The results of the calculations are presented in Table 1, which also shows the experimental results obtained in ref. 23.

It can be seen from the table that only calculations according to model No. 2 agree with experiment over the entire range of the parameters $[CF_3I]_0$ and γ. This means that only situation (10b) corresponds to reality as far as rate constants k_{60} and k_{26} are concerned. It was not possible, however, to achieve complete coincidence (within the limits of experimental error). This is hardly surprising since, on the one hand, the presence in the experimental results of hidden systematic errors cannot be excluded. On the other hand, the theoretical calculations for model No. 2 make the manifestly coarse assumption that k_{60} and k_{700} are independent of temperature. Unfortunately, there are no experimental data on the functions $k_{60}(T)$ and $k_{700}(T)$, while the present state of the theory of rate constants does not yield even a guess at the form of these functions.

Thus, on the whole, model (1)-(8) with rate constants (10b) works satisfactorily over a wider range of varia-

TABLE 1. Theoretical and Experimental Dependence of t_{qu} and Γ_Σ of Small-Volume (transparent for pumping radiation) CF_3I Laser on Initial Pressure p_0 of Working Gas and on Pumping Rate γ, Equal to $1.6 \cdot 10^i$ sec^{-1}

p_0, torr	Model No.	t_{qu}, μsec					$\Gamma_\Sigma(\%)=100\cdot\frac{1.5}{[CF_3I]_0}\int_0^{t_{qu}}G(t)\,dt$				
		i = 1	i = 2	i = 3	i = 4	i = 5	i = 1	i = 2	i = 3	i = 4	i = 5
10	1	1973	224	27.7	4.46	0.855	1.47	1.79	2.54	4.52	9.00
	2	4471	476	53.0	6.52	1.097	4.02	4.25	4.74	6.31	11.03
	3	21410	2186	229.2	25.10	2.933	19.99	20.06	20.24	20.72	22.76
	4	3460	3766	1262	126.5		3.30	35.21	83.48	86.37	
	5	1093	336	108.7	35.54	12.037	1.32	4.09	12.60	35.57	77.89
	*	2800	500	70	11		2.3	3.6	4.9	6.3	
80	1	1656	202	22.9	2.83	0.462	1.10	1.52	1.86	2.67	4.82
	2	4280	453	48.2	5.40	0.687	3.56	4.06	4.31	4.83	6.61
	3	21250	2155	220.0	22.98	2.539	19.67	20.03	20.11	20.30	20.82
	4	307	184	262.6	125.2		0.38	1.90	24.75	85.45	
	5	253	82	25.9	8.07	2.518	0.32	1.02	3.20	9.79	28.27
	*		300	60	11	1.5		2.7	4.3	5.8	7.2
640	1	382	171	22.5	2.54	0.300	0.28	1.08	1.76	2.10	2.88
	2	2200	444	48.1	5.02	0.556	0.79	3.35	4.31	4.58	5.04
	3	20400	2201	222.6	22.48	2.349	15.56	19.51	20.43	20.48	20.53
	4	89	33	29.6	114.3		0.11	0.40	2.36	55.45	
	5	84	27	8.5	2.86	1.087	0.11	0.34	1.09	3.50	11.93
	*				3	0.6				1.5	3.3

Note: Nos. 1, 2, 3 correspond to model (1)-(8) for cases (10a), (10b), and (10c), respectively and temperature dependence (20); No. 4 corresponds to model (1)-(4) with temperature dependence (20); No. 5 corresponds to model (1)-(4) with temperature T(t) = const = T_0 = 293°K. The asterisks denote experimental values obtained through interpolation and extrapolation of the results of ref. 23; the relative error of the experimental data is ± 15% for Γ_Σ and ± 25% for t_{qu}.

tions of the parameters $[CF_3I]_0$ and γ than any other model. The value of $k_{60} = 2.10^{-11}$ cm^3/mole·sec obtained by us is, in fact, a certain "average value" of $k_{60}(T)$ in the temperature interval 300–700°K.

It is clear also from the data of the table that the "recombination mechanism" (1)–(4) (model No. 4) does not give remote agreement between calculation and experiment. It can also be seen that the recombination mechanism with fixed rate constant (model No. 5), which manifestly does not correspond to reality, gives for $160 < \gamma < 1600$ and 50 torr $< p_0 <$ 100 torr the illusion for coincidence of theoretical and experimental data. (The calculations of refs. 8 and 12 pertain to just such values of the parameters γ and p_0.) Model No. 5 does not work, however, for $p_0 <$ 20 torr and $160 < \gamma < 1600$, and gives values of Γ_Σ and t_{qu} that are too high compared with experiment. Mention is made of these high values both in ref. 8 and in ref. 12. This demonstrates again the methodological incorrectness of drawing conclusions on the validity of a given model for the photodissociation laser solely on the grounds that the calculated and experimental data coincidence for certain randomly chosen values of the pressure (p_0) and the pump rate (γ). Before such a conclusion can be drawn it is necessary, at the very least, that the calculated and experimental data coincide in the entire experimentally accessible range of variation of the parameters p_0 and γ.

This remark also applies to the recent paper by Hohla and Kompa.[24] The merit of the kinetic model of the CF_3I laser constructed in ref. 24 is that it incorporates reactions (5)–(7) [but not (8)]. However, all rate constants in ref. 24 are assumed to be temperature independent, most of them differ appreciably from their true values, and the calculation is carried out only for a single value of the parameters p_0 and γ.

---

[1] J. V. V. Kasper and G. C. Pimentel, Appl. Phys. Lett., 5, 231 (1964).

[2] J. V. V. Kasper, J. H. Parker, and G. C. Pimentel, J. Chem. Phys., 43, 1827 (1965).

[3] G. A. Skorobogatov, Vestn. LGU, No. 4, 144 (1970).

[4] V. Yu. Zalesskii and A. A. Venediktov, Zh. Eksp. Teor. Fiz., 55, 2088 (1968) [Sov. Phys. – JETP, 28, 1104 (1969)].

[5] M. A. Pollack, Appl. Phys. Lett., 8, 36 (1966).

[6] V. Yu. Zalesskii and E. I. Moskalev, Zh. Eksp. Teor. Fiz., 57, 1884 (1969) [Sov. Phys. – JETP, 30, 1019 (1970)].

[7] G. A. Skorobogatov and V. E. Khomenko, Vestn. LGU, No. 10, 170 (1970).

[8] V. Yu. Zalesskii, Zh. Eksp. Teor. Fiz., 61, 892 (1971) [Sov. Phys. – JETP, 34, 474 (1972)].

[9] B. P. Dymov and G. A. Skorobogatov, ZhOKh, 44, No. 5 (1974).

[10] R. J. Donovan and D. Husain, Nature, 206, 171 (1965).

[11] I. I. Deakin and D. Husain, J. Chem. Soc. (Far. Trans.), II, 68, 1603 (1972).

[12] A. A. Filyukov and V. Ya. Karpov, Zh. Eksp. Teor. Fiz., 62, 119 (1972) [Sov. Phys. – JETP, 35, 63 (1972)]; Khimiya Vysokikh Energii, 7, 235 (1973).

[13] R. J. Donovan and D. Husain, Trans. Far. Soc., 62, 11 (1966); E. W. Abrahamson, L. J. Andrews, D. Husain, and J. R. Wiesenfeld, J. Chem. Soc. (Far. Trans.), II, 68, 48 (1972).

[14] V. Yu. Zalesskii and T. I. Krupenikova, Opt. Spektrosk., 30, 813 (1971).

[15] G. A. Skorobogatov and V. E. Khomenko, Vestn. LGU, No. 16, 109 (1972).

[16] G. A. Skorobogatov, Vestn. LGU, No. 22, 84 (1972).

[17] T. Ogawa, G. A. Carlson, and G. C. Pimentel, J. Chem. Phys., 74, 2090 (1970).

[18] V. N. Kondrat'ev, Rate Constants of Gas-Phase Reactions [in Russian], Izd. Nauka, Moscow (1970).

[19] D. L. Bunker and N. Davidson, J. Am. Chem. Soc., 80, 5085 (1958).

[20] N. Basco and F. G. M. Hathorn, Chem. Phys. Lett., 8, 291 (1971).

[21] A. P. Modica and S. J. Sillers, J. Chem. Phys., 48, 3283 (1968).

[22] P. B. Auscough, J. Chem. Phys., 24, 944 (1956).

[23] V. S. Komarov, V. G. Seleznev, and G. A. Skorobogatov, Zh. Tekh. Fiz., 44, 875 (1974) [Sov. Phys. – Tech., Phys., 19, 558 (1974)].

[24] K. Hohla and K. L. Kompa, Z. Naturforsch., 27a, 938 (1972).

Energy input in electrical ionization lasers

Yu. I. Bychkov, Yu. D. Korolev, Yu. A. Kurbatov, and G. A. Mesyats
Institute of Atmospheric Optics, Siberian Branch,
Academy of Sciences of the USSR, Tomsk
(Submitted May 17, 1973)
Zh. Tekh. Fiz., 44, 791-796 (April 1974)

The development of a volume discharge excited by a beam of fast electrons is studied at pressures $P \geq 1$ atm. The current characteristics are calculated allowing for the parameters of the discharge circuit and the energy input to the gas is analyzed. For $P \approx 2$ atm the specific energy introduced into a mixture of N_2 and CO_2 is $W_g \sim 1$ J/cm^3. These values are achieved at a current density in the electron beam $j_{beam} \sim 5$-10 A/cm^2 and a beam lifetime $\tau_{beam} \sim 4 \cdot 10^{-8}$ sec. It is shown that maintenance of the discharge by ionization processes permits a substantial reduction in the beam current while maintaining acceptable energy characteristics and sparkless operation. For example, $W_{gas} \sim 0.1$ J/cm^3 with $j_{beam} \sim 0.1$ A/cm^2 amd $\tau_{beam} \sim 2 \cdot 10^{-8}$ sec.

1. INTRODUCTION

The problem of constructing a gas laser with a high light energy per unit volume is closely linked to the problem of obtaining a volume discharge at pressures of the order of an atmosphere or higher. Such discharges have been obtained with the aid of a beam of fast electrons.[1] Lasers that use a volume discharge are called electrical ionization lasers.[2,3] In the design of such lasers it is important to find regimes in which large specific energies are dissipated in the gas, a matter to which a number of papers have been devoted.[3-6]

Until now, however, little attention has been given to the effect of the characteristics of the discharge circuit on the passage of the current. An understanding of this feature is necessary in order to optimize the transfer of energy to the gas. An analysis of the introduction of energy into the gas volume allowing for the parameters of the discharge circuit is given in the present paper.

THE FUNDAMENTAL EQUATIONS

The equations that describe the input of energy into the gas are

$$\frac{dn}{dt} = (\alpha - \eta)\mu E n - \beta n^2, \tag{1}$$

$$j = en\mu E, \tag{2}$$

$$j = -C\frac{d}{S}\frac{dE}{dt}, \tag{3}$$

$$W_g = \int_0^t E j dt, \tag{4}$$

where n is the electron density, E is the electric field in the gap, μ is the electron mobility, α, η, β are the coefficients of ionization, attachment, and combination, j is the discharge current density, W_{gas} is the specific (i.e., per unit volume) energy released in the gas, C is the capacitance of the condenser bank, d/S is the ratio of the height of the discharge column to its area, and e is the electron charge.

The equations are subject to the following limitations. Equations (1)-(2) are valid for $n > 10^{11}$ cm^{-3}, since it is only at high electron densities that a cathode drop is formed with length $l_{cath} \ll d$ and the conductivity of the gap is determined by electron drift.[4]

For most cases of practical importance the resistance of the plasma is ohmic in character so that the effect of inductance can be neglected in the Kirchhoff equation (3).

In the experiments, the discharge is initiated by a beam of short lifetime $\sim 10^{-8}$ sec, and the ionizing effect of the beam is allowed for in the initial conditions $n(0) = n_0$, $E(0) = E_0$, $j(0) = j_0$.

There are two regimes of interest in connection with the introduction of energy into the gas, namely: 1) no impact ionization in the gas, $(\alpha - \eta)\mu E \ll \beta n$; and 2) ionization operates and the incremental electron density due to electron multiplication in the gas is important.

DISCHARGE WITHOUT IMPACT IONIZATION IN THE GAS

This regime can be realized in practice at low values of the electric field E, for example, when $E \leq 0.3E_{st}$ (E_{st} is the static breakdown electric field).

However, remembering that the energy introduced into the gas increases with increasing field, there is clearly practical interest in the possibility of operating at high E up to the breakdown value E_{bd}. In order to realize a regime without ionization enhancement the electron density must be large.

Subject to the condition $(\alpha - \eta)$ vn = 0 Eqs. (1)-(4) can be solved analytically to give

$$E = E_0(1 + \beta n_0 t)^{-\frac{Se\mu}{Cd\beta}}, \tag{5}$$

$$j = en_0\mu E(1 + \beta n_0 t)^{-\left(1 + \frac{Se\mu}{Cd\beta}\right)}, \tag{6}$$

$$W_g = \frac{CE^2}{2}\frac{d}{S}\left[1 - (1 + \beta n_0 t)^{-\frac{2Se\mu}{Cd\beta}}\right]. \tag{7}$$

It is meaningful to consider the energy released only up to a certain critical time $t_{cr} = [(n_0/n_{cr}) - 1]/\beta n_0$, when the electron density has fallen to n_{cr}, the value of n at which the length of the cathode drop becomes comparable with the length of the discharge gap. The input of energy to the gas then effectively ceases.[4-6] Experimental estimates give $n_{cr} \sim 5 \cdot 10^{10}$-$10^{11}$ cm^{-3}.

The energy introduced into the laser medium is obtained by inserting the expression for t_{cr} into (7):

$$W_g = \frac{CE_0^2}{2}\frac{d}{S}\left[1 - \left(\frac{n_{cr}}{n_0}\right)^{A/\theta}\right], \tag{8}$$

where $A = (2se\mu)/d\beta$.

The energy input increases in proportion to E^2. If $E_0/P = \text{const}$, then, remembering that $\mu \sim 1/P$ and that $U_0 \sim P$, the function $W_g = W_g(P)$ varies somewhat more slowly than a quadratic. Let us consider in more detail the dependence of W_g on C. It is readily seen that when $n_{cr}/n_0 \ll 1$ and $A > C$, the energy input increases linearly with increasing C. This result means that the conductivity of the gap is sufficient to allow the capacitor to discharge completely in a time t_{cr}. Strictly speaking, the discharge time of the capacitor depends on the relationship between the geometrical dimensions of the discharge column and the value of the capacitance. A universal parameter characterizing the rate of voltage drop is given by (Cd)/S. When this parameter is increased (e.g., by increasing C) the linear growth of W_g is maintained so long as $(n_{cr}/n_0)^{A/C} \ll 1$, after which it slows down. The limiting energy as $C \to \infty$ can be written

$$W_{\text{lim}} = \frac{e\mu E_0^2}{\beta} \ln \frac{n_0}{n_{cr}}. \tag{9}$$

The input energy is thus effectively increased with increasing C up to a certain value slightly greater than the parameter A. The energy can be increased at larger values of C by increasing n_0, although this dependence is very weak since n_0 appears under the logarithm sign. This means that increasing the beam current density is not accompanied by a growth of the input energy. Experiments have shown that it is pointless to increase the current density of the beam beyond 5 A/cm², which corresponds to a density $n_0 \sim 5 \cdot 10^{13}$ cm^{-3} at P = 1 atm.

Curves of specific energy versus E/P are shown in Fig. 1 for various mixtures. Spark breakdown is absent in all cases. It is characteristic that by suitably choosing the values of C a sparkless discharge regime can be obtained for values of E/P close to breakdown. This fact acquires special significance in the case of a discharge in a mixture with a large CO_2 content. Data on the initiation of a discharge at high pressures but at low values of $E/P \leqslant 20$ V/cm · mm Hg are given in ref. 7, where it is shown that electrons are lost from the discharge mainly through attachment to CO_2 molecules. The high values of $E/P > 20$ V/cm · mm Hg in our case and the resulting insignificant losses due to attachment[8] mean that more effective use can be made of the electron beam. The drop of electron density to n_{cr} takes place over a longer time and the energy introduced into the volume increases. For example, with a 5 A/cm² electron beam the energy input to a CO_2-N_2 (1:3) mixture at P = 2 atm is $W_g \sim 1$ J/cm³. A laser operating in the described regime gave an output light energy of ~ 2.5 J. The total volume of the active region is ~ 40 cm³ with a length of 40 cm (see ref. 9).

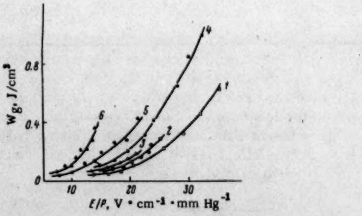

Fig. 1. Curves of $W_g = f(E_0/P)$ for regime without ionization enhancement (spark breakdown absent in all cases). CO_2:N_2:He ratio 1:3:10. 3) 1 atm; 6) 3 atm. Ratio 1 : 3 : 0.1) 1 atm; 4) 2 atm. Ratio 1 : 3 : 3.2) 1 atm; 5) 2 atm.

DISCHARGE WITH ELECTRON MULTIPLICATION IN THE GAS

The main advantage of a discharge without ionization enhancement is its stability in all mixtures at pressures up to tens of atmospheres. The production of high specific energies, however, requires the use of electron beams of high current density, j_{beam}. The values of j_{beam} can be reduced if the initial electrons participate in ionization enhancement.

Let us consider the energy input process, allowing for impact ionization and assuming the field in the gap remains constant during the discharge, i.e., $E(t) = E_0$, or, what is the same thing, $C \to \infty$. The time variation of electron density can then be written

$$n = n_{st} \frac{e^{(\alpha-\eta)vt}}{e^{(\alpha-\eta)vt} - 1 + \frac{n_{st}}{n_0}}, \tag{10}$$

where n_{st} is the stationary electron density, determined from the condition $t \to \infty$,

$$n_{st} = \frac{\alpha - \eta}{\beta} \mu E. \tag{11}$$

The energy introduced per unit volume of the laser medium is given by

$$W_g = \frac{e\mu_- E^2}{\beta} \ln \frac{e^{(\alpha-\eta)vt} - 1 + \frac{n_{st}}{n_0}}{\frac{n_{st}}{n_0}}. \tag{12}$$

It follows from (12) that the energy introduced into the gas increases with time the more rapidly, the larger the quantity $(\alpha - \eta)v$.

An experimental study of this regime has been reported by Korolev and Khuzeev[10] for pure nitrogen and for a mixture of CO_2, N_2, and He. In all cases there is a definite time delay t_d between the time at which the beam is injected and the time at which spark breakdown occurs; a volume discharge exists during this time and energy input to the gas takes place. The time t_d varies from fractions to tens of microseconds and depends strongly on E/P and the gas pressure P. For optimum values of these parameters and an injection current density of 0.1 A/cm² the experimentally measured energy introduced into a

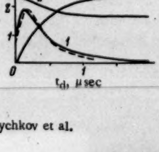

Fig. 2. Theoretical (solid curves) and experimental (dashed curve) variation with delay t_d of (1) current density, (2) voltage, and (3) specific energy input for: $n_0 = 5 \cdot 10^{12}$ cm^{-3}, S = 80 cm², d = 1 cm, C = 10^{-7} F.

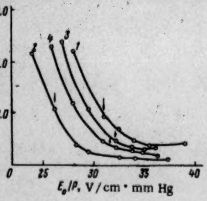

Fig. 3. Delay t_d under various conditions. 1) N_2, $C = 5.6 \cdot 10^{-9}$ F, d = 0.85 cm, S = 5 cm^2, P = 1 atm, $n_0 = 10^{13}$ cm^{-3}; 2) as for curve 1 but with $n_0 = 2 \cdot 10^{12}$ cm^{-3}; 3) $CO_2:N_2 \cdot 10^3$, $C = 5.6 \cdot 10^{-9}$ F, d = 0.85 cm, S = 5 cm^2, P = 1 atm, $n_0 = 6 \cdot 10^{12}$ cm^{-3}; 4) as for curve 3 but with $C = 3.9 \cdot 10^{-9}$ F.

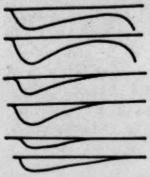

Fig. 4. Oscillograms of discharge current for conditions in the table.

CO_2-N_2 mixture is 0.1-0.2 J/cm^3 for a discharge lifetime 10^{-6}-10^{-5} sec.

Thus, by keeping the field in the gap constant and utilizing electron multiplication it is possible to reduce the current density of the electron beam substantially and to obtain a uniform discharge for times up to 10 μsec. A serious disadvantage of this regime, however, is the fact that the discharge goes over into the spark phase.

With a view to investigating conditions under which the spark phase can be avoided we have analyzed the case with a varying voltage across the capacitor. The initial intensity is high to assure electron multiplication; the field intensity falls as the discharge proceeds. Equations (1)-(4) are solved numerically for these conditions.

A solution for a mixture of the gases CO_2, N_2, and He would be of the greatest interest. However, since the values of the ionization and recombination coefficients are not known over a wide range of variation of E/P for such mixtures, the analysis is performed for nitrogen. The recombination coefficient $\beta = \beta(E/P)$ is taken from the experimental data of Korolev and Khuzeev[10] ($\beta \sim 10^{-6}$ cm^3/sec). The tabulated values are used for α. Typical curves for $n_0 = 5 \cdot 10^{12}$ cm^{-3} are shown in Fig. 2. For sufficiently small n_0, where $(\alpha - \eta)\, vn_0 > \beta n_0^2$, in accordance with (1) we have an increase of electron density and current (curve 1 of Fig. 2).

Recombination losses subsequently begin to balance ionization multiplication, and the drop in voltage is accompanied by a drop in current.

Experiments conducted in pure nitrogen and also in a $CO_2:N_2$ mixture show that a real fivefold enhancement of current can be obtained by impact ionization. The delay t_d before the onset of spark discharge falls sharply when the enhancement is large. Figure 3 shows experimental curves of t_d versus /P for a 1:3 mixture of $CO_2:N_2$.

Discharges in mixtures containing helium prove to be more interesting for practical use. Oscillograms of the discharge current are shown in Fig. 4. In a 1:3:10 mixture of $CO_2:N_2:He$ it is possible to achieve a current enhancement of 10 without spark breakdown.

Table 1 lists the experimental data on the delay t_d, the maximum electron density n_m obtained in the discharge, and the specific energy introduced into the discharge, for various values of E/P and capacitance C. In this experiment the initial electron density produced by the injected beam is $5 \cdot 10^{11}$-10^{12} cm^{-3}, i.e., the current density is 0.1 A/cm^2. It can be seen from the table that at this small value of beam current the energy input to the gas is ~ 0.1 J/cm^3.

The idea of preventing spark discharge by rapidly reducing the voltage across the gap can be realized by means of special circuits. The results of experiments are shown in Figs. 4 and 5. Here, a voltage $U_0 < U_{st}$ is applied to the gap. At beam injection a pulse ΔU of length $\Delta\tau$ is applied so that the total voltage across the gap is $U_0 + \Delta U$. Ionization multiplication occurs for a time $\Delta\tau$. It can be seen that the enhancement k of the initial electron density can be varied by varying ΔU and $\Delta\tau$, and regimes occur ($U_0 \le 0.3U_{st}$) in which spark breakdown does not occur.

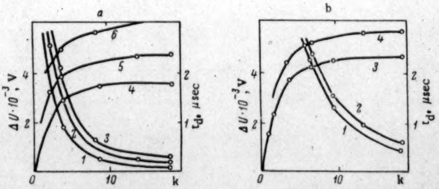

Fig. 5. Curves of ΔU and t_d versus enhancement k for various conditions. a: $n_0 = 5 \cdot 10^{11}$ cm^{-3}, $U_0 = 5.53 \cdot 10^3$ V, d = 0.3 cm, P = 1 atm, $CO_2:N_2$ = 1:3; $\Delta\tau$, nsec: 1) 80; 2) 40; 3) 20; 4) 80; 5) 40; 6) 20. b: As for a, but with $U_0 = 4.5 \cdot 10^3$ V; $\Delta\tau$, nsec: 1) 80; 2) 40; 3) 80; 4) 40.

TABLE 1

C, F	E/P, V/cm · mm Hg	t_d, μsec	$\sim n_{max}$, cm^{-3}	W, J/cm^3	W_{store}, J/cm^3
$5.9 \cdot 10^{-9}$	18.4	1.1	$7.8 \cdot 10^{12}$	0.10	0.173
	19.7	1.0	$1.3 \cdot 10^{13}$	0.13	0.20
$3.9 \cdot 10^{-9}$	18.4	2.6	$7 \cdot 10^{12}$	0.08	0.115
	19.7	$\geqslant 3$	$1.1 \cdot 10^{13}$	0.10	0.132
$2.6 \cdot 10^{-9}$	18.4	> 3	$5.1 \cdot 10^{12}$	0.06	0.0765
	19.7	> 3	$8.3 \cdot 10^{12}$	0.07	0.088

In effect, here a high-power electron injector is replaced by a low-power injector combined with a special circuit for powering the gap. The pulse ΔU can be fed to the gap several times at ~ 1 μsec intervals, when the electron density can fall on account of recombination. Experiments with two pulses have demonstrated the possibility, in principle, of increasing the energy input to the gas by this method.

---

[1] B. M. Koval'chuk, V. V. Kremnev, and G. A. Mesyats, Dokl. Akad. Nauk SSSR, 191, 76 (1970) [Sov. Phys. – Dokl., 15, 267 (1970)]; G. A. Mesyats, B. M. Koval'chuk, and Yu. F. Potalitsin, Author's Certificate No. 356824, Byull. Izobr., No. 32 (1972).

[2] Yu. V. Afanas'ev, É. M. Belenov, O. V. Bogdankevich, V. A. Danilychev, S. G. Darznek, and A. F. Suchkov, Kr. Soobshch. Fiz., No. 11, 23 (1970).

[3] N. G. Basov, É. M. Belenov, V. A. Danilychev, and A. F. Suchkov, Kvant. Elecktron. (Mosc.), No. 3. 121 (1971).

[4] N. G. Basov, É. M. Belenov, V. A. Danilychev, O. M. Kerimov, I. B. Kovsh, and A. F. Suchkov, ZhETF Pis. Red., 14, 421 (1971) [JETP Lett., 14, 285 (1971)].

[5] B. M. Koval'chuk, V. V. Kremnev, G. A. Mesyats, Yu. V. Potalitsin, ZhPMTF, No. 6, 21 (1971).

[6] G. A. Mesyats, Yu. I. Bychkov, V. V. Kremnev, Yu. D. Korolev, Yu. A. Kurbatov, and V. V. Savin, Preprint [in Russian], Institute of Atmospheric Optics, Siberian Branch,, Academy of Sciences of the USSR, No. 3 (1972).

[7] N. G. Basov, É. M. Belenov, V. A. Danilychev, O. M. Kerimov, I. B. Kovsh, and A. F. Suchkov, Zh. Tekh. Fiz., 42, 2540 (1972) [Sov. Phys. – Tech. Phys., 17, 1976 (1973)].

[8] S. C. Brown, Elementary Processes in Gas Discharges, Wiley, New York (1961).

[9] G. A. Mesyats, Yu. I. Bychkov, and Yu. A. Kurbatov, in: High-Power Impulsive Nanonsecond Sources of Accelerated Electrons (G. A. Mesyats, ed.) [in Russian], Izd. Nauka, Novosibirsk (1973).

[10] Yu. D. Korolev and A. P. Khuzeev, in: High-Power Impulsive Nanosecond Sources of Accelerated Electrons (G. A. Mesyats, ed.) [in Russian], Izd. Nauka, Novosibirsk (1973).

Pulsed neodymium-glass laser with periodic Q switching

T. A. Kuzovkova, E. V. Nilov, V. A. Rusov, I. N. Semenov, and A. A. Chertkov

(Submitted January 11, 1973; resubmitted July 5, 1973)
Zh. Tekh. Fiz., 44, 797-802 (April 1974)

A pulsed neodymium-glass laser with periodic Q switching is described; high-frequency giant pulses are generated by this laser. The operation is analyzed and approximate expressions are derived to relate the laser parameters to the apparatus parameters. Experimental investigations are described.

1. INTRODUCTION

In many physics problems it is useful to have a source of light which gives a series of short, high-frequency, high-power pulses. This kind of operation can be obtained by means of a pulsed solid-state laser that uses multiple Q switching of the laser resonator. Well-known examples of such lasers are the ruby laser,[1-4] the neodymium-glass laser,[5,6] the neodymium-doped YAG laser,[7-9] and also neodymium lasers in which infrared radiation is converted into the second harmonic.[5-9] The resonators of these lasers are periodically Q-switched by devices similar to those used for Q switching under single-pulse conditions; optomechanical,[1,5,7] electrooptical,[2-4,8] and optoacoustic[6,9] devices are used for this purpose.

Pulsed lasers operating with a periodically Q-switched resonator have so far only been used in practice for high-speed filming,[2,3,5] but they can also be used for plasma diagnostics,[10] for microprocessing materials[9] and in other cases where giant light pulses and high repetition frequencies are required over comparatively short time intervals.

It should be noted that since no other methods of obtaining high repetition frequencies of giant pulses exist presently (insufficient mean source powers of the pump and the power limitations of the active material), the problem of designing and developing periodically Q-switched pulsed lasers is an urgent one.

The present paper gives an analysis of certain processes which occur in lasers in which neodymium glass is used as the active medium.

2. ANALYSIS OF PERIODIC LASING OF A NEODYMIUM LASER WITH A PULSED PUMP

When the resonator is subjected to periodic Q switching, while the quasistationary pumping pulse is acting, a synchronous process of pulse generation occurs which is accompanied by an alternate rise and fall in the population inversion. At low Q-switching frequencies ($f < 1/\tau$, where τ is the lifetime in the metastable level) the amplitude of the pulses generated remains constant. This result is due to the constancy of the population inversion until each pulse starts, which is ensured by stabilizing the pumping power level, and is achieved in practice by using as the pumping tube supply the discharge of a long artificial line matched to the internal impedance of the tube during the period in which it flashes. Under these conditions the parameters of the pulses generated are similar to the parameters of the pulses obtained under single-pulse conditions.

As the Q-switching frequency is increased the lasing frequency increases; beginning at a certain frequency $f \approx 1/\tau$, the amplitude decreases. At a certain frequency ($f = f_t$), which depends on the laser parameters, the value of the initial population inversion becomes equal to the threshold value. A further increase in the Q-switching frequency will cause gaps to occur in the lasing.

The analysis of the processes which occur when the laser is periodically Q-switched applies for the single-mode approximation. It enables us to explain the physical behavior of periodic high-frequency lasing, and to make positive estimates of the expected power characteristics of the laser from the known parameters of the apparatus.[9,11]

The process of the periodic generation of pulses which have parameters close to the parameters of giant pulses, is described by the well-known rate equations for the relative density of the population inversion and the density of the radiation emitted.[11]

Values of the relative density of the population inversion at the beginning of each pulse, y_0, and at the end $y_{\min}$, for a rectangular pump pulse, can be obtained from the following set of equations:

$$y_0 - y_{\min} = \frac{k_1}{\varkappa} \ln \frac{y_0}{y_{\min}}, \tag{1}$$

$$y_0 = \frac{G}{D}\left(1 - e^{-D/2f}\right) + y_{\min} e^{-D/2f}, \tag{2}$$

where f is the repetition frequency of the pulses, k_1 is the overall loss factor, $\varkappa$ is the maximum gain, and G and D are quantities which are proportional to the pump power, being given by the following expressions:

$$D = 2(\eta B U_H + P_{32} + P_{31}), \tag{3}$$

$$G = 2\eta B U_H. \tag{4}$$

In these expressions $\eta = P_{43}/(P_{43} - P_{41})$, U_H is the density of the pump radiation, P_{ij} is the probability of the corresponding interlevel transition, and B is the Einstein coefficient.

It is difficult to obtain accurate values of y_0 and $y_{\min}$, in Eqs. (1) and (2), because of the complexity of the calculations. For practical purposes, however, it is sufficient to use approximate values of these quantities, which can be obtained as follows.

Consider the region of lasing frequencies in the range 10-100 kHz. Below 10 kHz the processes by which the pulses develop are identical with the processes under single-pulse conditions. The number of pulses in this case is small, due to the power limitations of the flash tube. Above 100-150 kHz the development of the pulses is similar to the development of pulses under regular free-running conditions.

At frequencies $f \geq 10$ kHz the quantity $D/(2f)$ in Eq. (2) is very much smaller than unity. Expanding the function $\exp(-D/2f)$ in a Taylor series, and using the first three terms of this expansion, we can transform expression (2) as follows:

$$y_0=\frac{G}{2f}\left(1-\frac{D}{4f}\right)+y_{\min}\left(1-\frac{D}{2f}+\frac{D^2}{8f^2}\right). \qquad (5)$$

The quantity $y_{\min}$ is found from Eq. (1) by substituting Eq. (5):

$$\delta \ln \frac{a+by_{\min}}{y_{\min}}=a-y_{\min}C, \qquad (6)$$

where

$$\delta=\frac{k_1}{\varkappa};\ a=\frac{G}{2f}\left(1-\frac{D}{4f}\right);$$

$$b=1-\frac{D}{2f}+\frac{D^2}{8f^2};\ C=\frac{D}{2f}-\frac{D^2}{8f^2}.$$

Since $a \gg y_{\min}C$, we can write expressions for y_0 and $y_{\min}$ which depend on the frequency,

$$y_{\min}=\frac{a}{e^{a/\delta}-b}, \qquad (7)$$

$$y_0=a+\frac{ab}{e^{a/\delta}-b}. \qquad (8)$$

Using these equations, expressions can be derived to relate the energy, the power, the pulse length and the laser efficiency with the parameters of the apparatus. These are

$$W_{1a}=\frac{nh\nu lS}{2}\frac{k_r}{k_1}\left(a-\frac{aC}{e^{a/\delta}-b}\right); \qquad (9)$$

$$\overline{P_{\max}}=\frac{nh\nu\mu vk_r lS}{2}\left(a+\frac{a}{e^{a/\delta}-b}-\delta-\delta\ln\frac{a+\frac{ab}{e^{a/\delta}-b}}{\delta}\right); \qquad (10)$$

$$\Delta t=\frac{a-\frac{aC}{e^{a/\delta}-b}}{\mu vk_1\left(a+\frac{aB}{e^{a/\delta}-b}-\delta-\delta\ln\frac{a+\frac{ab}{e^{a/\delta}-b}}{\delta}\right)}; \qquad (11)$$

$$\eta=\frac{nh\nu lSNk_r}{2k_1E_p}\left(a-\frac{aC}{e^{a/\delta}-b}\right), \qquad (12)$$

where n is the density of the active particles, h is Planck's constant, ν is the frequency of the emission, v is the velocity of light in the active medium, μ is the filling factor of the resonator, l is the length of the active element, S is the transverse cross-section, k_r is the transmittance of the exit mirror, N is the number of pulses in a series, and E_p is the pump power.

The error involved in using these equations is below 25%.

Using Eq. (9) we can find the transmittance of the exit mirror for maximum output energy:

$$k_r=\sqrt{\frac{G\varkappa\rho}{D}\left(1-\frac{D}{4f}\right)}-\rho, \qquad (13)$$

where ρ is the loss the resonator.

It should be noted that for the region of high frequencies in the band used (f = 40-100 kHz), Eqs. (9)-(13) can be simplified considerably without increasing the error, if we neglect the quantities $D/2f$ on account of their smallness. We obtain

$$W_{1a}=\frac{nh\nu lS}{2}\frac{k_r}{k_1}\frac{G}{2f}; \qquad (14)$$

$$\overline{P_{\max}}=\frac{nh\nu\mu vk_r lS}{2}\left[\frac{G}{2f}-\delta\ln\left(1+\frac{G}{2f\delta}\right)\right]; \qquad (15)$$

$$\Delta t=\frac{\frac{G}{2f}}{\mu vk_1\left[\frac{G}{2f}-\delta\ln\left(1+\frac{G}{2f\delta}\right)\right]}; \qquad (16)$$

$$\eta=\frac{nh\nu lSN}{2}\frac{k_r}{k_1E_p}\frac{G}{2f}. \qquad (17)$$

3. EXPERIMENTAL INVESTIGATIONS OF A PERIODICALLY Q-SWITCHED LASER

The purpose of the experimental investigations is to establish the relationship between the main power parameters of the laser and the Q-switching frequency.

The arrangement consists of the usual solid-state laser system with a controlled Q. The active element consists of GLS-1 neodymium glass ($n = 2 \cdot 10^{20}$ cm^{-3}) of diameter 15 mm and with a length of the active part of 240 mm. The ends of the element are tapered at the Brewster angle.

An IFP-8000 flash tube is used for pumping. A long artificial line consisting of capacitors and inductors matched to the internal impedance of the tube is discharged through the tube.

The limiting value of the discharge energy is 5 kJ. The pumping light pulse length is 1.5 μsec.

The resonator is Q switched using a quarter-wave Pockels cell, which uses the transverse electrooptical effect in a KDP crystal. The cell is controlled by means of a high-voltage rectangular pulse generator similar to that described in ref. 12.

A total-internal-reflection prism and a stack of glass plates with reflectance 30% are used as the resonator mirror.

The experimental investigations are made at a pumping power of 3 kJ, which corresponds to a threefold excess over the lasing threshold for the case when the Q switch introduced into the resonator is completely trans-

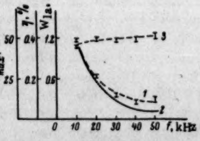

Fig. 1. Laser emission parameters as a function of the Q switching frequency. 1) The pulse energy; 2) the pulse power; 3) the efficiency. The solid line represents the theoretical curve, and the dashed lines represent the theoretical relations compared with the experimental relations.

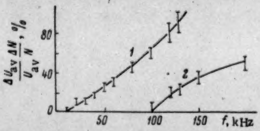

Fig. 2. Amplitude fluctuations of the emission (1) and the number of pulse gaps (2) as a function of the Q-switching frequency.

Fig. 3. Oscillogram of a series of laser pulses with repetition frequency 25 kHz.

mitting, and is in fact one of the sources of passive loss.

It is established that the emission is a regular sequence of giant pulses, the envelope of which quite accurately repeats the time behavior of the light pump pulse. When the Q-switching frequency is increased from a few kilohertz to tens or even hundreds of kilohertz, the power parameters change from values which are specific for single-pulse operation to values close to free-running conditions. In the latter case, the emission is regular free-running emission. The frequency dependences of certain power parameters are shown in Fig. 1.

The experimental results, agree with the theoretical curves calculated using Eq. (9) and (12).

The values of a number of the parameters in these equations are measured or calculated. Thus, the total losses in the resonator are found using the method described in ref. 11, and are as follows: $\rho \approx 0.07\ \text{cm}^{-1}$, maximum gain $\varkappa \approx 6.7\ \text{cm}^{-1}$, cross section of stimulated absorption measured using the method described in ref. 13, $\sigma_{32} = 3.35 \cdot 10^{-20}\ \text{cm}^2$; the threshold pump power is $\cdot \eta B U_{H_k} \simeq 20\ \text{sec}^{-1}$, and the energy characteristics are measured for a threefold excess of the pump power above the threshold value.

The dependence of the efficiency on the frequency is worth noting. At frequencies higher than 20 kHz the value remains unchanged and approximately 2.5 times higher than the efficiency under single-pulse conditions. The efficiency obtained in the experiments for a 5.5-fold excess above the threshold is 0.6%. This is due to the high losses introduced into the resonator by the KDP crystal. Thus, without the crystals, the power under free-running conditions is 100 J for a pump power of 5 kJ. When the crystals are introduced into the resonator, the power is reduced to 30 J.

The stability of the amplitude of the emitted pulses is investigated from oscillograms taken at different lasing frequencies.

It is established that as the Q-switching frequency is increased the level of fluctuations increases, and starting at a frequency of the order of 100 kHz, gaps in the emission occur. This is shown in Fig. 2, in which the frequency dependence of the change in the fluctuation intensity and the change in the number of pulse gaps is shown in relative units. The curves are constructed by processing the results of a large number of oscillograms.

As an illustration, Fig. 3 shows one of the oscillograms corresponding to a Q-switching frequency of 25 kHz.

---

[1] J. W. Gates, R. G. N. Hall, and I. N. Ross, Proc. Eighth Intern. Congress on High-Speed Photography, 299, Stockholm (1968).

[2] D. Ebeling, Seventh Intern. Congress 554, Zurich (1965).

[3] R. E. Roulands, C. E. Taylor and I. M. Daniel, Proc. Eighth Intern. Congress on High-Speed Photography, 275, Stockholm (1968).

[4] V. E. Terent'ev and A. A. Chertkov, Kvant. Elektron. (Mosc.), 7, 88 (1972) [Sov. J. Quant. Electron., 2, 81 (1972)].

[5] M. P. Vanyukov, S. V. Evdokimov, E. V. Nilov and A. A. Chertkov, in: Quantum Electronics, (ed. N. G. Basov,), 3, 108 (1971).

[6] V. E. Terent'ev, Opt. Spektrosk., 27, 705 (1969).

[7] W. Buchman, W. Koichner and D. Rice, IEEE J. Quant. Electron., 6, 747 (1970).

[8] I. C. Chang, E. G. H. Lean and C. G. Powell, IEEE J. Quant. Electron., 6, 436 (1970).

[9] R. B. Chesler, M. A. Karr and I. E. Geusic, IEEE J. Quant. Electron., 5, 345 (1970)

[10] Laser Focus, 7, 36 (1971)

[11] B. I. Stepanov (ed.) Methods of Designing Lasers, Vol. 2 [in Russian], Nauka i Tekhnika, Minsk (1968).

[12] G. A. Aver'yanov, S. V. Evdokimov, E. V. Nilov, B. M. Savichev, and A. A. Chertkov, Kvant. Elektron., (Mosc.), 6, 133 (1971) [Sov. J. Quant. Electron., 1, 682 (1972)].

[13] V. R. Belan, V. V. Grigor'yants, and M. E. Zhabotinskii, ZhETF Pis. Red., 6, 721 (1967) [JETP Lett., 6, 200 (1967)]

Characteristics of the electrical ionization CO_2 laser

Yu. I. Bychkov, Yu. A. Kurbatov, and V. V. Savin

Institute of Atmospheric Optics, Siberian Branch,
Academy of Sciences of the USSR, Tomsk

(Submitted May 21, 1973)
Zh. Tekh. Fiz., 44, 803-807 (April 1974)

Theoretical estimates of the input energy to the gas are derived and oscilloscope traces of the current and voltage of a pulsed electrical ionization CO_2:N_2 laser and the output pulses are analyzed. The experimental and theoretical dependence of the spectral composition and efficiency on the pumping energy are obtained. The effect of helium efficiency is indicated. Threshold and cutoff values of the pump power are considered for different cavities.

The recent development of electrical ionization CO_2 lasers[1,2] has stimulated interest in the processes involving delivery of energy to the gaseous medium at high pressure as well as the energy and spectral characteristics of the laser emission. We have investigated these problems and have also studied the dependence of the threshold and cutoff pumping energy of an electrical ionization CO_2 laser on the parameters of the cavity and the gaseous mixture.

To analyze the energy and spectral characteristics of the electrical ionization CO_2 gas laser we employ a system of equations which describes the energy input to the gaseous medium, the energy distribution among the vibrational levels of CO_2 and N_2, and lasing at transitions of the P branch of the 00^01-10^00 and 00^01-02^00 bands. The variation in electron density n and electric field E in the discharge gap for a storage capacity C is described by the equations

$$\left.\begin{aligned}\frac{dn}{dt}&=(\alpha-\eta)\mu nE-\beta n^2,\\ \frac{dE}{dt}&=-\frac{Se\mu En}{Cd},\end{aligned}\right\}\tag{1}$$

where α, β, and η are the (field-dependent) coefficients of impact ionization, recombination, and attachment, μ is the electron mobility, e is the electron charge, S is the cathode area, and d is the electrode spacing.

The initial conditions for (1) are

$$n|_{t=0}=n_0,\quad E|_{t=0}=\frac{U_0}{d},$$

where n_0 is the electron density in the gap after injection of a short-duration high-energy electron beam and U_0 is the charging voltage of the pump circuit.

Thus, the specific pumping power (per unit volume) is $P_g = Ej_-$, where $j_- = enE\mu$ is the current density.

The quantity N is the total number of particles per unit volume and N_μ is the population of the μ-th energy level; we introduce the variables $n_\mu = N_\mu/N^\mu$. Let $dP_0(\nu)/d\nu$ be the spectral density of the laser output power.

We set

$$\varphi(\nu)=\frac{[dP_0(\nu)/d\nu]}{S_a NCh\nu},$$

where S_a is the active cross section of the laser and $Ch\nu$ is the energy of a photon at frequency ν cm^{-1}. Then

$$\frac{d\varphi}{dt}=\frac{S_a}{4\pi L^2}\sum_{\mu\mu'}A_{\mu\mu'}n_\mu\frac{\Delta\nu_{\mu'\mu}}{(\Delta\nu_{\mu'\mu})^2+(\nu-\nu_{\mu'\mu})^2}+[\varkappa(\nu)-\alpha(\nu)]\varphi(\nu).\tag{2}$$

Here, L is the cavity length $A_{\mu'\mu}$, $\nu_{\mu'\mu}$, and $\Delta\nu_{\mu'\mu}$ are the Einstein coefficient, the frequency, and the Lorentz half-width of the spectral line $\mu'-\mu$,

$$\varkappa(\nu)=\frac{lN}{8\pi L\nu^2}\frac{\Delta\nu_{\mu'\mu}\left(\frac{g_\mu n_{\mu'}-g_{\mu'}n_\mu}{g_\mu}\right)}{(\Delta\nu_{\mu'\mu})^2+(\nu-\nu_{\mu'\mu})^2},$$

$$\alpha(\nu)=-\frac{1}{2L}\ln[r_1(\nu)r_2(\nu)],$$

l is the length of the active medium, g_μ is the multiplicity of the degeneracy of the μ-th level, and $r_1(\nu)_1r_2(\nu)$ are the reflection coefficients of the cavity mirrors, which, in the general case, depend on the frequency.

The population of the vibrational and, consequently, the vibrational–rotational levels can be determined by using the method proposed in refs. 3 and 4, which involves the determination of the populations of the vibrational levels in the i-th mode of the Boltzmann distribution, characterized by a vibrational temperature T_i. If the vibrational temperature is known, the population of any CO_2 or N_2 vibrational level can be determined. The equations for $x_i = \exp\{-E_i/kT_i\}$, where i = 1, ..., 4, E_i is the photon energy of the i-th mode (i = 1, 2, 3 refs to CO_2, i = 4 to N_2), and k is the Boltzmann constant, are similar to those given in ref. 3 and contain extra terms to describe the variation in x_i due to the emission processes. The system also includes an equation to describe the variation in the translational temperature of the gaseous medium. The rate constants for relaxation and exchange of vibrational energy are taken from ref. 4.

A computer solution of the above system of equations, which is not given in full because of its complexity, gives the time dependences of the discharge characteristics $j_-(t)$ and E(t), and the laser output:

$$P_0(t)=\int\limits_\nu\left(\frac{dP_0(\nu)}{d\nu}\right)d\nu,\quad W_0(t)=\int\limits_0^t P_0(t)\,dt,$$

as well as the spectral composition of the output energy:

$$\frac{dW_0}{d\nu}=\int\limits_\nu\left[\frac{dP_0(\nu)}{d\nu}\right]dt.$$

The calculations are performed for a laser with the parameters l = 40 cm, L = 100 cm, $r_1 = 0.9$, $r_2 = 0.4$, $S_a = 1$ cm^2, S = 80 cm^2, and d = 1 cm; these correspond to the parameters of the experimental device described in ref. 2.

Figure 1 gives a solution of the system of equations for a laser with $CO_2:N_2:He = 1:3:0$ at a pressure of 1 atm, excited by a $C = 10^{-7}$ F discharge with $U_0 = 15$ kV for an initial electron density $n_0 = 5 \cdot 10^{12}$ cm^{-3}. The dependence of $(\alpha - \eta)$ and β on E is obtained by interpolation of the experimental data of ref. 2 for $CO_2:N_2$ mixtures. The density of the input energy is 0.1 J $\cdot$ cm^{-3}, and the output energy is $W_0 \sim 5.6 \cdot 10^{-3}$ J $\cdot$ cm^{-3} with a peak power of $2.7 \cdot 10^5$ W. It is assumed in the calculations that the cavity does not have mode-selecting properties and lasing occurs at transitions in the 00^01-10^00 band. The spectral density of the output energy for this case is shown in Fig. 2a. Lasing occurs in practice, at one rotational line of the 00^01-10^00 band, and the ratio of the energy input into the gas to the threshold pumping energy is $W_g/W_{th} \sim 2.5$. At high threshold pump energy lasing occurs on several lines; because of the increase in gas temperature, the maximum $dW_0/d\nu$ shifts toward higher j. In Fig. 2b the emission spectrum is calculated for $U_0 = 25$ kV, giving $W_g = 0.3$ J $\cdot$ cm^{-3} and $W_g/W_{th} \sim 7.5$. Thus, the calculations indicate that even in a non-mode-selecting cavity the frequency of laser emission can be regulated by varying just the pump energy. The experimental values for laser efficiency $\tilde{\eta} = W_0/W_g$ are given in Fig. 3 for different compositions of the gas mixture at a pressure of 1 atm. Variation of W_g is accomplished by varying the charging voltage U_0 for a fixed electron beam, or by varying the beam density for a fixed U_0, i.e., by varying n_0. The calculation performed for a $CO_2:N_2 = 1:3$ mixture indicates that the decrease in efficiency for high W_g values is due to the more intense heating of the gas due to a transfer of a portion of the discharge energy through symmetric and bending vibrations of CO_2 to translational degrees of freedom. The presence of He in the mixture shifts the maximum $\tilde{\eta}(W_g)$ toward smaller W_g. This is due to the increase in the gain, and, consequently, to the reduction in the threshold pump energy as a result of the decrease, by comparison with CO_2, in the broadening of the spectral lines of the laser transitions. For large W_g a gaseous mixture containing He is heated more strongly due to the smaller specific heat of He; consequently the dropoff in efficiency occurs for smaller W_g values.

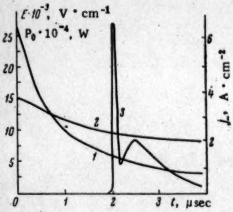

Fig. 1. Time characteristics of the discharge and laser output. A mixture $CO_2:N_2 = 1.3$ for P = 1 atm: 1) discharge current density j_-; 2) field voltage E; 3) laser output power P_0.

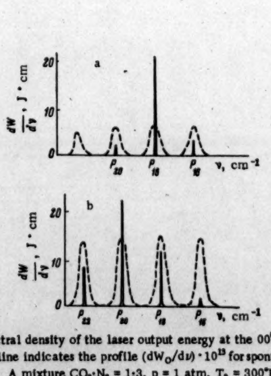

Fig. 2. Spectral density of the laser output energy at the 00^01-10^00 band. The dashed line indicates the profile $(dW_0/d\nu) \cdot 10^{13}$ for spontaneous emission $r_1r_2 = 0$. A mixture $CO_2:N_2 = 1:3$, p = 1 atm, $T_0 = 300$°K. a) $U_0 = 15$ kV, $W_g = 0.1$ J $\cdot$ cm^{-3}; b) $U_0 = 25$ kV, $W_g = 0.3$ J $\cdot$ cm^{-3}.

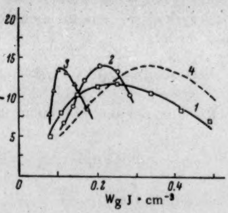

Fig. 3. Laser efficiency as a function of energy input to the gas. The experimental data are for a $CO_2:N_2:He$ mixture. 1) 1 : 3 : 0; 2) 1 : 3 : 3; 3) 1 : 3 : 10; 4) calculation for a 1 : 3 : 0 mixture.

The experimental[2] and calculated data indicate that with increasing W_g, W_0 also passes through a maximum more appropriate to higher W_g than to a maximum $\tilde{\eta}(W_g)$. Therefore, the operating modes of a CO_2 laser with maximum efficiency and with maximum output energy correspond to different ranges of W_g values.

We also investigate the dependence of the threshold pumping energy of an electrical ionization CO_2 laser on the parameters of the cavity and the composition of the gas mixture. It is noted that the gas temperature increases with increasing W_g, and this increases the threshold pump energy. If one continues to increase W_g after the threshold has been reached a situation can arise in which the gas will be heated to a temperature for which the population inversion threshold cannot be attained due to the large population of the lower-lying laser level, the population being determined by the Boltzmann distribution with a translational gas temperature T. This is indirectly indicated by the dropoff in efficiency for high W_g. The equations giving the threshold and cutoff values of the pump energy for the CO_2 laser are

$$\left.\begin{aligned} W_0 &= P1.25\Phi_1 \frac{1}{2}\left\{\frac{1-x_1-\delta(a+1)}{\delta}\right. \\ &\quad \times \left.\left[1 \pm \sqrt{1-4\frac{(a\delta - x_1)\delta}{1-x_1-\delta(a+1)}}\right]\right\}, \\ T &= T_0 + \frac{\Phi_2 W_0}{C^*}. \end{aligned}\right\} \qquad (5)$$

Here, Φ_1 is the portion of the discharge energy exciting the 00^0v levels of CO_2 and N_2, Φ_2 is the portion of the discharge energy exciting the symmetric and bending vibrations of

CO_2, $\bar{x}_i = \exp\{-E_i/kT\}$ ($i = 1$ is the symmetric and $i = 2$ is the bending mode),

$$a = 1 + x_1(1 - x_1)^{-1} + 2x_2(1 - x_2)^{-1},$$

C^* is the specific heat per unit volume of the gas mixture,

$$\delta = 1.25 \cdot 10^{-2}\psi \frac{Z}{fC_3},$$

$$f = 1.12(2j + 1)\exp\left\{-\frac{0.56j(j + 1)}{T}\right\}T^{-1},$$

f is the population distribution function of the vibrational level with respect to the sublevel j, $\psi = C_3 + 0.78C_4 + 0.5C_5$ is a function determining the broadening of the spectral line of the laser transition in the gas mixture, C_3 is the concentration of CO_2, C_4 of N_2, C_5 of He, P is the pressure of the gas mixture (atm), and $Z = -[\ln(r_1r_2)]/l$.

The square root in Eq. (5) gives two values of W_0. It is clear from physical considerations that taking the square root in (5) with the minus sign yields the threshold pump energy – with the plus sign it yields the cutoff value. The system of equations (5) is solved on a computer by successive approximations. Figure 4 gives the threshold and cutoff values of the pump energy as a function of the cavity parameter Z for a $CO_2 : N_2 : He = 1 : 3 : 0$ mixture at a pressure of 1 atm and with different initial temperatures T_0 of the gas mixture. The range of allowable values for W_0, limited below by the threshold and above by the cutoff, narrows with an increasing Z. At a certain value Z_n we have $W_{th} = W_{cut}$, which means that for $Z > Z_n$ lasing can be obtained for a lower initial temperature T_0.

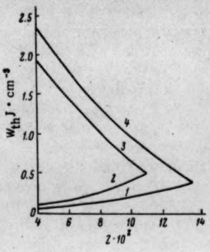

Fig. 4. Threshold (1, 2) and cutoff (3, 4) values of the pump energy vs the cavity parameter Z. T_0, °K: 1, 4) 300; 2, 3) 400.

A satisfactory agreement between the calculated and experimental values of W_{th} is observed for different mixtures.[2] The cutoff values of the pump energy are not attained in the experimental apparatus because of the limitations of the pump source. The estimates given above indicate the upper and lower limits of the pump energy for specific CO_2 laser cavities.

---

[1] N. G. Basov, É. M. Belenov, V. A. Danilychev, O. M. Kerimov, I. B. Kovsh, and A. F. Suchkov, ZhETF Pis. Red., 14, 421 (1971) [JETP Lett., 14, 285 (1971)].

[2] G. A. Mesyats, Yu. I. Bychkov, V. V. Kremnev, Yu. D. Korolev, Yu. A. Kurbatov, and V. V. Savin, Preprint, Inst. Opt. Atmos. Sib. Otdel. Akad. Nauk SSSR, No. 3, Tomsk (1972).

[3] A. S. Biryukov, B. F. Gordiets, and L. A. Shelepin, Zh. Eksp. Teor. Fiz., 57, 585 (1969) [Sov. Phys. – JETP, 30, 321 (1970)].

[4] E. N. Lotkova, V. N. Ochkin, and N. N. Sobolev, Zh. Tekh. Fiz., 40, 1402 (1970) [Sov. Phys. – Tech. Phys., 15, 1085 (1971)].

Linear accelerator for beam injection into a slowly rising magnetic field

D. G. Borisov, A. I. Gryzlov, V. M. Levin, and A. V. Ryabtsov

(Submitted December 26, 1972)
Zh. Tekh. Fiz., 44, 808-811 (April 1974)

A linear electron accelerator is described which is intended for the injection of a relativistic beam into the slowly rising magnetic field of a synchrotron. Monochromatization of the particle beam is accomplished in each bunch along with modulation of the mean energy in each bunch with the energy increasing from bunch to bunch. A high-frequency field is used for modulation of particle energy. The disparity between the curve for energy modulation and the curve for the rise in the magnetic field is insignificant for the slowly rising steering magnetic field in a synchrotron. This situation offers an opportunity to excite the modulating and equalizing sections from a single source at a frequency different from the excitation frequency of the main accelerator sections.

It is well known that the best results for particle injection into a circular accelerator can be obtained when the energy of the injected particles varies synchronously with the rising magnetic field of the circular accelerator.[1] This problem has been solved for nonrelativistic injection energies.[2] This problem has, in general, also been solved for proton accelerators.[3-5]

However, this problem has not yet been solved in a practical way for electrons with energies of the order of 10 MeV and above. There is a well-known proposal[6] to use for modulation of particle energy a section of a linear induction accelerator in which the amplitude of the eddy field rises continuously over the duration of a pulse in accordance with a specified relation. This solution is ideal from the standpoint of a match between the energy modulation curve and the magnetic field variation. As was shown,[6] its application in this case (despite the low efficiency of a linear induction accelerator at low currents) is more suitable than the use of a linear waveguide accelerator of excessive length.

However, the situation shifts in favor of a traveling-wave accelerator when the rise in the steering magnetic field in a circular accelerator is small over the injection time. Assuming the rise in the field is linear in such a case, one can use the linear portion of the sinusoidal accelerating field in the traveling-wave accelerator for modulation of particle energy.

Linear electron accelerators at the exit of which particle beams can be produced with energies rising during the pulse are well-known.[7] One of their characteristic features is the inequality of the electromagnetic field frequencies in the main accelerating sections and the sections for particle energy modulation.[8]

The advantage of such an accelerator can be realized even more completely during injection if the instantaneous width of the beam energy spectrum is made smaller. The most convenient solution for the problem of beam spectrum compression is the use of special monochromatizing devices, which ensure in their operation an unchanged beam intensity relative to the original values.

There are several monochromators that are used in electron accelerators at the present time.[9-11] A characteristic feature is excitation of the sections for equalizing particle energy, or of a resonator, at the frequency of the main accelerating sections.

However, the latter situation is unsuitable for an accelerator with modulation of beam energy. We first show that it is necessary to carry out modulation of mean bunch energy before bunch monochromatization. Equalization of particle energies in the bunches in both proton and electron accelerators is carried out after considerable elongation of the bunches. On the other hand, it is clear that with modulation of the mean energy of a bunch the quality of the monochromatization will be so much the worse the more a bunch is elongated. Also in favor of modulation before monochromatization is the fact that the energy spread introduced by modulation for bunches narrow in phase is not outside the limits acceptable for a monochromator, i.e., it can be compensated for in the monochromator.

Returning to the question of the choice of excitation frequency for the equalizing section, it is timely to emphasize that bunches with different mean energies either pass through a drift space in different times (for nonrelativistic energies) or pass through the magnetic channel of a debuncher along trajectories of different lengths at identical velocities. This means that in an accelerator with modulation, the equalizing section must be excited at a frequency different from the main section frequency and matching the frequency of bunch arrival, which is in contrast to the generally accepted method for monochromatization.

Otherwise, additional modulation of the mean bunch energy is initiated in the equalizing section with monochromatization being different for each bunch and completely absent for some bunches.

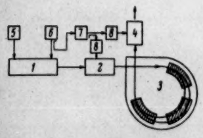

Fig. 1. Block diagram of accelerator. 1) Main section of accelerator; 2) modulation section; 3) magnetic debuncher; 4) equalizing section; 5, 6) klystron amplifiers; 7) phase modulator; 8) phase shifter.

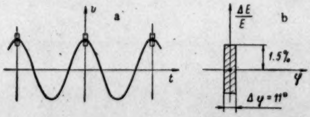

Fig. 2. Bunch position relative to accelerating wave (a), and energy and phase distribution of bunch particles (b).

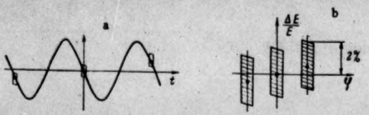

Fig. 3. Bunch position relative to modulating wave (a), energy distribution of bunches in a pulse, and phase and energy distribution of bunch particles (b).

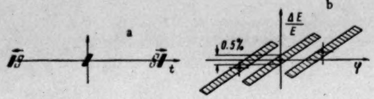

Fig. 4. Energy and phase distribution of particles after the magnetic debuncher.

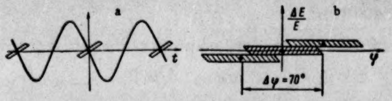

Fig. 5. Bunch position relative to equalizing wave (a), and phase and energy distribution of particles after equalizing section (b).

A linear electron accelerator intended to achieve optimal multiturn injection of a beam into a slowly rising steering magnetic field in a 1.2 MeV synchrotron can be pictured in the following form (Fig. 1). Element 1 is a linear traveling-wave electron accelerator with an energy of 40-50 MeV, a relative spectral width at exit $\Delta E/E = \pm 1.5\%$, in which $f_0 = 1818$ MHz in the sections. Figure 2a shows schematically the position of electron bunches relative to the accelerating wave at the accelerator exit. Figure 2b shows the idealized distribution of bunch particles over energy and phase. Element 2 is a section for modulation of mean bunch energy. The rise in mean energy during a pulse is + 1% and the length of the section is 40 cm. The electromagnetic frequency in the section, $f_1 = f_0 - 11$ kHz, is chosen to match the frequency in the equalizing section. Because of this choice, a rise in energy from bunch to bunch is provided in an accelerating field decreasing with time, as shown in Fig. 3a. The energy distribution of the bunches in a pulse at the exit section and the phase and energy distributions of bunch particles are shown in Fig. 3b for the first, middle, and last bunches in a pulse. Element 3 is a magnetic debuncher occupying an area of 1 m^2. Three magnets with uniform field and tapered pole tips provide a beam deflection of 270°, a sevenfold longitudinal dispersion of the bunches, establish a correlation between particle phase and energy, and provide vertical stability of the beam. Energy and phase distributions of the particle beyond the magnetic debuncher are shown in Fig. 4. Element 4 is the section which equalizes the energy of particles in a bunch. At the exit the relative spectral width $\Delta E/E = 0.25\%$, and the length of the section is 60 cm. The electromagnetic frequency in the section, $f_1 = f_0 - 11$ kHz, is determined by the need for delaying higher-energy bunches relative to bunches with lower energies during passage through the debuncher of a pulse of particles with energies which increase with time. The energy and phase distribution of the particles in the first, middle, and last bunches of a pulse are shown in Fig. 5b. Figure 5a shows the position of electron bunches relative to the traveling wave in the equalizing section. Equalization of particle energy in the bunches is provided by location of the bunches in a field decreasing with time. Elements 5 and 6 are klystron amplifiers, 7 is a phase modulator, and 8 is a phase shifter.

Use of an accelerator with beam energy modulation and bunch monochromatization as an injector for a synchrotron makes it possible to double the injection time in comparison with a monochromatic beam, to optimize the conditions for particle capture in the circular chamber of the synchrotron, to reduce the Coulomb interaction because of longitudinal dispersion of the bunches, and, in the final analysis, to increase the particle current emerging from the synchrotron.

---

[1] M. H. Blewett, G. K. Green, R. R. Kasner, W. H. Moore, L. W. Smith, and H. S. Snyder, Rev. Sci. Instr., 24, 861 (1953).

[2] D. K. Wells and Rudin Johnson, Rev. Sci. Instr., 31, 942 (1960).

[3] W. Myers and J. Abraham, IEEE Trans. Nuc. Sci. (June 1967), p. 666.

[4] L. P. Zinov'ev, R. B. Kadyrov, N. N. Plyashkevich, V. A. Popov, I. N. Semenyushkin, and V. L. Stepanyuk, Abstracts of Papers at Second All-Union Conference on Charged-Particle Accelerators [in Russian], GKIAÉ, AN SSSR, Moscow (1970), p. 72.

[5] J. Faure et al., Proc. Eighth International Conference on High-Energy Accelerators, Geneva (1971), p. 91.

[6] D. G. Borisov and A. I. Grizlov, Particle Acc., 2, 313 (1971).

[7] D. G. Borisov, A. I. Gryzlov, and I. A. Prudnikov, Byull. Izobr., No. 9, 227 (1971). Inventor's Certificate 276268.

[8] D. G. Borisov, A. I. Gryzlov, and É. Kh. Émirov, Byull. Izobr., No. 10, 238 (1971); Inventor's Certificate 270918.

[9] French Patent 1205220, Class HO5. "Magnetic separator for electrons of various energies composing an electron beam."

[10] A. N. Dovbnya, E. M. Kolot, and V. V. Petrenko, Paper 70/12, Papers at Seventh Closing Conference, Khar'kov Physicotechnical Institute, Khar'kov, (1970), p. 5.

[11] M. C. Crowley-Milling and G. Saxon, IEEE Trans. Nucl. Sci., NS-18, No. 3, 968, June, 1971.

[12] A. V. Ryabtsov, Byull. Izobr. Inventor's Certificate 351484, No. 15 (1974).

[13] A. V. Ryabtsov, D. G. Borisov, A. I. Gryzlov, and V. M. Levin, Byull. Izobr. No. 48, 148 (1973). Inventor's Certificate 409401.

Use of the distribution function to describe free molecular beams

I. G. Neudachin, B. T. Porodnov, and P. E. Suetin

S. M. Kirov Ural Polytechnic Institute, Sverdlovsk

(Submitted May 15, 1973)
Zh. Tekh. Fiz., 44, 812-817 (April 1974)

We have determined the characteristics of molecular beams shaped by cylindrical and infinitely wide channels under free molecular conditions. The density, flux, and temperature have been calculated by using the molecular velocity distribution function. It has been established that Clausing's angular distribution is obtained at large distances from the source. The effect of the nonlinearity of the distribution of molecular collisions with the channel walls on the beam characteristics has been estimated.

1. INTRODUCTION

The molecular beam method has been widely used in studies of the interaction of gas molecules with solid surfaces in masers[1-3] and therefore a detailed study of beam characteristics is of interest. Investigations of this kind have been performed under free molecular conditions using the cosine law, as in refs. 4 and 5, to calculate fluxes. Gadamer[6] attempted to calculate the molecular density close to the exit cross section of a cylindrical channel by using the distribution function.

We propose a calculational method using the distribution function which enables one to find any macroscopic characteristics of gas flow in the collisionless regime both inside and outside the channel. The shaping of beams by circular and little-studied slotted channels of finite length is discussed.

2. STATEMENT OF THE PROBLEMS

We consider the free molecular flow of a gas from a chamber with a gas density n_1 and temperature T_1 through a channel into a chamber with gas density n_2 and temperature T_2. Since the molecules do not collide it is sufficient to consider the case $n_2 = 0$. The results can easily be generalized for an arbitrary gas density in the second container. The chambers are so large in comparison with the channel that the gas in the chambers is in equilibrium and the molecules are incident on the channel with an equilibrium Maxwellian distribution f_{00}:

$$f_{00}=n_1\left(\frac{m}{2\pi kT_1}\right)^{3/2}\exp(-c^2),\quad c=\sqrt{\frac{m}{2kT_1}}\,v, \tag{1}$$

where c is the dimensionless velocity. Under stationary conditions equilibrium is established between the flux of incident molecules and those reflected from the walls. Molecules which are diffusely scattered by the channel surface are described by a distribution function f_0 of the form

$$f_0=Nf_{00}. \tag{2}$$

The quantity N in Eq. (2) is a solution of the equation for the blance of fluxes normal to the wall, or the well known Clausing equation.[7]

Consequently the problem consists of two parts: the solution of the Clausing equation, which enables to find the distribution function f_0, and the subsequent use of the distribution functions f_0 and f_{00} to calculate various characteristics of the molecular beam shaped by the channel.

Under free molecular conditions of flow in the absence of external forces the Boltzmann equation can be written in the form

$$\mathbf{c}\frac{\partial f}{\partial \mathbf{r}}=0. \tag{3}$$

Consequently the distribution function is preserved along the molecular trajectories. In order to determine the distribution function of molecules with velocities in a given direction at a given point a ray must be constructed in the opposite direction. If this ray intersects the channel surface the distribution function for such molecules will be f_0; if the molecules came from the volume their distribution function will be f_{00}. Knowing the distribution function we use the kinetic definitions of density n, flux nu, and temperature T

$$(n,\ n\mathbf{u},\ nkT)=\left(\frac{2kT_1}{m}\right)^{3/2}\int f\left(1,\ \mathbf{c},\ \frac{2kT_1(\mathbf{c}-\mathbf{u})^2}{3}\right)d\mathbf{c}, \tag{4}$$

where $\mathbf{u} = (m/2kT_1)^{1/2}\mathbf{V}$ is the dimensionless macroscopic velocity of the gas at the given point.

Because of symmetry the problem can be solved for one quarter of the plane of an axial cross section of the channel.

3. PLANE SOURCE

We introduce a rectangular coordinate system. We consider the outflow of gas from a plane channel into a vacuum. Let the x axis be directed along the gas flow with the plates confining the flow placed at the planes y = ± 0.5. The molecules are incident on the channel through the cross section x = 0, and emerge from it through the cross section x = L. All lengths are measured in units of the distance between the plates.

The integration in velocity space in Eq. (4) is performed in cylindrical coordinates, in which the element $d\mathbf{c} = c_\rho dc_\rho dc_z d_\varphi$ and $c_\rho = (c_x^2 + c_y^2)^{1/2}$. At points with coordinates $0 \le y \le 0.5 + (x - L)/L$ the total molecular flux density is determined not only by the molecules scattered by the walls but also by those traversing the channel without colliding with the walls. Therefore it is more convenient to transform from the integration over the angle φ to integration over x_1 by the obvious relation

$$x_1=x-(0.5+y)\operatorname{ctg}\varphi. \tag{5}$$

In accordance with this the flow field outside the chan-

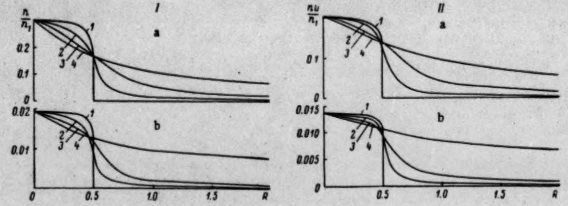

Fig. 1. Plane source. I) Normalized density; II) reduced flux. Here and in Fig. 2 φ in deg : 1) 90; 2) 80; 3) 60; 4) 0; a) L = 1; b) L = 100.

nel is divided into three zones with the following ranges of y: $0 \le y \le 0.5$, $0.5 \le y \le 0.5 + (x - L)/L$, and $0.5 + (x - L)/L \le y$. The results are too cumbersome to be written down in detail, and therefore, in the example below we give only the expression for the molecular number density in the $0 \le y \le 0.5$ zone:

$$n = \frac{n_1}{2\pi}\left[\operatorname{arc\,tg}\frac{0.5+y}{x} + \operatorname{arc\,tg}\frac{0.5-y}{x} + \int_0^L \left(\frac{0.5-y}{(0.5-y)^2+(x-x_1)^2} + \frac{0.5+y}{(0.5+y)^2+(x-x_1)^2}\right) N(x_1)\,dx_1\right]. \quad (6)$$

Since the solution of Clausing's equation[8] obtained by a variational method converges well,[9] N(x) can be determined in the linear approximation:

$$N(x) = 0.5[1 + A(0.5L - x)],$$
$$A = \frac{6(L - \operatorname{Arsh} L)}{L^3 + 3L^2 + 4 - (L^2+4)\sqrt{1+L^2}}. \quad (7)$$

The results of a machine calculation of the molecular number density and the molecular flux at points a distance R along rays from the point (x = L, y = 0, z = 0) making various angles φ with the x axis are shown in Fig. 1, I and II respectively. The molecular flux density is given by

$$nu = \sqrt{(nu_x)^2 + (nu_y)^2}. \quad (8)$$

4. CYLINDRICAL SOURCE

We consider the flow field from a cylindrical pipe. We take the z axis along the channel of length L, and the x and y axes in the entrance cross section. All lengths are measured in units of the radius of the pipe. The determination of the macroscopic moments (4) requires integrating the distribution function with various weights in velocity space, but for convenience in introducing the limits of integration it is necessary to transform the integration variables.

We transform from the cylindrical coordinate system in velocity space used in the last section to polar coordinates at the center of the entrance cross section z = 0. Then the contribution of "straight-through" molecules, i.e., molecules which traverse the channel without colliding with the walls, is taken into account by integrating over the area S of the entrance opening visible from the observation point (ρ, φ, z)

We introduce new variables ρ_1 and φ_1 by the relations

$$c_z = \frac{z}{m} c_\rho, \quad \varphi = 2\pi - \arcsin\left(\frac{\rho_1}{m}\sin\varphi_1\right), \quad (9)$$

where $m^2 = \rho^2 + \rho_1^2 - 2\rho\rho_1\cos\varphi_1$.

Then the element of volume in velocity space is

$$dc = c_\rho dc_\rho dc_z d\varphi = \frac{z\rho_1}{m^3} c_\rho^2 dc_\rho d\rho_1 d\varphi_1. \quad (10)$$

The fraction of the molecules reflected from the walls is found by integrating over the part of the inner surface of the cylinder C visible from the point of observation. We define the transformation of integration variables by

$$c_z = \frac{z - z_1}{m_1} c_\rho, \quad \varphi = -\arcsin\frac{\sin\varphi_1}{m_1}, \quad (11)$$

where $m_1^2 = 1 + \rho^2 - 2\rho\cos\varphi_1$.

Then the element of volume dc for molecules reflected by the wall is

$$dc = c_\rho dc_\rho dc_z d\varphi = \frac{1 - \rho\cos\varphi_1}{m_1^3} c_\rho^2 dc_\rho dz_1 d\varphi_1. \quad (12)$$

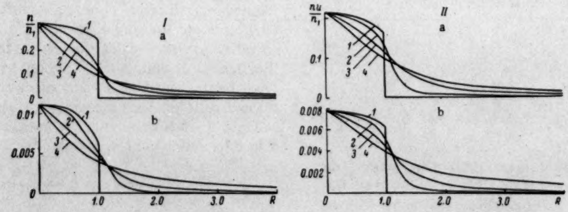

Fig. 2. Cylindrical source. I) normalized density; II) reduced flux.

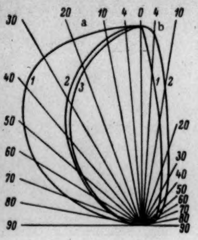

Fig. 3. Cylindrical source. Asymptotic behavior of normalized flux $nu(\varphi)/nu(0)$. a: L = 1; 1) R = 2; 2) 20; 3) ∞. b: L = 10; 1) R = 20; 2) ∞.

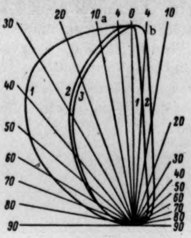

Fig. 4. Plane source. Asymptotic behavior of normalized flux $nu(\varphi)/nu(0)$. a: L = 1; 1) R = 1; 2) 10; 3) ∞ b: L = 10; 1) R = 10; 2) ∞.

The molecular density, for example, is given by

$$n=\frac{n_1 z}{4\pi}\iint_S \frac{\rho_1}{A_1^3}\,d\rho_1 d\varphi_1+\frac{n_1}{4\pi}\iint_C \frac{1-\rho\cos\varphi_1}{A_2^3}N(z_1)\,dz_1 d\varphi_1, \qquad (13)$$

where $A_1^2 = z^2 + \rho_1^2 + \rho^2 - 2\rho\rho_1 \cos\varphi_1$ and $A_2^2 = (z - z_1)^2 + 1 + \rho^2 - 2\rho\cos\varphi_1$.

The flow field is divided into several zones. Since a detailed report of the results would be too cumbersome we present below as an example only the expression for the molecular flux density in the axial direction for $0 \le \rho \le 1$:

$$nu_z=\frac{n_1}{4\sqrt{\pi}}\left[1-\frac{\rho^2+z^2-1}{\sqrt{(1+\rho^2+z^2)^2-4\rho^2}}\right.$$
$$\left.+4\int_0^L\frac{a-2\rho^2}{(a-4\rho^2)^{3/2}}(z-z_1)N(z_1)\,dz_1\right], \qquad (14)$$

where $a = (z - z_1)^2 + \rho^2 + 1$.

Using a variational method[8] we find for N(z)

$$N(z)=0.5+A(0.5L-z),$$
$$A=\frac{1}{3}\,\frac{(0.5L)^3-2+(2-0.25L^2)\sqrt{1+0.25L^2}}{0.5L\sqrt{1+0.25L^2}-\operatorname{Arsh}(0.5L)}. \qquad (15)$$

The results shown in Fig. 2 are obtained with a computer program written to calculate macroscopic characteristics of a molecular beam. This figure shows the molecular density n and the molecular flux

$$nu=\sqrt{(nu_\rho^2)+(nu_z^2)} \qquad (16)$$

as functions of the distance R along a ray from the point (x = 0, y = 0, z = L) making an angle φ with the z axis.

Calculations show that the computing time depends strongly on the position of the point of observation and increases significantly close to the edge of the exit opening of the pipe.

It is interesting to note that for both plane and cylindrical channels the temperature T as a function of the average molecular velocity u is given by

$$T=T_1\left(1-\frac{2}{3}u^2\right). \qquad (17)$$

The same result was obtained by Narasimha[10] for flow through an opening, and by Shakhov[11] for a spherical source.

5. DISCUSSION OF RESULTS AND CONCLUSION

The fluxes obtained by using the distribution function and making a change of variables are identical with those obtained by using the cosine law.[4,5] However, the introduction of this method of describing molecular beams leads to considerably more information on the flow field outside the channel (density, velocity, temperature) on the basis of the usual kinetic definitions of macroscopic characteristics (4).

We consider limiting cases. For L = 0 our results agree with Narasimha's equation[10] for a circuit opening and for a slot in a thin wall. Clausing's angular distribution[4,12] is asymptotic in comparison with ours, i.e., it is valid for $R \gg 1$ and $R \gg L$. This must be taken into account in experiments with molecular beams.

A comparison of the results, part of which are shown in Fig. 3, shows that the normalized flux density $nu(\varphi)/nu(0)$ differs from the limiting Clausing diagram for an axisymmetric beam by less than 7% for R = 20L ($L \ge 1$). The limiting angular diagram for a plane source and the normalized flux density $nu(\varphi)/nu(0)$ given by our calculations (Fig. 4) differ by no more than 10% for R = 10L($L \ge 1$). The fluxes in actual and limiting cases differ the most (by about 5%) on the axis for R = 20L (cylindrical source) and for R = 10L (plane channel). The direction of the fluxes varies from axial in the output cross section to radial when the limiting diagram is reached at large distances.

The average molecular velocity u and the temperature T in a beam with axial symmetry approach the limiting values

$$u'=\frac{2}{\sqrt{\pi}},\quad T'=T_1\left(1-\frac{8}{3\pi}\right) \qquad (18)$$

as $R \to \infty$.

The macroscopic velocity u differs from the limiting velocity u' at R = 20 by less than 0.1%. The corresponding limits in the plane case are

$$u''=\frac{\sqrt{\pi}}{2},\quad T''=T_1\left(1-\frac{\pi}{6}\right). \qquad (19)$$

At R = 10 the velocity differs from its limiting value by less than 0.1%.

The flux parameters are also calculated using the second approximation of the variational method for N[9,12] [cf. Eq. (7)] in order to estimate the accuracy of the quantities obtained. For short and rather long channels the results are practically the same. A difference is observed only for intermediate length channels and large angles. For example, for a cylindrical source the difference in the two approximations for the flux density nu ($\varphi = 80°$) is 2.3% for L = 8, 4.6% for L = 32, and 3.7% for L = 80.

---

[1] Molecular Beam Studies (A. M. Brodskii and V. B. Leonas, eds.) [in Russian], Mir, Moscow (1969).

[2] A. I. Livshits, Zh. Tekh. Fiz., 37, 1304 (1967) [Sov. Phys. – Tech. Phys., 12, 947 (1968)].

[3] A. I. Livshits, I. M. Metter, and L. É. Rikenglaz, Zh. Tekh. Fiz., 41, 368 (1971) [Sov. Phys. – Tech. Phys., 16, 276 (1971)].

[4] P. Clausing, Zeits. Phys., 66, 471 (1930).

[5] W. L. Winterbottom, J. Chem. Phys., 49, 106 (1968).

[6] E. O. Gadamer, C. A. S. I. Trans., 3, 84 (1970).

[7] P. Clausing, Ann. Phys., 12, 961 (1932).

[8] W. C. DeMarcus, Report K-1302, Oak Ridge, Tenn. (1957).

[9] I. G. Neudachin, I. Nauchn. Konf. Molodykh Uchenykh Aspirantov Fizikotekhn. Fak., Tez., 105 (1972).

[10] R. Narashimha, J. Fluid Mech., 10, 371 (1961).

[11] E. M. Shakhov, MZhG, 2, 58 (1971).

[12] I. G. Neudachin, B. T. Porodnov, and P. E. Suetin, Zh. Tekh. Fiz., 42, 1069 (1972) [Sov. Phys. – Tech. Phys., 17, 848 (1972)].

Flow of low-density gases in a capillary grid

B. T. Porodnov, V. D. Akin'shin, V. I. Kichaev, S. F. Borisov, and P. E. Suetin
S. M. Kirov Ural Polytechnical Institute, Sverdlovsk

(Submitted May 14, 1973)
Zh. Tekh. Fiz., 44, 818-823 (April 1974)

An experimental study has been made of the flow of the gases He, Ne, Ar, Kr, Xe, H_2, D_2, N_2, CO_2, and CH_4 over the Knudsen-number range $5 \cdot 10^{-1}$-10^4. The experiments are carried out at room temperature with a capillary grid made from glass capillaries with fused walls. The free-molecule values of the reduced flow rates are determined for all the gases. The accommodation coefficients for the tangential momentum of the molecules incident on the wall are calculated under the assumption that the xenon molecules are scattered diffusively by the wall. The accommodation coefficients found for He, Ne, and Ar agree with the values found previously with single capillaries.

INTRODUCTION

Berman and Maegley[1,2] have recently attempted to explain a phenomenon observed by them and other investigators:[3,4] the experimental flow rates in the free-molecule regime and in intermediate regimes are found to be lower than the theoretical values based on the assumption of complete diffuse scattering of molecules by the walls. Channels with artificially roughened walls were used in these experiments.

Berman and Maegley have suggested that among the molecules scattered by a smooth wall it is possible to distinguish a group which are probably scattered predominantly backward, in the direction opposite the direction of incidence. They describe this group of molecules by means of a "back-scattering coefficient." This coefficient is incorporated into the boundary conditions in a numerical solution of the Boltzmann equation with the Bhatnager–Gross–Krook collision operator.

We believe that the use of the concept of backscattering of molecules by a smooth wall in boundary-value problems of the kinetic theory of gases is not justified, for the following reasons.

First, it has been shown[5] that a Monte Carlo description of free-molecule flow of gases in circular capillaries with artificial regular wall corrugations with various shapes and parameters agrees with the observed flows, within the experimental and theoretical errors, if the rough walls are assumed to scatter molecules completely diffusely. An analogous result has been obtained[6] for a planar channel with triangular roughness features.

Second, analysis of the molecular-scattering characteristics obtained from experiments on the interaction of molecular beams with solid surfaces[7] supports the Maxwell-boundary condition scheme, according to which some of the molecules incident on a smooth wall undergo specular reflection.

Third, it follows from experimental studies of the intermediate flow regime and of viscous flow with slip in various channels[4,8-10] that the observed slip flows are larger than the theoretical flows calculated for diffuse scattering of molecules by the rigorous methods of the kinetic theory of gases. In this case, the discrepancy between theory and experiment can be attributed to the introduction of a diffuse-mirror boundary-condition scheme or an accommodation coefficient for the tangential momentum of the molecules incident on the walls.

Accordingly, the available experimental and theoretical information shows that each smooth element of the wall surface apparently is responsible for the mirror-reflection of a certain fraction of the molecules incident on it.

It is therefore worthwhile to carry out a systematic study of free-molecule and intermediate flow regimes for a wide range of gases. Under these conditions the interaction of the gas with the surface has the clearest effect on the macroscopic flow characteristics. These experiments are extremely difficult to carry out, primarily because it is necessary to detect very small flows if a single capillary or a packet of capillaries is used; the problem can be simplified considerably by using a capillary microscreen as the channel.

We report here on an experimental study of free-molecule and intermediate flow regimen for several inert and polyatomic gases in a capillary screen. We compare the results with the other information available.

EXPERIMENTAL PROCEDURE

The measurement procedure and the experimental apparatus for this study of intermediate and free-molecule flow regimes are described in detail in ref. 10. The only difference in the apparatus is that slight structural changes have been made in the injection system and in the working chamber in connection with the use of a different channel. Accordingly, we describe only the basis features of the working channel and the procedure for determining the flows.

The working channel is a capillary screen, fabricated

TABLE 1. Purity of the Gases Studied

	He	Ne	Ar	Kr	Xe	H_2	D_2	N_2	CO_2	CH_4
Impurity content, %	0.015	0.02	0.04	0.3	< 0.01	0.3	0.3	0.001	0.5	~1
Impurity	N_2	N_2	N_2	Xe	—	N_2	N_2	O_2	N_2	N_2

from a set of thin-walled capillaries of the same diameter placed in a glass tube, heated, and stretched. The average capillary diameter is $(1.35 \pm 0.01) \cdot 10^{-3}$ cm, the capillary length is ~ 5.0 cm, the transparency of the screen is ~ 90%, and there are ~ 640 capillaries.

The screen is mounted in the following manner: A silver film of the necessary thickness is deposited on the outer surface of the glass tube of the screen. Then the screen is soldered by means of Wood's metal to a Kovar disk, soldered with ordinary solder beforehand to a stainless steel flange. This flange divides the working volume of the experimental apparatus into two approximately equal parts. This method for mounting the screen in a flange provides a good thermal contact between the flange and the metal and prevents the possible leakage of gas around the capillaries; it also permits experiments to be carried out over a broad temperature range, from 70 to 350°K.

We have studied the free-molecule and intermediate flow regimes of a wide variety of inert, diatomic, and polyatomic gases; the purity of the gases is shown in Table 1.

The results of the experiments carried out with spectrally pure helium and nitrogen and with samples of these gases of ordinary purity (an impurity of ~ 2%) agree within the experimental error.

All the gases are passed through a liquid-nitrogen trap before they enter the experimental apparatus. All measurements are carried out at room temperature, 290-292°K.

EXPERIMENTAL RESULTS AND CONCLUSIONS

The experimental results are analyzed on a computer by means of a nonlinear method of least squares, by the procedure described in ref. 10. The quantity which is the immediate result of the computer analysis of the experimental data is the constant C, which is related to the flow rate of the gas through the channel per unit pressure difference across the ends of the channel, M:

$$C = \frac{M}{V\left(1 + \frac{a}{V} p\right)}. \tag{1}$$

Here $V = V_1V_2/(V_1 + V_2)$ is the reduced volume of the system, 146.5 cm^3, which is measured by a comparison method within 0.1%; the quantity $a = 0.136 \pm 0.002$ c^3/torr is the correction for the membrane curvature of the differential capacitance micromanometer. Since the measurements are carried out over an intermediate pressure range, $\bar{p} \simeq (5 \cdot 10^{-4}\text{–}10^{-1})$ torr, their contribution to the flow rate of the term associated with this membrane curvature is negligibly small over the entire $\bar{p}$ range.

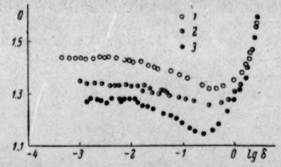

Fig. 1. Reduced gas flow rate Q as a function of the parameter δ. 1) He; 2) H_2; 3) Xe.

The relative error in the calculation of the gas flow rate M is less than 0.5% for He, Ne, and D_2 or 1% for the other gases in the entire pressure range studied. All the measurements were repeated after an interval of about two months; the results agree within the specified errors.

The experimental data for the various gases are conveniently compared on the basis of the reduced volume flow rate Q as a function of the parameter δ, which is related to the Knudsen number Kn by

$$\delta = \frac{\sqrt{\pi}}{2} \frac{R}{\lambda} = \frac{\sqrt{\pi}}{2} \frac{1}{\mathrm{Kn}}, \tag{2}$$

where R is the average capillary radius and λ is the mean free path of the molecules; this mean free path is calculated on the basis of the hard-sphere model and the equation for the viscosity coefficient in the second Chapman–Enskog approximation.

Since there is an uncertainty in the channel geometry for the capillary screen used here (the cross sections of several of the capillaries are not circular), and since we do not know the exact number of capillaries, we use the following definition of the reduced flow rate, in contrast with that used in refs. 9 and 10:

$$Q = \frac{M}{\left(\frac{T}{\mu}\right)^{1/2}}, \tag{3}$$

where T is the experimental temperature and μ is the molecular weight. This definition of Q suppresses a sensitivity of the gas flow rate in the free-molecule and intermediate flow regimes to the temperature and the nature of the gas. It also allows all the differences in the values of Q for the various gases in these flow regimes to be attributed to interactions of the gases with the surface alone.

To illustrate the results we show in Fig. 1 the reduced flow rate Q as a function of the parameter δ for He, H_2, and Xe.

In the intermediate flow regime (δ ~ 1) as well as in the free-molecule and adjacent regimes (δ < 0.1), there is

TABLE 2. Experimental Values of the Reduced Free-Molecule Gas Flow Rate Q_{fm} and of the Tangential-Momentum Accommodation Coefficient α

	He	Ne	Ar	Kr	Xe	H_2	D_2	N_2	CO_2	CH_4
Q_{fm}	1.442	1.471	1.337	1.312	1.289	1.354	1.372	1.351	1.296	1.309
$\pm\Delta Q_{fm} \cdot 10^3$	7	7	13	10	15	13	5	14	13	11
α	0.944	0.934	0.982	0.991	1	0.976	0.969	0.977	0.998	0.992
$\pm\Delta\alpha \cdot 10^3$	4	4	6	5	—	7	3	7	6	6

a significant difference between the values of the reduced flow rates Q for the various gases.

To calculate the free-molecule flow rate Q_{fm} we use

$$Q = Q_{fm}(1 + 0.7\delta \lg\delta). \tag{4}$$

The functional dependence of Q on δ described by (4) is analogous to the theoretical function $Q(\delta)$ for approximately free-molecule flow ($\delta \leqslant 10^{-2}$) (refs. 11, 12). Calculations show that the values of Q calculated from Eq. (4) agree with the exact values[11,12] within $< 0.2\%$ for $\delta < 5 \cdot 10^{-2}$.

We analyze all the experimental data in this range of δ by the method of least squares, using Eq. (4). Table 2 shows the values of Q_{fm} and the corresponding standard deviations found for the various gases.

We see from Table 2 that Q_{fm} is a strong function of the nature of the gas; the most pronounced difference, ~ 16%, is observed between the results for Ne and Xe.

According to ref. 10, the experimental data for xenon agree with the theoretical data within the experimental error for both viscous flow with slip (with a slip constant) and for approximately free-molecule flow (a reduced flow rate), provided that all the molecules are assumed to be scattered diffusely by the wall in the theory. Since a screen of glass capillaries with fused walls is used in our experiments, and since the lowest value of Q_{fm} found is that for xenon, we can quite confidently assert that the xenon molecules in our experiments are scattered diffusely by the fused glass surface. Then all the differences among the values of Q_{fm} for these gases can be attributed to differences in the relative number of molecules which are scattered diffusely by the wall, Q_{fm}. This relative number can be calculated from the experimental values of Q_{fm} through the equation[12]

$$Q_{fm}(\alpha) = Q_{fm}(\alpha = 1)\frac{2-\alpha}{\alpha}. \tag{5}$$

According to our assumptions, the quantity $Q_{fm} \cdot \alpha = 1)$ in (5) is the reduced flow rate for xenon. In this procedure, the values of α calculated for all the gases are relative values.

The observed values of α are shown along with the corresponding errors in Table 2. The error in the determination of α is governed solely by the error ΔQ_{fm} for each gas since the error in the determination of Q_{fm} for xenon is a systematic error.

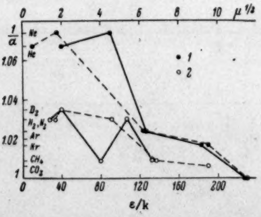

Fig. 2. The quantity $1/\alpha$ as a function of the molecular weight μ and the depth of the potential well, ε/k. 1) Inert gases; 2) polyatomic gases. Dashed lines) $1/\alpha = f_1(\varepsilon/k)$; solid lines) $1/\alpha = f_1(\mu^{1/2})$.

In ref. 10 the values $\alpha = 0.935$, 0.929, and 0.975 are founde for He, Ne, and Ar, respectively, in good agreement with the data in Table 2. This agreement strengthens our confidence in the interpretation of these experimental results.

Figure 2 shows $1/\alpha$ as a function of the molecular weight μ of the gases studied. We see that as the molecular weight is increased the quantity $1/\alpha$ falls off monotonically for the inert gases, except for helium. For the polyatomic gases the functional dependence $1/\alpha = f_1(\mu^{1/2})$ is satisfied on the whole, although there are anomalous values of $1/\alpha$ for hydrogen and methane.

It seems worthwhile to attempt to find another parameter characterizing either the individual or collective properties of the atoms or molecules and which could be used to eliminate this anomalous behavior of the values of $1/\alpha$. Such a parameter could be, e.g., the diameter of the molecule or the depth of the potential well, ε/k, in the Lennard Jones (6-12) potential. An attempt to use the molecular diameter as this parameter has been unsuccessful.

For comparison, Figure 2 shows the experimental values of $1/\alpha$ as a function of the depth of the potential well, ε/k. These depths, given in ref. 13, are determined from the functional dependences of the viscosity coefficients on the temperature, in which the quantum-mechanical corrections are taken into account. We see that the anomalous behavior for methane vanishes, although that for helium and hydrogen does not.

We can draw the following conclusions from these experimental results.

First, it has been shown experimentally that the observed flow rates for all the gases in free-molecule and adjacent flow regimes in glass capillaries with fused walls are higher than the theoretical values obtained under the assumption of completely diffuse scattering of molecules by the wall. This difference supports the Maxwell diffuse-mirror scheme for the interaction of gases with a surface.

Second, the agreement between the calculated values of the coefficient α and the available data from single capillaries is evidence in favor of the procedure of extracting these coefficients from the experimental data by a relative method, in which xenon is chosen as a diffusely scattered gas.

Third, the fact that α does not behave anomalously as a function of the depth of the potential well for the inert and polyatomic gases studied here, except for helium and hydrogen, allows us to conclude that heavy-gas molecules, for which the depth of the potential well is greater, are reflected more diffusely than light-gas molecules, since they spent more time interacting with the wall (and thus have a longer lifetime in the adsorbed state).

Taking account of surface diffusion would undoubtedly improve the agreement between the experimental and theoretical results. However, at present it is difficult to distinguish between mirror reflection and surface diffusion in the absence of appropriate experimental information, in particular, information obtained at various temperatures.

---

[1] A. S. Berman and W. J. Maegley, Phys. Fluids, 15, 772 (1972)

[2] W. J. Maegley and A. S. Berman, Phys. Fluids, 15, 780 (1972).

[3] L. A. W. Huggel, Proc. R. Soc. A, 212, 123 (1952).

[4] L. M. Lund and A. S. Berman, J. Appl. Phys., 37, 2496 (1966).

[5] D. H. Davis, L. L. Levenson, and M. Milleron, J. Appl. Phys., 35, 529 (1964).

[6] B. T. Porodnov, P. E. Suetin, S. F. Borisov, and M. V. Nevolin, Izv. VUZ. Fiz., No. 10, 150 (1972).

[7] F. Herblat, in: Interaction of Gases With Surfaces [Russian translation], Izd. Mir, Moscow (1965), p. 13.

[8] R. M. Barrer and D. Nicholson, Can. J. Chem., 43, 896 (1965).

[9] B. T. Porodnov, P. E. Suetin, and S. F. Borisov, Zh. Tekh. Fiz., 40, 2383 (1970) [Sov. Phys. – Tech. Phys., 15, 1863 (1971)].

[10] S. F. Borisov, B. T. Porodnov, and P. E. Suetin, Zh. Tekh. Fiz., 42, 1310 (1972) [Sov. Phys. – Tech. Phys., 17, 1039 (1972)].

[11] Y. Sone and K. Yamamoto, Phys. Fluids, 11, 1672 (1968).

[12] V. G. Chernyak, B. T. Porodnov, and P. E. Suetin, Inzh.-Fiz. Zh., No. 2, 227 (1973).

[13] J. O. Hirschfelder, C. F. Curtiss, and R. B. Bird, Molecular Theory of Gases and Liquids, Wiley, New York (1954).

Transient molecular effusion characteristics

Yu. N. Lyubitov and V. Z. Belen'kii

Institute of Crystallography,
Academy of Sciences of the USSR, Moscow

(Submitted April 17, 1973; resubmitted October 8, 1973)
Zh. Tekh. Fiz., 44, 824-829 (April 1974)

Numerical solutions are found for several two-dimensional problems in the Knudsen pressure range using the Langmuir adsorption model in the transient state: These include the distribution of the molecular flow within a cylindrical effusion vessel, the distribution of coverage of the adsorbed film on the walls of this vessel, and the signal from an ideal detector for molecular flows from the cylinder for various geometries. The time constants of the vessel–collimator–detector systems are functions of the ratio of the angular dimensions of the collimator and vessel and of their relative arrangement. The time constant of this system is also a function of combinations of characteristic times involved in this problem, e.g., the transit time in the vessel, the lifetime on the wall, the frequency of particle–wall collisions, and the time constant of the detector. The characteristics (like the real characteristics) deviate significantly from one-dimensional behavior and are transient. Programs which have been worked out provide realistic simulations of the evolution of the effusion characteristics over a broad range of the governing parameters.

The use of molecular effusion from various vessels and the closely related problems of the molecular distribution within these vessels play an important role in applied physics. An understanding of these processes is important in high-temperature evaporation, in the use of molecular guns in molecular-beam experiments, in problems that arise in ion engines and vacuum communication systems, and in problems involving porous adsorbents, deposited films, and catalysts.[1-4] Clausing's work in the 1930's has apparently been the most important in this field, although there has been some recent work.[5,6]

In this work we use a system of transient equations [Eqs. (1)-(3)], introduced previously,[7] which relate the distribution of the incident particle flux per surface position per unit time, $\sigma = \sigma(P, t)$, the distribution of the departing particle flux, $\varphi = \varphi(P, t)$; and the distribution of the degree of coverage, $\theta = \theta(P, t)$. Here, t is the time and P specifies a point on the internal surface of the cylinder. The lifetime of the particles on the surface and the time spent in flight (in the single-velocity approximation) are taken into account. In constructing these equations we adopt the Knudsen cosine law and neglect collisions between particles (we assume Knudsen flow). We assume the unknown distributions to be axisymmetric, so the problems solved here are two-dimensional, being much more complicated than the one-dimensional ones solved by Clausing[8] but simpler than actual three-dimensional systems. We do not use Clausing's[9] replacement of approximation integral equation (2) by a partial-derivative diffusion equation; this simplification is valid only for infinitely long (or very long) capillaries.[3]

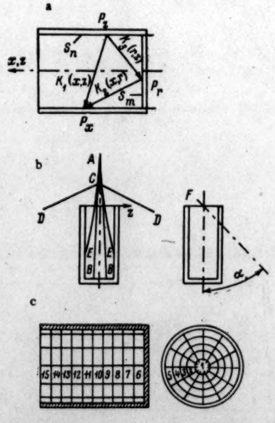

Fig. 1. The coordinate systems. a) For Eqs. (1)-(4). Here S_m is the base and S_n is the lateral surface of a cylinder; b) relative arrangement and motion of the vessel and the collimator. Here, point F is the intersection of the z axis and the plane of the figure; c) scheme for partitioning the internal surface into mutual-irradiation zones.

The system of equations which we use below can be written:

$$\varphi = (\sigma + \mu)\,\Theta, \tag{1}$$

$$\sigma(P,\ t) = \int_s \varphi\left(P',\ t - \frac{\|P' - P\|}{v}\right) K(P,\ P')\,dS(P'), \tag{2}$$

$$\dot{\Theta} = \sigma - \varphi, \tag{3}$$

$$\Theta(P,\ 0) = \begin{cases} \Theta_0, & P \in S_m, \\ 0, & P \in S_n. \end{cases} \tag{4}$$

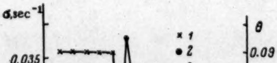

Fig. 2. Distributions of the degree of coverage θ and the intensity of the incident flux σ over the internal surface of the cylinder. Here (m + n) is the index of the zone (see Fig. 1c). t = 0.116 sec: 1) θ; 2) σ. t = 1.15 sec: 3) θ; 4) σ.

where

$$K(P,\ P')=\begin{cases}K_1(x,\ z);\ P,\ P'\in S_n;\ P=P_x;\ P'=P_z,\\ K_2(x,\ r);\ P\in S_n;\ P'\in S_m;\ P=P_x;\ P'=P_r,\\ K_3(r,\ z);\ P\in S_m;\ P'\in S_n;\ P=P_r;\ P'=P_z.\end{cases}$$

$$K_1(x,\ z)=\frac{1}{2}\left[1-\frac{|x-z|(6R^2+|x-z|^2)}{(4R^2+|x-z|^2)^{3/2}}\right];$$

$$K_2(x,\ r)=\frac{2xr\,(R^2-r^2+x^2)\,R^2}{[(R^2+r^2+x^2)^2-4r^2R^2]^{3/2}};$$

$$K_3(r,\ z)=\frac{2z\,(R^2-r^2+z^2)\,R^3}{[(R^2+r^2+z^2)^2-4r^2R^2]^{3/2}}.$$

In Eqs. (1)-(3), μ is the average rate at which particles leave the surface. This quantity is a function of the temperature and the heat of adsorption and is assumed to be constant in these calculations. Also, v is the particle velocity, R is the cylinder radius, r is the radial coordinate, and x and z are the axial coordinates. All the numerical examples are calculated for $\mu = 1\ \mathrm{sec}^{-1}$, R = 1 cm, and $v = 10^4$ cm/sec for a cylinder 5 cm long; the other dimensions are chosen according to scale on the basis of Fig. 1. The quantity K(P, P') is the probability that a particle will be incident from the region near point P' on the region near point P. The nature of this probability has been discussed widely (see, e.g., ref. 3). Equation (1) describes the balance between the fluxes arriving at and departing from a given point, Eq. (2) describes the balance between the fluxes between a given point and other points on the cylinder, taking account of the delays involved, and Eq. (3) is found from the ordinary Langmuir equation for the adsorption φ kinetics. The departing flux φ consists of the reflected part of the incident flux $\sigma(\Theta)$ (we assume that a particle incident on a filled position is reflected, while one incident on a vacant position is captured), and the desorbed flux, $\mu(\Theta)$; and Eq. (4) is the initial condition. If we set $\Theta = 0$ in Eq. (3) (corresponding to the steady state), we find $\sigma = \varphi$, and Eq. (2) becomes a an integral Fredholm equation of the second kind (if we also assume $\|P'-P\|/v = 0$), which we manipulate in the ordinary manner with the Clausing times. If we do not assume $\|P'-P\|/v = 0$, we find from Eq. (2), in the case of sufficiently rapid adsorption, integral equations with a retarded argument, introduced in ref. 3. Surface diffusion, which has been discussed from time to time in the literature (beginning with Volmer) is inconsequential in our problem; According to the Clausing criterion,[9] this process is negligible when the quantity

$$\frac{3D_s}{4R^2\mu},$$

where D_s is the surface-diffusion coefficient, is small in comparison with unity.

We assume that the cylinder has been brought to

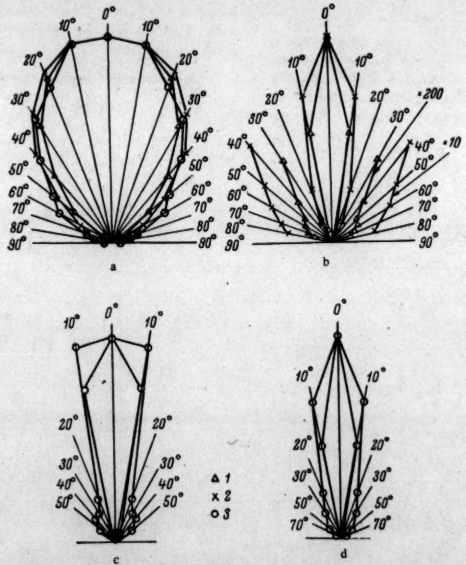

Fig. 3. Time evolution of the characteristics for various collimators. a) CDD; b) CEE; c) ABB according to Fig. 1b; d) "infinitely" remote collimator. a (CDD): 1) z = 0, t = 0.116 sec; 2) z = 0, t = 1.4 sec; 3) z = 2.66 cm, t = 0.116 sec. c) (ABB): inner curve) z = 0, t = 0.116 sec; outer curve) z = 0, t = 1.99 sec. d("infinitely" remote collimator): inner curve) z = 0, t = 0.116 sec; outer curve) z = 0, t = 1.99 sec.

that temperature at which the average particle lifetime in the adsorbed film is μ^{-1} sec. Then, as in ref. 7, we place a certain amount of the material, Θ_0, at the base of the cylinder (Fig. 1). The numerical examples are carried out for $\Theta_0 = 0.1$ monolayer.

Using a difference approximation of Eqs. (2) and (3) we can calculate the values of σ, φ, and Θ in all zones of the cylinder in successive time layers; the results of such a calculation for σ and Θ are shown in Fig. 2. However, it is difficult to compare these results with the measured values of Θ and σ within the cylinder because of the difficulty in carrying out such experiments. It is simpler to measure the fluxes I from the cylinder through some collimator system to a detector. The rest of this paper is devoted to a calculation of such effusion fluxes, but this calculation can be carried out only after σ and Θ are found).[1)]

Figure 1b shows the relative arrangement of the effusion cylinder and the three samples used as collimators in the calculations. The collimators are a system of two coaxial circular irises which determine the right circular "visibility cones" ABB, CDD, and CEE in the figure. These cones bound that part of the surface of the cylinder from which particles capable of passing through the collimator into the detector (among other particles) are desorbed. We assume that all the particles which pass through the collimator are detected.

Here, we have introduced a realistic collimating system. On the other hand, to match the system for which calculations were first carried out by Clausing[10] and for which many subsequent calculations have been carried out (see, ref. 6 and the bibliography there), we must construct something similar to the faceted eye of an insect. No such collimators have been described in the literature; nevertheless, our analysis of the emission characteristics of various points on the cross section of a cylinder is an important supplement to previously published work. This analysis converts the one-dimensional characteristics of Clausing and many of his successors into the two-dimensional characteristics of the present paper.

The program that we have worked out makes it possible to calculate the number of particles incident on the detector for various specified geometries of the cylinders and collimators, and it is possible to alter the relative arrangement of these units, e.g., by moving the cylinder a specified distance along the z axis with respect to the collimator and then rotating the cylinder around this axis through a specified angle α, while the other replaceable collimators are held in position.

We also calculate the signals from our ideal detector as a function of the time.

The detector signal is calculated for fixed values of all the parameters in the following manner: The internal surface of the cylinder is partitioned into hoops m, n and into a specified number of angular sectors (see Fig. 1c, where m = 5, n = 10 hoops, and there are 12 sectors for concrete calculations). The exit-window iris of the collimator is also partitioned into a specified number of radial and angular regions. We calculate the probabilities for incidence from each such region of the cylinder (assuming a cosine law) on all regions of the collimator in succession. We take into account only those pairs of regions which are in the line of sight. Then, through a summation over the corresponding regions, we find the probabilities for incidence on the detector of particles from each of the (m + n) regions of the cylinder. The detector signal is found through a summation (with these probabilities) of the distribution of the escaping flux, $\varphi(P)$, calculated by the program described above.

Figure 3 shows the effusion characteristics $I = I(\alpha)$ for various collimator schemes and for various relative arrangements of the cylinder, collimator, and detector. The curves in this figure are obtained by connecting points for which the coordinates are calculated, so the curves may differ slightly from those which would be calculated with a finer calculation step (this refinement can be made where necessary). Figure 3d shows data for an "infinitely" remote collimator (the cylinder–collimator separation used in the calculation is 50 cm), having the same dimensions as the collimator for CDD. This scheme is also a good approximation of the ideal Clausing collimator,[10] which we have discussed above.

In Fig. 3 we see a gradual broadening of the emission patterns and a broadening of the "pupil" of the collimator as time elapses; this behavior is, of course, a manifestation of an increase in the entropy of the system.

Figure 4 shows the detector signal as a function of the time for the various collimator versions and for various

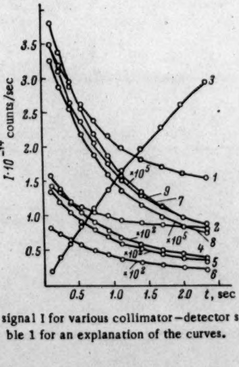

Fig. 4. Detector signal I for various collimator–detector systems. See Table 1 for an explanation of the curves.

TABLE 1. Signal Decay Over the Observation Interval from One to Two Seconds (from the data in Fig. 4)

Curve label in Fig. 4	$I(1)\cdot10^{-14}$, sec^{-1}	$I(2)\cdot10^{-14}$, sec^{-1}	$\frac{I(1)}{I(2)}$	Geometry (see Fig. 1b) z,cm	Type of collimator
1	2.1	1.55	1.35	0	CDD
2	0.97	0.84	1.15	1.33	
3*	1.47	2.6	0.56	2.66	
4	$0.75\cdot10^{-2}$	$0.45\cdot10^{-2}$	1.67	0	CEE
5	$0.67\cdot10^{-2}$	$0.40\cdot10^{-2}$	1.67	0.43	
6	$0.42\cdot10^{-2}$	$0.25\cdot10^{-2}$	1.68	0.87	
7	$1.8\cdot10^{-5}$	$1\cdot10^{-5}$	1.8	0	ABB
8	$1.04\cdot10^{-5}$	$0.58\cdot10^{-5}$	1.8	0.36	
9	$0.56\cdot10^{-5}$	$0.34\cdot10^{-5}$	1.64	0.72	

*No decay; instead, the signal increases.

positions of the cylinder along the z axis (Fig. 1b) (but without rotation). Particularly noteworthy is the increase in the detector signal in the case of curve 3, in the face of a decay of this signal for all other cases. This singular case is attributed to the combination of the wide "vision" angle of collimator CDD (Fig. 1b) and the extreme position of the cylinder, displaced 2.66 cm along the z axis. In this position the detector "sees" only the time-increasing emission from the mouth of the cylinder, where particles from the base of the cylinder are incident. Subsequently, of course, this signal must decay.

A direct analysis of Eqs. (1)-(4) does not yield any conclusions regarding the time constants of the system. On the basis of general considerations we conclude that the time characteristic of the system is a function of several characteristic times – the time a particle spends in flight, the time it spends at the surface, the time which elapses between collisions with the surface – as well as of the number of such collisions. The frequency and number of collisions with the surface are functions of the geometry of the system.

Let us analyze the curves in Fig. 4 as if we had obtained them experimentally. One possible result of this analysis is shown in Table 1.

Table 1 shows how the detector signal varies from 1 to 2 sec on the scale in Fig. 4 for various geometric arrangements. These data show that the time constants of the overall cylinder–collimator system are different, even though the same processes occur in the same cylinders and with the same boundary and initial conditions (Fig. 2). Accordingly, the construction and arrangement of the collimator affect the time constant of the system; this constant is shorter, the "stiffer" the collimation.

The significance of these results is clear. It would be useful to analyze the metrological features of these systems, which must also be taken into account in measurements and which may be used in further studies.

The authors thank V. Fedosimov for consultation on the calculations, and they thank the participants of the seminar supervised by É. Ya. Zandberg and N. I. Ionov for a detailed discussion of this work.

---

[1] We recognize that the inverse problem must be solved, but at the present stage we do not know how to proceed.

---

[1] A. I. Pipko, V. Ya. Pliskovskii, and E. A. Penchko, Design and Construction of Vacuum Systems [in Russian], Izd. Énergiya, Moscow (1970).
[2] Yu. N. Lyubitov, Calculations of the Interaction of Molecular Fluxes with Confining Vessels [in Russian], Izd. Nauka, Moscow (1964).
[3] Yu. N. Lyubitov (Ljubitov), Molecular Flow in Vessels, Plenum Press, New York (1967).
[4] É. Ya. Zandberg and N. I. Ionov, Surface Ionization [in Russian], Izd. Nauka, Moscow (1969).
[5] V. I. Lozgachev, Zh. Tekh. Fiz., 32, 1012, 1023, 1123 (1962) [Sov. Phys. – Tech. Phys., 7, 736, 745, 827 (1963)].
[6] G. F. Voronin, Zh. Fiz. Khim., 43, 1320 (1969).
[7] Yu. N. Lyubitov and V. A. Belen'kii, Elektronika (in press).
[8] P. Clausing, Zs. Physik., 66, 471 (1930).
[9] P. Clausing, Ann. Phys., 5E, No. 4, 489 (1930).
[10] P. Clausing, Ann. Phys., 5F, No. 5, 559 (1930).

A transaxial lens

V. M. Kel'man, L. M. Nazarenko, and E. M. Yakushev

(Submitted July 23, 1973)
Zh. Tekh. Fiz., 44, 830-834 (April 1974)

An experimental study has been made of a transaxial lens operating in the anamorphic regime. The focal length of the lens and the aberrational broadening of the image line in the focal point have been measured. Good agreement is found with calculated data.

Transaxial lenses, studied theoretically in refs. 1 and 2, have been suggested for use as collimators and focusing devices in symmetric prism energy focusing mass spectrometers.[3] An advantage of such lenses is the fact that the spherical aberration in the dispersion direction of the instrument is small; structurally, these lenses combine well with the reflecting elements of the instrument. We report here on an experimental test of such lenses. We have tested the lenses along with the electrostatic deflecting elements (three-electrode telescope systems) of a mass spectromer; in this way we are able to determine simultaneously the quality of the entire electrostatic part of the mass spectrometer (without the magnetic prism). Furthermore, the deflecting elements make it possible to construct an electron-optics bench, which is particularly useful for testing transaxial lenses.

Figure 1 shows the experimental apparatus, which consists of two identical systems, I and II, divided in this figure by line mm. In a symmetric prism mass spectrometer these systems lie in symmetric positions with respect to the magnetic prism and serve as its arms. In the mass spectrometer the edges of electrodes 6 of the two systems, which touch each other along line mm in this apparatus, are parallel to the direction in which the field of the magnetic prism is constant. Each arm (I or II) consists of a transaxial lens with electrodes 1-4 and a deflecting telescope system with electrodes 4-6. A single electrode consists of two identical plates arranged symmetrically with respect to the median plane of the system. The distance between the plates in each electrode d = 8 mm.

To avoid disturbing the desired field distribution we place all the supporting parts between the electrode plates at a distance of at least 5d from the axis of the ion beam. The lens electrodes are L = 100 mm in size. The gap between neighboring electrodes of the lenses and telescope systems is 1 mm. Limiter D, with a rectangular aperture, is placed 309 mm from ion source E. The dimensions of this aperture are 2.7×9 mm^2; the long dimension is parallel to the median plane of the system.

In the arrangement of electron-optics elements shown in this figure the gaps between the electrodes of the two telescope systems are parallel to each other. Accordingly, the two telescope systems together constitute an electron-optics analog of a plane-parallel plate, and for the case of a parallel beam in the median plane, these telescope systems are free of all types of geometric and angular chromatic aberrations.

Figure 2 shows a photograph of one part of the electron-optics bench (one arm of the mass spectrometer). All the electrodes are mounted on plate 7. Electrodes 1-5 and plate 7 are made of a nonmagnetic material (stainless steel). The plates of electrode 6 are made of soft magnetic materials, because this electrode is also a magnetic shield, used to keep the field of the deflecting magnet two-dimensional. Here we are concerned with this electrode only in regard to its effect in shaping the electrostatic field of the telescope system.

Certain requirements are imposed on the elements of an arm of a mass spectrometer,[3] and the parameters of the telescope system are chosen to meet these requirements. The incidence angle (Fig. 1) $i = 64°40'$, the refraction angle $j = 31°15'$, and the width of the intermediate electrode $l = 41$ mm. The ratio of the potentials at the extreme electrodes of the telescope system is $V_4/V_0 = 0.330$, while the potential at the central electrode is $V_{ce} = 0.530\ V_0$. The point at which the ions appear is assumed to be at zero potential, and the potential of grounded electrodes 1 and 6 is V_0. The effective refraction plane of the telescope system, bb, lies near central electrode 5, 9 mm from the plane passing through the center of the gap between electrodes 4 and 5. With these parameters of the telescope system the mass spectrometer is achromatic, and its spectral lines are straight when the beam enters the magnetic prism at an angle $\alpha = 51°$.

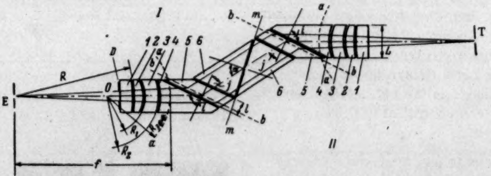

Fig. 1. Arrangement of the apparatus for testing transaxial lenses. 1-4) Electrodes of the transaxial lenses; 4-6) electrodes of the electrostatic telescope systems; E) exit slit of the ion source; T) detector slit of the recording instrument. Lines aa show the effective refraction surfaces of the transaxial lenses, while lines bb show the effective refraction planes of the telescope systems.

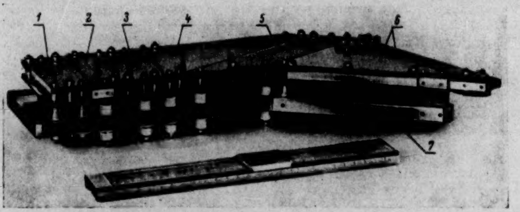

Fig. 2. Transaxial lens and deflecting telescope system. 1-4) Electrodes of the lens; 4-6) electrodes of the telescope system; 7) supporting plate.

The transaxial lenses, whose task is to produce a parallel, three-dimensional beam from the ions emerging from a point source and to then focus this beam to a point in the object plane, operate in the anamorphic regime. Accordingly, the calculations carried out for cylindrical transaxial lenses[4,5] can be used only as rough estimates. The parameters of the lenses used here are determined accurately through numerical computer calculations. For this purpose we assume electrodes 1 and 2 to be grounded, i.e., we assume the lenses to be three-electrode lenses. With potential V_4, given above, on the electrode 4, and with $R_1 = 121$ mm and $R_2 = 161$ mm, the potential of the central electrode of the transaxial lens, electrode 3, which provides lens operation in the anamorphic regime is calculated to be $V_3 = 2.19\ V_0$. Here R_1 and R_2 are the radii of curvature of the edges of electrode 3 with center at point 0. The corresponding focal length on the concave side of the lens is $f = 460$ mm, and the effective refracting surface is found to lie at a distance $R_{\text{eff}} = 195$ mm from the center of curvature of the transaxial lens, 0. This information is sufficient for determining the paths of rays in the median plane of the entire system. We note that this system has unit magnification in both the horizontal and vertical directions.

Electrode 2 is added to correct the position of the focus. The gap between electrodes 1 and 2 is cut along the arc of a circle of radius R = 350 cm, centered at the slit of the ion source E (or at that of the detector, T). Accordingly, the field in this gap does not alter the rectilinear nature of the ion trajectories from the source to the median plane of the system (or from this plane to the detector). When there is a slight change ΔV_2 in potential $V_2 = V_0 + \Delta V_2$ at electrode 2, the field in this gap also has essentially no effect on the vertical course of the trajectories because when the ratio $\Delta V_2/V_0$ is small the optical power of the lens in the vertical direction is proportional to the square of this ratio. Accordingly, the role of the extreme electrode of the three-electrode transaxial lens is assumed by electrode 2, and a change in the potential of this electrode leads to a change in the refractive index of the lens, providing the desired control of the position of the focus.

In preliminary experiments we observe the images visually by means of an ion-optical image converter. In these experiments the exit slit of the source is 1 × 0.1 mm^2 in size. The calculated potentials are supplied (within 0.1%) to the electrodes, and electrode 2 is grounded. The ion energy eV_0 is 2870 eV. Because of the low resolution of the image converter, the shape and dimensions of the image on the screen are governed largely by the quality of the converter. The observed image is a spot whose brightest part is a circle about 1 mm in diameter (Fig. 3a). This result is evidence that this ion-optics system is operating in the anamorphic regime when the source and detector are placed in their calculated positions. A change of ± 100 V in the potential on electrode 2 causes a significant expansion of the beam in the horizontal direction (parallel to the median plane), while a like change of the potential at electrode 3 has essentially no effect on the image shape. In addition to the central bright spot on the screen we observe fainter vertical bands issuing upward and downward from this bright spot; the intensity of these bands falls off rapidly from the central spot, and the bands essentially vanish at a distance of 10-12 mm from it. These bands may be due to vertical aberrations of the transaxial lenses and the telescope systems, as is implied by the circumstance that a reduction of the potential on electrode 3 can significantly contract the vertical dimension of the pattern as a whole, while the central bright spot stretches out in the vertical direction (Fig. 3b). This behavior corresponds to a coincidence of the plane in which the vertical spherical aberration is minimal[6] with the grid plane of the image converter. In this adjustment, the height of the image as a whole is about 10 mm, and that of the bright spot is about 6 mm.

When there is a simultaneous change in the potentials on both electrodes 4, the image does not move. It does move when the potential on only one of electrodes 4 is changed. In that case, the additional potential is fed to electrode 4 of system II, which is the one closer to the ion detector T. Measuring the resulting image displacement δl and the additional potential supplied to electrode 4, δV, we can determine experimentally the focal length of the transaxial lens:

$$f = 2 \operatorname{ctg} \iota \sqrt{V_0 V_4}\, \frac{\delta l}{\delta V}. \tag{1}$$

The focal length found in this manner turns out to be 468 ± 10 mm, in agreement with the calculated value.

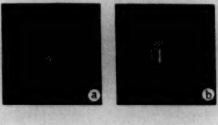

Fig. 3. Photograph of the image line. a) In the anamorphic regime; b) with the system adjusted for the shortest image.

We use the following procedure for a precise measurement of the width of the image line. We detect the ions with an SI-03 counter, the slit of whose detecting head is placed in the image plane. By smoothly changing the potential on electrode 4 of system II, we cause the image to move in the horizontal direction; we measure the intensity of the ion current passing through the detector slit as a function of the additional voltage fed to the electrode, δV. From the width of the peak ΔV determined in this manner and from Eq. (1) we determine the image width:

$$\Delta l = \frac{f\,\mathrm{tg}\,t}{2\sqrt{V_0 V_4}}\Delta V. \qquad (2)$$

The basic voltage on both electrodes 4 is supplied by a single source, so the deflection angle is independent of fluctuations in this voltage. In this manner we eliminate the errors due to the instability of the high-voltage source. On the other hand, the instability of the additional voltage fed to electrode 4 of system II, δV, cannot introduce any important errors since it is so small (up to 1 V).

We carry out measurements as argon is injected into the ion source. To improve the accuracy, we choose a slit width of 5 μ for both the source and the detector. In these experiments the apparatus is not shielded from the earth's field, so the apparatus has a certain slight mass dispersion. As a result, a small amount of residual gas causes a significant expansion of the base of the peak. Accordingly, in determining the image width from Eq. (2) we use twice the peak width at half-height as ΔV.

Measurements show the broadening of the image line per arm of the mass spectrometer to be 13 μ. This broadening is caused by aberrations of the transaxial lens, errors in the assembly of the ion-optics system, errors in adjustment, and all other experimental errors.

For comparison, the resultant calculated aberration of this transaxial lens in the horizontal direction, with the specified position of the aperture limiter, is

$$\Delta y = B_1 y_0^3 + B_2 y_0^2 y_D + B_3 y_0 y_D^2 + B_4 y_D^3 + B_5 y_0 z_0^2 + B_6 y_0 z_0 z_D + B_7 y_0 z_D^2 + B_8 y_D z_0 z_D + B_9 y_D z_0^2 + B_{10} y_D z_D^2. \qquad (3)$$

Here we have adopted a Cartesian coordinate system y, z with origin at the main optical axis of the lens. The y axis is in the median plane of the lens and runs perpendicular to the main optical axis. Coordinates in the object plane are given a subscript "O," while those in the limiter plane are given a subscript "D." The aberration coefficients B_1–B_{10}, which characterize the aberrations in the focal plane of this lens (i.e., in the object plane for the collimator lens or in the image plane for the focusing lens), are, in reciprocal square millimeters (mm^{-2}): $B_1 = 1.16 \cdot 10^{-6}$, $B_2 = 7.63 \cdot 10^{-6}$, $B_3 = 8.76 \cdot 10^{-6}$, $B_4 = 1.72 \cdot 10^{-5}$, $B_5 = 5.20 \cdot 10^{-5}$, $B_6 = 2.67 \cdot 10^{-5}$, $B_7 = 1.39 \cdot 10^{-4}$, $B_8 = 1.55 \cdot 10^{-4}$, $B_9 = 3.05 \cdot 10^{-4}$, $B_{10} = 8.20 \cdot 10^{-44}$ mm^{-2}.

Since the slit of the ion source (or detector) is very narrow, and the center of this slit is assumed to lie at the main optical axis of the lens, the terms in Eq. (3) containing y_0 are negligibly small. With the dimensions specified above for the ion source and the limiter, the total contribution of the other terms to the line width at its base is $2\Delta y$ = 18 μ. Most of this contribution is from spherical aberration, described by the two terms $2B_4 y_D^3$ = 3 μ and $2B_{10} y_D Z_D^2$ = 13 μ.

The theoretical broadening of the image in the transaxial lens (18 μ) turns out to be slightly higher than the experimental image broadening (13 μ). The explanation lies in the circumstance that the aberrations are calculated for the image in the Gaussian plane, while the image width is measured in the plane of the best focus, where the spherical aberration is known to be much less than in the Gaussian plane. Furthermore, the theoretical calculation neglects the distribution of the ion current density over the image width; i.e., the peak shape is not taken into account. A more accurate calculation shows that the width of the peak at its base is more than double its width at half-height. Accordingly, the assumption that the width of the peak at its base is equal to twice its half-height width, used in the experimental determination of ΔV, leads to an estimate of the image width which is slightly too low.

We note that the aberrations of the transaxial lenses fall off rapidly with decreasing limiter dimensions. For example, the calculated aberrations of the ion-optics system shown in Fig. 1 are about 1 μ when a circular limiter 2 mm in diameter is used; under these conditions the elements of this system (I and II) are completely suitable for use in a high-resolution prism mass spectrometer.

---

[1] S. P. Karetskaya, V. M. Kel'man, and E. M. Yakushev, Zh. Tekh. Fiz., 40, 2563 (1970) [Sov. Phys. – Tech. Phys., 15, 2010 (1971)].

[2] S. P. Karetskaya, M. V. Kel'man, and E. M. Yakushev, Zh. Tekh. Fiz., 41, 325 (1971) [Sov. Phys. – Tech. Phys., 16, 244 (1971)].

[3] V. M. Kel'man, L. M. Nazarenko, and E. M. Yakushev, Zh. Tekh. Fiz., 42, 963 (1972) [Sov. Phys. – Tech. Phys., 17, 761 (1972)].

[4] S. P. Karetskaya, V. M. Kel'man, and E. M. Yakushev, Zh. Tekh. Fiz., 41, 548 (1971) [Sov. Phys. – Tech. Phys., 16, 425 (1971)].

[5] L. G. Glikman, S. P. Karetskaya, V. M. Kel'man, and E. M. Yakushev, Zh. Tekh. Fiz., 41, 330 (1971) [Sov. Phys. – Tech. Phys., 16, 247 (1971)].

[6] P. A. Sturrock, Static and Dynamic Electron Optics, Cambridge, London (1955).

Differential electromagnetic characteristics at the interface between ice and water in the ocean

V. V. Bogorodskii and V. P. Tripol'nikov

Arctic and Antarctic Scientific-Research Institute, Leningrad

(Submitted July 31, 1973)
Zh. Tekh. Fiz., 44, 835-838 (April 1974)

Experimental data on the electromagnetic contrast of the interface between ice and water in the ocean are reported. The experiments were carried out on pack ice and ice one year old by the SP-19 drifting station through the use of video pulses of various length and radio pulses at 200 MHz.

A knowledge of the electromagnetic contrast at the interface between ice and water in the ocean is of fundamental importance for assessing the feasibility of radar sounding of ice formations in the ocean from various vehicles.

The power required for probing ice in the ocean is reported in ref. 1.

In calculations of the total loss it has been assumed that there is no electromagnetic matching between ice and water. The Fresnel reflection coefficient of an ice–water interface has been assumed equal to unity, since the modulus of the impedance of sea water is about 25 Ω, while that of ice is 180-220 Ω. This model is only approximate, and objections can be raised against it, since the complicated physical processes involved in the crystallization of sea water always provide a transitional ice layer having relatively high liquid-phase and salt content at the interface. It therefore becomes necessary to study the quantitative characteristics of the electromagnetic contrast between ice and water in the ocean under natural conditions.

An experimental study has been made of the electromagnetic contrast of the ice-water interface at the most typical formations of pack ice and 1-year ice in the Arctic.

Figure 1 shows the experimental arrangement. Two holes 10 mm in diameter, 10 cm apart, and parallel to each other are melted by a hot needle in the ice. Metal rods 5 mm in diameter with length greater than the thickness of the ice are inserted into the holes. The lower ends of these rods extend below the ice-water interface. After a certain time, the metal rods become frozen into the ice and form a two-conductor "ice" line with a characteristic impedance of about 200 Ω, short circuited by the sea water at the boundary of the ice. It has been established that this technique for preparing the holes does not alter the structure of the ice between the rods of the ice line. Then this line is sounded with video and radio pulses, through the use of an apparatus having an air delay line matched to the ice line (Fig. 1).

Figure 2 shows the pulses reflected from the short circuit of the ice line by the sea water and from a short circuit produced by the operator at the air–ice interface. These pulses are recorded through a multiple exposure of the film: First, the pulse reflected from the short circuit produced by the operator at the ice–air interface is recorded; then, with the camera shutter open, the short-circuit at the air end is removed, and the pulses due to reflection at the short circuit in the ice line are recorded. No additional amplification is used.

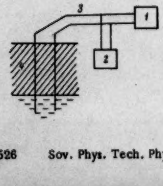

Fig. 1. Experimental apparatus for determining the electromagnetic contrast at the interface between ice and water in the ocean. 1) Oscillator; 2) detector; 3) delay line (400 nsec); 4) metal rods.

By comparing the signals reflected from the artificial short circuit at the air–ice interface with those reflected from the short circuit formed by the sea water we can evaluate the total loss in the ice line. This loss is due to absorption in the dielectric (natural sea water) and the loss due to reflection at the air–ice and ice–water interfaces. The latter can be adopted as a measure of the electromagnetic contrast at the lower boundary of the ice. Figure 3 shows the experimental values of the attenuation as a function of the ice thickness. Here the dashed curves correspond to the specified values of the specified absorption N (in decibels per meter). The measurements are carried out on pack ice many years old, with thickness up to 10 m, on 2-yr pack ice ranging in thickness from 2 to 3 m, and on young ice 1 m thick. The three groups are distinguished by different thickness distributions of the temperature and

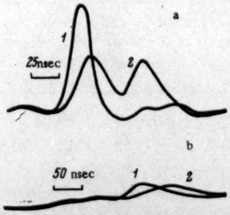

Fig. 2. 1) Reflection from an artificial short circuit; 2) reflection from the interface with water during the sounding of a line in pack ice 3.3 m thick. a) Video pulses 25 nsec long; b) radio pulses 50 nsec long at 440 MHz.

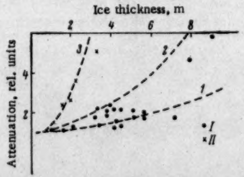

Fig. 3. Total signal attenuation in lines of various lengths. I) Video pulses 25 nsec long; II) radio pulses 50 nsec long at 200 MHz. 1) 1; 2) 2; 3) 5 dB/m.

TABLE 1

Depth, m	Salinity, ppt*	Temperature °C
0÷16	Fresh-water ice	>9
17	0.4	8.3
18	0.74	8.3
19	1.47	7.5
22	8.04	6.0
32	7.98	1.8

*Number of grams of salts per kilogram of ice.

salinity.[2] Despite the variety in the general characteristics of these ice formations, the results found by sounding with video pulses 25 nsec long show that the specific absorption usually lies in the range 0.9-0.2 dB/m. The reflection coefficient at the lower interface can be assumed equal to unity; otherwise the curves of N (in decibels per meter) would intersect the ordinate at values above unity. This is also true for the radial pulses at 200 MHz, and the specific absorption in this case is 4-5 dB/m. In sounding the lines described above with radial pulses at 440 MHz, we have also verified the existence of an appreciable electromagnetic contrast at the ice-water interface (Fig. 2b). However, it is difficult to quantitatively evaluate this difference at 440 MHz in this line arrangement. The preparation of ice lines in which the conductors are closer together would require a more complicated drilling technique.

These results do not tell us whether the actual reflecting interface is the sea water proper or the upper boundary of the layer in which the highly concentrated brine appears. This question is of practical importance in radar measurements of the thickness of ice in the ocean. To study this question further we have carried out a radar sounding of an ice island (at the ST-19 drifting station). This ice island, a fragment of an ice shelf, has been floating in the Arctic basin for many years. Its thickness was measured during the thermal drilling and found to range from 28 to 34 m. Samples of the ice were removed for salinity tests from various depths, from cores obtained during the thermal drilling with an annular thermal drill. The temperature of the ice was also measured at various depths.1) Table 1 shows the temperatures and the salinities of the ice at certain depths.

Since the temperature at depths of 17 mm below is higher than the eutectic temperature for most salts in sea water, the presence of salts at these depths implies the presence of a liquid phase in the ice.

The relative content of the liquid phase increases with increasing temperature and increasing salinity of the ice.[3]

The radar sounding of the ice island was carried out at a frequency of 200 MHz, a pulse length of 50 nsec, and a locator potential of 140 dB.

The antennas, half-wave radiators, were embedded in the ice 25 m apart; their lengths were reduced by a factor of $(\varepsilon)^{1/2}$. The reflectors were pieces of sheet metal 1.5 × 1.5 m in size, mounted behind the antennas on the surface of the ice. The results of the probing are shown in Fig. 4. Here pulse 1 is the forward signal in the air, 2 is the forward signal in the ice, 3 is the signal reflected from the salinity boundary at a depth of 17 m, 4 are the reflections due to the discontinuity in salinity at depths on the order of 20-22 m, and 5 is the reflection from the bottom of the ice. This interpretation is supported, in particular, by the circumstance that the amplitudes of the reflected signals fall off with decreasing directionality of the antennas (Fig. 4). To calculate the depth of the first reflecting boundary we use the equation

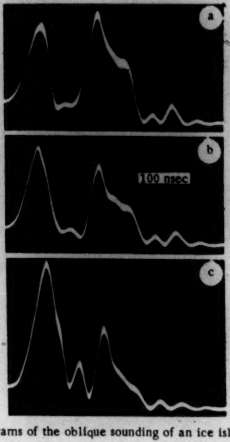

Fig. 4. Oscillograms of the oblique sounding of an ice island. a) Reflectors on both antennas; b) reflector on the transmitting antenna only; c) antennas without reflectors.

$$\Delta t = \frac{\sqrt{R^2 + (2H)^2}}{v} - \frac{R}{c},$$

where Δt is the delay of the reflected signal with respect to the forward signal in air, H is the height of the reflected boundary, c is the wave velocity in air, v is that in fresh-water ice (170 m/μsec), and R is the distance between antennas. To determine the depth of the lower boundary we use the approximate equation

$$2h \approx v_1 \Delta t_1,$$

where h is the thickness of the ice layer below the 17-m level, Δt_l is the delay between signals 3 and 5, and v_l is the wave velocity in the layer. If we assume the velocity in the layer to have an average value of[4] 100 m/μsec over the prevailing temperature and salinity distributions, we find a layer thickness of 11.5 m for the measured delay of Δt_l = 0.23 μsec. Accordingly, the total thickness of the ice according to the radar at our measurements is 28.5 m, in satisfactory agreement with the drilling results.

These experiments show that, despite the lack of contrast in terms of certain physical characteristics (e.g., the density and temperature), there is a good electromagnetic contrast between the layers in ice, which are characterized by variations in salinity and simultaneous variations in the relative amounts of liquid phase. Similar conditions arise at the lower boundary of ice in the ocean. In this connection, the signal received after the reflection from the lower boundary of the ice during radar sounding may begin to be formed slightly above this lower boundary: at the top of the transition layer. The thickness of this layer is governed by the temperature at the time of the ice formation as well as the temperature at the time of the radar sounding.

---

[1] A. P. Legen'kov measured the temperature.

[1] V. V. Bogorodskii and V. P. Tripol'nikov, Problems of the Arctic and the Antarctic [in Russian], No. 39 (1972), p. 135.

[2] V. V. Bogorodskii (ed.), Trans. of the Arctic and Antarctic Research Institute, Leningrad [in Russian], Vol. 295 (1970), pp. 108, 154.

[3] V. L. Tsurikov and A. P. Tsurikova, Okeanologiya, No. 5, 792 (1972).

[4] V. V. Bogorodskii and V. P. Tripol'nikov, Dokl. Akad. Nauk SSSR, 213, 577 (1973)

Evolution of monochromatic whistler and plasma-wave packets in a collisionless plasma

Ya. N. Istomin
Institute of Terrestrial Magnetism,
Ionosphere, and Radiowave Propagation,
Academy of Sciences of the USSR

(Submitted January 30, 1973)
Zh. Tekh. Fiz., 44, 839-840 (April 1974)

The evolution of wave packets is considered. The effect of the velocity spread on the electron distribution function is investigated. Expressions are found for the adiabatic invariants of the motion of the resonant particles taking the spread in velocity into account.

In refs. 1 and 2, the evolution of monochromatic wave packets (whistlers and plasma waves) due to the interaction with resonant particles is treated. This is a bounded problem, in contrast to the problem of the damping of an unbounded plane monochromatic wave.[3,4] A number of aspects of this problem are discussed in the present paper.

To be definite, we introduce the plasma-wave packet $E(x, t) = E_0(x, t) \sin (kx - \omega t + \varphi)$. We write the collisionless kinetic equation for the plasma electrons as

$$\frac{\partial f}{\partial t} + v\frac{\partial f}{\partial x} - \frac{eE_0(x, t)}{m}\sin(kx - \omega t + \varphi)\frac{\partial f}{\partial v} = 0. \tag{1}$$

In the nonlinear case [$\gamma_L \tau \ll 1$, where γ_L is the linear growth rate and τ is a characteristic oscillation time of the resonant particles, $\tau = (m/eE_0k)^{1/2}$], the wave amplitude $E_0(x, t)$ changes very slowly with time and it is therefore convenient to go over from the variables t, x, and v in (1) to the new independent variables: x, $2\xi = kx - \omega t + \varphi$, $2\dot{\xi} = kv - \omega$, and

$$\left(v_0 + \frac{2}{k}\dot{\xi}\right)\frac{\partial f}{\partial x} + \dot{\xi}\frac{\partial f}{\partial \xi} - \frac{1}{2\tau^2}\sin 2\xi\frac{\partial f}{\partial \dot{\xi}} = 0, \tag{2}$$

where $v_0 = \omega/k$ is the phase velocity. A similar kinetic equation is obtained for whistlers by introducing the analogous variables defined by Eq. (2.5) of ref. 1. In this reference, the divergence of the resonant particles is neglected, i.e., the first term in the kinetic equation (2) is written as $v_0 \partial f/\partial x$. The solution to (2) is found here without this simplification.

If the packet is rectangular, i.e., τ is constant in the packet, the particles move in such a way that the quantity $\varkappa = (\tau^2\dot{\xi}^2 + \sin^2 \xi)^{-1/2}$ is conserved. If $|\varkappa| < 1$, the particle is free and if $|\varkappa| > 1$, the particle is trapped by the wave. We now find the average values over x of the particle velocity and the square of this velocity for the cases above:

$$\bar{\psi} = \frac{\int \psi dx}{\int dx} = \frac{\int \psi\left(v_0 + \frac{2}{k}\dot{\xi}\right)\frac{d\xi}{\dot{\xi}}}{\int\left(v_0 + \frac{2}{k}\dot{\xi}\right)\frac{d\xi}{\dot{\xi}}},$$

$$\bar{\dot{\xi}} = \frac{\pi}{2\tau\varkappa K(\varkappa)}\,\frac{1 + \frac{4E(\varkappa)}{\pi k v_0 \tau\varkappa}}{1 + \frac{\pi}{kv_0\tau\varkappa K(\varkappa)}}, \quad \bar{\dot{\xi}^2} = \frac{E(\varkappa)}{\tau^2\varkappa^2 K(\varkappa)}\,\frac{1 + \frac{\pi}{kv_0\tau\varkappa E(\varkappa)}}{1 + \frac{\pi}{kv_0\tau\varkappa K(\varkappa)}}; \; |\varkappa| < 1,$$

$$\bar{\dot{\xi}} = \frac{2}{kv_0\tau^2}\,\frac{E\left(\frac{1}{\varkappa}\right) - (1 - \varkappa^{-2})K\left(\frac{1}{\varkappa}\right)}{K\left(\frac{1}{\varkappa}\right)}, \quad \bar{\dot{\xi}^2} = \frac{kv_0}{2}\bar{\dot{\xi}}; \quad |\varkappa| > 1, \tag{3}$$

K(ϰ) and E(ϰ) are elliptical integrals of the first and second kinds. We note that the expressions for the average quantities in the bounded problem are different from those in the initial-value problem by a quantity of the order of $1/kv_0\tau$, i.e., by the ratio of the spread in velocities $1/k\tau$ to the phase velocity. This difference is due to the fact that the oscillation period of the resonant particles depends only on τ and on the energy (i.e., on $\varkappa$) while the spatial period also depends on the particle velocity.

We now find the distribution function $f(x, \xi, \dot{\xi})$. From Liouville's theorem we obtain

$$f(x, \xi, \dot{\xi}) = f(0, \xi_0(x, \xi, \dot{\xi}), \; \dot{\xi}_0(x, \xi, \dot{\xi})), \tag{4}$$

where the right side contains the distribution function at the origin of the packet (x = 0). Assuming that $1/k\tau \ll v_T$, we expand v_0 in powers of $\dot{\xi}_0$ and limit ourselves to the first two terms:

$$f(x, \xi, \dot{\xi}) = f_0(v_0) + f_0'(v_0)\frac{2}{k}\dot{\xi}_0(x, \xi, \dot{\xi}), \tag{5}$$

where f_0 is the unperturbed distribution function.

Complete phase mixing of the particles takes place in a time of the order of a few τ, and a so-called ergodic state is established.[4] In order to find this ergodic distribution function, we substitute the average velocity $\bar{\dot{\xi}}$ into (5). Owing to the fact that $\bar{\dot{\xi}}$ contains a small correction which is even in $\varkappa$, the average resonant particle density over a wave period

$$\frac{2}{\pi k}\int\limits_{-\pi/2}^{\pi/2} d\xi \int\limits_{-\infty}^{\infty} (f - f_0)\, d\dot{\xi}$$

is nonzero. Knowing the particle distribution function, we can easily show that

$$\int\limits_{-\pi/2}^{\pi/2} d\xi \int\limits_{-\infty}^{\infty} (f - f_0)\, d\dot{\xi} = -\frac{2}{kv_0}\int\limits_{-\pi/2}^{\pi/2} d\xi \int\limits_{-\infty}^{\infty} (f - f_0)\,\dot{\xi}\, d\dot{\xi}. \tag{6}$$

Equation (6) is a result of the continuity condition, which can be obtained directly from the kinetic equation (2).

We consider a long packet ($l \gg v_0\tau$) of arbitrary shape. We will show how, even in this case, corrections which are even functions of the velocity appear in the distribution function as a result of the spread in velocity of the resonant particles. If the amplitude changes, the magnitude of $\varkappa$ is altered. However, as in ref. 1, we can find the adiabatic invariants.

$$\left.\begin{aligned} &\frac{E(\varkappa)}{\varkappa\tau}+\frac{\pi}{2kv_0\tau^2}\left(\frac{1}{\varkappa^2}-\frac{1}{2}\right)=\text{const}, \quad |\varkappa|<1; \\ &\frac{E\left(\frac{1}{\varkappa}\right)-(1-\varkappa^{-2})K\left(\frac{1}{\varkappa}\right)}{\tau}\equiv\frac{\nu(\varkappa)}{\tau}=\text{const}, \quad |\varkappa|>1. \end{aligned}\right\} \tag{7}$$

By using (7), we can easily find the distribution function for the particles in transit:

$$f(x,\varkappa)=f_0(v_0)+f_0'(v_0)\frac{2}{k}\left\{\frac{2}{\pi}\frac{E(\varkappa)}{\varkappa\tau}+\frac{1}{2kv_0\tau^2}\left[\frac{1}{\varkappa^2}-\frac{1}{2}-\frac{4}{\pi^2}\frac{E^2(\varkappa)}{\varkappa^2}\right]\right\}. \tag{8}$$

In order to find the distribution function for the trapped particles we recall that into a given region of the phase space of these particles, there enter particles which were originally in two different regions of transit-particle phase space, i.e., the regions $\varkappa_0^+ > 0$ and $\varkappa_0^- < 0$. We make use of the differential form of the particle conservation law (see ref. 5):

$$\begin{aligned} f(x,\xi)\left(v_0+\frac{2}{k}\xi\right)d\xi d\xi &= f(0,\xi_0^+)\left(v_0+\frac{2}{k}\xi_0^+\right)d\xi d\xi_0^+ \\ &+ f(0,\xi_0^-)\left(v_0+\frac{2}{k}\xi_0^-\right)d\xi d\xi_0^-. \end{aligned} \tag{9}$$

Transforming to the variables ξ and $\varkappa$, integrating (9) over ξ and using (7), we obtain

$$\begin{aligned} f(x,\nu) &= \frac{1}{2}f(0,\varkappa_0^+)\left(1+\frac{\pi\nu}{2kv_0\tau}\right)+\frac{1}{2}f(0,\varkappa_0^-)\left(1-\frac{\pi\nu}{2kv_0\tau}\right) \\ &= f_0(v_0)+\frac{2}{k}f_0'(v_0)\frac{\nu^2}{kv_0\tau^2}\left(\frac{3}{2}-\frac{4}{\pi^2}\right). \end{aligned} \tag{10}$$

To get a closed equation for the amplitude of the packet we use conservation of energy:

$$\frac{\partial}{\partial t}\left(\frac{E_0^2}{8\pi}\right)+\frac{\partial}{\partial x}I=0, \tag{11}$$

where I is the energy flux of the resonant particles:

$$I=\frac{m}{\pi k}\int_{-\pi/2}^{\pi/2}d\xi\int_{-\infty}^{\infty}(f-f_0)\left(v_0+\frac{2}{k}\xi\right)^3 d\xi.$$

Using (6) we get

$$I=\frac{2m}{\pi k}v_0\int_{-\pi/2}^{\pi/2}d\xi\int_{-\infty}^{\infty}(f-f_0)\frac{2}{k}\xi d\xi. \tag{12}$$

Substituting (8) and (10) into (12), and then (12) into (11), we obtain the equation

$$\frac{\partial E_0}{\partial t}-C(E_0)\frac{\partial E_0}{\partial x}=0,$$

where $C(E_0)$ is identical with expression (5.11) from ref. 1. Thus allowance for the term $2\xi/k$ in (2) does not affect the form of the final equation for the field as obtained in ref. 1. This is because the inclusion of this term leads to even corrections in the distribution function and these do not make any contribution to the integral (12).

The author is grateful to V. I. Karpman for suggesting the problem and for useful discussions.

---

[1] Ya. N. Istomin and V. I. Karpman, Zh. Eksp. Teor. Fiz., 63, 131 (1972) [Sov. Phys. – JETP, 36, 69 (1973)].

[2] D. D. Ryutov and V. N. Khudik, Zh. Eksp. Teor. Fiz., 64, 1252 (1973).

[3] R. K. Mazitov, Prikl. Matem. Teor. Fiz., 1, 27 (1965).

[4] T. M. O'Neil, Phys. Fluids, 8, 2255 (1965).

[5] Ya. N. Istomin, V. I. Karpman, and D. R. Shklyar, Zh. Eksp. Teor. Fiz., 64, 2072 (1973).

Diffraction of a plane electromagnetic wave by a conducting plane with a projection

A. A. Zilbergleit

A. F. Ioffe Physicotechnical Institute,
Academy of Sciences of the USSR, Leningrad

(Submitted August 6, 1973)
Zh. Tekh. Fiz., 44, 841-844 (April 1974)

The diffraction of an E-polarized electromagnetic wave incident at an arbitrary angle on a conducting plane with a perpendicular projection of height a is discussed. The dual integral equations of the problem are reducted to a Fredholm integral equation of the second kind with a symmetric kernel, which is solved by an expansion in terms of the small parameter $(ka)^{-1} \ll 1$, where $k = 2\pi/\lambda$ is the wave number, which corresponds to short waves. Equations are derived for the current density and the coefficient of scattering from the projection, and asymptotic expansions of these quantities which are applicable for any angle of incidence are found.

A method for solving certain problems in the diffraction of short waves based on the use of dual integral equations was proposed recently.[1,2] We employ a variation of this method to solve the problem of the diffraction of a plane electromagnetic wave by a conducting plane with a projection. Equations are obtained for the current density on the projection and for the scattering factor, and the short-wave asymptotic forms of these quantities are presented.

1. Suppose a plane wave polarized with its E vector along OZ is incident on the system shown in Fig. 1 at the angle of incidence γ, $0 < \gamma \leq \pi/2$. The calculation of the plane field produced is reduced to finding the function $E_z = E(x, y)$:

$$\Delta E + k^2 E = 0, \quad -\infty < x < \infty, \quad 0 < y < \infty \tag{1}$$

where $k = 2\pi/\lambda$ is the wave number. The solution of Eq. (1) which goes to zero at infinity and vanishes at y = 0 has the form

$$E(x, y) = E_0 \Big\{ e^{ik(x\cos\gamma + y\sin\gamma)} - e^{ik(x\cos\gamma - y\sin\gamma)} - 2i \int_0^\infty A(\nu)\, e^{\mp x\sqrt{\nu^2 - k^2}} \sin \nu y\, d\nu \Big\}, \quad x \gtrless 0. \tag{2}$$

By using (2) to satisfy the condition on the projection and the requirement of the continuity of $\partial E/\partial x$ on the ray $x = 0$, $a < y < \infty$, and making the substitutions

$$A(\nu) = \frac{2}{\pi} f(\nu) - N(\nu), \quad \varkappa = k \sin\gamma, \tag{3}$$

$$f(\nu) = \frac{k}{2} \Big\{ \frac{(\varkappa - \nu)\cos(\varkappa - \nu)a + k \sin(\varkappa - \nu)a}{(\varkappa - \nu)[k^2 + (\varkappa - \nu)^2]} - \frac{(\varkappa + \nu)\cos(\varkappa + \nu)a + k\sin(\varkappa + \nu)a}{(\varkappa + \nu)[k^2 + (\varkappa + \nu)^2]} \Big\} \tag{4}$$

we obtain the dual integral equations for $N(\nu)$:

$$\int_0^\infty N(\nu) \sin \nu y\, d\nu = 0, \quad 0 < y < a; \tag{5}$$

$$\int_0^\infty N(\nu) \sqrt{\nu^2 - k^2} \sin \nu y\, d\nu = g(y), \quad a < y < \infty, \tag{6}$$

where

$$g(y) = \frac{2}{\pi} \int_0^\infty f(\nu) \sqrt{\nu^2 - k^2} \sin \nu y\, d\nu. \tag{7}$$

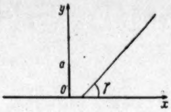

Fig. 1

2. When $ka \gg 1$ we seek the solution of Eqs. (5) and (6) in the form

$$N(\nu) = \sqrt{\frac{ik}{\pi}} \int_a^\infty \psi(t) \Big[\frac{e^{i\nu t}}{\sqrt{k - \nu}} - \frac{e^{-i\nu t}}{\sqrt{k + \nu}} \Big] dt. \tag{8}$$

Here, $\psi(t)$ is a continuous differentiable function for $a < t < \infty$; it is to be determined so that $\psi(t) \to 0$ as $t \to \infty$. Starting from the relations on p. 201 of ref. 3

$$\frac{i}{\sqrt{\pi}} \int_0^\infty \Big[\frac{e^{i\nu t}}{\sqrt{i(k - \nu)}} - \frac{e^{-i\nu t}}{\sqrt{i(k + \nu)}} \Big] \sin \nu x\, d\nu = \begin{cases} 0, & x < t, \\ -\dfrac{e^{-ik(x-t)}}{\sqrt{x - t}}, & x > t, \end{cases} \tag{9}$$

$$\frac{i}{\sqrt{\pi}} \int_0^\infty \Big[\frac{e^{i\nu t}}{\sqrt{i(k + \nu)}} - \frac{e^{-i\nu t}}{\sqrt{i(k - \nu)}} \Big] \sin \nu x\, d\nu = \begin{cases} \dfrac{e^{-ik(t+x)}}{\sqrt{t + x}} - \dfrac{e^{-ik(t-x)}}{\sqrt{t - x}}, & x < t, \\ \dfrac{e^{-ik(t+x)}}{\sqrt{t + x}}, & x > t, \end{cases} \tag{10}$$

it can be shown that Eq. (8) satisfies (5) identically, and it follows from (6) that $\psi(t)$ is the solution of a Fredholm integral equation of the second kind with a symmetric kernel. After transformation to the dimensionless quantities

$$\tau = t/a; \quad \psi(\tau) = \psi(t)$$

$$\Psi(\tau) = e^{-ka(\tau - 1)} [v_+ e^{i\varkappa a\tau} + v_- e^{-i\varkappa a\tau}] \tag{11}$$

the latter takes the form

$$+ \frac{ka}{2} \int_1^\infty \Psi(\sigma) [H_0^{(2)}(ka(\tau + \sigma)) + iH_1^{(2)}(ka(\tau + \sigma))]\, d\sigma, \quad 1 \leqslant \tau < \infty; \tag{12}$$

$$v_\pm(\gamma) = 0.5 (1 + i \pm \sin\gamma)^{1/2} (\pi i)^{-1/2}. \tag{13}$$

Solving (12) by the method of asymptotic iteration ($ka \gg 1$) gives

$$\Psi(\tau) = \Psi_+(\tau) + \Psi_-(\tau); \quad \varphi_\pm(\gamma) = 1 \pm \sin\gamma;$$

$$\Psi_\pm(\tau) = v_\pm \Big[e^{\pm i\varkappa a\tau - ka(\tau - 1)} + \frac{1}{(ika)^{1/2}} \frac{e^{-ika\tau}}{(\tau + 1)^{1/2}} \frac{e^{-ika\varphi_\mp}}{2\sqrt{2\pi}(i - \varphi_\mp)} + \ldots \Big]. \tag{14}$$

Equations (2)-(4), (8), and (14) completely determine the solution of the problem.

3. We calculate the current density $j_z(y)$ induced on the projection. Starting with the expression

$$j_z(y)=\frac{c}{4\pi ik}\left[\frac{\partial E}{\partial x}\bigg|_{x\to+0}-\frac{\partial E}{\partial x}\bigg|_{x\to-0}\right],\quad 0<y<a \tag{15}$$

we use (2), (3), and (8)-(10) to find

$$\begin{aligned}j_z(y)=\frac{cE_0}{\pi}\Bigg\{&k^{-1}g(y)+k^{-3/2}\psi(a)\left[\frac{e^{-ik(a+y)}}{\sqrt{a+y}}-\frac{e^{-ik(a-y)}}{\sqrt{a-y}}\right]\\&+k^{-1/2}\int\limits_a^\infty(e^{-ikt}\psi(t))'\left[\frac{e^{-iky}}{\sqrt{t+y}}-\frac{e^{iky}}{\sqrt{t-y}}\right]dt\Bigg\},\quad 0<y<a.\end{aligned} \tag{16}$$

Setting

$$\eta=y/a,\quad j_z(y)=j(\eta) \tag{17}$$

and using (14) we obtain the asymptotic formula

$$\begin{aligned}j(\eta)={}&\frac{cE_0}{\pi}\left(i\cos\gamma\left[\sin\varkappa a\eta-0.5e^{-ka(1-\eta)+i\varkappa a\eta}\right]+j_+(\eta)+j_-(\eta)\right);\\ j_\pm(\eta)={}&v_\pm\Bigg\{e^{ka(1-\eta)\pm i\varkappa a}\sqrt{\pi i(\varphi_\mp-i)}\left[1-\Phi\left(\sqrt{ika(\varphi_\mp-i)(1-\eta)}\right)\right]\\&+\frac{e^{-ika(\eta+\varphi_\mp)+i\pi/4}}{2(ika)^{1/2}(1+\eta)^{3/2}(i-\varphi_\mp)}\left[1-\Phi\left(\sqrt{2ika(1-\eta)}\right)\right]\\&-\frac{e^{-ika(1+\eta)\pm i\varkappa a+i\pi/4}}{2(ika)^{3/2}(1+\eta)^{3/2}(i-\varphi_\mp)}\\&-\frac{e^{-ika(1-\eta)\pm i\varkappa a+i\pi/4}}{(ika)^{1/2}(1-\eta)^{1/2}}+\ldots\Bigg\},\end{aligned} \tag{18}$$

where $\Phi(z)$ is the probability integral.

Equation (18) is valid for all η, $0<\eta<1$, and is simplified if η lies in the range $0<\eta\le\eta_0<1$.

4. We find the coefficient of scattering from the projection. The average power scattered per unit length is related to the current density $j_z(y)$ by the equation

$$P=2E_0\operatorname{Im}\int\limits_0^a j_z(y)\sin\varkappa y\,dy, \tag{19}$$

which gives P in terms of $\bar{\psi}(\tau)$:

$$\begin{aligned}P=\frac{E_0^2ac}{\pi}\operatorname{Im}\Bigg\{&2k^{-1}\int\limits_0^1 g(a\eta)\sin\varkappa a\eta\,d\eta-\sqrt{\frac{\pi}{i}}\\&\times\int\limits_1^\infty\bar{\psi}(\tau)\Big(\sqrt{\varphi_-}e^{-i\varkappa a\tau}\left[\Phi\left(\sqrt{ika\varphi_-(\tau+1)}\right)-\Phi\left(\sqrt{ika\varphi_-(\tau-1)}\right)\right]\\&-\sqrt{\varphi_+}e^{i\varkappa a\tau}\left[\Phi\left(\sqrt{ika\varphi_+(\tau+1)}\right)-\Phi\left(\sqrt{ika\varphi_+(\tau-1)}\right)\right]\Big)\,d\tau\\&-\frac{2\sin\varkappa a}{\sqrt{ka}}\int\limits_1^\infty\bar{\psi}(\tau)\left[\frac{e^{-ika(\tau+1)}}{\sqrt{\tau+1}}+\frac{e^{-ika(\tau-1)}}{\sqrt{\tau-1}}\right]d\tau\Bigg\}.\end{aligned} \tag{20}$$

Defining the scattering coefficient by the expression

$$R=\frac{P}{P_0};\qquad P_0=\frac{E_0^2ac}{\pi}, \tag{21}$$

we obtain the asymptotic expansion

$$\begin{aligned}\frac{R}{2}={}&\cos\gamma+\frac{R^{(1)}}{ka}+\frac{R^{(2)}}{(ka)^{3/2}}+\ldots;\\ R^{(1)}={}&-0.5\,(\cos\gamma-\operatorname{ctg}\gamma\,(1+4\sin^2\gamma)^{-1}[2\sin\gamma\cos2\varkappa a\\&-(1+2\sin^2\gamma)\sin2\varkappa a])\\&+\operatorname{Im}(2i)^{-1}\Big(\sqrt{(1-i\varphi_+)(1+i\varphi_-)}\left[1-e^{2i\varkappa a}(1-2i\sin\gamma)^{-1}\right]\\&-\sqrt{(1-i\varphi_-)(1+i\varphi_+)}\left[1-e^{-2i\varkappa a}(1+2i\sin\gamma)^{-1}\right]\\&+\sqrt{i\varphi_+}\,\Phi\left(\sqrt{2ika\varphi_+}\right)\left[\sqrt{1-i\varphi_-}+\sqrt{1-i\varphi_+}e^{2i\varkappa a}(1-2i\sin\gamma)^{-1}\right]\\&+\sqrt{i\varphi_-}\,\Phi\left(\sqrt{2ika\varphi_-}\right)\left[\sqrt{1-i\varphi_+}+\sqrt{1-i\varphi_-}e^{-2i\varkappa a}(1+2i\sin\gamma)^{-1}\right]\Big).\end{aligned} \tag{22}$$

The expansion (22) is applicable for all angles of incidence, $0<\gamma\le\pi/2$; for $\pi/2-\gamma_0\le\gamma\le\pi/2$, and for $0<\gamma\le\eta_0<\pi/2$ the expressions for the coefficients $R^{(n)}$ can simplified. Thus

$$\left.\begin{aligned}R^{(1)}\left(\gamma=\frac{\pi}{2}\right)=-0.5\left[1-(20)^{-1/4}\sin\left(2ka+\frac{a}{2}-\frac{\pi}{4}\right)\right],\\ a=\operatorname{arc\,tg}2,\end{aligned}\right\} \tag{23}$$

and for $0<\gamma\le\gamma_0<\pi/2$ we have

$$\begin{aligned}R^{(1)}=-0.5\Bigg\{&\cos\gamma-\operatorname{ctg}\gamma\,(1+4\sin^2\gamma)^{-1}[\sin\gamma\cos2\varkappa a\\&-(1+2\sin^2\gamma)\sin2\varkappa a]\\&+\sqrt{\varphi_+\rho_-}\sin\left(\frac{\beta_-}{2}+\frac{\pi}{4}\right)-\sqrt{\varphi_-\rho_+}\sin\left(\frac{\beta_+}{2}+\frac{\pi}{4}\right)\\&-(1+4\sin^2\gamma)^{-1/2}\Bigg[\sqrt{\varphi_+\rho_+}\sin\left(2\varkappa a+\theta-\frac{\beta_+}{2}-\frac{\pi}{4}\right)\\&+\sqrt{\varphi_-\rho_-}\sin\left(2\varkappa a+\theta+\frac{\beta_-}{2}+\frac{\pi}{4}\right)\Bigg]\Bigg\}.\end{aligned} \tag{24}$$

where

$$\left.\begin{aligned}\rho_\pm(\gamma)=[1+(1\pm\sin\gamma)^2]^{1/2};\quad\beta_\pm(\gamma)=\operatorname{arc\,tg}(1\pm\sin\gamma);\\ \theta(\gamma)=\operatorname{arc\,tg}(2\sin\gamma).\end{aligned}\right\} \tag{25}$$

These results may be of interest for the theory of propagation of radio waves around the irregular surface of the earth (cf., e.g., ref. 4 and the bibliography listed there).

The author thanks N. N. Lebedev and I. P. Skal'skaya for their interest.

[1] N. N. Lebedev and I. P. Skal'skaya, Zh. Tekh. Fiz., 41, 1329 (1971) [Sov. Phys. – Tech. Phys., 16, 1047 (1972)].
[2] N. N. Lebedev and I. P. Skal'skaya, Zh. Tekh. Fiz., 42, 681 (1972) [Sov. Phys. – Tech. Phys., 17, 539 (1972)].
[3] F. Oberhettinger, Tabellen zur Fourier Transformation, Springer Verlag, Berlin (1957).
[4] D. S. Jones, Quart. J. Mech. Appl. Math., 26, 1 (1973).

Reflection of electromagnetic waves by a moving plasma

V. I. Miroshnichenko

(Submitted June 27, 1973)
Zh. Tekh. Fiz., 44, 844-847 (April 1974)

The kinetic theory of the reflection of electromagnetic waves from a moving plasma in a homogeneous magnetostatic field H_0 perpendicular to the boundary is discussed. It is assumed that the incident wave is slowed down by a plasma which fills all space. The general form of the field penetrating the reflecting plasma is determined under the assumption of a sharp boundary of the reflecting plasma and the diffusion character of the reflection of electrons from the boundary. The coefficient of reflection of the incident electromagnetic wave is calculated.

The reflection of electromagnetic waves by a semibounded moving plasma under the assumption that the incident wave is slowed down by a stationary plasma filling all of space in a steady uniform magnetic field H_0 parallel to the velocity v_0 of the reflecting plasma is treated in ref. 1. The boundary of the reflecting plasma is assumed to be sharp, and the boundary condition for the high-frequency contribution to the equilibrium electron distribution function is taken as[2]

$$f(0,\, v_z) = pf(0,\, -v_z). \tag{1}$$

Then, as shown in ref. 1, the initial system of equations, consisting of Maxwell's equations for the electromagnetic field, the equation of motion of the electrons of the moderating plasma, and the kinetic equation for the high-frequency contribution to the equilibrium distribution function of the electrons in the reflecting plasma, can be reduced to a single integrodifferential equation for the intensity of the electric field

$$\frac{d^2E}{dz^2} + k^2E = -k^2\Bigg\{\int_0^{+\infty} k_1(|z-z'|)E(z')dz' + p\int_0^{+\infty} k_1(z+z')E(z')dz' + \int_0^{z} k_2(z-z')\Big[E(z') + \frac{iV_0}{\omega}\frac{\partial E(z')}{\partial z'}\Big]dz' + F(z)\Bigg\}, \tag{2}$$

where we have introduced the notation

$$k_1(z) = \frac{i\omega_{01}^2}{\sqrt{\pi}\,\omega v_T}\int_0^{+\infty}\frac{dv_z}{v_z}\exp\Big[-\frac{v_z^2}{v_T^2} + \frac{i}{v_z}(\omega + i\nu_1 - \omega_H)z\Big],$$

$$k_2(z) = \frac{i\omega_{02}^2}{\omega V_0}\exp\Big[\frac{i}{V_0}(\omega + i\nu_2 - \omega_H')z\Big],$$

$$F(z) = -\frac{im\gamma_0\omega_{02}^2 u(0)}{e\omega}\exp\Big[\frac{iz}{V_0}(\omega + i\nu_2 - \omega_H')\Big], \quad \omega_H' = \omega_H\sqrt{1-\beta^2} \equiv \omega_H\gamma_0^{-1},$$

$E = E_x - iE_y$, $u = u_x - iu_y$, and u(0) is the value of the transverse high-frequency velocity of the electrons of the retarding plasma at the reflector boundary, and the remaining notation is standard. Equation (2) is solved in ref. 1 for specular reflection of electrons from the boundary (p = 1).

In this note we present the solution of Eq. (2) for diffuse reflection of electrons from the boundary when p = 0.

To solve Eq. (2) in this case we introduce functions $\bar{E}(x)$ and $\bar{F}(z)$, which coincide with E(z) and F(z) for $z \geq 0$, and are zero for $z < 0$,

$$\bar{E}(z) = \begin{cases} E(z) & z \geqslant 0, \\ 0 & z < 0, \end{cases} \quad \bar{F}(z) = \begin{cases} F(z) & z \geqslant 0, \\ 0 & z < 0. \end{cases} \tag{3}$$

It is convenient to continue the kernel $k_1(z)$ of the integral equation (2) onto the left semiaxis by defining it to be even, $k_1(z) = k_1(-z)$, and to take $k_2(z)$ to be zero.

The function $\bar{E}(z)$ introduced in this way is expanded in a Fourier integral:

$$\bar{E}(z) = \frac{1}{2\pi}\int_{-\infty}^{+\infty}\mathcal{E}(t)e^{itz}dt, \quad \mathcal{E}(t) = \int_0^{+\infty}E(z)e^{itz}dz \tag{4}$$

and used with Eq. (2) to obtain the relation

$$\int_{-\infty}^{+\infty}\{[t^2 - k^2\varepsilon(t)]\mathcal{E}(t) + f(t)\}e^{itz}dt = 0 \quad (z \geqslant 0), \tag{5}$$

where

$$\begin{gathered}\varepsilon(t) = 1 + k_1(t) + \frac{\omega - tV_0}{\omega}k_2(t), \\ f(t) = k^2\Big[E'(0) + itE(0) + \frac{iV_0}{\omega}k_2(t)E(0) - F(t)\Big], \\ k_1(t) = \frac{i\sqrt{\pi}\,\omega_{01}^2}{\omega v_T|t|}\exp\Big[-\Big(\frac{\omega-\omega_H}{tv_T}\Big)^2\Big] - \frac{\omega_{01}^2}{\omega(\omega-\omega_H)}\varphi\Big(\frac{\omega-\omega_H}{tv_T}\Big), \\ \varphi(t) = 2te^{-t^2}\int_0^t e^{x^2}dx, \quad k_2(t) = -\frac{\omega_{02}^2}{\omega(\omega + i\nu_2 - \omega_H' - tV_0)}, \\ F(t) = \frac{m\gamma_0 V_0 u(0)}{e}\,\frac{\omega_{02}^2}{\omega(\omega + i\nu_2 - \omega_H' - tV_0)}\end{gathered} \tag{6}$$

E(0) and E'(0) are the values of the electric field and its derivative on the boundary of the reflecting plasma.

It follows from Eq. (5) and the lemma of ref. 3 that the part of the integrand in (5) in the braces is the limiting value along the axis $-\infty < t < \infty$ of the function $\Phi^+(t)$, analytic in the upper half-plane of the complex variable

$$\left.\begin{aligned}\Delta(t)\mathcal{E}(t) + f(t) = \Phi^+(t) \quad (-\infty < t < +\infty), \\ \Delta(t) \equiv t^2 - k^2\varepsilon(t).\end{aligned}\right\} \tag{7}$$

According to (4), $\mathcal{E}(t)$ is the limiting value along the real axis of a function analytic in the lower half-plane, $\mathcal{E}(t) = \Phi^-(t)$; thus, the solution of Eq. (5) can be reduced to the solution of the following inhomogeneous Hilbert problem for two functions:[4,5]

$$\Phi^+(t) = \Delta(t)\Phi^-(t) + f(t) \quad (-\infty < t < +\infty). \tag{8}$$

It can be shown[1] that the index of Δ(t), defined as 1/2π times the increment of the argument of Δ(t) as t varies from −∞ to +∞,

$$n = \frac{1}{2\pi}\arg\Delta(t)\Big|_{-\infty}^{+\infty} \tag{9}$$

is zero in the sub-Cerenkov case, for which the inequality

$$1-\beta^2\left[1-\frac{\omega_{01}^2}{\omega(\omega-\omega_H)}\right]>0, \tag{10}$$

is satisfied.

The solution of the boundary-value problem (8) is standard, and we give the final result:

$$\mathcal{E}(t)=-\frac{f(t)}{2\Delta(t)}+\frac{\Phi_0^+(t)}{2\pi i}\int\limits_{-\infty}^{+\infty}\frac{f(\tau)\,d\tau}{\Phi_0^+(\tau)(\tau-t)}+P(t)\,\Phi_0^-(t), \tag{11}$$

where

$$\left.\begin{aligned}&\Phi_0^+(t)=(t+ia)\sqrt{g(t)}\,H(t),\quad \Phi_0^-(t)=\frac{H(t)}{(t-ia)\sqrt{g(t)}},\\&H(t)=\exp\left[\frac{1}{2\pi i}\int\limits_{-\infty}^{+\infty}\frac{\log g(\tau)\,d\tau}{\tau-t}\right],\quad g(t)=\frac{\Delta(t)}{t^2+a^2},\quad a>0,\end{aligned}\right\} \tag{12}$$

P(t) is a polynomial to be determined.

By comparing the asymptotic forms of the left- and right-hand sides of Eq. (11),

$$\mathcal{E}(t)=\frac{E(0)}{it}+\frac{E'(0)}{(it)^2}+\ldots, \tag{13}$$

we find that in our case the polynomial P(t) is a constant $P(t) = -i\,E(0)$.

Equations (11), (12), and (4) enable us to determine the general form of the field penetrating into the plasma half-space for diffuse reflection of electrons from the boundary.

By comparing the asymptotic forms of the left-and right-hand sides of Eq. (11) to terms of the order t^{-2} we establish the following relation between the field and its derivative at the plasma boundary:

$$E'(0)=CE(0)+D\left[E(0)-\frac{i\omega m\gamma_0}{e}u(0)\right], \tag{14}$$

$$C=-\left[a+\frac{1}{2\pi}\int\limits_{-\infty}^{+\infty}\log g(t)\,dt\right],$$

$$D=\frac{i\omega_{02}^2}{c^2}\frac{1}{\Phi_0^+(t)},\quad t_0=\frac{\omega+i\nu_2-\omega_H'}{V_0},\quad a>0.$$

We note that in the absence of a moderator ($\omega_{02} = 0$) and for an external magnetic field $H_0 = 0$ Eq. (14) reduces to the result obtained earlier.[6]

The coefficient of reflection of an electromagnetic wave from the plasma half-space considered can be determined by adding to Eq. (14) the continuity conditions for the tangential components of the electric field E, the magnetic field H, and the transverse high-frequency velocity u of the electrons of the moderating plasma. Using Maxwell's equations and the equations of motion these can be written in the form

$$\left.\begin{aligned}E_i+E_r&=E(0))\\k_i'E_i+k_r'E_r&=-iE'(0),\\\frac{\omega_H'}{\omega-k_i'V_0-\omega_H'}E_i+\frac{\omega_H'}{\omega-k_r'V_0-\omega_H'}E_r&=-\left[E(0)-\frac{im\gamma_0\omega}{e}u(0)\right].\end{aligned}\right\} \tag{15}$$

Then the reflection coefficient is given by the following general expression:

$$\left.\begin{aligned}R=\frac{E_r}{E_i}=-\left[1-\frac{ik_i'}{C}-\frac{\omega_H'}{\omega-k_i'V_0-\omega_H'}\frac{D}{C}\right],\\\left[1-\frac{ik_r'}{C}-\frac{\omega_H'}{\omega-k_r'V_0-\omega_H'}\frac{D}{C}\right]^{-1}\end{aligned}\right\} \tag{16}$$

C and D are determined by (14). We give the expression for the reflection coefficient R for the case of a "super-anomalous" skin when the relation

$$\frac{\omega_{01}v_T}{\omega c}\gg 1 \tag{17}$$

is satisfied.

In this case the values of C and D are

$$C\simeq\left(-1+\frac{i}{\sqrt{3}}\right)\left(\frac{\sqrt{\pi}\,\omega_{01}^2}{\omega^2\beta_T}\right)^{1/3}\frac{\omega}{c},\quad D\simeq\frac{\omega_{02}^2}{\omega_{01}c}. \tag{18}$$

Substituting the values of C and D from (18) into (16) gives for the reflection coefficient R

$$R=-\left[1+\frac{3}{4}\left(i-\frac{1}{\sqrt{3}}\right)\frac{1}{\beta_0}\left(\frac{\omega^2\beta_T}{\sqrt{\pi}\,\omega_{01}^2}\right)^{1/3}\right.$$
$$\left.+\frac{3}{4}\left(1+\frac{i}{\sqrt{3}}\right)\left(\frac{\omega^2\beta_T}{\sqrt{\pi}\,\omega_{01}^2}\right)^{1/3}\frac{\omega_{02}^2}{\omega\omega_{01}}\frac{\omega_H}{\omega_i-\omega_H}\right]. \tag{19}$$

The second term of Eq. (19) is due to the absorption of part of the energy of the incident electromagnetic wave by electrons of the reflecting plasma having a thermal spread. A comparison of this term with the analogous term of Eq. (50) of ref. 1, where specular reflection of electrons from the boundary is assumed, shows that they differ only by a numerical factor.

The second term in Eq. (19) is related to the part of the part of the electromagnetic wave energy which penetrates the reflecting plasma due to the penetration of the moderating plasma into the reflecting plasma. For diffuse reflection of electrons from the boundary this term is $(\omega_{01}/\omega)\beta_T$ ($\gg 1$) times as large as for specular reflection.

In conclusion the author thanks Ya. B. Fainberg for a discussion of the results of this paper.

---

[1] V. I. Miroshnichenko, Zh. Tekh. Fiz., 43, 467 (1973) [Sov. Phys. – Tech. Phys., 18, 299 (1972)].

[2] G. Euter and E. Sondheimer, Proc. Roy. Soc., 195, 336 (1949).

[3] I. I. Rapoport, Dokl. Akad. Nauk SSSR, 59, 1403 (1948).

[4] V. I. Smirnov, Course in Higher Mathematics, Vol. 4 [in Russian], GITTL, Moscow (1951).

[5] N. I. Muskhelishvili, Singular Integral Equations [in Russian], GIFML, Moscow (1962).

[6] V. P. Silin, Zh. Eksp. Teor. Fiz., 40, 616 (1961) [Sov. Phys. – JETP, 13, 430 (1961)].

A useful function in the thermodynamics of irreversible processes

A. V. Pamfilov, A. I. Lopushanskaya, and L. B. Tsvetkova
Chernovtsy State University
Thernopol' Finance-Economics Institute

(Submitted April 2, 1973)
Zh. Tekh. Fiz., 44, 848-851 (April 1974)

It is shown on the basis of the time axiom and the integrability theorem that the difference of the functions F_2-F_1 gives the part of the entropy production due to the change in thermodynamic forces. The quantity $\sum\limits_{i=1}^{n}\int\limits_{0}^{x_i} I_i\,dX_i$ which is derived contains the thermodynamic forces and coefficients with two and three indices which are functions of the state parameters and which can be written in terms of measurable quantities.

The two most familiar methods of nonequilibrium thermodynamics which go beyond the scope of the linear relations are the approach based on the time axiom and a theorem of integrability[1] and an approach which does not adopt the principle of a local equilibrium.[2] In the first approach, the function F is adopted as the basic function; knowledge of this function for forward and reverse processes is sufficient for describing the time behavior of a system

Using F, we can state a system of n time axioms characterizing the simultaneous occurrence of n processes.

For processes i and k, e.g., the differential form of the time axiom is

$$\frac{dc_i}{dt}=-J_{i1}(r_{11},\ \ldots,\ r_{n1})+J_{i2}(r_{12},\ \ldots,\ r_{n2})=\frac{\partial F_1}{\partial r_{i1}}+\frac{\partial F_2}{\partial r_{i2}}, \qquad (1)$$

where $i = 1, 2, \ldots, n$; c_i is the variable (the state coordinate); t is the time; r_{i1} and r_{i2} are specific variables of component i, related to parameters of the subsystems; and J_{i1}, J_{i2}, F_1, and F_2 are functions of the state parameters. The first index gives the process, and the second shows whether the forward or reverse half-process is meant.

According to this theory, we have

$$J_{i1}=\mu_{i1}\exp\frac{\left(\frac{\partial S}{\partial\lambda_i}\right)^{*}_{01}-\left(\frac{\partial S}{\partial\lambda_i}\right)_{1}}{R};\quad J_{i2}=\mu_{i2}\exp\frac{\left(\frac{\partial S}{\partial\lambda_i}\right)^{*}_{02}-\left(\frac{\partial S}{\partial\lambda_i}\right)_{2}}{R}. \qquad (2)$$

Here, μ_{i1} and μ_{i2} are transition functions, $(\partial S/\partial\lambda_i)_1$ and $(\partial S/\partial\lambda_i)_2$ are the entropy changes of the matter in the initial and final states in the case $\lambda = 1$, λ is the number of reaction runs, $(\partial S/\partial\lambda_i)_0^*$ is the change in the entropy for the intermediate state, and R is the gas constant.

We can also write an integrability theorem in terms of the function F:

$$\frac{\partial^2 F_1}{\partial r_{i1}\partial r_{k1}}=\frac{\partial^2 F_1}{\partial r_{k1}\partial r_{i1}},\quad \frac{\partial^2 F_2}{\partial r_{i2}\partial r_{k2}}=\frac{\partial^2 F_2}{\partial r_{k2}\partial r_{i2}}. \qquad (3)$$

We find an expression for F by using the vector and scalar forms. We introduce the following vectors:

$$\left.\begin{aligned}
\mathbf{r}_0&=(r_{10},\ \ldots,\ r_{i0},\ \ldots,\ r_{n0}),\\
\mathbf{r}_1&=(r_{11},\ \ldots,\ r_{i1},\ \ldots,\ r_{n1}),\\
\mathbf{r}_2&=(r_{12},\ \ldots,\ r_{i2},\ \ldots,\ r_{n2}),\\
\Delta\mathbf{r}_1&=(\Delta r_{11},\ \ldots,\ \Delta r_{i1},\ \ldots,\ \Delta r_{n1}),\\
\Delta\mathbf{r}_2&=(\Delta r_{12},\ \ldots,\ \Delta r_{i2},\ \ldots,\ \Delta r_{n2}),
\end{aligned}\right\} \qquad (4)$$

where the subscript "0" denotes equilibrium.

Expanding the functions J_{i1} and J_{i2} in Taylor series, and using the notation in (4), we find

$$\begin{aligned}
J_{i1}&=J_{i1}(\mathbf{r}_0)+DJ_{i1}\Big|_{\mathbf{r}=\mathbf{r}_0}(\Delta\mathbf{r}_1)^{(1)}+\ldots\\
&+\frac{1}{k!}D^{(k)}J_{i1}\Big|_{\mathbf{r}=\mathbf{r}_0}(\Delta\mathbf{r}_1)^{(k)}+R_{i+1},\\
J_{i2}&=J_{i2}(\mathbf{r}_0)+DJ_{i2}\Big|_{\mathbf{r}=\mathbf{r}_0}(\Delta\mathbf{r}_2)^{(1)}+\ldots\\
&+\frac{1}{k!}D^{(k)}J_{i2}\Big|_{\mathbf{r}=\mathbf{r}_0}(\Delta\mathbf{r}_2)^{(k)}+R'_{i+1},
\end{aligned} \qquad (5)$$

where $D^{(k)}$ is the operator representing k-th order differentiation with respect to the vectors $\mathbf{r}_1$ and $\mathbf{r}_2$; $(\Delta\mathbf{r}_1)^{(k)}$ and $(\Delta\mathbf{r}_2)^{(k)}$ are linear forms of order k, and R_{i+1} and R'_{i+1} are the remaining terms.

In the second approximation these functions are given in scalar form by

$$\begin{aligned}
J_{i1}(r_{11},\ \ldots,\ r_{n1})&=J_{i1}[(r_{10}+\Delta r_{11}),\ \ldots,\ (r_{n0}+\Delta r_{n1})]\\
&=J_{i1}(r_{10},\ \ldots,\ r_{n0})+\sum_{k=1}^{n}\frac{\partial J_{i1}}{\partial r_{k1}}\Big|_{r_{10},\ldots,r_{n0}}\Delta r_{k1}+\frac{1}{2!}\Bigg[\sum_{k=1}^{n}\frac{\partial^2 J_{i1}}{\partial r_{k1}^2}\Big|_{r_{10},\ldots,r_{n0}}\Delta r_{k1}^2\\
&+2\sum_{k=i+1}^{n}\frac{\partial^2 J_{i1}}{\partial r_{i1}\partial r_{k1}}\Big|_{r_{10},\ldots,r_{n0}}\Delta r_{i1}\Delta r_{k1}\Bigg],
\end{aligned} \qquad (6)$$

where $i, k = 1, 2, \ldots, i, \ldots, n$.

In (6) r_{i1} is written in the form $r_{i0} + \Delta r_{i1}$, since $r_{i1} - r_{i0} = \Delta r_{i1}$. The function $J_{i2}(r_{12}, \ldots, r_{n2})$ appears in analogous form.

Using the system of equations

$$\frac{\partial F_1(r_{11},\ \ldots,\ r_{n1})}{\partial r_{i1}}=J_{i1},\quad \frac{\partial F_2(r_{12},\ \ldots,\ r_{n2})}{\partial r_{i2}}=J_{i2},$$

and taking account of the continuity and differentiability of the functions F_1 and F_2, we can write

$$\left.\begin{aligned}
\int_{\mathbf{r}_0}^{\mathbf{r}_1}dF_1&=F_1\Big|_{\mathbf{r}_1}-F_1\Big|_{\mathbf{r}_0}=\int_{\mathbf{r}_0}^{\mathbf{r}_1}\mathbf{J}_1 d\mathbf{r}_1,\quad \mathbf{J}_1=(J_{11},\ \ldots,\ J_{n1}),\\
\int_{\mathbf{r}_0}^{\mathbf{r}_2}dF_2&=F_2\Big|_{\mathbf{r}_2}-F_2\Big|_{\mathbf{r}_0}=\int_{\mathbf{r}_0}^{\mathbf{r}_2}\mathbf{J}_2 d\mathbf{r}_2,\quad \mathbf{J}_2=(J_{12},\ \ldots,\ J_{n2}),
\end{aligned}\right\} \qquad (7)$$

or, in scalar form,

$$\int\limits_{r_{10},\ldots,r_{n0}}^{r_{11},\ldots,r_{n1}} dF_1 = \int\limits_{r_{10},\ldots,r_{n0}}^{r_{11},\ldots,r_{n1}} (J_{11}dr_{11} + \ldots + J_{i1}dr_{i1} + \ldots + J_{n1}dr_{n1}). \quad (7')$$

For the F_2 case we find an equation analogous to (7'), in which the second indices are replaced by "2."

To find the difference of functions $F(X) = F_2(\mathbf{r}_2) - F_1(\mathbf{r}_1)$, where $X = \Delta\mathbf{r}_2 - \Delta\mathbf{r}_1$, we substitute in the corresponding values of J from Eqs. (5) and (6); integrating the left sides of (7) and (7') and collecting terms, we can write F(X) as

$$F(\mathbf{X}) = \sum_{k=1}^{n} \frac{1}{k!} D^{(k)} \mathbf{J}_1 \Big|_{\mathbf{r}=\mathbf{r}_0} \left\{ \int\limits_{\mathbf{r}_0}^{\mathbf{r}_2} (\Delta\mathbf{r}_2)^{(k)}\, d\mathbf{r}_2 - \int\limits_{\mathbf{r}_0}^{\mathbf{r}_1} (\Delta\mathbf{r}_1)^{(k)}\, d\mathbf{r}_1 \right\}. \quad (8)$$

In the second approximation the difference $F_2 - F_1$ is written in scalar form as

$$\begin{aligned} F(X) &= F_2(r_{12}, \ldots, r_{n2}) - F_1(r_{11}, \ldots, r_{n1}) \\ &= \sum_{i,k=1}^{n} \left[\int\limits_{r_{i0}}^{r_{i2}} \frac{\partial J_{i2}}{\partial r_{k2}} \Big|_{r_{10},\ldots,r_{n0}} \Delta r_{k2} dr_{i2} - \int\limits_{r_{i0}}^{r_{i1}} \frac{\partial J_{i1}}{\partial r_{k1}} \Big|_{r_{10},\ldots,r_{n0}} \Delta r_{k1} dr_{i1} \right] \\ &\quad + \frac{1}{2!} \left[\sum_{i=1}^{n} \int\limits_{r_{i0}}^{r_{i2}} \left\{ \sum_{k=1}^{n} \frac{\partial^2 J_{i2}}{\partial r_{k2}^2} \Big|_{r_{10},\ldots,r_{n0}} \Delta r_{k2}^2 \right. \right. \\ &\quad \left. + 2 \sum_{k=i+1}^{n} \frac{\partial^2 J_{i2}}{\partial r_{i2} \partial r_{k2}} \Big|_{r_{10},\ldots,r_{n0}} \Delta r_{i2} \Delta r_{k2} \right\} dr_{i2} \\ &\quad \left. - \sum_{i=1}^{n} \int\limits_{r_{i0}}^{r_{i1}} \left\{ \sum_{k=1}^{n} \frac{\partial^2 J_{1i}}{\partial r_{k1}^2} \Big|_{r_{10},\ldots,r_{n0}} \Delta r_{k1}^2 + 2 \sum_{k=i+1}^{n} \frac{\partial^2 J_{i1}}{\partial r_{i1} \partial r_{k1}} \Big|_{r_{10},\ldots,r_{n0}} \Delta r_{i1} \Delta r_{k1} \right\} dr_{i1} \right]. \end{aligned} \quad (9)$$

We note that in (8) and (9) the difference $F_2(\mathbf{r}_0) - F_1(\mathbf{r}_0)$ vanishes at equilibrium.

Before we use (8) and (9) we note that a quantity of the type

$$\int\limits_{\mathbf{r}_0}^{\mathbf{r}_2} (\Delta\mathbf{r}_2)^{(k)}\, d\mathbf{r}_2 - \int\limits_{\mathbf{r}_0}^{\mathbf{r}_1} (\Delta\mathbf{r}_1)^{(k)}\, d\mathbf{r}_1 \quad (10)$$

can be written

$$\int\limits_{0}^{\mathbf{r}_2 - \mathbf{r}_1} \{(\Delta\mathbf{r}_2)^{(k)} - (\Delta\mathbf{r}_1)^{(k)}\}\, d(\mathbf{r}_2 - \mathbf{r}_1). \quad (11)$$

Introducing the notation $(\Delta\mathbf{r}_2)^{(k)} - (\Delta\mathbf{r}_1)^{(k)} = \mathbf{X}^{(k)}$ we write integral (11) as

$$\int\limits_{0}^{\mathbf{X}} \mathbf{X}^{(k)} d\mathbf{X}. \quad (11')$$

Using (11') we can rewrite (8) as

$$F(\mathbf{X}) = \int\limits_{0}^{\mathbf{X}} \sum_{i=1}^{n} \frac{1}{k!} D^{(k)} \mathbf{J}_1 \Big|_{\mathbf{r}=\mathbf{r}_0} X^{(k)} d\mathbf{X} = \int\limits_{0}^{\mathbf{X}} \sum_{i=1}^{n} \mathbf{I}_k d\mathbf{X}, \quad (12)$$

where $\mathbf{I}_k = f(\mathbf{X}, \ldots, \mathbf{X}^{(k)})$.

In Eq. (12) the quantity $\mathbf{I}_{ki} = \frac{1}{k!} D^{(k)} \mathbf{J}_1 \Big|_{\mathbf{r}=\mathbf{r}_0} \mathbf{X}^{(k)}$ represents a thermodynamic flux, while X represents a thermodynamic force.

Using (10) and (11), we can treat (9) in analogous manner. Collecting like terms in (9), and denoting the coefficients by L_{ik} and L_{ikj}, we find

$$\begin{aligned} F_2 - F_1 = \sum_{i,k=1}^{n} L_{ik} \int\limits_{0}^{X_i} X_k dX_i + \frac{1}{2!} \sum_{i,k=1}^{n} L_{ikk} \int\limits_{0}^{X_i} (\Delta r_{k2}^2 - \Delta r_{k1}^2)\, dX_i \\ + \sum_{i=1,\, k=i+1}^{n} L_{iik} \int\limits_{0}^{X_i} (\Delta r_{i2} \Delta r_{k2} - \Delta r_{i1} \Delta r_{k1})\, dX_i. \end{aligned} \quad (13)$$

Introducing

$$\left.\begin{aligned} X'_k &= \Delta r_{k2}^2 - \Delta r_{k1}^2, \\ X_{ik} &= \Delta r_{i2} \Delta r_{k2} - \Delta r_{i1} \Delta r_{k1}, \end{aligned}\right\} \quad (13')$$

we can write (13) as

$$F_2 - F_1 = \int\limits_{0}^{X_i} \sum_{i=1}^{n} \left\{ \sum_{k=1}^{n} \left(L_{ik} X_k + \frac{1}{2!} L_{ikk} X'_k \right) + \sum_{k=i+1}^{n} L_{iik} X_{ik} \right\} dX_i. \quad (14)$$

The expression in braces in (14) is the thermodynamic flux J_i and (14) becomes

$$F(X) = F_2 - F_1 = \sum_{i=1}^{n} \int\limits_{0}^{X_i} \mathbf{I}_i dX_i. \quad (15)$$

It follows from (12) and (15) that F, which has the dimensionality of entropy per unit time, is the part of the entropy production which is due to the changes in the thermodynamic forces.[3] The function $\sum_{i=1}^{n} \int_0^{X_i} I_i dX_i$ is used in the second approach, whose theory is justified on the basis of the principle of a local equilibrium. Accordingly, we have the inequality $dF \leq 0$, which describes the time evolution of the system with the specified constraints.

We note that the coefficients having three indices are related by equations like the Onsager relations:

$$\left.\begin{aligned} L_{ikk} &= L_{kki} = L_{kik}, \\ L_{ikj} &= L_{kij} = L_{jik}. \end{aligned}\right\} \quad (16)$$

Using (16), we are to select from the set of coefficients having three indices in (14) the coefficients L_{iii}, L_{ikk}, and L_{ikj}.

Then, using (16), we rewrite (14) as

$$\begin{aligned} F_2 - F_1 = \sum_{i,k=1}^{n} \int\limits_{0}^{X_i} L_{ik} X_k dX_i + \frac{1}{2!} \sum_{i,k,j=1}^{n} \int\limits_{0}^{X_i} \{L_{iii} X'_i + \sigma_{ik} L_{ikk} (X'_k + 2X_{ik}) \\ + \sigma_{ikj} L_{ikj} (X_{kj} + X_{ij} + X_{ik})\}\, dX_i, \end{aligned} \quad (17)$$

where σ_{ik} and σ_{ikj} are defined by

$$\begin{aligned} &\sigma_{ik} = 1, \quad i \neq k; \quad \sigma_{ikj} = 1, \quad i \neq k \neq j; \\ &\sigma_{ik} = 0, \quad i = k; \quad \sigma_{ikj} = 0, \quad i = k = j. \end{aligned}$$

Equations (12) and (14) are not convenient for use because they contain the variables X'_k and X_{ik}, whose physical meaning is not clear. If we neglect the reverse process, we can simplify (14) and determine the meaning of X'_k and X_{ik}. In fact it can be shown that in this case we have

$$X'_k \cong X_k^2, \quad X_{ik} \cong X_i X_k. \quad (18)$$

To prove this we write X_k^2 as $X_k^2 = \Delta r_{k2}^2 - 2\Delta r_{k2}\Delta r_{k1} + \Delta r_{k1}^2$. Since we have $\Delta r_{k1} \to 0$, we can neglect the second and third terms; then, using (13'), we find $X_k^2 \cong \Delta r_{k2}^2 \cong x_k'$, i.e., $X_k^1 \cong X_k^2$.

Analogously we can show that, far from equilibrium, $X_{ik} \cong X_i X_k$; since $X_i X_k = (\Delta r_{i2} - \Delta r_{i1})(\Delta r_{k2} - \Delta r_{k1}) = \Delta r_{i2}\Delta r_{k2} - \Delta r_{i1}\Delta r_{k2} - \Delta r_{i2}\Delta r_{k1} + \Delta r_{i1}\Delta r_{k1}$, we can neglect all terms containing Δr_{i1}, $\Delta r_{k1} \to 0$. Then, using (13'), we find $X_i X_k \cong \Delta r_{i2}\Delta r_{k2} = X_{ik}$, i.e., $X_{ik} \cong X_i X_k$.

Using (18), we can rewrite (17) as

$$F(X) = \sum_{i,k,j=1}^{n} \int_0^{X_i} \Big\{ L_{ik} X_k + \frac{1}{2!} [L_{iii} X_i^2 + \sigma_{ik} L_{ikk} (X_k^2 + 2X_i X_k) + \sigma_{ikj} L_{ikj} (X_k X_j + X_i X_j + X_i X_k)] \Big\} dX_i. \qquad (19)$$

Equation (19) contains the ordinary thermodynamic forces and phenomenological coefficients having two and three indices, which are given explicitly by (9) and could be obtained directly from the time axiom.[4]

---

[1] H. G. Reik, Ann. Physik, 13, 73 (1953).

[2] I. Prigogine, Introduction to the Thermodynamics of Irreversible Processes, Wiley, New York (1962).

[3] P. Glansdorff and I. Prigogine, Physica, 20, 773 (1954).

[4] A. V. Pamfilov, A. I. Lopushanskaya, and L. B. Tsvetkova, Zh. Fiz. Khim., 42, 238 (1968).

Effect of ion current on the measurement of the electron energy distribution function by the second-derivative method

V. A. Dovzhenko, A. P. Ershov, and G. S. Solntsev

M. V. Lomonosov Moscow State University

(Submitted August 13, 1973)
Zh. Tekh. Fiz., 44, 851-853 (April 1974)

Conditions are investigated for which it is necessary to take account of the second derivative of the ion current in the second derivative of the total current. The ratio of the second derivative of the electron current to the second derivative of the ion current to a probe is calculated for "thin" and "thick" cylindrical probes on the assumption of a Maxwellian energy distribution for the electrons. It is shown that in helium, the contribution of the second derivative of the ion current is greater than 10% when the ratio of the probe potential to the electron temperature (in electron volts) is higher than 6. The results explain the experimental observation that the second derivative of the total probe current varies slowly at high probe potentials.

Electron energy distribution functions are often measured by the second-derivative method,[1,2] which makes use of the well-known Druyvesteyn equation

$$f_0(V)=\frac{2\sqrt{2}}{Sen}\sqrt{\frac{m}{e}}\sqrt{V_p}\cdot\frac{d^2i_e}{dV_p^2}, \tag{1}$$

where $f_0(V)$ is the distribution function defined by the relation $dn = nf_0(V)dV$, V_p is the potential of the probe relative to the plasma, $V = V_p = (mv^2)/(2e)$ is the potential corresponding to the electron energy in eV, S is the area of the probe, and e, m, and n are the charge, mass, and density of the electron. The quantity $i_e'' = d^2i_e/dV_p^2$ is measured electronically[1,2] and identified with the second derivative of the total probe current $i_p'' = i_e'' + i_p''$. It is assumed that

$$i_p''\ll i_e''. \tag{2}$$

It has in fact been shown experimentally[3] that this inequality holds in the plasma of a mercury vapor positive column at pressures of $\sim 10^{-3}$ torr. On the other hand, it has been noted in ref. 2 that the inequality (2) is not valid at very high probe potentials. This is understandable because i_p'' is small and increases slowly with V_p, whereas i_e'' decreases exponentially to zero. However, the value of V_p at which (2) no longer holds is not estimated in ref. 2.

The aim of the present paper is to investigate the conditions under which the contribution from the second derivative of the ion current must be taken into account.

We assume that the electron distribution is Maxwellian and limit ourselves to low pressures. This case has been considered in detail in a review[4] and the equations for the electron and ion currents per unit length of a cylindrical probe are given there as

$$i_e=-en\sqrt{\frac{kT_e}{2\pi m}}\,2\pi a e^{-\eta}, \tag{3}$$

$$i_p=2\pi r_p en\sqrt{\frac{2kT_e}{M}}\,\alpha', \tag{4}$$

$$i_p=\frac{2\sqrt{2}}{9}\sqrt{\frac{e}{M}}\,\frac{V_p^{3/2}}{a\beta^2\left(\frac{r_p}{a}\right)}, \tag{5}$$

where $\eta = (eV_p)/(kT_e)$, k is the Boltzmann constant, a is the radius of the probe, r_p is the sheath radius, M is the ion mass, $\beta^2(r_p/a)$ is a tabulated function, $\alpha' = 0.37$ for $T_e \gg T_p$, T_e and T_p are the electron and ion temperatures. We use the notation $x = r_p/a$, $\varphi(x) = x\beta^2(x)$ and $\lambda_{De} = (kT_e/4\pi ne^2)^{1/2}$. It can be seen from (4) that i_p'' is proportional to r_p''. In order to find r_p'' and r_p from (4) and (5) we must eliminate i_p. Then the ratio $\chi \equiv i_e''/i_p''$ is

$$\chi=\frac{\dfrac{d^2i_e}{d\eta^2}}{\dfrac{d^2i_p}{d\eta^2}}=\frac{3}{4\sqrt{\pi}}\sqrt{\frac{M}{m}}\left(\frac{a}{\lambda_{De}}\right)^2\Phi(x)\,\eta^{1/2}e^{-\eta}, \tag{6}$$

TABLE 1. Variation of the Functions φ and Φ with x

	values											
	1.00	1.01	1.04	1.06	1.1	1.4	2.0	3.0	5.0	10	14	20
$\varphi(x)$	0	$1.01\cdot10^{-4}$	$1.65\cdot10^{-3}$	$3.78\cdot10^{-3}$	$1.08\cdot10^{-2}$	$2.08\cdot10^{-1}$	1.69	8.94	49.4	$3.7\cdot10^{2}$	$9.15\cdot10^{2}$	$2.3\cdot10^{3}$
$\Phi(x)$	0	0.04	0.18	0.24	0.34	2.0	4.67	13.7	36.0	130	248	400

TABLE 2. Variation of $\chi \equiv (d^2i_e/dV_p^2)/(d^2i_p/dV_p^2)$ with η for Various λ_{De}/a in Helium

λ_{De}/a	η								
	2	3	4	5	6	7	8	9	10
10^{-2}	$9.8\cdot10^{3}$	$7.0\cdot10^{3}$	$3.4\cdot10^{3}$	$1.8\cdot10^{3}$	$7.9\cdot10^{2}$	$3.5\cdot10^{2}$	$1.5\cdot10^{2}$	$6.2\cdot10^{1}$	$2.5\cdot10^{1}$
10^{-1}	$8.3\cdot10^{2}$	$5.7\cdot10^{2}$	$2.9\cdot10^{2}$	$1.6\cdot10^{2}$	$7.2\cdot10^{1}$	$3.5\cdot10^{1}$	$1.5\cdot10^{1}$	6.4	2.8
1	$1.1\cdot10^{2}$	$7.6\cdot10^{1}$	$3.7\cdot10^{1}$	$1.9\cdot10^{1}$	8.7	3.9	1.75	0.75	0.32

TABLE 3. Variation of χ with η when $\lambda_{De}/a > 1$ in Helium

	η								
	2	3	4	5	6	7	8	9	10
χ	$1.2 \cdot 10^2$	$7.9 \cdot 10^1$	$4.5 \cdot 10^1$	$2.3 \cdot 10^1$	$1.13 \cdot 10^1$	5.2	2.4	1.04	0.45

where

$$\Phi(x) = \frac{\left(\frac{d\varphi}{dx}\right)^3}{\left[-\left(\frac{d\varphi}{dx}\right)^2 + 3\varphi(x)\frac{d^2\varphi}{dx^2}\right]}. \tag{7}$$

The value of x is determined from the expression

$$\varphi(x) = 1.2\left(\frac{\lambda_{De}}{a}\right)^2 \eta^{3/2}. \tag{8}$$

The functions $\varphi(x)$ and $\Phi(x)$ are given in Table 1. In the calculation of $\Phi(x)$, we use the representation of $\beta^2(x)$ in the form of a Langmuir series.[5] It can be seen from (6) that χ depends on the type of gas, the ratio λ_{De}/a, and the probe potential. Since (4) and (5) are derived for high probe potentials, we limit ourselves to $\eta \geq 2$. The variation of χ with η for various λ_{De}/a is shown in Table 2 for helium.

It is evident from Table 2 that when $\lambda_{De}/a \ll 1$ the effect of i_p'' can be neglected. Since $\chi \propto (M)^{1/2}$, it is even more reasonable to neglect the second derivative of the ion current for heavier gases (mercury vapor, for example). At the limits of applicability of (4) and (5), where $\lambda_{De} \simeq 1$, the contribution due to the second derivative of the ion current is greater than 10% for $\eta \geq 6$.

When the theory does not hold, it is possible to use the following equation[6] for the analysis of the ratio i_e''/i_p'' with $\lambda_{De}/a > 1$:

$$i_p = 2ena\sqrt{\frac{2eV_p}{M}}. \tag{9}$$

The ratio of second derivatives is then

$$\chi = \sqrt{4\pi}\sqrt{\frac{M}{m}}\,\eta^{3/2}e^{-\eta}. \tag{10}$$

The results of calculations using this equation are given in Table 3. When $\lambda_{De}/a > 1$ the contribution due to the second derivative of the ion current is 10% or more for $\eta \geq 6$ (in helium), whatever the value of the electron density.

Thus results of measurements of the second derivative of electron current can be trusted at least up to potentials of the order of six electron temperatures.

The results obtained here explain the experimentally observed fact that the second derivative of the total current varies slowly at high probe potentials.

---

[1] Yu. M. Kagan, Beitr. Plasma Phys., 5, 479 (1965).

[2] Yu. M. Kagan, in: Spectroscopy of a Gas-Discharge Plasma [in Russian], Nauka, Moscow (1970), p. 201.

[3] R. L. F. Boyd and N. D. Twiddy, Proc. R. Soc. A, 250, 53 (1959).

[4] Yu. M. Kagan and V. I. Perel', Usp. Fiz. Nauk, 81, 409 (1963) [Sov. Phys. – Usp., 6, 767 (1964)].

[5] N. A. Kaptsov, Electronics [in Russian], GITTL, Moscow (1953).

[6] Yu. M. Kagan and V. I. Perel', Zh. Tekh. Fiz., 39, 2238 (1969) [Sov. Phys. – Tech. Phys., 14, 1689 (1970)].

Energy dependence of the focusing of ions by crystals

E. S. Mashkova, V. A. Molchanov, and A. D. Pavlova

(Submitted July 30, 1973)
Zh. Tekh. Fiz., 44, 854-855 (April 1974)

The number of particles scattered at an angle of 25° from the (110) face of a copper crystal has been measured as a function of the azimuthal angle of rotation of the target for 5-30 keV incident argon ions. The sharp oscillations of the number of scattered particles diminish appreciably when the energy of the incident ions lies below 10 keV.

It is known[1] that under certain conditions a focusing effect obtains when ions are scattered by the crystal surfaces. Under these conditions a beam of ions scattered by a crystal is appreciably narrower than when scattered by surfaces of disordered solids, or for an orientation of the crystal target relative to the beam of primary ions which is arbitrary in the Lindhard sense. In particular, focusing leads to a characteristic shape of the curve for the number of particles scattered in a given direction in the plane of incidence of the beam of primary ions as a function of the azimuthal angle of rotation of this plane, i.e., about an axis perpendicular to the surface of the target. When the plane of incidence of the ions is parallel to certain crystallographic axes on the surface of the target there are sharp maxima in the number of particles reaching the analyzer in spite of the fact that the integrated scattering coefficient is not a maximum.[2]

The present experiment is undertaken to find the effect of the incident ion energy on the character of the dependence of the number of particles scattered on the azimuthal angle of rotation of the target (Fig. 1). The experiment is performed in the following way. A well-collimated beam of singly charged argon ions (5-30 keV) is directed onto the (110) face of a single-crystal copper target at a small angle α with the surface. The scattered particles are recorded by a fast particle detector.[3] The detector current is proportional to the number of fast particles reaching the detector, but depends somewhat on their energy distribution. In the present experiment, however, the scattering angle is constant and the energy distributions of both ions and neutrals are rather narrow[4] and this dependence can be neglected. The angular resolution of the detector is ± 1°.

Figure 2 shows the dependence of the number of scattered particles on the azimuthal angle of rotation of the target β for various energies of the incident ions. In the range of azimuthal angles of rotation of the target investigated ($-110° \leq \beta \leq 110°$) the maximum number of scattered particles is in all cases taken as unity for convenience in comparing the shapes of the angular distributions. The glancing angle α is 12°, and the scattering angle $\theta = 25°$. The dependence of the number of scattered particles on the azimuthal angle of rotation of the target is sharply nonmonotonic, exhibiting maxima and minima, and is symmetric about $\beta = 0°$, which corresponds to the plane of incidence and scattering being parallel to the (110) directions in the target surface. In this case the principal maximum in the number of scattered particles is observed. When the plane of incidence and scattering is parallel to the (100) directions ($\beta = \pm 90°$) there is also an increase in the number of scattered particles, but not so large as at $\beta = 0°$. Thus for 30 keV incident ions the corresponding maxima in the number of scattered particles differ by about a factor of 2, as do their half-widths. It should also be noted that the maximum at $\beta = 0°$ is split into two components. If the ratio of the maximum intensity to the minimum in the angular range under investigation is taken as a measure of the orientation effect, it is a maximum for an ion energy of 25 keV and decreases by about a factor of 5 when the energy is decreased to 5 keV. The decrease in energy leads to a decrease in the intensity relative to the principal maximum, and to an increase in the half-width of all maxima. The depth of the intensity dip at $\beta = 0°$ (the depth of splitting of the principal peak) is approximately constant for incident ion energies of 30-20 keV, but decreases sharply for lower energies and disappears altogether below 15 keV. Nevertheless, the general qualitative picture of the angular dependences investigated is preserved in the 30-10 keV energy range. When the energy is decreased further the angular dependence of the intensity changes appreciably, as shown by the curve for 5 keV incident ions. The preferential directions of scattering related to the (110) and (100) directions are still preserved, but the sharpness of the directional effect is much decreased and there is a tendency toward a relative increase in the number of particles scattered in other directions.

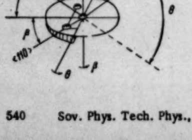

Fig. 1. Scattering scheme.

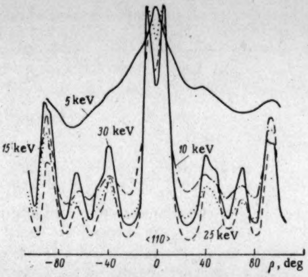

Fig. 2. Ar^+−Cu(110), $\alpha = 12°$, $\theta = 25°$.

---

[1] E. S. Mashkova and V. A. Molchanov, Rad. Eff., 13, 183 (1972).
[2] M. W. Thompson, Contemp. Phys., 9, 375 (1968).
[3] E. S. Mashkova and V. A. Molchanov, Rad. Eff., 16, 143 (1972).
[4] V. M. Chicherov, ZhETF Pis. Red., 16, 328 (1972) [JETP Lett., 16, 231 (1972)].

Steady-state study of the temperature dependence of the mutual-diffusion coefficients of certain gases

N. D. Kosov and B. P. Solonitsyn

S. M. Kirov Kazakh State University, Alma-Ata

(Submitted April 17, 1973)
Zh. Tekh. Fiz., 44, 855-857 (April 1974)

A steady-state, continuous-flow method is used to study the mutual-diffusion coeficients of the hydrogen−nitrogen, helium−nitrogen, and helium−carbon dioxide systems over the temperature range 300-810°K. The data are compared with the experimental data reported elsewhere and with theoretical values calculated on the basis of the Chapman−Enskog and Maxwell−Boltzmann−Jeans theories.

Most methods available for measuring the mutual-diffusion coefficients of gases are nonsteady-state methods. The equations used in these methods are derived from Fick's second law under various assumptions regarding the diffusion. In steady-state methods these equations are derived from Fick's first law. The steady-state method proposed in ref. 1 for measuring the mutual-diffusion coefficients of gases has several advantages (there is no redundant apparatus, and the results are highly reproducible) and has been used to study the mutual-diffusion coefficients of gases at temperatures below room temperature.[2] In this work we report the use of a steady-state continuous-flow method to study the mutual-diffusion coefficients of gases at temperatures above room temperature (up to 814°K).

The apparatus does not differ fundamentally from that described in refs. 1-3. The diffusion cell is a set of 58 identical capillaries 5.000 ± .002 cm long with a total cross-sectional area of 0.1360 ± 0.0002 cm^2. The volume flow rate of the pure gases is 1.116 ± 0.002 cm^3/sec at T = 298.0°K. The experiments are carried out at atmospheric pressure. The results for the three binary systems studied (hydrogen−nitrogen, helium−nitrogen, and helium−carbon dioxide) are shown in Table 1. To the best of our knowledge, this is the first reported measurement of the mutual-diffusion coefficients for the helium−carbon dioxide system above 498°K. The experimental error is less than 2%.

Using the method of least squares, we find the following empirical relations between the experimental mutual-diffusion coefficients and the temperature:

$$H_2—N_2 : \lg D = 1.645 \lg T - 4.1556, \tag{1}$$

$$He—N_2 : \lg D = 1.634 \lg T - 4.1887, \tag{2}$$

TABLE 1. Mutual-Diffusion Coefficients of Three Binary Gaseous Mixtures Measured by the Steady-State Method (the results are referred to normal pressure).

H_2—N_2		He—N_2		He—CO_2	
T, °K	D, cm^2/sec	T, °K	D, cm^2/sec	T, °K	D, cm^2/sec
297.0	0.809	296.0	0.707	297.5	0.605
362.0	1.12	355.0	0.948	361.5	0.838
427.0	1.48	416.5	1.22	414.5	1.06
478.5	1.79	464.5	1.48	463.5	1.28
512.0	2.00	509.5	1.71	510.0	1.48
566.5	2.37	557.5	2.00	555.0	1.74
600.0	2.61	601.5	2.26	598.0	1.98
649.0	2.95	640.5	2.50	641.0	2.21
684.0	3.22	686.0	2.79	683.5	2.47
728.0	3.56	717.0	3.00	725.5	2.74
770.0	3.91	771.0	3.38	766.0	3.01
814.0	4.27	812.0	3.66	810.5	3.30

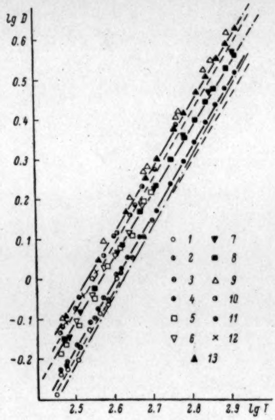

Fig. 1. Mutual-diffusion coefficients measured by the steady-state continous-flow method, experimental data of other workers, and theoretical functional dependences calculated from the Chapman−Enskog theory (dashed lines) and the Maxwell−Boltzmann−Jeans theory (dot−dash lines). The solid lines correspond to Eqs. (1)-(3). He−CO_2: 1) ref. 4; 2) ref. 5; 3) ref. 6; 4) the present work. He−N_2: 5) ref. 6; 6) ref. 5; 7) ref. 7; 8) the present work. H_2−N_2: 9) ref. 8; 10) ref. 5; 11) ref. 9; 12) ref. 10; 13) the present work.

$$He—CO_2 : \lg D = 1.691 \lg T - 4.4005. \tag{3}$$

The average deviation of the experimental coefficients from those calculated from Eqs. (1)-(3) is less than 0.4%.

Our data are compared with the experimental data of other workers[4-10] and with the theoretical functional dependences derived on the basis of the rigorous Chapman−Enskog kinetic theory with the Lennard−Jones (6-12) potential[11] and on the basis of the Maxwell−Boltzmann−Jeans theory, in which the functional dependence of the effective molecular diameter is taken into account,[12] in Fig. 1. For the hydrogen−nitrogen system the Maxwell−Boltzmann−Jeans theory agrees completely with our experimental results, while the Chapman−Enskog theory predicts results which average 6% lower than our experimental results. For the helium−nitrogen system both theories agree with experiment within the experimental error. For the helium−carbon dioxide system both theories predict results which average 6% lower than the experimental results.

The mutual-diffusion coefficients measured by the steady-state continuous-flow method have a small scatter and agree with data reported previously; this method seems to be extremely promising for studying the mutual-diffusion coefficients of gases over broad temperature ranges.

---

[1] L. I. Kurlapov and N. D. Kosov, in: Physics [in Russian], No. 3, Izd. MVISSO KazSSR, Alma-Ata (1968), p. 224.

[2] N. D. Kosov and A. Zh. Zhalgasov, Zh. Tekh. Fiz., 40, 1325 (1970) [Sov. Phys. – Tech. Phys., 15, 1024 (1970)].

[3] B. P. Solonitsyn and N. D. Kosov, in: Diffusion in Gases and Liquids [in Russian], Alma-Ata (1972), p. 66.

[4] S. C. Saxena and E. A. Mason, Molec. Phys., 2, 379 (1959).

[5] B. A. Ivakin and P. E. Suetin, Zh. Tekh. Fiz., 34, 1115 (1964) [Sov. Phys. – Tech. Phys., 9, 866 (1964)].

[6] S. L. Seager, L. R. Geertson, and J. C. Giddings, J. Chem. and Eng. Data, 8, 168 (1963).

[7] J. C. Liner and S. Weissman, J. Chem. Phys., 56, 2288 (1972).

[8] V. F. Vyshenskaya and N. D. Kosov, in: Heat and Mass Transfer [in Russian], Vol. 1, Izd. Akad. Nauk BSSR, Minsk (1962), p. 181.

[9] D. S. Scott and K. E. Cox, Can. J. Chem. Eng., 38, 201 (1960).

[10] E. A. Mason and L. Monchick, J. Chem. Phys., 36, 2746 (1962).

[11] J. O. Hirschfelder, C. F. Curtiss, and R. B. Bird, Molecular Theory of Gases and Liquids, Wiley, New York (1954).

[12] N. D. Kosov, A. F. Bogatyrev, and B. P. Solonitsyn, in: Thermophysical Properties of Gases [in Russian], Izd. Nauka, Moscow (1970), p. 197.

Statistical characteristics of the turbulent wake behind a supersonic sphere

V. G. Ivanov, G. I. Mishin, and S. N. Palkin

A. F. Ioffe Physicotechnical Institute,
Academy of Sciences of the USSR, Leningrad

(Submitted July 9, 1973)
Zh. Tekh. Fiz., 44, 857-861 (April 1974)

An experimental study has been made of the characteristics of the boundaries of turbulent wakes in a ballistic apparatus using a Schlieren method. The correlation function, roughness dimension, intermittence coefficient, and microscopic scale of the fluctuations in the wake boundaries are found as functions of the downstream distance. The results are compared with those of other workers.

Serious difficulties have been encountered in attempts to find a theoretical explanation for the characteristics of free turbulence.[1] We report here on an experimental study of the statistical characteristics of fluctuations in the boundary of a turbulent wake; these are of considerable importance in connection with the understanding of free turbulence. The experiments are carried out by using a Schlieren method to study the wake behind a sphere 20.7 mm in diameter moving at 675 m/sec ($M_\infty = 2$) in air at a pressure of 760 torr ($Re_\infty = 10^6$). The flow becomes turbulent upon the separation of the boundary layer. The wake in the photographs is 125 mm long.

Data for the statistical analysis are obtained from the part of the wake being studied by measuring the distances y_{bo} from a baseline, which corresponds approximately to the axis of the wake, to the upper and lower boundaries of the wake. In this case the asymmetry of the turbulent wake can be neglected,[2] since the boundary contour of the viscous wake visible on the shadow and Schlieren photographs corresponds primarily to points on the boundary which are near the meridian plane of the wake, parallel to the image plane.

The length of the part of the wake for which the measurements are used to calculate the statistical characteristics is 30 mm (~ 1.5 diameters of the object), and the measurement step is 0.5 mm.

To eliminate the rms value of y_{bo} and its linear change along the wake, we use the method of least squares to find the line corresponding to the average wake boundary. We calculate the deviations of the boundary from this line, Δy_{bo}, and from the results of these calculations we determine the statistical characteristics of the fluctuations in the boundary of the turbulent wake. We then average the results of 10 experiments for each part of the wake.

Figure 1 shows the normalized correlation function of the boundary fluctuations of the turbulent wake calculated for eight parts of the wake. We see that the functional dependence of the normalized correlation function $R(\xi)$ on the delay length ξ weakens with distance along the wake, i.e., the scale of the boundary roughness increases.

A measure of the boundary roughness of the turbulent wake is the rms deviation from the average wake boundary, found by the method of least squares. Figure 2 shows the rms deviation γ divided by the object diameter d as a function of the dimensionless distance downstream from the object, x/d. According to the experimental data shown in Fig. 2, the dimension of the boundary roughness of the

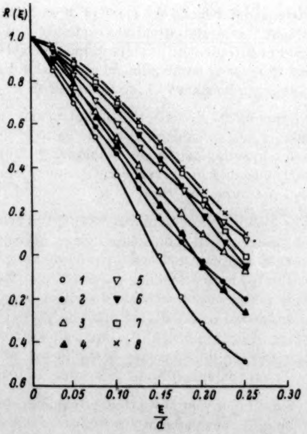

Fig. 1. Here and in Fig. 7, x/d: 1) 4.1-5.6; 2) 5.6-7.1; 3) 7.1-8.6; 4) 8.9-10.4; 5) 10.4-11.9; 6) 11.9-13.4; 7) 14.4-15.9; 8) 15.9-17.4.

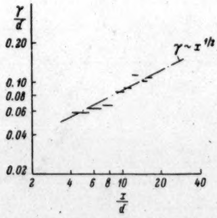

Fig. 2.

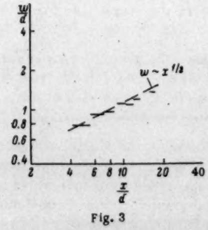

Fig. 3

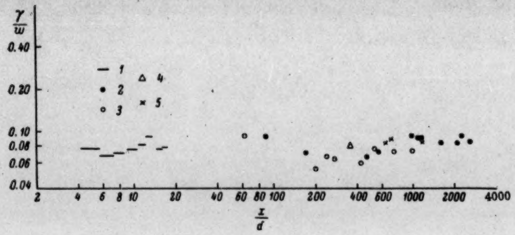

Fig. 4.

TABLE 1

Curve	Sphere diameter, mm	M_∞	Re_∞	Reference
1	20.7	1.97	10^6	The present work
2	3.2	3.2	$2.5 \cdot 10^5$	[2]
3	6.4	4.7	$7.1 \cdot 10^5$	
4	76.2	6.0	$1.1 \cdot 10^7$	[4]
5	6.4	13.6	$2.6 \cdot 10^5$	[2]

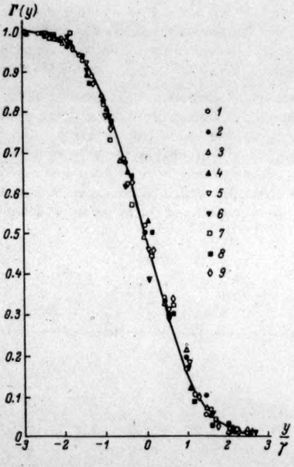

Fig. 5. x/d: 1) 4.1-5.6; 2) 5.6-7.1; 3) 7.1-8.6; 4) 8.9-10.4; 5) 10.4-11.9; 6) 11.9-13.4; 7) 14.4-15.9; 8) 15.9-17.4; 9) 17.4-18.9.

turbulent wake over the range $4 \leq \chi/d \leq 17$ increases approximately according to $\gamma \sim x^{1/2}$.

Figure 3 shows the average wake diameter w, defined as the average distance between the least-squares lines for the upper and lower boundaries of the wake, as a function of the distance from the object.

Since the average wake diameter and the dimension of the boundary roughness increase at the same rate, the rms deviation converted to dimensionless form by dividing by the wake diameter remains constant with distance along the flow (Fig. 4 and Table 1).

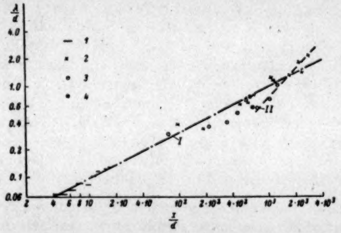

Fig. 6. λ: I) $x^{1/2}$; II) $x^{13/12}$ (ref. 2).

TABLE 2

Curve	Sphere diameter, mm	M_∞	R_∞	Reference
1	20.7	1.97	10^6	The present work
2	3.2	3.2	$2.5 \cdot 10^5$	[2]
3	6.4	4.7	$7.1 \cdot 10^5$	
4	6.4	13.6	$2.6 \cdot 10^5$	

This result agrees well with the experimental data of ref. 2.

Townsend[3] introduced the concept of an "intermittency coefficient," as a statistical characteristic of the intermittence of turbulence; this gives the probability for turbulence to exist at some point in space at a distance y from the average boundary of the turbulent flow.

The intermittency coefficient of the boundary of the turbulent wake, Γ (y), is calculated as the ratio of the time over which a hypothetical probe a distance y from the least-squares line is in the turbulent wake to the total (quite long) measurement time.

Figure 5 shows the calculated intermittency coefficient of the boundary of a turubulent wake. The coordinate y is converted to dimensionless form by dividing it by the rms deviation γ; in this manner we can display the results obtained for different downstream distances. Comparison of the experimental data with the function $\Gamma(y) = (1/2)\,[1 - \Phi(y/\gamma)]$, where Φ is the probability integral, shows that the distribution law for the boundary of the turbulent wake is Gaussian, in agreement with the data of refs. 2 and 4.

One of the important statistical parameters of the fluctuations in the boundary of a turbulent wake is the microscale λ. Since the wake boundary is described by a Gaussian distribution, the microscale λ is, according

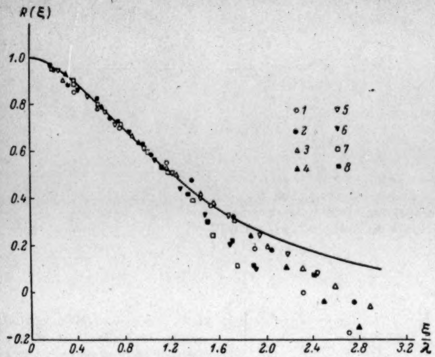

Fig. 7. The solid curve[2] shows $R(\xi) = \sin[(\pi/2)\exp(-2\sqrt{2}\,\xi/\pi\lambda)]$.

to Corrsin and Kistler[3]

$$\lambda=\frac{\sqrt{2}}{\pi}\frac{1}{N_0},$$

where N_0 is the average number of intersections of Δy_{b0} with the zero line per unit length.

It follows from the experimental data in Fig. 6 and Table 2 that the microscale λ converted to dimensionless form by dividing it by the object diameter d increases with increasing dimensionless downstream distance x/d according to $\lambda \sim x^{1/2}$. The functional dependence agrees with the experimental data of Shapker,[2] obtained at large values of x/d. On the other hand, the theoretical function $\lambda \sim x^{13/12}$ proposed by Shapker does not agree with our experimental results. Furthermore, as is pointed out in ref. 5, the values of the displacement lengths obtained on the basis of the theoretical functional dependences of the statistical characteristics of the wake boundaries on the downstream distance proposed by Shapker "are apparently unlikely."

Figure 7 shows the normalized correlation function $R(\xi/\lambda)$, which agrees well with the empirical functional dependence obtained by Corrsin and Kistler[2] on the basis of the results of thermoanemometric measurements:

$$R(\xi)=\sin\left(\frac{\pi}{2}e^{-\frac{2\sqrt{2}}{\pi}\frac{\xi}{\lambda}}\right).$$

---

[1] A. S. Monin and A. M. Yaglom, Statistical Fluid Mechanics [in Russian]. Part 1, Izd. Nauka, Moscow (1965).

[2] Shapker, RTK, 4, 119 (1966).

[3] I. O. Khintse, Turbulence [in Russian], GIFML, Moscow (1963).

[4] Levenshteins and Krumins, RTK, 5, 76 (1967).

[5] Satton, RTK, 6, 231 (1968).

Gas focusing of a negative-ion beam

M. D. Gabovich, A. P. Naida, I. M. Protsenko, L. S. Simonenko, and I. A. Soloshenko

Institute of Physics,
Academy of Sciences of the Ukrainian SSR, Kiev

(Submitted July 23, 1973)
Zh. Tekh. Fiz., 44, 861-863 (April 1974)

Gas focusing of a negative beam of H_1^- ions has been studied at beam currents up to 10 mA and at energies up to $eV_0 = 10$ keV. The potential at the beam axis becomes positive, and focusing occurs at a pressure of $p_0 \sim 10^{-4}$ torr in agreement with the calculated value. At $p > p_0$ the radial potential distribution displays two steps. The measured potential drops near the wall and at the beam boundary agrees with the corresponding calculated values.

Focusing of electron beams by the field produced by positive ions formed as the beam passes through a gas was detected a long time ago, but the analogous focusing of negative-ion beams has not previously been reported. The development of accelerator technology and effective plasma-heating methods has stimulated study of the conditions for the transport of such ion beams. Below we report the first observation of gas focusing of intense negative-ion beams and a study of the features of this focusing.

In an effort to observe this effect we produce intense beams of negative hydrogen ions at currents up to 10 mA and energies up to 10 keV converging at an angle ~ 1° toward the crossover point, which is in the entrance aperture of a chamber filled with argon to a pressure of 10^{-5}-10^{-3} torr. Curve 1 in Fig. 1 shows the potential at the axis of the negative-ion beam as a function of the argon pressure in the chamber. This fundamental dependence is obtained by means of a thermal probe; the beam travels a path length of 100 cm in the chamber. We see that as the pressure is raised above a certain value p_0 the negative potential becomes positive. At the same time a thermocouple in this region indicates an increase in the specific power w at the beam axis (curve 2), which is evidence of the desired effect. The value of p_0 agrees with the calculated value of the argon-atom density at which the space charge of the positive ions formed during ionization of the gas by the beam balances the space charge of the beam: $n_{a0} \approx (2/R)(\bar{v}_{\pm}/v_-)(1/\sigma_i)$, where R is the beam radius, $\bar{v}_+$ is the average velocity of the ions produced, v_- is the velocity of the beam ions, and σ_i-is the ionization cross section.

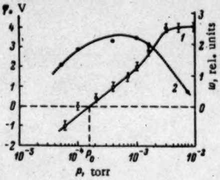

Fig. 1. Space potential (curve 1) and specific power (curve 2) at the beam axis as functions of the argon pressure in the chamber. The current of the beam of H_1^- ions is $I_- = 5$ mA; the energy is $eU_0 = 10$ keV.

To clarify the mechanism and features of this effect consider Fig. 2, which shows the radial profile of the potential over the entire chamber cross section at a pressure $p \gg p_0$, along with the corresponding radial distribution of the current density in the beam. Since the potential profile has two steps, we conclude that the field at the boundary of the beam, which contracts the beam, is due not to the total potential drop $\varphi_1 + \varphi_2$, but only to the small potential drop in the beam zone, φ_2. This circumstance is partially responsible for the relative weakness of the contraction. Another factor is the loss of electrons by negative ions, which is appreciable at $p > p_0$, and which also explains the peak on curve 2 in Fig. 1. Even at the pressure $p = p_0$ the mean free path for this detachment of electrons,

$$\lambda_{-10} = \frac{1}{n_{a0}\sigma_{-10}} = \frac{Rv_-\sigma_i}{2v_+\sigma_{-10}},$$

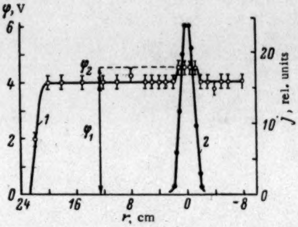

Fig. 2. Radial profiles of the potential (curve 1) and the negative-ion current density (curve 2). The current of the H_1^- beam is $I_- = 5$ mA, and the energy is $eU_0 = 10$ keV.

turns out to be comparable to the distance covered by the beam in the gas. The important role of electron detachment governs our choice of a thermocouple as a probe to detect this effect. This thermocouple detects both fast charged particles and fast atoms, which move toward the axis before they undergo charge exchange. This latter circumstance explains why a probe which detects charged particles only is less sensitive to the beam contraction.

It is important to note that the two-stepped potential profile found experimentally also follows from the Poisson equation, which is solved numerically in refs. 1 and 2 for the case of the passage of an electron beam (although a distribution of this type has not been detected for the case of an electron beam). Considering the condition for the quasineutrality of the plasma formed in a two-stepped well, the capture of the slowest electrons in this well, and the loss of electrons from this well due to Coulomb collisions with ions, we can estimate the order of magnitude of the potential drops without resorting to this solution. The potential drop in the beam is of order

$$\varphi_2 \approx a^{1/3} e \left(\frac{U_i}{U_0}\right)^{1/3} \left(\frac{M}{m}\right)^{1/3} \frac{1}{n_{a0}^{1/3} (\sigma_i + \sigma_{-10})^{1/3}} \left(1 - \frac{n_{a0}}{n_a}\right)^{1/3} n_-^{1/3},$$

where n_- is the ion density in the beam, eU_0 is the ion energy, M is the mass, and U_i is the ionization potential of the atoms. Estimates reveal a correspondence between the calculated and measured values of φ_1 and φ_2.

We note in conclusion that a more or less well-defined two-stepped potential profile should also be observed when an intense beam of any type of fast particles passes through a gas with a sufficiently high density. In the passage of electrons or negative ions the field at the beam boundary is a focusing field under these conditions; in the case of the free propagation of a positive-ion beam it is always a defocusing field.

---

[1] D. A. Dunn and S. A. Self, J. Appl. Phys., 35, 113 (1964).

[2] R. A. McCorkle and W. H. Bennett, Plasma Phys., 13, 1153 (1971).

Time characteristics of the near radiation field of the injection laser

Zh. I. Alferov, V. N. Deryagin, L. E. Marasin, Yu. V. Popov, and E. L. Portnoi

(Submitted July 18, 1973)
Zh. Tekh. Fiz., 44, 863-864 (April 1974)

Semiconductor lasers are finding increasing use in optical location systems,[1] in which the operating accuracy is governed largely by the time structure of the laser radiation. It has been pointed out[2] that there is a significant temporal inhomogeneity over the emitting surface of an injection laser with a diffuse p−n junction in GaAs.

We report here a study of the temporal characteristics of the near radiation field of injection heterolasers. The active region of the samples is made from lightly doped n-type GaAs ($n \simeq 5 \cdot 10^{16}$ cm^{-3}), and is enclosed between wide-band p-type and n-type $Al_xGa_{1-x}As$ emitters with $x \simeq 0.2$ (refs. 3, 4). Some of the samples have a thin active layer ($d \leq 1\ \mu$), which corresponds to the generation of the fundamental transverse mode, while others have thicker active layers, corresponding to the generation of higher-order transverse modes.[5]

The temporal characteristics of the near field are studied by a pulsed phase method involving the measurement of short time intervals[6] as an iris is moved over a magnified image of the emitting surface. The time resolution is about 0.05 nsec, and the spatial resolution is $\simeq 0.05\ \mu$.

Figure 1 shows typical distributions of the radiation intensity and the delay times in the direction perpendicular to the plane of the active layer. Comparison of these data with those of ref. 2 shows that heterolayers display a near-field structure which is much more homogeneous than that of p−n junction lasers. This circumstance could be due to the absence from the heterolaser structure of traps of the double-acceptor type,[7] which are responsible for the delay times in lasers having a diffuse p−n junction.

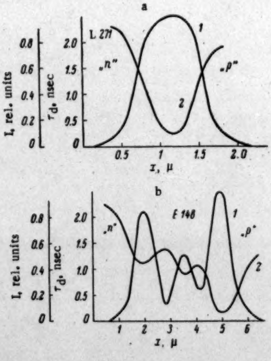

Fig. 1. Distributions of the intensity (1) and delay time of the radiation (2) for a heterolaser with a thin active layer (a) and a thick active layer (b).

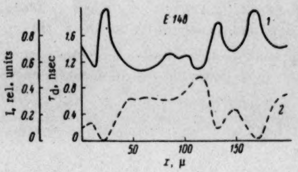

Fig. 2. Distributions of the intensity (1) and radiation delay time (2) in the direction along the active layer for a laser with a thin active layer.

It is extremely interesting to consider the correlation observed between the intensity of the near-field radiation and the temporal distribution; this correlation is found both for heterolasers with the fundamental transverse mode (Fig. 1a) and in those having higher-order transverse modes (Fig. 1b). Here the delay time is evidently decreasing as the amplitude of the radiation field is increasing, leading to an increase in the rate of stimulated radiative transitions. On the basis of this result we can conclude that there is a direct connection between the time intervals measured by the pulsed-phase method and the lifetime of the minority carriers in the active layer of a heterolaser.

Measurements of the temporal distribution along the active layer of the heterolasers (Fig. 2) also reveal a structure which is much more homogeneous than that of diffuse lasers.[2] The explanation apparently lies in the much more homogeneous generation pattern in this direction, which is characteristic of heterolasers.[8]

These results show that heterolasers are promising for use as radiation sources in highly accurate optical range finders.

The authors thank V. M. Tuchkevich for his continued interest in this work.

---

[1] V. N. Deryagin, L. E. Marasin, and Yu. V. Popov, OMP, No. 7, 23 (1972).
[2] V. N. Deryagin and L. E. Marasin, Fiz. Tekh. Poluprovodn., 5, 1981 (1971). [Sov. Phys. – Semicond., 5, 1716 (1972)].
[3] Zh. I. Alferov, V. M. Andreev, E. L. Portnoi, and M. K. Turkan, Fiz. Tekh. Poluprovodn., 3, 1328 (1969) [Sov. Phys. – Semicond., 3, 1107 (1970)].
[4] Zh. I. Alferov, V. M. Andreev, D. Z. Garbuzov, Yu. V. Zhilyaev, E. P. Morozov, E. L. Portnoi, and V. G. Trofim, Fiz. Tekh. Poluprovodn., 4, 1826 (1970) [Sov. Phys. – Semicond., 4, 1573 (1971)].
[5] V. M. Andreev, V. I. Borodulin, V. P. Konyaev, G. T. Pak, A. I. Petrov, E. L. Portnoi, and V. I. Shveikin, Fiz. Tekh. Poluprovodn., 6, 1739 (1972) [Sov. Phys. – Semicond., 6, 1500 (1973)].
[6] V. N. Deryagin, L. E. Marasin, and Yu. V. Popov, Prib. Tekh. Eksp., No. 2, 112 (1974).
[7] C. Dyment and J. E. Ripper, J. Quant. Electron., 4, 155 (1968).
[8] Zh. I. Alferov, V. M. Andreev, F. A. Gimmel'fart, L. M. Dolginov, Yu. A. Zhitkov, L. D. Libov, E. L. Portnoi, V. G. Trofim, M. K. Turkan, and E. G. Shevchenko, Fiz. Tekh. Poluprovodn., 4, 1697 (1970) [Sov. Phys. – Semicond., 4, 1457 (1971)].

Frequency-doubling single-mode laser for picosecond pulses

A. M. Bonch-Bruevich, A. M. Tkachuk, and A. A. Fedorov

(Submitted July 10, 1973)
Zh. Tekh. Fiz., 44, 864-867 (April 1974)

A frequency-doubling single-mode neodymium-glass laser that provides picosecond pulses has been designed using a KDP crystal. The energy distribution, lifetime, and spectral distribution of the generated pulses have been investigated. It is shown that the laser output consists of a train of 10-15 nanosecond or subnanosecond pulses with a period of 16 nsec. With self-mode-locking the divergence is 15″ for the first harmonic and 21″ for the second harmonic. Each subnanosecond pulse consists of two ~ 5 · 10^{-12} sec spikes separated by a 200 nsec interval. The maximum radiated power in one picosecond pulse is ~ 3 · 10^{11} and ~ 10^{11} W in the first and second harmonics respectively.

A neodymium-glass self-mode-locked laser with a telescopic resonator is described which uses a KDP crystal for frequency doubling. The low radiation divergence of such a laser and the high power density due to self-mode-locking make it possible to obtain frequency doubling with a KDP crystal with a conversion efficiency of about 30% without the aid of special optical devices. Figure 1 shows the experimental arrangement used to obtain the radiation

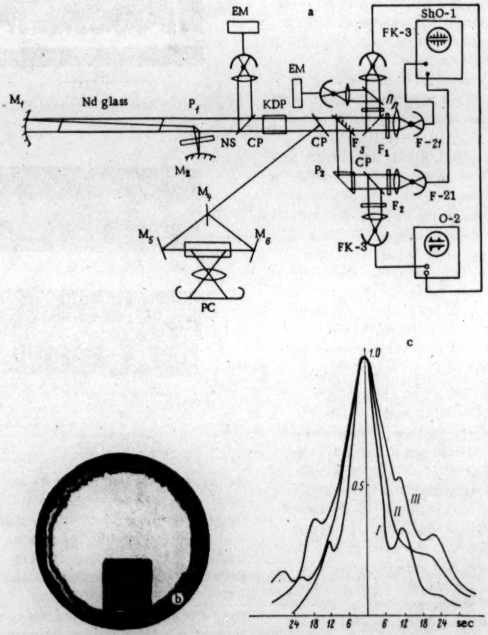

Fig. 1. a: Experimental arrangement for measuring the first- and second-harmonic characteristics of a neodymium glass single-mode picosecond laser: M) dielectric mirrors with reflection coefficients R = 99.5 ± 0.5% (M_1, M_2, M_3, M_5, and M_6) and R = 50 ± 0.5% (M_4) at λ = 1.06 μ. The reflection coefficient of M_3 at λ = 530 nm is R ≈ 25%; PC) photocamera; P_1, P_2) total internal reflection prisms; NS) nonlinear shutter; CP) color-selective plates; KDP) KDP crystal; FM) energy meter; FK-3) coaxial photocell; F-21) photocell; F_1) SZS-10, ZS-1 filter; F_2) IKS-1 filter; ShO) 6LOR-2M wide-band; O-2) S1-8 oscilloscope. b: Radiation distribution at a distance of 40 cm from the active element (normal generation mode). c: Radiation intensity distribution in normal generation mode (I) and in self-mode-locking operation at 1.06 μ (II) and 530 nm (III).

characteristics of the single-mode subnanosecond pulse laser. We have investigated the short- and long-range energy distribution and the spectral distribution of the first- and second-harmonic pulses. The active element is a neodymium-glass cylinder 45 mm in diameter and 710 mm long with end faces cut at an angle of 87° to the resonator axis. Pumping is provided by four linear IFP-20000 lamps with cylindrical reflectors. The telescopic resonator[1] is formed by two mirrors with radii of curvature $r_1 = -500$ cm and $r_2 = +125$ cm with a reflection coefficient $R_1 = R_2 = 99.5 \pm 0.5\%$ at $\lambda = 1.06\ \mu$ and a prism. A test cell with an initial transmission of 0.7 is used as a passive shutter for Q modulation. The cell filled with a solution of polymethine dye in nitrobenzene is placed close to the opaque mirror so that its surface makes an angle of 85-82° with the resonator axis. The radiation exits from the resonator asymmetrically at the prism side. Figure 1b shows a photograph of the radiation in the near region (at a distance 40 cm from the active element end face). An analysis of the angular distribution of radiation intensity in the far region indicates that the intensity distribution of the free lasing radiation at the focus of an optical system with an equivalent focal length of 50 m is of a diffraction nature and that the half-width of the central distribution spot corresponds to an angular divergence of about 11" (Fig. 1c, curve 1). This is almost twice the diffraction limit. The self-mode-locking half-width of the central spot in the radiation intensity distribution increases to 15" (Fig. 1c, curve II), which is apparently associated with wave-front distortion caused by insertion of the cell into the resonator. After conversion to second harmonic the half-width of the central spot of the radiation intensity distribution at $\lambda = 530$ nm is about 21", the distribution of intensity between the central spot and the side peaks being somewhat less uniform, as indicated by curve III in Fig. 1c. However, it can be assumed that transmission through a KDP crystal placed outside the resonator does not change the radiation mode composition and that the observed waveform distortion is associated with optical imperfections of the crystal.

An oscilloscope study of 1.06 μ and 530 nm output signals with the aid of F-21 photocells and a 6LOR-2M high-speed oscilloscope indicates that as the transmission of the nonlinear filter is varied between 0.5 and 0.7 the radiation consists either of a single pulse or of a train of 10-15 nanosecond or subnanosecond pulses following each other at an interval $2L/c = 16$ nsec, where L is the optical length of the resonator. The time resolution of the photoelectric system is about 0.5 nsec. As seen in Fig. 2, a-d, the first- and second-harmonic pulse trains, as well as the individual pulses in the trains, are of the same form. The actual structure of the nanosecond pulses and the length of the subnanosecond pulses have been determined by the two-photon luminescence method.[2] It has been found that the nanosecond pulses in the trains have no fine structure. Their lengths have been determined from oscillograms and found to depend on the nonlinear-shutter transmission, varying from one to several nanoseconds (Fig. 2a, b). Subnanosecond pulses (Fig. 2c, d) consist of two (sometimes one) spikes of $T = (2-5) \cdot 10^{-12}$ sec at an interval of about 200 psec. A photograph of rhodamine 6G fluorescence produced by the transmission of two opposing pulses is shown in Fig. 3a, b. Simultaneous measurement of first- and second-harmonic oscillation spectra with a spectrum analyzer (second-order dispersion 6.5 A/mm) shows that pulses having a picosecond structure contain a spectral line of width $2\Delta\nu \approx 10$ cm^{-1} at 1.06 μ and $2\Delta\nu \approx 24$ cm^{-1} at 530 nm. The expression[3] $T = 0.88/(c\,2\Delta\nu)$, where $\Delta\nu$ is the line half-width, gives $T_1 = 3 \cdot 10^{-12}$ sec and $T_2 = 1.2 \cdot 10^{-12}$ sec for the first and second harmonics respectively. The oscillations spectrum of structureless nanosecond pulses shows narrow lines whose width is comparable with the instrumental slit width. The values agree with data on two-photon luminescence and with data on the duration of picosecond pulses produced by neodymium-glass lasers described in refs. 2 and 4-6. The obtained pulse length $T = 3 \cdot 10^{-12}$ sec is used to calculate the number of locked modes $\Delta = 5 \cdot 10^3$.

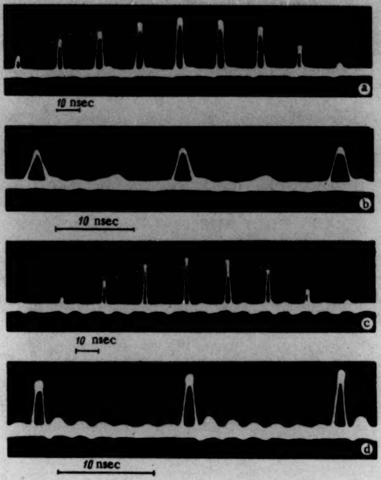

Fig. 2. Oscillograms of nanosecond (a, b) and subnanosecond (c, d) pulses generated in self-mode-locking.

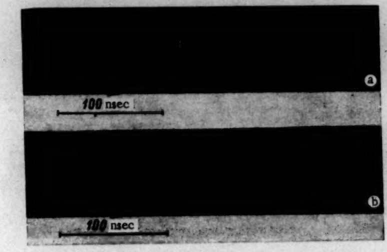

Fig. 3. Two-photon luminescence subnanosecond pulses.

The radiation energy is measured with a calorimeter and calibrated photocells whose output has been observed on an oscilloscope (for checking the number and amplitude of nanosecond pulses in a train as well as the number of relative giant-pulse amplitudes per flash). The average energy of one giant pulse is 14-15 J at the first harmonic and 4-5 J at the second harmonic. It should be noted that the conversion factor is significantly affected by the presence of internal structure in a nanosecond spike. Maximum first-to-second harmonic conversion efficiency is about 30% for a beam cross section of 12 cm^2. Maximum power in one picosecond pulse is $3 \cdot 10^{11}$ W at the first harmonic and about 10^{11} W at the second harmonic.

---

[1] Yu. A. Anan'ev, N. A. Sventsitskaya, and V. E. Sherstobitov, Zh. Eksp. Teor. Fiz., 39, 1325 (1969).

[2] P. M. Rentzepis and M. A. Duguay, Appl. Phys. Lett., 11, 218 (1967).

[3] A. S. Malkin, Trudy FIAN, 56, 57 (1971).

[4] S. D. Kaitamazov, I. K. Krasyuk, P. P. Panshin, and A. M. Prokhorov, Dokl. Akad. Nauk SSSR, 180, 1331 (1968) [Sov. Phys. – Dokl., 13, 591 (1968)].

[5] T. A. Giordmaine, P. M. Rentzepis, S. H. Shapiro, and K. W. Wecht, Appl. Phys. Lett., 11, 216 (1967).

[6] M. P. Vanyukov, V. I. Kryzhanovskii, V. A. Serebryakov, and A. D. Starikov, Kvant. Elektron. (Mosc.), No. 5, 69 (1971) [Sov. J. Quant. Electron., 1, 483 (1972)].

Unidirectional cw oscillation in a solid state ring laser with a return mirror

A. A. Mak, V. I. Ustyugov, V. A. Fromzel', and M. M. Khaleev

(Submitted September 3, 1973)
Zh. Tekh. Fiz., 44, 868-870 (April 1974)

Single-frequency cw operation is analyzed in a ring laser with an additional return mirror. Strong spectral broadening of axial modes is observed in a YAG:Nd^{3+} cw laser; insertion of the mirror also causes the laser to operate in the pulsed mode rather than the cw mode. The intensity ratio of the opposing modes is $3 \cdot 10^3$; however, a single-frequency operation is achieved only with an additional frequency selector in the form of a plane-parallel glass plate 8 mm thick. The output power of the single TEM$_{00}$ mode is 0.43 W for a mode ratio of 600.

In refs. 1 and 2 it is proposed to use a ring resonator with an additional return mirror as a simple means of achieving a traveling wave regime and removing the spatial inhomogeneity of the field in the active medium, thus obtaining single-frequency operation,[1] in refs. 1 and 2. Limiting ourselves to solid-state lasers we note that experiments have shown the difficulty of achieving single-frequency operation by this method. In the published papers, which all are devoted to the study of pulsed excitation (a survey of these papers is contained, for example, in ref. 3), a single-frequency spectrum is not achieved over the entire pulse length; however, single-frequency operation over a portion of the pulses is reported in refs. 4 and 5.

In this note we analyze the conditions necessary for stationary single-frequency lasing in a ring resonator with a return mirror; the results of an experimental study of cw operation of a YAG:Nd^{3+} laser are also described. Considering the case of low transmission through the output mirror 3 (Fig. 1), we assume that two opposing modes are supported in the resonator with the intensities I_1 and I_2, which are constant along the resonator axis; the fields at the surface of the output mirror at the point x = 0 have the form $E_1 = |E_1| \exp[i(\omega t + \varphi_1)]$, $E_2 = |E_2| \exp[i(\omega t + \varphi_2)]$, respectively. Since the wave directed into the resonator by the return mirror is formed from the wave E_2, its field at the point x = 0 has the form $E_3 = |E_3| \exp \cdot [i(\omega t + \varphi_2 - 2kd - \pi)]$, where $(2kd + \pi)$ is the phase shift due to reflection and the two-way passage through the optical path length d. For constructive interference of the waves E_1 and E_3 it is necessary that $\varphi_2 - 2kd - \pi = \varphi_1$. This condition phases the opposing waves with respect to each other (it is assumed that scattering of wave I_1 into the wave I_2 does not disturb it), producing localized maxima and minima of the field along the resonator axis; in particular, it is easy to verify that a minimum of the fields of all axial modes, independent of their index, exists at the point $x_1 = -d$, and also at the point x_2 separated from x_1 by the optical length L/2, where L is the optical length of the resonator. The optimum configuration for flat-mirror resonator for unidirectional operation and frequency selection is obtained when the center of the active medium coincides with the point x_2 (as in Fig. 1). This location of the active element ensures that in the presence of a thermal lens in the medium the wave E_3 coincides with the field in the resonator (in terms of curvature of the phase front) regardless of the pump power. This configuration is best for frequency selection because the spatial difference of the fields of different axial modes near the point x_2 (and the point x_1 also) is a minimum. The presence of spatial localization of the field minima and maxima in the stationary regime makes this case to some extent analogous to a linear resonator, and amenable to a calculation whose starting point is formulated in ref. 6. In the plane wave approximation the energy density of the field of an axial mode of index $m = j + \xi$ in the active medium can be represented in the form $u_\xi(z) = u_\xi \varphi_\xi(z)$, where $\varphi_\xi(z) = 1 - \mu \cos[4\pi\varkappa \times (j + \xi) z/L]$, $\mu = 2(\chi)^{1/2}/(1 + \chi)$, $\chi = I_1/I_2$ is the ratio of opposing modes in the resonator in the stationary regime, and $\varkappa$ is the refractive index of the active medium. For stationary oscillation in a single axial mode with $\xi = 0$, whose energy density is proportional to A_0 (see the notation in ref. 6) and whose frequency coincides with the center of the homogeneously broadened luminescence line, we require

$$\frac{g_\xi n \gamma_0}{l \gamma_\xi} \int\limits_{-l/2}^{l/2} \frac{\varphi_\xi(z)}{1 + A_0 \varphi_0(z)} dz < 1 \tag{1}$$

for all $\xi \neq 0$. Here, n is the excess pumping above threshold, and g_ξ and γ_ξ are the shape factor of the emission line and the resonator losses at the frequency of the mode, respectively (at the line center $g_0 = 1$). Evaluation of the integral (without constraint on the pumping for $\xi \ll j$, $\chi \gg 4$, $g_\xi^{-1} - 1 \ll 1$, and $(\gamma_\xi - \gamma_0)/\gamma_0 \ll 1$ gives

$$n < \left\{1 - \frac{\chi\,[g_\xi^{-1} + (\gamma_\xi - \gamma_0)/\gamma_0 - 1]}{2\,(1 - \sin 2\pi\zeta\xi/2\pi\zeta\xi)}\right\}^{-1}, \tag{2}$$

where $\zeta = l\varkappa/L$. Setting $\zeta = 1/2, 1$, we find that the inequality (2) is satisfied for any pumping level if

$$\chi > \chi_1 = \frac{2}{[g_\xi^{-1} + (\gamma_\xi - \gamma_0)/\gamma_0 - 1]}. \tag{3}$$

In the absence of a frequency selector in the resonator $(\gamma_\xi - \gamma_0 = 0)$ we obtain $\chi_1 = 6 \cdot 10^4$, as applied to a YAG:Nd^{3+} laser with an emission linewidth of 7 Å and L = 55 cm. The introduction of even a very weak selector into the resonator lowers this value. Thus, in the case of a plane-parallel glass plate with refractive index of 1.5 and 8 mm thick, $\chi_1 = 150$ according to Eq. (3).

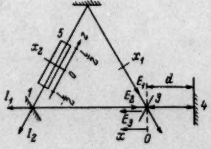

Fig. 1. Resonator diagram. 1, 3) Ring resonator mirrors; 4) return mirror; 5) active medium.

The basic experiments are performed with a three-mirror ring resonator with optical length of 55 cm, which operates in the TEM_{00} mode; the YAG : Nd^{3+} active element (5 × 50 mm) is located along the resonator axis as shown in Fig. 1. A four-mirror resonator scheme has also been investigated. The shape of the mirror backings and the tilt of the active element with plane-parallel coated faces at an angle which precludes interference of the beams reflected from the faces ensures the absence of parasitic frequency selection. The spectrum is studied with a Fabry–Perot interferometer with 5 and 16 mm spacings with image-converter tube or photographic recording. An important result is the sharp broadening of the spectrum with the introduction of the return mirror; the output also goes from cw to spiked (Fig. 3a and Fig. 2). With the results of ref. 7 in mind relative to the exceptionally high sensitivity of the radiation kinetics to the fluctuations in the resonator Q value, we note, as is evident from Fig. 3a, that in our case the mechanical stability of the resonator elements is good enough for the laser to operate without the return mirror in the stationary single-frequency regime with a low level of amplitude noise. The mode ratio at the lasing threshold $\chi_{th} = 200$, and increases with increasing pumping (Fig. 2). In some cases (with the smallest scattering at the optical surfaces) we achieve $\chi = 3 \cdot 10^3$, but the spectrum is multifrequency and nonstationary; the same result relative to the spectral width is obtained by photographing the spectrum at exposures up to 1/500 sec. A comparison of the experimental data with the considerations developed above shows that the multifrequency spectrum corresponds to the condition[2] according to which for $\chi = 200$ and $\zeta = 0.17$ and stationary single-frequency lasing is not possible even with $n-1 > 0.02$. The persistence of the multifrequency regime despite the increase of χ with increasing pumping is evidently related to the peculiarities of the nonstationary processes occurring at the time. It is clear that the observed high sensitivity of the laser to the misalignment of the return mirror, noted also in all previous publications, should play a dominant role in the generation kinetics. As noted earlier, single-frequency lasing is observed in portions of the radiation spikes in some experiments on pulsed excitation, when the wave ratio is below that required by condition (2). This result does not contradict the foregoing if we consider that the treatment of the spike regime within the framework of the stationary model has meaning only as applied to the integrated spectrum over a sufficiently large period of time, the width of which, as we noted, is always large.

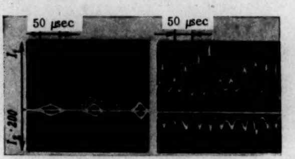

Fig. 2. Kinetics of multifrequency lasing with return mirror. 1) Pumping near threshold; 2) excess above threshold 1.13.

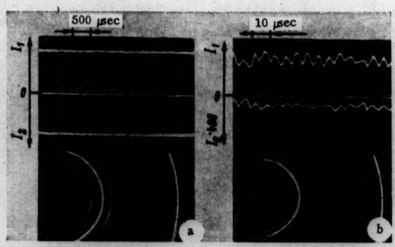

Fig. 3. Kinetics and spectrum of axial modes. a) Without frequency selector and return mirror; b) with frequency selector and return mirror; excess above pumping 1.25. The Fabry–Perot interferometer spacing is 16 mm.

The relatively high value of χ_{th} obtained in our experiments permits (2) to be satisfied for any pumping level by introducing the selective glass plate considered above. In fact, the use of this plate 8 mm thick results in single-frequency lasing and also in a reduction of the fluctuations of the radiation (Fig. 3b). It is interesting to note that at the same time the modulation of the opposing wave intensities became of opposite phase as compared to the spike lasing.

The output power of the single-frequency radiation obtained with the selective plate is limited primarily by the appearance of higher transverse modes. In the TEM_{00} mode it is 0.43 W with $\chi = 600$, and can be increased with the onset of higher transverse modes of 0.65 W.

---

1) Here and below single-frequency lasing is understood to mean the excitation of one axial mode when the laser operates in a single transverse mode.

[1] S. N. Bagaev, V. S. Kuznetsov, V. Yu. Troitskii, and B. I. Troshin, ZhETF Pis. Red., 1, 21 (1965).
[2] M. Hercher, M. Young, and C. B. Smoyer, J. Appl. Phys., 36, 3351 (1965).
[3] S. V. Kruzhalov, Thesis, LPI (1972).
[4] V. I. Malyshev, A. S. Markin, and A. A. Sychev, ZhETF Pis. Red., 9, 3 (1969) [JETP Lett., 9, 1 (1969)].
[5] V. I. Kravchenko and V. V. Tarabrov, Zh. Prikl. Spektrosk., 13, 719 (1970).
[6] N. M. Galaktionova, G. A. Garkavi, V. F. Egorova, A. A. Mak, and V. A. Fromzel', Opt. Spektrosk., 28, 751 (1970).
[7] G. N. Vinokurov, N. M. Galaktionova, V. F. Egorova, A. A. Mak, B. M. Sedov, and Ya. I. Khanin, Zh. Eksp. Teor. Fiz., 60, 489 (1971) [Sov. Phys.–JETP, 33, 262 (1971)].

Measurement of plasma ion temperature by a thin probe with $T_i \gtrsim T_e$

B. I. Kanaev and E. E. Yushmanov

(Submitted August 15, 1973)
Zh. Tekh. Fiz., 44, 870-873 (April 1974)

A method is described for measuring ion temperatures using the ion branch of the volt–ampere characteristic of a cylindrical Langmuir probe operating in the "orbit-limited" regime. The method is applicable for $n \in (10^{12}\text{-}10^{13})\ \text{cm}^{-3}$ and $T \in 200$ eV (in hydrogen); under the proper conditions the absolute error is less than 20%.

INTRODUCTION

Plasmas with ion temperatures higher than electron temperatures are the object of investigation in a number of areas of modern physics, e.g., thermonuclear fusion. The measurement of the ion temperature presents a complicated problem in diagnostics; at energies of several hundreds of electron volts and higher (hydrogen plasma) it is appropriate to use energy analysis of charge-exchange neutrals; on the other hand, reliable methods are not available below 100 eV. In this work we describe a probe method which is especially suitable for the above purpose.

The method is based on the properties of the volt–ampere characteristic of the ion saturation current of a cylindrical Langmuir probe operating in the "orbit-limited" regime. Let us briefly recall the main features of the problem (see, e.g., ref. 1). If the thickness of the probe sheath d is much smaller than r_0, the probe radius, the current of particles collected by the probe (for an attractive potential) is determined by the random flux at the outer surface of the sheath essentially independent of the probe potential, due to the fact that the effective collection radius remains almost constant, i.e., $r_0 + d \approx r_0$. If, on the other hand, the radius of the probe is much smaller than the thickness of the sheath, the current to the probe is determined by the orbital motion of the particles in the field of the probe, and the effective radius is given by $r_0(1 + e\varphi/\varepsilon_\perp)^{1/2}$, where φ is the potential difference (attractive) between the probe and the plasma, and $\varepsilon_\perp$ is the energy of the particles at infinity in the direction perpendicular to the probe axis.

This relationship, given by Langmuir, has been confirmed using the electron saturation current. For the ion current the situation is much more complicated, because of the sheath (for $T_i \ll T_e$, a condition which usually holds for gas discharges), and the ion current does not satisfy the above relationship. This question has been studied in detail in ref. 2; however, experiment shows[3] that it is not completely correct.

In a hot-ion plasma ($T_i \gg T_e$) the theory of orbital collection can be applied to the ion saturation current in simple form, offering the possibility of determining T_i as follows: The plot of the square of the probe current $I_i^2(\varphi) = \text{const}\,(1 + e\varphi/\varepsilon_\perp)$ is linear, and its intersection with the horizontal axis gives $\varepsilon_\perp$, which is related to T_i.

SOURCES OF ERROR

1. Spectral broadening. The effective radius of the probe is different for particles with different energies and one must integrate over all energies of the collected particles. Because it depends on the form of the spectrum, the volt–ampere characteristic is not linear when plotted on a quadratic scale. The results of the integration are given in ref. 1 for the case of a Maxwellian distribution. The plot shows that an appreciable deviation from linearity occurs only in the region of small attractive potentials, i.e., $0 < e\varphi < 0.5T$ (here and in what follows the temperature will be expressed in energy units). As far as ion collection is concerned this region is not useful anyway, because of incomplete blocking of the electron current. In the region of attractive potentials from 0.5T to 5T the quadratic characteristic is linear; however, the value of $\varepsilon_\perp$ which is determined by it is not equal to the true average value of perpendicular energy T, but rather to a somewhat smaller value, namely 0.85T. The complete form of the expression which describes the ion current in this range is

$$I_i \simeq \frac{env}{4} S \left(1 + \frac{e\varphi}{0.85T_i}\right)^{1/2}. \tag{1}$$

Here, n is the plasma density, $v = [8T_i(\pi M_i)^{1/2}]$ is the average speed of the ions, $S = 2\pi r_0 L$ is the area of the probe, and φ is the absolute value of the negative potential of the probe relative to the plasma.

2. Effect of the finite thickness of the sheath. As noted earlier, orbital collection occurs when the condition $r_0 \ll d$ is satisfied. If the sheath thickness d is finite, the difference between the true value of current and that given by Eq. (1) is of order $(r_0/d)^2$, according to the calculation cited above. An estimate for d is obtained from the Debye distance: $d \simeq (T_i/4\pi m e^2)^{1/2}$. For $n \simeq 10^{12}$ cm^{-3} and $T_i \simeq 100$ eV, d is of the order of 0.1 mm, and in order to make the error small the probe should be 10 to 20 μ thick, which causes no technical complications.

3. Magnetization. If the plasma is located in a magnetic field, then the obvious condition for the applicability of orbital considerations is the smallness of r_0 compared with the Larmor ion radius ρ. This condition is more easily satisfied than the previous one, since even in a field of 10 kG, $\rho = 1.4$ mm for a hundred-volt proton.

4. Secondary emission. The ions which strike the probe knock out secondary electrons which leave the probe and thereby give rise to a fictitious ion current. For incident ion energies of about 500 eV (for protons), the coefficient of secondary emission is clearly larger than unity, and the form of the volt–ampere characteristic deviates from Eq. (1). This puts an upper limit on the value of the temperature measured by this method.

5. Plasma potential. A realistically measurable volt–ampere characteristic has for its argument the value of potential with respect to a certain reference value (for example, zero), not with respect to the plasma potential. Therefore, the horizontal intercept of the straight line $I_i^2(\varphi)$ is not the quantity $0.85T_i$ itself, but in-

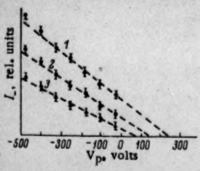

Fig. 1. Quadratic volt–ampere characteristics of the ion current of a thin probe operating at various values of the ion temperature. $U_1 > U_2 > U_3$; T_i, eV. 1) 220; 2) 130; 3) 65.

stead is a correction equal to the potential of the plasma taken with respect to the reference value. The magnitude of this correction can usually be estimated to an accuracy of ± T_e, and if $T_e \ll T_i$, the error in the estimate is not large. If T_e and T_i and comparable a special measurement must be made.

6. Excess heating and disintegration of the probe. Apart from the other considerations, the applicability of the present method in a dense and hot plasma is limited by the need to avoid excess heating of the probe (resulting in thermal emission noise), not to mention disintegration. This requirement imposes a limit on the duration of the process under study. It is not difficult to make a quantitative estimate of this limitation.

EXPERIMENTAL APPLICATION

Our method for measuring T_i has been used in experimental studies of the confinement of a plasma in a minimum-B mirror device[4]. A hot-ion plasma is established by a radio-frequency ion magnetron, using the following as initial parameters: $n \geq 10^{12}$ cm^{-3}, $T_i \simeq 50$-250 eV, and $T_e \simeq 3$-15 eV. The probe for the measurement of T_i is located in a region of reduced density ($n \simeq 10^{11}$ cm^{-3}) at the periphery so that the loss of ions to the probe does not result in a significant reduction of the confinement time. The active portion of the probe is a tungsten wire 20 μ thick and 1 cm long. Data for the volt–ampere characteristics are obtained by making a number of measurements for various values of the negative probe potential.

Figure 1 shows the volt–ampere characteristics (on a quadratic current scale) for various values of the rf voltage U which causes the heating of the plasma introduced into the collector. The curves are nearly linear, and show the various ion temperatures. Some distortion seen at high potentials is probably caused by secondary emission. The errors shown in Fig. 1 refer to the deviation in the values of current from one shot to another. The values of the plasma potentials which are measured approximately for the given regimes, amount to about 20% of the intercepts of the linear sections on the horizontal axis; the error caused by inaccurate knowledge of the potential (± 5-10 V) is therefore small, as noted earlier.

In addition to using the probe method to measure T_i, it was estimated in these experiments by using the spectra of the electrostatic trapping of ions escaping along the magnetic field and by extrapolating the charge-exchange spectrum to the low energy region. Although the results obtained by both of these methods show a greater spread, they are in satisfactory qualitative and quantitative agreement with the probe results given above.

CONCLUSION

In principle, it is possible to use the method described above to measure the local ion temperature in a plasma with $T_i \gg T_e$ in the temperature region (for a hydrogen plasma) from about 200 eV on down and for densities up to 10^{12}-10^{13} cm^{-3}. Although the method is of relatively low accuracy (10-20%), it is useful because of the lack of other methods of comparable simplicity.

The authors thank M. S. Ioffe for a number of useful comments.

---

[1] F. Chen, in: Plasma Diagnostic Techniques, R. Huddlestone and S. L. Leonard, Academic Press, New York.

[2] J. C. Laframboise, Adv. Appl. Mech. (suppl.), 3(2), 22 (1966).

[3] D. Smith and I. C. Plumb, J. Phys. D; Appl. Phys., 6, 196 (1973).

[4] Yu. T. Baiborodov, M. S. Ioffe, B. I. Kanaev, R. I. Sobolev, and E. E. Yushmanov, Plasma Physics and Controlled Nuclear Fusion Research, 2, 647, Vienna (1971).

Effect of instrumental noise on a system with two spin oscillators using Cs^{133} and He^3

R. A. Zhitnikov, V. V. Semenov, and P. A. Klyushkin

M. I. Kalinin Polytechnic Institute, Leningrad

(Submitted September 28, 1973)
Zh. Tekh. Fiz., 44, 873-875 (April 1974)

We describe the effect of instrumental noise on the operation of a system with two spin oscillators, He^3 and Cs^{133}, one of which (Cs^{133}) is used to stabilize the magnetic field by means of a phase-locked loop. The experimental instrumental noise power spectrum in the frequency range 0.03-1 Hz is given. The frequency drift of the He^3 and Cs^{133} spin oscillators is calculated and compared with the experimental data.

Instrumental noise, which is generated by nearly all electronic equipment, has a significant effect on the operation of an optically pumped spin oscillator.[1] Manifesting itself primarily at low frequencies, line noise modulates the frequency and phase of the oscillations.[2]

In an optically pumped spin oscillator the sources of low-frequency instrumental noise are the intensity fluctuations of the spectral pump lamp, flicker noise current in the photodetector circuit and in the first amplifier stage of the feedback loop, and instability of the power supply. Assuming the sources to be uncorrelated, we can combine them into one equivalent noise generator acting on the input of the feedback amplifier in the form of photodetector flicker noise currents, whose variance is the sum of variances of all noise components in the oscillator circuit. This total noise has a spectral density S_Σ given by the well-known expression[2]

$$\frac{4}{A} > t > \left(\frac{\omega^2\tau_3^4}{A}\right)^{1/n}. \qquad (1)$$

where A is a constant characterizing the noise intensity, and n is a number between 0.6 and 3. Values $n < 1$ correspond to stationary instrumental noise, which leads to a line broadening that is independent of time. For $n > 1$ the noise is nonstationary, and manifests itself in spectral line broadening $\Delta\omega(t)$, which increases with time. The value of $\Delta\omega(t)$ for optically pumped spin oscillators can be determined from the expressions in ref. 1, if the coefficients A and n are known.

In this paper we study the effect of instrumental noise on the operation of a system containing two spin oscillators with optical orientation of Cs^{133} and He^3 in the same cell; the cesium spin oscillator is used in a phase-lock loop to stabilize the magnetic field.[3] The system operates in a magnetic field of about 10 mOe; the Q factor of the Cs^{133} resonance line ~ 4, and that of the He^3 line ~ 500. The mean-square frequency fluctuation of the cesium spin oscillator is less than $5 \cdot 10^{-3}$ Hz over several hours, and is determined mainly by the instability of the reference quartz oscillator in the phase-locked loop. The magnitude and stability of the magnetic field are controlled with the He^3 signal, whose fluctuations are less than $5 \cdot 10^{-5}$ Hz over 30 sec at a signal-to-noise ratio ~ 20 in the 200 kHz bandwidth of the feedback amplifier. The mean value of the fluctuation amplitude of the He^3 spin oscillator frequency increases to $5 \cdot 10^{-4}$ Hz after one hour of operation. We assume that this effect is due to magnetic field variations due to instrumental noise in the Cs^{133} spin oscillator circuit, which cause fluctuations of the oscillator frequency affecting the phase-locked loop. This assumption is verified experimentally by measuring the spectral power density of the instrumental noise in the He^3 and Cs^{133} circuits. The measurements are made with an ultralow-frequency spectrum analyzer, which operates in the 0.01-1 Hz range and has a noise level of ~ $5 \cdot 10^{-6}$ W^2/Hz at 1 Hz. Two photodiodes are connected to the analyzer through a differential input, which either subtracts or adds the signals. In the subtraction mode the analyzer measures the spectral density of the photodetector noise S_p; in the addition mode we measure S_Σ, i.e., the total noise spectral density due to the instability of the pump lamp power supply and the photodetectors (these are the principal noise sources in a spin oscillator).[1)] The experimental values of S_Σ and S_p are plotted versus frequency in Fig. 1 for the He^3 (curves 1 and 3) and Cs^{133} (curves 2 and 4) spin oscillators. The dashed line shows the internal noise level of the analyzer. The He^3 and Cs^{133} spin oscillators employ an FD-7K silicon photodetector connected to a 20 kΩ load and operating as a photodiode with a bias voltage ~ 5 V, and ~ 100 μA (Cs^{133}) and ~ 150 μA (He^3) at constant illumination flux. As follows from Fig. 1, the noise level in the He^3 spin oscillator is about twice as high as in the Cs^{133} oscillator, due to the different values of the dc current flowing through the diodes. At the same time the same slope of the S_Σ and S_p curves indicates that the instrumental noise in both spin oscillators has the same character. The coincidence of the values of S_Σ and S_p at $f = 1$ Hz shows that at this frequency the photodetector flicker current is the main contribution to the instrumen-

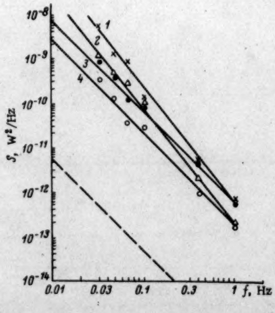

Fig. 1. Curves of the spectral power density of the flicker noise in the Cs^{133} and He^3 spin oscillators as a function of frequency. 1 and 2 represent S_Σ for the He^3 and Cs^{133} spin oscillators, respectively; 3 and 4 show S_p for the same He^3 and Cs^{133} spin oscillators. The dashed curve is the internal noise level of the spectrum analyzer.

tal noise of the spin oscillators. With decreasing frequency other souces of instrumental noise related mainly to the instability of the supply voltages begin to play the predominant role (the curves S_p and S_Σ have different slopes). The pump lamp noise of the He^3 and Cs^{133} spin oscillators turns out to be much smaller than the FD-7K photodetector noise, and is therefore not determined.

The measurements of S_Σ and S_p show that instrumental noise in a system with two spin oscillators, He^3 and Cs^{133}, is of nonstationary character ($n > 1$), and causes broadening of the line with time. Let us evaluate the linewidth $\Delta\omega(t)$ at time t. We use the expression for the instrumental linewidth of a spin oscillator given in ref. 1. It is evident from Fig. 1 that $n \geq 2$. For this case we have

$$\Delta\omega(t) = \frac{1}{2Q}\left\{2A\left[\frac{\pi t^{n-1}}{\tau_2^2\Gamma(n)\sin\frac{\pi(n-1)}{2}} - 2\Gamma(3-n)\,t^{n-3}\sin\frac{\pi(n-2)}{2}\right]\right\}^{1/2}, \qquad (2)$$

where $Q = \omega\tau_2/2$ is the Q of the magnetic resonance line; ω is the Larmor frequency, τ_2 is the transverse relaxation time, including the effect of the pumping light, Γ is the gamma function, which depends on n, and t is the observation time, which satisfies

$$\frac{4}{A} > t > \left(\frac{\omega^2\tau_2^4}{A}\right)^{1/n}.$$

The coefficient A, determined by the value of the spectral density S_Σ at 1 Hz, is $2.5 \cdot 10^{n-14}$ sec^{n-1} for the He^3 and Cs^{133} spin oscillators as determined for $n = 2.5$ from the slope of the curves 1 and 3 in Fig. 1. Substituting these values of A and n into Eq. (2) and using the experimental data, we obtain the following values for the linewidths of the spin oscillators in a magnetic field of 10 mOe: $3 \cdot 10^{-2}$ Hz after one hour for Cs^{133}, and $\sim 10^{-5}$ Hz after 10^7 sec for He^3. It is assumed in the calculation that the character of the curves in Fig. 1 is preserved at lower frequencies. A comparison of these values with the experimental data shows that the magnetic field variations corresponding to the calculated broadening of the cesium spin oscillator linewidth ($\sim 9 \cdot 10^{-3}$ gamma/h) are about of the same order of magnitude as the increased mean fluctuation of the magnetic field obtained in the experiment from the He^3 spin oscillator signal ($16 \cdot 10^{-3}$ gamma/h). The measurements are made with thermostatic control of the cell and of the cesium spectral pump lamp operation. This makes it possible to lower the measurement errors due to thermal frequency shifts of the Cs^{133} spin oscillator.[4,5]

---

1) The spectrum analyzer and the method of measurement of the quantities S_Σ and S_p will be described in a separate paper.

---

[1] R. A. Zhitnikov, P. A. Klyushkin, V. V. Semenov, and G. V. Fomin, Zh. Tekh. Fiz., 43, 1965 (1973) [Sov. Phys. – Tech. Phys., 18, 1238 (1974)].

[2] A. N. Malakhov, Fluctuations in Self-Oscillating Systems [in Russian], Nauka, Moscow (1968).

[3] R. A. Zhitnikov and V. V. Semenov, Zh. Tekh. Fiz., 44, 177 (1974) [Sov. Phys. – Tech. Phys., 19, 105 (1974)].

[4] S. Ando, Japan. J. Appl. Phys., 4, 793 (1965).

[5] E. I. Dashevskaya, A. N. Kozlov, and E. N. Pestov, in: Instruments and Methods for the Measurement of Magnetic Fields [in Russian], Ilim, Frunze (1971), p. 91.

Method for determining the absolute characteristics of CF_3I laser emission

V. S. Komarov, V. G. Seleznev, and G. A. Skorobogatov

A. A. Zhdanov Leningrad University

(Submitted April 26, 1973)
Zh. Tekh. Fiz., 44, 875-878 (April 1974)

A method is proposed for calculating the absolute pump radiative flux from the absolute energy and the shape of the stimulated emission pulse of a CF_3I laser. This method is used to measure the absolute characteristics of the stimulated emission and pump radiation for a CF_3I laser with initial CF_3I pressures ranging from 20 to 370 torr for pump fluxes (10^{22}-10^{23} photon/cm^2 · sec in the CF_3I absorption band) that exceed by one order of magnitude the values attained by previous researchers. Our data and those of other authors for four values of the initial CF_3I pressure (20, 74, 185, and 370 torr) are used to plot the absolute quantum yield of the CF_3I laser emission as a function of the absolute pump rate.

1. Since the discovery by Kasper and Pimentel[1] of the iodine CF_3I laser, there have been about 10 published papers[2-9] which studied the dependence of stimulated emission on the initial concentration $[CF_3I]_0$ of the active medium, the pump energy, and other parameters. It was established in these papers that for a sufficiently long pump pulse CF_3I lasing always cuts off due to some internal mechanism, so that only 2-5% of all CF_3I molecules in the working volume contribute even one photon of stimulated emission. The possible chemical processes leading to quenching of CF_3I laser action have been widely discussed in the literature.[4-6,8-13] These discussions, which are based on a comparison between the stimulated emission characteristics derived from some model and the experimental data suffer from the fact that, there is nothing to compare the calculations with. Almost all of the experimental papers measure only the relative stimulated emission energy; the pump fluxes are not determined. The absolute stimulated emission energies are measured in only four papers[3,6-8] for several isolated $[CF_3I]_0$ values, and only in refs. 6 and 8 are the pump fluxes estimated.

Considering the experimental difficulties of direct measurements of the absolute light fluxes, on the one hand, and the decisive role of these data in choosing a model for CF_3I laser action, on the other, we have devised a method for determining these parameters. The method has been employed to measure the absolute characteristics of stimulated emission of the CF_3I laser and the pump radiation over a broad range of $[CF_3I]_0$ values with pump fluxes (in the CF_3I absorption band) that exceed those attained previously by more than one order of magnitude.

2. The quartz laser cell (inner diameter 5.4 mm, l = 250 mm, and working volume V = 5.7 cm^3) with end windows tilted at 90° to the cell axis, is surrounded by four IFP-5000 lamps wrapped in aluminum foil. The pump pulse, which passes through a coaxial air discharge gap, is obtained by delivering voltage of 10 to 30 kV to the lamp from two KMK-40-4 capacitors (C_{tot} = 7.6 μF, L = 15 nH). For a discharge energy of 500 J the pump pulse length in the uv region at half-height is 10 μsec; for 3600 J it is 20 μsec.

The cavity is formed by an opaque mirror and a mirror with a dielectric coating with 10% reflection at 1300 nm. The radius of curvature of the mirrors is 1 m and they are 750 mm apart. A portion (20%) of the stimulated emission is reflected by a quartz plate and, after attenuation by approximately a factor of 100 passes through the waveguide to the sensor (a FD9E111B photodiode) of an S1-29 recording oscilloscope. The remaining 80% falls on the input to an IKT-1M calorimeter. The use of cells with Brewster windows does not increase the yield of stimulated emission energy per 1 cm^3 of working volume.

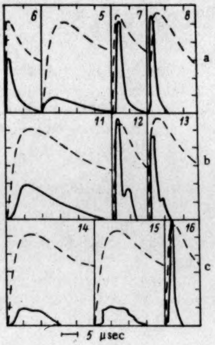

Fig. 1. Pump (dashed lines) and stimulated emission (solid lines) pulses of a CF_3I laser for $[CF_3I]_0$ = 74, 185, and 370 torr (a, b, and c, respectively). The numbers in the figure correspond to the numbers in the table.

Trifluoridemethane (99.8% of the basic product) is purified by 10 vacuum distillations with sampling in each case of 4/5 of the volume of the substance during the middle of the distillation. The purity of the product is monitored by using a gas chromatograph and the IR spectra.

3. The measured pump and stimulated emission pulses are shown in Fig. 1. It can be seen from Fig. 1 that in all cases lasing cuts off due to true chemical quenching before the pumping radiation drops 20-40% below its peak. For each initial pressure $(CF_3I)_0$ given in Table 1, we also give the pump energy (E_{pump}), the measured yield of stimulated emission energy per 1 cm^3 of working volume (E_{las}), the time at which maximum lasing is reached (t_{max}), and the lasing cutoff time (t_{quen}). The table also gives values, calculated from

$$\Gamma_\Sigma (\%) = \frac{0.988 \cdot 10^{19} E_{las}\ (\mathrm{J/cm^3})}{[CF_3I]_0\ (\mathrm{mole/cm^3})} \cdot 100 \qquad (1)$$

for the integrated stimulated emission yield (Γ_Σ) in per-

TABLE 1. Absolute Stimulated Emission Characteristics of the CF_3I Laser Calculated from Experimental Data

Numbers as in graphs	$[CF_3I]_0$		E_{pump}, J	E_{las}, mJ/cm^3	t_{max}, μsec.	t_{quen}, μsec	Γ_Σ, %	$G_{max} \cdot 10^{-23}$, photon/cm^3 · sec	$\varphi\varphi\ (t_{max})$, sec^{-1}	$\varphi\varphi$ sec^{-1}	$n(t_{max})$	references
	torr	mole/cm^3										
1	15	$4.9 \cdot 10^{17}$	40500	1.22	200	1400	2.31	0.0009	26	~26	0.995	[3]
2	20	$6.6 \cdot 10^{17}$	—	—	15	50	5.2	—	3300	3300	0.956	[6]
3	22	$7.2 \cdot 10^{17}$	3420	4.6	0.5	5	6.21	1.39	28500	30000	0.986	**
4	37	$1.22 \cdot 10^{18}$	1840	5.0	—	20	4.01	0.163	2000	2000	0.987	[7]
5	74	$2.44 \cdot 10^{18}$	1520*	13.5	2.5	20	5.46	1.10	6760	6460	0.984	**
6			855	15.1	1.0	10	6.11	3.35	20600	16300	0.979	**
7			1840	15.4	1.8	9	6.2	4.64	28500	24000	0.950	**
8			2570	15.4	1.0	5	6.2	5.76	35500	38000	0.965	**
9	100	$3.29 \cdot 10^{18}$	—	—	38	73	4.3	—	2100	1780	0.934	[8]
10	111	$3.65 \cdot 10^{18}$	1840	14.8	—	20	4.01	0.488	2000	2000	0.987	[7]
11	185	$6.1 \cdot 10^{18}$	2375*	23.9	4.0	27	3.86	1.41	3470	2900	0.986	**
12			1840	30.5	1.5	7	4.94	9.16	22500	19800	0.967	**
13			2570	35.1	1.5	6	5.68	10.02	24650	24600	0.964	**
14	370	$1.22 \cdot 10^{19}$	1600*	21.4	4.0	16	1.73	1.80	2215	2215	0.991	**
15			2280*	27.0	2.5	13	2.19	2.12	2600	2600	0.993	**
16			3420	39.9	2.0	5	3.23	14.7	18000	17400	0.965	**

Note: One asterisk denotes the results obtained by long-term operation of lamps[14] and with a reflector having a lower light efficiency, two asterisks refers to the present paper.

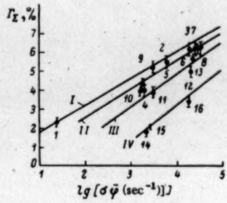

Fig. 2. Integrated quantum yield Γ_Σ (%) of stimulated emission of the CF_3I laser as a function of the logarithm (base 10) of the absolute pump rate $\sigma\tilde{\varphi}$ (sec^{-1}) averaged over the lasing time. The numbers next to the points correspond to the numbers in the table. torr: I) 20; II) 74; III) 185; IV) 370.

cent of the maximum possible value $2/3[CF_3I]_0$. Also, the measured values of E_{las} and the shapes of the lasing pulses are used to calculate the maximum stimulated emission power E_{max}(J/cm^3 · sec) per unit working volume. These values are given in the table in units of photon/cm^3 · sec (G_{max}). The table also contains the values obtained from

$$\sigma\varphi\,(t_{max})\,\frac{1}{\sec.} = \frac{1.5G_{max}\,(\text{photon/cm}^3 \cdot \sec)}{[CF_3I]_0} \tag{2}$$

for the flux (φ) of pump radiation in the CF_3I absorption band at maximum lasing (t_{max}) multiplied by the cross section (σ), averaged over the band, of the absorption of photons by the CF_3I molecules[12] ($\sigma \simeq 4 \cdot 10^{-19}$ cm^2/mole). The justification for using Eq. (2) [the basic equation of this paper] is based on the following four considerations.

First, in contrast to earlier ideas about the operation of photodissociation lasers,[15,9,11] recent experimental work[6,12,16-18] has established that no chemical process can raise the output of a CF_3I laser by more than 10-13% in comparison to the peak output [see Eq. (20) ref. 13]

$$G(t) = \frac{2}{3}\,\sigma\varphi\,(t)\,[CF_3I]. \tag{3}$$

Second, quantitative estimates indicate that for sufficiently high Q of the cavity and sufficiently high pumping energies, the output energy density increases to values in accordance with Eq. (3) even for a short time ε after onset of lasing (t_{las}).

Third, investigations[9,10,13,19] undertaken by us indicate that for a time $t \leq \min\{t_{las} + 1\ 3(t_{quen} - t_{las}), t_{max}\}$ and for any possible quenching mechanism, CF_3I laser action is not reduced by more than 2-5% in comparison with (3).

Fourth, in the CF_3I laser at t_{max} not more than 2-4% of the initial amount of the active medium has been consumed, so that one can set $[CF_3I] = [CF_3I]_0$ in Eq. (3):

$$G(t) = \frac{2}{3}\,\sigma\varphi\,(t)\,[CF_3I]_0 \Big\{ t_{las} + \varepsilon < t \leq \min\Big[t_{las} + \frac{1}{3}(t_{quen} - t_{las}),\ t_{max}\Big]\Big\}. \tag{4}$$

Equation (2) is obtained from Eq. (4) for $t = t_{max}$.

The table also contains values of σ multiplied by the fluxes $\tilde{\varphi}$, averaged over the lasing time, of the pump radiation in the CF_3I absorption band

$$\sigma\tilde{\varphi} = \frac{1}{t_{quen} - t_{las}} \int\limits_{t_{las}}^{t_{quen}} \sigma\varphi\,(t)\,dt, \tag{5}$$

which are calculated for fixed shapes of the pump pulses and values of $\varphi(t_{max})$. Allowing for experimental error and the assumptions made in deriving Eq. (4), we can assume that the values of $\sigma\tilde{\varphi}$ have a relative error of 20-25%. The relative amount of active CF_3I at maximum lasing is

$$n\,(t_{max}) = \frac{[CF_3I]_{t_{max}}}{[CF_3I]_0} = \exp(-\sigma\tilde{\varphi} t_{max}). \tag{6}$$

It is evident from these values that the assumption $[CF_3I] = [CF_3I]_0$ made in the derivation of Eq. (4) is valid in all cases.

In addition to our data, Table 1 gives the experimental results of other authors after processing by our method. On the basis of the values obtained for Γ_Σ and $\sigma\tilde{\varphi}$ the dependence of Γ_Σ(%) on the product of σ and the average absolute fluxes of $\tilde{\varphi}$ of pumping radiation in the CF_3I absorption band is given in Fig. 2 for different values of $[CF_3I]_0$.

In conclusion, the authors thank A. G. Morachevskii, whose support made the present work possible.

---

[1] J. V. Kasper and G. C. Pimentel, Appl. Phys. Lett., 5, 231 (1964).

[2] J. V. Kasper, J. H. Parker, and G. C. Pimentel, J. Chem. Phys., 43, 1827 (1965).

[3] A. J. DeMaria and C. J. Ultee, Appl. Phys. Lett., 9, 67 (1966).

[4] M. A. Pollack, Appl. Phys. Lett., 8, 36 (1966)

[5] D. E. O'Brien and J. R. Bowen, J. Appl. Phys., 42, 1010 (1971).

[6] V. Yu. Zalesskii and E. I. Moskalev, Zh. Eksp. Teor. Fiz., 57, 1884 (1969) [Sov. Phys. – JETP, 30, 1019 (1970)].

[7] T. L. Andreeva, V. I. Malyshev, M. I. Maslov, G. Ya. Solov'ev, and V. N. Sorokin, Krakt. Soobsch. Fiz., No. 5, 71 (1970).

[8] V. Yu. Zalesskii, Zh. Eksp. Teor. Fiz., 61, 892 (1971) [Sov. Phys. – JETP, 34, 474 (1972)].

[9] G. A. Skorobogatov and V. E. Khomen'ko, Vestn. Leningr. Univ., No. 10, 170 (1970)].

[10] G. A. Skorobogatov and V. E. Khomenko, Vestn. Leningr. Univ., No. 16, 109 (1972).

[11] D. E. O'Brien and J. R. Bowen, J. Appl. Phys., 40, 4767 (1969).

[12] K. Hohla and K. L. Kompa, Z. Natuforsch., 27a, 938 (1972).

[13] G. A. Skorobogatov, Vestn. Leningr. Univ., No. 4, 144 (1970).

[14] B. F. Rud'ko, V. V. Stefanyak, and Yu. P. Koval', Zh. Prikl. Spektrosk., 11, 1148 (1969).

[15] N. G. Basov, L. K. Gavrilina, Yu. S. Leonov, and V. A. Sautkin, ZhETF Pis. Red., 8, 178 (1968) [JETP Lett., 8, 106 (1968)]; T. L. Andreeva, V. I. Malyshev, A. I. Maslov, I. I. Sobel'man, and V. N. Sorokin, ZhETF Pis. Red., 10, 423 (1969) [JETP Lett., 10, 271 (1969)].

[16] P. Gensel, K. Hohla, and K. L. Kompa, Appl. Phys. Lett., 18, 48 (1971).

[17] V. N. Volkov, and I. G. Zubarev, Krakt. Soobshch. Fiz., No. 6, 24 (1972).

[18] V. Yu. Zalesskii and T. I. Krupenikova, Opt. Spektrosk., 30, 813 (1971).

[19] G. A. Skorobogatov, Vestn. Leningr. Univ., No. 22, 84 (1972).

Electrostatic analyzer for wide beams

V. G. Kovalenko and B. V. Polenov

(Submitted July 21, 1972; resubmitted January 12, 1973)
Zh. Tekh. Fiz., 44, 878-880 (April 1974)

The design of a novel electrostatic analyzer is proposed in which the electrodes are shaped like logarithmic spirals to increase sensitivity and to reduce size and weight.

Cylindrical electrostatic analyzers in which the electrode gap and curvature are independent of the deflection angle of the particle beam are currently used widely for energy selection of widely charged particles.[1] However, the sensitivity of the corresponding measurements in terms of the flux density turns out to be inadequate for several problems because of the small area of the entrance of the analyzer. The analyzer dimension or the gap between the electrodes can be increased only at the cost of a significant increase in the overall dimensions of the apparatus. Furthermore, an increase in the gap alone leads to a degradation of the resolution and the selectivity of the analyzer in terms of the type of radiation being detected, and higher working voltages are required.

We report here on the design and characteristics of a cylindrical electrostatic analyzer[2] in which the sensitivity of the measurements in terms of the flux density is increased and the dimensions of the apparatus are reduced through the use of electrodes whose directrices are described by the logarithmic spiral

$$r(\varphi) = ae^{-k\varphi},$$

where a = const, r and φ are polar coordinates, $k = \cot\psi$, and ψ is the angle between radius vector r and the tangent at an arbitrary point of the line $r(\varphi)$ (Fig. 1).

Neglecting the fringing fields, we can determine the potential distribution between the analyzer electrodes, $V(r, \varphi)$, in the r, φ coordinate plane through a conformal mapping:

$$W(z) = U(z) + iV(z) = ie^{i\beta}(A \ln z + B),$$

where A and B are constants governed by the potentials on the analyzer electrodes, $\tan\beta = k = \cot\psi$, and z is the complex variable.

In the case of in-phase voltage on the analyzer electrodes ($V = \pm V_0/2$), the potential distribution between the electrodes is given by

$$V(r, \varphi) = V_0 \frac{\ln \frac{r}{\sqrt{a_1 a_2}} + k\varphi}{\ln \frac{a_2}{a_1}}.$$

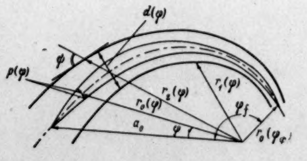

Fig. 1. Electrostatic analyzer with electrodes shaped like logarithmic spirals.

It follows from this equation that the equipotentials are also logarithmic spirals. The radius vector $\mathbf{r}_0 = (\varphi) = \sqrt{\mathbf{r}_1(\varphi)\mathbf{r}_2(\varphi)}$ specifies the equilibrium trajectory, at which the potential is zero.

In an analyzer whose electrodes are shaped like logarithmic spirals the ratio of the gap between the electrodes $\mathbf{d}(\varphi)$ to the radius of curvature of the equilibrium trajectory, $\rho_0(\varphi)$, is a constant:

$$\frac{\mathbf{d}(\varphi)}{\rho_0(\varphi)} \approx \frac{(a_2 - a_1)\sin\psi}{\sqrt{a_1 a_2 (1 + \mathbf{k}^2)}} = \text{const.}$$

Because of the constancy of the ratio $[\mathbf{d}(\varphi)]/[\rho_0(\varphi)]$, particles having energies of approximately $\mathbf{E}_0 = \mathbf{q}[(\mathbf{V}_0\rho_0)/2\mathbf{d}]$, where **q** is the particle charge, can pass through the analyzer.

Since the lines of force intersect the equilibrium trajectory at right angles, the electrodes should be cut off at the entrance and exit of the analyzer along the normal to the equilibrium trajectory, rather than along the radius vector, even though the second approach is in principle possible.

To determine the focusing angle φ_f we use the equation for the displacement $\rho(l)$ (Fig. 1) with respect to a trajectory coinciding with an equipotential. The displacement $\mathbf{p}(l)$ is a function of the path length along this trajectory, l, and is found from[3]

$$\frac{d^2\mathbf{p}(l)}{dl^2} + \frac{2}{\rho(l)^2}\mathbf{p}(l) = 0$$

and the boundary condition $\mathbf{p}(0) = 0$.

Taking into account the relations among l, ρ, and $\mathbf{r}$ [$l = (\sqrt{1 + \mathbf{k}^2})/\mathbf{k}(a - \mathbf{r})$ and $\rho = \sqrt{1 + \mathbf{k}^2}\mathbf{r}$], we can rewrite this equation

$$\frac{d^2\mathbf{p}(r)}{dr^2} + \frac{2}{r^2\mathbf{k}^2}\mathbf{p}(r) = 0$$

with the boundary condition $\mathbf{p}(a) = 0$. Particle focusing is achieved if the solution of this equation is a periodic function, as it is in the case[4] $k < 2\sqrt{2}$. In this case, using $\mathbf{r} = ae^{-\mathbf{k}\varphi}$, we find $\mathbf{p}(\varphi) = \mathbf{C}e^{-\mathbf{k}\varphi/2}\sin\sqrt{(8 - \mathbf{k}^2)}/2\varphi$, where C is a constant. Hence we have $\varphi_f = (2\pi/\sqrt{8 - \mathbf{k}^2})\mathbf{n}$, where **n** is an integer.

With $\mathbf{k} \geq 2\sqrt{2}$, the analyzer has no focusing properties, so when the experimental conditions require no focusing the analyzer can have a large value of k, so that the analyzer dimensions can be reduced further.

To study the analyzer characteristics, we have calculated the electrode shapes and constructed an electron spectrometer with cylindrical electrodes and entrance and exit cuts along the normal to the equilibrium trajectory. This analyzer has the following dimensions: a_1 = 85 mm,

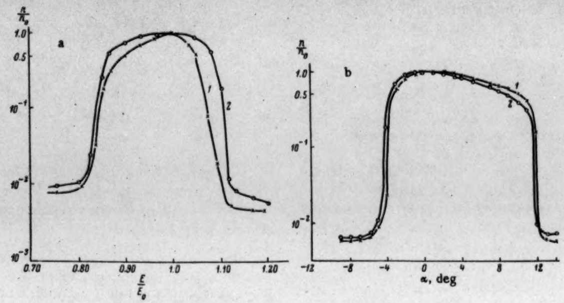

Fig. 2. Energy (a) and angular (b) characteristics of the analyzer E, keV: 1) 1; 2) 3.6.

$a_2 = 118$ mm, an electrode height of $h = 110$ mm, $d/\rho_0 = 0.24$, $\varphi_p = \varphi_f = 130°$, $\psi = 60°$, $S_{en}/S_{exi} = 3.6$, and $k = 1/\sqrt{3}$. The effects of the fringing fields at the entrance and exit are suppressed by means of limiters with rectangular apertures having a height of 55 mm and a width equal to the entrance or exit gap (the centers of these apertures coincide with the centers of the entrance and exit windows). For the case of a broad, unidirectional electron flux at an energy of $E_0 = 1.0$ or 3.6 keV, incident normal to the entrance window of the analyzer, the ratio of the particle flux density at the exit of the analyzer to that at its entrance is 1.6 or 1.7, respectively, about 3.5 times higher than in the case of an ordinary cylindrical electrostatic analyzer. Typical energy and angular characteristics of the analyzer are shown in Fig. 2.

In conclusion we should note that analyzers which collimate broad particle beams can be used with discrete detectors with a relatively small entrance window and a restricted field of view (e.g., with secondary-electron multipliers with discrete and continuous dynodes). The shapes of the analyzer electrodes can correspond to parts of a sphere or torus.

---

[1] G. C. Theodoridis and F. R. Paolini, Rev. Sci. Instr., 39, 326 (1968).

[2] V. G. Kovalenko, P. A. Kovrazhkin, E. L. Lein, B. V. Polenov, V. V. Temnyi, and B. I. Khazanov, USSR Patent No. 286 855, Ofitsial'nyi Byulleten' OIPOTZ, No. 36 (1971).

[3] V. M. Kel'man and S. Ya. Yavor, Electron Optics, [in Russian], Izd. Akad Nauk SSSR, Moscow—Leningrad (1963).

[4] E. Kamke, Handbook of Ordinary Differential Equations [Russian translation[, Izd. Nauka, Moscow (1965).

Vacuum-UV and soft x-ray emission in a magnetoplasma compressor

P. E. Kovrov and L. G. Tokarev

(Submitted April 13, 1973)
Zh. Tekh. Fiz., 44, 881-883 (April 1974)

The emission in the range 150-200 Å and below 20 Å of magnetoplasma compressors of the rod and radial types is studied by means of absorbing filters. It is found that UV emission continues for a time comparable to the discharge time, while the x-ray emission (energy of 2.5-4 keV) is irregular. The emission intensity is given as a function of the discharge parameters.

There is general agreement in the importance of studying the short-wavelength emission in high-current discharges; such studies not only furnish the necessary complement to spectral studies in the visible region, but are also of decisive importance for the understanding of certain physical processes and can reveal several of the most important plasma characteristics.

On several occasions measurements of this type have been carried out in connection with a study of coaxial plasma guns.[1-4] Both soft and hard x-ray emission have been demonstrated, both at an energy several times higher than that corresponding to the applied voltage. In coaxial guns, however, and in z pinches[5] and in the plasma focus,[6] the hard x-ray emission lasts for only a fraction of a microsecond, a time much shorter than the length of the discharge.

On the other hand, the theory of ref. 7 predicts that high plasma parameters can be attained in steady-state operation of a magnetoplasma compressor. Experimental work on these compressors[8] has demonstrated the presence of ions with a high degree of ionization in the compression zone; these ions have a long lifetime.

In this note we report on a study of the vacuum-UV and soft-x-ray emission. We use two types of magnetoplasma compressors: a conical type and a radial type (Fig. 1). In the conical version the compressor consists of a cylindrical central electrode (d = 12 cm), one end of which is tapered into a cone, and an external electrode, consisting of 12 rods spaced uniformly at a distance D = 21 cm. In the radial version both electrodes are a system of rods arranged along the radii of two coaxial circles, at a distance z = 4 cm apart. The current is supplied by a coaxial cable.

The working gas is hydrogen, which is injected into the vacuum chamber before the experiment, at a pressure of 0.1-5 torr; in the conical version, there is also a pulsed injection of gas.

The discharge current is 250-500 kA, the bank voltage is 5 kV, and the current pulse is 75-150 μsec long. The polarities of the electrodes can be reversed. A detailed experimental study of the magnetoplasma compressor is reported in ref. 8.

The emission is analyzed by a method involving absorbing filters and detection by a plastic scintillator with a photomultiplier. The filters are made from aluminum foil ranging from 6 to 70 μ in thickness from beryllium foil, 100, 150, and 500 μ thick, and various combinations of these foils. The resolving time of the apparatus is 0.1 μsec.

We are interested primarily in the zone of maximum density – the plasma focus; in the conical version this is the axial zone beyond the end of the central electrode; in the radial version this is the axial zone between the electrodes.

EXPERIMENTAL RESULTS

Figure 2 shows characteristic oscillograms of the emission recorded with various filters. We see that the nature of the oscillogram is strongly influenced by the filter used, because the emission detected in these cases falls in different spectral regions.

The oscillogram in Fig. 2b corresponds to the case in which the total radiation in the visible and UV regions is detected. The first large peak on this oscillogram results from the appearance of a dense plasma piston, which precedes the formation of the plasma focus in the region being observed. This peak lasts about 5 μsec and is always observed before the feature in the discharge current. The

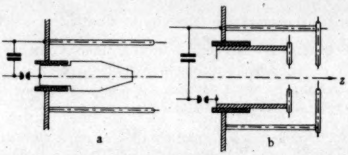

Fig. 1. Magnetoplasma compressors. a) Conical type; b) radial type.

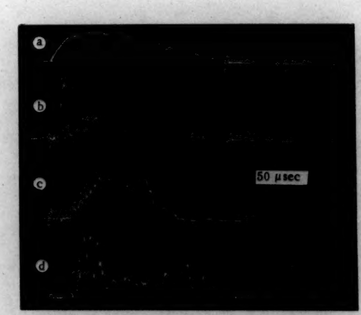

Fig. 2. Oscillograms of the discharge current (a) and of the emission detected through various filters (b-d). a) Discharge current, I_m = 350 kA; b) Al (thickness of 800 Å); c) Al (5.85 μ); d) Al (3 × 5.85 μ).

intensity of the visible emission at this time is much higher than that at later times.

The far-UV region poses serious experimental difficulties. We only study the emission in a narrow spectral region, $\lambda = 150\text{–}200$ Å, corresponding to a transmission "window" of the aluminum foils. The spectral interval studied is determined by the combination of aluminum, beryllium, and hydrogen filters. The oscillogram in Fig. 2c is typical of the emission intensity in this spectral range.

The UV emission always begins with the appearance of the feature in the discharge current and lasts for a long time (for a time of the order of the lifetime of the discharge current). The oscillograms display a deep, irregular modulation. The modulation depth in the conical version is influenced only slightly by the collimation of the measuring system, while that in the radial version increases as the collimation is improved. In both cases the modulation intensifies when the hydrogen pressure in the discharge cap is reduced or when the inner electrode is made the anode (this arrangement has the positive polarity).

The emission intensity in this spectral range is approximately the same for the radial and conical versions, changes slightly as a function of the gas pressure, and is essentially independent of the polarity. The emission intensity is a very strong function of the bank voltage:

$$\frac{I_2}{I_1} = \left(\frac{U_2}{U_1}\right)^n, \quad 3 < n < 4,$$

where I is the emission intensity at a bank voltage of U.

Experiments carried out with a pinhole camera and a scintillation method with various degrees of collimation show the source of the UV emission to be the zone in which the plasma density is a maximum.

According to our experiments, the energy emitted in the range 150-200 Å by these magnetoplasma compressors is about 1 J per discharge when the input energy is ≈ 20 kJ. This is the sum of the energies corresponding to the line, recombination, and bremsstrahlung emission; we do not know the relative contributions. Measurements with thicker filters allow us to study the emission in the soft x-ray region; Fig. 2d shows a characteristic oscillogram of the emission in this region. As in the UV region, the emission begins when the feature appears in the discharge current and lasts for 10-90 μsec. The oscillograms of the emission intensity are less regular and are dominated by bursts lasting an average of ≈ 1 μsec. The intensity also varies markedly from discharge to discharge, in both length and amplitude. In the positive-polarity case, the intensity of this emission increases by nearly an order of magnitude, other conditions being the same. The increase in the x-ray intensity as a function of the bank voltage is analogous to that of the UV intensity.

The energy of the x-ray emission is determined in a two-channel setup by means of a combination of aluminum and beryllium filters. The spectral range of this emission turned out to have a narrow band corresponding to an energy of 2.5-4 keV and to be essentially independent of the compressor design and the discharge parameters, including the bank voltage.

This behavior distinguishes this emission in a magnetoplasma compressor from the emission described in refs. 1-6, where the x-ray emission is observed at an energy lower than that corresponding to the applied voltage by a factor of 10, and the emission lasts for a fraction of a microsecond.

The x-ray emission is most probably due to an instability of the plasma formation.

In conclusion the authors thank A. I. Morozov for his interest in this work, they thank A. I. Yaroslavskii, A. K. Vinogradova, V. I. Berkov, and E. N. Gavrilovskaya for useful discussions, and they thank M. A. Tsibizov and V. P. Trofimov for assistance in the experiments.

---

[1] J. W. Mather, Phys. Fluids, 7, 366 (1964).

[2] M. I. Pergament and A. I. Yaroslavskii, Plasma Diagnostics [in Russian], No. 2, Atomizdat, Moscow (1968), p. 89.

[3] I. M. Zolototrubnikov, Study of Plasmoids [in Russian], Izd. Naukova Dumka, Kiev (1968).

[4] A. A. Kalmykov, A. D. Timofeev, and B. A. Shevchuk, Plasma Physics and Problems of Controlled Thermonuclear Fusion [in Russian], Izd. Naukova Dumka, Kiev (1971), p. 2.

[5] L. A. Artsimovich, A. M. Andrianov, E. I. Dobrokhotov, S. Yu. Luk'yanov, I. M. Podgornyi, V. I. Sinitsyn, and N. V. Filippov, At. Energ., 3, 84 (1956).

[6] N. V. Filippov, T. I. Filippova, and V. P. Vinogradov, Nucl. Fusion, Suppl., Part 2, 577 (1962).

[7] A. I. Morozov, Zh. Tekh. Fiz., 37, 2147 (1967) [Sov. Phys. – Tech. Phys., 12, 1580 (1968)].

[8] V. I. Berkov and A. K. Vinogradova, Report to the First All-Union Conference on Plasma Accelerators, Moscow, 1971.

Multiple recording and erasure of optical information in certain glassy chalcogenides

V. V. Korsakov, V. I. Nalivaiko, V. G. Remesnik, and V. G. Tsukerman

(Submitted July 24, 1973)
Zh. Tekh. Fiz., 44, 883-885 (April 1974)

Glassy chalcogenide semiconductors are completely new recording media, used in holography.[1-5] In addition, they are extremely promising materials because of their capability of recording holograms with a high diffraction efficiency and with essentially unlimited resolution. Workers describing the properties of these materials have also pointed out the possibility of a reversible recording of holograms; the optical information is erased by heating part of the semiconducting layer. No information has been reported on the changes in the properties of the material over repeated cycles of recording and erasure. These properties are extremely important in an evaluation of the operation of chalogenide semiconductors as operational storage media. In this note we report the preliminary results obtained in a study of the multiple recording and erasure of optical information in certain glassy chalcogenides.

We have studied compounds of the systems As–S, As–Se, As–S–Se, As–S–I, As–Se–I, and As–S–Se–I. The samples, ranging in thickness from a few microns to 20μ, are prepared by a vacuum deposition of the stock material on a substrate by pulsed thermal evaporation or by the electron-beam method. The substrates are polished plates of BaF_2 and CaF_2 crystals, whose linear expansion coefficients are approximately equal to those of the material being deposited. This matching avoids cracks and other types of damage which occur in the material when films on glass substrates are heated and cooled; it permits a repeated study of cycles of optical recording and thermal erasure of information. The information is recorded by means of a helium–neon laser in films based on antimony selenide and by an argon laser in films based on antimony sulfide. The film composition is chosen on the basis of the position of the fundamental absorption edge, which lies in the range of wavelengths generated by the lasers ($\lambda_{He-Ne} = 6328$ Å and $\lambda_{Ar} = 5145$ Å). Under the influence of the radiation or the heating the fundamental absorption edge shifts toward longer wavelengths; there is a concomitant change in both the transmission coefficient and the refractive index of the material. These quantities are found to be interrelated (Fig. 1). The abscissa in Fig. 1 shows the change in the relative film transmission ($\Delta T = T_0 - T_1$, where T_0 is the transmission of the part of the film at the given wavelength, assigned the value of 100%, and T_1 is the relative transmission of the exposed or heated region). The ordinate shows the change in the refractive index, determined from the shift of the fringes observed in a dual-beam interferometer. The exposed sample is placed in one arm of the interferometer, and the light source is a helium–neon laser.

We see from this figure that the shift in the edge of the absorption band is accompanied by a significant change in the refractive index, due to the high diffractive efficiency of the recorded diffraction grating. In our experiments the diffraction efficiency reaches 30% in the case of recording by a helium–neon laser and 80% with an argon laser. However, the first thermal erasure causes significant changes in the properties of the material. Figure 2 shows the decrease in the changes of the optical properties of the material during exposure after the first erasure of the information in the film through a heating of the film to a temperature of 200°C and subsequent cooling to room temperature. We see from this figure that the change in the transmission (Fig. 2a) and that in the refractive index (Fig. 2b) during the irradiation reach saturation, but the limiting changes in these parameters decrease rapidly after the first erasure cycle. After more of these cycles, the values of these quantities do not change, and the properties of the material remain essentially constant (Fig. 3). The extent of the changes in the optical properties of the recording film depends on the film composition and the deposition technique. As a rule, films having a relatively high sensitivity to radiation (i.e., films displaying relatively large changes in Δn and ΔT) suffer a more pronounced loss in sensitivity after the first erasure cycle.

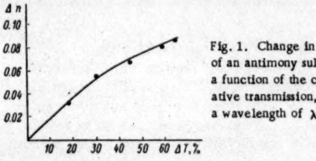

Fig. 1. Change in the refractive index of an antimony sulfide film, Δn, as a function of the change in the relative transmission, ΔT, measured at a wavelength of $\lambda = 5200$ Å.

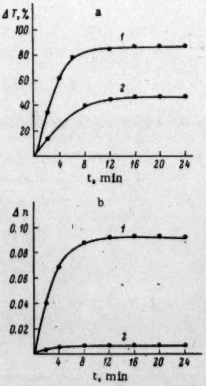

Fig. 2. Changes in the relative transmission (a) and in the refractive index (b) of an $As_2S_3 \cdot As_2Se_3$ film during its irradiation by a helium–neon laser (intensity of $p = 6.5$ mW/mm^2). 1) After film deposition; 2) after the first erasure cycle.

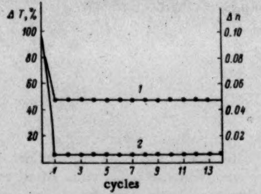

Fig. 3. Change in the relative transmission ΔT (1) and change in the refractive index Δn (2) of an As_2S_3. As_2Se_3 film as a function of the number of recording–erasure cycles N. The film was irradiated by a helium–neon laser at an intensity of p = 6.5 mW/mm² for 10 μsec.

It could be suggested that the loss of optical sensitivity is due to oxidation of the surface with heating in air; however, the materials do not retain their properties when they are heated in high vacuum (a residual gas pressure lower than 10^{-6} torr) or when special brightening or protective coatings are applied.

Since the deposition technique strongly affects the sensitivity of a film, it could be argued that the film structure after the deposition is extremely disordered. Photochemical processes in the film caused by the illumination[4] improve the structure, thereby significantly changing the optical properties of the material. Erasure of the stored information requires heating the material to its softening point. The film structure becomes more ordered in this process, so the changes displayed in the optical properties upon a repeated illumination are not as pronounced.

Figure 4 shows that the film must be heated to its softening point (180–200°C) for erasure of the stored information. We see that the diffractive efficiency of the grating recorded by an argon laser in an antimony sulfide film does not change at temperatures up to 180°C. At higher temperatures the diffractive efficiency falls off sharply, implying erasure. When the grating is rerecorded, the diffractive efficiency is below 5–7%.

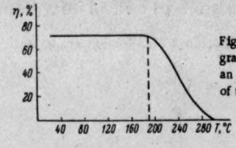

Fig. 4. Diffractive efficiency η of a grating recorded by an argon laser in an antimony sulfide film as a function of the erasure temperature.

Accordingly, the second and subsequent erasures of the information stored in thin glassy chalcogenide films cause the diffractive efficiency of the recorded grating to fall off by an order of magnitude. If we assume that the responsible mechanism involves an improvement in the structure of the material upon slow heating and cooling, we can assume that a more rapid process, e.g., local heating by a powerful laser or pulsed illumination, would help stabilize the properties of the material. We have observed this effect during pulsed recording and erasure of information bits in such materials.[6] Obviously, the question of the optimum program of multiple erasure of the optical information in glassy chalcogenide films requires further study.

The authors thank V. M. Lyubin and M. N. Korotkevich for synthesizing the stock materials and for support.

---

[1] S. A. Keneman, Appl. Phys. Lett., 19, 205 (1971).

[2] R. G. Brands, F. P. Laming, and A. D. Pearson, Appl. Opt., 9, 1712 (1970).

[3] Y. Ohmachi and T. Igo, Appl. Phys. Lett., 20, 506 (1972).

[4] J. C. Berkes, S. W. Ing, and W. J. Hillegas, J. Appl. Phys., 42, 4908 (1971).

[5] S. B. Gurevich, N. N. Il'yashenko, B. T. Kolomiets, V. M. Lyubin, V. I. Nalivaiko, Yu. E. Nesterikhin, V. G. Tsukerman, and D. F. Chernykh, in: Reports to the first All-Union Conference on Holography, Tbilisi, 1972 (in press).

[6] T. S. Karakulova, V. I. Nalivaiko, V. G. Remesnik, and V. G. Tsukerman, in: Quantum Electronics [in Russian] (1973) (in press).

Temperature dependence of the dielectric permittivity of single-crystal TiO_2 in the submillimeter range

A. A. Volkov, N. A. Irisova, and G. V. Kozlov

P. N. Lebedev Physics Institute,
Academy of Sciences of the USSR, Moscow

(Submitted April 27, 1973; resubmitted August 31, 1973)
Zh. Tekh. Fiz., 44, 886-888 (April 1974)

A procedure is described for obtaining the dielectric characteristics of transparent dielectrics as functions of the temperature in the submillimeter range of wavelengths. Measurements of ε' and tan δ are reported for single-crystal TiO_2 for λ = 0.8-3.5 mm at temperatures from 4.2 to 1000°K.

The dielectric properties of single-crystal TiO_2 are of interest because the structural formation of TiO_2 represents a basic structural element of ferroelectric titanates, whose properties have been the subject of extensive research. In addition, crystalline rutile has wide technical applications in optics, microwave technology, and radio engineering. Its dielectric properties in these ranges have been thoroughly studied.[1]

Recent rapid developments in physics and engineering require broadening our knowledge of the properties of rutile in the submillimeter range.

We have measured the permittivity and loss tangent of single-crystal TiO_2 at wavelengths from 0.8 to 3.5 mm at temperatures from 4.2 to 1000°K. The measurements are performed on a quasioptical setup using monochromatic backward-wave oscillators and wire mesh optical elements. Measurements are made of the transmission of a plane slab of TiO_2 15 mm square and 1.32 mm thick, with the optic axis in the plane of the sample, placed in a thermostat in a nitrogen[3] or helium cryostat.

Figure 1 shows a block diagram of the experimental arrangement.

Monochromatic radiation from a backward-wave tube is shaped by a horn and a Teflon lens into a parallel beam, polarized by a mesh element, passed through the sample in the cryostat (thermostat), and recorded by an OAP-5 optical–acoustic receiver. A grid polarizer can polarize the incident radiation with the **E** vector parallel to or perpendicular to the optic axis of the crystal under study.

The fixed-frequency signal to the receiver, recorded on a two-coordinate recording instrument while the sample in the cryostat is cooled from room temperature to the temperature of liquid nitrogen, is shown in Fig. 2. The oscillatory character of the curve is a result of the interference of radiation inside the sample. The distance between interference maxima is determined by the change of the index or refraction with temperature, and the widths of the curves depend on the index of refraction n and tan δ, which characterize the absorption in the sample.

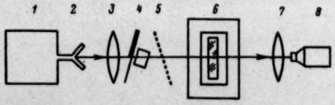

Fig. 1. Schematic diagram of experimental arrangement. 1, 2) Monochromatic oscillator with horn; 3, 7) Teflon lenses; 4) modulator; 5) polarizer; 6) thermostat (cryostat) with sample; 8) optical–acoustic receiver.

Considering the slab of TiO_2 as a Fabry–Perot interferometer, its transmission τ as a function of the wavelength λ and the index of refraction n for a sample thickness d can be described by the well-known Airy equation,[4] which is valid when the index of refraction of the sample n is independent of λ:

$$\tau=\left(1-\frac{A}{1-R}\right)^2\frac{1}{1+[4R/(1-R)^2]\sin^2\frac{2\pi nd}{\lambda}},$$

where R is the reflection from the sample and A is the absorption in it.

The interference maxima in the transmission of a slab appear when

$$nd=\frac{m\lambda}{2},$$

where m = 1, 2, 3, ... is the number of the maximum.

If the index of refraction of the sample depends on the temperature, this condition is satisfied periodically for a certain fixed wavelength λ_1 and for slow cooling or heating of the sample, and at certain temperatures the sample becomes transparent. By changing the wavelength we obtain the same maxima but at different temperatures (Fig. 2, curve 2). Thus, having experimental curves of the temperature dependence of the transmission of the sample $\tau(T)$ taken at various wavelengths it is possible to trace the displacement of any maximum with temperature and to determine its number, m. When the position of the m-th maximum for λ_1 coincides with the (m + k)-th maximum (where k is an integer) obtained with another wavelength λ_2, the condition

$$m\lambda_1=(m+k)\lambda_2$$

is satisfied and the number corresponding to maximum m is determined. Many measurements made with various

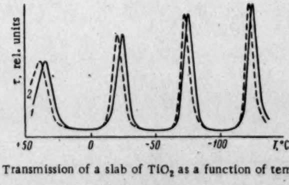

Fig. 2. Transmission of a slab of TiO_2 as a function of temperature.

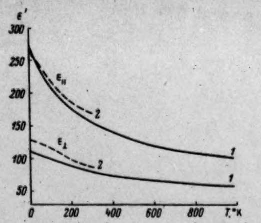

Fig. 3. Temperature dependence of permittivity of rutile. λ, mm: 1) 0.8-3.5; 2) 10 (ref. 5).

wavelengths for various values of k always give accurately integral values of the numbers m of the maxima. This indicates there is not much dispersion and one can assume that the numbers of the maxima m are determined with absolute accuracy. By varying the wavelength we obtain the m-th maximum at a different temperature each time, and in each case we determine the index of refraction n from the condition on the behavior of the interference maximum.

A sample of rutile is studied in this way in a thermostat up to a temperature of 1000°K. In all the temperature measurements the temperature gradient in the sample does not exceed 0.03 deg/mm. However, in the measurements in the helium cryostat, where the temperature can be varied smoothly from 4.2°K to the liquid-nitrogen temperature, the pronounced nonlinearity of the temperature gages prevents us from obtaining interference maxima suitable for processing by the procedure we have described. Therefore in this case we measure the transmission of the sample, not as a function of temperature, but of the wavelength of the transmitted radiation at fixed temperatures, and observe the displacement of the maxima. The number of a maximum can be obtained by using measurements made in the nitrogen cryostat. To do this it is sufficient to know the number of the maximum of the $\tau(T)$ relation at the liquid-nitrogen temperature and the wavelength at which it is obtained, and then to find this maximum on the $\tau(\lambda)$ relation obtained at the liquid-nitrogen temperature in the helium cryostat.

We note that it is difficult to determine $\tau(\lambda)$ since retuning the backward-wave tube changes its power output and prevents a direct determination of $\tau(\lambda)$ by using the scheme shown in Fig. 1. Another receiver is required to measure the power incident on the sample. The final determination of $\tau(\lambda)$ is made by dividing the reading of the receiver beyond the sample under study by the reading of the receiver before it.

Measurements made at wavelengths from 3.5 to 0.8 mm show that within the experimental error n is independent of the wavelength at all temperatures.

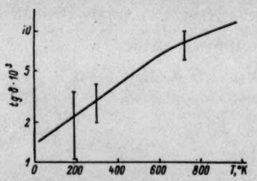

Fig. 4. Temperature dependence of tan δ for rutile at a wavelength λ = 1.9 mm.

Figure 3 shows the permittivity of a single crystal of rutile along two axes using 1 mm waves at temperatures from 4.2 to 1000°K. For comparison the figure also shows the values of the permittivity of rutile obtained[5] for λ = 10 mm.

The accuracy of the measurement of n is determined by the quality of the interference maxima on the transmission curve. For the frequency and temperature ranges studied the interference maxima have Q values from 50 to 300, ensuring an error of no more than 1% in n.

The loss in the sample is calculated from the half-widths of the maxima of the $\tau(T)$ and $\tau(\lambda)$ curves discussed above. The error in measuring tan δ for rutile increases to 100% as the temperature is lowered, since the TiO_2 sample becomes highly transparent and the maxima are noticeably narrowed. The quality of the equivalent resonator is now determined mainly by the reflection from the faces of the sample and becomes very large in comparison with the small changes due to the decrease of absorption in the sample at lower temperatures.

Figure 4 shows the temperature dependence of tan δ obtained for a single crystal of rutile at a wavelength of 1.9 mm. This variation of tan δ with temperature agrees with the results of temperature measurement using microwaves.[5] It is clear that in the submillimeter range rutile is highly transparent and becomes even more so as the temperature is lowered.

Taking account of this fact, the high permittivity, the good mechanical propoerties, and the well-developed technology of obtaining large single crystals makes rutile a promising material for cryogenic technology in the submillimeter region.

---

[1] E. M. Voronkova, B. N. Grechushnikov, G. I. Distler, and I. P. Petrov, Optical Materials for Infrared Technology [in Russian], Nauka, Moscow (1964).

[2] N. A. Irisova, Vestn. AN SSSR, 10, 63 (1968).

[3] A. A. Volkov, G. V. Kozlov, and I. M. Chernushev, Prib. Tekh. Eksp., 4, 237 (1972).

[4] Long-Wave Infrared Spectroscopy (V. N. Murzin, ed.) [in Russian], Mir, Moscow (1966).

[5] E. S. Sabisky and H. J. Gerrtsen, J. Appl. Phys., 33, 1450 (1962).

Low-voltage gun with a resonator for formation of electron bunches in a linear accelerator

V. A. Boiko, R. M. Voronkov, and V. A. Danilichev

(Submitted May 3, 1973; resubmitted October 10, 1973)
Zh. Tekh. Fiz., 44, 888-891 (April 1974)

Results are given for an investigation of the beam parameters at the exit of an experimental 10-MeV electron linear accelerator in which a device consisting of a low-voltage gun and an accelerating resonator is used as an injector. For operation of the accelerator with a pulse length of 6 μsec and a current of 1.6 A, an energy-spectrum width based on a half-drop in current of 4% is obtained.

For effective operation of an electron linear accelerator it is necessary that even in its initial part the electron stream should consist of bunches which follow the frequency of the accelerating microwave field and are phased properly with respect to the crest of the traveling wave. Usually such bunches are formed from the continuous beam from an electron gun using a waveguide buncher; in the latter the phase velocity of the wave increases along the length from the velocity corresponding to the gun voltage to the velocity of light according to a specially calculated relation. It is preferable to use an accelerating structure which initially has a phase velocity of the wave equal to the velocity of light. With a sufficiently high accelerating microwave field (100 kV/cm) in such a structure, compact bunches located near the wave crest form very rapidly (over a length of several tens of centimeters) from a continuous electron beam. However, it is necessary that the energy of the injected electrons be more than 100 keV. In acceleration fewer than 50% of the injected electrons are captured, and those that remain fall on the wall of the waveguide. This has motivated us to carry out a preliminary processing of the electron beam so that a bunch with phase length of at least 120° is formed before it is introduced into the accelerating structure; thus we can eliminate the "superfluous" electrons. One of the methods for processing the beam is to pass it through a resonator with a transverse deflecting electric (or magnetic) microwave field and collimator which enables us to eliminate the improperly phased part of the electron beam. Another method uses a klystron-type buncher, i.e., a resonator in which the continuous electron beam from the gun is modulated according to the velocity of the microwave voltage, which is small in comparison with the gun voltage.

A very attractive idea for forming electron bunches is the use of a combination that is similar to a klystron-type buncher, but differs in the fact that the electron gun operates at a very low voltage (10-20 kV) and the microwave voltage on the resonator is many times greater (300-500 kV). In this case, approximately 30% of the electrons that enter the resonator form a bunch with length of about 90° and energy up to 500 keV, which is highly suitable for introduction into the accelerating structure with constant phase velocity equal to the velocity of light. The remaining approximately 70% of the electrons enter at unfavorable phases and fall on the resonator walls, but these are low-energy electrons, so that the effect is not harmful.

The aim of the present work is to investigate the operation conditions of an experimental electron linear accelerator at an energy of about 10 MeV, using as an injector a low-voltage gun and resonator with high microwave voltage.

The dynamics of electrons in such resonators for high fields has been thoroughly investigated in a number of papers, e.g., refs. 1 and 2. Therefore within the framework of the present work we do not discuss the electron dynamics, but consider briefly the application of such a resonator in an injector for an electron linear accelerator. The principal advantage of an injector with an accelerating resonator is that it allows us to use a comparatively low-voltage gun and to obtain a beam consisting of separate bunches with high energy. The reduction of the voltage on the electron gun to 10-20 kV makes it possible to simplify the power supply scheme and the gun. If we require several pulse lengths of beam current, including nanosecond pulses, then for a voltage of 10-20 kV such pulses can form directly on the cathode, without using any additional devices, such as a grid or an inflector.

A schematic diagram of the injector with accelerating resonator is shown in Fig. 1. The electron gun consists of a cathode node 1 and an anode 2. In the present structure we select a system of plane electrodes. The cathode of the gun is a disk of lanthanum hexaboride about 1.4 cm in diameter. To obtain large currents from the cathode (tens of amperes for nanosecond pulses) the anode−cathode distance, calculated from the equation for a plane diode, is made several times smaller than the anode aperture. Therefore, to improve the current extraction from the cathode, the anode is made from a high-transmission tungsten grid with grid size several times smaller than the anode−cathode distance.

The cylindrical resonator of the injector 3 is made from oxygen-free copper. To prevent penetration of the

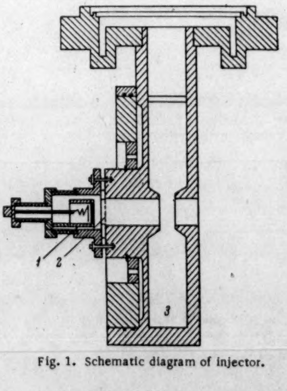

Fig. 1. Schematic diagram of injector.

microwave field into the anode–cathode region, the beam is introduced into the resonator through a small drift tube, which is a section of a waveguide beyond cutoff. The beam is extracted from the resonator through the same tube. The power to the resonator is supplied by the waveguide through a rectangular aperture in the cylindrical wall.

The injector is investigated for operation of the accelerator both in the quasistationary regime (i.e., for pulse length of the beam current considerably greater than the time of filling of the waveguide by microwave energy), and also in the stored-energy regime (when the pulse length of the beam current is less than the filling time). In the first case the power engineering of the injector resonator is very simple and a resonator efficiency of about 30% is obtained. In the second case the engineering of the resonator has a number of distinctive features, and we discuss these in detail.

We carry out a preliminary estimate of the quality factor of the resonator Q and the power P_0 needed to supply the resonator, using the following example. The mean electron energy at the injector exit E = 500 keV, the current of accelerated electrons I = 10 A, the current pulse length t = 10 nsec, the admissible energy drop per current pulse $\delta E = 0.1$ (10%), the microwave-generator pulse length $\tau = 1.5$ μsec, and the generator frequency $f_0 = 1820$ MHz. In this case we can assume that the electrons are accelerated in the resonator and the sections because of the stored energy, and the injection of energy during the current pulse can be neglected. Electrons should be injected into the accelerator when the energy storage is completed. In order for this to occur the quality factor of the resonator Q must be such that a stationary regime is established in the resonator during the pulse. We can assume that this condition is satisfied if

$$Q \leqslant \frac{2\pi f_0 \tau}{5}.$$

For our example Q ≤ 3000. The energy removed by the beam per pulse $W_b = I \cdot E \cdot t$; in our case $W_b = 0.05$ J.

For small decreases in electron energy during a current pulse we can assume that the allowable drop in energy stored in the resonator is $\delta W_r \approx 2\delta E$; hence, the energy stored in the resonator is

$$W_r = \frac{W_b}{2\delta E}.$$

In our case $W_r = 0.25$ J. Acceleration of electrons by the stored energy requires that $P_0 \approx P_{loss}$, where P_{loss} is the power loss in the resonator.

Using the definition of the quality factor of the resonator and taking account of the fact that $P_0 = P_{loss}$, we obtain

$$P_0 \approx \frac{2\pi f_0 W_r}{Q}.$$

For this example, $P_0 = 1$ MW. The coefficient of coupling between the waveguide and the resonator for large beam-current pulse lengths is chosen taking account of the shunting action of the electron beam.

The height of the accelerating gap in the resonator is chosen on the basis of the calculation of electron dynamics, carried out according to the method discussed in ref. 1. A gap height of about 3 cm is chosen. The coupling between the resonator and the waveguide is selected so that a current of 1.5 A can be accelerated for large pulse lengths.

The injector is investigated for the following operational regime. The power fed to the resonator is up to 2 MW, the microwave pulse length is 6 μsec, the voltage on the gun cathode is 15 kV, the operating frequency is 1818 MHz. The current at the resonator exit is measured with a Faraday cup, and the energy is measured with an electrostatic spectrometer.

Figure 2 shows the electron energy spectrum obtained at the resonator exit for a pulsed accelerated-electron current of 1.5 A. The mean energy of accelerated electrons is about 500 keV and the energy-spectrum width based on the half-drop in current is 120 keV.

After the injector is investigated above, its operation is checked together with the accelerating sections having phase velocity equal to the velocity of light. The length of the section is 1.65 m; the mean field for an input microwave power of 18 MW for an unloaded regime is about 10 kV/cm. The power is introduced into the resonator through an iris with about 10 dB loss and a remotely controlled phase shifter. Focusing of the beam is accomplished by short coils in the injector and by a solenoid in the accelerating section. The current at the exit is measured with a Faraday cup, and the energy is measured with a magnetic spectrometer with a resolution better than 1%.

Curve 1 of Fig. 3 shows the energy spectrum of the electron beam at the exit of the section for a pulse length of 5.5 μsec. The energy at the maximum is 10.3 MeV. The width of the energy spectrum based on the half-drop

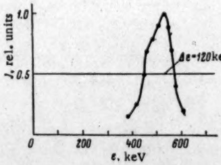

Fig. 2. Energy spectrum of electron beam at injector exit.

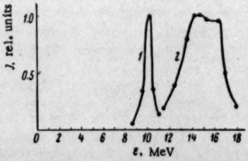

Fig. 3. Energy spectra of electron beam at accelerator exit. 1) For current pulse length 5.5 μsec; 2) for pulse length 150 nsec.

in the current is about 4%. The current in a pulse at the exit of the section is 1.5 A. The coefficient for conversion of energy of the microwave field into energy of the electrons is about 80%. The beam parameters obtained at the exit of the section with the described injector are considerably better than the parameters obtained with other types of injectors under the same conditions.

Curve 2 of Fig. 3 shows the energy spectrum of the beam at the exit of the section for a beam-current pulse length of 150 nsec and an exit current of about 1 A. This spectrum has a rather clearly expressed flat peak, characteristic of accelerators operating in a stored-energy regime. The flat part of the peak of the spectrum is due to the fact that the electron energy decreases from bunch to bunch essentially linearly as the energy stored in the section is expended in accelerating the beam.

The experiments that have been carried out show that a low-voltage gun with an accelerating resonator can, with some further developments, be used as an injector for an electron linear accelerator. Such an injector can be used both in an accelerator operating in a stored-energy regime, and also in an accelerator operating in a quasistationary regime. The use of this injector enables us to simplify the power supply scheme and to eliminate the bunching waveguide section from the accelerator.

---

[1] R. G. Mirimanov (ed.), Millimeter and Submillimeter Waves [Russian translation], IL, Moscow (1969).

[2] N. A. Khizhnyak, V. T. Tolok, V. V. Chechkin, and N. I. Nazarov, At. Energ., 11, 34 (1961).

Parametric excitation of surface waves in a spatially modulated electron beam

A. I. Pasynok and N. S. Repalov

Physicotechnical Institute,
Academy of Sciences of the Ukrainian SSR, Khar'kov

(Submitted September 10, 1973; resubmitted December 7, 1973)
Zh. Tekh. Fiz., 44, 891-894 (April 1974)

The parametric stability of surface waves in an electron beam modulated by a spatially periodic electrostatic field is investigated. It is shown that the instability develops at frequencies above a critical value. In this case the excitation of surface waves is comparable in efficiency to the excitation of volume waves. The effect of an external magnetic field on the excitation of such waves is discussed, and the growth rate is given as a function of the angle between the direction of propagation of the surface wave and the wave vector of the modulating wave.

The parametric excitation of slow waves ($u_p \ll c$) in an electron beam subject to an external spatially periodic electrostatic field has been investigated[1] on the assumption that the beam completely fills the transverse cross-section of the waveguide. This formulation of the problem obviously does not treat effects connected with a free surface of the beam and phenomena in which surface waves are important. In this paper we show that in an electron beam whose boundary is far from the walls of the waveguide, parametric excitation of surface waves is comparable in efficiency with the excitation of volume waves (in a moderate external magnetic field $\omega_0 \gtrsim \omega_H$).

We use the equations obtained in ref. 1. In order to avoid unwieldy equations, we confine ourselves to wavelengths much smaller than the radius of the beam and the thickness of the gap between the boundaries of the beam and the wall. With these assumptions the equations that describe the perturbation of the potential in the beam are

$$\left.\begin{aligned} \frac{d^2\varphi(k,x)}{dx^2} - p^2\varphi(k,x) &= \alpha\varphi(k-k_0,x) \\ \frac{d^2\varphi(k-k_0,x)}{dx^2} - p_-^2\varphi(k-k_0,x) &= \beta\varphi(k,x) \end{aligned}\right\} x>0, \tag{1}$$

where k_0 is the wave number of the modulated wave,

$$p^2 = k_z^2 + \frac{\varepsilon_3(k)}{\varepsilon_1(k)}k_y^2,\quad p_-^2 = k_z^2 + \frac{\varepsilon_3(k-k_0)}{\varepsilon_1(k-k_0)}(k-k_0)_y^2,$$

$$\alpha = \frac{\xi}{2\varepsilon_1(k)}[a_{-1} + b_{-1}(p_-^2 - k_z^2)],$$

$$\beta = \frac{\xi}{2\varepsilon_1(k-k_0)}[a_{+1}(k-k_0) + b_{+1}(k-k_0)(p^2 - k_z^2)].$$

Expressions for the coefficients $a_{\pm 1}$, $b_{\pm 1}$, and ξ are given in ref. 1. Equation (1) can be written in a Cartesian system of coordinates in which the ZOY plane is the surface of separation, the Y axis coincides with the direction of the external magnetic field, H_0, and the X axis is directed into the plasma. In the region free from plasma ($x < 0$) the potential perturbations satisfy Eqs. (1), in which

$$\alpha = \beta = 0,\quad p_0^2 = k_y^2 + k_z^2,\quad (p_-^0)^2 = (k-k_0)_y^2 + k_z^2.$$

To solve (1) we proceed as follows: We differentiate the first equation twice, and eliminate from it the function $\varphi(k-k_0, x)$ using the second equation. We then obtain

$$\frac{d^4\varphi(k,x)}{dx^4} - (p^2 + p_-^2)\frac{d^2\varphi(k,x)}{dx^2} + (p^2p_-^2 - \alpha\beta)\varphi(k,x) = 0. \tag{2}$$

The function $\varphi(k-k_0, x)$ also satisfies this equation. The solution of Eq. (2) will be sought in the form

$$\varphi(k,x) = e^{\lambda x}. \tag{3}$$

Substituting Eq. (3) in Eq. (2) and solving the characteristic equation we obtain

$$\lambda_{1,2}^2 = \frac{p^2 + p_-^2}{2} \pm \frac{1}{2}\sqrt{(p^2 - p_-^2)^2 + 4\alpha\beta}. \tag{4}$$

We will not consider the case $p \to p_-$ ($k_0 \to 0$). Assuming that $\alpha\beta \sim \xi^2 \ll 1$, we obtain

$$\lambda_1^2 = p^2 + \frac{\alpha\beta}{p^2 - p_-^2},\quad \lambda_2^2 = p_-^2 - \frac{\alpha\beta}{p^2 - p_-^2}. \tag{5}$$

Hence, the solution of (1) which vanishes as one goes away from the boundary when $\lambda_{1,2} > 0$, has the following form:

$$\left.\begin{aligned} \varphi(k,x) &= A_1e^{-\lambda_1 x} + A_2e^{-\lambda_2 x}; & x>0, \\ \varphi(k,x) &= Be^{p_0 x}; & x<0. \end{aligned}\right\} \tag{6}$$

The function $\varphi(k-k_0, x)$ is

$$\left.\begin{aligned} \varphi(k-k_0,x) &= a_1e^{-\lambda_1 x} + a_2e^{-\lambda_2 x}; & x>0, \\ \varphi(k-k_0,x) &= be^{(p_-^0)x}; & x<0. \end{aligned}\right\} \tag{7}$$

The coefficients A_i and a_i in (6) and (7) are not independent. Substituting Eqs. (6) and (7) in the first equation of Eqs. (1) we obtain the following relation:

$$A_1 = \frac{p^2 - p_-^2}{\beta}a_1,\quad A_2 = \frac{-\alpha}{p^2 - p_-^2}a_2. \tag{8}$$

A similar procedure using the second of Eqs. (1) leads to the same result.

In order to obtain a dispersion equation for the surface waves in the modulated beam it is necessary to match the solutions (6) and (7) using the appropriate boundary conditions. The boundary conditions are as follows:[2]

$$x = 0:\ \{\varphi\} = 0,\quad \left\{\varepsilon_1\frac{d\varphi}{dx}\right\} = 0. \tag{9}$$

Substituting (6) and (7) in (9) and expanding the coefficients which form the determinant, we obtain

$$(p_0 + \lambda_1\varepsilon_1)(p_-^0 + \lambda_2\varepsilon_1^-) = -\frac{\alpha\beta}{(p^2 - p_-^2)^2}(p_0 + \lambda_2\varepsilon_1)(p_-^0 + \lambda_1\varepsilon_1^-), \tag{10}$$

where

$$\lambda_1 = p + \frac{1}{2}\frac{\alpha\beta}{p(p^2 - p_-^2)},\quad \lambda_2 = p_- - \frac{1}{2}\frac{\alpha\beta}{p_-(p^2 - p_-^2)},\quad \varepsilon_1^- \equiv \varepsilon_1(k-k_0).$$

Introducing the quantities Θ and Θ_1, the angles between the vectors **k**, and **k** − $\mathbf{k}_0$ and the direction of the external magnetic field, and taking account of the fact that $k_z = k\cos\Theta$, $k_y = k\sin\Theta$, in the zeroth approximation with respect to ξ, for the frequencies of the surface waves we have from (10)

$$\left.\begin{aligned}\omega_{1,2} &= kv_0 + \frac{1}{2}\left[\omega_H\cos\Theta \pm \sqrt{2\omega_0^2 + \omega_H^2(1+\sin^2\Theta)}\right],\\ \omega_{3,4} &= (k-k_0)U_0 + \frac{1}{2}\left[\omega_H\cos\Theta_1 \pm \sqrt{2\omega_0^2 + \omega_H^2(1+\sin^2\Theta_1)}\right],\end{aligned}\right\} \quad (11)$$

where $\omega_H = eH_0/(mc)$ is the cyclotron frequency.

We confine our investigation of the parametric interaction of surface waves in a spatially-modulated electron beam to a few special cases.

1. The waves propagate parallel to the boundary in the absence of an external magnetic field ($\Theta = \Theta_1 = \pi/2$, $H_0 = 0$). In this case the dispersion equation (10), taking into account the fact that we have substituted in its right-hand side the frequencies of the surface waves in the zeroth approximation with respect to ξ given by Eqs. (11), takes the form

$$(1+\varepsilon_3)(1+\varepsilon_3^-) = \xi^2\frac{(k+3k^-)(k^-+3k)}{(k+k^-)^2},\quad k^- \equiv k-k_0. \quad (12)$$

Assuming further that the modulation of the beam leads to a deviation of the surface-wave frequencies from the resonance value given by Eq. (11) by an amount $\Delta\omega \ll \omega$, and expanding the left-hand side of Eq. (12) in powers of $\Delta\omega$, we obtain

$$(\Delta\omega)^2 = \xi^2\frac{(k+3k^-)(k^-+3k)}{(k+k^-)^2}\,\frac{1}{\varepsilon_3'(\varepsilon_3^-)'}.$$

The imaginary part of this equation defines the growth rate of the parametric instability:

$$\gamma = \frac{\xi}{2\sqrt{2}}\,\frac{\omega_0}{\omega}\left(\omega^2 - \frac{\omega_0^2}{8}\right)^{1/2};\quad \omega > \frac{\omega_0}{\sqrt{2}}. \quad (13)$$

It follows from (13) that in the frequency range $\omega > \omega_{gr} = \omega_0/\sqrt{2}$ the growth rate is identical with that obtained in ref. 1, apart from a numerical factor.

2. In the presence of a finite external magnetic field for waves which propagate along the boundary of the beam, Eq. (10) takes the form

$$k(k^-)\left[1+(\varepsilon_1\varepsilon_3)^{1/2}\right]\left[1+(\varepsilon_1^-\varepsilon_3^-)^{1/2}\right]$$
$$= -\frac{\alpha\beta}{\left[k^2\frac{\varepsilon_3}{\varepsilon_1} - (k^-)^2\frac{\varepsilon_3^-}{\varepsilon_1^-}\right]^2}\left[k + (k^-)\varepsilon_1\left(\frac{\varepsilon_3^-}{\varepsilon_1^-}\right)^{1/2}\right]\left[k^- + k\varepsilon_3^-\left(\frac{\varepsilon_3}{\varepsilon_1}\right)^{1/2}\right], \quad (14)$$

while the growth rate is given by

$$\gamma = \frac{\xi}{4\sqrt{2}}\,\frac{\left[\omega^2(2\omega_0^2+\omega_H^2)^2 - \frac{\omega_0^2+\omega_H^2}{2}(\omega_0^2+2\omega_H^2)\right]^{1/2}}{\omega(\omega_0^2+\omega_H^2)^{1/2}};\quad \omega > \frac{(\omega_0^2+\omega_H^2)^{1/2}}{\sqrt{2}}. \quad (15)$$

Comparing Eqs. (13) and (15) it is easy to show that the magnetic field increases the lower limiting frequency of the instability region, while the growth rate is reduced.

3. In conclusion we consider the propagation of surface waves in a beam when the wave vectors **k** and **k** − $\mathbf{k}_0$ are directed at angles Θ and Θ_1 respectively to the wave vector of the modulating wave $\mathbf{k}_0$ in the absence of a focusing magnetic field. Bearing in mind that in this case $k_z = k_z^-$, i.e., $k_y^2 - (k_y^-) = k^2 - (k^-)^2$, Eq. (10) takes the form

$$(1+\varepsilon_3)(1+\varepsilon_3^-) = \xi^2\frac{1}{(k+k^-)^2}\,\frac{k_yk_y^-}{kk^-}\left[k_y+3k_y^-\right]\left[k_y^-+3k_y\right]. \quad (16)$$

The expression for the growth rate then takes the form

$$\gamma = \frac{\xi}{2\sqrt{2}}\,\frac{\omega_0}{\omega}\left(\omega^2 - \frac{\omega_0^2}{8}\right)^{1/2}\sqrt{\sin\Theta\sin\Theta_1};\quad \omega > \frac{\omega_0}{\sqrt{2}}. \quad (17)$$

The angles Θ and Θ_1 are related by the following expression:

$$\operatorname{tg}\Theta_1 = \operatorname{tg}\Theta - \frac{k_0}{k}\sqrt{1+\operatorname{tg}^2\Theta}. \quad (18)$$

The analysis shows that parametric excitation of surface waves in a spatially modulated electron beam in the frequency range $\omega > \omega_0/\sqrt{2}$ is comparable in efficiency with the excitation of volume waves. The solutions (11) correspond to surface waves only when k and k − k_0 are positive. At frequencies $\omega < \omega_0/\sqrt{2}$ the quantity k − k_0 becomes negative, which is easily shown using the resonance condition. Calculations similar to those given above show that the surface-wave parametric instability is not excited in this range.

---

[1] A. I. Pasynok and N. S. Repalov, Zh. Tekh. Fiz., 44, 277 (1974) [Sov. Phys. – Tech. Phys., 19, 177 (1974)].

[2] L. D. Landau and E. M. Lifshitz, Electrodynamics of Continuous Media, Addison-Wesley (1960).

250 years of the Academy of Sciences of the USSR

Zh. Tekh. Fiz., 44, 897-905 (May 1974)

In May 1974, The Academy of Sciences of the USSR – acknowledged leader of Soviet Science – celebrates its 250th anniversary. In a resolution on October 17, 1973 concerning this anniversary, the Central Committee of the Communist Party of the Soviet Union noted, in particular, the outstanding role played by the Academy, its institutes, and numerous groups of collaborators in the development of the basic and applied research which is being carried on at an ever increasing tempo and which is now leading to an era of scientific and technical revolution in our country.

Little more than a fifth of the lifetime of the Academy of Sciences falls within the Soviet period of the history of our country. But those years are marked by the greatest of achievements which gained international prestige for our Academy and all Soviet science. Science in the Soviet Union enjoys exceptional consideration and support from the Party and the government. The expenditures on science grow every year, as does the number of scientists.

The national regard for the Academy is especially marked when one considers the position the Academy occupied, particularly with regard to physical research, in the prerevolutionary period, especially at the end of the 18th and the greater part of the 19th centuries. In those far-off years, the Academy, of course, might invite outstanding physicists to work within its walls; however, one can say that any definite successes they managed to achieve were not due to help from the Tsarist government and to some extent even despite its indifference to the needs of native science.

Conditions were different in the years of immediate preparation for the establishment of an Academy and in the first decades of its existence.

The founder of our Academy was Peter I, a man of vast and powerful intellect who understood that consolidation of the victories of Russian arms, future strengthening of the government, and the development of its industries were unthinkable without education and science in the land. Acquaintance with the economics and industry of European governments – England, Germany, France, and Holland, which he visited many times and for extended periods – convinced Peter of this. At the very beginning of the 18th century he took energetic steps directed toward organization of an Academy. He carried on negotiations involving the invitation of European scientists – physicists, chemists, mathematicians, naturalists, and humanists – to the Academy created in St. Petersburg. There were almost no such specialists in Russia at the time; despite the relatively high level of literacy and the development of printing, there were no universities in the country.

Preparation for the opening of the Academy was in full swing. L. L. Blyumentrost, physician to Peter, author of the rules and regulations for the St. Petersburg Academy, and its future first president, asked Tatishchev (one of the most illustrious people of that time, a historian and geographer, who left St. Petersburg for Sweden in 1724) to find out if there were Swedish scientists who might wish to work in the Russian Academy. Tatishchev replied, "It is useless to plant seed when the earth in which it is sown is not prepared." Peter, who was present at this conversation, answered Tatishchev for Blyumentrost with the following parable: "A certain nobleman wished to build a mill in his village but had no water. Seeing lakes and marshes near his neighbors, who had an abundance of water, he quickly conceived a plan to build a canal, with their consent, and to lay up stores at the mill; although he was not able to bring the project to completion by himself, his children, pitying the enforced dependence of their parents, accepted the need for the project and completed it."

In the draft of the decree establishing an Academy of Sciences and Arts, which was approved by Peter on January 22, 1724 an organizational basis of the Academy was laid out which in his idea would assure in Russia for many years in the future the development of three classes of sciences: mathematical sciences (pure mathematics, astronomy, geography, navigation, mechanics), physical sciences (theoretical and experimental physics, anatomy, chemistry, botany), and the humanities (oratory, history, politics, and law).

The initial momentum the Academy received (which was the result of the efforts put forth by Peter during the last 10-15 years of his life) was so powerful that the Academy of Sciences in St. Petersburg based on his plans proved to be viable, even after his death, in the first year of the reign of Catherine I, got through the very difficult years under Biron, and acquired a European reputation in the years 1740-1760. The crop planted by Peter yielded a remarkable harvest; the very existence of the great Lomonosov, pupil of the Academy and the first Russian physicist-academician, was sufficient to justify everything that was done to establish the Academy![1)]

In the draft of Peter's decree concerning the Academy (still preseving traces of corrections in his own hand), he speaks of an Academy of Sciences and Arts. At that time, the "arts" were understood to be the application of "pure science" in practical matters (and also in the professions). In other words, the arts were applied sciences. The problem of the interrelation between the basic and applied sciences concerned the organizers of the St. Petersburg Academy even at that time and the necessity for this sort of application, which was provided for from the very beginning, was one of the features of the Academy. One should note here that from the dictionary definition (particularly the dictionary of Brockhouse and Efron), academies are scientific societies which "are concerned with science not for practical purposes, but for science itself".[2)]

Many of the first academicians arriving in St. Petersburg in 1725 displayed a devotion to "pure science". In view of this, it is interesting to follow the activities of Daniel Bernoulli, who began his work in Russia in 1725 and who maintained his connection with the Academy to the end of his life. Shortly before his arrival in St. Petersburg, Bernouilli wrote the mathematician Goldbach,[3)] who furthered Bernouilli's invitation, that he hoped "nothing would be required from him other than that which relates to pure theory". At the same time, he repeatedly reported at St. Petersburg, without urging by anyone, on his work of an applied nature. Thus, Vol. I of the "Proceedings of the Sessions of the Conference of the Imperial Academy of Sciences" indicates that on November 2, 1731, Bernouilli read a paper on the circulation of air in the stoves usually used in Russia. In 1732, he told a Conference (meeting of academicians) of his "Views on raising the great Moscow bell into a bell tower"; he also expounded repeatedly on the principles for the construction or improvement of physical instruments (barometers, hydrometers, etc.).

This understanding of the unity of science and its applications, their mutually enriching effect, is outstandingly characteristic of Lomonosov – the pride of our country. He performed exceptionally great service for Russian science. From studies of creative works and biography, Lomonosov is second only to Pushkin. There is therefore no need to speak of his scientific discoveries in physics and chemistry, of his role in the development of Russian literary language and also of scientific language (including here both physical and chemical terminology; a number of the terms which we use today were introduced by Lomonosov) as well as the language in government documents – decrees, messages, etc. Although Lomonosov wrote numerous works not only in Russian but also in Latin, which he mastered completely in the opinion of specialists, and these works were well known to his contemporaries (in particular, Euler had an extremely high opinion of them),[4] he was rediscovered at the beginning of this century primarily because of the studies of his work by Prof. B. N. Menshutkin of the Leningrad Polytechnic Institue published both here and abroad (in the well-known publication "Science Classics" by W. Ostwald). In the preface to the "Biography of Mikhail Vasil'evich Lomonosov" by B. N. Menshutkin, S. I. Vavilov cited the remarkable statement of A. Smith, president of the American Chemical Soviety, "the rediscovery of Lomonosov straight away added a chemist of first magnitude and an individual of astonishing vigor to be exclusive circle of the greatest people in the world". B. N. Menshutkin himself wrote, "It was with amazement that I became acquainted with the physical chemistry of Lomonosov, which completely corresponds to modern chemistry with its atomistic hypothesis and a number of theories based on that hypothesis having to do with the principle of energy conservation, the theory of heat, the kinetic theory of gases, etc. All these theories were formulated 100-120 years after his death."

Lomonosov is deserving of even greater credit because he had to pursue physics and chemistry at irregular intervals; even people of importance kindly disposed toward him, in particular I. I. Shuvalov, considered the creation of poetry and work on the Russian language and its grammar to be his principal activities. Lomonosov pointed out in the preface to this "Grammar" (1755), "Versifying is my delight, physics is my exercise." Two years earlier, he wrote Shuvalov, "As far as my other activities in physics and chemistry are concerned, there is no need or possibility at all that they be abandoned. Every man needs relaxation from work; for that purpose, putting aside the business at hand, he, together with guest or family, turns to pastimes such as cards, checkers, or other amusements, and even to smoking tobacco, all of which I have long ago renounced because I find in them nothing but boredom. So I hope that as relaxation from the work which I report on and present at conferences on Russian history and the work on ornamentation of the Russian word, several hours a day will be allowed me to use not for billiards but for physical and chemical experiments, which are to me not only excellent matters to replace amusement but also serve as exercise in place of medicine, and more than that, may of course lead to a usefulness and honor for the Motherland hardly less than my principal activity."

Leonard Euler was another scientist of the 18th century of whom we can rightfully be proud and who worked at the Academy in St. Petersburg for more than 20 years before his death. Daniel Bernouilli, Euler, Lomonosov – their names are inseparably linked with the establishment of science in Russia and with the general recognition of the Academy of Sciences at St. Petersburg.

The names of the first Russian inventors are also firmly associated with the activities of the Academy in the first years of its existence – A. K. Nartov (his original machine can now be seen at the Hermitage), I. P. Kulibin who worked at the Academy for more than 30 years and who became famous for a number of investigations, and many others.

The 19th century appears in the history of Russian science and of the Academy primarily as a time when the mathematics and chemical schools flourished. It is significant not only that P. L. Chebyshev was one of the most powerful mathematicians of his time but also that his appearance preceded the fruitful work of the mathematicians Ostrogradskii and Bunyakovskii, who were also academicians. It is important that from the middle of the 19th century there was a direct continuity of the mathematical studies carried on in Russia within either the Academy or in the universities which were established at the beginning of the century [in Kazan', Derpt (Tartu), St. Petersburg, Khar'kov, and later other cities as well]. P. L. Chebyshev, A. M. Lyapunov, A. A. Markov, V. A. Steklov – from them, from their students, from the students of their students, one can draw a direct line, a continuous chain which leads directly to the outstanding Soviet mathematicians who are our contemporaries. One cannot trace the line in the opposite direction, say from Ostrogradskii to Euler. The genius Lobachvskii[5] was understood by few of his contemporaties (primarily by Gauss). His activities took place outside the Academy, to which he was not elected a member.

Approximately the same thing can be said about the chemists; there is a direct line leading from the remarkable work and famous names of N. N. Zinin and A. M. Butlerov to the present-day far-flung schools of chemistry in the Soviet Union, but before them (excepting, of course, Lomonosov) we had no great chemist or "chemical traditions". It is worth noting that here also (as in the case of mathematics), one of the most brilliant and splendid representatives of Russian science, D. I. Mendeleev, was not elected to the Academy of Sciences.

As far as physics is concerned, the 19th century had several outstanding academicians: V. V. Petrov (who discovered the electric arc), B. S. Yakobi (electric motor, galvanoplastics), E. Kh. Lenz (Lenz's law, the Joule-Lenz law, remembered by us from school days), but the beginnings of the Russian schools of physics appeared in the last decades of the 19th and the beginning of the 20th century.

In the Academy of Sciences, the start of new work was marked by the activity of B. B. Golitsyn, who because of his brilliant talent in physics (work on radiant energy, molecular and mathematical physics, classical studies in geophysics and seismic waves) and his organizational ability was able to expand the research in the physics laboratories of the Academy and to attract a number of capable young people to the Academy. The physics laboratories were thereby prepared for the role which fell to them in the immediate future, in the first postrevolutionary years. Directed in those years by V. A. Steklov, A. N. Krylov, and S. I. Vavilov, they served as a distinctive seed from which crystallized the V. A. Steklov Mathematics Institute and the P. N. Lebedev Physics Institute (FIAN).

However, as graphically reported in the second volume of "The History of the Academy of Sciences of the USSR" (Moscow, 1964), "The main flow in the development of Russian Physics passed around the walls of the Academy." Indeed, P. N. Lebedev, very likely the first of our own physicists, who obtained in his lifetime recognition of this merit both here and abroad (W. Thompson, for example, in a conversation with K. A. Timiryazev confessed that precisely the work on light pressure[6] convinced him of the validity of Maxwell's electromagnetic theory), was not a member of the Academy; a group of academicians including G. I. Vil'd, F. A. Bredikhin, and P. L. Chebyshev, was unable to achieve election to the Academy of A. N. Stoletov who agreed to the balloting,[7] and neither N. A. Umov nor A. S. Popov were members of the Academy.

The October Revolution opened a new era in the history of the Academy of Sciences. One can say that the Soviet government and Vladimir Il'ich Lenin supporting and stimulating the activities of the Academy from the very beginning strove to direct the main flow in the development of our science into the channels of the Academy.

At an extraordinary general session of the Academy of Sciences on January 24 (February 6), 1918, its permanent secretary, Academician S. F. Ol'denburg, reported that a representative of the People's Commisariat for Education had called on him "in reference to the question of possible scientific work by the Academy in connection with various government problems of the time." Somewhat later, the permanent secretary became acquainted with the "Proposed plan for the mobilization of science for the needs of government construction," opening with the following words which were meaningful for the future of the Academy: "a special commision of the Academy of Sciences staffed by those participating most closely in the work of the organization will be the organizational center for the mobilization of science."

Replying to this proposal, the president of the Academy, A. O. Karpinskii, in a letter of March 5, 1918 to the People's Commissar for Education, A. V. Lunarcharskii, on the problems of the Academy in the study of the national economy of the country spoke of the activity organized in 1915 under the Academy's Commission on the Study of the Productive Forces of Russia (KEPS). In the name of the members of the Academy, he expressed a readiness to collaborate with the Soviet government both in the field of further study of the natural resources of the country and in respect to an analysis of a technical and economic nature in order to facilitate the selection of paths which, when followed, would ensure the most rapid increase in the most important sections of the national economy. In the list of areas of the economic life of the country subject to study and development compiled under the direction of the president of the Academy, there was outlined the creation of scientific bases for commercial methods of producing precious and rare metals, structural materials, salt (in particular, a study of the Kara Bogaz Gol Bay), gaseous fuels, along with planning and development of irrigation and land reclamation work, and the study of waterways as future means of communication. A third group of problems encompassed the needs of agriculture (cultured plants, soil, mineral fertilizers; physicists were brought in later, in the 1930's, to participate in the solution with the Agrophysical Institute organized in Leningrad being the center of their activity).

The next very important step was the compilation by V. I. Lenin of the famous "Draft Plan for Scientific and Technical Operations" (April 1918) addressed to the Academy of Sciences. In this document of paramount importance, it was pointed out that any plan considered "... must include rational distribution of inductry in Russian from the viewpoint of closeness to raw materials and the possibility of least loss of labor in the transition from processing of raw materials through all subsequent stages of processing the semifabricated products to the production of the final product ... special attention to the electrification of industry and transport and the use of electricity in agriculture... the use of low-grade fuels (peat and low-grade coal) for the production of electrical energy with minimum expenditure on extraction and transport of the fuel." The "Draft" of V. I. Lenin was the answer to the suggestions mentioned above which came from the Academy. In that same month, the Council of People's Commissars decided "to meet this proposal, to acknowledge in principle the necessity for financing the appropriate work of the Academy, and to indicate to it as a particularly important and urgent problem the question of the correct distribution of industry in the country and the most rational use of its economic forces."

These proposals began to be realized practically immediately. A whole series of new institutes was created (Institute of Physicochemical Analysis, Institute for the Study of Platinum and Other Precious Metals, State Ceramics Research Institute, Hydrological Institute, State Radium Institute, etc.).

It should be pointed out here that although the physicists were extensively brought into the work (it is sufficient to note among them the direct participation in work on the study of the Kursk magnetic anomaly directed by Academician P. P. Lazarev and active participation in work under the GOÉLRO plan for the creation of a radio industry), the physics institutes formed inmmediately after the October revolution and particularly the State Physicotechnical Roentgen Institute (A. F. Ioffe), the State Optical Institute (D. S. Rozhdestvenskii), and the Institute of Physics and Biophysics (P. P. Lazarev) at first functioned outside the system of the Academy of Sciences.

Besides the encouragement and initiation of every kind of applied work, the Soviet government from the very first years of Soviet power also encouraged the performance of basic research not having a direct and obvious result of consequence for industry but of general scientific interest. The government supported and financed the fruitful activity of the Atomic Commission, in the work of which D. S. Rozhdestvenskii, A. M. Krylov, A. A. Fridman and others participated; large amounts were allotted to studies in quantum theory, atomic physics, crystal physics, and biophysics.

A special resolution of the Central Executive Committe and of the Council of People's Commissars of the USSR on June 25, 1925 referring to the Academy was timed to the 200th aniversary of the Academy, which was to be observed in September 1925. The resolution said in part, "We recognize the Russian Academy of Sciences as the highest all-union scientific institution under the jurisdiction of Council of People's Commissars of the USSR and operating under regulations approved by the latter. We confer on the aforesaid Academy the name Academy of Sciences of the Union of Soviet Socialist Republics'."

This resolution recognized the leading role of the Academy of Sciences in the development of science, which was so brilliantly demonstrated by it during the first postrevolutionary years. To bring into being the sense of this resolution, the Presidium of the Academy of Sciences of the USSR and a number of other academic institutions were moved to Moscow in 1934.

The 1930's appear in the history of Soviet science as years of vigorous growth of the Academy and its institutes. The Physicotechnical Institute was included in the Academy system; a Physical Institute organized by S. I. Vavilov and an Institute of Physical Problems organized by P. L. Kapitsa were opened in Moscow. Where there were 22 institutes in the Academy in 1930, the number had increased to 53 by January 1, 1945 (this does not include the separate laboratories, committees of the Academy of Sciences, its observatories, etc.).

The systematic development of the Academy of Sciences of the USSR and the work being pursued intensively in it were interrupted in June 1941 after the treacherous attack on our country by fascist Germany. The institutes of the Academy adjusted extraordinarily rapidly to the new problems and the new conditions which were especially serious in the first year of the war. Academy scientists joined in the national battle against fascism, working on defense needs and in close collaboration with the defense industries established to serve the cause of victory. The widely known work performed by Soviet physicists included radar, ship degaussing for protection against magnetic mines, participation of Academy scientists in the creation of new types of armament, and in the relocation and speedy startup of war industries in the Urals and in Siberia (in this connection, we mention the committee on mobilization of the resources of the Urals, Western Siberia, and Kazakhstan for defense needs headed by the president of the Academy of Sciences of the USSR, V. L. Komarov, the committee on scientific and technical naval problems under A. F. Ioffe, and the committee on military health under L. A. Orbeli.)

Under difficult wartime conditions, work was started under the leadership of I. V. Kurchatov on the creation of an atomic industry with the consequence by 1949 that the armed forces of the Soviet Union had a powerful new weapon for the defense of the peaceful pursuits of the Soviet people.

The Academy of Sciences of the USSR made its solid contribution to the cause of victory over Hitler's invaders. A resolution of the Council of People's Commissars of the USSR adopted on January 21, 1945, i.e., even before the end of the war, concerning the celebration of the 220th anniversary of the Academy was but an acknowledgement of the services of the Academy and its workers in the efforts directed toward the achievement of victory, the day of which, it was felt, was not far off.

Shortly after this great day, June 10, 1945, a large group of workers at the Academy was decorated with orders and medals by decree of the Presidium of the Supreme Soviet of the USSR for outstanding services in the development of science and technology and in connection with the 220th anniversary of the Academy. On June 16, in greetings from the Council of People's Commissars of the USSR and from the Central Committee of the Communist Party of the Soviet Union (Bolshevik) directed to the Academy of Sciences, they said, " The Academy of Sciences of the USSR marks its anniversary in a period when the Soviet people victoriously concluded the war with the German invaders. In the days of the war, Soviet scientists carried out successful work, helping the military' front and the national economy by their efforts. Soviet scientists made valuable contributions to the job of crushing the enemy. In the institutes of the Academy, Soviet scientists worked frutifully – physicists and chemists, mathematicians and astronomers, biologists and doctors, geologists and geographers, historians and philosophers, lawyers and philologists... the Council of People's Commissars of the USSR and the Central Committee of the CPSU(B) are confident that in its future activities the Academy of Sciences of the USSR will further develop the traditions of our peaceful science, will use its achievements in every way possible for the development of the economy and culture of the peoples of the USSR, and will raise the prestige of Soviet science among the peoples of the world even higher."

Anniversary celebrations of the Academy of Sciences took place in Moscow and Leningrad during June 16–30, 1945; more than 100 scientists from many countries were invited, and this was the first international meeting of scientists on ending world wars.

A new problem faced the Soviet people: restoration of industry and its transfer to peaceful activities; ahead were years of strenuous, and joyful, peaceful labor.

Directed in its activities by the Party and Soviet government, the Academy of Sciences of the USSR in close interaction and collaboration with the Academies of Sciences of the Republics did its sizeable bit toward the construction of a communist society in our country.

sizeable bit toward the construction of a communist society in our country.

Within the confines of a short paper it is not possible to enumerate in any detail the successes achieved by Soviet scientists in the development of physics and its applications; the following review is a rough guide (detailed analysis of the development of physics in Russia over the past halfcentury is given in a number of publications issued on the 50th anniversary of the Soviet government, on the 100th birthday of V. I. Lenin, and on the 50th anniversary of the Great October Socialist Revolution; see the two-volume edition of "Development of Physics in the USSR," Moscow, 1967, the collections "October and Scientific Progress," "Lenin and the Academy of Sciences", and "Academy of Sciences of the USSR—Headquarters of Soviet Science", see also the anniversary issues of Uspekhi Fizicheskikii Nauk and Zhurnal Tekhnicheskoi Fiziki of October 1967).

Theoretical physics achieved fantastic growth in the years of Soviet rule. A large group of Soviet theoreticians work in the institutes of the Academy, students of L. I. Mandel'shtam and I. E. Tamm, students of L. D. Landau, and students of N. N. Bogolyubov.

With the names of A. I. Alikhanov, L. A. Artsimovich, V. I. Veksler, I. V. Kurchatov, D. V. Skobel'tsyn, and G. N. Flerov is associated the research on elementary-particle physics so fruitfully developed in our country as well as work on accelerator physics and technology directly connected with that advanced field of science. The discoveries made at the large accelerators at Serpukhov and Dubna have received worldwide recongnition.

The successes of prewar nuclear physicists (A. K. Val'ter, Ya. B. Zel'dovich, I. V. Kurchatov, L. V. Mysovskii, K. D. Sinel'nikov, D. V. Skobel'tsyn, and Yu. V. Khariton) determined the creation of nuclear power installations in our country; reactors and nuclear power stations (I. V. Kurchatov, A. I. Alikhanov, A. P. Aleksandrov, and A. I. Leipunskii); our country is indebted to L. A. Artsimovich and his numerous associates and students for successful research in plasma physics which, in the final analysis, is called upon to solve the problem of energy sources.

A whole series of important results in the physics of the condensed state belongs to Soviet scientists. Here, one should first mention the work on the physics of crystals and their stability which had its start in the work carried out at the Leningrad school of A. F. Ioffe and by its head, one of the founders of Soviet physics, A. F. Ioffe, first editor-in-chief of Zhurnal Tekhnicheskoi Fiziki. The researches of L. F. Vereshchagin, N. N. Davidenkov, S. N. Zhurkov, G. V. Kurdyumov, I. V. Obreimov, A. V. Stepanov, and Ya. I. Frenkel' provided the basis for a picture of an actual crystal, served as a foundation on which the present physical theory of stability was constructed, and pointed out means for increasing it which have now been realized in a number of institutes.

Among the precious possessions of Soviet science is the research on nonlinear oscillations by L. I. Mandel'shtam, N. D. Papaleksi, N. M. Krylov, and their students. The work of A. A. Chernyshev, S. A. Vekshinskii, G. A. Grinberg, N. D. Devyatkov, Yu. B. Kobzarev, and S. M. Rytov served as a solid foundation for the development of our radio engineering and the physics of electronic instruments. B. A. Vvedenskii, G. A. Grinberg, D. A. Rozhanskii, and V. A. Fok made a great contribution to research in the propagation of radio waves by their work.

It is well known that our times are characterized by exceptional subdivision and differentiation of science. Perhaps this is explained by the ever-increasing complexity of "final products of production" which incorporate achievements reached in many widely separated fields of science and technology. To the greatest extent, such an assertion is valid for the elements of space technology, and the successes of our country in mastering and studying outer space encompasses the progress achieved in mechanics, physical gas dynamics, computer technology, fuel chemistry, electronics, and radio technology. The name of Academician S. P. Korolev is inseparably associated with these remarkable achievements.

The high regard for radiophysical research fostered primarily at the P. N. Lebedev Physics Institute even in the first years of its existence determined its leading position in such new and revolutionary fields of physics as quantum radiophysics and electronics. The work of A. M. Prokhorov and N. G. Basov and of their numerous associates and followers receives worldwide recognition and fame. Another product of this "hot" field of modern science is semiconductor research which was initially performed at the Physicotechnical Institute in Leningrad and is now being successfully developed in the entire country. From the Leningrad school came work of great economic importance on high-power semiconductor instruments which find application in many branches of industry and transport (V. M. Tuchkevich and associates). Work on the physics of doped transistors (Zh. I. Alferov) appears very promising (and is already finding technical application).

The physics of quasiparticles was born in the Soviet Union (I. E. Tamm, Ya. I. Frenkel', I. M. Lifshits, and others) becoming an integral part of the physics and optics of the solid state and a powerful tool in the study of its electronic properties.

The work of D. S. Rozhdestvenskii, S. I. Vavilov, L. I. Mandel' shtam, G . S. Landsberg, E. F. Gross, A. N. Terenin, and S. E. Frish in optics and spectroscopy brought worldwide fame to this field of Soviet physics. The discovery of the phenomenon of combination scattering, the discovery of the Vavilov—Cerenkov effect (which was explained in the theoretical work of I. E. Tamm and I. M. Frank) became valuable assets in the physics of our century.

For many years, a single Academy of Sciences existed in our country. During the years of Soviet rule, local Academies of Sciences were organized in all the Republics. In addition, a number of specialized Academies were created. The specialized and local Academies made sizeable contributions to scientific and technical progress.

One of the main factors ensuring the success of scientific development is scientific information. In our time, numerous journals in all branches of knowledge have become the main means for regular scientific information.

Where in prerevolutionary years in our country, the single physical journal was essentially the Journal of the Russian Physicochemical Society, and Russian physicists preferred to publish their papers in foreign journals, we now publish tens of journals in all fields of scientific research. Yet despite the considerable expansion of international scientific relations Soviet scientists, as a rule, publish the results of their work in our periodicals; the international prestige of Soviet scientific periodicals increases each day.

At the anniversary celebrations connected with the 250th anniversary of the Academy of Sciences of the USSR, the achievements of Russian physics, its traditions, and new paths added to it by the work of Soviet scientists will be demonstrated to the people of the world.

In the resolution of the Central Committee of the CPSU on the 250th anniversary of the Academy, confidence is expressed that "in observing the anniversary of the Academy of Sciences of the USSR, scientists and groups of scientific research institutions of the country will make every effort to solve the problems formulated by the XXIV Congress of the CPSU, will add new successes in future development of the leading scientific fields and in the introduction of scientific achievements into the sphere of material production, and thereby make a worthy contribution to the national battle for communism." The services of the Academy of Sciences of the USSR were noted by the awarding of two Orders of Lenin (1967 and February 1974).

One can assert with confidence that Soviet scientists will be equal to the problems set before them by the Party and the people.

---

[1] The first Russian elected to the Academy (in October 1733) as assistant in higher mathematics was Vasilii Evdokimovich Adadurov who is remembered for his works in Russian and was known as a writer and translator (subsequently, trustee of Moscow University and honorary member of the St. Petersburg Academy of Sciences.)

[2] It is interesting to recall that Academy was the name of a locality near Athens where there were areas for gymnastic exercises developed for the use of wealthy inhabitants of the Greek capitol. Plato often strolled along the picturesque avenues separating these areas in 388 B. C. surrounded by numerous pupils and admirers, conversing with them on philosphic and scientific subjects. Hence there arose the name "Academic School of Plato" which became the prototype for the modern meaning of this word.

[3] Christian Goldbach himself was an academician in Mathematics in St. Petersburg. His name is well-known even now mainly in connection with the "Goldbach problem" formulated by him in a letter to Euler in 1742. This problem was solved by I. M. Vinogradov, member of the Academy of Sciences of the USSR, in 1937, after two centuries.

[4] It was established that the "physics dissertation" of Lomonosov was read by Lavoisier in particular.

[5] M. V. Ostrogradskii, whom it is impossible to suspect of bias or hostility, said, "Everything I understood in the geometry of Lobachevskii was less than mediocre." It is therefore not surprising that in Bulgarin's "Son of the Motherland" in 1834, there appeared a flippant review of the work of Lobachevskii in which, after recalling the author of the work was an ordinary professor of mathematics, it was said, "Considering everything, I conclude with great probability that the true purpose for which Lobachevskii built and published his Geometry is simply a joke, or better a satire, on mathematicians and perhaps on the scientific writers of our time in general."

[6] P. N. Lebedev was awarded the prize of the Russian Academy of Sciences for this research and was elected an honorary member of the London Royal Society.

[7] This agreement signified a readiness (upon favorable outcome of the balloting) to transfer to St. Petersburg; N. E. Zhukovskii, not desiring to break off his connections in Moscow, turned down the balloting when he was put up for membership in the Academy in 1900 (he was a corresponding member).

Two-dimensional diffraction on a system of straight segments (shields)

G. A. Grinberg

A. F. Ioffe Physicotechnical Institute, Academy of Sciences of the USSR, Leningrad

(Submitted November 13, 1973)
Zh. Tekh. Fiz., 44, 906-915 (May 1974)

The diffraction electromagnetic field created by an arbitrary, sinusoidally time-varying external field with components $E_z^0(x, y)$, $H_x^0(x, y)$, and $H_y^0(x, y)$ is analyzed for a system of perfectly conducting, infinitesimally thin plane shields (bands or strips) of finite or semiinfinite width whose edges are parallel to the z axis; these can touch each other and the planes of the shields form arbitrary angles. In the general case the problem is reduced to a system of Fredholm integral equations of the second kind for the current densities induced in the shields by an arbitrarily located line current. A new method for solving the currents induced by an arbitrary external field in a plate of finite width h is given; this solution is a natural one and has an obvious physical meaning and can be used to get the asymptotic expression for kh ≫ 1 in simple form. As an example, the case of a shield in the shape of a right-angled corner piece is considered; it is shown that certain simplifications are possible.

1. We consider the diffraction of electromagnetic waves coming from a line current source I of frequency ω incident on a system of n straight segments (perfectly conducting shelds) of finite or semiinfinite width; the ends of some of the segments can touch each other to form segments of broken lines (Fig. 1). The current filament I and all the plates (strips) A_1A_1', A_2A_3, A_3A_4, etc., are assumed to be unbounded in the direction perpendicular to the plane of the drawing (OZ axis) and the current distribution in the strips is independent of z. The time variation of the fields and currents is given by the factor $e^{i\omega t}$.

We start from the solution for a single plate of arbitrary width h and we put I = 1, i.e., the primary current is of unit strength. We denote by j(r, α, ξ, h) the density of the total induced current at a point in the plate[1)] at a distance ξ from the left side; r is the distance of the edge from the primary current and α is the angle between the direction of r and the plate.[2)] The density j(r, α, ξ, h) satisfies the integral equation[1]

$$\int_0^h j(r,\ \alpha,\ \xi,\ h)\, H_0^{(2)}(k\,|x-\xi|)\, d\xi = -H_0^{(2)}(k\rho),$$
$$\rho = \sqrt{r^2 - 2rx\cos\alpha + x^2},\quad 0 < x < h,\quad r > 0, \tag{1}$$

where k is the wave number and $H_0^{(2)}(t)$ is the zero-order Hankel function of the second kind of argument t. Condition (1) reflects the requirement that the total electric field at the surface of the plate (shield) should be equal to zero. This field is made up of the contributions from the primary line current and from the induced currents in the shield. We use the well-known expression $E = (-I\pi k/c) \cdot H_0^{(2)}(kR)$ for the field created by a line current I of frequency ω at a distance R.

Knowing the function j (r, α, ξ, h) we can easily set up a system of Fredholm integral equations of the second kind for the current densities induced in the plates. Thus denoting by $j_k(\xi_k)$ (k = 1, 2, . . . , n) the total density of the current induced at point M_k of the k-th plate at a distance $A_kM_k = \xi_k$ from its left edge A_k, and by $r_{ik} = M_iA_k$ the distance from A_k to the point M_i of the i-th plate at a distance $A_iM_i = \xi_i$ from its left edge A_i, putting $\alpha_{ik} = \angle M_iA_kM_k$, denoting by h_k the width of the k-th plate and taking the primary current I to be at the point M_0 (with $M_0A_k = r_{0k}$ and $\angle M_0A_kM_k = \alpha_{0k}$), we get the following relations for $j_k(\xi_k)$:

$$j_k(\xi_k) = Ij(r_{0k},\ \alpha_{0k},\ \xi_k,\ h_k) + \sum_{i \neq k} \int_0^{h_i} j_i(\xi_i)\, j(r_{ik},\ \alpha_{ik},\ \xi_k,\ h_k)\, d\xi_i, \tag{2}$$

where the summation is over all plates except the k-th. The first term on the right side gives the magnitude of the current density induced directly at point M_k of the plate by the primary current I. The second term is obtained by summing the current densities induced at this point by all the elementary (line) currents $j_i(\xi_i)d\xi_i$ flowing in the surfaces of all the other plates. Since these equations can be written for all the plates in the system, they give n interrelated linear Fredholm-type integral equations of the second kind for the n currents $j_k(\xi_k)$, k = 1, 2, 3, . . . , n. The problem can be solved if these currents are found because the electromagnetic fields produced by these currents can be determined by standard techniques. The same considerations hold for the solution of the general problem of diffraction on a given system of perfectly conducting shields of two-dimensional electromagnetic waves, in which only the E_z^0, H_x^0, and H_y^0 components are nonzero because the solution of the above problem as formulated by Eqs. (2) for k = 1, 2, . . . , n gives the Green's function for this class of problem.

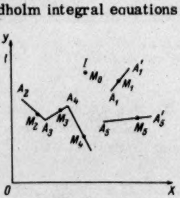

Fig. 1

2. The method requires a knowledge of the function j(r, α, ξ, h). It is well known that it is possible to obtain an exact expression for this in the form of series in Mathieu functions; however, these series are only convenient for numerical calculations when γ = kh is small and we are interested mainly in the question of the asymptotic form of the function j(r, α, ξ, h) when $\gamma \gg 1$. In earlier papers,[2,3] we suggested another approach to the solution of the problem of electromagnetic-wave diffraction on perfectly conducting plane shields and we showed, in particular, that the solution of the most general two-

dimensional problem of diffraction[3] for a strip reduces to an integration if the solution to the prototype problem, formulated by the integral equation

$$\int_0^h j(R,\ \xi,\ h)\, H_0^{(2)}(k|x-\xi|)\, d\xi = -H_0^{(2)}[k(R+x)],$$

$$0<x<h,\ R>0, \tag{3}$$

where $j(R,\ \xi,\ h) = j(R,\ \pi,\ \xi,\ h)$, is known.

In a subsequent paper,[4] the determination of the function $j(R,\ \xi,\ h)$ was reduced to the solution of two independent Fredholm integral equations of the second kind, which could supply the required result for any value of γ and in particular for $\gamma \gg 1$. In this last case, the solution was found in explicit form by iteration to accuracy of $O(\gamma^{-2})$. On the basis of these results, there would be no great difficulty in obtaining a good approximate expression for the function $j(r,\ \alpha,\ \xi,\ h)$ in the case which is of most interest to us, in which γ is not small. This approach, however, leads to rather cumbersome calculations. We have therefore chosen a completely different method of solving the problem, which seems to give quicker results and which provides the solution in the principal approximation in an extremely simple and physically obvious form. We take as our starting point the solution[5] to the problem of electromagnetic-wave diffraction on a perfectly conducting half-plane when the source is a parallel line current I of frequency ω at a distance r from the edge of the half-plane and parallel to it. The direction of r makes an angle α with the half-plane.

The expression for the vector potential $\mathbf{A} = \mathbf{i}_z A_z$ corresponding to the total field is[5]

$$A_z = A(\rho,\ \theta) = \frac{I}{c}\left\{\int_{-b_1}^{\infty} \frac{e^{-ikR_1}}{R_1} d\eta - \int_{-b_2}^{\infty} \frac{e^{-ikR_2}}{R_2} d\eta\right\}, \tag{4}$$

where ρ and θ are the polar coordinates of the point M at which the vector potential is considered (Fig. 2) and

$$\left.\begin{aligned} R_1^2 &= r^2+\rho^2-2r\rho\cos(\theta-\alpha)+\eta^2, \\ R_2^2 &= r^2+\rho^2-2r\rho\cos(\theta+\alpha)+\eta^2, \end{aligned}\right\} \tag{5}$$

$$\left.\begin{aligned} b_1 &= 2\sqrt{r\rho}\cos\frac{\theta-\alpha}{2}, \\ b_2 &= 2\sqrt{r\rho}\cos\frac{\theta+\alpha}{2}. \end{aligned}\right\} \tag{6}$$

We take I = 1.

Remembering that H = curl A, we can easily find the current densities $j_1(\xi)$ and $j_2(\xi)$ induced at the upper (θ = 0) and lower ($\theta = 2\pi$) sides of the half-plane at points distant $\rho = \xi$ from the edge:

$$j_1(\xi) = -\frac{c}{4\pi}(H_r)_{\theta=0} = -\frac{c}{4\pi r}\left(\frac{\partial A}{\partial\theta}\right)_{\theta=0}$$

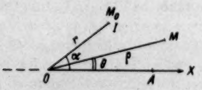

Fig. 2

$$= -\frac{1}{2\pi}\left\{\sqrt{\frac{r}{\xi}}\frac{e^{-ik(r+\xi)}}{r+\xi}\sin\frac{\alpha}{2} + r\sin\alpha\,\psi(-b_0)\right\}, \tag{7}$$

$$j_2(\xi) = \frac{c}{4\pi r}\left(\frac{\partial A}{\partial\theta}\right)_{\theta=2\pi} = -\frac{1}{2\pi}\left\{\sqrt{\frac{r}{\xi}}\frac{e^{-ik(r+\xi)}}{r+\xi}\sin\frac{\alpha}{2} - r\sin\alpha\,\psi(b_0)\right\}$$

$$= -\frac{r\sin\alpha}{2\pi}\int_{r+\xi}^{\infty}\frac{e^{-ikR_0}}{\eta^3}dR_0 = \frac{ir\sin\alpha e^{-ik(r+\xi)}}{2\pi k b_0^3}$$

$$\times\left\{1+\frac{3i}{4\cos^2\frac{\alpha}{2}}\left(\frac{1}{kr}+\frac{1}{k\xi}\right)(1-e^{-ik\mu})\right\}, \tag{8}$$

where μ is some close unknown real number and

$$b_0 = 2\sqrt{r\xi}\cos\frac{\alpha}{2}, \tag{9}$$

$$\psi(b) = \int_b^{\infty}\left(ik+\frac{1}{R_0}\right)\frac{e^{-ikR_0}}{R_0^2}d\eta, \tag{10}$$

$$R_0 = \sqrt{r^2+\xi^2-2r\xi\cos\alpha+\eta^2} \equiv \sqrt{d^2+\eta^2}. \tag{11}$$

Here $d = \sqrt{r^2+\xi^2-2r\xi\cos\alpha}$ is the distance from the current I to the given point of the half-plane.

The total current density induced at a point ξ in the half-plane is[4]

$$j(r,\ \alpha,\ \xi,\ \infty) = j_1(\xi)+j_2(\xi)$$

$$= -\frac{1}{\pi}\left\{\sqrt{\frac{r}{\xi}}\frac{e^{-ik(r+\xi)}}{r+\xi}\sin\frac{\alpha}{2} + \frac{r\sin\alpha}{2}[\psi(-b_0)-\psi(b_0)]\right\}$$

$$= -\frac{1}{\pi}\left\{\sqrt{\frac{r}{\xi}}\frac{e^{-ik(r+\xi)}}{r+\xi}\sin\frac{\alpha}{2} - r\sin\alpha\left[\frac{\pi ki}{2d}H_1^{(2)}(kd)+\psi(b_0)\right]\right\}, \tag{12}$$

where we have used[5]

$$2\psi(0) = \int_{-\infty}^{\infty}\left(ik+\frac{1}{R_0}\right)\frac{e^{-ikR_0}}{R_0^2}d\eta = \psi(b_0)+\psi(-b_0) = -\frac{\pi ki}{d}H_1^{(2)}(kd), \tag{13}$$

so that the difference of the currents is

$$j_1(\xi)-j_2(\xi) = -\frac{r\sin\alpha}{2\pi}[\psi(b_0)+\psi(-b_0)] = -\frac{kir\sin\alpha}{2d}H_1^{(2)}(kd). \tag{14}$$

This last equation can also be obtained directly without use of (7) and (8) because, as is shown in ref. 1, the difference in the current densities $j_1(\xi)$ and $j_2(\xi)$ induced in the two sides of an element of any flat, perfectly conducting shield in the plane y = 0 and placed in an external, time-varying magnetic field $H^0(x,\ y)$ is always subject to the condition

$$j_1(\xi)-j_2(\xi) = -\frac{c}{2\pi}H_x^0(\xi,\ 0); \tag{15}$$

in our case H^0 is the magnetic field of the line current I = 1 passing through the point $M_0(r,\ \alpha)$, so that

$$H_x^0(\xi,\ 0) = -\frac{\pi kir\sin\alpha}{cd}H_1^{(2)}(kd). \tag{16}$$

If we substitute (16) into (15), we obtain (14) and also get the value of the sum $\psi(b_0)+\psi(-b_0)$ in agreement with Eq. (13).

When r > 0 and $\alpha = \pi$, i.e., when I lies on the x axis to the left of the conducting half-plane, the currents $j_1(\xi)$ and $j_2(\xi)$ are equal and are given by

$$j_1(\xi) = j_2(\xi) = -\frac{1}{2\pi}\sqrt{\frac{r}{\xi}}\frac{e^{-ik(r+\xi)}}{r+\xi}. \tag{17}$$

When I is above the half-plane, $j_1(\xi)$ tends with increasing ξ to the value which it would have for the same position of I if the half-plane were replaced by a full plane; the "shadow" current $j_2(\xi)$ decreases rapidly away from the edge.[6] The asymptotic form of this decrease for $kr\cos^2\alpha/2 \gg 1$ and $k\xi\cos^2\alpha/2 \gg 1$ can be obtained from (8) as

$$j_2(\xi) = \frac{i\sin\frac{\alpha}{2}}{8\pi k\sqrt{r}\,\xi^{3/2}\cos^2\frac{\alpha}{2}}\,e^{-ik(r+\xi)}, \tag{18}$$

while for $j_1(\xi)$ under these same conditions we find

$$j_1(\xi) = \frac{\sqrt{k}\,r\sin\alpha}{\sqrt{2\pi}\,d^{3/2}}\,e^{-i\left(kd-\frac{\pi}{4}\right)}. \tag{19}$$

We now find $j(r, \alpha, \xi, h)$. Suppose that the segment OA in Fig. 2 represents a plate of width h on which $0 \le x \le h$. In addition we consider the two including half-planes $0 \le x \le \infty$ and $-\infty \le x \le h$, with edges which correspond respectively with the left and right edges of the given plate and also the full plane $-\infty \le x \le \infty$. We take the plate, the half-planes, and the full plane to be perfectly conducting and we consider the total current densities induced in each of them separately, assuming that the primary field is in all cases produced by the same current $I = 1$ at the point $M_0(r, \alpha)$, $0 < \alpha < \pi$ (Fig. 2). Equation (1) holds for the current density $j(r, \alpha, \xi, h)$ on the plate; the density $j(r, \alpha, \xi, \infty)$ on the first half-plane is

$$\int_0^\infty j(r, \alpha, \xi, \infty)\,H_0^{(2)}(k|x-\xi|)\,d\xi = -H_0^{(2)}(k\rho), \quad 0 < x < \infty, \tag{20}$$

where ρ here and in what follows has the same meaning as in (1); for the second half-plane we obtain[7]

$$\int_{-\infty}^{h} j(r', \alpha', h-\xi, \infty)\,H_0^{(2)}(k|x-\xi|)\,d\xi$$
$$= -H_0^{(2)}(k\rho), \quad -\infty < x < h, \tag{21}$$

where $r' = M_0A$, $\alpha' = \angle M_0AO$; finally, the density $j_0(\xi)$ on the full plane is

$$\int_{-\infty}^{\infty} j_0(\xi)\,H_0^{(2)}(k|x-\xi|)\,d\xi = -H_0^{(2)}(k\rho), \quad -\infty < x < \infty. \tag{22}$$

We now note that it follows directly from (15), which is valid for any plane shield in any electromagnetic field of the type considered in this paper when the shield is a full plane and the sources of external field all lie in the upper half-plane, the total induced current density $\bar{j}_0(\xi)$ is

$$j_0(\xi) = j_1(\xi) = -\frac{c}{2\pi}H_x^0(\xi, 0), \tag{23}$$

since $j_2(\xi) = 0$ (total shielding). Thus (15) can be rewritten as

$$j_1(\xi) - j_2(\xi) = j_0(\xi); \tag{24}$$

this equation relates the difference in the current densities induced on the two sides of any plane shield to the current density induced by the same external field at the same point of the full plane and is of a general nature. In particular, the value of $j_0(\xi)$ for (22) can be obtained from (23) by substituting into this latter equation the value of $H_x^0(\xi, 0)$ given by (16), i.e.,

$$j_0(\xi) = \frac{kir\sin\alpha}{2d}H_1^{(2)}(kd), \quad -\infty \leqslant \xi \leqslant \infty. \tag{25}$$

In what follows we assume that the variable x in (20)-(22) has a value in the interval $0 < x < h$. Subtracting the appropriate terms of (20) from the right and left sides of (1), we get

$$\int_0^h [j(r, \alpha, \xi, h) - j(r, \alpha, \xi, \infty)]\,H_0^{(2)}(k|x-\xi|)\,d\xi$$
$$= \int_h^\infty j(r, \alpha, \xi, \infty)\,H_0^{(2)}(k|x-\xi|)\,d\xi = \int_h^\infty j_0(\xi)\,H_0^{(2)}(k|x-\xi|)\,d\xi$$
$$+ 2\int_h^\infty j_2(\xi)\,H_0^{(2)}(k|x-\xi|)\,d\xi, \quad 0 < x < h, \tag{26}$$

since it follows from (12) and (24) that

$$j(r, \alpha, \xi, \infty) = [j_1(\xi) - j_2(\xi)] + 2j_2(\xi) = j_0(\xi) + 2j_2(\xi).$$

Similarly, subtracting (21) from (1) term by term, we obtain the relationship

$$\int_0^h [j(r, \alpha, \xi, h) - j(r', \alpha', h-\xi, \infty)]\,H_0^{(2)}(k|x-\xi|)\,d\xi$$
$$= \int_{-\infty}^{0} j(r', \alpha', h-\xi, \infty)\,H_0^{(2)}(k|x-\xi|)\,d\xi$$
$$= \int_{-\infty}^{0} j_0(\xi)\,H_0^{(2)}(k|x-\xi|)\,d\xi$$
$$+ 2\int_{-\infty}^{0} j_2'(h-\xi)\,H_0^{(2)}(k|x-\xi|)\,d\xi, \quad 0 < x < h, \tag{27}$$

because

$$j(r', \alpha', h-\xi, \infty) = j_1'(h-\xi) + j_2'(h-\xi), \tag{28}$$

where $j_1'(h-\xi)$ and $j_2'(h-\xi)$ denote the densities of the surface currents induced[8] on the half-plane $(-\infty, h)$.

Finally, subtracting (22) from (1), we get

$$\int_0^h [j(r, \alpha, \xi, h) - j_0(\xi)]\,H_0^{(2)}(k|x-\xi|)\,d\xi$$
$$= \int_h^\infty j_0(\xi)\,H_0^{(2)}(k|x-\xi|)\,d\xi + \int_{-\infty}^{0} j_0(\xi)\,H_0^{(2)}(k|x-\xi|)\,d\xi, \quad 0 < x < h, \tag{29}$$

and adding (26) to (27) and then subtracting (29) we obtain

$$\int_0^h \{j(r, \alpha, \xi, h) - [j(r, \alpha, \xi, \infty) + j(r', \alpha', h-\xi, \infty) - j_0(\xi)]\}$$
$$\times H_0^{(2)}(k|x-\xi|)\,d\xi = 2\int_h^\infty j_2(\xi)\,H_0^{(2)}(k|x-\xi|)\,d\xi$$
$$+ 2\int_{-\infty}^{0} j_2'(h-\xi)\,H_0^{(2)}(k|x-\xi|)\,d\xi$$

$$= 2\left\{\int_0^\infty j_2(h+\eta) H_0^{(2)}(k[\eta + x_1])\,d\eta \right.$$
$$\left. + \int_0^\infty j_2'(h+\eta) H_0^{(2)}(k[\eta + x])\,d\eta]\right\}, \quad 0 < x < h, \tag{30}$$

where $x_1 = h - x$.

If we make use of (3) and the equation which results from it when x is replaced by $x_1 = h - x$ and ξ by $(h - \xi)$

$$\int_0^h j(R, h-\xi, h) H_0^{(2)}(k|x-\xi|)\,d\xi = -H_0^{(2)}[k(R + x_1)], \quad 0 < x < h \tag{31}$$

and introduce the notation

$$w(\xi) = j(r, \alpha, \xi, \infty) + j(r', \alpha', h-\xi, \infty) - j_0(\xi), \quad 0 < \xi < h, \tag{32}$$

for the known quantity which appears in the right side, we find by comparing the right and left sides of (30), (3), and (31) that

$$j(r, \alpha, \xi, h) = w(\xi) - 2\left\{\int_0^\infty j_2(h+\eta)\, j(\eta, h-\xi, h)\,d\eta \right.$$
$$\left. + \int_0^\infty j_2'(h+\eta)\, j(\eta, \xi, h)\,d\eta\right\}, \quad 0 < \xi < h. \tag{33}$$

This is an exact equation, valid for any value of γ. The function $j(\eta, \xi, h)$ has been studied, as noted above, in our earlier paper,[4] where, in particular, the first few terms are calculated for the asymptotic expansion in the case of interest here, $\gamma \gg 1$. It can easily be seen, however, that under this condition Eq. (33) gives the principal asymptotic value directly as

$$j(r, \alpha, \xi, h) = w(\xi) = j(r, \alpha, \xi, \infty) + j(r', \alpha', h-\xi, \infty) - j_0(\xi), \tag{34}$$

since the integrand on the right side of (33) contains only the values of the "shadow" currents $j_2(h + \eta)$ and $j_2'(h + \eta)$ on the corresponding half-planes and there only at distances greater than h from the edges, i.e., where they arise only as a result of diffraction and where for $kh \gg 1$ they are of negligible amplitude.[9] If the integral terms in (33) are taken into account, then the results of ref. 4 must be used; the first approximation to the function $j(\eta, \xi, h)$ can be taken as

$$j(\eta, \xi, h) \cong j(\eta, \xi, \infty) = -\frac{\sqrt{\eta}}{\pi}\frac{e^{-ik(\xi+\eta)}}{(\xi+\eta)\sqrt{\xi}}. \tag{35}$$

We add the following comment. Although (33) has been derived only for the case in which the external field is created by a single line current, it is in fact valid for the case of an arbitrary external field which has only one electric field component $E_z^0(x, y)$ provided that $j(r, \alpha, \xi, h)$ is replaced by the total density $\bar{j}(\xi, h)$ of the currents induced by the external field in a plate lying on the segment $0 \le x \le h$, $j(r, \alpha, \xi, \infty)$ and $j(r', \alpha, h - \xi, \infty)$ are replaced by the current densities induced by the same field in the half-planes $(0, \infty)$ and $(-\infty, h)$ respectively and $j_0(\xi)$ by the density $\bar{j}_0(\xi)$ induced in the plane $(-\infty, \infty)$; $j_2(h + \eta)$ and $j_2'(h + \eta)$ must be taken as the values of the shadow currents in the half-planes.[10] The truth of this statement is obvious, since any external field of this type can be represented as the result of the superposition of fields from current filaments which are discretely or continuously distributed in space around the plate at a finite or infinite distance from it. Formally, it follows from the fact that for any field, all the starting equations (1), (20), (21), and (22) for deriving (33) contain (in their right sides) the function $H_0^{(2)}(k\rho)$, which is equal to $(-c/\pi k)E_z^0$ in the case of a single line current but is replaced by a new function $(-c/\pi k)E_z^0(x, 0)$ for a different field. But since these equations are subtracted from each other in the derivation of (33) and the right sides are generally lost, it is clear that the form of the final equation of the type (33) does not change in the general case.

3. We now apply the method to find the field of a perfectly conducting corner reflector AOB with a cross section (Fig. 3), located in an external field of frequency ω. We show how the solution here and in similar problems can be simplified by using additional considerations. For simplicity we take OA = OB = h and assume that all the external field sources, for which $\mathbf{E} = \mathbf{i}_z E^0(x, y)$, lie in the first quadrant. We denote by $j_x(\xi, h)$ and $j_y(\eta, h)$ the total current densities induced in the sides OA $(0 \le \xi \le h)$ and OB $(0 \le \eta \le h)$ respectively. Writing the condition that the tangential component of the total electric field at the surface of a perfect conductor is zero, we get

$$\int_0^h j_x(\xi, h) H_0^{(2)}(k|x-\xi|)\,d\xi + \int_0^h j_y(\eta, h) H_0^{(2)}(k\sqrt{x^2+\eta^2})\,d\eta$$
$$= E^0(x, 0), \quad 0 < x < h, \tag{36}$$

$$\int_0^h j_x(\xi, h) H_0^{(2)}(k(\sqrt{y^2+\xi^2})\,d\xi + \int_0^h j_y(\eta, h) H_0^{(2)}(k|y-\eta|)\,d\eta$$
$$= E^0(0, y), \quad 0 < y < h. \tag{37}$$

Comparing these equations with those for h = ∞, when the sides OA and OB are two half-planes and when the solution can be obtained directly from the reflection method, we denote the known induced currents by $j_x(\xi, \infty)$ and $j_y(\eta, \infty)$ and find by subtracting (36) and (37) from the corresponding equations with h = ∞, that (say)

$$j_x(\xi, \infty) - j_x(\xi, h) = u(\xi), \quad 0 < \xi < h, \tag{38}$$

$$j_y(\eta, \infty) - j_y(\eta, h) = v(\eta), \quad 0 < \eta < h, \tag{39}$$

and putting $h - x = x_1$, $h - y = y_1$,

$$\int_0^h u(\xi) H_0^{(2)}(k|x-\xi|)\,d\xi = -\int_0^h v(\eta) H_0^{(2)}(k\sqrt{x^2+\eta^2})\,d\eta$$

$$-\int_h^\infty j_x(\xi, \infty) H_0^{(2)}(k|x-\xi|)\,d\xi - \int_h^\infty j_y(\eta, \infty) H_0^{(2)}(k\sqrt{x^2+\eta^2})\,d\eta$$

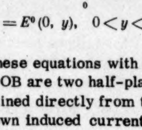

Fig. 3

$$= -\int_0^h v(\eta) H_0^{(2)}(k\sqrt{x^2+\eta^2})\,d\eta - \int_0^\infty j_x(h+\zeta,\ \infty) H_0^{(2)}(k[\zeta+x_1])\,d\zeta$$

$$-\int_h^\infty j_y(\eta,\ \infty) H_0^{(2)}(k\sqrt{x^2+\eta^2})\,d\eta,\quad 0<x<h, \tag{40}$$

$$\int_0^h v(\eta) H_0^{(2)}(k|y-\eta|)\,d\eta = -\int_0^h u(\xi) H_0^{(2)}(k\sqrt{y^2+\xi^2})\,d\xi$$

$$-\int_0^\infty j_y(h+\zeta,\ \infty) H_0^{(2)}(k[\zeta+y_1])\,d\zeta$$

$$-\int_h^\infty j_x(\xi,\ \infty) H_0^{(2)}(k\sqrt{y^2+\xi^2})\,d\xi,\quad 0<y<h. \tag{41}$$

We note that for $\alpha = \pi/2$, Eq. (1) gives

$$\int_0^h j\left(r,\ \frac{\pi}{2},\ \xi,\ h\right) H_0^{(2)}(k|x-\xi|)\,d\xi = -H_0^{(2)}(k\sqrt{x^2+r^2}),\quad 0<x<h, \tag{42}$$

and we use (31) to show that the following relationships follow from (40) and (41) [as in the transition from (30) to (33)]:

$$u(\xi) = \int_0^\infty j_x(h+\zeta,\ \infty)\, j(\zeta,\ h-\xi,\ h)\,d\zeta$$

$$+\int_h^\infty j_y(\eta,\ \infty)\, j\left(\eta,\ \frac{\pi}{2},\ \xi,\ h\right) d\eta$$

$$+\int_0^h j\left(\eta,\ \frac{\pi}{2},\ \xi,\ h\right) v(\eta)\,d\eta,\quad 0<\xi<h, \tag{43}$$

$$v(\xi) = \int_0^\infty j_y(h+\zeta,\ \infty)\, j(\zeta,\ h-\xi,\ h)\,d\zeta$$

$$+\int_h^\infty j_x(\eta,\ \infty)\, j\left(\eta,\ \frac{\pi}{2},\ \xi,\ h\right) d\eta$$

$$+\int_0^h u(\eta)\, j\left(\eta,\ \frac{\pi}{2},\ \xi,\ h\right) d\eta,\quad 0<\xi<h. \tag{44}$$

Introducing the notation

$$f_1(\xi) = \int_0^\infty j_x(h+\zeta,\ \infty)\, j(\zeta,\ h-\xi,\ h)\,d\zeta$$

$$+\int_h^\infty j_y(\eta,\ \infty)\, j\left(\eta,\ \frac{\pi}{2},\ \xi,\ h\right) d\eta, \tag{45}$$

$$f_2(\xi) = \int_0^\infty j_y(h+\zeta,\ \infty)\, j(\zeta,\ h-\xi,\ h)\,d\zeta$$

$$+\int_h^\infty j_x(\eta,\ \infty)\, j\left(\eta,\ \frac{\pi}{2},\ \xi,\ h\right) d\eta, \tag{46}$$

where the given functions may be taken as known,[11] we add and subtract (43) and (44) and put

$$w_\pm(\xi) = u(\xi) \pm v(\xi),\quad 0<\xi<h, \tag{47}$$

to get two independent Fredholm integral equations of the second kind for the functions

$$w_\pm(\xi) = [f_1(\xi) \pm f_2(\xi)] \pm \int_0^h j\left(\eta,\ \frac{\pi}{2},\ \xi,\ h\right) w_\pm(\eta)\,d\eta,\quad 0<\xi<h, \tag{48}$$

where for $\gamma \gg 1$, the function $j(\eta,\ \pi/2,\ \xi,\ h)$ with the plus or minus sign, which plays the role of the kernel and which satisfies the exact equation (33), is given in the main approximation by (34) with $\alpha = \pi/2$. When $\gamma \gg 1$, Eq. (48) can be solved by the method of successive approximations with the functions $\alpha^0_\pm(\xi) = f_1(\xi) \pm f_2(\xi)$ taken as the initial solutions.

We have considered the case of a rectangular corner reflector with equal sides. A similar method can be used for acute angles, corner reflectors with unequal sides, and so on, and the results can be used to solve more complex problems, in which the number of straight-line segments forming the system is greater than 2.

---

[1] That is, the sum of the densities of the currents induced on the two sides of the element of the plate.

[2] We note that when h = ∞ the plate is transformed into a half-plane and the total induced current density at a point is equal to $j(r,\ \alpha,\ \xi,\ \infty)$.

[3] That is, when the external field is independent of the coordinate parallel to the length of the strip.

[4] Compare footnote 2.

[5] The validity of (13) can be tested by putting $\eta = \sinh t$ under the integral sign and using the well-known representation of the Hankel function $H^2_\nu(x) = \left(e^{\frac{i\pi\nu}{2}}/\pi\right)i \int_{-\infty}^{\infty} e^{-ix\,\mathrm{ch}\,\eta-\nu\eta}\,d\eta$, $\mathrm{Im}(x) < 0$. See also the note in the text on Eq. (14).

[6] Providing that the angle α is not too close to zero or π (grazing incidence).

[7] The validity of this equation becomes obvious if we look at Fig. 2 from the plane of the drawing itself; the semiinfinite line $-\infty \le x \le h$ is then directed to the right from point A, where its edge occurs and the line current I = 1 which passes through the point M is at a distance r' from A and is seen from this point to be at an angle α' to AO. But this is exactly the same situation as for the half-plane $(0,\ \infty)$ in Fig. 2 with the sole difference that r is replaced by r', α by α' and that the distance $\xi_1 = h - \xi$ of the given point to A must be taken instead of ξ. The required density is therefore equal to $j(r,\ \alpha',\ \xi_1,\ \infty)$ and this is what is found in Eq. (21).

[8] $j_1'(h-\xi)$ and $j_2'(h-\xi)$ can be obtained from (7) and (8) for $j_1(\xi)$ and $j_2(\xi)$ by replacing r with r', α with α', and ξ with $h-\xi$.

[9] Apart from the cases when the angle α is close to zero or π. Compare the conditions for (18).

[10] It is assumed that the external field sources are all above the plate. If there are also sources below it, the effect of each group can be considered separately as described in the text to give the total effect of a simple arrangement.

[11] At least in the case which interests us when $\gamma \gg 1$.

1. G. A. Grinberg, Zh. Tekh. Fiz., 27, 2595 (1957) [Sov. Phys. – Tech. Phys., 2, 2410 (1957)].
2. G. A. Grinberg, Zh. Tekh. Fiz., 28, 542 (1958) [Sov. Phys. – Tech. Phys., 3, 509 (1958)].
3. G. A. Grinberg, Zh. Tekh. Fiz., 28, 555 (1958) [Sov. Phys. – Tech. Phys., 3, 52 (1958)].
4. G. A. Grinberg, Dokl. Akad. Nauk SSSR, 129, 295 (1959) [Sov. Phys. – Dokl., 4, 1222 (1960)].
5. Yu. V. Vandakurov, Zh. Eksp. Teor. Fiz., 26, 3 (1954).

Conductivity of a medium with inhomogeneous inclusions in a magnetic field

Yu. P. Emets

Institute of Electrodynamics,
Academy of Sciences of the Ukrainian SSR, Kiev

(Submitted July 3, 1973)
Zh. Tekh. Fiz., 44, 916-921 (May 1974)

The two-dimensional electric field in a continuous medium with a low density of inhomogeneous inclusions and an anisotropic conductivity is analyzed. An analytic solution is found for the current distribution near an inhomogeneity; this is used to determine the average macroscopic characteristics of the medium. As the magnetic field is strengthened the current is displaced from the neighborhood of the inhomogeneity, and in a strong magnetic field the effective parameters σ_{eff} and β_{eff} are independent of the magnitude and sign of fluctuations in the system; these become functions of the volume of the inhomogeneous inclusions.

In this work we analyze the electric field in a continuous medium containing inhomogeneous inclusions and which is in a homogeneous magnetic field. We determine the average macroscopic characteristics of such a medium, which has an anisotropic conductivity. We find that for inclusions which are cylinders parallel to the magnetic lines of force or, equivalently, films and plates with inclusions, the current is displaced from the neighborhood of an inhomogeneity as the magnetic field is strengthened. A solution is obtained for the case of a low density of inclusions for an arbitrary difference between the conductivities and Hall parameters of the host (σ_1, β_1) and the disperse phase (σ_2, β_2). In a strong magnetic field the effective parameters σ_{eff} and β_{eff} are independent of the magnitude and sign of the fluctuations in the system and are functions of the volume of inhomogeneous inclusions alone.

In a plasma or a semiconductor in a magnetic field the conductivity is a tensor quantity, and the current distribution is sensitive to inhomogeneities in the medium. At large values of the Hall parameter ($\beta_1 \gg 1$) the appearance of even extremely slight fluctuations in the parameters can lead to a significant perturbation of the electric fields and thus changes in the properties of the medium as a whole.

For the electric fields averaged over a region, the influence of the inhomogeneities can be related to the changes in the electrical properties of the medium; quantitative characteristics of these properties are the effective values σ_{eff} and β_{eff}. It has been shown for stratified media[1-4] and for systems in which regions having different properties are distributed equiprobably[5] that these parameters are quite sensitive to the specific structure of the inhomogeneities. We consider a system consisting of a continuous medium with conductivity σ_1 and a Hall parameter β_1 containing inclusions extended along the lines of force of the external magnetic field and which has parameters σ_2 and β_2. Plates and films can also be described on the basis of this model; in these cases the fluctuation pattern is two-dimensional. We assume the dimensions of the inhomogeneities to be small in comparison with the distances between them, and we assume that the inhomogeneities do not interact with each other. In other words, we assume a low density of inclusions. Under these conditions, as in the papers cited above, the problem of determining σ_{eff} and β_{eff} can be solved analytically for arbitrary differences between the parameters σ_1, β_1, and σ_2, β_2.

1. CURRENT DISTRIBUTION NEAR AN INHOMOGENEITY

Under the conditions of this problem calculation of the field in the medium reduces to calculation of the current distribution near a single inhomogeneous inclusion and averaging of the field over the entire system.

We are to find the current distribution by working from the system of equations

$$\left.\begin{aligned} \mathbf{j}+\frac{\beta}{B}\mathbf{j}\times\mathbf{B}-\sigma\mathbf{E}=0,\\ \nabla\mathbf{j}=0,\quad \nabla\times\mathbf{E}=0. \end{aligned}\right\} \tag{1.1}$$

The Hall effect is taken into account in Ohm's law.

The external magnetic field is assumed to be homogeneous everywhere, and the self magnetic field of the current in the system is assumed to be negligible. At the interface between the two media we have the ordinary electrodynamic conditions: continuity of the current component normal to the boundary and continuity of the tangential component of the electric field. The field is assumed to be homogeneous at infinity and equal to some effective field; this effective field is set up by (in addition to the external sources) all inhomogeneous inclusions other than the one under consideration.

System (1.1) permits the introduction in the complex $\zeta = \rho e^{i\theta}$ plane of the analytic function $j(\zeta) = e^{i\theta}[j_\rho(\rho, \theta) + ij_\theta(\rho, \theta)]$. The theory of the Riemann boundary-value problem[6,7] furnishes a convenient apparatus for determining $j(\zeta)$.

We represent the inhomogeneous inclusion by the area S^+ ($|\zeta| < 1$) enclosed by circle L ($|\zeta| = 1$). We adopt as the positive direction on L that for which the exterior of the circle, S^-, is on the right.

This model is quite general, since any case involving an inhomogeneous inclusion specified by a finite region Σ, bounded by a smooth closed contour l which satisfies the Lyapunov condition can be transformed to the case considered here by means of a conformal mapping $z = \omega(\zeta)$ of Σ into S^+.

We introduce the piecewise-holomorphic function

$$\Psi_1(\zeta)=\begin{cases}\Psi_1^+(\zeta)=j_1(\zeta) & \text{for } |\zeta|<1,\\ \Psi_1^-(\zeta)=\overline{j_1(1/\bar{\zeta})} & \text{for } |\zeta|>1,\end{cases} \tag{1.2}$$

where $\Psi_1^-(\zeta)$ takes on the values which are the conjugates of $\Psi_1^+(\zeta)$ at the points which are the reflections of the points ζ with respect to the circle L. Similarly, we introduce the function $\Psi_2(\zeta)$:

$$\Psi_2(\zeta)=\begin{cases}\Psi_2^+(\zeta)=\overline{j_2(1/\bar\zeta)} & \text{for } |\zeta|<1,\\ \Psi_2^-(\zeta)=j_2(\zeta) & \text{for } |\zeta|>1.\end{cases} \tag{1.3}$$

The components of the functions $\Psi_1^-(\zeta)$ and $\Psi_2^+(\zeta)$ are the unknown values of the complex current outside and inside an inhomogeneity. In all the equations below, subscripts "1" and "2" refer to the host and disperse phases, respectively.

Using one of the two boundary conditions at L,

$$j_{\rho1}(1,\ \theta)=j_{\rho2}(1,\ \theta)=\gamma(\theta), \tag{1.4}$$

and using the functions $\Psi_1(\zeta)$ and $\Psi_2(\zeta)$ introduced here, we can construct two Riemann boundary-value problems:

$$\left.\begin{aligned}\Psi_1^+(t)&=-t^2\Psi_1^-(t)+2t\gamma(\theta),\\ \Psi_2^+(t)&=-\frac{1}{t^2}\Psi_2^-(t)+\frac{2}{t}\gamma(\theta)\end{aligned}\right\} \tag{1.5}$$

($t = e^{i\theta}$, $0 \le \theta \le 2\pi$).

The implicit solution of these problems [in which $\gamma(\theta)$ remains unknown] yields equations which we need below to relate the tangential current components at the interface between the media.

In the first problem in (1.5) the index is positive ($\varkappa = 2$) so that a solution bounded at infinity is given by

$$\Psi_1(\zeta)=\frac{1}{\pi i}\int_L\frac{t\gamma(\theta)\,dt}{t-\zeta}-\bar a\zeta^2-\bar b\zeta-\bar c. \tag{1.6}$$

Here, a, b, and c are complex constants. It can be shown, by exploiting the properties of Cauchy integrals, that these constants are governed by the value of $\Psi_1(\zeta)$ at the origin (the primes denote differentiation with respect to ζ):

$$a=\Psi_1(0),\quad b=\Psi_1'(0),\quad c=\frac{1}{2}\Psi_1''(0). \tag{1.7}$$

In (1.6) we have

$$\left.\begin{aligned}a+\bar c&=\frac{1}{\pi i}\int_L\gamma(\theta)\,dt,\\ b+\bar b&=\frac{1}{\pi i}\int_L\gamma(\theta)\frac{dt}{t}=\frac{1}{\pi i}\int_L\gamma(\theta)\,d\theta.\end{aligned}\right\} \tag{1.8}$$

The solution of the second Riemann boundary-value problem in (1.5) is

$$\Psi_2(\zeta)=\frac{1}{\pi i}\int_L\frac{\gamma(\theta)\,dt}{t(t-\zeta)}. \tag{1.9}$$

Since the index of this problem is negative ($\varkappa = -2$), solution (1.9) exists only if an additional condition is satisfied; in this case, this condition reduces to the vanishing of the quantity in the second equation in (1.8). Accordingly, b can take on only purely imaginary values. The integral on the right-hand side of this equation gives the total current flowing across the interface between the two media. This current vanishes since there are no current sources or sinks in region S^+. We see that the formal condition for the solvability of the inhomogeneous Riemann boundary-value problem with the negative index takes on a completely definite physical meaning.

Using (1.8) we convert the equations for $\Psi_1(\zeta)$ and $\Psi_2(\zeta)$ to

$$\left.\begin{aligned}\Psi_1(\zeta)&=\frac{\zeta}{\pi i}\int_L\frac{\gamma(\theta)\,dt}{t-\zeta}-\bar a\zeta^2+a-\bar b\zeta,\\ \Psi_2(\zeta)&=\frac{\zeta^{-1}}{\pi i}\int_L\frac{\gamma(\theta)\,dt}{t-\zeta}.\end{aligned}\right\} \tag{1.10}$$

Now, comparing the limiting values of $\Psi_1(\zeta)$ and $\Psi_2(\zeta)$ found by means of the Plemelj equations as ζ approaches L, e.g., from within the circle,

$$\frac{1}{t}\Psi_1^+(t)=\gamma(\theta)+\frac{1}{\pi i}\int_L\frac{\gamma(\theta)\,d\tau}{\tau-t}-\bar a t+a\frac{1}{t}-\bar b,$$

$$t\Psi_2^+(t)=\gamma(\theta)+\frac{1}{\pi i}\int_L\frac{\gamma(\theta)\,d\tau}{\tau-t},$$

we find an equation relating the tangential current components $j_{\theta1}$ and $j_{\theta2}$ at the interface:

$$j_{\theta1}(t)+j_{\theta2}(t)=t\left(-a\frac{1}{t}+\bar a t+b\right). \tag{1.11}$$

Turning to the second boundary condition at L,

$$E_{\theta1}(1,\ \theta)=E_{\theta2}(1,\ \theta),$$

we note that we can write it in the following manner by using Ohm's law:

$$-\frac{\beta_1}{\sigma_1}j_{\rho1}+\frac{1}{\sigma_1}j_{\theta1}=-\frac{\beta_2}{\sigma_2}j_{\rho2}+\frac{1}{\sigma_2}j_{\theta2}.$$

Using the limiting values of the current on L and Eqs. (1.2) and (1.3) we find two Riemann boundary-value problems:

$$\left.\begin{aligned}\Psi_1^+(t)&=\frac{\sigma_1+\sigma_2-i(\sigma_2\beta_1-\sigma_1\beta_2)}{\sigma_1+\sigma_2+i(\sigma_2\beta_1-\sigma_1\beta_2)}t^2\Psi_1^-(t)\\ &\quad-\frac{2\sigma_1(\bar a t^2+\bar b t-a)}{\sigma_1+\sigma_2+i(\sigma_2\beta_1-\sigma_1\beta_2)},\\ \Psi_2^+(t)&=\frac{\sigma_1+\sigma_2-i(\sigma_2\beta_1-\sigma_1\beta_2)}{\sigma_1+\sigma_2+i(\sigma_2\beta_1-\sigma_1\beta_2)}\frac{1}{t^2}\Psi_1^-(t)\\ &\quad+\frac{2\sigma_1(\bar a t^2+\bar b t-a)}{\sigma_1+\sigma_2+i(\sigma_2\beta_1-\sigma_1\beta_2)}.\end{aligned}\right\} \tag{1.12}$$

The solution for $\Psi_2(\zeta)$ in region S^+ is

$$\Psi_2(\zeta)=\frac{2\sigma_2}{\sigma_1+\sigma_2+i(\sigma_2\beta_1-\sigma_1\beta_2)}\left(\bar a-\frac{b}{\zeta}\right).$$

All the conditions of the original boundary-value problem are satisfied if we set b = 0. The physical meaning of this condition is that there is no circulation of current around the cylinder. Using this condition we find a solution for the second boundary-value problem in (1.12) for the region S^-:

$$\Psi_1(\zeta)=\frac{\sigma_2-\sigma_1+i(\sigma_2\beta_1-\sigma_1\beta_2)}{\sigma_1+\sigma_2-i(\sigma_2\beta_1-\sigma_1\beta_2)}\frac{a}{\zeta^2}+\bar a.$$

The constant a is determined from the condition of the specified homogeneous current at infinity, $\Psi_1(\infty) = J_0$.

Accordingly, the current distribution in the neighborhood of a circular inhomogeneity of radius R is

$$j(\zeta)=\begin{cases}\dfrac{\sigma_2-\sigma_1+i(\sigma_2\beta_1-\sigma_1\beta_2)}{\sigma_1+\sigma_2-i(\sigma_2\beta_1-\sigma_1\beta_2)}J_0\dfrac{R^2}{\zeta^2}+J_0 & \text{for } |\zeta|>R,\\ \dfrac{2\sigma_2}{\sigma_1+\sigma_2+i(\sigma_2\beta_1-\sigma_1\beta_2)} & \text{for } |\zeta|<R,\end{cases} \tag{1.13}$$

$$j(\zeta)=j_\xi(\xi,\ \eta)-ij_\eta(\xi,\ \eta)=e^{-i\theta}(j_\rho(\rho,\ \theta)-ij_\theta(\rho,\ \theta)).$$

A characteristic property of this solution is that the current distribution within the circle is homogeneous. If the conductivity is isotropic ($\beta_1 = \beta_2 = 0$) or $B=0$ the current within the circle, j_2, flows in the same direction as the current at infinity, J_0, differing from the latter only in magnitude. The current is drawn toward or repelled from the inhomogeneity, depending on the ratio between the conductivities and inclusions, σ_1 and σ_2.

If there is a Hall effect the current j_2, while remaining homogeneous, is rotated around J_0 through an angle (the reduced Hall angle)

$$\pi\varepsilon = \operatorname{arc\,tg}\frac{\sigma_2\beta_1 - \sigma_1\beta_2}{\sigma_1 + \sigma_2}, \quad 0 \leqslant |\varepsilon| < \frac{1}{2}. \tag{1.14}$$

We see from Eq. (1.13) that as the magnetic field is strengthened the current near the inclusion always decreases, regardless of the difference between σ_1 and σ_2. This decrease, by a factor of $(1 + \tan^2 \pi\varepsilon)^{1/2}$, is governed solely by the difference between the Hall constants $R_{Bi} = \beta_i/\sigma_i B_i$ ($i = 1, 2$) and the magnitude of the external magnetic field. For example, when σ_1 is finite but $\sigma_2 \to \infty$, we have $|j_2| \to 2J_0/(1 + \beta_1^2)^{1/2}$, i.e., in a strong magnetic field the current is displaced, even from ideally conducting inclusions, by an amount which is proportional to the Hall parameter of the host (β_1).

2. EFFECTIVITY CONDUCTIVITY OF AN INHOMOGENEOUS MEDIUM WITH AN ANISOTROPIC CONDUCTIVITY

Using the current distribution found here we can determine the effective conductivity σ_{eff} and the effective Hall parameter β_{eff} of a medium using inhomogeneous inclusions.

We must find the complex (because of the anisotropy in the conductivity) proportionality coefficient between the space averages of the field quantities J_{eff} and E_{eff}.

Using the complex form of Ohm's law

$$j_k(\zeta) = \frac{\sigma_k}{1 + i\beta_k} E_k(\zeta) \quad (k = 1, 2),$$

we consider the following integral for averaging over the volume:

$$\frac{1}{S}\int\left(E - \frac{1 + i\beta_1}{\sigma_1} j\right) ds \equiv E_{\text{eff}} - \frac{1 + i\beta_1}{\sigma_1} J_{\text{eff}}.$$

Here we have assumed that a homogeneous current equal to the effective current J_{eff} flows with respect to impurities in the medium. The integrand is nonvanishing only within the inhomogeneities. The contribution of the overall field from the component of the field within the inclusions is proportional to the inclusion volume λ. We therefore have

$$E_{\text{eff}} = \frac{1 + i\beta_1}{\sigma_1} J_{\text{eff}} + \lambda\left(E_2 - \frac{1 + i\beta_1}{\sigma_1} j_2\right),$$

from which we find, using Eq. (1.13) (where we must use J_{eff} instead of J_0), the equation

$$\frac{1 + i\beta_{\text{eff}}}{\sigma_{\text{eff}}} = \frac{1}{\sigma_1}\Big[1 + i\beta_1 + 2\lambda\frac{(\sigma_1 - \sigma_2)(\sigma_1 + \sigma_2) + (\sigma_2\beta_1 - \sigma_1\beta_2)^2 - 2i\sigma_2(\sigma_2\beta_1 - \sigma_1\beta_2)}{(\sigma_1 + \sigma_2)^2 + (\sigma_2\beta_1 - \sigma_1\beta_2)^2}\Big].$$

Hence

$$\left.\begin{aligned} \sigma_{\text{eff}} &= \sigma_1\left(1 + 2\lambda\frac{\Delta + \operatorname{tg}^2\pi\varepsilon}{1 + \operatorname{tg}^2\pi\varepsilon}\right)^{-1}, \\ \beta_{\text{eff}} &= \left(\beta_1 - \frac{4\lambda\sigma_2}{\sigma_1 + \sigma_2}\frac{\operatorname{tg}\pi\varepsilon}{1 + \operatorname{tg}^2\pi\varepsilon}\right)\left(1 + 2\lambda\frac{\Delta + \operatorname{tg}^2\pi\varepsilon}{1 + \operatorname{tg}^2\pi\varepsilon}\right)^{-1}. \end{aligned}\right\} \tag{1.15}$$

Here $\Delta = (\sigma_1 - \sigma_2)/(\sigma_1 + \sigma_2)$ is the relative magnitude of the conductivity fluctuation and $\pi\varepsilon$ is the reduced Hall angle given by Eq. (1.14).

If the conductivity is isotropic ($\beta_1 = \beta_2 = 0$) the quantity σ_{eff} is a function not only of the magnitude, but also the sign of the fluctuation Δ:

$$\sigma_{\text{eff}} = \frac{\sigma_1}{1 + 2\lambda\Delta} \quad (-1 \leqslant \Delta \leqslant 1).$$

These results are valid to first order in λ, so the equation given above can also be written as

$$\sigma_{\text{eff}} = \sigma_1(1 - 2\lambda\Delta).$$

If, on the other hand, there is a Hall effect in the medium, we find that in a strong magnetic field ($\tan^2 \pi\varepsilon \gg 1$), according to (1.15), the effective parameters are altogether independent of the fluctuations in the properties of the medium:

$$\sigma_{\text{eff}} = \frac{\sigma_1}{1 + 2\lambda}, \quad \beta_{\text{eff}} = \frac{\beta_1}{1 + 2\lambda}. \tag{1.16}$$

We see that in the cases of the limiting values of the fields both σ_{eff} and β_{eff} are always smaller than the corresponding parameters of the host phase (σ_1, β_1), regardless of the properties of the inhomogeneous inclusions. The only governing factor is the volume of these inclusions.

---

[1] E. P. Velikhov, Proceedings of the Conference on MHD, Newcastle, 1962.

[2] D. J. Rose, Phys. Fluids, 5, 9 (1962).

[3] C. Herring, J. Appl. Phys., 31, 1939 (1960).

[4] Yu. P. Emets, Prikl. Matem. Mekh., 36, 617 (1972).

[5] A. M. Dykhne, Zh. Eksp. Teor. Fiz., 59, 641 (1970) [Sov. Phys. – JETP, 32, 348 (1971)].

[6] F. D. Gakhov, Boundary-Value Problems [in Russian], GIFML, Moscow (1963).

[7] N. I. Muskhelishvili, Singular Integral Equations [in Russian], GIFML, Moscow (1962).

Nonlinear polarizability of a gaseous medium in a longitudinal magnetic field

V. A. Sokolov and L. M. Khayutin

A. A. Zhdanov Leningrad State University

(Submitted June 25, 1973)
Zh. Tekh. Fiz., 44, 922-927 (May 1974)

The polarizability of an active (single-isotope) gaseous medium in a fixed magnetic field is calculated in third order in the electric field. The two-mode linear and nonlinear interaction coefficients are calculated for modes with different polarization states. In ring gas lasers with broad Doppler gain spectrum, in a fixed longitudinal magnetic field the nonlinear interaction between modes is due primarily to three effects: 1) the formation of Bennett dips (or peaks), 2) modulation of the population, and 3) excitation of atoms in a coherent superposition of Zeeman sublevels (Hertz coherence).

INTRODUCTION

Several experimental and theoretical papers have appeared recently on the nonlinear interaction of traveling waves with different polarization states in an active gaseous medium in a fixed magnetic field.[1-5] In two-mode ring lasers the electromagnetic field can be represented by eight traveling waves with different polarization states [see Eq. (1) and Fig. 1]. The nonlinear polarizability of a gaseous medium in a magnetic field must be calculated, and the linear and nonlinear coefficients for the traveling-wave interaction must be found, in order to determine the stability regions for various lasing regimes in a ring laser and to determine the frequency characteristics of a ring laser for several problems in laser spectroscopy.[6] The effect of a magnetic field on the operation of a ring laser is of experimental as well as theoretical interest (e.g., in connection with the ring laser in the geomagnetic field and the laser gyroscope). The polarization of the modes in a ring laser is governed by both the properties of the cavity (including those of asymmetric elements inserted in the cavity) and the characteristics of the active medium. The calculated interaction coefficients, given in Eqs. (8) below, can be used to analyze cases of various mode polarizations.[1)]

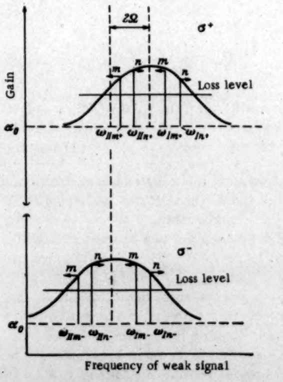

Fig. 1. Splitting of the Doppler gain spectrum in a fixed longitudinal magnetic field (Ω) into two spectra (the Landé g factors are assumed to be identical) corresponding to the σ^+ and σ^- transitions. In a two-mode ring laser (ω_I and ω_{II}) the frequencies of oppositely directed waves of each mode split, because of rotation or because of the insertion of noninteracting element into the cavity, into a total of four waves with right-hand circular polarization (+) and four waves with left-hand circular polarization (−) (here n and m give the propagation directions).

We use the semiclassical approach[8] to analyze the nonlinear polarizability of a single-isotope active gaseous medium. We treat the active medium as a set of atoms in which a dipole transition can occur between two excited states, a and b (with total angular momenta j_a and j_b). The gaseous medium is in a fixed magnetic field along the laser axis, the z axis (z and −z are the propagation directions of the traveling waves). We also choose the z axis as the quantization axis. We find the coefficients for the linear and nonlinear interactions [see Eqs. (8)] for eight traveling waves with various polarization states (Fig. 1) in third-order perturbation theory in the laser field [see (3)].

NONLINEAR POLARIZABILITY OF A GASEOUS MEDIUM

We assume an active gaseous medium in a fixed magnetic field H. We assume the Zeeman splitting $\Omega = g\mu_\beta H$ to be the same for the upper (a) and lower (b) levels (g is the Landé g factor and μ_β is the Bohr magneton).

We write the field in the two-mode ring laser, E(z, t), as eight traveling waves (Fig. 1) in a circular coordinate system:

$$\left.\begin{aligned} E(z,\ t) &= \sum_{p=(I,II)} \sum_{\binom{r=(n,m)}{s=(+1,-1)}} \{(-1)^s \hat{e}_{-s} \mathcal{E}_{prs}(t) \\ &\quad \times \exp[-i(\omega_{prs} t - k_{prs} z)] + \text{c.c.}\}, \\ \mathcal{E}_{prs}(t) &= E_{prs}(t) \exp[-i\varphi_{prs}(t)],\ k_{pns} = -k_{pms} > 0, \\ \hat{e}_s &= -\frac{s}{\sqrt{2}}(\hat{e}_x + is\hat{e}_y),\ s = (\pm 1), \end{aligned}\right\} \tag{1}$$

where $s = \pm 1$ is the index of the circular coordinate; p = I, II is the mode index, r = n, m is the propagation direction of the wave; and $k_{pns} = (2\pi q_n)/L$, where q_n is a large integer, L is the perimeter of the cavity, and ω_{prs} is the circular frequency of wave "prs."

The system of truncated equations for the electric field is

$$\left.\begin{aligned} \frac{d\mathcal{E}_{prs}}{dt} &= i(\omega_{prs} - \nu_{prs})\mathcal{E}_{prs} - \frac{\delta\omega_p}{2}\mathcal{E}_{prs} + \frac{2\pi i\omega_{prs}}{\varepsilon} P_{prs}(t), \\ p &= (I,\ II),\ r = (n,\ m),\ s = (\pm 1), \end{aligned}\right\} \tag{2}$$

where ν_{prs} is the cavity frequency of wave "prs," and ε is the dielectric constant of the medium, neglecting the transition under consideration.

To third order in perturbation theory in the laser field, for which case

$$\frac{|(j_a\|d\|j_b)E|^2}{\hbar^2\gamma_{ab}}\left(\frac{1}{\gamma_a}+\frac{1}{\gamma_b}\right)\ll 1, \tag{3}$$

where $(j_a\|d\|j_b)$ is the reduced matrix element of the dipole transition between working levels *a* and b, we can write the polarizability of the active medium $P_{prs}(t)$ as

$$\left.\begin{aligned}
P_{prs}(t)&=\frac{s\mathcal{E}_{prs}}{2\pi i\omega_{prs}}\Big\{i\chi^{(p)}_{rs}+i\sum_{(p_1,r_1,s_1)}\chi^{(p,p_1)}_{rsr_1s_1}|\mathcal{E}_{p_1r_1s_1}|^2\Big\}\\
&+\frac{s}{2\pi i\omega_{prs}}\{i\mathcal{E}_{pr-s}\mathcal{E}_{pr's}\mathcal{E}^*_{pr'-s}\chi^{(p,p')}_{rsr-sr'sr'-s}\\
&+i\mathcal{E}_{pr-s}\sum_{(r_1)}\chi^{(p,p')}_{rsr-sr_1sr_1-s}\mathcal{E}_{p'r_1s}\mathcal{E}^*_{p'r_1-s}\\
&+i\frac{N_2}{N}\mathcal{E}^*_{p'r'-s}\sum_{(s_1)}\chi^{(p,p')}_{rsr's_1r-s_1r'-s}\mathcal{E}_{pr's}\mathcal{E}_{p'r-s_1}\exp(i\omega_{pp'}t)\\
&+i\frac{N_2}{N}\chi^{(p,p')}_{rsr'srsr's}\mathcal{E}_{pr'r}\mathcal{E}_{p'rs}\mathcal{E}^*_{p'r's}\exp(i\omega_{pp'}t),\\
&p\neq p'=(\mathrm{I},\ \mathrm{II}),\qquad p_1=(p,\ p')\\
&r\neq r'=(n,\ m),\qquad r_1=(r,\ r')\\
&s=(\pm 1),\qquad s_2=(s,\ -s),
\end{aligned}\right\} \tag{4}$$

where $\omega_{pp'}=(\omega_{pr}-\omega_{pr'})-(\omega_{p'r}-\omega_{p'r'})$; $\omega_{pr}=(1/2)\cdot(\omega_{prs}+\omega_{pr-s})$, and N_2/N is the Fourier component of the relative amount by which the pumping exceeds the threshold level. This component is a function of the difference between the wave numbers and the relative arrangement and length of the tubes containing the active medium. In the approximation

$$\left\{\begin{aligned}k_{prs}=k_{pr-s}\equiv k_{pr},\\ k_{pn}=-k_{pm}\equiv k_p>0\end{aligned}\right\} \tag{5}$$

we can write N_2/N as (see ref. 7 for more details)

$$\frac{N_2}{N}=\frac{\frac{1}{L}\int\limits_0^L N(z)\exp[-i(k_p-k_{p'})z]\,dz}{\frac{1}{L}\int\limits_0^L N(z)\,dz}. \tag{6}$$

Taking account of the total angular momenta j_a and j_b for a single-isotope gaseous medium in the case

$$\left.\begin{aligned}\eta^2=\left(\frac{\gamma_{ab}}{ku}\right)^2\ll 1,\\ (\omega_{\mathrm{I}}-\omega_{\mathrm{II}})^2\ll(ku)^2\end{aligned}\right\} \tag{7}$$

[where $\gamma_{ab}\geq 1/2(\gamma_a+\gamma_b)$ is the homogeneous half-width of the radiation line, $1/\gamma_a$ and $1/\gamma_b$ are the lifetimes of excited levels *a* and b, and ku is the half-width of the Doppler amplification spectrum], we can write the coefficients for the linear and nonlinear wave interactions in Eq. (4) as

$$\begin{aligned}
\chi^{(p)}_{rs}&=-i\frac{N\delta\omega_p}{2N_{\mathrm{thr}}}(1-\eta^2f^2_{prs})+\frac{\eta}{2\sqrt{\pi}}\frac{N\delta\omega_p}{N_{\mathrm{thr}}}f_{prs},\\
\chi^{(p,p)}_{rsrs}&=iB_0\left(\frac{1}{\varkappa_a}+\frac{1}{\varkappa_b}\right),\\
\chi^{(p,p)}_{rsr-s}&=iB_1\left(\frac{1}{\varkappa_a\zeta^{pr-s}_{prs}}+\frac{1}{\varkappa_b\zeta^{pr-s}_{prs}\zeta^{pr-s(b)}_{prs}}\right)+iB_2\,(a\leftrightarrow b),\\
\chi^{(p,p)}_{rsr's}&=\frac{iB_0}{\xi^{pr's}_{prs}}\left(\frac{1}{\varkappa_a}+\frac{1}{\varkappa_b}\right),\\
\chi^{(p,p)}_{rsr'-s}&=\frac{i}{\xi^{pr'-s}_{prs}}\left(\frac{B_1}{\varkappa_a}+\frac{B_2}{\varkappa_b}\right),\\
\chi^{(p,p')}_{rsrs}&=\frac{iB_0}{\zeta^{p'rs}_{prs}}\left(\frac{1}{\varkappa_a}+\frac{1}{\varkappa_a\zeta^{p'rs(a)}_{prs}}\right)+iB_0\,(a\leftrightarrow b),\\
\chi^{(p,p')}_{rsr-s}&=\frac{iB_1}{\zeta^{p'r-s}_{prs}}\left(\frac{1}{\varkappa_a}+\frac{1}{\varkappa_b\zeta^{p'r-s(b)}_{prs}}\right)+iB_2\,(a\leftrightarrow b),\\
\chi^{(p,p')}_{rsr's}&=\frac{iB_0}{\xi^{p'r's}_{prs}}\left(\frac{1}{\varkappa_a}+\frac{1}{\varkappa_b}\right),\\
\chi^{(p,p')}_{rsr'-s}&=i\left(\frac{B_2}{\varkappa_b}+\frac{B_1}{\varkappa_a}\right)\frac{1}{\xi^{p'r'-s}_{prs}},\\
\chi^{(p,p)}_{rsr-sr'sr'-s}&=\frac{iB_1}{\xi^{pr's}_{prs}}\left(\frac{1}{\varkappa_b\zeta^{pr-s(b)}_{prs}}\right)+iB_2\,(a\leftrightarrow b),\\
\chi^{(p,p')}_{rsr-srsr-s}&=\frac{iB_1}{\zeta^{p'r-s}_{prs}}\left(\frac{1}{\varkappa_a\zeta^{p'r-s(a)}_{prs}}+\frac{1}{\varkappa_b\zeta^{pr-s(b)}_{prs}}\right)+iB_2\,(a\leftrightarrow b),\\
\chi^{(p,p')}_{rsr-sr'sr'-s}&=iB_1\left(\frac{1}{\varkappa_b\zeta^{pr-s(b)}_{prs}\xi^{p'r's}_{prs}}\right)+iB_2\,(a\leftrightarrow b),\\
\chi^{(p,p')}_{rsr'srsr's}&=iB_0\left(\frac{1}{\varkappa_a\zeta^{p'r's(a)}_{pr's}\left(\xi^{pr's}_{prs}+\frac{i\Delta_{pp'}}{2}\right)}\right)+iB_0\,(a\leftrightarrow b),\\
\chi^{(p,p')}_{rsr'sr-sr'-s}&=iB_1\left(\frac{1}{\varkappa_b\zeta^{p'r'-s(b)}_{pr's}\left(\xi^{pr's}_{prs}+\frac{i\Delta_{pp'}}{2}\right)}\right)+iB_2\,(a\leftrightarrow b),\\
\chi^{(p,p')}_{rsr'-srsr'-s}&=iB_1\left(\frac{1}{\varkappa_a\zeta^{p'r'-s(a)}_{pr'-s}\left(\xi^{pr'-s}_{prs}+\frac{i\Delta_{pp'}}{2}\right)}\right)+iB_2\,(a\leftrightarrow b),\\
&p\neq p',\quad r\neq r'.
\end{aligned} \tag{8}$$

In Eq. (8) we have used

$$\left.\begin{aligned}
\frac{N}{N_{\mathrm{thr}}}&=\frac{(N_a-N_b)4\pi^{3/2}Q_{pr}|(j_a\|d\|j_b)|^2}{3\hbar ku\varepsilon},\\
B_i(j_a,\ j_b)&=\frac{3}{2}\frac{N\delta\omega_p}{N_{\mathrm{thr}}}\frac{|(j_a\|d\|j_b)|^2}{\hbar^2\gamma^2_{ab}}G_i(j_a,\ j_b)\quad(i=0,\ 1,\ 2),\\
f_{prs}&=\frac{\omega_{prs}-\omega_0+s\Omega}{\gamma_{ab}},\ \zeta_{prs}=1-if_{prs},\\
f^{p'r's'}_{prs}&=f_{prs}-f_{p'r's'},\quad \zeta^{p'r's'}_{prs}=1-\frac{i}{2}f^{p'r's'}_{prs},\\
\xi^{p'r's'}_{prs}&=1-\frac{i}{2}(f_{prs}+f_{p'r's'}),\ \zeta^{p'r's'(a)}_{prs}=1-\frac{i}{\varkappa_a}f^{p'r's'}_{prs},\\
\varkappa_a&=\frac{\gamma_a}{\gamma_{ab}},\quad \Delta_{pp'}=\frac{\omega_{pp'}}{\gamma_{ab}},\\
Q_{pr}&=\frac{\omega_{pr}}{\delta\omega_p},\quad \frac{\Delta Q_p}{Q_p}=\frac{Q_{pr}-Q_{pr'}}{Q_{pr}+Q_{pr'}}.
\end{aligned}\right\}. \tag{9}$$

The coefficients $G_i(j_a,\ j_b)$ ($i=0,\ 1,\ 2$) are the sums of the products of the Wigner 3j symbols. These are given in Table 1 for the cases $|j_a-j_b|=(0;1)$ (see also refs. 2, 3).

The physical meaning of interaction coefficients (8) is clear from the solution of the system of equations for the density matrix describing a set of atoms in a fixed magnetic field between the two excited states of which a dipole transition is allowed.[1] The field (1) consists of waves of different origins, $\mathcal{E}_{p_1r_1s}$ and $\mathcal{E}_{p_2r_2-s}$ (ref. 2), propagating in the same and different directions, i.e., the laser field is a mixture of the σ^+ and σ^- polarization components ("coherent" polarization[1]). Under the influence of the pump the atoms are in the Zeeman sublevels of the excited upper (*a*) and lower (b) levels. As they interact with the field of coherent polarization the atoms convert from the Zeeman sublevels to a coherent superposition of sublevels (a Hertz coherence). Dips (Bennett peaks[9]) form in the Maxwell velocity distributions of the atoms in the Zeeman sublevels. In two-mode lasing, the population difference consists of two terms, one is constant in space and time and the other is a function of the phase difference between the

TABLE 1

$G_i(j_a, j_b)$	$\lvert j_a - j_b \rvert = 0$	$\lvert j_a - j_b \rvert = 1$
$G_0(j_a, j_b)$	$G_0(j, j) = \frac{2j^2 + 2j + 1}{15j(j+1)(2j+1)}$	$G_0(j, j+1) = \frac{6j^2 + 12j + 5}{15(j+1)(2j+1)(2j+3)}$ $G_0(j+1, j) = G_0(j, j+1)$
$G_1(j_a, j_b)$	$G_1(j, j) = \frac{(2j-1)(2j+3)}{30j(j+1)(2j+1)}$	$G_1(j, j+1) = \frac{(j+2)(2j+5)}{30(j+1)(2j+1)(2j+3)}$ $G_1(j+1, j) = \frac{j(2j-1)}{30(j+1)(2j+1)(2j+3)}$
$G_2(j_a, j_b)$	$G_2(j, j) = G_1(j, j)$	$G_2(j+1, j) = G_1(j, j+1)$ $G_2(j, j+1) = G_1(j+1, j)$

traveling waves and varies in space and time (the modulation of the population) (ref. 10). These effects are described by nonlinear polarizability $P_{prs}(t)$ [see Eq. (14)]. The nonlinear susceptibilities in polarizability (4), $\chi^{(p,p')}_{rsr_1s_1r_2s_2r_3s_3}$, are fourth-rank tensors and characterize the linear properties of the active medium.[2]

The susceptibilities which describe the interactions between waves (of different modes) travelingin the opposite directions are not functions of the population modulation; all the other nonlinear two-mode interaction coefficients are functions of this modulation.[10] Furthermore, it can be shown that in the Doppler limit the quantities $\chi^{(p,p')}_{rsrsr'sr's}$ and $\chi^{(p,p')}_{rsrsr'-sr'-s}$ describe Bennett dips (or peaks); the terms in the susceptibilities which are proportional to $G_0(j_a, j_b)$, and $G_1(j_a, j_b)$ correspond to Bennett dips, while those which are proportional to $G_0(j_b, j_a)$ and $G_1(j_b, j_a)$ corresponds to Bennett peaks. The nonlinear susceptibility $\chi^{(p,p')}_{rsrsr-sr-s}$ describes both Bennett dips and Hertz coherence, while $\chi^{(p,p')}_{rsr-sr'sr'-s}$ describes Hertz coherence, where the terms proportional to $G_2(j_a, j_b)$ correspond to Hertz coherence of the upper level, and those proportional to $G_2(j_b, j_a)$ correspond to that of the lower level. The condition for the appearance of coherent terms in the emission is the existence of Zeeman sublevels of lower level b which are common to the σ^+ and σ^- transitions, and the condition for the appearance of coherent terms in the absorption is the existence of analogous sublevels of upper level *a*. As the magnetic field H is strengthened, the Hertz coherence is disrupted, and the effect of H on the polarizability $P_{prs}(t)$ decreases.

Accordingly, the nonlinear interaction of modes in a gas ring laser with a broad Doppler gain spectrum is due primarily to three effects: 1) the formation of Bennett dips (or peaks), 2) modulation of the population, and 3) the excitation of atoms in a coherent superposition of Zeeman sublevels (a Hertz coherence).

The authors thank É. E. Fradkin for useful discussions.

---

[1] The two-mode interaction coefficients in (8) differ from those given in ref. 4.

[2] The quantities $\chi^{(p)}_{rs}$ and $\chi^{p,p'}_{rsr's}$ were analyzed in detail previously.[2,3]

[1] M. I. D'yakonov and V. I. Perel', Opt. Spektrosk., 20, 472 (1966).
[2] É. E. Fradkin and L. M. Khayutin, Zh. Eksp. Teor. Fiz., 59, 1634 (1970) [Sov. Phys. – JETP, 32, 891 (1971)].
[3] L. M. Khayutin, Zh. Eksp. Teor. Fiz., 62, 1321 (1972) [Sov. Phys. – JETP, 35, 696 (1972)].
[4] V. A. Vetkin and A. M. Khromykh, Quantum Electronics, N. G. Basov (ed.) [in Russian], Vol. 3 (9) (1972), p. 59.
[5] V. S. Rubanov and L. N. Orlov, Preprint, Minsk (1971).
[6] V. A. Sokolov and L. M. Khayutin, Proceedings of the Siberian Symposium on Laser Spectroscopy, Krasnoyarsk (1973), p. 16.
[7] V. A. Sokolov and É. E. Fradkin, Zh. Tekh. Fiz., 43, 2367 (1973) [Sov. Phys. – Tech. Phys., 18, 1494 (1974)].
[8] W. E. Lamb, Phys. Rev., 134A, 1429 (1964).
[9] W. A. Bennett, Phys. Rev., 126, 520 (1962).
[10] S. G. Zeiger, Izv. VUZ. Radiofiz., 10, 1671 (1967).

Theory of the cathode lens.
III. Derivation of equations for composite cathode lenses

V. M. Kel'man, A. A. Sapargaliev, and E. M. Yakushev

Institute of Nuclear Physics,
Academy of Sciences of the Kazakh SSR, Alma-Ata

(Submitted July 30, 1973)
Zh. Tekh. Fiz., 44, 928-937 (May 1974)

We consider the motion of charged particles in a composite cathode lens formed by an electric field and a superimposed magnetic field with a common z axis of symmetry. By means of the substitution $z = \zeta + \eta(\zeta)$ where $\zeta = [-(2e/m)\Phi(\zeta)]^{1/2}$, and $\eta(\zeta)$ is a small quantity, time is eliminated from the differential equations of motion written in the cylindrical coordinate system r, ψ, z. The quantity $\Phi(z)$ is the distribution of the scalar potential along the lens axis. The specified substitution makes it possible to bring the equations for the trajectories to a form in which the smallness of the nonlinear terms in the paraxial region is preserved when the initial angles of the trajectories with the axis of the lens reach $\pi/2$ and the spread in particle energies is of the order of the initial energy. The resulting equations are solved by successive approximations to third order. The solution is obtained in the form of coordinate dependence on the variable ζ. However, because of the smallness of the quantity $\eta(\zeta)$, all the functions of the variable ζ appearing in the solution far from the cathode surface can be expanded in powers of this quantity and are represented in a trajectory in the form of explicit dependence of the coordinates r and ψ on z. The solution thus obtained is suitable for investigation of the electron-optical properties of cathode lenses, including aberration.

As has been shown,[1-4] the quality of an image obtained with a cathode lens is improved considerably if a magnetic field is used together with the electrostatic field. The use of magnetic cathode lenses in an emission electron microscope made it possible to obtain resolutions[5] down to 100 Å. For this reason, there is considerable interest in the electron-optical properties of such lenses, including their aberration. Studies in this field have been made by a number of authors within the limits of geometric electron optics.[6,7] However, the assumption introduced in these papers – a finite (though small) value for the initial longitudinal velocity of the electrons – is at variance with a characteristic of a cathode lens where electrons with infinitely small, and even zero, initial energy can, in principle, participate in image formation.

In a cathode lens the initial particle energy ε and the distance from the symmetry axis r are considered small quantities. Although these quantities are unlike by their very nature, when ε is not equal to zero it can be considered a quantity of second-order smallness[8,9] with respect to r. The theory of the cathode lens must also include the case in which ε becomes an infinitesimally small quantity.

In studies of cathode lenses it is necessary to bring the equation for the trajectory of charged particles to a form in which the contribution of nonlinear terms is of higher order than r. By using successive approximations one can then determine the paraxial properties of cathode lenses and their aberrations just as is done for immersion and unipotential lenses.

Since we are considering third-order aberrations in this paper the contribution of nonlinear terms must be taken into account to third order in deriving equations for the trajectories. Orders of magnitude are indicated with reference to r, with ε being considered a quantity of second order. The total magnitude of nonlinear terms must remain small even when the slope of a trajectory relative to the lens axis becomes infinitely large near the cathode surface.

We locate the origin of a cylindrical coordinate system r, ψ, z on the cathode surface and make the z axis coincide with the principal optical axis of the cathode lens. The electric field will be characterized by a scalar potential $\varphi = \varphi(r, z)$ and the magnetic field by a vector potential with the components $A_r = A_z = 0$, $A_\psi = A(r, z)$. We assume the potential of the cathode to be zero so that the equation

$$\varphi(r_0, z_0) = 0 \tag{1}$$

will determine the cathode surface, which need not be planar in the general case. The subscript "0" indicates the value of a quantity at the cathode.

The equations of motion for a particle of charge e and mass m leaving the cathode with an energy $\varepsilon = e\varphi_z$ take the form

$$\ddot{r} = r\dot{\psi}^2 - \frac{e}{m}\frac{\partial\varphi}{\partial r} + \frac{e}{m}\dot{\psi}\frac{\partial}{\partial r}(rA), \tag{2}$$

$$\dot{z}^2 + \dot{r}^2 + r^2\dot{\psi}^2 = -\frac{2e}{mc}[\varphi(r, z) + \varphi_1], \tag{3}$$

$$mr^2\dot{\psi} + \frac{e}{c}rA = -\frac{e}{c}C, \tag{4}$$

where C is a constant and c is a quantity numerically equal to the speed of light.

We introduce the complex variable

$$u = re^{i\varkappa} \tag{5}$$

with

$$\varkappa = \psi + \frac{e}{mc}\int\frac{A}{r}\,dt, \tag{6}$$

where t is the time. The system of equations (2), (3), and (4) then takes the following form:

$$\frac{m}{e}\ddot{u} + 2\left[\frac{\partial\varphi}{\partial(r^2)} - k^2\frac{A^2}{r^2}\right]u = 4k^2(C + Ar)u\frac{\partial}{\partial(r^2)}\left(\frac{A}{r}\right), \tag{7}$$

$$\frac{m}{2e}\dot{z}^2+\varphi(r,\ z)=-\frac{m}{2e}\dot{u}\dot{\bar{u}}-\varphi_i+k^2\left(\frac{2C}{r^2}+\frac{A}{r}\right)\frac{A}{r}u\bar{u}, \tag{8}$$

where $k = 1/c\,(-e/2m)^{1/2}$ and

$$C=\frac{imc}{2e}(\dot{u}\bar{u}-u\dot{\bar{u}}). \tag{9}$$

The next problem is the elimination of time from the system of equations (7) and (8). To do this, we introduce a new variable ζ, which satisfies

$$\zeta=\sqrt{-\frac{2e}{m}\Phi(\zeta)} \tag{10}$$

and assume

$$z=\zeta+\eta, \tag{11}$$

where η is a function of ζ in which the initial conditions appear as parameters. The quantity $\Phi(z) = \zeta(0, z)$ is the φ potential distribution function along the lens axis and $\Phi(\zeta)$ is the same function for the argument ζ. Using Eqs. (10) and (11), we eliminate the time t and the coordinate z from Eqs. (7) and (8) by introducing ζ as an independent variable,

$$\Phi(\zeta)\frac{d^2u}{d\zeta^2}+\frac{1}{2}\frac{d\Phi(\zeta)}{d\zeta}\frac{du}{d\zeta}+\frac{1}{4}\left[\frac{d^2\Phi(\zeta)}{d\zeta^2}+k^2H^2(\zeta)\right]u=F_n, \tag{12}$$

$$2\Phi(\zeta)\frac{d\eta}{d\zeta}-\frac{d\Phi(\zeta)}{d\zeta}\eta=f_n. \tag{13}$$

Here

$$F_n=\left[\frac{\partial\varphi(r,\ \zeta+\eta)}{\partial(r^2)}+\frac{1}{4}\frac{d^2\Phi(\zeta)}{d\zeta^2}-k^2\frac{A^2(r,\ \zeta+\eta)}{r^2}+\frac{k^2}{4}H^2(\zeta)\right]u$$
$$+2k\left\{\frac{i}{2}\sqrt{\Phi(\zeta)}\left[\bar{u}\frac{du}{d\zeta}-u\frac{d\bar{u}}{d\zeta}\right]-kA(r,\ \zeta+\eta)r\right\}u\frac{\partial}{\partial(r^2)}\left[\frac{A(r,\ \zeta+\eta)}{r}\right], \tag{14}$$

$$f_n=\varphi(r,\ \zeta+\eta)-\frac{d\Phi(\zeta)}{d\zeta}\eta-\Phi(\zeta)\left(\frac{d\eta}{d\zeta}\right)^2+\varphi_i-\Phi(\zeta)\left(1+\frac{du}{d\zeta}\frac{d\bar{u}}{d\zeta}\right)$$
$$+k\left[i\frac{\sqrt{\Phi(\zeta)}}{u\bar{u}}\left(\bar{u}\frac{du}{d\zeta}-u\frac{d\bar{u}}{d\zeta}\right)-k\frac{A(r,\ \zeta+\eta)}{r}\right]\frac{A(r,\ \zeta+\eta)}{r}u\bar{u}, \tag{15}$$

H(z) is the distribution function for the magnetic field along the principal optical axis of the lens and $H(\zeta)$ is the same function for the argument ζ.

Equation (13) indicates that the quantity η can be assumed to be zero for particles moving along the principal optical axis of the lens when $\varphi_i = 0$. This means that there is a particular solution of Eq. (13) $\eta = \eta(\zeta)$ which is small for small values of φ_i and r. We use this solution. In addition, we require that $d\eta/d\zeta$ remain a bounded quantity near the cathode. No approximations are introduced in the derivation of Eqs. (12) and (13); therefore these equations are valid for any values of r and φ_i. We seek solutions of these equations for a region near the principal optical axis of the lens and for small values of the initial energies. Equations (12) and (13) are written in a form such that they allow solution by successive approximation under the conditions specified.

Using the well-known representations of field potentials near the symmetry axis of the system

$$\varphi(r,\ z)=\Phi(z)-\frac{r^2}{4}\frac{d^2\Phi(z)}{dz^2}+\frac{r^4}{64}\frac{d^4\Phi(z)}{dz^4}-\dots, \tag{16}$$

$$\frac{A(r,z)}{r}=\frac{1}{2}H(z)-\frac{r^2}{16}\frac{d^2H(z)}{dz^2}+\dots \tag{17}$$

and the expansions

$$\Phi(z)=\Phi(\zeta)+\frac{d\Phi(\zeta)}{d\zeta}\eta+\dots, \tag{18}$$

$$H(z)=H(\zeta)+\frac{dH(\zeta)}{d\zeta}\eta+\dots, \tag{19}$$

we write Eqs. (12) and (13) in the form

$$\Phi u''+\frac{1}{2}\Phi'u'+\frac{1}{4}Q_2u=F_n^{(3)}, \tag{20}$$

$$2\Phi\eta'-\Phi'\eta=f_n^{(3)} \tag{21}$$

with

$$F_n^{(3)}=-\frac{Q_2'}{4}\eta u+\frac{Q_4}{32}u^2\bar{u}-\frac{ik}{16}H''\sqrt{\Phi}(u'\bar{u}-u\bar{u}')u, \tag{22}$$

$$f_n^{(3)}=-\Phi u'\bar{u}'-\frac{Q_2}{4}u\bar{u}+\frac{ik}{2}H\sqrt{\Phi}(u'\bar{u}-u\bar{u}')+\varphi_n. \tag{23}$$

Here

$$Q_2=\Phi''+k^2H^2, \tag{24}$$

$$Q_4=\Phi^{\mathrm{IV}}+4k^2HH''. \tag{25}$$

Primes indicate differentiation with respect to the independent variable ζ.

In the derivation of Eqs. (20) and (21) terms above third order relative to r are dropped. The quantity $f_n^{(3)}$ is second order. The fact that u' can become infinite near the cathode does not contradict this statement since $\Phi \to 0$. The term in Eq. (23)

$$\Phi u'\bar{u}' = -\frac{m}{2e}(\dot{r}^2+r^2\dot{\psi}^2),$$

i.e., it is proportional to the square of the transverse velocity. The magnitude of this term near the cathode, like that of φ_i, is of second-order smallness. This same order is also maintained with particle separation from the cathode because the variation of the quantity $\Phi u'\bar{u}'$ is quadratic with respect to r. The other term in Eq. (23) containing u' and ū' is also of second-order smallness. Since the quantity η will be of the same order of smallness as $f_n^{(3)}$, i.e., second order, the right side of Eq. (20) is a quantity of third order. Note that on the right side of Eqs. (20) and (21), the product $u'(\Phi)^{1/2}$, and the quantity u' itself, appear as quantities of small magnitude. Therefore, the smallness of the quantities $F_n^{(3)}$ and $f_n^{(3)}$, which is necessary for the use of successive approximation, is ensured either by the smallness of Φ, which occurs near the cathode surface, or by the smallness of u' at sufficient separation from that surface. The equations (20) and (21) differ from the corresponding equations written for immersion and unipotential lenses[10] in which the smallness of the right sides is ensured only by the smallness of the slope of the trajectory; these are therefore unsuitable for the analysis of cathode systems.

To solve the equations (20) and (21) we first find a quantity U which determines u in first approximation by setting $F_n^{(3)} = 0$ in Eq. (20) and then compute η by substituting U in the right side of Eq. (21); then, by substituting U and η in the right side of Eq. (20), we obtain a linear inhomogeneous equation for the third-order correction:

$$\chi = u - U. \tag{26}$$

When $F_n^{(3)} = 0$, we have

$$\Phi U'' + \frac{1}{2}\Phi' U' + \frac{1}{4} Q_2 U = 0. \tag{27}$$

This equation has a singularity at $\zeta = 0$ which is a pole of first order for the coefficients of U' and U since it is assumed that the electric field is different from zero at the cathode surface. According to the theory for this type of equation, there are two linearly independent real particular solutions of Eq. (27) of which one, $p(\zeta)$, is an analytic function; the other is

$$g(\zeta) = q(\zeta)\sqrt{\Phi(\zeta)}, \tag{28}$$

where $q(\zeta)$ is an analytic function satisfying

$$\Phi q'' + \frac{3}{2}\Phi' q' + \frac{1}{4}(3\Phi'' + k^2 H^2)\, q = 0. \tag{29}$$

We assign the initial conditions

$$p(0) = q(0) = 1. \tag{30}$$

Then, from Eqs. (27) and (29)

$$p'(0) = -\frac{1}{2\Phi_0'} Q_{20} = \frac{1}{R} - \frac{k^2 H_0^2}{2\Phi_0'}, \tag{31}$$

$$q'(0) = \frac{1}{R} - \frac{k^2 H_0^2}{6\Phi_0'}. \tag{32}$$

Here, H_0 is the magnetic field and Φ_0' is the electric field on the lens axis at the cathode surface. The quantity

$$R = -\frac{2\Phi_0'}{\Phi_0''} \tag{33}$$

is the radius of curvature of the cathode surface when r = 0. We take R > 0 for a convex cathode and R < 0 for a concave cathode.

Note that by using Eqs. (27) and (29) one can determine derivatives of any order with respect to p and q for $\zeta = 0$; this can be necessary in the numerical integration of these equations.

The particular solutions p and g are connected by the following relation:

$$\sqrt{\Phi}\,(pg' - p'g) = \frac{\Phi_0'}{2}. \tag{34}$$

The general solution of Eq. (27) will be

$$U = ap + bg, \tag{35}$$

where *a* and b are arbitrary constants, generally complex, and of first-order smallness. Substituting this solution in place of u in Eq. (23) and keeping Eq. (34) in mind, we obtain

$$f_n^{(3)} = -a\bar{a}\left(\Phi p'^2 + \frac{1}{4} Q_2 p^2\right) - \bar{a}b\left(\Phi p'g' + \frac{1}{4} Q_2 pg - \frac{ik}{4}\Phi_0' H\right) - a\bar{b}\left(\Phi p'g' + \frac{1}{4} Q_2 pg + \frac{ik}{4}\Phi_0' H\right) - bb\left(\Phi g'^2 + \frac{1}{4} Q_2 g^2\right) + \varphi_H. \tag{36}$$

A solution of Eq. (21) will be sought in the form

$$\eta = a\bar{a}\eta_1 + a\bar{b}(\eta_2 - i\eta_5) + \bar{a}b(\eta_2 + i\eta_5) + b\bar{b}\eta_3 + \varphi_H\,\eta_4. \tag{37}$$

Equation (21) then breaks down into a number of equations for which the solutions are

$$\eta_1 = -\frac{pp'}{2} + \sqrt{\Phi}\int_0^{\zeta} \frac{pp''}{\sqrt{\Phi}}\, d\zeta, \tag{38}$$

$$\eta_2 = \frac{\sqrt{\Phi}}{2}\int_0^{\zeta} (p''q - p'q')\, d\zeta, \tag{39}$$

$$\eta_3 = \frac{\Phi'}{4} q^2 - \frac{\Phi}{2} q'q + \sqrt{\Phi}\int_0^{\zeta} \sqrt{\Phi}\, qq''\, d\zeta, \tag{40}$$

$$\eta_4 = -\frac{1}{\Phi_0'} + \frac{\sqrt{\Phi}}{2\Phi_0'}\int_0^{\zeta} \frac{\Phi_0' - \Phi}{\Phi\sqrt{\Phi}}\, d\zeta, \tag{41}$$

$$\eta_5 = -\frac{k}{4} H_0 + \frac{k}{8}\sqrt{\Phi}\int_0^{\zeta} \frac{\Phi_0' H - \Phi' H_0}{\Phi\sqrt{\Phi}}\, d\zeta. \tag{42}$$

The quantities η_1-η_5 are finite everywhere together with their first derivatives. This ensures second-order smallness of the functions η and η' according to Eq. (37).

Substituting Eqs. (35) and (37) into Eq. (22), on the basis of Eqs. (20) and (26) we obtain an equation for χ, a solution of which will be sought in the form

$$\chi = a^2\bar{a}\chi_1 + a^2\bar{b}\chi_2 + a\bar{a}b\chi_3 + \bar{a}a^2\chi_4 + ab\bar{b}\chi_5 + b^2\bar{b}\chi_6 + \varphi_H(a\chi_7 + b\chi_8). \tag{43}$$

In this case, Eq. (20) breaks down into a series of equations

$$\Phi\chi_j'' + \frac{1}{2}\Phi'\chi_j' + \frac{1}{4} Q_2 \chi_j = F_{nj}^{(3)}, \quad (j = 1, 2, \ldots, 8), \tag{44}$$

where

$$F_{n1}^{(3)} = \frac{Q_4}{32} p^3 - \frac{Q_2'}{4}\eta_1 p, \tag{45}$$

$$F_{n2}^{(3)} = \frac{Q_4}{32} p^2 g - \frac{Q_2'}{4}(\eta_2 - i\eta_5)\, p + \frac{ik}{32}\Phi_0' H'' p, \tag{46}$$

$$F_{n3}^{(3)} = \frac{Q_4}{16} p^2 g - \frac{Q_2'}{4}[(\eta_2 + i\eta_5)\, p + \eta_1 g] - \frac{ik}{32}\Phi_0' H'' p, \tag{47}$$

$$F_{n4}^{(3)} = \frac{Q_4}{32} pg^2 - \frac{Q_2'}{4}\Big[(\eta_2 + i\eta_5)\, g - \frac{ik}{32}\Phi_0' H'' g, \tag{48}$$

$$F_{n5}^{(3)} = \frac{Q_4}{16} pg^2 - \frac{Q_2'}{4}[(\eta_2 - i\eta_5)\, g + \eta_3 p] + \frac{ik}{32}\Phi_0' H'' g, \tag{49}$$

$$F_{n6}^{(3)} = \frac{Q_4}{32} g^3 - \frac{Q_2'}{4}\eta_3 g, \tag{50}$$

$$F^{(3)}_{n7} = -\frac{Q_2'}{4}\eta_4 p, \tag{51}$$

$$F^{(3)}_{n8} = -\frac{Q_2'}{4}\eta_4 g. \tag{52}$$

Solving Eq. (44) we find

$$\chi_j = -\frac{2}{\Phi_0'}\left\{p\int_0^{\zeta}\frac{F^{(3)}_{nj}}{\sqrt{\Phi}}g\,d\zeta - g\int_0^{\zeta}\frac{F^{(3)}_{nj}}{\sqrt{\Phi}}p\,d\zeta\right\} \quad (j = 1, 2, \ldots, 8). \tag{53}$$

Equations (26), (35), and (43) together with Eq. (53) determine the quantity u as a function of ζ. In order to determine r and ψ as functions of ζ on the basis of these equations, it is necessary to eliminate the time t from Eq. (6). Using the relations (10) and (17) and eliminating unnecessary terms, we write

$$\varkappa = \phi - \theta - \varkappa_1, \tag{54}$$

where

$$\Theta = \frac{ik}{2}\int_0^{\zeta}\frac{H}{\sqrt{\Phi}}\,d\zeta, \tag{55}$$

$$\varkappa_1 = \frac{k}{2}\int_0^{\zeta}\left(H'\eta - \frac{H''}{8}u\bar{u}\right)\frac{d\zeta}{\sqrt{\Phi}}. \tag{56}$$

The constant of integration in Eq. (54) is set equal to zero, which does not limit the generality of the discussion because of the arbitrariness of *a* and b.

From Eq. (5) we have

$$u = re^{i(\psi - \Theta - \varkappa_1)} = U + \chi, \tag{57}$$

whence

$$re^{i(\psi - \Theta)} = U + \chi + i\varkappa_1 U. \tag{58}$$

We transform Eq. (56) by subtituting U and η into it. From Eqs. (35) and (37) we have

$$\varkappa_1 = a\bar{a}\varkappa_{11} + a\bar{b}(\varkappa_{12} - i\varkappa_{15}) + \bar{a}b(\varkappa_{12} + i\varkappa_{15}) + b\bar{b}\varkappa_{13} + \varphi_1\varkappa_{14}. \tag{59}$$

Here

$$\varkappa_{11} = \frac{k}{2}\int_0^{\zeta}\left(H'\eta_1 - \frac{H''}{8}p^2\right)\frac{d\zeta}{\sqrt{\Phi}}, \tag{60}$$

$$\varkappa_{12} = \frac{k}{2}\int_0^{\zeta}\left(H'\eta_2 - \frac{H''}{8}pg\right)\frac{d\zeta}{\sqrt{\Phi}}, \tag{61}$$

$$\varkappa_{13} = \frac{k}{2}\int_0^{\zeta}\left(H'\eta_3 - \frac{H''}{8}g^2\right)\frac{d\zeta}{\sqrt{\Phi}}. \tag{62}$$

$$\varkappa_{14} = \frac{k}{2}\int_0^{\zeta}H'\eta_4\frac{d\zeta}{\sqrt{\Phi}}, \tag{63}$$

$$\varkappa_{15} = \frac{k}{2}\int_0^{\zeta}H'\eta_5\frac{d\zeta}{\sqrt{\Phi}}. \tag{64}$$

Using Eqs. (35), (37), (43), and (59), we write in parametric form the equations for the trajectory of a charged particle in the field of a composite cathode lens

$$\begin{aligned} re^{i(\psi - \Theta)} = {} & ap(\zeta) + bg(\zeta) + a^2\bar{a}[\chi_1(\zeta) + i\varkappa_{11}(\zeta)p(\zeta)] \\ & + a^2\bar{b}\{\chi_2(\zeta) + i[\varkappa_{12}(\zeta) - i\varkappa_{15}(\zeta)]p(\zeta)\} \\ & + a\bar{a}b\{\chi_3(\zeta) + i[\varkappa_{12}(\zeta) + i\varkappa_{15}(\zeta)]p(\zeta) + i\varkappa_{11}(\zeta)g(\zeta)\} \\ & + \bar{a}b^2\{\chi_4(\zeta) + i[\varkappa_{12}(\zeta) + i\varkappa_{15}(\zeta)]g(\zeta)\} \\ & + ab\bar{b}\{\chi_5(\zeta) + i[\varkappa_{12}(\zeta) - i\varkappa_{15}(\zeta)]g(\zeta) + i\varkappa_{13}(\zeta)p(\zeta)\} \\ & + b^2\bar{b}[\chi_6(\zeta) + i\varkappa_{13}(\zeta)g(\zeta)] + a\varphi_1[\chi_7(\zeta) + i\varkappa_{14}(\zeta)p(\zeta)] \\ & + b\varphi_1[\chi_8(\zeta) + i\varkappa_{14}(\zeta)g(\zeta)], \end{aligned} \tag{65}$$

$$\begin{aligned} z = {} & \zeta + a\bar{a}\eta_1(\zeta) + a\bar{b}[\eta_2(\zeta) - i\eta_5(\zeta)] + \bar{a}b[\eta_2(\zeta) + i\eta_5(\zeta)] \\ & + b\bar{b}\eta_3(\zeta) + \varphi_1\eta_4(\zeta). \end{aligned} \tag{66}$$

We determine the arbitrary constants *a* and b on the basis of the initial conditions at the cathode surface. We first determine the value $\zeta = \zeta_0$ at the point of particle emission. At this point,

$$\dot{z}_0^2 = -\frac{2e}{m}\varphi_1\cos^2\vartheta_0, \tag{67}$$

where ϑ_0 is the angle between the initial velocity of the emerging particle and the z axis. On the other hand, we have on the basis of Eqs. (10) and (11)

$$\dot{z}_0 = \left(\dot{\zeta}\frac{dz}{d\zeta}\right)_{\zeta = \zeta_0} = [1 + \eta'(\zeta_0)]\sqrt{-\frac{2e}{m}\Phi(\zeta_0)}. \tag{68}$$

On the basis of the last two equations we write

$$\Phi(\zeta_0) = \frac{\varphi_1\cos^2\vartheta_0}{[1 + \eta'(\zeta_0)]^2}, \tag{69}$$

whence it follows that to third order

$$\zeta_0 = \frac{\varphi_1}{\Phi_0'}\cos^2\vartheta_0. \tag{70}$$

The direction of particle emission from the cathode is characterized by the two angles γ_0 and ω_0. When $\psi_0 = 0$, γ_0 is the angle between the initial velocity of the particle and the normal to the surface of the cathode at the emission point. These directions define a plane; the angle of this plane with respect to the plane $\psi = 0$ is designated by ω_0. Using the notation introduced for the angle we write

$$\cos\vartheta_0 = \cos\gamma_0 - \frac{r_0}{R}\cos\omega_0\sin\gamma_0. \tag{71}$$

In our approximation the angle between the normal and the z axis is r_0/R. At the point of particle emission, Eq. (65) is

$$r_0e^{-i\Theta(\zeta_0)} = ap(\zeta_0) + bg(\zeta_0) + \chi(\zeta_0) + i\varkappa_1(\zeta_0)[ap(\zeta_0) + bg(\zeta_0)]. \tag{72}$$

Differentiation of Eq. (65) with respect to time yields for the same point

$$\begin{aligned} & \left[\dot{r}_0 + ir_0\dot{\psi}_0 - ir_0\theta'(\zeta_0)\sqrt{-\frac{2e}{m}\Phi(\zeta_0)}\right]e^{-i\Theta(\zeta_0)} \\ & = \{ap'(\zeta_0) + bg'(\zeta_0) + \chi'(\zeta_0) + i[ap'(\zeta_0) + bg'(\zeta_0)]\varkappa_1(\zeta_0) \\ & \quad + i[ap(\zeta_0) + bg(\zeta_0)]\varkappa_1'(\zeta_0)\}\sqrt{-\frac{2e}{m}\Phi(\zeta_0)}. \end{aligned} \tag{73}$$

Equations (72) and (73) must be solved with respect to the constants *a* and b. This solution must be carried out to third-order. For convenience in calculation we convert these equations to the forms

$$a=\frac{1}{p(\zeta_0)}[r_0e^{i-\Theta(\zeta_0)}-bg(\zeta_0)], \tag{74}$$

$$b=\frac{2\sqrt{\Phi(\zeta_0)}}{\Phi_0'}\left\{\left[\frac{\dot{r}_0+ir_0\dot{\psi}_0}{\sqrt{-\frac{2e}{m}\Phi(\zeta_0)}}-ir_0\theta'(\zeta_0)\right]p(\zeta_0)\cdot\right.$$
$$\left.-r_0p'(\zeta_0)\right\}e^{-i\Theta(\zeta_0)}-\frac{i2a}{\Phi_0'}\varkappa_1'(\zeta_0)\sqrt{\Phi(\zeta_0)}. \tag{75}$$

Here, Eq. (34) is used. The quantities $\dot{r}_0$ and $r_0\dot{\psi}$ appearing in the last equation can be expressed in terms of the initial energy of the particle

$$\dot{r}_0=\sqrt{-\frac{2e}{m}\varphi_1}\left(\sin\gamma_0\cos\omega_0+\frac{r_0}{R}\cos\gamma_0-\frac{r_0^2}{2R^2}\sin\gamma_0\cos\omega_0\right), \tag{76}$$

$$r_0\dot{\psi}=\sqrt{-\frac{2e}{m}\varphi_1}\,\sin\gamma_0\sin\omega_0. \tag{77}$$

The quantities $\Theta(\zeta_0)$ and $g(\zeta_0)$ in this approximation can be represented by

$$\Theta(\zeta_0)=\frac{k}{2}\int_0^{\zeta_0}\frac{H}{\sqrt{\Phi}}d\zeta=\frac{kH_0}{\Phi_0'}\sqrt{\varphi_1}\left(\cos\gamma_0-\frac{r_0}{R}\sin\gamma_0\cos\omega_0\right), \tag{78}$$

$$g(\zeta_0)=q(\zeta_0)\sqrt{\Phi(\zeta_0)}=\sqrt{\varphi_1}\left(\cos\gamma_0-\frac{r_0}{R}\sin\gamma_0\cos\omega_0\right). \tag{79}$$

Substituting Eqs. (70), (76)-(79) into Eqs. (74) and (75) and carrying out the expansion over small quantities, we find

$$a=r_0-\frac{\varphi_1}{\Phi_0'}e^{i\omega_0}\sin 2\gamma_0+r_0^3\left(\frac{k^4H_0^4}{4\Phi_0'^2}+\frac{k^2H_0^2}{4R\Phi_0'}\right)$$
$$+ir_0^2\left[\left(\frac{kH_0}{2R}+\frac{k^3H_0^3}{4\Phi_0'}\right)\bar{b}_1-\frac{k^3H_0^3}{2\Phi_0'}b_1\right]$$
$$+r_0\left[\left(\frac{\Phi_0'}{4R}-\frac{k^2H_0^2}{4}\right)b_1^2+\left(\frac{\Phi_0'}{2R}+\frac{k^2H_0^2}{2}\right)b_1\bar{b}_1\right]$$
$$-ib_1^2\bar{b}_1\frac{k}{4}H_0\Phi_0'-r_0\frac{\varphi_1}{\Phi_0'}\left(\frac{k^2H_0^2}{\Phi_0'}+\frac{1}{R}\right)+ib\varphi_1\frac{kH_0}{\Phi_0'}, \tag{80}$$

$$b=b_1-i\varphi_1k\frac{H_0}{\Phi_0'^2}e^{i\omega_0}\sin 2\gamma_0+ir_0^3\left(\frac{k^5H_0^5}{4\Phi_0'^3}+\frac{kH_0'}{2R\Phi_0'}+\frac{kH_0''}{8\Phi_0'}\right)$$
$$+r_0^2\left[\left(\frac{k^4H_0^4}{2\Phi_0'^2}-\frac{k^2H_0^2}{2R\Phi_0'}+\frac{1}{4R^2}\right)b_1+\left(\frac{1}{4R^2}-\frac{k^4H_0^4}{4\Phi_0'^2}-\frac{k^2H_0^2}{4R\Phi_0'}\right)\bar{b}_1\right]$$
$$+ir_0\left[\left(\frac{kH_0}{2R}-\frac{k^3H_0^3}{4\Phi_0'}\right)b_1^2+\frac{k^3H_0^3}{2\Phi_0'}b_1\bar{b}_1\right]+\left(k^2\frac{H_0^2}{4}-\frac{\Phi_0'}{4R}\right)b_1^2\bar{b}_1$$
$$-ir_0\varphi_H\frac{k^3H_0^3}{\Phi_0'^3}+b_1\frac{\varphi_1}{\Phi_0'}\left(\frac{1}{R}-\frac{k^2H_0^2}{\Phi_0'}\right), \tag{81}$$

where

$$b_1=\frac{2\sqrt{\varphi_1}}{\Phi_0'}e^{i\omega_0}\sin\gamma_0-ir_0\frac{kH_0}{\Phi_0'}. \tag{82}$$

Equations (65) and (66) are valid over the entire length of the trajectory, including the cathode region. Therefore these equations can be used to determine the constants a and b through the initial conditions at the cathode.

We now turn to the determination of the explicit dependence of r and ψ on z. Solving Eq. (66) by successive approximation and eliminating terms of order higher than third, we find

$$\zeta=z-\eta[z-\eta(\zeta)]=z-\eta(z). \tag{83}$$

Substituting Eq. (83) into Eq. (65) and expanding functions with argument $z-\eta(z)$ with respect to $\eta(z)$, we find

$$re^{i\Psi}=ap(z)+bg(z)+\chi(z)-\eta(z)[ap'(z)+bg'(z)]$$
$$+i[ap(z)+bg(z)]\left[\varkappa_1(z)-\frac{kH(z)\eta(z)}{2\sqrt{\Phi(z)}}\right], \tag{84}$$

where

$$\Psi=\psi-\frac{k}{2}\int_0^z\frac{H(z)}{\sqrt{\Phi(z)}}dz. \tag{85}$$

The functions p(z), g(z), η(z), χ(z), and $\varkappa_1$(z) in Eq. (84) were defined earlier as functions of ζ. Equation (84) determines the trajectory of a charged particle in a rotating coordinate system; the angle of rotation as a function of z is given by

$$\Theta(z)=\frac{k}{2}\int_0^z\frac{H(z)}{\sqrt{\Phi(z)}}dz. \tag{86}$$

Expansion of the functions $g[z-\eta(z)]$, $\theta[z-\eta(z)]$, and $\varkappa_1[z-\eta(z)]$ with respect to $\eta(z)$ will not be valid in the cathode region, where the derivatives of these functions increase without limit. Therefore Eqs. (84) and (85), which are determined with the help of the expansion, describe the trajectory at some distance from the cathode surface, i.e., in the region where the condition $\Phi(z)\gg\varphi_1$ is satisfied. Investigation of trajectories in this region is of greatest practical interest because it contains the position of the minimum beam cross section in electron guns and the image plane in emission electron microscopes. In view of the fact that the constants a and b are already determined by Eqs. (80) and (81), the simpler equation (84) can be used in a subsequent study of aberrations at sufficient separation from the cathode surface without recourse to analysis of Eqs. (65) and (66) which are valid everywhere, including the near-cathode region.

---

[1] C. Fert and R. Simon, J. Phys. Radium, 18, 875 (1957).

[2] G. V. Spivak and V. P. Lyubchenko, Izv. Akad. Nauk SSSR, Ser. Fiz., 23, 697 (1959).

[3] A. M. Rozenfel'd and P. V. Zaitsev, Izv. Akad. Nauk SSSR, Ser. Fiz., 25, 713 (1961).

[4] V. G. Dyukov, A. I. Nevzorov, N. N. Sedov, and G. V. Spivak, Izv. Akad. Nauk SSSR, Ser. Fiz., 32, 972 (1968).

[5] E. A. Soa, Optik., 22, 66 (1965).

[6] B. E. Bonshtedt, Radiotekh. Elektron., 9, 844 (1964).

[7] P. P. Kasyankov, Tr. GOI, 33, 62 (1962).

[8] L. A. Artsimovich, Izv. Akad. Nauk SSSR, Ser. Fiz., 8, 313 (1944).

[9] E. Hahn, Jenaer Jahrbuch, 1, 184 (1959).

[10] E. Bruche and O. Shertzer, Geometric Electron Optics [Russian translation], Gazetno-Zhurnalnoe i Knizhnoe Izd., Leningrad (1943).

Theory of the cathode lens.
IV. Aberrations of composite cathode lens

V. M. Kel'man, A. A. Sapargaliev, and E. M. Yakushev
Institute of Nuclear Physics,
Academy of Sciences of the Kazakh SSR, Alma-Ata

(Submitted August 10, 1973)
Zh. Tekh. Fiz., 44, 938-943 (May 1974)

Aberrations are classifed and aberration coefficients calculated for a composite cathode lens formed by superposition of axisymmetric electric and magnetic fields. All types of aberrations characteristic of ordinary electron lenses are present in a composite cathode lens. In addition, if the magnetic field at the cathode surface is nonzero four additional terms appear in the expression for the total aberration of the cathode lens.

This paper is a continuation of ref. 1. The same notation is used and the numbering of the equations is continued so that it is possible to refer to previously derived relations without indicating the source. We investigate aberrations at considerable separation from the cathode surface, making it possible to analyze trajectories on the basis of Eqs. (84) and (85), which determine the explicit dependence of the coordinates r and ψ on z. The functions of z appearing in Eq. (84) have been defined[1] as functions of the argument ζ. In subsequent use of equations given in ref. 1 it is necessary to take this situation into account by replacing the argument ζ by the coordinate z everywhere.

All functions appearing in subsequent expressions are given as functions of this coordinate and the primes indicate differentiation with respect to it.

In the analysis of aberrations it is necessary to represent Eq. (84) in the form of a sum, from which the dependence of the trajectory on the initial conditions r_0 and

$$b_1=\frac{2\sqrt{\varphi_1}}{\Phi_0'}e^{i\omega_0}\sin\gamma_0-ir_0\frac{kH_0}{\Phi_0'}$$

can be seen explicitly.

Substituting for the functions $\eta(z)$, $\chi(z)$, and $\varkappa_1(z)$ in Eq. (84) in accordance with Eqs. (37), (43), and (59) and the values of the constants a and b from Eqs. (80) and (81), after performing a number of complicated transformations we obtain

$$\begin{gathered}w(z)=re^{i\Psi}=r_0p(z)+b_1g(z)\\
-p(z)\frac{\varphi_1}{\Phi_0'}e^{i\omega_0}\sin 2\gamma_0-ig(z)\frac{kH_0}{\Phi_0'^2}\varphi_1e^{i\omega_0}\sin 2\gamma_0\\
+r_0^3[B_1(z)+ic_1(z)]+r_0^2\{[B_2(z)+ic_2(z)]\bar{b}_1+[B_3(z)+ic_3(z)]b_1\}\\
+r_0\{[B_4(z)+ic_4(z)]b_1^2+[B_5(z)+ic_5(z)]b_1\bar{b}_1\}\\
+[B_6(z)+ic_6(z)]b_1^2\bar{b}_1+\varphi_H\{[B_7(z)+ic_7(z)]r_0\\
+[B_8(z)+ic_8(z)]b_1\}.\end{gathered}\tag{87}$$

Here,

$$B_1(z)=p\left(\frac{1}{2R^2}-\frac{k^2H_0^2}{4R\Phi_0'}+\frac{3k^4H_0^4}{8\Phi_0'^2}-J_1\right)+gJ_2,\tag{88}$$

$$B_2(z)=p\left(\frac{k^2H_0H}{8\sqrt{\Phi}}-J_3\right)+g\left(J_1+\frac{1}{2}p'^2-\frac{1}{4R^2}+\frac{k^2H_0^2}{4R\Phi_0'}-\frac{3k^4H_0^4}{8\Phi_0'^2}\right),\tag{89}$$

$$\begin{gathered}B_3(z)=-p\left(\frac{k^2H_0H}{8\sqrt{\Phi}}+2J_4\right)+p'\frac{\Phi_0'}{4\sqrt{\Phi}}\\
+g\left(2J_1+\frac{3}{2}p'^2-\frac{3}{4R^2}+\frac{k^2H_0^2}{2R\Phi_0'}+\frac{k^4H_0^4}{4\Phi_0'^2}\right),\end{gathered}\tag{90}$$

$$B_4(z)=-p\left(\frac{k^3H_0^2}{8}+J_5\right)+g\left(J_3-k^2\frac{H_0H}{8\sqrt{\Phi}}+\frac{1}{2}p'g'\right),\tag{91}$$

$$B_5(z)=p\left(\frac{3}{4}k^3H_0^2-2J_5\right)+g\left(2J_4+\frac{1}{2}p'g'+k^2\frac{H_0H}{8\sqrt{\Phi}}\right),\tag{92}$$

$$\begin{gathered}B_6(z)=-pJ_6+g\Big[J_5+\frac{1}{2}g'^2-\frac{1}{2}gg'\frac{\Phi'}{\Phi}+\frac{k^2H_0^2}{8}\\
-\frac{\Phi'}{\Phi_0'\sqrt{\Phi}}p'g^2g'+\frac{Q_2}{\Phi}g^2\left(\frac{1}{8}-\frac{\Phi'}{4\Phi_0'\sqrt{\Phi}}pg\right)\Big],\end{gathered}\tag{93}$$

$$B_7(z)=p\left(J_7-\frac{3k^2H_0^2}{2\Phi_0'^2}\right)-gJ_8,\tag{94}$$

$$B_8(z)=pJ_9+g\left[\frac{\Phi'}{2\Phi_0'\Phi\sqrt{\Phi}}pg-\frac{p}{\Phi_0'}\frac{d}{dz}\left(\frac{g}{\sqrt{\Phi}}\right)+\frac{p'g}{\Phi_0'\sqrt{\Phi}}-\frac{k^2H_0^2}{2\Phi_0'^2}-J_7\right],\tag{95}$$

$$c_1(z)=p\left(\frac{kH}{4\sqrt{\Phi}}pp'-\mu_1\right)+g\left(\frac{kH_0'}{2R\Phi_0'}+\frac{kH_0''}{8\Phi_0'}+\frac{k^5H_0^5}{4\Phi_0'^3}\right),\tag{96}$$

$$c_2(z)=p\left(\frac{k^3H_0^3}{4\Phi_0'}+\frac{kH_0}{2R}-\mu_2\right)+g\left(\mu_1-\frac{kH}{4\sqrt{\Phi}}pp'\right),\tag{97}$$

$$c_3(z)=-p\frac{k^3H_0^3}{2\Phi_0'}+g\left(\frac{kH}{2\sqrt{\Phi}}pp'-2\mu_1\right),\tag{98}$$

$$\begin{gathered}C_4(z)=p\mu_3\\
+g\left\{p\frac{kH}{4}\left[\frac{\Phi'}{2\Phi\sqrt{\Phi}}g-\frac{d}{dz}\left(\frac{g}{\sqrt{\Phi}}\right)\right]+\frac{kH_0}{2R}-\frac{k^3H_0^3}{4\Phi_0'}-\mu_2\right\},\end{gathered}\tag{99}$$

$$C_5(z)=-2p\mu_3+g\left\{\frac{k^3H_0^3}{2\Phi_0'}-p\frac{kH}{2}\left[\frac{\Phi'}{2\Phi\sqrt{\Phi}}g-\frac{d}{dz}\left(\frac{g}{\sqrt{\Phi}}\right)\right]\right\},\tag{100}$$

$$c_6(z)=-pkH_0\frac{\Phi_0'}{4}-g\left\{\frac{kH}{4}\left[\frac{\Phi'}{2\Phi\sqrt{\Phi}}g^2-g\frac{d}{dz}\left(\frac{g}{\sqrt{\Phi}}\right)\right]+\mu_3\right\},\tag{101}$$

$$c_7(z)=p\left(\frac{kH}{2\Phi_0'\sqrt{\Phi}}-\mu_4\right)-g\frac{k^3H_0^3}{\Phi_0'^3},\tag{102}$$

$$c_8(z)=p\frac{kH_0}{\Phi_0'}+g\left(\frac{kH}{2\Phi_0'\sqrt{\Phi}}-\mu_4\right).\tag{103}$$

The integrals J_1-J_9 and μ_1-μ_4 in the equations above have the form

$$J_1=\frac{1}{16\Phi_0'}\int_0^z\frac{g}{\sqrt{\Phi}}[p^2(Q_4p+4Q_2'p')+8p''(4\Phi p'^2+Q_2p^2)]\,dz,\tag{104}$$

$$J_2=\frac{1}{16\Phi_0'}\int_0^z\frac{p}{\sqrt{\Phi}}[p^2(Q_4p+4Q_2'p')+8p''(4\Phi p'^2+Q_2p^2)]\,dz,\tag{105}$$

$$\begin{gathered}J_3=\frac{1}{16\Phi_0'}\int_0^z\frac{1}{\sqrt{\Phi}}\Big[pg^2(Q_4p+4Q_2'p')+8p''g(4\Phi p'g'+Q_2pg)\\
+k^2\Phi_0'\left(2H_0H'+H\frac{\Phi_0'H-\Phi'H_0}{\Phi}\right)\Big]dz,\end{gathered}\tag{106}$$

$$\begin{gathered}J_4=\frac{1}{16\Phi_0'}\int_0^z\frac{1}{\sqrt{\Phi}}\Big[pg^2(Q_4p+4Q_2'p')+4p''g(4\Phi p'g'+Q_2pg)\\
+4pp''(4\Phi g'^2+Q_2g^2)-k^2\Phi_0'\left(H_0H'+H\frac{\Phi_0'H-\Phi'H_0}{2\Phi}\right)\Big]dz,\end{gathered}\tag{107}$$

$$J_5=\frac{1}{16\Phi_0'}\int_0^z\frac{g}{\sqrt{\Phi}}[g^2(Q_4p+4Q_2'p')+8p''(4\Phi g'^2+Q_2g^2)]\,dz,\tag{108}$$

$$\begin{gathered}J_6=\frac{1}{16\Phi_0'}\int_0^z g\Big[\frac{g^2}{\sqrt{\Phi}}\left(Q_4g-4\frac{\Phi'}{\Phi}Q_2'g+4Q_2'g'\right)\\
+8(4\Phi g'^2+Q_2g^2)\frac{d^2}{dz^2}\left(\frac{g}{\sqrt{\Phi}}\right)\Big]dz,\end{gathered}\tag{109}$$

$$J_7=\frac{2}{\Phi_0'}\int_0^z p''\frac{g}{\sqrt{\Phi}}dz, \tag{110}$$

$$J_8=\frac{2}{\Phi_0'}\int_0^z \frac{pp''}{\sqrt{\Phi}}dz, \tag{111}$$

$$J_9=\frac{2}{\Phi_0'}\int_0^z g\left[\frac{d^2}{dz^2}\left(\frac{g}{\sqrt{\Phi}}\right)\right]dz, \tag{112}$$

$$\mu_1=\frac{k}{2}\int_0^z\left(\frac{H''}{8}p^2+\frac{H'}{2}pp'+Hpp''\right)\frac{dz}{\sqrt{\Phi}}, \tag{113}$$

$$\mu_2=k\int_0^z\left[\frac{H''}{8\sqrt{\Phi}}pg+\frac{H}{2\sqrt{\Phi}}p''g-Hp'\frac{d}{dz}\left(\frac{g}{2\sqrt{\Phi}}\right)\right]dz, \tag{114}$$

$$\mu_3=\frac{k}{2}\int_0^z\left[\frac{H''}{8\sqrt{\Phi}}g^2-\frac{H'\Phi'}{4\Phi\sqrt{\Phi}}g^2\right.$$
$$\left.+H'g\frac{d}{dz}\left(\frac{g}{2\sqrt{\Phi}}\right)+Hg\frac{d^2}{dz^2}\left(\frac{g}{\sqrt{\Phi}}\right)\right]dz, \tag{115}$$

$$\mu_4=\frac{k}{2\Phi_0'}\int_0^z\left[H'+H\left(\frac{\Phi_0'-\Phi'}{2\Phi}\right)\right]\frac{dz}{\sqrt{\Phi}}. \tag{116}$$

These integrals assume constant values if the upper limit of integration falls outside the field of the lens. Double integrals obtained in the transformations are reduced to single integrals by integration by parts and use of the following relations:

$$\frac{d}{dz}(4\Phi p'^2+Q_2p^2)=Q_2'p^2, \tag{117}$$

$$\frac{d}{dz}(4\Phi p'g'+Q_2pg)=Q_2'pg, \tag{118}$$

$$\frac{d}{dz}(4\Phi g'^2+Q_2g^2)=Q_2'g^2. \tag{119}$$

We first consider paraxial trajectories, which are limited to terms of first order relative to r. In this approximation, the equation for a trajectory is

$$W(z)=re^{i\Psi}=r_0p+\left(\frac{2\sqrt{\varphi_1}}{\Phi_0'}e^{i\omega_0}\sin\gamma_0-ir_0\frac{kH_0}{\Phi_0'}\right)g. \tag{120}$$

We consider the plane z = 0 (tangent to the cathode surface) as the object plane. According to the definition (28), g(0) = 0 in this plane since the potential at the cathode surface is assumed to be zero.

The image plane $z = z_b$ will be determined by the relation $g(z_b) = 0$. As is obvious from Eq. (120), a true image of the cathode surface is obtained in this plane.

In accordance with Eq. (85), the presence of a magnetic field gives rise to a rotation of this image by an angle

$$\Theta_b=\frac{k}{2}\int_0^{z_b}\frac{H}{\sqrt{\Phi}}dz. \tag{121}$$

In this approximation, the variation of initial energy φ_1 of emerging particles from zero to a maximum value and also the variation in the emergence angles γ_0 and ω_0 from zero to $\pi/2$ cause neither distortion nor smearing of the image. Since p(0) = 1 from Eq. (30), the lateral magnification of the system is

$$M=p(z_b). \tag{122}$$

In an electrostatic cathode lens, there is considerable interest in the determination of the size of the beam cross section in the crossover plane $z = z_k$, where z_k satisfies the equation $p(z_k) = 0$.

In this plane, the area of the beam cross section is independent of the cathode dimensions and can be made considerably smaller than the area of the latter.

With a magnetic field the analogous situation will occur only when the magnetic field is $H_0 = 0$ at the cathode surface, as can be seen from Eq. (120).

If $H_0 \neq 0$, the distance from the axis at which a charged particle crosses the plane $z = z_k$ is

$$r_k^{(1)}=\frac{g(z_k)}{\Phi_0'}\sqrt{4\varphi_H\sin^2\gamma_0+r_0^2k^2H_0^2-4r_0\sqrt{\varphi_H}kH_0\sin\omega_0\sin\gamma_0}. \tag{123}$$

Aberrations of a cathode lens in the image plane are determined by

$$\Delta w=\Delta w^{(2)}+\Delta w^{(3)}, \tag{124}$$

where aberrations of the second order are

$$\Delta w^{(2)}=-M\frac{\varphi_H}{\Phi_0'}e^{i\omega_0}\sin 2\gamma_0, \tag{125}$$

and aberrations of the third order are

$$\begin{aligned}\Delta w^{(3)}=&\,r_0^3[B_1(z_b)+ic_1(z_b)]+r_0^2\{[B_2(z_b)\\&+ic_2(z_b)]\bar{b}_1+[B_3(z_b)+ic_3(z_b)]b_1\}\\&+r_0\{[B_4(z_b)+ic_4(z_b)]b_1^2+[B_5(z_b)\\&+ic_5(z_b)]b_1\bar{b}_1\}+[B_6(z_b)+ic_6(z_b)]b_1^2\bar{b}_1\\&+\varphi_H\{[B_7(z_b)+ic_7(z_b)]r_0+[B_8(z_b)+ic_8(z_b)]\bar{b}_1\}.\end{aligned} \tag{126}$$

Here,

$$\left.\begin{aligned}B_1(z_b)&=M\left[\frac{1}{2R^2}-\frac{k^2H_0^2}{4R\Phi_0'}+\frac{3k^4H_0^4}{8\Phi_0'^2}-J_1(z_b)\right],\\B_2(z_b)&=M\left[k^2\frac{H_0H_b}{8\sqrt{\Phi_b}}-J_3(z_b)\right],\\B_3(z_b)&=p_b'\frac{\Phi_0'}{4\sqrt{\Phi_b}}-M\left[k^2\frac{H_0H_b}{8\sqrt{\Phi_b}}+2J_4(z_b)\right],\\B_4(z_b)&=-M\left[\frac{k^2H_0^2}{8}+J_5(z_b)\right],\\B_5(z_b)&=M\left[\frac{3}{4}k^2H_0^2-2J_5(z_b)\right],\\B_6(z_b)&=-MJ_b(z_b),\\B_7(z_b)&=M\left[J_7(z_b)-\frac{3k^2H_0^2}{2\Phi_0'^2}\right],\\B_8(z_b)&=MJ_9(z_b),\end{aligned}\right\} \tag{127}$$

$$\left.\begin{aligned}c_1(z_b)&=M\left[\frac{kH_b}{4\sqrt{\Phi_b}}Mp_b'-\mu_1(z_b)\right],\\c_2(z_b)&=M\left[\frac{k^3H_0^3}{4\Phi_0'}+\frac{kH_0}{2R}-\mu_2(z_b)\right],\quad c_3(z_b)=-M\frac{k^3H_0^3}{2\Phi_0'},\\2c_4(z_b)&=-c_5(z_b)=2M\mu_3(z_b),\quad c_6(z_b)=-MkH_0\frac{\Phi_0'}{4},\\c_7(z_b)&=M\left[\frac{kH_b}{2\Phi_0'\sqrt{\Phi_b}}-\mu_4(z_b)\right],\quad c_8(z_b)=M\frac{kH_0}{\Phi_0'}.\end{aligned}\right\} \tag{128}$$

We obtain the radius of the circle of confusion resulting from the presence of aberrations of second order by setting $\gamma_0 = 45°$ in Eq. (125),

$$\Delta r^{(2)}=\frac{M\varphi_H}{\Phi_0'}. \tag{129}$$

It is then clear that the size of the circle of confusion referred to the object plane is independent of the existence of a magnetic field.

The quantity $\Delta w^{(3)}$ represents the total aberration of third order of a beam not defined by a diaphragm. We introduce a defining diaphragm in the plane $z = z_d$. In accordance with Eq. (120), we shall have in this plane

$$b_1 = \frac{W_d - r_0 p_d}{g_d}. \tag{130}$$

The subscript d denotes values of quantities in the plane of the diaphragm. We substitute the value of b_1 expressed in this manner in Eq. (126), and having grouped terms of the sum in the appropriate manner, we find

$$\begin{aligned}\Delta W_d^{(3)} = {}& (B + ib_m) W_d^2 \bar{W}_d + r_0 \{(F - if) W_d^2 + [2F + F_m \\ & + i(2f + f_m)] W_d \bar{W}_d\} + r_0^2 [(C + D + id_m) W_d + (C + ic) \bar{W}_d] \\ & + r_0^3 (E + ie) + \varphi_H [(G + ig_m) W_d + (J + ij) r_0],\end{aligned} \tag{131}$$

where

$$B = -\frac{M}{g_d^3} J_6(z_b), \tag{132}$$

$$F = \frac{M}{g_d^2}\left[J_6(z_b)\frac{p_d}{g_d} - J_5(z_b) - \frac{k^2 H_0^2}{8}\right], \tag{133}$$

$$\begin{aligned}C = \frac{M}{g_d}\Big\{& k^2 \frac{H_0 H_b}{8\sqrt{\Phi_b}} - J_3(z_b) \\ & + \left[2J_5(z_b) - \frac{3}{4}k^2 H_0^2\right]\frac{p_d}{g_d} - J_6(z_b)\frac{p_d^2}{g_d^2}\Big\},\end{aligned} \tag{134}$$

$$\begin{aligned}D = \frac{M}{g_d}\Big\{& J_3(z_b) - 2J_4(z_b) - \frac{k^2 H_0 H_b}{4\sqrt{\Phi_b}} \\ & + \left[2J_5(z_b) + \frac{k^2 H_0^2}{4}\right]\frac{p_d}{g_d} - J_6(z_b)\frac{p_d^2}{g_d^2}\Big\} + \frac{p_b' \Phi_0'}{4 g_d \sqrt{\Phi_b}},\end{aligned} \tag{135}$$

$$\begin{aligned}E = M\Big\{& \frac{1}{2R^2} - \frac{k^2 H_0^2}{4R\Phi_0'} + \frac{3k^4 H_0^4}{8\Phi_0'^2} - J_1(z_b) + [J_3(z_b) + 2J_4(z_b)]\frac{p_d}{g_d} \\ & + \left[\frac{5}{8}k^2 H_0^2 - 3J_5(z_b)\right]\frac{p_d^2}{g_d^2} + J_6(z_b)\frac{p_d^3}{g_d^3}\Big\} - p_b' \frac{\Phi_0'}{4\sqrt{\Phi_b}}\frac{p_d}{g_d},\end{aligned} \tag{136}$$

$$f = -\frac{M}{g_d^2}\left[\mu_3(z_b) + kH_0\Phi_0'\frac{p_d}{4g_d}\right], \tag{137}$$

$$c = \frac{M}{g_d}\left\{\frac{k^3 H_0^3}{4\Phi_0'} + \frac{kH_0}{2R} - \mu_2(z_b) + 2\mu_3(z_b)\frac{p_d}{g_d} - kH_0\Phi_0'\frac{p_d^2}{4g_d^2}\right\}, \tag{138}$$

$$\begin{aligned}e = M\Big\{& Mp_b' \frac{kH_b}{4\sqrt{\Phi_b}} - \mu_1(z_b) + \left[\mu_2(z_b) - \frac{kH_0}{2R} + \frac{k^3 H_0^3}{4\Phi_0'}\right]\frac{p_d}{g_d} \\ & - \mu_3(z_b)\frac{p_d^2}{g_d^2} + kH_0\Phi_0\frac{p_d^3}{4g_d^3}\Big\},\end{aligned} \tag{139}$$

$$G = \frac{M}{g_d} J_g(z_b), \tag{140}$$

$$J = M\left[J_7(z_b) - \frac{3}{2}\frac{k^2 H_0^2}{\Phi_0'^2} - J_9(z_b)\frac{p_d}{g_d}\right], \tag{141}$$

$$j = M\left[\frac{kH_b}{2\Phi_0'\sqrt{\Phi_b}} - \mu_4(z_b) - \frac{kH_0}{\Phi_0'}\frac{p_d}{g_d}\right], \tag{142}$$

$$F_m = \frac{M}{g_d^2} k^2 H_0^2, \tag{143}$$

$$b_m = -\frac{M}{4g_d^3} kH_0\Phi_0', \tag{144}$$

$$f_m = MkH_0\Phi_0'\frac{p_d}{g_d^3}, \tag{145}$$

$$d_m = -\frac{M}{g_d}\left(\frac{k^3 H_0^3}{2\Phi_0'} + kH_0\Phi_0'\frac{p_d^2}{2g_d^2}\right), \tag{146}$$

$$g_m = M\frac{kH_0}{\Phi_0' g_d}. \tag{147}$$

Geometric aberrations are determined by the coefficients B, F, C, D, E, *f*, c, and e: spherical aberration, coma, astigmatism, curvature of image field, distortion, anisotropic coma, anisotropic astigmatism, and anisotropic distortion, respectively, which are also characteristic of ordinary electron lenses.[2] The coefficient G determines aperture chromatic aberration, and J and j, the variations in magnification and angular rotation of the image, respectively, which are associated with particles leaving the cathode with some energy.

Similar forms of chromatic aberration appear in ordinary lenses. The remaining four terms involving geometric aberrations, F_m, b_m, f_m, and d_m, and the one form of chromatic aberration, g_m, are not encountered in ordinary lenses. Furthermore, they are not found in composite cathode lenses if there is no magnetic field at the cathode surface ($H_0 = 0$).

---

[1] V. M. Kel'man, A. A Sapargaliev, and E. M. Yakushev, Zh. Tekh. Fiz., 44, 918 (1974) [Sov. Phys. – Tech. Phys., 19, 586 (1974)].

[2] W. Glaser, Fundamentals of Electron Optics [Russian translation], GITTL, Moscow (1957).

Variational analysis of thermal breakdown of a semiconductor irradiated by light

V. L. Komolov

A. F. Ioffe Physicotechnical Institute,
Academy of Sciences of the USSR, Leningrad
(Submitted September 25, 1973)
Zh. Tekh. Fiz., 44, 944-949 (May 1974)

A variational method is given for solving problems involving the thermal breakdown of a semiconductor caused by light. Solutions are found for two simple one-dimensional problems; a disk of finite dimensions illuminated by a light beam with a Gaussian intensity distribution and boundary conditions of the third kind is also treated.

1. In this work we present a variational approach for solving problems involved in the thermal instability of a semiconductor irradiated by light. A mechanism leading to such an instability was proposed by Épshtein,[1] who also calculated the instability threshold for a long cylinder whose lateral surface is at a fixed temperature. Volod'kina and Komolov[2] solved two simple thermal-breakdown problems, using more general heat-transfer conditions at the boundary of a semiconductor; it turns out that the reasonable assumption of heat transfer due to air convection at the surface of the sample leads to a significant discrepancy with the threshold calculated in ref. 1.

Exact solutions can be found for the thermal-breakdown problem only for one-dimensional cases (infinite plate, long cylinder, sphere), but the problems of most practical interest are those involved in the design of the optical elements of CO_2 lasers (exit windows, filters, etc.), in which case it is necessary to deal with three-dimensional regions (which, however, show axial symmetry in the light-propagation direction). In certain cases it is also important to take account of the intensity distribution in the light beam. As shown below, all these features can be easily incorporated in a variational approach to the solution of the thermal-breakdown problem. Furthermore, the variational approach can also be used to solve idealized one-dimensional problems like those of refs. 1 and 2 since it yields results in a simple form – an important consideration for numerical calculations.

2. The threshold for the thermal breakdown of a semiconductor is defined as the light intensity above which there is no steady-state solution of the heat-conduction equation:

$$\lambda\nabla^2 T+\varkappa(T)\,q(r_\perp)=0 \qquad (1)$$

in region D for the specified heat-transfer conditions at boundary B. [Here λ is the thermal conductivity, $\varkappa(T)$ is the absorptivity, and $q(r_\perp)$ is the intensity profile of the light beam.] In the calculations below we use boundary conditions of the third kind:

$$\left[\lambda\frac{dT}{dn}+H(T-T_0)\right]_B=0, \qquad (2)$$

where n is the direction normal to the surface, H is the heat transfer coefficient, and T_0 is the temperature of the surrounding medium.

The stability conditions for the solutions of boundary-value problem (1), (2) can be obtained from a variational principle for the functional I, for which Eq. (1) is an Euler equation. It is necessary to choose trial functions satisfying boundary condition (2). A similar method has been used[3] to calculate the thresholds for the thermal explosion of a gas in which an exothermic chemical reaction occurs. An important feature of the semiconductor breakdown problem is the use of boundary conditions of the third kind. The boundary conditions must be written in the form of (2) because the surface of the semiconductor is ordinarily in contact with a gas (air or CO_2) whose thermal conductivity and heat capacity are much lower than those of the semiconductor; thus, the boundary temperature cannot be assumed to be constant, as in the case of the thermal explosion in an exothermic reaction; in this latter case, the gas, which conducts heat poorly, is enclosed in a massive metal vessel, which is a good thermal regulator. When boundary condition (2) is used it is necessary to seek a solution of the variational problem among functions which do not vanish at the boundary; accordingly, the form of the functional I would be different from that in ref. 3.

In analyzing the thermal breakdown of a semiconductor we assume that the light absorption is due to conduction electrons and is described as a function of the temperature by

$$\varkappa(T)=\varkappa_0\exp\left\{-\frac{E_g}{2kT}\right\}. \qquad (3)$$

This absorption relation leads to serious difficulties in the calculations; these can be avoided by approximating (3) by the power function

$$\left.\begin{aligned}\varkappa(T)&\approx\varkappa_0 e^{-\frac{E_g}{2kT_0}}(1+0.72\Theta+\Theta^2),\\ \Theta&=\frac{(T-T_0)E_g}{2kT_0^2},\end{aligned}\right\} \qquad (4)$$

which, according to ref. 4, is a good approximation over the interval $0\le\Theta\le 2.5$. It follows from the results of refs. 1 and 2 that Θ usually falls in this interval anywhere below the instability threshold.

Below we present the solutions for a plate and for a long cylinder as found by the variational method; we also present the solution of the problem of thermal breakdown of a cylinder of finite length irradiated by a light beam with a Gaussian intensity distribution.

3. In the case of an unbounded flat plate of thickness $2l$ Eqs. (1) and (2) become

$$\left.\begin{aligned}&\frac{d^2\Theta}{dz^2}+\mu(1+0.72\Theta+\Theta^2)=0,\\ &\left[\pm\frac{d\Theta}{dz}+\beta\Theta\right]_{z=\pm1}=0,\end{aligned}\right\} \qquad (5)$$

where $z = x/l$; $q(r_\perp) \equiv q_0$, $\beta = Hl/\lambda$, and $\mu = [\varkappa(T_0)q(r_\perp)]\cdot[\lambda(E_g l^2)/(2kT_0^2)]^{-1}$.

The functional I corresponding to this equation is

$$I=\frac{1}{\beta}\left(\frac{d\Theta}{dz}\right)^2\Big|_{z=1}+\int_0^1\left[\left(\frac{d\Theta}{dz}\right)^2-2\mu\left(\Theta+0.36\Theta^2+0.33\Theta^3\right)\right]dz. \quad (6)$$

Choosing the simplest trial function which satisfies the boundary condition

$$\Theta=C\left(1+\frac{2}{\beta}-z^2\right), \quad (7)$$

where C is an adjustable parameter, and substituting in (6), we find

$$I=2aC^2-2\mu\left(aC+bC^2+pC^3\right). \quad (8)$$

Here

$$\left.\begin{aligned}a&=2\left(\frac{1}{\beta}+\frac{1}{3}\right),\\ b&=0.72\left[\frac{1}{2}\left(1+\frac{2}{\beta}\right)^2-\frac{1}{3}\left(1+\frac{2}{\beta}\right)+\frac{1}{10}\right],\\ p&=\left[\frac{1}{3}\left(1+\frac{2}{\beta}\right)^3-\frac{1}{3}\left(1+\frac{2}{\beta}\right)^2+\frac{1}{5}\left(1+\frac{2}{\beta}\right)-\frac{1}{21}\right].\end{aligned}\right\} \quad (9)$$

The condition that the variation vanish,

$$\delta I=\frac{dI}{dC}=4aC-2\mu\left(a+2bC+3pC^2\right)=0, \quad (10)$$

leads to a quadratic equation in C which has real roots only when $\mu < \mu_{cr}$, where the dimensionless threshold for thermal breakdown is

$$\mu_{cr}=\frac{a}{b+\sqrt{3ap}}. \quad (11)$$

The maximum temperature in the steady state, which corresponds to (11), is

$$\Theta_{max}=\sqrt{\frac{a}{3p}}\left(1+\frac{2}{\beta}-z^2\right). \quad (7a)$$

For small values of β we find $\mu_{cr} \approx \beta/2.72$ from Eqs. (9) and (11); in the opposite limiting case, $\beta=\infty$, we find $\mu_{cr} \approx 0.89$. Both these results agree with those found through an exact solution of the problem.[2]

As another example of the application of this variational procedure we consider a long cylinder; in this case we can take account of the effect of the generating surface alone and can neglect heat transfer at the ends of the cylinder. In this case the breakdown is described by

$$\left.\begin{aligned}&\frac{d^2\Theta}{dz^2}+\frac{1}{z}\frac{d\Theta}{dz}+\mu\left(1+0.72\Theta+\Theta^2\right)=0,\\ &\left[\pm\frac{d\Theta}{dz}+\beta\Theta\right]_{z=\pm1}=0,\end{aligned}\right\} \quad (12)$$

where the notation is the same as that of (5), except that l is the radius of the cylinder. The functional for (12) is

$$I=\frac{1}{\beta}\left(\frac{d\Theta}{dz}\right)^2\Big|_{z=1}+\int_0^1 z\,dz\left[\left(\frac{d\Theta}{dz}\right)^2-2\mu\left(\Theta+0.36\Theta^2+0.33\Theta^3\right)\right]; \quad (13)$$

substituting trial function (7) we find an equation like (11) for μ_{cr}:

$$\mu^0_{cr}=\frac{2a_0}{b_0+\sqrt{3a_0p_0}}, \quad (14)$$

where

$$\left.\begin{aligned}a_0&=\frac{1}{\beta}+\frac{1}{4},\\ b_0&=0.36\left[\frac{1}{2}\left(1+\frac{2}{\beta}\right)^2-\frac{1}{2}\left(1+\frac{2}{3}\right)+\frac{1}{6}\right],\\ p_0&=\frac{1}{3}\left[\frac{1}{2}\left(1+\frac{2}{\beta}\right)^3-\frac{3}{4}\left(1+\frac{2}{\beta}\right)^2+\frac{1}{2}\left(1+\frac{2}{3}\right)-\frac{1}{8}\right].\end{aligned}\right\} \quad (15)$$

Equations (14) and (15) are obtained for the case $q(r_\perp)=q_0$, but we could obviously substitute any distribution $q(r_\perp)$ into (13); if the corresponding integrals exist, we can find an expression for the threshold value of μ. As an example we give the solution of the problem for a Gaussian distribution $q(z)=q_0\exp(-z^2/z_0^2)$, with $z_0 \gg 1$ (a more general case is analyzed below). For a broad Gaussian beam the value of μ_{cr} is again given by Eq. (14), where the quantities a_0, b_0, and p_0 are replaced by

$$\left.\begin{aligned}a_0'&=a_0-\frac{1}{2z_0^2}\left(\frac{1}{6}+\frac{1}{\beta}\right),\\ b_0'&=b_0-\frac{0.36}{z_0^2}\left[\frac{1}{4}\Pi^2-\frac{1}{3}\Pi+\frac{1}{8}\right],\\ p_0'&=p_0-\frac{1}{3z_0^2}\left[\frac{1}{4}\Pi^3-\frac{1}{2}\Pi^2+\frac{3}{8}\Pi-\frac{1}{10}\right];\ \ \Pi=1+\frac{2}{\beta}.\end{aligned}\right\} \quad (16)$$

It is evident that the results obtained for a long cylinder also agree with the results of the exact solutions, where the latter can be found. For example, with $\beta=\infty$ we find $\mu_{cr}=2.1$ and $\Theta_{max}|_{z=0}=1.41$, and the corresponding exact values[1] are 2.0 and 1.39.

4. We turn now to the solution of the problem of the thermal breakdown of a semiconductor which is a cylinder of length $2l$ and radius R. In the solution of this problem we assume that the heat-transfer conditions at the bases and generating surface of the cylinder are different, being characterized by heat-transfer coefficients H_1 and H_2, respectively. This assumption corresponds to the usual experimental conditions, under which the sample is placed in a holder (which is usually a good heat conductor), or to the operating conditions of the exit window of a CO_2 laser. Furthermore, we incorporate in the absorptivity an additional term $\varkappa_1$, which is not a function of the temperature, in order to take account of possible absorption by impurities or other absorption processes not involving conduction electrons.

Under these assumptions Eqs. (1) and (2) become

$$\left.\begin{aligned}&\frac{\partial^2\Theta}{\partial z^2}+b^2\frac{1}{\rho}\frac{\partial}{\partial\rho}\left(\rho\frac{\partial\Theta}{\partial\rho}\right)+\mu_1+\mu_2\left(1+0.72\Theta+\Theta^2\right)=0,\\ &\left[\pm\frac{\partial\Theta}{\partial z}+\beta_1\Theta\right]\Big|_{z=\pm1}=0;\ \left[\pm\frac{\partial\Theta}{\partial\rho}+\frac{\beta_2}{b}\Theta\right]_{\rho=\pm1}=0.\end{aligned}\right\} \quad (17)$$

Here,

$$\left.\begin{aligned}&z=\frac{x}{l},\ \ \rho=\frac{r}{R},\ \ b=\frac{l}{R},\\ &\Theta=\frac{(T-T_0)E_g}{2kT_0^2},\ \ \beta_1=\frac{H_1l}{\lambda},\ \ \beta_2=\frac{H_2l}{\lambda},\\ &\mu_1=\varkappa_1\frac{q(\rho)}{\lambda}\frac{E_gl^2}{2kT_0^2},\ \ \mu_2=\varkappa(T_0)\frac{q(\rho)}{\lambda}\frac{E_gl^2}{2kT_0^2}.\end{aligned}\right\} \quad (18)$$

It is easy to see that the following functional corresponds to Eq. (17):

$$
\begin{aligned}
I = &-\frac{1}{2\beta_1}\int\limits_0^1\left(\frac{\partial\Theta}{\partial z}\right)^2\Big|_{z=1}\rho d\rho - \frac{b^3}{2\beta_2}\int\limits_0^1\left(\frac{\partial\Theta}{\partial\rho}\right)^2\Big|_{\rho=1}dz \\
&+\int\limits_0^1\int\limits_0^1\rho d\rho dz\left\{-\frac{1}{2}\left[\left(\frac{\partial\Theta}{\partial z}\right)^2 + b^2\left(\frac{\partial\Theta}{\partial\rho}\right)^2\right]\right. \\
&\left.+\mu_1\Theta + \mu_2(\Theta + 0.36\Theta^2 + 0.33\Theta^3)\right\}. \qquad (19)
\end{aligned}
$$

As a trial function we choose $\Theta = C(1 + 2/\beta_1 - z^2)(1 + 2/\beta_2 - \rho^2)$, and for definiteness we assume a Gausian intensity distribution

$$
q(\rho) = q_0\exp\left\{-\frac{\rho^2}{\rho_0^2}\right\}. \qquad (20)
$$

Here we have

$$
\left.\begin{aligned}
\mu_1(\rho) &= \mu_1^0\exp\left\{-\frac{\rho^2}{\rho_0^2}\right\}, \\
\mu_2(\rho) &= \mu_2^0\exp\left\{-\frac{\rho^2}{\rho_0^2}\right\},
\end{aligned}\right\} \qquad (21)
$$

where the values of $\mu_{1,2}^0$ are found from Eq. (18) with $q(\rho) = q_0$. This problem can be solved in the same way as the one-dimensional problems treated above. The critical value of μ_2^0 is

$$
\mu_{cr}^0 = \frac{A}{D + \sqrt{3BF\left(1 + \frac{\varkappa_1}{\varkappa(T_0)}\right)}}. \qquad (22)
$$

The coefficients in (22) are given in the Appendix.

5. We turn now to numerical estimates of the threshold for the thermal instability. We first write an explicit equation for the threshold density of the light flux. According to (5) and (18), and under the assumption that no light is reflected from the surface, we find this critical density to be

$$
q_{cr} = \frac{2\lambda k T_0^2}{\varkappa(T_0) E_g l^2}\mu_{cr}, \qquad (23)
$$

where μ_{cr} is given by the equations derived in the preceding sections. Since these equations are cumbersome, we carry out numerical estimates for only two limiting cases:

1. $\varkappa_1 = 0$, $q(\rho) = q_0$, $\beta_1 = \beta_2 = \infty$. In this case we obtain

$$
\mu_{cr} \approx 0.9 + 2.1 b^2. \qquad (24)
$$

2. $\varkappa_1 = 0$, $q(\rho) = q_0$, $\beta_1 = 1$, $\beta_2 = \infty$. In this case we obtain

$$
\mu_{cr} \approx 0.3 + 2.1 b^2. \qquad (25)
$$

Obviously, although the first case does not arise ordinarily, it gives us an upper limit on the breakdown threshold, since any degradation of the heat transfer would lead to an instability at a lower light intensity. The second case, on the other hand, corresponds to a situation frequently met in practice, in which the heat transfer at the ends occurs as a result of the natural convection of air while the heat transfer at the generating surface is due to contact with a massive metal holder. It is interesting to compare the threshold predicted by Eqs. (23) and (25) with the experimental data available on the breakdown threshhold for germanium irradiated by a CO_2 laser.[5] We should stipulate, however, that the experimental boundary conditions are slightly different from those we have assumed here, so that we can expect only an order-of-magnitude agreement between theory and experiment.

Substituting the values $T_0 = 20°C$, $\varkappa(T_0) = 0.07\ cm^{-1}$, and $l = 0.3$ cm from ref. 5 into Eqs. (23) and (25), we find $q_{cr} \approx 410\ W/cm^2$; for comparison, the experimental thresholds vary over the range 20-90 W/cm^2, depending on the cooling efficiency. In view of our reservation above we conclude that this agreement is satisfactory; this method should be useful for designing the elements of CO_2 lasers.

In conclusion the author thanks S. I. Anisimov for useful comments and I. N. Yassievich for discussion.

APPENDIX

The coefficients in Eq. (2) are

$$
\left.\begin{aligned}
A = {} & 2\left[\frac{1}{\beta_1}\left(\frac{1}{4}+\frac{b}{\beta_2}\right)+\frac{2b^3}{\beta_2}\left(\frac{1}{3}+\frac{1}{\beta_1}\right)\right] \\
& +\frac{2}{3}\left[\frac{1}{2}\Pi_2^2-\frac{1}{2}\Pi_2+\frac{1}{6}\right]+\frac{1}{2}b^2\left[\Pi_1^2-\frac{2}{3}\Pi_1+\frac{1}{5}\right], \\
B = {} & \left(\frac{1}{3}+\frac{1}{\beta_1}\right)\rho_0^2\left[(\Pi_2-\rho_0^2)(1-e^{-1/\rho_0^2})+e^{-1/\rho_0^2}\right], \\
D = {} & 0.36\left[\Pi_1^2-\frac{2}{3}\Pi_1+\frac{1}{5}\right]\left\{\frac{1}{2}\Pi_2^2\rho_0^2(1-e^{-1/\rho_0^2})\right. \\
& \left.-\Pi_2\rho_0^2\left[\rho_0^2(1-e^{-1/\rho_0^2})-e^{-1/\rho_0^2}\right]-\rho_0^6-\frac{1}{2}e^{-1/\rho_0^2}(\rho_0^2+2\rho_0^4+2\rho_0^6)\right\}, \\
F = {} & \frac{1}{6}\left[\Pi_1^3-\Pi_1^2+\frac{3}{5}\Pi_1-\frac{1}{7}\right]\rho_0^2\left\{\Pi_2^3(1-e^{-1/\rho_0^2})\right. \\
& -3\Pi_2^2\left[\rho_0^2(1-e^{-1/\rho_0^2})-e^{-1/\rho_0^2}\right]+3\Pi_2 \\
& \times\left[2\rho_0^4(1-e^{-1/\rho_0^2})-(1+2\rho_0^2)e^{-1/\rho_0^2}\right]-6\rho_0^6 \\
& \left.+e^{-1/\rho_0^2}(1+3\rho_0^2+6\rho_0^4+6\rho_0^6)\right\}, \\
\Pi_1 = {} & 1+\frac{2}{\beta_1};\quad \Pi_2 = 1+\frac{2b}{\beta_2}.
\end{aligned}\right\} \qquad (A.1)
$$

In the case of a broad Gaussian distribution ($\rho_0 \gg 1$) we can use $\exp(-\rho^2/\rho_0^2) = 1 - (\rho^2/\rho_0^2) + \ldots$, so Eqs. (A.1) are simplified; to terms of order $1/\rho_0^2$ the coefficients are

$$
\left.\begin{aligned}
A' = {} & A, \\
B' = {} & \left(\frac{1}{3}+\frac{1}{\beta_1}\right)\left[\Pi_2\left(1-\frac{1}{2\rho_0^2}\right)-\frac{1}{2}+\frac{1}{3\rho_0^2}\right], \\
D' = {} & 0.36\left[\Pi_1^2-\frac{2}{3}\Pi_1+\frac{1}{5}\right] \\
& \times\left[\frac{1}{2}\Pi_2^2\left(1-\frac{1}{2\rho_0^2}\right)-\Pi_2\left(\frac{1}{2}-\frac{1}{3\rho_0^2}\right)+\frac{1}{2}\left(\frac{1}{3}-\frac{1}{4\rho_0^2}\right)\right], \\
F' = {} & \frac{1}{6}\left[\Pi_1^3-\Pi_1^2+\frac{3}{5}\Pi_1-\frac{1}{7}\right]\left[\Pi_2^3\left(1-\frac{1}{2\rho_0^2}\right)\right. \\
& \left.-3\Pi_2^2\left(\frac{1}{2}-\frac{1}{3\rho_0^2}\right)+3\Pi_2\left(\frac{1}{3}-\frac{1}{4\rho_0^2}\right)-\frac{1}{4}+\frac{1}{5\rho_0^2}\right].
\end{aligned}\right\} \qquad (A.2)
$$

In the limit $\rho_0 = \infty$ Eqs. (A.2) hold for the case of a uniform illumination of the entire end of the cylinder.

---

[1] É. M. Épshtein, Izv. VUZ. Radiofiz., 15, 33 (1972).

[2] V. L. Volod'kina and V. L. Komolov, Zh. Tekh. Fiz., 43, 1766 (1973) [Sov. Phys. – Tech. Phys., 18, 1117 (1974)].

[3] S. I. Anisimov and É. I. Vitkin, Zh. Prikl. Mekhan. Tekh. Fiz., No. 4, 150 (1966).

[4] P. H. Thomas, Trans. Faraday Soc., 54, 60 (1958).

[5] P. A. Young, Appl. Opt., 10, 638 (1971).

Reflection of finite amplitude electromagnetic waves from a semiconductor plasma

Yu. F. Filippov
Institute of Radiophysics and Electronics,
Academy of Sciences of the USSR, Khar'kov

(Submitted June 25, 1973)
Zh. Tekh. Fiz., 44, 950-955 (May 1974)

The present work considers two circularly polarized waves of finite but small amplitude with arbitrary frequencies incident on a plasma–vacuum boundary. It is shown that nonlinear effects lead to an intensity dependence of the Fresnel coefficients and to the appearance of waves at combination frequencies. The effects are most pronounced at the plasma cyclotron resonance.

The nonlinear effects which occur in the interaction of strong electromagnetic waves with semiconductors are utilized in a variety of devices: detectors, multipliers, mixers, and so on. For small pump powers (of the order of a tenth of a watt), the effects away from resonance are small. However, near resonance (cyclotron resonance, for example), the waves are strongly attenuated in the plasma. When there is a plasma–vacuum interface, reflected waves appear in the vacuum at the fundamental and at combination frequencies. It is shown below that at the cyclotron and plasma cyclotron frequencies there is a significant increase in the amplitudes of these waves and in the dependence of the Fresnel coefficients on the incident amplitude.

WAVE INTERACTION IN A PLASMA

Assume that a multicomponent collisionless cold plasma occupies the half-space $z \geq 0$. The properties of a finite-amplitude wave propagating in this plasma can be described by the solutions of the following nonlinear system:

$$\left.\begin{aligned} &C\,\mathrm{curl}\,\mathbf{E} = -\frac{\partial \mathbf{H}}{\partial t}, \quad C\,\mathrm{curl}\,\mathbf{H} = \varepsilon_l \frac{\partial \mathbf{E}}{\partial t} + \sum 4\pi \mathbf{j}_\alpha, \\ &\mathrm{div}\,\mathbf{H} = 0, \quad e_\alpha \frac{\partial n_\alpha}{\partial t} + \mathrm{div}\,\mathbf{j}_\alpha = 0, \\ &\frac{\partial \mathbf{j}_\alpha}{\partial t} - \frac{\omega_{p\alpha}^2}{4\pi}\mathbf{E} - \frac{\omega_{H\alpha}}{H_0}[\mathbf{j}_\alpha \mathbf{H}_0] = \frac{4\pi}{c}\phi_\alpha. \end{aligned}\right\} \qquad (1)$$

Here E and H are the wave fields; e_α, m_α, $N_{0\alpha}$, $\omega_{p\alpha}$ and $\omega_{H\alpha}$, n_α and j_α are respectively the charge, effective mass, equilibrium density, plasma and cyclotron frequencies, and the varying density and current density components for particles of species α caused by the wave fields; ε_e is the dielectric constant due to the lattice; $\sum_\alpha$ denotes summation over all particles α. We consider a quasineutral plasma, for which $\sum_\alpha e_\alpha N_{0\alpha} = 0$.

The influence of the nonlinear effects on the wave is determined by the function ψ_α

$$\frac{4\pi}{c}\phi_\alpha = \frac{e_\alpha}{m_\alpha}\left\{e_\alpha n_\alpha \mathbf{E} + \frac{1}{c}[\mathbf{j}_\alpha \mathbf{H}] - \sum_i \frac{\partial}{\partial x_i}(\mathbf{j}_\alpha j_{\alpha i})\right\} \qquad (1a)$$

($\sum_i$ denotes summation over coordinates).

We choose the z axis in the direction of propagation of the wave. In a longitudinal field ($\mathbf{H}_0 \parallel \mathbf{i}_z$), the system (1) admits the following exact solution describing the propagation of a single transverse wave of finite amplitude:

$$H_x = h_0 \cos(\omega t - kz), \quad H_y = \frac{\eta}{\omega}\frac{\partial H_x}{\partial t},$$

$$\frac{4\pi}{c}\mathbf{j}_{\alpha\perp} = -\frac{\omega\omega_{p\alpha}^2}{kc^2(\omega_{H\alpha} - \eta\omega)}\mathbf{H}_\perp,$$

$$j_{z\alpha} = n_\alpha = E_z = \phi_\alpha = 0, \qquad (2)$$

where k and ω are the propagation constant and frequency of the wave and are related by the usual dispersion equation:

$$k^2c^2 = \omega^2\left[\varepsilon_l - \sum_\alpha \frac{\omega_{p\alpha}^2(\omega - \eta\omega_{H\alpha})^{-1}}{\omega}\right]. \qquad (2a)$$

The solutions (2) and (2a) describe the properties of the ordinary ($\eta = -1$) or extraordinary ($\eta = 1$) wave and show that the propagation of one of these waves along the magnetic field does not produce any change in the plasma parameters. Thus an intense wave propagates in exactly the same way as a wave of infinitesimal amplitude. This result does not contradict the conclusions reached in other papers which consider the nonlinearity produced by electron heating leading to a dependence of the dielectric constant on the power even when only one wave propagates (see, for example, ref. 1). In our case $\nu \ll \omega$, ω_H, and so the effect of heating on the wave can be neglected. Nonlinear effects occur in a longitudinal magnetic field only when several waves propagate.

We limit ourselves here to a study of the case in which the wave is normally incident from vacuum on a vacuum–plasma interface. For longitudinal incidence of a circularly polarized wave ($\mathbf{k} \parallel \mathbf{H}_0$) there is no change of polarization across the boundary and hence nonlinear effects do not occur. If the incident wave is linearly polarized, it splits into two waves, circularly polarized in opposite directions, and these propagate into the plasma with different phase velocities. For sufficiently high incident power an interaction is set up between the waves and this leads to the appearance of longitudinal and transverse waves at twice and three times the frequency respectively. The phase velocities and the Fresnel coefficients then depend on the amplitude of the primary wave. It is not possible to analyze these effects in the general case. We therefore limit ourselves to waves of finite, but small, amplitude.

We expand the system (1) in a series in the small parameter defined as the ratio of the wave amplitude to the strength of the external magnetic field; retaining terms up to the third order in small quantities, we reduce (1) to the form

$$(\hat{L}_1^2 + \hat{L}_2^2)H_x = -\frac{\partial}{\partial z}\left\{\sum_\alpha \hat{L}_{H\alpha}\left[\frac{\partial}{\partial t}(\hat{L}_1 + \hat{L}_2\omega_{H\alpha})\psi_{y\alpha} + \left(\hat{L}_2\frac{\partial^2}{\partial t^2} - \hat{L}_1\omega_{H\alpha}\right)\psi_{x\alpha}\right]\right\}, \qquad (3a)$$

$$\varepsilon_l\frac{\partial^2 E_z}{\partial t^2} + \sum_\alpha \omega_{p\alpha}^2 E_z = -c\sum \psi_{z\alpha}, \qquad (3b)$$

$$\frac{\partial j_{z\alpha}}{\partial t} = \frac{\omega_{p\alpha}^2}{4\pi} E_z + \frac{c}{4\pi} \psi_{z\alpha}, \qquad (3c)$$

where ψ_α is defined by (1a) and

$$c^2 \hat{L}_1 = \left(\varepsilon_l \frac{\partial^2}{\partial t^2} - c^2 \frac{\partial^2}{\partial z^2}\right) + \sum_\alpha \omega_{p\alpha}^2 \hat{L}_{H\alpha}^{-1} \frac{\partial^2}{\partial t^2},$$
$$c^2 \hat{L}_2 = \sum \omega_{H\alpha} \omega_{p\alpha}^2 \hat{L}_{H\alpha}^{-1}, \quad \hat{L}_{H\alpha} = \omega_{H\alpha}^2 + \frac{\partial^2}{\partial t^2}.$$

Since the nonlinear effects are small, all the field and current components in ψ_α can be expressed in terms of H_x from (2).

We first consider the interaction of circular waves with different amplitudes and frequencies and arbitrary directions of rotation (as given by the parameter η)

$$H_x = \sum_{j=1}^{2} \frac{a_j}{2} e^{i\eta_j\varphi_j} + \text{c.c.}, \qquad (4)$$

where $\varphi_j = \omega_j t - k_j z_j$, $\eta_j = \pm 1$.

Substituting (4) into (3b), we see that a longitudinal wave is produced at the combination frequency $\eta_1\omega_1 - \eta_2\omega_2$

$$E_z = a_1 a_2 \sum_\alpha \left(\frac{\omega_{H\alpha}\omega_{p\alpha}^2}{2icH_0}\right) \left[\sum_{\alpha'} \omega_{p\alpha'}^2 - \varepsilon_l (\eta_1\omega_1 - \eta_2\omega_2)^2\right]^{-1}$$
$$\times \left\{\omega_1 \frac{(\omega_{H\alpha} - \eta_1\omega_1)^{-1}}{k_1 - \omega_2 (\omega_{H\alpha} - \eta_2\omega_2)^{-1}/k_2}\right\} e^{i(\eta_1\varphi_1 - \eta_2\varphi_2)} + \text{c.c.} \qquad (5)$$

We can conclude from (5) that if the original waves have the same sense ($\eta_1 = \eta_2$), they give rise to a longitudinal wave at the difference frequency ($\omega_{l0} = |\omega_1 - \omega_2|$); whereas if they have opposite senses ($\eta_1 = -\eta_2$), the resultant wave is at the sum frequency ($\omega_{l0} = \omega_1 + \omega_2$). The amplitude becomes significantly greater near resonance.

Cyclotron resonances are observed in a two-component plasma: ion cyclotron in the ordinary wave (α = i, e) and electron cyclotron in the extraordinary wave ($\omega_{Hi} = \omega$, $\eta = -1$). It is also possible to have a nonlinear plasma resonance when $\varepsilon_l(\eta_1\omega_1 - \eta_2\omega_2)^2 = \omega_{pe}^2 + \omega_{pi}^2$. The longitudinal wave reaches its greatest amplitude at the double resonance $\varepsilon_l(\omega_1 = \eta_2\omega_2)^2 = \omega_{pe}^2 + \omega_{pi}^2$, $\omega_1 = \omega_{He}$, $\eta_1 = 1$. The inverse effect of a longitudinal wave on transverse waves results in the dependence of the phase velocities on intensity and to the appearance of transverse waves at the combination frequencies

$$H_{x1}(\omega_1^+) = b_1^+ \exp[i(2\eta_1\varphi_1 - \eta_2\varphi_2)] + \text{c.c.},$$
$$H_{x2}(\omega_2^-) = b_2^- \exp[i(2\eta_2\varphi_2 - \eta_1\varphi_1)] + \text{c.c.},$$
$$\omega_j^\pm = \eta_j\omega_j \pm (\eta_1\omega_1 - \eta_2\omega_2).$$

We omit the cumbersome intermediate steps and quote the results for the nonlinear corrections to the wave vectors and for the amplitudes $b_j^\pm$:

$$\left.\begin{aligned} \Delta k_1 &= -\frac{\eta_1}{2} \sum_\alpha \psi_{2\alpha}^\pm (\omega_{H\alpha} - \eta_1\omega_1)^{-1} \frac{a_1}{a_2}; \\ \Delta k_2 &= -\frac{\eta_2}{2} \sum_\alpha \psi_{1\alpha}^- (\omega_{H\alpha} - \eta_2\omega_2)^{-1} \frac{a_2}{a_1}; \end{aligned}\right\} \qquad (6a)$$

$$b_j^\pm = -\sum_\alpha \frac{a_j k_j^\pm \psi_{j\alpha}^\pm (\omega_{H\alpha} - \omega_j^\pm)^{-1}}{\Delta_j^\pm}, \qquad (6b)$$

where

$$k_j^\pm = \eta_j k_j \pm (\eta_1 k_1 - \eta_2 k_2), \qquad (7a)$$

$$\Delta_j^\pm c^2 = k_j^{\pm 2} c^2 - \omega_j^{\pm 2} \left[\varepsilon_e + \sum_\alpha \frac{\omega_{p\alpha}^2 (\omega_{H\alpha} - \omega_j^\pm)^{-1}}{\omega_j^\pm}\right], \qquad (7b)$$

$$\psi_{j\alpha}^\pm = \left(\frac{a_1 a_2 \omega_{H\alpha}}{2H_0^2 C^2}\right) (\eta_1\omega_1 - \eta_2\omega_2)^{-1} \left[1 - \frac{\omega_j}{k_j} \frac{\eta_1 k_1 - \eta_2 k_2}{\eta_1\omega_1 - \eta_2\omega_2}\right.$$
$$\left. + \frac{\omega_j}{k_j} k_j^\pm (\omega_{H\alpha} - \eta_j\omega_j)^{-1}\right] \left[R_{z\alpha} - \frac{\omega_{p\alpha}^2 \sum_{\alpha'} R_{z\alpha'}}{\left[\sum_{\alpha'} \omega_{p\alpha'}^2 - \varepsilon_e (\eta_1\omega_1 - \eta_2\omega_2)^2\right]}\right], \qquad (7c)$$

$$R_{z\alpha} = \omega_{H\alpha}\omega_{p\alpha}^2 \left[\frac{\omega_1 (\omega_{H\alpha} - \eta_1\omega_1)^{-1}}{k_1 - \omega_2 (\omega_{H\alpha} - \eta_2\omega_2)^{-1}/k_2}\right]. \qquad (7d)$$

Interaction in a longitudinal magnetic field leads to the appearance of a virtual longitudinal wave characterized by a frequency $|\eta_2\omega_2 - \eta_1\omega_1|$ and a propagation constant $\eta_1 k_1 - \eta_2 k_2$. This is not a characteristic wave in a magnetoactive plasma: If thermal effects are neglected the only waves which can occur are plasma oscillations. The reaction of these waves on the primary waves leads to a dependence of the phase velocities on the power of the interacting waves and to the appearance of transverse waves at frequencies ω_1^+ and ω_2^- with propagation constants which can be expressed in terms of k_1 and k_2. The frequency and propagation constant of the characteristic wave are related by the dispersion equation (2a). Since the wave vectors $H_{x1}(\omega_1^+)$ and $H_{x2}(\omega_2^-)$ do not satisfy this condition, the above interaction does not apply to the resonance wave, which is characterized by the possibility of a total jump in energy from one wave to another. All of these effects are in general small. Thus, for example, in the "opposed" interaction ($\eta_2 = -\eta_1$) when the frequencies are such that $\omega_{Hi} \ll \omega_1$, $\omega_2 \ll \omega_{He}$, ω_{pe} the relative change in the propagation constant of the helicon ($\eta_2 = 1$) is

$$\frac{\Delta k_2}{k_2} \approx \frac{a_1^2}{4H_0^2} \varepsilon_l \left[\varepsilon_e - \frac{\omega_{pe}^2}{\omega\omega_{He}}\right]^{1/2} = \left(\frac{\pi\varepsilon_l P_\omega}{cH_0^2 S_0}\right) \left(\varepsilon_l - \frac{\omega_{pe}^2}{\omega\omega_{He}}\right)^{-1/2}, \qquad (8)$$

where k_2 is the propagation constant of the ordinary wave, P_ω is the power of this wave ($\eta_1 = -1$) through the cross section S_0. With $\varepsilon_l = 16$, $H_0 \sim 1$ kOe, $S_0 = 1\ \text{mm}^2$, $\omega^2_{pe} \cdot (\omega\omega_{He}\varepsilon_e)^{-1} \sim 15$, we find from (8) that the relative shift in the helicon wave vector for $P_\omega = 10$ W is of the order of $(\Delta k_2)/k_2 \sim 10^{-6}$.

It can be shown in a similar way that the power of the harmonics is very small. This is in agreement with experimental results[2] at $\lambda = 3.2$ cm, where with $P_\omega = 20$ kW, the power of the third harmonic is $5 \cdot 10^{-5}$ W with pulsed excitation.

RESONANCES IN THE PLASMA

The strongest nonlinear effects occur at the resonances. We first consider the interaction between ordinary and extraordinary waves with the same frequency ($\eta_1 = -\eta_2 = 1$, $\omega_1 = \omega_2 = \omega$) and neglect the effect on these waves of all the charged particles except electrons ($\omega \gg \omega_{H\alpha}$ when $\alpha \neq e$).

Electron cyclotron resonance ($\omega = \omega_{He}$). When $\omega = \omega_{He}$, a singularity appears in (7) and the expressions for Δk_j and the harmonic amplitudes go to infinity. The singularity results from neglecting the particle collisions, which always occur in a real plasma. It can be shown that the inclusion of collisions in the original equations leads to finite values of Δk and b_j

$$\left.\begin{aligned}\frac{\Delta k_1}{k_1} &\approx \frac{a_2^2}{4H_0^2}\frac{\omega}{i\nu}\varepsilon_l\omega^2(\omega_{pe}^2-4\varepsilon_l\omega^2)^{-1},\\ \frac{\Delta k_2}{k_2} &\approx \frac{a_1^2}{4H_0^2}\frac{\omega}{i\nu}\varepsilon_l\omega^2(\omega_{pe}^2-4\varepsilon_l\omega^2)^{-1};\end{aligned}\right\} \tag{9a}$$

$$\left.\begin{aligned}b_1^+ &\approx -\frac{a_1^2a_2}{2H_0^2}\frac{\omega}{i\nu}\varepsilon_l\omega^2(\omega_{pe}^2-4\varepsilon_l\omega^2)^{-1},\\ b_2^- &\approx \frac{a_1a_2^2}{4H_0^2}\frac{\omega_{pe}^2}{k_1k_2c^2}\frac{\omega}{i\nu}\frac{\varepsilon_l\omega_p^2}{1}(\omega_{pe}^2-4\varepsilon_l\omega^2)^{-1}.\end{aligned}\right\} \tag{9b}$$

Here, ν_e is the effective collision frequency, b_1 and b_2 are the amplitudes of the ordinary and extraordinary waves, and k_1 and k_2 are given by $\sqrt{2}k_1 \approx (1-i)\left(\frac{\omega_{pe}^2\omega}{\nu c^2}\right)^{1/2}$ and $k_2 \approx \frac{\omega}{c}\left(\frac{\varepsilon_l-\omega_{pe}^2}{2\omega^2}\right)^{1/2}$. Equation (9a), which describes the nonlinear shift in the wave vector, shows that the nonlinear effects produce wave attentuation in the plasma. Expressions (9b) describe the amplitude of the two third harmonics which propagate with different phase velocities. Since the propagation constants depend on k_1, these waves are also strongly attenuated inside the plasma.

Cyclotron plasma resonance ($\omega = \omega_{He} = \omega_{pe}/2\sqrt{\varepsilon_e}$). We note from (9a) and (9b) that the amount of shift and the amplitudes of the harmonics are significantly greater than $\omega_{pe} = 2\sqrt{\varepsilon_e}\omega$. It follows from (5) that under these conditions there will be a nonlinear plasma resonance in the longitudinal wave. In order to obtain finite amplitudes at the double resonance we must take account of the effect of collisions on the propagation of the longitudinal wave. It can be shown that (9a) and (9b) then reduce to

$$2\frac{\Delta k_1}{k_1} \approx -\left(\frac{a_2\omega}{2H_0\nu}\right)^2,\quad 2\frac{\Delta k_2}{k_2} \approx -\left(\frac{a_1\omega}{2H_0\nu}\right)^2; \tag{10a}$$

$$b_1^+ \approx a_2\left(\frac{a_1\omega}{2H_0\nu}\right)^2,\quad b_2^- \approx \frac{i-1}{\sqrt{2}}a_1\left(\frac{a_2\omega}{2H_0\nu}\right)^2\sqrt{\frac{\nu}{\omega}}. \tag{10b}$$

Thus, when $\omega \gg \nu$ the nonlinear shift in the wave vector and the amplitude of the harmonics are much greater at resonance than in normal cases.

The other resonances can be studied in the same way. In particular, a triple resonance is possible when $\omega_{Hi} = \omega_2 \ll \omega_1 = (\omega_{0e}^2 + \omega_{0i}^2)^{1/2}/\sqrt{\varepsilon_l}$. Estimates show, however, that the values of Δk_j and b_j are of the same order as in the double resonance and so we will not go into the details here.

As a result of the strong wave attenuation in the plasma at the resonances, the effects cannot be utilized to construct semiconductor devices. It is therefore necessary to investigate the influence of the nonlinear effects on the waves which are reflected from the plasma.

THE INFLUENCE OF THE BOUNDARY ON THE WAVE INTERACTION

We consider normal incidence of circularly polarized waves of arbitrary sense with frequencies ω_1 and ω_2 and amplitudes h_{01} and h_{02}. As a result of the interaction reflected waves are produced in the vacuum at the fundamentals and at the combination frequencies $|2\eta_1\omega_1-\omega_2\eta_2|$ and $|2\eta_2\omega_2-\eta_1\omega_1|$. Since circularly polarized waves propagating longitudinally in a magnetized plasma ($\mathbf{k} \parallel \mathbf{H}_0$) are normal waves, there is no transformation into waves of the opposite sense at the vacuum – plasma boundary. Thus the tangential components of the E and H fields of each type must be continuous at this boundary. We also note that in order to satisfy these conditions for the fields at the frequencies ω_1^+ and ω_2^- we must use the full solution of (3a) consisting of the particular solution (7) which we have already discussed and the solution of the homogeneous equation

$$(\hat{L}_1^2+\hat{L}_2^2)H_x = 0.$$

With these preliminary remarks, we now quote the expressions for the amplitudes of the H_x field components:

$$a_j = \frac{2h_{0j}k_jc}{(\omega_j+k_jc)}, \tag{11a}$$

$$b_j^\pm = -2k_jk_j^\pm ch_{0j}(k_jc+\omega_j)^{-1}\sum\frac{\psi_{\alpha j}^\pm(\omega_{H\alpha}-\omega_j^\pm)^{-1}}{\Delta_j^\pm}, \tag{11b}$$

$$\tilde{b}_j^\pm = (k_j^\pm c+\omega_j^\pm)(\tilde{k}_j^\pm c+\omega_j^\pm)^{-1}\frac{b_j^\pm \tilde{k}_j^\pm}{k_j^\pm}, \tag{11c}$$

$$f_j = (k_jc-\omega_j)(k_jc+\omega_j)^{-1}h_{0j}, \tag{11d}$$

$$g_j^\pm = \omega_j^\pm(k_j^\pm-\tilde{k}_j^\pm)(\omega_j^\pm \mp k_j^\pm c)^{-1}\frac{b_j^\pm}{k_j^\pm}. \tag{11e}$$

Here h_{0j}, a, b_1^+, b_2^-, $\tilde{b}_1^+$, $\tilde{b}_2^-$ and f_j, g_1^+, g_2^- are respectively the amplitudes of the incident, transmitted (plasma) and reflected (vacuum) waves at the frequencies ω_1, ω_2, $\omega_1^+ = |2\eta_1\omega_1-\eta_2\omega_2|$, $\omega_2^- = |2\eta_2\omega_2-\eta_1\omega_1|$,

$$\tilde{k}_j^\pm = \left(\frac{|\omega_j^\pm|}{c}\right)\left[\varepsilon_l-\sum_\alpha\frac{\omega_{p\alpha}^2(\omega_j^\pm-\omega_{H\alpha})^{-1}}{\omega_j^\pm}\right]^{1/2}$$

are the propagation constants of the normal waves of frequency ω_1^+ (ω_2^-) and amplitude $\tilde{b}_1^+$ ($\tilde{b}_2^-$).

The effect of the boundary is that in addition to the forced waves b_1^+ and b_2^- in the plasma, natural waves b_1^+ and b_2^- are also formed with the same frequencies but with wave numbers k_1^+ and k_2^-. The sense of the rotation in the plane of rotation is determined by the signs of ω_1^+ and ω_2^-. As for the other waves, the amplitudes are significantly higher near the resonances. In particular, if a linearly polarized wave of frequency ω is incident, the third harmonic is produced in the plasma. At the cyclotron plasma resonance ($\omega_{Hi} \ll \omega = \omega_{He} = \omega_{pe}/2\sqrt{\varepsilon_l}$), the forced third harmonic waves are rapidly attenuated away from the boundary, but this is not true of the natural waves, for which

$$b_2^- \approx \frac{h_0}{2}\sqrt{\frac{\nu}{i\omega}}(1+i\sqrt{\varepsilon_l})^{-2}\left(\frac{h_0\omega}{H_0\nu}\right)^2,\quad \tilde{k}_2^- \approx \sqrt{6\varepsilon_l}\frac{\omega}{c}$$

for the ordinary wave,

$$b_1^+ \approx 2i\sqrt{\varepsilon_l}h_0(1+i\sqrt{\varepsilon_l})^{-1}\left(\frac{h_0\omega}{H_0\nu}\right)^2,\quad \tilde{k}_1^+ \approx \sqrt{3\varepsilon_l}\frac{\omega}{c}$$

for the helicon.

If $\varepsilon_l = 16$, $\omega = 10^{12}$ sec^{-1}, $S_0 = 1$ mm^2, $H_0 = 0.7 \cdot 10^3$

Oe, $\nu = 10^{10}$ sec^{-1} and the incident power $P_\omega = 10$ W, the output power of the helicon will be of the order of $P_{3\omega} \approx 10^{-3}$ W and this is considerably higher than the effect observed experimentally in ref. 2. Similar estimates can be made for the powers reflected from the plasma.

The nonlinear effects also cause the Fresnel coefficients to depend on the incident power. In particular, at the double resonance

$$2\Delta R_1 = \sqrt{\frac{i\nu}{\omega}}\left(\frac{h_0\omega_p}{2\nu H_0}\right)^2 (1 + i\sqrt{\varepsilon_l})^{-2} R_1,$$

$$\Delta R_2 = i\sqrt{\varepsilon_l}\,(1 + \varepsilon_l)^{-1}\left(\frac{h_0\omega}{H_0\nu}\right)^2 R_2,$$

where R_j is the reflection coefficient in the linear approximation. The change is of the order of a few per cent for the parameter values given above.

---

[1] V. L. Ginzburg and A. V. Gurevich, Usp. Fiz. Nauk, 70, 201 (1960) [Sov. Phys.–Usp., 3, 115 (1960)].

[2] J. Maurer, A. Libchaber, and J. Bok, Plasma Effects in Solids, Paris (1964).

Cerenkov instabilities of a relativistic beam in a periodic plasma-filled waveguide

V. I. Kurilko, Yu. V. Tkach, and V. A. Shendrik

(Submitted July 4, 1973; resubmitted October 1, 1973)
Zh. Tekh. Fiz., 44, 956-964 (May 1974)

A hydrodynamic theory is derived for the Cerenkov instability of a monoenergetic, relativistic electron beam in a periodic plasma-filled waveguide. The frequencies and growth rates are found for the limiting cases of strong and weak magnetic fields. Under certain conditions the presence of a plasma can strongly influence the interaction of the beam with a periodic waveguide.

INTRODUCTION

The theory of collective interactions of a relativistic electron beam with slow-wave structures and plasmas is of interest in connection with the development of methods for accelerating ions by charge-density waves and the resulting electromagnetic waves,[1,2] with the development of new microwave-generation methods based on the use of the collective interaction of intense relativistic electron beams with a plasma1) (refs. 3, 4), with the possibility of increasing the efficiency of this interaction by premodulation of the beam,[7] and with the determination of the threshold and critical currents and their functional dependences on the beam and plasma parameters.[8] We report here on a comparative analysis of the optimum conditions and efficiency of the collective Cerenkov interaction of a cylindrical, monoenergetic electron beam with a slow-wave structure in the form of a periodic waveguide filled with the plasma.

The collective interaction of a beam with a periodic retarding structure was first studied by Akhiezer et al.,[9] who calculated the growth rates for the Cerenkov instability of a beam in a chain of cavities for an axisymmetric mode (m = 0). Experiments carried out in linear electron accelerators[10-12] have shown that an axially asymmetric wave can also be excited in an accelerating structure with a single field cycle in the azimuthal direction; this mode throws the beam against the accelerator walls.[12-14] Furthermore, a dense plasma can form when high-current beams pass through such structures; the collective interaction of the beam with this plasma can compete with the excitation of waveguide modes. Accordingly, effective control of the instabilities of a relativistic beam in this system requires a theoretical study of the conditions under which a collective interaction can occur between the beam and the plasma and waveguide modes; it is also necessary to calculate the functional dependences of the corresponding growth rates on the parameters of the beam and the system. This problem is the subject of the present paper.

STATEMENT OF THE PROBLEM

We consider a waveguide with conducting walls of radius R, loaded periodically (at a spacing of d) with infinitesimally thin conducting disks with inner radius b. A monoenergetic beam moves along the z axis with velocity v_0, and the equilibrium density $n_b(r)$ of the beam falls off radially, so $n_b(a) = 0$. With no external magnetic field or plasma the Coulomb charge of the beam in the equilibrium state is partially neutralized by the ion background whose density $n_+(r)$ is such that the radial force acting on a beam particle vanishes: $n_+(r) \equiv n_b(r)/\gamma^2$ $[\gamma \equiv (1 - v_0^2/c^2)^{-1/2}]$.

The starting point for this problem is the system of hydrodynamic equations of motion, the continuity equation for the beam particles,2) and the Maxwell equations for the field:

$$\frac{d}{dt}\frac{m_0}{\left(1-\frac{v_0^2}{c^2}\right)^{1/2}}\mathbf{v} = e\mathbf{E} + \frac{e}{c}[\mathbf{vH}], \quad \frac{\partial\rho}{dt} + \operatorname{div}\mathbf{j} = 0, \tag{1}$$

$$\operatorname{curl}\mathbf{E} = -\frac{1}{c}\partial\mathbf{H}, \operatorname{curl}\mathbf{H} = \frac{1}{c}\frac{\partial\mathbf{D}}{\partial t} + \frac{4\pi}{c}\mathbf{j}, \tag{2}$$

where ρ and $\mathbf{j}$ are the beam charge density and current; $D_i \equiv \hat{\varepsilon}_{ik}E_k$, and $\hat{\varepsilon}_{ik}$ is the dielectric tensor of the plasma in an external magnetic field, given by

$$\hat{\varepsilon}_{ik} \equiv \begin{pmatrix} \varepsilon_1 & i\varepsilon_2 & 0 \\ i\varepsilon_2 & \varepsilon_1 & 0 \\ 0 & 0 & \varepsilon_3 \end{pmatrix} \begin{array}{l} \varepsilon_1 \equiv 1 + \sum\limits_\alpha \frac{\omega_{p\alpha}^2}{\omega_{H\alpha}^2 - \omega^2}, \quad \varepsilon_2 \equiv \sum\limits_\alpha \frac{\omega_{H\alpha}\omega_{p\alpha}^2}{(\omega_{H\alpha}^2 - \omega^2)\,\omega}, \\ \varepsilon_3 \equiv 1 - \sum\limits_\alpha \frac{\omega_{p\alpha}^2}{\omega^2}, \end{array}$$

where $\omega_{p\alpha} \equiv (4\pi e n_{p\alpha}/m_\alpha)^{1/2}$ is the plasma frequency for particles of species α, and $\omega_{H\alpha} = (eH_0/m_\alpha c)$ is the Larmor frequency for particles of species α.

Equations (1), (2) must be solved taking account of the boundary conditions at the surface of the plasma and of the slow-wave structure. Solving this problem for the general case is quite complicated, so we consider separately the collective interaction of the beam with the periodic waveguide and with the plasma.

COLLECTIVE INTERACTION OF A RELATIVISTIC BEAM WITH A PERIODIC STRUCTURE IN THE ABSENCE OF A PLASMA

In the absence of a plasma ($n_p = 0$, $\hat{\varepsilon}_{ik} = 1$), Eqs. (1), (2) describe the collective interaction of a beam with a slow-wave structure. If the beam current is not too high, so that the growth rate δ is small in comparison with the frequency of the excited waves, ω_0, we can use a variational method,[15,16] finding an analytic expression for the growth rate which is valid to terms of order $(\delta/\omega_0)^2$. The calculations are very complicated for an arbitrary value of the external magnetic field H_0; hence we consider the limiting cases of strong and weak fields, in which it is possible to obtain relatively simple analytic expressions. We analyze the interaction of the beam with axially symmetric and axially asymmetric modes.

1. Symmetric Waves (m = 0)

The field profile and the dispersion in a waveguide with relatively thick disks ($d \ll \lambda_g$) are studied in refs. 17 and 18. Accordingly, we give only the equations for the growth rates of Cerenkov instabilities excited in the system by a monoenergetic beam.

a. Strong magnetic field. For a strong external field the high-frequency beam current j induced by the field of this wave contains only one nonvanishing component, the longitudinal component,

$$j_z = \frac{ie^2 n_b \omega E_z}{m_z (\omega - k_z v_0)^2}.$$

The corresponding equation for the growth rate of the Cerenkov instability of the symmetric mode is

$$\delta = \frac{3^{1/3}}{2}\omega_0 \left(\frac{2\pi r_0 \lambda_0^2 N}{\gamma^3 W_0}\right)^{1/3}, \qquad (3)$$

where $r_0 \equiv e^2/m_0c^2$ is the classical radius of the electron, $N \equiv 2\pi \int_0^a r n_b(r) dr$ is the density of beam particles per unit length, and $W_0 \equiv 2\pi \int_0^R E_z^2(r) r dr$ is the normalization field.

Equation (3) is the same as the corresponding equation of ref. 9, except that the beam density n_b is replaced by its average value $\bar{n}_b = N/W_0$.

To determine the functional dependence of the growth rate on the profile of the beam density, we consider the case of a beam of homogeneous density (n_b = const for $r < a$, $n_b = 0$ for $r > a$), for which the dispersion relation can be derived in analytic form (for the case of thick disks and axisymmetric waves) for an arbitrary value of the total beam current. In this case the growth rate is[19]

$$\delta = \frac{3^{1/3}}{2}\omega_0 \left\{\frac{2r_0 N}{\gamma^3} \frac{Z_0^2(k_0 b)}{I_0^2\left(k_0 \frac{b}{\gamma}\right)} \left[\frac{dZ_0(k_0 b)}{dk_0 b} Z_1(k_0 b) - \frac{dZ_1(k_0 b)}{dk_0 b} Z_0(k_0 b)\right]\right\}^{1/3}. \qquad (4)$$

A comparison shows that when both (3) and (4) are applicable the predicted growth rates are identical in terms of functional dependence on the parameters of the beam and the system, differing only in numerical factors of order unity.

b. Vanishing magnetic field. We recall that in this case the beam is held in equilibrium in the steady state by the ion background, whose density n+ is $n_+ = n_b/\gamma^2$. When the beam density $n_b(r)$ is radially inhomogeneous, the growth rate of the Cerenkov instability can be found by a variational method. Writing the longitudinal current in terms of the field on the basis of the continuity equation and the equation of motion, we find

$$j_z = \frac{ie^2 n_b E_z \omega}{m_0 \gamma^3 (\omega - k_z v_0)^2} + \frac{e^2 v_0}{m_0 \gamma (\omega - k_z v_0)^2} \frac{1}{r} \frac{\partial}{\partial r} [r n_b(r)(E_r - \beta_0 H_\varphi)].$$

Substituting this result into the equations for the field, we find the growth rate as given by (3).

To determine the influence of the shape of the beam-density profile on the growth rate we again consider the case of a homogeneous density, for which the dispersion relation can be obtained in analytic form.[19] Analysis of this equation shows that for beam currents which are not too high, $\omega a_{b\perp}/c < 1$, the frequency spectrum and the growth rate are the same as in a strong magnetic field. The physical interpretation of this result is that the condition $\omega a_{b\perp}/c < 1$ is equivalent to the requirement that the beam radius be small in comparison with the skin depth $\delta_{sk} = c/\omega_{b\perp}$. In this case the field penetrates well into the beam, so that the frequency and growth rate are the same as in a strong magnetic field. When $\omega_{b\perp} a/c > 1$, and the beam radius is larger than the skin depth, the high-frequency field does not penetrate into the beam, which serves as a conductor in this case. Accordingly, the skin effect of the field in the beam region $r < a$ leads to a frequency spectrum different from that for the case of a strong magnetic field and to a reduction proportional to $(a\omega_{b\perp}/c)^{1/3}$ in the growth rate.

2. Asymmetric Modes (m = 1)

These modes are particularly interesting, since they lead to beam collapse. When the wave field is characterized by the m = 1 azimuthal mode the amplitude of its transverse components does not vanish at the axis as $v_\Phi \to c$. The field profile and the dispersion relation of this wave (for the case of thick disks) are studied in ref. 20.

The excitation of an asymmetric mode by a relativistic beam in the absence of an external magnetic field is solved by a variational method since the exact solution requires finding the roots of a seventh-order determinant.

Substituting the expression for the longitudinal current,

$$j_z = \frac{ie^2}{m_0(\omega - k_z v_0)^2}\left\{\frac{n_b \omega E_z}{\gamma^3} - \frac{iv_0}{\gamma}\frac{1}{r}\frac{\partial}{\partial r} \times [r n_b(r)(E_r - \beta_0 H_\varphi)] + \frac{n_b v_0}{\gamma}\frac{1}{r}(E_\varphi + \beta_0 H_r)\right\}$$

into the equation for the field, and integrating the result over the waveguide cross section, we find the growth rate to be

$$\delta = \frac{3^{1/3}}{2}\omega_1 \left(\frac{4\pi r_0 \lambda_1^2 N}{W_1 \gamma}\right)^{1/3}. \qquad (5)$$

Accordingly, the growth rate of the Cerenkov instability for an axially asymmetric mode, which causes beam collapse, falls off more slowly with increasing energy than the growth rate for a symmetric mode.[21] It must be emphasized that this result holds for the case of minimum neutralization of the beam space charge by the ion background ($n_+ = n_{cr} = n_b/\gamma^2$), with no synchrotron oscillations of the beam particles. With $n_+ > n_{cr}$ the additional focusing of the beam by the ion background can suppress the transverse instability; however, in the steady state the beam particles move along nonlinear trajectories so that a special investigation is required to determine the equilibrium configurations of the system and the stability in this case. An external magnetic field can also suppress the transverse instability of a beam in a slow-wave structure.

COLLECTIVE INTERACTION OF A RELATIVISTIC BEAM WITH SLOW WAVES IN A GYROTROPIC PLASMA WAVEGUIDE

We have neglected the electron plasma in the waveguide, even though ionization of the residual gas leads to the formation of a plasma in the interaction region in a real experiment. The result is that plasma and waveguide modes begin to compete. It is therefore worthwhile to determine the conditions under which the collective interaction of the beam with the plasma is stronger than the interaction with the slow-wave structure.

1. Plasma Instabilities

We consider a circular waveguide of radius a filled with a plasma of density n_p. A fixed magnetic field H_0 is imposed along the axis of the waveguide. A relativistic electron beam with density $n_b(r)$ = const and radius equal to that of the waveguide moves at a velocity v_0 parallel to the axis of the system. Solving Eqs. (1) and (2), we find the following equations for the longitudinal field components:

$$E_z = \sum_{s=1}^{2} A_s J_m(k_s r), \quad H_z = \sum_{s=1}^{2} B_s J_m(k_s r),$$

where k_s is the transverse wave number, which satisfies the biquadratic equation

$$Ak_s^4 + Bk_s^2 + C = 0, \tag{6}$$

where

$$A \equiv \varepsilon_1 - \frac{\omega_{b\perp}^2 (1 - \beta_0^2 \varepsilon_1)}{(\omega_x^2 - \omega_{Hb}^2)},$$

$$B \equiv -k_{\perp p}^2 \left[\frac{\omega_{b\parallel}^2}{\omega_x^2} + \frac{\omega_{b\perp}^2 (1 - \beta_0^2 \varepsilon_1)}{\omega_x^2 - \omega_{Hb}^2}\right] + (\varepsilon_1 + \varepsilon_3)\left[k_{\perp p}^2 + \frac{\omega_{b\perp}^2 \omega_x^2}{(\omega_x^2 - \omega_{Hb}^2) c^2}\right]$$
$$- \frac{\omega_{b\perp}^2 \omega_{b\parallel}^2}{(\omega_x^2 - \omega_{Hb}^2) c^2} - \frac{\omega_{b\perp}^4 (1 - \beta_0^2 \varepsilon_1)}{(\omega_x^2 - \omega_{Hb}^2) c^2}$$
$$+ \varepsilon_2 \left[k^2 \varepsilon_2 \left(1 + \frac{\omega_{b\perp}^2 \beta_0^2}{\omega_x^2 - \omega_{Hb}^2}\right) - 2k \frac{\omega_{b\perp}^2 \omega_{Hb}}{(\omega_x^2 - \omega_{Hb}^2) c}\right],$$

$$C \equiv \left(\varepsilon_3 - \frac{\omega_{b\parallel}^2}{\omega_x^2}\right)\left\{k_{\perp p}^4 + (2k_{\perp p}^2 c^2 + \omega_{b\perp}^2) \frac{\omega_{b\perp}^2 \omega_x^2}{(\omega_x^2 - \omega_{Hb}^2) c^4}\right.$$
$$\left. + \varepsilon_2 k^2 \left[\frac{2\omega_{b\perp}^2 \omega_x \omega_{Hb}}{(\omega_x^2 - \omega_{Hb}^2) c^2} - \varepsilon_2 k^2\right]\right\},$$

$$k_{\perp p}^2 \equiv k_s^2 - k^2 \varepsilon_1, \quad \omega_x \equiv \omega - k_z v_0, \quad \omega_{Hb} \equiv \frac{eH_0}{m_0 \gamma c}.$$

In the case of a limited gyrotropic beam–plasma waveguide an equation for the spectrum of transverse wave numbers can be derived from the condition that the tangential components of the electromagnetic field vanish at the waveguide wall:

$$J_m(k_1 a) = \frac{R_1 k_1 a J_m(k_2 a) J_m'(k_1 a)}{m (P_2 - P_1) J_m(k_2 a) + R_2 k_2 a J_m'(k_2 a)} \tag{7}$$

(we omit the equations for P_s and R_s because of their length). Together with (6) this equation determines the dispersion of the characteristic modes of the system. To find analytic solutions of (6) and (7), we consider the limiting cases of strong and weak external magnetic fields.

a. Strong magnetic field. The magnetic field is such that the inequalities $\omega_p^2 \ll \omega_{Hp}^2$ and $\omega^2 \ll \omega_{Hp}^2$ are satisfied.

Expanding (6) and (7) in terms of these small parameters, we find the frequency spectrum of the waves in the absence of a beam:

$$\omega_{0H}^2 = \omega_p^2 \left\{\left(1 - \frac{\gamma^2}{N_s}\right) + \frac{\omega_p^2}{\omega_{Hp}^2} \gamma^4 \frac{(\gamma^2 + 2)}{N_s}\right\}, \tag{8}$$

where

$$N_s \equiv \frac{4\pi r_0 n_p a^2}{\lambda_{s\infty}^m}, \quad J_m(\lambda_{s\infty}) = 0.$$

We see from this equation that there exists a threshold density per unit length of the beam above which the beam becomes influential. At $N_s < \gamma^2$, in which case the phase velocity of the wave is lower than the beam velocity, and the condition $V_\Phi = V_0$ does not hold,[22,23] the Cerenkov instability does not occur.[3)]

It follows from (8) that in the relativistic case with high-frequency waves ($\omega^2 \gg \omega_{Hp}^2 m_0/M_0$, where m_0 and M_0 are the electron and ion masses), the beam can be considered magnetized only in strong magnetic fields, for which the inequality $\omega_p^2 \gamma^4 \ll \omega_{Hp}^2$ holds. Analysis of Eq. (6) shows that the off-diagonal (gyrotropic) components of tensor $\hat{\varepsilon}_{ik}$ make the most important contribution to the dispersion of relativistic waves of a plasma waveguide in a strong field.

The corrections to (8) due to the finite beam current lead to the growth rate

$$\delta = \frac{3^{1/2}}{2^{4/3}} \omega_{0H} \left(\frac{\omega_{b\parallel}^2}{\omega_{0H}^2}\right)^{1/3}. \tag{9}$$

b. Weak magnetic field. We assume that the magnetic field is such that the inequalities $\omega_{Hp}^2/\omega_p^2 = \mu \ll 1$ and $(\omega - \omega_p)/\omega_p = \eta \ll 1$ hold.

Expanding (6) in terms of these small parameters, we find $k_1^2 a^2 = \lambda_s^2$,

$$\eta(\mu) = \mu/[2(1 + N_s)^2], \quad a^2 k_2^2 = -N/(2 + N_s), \tag{10}$$

where $N \equiv \omega_p^2 a^2/c^2$, and $N_s \equiv N/\lambda_s^2$.

The spectrum of this system is thus governed by the single parameter λ_s, which must be found from dispersion relation (7). In this particular limiting case this dispersion relation can be reduced to

$$\frac{\lambda_s J_m'(\lambda_s)}{J_m(\lambda_s)} = \frac{\varkappa_s^2 I_m'(\varkappa_s a)}{I_m(\varkappa_s a)} \frac{\gamma^2 (1 + N_s) - \varkappa_s^2}{\gamma^2 (1 + N_s) - \lambda_s^2}, \tag{11}$$

where $\varkappa_s^2 \equiv \lambda_s^2 N_s/(2 + N_s)$.

Knowing the solutions λ_s of transcendental equation (11), we can easily calculate the frequencies of the waves excited by the beam in this system and the corresponding growth rates:

$$\omega_{0s}^2 = \omega_p^2 \left[1 + \frac{\omega_{Hp}^2}{\omega_p^2} \frac{1}{(1 + N_s)^2}\right], \tag{12}$$

$$\left.\begin{aligned} &\delta = \frac{3^{1/2}}{2^{4/3}} \omega_p \left(\frac{\omega_{bs}^2}{\omega_p^2}\right)^{1/3} \left[\frac{N_s^2 (2 + N_s)}{2(1 + N_s)^2}\right]^{1/3}, \\ &1 \gg \frac{\omega_{Hp}^2}{\omega_p^2} \gg \left(\frac{n_b}{n_p}\right)^{1/3} \frac{1}{\gamma}\left[1 + \gamma\left(\frac{n_b}{n_p}\right)^{1/3}\right]. \end{aligned}\right\} \tag{13}$$

In the case of a weak magnetic field the frequencies of the excited waves are concentrated near the upper hybrid frequency,[27] and the growth rates are of the same order of magnitude as those for a strong external magnetic field.

2. Budker Instabilities of a Bounded Relativistic Beam in the Absence of an External Magnetic Field

A high-current electron beam held in an equilibrium state by the charge of the ion background ($n_+ = n_b/\gamma^2$) can be unstable with respect to the excitation of ion waves. The corresponding analysis for the case of an infinitely strong external magnetic field ($\omega_{Hi}^2 \gg \omega^2$) is given in ref. 22. We consider the stability of an electron beam neutralized by an ion background in the absence of an external magnetic field.

We consider a bounded relativistic electron beam of radius a moving along the z axis through an ion background whose density is radially homogeneous, $n_+ \equiv n_b/\gamma^2$. Assuming $\hat{\varepsilon}_{ik} = \delta_{ik}\varepsilon_+$ [$\varepsilon_+ \equiv 1 - 4\pi e^2 n_+/(M_0\omega^2)$, where M_0 is the ion mass] in Eqs. (1) and (2) for this case, and incorporating the surface currents[28] in the boundary conditions at $r = a$, we find the dispersion relation (m = 0):

$$\left.\begin{aligned} &F_0 \frac{I_1(\varkappa_1 a)}{\varkappa_1 a I_0(\varkappa_1 a)} = \frac{K_1(k_\perp a)}{k_\perp a K_0(k_\perp a)},\\ &F_0 \equiv \nu\left\{1 + \frac{\beta_0^2\omega_{b\perp}^2(1-\varepsilon_+)}{\varepsilon_+\omega_z^2 - \omega_{b\perp}^2(1-\beta_0^2\varepsilon_+)}\right\} \equiv \nu\frac{\varkappa_1^2}{\varkappa^2},\\ &\varkappa^2 \equiv k_s^2 - k^2\varepsilon_+ + \frac{\omega_{b\perp}^2}{c^2}, \quad \nu \equiv \frac{\omega_{b\perp}^2}{\omega_z^2} - \varepsilon_+\left(1 + \frac{\beta_0^2\omega_{b\perp}^2}{\omega_z^2}\right). \end{aligned}\right\} \tag{14}$$

This equation has two kinds of solutions, corresponding to the surface modes and volume modes. The fields of the volume modes are oscillatory in the radial direction and the corresponding dispersion relation is

$$\varkappa_1^2 a^2 = -\lambda_s^2. \tag{15}$$

The field of the surface waves decays toward the waveguide axis, $\varkappa_1^2 > 0$, so these waves can exist only at values of the parameters such that the condition $F_0 > 1$ is satisfied.

It can be shown that at beam-particle densities (per unit length) such that $\omega_{b\perp}^2 a^2 \ll c^2\lambda_s^2$ the solutions of (15) are concentrated near the pole $\varkappa_1^2 a^2$ and are given by (cf. refs. 22, 29)

$$\left.\begin{aligned} &k_s = \pm\omega_{bs}/v_0, \quad \delta = \frac{3^{1/2}}{2^{4/3}}\omega_{bs}\left(\frac{m_0}{M_0}\gamma^3\right)^{1/3},\\ &m_0\gamma^3 \ll M_0, \quad \operatorname{Re}\omega \sim \delta. \end{aligned}\right\} \tag{16}$$

The growth rate in (16) is of the same order as the analogous quantity for the case of a strong longitudinal magnetic field.[22] The explanation is that in the absence of a magnetic field the increase in the growth rate due to the transverse mass of the beam electrons[21] is offset by a corresponding decrease in the density of the ion background ($n_+ \equiv n_b/\gamma^2$).

Analysis of Eq. (14) shows that the corresponding results for surface waves in the case $k_\parallel a \ll 1$ differ from the results in (16) only by corrections of order $k_\parallel^2 a^2$.

The growth rate of the volume modes is a weak function of the index of the azimuthal harmonic; hence axially asymmetric modes (m = ± 1) are also characterized by growth rates of the order of (16).

Since the radial defocusing force does not vanish for m = ± 1,

$$\left.\begin{aligned} &F_r = e(E_r - \beta_0 H_\varphi) \simeq \frac{ie(k\beta_0\varepsilon_+ - k_s)}{\varkappa^2}\frac{\partial E_z}{\partial r},\\ &\frac{F_r}{eA_r} = \frac{c\lambda_s}{\gamma\omega_{b\perp}a}J_0(\lambda_s) \gg 1, \quad J_1(\lambda_s) = 0, \end{aligned}\right\} \tag{17}$$

this wave defocuses the beam, as in the case of a collective interaction of the beam with the structure, considered above. This steady state is thus disrupted by the onset of a transverse instability. Comparison of (16) with the analogous result for the firehose instability[30,31] shows that the transverse instability, in contrast with the firehose instability, can appear even if there is no spread in transverse velocities ($\langle\Theta\rangle = 0$); in the case $\langle\Theta\rangle \neq 0$, the growth rate turns out to be larger than that of the firehose instability[32] when the inequality $\langle\Theta\rangle < (\omega_{b\perp}a/c)(M_0 - m_0)^{1/6}$ is satisfied.

CONCLUSION

This analysis thus shows that collective Cerenkov excitation of waveguide and plasma waves can occur in this system.

In a strong external magnetic field ($\omega_p^2\gamma^4 \ll \omega_{Hp}^2$), plasma waves can be excited only at sufficiently large densities per unit length of the plasma ($\omega_0^2 \geq \omega_{sk}^2 = \omega_0^2 + \gamma^2c^2\lambda_1^2/a^2$); at lower densities, the beam interacts only with the slow-wave structure, if the disk radius is not too large ($\omega_0 b < \gamma c$). At strong, but finite magnetic fields the most important contribution to the change in the dispersion characteristics of the plasma waveguide at relativistic phase velocities comes from the plasma gyrotropy, $\varepsilon_2 \neq 0$ [see Eqs. (6)-(8)]. In the case of a relatively weak external field ($\omega_{Hp}^2 \ll \omega_0^2$) the spectrum of excited frequencies is concentrated near the upper hybrid frequency [Eq. (12)]; as the plasma density is reduced the corresponding frequencies and growth rates decrease, so that the transition to the excitation of waveguide modes occurs at the plasma density n_{pcr} found from the condition $\delta_{volum}(n_{pcr}) = \delta_{str}(\omega_0)$: $n_{pcr} = \omega_0^2 m_0/(4\pi e^2)$.

In the absence of an external magnetic field the beam particles can move along straight trajectories in the equilibrium state only at the equilibrium density of the ion background, $n_+ = n_b/\gamma^2$. An equilibrium state of this type is unstable against excitation of an axially asymmetric mode of a limiting waveguide [see (5)], which throws the beam against the walls of the waveguide as it builds up. If the radius of the limiters is large enough so that there is no collective interaction between the beam and the limiting waveguide, the beam is unstable against collective excitation of waves of the ion background. The corresponding growth rates are comparable to those of Budker waves (cf. refs. 22, 29). The excitation of an axially asymmetric wave of this type also defocuses the beam.

This analysis has been based on the hydrodynamic approximation and has neglected the thermal spread in the energies of the beam particles and the increase in the plasma-density gradient over the cross section and the length of the waveguide.[32,33] The results can thus be used to evaluate the practical use of the beam–plasma interaction under optimum conditions, i.e., when the gradients and thermal energy spread are small.

---

1) The possibilities of using relativistic beams in vacuum electron systems are examined in refs. 5 and 6.

2) In the relativistic case ($\gamma \gg 1$) the kinetic effects are important only at relatively low currents.

3) Excitation of a plasma by a relativistic beam is also studied in refs. 24-26.

[1] V. I. Veksler, Proc. Symp. CERN, 1, 80 (1956).

[2] Ya. B. Fainberg, Proc. Symp. Cern, 1, 84 (1956).

[3] J. A. Nation, Appl. Phys. Lett., 17, 491 (1970).

[4] Yu. V. Tkach, Ya. B. Fainberg, I. I. Magda, V. D. Shapiro, V. I. Shevchenko, A. I. Zykov, E. A. Lemberg, I. N. Mondrus, and N. P. Gadetskii, ZhETF Pis. Red., 16, 168 (1972) [JETP Lett., 16, 116 (1972)].

[5] M. I. Petelin, Izv. Vuz. Radiofiz., 13, 1586 (1970).

[6] V. K. Yulpatov, Izv. Vuz., Radiofiz., 13, 1784 (1970).

[7] Ya. B. Fainberg, At. Energ., 11, 313 (1961); in: Invited Papers, International Conference on Plasma Physics, Vienna, 1967 [in Russian], IAEA (1968), p. 149

[8] L. S. Bogdankevich and A. A. Rukhadze, Usp. Fiz. Nauk, 103, 609 (1971) [Sov. Phys. – Usp., 14, 163 (1971)].

[9] A. I. Akhiezer, Ya. B. Fainberg, and G. Ya. Lyubarskii, Proc. Symp. CERN, 1, 220 (1956).

[10] M. Kelliher and R. Beadle, Nature, 187, 1099 (1960); H. Hirakawa, Japan. J. Appl. Phys., 3, 27 (1964).

[11] A. K. Val'ter (Valter), I. A. Grishaev (Grishayev), E. V. Eremenko, Dobrolyubov (J. I. Dobroljubov), A. I. Zykov, V. V. Kondratenko, F. G. Kuznetsov (Kuznetzov), Bazaev (J. M. Bazajev), F. A. Goroshovatskii (Goroshovatsky), V. B. Mufel, N. I. Motcheshnikov, V. V. Petrenko, V. I. Kolosov, N. A. Kovalenko, G. A. Tseitlenok (Zeitlenok), V. M. Levin, I. F. Malishev, E. G. Komar, V. V. Rumyantsev (Rumjantzev), F. F. Turkin, and V. K. Chochlov, Proceedings of the Fifth International Conference on High Energy Accelerators, Frascati, Italy, 1965, CNEN, Rome (1966), p. 233.

[12] W. K. H. Panofsky, SLAC Int. Rept. TN-66-27, 1966; W. K. H. Panofsky and M. Bander, Rev. Sci. Instr., 39, 206 (1968).

[13] G. V. Voskresenskii, V. I. Koroza, and Yu. N. Serebryakov, At. Energ., 20, 3 (1966).

[14] V. I. Kurilko and A. P. Tolstoluzhskii, At. Energ., 28, 498 (1970); G. D. Kramskoi, V. I. Kurilko, and V. A. Shendrik, Ukr. Fiz. Zh., 17, 1608 (1972).

[15] M. A. Miller, Izv. Vuz. Radiofiz., 1, 110 (1958).

[16] A. B. Mikhailovskii and K. Jungwirt, Zh. Tekh. Fiz., 36, 777 (1966) [Sov. Phys. – Tech. Phys., 11, 581 (1966)].

[17] E. L. Chu and W. W. Hausen, J. Appl. Phys., 18, 966 (1947).

[18] A. I. Akhiezer and Ya. B. Fainberg, Usp. Fiz. Nauk, 44, 321 (1951).

[19] V. I. Kurilko and V. A. Shendrik, Symposium on Collective Acceleration Methods [in Russian], Izd. OIYaI, Dubna (1972), p. 122.

[20] H. Hahn, Rev. Sci. Instr., 34, 1094 (1963).

[21] E. E. Lovetskii and A. A. Rukhadze, Zh. Eksp. Teor. Fiz., 48, 514 (1965) [Sov. Phys. – JETP, 21, 342 (1965)].

[22] G. I. Budker, At. Energ., 1, 9 (1956).

[23] A. K. Berezin, Ya. B. Fainberg, L. I. Bolotin, G. P. Berezina, I. A. Bezyazychnyi, V. I. Kurilko, V. D. Shapiro, and V. P. Zeidlits, Nuclear Fusion (Special Supplement), 251 (1969).

[24] B. I. Aronov and A. A. Rukhadze, Zh. Tekh. Fiz., 42, 1606 (1972) [Sov. Phys. – Tech. Phys., 17, 1283 (1973)].

[25] V. K. Grishin and A. A. Kolomenskii, Zh. Tekh. Fiz., 42, 2604 (1972) [Sov. Phys. – Tech. Phys., 17, 2022 (1973)].

[26] V. E. Nechaev, Izv. Vuz. Radiofiz., 16, 613 (1973).

[27] A. K. Berezin, Ya. B. Fainberg, L. I. Bolotin, A. M. Egorov, V. A. Kiselev, V. A. Buts, V. I. Kurilko, and A. P. Tolstoluzhskii, Zh. Eksp. Teor. Fiz., 63, 861 (1972) [Sov. Phys. – JETP, 36, 453 (1973)].

[28] V. I. Kurilko, Zh. Tekh. Fiz., 31, 899 (1961) [Sov. Phys. – Tech. Phys., 6, 655 (1962)].

[29] B. V. Chirikov, At. Energ., 19, 239 (1965).

[30] A. A. Vedenov and R. Z. Sagdeev, in: Plasma Physics and the Problem of Controlled Thermonuclear Reactions [in Russian], Vol. 3, Izd. Akad. Nauk SSSR, Moscow (1958), p. 278.

[31] A. A. Ivanov and L. I. Rudakov, Zh. Eksp. Teor. Fiz., 58, 1332 (1970) [Sov. Phys. – JETP, 31, 715 (1970)].

[32] A. A. Vedenov and D. D. Ryutov, in: Problems of Plasma Theory, Vol. 9 (1972), p. 3.

[33] L. S. Bogdankevich and A. A. Rukhadze, Zh. Eksp. Teor. Fiz., 63, 899 (1972) [Sov. Phys. – JETP, 36, 473 (1973)].

Local-potential study of the Bénard problem in a homogeneous magnetic field

A. I. Lopushanskaya and V. N. Kapranov

Chernovtsy State University

(Submitted August 2, 1973)
Zh. Tekh. Fiz., 44, 965-970 (May 1974)

A variational procedure related to the concept of a local potential is used to solve the Bénard problem in a homogeneous magnetic field for the case of fixed boundaries.

Steady states are usually established when time-independent boundary conditions are imposed on a system; whether these states are stable or unstable depends on the kinetics of the process and the imposed constraints. Since only stable states can actually be observed those are the ones of practical interest.

For motion to be stable any small perturbation must be damped; if an arbitrarily small perturbation grows in time, the system is absolutely unstable and cannot exist.

Thermodynamic approaches are being used with increasing frequency in stability studies; the approach we use below, the potential method, is of this class.[1-3]

We consider a thin layer of an electrically neutral, incompressible, conducting fluid of thickness d, in gravitational and homogenous magnetic fields, which is heated from below. The liquid is unpolarizable, and the displacement current is negligible. We use the Maxwell equations

$$\left.\begin{aligned} &\frac{\partial H_i}{\partial x_i}=0,\\ &\varepsilon_{ijk}\frac{\partial}{\partial x_j}H_k=4\pi I_1,\\ &\varepsilon_{ijk}\frac{\partial}{\partial x_j}E_k=-\mu\frac{\partial H_i}{\partial t}\end{aligned}\right\}\qquad(1)$$

and introduce the dimensionless variables

$$x_i=\frac{x_i}{d},\ v_i=v_i\frac{d}{\nu},\ t=t\frac{\nu}{d^2};\ H_i=\frac{H_i}{H^+};\ T=\frac{T}{\Delta T}.\qquad(2)$$

The balance equations for the mass, momentum, internal energy, and magnetic field take the following form in the Boussinesq approximation:[4]

$$\left.\begin{aligned} &\frac{\partial v_i}{\partial x_i}=0,\\ &P_1\frac{\partial V_i}{\partial t}+P_1V_j\frac{\partial V_i}{\partial x_j}-\frac{P_1}{P_2}QH_j\frac{\partial H_i}{\partial x_j}=-\frac{\partial}{\partial x_i}\left(P+\frac{P_1}{P_2}Q\frac{H^2}{2}\right)\\ &\qquad+P_1\nabla^2v_i+\frac{d^3}{\sigma x}(1+\alpha\Delta T)F_i,\\ &P_1\frac{\partial T}{\partial t}+P_1\frac{\partial T}{\partial x_j}V_j=\nabla^2T,\\ &P_1\frac{\partial H_i}{\partial t}=P_1H_j\frac{\partial V_i}{\partial x_j}+\frac{P_1}{P_2}\nabla^2H_i,\end{aligned}\right\}\qquad(3)$$

where V_i and H_i are the components of the barycentric velocity and the magnetic field intensity, ρ is the density, P is the pressure, μ is the permeability, $\varkappa$ is the thermal diffusivity, σ is the electrical conductivity, α is the thermal-expansion coefficient, ΔT is the temperature differential between the lower and upper boundaries, ν is the kinematic viscosity, ε_{ijk} is a unit antisymmetric tensor of rank 3 and

$$P_1=\frac{\nu}{\varkappa},\quad P_2=\frac{\nu}{\eta}=4\pi\sigma\nu\mu;\quad Q=\frac{\mu(H^+)^2}{4\pi\rho\nu\eta}d^2,\quad H^+=H_z.$$

We consider the stability of the steady state of a quiescent fluid layer between two fixed surfaces at temperatures T_0 and T_1, in a homogeneous magnetic field along the x axis; the state is described by

$$\left.\begin{aligned} &H_i^{st}=\lambda_i,\\ &T^{st}=T_0-z,\\ &\frac{\rho^{st}}{\rho_0}=[1-\alpha\Delta T(T^{st}-T_0)],\end{aligned}\right\}\qquad(4)$$

where T_0 and ρ_0 are the temperature and density at the lower boundary and where

$$\boldsymbol{\lambda}=\{0,0,1\}.$$

Setting

$$\left.\begin{aligned} &V_i=u_i,\quad H_i=H_i^{st}+h_i,\quad P=P^{st}+\delta P;\\ &T=T^{st}+\theta,\quad \rho=\rho^{st}+\delta\rho,\end{aligned}\right\}\qquad(5)$$

we find a system of equations for the perturbed motion:

$$\left.\begin{aligned} &\frac{\partial u_i}{\partial x_i}=0,\\ &P_1\frac{\partial\theta}{\partial t}-P_1u_i\lambda_i=\nabla^2\theta,\\ &P_1\frac{\partial u_i}{\partial t}=\frac{\partial}{\partial x_i}\left(\delta P+\frac{P_1}{P_2}Q\lambda_ih_i\right)+R\lambda_i\theta+P_1\nabla^2u_i+\frac{P_1}{P_2}Q\lambda_j\frac{\partial h_i}{\partial x_j},\\ &P_1\frac{\partial h_i}{\partial t}=P_1\lambda_j\frac{\partial u_i}{\partial x_j}+\frac{P_1}{P_2}\nabla^2h_i\end{aligned}\right\}\qquad(6)$$

where $R=d^3\Delta T\alpha g/\nu\varkappa$ is the Rayleigh number.

Taking the curl of the second equation twice and multiplying λ_i, we find

$$\left.\begin{aligned} &P_1\frac{\partial}{\partial t}\nabla^4u_z=R\left(\frac{\partial^2\theta}{\partial x^2}+\frac{\partial^2\theta}{\partial y^2}\right)+P_1\nabla^4u_z+\frac{P_1}{P_2}Q\frac{\partial}{\partial z}\nabla^2h_z,\\ &P_1\frac{\partial\theta}{\partial t}-P_1u_z=\nabla^2\theta,\\ &P_1\frac{\partial h_z}{\partial t}=P_1\frac{\partial u_z}{\partial z}+\frac{P_1}{P_2}\nabla^2h_z.\end{aligned}\right\}\qquad(7)$$

Substituting the perturbations

$$A_z=A(z)\cos k_xx\cos k_yy\exp\beta t$$

into (7), we find

$$\left.\begin{aligned} &P_1(D^2-k^2)(D^2-k^2-\beta)u+\frac{P_1}{P_2}QD(D^2-k^2)h=k^2R\theta,\\ &(D^2-k^2-P_1\beta)\theta=-P_1u,\\ &(D^2-k^2-P_2\beta)h=-P_2Du,\end{aligned}\right\}\qquad(8)$$

where $D^n=d^n/dz$ and $k^2=k_x^2+k_y^2$. The solution of this equation must satisfy the boundary conditions

$$\theta=u=h=0,\ Du=0\ \text{at}\ z=0,\ z=1.$$

The steady state described by (4) is unstable if $\mathrm{Re}\,\beta>0$ and stable if $\mathrm{Re}\,\beta<0$; the case $\mathrm{Re}\,\beta=0$ corresponds to the state of neutral stability, which separates the regions of stability and instability. If $\mathrm{Im}\,\beta=0$ (if the principle of the exchange of stabilities holds), the critical state is a steady state; otherwise, it is oscillatory.

When the principle of the exchange of stabilities holds, we find, by setting $\beta = 0$ in (8),

$$\left.\begin{aligned} P_1(D^2-k^2)^2u+\frac{P_1}{P_2}QD(D^2-k^2)h&=Rk^2\theta,\\ (D^2-k^2)\theta&=-P_1u,\\ (D^2-k^2)h&=-P_2Du; \end{aligned}\right\} \tag{9}$$

substituting the second equation into the first, we can reduce this system to

$$\left.\begin{aligned} P_1[(D^2-k^2)^2-QD^2]u&=+k^2R\theta,\\ (D^2-k^2)\theta&=-P_1u \end{aligned}\right\} \tag{10}$$

with the boundary conditions

$$\theta=u=Du=0 \quad\text{at}\quad z=0,\ z=1.$$

As a rule it is difficult or even impossible to find the exact eigenfunctions and eigenfrequencies, so we use a variational procedure which involves the concept of a local potential, a characteristic feature of which is a functional dependence on two types of variables: average and fluctuating.[5]

By definition,[2,6] a functional $\Phi(A_i, A_{i0}) = \int dVL(A_i, A_{i0})$ is a local potential if

$$\Phi(A_{i1}, A_{i0})-\Phi(A_{i0}, A_{i0})=\Delta\Phi>0 \tag{11}$$

and

$$\left(\frac{\delta L}{\delta A_i}\right)_{A_{i0},A_k}=0 \quad\text{for}\quad A_i=A_{i0}, \tag{12}$$

where i = 1, 2, ... denotes the differential equation of the original problem.

To find the local potential we multiply the second, third, and fourth equations in (6) by $-\delta\theta$, $-\delta u_i$, and $-\delta h_i$, respectively. We then combine them and integrate over the volume of the system. Using the boundary conditions and the equation

$$A_i=A_{i0}+\delta A_i, \tag{13}$$

and integrating by parts, we find the desired functional (the local potential):

$$\begin{aligned} \Phi=\int dV\Big\{&-\Big(\delta P_0+\frac{P_1}{P_2}\lambda_j h_{j0}Q\Big)\frac{\partial u_i}{dx_i}-R\theta_0\lambda_i u_i+\frac{P_1}{2P_2}\Big(\frac{\partial}{\partial x_j}h_i\Big)^2\\ &+\frac{P_1}{2}\Big(\frac{\partial u_i}{\partial x_j}\Big)^2+\frac{P_1}{P_2}Q\lambda_j h_{i0}\frac{\partial u_i}{\partial x_j}+\frac{1}{2}\Big(\frac{\partial\theta}{\partial x_j}\Big)^2+P_1\lambda_j u_{i0}\frac{\partial h_i}{\partial x_j}\\ &+P_1\Big[h_i\frac{\partial h_{i0}}{\partial t}+u_i\frac{\partial u_{i0}}{\partial t}+\theta_0\frac{\partial\theta}{\partial t}\Big]-P_1u_{i0}\lambda_i\theta\Big\}. \end{aligned} \tag{14}$$

We note that

$$\left.\begin{aligned} \Big(\frac{\partial L}{\delta u_i}\Big)_{h_i,\theta,u_{i0}}&=0=\frac{\partial}{\partial x_i}\Big(\delta P+\frac{P_1}{P_2}Q\lambda_i h_j\Big)_0-R\theta_0\lambda_i-P_1\nabla^2u_i\\ &\qquad-\frac{P_1}{P_2}Q\lambda_j\frac{\partial h_{i0}}{\partial x_j}+P_1\frac{\partial u_{i0}}{\partial t},\\ \Big(\frac{\delta L}{\delta\theta}\Big)_{h_i,u_i,\theta_0}&=0=-P_1u_{i0}\lambda_i-\nabla^2\theta_0+P_1\frac{\partial\theta_0}{\partial t},\\ \Big(\frac{\partial L}{\delta h_i}\Big)_{h_{i0},\theta,u_i}&=0=-P_1\lambda_j\frac{\partial u_{i0}}{\partial x_j}-\frac{P_1}{P_2}\nabla^2h_i+P_1\frac{\partial h_{i0}}{\partial E}, \end{aligned}\right\} \tag{15}$$

or the same as system (6) for $A_i = A_{i0}$.

Integrating the terms linear in $\delta\theta$, δu_i, and δh_i by parts, using (15), and the fact that the variations of the state variables vanish at the boundary, we find

$$\Delta\Phi=\frac{1}{2}\int\Big[\frac{P_1}{P_2}\Big(\frac{\partial\delta h_i}{\partial x_j}\Big)^2+\Big(\frac{\partial\delta\theta}{\partial x_j}\Big)^2+P_1\Big(\frac{\partial\delta u_i}{\partial x_j}\Big)^2\Big]dV>0. \tag{16}$$

Substituting the perturbations[4]

$$\left.\begin{aligned} u_z=u(z)\cos k_x x\cos k_y ye^{\beta t},\quad h_1&=h(z)\cos k_x x\cos k_y ye^{\beta t},\\ u_x&=-\frac{k_x}{k^2}Du\sin k_x x\cos k_y ye^{\beta t},\\ h_x&=-\frac{k_x}{k^2}Dh\sin k_x x\cos k_y ye^{\beta t},\\ u_y&=-\frac{k_y}{k^2}Du\cos k_x x\sin k_y ye^{\beta t},\\ h_y&=-\frac{k_y}{k^2}Dh\cos k_x x\sin k_y ye^{\beta t},\\ \theta&=\theta(z)\cos k_x x\cos k_y ye^{\beta t}. \end{aligned}\right\} \tag{17}$$

into (14) (analogous equations are written for the quantities not being varied), we find

$$\begin{aligned} \Phi=\int dz\Big\{&-R\theta_0u+\frac{P_1}{2}\Big[k^2u^2+\frac{1}{k^2}(D^2u)^2+2(Dh)^2\Big]\\ &-P_1u_0\theta+\frac{P_1}{2P_2}\Big[k^2h^2+\frac{1}{k^2}(D^2h)^2+2(Du)^2\Big]\\ &-\frac{P_1}{k^2}(D^2-k^2)hDu_0+\frac{1}{2}[k^2\theta^2+(D\theta)^2]-\frac{P_1}{P_2k^2}Q(D^2-k^2)h_0Du\\ &+P_1\beta_0\Big[\theta_0\theta+u_0u+h_0h+\frac{1}{k^2}Du_0Du+\frac{1}{k^2}Dh_0Dh\Big]\Big\}, \end{aligned} \tag{18}$$

whose Euler–Lagrange equations are the equations of system (8), with the auxiliary conditions $A_i = A_{i0}$; or

$$\begin{aligned} \Phi_1=\int dz\Big\{&-R\theta_0u+\frac{P_1}{2}\Big[k^2u^2+\frac{1}{k^2}(D^2u)^2+2(Du)^2\Big]\\ &+\frac{P_1}{2P_2}\Big[k^2h^2+\frac{1}{k^2}(D^2h)^2+2(Dh)^2\Big]-\frac{P_1}{k^2}(D^2-k^2)hDu_0-P_1u_0\theta\\ &-\frac{P_1}{k^2P_2}Q[D^2-k^2]h_0Du+\frac{1}{2}[k^2\theta^2+(D\theta)^2]\Big\}, \end{aligned} \tag{19}$$

corresponding to (9).

Integrating the term $(Dh)^2$ by parts, and setting h equal to zero at the boundary, we find

$$[k^4h^2-2k^2D^2hh+(D^2h)^2]=[k^2h-D^2h]^2=[(D^2-k^2)h]^2. \tag{20}$$

Accordingly, by using the third equation in system (9) to eliminate the terms containing the magnetic field, we find the local potential

$$\begin{aligned} \Phi_2=\int dz\Big\{&-R\theta_0u+\frac{P_1}{2}\Big[k^2u^2+\frac{1}{k^2}(D^2u)^2+2(Du)^2\Big]+\frac{P_1P_2}{2k^2}(Du)^2\\ &-\frac{P_1P_2}{k^2}DuDu_0+\frac{P_1}{k^2}QDu_0Du+\frac{1}{2}(k^2\theta^2+(D\theta)^2\Big\} \end{aligned} \tag{21}$$

of problem (10), or because with $u_0 = u$, we have $\theta = \theta_0$, so that

$$\Big(\frac{\delta L_1}{\delta u}\Big)_{u_0,\theta}=-R\theta_0+P_1k^2u_0+\frac{P_1}{k^2}D^4u_0-2P_1D^2u_0-\frac{P_1}{k^2}QD^2u_0=0, \tag{22}$$

$$\Big(\frac{\delta L_2}{\delta\theta}\Big)_{u,\theta_0}=P_1u_0+k^2\theta_0-D^2\theta_0=0; \tag{23}$$

setting

$$\theta=\theta_0+\delta\theta,$$
$$u=u_0+\delta u$$

TABLE 1. Critical Values of the Wave Numbers and Rayleigh Numbers

Q	k_{cr}	R	R [4]	$\frac{\Delta R}{R}$, %	$\frac{R}{R_1}$
0	3.117	1750	1707.8	2.45	1
10	3.26	1996.7	1945.9	2.62	1.14
50	3.69	2906.8	2802.1	3.71	1.66
100	4.00	3950	3757.4	5.13	2.26
200	4.46	5856	5488.6	6.68	3.36
500	5.21	11200	10119	10.7	6.4
1000	5.9	19445	17103	13.58	11.1
2000	6.68	34993	30125	16	20
4000	7.56	64752	54697	18.38	37
6000	8.13	93674	78391	19.5	53.5
8000	8.55	122137	101606	20.2	69.79
10000	8.9	150292	124509	20.7	85.88

and using (22), (23), and the boundary conditions, we find

$$\Delta\Phi_2 = \int dz \left\{ \frac{P_1}{2}\left[k^2(\delta u)^2 + \frac{(D^2\delta u)}{k^2} + 2\,(D\delta u)^2\right] + \frac{P_1P_2}{2k^2}(D\delta u)^2 + \frac{1}{2}\left[k^2(\delta\theta)^2 + (D\delta\theta)^2\right]\right\} > 0. \qquad (24)$$

We specify the unknown functions to be of the form

$$\left.\begin{aligned} u = A\,(1-z)^2 z^2, \quad u_0 = A_0\,(1-z)^2 z^2,\\ \theta = B\,(1-z)\,z, \quad \theta_0 = B_0\,(1-z)\,z, \end{aligned}\right\} \qquad (25)$$

where the constants A and B are governed by the conditions

$$\left.\begin{aligned} \left(\frac{\partial\Phi_2}{\partial A}\right)_{B_0, A_0, B} = 0\\ \left(\frac{\partial\Phi_2}{\partial B}\right)_{A_0, A, B_0} = 0 \end{aligned}\right\} \quad \begin{aligned} A_0 = A,\\ B_0 = B. \end{aligned} \qquad (26)$$

We thus find the following system of linear, homogeneous algebraic equations:

$$\left.\begin{aligned} P_1\left[\frac{4}{5k^2} + \frac{4}{105} + \frac{k^2}{630} + \frac{2Q}{105k^2}\right]A - \frac{R}{140}B = 0,\\ -\frac{P_1}{140}A + \frac{1}{3}\left[\frac{k^2}{10} + 1\right]B = 0, \end{aligned}\right\} \qquad (27)$$

which have a nontrivial solution if

$$\left[\frac{4}{5x} + \frac{4}{105} + \frac{2Q}{105x} + \frac{x}{630}\right]\left[\frac{x}{30} + \frac{1}{3}\right] = \frac{R}{(140)^2} \qquad (28)$$

$(x = k^2)$.

Equation (28) gives the values of the Rayleigh numbers corresponding to the stability limit as a function of the wave number k and the parameter Q, related to the magnetic field. The Rayleigh number determined for a fixed Q and for the critical wave number is lower than for all other wave numbers, and it determines the largest temperature gradients which do not disrupt the stability of the system.

The critical wave number is found from the condition dR/dx = 0. Differentiating (28) we find

$$x^3 + 17x^2 - 60\,(42 + Q) = 0. \qquad (29)$$

Table 1 shows the solutions of Eqs. (29) and (28), along with data obtained through the use of a variational formulation of the classical structure. However, finding a variational functional for which the characteristic-value problem is written in the form of the corresponding Euler–Lagrange equations in the latter case is actually more heuristic than an approach based on physical principles; hence, certain unique difficulties arise in each problem. On the other hand, the variational formulation based on the local-potential concept is extremely general in nature and can be used to solve a broad class of problems, including nonlinear and non-self-adjoint problems.[7]

We see from this table that even the first approximation gives comparatively satisfactory results, at least up to Q = 500, at which point the critical temperature gradient is six times above the Bénard point in the absence of a magnetic field. The agreement could undoubtedly be improved by increasing the number of parameters in the trial functions.

---

[1] R. S. Schechter, The Variational Method in Engineering, McGraw-Hill, New York (1967).

[2] P. Glansdorff and I. Prigogine, Thermodynamic Theory of Structure, Stability, and Fluctuation, Wiley–Interscience, New York (1971).

[3] R. S. Schechter and D. M. Himmelblau, Phys. Fluids, 8, 1431 (1965).

[4] S. Chandrasekhar, Hydrodynamic and Hydromagnetic Stability, Clarendon Press, Oxford (1961).

[5] I. Prigogine and P. Glansdorff, Physica, 31, 1242 (1965).

[6] S. M. Rohde, Physica, 61, 53 (1972).

[7] L. C. Legros, I. K. Plattem, and P. G. Roty, Phys. Fluids, 13, 1383 (1972).

Plasma

Linear theory for the low-frequency electromagnetic properties of an isotropic turbulent plasma

K. Komilov, F. Kh. Khakimov, and V. N. Tsytovich

V. I. Lenin Tadzhik State University, Dushanbe

(Submitted August 29, 1973)
Zh. Tekh. Fiz., 44, 971-976 (May 1974)

The low-frequency electromagnetic properties of an isotropic turbulent plasma are studied. An expression is obtained for the permittivity by expanding the collision integrals of the plasma particles and the fluctuations in terms of the turbulence energy, allowance being made for a weak correlation between the turbulent fluctuations. Spectra are found for the longitudinal perturbations of an isotropic turbulent plasma.

GENERAL STATEMENT OF THE PROBLEM

At the present time, one of the important theoretical and experimental problems of the physics of the turbulent plasma is the study of its electromagnetic properties. The radical changes in the electromagnetic properties of a plasma in the low-frequency region caused by high-frequency turbulence are of great importance; in particular, this is true for low-frequency instabilities, which are the most dangerous from the point of view of plasma containment. The low-frequency properties of a turbulent plasma can be described by means of the electrical conductivity tensor σ_{ij} when an expansion in the turbulence energy W is impossible and one must take account of a continuous series of terms of the expansion in W. A criterion for choosing these is the smallness of the frequency ω and the wave number **k** of the low-frequency perturbation.

The main aim of the present investigation is to find the actual form of the tensor σ_{ij} or the permittivity tensor ε_{ij} as a function of the frequency ω and wave number **k** of the perturbing electromagnetic field[1-4] $\varepsilon_{ij} = \varepsilon_{ij}(\omega, \mathbf{k})$ in a form convenient for investigating the low-frequency properties of the plasma. Let us elucidate the meaning of our physical assumptions. In a turbulent plasma the tensor ε_{ij} depends functionally on the spectral energy density $W_{\mathbf{k}_1}$ of the turbulence,[5,6] which is defined by the equation

$$W = \int W_{\mathbf{k}_1} d\mathbf{k}_1, \tag{1}$$

where W is the total energy of the turbulence per cubic centimeter of plasma.

In what follows, to be specific, we shall consider turbulence due to electron plasma waves. We note that the effective collision frequencies in a turbulent plasma depend on $W_{\mathbf{k}_1}$: $\nu_{\text{eff}} = \nu_{\text{eff}}(W_{\mathbf{k}_1})$.

The problem is to find an analytic form of the low-frequency permittivity tensor of an isotropic turbulent plasma:

$$\varepsilon_{ij} = \varepsilon_{ij}(\omega, \mathbf{k}, W_{\mathbf{k}_1}) \tag{2}$$

for frequencies ω appreciably smaller than ν_{eff}. It can be shown that in this case ε_{ij} cannot be expanded with respect to $W_{\mathbf{k}_1}$. A similar problem for one-dimensional motion of the particles is the subject of ref. 6. These results cannot be transferred directly to the three-dimensional case. The task of the present paper is to construct a theory for the low-frequency properties of longitudinal plasma perturbations suitable for isotropic distributions of the particles and longitudinal turbulent oscillations. To construct the theory we use the method of ref. 7, in which an expansion is made with respect to the turbulence energy in the kernels of the collision integrals and allowance is made for renormalization processes by summing terms with an ever-increasing number of nonlinear interactions. The distribution function f and the longitudinal electric field **E** are split into the sum of turbulent, f^T, $\mathbf{E}^T$, and regular, f^R, $\mathbf{E}^R$, components:

$$f = f^T + f^R, \quad \mathbf{E} = \mathbf{E}^T + \mathbf{E}^R, \tag{3}$$

where $\langle f^T \rangle = 0$, $\langle \mathbf{E}^{T(0)} \rangle = 0$, and the averaging is taken over a statistical ensemble. Further, all the quantities ($\mathbf{E}^T$, $\mathbf{E}^R$, f^T, f^R are expanded with respect to $\mathbf{E}^R$ and the terms linear in $\mathbf{E}^R$ are retained. We give the treatment for longitudinal turbulent perturbations of an isotropic plasma. In contrast to ref. 6, in which the case $H \to \infty$ was considered, we assume $H_0 = 0$ here.

PERMITTIVITY TENSOR FOR AN ISOTROPIC TURBULENT PLASMA

We use the kinetic self-consistent field equation with $H_0 = 0$:

$$\frac{\partial f}{\partial t} + \mathbf{v}\frac{\partial f}{\partial \mathbf{r}} - \frac{e}{m_e}\mathbf{E}\frac{\partial f}{\partial \mathbf{v}} = 0, \tag{4}$$

where **v** is the particle velocity and **E** is the electric field. Using the method described above, from Eq. (4) we obtain a system of equations for the ground turbulent state (superscript (0)] and perturbations of this state (superscript (1)]:

$$-i(\omega - \mathbf{kv}) f_k^{R(1)} - \frac{eE_k^R}{m_e|\mathbf{k}|}\left(\mathbf{k}\frac{\partial \Phi}{\partial \mathbf{v}}\right) - \frac{\partial}{\partial \mathbf{v}}\langle D^* \rangle \frac{\partial \Phi}{\partial \mathbf{v}} = \frac{e}{m_e|\mathbf{k}|}\left(\mathbf{k}\frac{\partial}{\partial \mathbf{v}}\right) \times \int \delta(k - k_1 - k_2)\, dk_1 dk_2 (\langle E_{k_1}^{T(0)} f_{k_2}^{T(1)} + E_{k_1}^{T(1)} f_{k_2}^{T(0)} \rangle), \tag{5}$$

$$\varepsilon(k) E_k^{T(1)} = \frac{4\pi i e}{|\mathbf{k}|} \int f_k^{T(1)} d\mathbf{v}, \tag{6}$$

$$-i(\omega - \mathbf{kv}) f_k^{T(0)} - \frac{e}{m_e|\mathbf{k}|}\left(\mathbf{k}\frac{\partial}{\partial \mathbf{v}}\right) \int \delta(k - k_1 - k_2)\, dk_1 dk_2 \times (E_{k_1}^{T(0)} f_{k_2}^{T(0)} - \langle E_{k_1}^{T(0)} f_{k_2}^{T(0)} \rangle), \tag{7}$$

$$-i(\omega - \mathbf{kv}) f_x^{T(1)} - \frac{e}{m_e|\mathbf{k}|} \int \delta(k - k_1 - k_2)\, dk_1 dk_2 E_{k_1}^{T(0)} \left(\mathbf{k}_1 \frac{\partial f_{k_2}^{R(1)}}{\partial \mathbf{v}}\right) - \frac{\partial}{\partial \mathbf{v}}(D^* - \langle D^* \rangle)\frac{\partial \Phi}{\partial \mathbf{v}} - \frac{e}{m_e|\mathbf{k}_1|}\left(\mathbf{k}_1 \frac{\partial}{\partial \mathbf{v}}\right) \int \delta(k - k_1 - k_2)\, dk_1 dk_2$$

$$\times\left(E^{R}_{k_1} f^{T(0)}_{k_2} + E^{T(0)}_{k_1} \tilde f^{T(1)}_{k_2} - E^{T(1)}_{k_1} \tilde f^{T(0)}_{k_2} - \langle E^{T(0)}_{k_1} \tilde f^{T(1)}_{k_2} + E^{T(1)}_{k_1} \tilde f^{T(0)}_{k_2}\rangle\right) = 0. \tag{8}$$

Here, $\tilde f^{T(0)}_{k}$ and $\tilde f^{T(1)}_{k}$ are the renormalized distribution functions for the turbulent state,[6]

$$D^{*} = i(\omega - \mathbf{kv})\left(\frac{e}{m_e}\right)^2 \int \frac{\delta(k - k_1 - k_2)\, dk_1 dk_2}{(\omega_1 - \mathbf{k}_1\mathbf{v})(\omega_2 - \mathbf{k}_2\mathbf{v})} \frac{(\mathbf{k}_1\mathbf{k}_2)}{|\mathbf{k}_1||\mathbf{k}_2|} E^{T(0)}_{k_1} E^{T(1)}_{k_2} \tag{9}$$

and dk = dkdω. At low frequencies (k → 0) the collision integral in Eq. (5), which contains D*, is much greater than the remaining terms of the right-hand side of Eq. (5). We now derive an equation for D*, taking account of correlation effects and the renormalizations used in ref. 6.

Using Eqs. (6) and (8), we form an expression for $\langle E^{T(0)}_{k_1} E^{T(1)}_{k_2}\rangle$:

$$\varepsilon(k_2)\langle E^{T(0)}_{k_1} E^{T(1)}_{k_2}\rangle + \frac{ie}{m_e}\int dk_1' dk_2' \delta(k_2 - k_1' - k_2')\left(S_{k_2, k_1', k_2'} + \delta S_{k_2, k_1', k_2'}\right)$$
$$\times \langle E^{T(0)}_{k_1} E^{T(0)}_{k_1'} E^{T(1)}_{k_2'}\rangle + \frac{\omega_{pe}^2}{n_0|\mathbf{k}_2||\mathbf{k}_1'|}\int \frac{d\mathbf{v}\,\delta(k_2 - k_1' - k_2')\, dk_1' dk_2'}{\omega_2 - \mathbf{k}_2\mathbf{v}}$$
$$\times\left(\mathbf{k}_1' \frac{\partial}{\partial \mathbf{v}}\right)\left(\langle \tilde f^{T(0)}_{k_1'} E^{T(0)}_{k_1} E^{T(1)}_{k_2'}\rangle + \langle E^{T(0)}_{k_1} E^{T(0)}_{k_1'} \tilde f^{T(1)}_{k_2'}\rangle\right) \equiv G, \tag{10}$$

where

$$S_{k, k_1, k_2} = \frac{\omega_{pe}^2}{n_0|\mathbf{k}||\mathbf{k}_1||\mathbf{k}_2|}\int \frac{d\mathbf{v}}{(\omega - \mathbf{kv})} \frac{(\mathbf{k}_1\mathbf{k}_2)}{(\omega_1 - \mathbf{k}_1\mathbf{v})(\omega_2 - \mathbf{k}_2\mathbf{v})}\left(\mathbf{k}\frac{\partial\Phi}{\partial \mathbf{v}}\right), \tag{11}$$

$$\delta S_{k, k_1, k_2} = \frac{\omega_{pe}^2}{n_0|\mathbf{k}||\mathbf{k}_1||\mathbf{k}_2|}\int \frac{d\mathbf{v}}{(\omega_1 - \mathbf{k}_1\mathbf{v})^2} \frac{[\mathbf{k}_1\mathbf{k}_2]}{(\omega_2 - \mathbf{k}_2\mathbf{v})^2}\Phi.$$

Analysis shows that in the region of phase velocities comparable to those of the plasma waves, in which the instability is considered, $v_p > v_{Te}\sqrt{m_i/m_e}$, the quantity $\delta S_{k,k_1,k_2}$ is smaller than $S_{kk_1k_2}$ by a factor m_e/m_i; therefore (12) can be ignored in what follows.

The right-hand side of (10) does not contain $E^{T(1)}_{k}$, and it can therefore be calculated using (7):

$$G = -\frac{\omega_{pe}^2 J_{k_1}}{n_0|\mathbf{k}_1||\mathbf{k}_2|}\int \frac{d\mathbf{v}}{\omega_2 - \mathbf{k}_2\mathbf{v}}\left(\left(\mathbf{k}_1\frac{\partial f^{R(1)}_{k}}{\partial \mathbf{v}}\right)\right. \tag{12}$$

$$\left. + \frac{ieE^{R}_{k}}{m_0|\mathbf{k}|}\left(\mathbf{k}\frac{\partial}{\partial \mathbf{v}}\right)\frac{1}{(\omega_1 - \mathbf{k}_1\mathbf{v})}\left(\mathbf{k}_1\frac{\partial\Phi}{\partial \mathbf{v}}\right)\right). \tag{13}$$

Making more precise the mean value of the three fields in Eq. (10), using the assumption of a weak correlation of the fields, and splitting the mean value of four fields into binary products, we obtain

$$G = \tilde\varepsilon(k_2)\langle E^{T(0)}_{k_1} E^{T(1)}_{k_2}\rangle - \left(\frac{e}{m_e}\right)^2 J_{k_1}\int dk_1' \tilde\Sigma_{k_2, k_1', -k_1, k-k_2'}$$
$$\times\left(\langle E^{T(0)}_{k_1'} E^{T(1)}_{k-k_1'}\rangle + \langle E^{T(0)}_{k-k_1'} E^{T(1)}_{k_1'}\rangle\right) + \left(\frac{e}{m_e}\right)^2\int dk_2' J_{k_2-k_2'} S_{k_2, k_2', k_2-k_2'}$$
$$\times\frac{1}{\varepsilon(k_1)} S_{k_1, k_2'-k_2, k-k_2'}\langle E^{T(0)}_{k-k_2'} E^{T(1)}_{k_2'}\rangle, \tag{14}$$

where

$$\tilde\Sigma_{k_2, k_1', -k_1, k-k_1'} = \Sigma_{k_2, k_1', -k_1, k-k_1'}$$

$$- S_{k_2, k_1', k_2-k_1'}\frac{1}{\varepsilon(k_2 - k_1')} S_{k_2-k_1'', -k_1, k-k_1'}, \tag{15}$$

$$\tilde\varepsilon(k_2) = \varepsilon(k_2) - \left(\frac{e}{m_e}\right)^2\int J_{k_1'} dk_1' \tilde\Sigma_{k_2, k_1', -k_1', k_2}, \tag{16}$$

$$\Sigma_{k_2, k_1', -k_1, k-k_1'} = \frac{\omega_{pe}^2}{n_0|\mathbf{k}_2||\mathbf{k}_1'||\mathbf{k}_1||\mathbf{k} - \mathbf{k}_1'|}\int \frac{d\mathbf{v}\,(\mathbf{k}_1'\mathbf{k}_2)}{(\omega_2 - \mathbf{k}_2\mathbf{v})^2}\left[\frac{2(\mathbf{k}_1\mathbf{k}_2)}{(\omega_2 - \mathbf{k}_2\mathbf{v})}\right.$$
$$\left. + \frac{\mathbf{k}_1(\mathbf{k}_2 + \mathbf{k}_1')}{\omega_2 + \omega_1' - (\mathbf{k}_2 + \mathbf{k}_1')\mathbf{v}}\right]\frac{1}{(\omega_1 - \mathbf{k}_1\mathbf{v})(\omega - \omega_1' - (\mathbf{k} - \mathbf{k}_1')\mathbf{v})}(\mathbf{k} - \mathbf{k}_1')\frac{\partial\Phi}{\partial \mathbf{v}}. \tag{17}$$

We emphasize that (14) contains the operator $\tilde\varepsilon(k_2)$ and additional terms $\sim J_{k_1}$, which are of the same order as $\tilde\varepsilon(k_2)$ or $\varepsilon(k_2)$. Ignoring the last term of (14), which is equal to zero for nondecay turbulence, we obtain the equation

$$\tilde\varepsilon(k - k_1)\langle E^{T(0)}_{k_1} E^{T(1)}_{k-k_1}\rangle = -\frac{\omega_{pe}^2 J_{k_1}}{n_0|\mathbf{k}_1||\mathbf{k} - \mathbf{k}_1|}$$
$$\times\int \frac{d\mathbf{v}}{(\omega - \omega_1 - (\mathbf{k} - \mathbf{k}_1)\mathbf{v})}\left\{\left(\mathbf{k}_1\frac{\partial f^{R(1)}_{k}}{\partial \mathbf{v}}\right)\right.$$
$$\left. + \frac{ieE^{R}_{k}}{m_e|\mathbf{k}|}\left(\mathbf{k}\frac{\partial}{\partial \mathbf{v}}\right)\frac{1}{\omega_1 - \mathbf{k}_1\mathbf{v}}\left(\mathbf{k}_1\frac{\partial\Phi}{\partial \mathbf{v}}\right)\right\} + \left(\frac{e}{m_e}\right)^2 J_{k_1}\int dk_1'\langle E^{T(0)}_{k_1'} E^{T(1)}_{k-k_1'}\rangle$$
$$\times\left[\tilde\Sigma_{k-k_1, k_1', -k_1, k-k_1'} + \tilde\Sigma_{k-k_1, k-k_1', -k_1, k_1'}\right]. \tag{18}$$

If we solve the integral equation (18), we can also readily find the collision integral that contains ⟨D*⟩. Note that the collision integral on the right-hand side of (5) containing $\langle E^{T(1)}_{k_1} f^{T(0)}_{k_2}\rangle$ is of order W/n_0T_e with respect to the term with D*. This is the justification for only keeping the term with D* on the right-hand side.

We solve the resulting integral equation (18) in the limiting case $|\omega_1 - \omega'_1| \ll |\mathbf{k}_1 - \mathbf{k}'_1| v_{Ti}$, $\omega \ll k_1 v_{Ti}$. From (15), for this case we obtain the following approximate expression for $\tilde\Sigma$:

$$\tilde\Sigma_{k-k_1, k_1', -k_1, k-k_1'} \approx -\frac{\omega_{pe}^2 T_e \mathbf{k}_1'(\mathbf{k}_1' - \mathbf{k})}{(T_e + T_i) v_{Te}^2 |\mathbf{k}_1'||\mathbf{k}_1' - \mathbf{k}|\omega_1\omega_1'(\omega_1' - \omega)(\omega_1 - \omega)}. \tag{19}$$

This result holds for opposite signs of the frequencies ω_1 and ω_1'; when the signs of ω_1 and ω_1' are the same, (19) is equal to zero. Dividing (18) by $\tilde\varepsilon(k - k_1)$, [cf. ref. 6, where $S_\pm$ is different from (20)] we find an equation for

$$S_\pm(k) = \int \frac{\mathbf{k}_1(\mathbf{k}_1 - \mathbf{k})\langle E^{T(0)}_{k_1} E^{T(1)}_{k-k_1}\rangle}{|\mathbf{k}_1||\mathbf{k}_1 - \mathbf{k}|\omega_1(\omega - \omega)} dk_{1,\pm}, \tag{20}$$

where the integration in $S_+(k)$ is over positive frequencies, while in $S_-(k)$ it is over negative frequencies. From Eq. (18) we obtain a linear algebraic system of equations for $S_\pm(k)$; the solution is

$$S_+(k) + S_-(k) = -\left[1 + \frac{\omega_{pe}^4}{4\pi n_0(T_e + T_i)}\right.$$
$$\left.\times\int \frac{\mathbf{k}_1(\mathbf{k}_1 + \mathbf{k}) J_{k_1} dk_1}{|\mathbf{k}_1||\mathbf{k}_1 + \mathbf{k}|\omega_1^2(\omega_1 + \omega)^2\tilde\varepsilon(k_1 + k)}\right]^{-1}$$
$$\times\frac{\omega_{pe}^2}{n_0}\int \frac{\mathbf{k}_1(\mathbf{k}_1 + \mathbf{k}) J_{k_1} dk_1}{|\mathbf{k}_1|^2|\mathbf{k}_1 + \mathbf{k}|^2\omega_1(\omega_1 + \omega)^3\tilde\varepsilon(k_1 + k)}\int \frac{d\mathbf{v}}{(\omega_1 + \omega) - (\mathbf{k}_1 + \mathbf{k})\mathbf{v}}$$
$$\times\left\{\left(\mathbf{k}_1\frac{\partial f^{R(1)}_{k}}{\partial \mathbf{v}}\right) + \frac{ieE^{R}_{k}}{m_e|\mathbf{k}|}\left(\mathbf{k}\frac{\partial}{\partial \mathbf{v}}\right)\frac{1}{(\omega_1 - \mathbf{k}_1\mathbf{v})}\left(\mathbf{k}_1\frac{\partial\Phi}{\partial \mathbf{v}}\right)\right\}. \tag{21}$$

On the other hand, using Eq. (9) to the necessary accuracy we obtain

$$\langle D^{*}\rangle = -i(\omega - \mathbf{kv})\left(\frac{e}{m_e}\right)^2\left(S_+(k) + S_-(k)\right), \tag{22}$$

by means of which the diffusion coefficient can be determined:

$$D_1 = -i\frac{\omega_{pe}^2}{n_0}(\omega - \mathbf{kv})\, n_k^{(1)} \left(\frac{e}{m_e}\right)^2 \int \frac{J_{k_1} dk_1}{\tilde{\varepsilon}(k_1+k)\,\omega_1(\omega_1+\omega)^3}$$
$$\times\left[1 + \frac{\omega_{pe}^4}{4\pi n_0 (T_e+T_i)} \int \frac{\mathbf{k}_1(\mathbf{k}_1+\mathbf{k})\, J_{k_1} dk_1}{|\mathbf{k}_1|\,|\mathbf{k}_1+\mathbf{k}|\,\omega_1^2(\omega_1+\omega)^2\,\tilde{\varepsilon}(k_1+k)}\right]^{-1}. \quad (23)$$

From (23) and (5) we obtain the permittivity of the isotropic plasma in the form

$$\varepsilon(k) = \varepsilon_0^i(k) + (\varepsilon_0^e(k) - 1)\left(1 + \frac{n_0 m_e}{T_e+T_i} d_2\right)$$
$$\times\left(1 + \frac{(\varepsilon_0^e(k)-1)\, n_0 k^2}{\omega_{pe}^2} d_1 - \frac{n_0 m_e}{(T_e+T_i)} d_2\right)^{-1}, \quad (24)$$

where

$$d_1 = \frac{e^2\omega_{pe}^2}{n_0 m_e^2} \int \frac{J_{k_1} dk_1}{\tilde{\varepsilon}(k_1+k)\,\omega_1(\omega_1+\omega)^3}, \quad (25)$$

$$d_2 = \frac{e^2\omega_{pe}^2}{n_0 m_e^2} \int \frac{\mathbf{k}_1(\mathbf{k}_1+\mathbf{k})\, J_{k_1} dk_1}{|\mathbf{k}_1|\,|\mathbf{k}_1+\mathbf{k}|\,\omega_1^2(\omega_1+\omega)^2\,\tilde{\varepsilon}(k_1+k)}. \quad (26)$$

This result differs from the one-dimensional case[6] in that d_2 contains the factor $\frac{\mathbf{k}_1(\mathbf{k}_1+\mathbf{k})}{|\mathbf{k}_1|\,|\mathbf{k}_1+\mathbf{k}|}$.

INSTABILITIES OF LONGITUDINAL TURBULENT FLUCTUATIONS OF AN ISOTROPIC PLASMA

It is well known[6] that there is a radical change of the dispersion properties of an isotropic plasma in the region of low frequencies under the influence of high-frequency perturbations. As an example, let us consider turbulence due to electron plasma waves: $\omega_{\mathbf{k}_1} = \omega_{pe} + (3/2)(k_1^2 v_{Te}^2/\omega_{pe})$. In the region $v_p > (3v_{Te}^2)/v_{Ti}$ the group velocities of the plasmons change slowly. Using this fact and the inequalities $\omega \ll \omega_{\mathbf{k}_1}$, $\mathbf{k} \ll \mathbf{k}_1$, $\frac{\omega}{\mathbf{k}} \ll \frac{\omega_1}{\mathbf{k}}$, $\omega \ll \mathbf{k}_1 v_{Ti}$, we find that (25) and (26) take the approximate form

$$d_1 \approx -\frac{\omega_{pe}^4}{n_0^2 m_e} \int \frac{d\mathbf{k}_1}{(\omega - \mathbf{kv}_g)} \left(\mathbf{k}\frac{\partial}{\partial \mathbf{k}_1}\right) \frac{W_{\mathbf{k}_1}}{\omega_{\mathbf{k}_1}} \left(\frac{\partial}{\partial\omega_1}\omega_1^2\tilde{\varepsilon}(k_1)\right)^{-2}_{\omega_1=\omega_{\mathbf{k}_1}}, \quad (27)$$

$$d_2 \approx -\frac{\omega_{pe}^4}{n_0^2 m_e} \int \frac{d\mathbf{k}_1}{(\omega - \mathbf{kv}_g)} \left(\mathbf{k}\frac{\partial}{\partial \mathbf{k}_1}\right) \frac{W_{\mathbf{k}_1}}{\omega_{\mathbf{k}_1}} \left(\frac{\partial}{\partial\omega_1}\omega_1^2\tilde{\varepsilon}(k_1)\right)^{-2}_{\omega_1=\omega_{\mathbf{k}_1}}$$
$$+ \frac{\omega_{pe}^4}{n_0^2 m_e} \int \frac{(\mathbf{kk}_1)}{k_1^2} \frac{W_{\mathbf{k}_1} d\mathbf{k}_1}{(\omega - \mathbf{kv}_g)\,\omega_{\mathbf{k}_1}} \left(\frac{\partial}{\partial\omega_1}\omega_1^2\tilde{\varepsilon}(k_1)\right)^{-2}_{\omega_1=\omega_{\mathbf{k}_1}}, \quad (28)$$

where $\mathbf{v}_g = (\partial\omega_{\mathbf{k}_1}^l)/\partial\mathbf{k}_1$ is the group velocity for the linear spectrum. In deriving Eqs. (27) and (28) we have assumed that $\tilde{\varepsilon}(\mathbf{k}_1) = 0$ and $\tilde{\varepsilon}(\mathbf{k}_1 + \mathbf{k}) \approx (\omega - \mathbf{kv}_g) \left.\frac{\partial\tilde{\varepsilon}}{\partial\omega_1}\right|_{\omega_1=\omega_{\mathbf{k}_1}}$ for the linear spectrum. If we assume $\omega \gg \mathbf{kv}_g$, from (27) and (28) we obtain approximately

$$d_1 \approx \frac{k^2 v_{Te}^2 v_\sim^2}{n_0\omega^2};\quad d_2 \approx \frac{4}{3}\frac{k^2 v_{Te}^2 v_\sim^2}{n_0\omega^2};\quad v_\sim^2 = \frac{3W}{4n_0 m_e}. \quad (29)$$

For the region $\mathbf{k}v_{Ti} \ll \omega \ll \mathbf{k}v_{Te}$, from (24) we obtain

$$\varepsilon(k) \approx -\frac{\omega_{pi}^2}{\omega^2} + \frac{\omega_{pe}^2}{k^2 v_{Te}^2}\left(1 + \frac{4}{3}\frac{k^2 v_\sim^2 T_e}{\omega^2(T_e+T_i)}\right)\left(1 + \frac{k^2 v_\sim^2(7T_e+3T_i)}{3\omega^2(T_e+T_i)}\right)^{-1}. \quad (30)$$

Hence

$$\omega^2 = k^2\tilde{v}_\pm^2,$$

$$\tilde{v}_\pm^2 = \frac{1}{2}\left(v_s^2 - \frac{4}{3}\frac{v_\sim^2 T_e}{(T_e+T_i)}\right)$$
$$\pm\sqrt{\frac{1}{4}\left(v_s^2 - \frac{4v_\sim^2 T_e}{3(T_e+T_i)}\right)^2 + v_s^2 v_\sim^2\frac{(4T_e+3T_i)}{3(T_e+T_i)}}. \quad (31)$$

The minus sign in (31) corresponds to an unstable root. This instability differs quantitatively from the instability obtained in ref. 6 for the one-dimensional case, although the qualitative features remain the same as in ref. 6. In the special case $v_\sim^2 \gg v_s^2$, the square of the growth rate (31) is proportional to W, i.e.,

$$\gamma_k^2 = k^2 v_{Te}^2\frac{W}{n_0(T_e+T_i)}. \quad (32)$$

For $\omega \gg \mathbf{k}v_g$ and $\omega \ll \mathbf{k}v_{Ti}$, $\mathbf{k}v_{Te}$, we obtain

$$\varepsilon(k) = \frac{\omega_{pi}^2}{k^2 v_{Ti}^2} + \frac{\omega_{pe}^2}{k^2 v_{Te}^2}\left(1 + \frac{4}{3}\frac{k^2 v_\sim^2 T_e}{\omega^2(T_e+T_i)}\right)\left(1 + \frac{k^2 v_\sim^2(7T_e+3T_i)}{3\omega^2(T_e+T_i)}\right)^{-1}, \quad (33)$$

$$\omega^2 = -\frac{7}{3}k^2 v_\sim^2\frac{T_e}{T_e+T_i}. \quad (34)$$

Note that in this case too the square of the growth rate of the instability is proportional to W, i.e.,

$$\gamma_k^2 = \frac{7}{4}k^2 v_{Te}^2\frac{W}{n_0(T_e+T_i)}. \quad (35)$$

Note that in the cases investigated here the existing instabilities (31) and (34) differ from the instabilities considered for the one-dimensional case[6] by the numerical coefficient 1/3. Obviously, this is due to the isotropy of the original turbulent state.

Thus, isotropic and one-dimensional turbulence lead to instabilities described by similar expressions, and they differ only by numerical coefficients of order unity. This gives one reason to believe that in the case of arbitrary nonisotropic turbulence the results will be qualitatively similar. One can also write down general relations for the instability of nonisotropic turbulence, since the assumption of isotropy is used only at the end of the calculations to obtain the actual expressions for d_1 and d_2 [see (29)]. It is also easy to generalize the results to the case of an external magnetic field that is not infinitely strong. The present investigation also reveals errors in the results of ref. 8 on the decay of plasmons associated with electron plasma waves.

---

[1] B. B. Kadomtsev, Plasma Turbulence, Academic Press, London (1965).

[2] V. L. Ginzburg (Ginsburg), The Propagation of Electromagnetic Waves in Plasma, Pergamon Press, Oxford (1964).

[3] L. D. Landau and E. M. Lifshitz, Electrodynamics of Continuous Media, Pergamon Press, Oxford (1960).

[4] V. P. Silin and A. A. Rukhadze, Electromagnetic Properties of Plasmas and Similar Media [in Russian], Atomizdat, Moscow (1961).

[5] V. N. Tsytovich, Theory of Turbulent Plasma, Consultants Bureau, New York (1973).

[6] V. N. Tsytovich, Zh. Eksp. Teor. Fiz., 57, 141 (1969) [Sov. Phys. – JETP, 30, 83 (1970)].

[7] V. N. Tsytovich, Nonlinear Effects in Plasma, Consultants Bureau, New York (1970)].

[8] V. E. Zakharov, Zh. Eksp. Teor. Fiz., 62, 1745 (1972).

Excitation of surface electromagnetic waves in a plasma cylinder surrounded by a hollow electron beam

O. V. Dolzhenko, A. V. Zosimov, and A. A. Rukhadze
P. N. Lebedev Physics Institute,
Academy of Sciences of the USSR, Moscow
(Submitted September 7, 1973)
Zh. Tekh. Fiz., 44, 977-984 (May 1974)

The interaction of a hollow relativistic electron beam with the surface oscillations of a plasma cylinder with a free surface is analyzed. It is shown that surface waves can be excited only if the axial magnetic field is relatively weak, so that the plasma electrons are unmagnetized. If, in addition, the beam electrons are unmagnetized as well, then a large number of surface-wave modes are excited. If the beam electrons are magnetized, in a dense plasma many modes are excited; in a rarefied plasma only one axially symmetric surface-wave mode is excited, i.e., the excitation has a single-mode character. The frequencies and linear growth rates are found. Estimates are made of the amplitudes of the steady-state nonlinear waves and of the flux of electromagnetic radiation (Poynting vector) associated with the excited modes.

INTRODUCTION

It is well known that both volume and surface electromagnetic waves can exist in a plasma cylinder with a free surface. The spectrum of characteristic frequencies and the phase velocity along the cylinder axis of volume electromagnetic waves are weak functions of the wave numbers and are of almost the same order for all modes. As a result, when an electron beam interacts with the volume oscillations of a plasma a large number of electromagnetic modes are excited. The situation is different for surface electromagnetic waves in a plasma cylinder, for which the frequency spectrum and the phase velocities are sensitive functions of the wave number. Accordingly, in this case one can always specify conditions in which an electron beam will only excite one surface electromagnetic mode.

In refs. 1-4, the excitation of electromagnetic waves in a plasma cylinder due to the motion of a relativistic electron beam through the plasma is investigated. In this formulation of the problem the beam always excites surface modes and volume modes; as a result the excitation is of a multimode character. With a view to avoiding the excitation of volume waves, in the present paper we examine the interaction of a hollow electron beam with a plasma under conditions such that the beam surrounds the plasma but does not intersect it.

In ref. 4 an expression is obtained in the linear hydrodynamic approximation for the dielectric tensor for a beam–plasma system in cylindrical coordinates; the expression holds for any degree of radial inhomogeneity of the beam and plasma:

$$\varepsilon_{ij}=\begin{pmatrix} \varepsilon_1 & i\varepsilon_2 & \sum\limits_\alpha \alpha_{rz}\left(\frac{\partial}{\partial r}-\frac{l}{r}\frac{\Omega_\alpha}{\omega'_\alpha}\right) \\ -\nu i\varepsilon_2 & \varepsilon_1 & \sum\limits_\alpha i\alpha_{rz}\left(\frac{l}{r}-\frac{\Omega_\alpha}{\omega'_\alpha}\frac{\partial}{\partial r}\right) \\ \sum\limits_\alpha\left(\frac{l}{r}\frac{\Omega_\alpha}{\omega'_\alpha}+\frac{1}{r}\frac{\partial}{\partial r}r\right)\alpha_{rz} & i\sum\limits_\alpha\left(\frac{l}{r}+\frac{\Omega_\alpha}{\omega'_\alpha}\frac{1}{r}\frac{\partial}{\partial r}r\right)\alpha_{rz} & \varepsilon_{\parallel} \end{pmatrix}, \tag{1}$$

where α is the particle species, k and l are the longitudinal and azimuthal wave numbers, u_α is the directed velocity of particles of species α, $\omega'_\alpha=(\omega-ku_\alpha)\gamma_\alpha$, $\gamma_\alpha=(1-u_\alpha^2/c^2)^{-1/2}$, Ω_α is the gyrofrequency and $\omega_{L\alpha}$ is the plasma frequency of particles of species α, and

$$\varepsilon_1=1-\sum_\alpha\frac{\omega_{L\alpha}^2\omega_\alpha'^2\gamma_\alpha^{-1}}{\omega^2(\omega_\alpha'^2-\Omega_\alpha^2)},\quad \varepsilon_2=-\sum_\alpha\frac{\omega_{L\alpha}^2\omega'_\alpha\Omega_\alpha\gamma_\alpha^{-1}}{\omega^2(\omega_\alpha'^2-\Omega_\alpha^2)},$$

$$\varepsilon_3=1-\sum_\alpha\frac{\omega_{L\alpha}^2\gamma_\alpha^{-1}}{\omega_\alpha'^2},\quad \alpha_{rz}=i\frac{\omega_{L\alpha}^2u_\alpha\omega'_\alpha}{\omega^2(\omega_\alpha'^2-\Omega_\alpha^2)},$$

$$\alpha_{zz}=\frac{\omega_{L\alpha}^2u_\alpha^2\gamma_\alpha}{\omega^2(\omega_\alpha'^2-\Omega_\alpha^2)},$$

$$\varepsilon_{\parallel}=\varepsilon_3+\sum_\alpha\frac{1}{r}\frac{\partial}{\partial r}r\alpha_{zz}\frac{\partial}{\partial r}-\frac{l^2}{r^2}\alpha_{zz}+\frac{l}{r}\frac{\Omega_\alpha}{\omega'_\alpha}\left(\alpha_{rz}\frac{\partial}{\partial r}-\frac{\partial}{\partial r}\alpha_{rz}\right).$$

When the tensor (1) is used the field equations

$$\left.\begin{aligned}[\mathrm{curl}\,\mathbf{B}]_i&=-\frac{i\omega}{c}\varepsilon_{ij}E_j,\quad \mathrm{div}\,\mathbf{B}=0,\\ \mathbf{B}&=-i\frac{c}{\omega}\mathrm{curl}\,\mathbf{E},\ \frac{\partial}{\partial r_i}\varepsilon_{ij}E_j=0\end{aligned}\right\} \tag{2}$$

appear in the same form for any degree of inhomogeneity of the density $n_\alpha(r)$.

The following geometry will be considered: A plasma cylinder of radius r_0 is located in a waveguide of radius $R > r_0$; the space between the walls of the waveguide and the plasma cylinder is completely filled by the electron beam; an external magnetic field is directed along the axis of the waveguide; the particle density is constant with a sharp drop to zero at the boundaries r_0 and R.

The boundary conditions have the following form: At the surface of the plasma cylinder

$$\left.\begin{aligned}&\{E_z\}_{r=r_0}=\{E_\varphi\}_{r=r_0}=\{B_z\}_{r=r_0}=0,\\ &\{B_\varphi\}_{r=r_0}=-\frac{i\omega}{c}\Big\{\sum_\alpha\alpha_{rz}E_r+i\sum_\alpha\frac{\Omega_\alpha}{\omega'_\alpha}d_{rz}E_\varphi\\ &\qquad+\sum_\alpha\alpha_{zz}\frac{\partial E_z}{\partial r}+\sum_\alpha\frac{l}{r}\frac{\Omega_\alpha}{\omega'_\alpha}\alpha_{rz}E_z\Big\}_{r=r_0}=0;\end{aligned}\right\} \tag{3}$$

at the surface of the metal waveguide

$$E_z|_{r=R}=E_\varphi|_{r=R}=0. \tag{3$^{\mathrm{I}}$}$$

The dispersion relation proves to be very intractable in the general case of an arbitrary external magnetic field and an arbitrary waveguide radius. Therefore, we assume the waveguide radius to be very large ($R \gg r_0$), and we limit ourselves to three simple limiting cases: a) Neither the plasma nor the beam is magnetized, i.e., $\omega_{L\alpha} \gg \Omega_\alpha$; b) both the plasma and the beam are magnetized, i.e., $\Omega_\alpha \gg \omega_{L\alpha}$; c) the beam is magnetized and the plasma is unmagnetized, i.e., $\omega_{L0} \gg \Omega_e \gg \omega_{L1}$, where ω_{L0} is the electron plasma frequency for the plasma and ω_{L1} is the electron plasma frequency for the beam.

ANALYSIS OF DISPERSION RELATION

The operator ε_{ij} simplifies greatly in the aforementioned limiting cases. In case a) the nonzero components of ε_{ij} are: in the plasma

$$\varepsilon_1 = \varepsilon_3 = \varepsilon_\parallel \equiv \varepsilon_I = 1 - \frac{\omega_{L0}^2}{\omega^2}, \tag{4}$$

in the beam

$$\left.\begin{aligned} \varepsilon_1 = \varepsilon_{II} = 1 - \frac{\omega_{L1}^2}{\gamma\omega^2}, \\ \varepsilon_\parallel = 1 - \frac{\omega_{L1}^2\gamma^{-3}}{(\omega - ku)^2} + \frac{1}{r}\frac{\partial}{\partial r} r\alpha_{zz}\frac{\partial}{\partial r} - \frac{l^2}{r^2}\alpha_{zz}. \end{aligned}\right\} \tag{4^I}$$

The field equations reduce to two equations for E_z and B_z:

$$\begin{aligned} \left(\frac{1}{r}\frac{\partial}{\partial r} r \frac{\partial}{\partial r} - \frac{l^2}{r^2} - \varkappa^2\right) E_z = 0, \\ \left(\frac{1}{r}\frac{\partial}{\partial r} r \frac{\partial}{\partial r} - \frac{l^2}{r^2} - \varkappa^2\right) B_z = 0, \end{aligned} \tag{5}$$

where

$$\varkappa_{I,\,II}^2 = k^2 - \frac{\omega^2}{c^2}\varepsilon_{I,\,II}.$$

The index I refers to the plasma and II to the beam. The other field components are expressed in terms of E_z and B_z through the relationships[3]

$$\begin{aligned} E_\varphi &= \frac{1}{\varkappa^2}\left[\frac{i\omega}{c}\frac{\partial B_z}{\partial r} + \frac{l}{r}\left(k + i\frac{\omega^2}{c^2}\alpha_{rz}\right)E_z\right], \\ E_r &= \frac{1}{\varkappa^2}\left[\frac{\omega}{c}\frac{l}{r}B_z + \left(\frac{\omega^2}{c^2}\alpha_{rz} - ik\right)\frac{\partial E_z}{\partial r}\right], \\ B_\varphi &= \frac{1}{\varkappa^2}\left[k\frac{l}{r}B_z + \frac{\omega}{c}(k\alpha_{rz} - i\varepsilon_1)\frac{\partial E_z}{\partial r}\right], \\ B_r &= \frac{1}{\varkappa^2}\left[-ik\frac{\partial B_z}{\partial r} - \frac{l}{r}\frac{\omega}{c}(\varepsilon_1 + ik\alpha_{rz})E_z\right]. \end{aligned} \tag{6}$$

Boundary condition (3) for B_φ now assumes the form

$$(B_\varphi)_{r=r_0} = -\frac{i\omega}{c}\left\{\alpha_{rz}E_z + \alpha_{zz}\frac{\partial E_z}{\partial r}\right\}_{r=r_0}.$$

Utilizing the requirement that the field be bounded, the solution of Eqs. (5) can be written in the form

$$\left.\begin{aligned} E_{zI} = C_{II}I_l(\varkappa_I r), \quad B_{zI} = D_{II}I_l(\varkappa_I r), \\ E_{zII} = C_{III}K_l(\varkappa_{II} r), \quad B_{zII} = D_{III}K_l(\varkappa_{II} s), \end{aligned}\right\} \tag{7}$$

where $I_l(x)$, $K_l(x)$ are the cylindrical functions of imaginary argument. Inserting these solutions into the boundary conditions yields the dispersion relation

$$\begin{aligned} &\left[\frac{\varepsilon_I}{\varkappa_I}I_l'(\varkappa_I r_0)K_l(\varkappa_{II} r_0) - \frac{\varepsilon_{3II}}{\varkappa_{II}}I_l(\varkappa_I r_0)K_l'(\varkappa_{II} r_0)\right] \\ &\times\left[\frac{1}{\varkappa_I}I_l'(\varkappa_I r_0)K_l(\varkappa_{II} r_0) - \frac{1}{\varkappa_{II}}I_l(\varkappa_I r_0)K_l'(\varkappa_{II} r_0)\right] \\ &-\frac{l^2c^2}{\omega^2 r_0^2}\left[\frac{k}{\varkappa_I^2} - \frac{1}{\varkappa_{II}^2}\left(k + i\frac{\omega^2}{c^2}\alpha_{rz}\right)\right]^2 I_l^2(\varkappa_I r_0)K_l^2(\varkappa_{II} r_0) = 0. \end{aligned} \tag{8}$$

For waves with a phase velocity close to the velocity of the beam electrons (Cerenkov excitation mechanism), i.e., for $\omega \simeq ku$, and for low-density beams, when $\omega_{L1} \ll \omega_{L0}$, this equation is readily solved in the two limiting cases: ($\varkappa_{II}r_0 \gg 1$) and ($\varkappa_{II}r_0 \ll 1$).

In the short-wave limit ($\varkappa_{II}r_0 \gg 1$, so that $\varkappa_I r_0 \gg 1$) we obtain

$$\omega = \frac{\omega_{L0}}{\sqrt{1+\gamma^2}}\left[1 + \frac{-1 + i\sqrt{3}}{2}\left(\frac{n_1}{n_0}\frac{\gamma}{\gamma^4 + 1}\right)^{1/3}\right] \tag{9}$$

for all axial modes l.

In the long-wave limit ($\varkappa_{II}r_0 \ll 1$) for the mode with $l = 0$ we have

$$\begin{aligned} \omega = \frac{u\gamma}{r_0}\left\{1 + \frac{-1 + i\sqrt{3}}{2}\left(\frac{\omega_{L1}^2 r_0^2}{2u^2\gamma^7}\exp\left[2\frac{(\gamma^2 - 1)c}{\omega_{L0}r_0}\frac{I_0\left(\frac{\omega_{L0}r_0}{c}\right)}{I_1\left(\frac{\omega_{L0}r_0}{c}\right)}\right]\right)^{1/3}\right\} \\ \times\exp\left[-\frac{(\gamma^2 - 1)c}{\omega_{L0}r_0}\frac{I_0\left(\frac{\omega_{L0}r_0}{c}\right)}{I_1\left(\frac{\omega_{L0}r_0}{c}\right)}\right], \end{aligned} \tag{10}$$

and for modes with $l \geq 1$

$$\omega = \frac{\omega_{L0}}{\sqrt{2}}\left\{1 + \frac{-1 + i\sqrt{3}}{2}\left[\frac{n_1}{2n_0}\frac{1}{\gamma}\right]^{1/3}\right\}, \tag{11}$$

where n_1 and n_0 are the densities of beam and plasma electrons.

Short-wave modes are possible only in a dense plasma when $\omega_{L0}^2 r_0^3 \gg 2u^2\gamma^2$, while long-wave modes are only excited in a rarefied plasma when

$$\frac{(\gamma^2 - 1)c}{\omega_{L0}r_0} \gg \frac{I_0\left(\frac{\omega_{L0}r_0}{c}\right)}{I_1\left(\frac{\omega_{L0}r_0}{c}\right)}.$$

It follows from a comparison of Eq. (8) with the dispersion relation for a waveguide of finite radius that Eq. (9) (short-wave limit or a dense plasma) holds effectively for any $R > r_0$, while expressions (10) and (11) (long-wave limit or rarefied plasma) are valid for

$$\frac{R}{r_0} > \exp\left[(\gamma^2 - 1)\frac{c}{\omega_{L0}r_0}\frac{I_0\left(\frac{\omega_{L0}r_0}{c}\right)}{I_1\left(\frac{\omega_{L0}r_0}{c}\right)}\right] \gg 1.$$

The growth rates $\delta = \mathrm{Im}\,\omega$ are independent of the mode index l in the short-wave limit ($\varkappa_{II}r_0 \gg 1$); while in the long-wave limit ($\varkappa_{II}r_0 \ll 1$) the growth rates of modes with $l \geq 1$ are much greater than the growth rate of the mode with $l = 0$ and are also independent of l, i.e., in both cases many modes are excited simultaneously. However, as will be shown below, the flux of microwave energy is determined mainly by a single mode. The flux of microwave energy is small in the case of nonrelativistic beams ($u \ll c$, $\gamma \gg 1$), since the excited field is almost electrostatic in character; in the case of ultrarelativistic beams ($\gamma \gg$

1) the waves excited by the beam are almost transverse and the flux of radiation energy is significant.

Let us consider case b), when both the plasma and the beam are magnetized (ω_{L0}, $\omega_{L1} \ll \Omega_e$) and case c), when the beam is magnetized and the plasma is not ($\omega_{L0} \gg \Omega_e \gg \omega_{L1}$). The operator $\hat{\varepsilon}_{ij}$ has the following nonzero components. For case b): in the plasma

$$\varepsilon_1 = 1,\quad \varepsilon_2 = \frac{\omega_{L0}^2}{\omega\Omega_e},\quad \varepsilon_3 = 1 - \frac{\omega_{L0}^2}{\omega^2},$$

in the beam

$$\varepsilon_1 = 1,\quad \varepsilon_3 = 1 - \frac{\omega_{L1}^2\gamma^{-3}}{(\omega - ku)^2}.$$

For case c): in the plasma

$$\varepsilon_1 = \varepsilon_3 = 1 - \frac{\omega_{L0}^2}{\omega^2},\quad \varepsilon_2 = -\frac{\omega_{L0}^2\Omega_e}{\omega^3},$$

in the beam

$$\varepsilon_1 = 1,\quad \varepsilon_3 = 1 - \frac{\omega_{L1}^2\gamma^{-3}}{(\omega - ku)^2}.$$

The boundary conditions for B_φ now assume the form $\{B_\varphi\}_{r=r_0} = 0$, and the field equations reduce to two equations for E_z and B_z:

$$\left.\begin{aligned} &\left(\varkappa^2 + \frac{\omega^2}{c^2}\frac{\varepsilon_2^2}{\varepsilon_1}\right)\Delta_\perp E_z + \frac{\varepsilon_3}{\varepsilon_1}\left(\frac{\omega^4}{c^4}\varepsilon_2^2 - \varkappa^4\right)E_z = i\frac{\varepsilon_2}{\varepsilon_1}\frac{\omega k}{c}\Delta_\perp B_z, \\ &\varkappa^2\Delta_\perp B_z + \left(\frac{\omega^4}{c^4}\varepsilon_2^2 - \varkappa^4\right)B_z = -i\frac{\omega k}{c}\varepsilon_2\Delta_\perp E_z, \end{aligned}\right\} \tag{12}$$

where

$$\Delta_\perp = \frac{1}{r}\frac{\partial}{\partial r} r \frac{\partial}{\partial r} - \frac{l^2}{r^2},$$

$$\varkappa^2 = k^2 - \frac{\omega^2}{c^2}\varepsilon_1.$$

The remaining field components are connected with E_z and B_z by the relationships[4]

$$\begin{aligned} E_r &= \left(\varkappa^4 - \varepsilon_2^2\frac{\omega^4}{c^4}\right)^{-1}\left(-ik\varkappa^2\frac{\partial E_z}{\partial r} + \frac{l}{r}\frac{\omega}{c}\varkappa^2 B_z - \frac{\omega^3}{c^3}\varepsilon_2\frac{\partial B_z}{\partial r} + ik\frac{l}{r}\frac{\omega^2}{c^2}\varepsilon_2 E_z\right), \\ E_\varphi &= \left(\varkappa^4 - \varepsilon_2^2\frac{\omega^4}{c^4}\right)^{-1}\left(i\frac{\omega}{c}\varkappa^2\frac{\partial B_z}{\partial r} + \frac{l}{r}k\varkappa^2 E_z - k\varepsilon_2\frac{\omega^2}{c^2}\frac{\partial E_z}{\partial r} - i\frac{l}{r}\frac{\omega^3}{c^3}\varepsilon_2 B_z\right), \\ B_r &= \left(\varkappa^4 - \varepsilon_2^2\frac{\omega^4}{c^4}\right)^{-1}\Big[-ik\varkappa^2\frac{\partial B_z}{\partial r} - \frac{\omega}{c}\varepsilon_1\left(\varkappa^2 + \frac{\omega^2}{c^2}\frac{\varepsilon_2^2}{\varepsilon_1}\right)E_z \\ &\quad + k\frac{\omega}{c}\varepsilon_2\frac{\partial E_z}{\partial r} + i\frac{l}{r}\frac{\omega^2}{c^2}k\varepsilon_2 B_z\Big], \\ B_\varphi &= \left(\varkappa^4 - \varepsilon_2^2\frac{\omega^4}{c^4}\right)^{-1}\Big[-i\frac{\omega}{c}\varepsilon_1\left(\varkappa^2 + \frac{\omega^2}{c^2}\frac{\varepsilon_2^2}{\varepsilon_1}\right)\frac{\partial E_z}{\partial r} \\ &\quad + \frac{l}{r}k\varkappa^2 B_z - k^2\frac{\omega^2}{c^2}\varepsilon_2\frac{\partial B_z}{\partial r} + i\frac{l}{r}\frac{\omega}{c}k^2\varepsilon_2 E_z\Big]. \end{aligned} \tag{13}$$

In the beam region Eqs. (12) decouple and reduce to set (5), the solution of which can be written in the form

$$E_{zII} = A_{IIl}K_l\left(\sqrt{\frac{\varepsilon_{3II}}{\varepsilon_{1II}}}\varkappa_{II}r\right),\quad B_{zII} = B_{IIl}K_l(\varkappa_{II}r). \tag{14}$$

In the plasma region the solution of set (12) will be

$$E_{zI} = A_{Il}I_l(k_1r) + B_{Il}K_l(k_1r),$$

$$B_{zI} = i\frac{c}{\omega k}\left[\left(\frac{\varepsilon_3\varkappa^2}{\varepsilon_2} - k_1^2\frac{\varepsilon_1}{\varepsilon_2}\right)A_{Il}I_l(k_1r) + \left(\frac{\varepsilon_3\varkappa^2}{\varepsilon_2} - k_2^2\frac{\varepsilon_1}{\varepsilon_2}\right)B_{Il}K_l(k_1r)\right], \tag{15}$$

where

$$\left.\begin{aligned} &k_{1,2}^2 = \frac{\varepsilon_1 + \varepsilon_3}{2\varepsilon_1}\varkappa^2 + \frac{\omega^2}{2c^2}\frac{\varepsilon_2^2}{\varepsilon_1} \pm \frac{1}{2}\sqrt{\left[\left(1 - \frac{\varepsilon_3}{\varepsilon_1}\right)\varkappa^2 + \frac{\omega^2}{c^2}\frac{\varepsilon_2}{\varepsilon_1}\right]^2 + 4k^2\frac{\omega^2}{c^2}\frac{\varepsilon_3\varepsilon_2^2}{\varepsilon_1^2}}, \\ &\varkappa_{II}^2 = k^2 - \frac{\omega^2}{c^2}\varepsilon_{1II}. \end{aligned}\right\} \tag{16}$$

The dispersion relation obtained by inserting these solutions into the boundary conditions proves to be very cumbersome. It is readily shown, however, that in case b), when $\omega_{L0} \ll \Omega_e$, the dispersion relation has no solutions, i.e., the beam excites no waves in a magnetized plasma. In case c), however, when the beam is magnetized and the plasma is not ($\omega_{L0} \gg \Omega_e \gg \omega_{L1}$), $\varepsilon_{1I} = \varepsilon_{3I}$ and the roots $k_{1,2}$ become almost degenerate, i.e.,

$$k_{1,2} = \frac{\varepsilon_1 + \varepsilon_3}{2\varepsilon_1}\varkappa^2 \pm \sqrt{k^2\frac{\omega^2}{c^2}\varepsilon_3\frac{\varepsilon_2^2}{\varepsilon_1^2}},$$

where the second term is negligibly small. The dispersion relation in this case reduces to the form

$$\begin{aligned} &\left[\frac{\varepsilon_{1I}}{\varkappa_I}I_l'(\varkappa_Ir_0)K_l(\sqrt{\varepsilon_{3II}}\varkappa_{II}r_0) - \frac{\sqrt{\varepsilon_{3II}}}{\varkappa_{II}}I_l(\varkappa_Ir_0)K_l'(\sqrt{\varepsilon_{3II}}\varkappa_{II}r_0)\right] \\ &\quad \times\left[\frac{1}{\varkappa_I}I_l'(\varkappa_Ir_0)K_l(\varkappa_{II}r_0) - \frac{1}{\varkappa_{II}}I_l(\varkappa_Ir_0)K_l'(\varkappa_{II}r_0)\right] \\ &\quad - \frac{l^2k^2c^2}{\omega^2r_0^2}\left(\frac{1}{\varkappa_I^2} - \frac{1}{\varkappa_{II}^2}\right)^2 I_l^2(\varkappa_Ir_0)K_l(\varkappa_{II}r_0)K_l(\sqrt{\varepsilon_{3II}}\varkappa_{II}r_0) = 0. \end{aligned} \tag{19}$$

In the absence of a beam Eq. (19)* coincides with Eq. (8), i.e., the characteristic frequencies in this case can differ from case a) only in imaginary parts (in the growth rates of the oscillations). The conditions on the plasma density for the excitation of short-wave and long-wave modes are maintained, as is the condition on the ratio of the waveguide radius R to the plasma cylinder radius r_0 for which the long-wave and short-wave approximations are valid. However, the difference in the growth rates for cases a) and c) introduces changes in case c) in the manner in which the oscillations grow and in the character of the nonlinear saturation of the generated waves.

In the short-wave limit ($\varkappa_{II}r_0 \gg 1$) the growth rates are independent of the mode index l:

$$\delta = \operatorname{Im}\omega = \frac{\sqrt{3}}{2}\left(\frac{n_1}{2n_0}\frac{\gamma}{\gamma^4 + 1}\right)^{1/3}\frac{\omega_{L0}}{\sqrt{1 + \gamma^2}},$$

i.e., they are smaller than the growth rates in case a) by a factor of $2^{1/3}$.

In the long-wave limit ($\varkappa_{II}r_0 \ll 1$) axially nonsymmetric modes are not excited by a magnetized beam since the growth rate is positive only for the symmetric mode with $l = 0$:

$$\delta = \frac{\sqrt{3}}{2}\left\{\frac{\omega_{L1}^2\omega_{L0}c}{4\gamma^6u}\frac{I_1\left(\frac{\omega_{L0}r_0}{c}\right)}{I_0\left(\frac{\omega_{L0}r_0}{c}\right)}\exp\left[-\frac{(\gamma^2 - 1)c}{\omega_{L0}r_0}\frac{I_0\left(\frac{\omega_{L0}r_0}{c}\right)}{I_1\left(\frac{\omega_{L0}r_0}{c}\right)}\right]\right\}^{1/3}.$$

RADIATION EFFICIENCY AND DISCUSSION

Having analyzed the excitation of surface waves, we are now faced with the problem of the output of this radiation from the waveguide. An output of radiation is possible if the axial component of the Poynting vector

$$P_z = \frac{c}{4\pi}\int_0^R r\,dr\int_0^{2\pi} d\varphi\,[\overline{\mathbf{E}\times\mathbf{B}}],$$

is nonzero.

Utilizing (6) and (13) we can calculate the electromagnetic energy flux P_z correct to the constants $A_{II l}$, indeterminate in the linear theory, entering into the amplitude of the axial component of the electric field E_z in the beam region $[E_{z}\text{II} = A_{IIl}(\varkappa_{II}r),\ E_z\text{II} = A_{IIl}K_l(\varepsilon_{3II}\varkappa_{II}r)^{1/2}]$. In order to determine the maximum value of these constants recourse must be made to a model for the nonlinear saturation of the wave.

It can be shown from (6) and (13) that the short waves excited in a dense plasma will be almost electrostatic at small velocities of the beam electrons ($u \ll c$) and will be almost transverse for ultrarelativistic beams ($\gamma \gg 1$); the long-wave modes in a rarefied plasma are, however, always almost transverse.

An upper limit on the growth of the amplitude of potential waves can be established in terms of the capture of the beam electrons by the potential field of the wave. A condition of such capture, when relative motion between the wave and the beam electrons ceases, is given by[5]

$$e\Phi = \frac{m}{2}\gamma^3\,\mathrm{Re}\left(\frac{\omega}{k}-u\right)^2,$$

where Φ is the wave potential ($E_z = -ik\Phi$).

In the case of transverse waves the results of Kovtun and Rukhadze[6] can be used to estimate the nonlinear conversion of a transverse field into electrostatic waves, and the maximum amplitude of the latter estimated through the capture of beam electrons.

The ratio of the maximum flux of electromagnetic energy determined in this manner to the flux of kinetic energy of the beam electrons $\pi(R^2-r_0^2)mn_1c^2u(\gamma-1)$ gives a measure of the efficiency of a radiator (generator) based on the investigated beam–plasma interaction.

In the short-wave limit the energy flux is removed mainly by the mode $l = 0$ (the flux removed by the remaining modes is smaller by a factor of $\omega^2_{L0}r_0^2/2u^2\gamma^2$), and we have for the efficiency in the case of an unmagnetized beam

$$\eta = \frac{r_0u\gamma^2(\gamma+1)(\gamma^6-1)}{16\omega_{L0}(R^2-r_0^2)\sqrt{\gamma^2+1}}\left(\frac{\gamma}{\gamma^4+1}\right)^{1/3}\left(\frac{n_1}{n_0}\right)^{1/3}.$$

The efficiency for a magnetized beam is smaller by a factor $2^{4/3}$.

In the long-wave limit in the case of an unmagnetized beam the flux of electromagnetic energy is removed mainly by the mode $l = 1$ (the contribution from the other modes is smaller by a factor of $2u^2\gamma^2/\omega^2_{L0}r_0^2$), and the generator efficiency is

$$\eta = \frac{u^3}{6uc^2}\left(\frac{n_1}{2n_0\gamma}\right)^{1/3}\frac{\gamma^5(2\gamma^2-1)}{(\gamma-1)}\frac{r_0^2}{R^2-r_0^2}.$$

If, however, the beam is magnetized and only the mode with $l = 0$ is excited, then the generator efficiency is given by the expression

$$\eta = \frac{1}{4\gamma^2(\gamma-1)}\left[\frac{2I_1^2\left(\frac{\omega_{L0}r_0}{c}\right)}{I_0^2\left(\frac{\omega_{L0}r_0}{c}\right)}\right].$$

The following conclusions can be drawn from our analysis.

1. In a magnetized plasma oscillations are not generally excited. In an unmagnetized dense plasma the beam excites a large number of short-wave modes with the same frequency $\omega = \omega_{L0}(\gamma^2+1)^{1/2}$, but electromagnetic energy is removed mainly by the axially symmetric mode. The cases of a magnetized and an unmagnetized beam differ only in the growth rates and in the radiation efficiency. For ultrarelativistic beams the excited waves are almost transverse and the radiation efficiency is appreciably greater than for slow beams.

2. In a rarefied unmagnetized plasma an unmagnetized beam excites a large number of nonsymmetric modes with $l \geq 1$ and the same frequency $\omega = \omega_{L0}/\sqrt{2}$. The oscillations are almost transverse, and in the case of many modes electromagnetic energy is removed mainly by the mode with $l = 1$. A magnetized beam, on the other hand, excites only one axially symmetric mode with frequency

$$\omega = \frac{u\gamma}{r_0}\exp\left[-\frac{(\gamma^2-1)c}{\omega_{L0}r_0}\frac{I_0\left(\frac{\omega_{L0}r_0}{c}\right)}{I_1\left(\frac{\omega_{L0}r_0}{c}\right)}\right].$$

3. Excitation of waves in a rarefied plasma by a magnetized beam is advantageous not only because just one mode of oscillation is excited. In this regime the frequency depends very strongly (exponentially) on the velocity of the beam electrons and can readily be varied over a wide range by varying the latter. The limitations on the plasma density may, however, be an obstacle to obtaining a high radiation power.

The authors are grateful to B. I. Aronov for a number of remarks.

---

* Publishers Note: There were no equations labelled (17) and (18) in the original Russian.

---

[1] L. S. Bogdankevich and A. A. Rukhadze, Zh. Eksp. Teor. Fiz., 62, 233 (1972) [Sov. Phys. – JETP, 35, 126 (1972)]; L. S. Bogdankevich, O. V. Dolzhenko, and A. A. Rukhadze, Radiotekh. Elektron., 17, 1647 (1972).

[2] B. I. Aronov, A. A. Rukhadze, and M. E. Chegovadze, Zh. Tekh. Fiz., 42, 1097 (1972) [Sov. Phys. – Tech. Phys., 17, 877 (1972); B. I. Aronov and A. A. Rukhadze, Zh. Eksp. Teor. Fiz., 42, 1606 (1972) [Sov. Phys. – JETP, 15, 758 (1962)].

[3] B. I. Aronov, L. S. Bogdankevich, and A. A. Rukhadze, Zh. Tekh. Fiz., 42, 716 (1973) [Sov. Phys. – Tech. Phys., 17, 564 (1972)].

[4] V. N. Tsytovich, Nonlinear Effects in Plasma, Plenum, New York (1970).

[5] L. S. Bogdankevich and A. A. Rukhadze, Preprint No. 18 [in Russian], Physics Institute of the Academy of Sciences of the USSR (1973).

[6] R. I. Kovtun and A. A. Rukhadze, Zh. Eksp. Teor. Fiz., 58, 1709 (1970) [Sov. Phys. – JETP, 31, 915 (1970)].

Launching and propagation of regular nonlinear waves in an anisotropic plasma-filled waveguide

V. I. Kurilko, A. P. Tols-toluzhskii and Ya. B. Fainberg

Physicotechnical Institute,
Academy of Sciences of the Ukrainian SSR, Khar'kov

(Submitted September 17, 1973)
Zh. Tekh. Fiz., 44, 985-944 (May 1974)

Hydrodynamic theory is derived for the launching and propagation of regular periodic waves of finite amplitude propagating along the axis of a cylindrical plasma-filled waveguide in a strong external magnetic field. It is shown that the problem of seeking the field configuration dispersion of such waves reduces to the solution of a quasilinear equation of the elliptic type for the high-frequency potential. The slightly nonlinear solutions of this equation are classified. The conditions under which periodic waves of finite amplitude exist are determined. Analytic expressions are found for the dispersion and wave configuration at Mach numbers near unity. The Cerenkov excitation of a nonlinear plasma-filled waveguide by a train of charged disks is analyzed. The plasma nonlinearity stabilizes the Budker and Cerenkov instabilities of a relativistic beam injected into a bounded plasma.

The launching and propagation of regular waves of finite amplitude in a bounded plasma are of interest in connection with the development of collective acceleration methods[1-3] and beam methods for producing and controlling the spectra of microwaves.[4,5] In the present paper we analyze the dispersion, field configuration, and launching efficiency for regular nonlinear waves in an anisotropic cylindrical plasma waveguide.

1. STATEMENT OF THE PROBLEM

We consider a cylindrical waveguide having conducting walls of radius a and filled with a magnetized plasma ($\omega_p^2 \ll \omega_H^2$). The self-consistent system of equations describing the propagation of high-frequency electromagnetic waves in such a waveguide consists of the equation of longitudinal motion, the continuity equation for the plasma electrons, and the Maxwell equations for the field. In the simplest case of axisymmetric TM waves these equations are

$$\left.\begin{gathered}\frac{dp_z}{dt}=eE_z,\quad \frac{\partial\rho}{\partial t}+\frac{\partial}{\partial z}(\rho v_z)=0,\\ \frac{\partial H_\perp}{\partial z}+\frac{1}{c}\frac{\partial E_\perp}{\partial t}=0,\quad \frac{1}{c}\frac{\partial H_\perp}{\partial t}+\frac{\partial E_\perp}{\partial z}-\frac{\partial E_z}{\partial r}=0,\\ \frac{1}{r}\frac{\partial}{\partial r}rH_\perp-\frac{1}{c}\frac{\partial E_z}{\partial t}=\frac{4\pi e}{c}\rho v_\parallel.\end{gathered}\right\}\qquad(1)$$

We seek solutions of these equations in the form of waves propagating along the waveguide axis at a constant phase velocity V. In this case, introducing the high-frequency wave potential $\varphi(r, z-Vt)$, we can reduce the order of system (1) by using its first integrals

$$\left.\begin{gathered}\rho(r,z')[u(r,z')-\beta]=I_1(r),\\ \frac{1-\beta u}{(1-u^2)^{1/2}}+\frac{e\varphi}{m_0c^2}=\frac{eI_2(r)}{m_0c^2},\quad \beta\equiv\frac{V}{c},\\ H_\perp(r,z')-\beta E_\perp(r,z')=\beta I_3(r),\quad \gamma\equiv(1-\beta^2)^{-1/2},\\ E_\perp\equiv-\gamma^2\frac{\partial\varphi}{\partial r},\quad E_z\equiv-\frac{\partial\varphi}{\partial z'},\quad z'\equiv z-Vt,\ u\equiv\frac{v_z}{c}.\end{gathered}\right\}\qquad(2)$$

The functions $I_s(r)$, which are not functions of z', must be found from the boundary conditions on z'. The first is unambiguously determined by the known value of ρ_+V for the total flow at the points z' where the electron velocity vanishes:

$$\rho(r,z')u(r,z')=\beta[\rho(r,z')-\rho_+].\qquad(2a)$$

The other two first integrals appear in the final equation for the high-frequency potential, $\Phi(\eta,\xi)\equiv e/(m_0V^2)\cdot[\varphi(r,z')-I_2(r)]$ (cf. ref. 6),

$$\left.\begin{gathered}M_0^2\frac{1}{\eta}\frac{\partial}{\partial\eta}\eta\frac{\partial\Phi}{\partial\eta}+\frac{\partial^2\Phi}{\partial\xi^2}+R(\Phi)=0,\quad \Phi<\Phi_{\max}\equiv\frac{\gamma}{\gamma+1};\\ R(\Phi)\equiv\frac{w(\Phi)}{1-w(\Phi)}+G(\eta),\\ w(\Phi)\equiv\frac{u}{\beta}=\frac{1-(1-\beta^2\Phi)\sqrt{1-2\Phi+\beta^2\Phi^2}}{(1-\beta^2\Phi)^2+\beta^2},\\ \eta\equiv\frac{r}{a}\leqslant1,\ \xi\equiv\frac{\omega_p}{V}z',\ M_0^2\equiv\frac{V^2\gamma^2}{\omega_p^2a^2},\ \omega_p^2\equiv\frac{4\pi e^2n_p}{m_0}\end{gathered}\right\}\qquad(3)$$

as the linear superposition

$$G(\eta)\equiv M_0^2\frac{1}{\eta}\frac{d}{d\eta}\left\{\eta\left[\frac{e}{m_0V^2}\left(\frac{\partial I_2}{\partial r}-I_3\right)\right]\right\}.$$

Physically, this latter function represents the perturbation of the average charge density in the plasma due to the finite amplitude of the potential. In our case of periodic waves in a current-free plasma, the average value of the total charge density over a period along z is $R(\Phi)\sim\rho_- - \rho_+$, and the current ρu [see (2a)] vanishes.[2] According to (3), this condition is equivalent to the equation

$$\bar{R}(\Phi)\equiv\int_{-L/2}^{+L/2}d\xi R[\Phi(\eta,\xi)]=-\frac{M_0^2}{\eta}\frac{d}{d\eta}\left(\eta\frac{d}{d\eta}\bar{\Phi}\right)=0,\qquad(3a)$$

which holds automatically in the one-dimensional case and which gives the unknown function $G(\eta)$ in the two-dimensional case (see below).

To determine unambiguously the potential $\Phi(\eta,\xi)$ we must also specify the boundary conditions with respect to the transverse coordinate. For purposes of acceleration, e.g., the most interesting solutions (3) are those corresponding to the maximum longitudinal field at the axis. The longitudinal field and the potential vanish at the conducting walls. The boundary conditions with respect to η are thus

$$\Phi(1, \xi) = \frac{\partial \Phi}{\partial \eta}(0, \xi) = 0. \tag{3b}$$

2. LINEAR THEORY

Before we turn to the nonlinear solutions of Eq. (2) we will briefly discuss those results of the corresponding linear theory which we will need below.

In the linear approximation we have $R(\Phi) = \Phi$, $G = 0$, so that periodic natural modes of this waveguide can be analyzed through separation of variables. Substituting into (3) the potential Φ in the form

$$\Phi(\eta, \xi) = AP(\eta)\exp(ik\xi) \tag{4a}$$

we find Bessel's equation for the radial function $P(\eta)$:

$$\left[M_0^2 \frac{1}{\eta}\frac{d}{d\eta}\eta\frac{d}{d\eta} + 1 - k^2\right]P(\eta) = 0. \tag{4b}$$

Using this equation and the boundary conditions at the walls and the waveguide axis, we find the field configuration and dispersion relation for these waves:

$$\begin{gathered} P_s(\eta) = J_0(\lambda_s \eta), \quad J_0(\lambda_s) = 0, \\ k_s^2 \equiv 1 - M_s^2, \quad M_s^2 \equiv M_0^2 \lambda_s^2, \end{gathered} \tag{4c}$$

where $s = 1, 2, 3, \ldots$ is the wave index ($\lambda_1 = 2.405$).

For the analysis below it is important to note that the phase velocity of the wave of index s,

$$V_s(\omega) \equiv \frac{c}{\left[1 + \frac{\lambda_s^2 c^2}{(\omega_p^2 - \omega^2)a^2}\right]^{1/2}}\,, \tag{4d}$$

falls off with increasing frequency, from the constant value $V_s(0) \equiv c[1 + \lambda_s^2/\nu]^{-1/2}$ at $\omega \to 0$ [$\nu \equiv (\omega_p^2 a^2)/c^2$ is the Budker "instantaneous electron"], to zero at $\omega \to \omega p$. Phase velocities on the order of the velocity of light can be obtained in the low-frequency range ($\omega_p^2 \gg \omega^2 \gg \omega_{ce}\omega_{ci}$) only with a sufficiently large instantaneous plasma density ($\nu \gg \lambda_s^2$).

3. SLIGHTLY NONLINEAR PERIODIC WAVES

In general, the Mach number M_s for wave s is on the order of unity ($M_s \sim 1$), so that Eq. (3) contains no small parameter. We can thus find analytic solutions of (3) only for potential amplitudes which are not too large, in which case the solutions can be obtained by an appropriate modification of the Bogolyubov method (see also ref. 7). We expand the potential $\Phi(\xi, \eta)$ in a series in radial harmonics of the linear theory satisfying the boundary conditions at the axis and walls of the waveguide:

$$\Phi(\eta, \xi) = \sum_s P_s(\eta) Z_s(\xi), \tag{5}$$

where $Z_s(\xi)$ are the unknown amplitudes of these harmonics. Substituting (5) into (3), and integrating over η, we find for $Z_s(\xi)$ a complete system of coupled nonlinear differential equations:

$$\left(\frac{d^2}{d\xi^2} + k_s^2\right)Z_s(\xi) = f_s(\xi) \equiv \frac{1}{N_s}\int_0^1 \eta d\eta P_s(\eta) f(\xi, \eta), \tag{6}$$

$$f(\xi, \eta) \equiv \Phi(\xi, \eta) - R[\Phi(\eta, \xi)],$$

$$N_s \equiv \int_0^1 \eta d\eta P_s^2(\eta) = \frac{1}{2} J_1^2(\lambda_s).$$

Analysis of these equations shows that under the condition $|\Phi| \ll 1$ we can associate with each linear traveling wave of type (4) a slightly nonlinear wave

$$Z_s(\xi) = A_s \cos[K_s \xi + \psi_s] + \delta_s(\xi) A_s^2, \tag{7a}$$

whose spatial period $L_s \equiv 2\pi/K_s$ is governed unambiguously by the requirement that there be no secular terms in the driving force $f_s(\xi)$ of Eq. (6) for the amplitude of this wave. The amplitudes of the other radial harmonics of the field of this wave ($m \neq s$) are also unambiguously determined from the condition that there be no homogeneous (undriven) solutions of Eqs. (6) for their amplitudes $Z_m(\xi)$. Within terms quadratic in the amplitude A_s we can write the dispersion and field configuration for the wave of index s as

$$K_s^2 = k_s^2 + \mu_s A_s^2, \tag{7b}$$

$$\left.\begin{gathered} \delta_s(\xi) = \frac{3}{4}\frac{Q_{ss}^{(s)}}{4K_s^2 - k_s^2}\cos[2(K_s\xi + \psi_s)], \\ \mu_s \equiv -\frac{9}{8}\sum_{m=1}^{\infty} Q_{ss}^{(m)} Q_{ms}^{(s)} \frac{1}{k_m^2 - 4K_s^2} + \frac{3}{4}\frac{4\gamma^2+1}{\gamma^2} T_s < 0, \\ N_\gamma Q_{\alpha\beta}^{(\gamma)} \equiv \int_0^1 \eta d\eta P_\alpha(\eta) P_\beta(\eta) P_\gamma(\eta), \quad T_\alpha N_\alpha \equiv \int_0^1 P_\alpha^4(\eta)\eta d\eta, \end{gathered}\right\} \tag{7c}$$

where the constant component of the potential has been eliminated by means of quasineutrality condition (3a).

We see from (7b) that the phase velocity of the wave increases with increasing amplitude of the potential; this result, first found in ref. 2, has recently been verified experimentally.[8]

4. PERIODIC WAVES OF FINITE AMPLITUDE

It follows from Eqs. (7) that the nonlinear wave index s in general contains contributions from all the radial harmonics having different roots of the Bessel function. However, the condition for the applicability of these equations, $A_s^2 \ll k_s^2$, does not hold at low frequencies ($\omega \ll \omega_p$), where the phase velocity for wave s is approximately equal to $V_s(0)$. Here we have $k_s^2 \equiv 1 - M_s^2 \ll 1$, so that the iteration procedure used in the derivation of (7) turns out to be inapplicable even at $A_s \sim 1 - M_s^2 \ll 1$. Nevertheless, even in this case we can find an approximate analytic solution of system (6) by exploiting the smallness of the parameter $(1 - M_s^2)$.

We see from (7a) and (7b) that with $k_s^2 \ll 1$ the most important contribution to the right-hand sides of these equations comes from the terms corresponding to the field of the given radial harmonic. This means that under these conditions the dispersion and the field configuration for nonlinear wave s can be found directly from the nonlinear equation of system (6) for the amplitude of this harmonic, $Z_s(\xi)$:

$$Z_s'' - M_s^2 Z_s = \frac{1}{N_s}\int_0^1 \eta d\eta J_0(\lambda_s\eta)$$

$$\times\left\{1-\left[1-2\sum_{m=1}^{\infty} Z_m(\xi) J_0(\lambda_m\eta)\right]^{-1/2}\right\} - g_s; \qquad (8a)$$

$$g_s \equiv \frac{1}{N_s}\int_0^1 \eta d\eta G(\eta) J_0(\lambda_s\eta), \quad \beta^2 \ll 1,$$

where the amplitudes $Z_m(\xi)$ of the other radial field harmonics ($m \neq s$) are found from

$$-M_m^2 Z_m^{(s)}(\xi) = \frac{1}{N_m}\int_0^1 \eta d\eta J_0(\lambda_m\eta)\,\{1-[1-2J_0(\lambda_s\eta)\,Z_s(\xi)]^{-1/2}\} - g_m.$$

The Fourier amplitudes for the function $G(\eta)$, and thus the entire function, are determined unambiguously from quasineutrality condition (3a), which in this case becomes

$$\bar{Z}_m^{(s)} \equiv \int_{-L_s/2}^{+L_s/2} d\xi Z_m^{(s)}(\xi) = 0. \qquad (8b)$$

We have thus shown that in the case $1 - M_s^2 \ll 1$ we can use (8) to reduce the problem of finding the potential for wave s to the solution of the equation of motion for a particle having a coordinate $Z_s(\xi)$ in the field of the nonlinear electrostatic force:

$$F(Z_s) \equiv +M_s^2 Z_s + \frac{1}{N_s}\int_0^1 \eta d\eta J_0(\lambda_s\eta)$$

$$\times\left\{1-\left[1-2\sum_{m=1}^{\infty} Z_m(\xi) J_0(\lambda_m\xi)\right]^{-1/2}\right\} - g_s. \qquad (8c)$$

If the amplitude of this wave, A_s, is not too close to the maximum possible amplitude ($\Phi_{max} = 0.5$, $\beta^2 \ll 1$), then we can neglect the terms with $m \neq s$ in (8a) and (8c), according to (8b). We can then find an analytic expression for first integral (8a):

$$Z_s'^2 - M_s^2 Z_s^2 - \frac{2}{N_s}\int_0^1 \eta d\eta\,[\sqrt{1-2Z_s J_0(\lambda_s\eta)})$$

$$+ Z_s J_0(\lambda_s\eta)] + 2g_s Z_s = G_s \qquad (9)$$

We can thus find the function $Z_s(\xi)$ explicitly. Furthermore, from the known amplitude of this wave, $A_s \equiv \max \Phi(0, \xi)$, and its phase velocity $V_s \equiv (\omega_p a/\lambda_s) M_s$ we can calculate its frequency:

$$\left.\begin{aligned} \Omega_s(A_s) &\equiv K_s = \frac{2\pi}{L_s(A_s)}, \\ L_s(A_s) &\equiv 2\int_{a_s}^{A_s} dZ_s\,[Z_s'^2]^{-1/2}, \end{aligned}\right\} \qquad (10)$$

where $a_s(A_s)$ is the minimum potential in the given wave, determined from the condition $Z'_s(a_s) = 0$, where the constant g_s is eliminated by means of quasineutrality condition (3a).

These equations hold for arbitrary s, provided that the condition $1 - M_s^2 \ll 1$ is satisfied. We turn now to a more detailed analysis of the case of most applied interest – that of the first radial harmonic (s = 1). In this case, as we see from (8b), our neglect of the higher radial harmonics ($m \geq 2$) in (9) and (10) causes an error no larger than 10%, even for the case in which the amplitude of the potential is comparable to the maximum possible value [$A_1 \lessapprox (0.7\text{–}0.8)\Phi_{max}$]. If, on the other hand, this amplitude is slightly lower [$A_1 \lessapprox (0.5\text{–}0.6)\Phi_{max}$], the functions $Z_1'(\xi)$ and $\Omega_{NL}(A_1)$ can be found analytically. Expanding the integrand in (9) in a series in Z_1 and retaining the first nonlinear term, we find the function $(Z_1')^2(Z_1)$:

$$Z_1'^2 = (A_1 - Z_1)(Z_1 - a_1)[1 - M_1^2 + Q_{11}^{(1)}(Z_1 + A_1 + a_1)],$$

$$+ \quad Q_{11}^{(1)} \simeq 0.72, \qquad (11)$$

where the constants C_1 and g_1 are expressed in terms of the maximum and minimum wave potentials, A_1 and a_1, respectively.

Using Eq. (11a) and the quasineutrality condition

$$\int_{a_1}^{A_1} x dx\,\{(A_1 - x)(x - a_1)[1 - M_1^2 + Q_{11}^{(1)}(A_1 + a_1 + x)]\}^{-1/2} = 0, \qquad (11b)$$

which determines the function $a_1(A_1)$, we can also use analytic methods to analyze the behavior of the dispersion and field configuration of the period wave. In particular, at small amplitudes ($A_1 \ll 1 - M_1^2$) we find from these equations explicit equations for the minimum potential a_1 and the wave period Z_1:

$$a_1(A_1) = -A_1\left[1 - \frac{1}{2}\frac{Q_{11}^{(1)} A_1}{1 - M_1^2}\right], \qquad (12a)$$

$$L_1(A_1) = \frac{2\pi}{(1 - M_1^2)^{1/2}}\left[1 - \frac{3}{L\pi}\frac{(Q_{11}^{(1)} A_1)^2}{(1 - M_1^2)^2}\right]. \qquad (12b)$$

Accordingly, at small amplitudes of the potential and for a fixed wave phase velocity (M_1 = const), the spatial period of the wave decreases (the frequency increases) with increasing amplitude. If, on the other hand, the wave frequency is held constant (L_1 = const), an increase in the potential amplitude is accompanied by an increase in the velocity. With $A_1 \sim (1 - M_1^2)$, Eqs. (12) do not hold, so we must use numerical methods to calculate the shape of the wave potential and its phase velocity under these conditions. Figure 1 shows the frequency of the first radial harmonic (s = 1) as a function of the potential amplitude as calculated from Eqs. (9)–(11) and (3a). We see that the phase velocity continues to increase with increasing potential amplitude even at high potential amplitudes – but not so high that the condition allowing us to neglect the

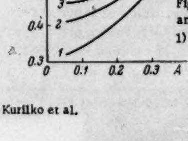

Fig. 1. Frequency as a function of the amplitude of the first harmonic M_1: 1) 0.95; 2) 0.9; 3) 0.85; 4) 0.8.

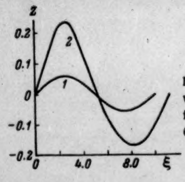

Fig. 2. Longitudinal profile of the wave potential at the waveguide axis for a fixed frequency, $\Omega = 0.5$. A_1: 1) $6 \cdot 10^{-2}$; 2) 0.24.

higher radial harmonics [$A_1 < (0.5\text{-}0.6)\Phi_{\max}$] breaks down. Furthermore, as the phase velocity decreases (or the Mach number M_1 decreases), and the potential amplitude increases, there is an increase in the nonlinearity of the dispersion (the derivative of the phase velocity with respect to amplitude at fixed frequency). The curves in Fig. 2 show the shape of the wave potential at the waveguide axis as a function of the wave amplitude at a fixed frequency.

5. CERENKOV EXCITATION OF A NONLINEAR PLASMA-FILLED WAVEGUIDE BY A PERIOD TRAIN OF CHARGED DISKS

The functional dependence of the phase velocity of the period wave on its amplitude, analyzed above, turns out to be important in the Cerenkov excitation of this wave by specified sources.[1)] Let us assume, for example, that a periodic train of thin charged disks carrying a charge density

$$\rho(r, z, t) = \sigma_0 J_0\left(\lambda_1 \frac{r}{a}\right) \sum_{s=1}^{N} \delta[z - V_0 t + (s-1) l] \tag{13}$$

is moving along the axis of a waveguide of the type considered here; here σ_0 is the amplitude of the surface charge density on each disk, $J_0(\lambda_1 \eta)$ is its functional dependence on the radius, and l is the repetition period of the disks.

The field configuration excited in the waveguide by such disks can be found from Eqs. (6)-(10) by setting $V = V_0$ ($1 - M_1^2 \ll 1$) and determining the integration constants from the boundary conditions at the disk surfaces:

$$\begin{gathered} Z_1[z = V_0 t - (s-1) l + 0] - Z_1[z = V_0 t - (s-1) l - 0] = 0; \\ Z_1'[z = V_0 t - (s-1) l + 0] - Z_1'[z = V_0 t - (s-1) l - 0] \\ = \varepsilon \equiv \frac{4\pi\sigma_0 |e|}{m_0 \omega_p V_0},\ Z_1(+\infty) = Z_1'(+\infty) = 0. \end{gathered} \tag{14}$$

If the charge on a disk is small ($\varepsilon \to 0$) and the functional dependence of the period of the excited wave on its amplitude can be neglected, each disk excited a wave at frequency Ω given by the dispersion relation $V^{(1)}(\Omega) = V_0$. If the repetition period of the disks, l, is equal to the wavelength of this wave, the Cerenkov fields of the disks combine coherently, so that the amplitude of the total field increases linearly with the disk index. It has been shown experimentally[11,12] and theoretically[4,12,13] that this effect is the basis of the collective Cerenkov interaction between charged-particle beams and plasmas. However, as the number of disks N increases, or the charge on each disk σ_0 increases, the condition for the applicability of the linear theory [$\varepsilon N \ll 1 - M_1^2(V_0) \ll 1$] is violated.

Because of the increase in the wavelength of the excited wave with increasing potential amplitude, the later disks begin to lag behind the maximum of the field excited by the earlier disks. As a result, the coherence of their radiation is disrupted, and the increase in the resultant field amplitude ends. The maximum number of coherently radiating disks, $N_{\max}$, can be evaluated from Eqs. (11)-(12). From the requirement that the nonlinear change in the wave period be small in comparison with the bunch repetition period $l = 2\pi(1 - M_1^2)^{1/2}$ we find

$$\left.\begin{aligned} N_{\max} &\sim \frac{1}{\varepsilon}(1 - M_1^2)^{3/2}, \\ E_{\max} &\simeq \sqrt{4\pi n_p m_0 V_0^2}\left(1 - \frac{\lambda_1^2 V_0^2}{\omega_p^2 a^2}\right)^{3/4} \ll 1. \end{aligned}\right\} \tag{15}$$

6. CERENKOV EXCITATION OF A NONLINEAR PLASMA (SELF-CONSISTENT APPROXIMATION)

The functional dependence of the dispersion characteristics of a plasma on the field amplitude can lead to a stabilization of two-stream instabilities, as a result of the violation of the condition for the efficient interaction of the wave with the beam particles, $\omega = kV_0$ (ref. 4). However, at relatively low beam energy densities this effect turns out to be weaker than the inverse effect of the field on the beam, which leads to a violation of this condition because of the change in the velocity of the beam particles. Accordingly, the plasma dispersion can be nonlinear only if the inverse effect of the field on the beam is negligible, as in the case of the Budker instability.[14,15] To see that this is so, we transform to the reference frame in which the beam electrons are at rest and in which the ions move, exciting longitudinal waves in the electronic background. In the simplest case of an unbounded beam the dispersion relation for these waves,

$$1 - \frac{\omega_-'^2}{\omega^2} - \frac{\omega_+'^2}{(\omega - kV_0')^2} = 0,\quad \omega_\pm'^2 \equiv \frac{4\pi^2 n_\pm'}{m_\pm'} \tag{16}$$

(the primes denote quantities referring to the rest system of the electrons), has growing solutions, for which the growth rate is

$$\delta' \equiv \omega_-'\left(\frac{n_+' m_-'}{n_-' m_+'}\right)^{1/3} \frac{\sqrt{3}}{2^{4/3}}.$$

The plasma nonlinearity becomes important at the field amplitude E_- at which the nonlinear frequency shift $\Delta\omega_- \sim \omega_-'(v_E^2/c^2)$ becomes comparable to the growth rate δ'. The inverse effect of the field on the ion beam becomes appreciable at the field amplitude E_+ at which the displacement of an ion during the characteristic time of the instability growth is comparable to the wavelength $\lambda_g' = V_0'/\omega_-'$. Comparing E_- and E_+, we find

$$\frac{E_+^2}{E_-^2} \simeq \frac{n_+' m_+' V_0'^2}{n_-' m_-' c^2}. \tag{17}$$

Accordingly, because of the large ratio of the ion mass to the electron mass, the nonlinearity of the dis-

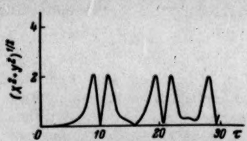

Fig. 3. Electron oscillation amplitude for the Budker instability as a function of the dimensionless time τ.

persion properties of the plasma becomes apparent much earlier than the inverse effect of the field on the beam, even for relatively low beam energies.

For a quantitative evaluation of the maximum amplitude of the field excited in this system it is convenient to use the method in which the kinetic equation is integrated in terms of Lagrange variables.[10,11,16] Since the instability is stabilized before the electron trajectories intersect, we find the following system of coupled nonlinear equations for the deviations $\Delta_{\pm}(t, z_0) \equiv Z_{\pm}(t, z_0) - V_{\pm}t - z_0$ of electrons and ions from the trajectories $Z_{\pm}^{(0)} \equiv z_0 + V_{\pm}t$ in the case of a monoenergetic beam without an interaction:

$$\left.\begin{aligned}\left\{\left(1-\frac{\Delta_-^2}{c^2}\right)^{-3/2}\frac{\partial^2}{\partial t^2}+\omega_-'^2\right\}\Delta_-(t,\ z_0)=\frac{n_+'}{n_-'}\Delta_+(t,\ z_0-V_0't),\\ \frac{\partial^2}{\partial t^2}\Delta_+(t,\ Z_0)=\frac{m_-'}{m_+'}\Delta_-(t,\ z_0+V_0t).\end{aligned}\right\}\quad(18)$$

In the linear approximation we find from this equation a complete system of coupled differential equations for the Fourier amplitudes $a_{\pm}(t) \equiv \Delta_{\pm}(t, z_0)\exp(-ikz_0)$ of the unknown displacements; the condition that there be no trivial solutions of this system yields dispersion relation (16) for the corresponding natural frequencies $[a_+(t) = a_-(t)\exp(-ikV_0t)]$. Exploiting the smallness of the growth rate ($\delta' \ll \omega_-'$), we can seek nonlinear solutions of system (18) by the Bogolyubov method:

$$\left.\begin{aligned}\Delta_-(t,\ z_0)=\mu\,[(x+iy)(\tau)]\exp[i(kz_0-\omega_0t)]+\text{c.c.},\\ \mu\equiv\left[\frac{2}{3}\left(\frac{n_+'m_-'}{2n_-'m_+'}\right)^{1/3}\right]^{1/2},\quad \tau\equiv\delta't,\ kV_0'\simeq\omega_0\simeq\omega_-'.\end{aligned}\right\}\quad(18a)$$

Then for the functions $x(\tau)$ and $y(\tau)$, which vary slowly with the time, we find a system of coupled, nonlinear, third-order equations not containing a small parameter:

$$\left.\begin{aligned}\dot{\bar{x}}+y=\frac{d^2}{d\tau^2}[(x^2+y^2)y],\\ \dot{\bar{y}}-x=\frac{d^2}{d\tau^2}[(x^2+y^2)x].\end{aligned}\right\}\quad(19)$$

Numerical solution of these equations shows that the change in amplitude which they describe is a periodic function of the time τ with a maximum amplitude on the order of two, and a characteristic period on the order of ten, times the reciprocal growth rate (Fig. 3). Hence we find the following expressions for the maximum oscillatory velocity of the electrons and for the field intensity:

$$\left.\begin{aligned}\left(\frac{v_E'^2}{c^2}\right)_{\max}\simeq\frac{8}{3}\left(\frac{\delta'}{\omega_-'}\right)\ll 1,\\ E_{\max}^2\simeq\frac{2^{5/3}}{3}16\pi\left(n_-'^2n_+'^2\frac{m_-'}{m_+'}\right)^{1/3}m_-'c^2.\end{aligned}\right.\quad(20)$$

The nonlinearity of the dispersion characteristics of the plasma can lead to a stabilization of the amplitude of the field excited by the beam, even in the case of an electron beam, provided that the beam energy is sufficiently high. For example, in an experiment involving the injection of a periodic train of electron bunches into a plasma resonator having a fixed spatial field configuration[12] (z = const), the increase in the field amplitude leads to a change in the natural frequency of the resonator, according to (12b). Accordingly, as the injection energy is raised, and the inverse effect of the field on the motion of the beam particles is weakened, the growth of the field amplitude reaches saturation as a result of the nonlinear phase drift of the field as time elapses. Figure 4 shows the energy of the periodic train of electron bunches at the exit from the resonator as a function of the bunch index N calculated for various injection energies and taking into account the nonlinear frequency shift $\Delta\Omega \equiv -\sigma A^2$ in Eqs. (6b) of ref. 12. We see that as the injection energy is raised the role of the nonlinear frequency shift in stabilizing the amplitude growth becomes more important.

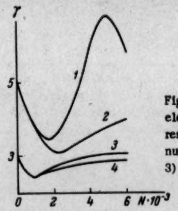

Fig. 4. Energy of the periodic train of electron bunches at the exit from the resonator as a function of the bunch number N. γ: 1, 2) 5; 3, 4) 3. α: 1, 3) 0.3; 2, 4) 0.

We can summarize the basic results of this analysis as follows:

1. We have analyzed the dispersion and field configuration of regular periodic waves of finite amplitude propagating along the axis of an anisotropic plasma-filled waveguide having conducting walls. We have shown that at low frequencies ($\omega < \omega_{pe}$) the field configuration and dispersion of these waves are governed primarily by only a single radial field harmonic – that describing that radial potential profile in the corresponding linear wave. The phase velocities of these waves and the nonlinearity of the dispersion increase monotonically with increasing amplitude of the potential.

2. We have analyzed the problem of the Cerenkov excitation of a nonlinear plasma-filled waveguide by a periodic train of charged disks, finding that the disruption of the coherence of the disk radiation due to the increase in the wavelength with increasing amplitude limits the role of this amplitude.

3. We have studied the effect of a nonlinearity of the plasma dispersion characteristics on the stabilization of the two-stream instabilities, finding that this mechanism limits the growth of the Budker instability. We have calculated the maximum amplitude of the Budker-instability field and the characteristic time required for its establishment. We have also shown that an analogous effect can have a decisive influence on the interaction of a modulated relativistic beam with a plasma resonator, especially at high energies of the injected beam.

We note in conclusion that we have restricted this analysis to the steady-state solutions of the original equations, (1)-(3), and we have not taken up the stability of these solutions.[17–19] Recent experiments at a high microwave power level[8] have shown that under certain conditions these regular waves are stable.

The authors thank M. A. Leontovich and B. B. Kadomtsev for discussion of these results.

[1)] Miroshnichenko[9] and Kurilko et al.[10] analyzed the polarization loss in a nonlinear plasma in this approximation.

---

[1] V. I. Veksler, Proceedings of the CERN Symposium, Vol. 1 (1956), p. 80; At. Energ., 2, 427 (1957).

[2] Ya. B. Fainberg, Proceedings of the CERN Symposium, Vol. 1 (1956), p. 84; At. Energ., 6, 431 (1959); Usp. Fiz. Nauk, 93, 617 (1967) [Sov. Phys.—Usp., 10, 750 (1968)].

[3] M. S. Rabinovich, Proceedings of the All-Union Conference on Accelerators (Moscow, 1968) [in Russian], Vol. 1, Izd. VINITI, Moscow (1970), p. 473.

[4] Ya. B. Fainberg, At. Energ., 11, 313 (1961).

[5] Ya. B. Fainberg, Survey of Phenomena in Ionized Gases (Vienna, 1967), IAEA, Vienna (1969), p. 149.

[6] V. I. Kurilko and A. P. Tols-toluzhskii, Symposium on Collective Acceleration Methods (Dubna, 1972) [in Russian], Izd. OIYaI, Dubna (1972), p. 111.

[7] A. V. Gaponov, L. A. Ostrovskii, and M. I. Rabinovich, Izv. Vuz., Radiofiz., 13, 163 (1970).

[8] A. M. Egorov, Ya. B. Fainberg, V. I. Kurilko, A. F. Kivshik, L. I. Bolotin, and A. F. Bats, At. Energ., 34, 181 (1973).

[9] V. I. Miroshnichenko, UZhF, 8, 1268 (1973); Zh. Tekh. Fiz., 34, 1537 (1964) [Sov. Phys.—Tech. Phys., 9, 1192 (1965)].

[10] V. I. Kurilko, A. P. Tols-toluzhskii, and Ya. B. Fainberg, Problems of Plasma Theory [in Russian], ITF Akad. Nauk SSSR, Kiev (1972), p. 245.

[11] I. F. Kharchenko, Ya. B. Fainberg, E. A. Kornilov, E. I. Lutsenko, and N. S. Pedenko, Zh. Eksp. Teor. Fiz., 38, 685 (1960) [Sov. Phys.—JETP, 11, 493 (1960)].

[12] A. K. Berezin, Ya. B. Fainberg, L.I. Bolotin, A. M. Egorov, V. A. Kiselev, V. A. Buts, V. I. Kurilko, and A. P. Tols-toluzhskii, Zh. Eksp. Teor. Fiz., 63, 861 (1972) [Sov. Phys.—JETP, 36, 453 (1973)].

[13] V. I. Kurilko, Zh. Eksp. Teor. Fiz., 57, 885 (1969) [Sov. Phys.—JETP, 30, 484 (1970); Dokl. Akad. Nauk SSSR, 208, 1059 (1973) [Sov. Phys.—Dokl., 18, 132 (1973)].

[14] G. I. Budker, At. Energ., 1, 9 (1957).

[15] O. Buneman, Phys. Rev. Lett., 1, 8 (1958); Phys. Rev., 115, 603 (1959).

[16] V. I. Kurilko, International Conference on Accelerators (Erevan, 1969) [in Russian], Vol. 2, Izd. Akad. Nauk ArmSSR, Erevan (1971), p. 498.

[17] V. N. Oraevskii and R. Z. Sagdeev, Zh. Tekh. Fiz., 32, 1291 (1962) [Sov. Phys.—Tech. Phys., 7, 955 (1963)].

[18] V. N. Oraevskii, Problems of Plasma Theory [in Russian], ITF Akad. Nauk UkrSSR, Kiev (1972), p. 219.

[19] V. P. Silin, Zh. Eksp. Teor. Fiz., 47, 2254 (1964) [Sov. Phys.—JETP, 20, 1510 (1965)]; Usp. Fiz. Nauk, 108, 625 (1972) [Sov. Phys.—Usp., 15, 742 (1973)].

Kinetic plasma instabilities excited by a monoenergetic beam

A. I. Ranyuk and V. L. Sizonenko

Physicotechnical Institute,
Academy of Sciences of the Ukrainian SSR, Khar'kov

(Submitted September 12, 1973)
Zh. Tekh. Fiz., 44, 995-997 (May 1974)

The solutions of the dispersion equation describing the excitation of kinetic branches in a beam–plasma system with a monoenergetic beam are investigated by numerical methods. Solutions for a wide range of wavelengths and plasma parameters are obtained.

It has been found in refs. 1-3 that, along with the well-known hydrodynamic instabilities, kinetic oscillation branches are also excited in a beam–plasma system in spite of the fact that the energy homogeneity condition for the beam is satisfied: $u/v_b \gg (n_p/n_b)^{1/3}$; where u is the directed velocity of the beam, v_b is the beam thermal velocity, and n_b and n_p are the densities of the beam and the plasma, respectively. These instabilities have a growth rate γ, whose magnitude is comparable to the maximum growth rate of the hydrodynamic modes. These are excited with either relativistic or nonrelativistic beams.

According to refs. 1-3, the pertinent dispersion equation is

$$z_0 - z + \eta\left[1 + i\sqrt{\pi}\, z w(z)\right] = 0, \tag{1}$$

where, in the case of a nonrelativistic beam.

$$z = \frac{\omega - \mathbf{k}\mathbf{u}}{\sqrt{2}\, k v_b}, \quad z_0 = \frac{-(\mathbf{k}\mathbf{u})}{2\sqrt{2}\, k v_b}\left[\frac{\omega_p^2}{(\mathbf{k}\mathbf{u})^2} - 1\right],$$

$$\eta = -\frac{\omega_b^2(\mathbf{k}\mathbf{u})}{(\sqrt{2}\, k v_b)^3}, \quad w(z) = e^{-z^2}\left(1 + \frac{2i}{\sqrt{\pi}}\int\limits_0^z e^{t^2} dt\right),$$

while, for a relativistic beam (and $z_0 = 0$),

$$z = \frac{\omega - \mathbf{k}\mathbf{u}}{\sqrt{2}\,\Gamma k' v_b}, \quad \eta = -\frac{\omega_b'^2(\mathbf{k}\mathbf{u})}{(\sqrt{2}\,\Gamma k v_b)^3}, \quad \Gamma = \sqrt{1 - \frac{u^2}{c^2}}.$$

Here, ω_p and ω_b are the plasma frequencies of the plasma and the beam, respectively, and ω and $\mathbf{k}$ are the frequency and the wave vector, respectively; the primed quantities pertain to the reference system in which the relativistic beam is at rest.

In addition to the beam–plasma instabilities, the dispersion equation (1) also holds for certain current-driven instabilities, where electrons move relative to ions with the velocity **u** (see ref. 4). In this case, as shown in ref. 4, for a nonmagnetized plasma

$$z_0 = -\frac{\mathbf{k}\mathbf{u}}{2\sqrt{2}\, k v_{Ti}}\left(\frac{\omega_{pe}^2}{(\mathbf{k}\mathbf{u})^2} - 1\right), \quad z = \frac{\omega}{\sqrt{2}\, k v_{Ti}}, \quad \eta = \frac{(\mathbf{k}\mathbf{u})\omega_{pi}^2}{(\sqrt{2}\, k v_{Ti})^3};$$

for a magnetoactive plasma with the current in the direction of the magnetic field the expressions for z and η are more cumbersome and are, therefore, not given here. Here, $\omega_{p\alpha}$ is the plasma frequency for species α (e, i), and v_{Ti} is the ion thermal velocity.

The dispersion equation (1) has been investigated analytically in refs. 1-4 for large and small values of η. It is also interesting to solve this equation for arbitrary values $\eta \sim 1$ and $z_0 \sim 1$, since the phase velocities of unstable modes are then comparable to the thermal velocities of particles ($z \sim 1$).

We have determined the roots of Eq. (1) numerically, using the M-220 and M-222 computers and the calculation method described in refs. 5 and 6.

The transient solutions of Eq. (1) are given in Figs. 1-3 as curves of the functions x and y, where $x \equiv \mathrm{Re}\, z$ and $y \equiv \mathrm{Im}\, z$.

Equation (1) has also damped solutions, which are shown in Fig. 4. Figure 5 shows both the growing and damped solutions for $\eta = 0.7$.

The numerical results are checked by using the analytical solutions x and y for small and large values of η.

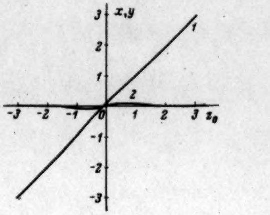

Fig. 1. Dependences of x (curve 1) and y (curve 2) on z_0 for $\eta = 0.1$.

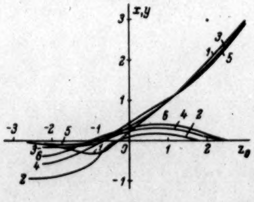

Fig. 2. 1, 3, and 5) x; 2, 4, and 6) y. 1 and 2) $\eta = 0.3$; 3 and 4) $\eta = 0.7$; 5 and 6) $\eta = 1$.

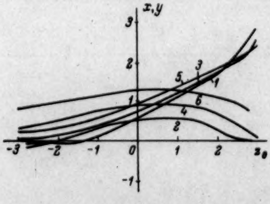

Fig. 3. 1, 3, and 5) x; 2, 4, and 6) y. 1 and 2) $\eta = 2$; 3 and 4) $\eta = 5$; 5 and 6) $\eta = 10$.

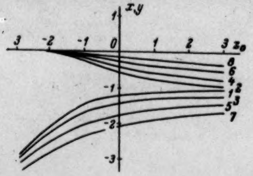

Fig. 4. 1, 3, 5, and 7) x; 2, 4, 6, and 8) y. 1 and 2) $\eta = 1$; 3 and 4) $\eta = 2$; 5 and 6) $\eta = 5$; 7 and 8) $\eta = 10$.

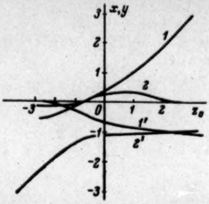

Fig. 5. Solutions for $\eta = 0.7$. 1) x; 2) y (increasing solution); 1', and 2') x and y, respectively (damped solution).

Putting $z_0 = 0$ and $\eta \ll 1$, we obtain

$$z = \eta + i\sqrt{\pi}\,\eta^2.$$

This expression describes the solutions obtained numerically for $\eta = 0.1$ and $\eta = 0.3$.

Assuming that $\eta \gg 1$, $|z_0| = 0$, and $|z| \gg 1$, we obtain the following equation instead of (1):

$$z^3 + \frac{\eta}{2} = 0, \tag{2}$$

which yields the transient solution

$$z = \frac{1 + i\sqrt{3}}{2}\left(\frac{\eta}{2}\right)^{1/3}. \tag{3}$$

For $\eta = 10$, we obtain $x \simeq 0.86$ and $y \simeq 1.46$. It should be noted that solution (3) for $\eta = 10$ is in good agreement with the data given in Fig. 4, although, strictly speaking, the asymptotic behavior of $|z| \gg 1$, for $\eta = 10$ cannot be utilized.

Thus it has been shown that, for $z_0 \sim 1$ and $\eta \sim 1$, Eq. (1) does have transient solutions with Re z ~ Im z ~ 1.

---

[1] V. L. Sizonenko and K. N. Stepanov, Izv. Vuzov. Radiofizika, 15, 144 (1972).

[2] V. I. Pakhomov, V. L. Sizonenko, and K. N. Stepanov, All-Union Conference on Plasma Theory, Kiev, October 19-23, 1971.

[3] V. I. Pakhomov and V. L. Sizonenko, Zh. Tekh. Fiz., 42, 1088 (1972) [Sov. Phys. – Tech. Phys., 17, 866 (1972)].

[4] V. L. Sizonenko and K. N. Stepanov, Zh. Tekh. Fiz., 42, 484 (1972) [Sov. Phys. – Tech. Phys., 17, 385 (1972)].

[5] B. P. Demidovich and I. A. Moron, Fundamentals of Computational Mathematics [in Russian], Fizmatgiz, Moscow (1960).

[6] B. P. Demidovich, I. A. Moron, and É. Z. Shuvalova, Numerical Methods of Analysis [in Russian], Fizmatgiz, Moscow (1962).

Quasilinear theory of beam-generated surface waves in a plasma

V. I. Pakhomov and V. L. Sizonenko

(Submitted May 16, 1973; resubmitted August 13, 1973)
Zh. Tekh. Fiz., 44, 998-1005 (May 1974)

A system of quasilinear equations is obtained that describes the interaction of a beam of charged particles with electrostatic surface waves in a semiinfinite magnetoactive plasma. The quasilinear integral and the spectrum in the final stage are found.

1. INTRODUCTION

Investigations of the interaction of beams of charged particles with surface waves in the linear approximation have been reported in many papers.[1,2] If the beam density is low and the velocity spread of the beam particles is large the quasilinear approximation,[3] which takes account of the reaction of the waves on the distribution function of the beam particles, can be used to investigate the nonlinear stage of the interaction of the beam with the surface waves.

In this case the quasilinear relaxation of the beam has certain distinctive features due to the exponential reduction of the amplitude of the surface wave as a function of distance from the boundary. Thus the diffusion coefficient of particles in velocity space, which is proportional to the wave energy, will also decrease exponentially with the distance from the boundary. Consequently in the quasilinear relaxation process a beam which is initially homogeneous in ordinary space becomes inhomogeneous. This feature must be taken into account even in the linear theory, i.e., an inhomogeneous beam must be considered in obtaining the expression for the linear growth rate of surface waves.

In general the quasilinear relaxation of a beam interacting with surface waves is a very complex process. A beam moving parallel to the boundary excites waves with a large range of phase velocities. This feature and the inhomogeneity of the beam and the nonuniformity of the field of the excited waves are attributable essentially to the multidimensional character of the quasilinear relaxation process. The relaxation of the beam is accompanied by the diffusion of particles in velocity space and in ordinary space. It is known[4] that in the simpler case of an unbounded homogeneous beam moving in an isotropic plasma, the three-dimensional quasilinear relaxation of the beam cannot be described analytically.

We treat here the simplest one-dimensional quasilinear relaxation of a beam interacting with high-frequency electrostatic surface waves in a semiinfinite plasma ($y < 0$). The beam moves outside the plasma ($y > 0$) along the z axis, which is directed along a uniform external magnetic field $\mathbf{H}_0$ which fills all space. The beam density n_0 and the beam velocity v_0 are assumed to be arbitrary functions of the y coordinate. The beam particles have a certain spread in longitudinal velocity.1) The value of the spread can also depend on the distance from the boundary. We consider surface waves that propagate along the magnetic field and the reaction of the waves on the average distribution function of the beam particles. The fact that these waves are most strongly excited by the beam justifies the use of a "one-dimensional" model.

We derive a set of quasilinear equations, find the "quasilinear" integral, and determine the intensity of the surface waves in the final stage.

2. LINEAR GROWTH RATE OF EXCITED SURFACE WAVES

The initial equations of the problem are the kinetic equation

$$\frac{\partial F}{\partial t}+\mathbf{v}\frac{\partial F}{\partial \mathbf{r}}+\frac{e}{m}\left(\nabla\psi-\frac{[\mathbf{v}\mathbf{H}_0]}{c}\right)\frac{\partial F}{\partial \mathbf{v}}=0 \tag{1}$$

and Poisson's equation

$$\Delta\psi=4\pi e\left(\int F d\mathbf{v}-n\right). \tag{2}$$

Equations (1) and (2) describe both the plasma ($y < 0$) and the beam ($y > 0$). We consider high-frequency waves and neglect the effect of beam and plasma ions.

We assume that in the initial state the particles have only a longitudinal velocity component [$\mathbf{v} = (0, 0, v)$] and that the beam and plasma are inhomogeneous in the direction of the normal to the boundary (the y axis).

Assuming that the perturbations are small,

$$F=F_0+F', \quad |F'|\ll F_0,$$

linearizing the kinetic equation, and considering plane waves $\exp i(kz - \omega t)$ propagating in the direction of the external magnetic field $\mathbf{H}_0$, we find the correction to the distribution function

$$f=\int F' v_\perp dv_\perp d\varphi$$
$$=\frac{e}{m}\left\{\frac{k\psi}{\omega-kv}\frac{\partial f_0}{\partial v}-\frac{1}{2\omega_H}\frac{\partial}{\partial y}\left[\left(\frac{1}{\omega-kv+\omega_H}-\frac{1}{\omega-kv-\omega_H}\right)f_0\frac{\partial\psi}{\partial y}\right]\right\}, \tag{3}$$

where $f_0 = f_0(y, v)$, $\omega_H = e\mathbf{H}_0/mc > 0$ is the electron cyclotron frequency, and φ is the azimuthal angle in velocity space.

Using (3) we write Poisson's equation in the form

$$\frac{d}{dy}\left(\varepsilon_1\frac{d\psi}{dy}\right)-k^2\varepsilon_3\psi=0, \tag{4}$$

where

$$\varepsilon_1=1+A_1(y), \quad A_1=\frac{2\pi e^2}{m\omega_H}(I_+-I_-), \quad I_\pm=\int_{-\infty}^{\infty}\frac{f_0 dv}{\omega-kv\pm\omega_H},$$

$$\varepsilon_3=1+A_2(y)\equiv 1+\frac{4\pi e^2}{mk}\int_{-\infty}^{\infty}\frac{\frac{\partial f_0}{\partial v}}{\omega-kv}dv. \tag{5}$$

We obtain the dispersion equation from the matching condition for the solutions of Eq. (4) and $\varepsilon_1(d\psi/dy)$ for the beam and plasma at the boundary y = 0.

Assuming that the plasma is cold and uniform, from (5) we have

$$\varepsilon_1 = 1 - \frac{\omega_p^2}{\omega^2 - \omega_H^2}, \quad \varepsilon_3 = 1 - \frac{\omega_p^2}{\omega^2}, \quad \left(\omega_p^2 = \frac{4\pi e^2 n_p}{m}\right); \tag{6}$$

consequently the solution of Eq. (4) for a surface wave in the region occupied by the plasma (y < 0) has the form

$$\psi = C_- e^{\varkappa y}, \quad \left(\varkappa = k\sqrt{\frac{\varepsilon_3}{\varepsilon_1}} > 0\right). \tag{7}$$

It follows from (7) that the condition for the existence of a surface wave in the plasma is $\varepsilon_3/\varepsilon_1 > 0$.

It is impossible to obtain an analytic solution of Eq. (4) in the region of the inhomogeneous beam (y > 0) in the general case. However, when the beam density n_b is small in comparison with the plasma density n_p the method of successive approximations[1,7] can be used to solve Eq. (4). In our problem the assumption $n_b \ll n_p$ is unavoidable since the quasilinear approximation can only be used to investigate a system with a small growth rate. For $n_b \ll n_p$ the field of a surface wave in the region y > 0 will differ only slightly from the vacuum field described by the function exp(− ky). Without going into the calculations we present the dispersion relation for surface waves on the plane boundary between the uniform cold plasma and an inhomogeneous hot beam of low density

$$\varepsilon_1\varkappa + k = -k\int_0^\infty (A_1 + A_2)\, e^{-2ky}dy, \tag{8}$$

where A_1 and A_2 are given by (5) and refer to the beam.

In the absence of a beam ($A_1 = A_2 = 0$) Eq. (8) takes the form

$$\varepsilon_1\varkappa + k = 0. \tag{9}$$

From (9) we find the frequency of the electrostatic surface waves on the plane plasma−vacuum boundary:

$$\omega_0 = \sqrt{\frac{\omega_p^2 + \omega_H^2}{2}}. \tag{10}$$

The solution (10) exists for $\omega_p > \omega_H$.

An inhomogeneous low-density beam excites surface waves with the frequency (10). For a sufficiently large thermal spread of the longitudinal velocities of the beam particles, we find the following expression for the growth rate $\gamma(\omega = \omega_0 + i\gamma)$ from (18):

$$\gamma = \frac{\pi\omega_0(\omega_p^2 - \omega_H^2)}{4kn_p\omega_H}\left\{\frac{\omega_H}{k}\left\langle\frac{\partial f_0}{\partial v}\right\rangle\Big|_{v=\frac{\omega_0}{k}} + \frac{1}{2}\left(\langle f_0\rangle\Big|_{v=\frac{\omega_0+\omega_H}{k}} - \langle f_0\rangle\Big|_{v=\frac{\omega_0-\omega_H}{k}}\right)\right\}, \tag{11}$$

where

$$\langle f_0\rangle = 2k\int_0^\infty f_0 e^{-2ky}dy. \tag{12}$$

Three groups of resonance particles of the beam contribute to the growth (or damping) rate (11) of surface waves with a given wave vector k, or a given phase velocity ω_0/k: 1) particles in Cerenkov resonance with the wave; their velocity coincides with the phase velocity of the wave; 2) particles in cyclotron resonance with the wave under conditions of the anomalous Doppler effect; their velocity is higher than the phase velocity of the wave; 3) particles in cyclotron resonance with the wave under conditions of the normal Doppler effect; their velocity is lower than the phase velocity of the wave.

We consider a beam with a small velocity spread v_T ($v_T \ll v_0$). Through the Cerenkov mechanism such a beam will excite waves with a range of phase velocities $\Delta v_p \sim v_T$ immediately below the value of $v_0 (v_p < v_0)$. If $\omega_p \gg \omega_H$, $\omega_0 \sim \omega_p \sim \omega_H$. In this case beam particles from the tail of the distribution, whose velocities differ from v_0 by amounts of the order of $v_0 \gg v_T$, will be in cyclotron resonance with waves having phase velocities in the range Δv_p. Their contribution can be neglected.

Through the cyclotron mechanism the bulk of the beam particles will excite waves in the range $\Delta v_p' \sim v_T$ lying to the left of v_0 by an amount of the order of v_0; the beam particles must be "superluminal". Also through the cyclotron mechanism, under conditions of the normal Doppler effect, the beam particles with thermal velocities will damp out waves from the range of phase velocities $\Delta v_p'' \sim v_T$ lying to the right of v_0 by an amount of the order of v_0. The growth (or damping) rate due to the cyclotron mechanism is of the order of magnitude of v_0/v_T times smaller than that due to the Cerenkov mechanism.

The preceding discussion shows that when the velocity spread of the beam particles is small ($v_T \ll v_0$) and the relation $\omega_p \gg \omega_H$ holds for the plasma, all three particle−wave interaction mechanisms can be considered separately, with the Cerenkov interaction playing the leading role. We consider this case in the investigation of the quasilinear relaxation of the beam presented below.

For an increase in the plasma density or a decrease in the external magnetic field the intervals between Δv_p, $\Delta v_p'$, and $\Delta v_p''$ are decreased, and for $\omega_p/\omega_H \sim v_0/v_T \gg 1$ these intervals are of order v_T and the spectra overlap. In this case all three mechanisms can make approximately equal contributions to the growth rate.

When the velocity spread of the beam particles is large ($v_T \sim v_0$) it is necessary to take account of all three interaction mechanisms.

We note that the expression for γ does not contain spatial derivatives of the distribution function of the beam particles since the waves propagate along the beam velocity v_0. These derivatives appear for oblique wave propagation.

The contributions of the separate parts of the beam to the growth rate (11) depend on how far these particles are from the boundary. This fact appears explicitly in the averaging with an appropriate weight in (12). The fact that the growth rate is a spatial integral of a quantity is a characteristic feature of the problem under consideration.

3. QUASILINEAR RELAXATION OF THE BEAM

We continue the investigation of the problem posed in the quasilinear approximation, i.e., we take account of the effect of the excited waves on the distribution function of the beam particles in the first nonvanishing approximation in the wave energy.

It is known[3] that the quasilinear approximation can be used to investigate the instabilities of beam systems when the growth rate γ is appreciably smaller than kv_T and the frequency ω. From Eq. (11) we obtain the condition

$$\left(\frac{v_T}{v_0}\right)^3 \gg \frac{n_b}{n_p}. \tag{13}$$

We assume that the conditions $v_T \ll v_0$ and $\omega_p \gg \omega_H$ are satisfied. Then, as noted above, we need take account only of the Cerenkov interaction of the particles with the waves, i.e., in Eq. (11) for the growth rate we take account only of the first term on the right-hand side.

In the usual way we represent the rapidly oscillating part of the distribution function and the field of the excited waves by a superposition of plane waves $\exp i(kz - \omega_k t)$ with random phases. The amplitudes of these waves are related by the linear theory, equation (3). In the case under consideration only the first term on the right-hand side of (3) need be taken into account. We obtain the equation for the slowly varying distribution function of the beam particles by averaging the kinetic equation over the fast oscillations. Since only the Cerenkov interaction is taken into account the particle velocity v is uniquely determined by the wave vector $k = \omega_0/v$.

As a result we obtain the one-dimensional diffusion equation

$$\frac{\partial f_0(y,\ v,\ t)}{\partial t} = \frac{\partial}{\partial v} D \frac{\partial f_0(y,\ v,\ t)}{\partial v}, \tag{14}$$

where the diffusion coefficient D is given by

$$D = \frac{8\pi^2 e^2}{m^2} \frac{W(y,\ v,\ t)}{v}. \tag{15}$$

If f_0 varies slowly with the time, the spectral energy density of the electrostatic surface oscillations $W = k^2|\psi|^2 \cdot (4\pi)^{-1}$ varies according to the equation

$$\frac{\partial W(y,\ v,\ t)}{\partial t} = 2\gamma(v,\ t)\, W(y,\ v,\ t), \tag{16}$$

where γ is given by the linear theory equation

$$\gamma(v,\ t) = \frac{\pi}{4} \frac{\omega_p^2 - \omega_H^2}{\omega_0} \frac{v^2}{n_p} \left\langle \frac{\partial f_0(y,\ v,\ t)}{\partial v} \right\rangle, \tag{17}$$

in which the distribution function averaged over the fast waves must appear instead of the initial distribution function.

The quantity $W(y,\ k,\ t)dk = W(y,\ v,\ t)(\omega_0/v^2)dv$ is the energy density of the electrostatic surface waves whose phase velocity lies between v and v + dv at a distance y from the boundary on the beam side. Integrating over all v we obtain the volume energy density of the oscillations. The dependence of W on y is given by

$$W(y,\ v,\ t) = W(y=0,\ v,\ t)\, e^{-2\frac{\omega_0}{v}y}. \tag{18}$$

The system of equations (14)-(17) describes the quasilinear relaxation of the beam interacting with the surface waves. The distribution function of the beam particles is "eroded" on the low velocity side. Since collisions are not taken into account the beam must relax to a plateau state.

A characteristic feature of the quasilinear relaxation of a beam exciting surface waves is the spatial nonuniformity of the relaxation process. Clearly at a certain instant in the quasilinear relaxation process the degree of "erosion" of the beam particle distribution function will decrease with the distance from the boundary. For example, an initially spatially homogeneous beam develops a certain profile of the average velocity during the relaxation process, with v_0 increasing with the distance from the boundary. Subsequently, as the plateau state is established, the directed velocity profile disappears, starting from the boundary.

Equations (14)-(17) describe the simplest form of the quasilinear relaxation of a beam exciting surface waves. In the case considered there is neither heating of the beam in the transverse direction, nor diffusion of particles in ordinary space. The interdependence of the relaxation of layers of the beam at various distances from the boundary is contained only in the averaging of γ over y (Eq. 12).

The system of quasilinear equations (14)-(17) has a time integral. From these equations there follows the relation

$$\frac{\partial f_0}{\partial t} = \frac{16\pi e^2 n_p}{m^2} \frac{\omega_0}{\omega_p^2 - \omega_H^2} \frac{\partial}{\partial v}\left[\frac{1}{v^3} \frac{\partial W(y,\ v,\ t)}{\partial t} \frac{\dfrac{\partial f_0}{\partial v}}{\left\langle \dfrac{\partial t_0}{\partial v} \right\rangle}\right]. \tag{19}$$

Integrating (19) with respect to y from zero to infinity and using (18) we obtain

$$\frac{\partial}{\partial t}\left\{\int_0^\infty f_0 dy - \frac{2\omega_p^2}{m(\omega_p^2 - \omega_H^2)} \frac{\partial}{\partial v}\left[\frac{W(y=0,\ v,\ t)}{v^2}\right]\right\} = 0. \tag{20}$$

Thus the quantity in braces in (20) is conserved in the quasilinear relaxation of the beam.

We make the usual assumption that at zero time the fluctuations of the surface oscillations are thermal and that their energy can be neglected in comparison with the beam energy, i.e., we assume that W(y = 0, v, t = 0) = 0. Then, from (20)

$$\frac{\partial}{\partial v}\left[\frac{W(y=0,\ v,\ t)}{v^2}\right] = \frac{m(\omega_p^2 - \omega_H^2)}{4\omega_p^2} \int_0^\infty [f_0(y,\ v,\ t) - f_0(y,\ v,\ t=0)]\, dy. \tag{21}$$

Since $v_T \ll v_0$ we can set

$$f_0(y, v, t=0) = n_b(y)\,\delta(v - v_0). \tag{22}$$

Assume that the quasilinear relaxation is terminated in time $t = t_R$, i.e., the plateau on the distribution function has been established for any y. Then

$$f_0(y, v, t_R) = \begin{cases} \dfrac{n_b(y)}{v_0}, & 0 < v < v_0; \\ 0, & v > v_0. \end{cases} \tag{23}$$

For simplicity we assume that v_0 does not depend on y. It is clear that if $n_b(y)$ is finite as $y \to \infty$, $t_R = \infty$.

Substituting (22) and (23) into (21) and integrating with respect to v from 0 to v_0, we find the spectral energy density of the electrostatic waves at the boundary y = 0 in the final state:

$$W(y=0, v, t_R) = \begin{cases} \dfrac{m(\omega_p^2 - \omega_H^2)}{2\omega_p^2}\dfrac{v^3}{v_0}\displaystyle\int_0^\infty n_b(y)\,dy, & 0 < v < v_0; \\ 0 & v > v_0. \end{cases} \tag{24}$$

The quantity $W(y = 0, v, t_R)$ does not change if the beam is at various distances from the boundary; as this distance is increased, only the time t_R to establish a stationary state is increased.

Multiplying (24) by $\exp[-2(\omega_0/v)y](\omega_0/v^2)$ and integrating with respect to v from 0 to v_0 and with respect to y from 0 to ∞, we obtain the total energy U_b of the electrostatic waves in the final state contained in a semiinfinite ($y > 0$) column with unit cross-sectional area:

$$U_b = \frac{1}{6}\frac{\omega_p^2 - \omega_H^2}{\omega_p^2} U_0, \tag{25}$$

where $U_0 = (mv_0^2/2)\int\limits_0^\infty n_b(y)dy$ is the initial kinetic energy of the beam in that column.

It is not difficult to calculate the energy U of the electric field contained in a similar column on the plasma side ($y < 0$). Taking account of the fact that the ratio of the energy density of the field in the plasma (at $y = -0$) to the energy density of the field in the beam (at $y = +0$) is $(\varepsilon_1 + \varepsilon_3)/2\varepsilon_1$, and also the fact that the damping rate of the field of the surface wave in the plasma is $\sqrt{\varepsilon_1/\varepsilon_3} = (\omega_p^2 + \omega_H^2)/(\omega_p^2 - \omega_H^2)$ times larger than in the beam region, we obtain

$$U_p = \frac{1}{6}\frac{\omega_p^4 + \omega_H^4}{\omega_p^2(\omega_p^2 + \omega_H^2)} U_0. \tag{26}$$

The total energy contained in the electric field in the final state is therefore

$$U = U_b + U_p = \frac{1}{3}\frac{\omega_p^2}{\omega_p^2 + \omega_H^2} U_0. \tag{27}$$

In the final state 1/3 of the initial energy remains in the beam and 2/3 has been transformed into waves. Using this fact we find the wave energy U_k of the plasma particles in the final state:

$$U_k = \frac{2}{3}U_0 - \frac{1}{3}\frac{\omega_p^2}{\omega_p^2 + \omega_H^2}U_0 = \frac{1}{3}\frac{\omega_p^2 + 2\omega_H^2}{\omega_p^2 + \omega_H^2}U_0. \tag{28}$$

The value of $(U_p + U_k)$ can be obtained by using the familiar expression for the average electrostatic energy density in a plasma:

$$\bar{U} = \frac{d(\omega\varepsilon_{\alpha\beta})}{d\omega}\frac{E_\alpha^* E_\beta}{16\pi}. \tag{29}$$

The problem of the dynamics of the one-dimensional quasilinear relaxation of a beam is solved in ref. 8. The solution is obtained by using the small parameter representing the ratio of the energy density of thermal fluctuations U_T to the energy density of oscillations in the final state U_∞. The solution for the distribution function of the beam electrons is a step function, describing the process when the boundary of the relaxation region moves slowly toward lower velocities, and the plateau state has time to be established to the right of the boundary.

We are unable to obtain an analogous solution for our problem. One can expect, however, that the relaxation process goes on in a similar way in beam layers near the boundary. It is clear that the velocity of the boundary of the relaxation region must decrease with distance from the boundary. At large distances from the boundary the ratio U_T/U_∞ ceases to be small and the step function solution is not realized.

It was indicated above that the beam particles excite surface waves with phase velocities in the range $v_p \lessgtr v_0 - (\omega_H/\omega_0)v_0$ by the cyclotron mechanism. When the boundary of the relaxation region reaches these velocities, it is necessary to account for the cyclotron interaction of particles with waves under conditions of the anomalous Doppler effect in the quasilinear equations. Instead of using Eq. (17) for the growth rate it is necessary to use the expression

$$\gamma(v, t) = \frac{\pi}{4}\frac{\omega_p^2 - \omega_H^2}{\omega_H}\frac{v}{n_p}\left[\frac{\omega_H}{\omega_0}v\left\langle\frac{\partial f_0(v, t)}{\partial v}\right\rangle + \frac{1}{2}\left\langle f_0\left(v + \frac{\omega_H}{\omega_0}v, t\right)\right\rangle\right]. \tag{30}$$

The term

$$\frac{1}{\omega_H}\frac{\partial}{\partial v}D\left(\frac{\partial f_0}{\partial y} - \frac{\omega_0 + \omega_H}{v}f_0\right).$$

must be added to the right-hand side of the diffusion equation (14).

Taking account of the cyclotron interaction in the quasilinear approximation leads to the motion of the beam as a whole. When the Cerenkov excitation of waves causes the sharp boundary of the relaxation region to move at a velocity which necessitates taking account of the cyclotron excitation of waves, the diffusion coefficient is obviously increased. In this case the conditions for the existence of a step function solution can be violated.

The authors are grateful to K. N. Stepanov for discussion.

---

[1] The quasilinear relaxation of a monoenergetic beam in a plasma waveguide is treated in refs. 5 and 6.

---

[1] V. I. Pakhomov and K. N. Stepanov, Zh. Tekh. Fiz., 38, 796 (1968) [Sov. Phys.-Tech. Phys., 13, 599 (1968)].

[2] N. M. El-Siragy and V. I. Pakhomov, Plasma Physics, 11, 707 (1969).

[3] A. A. Vedenov, E. P. Velikhov, and P. Z. Sagdeev, Yadernyi Sintez, 1, 82 (1962).

[4] A. A. Vedenov and D. D. Ryutov, in: Problems of Plasma Theory, Vol. 6 [in Russian], Gosatomizdat, Moscow (1972).

[5] B. I. Aronov, A. A. Rukhadze, and M. E. Chogovadze, Zh. Tekh. Fiz., 42, 1097 (1972) [Sov. Phys.-Tech. Phys., 17, 877 (1972)].

[6] M. E. Chogovadze, Zh. Tekh. Fiz., 42, 2022 (1972) [Sov. Phys.-Tech. Phys., 17, 1620 (1973)].

[7] A. B. Mikhailovskii, Zh. Eksp. Teor. Fiz., 48, 380 (1965) [Sov. Phys.-JETP, 21, 250 (1965)].

[8] A. A. Ivanov and L. I. Rudakov, Zh. Eksp. Teor. Fiz., 51, 1522 (1966) [Sov. Phys.-JETP, 24, 1027 (1967)].

Instabilities in a finite-β plasma with transverse current. I

A. I. Pyatak and V. L. Sizonenko

(Submitted July 30, 1973)
Zh. Tekh. Fiz., 44, 1006-1013 (May 1974)

We consider a plasma with current that flows at right angles to the confining magnetic field; the high-frequency small-scale instabilities that propagate with a phase velocity along the magnetic field that is appreciably lower than the electron thermal velocity are analyzed. Allowance is made for inhomogeneity of the magnetic field. The instabilities are electromagnetic; frequencies and growth rates are determined.

1. INTRODUCTION

Interest in the stability of a plasma with a current that flows at right angles to an external magnetic field arises from the important role that related instabilities play in plasma containment, turbulent heating and anomalous resistance, and radiation from a plasma. Such instabilities can develop in theta pinches, in shock waves, in various kinds of plasma injectors, in plasmoids that enter an inhomogeneous magnetic field, when ion cyclotron and fast magnetoacoustic waves of large amplitude are excited in a plasma, and in other cases.

At the present time the excitation of high-frequency ($\omega \gg \omega_{Hi}$) electrostatic instabilities in a low-pressure plasma [$\beta = 4\pi n_0(T_e + T_i)/H_0^2 \ll 1$] has been investigated fairly fully. The existence of various instabilities has been established; these include the Bernstein modes ($\omega \equiv n\omega_{He}$, $\gamma \gg \sqrt{\omega_{He}\omega_{Hi}}$), which propagate precisely at right angles to the magnetic field,[1] and various instabilities ($\omega < \omega_{He}$, $\gamma \sim \sqrt{\omega_{He}\omega_{Hi}}$) which propagate almost at right angles to the magnetic field.[2-6]

The conjecture that Bernstein modes can play an important role in the structure of a shock front calls for a detailed study of the excitation of these instabilities in a finite-pressure plasma[7,8] ($\beta \sim 1$). At the same time, in a number of experimental situations the Bernstein modes play a secondary role. It is of interest to investigate the influence of the effects that the finite pressure has on the excitation of these current-driven instabilities. As is shown in ref. 9, allowance for a small but finite pressure leads to the appearance of electromagnetic branches with a growth rate $\gamma \sim \sqrt{\omega_{He}\omega_{Hi}\beta}$. In ref. 10, a study is made of the influence of a finite pressure on the development of electron acoustic and drift instabilities in a plasma with hot ions and cold electrons.

In the present paper we investigate the excitation of high-frequency ($\omega_{Hi} \ll \omega$, $\gamma \ll \omega_{He}$) short-wave ($kv_{Ti} \gg \omega_{Hi}$) oscillations in a finite-β plasma ($\beta \sim 1$) with transverse current. It is assumed that the current velocity u is appreciably greater than the drift velocities due to the inhomogeneity of the density and temperature of the plasma, so that terms $\sim \nabla n_0$, ∇T in the dispersion equation can be ignored. At the same time terms associated with the particle drift due to inhomogeneity of the magnetic field are retained and make an important contribution to the dispersion equation..

In Sec. 1 of this paper we study the excitation of oscillations whose phase velocities along the magnetic field are less than the electron thermal velocity ($\omega/k_{\parallel}v_{Te} \lesssim 1$). Such waves propagate at an angle θ to the magnetic field that is not too near $\pi/2$, so that $\cos\theta \gtrsim u/v_{Te}$. We show that in a hot electron plasma ($T_e \gg T_i$) the most rapidly growing modes are those with $\cos\theta \sim u/v_{Te}$, whose growth rate is approximately

$$\gamma \sim \sqrt{\omega_{He}\omega_{Hi}}. \qquad (1.1)$$

In the region of wavelengths of the order of the electron Larmor radius ($kv_{Te} \sim \omega_{He}$) this instability is a branch of the electromagnetic ion-acoustic oscillations in a magnetic field.

In an isothermal plasma ($T_e \sim T_i$) and in a plasma with hot ions ($T_i \gg T_e$) the unstable modes are also essentially electromagnetic and their growth rates are smaller than (1.1).

An important feature is the rapid decrease of the growth rates with increasing β in the region $\beta > 1$.

2. DISPERSION EQUATION

We first obtain a dispersion equation for unstable modes in a finite-β plasma. For simplicity we assume that the lines of force of the magnetic field $\mathbf{H}_0$ that confines the plasma are parallel to the z axis, while the field strength H_0 varies slowly with the y coordinate:

$$\frac{\varkappa_H v_{Ti}}{\omega_{Hi}} \ll 1, \quad \varkappa_H = \frac{1}{H_0}\frac{\partial H_0}{\partial y}.$$

We investigate the case in which the current velocity u, which is directed along the z axis, exceeds appreciably the Larmor drift velocity of the particles due to the inhomogeneity of the density and temperature of the plasma, so that terms $\sim \nabla n_0$, ∇T in the dispersion equation can be ignored.

It is convenient to introduce the scalar ψ and vector **A** potentials instead of the vectors **E** and **H**. Then the dispersion equation in the local approximation has the form[11]

$$\begin{aligned}\varepsilon_{00}N^4 + [\varepsilon_{03}^2 - \varepsilon_{02}^2 - \varepsilon_{00}(\varepsilon_{33} + \varepsilon_{22})]N^2 + \varepsilon_{00}\varepsilon_{23}^2 + \varepsilon_{02}^2\varepsilon_{33} \\ + 2\varepsilon_{02}\varepsilon_{03}\varepsilon_{23} + \varepsilon_{22}(\varepsilon_{00}\varepsilon_{33} - \varepsilon_{03}^2) = 0, \quad N \equiv kc/\omega, \qquad (2.1)\end{aligned}$$

where, for Maxwell ion distributions the components ε_{ij} are given by the expressions[9]

$$\varepsilon_{00} = 1 + \frac{\omega_{pe}^2}{k^2 v_{Te}^2}\left[1 - \int d\mathbf{v} f_{0e}\frac{J_0^2}{\Delta_e}\omega\right] + \delta\varepsilon_{00}^i,$$

$$\varepsilon_{02} = -\varepsilon_{20} = i\frac{\omega_{pe}^2}{k_z v_{Te}^2}\int d\mathbf{v} f_{0e}\frac{v_\perp}{\Delta_e}J_0 J_0',$$

$$\varepsilon_{03} = \varepsilon_{30} = -\frac{\omega_{pe}^2}{k_z v_{Te}^2}\int d\mathbf{v} f_{0e}\frac{v_\parallel}{\Delta_e}J_0^2,$$

$$\varepsilon_{23} = -\varepsilon_{32} = -i\frac{\omega_{pe}^2}{\omega v_{Te}^2}\int d\mathbf{v} f_{0e}\frac{v_\parallel v_\perp}{\Delta_e}J_0 J_0',$$

$$\varepsilon_{22}=1+\frac{\omega_{pe}^2}{\omega_{He}^2}-\frac{\omega_{pe}^2}{\omega v_{Te}^2}\int d\mathbf{v} f_{0e}\frac{v_\perp^2}{\Lambda_e}(J_0')^2,$$

$$\varepsilon_{33}=1-\frac{\omega_{pe}^2}{\omega v_{Te}^2}\int d\mathbf{v} f_{0e}\frac{v_\parallel^2}{\Lambda_e}J_0^2,$$

$$\delta\varepsilon_{00}^i=\frac{\omega_{pi}^2}{k^2v_{Ti}^2}[1+i\sqrt{\pi}\,z_iw_i],$$

where

$$\Lambda_e=\omega-k_\parallel v_\parallel-\frac{k_x\varkappa_H v_\perp^2}{2\omega_{He}},\quad z_i=\frac{\omega-k_xu}{\sqrt{2}\,kv_{Ti}},\quad k_\parallel=k\cos\theta,$$

$$\omega_{He}=\frac{eH_0}{m_ec}>0,\quad \omega_{pe}=\left(\frac{4\pi e^2n_0}{m_e}\right)^{1/2},$$

$$v_{Te}=\left(\frac{T_e}{m_e}\right)^{1/2},\quad J_0'=-J_1,\quad J_0\left(\frac{k_xv_\perp}{\omega_{He}}\right)$$

is the Bessel function, $w_i = w(z_i)$ is the Cramp function of complex argument.

The dispersion equation holds for frequencies ω and wave vectors **k** for which the ions can be assumed to be unmagnetized ($kv_{Ti}/\omega_{Hi} \gg 1$, $|\omega| \gg \omega_{Hi}$) and the electrons magnetized[1)] ($kv_{Te} \lessgtr \omega_{He}$, $|\omega| \ll \omega_{He}$). The current velocity u, which is associated with the relative motion of the ions and the electrons, is introduced into the ion distribution function. We also give the following relation between u and $\varkappa_H$, which follows from the Maxwell equation curl $H_0 = 4\pi/cj$:

$$u=\frac{cH_0\varkappa_H}{4\pi en_0}.\tag{2.2}$$

Equation (2.1) is simplified appreciably in the limiting case of fairly large $k_\parallel$, where $|\omega - k_x\varkappa_H v_{Te}^2/\omega_{He}| \ll k_\parallel v_{Te}$:

$$\left[1+i\sqrt{\pi}z_0A_0+\frac{T_e}{T_i}(1+i\sqrt{\pi}z_iW_i)\right]$$
$$\times\left\{1-2z_0^2q\left[A_0-\frac{k_xu_H}{\omega}(A_0+\mu A_0')+\beta_e(A_0')^2\right]\right.$$
$$\left.+2i\sqrt{\pi}z_0(\beta_eA_0'+z_0^2q\eta_1)\right\}+2z_0^2qA_0(A_0+2i\sqrt{\pi}z_0\eta_2)=0,\tag{2.3}$$

where

$$\eta_1=-A_0\left(1-\frac{k_xu_H}{\omega}\right)^2+2\mu A_0'\frac{k_xu_H}{\omega}(1+\beta_eA_0')$$
$$-\frac{k_x^2u_H^2}{\omega^2}(2A_0+4\mu A_0'+\mu^2A_0'')$$
$$-2\beta_eA_0'\left[A_0+A_0'-\frac{k_xu_H}{\omega}(A_0+2A_0'+\mu A_0'')\right],$$
$$\eta_2=A_0+\beta_eA_0'(A_0+A_0')-\frac{k_xu_H}{\omega}(A_0+\mu A_0'),$$
$$A_0=e^{-\mu}I_0(\mu),\quad A_0'=\frac{d}{d\mu}A_0,\quad \mu=k^2\rho^2\equiv\frac{k^2v_{Te}^2}{\omega_{He}^2},$$
$$u_H=\frac{\varkappa_Hv_{Te}^2}{\omega_{He}}=u\beta_e,\quad \beta_e=\frac{4\pi n_0T_e}{H_0^2},\quad q=\frac{\omega_{pe}^2}{k^2c^2},\quad z_0=\frac{\omega}{\sqrt{2}|k_z|v_{Te}},$$

and $I_0(\mu)$ is a modified Bessel function.

In what follows we analyze the dispersion equation (2.3).

3. HOT-ELECTRON PLASMA ($T_e \gg T_i$)

We first consider a plasma with hot electrons and cold ions. We assume that $|z_i| \gg 1$. In the case $\mu \ll 1$, Eq. (2.3) is simplified considerably and takes the form

$$\left[1-\frac{k^2v_s^2}{(\omega-k_xu)^2}+i\sqrt{\pi}z_0\right]\left\{1-2z_0^2q\left[1+\beta_e\left(1-\frac{k_xu}{\omega}\right)\right]\right.$$
$$\left.+2i\sqrt{\pi}z_0(-\beta_e+z_0^2q\eta_1)\right\}+2z_0^2q(1+2i\sqrt{\pi}z_0\eta_2)=0,\tag{3.1}$$

where

$$\eta_1=-\left(1-\frac{k_xu}{\omega}\beta_e\right)^2-2\beta_e^2\frac{k_xu}{\omega}\left(\frac{k_xu}{\omega}-1\right),$$
$$\eta_2=1-\frac{k_xu}{\omega}\beta_e,\quad v_s=\left(\frac{T_e}{m_i}\right)^{1/2}.$$

Equations (2.3) and (3.1) are valid only in the approximation $|z_0| \ll 1$ and terms proportional to iz_0 in Eq. (3.1) are small. Since $q = \beta_e/\mu \gg 1$, terms $\sim z_0^2q$ can be comparable with the remaining principal terms in (3.1). We therefore investigate the solutions of Eq. (3.1) in the first approximation, ignoring small terms $\sim iz_0$. Then Eq. (3.1) takes the form

$$[(\omega-k_xu)^2-k^2v_s^2][k_z^2v_{Te}^2-\omega^2(1+\beta_e)q$$
$$+\omega k_xu\beta_eq]+\omega^2(\omega-k_xu)^2q=0.\tag{3.2}$$

When $u \gg v_s$ the roots of Eq. (3.2) are

$$\omega_{1,2}=k_xu\left[1\pm i\sqrt{\frac{q}{\cos^2\theta}-\frac{v_{Te}^2}{u^2}\left(\frac{m_e}{m_i}\right)^{1/2}}\right],\tag{3.3}$$

$$\omega_{3,4}=\frac{k_xu}{2}\left(1\pm\sqrt{1+\frac{\cos^2\theta v_{Te}^2}{u^2q\beta_e}}\right),\tag{3.4}$$

where

$$\cos\theta=\frac{k_z}{k_x}.$$

It follows from (3.3) that when $|k_\parallel| < k_0 \equiv (u/c)\cdot(\omega_{pe}/v_{Te})^{-1}$ one of the roots is unstable; when $k_\parallel \ll k_0$ the growth rate of the instability is

$$\gamma\equiv\operatorname{Im}\omega=\frac{u}{v_{Te}|\cos\theta|}\sqrt{\omega_{He}\omega_{Hi}\beta_e}.\tag{3.5}$$

In this case the condition $|z_0| \ll 1$ means that $u/v_{Te}\cdot|\cos\theta| \ll 1$. Thus, the growth rate (3.5) increases with decreasing $|\cos\theta|$, and the oscillations that must be most rapidly excited are those that propagate in the interval of angles $|\theta-\pi/2| \lessgtr u/v_{Te}$.

When $|k_\parallel| > k_0$ all the solutions of Eq. (3.2) are stable and to determine the growth rate or the decay rate one must take account of the small residue terms $\sim i\sqrt{\pi}z_0$ in Eq. (3.1). For each of the oscillation branches we obtain the following values of γ:

$$\gamma_{1,2}=\mp\sqrt{\frac{\pi}{8}\frac{m_e}{m_i}}\frac{|k_x|u}{|\cos\theta|}\left(1-\frac{k_0^2}{k_z^2}\right)^{-1/2}\left[1-2\beta_e+2(1-\beta_e)\frac{k_0^2}{k_z^2}\right.\tag{3.6}$$
$$\left.+(\beta_e^2+2\beta_e-2)\frac{k_0^4}{k_z^4}\right],$$

$$\gamma_{3,4}=-3\sqrt{\frac{\pi}{2}}\beta_e\frac{\omega_{3,4}}{|k_z|v_{Te}}\left[\left(\frac{k_xu}{\omega_{3,4}}-\frac{2}{3}\right)^2\right.$$

$$+\frac{2}{9}\Big]\left(1-\frac{k_x u}{\omega_{3,4}}\right)\left(2-\frac{k_x u}{\omega_{3,4}}\right)^{-1}. \quad (3.7)$$

It follows from (3.6) that one of the branches is always unstable, although the growth rate (3.6) for $|k_{\parallel}| > k_0$ is smaller by a factor $1/|z_0|$ than the growth rate (3.5) obtained in the case $|k_{\parallel}| < k_0$. The branches (3.4) and (3.7) are always stable. It is interesting to note that the branches ω_3 and ω_4 are purely electron oscillations for $u \gg v_s$; in the absence of resonant ions, these are damped.

Solutions of Eq. (3.2) can also be readily be found in the case $u - v_s \ll v_s$:

$$\omega_{1,2}=\frac{\sqrt{2}\,u^2\kappa_x}{2|\cos\theta|v_{Te}q(1-2\beta_e)}\left\{\cos^2\theta\frac{v_{Te}^2}{u^2}-\frac{q\beta_e}{2}\left(1-\frac{v_s^2}{u^2}\right)\right. \quad (3.8)$$

$$\left.\pm\sqrt{\left[\cos^2\theta\frac{v_{Te}^2}{u^2}+\frac{\beta_e q}{2}\left(1-\frac{v_s^2}{u^2}\right)\right]^2-\cos^2\theta\frac{v_{Te}^2}{u^2}q\left(1-\frac{v_s^2}{u^2}\right)}\right\},$$

$$\omega_{3,4}=\frac{k_x v_s}{2}\left(3\beta_e\pm\sqrt{9\beta_e^2-8\beta_e+4}\right). \quad (3.9)$$

It follows from the form of the radicand in (3.8) that these solutions are unstable only when $u > v_s$ and $\beta_e < 0.5$. In the region of instability of the roots (3.8) the growth rate is a maximum when

$$q\left(1-\frac{v_s^2}{u^2}\right)=4\frac{v_{Te}^2\cos^2\theta}{\beta^2u^2}\left(1-\beta_e-\sqrt{(1-\beta_e)^2-\frac{3}{4}\beta_e^2}\right),$$

this maximum being equal to

$$\gamma_m=\frac{u(1-\beta_e)^{-3/2}\left(1-\frac{v_s^2}{u^2}\right)^{3/2}}{8v_{Te}|\cos\theta|\sqrt{1-2\beta_e}}\left[1-\sqrt{1-\frac{3}{4}\frac{\beta^2}{(1-\beta)^2}}\right]^{-3/2}$$

$$\times\left[1-2\beta_e+\frac{\beta_e^2}{2}+(1-\beta_e)\sqrt{1-2\beta_e+\frac{\beta_e^2}{4}}\right]^{-1/2}\sqrt{\omega_{He}\omega_{Hi}\beta_e}. \quad (3.10)$$

When $\beta_e > 0.5$ all solutions of Eq. (3.2) are stable. A growth rate appears in this case only when allowance is made for the small residue terms $\sim iz_0$ in Eq. (3.1). Analysis of the solutions obtained in this manner shows that the branches (3.9) are always damped (for any β_e).

One of the branches (3.8) for $\beta_e > 0.5$ is unstable, its growth rate being smaller by a factor $|\cos\theta|\,v_{Te}/u$ than the growth rate (3.10).

An exceptional case arises when $\beta_e = 0.5$ since the growth rate (3.10) increases rapidly. However, one cannot use Eq. (3.2), because all the terms $\sim iz_0$ in Eq. (3.1) are then not small. Bearing this in mind, from Eq. (3.1) we have

$$z_0^2+i\frac{\sqrt{\pi}}{6}\frac{u^2}{v_{Te}^2\cos^2\theta}z_0+\left[\left(1-\frac{v_s^2}{u^2}\right)\frac{u^2}{12\cos^2\theta v_{Te}^2}-\frac{1}{3q}\right]=0.$$

It is not difficult to make an extremum investigation of this equation. The growth rate is a maximum when

$$q=\frac{48\alpha^4}{\pi a(a-1)}\left[2a+\sqrt{2a}-\frac{1}{2}\right],$$

$$a\equiv1+\frac{12\cos^2\theta v_{Te}^2}{\pi u^2}\left(1-\frac{v_s^2}{u^2}\right),\quad \alpha=\cos\theta\frac{v_{Te}}{u}$$

and is equal to

$$\gamma_m=\frac{\sqrt{\omega_{He}\omega_{Hi}}}{4\sqrt{\pi}}\left(1-\frac{v_s^2}{u^2}\right)^{3/2}x(a)^{1/4}\left[(a)^{1/2}+\frac{\sqrt{2}}{2}\right]^{-3/2}. \quad (3.11)$$

Thus, when $\beta_e = 0.5$ the growth rate is larger by at least a factor $(1-v_s^2/u^2)^{-1/2}$ than the growth rate when $\beta_e \neq 0.5$.

There are of course unstable solutions of Eq. (3.2) when $u \gtrsim v_s$. In particular, for angles θ defined by the relation

$$\cos^2\theta=q\left[(\beta_e+3)\frac{m_e}{m_i}-\frac{u^2}{v_{Te}^2}\beta_e\right],$$

one can readily obtain solutions of Eq. (3.2) in explicit form:

$$\left(\omega-\frac{3}{4}k_x u\right)^2=\left(\frac{k_x^2u^2}{16}+k^2v_s^2+2k^2v_A^2\right)$$

$$\times\left(1\pm\left\{1-\left[\left(1-\frac{16v_s^2}{u^2}\right)^2+\frac{3}{4}16^2\frac{v_A^2}{u^2}\left(4\frac{v_s^2}{u^2}-1\right)\right]\right.\right.$$

$$\left.\left.\times\left[1+16\frac{v_s^2}{u^2}+32\frac{v_A^2}{u^2}\right]^{-2}\right\}^{1/2}\right),\quad v_A^2=\frac{v_s^2}{\beta_i}. \quad (3.12)$$

It follows, for example, that the expression in the braces in (3.12) is negative (there is an unstable solution) if tion) if

$$\frac{8(\beta_e+3)}{\beta_e+6}<\frac{u^2}{v_s^2}<4\left(1+\frac{3}{\beta_e}\right),\quad (\beta_e<6).$$

Thus, our investigation of the instabilities shows that electromagnetic modes, like electrostatic modes, are excited by a transverse current only when $u > v_s$; the growth rate increase in proportion to $u(1+\beta_e)/v_{Te}|\cos\theta|$. The maximum growth rate obviously arises in the case $|\cos\theta| \sim u/v_{Te}$, $\mu \sim 1$, when Eq. (2.3) can no longer be used.

Unstable electrostatic modes for such angles and wavelengths in a low-pressure plasma ($\beta \to 0$) are investigated in ref. 5, and called magnetized ion sound waves. Naturally, in a finite-B plasma ($\beta_e \sim 1$) this branch must become essentially electromagnetic.

Below we shall investigate the excitation of this branch of oscillations when $\beta_e \sim 1$ in the limiting case of fairly large current velocities $u \gg v_s$.

An important circumstance facilitating the finding of unstable solutions is the fact that the ion terms need be taken into account only in the component ε_{00} in Eq. (2.1):

$$\varepsilon_{00}^i=-\frac{\omega_{pi}^2}{(\omega-k_x u)^2}.$$

In this case the complex frequency can be sought in the form $\omega = k_x u + \Delta\omega$, where $\Delta\omega \ll k_x u$. Then, substituting into the electron part of the tensor ε_{ij} the value $\omega = k_x u$ and ignoring the correction $\Delta\omega$, from Eq. (2.1) we have

$$\Delta\omega=\pm\omega_{pi}\left[\frac{c^4}{u^4}-\frac{c^2}{u^2}(\varepsilon_{33}+\varepsilon_{22})+\varepsilon_{23}^2+\varepsilon_{22}\varepsilon_{33}\right]^{1/2}\left\{\frac{c^4}{u^4}\varepsilon_{00}^e\right.$$

$$+\frac{c^2}{u^2}\left[\varepsilon_{03}^2-\varepsilon_{02}^2-\varepsilon_{00}^e(\varepsilon_{33}+\varepsilon_{22})\right]+\varepsilon_{00}^e\varepsilon_{23}^2+\varepsilon_{02}^2\varepsilon_{33}$$

$$\left.+2\varepsilon_{02}\varepsilon_{03}\varepsilon_{23}+\varepsilon_{22}(\varepsilon_{00}^e\varepsilon_{33}-\varepsilon_{03}^2)\right\}^{-1/2}. \quad (3.13$$

As we have noted above, the right-hand side of (3.13) does not contain the frequency $\Delta\omega$. This quantity can be ignored in the electron terms since the terms in the resonance denominators associated with the drift in the inhomogeneous magnetic field are large compared with $\Delta\omega$:

$$\Lambda_e \sim \frac{k_x \varkappa_H v_\perp^2}{\omega_{He}} \sim k_x u \beta_e \gg \Delta\omega, \quad (\beta_e \sim 1).$$

Since $\mu \sim 1$ the integrals in ε_{ij} cannot be expressed in terms of known functions. However, when $\mu \sim 1$, $k_x u \sim k_\parallel v_{Te} \sim k_x \varkappa_H v_\perp^2/\omega_{He}$, we have the estimate $\mathrm{Im}\,\varepsilon_{ij} \sim \mathrm{Re}\,\varepsilon_{ij}$, so that the components of the tensor ε_{ij} are of order

$$|\varepsilon_{00}^e| \sim \frac{\omega_{pe}^2}{\omega_{He}^2}, \; |\varepsilon_{33}| \sim |\varepsilon_{22}| \sim |\varepsilon_{23}| \sim \frac{c^2}{u^2}, \; |\varepsilon_{02}| \sim |\varepsilon_{03}| \sim \frac{c}{u}\frac{\omega_{pe}}{\omega_{He}}.$$

Since the expression on the right-hand side of (3.13) is complex, with a real part of the same order as the imaginary part, one of the roots $\Delta\omega$ will always correspond to instability with growth rate of order $\gamma \sim \sqrt{\omega_{He}\omega_{Hi}}$.

Thus, in a finite-β plasma the magnetized ion sound wave with wavelength of the order of electron Larmor radius is an electromagnetic branch whose growth rate, as in a low-β plasma,[2,5] is of the order of magnitude given by (1.1). It should be pointed out that a magnetized ion sound wave in the short-wave region $\mu \gg 1$ is an electrostatic mode even in a finite-β plasma.

4. HOT-ION PLASMA

Let us now consider a hot-ion plasma in which one can assume $|z_i| \ll 1$, $\mu \ll 1$. Then, from Eq. (2.3) we have

$$\Big[1 + \frac{T_e}{T_i}(1 + i\sqrt{\pi}z_i) + i\sqrt{\pi}z_0\Big]\Big[1 - 2z_0^2 q\Big(1 + \beta_e - \beta_e\frac{k_x u}{\omega}\Big) + 2i\sqrt{\pi}z_0(-\beta_e + z_0^2 q\eta_1)\Big] + 2z_0^2 q(1 + 2i\sqrt{\pi}z_0\eta_2) = 0, \qquad 4.1)$$

where

$$\eta_1 = -\Big(1 - \frac{k_x u}{\omega}\beta_e\Big)^2 + 2\beta_e^2\frac{k_x u}{\omega}\Big(1 - \frac{k_x u}{\omega}\Big), \quad \eta_2 = 1 - \frac{k_x u}{\omega}\beta_e.$$

Using the fact that the imaginary terms are small in (4.1) we can readily obtain expressions for the frequency and growth rate:

$$\mathrm{Re}\,\omega \equiv \omega_\pm = \mathrm{sgn}\,k_x\Big(\frac{b}{2}k_x u \pm \sqrt{\frac{b^2k_x^2u^2}{4} + b\frac{k_\parallel^2 v_{Te}^2}{q}}\Big),$$
$$\gamma = -\sqrt{\pi}z_0\frac{q\omega^3}{q\omega^2\beta_e + k_\parallel^2 v_{Te}^2}\Big[|\cos\theta|\sqrt{\frac{m_i}{m_e}}\Big(\frac{T_e}{T_i}\Big)^{3/2}\Big(1 - \frac{k_x u}{\omega}\Big) + \beta_e^2\Big(\frac{k_x u}{\omega}\Big)^2 + 2\beta_e\Big(1 - \frac{k_x u}{\omega}\Big)\Big], \qquad (4.2)$$

where

$$b \equiv \beta_e\Big(1 + \frac{T_e}{T_i}\Big)\Big[\beta_e + (1 + \beta_e)\frac{T_e}{T_i}\Big]^{-1} \simeq 1 - \frac{T_e}{T_i\beta_e}. \qquad (4.3)$$

It follows from (4.3) that waves with frequency ω_- are damped, since $k_x u/\omega_- < 0$; excitation of waves with frequency ω_+ requires the condition $k_x u > \omega_+$, i.e., $k_\parallel^2 v_{Te}^2 \cdot q^{-1} < k_x^2 u^2/\beta_e(T_e/T_i) \ll k_x^2 u^2$. Thus from (4.2) and (4.3) we have

$$\mathrm{Re}\,\omega = \omega_+ = \Big(1 - \frac{T_e}{T_i\beta_e}\Big)k_x u + \frac{k_\parallel^2 v_{Te}^2}{q k_x u},$$
$$\gamma = \sqrt{\frac{\pi}{2}}\frac{|k_x|u^2}{v_{Te}\beta_e|\cos\theta|}\Big\{|\cos\theta|\sqrt{\frac{m_i}{m_e}}\Big(\frac{T_e}{T_i}\Big)^{3/2}\Big[\frac{T_e}{T_i\beta_e} - \frac{k_\parallel^2 v_{Te}^2}{k_x^2 u^2 q}\Big] - \beta_e^2\Big\}. \qquad (4.4)$$

It is evident that the growth rate (4.4) is a maximum when

$$|\cos\theta| = \Big[\frac{3\sqrt{3}}{4}\beta_e^{11/3}\frac{m_e}{m_i}\frac{u}{v_{Te}}\Big(\frac{T_i}{T_e}\Big)^{3/2}\Big]^{1/3},$$

$$k = \frac{2}{3\sqrt{3}}\beta_e^{-7/3}\frac{u}{v_{Te}}\sqrt{\frac{m_i}{m_e}}\Big(\frac{T_e}{T_i}\Big)^3\frac{\omega_{pe}}{c}$$

being equal to

$$\gamma_m = \sqrt{\frac{\pi}{10}}\frac{4}{25}\beta_e^{-8}\Big(\frac{u}{v_{Ti}}\Big)^3\Big(\frac{T_e}{T_i}\Big)^4\sqrt{\omega_{He}\omega_{Hi}}. \qquad (4.5)$$

In this case, to satisfy the inequalities $z_0 \ll 1$, $\mu \ll 1$, and $z_i < 1$ it is necessary that $u/v_{Ti} < \beta_i = \beta_e T_i/T_e$.

We introduce a certain limiting value for the current velocity $u = u^*$, for which the condition $\gamma_m \sim \omega_{Hi}$ is satisfied:

$$u^* \simeq 2v_{Ti}\Big(\frac{m_e}{m_i}\Big)^{1/6}\beta_e^{8/3}\Big(\frac{T_i}{T_e}\Big)^{4/3}. \qquad (4.6)$$

Then the above instability exists in the range of current velocities $u^* < u < \beta_i v_{Ti}$.

5. ISOTHERMAL PLASMA ($T_e \sim T_i$)

In an isothermal plasma one can investigate analytically only the case in which the phase velocity of the wave at right angles to the magnetic field is smaller than the ion thermal velocity ($z_i < 1$). Then the dispersion equation has the form (4.1), in which $T_e/T_i \sim 1$. As in the case of a plasma with hot ions, the unstable branch is the one with frequency $\omega = \omega_+$ defined by the expression (4.2), and the growth rate γ is equal to

$$\gamma = \sqrt{\pi}z_0\Big(1 + \frac{T_e}{T_i}\Big)^{-1}\omega\Big[\Big(1 + \frac{T_e}{T_i}\Big)\Big(1 + \beta_e + \frac{k_\parallel^2 v_{Te}^2}{q\omega^2}\Big) - 1\Big]^{-1}$$
$$\times\Big\{|\cos\theta|\sqrt{\frac{m_i}{m_e}}\Big(\frac{T_e}{T_i}\Big)^{3/2}\Big(\frac{k_x u}{\omega} - 1\Big) - \Big[\Big(1 + \frac{T_e}{T_i}\Big)\Big(1 - \frac{k_x u}{\omega}\beta_e\Big) - 1\Big]^2 - 2\beta_e\Big(1 + \frac{T_e}{T_i}\Big)^2\Big[\Big(1 - \frac{k_x u}{\omega}\Big)^2\beta_e + \frac{T_e}{T_i}\Big(1 + \frac{T_e}{T_i}\Big)^{-1}\Big]\Big\}. \qquad (5.1)$$

The growth rate (5.1) has a maximum at certain values of $k_\parallel$ and k, although an extremum investigation is very cumbersome. In order to elucidate the characteristic features of the excitation of oscillations in an isothermal finite-β plasma, let us consider the special case $T_e = T_i$, $qu^2/\cos^2\theta\, v_{Te}^2 \gg 1$. Then the expression (5.1) is simplified and takes the form

$$\gamma = \sqrt{\frac{\pi}{2}}\frac{\beta_e}{(2\beta_e + 1)^3}|k_x|u\frac{u}{v_{Ti}}\Big[1 - \frac{4\beta_e}{|\cos\theta|}\sqrt{\frac{m_e}{m_i}}(2\beta_e^2 + 2\beta_e + 1)\Big], \qquad (5.2)$$

where $\beta_e = \beta_i \equiv \beta$.

The growth rate (5.2) will be positive when $1 \gg |\cos\theta| > 4\beta_e\sqrt{m_e/m_i}(2\beta^2+2\beta+1)$. For a hydrogen plasma when $\beta = 1$ it is difficult to satisfy these inequalities because the growth rate (5.2) is positive only for $|\cos\theta| \sim 1$. On the basis of this observation, we can introduce a certain limiting pressure $\beta = \beta^*$ above which instability is impossible:

$$4\beta^*(2\beta^{*2}+2\beta^*+1)\sqrt{\frac{m_e}{m_i}} \approx 0.3. \qquad (5.3)$$

To satisfy the condition $|z_i| < 1$ one requires $u/v_{Ti} < 1$ and this reduces the value of the growth rate. It is obvious that when $\beta \sim 1$ the solutions (5.1) and (5.2) are valid only in a plasma with heavy ions (for example, for the gas Xe), since it is only in this case that the conditions $\gamma \gg \omega_{Hi}$, $\beta^* > \beta > 1$ can be satisfied.

---

1) The condition $|\omega| \ll \omega_{He}$ enables us to retain only the term with $n = 0$ in ε_{ij} and to ignore effects associated with electron cyclotron resonances.

[1] V. I. Kurilko and V. I. Miroshnichenko, in: Plasma Physics and Problems of Controlled Thermonuclear Fusion, Vol. 3 [in Russian], Izd. Akad. Nauk UkrSSR, Kiev (1963), p. 161.

[2] K. N. Stepanov, Zh. Tekh. Fiz., 34, 2146 (1964) [Sov. Phys.-Tech. Phys., 9, 1653 (1965)].

[3] V. L. Sizonenko and K. N. Stepanov, Nucl. Fusion, 7, 131 (1967).

[4] V. I. Aref'ev, I. A. Kovan, and L. I. Rudakov, ZhETF Pis. Red., 8, 286 (1968) [JETP Lett., 8, 176 (1968)].

[5] L. I. Grigor'eva, A. V. Longinov, A. I. Pyatak, V. L. Sizonenko, B. I. Smerdov, K. N. Stepanov, and V. V. Chechkin, Zh. Eksp. Teor. Fiz., 60, 605 (1971) [Sov. Phys.-JETP, 33, 329 (1971)].

[6] L. I. Grigor'eva, A. V. Longinov, A. I. Pyatak, V. L. Sizonenko, B. I. Smerdov, K. N. Stepanov, and V. V. Chechkin, Report IAEA [CN-28]L7, Fourth International Conference on Investigations in Plasma Physics and Controlled Thermonuclear Reactions, Madison, Wisconsin, USA, 17-23 June 1971.

[7] J. J. Sanderson and E. R. Priest, Plasma Phys., 14, 959 (1972).

[8] S. P. Gary, Plasma Phys., 15, 393 (1973).

[9] A. I. Pyatak, V. L. Sizonenko, and K. N. Stepanov, Zh. Tekh. Fiz., 43, 475 (1973) [Sov. Phys.-Tech. Phys., 18, 304 (1973)].

[10] L. P. Gudblud, A. I. Pyatak, and V. L. Sizonenko, Zh. Eksp. Teor. Fiz., 64, 2084 (1973) [Sov. Phys.-JETP, 37 (in press)].

[11] A. B. Mikhailovskii, in: Reviews of Plasma Physics, Vol. 3, Consultants Bureau, New York (1967), p. 159.

Instabilities in a finite-β plasma with transverse current. II

A. I. Pyatak and V. L. Sizonenko

(Submitted July 30, 1973)
Zh. Tekh. Fiz., 44, 1014-1021 (May 1974)

We treat a finite-β plasma with current that flows at right angles to the confining magnetic field; high-frequency small-scale instabilities that propagate at right angles to the magnetic field are analyzed. Allowance is made for the inhomogeneity of the magnetic field due to the flowing current. The instabilities are electromagnetic; frequencies and growth rates are determined.

1. INTRODUCTION

In the second part of the present paper, which is a continuation of ref. 1, we investigate high-frequency (γ, $\omega \gg \omega_{Hi}$) small-scale ($k_\perp v_{Ti} \gg \omega_{Hi}$) instabilities of a finite-β plasma $\beta = 4\pi n_0 (T_e + T_i/H_0^2 \gtrsim 1)$ with transverse current. In the linear approximation we consider modes that propagate exactly at right angles to the external magnetic field ($\theta = \pi/2$). It is assumed, as before, that the current velocity u responsible for the instabilities is appreciably greater than the Larmor drift velocity due to the inhomogeneity of the density and temperature of the electrons, so that the terms ∇n_0 and ∇T in the dispersion equation can be ignored. The inhomogeneity of the magnetic field due to the transverse current is taken into account and plays an important role in the excitation of instabilities in a finite-β plasma. In the considered range of frequencies and wavelengths the ions can be assumed to be unmagnetized so that the effects associated with gradients of the density, temperature, and magnetic field in the ion terms can be ignored.

It is shown that in a hot-electron plasma ($T_e \gg T_i$) one can have the excitation of hydrodynamic electromagnetic modes with wave vectors $k \sim \omega_{pe}/c(v_A/u)^{1/3}$, whose growth rates are of order

$$\gamma \sim \sqrt{\omega_{He}\omega_{Hi}} \quad (u \gtrsim v_A). \tag{1.1}$$

We find a threshold value of the current velocity below which the solutions we obtain do not apply.

In the region of shorter wavelengths kinetic instabilities are excited by the Cerenkov resonance between the waves and electrons drifting in the inhomogeneous magnetic field. The growth rate of these instabilities increases with increasing plasma pressure, reaching the value in (1.1) when $\beta \approx 0.25$.

Unstable modes propagating at right angles to the magnetic field in a plasma with hot ions ($T_i \gg T_e$) and finite ion pressure ($\beta_i = 4\pi n_0 T_i/H_0^2 \sim 1$, $\beta_e = 4\pi n_0 T_e/H_0^2 \ll 1$) are investigated in ref. 1. Here, we investigate the excitation of such modes for a finite electron pressure. ($\beta_e \sim 1$, $\beta_i \gg 1$). It is shown that allowance for the residue terms associated with the magnetic drift of the electrons has a stabilizing influence on the instability.

We also consider the excitation of instabilities in an isothermal plasma ($T_e \sim T_i$) at high pressure ($\beta \gg 1$). We determine the boundaries of the instability region with respect to the current velocity and we find expressions for the frequencies and growth rates.

It is shown that all these instabilities disappear in a plasma of infinitely high pressure ($\beta \to \infty$) because of the rapid decrease of the growth rate with increasing β.

2. DISPERSION EQUATION

We obtain first a dispersion equation, assuming that the equilibrium distribution functions of the electrons and the ions are Maxwellian in the first approximation in the weak inhomogeneity parameter. The electromagnetic field will be described by the scalar and vector potentials. Then, taking $k_\parallel = 0$ ($\theta = \pi/2$) in the tensor ε_{ij} given in Part 1 of the present work, we find that

$$\left.\begin{aligned} &\varepsilon_{03} = \varepsilon_{23} = 0,\\ &\varepsilon_{33} = N^2 \equiv \frac{k^2c^2}{\omega^2},\\ &\varepsilon_{00}(\varepsilon_{22} - N^2) + \varepsilon_{02}^2 = 0, \end{aligned}\right\}. \tag{2.1}$$

where

$$\left.\begin{aligned} &\varepsilon_{33} = 1 - 2\frac{\omega_{pe}^2}{\omega v_{Te}^2}\int d\mathbf{v} f_{0e}\frac{v_\perp^2 J_0^2}{2\omega - k_x\varkappa_H v_\perp^2\omega_{He}^{-1}},\\ &\varepsilon_{00} = 1 + \frac{\omega_{pe}^2}{k^2v_{Te}^2}\left[1 - 2\int d\mathbf{v} f_{0e}\frac{\omega J_0^2}{2\omega - k_x\varkappa_H v_\perp^2\omega_{He}^{-1}}\right] + \delta\varepsilon_{00}^i,\\ &\varepsilon_{02} = 2i\frac{\omega_{pe}^2}{k_x v_{Te}^2}\int d\mathbf{v} f_{0e}\frac{v_\perp J_0 J_0'}{2\omega - k_x\varkappa_H v_\perp^2\omega_{He}^{-1}},\\ &\varepsilon_{22} = 1 + \frac{\omega_{pe}^2}{\omega_{He}^2} - 2\frac{\omega_{pe}^2}{\omega v_{Te}^2}\int d\mathbf{v} f_{0e}\frac{v_\perp^2 (J_0')^2}{2\omega - k_x\varkappa_H v_\perp^2\omega_{He}^{-1}},\\ &\delta\varepsilon_{00}^i = \frac{\omega_{pi}^2}{k^2v_{Ti}^2}[1 + i\sqrt{\pi}z_i w_i]. \end{aligned}\right\} \tag{2.2}$$

When $\mu \ll 1$, the Bessel functions can be expanded in the small parameter $k_\perp v_\perp/\omega_{He}$. Then the integrals in the components of the tensor ε_{ij} can be readily expressed in terms of the exponential integral $Ei(\zeta)$, where

$$Ei(\zeta) \equiv e^\zeta \int_0^\infty \frac{e^{-x}dx}{\zeta - x}, \quad \zeta = \frac{\omega\omega_{He}}{k_x\varkappa_H v_{Te}^2} = \frac{\omega}{k_x u\beta_e}. \tag{2.3}$$

This function shows the following aymptotic behavior:

$$Ei(\zeta) = e^\zeta \sum_{n=0}^\infty \frac{n!}{\zeta^{n+1}} - i\pi\,\mathrm{sgn}\,k_x \quad \text{for} \quad |\zeta| \gg 1,\ \omega \gg \gamma, \tag{2.4}$$

$$Ei(\zeta) \simeq C + \ln(-\zeta) \quad \text{for} \quad |\zeta| \ll 1, \tag{2.5}$$

where C ≈ 0.57 is Euler's constant.

If $|\zeta| \gg 1$ but $\gamma \gtrsim \omega$, in the asymptotic expression (2.4) one must ignore the imaginary part, because the residue terms vanish in the integrand of (2.3). The dispersion equations (2.1) and (2.2) take the following form:

$$1 + q\zeta e^{-\zeta}Ei = 0; \tag{2.6}$$

$$\left[(1-\zeta e^{-\zeta}Ei)\left(1-\zeta\mu+\frac{3}{8}\zeta^2\mu^2\right)+\frac{3}{8}\zeta\mu^2+\frac{T_e}{T_i}(1+i\sqrt{\pi}z_iw_i)\right]$$
$$\times\left\{\frac{\omega}{k_xu}\left[1+\zeta(1-\zeta e^{-\zeta}Ei)\left(1-\frac{\mu}{2}\zeta+\frac{5}{48}\mu^2\zeta^2\right)-\frac{\mu}{2}(2+\zeta)\right.\right.$$
$$\left.\left.+\frac{5}{48}\mu^2(\zeta^2+2\zeta+6)\right]-1\right\}$$
$$-\frac{\omega}{k_xu}\zeta\left\{(1-\zeta e^{-\zeta}E_i)\left(1-\frac{3}{4}\zeta\mu-\frac{5}{24}\mu^2\zeta^2\right)\right.$$
$$\left.-\frac{3}{4}\mu-\frac{5}{24}\mu^2(\zeta+2)\right\}^2=0. \qquad (2.7)$$

Here and in what follows Ei ≡ Ei(ζ).

In Eq. (2.6) we have retained only the highest terms in the expansion in the parameter μ, and in Eq. (2.7) we have omitted the terms $\sim\mu^3$ and higher.

Analysis shows that Eq. (2.6) has only a damped solution, since the contribution of the ions to ε_{33} is ignored. Therefore, in what follows we investigate the solutions of Eq. (2.7).

3. HOT-ION PLASMA ($T_e \gg T_i$)

If the ion temperature is low one can assume that $|z_i| \gg 1$, so that the ion term takes the form

$$\frac{T_e}{T_i}(1+i\sqrt{\pi}z_iw_i)=-\frac{k^2v_s^2}{(\omega-k_xu)^2}.$$

Let us investigate the instabilities in a low-β plasma ($\beta_e \ll 1$), in which $|\zeta| \gg 1$. In this case Eq. (2.7) becomes

$$1+q\left(1-\frac{k_xu}{\omega}\right)-\frac{\omega_{He}\omega_{Hi}}{(\omega-k_xu)^2}=\frac{\pi^2}{16}\frac{\omega^2}{k_x^2u^2q}\zeta^4e^{-2\zeta}+i\pi\zeta^2e^{-\zeta}$$
$$\times\left\{1+q\left(1-\frac{k_xu}{\omega}\right)-\frac{\omega}{k_xu}\frac{\omega_{He}\omega_{Hi}}{(\omega-k_xu)^2}-\frac{\omega^2}{2k_x^2u^2q}\left[1-\frac{\omega_{He}\omega_{Hi}}{(\omega-k_xu)^2}\right]\right\}. \qquad (3.1)$$

It must be remembered that the right-hand side of Eq. (3.1) is nonvanishing only in the case Re $\omega \gg$ Im ω and is equal to zero if Re $\omega \lessgtr$ Im ω.

Let us first consider the solutions of Eq. (3.1) for which the right-hand side of this equation can be ignored (this is the case for which Im $\omega \sim$ Re ω or small β_e). The problem now reduces to finding the roots of a cubic equation. It is not difficult to show that one of the roots of this equation will give an instability when

$$\left[1+\frac{u^2}{3qv_A^2}\frac{1}{(1+q)}\right]\left(1+\sqrt{1+3q\frac{v_A^2}{u^2}(1+q)}\right)<\frac{9}{2}\left(q+\frac{8}{9}\right). \qquad (3.2)$$

The limits of the stability region ($q = q_0$) can now be readily determined by replacing the inequality sign in (3.2) by the equality sign.

The growth rate of the instability can be written explicitly in certain limiting cases.

When $u \gg v_A$, from (3.2) we have $q_0 = 2^{2/3}/3(u/v_A)^{2/3}$. In this case, in the region $q-q_0 \ll q_0$ the growth rate has the form

$$\gamma=\sqrt{\omega_{He}\omega_{Hi}}\left(\frac{q-q_0}{q_0}\right)^{1/3}, \qquad (3.3)$$

in the region $q \gg q_0$ it is

$$\gamma=\left(\frac{27}{16}\right)^{1/3}\sqrt{\omega_{He}\omega_{Hi}}\left(\frac{q_0}{q}\right)^{1/3}. \qquad (3.4)$$

Thus, the growth rate attains a maximum value for wave vectors $k \sim \omega_{pe}/c(v_A/u)^{1/3}$ and is of order

$$\gamma_m \simeq \sqrt{\omega_{He}\omega_{Hi}} \quad (q \geqslant q_0). \qquad (3.5)$$

When $u \ll v_A$ the unstable solutions lie in the region $|\omega| \ll |k_xu|$ and are determined by the expressions

$$\omega=\frac{k_xu}{4}\left(\frac{u^2}{v_A^2q}-1\right)\pm i\frac{u}{4}\frac{\omega_{pe}}{c}\sqrt{\frac{8}{q}\frac{u^2}{v_A^2}-\frac{1}{q}\left(\frac{u^2}{v_A^2q}-1\right)^2}. \qquad (3.6)$$

When $k = (v_A/u)(\omega_{pe}/c)$ the growth rate is a maximum:

$$\gamma_m=\frac{1}{2}\frac{u}{v_A}\sqrt{\omega_{He}\omega_{Hi}}. \qquad (3.7)$$

Finally, we give the solutions of Eq. (3.1) in the following special case:

$$\omega=\left\{\frac{1}{2}+i\left[\frac{3\sqrt{2}-2}{4(2+\sqrt{2})}\right]^{1/2}\right\}\sqrt{\omega_{He}\omega_{Hi}},\quad q=\frac{u^2}{v_A^2}=1+\sqrt{2}. \qquad (3.8)$$

It follows from (3.5)-(3.8) that the growth rates increase with increasing u and reach saturation ($\gamma \simeq \sqrt{\omega_{He}\omega_{Hi}}$) in the region $u \gtrsim v_A$.

The threshold value $u = u^*$ of the velocity below which these solutions become inapplicable can be determined from the conditions $\gamma > kv_{Ti}, \omega_{Hi}$. Taking the smallest γ to be that from (3.7) we find

$$u^*\simeq\max\left\{v_A\sqrt{\frac{m_e}{m_i}};\ v_A\beta_i^{1/2}\right\},\quad \beta_i=\frac{4\pi n_0T_i}{H_0^2}. \qquad (3.9)$$

We now investigate the solutions of Eq. (3.1) that give a nonvanishing growth rate only when allowance is made for the right-hand side of (3.1). In the case $u \gg v_A$ we set $\omega = k_xu + \Delta\omega$, where the small correction $\Delta\omega$ is determined by

$$(\Delta\omega)^2=\omega_{He}\omega_{Hi}\frac{16q+8i\pi\zeta^2e^{-\zeta}(1-2q)}{16q+8i\pi\zeta^2e^{-\zeta}-i\pi\zeta^2e^{-\zeta}(16q-i\pi\zeta^2e^{-\zeta})},\quad \zeta=\frac{1}{\beta_e}. \qquad (3.10)$$

It follows from (3.10) that Im $\omega \sim \zeta^2e^{-\zeta} \to 0$ in the limit $\beta_e \to 0$. However, even in the region $\beta_e \ll 1$ the growth rate determined by the residue terms can become large if $\beta_e > \beta_{cr}$:

$$\mathrm{Im}\,\Delta\omega \sim \mathrm{Re}\,\Delta\omega \sim \sqrt{\omega_{He}\omega_{Hi}},\quad q \leqslant 1. \qquad (3.11)$$

Here, $\beta_{cr} \simeq 0.25$ is determined from the condition

$$\pi\beta_{cr}^{-2}\exp\left(-\frac{1}{\beta_{cr}}\right)\simeq 1.$$

The solution found above satisfies the conditions $|\zeta| \gg 1$, Im ω/Re $\omega \lessgtr v_A/u \ll 1$ and lies in the region of wavelengths in which the hydrodynamic instability (3.3)-(3.5) vanishes. It is interesting to note that when $\beta_e \approx \beta_{cr}$ the growth rate (3.11) is of the order of the maximum hydrodynamic growth rate (3.5).

In the case $u \ll v_A$ and $|1-q(v_A^2/u^2)| > 2\sqrt{2}(u/v_A)$, the hydrodynamic solutions (3.6) become stable. Allowance for the residue terms in (3.1) for these roots gives the following value of the growth rate:

$$\gamma=\sqrt{\frac{\pi}{2}}\zeta^2e^{-\zeta}q^{3/2}\frac{u}{v_A}\left[2\frac{v_A^2}{u^2}\left(1-q\frac{v_A^2}{u^2}\right)-1\right]\left(1-q\frac{v_A^2}{u^2}\right)^{-3}\sqrt{\omega_{He}\omega_{Hi}}. \tag{3.12}$$

When the right-hand side is ignored, the third root of Eq. (3.13) is always stable:

$$\omega=k_xu+\Delta\omega,\ \Delta\omega=\pm\sqrt{\omega_{He}\omega_{Hi}},\ \ q\ll 1.$$

With allowance for the residue terms, this root of the equation also gives an instability with growth rate equal to

$$\gamma=\frac{\pi}{16}\sqrt{\omega_{He}\omega_{Hi}}\frac{1}{\beta_e^2}\exp\left(-\frac{1}{\beta_e}\right). \tag{3.13}$$

In a plasma with a reasonably high pressure (for example, for $\beta_e \sim \beta_{cr}$) the growth rate (3.13) can exceed the growth rate (3.7).

Finally, we give the solutions of (3.1) when $u \sim v_A$ for waves with $q \ll 1$, which are not excited in the hydrodynamic approximation. Then two solutions can be sought in the form $\omega = k_xu + \Delta\omega$ ($\Delta\omega \ll k_xu$), where

$$\Delta\omega=\pm\sqrt{\omega_{He}\omega_{Hi}}\left[1-i\frac{\pi}{16}\frac{1}{\beta_e^2}\exp\left(-\frac{1}{\beta_e}\right)\right]. \tag{3.14}$$

The third root of Eq. (3.1) lies in the region of frequencies $|\omega| \ll |k_xu|$ and is determined by the expression

$$\left.\begin{aligned}\omega&=k_xuq+i\gamma,\\ \gamma&=k_xuq^2\left(\frac{v_A^2}{u^2}-\frac{1}{2}\right)\pi\zeta^2e^{-\zeta}.\end{aligned}\right\} \tag{3.15}$$

It follows from (3.15) that this solution gives an instability only when $u < \sqrt{2}v_A$. Nothing that $\zeta = q/\beta_e$, we can readily find the maximum value of the growth rate (3.15), which is attained when $q = (7/2)\beta_e \ll 1$ and is equal to

$$\gamma_m=8\beta_e^{3/2}\frac{u}{v_A}\left(\frac{v_A^2}{u^2}-\frac{1}{2}\right)\sqrt{\omega_{He}\omega_{Hi}}. \tag{3.16}$$

We now turn to the investigation of instabilities in a hot-electron plasma at finite pressure ($\beta_e \gtrsim 1$).

When $\beta_e \sim 1$ and $u \gg v_s$, a solution of Eq. (2.7) can be sought in the form $\omega = k_xu + \Delta\omega$ ($\Delta\omega \ll k_xu$). Then, bearing in mind that $\zeta = 1/\beta_e \gg \mu$, from (2.7) we have

$$\left(\frac{\Delta\omega}{k_xu}\right)^3+\left(\frac{1-\beta_e}{\beta_e}\right)\mu\left(\frac{\Delta\omega}{k_xu}\right)^2-\frac{v_A^2}{u^2}=0. \tag{3.17}$$

It is evident that when $\beta_e < 1$ Eq. (3.17) has unstable solutions if

$$\mu<\frac{3}{2^{2/3}}\frac{\beta_e}{1-\beta_e}\left(\frac{v_A}{u}\right)^{4/3}, \tag{3.18}$$

and that when $\beta_e > 1$ an instability occurs for all values $\mu < 1$. We give a solution of Eq. (3.17) when $\beta_e > 1$ in certain limiting cases. If $\mu \gg (v_A/u)^{4/3}$, we can ignore the first term in (3.17) and find that

$$\Delta\omega=\pm i\sqrt{\frac{\omega_{He}\omega_{Hi}}{\beta_e-1}}. \tag{3.19}$$

If $\mu \ll (v_A/u)^{4/3}$, the complex roots have the form

$$\Delta\omega=-\sqrt{\mu}\left(\frac{u}{v_A}\right)^{1/3}\left(\frac{1}{2}\pm i\frac{\sqrt{3}}{2}\right)\sqrt{\frac{\omega_{He}\omega_{Hi}}{\beta_e}}\frac{k_x}{|k_x|}. \tag{3.20}$$

It follows from the form of (3.19) and (3.20) that the growth rate of the instability increases with increasing μ and becomes saturated in the region $\mu \gtrsim (v_A/u)^{4/3}$ (there is a plateau region). On the plateau, the growth rate is of order $\gamma \sim \sqrt{\omega_{He}\omega_{Hi}}$.

When $\beta_e \gg 1$ and $u \gg v_s$, Eq. (3.17) becomes inapplicable in the region $\mu \gtrsim \zeta = 1/\beta_e$. It is not difficult to see that in this case one must replace (3.17) by the following equation:

$$\left(\frac{\Delta\omega}{k_xu}\right)^3-\mu\left(\frac{\Delta\omega}{k_xu}\right)^2-\frac{v_A^2}{u^2}(1-\mu\beta_e)=0. \tag{3.21}$$

Equation (3.21) will have complex-conjugate roots when

$$\mu<\frac{1}{\beta_e}\quad\text{or}\quad\mu-\frac{1}{\beta_e}>\frac{4}{27}\frac{u^2}{v_s^2}\mu^3. \tag{3.22}$$

In the case $\beta_e \gg u/v_s$, the inequalities are satisfied when $\mu < 1/\beta_e$ or when $(1/\beta_e)[1+ 4/27\beta_e^2(u^2/v_s^2)] < \mu < \sqrt{27}/2(v_s/u)$. In the region $\mu < 1/\beta_e$ one can ignore the second term in Eq. (3.21).

Then the growth rate is

$$\gamma=\frac{\sqrt{3}}{2}\left(\frac{u}{v_A}\right)^{1/3}\sqrt{\frac{\omega_{He}\omega_{Hi}}{\beta_e}}\sqrt{\mu}(1-\beta_e\mu)^{1/2}. \tag{3.23}$$

The growth rate (3.23) reaches a maximum when $\mu \doteq 3/5\beta_e$; this maximum is

$$\gamma_m=\frac{3}{5\sqrt{5}}\left(\frac{u}{v_A}\right)^{1/3}\frac{1}{\beta_e}\sqrt{\omega_{He}\omega_{Hi}}. \tag{3.24}$$

In the region $1/\beta_e < \mu < \sqrt{27}/2(v_s/u)$ all the terms in (3.21) are of the same order; hence

$$\gamma\sim\operatorname{Re}\Delta\omega\sim\sqrt{\mu\omega_{He}\omega_{Hi}}<\sqrt{\omega_{He}\omega_{Hi}}\left(\frac{v_s}{u}\right)^{1/2}. \tag{3.25}$$

The solutions of Eq. (2.7) can also be found in the case $u \sim v_s$, $\beta_e \gg 1$:

$$\omega=\frac{u-v_s}{v_s}\left(1+i\frac{\pi}{2\beta_e}\operatorname{sgn}k_z\right)\sqrt{\omega_{He}\omega_{Hi}}\,k_z\rho_e. \tag{3.26}$$

It follows that the modes are unstable only when $u > v_s$.

Comparison of the growth rates (3.19) and (3.20) for $\beta_e \sim 1$ with the growth rates (3.23)-(3.26) for $\beta_e \gg 1$ shows that the instability growth rates decrease with increasing β_e and become appreciably smaller than $\sqrt{\omega_{He}\omega_{Hi}}$.

It should be emphasized that all of the above instabilities in a hot-electron plasma are due to the finite plasma pressure; as a rule, these are electromagnetic modes (electrostatic instabilities do not appear in the limiting cases $\beta_e \to 0$ and $\theta = \pi/2$). An important feature of these instabilities is the high growth rate ($\gamma \sim \sqrt{\omega_{He}\omega_{Hi}}$), which is comparable with the maximum growth rate of electrostatic modes of a zero-pressure plasma, which propagate at oblique angles to the external magnetic field.[2]

HOT-ION PLASMA ($T_i \gg T_e$)

We now consider instabilities in a hot-ion plasma when the influence of the finite electron pressures must be included. In the case $\beta_e \gg 1$ (β_i is arbitrary) the quantity $\zeta \sim 1/\beta_e$ is large in Eq. (2.7). Then Eq. (2.7) can be simplified and reduced to the dispersion equation

$$1 + q\left(1 - \frac{k_x u}{\omega}\right) + \frac{q}{\beta_i}\left(1 + i\sqrt{\pi} z_i w_i\right) - \frac{\pi^2}{16}\frac{\omega^4}{k_x^2 u^2 q}\zeta^4 e^{-2\zeta}$$
$$- i\pi\zeta^2 e^{-\zeta}\left\{1 + q\left(1 - \frac{k_x u}{\omega}\right) + \frac{\omega}{k_x u}\frac{q}{\beta_i}\left(1 + i\sqrt{\pi} z_i w_i\right)\right.$$
$$\left.\times\left(1 - \frac{\omega}{2k_x u q}\right) - \frac{\omega^2}{2k_x^2 u^2 q}\right\} = 0. \qquad (4.1)$$

If we ignore the residue terms $\sim e^{-\zeta}$, Eq. (4.1) reduces to the dispersion equation investigated in ref. 1, in which it is shown that drift waves propagating at an angle $\theta = \pi/2$ in a plasma with $\beta_i \sim 1$ have a high growth rate; this growth rate can be higher than for electron-acoustic oscillations ($\gamma \sim 0.1\,(u^2/v_{Ti}^2)\sqrt{\omega_{He}\omega_{Hi}}$).

Let us now investigate the role of the residue terms in (4.1). Assuming that the terms $\sim e^{-\zeta}$ make a contribution only to the growth rate, from (4.1) we have

$$\left.\begin{aligned}\omega &= \frac{k_x u q \beta_i}{\beta_i + q(1+\beta_i)},\\ \gamma &= \sqrt{\frac{\pi}{2}}\, u\frac{\omega_{pe}}{c}\frac{q^{3/2}\beta_i(\beta_i + q)}{[\beta_i + q(1+\beta_i)]^3}\\ &\times\left\{\frac{u}{v_{Ti}} - \sqrt{\frac{\pi}{2}}\zeta^2 e^{-\zeta}\left[2 + \frac{\beta_i^2}{\beta_i + q(1+\beta_i)}\right]\right\},\end{aligned}\right\} \qquad (4.2)$$

where

$$\zeta = \frac{q}{\beta_i + q(1+\beta_i)}\frac{T_i}{T_e}.$$

Therefore, allowance for the residue terms in (4.1) has a stabilizing influence on the instability, since it reduces the growth rate. There exists a certain critical value $\beta_e = \beta_{cr} \ll 1$ at which the maximum growth rate (4.2) becomes equal to zero. This β_{cr} can be found from the following arguments. The residue term in (4.2) is a minimum for $q \gg 1$, so that in this case $\zeta = \beta_i/(1+\beta_i)\,1/\beta_e$. The vanishing of the maximum growth rate is possible when

$$\left(\frac{\beta_i}{1+\beta_i}\right)^2\frac{1}{\beta_{cr}^2}\exp\left[-\frac{\beta_i}{1+\beta_i}\frac{1}{\beta_{cr}}\right] = \frac{1}{\sqrt{2\pi}}\frac{u}{v_{Ti}} \ll 1. \qquad (4.3)$$

It follows from (4.2) and (4.3) that in a plasma with $\beta_e \sim 1$ instability occurs only when $u \gtrsim v_{Ti}$.

Let us now investigate the instability in a plasma with $\beta_e \gtrsim 1$ ($\beta_i \gg 1$). Setting $|z_i| \ll 1$, $\omega = k_x u + \Delta\omega$ ($\Delta\omega \ll k_x u$), $\zeta = 1/\beta_e \lesssim 1$ we obtain from Eq. (2.7)

$$\mathrm{Re}\,\Delta\omega = -\frac{k_x u}{\beta_i} + k_x u\frac{(\beta_e - 1)}{q},$$

$$\frac{\gamma}{|k_x|u} = \sqrt{\frac{\pi}{2}}\frac{u}{v_{Ti}\beta_i^2}\left[1 + (1-\beta_e)\mu\frac{T_i}{T_e}\right]$$
$$- \frac{\pi e^{-1/\beta_e}}{\beta_i^2}\frac{\left(1 + \frac{3}{2}\mu\frac{T_i}{T_e}\right)^2\beta_e^2}{(\beta_e - e^{-1/\beta_e}\,\mathrm{Re}\,Ei)^2 + \pi^2 e^{-2/\beta_e}} - \frac{5}{6}\frac{\pi e^{-1/\beta_e}}{q}. \qquad (4.4)$$

For $\mu \ll 1/\beta_i$ the growth rate (4.4) has the form

$$\gamma = \sqrt{\frac{\pi}{2}}\frac{u}{v_{Ti}\beta_i^2}\sqrt{\frac{T_i}{T_e}\mu}\left[\frac{u}{v_{Ti}} - \frac{\sqrt{2\pi}e^{-1/\beta_e}\beta_e^2}{(\beta_e - e^{-1/\beta_e}\,\mathrm{Re}\,Ei)^2 + \pi^2 e^{-2/\beta_e}}\right]\sqrt{\omega_{He}\omega_{Hi}}$$

and increases with increasing μ. When $\mu \gg 1/\beta_i$, the modes are absorbed by resonant electrons more strongly than they are excited by the resonant ions, so that the growth rate (4.4) becomes negative. The waves that are most rapidly excited are those with $\mu \sim (T_e/T_i)(1/\beta_e) = 1/\beta_i$, whose growth rate is of order

$$\gamma_m \sim \left(\frac{T_e}{T_i}\right)^2\beta_e^{-3/2}\sqrt{\omega_{He}\omega_{Hi}}\left(\frac{u}{v_{Ti}}\right)^2. \qquad (4.5)$$

The condition $z_i \ll 1$ is then satisfied for $u/v_{Te} \ll \beta_i$.

It is interesting to note that the growth rate (4.5) decreases rapidly with increasing β_e; in a plasma at very high pressure ($\beta_e \gg 1$) the condition $\gamma > \omega_{Hi}$ breaks down and the above instabilities disappear.

5. ISOTHERMAL PLASMA ($T_e \sim T_i$)

We now investigate the excitation of modes propagating at right angles to a magnetic field in an isothermal plasma at high pressure $\beta \gg 1$. Assuming in this case $\omega = k_x u + \Delta\omega$ ($\Delta\omega \ll k_x u$), $\zeta \simeq 1/\beta_e \ll 1$ and ignoring the terms $\sim \mu^2$, we find from Eq. (2.7) that

$$\mathrm{Re}\,\Delta\omega = k_x u\left[\mu - \frac{1}{\beta_i}\left(1 + \frac{T_e}{T_i}\right)^{-1}\right],$$

$$\gamma = \sqrt{\frac{\pi}{2}}\left(1 + \frac{T_e}{T_i}\right)^{-3}\frac{|k_x|u}{\beta_i^2}\left\{\frac{u}{v_{Ti}}\left[1 - \mu\beta_e\left(1 + \frac{T_i}{T_e}\right)\right] - \sqrt{2\pi}\left(1 + \frac{T_e}{T_i}\right)\right\}.$$

The quantity γ attains a maximum value when $\mu = 1/3\,(v_{Ti}/u\beta_e)(1 + T_i/T_e)^{-1}[u/v_{Ti} - \sqrt{2\pi}(1 + T_e/T_i)]$ and is then equal to

$$\gamma_m = \frac{1}{3}\sqrt{\frac{2\pi}{3}}\beta_e^{-5/3}\left(\frac{T_e}{T_i}\right)^2\left(1 + \frac{T_e}{T_i}\right)^{-7/3}\left(\frac{u}{v_{Ti}}\right)^{1/3}$$
$$\times\left[\frac{u}{v_{Ti}} - \sqrt{2\pi}\left(1 + \frac{T_e}{T_i}\right)\right]^{3/2}\sqrt{\omega_{He}\omega_{Hi}}. \qquad (5.1)$$

It follows from (5.1) that the instability occurs when the current velocity exceeds a certain value:

$$u > u^* = \sqrt{2\pi}\left(1 + \frac{T_e}{T_i}\right)v_{Ti}. \qquad (5.2)$$

At the same time, the condition $z_i \ll 1$ is satisfied for $u < u^*\beta_i$, so that the solution obtained above is valid if the current velocity lies in the range $u^* < u < u^*\beta_i$. Let us estimate the value of γ_m in the limiting case $u \sim u^*\beta_i$, for which the growth rate takes its largest value. We find that

$$\gamma_m \sim \frac{1}{\sqrt{\beta}}\sqrt{\omega_{He}\omega_{Hi}}. \qquad (5.3)$$

Thus, in an isothermal plasma at high pressure ($\beta \gg 1$), as in a nonisothermal plasma, the growth rates decrease with increasing pressure.

We thank K. N. Stepanov for helpful comments.

---

[1] I. P. Gudblud, A. I. Pyatak, and V. L. Sizonenko, Zh. Eksp. Teor. Fiz., 64, 2084 (1973).

[2] L. I. Grigor'eva, V. L. Sizonenko, B. I. Smerdov, K. N. Stepanov, and V. V. Chechkin, Zh. Eksp. Teor. Fiz., 60, 605 (1971) [Sov. Phys.-JETP, 33, 329 (1971)].

Charge-carrier density of the plasma produced in a Penning mixture by irradiation by uranium fission fragments and reactor radiation

G. A. Batyrbekov, Yu. D. Kuznetsov, and Zh. S. Takibaev

(Submitted June 27, 1973; resubmitted November 2, 1973)
Zh. Tekh. Fiz., 44, 1022-1024 (May 1974)

An experimental study has been made of a plasma produced in a Penning mixture (Ar/Ne $\sim 10^{-3}$) under the influence of uranium fission fragments and of reactor radiation. The apparatus for producing and diagnosing the plasma is described, and measurements of the electron density and temperature in the plasma for a neutron flux of $2\cdot 10^{13}$ neutrons/cm^2 are reported.

A question which arises in connection with efforts to achieve direct conversion of the thermal energy in a nuclear reactor into electrical energy is that of producing a plasma under reactor conditions. This plasma is required in a thermionic converter in order to neutralize the electronic space charge between the electrodes; it is required in MHD generators to produce a gas which is a good electrical conductor.[1,2]

It has been suggested[3,4] that a thermionic converter with an inert-gas plasma can be obtained by ionization of the gas by reactor radiation and uranium fission fragments.

It is therefore of interest to study a plasma produced under reactor conditions and to optimize the plasma-production conditions (the composition and pressure of the gas and the neutron flux) in order to produce a plasma of maximum possible density in the active zone of a reactor.

We report here on the construction of apparatus suitable for plasma diagnostics within a reactor and a study of the plasma produced in a Penning mixture in ionization caused by uranium fission fragments and reactor radiation.

EXPERIMENTAL PROCEDURE

The properties of the plasma produced under the reactor conditions are studied by means of electrostatic probes. The probe method is used most frequently for plasma diagnostics at low gas pressures, in which case the probe radius is much shorter than the electron mean free path ($R_p \ll \lambda_e$). Since relatively high inert-gas pressures (above 100 torr) are required to produce a plasma of the maximum density, we use the theory derived in ref. 5 for the operation of electrostatic probes in a dense plasma.

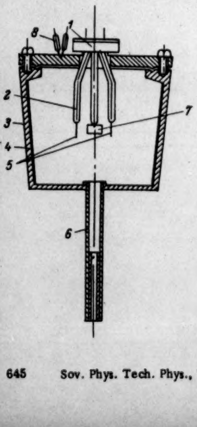

Fig. 1. The ampoule. 1) Radiation-resistant vacuum-tight connector; 2) quartz insulator; 3) body of ampoule; 4) uranium layer; 5) cylindrical probes; 6) fitting for evacuation; 7) flat probe; 8) thermocouple.

In accordance with this theory, we use three probes – two cylindrical probes and one flat probe – for the measurements.

The two cylindrical probes (the "probe" and the "counterprobe") are used to determine the electron temperature,[6] while the flat probe and the cylindrical probes are used to determine the ion and electron densities.

To perform tests on plasma within the reactor by the probe method, we constructed an apparatus consisting of the following basic elements:

1. An ampoule of Kh18N9T steel, which holds the electrostatic probe and a layer of uranium enriched to 90% U^{235}, filled with the inert gas (Fig. 1). The probes are connected electrically to the apparatus outside the chamber through a radiation-resistant, vacuum-tight multiconductor connector. The working surfaces of the probes are convered by quartz insulators. The uranium layer is deposited on a thin tungsten substrate, which is itself mounted on the lateral inner surface of the ampoule. The uranium layer is at least 15 mg/cm^2 thick. The ampoule is evacuated and filled with gas through fittings welded to its bottom. After the ampoule is filled with the gas mixture it is sealed off.

2. A vacuum channel 60 mm in diameter of type SAV alloy, in which the ampoule with the gas mixture is placed and through which the probe leads run from the ampoule to the measuring apparatus. The probe circuit is shielded by radiation-resistant insulation (alundum shavings) within the vacuum channel. The top of the vacuum channel is finished in a flange having an end cap, which holds a vacuum-tight connector for electrical connection between the probe and the measuring apparatus. The end cap can be removed or replaced by a special wrench during an experiment.

The channel has a conical recess which holds the ampoule, whose lateral surface has the same taper. This arrangement provides good thermal contact so that heat can be transferred from the ampoule to the channel and to the coolant water which flows around the channel.

3. A tube 90 mm in diameter and 15 m long which connects the vacuum pumps with the vacuum channel.

4. A system of pumps consisting of a TMN-200 turbomolecular pump and a VN-2MG forevacuum pump, which evacuates the vacuum chamber after the ampoule is replaced.

The channel with the ampoule is placed in the center of the active zone of a VVR-K reactor.

EXPERIMENTAL RESULTS

We measured the properties of the plasma in a Penning mixture with an argon : neon concentration ratio of 10^{-3} and a pressure of 200 torr. The ion branches of the probe characteristic are analyzed on the basis of the Ul'yanov theory cited above. The values of the recombination coefficient in the Penning mixture, 10^{-9}, are taken from ref. 7. In calculating the ambipolar-diffusion coefficient we take into account only the mobility of the predominant gas in the mixture.

The electron or ion density in the plasma determined in this manner for a reactor power of 2 MW and a thermal-neutron flux of $\sim 2 \cdot 10^{13}$ neutrons/(cm^2 · sec) in the central channel turns out to be

$$n_i = n_e = (6 \pm 2) \cdot 10^{12}\ \text{cm}^{-3}$$

The electron temperature is $T_e = 1200$°K.

This electron density is apparently close to the optimum value for the given reactor power; it can be raised by increasing the power.

---

[1] F. Jamerson, in: Thermionic Energy Conversion [Russian translation], Atomizdat, Moscow (1964).

[2] E. I. Yantovskii and I. M. Tolmach, MHD Generators [in Russian], Izd. Nauka, Moscow (1972).

[3] R. Forman and R. Tolman, in: Thermionic Energy Conversion [Russian translation] Atomizdat, Moscow (1964).

[4] K. M. Aref'ev and I. I. Paleev, Fundamentals of Thermionic and MHD Energy Conversion [in Russian], Atomizdat, Moscow (1970).

[5] K. N. Ul'yanov, Zh. Tekh. Fiz., 40, 4 (1970).

[6] E. Johnson and L. Malter, Phys. Rev., 80, 58 (1950).

[7] M. A. Biondi, Phys. Rev., 83, 1078 (1951).

Expansion of a recombining plasma in vacuum

E. E. Lovetskii, A. N. Polyanichev, and V. S. Fetisov
Moscow Engineering Physics Institute
(Submitted April 20, 1973; resubmitted September 7, 1973)
Zh. Tekh. Fiz., 44, 1025-1031 (May 1974)

The expansion, in vacuum, of a recombining lithium plasma initially in a state of ionization equilibrium is treated by numerical solution of gas-dynamic equations. If the characteristic recombination length of singly charged particles exceeds the initial radius of the cloud, the number density of the particles of given charge is a monotonic function of the radius. An inverse relationship between the recombination length and the initial radius produces nonuniform heating due to recombination. As a result, the ion distribution along the coordinate is characterized by maxima at the periphery of the cloud. The density maxima corresponding to ions of different charge are separate; the maxima for ions of smaller charge are shifted toward smaller radii and velocities. The solution indicates that recombination heating produces additional acceleration of the ions.

INTRODUCTION

In this paper we examine the spatial distribution of ions of different charge in a vacuum. An example of this process is the plasma generated by the action of a powerful laser beam on the surface of a solid target. Mass-spectroscopic techniques are used in refs. 1 and 2 to obtain the energy distributions of ions of different charge in a late stage of expansion of a laser plasma. It turns out that the ion energy distribution has sharp maxima, with the maxima for ions of high charge shifted toward high energies. Another important feature of the ion energy distribution is noted in refs. 1 and 2: the distributions for ions of different charge (with $Z \leqslant 5$) have a common upper limit. The interpretation of the experimental results given in ref. 2 ascribes the shape of the ion distributions to recombination in the expanding plasma; however, the results only give a qualitative picture of the expansion. In ref. 3, the formation of ion energy spectra and the spatial distribution are analyzed on the basis of a self-similar solution of the gas-dynamic equations describing the expansion of a recombining plasma. The results obtained in ref. 3 are limited to the case of photorecombination and refer to a plasma in which ionization equilibrium has completely broken down at the initial time. In the present paper, the problem of expansion of a plasma cloud in vacuum is solved by numerical integration of the gas-dynamic equations allowing for ionization and recombination. It is established that the recombination process is different in different regions of the cloud and that it depends sensitively on the initial plasma dimension.

If the initial cloud dimension R_0 is smaller than the characteristic length for recombination of singly charged ions l_1, the plasma is set in motion until there is an appreciable recombination of ions with $Z > 1$. Strong recombination occuring after ionization equilibrium breaks down produces an intense heating of the entire mass of the cloud; as a result the degree of ionization and the charged particle densities vary almost monotonically from the center to the periphery. When $R_0 > l_1$, a small plasma layer near the plasma–vacuum interface is subjected to strong recombination heating. The major portion of the ions with $Z > 1$ succeed in recombining until ionization equilibrium breaks down due to rarefaction, and the stored potential ion energy becomes small. Therefore, heat release in the plasma core is small and is not able to retard the recombination process. Freezing of the degree of ionization occurs only in the periphery of the plasma. The spatial distributions of the ions have separate maxima.

1. INITIAL EQUATIONS

Expansion of a multicomponent plasma in a vacuum can be described by using multifluid gas-dynamic equations including ionization and recombination processes. Then the ions are driven by the electric field, the pressure, and the friction between the different groups of ions.[4] In the electric field ions of different charge are accelerated to different velocities. However, the strong friction between ion species equalizes these velocities. The numerical calculations performed in ref. 5 indicate that for parameters corresponding to a laser-produced plasma the ion–ion collisions equalize the velocities of ions of different species. In the initial stage of the expansion this assertion is valid for the entire volume of the expanding plasma, excluding only a small region on the periphery of the cloud with dimensions of the order of the ion mean free path for ion–ion collisions. In this region the ion friction is small, and the electric field forces can lead to a relative acceleration of charges with different Z. We note that for the approximate experimental conditions the ratio between the ion mean free path and the initial cloud dimension is less than 10^{-3}.

In the present paper recombination effects are included in the analysis of plasma expansion. The behavior of the plasma in the peripherial region is neglected. Therefore, the relative motion of ions of different charge can be neglected and the expansion of the plasma can be considered as a whole.

We consider radiative recombination with electron capture in the ground state[6] and three-body recombination to a highly excited level with the electron as the third particle.[7] It is well known[8] that a portion of the energy freed in three-body recombination heats the electron gas.

Assuming that all the plasma particles have the same temperature, we include recombination heating in the equation for the total plasma pressure. Thermal conductivity effects are neglected; this procedure is valid if the following condition is satisfied:

$$R_0 > \sqrt{\frac{M}{m}}\,\frac{6\sqrt{2}\,\pi^{3/2}}{L}\,(n_a r_D^3)\, r_D,$$

where L is the Coulomb logarithm and r_D is the Debye radius. This condition is satisfied for the values of the parameters given below.

Assuming neutrality and neglecting electron inertia and electron–ion collisions in the equations of motion, we can write the system of equations describing spherically symmetric expansion of the plasma in a vacuum as

$$\left.\begin{aligned} &\frac{\partial u}{\partial t}+u\frac{\partial u}{\partial r}=-\frac{1}{\rho}\frac{\partial P}{\partial r},\\ &\frac{\partial n_z}{\partial t}+\frac{1}{r^2}\frac{\partial}{\partial r}(r^2un_z)=A_z,\\ &\frac{\partial P}{\partial t}+u\frac{\partial P}{\partial r}+\frac{5}{3}\frac{P}{r^2}\frac{\partial}{\partial r}(ur^2)=\frac{2}{3}Q. \end{aligned}\right\} \quad (1)$$

The expression for A_Z and Q is

$$\left.\begin{aligned} A_z&=n_e\{n_{z+1}\Gamma_2(Z+1)+n_{z-1}\Gamma_1(Z-1)-n_z[\Gamma_1(Z)+\Gamma_2(Z)]\},\\ Q&=n_e\sum_{Z=0}^{Z_m}n_z\left\{E(Z)\Gamma_4(Z)-I(Z)\Gamma_1(Z)-\frac{3}{2}T\Gamma_3(Z)\right\}. \end{aligned}\right\} (2)$$

Here, P is the total plasma pressure, n_Z is the number density of particles with charge $Z(0 \leq Z \leq Z_m)$, Z_m is the maximum ionization multiplicity, I(Z) is the ionization potential of a Z-fold ionized ion, $n_e = \sum_{Z=0}^{Z_m} Zn_Z$ is the number of electrons per unit volume, $\rho = \sum_{Z=0}^{Z_m} n_Z M$ is the plasma density, and M is the ion mass.

The ionization coefficient is determined from the condition for detailed balance of the ionization and recombination process

$$\left.\begin{aligned} \Gamma_1(Z)&=2\left(\frac{2\pi mk}{h^2}\right)^{3/2}\frac{T^{3/2}}{n_e}e^{-\frac{I(Z)}{T}}\Gamma_4(Z),\\ \Gamma_2(Z)&=\Gamma_3(Z)+\Gamma_4(Z), \end{aligned}\right\} \quad (3)$$

and Γ_3 is the radiative recombination coefficient[6]

$$\Gamma_3(\Gamma)=2\cdot10^{-13}\frac{Z^2}{\sqrt{T}}. \quad (4)$$

The three-body recombination coefficient is taken in the form proposed in ref. 7:

$$\Gamma_4(Z)=\frac{4\pi\sqrt{2\pi}}{9}\frac{e^{10}Z^3}{\sqrt{m}\,T^{9/2}}n_e. \quad (5)$$

Finally, E(Z) is the energy released in the gas by a three-body recombination event:

$$E(Z)=\begin{cases} 6\cdot10^{-4}n_e^{1/6}T^{1/18} & E(Z)>T,\\ T & E(Z)<T,\\ I(Z-1) & E(Z)>I(Z-1). \end{cases} \quad (6)$$

The energy radiated from the plasma which is assumed to be optically thin, is I(Z − 1) − E(Z). The latter assumption is valid since the radiative mean free path exceeds the plasma dimension for our case. The approximate estimates are given in ref. 6.

After the appropriate transformations the system of equations (1) is replaced by a system of difference equations which is solved numerically for a lithium plasma with T_0 = 9 eV and $n_a = 10^{19}$ cm^{-3} (T_0 is the initial plasma temperature, which is assumed to be radially homogeneous, and $n_a = \sum_{Z=0}^{Z_m} n_Z(r, t = 0)$. The initial densities of all particles are independent of the radius.

We assume that when t = 0 the plasma is in a state of ionization equilibrium. Computer calculations for the ion and neutral-particle densities give

$$n_0=3.2\cdot10^{-7}n_a,\quad n_1=2.5\cdot10^{-2}n_a,$$
$$n_2=0.824n_a,\quad n_3=0.151n_a.$$

The boundary conditions selected are as follows: zero velocity in the center of the cloud and free expansion to the boundary with the vacuum.

2. NUMERICAL CALCULATIONS

In this section the results of a numerical solution of system (1) are given for a lithium plasma.

When the plasma expands from the boundary with the vacuum to the center, a spherical rarefaction wave arises in which the plasma density and temperature decline. Because of the exponential temperature dependence of the ionization coefficient, ionization equilibrium breaks down and recombination begins to dominate. The heat released by recombination increases the temperature and, thus, the rate of expansion of the plasma. This process is sensitive to the initial dimension of the cloud. Recombination occurs in all the cloud regions which are not yet in motion.

At the initial time the right-hand terms in the continuity equations are zero since the plasma is in a state of ionization equilibrium when t = 0. Three-body recombination is accompanied by heating and an increase in the temperature. This process is represented by the first term in the expression for Q. The second term is the energy expended on ionization and reduces the temperature (the third term, the radiative recombination, does not generally change the plasma temperature). Estimates from Eq. (6) indicate that the heating E(Z) is smaller than the ionization potential I(Z − 1), and this means that the difference between the first two terms in the expression for Q is negative. The temperature of the quiescent plasma declines, and A_α becomes nonzero. The most rapid recombination is for ions with Z = 2, 3.

Thus, if the initial radius of the cloud is small, the rarefaction wave covers the entire plasma volume until recombination of doubly and triply charged ions becomes appreciable. Ions with Z = 2, 3 recombine strongly in the rarefaction wave and produce a significant amount of heating. Since there are many doubly and triply charged ions in the entire volume, the heating produces a marked freezing of the degree of ionization over the entire cloud volume (curve 1 in Fig. 1). The plasma velocity is two or three times greater than the adiabatic expansion rate.

A different situation obtains when a cloud with large radius expands. When $R_0 \gg l_1$ (l_1 is the characteristic recombination length of singly charged ions), the time it takes for the rarefaction wave to reach the center of the cloud exceeds considerably the characteristic time for recombination of doubly and triply charged ions.

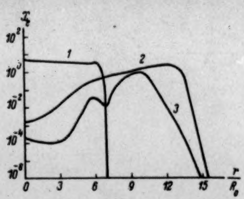

Fig. 1. Degree of ionization x_e as a function of radius. 1) $R_0 = l_1/2$, $t = 1.1\ t_p$; 2) $R_0 = l_1$, $t = 2.45\ t_p$; 3) $R_0 = 3\ l_1$, $t = 2.6\ t_p$.

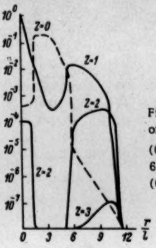

Fig. 3. Number density of particles of different charge in units of $\sum_n n_z \cdot (0, t)$. $R_0 = 3\ l_1$; $t = 0.6\ t_p$; $n_0(0, t) = 6.3 \cdot 10^{-4} n_a$; $n_1(0, t) = 0.99\ n_a$; $n_2 \cdot (0, t) = 1.74 \cdot 10^{-4} n_a$; $n_3 = 5.9 \cdot 10^{-3} n_a$.

Because of recombination the densities of doubly and triply charged ions in the core of the cloud are reduced until the disturbance from the boundary reaches the center. Therefore, strong heating occurs only in the periphery of the cloud, where there is an exponential breakdown of ionization equilibrium, due to the expansion, until appreciable recombination of ions with Z = 2, 3 occurs. The temperature near the vacuum boundary exceeds the temperature at the center of the plasmoid, which is already in motion. This effect can be seen clearly in Fig. 2 (curve 1). The temperature-dip region moves toward the center as time increases. The temperature peak produced at the periphery by strong recombination heating is retained, although its magnitude decreases with the expansion (curve 2 in Fig. 2). The strong heating at the periphery means that freezing of the degree of ionization occurs precisely in this region. The degree of ionization in the core of the cloud is several orders of magnitude lower (curves 2 and 3 in Fig. 1). It can be seen that the freezing effect at the periphery becomes sharper as R_0 increases. The radial particle density distribution is shown in Fig. 3. It is clear that "recombination" waves follow in the wake of the rarefaction wave. Strong recombination occurs within the recombination wave front. Due to the exponential dependence of $\Gamma_1(Z)$ on I(Z), ionization equilibrium breaks down faster for ions with large Z; therefore, different recombination waves correspond to ions with different charge. The recombination wave of ions with Z = 3 has already reached the center, and their density is nonzero only near the vacuum boundary. Recombination waves of ions with Z = 1, 2 have not yet reached the center. Recombination of ions with higher charge exceeds recombination of ions with smaller charge; this is due to the following dependence of the characteristic recombination time τ_Z of ions with charge Z:

$$\tau_z \sim Z^{-3}.$$

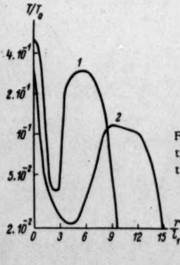

Fig. 2. Radial temperature distribution at different times. $R_0 = 3\ l_1$; 1) $t = 0.46\ t_p$; 2) $t = 0.6\ t_p$.

The dips in the curves of Fig. 3 correspond to the temperature dip.

The influence of the initial plasma parameter on the integrated ion yield for a given charge is shown in Fig. 4. The effective yield increases with decreasing radius. In the inertial stage of expansion the ion densities are frozen.

The energy characteristics of the plasma indicate the manner in which the potential ion energy is redistributed during expansion (Fig. 5). As the radius decreases the kinetic energy of the plasma, per initial unit volume,

$$\varepsilon_k(t) = \left(\frac{l_1}{R_0}\right)^3 \int dV \frac{\rho u^2}{2}$$

increases because of strong recombination heating for the expansion of a cloud with smaller radius. The origin of this effect is discussed above. The thermal energy

$$\varepsilon_T(t) = \left(\frac{l_1}{R_0}\right)^3 \int dV \frac{3}{2} P$$

decreases much faster for $R_0 = 3l_1$ by comparison with cloud with $R_0 = l_1/2$; again, this is due to the decrease in heating for the expansion of a large cloud. The total energy emitted by the plasma per initial unit volume for time t is

$$\varepsilon_{\text{rad}}(t) = \left(\frac{l_1}{R_0}\right)^3 \sum_{Z=0}^{Z_m} \int_0^t dt' \int dV n_z \{I(Z-1)\Gamma_4(Z)$$

$$+ (I(Z-1) - E(Z))\Gamma_z n_e\}.$$

The energy is composed of the energy radiated in photorecombination and three-body recombination. When $R_0 \gg l_1$, $\varepsilon_{\text{rad}}(t)$ is largely determined by three-body recombination, and when $R_0 = l_1/2$ photorecombination predominates.

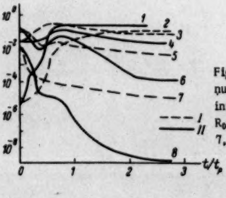

Fig. 4. Time variation of the total number of particles with charge Z per initial unit volume. I) $R_0 = l_1$; II) $R_0 = 3\ l_1$; Z: 1, 2) 0; 3, 4) 1; 5, 6) 2; 7, 8) 3.

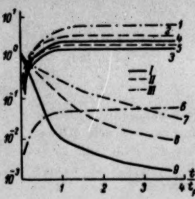

Fig. 5. Energy characteristics of the plasma. I) $R_0 = 3l_1$, II) $R_0 = l_1$, III) $R_0 = l_1/2$; 1, 2, 3) $\varepsilon_k(t)$; 4, 5, 6) $\varepsilon_{rad}(t)$; 7, 8, 9) $\varepsilon_T(t)$. All values refer to the initial unit volume.

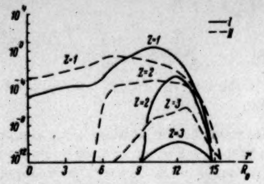

Fig. 6. Asymptotic behavior of ion densities in units of $N_0 = \sum_{z=0}^{z_m} n_z(0; t)$. I) $R_0 = 3l_1$, $t = 2.6t_p$, $N_0 = 5\cdot10^{-3}n_a$; II) $R_0 = l_1$, $t = 2.5t_p$, $N_0 = 4.8\cdot10^{-3}n_a$.

Curves 4, 5, and 6 in Fig. 5 indicate that the energy radiated by the plasma (per initial unit volume) increases with the initial cloud radius, as shown by the fact that the fraction of the potential energy expended in heating decreases with increasing initial plasma dimensions.

We now consider the densities of ions with different charge for times ($t > t_p = R_0\sqrt{M/T_0}$) sufficiently large so that the ion densities are already frozen (Fig. 6). Strong freezing is experienced only by the ions at the periphery of the cloud. Intense ion recombination occurs in the plasma core, and doubly and triply charged ions disappear from this region. It is clear that the maxima of the asymptotic distributions are shifted toward the center with decreasing Z. Since the radial dependence of the velocity in the calculated cases is almost linear the ion energy distribution has similar properties, namely: The maxima of the energy distributions are shifted toward lower energies with decreasing ion charge. It is characteristic that all the spectra have a common right-hand limit.

It should be noted that the periphery ions are appreciably accelerated, and their energy increases by a factor of 30-50 (for adiabatic expansion the acceleration of the boundary is relatively small and the particle energy increases by less than a factor of 10). Similar data agree with the data of ref. 9, in which a 400-eV lithium plasma is investigated.

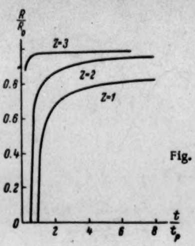

Fig. 7. Time variation of ion density maxima ($R_0 = l_1$).

The behavior of the ion density maxima is shown in Fig. 7 in Lagrange coordinates.

It is clear that when $t > 6t_p$ the curves form a plateau corresponding to a steady motion of the maxima. The resolution between the individual maxima is fairly good.

The results of the numerical calculation indicate that the presence of accelerated ions and the shape of the energy spectra in the experiments[1,2] can be attributed to recombination in the expanding plasma.

In conclusion the authors thank V. E. Kondrashov for help with the programming.

---

[1] Yu. A. Bykovskii, N. N. Degtyarenko, V. F. Elesin, Yu. P. Kozyrev, and S. M. Sil'nov, Zh. Eksp. Teor. Fiz., 60, 1306 (1971) [Sov. Phys.-JETP, 33, 706 (1971); ZhETF Pis. Red., 14, 238 (1971) [JETP Let., 14, 157 (1971)].

[2] O. B. Anan'in, Yu. A. Bykovskii, N. N. Degtyarenko, Yu. P. Kozyrev, S. M. Sil'nov, and B. Yu. Sharkov, ZhETF Pis. Red., 16, 543 (1972) [JETP Lett., 16, 384 (1972)].

[3] Yu. V. Afanas'ev and V. B. Rozanov, Zh. Eksp. Teor. Fiz., 62, 247 (1972) [Sov. Phys.-JETP, 35, 133 (1972)].

[4] S. I. Braginskii, Reviews of Plasma Physics, Vol. 1, Consultants Bureau, New York (1965).

[5] R. Sigel, S. Witowskii, Kh. Baumkhacker, K. Büchl, K. Eidmann, H. Hora, H. Mennike, P. Mulser, D. Pfirsch, and H. Salzmann, Kvant. Elektron. (Mosc.), No. 2, 37 (1972) [Sov. J. Quant. Electron., 2, 117 (1972)].

[6] Ya. B. Zel'dovich and Yu. P. Raizer, Physics of Shock Waves and High-Temperature Hydrodynamic Phenomena [in Russian], Nauka, Moscow (1966).

[7] A. V. Gurevich and L. P. Pitaevski, Zh. Eksp. Teor. Fiz., 46, 1281 (1964) [Sov. Phys.-JETP, 19, 870 (1964)].

[8] N. M. Kuznetsov and Yu. P. Raizer, Prikl. Mekh. Tekh. Fiz., 10, No. 4 (1965).

[9] C. Yamanaka, T. Yamanaka, H. Kang, T. Sasaki, K. Yoshida, K. Ueda, M. Hongyo, and M. Waki, Kvant. Electron. (Mosc.), No. 2, 45 (1972) [Sov. J. Quant Electron., 2, 127 (1972)].

Investigation of ionization processes behind strong shock waves using an electrical conductivity probe

V. A. Tishchenko, N. V. Khandurov, and É. K. Chekalin

G. M. Krzhizhanovskii Power Research, and Engineering Institute, Moscow

(Submitted August 6, 1973)
Zh. Tekh. Fiz., 44, 1032-1036 (May 1974)

Results are presented of investigations of ionization properties of an argon plasma, in a shock tube, obtained from measurements of the electrical conductivity ion behind the incident shock. The investigations pertain to the initial pressure range P_1 = 5 to 14 torr and the Mach number range M_1 = 8 to 10. It is shown that the addition of about $2 \cdot 10^{-2}$ parts of air leads to contraction of the ionization relaxation zone.

The flush-mounted wall gauge for measurement of electrical conductivity of shock-heated gas flows described in ref. 1 has a number of advantages over the other type consisting of a high-frequency coil which either surrounds a stream of conducting gas[2,3] or is inserted into the stream.[4] The flush gauge allows measurement of the conductivity of supersonic plasma flow with good temporal and spatial resolution, does not introduce gasdynamic perturbations into the stream, and has good sensitivity over a wide range of electrical conductivity. The gauge can easily be calibrated by means of electrolytes and slabs of graphite and metals. When there is no skin effect the gauge probe field penetrates into the plasma to a depth of the order of the coil diameter. The readings of a wall gauge of relatively small size depend appreciably on the properties of the boundary layer near the gauge surface. Direct measurement of the electrical conductivity of the unperturbed plasma stream is only possible when the wall gauge diameter is much greater than the boundary layer thickness.[1] If the gauge and the boundary layer are comparable in dimension, or if an easily ionized impurity is present, it is difficult to interpret the readings of the wall conductivity gauge.

The aim of the present work is to explore the possibility of measuring conductivity and ionization relaxation time in a gas behind strong shock waves in a plasma with relatively high impurity content using a high-frequency coil located in the shock tube wall.

EXPERIMENTAL ARRANGEMENT

The investigations are conducted in a shock tube consisting of a high-pressure driver 100 mm in diameter and 1.0 m long, and a driven section 5.4 m long, separated by a copper diaphragm 1.5 mm thick. At a distance of 3.5 m from the diaphragm the driver section is connected through a transition section (0.2 m long) to a section of square channel, 72 × 72 mm in size and 1.8 m long. The square channel has a clear plastic measurement section (Fig. 1), 100 mm long, distant 0.8 m from the transition section and 0.9 m from the end of the tube; this section corresponds to the steady shock speed region. The reflected shock does not reach the measuring section during the experiment. The investigations are carried out with an initial pressure of 40 to 50 atm of hydrogen in the driver section, and an initial pressure of p_1 = 5 to 14 torr of argon in the driven section. Before filling, the driven section is pumped down to $5 \cdot 10^{-2}$ torr. Taking leakage into account, the relative air impurity in the test gas is $2 \cdot 10^{-2}$. The incident shock speed is measured by means of two ionization gauges. The signal from a third gauge is used to trigger the recorders. The accuracy of Mach number measurement in the range 8 to 10 is 2.5%. The error in meassurement of the initial pressure p_1 does not exceed 1%.

EXPERIMENTAL METHOD

In this work we use the high-frequency wall-mounted conductivity gauge described in ref. 1. The sensor coil is mounted on a ferrite rod, flush with the metal shock tube wall. The sensor is connected to an oscillator.[5,6] When the coil is in contact with a conducting medium the "Q" of the coil is reduced, reducing the amplitude of the oscillations. The change in the amplitude of oscillation ΔU_σ is detected by a balanced detector and recorded by an S1-16 oscilloscope. The sensor parameters: R_k = 0.3 cm, $f = \omega/2\pi$ = 5.3 MHz are chosen to suit the condition for zero skin effect, according to ref. 1, i.e., $R_k\sqrt{\sigma\mu\omega} \leq$

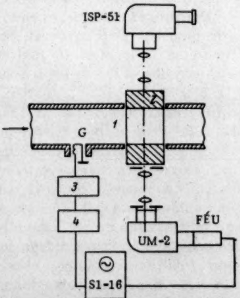

Fig. 1. Schematic diagram of the measurements. 1) Driven section; 2) measuring section; 3) oscillator; 4) balance detector; G is the conductivity gauge.

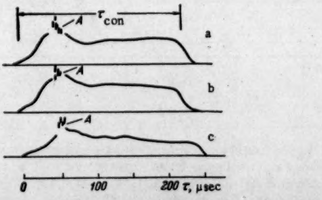

Fig. 2. Oscillograms of conductivity gauge signals (first series of experiments). p_1 = 7 torr; a) M_1 = 9.28; b) M_1 = 9.14; c) M_1 = 8.75. "A" indicates interference from the ionization gauge.

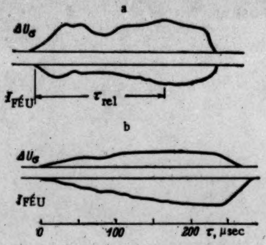

Fig. 3. Oscillograms of conductivity gauge signals ΔU_σ and continuum radiative intensity $I_{FÉU}$. a) First series of experiments, $p_1 = 10$ torr; $M_1 = 9$; b) second series, $p_1 = 7$ torr, $M_1 = 8.9$.

0.8 (R_k is the coil radius, σ is the electrical conductivity; μ is the magnetic permeability; ω is the angular frequency), for a maximum conductivity of $\sigma_{max} \sim 2000$ mho/m. The spatial resolution of the gauge is 0.8 cm.

Simultaneously with the recording of the electrical conductivity, measurements are taken of the relative intensity of the continuum spectra, which depends on the density of free electrons and ions. The axial region of the shock tube is imaged on the entrance slit of a type UM-2 monochromator with slit width 0.3 mm. The optical system comprises two lenses with focal lengths 94 and 110 mm. The spectral region selected is recorded by means of a type FÉU-19 M photomultiplier, and the output signal goes to the S1-16 oscilloscope through a cathode follower.

The investigation of the spectra composition of the gas radiation behind the shock is performed using a type ISP-51 spectrograph. Besides the argon lines, the spectrum shows lines of Na, and also Fe and Cu. The continuum is recorded in the 5300 Å region where there are no strong argon and impurity lines.

For the present experimental conditions the boundary layer is laminar.[1] Two series of experiments are made to elucidate the effect of easily ionized impurities, coming from the shock tube walls, on the nature of the conductivity gauge signal. In the first series no special measures are taken to keep the shock tube walls free from impurities; in the second series the inside surface of the shock tube is carefully cleaned and flushed out.

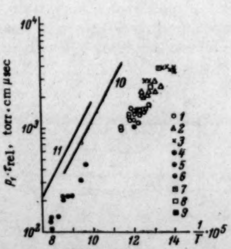

Fig. 4. Temperature dependence of the product $p_1 \cdot \tau_{rel}$ behind the incident shock in argon with air impurity. The time is in laboratory coordinates, and the temperature in °K. 1-4) $p_1 = 7$, 10, 14, and 5 torr, respectively, and air impurity of $2 \cdot 10^{-2}$ (our data); 5) $p_1 = 5$ torr, impurity $3.5 \cdot 10^{-3}$, 10^{-2} (ref. 9); 6) $p_1 = 5$ torr, impurity $8 \cdot 10^{-3}$ (ref. 10); 7-9) $p_1 =$ 9, 7, and 5 torr, impurity 10^{-2} (ref. 11); 10, 11) $p_1 = 50$ torr, impurity $2 \cdot 10^{-2}$ and $7 \cdot 10^{-4}$ (ref. 12).

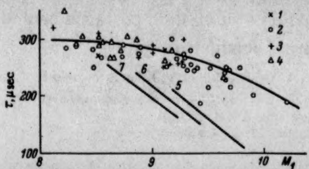

Fig. 5. Duration of the conductivity signal τ_{con} (1-4) and the ionization relaxation time $\tau_{rel.}$ (5-7), as a function of M_1. 1) $p_1 = 5$ torr; 2,5) $p_1 =$ 7 torr; 3,6) $p_1 = 10$ torr; 4,7) $p_1 = 14$ torr.

EXPERIMENTAL RESULTS AND DISCUSSION

Figure 2 shows three typical oscillograms of conductivity gauge signals behind the incident shock, for different Mach numbers (M_1). Earlier experiments with a thin-film temperature gauge[1] showed that the shock front coincides with the start of growth of the conductivity gauge signal ΔU_σ. There is a characteristic sharp fall in conductivity in the region of the shock-heated gas at the contact surface between the driver gas and the heated gas. The signal length from the shock front to the contact zone τ_{con} is taken to indicate the extent of shock-heated argon (test sample length). The oscillograms (Fig. 2) show a rapid signal increase up to a maximum. After the first maximum, depending on the Mach number M_1, the signal either decreases as the contact zone is approached (Fig. 2, c), or stays constant (Fig. 2, b). At the higher M_1 values (Fig. 2, a) a second weak maximum is observed. Sometimes the signal increases at the plateau. These features are typical of all the initial pressure p_1 levels tested.

Figure 3, a shows an oscillogram of the photomultiplier signal for the first series of experiments. The oscillograms of $I_{FÉU}$ typically show a first maximum, like that on the conductivity oscillograms. In the second series the inside walls of the shock tube are carefully cleaned. No first maxima are seen (Fig. 3, b) on the conductivity and intensity oscillograms in the first experiments after cleaning the walls. Analysis of the experimental data show that the first maximum on the oscillograms (Figs. 2 and 3, a) is probably due to the efflux of easily ionized impurities (Na) from the shock tube wall into the boundary layer. The fall in intensity of continuum radiation of the photomultiplier oscillogram following the first maximum is apparently due to the drop in the effective gas temperature in the boundary layer as its thickness increases, which leads to a decrease in charged-particle concentration. The falloff in conductivity gauge signal after the first maximum is also due to fall of temperature in the boundary layer as the latter grows. The effective conductivity in the boundary layer decreases sharply. The sharp maximum of distributed current observed in shock-heated argon in ref. 7 is probably also due to processes involving ionization of easily ionized impurities coming from the shock tube walls.

The subsequent growth of the continuum intensity and of the gauge signal, as well as the rise to the second maximum, are evidently connected with the process of ionization of argon in the flow core. In Fig. 3,a the zone of ionization relaxation for argon (τ_{rel}) is located between the shock front and the second maximum of the radiation (see the $I_{\text{FÉU}}$ signal). Since the time to equilibrate the electron and gas temperatures is relatively short (for $M_1 \sim$ 8 to 10), we can assume that the increase in conductivity behind the shock is determined uniquely by the increase in electron density.[8] Therefore, the gauge oscillogram can also be used to determine the ionization relaxation time. The relaxation time for argon, determined from the ΔU_σ signal as being the time from arrival of the shock up to the second maximum, is equal to the relaxation time τ_{rel} measured from the intensity FÉU oscillogram Fig. 3,a). Ionization equilibrium is not reached in the shock-heated argon in Fig. 3,b, since the photomultiplier signal increases throughout the entire test slug.

Figure 4 shows the results of measurements of the ionization relaxation time τ_{rel}. behind the incident shock, obtained from reduction of the oscillograms of the first and second experimental series. Good agreement is observed between the results obtained and individual data points of ref. 11, in which measurements were made of the absolute electron densities and the ionization relaxation time in argon with about 1% impurity.

The data of the present investigations are referred to the theoretical equilibrium temperatures of the flow core, without allowance for possible reduction of temperature due to dissociation and partial ionization of impurities (such estimates were made in refs. 1 and 10). The effect of air impurity on the relaxation time can be clearly seen by comparing with curves 10 and 11 for the relatively pure argon of Fig. 4.

Figure 5 shows the relaxation times τ_{rel} as averaged by straight lines, as a function of M_1 (points 1-3 of Fig. 4). Evidently, ionization equilibrium is reached for $M_1 < 10$ in the second half of the gas sample, for all test values of the initial pressure p_1. The duration of the shock-heated argon region τ_{con} is practically independent of the initial pressure, but decreases noticeably with increase of M_1. Ionization equilibrium is reached along the test slug for $p_1 = 7$ torr at $M_1 \geq 9.2$, for $p_1 = 10$ torr at $M_1 \geq 8.9$, and for $p_1 = 14$ torr at $M_1 \geq 8.6$.

Thus, we have used a conductivity gauge to show that, behind shock waves at $M_1 = 8$ to 10 in argon, an air impurity ($\sim 2 \cdot 10^{-2}$) reduces the extent of the ionization relaxation region appreciably.

---

[1] M. A. Novgorodov, Yu. A. Polyakov, V. A. Tishchenko, and É.K. Chekalin, Zh. Tekh. Fiz., 43, 1196 (1973) [Sov. Phys.—Tech. Phys., 18, 759 (1973)].

[2] L. P. Poberenzhiskii, Teplofiz.Vys. Temp., 6, 973 (1968).

[3] R. V. Vasil'eva, K. V. Donskoi, B. M. Dobrynin, V. Kh. Manerov, G. K. Tumakaev, and V. A. Shingarkina, Zh. Tekh. Fiz., 40, 605 (1970) [Sov. Phys.—Tech. Phys., 15, 467 (1970)].

[4] E. J. Stubbe, AIAA J., 10, 92 (1972).

[5] S. Aizenberg, and Chen-Vei-Kuo, Proc. IEEE, 591 291 (1971).

[6] I. M. Gaponov, Yu. M. Zelikson, A. V. Zrodnikov, A. D. Isérov, L. P. Poberezhskii, M. S. Semenov, A. F. Tokarev, in: MHD Method of Generating Electrical Power [in Russian], Izd. Energiya, Moscow (1972), p. 124.

[7] É.K. Chekalin, and M. A. Novgorodov, Zh. Tekh. Fiz., 42, 1519 (1972) [Sov. Phys.—Tech. Phys., 17, 1212 (1973)].

[8] E. V. Stupochenko, S. A. Losev, and A. I. Osipov, Relaxation Processes in Shock Tubes [in Russian], Izd. Nauka, Moscow (1965).

[9] N. R. Jones, and M. McChesney, Nature, 209, No. 5028, 1080 (1966).

[10] G. I. Kozlov, Yu. P. Raizer, and D. I. Roitenburg, Zh. Prikl. Mekh. Tekh. Fiz., No. 1, 140 (1968).

[11] L. V. Kochmanova, Ts. G. Breido, V. L. Goryachev, and G. S. Sukhov, Zh. Tekh. Fiz., 40, 600 (1970) [Sov. Phys.—Tech. Phys., 15, 463 (1970)].

[12] G. Petchek, and S. Bairon, in: Shock Tubes, Kh. A. Rakhmatullin and S. S. Semenov, (eds.) [Russian translation], IL, Moscow (1962), p. 471.

Theory of the low-voltage arc in a narrow gap

F. G. Baksht, A. A. Kostin, and V. A. Nemchinskii

A. F. Ioffe Physicotechnical Institute,
Academy of Sciences of the USSR, Leningrad

(Submitted September 5, 1973)
Zh. Tekh. Fiz., 44, 1037-1043 (May 1974)

The low-voltage arc in a planar cesium diode is treated for the case in which the cathode current is comparable to the random electron current of the plasma. Numerical calculations for the voltage–current characteristic and plasma state are given.

1. Much attention is currently being given to the study of low-voltage arc discharges in highly ionized plasmas. In particular, Baksht et al.[1] and Dyuzhev et al.[2] have studied theoretically and experimentally a low-voltage arc in cesium at pressures $p \lessdot 1$ torr, between electrodes $d \sim 1$ mm apart, and current densities of the order of several tens of amperes per square centimeter. There is now considerable practical interest in arc discharges in highly ionized plasma with the same values of p and d but with current densities j of the order of hundreds of amperes per square centimeter. A theoretical study of such discharges is the subject of the present work.

2. When the interelectrode distances are great in comparison with the mean free paths and the plasma is in a state of local thermodynamic equilibrium, the plasma in the gap is described by the system of equations

$$j = -u_e n\left[q\frac{d\varphi}{dx} + 1.7k\frac{dT_e}{dx}\right] - qD_e\frac{dn}{dx}, \qquad (1)$$

$$Q_e = j\left(3.2\frac{kT_e}{q} + \varphi\right) - 1.6D_e nk\frac{dT_e}{dx}, \qquad (2)$$

$$-\frac{d}{dx}\left(\varkappa\frac{dT}{dx}\right) = \Delta q_{ei} + \Delta q_{ea}, \qquad (3)$$

$$p_e + p_i + p_a = p. \qquad (4)$$

Here Q_e is the energy flux transported by electrons, p is the plasma pressure, n is the charged particle density, T_e and T are the temperatures of electrons and heavy particles respectively, u_e and D_e are the electron mobility and diffusion coefficient, $p_e = nkT_e$, $P_i = nkT$, and $p_a = n_a kT$ are partial pressures of electrons, ions, and atoms respectively, φ is the electric potential, Δq_{ei} and Δq_{ea} is the energy transferred by electrons to ions and atoms in collision, and $\varkappa$ is the thermal conductivity of the heavy component (see ref. 1).

The atomic density n_a is related to the density of charged particles n through the Saha equation:

$$\frac{n^2}{n_a} = \frac{(2\pi m_e kT_e)^{3/2}}{h^3} e^{-\frac{\varepsilon_i}{kT_e}}.$$

Here, $\varepsilon_i = 3.89$ eV is the ionization energy of Cs.

The system (1)–(3) has the following boundary conditions.

At the cathode boundary of the plasma (x = 0) we have

$$j = j_s - \frac{1}{4} qn_k\bar{v}_{ek}e^{-\frac{q\varphi_k}{kT_{ek}}} + j_{ik}, \qquad (5)$$

$$Q_e = j_s\left(\frac{2kT_k}{q} + \varphi_0\right) - \frac{1}{4} n_k\bar{v}_{ek}e^{-\frac{q\varphi_k}{kT_{ek}}}(2kT_{ek} + q\varphi_0)$$

$$-\frac{j_{ik}}{q}[\varepsilon_i + q(\varphi_k - \varphi_0)], \qquad (6)$$

$$T(0) = T_k. \qquad (7)$$

At the anode boundary (x = d) we have

$$j = \frac{1}{4(1-f_0)} qn_a\bar{v}_{ea}e^{-\frac{q\varphi_a}{kT_{ea}}} - j_{ia} \qquad (8)$$

$$Q_e = \frac{1}{4(1-f_1)} n_a\bar{v}_{ea}e^{-\frac{q\varphi_a}{kT_{ea}}} 2kT_{ea} + \frac{j_{ia}}{q}(\varepsilon_i + q\varphi_a), \qquad (9)$$

$$T(d) = T_a. \qquad (10)$$

Here, j_s is the cathode emission, $n_k = n(0)$ and $n_a = n(d)$, $T_{ek} = T_e(0)$ and $T_{ea} = T_e(d)$ are the density and electron temperature at the cathode and anode plasma boundary respectively, T_k and T_a are the cathode and anode temperatures, φ_0 is the voltage drop across the arc (with respect to the anode surface), $\bar{v}_{ek,a} = \sqrt{8kT_{ek,a}/(\pi m_e)}$, and functions $f_0[q\varphi_a/(kT_{ea})]$ and $f_1[q\varphi_a/(kT_{ea})]$ are defined in ref. 3.

If the ionization length $L_i = \sqrt{D_i[1 + (T_e/T)]/[v_e n_a \sigma_0(Te)]}$ is large in comparison with the ion mean free path in the electrode regions, the ion currents to the cathode and anode are given by[4]

$$j_{ik,a} = \frac{qD_i\left(1 + \frac{T_{ek,a}}{T_{k,a}}\right)}{\sqrt{2}L_{ik,a}}. \qquad (11)$$

where D_i is the diffusion coefficient for ions in atoms, and $\sigma_0(T_e)$ is the effective ionization cross section.[5,6]

If the ionization length $L'_i = \bar{v}_a/n\bar{v}_e\sigma_0(T_e)$ is less[1)] than the ion–atom (atom–ion) mean free path the ion currents to the electrodes are given by[7]

$$j_{ik,a} = 0.61q\sqrt{\frac{kT_{ek,a}}{m_i}} n_{k,a}. \qquad (12)$$

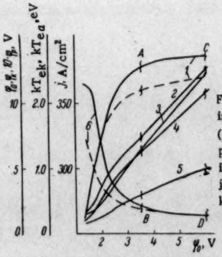

Fig. 1. Voltage–current characteristic of arc (1), T_{ek}(2), T_{ea}(3), φ_k(4), φ_a(5), and φ_p(6). Dashed curves plotted without taking ionization loss into account. d = 0.5 mm, p = 2 torr, $j_s = 409$ A/cm², $kT_k = 0.15$ eV, and $kT_a = 0.08$ eV.

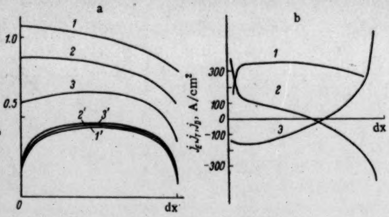

Fig. 2. a) Electron (1, 2, 3) and ion 1', 2', 3') temperatures: j = 357 (1, 1'), 340 (2, 2'), and 310 (3, 3') A/cm². b) Current components in the gap: j_E (1), j_D (2), j_T (3), $j = j_E + j_D + j_T = 320$ A/cm².

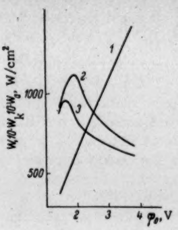

Fig. 3. W(1), W_a(2), and W_k(3).

The results depend on the relationship between the emission current and the random current of plasma electrons $j_r = (q/4)n\bar{v}_e$. The cases $j_s < j_r$ and $j_s > j_r$ are considered below.

3. If $j_s < j_r$, the anode fall retards the electrons moving from the plasma towards the anode so that the arc current does not exceed j_s. The voltage–current characteristic of a planar Cs diode was calculated for this case [d = 0.5 mm, p = 2 torr, j_s = 409 A/cm. In a low-voltage arc in a highly ionized plasma the current j_s increases because of the Schottky effect at the cathode and decreases because of falling ion density near the cathode and decreasing cathode coating. These factors are assumed to compensate each other so that j_s = const]. The voltage–current characteristic is shown in Fig. 1, which also indicates the plasma parameters near the electrode regions. At high currents $T_{ek} \approx T_{ea} \approx q\varphi_0/(2k)$. T_{ek} and T_{ea} increase smoothly with increasing φ_0, φ_k, φ_a, and the voltage drop across the region $\varphi_p = \varphi_a + \varphi_0 - \varphi_k$ decreases.

Figure 2a shows the electron temperature distribution $T_e(x)$ and the temperature distribution for heavy particles T(x) in the gap. The temperature T shows significant variation only in narrow regions near the electrodes. The small variations of T in the main portion of the gas are due to the fact that the heat conductivity of the heavy component is governed by the heat conductivity of ions[8] $\varkappa_i$, which increases rapidly: $\varkappa_i \sim T^{5/2}$. The relatively small change of T_e and T in a completely ionized plasma results in an approximately constant density in the main part of the gap. Significant density gradients appear only in narrow regions near the electrodes.

Figure 2b shows the current components in the gap: $j_E = -u_e n(d\varphi/dx)$, $j_T = -1.7u_e nk(dT_e/dx)$, and $j_D = -qD_e \cdot (dn/dx)$. It is obvious that although all three current components are relatively large, the total current in the main part of the gap $j \approx j_E$. The electric field is nearly constant. However, near the electrodes, where the density gradients (and near the anode also the electron temperature gradient) are high, j differs appreciably from j_E.

4. The principal difference between the present results and those obtained in ref. 1 is the higher electron temperature; this is due to the fact that the energy lost in ionization is a small fraction of the electric power $j\varphi_0$. This result is illustrated in Fig. 3, which shows the ionization loss at the cathode $W_k = (j_{ik}/q)\varepsilon_i$ and anode $W_a = (j_{ia}/q)\varepsilon_i$, and the total power $W = j\varphi_0$. The relatively minor importance of ionization loss is also observed in Fig. 1, where the dashed curves have been plotted neglecting these losses.

Another difference is the nature of variation of the heavy-particle temperature T with increasing φ_0. Whereas for the relatively small currents discussed in ref. 1 T(x) increases with increasing φ_0, in the case discussed here²⁾ T(x) decreases with increasing φ_0.

5. The principal factor which limits the applicability of the discussed approximation[9] is the increase of the Coulomb relaxation length l_ε of the cathode electron beam with the applied voltage φ_0:

$$l_\varepsilon = \frac{1}{2\pi q^4 \lambda} \frac{(q\varphi_k)^2}{n}, \tag{13}$$

where λ is the Coulomb logarithm, and $q\varphi_k$ is the energy of emission electrons accelerated by the cathode voltage fall.

The line AB in Fig. 1 corresponds to the φ_0 for which $l_\varepsilon = d$.

If the energy and momentum relaxation of the cathode beam electrons is provided by Coulomb binary collisions, applicability of the described system requires that $l_\varepsilon < d$. Actually, however, the described conditions cause the excitation of strong oscillations in the cathode region of the plasma, whose excitation length $l_1 \approx r_D(n/n_b)(v_{eT}/v_b) \ll d$. Here, r_D is the Debye radius, n_b and $v_b = \sqrt{2q\varphi_k/m_e}$ are the electron density and velocity in the beam,[10] and $v_{eT} = \sqrt{2kT_e/m_e}$. At a distance from the cathode nearly equal to l_1 the electron velocity distribution function changes, forming a plateau.[11-14] After passing the region of strong oscillations the beam relaxes by binary collisions, as before. However, the relaxation length can change considerably because of the distortion of the distribution function. In particular, assuming that (in accordance with the quasilinear theory) the electron velocity distribution is uniform in the interval from v_{eT} to v_b, the relaxation length L_ε, given by

$$\frac{1}{L_\varepsilon} = \left\langle \frac{\varepsilon}{v\tau_\varepsilon(\varepsilon)} \right\rangle \langle \varepsilon \rangle^{-1} \tag{14}$$

(where τ_ε is the energy relaxation time, and the symbol <> denotes averaging over the distribution function), is

$$L_\varepsilon = \frac{1}{3} \tau_\varepsilon (q\varphi_k) v_{eT}, \tag{15}$$

i.e., noticeably smaller than l_ε. The line CD in Fig. 1

marks the point on the voltage–current characteristics where $L_\varepsilon = d$.

With higher φ_0 and φ_k it is necessary to distinguish between two groups of electrons: fast electrons of the beam and slow randomized plasma electrons. The lack of randomization of fast electrons should, in particular, result in the temperature of slow electrons T_e being significantly lower than $q\varphi_0/2k$, as the energy provided by the electric field is mainly carried out to the anode by the electrons. A T_e lower than that predicted by theory indicates that no fast-electron randomization takes place in the gap.

6. The case $j_r \ll j_s$ can occur at relatively low pressures. In this case the polarity of the anode voltage fall can, in principle, change with increasing φ_0. To analyze such an arc let us consider the case $\varphi_a = 0$.

Assume that the electron temperature is so much higher than the ion temperature that

$$p = n(x)\,kT_e(x). \qquad (16)$$

Using (16) and eliminating $\varphi(x)$ from (1) and (2), we obtain an equation from which $T_e(x)$ can be determined:

$$\Theta_e^{3/2}\left[1.6\,\frac{d}{d\xi}\left(\Theta_e^{5/2}\frac{d\Theta_e}{d\xi}\right) - \frac{5}{2}\frac{d\Theta_e}{d\xi}\right] = -1. \qquad (17)$$

Here, we use the dimensionless quantities $\theta_e = T_e/T_{ea}$ and $\xi = x/L$, where

$$L = \frac{u_e n k T_{ea}}{j} = 194\,\frac{(kT_{ea})^{5/2}}{\lambda j}. \qquad (18)$$

In (18) L is expressed in centimeters, kT_{ea} in electron volts, and j in amperes per square centimeter. The product $u_e n = 1.96\,qn\tau_e/m_e$ (see ref. 8) depends on T_e only and is computed in (18) for $T_e = T_{ea}$. It is convenient to specify the boundary conditions for (17) at the plasma interface with the anode and to integrate the equation beginning at the anode, i.e., in the direction of negative ξ. Let $\xi = 0$ and $x = d$. Then, neglecting the ion current and ionization loss, Eqs. (8) and (9) give

$$\Theta_e(0) = 1,\quad \left.\frac{d\Theta_e}{d\xi}\right|_{\xi=0} = \frac{3}{4}. \qquad (19)$$

The solution of (17) with the boundary conditions (19) is plotted in Fig. 4a. It is seen that there is a critical gap $\xi \approx 0.53$ [or $d_0 = 103\,(kT_{ea})^{5/2}/\lambda j$] at which $\theta_e(\xi)$ vanishes. An arc $\varphi_a = 0$ can hold only for $d < d_0$. Let us now compare the mean free path $l_e = \bar{v}_e\tau_e$ of electrons in a highly ionized plasma with d_0. Finding l_e for $n = n_a$ and $T_e = T_{ea}$, we get $l_e = 125\,(kT_{ea})^{5/2}/\lambda j$, i.e., $l_e \approx d_0$. Thus under the above assumptions it is impossible to form an arc in a dense plasma ($d \gg l_e$) with a zero or accelerating voltage fall at the anode.

Let us now see how the result is affected by accuracy of the boundary conditions at the anode. The second boundary condition in (19) should be written in the general case as $(d\Theta_e/d\xi)|_{\xi=0} = (\beta - \delta)/\alpha$, the factors β and α depending on the electron scattering mechanism (for Coulomb scattering $\beta = 3.2$ and $\alpha = 1.6$), and the factor δ of the electron distribution function at the electrode boundary (in the above we have assumed $\delta = 2$). The function $d_0(\delta)$, plotted from numerical calculations, is shown in Fig. 4b. It is seen that varying δ within reasonable limits does not appreciably change the pattern.

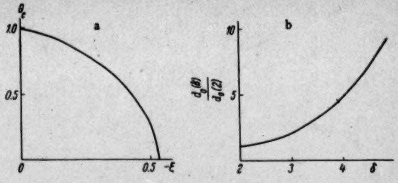

Fig. 4

7. Let us now evaluate the effect of the self magnetic field on the discharge. The interaction of a current j with its self magnetic field B gives rise to a radial pressure gradient which balances the Lorentz force:

$$-\frac{dp(r)}{dr} = \frac{1}{c}\,j(r)\,B(r). \qquad (20)$$

Using the equation

$$\frac{1}{r}\frac{d(rB)}{dr} = \frac{4\pi}{c}\,j, \qquad (21)$$

we get a connection between plasma pressure in the arc averaged over the cross-sectional area $\bar{p} = (2/R^2)\int_0^R p(r)\cdot r\,dr$, the pressure $p_0 = p(R)$, and the magnetic field $B_0 = B(R)$ at the discharge boundary (where R is the discharge radius for $r > R$ and $j = 0$).

$$\bar{p} - p_0 = \frac{B_0^2}{8\pi}. \qquad (22)$$

B_0 is determined by the total arc current I. Assuming that φ and T_e do not vary along the radius, and that the pressure gradient is due to the change in density, neglecting the contribution of ions to pressure, we get from (8)

$$B_0 = \frac{2I}{cR} = \frac{2q\pi R}{c(1-f_0)}\,\frac{\bar{p}}{\sqrt{2\pi m_e kT_{ea}}}\,e^{-\frac{q\varphi_a}{kT_{ea}}}. \qquad (23)$$

Substituting (23) into (22), we have

$$\bar{p} = \frac{1}{2}\left[p_1 - \sqrt{p_1^2 - 4p_0 p_1}\right], \qquad (24)$$

where

$$p_1 = \frac{4(1-f_0)^2 c^2 m_e kT_{ea}}{q^2 R^2}\,e^{\frac{2q\varphi_a}{kT_{ea}}}. \qquad (25)$$

The condition $p_1 \geq 4p_0$ must be obeyed. The condition $p_1 = 4p_0$ gives the maximum discharge radius R_m:

$$R_m = \frac{c}{q}(1-f_0)\sqrt{\frac{m_e kT_{ea}}{p_0}}\,e^{\frac{q\varphi_a}{kT_{ea}}}. \qquad (26)$$

If $R = R_m$, $\bar{p} = (p_1/2) = 2p_0$, i.e., the average arc pressure can be at most twice as high as the gas pressure outside the discharge.

Let us find R_m after the saturation current is removed.

If $j_s < j_r$, the saturation current is $I = \pi R_m^2 j_s$. Eliminating φ_a from (23) and (26), we have

$$R_m = c\sqrt{\frac{2p_0}{\pi}}\frac{1}{j_s}, \tag{27}$$

for p = 2 torr and j_s = 400 A/cm², $R_m \approx 3$ cm, i.e., $R_m \gg d$.

If $j_s \geqslant j_r$, the saturation current is governed by the random current of plasma electrons. If $\varphi_a = 0$ ($f_0 = 1/2$), we have from (26)

$$R_m = \frac{c}{2q}\sqrt{\frac{m_e kT_{ea}}{p_0}} \tag{28}$$

for p = 1 torr, $p_0 = 1$ eV, and $R_m \approx 3 \cdot 10^{-2}$ cm.

Under these conditions the radius R_m is of the same order as the interelectrode distance d, i.e., should such an arc appear, strong self-pinching would be observed.

In conclusion the authors thank G. A. Dyuzhev for discussion.

---

1) If the electron temperature is high enough, a Cs atom evaporated from an electrode can be ionized even before encountering a second atom or ion. The corresponding ionization length L_i' differs from L_i.

2) The energy imparted by electrons to ions in collision[8] is given by $\Delta q_{ei} = (3m_e/m_i)k(T_e - T)(n/\tau_e)$. Since $\tau_e \sim T_e^{3/2}n^{-1}$, and since in a highly ionized plasma $n = p/[k(T_e + T)]$, Δq_{ei} decreases with increasing T_e when the electron temperature is sufficiently high.

[1] F. G. Baksht, I. L. Korobova, and B. Ya. Moizhes, Zh. Tekh. Fiz., 41, 387 (1971) [Sov. Phys.—Tech. Phys., 16, 292 (1971)].

[2] G. A. Dyuzhev, V. B. Kaplan, B. Ya. Moizhes, and V. G. Yur'ev, Zh. Tekh. Fiz., 41, 453 (1971) [Sov. Phys.—Tech. Phys., 16, 350 (1971)].

[3] Thermionic Converters and Low-Temperature Plasma [in Russian], B. Ya. Moizhes and G. E. Pikus, (eds.), Nauka, Moscow (1973), Chap. 6.

[4] F. G. Baksht and B. Ya. Moizhes, Zh. Tekh. Fiz., 38, 724 (1968) [Sov. Phys.—Tech. Phys., 13, 540 (1968)].

[5] É. B. Sonin, Zh. Tekh. Fiz., 37, 1840 (1967) [Sov. Phys.—Tech. Phys., 12, 1347 (1968)].

[6] F. G. Baksht, B. Ya. Moizhes, and V. A. Nemchinskii, Zh. Tekh. Fiz., 38, 1731 (1968) [Sov. Phys.—Tech. Phys., 13, 1401 (1969)].

[7] F. G. Bakst, G. A. Dyuzhev, N. K. Mitrofanov, S. M. Shkol'nik, and V. G. Yur'ev, Zh. Tekh. Fiz., 43, 2574 (1973) [Sov. Phys.—Tech. Phys., 18, 1617 (1974)].

[8] S. I. Braginskii, in: Reviews of Plasma Physics, Vol. 1, Consultants Bureau, New York (1965).

[9] B. A. Trubnikov, in: Reviews of Plasma Physics, Vol. 1, Consultants Bureau, New York (1965).

[10] V. N. Tsytovich, Nonlinear Effects in Plasma, Plenum, New York (1970).

[11] V. A. Nemchinskii, Zh. Tekh. Fiz., 40, 2462 (1970) [Sov. Phys.—Tech. Phys., 15, 1927 (1971)].

[12] N. D. Margulis, Yu. P. Korchevoi, and D. Ya. Dudko, Zh. Tekh. Fiz., 38, 1065 (1968) [Sov. Phys.—Tech. Phys., 13, 886 (1969)].

[13] G. A. Dyuzhev, B. Ya. Moizhes, V. A. Nemchinskii, E. A. Startsev, S. M. Shkol'nik, and V. G. Yur'ev, Zh. Tekh. Fiz., 41, 2406 (1971) [Sov. Phys.—Tech. Phys., 16, 1910 (1972)].

[14] U. K. Guskov, A. I. Kiryishchenko, M. I. Lebedev, and V. E. Cherkovets, Proc. Third Intern. Conf. on Thermionic Electrical Power Generation, Juelich, 3, 1663 (1972).

Continuous electron acceleration in a gas discharge

G. D. Alkhazov

(Submitted August 24, 1973)
Zh. Tekh. Fiz., 44, 1044-1046 (May 1974)

The possible transition from electron avalanche to continuous acceleration because of the statistical nature of the energy loss is analyzed. On the basis of calculations of the electron energy spectra in Townsend avalanches it is concluded that the electron runaway due to the statistical mechanism begins effectively at a field $E \approx (^1/_2 f)E^*$, where eE^* is the maximum electron energy loss per unit length along the drift path to the anode, and f is the field intensification coefficient near the head of the avalanche.

In strong electric fields the energy imparted to electrons by the field can exceed the energy loss due to inelastic collisions with gas molecules, so that electrons undergo a transition to continuous acceleration, thereby acquiring an energy of the order of eU_0, where U_0 is the applied voltage. It is natural to identify the critical field, i.e., that at which electrons begin acceleration, as the field $E^* = (\gamma/e)(d\varepsilon/dx^{\max})$, where $(d\varepsilon/dx^{\max})$ is the maximum energy loss per unit length of the complete path, and γ is a coefficient equal to the ratio of the average length of the complete path to the distance the electron has moved toward the anode (in strong fields, γ is approximately unity). Fast electrons can appear in gas discharges at fields[1] $E < E^*$, as shown in ref. 2, because electrons are accelerated as a result of the field intensification in the space-charge region. If the electron energy exceeds a certain critical value ε^* in a field $E < E^*$ (Fig. 1), the electrons begin continuous acceleration and acquire an energy of order eU_0. Even if there were no field inhomogeneities, "runaway" electrons could, in principle, appear at $E < E^*$ because of the statistical nature of the energy loss of electrons in a gas. Although the average energy of the avalanche electrons in a field $E < E^*$ is less than ε^*, if the energy lost by an electron is lower than the average over a few mean free paths this electron can acquire an energy greater than ε^* (due to the applied field) and can undergo a transition to continuous acceleration. To get an idea of the importance of the statistical mechanism for accelerating electrons we have now calculated the electron energy distributions for an avalanche in helium moving through a potential difference of $U_0 = 3$ kV.

If we assume that impact ionization is primarily responsible for the growth of the avalanche, and if we neglect space-charge effects, we can find the electron energy distribution on the basis of the model of a one-dimensional avalanche by solving the kinetic equation,

$$\frac{\partial}{\partial x} N(x, \varepsilon) = -\frac{\partial}{\partial \varepsilon} N(x, \varepsilon) eE - n\gamma (Q_\varepsilon^i + Q_\varepsilon^{ex}) N(x, \varepsilon) + \sum_k n\gamma Q_{\varepsilon+eU_k}^{ex}(U_k) N(x, \varepsilon + eU_k) + \int_{eI}^{\varepsilon} n\gamma Q_{\varepsilon+\varepsilon_i}^{i}(\varepsilon_i) N(x, \varepsilon + \varepsilon_i)\, d\varepsilon_i\,, \tag{1}$$

under the initial condition $N(0, \varepsilon) = \delta(\varepsilon)$. Here, $N(x, \varepsilon)d\varepsilon$ is the average number of electrons in an avalanche (which has moved a distance x) which have energies ε in the interval $d\varepsilon$, $Q_\varepsilon^{ex}(U_k)$ is the cross section for the excitation of level k of the helium atom, $Q_\varepsilon^{I}(\varepsilon_i)$ is the differential cross section for the ionization of a helium atom by electrons at energy ε, ε_i is the energy lost in an ionization event, $Q_\varepsilon^{ex} = \sum_k Q_\varepsilon^{ex}(U_k)$ and $Q_\varepsilon^{i} = \int_{eI}^{\frac{\varepsilon+eI}{2}} Q_\varepsilon^{i}(\varepsilon_i)d\varepsilon_i$ are the total excitation and ionization cross sections, I is the ionization potential, and n is the density of helium atoms. In strong fields we can neglect the energy lost in elastic collisions; nevertheless, elastic scattering must be taken into account in our problem. Elastic collisions between electrons and atoms increase the angular spread, i.e., the total distances traveled by the electrons, and thereby increase the probability for energy loss in inelastic collisions. The angular spread of the electrons which results from elastic and inelastic collisions of electrons with atoms is effectively incorporated in Eq. (1) by the coefficient γ, which is larger than unity. Equation (1) is solved by successive iterations.[1)] The ionization and excitation cross sections for the helium atoms are calculated by the semiempirical equations given in ref. 4. Over the range of values of E/E^* considered here the calculated values of the first Townsend coefficient are in good agreement with experiment with $\gamma = \text{const} = 1.4$. The calculated value of E^*/p is[2)] $E^*/p = 7 \cdot 10^4$ V/(cm · atom). Because of the important simplifications used in the model for the shower development (space-charge effects are neglected, elastic scattering is taken into account in a simplified manner, etc.), and because of the uncertainty in the values used for the cross sections, our calculation is of a particularly qualitative nature. Nevertheless, we can conclude on the basis of our results (Fig. 2) that electron acceleration due to the statistical mechanism is possible even when $E = gE^*$, where $g = 0.5$-0.6. Although the relative number

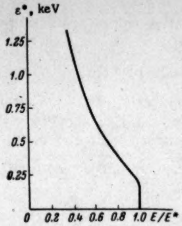

Fig. 1. Critical energy ε^* as a function of the field intensity E. At $\varepsilon > \varepsilon^*$ the increment in the electron energy due to the field exceeds the loss due to inelastic collisions. Here $E^*/p = 7 \cdot 10^4$ V/(cm · atom), where p is the gas pressure.

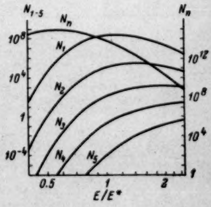

Fig. 2. Results of a numerical solution of Eq. (1) for the case of helium for an applied potential difference of $U_0 = 3$ kV. Here N_n is the total number of electrons formed in the avalanche, and N_{1-5} are the numbers of avalanche electrons having energies in the ranges 0.5-1.0, 1.0-1.5, 1.5-2.0, 2.0-2.5, and 2.5-3.0, respectively.

of electrons which undergo the transition to continuous acceleration is vanishingly small at these fields (only a few electrons "run away"), the appearance of these runaway electrons can alter the development of the discharge significantly: Secondary avalanches appear along the trajectory of a fast electron; the discharge-formation time is reduced; and the discharge can acquire a diffusive or multichannel nature. The calculated total number of electrons in an avalanche (Fig. 2) reaches the large value $N_n \approx 10^{15}$, implying that the calculations are not valid for dense gases. In fact, in dense gases (at atmospheric pressure) the distortion of the field by the space charge causes the growth of the avalanche to deviate from the Townsend law at only $N_n \approx 10^7$, and the avalanche becomes a streamer at $N > 10^8$ in strong fields. Strictly speaking, therefore, these calculations are valid only for low pressures, but it should be noted that fast electrons appear as a result of the acceleration of slow electrons present in the avalanche in an earlier stage of its development, in this case when the avalanche has not yet reached its critical size. Thus taking account of the nonexponential nature of the avalanche growth in this problem has a significant effect on only the total number of electrons; the number of fast electrons is changed only slightly.

When we take account of the field intensification in the space-charge region we find that the minimum field at which fast electrons can appear is reduced to $E = (g/f) \cdot E^*$. According to the calculations of ref. 2, the field-intensification factor f can reach $f = 3$. The x-ray bremsstrahlung detected in ref. 1 in helium discharges at $E \approx 1.5 \cdot 10^4$ V/(cm · atom) is evidence of the appearance of fast electrons in discharges. The appearance of fast electrons at these relatively weak fields ($E \approx 0.2E^*$) can be attributed to the combined effects of the statistical mechanism for electron runaway and the field-intensification effect. A qualitative study of electron runaway in helium discharges was reported in ref. 6, but in those measurements the external field was significantly inhomogeneous. Analogous measurements in homogeneous external fields at various pressures could apparently allow us to distinguish between the contribution of the statistical mechanism for electron runaway and the mechanism involving field intensification near the head of the avalanche.

---

1) The method used is the same as that used in ref. 3.

2) The value $E^*/p = 5 \cdot 10^4$ V/(cm · atom) given in ref. 3 for the case of helium (for the case of no field intensification) is obviously too low, because the authors set $\gamma = 1$.

[1] S. Frankel, V. Highland, T. Sloan, O. von Dyke, and W. Wales, Nucl. Instr. Meth., 44, 345 (1966).

[2] L. P. Babich and Yu. L. Stankevich, Zh. Tekh. Fiz., 42, 1674 (1972) [Sov. Phys.-Tech. Phys., 17, 1333 (1973)].

[3] G. D. Alkhazov, Preprint FTI-207, Leningrad, 1969.

[4] G. D. Alkhazov, Zh. Tekh. Fiz., 40, 97 (1970) [Sov. Phys.-Tech. Phys., 15, 66 (1970)].

[5] J. M. Meek and J. D. Craggs, Electrical Breakdown of Gases, Oxford, London (1953).

[6] R. C. Noggle, E. P. Krider, and J. R. Wayland, J. Appl. Phys., 39, 4746 (1968).

Accelerators

Inductive energy storage in pulsed accelerators

V. A. Glukhikh, O. A. Gusev, E. G. Komar, and M. P. Svin'in

(Submitted July 23, 1973)
Zh. Tekh. Fiz., 44, 1047-1050 (May 1974)

The outlook for the use of inductive energy-storage banks as pulsed high-voltage sources for direct accelerators is discussed. Electrical circuits are given, and the results of experiments with prototype accelerators are reported.

In recent years, stimulated by the needs of several branches of science and technology for intense charged-particle and x-ray beams, rapid progress has been made in the development of high-current pulsed accelerators. At present, the energy per pulse carried by the particle beam in the most powerful accelerators[1] is as high as 1 MJ at an accelerating voltage of 10^6-10^7 V. Nevertheless, there is a real need for substantial increases in these parameters.

Most high-current accelerators use capacitive storage banks; these more or less determine the geometric dimensions and cost of the installations. Electric fields up to 10^6 V/cm and energy densities up to 0.1 J/cm^3 are achieved in modern oil-filled paper capacitors. In water-filled capacitors, electric fields up to $3 \cdot 10^5$ V/cm and energy densities up to 0.3 J/cm^3 have been achieved for storage times of the order of 10^{-6} sec. Accordingly, capacitive banks for energies of 10^7-10^{10} J are extremely bulky and expensive.

In addition to capacitive banks, however, there are inductive banks. Even at fields on the order of 10^5 Oe, far from the highest possible, the energy density in these banks reaches 40 J/cm^3, i.e., some 150-400 times the energy density which has been reached in an electric field. At the fields of (5-6)$\cdot 10^5$ Oe which have now been achieved in small volumes the energy density reaches more than 1000 J/cm^3.

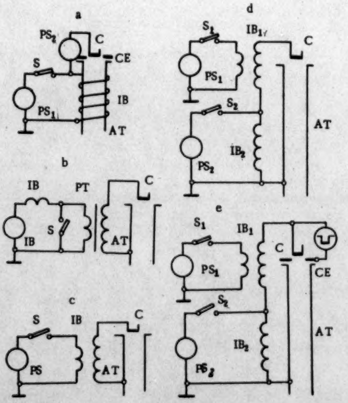

Fig. 1. Schematic circuits of direct-action charged-particle accelerators with inductive storage banks.

It therefore seems worthwhile to evalute the possible use of inductive banks in pulsed charged-particle, e.g., electron, accelerators.

The present authors have offered several suggestions regarding the circuits and construction of direct-action accelerators with inductive banks.

The simplest circuit is that in which the bank is connected directly to the accelerating gap[2] (Fig. 1a). After energy from power supply PS$_1$ has been stored in the inductive bank (IB), switch S cuts off the power supply. The emf of the inductive bank is applied to the gap through accelerating tube AT and cathode C. The energy stored in the bank is expended in accelerating electrons.

The opening of the charging circuit by mechanical or other means can be simplified significantly if the particle beam passes through the accelerating tube before switch S is thrown by PS$_2$ and control electrode CE.

Since the electrons are incident on a grounded collector at the point at which they are used, the electron beam shunts the charging circuit of the bank. If the beam current is made equal to the current in the bank winding, the current passing through switch S vanishes, and the charging circuit can be opened without causing an arc. If the voltage on control electrode CE is then reduced, a voltage of any magnitude can be produced between the bank terminals. Obviously, this voltage will be equal to the product of the bank inductance and the derivative of the electron-beam current. By adjusting this derivative one can shape rectangular pulses or any other accelerating voltage pulses. A fundamental characteristic of an inductive bank is the fact that there is a magnetic field throughout the acceleration process. Under certain conditions, this field can be used for focusing if the solenoid axis and that of the accelerating tube coincide. The beam current at which the beam is focused by the magnetic field of an inductive bank can be found from the familiar equation giving the focusing conditions for a magnetically confined beam.[3] If the focusing field is expressed in terms of the beam current and the parameters of the solenoid by means of B = μNI, where B is the magnetic induction, N is the number of solenoid turns per unit length, and μ is the permeability, the focusing condition is

$$I \geqslant \frac{1}{2\pi\varepsilon\mu^2 q^{3/2} N^2 U^{1/2} r^2 \left(\frac{\Delta r}{r}\right)}.$$

Here, U is the potential corresponding to the particle energy at the beam axis, ε is the dielectric constant, q is the charge-to-mass ratio of the particle, and $\Delta r/r$ is the relative pulsation in the beam edge.

In this accelerator circuit nearly all the energy stored in the bank is expended in accelerating the particles; the only other energy expenditure is that in heating the winding of the bank.

The energy loss is much higher if exploding wires, foils, etc., are used to open the charging circuit of the bank instead of the method suggested above (shunting the switch by the particle beam).

If we neglect the functional dependence of the resistance of the accelerating gap on the applied voltage, and if we assume an exponential behavior of the current in switch S, we find the energy transferred from the bank to the particle beam to be

$$W = W_{\text{in}} \left(1 - \frac{\tau_{\text{b}}}{\tau_{\text{b}} + \tau_{\text{s}}}\right) \text{ for } \tau_{\text{s}} \neq \tau_{\text{b}},$$

$$W = 0.5 W_{\text{in}} \text{ for } \tau_{\text{s}} = \tau_{\text{b}}$$

Here, W_{in} is the energy stored in the bank, and τ_{s} and τ_{b} are the time constants of the switch and beam circuits.

There are other possible circuits for accelerators with inductive banks; for example, the bank can be connected to the accelerating gap through a steel-core step-up transformer (Fig. 1b), or the bank itself can be part of the transformer (Fig. 1c).

Specifying a maximum recovery voltage across the switch, we can find the beam current and efficiency of the energy transfer as functions of the coupling coefficient:

$$I_{\text{b max}} = \frac{k n I_0}{1 + \frac{n^2 r_{\text{b}} \tau_{\text{s}}}{L_{\text{in}}}},$$

$$\eta = \frac{k^2}{1 + \frac{n^2 r_{\text{b}} \tau_{\text{s}}}{L_{\text{in}}}}.$$

Here, k is the coupling coefficient of the transformer windings, n is the ratio of the number of turns in the primary winding to that of the secondary winding, and r_{b} is the equivalent resistance of the accelerating gap.

The beam energy can be increased further by cascading inductive banks (Fig. 1d). After inductive banks IB_1 and IB_2 are charged and the circuit is opened by switch S_1, the current through the secondary winding of IB_1 flows through switch S_2. When the beam current reaches the level of the current in the second winding, the current through switch S_2 drops to zero, facilitating the opening of the circuit of the second bank.

Here, the beam energy is increased by increasing the length of the common discharge of two banks across a single accelerating gap.

If a control electrode is placed in the accelerating gap (Fig. 1e) the advantages of cascading banks can be exploited more fully. In this case, after the circuit of bank IB_2 is opened, the control electrode can be used to adjust the resistance of the accelerating gap, thereby controlling the bank discharge rate and the beam power.

The use of inductive bank pulsed accelerators seems extremely promising.

The most important question here is that of switching the bank current as rapidly as possible. An extremely interesting and promising method is that described above, involving the use of the current carried by the charged-particle beam in the switching.[2] It also seems possible to exploit current instabilities in a plasma, which cause sharp changes in its conductivity.[4]

Experimental accelerators with the circuits in Figs. 1a and 1c have been constructed at the D. V. Efremov Scientific-Research Institute of Electrophysical Apparatus, Leningrad.

The first accelerator is being used to test the conditions for the focusing of the beam by the magnetic field of an inductive bank, the conditions for the formation of rectangular accelerating-voltage pulses, and the switching by means of a controllable charged-particle beam at a recovery voltage of up to 1000 kV.

A field-emission cathode and a high-speed exploding-foil switch are used in the second accelerator. The inductive bank is coaxial with the accelerating tube. An electron beam with a current up to 1 kA, a diameter of 2 cm, and a pulse length of 7 μsec has been obtained at a distance of 0.5 cm from the aperture of the accelerating gap. The voltage across the accelerating gap reaches 300 kV.

---

[1] I. D. Shipman and J. D. Shipman, IEEE Trans. Nucl. Sci., NS-18, No. 4, 243 (1971).

[2] O. A. Gusev and E. G. Komar, Author's certificate No. 307743, TsNIILI; Buyll. Izobr., No. 8 (1972).

[3] J. R. Pierce, Theory and Design of Electron Beams, Van Nostrand, Princeton, New Jersey (1949).

[4] V. I. Agafonov, G. V. Golub, L. G. Golubchikov, V. F. D'yachenko, V. D. Ivanov, V. S. Imshennik, Yu. A. Kolesnikov, É. B. Svirskii, N. V. Filippov, and T. I. Filippova, Third International Conference on Plasma Physics, Report CN-24/G-1, Novosibirsk, 1968 [in Russian], IAEA, Vienna (1969).

Shaping of voltage pulses by discharging an inductive storage bank with a charged-particle beam

O. A. Gusev, E. G. Komar, V. B. Markov, and E. M. Mellekh

D. V. Efremov Scientific-Research Institute of Electrophysical Apparatus, Leningrad

(Submitted July 23, 1973)
Zh. Tekh. Fiz., 44, 1051-1054 (May 1974)

Calculations and experimental data are reported on the conditions for the formation of a rectangular accelerating-voltage pulse in a direct-action charged-particle accelerator in which energy is supplied from an inductive bank.

The use of an inductive energy bank as a high-voltage source for a direct-action accelerator is particularly effective when the intensity of the charged-particle beam can be varied to suit the relation required for shaping a rectangular accelerating-voltage pulse. In this case the charging circuit of the bank can be opened without causing an arc, and the bank can be charged by means of a beam of low-energy charged particles.[1] A necessary condition here is that the beam current be equal to that in the bank.

The limitation on the beam current transported through the accelerating tube and on the bank current makes it necessary to achieve the necessary energy storage by increasing the number of turns in the bank; this leads to an increase in the parasitic capacitance, which affects the current regulation.

Figure 1 shows the equivalent circuit of the regulation of the charged-particle current in an accelerator with an inductive energy bank for the shaping of a flat-topped accelerating-voltage pulse. The transfer impedance of this circuit is

$$h(p)=\frac{U_{\text{acc}}(p)}{i(p)}=\frac{1}{\omega_0}\frac{r+pL}{p^2+2\delta p+g\omega_0},$$

$$\omega_0=\frac{1}{\sqrt{LC}},\quad g=1+\frac{r}{R},\quad \delta=\frac{r}{2L}+\frac{1}{2RC}.$$

The transfer characteristic of the circuit is

$$h(t)=\frac{r}{g}\left[1-\left(\cos\omega t+\frac{\delta}{\omega}\sin\omega t\right)\exp(-\delta t)\right]+\frac{\sin\omega t}{\omega C}\exp(-\delta t),$$

where $\omega = \sqrt{g\omega_0^2 - \delta^2}$; when $r/R \ll 1$, this equation can be simplified to

$$h(t)\approx\frac{\sin\omega t}{\omega C}\exp(-\delta t). \tag{1}$$

From (1) we can determine the amplitude I_1 and length t_r of the input stepped signal required to rapidly charge the parasitic capacitance to the value $U_{\max}$:

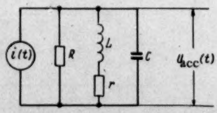

Fig. 1. Equivalent circuit for the shaping of the accelerating-voltage pulse. L) Inductance of bank; r) resistance of the bank; C) total parasitic capacitance of the current regulator and bank; R) dynamic output resistance of the current regulator i(t). I_0 is the initial bank current; and $U_{\text{acc}}(t)$ is the pulsed accelerating voltage.

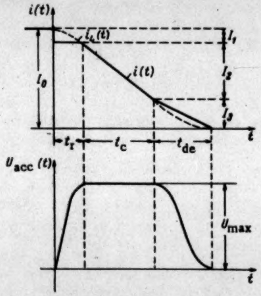

Fig. 2. The functions i(t), $i_L(t)$, and $U_{\text{acc}}(t)$ for r = 0 and R → ∞.

$$I_1=\exp\left[\frac{\delta}{\omega}\operatorname{arc\,tg}\frac{\omega}{\delta}\right]\frac{U_{\max}\sqrt{C}}{\sqrt{L}}, \tag{2}$$

$$t_r=\frac{1}{\omega}\operatorname{arc\,tg}\frac{\omega}{\delta}. \tag{3}$$

It can be shown that the current in the inductive bank is reduced by an amount

$$\Delta i_L=I_1\left[1-\frac{\sqrt{L}}{R\sqrt{C}}\exp\left(-\frac{\delta}{\omega}\operatorname{arc\,tg}\frac{\omega}{\delta}\right)\right]. \tag{4}$$

We see from (2)-(4) that the values of Δi_L and t_r decrease, and that of I_1 increases, as the output resistance of the beam current regulator is reduced.

After an interval $t = t_r$ the accelerating-voltage pulse

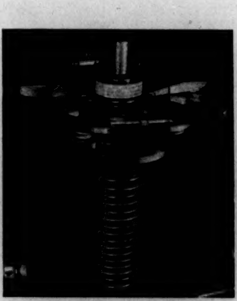

Fig. 3. Inductive storage bank and proton source.

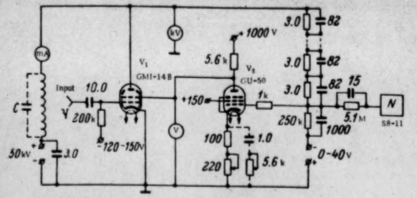

Fig. 4. Schematic of the experimental apparatus.

is given a flat top by cutting off the beam current in a sawtooth fashion from $I_0 - \Delta i_L$ to the value determined from the condition for total extraction of energy from the bank, including the energy stored in its parasitic capacitance, without the return voltage half-wave. The amplitude of this half-wave can be large because of the gain in the accelerating tube. Figure 2 shows the current and voltage for the circuit of Fig. 1 for the conditions $r = 0$ and $R \to \infty$; we see that the energy can be extracted from the inductive bank in a time t_{de} without a change in the voltage polarity when the current is also of sawthooth shape, but not as steep as in the interval t_c. If R is finite, with $r/R \ll 1$, and with the sawtooth law

$$i(t) = \frac{I_3}{t_{de}} t$$

the voltage falls off according to

$$U_{acc}(t) = \frac{I_3}{t_{de}} L + \left(U_{max} - \frac{I_3}{t_{de}} L\right)\left(\cos \omega t + \frac{\delta}{\omega} \sin \omega t\right) \exp(-\delta t), \tag{5}$$

where $t_{de} = \pi/\omega$.

The current in the inductance in this interval varies according to

$$i_L(t) = I_3\left(1 - \frac{t}{t_{de}}\right) - \frac{\sin \omega t}{\omega L}\left(U_{max} - \frac{I_3}{t_{de}} L\right) \exp(-\delta t). \tag{6}$$

Equating (5) and (6) to zero, we find the condition for total extraction of the remaining energy from the bank:

$$I_3 = \frac{U_{max}}{\omega L} \pi \frac{\exp\left(-\frac{\delta\pi}{\omega}\right)}{1 + \exp\left(-\frac{\delta\pi}{\omega}\right)}.$$

As R is reduced, I_3 decreases, and the flat part of the pulse, t_c, becomes longer. Accordingly, a reduction of the output resistance of the regulator for the charged-particle beam current leads to a reduction of the loss of energy stored in the inductive bank associated with the need to charge and discharge the parasitic bank capacitance.

Experimental information on the shaping of high-voltage pulses is obtained in discharges of an inductive bank designed for a 1-MeV proton accelerator with a pulsed beam current up to 1 A. Figure 3 shows the inductive bank and the proton source. The frequency characteristic of the bank has a sharp resonance near 205 Hz; no other resonant frequencies, which could have resulted from the sectioned construction of the bank, are found.

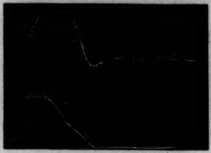

Fig. 5. Oscillograms of the high-voltage (upper curve) and input-signal (lower curve) pulses. The vertical scale for the upper curve is 3.7 kV/div, and the horizontal scale is 5 msec/div.

The inductance of the bank is L = 5270 H, and the resistance is r = 51.4 kΩ. The characteristic impedance of the circuit formed by the inductance and the parasitic capacitance of the bank is on the order of several megohms, so we have constructed the experimental apparatus shown in Fig. 4 in order to simulate the shaping of the accelerating-voltage pulses with an adjustable bank discharge. Here the current regulator is a GMI-14B modulator tube (V_1), whose internal resistance can be increased by introducing positive feedback from the anode of V_1 to the screen grid through the GU-50 (V_2) amplifier cascade.

Figure 5 shows an oscillogram of the high-voltage pulse (upper curve) obtained when the input of the current regulator, which has a high output resistance, is fed the voltage pulse shaped by combining step and sawtooth signals (lower curve). The height of the voltage pulse is 10 kV, and the characteristic times are t_r = 6 msec, t_c = 5.5 msec, and t_{de} = 9 msec. In the interval in which the top of the pulse is shaped the input signal has a variable steepness, to compensate for the nonlinearity of the tube characteristics.

CONCLUSION

1. If an inductive energy bank has a single resonance the required functional dependence of the beam current on the time can be arranged by using simple components: sawtooth and stepped waveforms.

2. Variations in the output resistance of the regulator for the charged-particle beam do not affect these functions; they only change the amplitude and temporal relations.

3. By reducing the output resistance of the beam-current regulator one can reduce the loss of energy stored in the inductive bank due to the charging and discharging of the parasitic bank capacitance.

---

[1] O. A. Gusev and E. G. Komar, Author's certificate No. 307743, TsNIIPI; Byull. Izobr., No. 8 (1972).

[2] S. G. Ginzburg, Methods for Solving Problems Involving Transient Processes in Experimental Circuits [in Russian], Izd. Vysshaya Shkola, Moscow (1967).

General

Polarization of a cavity with a thermally deformed active element

I. B. Vitrishchak, L. N. Soms, and A. A. Tarasov

(Submitted June 6, 1973)
Zh. Tekh. Fiz., 44, 1055-1062 (May 1974)

The form of the Jones matrix is found for thermally deformed active laser elements. The polarization states of linear cavities is analyzed for particular cases of practical importance; cavities with active elements in the form of cylinders and rectangular plates. The optical pumping is assumed to be continuous or in periodic pulses. The heat evolution is assumed to be homogeneous and heat is assumed to be removed rapidly from the surface. The cavities also contain various phase plates. The polarization at each point on the cross section of the emitting aperture is shown to be linear. There is an analysis of the compensation for the phase shift between the orthogonal polarizations in reflection from a total-internal-reflection prism. The applicability of the Jones method is discussed.

The Jones matrix method is widely used in calculations of the polarization characteristics of laser cavities with anisotropic elements (phase plates, polarizers, and shifters in various combinations) (see, e.g., refs. 1-3).

In this note we use the Jones method to analyze a cavity with a thermally deformed active element.

When the active element of a solid-state laser is pumped optically an inhomogeneous temperature field is produced, causing thermal stress. When a light beam passes through a stressed active element, the optical path length can be different for the two orthogonal polarizations of the light, which coincide with the directions of the principal stresses σ_1, σ_2 and σ_3 at a given point, if the light propagates along one of them, or in the directions of the quasiprincipal stresses, for an arbitrary propagation direction[4] (Fig. 1).

Accordingly, in the coordinate system x'y', which coincides with the direction of the principal stresses, the Jones matrix for an arbitrary point is

$$A'=\begin{pmatrix}\exp\left(\frac{j\varphi}{2}\right) & 0\\ 0 & \exp\left(-\frac{j\varphi}{2}\right)\end{pmatrix}, \tag{1}$$

where φ is the phase shift between two polarizations when the light passes through a given point along the entire length of the active element.

Transforming to coordinate system xy by means of the familiar equation

$$A=S(-\theta)A'S(\theta),$$

where $S(\theta)$ is the matrix which rotates the coordinate system through an angle θ, we find the Jones matrix for the active element to be[5]

$$A(x,\ y)=\begin{vmatrix}\cos\frac{\varphi(x,\ y)}{2}+j\cos[2\theta(x,\ y)]\sin\frac{\varphi(x,\ y)}{2}, & j\sin[2\theta(x,\ y)]\sin\frac{\varphi(x,\ y)}{2}\\ j\sin[2\theta(x,\ y)]\sin\frac{\varphi(x,\ y)}{2}, & \cos\frac{\varphi(x,\ y)}{2}-j\cos[2\theta(x,\ y)]\sin\frac{\varphi(x,\ y)}{2}\end{vmatrix}. \tag{2}$$

Accordingly, from the polarization standpoint, a thermally deformed active element is a linear phase plate with phase difference and directions of the principal axes which vary over the cross section.

It follows immediately from (1) that the polarizations of the active element at any point coincide with the directions of the principal (or quasiprincipal) stresses at that point; the eigenvalues, whose argument gives the phase shift for the polarizations for passage through such an element, are

$$\lambda_{1,2}=\exp\left(\pm j\frac{\varphi}{2}\right). \tag{3}$$

Analysis of the polarization of cavities containing such an active element and other anisotropic elements reduces to an analysis of the combination of the phase plate plus the anisotropic elements incorporating the coordinate dependence of the phase shift in the active element.

We consider two particular cases of practical importance: a cylindrical active element and an active element in the form of a thin plate (see Fig. 2 and ref. 6). The length of the active element is much larger than the transverse dimensions; the heat evolution is homogeneous throughout the volume of the active element and constant over time (this is the situation in lasers with continuous or pulsed periodic pumping); we assume rapid heat transfer at the lateral surface. The principal stresses at each

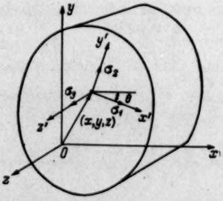

Fig. 1

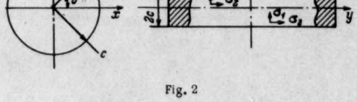

Fig. 2

point of a cylindrical active element are parallel to the axes of a cylindrical coordinate system (the z axis coincides with the cylinder axis); at each point of the plate these are parallel to the x and y axes (except in the boundary regions hatched in Fig. 2, in which edge effects are important; we neglect these regions below).

The temperature distribution is described by the parabolic relation

$$\left.\begin{aligned} T(r) &= T_0 + T_{1c}\left(1-\frac{r^2}{c^2}\right),\\ T(x) &= T_0 + T_{1p}\left(1-\frac{x^2}{c^2}\right), \end{aligned}\right\} \tag{4}$$

where I_{1c} and T_{1p} are the temperature drops between the centers of the cylinder and plate, respectively, and the corresponding surfaces.

The difference between the optical path lengths, ΔP, between the center of the active element and any point for the rays of orthogonal polarizations is

$$\left.\begin{aligned} \Delta P_{r,\theta}(0)-\Delta P_{r,\theta}(r) &= L\left(P\pm\frac{Q}{2}\right)T_{1c}\frac{r^2}{c^2},\\ \Delta P_{x,y}(0)-\Delta P_{x,y}(x) &= L(P\pm Q)\,T_{1p}\frac{x^2}{c^2}, \end{aligned}\right\} \tag{5}$$

Here, P and Q are the thermooptical constants introduced in ref. 7.

At the point under consideration the optical path difference for the rays of these orthogonal polarizations is

$$\left.\begin{aligned} \Delta P_r(r)-\Delta P_\theta(r) &= LT_{1c}Q\frac{r^2}{c^2},\\ \Delta P_x(x)-\Delta P_y(x) &= 2LT_{1p}Q\frac{x^2}{c^2}. \end{aligned}\right\} \tag{6}$$

The phase shift between these rays is given by

$$\left.\begin{aligned} \varphi_c(r) &= 2\pi\frac{LI_{1c}Q}{\lambda}\frac{r^2}{c^2},\\ \varphi_p(x) &= 4\pi\frac{LI_{1p}Q}{\lambda}\frac{x^2}{c^2}. \end{aligned}\right\} \tag{7}$$

The Jones matrix for the cylindrical active element becomes

$$A(r,\theta)=\begin{pmatrix} \cos\frac{\varphi(r)}{2}+j\cos 2\theta\sin\frac{\varphi(r)}{2} & j\sin 2\theta\sin\frac{\varphi(r)}{2}\\ j\sin 2\theta\sin\frac{\varphi(r)}{2}, & \cos\frac{\varphi(r)}{2}-j\cos 2\theta\sin\frac{\varphi(r)}{2} \end{pmatrix}. \tag{8}$$

The corresponding polarizations for the active element are

$$\begin{pmatrix}E_x\\E_y\end{pmatrix}_1=E_0\begin{pmatrix}\cos\theta\\ \sin\theta\end{pmatrix};\quad \begin{pmatrix}E_x\\E_y\end{pmatrix}_2=E_0\begin{pmatrix}\sin\theta\\ -\cos\theta\end{pmatrix}. \tag{9}$$

The Jones matrix for the plate becomes

$$A(x)=\begin{pmatrix}\exp\left(j\frac{\varphi(x)}{2}\right) & 0\\ 0 & \exp\left(-j\frac{\varphi(x)}{2}\right)\end{pmatrix}. \tag{10}$$

The corresponding polarizations of the active element are

$$\begin{pmatrix}E_x\\E_y\end{pmatrix}_1=\begin{pmatrix}1\\0\end{pmatrix};\quad \begin{pmatrix}E_x\\E_y\end{pmatrix}_2=\begin{pmatrix}0\\1\end{pmatrix}. \tag{11}$$

The eigenvalues for both configurations are found from (3):

$$\left.\begin{aligned} \lambda_{1,2} &= \exp\left(\pm j\frac{\varphi_c(r)}{2}\right),\\ \lambda_{1,2} &= \exp\left(\pm j\frac{\varphi_p(x)}{2}\right). \end{aligned}\right\} \tag{12}$$

The arguments $\lambda_{1,2}$ in (12) do not take account of the phase shift resulting from the passage of the light through the active element, which is common to both polarizations; this shift is also a quadratic constant P [see Eq. (5)].

To take this phase shift into account we multiply the right sides of (12) and matrices (8) and (10) by

$$\left.\begin{aligned} &\exp\left(2\pi j\frac{T_{1c}P}{\lambda}\frac{r^2}{c^2}\right),\\ &\exp\left(2\pi j\frac{T_{1p}P}{\lambda}\frac{x^2}{c^2}\right). \end{aligned}\right\} \tag{13}$$

The polarization states are obviously not affected.

The quadratic functional dependences of the phase shift imply that these active elements are equivalent to lenses for each of the polarizations: a spherical lens for the cylinder and a cylindrical lens for the plate.[6]

For the simplest cases of a linear cavity or a ring cavity with an even number of mirrors the polarization is also given by (9) and (11).

We have in fact observed these polarization states experimentally (linear polarization of the radiation of a laser with a plate-shaped active element[6] and transverse electric and transverse magnetic modes $E^{(r)}$ and $E^{(\varphi)}$ in ref. 8).

We now turn to more complicated situations, in which the cavity contains other anisotropic elements in addition to the active element (Fig. 3).

The three variants in Fig. 3 are essentially equivalent and coincide with the variant in Fig. 3B when the phase shift in the phase plate is chosen appropriately. However,

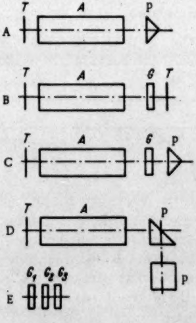

Fig. 3. Optical arrangement of the cavities. The matrices of the anisotropic elements correspond to Eqs. (8), (10) and (14)-(16).

the variant in Fig. 3A merits separate study, since this arrangement is frequently used in Q-spoiled lasers; the arrangement of Fig. 3C, on the other hand, can be useful when it is necessary to compensate for the phase shift at a prism.

The Jones matrices for the elements of the cavity are as follows:[2,3] for a phase plate,

$$G=\begin{pmatrix}\exp\left(j\frac{\psi_g}{2}\right) & 0\\ 0 & \exp\left(-j\frac{\psi_g}{2}\right)\end{pmatrix}; \tag{14}$$

for a prism,

$$\Pi=\begin{pmatrix}\exp\left(j\frac{\psi_p}{2}\right) & 0\\ 0 & \exp\left(-j\frac{\psi_p}{2}\right)\end{pmatrix}; \tag{15}$$

for a mirror,

$$T=\begin{pmatrix}1 & 0\\ 0 & 1\end{pmatrix}. \tag{16}$$

In the calculations below we use ψ_p = 82°, corresponding to a refractive index of n = 1.53 for the prism.

The matrices of the cavities are

$$\left.\begin{aligned}D_A&=A\cdot \mathrm{P}\cdot A\cdot T,\\ D_B&=A\cdot G\cdot G\cdot A,\\ D_C&=A\cdot G\cdot \mathrm{P}\cdot T\cdot G\cdot A\end{aligned}\right\} \tag{17}$$

where the subscripts on matrices D correspond to the arrangements in Fig. 3.

It is easy to see that all the matrices in (17) are diagonal for the plate-shaped active element, so the polarization states remain linear, but their directions are along the x and y axes. The eigenvalues of the cavity matrices are equal to the corresponding diagonal terms, and since the elements of matrices (14)-(16) are not functions of the coordinate x, the coordinate dependence of the phase shift of the polarizations of the cavities in Fig. 3 is governed by the same parabolic relation [Eq. (7) with (13)].

For the cylindrical element the components of the cavity have different symmetries, and the question of the polarizations is much more complicated.

We note first that by using the familiar equations[3] for the eigenvalues $\lambda_{1,2}$ and the ratio of the components of the polarizations, E_x and E_y,

$$\left.\begin{aligned}\lambda_{1,2}&=\frac{1}{2}[(D_{11}+D_{22}\pm\sqrt{(D_{11}-D_{22})^2+4D_{12}D_{21}}],\\ \frac{E_x}{E_y}\Big|_{1,2}&=\frac{D_{12}}{\lambda_{1,2}-D_{11}},\end{aligned}\right\} \tag{18}$$

where D_{ik} is the corresponding element of matrix D from (17), we can show that the polarization states of the system of phase plates in Fig. 3E (where $G_1 = G_3$ and where the axes of plate G_2 are rotated through an arbitrary angle with respect to the axes of G_1 and G_3) are linear.

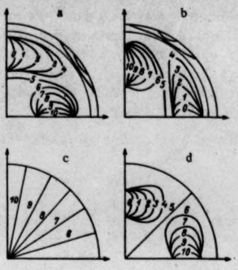

Fig. 4. Distribution of the azimuths of the polarization over the cross section of the cavity. T_{1c} = 23°K, Q = $7\cdot10^{-7}$, L = 8 cm. The contours labeled 0-10 correspond to azimuths from −75 to + 75° at 15° steps.

It follows that for matrix A(x, y) of the most general form, (2), the polarization states of any of the cavities in Figs. 3A-3C are linear, and the only parameter distinguishing these states is the azimuth of the polarization direction.

We use Eqs. (18) to calculate the polarization states of the cavities in Figs. 3A-3D with cylindrical active elements. The results are shown in Figs. 4a-4c as contours of equal azimuth; Fig. 4a shows the azimuth field of one of the polarizations of the cavity in Fig. 3A.

At the center of the cavity, where there is no anisotropy of the active element, the azimuth of the polarization is governed completely by the prism, and it coincides with one of the principal axes of the prism, that running parallel to the x axis, which is itself parallel to an edge of the prism.

We note that there are points at which the contours converge; here there is a compensation for the phase shift in the prism by the phase plate corresponding to the given point of the active element. At these points the cavity is equivalent to an isotropic cavity. The compensation can occur only when the principal axes of the phase plates coincide, so these points lie on lines passing through the center of the active element, parallel and perpendicular to the edge of the prism.

Figure 4b shows the field of azimuths of one of the polarizations of the cavity of Fig. 3B; the phase shift at the plate is chosen to be 41°. Although the phase shift at the plate is 82°, after two passes, like the phase shift at the prism, the field of polarization azimuths is quite different in these cases. The reason is that the right-handed coordinate system is converted into a left-handed system in reflection from the mirror; this does not happen in reflection from the prism, and the mirror is equivalent to a half-wave phase plate in any coordinate system [see (16)]. Accordingly, when the phase shift at the prism is compensated (Fig. 3C) the phase shift between the orthogonal polarizations must be 180° after two passes through the phase plate and the prism, i.e., the phase shift at the plate is

$$\psi_g=\frac{180^\circ-82^\circ}{2}=49^\circ.$$

Figure 4c shows the field of azimuths of one of the polarizations of such a cavity, with this value of ψ_g. We see that the direction of the azimuths corresponds to the mode $E^{(r)}$, i.e., compensation occurs.

On the other hand, when ψ_g is chosen such that the total phase shift vanishes (or is equal to 360°), i.e., when

$$\psi_g = \frac{360^\circ - 82^\circ}{2} = 139^\circ,$$

the picture is quite different (this case can occur when opticomechanical spoilers with rotation-rate doubling are used; Fig. 3D). Figure 4b shows the results calculated for such a cavity; we see that the distribution of polarization over the cavity aperture is quite different from that in the compensation case (Fig. 4b).

We turn now to the range of applicability of the Jones method for calculating the polarization states of anisotropic elements with the coordinate dependence specified above for the phase advance in the cross section of the element.

One condition for the applicability of the Jones method is that the front of the light wave transmitted by the anisotropic element be planar.[3] It is not difficult to show, however, that this requirement is imposed simply so that it is possible to reduce the transformation of the polarization in extended anisotropic elements to the transformation by a certain plane described by the Jones matrix, so that it would not be necessary to follow actual trajectories of the rays through these elements when the wave front is nonplanar.

Obviously this requirement can be lifted if we introduce these trajectories and calculate the transformation of the polarization. As an example we note that the anisotropic device used in ref. 9 to produce $E^{(r)}$ modes (a Galilean telescope into which a calcite plate has been inserted; the optic axis of this plate is parallel to the telescope axis) is described by a matrix like (8); it is simply necessary to take account of the scaling ratio of the coordinate transformation on the different sides of the telescope, which is equal to the magnification of the telescope.

For the thermally deformed active elements with which we are concerned here we can easily derive the condition for which the trajectories discussed above can be neglected and for which the error resulting from the use of the Jones matrices in their simplest form, (8) and (10), is small (Fig. 5).

The phase advance between two polarizations for propagation along the actual trajectory is

$$\varphi_1(r_0) = \frac{1}{L}\int_0^L \varphi(r(r_0, z))\,dz,$$

where $r(r_0, z)$ is the trajectory of the ray which enters the active element at point r_0, propagating parallel to the z axis,[10] and the function $\varphi(r)$ in the integrand is that in (7).

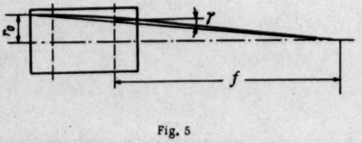

Fig. 5

The phase advance $\varphi_0(r_0)$ in the plane-wave approximation is given by Eqs. (7) with $r = r_0$; matrix (8) can be used when

$$\frac{r}{r_0} \approx 1, \tag{19}$$

$$\frac{\varphi_1(r_0)}{\varphi_0(r_0)} \approx 1. \tag{20}$$

We see from Fig. 5 that

$$1 \geqslant \frac{r}{r_0} \geqslant \frac{r_0 - L\sin\gamma}{r_0} = 1 - \frac{L}{r_0}\sin\gamma.$$

For small γ we have

$$1 \geqslant \frac{r}{r_0} \geqslant 1 - \frac{L}{r_0}\frac{r_0}{f} = 1 - \frac{L}{f},$$

and using (19) we find

$$L \ll f. \tag{21}$$

Similarly, using (7), we find

$$1 \geqslant \frac{\varphi_1(r_0)}{\varphi_0(r_0)} \geqslant \left(1 - \frac{L}{2f}\right)^2 \approx 1 - \frac{L}{f},$$

which is seen to be the same as (21) when (20) is taken into account.

The focal length of the thermal lens of a cylindrical active element of type GLS-2 glass under the conditions assumed in this calculation[10,11] is about 2 m, so that condition (21) is satisfied.

We note in conclusion that the Jones method, which allows us to find the polarization states of cavities containing thermally deformed active elements in a comparatively simple manner, does not give us information about the modes actually excited in such cavities or about their loss.

This information can apparently be found by combining this method with the Fox–Li method[12] for solving diffraction problems. In this case the problem is obviously complicated: instead of solving a single integral equation, it is necessary to solve a system of equations corresponding to an iterative process of the type

$$\mathrm{E}'(\mathbf{r}) = \int K(\mathbf{r}, \mathbf{r}')\,D\mathrm{E}(\mathbf{r}')\,d\mathbf{r},$$

where D is the Jones matrix for the anisotropic cavity.

---

[1] W. A. Shurcliff, Polarized Light, Harvard Univ. Press, Cambridge (1962).

[2] É. I. Ivanov and N. P. Chaika, The Physics of Gas Lasers [in Russian], Izd. LGU (1969).

[3] V. Ya. Molchanov and G. V. Skrotskii, Kvant. Elektron (Mosc.), No. 4, 3 (1971).

[4] A. J. Durelli and W. F. Riley, Introduction to Photomechanics, Prentice-Hall, Englewood Cliffs, New Jersey (1965).

[5] G. A. Massey, Appl. Phys. Lett., 17, 213 (1970).

[6] A. A. Mak, L. N. Soms, A. I. Stepanov, and A. B. Sudakov, Opt. Spektrosk., 30, 1081 (1971).

[7] Yu. A. Anan'ev and N. N. Grishmanova, Zh. Prikl. Spektrosk., 12, 668 (1970).

[8] A. A. Mak, V. M. Mit'kin, and L. N. Soms, Opt. Spektrosk., 32, 996 (1972).

[9] D. Pohl, Appl. Phys. Lett., 20, 226 (1972).

[10] H. Kogelnick, BSTJ, 44, 465 (1965).

[11] A. A. Mak, V. M. Mit'kin, L. N. Soms, A. I. Stepanov, and O. S. Shavelev, Opt.-Mekh. Prom., No. 9, 42 (1971).

[12] A. G. Fox, Appl. Phys. Lett., 17, 213 (1970).

Gas cooling in transmission of high-power CO_2 laser radiation through the atmosphere

B. F. Gordiets, A. I. Osipov, and R. V. Khokhlov

M. V. Lomonosov Moscow University

(Submitted July 16, 1973)
Zh. Tekh. Fiz., 44, 1063-1069 (May 1974)

The rate of change of the gas temperature in the laser beam path when radiation is transmitted through the atmosphere and the time dependence of the populations of CO_2 and N_2 molecular vibration levels are calculated for a broad range (0.3-10^5 kW/cm^2) of CO_2 laser power densities and altitudes of 0-20 km. The basic parameters of the cooling which can occur immediately following absorption of the radiation are determined. It is shown that for a humid atmosphere there are critical laser power densities which, if exceeded, cause the cooling effect to disappear. For a standard atmosphere these critical power densities range from $2\cdot10^3$-10^5 W/cm^2 (depending on the altitude and atmospheric humidity).

When laser radiation propagates through the atmosphere thermal defocusing occurs due to heating of the gas caused by partial absorption of the radiation and the resulting temperature gradients and refractive index over the beam cross section.[1]

It is shown in ref. 2, however, that when CO_2 laser radiation is transmitted the gas may be cooled, rather than heated, in the initial period following the absorption. This result is due to the fact that the rate of vibrational–translational relaxation of the 10^00 (CO_2) level, which is the lower level for radiative absorption, is large in comparison to the relaxation rate of the populations of the 00^01 upper level and the $\vartheta = 1$ (N_2) molecular vibrational level resonant with it. In this case, absorption of the radiation is associated with energy pumping from the translational degrees of freedom to the 00^01 (CO_2) and $\vartheta = 1$ (N_2) levels, which cools the gas during the initial period. This cooling mechanism is advantageous for transmission of radiation since it is accompanied by thermal self-focusing. In ref. 2, however, the dependence of this effect on laser power density is not considered, although it is important for the selection of the most appropriate conditions for laser energy transfer (for example, in selecting the optimum length of the lasing pulses).

The dependence of cooling effects on laser power density is considered in ref. 3. However, the equations derived in ref. 3 have a limited range of validity and lead to erroneous results for high power densities in a humid atmosphere.

In the present paper we determine the cooling parameters resulting from the transmission of CO_2 laser radiation through the atmosphere for a broad range (0.3-10^5 kW/cm^2) of power densities and altitudes of 0-20 km.

A pure-atmosphere model, i.e., an atmosphere not containing drops of condensed water and other microparticles, is used to solve the problem. In this case one can assume that the CO_2 laser radiation is absorbed only by atmospheric CO_2 (through the $10^00 \rightarrow 00^01$ transition) and water vapor (in the wing of the 6.3 μ absorption band of H_2O).

To determine the time dependence of the gas temperature for CO_2 absorption we begin with the gas-kinetic equations describing vibrational–translational energy exchange in a $CO_2-N_2-O_2-H_2O$ mixture. In the general case this approach requires that one consider a large number of equations for the populations of the lower vibrational states of these molecules. We note that under atmospheric conditions it is improper to base the analysis of CO_2 laser processes on the often-used kinetic model in which different CO_2 vibrational modes have different temperatures, i.e., a local Boltzmann distribution is assumed in each mode. Because of the small amount of CO_2 in the atmosphere the vibrational–vibrational exchange processes which establish a quasiequilibrium are not effective and occur more slowly than, for example, vibrational–translational relaxation. The problem is simplified considerably if it is noted that the following condition always holds for the atmospheric gas temperature T:

$$kT \ll h\nu, \tag{1}$$

where ν is the smallest vibrational frequency in the molecular system under consideration, i.e., the frequency of CO_2 bending vibrations. If (1) is satisfied, all the vibrational partition functions can be set equal to unity and it can be assumed that the population of the 01^00 level is always in equilibrium in the absorption of radiation of any power and that only the populations of the 020, 10^00, and 00^01 levels, responsible for the absorption of the radiation and the population of the first N_2 vibrational level, show any change. This is the case because the negative source of molecules (in our case the radiation converting the molecules from the 10^00 to the 00^01 state) distorts the distribution function only in the energy region $\sim$kT, near the level on which it acts.[4,5] The 01^00 level is separated by $h\nu \gg kT$ from the 02^00 and 10^00 levels.

The problem can be simplified further by noting that the fastest molecular processes under atmospheric conditions are resonant energy exchange between the 10^00 and 02^00 states in CO_2, vibrational exchange between O_2 and H_2O, and vibrational–translational relaxation in H_2O. In this case, it can be assumed that the populations of the 10^00 and 020 (CO_2) levels are always equal (allowing for the statistical weight of the 020 level), and the stored vibrational energy in O_2 and H_2O is in equilibrium; thus, vibrational exchange between O_2 and H_2O and the CO_2 and N_2 molecules only increases the usual vibrational–translational relaxation of the latter two species.

With allowance for the above considerations, the system of gas-kinetic equations describing the vibrational relaxation and accounting for the vibrational–translational energy exchange in the atmosphere in the presence of absorbed CO_2 laser radiation reduces to a system of three linear equations

$$\left.\begin{aligned}\frac{dx_1}{dt}&=-\beta(w+2gP_{10})x_1+\beta wx_2+2\beta gP_{10}x_1^0,\\ \frac{dx_2}{dt}&=wx_1-(w+Q+P_{20})x_2+Qx_3+P_{20}x_2^0,\\ \frac{dx_3}{dt}&=\delta Qx_2-(\delta Q+P_{30})x_3+P_{30}x_3^0.\end{aligned}\right\}\qquad(2)$$

Here, x_1, x_2, and x_3 are the relative populations of the 10^00, 00^01 (CO_2), and $\vartheta = 1$ (N_2) levels; x_1^0, x_2^0, x_3^0 are the equilibrium values of these populations corresponding to a gas temperature T, i.e., $x_1^0 = \exp\{-E_1/T\}$, $x_2^0 = x_3^0 = \exp \cdot \{-E_2/T\}$ [E_1 and E_2 are the energies (in deg) of the 10^00 and 00^01 levels; it is assumed that the energy of an N_2 photon is E_2]; P_{10}, P_{20}, and P_{30} are the probabilities (in sec^{-1}) of collisional quenching of the 01^00, 00^01 (CO_2), and $\vartheta = 1$ (N_2) levels; Q is the probability (in sec^{-1}) of resonant transfer of excitation from 00^01 (CO_2) to the $\vartheta = 1$ (N_2) level; w is the probability (in sec^{-1}) of optical excitation of CO_2 by the laser radiation; g = 3 is the statistical weight of the 020 level; $\beta = (1 + g)^{-1} = 1/4$; $\delta = 3.85 \cdot 10^{-4}$ is the ratio of the total CO_2 concentration to the total N_2 concentration in the atmosphere. In writing (2) it is assumed that collisional relaxation of the 10^00 state occurs through a bending vibration. Spontaneous radiative transitions in CO_2 are not taken into account in (2) because at altitudes of 0-20 km the transition probability is considerably smaller than the probabilities of the collisional processes.

If thermal conductivity and convective heat transfer are neglected, the variation in gas temperature due to the laser radiation is determined by

$$\left.\begin{aligned}&\frac{c_p}{R}N\frac{dT}{dt}=F+\alpha^0_{H_2O}(E_2-E_1)\Phi;\\ &F=N_{CO_2}\Big[E_1 2gP_{10}(x_1-x_1^0)\\ &+E_2P_{20}(x_2-x_2^0)+E_2\frac{P_{30}}{\delta}(x_3-x_3^0)\Big].\end{aligned}\right\}\qquad(3)$$

Here, R is the gas constant, c_p is the specific heat capacity at constant pressure, N and N_{CO_2} are the total number of molecules and the total number of CO_2 molecules per unit volume, F is the energy flux to vibrational degrees of freedom from vibrational relaxation of CO_2 and N_2, Φ is the photon flux in the laser beam, and $\alpha^0_{H_2O}$ is the absorption coefficient of water vapor. It is understood in (3) that due to the rapid rotational relaxation of water vapor saturation effects do not appear for H_2O absorption and that the adsorbed energy is rapidly converted to rotational degrees of freedom. Simple estimates indicate that for altitudes of 0-20 km this assumption is valid for laser power densities $I < 10^{10}$ kW/cm^2.

The radiative photon flux Φ in (3) is related to the probability w of optical excitation of CO_2 by

$$w=\frac{\alpha^0_{CO_2}}{(x_1^0-x_2^0)N_{CO_2}}\Phi,\qquad(4)$$

where $\alpha^0_{CO_2}$ is the absorption coefficient (in cm^{-1}) of atmospheric CO_2 in the absence of saturation effects, i.e., for weak radiative intensities.

We now consider the solution of system (2). Remembering that under atmospheric conditions it is always true that βQ; $2\beta gP_{10} \gg P_{20}/\delta$; P_{30}, we can find the explicit form of the solution for the following case of practical interest.

The negative terms in square brackets in (6), which exceed the other terms during the initial time period, describe the cooling the gas after absorption of the radiation. If the second rapidly damping term in square brackets in (6a) is neglected, the expression for F is the same as that obtained in ref. 2. In this case, such important cooling parameters as the maximum degree of cooling ΔT, the time for attaining this cooling t_{min}, and the time duration of the cooling Δt are determined by the probability P' and the ratio between the CO_2 and H_2O absorption coefficients, i.e., by the atmospheric humidity. It is easy to show from the solution of (3), with (6a), that the maximum degree of cooling ΔT increases linearly with increasing power density I, and t_{min} and Δt are independent of I. We note that the cooling effect itself is possible for atmospheric humidity such that $\alpha^0_{H_2O} < [E_1/(E_2 - E_1)]\alpha^0_{CO_2} = 1.29\alpha^0_{CO_2}$. At sea level this inequality holds for a relative humidity of $\leq$ 50% (at a temperature of 15°C). However, cooling can occur for 100% humidity at altitudes as low as 1.5 km (for a standard-atmosphere temperature).

1. LOW LASER POWER DENSITIES
$w \ll 2gP_{10}$; Q

The above inequality holds in the atmosphere for power densities $I \ll 10^3$ kW/cm^2; 10 kW/cm^2 (for 100% humidity and altitudes of 0 and 18 km, respectively). If we recall that in many cases $Q > 2gP_{10}$ the solution of system (2) is simplified further and becomes

$$\left.\begin{aligned}&x_1\approx x_1^0-\frac{wP'(x_1^0-x_2^0)}{2gP_{10}(\delta w+P')}\\ &+\frac{w}{2gP_{10}}(x_1^0-x_2^0)\Big[\exp\{-2\beta gP_{10}t\}\\ &-\frac{\delta w}{\delta w+P'}\exp\{-(\delta w+P')t\}\Big],\\ &x_2\approx x_3\approx\frac{\delta wx_1^0+P'x_2^0}{\delta w+P'}-\frac{\delta w}{\delta w+P'}(x_1^0-x_2^0)\exp\{-(\delta w+P')t\}.\end{aligned}\right\}\qquad(5)$$

Here and below, $P' = P_{30} + \delta P_{20}$.

By substituting (5) into (3), we find the energy flux F to translational degrees of freedom resulting from CO_2 absorption of laser beam radiation. For the two characteristic cases we have

$$\left.\begin{aligned}&F\approx N_{CO_2}(x_1^0-x_2^0)w[(E_2-E_1)\\ &+E_1\exp\{-2\beta gP_{10}t\}-E_2\exp\{-P't\}]\\ &\text{when }\ \delta W\ll P'\ \text{(a)}\\ &F\approx N_{CO_2}(x_1^0-x_2^0)\Big[\frac{P'}{\delta}(E_2-E_1)\\ &+wE_1(\exp\{-2\beta gP_{10}t\}-\exp\{-\delta wt\})\Big]\\ &\text{when }\ \delta w\gg P'\ \text{(b)}.\end{aligned}\right\}\qquad(6)$$

When $\delta w \gg P'$ one of the saturation mechanisms operates. It follows from (6b) that in the steady state as $t \to \infty$ the energy flux to translational degrees of freedom becomes independent of the laser radiative intensity and is determined by the probability of vibrational deactivation P'/δ. In the transient period, however, at a time $t \leq 1/\delta w$ the flux F is still a function of w. For the present case the cooling parameters ΔT, t_{min}, and Δt are determined for a dry atmosphere by

$$\Delta T \approx -E_1 \frac{R}{c_p}(x_1^0 - x_2^0)\frac{N_{CO_2}}{\delta N}; \qquad (7)$$

$$t_{min} \approx \frac{1}{\delta w}\ln\left[\frac{E_1}{E_2 - E_1}\frac{\delta w}{P'}\right]; \ \Delta t = \frac{E_1}{E_2 - E_1}\frac{1}{P'}.$$

If the atmosphere is humid we obtain

$$\left.\begin{aligned}\Delta T &= \frac{R}{c_p}\frac{N_{CO_2}}{\delta N}(x_1^0 - x_2^0)\left[(E_2 - E_1)\frac{\alpha^0_{H_2O}}{\alpha^0_{CO_2}} - E_1\right];\\ t_{min} &= \frac{1}{\delta w}\ln\left[\frac{\alpha^0_{CO_2}}{\alpha^0_{H_2O}}\frac{E_1}{E_2 - E_1}\right];\\ \Delta t &\doteq \frac{1}{\delta w}\frac{\alpha^0_{CO_2}}{\alpha^0_{H_2O}}\frac{E_1}{E_2 - E_1}[1 - \exp\{-\delta w \Delta t\}].\end{aligned}\right\} \qquad (8)$$

It follows from (7) and (8) that for the indicated saturation mechanism maximum cooling ΔT is independent of the radiative intensity; the time for achieving this cooling is inversely proportional to this intensity. The time duration of cooling Δt is either independent of the intensity [for a dry atmosphere, (7)] or inversely proportional to it [for a humid atmosphere, (8)]. The indicated mechanism has been investigated in detail in ref. 3. It should be noted, however, that the results obtained in ref. 3, just as Eqs. (7) and (8), have a limited range of validity and are invalid for high power densities. Thus, for example, according to ref. 3 and Eqs. (7) and (8), the cooling effect will occur for any power density only if the atmospheric humidity is such that $\alpha^0_{H_2O} < [E_1/(E_2 - E_1)]\alpha^0_{CO_2}$. Actually, the cooling effect can disappear for laser power densities $w > 2gP_{10}; Q$. We consider this case in more detail.

2. HIGH POWER DENSITIES $\omega \gg 2gP_{10}; Q$

For the above relationships between the probabilities the solution of system (2) has the form

$$\left.\begin{aligned}x_1 &\approx x_1^0 - \frac{P'(x_1^0 - x_2^0)}{2\delta gP_{10} + P'} + (x_1^0 - x_2^0)\Big\{\frac{\beta}{1+\beta}\exp[-(1+\beta)wt]\\ &\quad -\left(\frac{\beta}{1+\beta} - \frac{Q}{2gP_{10}+Q}\right)\exp\left[-\frac{\beta}{1+\beta}(Q + 2gP_{10})t\right]\\ &\quad -\frac{Q}{2gP_{10}+Q}\exp\left[-\frac{2\delta gP_{10}Q}{2gP_{10}+Q}t\right]\Big\},\\ x_2 &\approx x_1^0 - (x_1^0 - x_2^0)\Big\{\frac{1}{1+\beta}\exp[-(1+\beta)wt]\\ &\quad +\left(\frac{\beta}{1+\beta} - \frac{Q}{2gP_{10}+Q}\right)\exp\left[-\frac{\beta}{1+\beta}(Q + 2gP_{10})t\right]\\ &\quad +\frac{Q}{2gP_{10}+Q}\exp\left[-\frac{2\delta gP_{10}Q}{2gP_{10}+Q}t\right]\Big\},\\ x_3 &\approx x_1^0 - (x_1^0 - x_2^0)\exp\left\{-\frac{2\delta gP_{10}Q}{2gP_{10}+Q}t\right\}.\end{aligned}\right\} \qquad (9)$$

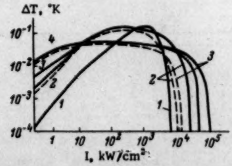

Fig. 1. Maximum cooling ΔT vs. power density I for different altitudes. Here and in Fig. 2, the solid curves represent 30% relative humidity, and the dashed curves 100%; standard atmosphere; H in km: 1) 0; 2) 6; 3) 12; 4) 18.

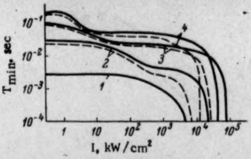

Fig. 2. Time t_{min} for attaining maximum cooling vs power density I for different altitudes.

Substituting (9) into (3) and neglecting the rapidly damping terms with $\exp\{-(1+\beta)wt\}$ and $\exp\{-[\beta/(1+\beta)]\cdot(Q + 2gP_{10})t\}$, we find the energy flux F:

$$F \approx N_{CO_2}(x_1^0 - x_2^0)\left[\frac{P'}{\delta}(E_2 - E_1) - E_1\frac{2gP_{10}Q}{2gP_{10}+Q}\exp\left\{-\frac{2\delta gP_{10}Q}{2gP_{10}+Q}t\right\}\right]. \qquad (10)$$

It follows from (10) that for laser power densities such that $w \gg 2gP_{10}; Q$ the energy flux to translational degrees of freedom from CO_2 absorption of laser radiation no longer depends on the power density over the entire time interval. This may be called the "total" saturation mechanism. Formally, Eq. (10) can be obtained from (6b) by replacing the probability w by the probability $2gP_{10}Q/(2gP_{10} + Q)$. Physically, the conversion from (6a) to (6b) and (10) is due to the presence of bottlenecks for gas heating and cooling. Actually, since the heating rate is limited by the relaxation rate in the 00^01 (CO_2) and $\vartheta = 1$ (N_2) levels (i.e., by the probability P'/δ), with power densities such that $w > P'/\delta$, the probability w in (6a) in the first term, which describes gas heating, is replaced by P'/δ. Similarly, since the cooling rate is limited by the probability of energy conversion from translational degrees of freedom to the 00^01 (CO_2) and $\vartheta = 1$ (N_2) levels (i.e., by the probabilities $2gP_{10}$ and Q), with power densities such that $w > 2gP_{10}; Q$, the term w in (6b) is replaced by $2gP_{10}Q/(2gP_{10} + Q)$. Combining Eqs. (10) and (3), we can find the cooling parameters

$$\Delta T = (E_2 - E_1)\frac{R}{c_p N}\left[\alpha^0_{H_2O}\Phi + (x_1^0 - x_2^0)N_{CO_2}\frac{P'}{\delta}\right]t_{min} - E_1\frac{R}{c_p}(x_1^0 - x_2^0)\frac{N_{CO_2}}{\delta N}\left[1 - \exp\left\{-\frac{2\delta gP_{10}Q}{2gP_{10}+Q}t_{min}\right\}\right];$$

$$t_{min} = \frac{2gP_{10}+Q}{2\delta gP_{10}\cdot Q}\ln\left[\frac{2\delta gP_{10}Q}{(2gP_{10}+Q)}\frac{\alpha^0_{CO_2}E_1}{(P'\alpha^0_{CO_2} + \delta w\alpha^0_{H_2O})(E_2 - E_1)}\right];$$

$$\Delta t = \frac{(x_1^0 - x_2^0)N_{CO_2}E_1}{[\delta\alpha^0_{H_2O}\Phi + (x_1^0 - x_2^0)N_{CO_2}P'](E_2 - E_1)}$$

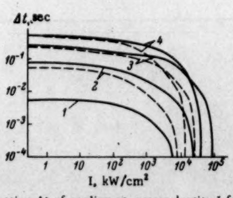

Fig. 3. Time duration Δt of cooling vs power density I for different frequencies.

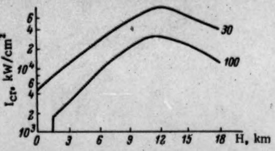

Fig. 4. Critical power density I_{cr} vs. atmospheric altitude for different relative humidities. Standard atmosphere; 30 and 100% humidities.

$$\times\left[1-\exp\left\{-\frac{2\delta gP_{10}Q}{2gP_{10}+Q}\Delta t\right\}\right]. \qquad (11)$$

For a dry atmosphere, ΔT and Δt determined from (11) are close to the values of (7); in contrast to (7), t_{min} does not depend on the radiative intensities and is determined by $2\delta gP_{10}Q/(2gP_{10}+Q)$. For a humid atmosphere, however, when $w > 2gP_{10}$; Q, all three cooling parameters depend on Φ (or I) in a way that is substantially different from that obtained in ref. 3 [see Eq. (8)]. These dependences are given in Figs. 1-3 for a broad range of power densities $0.3\text{-}10^5$ kW/cm² and for different altitudes 0-18 km. It follows from Fig. 1 that for a humidity $\gtrsim$ 30% and power densities $\gtrsim$ 10 kW/cm² the degree of cooling begins to decrease as the power density increases; for power densities $10^4\text{-}10^5$ kW/cm² (depending on the altitude and humidity) the cooling effect disappears. The time t_{min} for attaining maximum cooling (Fig. 2) is independent of the power density or is governed by Eqs. (7) and (8) only for comparatively low power densities ($\leq$ 300, 30, and 10 kW/cm² at altitudes of 6, 12, and 18 km, respectively). The time duration of the cooling for power densities $\gtrsim 10^3$ kW/cm² is not governed by Eqs. (7) and (8), and for a certain power density (determined by the humidity and altitude) it vanishes. The disappearance of cooling in a humid atmosphere comes about because for high power densities, when "total" saturation is attained for CO_2 absorption, the energy flux from translational to vibrational degrees of freedom associated with gas cooling ceases to depend on power density and reaches a maximum [see (10)]. However, the energy flux to translational degrees of freedom, which is induced by water vapor absorption and determines the gas heating, remains proportional to the power density. For this reason there is a certain power density at which gas heating begins to dominate the cooling for the entire time interval $0 < t < \infty$. It is easy to see from (11) that the critical power density I_{cr} at which the cooling effect disappears is determined by

$$w_{cr} = \frac{E_1}{E_2 - E_1}\frac{\alpha^0_{CO_2}}{\alpha^0_{H_2O}}\frac{2gP_{10}Q}{2gP_{10}+Q} - \frac{\alpha^0_{CO_2}}{\alpha^0_{H_2O}}\frac{P'}{\delta}, \qquad (12)$$

where w_{cr} is the critical probability of optical excitation associated with the critical photon flux by Eq. (4). The dependence of the critical power density I_{cr} on altitude for a standard atmosphere is shown in Fig. 4 for relative humidities of 30 and 100%. These power densities are extremely large but they are completely practical experimentally. We note that breakdown of the gas due to CO_2 laser radiation, which may compete with the cooling process, occurs[6,7] at power densities > 10^5 kW/cm², and thus has essentially no effect on the above conclusions.

Equations (7), (8), and (11), along with Fig. 1, indicate that the degree of cooling is small under atmospheric conditions and usually does not exceed ~0.5°K. When radiation propagates in the atmosphere, however, the most important quantity is not the degree of cooling, but the total duration Δt of this process, since during time Δt the propagation of radiation will not be harmed by thermal defocusing of the beam due to the absence of heating in the laser beam path. It is therefore clear that to avoid defocusing the length of the beam pulses must be chosen by starting with Δt.

In conclusion, we note that under laboratory conditions with a dry $CO_2 + N_2$ mixture (with a substantial N_2 excess), preliminary heating of the gas produces cooling in the laser beam path that substantially exceeds the ΔT values obtained in the ordinary atmosphere. Thus, it is easy to see from Eq. (7) that when T = 1000°K (when $x_1 = 0.143$) cooling with $\Delta T = 60$°K can be obtained.

---

[1] S. A. Akhmanov, A. P. Sukhorukov, and R. V. Khokhlov, Usp. Fiz. Nauk, 93, 19 (1967) [Sov. Phys. – Usp., 10, 609 (1968)]; S. A. Akhmanov, R. V. Khokhlov, and A. P. Sukhorukov, Laser Handbook, Vol. 2, North-Holland, Amsterdam (1972), p. 1151.

[2] A. D. Wood, M. Comac, and E. T. Gerry, Appl. Opt., 10, 1877 (1971).

[3] E. L. Breig, J. Opt. Soc. Am., 62, 518 (1972).

[4] E. V. Stupochenko, S. A. Losev, and A. I. Osipov, Relaxation Processes in Shock Waves [in Russian], Nauka, Moscow (1965).

[5] B. F. Gordiets, A. I. Osipov, E. V. Stupochenko, and L. A. Shelepin, Usp. Fiz. Nauk, 108, 655 (1972) [Sov. Phys. – Usp., 15, 759 (1973)].

[6] C. D. Moody, Appl. Phys. Lett., 22, 31 (1973).

[7] A. M. Robinson, Appl. Phys. Lett., 22, 33 (1973).

Nonlinear spherical aberrations and thermoelastic stresses in thermal self-focusing

A. A. Vigasin, Yu. A. Gorokhov, A. P. Sukhorukov, and A. M. Khachatryan

M. V. Lomonosov Moscow State University

(Submitted June 25, 1973)
Zh. Tekh. Fiz., 44, 1070-1075 (May 1974)

Experimental and theoretical investigations of thermal self-focusing of the continuum radiation of an argon laser in TF-105 glass are reported. The experimental results are compared quantitatively with an analysis of the effect of thermoelastic stresses on the nonlinear refraction. It is shown that steady-state thermal self-focusing can be described by using the aberration-free approximation up to the focus, applying the aberration correction only in the expression for R_{nl}. The distortion of the Gaussian profile of the laser beam caused by aberrations is investigated.

1. In the propagation of laser radiation through an absorbing medium nonuniform local heating of the medium occurs as a result of dissipation of the electromagnetic energy. The refraction index of the medium changes, leading to thermal self-stress effects [thermal self-focusing or defocusing, depending on the sign of the temperature gradient of the refraction index dn/(dT)], which are most pronounced in beams of high-power cw lasers.

Several papers treat the problem of thermal self-focusing.[1-5] We investigate here the behavior of a self-focusing beam taking account of thermoelastic stresses in the medium and nonlinear spherical aberrations.

The refraction index of an absorbing medium is

$$n(r)=n_0+\frac{dn}{dT}T(r). \tag{1}$$

where T(r) is the steady-state temperature distribution in the medium. However, it must be remembered that the refraction index does not depend only on the absolute temperature increment at a certain point in the medium. Strong temperature gradients produce thermoelastic stresses and these can change the optical characteristics of the medium. Thus, the total temperature-induced change in the refraction index is (see Appendix)

$$\frac{dn}{dT}=\left(\frac{\partial n}{\partial T}\right)_{\sigma=0}+\left(\frac{\partial n}{\partial T}\right)_{TH}$$

$$=\frac{\partial n}{\partial T}+\frac{\alpha n_0^3}{4(1-\nu)}[(p_{11}+p_{12})(1-3\nu)+2p_{12}(1-\nu)]. \tag{2}$$

Since nonlinear refraction accompanying thermal self-stresses is determined by the total derivative of the refraction index with respect to temperature, the effect of thermoelastic stresses can be significant in estimating the self-focusing length, the critical power, etc.

2. An experiment has been performed using an argon laser with an output power of 1 W. The nonlinear medium consists of TF-105 glass with the following characteristics: the length of the specimen, l = 17 cm; the refraction index, n_0 = 1.77; the coefficient of thermal conductivity, $\varkappa = 6.75\cdot 10^{-3}$ W/cm · deg; the relative temperature gradient of the refraction index, $[\partial n/(\partial T)]_{\sigma=0} = 116\cdot 10^{-7}$ deg^{-1}; the linear expansion coefficient, $\alpha = 8.1\cdot 10^{-6}\,\text{deg}^{-1}$; the absorption coefficient, δ = 0.11 cm^{-1}; the constants connected with thermoelastic stresses[6] (see Appendix), ν = 0.25, p_{11} = 0.232, and p_{12} = 0.256. Thus, the total derivative for the glass is $dn/(dT) = 192.10^{-7}\,\text{deg}^{-1}$.

The dispersion resonator of the laser separates the 5145 Å line. An iris is placed inside the laser resonator to isolate the TEM_{00} mode. The beam radius at the exit face of the glass a_0 = 275 μ. After emerging from glass, the light beam strikes the slit of the instrument, which uses an FDK-1 photodiode. The intensity distribution in the self-focusing beam is obtained by moving the instrument across the beam, using a micrometer feed. The beam width at exit from the glass is measured with respect to the level at which the intensity is $1/e^2$ of its maximum value. We thus obtain the diameter of the beam emerging from the specimen as a function of the power incident on the glass. The beam diminishes with increasing power. When the power exceeds a threshold value, the focus of the thermal lens moves inside the specimen, and the beam diameter starts to increase. The beam structure is distorted: Rings appear around the central spot as a consequence of nonlinear aberrations of the thermal lens.

3. The equation for the dimensionless beam width ($f = a(z)/a_0$) describing steady-state thermal self-focusing near the axis of a Gaussian beam (aberration-free approximation) has the following form:[2,7]

$$\frac{d^2f}{dz^2}=-\frac{\delta\exp(-\delta z)}{R_{nl}^{a-f}}+\frac{1}{R_g^2f^3}. \tag{3}$$

Here, $R_g = (ka_0^2)/2$ is the diffraction length of the beam, the quantity

$$R_{nl}^{a-f}=\frac{2n_0\varkappa}{\frac{dn}{dT}I_0}=\frac{\pi n_0\varkappa a_0^2}{\frac{dn}{dT}P_0} \tag{4}$$

characterizes the nonlinear refraction intensity as a function of the intensity I_0 at the axis of a Gaussian beam, a_0 is the radius of this beam at the entrance into the medium, P_0 is the initial power, $\varkappa$ is the thermal conductivity coefficient, and dn/(dT) is the total derivative (2).

The analysis of Eq. (3) is performed on the basis of a computer solution. In particular, this analysis has been performed for the parameters $\tilde{\delta} = \delta R_g = 5$ and $b = \tilde{\delta}(R_g)/(R_{nl}) = 0\text{–}100$, which pertain to the experimental conditions. At the focus, b = 19.5. For these parameters, the dependence $d(P_0)$, shown in Fig. 1 (curve 1), where $d = 2a$, can be obtained from the solution of Eq. (3). The minimum beam contraction for the above parameters can also be obtained from this solution. Calculations for our case yield f_Q = 0.243, which is in good agreement with ex-

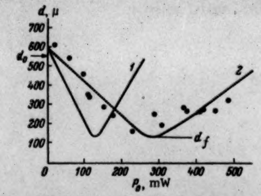

Fig. 1. Diameter of the laser beam at the exit from glass as a function of the power incident to the glass. 1) Aberration-free approximation; 2) with an allowance for aberrations; $d_f = d_0 f_f = 134\ \mu$.

perimental data. However, the general behavior of curve 1 is different from the experimental behavior, and, therefore, the spherical aberrations of a thermal lens must be taken into account in calculating the nonlinear refraction.

4. Nonlinear spherical aberrations are taken into account in the geometric optics approximation (k → ∞) on the basis of the equation for rays[8,9]

$$\frac{d^2 f_r}{dz^2} = -\frac{\delta \exp(-\delta z)}{R_{nl}^{ab}(r_0) f_r}. \qquad (5)$$

Here, $f_r = r(z)/r_0$ is the relative deviation of a ray from the beam axis, r_0 is the initial beam coordinate, and

$$R_{nl}(r_0) = \frac{2n_0\varkappa}{\frac{dn}{dT} \bar{I}(r_0)}, \qquad (6)$$

which characterizes the nonlinear refraction; the latter depends on the mean intensity in the beam tube,

$$\bar{I}(r_0) = \frac{P_0(r_0)}{\pi r_0^2},$$

where $P_0(r_0)$ is the initial power in the beam tube. For a Gaussian beam,

$$\bar{I}(r_0) = I_0 \frac{a_0^2}{2r_0^2}\left(1 - e^{-\frac{2r_0^2}{a_0^2}}\right),$$

where I_0 is the intensity at the axis. Then,

$$R_{nl}(r_0) = \frac{4n_0\varkappa r_0^2}{\frac{dn}{dT} I_0 a_0^2 \left(1 - e^{-\frac{2r_0^2}{a_0^2}}\right)}. \qquad (7)$$

For k → ∞, Eq. (3) is formally identical to Eq. (5), written for a beam tube with $r_0 = a_0$; however, in this case,

$$R_{nl}(a_0) \approx \frac{4.6 n_0\varkappa}{\frac{dn}{dT} I_0} = 2.3\, R_{nl}^{a-f}$$

i.e., if the aberrations are taken into account, the nonlinear refraction is reduced by a factor of approximately 2.3 (see also ref. 10). In Fig. 1, the measured dependence $d(P_0)$ is described adequately by curve 2, obtained by using this correction.

Hence we conclude that steady-state thermal self-focusing can be described by the aberration-free approximation up to the focus, considering the aberration correction only in the expression for R_{nl}.

Nonlinear aberrations must also be taken into account in investigating the beam profile in self-focusing. It has been found experimentally that the Gaussian profile of the beam is distorted; this can be explained by the effect of spherical aberrations. Figure 2 shows the experimental curves characterizing the degree of distortion of the Gaussian profile for different values of the input power. It is evident that, as the beam enters the medium, the Gaussian wings are distorted least, while the rays near the axis experience the greatest contraction.

The intensity distribution at the exit from the nonlinear medium is calculated by using an equation from aberration theory[9]

$$I(r) = \frac{I_0 e^{-\frac{2r_0^2}{a_0^2}} e^{-\delta l}}{f_r^2 + r_0 f_r \frac{df_r}{dr_0}}, \qquad (8)$$

where $f_r = r/r_0$ is the solution of Eq. (5). The functional dependence $f_r(r_0)$ is obtained on the basis of the computer solution of Eq. (5) allowing for the initial beam divergence $df_r/dz|_{z=0} = 1/R$ (under our experimental conditions, this value is $1/R = 6.45 \cdot 10^{-3}\ \mathrm{cm}^{-1}$). The beam profile calculated by means of (8) can be compared with the profile determined experimentally only for low values of the beam power, in which case the geometric optics approximation holds. Figure 2 illustrates the good agreement between experiment and the calculation for 18 and 61 mW (the theoretical and experimental results are indicated by solid and dashed curves, respectively).

Thus, Eq. (5) describes adequately the profile distortion in a Gaussian beam, which is absent if thermal self-focusing is considered in the aberration-free approximation.

APPENDIX

Let us calculate the correction for the refraction index connected with thermoelastic strain in a piezooptic crystal. Assume that the crystal is in the shape of a long cylinder with the radius R and that a narrow laser beam propagates along the z axis of the crystal. Neglecting end effects we assume that the cylinder heated by the laser beam is in a plane strained state. The components of the

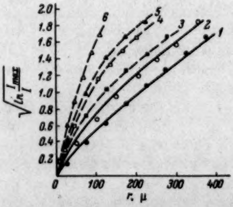

Fig. 2. Distortion of a laser beam with a Gaussian distribution at its entrance into glass. The power incident to glass P is the parameter of the curves: 1) 18; 2) 61; 3) 94; 4) 150; 5) 174; 6) 228 mW.

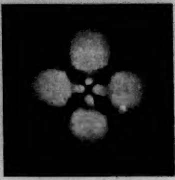

Fig. 3. Characteristic conoscope pattern obtained in a KS-13 glass filter by focusing it in the radiation of an argon laser. The photograph is taken through a microscope, while the filter is placed in crossed polaroids.

stress tensor are then[11]

$$\left.\begin{aligned}\sigma_r &= \frac{\alpha E}{1-\nu}\left[\frac{1}{R^2}\int_0^R T(r)\,r\,dr - \frac{1}{r^2}\int_0^r T(r)\,r\,dr\right],\\ \sigma_\varphi &= \frac{\alpha E}{1-\nu}\left[\frac{1}{R^2}\int_0^R T(r)\,r\,dr + \frac{1}{r^2}\int_0^r T(r)\,r\,dr - T(r)\right],\\ \sigma_z &= \sigma_r + \sigma_\varphi.\end{aligned}\right\} \quad (A.1)$$

Here, α is the linear expansion coefficient, E is Young's modulus, and ν is the Poisson bracket.

The components of σ are related linearly to the components of the elastic strain tensor:

$$\left.\begin{aligned}\varepsilon_r &= \frac{1}{E}[\sigma_r - \nu(\sigma_\varphi + \sigma_z)],\\ \varepsilon_\varphi &= \frac{1}{E}[\sigma_\varphi - \nu(\sigma_r + \sigma_z)],\\ \varepsilon_z &= \frac{1}{E}[\sigma_z - \nu(\sigma_r + \sigma_\varphi)] = \frac{1}{E}(1-\nu)\sigma_z.\end{aligned}\right\} \quad (A.2)$$

If we know the strain tensor we can calculate the permittivity tensor of the medium or the variation in the coefficients of the optical indicatrix[12]

$$\Delta B = \|P\|\hat{E}, \quad (A.3)$$

where $\|P\|$ is the matrix of elastooptical coefficients. The first-order piezooptical effect is also observed in isotropic materials, such as glass. In this case, the matrix $\|P\|$ has the same form as for class-m3m crystals of the cubic system:

$$\|P\| = \begin{vmatrix} p_{11} & p_{12} & p_{12} & 0 & 0 & 0\\ p_{12} & p_{11} & p_{12} & 0 & 0 & 0\\ p_{12} & p_{12} & p_{11} & 0 & 0 & 0\\ 0 & 0 & 0 & p_{44} & 0 & 0\\ 0 & 0 & 0 & 0 & p_{44} & 0\\ 0 & 0 & 0 & 0 & 0 & p_{44}\end{vmatrix}; \quad (A.4)$$

however, its coefficients are related by the expression $2p_{44} = p_{11} - p_{12}$. By substituting (A.4) in (A.3), we find

$$\left.\begin{aligned}\Delta B_r &= p_{11}\varepsilon_r + p_{12}(\varepsilon_\varphi + \varepsilon_z),\\ \Delta B_\varphi &= p_{11}\varepsilon_\varphi + p_{12}(\varepsilon_r + \varepsilon_z).\end{aligned}\right\} \quad (A.5)$$

Small changes in the refraction indices are related to changes in the indicatrix coefficients by the linear expression

$$\Delta n_i = -\frac{\Delta B_i}{2} n_0^3. \quad (A.6)$$

Artificial anisotropy generally arises as a result of thermoelastic stresses in the medium. The laser beam experiences partial depolarization. Figure 3 shows a typical interference pattern, obtained with crossed polaroids in a KS-13 glass filter 5 mm thick, which absorbs completely the argon laser radiation. Similar patterns are observed in other glasses, for instance, UFS-1, PS-13, TS-1, and TS-4.

If we neglect the polarization effects, the mean addition to the refraction index consists of two parts:

$$\Delta n_{\mathrm{me}} = -\frac{1}{4} n_0^3 (\Delta B_r + \Delta B_\varphi) = -\frac{\alpha n_0^3}{4(1-\nu)}[(p_{11} + p_{12})(1-3\nu) + 2p_{12}(1-\nu)]\left[\frac{2}{R^2}\int_0^R T(r)\,r\,dr - T(r)\right]. \quad (A.7)$$

The first term, which is independent of the coordinates, can be significant in nonlinear processes where the synchronism conditions are satisfied. The second term is proportional to the temperature. Therefore, the total nonuniform change in the refraction index is

$$\Delta n = \frac{dn}{dT} T, \quad (A.8)$$

where

$$\frac{dn}{dT} = \left(\frac{\partial n}{\partial T}\right)_{\sigma=0} + \left(\frac{\partial n}{\partial T}\right)_{TH} = \frac{\partial n}{\partial T} + \frac{\alpha n_0^3}{4(1-\nu)}[(p_{11} + p_{12})(1-3\nu) + 2p_{12}(1-\nu)]. \quad (2)$$

---

[1] S. A. Akhmanov, Yu. A. Gorokhov, D. P. Krindach, A. P. Sukhorukov, and R. V. Khokhlov, Fourth All-Union Conference on Nonlinear Optics, Abstracts of reports [in Russian], Kiev (1968).

[2] F. W. Dabby and J. R. Winnery, Appl. Phys. Lett., 13, 284 (1968).

[3] S. A. Akhmanov, Yu. A. Gorokhov, D. P. Krindach, A. P. Sukhorukov, and R. V. Khokhlov, Zh. Eksp. Teor. Fiz., 57, 16 (1969) [Sov. Phys. – JETP, 30, 9 (1970)].

[4] R. L. Carman, A. M. Mooradian, P. L. Kelly, and A. Tufts, Appl. Phys. Lett., 14, 136 (1969).

[5] Yu. A. Gorokhov, A. P. Sukhorukov, A. M. Khachatryan, and É. N. Shumilov, Fifth All-Union Conference on Nonlinear Optics, Abstracts of reports [in Russian], Kishinev (1970).

[6] E. R. Mustel' and V. N. Parygin, Methods of Modulation and Scanning of Light [in Russian], Izd. Nauka, Moscow (1970).

[7] S. A. Akhmanov, D. P. Krindach, A. V. Migulin, A. P. Sukhorukov, and R. V. Kokhlov, IEEE J. Quant. Electron., QE-4, 568 (1968).

[8] A. M. Khachatryan (Khachatrian) and A. P. Sukhorukov, Opto-Electron., 3, 49 (1971).

[9] A. P. Sukhorukov, S. Ya. Fel'd, A. M. Khachatryan, and É. N. Shumilov, Kvant. Elektron. (Mosc.), No. 8, 53 (1972) [Sov. J. Quant-Electron., 2, 133 (1972)].

[10] F. W. Dabby and H. A. Haus, J. Appl. Phys., 40, 439 (1969).

[11] A. D. Kovalenko, Introduction to Thermoelasticity [in Russian], Izd. Naukova Dumka, Kiev (1965).

[12] J. F. Nye, Physical Properties of Crystals, Oxford Univ. Press (1957).

Possible electrohydrodynamic effects in electrolytes

E. Z. Gak. É. Kh. Rokhinson, and N. F. Bondarenko

Agrophysical Scientific-Research Institute, Leningrad

(Submitted April 6, 1973; resubmitted September 13, 1973)
Zh. Tekh. Fiz., 44, 1076-1079 (May 1974)

The appearance of a macroscopic space charge in aqueous solutions of electrolytes is discussed. This effect can be used to produce various electrohydrodynamic effects in such solutions. This space charge appears only when limiting diffusion currents flow through the solution.

1. On the basis of arguments regarding the electrical neutrality of electrolytic solutions it is usually assumed that no space charge appears in such solutions except near interfaces, where there is a space-charge density[1] $\rho \neq 0$ in an electrical double layer with thickness of order of 10^2-10^3 Å. Electrohydrodynamic effects, e.g., electroosmosis and electrophoresis occur under the influence of external electric fields in a region with $\rho \neq 0$. Because of the microscopic surface nature of these phenomena, the use of electrohydrodynamic effects in electrolytes has been restricted primarily to capillary–pore systems.

When certain physicochemical conditions prevail in electrolytes electric-charge formations of macroscopic dimensions can appear outside the double layer, expanding the practical usefulness of electrohydrodynamic effects.

We report here a theoretical and experimental study of the effects of alternating electric fields on the space-charge region which arises outside the double layer when an electric current near the limiting strength is passed through a solution. Although the existence of such charge formation has a firm theoretical basis,[2] the absence of convincing experimental results has apparently been responsible for the general neglect of this theory. The magnitude of the charge, the regions in which it exists, and the effect on various heterogeneous processes in electrolytes have not been determined.

2. The idea that a macroscopic space charge can appear outside the double layer is based on the following arguments: When the rate at which ions are furnished determines the rate of a heterogeneous process, i.e., in the region of diffusion and mixed kinetics, a diffusion layer of thickness δ_{diff} is known to appear behind the electrical double layer of thickness δ_{do}; in this diffusion layer the ion density drops from some c to c_0, the density in the bulk electrolyte.

To be definite we consider the case in which the space charge arises in a binary electrolyte and in which there are diffusion limitations at the cathode. In the diffuse part of the double layer the anion concentration is a minimum; anions must accumulate in the diffusion layer adjacent to the electrical double layer, since the movement of cations through the cathode region under the influence of migration mechanisms is considerably more rapid than the movement of anions to the bulk solution by diffusion. Accordingly, in the immediate vicinity of the double layer a negative macroscopic space charge arises with density ρ_{sc} and dimension $\Delta x \gg \delta_{do}$.

In a medium at rest the density ρ_{sc} over a region $x \geq 2$-$3\delta_{do}$ is given by[2]

$$\rho_{sc} = \frac{\varepsilon RT}{4\pi z_2 F}\frac{1}{x^2}, \tag{1}$$

where z_2 is the valence of the anions, R is the Mendeleev–Clapeyron constant, F = 96 kC/g-eq is the Faraday number, T is the absolute temperature, ε is the dielectric constant of the medium, and x is the distance into the electrolyte from the cathode.

The structure of this space-charge formation is similar to that of the diffuse part of the double layer, but the charge ρ_{max} is much lower than that of the double layer.

The dimension of this macroscopic charge formation, Δx, must be a function of the electrolyte concentration: $\Delta x = f(1/\sqrt{c})$. According to an estimate in ref. 5, this dimension is $\Delta x > 10\delta_{do}$ and can reach 10^{-4}-10^{-2} cm at low concentrations. The maximum value of Δx is δ_{diff}.

Using these arguments we can represent the function $\rho = f(x)$ as in Fig. 1, where region I is the double layer (with which we are not concerned here), the space charge increases in region II, for $\delta_{do} \leq x \leq 3\delta_{do}$, and the space charge decreases in region III, in accordance with Eq. (1). The function $\rho(x)$ thus passes through a maximum ρ_{max}, some $(2$-$3)\delta_{do}$ from the cathode.

Let us consider certain consequences of the existence of this macroscopic space-charge formation outside the electrical double layer.

a) This space charge must produce a barrier to the motion of ions toward the cathode; the density ρ_{max} determines the barrier height, and the dimension Δx determines its width. The electric field produced by this charge is $E_{sc} = (dU_{sc})/(dx)$ or, in terms of average values,

$$E_{sc} = \frac{U_{sc}}{\Delta x}. \tag{2}$$

Together with the concentration limitations this electrical barrier is apparently responsible for the formation of limiting currents.

b) The magnitude of the space charge and the region in which it exists are governed largely by the hydrodynamic conditions. An increase in the ion concentration drop dc/dx reduces Δx, but ρ_{max} increases. For ρ_{sc} the following equation has been found:[2]

$$\rho = \frac{\varepsilon}{4\pi}\frac{D_1 - D_2}{z_1 D_1 + z_2 D_2}\frac{RT}{F}\Delta \ln c, \tag{3}$$

where D_1 and D_2 are the cation and anion diffusion coefficients.

We assume that the diffusion limitations cannot be fully lifted even by very rapid mixing. This mixing can be caused by directly perturbing the space charge, e.g., by means of an alternating electric field $E_\sim = E_0 \sin\omega t$, where $\omega = 2\pi f$. The imposition of such a field can lead to hydrodynamic oscillations in the region of the space charge and to deformation of this charge; the result would

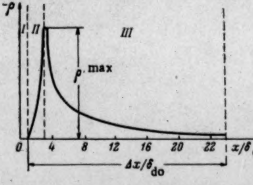

Fig. 1. Space-charge density as a function of the distance to the cathode, $\rho_{sc} = f(x)$. I) Electrical double layer; II) region of increasing space charge formed by anions; III) region in which the space charge falls off with distance from the cathode.

be a partial or complete dissipation of this charge and an increase in the current through the electrolyte. However, this effect of a field can be important only at $E_0 > E_{sc}$.

c) Physical factors should be influential only at current levels near the limiting current in the region in which $\rho_{sc} \neq 0$, i.e., at $x \leq \Delta x$. At currents far from the limiting value, which are thus governed primarily by electrochemical kinetics, an alternating electric field should not have any important effect on the electrode processes.

3. To study these phenomena experimentally we make use of the functional dependence $j_= = f(U_=)$, where $j_=$ is the density of the direct current and $U_=$ is the voltage across the electrochemical cell. Cells of two types are used: an annular electrochemical cell with electrodes 0.6 and 3 cm in radius and 1.5 cm high, and a rectangular cell whose (planar) cathode is 1 cm^2 in area, whose (planar) anode is 6 cm^2 in area, and whose electrodes are 6 cm apart.

To determine the region in which the space charge exists we use a movable electrode through which the liquid can pass freely (a grid electrode); with the annular cell we use a set of grids. We apply an alternating voltage $U_\sim = U_0 \sin \omega t$ between the cathode and the movable electrode, and we apply a constant voltage $U_=$ between the cathode and anode. The corresponding circuits are isolated by the usual circuit methods (RC and LC filters). The frequency of the alternating current is varied from 1 to 10^4 Hz.

The electrolytes are aqueous solutions of $CuSO_4$ and $NiSO_4$ at concentrations ranging from 0.01N to 1N. The electrodes and grids are copper or nickel to avoid chemical polarization of the electrodes.

As expected, the imposition of an alternating electric field lifts the diffusion limitations on the direct electric current through the electrolyte, causing a significant increase in the limiting current; it is in fact possible to displace the entire voltage–current characteristic into the region of electrochemical kinetics. This increase in the limiting current reaches 400–500% at low electrolyte concentrations, increasing with E_0 beyond a certain threshold, i.e., at $E_0 > (5\text{-}10)E_=$ (Fig. 2). From the experimental data we estimate $E_{sc} \approx 20$ V/cm.

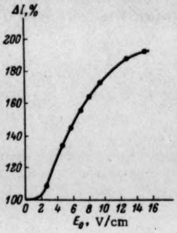

Fig. 2. Increase in the limiting direct current as a function of the amplitude of the applied alternating electric field, $\Delta I = f(E_0)$ for 0.01N $CuSO_4$. The frequency of the applied field is 50 Hz. Here $I = I_{li}(E_0 \neq 0)/I_{li}(E_0 = 0)$, where $I_{li}(E_0 \neq 0)$ and $I_{li}(E_0 = 0)$ are the limiting currents corresponding to $E_0 \neq 0$ and $E_0 = 0$.

As we move the movable grid electrode toward the cathode, to the closest position possible under our experimental conditions ($0.5 \cdot 10^{-2}$ cm), we observe the same effect, a current increase, at progressively lower voltages U_0. The effect is independent of the frequency at frequencies $f \geq 30$ Hz; at lower frequencies (f = 1-20 Hz) there is some increase in the effect. The results obtained with other electrolytes are similar to those shown here.

As expected, in the region in which the current is controlled by electrochemical kinetics, i.e., at currents far from the limiting current, the increase in the direct current does not exceed 10–15%, perhaps due to a change in the structure of the diffuse part of the double layer and to the circumstance that the process can occur under diffusion limitations. This circumstance is apparently responsible for the small changes observed elsewhere in the voltage–current characteristics under the influence of an alternating electric current.[3]

4. These phenomena deserve further study; they may find applications not only in experimental physics and electrochemistry but also in efforts to increase the rates of various heterogeneous processes involving the transport of one or several ion species across an interface when there is a concentration gradient in layers near a wall.

---

[1] A. I. Levin, Basic Theory of Electrochemistry [in Russian], Izd. Metallurgiya, Moscow (1972)

[2] V. G. Levich, Physicochemical Hydrodynamics, Prentice-Hall, Englewood Cliffs, N. J. (1962).

[3] V. I. Chernenko, M. A. Loshkarev, and Zh. N. Levitin, Zh. Fiz. Khim., 37, 1015 (1963).

Electron-scanning transformation of the potential distribution on an electrostatic target

V. L. Lentsman
Main Astrophysical Observatory, Academy of Sciences of the USSR, Leningrad
(Submitted June 19, 1973)
Zh. Tekh. Fiz., 44, 1080-1083 (May 1974)

The discharge of the electrostatic targets of television and crt storage devices in scanning by an electron beam whose density is uniform over the target surface is studied. There is a predominant attenuation of the lower spatial frequencies of the spectrum of the electronic image stored on the target. Experimental detection of this effect is reported.

Two basic kinds of electrostatic storage targets are used in television pickup tubes and in crt storage devices: a target formed by a dielectric film held under tension at a certain distance from a fine metal grid (the superorthicon and the izokon) and a target consisting of a metal substrate (signal plate) on which a dielectric film has been deposited (the vidicon, the SEC vidicon, the graphecon, etc.). Images are usually stored, read off, and erased from such targets by scanning with both focused and unfocused beams of electrons with various energies.

The transformations of the electronic images are conveniently described in terms of the mathematical apparatus of scattering functions and spatial frequency characteristics,[1-3] as in optics and photography. In particular, the transformation of the electronic image involved in the transition from the charge-density distribution on the target surface to the potential distribution in the same plane (the "charge-potential" transformation), which largely governs the target resolution, can be characterized by the following frequency characteristics:

For the first type of target,

$$\tau_1(\omega_r)=\frac{d}{\varepsilon_0}\frac{1-e^{-2\omega_r d}}{2\omega_r d}$$

$$\times 2\frac{(\varepsilon_1+1)+(\varepsilon_1-1)e^{-\omega_r\delta}}{(\varepsilon_1+1)^2-(\varepsilon_1-1)^2e^{-2\omega_r\delta}-(\varepsilon_1^2-1)e^{-2\omega_r d}+(\varepsilon_1^2-1)e^{-2\omega_r(d+\delta)}},$$

where d is the distance between the film and the grid, δ is the film thickness, ε_0 is the permittivity of free space, and ε_1 is the dielectric constant of the film material. The coefficient d/ε_0, which governs the value of the frequency characteristic at $\omega_r = 0$, is the reciprocal of the "specific storage capacitance" of the target, $c = \varepsilon_0/d$;

for the second type of target,

$$\tau_1(\omega_r)=\frac{d}{\varepsilon_0\varepsilon_1}\frac{1-e^{-2\omega_r d}}{2\omega_r d}\frac{2\varepsilon_1}{(\varepsilon_1+1)+(\varepsilon_1-1)e^{-2\omega_r d}},$$

where d is the thickness of the dielectric film, and ε_1 is the dielectric constant of the film material.

These frequency characteristics are obtained by integrating the Laplace equation and using the Hankel transform.[2,4] The corresponding scattering functions for the charge-potential transformation, which in this case are the potential distribution due to a point charge, can be found by an inverse Hankel transform.

Let us consider the change in the charge distribution q(x, y, t) and the potential relief V(x, y, t) on such targets in scanning by a beam of electrons whose density is uniform over the target surface. The continuity equation for this case can be written

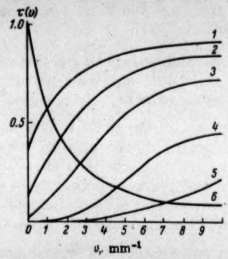

Fig. 1. Frequency characteristics for the transformation of the electronic image on the target. 1-5) For electron irradiation at $j_n b t/c \le 1, 2, 5, 10, 20$, 6) charge-potential transformation for d = 0.1 mm. Here $\nu = \omega_r/2\pi$.

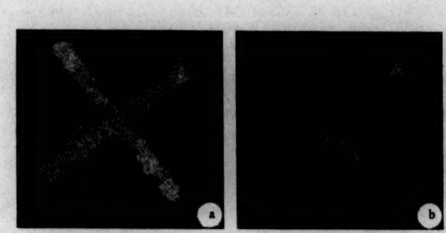

Fig. 2. Images photographed from the screen of a television video monitor.

$$\frac{\partial}{\partial t}q(x, y, t)=j_Q(x, y, t).$$

Here, $j_Q(x, y, t)$ is the instantaneous current-density distribution of the charge; this is governed by the current density of primary electrons and the instantaneous value of the secondary-emission yield, which in turn is a complicated function of the target potential. In certain cases this functional dependence can be approximated as a linear function, e.g., at a low primary-electron energy, in which case the secondary yield is governed by the electron-optics reflection of the primary electrons, or in the fast-electron regime, in which case the average target potential is approximately equal to the collector potential. For these cases the above equation can be written

$$\frac{\partial}{\partial t} q(x, y, t) + j_n \beta V(x, y, t) = 0,$$

where β is a coefficient describing the rate of change in the secondary yield as a function of the target potential. The relation between V(x, y, t) and q(x, y, t) is governed by this charge-potential transformation.

Solving this equation in frequency space through the use of Fourier or Hankel transforms, we can find the frequency characteristic governing the transformation of the spectrum of charge and potential distributions in scanning of the target by an electron beam of uniform density:

$$\tau_2(\omega_r) = \exp\left\{-\frac{j_n \beta t}{c} \tau_1^0(\omega_r)\right\},$$

where $\tau_1^0(\omega_r)$, is the frequency characteristic of the charge-potential transformation, is equal to unity at $\omega_r = 0$.

Curves 1-5 in Fig. 1 show frequency characteristic $\tau_2(\omega_r)$ for five values of the dimensionless parameter $j_n \tau t/c$: 1, 2, 510^0, and 20.

As $\tau_1^0(\omega_r)$ we adopt the frequency characteristic of a target of the first type with d = 0.1 mm (curve 6 in Fig. 1). We see that scanning of the target by a uniform-density electron beam causes a preferential attenuation of the lower spatial frequencies of the spectrum of the electronic image stored on the target. When the current density and scanning time are chosen appropriately, this effect can be exploited to isolate the outlines of objects and fine details in the original image, to correct electron-optics images, to reduce an excessive number of these images, etc. The advantages of two-dimensional transformations of electronic images over the methods basic to signal processing have been pointed out previously.[1,5,6]

Note should be taken of a distinction between this spatial-filtering method and one described previously,[5] based on the combination of electronic images of various signs on the target, one of which (the positive image) is stored in the fast-electron regime, while the other (negative) is stored in the slow-electron regime.

We have carried out an experimental study of this effect with a superorthicon television transmitting tube. The television system in which the tube operates can separate the storage and readout processes and perform various transformations of the electronic images.[6] After the potential distribution is recorded in the usual manner (in the fast-electron regime), the target of the superorthicon is scanned by a beam of slow photoelectrons obtained from the uniform illumination of the photocathode of the tube, whose potential has been changed accordingly. Figure 2 shows the original (a) and transformed (b) images, photographed on the screen of a video monitor. We see the influence of nonlinear effects; in particular, the intensities of the positive and negative excursions at the boundary of the object are not the same.

This transformation of the potential distribution must occur in a wide variety of television and storage tubes even when the target is being scanned by the readout beam, although the discharging of the target under these conditions is of course considerably more complicated. The potential distribution remaining on the target after readout, which corresponds primarily to the outlines of objects and to fine details, is built up from frame to frame during continuous operation of the apparatus, so the resolution of television transmitting tubes at low illumination is significantly improved in the transmission of fixed images. In particular, this mechanism can be used to explain the satisfactory resolution of superorthicons with a large grid–film separation, for which the frequency characteristic of the charge-potential transformation falls off significantly at high spatial frequencies.

---

[1] I. I. Tsukkerman, Conversion of Electronic Images [in Russian], Izd. Energiya, Leningrad (1972).

[2] V. L. Lentsman, Voprosy Radioelektroniki, Ser. TT, No. 5, 83 (1970).

[3] V. L. Lentsman, Radiotekh. Elektron., 16, 1927 (1971).

[4] L. A. Serebrov and S. A. Fridrikhov, Radiotekh. Elektron., 5, 1680 (1960).

[5] V. L. Lentsman, A. G. Matveeva, and I. I. Tsukkerman, Zh. Tekh. Fiz., 36, 1514 (1966) [Sov. Phys. – Tech. Phys., 11, 1131 (1967)].

[6] V. L. Lentsman and I. I. Tsukkerman, Tekhnika Kino i Televideniya, No. 4, 51 (1968).

Symmetric multielectrode tubular electrostatic lenses

L. G. Glikman, V. M. Kel'man, and M. Sh. Nurmanov
Institute of Nuclear Physics,
Academy of Sciences of the Kazakh SSR, Alma-Ata
(Submitted July 30, 1973)
Zh. Tekh. Fiz., 44, 1084-1087 (May 1974)

Curves are given for determining the cardinal elements and spherical aberration of symmetric multielectrode tubular lenses for three versions of the potential distribution. The electrodes have the same radius, which is equal to the axial dimension. The spherical aberration of the lens drops sharply as the number of electrodes is increased.

The positions of the cardinal elements and the spherical aberration of immersion tubular lenses with electrodes of the same diameter are calculated in refs. 1 and 2. The results show that increasing the number of electrodes reduces the spherical aberration and that, for a given number of electrodes, this aberration is generally a minimum when the lengths of the intermediate electrodes are equal to the radius. In this note we carry out similar calculations for single lenses. Since the spherical aberration is almost always a minimum when the length of the intermediate electrodes, λ, is equal to the radius R (the same for all the electrodes), we report the results for this case alone.

The electrostatic field is calculated from the exact equation given in ref. 1, which is derived under the assumption that the gaps between the electrodes are infinitesimally small. In all cases considered here the number of electrodes N is odd and the field is symmetric with respect to the middle of the lens. We denote by Φ_1 the potential at the extreme electrodes, measured with respect to that at the position at which the charged-particle velocity is zero, and we denote by Φ_c the potential at the central electrode. The electron-optics properties of the lenses are calculated for both $\Phi_c/\Phi_1 > 1$ and $\Phi_c/\Phi_1 < 1$. We consider the following versions of the potential distribution.

1. The ratio of the potentials at two adjacent electrodes in the first half of the lens (between the first and central electrodes) is constant and equal to

$$q = \sqrt[\frac{N+1}{2}]{\frac{\Phi_c}{\Phi_1}}. \tag{1}$$

The potential at the k-th electrode is

$$\Phi_k = \Phi_1 q^{k-1}, \quad k = 1,\ 2,\ \ldots,\ (N+1)/2. \tag{2}$$

The potential in the second half of the lens is determined from the symmetry of the field with respect to the center of the lens.

2. The potential difference between two adjacent electrodes in the first half of the lens is constant and equal to

$$\Delta\Phi = \frac{2(\Phi_c - \Phi_1)}{N-1}. \tag{3}$$

The potential at the k-th electrode is

$$\Phi_k = \Phi_1 + (k-1)\Delta\Phi, \quad k = 1,\ 2,\ \ldots,\ (N+1)/2. \tag{4}$$

The potentials in the second half of the lens are determined from the symmetry condition.

3. The potential distribution is described by

$$\Phi_k = 1 + \frac{m^2}{1 + \left(\frac{z_k - \frac{L}{2}}{d}\right)^2} \tag{5}$$

and

$$\Phi_k = 1 - \frac{m^2}{1 + \left(\frac{z_k - \frac{L}{2}}{d}\right)^2}, \quad k = 1,\ 2,\ \ldots,\ N. \tag{6}$$

Here, m and d are constant, L is the distance between

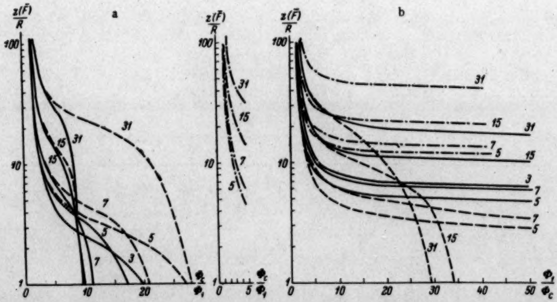

Fig. 1. Coordinates z(F) of the imaginary foci as functions of the ratio of the potentials at the central and extreme electrodes for $\Phi_c/\Phi_1 > 1$ (a) and $\Phi_c/\Phi_1 < 1$ (b).

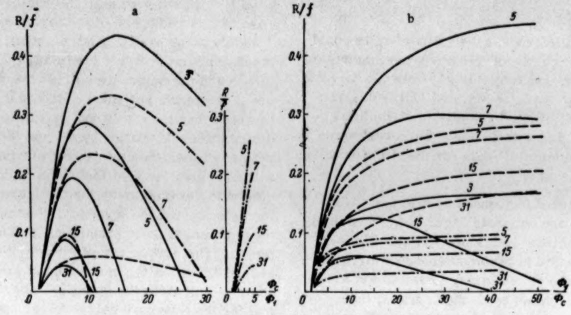

Fig. 2. Diagrams used to determine the focal length for $\Phi_c/\Phi_1 > 1$ (a) and $\Phi_c/\Phi_1 < 1$ (b).

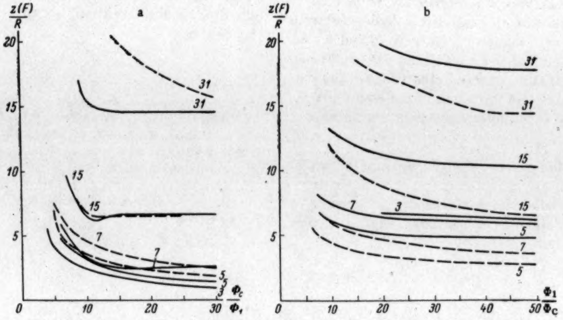

Fig. 3. Coordinates z(F) of the real foci as functions of the ratio of the potentials at the central and extreme electrodes for $\Phi_c/\Phi_1 > 1$ (a) and $\Phi_c/\Phi_1 < 1$ (b).

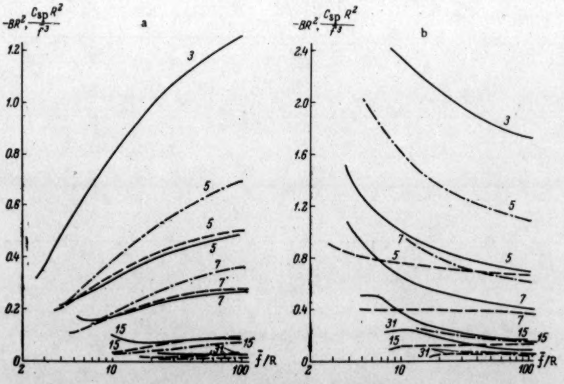

Fig. 4. Diagrams used to determine the spherical aberration coefficient B with the object at infinity and to determine the spherical aberration constant C_{sp} with the object at the real focus for $\Phi_c/\Phi_1 > 1$ (a) and $\Phi_c/\Phi_1 < 1$ (b).

the extreme electrodes, and $z_k = -L/2 + (k-1)\lambda$.

For intermediate electrode k the value of z_k is equal to the coordinate of the center of this electrode, measured along the axis of the system from the gap between the first and second electrodes. As $L/R \rightarrow \infty$ and $\lambda/R \rightarrow 0$, Eqs. (5) and (6) describe bell-shaped potential distributions. The calculations show that with $L/d = 4$ the lens aberrations are nearly a minimum; all data for specific lenses given here refer to this case.

The results calculated for lenses with the specified potential distributions are shown in Figs. 1-4. In each of these diagrams the electron-optics properties of lenses in which the potential ratio between adjacent electrodes is constant in each of the (symmetric) halves of the lens [potential ratio (1)] are shown by dashed curves; those corresponding to the constant potential difference (3) are shown by solid curves; those corresponding to distribution (5), (6) are shown by dot-dashed curves. The curves are labeled with the number of electrodes N. For comparison, these figures show the data for a three-electrode lens, which coincide with the data from refs. 3 and 4. As in ref. 2, it is assumed that the $z = 0$ plane passes through the gap between the first and second electrodes. The calculations are carried out on the basis of the equations given in ref. 5, whose terminology and notation we have adopted here.

Figure 1 shows the positions of the imaginary foci $\overline{F}$ [the coordinates $z(\overline{F})$] as functions of the potential ratio between the central and extreme electrodes. Figure 2 shows diagrams for determining the focal lengths $\bar{f}$. Beyond $N > 3$ an increase in the number of electrodes always results in a reduction of the lens power. The data in Figs. 1 and 2 can be used to find the positions of the principal planes and to construct the image of an object if both the image and the object lie outside the field of the lens. Figure 3 shows the positions of the real foci F for the case in which they lie within the lens field. For the potential distributions described by (5) and (6), and for the range of ratios between the central and extreme electrodes considered here, the real foci lie outside the field and coincide with the imaginary foci. Figure 4 shows diagrams for determining the spherical aberration of lenses, with these potential distributions as a function of the focal length. The curves are plotted for two object positions: at infinity and at the real focus of the lens. For the former case we calculate the spherical aberration coefficient B, and for the latter we calculate the spherical aberration constant C_{sp}. These curves can be used to determine B only when the lens focus lies outside its field. From Fig. 4 we see that increasing the value of N rapidly reduces the spherical aberration, because the size of the lens field increases.

---

[1] L. G. Glikman, V. M. Kel'man, and M. Sh. Nurmanov, Zh. Tekh. Fiz., 43, 1358 (1973) [Sov. Phys. – Tech. Phys., 18, 864 (1974)].

[2] L. G. Glikman, V. M. Kel'man, and M. Sh. Nurmanov, Zh. Tekh. Fiz., 43, 2278 (1973) [Sov. Phys. – Tech. Phys., 18, 1441 (1974)].

[3] D. Werner, Optik, 32, 320 (1971).

[4] A. Adams and F. H. Read, J. Phys. E: Sci. Instrum., 5, 150 (1972).

[5] W. Glaser, Fundamentals of Electron Optics [Russian translation], GITTL, Moscow (1957).

Upper and lower limits on the capacitance of a plane capacitor

R. F. Fikhmanas and P. Sh. Fridberg

(Submitted July 23, 1973)
Zh. Tekh. Fiz., 44, 1088-1090 (May 1974)

1. We consider a plane capacitor formed by two identical, infinitesimally thin, metal plates of arbitrary shape (Fig. 1a); we assign potentials of + 1 and − 1 to the plates.

Since the device is symmetric with respect to the z = h plane, we need only consider the "half" problem: that of a plate, charged to unit potential, above a grounded plane (Fig. 1b). The density of the surface charge σ on the plate D satisfies the integral equation

$$\int_D ds' G(\mathbf{x}, \mathbf{x}')\,\sigma(\mathbf{x}') = \varepsilon, \ \mathbf{x} \in D. \tag{1}$$

Here, $G(\mathbf{r}, \mathbf{r}')$ the Green's function of the Laplace equation for the half-space $z \le h$, satisfies homogeneous Dirichlet boundary conditions, and ε is the dielectric constant of the medium (in international units).

Using (1) and the standard procedure,[1] we find the capacitance

$$C = \frac{1}{2} \int_D ds\,\sigma(\mathbf{x}), \tag{2}$$

in a stationary Schwinger representation:

$$C = \frac{\varepsilon}{2} \max_{\sigma} \frac{\left[\int_D ds\,\sigma(\mathbf{x})\right]^2}{\int_D ds \int_D ds'\,\sigma(\mathbf{x})\,G(\mathbf{x}, \mathbf{x}')\,\sigma(\mathbf{x}')}. \tag{3}$$

Functional (3) can be used to find a lower limit on the capacitance.

An upper limit on the capacitance is known[2] to be given by the Dirichlet integral:

$$C = \frac{\varepsilon}{2} \min_{\varphi} \int_{(z<h)} dv\,|\mathrm{grad}\,\varphi(\mathbf{r})|^2, \quad \varphi|_D = 1. \tag{4}$$

However, the use of variational principle (5) runs into difficulties because of the need to specify the three-dimensional potential distribution $\varphi(\mathbf{r})$.

It is much more convenient to start from the equation

$$\lim_{z\to 0} \frac{\partial}{\partial z} \int_Q ds' \left\{\frac{\partial}{\partial z'} [G(\mathbf{r}, \mathbf{r}') + \Gamma(\mathbf{r}, \mathbf{r}')]\right\}_{z'=0} \varphi(\mathbf{x}') = 0, \ \mathbf{x} \in S; \ \varphi|_D = 1 \tag{5}$$

for the potential $\varphi(\mathbf{x})$ on the continuation S of plate D, (Q = S + D is an infinite plane). Here, Γ and G are the Green's functions for the region $0 \le z \le h$ and satisfy homogeneous Dirichlet boundary conditions. The variational principle based on this equation is

$$C = \frac{\varepsilon}{2} \min_{\varphi} \int_Q ds \int_Q ds'\,\varphi(\mathbf{x})\,K(\mathbf{x}, \mathbf{x}')\,\varphi(\mathbf{x}'), \quad \varphi|_D = 1, \tag{6}$$

where the role of kernel is played by the generalized "admittance"[1)]

$$K(\mathbf{x}, \mathbf{x}') = -\lim_{z\to 0} \frac{\partial}{\partial z} \left\{\frac{\partial}{\partial z'} [G(\mathbf{r}, \mathbf{r}') + \Gamma(\mathbf{r}, \mathbf{r}')]\right\}_{z'=0}. \tag{7}$$

Functional (6) leads to upper estimates on the capacitance in the class of continuous functions having uniformly continuous derivatives along plane Q nearly everywhere, which take on the specified value on the surface of the plate, and which fall off as $x^{-\nu}$ for $x \to \infty$, where $\nu \ge 3$; we denote this class as class F. The actual value of C thus lies on the interval $[C\{\sigma\}, C\{\varphi\}]$, where σ and φ are allowable trial functions.

In contrast with (4), functional (6) now contains information about the geometry of the problem (through the Green's functions of the volumes) and requires specification of only a two-dimensional potential distribution.

2. The most interesting case is that of a circular plate capacitor.

On the basis of physical considerations, Kirchhoff[4] has derived the following asymptotic equation for the capacitance in this case:

$$\frac{1}{4\pi\varepsilon a} C_K = \frac{1}{8\alpha} + \frac{1}{4\pi} \ln \frac{8\pi}{e\alpha}, \quad \alpha \ll 1, \tag{8}$$

where $\alpha = h/a$, and a is the disk radius. The first term of this equation corresponds to the capacitance of a plane capacitor for which edge effects are neglected, and the second, which holds within terms which do not vanish as $\alpha \to 0$, gives the correction for edge effects. Kirchhoff's equation is justified analytically in refs. 5 and 6.

Variational principle (7) has been used[2] with the trial distribution σ = const, i.e., in effect, the Howe method[7] is used to calculate the capacitance of this capacitor.

Noble[8] has refined the results of ref. 2 through the use of the trial function

$$\sigma(x) = A + B\left[1 - \left(\frac{x}{a}\right)^2\right]^{-1/2}. \tag{9}$$

The physical meaning of the second term is obvious: It gives the charge distribution on an isolated disk.

Variational principle (6), formulated in Sec. 1, can be

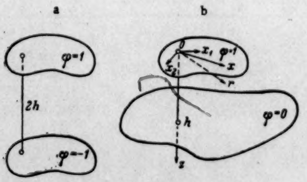

Fig. 1

α	$\frac{1}{4\pi\varepsilon a} C\{\sigma\}$	$\frac{1}{4\pi\varepsilon a} C\{\varphi\}$	$\delta = \frac{C\{\varphi\} - C\{\sigma\}}{C\{\varphi\} + C\{\sigma\}}$
0.001	125.5	134.7	0.035
0.005	25.52	27.17	0.031
0.010	13.02	13.73	0.026
0.050	2.915	2.997	0.014
0.1	1.616	1.660	0.013
0.2	0.978	0.990	0.006
0.3	0.759	0.765	0.004
0.4	0.647	0.652	0.004
0.5	0.579	0.584	0.004
0.6	0.533	0.539	0.006
0.7	0.501	0.508	0.007
0.8	0.476	0.484	0.008
0.9	0.457	0.467	0.011
1.0	0.442	0.453	0.012
1.2	0.420	0.434	0.016
1.4	0.403	0.421	0.022
1.6	0.391	0.412	0.026
1.8	0.383	0.406	0.029
2.0	0.375	0.401	0.032
2.5	0.365	0.394	0.038

used to find an upper limit on the capacitance; when this upper limit is combined with the lower limit, the error of the calculation can be determined.

Using the explicit representation for Green's functions G and Γ in a cylindrical coordinate system and exploiting the axial symmetry of the problem, we find

$$\frac{1}{4\pi\varepsilon} C = \frac{1}{4} \min_{\varphi \in F} \int_0^\infty d\lambda (1 + \operatorname{cth} \lambda h) \left[\int_0^\infty dx\, x J_1(\lambda x) \frac{d\varphi(x)}{dx} \right]^2. \qquad (10)$$

The numerical results found with the trial function[2]

$$\varphi(x) = \begin{cases} 1, & x \in D, \\ \left(\frac{a}{x}\right)^3 \left[1 + A\left(1 - \frac{a^2}{x^2}\right)^{1/2}\right], & x \in S \end{cases} \qquad (11)$$

are shown in Table 1, which also gives the lower limits on the capacitance, which we calculated[3] from the equations of ref. 8.

The calculations show that the plane-capacitor equation has an error certainly larger than 5% even with $\alpha = 0.2$, while the Kirchhoff equation has a corresponding error at $\alpha = 0.02$.

Serini[6] has proposed the following empirical equation for the case of small α:

$$\frac{1}{4\pi\varepsilon a} C_S = \frac{1}{8\alpha} + \frac{1}{\pi}, \quad \alpha \ll 1. \qquad (12)$$

Since the term $1/8\alpha$ is the principal term in the asymptotic behavior as $\alpha \to 0$, while the constant $1/\pi$ is the principal term as $\alpha \to \infty$ (ref. 2), it is interesting to estimate the error of this equation for intermediate values of α; it turns out that over the range $0.05 \leq \alpha \leq 2.5$ we have

$$\left| 1 - \frac{C\{\sigma\} + C\{\varphi\}}{2C_S} \right| < 0.03. \qquad (13)$$

---

[1] Methods for calculating such quantities are examined in ref. 3.

[2] We note that $\varphi(x)$ satisfies the condition at the cut and belongs to class F for any value of the adjustable factor A.

[3] Numerical values of $C\{\sigma\}$ are given in ref. 8 only for α = 0.05, 0.1, 0.2, and 0.4.

[1] J. Schwinger and D. S. Saxon, Inhomogeneities in Waveguides, Gordon and Breach, New York (1968).

[2] G. Pólya and G. Szegö, Isoperimetric Inequalities in Mathematical Physics, Princeton Univ. Press, Princeton, New Jersey (1951).

[3] I. B. Levinson and P. Sh. Fridberg, Dokl. Akad. Nauk SSSR, 158, 1064(1964) [Sov. Phys. – Dokl., 9, 897 (1965); Radiotekh. Elektron., 10, 260 (1965)].

[4] G. Kirchhoff, Monatsb. Deutsch. Akad. Wiss., Berlin (1877).

[5] V. Hutson, Proc. Cambridge Phil. Soc., 59, 211 (1963).

[6] F. Leppington and H. Levine, Proc. Cambridge Phil. Soc., 68, 235 (1970).

[7] R. F. Fikhmanas and P. Sh. Fridberg, Zh. Tekh. Fiz., 40, 1327 (1970) [Sov. Phys. – Tech. Phys., 15, 1027 (1970)].

[8] B. Noble, Proc. Edinburgh Math. Soc., 11, 115 (1958).

Impossibility of shielding against the rf radiation of a thermonuclear reactor with a cold-plasma sheath

A. S. Chikhachev

Moscow Engineering-Physics Institute

(Submitted August 22, 1973)
Zh. Tekh. Fiz., 44, 1090-1091 (May 1974)

The problem of shielding the first wall of a thermonuclear reactor against the highest-frequency part of the radiation of a thermonuclear plasma is analyzed. It is shown that this shielding cannot be achieved with a sheath of cooler plasma because the absorption coefficient α_ω is not a function of the temperature at frequencies $\omega > T_e/\hbar$, where ω is the frequency of the radiation and T_e is the temperature of the cooler plasma.

One of the primary factors preventing prolonged operation of thermonuclear reactors is the intense flux of electromagnetic energy, which destroys the wall.

Let us consider in this connection some estimates giving a qualitative description of the radiation of a reactor plasma in the rf range.

We assume that there are n ions (protons) per cm^3, which are at rest, and we assume that there are an equal number of electrons, moving at a velocity v. We denote by $\sigma_\omega(\varepsilon)d_\omega$ the probability of the emission of a photon with energy $\hbar\omega$ in the frequency range (w, w + $d\omega$) in the collision of an electron with energy ε with an ion at rest. Then the total number of collisions per 1 cm^3 resulting in the emission of energy $\hbar\omega$ is $n^2\sigma_\omega d\omega$, and the total energy radiated in the range $d\omega$ is

$$j_\omega d\omega \simeq \hbar\omega n^2 v\sigma_\omega(\varepsilon)\,d\omega. \tag{1}$$

The bremsstrahlung cross section is given by[1]

$$\sigma_\omega \frac{d\omega}{\varepsilon} = \frac{8}{3}\alpha r_0^2 \frac{d\omega}{\omega}\frac{m}{\varepsilon}\ln\frac{(\sqrt{\varepsilon}+\sqrt{\varepsilon-\omega})^2}{\varepsilon}, \tag{2}$$

where $\alpha = e^2/\hbar c = 1/137$, $r_0 = 2.8\cdot 10^{-13}$ cm is the classical radius, and ε is its energy. We see from Eq. (2) that the emission can, in principle, reach frequencies $\omega \lessdot \varepsilon/\hbar$; the characteristic energy ε here is taken to be electron thermal energy T_e.

An estimate of the rf part of the radiation for the total radiated power per 1 cm^3 yields

$$J \simeq \int^{T_e/\hbar} j_\omega d\omega \simeq \alpha n^2 v_{T_e} r_0^2 mc^2, \tag{3}$$

where ν_{Te} is the velocity of an electron with energy T_e, m is the electron mass, and c is the speed of light.

The radiation pressure, I, is the product of this quantity and the characteristic reactor dimension L. We note that (3) implies an extremely weak functional dependence of this pressure on the temperature. With $L \simeq 100$ cm, $T_e \simeq 50$ keV, and $n \simeq 10^{15}$ cm^{-3} we find I = 100 W/cm^2.

Taking account of the functional dependence on T_e and n, we find

$$\sqrt{\frac{T_e}{50}}\,L \text{ W/cm}^2. \tag{4}$$

Here, n is the number of particles per cubic centimeter, L is the characteristic dimension in meters, and T_e is the temperature in electron volts.

We turn now to the possibility of the absorption of the energy described by (3). The absorption occurs because of scattering processes involving photon absorption.

By definition, the absorption coefficient of the medium is $\alpha_\omega = j_\omega/I_\omega$, where j_ω is given by (1), and $I_\omega = (\hbar\omega^3/8\pi^3c^2)\cdot[\exp(\hbar\omega/T) -]^{-1}$.

It follows from the form of I_ω that the behavior of I_ω differs markedly at $\omega > T_e/\hbar$ and $\omega < T_e/\hbar$; taking account of this circumstance and of the presence of the important Gaunt factor[2] allows us to write a simple qualitative equation for α_ω:

$$a_\omega \simeq n^2 r_0^2\left(\frac{c}{\omega}\right)^2\left[\frac{mc^2}{\max(T_e, \hbar\omega)}\right]^2. \tag{5}$$

If $\hbar\omega \gg T_e$, i.e., if the temperature in some layer near the wall is lower than that corresponding to the radiation energy from the working zone, we can easily find a relation for the characteristic length over which absorption of the radiation can be significant:

$$l_\omega \simeq 10^{19}\left(\frac{\omega}{10^{19}}\right)^{7/3}\left(\frac{10^{18}}{n'}\right)^{2/3} \text{ cm}. \tag{6}$$

Here, ω is the frequency in reciprocal seconds, and n is the density of the cold plasma.

We see that it is unrealistic to try to absorb the rf radiation in a cold-plasma sheath for the conditions corresponding to a thermonuclear reactor, i.e., at $\omega \simeq 10^{19}$ sec^{-1} and $n' \sim 10^{20}$ cm^{-3}. This conclusion can be extended to a moving cold-plasma sheath, in which the radiation would propagate as in vacuum. Absorption is possible if there are more massive ions present. In the working zone of a reactor, however, heavy ions would produce even more radiation, so their presence is extremely undesirable. We are thus left with the possibility of absorption in a wall of a heavy metal, in which resonant transitions of electrons can occur which correspond to photon energies of 50 keV. This conclusion means that most of the load must be carried by the first wall of the reactor.

The author thanks V. M. Smirnov for useful comments.

---

[1] A. A. Sokolov, Introduction to Quantum Electrodynamics [in Russian], Fizmatgiz, Moscow (1958), Ch. II.

[2] G. Bekefi, Radiation Processes in Plasmas, Wiley, New York (1966).

Absolute decay instability of low-frequency waves in an inhomogeneous plasma

A. D. Piliya and V. I. Fedorov

A. F. Ioffe Physicotechnical Institute, Academy of Sciences of the USSR, Leningrad

(Submitted October 11, 1973)
Zh. Tekh. Fiz., 44, 1092-1093 (May 1974)

Parametric instabilities in a plasma have recently received wide attention in connection with the problem of rf heating and laser initiation of thermonuclear reactions. Since a real plasma is always inhomogeneous it is of interest to consider the effect of this inhomogeneity on the instabilities.

In a weakly inhomogeneous medium whose inhomogeneity is along a single coordinate, the decay conditions for the x components of the wave vectors of parametrically coupled waves can be satisfied only at certain points on the x axis (x is the coordinate along which the plasma parameters vary).[1,2] There is a finite swelling of waves near such points, in contrast with the absolute instability which arises under the corresponding conditions in a homogeneous plasma. If there are turning points, however, an absolute instability can arise for interacting waves even in an inhomogeneous plasma. The reason is that each of the parametrically coupled waves propagating through the interaction region not only interacts with this region but also generates a wave of a different type. A positive-feedback loop arises as a result of this nonlinear transformation and reflection of waves from the turning point in the plasma slab. It turns out that this situation arises whenever there is a point at which a high-frequency wave is cut off.

We assume for simplicity that the characteristic spatial dimension of the pumping field $E_0 = \mathcal{E}_0 e^{-i\omega_0 t}$ is much larger than all other dimensions of interest, so that $E_0 = \text{const}$. In the presence of field $\mathcal{E}_0$, the low-frequency wave $E_3 = f_3(x)\exp\cdot[-i\Omega t + ik_z z]$ $(\Omega \ll \omega_0)$ is parametrically coupled with two high-frequency waves: $E_1 = f_1(x)\exp\cdot[i(\omega_0-\Omega)t + ik_z z]$ and $E_2 = f_2(x)\exp[-i(\omega_0+\Omega)t + ik_z z]$. The equations describing the decay interaction of these waves can be written (e.g., ref. 2)

$$\left.\begin{aligned} f_1'' + k^2(x,\ \omega_0-\Omega)\, f_1 &= \nu_{13} f_3, \\ f_2'' + k^2(x,\ \omega_0+\Omega)\, f_2 &= \nu_{23} f_3, \\ f_3'' + \varkappa^2(\Omega)\, f_3 &= \nu_{31} f_1 + \nu_{32} f_2, \end{aligned}\right\} \tag{1}$$

where $k(x, \omega_0 \pm \Omega)$ and $\varkappa(\Omega)$ are the x components of the wave vectors of the high- and low-frequency waves, respectively, and $\nu_{23} \sim \nu_{13} \sim \mathcal{E}_0$ and $\nu_{31} \sim \nu_{32} \sim \mathcal{E}_0$. Considering a region near the high-frequency turning point whose dimension is small in comparison with the scale of the plasma inhomogeneity, we can write $k^2(x, \omega_0 \pm \Omega) = -\alpha(x \mp x_0)$, $(x_0 \sim \Omega)$ and neglect the function dependence of $\varkappa(\Omega)$ on the coordinate. The dispersion curves for this case are shown in Fig. 1. The arrows show the direction in which energy propagates for the case $dk/(d\omega) > 0$. This direction differs for the high-frequency waves f_1 and f_2 because their frequencies differ in sign. When the group velocity of the high-frequency or low-frequency waves is negative $[dk/(d\omega) < 0]$, the instability appears for the opposite sign of the frequencies $[-\Omega, -(\Omega+\omega_0), \omega_0-\Omega]$.

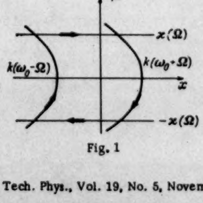

Fig. 1

A resonant decay interaction occurs near the intersections of the curves for $k(x, \omega_0 \pm \Omega)$ and $\varkappa(\Omega)$. If $\varkappa^3\alpha^{-1} \gg 1$, and $\varkappa x_0 \gg 1$ (if the distances between the decay points are large in comparison with the characteristic wavelengths), the interaction in each of the resonant regions proceeds independently of the interactions in the others and is described by the corresponding equations of ref. 3. If there is no absorption, the onset of instability requires that the product of all four "nonlinear-transformation" coefficients (corresponding to the four resonant points) be larger than unity. Using the equations of ref. 3, we can easily write this requirement as

$$4\,\mathrm{sh}^2\,\pi Z \geqslant 1, \tag{2}$$

where $Z = (\nu_{23}\nu_{32} + \nu_{13}\nu_{31})/4\alpha\varkappa$. Furthermore, the semiclassical phase advance over the entire feedback loop (taking into account the phase changes in the resonant regions and at the turning points) must be an integer times 2π:

$$4\varkappa x_0(\Omega) = (2m+1)\pi, \quad m = 0,\ 1,\ 2\ldots. \tag{3}$$

Accordingly, an absolute instability can appear in an inhomogeneous plasma for a certain discrete set of frequencies Ω_m. The instability threshold, given by an equation like (2) is finite, even in the absence of damping. It follows from Eqs. (2) and (3) that m = 0 mode can be the most unstable. In the interaction of plasma and ion-acoustic waves in a plasma without a magnetic field, the threshold pumping field $\mathcal{E}_0'$ for this mode is a minimum at $\Omega \lessapprox \omega_{pi}$, given by

$$\frac{\mathcal{E}_0^2}{4\pi nT} \simeq \frac{r_d^2}{l^2}\sqrt{\frac{m_i}{m_e}}, \tag{4}$$

where n and T are the plasma density and temperature, $l = [1/n|dn/dx|]^{-1}$ is the scale of the plasma inhomogeneity, and r_d is the Debye radius. Here condition (3) leads to the following restriction on l:

$$\frac{l}{r_d} > \sqrt{\frac{m_i}{m_e}}. \tag{5}$$

It should be kept in mind that in the m = 0 case Eqs. (2) and (3), derived in the semiclassical approximation, can be treated as rough approximations. Decay instabilities have been examined for similar conditions by Perkins and Flick,[2] but they take account only of one of the high-frequency waves, therefore reaching the conclusion that there is no absolute instability.

---

[1] A. D. Piliya, 10th Intern. Conf. on Phenomena in Ionized Gases, Oxford, England, 1971.

[2] F. W. Perkins and J. Flick, Phys. Fluids, 14, 2012 (1971).

[3] A. D. Piliya, Zh. Eksp. Teor. Fiz., 64, 1237 (1973) [Sov. Phys.–JETP, 37, 629 (1974)].

Effect of a high-frequency electric field on the energy loss of a charged particle in a medium

Zh. M. Diasamidze
Tbilisi State University
(Submitted October 5, 1973)
Zh. Tekh. Fiz., 44, 1093-1095 (May 1974)

The energy losses of a charged particle in an alternating electric field moving in an unbounded dielectric are considered. The effect of the external alternating electric field on the energy loss of the particles is investigated for an arbitrary value of the electric field.

The effect of an external alternating electric field on the energy loss of a charged particle moving through a medium (dielectric or a plasma), and when it moves in a dielectric above the boundary of separation of two dielectrics, has been considered in refs. 1-4.

In this paper we consider the energy loss of a charged particle which moves with a constant velocity along the z axis in an unbounded dielectric in the presence of an external high-frequency electric field $\mathbf{E} = \mathbf{E}_0 \sin \omega_0 t$, which is perpendicular to the motion of the particle.

The total energy lost by the particle per unit length of path is given by the well-known relation[5]

$$-\frac{\partial \mathcal{E}}{\partial z} = \frac{e(\mathbf{V}\cdot\mathbf{E})}{V},$$

where the electric field is taken at the particle location.

To determine the electromagnetic field of the particle we use Maxwell's equations with the charge density and the current:

$$\rho = e\delta(x)\,\delta(y - y(t))\,\delta(z - v_0 t),$$
$$\mathbf{j} = \rho\mathbf{V},$$

where

$$\mathbf{V} = \mathbf{V}_0 - \mathbf{V}_\sim \cos \omega_0 t,$$
$$y(t) = y_0 - \frac{v_\sim}{\omega_0} \sin \omega_0 t,$$

and the velocity and trajectory of the particle in the alternating electric field are $V_\sim = eE_0/m\omega_0$, $v_0 = V_{\sim y}$ and $y_0 = 0$, respectively.

The electromagnetic field of a particle which moves along a sinusoidal trajectory can be found in the usual way. Such calculations have been carried out many times (see, for example, refs. 4 and 6). Carrying out the appropriate calculations we obtain the following expression for the total energy loss of the particle of charge e in a field $\mathbf{E} = \mathbf{E}_0 \sin \omega_0 t$, moving in a medium of dielectric constant ε:

$$-\frac{\partial \mathcal{E}}{\partial z} = -\frac{e^2}{2\pi v_0^2}\,\mathrm{Re}\, i$$
$$\times \sum_l \iint \frac{\omega(\varepsilon\beta^2 - 1) J_l^2\left(\frac{k_y v_\sim}{\omega_0}\right)}{\varepsilon\sqrt{\left(\frac{\omega + l\omega_0}{v_0}\right)^2\left(\frac{\omega^2}{(\omega + l\omega_0)^2}\varepsilon\beta^2 - 1\right) - k_y^2}}\, dk_y d\omega$$
$$-\frac{e^2}{8\pi c^2}\frac{v_\sim^2}{v_0^2}\,\mathrm{Re}\, i$$
$$\times \sum_l \iint \frac{\omega J_l\left(\frac{k_y v_\sim}{\omega}\right)\left\{J_l\left(\frac{k_y v_\sim}{\omega_0}\right) + J_{l+2}\left(\frac{k_y v_\sim}{\omega_0}\right)\right\}}{\sqrt{\left(\frac{\omega + (l+1)\omega_0}{v_0}\right)^2\left(\frac{\omega^2}{(\omega + (l+1)\omega_0)^2}\varepsilon\beta^2 - 1\right) - k_y^2}}\, dk_y d\omega$$
$$-\frac{e^2}{8\pi c^2}\frac{v_\sim^2}{v_0^2}\,\mathrm{Re}\, i$$
$$\times \sum_l \iint \frac{\omega J_l\left(\frac{k_y v_\sim}{\omega_0}\right)\left\{J_l\left(\frac{k_y v_\sim}{\omega_0}\right) + J_{l-2}\left(\frac{k_y v_\sim}{\omega_0}\right)\right\}}{\sqrt{\left(\frac{\omega + (l-1)\omega_0}{v_0}\right)^2\left(\frac{\omega^2}{(\omega + (l-1)\omega_0)^2}\varepsilon\beta^2 - 1\right) - k_y^2}}\, dk_y d\omega. \quad (1)$$

Here, the first term with $l = 0$ gives the Cerenkov radiation ($\varepsilon\beta^2 > 1$), with $l \neq 0$ it gives the Doppler radiation with frequency $\omega = |-[l\omega_0/(1 - \beta\sqrt{\varepsilon}\cos\theta)]|$, ($l = \pm 1, \ldots$ $\varepsilon = \mathrm{const}$). The second and third terms for any l make a contribution to the Doppler radiation; for example, with $l = 0$, the next term gives Doppler radiation of frequency $\omega = \omega_0/\beta\sqrt{\varepsilon}\cos\theta - 1$ (the anomalous Doppler effect $\beta\sqrt{\varepsilon}\cos\theta > 1$), and the third term gives Doppler radiation of frequency $\omega = \omega_0/1 - \beta\sqrt{\varepsilon}\cos\theta$ (the normal Doppler effect $\beta\sqrt{\varepsilon}\cos\theta < 1$).

Evaluating (1) for weak alternating electric fields, $|k_y v_\sim|/\omega_0 \ll 1$, and integrating with respect to k_y, we obtain the energy loss of the charge:[4]

$$-\frac{\partial \mathcal{E}}{\partial z} = Q_0 - \frac{e^2}{4v_0^2}\frac{v_\sim^2}{\omega_0^2}\int \omega^3 \frac{(\varepsilon\beta^2 - 1)^2}{\varepsilon}\, d\omega$$
$$+\frac{e^2}{8v_0^4}\frac{v_\sim^2}{\omega_0^2}\int \omega\left\{(\omega + \omega_0)^2\left(\frac{\omega^2}{(\omega + \omega_0)^2}\varepsilon\beta^2 - 1\right)\frac{\varepsilon\beta^2 - 1}{\varepsilon} + 2\beta^2\omega_0^2\right\} d\omega$$
$$+\frac{e^2}{8v_0^4}\frac{v_\sim^2}{\omega_0^2}\int \omega\left\{(\omega - \omega_0)^2\left(\frac{\omega^2}{(\omega - \omega_0)^2}\varepsilon\beta^2 - 1\right)\frac{\varepsilon\beta^2 - 1}{\varepsilon} + 2\beta^2\omega_0^2\right\} d\omega, \quad (2)$$

where

$$Q_0 = \frac{e^2}{v_0^2}\int \frac{\omega(\varepsilon\beta^2 - 1)}{\varepsilon}\, d\omega \quad (3)$$

is the Cerenkov radiation for particle motion in the dielectric with no field. In Eq. (2) we have neglected terms of the order of $v_\sim^4$ and higher.

It is evident from Eq. (2) that the well-known expression for the energy loss by Cerenkov radiation in an unbounded dielectric Q_0, obtained by Tamm and Frank,[7] must be supplemented by terms which are quadratic in the electric field. The first of the terms is an addition to the Cerenkov radiation Q_0 in a weak electric field, and reduces the Cerenkov losses slightly. The last two terms define the Doppler radiation, which increases quadratically with the electric field.

It should be noted that the expression for the energy loss of a charged particle due to Doppler radiation (the normal Doppler effect) for weak electric fields is identical with the expression for the total energy radiated by an electron moving in a medium with refractive index n, obtained by Ginzburg[1] [Eq. (13) of ref. 1] in the dipole approximation. It is easy to show this by calculating the angular distribution of the energy of the normal Doppler radiation per solid angle $d\Omega$, changing in the last term of expression (2) from integration with respect to ω to integration over the angle θ, and using the equation $\omega = \omega_0/1 - \beta\sqrt{\varepsilon}\cos\theta$.

Evaluating (1) for strong alternating electric fields $|k_y v_\sim|/\omega_0 > 1$, and integrating over k_y, as in the previous case we obtain

$$-\frac{\partial \mathscr{E}}{\partial z} = \frac{e^2}{\pi v_0}\frac{\omega_0}{v_\sim}\int \frac{\sqrt{\varepsilon\beta^2 - 1}}{\varepsilon}\sin\left(2\frac{\omega}{\omega_0}\frac{v_\sim}{v_0}\sqrt{\varepsilon\beta^2 - 1}\right)d\omega$$

$$+\frac{e^2}{\pi v_0}\frac{\omega_0}{v_\sim}\sum_{l\neq 0}\int (-1)^l \frac{\omega(\varepsilon\beta^2 - 1)\sin\left(2\frac{\omega + l\omega_0}{\omega_0}\frac{v_\sim}{v_0}\sqrt{\frac{\omega^2}{(\omega + l\omega_0)^2}\varepsilon\beta^2 - 1}\right)}{\varepsilon(\omega + l\omega_0)\sqrt{\frac{\omega^2}{(\omega + l\omega_0)^2}\varepsilon\beta^2 - 1}}\,d\omega.$$

Hence, for strong alternating electric fields the energy loss of a charged particle is inversely proportional to the amplitude of the alternating electric field.

In conclusion we note that maximum radiation is obtained when $|k_y v_\sim|/\omega_0 \sim 1$.

We wish to thank N. L. Tsintsadze for guidance.

---

[1] V. L. Ginzburg, Dokl. Akad. Nauk SSSR, 56, 145 (1947).

[2] T. L. Tavdgiridze and N. L. Tsintsadze, Zh. Eksp. Teor. Fiz., 58, 975 (1970) [Sov. Phys. – JETP, 29, 526 (1969)].

[3] Zh. M. Diasamidze and N. L. Tsintsadze, Zh. Tekh. Fiz., 43, 1323 (1973) [Sov. Phys. – Tech. Phys., 18, 845 (1973)].

[4] Zh. M. Diasamidze and T. L. Tavdgiridze, Zh. Tekh., Fiz., 42, 28 (1972) [Sov. Phys. – Tech. Phys., 17, 30 (1972)].

[5] V. P. Silin and A. A. Rukhadze, Electromagnetic Properties of a Plasma and Plasma-Like Media [in Russian], Atomizdat, Moscow (1961).

[6] V. Ya. Eidman, Zh. Eksp. Teor. Fiz., 36, 1335 (1959) [Sov. Phys. – JETP, 9, 947 (1959)].

[7] I. E. Tamm and I. M. Frank, Dokl. Akad. Nauk SSSR, 14, 107 (1937); Usp. Fiz. Nauk, 93, 388 (1967).

Contraction of the positive column of a glow discharge due to the presence of negative ions

L. A. Mikhalev and L. N. Selin

(Submitted May 29, 1973)
Zh. Tekh. Fiz., 44, 1095-1097 (May 1974)

The contracted state of the discharge in a gas containing a small addition of electronegative impurities is investigated. The ionization of the impurity atoms is neglected compared with the ionization of the atoms of the main gas. The model gives a linear relationship between the contraction radius and the radius of the tube. The results show that the contraction of the positive column increases when the density of impurities increases.

It is known from experiment that a gas discharge at medium pressure can contract. The contraction of the positive column may be due to a difference in the temperature of the electrons in the axial region and the peripheral region of the discharge,[1] and a deviation of the electron energy distribution function from a Maxwell distribution at the periphery of the positive column.[2] Another reason may be the fact that the ambipolar diffusion coefficient D_{am} and the recombination coefficient α_r of the electrons is not constant along the radius of the tube.

This point of view has been developed in ref. 3, where the contraction of the positive column of a discharge in electronegative gases is considered.

In the present note we investigate the contracted state of the discharge in a gas which contains a small addition of electronegative impurities.

Consider a plasma layer which is uniform along its length, bounded by plane walls ($x = \pm l$). The plasma is assumed to be neutral, $n_+ = n_e + n_-$, and to be in a nonequilibrium state, $\gamma = T_e/T_+ = T_e/T_- \gg 1$. Here, T_+ and T_- are the temperatures of the positive and negative ions, respectively. The ionization of the impurity atoms is neglected compared with the ionization of the atom of the main gas. The mechanism by which the negative ions are created and destroyed is assumed to be as follows: The negative ions are formed as a result of electron attachment to impurity atoms, and are lost by recombination with positive ions of the main gas and by diffusion to the walls.

With these assumptions the behavior of the particles can be described by the following set of equations:[4]

$$\frac{d}{dx}\left[D_e^a\frac{dn_e}{dx}\right]+(\nu_i-\nu_p)\,n_e=0, \tag{1}$$

$$\frac{d}{dx}\left[D_-^a\frac{dn_-}{dx}\right]+\nu_p n_e-\alpha n_+n_-=0, \tag{2}$$

where

$$D_e^a=b_+T_+\frac{1+\gamma(1+2\varepsilon)}{1+\frac{b_+}{b_e}(1+\varepsilon)+\frac{b_-}{b_e}\varepsilon},\quad D_-^a=D_e^a\frac{1}{\gamma}\frac{b_-}{b_e},\quad \varepsilon=\frac{n_-}{n_e}.$$

We have used the following notation: ν_i is the rate of impact ionization by a single electron, ν_p is the electron attachment rate, α is the ion–ion recombination coefficient, and b_e, b_+ and b_- are the mobilities of the electrons, positive ions, and negative ions respectively.

Assuming that the charges particles recombine completely at the walls, we have the boundary conditions

$$n_e|_\Sigma=n_+|_\Sigma=n_-|_\Sigma=0. \tag{3}$$

In addition, the charged particle distribution must possess axial symmetry, i.e.,

$$\left.\frac{dn_e}{dx}\right|_{x=0}=\left.\frac{dn_-}{dx}\right|_{x=0}=\left.\frac{dn_+}{dx}\right|_{x=0}=0. \tag{4}$$

In view of the fact that $T_+ = T_- \ll T_e$ the diffusion of the negative ions can be neglected. Moreover, in the expression for the diffusion coefficient D_e^a we can, without loss of generality, neglect terms proportional to b_+/b_e and b_-/b_e. This corresponds to the inequality

$$\frac{b_+}{b_e}(1+\varepsilon),\ \frac{b_-}{b_e}\varepsilon\ll 1,$$

which is satisfied even when $\varepsilon \gg 1$.

With these assumptions Eqs. (1) and (2) reduce to the following:

$$\left.\begin{aligned}&\frac{d}{dx}\left[D_e^a\frac{dn_e}{dx}\right]+(\nu_i-\nu_p)\,n_e=0,\\ &\frac{\nu_p}{\alpha n_e}=\varepsilon(\varepsilon+1),\quad D_e^a=b_+T_e(1+2\varepsilon).\end{aligned}\right\} \tag{5}$$

In the case of small ε the radial density distribution of the electrons will be close to a Schottky distribution over a large part of the plasma layer:

$$n_e=n_e(0)\cos\frac{\pi x}{2l},\quad \nu_i-\nu_p=D_e^a\left(\frac{\pi}{2l}\right)^2. \tag{6}$$

The negative ion distribution over the radius will be close to a Π-shaped distribution, $n_- = (\nu_p/\alpha)[1/(1+\varepsilon)]$. Near the walls, in the region $\delta \sim (8/3\pi)l\,[\nu_p/\alpha n_e(0)]$, the negative ion density falls to zero.

Consider the case $\varepsilon \gg 1$ over the whole cross section of the plasma layer. We introduce the following dimensionless variables:

$$y=\sqrt{\frac{n_e}{n_e(0)}},\quad \xi=x\sqrt{\frac{\nu_i-\nu_p}{b_+T_e}\sqrt{\frac{\alpha n_e(0)}{4\nu_p}}}. \tag{7}$$

Equation (5) and the boundary conditions (3) and (4) can then be written in the form

$$2\frac{d^2y}{d\xi^2}+y^2=0,\quad y(\xi(l))=0,\quad y'_\xi(0)=0. \tag{8}$$

The solution of Eq. (8) which satisfies the above boundary conditions can be expressed in terms of the elliptic integral of the first kind (see Fig. 1)

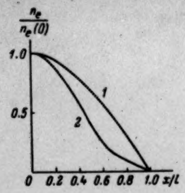

Fig. 1. $n_e/n_e(0)$ as a function of the coordinates. h: 1) 2/3; 2) 0.465.

$$\int_y^1 \frac{dz}{\sqrt{1-z^3}} = \frac{\xi}{\sqrt{3}}. \tag{9}$$

From the boundary conditions $y[\xi(l)] = 0$ we have

$$\frac{\xi(l)}{\sqrt{3}} = l\sqrt{\frac{\nu_i-\nu_p}{3b_+T_e}\sqrt{\frac{an_e(0)}{4\nu_p}}} = \frac{1}{\sqrt[4]{3}}F(\varphi,\ \sin 75°),\quad \cos\varphi = \frac{\sqrt{3}-1}{\sqrt{3}+1}. \tag{10}$$

Here, $F(\varphi, k)$ is the elliptic integral of the first kind.[5]

To estimate the degree of contraction we introduce the parameter $h = l_k/l$, which is equal to the relative half-width of the distribution over the radius. Then, for the Schottky distribution (6) the parameter h = 2/3. We obtain this parameter for the contracted state of the discharge. We have from Eq. (9)

$$\frac{\xi(l_k)}{\sqrt{3}} = l_k\sqrt{\frac{\nu_i-\nu_p}{3b_+T_e}\sqrt{\frac{an_e(0)}{4\nu_p}}} = \frac{1}{\sqrt[4]{3}}F(\varphi_k,\ \sin 75°),$$

$$\cos\varphi_k = \frac{\sqrt{3}-1+\frac{1}{\sqrt{2}}}{\sqrt{3}+1-\frac{1}{\sqrt{2}}}. \tag{11}$$

The parameter h in this case is

$$h = \frac{l_k}{l} = \frac{F(\varphi_k,\ \sin 75°)}{F(\varphi,\ \sin 75°)} = 0.465. \tag{12}$$

The contraction is due to the fact that in the region of the walls the diffusion coefficient D_e^a increases, i.e., the velocity with which the electrons drift to the walls increases.

We note also that the model considered gives a linear relationship between the contraction radius and the radius of the tube.

---

[1] A. T. Rakhimov and F. R. Ulinich, Dokl. Akad. Nauk SSSR, 187, 72 (1969) [Sov. Phys. – Dokl., 14, 655 (1970)].

[2] Yu. M. Kagan and R. I. Lyagushchenko, Zh. Tekh. Fiz., 34, 1873 (1964) [Sov. Phys. – Tech. Phys., 9, 1445 (1965)].

[3] G. Albrecht, G. Ecker, and K. G. Müller, Zs. Naturforsch., 17a, 854 (1962).

[4] J. B. Tompson, Proc. Phys. Soc., 73, 818 (1959).

[5] E. Yanke, F. Emde, and F. Leche, Special Functions [in Russian], Nauka, Moscow (1968).

Current-driven instability in a conducting fluid

A. M. Kovnatskii

M. A. Bonch-Bruevich Leningrad Electrotechnical Communications Institute

(Submitted June 29, 1973)
Zh. Tekh. Fiz., 44, 1097-1098 (May 1974)

Excitation of waves in an inhomogeneous conducting fluid carrying a current in a magnetic field is analyzed. It is shown that instability arises at a critical value of the current.

1. In this paper we consider the excitation of waves in an inhomogeneous medium carrying a current in a magnetic field. It is shown that a current which is sufficiently strong can lead to the excitation of waves which propagate in the medium. The instability condition is

$$j > (ck)(kL)\frac{H_{cr}}{4\pi} \tag{1}$$

when H $\nless$ H$_{cr}$, or

$$j > (ck)\frac{kL}{4\pi}\frac{H_{cr}^2}{H} \tag{2}$$

when H > H$_{cr}$, where j is the current density, c is the velocity of light in vacuum, k is the wave vector, L is the inhomogeneity length, $L^{-1} = |\nabla\eta/\eta|$, $H_{cr} = \eta/\eta_1$ is the critical magnetic field, η and η_1 are the normal and Hall resistances.

2. The equations describing this problem consist of an expression for the electric field

$$\mathbf{E} = \eta\mathbf{j} + \eta_1[\mathbf{j},\mathbf{H}] - \frac{1}{c}[\mathbf{v},\mathbf{H}] \tag{3}$$

and the equation of magnetohydrodynamics.[1] Here, and in what follows, **v** is the hydrodynamic velocity, ρ is the density of the medium and p is the pressure.

The system of equations has been studied by the usual method[1] in the linear approximation. The approximations are as follows: 1) Only the low-frequency case is considered: $\omega \ll \sigma$, where σ is the conductivity; 2) The inhomogeneity is assumed to be weak, $kL \gg 1$; 3) The self magnetic field H_{nat} is neglected as in ref. 2.

3) Suppose that j is directed along the x axis and H along the y axis. The gradient $\nabla\eta$ and the wave vector **k** can lie along any of the axes x, y or z. Out of all the possible orientations between **j**, **H**, $\nabla\eta$ and **k**, excitation is only found for $H \le H_{cr}$ in the following cases.

a) $\nabla\eta$ and **k** are parallel to j. In this case the dispersion equation has the form

$$\omega = -\left(\frac{c^2}{4\pi}\nabla\eta k + \eta_1 cjk\right) + i\left(c\nabla\eta_1 j - \frac{c^2\eta}{4\pi}k^2\right) \tag{4}$$

and H' = H'_z or

$$\omega = (ck)(sk)^2\frac{\left[\frac{c\nabla\eta}{4\pi} + j\left(\eta_1 + 2H^2\frac{\partial\eta_1}{\partial H^2}\right)\right] + ic(sk)^2\left[\frac{ck^2\eta}{4\pi} - \nabla\eta_1 j\right]}{k^2\left(\frac{H^2}{4\pi\rho} + s^2\right)} \tag{5}$$

and H' = H'$_y$ and $\omega \ll$ sk. For the case $\omega \gg$ sk,

$$\omega = -ck\left[\frac{c\nabla\eta}{4\pi} + j\left(\eta_1 + 2H^2\frac{\partial\eta_1}{\partial H^2}\right)\right] - ic\left[\frac{ck^2\eta}{4\pi} - \nabla\eta_1 j\right]. \tag{6}$$

b) $\nabla\eta$ is parallel to the current along the x axis and **k** lies along z. The dispersion equation is now

$$\omega = -\frac{s^2k^2\left\{\left[2c\frac{\partial\eta}{\partial H^2}Hkj + \frac{c^2}{4\pi}H\nabla\eta_1 k\right] - i\left[\frac{k^2c^2}{4\pi}\eta\right]\right\}}{\left(\frac{k^2H^2}{4\pi\rho} + s^2k^2\right) + i\left(\frac{Hkj}{c\rho}\right)}. \tag{7}$$

The instability condition is shown in (1).

c) When H > H$_{cr}$ and **k** ∥ H, $\nabla\eta_1$ ∥ **j**, H ⊥ **j**, the dispersion equation has the form

$$\omega = \frac{ck^2\eta_1 H}{4\pi} + i\left[c\nabla\eta_1 j - \frac{c^2k^2}{4\pi}\eta\right], \tag{8}$$

and the instability condition is given by (2).

4. We now estimate the critical current and the frequency of the excited waves. Excitation occurs if $j \ge j_{cr}$, where

$$j_{cr} = (ck)(kL)\frac{H_{cr}}{4\pi}.$$

with c = $3 \cdot 10^{10}$ cm/sec, k = 1 cm^{-1}, kL ≈ 3, H$_{cr}$ ≃ $3 \cdot 10^4$ Oe, j$_{cr}$ ≃ $3 \cdot 10^4$ A/cm^2.

For the frequency of the excited waves: in case a) $\omega \approx \eta_1 cjk \approx kv_{dr}$, and for $j_{cr} = 3 \cdot 10^4$ A/cm^2, $v_{dr} \approx 10^2$ cm/sec, $\omega \simeq 10^2$ sec^{-1}. For case b) $\omega \simeq (c^2k^2/\sigma) \cdot (H^2/4\pi\rho s^2)kL \approx k^3$ and for the above values $\omega \simeq 10^2$ sec^{-1}. In case c) with H ≃ 10^5 Oe, $j_{cr} \simeq 10^4$ A/cm^2 and n ≃ 10^{22} cm^{-3} (liquid metal), $\omega \sim 10^{-8}$ sec^{-1}, i.e., the instability is almost aperiodic.

---

[1] L. D. Landau and E. M. Lifshitz, Electrodynamics of Continuous Media, Pergamon Press, Oxford–New York (1960).

[2] L. E. Gurevich and I. V. Ioffe, Zh. Eksp. Teor. Fiz., 58, 2047 (1970) [Sov. Phys. – JETP, 31, 1102 (1970)].

Convection in a liquid dielectric in a longitudinal electric field

I. V. Ioffe and N. V. Kalinin

A. F. Ioffe Physicotechnical Institute, Academy of Sciences of the USSR, Leningrad

(Submitted October 29, 1973)
Zh. Tekh. Fiz., 44, 1099-1100 (May 1974)

It is shown that a uniform longitudinal electric field prevents convection; convection is possible only when the liquid is heated from below; in addition there is an upper limit on the critical temperature gradient in addition to the usual lower limit.

The effect of an electric field, parallel to the equilibrium-temperature gradient, on convection in a liquid dielectric has been investigated for nonconducting liquids[1,2] and conducting liquids.[2,3]

In this note we consider convection in a plane layer of a viscous incompressible liquid, situated between horizontal plates ($z = \pm h/2$). The external uniform electric field $\mathbf{E}_0$ is perpendicular to the force of gravity g, and has components $\mathbf{E}_0 = (E_0, 0, 0)$.

It is shown that the applied field prevents convection; convection is possible only when the liquid is heated from below, unlike the results obtained in refs. 1, 2. The set of equations which describes convection in the absence of conductivity, has the form[1,2]

$$\left.\begin{aligned}&\rho\left[\frac{\partial \mathbf{u}}{\partial t}+(\mathbf{u}\nabla)\,\mathbf{u}\right]=-\nabla p+\nu\rho\Delta\mathbf{u}+\mathbf{g}\rho+\mathbf{f}_e,\\&\frac{\partial T}{\partial t}+(\mathbf{u}\nabla)\,T=\chi\Delta T,\ \frac{d\rho}{\partial T}=-\beta\rho,\ \operatorname{div}\mathbf{u}=0,\\&\operatorname{div}(\varepsilon\mathbf{E})=0,\ \ \mathbf{E}=-\nabla\varphi,\ \ \varepsilon=\varepsilon\,(T,\ \rho\,(T)).\end{aligned}\right\}\qquad(1)$$

According to ref. 4

$$\mathbf{f}_e=\frac{1}{8\pi}\left\{\nabla\left[E^2\rho\left(\frac{\partial\varepsilon}{\partial\rho}\right)_T\right]-E^2\nabla\varepsilon\right\}$$

is the electrostriction force. The remaining symbols have the usual meaning.

We reduce the system (1) to dimensionless form, and obtain an equation for the temperature perturbation:

$$\left.\begin{aligned}&\left(\left(\frac{\partial}{\partial t}-\Delta\right)\left(Pr\frac{\partial}{\partial t}-\Delta\right)\Delta^2-R\left(\Delta-RN\frac{\partial^2}{\partial x^2}\right)\Delta_\perp\right)T=0,\\&\Delta_\perp=\Delta-\frac{\partial^2}{\partial z^2},\ \ Pr=\frac{\nu}{\chi},\ \ a=\left(\frac{d}{dT}\ln\varepsilon\right)_0,\end{aligned}\right\}$$

$$N=\frac{1}{4\pi}\frac{\varepsilon a^2E_0^2\chi\nu}{\rho g^2\beta^2h^4},\quad R=\frac{g\beta h^4\nabla T_0}{\nu\chi}$$

is the Rayleigh number.

Equation (2) has the solution $T \sim \exp\{i(k_x x + k_y y) - \omega t\}\,\Theta(z)$. For a layer of liquid with free boundaries (the boundary conditions with respect to z are the same as in the Rayleigh problem) $\Theta \sim \cos k_z z$, $k_z = \pi n$ (see refs. 1, 2, 5). The convection condition has the form $\mathrm{Im}(\omega) = 0$. Then $\mathrm{Re}(\omega) = 0$,

$$\left.\begin{aligned}&k^6+NR^2k_x^2k_\perp^2-\mathrm{R}\,k^2k_\perp^2=0,\\&k^2=k_x^2+k_y^2+k_z^2,\ \ k_\perp=k_x^2+k_y^2.\end{aligned}\right\}\qquad(3)$$

As can be seen from Eqs. (3), when the liquid is heated from above ($R < 0$) convection is impossible.

We write Eqs. (3) in the form

$$NR^2-\frac{1}{b}R+\frac{1}{b}R_0=0,\qquad(4)$$

$b = k_x/k^2$, $R_0 = k^6/k_\perp^2$ is the critical value of the Rayleigh number for ordinary convection.[5]

For $N = 0$, $R = R_0$. Convection is possible if

$$N\leqslant N_m=\frac{1}{4R_0b}=\frac{k_\perp^2}{k_x^2k^4}.\qquad(5)$$

It is evident from Eq. (5) that small values of N stabilize the oscillations with large k_x^2 and small k_y^2; large values of N stabilize oscillations with small k_x^2 and large k_y^2

$$R_{1,2}=\frac{1}{2Nb}\left(1\pm(1-4R_0Nb)^{1/2}\right).\qquad(6)$$

Obviously $R_{1,2} > R_0$, i.e., the applied field inhibits convection. Unlike the case $N = 0$, when the temperature gradient is greater than a certain value and convection always occurs, when $N \neq 0$ the region of instability is limited both from below and from above, $R_1 \leq R \leq R_2$. When $N = N_m$, $R_1 = R_2$ the region degenerates to a point.

The maximum value of the field for which convection occurs is of the order of 1 kV/cm for $h \approx 0.3$ cm.

---

[1] B. L. Gelmont and I. V. Ioffe, Phys. Lett., 26A, 253 (1968).
[2] P. H. Roberts, Quart. J. Mech. and Appl. Math., 22, 211 (1969).
[3] I. V. Ioffe and A. I. Saet, Phys. Lett., 43A, 423 (1973).
[4] L. D. Landau and E. M. Lifshitz, Electrodynamics of Continuous Media, Addison-Wesley (1960).
[5] G. Z. Gershuni and E. M. Zhukovitskii, Convection Stability of Incompressible Liquids [in Russian], Nauka, Moscow (1972).

Infrared nitrogen laser using a transverse discharge

V. F. Tarasenko and Yu. I. Bychkov

Institute of Atmospheric Optics, Siberian Branch, Academy of Sciences of the USSR, Tomsk

(Submitted April 23, 1973)
Zh. Tekh. Fiz., 44, 1100-1101 (May 1974)

Laser action is obtained in molecular nitrogen on the First Positive system using transverse excitation. The optimum pressure is 33 torr and the output pulse is delayed with respect to the exciting pulse by less than 10 nsec. Certain features of transverse excitation are considered.

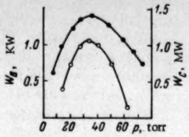

Fig. 1. Plots of output power versus pressure for First Positive (W_B) and Second Positive (W_C) systems of nitrogen.

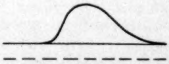

Fig. 2. Shape of output pulse for First Positive system; 8 nsec markers.

Laser action in molecular nitrogen was first obtained[1] in the infrared (0.75-1.2 μ) simultaneously on 30 lines assigned to the First Positive system of the band spectrum of nitrogen. A detailed study of the physical processes is given by Knyazev[2] along with spectral measurements. All known experiments in which laser action has been obtained on the First Positive system of nitrogen have been carried out in tubes in which an axial discharge is maintained at low gas pressures. The output power can be increased by increasing the pressure of the working gas, provided a high electric field can be maintained.

In the present work we investigate the possibility of using transverse excitation to obtain laser action on the First Positive system of nitrogen (the transition $B^3\pi_g \to A^3\Sigma_u^+$). The experimental arrangement is similar to that previously described[3] except that the characteristic impedance of the discharge circuit is 0.07 Ω. The laser chamber is 1 m long and has cross-sectional dimensions 24 × 3 mm. Figure 1 shows a plot of output power versus pressure for the lines of the First Positive system of nitrogen and, for comparison, an analogous plot obtained with the same apparatus for the Second Positive system of nitrogen (transition $C^3\pi_u \to B^3\pi_g$, wavelength λ = 3371 Å). No effort is made to optimize the resonator or the dimensions of the laser chamber. For transverse excitation the output pulse is delayed with respect to the current pulse by less than 10 nsec. There is no difficulty in obtaining laser action simultaneously in the ultraviolet and in the infrared. Figure 2 shows an oscillogram of the output pulse for laser action on the First Positive system of nitrogen. The short duration of the output pulse compared with previous results[1,2,4] is due to the transverse excitation and the high pressure of the working gas in the laser chamber. In systems with a transverse discharge a high electron temperature is maintained only during the switching period, i.e., while the current is building up in the laser chamber. Subsequently, due to the reduction of the voltage across the plasma, the electron energy becomes small and efficient excitation of the B state of molecular nitrogen ceases. The switching time for the transverse-discharge is ~ 10 nsec.

It is known[2] that the rate of change of the population of the upper working level begins to decrease sharply at a certain point as a result of deexcitation of the B state by electrons.

Let us estimate the maximum electron density commencing from which deexcitation by electron impact becomes important for pumping lengths of 10 nsec. The role of radiative decay can be neglected. Then,

$$\dot{N}_B = (N_0 - N_B) n_e \langle \sigma_{0B} v \rangle - N_B n_e \langle \sigma_{BA} v \rangle,$$

where $\langle \sigma_{EA} v \rangle$ is the average, over the electron velocity distribution, of the product of electron velocity v times the effective cross section for deexcitation by electrons of the B state to all lower-lying vibrational levels of the A state; $\langle \sigma_{0B} v \rangle$ is the average of the product of electron velocity times the effective cross section for excitation of the B state from the ground state; N_0 is the initial concentration of nitrogen molecules in the ground state; and n_e is the electron density.

For $\langle \sigma_{0B} v \rangle$ = const, $\langle \sigma_{BA} v \rangle$ = const and $n_e = at$, where a = const and t is time, we find

$$N_B = \frac{N_0 \langle \sigma_{0B} v \rangle}{\langle \sigma_{0B} v \rangle + \langle \sigma_{BA} v \rangle} \{1 - \exp[-0.5 n_e t (\langle \sigma_{0B} v \rangle + \langle \sigma_{BA} v \rangle)]\}.$$

The population of the B state is a maximum when

$$\exp[-0.5 n_e t (\langle \sigma_{0B} v \rangle + \langle \sigma_{BA} v \rangle)].$$

Then, setting $N_B = 0.95\ N_{B\,max}$, we obtain an electron density $n_e \approx 10^{16}$ cm^{-3} at which laser action is limited through deexcitation by electron impact. The values of $\langle \sigma_{0B} v \rangle$ and $\langle \sigma_{BA} v \rangle$ are taken from ref. 4. This value is to be compared with known systems of transverse-discharge excitation, when $n_e \approx 10^{15}$ cm^{-3} and less.[5]

In a nitrogen laser based on the First Positive system the output power can be increased by increasing the electron density, which can be effected by reducing the characteristic impedance of the discharge circuit.

In conclusion, transverse excitation of nitrogen can be used to obtain laser action on the First Positive system at a high optimum pressure and simultaneous laser action in the ultraviolet and the infrared.

---

[1] L. E. S. Mathias and J. T. Parker, Appl. Phys. Lett., 3, 16 (1963).
[2] I. N. Knyazev, Tr. Fiz. Inst. P. N. Lebedeva AN SSSR, 56, 119 (1971).
[3] V. F. Tarasenko and Yu. I. Bychkov, Prib. Tekh. Eksp., No. 1, 183 (1973).
[4] I. N. Knyazev, Zh. Eksp. Teor. Fiz., 61, 72 (1971) [Sov. Phys. – JETP, 34, 38 (1972)].
[5] J. D. Shipman, Appl. Phys. Lett., 10, 3 (1967).

Microwave maser with nonrelativistic electrons

A. S. Dement'ev and Yu. G. Pavlenko

M. V. Lomonosov Moscow State University

(Submitted June 18, 1973)
Zh. Tekh. Fiz., 44, 1101-1103 (May 1974)

It is shown by the methods of classical electrodynamics that nonrelativistic electrons moving in an electromagnetic field described by the vector potential A = (0, Hx, 0) and the scalar potential $\Phi = (1/2)(Ax^2 + By^2) - (1/2)(A + B)z^2$ are a source of stimulated emission in the microwave region.

Fundamental to the operation of lasers, masers, and amplifiers is the creation of an inverted population. However, the excited atom or molecule constituting the working medium in such devices delivers an energy equal to just one photon. It is well known that electrons moving in macroscopic electromagnetic fields continuously radiate electromagnetic waves. The reason, in all cases of practical interest, is that the energy of electrons performing a finite motion lies in the region of highly excited energy levels with quantum numbers $n \sim 10^5$. In radiation at submillimeter wavelengths the electron gives up an insignificant amount of energy and remains in an excited state. This has given rise to the concept of a device similar to the maser, but which utilizes electrons moving in periodic trajectories rather than excited atoms and molecules. Such devices are frequently called "electron masers" or "cyclotron-resonance masers".[1] It is also well known that the stimulated emission associated with the motion of electrons in a constant uniform magnetic field is due to relativistic effects. However, in magnetic and electrostatic fields of a certain configuration, stimulated emission occurs even at nonrelativistic electron energies.[2]

In the present work we consider the stimulated emission of nonrelativistic electrons moving in a uniform magnetic field with a vector potential A = (0, Hx, 0) and in an electrostatic field of rhombic symmetry, the potential of which is given by

$$\Phi = \frac{1}{2}(Ax^2 + By^2) - \frac{1}{2}(A + B)z^2, \quad A,\ B > 0. \tag{1}$$

Potential (1) satisfies Laplace's equation $\Delta\Phi = 0$ and can be realized by a suitable configuration of metallic surfaces.

It will be shown below that for fields attainable under laboratory conditions the frequency at which stimulated emission occurs lies in the microwave region and can be tuned by varying the fields.

As the problem is essentially classical, a purely classical approach will be used in the subsequent analysis. Accordingly, to investigate the possibility of stimulated emission we solve the set of equations

$$\left.\begin{aligned} \ddot{x} + \Omega\dot{y} - \Omega_1^2 x &= -\frac{e}{m}E_x(\mathbf{r},\ t), \\ \ddot{y} - \Omega\dot{x} - \Omega_2^2 y &= -\frac{e}{m}E_y(\mathbf{r},\ t), \\ \ddot{z} + \omega_3^2 z &= -\frac{e}{m}E_z(\mathbf{r},\ t). \end{aligned}\right\} \tag{2}$$

Here, m and e are, respectively, the mass and charge of the electron,

$$\Omega = \frac{eH}{mc}, \quad \Omega_1 = \sqrt{\frac{eA}{m}}, \quad \Omega_2 = \sqrt{\frac{eB}{m}}, \quad \omega_3 = \sqrt{\frac{e(A+B)}{m}}, \quad \Omega > \Omega_1 + \Omega_2,$$

and E(r, t) is the field of the wave being amplified.

The initial energies of the particles are assumed to be the same and the initial phases are assumed to be uncorrelated. If the solution of the equations of motion is sought as an expansion in powers of the electron position

$$\mathbf{r} = \mathbf{r}_0 + \mathbf{r}_1 + \ldots, \tag{3}$$

then the instantaneous power of the stimulated emission in the frequency range $d\omega$ and the angular interval do in the direction $\mathbf{n} = (\sin\theta\cos\varphi, \sin\theta\sin\varphi, \cos\theta)$, averaged over the initial phases of the particles and the field, is given by

$$dP^{\text{stim}} = P^{\text{stim}}(t)\frac{V\omega^2}{(2\pi c)^3}\,d\omega\, do,$$

where

$$P^{\text{stim}}(t) = eN\langle\dot{\mathbf{r}}\mathbf{E}(\mathbf{r},\ t)\rangle. \tag{4}$$

Here, N is the number of electrons per unit volume.

In zero order $\mathbf{r}_0$ satisfies a homogeneous set of equations; solving these gives

$$\left.\begin{aligned} x_0 &= R_1\cos(\omega_1 t - \delta_1) + R_2\cos(\omega_2 t - \delta_2), \\ y_0 &= a_1R_1\sin(\omega_1 t - \delta_1) + a_2R_2\sin(\omega_2 t - \delta_2), \\ z_0 &= R_3\cos(\omega_3 t - \delta_3). \end{aligned}\right\} \tag{5}$$

Here

$$\omega_{1,2} = \frac{1}{2}\left(\sqrt{\Omega^2 - (\Omega_1 - \Omega_2)^2} - \sqrt{\Omega^2 - (\Omega_1 + \Omega_2)^2}\right), \quad a_{1,2} = \frac{\omega_{1,2}^2 + \Omega_1^2}{\omega_{1,2}\Omega},$$

and R_i and δ_i are determined by the initial conditions.

It follows from (5) that bounded motion of the electrons is possible only when $\Omega > \Omega_1 + \Omega_2$. For nonrelativistic electron motion we can utilize the dipole approximation. Then, having determined $\mathbf{r}_1$ by variation of parameters, we obtain from (4) for an unpolarized incident wave

$$\begin{aligned} P^{\text{stim}}(t) = \frac{2\pi e^2 N u_{\mathbf{n}_1}(\omega)}{m(\omega_1^2 - \omega_2^2)}\Big\{&[(\omega_2^2 + \Omega_2^2)(1 - n_x^2) \\ &+ (\omega_2^2 + \Omega_1^2)(1 - n_y^2)]\frac{\sin(\omega - \omega_2)t}{\omega - \omega_2} - [(\omega_1^2 + \Omega_2^2)(1 - n_x^2) \\ &+ (\omega_1^2 + \Omega_1^2)(1 - n_y^2)]\frac{\sin(\omega - \omega_1)t}{\omega - \omega_1}\Big\} \\ &- \frac{2\pi e^2 N u_{\mathbf{n}}(\omega)}{m}(1 - n_z^2)\frac{\sin(\omega - \omega_3)t}{\omega - \omega_3}, \end{aligned} \tag{6}$$

where $u_{\mathbf{n}}(\omega)$ is the spectral-angular energy density of the external radiation. It follows from (6) that the incident electromagnetic wave is absorbed at frequencies ω_1 and ω_3 and is amplified at the frequency ω_2.

One is normally interested in the average power of the stimulated emission. If particle collisions constitute the main relaxation factor, the average power is given by[3]

$$P_{\mathrm{av}}^{\mathrm{stim}} = \int_0^\infty P^{\mathrm{stim}}(t) \frac{1}{\tau} \exp\left(-\frac{t}{\tau}\right) dt. \tag{7}$$

If $u_n(\omega)$ is nonzero only in the vicinity of the frequency ω_2, inserting (6) into (7) we have

$$P_{\mathrm{av}}^{\mathrm{stim}} = \frac{2\pi e^2 N u_n(\omega)}{m(\omega_1^2 - \omega_2^2)} [(\omega_2^2 + \Omega_2^2)(1 - \sin^2\theta \cos^2\varphi) + (\omega_2^2 + \Omega_1^2)(1 - \sin^2\theta \sin^2\varphi)] \frac{\tau}{1 + \tau^2(\omega - \omega_2)^2}. \tag{8}$$

It follows from (8) that the gain depends on the azimuthal angle φ and reaches a maximum at resonance ($\omega = \omega_2$). For a magnetic field $5 \cdot 10^4$ Oe and frequencies $\Omega_1 = 0.7\ \Omega$ and $\Omega_2 = 0.1\ \Omega$, we find from (5) that the frequency ω_2 at which amplification occurs satisfies $\omega_2 = 0.1\ \Omega$, which corresponds to a wavelength $\lambda_2 = 2\pi c/\omega_2 = 2.2$ cm. The system can thus be used as a generator of electromagnetic oscillations in the microwave region. Unlike the cyclotron resonance type of maser, which depends upon relativistic effects for its operation, the investigated quasiquantum generator has the advantage of using nonrelativistic electrons. It should be noted that only absorption of the incident electromagnetic wave can occur if the electrons move in a field (1) with A, B < 0. We mention another way of producing fields in which the incident wave can be amplified. To this end a waveguide is located in a homogeneous magnetic field directed along its axis and high-frequency oscillations are excited in it at a frequency much greater than the cyclotron frequency. In this case the electron moves along a smooth trajectory, simultaneously performing small oscillations around it. As shown by Gaponov and Miller[4] the smooth trajectory is formed by the static fields and by an additional force

$$\mathbf{F} = -\nabla U_{\mathrm{eff}}, \quad U_{\mathrm{eff}} = \frac{e^2}{2m} \left\langle \int_0^t \mathbf{E}_\sim^2(\mathbf{r}, t)\, dt \right\rangle,$$

where $\mathbf{E}_\sim$ is the intensity of the high-frequency electric field in the waveguide. It is not hard to see that for certain wave modes the "effective potential energy" U_{eff} has the necessary form. For example, for an electron moving near the axis of a circular waveguide of radius a in the field of a monochromatic H_{1n} wave we have

$$U_{\mathrm{eff}} = -\frac{e^2 |\mathbf{H}_{1n}|^2}{64 m c^2} (x^2 + 3y^2) + \mathrm{const},$$

where H_{1n} is the wave amplitude.

In conclusion we thank Professor A. A. Sokolov for his interest.

---

[1] A. V. Gaponov, M. I. Petelin, and V. K. Yulpatov, Izv. VUZ. Radiofizika, 10, 1414 (1967).

[2] Yu. G. Pavlenko and D. V. Gal'tsov, Izv. VUZ. Radiofizika, 9, 1232 (1967).

[3] Millimeter and Submillimeter Waves (Collected Papers) [Russian translation], IL, Moscow (1959), p. 262.

[4] A. V. Gaponov and M. A. Miller, Zh. Eksp. Teor. Fiz., 34, 242 (1958); 34, 751 (1958) [Sov. Phys. – JETP, 7, 168 (1959); 7, 515 (1958)].

Holography of raster objects

Sh. D. Kakichashvili

Institute of Cybernetics, Academy of Sciences of the Georgian SSR, Tbilisi

(Submitted August 2, 1973)
Zh. Tekh. Fiz., 44, 1104-1106 (May 1974)

A theoretical analysis is made of the reference-free holographic recording and reconstruction of objects forming two-dimensional periodic structures composed of identical elements. The analysis is carried out in the Fraunhofer approximation and it shows that virtual and real images are reconstructed from the hologram. A further analysis based on the Fresnel approximation demonstrates the existence of series of reconstructed images formed by the same wave front at multiples of a certain distance in front of and behind the hologram.

It has been shown experimentally that objects in the form of two-dimensional periodic structures composed of identical elements of arbitrary nature can be recorded holographically without a reference wave.[1] The geometrical-optics properties of holograms obtained in this way are discussed theoretically.

If the transparency function of an individual diffracting element is $\xi(x_0, y_0, z_0)$, the transparency function $\Xi(x_0, y_0, z_0)$ of a raster object formed by two-dimensional multiplication of a single element can be written as a Fourier series of the function $\xi(x_0, y_0, z_0)$ in an interval limited by the dimensions of the raster ($x_0, y_0 \le S_0$):

$$\Xi(x_0, y_0, z_0) \approx \sum_{n=-\infty}^{+\infty} \sum_{m=-\infty}^{+\infty} \exp i2\pi\left(\frac{n}{p_{x_0}} x_0 + \frac{m}{p_{y_0}} y_0\right) C_{n,m}. \tag{1}$$

Here, x_0 and y_0 are the coordinates in the plane of the raster object; p_{x_0} and p_{y_0} are the spatial periods along the x_0 and y_0 axes; $C_{n,m}$ are the Fourier coefficients.

We now use the Fraunhofer approximation in an analysis of the field diffracted by the structure (1). In this approximation the distance to the object located to the left of the origin can be expressed in the form

$$R(x_0, y_0, z_0) \approx -z_0 + \frac{xx_0 + yy_0}{z_0}. \tag{2}$$

In the $z = 0$ plane, where a light-sensitive film is located, the field scattered by the object is

$$\Psi(x, y, t) \approx \frac{i\varkappa}{2\pi z_0} \iint_{S_0} \Xi(x_0, y_0, z_0) \exp i[\omega t - \varkappa R(x_0, y_0, z_0, x, y)]\, dx_0 dy_0$$

$$\approx \frac{iz_0}{2\pi\varkappa} \exp i(\omega f + \varkappa z_0) \sum_{n=-\infty}^{+\infty} \sum_{m=-\infty}^{+\infty} C_{n,m} \delta\left(\frac{2\pi n z_0}{p_{x_0}\varkappa} - x, \frac{2\pi m z_0}{p_{y_0}\varkappa} - y\right). \tag{3}$$

The light-sensitive film records $(\Psi\Psi^*)\gamma/2$. Selecting $\gamma = 1$ and assuming that $\delta[f(x, y)] = \delta^*[f(x, y)]$, we find that the subsequent illumination of the resultant hologram with a plane-front beam yields (in the same approximation)

$$\Psi'(x', y', z', t) \approx -\frac{z_0}{z'} \exp i(\omega t - \varkappa z')$$

$$\times \sum_{n=-\infty}^{+\infty} \sum_{m=-\infty}^{+\infty} C_{n,m} \exp i\left(\frac{\varkappa x'}{z'} x + \frac{\varkappa y'}{z'} y\right)$$

$$\times \delta\left(\frac{2\pi n z_0}{p_{x_0}\varkappa} - x, \frac{2\pi m z_0}{p_{y_0}\varkappa} - y\right) \approx -\frac{z_0}{z'} \exp i(\omega t - \varkappa z')$$

$$\times \sum_{n=-\infty}^{+\infty} \sum_{m=-\infty}^{+\infty} C_{n,m} \exp i2\pi\left(\frac{n z_0}{z' p_{x_0}} x' + \frac{m z_0}{z' p_{y_0}} y'\right), \tag{4}$$

where x', y', and z' are the coordinates of the point of observation.

For distances to the point of observation satisfying the conditions $z' = z_0$ and $z' = -z_0$, it follows from Eq. (4) that

$$\Psi_1'(x', y', z', t) \approx -\exp i(\omega t - \varkappa z_0) \sum_{n=-\infty}^{+\infty} \sum_{m=-\infty}^{+\infty} C_{n,m} \exp i\,2\pi\left(\frac{nx'}{p_{x_0}} + \frac{my'}{p_{y_0}}\right), \tag{5}$$

$$\Psi_2'(x', y', z', t) \approx \exp i(\omega t - \varkappa z_0) \sum_{n=-\infty}^{+\infty} \sum_{m=-\infty}^{+\infty} C_{n,m} \exp i2\pi\left(\frac{nx'}{p_{x_0}} + \frac{my'}{p_{y_0}}\right). \tag{6}$$

Therefore, Eqs. (5) and (6) describe, respectively, the virtual and real images of the original raster object, formed by the same wave front in conjugate intervals along the z axis.

We supplement the Fraunhofer analysis by a discussion of the situation in the Fresnel diffraction zone. In this zone the field scattered by objects of the type (1) has interesting singularities first discovered by Talbot[2] and investigated theoretically by Rayleigh.[3] Recently these singularities have attracted the attention of many workers.[4-8]

When a raster object is illuminated with a parallel beam of coherent light, the diffracted field is (in the approximation quadratic in the distance)

$$\Psi(x, y, t) \approx \frac{i\varkappa}{2\pi z'} \exp i\left[\omega t + \varkappa\left(z' + \frac{x'^2 + y'^2}{2z'}\right)\right]$$

$$\times \sum_{n=-\infty}^{+\infty} \sum_{m=-\infty}^{+\infty} C_{n,m} \iint_{S_0} \exp i\left[\frac{\varkappa(x'^2 + y'^2)}{2z'} + \left(\frac{2\pi n}{p_{x_0}} - \frac{\varkappa x'}{z'}\right) x_0 \right. \tag{7}$$

$$\left. + \left(\frac{2\pi m}{p_{y_0}} - \frac{\varkappa y'}{z'}\right) y_0\right] dx_0 dy_0.$$

Evaluating the integral in the asymptotic approximation ($S_0 \to \pm\infty$), we obtain

$$\Psi(x, y, t) \approx -\exp i(\omega t + \varkappa z') \sum_{n=-\infty}^{+\infty} \sum_{m=-\infty}^{+\infty} C_{n,m} \exp i2\pi\left(\frac{n}{p_{x_0}} x' + \frac{m}{p_{y_0}} y'\right)$$

$$\times \exp - i2\pi\left(\frac{z'\pi n^2}{p_{x_0}^2 \varkappa} + \frac{z'\pi m^2}{p_{y_0}^2 \varkappa}\right).$$

It follows from Eq. (8) that when the conditions

$$\frac{z'\pi}{p_{x_0}^2 \varkappa} = N, \quad \frac{z'\pi}{p_{y_0}^2 \varkappa} = M \tag{9}$$

are satisfied simultaneously (here, N, M = 0, ± 1, ± 2,

± 3, ...), the third exponential term in Eq. (8) becomes unity irrespective of the value of n and m and the field — with the exception of its phase term $\exp i(\varkappa^2/2\pi)(p_{x_0}^2 + p_{y_0}^2 M)$ — is identical with the field immediately behind the raster object. Obviously, the phase term is not of great significance. Distances in such a self-reproduced image of a raster object can be found by satisfying simultaneously the conditions in Eq. (9). These conditions are compatible only if $p_{x_0} = p_{y_0}$, hence it follows that the required distances must obey

$$z' = \frac{\varkappa p_{x_0}^2 N}{2\pi} + \frac{\varkappa p_{y_0}^2 M}{2\pi}, \tag{10}$$

where the values of M and N are restricted by the conditions in Eq. (9).

Since a reference-free hologram of such an object is also a periodic structure with the same period as the object itself [compare Eqs. (1) and (3)], it follows that at distances specified by Eq. (10) the hologram produces a system of images reproducing the field directly behind the hologram to within the phase factor and also a system of reconstructed images shifted relative to the hologram by the amounts

$$\left.\begin{aligned} z'_{N,M} &= \left(z_0 - \frac{\varkappa p_{x_0}^2 N}{2\pi}\right) + \left(z_0 - \frac{\varkappa p_{y_0}^2 M}{2\pi}\right), \\ z'_{N,M} &= -\left(z_0 - \frac{\varkappa p_{x_0}^2 N}{2\pi}\right) - \left(z_0 - \frac{\varkappa p_{y_0}^2 M}{2\pi}\right) \end{aligned}\right\} \tag{11}$$

respectively, for virtual and real images.

Figure 1 shows schematically a hologram Q, a reconstructed virtual image of a raster object R_1, a reconstructed real image of the object R'_1, a self-reproduced virtual image of the hologram Q_1, a self-reproduced real image of the hologram Q'_1, a reconstructed virtual image of the object R_ν and a self-reproduced virtual image of the hologram Q_ν (ν is the serial number of the image), and a reconstructed real image of the object R'_ν and a self-reproduced real image of the hologram Q'_ν.

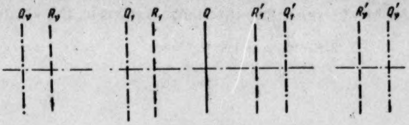

Fig. 1

A reference-free method can also be used in the holographic recording of a coherently emitting object with a spatially restricted spectrum when the formation of a reference wave is for some reason impossible. In this case the beam diffracted by an object must be multiplied by an optical device (see, for example, refs. 7 and 8) which divides the amplitude into a large number of identical spatially periodic cophasal beams of equal amplitudes. Obviously, the total field of such a system of multiplied beams is equivalent to the total field of the light diffracted by the raster object. If the resultant pattern is recorded in a light-sensitive film, the subsequent illumination of this film can be used to reconstruct a multiplied wave front, i.e., a system of multiplied images of the object. Depending on the requirements we can use one of the reconstructed images or we can pass the reconstructed front again through a multiplication system which then synthesizes in the reverse direction the original image of a single object.

---

[1] Sh. D. Kakichashvili, Zh. Tekh. Fiz., 42, 650 (1972) [Sov. Phys. – Tech. Phys., 17, 511 (1972)].

[2] H. F. Talbot, Phil. Mag., 9, 401 (1836).

[3] J. W. Rayleigh, Phil. Mag., 11, 196 (1881).

[4] H. G. Booker, J. A. Ratcliffe, and D. N. Shinn, Phil. Trans. R. Soc. London A, 242, 579 (1950).

[5] P. E. Edgar, Opt. Acta, 16, 281 (1969).

[6] Yu. N. Denisyuk, N. M. Ramishvili, and V. V. Chavchanidze, Opt. Spektrosk., 30, 1130 (1971).

[7] N. A. Valyus, Raster Optics [in Russian], GITTL, Moscow–Leningrad (1949).

[8] Sun Lu, Proc. IEEE, 56, 116 (1968).

NÉM–1T magnetic-discharge pumps in the vacuum system of the I-100 linear accelerator

O. N. Krokhina and K. G. Mirzoev

(Submitted July 16, 1973)
Zh. Tekh. Fiz., 44, 1106-1108 (May 1974)

The characteristics of NÉM-1T titanium pumps after prolonged use in the cavities of a linear accelerator are described. The effective sputtering ratio of the titanium in the cell of the electric-discharge pump is determined from measurements of craters on the cathode plates. Experience gained in the use of these pumps in the linear accelerator is used to determine the failure time, the time over which the vacuum system operates stably at a pressure of (0.5-1)·10^{-6} torr, and the useful lifetime of the pumps under these conditions.

Since magnetic-discharge pumps are increasing in popularity for physical-research apparatus, it is of interest to study the characteristics of these pumps after prolonged operation in the I-100 linear proton accelerator.[1]

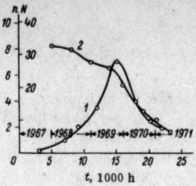

Fig. 1. 1) Number of instances n per 1000 h, in which the cavity pressure surged as a function of the time; 2) number of pumps N which had not been reassembled.

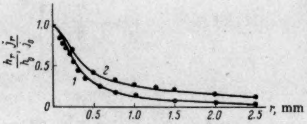

Fig. 2. 1) Characteristic crater profile; 2) distribution of the ion current density with respect to the cathode radius, from ref. 2.

The cavities of the accelerator, with a total volume of 100 m^3, are evacuated by NÉM-1T magnetic-discharge pumps (33 of them) at a pumping rate of 1000 liter/sec at the entrance flange at a pressure of $1 \cdot 10^{-6}$ torr. The basic components in the mass spectrum of the residual gas, measured by an IPDO-1 apparatus at a cavity pressure of (3-5)·10^{-7} torr, are H_2 (36%), N_2 + CO (30%), O_2 (4%), Ar (9%), H_2O (8%), and hydrocarbons (3%).

Most of the pumps operated in the accelerator for an average of 30,000 h, and some operated as long as 35,000 h, without replacement. The pumps operated continuously for 1000-1500 h per cycle. Some of the pumps failed during operation, and the failures were corrected by removing the pumps from the accelerator and reassembling them. A total of 29 pumps were reassembled at various times and tested. A typical cause of failure after prolonged operation is a short circuit in the electrod units due to metallization and splitting of the insulators or as a result of the peeling of films from the electrodes. The average operating time before failure is 8000-9000 h.

The pumps are restored to service by mechanically removing the films from the electrodes and the housing and by replacing the ceramic insulators or cleaning them, by etching in a dilute solution of hydrofluoric acid. After reassembly, the pumps are processed in a vacuum station at 400°C. Measurements of the pumping rate and the limiting vacuum for one of the pumps after 12,000 h of operation in the accelerator without reassembly show that these values are the same as those measured before the pump is installed in the accelerator.

There were several occasions on which the cavity pressure surged sharply for 3-5 min, from $5 \cdot 10^{-7}$ to (0.5-1)·10^{-4} torr, and then returned to its initial value over 25-30 min. The reason could be a brief breakdown in one of the pumps because a titanium film is peeled from the anode, and gas is evolved from this film as it burns. This gas evolution would raise the pressure in the pump and the discharge current, so the absorbed gas, including argon, would be evolved from the cathodes, and the pumping rate would fall off sharply. In some cases so much gas was evolved that the pressure increased throughout the cavity volume, leading to an increase in the discharge current in the other pumps and thus the evolution of gas from them. Because of the large number of pumps and the large cavity volume, the pressure does not exceed $1 \cdot 10^{-4}$ torr; although the pumping rate of the pumps fell off markedly, it remained sufficient to pump out the evolved gas. In some of the pumps an argon instability was observed in the pressure range (1-5)·10^{-5} torr. Figure 1 (curve 1) shows the number of instances of pressure increases per 1000 h of operation as a function of the average operating time of the pumps which had not been reassembled; the number of such pumps is shown by curve 2. Figure 1 shows that essentially no pressure surges are observed before the pumps operate for about 8000 h. Thereafter, the number of surges increases rapidly, and by the end of 1970, when most of the pumps had been cleaned and reassembled, the number of surges was falling approximately in proportion to the number of pumps which had not been cleaned. This behavior shows that the pressure surges in the cavities are initiated by pumps which have been operating for more than 8000-9000 h.

Accordingly, a periodic cleaning of the magnetic-discharge pumps at intervals of 8000-9000 h, for operation at (0.5-1)·10^{-6} torr, can ensure stable operation of the vacuum system.

Since the cathode plates determine the useful lifetime of the pumps, we have studied the craters formed as a result of titanium sputtering. During the reassembly of several pumps, we measure the depths of the craters within ± 0.01 mm at each point. Figure 2 shows the ratio of the crater depth at each point to the depth at the center, h_r/h_0, as a function of the crater radius r (curve 1). Curve 2 shows the distribution of the ion current density j_r/j_0 over the cathode radius,[2] obtained under approximately the same operating conditions. Comparison of these two curves shows that the shape of the craters is related to the ion current distribution; the shape should also be affected by the sputtering of titanium from the opposite cathode and by the incidence angle of the ions, which obviously vary as the shape of the crater changes.

We calculate the amount of sputtered titanium by calculating the crater volumes. Averaging over 10 cells of each of 10 pumps, we find the average rate of titanium sputtering from a single cathode of a cell to be (2 ± 0.5) × 10^{-7} g/h at a cavity pressure of $1 \cdot 10^{-6}$ torr. For each of these pumps we calculate the average pressure in the volume being evacuated over the entire operating history of the pump, and we experimentally determine the functional dependence of the discharge current on the pressure, from which we are able to determine the average ion current to a cathode of the cell within ± 30%. From these results we calculate the effective sputtering ratio for the titanium in a cell of the pump: 0.15 ± 0.04 atom/ion. On the basis of this sputtering ratio, we calculate that several decades would be required for an aperture to grow all the way through a cathode plate 2 mm thick at a pressure of $1 \cdot 10^{6}$ torr.

The authors thank V. G. Rogozinskii for discussion, S. A. Il'evskii for his constant interest in this work, and V. A. Butenko for carrying out the measurements.

---

[1] M. I. Basalaev, S. A. Il'evskii, K. G. Mirzoev, and V. G. Rogozinskii, Preprint 71-7, Institute of High-energy Physics, Serpukhov, 1971.

[2] E. M. Rudnitskii, Zh. Tekh. Fiz., 37, 927 (1967) [Sov. Phys. – Tech. Phys., 12, 666 (1967)].

Method for studying gas creep along a solid surface

B. M. Markeev

Institute of Problems of Mechanics,
Academy of Sciences of the USSR, Moscow

(Submitted September 24, 1973)
Zh. Tekh. Fiz., 44, 1108-1110 (May 1974)

Many authors have reported on the creep of a gas along a surface (see, e.g., refs. 1-7). Several assumptions have usually been used, but it has been shown[7] that these assumptions, in particular, lead to a discontinuity of the distribution function far from the wall when this function is calculated by the method of half-space moments: a physically meaningless result. Furthermore, the calculation difficulties which arise in the use of this method lead to a situation in which it is possible to analyze creep only of a Maxwellian gas or of a gas whose molecules have a hard-sphere interaction.

In this note we analyze the creep of a gas in a temperature gradient tangential to an infinite wall and in the absence of a gradient, calculating the creep velocities. We make no assumptions regarding the nature of the interaction between gas particles. We seek the particle distribution functions as series expansions in Hermite–Chebyshev polynomials, and we incorporate the boundary conditions into the right-hand side of the kinetic equation by means of sources concentrated at the boundary. The gas molecules in the Knudsen layer at distances on the order of a mean free path from the wall can have a discontinuous distribution function different from the volume function. However, this circumstance is not taken into account in an analysis of the problem on the basis of the moment equations.[3] The method proposed here can be used to take into account the discontinuity of the distribution function in the Knudsen layer.

1. We consider a gas in a temperature gradient tangential to the wall. The origin of our coordinate system is at the surface, the x axis is along the normal to the surface, and the z axis is along the surface. Under the conditions of steady-state flow the distribution function can be determined from a kinetic equation in which the boundary conditions are introduced into the right-hand side in the form of concentrated sources:[8]

$$(\mathbf{v}\nabla) f = J + v_x f(x=0)\,\delta(x), \tag{1.1}$$

where $J = \int d\mathbf{v}_1 d\Omega\sigma(w,\vartheta)\{f'f_1' - ff_1\}w$ is the elastic-collision integral, $\mathbf{w} = \mathbf{v} - \mathbf{v}_1$ is the relative velocity of the colliding particles, ϑ is the scattering angle, $\sigma(w,\vartheta)$ is the differential scattering cross section, and $\delta(x)$ is the Dirac δ function. In the usual manner,[1] we distinguish between molecules moving toward the surface and those moving away from it, i.e., we have $f(\mathbf{v}, \mathbf{r}) = f^+(\mathbf{v}, \mathbf{r})$ for $v_x > 0$ and $f(\mathbf{v}, \mathbf{r}) = f^-(\mathbf{v}, \mathbf{r})$ for $v_x < 0$. We write distribution functions $f^\pm$ over their ranges of definition as series in Hermite–Chebyshev polynomials:

$$f^\pm(\mathbf{v}, \mathbf{r}) = \frac{n}{\pi^{3/2} v_T^3}\exp\left\{-\frac{(v-u_{\pm z})^2}{v_T^2}\right\}\left\{1 - 2\frac{\sigma_{\pm xz}}{2nT}\frac{m}{T}(v-u_\pm)_z v_x - \frac{q_z(v-u_\pm)_z m}{nT}\left[1 - \frac{m(\mathbf{v}-\mathbf{u}_\pm)^2}{5T}\right]\right\}, \tag{1.2}$$

where n is the density, m is the mass, T is the temperature (in energy units), u_z is the average velocity, and q_z is the heat flux. Using the theory of integrals which are functions of parameters,[8] we write the equations for u_z, σ_{xz}, and q_z as follows:

$$\nabla_x \frac{1}{2}(\sigma_+ + \sigma_-)_{xz} = \frac{1}{2}(\sigma_+ + \sigma_-)_{0xz}\,\delta(x), \tag{1.3}$$

$$\mu\nabla_x \frac{1}{2}(u_+ + u_-)_z = \frac{1}{2}(\sigma_+ + \sigma_-)_{xz} + \left[\mu\frac{1}{2}(u_+ + u_-)_{0z} - \frac{2}{5}\nu_1^{-1}\frac{1}{2}(q_+ + q_-)_{0z}\right]\delta(x), \tag{1.4}$$

$$\frac{1}{2}(q_+ + q_-)_z = -\eta\nabla_z T; \tag{1.5}$$

$$\nabla_x \frac{1}{2}(\sigma_+ - \sigma_-)_{xz} = \nu_2 nm\frac{1}{2}(u_+ - u_-)_z + \left(\frac{\nu_3}{v_T^2}\right)\frac{1}{2}(q_+ - q_-)_z + \frac{1}{2}(\sigma_+ - \sigma_-)_{0xz}\,\delta(x), \tag{1.6}$$

$$\frac{2}{5}\nabla_x \frac{1}{2}(q_+ - q_-)_z + nT\nabla_x\frac{1}{2}(u_+ - u_-)_z = \frac{1}{2}(\sigma_+ - \sigma_-)_{xz}\nu_4 + \left(\frac{2}{5}\right)\frac{1}{2}(q_+ - q_-)_{0z}\,\delta(x) + nT\,\frac{1}{2}(u_+ - u_-)_{0z}\,\delta(x), \tag{1.7}$$

$$\frac{T}{m}\nabla_x \frac{1}{2}(\sigma_+ - \sigma_-)_{xz} = \frac{1}{2}nmv_T^2\nu_5\frac{1}{2}(u_+ - u_-)_z + \nu_6\frac{1}{2}(q_+ - q_-)_z + \frac{T}{m}\frac{1}{2}(\sigma_+ - \sigma_-)_{0xz}\,\delta(x). \tag{1.8}$$

The quantities μ, η, ν_1, ν_2, . . . , ν_7 are defined by

$$\left.\begin{aligned}
&\eta = \frac{5}{2}\frac{nT}{m\nu_7};\quad \mu = \frac{nT}{\nu_1};\quad \nu_1 = \frac{3}{10}\Omega^{(2,2)};\\
&\nu_2 = (\Omega^{(1,1)} + 2\tilde{\Omega}^{(1,1)});\quad \nu_3 = -(3\tilde{\Omega}^{(0,0)} - 2\tilde{\Omega}^{(0,1)})\\
&\quad - \left[(\Omega^{(1,1)} + 2\tilde{\Omega}^{(1,1)}) - \frac{2}{5}(\Omega^{(1,2)} + 2\tilde{\Omega}^{(1,2)})\right];\\
&\nu_4 = \left(\frac{3}{4}\tilde{\Omega}^{(0,0)} - \frac{1}{10}\tilde{\Omega}^{(0,2)}\right)\\
&\quad + \frac{1}{2}\left[(\Omega^{(1,1)} + 2\tilde{\Omega}^{(1,1)}) + \frac{3}{10}(\Omega^{(2,2)} + \tilde{\Omega}^{(2,2)})\right];\\
&\nu_5 = \frac{1}{2}\left[\frac{5}{2}(\Omega^{(1,1)} + 2\tilde{\Omega}^{(1,1)}) + (\Omega^{(1,2)} + 2\tilde{\Omega}^{(1,2)})\right];\\
&\nu_6 = -\frac{1}{8}\Omega^{(1,1)} - \frac{1}{5}\Omega^{(2,2)} - \frac{5}{2}\frac{\nu_3}{2};\quad \nu_7 = \frac{2}{5}\Omega^{(2,2)}.
\end{aligned}\right\} \tag{1.9}$$

Here

$$\Omega^{(l,s)} = (8\sqrt{2}/3\sqrt{\pi})\,nv_T\int dg\,d\Omega\sigma(w,\vartheta)(1\quad\cos^l\vartheta)\,g^{2s+3}e^{-g^2},$$

$$\tilde{\Omega}^{(l,s)} = (4\sqrt{2}/3\sqrt{\pi})\,nv_T\int dg\,d\Omega\sigma(w,\vartheta)\cos^l\vartheta\,g^{2s+3}e^{-g^2}.$$

2. We assume that a steady state characterized by a thermal creep velocity and an isothermal creep velocity of the gas with respect to the surface, u_T and u_{cr}, respectively, and by a gradient in the average velocity, $(\nabla_x u)_\infty$, is established in the volume; then we find the following solution for this system of equations

$$\frac{1}{2}(u_+ + u_-)_s = u_\tau + u_{\text{cr}} + (\nabla_x u)_\infty x, \tag{2.1}$$

$$\frac{1}{2}(\sigma_+ + \sigma_-)_{xs} = \mu\nabla_x \frac{1}{2}(u_+ + u_-)_s, \tag{2.2}$$

$$\frac{1}{2}(q_+ + q_-)_s = -\eta\nabla_s T, \tag{2.3}$$

$$\frac{1}{2}(u_+ - u_-)_s = \frac{1}{2}(u_+ - u_-)_{0s} \exp\left\{-\frac{x}{\lambda}\right\}, \tag{2.4}$$

$$\frac{1}{2}(\sigma_+ - \sigma_-)_{xs} = \mu_1\nabla_x \frac{1}{2}(u_+ - u_-)_s, \tag{2.5}$$

$$\frac{1}{2}(q_+ - q_-)_s = -nTS\,\frac{1}{2}(u_+ - u_-)_s, \tag{2.6}$$

where

$$\mu_1 = \frac{nT}{\nu_4}\left[1 - \frac{2}{5}S\right];\ \lambda^{-2} = \frac{nm}{\mu_1}\left[\nu_2 - \frac{1}{2}\nu_3 S\right],$$

$$S = \frac{\nu_5 - \nu_2}{\nu_6 - \frac{1}{2}\nu_3};\quad (\nabla_x u)_\infty = \mu^{-1}\frac{1}{2}(\sigma_+ + \sigma_-)_0,$$

$$u_\tau = \frac{2}{5}\frac{\eta}{\mu\nu_1} = \frac{3}{4}\frac{\mu}{\rho}\nabla \ln T,$$

$$u_{\text{cr}} = (\nu_1\mu)^{-1}\left[\left(\frac{2}{5}\right)\frac{1}{2}(q_+ + q_-)_{0s} + nT\,\frac{1}{2}(u_+ + u_-)_{0s}\right]. \tag{2.7}$$

When $(\nabla_x u)_\infty = u_{\text{cr}} = 0$, Eq. (2.1) takes the simple form

$$(1/2)(u_+ + u_-) = u_\tau. \tag{2.8}$$

Equations (2.4)-(2.6) vanish identically for partial reflection of molecules from the surface. Accordingly, an inhomogeneously heated gas moves along a surface at an average thermal creep velocity $u = u_T$, which is not a function of the distance from the wall. When $(\nabla_x u)_\infty \neq 0$, the creep velocity of the gas, as we see from (2.1)-(2.6), is the sum of the thermal and isothermal creep velocities. The latter, as follows directly from (2.4), is given by the following equation for the case of partial reflection of the molecules from the wall:

$$(\varepsilon/(2-\varepsilon))^2 u_{\text{cr}} = (\nu_4/\nu_1)\,\lambda\,(\nabla_x u)_\infty, \tag{2.9}$$

where ε is the accommodation coefficient. The creep coefficient determined from this equation for the particular case of Maxwell molecules is 1.06, in good agreement with the results, e.g., of ref. 7.

In conclusion we note that the method proposed here has two advantages over that of ref. 2: First, it can be used to analyze creep along a surface by a gas having an arbitrary intermolecular interaction, and the discontinuity of the distribution function near the surface can be taken into account simultaneously. Second, this method does not lead to such physical contradictions as a discontinuity in the distribution function far from the surface.[7]

The author thanks S. P. Bakanov for discussion.

---

[1] J. C. Maxwell, Phil. Trans. Roy. Soc., 170, 231 (1879).

[2] E. P. Gross and S. Ziering, Phys. Fluids, 1, 215 (1958).

[3] R. Ya. Kucherov and L. É. Rikenglaz, Zh. Eksp. Teor. Fiz., 36, 1758 (1959) [Sov. Phys. – JETP, 9, 1253 (1959)].

[4] I. N. Ivchenko and Yu. I. Yalamov, Izv. Akad. Nauk SSSR, Mekhan. Zhidk. Gaza, 59-66 (1969). ?

[5] S. K. Loyalka and J. W. Cippolla, Jr., Phys. Fluids, 14, 1656 (1971).

[6] Y. Sone, J. Phys. Soc. Japan, 21, 1836 (1966).

[7] S. P. Bakanov and B. V. Deryagin, Dokl. Akad. Nauk SSSR, 139, 71 (1961) [Sov. Phys.–Dokl., 6, 588 (1962)].

[8] V. S. Vladimirov, Equations of Mathematical Physics [in Russian], Izd. Nauka, Moscow (1971).

X-ray fluorescence of oxygen in H_2O

L. A. Smirnov

A. A. Zhdanov Leningrad State University

(Submitted April 4, 1973)
Zh. Tekh. Fiz., 44, 1110-1111 (May 1974)

The ratio of the x-ray fluorescence yields in H_2O and O_2 is found; the value of $\omega_K(H_2O)$ is larger than $\omega_K(O_2)$ by a factor of 1.8 ± 0.2. In addition the absolute values of ω_K for oxygen in O_2, CO_2, and H_2O are evaluated: These are 0.0073, 0.0094, and 0.0131 respectively. The maximum error in the determinations is estimated to be 30%.

We have reported previously[1] that the x-ray fluorescence yield of oxygen in CO_2 is 1.3 times that in O_2. We have now used the same procedure to compare these yields in H_2O and O_2. Since the room-temperature density of water vapor is extremely low, the x-ray fluorescence of oxygen is correspondingly extremely weak, amounting to only one third the background intensity. We have therefore carried out about a hundred measurements, to whose results we are able to apply statistical methods to obtain accurate ratios. We find the x-ray fluorescence yield of oxygen in H_2O to be 1.8 ± 0.2 times that in O_2; accordingly, the effect of the chemical binding on the value of ω_K for a light element can be extremely important. Hence, in reporting measurements of ω_K it is mandatory to state the chemical compound in which the element in question is studied.

Altering the experimental procedure slightly, we also determine the absolute values of ω_K for oxygen in H_2O, CO_2, and O_2. Holding constant the parameters of the x-ray tube producing the primary beam, we fill the chamber of the apparatus with oxygen (O_2) and chlorine (as CCl_4) alternately. Measuring the count rates for the x-ray fluorescence of oxygen and chlorine, we are able to find the ratio of the corresponding x-ray fluorescence yields from the obvious relation

$$\frac{N_{Cl}}{N_O}=\frac{n_{Cl}}{n_O}\frac{\omega_K(Cl)}{\omega_K(O_2)}\frac{Q_{Cl}}{Q_O}.$$

Here N_{Cl} and N_O are the count rates for the x-ray fluorescence of chlorine and oxygen, respectively, n_{Cl} and n_O are the numbers of K vacancies produced by the primary radiation per unit time, and Q_{Cl} and Q_O are coefficients which take into account the absorption of the x-ray fluorescence and the efficiency with which it is detected. The coefficients n_{Cl}, n_O, Q_{Cl}, and Q_O are calculated from the dimensions of the apparatus and tabulated absorption coefficients. Then assuming $\omega_K(Cl)$ to be 0.091, according to ref. 2, we find, for oxygen,

$$\omega_K(O_2)=0.0073,$$
$$\omega_K(CO_2)=0.0094,$$
$$\omega_K(H_2O)=0.0131.$$

These results agree with McGuire's calculations[3] for atomic oxygen ($\omega_K = 0.0095$) and with the curve of ref. 4, extrapolated to the light elements. On the other hand, these results are much higher than the data reported in ref. 5; the discrepancy exceeds the maximum possible errors, which can be estimated to be 30% for our data.

---

[1] L. A. Smirnov, Zh. Tekh. Fiz., 43, 2427 (1973) [Sov. Phys. – Tech. Phys., 18, 1530 (1974)].

[2] V. O. Kostroun, M. H. Chen, and B. Grasemann, Phys. Rev., A3, 533 (1971).

[3] E. J. McGuire, Phys. Rev., 185, 1 (1969).

[4] J. Byrne and N. Howarth, J. Phys. B, 3, 280 (1970).

[5] C. Broyles, D. Thomas, and S. Haynes, Phys. Rev., 89, 715 (1953).

Dispersion of the dielectric constant of crystalline KH_2PO_4 near the "soft" mode frequency

V. V. Meriakri, Yu. M. Poplavko, and E. F. Ushatkin

Institute of Radio Engineering and Electronics, Academy of Sciences of the USSR, Moscow

(Submitted June 18, 1973; resubmitted November 16, 1973)
Zh. Tekh. Fiz., 44, 1111-1113 (May 1974)

The dielectric properties of potassium dihydrophosphate are investigated at frequencies 0.3-15 cm^{-1} in the temperature range 80-300°K. The parameters of a dispersion oscillator which describe the dispersion of the dielectric constant of KH_2PO_4 in the paraelectric phase are determined.

Although potassium dihydrophosphate is one of the most studied ferroelectrics, direct measurements of the dispersion of the dielectric constant ε in the vicinity of the Curie point of this crystal have not been performed. The point is that the dispersion of ε in the nonpolar phase of KH_2PO_4 occurs at submillimeter wavelengths, midway between the microwave and infrared regions of the spectrum, and the technology of dielectric measurements of ferroelectrics at such wavelengths is still in the developmental stage.[1]

Investigation of the dispersion of ε near the phase transition is important in connection with the modern dynamical theory of ferroelectricity, which is based on the concept of a "soft" mode of vibration of the crystal lattice. In principle, the vibrational spectra of ferroelectric crystals, from which the character of the temperature dependence of the critical vibration frequency in the vicinity of the phase transition can be determined, can be studied in various ways. In the case of the KH_2PO_4 crystal, however, the damping of the coupled tunnel-phonon vibration (which plays the role of the "soft" mode) proves to be extremely large, precluding observation of a maximum in the scattered light[3,4] as well as in infrared reflection spectra.[5] All these methods only yield an estimate of the frequency and damping of the "soft" model. Accordingly, great importance attaches in crystals of KH_2PO_4 type to direct dielectric measurements in the region of dispersion of ε in a temperature range including the phase transition.

The frequency dependence of the complex dielectric constant of potassium dihydrophosphate along the fourfold axis, $\varepsilon_3 = \varepsilon'_3 - i\varepsilon''_3$, has previously been investigated in the microwave region.[6,7] It was found that in the nonpolar phase ε_3 exhibits no dispersion up to 30 GHz (1 cm^{-1}), although the dielectric losses are observed[7] to increase significantly as the Curie point is approached at millimeter wavelengths, indicating that the dispersion region is not far off. A study of the infrared reflection spectra of KH_2PO_4 crystals[5] has disclosed a low-frequency maximum of ε''_3 at a frequency of 46 cm^{-1} at 300°K, and at 30 cm^{-1} at 200°K. From a comparison of the microwave and infrared data one can expect the dispersion of ε_3 in KH_2PO_4 to occur near the critical temperature in the submillimeter waveband.

The temperature dependence of the transmittance and the reflectivity is measured at submillimeter wavelengths on the apparatus described in ref. 1. The investigated crystal samples are 0.15-0.3 mm thick and 3 cm^2 in area. The error in the measurement of the real and imaginary parts of the dielectric constant at frequencies 7-15 cm^{-1} does not exceed 10%. Microwave experiments are performed in waveguides by the usual method.[7]

Figure 1 shows the temperature variation of ε'_3 and ε''_3 of potassium dihydrophosphate at various frequencies. The temperature variation of ε'_3 at 1 kHz characterizes the properties of the free crystal and is described by the Curie–Weiss law

$$\varepsilon'_3 = \varepsilon'_\infty + C'(T - T_C)^{-1}$$

with parameters C' = 3000°, ε'_∞ = 5.5 and T_C = 123°K. Microwave measurements at 0.3 and 0.8 cm^{-1} yield the parameters describing $\varepsilon'_3(T)$ for a fixed crystal (KH_2PO_4 is piezoelectric above T_C): C = 2600° and Θ = 118°K. The maximum value of $\varepsilon'_3(T)$ at T = T_C reaches 550 ± 30 at microwave frequencies.[7] The onset of dispersion is observed at millimeter wavelengths (2.6 cm^{-1} in the figure). This dispersion is sharply expressed in the submillimeter range: At frequencies 11.3 and 14.6 cm^{-1} the sharp peak in the vicinity of the phase transition is replaced by shallow minima of $\varepsilon'_3(T)$; flat maxima of $\varepsilon'_3(T)$ occur at 170 and 210°K, respectively. Sharp maxima of $\varepsilon'_3(T)$ are conserved only in the ferroelectric phase, where the dispersion frequency of ε_3 is higher than in the nonpolar phase; accordingly, the value of ε'_3 near T_C in the ferroelectric phase is decreased much less than in the paraelectric phase.

The qualitative behavior of the dispersion of $\varepsilon_3(\nu, T)$ in the investigated crystals above T_C = 123°C can be described using a model of a dispersion oscillator with frequency ν_0 and damping γ:

$$\varepsilon_3(\nu, T) = \varepsilon_\infty + \frac{C\nu_0^2}{(T - \Theta)(\nu_0^2 - \nu^2 + i2\gamma\nu)},$$

where $\nu_0 = a(T - \Theta/T)^{1/2}$, in accordance with the dynamical theory of ferroelectricity, which is applicable to KH_2PO_4

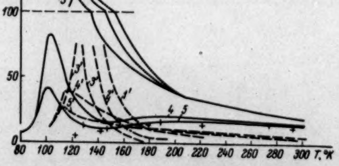

Fig. 1. Plots of ε'_3 (solid curves) and ε''_3 (dashed curves) versus temperature for various frequencies ν, cm^{-1}: 1) $3.3\cdot10^{-7}$ (1 GHz); 2) 0.3; 3) 2.6; 4) 11.3; 5) 14.6. The points denoted by + correspond to calculated values of ε'_3 for a = 85 cm^{-1}, γ = 100 cm^{-1}, ν = 14.6 cm^{-1}.

crystals.[3,8] Far from the Curie point ($T > T_C + 25°$) Eq. (1) gives a good description of the family of curves of the figure for $a = 85$ cm^{-1}, $\gamma = 100$ cm^{-1}, C and Θ as determined above, and $\varepsilon_\infty = 4.5$. Near T_C at submillimeter wavelengths there is a considerable discrepancy between the experimental and calculated data.

The authors are grateful to I. S. Rez and V. G. Vaks for discussion and to V. N. Aleshechkin and A. N. Pashkov for their assistance in preparing the samples.

---

[1] V. N. Aleshechkin, G. A. Kraftmakher, V. V. Meriakri, and E. F. Ushatkin, Prib. Tekh. Eksp., No. 4, 150 (1971); Izv. AN SSSR, Ser. Fiz., 35, 1924 (1971); Radiotekh. Elektron., 17, 209 (1972).

[2] G. Shirane, J. Phys. Soc. Japan, Suppl., 28, 20 (1970).

[3] I. P. Kaminow and T. C. Damen, Phys. Rev. Lett., 20, 1105 (1968).

[4] J. F. Ryan, R. S. Katiyar, and W. Taylor, J. Phys. Suppl., 33, C2-49 (1972).

[5] T. Kawamura, A. Mitsuichi, and H. Iochinaya, J. Phys. Soc. Japan, Suppl., 28, 227 (1970).

[6] I. P. Kaminow and G. O. Harding, Phys. Rev., 129, 1562 (1963).

[7] L. P. Pereverzeva, Yu. M. Poplavko, V. N. Petrov, E. V. Makarevskaya, and I. S. Rez, Kristallografiya, 18, 645 (1973) [Sov. Phys. – Crystallogr., 18, 407 (1973)].

[8] B. D. Silverman, Phys. Rev. Lett., 25, 107 (1970).

Formation of molecular ions in an alkali discharge

V. N. Paslen and A. M. Przhonskii

T. G. Shevchenko Kiev State University

(Submitted April 25, 1973)
Zh. Tekh. Fiz., 44, 1113-1115 (May 1974)

The ionic composition of a potassium discharge is measured in the range $p = 7 \cdot 10^{-3}$-$6 \cdot 10^{-2}$ mm Hg and $n_e = 10^9$-10^{11} cm^{-3}. It is shown that the main mechanism for the formation of K_2^+ ions is associative ionization: $2K^*(4P) \rightarrow K_2^+ + e$. The effective cross section for the reaction $q \approx 3 \cdot 10^{-16}$ cm^2.

The results of a mass-spectrometer analysis of the ion composition of a potassium discharge were used in a previous paper[1] to show that at pressures $p \geqslant 0.1$ mm Hg and densities $n_e > 10^{10}$ cm^{-3}, K_2^+ molecular ions are formed mainly as a result of binary ion–molecule collisions of the form

$$K^+ + K_2 \rightarrow K_2^+ + K. \qquad (1)$$

In the present work we present the results of a similar investigation performed at lower pressures $p = 7 \cdot 10^{-3}$-$6 \cdot 10^{-2}$ mm Hg in the density range $n_e = 10^9$-10^{11} cm^{-3} (where increasing n_e causes the electron temperature T_e to decrease monotonically from 10,000 to 4000°K). For these values of p and n_e the recombination of both atomic and diatomic ions takes place mainly at the wall following ambipolar diffusion.

Curves of the ratio J_2/J_1 measured at the mass-spectrometer output (and proportional to the ratio n_2/n_1 of the densities of K_2^+ and K^+ ions in the plasma) as a function of n_e are shown in Fig. 1 for various pressures. Evidently, a) increasing p leads to a growth of n_2/n_1, the growth slowing down significantly for $p > 0.03$ mm Hg; b) increasing n_e reduces n_2/n_1, although the density of diatomic ions n_2 is not decreased, but increases (curve 5'). The latter feature means that at higher n_e the efficiency for the formation of K^+ atomic ions (electron impact ionization) exceeds that of K_2^+ molecular ions.

From a consideration of the balance equation[1] it follows that the above features cannot be explained on the basis of the aforementioned reaction (1). Under the present conditions the governing mechanism for the formation of K_2^+ ions in the plasma appears to be the so-called associative ionization process, with participation of excited atoms. The following reaction of associative ionization is known[2] to be possible in potassium vapor:

$$K + K^{**} \rightarrow K_2^+ + e; \qquad (2)$$

where K is an atom in the ground state and K^{**} is an atom excited to a level no lower than 6P ($\varepsilon^{**} \geq 3.6$ eV). As in cesium vapor,[3,4] another possibility is ionization through the interaction of two potassium atoms excited to the first resonance level:

$$K^* + K^* \rightarrow K_2^+ + e. \qquad (3)$$

Investigations in cesium vapor[5] show that the effective cross section of a reaction of type (3) is about one and a half orders greater than for a reaction of type (2). Estimates made on this basis show that reaction (2) has a negligible effect compared with reaction (3). The balance equation between the rates of formation and disappearance of ions in the plasma must accordingly have the form

$$\frac{1}{2} q u_a n_a^{*2} = \frac{2}{R} \frac{j_{2W}}{e}.$$

In this equation q is the effective cross section of reaction (3), u_a is the mean relative velocity of atoms, n_a^* is the density of potassium atoms in the 4P resonance level, j_{2W} is the diffusion current density of diatomic ions to the side wall (the values of j_{2W} are found from the independently measured values of the total ion current density to the wall $j_W = j_{1W} + j_{2W}$ and $j_{2W}/j_{1W} \approx 1/\sqrt{2}(J_2/J_1)$ [see ref. 1]).

To analyze the balance equation the reversal temperature of the resonance line of potassium is used to determine the values of $n_a^*(4P)$ for the same discharge current $I = 20$ mA at different pressures p (Fig. 2). The curves are correlated; the peaks coincide in the region $p = 0.03$ mm Hg. Further, the data of Fig. 2 imply that $q = 3 \cdot 10^{-16}$ cm^2, which is very close to the effective cross section of the corresponding reaction in cesium vapor[5]

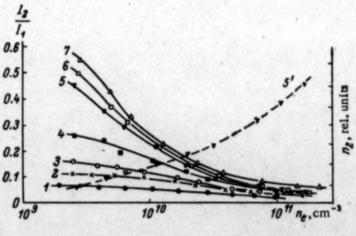

Fig. 1. Vapor pressure p (mm Hg): 1) 0.007; 2) 0.01; 3) 0.015; 4) 0.02; 5) 0.03; 6) 0.04; 7) 0.06; 5' shows n_2 as a function of n_e for p = 0.03 mm Hg.

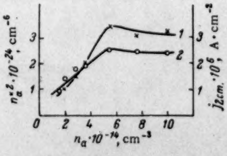

Fig. 2. 1) Graph of $n_a^{*2} = f(n_a)$; 2) graph of $j_{2W} = f(n_a)$. Curves obtained under the same conditions.

($1.1 \cdot 10^{-15}$ cm^2). All this speaks in favor of reaction (3).

We note finally that analogous measurements at pressures $p \sim 0.01$ mm Hg in a cesium plasma lead to a value $q \approx 1.5 \cdot 10^{-15}$ cm^2, which is almost the same as the value measured in ref. 5.

Thus, the formation of diatomic ions in discharge potassium and cesium plasmas in the investigated regimes proceeds mainly through reactions (1) and (3), the latter predominating at low pressures (0.01-0.05 mm Hg) and the former at elevated pressures ($p \geqslant 10^{-1}$ mm Hg).

In conclusion we thank N. D. Morgulis for guidance and A. I. Kravchenko for performing the optical measurements.

---

[1] N. D. Morgulis, A. M. Przhonskii, and V. Ya. Chernyak, Report presented at Fifth All-Union Conf. on Physics of Electronic and Atomic Collisions, Uzhgorod, 1972 [in Russian], p. 179; A. M. Przhonskii and V. Ya. Chernyak, Zh. Tekh. Fiz., 43, 1516 (1973) [Sov. Phys.–Tech. Phys., 18, 960 (1974)].

[2] Y. Lee and B. H. Mahan, J. Chem. Phys., 42, 2893 (1965).

[3] K. Freudenburg, Zs. Phys., 67, 417 (1931).

[4] N. D. Morgulis and A. M. Przhonskii, Zh. Eksp. Teor Fiz., 58, 1873 (1970) [Sov. Phys.–JETP, 31, 1005 (1970).

[5] A. N. Klyucharev and N. S. Ryazanov, Opt. Spektrosk., 31, 347 (1971); 33, 425 (1972).

Current density of thermionic-field emission into a plasma at moderate fields

I. N. Ostretsov, V. A. Petrosov, A. A. Porotnikov, and B. B. Rodnevich

(Submitted April 20, 1973)
Zh. Tekh. Fiz., 44, 1115-1117 (May 1974)

An analysis is made of the effect on thermionic-field emission at moderate fields of the individual fields of ions which form a nonneutralized space charge near the cathode. An analytic expression is obtained for the electron current density. Taking account of the discrete nature of the charge can increase the emission current significantly.

Guth and Mullin[1,2] have derived approximate analytic expressions for the current density of thermionic-field (T–F) emission into vacuum. Their equation for the case of moderate electric fields E can be written

$$j_{T-F}=AT^2\exp\left(-\frac{e\varphi_0}{kT}+\frac{e\Delta\varphi}{kT}\right)[1+\alpha(T,\ E)], \tag{1}$$

where A is the thermionic-emission constant, e is the electron charge, k is the Boltzmann constant, φ_0 is the work function of the cathode material, and $\Delta\varphi$ is the Schottky correction, which reduces the work function. In the case of a constant field this correction is $\Delta\varphi = \sqrt{e/E}$ The function $\alpha(T, E)$ is small, and is a weak function of E.

When there is a plasma near a hot cathode (e.g., in an arc discharge) the electron current density is usually calculated from Eq. (1) and the field E is determined on the basis of the Langmuir–Mackeown model of the cathode sheath.[3,4] In this model it is assumed that the actually discrete unbalanced space charge in the sheath is smeared into a continuous charge distribution; this simplification can have important effects in calculations for emission processes in several situations: In addition to the average field E there are fluctuations due to the fields of individual ions. Then the field at the cathode is a random quantity, which can take on values from $E_{\min}$ to $E_{\max}$, depending on the arrangement of ions in the sheath, and the work function can, correspondingly, take on values from $\varphi_{\max}$ to $\varphi_{\min}$.

Bauer[5] reported the first attempt to incorporate the effect of the fields of the individual ions on the current density of thermionic field emission, but he used crude assumptions, and his results are valid only for particular cases.

Ostretsov et al.[6] examined the effect of the field of individual ions on thermionic (T) emission; in particular, they derived the distribution function of the correction to the work function due to the discrete nature of the charge distribution in the cathode sheath, and they found the range of this correction:[1)]

$$\left.\begin{aligned} f(x)&=nr_*^3\left(\frac{3.36}{x^{5/2}}-8.23\right)\exp\left[-nr_*^3\left(\frac{2.24}{x^{3/2}}+8.23x+9.58\right)\right],\\ x&=\Delta\varphi\frac{r_*}{e}-0.5,\quad 0\leqslant x\leqslant 0.7.\end{aligned}\right\} \tag{2}$$

Here n is the ion concentration near the cathode surface, $r_* = 1/2\sqrt{e/E}$ is the Schottky distance, x is the dimensionless correction to the work function. When x = 0 the Schottky correction is obtained.

In moderate fields a characteristic feature of T–F emission is the fact that the increase in the electron current density occurs primarily because of a lowering of the potential barrier at the surface of the metal (as in T emission – the Schottky effect), and not because of a narrowing of the barrier, i.e., an increase in its transmission (as in field emission – the tunneling effect). Accordingly, the results of ref. 6 can be extended to this range of T–F emission.

To find the current density for T–F emission, taking account of the effects of the fields of the individual ions (I–T–F emission), we must average $j_{T-F}(x)$ over the distribution $f(x)$:

$$j_{I-T-F}=\int\limits_0^{0.7} j_{T-F}(x)\,f(x)\,dx. \tag{3}$$

Integral (3) cannot be evaluated exactly, so we represent $f(x)$ by a parabola whose vertex is at the maximum, $f(\bar{x})$: $y = f(\bar{x}) - K(x - \bar{x})^2$, where $\bar{x}$ is the coordinate of the maximum of $f(x)$. We find the coefficient K from the normalization condition

$$\int\limits_{\bar{x}-\delta}^{\bar{x}+\delta} y(x)\,dx=1,$$

where $x = \bar{x} + \delta$ and $x = \bar{x} - \delta$ are the points at which the parabola intersects the x axis.

Then

$$f(x)\approx y=f(\bar{x})-\frac{16}{9}f^3(\bar{x})(x-\bar{x})^2. \tag{4}$$

Substituting (4) into (3), we find

$$\left.\begin{aligned} j_{I-T-F}&=AT^2\exp\left(-\frac{e\varphi_0}{kT}+\frac{e\sqrt{eE}}{kT}\right)\\ &[1+\alpha(T,\ E)]\,e^{a\bar{x}}\left(\operatorname{ch}b-\frac{\operatorname{sh}b}{b}\right)\frac{3}{b^2},\\ a&=\frac{e^2}{kTr_*},\quad b=\frac{3a}{4f(\bar{x})}.\end{aligned}\right\} \tag{5}$$

To find $\bar{x}$ we use the approximations

$$\bar{x}=\begin{cases}1.22\,(nr_*^3)^{3/2}, & nr_*^3<0.1,\\ 0.73-0.22\,(nr_*^3)^{-1/2}, & 0.1\leqslant nr_*^3\leqslant 10,\\ 0.7-0.28\,(nr_*^3)^{-1/2}, & 10<nr_*^3.\end{cases} \tag{6}$$

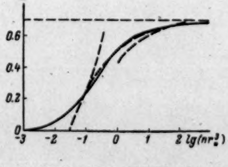

Fig. 1

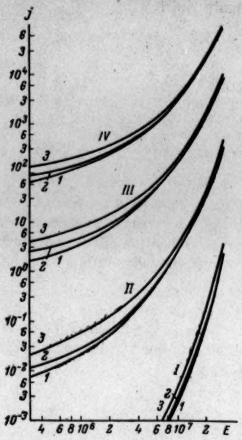

Fig. 2. n, cm^{-3}: 1) 0; 2) 10^{18}; 3) 10^{19}. T (°K): I) 1500; II) 2000; III) 2500; IV) 3000.

Functions (6) are shown in Fig. 1 by the dashed curves; the solid curve shows the exact functional dependence of the coordinate $\overline{x}$ on the parameter nr_*^3, found numerically.

Typical values for I–T–F emission are $nr_*^3 \sim 10^{-1}$. Figure 2 shows functions (5) for various values of T and n; the n = 0 curve corresponds to pure T–F emission. We see that in all cases $j_{I-T-F} > j_{T-F}$. As the temperature is lowered and the density increased this inequality is strengthened.

---

1) The expression in ref. 6 for $f(x)$ is slightly different in form: Eq. (2) differs from it in that $f(x)$ in Eq. (2) vanishes at X = 0.7.

[1] E. Guth and C. J. Mullin, Phys. Rev., 59, 575 (1941).
[2] E. Guth and C. J. Mullin, Phys. Rev., 61, 339 (1942).
[3] I. Langmuir, Phys. Rev., 33, 954 (1929).
[4] S. Mackeown, Phys. Rev., 34, 611 (1929).
[5] A. Bauer, Beitr. Plasmaphysik, No. 4 (1966).
[6] I. N. Ostretsov, V. A. Petrosov, A. A. Porotnikov, and B. B. Rodnevich, Zh. Tekh. Fiz., 43, 2201 (1973) [Sov. Phys. – Tech. Phys., 18, 1392 (1974)].

Preservation of semiconductor field-emission cathodes

N. V. Egorov, G. N. Fursei, and M. K. El'Nimr

A. A. Zhdanov Leningrad State University

(Submitted July 9, 1973)
Zh. Tekh. Fiz., 44, 1117-1118 (May 1974)

Direct experiments have shown that irreversible changes in the properties of semiconductor field-emission cathodes, which occur in heating to temperatures exceeding 150°C, are to a considerable degree due to metals which are deposited on the surface of an emitter during the sharpening process in an electrolyte and which alter the conductance of the surface region of the sample.

One of the greatest difficulties in the preparation and use of semiconductor field-emission cathodes is the great change in their properties due to heat treatment. These changes can occur at any stage: during electrolytic etching, in the course of outgassing of a vacuum device with a semiconductor emitter, and as a result of heating of the emitter by its own emission current. Distortions of the field-emission characteristics as a result of heat treatment have been reported for Ge (refs. 1,2), Si (ref. 3), GaAs (ref. 4), In_2S_3 (ref. 5), and other semiconductors.

It has been shown (see, for example, refs. 1-3) that nonlinear voltage—current characteristics can be obtained only if the heat treatment is confined to low temperatures (T ~150°C).

It has been suggested[3] that changes in the properties of semiconductor field emitters may be due to the presence of metal ions which remain following the electrochemical treatment. Solutions of alkalis, hydrofluoric and nitric acids, hydrogen peroxide, and other high-purity etchants are usually contaminated with ions of heavy metals (copper, silver, lead, iron, gold, etc.) in amounts from $1 \cdot 10^{-5}$ to $1 \cdot 10^{-3}$%. This also applies to distilled water, which is used to wash silicon, germanium, and other semiconductors. In the course of etching a semiconductor can absorb impurities present in an etchant. In view of the high ratio of the surface area to the volume of a field emitter, the diffusion of impurities can alter the nature and the degree of doping of the surface region of a semiconductor cathode.

We have investigated this hypothesis in series of experiments in which the concentration of metal impurities captured during etching is reduced by treatment in organic solutions (Trilon B or 2,4-pentadiene).[6] These compounds form stable complexes with copper and similar metal ions in basic solutions and are then easily removed by washing.

The temperature of a sample during vacuum processing lies within the range 150-500°C. After each heat-treatment cycle we record the voltage—current characteristic at a fixed temperature. The recording of the characteristic is preceded by a field-desorption treatment.

It is clear from a comparison of Figs. 1 and 2 that the critical temperature at which the voltage—current characteristic becomes linear, T_{cr}, increases when metals deposited during etching are removed by means of complex-forming agents.

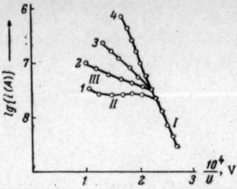

Fig. 1. Illustration of the distortion of the original properties of a silicon field emitter (p-type, ρ = 14 Ω·cm) during heat treatment in the course of vacuum processing of a field-emitting device. T (°C): 1) 150; 2) 250; 3) 300; 4) 350.

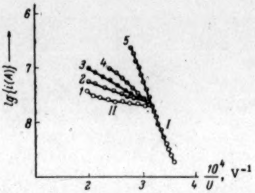

Fig. 2. Voltage—current characteristics of a silicon field emitter (p-type, 14 Ω·cm) recorded after different heat treatments for samples which are etched electrochemically and then treated in solutions forming stable complexes with metal ions. T (°C): 1) 250; 2) 300; 3) 350; 4) 400; 5) 500.

When a sample whose voltage—current characteristic becomes linear is subjected to a second etching, which removes a thin surface layer, the nonlinearity is fully restored. The process is irreversible when the sample is heated to a very high temperature (800-1000°K or above) and this is evidently due to the doping of the whole of the emitter.

Thus, our investigation indicates that the experimentally observed changes in the original properties of a silicon emitter resulting from heat treatments are, to a considerable degree, due to the presence of metal impurities deposited on the surface of the emitter in the course of the electrochemical treatment.

---

[1] J. R. Arthur, Jr., J. Appl. Phys., 36, 3221 (1965).

[2] G. N. Fursei and R. Z. Bakhtizin, Vestn. Leningr., Univ. Fiz. Khim., No. 22, 65 (1970).

[3] G. N. Fursei (Fursey) and N. V. Egorov, Phys. Status Solidi, 32, 23 (1969).

[4] J. R. Arthur, Jr., J. Appl. Phys., 37, 3057 (1966).

[5] H. Neumann, Z. Naturforsch., 22a, 1012 (1967).

[6] R. R. Stead Richardson, USA Patent, No. 2, 871, 111.

The magnetostatic problem for thin closed shells

I. P. Krasnov

(Submitted August 13, 1973)
Zh. Tekh. Fiz., 44, 1121-1124 (June 1974)

Integral equations are used to solve magnetostatic problems for thin closed shells, limiting cases of the equations are considered, and the relation of these equations to the Dirichlet and Neumann problems and the determination of eddy currents are discussed.

1. In the calculation of the magnetic field created by a thin closed shell of magnetic material with permeability μ located in a medium of permeability μ_1 the following approximate boundary conditions have been proposed[1] on the assumption that the field varies linearly across the thickness of the shell:

$$\left.\begin{aligned}\varphi^+ - \varphi^- &= -\Delta\frac{\mu_1}{\mu}\frac{\partial}{\partial n}\varphi^+,\\ \frac{\partial}{\partial n}\varphi^+ - \frac{\partial}{\partial n}\varphi^- &= \varkappa\Delta\frac{\partial}{\partial n}\varphi^+ + \Delta\frac{\mu}{\mu_1}\operatorname{div}_s\operatorname{grad}_s\varphi^+,\end{aligned}\right\} \qquad (1)$$

where n is the normal to the surface of the shell, div_s and grad_s are the surface divergence and gradient, $\varkappa$ is the curvature of the shell surface,[1)] and Δ is the thickness; the superscripts '+' and '−' denote the limiting values of the scalar magnetic potential φ on the inside and outside of the shell respectively. The fact that the boundary conditions (1) only contain the ratio of the permeabilities means that it is possible to separate the two cases $\mu_1 \ll \mu$ and $\mu_1 \gg \mu$ (the case $\mu_1 \simeq \mu$ is of no particular interest since it can be described simply in terms of a uniformly magnetized shell). The boundary conditions for the two cases are as follows: for $\mu_1 \ll \mu$ (see ref. 2)

$$\left.\begin{aligned}\varphi^+ - \varphi^- &= 0,\\ \frac{\partial}{\partial n}\varphi^+ - \frac{\partial}{\partial n}\varphi^- &= \varkappa\Delta\frac{\partial}{\partial n}\varphi^+ + \frac{\partial}{\partial n}\varphi^-\bigr) + \mu_s\operatorname{div}_s\operatorname{grad}_s\varphi^+,\end{aligned}\right\} \qquad (2)$$

and for $\mu_1 \gg \mu$,

$$\left.\begin{aligned}\frac{\partial}{\partial n}\varphi^+ - \frac{\partial}{\partial n}\varphi^- &= 0,\\ \varphi^+ - \varphi^- &= -\nu_s\frac{\partial}{\partial n}\varphi^+.\end{aligned}\right\} \qquad (3)$$

Here, for simplicity we have written $\mu_s \equiv \Delta\,(\mu/\mu_1)$, $\nu_s \equiv \Delta\,(\mu_1/\mu)$.

The only way of solving the boundary-value problem for the magnetic fields of shells with arbitrary shape is to use numerical or numerical-analytic methods; it is preferable to deal with integral equations. In this paper we given an equivalent formulation of the boundary-value problems (2) and (3) in the form of Fredholm integral equations of the second kind; integral equations equivalent to (2) for a two-dimensional space are considered in ref. 3.

2. In order to obtain integral equations corresponding to (2) and (3) it is convenient to represent the scalar magnetic potential as the sum of the potentials of a primary field φ_0 and a secondary field ψ:

$$\varphi = \varphi_0 + \psi, \qquad (4)$$

and to take as the secondary field the potential of a simple or double layer. It is clear from the properties of these potentials[4] that the first (homogeneous) parts of the boundary conditions (2) and (3) are satisfied if the secondary field in (2) is represented by the potential of a simple layer:

$$\psi(x) = \frac{1}{4\pi}\int_S g(s)\frac{1}{r_{sx}}\,ds, \qquad (5)$$

and in (3) by the potential of a double layer:

$$\psi(x) = \frac{1}{4\pi}\int_S \sigma(s)\frac{\partial}{\partial n_s}\frac{1}{r_{sx}}\,ds; \qquad (6)$$

here, r_{SX} denotes the distance between a points on the surface S of the shell and a point $x = (x_1x_2x_3)$ in space. We now substitute (5) and (6) into the remaining parts of the boundary conditions (2) and (3) respectively and use (4) to obtain singular integral equations which are equivalent to the original problems. Equation (2) is equivalent to

$$\begin{aligned}&g(s_2) - \mu_s\operatorname{div}_s\operatorname{grad}_s\frac{1}{4\pi}\int_S g(s_1)\frac{1}{r_{12}}\,ds_1\\ &-\frac{\varkappa\Delta}{4\pi}\int_S g(s_1)\frac{\partial}{\partial n_2}\frac{1}{r_{12}}\,ds_1 = \mu_s\operatorname{div}_s\operatorname{grad}_s\varphi_0.\end{aligned} \qquad (7)$$

For (3) we have

$$\sigma(s_2) - \nu_s\frac{1}{4\pi}\int_S \sigma(s_1)\frac{\partial}{\partial n_2}\frac{\partial}{\partial n_1}\frac{1}{r_{12}}\,ds_1 = \nu_s\frac{\partial}{\partial n_2}\varphi_0(s_2). \qquad (8)$$

In order to reduce these singular equations to the Fredholm form, we apply to each the integral operation

$$\frac{1}{\pi}\int_S \dots \frac{1}{r_{20}}\,ds_2.$$

We then change the order of integration in the resultant singular integrals in accordance with the commutation relations

$$-\frac{1}{4\pi^2}\int_S\left(\operatorname{div}_s\operatorname{grad}_s\int_S g(s_1)\frac{1}{r_{12}}\,ds_1\right)\frac{1}{r_{20}}\,ds_2$$

$$= g(s_0) + \frac{1}{2\pi}\int_S g(s_1)\,M(s_1s_0)\,ds_1;$$

$$-\frac{1}{4\pi^2}\int_S\left(\int_S \sigma(s_1)\frac{\partial}{\partial n_2}\frac{\partial}{\partial n_1}\frac{1}{r_{12}}\,ds_1\right)\frac{1}{r_{20}}\,ds_2$$

$$= \sigma(s_0) - \frac{1}{2\pi}\int_S \sigma(s_1)\,N(s_1s_0)\,ds_1,$$

$$M(s_1s_0) \equiv \frac{1}{2\pi}\int_S\left(\operatorname{grad}_s\frac{1}{r_{12}},\ \operatorname{grad}_s\frac{1}{r_{20}}\right)ds_2,$$

where

$$N(s_1 s_0) \equiv \frac{1}{2\pi}\int\limits_S \frac{\partial}{\partial n_1}\frac{1}{r_{12}}\frac{\partial}{\partial n_2}\frac{1}{r_{20}}\,ds_2,$$

of which the first can be obtained from the spatial analog of the Poincaré–Bertran equation[5] and the second from Green's theorem for a harmonic function.

Thus Eq. (7) for the boundary condition (2) can be transformed to

$$\mu_s g(s_2) + \frac{1}{2\pi}\int\limits_S g(s_1)\left(\frac{2}{r_{12}} + \mu_s M(s_1 s_2) - \varkappa\Delta P(s_1 s_2)\right) ds_1 = \frac{\mu_s}{\pi}\int\limits_S \operatorname{div}_s \operatorname{grad}_s \varphi_0(s_1)\frac{1}{r_{12}}\,ds_1, \qquad (9)$$

where

$$P(s_1 s_2) \equiv \frac{1}{2\pi}\int\limits_S \frac{1}{r_{20}}\frac{\partial}{\partial n_0}\frac{1}{r_{01}}\,ds_0,$$

and Eq. (8) for (3) to

$$\nu_s \sigma(s_2) + \frac{1}{2\pi}\int\limits_S \sigma(s_1)\left(\frac{2}{r_{12}} - \nu_s N(s_1 s_2)\right) ds_1 = \frac{\nu_s}{\pi}\int\limits_S \frac{\partial}{\partial n}\varphi_0\frac{1}{r_{12}}\,ds_1. \qquad (10)$$

Simple calculations show that the kernels $P(s_1s_2)$ and $N(s_1s_2)$ do not have more than a logarithmic singularity provided that S has a continuous curvature; it can also be shown that $M(s_1s_2)$ then also has a logarithmic singularity.

As a result, Eqs. (9) and (10) are of the Fredholm type (or more exactly, they are integral equations with a weak singularity for which Fredholm's theorem is valid).

We note the relation between the kernels

$$N(s_1 s_2) = \frac{\partial}{\partial n_2}P(s_1 s_2),$$

$$M(s_1 s_2) = \frac{1}{2\pi}\int\limits_S \left(\left[\mathbf{n}_0, \operatorname{grad}\frac{1}{r_{01}}\right]\left[\mathbf{n}_0 - \mathbf{n}_1, \operatorname{grad}\frac{1}{r_{20}}\right]\right) ds_0 - N(s_1 s_2),$$

which shows, in particular, that if S is a plane then P = N = M = 0. If S is a sphere of radius R, then we have

$$M(s_1 s_2) = -\frac{1}{4R^2}K\left(\cos\frac{\vartheta_{12}}{2}\right) = -N(s_1 s_2),$$

where K is the complete elliptical integral of the first kind and ϑ_{12} is the angle between the radii drawn to the points s_1 and s_2.

3. We now consider the limiting cases of (9) and (10). If $\mu_S \to \infty$ in (9), then

$$g(s_2) + \frac{1}{2\pi}\int\limits_S g(s_1) M(s_1 s_2)\,ds_1 = \frac{1}{\pi}\int\limits_S \operatorname{div}_s \operatorname{grad}_s \varphi_0\frac{1}{r_{12}}\,ds_1. \qquad (11)$$

This Fredholm equation can be considered as an integral equation for the solution of the Dirichlet problem

$$\psi|_s = -\varphi_0(s)$$

by means of a simple layer potential (the usual formulation of the Dirichlet problem by means of the potential of a simple layer leads to an equation of the first kind with a weak singularity). Similarly, Eq. (11) can be considered as an integral equation for the solution of the Poisson problem on the surface S:

$$\operatorname{div}_s \operatorname{grad}_s \psi = F\ (\equiv -\operatorname{div}_s \operatorname{grad}_s \varphi_0),$$

which occurs in the determination of eddy currents in thin shells.[6] If $\nu_S \to \infty$ in (10), then

$$\sigma(s_2) - \frac{1}{2\pi}\int\limits_S \sigma(s_1) N(s_1 s_2)\,ds_1 = \frac{1}{\pi}\int\limits_S \frac{\partial}{\partial n_1}\varphi_0(s_1)\frac{1}{r_{12}}\,ds_1. \qquad (12)$$

This equation can be considered as an integral equation for the solution by means of a double-layer potential of the Neuman problem

$$\frac{\partial}{\partial n}\psi|_s = -\frac{\partial}{\partial n_s}\varphi_0(s),$$

which is usually solved with the use of a single-layer potential.

The integral equations (9) and (10) and their limiting cases have been verified by the example of a surface S in the form of a spheriod; an analytical solution is obtained by expanding 1/r in a series of orthogonal functions on this surface and the solution identical to that given in ref. 1. Analytical solutions of (9) and (10) exist in cases in which separation of variables is possible for the boundary-value problems (2) and (3), but the advantage in using these equations appears when numerical methods are used for shells of arbitrary shape.

We note in conclusion that (2) and (3) are related in the two-dimensional case when $\varkappa\Delta \ll 1$. This follows the fact that the solutions of (2) and (3) are then the real and imaginary parts of a function of a complex variable; if g(s) is the density of the simple-layer potential with which (2) is solved and δ(s) is the density of the double-layer potential for solving (3), then

$$g(s) = \frac{d}{ds}\sigma(s).$$

Thus the methods suggested in ref. 3 for solving (2) are also suitable for solving (3). In the three-dimensional case, the relation between (2) and (3) no longer holds.

---

1) If u and v are orthogonal coordinates on the surface of the shell and h_u and h_v are the corresponding Lamé coefficients, then

$$\varkappa = \frac{1}{h_u h_v}\frac{\partial}{\partial n}(h_u h_v).$$

---

[1] L. A. Tseitlin, Zg. Tekh. Fiz., 28, 1326 (1958) [Sov. Phys.—Tech. Phys., 3, 1231 (1958)].

[2] S. V. Zhukov, Zh. Tekh. Fiz., 37, 1149 (1967).

[3] I. P. Krasnov, Zh. Tekh. Fiz., 42, 1545 (1972) [Sov. Phys.—Tech. Phys., 17, 1239 (1973)].

[4] V. I. Smirnov, Course in Advanced Mathematics, [in Russian], GITTL, Moscow–Leningrad (1951).

[5] A. V. Bitsadze, Boundary-Value Problems for Elliptical Equations of Second Order [in Russian], Nauka, Moscow (1966).

[6] L. A. Tseitlin, Zh. Tekh. Fiz., 39, 1733 (1969) [Sov. Phys.—Tech. Phys., 14, 1305 (1970)].

Microwave propagation in a low-loss dielectric

L. É. Rikenglaz

G. V. Plekhanov Leningrad Mining Institute

(Submitted September 4, 1973)
Zh. Tekh. Fiz., 44, 1125-1128 (June 1974)

The self-consistent problem of determining the electric and temperature fields in a semiinfinite dielectric is solved in the adiabatic approximation for the case of a plane wave at normal incidence; the parameters of the medium are arbitrary functions of temperature.

In this note the problem of determining the electric and temperature fields in a semiinfinite low-loss dielectric is solved in the adiabatic approximation for the case of normal incidence of a plane wave [$\sim\exp(i\omega t)$]. The parameters of the medium are arbitrary functions of temperature. The problem has been solved earlier[1] for the case in which the damping coefficient is a linear function of temperature and all other parameters are constants.

Since the characteristic heating time and the relaxation times of the electrical parameters of the medium are much greater than the oscillation period, the electric field in the medium can be written in the form

$$E(x,\ t)=y(x,\ t)\exp(i\omega t)\quad(x>0),\tag{1}$$

where y(x, t) is a slowly varying function of time that satisfies the equation

$$\frac{d^2y}{dx^2}+k_0^2\varepsilon(x,\ t)\,y=0,\tag{2}$$

in which the time is a parameter. Here, k_0 is the wave number in vacuum, and $\varepsilon = \varepsilon' - i\varepsilon''$ is the complex dielectric constant of the medium.

In the isothermal case the field penetration depth in a low-loss medium

$$h=\frac{2}{k_0\varepsilon'\operatorname{tg}\delta}\quad\left(\operatorname{tg}\delta=\frac{\varepsilon''}{\varepsilon'}\right)$$

is considerably greater than the wavelength in the medium. Since the temperature of the medium and the dielectric constant ε vary on a space scale of order h, the WKB method can be used to solve Eq. (2).

Neglecting the reflected wave, we have

$$y=D\frac{\varepsilon^{1/4}(0,\ t)}{\varepsilon^{1/4}(x,\ t)}\exp\left[-k_0\int\limits_0^x\varepsilon^{1/2}(x',\ t)\,dx'\right].\tag{3}$$

Using the continuity of the field vectors at the dielectric boundary x = 0, we find

$$y=\frac{2D_0}{1+\varepsilon^{1/2}(0,\ t)}\,\frac{\varepsilon^{1/4}(0,\ t)}{\varepsilon^{1/4}(x,\ t)}\exp\left[-k_0\int\limits_0^x\varepsilon^{1/2}(x',\ t)\,dx'\right],\tag{4}$$

where D_0 is the electric field of the incident wave.

The density of heat sources in the medium q(x, t) is

$$q(x,\ t)=0.5\omega\varepsilon_0\varepsilon'\operatorname{tg}\delta\,|E|^2=SD_{\rm en}(t)\,\alpha(x,t)\exp\left[-\int\limits_0^x\alpha(x't)\,dx'\right],\tag{5}$$

where S is the electromagnetic energy flux density, $D_{\rm en}(t) = 4\varepsilon'(0,\ t)[1+\varepsilon'^{1/2}(0,\ t)]^{-2}$ is the energy transmission coefficient, and $\alpha(x,\ t) = k_0\sqrt{\varepsilon'(x,\ t)}\tan\delta$ is twice the isothermal damping coefficient.

In the adiabatic approximation the heat-conduction equation assumes the form

$$c(T)\rho(T)\frac{\partial T}{\partial t}=SD_{\rm en}(t)\,\alpha(x,\ t)\exp\left[-\int\limits_0^x\alpha(x',\ t)\,dx'\right]\tag{6}$$

with the initial and boundary conditions

$$T(0,\ x)=T(t,\ \infty)=T_0.\tag{7}$$

If the experimental or theoretical temperature of the heat capacity c, density ρ, and complex dielectric constant ε of the medium are known, Eq. (6) is a nonlinear integrodifferential equation for the temperature. The explicit dependence of the temperature on the time and coordinate has been determined for the special case[1]

$$\alpha=\alpha_0+\gamma(T-T_0);\quad c=\text{const},\quad \rho=\text{const},\quad \varepsilon'=\text{const}.$$

We now solve Eq. (6) in the general case. We first determine the temperature at the boundary of the medium. At x = 0 we have

$$c\{T(0,\ t)\}\,\rho\{T(0,\ t)\}\,\frac{\partial T(0,\ t)}{\partial t}=SD_{\rm en}\{T(0,\ t)\}\,\alpha\{T(0,\ t)\},\tag{8}$$

so that

$$t=\int\limits_{T_0}^{T}\frac{c(T)\,\rho(T)\,dT}{SD_{\rm en}(T)\,\alpha(T)}.\tag{9}$$

The integral can be evaluated numerically for known temperature dependences of the parameters of the medium, making it possible to determine the temperature T(0, t) at the boundary of the medium and the energy transmission coefficient $D_{\rm en}(t)$.

When T(0, t) and $D_{\rm en}(t)$ are known it is possible to find T(x, t). We replace the time t by the new variable Q:

$$Q=S\int\limits_0^t D_{\rm en}(t)\,dt;\quad \frac{\partial Q}{\partial t}=SD_{\rm en}(t).\tag{10}$$

The meaning of the new variable is obvious; Q is the energy transferred across unit area in time t.

Using Eq. (10), we transform Eq. (6):

$$\frac{c(T)\,\rho(T)}{\alpha(T)}\,\frac{\partial T}{\partial Q}=\exp\left[-\int\limits_0^x\alpha(x',\ Q)\,dx'\right];$$

$$T(0,\ x)=T(Q,\ \infty)=T_0.\tag{11}$$

We define the new function H(Q, x) by the equation

$$H(Q,\ x)=\int\limits_{T_0}^{T}\frac{c(T)\,\rho(T)}{\alpha(T)}\,dT;\quad \frac{dH}{dT}=\frac{c(T)\,\rho(T)}{\alpha(T)}\tag{12}$$

and assume that $\alpha\{T(Q,x)\}$ can be expressed as $\alpha\{H(Q,x)\}$.

Substituting Eq. (12) into (11), we obtain

$$\frac{\partial H}{\partial Q}=\exp\left[-\int_0^x \alpha(x',\,Q)\,dx'\right]H(0,\,x)=H(Q,\,\infty)=0. \quad (13)$$

We differentiate Eq. (13) with respect to x:

$$\frac{\partial^2 H}{\partial x\partial Q}=-\alpha(H)\exp\left[-\int_0^x \alpha(x',\,Q)\,dx'\right]=-\alpha(H)\frac{\partial H}{\partial Q}. \quad (14)$$

Relation (14) can be written in the alternative form

$$\frac{\partial}{\partial Q}\left(\frac{\partial H}{\partial x}+\int_0^H \alpha(H)\,dH\right)=0,$$

so that

$$\frac{\partial H}{\partial x}+\int_0^H \alpha(H)\,dH=f(x), \quad (15)$$

where $f(x)$ is an arbitrary function.

For Q = 0 we have $H(0,\,x) = \partial H(0,\,x)/\partial x = 0$. Therefor, $f(x) = 0$, and Eq. (15) assumes the form of an equation with variables separable:

$$\partial x=-\frac{\partial H}{\int_0^H \alpha(H)\,dH}. \quad (16)$$

Integrating this relation, we find

$$x=\int_{H(Q,\,x)}^{H(Q,\,0)}\frac{dH'}{\int_0^{H'}\alpha(H'')\,dH''}. \quad (17)$$

Making a change of variables in this relation according to Eq. (12), we obtain the following implicit solution of the problem:

$$x=\int_{T(x,\,t)}^{T_s}\frac{c(T'')\rho(T'')\,dT''}{\alpha(T')\int_{T_0}^{T'} c(T'')\rho(T'')\,dT''}. \quad (18)$$

For the important case in which the density and heat capacity are constant Eq. (18) is greatly simplified:

$$x=\int_{T(x,\,T)}^{T(0,\,t)}\frac{dT'}{\alpha(T')(T'-T_0)}. \quad (19)$$

Equation (19) can be integrated analytically in many important cases; in any case it can be integrated numerically.

We now estimate the range of validity of the underlying assumptions. The adiabaticity conditions require that

$$c\rho\frac{\partial T}{\partial t}\gg\lambda\left|\frac{\partial^2 T}{\partial x^2}\right|, \quad (20)$$

where λ is the thermal conductivity of the medium.

Using Eqs. (8) and (19) we find that (20) holds for (x,t) satisfying the relation

$$\frac{SD_{\mathrm{en}}(t)}{T(0,\,t)-T_0}\gg a^2\left[\alpha(T)+(T-T_0)\frac{d\alpha}{dT}\right], \quad (21)$$

where $a^2 = \lambda/c\rho$ is the thermal diffusivity of the medium.

---

[1] L. B. Nekrasov and L. É. Rikenglaz, Zh. Tekh. Fiz., 43, 694 (1973) [Sov. Phys. – Tech. Phys., 18, 438 (1973)].

Maximum current of a beam with finite phase volume

G. I. Trubnikov and V. S. Kuznetsov

D. V. Efremov Scientific-Research Institute of Electrophysical Apparatus, Leningrad

(Submitted April 17, 1973)
Zh. Tekh. Fiz., 44, 1129-1132 (June 1974)

A universal curve giving the conditions for maximum current of an axisymmetric beam with finite phase volume is derived. This curve is the boundary of the region in which solutions for the beam envelope exist. Use of this curve to design a beam-transport channel is illustrated.

The familiar maximum-current problem is encountered in one form or another in many electronic devices and charged-particle accelerators.[1-3]

In the drift region this problem consists of determining the maximum current which can be transported through the drift tube in the absence of focusing fields. Formulated differently, it consists of determining the minimum number of lenses required in a drift tube of given length and bore to transport a given beam.

This problem has been solved previously only for one particular case: that in which the beam particles have zero thermal-velocity spread. In many cases, however, particularly in ion-beam calculations, this spread is important; frequently it is the decisive factor in beam spreading.[4] In this note we solve this problem for high-current beams, taking account of the thermal spread, which is characterized by the value of the beam emittance.

SOLUTION OF THE MAXIMUM-CURRENT PROBLEM

The spreading of an axisymmetric beam in an equipotential space is described by[4]

$$\frac{d^2r}{dz^2}-\frac{E^2}{r^3}-\frac{K}{r}=0. \qquad (1)$$

Here, r is the beam radius (envelope), z is the longitudinal coordinate, E is the beam emittance, and

$$K=\frac{e(1-\beta^2)^{3/2}}{2\pi\varepsilon_0 m_0 c^3\beta^3}I$$

is the Coulomb factor, where β is the relative longitudinal particle velocity and I is the beam current.

Integrating Eq. (1) twice, we find an integral equation relating z and r for initial conditions r_0 and r_0':

$$z=\int\limits_{r_0}^{r}\frac{dr}{\sqrt{E^2\left(\frac{1}{r_0^2}-\frac{1}{r^2}\right)+2K\ln\frac{r}{r_0}}}. \qquad (2)$$

The solution of Eq. (1) is symmetric with respect to the plane in which $r_0' = 0$; without any loss of generality we can then analyze the beam spreading with the initial conditions $r = r_0$ and $r_0' = 0$, where r_0 is now the beam radius at the crossover point:

$$z=\int\limits_{r_0}^{r}\frac{dr}{\sqrt{E^2\left(\frac{1}{r_0^2}-\frac{1}{r^2}\right)+2K\ln\frac{r}{r_0}+r_0'^2}}. \qquad (3)$$

We note that $E = r_0\alpha_0$ at the crossover point, where α_0 is the maximum inclination angle of a particle trajectory, a measure of the thermal spread.

To find the maximum distance the beam can propagate for a fixed maximum radius r as function of r_0, we differentiate (3) parametrically with respect to r_0 and equate the derivative to zero, using the new variable $x = r/r_0$; we find

$$\int\limits_{1}^{x}\frac{\partial}{\partial r_0}\left(\frac{r_0}{\sqrt{\frac{E}{r_0^2}\left(1-\frac{1}{x^2}\right)+2K\ln x}}\right)dx = \frac{x}{r_0}\,\frac{r_0}{\sqrt{\frac{E}{r_0^2}\left(1-\frac{1}{x^2}\right)+2K\ln x}}. \qquad (4)$$

Differentiating the integrand and introducing $2Kr_0^2/E^2 = A$, we find

$$\int\limits_{1}^{x}\frac{dx}{\sqrt{1-\frac{1}{x^2}+A\ln x}}+\int\limits_{1}^{x}\frac{\left(1-\frac{1}{x^2}\right)dx}{\left[1-\frac{1}{x^2}+A\ln x\right]^{3/2}}=\frac{x}{\sqrt{1-\frac{1}{x^2}+A\ln x}}. \qquad (5)$$

The solution of Eq. (5) is the quantity $x = x^*$, which

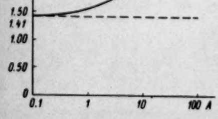

Fig. 1. The relative radius x* as a function of the parameter A for a maximum current.

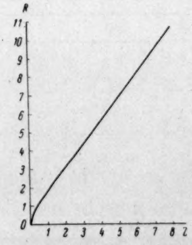

Fig. 2. The universal curve; here Z = z(K/E) and R = r($\sqrt{K/E}$).

is a function of the parameter A and which governs the condition for the maximum current. Figure 1 shows the functional dependence of x^* on A obtained through a numerical solution of Eq. (5).

At $A = 0$ Eq. (5) has the analytic solution $x^* = \sqrt{2}$; this case corresponds to a negligibly small Coulomb factor. As A is allowed to increase without bound, x^* asymptotically approaches the value 2.35, corresponding to the known solution of this problem for the case of a negligibly small thermal spread.

Integrating (3) up to the value x^* which we have found, we can find a functional relation between z and r, corresponding to the condition for maximum current.

Introducing the coordinates $R = r(\sqrt{K}/E)$ and $Z = z(K/E)$, we find a universal curve, which is the solution of our problem (Fig. 2).

PHYSICAL MEANING OF THE UNIVERSAL CURVE

For fixed values of E and K, the universal curve gives a functional relation between z and r which corresponds to the maximum current. For a given length of the drift tube, L, we can set $z = L/2$ and find the minimum tube radius r required to transport a beam with the parameters K and E.

The universal curve is the envelope of the family of all beam envelopes which can be obtained by solving Eq. (1) for $r_0' = 0$ and for various values of r_0. The beam envelopes fill the entire region above the universal curve; each envelope intersects each other envelope and is tangent to the universal curve at one point.

The fact that the envelopes intersect means that a crossover can be achieved at a given z by two methods by specifying the convergence angles to be equal to the derivatives of the envelopes at the intersection. The points lying on the universal curve correspond to the unique solution of this problem. The universal curve is thus the boundary of the definition region of the function specified by Eq. (1).

Since the universal curve is tangent to the envelopes, the angle of incidence of the beam at maximum current can be found from the derivative of this curve. The corresponding value of r_0 can be found from the curve in Fig. 1. Accordingly, we can determine all the basic beam parameters – the beam radius, its incidence angle (these two parameters unambigously determine the lens power), and the beam radius at the crossover point – without resorting to a solution of Eq. (1).

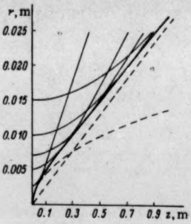

Fig. 3. Universal curve, degenerate curves, and beam envelopes for the case K = 0.0008 and E = 0.0001.

In the case of a small thermal spread, the universal curve degenerates into the straight line

$$r = \sqrt{2K \ln 2.35}\, z, \tag{6}$$

and in the case of a small Coulomb factor it becomes the parabola

$$r = \sqrt{2Ez}. \tag{7}$$

Figure 3 shows the universal curve for a 750-keV proton carrying a current of 0.4 A and having an emittance of 10^{-4} m · rad. The light curves show the beam envelopes, and the dashed curves show line (6) and parabola (7).

The authors thank E. K. Chistov for assistance in the computer calculation.

---

[1] V. S. Lukoshkov, Zh. Tekh. Fiz., 6, 26 (1936).

[2] P. Kirstein et al., Space-Charge Flow, McGraw-Hill, New York (1967).

[3] S. I. Molokovskii and A. D. Sushkov, High-Current Electron and Ion Beams [in Russian], Izd. Energiya, Leningrad (1972).

[4] I. M. Kapchinskii, Particle Dynamics in Linear Resonant Accelerators [in Russian], Atomizdat, Moscow (1966).

Symmetry of high-frequency plasma motions

A. A. Zhmudskii and V. B. Taranov

Institute of Nuclear Research,
Academy of Sciences of the Ukrainian SSR, Kiev

(Submitted July 17, 1973; resubmitted October 18, 1973)
Zh. Tekh. Fiz., 44, 1133-1136 (June 1974)

The high-frequency motion of a plasma is analyzed on the basis of the one-dimensional single-fluid model taking account of the finite electron temperature. The symmetry of the equations is analyzed by the theory of continuous transformation groups. Since the equations are invariant under a transformation to a coordinate system oscillating at the plasma frequency, equations for generalizing the solutions can be derived. In particular, generalization of traveling-wave solutions leads to new solutions in which the phase as a linear function of the time is supplemented by a term which oscillates at the plasma frequency and in which the velocity and electric field are supplemented by terms which result from the noninertial nature of the oscillating coordinate system.

The single-fluid model is usually used in the analysis of the high-frequency motion of a plasma. Several exact solutions of the nonlinear equations of the one-dimensional single-fluid model are derived in refs. 1-4, primarily traveling-wave time-independent solutions. In addition, a general solution has been found for these equations, written in Lagrange variables, for the case of a cold plasma.[1-3] Below we analyze the equations of the one-dimensional single-fluid model, taking account of the finite electron temperature, in a more general manner; specifically, we use a group method,[5] which leads to new exact solutions representing traveling waves in the coordinate system oscillating at the plasma frequency, and which leads to equations for generalizing these solutions. Taking account of the pressure alters the symmetry of the equations and, thus, the nature of the exact solutions.

1. We consider the one-dimensional, high-frequency motion of a plasma with electron temperature T, neglecting the ion motion ($n_i = n_0 = \text{const}$, $v_i = 0$). Adopting the standard notation, we introduce the dimensionless variables

$$\left.\begin{aligned} &t^* = \omega_p t, \quad x^* = \omega_p \sqrt{\frac{m}{T}}\,x, \quad n^* = \frac{n}{n_0}, \\ &v^* = \sqrt{\frac{m}{T}}\,v_e, \quad E^* = \frac{E}{\sqrt{4\pi n_0 T}}, \quad p^* = \frac{p}{n_0 T}, \end{aligned}\right\} \tag{1}$$

where

$$\omega_p = \sqrt{\frac{4\pi e^2 n_0}{m}}.$$

The system of equations for the electron component in the absence of a magnetic field is (we omit the asterisks below) is

$$\left.\begin{aligned} &\frac{\partial v}{\partial t} + \frac{\partial v}{\partial x} + f(n)\frac{\partial n}{\partial x} + E = 0, \\ &\frac{\partial n}{\partial t} + v\frac{\partial n}{\partial x} + n\frac{\partial v}{\partial x} = 0, \\ &\frac{\partial E}{\partial x} = 1 - n, \end{aligned}\right\} \tag{2}$$

where $f(n) = (1/n)(dp/dn)$ and where $n > 0$.

System (2) must be solved with the boundary condition

$$\left(\frac{\partial E}{\partial t} - nv\right)\Big|_{x=x_0} = 0, \tag{3}$$

where x_0 is an arbitrary fixed constant.

2. Analysis of the symmetry of Eqs. (2), whose results are given in Sec. 3 of this paper, shows that with $f(n) \neq 0$ we can find two types of solutions:

a) Self-similar solutions,

$$\left.\begin{aligned} &E = \frac{\alpha x \cos t}{1 + \alpha \cos t}, \quad v = \frac{-\alpha x \sin t}{1 + \alpha \cos t}, \\ &n = \frac{1}{1 + \alpha \cos t}, \quad |\alpha| < 1. \end{aligned}\right\} \tag{4}$$

For these solutions $\partial n/\partial x = 0$, i.e., they can easily be derived from the general solution of the cold-plasma equations (see, e.g., ref. 3).

b) Solutions of the type (the dot denotes differentiation with respect to t)

$$\left.\begin{aligned} &v(x, t) = v(\xi) + \dot{F}(t), \\ &E(x, t) = E(\xi) - \ddot{F}(t), \\ &n(x, t) = n(\xi), \end{aligned}\right\} \tag{5}$$

where $\xi = x - F(t)$, and F(t) is a function whose specific form is found below with the help of condition (3).

From (2) we find a system of equations for the functions v, E, and n of ξ (the prime denotes differentiation with respect to ξ):

$$\left.\begin{aligned} &vv' + f(n)n' + E = 0, \\ &(nv)' = 0, \\ &E' = 1 - n. \end{aligned}\right\} \tag{6}$$

The second equation in (6) yields

$$nv = -u_0 = \text{const}. \tag{7}$$

Using condition (3) along with (6) and (7), we find a specific equation for the function F(t):

$$F(t) = F_0 + u_0 t + (\dot{F}_0 - u_0)\sin t + \ddot{F}_0(1 - \cos t). \tag{8}$$

where F_0, $\dot{F}_0$, and $\ddot{F}_0$ are constants.

Using the equations in sec. 3 to generalize the solutions, we can distinguish among solutions (5) certain un-

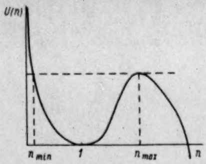

Fig. 1

usual solutions like

$$\left.\begin{aligned} v &= v(\xi) + u_0, \\ E &= E(\xi), \\ n &= n(\xi), \end{aligned}\right\} \qquad (9)$$

where $\xi = x - u_0 t$. Solutions of this type are traveling waves with a phase velocity u_0. New solutions can be generated from (9) by means of the generalization equations in Sec. 3.

Equations (6) and (7) allow the energy integral

$$W = \frac{1}{2} E^2 + \frac{1}{2} u_0^2 \left(\frac{1}{n} - 1\right)^2 + \int_1^n \left(\frac{1}{n} - 1\right) dp. \qquad (10)$$

Equations (7) and (10) give $v(\xi)$ and $E(\xi)$ as functions of $n(\xi)$; using the third equation in (6) we can then reduce the problem to quadratures. Exact traveling-wave solutions for the case $p = (1/3) n^3$ have been found previously.[4]

Using integral (10) we can analyze qualitatively the behavior of the solutions for an arbitrary functional dependence of p on n. We treat the function

$$U(n) = \frac{1}{2} u_0^2 \left(\frac{1}{n} - 1\right)^2 + \int_1^n \left(\frac{1}{n} - 1\right) dp \qquad (11)$$

as a "potential energy."

With $n = 1 + \varepsilon$, where $|\varepsilon| \ll 1$ we have

$$U(1+\varepsilon) \approx \frac{1}{2}\left(u_0^2 - \left.\frac{dp}{dn}\right|_{n=1}\right)\varepsilon^2. \qquad (12)$$

Since this model is applicable when the wave phase velocity u_0 is much larger than the electron thermal velocity $dp/dn|_{n=1}$, we see that U (n) has a minimum at n = 1.

Figure 1 shows the nature of the function U(n) for the case $p = (1/\gamma) n^\gamma$.

The function U(n) has a maximum at the point $n_{\max} = |u_0|^{2/(\gamma+1)}$. For $W < U(n_{\max})$, the solutions are periodic in ξ; for $W > U(n_{\max})$ we find the multistream motion analyzed in refs. 1 and 2. When $W = U(n_{\max})$, the solution is a soliton solution.

3. Here we list the results of a group analysis[5] of the symmetry of Eqs. (2).

With an arbitrary function $f(n)$, system (2) permits an infinite-dimensional transformation group with the infinitesimal operator

$$X = C_1 \frac{\partial}{\partial t} + F(t)\frac{\partial}{\partial x} + \dot{F}(t)\frac{\partial}{\partial v} - \ddot{F}(t)\frac{\partial}{\partial E}, \qquad (13)$$

where C_1 is a constant, and F(t) is an arbitrary function of t. The symmetry of (13) is markedly nonlinear, i.e., linearized equations (2) do not permit transformations (13).

In the case $f(n) = 0$ the group is more comprehensive; the operator

$$Y = x\frac{\partial}{\partial x} + v\frac{\partial}{\partial v} + E\frac{\partial}{\partial E} \qquad (14)$$

is added.

Because of the symmetry of (14) the phase velocity of the wave turns out to be an unimportant parameter in this case; in the linear theory, this corresponds to the fact that the dispersion relation is independent of the wave vector k.

Group (13) contains a subgroup which effects a mutual interchange of the solutions of system (2) with condition (3); this subgroup is found from (13) by setting

$$F(t) = A\cos t + B\sin t + C, \qquad (15)$$

where A, B, and C are constants.

Finite transformations of this subgroup yield the following equations for generalizing the solutions of system (2) with condition (3).

If $v = \varphi(x, t)$, $E = \chi(x, t)$, $n = \psi(x, t)$ is some solution of (2) which satisfies (3); then the functions

$$\left.\begin{aligned} v &= \varphi(\bar{x}, \bar{t}) - R\sin(t-\theta), \\ E &= \chi(\bar{x}, \bar{t}) + R\cos(t-\theta), \\ n &= \psi(\bar{x}, \bar{t}) \end{aligned}\right\} \qquad (16)$$

are also solutions of (2) which satisfy (3). Here

$$\bar{t} = t + a,$$
$$\bar{x} = x + b - R\cos(t-\theta),$$

and a, b, R, and θ are arbitrary constants.

A simple illustration of the use of Eqs. (16) is to generalize the trivial solution E = 0, v = 0, n = 1, from which we find

$$\left.\begin{aligned} E &= R\cos(t-\theta), \\ v &= -R\sin(t-\theta), \\ n &= 1, \end{aligned}\right\} \qquad (17)$$

i.e., a plasma wave with $\lambda \to \infty$.

We note in conclusion that solutions (9) can be generalized by means of Eqs. (16); in particular, this holds for the solutions found in ref. 4 and for any other solutions of system (2) which satisfy condition (3).

The authors thank V. N. Oraevskii for guidance.

---

[1] J. M. Dawson, Phys. Rev., 113, 383 (1959).

[2] A. A. Vedenov, E. P. Velikhov, and R. Z. Sagdeev, Nucl. Fusion, 1, 82 (1961).

[3] R. W. C. Davidson and P. P. J. M. Schram, Nucl. Fusion, 8, 183 (1968).

[4] T. P. Coffey, Phys. Fluids, 14, 1402 (1971).

[5] L. V. Ovsyannikov, Group Properties of Differential Equations [in Russian], Izd. SO Akad. Nauk SSSR, Novosibirsk (1962).

Aperiodic instability in a plasma gap with external feedback

A. N. Igritskii

Moscow Engineering-Physics Institute

(Submitted July 12, 1973)
Zh. Tekh. Fiz., 44, 1137-1142 (June 1974)

A complete numerical solution is found for the dispersion relation for nonlinear aperiodic electrostatic waves in a homogeneous plasma gap. The nonlinear instability of the stable solutions with an adiabatic change in the boundary conditions is discussed. The nonlinear growth rate is much larger than the linear growth rate. The sensitivity of the growth rate to C and R elements in the external feedback circuit is analyzed.

INTRODUCTION

When an electron beam passes through a system with electrodes on which an external feedback circuit maintains specified boundary conditions an electrostatic instability can be excited.[1-3] This instability limits the current that can be carried by a neutralized electron beam. In the case of nonrelativistic beams this current is only a few times larger than the limiting current in vacuum, which is limited by the space charge of the beam. The problem of limiting currents and the stability of relativistic electron beams in plasmas have been analyzed in detail.[4] The instability can be suppressed by introducing a suitable feedback circuit.[5] The effect of feedback on the wave spectrum of a plasma in a limited volume (generalized boundary conditions) is analyzed in ref. 6. The instability in a one-dimensional plasma-filled gap is treated only in the linear approximation in refs. 1-3. The stability of nonlinear, steady-state potential distributions in such a system is analyzed qualitatively in ref. 7 for arbitrary initial distribution functions of the emitted electrons and ions. The nonlinear theory of the instability of a monoenergetic electron beam in a system with electrodes is treated in ref. 8, where certain particular growth rates are determined. The effects associated with the introduction of an arbitrary external feedback circuit, the equivalent circuit of the plasma-filled gap at frequencies low in comparison with the plasma frequency, and the end result of the nonlinear evolution are analyzed in ref. 9.

In this work we discuss a numerical solution of the dispersion relation for a nonlinear aperiodic electrostatic instability in a one-dimensional plasma-filled gap; the nonlinear instability of the stable solutions with an adiabatic change in the boundary conditions is also described. The nonlinear growth rates are shown to be much larger than the growth rates of the linear theory. The effect of an external feedback circuit (an RC circuit) on the growth rates is analyzed qualitatively.

1. The nonlinear dispersion relation for the electrostatic mode[7,9]

$$\left.\begin{aligned}\varphi(\xi)&=\varepsilon\sin\psi\left(1-\frac{\varepsilon}{2}\sin\psi\right),\\ \psi&=\xi+\varepsilon(1-\cos\psi)\end{aligned}\right\}\qquad(1)$$

is[8,9]

$$F(\xi,\ \psi\,|\,z)\equiv\xi-\frac{\psi}{1+z^2}+\frac{2z}{(1+z^2)^2}-\frac{e^{-z\psi}}{(1+z^2)^2}\left[(z^2-1)\sin\psi+2z\cos\psi\right]=0,\qquad(2)$$

where $\xi = L/r_d$; $\varepsilon = (eE_0r_d)/(mv_0^2)$; $\varphi = (e\varphi_L)/(mv_0^2)$; $r_d = v_0[(4\pi e^2n_0)/m]^{-1/2}$, L is the distance between the electrodes between which a constant potential difference φ_L is maintained, E_0 is the steady-state value of the electric field at the emitter, and v_0 and n_0 are the initial velocity and density of the electron beam. Here, n_0 is the density of the homogeneous, fixed ion background. The small perturbations of steady-state distribution (1) are given by ~ exp(zt), with $z = \gamma + i\omega$.

The equation

$$|\operatorname{Im}F(\xi,\ \psi\,|\,\gamma\pm i)|=\int_0^{\psi}(\psi-\alpha)\sin^2\alpha\, e^{-\gamma\alpha}d\alpha=0$$

has no solutions for any finite γ; we can thus write (2) in the equivalent form

$$P_4(\xi,\ \psi\,|\,z)=e^{-z\psi}Q_2(\xi,\ \psi\,|\,z),\qquad(3)$$

where

$$\begin{aligned}P_4&\equiv\xi z^4+(2\xi-\psi)z^2+2z+\xi-\psi,\\ Q_2&\equiv(z^2-1)\sin\psi+2z\cos\psi.\end{aligned}$$

Dispersion relation (3) has a special branch of solutions corresponding to an aperiodic instability $\omega = 0$, $\gamma \neq 0$, with the asymptotic value

$$\gamma_{as}=-\operatorname{ctg}\left(\frac{\psi-k\pi}{2}\right).\qquad(4)$$

which is independent of ε. Furthermore, at points $\psi_{01} = 2\operatorname{arc\,cot}\varepsilon$ and $\psi_{02} = 2k\pi$ there are solutions with $\gamma = 0$. Treating small deviations of the growth rate from the value $\gamma = 0$, setting $\psi = \psi_{0i} + \lambda$, where $|\lambda| \ll \psi_{0i}$ (i = 1, 2), and expanding (3) in powers of the deviations γ and λ, we find

$$a_{10}\lambda+a_{01}\gamma+a_{11}\gamma\lambda+a_{20}\lambda^2+a_{02}\gamma^2=0,\qquad(5)$$

where

$$\left.\begin{aligned}a_{10}&=\cos\psi-\varepsilon\sin\psi,\\ a_{01}&=-\psi\sin\psi+2(1-\cos\psi),\\ a_{11}&=\sin\psi-\psi\cos\psi,\\ a_{20}&=-\frac{1}{2}(\varepsilon\cos\psi+\sin\psi),\\ a_{02}&=\frac{1}{2}\psi^2\sin\psi+\psi(1+2\cos\psi)-3\psi.\end{aligned}\right\}\qquad(5')$$

From (5) we find

$$\gamma=\frac{1+\varepsilon^2}{1-\frac{\varepsilon\psi}{2}}\frac{\lambda}{4}-\frac{1}{(a_{01})^2}\left[a_{20}a_{01}+a_{11}+\frac{a_{02}}{a_{01}}\right]\lambda^2+O(\lambda^3) \tag{6a}$$

for $\psi = \psi_{01}$, and

$$\gamma=\pm\sqrt{-\lambda/3\psi}+\frac{1}{9}\lambda+O(\lambda^{3/2}) \tag{6b}$$

for $\psi = \psi_{02}$, with $\lambda \leq 0$.

When $\psi = \psi_{02}$ the complex frequency is

$$\left.\begin{aligned}\omega&=\pm\frac{1}{\sqrt{3\psi}}\lambda^{1/2}\pm\frac{1}{\sqrt{3\psi}}\left(\frac{7}{108}\psi+\frac{\varepsilon}{4}+\frac{1}{3\psi}\right)\lambda^{3/2}+O(\lambda^{5/2}),\\ \gamma&=\frac{1}{9}\lambda-\frac{2}{27}\left(\frac{\psi}{3}+\frac{2}{\psi}\right)\lambda^2+O(\lambda^3);\ \lambda>0.\end{aligned}\right\} \tag{7}$$

Equation (7) shows that the points $\xi = \psi = 2k\pi$ are not boundary points separating the unstable from the stable regions, as was previously assumed.[7] In fact, when the sign of λ is changed, i.e., when the points $\xi = 2k\pi$ are passed, we find another branch, with $\omega \neq 0$ and $\gamma > 0$; in other words, the solution remains unstable, but quasiperiodic growing solutions appear, since $|\omega| \gg \gamma$. At the same points, $\xi = 2k\pi$, the solutions of the equation are also unstable and, for small perturbations, are of the form const·t. Thus, each solution of Eq. (3) has a quasiperiod of 2π in the sense that the solutions are qualitatively similar at these intervals. Furthermore, at the points $\xi = 2k\pi$ $(k \geq 1)$, solutions with $|\omega| \gg \gamma$ and $\gamma > 0$ are generated, at least near these points.

Figure 1 shows the complete numerical solution of the equation for the aperiodic instability for the limiting nonlinearity cases $\varepsilon = 0$ and ± 1. Let us discuss certain features of these $\gamma = \gamma(\xi)$ curves.

With $\psi = 2\,\text{arc cot}\,\varepsilon$ it follows from (6) that in the case $\varepsilon > 0$ there is always some ψ such that the coefficient of λ becomes negative: $(2-\varepsilon\psi)^{-1} < 0$. The result is the typically nonlinear functional dependence of the growth rate on the external parameters ξ (Fig. 2). This behavior of γ corresponds to the collapse of the stable solutions: By adiabatically changing n_0 and holding L = const, i.e., by changing $\xi \sim \sqrt{n_0}$, we find that there is an electron flux density $n_0 = n_{0\,cr}$ which cannot be exceeded without the rapid onset of instability. This effect cannot be observed in a real system, since a continuous transition to the unstable region is possible even at lower values of n_0. This conclusion follows from the circumstance that the collapse requires that the condition $\varepsilon\psi > 2$ be satisfied, while the first value $\psi \equiv 2\,\text{arc cot}\,\varepsilon$ does not satisfy this condition. Accordingly, collapse can occur only beyond a Debye length. It is not difficult to evaluate γ at the collapse point directly from (3): Assuming $\gamma > 0$ and $1/\psi \ll \gamma \ll 1$, we find

$$\gamma\approx\sqrt{\frac{\varepsilon(1-\cos\psi)}{\xi}}=\sqrt{\frac{2\varepsilon}{\varepsilon^2+1}}\,\xi^{-1/2}. \tag{8}$$

Analysis of Eq. (3) and Fig. 1 reveals two markedly different solution regions, $|z| \gg 1$ and $|z| \ll 1$. At $|z| \gg 1$, the plasma properties of the system become inconsequential, and only the stable vacuum properties are manifest; here, $\gamma < 0$ and the nonlinearity has a weak influence on the values of γ in this region. In region $|z| \ll 1$, we can distinguish between the two subregions $|z\psi| \ll 1$ and $|z\psi| \gg 1$: The first corresponds to a quasisteady-state change in the boundary conditions, for which the transit time of the particles through the system is much shorter than the characteristic time for this change in boundary conditions. The steady-state potential distributions transform continuously into the distributions which are most similar to the steady-state distributions.

Generally speaking, the second subregion can exist only when $\psi \gg 1$, at least beyond a Debye length. This subregion also corresponds to a critical change in the boundary conditions, but here the plasma sheath is so large that the signal cannot pass through it. The part of the plasma-filled gap nearest the emitter – the part through which the signal carrying information about the change in the boundary conditions has already passed – displays plasma properties, while the rest of the system is equivalent to a vacuum gap. At $\varepsilon > 0$ a large part of each plasma period is unstable with respect to the feedback chosen, while at $\varepsilon < 0$ we have the opposite situation. Accordingly, at $\varepsilon > 0$ those periods through which the signal has already propagated are unstable on the average and they amplify the signal more, the larger ε. In the case of pronounced nonlinearity ($|\varepsilon| \sim 1$) and a large plasma sheath, the instability predominates. This behavior is seen in the collapse regions, where $\gamma \sim 1/\sqrt{\psi}$ and where $\varepsilon\psi > 2$. A general manifestation of the nonlinearity is the appearance in the aperiodic instability of growth rates $\gamma \sim 1/\sqrt{\psi} > 0$, while as $|\varepsilon| \to 0$ we have $\max\gamma \sim 1/\psi$. Hence

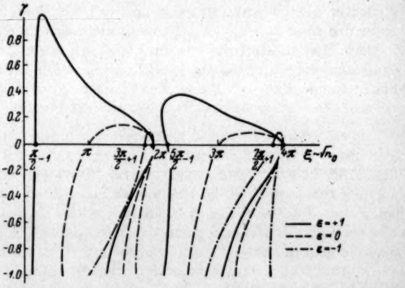

Fig. 1. Growth rate of the aperiodic instability γ/ω_0, as a function of the parameter $\xi\ [n_0/(mv_0^2/4\pi e^2L^2)]^{1/2}$ for the limiting cases of the nonlinearity: $\varepsilon = eE_0r_d/mv_0^2 = 0, \pm 1$.

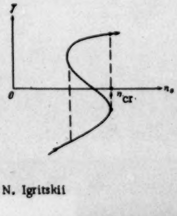

Fig. 2. Behavior of the growth rate for the aperiodic instability near the critical density (qualitative).

$\gamma_{\text{non}} \gg \gamma_{\text{lin}}$, and the nonlinear effects not only do not confine the growing instability; they even amplify it.

2. If we introduce a complex impedance

$$Z_{\text{fb}}(z)=\frac{1}{C}+Rz \tag{9}$$

in the feedback circuit, we can rewrite dispersion relation (3) as

$$F(\xi,\ \psi\,|\,z)+\frac{1}{C}+Rz=0. \tag{10}$$

The solutions z of this equation for $\omega = 0$ have the same asymptotic behavior as before [Eq. (4)]. The values of ψ_{01} and ψ_{02} corresponding to the value $\gamma = 0$ are now given by the equation

$$\sin\psi-\varepsilon(1-\cos\psi)+\frac{1}{C}=0. \tag{11}$$

It follows that with

$$\frac{1}{C}>\varepsilon+\sqrt{1+\varepsilon^2} \tag{12}$$

there are no values with $\gamma = 0$ in the aperiodic branch; by virtue of the continuity of the solution, all the values of γ are negative. This choice of C thus stabilizes the system with respect to perturbations with $\omega = 0$. This result cannot be extended to arbitrary z. Using $Z_{\text{fb}} = 1/C$ and (3), we rewrite (10) as

$$P_4\left(\xi+\frac{1}{C},\ \psi\,|\,z\right)=e^{-\varepsilon\psi}Q_2(\xi,\ \psi\,|\,z). \tag{13}$$

Apply Rouché's theorem to (13), we find that in the right half-plane ($\gamma > 0$) we have

$$\left|\left(\xi+\frac{1}{C}\right)(\omega^2-1)+\psi\right|>|\sin\psi|, \tag{14}$$

if this inequality holds at the $\gamma = 0$ axis even under condition (12). We conclude that the number of roots of Eq. (13) in the right half-plane is equal to the number of roots of the polynomial $P_4[\xi+(1/C),\ \psi|z)$ in this region, i.e., two, as is easily seen. The oscillatory instability with $\omega \neq 0$ is thus retained, so that additional elements must be used in the feedback circuit to make the system quasisteady-state.

To illustrate the consequence of a passive resistance R, we assume it to be large; then (6) becomes

$$\gamma\approx\begin{cases}\left(R+\dfrac{4-2\varepsilon\psi}{\varepsilon^2+1}\right)^{-1}\lambda; & \psi=\psi_{01},\\ -\dfrac{1}{R}\lambda; & \psi=\psi_{02}.\end{cases} \tag{15}$$

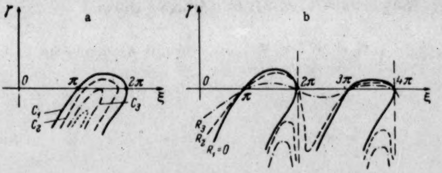

Fig. 3. Effect of capacitive feedback (a) and of a passive resistance (b) on the functional dependence of the growth rate on ξ (qualitative). a) $C_1 = \infty$; $C_3 < C_2 < C_1$; b) $0 = R_1 < R_2 < R_3$.

Figure 3a gives a qualitative idea of the effect of capacitive feedback and of a passive resistance R.

CONCLUSION

1. Numerical and approximate analytic solutions show that in the case of a pronounced nonlinearity the stable solutions collapse into the unstable region, after the first period.

2. The growth rates of the linear theory are increased when the nonlinearity is taken into account. Accordingly, nonlinear effects do not suppress a growing instability; on the contrary, they amplify it.

3. At the points $\xi = 2k\pi$ which are also unstable, small perturbations grow in proportion to the time. Furthermore, a quasiperiodic instability is generated at them under the condition $k \geq 1$ with $|\omega| \gg \gamma$ and $\gamma > 0$.

4. The introduction of small capacitances into the external feedback circuit makes the system completely stable with respect to aperiodic perturbations.

In conclusion the author thanks V. M. Smirnov for useful comments and fruitful discussion.

---

[1] J. R. Pierce, J. Appl. Phys., 15, 721 (1944).

[2] A. B. Mikhailovskii, Zh. Tekh. Fiz., 35, 1933, 1946 (1965) [Sov. Phys.-Tech. Phys., 10, 1490, 1498 (1966)].

[3] A. B. Mikhailovskii, Theory of Plasma Instabilities, Vol. 1, Consultants Bureau, New York (1973).

[4] L. S. Bogdankevich and A. A. Rukhadze, Usp. Fiz. Nauk, 103, 609 (1971) [Sov. Phys.-Usp., 14, 163 (1971)].

[5] V. V. Arsenin, Zh. Tekh. Fiz., 38, 1448 (1968) [Sov. Phys.-Tech. Phys., 13, 1186 (1969)].

[6] E. L. Lindman, Phys. Fluids, 13, 2367 (1970).

[7] V. M. Smirnov, Zh. Eksp. Teor. Fiz., 50, 4 (1966).

[8] V. D. Shapiro and V. I. Shevchenko, Zh. Eksp. Teor. Fiz., 52, 144 (1967) [Sov. Phys.-JETP, 25, 92 (1967)].

[9] A. N. Igritskii and V. M. Smirnov, in: Engineering-Mathematics Methods in Physics and Cybernetics [in Russian], No. 2, Atomizdat, Moscow (1973), p. 5.

[10] M. V. Konyukov, Zh. Eksp. Teor. Fiz., 37, 799 (1959) [Sov. Phys.-JETP, 10, 570 (1959)].

Magnetodrift waves in a finite-β plasma

N. M. Ryzhov, V. L. Sizonenko, V. A. Suprunenko, E. A. Sukhomlin, and Yu. V. Gutarev

(Submitted July 30, 1973)
Zh. Tekh. Fiz., 44, 1143-1150 (June 1974)

The low-frequency magnetodrift instability is studied in the finite-β plasma of an electrodeless induction discharge (a theta pinch). The instability is of a kinetic nature ($\omega \ll k_z v_{Te}$) and results from a mechanism that thermalizes the electrons accelerated by the induction electric field. The peak magnetic field of the waves is comparable to the main magnetic field.

INTRODUCTION

The excitation of electrostatic drift waves in a collisionless, low-β plasma ($\beta \equiv 8\pi n_0 T/H_z^2 \ll 1$) has been studied in detail (see, e.g., refs. 1 and 2 and the literature cited there). In a finite-β plasma ($\beta \geqslant 1$), on the other hand, it has been shown theoretically[3,4] that Alfvén and magnetosonic drift waves can also be excited; these waves, which are electromagnetic, have been called "magnetodrift waves." Although experiments on the excitation of drift waves in a finite-β plasma are of considerable interest in connection with several practical applications, they have received little attention.

We report here a study of magnetodrift waves in the plasma of an electrodeless induction discharge (a theta pinch). We show that the drift waves observed in the finite-β plasma have magnetic-field oscillations of a high amplitude, comparable to the main magnetic field.

EXPERIMENTAL PROCEDURE

A pulsed magnetic field with H_z up to 34 kOe is produced by discharging a 16-kJ capacitor bank into a single-turn coil 8 cm in diameter and 32 cm long. The half-period is 5.6 μsec.

The plasma is produced in a ceramic tube 150 cm long, with an inside diameter of 6.5 cm, filled with hydrogen at a pressure between 1 and 20 torr. Figure 1 shows the overall arrangement of the apparatus with the diagnostic devices. The geometric dimensions of the apparatus are chosen to provide minimum curvature of the magnetic lines of force in the working region and thus to prevent the possible excitation of the ordinary hydromagnetic instability, which has been studied in detail by many workers. In these experiments the condition

$$\frac{R}{a} > \left(\frac{a}{\rho_{Bi}}\right)^2$$

is satisfied easily, ensuring that there will be no hydromagnetic instability[2] (Fig. 2). Here R is the radius of curvature of the magnetic lines of force in the working part of the discharge, a is the plasma radius, and ρ_{Bi} is the ion gyroradius.

Figure 3 shows oscillograms of the magnetic field obtained by a magnetic probe for two cases: 1) The probe is in the central part of the discharge, where the magnetic field is homogeneous and where the hydromagnetic instability cannot be excited (curve 1 in Fig. 3); 2) the probe is near the edge of the coil, where the magnetic lines of force are highly curved (curve 2 in Fig. 3).

The low-frequency oscillations of the magnetic field observed on these two oscillograms clearly differ in shape and amplitude. We assume that in the region of high curvature the oscillations of the magnetic field are due to the excitation of the hydromagnetic instability at the ends of the discharge, while in the central part of the discharge we assume nonhydromagnetic instability, whose amplitude is of the order of the vacuum magnetic field at $\beta \sim 1$. Below, we identify this wave branch as corresponding to a magnetodrift wave of the magnetosonic type.

EXPERIMENTAL RESULTS

Curve 1 in Fig. 4 shows clearly that this low-frequency instability is excited only at a certain time t, at which completely definite relations have been established among the discharge parameters.

Analysis of the electron temperature as measured by the x-ray probes[5] (curve 3 in Fig. 4) and of the superthermal microwave emission from the discharge near the upper hybrid frequency (curve 2 in Fig. 4) shows that a high-frequency instability due to electron acceleration by the induction electric field of the theta pinch is excited in the plasma at time t, before the low-frequency magnetodrift instability is excited. This instability, which

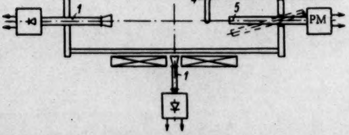

Fig. 1. Experimental apparatus and arrangement of the diagnostic devices. 1) Microwave detection horns; 2) field coils; 3) transmitting horn; 4) magnetic probes; 5) x-ray probe.

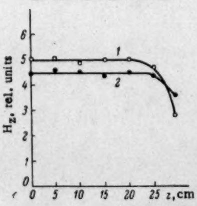

Fig. 2. Profile of the longitudinal magnetic field along the system. 1) Initial pressure of $1 \cdot 10^{-3}$ torr; 2) $2 \cdot 10^{-3}$ torr.

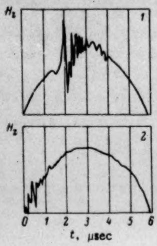

Fig. 3. Oscillograms of the magnetic field. 1) Magnetic probe in the homogeneous part of the magnetic field; 2) near the edge of the coil.

causes rapid turbulent heating of the plasma electrons in the central part of the discharge, is known[6] to be of a resonance nature and is excited when one of the even harmonics of the electron gyrofrequency lies near the upper hybrid frequency, $n\omega_{Be} = \sqrt{\omega_{pe}^2 + \omega_{Be}^2}$.

The thermalization of the accelerated electrons and the nearly instantaneous turbulent plasma heating in the central part of the discharge provide conditions suitable for the excitation of a low-frequency magnetodrift wave.

In these experiments, the plasma electron temperature reaches several keV at a plasma density of $10^{14}\,\text{cm}^{-3}$, corresponding to an equilibrium value $\beta_p \simeq 0.5$ [here $\beta_p \equiv 8\pi n_0(0)T_e(0)/H_z^2(a)$] before the low-frequency instability is excited. It should be noted that the ions remain essentially cold.

The diamagnetic effect related to this heating causes a pronounced radial gradient of the magnetic field (curve 1 in Fig. 5). Curve 2 in Fig. 5 shows the radial profile of the magnetic field 1 μsec after the excitation of the high-frequency starting instability, at which time the low-frequency instability has been excited. We see a wave structure whose half-wavelength is of the order of the magnetic field gradient. The corresponding radial wave vector k_r is

$$k_r = \frac{2\pi}{\lambda_r} \sim \frac{1}{H_z}\frac{\partial H_z}{\partial r} \simeq 1.7\ \text{cm}^{-1}.$$

Curve 3 in Fig. 5 shows the amplitude of this wave along the radius of the plasma column; this instability develops primarily in the central part of the discharge, where the electron heating is most pronounced (curve 4 in Fig. 5).

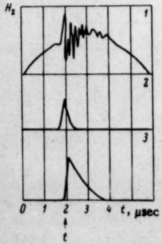

Fig. 4. 1) Oscillogram of the magnetic field; 2) microwave emission from the plasma at 8 mm; 3) signal from the x-ray probe.

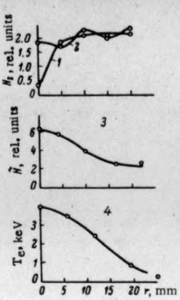

Fig. 5. Radial distribution of: 1) the magnetic field, before the excitation of the magnetodrift instability; 2) longitudinal magnetic field 1 μsec after the excitation of the magnetodrift instability; 3) amplitude of the magnetodrift waves; 4) electron temperature.

Figure 6 shows the amplitude and frequency of the low-frequency magnetodrift waves as functions of the initial hydrogen pressure. The bell-shaped functional dependence of the electron temperature on the initial pressure is due to the resonance properties of the initial high-frequency instability.[6] An important result of these experiments is the similarity of the functional dependences of all these quantities. On the basis of this similarity we conclude that the parameters of the low-frequency instability have the monotonic functional dependence on the electron temperature shown in Fig. 7.

A distinctive feature of this instability is the presence of a wave structure along the magnetic field ($k_z \neq 0$). The curves in part 1 of Fig. 8 are oscillograms of the signals from magnetic probes located 24 cm apart along the magnetic field. On the basis of a correlation analysis of these signals we can plot the phase of the first temporal harmonic of these waves along the axis of the system (curve 2 in Fig. 8). The wavelength found in this manner is 70 cm, i.e., the half-wavelength is roughly half the length of the coil. We find the corresponding value $k_z = 2\pi/\lambda_z \approx 0.1$. Over the interval of the phase measurements there is no appreciable axial gradient of the magnetic field before the waves appear (Fig. 2). The corresponding values for the second temporal harmonic are $\lambda_z = 35$ cm and $k_z \approx 0.2$ (curve 3 in Fig. 8).

The azimuthal structure of the instability is studied by means of three magnetic probes at various azimuthal positions and at equal distances from the center of the plasma. Figure 9 shows the wave phase as a function of the azimuthal angle.

This instability can be pictured as a cylindrical mag-

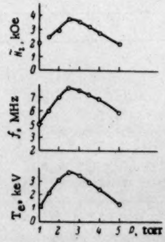

Fig. 6. Functional dependences on the initial hydrogen pressure. 1) Amplitude of the magnetodrift waves; 2) wave frequency; 3) electron temperature. Here p is given in units of 10^{-3} torr.

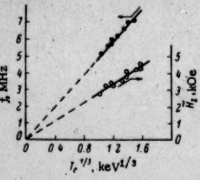

Fig. 7. Frequency (1) and amplitude (2) of the magnetodrift waves as functions of the plasma electron temperature.

netic tube with radius of the order of the dimension of the hot part of the plasma column, slightly bent in the radial direction and rotating around the geometric axis of the system at an angular velocity of the order of 10^7 sec^{-1}.

THEORY OF MAGNETODRIFT WAVES IN A FINITE-β PLASMA

Mikhailovskii and Fridman[4] have analyzed the excitation of magnetosonic drift waves in a finite-β plasma. We use their results to describe a possible mechanism for the excitation of the waves in these experiments. For this purpose, however, we require an analysis, more detailed than that of ref. 4, of the magnetodrift waves in a plasma with $T_e \gg T_i$, whose frequencies ω and wave vectors **k** satisfy

$$\omega \ll \omega_{Bi}, \quad k_\perp v_{Ti} \ll \omega_{Bi}, \quad k_z v_{Ti} \ll \omega \ll k_z v_{Te}. \tag{1}$$

Turning to this analysis, we start from the dispersion relation for unstable waves in the local approximation [Eq. (2.10) of ref. 4]:

$$k^2 \varepsilon_0 \left(\frac{k^2c^2}{\omega^2} - \varepsilon_2\right) + \alpha_2^2 = 0, \tag{2}$$

where ε_0, ε_2, and α_2 are determined with the help of inequalities (1):

$$\varepsilon_0 = \frac{\omega_{pi}^2}{\omega_{Bi}^2} - \frac{\omega_{pi}^2}{\omega^2}\cos^2\theta + \frac{\omega_{pi}^2(\varkappa_n - \varkappa_B)}{k_\perp \omega \omega_{Bi}}$$
$$+ \frac{\omega_{pe}^2}{k^2 v_{Te}^2}\left[1 + i\sqrt{\frac{\pi}{2}}\frac{\omega}{k_z v_{Te}}\left(1 - \frac{\omega_n}{\omega} + \frac{\omega_T}{2\omega}\right)\right],$$
$$\varepsilon_2 = -2\frac{k_\perp^2 v_{Ti}^2}{\omega_{Bi}^2}\frac{\omega_{pi}^2}{\omega^2} + i\sqrt{2\pi}\frac{\omega_{pe}^2}{\omega k_z v_{Te}}\frac{k_\perp^2 v_{Te}^2}{\omega_{Be}^2}\left(1 - \frac{\omega_n}{\omega} - \frac{3\omega_T}{2\omega}\right),$$
$$\alpha_2 = -\frac{k_\perp \omega_{pe}^2}{\omega \omega_{Be}}\left[1 + i\sqrt{\frac{\pi}{2}}\frac{\omega}{k_z v_{Te}}\left(1 - \frac{\omega_n}{\omega} - \frac{\omega_T}{2\omega}\right)\right].$$

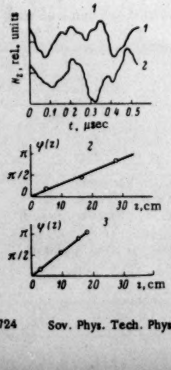

Fig. 8. Correlation analysis of the magnetodrift waves. 1) Magnetodrift waves according to probes 24 cm apart along the axis of the system, in the homogeneous part of the magnetic field; 2) profile of the phase of the standing wave along the axis, for the first temporal harmonic of the wave; 3) the same, for the second harmonic.

Here θ is the angle between **k** and H_z ($\cos\theta \equiv k_z/k \ll 1$), $\omega_{p\alpha} \equiv \sqrt{4\pi e_\alpha^2 n_0/m_\alpha}$ is the plasma frequency, $\omega_{B\alpha} \equiv e_\alpha H_z/m_\alpha c$ is the gyrofrequency of particles of species α (α = e,i; $e_e = -e_i < 0$), $\varkappa_{n,T,B} \equiv \mathrm{grad}\ln(n_0, T_e, H_z)$, and $\omega_{n,T} \equiv k_\perp T_e/(m_e\omega_{Be})\varkappa_{n,T}$.

We also use the equation $\varkappa_B = -(1/2)\beta(\varkappa_n + \varkappa_T)$, which follows from the pressure-balance equation $H_z^2/8\pi + n_0 + n_0T_e$ = const.

Using the condition $T_i \ll T_e$ and neglecting terms containing T_i in (2), we convert Eq. (2) to

$$\left[1 + \frac{k_\perp^2 v_s^2}{\omega_{Bi}^2} - \frac{k_z^2 v_s^2}{\omega^2} - \frac{\omega_n}{\omega}\left(1 - \frac{\varkappa_B}{\varkappa_n}\right) + i\sqrt{\frac{\pi}{2}}\frac{\omega}{k_z v_{Te}}\left(1 - \frac{\omega_n}{\omega} + \frac{\omega_T}{2\omega}\right)\right]$$
$$\times\left[1 - i\sqrt{\frac{\pi}{2}}\frac{\omega}{k_z v_{Te}}\beta\left(1 - \frac{\omega_n}{\omega} - \frac{3\omega_T}{2\omega}\right)\right]$$
$$+ \frac{\beta}{2}\left[1 + i\sqrt{\frac{\pi}{2}}\frac{\omega}{k_z v_{Te}}\left(1 - \frac{\omega_n}{\omega} - \frac{\omega_T}{2\omega}\right)\right]^2 = 0,$$
$$v_s \equiv \sqrt{\frac{T_e}{m_i}}. \tag{3}$$

Now, assuming the imaginary terms $\sim i(\omega/k_z v_{Te})$ in (3) to be small, we find that Eq. (3) has the two solutions $\omega = \omega_{1,2} + i\gamma_{1,2}$ ($|\gamma_{1,2}| \ll |\omega_{1,2}|$), where

$$\omega_{1,2} = \frac{1}{2}\omega_n\left(1 - \frac{\varkappa_B}{\varkappa_n}\right)\left(1 + \frac{\beta}{2} + \frac{k_\perp^2 v_s^2}{\omega_{Bi}^2}\right)^{-1}$$
$$\times\left\{1 \pm \left[1 + 4\frac{k_z^2 v_s^2}{\omega_n^2}\left(1 - \frac{\varkappa_B}{\varkappa_n}\right)^{-2}\left(1 + \frac{\beta}{2} + \frac{k_\perp^2 v_s^2}{\omega_{Bi}^2}\right)\right]^{1/2}\right\},$$
$$\gamma_{1,2} = -\sqrt{\frac{\pi}{8}}\frac{\omega_{1,2}^2}{k_z v_{Te}}\left(1 + \frac{\beta}{2} + \frac{k_\perp^2 v_s^2}{\omega_{Bi}^2}\right)^{-1}\left\{1 \pm \left[1 + 4\frac{k_z^2 v_s^2}{\omega_n^2}\left(1 - \frac{\varkappa_B}{\varkappa_n}\right)^{-2}\right.\right.$$
$$\left.\left.\times\left(1 + \frac{\beta}{2} + \frac{k_\perp^2 v_s^2}{\omega_{Bi}^2}\right)\right]^{-1/2}\right\}^{-1}\left[\left(1 + \beta + \frac{1}{2}\beta^2\right)\left(1 - \frac{\omega_n}{\omega_{1,2}}\right)\right.$$
$$\left. + \frac{\omega_T}{2\omega_{1,2}}\left(1 - \beta - \frac{3}{2}\beta^2\right)\right]. \tag{4}$$

The wave branch with frequency ω_1 in a low-β plasma ($\beta \to 0$, $\varkappa_B/\varkappa_n \to 0$) was first studied by Rudakov and Sagdeev,[7] who neglected the ion inertia ($k_\perp^2 v_s^2/\omega_{Bi}^2 \to 0$); Kadomtsev and Timofeev[8] took inertia into account.

It follows from (4) that the growth rate γ_1 increases with decreasing k_z, and under the condition

$$4\frac{k_z^2 v_s^2}{\omega_n^2}\left(1 - \frac{\varkappa_B}{\varkappa_n}\right)^{-2}\left(1 + \frac{1}{2}\beta + \frac{k_\perp^2 v_s^2}{\omega_{Bi}^2}\right) \ll 1$$

it is

$$\gamma_1 = \frac{1}{4}\sqrt{\frac{\pi}{2}\frac{m_e}{m_i}}\frac{\varkappa_n^2 v_s}{k_z}\frac{k_\perp^2 v_s^2}{\omega_{Bi}^2}\left(1 - \frac{\varkappa_B}{\varkappa_n}\right)\left(1 + \frac{1}{2}\beta + \frac{k_\perp^2 v_s^2}{\omega_{Bi}^2}\right)^{-3}$$
$$\times\left[\left(1 + \beta + \frac{1}{2}\beta^2\right)\left(\frac{\varkappa_B}{\varkappa_n} + \frac{1}{2}\beta + \frac{k_\perp^2 v_s^2}{\omega_{Bi}^2}\right)\right.$$
$$\left. + \frac{\varkappa_T}{2\varkappa_n}\left(\frac{3}{2}\beta^2 + \beta - 1\right)\left(1 + \frac{1}{2}\beta + \frac{k_\perp^2 v_s^2}{\omega_{Bi}^2}\right)\right]. \tag{5}$$

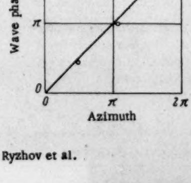

Fig. 9. Azimuthal profile of the phase of the magnetodrift wave for the first temporal harmonic.

The growth rate reaches a maximum at $k_\perp = k_0$, where k_0 is determined from

$$\left(\frac{k_0^2v_s^2}{\omega_{Bi}^2}\right)^2\left[1+\beta+\frac{1}{2}\beta^2+\frac{\varkappa_T}{2\varkappa_n}\left(\frac{3}{2}\beta^2+\beta-1\right)\right]-2\frac{k_0^2v_s^2}{\omega_{Bi}^2}\left(1-\frac{\varkappa_B}{\varkappa_n}\right)$$
$$\times\left(1+\beta+\frac{1}{2}\beta^2\right)-\left[\left(1+\frac{\beta}{2}\right)\left(1+\beta+\frac{1}{2}\beta^2\right)\left(\frac{\beta}{2}+\frac{\varkappa_B}{\varkappa_n}\right)\right.$$
$$\left.+\frac{\varkappa_T}{2\varkappa_n}\left(1+\frac{\beta}{2}\right)^2\left(\frac{3}{2}\beta^2+\beta-1\right)\right]=0. \tag{6}$$

When $\beta \gg 1$ and $\varkappa_n/\varkappa_T \sim 1$, we find $1 - \varkappa_B/\varkappa_n \approx \beta/2(1 + \varkappa_T/\varkappa_n)$, $k_0^2 = \beta(\omega_{Bi}^2/2v_s^2)p$, where

$$\left.\begin{aligned} p &\equiv \left(1+\frac{\varkappa_T}{\varkappa_n}\right)\left(1+\frac{3\varkappa_T}{2\varkappa_n}\right)^{-1}\\ &\times\left[1+\sqrt{1+\frac{\varkappa_T}{2\varkappa_n}\left(1+\frac{3\varkappa_T}{2\varkappa_n}\right)\left(1+\frac{\varkappa_T}{\varkappa_n}\right)^{-2}}\right],\\ \max\gamma_1 &= \sqrt{\frac{\pi}{8}\frac{m_e}{m_i}\frac{\varkappa_n^2v_s}{k_z}\frac{\beta^2}{4}\left(1+\frac{\varkappa_T}{\varkappa_n}\right)\frac{p}{(1+p)^3}\left[p+\frac{\varkappa_T}{2\varkappa_n}(1+3p)\right]},\\ \omega_1 &= -\varkappa_n v_s\sqrt{\frac{\beta}{2}\left(1+\frac{\varkappa_T}{\varkappa_n}\right)\frac{\sqrt{p}}{(1+p)}}. \end{aligned}\right\} \tag{7}$$

The second wave branch is easily seen to reach a maximum growth rate at

$$k_\perp \sim \frac{\omega_{Bi}}{v_s}\sqrt{1+\frac{1}{2}\beta},\quad k_z \sim \varkappa_n\sqrt{1+\frac{1}{2}\beta}, \tag{8}$$

and this growth rate is

$$\gamma_2 \sim |\varkappa_n| v_s\left(1+\frac{1}{2}\beta\right)^{3/2}\sqrt{\frac{m_e}{m_i}},\quad \omega_2 \sim \omega_n \sim \varkappa_n v_s\sqrt{1+\frac{1}{2}\beta}. \tag{9}$$

Obviously, only the first wave branch should be excited in our experiments, since the growth rate of the second branch is too small ($\gamma_2 \lessdot 10^6$ sec$^{-1} \ll \max\gamma_1$). The minimum values of k_z which can be used in (5) and (7) are governed by the length of the apparatus ($\min k_z \sim L^{-1}$), so that waves whose longitudinal wavelength is of the order of the length of the plasma column should be excited first. The conditions $\omega/k_zv_{Te} \ll 1$, $k_z^2v_s^2/\omega_n^2 \ll 1$ hold for these wavelengths. On the other hand, the condition $\gamma_1/\omega_1 \sim \sqrt{m_e/m_i\varkappa_n}L\beta^{2/3} \ll 1$ may not hold in the present experiments, since $\varkappa_nL \sim L/a \approx 10$ and since the local value of $\beta(r)$ at the center of the plasma is large: $\beta(0) \approx 5$–10. In this case Eq. (3) is also invalid, since the condition $\omega_{Me} \ll k_zv_{Te}$, no longer holds [here $\omega_{Me} = \varkappa_B k_\perp T_e/(m_e\omega_{Be})$ is the magnetodrift frequency, which appears in the resonant denominators $\omega - k_zv_z - \varepsilon\omega_{Me}$ of the dielectric tensor derived in ref. 4]. Since solutions (5), (7) constitute a limiting case of some more general solution of the dispersion relation, which also describes instabilities in the range $\omega_{Me} \sim k_zv_{Te}$, by extrapolating (5) and (7) to this range we find that in the present experiments magnetodrift waves with

$$\gamma \sim \omega \sim |\varkappa_n| v_s,\quad k_\perp \sim \frac{\omega_{Bi}}{v_s},\quad k_z \sim \frac{1}{L} \tag{10}$$

can be excited.

Estimates (10) agree with the experimental data: The wave growth is nearly aperiodic ($\gamma \sim \omega$), the wave frequency is a function of the temperature and a weak function of the amplitude of the external magnetic field, and the frequencies and wavelengths in (10) agree in order-of-magnitude terms with the experimental results. More precise agreement cannot be expected because the transverse wavelengths and the electron gyroradii are comparable to the radius of the plasma, so that the local approximation is not valid.

CONCLUSION

The instability in the present experiments is an electromagnetic wave whose frequency is much lower than the ion gyrofrequency, whose transverse wavelength is of the order of the plasma radius, whose longitudinal half-wavelength is of the order of the length of the homogeneous part of the magnetic field along the length of the coil, and whose azimuthal length is $2\pi a$. The amplitude of this instability has been shown experimentally to increase with increasing plasma electron temperature and to reach a large value after rapid turbulent plasma heating due to a high-frequency starting instability.

On the basis of this evidence we conclude that this instability is a branch of magnetodrift waves which are a natural continuation of electrostatic drift waves into the region of finite β.

The large wave amplitude observed indicates that this instability should strongly influence the plasma dynamics in a theta pinch.

The authors thank K. N. Stepanov for useful discussion of this work.

---

[1] L. I. Rudakov and R. Z. Sagdeev, Zh. Eksp. Teor. Fiz., 37, 1337 (1959) [Sov. Phys. – JETP, 10, 952 (1959)].

[2] A. B. Mikhailovskii, Theory of Plasma Instabilities, Vol. 2, Consultants Bureau, New York (1973).

[3] L. V. Mikhailovskaya and A. B. Mikhailovskii, Zh. Eksp. Teor. Fiz., 45, 1566 (1963) [Sov. Phys. – JETP, 18, 1077 (1964)].

[4] A. B. Mikhailovskii and A. M. Fridman, Zh. Eksp. Teor. Fiz., 51, 1430 (1966) [Sov. Phys. – JETP, 24, 965 (1967)].

[5] V. F. Aleksin and V. A. Suprunenko, Zh. Tekh. Fiz., 35, 1902 (1965) [Sov. Phys. – Tech. Phys., 10, 1465 (1966)].

[6] T. A. El-Khalafawy, V. A. Suprunenko (Souprunenko), A. M. Ternopol' (Ternopol), L. Khafis, and A. M. Yusef (Yousef), Plasma Physics, 11, 237 (1969).

[7] L. I. Rudakov and R. Z. Sagdeev, Dokl. Akad. Nauk SSSR, 138, 561 (1961).

[8] B. B. Kadomtsev and A. V. Timofeev, Dokl. Akad. Nauk SSSR, 146, 581 (1962) [Sov. Phys. – Dokl., 7, 826 (1963)].

Wave interaction in a thin plasma sheath

A. V. Pashchenko and B. N. Rutkevich

Physicotechnical Institute,
Academy of Sciences of the Ukrainian SSR, Khar'kov

(Submitted July 16, 1973)
Zh. Tekh. Fiz., 44, 1151-1160 (June 1974)

Electron oscillations in a plasma sheath in a strong longitudinal magnetic field are investigated. The model of a thin plasma sheath is substantiated, and solutions of the simple wave type are found and analyzed. The wave interaction in a thin plasma sheath is solved exactly. Simple asymptotic expressions are derived from the exact equations for a number of cases of practical importance.

1. INTRODUCTION

It is well known that wave interaction in a nonlinear medium, in a plasma in particular, produces combination frequencies; the spectrum changes in the course of wave propagation. The evolution of the spectrum has been studied theoretically and experimentally.[1–6]

Wave interaction is normally described by asymptotic methods,[7,8] which make it possible, in the case of a small nonlinearity, to reduce the problem to a system of approximate (truncated) equations for the amplitudes of the interacting waves. The solution of the approximate system yields the spectrum of combination frequencies and its evolution, at least in the initial stage of the interaction process. This approach is acceptable for a weakly turbulent plasma, in which case the phases of the waves are random variables. In situations where the phases can be regarded as deterministic, however, the indicated approximation becomes inapplicable for large times or coordinates. In this case, as in the case of large initial amplitudes, a rigorous analysis is needed to describe the evolution of the waves. This situation arises, in particular, in the investigation of simple waves.

We have shown previously[9] that simple-wave solutions occur in the study of a thin plasma sheath in a strong longitudinal magnetic field. The wave-interaction problem reduces to the solution of a transcendental equation describing a simple wave excited by sinusoidal oscillations.

In the present work an exact solution is obtained for the problem of the oscillation spectrum at any point z of a thin plasma sheath. Simple asymptotic representations are found for several cases of practical importance. The resulting expressions describe the familiar steepening of the simple wave front. The latter effect accompanies the generation of harmonics and combination-frequency oscillations. For small amplitudes and short distances the expression describing the oscillation spectrum agrees with the result obtained by the method of truncated equations.[4] The well-known Bessel–Fubini equation follows from the same relation when only one wave is excited in the sheath.[10,11]

Simple waves in a thin plasma sheath are investigated below; an exact solution is found for any distance from the point z = 0 at which oscillations are excited at frequencies ω_1 and ω_2. Calculations yielding a number of useful asymptotic expressions are described.

2. WAVES IN A THIN PLASMA SHEATH

Consider a cold plasma sheath of thickness 2d located symmetrically about the plane x = 0 in the space between two conducting planes x = ±D at zero potential. The system is assumed to be homogeneous in the y direction. A magnetic field strong enough to permit only longitudinal motions of the electrons is applied in the z direction. The density n_0 of the unperturbed plasma is assumed to be constant throughout the sheath.

The electron oscillations in the sheath are described by the equations

$$\frac{\partial v}{\partial t}+v\frac{\partial v}{\partial z}=\frac{e}{m}\frac{\partial \varphi}{\partial z}, \tag{1}$$

$$\frac{\partial n}{\partial t}+\frac{\partial}{\partial z}(nv)=0, \tag{2}$$

$$\frac{\partial^2\varphi}{\partial x^2}+\frac{\partial^2\varphi}{\partial z^2}=\begin{cases}4\pi e(n-n_0), & |x|<d,\\ 0, & d<|x|<D,\end{cases} \tag{3}$$

in which conventional notation is used.

Taking account of the symmetry of the problem and transforming to dimensionless variables $\eta = x/D$ and $\zeta = z/L$, where L is the characteristic scale of the perturbation in the z direction (wavelength), we write the potential φ as a series:

$$\varphi_1=\sum_{n=0}^{\infty}\frac{\partial^{2n}\varphi(\eta,\zeta)}{\partial\eta^{2n}}\bigg|_{\eta=0}\frac{\eta^{2n}}{(2n)!},\quad |\eta|\leqslant\eta_d\equiv\frac{d}{D},$$

$$\varphi_2=\sum_{n=0}^{\infty}\frac{\partial^{n}\varphi(\eta,\zeta)}{\partial\eta^{n}}\bigg|_{\eta=\eta_d}\frac{(\eta-\eta_d)^{n}}{n!},\quad \eta_d\leqslant\eta\leqslant 1.$$

According to the Laplace equation

$$\frac{\partial^2\varphi_2}{\partial\eta^2}+\zeta_D^2\frac{\partial^2\varphi_2}{\partial\zeta^2}=0\quad\left(\zeta_D=\frac{D}{L}\right),$$

terms beginning with n = 2 can be neglected with error $O(\zeta_D^2)$ in the series φ_2 for $\zeta_D \ll 1$. Only the first two terms need be retained in the series φ_1 for $\eta_d \ll 1$, with error $O(\eta_d^4)$. The application of the matching conditions

$$\left(\varphi_1(\eta_d,\zeta)=\varphi_2(\eta_d,\zeta);\quad \frac{\partial\varphi_1(\eta,\zeta)}{\partial\eta}\bigg|_{\eta=\eta_d}=\frac{\partial\varphi_2(\eta,\zeta)}{\partial\eta}\bigg|_{\eta=\eta_d}\right)$$

and the boundary condition $[\varphi_2(1,\zeta) = 0]$ to φ_1 and φ_2 and the substitution of φ_1 into Eq. (3) then gives

$$\varphi=\begin{cases}-4\pi e(n-n_0)dD\left(1-\frac{\eta_d}{2}-\frac{\eta^2}{2\eta_d}\right), & |\eta|\leqslant\eta_D,\\ -4\pi e(n-n_0)dD(1-|\eta|), & \eta_D\leqslant|\eta|\leqslant 1.\end{cases}$$

Inasmuch as $\eta_d \ll 1$, inside the sheath with error $O(\eta_d)$ we have

$$\varphi = -4\pi e(n - n_0)\,dD. \tag{4}$$

Substituting (4) into (1) and writing $\lambda = 4\pi e^2 dD/m$, we obtain the equation

$$\frac{\partial v}{\partial t} + v\frac{\partial v}{\partial z} + \lambda\frac{\partial n}{\partial z} = 0, \tag{5}$$

which, in conjunction with (2), determines n and v as functions of z and t.

The system of equations (2) and (5) has a solution in the form of simple waves. All variables in the simple waves are expressed in terms of one of them, for example the velocity v. In particular, the propagation velocity w of a point on the wave profile corresponding to a given value of the velocity v is itself a function of v. By definition

$$\frac{\partial v}{\partial t} + w\frac{\partial v}{\partial z} = 0, \tag{6}$$

so that the system (2)-(5) in combination with (6) implies the relations

$$\lambda n = (v - w)^2 \tag{7}$$

and

$$w = w_0\left(\pm 1 + \frac{3}{2}\frac{v}{w_0}\right), \tag{8}$$

in which $w_0 = \omega_0/\varkappa$, $\omega_0^2 = 4\pi e^2 n_0/m$, $\varkappa^2 = (dD)^{-1}$.

What is specific to the given problem is the designation of the particle velocity rather than the particle displacement as the primary function. Thus, the plasma is perturbed by the application of a modulating voltage at a certain point. It follows from (4), (7), and (8), however, that the velocity is then modulated by a corresponding relation at that point. Therefore, the problem of how to include the initial particle displacements having been eliminated, nonlinear "streaming" (a constant velocity component), which is directly attributable to that problem,[10,11] does not occur in the thin plasma sheath.

If an initial perturbation $v(0, t_0) = F(t_0)$ arises at the point $z_0 = 0$, the solution of Eq. (6) takes the form

$$v = F\left(t - \frac{z}{w(v)}\right). \tag{9}$$

Waves propagate in the plasma layer symmetrically about the excitation point $z_0 = 0$, so that we only consider $z > 0$ and, accordingly, choose the plus sign in (8).

If we consider the case of special significance, in which the initial perturbation is sinusoidal, we find that a wave with a changing profile propagates in the system; the slope of the wave front becomes steeper with increasing z, and harmonics of the fundamental frequency appear in the spectrum.[10,11]

With the intention of describing not only harmonic generation, but also wave interaction, we assume that the initial velocity perturbation represents a superposition of harmonics with frequencies ω_1 and ω_2 and amplitudes A_1 and A_2:

$$F(t_0) = \sum_{j=1}^{2} A_j \sin(\omega_j t_0). \tag{10}$$

Equation (9) then assumes the form

$$\xi = \sum_{j=1}^{2} a_j \sin\left(\psi_j + \frac{q_j\xi}{1+\xi}\right), \tag{11}$$

where

$$\xi = \frac{3}{2}\frac{v}{w_0},\quad a_j = \frac{3}{2}\frac{A_j}{w_0},\quad q_j = \frac{\omega_j z}{w_0},\quad \psi_j = \omega_j\tau,\quad \tau = t - \frac{z}{w_0}.$$

We now determine the values of ξ, τ, and z for which wave overturning takes place. In overturning $\partial\xi/(\partial z) = \infty$, the following equation follows from (11):

$$(1+\xi)^2 = \sum_{j=1}^{2} a_j q_j \cos\left(\psi_j + \frac{q_j\xi}{1+\xi}\right). \tag{12}$$

Since we are concerned with the minimum distance $z_{\min}$ at which overturning can take place, we augment (12) with the following expression, implied by the condition $\partial^2\xi/(\partial z^2) = 0$:

$$-2(1+\xi)^3 = \sum_{j=1}^{2} a_j q_j^2 \sin\left(\psi_j + \frac{q_j\xi}{1+\xi}\right). \tag{13}$$

The system of equations (11)-(13) determines $z_{\min}$ and the corresponding quantities $\xi_{\min}$ and $\tau_{\min}$.

We only estimate $z_{\min}$. We proceed from the fact that for any τ other than $\tau_{\min}$ the overturning distance calculated from Eqs. (11) and (12) must be greater than $z_{\min}$. If we choose $\tau = 0$, we infer from (11) that $\xi = 0$ as well, whereupon it follows from (12) that $z_{\min}$ and, thus, any z for which our solution is valid must satisfy the condition

$$a_1q_1 + a_2q_2 < 1. \tag{14}$$

If we regard ξ as a function of a_1 and a_2 we find that it has continuous partial derivatives $\partial^{n+m}\xi/(\partial a_1^n \partial a_2^m)$ (n, m ≥ 0) in the neighborhood of the point (0, 0). The derivatives all go to infinity "simultaneously" at a certain line in the plane $\{a_1, a_2\}$, and the condition for this event coincides with condition (12). This means that ξ is an analytic function of a_1 and a_2 up to overturning.

3. WAVE INTERACTION IN THE SHEATH

The problem at this stage is to derive the spectrum of combination frequencies from the transcendental equation (11) and to describe its evolution with z.

The analogous problem for the case of one harmonic perturbation has been solved[10,11] on the assumption that $a_1 \ll 1$.

The remainder of the analysis is carried out for the weaker condition $(a_1 + a_2) < 1$.

We rewrite (11), using an exponential relation for the sine:

$$\xi = \sum_{j=1}^{2} \frac{a_j}{2i} \left[e^{i\left(\psi_j + \frac{q_j \xi}{1+\xi}\right)} - e^{-i\left(\psi_j + \frac{q_j \xi}{1+\xi}\right)} \right], \tag{15}$$

and then we apply to (15) the equation for the generating function for Laguerre polynomials (see ref. 12, Table 8.975-1):

$$(1-z)^{-\alpha-1} \exp\left(\frac{xz}{z-1}\right) = \sum_{n=0}^{\infty} L_n^{\alpha}(x) z^n, \quad |z| < 1, \tag{16}$$

where

$$L_n^{\alpha}(x) \doteq \sum_{m=0}^{n} (-1)^m \binom{n+\alpha}{n-m} \frac{x^m}{m!}.$$

We find that

$$\xi = \sum_{n=0}^{\infty} \sum_{j=1}^{2} (-1)^n a_j G_n^{(j)} \xi^n, \tag{17}$$

where

$$G_n^{(j)} = \frac{e^{i\psi_j} L_n^{-1}(iq_j) - e^{-i\psi_j} L_n^{-1}(-iq_j)}{2i}. \tag{18}$$

As the condition for the applicability of (16) implies, Eq. (17) is valid for $(a_1 + a_2) < 1$.

We represent ξ as a double series:

$$\xi = \sum_{k,\, m=0}^{\infty} A_{km} a_1^k a_2^m, \tag{19}$$

which we use to obtain the relation

$$\xi^n = \sum_{k,\, m=0}^{\infty} \left(\sum_{\sum_{l=1}^{n} i_l = k,\ \sum_{l=1}^{n} j_l = m} \prod_{l=1}^{n} A_{i_l j_l} \right) a_1^k a_2^m. \tag{20}$$

Substituting (20) into (17) and comparing the result with (19), we have

$$\begin{aligned} \underset{k+m\neq 0;\ 1}{A_{km}} = \sum_{n=1}^{k+m-1} (-1)^n \Bigg\{ & G_n^{(1)} \sum_{\sum_{l=1}^{n} i_l = k-1,\ \sum_{l=1}^{n} j_l = m} \prod_{l=1}^{n} A_{i_l j_l} \\ & + G_n^{(2)} \sum_{\sum_{l=1}^{n} i_l = k,\ \sum_{l=1}^{n} j_l = m-1} \prod_{l=1}^{n} A_{i_l j_l} \Bigg\}. \end{aligned} \tag{21}$$

Equation (17) implies that

$$A_{00} = 0, \quad A_{10} = G_0^{(1)}, \quad A_{01} = G_0^{(2)}. \tag{22}$$

Using these values we obtain the coefficients A_{km} in explicit form from the recursion relation (21):

$$A_{km} = (-1)^{k+m-1} \frac{(k+m-1)!}{k!\,m!} \sum_{\sum_{l=1}^{k} i_l + \sum_{r=1}^{m} j_r = k+m-1} \prod_{l=1}^{k} G_{i_l}^{(1)} \prod_{r=1}^{m} G_{j_r}^{(2)}. \tag{23}$$

In (23) $k + m \neq 0$; all quantities associated with the index k(m) drop out for k = 0 (m = 0).

We use Eq. (18) to compute the derivative of the functions G:

$$\begin{aligned} \prod_{l=1}^{k} G_{i_l}^{(1)} \prod_{r=1}^{m} G_{j_r}^{(2)} = {} & \frac{1}{(2i)^{k+m}} \\ & \times \sum_{s=0}^{k} \sum_{f=0}^{m} (-1)^{s+f} \exp\{i[(k-2s)\psi_1 + (m-2f)\psi_2]\} \\ & \times \sum_{\sum_{l=1}^{k} x_l = (k-2s) i q_1,\ \sum_{r=1}^{m} y_r = (m-2f) i q_2} \prod_{l=1}^{k} L_{i_l}^{-1}(x_s) \prod_{r=1}^{m} L_{j_r}^{-1}(y_r), \end{aligned} \tag{24}$$

where each x and y in each term assumes one value from the respective sets $(iq_1, -iq_1)$ and $(iq_2, -iq_2)$.

The sum of the G products

$$P = \sum_{\sum_{l=1}^{k} i_l + \sum_{r=1}^{m} j_r = k+m-1} \prod_{l=1}^{k} G_{i_l}^{(1)} \prod_{r=1}^{m} G_{j_r}^{(2)}$$

acquires the following form after the substitution of (24) and a change in the order of summation:

$$\begin{aligned} P = \frac{1}{(2i)^{k+m}} & \sum_{s=0}^{k} \sum_{f=0}^{m} (-1)^{s+f} \exp\{i[(k-2s)\psi_1 + (m-2f)\psi_2]\} \\ & \times \sum_{\sum_{l=1}^{k} x_l = (k-2s) i q_1,\ \sum_{r=1}^{m} y_r = (m-2f) i q_2} \\ & \times \sum_{\sum_{l=1}^{k} i_s + \sum_{r=1}^{m} j_r = k+m-1} \prod_{l=1}^{k} L_{i_l}^{-1}(x_l) \prod_{r=1}^{m} L_{j_r}^{-1}(y_r). \end{aligned} \tag{25}$$

Applying the addition theorem for Laguerre polynomials:[12]

$$L_n^{\sum_{l=1}^{k} \alpha_l + k - 1} \left(\sum_{l=1}^{k} x_l \right) = \sum_{\sum_{l=1}^{k} i_l = n} \prod_{l=1}^{k} L_{i_l}^{\alpha_l}(x_l),$$

we find that the last sum in (25) is

$$L_{k+m-1}^{-1} \left(\sum_{l=1}^{k} x_l + \sum_{r=1}^{m} y_r \right).$$

After summation over x and y we find

$$\begin{aligned} P = \frac{1}{(2i)^{k+m}} & \sum_{s=0}^{k} \sum_{f=0}^{m} (-1)^{s+f} \exp\{i[(k-2s)\psi_1 + (m-2f)\psi_2]\} \\ & \times \binom{k}{s} \binom{m}{f} L_{k+m-1}^{-1} \{i[(k-2s) q_1 + (m-2f) q_2]\}. \end{aligned} \tag{26}$$

It then follows from (19), (23), and (26) that

$$\xi=\sum_{\substack{k=0\\ k+m\neq 0}}^{\infty}\sum_{m=0}^{\infty}\frac{(-1)^{k+m-1}(k+m-1)!}{(2i)^{k+m}k!\,m!}a_1^k a_2^m\sum_{s=0}^{k}\sum_{f=0}^{m}(-1)^{s+f}\exp\times\{i[(k-2s)\psi_1+(m-2f)\psi_2]\}\binom{k}{s}\binom{m}{f}L^{-1}_{k+m-1}\times\{i[(k-2s)q_1+(m-2f)q_2]\}. \tag{27}$$

Changing the order of summation on s, f and k, m in (27), we obtain ξ as a series in sines and cosines of the combination phase angles:

$$\xi=\sum_{\substack{l=0\\ l+p\neq 0}}^{\infty}\sum_{p=0}^{\infty}\sum_{k=0}^{\infty}\sum_{m=0}^{\infty}\frac{(-1)^{k+m-1}(2k+2m+l+p-1)!}{k!\,(k+l)!\,m!\,(m+p)!}\left(\frac{a_1}{2}\right)^{2k+l}\left(\frac{a_2}{2}\right)^{2m+p}\times\sum_{j=1}^{2}(-1)^{jp}\operatorname{Re}\{e^{i\psi_{lp}}(i)^{2m+2k+l+p}L^{-1}_{2k+2m+l+p-1}(iQ_{lp})\}, \tag{28}$$

where $Q_{lp} \equiv Q = lq_1 + (-1)^j pq_2$ is the combination argument describing the wave amplitude and $\psi_{lp} = l\psi_1 + (-1)^j p\psi_2$ is the combination phase.

Equation (28) is symmetric under the permutation of indices. This fact makes it possible to treat Q in the subsequent calculations as a positive quantity. The summation on j is not carried out in (28) for $l = 0$. The case in which $l = 0$ is obtained from the preceding case by a simple change of indices.

Equation (28) gives an explicit solution of the two-wave interaction problem. When $l = 1$ and $p = 0$ ($l = 0$, $p = 1$) we obtain the variation of the fundamental-frequency amplitudes with z. If p = 0 and m = 0 ($l = 0$, k = 0), we obtain the harmonic variation induced by the self-action of a wave; if p = 0 and m ≠ 0 ($l = 0$, k ≠ 0), we obtain the variation induced in the same harmonics by wave interaction. The case in which $l \neq 0$ and $p \neq 0$ gives the combination-frequency spectrum, where j = 1 corresponds to the red satellites, and j = 2 to the violet satellites.

Expression (28) can be simplified. We use the integral representation for the Laguerre polynomials (ref. 12, Table 6.631.10):

$$\int_0^{\infty}e^{-x^2}x^{2n+\mu+1}I_{\mu}(2x\sqrt{z})\,dx=\frac{n!}{2}e^{-z}z^{\frac{1}{2}\mu}L_n^{\mu}(z), \tag{29}$$

where

$$n=0,\ 1\ \ldots;\quad \operatorname{Re}\mu+n>-1. \tag{30}$$

The contour of integration in (29) is chosen so that the expression $e^{-x^2}x^{2n+\mu+2}I_{\mu}(2x\sqrt{z})$ is zero at its end points.[13]

Inasmuch as $\mu = -1$ and $n = 2m + 2k + l + p - 1$ in (28), the restriction (30) renders Eq. (29) invalid for the sets of indices (m = 0, k = 0, l = 1, p = 0) and (m = 0, k = 0, l = 0, p = 1), so that the case $l + p = 1$ requires special consideration.

Replacing the Laguerre polynomials in (28) in accordance with (29), changing the order of integration on x and of summation on k and m, and truncating the series thus formed, we obtain the expressions

$$\left.\begin{aligned}&\xi=\xi_1+\xi_2,\\ &\xi_1=2\sum_{m=1}^{2}\operatorname{Re}\left\{e^{i\psi_m}\left[\frac{a_m}{2i}(1-2R(q_m))+2M_{10}(q_m;\ a_m;\ a_k)\right]\right\},\\ &\xi_2=4\sum_{\substack{l=0\\ l+p\neq 0;\ 1}}^{\infty}\sum_{p=0}^{\infty}\sum_{j=1}^{2}(-1)^{jp+1}\operatorname{Re}\{e^{i\psi_{lp}}(-1)^{l+p}M_{lp}(Q;\ a_1;\ a_2)\},\end{aligned}\right\} \tag{31}$$

in which m + k = 3,

$$R(q_m)=e^{iq_m}(iq_m)^{1/2}\int_0^{\infty}e^{-x^2}I_{-1}(2x\sqrt{iq_m})\,dx, \tag{32}$$

$$M_{lp}(Q:a_1:a_2)=e^{iQ}(iQ)^{1/2}\int_0^{\infty}\frac{e^{-x^2}}{x^2}I_{-1}(2x\sqrt{iQ})\,I_s\left(\frac{a_1x^2}{i}\right)I_p\left(\frac{a_2x^2}{i}\right)dx. \tag{33}$$

The integration in (32) and (33) is carried out over the same contour; ξ_1 is the result obtained for cases with $l + p = 1$ when M_{10} is derived artificially without violating conditions (30) by the introduction of a term containing $R(g_m)$.

Because of the integral form of M_{lp} and R Eq. (31) provides a relatively simple means for obtaining asymptotic expressions and estimates.

4. ASYMPTOTIC REPRESENTATIONS

We first use the method of steepest descent to find asymptotic expressions for M_{lp} and R for $Q \gg 1$, making the change of variable $x = 2i\sqrt{iQy}$ in (32) and (33). If it is assumed that $y = \alpha + i\beta$, the change of variable makes it necessary to choose a contour of integration below the line $\beta = -\alpha$, and the expressions themselves assume the form

$$R(g_m)=2q_m e^{iq_m}\int_0^{\infty}e^{4iq_m y^2}I_1(-4q_m y)\,dy, \tag{32'}$$

$$M_{sp}=\frac{ie^{iQ}}{2}\int_0^{\infty}\frac{e^{4iQy^2}}{y^2}I_1(-4Qy)\,I_s(-4a_1Qy^2)\,I_p(-4a_2Qy^2)\,dy. \tag{33'}$$

The contour of integration C in (32') and (33') is assumed to consist of C_1 and C_2, where C_1 is the part of C on which $4Q|y| \ll 1$ and C_1 terminates inside the circular domain, in which $4Q|y^2| \ll 1$. It can be shown that M_{lp} can be made at least of order $O(1/Q^2)$ on C_1 for $l + p > 1$. Terms with R and M_{10} in ξ_1 cancel one another on C_1, because they become asymptotically equal and opposite in sign. Since $a_m q_m < 1$ in our problem, an error not greater than $O(1/q^2)$ is guaranteed.

The function $I_1(-4Qy)$ can be replaced on C_2 by its asymptotic representation

$$I_1(-4Qy)=\frac{1}{\sqrt{-2\pi Qy}}\cos\left(4Qy+\frac{3}{4}\pi\right)\left[1+O\left(\frac{1}{Q}\right)\right]. \tag{34}$$

The substitution of (34) into (32') and (33') yields

$$R(q_m)=\sqrt{\frac{q_m}{2\pi}}\,e^{iq_m+i3/4\pi}\left(\int_{C_1}+\int_{C_2'}\right)\left(e^{4iq_m(y^2+y)}\frac{dy}{\sqrt{-y}}\right), \tag{32''}$$

$$M_{lp}(Q,a_1,a_2)=\frac{ie^{iQ+i3/4\pi}}{4\sqrt{2\pi Q}}$$

$$\times\left(\int_{C_2}+\int_{C_2'}\right)\left(e^{4iQ(y^2+y)}\frac{I_l(-4a_1Qy^2)\,I_p(-4a_2Qy^2)}{y^2\sqrt{-y}}dy\right), \qquad (33'')$$

where C_2' is a contour above the line $\beta=-\alpha$. We assume that C_2 begins at the point (α_0, β_0) $(\alpha_0=-B/Q^{\eta};\ \beta_0=E/Q^{\eta};$ $B, E>0;\ 1/2<\eta<1)$ and then goes to infinity. Thus, C_2' begins at the point $(-\alpha_0, -\beta_0)$, from which it also goes to infinity. It can be shown that the integrals along C_2' are exponentially small. We compute the integral along C_2 by the method of steepest descent.

We first consider the case in which $a_m \ll 1$. The functions I_l and I_p vary only slightly in comparison with e^{4iQy^2}, and their dependence on Q can be neglected. The contour C_2 is drawn through the saddle point $y = 1/2$ along the line of the steepest cent $\beta=\alpha+1/2$. The integral along C_2 is of the type $F(Q)=\int_{C}\varphi(z)e^{Qh(z)}dz$, for which the contribution from the saddle point a is given by the expression[14,15]

$$V_a(Q)=\sqrt{-\frac{2\pi}{Qh''(a)}}\,\varphi(a)\,e^{Qh(a)}\left[1+O\left(\frac{1}{Q}\right)\right]. \qquad (35)$$

Inasmuch as the contribution of the beginning of the contour C_2 and the part of it with $|y|\gg 1$ to the integral is exponentially small and $\mathrm{Re}[4i(y^2+y)]$ is a maximum at the saddle point $y=-1/2$, the asymptotic behavior of M_{lp} and $R(q_m)$ for $Q\gg 1$ $(q_m\gg 1)$, according to a theorem given in ref. 14 (1.6.2), is determined by Eq. (35).

Carrying out the calculations, we obtain

$$R(q_m)=\frac{1}{2}\left[1+O\left(\frac{1}{q_m}\right)\right], \qquad (36a)$$

$$M_{lp}(Q,a_1,a_2)=\frac{i(-1)^{l+p}}{2Q}I_l(a_1,Q)\,I_p(a_2,Q)\left[1+O\left(\frac{1}{Q}\right)\right]. \qquad (36b)$$

In the case $a_m \not\ll 1$, when the dependence of I_l and I_p on Q cannot be neglected in (33"), integral representations are used for I_l and I_p in accordance with the relation

$$I_n(z)=\frac{1}{2\pi}\int_{-\pi}^{\pi}e^{-in\theta+iz\sin\theta}d\theta. \qquad (37)$$

Substituting I_l and I_p into (33") and integrating over y by the method of steepest descent, we obtain

$$M_{lp}=\frac{ie^{iQ}}{8\pi^2Q}\int_{-\pi}^{\pi}e^{-li\theta_1-pi\theta_2-\frac{iQ}{1-a_1\sin\theta_1-a_2\sin\theta_2}}$$

$$\times(1-a_1\sin\theta_1-a_2\sin\theta_2)^2\,d\theta_1 d\theta_2. \qquad (38)$$

Equation (36b) follows from the latter expression for $a_m \ll 1$, with error $O(a_m)$. For larger values of a_m the method of steepest descent is used $(Q\gg 1)$. The saddle points are $\theta_m=\pm\pi/2$. Applying Eq. (35) several times, we have

$$M_{lp}=\frac{ie^{iQ}}{4\pi Q^2\sqrt{a_1a_2}}\sum_{m,n=1}^{2}\exp\left\{i\frac{\pi}{2}[l(-1)^m+p(-1)^n]\right.$$

$$\left.-\frac{iQ}{1+(-1)^m a_1+(-1)^n a_2}+i\frac{\pi}{4}[(-1)^m+(-1)^n]\right\} \qquad (39)$$

$$\times[1+(-1)^m a_1+(-1)^n a_2]^4\,[1+O(1/Q)].$$

Equation (36b) holds not only for $Q\gg 1$, but also for $Q\ll 1$ and for $Q\sim 1$. This fact can be verified by applying Eq. (29) to (33') after differentiation with respect to a_m, replacement of I_p by the representation (37), and changing of the order of integration. It is then sufficient to assume that a_m and Qa_m^2 are small in order to obtain (36b). An error $O(\varepsilon)$ is guaranteed for small values of Q, where $\varepsilon=\max(a, Qa^2)$, $a=\max(a_1, a_2)$.

The substitution of (36a) and (36b) into (31) yields the asymptotic expression

$$\xi=2\sum_{\substack{l=0\\ l+p\neq 0}}^{\infty}\sum_{p=0}^{\infty}\sum_{j=0}^{2}(-1)^{jp}\frac{1+O(\delta)}{Q_{lp}}I_l(a_1Q_{lp})\,I_p(a_2Q_{lp})\sin\psi_{lp}, \qquad 40)$$

in which $\delta=\max(a,\sigma)$, $\sigma=\min(Qa^2, 1/Q)$.

For the case in which only one wave is excited, i.e., for $p=0$ and $a_2=0$, the classical Bessel–Fubini equation[10,11] is obtained from (40):

$$\xi=2a_1\sum_{l=1}^{\infty}\frac{I_l(la_1q_1)}{la_1q_1}\sin l\psi_1, \qquad (41)$$

so that (40) is the generalization of that equation to the case of wave interaction.

If we put $a_1Q_{ep}\ll 1$ in (40), we obtain the following expression for $p=x(p=1, 2, \ldots)$ satellites of the fundamental frequency ω_1:

$$\xi_{1p}=a_1\sum_{j=1}^{2}(-1)^{jp}I_p(a_2Q_{1p})\sin\psi_{1p}, \qquad (42)$$

which coincides with the result obtained by the method of truncated equations.[4]

If also $a_2Q_{1p}\ll 1$ in this case, then

$$\xi_{1p}=a_1\sum_{j=1}^{2}\frac{(-p)^{jp}}{p!}\left[\frac{a_2(\omega_1+(-1)^j p\omega_2)}{2w_0}z\right]^p\sin\psi_{1p}, \qquad (43)$$

whence it follows that energy is transferred predominantly into the high-frequency part of the spectrum under the conditions of applicability of Eqs. (42) and (43). The asymmetry in the amplitudes of the "red" and "violet" satellites increases as the frequencies ω_1 and ω_2 come closer together.

We obtain the following expression from (40) for oscillations at the fundamental frequency ω_1:

$$\xi_{10}=\frac{2}{q_1}I_1(a_1q_1)\,I_0(a_2q_1)\sin\psi_1, \qquad (44)$$

from which, by condition (14), it is inferred that the fundamental-frequency amplitudes decay monotonically up to inversion of the simple wave.

Another asymptotic representation for ξ in the case of small l and p, $Q \nless 1$, and $a_m \ll 1$ can be obtained from (28) by putting m = 0 and k = 0:

$$\xi = \sum_{\substack{l=0 \\ l+p\neq 0}}^{\infty} \sum_{p=0}^{\infty} \frac{(l+p-1)!}{e!\,p!} \left(\frac{a_1}{2}\right)^l \left(\frac{a_2}{2}\right)^p [1 + 0(p)] \times \sum_{j=1}^{2} (-1)^{jp+1} \mathrm{Re}\,\{e^{i\psi_{lp}} (i)^{l+p} L_{l+p-1}^{-1}(lQ)\}, \tag{45}$$

where

$$\xi = \sum_{\substack{l=0 \\ l+p\neq 0}}^{\infty} \sum_{p=0}^{\infty} \sum_{j=1}^{2} \frac{(-1)^{l+p+jp}[1 + 0(1/Q)]}{\pi Q_{lp}^{\frac{1}{2}} \sqrt{a_1 a_2}} \sum_{m,n=1}^{2} [C_{mn}]^{l} \sin(\psi_{lp} + \Phi_{mn}),$$

If Eq. (39) is substituted into (31), an asymptotic expression suitable for any a when $Q \gg 1$ is obtained:

$$C_{mn} = 1 + (-1)^m a_1 + (-1)^n a_2$$

$$\Phi_{mn} = \frac{\pi}{2}[l(-1)^m + p(-1)^n] + \frac{\pi}{4}[-1)^m + (-1)^n] + Q_{lp}\left(1 - \frac{1}{C_{mn}}\right).$$

where

$$C_{mn} = 1 + (-1)^m a_1 + (-1)^n a_2\ ,$$

$$\Phi_{mn} = \frac{\pi}{2}[l(-1)^m + p(-1)^n] + \frac{\pi}{4}[-1)^m + (-1)^n] + Q_{lp}\left(1 - \frac{1}{C_{mn}}\right).$$

In using Eq. (46) it is important to remember that $(a_1q_1 + a_2q_2) < 1$ in our problem, so that for small l and p the condition $Q \gg 1$ is not satisfied for arbitrary a ($a <$ 1), and (46) can have low accuracy. Moreover, the situation can arise in which Q is small for the "red" satellites, i.e., for j = 1, so that even though the "violet" satellites (j = 2) are described by Eq. (46), it is necessary to use another asymptotic expression.

When $Q \sim 1$ and a is not small, it is necessary to use Eq. (28) with however many terms are required to attain the necessary accuracy. Inasmuch as this asymptotic expression is needed for small l and p, only a few terms are required.

We point out that Eq. (40) is easily derived from (28) by replacing the Laguerre polynomial with its leading term for large values of Q.

We also note that oscillations with initial phases φ_1 and φ_2, which must be related by the condition $v|_{t=0} = 0$, can be specified at the driving point $z_0 = 0$. The introduction of φ_1 and φ_2 alters the determination of ψ_1 and ψ_2, but does not affect the form of any of the other expressions [except condition (14)].

The condition relating φ_1 and φ_2 has the form

$$a_1 \sin \varphi_1 + a_2 \sin \varphi_2 = 0.$$

The phases φ_1 and φ_2 are involved as terms in ψ_1 and ψ_2, respectively, and (14) goes over to the inequality

$$a_1 q_1 \cos \varphi_1 + a_2 q_2 \cos \varphi_2 < 1. \tag{14'}$$

Since the expressions derived above originate from an analysis of wave interaction in a thin plasma sheath, they must not be used for values of z close to the overturning distance, because the condition $D \ll L$ is violated in that case, i.e., the thin-sheath model becomes invalid.

---

[1] B. B. Kadomtsev and V. I. Karpman, Usp. Fiz. Nauk, 103, 193 (1971) [Sov. Phys.–Usp., 14, 40 (1971)].

[2] V. N. Tsytovich, Nonlinear Effects in Plasma, Plenum Press, New York (1970).

[3] I. S. Danilkin, Zh. Tekh. Fiz., 35, 667 (1965) [Sov. Phys.–Tech. Phys., 10, 524 (1965)].

[4] A. S. Bakai, Nucl. Fusion, 10, 53 (1970).

[5] K. S. Karplyuk, Ya. I. Kolesnichenko, É. N. Krivorutskii, V. G. Makhan'kov, V. N. Oraevskii, V. P. Pavlenko, and V. N. Tsytovich, Proc. Novosibirsk Conf., 1968 [in Russian], Vol. 1, Magate, Vienna (1969).

[6] V. D. Fedorchenko, V. I. Muratov, and B. N. Rutkevich, Yad. Sintez, 8, 37 (1968).

[7] S. A. Akhmanov and R. V. Khokhlov, Problems of Nonlinear Optics [in Russian], VINITI, Moscow (1964).

[8] N. Bloembergen, Nonlinear Optics, W. A. Benjamin, Menlo Park, Calif. (1965).

[9] B. N. Rutkevich, A. V. Pashchenko, V. D. Fedorchenko, and V. I. Muratov, Zh. Tekh. Fiz., 42, 493 (1972) [Sov. Phys.–Tech. Phys., 17, 391 (1972)].

[10] D. T. Blackstock, J. Acoust. Soc. Am., 34, 9 (1962).

[11] A. K. Zarembo and V. A. Krasil'nikov, Introduction to Nonlinear Acoustics [in Russian], Izd. Nauka, Moscow (1966).

[12] I. S. Gradshtein and I. M. Ryzhik, Tables of Integrals, Sums, Series, and Products [in Russian], Fizmatgiz, Moscow (1962).

[13] G. Szegö, Orthogonal Polymonials, Am. Math. Soc., Providence, Rhode Island (1959).

[14] M. A. Evgrafov, Asymptotic Estimates and Entire Functions [in Russian], Fizmatgiz, Moscow (1962), p. 66.

[15] N. G. de Bruijn, Asymptotic Methods in Analysis, Interscience, New York (1958).

Generation of drift waves by an rf field near the lower hybrid frequency

Yu. F. Baranov, D. G. Bulyginskii, M. I. Vil'dzhyunas, B. V. Galaktionov, and N. V. Shustova

A. F. Ioffe Physicotechnical Institute, Academy of Sciences of the USSR, Leningrad

(Submitted July 27, 1973)
Zh. Tekh. Fiz., 44, 1161-1167 (June 1974)

The generation of drift-waves in an argon plasma by rf fields at frequencies near the lower hybrid frequency is studied. Within a single pulse the nature of the spectrum changes gradually from a monochromatic spectrum near the beginning of the discharge to a noisy spectrum at the critical plasma parameters, corresponding to an abrupt change in the regime. At this abrupt change an equally abrupt restoration of the monochromatic drift-wave spectrum is observed. It is also found that when added, the spectra of two neighboring probes become different, apparently implying nonlinearity of the drift wave. It is suggested that the observed turbulence leads to additional charged-particle loss and is one of the factors responsible for the cutoff of the absorption of the rf radiation by the plasma.

Using a photomultiplier Galaktionov et al. have observed the emission from a plasma produced in a magnetic field by a source at frequencies between the electron, cyclotron, and lower hybrid frequencies.[1] During a pulse the magnetic field increases rapidly to its maximum value and then decays smoothly in a time of the order of 1 sec. The integrated emission also decays; however, this decay is not smooth, but proceeds in characteristic steps whose positions are governed by the field B and the plasma density n_e. The origin of these steps is not completely clear, but there is reason to believe that they are associated with the linear transformation of electromagnetic waves into plasma waves. It is also noted that the discharge is always characterized by low-frequency noise whose nature varies considerably during the pulse. We report here on a study of these waves and the relation between the stepped signal from the photomultiplier and the absorption of electromagnetic waves in the plasma.

EXPERIMENTAL PROCEDURE

The experimental apparatus (Fig. 1) consists of a glass tube 50 mm in diameter and more than 1 m long, located in a magnetic mirror. Around the middle of the tube there is a coil, which is connected to a source which produces pulses at 70 MHz which coincide in time with the magnetic field pulses (~ 1 sec). The overall characteristics of the discharge, such as the plasma density and the electron temperature, are measured by means of a double probe, which can be moved in the radial and axial directions without disrupting the vacuum. The probe characteristics are recorded point to point; a rectangular voltage pulse, whose amplitude is varied from discharge to discharge, is fed to the probes.

The oscillograms of the probe current reveal fluctuations at characteristic frequencies up to 30 kHz. The modulation of the probe saturation current reaches 20% to 50%, depending on conditions. These fluctuations and the imperfect reproducibility of the discharge conditions limit the accuracy of the measurements. The scatter in the temperature values measured under identical conditions is 25%, while the scatter in the absolute densities is 15%-20%. It should be noted that these absolute plasma densities, measured with the probe, agree within the specified experimental error with the densities measured previously[1] by a resonator method under similar conditions.

The plasma waves are studied with a system of miniature single probes of tungsten wire 0.1 mm in diameter which are inserted into the plasma in the radial direction to a position 6 mm from the inner wall. The lateral surfaces of the probes are insulated with alundum film. Only a part of the tip about 1 mm long remains exposed; this part serves as a local plasma-potential pickup. The probes are located in one cross section of the tube (Fig. 1) and are used to study the azimuthal propagation of the waves. There is also a pair of probes which are located 50 mm apart on a single magnetic line of force and used to detect the longitudinal component of the wave vector, k_z. The measurements are carried out in the floating-probe mode, i.e., the potential oscillations are measured with an instrument with an input impedance of 4 MΩ, which is large in comparison with the internal impedance of the probe–plasma system.

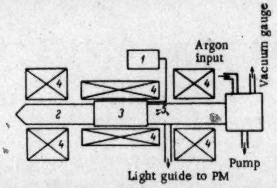

Fig. 1. The experimental apparatus. 1) rf oscillator; 2) glass tank; 3) rf circuit; 4) magnetic field coils; 5) probes.

The frequency characteristic of the measuring system is uniform over the entire frequency range studied.

The signals from the two probes, displayed as functions of the time, are photographed simultaneously from the screens of special high-resolution cathode-ray indicat-

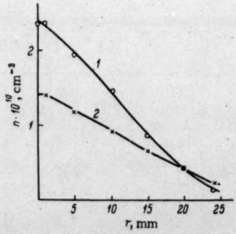

Fig. 2. Radial distribution of the plasma density. 1) Before the step; 2) 2) after the step.

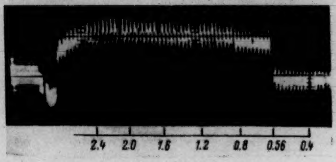

Fig. 3. Top) Photomultiplier signal as a function of the time; bottom) times at which the spectra are measured. The numbers show the strength of the magnetic field (in kOe) at the time of a measurement.

ing devices^2 and are then converted to digital form. A given sample lasts 1-2 msec and contains more than 1000 resolved points. Then the information is fed to a BÉSM-4 computer, which carries out a programmed correction of the systematic errors due to the nonlinear sweep of the indicating device and then produces Fourier transforms of the signals. By this procedure it is thus possible, in a single pulse, to find the oscillation spectra which prevail for a time of the order of 1 msec at two points in the plasma and to find the phase difference between these points for each of the spectral lines. All the experiments are carried out with argon.

Oscillation spectra are obtained for various discharge regimes in which the pressure and the rf power are varied. Below we report the results for only one regime, the one for which the light signal decays most rapidly. The corresponding pressure is $6.4 \cdot 10^{-4}$ torr and the voltage on the anode of the rf oscillator is about 400 V – the minimum value at which the discharge is stably triggered. We are interested in the data for successive times (and thus successive values of the magnetic field) before and after the first step in the photomultiplier signal. We are not able to proceed to the second or third step because of the limited sensitivity of the indicating device.

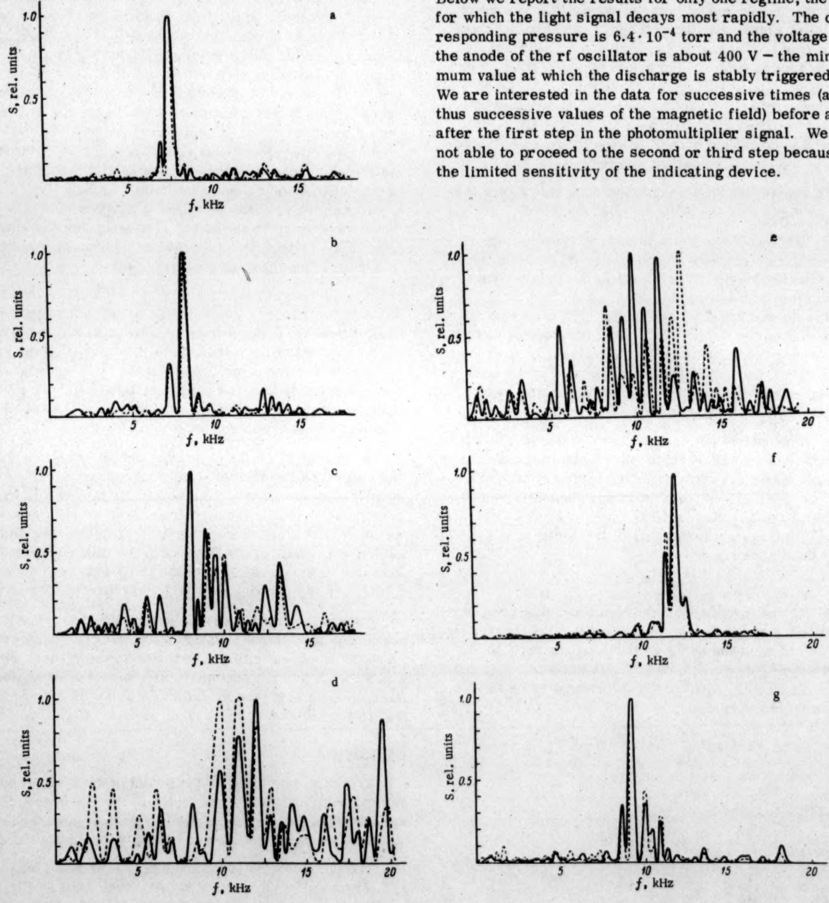

Fig. 4. Spectra of the probe-potential oscillations for various magnetic fields. a) H = 2.4 kOe; b) 2.0; c) 1.6; d) 1.2; e) 0.8 kOe; f) 0.56; g) 0.4.

EXPERIMENTAL RESULTS

Measurements with the movable double probe show that both the electron temperature and the plasma density remain essentially constant along the discharge. At the chamber axis the value of T_e before the jump is 5-7 eV; after the jump it is 10-15 eV. Figure 2 shows the radial profile of n_e before and after the jump.

The primary result of the oscillation measurements is the discovery that the signals from two probes separated in the azimuthal direction produce markedly different signals. These results imply $k_\parallel \ll k_\perp$, i.e., that the perturbations are considerably elongated along the magnetic field. In all subsequent measurements we therefore use two probes separated by an azimuthal angle of $\varphi = 40°$. The upper curve in Fig. 3 shows an oscillogram of a photomultiplier signal with the characteristic step; the total duration of the discharge is about 1 sec. Shown at the bottom are the times of the measurements; the results of the measurements are shown in Fig. 4. Here the ordinate axes show (in relative units) the absolute value squared of the oscillation amplitude as a function of frequency. The solid and dashed curves in each figure show the results of the computer calculation for the two probes.

In connection with the data shown in this figure it is interesting to note the following circumstance:

a. The spectrum has a line structure; the line halfwidth corresponds well in essentially all cases to the theoretical value of 1/T, where T is the observation time. The error in the determination of the line shape is monitored in an experiment in which part of a sine wave photographed from the screen of the indicating device is fed to the computer for processing and the result is compared with the Fourier integral of the same part of the wave, introduced mathematically. In both cases the results agreed within 1% with that shown in Fig. 5.

b. Comparison of the spectra obtained with this line shows that in the initial stages of the discharge the oscillations are almost purely sinusoidal. The phase shift between the oscillations from the two probes 40° apart is also 40°, implying that the first azimuthal mode predominates. Then the phase velocity of the perturbation can be easily determined from

$$v_{\text{p}} = m_\varphi R\omega,$$

where m_φ is the mode number, R is the radial position of the probes, and $\omega = 2\pi f$ is the oscillation frequency. The direction of v_{p} is the same as the Larmor drift of the electrons, and its magnitude is $9 \cdot 10^4$ cm/sec. This result is very nearly equal to the theoretical value for the drift-wave phase velocity:

$$v_0 = \frac{cT_e}{eB}\frac{\nabla n}{n} \approx 1 \cdot 10^5 \text{ cm/sec},$$

where T_e, ∇n, and n are evaluated from the data obtained by the double probe (Fig. 2). We note that in our case of a weakly ionized argon plasma the correction for the revolution velocity due to the radial ambipolar field is small:

$$u = \frac{c\theta}{eB}\frac{\nabla n}{n},$$

where

$$\theta = \frac{T_e m_e \nu_{e0} - T_i m_i \nu_{i0}}{m_e \nu_{e0} + m_i \nu_{i0}} \approx T_i \ll T_e.$$

c. On the basis of the line nature of the spectra we conclude that drift waves propagate in the azimuthal direction and that the wavelength is equal to the circumference of the circle divided by the integer m_φ. In principle, for the more complicated spectra, which, as Fig. 4 shows, are observed toward the step we can obtain a dispersion relation for the waves by constructing the functional dependence $m_\varphi(\omega)$. In this manner we could study the nature of the waves in more detail. However, two experimental circumstances rule out this procedure: First, it turns out that the phase shift between the oscillations of the two probes ceases to be a constant within a single line for the more complex spectra; second, a difference arises between the spectra from the two probes and increases in front of a step to such an extent that it becomes impossible to compare the different lines (Fig. 4e).

d. We record 15-20 spectra for each case; Fig. 4 shows typical examples from each group. The reproducibility of the spectra from discharge to discharge is very good for the first groups, but it worsens as the spectra becomes more complicated, so that, e.g., in Fig. 4e, the reproducibility of the individual lines has been lost completely. However, the overall nature of the spectrum is reproducible.

e. A typical result is that the abrupt change in the light signal to the photomultiplier is accompanied by an equally abrupt change in the nature of the oscillation spectrum, from a noisy spectrum (Fig. 4e) to a nearly monochromatic spectrum (Fig. 4f). Then the spectrum begins to broaden again, but we are not able to follow this behavior to the next step because the signal amplitude falls below the limiting sensitivity of the indicating device.

Generally, similar results are obtained in other experiments at different pressures and oscillator power levels. We can definitely assert that in those cases in which the step in the photomultiplier signal degenerates into a smooth slope the evolution of the oscillation spectra is also smooth.

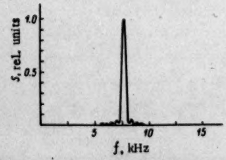

Fig. 5. Shape of the spectral line.

DISCUSSION

From the standpoint of the model of drift-wave propagating throughout the plasma volume, the significant difference between the spectra of the two probes, combined with the narrowness of the observed lines, is not understood.

The preservation of the natural line half-width $\Delta f \approx 1/T$, observed in all cases (the broadened lines in Fig. 4d result from a reduction of the sweep time T), implies that oscillations of a given frequency occur throughout the observation time. It is easy to see that over this time the wave front moves a distance three orders of magnitude larger than the distance between the probes (1.5 cm). The fact that the oscillation spectra are different under these conditions implies that each of the waves is azimuthally (or radially) localized in part of the plasma volume. Such a situation can arise because of nonlinear mechanisms when[3]

$$v_{\mathrm{dr}} \approx v_{\mathrm{p}},$$

where v_{dr} is the amplitude of the oscillatory velocity in the drift wave. If we adopt this possibility, we should interpret the divergence of the spectra from neighboring probes as indicating a transition of the wave into a nonlinear regime.

Turning to the role of drift waves in the mechanism for the maintenance of the discharge, in particular, to the relationship between these waves and the nature of the photomultiplier-signal steps, we note that, by itself, the coincidence of these steps with the abrupt change in the nature of the spectrum does not rule out the possibility that the drift waves are only a concomitant phenomenon and do not exert an inverse influence on the discharge regime. In this connection it is interesting to take into account the turbulent diffusion related to drift waves. While the regular oscillations observed in the initial stage do not contain an addition mechanism for particle loss across the magnetic field, the diffusion coefficient in pronounced turbulence can reach limiting values of the order of the Bohm value:[3]

$$D_{\perp \max} \approx \frac{1}{16} \frac{cT_e}{eB}.$$

An estimate shows that in this case the loss of charged particles, governed by their motion across H, is comparable to the loss due to ambipolar diffusion along the field, with the coefficient

$$D_a = \frac{T_e}{M_i \nu_{ia}},$$

where ν_{ia} is the frequency of resonance charge exchange in argon. On the basis of this circumstance we can suggest that if the turbulent oscillations are caused by the growth of drift waves and do not directly influence the mechanism for the absorption of the rf oscillations (it is assumed in ref. 1 that this mechanism is the linear transformation of electromagnetic into plasma waves), they can in any case be one of the factors governing the particle and energy balance in the plasma. In this sense, the low-frequency waves, along with the change in the magnetic field, can shape the functional dependence of the basic plasma parameters on the time, including the step observed in the light signal.

The experimental data available are not adequate for drawing more definite conclusions; it is necessary to measure the functional dependence of the density on the time, which is required for a solution of the balance equation.

In conclusion the authors thank A. D. Piliya, V. I. Fedorov, O. N. Shcherbinin, and V. V. D'yachenko for useful discussion.

---

[1] B. V. Galaktionov, V. E. Golant, V. V. D'yachenko, and O. N. Shcherbinin, Zh. Tekh. Fiz., 40, 2322 (1970) [Sov. Phys. – Tech. Phys., 11, 1813 (1971)].

[2] D. G. Bulyginskii, M. I. Vil'dzhyunas, and B. A. Utochkin, Prib. Tekh. Eksp., No. 3, 168 (1970).

[3] B. B. Kadomtsev, in: Reviews of Plasma Physics, No. 4, Consultants Bureau, New York (1966).

Coaxial plasma injector with programmed injection

V. A. Burtsev, V. N. Litunovskii, and M. P. Nadgornaya

D. V. Efremov Scientific-Research Institute of Electrophysical Apparatus, Leningrad

(Submitted December 26, 1972; resubmitted August 15, 1973)
Zh. Tekh. Fiz., 44, 1168-1175 (June 1974)

An experimental study has been made of the physical processes in the interelectrode region of a coaxial injector with closely spaced electrodes, a short ringing time, programmed injection, and preliminary ionization of the gas by an induction electric field. Phenomena which precede the current front and which were observed in previous work are also observed here. In addition, plasma-conductivity and emission fronts are observed; these move with velocities governed by the pressure gradient in the leading part of the initial gas distribution. The present results are compared with earlier results.

INTRODUCTION

We report here a continuation of the experiments reported in refs. 1-4 on the physical processes occurring in the interelectrode region of a coaxial injector with electrode diameter ratio of unity.

It was shown earlier[1,2] that the discharge (without preliminary gas ionization) develops from the very beginning as a current filament because of the channel nature of the initial gas breakdown and the subsequent influence of pinching forces.

The addition of a preliminary ionization system, homogeneous in the azimuthal direction,[4] causes the discharge to begin simultaneously at various points along the annular gap between the electrodes. The current sheaths formed in this manner remain azimuthally closed throughout the discharge, regardless of the initial gas distribution.

The azimuthal stability of the current sheaths in an injector with an electrode diameter ratio of unity, makes it possible to study the influence of the nature of the gas distribution on the phenomena preceding the current front detected earlier.[1-3]

EXPERIMENTAL APPARATUS AND PROCEDURE

The coaxial injector is described in detail in ref. 4. The outer diameter of the central electrode is 36 mm, the inner diameter of the outer electrode is 44 mm, the electrode length from the point at which the discharge is initiated to the aperture is 100 mm, and the distance to the insulator is 120 mm. The capacitor, with a capacitance of $C_0 = 3.6\ \mu F$, can be charged to $U_0 = 20$ kV, and the ringing time of the discharge circuit is $\tau_0 \simeq 1\ \mu sec$.

The programmed injection system and the system for the preliminary gas ionization are shown schematically at the left in Fig. 1. Gas is injected through a pulsed valve into the cavity within the central electrode. It then passes through longitudinal slits in this electrode to the interelectrode region. For a given gas-injection time the spatial distribution of the gas is governed primarily by the position of the movable partition and the variation of the transmission of the slits along the electrodes. This injection system permits study of various gas distributions with a fixed position of the inner edge. Current fronts are shaped at the inner edge of the distributions through preliminary gas ionization caused by the induction electric field. The length of this preliminary ionization step is varied from 0.3 to 1 μsec in the various experiments.

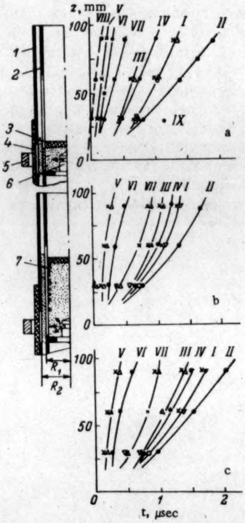

Fig. 1. Gas-injection system and curves showing the current, conductivity, and emission fronts of the plasma. $U_0 = 15$ kV. 1, 2) Outer and central electrodes; 3) movable partition; 4) porcelain tube; 5) preliminary-ionization loop; 6) pulsed valve; 7) cylindrical spiral with an adjustable pitch. Data are obtained by means of photomultipliers (1'), current probes with a shunt resistance of R = 75 Ω (2'), current probes with R = 0.6 Ω (3'), conductivity probes (4'), and magnetic probes (5'). I) Motion along the electrodes of the leading current front and the conductivity front of the first plasmoid; II) motion of the emission front of the first plasmoid; III-VII) motion of the conductivity and emission fronts due to preceding phenomena; VIII) motion of the emission front of the plasma produced by the preliminary-ionization system; IX) arrival time of the emission front of the slow plasma flow. a) Short gas distribution, $p_{z=0} = 1.5$ mm torr; regimes with a gas-pressure distribution characterized by a pressure drop toward the injector exit slower than in the interior of the interelectrode region. b) $p_{z=0} \simeq 1$ torr, $\Delta p_z \simeq 0.2$ torr/cm for z > 0. c) $p_{z=0} \simeq 1.5$ torr, $\Delta p_z \simeq 0.3$ torr/cm.

The voltage on the preliminary-ionization loop, U_{ion}, is detected by a magnetic probe.[4] The total discharge current between the injector electrodes, I_d, is measured by an integrating Rogowski loop,[1] and the voltage between the end parts of the electrodes, U_{el}, is measured by a low-inductance resitive divider.

The azimuthal and longitudinal magnetic fields in the interelectrode region are measured by magnetic probes[2] inserted in the radial direction; the diameter of the probe coils is 0.8 mm, the length is 0.8 mm, the conductor diameter is 0.03 mm, and there are 32 turns. The structure of the current fronts is studied by probes which detect local radial currents.[2,3] The current probes are surface elements of the outer electrode (the elements are 0.4 mm in diameter), connected to the discharge circuit of the injector through shunt resistances. These resistances are varied from 0.1 to 75 Ω in the various experiments.

The propagation of the ionized medium or the ionization wave through the gas is detected by coaxial conductivity probes[2,3], whose central electrodes are supplied a positive bias voltage. The end surfaces of the probe electrodes are flush with the working surface of the outer electrode of the injector.

The motion of the emission fronts is studied by photomultipliers which detect the emission in directions perpendicular to the injector axis, through the use of systems of irises and light guides.

The longitudinal electric field in the interelectrode gap is measured by a double probe inserted in the radial direction. The probe electrodes, made of tungsten wire 0.2 mm in diameter and insulated with alundum, are 1.5 mm apart.

The plasmoids in the region behind the electrode are studied with a plasma "absorber," which can be used to detect the plasma flux density nv (n is the plasma density and v is the flow velocity) on the basis of the dissipation in a transverse electric field. A coaxial absorber with a low-inductance capacitive power supply[5] which we have developed makes it possible to achieve the necessary time resolution (~ 50 nsec).

The pressure of the neutral gas in the interelectrode region of the injector is measured by ionization gauges and discharge gauges.

PRECURSOR PHENOMENA

Study of the propagation along the injector electrodes of the fronts of the radial discharge current, the conductivity, and the visible emission of the plasma reveals that the current front is preceded by faster conductivity and emission fronts whose velocities have different functional dependences on the gas distribution. Figure 1 shows the longitudinal motion of the fronts obtained in three operating regimes of the injector, differing in the gas-pressure gradient in the leading part of the distribution. Curve I shows the propagation of the current and conductivity fronts toward the injector exit, while curve II shows the motion of the emission front of the corresponding plasma front. The other curves in Fig. 1 correspond to phenomena preceding the current front.

On the basis of the experimental data obtained in the study of the propagation of the current, conductivity, and emission fronts for many operating regimes of the injector, including the regime with a homogeneous gas distribution in the interelectrode region, we can draw the following conclusions, and make the following assumptions regarding the mechanisms responsible for the observed pehnomena.

1. The observed phenomena can be divided into two groups. The first group includes the phenomena which occur in the leading part of the current sheath or in the gas ahead of the current front, so that they are assumed to precede the current front as it moves along the injector electrodes.

The second group includes the phenomena which occur shortly after the gas breakdown, while the electric field is still strong, and the plasma conductivity is low. We also treat these as precursor phenomena, since they cause changes in the interelectrode region of the injector before the current front begins to propagate through it.

2. To the first group we can assign the separation of the leading part of the current front, which occurs as the front moves through the gas at a pressure which falls off toward the injector exit. Figure 1 (curves III and IV) shows the motion of the separated current front along the injector electrodes, along with the conductivity and emission fronts of the accelerated plasma component. Figure 2 shows a typical oscillogram of the signals from the current probes to illustrate this phenomenon.

The separation of the leading part of the current sheath as it moves through a gas in which the pressure falls off, first predicted in ref. 6, can in fact be one of the mechanisms leading to the formation of the plasmoids observed by many workers in the case of short gas distributions.

3. We do not have an unambiguous interpretation for curves V-VII in Fig. 1. Conductivity front VII (Fig. 1, b

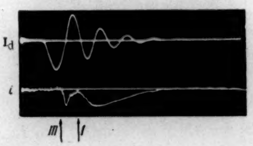

Fig. 2. Oscillograms of the signals from the Rogowski loop (I_d) and from the current probe (i) at z = 30 mm for the case of a short gas distribution with $p_{z=0} \approx 1.5$ torr.

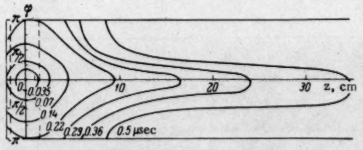

Fig. 3. Propagation of the emission front through the interelectrode region of an injector without a preliminary ionization system.[1] The dashed lines show the boundaries of the gas distribution ahead of the front.

and c) displays the most dynamic behavior; its velocity increases significantly with the pressure gradient in the leading part of the distribution, despite the slowing of current front I.

4. The second group of precursor phenomena includes the isotropic thermal expansion of the electron gas, which acquires a high temperature in the electric field immediately after the breakdown of the neutral gas (the heavy particles remain essentially cold because of the low efficiency with which energy is transferred to them by electrons). As the expanding electron gas entrains the ions it produces a plasma component which propagates in all directions away from the breakdown region.[7,8]

Figure 3 shows an expanded diagram of the propagation of the emission front through the interelectrode region of the injector without a preliminary ionization system.[1] This figure is plotted from an analysis of the measurements of the lateral photomultipliers at various positions along the φ and z coordinates. The origin of coordinates is at the point at which the original gas breakdown occurs. We see from this figure that the emission front propagates first uniformly in all directions, including the direction toward the insulator, going beyond the initial gas distribution. Only 0.2 μsec after the breakdown does an emission "tongue" begin to form rapidly in the direction toward the injector aperture (see ref. 2 for the results of a detailed study of this plasma tongue in the r, z cross section through the breakdown point).

In the present experiments the electron gas expands isotropically immediately after the breakdown, upon initiation of the preliminary discharge. However, this phenomenon is much less pronounced in the case of an azimuthal gas breakdown than in the case of a radial breakdown, and is thus not reflected in Fig. 1a. Curve VIII in this figure shows the thermal expansion of the plasma heated by the preliminary-discharge current.

5. Also among the phenomena preceding the formation of the current front is the longitudinal propagation of an avalanche discharge, discussed in detail in ref. 3: When the voltage is supplied to the discharge electrodes, electron avalanches of the Townsend stage of the discharge arise primary where the conditions are optimal, according to the Paschen-breakdown curve. Photons of the primary avalanches initiate adjacent secondary avalanches, leading to their rapid formation, i.e., to the propagation of the Townsend discharge along the electrodes.

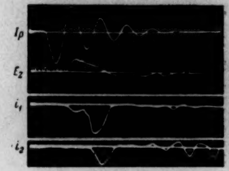

Fig. 5. Oscillograms of the signals from the Rogowski loop (I_d), the double electrostatic probe at z = 30 mm (E_z), and the current probes at z = 60 mm (i_1) and z = 90 mm (i_2). U_0 = 15 kV. Short gas distribution, $p_{z=0} \simeq$ 1.5 torr.

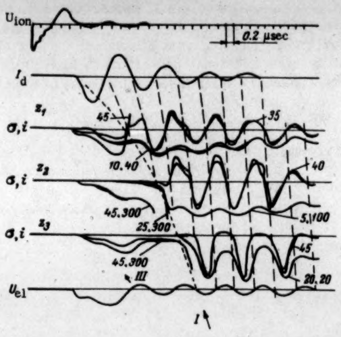

Fig. 6. Signals from the current probes (i), the conductivity probes (σ), the Rogowski loop (I_d), the magnetic ionization probe (U_{ion}), and the voltage divider at the ends of the electrodes (U_{el}) in the case of a short gas distribution. U_0 = 10 kV. The amplification (in decibels) is shown near the signals from the current probes, and the amplification (decibels) and the bias voltage (in volts) are shown near the signals from the conductivity probes. Dotted curve) Motion of the main plasma front, I; dashed curves) motion of the points of zero oscillation phase.

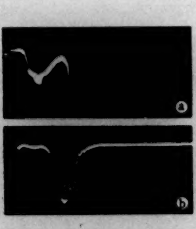

Fig. 4. Oscillograms of the signals from the plasma "absorber," which are proportional to the plasma flux density. Case of a short gas distribution, with $p_{z=0} \simeq$ 1.5 torr. The "absrober" is z = 65 cm from the ionization turn. a) Background plasma, sweep rate of 2 μsec/div, shunt resistance of R_s = 75 Ω; b) main plasmoid, 5 μsec/div, R_s = 0.07 Ω.

When the preliminary gas ionization takes place in a local zone (in the case of spark ignition, as in ref. 3, or in the case of spatially confined ionization by an induction electric field, as in ref. 4), the rapid formation of electron avalanches is triggered by gas ionization by photons emitted by the background. In the present experiments, in which the electrodes are shorter and the gap wider than in ref. 3, this phenomenon takes a slightly different form.

The avalanche discharge develops essentially simultaneously in the gas-filled interelectrode region, from the time at which the voltage is supplied to the injector electrodes (Fig. 1, b and c, t = 0) to the appearance of the fastest front V, due to the main discharge. The plasma emission intensity and conductivity increase monotonically over this time interval.

6. The precursor phenomena contribute to the formation of a background plasma, which is detected behind the electrode (short gas distribution) by means of the plasma absorber (Fig. 4). Its front velocity is equal to that of the fastest front, V, in Fig. 1a.

In the case of longer gas distributions the precursor phenomena lead to a situation in which the current front encounters a partially ionized gas, rather than a neutral gas, so that the snowplow behavior of the front can be affected.

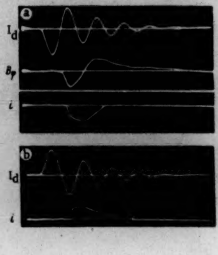

Fig. 7. Oscillograms of the signals from the Rogowski loop (I_d), the magnetic probe (I_p), and the current probes (i) for different electrode polarities. The probes are at z = 30mm. a) With central electrode as cathode; b) with central electrode as anode.

STRUCTURE OF THE CURRENT FRONT AND PLASMA FLOW

It is difficult to study the structure of the current front and the plasma flow behind it in this injector, with its interelectrode gap of ~4 mm, both from the diagnostic standpoint and because of the physical consequences of the strong influence of the electrode surfaces on the plasma properties. We therefore simply report some observations which we believe to be interesting and which illustrate the complexity of the physical processes in the injector.

1. Study of the distribution of the radial current in the interelectrode region reveals one or two movable current fronts corresponding to the fronts of current loops, and an essentially fixed sheath carrying most of the current in the discharge-formation region. Through the use of a double probe we find an opposite longitudinal field behind the moving current fronts, due to the existence of a potential well for ions (Fig. 5); this well is predicted in ref. 9 under the condition $v_0/v_A \sim 1$ (where v_0 is the velocity of the current front and v_A is the Alfvén velocity in the plasma behind the current front). A calculation of v_A based on the data from the magnetic measurements and an estimate of the plasma density based on the balance equation for the magnetic and gas-kinetic pressures shows that this condition is satisfied. However, the actual situation is more complicated than in the theory: In the inner part of the well the electric field oscillates at the frequency of the total current; these oscillations propagate in the plasma toward the injector exit. The magnetic and current probes show that these oscillations can be amplified both in time and in space as they propagate along the electrodes (Fig. 5). In experiments with relatively low discharge currents and a relatively large amount of gas in the interelectrode region, in which case the moving current fronts have much lower velocities and are rapidly disrupted (the ion potential well vanishes), the oscillations grow much more rapidly. The phase velocity of the oscillations propagating out of the fixed-discharge region toward the plasma front is much higher than that of the front, and the velocities of the subsequent oscillations are higher than those of the oscillations which precede them (Fig. 6).

2. The current fronts are studied with miniature magnetic probes inserted to the radial midpoint of the interelectrode region and with current probes at the walls. Comparison of the results found with the current probes for different initial polarities of the injector electrodes show that the motion of the current fronts is essentially independent of this polarity. It is thus possible to obtain information about processes occurring near the cathode and anode by switching the electrode polarity while the current probes are held at the outer electrode.

Figure 7 shows the signals from the magnetic and current probes for the different electrode polarities; comparison shows that the current front of the first loop is planar and perpendicular to the electrode surfaces. Behind the front, near the electrodes, there are current "tails," with those of the radial current more pronounced at the anode than at the cathode. The current front of the second loop is detected only by the magnetic probe in the center of the interelectrode gap. This result implies a bell-shaped second front.

CONCLUSION

1. The experimental results reported here represent a continuation of studies$^{1-4}$ of the possibility of accelerating plasma in a coaxial injector with an electrode diameter ratio of unity with a short ringing time. This paper is also a summary.

2. These experiments have shown that in a coaxial injector with closely spaced electrodes, in which it is more difficult for the current fronts to close in the azimuthal direction than in injectors of the usual geometry, the problem can be solved by arranging for azimuthally symmetric preliminary ionization of the gas.

3. A careful study of the propagation along the injector electrodes of the radial-current, plasma-conductivity, and plasma-emission fronts in various operating regimes of the accelerator and over a broad sensitivity range of the detectors (more than four orders of magnitude) has revealed several phenomena which precede the current front. Under the appropriate conditions, some of them contribute to the formation of the background plasmas which have been observed by many workers using pulsed coaxial injectors, while others alter the state of the gas in front of the current front. Which particular precursor phenomena appear is governed by many factors, including, to an important degree, the nature of the initial gas distribution.

4. Several interesting phenomena have been observed behind the current front, including an oscillatory process which is amplified in both time and space as it propagates along the electrodes; however, a detailed study of these phenomena is hindered by the small dimensions of the interelectrode gap.

5. We have not been able to fully exploit the advantages of the low-inductance power supply, the short ringing time of the discharge circuit, and the small change in the azimuthal magnetic field in the radial direction in this injector, because of the low dielectric strength of the interelectrode gap in the discharge-initiation region. These advantages can be exploited in a larger-scale injector of similar design.

---

[1] V. A. Burtsev and M. P. Nadgornaya, in: Electrophysical Apparatus [in Russian], No. 8, Atomizdat, Moscow (1969), p. 73.

[2] V. A. Burtsev, S. M. Klishevskii, V. N. Litunovskii, and M. P. Nadgornaya, in: Electrophysical Apparatus [in Russian], No. 8, Atomizdat, Moscow (1969), p. 81.
[3] V. A. Burtsev, V. N. Litunovskii, and M. P. Nadgornaya, Zh. Tekh. Fiz., 42, 1706 (1972) [Sov. Phys.–Tech. Phys., 17, 1363 (1973)].
[4] V. A. Burtsev, V. N. Litunovskii, and M. P. Nadgornaya, Zh. Tekh. Fiz., 42, 2105 (1972) [Sov. Phys.–Tech. Phys., 17, 1670 (1973)].
[5] V. A. Burtsev and V. N. Litunovskii, Author's certificate No. 327,407 Byull. Izobr., No. 5 (1972).
[6] V. F. Demichev and V. D. Matyukhin, Dokl. Akad. Nauk SSSR, 150, 179 (1963).
[7] A. A. Plyutto, Zh. Eksp. Teor. Fiz., 39, 1589 (1960) [Sov. Phys.–JETP, 12, 1106 (1961)].
[8] H. W. Hendel and T. T. Reboul, Phys. Fluids, 5, 360 (1962).
[9] N. A. Khizhnyak, Zh. Tekh. Fiz., 39, 2040 (1969) [Sov. Phys.–Tech. Phys., 14, 1534 (1970)].

Conversion of neutral hydrogen into protons in dense plasmas

T. A. Bazilevskaya, L. I. Krupnik, and N. G. Shulika

(Submitted December 29, 1972; resubmitted November 5, 1973)
Zh. Tekh. Fiz., 44, 1176-1182 (June 1974)

The efficiency of conversion of neutral hydrogen atoms with energies from 300 to 10,000 eV into protons by passage through plasma fluxes produced by a conical plasma injector with a pulsed hydrogen supply is studied. The plasma target density varies from 10^{12} to 10^{14} particles /cm^3. The efficiency of conversion into protons is compared for gaseous and plasma targets.

INTRODUCTION

Considerable attention has recently been given to the analysis of fluxes of neutral particles emitted by a plasma; these fluxes yield valuable information about the parameters and state of the plasma.[1]

In the neutral-particle analyzers developed thus far, the principle of partial ionization of the flux is used with subsequent analysis of the conversion ions. The most widely used method is stripping of hydrogen atoms in a gas target.[2]

This method is effective in the study of particles with energies above 1000 eV. The use of thin foils,[3] an electron beam,[4] and a gas-discharge plasma[5] as targets for the conversion of neutrals into charged particles does not lead to a significant increase in the efficiency for conversion of hydrogen atoms into protons in the low-energy region. In the present work, a hydrogen plasmoid with a charged-particle density of $\sim 10^{14}$ cm^{-3} is used as a target for the conversion of hydrogen atoms into protons.

The use of plasma as a conversion target offers an opportunity to take advantage of resonance charge exchange between hydrogen atoms and plasma protons, in which case the cross section rises sharply as the energy of the colliding particles decreases (Fig. 1).

EXPERIMENTAL ARRANGEMENT

Experimental measurements of the efficiency for conversion of hydrogen atoms into protons are made with the apparatus shown in Fig. 2.

A flux of neutral hydrogen atoms with energies in the range 300-10,000 eV is produced by means of the high-frequency ion source 1, the accelerating system 2, the magnetic mass monochromator 3, and the charge-exchange chamber 5. The charge exchange of protons into hydrogen atoms is accomplished in a gas target (air). Introduction of the beam into the charge-exchange chamber is made through the channel 4, which is 5 cm long and 5 mm in diameter. Protons which do not undergo change exchange are deflected by the electrostatic field of the plane condenser 18 and the primary beam of hydrogen atoms passes through the channel 7 into chamber 8, along which an accelerated plasma flux moves.

The plasma flux is produced by means of the conical plasma injector 9 with a pulsed hydrogen supply.[6]

The ion density in the flux is measured with the electrostatic probe 17.

From chamber 8, the beam of hydrogen atoms is directed through the channel 10 into the analyzer chamber 14. In this chamber, separation of the beam with respect to charge state takes place in the field of the plane condenser 11. The intensity of the undeflected beam is measured with the detector 16 through the number of secondary electrons ejected from a metal plate, and the intensity of charge-exchange protons is measured with detectors 12 or 13. The principle of particle detection in these detectors is similar to that described in ref. 2.

The test beam is incident on the bottom of the cylinder 19, and produces secondary electrons which are accelerated in the gap of the electrostatic lens formed by the two electrodes 19 and 20. The electrons are directed to the plastic scintillator 21, the light yield from which is recorded by the photomultiplier 22.

EXPERIMENTAL METHOD AND RESULTS

The conical plasma injector produces an accelerated plasmoid with an average particle velocity of $\sim 5 \cdot 10^6$ cm/sec and an electron temperature of $\sim$3-5 eV. The plasma density in the plasmoid can be varied over the range 10^{11}-10^{15} particles/cm^3.

The parameters of the plasma flux used as a target for the conversion of hydrogen atoms into protons are first studied by means of active particle diagnostics[10] and are checked during the course of an experiment by means of the electrostatic probe. Figure 3 shows an oscilloscope trace of the probe current obtained in a single picture covering 50 firing pulses of the plasma injector. The figure indicates that injector operation is satisfactorily stable, but some longitudinal nonuniformity of plasma is observed.

There are two density maxima in the flux. For the injector operating mode shown the plasma densities in the first and second maxima are 10^{12} and 10^{13} particles/cm^3 respectively. A characteristic feature of the plasma flux employed is a nonuniform degree of ionization of the plasma. The leading portion (first maximum) is characterized by a high degree of ionization (close to 100%). Then there is a decrease in the degree of ionization, which amounts to only 40-50% in the region of the second maximum.

The intensity of the beam of hydrogen atoms mea-

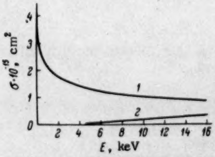

Fig. 1. Effective cross section for the conversion of hydrogen atoms into protons. 1) resonance charge-exchange cross section;[7,8] 2) cross section for stripping of hydrogen atoms in air.[9]

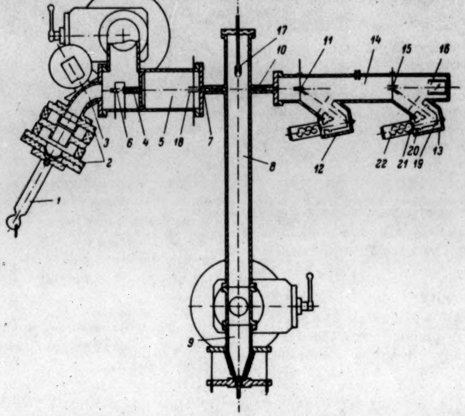

Fig. 2. Diagram of apparatus. 1) High-frequency ion source; 2) electrostatic lens; 3) mass monochromator; 4) entrance channel of charge-exchange chamber; 5) charge-exchange chamber; 6) correction plates; 7) exit channel of the charge-exchange chamber; 8) plasma guide; 9) plasma source; 10) entrance channel of analyzer; 11, 15, 18) deflection plates; 12, 13) particle detectors; 14) stripping chamber; 16) tuning detector; 17) electrostatic probe; 19) metal target; 20) electron lens; 21) scintillator; 22) photomultiplier.

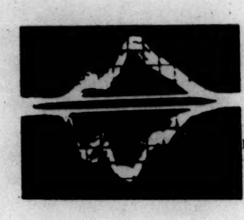

Fig. 3. Oscilloscope trace of signals from electrostatic probe.

sured at the end of the analyzer is 10^{-10} A for a beam energy of 300 eV and 10^{-7} A at 10 keV.

The efficiency for conversion of hydrogen atoms into protons is evaluated from the ratio between the intensity of the proton current in the beam, as measured by the detector 13, and the intensity of hydrogen atoms passing through the entire system with no plasma target present.

Figure 4 shows the dependence of conversion efficiency on the initial energy of the hydrogen atoms.

The target thickness nL, where n is the plasma density and L is the beam path length is plasma, is used as a parameter for the curves.

The energy dependence of the conversion efficiency correlates with the energy dependence of the effective resonance charge-exchange cross section (Fig. 1) only for two target thicknesses: $nL = 2.5 \cdot 10^{12}$ and $6 \cdot 10^{12}$ cm^{-2}. A variation in target thickness by a factor of 2.4 leads to a rise in conversion efficiency also by a factor 2.4.

However, an increase in conversion efficiency is not observed for nL values greater than 10^{13} cm^{-2} and for beam energy < 500 eV. This fact is explained by the increase in beam particle scattering at large target thicknesses and by the boundedness of the analyzer aperture.

Nevertheless, if one compares the conversion efficiency in a plasma target, even under these nonoptimum, conditions, with the conversion efficiency in a gas target obtained under the same conditions, which is shown in Fig. 4 by the dashed curve, a choice in favor of a plasma target must be made.

The dashed curve for a gas target is obtained under conditions such that the optimum value (for charge exchange) of gas density (hydrogen) in the chamber 8 is selected for each value of hydrogen-atom beam energy.

DISCUSSION OF RESULTS

Despite the obvious advantage in conversion of hydrogen atoms into protons at low energies (less than 1000 eV)

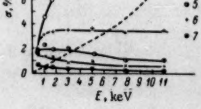

Fig. 4. Efficiency for conversion of hydrogen atoms into protons. 1) For a plasma target; 2) for a gas target; plasma density nL, cm^{-2}: 3) $2.5 \cdot 10^{12}$, 4) $6 \cdot 10^{12}$; 5) $1 \cdot 10^{13}$; 6) $1 \cdot 10^{14}$; 7) $1 \cdot 10^{15}$.

through collisions with protons (Fig. 1), we have not succeeded in completely realizing this advantage in experiments on the characteristics of neutrals emitted by a plasma. This is explained by the fact that distortion of the energy spectrum of the neutrals is not permissible in such experiments. Therefore an increase in target density to an optimum value from the viewpoint of producing maximum conversion efficiency is not always possible because of the large energy loss by the particles in collisions, particularly in the low-energy region.

The limits on the linear density nL of a plasma target for which the energy loss of a proton moving through the target will not exceed acceptable values can be determined from the expression[11]

$$\frac{dE}{dt}=-\frac{4\pi e^2}{v}\sum \lambda n_k e_k^2\left[\Phi\left(\frac{v}{v_k}\right)-\frac{2v}{\sqrt{\pi}\,v_k}\frac{m+m_k}{m\,m_k}e^{-\frac{v^2}{v_k^2}}\right]\ \ldots. \quad (1)$$

Here, dE/(dt) is the rate of change of the energy of an ion moving through the plasma; e, m, and v are the charge, mass, and velocity of the ion; e_k, v_k, m_k, and n_k are the charge, velocity (thermal), mass, and density of plasma particles; $\Phi(v/v_k)$ is the probability integral and λ is the Coulomb logarithm.

From Table 1, one can trace the magnitude of the quantities obtained by means of Eq. (1).

Table 1 gives the thicknesses of a plasma target for which there is a 1% change in energy of a proton passing through the target. Also given are values of $\Delta N/N$ corresponding to complete detection of protons created in the atomic flux by charge exchange with ions in the plasma target.

The calculation assumes that the plasma target consists of protons and electrons. The presence of neutral hydrogen atoms and of impurity atoms and ions in the plasma is not taken into account. In addition a value of 5 eV is assumed for the ion and electron temperatures of the plasma; this value is close to that obtained experimentally.

The values for target thickness presented are obtained under the assumption that the test particle passes through the plasma in a charged state. In the calculations, the average value of the Coulomb logarithm is assumed to be 15 for the entire range of particle energies and plasma densities.

A second factor, which reduces conversion efficiency at low energies, is large-angle particle scattering and the limited aperture capabilities of the analyzer.

We define the efficiency for conversion of hydrogen atoms into protons as the ratio

$$\alpha=\frac{J_1^+}{J_1^0} \quad (2)$$

for a device with a plasma target, where J_1^+ is the photon intensity recorded by the detector and J_1^0 is the intensity of the beam of atomic particles reaching the detector in the absence of plasma.

TABLE 1

	E, eV									
	20	50	100	200	300	400	500	1000	2000	5000
$nL\cdot 10^{-12}$, cm^{-3}	0.98	4.1	10	19	25.6	30.9	35.6	53.8	82.2	158
$\frac{\Delta N}{N}$, %	0.45	1.6	3.3	5.5	7.3	7.9	8.7	10.8	13.4	19

In turn, the quantity J_1^+ is related to J_0^+, the number of ions created in the target by charge exchange, by

$$J_1^+=kJ_0^+. \quad (3)$$

The coefficient k determines that portion of the protons which are scattered in collisions at angles greater than the aperture of the detection device.

The magnetude of particle deflection from the initial direction is conveniently characterized by the magnitude of the mean-square transverse component of the momentum, the mean rate of change of which for a Maxwellian velocity distribution of plasma particles is given by[11]

$$\frac{dp_\perp^2}{dt}=\frac{8\pi e^2}{v}\sum \lambda_k e_k n_k \Phi\left(\frac{v}{v_k}\right). \quad (4)$$

Here, $p_\perp$ is the perpendicular component of the particle momentum; e_k, n_k, and v_k are the charge, density, and velocity of plasma particles; e and v are the charge and velocity of scattered particles, λ is the Coulomb logarithm.

Assuming the deflection of particles from their initial direction is small, using Eq. (4) we obtain for the mean-square angle of deflection

$$\Theta^2=\frac{8\pi e^4 L}{m^2 v^4}\sum_k n_k \lambda_k \Phi\left(\frac{v}{v_k}\right), \quad (5)$$

where m is the mass of a particle moving through the plasma.

In the penetrating beam the angular distribution of particles in the neighborhood of $\varphi = 0$ obeys the Gauss law

$$N(\varphi)\,d\varphi=N_0\frac{\sqrt{2}}{\sqrt{\pi}}e^{-\left(\frac{\varphi}{\sqrt{2}\,\Theta_1}\right)^2}d\Theta. \quad (6)$$

The particle flux intensity $J_1^+(\varphi)$ reaching the detector is defined in the following manner, using Eq. (6):

$$J_1^+(\varphi)=J_0^+\frac{\sqrt{2}}{\sqrt{\pi}\,\Theta}\int_0^{\varphi} e^{-\left(\frac{\Theta_1}{\sqrt{2}\,\Theta}\right)}d\Theta_1 \quad (7)$$

or

$$J_1^+(\varphi)=\Phi(x)_1 J_0^+, \quad (8)$$

where $x = \varphi/\sqrt{2}\Theta$.

Comparing Eqs. (3) and (8), one can write

$$k=\Phi(x). \quad (9)$$

The defined parameter α can be written in the form

$$\alpha = \Phi(x)\left(1 - e^{-\sigma_n n L}\right) \tag{10}$$

(σ_n is the effective resonance charge-exchange cross section for hydrogen particles).

Where neutrals are present in the plasma it is necessary to consider in the calculation of α the possibility of secondary charge exchanges, which convert protons into neutral atoms and which lead to a decrease in the value of α. If the degree of ionization of the plasma used as a target is not very low, $n \gg n^0(\sigma_i/\sigma_n)$, Eq. (10) takes the form

$$\alpha = \frac{n}{n^0 + n}\Phi(x)\left(1 - e^{-\sigma_n (n^0+n) L}\right). \tag{11}$$

Here, n and n^0 are respectively the densities of charged and neutral particles in the plasma, and σ_i is the effective cross section for stripping of beam atoms by plasma atoms.

Equation (11) is valid in the region of low colliding-particle energies, where the effective resonance charge-exchange cross section is considerably greater than the effective cross sections for all other processes leading to the formation of protons in an atomic beam passing through the plasma.

Figure 5 shows the theoretical dependence for the detection efficiency for charge-exchange particles scattered at various angles. In the calculation of these curves and in all subsequent calculations, we select a plasma target thickness corresponding to a beam-particle energy loss of no more than 1%. Numerical values of all plasma parameters are selected on the basis of previously obtained experimental data.

Curves 1, 2, and 3 correspond to scattering at angles of 1, 2, and 3° respectively. Curve 4 is a graphical representation of the data in Table 1 and corresponds to the complete detection of all charge-exchange particles.

This figure indicates that an analyzer aperture of 2-3° is sufficient for satisfactory detection of secondary ions. The corresponding aperture for satisfactory collection of secondary protons which are converted in a gas target[12] is 15°. However, a rough calculation of the aperture of the analyzer used by us gives a value an order of magnitude less, ~ 0.2°.

A comparison of the experimental and theoretical data is shown in Fig. 6 which gives a graph of the energy dependence of the efficiency for conversion from atomic hydrogen into protons for several values of plasma target density. The solid lines are theoretical values and the points are experimental data. The results are obtained for various modes of plasma injector operation, producing different degrees of ionization in the plasma flux.

Satisfactory agreement of the calculations with experimental values justifies extrapolation of the results to a beam energy of 50 eV and permits comparison with data for conversion in a gas target.[12]

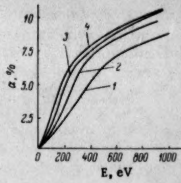

Fig. 5. Calculated values of the coefficient for conversion of atomic hydrogen into protons. 1) Particles recorded which are scattered by no more than 1°; 2) 2°; 3) 3°; 4) all charge-exchange particles recorded.

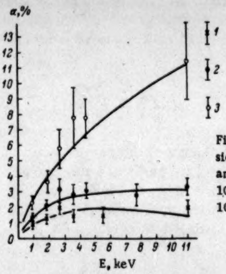

Fig. 6. Energy dependence of conversion efficiency. Target densities n^+L and n^0L (cm^{-2}), respectively: 1) $1.4 \cdot 10^{13}$ and $7 \cdot 10^{13}$; 2) $3.2 \cdot 10^{13}$ and $1 \cdot 10^{14}$; 3) $1.4 \cdot 10^{14}$ and $4.5 \cdot 10^{14}$.

For a beam energy of 50 eV and an analyzer angular aperture of ~ 1°, the coefficient for conversion of hydrogen atoms into protons is 10^{-3} for a plasma target and $5 \cdot 10^{-7}$ for a gas target.

The results presented here indicate the advantage of a plasma target for the conversion of hydrogen atoms into protons and are especially pertinent for experiments in the low-energy region.

---

[1] V. V. Afrosimov and I. P. Gladkovskii, Zh. Tekh. Fiz., 37, 1557 (1967) [Sov. Phys.–Tech. Phys., 12, 1135 (1968)].

[2] V. V. Afrosimov, I. P. Gladkovskii, Yu. S. Gordeev, I. F. Kalinkevich, and N. V. Fedorenko, Zh. Tekh. Fiz., 30, 1456 (1960) [Sov. Phys.–Tech. Phys., 5, 1378 (1961)].

[3] Yu. V. Gott and V. G. Tel'kovskii, Zh. Tekh. Fiz., 34, 2114 (1964) [Sov. Phys.–Tech. Phys., 9, 1628 (1965)].

[4] H. P. Eubank and T. D. Wilkerson, Rev. Sci. Instr., 34, 12 (1963).

[5] H. Fleischmann, R. E. Kribel, F. R. Scott, and R. Borochoff, Bull. Am. Phys. Soc., II, 10, 219 (1965).

[6] Yu. S. Azovskii, I. T. Guzhovskii, and B. G. Safronov, Zh. Tekh. Fiz., 34, 841 (1964) [Sov. Phys.–Tech. Phys., 9, 641 (1964)].

[7] V. A. Belyaev, B. G. Brezhnev, and E. M. Erastov, Zh. Eksp. Teor. Fiz., 52, 1170 (1967) [Sov. Phys.–JETP, 25, 777 (1967)].

[8] W. L. Fite, R. F. Brackman, and W. R. Snow, Phys. Rev., 112, 1161 (1958); D. G. Hummer, R. F. Stebbings, and W. L. Fite, Phys. Rev., 119, 663 (1960); W. L. Fite, A. H. Smith, and R. F. Stebbings, Proc. R. Soc. A, 268, 527 (1962).

[9] Ya. M. Fogel', D. V. Pelipenko, V. A. Ankudinov, and V. M. Topolya, Zh. Eksp. Teor. Fiz., 34, 579 (1958) [Sov. Phys.–JETP, 7, 400 (1958)].

[10] L. I. Krupnik and N. G. Shulika, in: Plasmoid Studies [in Russian], Izd. Naukova Dumka, Kiev (1967), p. 159.

[11] B. A. Trubnikov, in: Reviews of Plasma Physics, Vol. 4, Consultants Bureau, New York (1966).

[12] H. Fleischmann, Nucl. Fus., 8, 81 (1968).

Model for the low-voltage arc.
I. Stationary solution

Yu. Yu. Abramov and G. G. Gladush

(Submitted August 14, 1972; resubmitted September 7, 1973)
Zh. Tekh. Fiz., 44, 1183-1187 (June 1974)

1. It is well known from experimental studies (see, for example, refs. 1, 2 and citations therein) that at relatively high temperatures the transition from the diffusion mode in the thermionic converter to the arc mode is smooth, the striking and quenching voltages of the arc coincide, and the discharge is uniform along the electrodes. The picture changes with a reduction in temperature. The transition from the diffusion mode into the arc mode is accompanied by the appearance of luminosity at the anode and, subsequently, by a pronounced nonuniform distribution of plasma density and potential along the gap. The arc striking and quenching voltages do not coincide. These phenomena are associated with nonreproducibility of the volt–ampere characteristic (VAC). A theoretical description of the thermionic converter in the transition region requires an explanation of this effect; it is also necessary to have an "ideal" VAC, i.e., one calculated assuming uniformity along the electrodes. One would then investigate the solution for stability with respect to perturbations that are nonuniform along the electrodes and study the possibilities of describing a finite nonuniform state and the experimental VAC.

This paper is devoted to a theoretical description of an ideal VAC, which assumes a nonuniform distribution of plasma density and potential over the gap. It should be pointed out that a number of papers[1,3-5] have been devoted to a theoretical description of a VAC with a segment having a negative slope. All (except for ref. 5) are based on numerical calculations, and the general physical picture of the transition remains unclear; moreover, all obtain a VAC segment with negative differential resistance which is too small. The negative-resistance mechanism proposed in ref. 5 is associated with the energy balance of the system; a qualitatively different mechanism is proposed here. In addition, the region of applicability is relatively small in ref. 5.

2. Our calculation is based on the following model. It is assumed that ionization begins near the anode. As the current rises the ionization region spreads. The plasma gap is divided into two regions: a high-density region bordering on the anode, where ionization occurs, and a region near the cathode, in which there is no volume ionization and the electron space charge is neutralized by ions from the "arc" region. These regions are separated from one another by a double sheath of electric charge where there is a potential jump which accelerates electrons arriving from the diffusion region into the arc region, producing ionization there (see Fig. 1). We describe in qualitative fashion the reason for the creation of a negative slope in the VAC of such a model.

We first note that from the overall neutrality of the double layer it follows that the electron current from the diffusion region into the arc region is proportional to the counter ion current ($j_i \sim j_e \sqrt{m/M}$ is the Langmuir relation[6]). As the electron current increases (associated with a rise in the current emitted into the plasma, i.e., with a reduction in the cathode potential jump) the ion current also increases proportionately. On the other hand, the ion current at the cathode is proportional to the plasma density and, in addition, increases as the cathode jump decreases. It then follows that the plasma density at the cathode does not rise in proportion to the current, but more slowly. Therefore the size of the diffusion region, $x_0 \sim D_e n_0^{(1)}/j_e$ (where D_e is the electron diffusion coefficient and $n_0^{(1)}$ is the plasma density at the cathode), decreases with increasing current, and the size of the arc region increases. With a fixed potential jump in the double sheath, the plasma density in the arc region rises rapidly because of the increase in the current and the size of the region; it increases to such an extent that the ion current from the arc region increases more rapidly than the electron current. The rise in plasma density can be reduced by a reduction in the energy of the electrons producing ionization, i.e., by a reduction in the potential jump. Thus the potential jump decreases as the current increases, which is a basic reason for the reduction in the maintaining voltage of the arc. As a result a segment of the VAC has a negative differential resistance.

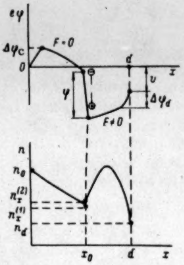

Fig. 1. Dependence of electron potential energy on the coordinate x. Schematic plasma density profile.

Certain assumptions are made in the following to obtain the analytic dependence of current on voltage: In particular, the electron temperature is assumed to be independent of coordinates. From the qualitative description and the results obtained below it follows that this assumption is not fundamental, but that makes it possible to simplify the calculations, which would otherwise be rather cumbersome. A number of other assumptions are specified in the text.

3. We consider the diffusion region. The x axis is directed from the cathode to the anode, and the plasma is uniform in the y and z directions. Since ionization and recombination do not occur in this region, the density profile of the quasineutral plasma must be linear:

$$n(x) = (n_x^{(1)} - n_0^{(1)})\frac{x}{x_0} + n_0^{(1)}, \tag{1}$$

where $n_x^{(1)}$ is the plasma density in the diffusion region at the boundary with the arc region. Substituting Eq. (1) in the usual boundary conditions for the ion and electron currents,[1] we obtain the following system of equations:

$$j_R \exp\left(\frac{-\Delta\varphi_k}{T}\right) - \frac{1}{2} n_0^{(1)} v_e = D_e \frac{n_0^{(1)} - n_x^{(1)}}{x_0} - u_e nE = \frac{1}{2} n_x^{(1)} v_e = j, \quad (2)$$

$$j_S - \frac{1}{4} n_0^{(1)} v_i \exp\left(-\frac{\Delta\varphi_C}{T}\right) = D_i \frac{n_0^{(1)} - n_x^{(1)}}{x_0} + u_i n(x) E(x) = -\frac{1}{2} n_x^{(2)} v_i, \quad (3)$$

where j_R is the Richardson emission current; T is the cathode temperature; j_S is the Saha–Langmuir current; $\Delta\varphi_C$ is the cathode potential jump, which retards electrons entering the plasma from the cathode; $n_x^{(2)}$ is the plasma density in the arc region at the boundary with the diffusion region; j is the current through the device.

The remaining notation is conventional. In the derivation of Eqs. (2) and (3), it is assumed that the potential drop at the jump is sufficiently great so that the ion current from the diffusion region into the arc region and the electron current from the arc region into the diffusion region can be neglected.

The ion and electron currents, which move in opposite directions through the collisionless double sheath, are coupled by the Langmuir relation

$$j_i = j_e \sqrt{\frac{m}{M}} \left(1 - \sqrt{\frac{T_e}{\varphi}}\right) (T_e \ll \varphi), \quad (4)$$

where T_e is the electron temperature.

This expression can be obtained from the Poisson equation on the basis of the overall neutrality of the sheath.

From Eq. (4) and the right-hand equations in the system (2)-(3), we obtain an expression for the current through the device by neglecting terms of order l/x_0 (l is the electron mean free path):

$$j = D_e \left(1 + \frac{T_i}{T_e}\right) \frac{n_0^{(1)}}{B x_0}, \quad (5)$$

where

$$B = 1 - \frac{\sigma_i}{\sigma_e} \sqrt{\frac{T_i}{T_e}} \left(1 - \sqrt{\frac{T_e}{\varphi}}\right),$$

$\sigma_{i,e}$ is respectively the scattering cross section for ions or electrons.

Since it is assumed that $j > 0$, it is necessary to satisfy the condition $B > 0$. Since $\sigma_i > \sigma_e$, this imposes certain conditions on the value of the electron temperature; these are assumed below. One can show that consideration of the finiteness of the width of the double sheath reduces these conditions, but consideration of a sheath with a dimension comparable with the mean free path complicates the problem tremendously (particularly the study of stability). Therefore the double sheath will be assumed to be collisionless and the quantity B is taken to be a constant of order unity.

Eliminating the quantity $\Delta\varphi_C$ from the left-hand equations of the system (2)-(3) and neglecting the Saha–Langmuir current, we obtain an expression for the plasma density at the cathode:

$$n_0^{(1)} = 2 \sqrt{\frac{j_R n_x^{(2)}}{v_e}}. \quad (6)$$

Substituting Eq. (6) in Eq. (5) and using Eq. (4), we obtain an expression for the current:

$$\frac{j}{j_R} = 8 \frac{D_e^2 \left(1 + \frac{T_i}{T_e}\right)}{B^2 x_0^2 v_e^2} \sqrt{\frac{T_e}{T_i}} \left(1 - \sqrt{\frac{T_e}{\varphi}}\right). \quad (7)$$

Since x_0 varies from quantities of the order of the mean free path l to the value d (size of the gap), it follows from Eq. (7) that $j_R (l/d)^2 \leqslant j \leqslant j_R$, i.e., the region of current variation is rather large.

The potential drop $\Delta\varphi_d$ in the diffusion region is found from the right-hand equations of the system (2)-(3) by integration of the quantity nE between the limits $(0, x_0)$ using Eq. (1),

$$\frac{\Delta\varphi_d}{T_e} = \frac{1-B}{B} \ln \frac{n_0^{(1)}}{n_x^{(1)}} = \frac{1-B}{B} \ln \frac{x_0 v_e B}{2D_e} \cong \frac{1-B}{B} \ln \frac{x_0}{l}. \quad (8)$$

The magnitude of the cathode potential jump is found from Eq. (3),

$$\frac{\Delta c_k}{T} = \ln \frac{1}{2} \sqrt{\frac{T_e}{T_i}} \frac{n_0^{(1)}}{n_x^{(1)}} \left(1 - \sqrt{\frac{T_e}{\varphi}}\right). \quad (9)$$

A comparison of Eqs. (8) and (9) indicates that $\Delta\varphi_d$ and $\Delta\varphi_C$ are quantities of the same order of magnitude.

4. To find the VAC it is necessary to determine the potential drop in the arc region and, in addition, the dimension of this region $d - x_0$. It is assumed that ionization in the arc region is produced by fast electrons which are accelerated in the potential drop of the double sheath, with the ionization length λ being greater[7] than d. In addition, we assume that excitation of the atom to some level E_1 is the limiting state.[3] This assumption is not essential for this model, but facilitates the analytic calculation.

Because of the assumption $\lambda > d$, the density of fast electrons decreases with distance, and in the diffusion limit

$$n_f = n_{fx} \left(1 - \frac{x - x_0}{d - x_0}\right), \quad (10)$$

where $n_{fx} = j(d - x_0)/D_{ef}$ is the density of fast electrons at the jump, $D_{ef} = D_e(\varphi / T_e)$ is the diffusion coefficient for fast electrons.

In this case, the expression for the generation function takes the form

$$F = \frac{3j}{\lambda^2} (d - x) \exp\left(\frac{\varphi - E_1}{T_e}\right) \quad (\varphi < E_1). \quad (11)$$

A relatively cold plasma is formed ($T_e \ll \varphi$) as a result of ionization in the arc region. From the equation

$$\operatorname{div} j_i = F$$

using quasineutrality and the standard boundary conditions for the ion current, we find a value for the density n(d) of the cold plasma at the anode and the density $n_x^{(2)}$ at the jump,

$$n_x^{(2)} = 2n(d) = \frac{2j}{\lambda^2 v_i}(d - x_0)^2 \exp\left(\frac{\varphi - E_1}{T_e}\right). \qquad (12)$$

The potential jump at the anode is found by integration of the continuity equation for slow electrons:

$$j_e = 2\int_{x_0}^{d} F(x)\,dx = \frac{1}{4} n(d) v_e \exp\left(-\frac{\Delta\varphi_a}{T_e}\right). \qquad (13)$$

From Eqs. (12) and (13), we have

$$\frac{\Delta\varphi_a}{T_e} = +\ln \frac{1}{12}\sqrt{\frac{M}{m}}\sqrt{\frac{T_e}{T_i}}. \qquad (14)$$

The size of the diffusion region, x_0, is found from Eqs. (4) and (12):

$$\frac{\varphi - E_1}{T_e} = \ln\left[\sqrt{\frac{m}{M}}\frac{\lambda^2}{(d - x_0)^2}\left(1 - \sqrt{T_e/\varphi}\right)\right]. \qquad (15)$$

The plasma potential drop in the arc region is determined by the ambipolar field, which is proportional to the logarithm of the density ratio. In view of Eq. (12), this means that

$$\frac{\Delta\varphi_p}{T_e} = -\ln 2. \qquad (16)$$

Equations (7)-(9) and (14)-(16) describe the VAC of a converter in the particular mode studied here. Since Eq. (7) indicates that x_0 decreases monotonically as the current rises, the simple relation which follows from these same equations,

$$\frac{\partial u}{\partial j} = \frac{T_e}{j}\left(\frac{d - 2x_0}{d - x_0} - \frac{1}{B}\right) \qquad (17)$$

shows that with a decrease in x_0 from d to a value of the order of the electron mean free path, the voltage u across the discharge gap decreases everywhere if $B < 0.5$.

Generally speaking, calculation of the VAC for such a system is a difficult problem. Difficulties arise primarily because of the complex form of the generation function, the necessity for considering heating of plasma electrons in the arc region, etc. It should be noted that the self-consistent problem of the calculation of a developed low-voltage arc in the parameter region where the cathode beam is important has not been solved at the present time, even with the help of a computer.[8] Therefore the simplifications made above are unavoidable.

Nevertheless, one can indicate the parameter region in which the model proposed above is strictly valid, although it appears possible that the actual region of applicability is broader.

We shall assume that ionization is mainly achieved by direct collision of fast electrons. In this case, the maximum voltage on the device is equal to the ionization potential of the gas, $E_1 = E_i$; $E_i = 3.89$ eV for Cs. The absence of fast-electron reflection from the arc region and also the requirement $\lambda > d$ limits analytic consideration to values $d \leqslant 20l$. In accordance with Eq. (15), the reduction in voltage does not exceed a quantity of the order of one volt. As an illustration, we consider a specific physical situation. Let $l \sim 0.1$ cm ($p \sim 3 \cdot 10^{-2}$ mm Hg), $d - x_0 = 0.5$ cm, $d = 0.8$ cm, and the maximum density $n_e = 2 \cdot 10^{11}$ cm^{-3}. In this case, the current is approximately 60 mA. From the balance between heating of cold plasma electrons by the beam and the cooling at the anode barrier, it follows that the temperature of the cold plasma is no more than 0.2 eV. Estimates show that in this case the effect of the cold plasma on ionization of Cs atoms can be neglected. One can estimate from Eq. (7) the Richardson current j_R which must be selected in order to obtain the assigned parameters; $j_R \sim 0.5$ A. Knowing j_R, one can estimate the current at maximum voltage, $j_V \sim 10$ mA. The voltage falls by 0.3 V when the current is increased to 60 mA. With further increase in current, the temperature and density of the cold plasma rises and its role in ionization becomes significant. The example presented is not inconsistent with available experimental data.

---

[1] G. A. Dyuzhev, A. M. Martsinovskii, G. E. Pikus, É. B. Sonin, and V. G. Yur'ev, Zh. Tekh. Fiz., 37, 1825 (1967) [Sov. Phys.—Tech. Phys., 12, 1336 (1968)].

[2] V. I. Derbilov, D. V. Karetnikov, and V. B. Turundaevskii, Abstracts of papers, 14th All-Union Conference on Emission Electronics, Tashkent (1970).

[3] F. G. Baksht and B. Ya. Moizhes, Zh. Tekh. Fiz., 35, 266 (1965) [Sov. Phys.—Tech. Phys., 10, 214 (1965)].

[4] A. A. Belokon' and É. B. Sonin, Zh. Tekh. Fiz., 39, 2105 (1969) [Sov. Phys.—Tech. Phys., 14, 1583 (1970)].

[5] V. A. Zherebtsov and I. P. Stakhanov, Zh. Tekh. Fiz., 40, 1729 (1970) [Sov. Phys.—Tech. Phys., 15, 1344 (1971)].

[6] V. L. Granovskii, Electrical Current in Gas [in Russian], Izd. Nauka, Moscow (1971).

[7] A. F. Nestoyashochiii, Zh. Tekh. Fiz., 38, 902 (1968) [Sov. Phys.—Tech. Phys., 13, 679 (1968)].

[8] I. P. Stakhanov and V. E. Cherkovets Zh. Tekh. Fiz., 41, 1400 (1971) [Sov. Phys.—Tech. Phys., 16, 1102 (1972)].

Model for the low-voltage arc.

II. Stability

Yu. Yu. Abramov and G. G. Gladush

(Submitted August 14, 1972; resubmitted September 7, 1973)
Zh. Tekh. Fiz., 44, 1188-1192 (June 1974)

The instability growth rate for the transition from the diffusion mode to the arc mode is calculated in the linear approximation. It is shown that homogeneous perturbations along the electrode can be stabilized by high external resistance; inhomogeneous perturbations can grow under these conditions.

In the preceding paper,[1] a model is proposed for the stationary state of the low-voltage hot-cathode arc. In this model, the negative segment in the volt–ampere characteristic (VAC) results from a nonuniform distribution of potential and plasma density over the gap. The plasma can be divided into two regions: a diffusion region close to the cathode in which there is no volume ionization and an arc region near the anode. The present paper considers the stability of this state.

The time-dependent equation for the variation of plasma density δn in the diffusion region is the ordinary equation for ambipolar diffusion (the notation used is the same as that in ref. 1):

$$\frac{\partial}{\partial t}\delta n - D_a\frac{\partial^2}{\partial x^2}\delta n = 0. \tag{1}$$

It is assumed here and in the following that the characteristic frequencies of these perturbations do not exceed the electron–neutral and ion–neutral collision frequencies or the electron and ion plasma frequencies. We seek a solution of Eq. (1) in the form

$$\delta n(x, t) = e^{-i\omega t}\delta n(x). \tag{2}$$

If we substitute the solution of Eq. (1) in the usual boundary conditions, we obtain equations which connect the perturbed densities at $x = 0$ and $x = x_0$ with the current variation δj. As in ref. 1, $x = 0$ is the plasma boundary at the cathode and $x = x_0$ is the boundary between the diffusion and arc regions. In the derivation of the boundary conditions one should consider the fact that the current variation at $x = x_0$ results not only from the change in plasma density at the boundary, but also from its displacement by an amount δx_0:

$$\delta j\,|_{x=x_0} = \frac{1}{2}\bar{v}_e\delta n_x^{(1)} + \left.\frac{\partial n}{\partial x}\right|_{x=x_0}\delta x.$$

The next two equations are obtained from the Langmuir condition (1.4) [here and in the following (1.4) denotes reference to Eq. (4) of ref. 1] and from the expression for the perturbation of the potential drop in the plasma, which is obtained by variation over the variables x_0, j, and n in the expression [see (1.8)]:

$$\Delta\varphi_d = \frac{j_e}{u_e}\int_0^{x_0}\frac{dx}{n(x)} + \frac{D_e}{u_e}\int_0^{x_0}\frac{\partial n}{\partial x}\frac{dx}{n(x)}.$$

By variation of the relation $j = j_R\exp(-\varphi_k/T) - {}^1\!/_2 n_0^{(1)}\bar{v}_e$ under the condition $j \ll {}^1\!/_2 n_0^{(1)}\bar{v}_e$, we obtain a relation between the current perturbation and the perturbation of the cathode potential jump:

$$\delta j = \frac{1}{2}\frac{n_0^{(1)}\bar{v}_e\delta\varphi_k}{T} + \frac{1}{2}\delta n_0^{(1)}\bar{v}_e.$$

Thus, we have six equations for the seven unknowns $\delta\varphi_k$, $\delta n_0^{(1)}$, $\delta n_x^{(1)}$, $\delta\varphi_d$, $\delta n_x^{(2)}$, δx_0, and δj. These equations are not presented in complete form because of their complexity.

The remaining unknown quantities are found from an analysis of the equations in the arc region. The equation for ambipolar diffusion in this region has the form

$$\frac{\partial}{\partial t}\delta n - D_a\frac{\partial^2}{\partial x^2}\delta n = \delta F, \tag{3}$$

where

$$\delta F = F(x)\left(\frac{\delta j}{j} + \frac{\delta\varphi}{T_e}\right) \tag{4}$$

is the variation of the generation function [see (1.11)].

One can represent δF in such a form if the ionization process is successfully established during the time of variation of the quantities δj and $\delta\varphi$. It is necessary that the characteristic time of the instability be greater than the fast-electron diffusion time over the distance $(d - x_0)$:

$$\omega \ll D_{e\varphi}\frac{D_{\mathrm{ef}}}{(d - x_0)^2}. \tag{5}$$

Substituting the solution of Eq. (3) in the boundary conditions at the left and right ends of the arc region, we obtain two equations in which the new unknowns $\delta\varphi$ and $\delta n(d)$ appear. Still another equation can be obtained from the condition for the continuity of the electron current of the cold plasma,

$$\delta j_e(d) = \frac{1}{4}\delta n(d)\bar{v}_e\exp\left(-\frac{\varphi_d}{T_e}\right) - \frac{1}{4}n(d)\bar{v}_e\exp\left(-\frac{\varphi_d}{T_e}\right)\frac{\delta\varphi_d}{T_e}$$

$$\delta j_e(d) = \frac{\partial}{\partial t}\int_{x_0}^{d}\delta n(x)\,dx + 2F\delta x_0 - 2\int_{x_0}^{d}\delta F(x)\,dx. \tag{6}$$

In the last equation the increase in electron current at the anode due to the increase in the size of the arc region is taken into account. For the plasma in the diffusion region this condition degenerates into an equality of the perturbed electron current at the cathode and at the jump. This difference is associated with the fact that the electron and ion currents are of the same order of magnitude in the arc region since the cold plasma does not transport current. Still another equation is the expression for the perturbation of the potential drop $\delta\varphi_p$ in the plasma of the arc region, which is obtained in a manner similar to that for $\delta\varphi_d$. A final equation is Ohm's law for the external circuit:

$$\delta u = -R\int\delta j ds = -R\delta I, \tag{7}$$

where δu is the perturbation of the potential drop in the interelectrode space, which is equal to the sum of the perturbations of the potential jumps and the perturbations of the potential drops in the plasma of the diffusion and arc regions, δI is the perturbation of the total current through the converter, and R is the external resistance.

The integral in Eq. (7) is taken over the area of the emitter.

Thus we have 11 equations for the 11 unknowns, and from the consistency conditions there follows an equation for ω (intermediate calculations are not given because of their complexity):

$$\Phi - 1 + \Psi\left[\frac{1}{2B} - \frac{x}{1-x} + \frac{1}{4}\varkappa^2 x(1-x) + \Phi\right]$$

$$-\frac{1}{2B}\Psi\int_0^1 (\cos\varkappa x\tau - 1)\frac{d\tau}{\tau^2}$$

$$\frac{1}{B}\int_0^1 \frac{d\tau}{\tau^2}\left[\frac{\sin\varkappa x\tau}{\varkappa x} - \tau\right] = -\frac{RI}{T_e}, \qquad (8)$$

where

$$\Phi = \left[\frac{1}{3} - \frac{1}{3}\cos\varkappa(1-x) + \frac{1}{2}\varkappa(1-x)\sin\varkappa(1-x)\right]$$

$$\times\left[\frac{\sin\varkappa(1-x)}{\varkappa(1-x)} - \cos\varkappa(1-x)\right]^{-1},$$

$$\Psi = [1 - B\cos\varkappa x - 2(1-B)\sin\varkappa x \mid \varkappa x]$$

$$\left[(1-B)\cos\varkappa x - \frac{1}{2}B\varkappa x\sin\varkappa x\right]^{-1},$$

$$\varkappa = \sqrt{\frac{\omega i}{D_a}}\,d, \quad x \equiv \frac{x_0}{d}.$$

Equation (8) can be simplified when $\varkappa \ll 1$. This condition means that during the growing time, all processes in the discharge plasma reach completion, i.e., a condition of quasistationarity exists. As expected, the variation of such quantities as φ_p, and φ_a, which do not depend on current in the stationary case, then goes to zero and Eq. (8) becomes the following equation:

$$\frac{j}{T_e}\frac{\partial u}{\partial j} - \varkappa^2\left[\frac{x^2}{4B} + \frac{11}{120}(1-x)^2 + \frac{19}{120}x(1-x)^2 + \frac{1}{6}\frac{x^3}{1-x}\right] = -\frac{RI}{T_e}. \qquad (9)$$

The condition $\varkappa \ll 1$ means that this equation is valid when the differential and external resistances are similar. Equation (9) indicates that the stability of the solutions for small $\varkappa$ is determined by the sign of the total (differential plus external) resistance. Since the differential resistance is negative in this case, the system is stable for $R > |\partial u/\partial I|$ and unstable for $R < |\partial u/\partial I|$. This condition is similar to that for any electronics instability and is perfectly reasonable, since the internal structure of the device itself does not manifest itself at low frequencies, and only the existence of a negative differential resistance is important (see Fig. 1).

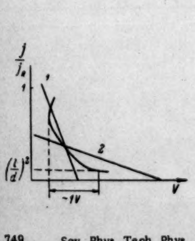

Fig. 1. Approximate form of volt–ampere characteristic and load lines. 1) $R < |du/dj|$; 2) $R > |du/dj|$.

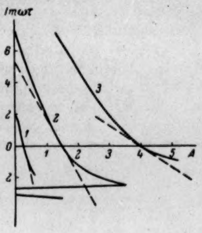

Fig. 2. Dependence of Im ω on $A = IR/T_e$ for various values of $x = x_0/d$, $\tau = d^2/D_a$. x: 1) 0.2; 2) 0.6; 3) 0.8.

Since all the terms in Eq. (9) are of order of unity when $R \sim |\partial u/\partial I|$, one can assume the characteristic roots of Eq. (8) are of the order of unity also, which corresponds to a characteristic growth rate $\Gamma \sim D_a/d^2$. This assumption is confirmed by numerical solution of Eq. (8), the results of which are shown[1] in Fig. 2. The dependence of Im ω on the quantity $A = RI/T_e$ is also shown in the figure.

The dashed curves correspond to the approximate equation (9). It is clear that when x is not very close to unity the approximate and exact solutions are similar up to $\varkappa \sim 1$. For $A < A_{cr} = |\partial u/\partial I|(I/T_e)$ (i.e., $R < |\partial u/\partial I|$), there are both positive and negative values of Im ω (Re ω = 0) and for $A > A_{cr}$, Im $\omega < 0$. The results shown indicate that the growth time is of the order of the time for ambipolar diffusion of an ion over a distance d, $\tau = d^2/D_a$, i.e., time for establishment of the stationary state.

The growth rate is a maximum for R = 0, which is reasonable since the resistance has a stabilizing effect.

It is of interest to consider the stability of the system with respect to perturbation with wave vector parallel to the plane of the electrodes. Such perturbations, on the one hand, will be stabilized by particle diffusion; on the other hand, the effect of resistance on such perturbations is not stabilizing since they do not change the total current in the circuit. For consideration of spatial dispersion along the y axis, the term $-k_y^2 D_a \delta_n$ appears in Eq. (1), which is equivalent to the substitution $i\omega \to i\omega + D_a k_y^2$, and the right sides of Eqs. (8) and (9) go to zero. For $k_y d \ll 1$, which is possible when $L \gg d$ where L is the dimension of the device, the system is absolutely unstable along the electrode, and even for resistances as high as desired can break down into regions with higher and lower current densities. In the nonlinear stages, this can lead to the formation of the current filament which is also observed experimentally.[2] Since the growth rate is greater than the reciprocal time for establishment of the stationary state, even for fast turn-on of the device, the stationary state should be established immediately as a nonuniform state (along the electrodes), bypassing the uniform stage, as has also been observed experimentally.[3] For devices with small longitudi-

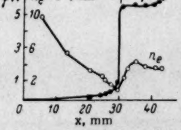

Fig. 3. Distribution of potential φ and density n on the axis of a discharge gap. L = 30 mm, d = 45 mm, $p = 2 \cdot 10^{-3}$ torr, $T_k = 950°K$.

nal dimensions, the quantity k_y can not be small, and transverse diffusion will be the significant stabilizing factor. In this case current flow along the electrodes can play an important role. Without considering such currents, however, one can estimate in order of magnitude the minimum dimension of the device for which the "transverse" instability will be quenched. Replacing $i\omega$ by $k_y^2 D_a$ in Eq. (9) and substituting for $\partial u/\partial j$ in accordance with (1.17), we obtain

$$L_{\min} = 2\pi d\,[x^2|4B + 11(1-x)^2|120$$

$$+ 19(1-x)x|120 + x^3|6(1-x)]^{1/2}$$

$$\times|(1-2x)|(1-x)-1|2B|^{-1/2}$$

$L_{\min} \sim d$ for $x \sim 0.5$.

This estimate agrees qualitatively with previous results[4] where for gaps of the order of the cathode dimension volt–ampere characteristics are obtained with a large segment of negative differential resistance with a plasmoid having sharply defined boundaries growing from anode to cathode as the current increases. A similar phenomenon is also observed in the development of the hot-cathode arc in inert gases.[5]

It should be noted that the assumptions upon which this theory is based and its results can find qualitative justification and confirmation in the phenomenon of anode spot formation in low-pressure arcs and in glow discharges.[6] Probe measurements show that the anode sheath (and after contraction, the anode spot also) is separated from the positive column by a double sheath of electric charge in which there is a potential drop of the order of the ionization potential of the gas. This plasma has a higher density and the rate of ion generation in it is greater than the rate of ion production in the plasma of the positive column. It is positively charged both with respect to the main plasma and with respect to the anode. The reason for the formation of an anode spot in this case may be the development of the transverse instability described here.

In conclusion, the authors thank D. V. Karetnikov for his interest.

Immediately after this paper was submitted an experimental paper of A. I. Kiryushchenko and M. A. Lebedev (Zh. Tekh. Fiz., 42, 1657 (1972) [Sov. Phys. – Tech. Phys., 17, 1322 (1973)] was published which confirms the basic assumptions of this model; in particular, the experimentally measured potential and plasma density profiles (Fig. 3) are in good agreement with the theoretical profiles (Fig. 1 of ref. 1). The arc region is separated from the diffusion region by a collisionless potential jump, and a beam of fast electrons is observed in the arc region.

---

1) The authors are grateful to L. Knizhnikova for the computer solution of the equation.

[1] Yu. Yu. Abramov and G. G. Gladush, Zh. Tekh. Fiz., 44, 1183 (1974) [Sov. Phys. – Tech. Phys., 19, 745 (1974)].

[2] G. A. Dyuzhev, A. M. Martsinovskii, G. E. Pikus, É. V. Sonin, and V. G. Yur'ev, Zh. Tekh. Fiz., 37, 1825 (1967 [Sov. Phys. – Tech. Phys., 12, 1336 (1968)].

[3] V. B. Kaplan, A. M. Martsinovskii, B. I. Tsirkel', and V. G. Yur'ev, Zh. Tekh. Fiz., 41, 1436 (1971) [Sov. Phys. – Tech. Phys., 16, 1130 (1972)].

[4] A. I. Kiryushchenko and M. A. Lebedev, Zh. Tekh. Fiz., 41, 1170 (1971) [Sov. Phys. – Tech. Phys., 16, 924 (1971)].

[5] E. O. Johnson, RCA Rev., 15, 498 (1955).

[6] B. N. Klyarfel'd and N. A. Neretina, Zh. Tekh. Fiz., 30, 186 (1960) [Sov. Phys. – Tech. Phys., 5, 169 (1960)].

Interferometer measurement of the neutral cesium distribution in a short low-voltage arc

Yu. L. Serov and I. P. Yavor

A. F. Ioffe Physicotechnical Institute, Academy of Sciences of the USSR, Leningrad

(Submitted July 19, 1973)
Zh. Tekh. Fiz., 44, 1193-1199 (June 1974)

An experimental study of the distribution of unexcited cesium atoms in a short low-voltage arc is described. The measurements use a Rozhdestvenskii interferometer and superposition of interference patterns. A significant radiation in the density of unexcited cesium atoms is observed in an arc in the interelectrode gap of a hot-cathode diode.

1. The short low-voltage cesium arc has been the subject of much experimental and theoretical study. Usually, however, attention has been focused on the charged components of the low-voltage plasma; the density and distribution of unexcited cesium atoms in the narrow gap of a thermionic converter or cesium diode are usually inferred from the thermal conditions in the apparatus and in the cesium reservoir. No direct measurements have been reported of the neutral cesium density. However, an important redistribution of neutrals can occur in a discharge plasma, and this redistribution can affect the plasma.[1]

In this work we describe measurements of the density and distribution of unexcited cesium atoms in the interelectrode gap of a hot-cathode planar diode. The measurements are carried out under various operating conditions of the diode by means of a dual-beam interferometer used with a spectrograph. We use the Rozhdestvenskii hook method[2] and the superposition of interference patterns.[3]

2. Figure 1 shows the experimental apparatus, including the dual-beam interferometer and the spectrograph. Continuum light from an arc lamp is focused by a lens onto the first semitransparent mirror of the interferometer. Here it is split into two beams of equal intensity. After one of these beams is reflected from a total-reflection mirror, it passes through the gap of the cesium diode. After the second beam is passed through a compensation tube and a glass plate to rotate the interference fringes, it strikes a second total-reflection mirror; then it strikes a second semitransparent mirror, beyond which the two beams are combined and directed to the slit of the spectrograph.

The hook method is usually used for measurement in homogeneous vapor or gas columns. The interferometer is adjusted by the classical method,[2] and the interference fringes are localized at infinity. It has been argued[1] that the hook method cannot be used to study objects in which there are strong density gradients: When the interference fringes are localized at infinity a large density gradient transverse to the axis of the light beam causes the hooks to become blurred.

In the narrow gap of a cesium diode with markedly different electrode temperatures the neutral density varies considerably over the gap, even in the free-running mode. Certain measures must be taken to avoid blurring of the hooks and to make it possible to determine the distribution of atoms over the gap from a single interferogram. The gap must be focused onto the spectrograph slit, and the spatial resolution in the direction perpendicular to the electrode surfaces (to the gap) must be good. In practice this second requirement can be met by using a narrow defining slit parallel to the gap to stop down the optical system in the specified direction. Furthermore, the interference fringes must be localized at the center of the diode gap. In this case the fringes and the gap are focused on the spectrograph slit. The interferometer is adjusted by the method of ref. 4 to localize the interference fringes at the center of the gap. Under the specified conditions, the interferogram contains a spectral sweep of the image of the gap with the interference fringes. The upper edge of the interferogram corresponds to the anode surface, while the lower edge corresponds to the cathode surface. Each narrow part of the interferogram parallel to the gap is formed by beams passing through the corresponding part of the gap and carries information about it.

The thermionic energy converter is a cesium diode with molybdenum electrodes. The working surfaces are the flat

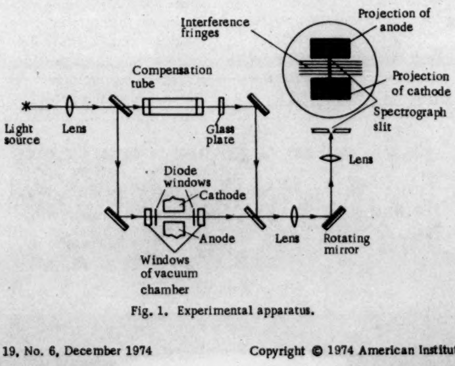

Fig. 1. Experimental apparatus.

ends of cylindrical electrodes, between which a gap from 0 to 2 mm can be established. The lateral electrode surfaces are covered by a BeO ceramic. The electrodes are 11 mm in diameter (this is the path length of the beam in the discharge region). The housing of the apparatus containing the electrodes has two windows through which the gap can be illuminated. The distance between these windows, i.e., the total path length of the light in the cesium vapor, is 50 mm. The diode housing is placed in a vacuum chamber, also fitted with windows.

The interferometer measurements yield information about the total neutral density along the path of the light, which is $\int_0^l N(x)dx$, where N(x) is the neutral density and l is the total length of the vapor column. It is necessary to take account of the comparatively cold layers of cesium vapor surrounding the interelectrode gap. To determine quantitatively the contribution to Nl from these layers and the changes in these layers which occur when conditions in the interelectrode gap are varied, we have an aperture 1 mm in diameter through the anode housing, parallel to its working surface and very close to it; part of the light beam passes through this aperture. The changes which occur in the neutral density in the gap upon, e.g., a change in the discharge current, are determined from the difference ΔNl along the paths of two light beams, one passing through this aperture, where there is no discharge, and the other passing through the interelectrode gap. Certain results obtained in this manner are monitored under conditions corresponding to the closest possible arrangement of windows (in which the distance between a window and the edge of the gap is 2 mm). However, this window arrangement causes difficulties so that it is used only in control experiments to check the validity of the basic series of measurements.

3. The hook method is used to measure the density of cesium atoms in the apparatus; the cesium vapor pressure can easily be determined from this density. Comparison of this pressure with that determined from the temperature of liquid cesium, on the basis of the data of ref. 5 shows the discrepancy to be less than 8% from 10^{-1} to 10 torr. This discrepancy lies within the total experimental error. The oscillator strength of the $6P_{3/2} - 6S_{1/2}$ transition (the line wavelength is λ_j = 8521 Å) used in these measurements f = 0.66 is calculated from the data of ref. 6.

A significant gradient in the neutral cesium density in the gap deforms the hooks. Figure 2 illustrates this behavior with three interferograms with hooks at the resonance line λ_j = 8521 Å. The cesium vapor pressure P = 4 torr and the interelectrode gap d = 1.6 mm. The lower interferogram is obtained under isothermal conditions, i.e., with the cathode, anode, and wall at the same temperature. The hooks have the usual shape. The central interferogram is obtained in the free-running mode (with the anode–cathode circuit opened), and at a cathode temperature T_c = 1600°K and an anode temperature T_a = 800°K. There is a significant density gradient in the gap; the densities at the electrodes differ by a factor of 2. The change in the neutral cesium density over the gap can be determined in the usual manner by measuring the distance between the hook vertices. The average gradient can be determined by counting the numbers of hooks to the right and left of the absorption line.[7] Taking account of the doublet structure of the cesium levels we can write

$$\overline{\frac{dN}{dy}} = \frac{m-n}{ald}\left(\sum_j \frac{f_j\lambda_m\lambda_j^2}{\lambda_m^2-\lambda_j^2} - \sum_j \frac{f_j\lambda_n\lambda_j^2}{\lambda_n^2-\lambda_j^2}\right)^{-1}, \tag{1}$$

$$a = \frac{e^2}{2\pi mc^2},$$

where m and n are the numbers of interference fringes or hooks along the vertical direction to the right and to the left, respectively, of absorption line λ_j, and λ_m and λ_n are the wavelengths at which the hooks or fringes are counted.

The upper interferogram is obtained with an arc discharge in the gap, at an arc current of i = 7 A. Here the hooks have contracted and become more deformed.

An important change in the density gradient over the gap can severely distort the hooks, which can become closed figures like the rings in Fig. 3.

From the condition $\partial\chi_{12}/(\partial y) = 0$ (χ_{12} is the phase difference between the interfering beams) we can find an equation for the neutral density gradient at the point at which, at wavelength λ_m, there is a "side" extremum on the interference fringe:

$$\frac{dN}{dy} = \frac{b}{al\lambda_m}\sum_j \frac{1}{f_j}\left(\frac{\lambda_m^2}{\lambda_j^2} - 1\right), \tag{2}$$

where b is the number of fringes per unit length at wavelength λ_m in the y direction in the absence of the vapor.

To determine the relative distributions of the neutral density in the interelectrode gap and the changes in these distributions with changes in the diode conditions it is more convenient to use a superposition method. From the blurs on the interferogram we can immediately determine the neutral distribution over the gap, since the distance $\lambda - \lambda_j$ from the blur at a given cross section of the gap to the center of the absorption line is proportional to the change in the product Nl along the beam in question:

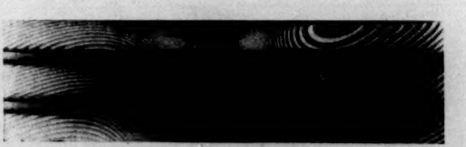

Fig. 2. Interferograms with hooks at the Cs λ = 8521 Å line. P = 4 torr, d = 1.6 mm.

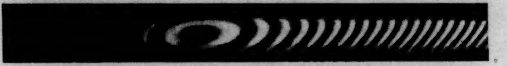

Fig. 3. Interferogram with closed fringes.

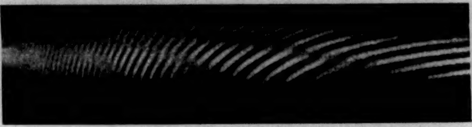

Fig. 4. Interferogram with blurs.

$\Delta(Nl) \sim \lambda - \lambda_j$. Figure 4 illustrates this situation with a blurred interferogram obtained by superimposing the interferogram corresponding to the free-running mode on the interferogram obtained with an arc.

When a resonant doublet is used it is necessary to take account of the total change in the dispersion near both absorption lines. Inspecting the interference pattern with blurs on both sides of the absorption line, we see that it is not symmetric with respect to the center of the line, because of the influence of the neighboring doublet component. The positions of the two neighboring blurs, of orders of m_1 and m_2, near the component λ_{j_1} of the resonance doublet are given by

$$\left.\begin{aligned} \Delta Nal\sum_j \frac{\lambda_{m1}^2\lambda_j f_j}{\lambda_{m1}^2-\lambda_j^2} &= \frac{2m_1+1}{2}\lambda_{m1}, \\ \Delta Nal\sum_j \frac{\lambda_{m2}^2\lambda_j f_j}{\lambda_{m2}^2-\lambda_j^2} &= \frac{2m_2+1}{2}\lambda_{m2}, \\ m_2 &= m_1+1. \end{aligned}\right\} \tag{3}$$

From these equations we can easily find an equation for the blurring order:

$$m_2=\frac{1}{2}\,\frac{\sum\limits_j \lambda_j^3 f_j\left[\frac{1}{\lambda_{m2}^2-\lambda_j^2}+\frac{1}{\lambda_{m1}^2-\lambda_j^2}\right]}{\sum\limits_j \lambda_j^3 f_j\left[\frac{1}{\lambda_{m2}^2-\lambda_j^2}-\frac{1}{\lambda_{m1}^2-\lambda_j^2}\right]}. \tag{4}$$

After rounding off the value of m_2 found from this equation to the nearest integer, we can determine the value of ΔN from (3). In addition, if we subtract the first equation in (3) from the second, we find

$$\Delta Nal\left[\lambda_{m2}^2\sum_j \frac{\lambda_j^3 f_j}{\lambda_{m2}^2-\lambda_j^2}-\lambda_{m1}^2\sum_j \frac{\lambda_j^3 f_j}{\lambda_{m1}^2-\lambda_j^2}\right] = \frac{(2m_1+1)(\lambda_{m2}-\lambda_{m1})+2\lambda_{m2}}{2}. \tag{5}$$

If the distance between the blurs satisfies $\lambda_{m2} - \lambda_{m1} < 50$ Å and if $\lambda_{m2} - \lambda_{j_0} < 100$ Å with $m_1 < 3$, we can neglect the first term on the right side of Eq. (5) for the resonant cesium doublet with an error of less than 1%. Then ΔN can be found without determining the order of the blur if the best-separated blurs are used:

$$\Delta N=\frac{\lambda_{m2}}{al}\left[\lambda_{m2}^2\sum_j \frac{\lambda_j^3 f_j}{\lambda_{m2}^2-\lambda_j^2}-\lambda_{m1}^2\sum_j \frac{\lambda_j^3 f_j}{\lambda_{m1}^2-\lambda_j^2}\right]^{-1}. \tag{6}$$

To incorporate the displacement of the interference pattern over the time between two exposures, we must insert identical terms (independent of λ) into the left sides of the first two equations of system (3). In this manner the displacement of the pattern between two exposures does not affect the value of ΔN determined from Eq. (5) or (6).

Figures 5a-5e show the distributions of the cesium-atom density in the arc discharge obtained by this method. These measurements are carried out at a fixed interelectrode gap of d = 1.6 mm and at a cathode temperature of 1400°K. We see that the density is governed by the vapor pressure and the current. As a current flow the neutral density in the discharge region falls off. As the vapor pressure is increased the relative change in the density at a fixed current increases. At a pressure of $P \approx 1$ torr the greatest change in the density occurs near the cathode; toward the anode surface, the neutral density approaches the level governed by the anode temperature. As the cesium vapor pressure is increased the maximum of the change in the neutral density shifts toward the anode, as can be clearly seen on the interferograms with blurs. The maximum value ΔN_{max} at a current of 10 A varies from 20% to 60% as the cesium vapor pressure is raised from 1 to 6 torr. The functional dependence on the current becomes smoother. We can assume (Fig. 5) that the neutral density in the arc near an electrode surface is governed by the electrode temperature, while that at the center of the gap is governed by processes occurring in the arc. To check this point, we carry out measurements using interferograms obtained with the spectrograph slit oriented parallel to the diode gap, and we determine the neutral density in a narrow (0.1mm) layer near the anode. These measurements show the density near the anode to be governed by the anode temperature.

The temperatures of the neutrals and ions in the arc can be compared if we take account of elastic scattering of electrons by ions and resonant charge exchange of ions. Over the time preceding the resonant charge exchange of an ion, the ion acquires from electrons an energy

$$\varepsilon=\frac{2m_e}{m_a}\frac{\tau_{ei}}{\tau_{ia}}k(T_e-T_i), \tag{7}$$

where τ_{ei} and τ_{ia} are the effective electron–ion and ion–neutral collision times.

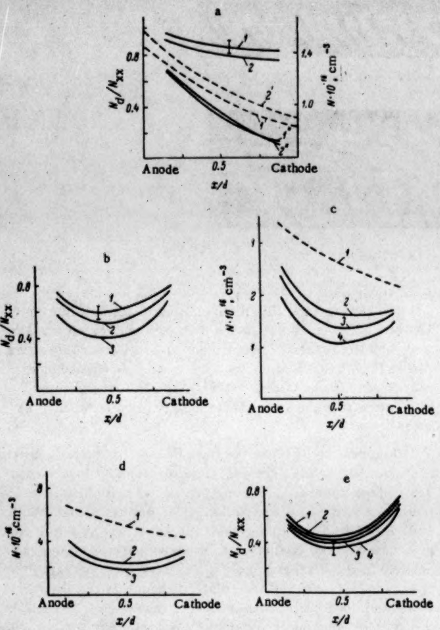

Fig. 5. Density distribution of the Cs atoms in the diode gap. a: 1-1") P = 1.15 torr. 1) $(N_d/N_{xx})(x/d)$, i = 5 A; 1') N(x/d), i = 0; 1") N(x/d), i = 5 A. 2-2") P = 1.3 torr. 2) $(N_d/N_{xx})(x/d)$, i = 10 A; 2') N(x/d), i = 0; 2") N(x/d), i = 10 A. b: P = 3 torr, $(N_d/N_{xx})(x/d)$. 1) i = 10 A; 2) 15 A; 3) 20 A. c: P = 3 torr, N(x/d). 1) i = 0; 2) 10 A; 3) 15 A; 4) 20 A. d: P = 6 torr, $N(x\cdot d)^{-1}$. 1) i = 0; 2) 5 A; 3) 20 A. e: P = 6 torr, $(N_d/N_{xx})(x/d)$. 1) 5 A; 2) 15 A; 3) 10 A; 4) 20 A.

At a pressure of a few torr and at an electron density of $N_e = 5\cdot 10^{14}$ cm^{-3} an ion manages to acquire an energy of $\varepsilon \sim 10^{-3}$ eV, i.e., the temperatures of the ions and neutrals become equal as a result of energy transfer, so that we can speak of a common heavy-particle temperature T. To evaluate the neutral temperature we use the heat-balance equation[8]

$$\frac{d}{dx}\left(\varkappa_a \frac{dT}{dx}\right) = -\frac{3m_e}{m_i}\frac{N_i}{\tau_{ei}}k(T_e - T)$$

$$4\frac{m_e}{m_a}k(T_e - T)\frac{v_e}{l_{ea}}N_e, \tag{8}$$

where $\varkappa_a$ is the thermal conductivity of the neutrals.

Assuming an interelectrode gap of d = 2 mm, a pressure of P = 4 torr, $N_e = 7\cdot 10^{14}$ cm^{-3}, T_e = 3000°K, T_c = 1400°K, T_a = 600°K, and $\bar{\varkappa} = 1.65\ T_{av}^{1/2}$, we find T = 2300°K from Eq. (8) for the center of the gap.

We can thus conclude from these measurements that in the weakly ionized plasma of a low-voltage arc there is an important redistribution of unexcited cesium atoms caused by the significant heat evolution in the discharge region. We believe that it would be worthwhile to carry out a more detailed comparison of the plasma parameters and neutral density by means of the appropriate calculations. We note that in our experiments we have observed hooks at lines corresponding to transitions from the $6P_j$ level; these can also be used for more detailed studies in a cesium plasma.

In conclusion the authors thank Yu. A. Dunaev for his constant interest in this work, for assistance, and for discussion.

---

[1] V. L. Granovskii, Electric Current in a Gas. Steady-State Current [in Russian], Izd. Nauka, Moscow (1971).

[2] D. S. Rozhdestvenskii, Works on Anomalous Dispersion in Metal Vapors [in Russian], Izd. Akad. Nauk SSSR, Moscow (1951).

[3] A. M. Shukhtin, Spectroscopy of a Gas-Discharge Plasma [in Russian], Izd. Nauka, Moscow (1971).

[4] G. K. Tumakaev and V. R. Lazovskaya, Aerophysical Studies of Supersonic Flow [in Russian], Izd. Nauka, Moscow (1967), p. 79.

[5] A. N. Nesmeyanov, Vapor Pressures of the Chemical Elements [in Russian], Izd. Akad. Nauk SSSR, Moscow (1961).

[6] N. P. Penkin, Spectroscopy of a Gas-Discharge Plasma [in Russian], Izd. Nauka, Moscow (1970).

[7] I. R. Yavor and Yu. L. Serov, Phys. Lett., 39A, 109 (1972).

[8] F. G. Baksht, I. L. Korobova, and B. Ya. Moizhes, Zh. Tekh. Fiz., 41, 387 (1971) [Sov. Phys. – Tech. Phys., 16, 292 (1971)].

Formation of a narrow gas jet in vacuum

G. I. Dimov and V. Ya. Savkin

(Submitted June 25, 1973)
Zh. Tekh. Fiz., 44, 1200-1205 (June 1974)

Experiments on the formation of a narrow hydrogen jet in vacuum in which the jet diameter and gas density remain constant are described. It is possible to form such a jet if a conical limiter is used to block the peripheral part of the jet from a Laval nozzle. A hydrogen jet whose diameter decreases from 1 to 0.3 cm over a length of 20 cm with density of 10^{16} molecules/cm^3 has been produced. Experimental data on the formation of thin gas jets which condense into a supersonic hydrogen jet are also reported.

The experimental apparatus described in ref. 1 has been used to study the influence of a conical limiter on a gas jet issuing from a Laval nozzle into vacuum with a Mach number of ~10. The Laval nozzle has an exit cone 44 mm long, and the diameters of the minimum and exit cross sections of the nozzle are 0.2 and 6 mm, respectively. Gas is supplied to the nozzle in pulses 1500 μsec long by means of an electromagnetic valve.[2] As it enters the nozzle, the gas is at room temperature and at a pressure between 10 and 100 absolute atmospheres.

The conical limiter (a truncated cone) is arranged coaxially with the Laval nozzle, at a distance s = 0-25 mm from the exit end of the nozzle (Fig. 1). The front edge of the cone is rounded off to a radius of ~0.01 mm, shorter than the local mean free path of the molecules in the jet. In the volume between the nozzle and the limiter, P_1, which is evacuated separately, the vacuum is better than 10^{-2} torr at the end of the gas pulse. The gas pressure in the working part of the chamber, P_2, does not exceed 10^{-3} torr at the end of the gas pulse.

The density of the gas flow is measured by the dividing-cone method, by means of a special ionization tube (Fig. 1). The front part of the tube housing, a truncated cone with a vertex angle of 45°, separates a small jet from the overall gas flow and directs it into the tube. Since the edge of the entrance aperture has a small radius of curvature ~0.01 mm, gas flows at densities up to 10^{18} molecules/cm^3 can be divided without shock waves. The entering gas reaches equilibrium in the tube, volume of 13 cm^3, over a time on the order of 10 μsec. The time required for the gas flow throught the entrance aperture, from 0.2 to 1 mm in diameter, is 20-500 times as long as the gas pulse. A three-electrode system with an external collector is used to measure the gas density in the tube; the current in the collector circuit is monitored by an oscilloscope through a matching amplifier. When a differentiating unit is inserted into the measuring circuit, the time behavior of the rate at which gas is supplied to the tube (which is proportional to the density in the channel) can be observed directly. The time constant of the measuring circuit is ~10 μsec. The sensitivity of the tube to air is 33 mA/torr. In control measurements with a homogeneous flow the readings from the tube are proportional to the area of the entrance aperture as the aperture diameter is varied from 0.2 to 1 mm, provided that the gas density in the tube does not exceed $3 \cdot 10^{15}$ molecules/cm^3. The gas density can be measured up to the point at which the tube enters the nonlinear region and the gas-discharge regime is approached. The distribution of the gas flow is found by moving the ionization tube in three directions between pulses. The error of these measurements is 20%. The spatial resolution is governed by the diameter of the entrance aperture of the tube, but the sensitivity of the tube falls off as this diameter is reduced.

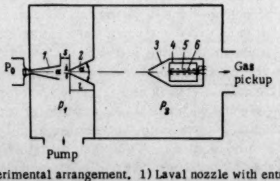

Fig. 1. Experimental arrangement. 1) Laval nozzle with entrance valve; 2) limiter (nickel); 3) housing of ionization tube (nickel, stainless steel); 4) ion collector (nickel); 5) grid (molybdenum); 6) cathode (thoriated tungsten).

Formation of a narrow jet of pure hydrogen. Under certain conditions, as the supersonic hydrogen jet passes through the conical limiter a narrow jet with a complex structure forms beyond the limiter. Figure 2a shows the jet structure beyond a conical limiter with an aperture diameter of d = 2 mm, a vertex angle of α = 45°, and a length of l = 40 mm for a hydrogen pressure of P_0 = 30 abs. atm at the entrance to the nozzle, as it appears τ = 850 μsec after the jet is turned on. The primary effect of the limiter is the formation of a tubular

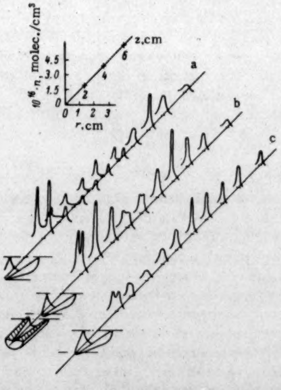

Fig. 2. Distribution of the hydrogen in the jets with respect to the radius r and the z axis. d = 2 mm, l = 40 mm, s = 6 mm, τ = 850 μsec. a) α = 45°, P_0 = 30 abs. atm; b) α = 35°, P_0 = 14 abs. atm; c) α = 40°, P_0 = 14 abs. atm).

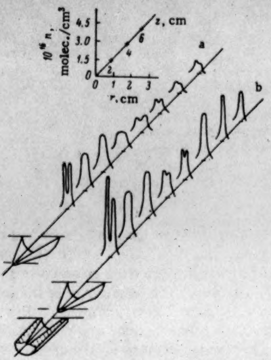

Fig. 3. Distribution of the hydrogen in the jet with respect to r and z. d = 3 mm, l = 40 mm, s = 6 mm, α = 40°, P_0 = 14 abs.atm. τ, μsec: a) 350; b) 850.

structure beyond the limiter; this structure contracts toward the axis. This tubular structure forms only if the diameter of the limiter aperture is much larger than the local mean free path of the molecules. With d < 1 mm the jet diverges significantly, and its intensity falls sharply. As the aperture is increased in size, the diameter of the gas tube at the exit from the limiter increases, as does the density of the jet at the point at which it contracts to the axis. With P_0 = 30 abs. atm, e.g., the tube diameter increases from 10 to 20 mm as the aperture diameter is increased from 2 to 15 mm. The vertex angle of the conical limiter, α, primarily affects the rate at which the jet contracts toward the axis. The point at which the jet contracts to the axis moves toward the limiter as the angle is reduced (in our experiments, to 30°). At the larger angles α = 55-60° the tubular structure becomes less well defined, and its diameter increases. As the cone is lengthened, the point at which the jet contracts to the axis moves toward the limiter, but with cones longer than 40 mm this effect weakens. As the entrance pressure P_0 is reduced, the gas jet beyond the limiter narrows, and the point at which it contracts to the axis moves toward the limiter, as the gas density in the jet falls off. At P_0 < 10 abs. atm the jet becomes blurred. Removing the limiter from the nozzle is equivalent to reducing the entrance pressure.

When the jet contracts toward the axis relatively rapidly (i.e., at small values of P_0 and α), the jet is observed to have a tubular structure with two successive necks (Fig. 2b; α = 35°, P_0 = 14 abs. atm, d = 2 mm). In Fig. 3, which shows the jet structure at 350 and 850 μsec after the beginning of the gas pulse, we see that as time elapses the jet slowly contracts toward the axis, and the contraction point moves toward the limiter. By 800-1000 μsec the jet becomes quite stationary. When flat or conical limiters are inserted beyond the conical shaping limiter, and if these additional limiters have aperture diameters which are less than the diameter of the jet at the point at which the density reaches 0.1 of its maximum in a given cross section, we observe partial or complete disruption of the fine jet, especially if the additional limiters are flat. When the apertures of these additional limiters are large the fine jet is not disrupted, but the rate at which it contracts toward the axis increases.

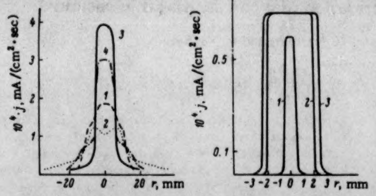

Fig. 4. Radial distribution of the jet density (expressed in milliamperes of the collector current of the tube per cm² per sec) at P_0 = 14 abs.atm. a: No limiter, z = 7 cm. 1) 100% H_2; 2) 100% CO_2; 3) 10% CO_2, 90% H_2; 4) 2% CO_2, 98% H_2. b: With a limiter, l = 20 mm, s = 5 mm, α = 45°, z = 10.5 cm, 10% CO_2 and 90% H_2. 1) d = 0.2 mm; 2) 1 mm; 3) 2 mm.

The narrowest hydrogen jets are formed when the vertex angle of the limiter is 40°. Figure 2c shows the jet structure for d = 2 mm, α = 40°, and P_0 = 14 abs. atm. The jet emerges from the limiter with a diameter of 10 mm and then gradually contracts toward the axis. In the 9-cm region, 11 cm from the exit of the limiter, the jet diameter is less than 3 mm (measured between the points at which the density is 0.2 of its maximum). In this part of the jet the radial distribution of the axial flow density is characterized by a 10-fold density drop at a radius of 5 mm and a 100-fold drop at a radius of 15 mm. If we assume the flow to be a supersonic hydrogen flow, we conclude that the gas density at the axis of the flow is $4.5 \cdot 10^{16}$ molecules/cm³ at the beginning of this part of the flow and $1.5 \cdot 10^{16}$ molecules/cm³ at the end of this part. While the flow density at the axis in the jet from a Laval nozzle without a limiter falls off roughly in proportion to the reciprocal square of the distance from the end of the nozzle, the density in the jet formed by the conical limiter varies only slightly. In the jet from a nozzle with the limiter shown in Fig. 2c the hydrogen density at the axis 24 cm from the end of the nozzle is 15 times higher than that in a jet from a nozzle without a limiter, for the same entrance pressure.

These experiments are carried out with liquid-nitrogen-cooled hydrogen of technical purity, with an impurity level of ~0.01%; similar results are obtained with pure helium. When a few hundredths of 1% of carbon dioxide is added to the hydrogen, the formation of a fine hydrogen jet is not observed.

From these experimental results we conclude that the formation of a nondiverging jet by the conical limiter and the contraction of this jet toward the axis are due to both the counterpressure of the scattered gas and "evaporation" from the jet surface of hydrogen molecules heated by the scattered molecules reflected from the cone (the mean free path in the jet is less than the thickness of the jet). Heating of the scattered molecules at the reflecting surface of the cone apparently plays an important role here. Before the jet contracts to the axis, its axial density falls off in proportion to the reciprocal square of the distance from the nozzle, because of the divergence of the supersonic jet. Because of this rapid decrease of the gas

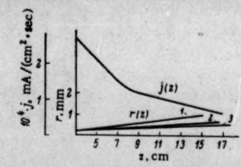

Fig. 5. Axial density of the jet, j(z), and jet radius, r(z), for various jet densities: 1) at the 0.1 level; 2) at the 0.5 level; 3) at the 0.8 level.

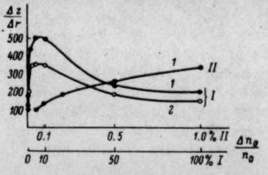

Fig. 6. Reciprocal vertex half-angle of the jet at the 0.5 level as a function of the relative volume concentration of CO_2 (curves 1) and of N_2 (curve 2) in mixtures with H_2. P_0 = 14 abs. atm, s = 25 mm, d = 0.2 mm.

density in the axial part of the jet and because of the radial contraction of the jet along its periphery, a tubular structure forms. The role of the entrance aperture of the conical limiter probably reduces to one of separating the central part of the jet from the Laval nozzle, by analogy with the limitation of a jet by freezing rings.[3]

This regular and quite pronounced effect on the structure of a jet of the surfaces surrounding it may be found useful in controlling the motion and deformation of gaseous formations in low vacuum.

Formation of narrow jets of condensing gases. When heavy gases are added to hydrogen in a supersonic jet, the heavy molecules are accelerated.[4] The divergence angle of the heavy impurity can be less than that of the hydrogen. If the impurity condenses in the jet the decrease in its divergence must be amplified. When the hydrogen condenses on the drops of impurity, the divergence of the jet as a whole must decrease. In this manner thin jets of a material in a "fog" can be produced.

We have attempted to form fine jets of carbon dioxide and nitrogen in a supersonic hydrogen jet. Figure 4a shows the distribution of the ionization-tube indications over the jet cross section 7 cm from the exit from the Laval nozzle. The jets of pure hydrogen and carbon dioxide (curves 1 and 2) diverge in similar ways. When carbon dioxide is added to the hydrogen, the jet contracts appreciably (curves 3 and 4), and the axial density increases significantly. Figure 4a shows that in a hydrogen jet with a CO_2 impurity the divergence of not only the carbon dioxide but also the hydrogen decreases. Jets with a very slight divergence cannot be obtained from the Laval nozzle used because of the large vertex angle of its exit cone.

Using a truncated cone to limit a jet of hydrogen with condensing impurities, we are able to produce jets with a very slight divergence in vacuum, and we are able to determine the "true" or thermal divergence of the slightly diverging component of the condensing jet from the Laval nozzle. The structure of a jet with condensing impurities has no features of any kind beyond the conical limiter over a broad range of diameters of the limiter aperture. Figure 4b shows the transverse distribution of a hydrogen jet containing 10% CO_2 (by volume) at a point 10 cm from the entrance to the conical limiter for various limiter apertures. The nature of the transverse distribution of the jet remains the same along the length of the jet, but the jet diameter increases essentially linearly with the length. The axial density of the jet is essentially independent of the diameter of the limiter aperture, falling off roughly in proportion to the reciprocal square of the distance from the nozzle and in proportion to the entrance pressure. The jet divergence beyond the limiter increases monotonically with increasing limiter aperture and is independent of the entrance pressure over the range 10-30 abs. atm. When the limiter is removed from the nozzle the axial density of the jet does not change, while the jet divergence beyond the limiter decreases. Figure 5 shows the axial density and radius of the jet, according to measurements made with the measuring tube, as functions of the distance from the end of the nozzle beyond a conical limiter with an aperture diameter of d = 0.2 mm (α = 45°, l = 20 mm, s = 25 mm, P_0 = 30 atm) for hydrogen with 10% CO_2. The axial density of the flow at 19.5 cm from the end of the nozzle ranges from $2 \cdot 10^{19}$ to $6 \cdot 10^{19}$ molecules/(cm^2·sec), depending on the relative amount of hydrogen at this point. The vertex angle of the jet is very small, less than 0.005 rad; the jet diameter 17 cm from the entrance to the limiter is 1.5 mm and at the 0.1 level, according to the indications of the tube.

Moving the conical limiter in the radial direction, we find that a jet consisting of a mixture of hydrogen with carbon dioxide has a component with an extremely slight thermal divergence not only at the axis but over the entire cross section, except in the outer layer, where the density falls off rapidly in the radial direction. For example 25 mm from the end of the nozzle a jet of H_2 with 10% CO_2 has a radius of 2.5 mm at the 0.5 level and a radius of 3.5 mm at the 0.05 level, according to the tube indications. A conical limiter placed in this cross section separates out a jet with a slight divergence, independent of the radial position of the limiter; in the central part of the cross section the density of this jet falls off radially more slowly than the density of the primary jet. At a radius of 2.5 mm the density of this smaller jet falls rapidly to zero. The axial density of the low-divergence jet formed by the limiter is several times lower than the corresponding density of the primary jet from the nozzle, according to the indications of the tube, when the CO_2 concentration is above $\sim 1\%$.

From the divergence of a jet beyond a limiter with a sufficiently small aperture we can determine the equivalent Mach number M $\sim \Delta z/\Delta r$, where Δr is the increase in the jet half-width over a length Δz. Figure 6 shows the ratio $\Delta z/\Delta r$ as a function of the volume concentration of CO_2 or N_2 in hydrogen for jets limited by a limiter with an aperture of d = 0.2 mm (α = 45°, l = 20 mm, s = 15 mm, P_0 = 14 abs. atm). The increase in the jet half-width is determined at the 0.5 level, from the indications of the tube. Figure 6 shows that CO_2 in a jet reduces the thermal divergence more effectively than does N_2. There is a weakly defined optimum impurity concentration in the range 2–10%. Jets of pure CO_2 and N_2 also have a high equivalent Mach number in the axial region. It follows from Fig. 6 that the gas composition plays an important role in reducing the thermal divergence in a jet. The rapid increase in the equivalent Mach number of the slightly divergent jet component with increasing concentration (up to an optimum concentration) is apparently due to accelerated condensation alone. Nevertheless, the acceleration of the impurity by the hydrogen contributes significantly to the reduction of the thermal divergence at a low impurity concentration.

The curves in Fig. 6 give only an approximate picture of the thermal divergence in the jet from a Laval nozzle, since the quantity $\Delta z/\Delta r$ is a function of d and s. Nevertheless, these experimental results show that it is possible in principle produce in vacuum an extremely slightly diverging jet of a material (e.g., pure hydrogen), in a "fog" by means of a Laval nozzle of the appropriate geometry, with the appropriate input temperature, and with a slight limitation of the jet from the nozzle.

The authors thank P. A. Zhuravlev for constructing the measuring tube and the conical limiters.

---

[1] G. I. Dimov, Zh. Tekh. Fiz., 39, 681 (1969) [Sov. Phys. – Tech. Phys., 14, 512 (1969)].

[2] G. I. Dimov, Prib. Tekh. Eksp., No. 5, 168 (1968).

[3] F. I. Busol, V. B. Yuferov, and E. I. Skibenko, Zh. Tekh. Fiz., 34, 2156 (1964) [Sov. Phys. – Tech. Phys., 9, 1661 (1965)].

[4] R. Klingelhofor and P. Lohse, Phys. Fluids, 7, 379 (1964).

Electron-beam excited crossed-field discharge

V. A. Saenko and M. M. Kasumov

Institute of Nuclear Research, Academy of Sciences of the Ukrainian SSR, Kiev

(Submitted February 12, 1973; resubmitted September 4, 1973)
Zh. Tekh. Fiz., 44, 1206-1209 (June 1974)

The ignition conditions and static characteristics of a discharge maintained by an electron beam (current 0-100 mA, energy 500-3000 V) in a longitudinal magnetic field (B = 0-800 G)and in a radial electric field (E_r = 0-100 V/cm) have been studied. The ignition curves of this discharge are similar to those of a magnetron discharge, and it is called a "beam-magnetron discharge." The critical electron-beam current, the working pressure in the ionization chamber ($p \approx 10^{-4}$ torr), and the magnetic and electric fields required for ignition have been determined. It may be possible to use this discharge in plasma injectors, ion sources, and other devices in which the working medium is a chemically active gas or a solid.

1. The most widely used low-pressure electron-beam excited discharges are direct discharges and reflex arc discharges. The fact that the cathode is in the ionization chamber inhibits the use of arc discharges in the ionization of chemically active gases or of materials which are usually in the solid phase. A beam–plasma discharge seems promising in this regard. An ion source that uses a beam–plasma discharge with a solid working medium is described in ref. 1; other advantages of beam–plasma sources are reported in ref. 2. However, the interaction of an electron beam with a plasma is effective only if the ionization chamber is long enough (L ~10 cm). To maintain a discharge in a short chamber we have recommended the use of a beam–plasma system in crossed electric and magnetic fields.[3] We report here on a study of the ignition conditions for an electron-beam excited crossed-field discharge and the possibility of increasing the ionization of the working medium.

2. Figure 1 shows the experimental apparatus. A steady-state electron beam, with current I_0 up to 100 mA and an energy of 3 kV, is produced by an annular electron gun, whose cathode is insulated from the grounded anode 4. The beam passes through a channel 12 mm long and 12 mm in diameter in the region of the magnetic field (B = 0-800 G) at an angle of 15° with respect to the axis of the discharge chamber. The radial inhomogeneity of the magnetic field in the discharge region is ~1%. The beam is collected by a movable water-cooled collector 11, 4.5 cm in diameter. The working gas (H_2, He, N_2, O_2) is injected (I) through a valve in the top flange of the discharge chamber and evacuated (E) on the electron-gun side. The limiting vacuum of the apparatus with the nitrogen trap in operation is $3 \cdot 10^{-6}$ torr. Most of the measurements are carried out in hydrogen. The radial electric field is produced by cylinder 10 with diameter $D_c = 2r_c$ of 9.5 cm and a length from 4 to 20 cm. The plasma parameters are determined by means of Langmuir probes 8, which can be moved in the axial and radial directions. The energy spectrum of the charged particles (Fig. 4) emerging from the discharge chamber through the beam-injection channel is determined by means of a four-grid analyzer 1 (ref. 4).

3. Ignition of an electron-beam excited discharge in crossed fields requires that the current of the injected beam, I_0, must exceed the critical value $I_{cr} \approx 0.5$ mA (Fig. 2a). Ignition of the discharge (beginning of gas ionization by secondary plasma electrons) is accompanied by a sharp increase in the current I_c to cylinder 10, a change in the current I_k to collector 11 (Fig. 1), from electronic to ionic, and by a jump in the ion current I_i to analyzer 1. This analyzer is at − 100 V with respect to the gun anode 4 and the electron collector 11, whose potential is defined as ground potential. At $I_0 > I_{cr}$ the currents I_c and I_k increase linearly with increasing I_0 (Fig. 2b), i.e., over the range of I_0 studied here, the mechanism for multiplication of the primary beam electrons is independent of the beam current. The nonlinearity observed in the

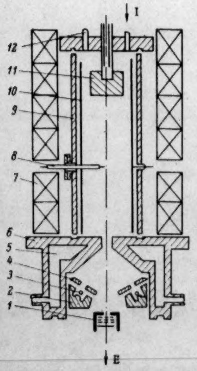

Fig. 1. The experimental apparatus. 1) Multigrid analyzers; 2) electrode near cathode; 3) tungsten cathode filament; 4) anode; 5) water-cooling cavity; 6) frame of the gun and the magnetic shield; 7) magnetic field coils; 8) system of mobile Langmuir probes; 9) walls of discharge chamber; 10) cylinder; 11) electron-beam collector; 12) pressure gauges; I) gas injection; E) evacuation.

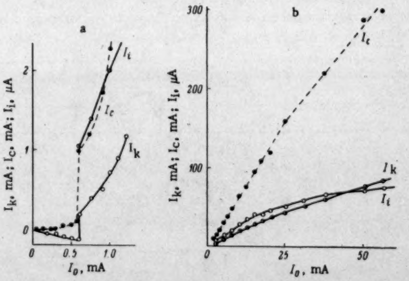

Fig. 2. Effect of the injection current I_0 on the discharge. E_0 = 1.2 kV; B = 180 G, $p = 2 \cdot 10^{-4}$ torr, V_c = 150 V, L = 10 cm.

function $I_i = f(I_0)$ is due primarily to a change in the plasma boundary from which the ions are incident on analyzer 1. The optimum beam energy is 600 eV.

Ionization in the volume can be increased by either increasing the injected current I_0 or by raising the potential V_c of the cylinder, (Fig. 3).

Energy measurements of the ions (Fig. 4) incident from the discharge on analyzer 1 show that the most probable ion energy E_i (in electron volts) is approximately equal to the cylinder potential ($E_i \approx eV_e$). Accordingly, an increase in V_c with $V_c > V_c^*$ has two consequences: an increase in the energy of the secondary electrons entering the plasma column (these electrons result from secondary electron emission from the electron-beam collector and ion– electron emission from both ends of the ionization chamber) and an increase in the number of secondary electrons (in the ion–electron emission yield). These phenomena increase the number and temperature (T_e) of the plasma electrons, whichare trapped at the ends and which cause most of the ionization in the discharge.

We call the cylinder potential V_c^* at which the jumps occur in the currents I_c, I_k, and I_i the ignition potential. Figure 5 shows this potential as a function of the magnetic field. The discharge is ignited at a magnetic field above the critical value, which is described satisfactorily by the approximate relation ($r_c \gg r_0$) (curve 1) given by Hull:[5]

$$B_{cr} \simeq \frac{2c}{r_c}\left(2\frac{m}{e}V_c\right)^{1/2}, \tag{1}$$

where c is the speed of light, e and m are the charge and mass of the electron, and r_0 is the distance from the electron to the axis when the electron is produced.

It follows from Eq. (1) that at low pressures ($p \sim 10^{-4}$ torr) the discharge is ignited when the slow electrons resulting from ionization at the axis (the beam region) no longer reach the collector under the influence of the electric field and begin to revolve along an epitrochoid in the azimuthal plane, effectively ionizing the gas. In a strong magnetic field $B \gg B_{cr}$ it is possible to reduce the height of the epitrochoid, ρ, to such an extent that the energy acquired by a slow electron in the field E_r, $\mathcal{E} = e\rho E_r$, becomes lower than the ionization energy eV_i:

$$\rho E_r \leqslant V_i. \tag{2}$$

In this case the discharge is cut off, as can be seen from Fig. 5 (the right-hand branch of the ignition curve). The calculated curve 4, for which inequality (2) holds, is

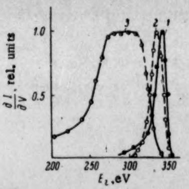

Fig. 4. Ion energy spectrum. Here $\partial I/\partial V$ is the differential functional dependence of the analyzer–collector current on the potential of the analyzer electrode; E_i is the ion energy; E_0 = 1.2 kV; p = $2 \cdot 10^{-4}$ torr; V_c = 350 V; L = 10 cm; I_0 = 2 mA. B, G: 1) 120; 2) 240; 3) 480.

shown in Fig. 5; it gives a qualitatively correct description of the experimental functional dependence of the ignition potential V_c^* on B.

Similar results are obtained when this annular gun (Fig. 1) is replaced by a Pierce gun, which produces a cylindrical electron beam. In addition to an electron beam, a powerful ion or electromagnetic (laser) beam can be used to evaporate a solid working medium and to cause primary ionization of the vapor or gas. The use of crossed electric and magnetic fields in this case also would presumably permit an increase of the ionization of the working medium, and the electron-beam excited electric discharge, which results would have characteristics similar to those of the discharge which we have studied.

The ignition curves of the discharge which we have studied are similar to those of a magnetron discharge,[6] so that we can call the electron-beam-maintained crossed-field discharge a "beam–magnetron discharge." The discharge which we have studied has certain features in common with a hot-cathode reflex discharge,[7] in which cutoff of the discharge by a strong magnetic field has also been observed (but not explained). Furthermore, in both types of discharges the currents I_c, I_k, and I_i are nonmonotonic functions of B. However, there are important differences between these discharges, which furnish a basis for identifying the electric discharge which we studied as a new type of electron-beam excited discharge. The most important difference is that in a beam–magnetron discharge the cathode is replaced by an electron gun outside the ionization chamber. This difference makes it possible 1) to protect the gun cathode from ion bombardment, 2) to limit the flux of neutral atoms to the cathode, 3) to independently regulate the energy and current of the electron beam over broad ranges, and 4) to use an electron beam to sup-

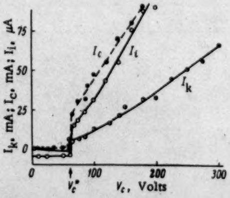

Fig. 3. Effect of the cylinder potential V_c on the discharge, L = 10 cm, B = 300 G, I_0 = 10 mA, E = 1.2 kV, p = $3 \cdot 10^{-4}$ torr.

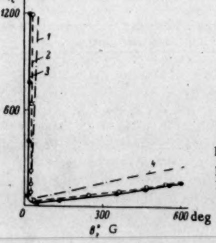

Fig. 5. Ignition curves. E_0 = 1.0 kV, p = $2 \cdot 10^{-4}$ torr, L = 10 cm. I_0, mA: 1, 4) calculated; 2) 2 mA; 3) 10 mA.

ply a solid-phase working medium to the ionization chamber.

The structural features of an apparatus which uses a beam—magnetron discharge are governed by the electron gun, the means for supplying working medium, and the direction in which the plasma or ions are collected. When the plasma or ions are collected parallel to the magnetic field, it is preferable to use an annular gun. The entire electron beam (an evaporating collector) or part of the beam can be used to evaporate a solid-phase working medium. In the latter case a rod of the working medium is placed beside the electron beam, and the rate at which the working medium is supplied to the ionization chamber is adjusted by adjusting the immersion of the rod into the beam region.

In conclusion the authors thank V. N. Vasil'kovskii for assistance and A. F. Linev for discussion.

---

[1] A. I. Vladimirov, V. A. Saenko, and Yu. P. Tret'yakov, Preprint R13-5559, JINR, Dubna (1971).

[2] R. A. Demirkhanov, L. V. Kursanov, and L. P. Skripal', Zh. Tekh. Fiz., 40, 1351 (1970) [Sov. Phys. — Tech. Phys., 15, 1047 (1971)].

[3] É. T. Kučerenko and V. A. Saenko, Author's Certificate No. 287494; Byull. Izob., No. 35 (1970).

[4] E. A. Lobikov and A. I. Nastyukha, Zh. Tekh. Fiz., 32, 1223 (1962) [Sov. Phys. — Tech. Phys., 7, 903 (1963)]; Yu. G. Zubov, E. A. Koltypin, E. A. Lobikov, and A. I. Nastuykha, Zh. Tekh. Fiz., 33, 686 (1963) [Sov. Phys. — Tech. Phys., 8, 513 (1963)].

[5] A. W. Hull, Phys. Rev., 18, 31 (1921).

[6] É. M. Reikhrudel' and Z. P. Sheretov, Radiotekh. Elektron., 9, 728 (1964); P. A. Redhead, Canad. J. Phys., 37, 1260 (1959).

[7] E. T. Kučerenko and V. A. Saenko, Czech. J. Phys., B17, 67 (1967).

Extraction of synchrotron radiation from a cyclic electron accelerator with a strong magnetic field

V. I. Kvochka, V. S. Panasyuk, V. F. Romanovskii, L. N. Samoilov, A. A. Sokolov, B. M. Stepanov, and Yu. M. Tereshkin

(Submitted June 25, 1973)
Zh. Tekh. Fiz., 44, 1210-1217 (June 1974)

An effective system for extracting synchrotron radiation from a cyclic electron accelerator with a strong magnetic field is described. This system uses a reflector in the accelerating chamber. The gains for a single reflecting surface of revolution and that for a system of two such surfaces are determined. The quality of the image of the electron orbit obtained through the use of a single reflecting surface of revolution is evaluated. Extraction of synchrotron radiation by means of a reflector outside the accelerator chamber and the use of composite reflectors are also examined.

INTRODUCTION

The properties of synchrotron radiation and its applications in vacuum-UV spectroscopy, solid state physics, metrology, and other fields of physical research have been discussed by many authors.[1-3]

In many applications of synchrotron radiation it is important that the intensity be high in the vacuum-UV region. In these cases it is important to extract as much of the radiation as possible from the accelerator chamber. Since the synchrotron radiation is focused near the plane of the electron orbit and since it is directed along a tangent to this orbit, the only way to extract the radiation in many accelerators with iron magnets is to use a vacuum light guide along the tangent to the orbit. In this case radiation from a small part of the orbit is used, so that the radiation-collection coefficient at the entrance to the collector, $\eta = I_c/I_0$, is small (here, I_c is the intensity of the radiation incident on the collector and I_0 is the total intensity of the synchrotron radiation). In the DESY accelerator,[4] this coefficient is 10^{-4}.

A comparatively simple and accessible source of synchrotron radiation can be realized with a cyclic electron accelerator with a strong magnetic field. An effective model for such an accelerator and the corresponding theory are given in refs. 4 and 5; certain aspects of the methods for developing and using such accelerators are discussed in ref. 6. In a cyclic electron accelerator with a strong magnetic field it is possible to construct light guides which can extract synchrotron radiation from all parts of the orbit.

EXTRACTION OF THE SYNCHROTRON RADIATION BY MEANS OF A REFLECTOR IN THE ACCELERATING CHAMBER

Let us consider the construction of the accelerator of refs. 4 and 6 and the light guide for synchrotron radiation (Fig. 1). A massive copper turn 1, which is both the electromagnet and the vacuum chamber of the accelerator, has an inner profile such that a magnetic field similar in shape to the field of an adiabatic trap is produced in the cavity within the turn. The decay index of the magnetic field over a relativistic orbit is 0.2. The electromagnet is fed with pulses from a capacitor bank. The cavity is simultaneously used as a volume resonator to produce a high-frequency accelerating E field in the H_{III} mode. The accelerating field is excited by rf oscillator 6, coupled to the cavity by turn 7. The electron source is a gun 5, which injects a low-voltage (100 eV) electron beam along the axis of the turn. This beam ionizes the residual gas near the axis of the turn. The radiation is extracted by means of reflector 2, in the accelerating chamber. The reflector is a surface of revolution, whose revolution axis coincides with the accelerator axis. Radiation passes through the vacuum light guide 3 to the entrance of collector 4. The use of thin reflecting films of platinum, gold, or tungsten on a glass substrate makes it possible to efficiently extract radiation in the vacuum-UV region up to a wavelength of 400 Å (ref. 7) without interfering with the normal operation of the accelerator.

We now use geometric-optics methods to examine the shape and quality of the image of the electron orbit formed by this reflector. Experiment[1] has shown that the synchrotron radiation from a local part of the orbit has a spherical wave front. Accordingly, a synchrotron reflector can be treated as a radiating circle, from each point of which a fine homocentric beam of rays is emitted along the tangent to the circle at the given point. The angle through which the extreme rays diverge from the central ray (along the tangent), β, for wavelengths near the maximum of the spectral distribution is of order γ^{-1}, where $\gamma = (1 -$

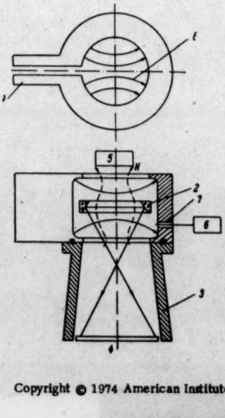

Fig. 1. Diagram of the accelerating chamber and the light guide. 1) Accelerating chamber; 2) reflector; 3) vacuum light guide; 4) radiation collector; 5) electron gun; 6) rf oscillator; 7) rf input.

$v^2/c^2)^{-1/2}$, v is the electron velocity, and c is the speed of light in vacuum. For this accelerator geometry and for a maximum electron energy of 50 MeV we have $\gamma \cong 100$ and thus $\beta \ll 1$. Since the synchrotron radiator is in a symmetric position with respect to the axis of the optical system, it is sufficient to consider the path of a beam of rays from any point of the emitting circle. The image of the other points can be easily found through a rotation around the axis of the system. These rays make an angle of approximately 90° with the optic axis and are not meridian rays; this circumstance rules out the use of the paraxial approximation, so that it is more convenient to use a direct method of constructing the beam paths.

Since this optical system is axially symmetric, the image of the circular electron orbit lies in a plane perpendicular to the optic axis. It is convenient to choose the origin of coordinates at the symmetry axis and to adopt this axis as the oz axis, which we characterize by the unit vector **k**. We locate the origin at the center of the orbit and assume the plane of the orbit to coincide with the xy plane (Fig. 2). We specify the position of the given point of the radiator by the vector A. For simplicity we consider a point radiator on the ox axis; in this case the vector A has the components $\{r, 0, 0\}$, where r is the radius of the electron orbit. We specify the beam of rays emerging from point A by the unit vector **s** with direction cosines $\{p, m, n\}$ $\mathbf{s}^2 = p^2 + m^2 + n^2 = 1$. The central ray of this beam is characterized by a unit vector $S_0\{0, 1, 0\}$, which is parallel to the tangent to the circle of the radiator at point A. In the general case the equation of a surface of revolution whose revolution axis coincides with the oz axis can be written

$$F(u^*, z) = 0;\ 2u^* = x^2 + y^2. \tag{1}$$

We write the vector equations for the ray paths as two systems of equations: 1) a system of two-dimensional equations relating the components of the vectors perpendicular to the oz axis, and 2) a system of equations for the projections of the vectors on the axis. Vectors perpendicular to the oz axis (i.e., vectors which have vanishing components along the oz axis), are denoted by capital letters. We use the vectors A with components $\{x, y, 0\}$ and S with components $\{p, m, 0\}$ so that

$$\mathbf{a} = \mathbf{A} + z\mathbf{k};\quad \mathbf{s} = S + n\mathbf{k}. \tag{2}$$

The path of a fine beam of rays can be determined by considering the path of the central ray, while the image quality can be analyzed by considering the divergence of the extreme rays from the central ray in the image plane. We consider the path of the central ray as shown in Fig. 2.

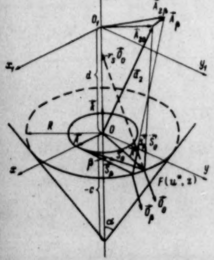

Fig. 2. Ray path for reflection from a conical surface.

With A_0^* as a vector from the origin to the point of incidence and $\mathbf{s}'_0$ as the unit vector along the reflected ray, the equations for calculating the ray path are, according to ref. 8,

$$\mathbf{A}_0^* = \mathbf{A} + l\mathbf{S}_0, \tag{3}$$

$\mathbf{s}'_0 = \mathbf{S}'_0 + \Gamma\mathbf{o}_0$ (the reflection law), and $\Gamma = -2(\mathbf{S}_0\mathbf{o}_0)$ (here $\mathbf{o}_0$ is the unit vector normal to the surface at the point of incidence).

To calculate l we square the first equation in (3):

$$\mathbf{A}_0^{*2} = 2u^* = \mathbf{A}^2 + 2\mathbf{A}\mathbf{S}_0 + l\mathbf{S}_0^2. \tag{4}$$

We consider this equation together with the equation of the reflecting surface, (1). Second-order surfaces of revolution are usually used in optics. We note that the path of the principal and other rays in the plane of the radiator (z = 0) are not affected by the general shape of the reflected surface, only by its curvature in the z = 0 plane, i.e., by the inclination with respect to the axis of the normal to the reflecting surface at any point at which it intersects the z = 0 plane. Accordingly, without any loss of generality we can consider the path of these rays upon reflection from a conical surface tangent to a second-order surface of revolution of a more general type.

The equation of a conical surface of revolution in this coordinate system (Fig. 2) is

$$F(u^*, z) = \frac{2u^*}{R_0^2} - \frac{(z+c)^2}{c^2} = 0;\quad c = R_0\,\mathrm{tg}\,\alpha; \tag{5}$$

where α is the angle between the direction cosine and the axis, and R_0 is the radius of the circle formed by the intersection of the cone with the z = 0 plane. From Eqs. (4) and (5) we find the coordinates of the vector A_0^* to be $\{r, \sqrt{R_0^2 - r^2}, 0\}$. In an axially symmetric system the vector normal to the surface intersects the oz axis so that

$$-r_s\mathbf{o}_0 = -\mathbf{A}_0^* + t\mathbf{k}, \tag{6}$$

where r_s is the sagittal radius of curvature or the distance along the normal from the point of incidence to the point at which the axis is intersected. The components of the normal at the point of incidence are proportional to the derivatives F_u^* and F_z, so that the vector $\mathbf{o}_0$ is parallel to the vector

$$F_{u^*}\mathbf{A}_0^* + F_z\mathbf{k}. \tag{7}$$

From Eqs. (6) and (7) we find the direction cosines of the vector; using Eqs. (1), we find the unit vector of the reflected ray, $\mathbf{s}'_0\{p'_0, m'_0, n'_0\}$:

$$\mathbf{s}'_0 = -\mathbf{i}\frac{2r\sqrt{R_0^2 - r^2}}{R_0^2(1 + \mathrm{tg}^2\alpha)} + \mathbf{j} \times \frac{R_0^2(\mathrm{tg}^2\alpha - 1) + 2r^2}{R_0^2(1 + \mathrm{tg}^2\alpha)} + \mathbf{k}\frac{2\,\mathrm{tg}\,\alpha\sqrt{R_0^2 - r^2}}{R_0(1 + \mathrm{tg}^2\alpha)}. \tag{8}$$

The reflected ray is governed completely by the unit vector $\mathbf{s}'_0$ and by the point of intersection with the z = 0 plane, i.e., by the vector A_0^*. To find the point at which the reflected ray intersects the z = d image plane we must find a vector $\mathbf{a}_2\{x_2, y_2, z\}$ such that

$$\mathbf{a}_2 = \mathbf{A}_0^* + l\mathbf{s}'_0.$$

We write the vector $\mathbf{a}_2$ as $\mathbf{a}_2 = \mathbf{A}_{20} + d\mathbf{k}$, where $\mathbf{A}_{20}$ lies in the z = d plane and runs from the axis of the system to the point at which the reflected ray intersects the z = d plane. Then we find

$$\mathbf{A}_{20} = \mathbf{A}_0^* + \frac{d}{n_0'}\mathbf{s}_0' - d\mathbf{k} = \mathbf{A}_0^* + \frac{d}{n_0'}\mathbf{S}_0', \tag{9}$$

where $\mathbf{s}'_0 = \mathbf{S}'_0 + n'_0\mathbf{k}$.

The length of vector $\mathbf{A}_{20}$ is equal to the radius of the circular image of the radiator, so that K, the magnification of the optical system in the z = d plane, is $K = |\mathbf{A}_{20}|/|\mathbf{A}|$. Squaring (9) and dividing by A^2, we find the square of the magnification in this plane to be

$$K^2 = 1 + \frac{1}{r^2}\Big[d^2 \frac{R_0^2(\mathrm{tg}^2\alpha - 1)^2 + 4r^2\,\mathrm{tg}^2\alpha}{4\,\mathrm{tg}^2\alpha\,(R_0^2 - r^2)} + d\frac{R_0(\mathrm{tg}^2\alpha - 1)}{\mathrm{tg}\,\alpha} + (R_0^2 - r^2)\Big]. \tag{10a}$$

The square of the radius of the image of the electron orbit is

$$R^2 = d^2 \frac{R_0^2(\mathrm{tg}^2\alpha - 1)^2 + 4r^2\,\mathrm{tg}^2\alpha}{4\,\mathrm{tg}^2\alpha\,(R_0^2 - r^2)} + d\frac{R_0(\mathrm{tg}^2\alpha - 1)}{\mathrm{tg}\,\alpha} + R_0^2. \tag{10b}$$

Analysis of the quantity in brackets in Eq. (10a) shows that it is always positive for any d, so that any reflecting surface of revolution provides a magnified image of the synchrotron radiation. From Eq. (10a) we find the value of d at which this magnification is minimized:

$$d_{\min} = \frac{2R_0(R_0^2 - r^2)(1 - \mathrm{tg}^2\alpha)\,\mathrm{tg}\,\alpha}{R_0^2(\mathrm{tg}^2\alpha - 1)^2 + 4r^2\,\mathrm{tg}^2\alpha}. \tag{11}$$

Substituting $d_{\min}$ into (10a) we find the minimum magnification for a single reflecting surface of revolution:

$$K^2_{\min} = 1 + \frac{4\,\mathrm{tg}^2\alpha\,(R_0^2 - r^2)}{R_0^2(\mathrm{tg}^2\alpha - 1)^2 + 4r^2\,\mathrm{tg}^2\alpha}, \tag{12a}$$

and we find the minimum square of the radius of the image of the electron orbit to be

$$R_{\min} = \frac{R_0 r(\mathrm{tg}^2\alpha + 1)}{\sqrt{R_0^2(\mathrm{tg}^2\alpha - 1)^2 + 4(\mathrm{tg}^2\alpha)\,r^2}}. \tag{12b}$$

As noted above, the quality of the image of an orbital point in the case of reflection from a single surface of revolution is independent of the nature of the surface for rays in the orbital plane. Accordingly, analysis of such rays is of general interest. Here it is sufficient to examine a ray in the plane of the synchrotron radiation (z = 0) and to examine its divergence from the central ray in the image plane.

We consider the extreme ray of the beam, which is emitted from point A and lies in the orbital plane. Its direction is governed by the unit vector $\mathbf{S}_\beta$, which makes an angle β with the central ray. The direction cosines of this ray, $\{p_\beta, m_\beta, 0\}$, can be expressed in terms of the angle β:

$$\left.\begin{aligned} p_\beta &= \cos\left(\frac{\pi}{2} - \beta\right) = \sin\beta, \\ m_\beta &= \cos\beta. \end{aligned}\right\} \tag{13}$$

Since $\beta \ll 1$, we expand the sine and cosine in powers of β, retaining only terms of first order in β. We can now write the direction cosines of $\mathbf{S}_\beta$ in the form $\{\beta, 1, 0\}$. Let us consider the reflection of this ray from the conical surface described by Eq. (5). Carrying out calculations analogous to those for the central ray, and retaining only terms of first order in β, we find the coordinates of the point at which the reflected ray (governed by the vector $\mathbf{A}_{2\beta}$; Fig. 2) intersects the image plane, at a distance d from the z = 0 plane. The divergence of this ray from the central ray in this plane is obviously given by $|\mathbf{A}_\beta| = |\mathbf{A}_{2\beta} - \mathbf{A}_{20}|$.

Calculations yield the following values for the projections of $\mathbf{A}_\beta$ onto the o_1x_1 and o_1y_1 axes:

$$\left.\begin{aligned} A_{\beta x} &= \beta\sqrt{R_0^2 - r^2}\Big[1 + d\frac{R_0^2(\mathrm{tg}^2\alpha - 1) + 2r^2}{2(\mathrm{tg}\,\alpha)R_0(R_0^2 - r^2)}\Big], \\ A_{\beta y} &= -r\beta\Big[1 - \frac{d}{R_0\,\mathrm{tg}\,\alpha}\Big]. \end{aligned}\right\} \tag{14}$$

We see from (14) that for no value of d does the quantity $|\mathbf{A}_\beta|$ vanish (its vanishing is the condition for a sharp image of point A). These equations for $|\mathbf{A}_\beta|$ show that $|\mathbf{A}_\beta|$ is a minimum at the value of d given by (11. Here, $|\mathbf{A}_\beta|$ is given to second order in β by

$$|\mathbf{A}_\beta| = \frac{\beta r R_0(1 + \mathrm{tg}^2\alpha)}{\sqrt{R_0^2(1 - \mathrm{tg}^2\alpha)^2 + 4r^2\,\mathrm{tg}^2\alpha}}. \tag{15}$$

We thus conclude that no reflecting surface of revolution can produce a sharp image of the synchrotron radiation. However, in many practical cases (because of the smallness of the angle β), the necessary image quality in the vacuum-UV region can be achieved by means of a conical surface.

Let us consider the possibility of obtaining a reduced image of the synchrotron radiation by introducing a second reflecting surface. Here we do not discuss the use of refraction optics since synchrotron radiation is of interest at wavelengths below 1000 Å, for which there are no transparent optical materials. Obviously, this second reflecting surface of revolution must have a radius of curvature at the point of incidence, which is directed opposite that of the first surface. We consider the reflection of the central ray from a conical surface of revolution with an angle of α_1 between the axis of the system and a line of the cone (Fig. 3). The equation of a conical surface of revolution in the coordinate system x_1y_1z, where the coordinate plane x_1y_1 contains the vector $\mathbf{A}_{20}$ corresponding to the minimal magnification given by the first reflecting surface, i.e.,

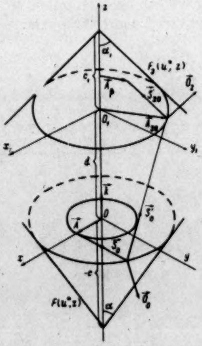

Fig. 3. Path of the central ray through a system of two conical reflecting surfaces.

the square of the length of the vector A_{20}, is governed by Eq. (12b):

$$F_2(u^*,\ z)=\frac{2u^*}{A_{20}^2}-\frac{(z-c_1)^2}{c_1^2}=0, \tag{16}$$

where $\tan\alpha_1 = |A_{20}|/c_1$.

The ray incident on the second surface is specified by the vector A_{20} and the unit vector s'_0. The unit vectors $s'_{20}\{p'_{20},\ m'_{20},\ n'_{20}\}$ and $S'_{20}\{p'_{20},\ m'_{20},\ 0\}$ of the reflected ray are found by analogy with the procedure above. The intersection of the reflected ray with an image plane perpendicular to the axis and at a distance d_2 from the x_1y_1 coordinate plane is given by the vector

$$\mathbf{A}_3=\mathbf{A}_{20}+\frac{d_2}{n'_{20}}S'_{20}. \tag{17}$$

The ratio $K_2 = |A_3|/|A|$ is the magnification of a system consisting of two reflecting conical surfaces of revolution. From Eqs. (12b) and (17) we find the square of the magnification of a system of two reflecting surfaces to be

$$\begin{gathered}K_2^2=1+(ad_2^2+bd_2+c),\\ a=\frac{1}{r^2}\left\{1+\frac{[R_0^2(\mathrm{tg}^2\alpha-1)^2+4r^2\,\mathrm{tg}^2\alpha](1+\mathrm{tg}^2\alpha)^2}{16\,\mathrm{tg}^2\alpha\,\mathrm{tg}^2\alpha_1(R_0^2-r^2)}\right\},\\ b=\frac{2R_0(\mathrm{tg}^2\alpha+1)}{r\sqrt{R_0^2(\mathrm{tg}^2\alpha-1)^2+4r^2\,\mathrm{tg}^2\alpha}},\\ c=\frac{4\,\mathrm{tg}^2\alpha(R_0^2-r^2)}{R_0^2(\mathrm{tg}^2\alpha-1)^2+4r^2\,\mathrm{tg}^2\alpha}.\end{gathered} \tag{18}$$

Analysis of Eq. (18) shows that a reduced image of the synchrotron radiator cannot be obtained for any value of d_2. The maximum magnification can be found by substituting the value $d_2 = -b/2a$ into Eq. (18); the largest magnification is unity at $\tan\alpha_1 = 1$.

USE OF AN EXTERNAL REFLECTOR

In most practical cases it is desirable to have a small image of the synchrotron radiator ($R_{\min} \sim r$) at a large distance from the plane of the electron orbit ($d_{\min} \gg r$). Analysis of Eq. (11) shows that this is the case when

$$R_0 \gg r, \tag{19a}$$

$$\tan < 1. \tag{19b}$$

Since the radius of the accelerator chamber is governed by the frequency of the H_{III} field and is equal to 2r (ref. 6), condition (19a) can be satisfied if the chamber and light guide are constructed as shown in Fig. 4. Here, reflector 4 has dimensions larger than those of the accelerator chamber, so that maximization of the radiation extraction requires that the accelerator chamber be constructed in two parts, separated from the plane of the electron orbit by a distance permitting complete extraction of the radiation from the accelerator to reflector 4 and then to collector 6.

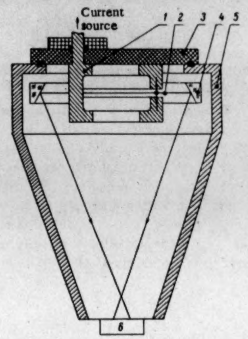

Fig. 4. Radiation-extraction method using a reflector outside the electromagnet–resonator. 1) Electromagnet–resonator; 2) gap in the resonator for extracting the radiation; 3) dielectric flange; 4) reflector; 5) vacuum light guide; 6) radiation collector.

EXTRACTION OF RADIATION BY MEANS OF A COMPOSITE REFLECTOR

A significant reduction of the dimensions of the synchrotron-radiation beam incident on the collector can be achieved by replacing the reflector in Fig. 1 by a composite reflector, e.g., one consisting of n identical plane mirrors, each of which is a distance R_0 from the center of the electron orbit and oriented as shown in Fig. 5a. The central ray of the beam, emerging from point A, strikes the center of mirror m at point M_1; after reflection, it reaches point M_2, which lies on the oz axis, a distance d from the orbital plane. It can be shown that the angle between the xy orbital plane and each element of the reflector is given by

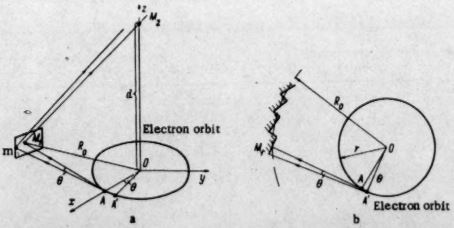

Fig. 5. Composite reflector. a) Reflection of the central ray from an element of the reflector; b) intersection of the surface of the composite reflector with the orbital plane.

$$\cos \varphi = \frac{d}{\sqrt{2}\sqrt{R_0^2 + d^2 + \sqrt{(R_0^2 + d^2)(R_0^2 - r^2)}}}. \quad (20)$$

The angular size of the beam reflected from each element of the reflector is, within terms on the order of β, equal to $2\theta = 2\pi/n$ and equal to the angular size of the electron orbit from which the radiation is incident on the given element. When the number of such elements making up the reflector, n, is sufficiently large, the size of the radiation spot incident on the collector a distance d from the orbital plane is $\simeq 2\pi d/n$. Figure 5b shows the intersection of the composite reflector with the xy plane of the electron orbit. These arguments obviously can be extended to the case of an external composite reflector.

---

[1] D. H. Tomboulian and P. L. Hartman, Phys. Rev., 102, 1423 (1956).

[2] R. Haensel and C. Kunz, Zs. Angew. Phys., 23, 276 (1967).

[3] R. P. Godwin, Springer Tracts in Modern Physics, Vol. 51 (1969), p. 1.

[4] A. V. Gryzlov, V. S. Panasyuk, V. M. Ryzhkov, A. A. Sokolov, Ya. M. Spektor, and B. M. Stepanov, Reports to the Second All-Union Conference on Charged-Particle Accelerators, Moscow, November 11, 1970.

[5] A. V. Gryzlov, V. S. Panasyuk, V. M. Ryzhkov, A. A. Sokolov, and Yu. M. Tereshkin, Zh. Tekh. Fiz., 42, 13 (1972) [Sov. Phys. – Tech. Phys., 17, 9 (1972)].

[6] V. S. Panasyuk, A. A. Sokolov, and B. M. Stepanov, At. Energ., 33, 907 (1972).

[7] A. N. Zaidel' and E. Ya. Shreider, Vacuum-UV Spectroscopy [in Russian], Izd. Nauka, Moscow (1967).

[8] M. Herzberger, Modern Geometric Optics, Interscience, New York (1958).

Resonator with azimuthally varying end plates

M. F. Vorogushin and V. I. Petrunin

D. V. Efremov Scientific-Research Institute of Electrophysical Apparatus, Leningrad

(Submitted November 9, 1972; resubmitted October 18, 1973)
Zh. Tekh. Fiz., 4, 1218-1221 (June 1974)

In the design of cyclotrons with an azimuthally varying electric field there is a need for analytic expressions for the field components in a resonator with azimuthally varying end plates. This problem cannot be solved exactly by the usual methods as the variables do not separate in any orthogonal coordinate system. In the present paper convenient expressions for the field components are found by constructing a solution in the form of the product of a certain scalar function of the radius and the vector static field of an azimuthally varying gap. It is shown that this representation is valid if the number of variations aound the azimuth is sufficiently large and the amount of variation is bounded.

The present problem is of interest in connection with the design of cyclotrons with an azimuthally varying electric field.[1] The accelerating system of such cyclotrons can have the form of a cylindrical or coaxial resonator of small height with large inphase variations of the end plates around the azimuth. The electrodynamic problem in this sort of structure cannot be solved exactly by any of the usual methods, e.g., by the method proposed by Kompaneets and Sayasov,[2] as the variables do not separate in any of the orthogonal coordinate systems.

Approximate expressions for the high-frequency fields in a resonator with azimuthally varying end plates are derived in the present paper. Also, it is shown that the field components can be represented as a combination of the static field of an azimuthally varying gap[3] and the high-frequency field of a smooth resonator, for which exact solutions are known.

Indeed, assuming a large number of variations around the azimuth, the solution of the wave equation for the electric field intensity is likely to be of the form

$$E = f(r)\,E_{st}, \tag{1}$$

where $f(r)$ is a scalar function normalized to unity which describes the radial variation of the high-frequency field, and $\bar{E}_{st}$ is the static field of an azimuthally varying gap.

Let us find conditions under which this sort of representation is possible. The wave equation for field (1) is

$$\nabla^2 (fE_{st}) + k_0^2 fE_{st} = 0. \tag{2}$$

Here k_0 is the wave number and ∇^2 is the Laplacian of a vector function

$$\nabla^2 (fE_{st}) = \nabla(\nabla(fE_{st})) - [\nabla[\nabla(fE_{st})]]. \tag{3}$$

Remembering that $(\nabla\bar{E}_{st}) = 0$ and $[\nabla\bar{E}_{st}] = 0$, we have

$$\left.\begin{aligned} \nabla(\nabla(fE_{st})) &= \nabla(f\nabla E_{st} + E_{st}\nabla f) = \nabla(E_{st}\nabla f) = \\ &= (E_{st}\nabla)\nabla f + (\nabla f\nabla)E_{st}, \\ [\nabla[\nabla(fE_{st})]] &= [\nabla(f[\nabla E_{st}] + [\nabla f E_{st}])] = \\ &= [\nabla[\nabla f E_{st}]] = (E_{st}\nabla)\nabla f - (\nabla f\nabla)E_{st} - E_{st}\nabla^2 f. \end{aligned}\right\} \tag{4}$$

Inserting these expressions into Eq. (2) gives

$$2(\nabla f\nabla)E_{st} + E_{st}(\nabla^2 f + k_0^2 f) = 0. \tag{5}$$

If the gradient of the vector $\bar{E}_{st}$ in the direction of the vector ∇f is zero

$$(\nabla f\nabla)E_{st} = 0, \tag{6}$$

then the function f satisfies the one-dimensional wave equation

$$\nabla^2 f + k_0^2 f = 0,$$

whose solution in cylindrical coordinates is expressed through the Bessel functions

$$f = AJ_0(k_0 r) + BN_0(k_0 r). \tag{7}$$

Condition (6) is satisfied, in particular, in a gap with no azimuthal variation of the boundaries; expression (7) along with the boundary conditions, determines the radial distribution of the high-frequency electric field in a cylindrical or coaxial resonator.

In the case of an azimuthally varying gap, condition (6) is satisfied exactly after averaging the fields over the azimuth φ, i.e., it holds in the mean.

Indeed, by definition

$$(\nabla f\nabla)E_{st} = \frac{\partial f}{\partial r}\frac{\partial E_{st}}{\partial r}. \tag{8}$$

Projecting this equality upon the unit vector of a cylindrical system of coordinates and remembering that the azimuth-averaged components of the static field[3] are independent of radius

$$\langle E_r\rangle = 0;\quad \langle E_\varphi\rangle = 0;\quad \langle E_z\rangle = \frac{U_0}{d},$$

we see that condition (6) is satisfied in the mean.

In the general case we represent the vector $\bar{E}_{st}$ in terms of its modulus and unit vector

$$E_{st} = |E_{st}|\,e.$$

Then

$$\frac{\partial E_{st}}{\partial r} = e\frac{\partial|E_{st}|}{\partial r} + B|E_{st}|\frac{\partial\alpha}{\partial r}, \tag{9}$$

where

$$B \perp e,\quad \alpha = \arccos\frac{E_r}{|E_{st}|}.$$

We use (8) and (9) to write Eq. (5) in the form

$$\varepsilon f'' + \frac{f'}{r}\left[\varepsilon + 2\varepsilon\frac{r\partial|\bar{E}_{st}|}{|\bar{E}_{st}|\partial r} + 2Br\frac{\partial\alpha}{\partial r}\right] + \varepsilon k_0^2 f = 0. \tag{10}$$

Let us estimate the terms in the square brackets of expression (10). We find that

$$2r\frac{1}{|\bar{E}_{st}|}\frac{\partial|\bar{E}_{st}|}{\partial r} = 2r\frac{E_r\frac{\partial E_r}{\partial r} + E_\varphi\frac{\partial E_\varphi}{\partial r} + E_z\frac{\partial E_z}{\partial r}}{E_r^2 + E_\varphi^2 + E_z^2}, \tag{11}$$

$$2r\frac{\partial\alpha}{\partial r} = 2r\frac{E_r\left(E_\varphi\frac{\partial E_\varphi}{\partial r} + E_z\frac{\partial E_z}{\partial r}\right) - \frac{\partial E_r}{\partial r}(E_\varphi^2 + E_z^2)}{(E_r^2 + E_\varphi^2 + E_z^2)\sqrt{E_\varphi^2 + E_z^2}}. \tag{12}$$

In a previous paper[3] an exact solution is found to the problem of the static field in a capacitor with azimuthally varying plates and it is shown that over a wide range of variation of the parameters the potential is given by the expression

$$U = U_0\frac{z}{d} + \cos\nu\varphi\frac{U_0\left(1 - \frac{2z_0}{d}\right)}{2\,\mathrm{ch}\frac{\nu z_0}{r}}\mathrm{ch}\frac{\nu z}{r}.$$

Calculating the corresponding derivatives in the midplane (z = 0) and inserting the results into (11) and (12), we obtain

$$\frac{2r}{|\bar{E}_{st}|}\frac{\partial|\bar{E}_{st}|}{\partial r} = -2\frac{\frac{\beta^3}{\nu^2}\mathrm{th}\,\beta\,(2M-1)\cos^2\nu\varphi + (1 - \beta\,\mathrm{th}\,\beta)\sin^2\nu\varphi}{\sin^2\nu\varphi + \Lambda^2 + \frac{\beta^2}{\nu^2}\mathrm{th}^2\beta\cos^2\nu\varphi}, \tag{13}$$

$$2r\frac{\partial\alpha}{\partial r} = -\frac{2\beta^2\cos\nu\varphi}{\nu}\frac{M(\sin^2\nu\varphi + 2\Lambda^2) - \Lambda^2}{\left[\sin^2\nu\varphi + \Lambda^2 + \frac{\beta^2}{\nu^2}\mathrm{th}^2\beta\cos^2\nu\varphi\right]\sqrt{\sin^2\nu\varphi + \Lambda^2}}, \tag{14}$$

where

$$\Lambda = \frac{\mathrm{ch}\beta}{\beta\left(\frac{d}{2z_0} - 1\right)}, \quad M = \frac{1 + \frac{\mathrm{sh}\,2\beta}{2\beta}}{\mathrm{ch}^2\beta}, \quad \beta = \frac{\nu z_0}{r}.$$

It can be seen from these expressions that these terms tend to zero in the limit of large and small radii ($\beta \to 0$, $\beta \to \infty$).

Thus, to estimate the error associated with representing the field in the form (1), we must determine the extremum values of (13) and (14).

It is not hard to show that expression (14), regarded as a function of two variables, has an extremum equal to

$$2r\frac{\partial\alpha}{\partial r}\bigg|_{\substack{\nu\varphi = k\pi \\ \beta = 1.2}} \cong -\frac{2\left(\frac{d}{2z_0} - 1\right)}{\nu}. \tag{15}$$

Similarly, (13) has the extremum

$$\frac{2r}{|\bar{E}_{st}|}\frac{\partial|E_{st}|}{\partial r}\bigg|_{\substack{\nu\varphi = \frac{(2k+1)\pi}{2} \\ \beta = 0.4}} \cong -\frac{1.7}{1 + \left(\frac{2.7}{\frac{d}{2z_0} - 1}\right)^2}. \tag{16}$$

It can be seen from these estimates that condition (6) is obeyed approximately for large ν($\nu > 10$) and $d/2z_0 < 2$, i.e., when the depth of variation is twice the aperture.

We note that this constraint is a consequence of the feature of the initial system of electrodes assuring a single harmonic field, as it is connected with the requirement that there be no satellites[1]. Accordingly, in a real resonator this constraint probably does not have any fundamental significance.

The high-frequency electric field in an azimuthally varying resonator is thus described by expression (1).

The components of the high-frequency magnetic fields in the resonator are found from the Maxwell equation

$$\nabla\bar{E} = -\frac{\partial\bar{B}}{\partial t},$$

where $\bar{E}$ has the form (1).

Remembering that

$$\nabla(f\bar{E}_{st}) = f\nabla\bar{E}_{st} + [\nabla f\bar{E}_{st}],$$
$$\nabla\bar{E}_{st} = 0,$$

we rewrite the vector product in the cylindrical coordinate system

$$\frac{\partial B_r}{\partial t} = 0,$$

$$\frac{\partial B_\varphi}{\partial t} = \frac{\partial f}{\partial r}(E_{st})_z,$$

$$\frac{\partial B_z}{\partial t} = -\frac{\partial f}{\partial r}(E_{st})_\varphi.$$

Assuming a sinusoidal variation of the field with time, we find the components of the high-frequency magnetic fields:

$$B_r = 0,$$
$$B_\varphi = -\frac{1}{\omega}\frac{\partial f}{\partial r}(E_{st})_z\cos(\omega t + \psi), \tag{17}$$

$$B_z = \frac{1}{\omega}\frac{\partial f}{\partial r}(E_{st})_\varphi\cos(\omega t + \psi). \tag{18}$$

In conclusion, we cite the expressions for all the components of the high-frequency fields in an azimuthally varying resonator in the vicinity of the midplane ($z < z_0$) allowing for the time factor:

$$E_r = -\frac{U_0\nu\left(1 - \frac{2z_0}{d}\right)}{2}\frac{f(r)}{r^2\,\mathrm{ch}^2\frac{\nu z_0}{r}}\left[z_0\,\mathrm{ch}\frac{\nu z}{r}\,\mathrm{sh}\frac{\nu z_0}{r} - z\,\mathrm{sh}\frac{\nu z}{r}\,\mathrm{ch}\frac{\nu z_0}{r}\right]$$
$$\times\cos\nu\varphi\sin(\omega t + \psi),$$

$$E_\varphi = \frac{U_0\nu\left(1 - \frac{2z_0}{d}\right)}{2}\frac{f(r)}{r\,\mathrm{ch}\frac{\nu z_0}{r}}\mathrm{ch}\frac{\nu z}{r}\sin\nu\varphi\sin(\omega t - \psi),$$

$$E_z = -f(r)\left[\frac{U_0\nu\left(1 - \frac{2z_0}{d}\right)}{2}\frac{\mathrm{sh}\frac{\nu z}{r}}{r\,\mathrm{ch}\frac{\nu z_0}{r}}\cos\nu\varphi + \frac{U_0}{d}\right]\sin(\omega t + \psi),$$

$$B_r = 0,$$

$$B_\varphi = \frac{1}{\omega}\frac{\partial f(r)}{\partial r}\left[\frac{U_0\nu\left(1 - \frac{2z_0}{d}\right)}{2}\frac{\mathrm{sh}\frac{\nu z}{r}}{r\,\mathrm{ch}\frac{\nu z_0}{r}}\cos\nu\varphi + \frac{U_0}{d}\right]\cos(\omega t + \psi),$$

$$B_z = \frac{1}{\omega}\frac{\partial f(r)}{\partial r}\frac{U_0\nu\left(1 - \frac{2z_0}{d}\right)}{2}\frac{\mathrm{ch}\frac{\nu z}{r}}{r\,\mathrm{ch}\frac{\nu z_0}{r}}\sin\nu\varphi\cos(\omega t + \psi, \tag{19}$$

where f(r) satisfies the Bessel equation. In particular, if $\nu = 0$ (no azimuthal variations), these expressions give the components B_φ and E_z defining the fields in a smooth resonator.

---

[1] V. I. Petrunin, Zh. Tekh. Fiz., 43, 782 (1973) [Sov. Phys.—Tech. Phys., 18, 491 (1973)].

[2] A. S. Kompaneets and Yu. S. Sayasov, Zh. Tekh. Fiz., 23, 2185 (1953).

[3] M. F. Vorogushin and V. I. Petrunin, Zh. Tekh. Fiz., 43, 628 (1973) [Sov. Phys.—Tech. Phys., 18, 394 (1973)].

Azimuthal and vertical motion in an accelerator with azimuthally varying electric field

M. F. Vorogushin and V. I. Petrunin

D. V. Efremov Scientific-Research Institute of Electrophysical Apparatus, Leningrad

(Submitted July 23, 1973)
Zh. Tekh. Fiz., 44, 1222-1227 (June 1974)

Power-series and Fourier-series expansions of the potential in an azimuthally varying accelerating structure which satisfies general symmetry conditions are used to derive simple relationships for the index of electrical focusing and the per-orbit energy increment. The advantage of using rectangular variations of the gap boundaries to optimize these parameters is indicated.

The motion of particles in high-frequency fields varying in the azimuthal direction has been studied in previous papers[1-3] on the basis of a model with a single azimuthal harmonic in the midplane (a monoharmonic field[1]). However, the required variation in gap boundary to give rise to such a field is quite complex as far as practical realization is concerned. This is especially true near the center of the structure, where an electrode discontinuity is necessary in order to meet the requirement that the field be monoharmonic.[2] On the other hand, a monoharmonic field is not the optimum field for particle acceleration and focusing.

Accordingly, it is of interest to investigate the particle dynamics in the more general case of an arbitrary variation of gap boundaries in the azimuth direction.

In a cylindrical coordinate system the electric potential U(r, φ, z) near the midplane is described[1] by the two-dimensional Laplace equation with a parameteric dependence on radius

$$U(r,\ \varphi,\ z)=f(r)\,U(\varphi,\ z);\quad \frac{\partial^2 U}{r^2\partial\varphi^2}+\frac{\partial^2 U}{\partial z^2}=0. \tag{1}$$

We substitute the power expansion[4] for U(φ, z)

$$U(\varphi,\ z)=\sum_{k=0}^{\infty} z^k U_k(\varphi) \tag{2}$$

into Eq. (1) and express the unknown functions U_k in terms of the potential U(φ, 0) = $U_0(\varphi)$ and the field in the midplane as $\partial U(\varphi, z)/\partial z|_{z=0} = U_1(\varphi)$. This gives

$$U(\varphi,\ z)=U_0(\varphi)+zU_1(\varphi)-\frac{z^2}{2r^2}U_0''(\varphi)-\frac{z^3}{6r^2}U_1''(\varphi)+\ldots. \tag{3}$$

The phase motion of the particles and possible stabilization are discussed in a previous paper.[3] The motion of the particles will thus be regarded here as isochronic, which in the earlier notation is equivalent to the condition

$$\psi_0=\psi-\nu(\varphi-\theta)=\text{const}. \tag{4}$$

Differentiating with respect to θ the equation for the instantaneous energy of the particle $U_m = m_0\omega_0^2 r^2/2e$ and utilizing expression (14) from ref. 3, we find the energy increment per orbit of a charge moving at a distance $z < z_0$ from the midplane:

$$U_{\mathrm{orb}}=-\int_0^{2\pi}\frac{\partial U(\varphi,\ z)}{\partial\varphi}\sin(\nu\theta+\psi)\,d\varphi.$$

Since the azimuthally varying boundaries must conform to a symmetry like

$$U(\varphi,\ z)=U(-\varphi,\ z);\quad U(\varphi,\ z)=U(\varphi+2\pi,\ z), \tag{5}$$

utilizing power expansion (3) and expression (4), we see that the integral above can be expressed as a sum of parts

$$U_{\mathrm{orb}}=\nu\cos\psi_0\int_0^{2\pi}\cos\nu\varphi\,[U_0(\varphi)+zU_1(\varphi)-\ldots]\,d\varphi.$$

The functions $U_0(\varphi)$ and $U_1(\varphi)$ are periodic in azimuth with a multiplicity (number of variations around the azimuth) ν. Accordingly, when they are expanded as Fourier series and integrated the orthogonality of the trigonometric functions means that the only contribution to the integral comes from the first harmonics. The other terms of the series convolute into the hyperbolic functions

$$U_{\mathrm{orb}}=\pi\nu\delta U_0\cos\psi_0\left[b_1\,\mathrm{ch}\,\frac{\nu z}{r}+a_1\frac{r}{\nu}\,\mathrm{sh}\,\frac{\nu z}{r}\right], \tag{6}$$

where the first coefficients of the Fourier expansion of $U_0(\varphi)$ and $U_1(\varphi)$ are respectively

$$b_1=\frac{\nu}{\pi\delta U_0}\int_0^{2\pi/\nu}U_0(\varphi)\cos\nu\varphi\,d\varphi, \tag{7}$$

$$a_1=\frac{\nu}{\pi\delta U_0}\int_0^{2\pi/\nu}U_1(\varphi)\cos\nu\varphi\,d\varphi. \tag{8}$$

The coefficients a_1 and b_1 are made dimensionless by means of scaling factors U_0 and δ, the significance of which will be explained below.

For antiphase variation of the gap boundaries the potential satisfies the condition

$$U(\varphi,\ z)=-U(\varphi,\ -z).$$

This condition, in conjunction with expression (3), implies that $U_0(\varphi) = 0$, $b_1 = 0$, and the energy increment per orbit is given by

$$U_{\mathrm{orb}}=\pi a_1\delta rU_0\cos\psi_0\,\mathrm{sh}\,\frac{\nu z}{r}. \tag{9}$$

The sign of the energy increment in this structure depends on the location of the particle relative to the midplane, a feature which may find practical application.

For inphase variation of the gap boundaries

$$U(\varphi,\ z)=-U\left[\varphi\pm(2k-1)\frac{\pi}{\nu},\ -z\right];\quad k=1,\ 2,3\ \ldots\ .$$

The component of the electric field in the midplane E_z is also symmetric

$$U_1(\varphi)=U_1\left[\varphi\pm(2k-1)\frac{\pi}{\nu}\right], \qquad (10)$$

which, in conjunction with the evenness of this function, determines its double periodicity $U_1(\varphi+\pi/\nu)=U_1(\varphi)$. Accordingly $a_1 = 0$, and the energy increment is given by

$$U_{\text{orb}}=\pi b_1\nu\delta U_0\cos\psi_0\,\text{ch}\,\frac{\nu z}{r}. \qquad (11)$$

It follows from (11) that the energy increment per orbit will be greatest in a structure with a rectangular variation of the boundaries, in which the limiting value of the coefficient b_1 is $4/\pi$.

We introduce two parameters characterizing the accelerating structure. The aperture coefficient

$$\delta=\frac{2\,|U_0(\varphi)|_{\max}}{U_0} \qquad (12)$$

and, in analogy with linear accelerators,[5] the time-of-flight factor η, which is the ratio of the first-harmonic amplitudes corresponding to the real and a stepwise variation of the potential in the midplane

$$\eta=\frac{\int\limits_0^{2\pi/\nu} s(\varphi)\cos\nu\varphi\,d\varphi}{\int\limits_0^{2\pi/\nu} s_{\text{st}}(\varphi)\cos\nu\varphi\,d\varphi}=\frac{\nu}{2}\int\limits_0^{\pi/\nu} s(\varphi)\cos\nu\varphi\,d\varphi. \qquad (13)$$

Here, U_0 is the peak high-frequency voltage across the gap, $s(\varphi) = U_0(\varphi)/|U_0(\varphi)|_{\max}$ is the dimensionless potential, and $s_{\text{ST}}(\varphi)$ is an even function of unit amplitude with the period of the structure. A change of variable in integral (13) shows that η is independent of ν.

Finally, utilizing (1), we find the energy increment per orbit:

$$U_{\text{orb}}=2\nu\delta\eta U_0 f(r)\cos\psi_0\,\text{ch}\,\frac{\nu z}{r}, \qquad (14)$$

where the parameters η and δ are determined by an electrolytic bath or by a numerical method.

For a monoharmonic field, in particular, these parameters are given analytically by

$$\eta=\frac{\pi}{4},\quad \delta=\frac{1-\frac{2z_0}{d}}{\text{ch}\,\frac{\nu z_0}{r}},$$

when U_{orb} coincides with the corresponding equation of ref. 2.

The vertical motion of a particle, which is described by the equation

$$\frac{d^2z}{d\theta^2}=\frac{ef(r)}{m_0\omega_0^2}\frac{\partial U(\varphi,\,z)}{\partial z}\sin(\nu\varphi+\psi_0)$$

is investigated through the power expansion (3) for the potential and the isochronicity condition (4). This leads, in the linear approximation in z, to an inhomogeneous Mathieu–Hill equation for the independent variable φ:

$$z''+Q(\varphi)\,z=-\frac{ef(r)}{m_0\omega_0^2}U_1(\varphi)\sin(\nu\varphi+\psi_0).$$

Here

$$Q(\varphi)=-\frac{f(r)}{2U_m}U_0''(\varphi)\sin(\nu\varphi+\psi_0).$$

The frequency of the vertical oscillations can be found from the homogeneous equation by the method of averaging.[6]

Following Kapchinskii,[7] we write the solution in the form

$$z(\varphi)=[1+q(\varphi)]\,X(\varphi), \qquad (15)$$

where $X(\varphi)$ is a slowly varying function, and $q(\varphi)$ is a rapidly oscillating function satisfying the equation

$$\frac{d^2q}{d\varphi^2}=\overline{Q(\varphi)}-Q(\varphi). \qquad (16)$$

Here, q and q' must not contain constant components, and $\overline{Q(\varphi)}$ is the mean value of the function over the period of the structure.

In successive integration of Eq. (16) we subtract the constant components from q and q':

$$q(\varphi)=\iint\overline{Q(\varphi)}\,d^2\varphi-\iint Q(\varphi)\,d^2\varphi$$

$$-\frac{\nu}{2\pi}\int\int\limits_0^{\frac{2\pi}{\nu}}\int\overline{Q(\varphi)}\,d^3\varphi+\frac{\nu}{2\pi}\int\int\limits_0^{\frac{2\pi}{\nu}}\int Q(\varphi)\,d^3\varphi$$

$$\frac{\nu}{2\pi}\int\limits_0^{\frac{2\pi}{\nu}}\iint\overline{Q(\varphi)}\,d^3\varphi+\frac{\nu}{2\pi}\int\limits_0^{\frac{2\pi}{\nu}}\iint Q(\varphi)\,d^3\varphi$$

$$+\frac{\nu^2}{4\pi^2}\int\limits_0^{\frac{2\pi}{\nu}}\int\int\limits_0^{\frac{2\pi}{\nu}}\int\overline{Q(\varphi)}\,d^4\varphi-\frac{\nu^2}{4\pi^2}\int\limits_0^{\frac{2\pi}{\nu}}\int\int\limits_0^{\frac{2\pi}{\nu}}\int Q(\varphi)\,d^4\varphi.$$

In order to evaluate $\overline{Q(\varphi)}$ and $q(\varphi)$ we expand $U_0(\varphi)$ as a Fourier series in orthogonal trigonometric functions. Finally

$$\begin{aligned}\overline{Q(\varphi)}&=-\frac{\nu\delta U_0 f(r)}{8\pi U_m}\int\limits_0^{2\pi/\nu}\left[\frac{d^2}{d\varphi^2}\sum_{n=1}^{\infty}b_n\cos n\nu\varphi\right]\sin(\nu\varphi+\psi_0)\,d\varphi\\&=\frac{b_1\nu^2\delta U_0 f(r)}{8U_m}\sin\psi_0,\end{aligned} \qquad (17)$$

$$\begin{aligned}q(\varphi)=\frac{Kb_1}{8\nu^2}\sin(2\nu\varphi+\psi_0)+\frac{K}{2\nu^2}\sum_{n=2}^{\infty}n^2b_n\Bigg\{&\frac{\sin[(n+1)\nu\varphi+\psi_0]}{(n+1)^2}\\&-\frac{\sin[(n-1)\nu\varphi-\psi_0]}{(n-1)^2}\Bigg\},\end{aligned} \qquad (18)$$

In accordance with ref. 7, the function $X(\varphi)$ is found from the equation

$$K=\frac{\delta\nu^2U_0}{4U_m}f(r).$$

where

$$\frac{d^2X}{d\varphi^2}+\mu^2X=0.$$

The number of vertical oscillations performed by the particle per orbit μ is given by the equation

$$\mu^2=\overline{Q(\varphi)}+\frac{\nu}{2\pi}\int_0^{2\pi/\nu} q(\varphi)Q(\varphi)\,d\varphi. \tag{19}$$

We use (16) to transform the integral in this expression

$$\int_0^{2\pi/\nu} qQd\varphi=\bar{Q}\int_0^{2\pi/\nu} qd\varphi-\int_0^{2\pi/\nu} qq''d\varphi.$$

The first term here vanishes, since $q(\varphi)$ has no constant component. Then, integrating the second term by parts and recalling the periodicity of $q(\varphi)$ and $q'(\varphi)$, we obtain

$$\int_0^{2\pi/\nu} qQd\varphi=\int_0^{2\pi/\nu}(q')^2\,d\varphi. \tag{20}$$

Differentiating (18), taking the first term under the summation sign, and utilizing the equality

$$\sum_{n=2}^{\infty}\frac{n^2b_n}{n-1}\cos\left[(n-1)\nu\varphi-\psi_0\right]=\sum_{n=0}^{\infty}\frac{(n+2)^2b_{n+2}}{n+1}\cos\left[(n+1)\nu\varphi-\psi_0\right],$$

we obtain the following expression for q':

$$q'=\frac{K}{2\nu}\sum_{n=0}^{\infty}\left\{\frac{n^2b_n}{n+1}\cos\left[(n+1)\nu\varphi+\psi_0\right]\right.$$
$$\left.-\frac{(n+2)^2b_{n+2}}{n+1}\cos\left[(n+1)\nu\varphi-\varphi_0\right]\right\}.$$

Integral (20), after some straightforward manipulations, can now be brought to the form

$$\int_0^{2\pi/\nu} qQd\varphi=\frac{K^2}{4\nu^2}\left\{\int_0^{2\pi/\nu}\sum_{n=0}^{\infty}\frac{[n^2b_n-(n+2)^2b_{n+2}]^2}{(n+1)^2}\cos^2\psi_0\cos^2(n+1)\nu\varphi d\varphi\right.$$
$$2\int_0^{2\pi/\nu}\sum_{n=0}^{\infty}\frac{[n^2b_n-(n+2)^2b_{n+2}]}{n+1}\cos\psi_0\cos(n+1)\nu\varphi$$
$$\times\left(\sum_{n=0}^{\infty}\frac{n^2b_n+(n+2)^2b_{n+2}}{n+1}\sin\psi_0\sin(n+1)\nu\varphi\right)d\varphi$$
$$\left.+\int_0^{2\pi/\nu}\sum_{n=0}^{\infty}\frac{[n^2b_n+(n+2)^2b_{n+2}]^2}{(n+1)^2}\sin^2\psi_0\sin^2(n+1)\nu\varphi d\varphi\right\}.$$

In this expression the second integral reduces to zero by orthogonality. Working out the remaining integrals and in using the results in (19), utilizing (1), we obtain

$$\mu^2=\frac{\nu^2b_1\delta U_0f(r)}{8U_m}\sin\psi_0+\frac{\nu^2\delta^2U_0^2f^2(r)}{128U_m^2}$$
$$\times\sum_{n=0}^{\infty}\frac{1}{(n+1)^2}\left[n^4b_n^2+(n+2)^4b_{n+2}^2-2n^2(n+2)^2b_nb_{n+2}\cos 2\psi_0\right]. \tag{21}$$

An analysis of this expression shows that the first term, which depends on the particle phase ψ_θ, corresponds to soft focusing and is proportional to the coefficient of the first harmonic in the expansion of the potential in the midplane. This term has a dominant effect on the focusing at large particle energies.

The terms independent of the phase ψ_θ correspond to hard focusing by the corresponding field harmonics. They can become predominant at low energies.

The expression in the square brackets of (21) is always greater than zero. Accordingly, within the limits of applicability of the method of averaging ($\mu \ll \nu$), the higher harmonics have the effect of increasing μ.

For a monoharmonic field[1] we have $b_1 = 1$ and $b_{n|n\neq 1} = 0$, and expression (21) reduces to

$$\mu^2=\frac{\nu^2\delta U_0f(r)}{8U_m}\sin\psi_0+\frac{\nu^2\delta^2U_0^2f^2(r)}{512U_m^2}.$$

The main contribution comes from the first term, which coincides with the index of electrical focusing n_{el} (see ref. 3). The second term is responsible for the hard-focusing effect.

Thus, for gap boundaries varying according to an arbitrary law subject to general symmetry conditions we see that the per-orbit energy increment (14) and number of vertical oscillations (21) are determined with adequate accuracy by the first harmonic of the Fourier expansion of the potential in azimuth. In particular, the use of an accelerating structure with a rectangular variation of the boundaries gives an increase of these parameters by a factor of $4/\pi$ compared with the monoharmonic case.

---

[1] M. F. Vorogushin and V. I. Petrunin, Zh. Tekh. Fiz., 43, 628 (1973)[Sov. Phys.-Tech. Phys., 18, 394 (1973)].

[2] V. I. Petrunin, Zh. Tekh. Fiz., 43, 782 (1973)[Sov. Phys.-Tech. Phys., 18, 491 (1973)].

[3] M. F. Vorogushin and V. I. Petrunin, Zh. Tekh. Fiz., 44, (1974) (in press).

[4] A. Rusterholtz, Electron Optics [Russian translation], Izd. IL, Moscow (1952).

[5] D. V. Karetnikov, Linear Ion Accelerators [in Russian], Gosatomizdat, Moscow (1962).

[6] N. N. Bogolyubov and Yu. A. Mitropol'skii, Asymptotic Methods in the Theory of Nonlinear Oscillations [in Russian], Fizmatgiz, Moscow (1958).

[7] I. M. Kapchinskii, The Dynamics of Particles in Linear Resonance Accelerators [in Russian], Atomizdat, Moscow (1966).

Spatial and energy parameters of the relativistic electron beam of the Rius-5 accelerator

A. T. Altyntsev and V. I. Koroteev

(Submitted July 17, 1973)
Zh. Tekh. Fiz., 44, 1228-1231 (June 1974)

The parameters of the relativistic electron beam in the Rius-5 accelerator have been studied in an effort to evaluate the use of this accelerator in plasma-heating experiments. The optimum conditions correspond to a beam energy of 450-500 J, a maximum electron energy of ~2 MeV, a beam particle density $n_e \sim 5 \cdot 10^{10}$ cm^{-3}, a beam divergence of ~ 6-7°, and a pulse length ~60 nsec.

A detailed study of the parameters of the electron beam of the Rius-5 accelerator,[1] built at the Institute of Nuclear Physics, Siberian Branch, Academy of Sciences of the USSR, has been undertaken in an effort to evaluate the use of this accelerator in plasma-heating experiments.[2] Theory[3] predicts that the effective transfer of beam energy to a plasma requires a highly dense beam (beam density comparable to that of the plasma) and a low beam divergence as the beam enters the plasma and moves through it.

Figure 1 shows the experimental apparatus. The electron beam is extracted from the accelerator through anode 2 (made of Al or Ti foil 10-50 μ thick) into a stainless steel cylinder 9, 160 mm in diameter and 250 mm long. Anode holder 4 is designed to accommodate anodes of various shapes (flat, concave, or convex). In addition, there are sector apertures 5 in the anode which connect the evacuated volumes of the discharge tube of the accelerator and the experimental apparatus.

The detectors which measure the beam parameters are mounted on disk 7. Disk holder 14 is designed so that the detectors can be moved along the axis of the chamber and the disk can be rotated around its axis without disruption of the vacuum. Phosphor bronze leaves 8 provide a reliable contact between the disk and the inner surface of the chamber.

The average charge density and the radial density profile are studied with 50 Faraday cups 10, 2.5 mm in diameter, arranged in a cross on the disk. The cups are loaded with low-leakage, low-inductance capacitors 11.

The voltage from the capacitors is measured through the use of a sequential scanner by an S1-29 storage oscilloscope. The signals from the series of detectors are displayed in a row on the oscilloscope; the charge-density profile along any direction can be monitored visually on the oscilloscope screen when the appropriate reading sequence is chosen.

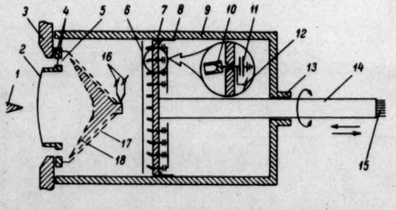

Fig. 1. 1) Cathode; 2) anode; 3) accelerator flange; 4) anode holder; 5) sector apertures in the anode holder; 6) shielding foil; 7) metal disk used as a support for the detectors; 8) phosphor bronze leaves; 9) housing; 10) Faraday cup; 11) capacitor; 12) capacitor terminal; 13) seal; 14) disk holder; 15) electrical leads from the detector elements to the external circuit; 16) leads to a copper–constantan thermocouple; 17) return conductor of the calorimeter; 18) calorimeter.

The Faraday cups are shielded by a grounded thin metal foil (copper, 30 μ thick) 6, and a positive potential (+100 V) is supplied to the capacitors before a pulse. In this manner signal distortion due to secondary-electron emission is avoided. Only the flux of electrons backscattered by the detector, some 15-20% of the basic flux,[4] is taken into account.

The total beam energy is measured by a calorimetric detector, a massive copper calorimeter 18 connected to the accelerator by a stainless steel return conductor 17, 0.05 mm thick. The change in the collector temperature is measured by a copper–constantan thermocouple 16 in a comparison circuit. The thermocouple indications go to a PSR1-13 electronic chart recorder.

Transparent films of chlorovinylmethylmethacrylate, darkened by bombardment by high-energy electrons, are used to obtain a qualitative estimate of the density and energy distributions of the electron beam integrated over a pulse (see ref. 5 for a detailed discussion). The films are arranged in a packet or sandwich and stacked with 7 μ aluminum foil, connected to the anode, to remove space charge. The sandwiches are placed behind the anode, and the relative density distribution and the maximum energy of the electrons in the beam can be determined from the shape and depth of the position of the darkening boundary.

The electron energy is measured with a high time resolution (~10^{-9} sec) by current collectors covered by foils of various thicknesses. The energy measurements are reliable and accurate because the accelerator beam is monoenergetic at each measurement time, as expected on the basis of the method used to extract the beam.

Cathodes of three types are used in the experiments: conical, three-ring (20 mm in diameter, consisting of a point and three concentric rings with acute vertices), and multi-ring (20 mm in diameter, consisting of six rings). The most efficient and stable operation results from the use of the three-ring cathode combined with an anode of aluminum foil, convex toward the cathode (radius of curvature of R ~13 cm).

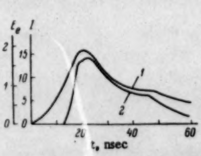

Fig. 2. Electron energy E_e (MeV) (1) and beam current I (kA) (2) as functions of the time.

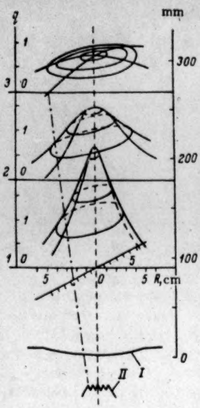

Fig. 3. Transformation of the charge-density distribution, averaged over a pulse, as the beam moves through the experimental chamber. The right-hand ordinate shows the distance to the anode, and the left-hand ordinate shows the cross sections (1, 2, 3) in which the measurements are made and the integrated surface-charge density q (relative units per square centimeter). I) Anode; II) cathode.

Experiments show that the total electron energy should be 2 MeV for prolonged maintenance-free use of the Rius-5 (several thousand pulses). The electron-current pulse, having a sharp front (5-10 nsec) and a slower decay (Fig. 2), has a length of the order of 50 nsec and is delayed ~10 nsec with respect to the voltage pulse. The delay apparently results from the fact that a critical electric field ($\sim 10^6$ V/cm) must be reached at the accelerator cathode for explosive field emission to occur.[6]

The electron density distribution is axially symmetric; the current density reaches 220 A/cm^2 (at the axis in the second cross section; Fig. 3), corresponding to a beam density of $n_e \sim 5 \cdot 10^{10}$ cm^{-3}.

Figure 3 illustrates the transformation of the charge-density distribution, averaged over a pulse, as the beam moves through the experimental chamber. The average density distribution is shown isometrically and has a Gaussian cross section. The beam divergence is taken to be half the magnitude of the plane angle at the vertex of the solid angle containing half the charge detected at the anode. With an aluminum-foil anode 50 μ thick the divergence does not exceed 7°. Calculations show that the divergence is due primarily to scattering by the foil, since[7] the corresponding scattering angle for electrons at ~1 MeV is ~6°.

As the maximum electric field in the discharge gap is raised (above 1 MeV/cm), electron-density rings appear in the distribution function along with the main peak. In this case the electron distribution is a multipeak curve (in cross section), whose shape hinders an evaluation of the beam divergence.

The experiments with the Rius-5 beam show that the basic beam parameters [the total energy (~450-500 J), the maximum electron energy (~2 MeV), the beam density ($n_e \sim 5 \cdot 10^{10}$ cm^{-3}), the length of the current pulse (~60 nsec), and the beam divergence (~7°)] are adequate for the initiation of an experimental study of the interaction of a relativistic electron beam with a plasma.

The authors thank R. Kh. Kurtmullaev for interest in this work and for useful discussion; they also thank E. A. Abramyan and S. B. Vasserman for the opportunity to use the Rius-5 accelerator.

---

[1] E. A. Abramyan, S. B. Vasserman, V. M. Dolgushin, L. A. Morkin, O. P. Pecherskii, and V. A. Tsukerman, Dokl. Akad. Nauk SSSR, 192, 76 (1970) [Sov. Phys. – Dokl., 15, 490 (1970)].

[2] A. T. Altyntsev, B. N. Breizman, A. G. Eskov, O. A. Zolotovskii (Zolotovsky), V. I. Koroteev, R. Kh. Kurtmullaev, V. L. Masalov, D. D. Ryutov, and V. N. Semenov, Nucl. Fusion, Suppl., 12, 161 (1972).

[3] B. N. Breizman and D. D. Ryutov, Zh. Eksp. Teor. Fiz., 60, 408 (1971) [Sov. Phys. – JETP, 33, 220 (1971)].

[4] W. Bothe, Z. Naturforsch., 4a, 542 (1949).

[5] B. P. Sannikov, Symposium on High-Current Plasma Emission Electronics, Tomsk, March, 1973.

[6] G. K. Kartsev, G. A. Mesyats, D. I. Proskurovskii, and G. N. Fursei, Dokl. Akad. Nauk SSSR, 192, 309 (1970) [Sov. Phys. – Dokl., 15, 475 (1970)].

[7] G. Moliere, Z. Naturforsch., 3a, 78 (1948).

General

Kinetics of gasdynamic lasers. Effect of nozzle geometry on inversion

A. S. Biryukov and L. A. Shelepin

P. N. Lebedev Physics Institute, Academy of Sciences of the USSR, Moscow

(Submitted June 8, 1973; resubmitted November 16, 1973)
Zh. Tekh. Fiz., 44, 1232-1243 (June 1974)

A detailed analysis is made of the effect of supersonic nozzle geometry on the parameters of a CO_2 gasdynamic laser. It is shown that each of the elements characterizing the nozzle (throat half-height or radius, divergence angle of expansion section, length and shape of expansion section, character of the transition from subsonic to supersonic flow, and so on) has its own specific effect on the population inversion and the kinetics of vibrational relaxation. A study is also made of the case of high (up to ~ 4000°K) initial temperatures, allowing for the variation of the composition and the gasdynamic parameters as a result of chemical reactions. It is shown that equilibrium reactions do not lead to additional nonequilibrium effects in the vibrational levels. Such nonequilibrium effects can result from the combustion of carbon-containing mixtures.

I. INTRODUCTION

Gasdynamic lasers have received much attention in recent years. Vibrational relaxation and laser action on the 00^01-02^00 and 00^01-10^00 transitions of the CO_2 molecule have been studied in many papers, both theoretical[1-13] and experimental[14-20] (see also the reviews in refs. 21 and 22). Gasdynamic lasers can be divided into two types, depending on the mechanism of operation and the characteristics of the kinetic processes: lasers operating in the low-temperature region at an initial temperature of the gas mixture $T_0 < 2500°K$, and high-temperature lasers $T_0 > 2500°K$).

The manner in which the population inversion depends on the initial parameters (stagnation temperature and pressure, mixture composition) has been investigated thoroughly in the case of low-temperature lasers. Work remains to be done, however, on the role played by nozzle size and geometry, factors which are often crucial in design. In most papers the work pertains to one particular nozzle geometry. Thus, Basov et al.[4] investigated the relaxation of a binary CO_2-N_2 mixture in a Laval nozzle. Generalov et al.[11] varied the temperature and the pressure, and, to some extent, the shape of the nozzle (Laval nozzle going over into a cylinder, a two-dimensional hyperbolic nozzle going over into a plane-parallel channel). Anderson and Harris[12] used a simplified relaxation scheme to calculate the variation of the gain along the flow axis of a $CO_2-N_2-H_2O$ mixture in a nozzle having a somewhat different profile than in refs. 4 and 11.

Of the various experimental papers[14-20] that by Kuehn[20] contains the most complete description of the effect of nozzle geometry on the output power of a gasdynamic laser (GDL). These papers are rather disconnected in character, however, and even when taken together do not lend themselves to systematic study of the effect of the nozzle.

In the present paper we have carried out a detailed study of the effect of nozzle geometry on the kinetics of vibrational relaxation and the appearance of an inverted population in low-temperature gasdynamic lasers. The nozzle is divided into separate sections and the effect of each (in particular, the dimensions and shape of the throat, the angle of divergence, the geometry of the transition to the expansion section, the presence or absence of a constant-area duct) is investigated with a view to drawing conclusions concerning the operation and usefulness of particular nozzles.

Little work has been done on high-temperature gasdynamic lasers. The kinetics of the physical processes in such lasers can differ strongly from the low-temperature case ($T_0 \leqslant 2500°K$). In particular, the CO_2 can be more than half dissociated, and thermal ionization begins to play a role ($T_0 > 3000°K$). Yushchenkova and Kalenov[6] noted that, upon expansion of the mixture, the chemical composition differs from the equilibrium value as a result of the "freezing" of the chemistry. The effect of chemical reactions on the vibrational kinetics in the low-temperature region ($T_0 \leqslant 3000°K$) is considered in refs. 8 and 13. The role of nonequilibrium recombination reactions is studied in ref. 23. Tulip and Seguin[10] calculated the inverse population distribution along the nozzle axis at temperatures up to ~4000°K but ignored the chemistry. The output power at high stagnation temperatures (up to ~4000°K) has been measured by Kuehn[20] but no explanation of his results is given.

Another aim of the work reported here is to investigate the role of chemical processes at temperatures $T_0 \geqslant 3000°K$ and to explain the operation of high-temperature gasdynamic lasers.

II. BASIC EQUATIONS AND METHOD OF CALCULATION

The analysis of the kinetics in a moving and expanding gas at high initial temperatures require the simultaneous consideration of the gas dynamics, the chemical processes and the chemical kinetics. Let us being with the chemical kinetics.

All chemical conversions in the ternary mixture CO_2-N_2-He at initial temperatures 2500-4000°K involve only the CO_2 molecule (N_2 dissociates to some extent at higher temperatures). Accordingly, the six main components of interest are O_2, CO, O, CO_2, N_2, and He. We denote the molar fractions by $\gamma_i = n_i/n$, where n_i is the concentration of the i-th component and n is the total number of particles per unit volume. To determine the six unknowns γ_i we have the following four relationships:

$$\left.\begin{array}{c}\sum_i \gamma_i(t)=1,\ \dfrac{\gamma_{CO}(t)+\gamma_{CO_2}(t)}{\gamma_{CO}(t)+\gamma_O(t)+2\gamma_{O_2}(t)+2\gamma_{CO_2}(t)}=b,\\ \gamma_{N_2}(t)=\dfrac{\mu(t)}{\mu_{N_2}}\alpha_{N_2},\ \gamma_{He}(t)=\dfrac{\mu(t)}{\mu_{He}}\alpha_{He},\end{array}\right\} \qquad (1)$$

where $\mu(t)$ is the molecular weight of the mixture; b, α_{N_2}, α_{He} are constants that depend on the initial conditions. The first of relationships (1) comes from the definition of γ_i; the second reflects the fact that the ratio of the number of carbon atoms to the number of oxygen atoms is a constant for all chemical conversions; the third and the fourth are connected with the fact that N_2 and He do not participate in the chemical reactions and that the mass of each relative to the total mass of gas must remain constant.

For a mixture of equilibrium chemical composition b = 1/2. If a composition with definite ratios of the molar fractions at some (initial) time is in a state of nonequilibrium, we have for α_{N_2}, α_{He}, b

$$\alpha_{N_2}=\frac{\gamma_{N_2}(0)\,\mu_{N_2}}{\sum\limits_i \gamma_i(0)\,\mu_i},\quad \alpha_{He}=\frac{\gamma_{He}(0)\,\mu_{He}}{\sum\limits_i \gamma_i(0)\,\mu_i},$$
$$b=\frac{\gamma_{CO}(0)+\gamma_{CO_2}(0)}{\gamma_{CO}(0)+\gamma_O(t)+2\gamma_{O_2}(0)+2\gamma_{CO_2}(0)}. \tag{2}$$

Thus, having four relationships with which to find the six unknown molar fractions, we must solve a set of two equations in all. For definiteness, let us take γ_{O_2} and γ_{CO_2} to be the independent variables in this set. We write the equations determining γ_{O_2} and γ_{CO_2} as a result of gasdynamic expansion in the presence of chemical reactions. Under these conditions, the concentration of the i-th component n_i is given by the equation[24]

$$\frac{d\gamma_i}{dt}=\frac{1}{n}\left(\frac{dn_i}{dt}\right)_*+\frac{\gamma_i}{\mu}\frac{d\mu}{dt}, \tag{3}$$

where $(dn_i/dt)_*$ is the rate of change of the i-th component as a result of the chemical reactions. The required set of equations can now, with the aid of (1), be represented in the form[25]

$$\left.\begin{aligned}\frac{d\gamma_{O_2}}{dt}&=\frac{1+\gamma_{O_2}}{n}\left(\frac{dn_{O_2}}{dt}\right)_*+\frac{\gamma_{O_2}}{n}\left(\frac{dn_{CO_2}}{dt}\right)_*,\\ \frac{d\gamma_{CO_2}}{dt}&=\frac{\gamma_{CO_2}}{n}\left(\frac{dn_{O_2}}{dt}\right)_*+\frac{1+\gamma_{CO_2}}{n}\left(\frac{dn_{CO_2}}{dt}\right)_*.\end{aligned}\right\} \tag{4}$$

To make (4) more specific we must restrict the discussion to a definite set of reactions responsible for the variation of the chemical composition. The most important reactions in this case include[25]

$$\left.\begin{aligned}&CO_2+M \underset{k_{-1}^M}{\overset{k_1^M}{\rightleftarrows}} CO+O+M,\\ &CO_2+O \underset{k_{-2}}{\overset{k_2}{\rightleftarrows}} CO+O_2,\\ &O_2+M \underset{k_{-3}^M}{\overset{k_3^M}{\rightleftarrows}} O+O+M.\end{aligned}\right\} \tag{5}$$

Here M is any of the six components of the mixture; k_i^M, k_{-i}^M are the rate constants of the forward and reverse reactions respectively. The particle-number balance equations determining the right sides of (4) have the form

$$\left.\begin{aligned}\frac{1}{n}\left(\frac{dn_{O_2}}{dt}\right)_*=\frac{P}{kT}\Big(&\frac{P}{kT}\gamma_O^2\sum_M k_{-3}^M\gamma_M+\gamma_{CO_2}\gamma_O k_2\\ &-\gamma_{O_2}\sum_M k_3^M\gamma_M-\gamma_{CO}\gamma_{O_2}k_{-2}\Big),\\ \frac{1}{n}\left(\frac{dn_{CO_2}}{dt}\right)_*=\frac{P}{kT}\Big(&\frac{P}{kT}\gamma_{CO}\gamma_O\sum_M k_{-1}^M\gamma_M\\ &+\gamma_{CO}\gamma_{O_2}k_{-2}-\gamma_{CO_2}\sum_M k_1^M\gamma_M-\gamma_{CO_2}\gamma_O k_2\Big),\end{aligned}\right\} \tag{6}$$

where P is the pressure and T the temperature of the gas.

The variation of the gasdynamic parameters is described by the equations of motion, energy conservation, and continuity. The analysis of the motion of a mixture of gases in a supersonic nozzle usually proceeds on the assumption that the flow is one-dimensional and that the gasdynamic parameters depend only on the one coordinate, x, along the axis of the nozzle. This assumption is usually justified in the great majority of cases (see also ref. 12).

We assume further that the rotational degrees of freedom are in equilibrium with the translational degrees of freedom and utilize the equation of state $P = \rho RT/\mu$. The set of gasdynamic equations then becomes

$$\left.\begin{aligned}&\frac{P\mu Vf}{RT}=\text{const},\\ &\frac{dP}{dx}=-\frac{P\mu V}{RT}\frac{dV}{dx},\\ &\frac{RT}{\mu}\left(\frac{5}{2}+\sum_i\gamma_i\right)+\sum_i e_v^i+\frac{V^2}{2}=\text{const},\end{aligned}\right\} \tag{7}$$

where $\rho(x)$ is the mass per unit volume of the gas; $f(x)$ is the ratio of the cross-sectional area at x to the nozzle area at the throat; R is the gas constant; e_v^i is the vibrational energy per unit mass of the i-th component. In (7) and in all relationships of this section the summation is taken over the molecular components.

The system (7) can be solved for the derivatives, and the equations determining the gasdynamic parameters take the form

$$\left.\begin{aligned}\frac{dT}{dx}&=-T\,\frac{\left\{(1-z)\sum\limits_i\frac{d\gamma_i}{dx}+\frac{1-z}{zV^2}\sum\limits_i\frac{de_v^i}{dx}+\frac{1}{f}\frac{df}{dx}-\left[\left(\frac{5}{2}+\sum\limits_i\gamma_i\right)(1-z)-1\right]\frac{1}{\mu}\frac{d\mu}{dx}\right\}}{\left(\frac{5}{2}+\sum\limits_i\gamma_i\right)(1-z)-1},\\ \frac{dV}{dx}&=V\,\frac{z\sum\limits_i\frac{d\gamma_i}{dx}+\frac{1}{V^2}\sum\limits_i\frac{de_v^i}{dx}+z\left(\frac{5}{2}+\sum\limits_i\gamma_i\right)\frac{1}{f}\frac{df}{dx}}{\left(\frac{5}{2}+\sum\limits_i\gamma_i\right)(1-z)-1},\\ \frac{dP}{dx}&=-\frac{P}{Vz}\frac{dV}{dx},\quad z=\frac{RT}{\mu V^2}.\end{aligned}\right\} \tag{8}$$

It can be seen from (8) that the nozzle geometry can have a significant effect on the rate of change of the gasdynamic parameters of the flow, which, in turn, determine the rates of all relaxation processes. The geometry of the nozzle is not only important beyond the throat, but also before it.

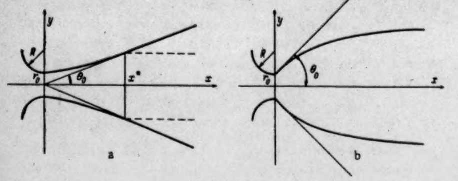

Fig. 1. Nozzle profiles.

The calculations were performed for two nozzle geometries, hyperbolic and logarithmic (see Fig. 1 for the shape for $x \geq 0$).

For a hyperbolic nozzle, in (x, y) coordinates (Fig. 1a) we have

$$y = r_0\sqrt{1+\left(\frac{x}{r_0}\operatorname{tg}\theta_0\right)^2}, \tag{9}$$

where r_0 is the half-height (or radius) of the throat, and θ_0 is the limiting angle of divergence of the nozzle. The area ratio f can be represented by a common expression for both circular and rectangular nozzle cross sections:

$$f = \sqrt{1+\left(\frac{x}{r_{01}}\operatorname{tg}\theta_{01}\right)^2}\sqrt{1+\left(\frac{x}{r_{02}}\operatorname{tg}\theta_{02}\right)^2}. \tag{10}$$

For $r_{01} = r_{02} = r_0$ and $\theta_{01} = \theta_{02} = \theta_0$ this expression corresponds to a circular (throat radius r_0) or square (half-height at throat r_0) nozzle, and otherwise to a rectangular-section nozzle.

It is of interest to consider a nozzle (10) going over, at some distance x^* from the throat, into a duct of constant cross-sectional area, i.e., f = const for $x \geq x^*$.

The nozzle geometry of Fig. 1b is most conveniently represented by an expression of the form

$$y = m\ln(ax + c). \tag{11}$$

The constants a and c are expressed in terms of m and the usual characteristics r_0 and θ_0 by

$$a = c\,\frac{\operatorname{tg}\theta_0}{m}, \quad c = e^{\frac{r_0}{m}}.$$

For large angles $\theta_0(\sim 45°)$ nozzles of this type resemble a slit with a half-height r_0 treated by us in ref. 5. For angles greater than this the quasi-one-dimensional character of the flow can be violated.

It can be seen from (10) and (11) that nozzles a and b differ fundamentally from each other in the manner in which the transition to expansion occurs.

The nozzle input profile is taken to be the same in both cases, a quarter arc of a circle of radius $R = 2r_0$ (Fig. 1).

For the chosen mixture composition and chemical reactions (5), we deal with only four molecular components: CO_2, CO, O_2, and N_2. Accordingly, besides those considered in ref. 26, the main channels of vibrational relaxation are the following:

$$\left.\begin{aligned}
&CO_2(00^01) + CO(v=0) \rightleftarrows CO_2(00^00) + CO(v=1), && W_{3.5},\\
&CO_2(00^00) + CO(v=1) \rightleftarrows \begin{cases} CO_2(11^10) + CO(v=0), & W_{5.12},\\ CO_2(03^10) + CO(v=0), & W_{5.2},\end{cases}\\
&CO_2(00^00) + O_2(v=1) \rightleftarrows CO_2(10^00) + O_2(v=0), && W_{6.1},\\
&N_2(v=1) + CO(v=0) \rightleftarrows N_2(v=0) + CO(v=1), && W_{4.5},\\
&N_2(v=1) + O \rightleftarrows N_2(v=0) + O, && W_{4.0},\\
&O_2(v=1) + M \rightleftarrows O_2(v=0) + M, && W^{M}_{6.0}.
\end{aligned}\right\} \tag{12}$$

The probabilities of the forward basic processes are indicated on the right; the indices from 1 to 3 denote respectively the symmetric stretching, the bending, and the asymmetric stretching modes of vibration of CO_2; the index 4 refers to the N_2 molecule, the index 5 to the CO molecule, and the index 6 to O_2.

When the chemical reactions occur in a moving flow of gas the variation of the average energy stored per unit mass in the i-th vibrational degree of freedom is given by the equation[27]

$$\frac{de_v^i}{dt} = \frac{\theta_i R}{\mu_i}\left[\frac{d\varepsilon_v^i}{dt} + \sum_j \left(\varepsilon_{i*}^{(j)} - \varepsilon_v^i\right)\frac{1}{n_i}\left(\frac{dn_i}{dt}\right)_*^{(j)}\right], \tag{13}$$

where the summation is understood to extend over all chemical reactions in which a given molecule participates; $\varepsilon_{i*}^{(j)}$ is the average energy, expressed in the number of photons $h\nu_i$ going into the i-th oscillator as a result of a single act of the j-th reaction; $\theta_i = h\nu_i/k$; k is Boltzmann's constant; $e_v^i = \varepsilon_v^i(\theta_i R/\mu_i)$; ε_v^i is the mean energy (number of photons) stored in the i-th vibration.[26]

Let us assume further that the reactions of dissociation and recombination go mainly through the upper vibrational levels. The magnitude of the vibrational energy lost or acquired by molecules participating in these processes is then approximately equal to the dissociation energy. In the case of the exchange reaction in (5) we set $\varepsilon_{i*} = 0$ for simplicity for all the components CO, O_2, CO_2. We assume that the vibrational energy of the chemical reactions in the case of CO_2 is uniformly distributed over its four vibrational modes, i.e., $\varepsilon_{i*} = D\alpha_i$, where D is the dissociation energy of CO_2, $\alpha_i = 0.25$ for the asymmetric and symmetric stretching modes, $\alpha_2 = 0.5$ for the doubly degenerate bending mode.

The rates of change of the concentrations of the mixture components are described by equations of the form (6)[24] but with the rate constants of the reactions (5) taken from ref. 28. The first term on the right side of (13) describes the normal collisional relaxation over the vibrational levels. The general expression for this process is obtained in ref. 26.

Thus, Eqs. (4), (8), and (13) along with (6) completely determine vibrational relaxation in a gas expanding through a nozzle and in which chemical reactions (5) can take place.

The calculations are performed on a computer, first for low-temperature mixtures ($T_0 \leqslant 2300°K$). It turns out that even at high pressures the chemical reactions are weak and their effect on the vibrational relaxation can be neglected. The acceleration of the gas from the nozzle input to the throat, as shown in ref. 11, can be regarded as taking place in complete thermodynamic equilibrium (an isentropic process). This is confirmed by our calculation, as the maximum deviation of the vibrational temperature from the gas temperature is less than ~80°K at T ~2000°K. The flow up to the throat is thus regarded as independent of the input geometry, and the parameters in the throat are found from the equations[29]

$$P_{\text{th}} = P_0\left(\frac{2}{\gamma+1}\right)^{\frac{\gamma}{(\gamma-1)}}, \quad T_{\text{th}} = T_0\frac{2}{\gamma+1}. \tag{14}$$

Here, P_0 and T_0 are the stagnation parameters; γ is the adiabatic ratio, defined in our case as

$$\gamma = \left(\frac{5}{2} + \sum_i \gamma_i\right) / \left(\frac{3}{2} + \sum_i \gamma_i\right).$$

This expression leads to a temperature-independent γ for a fixed chemical composition of the mixture, as it ignores the contribution to the specific heat of the gas from the vibrational degrees of freedom. The drop of gas temperature accompanying the acceleration of the gas from the input to the throat causes the adiabatic ratio to increase slightly. However, estimates allowing for the possible contribution from the symmetric and bending modes for a mixture containing He in a quantity $\gamma_{\text{He}} \gtrsim 0.5$ in the temperature range $T_0 = 3500$–2500°K show that the variation of γ is less than ~5%.

It can be seen from (8) that in supersonic operation of the nozzle the numerator and the denominator in the equations for T and V change sign simultaneously. This change occurs at a critical point x_1 located slightly downstream from the throat for nozzles of type a (Fig. 1a) and, as a rule, directly in the throat for nozzles of type b. For equilibrium initial stagnation conditions the distance x_1 is very small; accordingly, in the low-temperature calculations, the origin is taken to be in the throat. The equilibrium composition at P_{th}, T_{th} is calculated for various assigned α_{N_2}, α_{He} through (4) and (1) with the derivatives set equal to zero. The composition of the mixture and the temperature are used to find the initial velocity of the gas, which is assumed to be equal to the local (in the throat) velocity of sound.

The calculations for high-temperature mixtures are carried out for both equilibrium and nonequilibrium composition stagnation conditions. A type b nozzle geometry is used in both cases. At temperature T > 3000°K the chemical reactions can proceed intensively and the composition vary rapidly (especially under nonequilibrium conditions), and accordingly the choice of the initial value of the velocity in (8) is not a trivial one. It is chosen by the "ranging method" (see refs. 4, 24).

The probabilities of the processes entering into Eqs. (13) are taken from the data of ref. 30 with allowance for ref. 31.

III. RELAXATION PROCESSES AND MECHANISM OF OPERATION OF GASDYNAMIC LASERS

Our calculations on low-temperature mixtures demonstrate the profound effect of nozzle geometry on the parameters of gasdynamic lasers. This effect is systematically studied by dividing the nozzle into separate elements: the section up to the throat; the shape of the throat (circular or rectangular); the half-height (radius) of the throat r_0; the angle of divergence of the expansion section θ_0; the character of the transition to expansion (nozzle type *a* or b); length of expansion section x*.

It can be seen from (10) and (11) that each of these elements has its own specific effect on the laser characteristics, the maximum inversion, the position of this maximum along the nozzle axis, the width of the region in which inversion ΔN exists, and the manner in which the inversion depends on pressure and temperature. The calculations have the aim of investigating the effect of each of these closely interrelated factors for different stagnation conditions in order to permit an appraisal of the possibilities of particular nozzles as a whole. The results of the calculations are presented in Figs. 2–7. The effect of the character of the transition from the throat to the expansion section is analyzed on the basis of a type-*a* nozzle (Fig. 1a).

Figure 2 shows typical on-axis variations of the inversion $\Delta N = N_{00^01} - N_{10^00}$, and the vibrational and gas temperatures for complete thermodynamic equilibrium in the throat. It can be seen (the dashed curves) that at a certain distance from the throat the vibrational temperatures in N_2 and in the asymmetric CO_2 mode are "frozen," while T_2 continues to fall. The inversion, which occurs when the difference between T_3 and T_2 reaches a certain value (the ratio T_3/T_2 must be ~1.73), passes through a maximum and subsequently falls. The presence of a maximum is due, on the one hand, to the increase in the difference between T_3 and T_2 and, on the other, to the reduction in density upon expansion.

Calculations have also been performed for the same conditions but with the nozzle going over, at a distance x* from the throat, into a constant-area cylindrical duct (the solid curves). The picture here is somewhat different. Commencing from this point the gas temperature T increases as a result of the termination of expansion and the arrival of energy from the vibrational degrees of freedom to the translational. This increase of T enables T_2 to continue falling, and subsequently leads to a speeding up of the relaxation of T_3 and T_4. The region of increasing difference between T_3 and T_2 can be much more drawn out in this case, and since the particle density for x ≥ x* is constant it follows that the maximum inversion, under otherwise equal conditions, can be much higher than in the first case. The fall-off in inversion is due not to a reduction in density, but to a diminution in the rate of decrease of T_2 and its subsequent increase for a simultane-

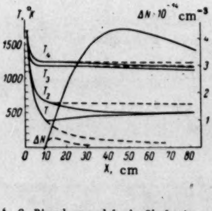

Fig. 2. Variation of inversion ΔN and vibrational and gas temperatures along axis of axially symmetric nozzle (type a). $T_{\text{th}} = 2000$°K, $P_{\text{th}} = 15$ atm, $\tan \theta_0/k_0 = 1.25$, $\alpha_{N_2} = 0.6$, $\alpha_{\text{He}} = 0.085$.

ous relaxation of T_3 and T_4. The process whereby T_3 and T_2 approach is a comparatively slow one, and accordingly the region in which the inversion is high can extend over a considerable distance (sometimes more than 1-2 m). The chosen values of α_{N_2} and α_{He} correspond under our conditions to a composition $CO_2:N_2:He \approx 1:3:3$ (the remaining components amount on the whole to less than one percent).

Figure 3a shows plots of the inversion along the axis of a nozzle going over into a constant-area duct for various values of the pressure in the throat P_{th}. It can be seen that for the specified parameters of the system the optimum value of $P_{th} \approx 27$ atm. This is due to the increase in the number of working particles with increasing pressure and to the accompanying speeding up of vibrational relaxation. The increase in the relaxation rate leads to a more rapid rise of the gas temperature, and as a result the region in which inversion exists contracts greatly with increasing P_{th}.

The role played by the expansion parameter tan θ_0/r_0 can be seen from Fig. 3b, which shows similar plots for a nozzle with larger tan θ_0/r_0. The optimum value of the inversion now occurs in the expansion section of the nozzle. However, inclusion of a transition to a constant-area duct enables the CO_2 bending modes to continue relaxing and the difference between T_3 and T_2 to increase, which, for a constant density, results in an increase in the inversion and attainment of a higher second maximum. The maximum value of ΔN increases up to pressures $P_{th} \sim 300$ atm and approaches x* with increasing pressure. The region in which inversion exists correspondingly contracts, as in the case of Fig. 3a.

With a view to establishing the effect of throat shape, we calculate the inversion along the axis of a two-dimensional type-*a* nozzle. The vibrational temperatures and the inversion in this case are distributed along the axis in much the same manner as in Fig. 2. However, the region of optimum pressures (Fig. 4a) occurs at much lower values of P_{th} as a result of the smaller rate of expansion. It can be seen from Fig. 4a that the higher the expansion parameter tan θ_0/r_0 the higher the pressure corresponding to optimum inversion and the greater the absolute value of the latter (the solid curves).

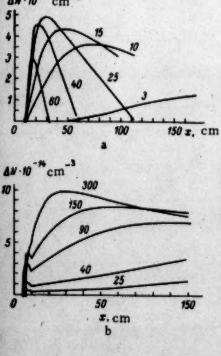

Fig. 3. Plots of inversion ΔN versus distance along axis of axially symmetric type-*a* nozzle for various throat pressures P_{th}. $T_{th} = 2000$°K, $\alpha_{N_2} = 0.6$, $\alpha_{He} = 0.085$, x* = 10 cm; tan θ_0/r_0: a) 1.25; b) 2.5.

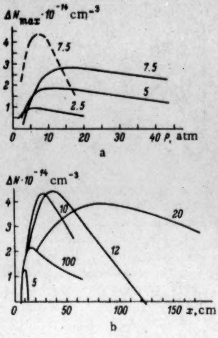

Fig. 4. a) Plots of a maximum inversion ΔN_{max} versus pressure P_{th} for two-dimensional type-*a* nozzle for various values of the expansion parameter tan θ_0/r_0 (solid curves). The dashed curves correspond to the same conditions but for a nozzle going over at x* = 10 cm into a constant-area duct. b) Plots of inversion along axis of two-dimensional type-*a* nozzle going over at x = x* into a constant area channel for various values of x*. $R_{th} = 7.65$ atm, tan $\theta_0/r_0 = 7.5$. In both cases $T_{th} = 2000$°K, $\alpha_{N_2} = 0.6$, $\alpha_{He} = 0.085$.

Figure 4b shows the variation of the inversion along the axis for various lengths x* of the expansion section of the nozzle. The presence of an optimum value x^*_{opt} is explained, on the one hand, by the fact that at $x^* < x^*_{opt}$ the role of relaxation is large, while at $x^* > x^*_{opt}$ the number of working particles is small on account of the appreciable expansion. As in the case of Fig. 3, the maximum inversion can be greater than for a nozzle with $x^* \to \infty$.

The effect of the manner in which the throat goes over into the expansion section can be seen by comparison with the results obtained for type-b nozzles (Fig. 1b). High initial cooling rates can occur here. As can be seen from Fig. 5, no "freezing" of T_3 and T_4 occurs. The difference between t_3 and t_2, established even at x ~ 1-2 cm, proves, however, to be sufficient for the occurrence of inversion. The subsequent increase of this difference resulting from the different relaxation times of the vibrational degrees of freedom of CO_2 leads, for a weakly varying density, to an increasing inversion ΔN (Fig. 6a). As the expansion rate of the nozzle falls off the gas temperature not only ceases to drop, but indeed even begins to rise on account of the accelerated relaxation of T_3 and T_4 (T_2 here is already close to T). This, along with a weak diminution of density, results in the inversion ΔN falling off.

Figure 6b shows plots of maximum inversion versus throat pressure for various nozzle characteristics. Curves 1 and 2 differ in the value of m by a factor of 3, the higher the value of m the more the optimum values of ΔN_{max} are displaced towards higher pressures. Calculations show

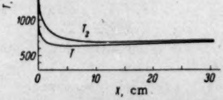

Fig. 5. Vibrational temperatures and gas temperature versus distance along axis of logarithmic type-b nozzle. $T_{th} = 2000$°K, $P_{th} = 15$ atm, tan $\theta_0/m = 2.663$, $/m = 0.0525$, $\alpha_{N_2} = 0.6$, $\alpha_{He} = 0.085$.

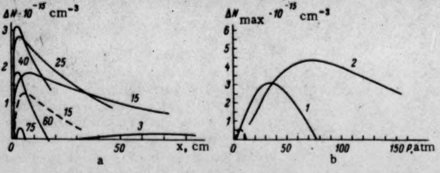

Fig. 6. a) Plots of inversion ΔN along axis of type-b nozzle for various values of the pressure in the throat. T_{th} = 2000°K, $\tan\theta_0/m$ = 2.663, r_0/m = 0.0525, α_{N_2} = 0.631, α_{He} = 0.1122 (corresponds to a composition $CO_2 : N_2 : He$ = 1 : 4 : 5). The dashed curve corresponds to α_{N_2} = 0.6, α_{He} = 0.085 (composition 1 : 3 : 3). b) Maximum inversion ΔN_{max} achieved on axis of logarithmic nozzle versus throat pressure T_{th} = 2000°K, α_{N_2} = 0.631, α_{He} = 0.122; $\tan\theta_0/m$: 1) 2.663; 2) 0.888; r_0/m: 1) 0.0525, 2) 0.0175. Dashed curve corresponds to $\tan\theta_0/m$ = 0.662, r_0/m = 0.065.

that the greater the ratio $\tan\theta_0/r_0$, the more efficiently is the gas cooled (compare, for example, with the dashed curve of Fig. 6b). Also, higher initial temperatures call for larger values of m (to achieve a sufficient depth of cooling). The absolute values of the optimum ΔN are around four to eight times greater than in the best variants of hyperbolic nozzles (correct to the small difference in the compositions of the mixtures).

Initial temperatures $T_0 \sim 1800$°K appear to be the optimum for gasdynamic lasers; higher values are regarded as inefficient on account of the high relaxation rate. The theoretical analysis ignores, however, a number of physical processes (for example the dissociation of CO_2, thermal ionization). Each of these factors demands a detailed study of the kinetics. To investigate the effect of the chemistry on the operation of high-temperature gasdynamic lasers, the inversion is calculated allowing for the chemical kinetics in a type-b nozzle at high temperatures T_0 = 3200-4000°K. The calculations are performed for equilibrium (in chemical composition) conditions at P_0, T_0 and also for a deliberately introduced degree of nonequilibrium. Velocity "ranging" is carried out for r_0 = 0.025 and 0.05 cm in both cases. In the case of equilibrium stagnation conditions over a wide range of pressures, the vibrational temperatures fall monotonically for both values of r_0 and, for $x = 2r_0$, are very close to the gas temperature (difference is ~90-120°K); the chemical compositions, however, are close to the equilibrium compositions at (P_{th}, T_{th}). This means that reactions (5) are able to establish a state of chemical equilibrium under conditions of varying gasdynamic parameters in the entire distance from x = 0 to $x = 2r_0$. The variation of the composition as a result of chemical reactions for a temperature drop from T_0 to T_{th} is small.[24]

In the case of a nonequilibrium chemical composition at (P_0, T_0), the temperature is found to vary in a nonmonotonic manner along the axis as a result of the reactions. A temperature difference between T_3 and T_2 of ~100°K is achieved, which is far from sufficient to obtain inversion.[24] Even this difference, however, is not maintained up to the throat, as T_3 and T_2 approach T as a result of intense relaxation. The absolute values of the temperatures in the throat are $T_{th} \sim 2800$-2900°K for T_0 = 3200°K (for T_0 = 4000°K, $T_{th} \sim 3500$-3700°K).

The subsequent motion of the mixture of almost equilibrium composition through the nozzle is accompanied, as a result of the sharp drop in P and T, by a rapid (for $x \gtrsim 1$ cm) "freezing" of the chemical reactions. In both cases therefore, equilibrium and nonequilibrium at (P_0, T_0, the composition at distances x ~1 cm differs from that at the throat by not more than 2% (in terms of the amount of CO_2). Thus, one can assume with good accuracy that the gas from the throat is a mixture of constant chemical composition in almost complete thermodynamic equilibrium.

As in low-temperature gasdynamic lasers, the use in the high-temperature case of a type-b nozzle does not result in the appearance of inversion since, for otherwise equal conditions, larger T_{th} calls for larger m. Figure 7 illustrates how the parameter m affects the maximum inversion in the case of high initial temperatures of the gas. This effect is significant for nozzles with small r_0, and better results are obtained with m ~5-7. Increasing r_0 requires larger m, and conversely. The optimum values of the inversion are smaller than at $T_0 \sim 2000$°K.

The above calculations, in which reactions (5) are taken into account, still do not permit a complete estimate to be made of the role of the chemistry. The fact is that real GDL mixtures contain a certain amount of water vapor, which can radically affect the chemical kinetics. The CO oxidation reaction catalyzed by water has the character of a chain reaction, and proceeds according to quite a different scheme than (5) (see ref. 32, for example). Also, it is exothermal, and probably makes a large energy contribution to the vibrational degrees of freedom of the CO_2 molecules formed as a result of the reaction. A detailed analysis of the kinetics of this reaction and of its effect on the vibrational relaxation is rendered difficult by several factors, namely, the fraction of the energy of the reaction going into vibrations is unknown, there are no rate constants for the various links of the reaction, and the role of the bounding surfaces, on which active centers may be created, is unclear. Under such conditions one can only make qualitative estimates, and these showed[24] that inversion can be an order greater than in the case of the ordinary oxidation reaction of CO. This may be the theoretical explanation of the experimental fact[20] that the output power of a gasdynamic laser increases with increasing stagnation temperature.

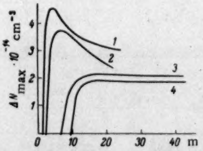

Fig. 7. Plots of ΔN_{max} versus the parameter m (logarithmic type-b nozzle). Curves 2 (r_0 = 0.025 cm and(r_0 = 0.025cm) and (R_0 = 0.05 cm) pertain to equilibrium stagnation conditions will α_{N_2} = 0, α_{He} = 0.178 (corresponds to composition $CO_2 : CO : O : O_2 : N_2 : He$ = 1 : 0.37 : 0.02 : 0.17 : 0 : 3.26 at P_0, T_0). Curves 1(r_0 = 0.025 cm) and 3 (r_0 = 0.05 cm) pertain to nonequilibrium composition $CO_2:CO:O:O_2:N_2:He$ = 1 : 2 : 1 : 1 : 0 : 8 at P_0, T_0. T_0 = 3200°K, P_0 = 90 atm, and θ_0 = 45°.

We note that in the high-temperature laser, on account of the high degree of thermal ionization, a discharge can be used to effect additional excitation of the working gas (in the throat the degree of thermal ionization amounts to 10^{-6}–10^{-7} at $P'_{th} \sim 10^2$ atm and $T_{th} \approx 3500°K$). Also, the large number of electrons greatly facilitates the striking of a discharge across the flow and gives rise to the electrical gasdynamic laser. The kinetics of the physical processes in such lasers at low initial temperatures ($T_0 \leqslant 2000°K$) are discussed in ref. 33.

On the whole, the data obtained in the present work on the dependence of the inversion on the individual elements of the nozzle in the low-temperature case can be used to obtain semiquantitative characteristics for a broad class of specific nozzles. The results can be refined by allowing for possible differences between the real and the calculated flows. Our analysis also shows the possibilities of high-temperature lasers based on the reactions of combustion.

In conclusion we should like to thank B. F. Gordiets for a useful discussion.

---

[1] V. K. Konyukhov and A. M. Prokhorov, Author's Certificate No. 223954 (1966).

[2] V. K. Konyukhov and A. M. Prokhorov, ZhETF Pis. Red., 3, 436 (1966) [JETP Lett., 3, 286 (1966)].

[3] N. G. Basov, A. N. Oraevskii, and V. A. Shcheglov, Zh. Tekh. Fiz., 37, 339 (1967) [Sov. Phys. – Tech. Phys., 12, 243 (1967)].

[4] N. G. Basov, V. G. Mikhailov, A. N. Oraevskii, and V. A. Shcheglov, Zh. Tekh. Fiz., 38, 2031 (1968) [Sov. Phys. – Tech. Phys., 13, 1630 (1969)].

[5] A. S. Biryukov, B. F. Gordiets, and L. A. Shelepin, Zh. Eksp. Teor. Fiz., 57, 585 (1969) [Sov. Phys. – JETP, 30, 321 (1970)].

[6] N. I. Yushchenkova and Yu. A. Kalenov, Zh. Prikl. Spektrosk., 11, 417 (1969).

[7] J. D. Anderson, Jr., Phys. Fluids, 13, 1983 (1970).

[8] J. D. Anderson, Jr., AIAA J., No. 3, 545 (1970).

[9] J. D. Anderson, Jr., R. L. Humphrey, J. S. Vamos, M. J. Plummer, and R. E. Jensen, Phys. Fluids, 14, 2620 (1971).

[10] J. Tulip and H. Seguin, J. Appl. Phys., 42, 3393 (1971).

[11] N. A. Generalov, G. I. Kozlov, and I. K. Selezneva, Prikl. Mekh. Tech. Fiz., No. 5, 24 (1971).

[12] J. D. Anderson, Jr., and F. L. Harris, Laser Focus, 8, 32 (1972); AIAA Paper No. 72-143 (1972).

[13] N. I. Yushchenkova and Yu. A. Kalenov, Zh. Prikl. Spektrosk., 16, 39 (1972).

[14] A. P. Dronov, A. S. D'yakov, E. M. Kudryavtsev, and N. N. Sobolev, ZhETF Pis. Red., 11, 516 (1970) [JETP Lett., 11, 353 (1970)].

[15] D. M. Kuehn and D. J. Monson, Appl. Phys. Lett., 16, 48 (1970).

[16] E. T. Gerry, Laser Focus, December, 27 (1970); AIAA Paper No. 71-23 (1971).

[17] S. Yatsiv, E. Greenfield, F. Dothan-Deutsch, D. Chuchem, and E. Bin Nun, Appl. Phys. Lett., 19, 65 (1971).

[18] W. H. Christiansen and G. A. Tsongas, AIAA Paper, No. 572 (1971).

[19] A. S. Biryukov (Biriukov), A. P. Dronov, E. M. Kudryavtsev (Kudriavtsev), and N. N. Sobolev, IEEE J. Quantum Electron., QE-7, 388 (1971).

[20] D. M. Kuehn, Appl. Phys. Lett., 21, 112 (1972).

[21] V. N. Karnyushin and R. I. Soloukhin, Fiz. Goreniya i Vzryva, 8, 163 (1972).

[22] B. F. Gordiets, A. I. Osipov, E. V. Stupochenko, and L. A. Shelepin, Usp. Fiz. Nauk, 108, 655 (1972) [Sov. Phys. – Usp., 15, 759 (1973)].

[23] A. S. Biryukov, B. F. Gordiets, and L. A. Shelepin, Kr. Soobshch. Fiz., No. 6, 13 (1971).

[24] A. S. Biryukov and L. A. Shelepin, Preprint FIAN, No. 59 (1973).

[25] E. V. Stupochenko, S. A. Losev, and A. I. Osipov, Relaxation Processes in Shock Waves [in Russian], Izd. Nauka, Moscow (1965).

[26] A. S. Biryukov and B. F. Gordiets, Prikl. Mekh. Tekh. Fiz., No. 6, 29 (1972); Preprint FIAN, No. 32 (1972).

[27] C. E. Treanor and P. V. Marrone, Phys. Fluids, 5, 1022 (1962).

[28] V. N. Kondrat'ev, The Rate Constants of Gas Phase Reactions [in Russian], Izd. Nauka, Moscow (1970).

[29] G. N. Abramovich, Applied Gas Dynamics [in Russian], Izd. Nauka, Moscow (1969).

[30] R. L. Taylor and S. Bitterman, Rev. Mod. Phys., 41, 26 (1969); E. E. Nikitin and S. Ya. Umanskii, Dokl. Akad. Nauk SSSR, 196, 145 (1971).

[31] A. S. Biryukov, V. K. Konyukhov, A. I. Lukovnikov, and R. I. Serikov, Preprint FIAN, No. 9 (1973).

[32] B. Lewis and G. Elbe, Burning, Flames, and Explosions in Gases [Russian translation], Izd. Mir, Moscow (1968).

[33] A. S. Biryukov and L. A. Shepelin, Zh. Tekh. Fiz., 43, 355 (1973) [Sov. Phys. – Tech. Phys., 18, 229 (1973)]; Preprint FIAN, No. 130 (1972).

Photochemical waves in a medium with a branch-chain conversion mechanism

A. N. Oraevskii, V. P. Pimenov, and V. A. Shcheglov

P. N. Lebedev Physics Institute,
Academy of Sciences of the USSR, Moscow

(Submitted September 27, 1973)
Zh. Tekh. Fiz., 44, 1244-1252 (June 1974)

Processes which are related to the propagation of blast waves in a gaseous medium characterized by a branch-chain conversion mechanism are considered. It is shown that under certain conditions the wave velocity exceeds substantially the wave velocity of nonbranching chain reactions. Expressions are found for the wave profile. These expressions differ from expressions for both the photolysis wave and the photochemical wave when no branching occurs.

I. INTRODUCTION

The propagation of photodissociation waves in gaseous media has been considered in refs. 1-3. Several papers[4-7] have reported on investigations of photochemical waves which propagate in gaseous media characterized by a chain conversion mechanism. The present work is a theoretical investigation of similar waves in media in which branch-chain reactions can take place. The interest in these waves results from the fact that chain reactions with branching (oxidation of hydrogen, burning of carbon dioxide in the presence of hydrogen-containing compounds, chlorination of acetylene, etc.) are characteristic of a large number of gas mixtures.

According to the theoretical concepts developed by Semenov and his school,[8-10] two basic chemical branching reactions can be distinguished. In the first type the branching of chains takes place without formation of induced particles ("material" branching), and the mechanism of the process proper consists of the formation of two active centers (radical and biradical) in the interaction of the radical with the initial molecule).

In the second type of chemical branching reaction the branching process takes place at the expense of the energy liberated during a chain reaction which is localized at a certain bond of the reaction product. In principle, monomolecular decomposition of an excited product can result in the branching of chains. Obviously, a rather low binding energy is associated with this process. If the excitation energy does not suffice for the rupture of bonds according to the monomolecular mechanism, branching can take place in a bimolecular reaction of an excited molecule on the one hand and one of the initial agents on the other. It is emphasized in refs. 9 and 10 that the branching process occurs in this case through formation of a chemical complex and through a strong perturbation of the energy levels of the interacting particles, rather than at the expense of migration of excitation energy to the bond of the initial agent and subsequent decomposition of the same.

2. FORMATION OF THE PROBLEM

The present work deals with photochemical waves in gaseous media which are characterized by a mechanism of bimolecular energy branching.

As in previous papers,[4-7] we assume that the mixture of gases A_2-B_2 is irradiated by quasimonochromatic radiation of frequency ν and intensity I_0, and that the B_2 molecules and the reaction products do not absorb radiation at this frequency. It is assumed that the reactions in the medium occur according to the following scheme:

$$\left.\begin{aligned}
A_2+h\nu &\xrightarrow{\sigma} 2A,\\
A+B_2 &\xrightarrow{k_1} AB+B,\\
B+A_2 &\xrightarrow{k_2} (1-\mu)\,AB+\mu AB^{+}+A,\\
AB^{+}+A_2 &\xrightarrow{k_3} AB+2A,\\
B+R &\xrightarrow{\gamma} BR,\\
A+Q &\xrightarrow{\gamma_1} AQ.
\end{aligned}\right\} \qquad (2.1)$$

The first link of Eq. (2.1) corresponds to the photoinitiation processs;the following two links correspond to the development of the chain; the fourth link corresponds to the branching process; the chain rupture is described by the next two links. The following notation is introduced in the scheme (2.1): A_2 and B_2 denote the molecules of the initial agents; A and B denote active centers; AB^+ and AB correspond to excited and nonexcited products of the chain reaction, respectively; R and Q are inhibitors; BR and AQ are inhibition products; σ denotes the cross section of photolysis; k_1 and k_2 denote the constants of the links in the chain reaction; k_3 denotes the constant of branching; μ denotes the probability of the appearance of an excited product; γ and γ_1 denote the constants of the chain-rupture processes. In our ensuing discussion, square brackets will be used to denote the densities of the corresponding agents, e.g., $[A_2]$, $[B_2]$, etc.

Thermal effects are ignored in the present paper.[1)]

To describe the propagation of a photochemical wave we used the radiation-transfer equation and equations of chemical kinetics. A solution to the system in the form of a stationary wave is determined, i.e., it is assumed that all dynamic variables depend upon the argument $x' = x - Dt$, where D denotes the wave velocity, which is to be determined. The system of ordinary differential equations which describes this wave has the form

$$\left.\begin{aligned}
u' &= -\sigma a_2 u,\\
a_2' &= \sigma a_2 u + b a_2 + \delta_3\varphi_2 a_2,\\
b_2' &= \delta_1 a b_2,\\
a' &= -2\sigma a_2 u + \delta_1 a b_2 - b a_2 - 2\delta_3\varphi_2 a_2,\\
b' &= -\delta_1 a b_2 + b a_2 + \delta_2 b r,\\
\varphi_1' &= -\delta_1 a b_2 - (1-\mu)\,b a_2 - \delta_3\varphi_2 a_2,\\
\varphi_2' &= -\mu b a_2 + \delta_3\varphi_2 a_2,\\
r' &= \delta_2 b r,\\
\psi' &= -\delta_2 b r,\\
q' &= \delta_4 a q,\\
\psi_1' &= -\delta_4 a q,
\end{aligned}\right\} \qquad (2.2)$$

where differentiation with respect to $\eta = x'(k_2[A_2^0])/D$ is performed; the following notation is introduced:

$$\left.\begin{gathered}\alpha=\sigma D/k_2,\ \delta_1=k_1/k_2,\ \delta_3=k_3/k_2,\ \delta_2=\gamma/k_2,\\ \delta_4=\gamma_1/k_2,\ a_2=[A_2]/[A_2^0],\ b_2=[B_2]/[A_2^0],\\ a=[A]/[A_2^0],\ b=[B]/[A_2^0],\ \varphi_1=[AB]/[A_2^0],\\ \varphi_2=[AB^+]/[A_2^0],\ r=[R]/[A_2^0],\\ \psi=[BR]/[A_2^0],\ q=[Q]/[A_2^0],\ \psi_1=[AQ]/[A_2^0],\ u=I/D[A_2^0]\end{gathered}\right\}$$

with I denoting the radiation flux expressed in photons $\cdot$ $cm^{-2} \cdot sec^{-1}$.

The solution of the problem is reduced to the integration of system (2.2) under the following boundary conditions:

$$\left.\begin{gathered}\eta=+\infty:u=0,\ a_2=1,\ r=r_0,\ q=q_0,\\ a=b=\varphi_1=\varphi_2=\psi=\psi_1=0,\\ b_2=b_2^0.\ \eta=-\infty:u=u_0,\ a_2=0.\end{gathered}\right\}$$

3. STABILITY OF THE UNPERTURBED GAS

We assume in our formulation of the problem that the front of the photochemical wave moves toward the gas medium which has not entered into the reaction. According to the theory of Semenov, this involves a situation in which the image point of the unperturbed state of the mixture is beyond the region of spontaneous (self-) ignition. Let us determine the conditions which the parameters of the problem must satisfy for the initial medium to be stable in this sense. To do this, we consider the front of the wave in the region of large $\eta > 0$ values, where the inequalities $(1-a_2) \ll 1$, $(b_2^0-b_2) \ll b_2^0$, $(r_0-r) \ll r_0$, $(q_0-q) \ll q_0$ hold. By linearizing the equations of the initial system in the neighborhood of the point corresponding to the unperturbed state, we obtain a relation between the intensity and the concentration of the active centers A:

$$2\alpha u=a\frac{(\alpha+\delta_2r_0)(\alpha+\delta_3)(\alpha+\delta_1b_2^0+\delta_4q_0)+{}+(\alpha+\delta_3)(\alpha+\delta_4q_0)-2\mu\delta_1\delta_3b_2^0}{(1+\alpha+\delta_2r_0)(\alpha+\delta_3)}. \tag{3.1}$$

Obviously, the proportionality coefficient in a linear relation between a and $2\alpha u$ must be positive. Since the stability condition is independent of the velocity of the wave propagating toward the gas, the minimum of the coefficient, which obtains for $\alpha = 0$ (i.e., $D = 0$), must be nonvanishing. Thus, the general stability condition, for the initial mixture corresponding to the reaction scheme (2.1), has the following form:

$$F=\frac{\gamma[R_0]}{k_2[A_2^0]}+\frac{\gamma_1[Q_0]}{k_1[B_2^0]}+\frac{\gamma_1[Q_0]}{k_1[B_2^0]}\frac{\gamma[R_0]}{k_2[A_2^0]}-2\mu>0. \tag{3.2}$$

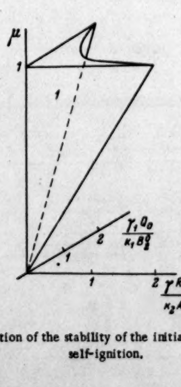

Fig. 1. Determination of the stability of the initial mixture. 1) Region of self-ignition.

The surface F = 0 splits the phase space into two regions: a region of self-ignition and a region of stability (Fig. 1).

To simplify the analysis we will restrict our considerations to cases in which chain rupture occurs only by virtue of the reaction of an active center B with an admixture R. In this case, inequality (3.2) assumes the simpler form

$$\gamma[R_0]-2\mu k_2[A_2^0]>0, \tag{3.3}$$

i.e., the chain length is bounded by the value $1/2\ \mu$.

4. CONDITIONS FOR A FAST TRANSITION INTO THE SELF-IGNITION REGION

The system of equations (2.2) (with Q = 0), which describes a stationary wave, has four integrals. This means that three types of particles and photon-particles are conserved:

$$\left.\begin{gathered}\psi=r_0-r,\\ (1+\mu)b=u+(1+\mu)(b_2^0-b_2)\\ -(1-a_2)-(1+\mu)(r_0-r)-\varphi_2,\\ a=2(1-a_2)+b-2(b_2^0-b_2)+(r_0-r),\\ \varphi_1=2(1-a_2)-a-\varphi_2.\end{gathered}\right\} \tag{4.1}$$

Equations (4.1) make it possible to reduce the initial system to the simpler system

$$\left.\begin{gathered}u'=-\alpha a_2u,\\ a_2'=\alpha a_2u+ba_2+\delta_3\varphi_2a_2,\\ \varphi_2'=-\mu ba_2+\delta_3\varphi_2a_2,\\ r'=\delta_2br,\\ \varepsilon b_2'=ab_2,\end{gathered}\right\} \tag{4.2}$$

where $\varepsilon = 1/\delta_1 = k_2/k_1$. The solution is greatly simplified when the reaction rate in one of the links of the chain reactions greatly exceeds the reaction rate in another link. This situation is frequently encountered in practice. In our subsequent discussion, we consider the case $\varepsilon = k_2/k_1 \ll 1$. It is possible to show[11] that for sufficiently small ε, the solution of the system resembles the solution of the system in which the last equation is replaced by

$$0=ab_2. \tag{4.3}$$

When an excess of agent B_2 is present (first condition of ref. 6), $a = 0$ is the solution to (4.3). This situation is of greatest interest. As a matter of fact, in the case of the second condition (B_2 deficiency), it is possible to show for a sufficiently small concentration of the inhibitor ($[R_0] \ll I_0/D$) that the wave velocity differs only slightly from the wave velocity of photodissociation of products from the instantaneously occurring chemical reactions, i.e., from the wave velocity $D = I_0/([A_2^0]-(1+\mu)[B_2^0])$ (it is assumed that $\xi = 2K_2[A_2^0]/\sigma I_0 \gg 1$, ref. 6). We consider below the first condition in which the wave propagation process is described by a system including the first four equations of (4.2), the integrals (4.1), and the equality $a = 0$.

The behavior of a medium characterized by a branch-chain conversion mechanism depends upon the form in which the concentration of the active centers changes. The following differential equation for the active center B can be obtained from system (2.2) (taking into account that $a = 0$):

$$b' = -2\alpha a_2 u + \delta_2 br - 2\delta_3\varphi_2 a_2. \tag{4.4}$$

In order to make our considerations clearer we assume for the time being $\delta_3 = k_3/k_2 \gg 1$ (fast branching reaction); then Eq. (4.4) assumes the form

$$b' = -2\alpha a_2 u + b(\delta_2 r - 2\mu a_2). \tag{4.5}$$

When we assume that Eq. (4.5) describes the kinetics of a reaction which occurs at some fixed point $x = x_1$ and when we recall the equality $\partial/(\partial t) = -Dd/(d\eta)$, it becomes obvious that Eq. (4.5) is equivalent to the equation which was obtained by Semenov.[9] It is shown in ref. 9 that self-ignition of the gas does not occur when the inequality $l_0 = \delta_2 r_0 - 2\mu > 0$ is satisfied. This coincides with the particular case of the previously considered stability condition (3.3) of the mixture.

The quantity $l = \delta_2 r - 2\mu a_2$ which appears in parentheses in Eq. (4.5) can be treated as "distance" between the image point and the region of self-ignition. As has been noted above, the inequality $l \approx l_0 > 0$ must be satisfied for large $\eta > 0$. The concentrations of both agent A_2 and admixture R decrease in the wave front and, hence, a cross section $\eta \equiv 0$, in which the representing point reaches the region of self-ignition, must not necessarily exist. This situation $[l(\eta) > 0, -\infty < \eta < \infty]$ corresponds to a wave propagating in a medium in which chain reactions with rupture occur.[6,12]

When we use the solution of the linearized system (4.2), (4.4), we can in the general case (arbitrary δ_3 value) determine the change in the distance L between the representing point and the region of self-ignition during changes in the dynamic variables in the wave front:

$$L = \delta_2 br - 2\delta_3\varphi_2 a_2 = \frac{2\alpha a_2 u}{(\delta_2 r_0 + \alpha)(\delta_3 + \alpha) - 2\delta_3\mu}[\delta_2 r_0(\delta_3 + \alpha)a_2^{\varkappa-1} - 2\delta_3\mu], \tag{4.6}$$

where

$$\varkappa = \frac{\frac{\gamma}{k_2}}{1 + \frac{1}{2}\left(\frac{\gamma R_0}{k_2 A_2^0} + \frac{\sigma D}{k_2}\right)}.$$

If $\varkappa < 1$, the decrease in the concentration of A_2 only enhances the inequality $L > 0$. If the inequality $\varkappa \gg 1$ is satisfied, a slight reduction of a_2 sharply reduces the term which in Eq. (4.6) corresponds to chain rupture, i.e., the representing point rapidly "enters" into the region of autoignition. We assume the point $\eta = 0$ at which L tends to zero $[L(o) = 0]$ as the origin of the coordinate system. For positive L values, the number of active centers in the medium is smaller than twice the number of absorbed photons; in the region of negative L values, active centers are generated by the medium. This implies that b(t), the number of active centers which are present at a particular time in a unit volume of the gas, can greatly exceed the number of photons N(t) absorbed by this volume. The quantity b(t) depends to a larger extent upon the time $\tau(t)$ during which the image point of the volume is within the self-ignition region than upon N(t). The quantity b(t) increases qualitatively in exponential form with increasing $\tau(t)$ (the factor before the exponential is $\sim N(t)$).

5. PROFILE AND VELOCITY OF THE WAVE

In order to investigate in explicit form the details of the waves which depend upon the properties of the branching reaction, it is interesting to consider the case in which the main fraction of agent A_2 is annihilated in the region of negative η values. To do this we consider a mixture which is close to the self-ignition region due to the presence of a small amount of a chemically active inhibitor R in the gas. We assume that the developing active centers B rapidly enter into reactions with molecules R, as long as molecules R are present in the gas. This means that the wave profile in the region of positive η values is of the photolysis type:

$$\eta > 0: r = r_0 - 2u,\ a_2 = 1 - u,\ \psi = 2u,$$

$$\varphi_1 = 2u,\ b_2 = b_2^0 = 2u,\ b = \varphi_2 = a = 0.$$

In the region of negative values of wave front coordinates, the concentration of admixture R becomes zero and the wave is described by a system which comprises the first three equations of (4.3) and the integrals

$$\left.\begin{aligned} &r = a = 0;\ \psi = r_0;\ \varphi_1 = 2(1 - a_2) - \varphi_2;\\ &b_2 = b_2^0 - \frac{1+2\mu}{1+\mu}(1 - a_2) - \frac{u}{1+\mu} + \frac{\varphi_2}{1+\mu},\\ &b = \frac{2u}{1+\mu} + \frac{2\mu}{1+\mu}(1 - a_2) - \frac{2}{1+\mu}\varphi_2 - r_0. \end{aligned}\right\}$$

The boundary conditions of this system are as follows: $\eta = 0$; $u = r_0/2$, $a_2 = 1 - r_0/2$, $r_2 = 0$.

We introduce for convenience $r_2 \equiv r_0/2$.

We obtain the following equation from Eq. (4.2):

$$\frac{d^2a_2}{du^2} + \frac{c_1}{u}\frac{da_2}{du} + \frac{c_2}{u^2}a_2 = \frac{c_3}{u} + \frac{c_4}{u^2} \tag{5.1}$$

with the boundary conditions

$$a_2(u = r_2) = 1 - r_2,$$

$$(da_2/du)(u = r_2) = -1,$$

where

$$\left.\begin{aligned} &c_1 = 1 + \frac{\delta}{z};\ c_2 = -\frac{\mu\delta}{z^2};\ c_3 = -\left(1 + \frac{\delta}{z}\right)\left(1 + \frac{1}{z}\right);\\ &c_4 = [r_2(1+\mu) - \mu]\frac{\delta}{z^2};\ \delta = \frac{k_3}{2k_2};\ \xi = \frac{2k_2[A_2^0]}{\sigma I_0};\ z = \frac{D}{\frac{2k_2}{\sigma}}. \end{aligned}\right\}$$

The solution of Eq. (5.1) has the form

$$a_2 = 1 - r_2 - \frac{r_2}{\mu} - m_1 u + \frac{r_2}{y_1 - y_2}\left\{\left(m_1 + \frac{1}{\mu}\right)\left[y_1\left(\frac{u}{r_2}\right)^{y_2} - y_2\left(\frac{u}{r_2}\right)^{y_1}\right] + (m_1 - 1)\left[\left(\frac{u}{r_2}\right)^{y_2} - \left(\frac{u}{r_2}\right)^{y_1}\right]\right\}, \tag{5.2}$$

where

$$m_1 = \frac{(z+\delta)(z+1)}{z^2 + \delta z - \mu\delta};\ y_{1,2} = \frac{\delta}{2z}\left(-1 \pm \sqrt{1 + \frac{4\mu}{\delta}}\right).$$

When we use the well-known conditions for $\eta = -\infty$: $u = u_0 = 1/\xi z$, and $a_2 = 0$, we can obtain, from Eq. (5.2), an equation establishing a relation between the velocity of the photochemical wave and the parameters of our problem:

$$E(z, \xi, \delta, \mu, r_2) = 0. \tag{5.3}$$

It is possible to show that Eq. (5.3) has two roots, one of which is

$$z^* = \frac{\delta}{2}\left[-1 + \sqrt{1 + \frac{4\mu}{\delta}}\right].$$

This root is independent of the intensity of the external radiation flux. Obviously, this root has no physical meaning. The velocity of the wave is given by the second root of Eq. (5.3).

Nonbranching chain reactions occur in the gas for $k_3 = 0$ or $\mu = 0$ in the region of negative η values. It is then possible to show that Eq. (5.3) is reduced to the following equation for the wave velocity:

$$0 = 1 - r_2 - \left(1 + \frac{1}{z}\right)\left(\frac{1}{\xi z} - r_2\right) + \frac{r_2}{z}\ln\left(\frac{1}{r_2 \xi z}\right). \tag{5.4}$$

In the limit $r_2 \to 0$, we obtain the well-known expression for the velocity[6,7]

$$D = \frac{1}{2}\frac{I_0}{[A_2^0]} + \sqrt{\left(\frac{1}{2}\frac{I_0}{[A_2^0]}\right)^2 + \frac{2k_2 I_0}{\sigma [A_2^0]}}. \tag{5.5}$$

It follows from a numerical solution of Eq. (5.4) that even for $r_2 = 10^{-4}$–10^{-6} the wave velocity differs only slightly from the limit value defined by Eq. (5.5).

The results of a numerical solution of the general equation (5.3) are displayed in Fig. 2 [a family of curves $D/D_0 = f_\delta(\xi)$ is shown for $\mu = 1$ and $r_2 = 10^{-4}$, $D_0 \equiv I_0/[A_2^0]$ denotes the velocity of the photodissociation wave[1]].

First of all, let us note that when the intensity decreases (ξ increases), the influence of branching upon the wave velocity increases. The branching effect in the reaction becomes important in this case, provided that the branching constant amounts to at least one per cent of the constant of the chain reaction. When the branching constant increases in the interval $0 < k_3 \leqslant k_2$ $(0 < \delta \leqslant 1)$, the wave velocity increases sharply and a further change in k_3 does not lead to a substantial increase in the velocity [for $\delta \geqslant 5$ the wave velocity is close to the limit value $D \approx D$ $(\delta = \infty)$]. When the branching constant is unbounded ($\delta \to \infty$) Eq. (5.3) assumes the simpler form

$$0 = 1 - r_2 - \frac{r_2}{\mu} - \frac{z+1}{z-\mu}\frac{1}{\xi z} + r_2 \frac{z(1+\mu)}{\mu(z-\mu)}(r_2 \xi z)^{-\mu/z}. \tag{5.6}$$

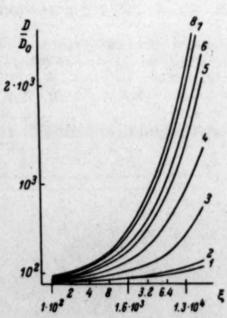

Fig. 2. Family of curves which define the velocity of the wave for various $\delta = \bar{k}_3/2\bar{k}_2$ values. $r_2 = 10^{-4}$, $\mu = 1$; 1) $\delta = 0$; 2) $\delta = 10^{-4}$; 3) $\delta = 10^{-2}$; 4) $\delta = 10^{-1}$; 5) $\delta = 0.5$; 6) $\delta = 1$; 7) $\delta = 5$; 8) $\delta = \infty$.

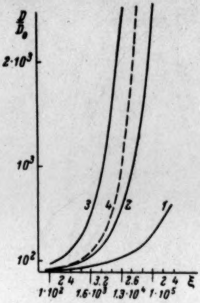

Fig. 3. Family of curves which determine the wave velocity for $\bar{k}_3 = \infty$. $r_2 = 10^{-4}$, 1) $\mu = 0$; 2) $\mu = 0.1$; 3) $\mu = 1$; 4) $r_2 = 10^{-6}$, $\mu = 0.1$.

It follows from reaction scheme (2.1) that in this case, the quantity 2μ has the meaning of the number of active centers generated by the medium per link of the chain reaction. By varying μ we can observe the way the degree of branching in the chain reaction affects the characteristics of the wave. Figure 3 displays the numerical solution of Eq. (5.6) for $r_2 = 10^{-4}$ and $\mu = 0$, 0.1, and 1. When the branching is "switched on", the velocity of the wave is greatly increased. For example we have for $\xi = 10^4$ the results $D(\mu = 0) = 10^2 D_0$, $D(\mu = 0.1) = 5 \cdot 10^2 D_0$, and $D(\mu = 1) = 2 \cdot 10^3 D_0$. Figure 2 includes the curve which corresponds to $r_2 = 10^{-6}$ and $\mu = 0.1$. In contrast with the nonbranching chain reactions, the velocity of the wave increases sharply with increasing concentration of the admixtures, even when the admixture concentration is low. This detail can be understood when we consider a unit volume of the gas located at a large distance before the wave front. The number of photons which are absorbed by the unit volume must decrease with decreasing admixture concentration for a branching chain reaction to be initiated in that volume. The time between the beginning of the reaction and the moment at which the wave front arrives at the particular point of the medium increases. The exponential increase in the rate of the branching reaction overcomes the reduction of the initiation rate with increasing η. One can show that when r_2 is decreased the wave velocity defined by Eq. (5.6) tends to the value D_{lim}:

$$D_{\mathrm{lim}} = \frac{1}{2}\frac{I_0}{[A_2^0]} + \mu\frac{k_2}{\sigma} + \sqrt{\left(\frac{1}{2}\frac{I_0}{[A_2^0]}\right)^2 + \frac{(2+\mu)k_2 I_0}{\sigma [A_2^0]} + \left(\mu\frac{k_2}{\sigma}\right)^2}. \tag{5.7}$$

However, let us note that the stability condition (Eq. 3.3) for the initial mixture implies a restriction of the minimum of the concentration of admixtures R, because the rate of the rupture reaction cannot exceed the gas-ki-

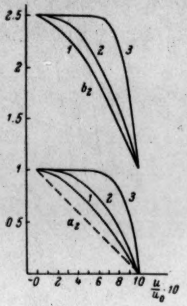

Fig. 4. Wave profiles ($\mu = 1$, $r_2 = 10^{-4}$). ξ values: 1) 100; 2) 800; 3) 10^5.

netic collision frequency ($r_0 > r_{0\,\min} = 2\gamma k_2/\gamma_{\max}$). The order of magnitude of $r_{0\min}$ is 10^{-2}–10^{-4} in fast chain reactions ($\mu k_2 \simeq 10^{-12}$–10^{-14} cm^3/sec). Figure 3 displays the curves which correspond to the greatest possible wave velocities in a medium which is characterized by a branch-type conversion mechanism. In the limit ($k_3 \gg k_2$), the expressions determining the wave profile have the form

$$\left.\begin{array}{c} a_2 = 1 - r_2 - \dfrac{r_2}{\mu} - \dfrac{z+1}{z-\mu}u + r_2\dfrac{z(1+\mu)}{\mu(z-\mu)}\left(\dfrac{u}{r_2}\right)^{\mu/z}; \\ r = \varphi_2 = a = 0;\ \psi = r_0;\ \varphi_1 = 2(1-a_2), \\ b_2 = b_2^0 - \dfrac{1+2\mu}{1+\mu}(1-a_2) - \dfrac{u}{1+\mu}, \\ b = \dfrac{2u}{1+\mu} + \dfrac{2\mu}{1+\mu}(1-a_2) - r_0, \\ \eta = -\dfrac{1}{a}\displaystyle\int_{r_2}^{\infty}\dfrac{du}{a_2(u)\,u}. \end{array}\right\}$$

Figure 4 shows the functions $a_2 = a_2(u/u_0)$, $b_2 = b_2(u/u_0)$. In the case of nonbranching reactions, the wave front is not distinguished from the front of the photolysis wave, and the relation between a_2 and u is linear: $a_2 = 1 - (u/u_0)$. When branching is "switched on", the wave front is distorted, i.e., the wave front begins to depend upon the ratio of the rate of chemical reactions to the rate of photolysis. When the intensity decreases, the wave front section on which the photons initiate reactions is more clearly separated. A considerable fraction of the photons are spent for the initiation process, and the change in the concentration of the agents is small in this range. The photodissociating agent is basically annihilated on the rear wave front section, where the rate of the chemical reaction reaches high values. For example, for $\xi = 10^5$, the concentration of A_2 and B_2 decreases less than 1% at the wave front point at which $u = u_0/2$.

6. CONCLUSION

It follows from our analysis that, in principle, the wave velocity in a medium characterized by a branch-chain conversion mechanism can be very high. The wave velocity can exceed by one order of magnitude the velocity of the corresponding wave in a medium without branching. However, for this to occur the image point of the initial gas mixture must be close to the region of self-ignition (the mixture is stabilized with the aid of a small amount of a chemically active inhibitor $\gamma > k_2$). When the medium is intensively heated by the heat liberated during the reaction, the condition for the entry of the representing point into the self-ignition region is less rigorous. The reason is that chain rupture frequently occurs as a consequence of triple collisions with activation energy zero, i.e., chain rupture depends only slightly upon temperature, contrary to the exponential temperature dependence of the rate of a chain reaction. The gas-dynamic motions which are caused by the external radiation flux and the possible formation of shock and explosion waves before the front of the photochemical wave are other interesting aspects of the problem. We propose that these specific questions be investigated in future work.

---

[1] As to the applicability conditions of the isothermal model, see refs. 2, 6.

---

[1] V. E. Khartsiev, Zh. Eksp. Teor. Fiz., 54, 867 (1968) [Sov. Phys. – JETP, 27, 464 (1968)].
[2] B. L. Borovich, V. S. Zuev, and O. N. Krokhin. Zh. Eksp. Teor. Fiz., 64, 1184 (1973)[Sov. Phys.–JETP, 37, 602 (1973)].
[3] B. L. Borovich, V. Ya. Karpov, N. I. Kozlov, Yu. Yu. Stoilov, and A. A. Filyukov, Zh. Eksp. Teor. Fiz., 64, 1211 (1973) [Sov. Phys.–JETP, 37, 616 (1973)].
[4] A. N. Oraevskii and V. A. Shcheglov, Zh. Eksp. Teor. Fiz., 59, 845 (1970) [Sov. Phys. – JETP, 32, 462 (1971)].
[5] A. N. Oraevskii and V. A. Shcheglov, Krat. Soobshch. Fiz., Sb. FIAN, No. 5 (1970).
[6] A. N. Oraevskii, V. P. Pimenov, and V. A. Shcheglov, Zh. Eksp. Teor. Fiz., 62, 89 (1972) [Sov. Phys. – JETP, 35, 48 (1972)].
[7] A. N. Oraevskii, V. P. Pimenov, and V. A. Shcheglov, Krat. Soobshch. Fiz., Sb. FIAN, No. 9, 7 (1971).
[8] N. N. Semenov, Chain Reactions [in Russian], Goskhimetkhizdat, Leningrad (1934).
[9] N. N. Semenov, Development of the Theory of Chain Reactions and Thermal Ignition [in Russian], Izd. Znanie, Moscow (1969).
[10] N. N. Semenov and A. E. Shilov, Kinet. Katal., 6, 3 (1965).
[11] A. A. Andronov, A. A. Vitt, and S. É. Khaikin, Theory of Oscillations [in Russian], GIMFL, Moscow (1959).
[12] A. N. Oraevskii, V. P. Pimenov, and V. A. Shcheglov, Preprint FIAN [in Russian], No. 115 (1972).

Direct and cascade four-photon parametric scattering of light in $LiIO_3$ crystals

S. M. Arakelyan, V. G. Tunkin, A. I. Kholodnykh, and A. S. Chirkin

M. V. Lomonosov Moscow State University

(Submitted August 27, 1973)
Zh. Tekh. Fiz., 44, 1253-1261 (June 1974)

Spontaneous parametric scattering of light (PSL) is a source of noise in parametric lasers and infrared frequency converters with nonlinear crystals. The present paper investigates the characteristics of four-photon PSL in one of the most interesting nonlinear crystals, $LiIO_3$. The results of experiments on the pumping of this crystal by a He−Ne laser ($\lambda_1 = 0.63\ \mu$) are presented. In noncentrosymmetric media, to which $LiIO_3$ belongs, three four-photon PSL mechanisms are possible: direct scattering on the cubic nonlinearity and two cascade processes on the quadratic nonlinearity through second-harmonic and idler generation. The principal aim of the work is to establish the dominant mechanism responsible for the scattering in $LiIO_3$. The effect is recorded using a coincidence-circuit technique. This technique gives a great improvement in the sensitivity of the measuring system over the usual one-channel recording, and enables pairs of correlated four-photon PSL photons to be distinguished against background phenomena. The experimental results in conjunction with a theoretical calculation indicate that the main scattering mechanism in the present case is a cascade process going through generation of an idler frequency.

INTRODUCTION. FORMULATION OF THE PROBLEM

Experimental investigations on the parametric scattering of light (PSL) date from 1967.[1-3] Since the publication of these papers much work has been carried out on this phenomenon in media with quadratic ($\hat{\chi}$) and cubic ($\hat{\theta}$) nonlinear susceptibilities. There are a number of reasons for the interest in PSL. First, it is a convenient tool for measuring the magnitudes of the nonlinear susceptibilities and their dispersion. This phenomenon can also be used to determine the tuning curves of parametric lasers, in which it plays the role of the initiating sources. Also, PSL limits the sensitivity of optical detectors that use nonlinear frequency conversion.

In connection with the interest manifest in recent times in processes involving nonlinear susceptibilities of higher order, considerable importance attaches to the question of the competition of different cascade transformations in multiphoton processes. For example, the magnitude of the pump threshold in four-photon parametric lasers utilizing cascade processes can be appreciably less than in the case of direct four-photon processes.[4-6]

Three-photon PSL processes are associated with the quadratic nonlinearity $\hat{\chi}$ of the medium, and four-photon processes with the cubic nonlinearity $\hat{\theta}$. Of the latter processes we mention in particular the process

$$\omega_1+\omega_1=\omega_s+\omega_a,\quad 2\mathbf{k}=\mathbf{k}_s+\mathbf{k}_a+\Delta, \tag{1}$$

where ω_1 is the pump frequency, ω_s and ω_a are the Stokes and antistokes frequencies of the scattered radiation, k_j are the wave numbers and Δ is the wave vector mismatch. Processes like (1) have been observed experimentally in refs. 7-12.

In noncentrosymmetric crystals ($\hat{\chi} \neq 0$) in addition to (1), there is the so-called cascade mechanism of four-photon scattering. This process is the result of two successive three-photon PSL processes. Such processes can go through excitation of the second harmonic ω_2

$$\left.\begin{aligned} &2\omega_1=\omega_2, && 2\mathbf{k}_1=\mathbf{k}_2+\Delta_2;\\ &\omega_2=\omega_s+\omega_a, && \mathbf{k}_2=\mathbf{k}_s+\mathbf{k}_a+\Delta' \end{aligned}\right\} \tag{2}$$

or through generation of the idler frequency ω_0

$$\left.\begin{aligned} &\omega_1=\omega_0+\omega_s, && \mathbf{k}_1=\mathbf{k}_s+\mathbf{k}_0+\Delta_s;\\ &\omega_0+\omega_1=\omega_a, && \mathbf{k}_0+\mathbf{k}_1=\mathbf{k}_a+\Delta_a. \end{aligned}\right\} \tag{3}$$

Process (3) in the ADP crystal has been studied by Andrews et al.[13] A detailed theoretical discussion of processes of the form (2) and (3) is given by Klyshko and Nazarova.[4] These authors also estimate the ratio of the scattering amplitudes in processes (1) and (3) and conclude that in certain cases cascade scattering on $\hat{\chi}$ is more efficient compared with direct scattering on θ.

Very little has been published on the experimental aspects of this problem. It is therefore of interest to establish the mechanism of four-photon PSL in one of the most promising nonlinear crystals, lithium iodate ($LiIO_3$). The bulk of the work reported in the present paper is devoted to this topic.

Another aim of the work is to develop a sensitive recording system for PSL processes. The usual single-channel photoelectric recording system makes essentially no use of such properties of PSL as the creation of completely correlated photon pairs. Single-channel detection does not offer much promise as far as improvement of the sensitivity is concerned. On the other hand, the correlation of the photon pairs can be used to experimentally distinguish PSL from other forms of scattering and to determine the specific scattering mechanism. Accordingly,

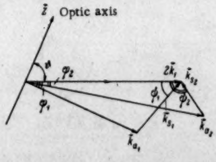

Fig. 1. Four-photon wavevector matching in principal plane of crystal for a varying frequency ω_a. φ_1, φ_2 are the angles between the direction of propagation of the pump wave $\mathbf{k}_1$ and the antistokes wave $\mathbf{k}_a$ for the different values of ω_a; ψ_1, ψ_2 are the angles for the Stokes wave; θ is the angle between the optic axis of the crystal $\mathbf{z}$ and $\mathbf{k}_1$.

in the present work we utilize a two-channel counting technique with subsequent application of a coincidence circuit. As a result, we can experimentally record four-photon PSL in $\mathrm{LiIO_3}$ using pumping with a cw He–Ne laser ($\lambda_1 = 0.63\mu$) with a power of 20 mW. (For comparison we mention that to date, on account of the small conversion coefficient, four-photon PSL has been investigated only in the field of pulsed Q-switched lasers with powers of the order of several megawatts). The scattering power at the antistokes frequency ω_a is $P_a = 9 \cdot 10^{-16}$ W. A corresponding theoretical calculation of the tuning and power characteristics of the various four-photon PSL mechanisms implies that the detected P_a corresponds to cascade PSL on the quadratic nonlinearity, the scattering proceeding through generation of the idler frequency.

TUNING CURVES

This section deals with the tuning curves for four-photon parametric scattering in $\mathrm{LiIO_3}$. As is well known, in PSL the intensity of the radiation at a given frequency has a sharp maximum in directions defined by the phase-matching condition (1)-(3). The parametric frequencies ω_s and ω_a are arbitrary in principle and lie in the transparency bands of the medium. For noncollinear interaction, when the direction of the radiation at the scattered frequency makes a certain angle φ with the direction of the pump radiation, a continuous spectrum of frequencies is emitted in the φ direction. This contrasts with the case of collinear interaction ($\varphi = 0$), in which the frequencies ω_s and ω_a are determined by the orientation of the nonlinear medium relative to the direction of propagation of the pump wave.

The tuning curves for direct four-photon PSL (1) are calculated from the condition that $\Delta = 0$, which determines a certain conical surface. This condition limits the possible frequencies of emitted photons. Formally, this follows from the requirement that $|\cos \varphi| \leq 1$; the sign of the equality corresponds to the limiting values of the frequencies for photons emitted along the direction of the incident light.

1. First we consider the tuning curves when the interacting waves have the same polarization; this analysis also holds for an isotropic medium. If all the interacting waves have ordinary polarization, the phase-match surface $\Delta = 0$ is a circular cone whose axis is directed in the direction of propagation of the pump wave. A straightforward analysis leads to the following picture of the emission of the parametric frequencies ω_s and ω_a in the region of transparency of the crystal. When $\omega_s = \omega_a = \omega_1$ both the created photons are emitted in the forward direction (degenerate collinear interaction). As ω_a is increased a deviation from this direction is observed: With increasing ω_a the angle φ first increases and then decreases (Fig. 1). Finally, at a certain frequency $\omega_a' = \omega_1 + \tilde{\omega}$ ($\tilde{\omega} > 0$) determined by the scalar condition $k_a(\omega_1 + \tilde{\omega}) - k_s(\omega_1 - \tilde{\omega}) = 2k_1(\omega_1)$, the wave vectors $\mathbf{k}_a$ and $\mathbf{k}_s$ are antiparallel. The angle ψ between the directions of propagation of the photons ω_s and ω_1 varies from 0 to 180°; scattering for $\psi > 90°$ is called backward-wave scattering. (This sort of scattering was observed by Weinberg[8] in water). A frequency $\omega_a'(\omega_a' \leq 2\omega_1)$ at which scattering occurs at an angle $\psi = 180°$ always exists for transparent media.

2. If waves of different polarization participate in four-photon PSL, the region of variation of the antistokes frequencies ω_a is reduced as compared with the case considered above. Separate allowed regions of ω_a are possible here; the boundaries are given for values below ω_a'. In all these cases the boundary value of the frequencies ω_a and ω_s corresponds to propagation of the scattered waves in the pump direction.

The family of calculated tuning curves for process (1) in the $\mathrm{LiIO_3}$ crystal at a pump wavelength $\lambda_1 = 0.63\,\mu$ is shown in Fig. 2a (collinear interaction) and in Fig. 2b (noncollinear interaction). In the first case tuning is accomplished by varying the angle θ between the crystal optic axis and the direction of propagation of the pump wave. In the second, tuning is accomplished by varying the angles of observation φ and ψ. The curves of Fig. 2 are calculated utilizing the refractive index values of Nath and Haussühl.[14]

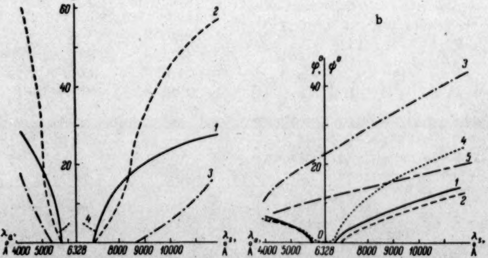

Fig. 2. a) Tuning curves for direct four-photon parametric scattering for different types of collinear interaction in $\mathrm{LiIO_3}$ crystal ($\lambda_1 = 0.63\ \mu$): $2k_1^0$: 1) $k_s^0 + k_a^e$; 2) $k_s^e + k_a^0$; 3) $k_s^e + k_a^e$; 4) $k_s^0 + k_a^0$; o and e denote ordinary and extraordinary waves respectively. b) Case of noncollinear interaction ($\lambda_1 = 0.63\ \mu$): 1) $2\mathbf{k}_1^e = \mathbf{k}_s^e + \mathbf{k}_a^e$, $\vartheta = 45°$; 2) $2\mathbf{k}_1^e = \mathbf{k}_s^e + \mathbf{k}_a^e$, $\vartheta = 90°$; 3) $2\mathbf{k}_1^e = \mathbf{k}_s^0 = \mathbf{k}_a^0$, $\vartheta = 90°$; 4) $2\mathbf{k}_1^0 = \mathbf{k}_s^0 + \mathbf{k}_a^0$, ϑ arbitrary; 5) $2\mathbf{k}_1^e = \mathbf{k}_s^0 + \mathbf{k}_a^e$, $\vartheta = 45°$; the values of the angles are given internal to the crystal.

In order to obtain a wide tuning range for collinear interaction in negative crystals ($LiIO_3$, for example), a pump wave with ordinary polarization must be used; for positive crystals, the pump wave must be polarized as an extraordinary wave.[10]

3. For the same pump waves and Stokes and antistokes waves, an obvious relationship holds between the wave-vector mismatches in the case of processes (1) and (2), (3), namely: $\Delta = \Delta_s + \Delta_a = \Delta_2 + \Delta'$. The tuning curves of process (1) ($\Delta = 0$) are thus the locus of points satisfying the condition $\Delta_s = -\Delta_a$ and $\Delta_2 = -\Delta'$. For processes (2) and (3) the case of double resonance is possible, when $\Delta_s = \Delta_a = 0$ and $\Delta_2 = \Delta' = 0$, which occurs on the curve of the intersection of the matching surfaces $\Delta_a = 0$ and $\Delta_s = 0$ or $\Delta_2 = 0$ and $\Delta' = 0$. In this case the matching condition of process (1) is automatically satisfied on this curve (compare with ref. 13). Thus, situations are possible in which the same frequencies ω_a and ω_s are created synchronously at the same angles for the cascade and the direct mechanisms of four-photon PSL.

It should be noted that in cascade processes (2) and (3), the frequency ω_0 or ω_2 may fall within the absorption band of the medium, making the calculation of the tuning curves more difficult.

EXPERIMENTAL METHOD AND RESULTS

1. As mentioned in the introduction, we measure four-photon parametric scattering in the $LiIO_3$ crystal by a photocounting technique in which signals at the frequencies ω_s and ω_a are recorded through separate channels with subsequent extraction of time-correlated pulses from both channels by a coincidence circuit.[15-17] A great improvement in the sensitivity of the system over the usual single-channel recording method is achieved by reduction of the noise level through the use of the coincidence circuit. An especially important feature of the present method is that the Stokes and anti-Stokes frequencies created simultaneously in the one event can be recorded. This becomes very significant in the case of cascade processes, when the scattering intensity at the frequency ω_a appearing in the second stage of the scattering is much smaller than the scattering intensity at frequency ω_s.

It should be noted that three-photon parametric scattering can not give coincidences; both the photons created in this case are Stokes photons and, after the spectrograph used in the experiment, they enter the same channel of the recording system. What is recorded in fact is the scattering power at the anti-Stokes frequency as the coincidence circuit generates a useful pulse only when an antistokes photon appears in one of the channels; this photon is correlated with the Stokes photon in the other channel. The detectors are two FÉU-79 photomultipliers, the measured quantum efficiencies of which are 5 and 1%, respectively. The resolving time of the coincidence circuit is 6 nsec.

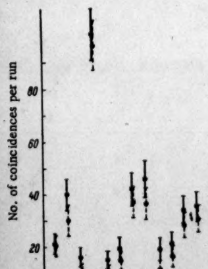

Fig. 3. Number of coincidences with crystal n_0 (solid bars) and normalized number of (noise) coincidences without crystal n_N (dashed bars) in various runs. The lengths of the bars correspond to the dispersion of the number of coincidences $2\sqrt{n_0}$ and $2\sqrt{n_N}$.

The sensitivity threshold of the recording system (the signal/noise ratio is unity) is determined in the experiment by the level of stray illumination from the laser, being 10^{-19} W for red light ($\hbar\omega = 3 \cdot 10^{-19}$ w). With this sensitivity it is possible to use the beam from a cw He–Ne laser ($\lambda_1 = 0.63\ \mu$); the power at the input to the nonlinear crystal $P_1 = 18$ mW.

2. In the experiment we observe the transformation $2\mathbf{k}_1 \rightarrow \mathbf{k}_s + \mathbf{k}_a$ in the $LiIO_3$ crystal. The optic axis of the crystal subtends an angle of 45° with the direction of propagation of the pump wave, which is an extraordinary wave. The geometry of the experiment is dictated by the need to satisfy two conditions: First, the frequencies ω_a and ω_s, for which the matching condition is satisfied, must lie within the region of sensitivity of the recording system; second, the magnitude of the working component of the nonlinear susceptibility tensor must be a maximum. The latter condition is satisfied when the parametric waves are also waves of extraordinary polarization. Accordingly, the main difficulty consists of reducing the stray illumination from the laser to a level comparable with the intrinsic noise of the photomultipliers. Two successive Fabry–Perot reflection etalons are used as a narrow-band light filter with selective absorption at the pump frequency. This reduces the number of coincidences from laser illumination by eight orders of magnitude. The illumination is reduced further by using a high-transmission spectrograph, at the output of which is located a mirror slot tuned for transmission of the pump radiation. The parametric radiation reflected from the planes of the slot goes to the photomultipliers through bandpass interference filters. The transmission coefficient of the entire optical system (the attenuation of the signal by the system) is 800 for the parametric frequencies.

The scattered radiation is collected in the range of angles from $\varphi_0 \simeq 0.3$ to $\varphi \simeq 3°$ within the crystal, which corresponds to wavelengths 0.68–0.75 μ for the Stokes components and to wavelengths 0.53–0.58 μ (Fig. 2b) for the anti-Stokes components.

3. The experimental procedure requires statistical processing of the results. The experiment consists of several runs of 45 min each. We measure the total number of coincidences n_0 (i.e., including both true coincidences from the parametric frequencies and noise coincidences) and the number of coincidences without the crystal n_N (noise coincidences). The intensity of the anti-Stokes scattering is determined from the amount by which n_0 exceeds n_N, i.e., from $n_a = n_0 - n_N$. The quantities n_0 and n_N are normalized to the same value of the product[1)] $n_{N1}n_{N2}$, where n_{Nj} is the number of noise pulses in each recording channel. (The number of coincidences n_N de-

pends only on the product $n_{N1}n_{N2}$ for small loading of the channels[18].

The experimental values of n_0 and n_N in various runs are given in Fig. 3. The value of n_a averaged over all runs is six coincidences per run. An estimate of the reliability of this experimental quantity n_a using Student's criterion (see ref. 18) gives a 98% confidence limit. We can thus assert that $n_a = 6$ coincidences per run is statistically significant. This value of n_a corresponds to a scattering power at the anti-Stokes frequency ω_a of $P_a^{\exp} = 9 \cdot 10^{-16}$ W measured immediately after the crystal (pump power $P_1 = 18$ mW). When allowance is made for the accuracy of measurement of the transmission coefficient of the optical system and the accuracy with which the quantum efficiency of the radiation detectors is determined, we find $P_a^{\exp} = (9 \pm 3) \cdot 10^{-16}$ W.

We conclude this section by pointing out an important experimental fact: Within the limits of accuracy of the experiment, the observed scattering power does not depend on the focusing of the pump radiation in the crystal.

DISCUSSION

In order to interpret the experimentally obtained value of the scattering power and to ascertain the specific scattering mechanism, the conditions of the experiment must be analyzed and the scattering intensity for the various four-photon parametric-scattering mechanisms (1)-(3) estimated.

However, we recall that our coincidence system discriminates against other possible mechanisms of creating both Stokes and anti-Stokes light photons in addition to (1)-(3) (thermal noise processes,[4,19] for example, which give rise to uncorrelated photons).

Let us now consider the power characteristics of four-photon PSL.

1. In the case of direct four-photon PSL on the cubic nonlinearity $\hat{\theta}$, the power P_Ω scattered per unit solid angle at the anti-Stokes frequency is given by the expression[20] (in the approximation of plane monochromatic waves)

$$P_\Omega = \frac{4\pi^2 \hbar \omega_a^4 \omega_s n(\omega_a) \theta^2 |v|}{c^6 n^2(\omega_1) n(\omega_s)} V S_1^2, \tag{4}$$

where $\theta = \Sigma e_{ai}\theta_{ijkl}e_{1j}e_{1k}e_{sl}$, e_m are the components of the unit polarization vector; $v = [(1/v_a)\cos(\varphi + \psi) - (1/v_s)]^{-1}$; v_s, v_a are the group velocities of the Stokes and anti-Stokes waves; V is the scattering volume; S_1 is the pump intensity and $S_1 = P_1/\pi r^2$, where P_1 is the pump power; πr^2 is the cross-sectional area of the pump beam; and $n(\omega)$ are the indices of refraction. The scattering power is thus proportional to the square of the pump power, is linearly dependent on the length of the nonlinear medium, and is inversely proportional to the area of the pump beam. Focusing of the pump beam can thus be used to increase the scattering intensity, unlike the case of three-photon PSL. For noncollinear interaction, however, the situation is complicated by the emergence of the rays from the interaction volume, which leads to a reduction of the coherence length in focusing. Allowance must be made for the effect of these two factors. Figure 4a shows the general form of the variation of anti-Stokes scattering power P_Ω with angle of observation φ for noncollinear interaction.

The total power P_a emitted at all anti-Stokes frequencies within a given receiver solid angle $\Delta\Omega$ is obtained by integrating expression (4). For small φ, allowing for the emergence of the rays from the interaction volume, we obtain

$$P_a = \frac{64\pi\hbar\omega_a^4\omega_s n(\omega_a)}{3c^5 n^2(\omega_s) n^2(\omega_1)} \left(\frac{1}{\varphi_0} - \frac{1}{\varphi}\right) \frac{\theta^2}{2r} P_1^2, \tag{5}$$

where P_1 is the power of the pump wave, 2r is the diameter of the pump beam, and φ_0 is the lower limit of integration (it is assumed that $\varphi_0 \geq 2r/L$, where L is the length of the crystal).

The quantity P_a represents the integrated scattering power collected in the angular range from φ_0 to φ. It can be seen from (5) that the scattering power can be increased by focusing the pump beam (compare with ref. 4). Figure 4b shows a plot of P_a as a function of the parameter φ/φ_0. Evidently, 90% of the total scattering power lies within an angle $\varphi \simeq 10\,\varphi_0$. Under the conditions of our experiment ($r = 60\,\mu$ and L = 3 cm) this corresponds to an angle $\varphi \simeq 3°$ (angles are given within the crystal).

2. For the case of cascade four-photon PSL on the quadratic nonlinearity $\hat{\chi}$, the scattering power does not depend on the focusing.[4] A theoretical comparison of the efficiency of cascade and direct four-photon PSL is given in refs. 4 and 21. It is shown in ref. 4 that for a transparent medium and a planar monochromatic pump wave, the ratio of the scattering amplitudes at the anti-Stokes frequency due to $\hat{\chi}$ (for example, through the idler wave λ_0) and due to $\hat{\theta}$ is given (for $\Delta = 0$) by

$$\frac{A_\chi}{A_\theta} = \frac{4\pi^2}{n(\omega_0)\Delta_a\lambda_0} \frac{\chi^2}{\theta} \tag{6}$$

(for $\Delta_a = 0$ the quantity Δ_a^{-1} is formally replaced by L/2).

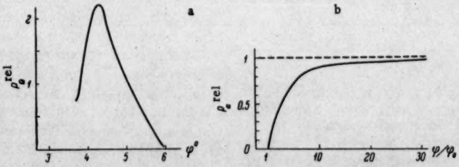

Fig. 4. a) Relative scattering power per unit solid angle P_Ω^{rel} versus angle of observation φ within $LiIO_3$ crystal for propagation of pump wave ($\lambda_1 = 0.63\,\mu$) along optic axis. b) Relative integral scattering power P_a^{rel} collected from scattering angles from φ_0 to φ versus ratio φ/φ_0.

Cascade conversion through the second harmonic [process (2)] in the present case goes more efficiently than conversion through the idler wave [process (3)] because of the joint effect of the strong absorption at the harmonic wavelength and the large wavevector mismatch in the $LiIO_3$ crystal at double the frequency of the pump wave $\lambda_1 = 0.63\ \mu$. Accordingly, we compare the efficiencies of the cascade process through the idler wave λ_0 and of direct four-photon PSL.

When all the interacting waves are extraordinary,[2] the maximum values of the working components of the nonlinear susceptibility tensors of $LiIO_3$ are $\chi \simeq 2.4 \cdot 10^{-8}$ cgs esu for the cascade process through the idler wave λ_0, and $\theta \simeq 2.1 \cdot 10^{-13}$ cgs esu for direct scattering. (The numerical values of the components of tensors $\hat{\chi}$ and $\hat{\theta}$ are taken from refs. 22-24; dispersion is ignored). These estimates assume that the Stokes and anti-Stokes photons are created at small angles relative to the direction of propagation of the pump wave. The angle between the direction of emission of the idler frequency and the pump frequency for $\Delta_a = \Delta_s = 0_s$ is about 10°, and the refractive index at the idler frequency (for example, $\lambda_0 \simeq 6\ \mu$) $n(\omega_0) \simeq 1.9$.

In the present case (6) is given by

$$\frac{A_\chi}{A_\theta} \simeq 1.4 \cdot 10^2. \tag{7}$$

Estimate (7) shows that in the present case cascade conversion in $LiIO_3$ goes much more efficiently than direct scattering.

3. Let us now compare the experimentally measured scattering power, $P_a^{\exp}$, with the powers calculated for direct scattering (P_a) and for cascade scattering through the idler wave ($P_{a,\chi}$).

In the case of four-photon parametric scattering on the cubic nonlinearity $\hat{\theta}$, the power of the radiation at the anti-Stokes frequency is given by expression (5). Under the conditions of the experiment [$P_1 = 18$ mW, $r = 60\ \mu$, $\theta = 2.1 \cdot 10^{-13}$ cgs esu, $\varphi_0 = 0.3°$, $\varphi = 3°$, $\omega_a \simeq \omega_s \simeq 3 \cdot 10^{15}\ \sec^{-1}$, $n(\omega_1) \simeq n(\omega_s) \simeq 1.8$] this leads to the value $P_a \simeq 2.5 \cdot 10^{-19}$ W. Thus, the experimentally measured power exceeds the power of scattering on $\hat{\theta}$ by more than three orders of magnitude:

$$P_a^{\exp}/P_a \simeq 3.6 \cdot 10^3. \tag{8}$$

A theoretical estimate for $P_{a,\chi}$ can be obtained with the aid of (7). In the cascade process, if the double matching condition is satisfied for one set of frequencies ω_s, ω_a, and ω_0, the power of the anti-Stokes emission is determined[20] by the angular width of the tuning curve $\Delta\theta$; in the direct process it is determined by the detection solid angle $\Delta\Omega$. As a result, for $\varphi \simeq 3°$

$$\frac{P_{a,\chi}}{P_a} = \frac{A_\chi^2}{A_\theta^2} \frac{\Delta\theta}{\Delta\Omega} \simeq 4.8 \cdot 10^3. \tag{9}$$

It can be seen that (8) and (9) are close in value. The difference is probably due to the fact that absorption at the idler frequency is ignored in (9). (For $LiIO_3$ the absorption coefficient is around $0.8\ \text{cm}^{-1}$ at $\lambda \simeq 6.0\ \mu$).

Thus, the measured power $P_a^{\exp}$ agrees with the model of a cascade process going through the idler wave.

The above estimates assume that cascade process (3) proceeds synchronously ($\Delta_a = \Delta_s = 0$); as already mentioned, this condition is satisfied if the refractive index $n(\omega_0) \simeq 1.9$ at $\lambda_0 \simeq 6\ \mu$, for example. Further, the $LiIO_3$ crystal has an absorption band from $\simeq 5.6$ to $6.5\ \mu$, for which the value of $n(\omega)$ is unknown; however, near the absorption band, at $\lambda \simeq 5.0\ \mu$, the refractive index $n \simeq 1.82$ (see ref. 25).

The double-matching conditions $\Delta_a = \Delta_s = 0$ must be satisfied, however, on account of the anomalous dispersion in the absorption region and the broad recorded spectrum of scattered waves, corresponding to a range of idler wavelengths from 3.3 to 6.7 μ. Also, an idler wave satisfying the double-matching condition can have extraordinary or ordinary polarization. However, for a cascade process involving an ordinary idler wave, the working component of the tensor $\chi = 2.8 \cdot 10^{-9}$ cgs esu is less than for an extraordinary wave $\chi = 2.4 \cdot 10^{-8}$ cgs esu. Thus, the main process in four-photon PSL in $LiIO_3$ is a cascade process going through an idler wave with extraordinary polization.

CONCLUSION

The results of our experiments can be summarized as follows.

1. The anti-Stokes and Stokes frequencies ω_a and ω_s are recorded by the measuring system. The corresponding photons go to different channels of the system (inorcoporating two photomultipliers) after separation in the spectrograph.

2. The frequencies ω_a and ω_s are correlated in time by feeding the signals from the photomultiplier outputs to a coincidence circuit.

3. The scattering power is determined from the amount by which the total number of coincidences exceeds the number of coincidences obtained with the crystal removed; it is $P_a^{\exp} = (6\text{–}12) \cdot 10^{-16}$ W. Within the limits of experimental error $P_a^{\exp}$ does not depend on the focusing of the pump radiation in the crystal.

These facts, in conjunction with the theoretical estimates (8) and (9), indicate that the recorded process in $LiIO_3$ is one of cascade parametric scattering through the idler wave [process (3)].

In order to observe direct scattering on the cubic nonlinearity $\hat{\theta}$, one must use a centrosymmetric medium, in which $\hat{\chi} = 0$ (see refs. 8-12), or a different experimental geometry such that two pump quanta are directed at a large angle to each other.[7] The experimental value of the observed scattering power coincides in this case with estimates via expression (5).

We thank S. A. Akhmanov for critical remarks and assitance, and D. N. Klyshko for discussion.

---

[1] The values of n_{N1} and n_{N2} averaged over 10 sec are measured in turn in the course of each run. Even slight drifts in laser power in the time of a run can be monitored in this manner.

[2)] It is shown later in this section that in our experiment the matching conditions for three-photon processes can be satisfied for such waves as a result of anomalous dispersion.

---

[1] S. A. Akhmanov, V. V. Fadeev, R. V. Khokhlov, and O. N. Chunaev, ZhETF Pis. Red., 6, 575 (1967) [JETP Lett., 6, 85 (1967)].
[2] D. Magde and H. Mahr, Phys. Rev. Lett., 18, 905 (1967).
[3] S. E. Harris, M. K. Oshman, and R. L. Byer, Phys. Rev. Lett., 18, 732 (1967).
[4] D. N. Klyshko and N. I. Nazarova, Zh. Eksp. Teor. Fiz., 58, 878 (1970) [Sov. Phys.—JETP, 31, 472 (1970)].
[5] I. V. Tomov, Vestn. MGU, No. 1, 47 (1969).
[6] A. P. Veduta and B. P. Krisanov, Zh. Eksp. Teor. Fiz., 56, 1175 (1969) [Sov. Phys.—JETP, 29, 632 (1969)].
[7] A. A. Grinberg, S. M. Ryvkin, P. M. Fishman, and I. D. Yaroshevskii, ZhETF Pis. Red., 7, 324 (1968) [JETP Lett., 7, 253 (1968)].
[8] D. L. Weinberg, Appl. Phys. Lett., 14, 32 (1969).
[9] J. G. Meadors, W. T. Kavage, and E. K. Damon, Appl. Phys. Lett., 14, 360 (1969).
[10] H. Ito and H. Inaba, Opto-Electron., 2, 81 (1970).
[11] H. Eichler and J. Knof, Zs. Phys., 241, 271 (1971).
[12] S. F. Giuliani, IEEE J., Quant. Electron., 8 (1972).
[13] R. A. Andrews, H. Rabin, and C. L. Tang, Phys. Rev. Lett., 25, 605 (1970).
[14] G. Nath and S. Haussühl, Appl. Phys. Lett., 14, 154 (1969).
[15] S. M. Arakelyan, V. G. Tunkin, A. I. Kholodnykh, and E. I. Shirkov, Sixth All-Union Conf. on Nonlinear Optics, Minsk, 1972.
[16] D. Bergnan and D. Weinberg, Phys. Rev. Lett., 25, 84 (1970).
[17] B. Ya. Zel'dovich and D. N. Klyshko, ZhETF Pis. Red., 9, 69 (1969) [JETP Lett., 9, 40 (1969)].
[18] V. I. Gol'danskii, A. B. Kutsenko, and M. I. Podgoretskii, The Statistics of Counts in the Recording of Nuclear Particles [in Russian], GIFML, Moscow (1959).
[19] Yu. A. Il'inskii and V. M. Petnikova, in: Quantum Electronics [in Russian], No. 5(11), 124, Izd. Sov. Radio, Moscow (1972).
[20] D. N. Klyshko, Zh. Eksp. Teor. Fiz., 55, 1006 (1968) [Sov. Phys.—JETP, 28, 522 (1969)].
[21] V. A. Bushuev. Vestn. MGU, No. 2, 177 (1973).
[22] L. B. Meisner, Fiz. Tverd. Tela, 14, 2220 (1972) [Sov. Phys.—Solid State, 14, 1922 (1973)].
[23] F. R. Nash, J. G. Bergman, G. D. Boyd, and E. H. Turner, J. Appl. Phys., 20, 520 (1969).
[24] M. Okada, Appl. Phys. Lett., 18, 451 (1971).
[25] A. S. Campilo and C. L. Tang, Appl. Phys. Lett., 16, 242 (1970).

Vaporization and boiling of liquid metal in an exploding wire

M. M. Martynyuk

Patrice Lumumba People's Friendship University, Moscow

(Submitted November 28, 1972; resubmitted August 9, 1973)
Zh. Tekh. Fiz., 44, 1262-1270 (June 1974)

Using the thermodynamics and kinetics of vaporization and boiling it is shown that the main factor in the electrical explosion of a wire is explosive boiling of superheated liquid metal. When certain conditions are satisfied the initial point of the electrical explosion must be in the neighborhood of the boundary for thermodynamic stability of the liquid metal phase.

Electrical explosion of a wire occurs in heating by a sufficiently strong current pulse. Thus far, there is no single theory which can explain all the phenomena observed in this process. At the same time, an explanation of the nature of an electrical explosion is important not only from the purely scientific point of view, but for the practical use of exploding wires (plasmotrons, pulsed tubes for laser pumping).

The experimental data indicate that the electrical explosion of a wire is associated with the conversion of a portion of the liquid metal into vapor and then into the plasma state; therefore, it is important to consider this phenomenon from the viewpoint of the thermodynamics and kinetics of the liquid–vapor phase transition, which is the purpose of the present study. To simplify the problem, we first neglect many factors which accompany the pulsed heating of a wire by a current (skin effect, magnetic pressure, and MHD instabilities); their effect will be discussed at the end of the paper in a description of the nature of an electrical explosion. The one factor on which we concentrate is the heating rate. It will be shown that for a given rate of heating considerable superheating of the liquid metal phase above its boiling point is possible; we therefore consider first certain problems in the thermodynamics of superheated liquids.

1. SUPERHEATED LIQUID AND ITS THERMODYNAMIC STABILITY BOUNDARY

According to Gibbs' thermodynamic theory,[1] there are two upper limits to the existence of the liquid phase; the binodal line, the equilibrium curve for the liquid and vapor, and the spinodal line, the boundary of thermodynamic stability of the liquid phase in continuous change. Between these boundaries there is a region of metastable (superheated, overexpanded) liquid. In crossing the spinodal line loss of stability of the liquid phase occurs; therefore at points on the spinodal line the thermodynamic stability coefficients go through zero:[2]

$$-\left(\frac{\partial p}{\partial V}\right)_T=0,\quad \left(\frac{\partial T}{\partial S}\right)_p=0 \tag{1.1}$$

(T is the temperature, S the entropy, p the pressure, and V the volume).

Since these coefficients are inversely proportional to the fluctuations[3]

$$-\left(\frac{\partial p}{\partial V}\right)_T=\frac{kT}{\overline{V^2}-\overline{V}^2},\quad \left(\frac{\partial T}{\partial S}\right)_p=\frac{kT^3}{\overline{H^2}-\overline{H}^2} \tag{1.2}$$

(k is the Boltzmann constant and H is the enthalpy), a sharp rise in the fluctuations in the liquid occurs near the spinodal line, which is also a reason for its breakdown over the entire volume. In the neighborhood of the spinodal line the electrical resistance of a liquid metal should rise sharply because of electron scattering by density fluctuations and because of localization of electron conductivity in small volumes of the liquid. To the right of the spinodal line (see Fig. 1) there is a region of unstable states for which the phase stability coefficients are negative; these states can only be realized in pronounced nonequilibrium processes such as explosions.

The van der Waals equation

$$\pi=\frac{8\tau}{3\varphi-1}-\frac{3}{\varphi^2} \tag{1.3}$$

($\pi = p/p_k$, $\tau = T/T_k$, $\varphi = V/V_k$; the subscript "k" refers to critical parameters) according to Eq. (1.1) yields the following equation for the spinodal line;

$$4\tau_c\varphi_c^3-9\varphi_c^2+6\varphi_c-1=0 \tag{1.4}$$

(the subscript "c" refers to the spinodal line). Fürth[4] obtained the following expression for the spinodal line on the basis of the statistical theory for vacancies in a superheated liquid:

$$p-p_c=1.32\sigma^{3/2}(kT)^{-1/2}, \tag{1.5}$$

where p and p_c are the pressures at points on the binodal and spinodal lines for the temperature T; σ is the surface tension at the vapor–liquid boundary for that temperature. Skripov has pointed out a number of important properties of the spinodal line.[5]

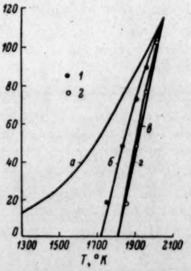

Fig. 1. State diagram for cesium in the high-temperature region. a) Binodal line from experimental data[6]; b) van der Waals spinodal line; c) Fürth spinodal line; d) straight-line approximation to spinodal line. Points are calculated from the theory for homogeneous nucleation; 1) 1; 2) $4\cdot10^{23}$.

Figure 1 is a state diagram for liquid cesium showing the binodal line according to experimental data[6] and the spinodal lines calculated from the van der Waals and Fürth equations. The values of σ needed for the calculation are obtained by linear extrapolation of data from ref. 7. As is evident, the Fürth and van der Waals lines in the figure do not coincide. It has been shown[5] that the Fürth spinodal line agrees better with experimental data in the case of organic liquids and thus one can assume that the Fürth spinodal line is also closer to reality in the case of liquid metals. The cesium spinodal line can be closely approximated by a straight line passing through the intersection of the Fürth spinodal line with the T axis (T_c = 1806°K = $0.9T_k$) and through the critical point (see Fig. 1). [For cesium, T_k = 2033°K and p_k = 116 bars (ref. 6).] The slope of this line in the reduced coordinates π, τ is 10, which is in practical agreement with the slope of the experimentally measured line for maximum superheating of organic liquids.[5] Thus one can write for the cesium spinodal line

$$\frac{p_c}{p_k}=\frac{10T_c}{T_k}-9. \tag{1.6}$$

For cesium, the melting temperature T_f = 301.8°K and the temperature for normal boiling T_0 = 955°K; Eq. (1.6) indicates that the maximum relative superheating for a continuous change in the liquid phase of cesium at p = 1 atm is $\beta_c = (T_c - T_0)/T_0 = (\tau_c - \tau_0)/\tau_0 = 0.89$; in this case the temperature range of the liquid state increases by a factor $(T_c - T_f)/(T_0 - T_f) = 2.3$ as compared to the range for discontinuous change.

2. HOMOGENEOUS NUCLEATION IN A SUPERHEATED LIQUID AND REALIZATION BY PULSED HEATING

The creation of homogeneous vapor nuclei in a defect-free volume of superheated liquid is accompanied by an increase in the Gibbs free energy; this process is possible because of fluctuations in the superheated liquid. In the formation of a spherical critical nucleus this increase is[8]

$$\Delta G_k=\frac{16\pi\sigma^3}{3g^2}, \tag{2.1}$$

where g is the difference between G_L the free energy per unit mass of the superheated liquid and G the free energy of the vapor, calculated per unit volume of the vapor; the parameter g characterizes the depth of penetration into the region of metastable states.

A given metastable state at the point (p_0, T) can be reached in two ways: a) by reducing the pressure from p to p_0 at constant T (p is the pressure of saturated vapor at the temperature T); b) by raising the temperature from T_0 to T at constant p_0 (T_0 is the boiling point at the pressure p_0). In the first case we obtain an expression for g by expansion of G_L and G in a series at the point (p, T) over the range ($p - P_0$); the linear approximation yields

$$\Delta G_k=\frac{16\pi\sigma^3}{3\left[\left(1-\frac{\rho}{\rho_L}\right)(p-p_0)\right]^2}, \tag{2.2}$$

where ρ_L and ρ are the liquid and vapor densities at the point (p, T). For the second case, a similar expansion of G_L and G at the point (p_0, T_0) over the range $T - T_0$ with $p = p_0$ constant leads to

$$\Delta G_k=\frac{16\pi\sigma^3}{(3\rho_0\lambda_0\beta)^2}, \tag{2.3}$$

where ρ_0 is the density of saturated vapor, λ_0 is the specific heat of vaporization at the point (p_0, T_0) and $\beta = (T - T_0)/T_0$ is the relative superheat. Equation (2.3) indicates that a reduction in G_k occurs as the superheating increases; consequently the probability for the formation of a homogeneous nucleus increases.

The rate of homogeneous nucleation at a temperature T is, according to classical theory,[9]

$$I=B\exp\left[-\frac{\Delta G_k}{kT}\right], \tag{2.4}$$

where B is a function which depends weakly on temperature and pressure in comparison with the exponential factor; only the order of magnitude of B is important in the calculation of I. The Becker–Dehring–Volmer theory[9] using experimental data for Fürth spinodal points far from the cesium critical point gives $B = 1.5 \cdot 10^{32}$ cm^{-3} · sec^{-1}. For this value of B two series of points on the cesium p–T diagram are calculated using Eqs. (2.2) and (2.4) (see Fig. 1) for two values of I; in the calculation, experimental data are used for σ (ref. 7), λ (ref. 10), ρ and ρ_L (refs. 6, 11). The first series corresponds to a value I = 1 cm^{-3} · sec^{-1} and the second to I = $4 \cdot 10^{23}$ cm^{-3} · sec^{-1} (for the laser value of I, there arises in liquid Cs in 1 μsec a number of homogeneous nuclei which is 0.01% of the total number of atoms and approximately corresponds to the condition for an electrical explosion). In the first case the points fall on the van der Waals spinodal line and in the second case, on the Fürth spinodal line. These calculations show that I increases rapidly during heating of a superheated liquid: for p = 1 atm, I for Cs varies from 1 to $4 \cdot 10^{23}$ · cm^{-3} · sec^{-1} over the comparatively narrow temperature range from 1720 to 1806°K. The calculations also show that considerable superheating above the boiling point is necessary for the realization of homogeneous nucleation in liquid metal ($I \geq 1$ cm^{-3} · sec^{-1}).

Equation (2.4) is applicable to stationary homogeneous nucleation. The nucleation rate I(t) under nonstationary conditions is related to I by[12]

$$I(t)=I\exp\left[-\frac{\tau}{t}\right], \tag{2.5}$$

where t is time and τ is the time for establishment of stationary nucleation after instantaneous superheating of the liquid. For ordinary liquids and moderate superheating, estimates[5,8] of τ give value of 10^{-8}–10^{-7} sec.

Significant superheating of the liquid and homogeneous nucleation are not achieved at low rates of heat deposition, since practically all the heat goes into the growth of heterogeneous vapor nuclei (ordinary boiling) which arise in the liquid at already existing centers (for example, gaseous inclusions) at insignificant superheating. The number of these centers in the liquid is comparatively small and depends weakly on temperature. At a sufficiently high heating rate the time for superheating the liquid is small and the mass of material which is vaporized within heterogeneous nuclei will be insignificant; therfore, the achievement of high superheating and intense homogeneous nucleation is possible. This boiling mode (shock mode) is discussed by Skripov and Pavlov.[13] In organic liquids and water this mode is realized by through pulsed heating of a platinum wire submerged in the liquid; in this case the points of violent boiling of the superheated liquid are in good agreement with the Fürth spinodal line.

We estimate the heating rate for which significant superheating of the liquid metal is achieved along with explosive boiling created by a sharp increase in the number of homogeneous vapor nuclei. We assume that the growth rate of the vapor bubbles is limited only by the vaporization kinetics; this assumption is obviously completely valid for an exploding wire. According to the Hertz–Knudsen equation,J, the molecular flux of material vaporized from the surface of a liquid at temperature T is[8]

$$J=\frac{\alpha(p-p_0)}{(2\pi mkT)^{1/2}}, \tag{2.6}$$

where α is the vaporization coefficient, m is the mass of the vapor molecule, k is the Boltzmann constant, p is the pressure of saturated vapor at the temperature T, and p_0 is the vapor pressure above the surface of the liquid. If the liquid is superheated instantaneously from the boiling point T_0 to T with $p = p_0 = \text{const}$, Eqs. (2.2) and (2.6) show that the rate of vaporization within a spherical bubble produced far from the critical point is

$$\frac{dM}{dt}\frac{\alpha m\lambda_0\rho_0 S\beta}{(2\pi mkT)^{1/2}},$$

where dM is the mass of material vaporized in time dt. If the volume of the bubble is V and the mass of vapor is M, the surface area S is

$$S=(36\pi V^2)^{1/3}=\left(\frac{36\pi}{\rho^2}\right)^{1/3}M^{2/3},$$

where ρ is the vapor density in the bubble at a temperature T. Making the substitution $\beta = \gamma t^n/T_0$ (t is the time taken in heating liquid metal from T_0 to T; γ and n are constant), we obtain

$$M^{-2/3}dM=\frac{K\gamma t^n}{T_0}dt, \tag{2.7}$$

where

$$K=\frac{\alpha m\lambda_0\rho_0(36\pi)^{1/3}}{(2\pi mkT)^{1/2}\rho^{2/3}}, \tag{2.8}$$

K is a weakly varying function of T and we shall take it to be a constant. Through integration of Eq. (2.7) we obtain an expression for ε, the fraction of the liquid which is vaporized within all heterogeneous nuclei in heating from T_0 to T,

$$\varepsilon=C\left[\frac{3K\gamma}{T_0(n+1)}\right]^3 t^{3(n+1)}, \tag{2.9}$$

where C is the number of identical heterogeneous nuclei per unit mass of liquid; it is assumed C is independent of temperature. If ε_0 is the maximum permissible value of ε, then for $\varepsilon \le \varepsilon_0$ and $n = 1$ we find a condition for the heating rate γ for which a superheat β_C close to the maximum is possible,

$$\gamma \geqslant \frac{3kT_0C^{1/3}\beta_c^2}{2\varepsilon_0^{1/3}}. \tag{2.10}$$

When cesium is heated at a pressure p = 1 atm, $\beta_C = 0.89$ and $k = 5.2\cdot10^4\ \text{deg}^{1/3}\cdot\text{sec}^{-1}$ (for $\alpha = 1$). Assuming $C = 10^2\ \text{deg}^{-1}$ and $\varepsilon \le 10^{-2}$, from Eq. (2.10) we find that $\gamma \ge 10^9$ deg/sec, which corresponds to a pulse heating time of about 1 μsec.

To evaluate the sufficiency of the condition $\gamma \ge 10^9$ deg/sec it still is necessary to consider vaporization from the free surface of the metal. The Hertz–Knudsen equation shows that the rate of displacement of the interphase boundary, $U = I/n_L$ (n_L is the number of atoms of liquid per unit volume), for cesium near the spinodal line and p = 1 atm is about 10 m/sec. At this velocity the interphase boundary shifts by 10^{-3} mm in 0.1 μsec and this means that vaporization of metal from the free surface of the liquid can be neglected when $\gamma \ge 10$ deg/sec.

Equations (2.8) and (2.10) show that for metals containing impurities which are adsorbed on the surface, explosive boiling can be realized at lower values of γ than for pure metals; this is explained by the effect of those impurities on the reduction of the vaporization coefficient α. (Knudsen[14] has observed a reduction in α from 1 to 10^{-3} for mercury contaminated by surface impurities.)

3. NATURE OF ELECTRICAL EXPLOSION

The entire process of heating a wire with a current pulse lasting 10^{-6}–10^{-4} sec is often called an electrical explosion, but experimental facts indicate that the true explosion begins at a time at which the voltage on the specimen increases abruptly, and the current falls under conditions which exclude surface discharge and mechanical breakdown of the specimen. At this point a sharp increase is observed in the velocity of the shock wave created in the surrounding medium;[15] this is then taken to be the initial point of the electrical explosion.

In the description of the electrical explosion of a wire it is important to know the pressure acting on the surface of the wire during the heating pulse; only when this pressure is below the critical value are superheating and explosive boiling of the liquid phase possible (see Fig. 1). We now estimate this pressure for a wire heated in air.

In this case the equilibrium pressure of saturated vapor cannot be established above the surface of the wire because the heating time is short and the vapor can expand into the surrounding air. However, the vapor flux leaving the surface of the metal will produce a reactive pressure given by

$$p_J=\frac{\alpha p}{2\pi}. \tag{3.1}$$

as follows from Eq. (2.6) when $p_0 = 0$.

In a liquid conductor of radius r_0 carrying a current i, the magnetic pressure at a distance r from the axis is

$$p_m=\frac{\mu\mu_0 i^2}{4\pi^2 r_0^2}\left(1-\frac{r^2}{r_0^2}\right) \tag{3.2}$$

(μ is the magnetic permeability of the conductor material, $\mu_0 = 4\cdot10^{-7}$ H/m). When $r \to r_0$, $p_m \to 0$, i.e., the magnetic pressure is close to zero in the surface layer of the metal. The pressure p_{in} produced by the inertia of the surrounding air in thermal radial expansion of the wire by an amount Δr is $p_{in} = \rho_a v \Delta r$ in accordance with the acoustic equation (ρ_a is the air density and v is the velocity of sound in air); this quantity is small and can be neglected. Thus, only the reactive pressure p_p and atmospheric pressure p_{at} act on the surface of the wire. The reactive pressure is a maximum for pure conductors ($\alpha = 1$); for "dirty" conductors, $\alpha \leq 1$ and p_p is insignificant. In any case, $p_p < p$ and therefore the process of pulsed heating of the surface of a conductor in air, contrary to the ideas of David,[16] does not go along the binodal line, but crosses it and penetrates into the region of metastable liquids (see Fig. 1). Heating of the surface of a "dirty" conductor is roughly isobaric for $p_0 = p_{at}$.

To explain the nature of an electrical explosion from the viewpoint of the kinetics of the liquid–vapor phase transition, we start with the following simplifying assumptions: 1) MHD instabilities, magnetic pressure, and skin effect are unimportant; 2) the heating rate satisfies the condition (2.10) but is not so large as to break down the stationarity of homogeneous nucleation [see Eq. (2.5)]. We now show that under these assumptions the explosion point must lie in the neighborhood of the spinodal line.

As was shown above, pulsed heating must be accompanied by crossing of the binodal line and penetration into the region of metastable states. The heating of the metastable phase proceeds for a comparatively long time when only heterogeneous vapor nuclei are present; these have an insignificant effect on vaporization and boiling when the condition (2.10) is satisfied. Considerable superheating is required before the first homogeneous nuclei are created in the metal; thereafter the number of such nuclei increases in avalanche fashion. This state in the metastable phase can be achieved by nearly maximum superheating (see Fig. 1), in which the activation energy for the formation of a homogeneous critical nucleus (2.3) is reduced so much because of superheating that it becomes comparable with the fluctuation energy (1.2); therefore the dominant boiling effect is the fluctuation mechanism for the formation of vapor nuclei. A sharp rise in the number of homogeneous nuclei produces a rapid increase in the volume of the specimen, leading to the creation of a shock wave in the surrounding medium. At the same time, there is a pronounced increase in the electrical resistance of the conductor which also leads to a current discontinuity under suitable conditions (for example, an explosion in a dense atmosphere of inert gas). At the beginning of the discontinuity the specimen is in the form of a dense metallic vapor containing drops of superheated liquid; vaporization of these drops continues because of superheat energy. When the metal vapor expands to the extent that ionization becomes possible, a second current pulse occurs.

If an explosion occurs in a liquid dielectric and is accompanied by current cutoff at the point of explosion, an aerosol consisting of fine metal particles 0.01-0.06 μ in size remains in the dielectric.[17] The later in the explosion the current is cut off, the finer the aerosol particles, since the greater number of homogeneous nuclei leads to a finer subdivision of the metal.

For the conditions assumed above, therefore, the initial point of an electrical explosion must be in the immediate vicinity of a point on the spinodal line; this gives the point a completely definite thermodynamic meaning and is in agreement with the existence of an "energy threshold" for an electrical explosion.[19] An electrical explosion is, in fact, a thermodynamic explosion which consists of the transition of a metastable superheated liquid into a two-phase state. If the external pressure varies, the curve produced by the electrical explosion points lies close to the spinodal line. The spinodal line calculated above for cesium satisfies the rule for thermodynamic similarity when compared with the spinodal line found experimentally for a number of organic liquids.[5] If the existence of thermodynamic similarity for metals is assumed by analogy the electrical explosion of a metal should occur at temperatures satisfying Eq. (1.6).

A measure of the metastability of a liquid heated from the boiling point T_0 to T at a constant pressure p_0 is the quantity g_L, which is the difference between the free energy of the liquid and that of its saturated vapor at the temperature T calculated per unit mass. By analogy with Eq. (2.3)

$$g_L = \lambda_0 \beta. \tag{3.3}$$

For maximum superheating of cesium at p_0 = 1 atm, $g_L = 0.89\,\lambda_0$.

A measure of energy deposition during the transition of a metastable liquid into the two-phase state is the excess enthalpy of the superheated liquid $H(T) - H(T_0)$ which leads to vaporization of the liquid. In a rapid transition to the state defined by the point p_0 the fraction of vaporized liquid $x = [H(T) - H(T_0)]/\lambda_0$. For Cs, $x \approx 0.4$ at p = 1 atm. Thus in the electrical explosion of a wire in air the energy released can be roughly 40% of the heat of vaporization. With conversion to unit initial volume this amounts to ~ 4500 cal/cm^3 for Cu and ~ 8000 cal/cm^3 for W, which exceeds the energy release in the explosion of TNT (1460 cal/cm^3). If one recalls that the electrical explosion occurs in a time less than 1 μsec and that the duration of a chemical explosion is greater,[18] it follows that the power in an electrical explosion is greater than the power of conventional chemical explosives.

As follows from Fig. 1 and Eq. (3.3), the energy β_L released in an electrical explosion is reduced by the reduction in λ_0 and β_c when the external pressure is increased. When $p \geq p_k$ then $\beta_L = 0$, i.e., critical and supercritical transition of a liquid metal into the gaseous state[21] is not accompanied by superheating of the liquid phase and by the release of energy during pulsed heating; therefore it should not be called an explosion.

The possibilities of superheating of the liquid metal and explosive boiling in an electrical explosion have been discussed qualitatively by Chace;[22] however, Chace does not discuss kinematics of the liquid metal–vapor transition. Subsequently, Chace rejected this idea[23] and adopted the David viewpoint of the nature of an electrical explosion,[16] which does not agree with the present paper.

The picture of an electrical explosion given above is somewhat idealized since various factors are not taken into account. We first consider the effect of magnetic pressure on the process. As follows from Eqs. (3.1) and (3.2), in pulsed heating of a wire by a current only a thin layer of metal near the surface of the wire is at a pressure equal to $p_{at} + p_p$; the pressure increases toward the axis. Consequently, the explosive boiling of superheated liquid metal first occurs in this layer, after which the boiling front is rapdily displaced toward the axis of the wire. The time at which the boiling front reaches the axis also corresponds of the boiling front, which is determined by the rate of homogeneous nucleation (2.4), must be somewhat greater, in the neighborhood of a spinodal point, than the rate of displacement of the interface boundary during vaporization, $u = J/n_L$, which is determined by the Hertz–Knudsen equation (2.6). It is obvious that the displacement of the boiling front we have discussed is significantly different from the so-called "ablation"[23] which is observed with pronounced skin effect.

A stratification structure has been observed in x-ray shadowgraphs of exploding wires after the initiation of explosion. These pictures indicate that the explosion of a wire does not occur simultaneously along its length, but rather in separate cross sections with an alternation of exploding sections, and sections in which the metal remains liquid. From the standpoint of the theory developed here, the creation of a stratified structure can be explained as follows. In pulsed heating of a liquid conductor a sausage MHD instability can be excited for a short time (0.1-0.2 μsec). At the constrictions the specific rate of heat deposition and the temperature are greater; therefore maximum superheating will be achieved earlier at those points, and these become local centers for electrical explosion.

Explosive boiling of a metal is obviously not restricted to the surface of a conductor but can also occur in deeper layers. The latter is possible in the case where current cutoff in the circuit occurs as the surface layer approaches the spinodal. This leads to a disappearance of the magnetic compression at the internal layers and to a displacement of material from the axis in a radial direction. As a result of this displacement and the effects of inertial forces, the initial compression of material on the axis is replaced by rarefaction,[24] leading to earlier intense homogeneous nucleation in that region. The magnetic pressure itself may also be a cause for the "internal" explosion; the internal, more compressed layer has a higher electrical conductivity and consequently can be superheated more than layers near the surface.

What has been said here indicates the effect of magnetic pressure on an electrical explosion may appear in various forms. However, one can show on the basis of Eq. (1.6) that in any case, electrical explosion of any layer of the metal under positive pressure should occur in the comparatively narrow temperature range from $0.9T_k$ to T_k.

In conclusion, we point out once more that the scheme proposed here for an electrical explosion is realistic only when the heating rate satisfies the conditions specified above. For rates smaller than the value given by Eq. (2.10) the liquid conductor breaks down at insignificant superheating because of the growth of heterogeneous vapor nuclei. Breakdown can also occur at an earlier stage because of the screw instability.[19] In this case the abrupt increase in voltage may not have any thermodynamic meaning.

If the heating rate is so great that the stationarity (2.5) for homogeneous nucleation breaks down, it is impossible to apply any results from equilibrium thermodynamics to the system. In that case, the initial point for the abrupt rise in electrical resistance will be located in the region of unstable states to the right of the spinodal line. These states can be realized with current pulse lengths below 10^{-7} sec.

---

[1] J. W. Gibbs, Scientific Papers, Vol. 1, Thermodynamics, Dover, New York.

[2] V. K. Semenchenko, Selected Topics in Theoretical Physics [in Russian], Izd. Prosveshchenie, Moscow (1966).

[3] T. L. Hill, Thermodynamics of Small Systems, Part 2, Benjamin, N. J. (1964).

[4] R. Fürth, Proc. Cambridge Phil. Soc., 37, 252 (1944).

[5] V. P. Skripov, Metastable Liquids [in Russian], Izd. Nauka, Moscow (1972).

[6] V. A. Alekseev, V. G. Ovcharenko, Yu. F. Ryzhakov, and A. P. Senchenkov, Equation of State for Cesium in the Pressure Range 20-600 Atm and the Temperature Range 500-2500°C [in Russian], I. V. Kurchatov Institute of Atomic Energy, Moscow (1970).

[7] I. Bohdansky and H. E. I. Achins, J. Inorg. Chem., 29, 2173 (1967).

[8] D. Hirs and G. Pound, Evaporation and Condensation, Usp. Fiz. Met., 11, Izd. Metallurgiya, Moscow (1966).

[9] O. Volmer, Kinetik der Phasenbildung, Steinkopf, Leipzig (1939).

[10] R. G. Ross and D. A. Greenwood, Prog. Mater. Sci., 14, 173 (1969).

[11] V. S. Korshunov, A. P. Senchenkov, E. I. Asinovskii, and A. G. Kynavi, Teplofiz, Vys. Temp., No. 6, 1288 (1970).

[12] Ya. B. Zel'dovich, Zh. Eksp. Teor. Fiz., 12, 525 (1942).

[13] P. A. Pavlov and V. P. Skripov, Teplofiz. Vys. Temp., 3, 109 (1965); 8, 579, 833 (1970).

[14] M. Knudsen, Ann. Phys., Fourth Series, 47, 697 (1915).

[15] F. D. Bennett, in: Progress in High Temperature Physics and Chemistry, 2, (C. A. Rouse, ed.), Pergamon, New York (1966).

[16] E. David, Zs. Phys., 150, 162 (1958).

[17] S. V. Lebedev and A. I. Savvatimskii, Teplofiz. Vys. Tem., 8, 524 (1970).

[18] A. G. Gorst, Powder and Explosives [in Russian], Oborongiz, Moscow (1957).

[19] K. B. Abramova, V. P. Valitskii, Yu. V. Vandakurov, N. A. Zlatin, and B. P. Peregud, Dokl. Akad. Nauk SSSR, 167, 778 (1966) [Sov. Phys. – Dokl. 11, 301 (1966)].

[20] V. M. Kul'gavchuk and G. A. Novoskol'tseva, Zh. Tekh. Fiz., 36, 549 (1966) [Sov. Phys. – Tech. Phys., 11, 406 (1966)].

[21] M. M. Martynyuk and N. F. Ganzhela, Izv. Vuz. Fizika, No. 3, 30 (1970).

[22] W. Chace, in: Exploding Wires, Vol. 1, Plenum, New York (1959).

[23] W. Chace, Przeglad Electrotechniczny, 43, 134 (1967).

[24] T. Korneff and W. Chace, Rev. Sci. Inst., 42, 1184 (1971).

Approximate similarity relations in the electrical explosions of underwater conductors

E. V. Krivitskii and V. K. Sholom

Design and Construction Bureau of Electrohydraulics,
Academy of Sciences of the Ukrainian SSR, Nikolaev

(Submitted November 9, 1973; resubmitted August 13, 1973)
Zh. Tekh. Fiz., 44, 1271-1276 (June 1974)

An attempt is made to generalize the available experimental data to obtain similarity conditions for the electrical characteristics for the explosion of conductors for the case in which the conductors do not explode and for the case in which there is no current pause. The explosion of a conductor can be arbitrarily divided into three basic stages on the basis of the behavior of the current. Three similarity criteria are obtained for these stages through an analysis of the differential equation of the discharge circuit and the energy balance during the destruction of the conductor. Analysis of the experimental data reveals that at corresponding times (determined by normalizing the time axis on the basis of the length of the half-period of the short-circuit current) the dimensionless discharge-current curves indicate approximate similarity relations. Experiments involving the explosion of copper and aluminum conductors have been carried out for broad ranges of the parameters.

Despite the many papers which have appeared on the explosion of conductors, relatively little is known about the mechanism for such explosions, and certain details of the process have not been explained.

The destruction of a conductor caused by the passage of a high-density current can be attributed qualitatively to the development of MHD instabilities, which change the shape of the conductor and ultimately cause fractures in it.[1]

If a current which produces a nearly critical pressure at the surface flows in the conductor during the growth of the instability, the conductor could undergo homogeneous vaporization.[2]

We restrict the discussion below to these two characteristic cases, although the actual explosion is more complicated.

From the standpoint of the electrical characteristics, the explosion of a conductor, which disrupts the metallic conductivity in part of the discharge circuit, is accompanied by a rapid decay of the discharge current and the appearance of an inductive overvoltage.[3]

In some cases the current decay ends with a complete current cutoff, which causes a "current pause" or "dark pause." The current increase which follows the pause or a partial current decay begins as a result of the breakdown of the explosion products of the conductor, and displays the behavior characteristic of a gas discharge.

During the explosion of a conductor the electrical characteristics [the discharge current i(t), the voltage across the discharge gap U(t), etc.] are governed by the voltage associated with the charge on the capacitor bank, U_0; the capacitance of this bank, C; the inductance of the discharge circuit, L; the length of the conductor, l; the conductor diameter d; the conductor material; and the properties of the medium in which the explosion occurs.

Many experiments on the electrical characteristics of conductor explosions[3–6] have shown that identical oscillograms (with identical decay phases, decay depths, and magnitudes of the secondary discharge-current pulse) can be obtained with various combinations of the discharge-circuit and conductor parameters.

We report here an attempt to obtain approximate similarity criteria for the electrical characteristics of the underwater explosion of conductors in the high-voltage discharge of a capacitor bank.

Since many parameters govern the several successive stages of the conversion of the conductor and the corresponding processes in the discharge circuit, we seek the similarity criteria through analysis and control experiments.

The equation of a discharge circuit consisting of a series connection of a charged capacitor bank, the inductance of the leads, and a nonlinear resistance can be written in general as

$$L\frac{di}{dt}+iR+\frac{1}{C}\int i dt=0, \tag{1}$$

where R is the sum of the resistance of the elements of the discharge circuit, R_d, and that of the conductor, R_n.

Using the similarity or scaling factors $m_i = U_0\sqrt{C/L}$ for the current and $m_i = \pi\sqrt{LC}$ for the time, we can rewrite Eq. (1) in dimensionless form with the single similarity criterion $S_1 = R\sqrt{C/L}$.

The resistance of the discharge-circuit elements is governed primarily by the resistance which is equivalent to the dielectric loss in the capacitor.[7] Its value is usually 0.1 of the characteristic impedance of the discharge circuit, $\sqrt{L/C}$.

For conductors which are not too thin, the value of R_c is comparable to that of R_d.

Since the temperature coefficients of the resistances of various metals (mercury is an exception) are almost the same, we can use the following approximate similarity criterion for the initial stage of the explosion (for the first current pulse):

$$S_1=(R_d+R_0)\sqrt{\frac{C}{L}}, \tag{2}$$

where R_0 is the initial resistance of the conductor.

Dimensionless combinations governing the phase of the rapid decay of the discharge current can be obtained from the energy-balance equation for the explosion which, according to ref. 4, can be written

$$\frac{d(w)}{g(w)}=\frac{R_0 i^2}{m}dt. \tag{3}$$

Here, w is the energy per unit mass of the conductor,

$g(w) = R_n/R_0$, $g(w_0) = 1$, and m is the mass of the conductor.

Integration of the left side of Eq. (3) from w_0 to w_1, which is set by the instant of explosion, gives a Stieltjes integral which is a function of the properties of the material alone, and is therefore constant.

Normalizing both parts of the equation to the specific energy required to heat, melt, and evaporate the conductor (w_c), we find (in dimensionless form)

$$\text{const} - \frac{R_0}{mw_e}\int_0^{t_e} i^2 dt = 0. \quad (4)$$

If we neglect the energy loss due to the heating of the conductor and the increase in its volume before destruction, define $I = i/m_i$ and $\tau = t/m_t$ and write the initial resistance in terms of the electrical conductivity σ and the mass, m, in terms of the geometric dimensions and the density ρ, then

$$\text{const} - \frac{1}{d^4\rho\sigma(\lambda + r)}\frac{U_0^2 C^{3/2}}{L^{1/2}} f(\tau_e) = 0. \quad (5)$$

Here, λ and r are the specific heats of fusion and vaporization, respectively, and

$$f(\tau_e) = \int_0^{\tau_e} I^2 d$$

is the dimensionless phase function of the explosion.

This dimensionless expression, which is a combination of dimensional quantities characterizing the circuit and the conductor, thus determines the explosion phase unambiguously and can serve as a second similarity criterion during the explosion:

$$S_2 = \frac{1}{d^4\rho\sigma(\lambda + r)}\frac{C^{3/2}U_0^2}{L^{1/2}}. \quad (6)$$

When the conductor is destroyed as a result of MHD instabilities, evaporation occurs locally, and only a negligible part of the conductor material manages to evaporate before the destruction. The energy-balance equation must be normalized, taking account only of the energy required for the heating and the melting. The function $f(\tau_e)$, a dimensionless function of the time, becomes a function of the time required for the growth of the instability.[1]

Experiments showing that the properties of an underwater spark discharge are similar to those of a discharge in the explosion products of a conductor in the stage following the explosion[8,9]

$$S_3 = \frac{Al^2}{U_0^2 \pi \sqrt{LC}} \quad (7)$$

is a third criterion. Here A, the spark constant, which is not a function of the conductor material, is $10^4\ V^2 \cdot sec/m^2$.

From (2), (6), and (7), we see that for similarity of the electrical characteristics as the diameter of the conductor is increased by a factor of n the bank capacitance C, the discharge voltage U_0, and the conductor length l, must be increased by a factor of n, while the inductance L and the resistance of the discharge-circuit elements must be reduced by a factor of n.

In these experiments the conductors are exploded by current pulses from the discharge of a capacitor bank charged to 8-40 kV. To determine the influence of the rate at which the energy is supplied to the conductor, we vary the inductance of the discharge circuit and the bank capacitance in such a way that the short-circuit length of the current half-period varies by a factor of about 10 (from ~ 8 to ~ 70.0 μsec).

Copper and aluminum conductors are used in most of the experiments; the discharge current is displayed on an oscilloscope by means of a coaxial shunt, while the voltage drop across the electrodes of the test sample is taken from a capacitive voltage divider.

The inductive component of the voltage drop is balanced out.

The system used to measure the current (the shunt and oscilloscope) is calibrated on the basis of a calculation of the peak short-circuit discharge current from the parameters of the discharge circuit for a specified bank voltage. The resistance is assumed to be constant. In this way we avoid errors in the determination of the conversion coefficients which incorporate the sensitivity of the oscilloscope, and of the properties of the shunt resistance.

The measurement system (the voltage divider and oscilloscope) is calibrated on the basis of the deflection of the oscilloscope trace during the discharge of the capacitor bank into a resistance chosen to provide a time constant of the RC circuit much longer than the length of the short-circuit current half-period. The similarity coefficients m_i and m_t are used to convert the oscillograms to dimensionless form.

The accuracy with which the electrical characteristics are determined is monitored on the basis of the energy balance in the discharge circuit, through the use of

$$\int_0^\infty P_R dt = \frac{CU_0^2}{2},$$

where P_R is the total power evolved in the resistance of the discharge circuit and the conductor. The deviation from an energy balance usually does not exceed 5%-7%.

The phase change of the rapid current decay accompanying the explosion of the conductor as S_2 is varied (with S_3 = idem), by means of a change in the conductor diame-

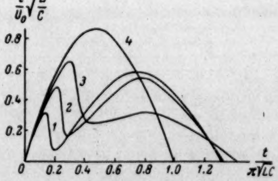

Fig. 1. Dimensionless discharge current during the explosion of copper conductors. $C = 99 \cdot 10^{-6}$ F, $U_0 = 14$ kV, $L = 3 \cdot 10^{-6}$ H. d, mm: 1) 0.4; 2) 0.5; 3) 0.68; 4) discharge current when the discharge gap is shorted by a copper rod.

TABLE 1

Curve in Fig. 3	U_0, kV	C, μF	L, μH	Material	d, mm	l, mm	S_2	$10^2 S_3$	$\frac{U_n}{U_0}$
1	40	3	2.26	Copper	0.30	116	0.24	1.01	3.2
2	18	34.6	2.53	Copper	0.51	100	0.22	1.05	3.7
3	14	99	3.0	Copper	0.66	100	0.22	1.95	3.6
4	8	48	10.6	Copper	0.33	67	0.22	0.97	3.7
5	8	47.6	11.8	Aluminum	0.41	68	0.24	1.00	3.3

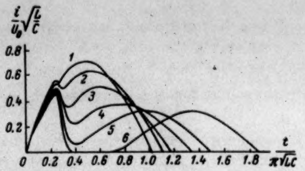

Fig. 2. Discharge current during the explosion of copper conductors d = 0.5 mm in diameter. $C = 99 \cdot 10^{-6}$ F, $U_0 = 14$ kV, L = 10 μH. l, mm: 1) 20; 2) 40; 3) 100; 4) 140; 5) 180; 6) 260.

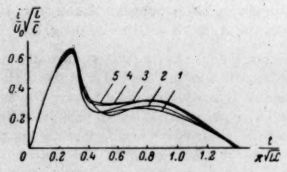

Fig. 3. Similarity of the current curve for the discharges being compared (Table 1) with S_2 = idem and S_3 = idem.

ter, is illustrated by the dimensionless oscillograms in Fig. 1. From the very slight deviation of the initial stage of the current increases from the short-circuit curve, we conclude that criterion S_1 has only a slight effect on the similarity of the discharge.

The differences in the second discharge pulse (despite the condition S_3 = idem) can be easily explained by noting that the initial conditions for this stage, which are governed by the depth of the discharge-current decay and by the relative energy expenditures in the first pulse, are different.

Figure 2 shows a family of discharge-current curves obtained in the explosion of copper conductors of the same diameter (d = 0.5 mm) but different length. Here, the condition S_2 = idem is satisfied.

Turning to the phase of the explosion, we see from these curves that it is essentially independent of the length of the conductor, which in this case governs the value of S_3. The discrepancies in the peak values of the first discharge current pulse (ranging up to 14%) can be attributed to the circumstance that with conductors 100 mm and longer the initial impedance of the conductor reaches 5%–10% of the characteristic impedance of the discharge circuit.

Heating the conductor to the melting point or above strongly affects the value of R_n (refs. 10, 11) and thus S_1.

Nevertheless, in this analysis of approximate similarity we use S_2 and S_3 as the basic criteria.

Figure 3 illustrates the situation with the dimensionless discharge-current curves for the case S_2 = idem and S_3 = idem as essentially all the dimensional properties of both the discharge circuit and the sample itself are varied.

Table 1 shows the basic electrical parameters and the properties of the conductor, along with the relative inductive peak of the overvoltage U_n/U_0 for the corresponding oscillograms in Fig. 3. In calculating S_2 and S_3 we express all the dimensional quantities in International Units.

From the satisfactory coincidence of the normalized discharge-current curves and overvoltage peaks we conclude that our similarity criteria can be used to model discharges in the underwater explosion of conductors.

It should be noted, however, that the similarity which we observe here is characteristic of the two metals which we have studied, for which the voltage curve does not display the continuities observed in the explosion of steel or iron conductors during current flow before the disruption of metallic conductivity.

These anomalies are apparently due to certain features of the conductor material itself which lead to an abrupt change in the conductivity at the transition from the solid phase to the liquid phase during melting.

Furthermore, these results refer primarily to discharges not accompanied by a pause after the first current pulse.

The presence of such a pause during the explosion of comparatively thin conductors, in which case the energy expended in the first current pulse can be neglected, does not play a special role, and the similarity of the discharges initiated by such conductors is discussed in ref. 12.

A current pause can be observed for large-diameter conductors (curve 6 in Fig. 2) if the length of the first pulse becomes comparable to the length of the half-period of the short-circuit current. In this case the energy evolved in the conductor during the first current pulse can be so large that expansion of the vapor–gas cavity toward the end of the current pause and toward the beginning of the second breakdown (the arc stage of the discharge) cannot be neglected. In this case the use of the criterion S_3, derived for the case in which the channel radius is a = 0 toward the beginning of the discharge, requires a further experimental check.

In conclusion, the authors thank B. P. Peregud for discussion.

---

[1] K. B. Abramova, V. P. Valitskii, Yu. V. Vandakurov, N. A. Zlatin, and B. P. Peregud, Dokl. Akad. Nauk SSSR, 167, 778 (1966) [Sov. Phys. – Dokl., 11, 301 (1966)].

[2] A. G. Lesnik, Dokl. Akad. Nauk SSSR, 170, 1059 (1966) [Sov. Phys. – Dokl.,

11, 902 (1967)].

[3] I. F. Kvartskhava, V. V. Bondarenko, A. A. Plyutto, and A. A. Chernov, Zh. Tekh. Fiz., 31, 45 (1956).

[4] F. D. Bennet, Prib. Nauch. Issled., No. 2, 134 (1967).

[5] E. V. Krivitskii, V. K. Sholom, and P. P. Dainis, Elektronnaya Obrabotka Materialov, No. 6, 47 (1969).

[6] K. B. Abramova and B. P. Peregud, Zh. Tekh. Fiz., 41, 2216 (1971) [Sov. Phys. – Tech. Phys., 16, 1758 (1972)].

[7] S. I. Andreev and M. P. Vanyukov, Zh. Tekh. Fiz., 31, 961 (1961) [Sov. Phys. – Tech. Phys., 6, 700 (1962)].

[8] E. Vlastos, 10th Intern. Conf. on Phenomena in Ionized Gases (Oxford, 1971), Contributed papers, Oxford (1971), p. 156.

[9] E. V. Krivitskii and V. V. Shamko, Zh. Tekh. Fiz., 42, 86 (1972) [Sov. Phys. – Tech. Phys., 17, 62 (1972)].

[10] M. M. Martynyuk, O. G. Panteleichuk, and V. I. Tsapkov, Zh. Prikl. Mekh. Tekh. Fiz., No. 4, 109 (1972).

[11] S. V. Lebedev, A. I. Savvatimskii, and Yu. B. Smirnov, Zh. Tekh. Fiz., 42, 1752 (1972) [Sov. Phys. – Tech. Phys., 17, 1400 (1973)].

[12] I. Z. Okun', Zh. Tekh. Fiz., 39, 837 (1969 [Sov. Phys. – Tech. Phys., 14, 627 (1969)]; A. P. Baikov.

Breakdown caused by electron bombardment of the surface of an alloy electrode

N. V. Belan, G. I. Kostyuk, and V. A. Pimkin

(Submitted September 17, 1973)
Zh. Tekh. Fiz., 44, 1277-1279 (June 1974)

An experimental study has been made of the conditions governing the development of a vacuum discharge when an electron beam is incident on the surface of the ternary alloy 50% Bi + 25% Sn + 25% Pb or on the surface of the quaternary alloy 50.1% Bi + 14.2% Sn + 24.9% Pb + 10.8% Cd. Study of the discharge delay time and the mass composition of the ions produced in the discharge reveals selective evaporation of the alloy components which leads to a change in the discharge delay time with the number of breakdown events.

An understanding of the developments of a discharge in the case of an alloy electrode is important in connection with the use of breaker contacts of alloys, the use of alloys as working media in accelerators, and the electric-spark processing of alloys.

Conditions governing the development of a discharge which occurs when an electron beam is incident on the surface of a pure metal are derived in refs. 2 and 3 on the basis of the assumption that the anode breakdown mechanism[1] operates when an electron beam affects the surface of an anode. It is shown[2,3] that the breakdown conditions are satisfied when the evaporated material at the electode surface reaches a pressure of $2 \cdot 10^{-3}$ torr. These conditions correspond to a redistribution of the heat flux over the surface as a result of ion (gas) focusing, which leads to heat fluxes for which the vapor pressure at the surface reaches the value required for the ignition of a discharge in the vapor of the anode.

We have studied the development of a discharge as an electron beam is incident on the surface of an alloy in a prototype pulsed coaxial plasma accelerator with electron-beam ignition of the discharge.[4] Figure 1 shows the experimental apparatus, which consists of a dish 1 which holds the alloy 3; accelerator electrodes 2 and 10, separated by dielectric 9; the anode of the electron source 4; a thermionic cathode 5; a focusing electrode 6; the heater of the electron emitter, 7; the power supply for the electron source, 8; and a time-of-flight mass spectrometer.

The experiments are carried out in a vacuum chamber at a residual gas pressure $5 \cdot 10\text{-}10^{-5}$ torr. We study the alloys 50% Bi + 25% Sn + 25% Pb (Rose metal) and 50.1% Bi + 14.2% Sn + 24.9% Pb + 10.8% Cd (Wood's alloy) and the pure metals Bi, Sn, Pb, and Cd.

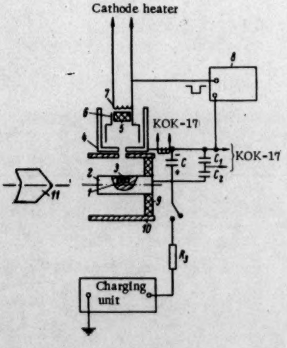

Fig. 1

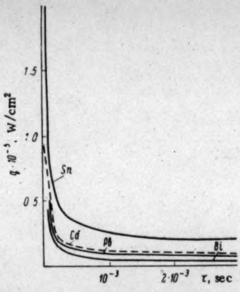

Fig. 2

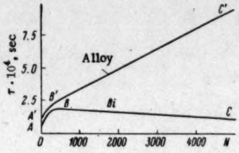

Fig. 3. $q = 1.5 \cdot 10^4$ W/cm².

The beginning of breakdown is determined from the display of the current and voltage on the screen of an OK-17M oscilloscope, which is triggered when the voltage is supplied to the electrodes of the electron source.

The mass-spectrometry experiments are carried out with a time-of-flight mass spectrometer; the measurement circuit is similar to that of ref. 5.

Study of the delay time for the discharge development when an electron beam is incident on the surface of a pure metal has shown that the discharge delay time τ is related to q, the heat flux produced by the electron beam by[2]

$$q = A \frac{1}{\sqrt{\tau}},$$

where A is a constant governed by the thermophysical properties of the bombarded material and by its initial temperature. For lead, tin, bismuth, and cadmium this functional dependence is shown in Fig. 2. A satisfactory agreement is found between the experimental and calculated results. As the number of breakdowns is increased, the discharge delay time falls off slightly, due to an in-

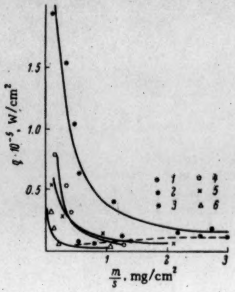

Fig. 4

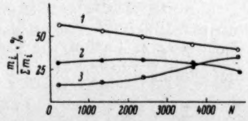

Fig. 5

crease in the initial temperature of the metal before breakdown; this increase reduces the time required for the vapor pressure above the metal surface to reach $2 \cdot 10^{-3}$ torr (Fig. 3). Figure 3 shows the discharge delay time as a function of the number of breakdowns for bismuth (the surface is not outgassed).

In region AB of the curve the metal surface is outgassed, i.e., from point A to point B a progressively smaller relative number of gaseous inclusions contributes to reaching breakdown conditions. In region BC there is some decrease in the discharge delay time because the alloy temperature increases.

As the electron beam affects the surface of the Rose alloy the functional dependence of the discharge delay time on the number of breakdowns changes (Fig. 3); there are two characteristic regions, A'B' corresponding to the outgassing of the surface (here the curve is of the same nature as that in region AB), and B'C', in which the behavior of the curve is different from that in region BC. It would be natural to assume that this feature is a reflection of the nature of the alloy evaporation during pulsed heating.

To clarify this situation we carry out experiments in which we determine the generation characteristics (the mass removed from a unit surface area as a function of the heat flux) for one filling of the dish with the alloy. To compare the experimental results for the alloys and the pure metals, we study the alloy components (Bi, Pb, Sn, and Cd) (Fig. 4).

In the first experiment the expenditure characteristics of the Rose metal and the Wood's alloy are similar to those for bismuth; in the second experiment, they are similar to those for lead or cadmium; and in the subsequent experiments they are similar to those for tin. This functional dependence $m/s = f(\tau)$ for the alloys implies that, after only a few breakdowns, bismuth, the most easily evaporated component, has been removed from the surface layer of the alloy, and the breakdown conditions correspond primarily to the vapor of this metal over the time required to reach the saturation vapor pressure above a bismuth surface. After more breakdowns the surface layer is depleted of bismuth, so that the role of lead and cadmium vapor in governing the breakdown conditions becomes more important; however, since this increased importance can result from an increase in the surface temperature, the time required to reach breakdown conditions is increased. Thereafter, the discharge delay time increases because of an increase in the relative amount of tin vapor. All these results point to the selective nature of the escape of the alloy components.

To check the selectivity of this evolution from the Rose metal, we subject the ion fluxes after various numbers of breakdowns to a mass-spectrometry study. For this purpose we use a time-of-flight mass spectrometer with time and natural modulation of the ion beam, so that the energy and velocity distributions of ions of various masses can be obtained. In this manner we are able to determine the nature of the ion and the relative number of ions of each species. Figure 5 shows the relative number of ions of each species as a function of the number of operations of the ignition system. The relative number of bismuth ions falls off as the number of breakdowns increases, while the relative number of lead ions at first increases and then decays. The relative number of tin ions increases as the number of breakdowns increases. The mass-spectrometry results verify the selective escape of the components during electron-beam ignition of the discharge. Study of the discharge development as an electron beam is incident on the surfaces of ternary and quaternary alloys showed that (1) the discharge delay time increases with an increase in the number of breakdowns and (2) selective evaporation of the components is observed. This selective evaporation explains the changes in the discharge delay time.

---

[1] I. N. Slivkov, Zh. Tekh. Fiz., 38, 1385 (1968) [Sov. Phys. – Tech. Phys., 13, 1131 (1969)].

[2] N. V. Belan, V. F. Gaidukov, G. L. Kostyuk, and E. K. Ostrovskii, Zh. Tekh. Fiz., 42, 1270 (1972) [Sov. Phys. – Tech. Phys., 17, 1010 (1972)].

[3] N. B. Belan, V. F. Gaidukov, G. L. Kostyuk, E. K. Ostrovskii, and L. V. Strelkov, Zh. Tekh. Fiz., 42, 382 (1972) [Sov. Phys. – Tech. Phys., 17, 303 (1972)].

[4] N. V. Belan, V. F. Gaidukov, G. L. Kostyuk, E. Ostrovskii, and L. V. Strelkov, First All-Union Conference on Plasma Accelerators, Moscow, 1971.

[5] A. A. Kalmykov, V. I. Tereshin, and N. S. Poltavtsev, Zh. Tekh. Fiz., 34, 1425 (1964) [Sov. Phys. – Tech. Phys., 9, 1101 (1965)].

Emission characteristics of an explosive gallium cathode*

G. N. Fursei and V. M. Zhukov

A. A. Zhdanov Leningrad State University

(Submitted July 9, 1973; resubmitted November 30, 1973)
Zh. Tekh. Fiz., 44, 1280-1286 (June 1974)

The temporal characteristics and emission properties of the initial stages of vacuum breakdown are studied. An attempt is made to distinguish processes related to the parameters of the external circuit from those due directly to the emission properties of the cathode. The delay times and switching times are measured during the development of vacuum breakdown on the surfaces of liquid and solid gallium with a limited emitting surface and on extended electrodes. The explosive-emission current displays saturation due to the limited cathode emissivity.

In the initial stages of vacuum breakdown explosive emission of electrons occurs as a result of the explosion of microscopic inhomogeneities on the cathode of the evacuated gap by the field-emission current.[1-2]

Until now it has been assumed[2-4] that the increase of the current as a function of the time and the voltage-current characteristics of explosive-emission diodes are governed primarily by the conditions under which the plasma bridges the evacuated gap. On the other hand, experiments with separate field emitters and studies of the microrelief of the cathode surface after breakdown[5] are consistent with the assumption that an equally important role is played by the growth of the emitting surface of the cathode as a function of the time[1]; this growth is a result of the propagation of plasma along this surface. An important role is also played by the strength of the explosion process, which is governed by the electric field and, correspondingly, by the density of the field-emission current. We report here on an attempt to distinguish these fundamental processes more clearly and to show why these processes are masked in most experiments with macroscopic surfaces.

1. EXPERIMENTAL PROCEDURE

Figure 1 shows a block diagram of the experimental apparatus. The experiments are carried out in sealed vessels at a residual pressure of 10^{-7}-10^{-6} torr. The vessels are pumped by titanium electric-discharge pumps. The anode-cathode separation can be adjusted continuously over a range of 20 mm. The cathodes are made of "Ga-00" gallium. Gallium is selected because it can be used to study both solid and liquid cathodes in ultrahigh vacuum.[6]

Since the explosive-emission current density can reach values up to 10^6-10^8 A/cm^2 at microscopic points (ref. 5), the total current for macroscopic cathode surfaces of the usual size (0.1 cm^2 and larger) is not limited by emission, but by the parameters of the external circuit and the space charge in the evacuated diode. To isolate the emission characteristics it is necessary to restrict the current increase resulting from the increase in the emitting surface area[1] during the explosive emission. A particular case with this limitation is the explosive emission of single microscopic points.[5] For this reason, in the present study we use Ga cathodes with a small, specially limited surface area [$S \sim 7 \cdot (10^{-4}$-10^{-3} cm^2)]. The results are compared with those for cathodes with extended surfaces (with S up to 1 cm^2). In most of the experiments the length of the rectangular voltage pulses (τ_p) is 130 nsec, the rise time (τ_r) is 5 nsec, and the peak value is 12-50 kV. In the experiments with extended cathodes we use voltage pulses of 60-120 kV, (τ_p) ≈ 100 nsec, and (τ_r) = 1 nsec.

EXPERIMENTAL RESULTS

Temporal characteristics. a) Explosive emission is customarily characterized by two times:[3-4] the delay time for the appearance of the explosive-emission current with respect to the leading edge of the voltage pulse, t_d, and the time required for the current to grow to values limited by the parameters of the external circuit, which has been called the "switching time" t_s (Fig. 2a).

In our experiments we also attempt to provide a cathode with a small emitting surface, so that the explosive-emission current will be governed not only by the parameters of the external circuit and the effect of the electron space charge, but also (and primarily) by the cathode emissivity. We find that the current oscillogram does in fact display a saturation region (Fig. 2b). In this case it is convenient to introduce the time required for the current to grow to its quasisteady-state value, t_g.

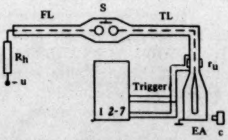

Fig. 1. Block diagram of the measurement apparatus. R_h) Charging resistance; FL) forming line; S) switch; TL) transmitting line; r_u) measuring resistance; EA) experimental apparatus; I2-7) time-interval meter; C) camera.

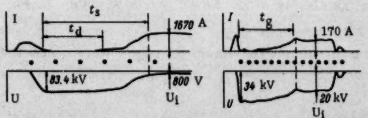

Fig. 2. Oscillograms of the explosive-emission current and voltage for cathodes with extended (a) and limited (b) emitting surfaces. U_{gap}) Discharge voltage. The time markers indicate intervals of 10 nsec.

Below we clearly distinguish between t_s and t_g, since their physical meanings are significantly different.

b) The value of t_d for a liquid cathode varies from hundreds of nanoseconds to several nanoseconds (Fig. 3a) over the ranges of the voltage U, the gap d, and thus the electric field F which we have studied. This result agrees well with the results obtained previously with solid metals[4,7] (Table 1). The scatter in the values of t_d for a cathode with an extended liquid surface is much smaller than that for solid electrodes. For liquid Ga the scatter does not exceed 5-10% (Fig. 3c), while for solid metallic cathodes under approximately the same conditions[4-7] the values of t_d can vary by a factor of 2-3.

The general behavior of t during the first few switchings on solid Ga is the same (Fig. 3b, I). A characteristic effect is the formation of the surface: After a few dozen switching events, t_d contracts rapidly to values shorter than 1 nsec (Fig. 3b, II). The formation effect can be related unambiguously to the formation of a large number of microscopic points on the solid gallium cathode under the influence of the preceding breakdowns. The formation of microscopic points on the surface of solid Ga under the influence of single breakdowns has been studied previously.[8] Conversion of the formed cathode to the liquid state and its subsequent "freezing" make it possible to restore the original functional dependence of t_d on U (Fig. 3b, I).

The time t_d is not a function of the magnitude of the voltage, being governed by F alone (Fig. 3a).

The absolute values of t_d on a gallium cathode are considerably shorter than for more refractory materials under similar conditions (Table 1). This difference can be naturally attributed to the low melting point of Ga and the change in the cathode geometry which occurs as the microscopic protuberances are drawn from the liquid phase.[6]

c) Figure 4 shows the functional dependence of t_s on the applied voltage U. A result not found earlier with solid cathodes[3,4,7] is the strong functional dependence of t_s on U (region I in Fib. 4) and, thus, on F. We believe that this functional dependence was not observed in the earlier experiments because most of these experiments were carried out at stronger fields. In our experiments we also observe a region in which t_s is actually independent of U (region II in Fig. 4).

Accordingly, in the functional dependence of t_s on U we can distinguish two branches, characterized by a decrease in t_s with increasing U (region I) and constancy of t_s with a further increase in U (region II). We attribute the decrease in t_s with increasing U to an increase in the number of explosive-emission centers accompanying an increase in F. This functional dependence is manifested only at comparatively small values of F, at which the switching process is a function of the growth of the effective emitting surface as well as of the conditions governing the bridging of the evacuated gap by the plasma. This effect should obviously be displayed most clearly at large electrode separations d, when one or several microscopic points explode. It is precisely this favorable situation which arises in experiments with a liquid gallium cathode.

TABLE 1

Material	t_d, nsec	t_s, nsec	d, mm	Reference
Cu	4—8	10—15	0.35	[4, 7]
Al	~8	17	0.35	
Al	~20	25	0.5	
Mo	2.5—3	4	0.2	
Ga	~2	18	0.70	The present work
Ga	~2	31	1.35	
Ga solid	~1	20	0.55	

Note: The voltage is U = 40 kV in all the experiments.

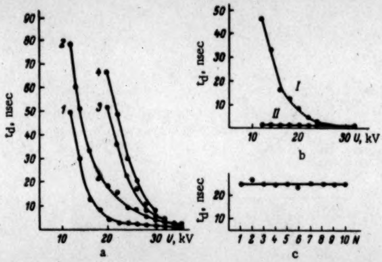

Fig. 3. Delay time as a function of the voltage on the liquid cathode (a, b) and reproducibility of the delay time for a cathode with an extended emitting surface (c). a: 1) d = 0.55 mm; 2) 0.70; 3) 1.35; 4) 3.2. b: d = 0.55 mm. c: U = 83.4 kV.

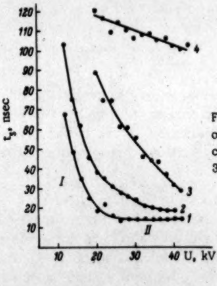

Fig. 4. Switching time as a function of the applied voltage on a liquid cathode. d, mm: 1) 0.55; 2) 0.70; 3) 1.35; 4) 3.2.

At small values of d and at large overvoltages, from the very beginning the number of centers is sufficient for the current increase in the gap to be governed entirely by space charge.

The data obtained for Ga agree well with the data from other works (Table 1).

Mesyats el at.[3] attempted to calculate t_s, taking account of the space-charge effect, in a model with an evacuated gap which contracts with the plasma expansion. The calculated results agree with the experimental data in region II of the $t_s = f(U)$ curve (Fig. 4).

We note that the decrease in t_s with increasing U can also be observed with a solid cathode. The cathode must be smooth and cannot have a large number of microscopic protuberances. Such conditions can be arranged by

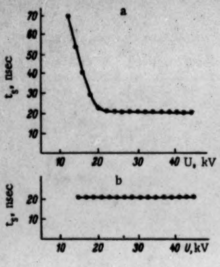

Fig. 5. Switching time as a function of the applied voltage during (a) and after (b) the forming of the solid cathode. d = 0.55 mm.

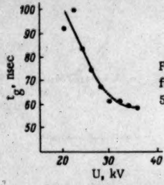

Fig. 6. Current-growth time t_g as a function of the applied voltage. d = 5.5 mm, S = $0.7 \cdot 10^{-3}$ cm^2.

solidifying liquid Ga (Fig. 5a). After several successive breakdowns we find the formation effect described above, which results from the formation of a large number of microscopic protuberances. In this case we observe the independence of t_s from U, which has been noted in several works (Fig. 5b). A formation process of this type apparently occurred in most of the experiments reported previously, in which the electrodes were almost always conditioned beforehand by breakdowns.

On a liquid-gallium cathode and on a smooth solid gallium cathode, as we see from Fig. 4, I, and in the region which is the transition to region II the linear functional dependence of t_s on U which is usually observed[3,4] is not found.

d) Comparison shows that t_g is much smaller than t_s for each voltage (Figs. 4 and 6). We see from these figures that this feature holds even when t_s is determined at a slightly smaller anode−cathode separation d. On the basis of this observed difference between t_s and t_g we can conclude that when the avalanche current increase at the cathode is artificially cut off (for the specified parameters of the external circuit) by a limitation on S, there is an important reduction of the formation time for the explosive-emission pulse.

Voltage−current characteristics. a) The use of an extended cathode to obtain electron beams by means of explosive emission suffers from the disadvantage that the voltage across the gap (U_{gap}) decays rapidly as a function of the time (Fig. 2a). This decay results from the rapid growth of the emitting surface area and from the high density of the explosive emission, which leads to a very rapid increase in the conductivity of the gap. Accordingly, a high-energy electron beam can be obtained only in a comparatively brief time interval during the initial stage of the discharge. Limitation of S permits us to overcome this difficulty and obtain an essentially rectangular pulse of a high-energy electron current (Fig. 2b).

b) Figure 7 shows the voltage−current characteristics of the discharge for various values of S and d. For large S these characteristics are the typical decaying characteristics of a self-maintained discharge[9] (Fig. 7a), limited by the resistance of the discharge circuit (in our case, $\rho = 75\ \Omega$). This typical voltage−current characteristic of the discharge shows that here we are apparently dealing with a cathode spot which has already formed; the elementary mechanism for the operation of such a spot is the explosion of a microscopic inhomogeneity under the influence of the field-emission current which is flowing. Emission at a cathode spot is the essence of explosive emission. The quantity U_{gap} is in fact the arcing voltage for the given circuit resistance.

When the cathode surface area is limited we find increasing voltage−current characteristics (Fig. 7b).

All the characteristics are plotted according to the current values measured in the quasisteady-state part of the functional dependence of the current on the time (Fig. 2).

Emission properties of a liquid cathode. a) The emission current density j obtained from a cathode with a limited surface area is $\sim (1\text{-}5) \cdot 10^5$ A/cm^2. The magnitude of the current is determined from oscillograms, and the emitting surface area is assumed to be the total surface area of the cathode. The average values of j are approximately equal to those obtained recently from the cathode spot of a self-maintained discharge.[9,10] We note that this is the average current density. The local value of j can be much larger in the region in which the microscopic explosion occurs.[5] The emission current density is a function of the average electric field1) F (Fig. 8). This functional dependence can be attributed to the different growth of explosive emission.[5]

b) The glow of a discharge on a cathode with a limited surface area is localized near the axis of the cathode. The expansion rate of the plasma, determined from the measured values of t_s and d by the procedure of ref. 3, is $(2\text{-}4) \cdot 10^6$ cm/sec for a liquid cathode.

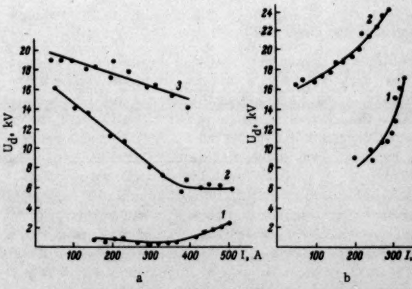

a

b

Fig. 7. Voltage−current characteristics for extended (a) and limited (b) cathode surfaces. a: S = $3.8 \cdot 10^{-3}$ cm^2. d, mm: 1) 0.7; 2) 3.2; 3) 5.2. b: S = $0.7 \cdot 10^{-3}$ cm^2. d, mm: 1) 2.5; 2) 5.5.

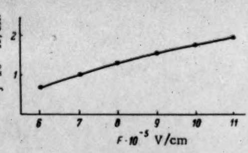

Fig. 8. Emission current density as a function of the average electric field.

CONCLUSION

1. The switching time has been found to decrease with increasing electric field F. This decrease has been shown to be the result of the growth of the effective emitting surface area and the increase in the number of cathode bursts with increasing F.

2. It has been shown that by limiting the emitting surface area of the cathode one can obtain high-energy electron beams with a specified impedance and with short rise times.

3. The voltage–current characteristics of the initial stages of vacuum discharge have been found to display two branches with decaying and increasing voltages. The behavior of the characteristics as a function of the parameters of the external circuit shows that we are dealing with the formation of a cathode spot from essentially the first few nanoseconds. The mechanism for the emission at a cathode spot is explosive emission of electrons.

4. Successive breakdowns lead to the formation, on a solid gallium cathode, of a large number of microscopic points, which are drawn from the molten metal during breakdown by the ponderomotive forces associated with the electric field. As a result the switching and delay times are shortened, and the switching time becomes independent of the applied voltage.

5. The measured average current densities on a liquid gallium cathode with a limited surface area are $(1\text{–}5) \cdot 10^5$ A/cm^2, in good agreement with recent data on the average current density at a cathode spot.[10]

6. The results agree with the model proposed in ref. 1 for the formation of a cathode spot.

---

*Reported to the Symposium on High-Current Plasma Emission Electronics in May, 1973 [Abstracts of the Symposium (in Russian), Tomsk (1973), p. 13].

1)In this case the cathode is conical; the quantity F is evaluated from the equations for an isolated point.

[1] G. N. Fursei and P. N. Vorontsov-Vel'yaminov, Zh. Tekh. Fiz., 37, 1880 (1967) [Sov. Phys.–Tech. Phys., 12, 1377 (1968)].

[2] S. P. Bugaev, A. M. Iskol'dskii, G. A. Mesyats, and D. I. Proskurovskii, Zh. Tekh. Fiz., 37, 2206 (1967) [Sov. Phys.–Tech. Phys., 12, 1625 (1968)].

[3] G. A. Mesyats and D. I. Proskurovskii, Izv. VUZ. Fiz., 1, 81 (1968).

[4] G. A. Mesyats, S. P. Bugaev, D. I. Proskurovskii, V. I. Eshkenazi, and Ya. Ya. Yurike, Radiotekh. Elektron., 14, 2223 (1969).

[5] G. N. Fursei (Fursey), V. M. Zhukov, B. F. Gulin, and I. D. Ventova, Proc. Fifth Intern. Symposium on Discharges and Electrical Insulation in Vacuum, Poznań, Poland (1972).

[6] I. Yu. Bartashyus, L. I. Pranevichyus, and G. N. Fursei, Zh. Tekh. Fiz., 41, 1943 (1971) [Sov. Phys.–Tech. Phys., 16, 1535 (1972)].

[7] D. I. Proskurovskii, Candidate's Dissertation [in Russian], Tomskii Politekh. Inst. (1968).

[8] L. A. Sena, L. I. Pranevychius, and G. N. Fursei (Fursey), Proceedings of the 10th Intern. Conf. on Phenomena in Ionized Gases, Cambridge, England (1971), p. 105.

[9] I. G. Kesaev, Cathode Processes in an Electric Arc [in Russian], Izd. Nauka, Moscow (1968).

[10] V. I. Rakhovsky, Proceedings of the Fifth Intern. Symposium on Discharges and Electrical Insulation in Vacuum, Poznan, Poland (1972), p. 207.

Atomic recombination on a solid surface

V. P. Pinchuk, A. N. Gorban', and V. G. Kornich

V. Ya. Chubar' Zapopozh'e Machine Construction Institute

(Submitted July 2, 1973)
Zh. Tekh. Fiz., 44, 1287-1291 (June 1974)

A study of the effect of atomic hydrogen on the surfaces of several materials has shown that the recombination of hydrogen atoms leads to effects such as the sputtering of certain metals and semiconducting compounds (without any important change in the stoichiometric composition); the appearance of characteristic microscopic swelling on the surface of certain metals; and electron emission. The temperature dependence of the emission current has been determined.

A comparatively large amount of energy is evolved (up to 10 eV per recombination event[1] in the recombination of free radicals at the surface of a solid). This energy is transferred either to the lattice or to individual atoms and electrons. In the first case the solid surface is heated, in certain cases by tens or even hundreds of degrees.[2] Under certain conditions we have observed the heating of platinum, nickel, and copper, which are active catalysts for the recombination of atomic hydrogen, to 650–700°C.

Transfer of the recombination energy to individual atoms of a semiconductor, resulting in the ionization of the atoms and the appearance of free charge carriers, leads to such effects as a change in the electrical conductivity, radical-recombination luminescence,[6] etc. It can be assumed that the recombination of radicals on a surface can also stimulate electron emission and the conversion of atoms of a solid into the gas phase. This conversion could of course also be related to the formation of highly volatile chemical compounds. (We note the familiar Panet mirror method, which can be used to determine the concentration of free radicals from the rate at which films of certain materials disappear).

We have studied the interaction of atomic hydrogen (recombination energy of 4.48 eV) with the surface of several materials – metals, elemental semiconductors, and semiconducting compounds.

The atomic hydrogen is produced by an rf electrodeless discharge. The hydrogen atoms defuse from the discharge region into the working chamber over a distance longer than 20 cm. The working chamber is a cup 1500 cm^3 in volume mounted on a plate. The hydrogen-atom density in the working volume is 10^{14} cm^{-3}.

Visual observations show that the exposure of a solid surface to atomic hydrogen usually leads to a change in the surface state. The nature of this change is governed by several surface processes. Previously oxidized metal surfaces (copper and molybdenum) are reduced even at room temperature. Increasing the temperature to 250°C raises the reduction rate. Magnesium oxide and zinc sulfide films as thick as 1.5 μ are evaporated essentially without change of the stoichiometric composition for 1-2 h. Since no change occurs in the stoichiometric composition in this case, as can be seen from the rate and nature of the radical-recombination luminescence, we conclude that the disappearance of the films results from sublimation of the material, rather than from a chemical interaction.

The exposure of pure molybdenum, copper, and platinum to atomic hydrogen leads to the appearance of characteristic formations on the surfaces. Photomicrographs (Fig. 1) show previously polished surfaces of these metals after exposure to atomic hydrogen. The atomic hydrogen leads to the appearance of areas of microscopic swelling on the metal surfaces. The rate at which these formations grow is largest for molybdenum and smallest for platinum.

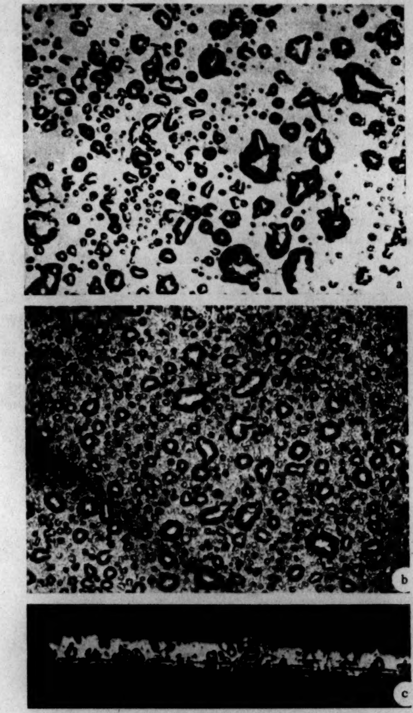

Fig. 1. Photomicrographs of the metal surfaces after exposure to atomic hydrogen. a) Molybenum (× 100); b) copper (× 100); c) platinum wire (× 200).

It is interesting to note that the appearance of similar bubbles on an iron surface during electrolysis has been described in ref. 7, in which the bubbles are attributed to the adsorption on the iron surface of atomic hydrogen evolved during electrolysis. By analogy with the explanation in ref. 7, it could be suggested that the appearance of the microscopic swelling shown in Fig. 1 results from the diffusion of hydrogen atoms adsorbed on the surface into the interior of the sample and the subsequent concentration of these atoms near volume defects (microscopic pores and inclusions). As it recombines into molecules, the hydrogen rapidly loses its mobility and produces a high pressure near the defects which in turn leads to the appearance of the characteristic swelling. The circumstance that the bubble-nucleation rate is highest in molybdenum can be attributed to the layered structure of the samples, which were prepared from rolled molybdenum and which therefore have a large number of microscopic pores.

Special experiments show that the effect of atomic hydrogen on many materials is to cause electron emission. Figure 2 shows a block diagram of the apparatus used to study this emission. In the emission experiment we apply a negative potential to the sample; the potential is chosen to lie in the saturation region of the voltage–current characteristic of the emission current. The heat-transfer conditions are such that the sample is warmed only slightly if the heater is turned off. The samples are 34 mm in diameter and not more than 0.5 mm thick.

The sample temperature can be held constant or varied according to a specified program by means of a heater and regulator. The emission current is measured by a V2-5 millivoltmeter–electrometer, which provides a current sensitivity of 10^{-15} A. Since the atomic hydrogen is produced in an rf discharge, particular care is taken to shield the generator, the rf feeder, and the measuring part of the apparatus. The density of atomic hydrogen is monitored with a platinum–Chromel–Copel thermocouple, which permits absolute measurements of the atomic density at some standard pressure (the system for monitoring the atomic density is not shown in the diagram).

Electron emission is observed in the recombination of hydrogen atoms on the surfaces of molybdenum, nickel, silver, copper, tantalum, magnesium, aluminum, germanium, the oxides of molybdenum and copper, and zinc sulfide. We have not been able to detect electron emission from a silicon surface. The steady-state emission current in the case of the metallic samples falls off slowly with increasing temperature (the emission current decreases 30%-40% upon heating to 250°C) and near 100°C is 0.37 pA for Mo, 0.145 pA for Ni, 0.125 pA for Ag, 0.090 pA for Cu, 0.075 pA for Ta, 0.064 pA for Mg and 0.061 pA for Al.

The change in the magnitude of the emission current as a function of the temperature in the recombination of atomic hydrogen on the surface of zinc sulfide and on the surface of molybdenum oxidized in air for 5 min at 260°C is shown in Fig. 3. The temperature dependence of the emission current from the surface of a zinc sulfide film 1.5 μ thick is easily reproducible upon cooling and repeated heating. For the oxidized molybdenum samples, on the other hand, the peak on the temperature dependence of the emission current is not observed after a cooling and repeated heating. This peak vanishes because the surface is reduced during the interaction with atomic hydrogen. After complete reduction of the surface a steady-state emission current is established; this current falls off slightly with increasing temperature, in the manner typical of pure metals. In those cases in which the oxide layer on the surface is thick (after oxidation for 5 min at 800°C in air), so that the sample is not reduced in a single heating cycle, the temperature peaks are observed for several cycles. The peak emission intensity falls off with each cycle.

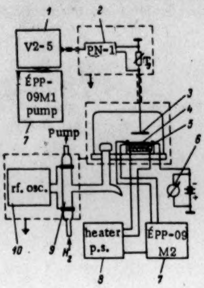

Fig. 2. Block diagram of the apparatus for measuring the electron emission stimulated by the recombination of hydrogen atoms. 1) V2-5 millivoltmeter–electrometer; 2) capacitance voltage transformer; 3) aluminum electron collector; 4) sample; 5) heater; 6) meter for measuring the voltage applied to the sample; 7) ÉPP-09M2 recording potentiometer; 8) power supply for heater; 9) discharge tube; 10) rf oscillator.

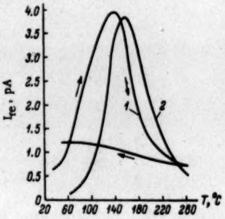

Fig. 3. Temperature dependence of the electron emission stimulated by recombination of hydrogen atoms with a molybdenum surface oxidized for 5 min at 260°C in air (1) and on the surface of a zinc sulfide film (2).

According to preliminary data the magnitude of the emission current varies from sample to sample and with a change in the temperature according to the rate at which atomic hydrogen recombines, i.e., according to how effectively the materials catalyze the recombination of hydrogen atoms into molecules.

CONCLUSIONS

Recombination of hydrogen atoms on the surfaces of metals and semiconductors can have several consequences, among which the following must be included:

a) sublimation of the atoms of the material (in the cases of zinc sulfide and magnesium oxide the evaporation occurs without any change in the stoichiometric composition);

b) the microscopic swelling of the surfaces of certain metals, which occurs because hydrogen atoms diffuse toward volume defects and lead toward the accumulation of molecular hydrogen there;

c) electron emission from the surface, governed by the surface state.

---

[1] Chemical Handbook [in Russian], Vol. 1, GKhI, Moscow (1951).

[2] A. N. Gorban' and V. A. Sokolov, Opt. Spektrosk., 7, 259 (1969).

[3] I. A. Myasnikov and S. Ya. Pshezhetskii, in: Problems of Kinetics and Catalysis [in Russian], Vol. 8 (1955), p. 175.

[4] N. P. Keier, S. Z. Roginskii, and E. A. Fokina, Izv. Akad. Nauk SSSR, Ser. Khim., No. 2, 422 (1957).

[5] G. Heiland, Z. Phys., 148, 15 (1957).

[6] V. A. Sokolov and A. N. Gorban', Luminescence and Adsorption [in Russian], Izd. Nauka, Moscow (1969).

[7] A. V. Cherepnin Principles of Cleaning, Outgassing, and Pumping for Vacuum Work [in Russian], Izd. Sovet-skoe Radio, Moscow (1967).

Adsorption of bismuth on tungsten.
I. Steady-state processes

M. A. Mittsev
A. F. Ioffe Physicotechnical Institute,
Academy of Sciences of the USSR, Leningrad
(Submitted July 23, 1973)
Zh. Tekh. Fiz. 44, 1292-1297 (June 1974)

The flux of particles desorbed from a heated tungsten ribbon on which a steady-state bismuth beam impinges is investigated by means of a mass spectrometer. Only Bi atoms are desorbed from the surface of the ribbon if its temperature is higher than 850°K. In addition to the desorption of Bi atoms, desorption of Bi_2 and Bi_4 occurs in the range 490-850°K. Analysis of the temperature dependences of atomic and molecular fluxes shows that, in contrast to tungsten–alkali-halide salt systems, the condition of equilibrium at the surface, where the evaporation rate is much lower than the molecular dissociation rate, is not satisfied for the W–Bi system.

INTRODUCTION

Investigations of the dissociation of NaCl and NaI molecules on a tungsten surface in ref. 1 have shown that quasiequilibrium processes occur in the adsorbed layer under the experimental conditions. The molecular dissociation energy MX of the salts used in the above work is considerably higher than the sublimation heat, so that surface molecular dissociation under equilibrium conditions occurs at a temperature above the temperature at which the crystalline phase obtains at the surface. The results given in ref. 1 support this conclusion.

We report here on the composition of desorption products from a tungsten surface exposed to a steady-state bismuth beam as a function of the tungsten temperature. In contrast to the alkali halide salts bismuth is characterized by the fact that the dissociation energy D of the Bi_2 molecule is approximately equal to the sublimation heats l of the monomer and the dimer[2,3] [$D_0(Bi_2)$ = 47 kcal/mole; $l_0(Bi)$ = 50 kcal/mole; $l_0(Bi_2)$ = 53 kcal/mole]. Therefore, in the case of equilibrium for bismuth, the dissociation temperature range for the Bi_2 molecule either coincides with the temperature range in which the condensed phase forms on the surface or is close to it. It is interesting to determine the characteristics of the dissociation and formation of molecules at the surface in this case.

DESCRIPTION OF THE DEVICE

The experiments are performed by means of a 90° mass spectrometer with an ion source similar to that used in ref. 1 (Fig. 1). A molecular beam of bismuth from the tantalum-foil evaporator 1 impinges on the tungsten ribbon 2. Atoms or molecules desorbed from the ribbon enter the region of electron-impact ionization 3 through a number of collimating slits. Usually, the ionizing electron energy is 2-4 V higher than the threshold energy for each component of the beam desorbed from the ribbon. The dissociative ion currents are negligible at these energies.

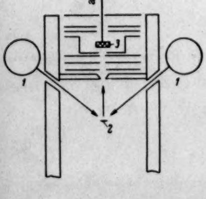

Fig. 1. Ion source of the mass spectrometer. 1) Evaporators; 2) tungsten ribbon; 3) cross section of the ionizing electron beam.

The ion current at the output of the mass spectrometer is recorded by means of a VÉU-1A electron multiplier, to which a U1-6 electrometric amplifier is connected.

The ribbon temperature T is determined by means of an optical pyrometer in the 1100-2500°K range or from the T = f(i) calibration curve, where i is the heating current, in the range below 1100°K. This curve is obtained in a separate experiment by measuring the temperature of a control ribbon by means of a Pt–Pt+10% Rh thermocouple. The control ribbon has the same dimensions as the operating ribbons (60 × 1 × 0.10 mm). The operating ribbons are chosen so that their temperature in the pyrometer range coincides with the temperature of the control ribbon. The accuracy of temperature measurements is also checked by determining the sublimation heats of magnesium and bismuth, which are evaporated from thick layers deposited on the ribbon.[4] The discrepancies between our sublimation heat values and those given by other authors are smaller than ± 2 kcal/mole.

The residual gas pressure in the vacuum system of the mass spectrometer is less than $(4\text{-}8)\cdot 10^{-9}$ torr.

DISCUSSION OF THE MEASUREMENT RESULTS

The mass spectrum of the ions produced by electron ionization of the neutrals desorbed from ribbon 1 as a steady bismuth beam strikes its surface shows peaks due to Bi^+, Bi_2^+, Bi_3^+, and Bi_4^+.

For a Maxwellian velocity distribution in the flux ν desorbed from the ribbon, the ion current I^+ is related to ν by[5,1]

$$\nu = kI^+T^{1/2}, \tag{1}$$

where k is a proportionality factor, which depends on the instrumental geometry, the electron ionization cross sec-

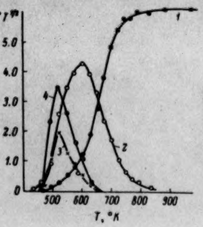

Fig. 2. Atomic and molecular fluxes (relative units) desorbed from a tungsten ribbon as functions of temperature for a steady flux arriving at the ribbon from the evaporator. 1) Bi; 2) Bi$_2$; 3) Bi$_3$; 4) Bi$_4$.

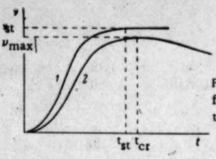

Fig. 3. Atomic and molecular fluxes from a tungsten ribbon as functions of time. 1) T > 520°K; 2) T < 520°K.

tion, and other factors, but is independent of T. We have been able to measure only the values of $I^+T^{1/2}$, proportional to the fluxes, since the coefficients k have not been determined in these experiments.

Figure 2 shows the value of $I^+T^{1/2}$ in relative units as a function of T for Bi^+, Bi_2^+, Bi_3^+, and Bi_4^+. These functions are measured in the following manner. Adsorbed gases are removed from the ribbon by pulsed heating at T = 2400°K, and the ribbon heating current is then changed abruptly to correspond to the ribbon temperature at which the ion current I^+ is to be measured.

The functions in Fig. 2 pertain to the molecular flux incident on the ribbon $\nu_0 \sim 10^{14}$ atoms/cm^2. The value of ν_0 is estimated with respect to the evaporator temperature, which is measured by means of a thermocouple, the bismuth vapor pressure, and the geometry of the ion source.

It is evident from Fig. 2 that only Bi atoms are desorbed at temperatures higher than 850°K. The atomic flux diminishes for T < 850°K, which is connected with an increase first in the flux of Bi$_2$ molecules and then in the flux of Bi$_4$ molecules. The Bi_3^+ ions in the mass spectrum evidently are of dissociative origin, since the ratio $I^+(Bi_3^+)\cdot T^{1/2}/I^+(Bi_4^+)\cdot T^{1/2}$ is independent of the ribbon temperature within the limits of experimental error, while the maxima of the curves $I^+(Bi_3^+)\cdot T^{1/2} = f(T)$ and $I^+(Bi_4{}^+)\cdot T^{1/2} = f(T)$ correspond to the same values of T.

Curve 1 of Fig. 3 illustrates schematically for T > 520°K the dependence of the flux of any beam component desorbed from the strip on the time t after the ribbon temperature reaches a steady-state value. After a time t_{st}, which depends on T and ν_0, the flux assumes the steady-state value ν_{st}. For T < 520°K, the dependence of ν on t is illustrated by curve 2 in Fig. 3. The flux ν decreases after it has reached its maximum value at the time t_{cr}. The variation rate is higher for low values of T. The value of ν decreases for $t > t_{cr}$ because the crystalline phase forms on the ribbon surface at these temperatures. From this point of view, desorption of Bi$_2$ and Bi$_4$ from the ribbon surface at T > 520°K is caused by the development of crystalline phase nuclei of subcritical size on the surface.

In Fig. 2, the steady-state flux values are given for T > 520°K, and the flux values $\nu = f(T)$ corresponding to the time t = 2 min > t_{cr} after the ribbon temperature has become steady are given for T < 520°K.

Investigations[1] of molecular dissociation MX of alkali halide salts on tungsten show that the dependence of the experimental values of $\nu(M)\nu(X)/\nu(MX)$ on T can be written in the following form:

$$\ln\frac{\nu M\,()\,\nu\,(x)}{\nu\,(Mx)} = \ln A - \frac{E}{RT}, \tag{2}$$

where A is a quantity which depends weakly on T, R is the gas constant, and E is equal to the molecular dissociation energy MX within the limits of experimental error. Figure 4 shows similar dependences for bismuth on tungsten: curve 1 for the reaction $Bi_2 \rightleftharpoons 2Bi$ and curve 2 for the reaction $Bi_4 \rightleftharpoons 2Bi_2$. It is evident that the experimental points lie on straight lines. The function $\log[\nu^2(Bi)/\nu(Bi_2)] = f(1/T)$ is observed only for low values of T. However, the values of E calculated from the slopes of these straight lines are much smaller than the bond breaking energies in the corresponding molecules. Thus, the mean of a number of E values calculated from the slope of curves similar to curve 1 is equal to E = 34 ± 3 kcal/mole, while the dissociation energy of Bi$_2$ molecules, calculated with respect to the evaporation heats[2] of Bi and Bi$_2$ and determined by mass spectrometry,[3] is equal to $D_0(Bi_2) = 47$ kcal/mole.

There is an even larger difference between the Bi$_2$–Bi$_2$ bond-breaking energy[3] $D_0(Bi_2 - Bi_2) = 47$ kcal/mole and the value E = 17 kcal/mole, calculated from the slope of the curve $\log \nu^2(Bi_2)/\nu(Bi_4)] = f(1/T)$.

To explain the above discrepancies let us consider the kinetics of surface phenomena under steady-state conditions, as in refs. 6 and 7. Such an analysis is rather complicated in the temperature range where simultaneous desorption of all three types of particles, i.e., Bi, Bi$_2$, and Bi$_4$, occurs. Therefore, we consider values of T for which the formation and dissociation of Bi$_2$ molecules are the only significant processes.

Assume that a beam consisting of Bi atoms and Bi$_2$ molecules strikes the surface, which is at a temperature

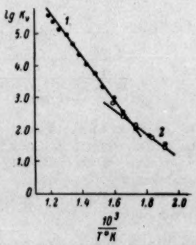

Fig. 4. Curves of log $K_\nu = f(1/T)$. 1) $K_\nu = \nu^2(Bi)/\nu(Bi_2)$ for the reaction $Bi_2 \rightleftharpoons 2Bi$; 2) $K_\nu = \nu^2(Bi_2)/\nu(Bi_4)$ for the reaction $Bi_4 \rightleftharpoons 2Bi_2$.

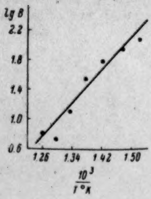

Fig. 5. Graph of log B = f(1/T).

T. We denote the atomic flux on the surface by ν_{01}, the atomic flux from the surface by ν_1, and the Bi_2 molecular flux from the surface by ν_2. Then, under steady-state conditions, we have the following equation for the atomic density N_1 at the surface:

$$\frac{dN_1}{dt} = \nu_{01} + 2kN_2 - \frac{1}{2}k'N_1^2 - \nu_1 = 0, \tag{3}$$

where k is the dissociation rate of diatomic molecules, k' is the atomic association rate, and N_2 is the surface density of Bi_2 molecules. Passing from densities to fluxes by using the relationships $C_iN_i = \nu_i$, we obtain the following after simple transformations:

$$\frac{\nu_1^2}{\nu_2} = 4\frac{k}{k'}\frac{C_1^2}{C_2}\left(1 - \frac{\nu_1 - \nu_{01}}{2\nu_2}\frac{C_2}{k}\right). \tag{4}$$

Under equilibrium conditions, we have

$$\frac{\nu_1^2}{\nu_2} = 4\frac{k}{k'}\frac{C_1^2}{C_2} \equiv K_{\nu p}, \tag{5}$$

which is readily shown by putting $\nu_1 = \nu_{01}$ according to the detailed balancing principle. Then, (4) assumes the following form:

$$K_\nu = \frac{\nu_1^2}{\nu_2} = K_{\nu p}\left(1 - \frac{\nu_1 - \nu_{01}}{2\nu_2}\frac{C_2}{k}\right). \tag{6}$$

In the case of alkali halide salts on tungsten, the slope of $\log K_\nu = f(1/T)$ is identical to the slope of a similar dependence under thermodynamic equilibrium conditions. According to (6), this is possible if $K_\nu \simeq K_{\nu p}$. We note in passing that for $K_\nu = K_{\nu p}$ the value of E from (2) is $E = D_T - 1/2\ RT$, where D_T is the molecular dissociation energy MX at temperature T. As mentioned earlier, the temperature dependence of K_ν is substantially different from the dependence $K_{\nu p} = f(1/T)$.

By using (6) we can determine C_2/k as a function of T if we know the temperature dependence of all the other quantities figuring in (6). For a certain $T = T_0$, $\nu_1 = \nu_{01}$ and

$$K_\nu = K_{\nu p}. \tag{7}$$

By subtracting (7) from (6), we obtain

$$\left(\frac{K_\nu}{K_{\nu p}}\right)_T - \left(\frac{K_\nu}{K_{\nu p}}\right)_{T_0} = -\frac{\nu_1 - \nu_{01}}{2\nu_2}\frac{C_2}{k}$$

and

$$\ln B \equiv \ln\left\{\frac{2\nu_2}{\nu_1 - \nu_{01}}\left[\left(\frac{K_\nu}{K_{\nu p}}\right)_{T_0} - \left(\frac{K_\nu}{K_{\nu p}}\right)_T\right]\right\} = \ln\frac{C_2^0}{k^0} - \frac{E_C - E_k}{RT}, \tag{8}$$

where C_2^0 and k^0 multiply the exponential factors, while E_C and E_k are the desorption activation energy and the dissociation activation energy of diatomic molecules, respectively.

To process experimental results by means of (8) it is necessary to know the percentage of atoms in the beam incident on the ribbon surface, i.e., the ratio ν_{01}/ν_0. This value is determined in a special experiment. An evaporator is substituted for ribbon 2 (Fig. 1), and the composition of the beam from the evaporator is determined for low ionizing electron energies. The ratio of efficiencies in mass-spectrometric detection of Bi atomic and Bi_2 molecular fluxes is determined by means of the steady-state temperature dependences of ν_1 and ν_2, similar to those given in Fig. 2 and the stationarity equation

$$\nu_0 = \nu_{01} + 2\nu_{02}. \tag{9}$$

For the evaporator temperatures at which the basic measurements are performed, the ratio ν_{01}/ν_0 is equal to 0.78.

The dependence of $K_{\nu p}$ on T is approximated by the function

$$K_{\nu p} = A\exp\left(-\frac{D_T}{RT}\right), \tag{10}$$

where A is assumed to be independent of T, while D_T = 48 kcal/mole, where T ~~= 720°C~~ is the mean value of the range of T used in calculations: 650-790°K.

Figure 5 shows the results of calculations based on (8) for one measurement of $\log K_\nu = (1/T)$. The mean of the six values of $E_k - E_C$ calculated from the slopes of graphs similar to that in Fig. 5 is equal to $E_k - E_C = 26 \pm 4$ kcal/mole.

It follows from these results that the dissociation activation energy of Bi_2 molecules at the surface is much higher than the desorption activation energy for these molecules. By using the obtained value of $E_k - E_C$ we estimate the order of magnitude of C_2^0/k^0.

By approximating K_ν and $K_{\nu p}$ by a function of the type (10) and using (6) and (7), we obtain

$$\frac{K_{\nu T}}{K_{\nu T_0}} = \frac{K_{\nu p T}}{K_{\nu p T_0}}\left(1 - \frac{\nu_1 - \nu_{01}}{2\nu_2}\frac{C_2}{k}\right)$$

and

$$\frac{C_2^0}{k^0} = \frac{2\nu_2}{\nu_1 - \nu_{01}}\exp\left(\frac{E_C - E_k}{RT}\right)\left\{1 - \exp\left[\frac{D_T - E}{R}\left(\frac{1}{T} - \frac{1}{T_0}\right)\right]\right\}. \tag{11}$$

For different measurement series, estimates of $C_2^0 \cdot (k^0)^{-1}$ based on (11) yield values in the range 10^{-7}-10^{-9}. For comparison it should be noted that Re–LiCl has been obtained in ref. 7 for the system $C_2^0/k^0 \approx 2 \cdot 10^{-2}$ on the basis of absolute reaction rate theory. The assumptions made in ref. 7 in estimating C_2^0/k^0 apparently also hold for bismuth on tungsten, so that $C_2^0/k^0 \sim 10^{-2}$ for this system.

The available experimental data on the system W–Bi are inadequate for an explanation of the large difference between C_2^0 and k^0 and the fact that the calculated value of C_2^0/k^0 exceeds the experimental value by a factor of 10^5-10^7.

The author is grateful to N. I. Ionov for discussion.

---

[1] N.I. Ionov and M. A. Mittsev, Zh. Tekh. Fiz., 35, 1863 (1965) [Sov. Phys.–Tech. Phys., 10, 1436 (1966)].
[2] A. T. Aldred and J. N. Pratt, J. Chem. Phys., 38, 1085 (1963).
[3] L. Rovner, A. Drowart, and J. Drowart, Trans. Faraday Soc., 63, 2906 (1967).
[4] J. B. Hudson and J. S. Sondejas, J. Vacuum Sci. Technol., 4, 238 (1967).
[5] J. D. McKinley, J. Chem. Phys., 41, 2814 (1964).
[6] N. D. Potekhina, Zh. Tekh. Fiz., 35, 1658 (1965) [Sov. Phys.–Tech. Phys., 10, 1280 (1966)].
[7] N. D. Potekhina, Zh. Tekh. Fiz., 40, 620 (1970) [Sov. Phys.–Tech. Phys., 15, 479 (1970)].

Effects of cleaning on adsorption by germanium single crystals

Yu. I. Belyakov, M. P. Volkov, and T. N. Kompaniets

A. A. Zhdanov Leningrad University
(Submitted July 6, 1973)
Zh. Tekh. Fiz., 44, 1298-1301 (June 1974)

Shock desorption has been used in a time-of-flight mass spectrometer to examine the adsorption of hydrogen and oxygen by germanium single crystals whose surfaces have been purified by reduction in atomic hydrogen or by bombardment with argon ions and subsequent brief or prolonged annealing. It is found that argon bombardment of a surface produced by reduction in hydrogen increases the rate of adsorption for molecular oxygen by a factor 5-6, while the rates of adsorption of atomic hydrogen and oxygen are only affected slightly. After prolonged annealing the adsorption behavior of surfaces after bombardment is the same as for surfaces obtained by reduction in atomic hydrogen.

We have examined the adsorption of hydrogen and oxygen on single crystals of germanium whose surfaces have been cleaned by various methods. The purity of the adsorbed gases and the cleanliness of the surfaces are recorded with a pulsed time-of-flight mass spectrometer, which records the desorption products. The amounts of adsorbed gas are determined by shock desorption.[1] See ref. 2 for details of the experimental methods.

The specimens are plates fabricated from single crystals 25 × 5 × 0.2 mm with (111) or (100) surfaces. The criterion for surface cleanliness in all cases is evaporation of the pure substance in the absence of desorption of any other products.

METHODS OF SURFACE CLEANING

Before installation in the mass spectrometer, the specimens are polished, etched in SR-4 solution, and washed with distilled water. During baking of the vacuum system the temperature of the specimen is kept above that of the walls. When the vacuum has attained $2\text{-}3 \cdot 10^{-9}$ torr, the surfaces are processed in three different ways.

a. Reduction in atomic hydrogen. It has been shown[3,4] that adsorption of atomic hydrogen on oxidized germanium makes it possible to remove oxygen as H_2O molecules at temperatures well below the desorption temperature for germanium monoxide. This result indicates that atomic hydrogen can clean germanium, removing nonvolatile films which usually remain after etching in SR-4.

The initial stages of cleaning with atomic hydrogen give rise to thermal desorption of water molecules, while desorption of atoms or molecules of hydrogen is not observed. The atomic hydrogen is produced by dissociation of H_2 molecules at a heated tungsten filament.[2-4] With the passage of time, the numbers of desorbed H_2O molecules falls and molecular hydrogen begins to dissolve. At the same time, thermal desorption of the germanium monoxide follows adsorption of the oxygen. After reduction in atomic hydrogen at $p\ (H_2) \sim 10^{-7}$ torr, there follows annealing under a very high vacuum, which reveals that no more H_2O molecules are desorbed. Then the specimens are annealed additionally for several hours at very low pressures with constant mass spectrometer monitoring of the evaporation products. The cleaning is terminated when the mass spectra only show peaks corresponding to germanium isotopes.

b. Bombardment with argon ions. A surface cleaned by reduction in hydrogen is bombarded with ions with energies of about 500 eV, the argon pressure in the system being about 10^{-3} torr. After bombardment for 10 min at 50-60 $\mu A/cm^2$, the specimen is given a 30 min annealing. The argon trapped by the specimen during bombardment is released during the first few minutes of annealing, and no subsequent desorption of argon is observed. This cycle is repeated several times, and is followed by annealing for 1-2 h at about 1000°K.

c. Annealing. The surface purified by bombardment is subjected to prolonged annealing in a very high vacuum at about 1000°K for several days.

The surface of each specimen thus undergoes all three stages of processing, after each of which we measure the amounts of adsorbed hydrogen and oxygen under standard conditions (constant gas pressure and temperature in the dissociation apparatus).

RESULTS

Surfaces cleaned by reduction in hydrogen give sticking coefficients[3] for O_2 of about 10^{-5}, with a substantial increase when the adsorption is performed in the presence of a hot tungsten filament. The amount of adsorbed oxygen is deduced from the number of GeO molecules released, and this depends substantially on the geometry of the specimen in relation to the tungsten filament as well as the temperature of the latter. This effect is not due to exposure of the surface to electrons, to the action of the light, to heating, to a deposition of tungsten or tungsten oxide on the surface, or to the generation of CO, CO_2, or H_2O at the hot tungsten. We conclude that the longer sticking coefficient is due to atomization of the O_2 at the hot tungsten and the easier adsorption of oxygen atoms; this result agrees with the results of ref. 5, where molecular beam methods are used to show that the rate of adsorption of oxygen atoms on germanium is larger by an order of magnitude than that for molecules.

Figure 1 shows the amount of desorbed GeO as a function of oxygen adsorption time for the adsorption of molecules (case 1) and common adsorption of atoms and molecules (case 2), the surface having been cleaned in hydrogen. The molecules make only a small contribution to the adsorption when atoms and molecules are present together, so in what follows we only consider adsorption of atomic oxygen.

When the surfaces have also been cleaned by bombardment, the O_2 is adsorbed much more rapidly (Fig. 2), while

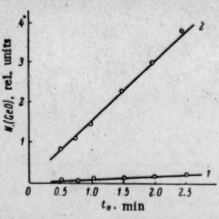

Fig. 1. Number of desorbed GeO molecules as a function of oxygen adsorption time for a germanium surface reduced in atomic hydrogen for adsorption of: 1) molecular oxygen; 2) atomic and molecular oxygen, P(O_2) ≈ $2 \cdot 10^{-6}$ torr.

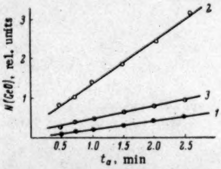

Fig. 2. Number of desorbed GeO molecules as a function of molecular oxygen adsorption time after: 1) reduction in atomic hydrogen; 2) additional bombardment by argon ions; 3) annealing (~ 30 h).

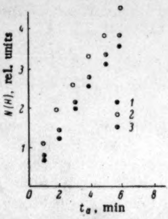

Fig. 3. Number of adsorbed hydrogen atoms as a function of time after: 1) reduction in atomic hydrogen; 2) additional bombardment by argon ions; 3) annealing (~ 30 h).

the amount of adsorbed oxygen is increased by less than 30-40%, the differences being within the limits of experimental error. The amount of adsorbed O_2 falls as the annealing time increases (Fig. 2), and after annealing for 50 h the value is approximately the same as for a surface cleaned by reduction in hydrogen.

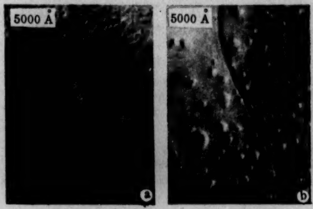

Fig. 4. Germanium surfaces made by: a) reduction in atomic hydrogen; b) bombardment with argon ions.

No adsorption of molecular hydrogen is found in any case. Figure 3 shows the amount of adsorbed hydrogen atoms as a function of adsorption time for surfaces cleaned in various ways. There is some increase in the amount of hydrogen adsorbed on the surface cleaned by bombardment because of the change in the surface relief, as is clear from photographs obtained by means of carbon replicas and an ÉM-5 electron microscope (Fig. 4).

Ion-bombarded surfaces show uptakes of O_2 molecules increased by factors of 5-6, which appear not to be related to additional purification of the germanium since we do not find a similar increase in the number of desorbed GeO molecules after adsorption of atomic oxygen. We assume that the more rapid adsorption of O_2 molecules on surfaces cleaned by bombardment is due either to increased microdefect concentrations, which heal only on prolonged annealing,[6] or to a change in the structure of the bonds at the surface during the bombardment—annealing cycle.[7]

We are indebted to N. I. Ionov for discussion and to M.I. Rudenko for the electron microscopy.

---

[1] V. N. Ageev, N. I. Ionov, and Yu. K. Ustinov, Zh. Tekh. Fiz., 34, 546 (1964) [Sov. Phys. – Tech. Phys., 9, 424 (1964)].

[2] Yu. I. Belyakov and T. N. Kompaniets, Zh. Tekh. Fiz., 42, 855 (1972) [Sov. Phys. – Tech. Phys., 17, 674 (1972)].

[3] Yu. I. Belyakov and T. N. Kompaniets, Zh. Tekh. Fiz., 42, 1278 (1972) [Sov. Phys. – Tech. Phys., 17, 1016 (1972)].

[4] Yu. I. Belyakov and T. N. Kompaniets, Zh. Tekh. Fiz., 43, 1317 (1973) [Sov. Phys. – Tech. Phys., 18, 839 (1973)].

[5] R. J. Madix and A. A. Susu, Surf. Sci., 20, 377 (1970).

[6] H. Farnsworth, Physics of Semiconductor Surfaces [Russian translation], IL, Moscow (1959), p. 55.

[7] J. J. Lander, G. W. Gobeli, and J. Morrison, J. Appl. Phys., 34, 2298 (1963).

Monte Carlo analysis of ion scattering in a mass spectrometer

M. L. Aleksandrov, L. N. Gall', and N. S. Pliss

(Submitted April 26, 1973)
Zh. Tekh. Fiz., 44, 1302-1305 (June 1974)

A Monte Carlo method is proposed for calculating the ion scattering by the residual gas and thus, the isotopic sensitivity of a mass spectrometer. Use of this method on a computer shows that the results are simple to interpret. It can be applied to various spectrometers and particular geometric features can be incorporated in the method. It can be used to optimize ion-optics systems. A calculation of the ion-scattering background in a static magnetic mass analyzer on a Minsk-22 computer and an experimental check of the results are reported.

In nuclear physics, semiconductor physics, and in chemical kinetics it is frequently necessary to analyze microscopic amounts of a material, this material frequently appearing as a microscopic impurity in some other material. When mass-spectrometric methods are used for this analysis, the most crucial aspect of the spectrometer is its isotopic sensitivity, i.e., its ability to measure microscopic amounts of material at high intensity ratios of peaks corresponding to adjacent masses. This sensitivity can be defined as the ratio of the background current at a point M±1 in the mass spectrum to the current of unscattered ions with mass M (ref. 1). If the analyzer is capable of completely resolving ion beams with masses M and M±1, the background current at the mass positions adjacent to the main peak results from two effects: scattering of ions of the main beam by residual-gas molecules and the reflection of these ions from the walls of the analyzer chamber.

Efforts to reduce the scattering effect and to increase the isotopic sensitivity have been based on several methods, primarily those involving improvement of the vacuum, tandem analyzers, and retarding-potential electrostatic systems.[2-4] As a rule, the choice of a method depends on the materials being studied and on the intuition of the person designing the apparatus, since no methods have been available for calculating ion scattering. Theoretical papers[5,6] which appeared in the 1960s did not find practical applications because of serious calculation difficulties and several important limitations; in particular, the theories neglected the aberrations of the beam focusing, the energy lost by an ion in a collision, and the geometric structure of the interior of the analyzer chamber. We have now worked out a versatile method for calculating the background due to ion scattering by the residual gas in a mass spectrometer.

METHOD FOR CALCULATING ION SCATTERING

In working out this method we have been guided by the following considerations:

1. The method must be versatile, i.e., applicable to both static and dynamic instruments; it must be easily adaptable for computer calculations; and the results must be easy to interpret.

2. In the choice of the optimum ion-optics systems for mass spectrometers[7] with high isotopic sensitivity it is clearly necessary to put the same emphasis on the ion scattering as on the focusing properties of the analyzer. The method must therefore be flexible enough to incorporate easily the geometric structure of the particular analyzer.

3. The scattering of ions in an analyzer is a random process, in that the initial conditions under which the ion enters the analyzer chamber are random, the point at which an ion meets a residual-gas molecule is random, and the number of possible encounters, i.e., the angle through which the ion is deflected as a result of the first collision, is random. The method must therefore be based on statistical probabilities.

With these considerations in mind, we choose the Monte Carlo method, whose use on a computer requires analytic expressions for the ion trajectories in the analyzer for specified initial conditions and for specified distributions of the several random quantities. Then the computer can be used to simulate "histories" of the motion and scattering of individual ions, to determine the coordinates of the points at which the ions are incident on the plane of the detector slit, and thus to construct the appropriate histogram, which can then be analyzed to study the effect in question.

We can briefly review the basic steps and features of the simulation of ion scattering by the residual gas; the corresponding simulation for scattering of ions by the chamber walls is not fundamentally different, but does have certain unique features.

Simulation of the injection of ions into the vacuum chamber of the analyzer. Here we need to know the combined distributions of certain random quantities: the angles describing the direction of the ion velocity at the entrance into the chamber, the ion energy at the entrance, and the coordinates of the entrance point. This information can be extracted from a statistical analysis of the processes occurring in the ion source. The purpose of this step is to simulate the initial conditions under which the ion enters the chamber, i.e., to construct the random vector $\mathfrak{A}_0$, whose components are the random quantities listed above.

Determination of the coordinates of the point at which the next scattering event occurs. Here we need the distribution of the random quantity l, the mean free path of the ion between successive collisions. After constructing this distribution and plotting it along the ion trajectory, we can easily find the coordinates of the scattering point.

The distribution of the quantity l can be assumed to be exponential:

$$F(l)=\begin{cases} 1-\exp(-\lambda l), & l\geqslant 0, \\ 0 & l<0, \end{cases} \qquad (1)$$

where $\lambda = \sqrt{2}n\sigma_{tot}$, n is the number of residual-gas molecules per unit volume, and σ_{tot} is the total scattering cross section.

It is important to note that at the vacuum levels used in modern mass spectrometry, the mean free path of an ion is much longer than its path in the apparatus. Therefore, only a small number of the histories generated on the basis of distribution (1) will contribute useful information; the overwhelming majority of the ions reach the collector without having undergone any collisions. To avoid the unproductive expenditure of computer time which would result from this direct simulation of the mean free path, we simulate a nominal mean free path which is defined for our purposes.

We denote by $S(\tilde{\alpha}_0)$ the length of the trajectory of an unscattered ion which enters the analyzer chamber under initial conditions $\tilde{\alpha}_0$; then the distribution of the nominal mean free path between collisions can be specified as

$$G(l)=\frac{F(l)}{F[S(\alpha_0)]},$$

with $F(l)$ given by (1).

Analysis of this second step of the calculation reveals another important advantage of this method: The ion-scattering background can be evaluated by varying the pressure at various parts of the apparatus. For example, in the case of an exponential distribution of the mean free path, we can do this by introducing scaling factors for various parts of the apparatus as functions of the pressure.

Simulation of the initial conditions of the ion motion after a scattering event. Here we need to know the distributions of the angles specifying the direction in which the ion moves after a collision; these angles are measured with respect to the direction in which the ion was moving initially. Here it is convenient to analyze the scattering event itself, in the spherical coordinate system fixed in the center of mass. If we adopt as the polar axis the vector of the relative velocity of the ion and the target molecule before the scattering, we can assume the azimuthal angle of the new relative velocity to be distributed homogeneously over the interval $[0, 2\pi]$ by virtue of the axial symmetry of the scattering.

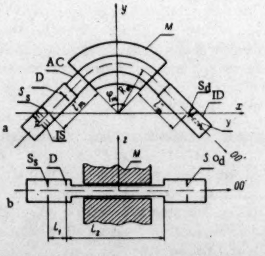

Fig. 1. Arrangement and basic structural parameters of a magnetic analyzer. a) Diagram of the analyzer in the xy plane; here φ_m = 90° and $R_m = l'_m = l''_m$ = 500 mm. b) Diagram of the analyzer in the $x\dot{z}$ plane along the axis of the central trajectory; here L_1 = 300 mm and L_2 = 1040 mm. IS) Ion source; S_s) exit slit of the ion source (0.1 × 4 mm); D) diaphragm which limits the beam to a height h_D = 7 mm; AC) analyzer chamber (70 × 11 mm); S_d) slit of ion detector (0.4 × 7.6 mm); ID) ion detector with movable collector; M) multiplier.

The polar angle θ, on the other hand, is a function $\theta(b)$ of the impact parameter b. For the scattering of a spatially homogeneous ion beam by a single scattering center, the impact parameter has the distribution

$$f(b)=\begin{cases} cb, & b\in[b_1, b_2], \\ 0, & b\notin[b_1, b_2], \end{cases} \tag{2}$$

where c is a normalization factor, and b_1 and b_2 are determined from the equations $\theta(b_1) = \theta_{max}$ and $\theta(b_2) = \theta_{min}$. The angle θ_{max} is governed by the total length of the interval over which the histogram is constructed, while θ_{min} is governed by the length of the partitioning interval. As the quantity σ_{tot} in (1) we adopt $\sigma_{tot} = \pi b_2^2$. The random quantity b with distribution (2) can be simulated easily, while the function $\theta(b)$ is governed by the nature of the ion, the nature of the molecule, and the ion energy, and thus requires a special study.

After calculating θ and transforming the velocity vector to the laboratory system, we can easily determine the trajectory along which the ion subsequently moves.

Plotting of the scattered-ion histograms. We consider the xz plane of the detector; we draw axis Ox through the midpoint along the long dimension of the detector slit, and we draw axis Oz, perpendicular to it. If the detector slit has a length h, we consider the band in this plane defined by $(-h/2) \leq z \leq (h/2)$; it is in this band that we record the coordinates of all the incident ions. As a result we find a sample $x_1, x_2, \ldots, x_N$, where N is the number of "histories"; according to the rules of statistics, we use this sample to construct the histogram for evaluating the scattered-ion background.

Example. As an example we calculate and compare by experiment the scattered-ion background in a static magnetic mass analyzer (Fig. 1).

Figure 2 shows the "tail" of the K^{39} peak for scatter-

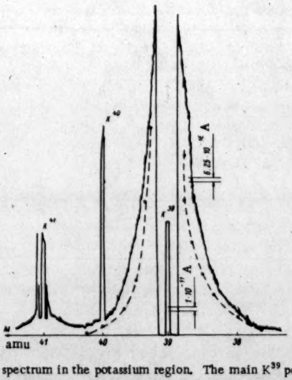

Fig. 2. Mass spectrum in the potassium region. The main K^{39} peak and the scattered-ion peak are plotted with different scales (the scale divisions are $1 \cdot 10^{-11}$ and $6.25 \cdot 10^{-16}$ A, respectively). The dashed curve is plotted by smoothing the scattered-ion histogram calculated by the method of the present paper.

ing by residual air, measured in an apparatus having U_{acc} = 3 keV and an analyzer-chamber pressure of $p = 3 \cdot 10^{-7}$ torr. The dashed curve in this figure is the calculated background found by the simulation of 4000 histories in 40 min on a Minsk-22 computer.

We see that the results agree well. The apparent reason that the calculated curve lies below the experimental curve is that our calculation takes into account only the elastic scattering of ions by residual-gas molecules, while there are other effects which influence the background.

CONCLUSIONS

1. An effective and versatile Monte Carlo method has been worked out for calculating the ion scattering by the residual gas and walls of an analyzer chamber of a mass spectrometer. No such method has been reported previously.

2. Since the method can incorporate any geometric structure of the analyzer chamber and the features of the ion-beam focusing, it can be used to select and optimize ion-optics systems for mass-spectrometer.

---

[1] F. A. White and L. Forman, Rev. Sci. Instr., 38, 355 (1967).

[2] R. G. Ridly, R. Munro, W. A. P. Young, R. Hayes, R. W. D. Hardy, and H. W. Wilson, Adv. Mass. Spectrom., 3, 553 (1965).

[3] R. N. Gall', Zh. Tekh. Fiz., 39, 360 (1969) [Sov. Phys. – Tech. Phys., 14, 263 (1969)].

[4] N. J. Freeman, N. R. Daly, and R. E. Powell, Rev. Sci. Instr., 38, 945 (1967).

[5] M. Menat, Canad. J. Phys., 42, 164 (1964).

[6] D. Joanoviciu, Canad. J. Phys., 48, 1735 (1970).

[7] M. L. Aleksandrov, L. N. Gall', and V. F. Denisov, Zh. Tekh. Fiz., 43, 829 (1973) [Sov. Phys. – Tech. Phys., 18, 520 (1973)].

Behavior of molten salts in strong electric fields

A. Z. Éfendiev, O. M. Shabanov, S. M. Gadzhiev, and S. M. Tagirov

V. I. Lenin Dagestan State University

(Submitted April 10, 1973)
Zh. Tekh. Fiz., 44, 1306-1311 (June 1974)

In an effort to fill a gap in the literature on the behavior of molten electrolytes (salts) in strong electric fields, a study is made of the electrical conductivity of molten lithium chloride at 630, 660, 735, and 800°C, of sodium chloride at 830 and 885°C, and of potassium chloride at 800, 840, and 885°C. Various field intensities are used. At fields above 40 kV/cm the discharge is accompanied by a glow of the salt, not due to breakdown. The electrical conductivity increases with increasing field, approaching a limiting value at a certain field which is a function of the temperature and the nature of the salt. The high-voltage conductivities agree with the Nernst–Einstein equation, so that the self-diffusion coefficients of the ions in the various salts can be calculated. The activation energy for the conductivity is higher in strong fields than in weak fields.

The few works which have been reported on the high-voltage behavior of conducting liquids can be classified into two groups; in the first group[1–3] it has been established that the electrical conductivity of molten electrolytes increases with increasing electric field, reaching saturation in fields of the order of 10^5 V/cm. These results constitute experimental confirmation of the existence of ion environments, in accordance with the Debye–Hückel–Onsager theory. In the second group, comparatively recent work,[4–6] a first attempt has been made to establish the physical nature of a high-voltage discharge in a conducting liquid. It was concluded that the discharge can be of the nature of an exponential decay, an oscillatory discharge, or a voltage cutoff (breakdown), depending on the high-voltage conductivity and the intensity of the electric field. The high-voltage behavior is found to be a function of the low-voltage conductivity, but not the nature of the electrolyte.

Our search of the literature has revealed no work on the behavior of molten electrolytes in strong electric fields, even though ionic liquids, of which molten salts are typical, are the most interesting, (from the theoretical standpoint) class of liquids displaying a long-range structural-particle potential. Furthermore, such liquids are widely used in atomic power and metallurgy. Study of the high-voltage behavior of molten salts can yield valuable information about the structures and transport properties of these liquids; in particular, as pointed out in ref. 7, a knowledge of the limiting conductivity of an electrolyte can shed light on the discrepancy in the Nernst–Einstein equation and can make it possible to use this equation to determine the self-diffusion coefficients of ions in melts. This latter result would greatly facilitate study of the kinetics of electrode processes.

We have therefore begun a study of molten salts in strong electric fields.

EXPERIMENTAL PROCEDURE

The apparatus used to measure the electrical conductivity of the molten salts as a function of the electric field is similar to that described in ref. 6, but the current is measured by a Rogowski loop instead of a current shunt. A generator with a controllable switch produces pulses, whose amplitude is adjustable up to 30 kV. The oscilloscope sweep is synchronized with the generator switch by means of a special single-pulse unit with delay adjustable from 0.3 to 50 μsec. The voltage drop across the sample and the current through it are recorded by means of an OK-21 dual-beam high-speed oscilloscope. The oscillograms are taken with a Zenit S camera using high-speed film. Mel'nikov et al.[6] did not state whether the electrolyte impedance was monitored in the course of their experiments. In the present experiments the low-voltage impedance of the sample is measured with an ac bridge after each pulse. The succeeding pulse is supplied only after the low-voltage impedance returns to its original value.

The maximum voltage drop across the melts is about 15 kV, and the currents do not exceed 6000 A. The electrodes are molybdenum conductors 1-2 mm in diameter, enclosed in long porcelain tubes. The ends of the electrodes are bent at a 90° angle and held tightly in a short (2 cm) porcelain tube to keep the polished bare surfaces strictly parallel. This short tube is ground off near the ends of the electrodes to allow free access of the melt to the interelectrode volume. The procelain tubes are reinforced with platinum wire at several points to keep the electrodes from being driven apart by the shock wave which arises in the discharge. The samples are prepared from "chemically pure" stock, recrystallized, and dried for 10-15 h. The salt is held in a porcelain or alundum crucible, which is lowered into position on the bottom of the quartz tube. The tube is filled with argon. The temperature of the melt is measured by a platinum/platinum–rhodium thermocouple. The entire system is placed in a muffle furnace.

RESULTS AND DISCUSSION

We have studied the electrical conductivity of the salts as a function of the electric field at several temperatures: 630, 660, 735, and 800°C for lithium chloride, 830 and 876°C for sodium chloride, and 800, 840, and 885°C for potassium chloride.

Because of the high conductivity of molten salts the impedance of the discharge gap can be lower than the critical impedance of the discharge circuit, in which case the

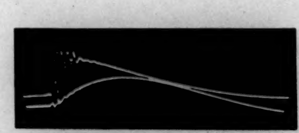

Fig. 1. Typical oscillograms of the voltage (upper trace) and current in the molten salts in strong electric fields.

TABLE 1

Salt	t, °C	λ_{expt}, cm²/Ω · g-eq(ref.8)	λ_{lim}, cm²/Ω · g-eq	$\frac{\Delta\lambda \cdot 100\%}{\lambda_{expt}}$	$\frac{\lambda_{expt}}{\lambda_{lim}}$	E_{lim}, kV/cm
LiCl	630	168	224	33.3	0.75	67
	660	170.9	231.8	35.6	0.737	55
	735	184.7	256.7	39.5	0.715	42
	800	199	287	44.2	0.693	33
NaCl	830	139.7	175	25.3	0.798	100
	876	147.1	195	32.6	0.754	75
KCl	800	110.3	125.3	13.3	0.872	167
	840	116.8	135.2	15.5	0.866	155
	885	124.0	148.4	19.6	0.835	145

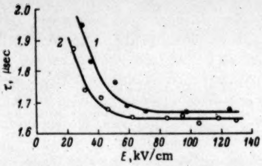

Fig. 2. Voltage-discharge time as a function of the electric field in LiCl at various temperatures. t, °C: 1) 735; 2) 800.

discharge becomes oscillatory. We therefore connect a 3.58 Ω noninductive resistor in series with the discharge gap; this resistor also limits the discharge current. Figure 1 shows typical oscillograms. The time constant of the discharge circuit is a function of the capacitance of the capacitor, the 3.58 Ω resistor in series with the salt, and the impedance of the salt itself. In the present experiments, this time decreases with increasing voltage. Figure 2 shows the discharge time of the first half-period of the aperiodic voltage oscillations for LiCl at 735 and 800°C as a function of the electric field. Other conditions being equal, a decrease in this time should be the result of a decrease in the resistance of the molten salts accompanying an increase in the electric field. The discharge time becomes constant at a certain value of E, which is a function of the temperature and the nature of the salt.

At fields above 40 kV/cm the salts glow; the oscillograms reveal no corresponding rapid voltage drop or current discontinuity. The glow becomes more intense as the field is strengthened (we did not take photographs of the glow). The oscillograms show that over the field and temperature ranges in question the glow is not due to a breakdown; it might be electroluminescence. Over a time of the order of 10^{-6} sec the Joule heat and the discharge products do not change the temperature or composition perceptibly.

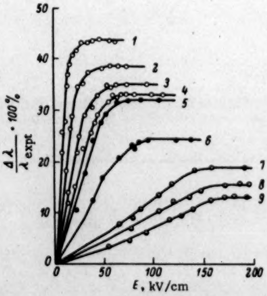

Fig. 3. The quantity $(\Delta\lambda/\lambda_{expt}) \cdot 100\%$ as function of the electric field. t, °C: 1-4) LiCl; 1) 800; 2) 735; 3) 660; 4) 630; 5, 6) NaCl; 5) 876; 6) 830; 7-9) KCl; 7) 885; 8) 840; 9) 800.

The electrical conductivities of LiCl, NaCl, and KCl at the stated temperatures, calculated from the oscillograms, increase with increasing field, tending toward a limiting value at a field value governed by the temperature and the nature of the salt. Figure 3 shows the relative change in the equivalent conductivity of these salts as a function of the electric field; at a certain field (E_{lim}) this conductivity becomes constant (the equivalent conductivity reaches its limiting value). Table 1 shows the limiting conductivities λ_{lim} along with the fields at which they are reached (E_{lim}), the relative change in the equivalent conductivity $(\Delta\lambda/\lambda_{expt}) \cdot 100\%$, the ordinary low-voltage conductivity λ_{expt}, and the ratio $\lambda_{lim}/\lambda_{expt}$.

The data in Fig. 3 and Table 1 show that for a given salt the quantities λ_{lim} and $(\Delta\lambda/\lambda_{expt}) \cdot 100\%$ increase while the quantities $\lambda_{expt}/\lambda_{lim}$ and E_{lim} decrease with increasing temperature. The relative change at a given temperature decreases from LiCl to KCl, while E_{lim} and $\lambda_{expt}/\lambda_{lim}$ increase (the latter quantity is adopted as the degree of dissociation of the electrolyte in the case of electrolytic solutions; then λ_{lim} is the equivalent conductivity at infinite dilution).

We believe there are two reasons for the increase in the conductivity of the molten salts with increasing electric field. The structure of the molten chloride of an alkali metal can be described by[9, 10]

$$\mathrm{MeCl}_n^{(n-1)-} + (n-1)\,\mathrm{Me}^+ \quad (\mathrm{Me}^+ = \mathrm{Li}^+,\ \mathrm{Na}^+,\ \mathrm{K}^+). \tag{1}$$

The conductivity is governed principally by the free cations in the second coordination sphere, which, like the complex $\mathrm{MeCl}_n^{(n-1)-}$ ions, have ion environments. In certain molten salts the motion of an ion in the electric field is prevented by the relaxational damping which results from a Coulomb interaction between the moving ion and the environment, whose symmetry is disrupted.[11] As the field is strengthened the drift velocity increases and can reach a value such that the ion environment does not manage to form along the path of the ion, i.e., the relaxational damping is removed. This case corresponds to the condition

$$l \leqslant \tau v, \tag{2}$$

TABLE 2

Salt	t, °C	λ_p	λ_{lim}	$D_+ \cdot 10^4$, cm²/sec		$D_- \cdot 10^4$, cm²/sec	
				[12]	from λ_{lim}	[12]	from λ_{lim}
LiCl	630	—	224.0	—	1.35	—	0.45
	660	—	231.8	—	1.45	—	0.48
	735	—	256.7	—	1.73	—	0.58
	800	—	287.0	—	2.06	—	0.69
NaCl	830	167.8	175.0	0.92	1.01	0.69	0.71
	876	186.5	195.0	1.11	1.17	0.80	0.84
KCl	800	—	125.3	—	0.74	—	0.46
	840	—	135.2	—	0.83	—	0.51
	885	—	148.4	—	0.96	—	0.59

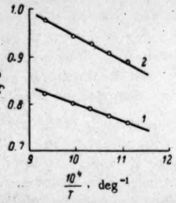

Fig. 4. log σ as a function of 1/T.

where l is the thickness of the ion environments (the Debye shielding length), τ is the relaxation time, and v is the ion velocity.

On the other hand, the ion energy in the field can be equal to or larger than the energy with which the ions are bound in the complex, so that the complex ions can decay, increasing the concentration of current carriers. Thus an increase in the field can increase both the mobility and the concentration of the carriers. These increases can continue until a field E_{lim} is reached, above which the mobility and concentration remain constant and Ohm's law holds.

Comparison shows that the values of E_{lim} for molten salts are low in comparison with those for electrolytic solutions,[1,3] apparently because solvation and electrophoretic damping do not occur in the molten salts. The functional dependence of E_{lim} on the temperature for a given melt can be described by the empirical equation

$$\ln E_{\text{lim}} = A - BT, \tag{3}$$

where E_{lim} is in volts per centimeter, T is in deg K, and A and B are constants for a given salt. For LiCl, e.g., the constants are A = 15.15 and B = $4.6 \cdot 10^{-3}$.

We can find an explanation for this functional dependence of the relative conductivity change on the temperature by considering the way in which the structure of the molten salt varies with temperature. As the temperature is raised the first coordination number, n, in Eq. (1) must decrease; then the relative number of free ions in the second coordination sphere decreases, and the relative number of ions bound in the complex increases. These changes explain the increase in $\Delta\lambda \cdot 100\%/\lambda_{\text{expt}}$ with increasing temperature: At high fields the relaxational damping is weakened and the complexes decay. The observed change in $\lambda_{\text{expt}}/\lambda_{\text{lim}}$ for a given salt as a function of the temperature can also be explained in this manner. The relative change in the conductivity decreases from LiCl to KCl at a given temperature because the relative stability of the complexes and the extent of binding in complexes decrease from LiCl to KCl, as follows from an analysis of the radial-distribution curves.

In weak fields the logarithm of the conductivity is a linear function of 1/T for alkali chlorides.[8] To check this functional dependence for strong fields we have plotted the corresponding data from the present experiments in Fig. 4, where the weak-field data from ref. 8 are shown for comparison. We see that ln σ is again a linear function of 1/T in strong fields, but that the activation energy is higher than in weak fields. This increase in the activation energy corresponds to an increase in the height of the potential barrier, which hinders ion migration.

According to the Nernst–Einstein equation,

$$\lambda_D = \frac{F^2}{RT}(D_+ + D_-), \tag{4}$$

the self-diffusion coefficients of the ion of a salt are unambiguously related to the equivalent conductivity; however, in the case of molten salts the conductivity calculated from the experimental self-diffusion coefficients is 40% higher than the (directly measured) weak-field conductivity. Nevertheless, the strong-field values of λ_{lim} agree with the values calculated from the self-diffusion coefficients by means of Eq. (4). The values of λ_{lim} can thus be used to calculate the self-diffusion coefficients of the various ions, if t and λ_{lim}, and the transition number are known. Table 2 shows the coefficients calculated from

$$D_i = t_i \sum D_i = t_i \frac{RT}{F^2} \lambda_{\text{lim}} \tag{5}$$

along with the experimental coefficients for LiCl, NaCl, and KCl. The literature reveals no data on self-diffusion for the cases of LiCl and KCl, but the agreement between the coefficients measured directly and calculated from λ_{lim} for NaCl is quite satisfactory, so that we can hope that experiment will confirm the values calculated for LiCl and KCl.

In calculating the self-diffusion coefficients we use the transition numbers for NaCl, calculated from

$$t_\pm = \frac{D_\pm}{D_+ + D_-}.$$

The values of D_+ and D_- are taken from ref. 12. In the calculations for LiCl and KCl the transition numbers are taken from ref. 13.

SUMMARY

1. The electrical conductivity of molten salts (alkali chlorides) has been measured as a function of the electric field for the first time. The conductivity has been shown to increase with increasing field, reaching a limiting value.

2. Breakdown is not observed in the molten salts. The discharge is accompanied by a glow.

3. The limiting conductivities, used in the Nernst–Einstein equation, give values for the self-diffusion coefficients of the ions which agree well with the values measured directly.

4. The activation energy for the conductivity increases with increasing field.

---

[1] J. Malsch and M. Wien, Physik. Z., 25, 559 (1924).

[2] M. Wien, Ann. Physik, 83, 327 (1927); Ann. Physik, 85, 795 (1928).

[3] J. A. Gladhill and A. Paterson, J. Phys. Chem., 56, 999 (1952).

[4] N. P. Mel'nikov, G. A. Ostroumov, and M. Yu. Stoyak, in: Breakdown of Dielectrics and Semiconductors [in Russian], Izd. Énergiya, Moscow–Leningrad (1964), p. 250.

[5] N. P. Mel'nikov, G. A. Ostroumov, and A. A. Shteinberg, in: Breakdown of Dielectrics and Semiconductors [in Russian], Izd. Énergiya, Moscow–Leningrad (1964), p. 236.

[6] N. P. Mel'nikov, G. A. Ostroumov, and A. A. Shteinberg, Dokl. Akad. Nauk SSSR, 147, 882 (1962).

[7] A. V. Gorodyskii and É. V. Panov, in: Physical Chemistry of Molten Salts [in Russian], Izd. Metallurgiya, Moscow (1965), p. 193.

[8] Jaffe and Van Artsdallen, J. Phys. Chem., 60, 1125 (1956).

[9] M. V. Smirnov, O. M. Shabanov, and A. P. Khaimenov, Élektrokhimii 2, 1240 (1966).

[10] M. V. Smirnov and O. M. Shabanov, Tr. Inst. Élektrokhimii UF Akad. Nauk SSSR, No. 8, 55 (1966).

[11] W. Oldekop, Z. Physik, 2, 181 (1955).

[12] J. O'M. Bockris and G. W. Hooper, Disc. Faraday Soc., 32, 218 (1961).

[13] F. Duke and A. Bowman, J. Electrochem., 106, 622 (1959).

Shielding properties of superconducting shields

S. I. Bondarenko, S. S. Vinogradov, G. A. Gogadze, S. S. Perepelkin, and V. I. Sheremet

Physicotechnical Institute of Low Temperatures,
Academy of Sciences of the Ukrainian SSR, Khar'kov

(Submitted July 31, 1973)
Zh. Tekh. Fiz., 44, 1312-1320 (June 1974)

A theoretical and experimental study has been made of the effect of the shape of a superconducting shield on its shielding properties. Axisymmetric shields (cylindrical shield with a bottom or spherical shield with a circular aperture) are shown to be effective. The calculated shielding coefficients agree with the experimental data.

In modern physics experiments it is frequently necessary to produce a homogeneous magnetic field which is highly stable in time or to reduce the magnetic field to zero in some volume. Both problems can be handled successfully by means of superconducting shields. The Meissner effect induces superconducting currents at the surface of such a shield and these currents prevent the magnetic flux from penetrating into the region enclosed by the shield. The shielding properties are governed by several factors: the shape of the shield, the configuration of the external magnetic field, and the physical and chemical properties of the shield material (the purity of the metal, the surface state, strain, etc.). We report below a theoretical and experimental study of the effect of shape on the shielding properties of a superconducting shield.

A rigorous approach to this problem would involve the solution of Maxwell's equations outside and inside the superconductor and matching the solutions at the interface, but this approach is complicated by the need to know the distribution of the currents induced on the surface of the superconductor. Alternatively, in shielding problems it is possible to use the model of an ideal Meissner effect, letting the London penetration depth of the magnetic field, δ_L, approach zero. Then the analytic problem becomes a boundary-value problem with a vanishing normal derivative of the magnetostatic potential.[1)]

If the results of this analysis are to be correct, the value of δ_L must be much smaller than all characteristic dimensions of the problem (e.g., the radius of curvature ρ of the convex parts of the shell); otherwise, as follows from potential theory, divergences can occur at certain points. It is convenient to exploit the strong analogy between the current distribution over the surface of a superconductor and the distribution of electrostatic charge in a conductor. The magnetic field produced by the surface current has equipotentials which are coupled to surface charges. When there are convex areas on the surface of the superconductor, the magnetic lines of force become dense near them, as if the surface current were increased locally. On the other hand, there is an important distinction between our problem and the electrostatic problem: This increase in the magnetic field cannot continue without limit. Each superconductor is characterized by a definite value of the critical field H_k so that we can work from the requirement that the field near convex regions cannot exceed the critical field to find a rough estimate of the applicability range of this calculation method:

$$H < H_k \frac{\rho}{a}, \tag{1}$$

where H is the external field, and a is the characteristic width of the aperture in the shield. We conclude from this estimate that an effort should be made in the design of a shield to smooth out any corners.

In this work we consider superconducting shields of simple shape: plane shields and axisymmetric shields.[4,5] Evaluation of the shielding coefficients shows that the axisymmetric shields are more effective, so that only such shields are studied in the experiments: cylindrical shields (with closed bottoms) and spherical shells with apertures. We describe the experimental apparatus and report on the results of measurements for lead shields.

CALCULATION OF SHIELDING PROPERTIES

Superconducting plane with an aperture. We assume that a homogeneous magnetic field is produced far from a superconducting plane with an aperture and that the field is parallel to the plane of the shield, in the x direction. The field in the volume occupied by the superconductor is described by the Maxwell equations

$$\left.\begin{aligned}\operatorname{curl}\mathbf{H}=0,\\ \operatorname{div}\mathbf{H}=0.\end{aligned}\right\} \tag{2}$$

Introducing the potential φ and exploiting the symmetry of the problem, we reduce system (2) to the Laplace equation

$$\frac{\partial^2\varphi}{\partial x^2}+\frac{\partial^2\varphi}{\partial y^2}=0,\ \mathbf{H}=-\operatorname{grad}\varphi. \tag{3}$$

This equation is solved with the boundary condition that the normal derivative of the potential $\partial\varphi/\partial n$ must vanish at the boundary of the superconductor. It is convenient to use the conformal-mapping method of ref. 6, which does not alter the Laplace equation but simply transforms the boundary condition (see, e.g., ref. 7):

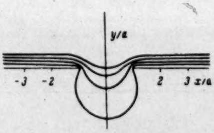

Fig. 1. Distribution of magnetic lines of force for a plane shield with an aperture.

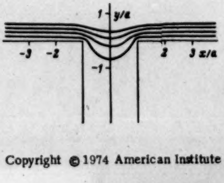

Fig. 2. Distribution of magnetic lines of force for a superconducting half-space with a groove.

$$\left.\frac{\partial\varphi_1}{\partial n_1}\right|_{S_1}=\left.\frac{\partial\varphi}{\partial n}\right|_S|z'(z_1)|=0, \tag{4}$$

where the complex quantity is $z = x + iy$, and the subscript "S" indicates that the derivative is to be evaluated at the boundary of the superconductor. Solving Eq. (4), we use the Cauchy–Riemann conditions to construct the complex potential $W_1 = \varphi_1 + i\psi_1 = A_1 z_1 + B_1$. To find the potential $W(z) = W_1[z_1(z)]$ in the z plane it is sufficient to know the function $z_1 = z_1(z)$. Using a Schwarz–Christoffel transformation,[6] we find

$$z_1=\frac{C}{a}\left(z+\sqrt{z^2-a^2}\right), \tag{5}$$

where $2a$ is the width of the aperture and C is a constant. The sign in front of the radical is chosen so that the transformation maps all points z into the upper half-plane of z_1. In this way we find the complex potential W(z). Then we use Eqs. (3) to calculate the components of the magnetic field around the shield:2)

$$H_x=-\frac{\partial\,\mathrm{Re}\,W}{\partial x},\quad H_y=-\frac{\partial\,\mathrm{Re}\,W}{\partial y}. \tag{6}$$

After lengthy but simple calculations we find

$$\begin{aligned}H_x=\frac{1}{2}\Bigg\{1+\Bigg[&\frac{x\,\mathrm{sign}\,(xy)\,(x^2+y^2-a^2)}{[(x^2-y^2-a^2)^2+4x^2y^2]^{3/4}}\\ &\times\frac{1}{\sqrt{2}}\sqrt{1+\frac{x^2-y^2-a^2}{\sqrt{(x^2-y^2-a^2)^2+4x^2y^2}}}\\ &+\frac{y\,(x^2+y^2+a^2)}{[(x^2-y^2-a^2)^2+4x^2y^2]^{3/4}}\frac{1}{\sqrt{2}}\sqrt{1-\frac{x^2-y^2-a^2}{\sqrt{(x^2-y^2-a^2)^2+4x^2y^2}}}\Bigg]\Bigg\};\\ H_y=\frac{H}{2}\Bigg\{&\frac{y\,\mathrm{sign}\,(xy)\,(x^2+y^2+a^2)}{[(x^2-y^2-a^2)^2+4x^2y^2]^{3/4}}\frac{1}{\sqrt{2}}\sqrt{1+\frac{x^2-y^2-a^2}{\sqrt{(x^2-y^2-a^2)^2+4x^2y^2}}}\\ &-\frac{x\,(x^2+y^2-a^2)}{[(x^2-y^2-a^2)^2+4x^2y^2]^{3/4}}\frac{1}{\sqrt{2}}\sqrt{1-\frac{x^2-y^2-a^2}{\sqrt{(x^2-y^2-a^2)^2+4x^2y^2}}}\Bigg\}.\end{aligned} \tag{7}$$

Let us consider the behavior of the field components along the x and y symmetry axes; according to (7), for example, we have $H_y = 0$ at the y axis, while H_x is described by

$$H_x=\frac{H}{2}\left(1+\frac{y}{\sqrt{y^2+a^2}}\right). \tag{8}$$

The shielding properties are customarily expressed in terms of a shielding coefficient K_S, which is the factor by which the magnetic field in the shielded volume is reduced at a distance equal to the width of the aperture in the shield.3) For a shield which is a superconducting plane with an aperture $2a$ wide we find $K_S \simeq 20$. As we move along the x axis we find

$$\left.\begin{aligned}&H_x=\frac{H}{2},\quad H_y=\frac{H}{2}\frac{x}{\sqrt{a^2-x^2}},\quad |x|<a,\\ &H_x=\frac{H}{2}\left\{1+\mathrm{sign}\,(y\to\pm 0)\frac{x\,[\theta(x-a)-\theta(-x-a)]}{\sqrt{x^2-a^2}}\right\},\\ &H_y=0,\quad |x|>a,\end{aligned}\right\} \tag{9}$$

where

$$\theta(x)=\begin{cases}1, & x>0,\\ 0, & x<0.\end{cases}$$

The reason for the divergences is noted above; The shield under consideration here is a plane with an aperture, near whose edge the condition $\delta_L \ll \rho$ does not hold. Figure 1 shows the distribution of the magnetic lines of force for this case. The principal drawback of such a shield is that if the field to be shielded against is not strictly parallel to the plane of the superconductor (if the component H_y does not vanish strictly) this field "falls into" the gap.4)

Superconducting half-space with a groove. Another possible version of the plane shield is a superconducting half-space with a groove; here we consider only the case of an infinitely deep groove. Again writing Maxwell equations (2), we conformally map the z plane into the upper half-plane of z_1. The Schwarz–Christoffel equation yields the relation

$$z=\frac{2a}{\pi}\left[\sqrt{z_1^2-1}+\arcsin\frac{1}{z_1}\right]. \tag{10}$$

Separating the real and imaginary parts in (10), we find a system of equations from which we can determine $x_1(x, y)$ and $y_1(x, y)$; these are used to construct the potential W(z):

$$\left.\begin{aligned}&x=\frac{2a}{\pi}\left[\sqrt{\rho}\,\frac{\theta}{2}+\mathrm{arc\,tg}\,\frac{x_1+\sqrt{\rho}\left(x_1\sin\frac{\theta}{2}-y_1\cos\frac{\theta}{2}\right)}{y_1+\sqrt{\rho}\left(x_1\cos\frac{\theta}{2}+y_1\sin\frac{\theta}{2}\right)}\right],\\ &y=\frac{2a}{\pi}\left[\sqrt{\rho}\,\sin\frac{\theta}{2}-\ln\sqrt{\frac{\rho+2\sqrt{\rho}\,\sin\frac{\theta}{2}+1}{x_1^2+y_1^2}}\right],\end{aligned}\right\} \tag{11}$$

where

$$\rho=\sqrt{(x_1^2-y_1^2-1)^2+4x_1^2y_1^2},\quad \theta=\theta_1+\theta_2,$$

$$\theta_1=\begin{cases}\mathrm{arc\,tg}\,\dfrac{y_1}{x_1-1}, & x_1>1,\\ \pi+\mathrm{arc\,tg}\,\dfrac{y_1}{x_1-1}, & x_1<1,\end{cases}$$

$$\theta_2=\begin{cases}\mathrm{arc\,tg}\,\dfrac{y_1}{x_1+1}, & x_1>-1\\ \pi+\mathrm{arc\,tg}\,\dfrac{y_1}{x_1+1}, & x_1<-1.\end{cases}$$

According to (11), at $x_1 = 0$ we have

$$x=0,\quad y=\frac{2a}{\pi}\left[\sqrt{y_1^2+1}+\ln\frac{y_1}{1+\sqrt{1+y_1^2}}\right]. \tag{12}$$

Noting that the left side of Eq. (12) vanishes at $y_1 \simeq 2/3$, we can find the analytic function $y_1 = y_1(0, y)$ within the shielded region by expanding (12) in powers of y_1. Retaining first-order terms and using (6), we find the behavior of the field components along the y axis:

$$H_x\cong\frac{2H}{e}e^{-\frac{\pi}{2a}|y|},\quad H_y=0, \tag{13}$$

from which we find $K_S \simeq 32$. Figure 2 shows the distribution of magnetic lines of force calculated from (11). Figure 3 shows the exact behavior of H_x along the y axis, plotted with the help of a computer.

Cylindrical superconducting shield. We turn now to axisymmetric shields, the simplest version of which is a superconducting cylinder. We assume the outer and inner radii of the cylinder to be a and b, respectively, and we assume the magnetic field to be directed along the z axis, the axis of the cylinder. We again begin the solution with the Laplace equation, which can be written as follows in the case of axial symmetry:

$$\frac{1}{r}\frac{\partial}{\partial r}\left(r\frac{\partial\varphi}{\partial r}\right)+\frac{\partial^2\varphi}{\partial z^2}=0. \tag{14}$$

We use the boundary conditions

$$\left.\frac{\partial\varphi}{\partial n}\right|_s=0,\quad -\left.\frac{\partial\varphi}{\partial z}\right|_{r=\infty}=H,\quad \left.\frac{\partial\varphi}{\partial z}\right|_{\substack{z=-\infty\\ r\leqslant a}}=0. \tag{15}$$

The last of these conditions reflects the circumstance that we are interested in a single connected shield: Experimentally, a superconducting shield is usually a long cylinder with a closed end. We divide the volume outside the superconductor into three volumes: (1) $0 \leq r \leq a$, $z \leq 0$; (2) the volume $r \geq 0$, $z \geq 0$; and (3) the volume $r \geq b$, $z \leq 0$.

We solve Eq. (14) by separation of variables. Using boundary conditions (15) we find the explicit form of the potential $\varphi(r, z)$ in these three volumes. We write the solution as a Fourier series (in the first volume) and as Fourier integrals (in the second and third volumes). The magnetic field components calculated from this solution ($H_r = -\partial\varphi/\partial r$, $H_z = -\partial\varphi/\partial z$) are, for the first two volumes,

$$\left.\begin{aligned} H_r^{(1)}&=H\sum_{m=1}^{\infty}A_m p'_m J_1\left(p'_m\frac{r}{a}\right)e^{\frac{p'_m}{a}z},\\ H_z^{(1)}&=-H\sum_{m=1}^{\infty}A_m p'_m J_0\left(p'_m\frac{r}{a}\right)e^{\frac{p'_m}{a}z}, \end{aligned}\right\} \tag{16}$$

$$\left.\begin{aligned} H_r^{(2)}&=H\int_0^{\infty}d\nu\,\nu F(\nu)\,J_1\left(\nu\frac{r}{a}\right)e^{-\frac{\nu}{a}z},\\ H_z^{(2)}&=H+H\int_0^{\infty}d\nu\,\nu F(\nu)\,J_0\left(\nu\frac{r}{a}\right)e^{-\frac{\nu}{a}z}. \end{aligned}\right\} \tag{17}$$

Here, J_n is the Bessel function of order n; p'_m are the zeros of J_1. Since we are only interested in the shielding properties of a cylindrical shell, we omit the field components in the third volume, which are functions of the unknown function $G(\nu)$. It turns out that both the coefficients A_m and the function $G(\nu)$ can be expressed in terms of $F(\nu)$; thus, the problem of calculating the field distribution reduces to that of finding $F(\nu)$. Using the continuity conditions on the potential at the boundaries of the volumes and using boundary conditions (15), we can use a Hankel transformation to find an integral Fredholm equation of the first kind for the function $F(\nu)$:

$$\int_0^{\infty}d\nu' F(\nu')\,K(\nu,\nu')=-\left(\frac{b}{a}\right)\frac{J_1\left(\nu\frac{b}{a}\right)}{\nu}. \tag{18}$$

The kernel of this equation is $K(\nu,\nu') = \xi(\nu,\nu') + \nu'\eta(\nu',\nu)$, where

$$\xi(\nu\nu')=2\sum_{m=1}^{\infty}p'_m\Gamma_m(\nu')\,\Gamma_m(\nu),$$

$$\eta(\nu,\nu')=\begin{cases}\dfrac{\left(\frac{b}{a}\right)\left[-\nu J_0\left(\nu'\frac{b}{a}\right)J_1\left(\nu\frac{b}{a}\right)+\nu' J_1\left(\nu'\frac{b}{a}\right)J_0\left(\nu\frac{b}{a}\right)\right]}{\nu'^2-\nu^2}, & \nu'\neq\nu,\\[2ex] \dfrac{1}{2}\left(\dfrac{b}{a}\right)^2\left\{J_0^2\left(\nu\dfrac{b}{a}\right)+J_1^2\left(\nu\dfrac{b}{a}\right)\right\}, & \nu'=\nu,\end{cases}$$

$$\Gamma_m(\nu)=\begin{cases}\dfrac{\nu J_1(\nu)}{\nu^2-p_m'^2}, & \nu\neq p'_m,\\[2ex] \dfrac{J_0(p'_m)}{2}, & \nu=p'_m.\end{cases}$$

This equation can be solved on a computer; the coefficients A_m are given by

$$A_m=\frac{2}{J_0(p'_m)}\int_0^{\infty}d\nu F(\nu)\,\Gamma_m(\nu). \tag{19}$$

In evaluating the shielding coefficient we need retain only the first term in the Fourier series, $H_z \sim He^{-7.6}$; the longitudinal field is then found to be $K_s \simeq 2000$ for this case.

In a transverse magnetic field (along the normal to the cylinder axis) the solution is written as a double Fourier series; an estimate shows that in this case the shielding coefficient is of the order of 40.

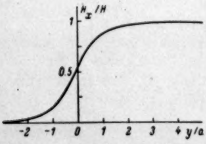

Fig. 3. The function $H_x = H_x(y)$ calculated on a computer for a shield which is a half-space with a groove.

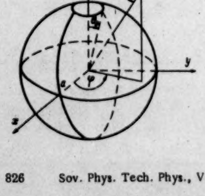

Fig. 4. Spherical shield with aperture.

Superconducting sphere with a circular aperture. We consider an infinitesimally thin superconducting sphere of radius a with a circular aperture $\theta = \theta_0$ in a homogeneous and fixed field $\mathbf{H}_0 \| 0z$ (Fig. 4). We seek a solution in the spherical coordinate system r, θ, φ, in which the potential of a homogeneous, azimuthally symmetric field is $U^{(0)} = -H_0 r P_1(\cos\theta)$, where $P_1(\cos\theta)$ is the Legendre polynomial of degree 1. We seek the total field potential in the form

$$U^{(e)}=U^{(0)}+V^{(0)},\quad U^{(i)}=V^{(i)}, \tag{20}$$

where the superscripts "e" and "i" refer to the exterior ($r > a$) and interior ($r < a$) of the sphere. We require that potential (20) satisfy the continuity conditions and the following boundary conditions:

$$\left.\begin{aligned} U^{(i)}|_{r=a-0}&=U^{(e)}|_{r=a+0},\quad 0\leqslant\theta\leqslant\theta_0,\\ \left.\frac{\partial U^{(i)}}{\partial r}\right|_{r=a-0}&=\left.\frac{\partial U^{(e)}}{\partial r}\right|_{r=a+0}=0,\quad \theta_0\leqslant\theta\leqslant\pi. \end{aligned}\right\} \tag{21}$$

The potentials themselves are sought in the form

$$U^{(e)}=-H_0 rP_1(\cos\theta)+H_0 a\sum_{n=0}^{\infty}A_n\left(\frac{a}{r}\right)^{n+1}P_n(\cos\theta), \tag{22}$$

TABLE 1

Diameter of aperture in sphere, mm	r, mm	Shielding coefficient		Sphere diameter mm
		longitudinal component	transverse component	
	40	$4.6 \cdot 10^4$	—	130
7	30	$8 \cdot 10^4$	—	—
14	30	$1.5 \cdot 10^4$	—	—
	25	$2.4 \cdot 10^4$	89	—
24	0	—	$4.5 \cdot 10^2$	—
49	0	$1.8 \cdot 10^3$	36	—
67	0	$4.5 \cdot 10^3$	18	—

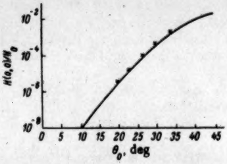

Fig. 5. Ratio of the field at the center of the sphere to the homogeneous external field H_0 as a function of the angle θ_0.

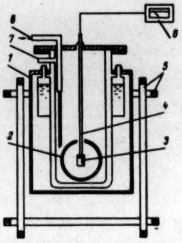

Fig. 6. The experimental apparatus. 1) Helium cryostat; 2) superconducting shield; 3) two-component pickup of the ferroprobe magnetometer; 4) calibrated rod; 5) Helmholtz coils; 6, 7) fittings for helium overflow and drainage; 8) ferroprobe magnetometer.

$$U^{(i)} = H_0 a \sum_{n=0}^{\infty} B_n \left(\frac{r}{a}\right)^n P_n(\cos\theta). \tag{23}$$

From the continuity condition we find a relation between expansion coefficients A_n and B_n:

$$-\delta_{1n} - (n+1) A_n = nB_n. \tag{24}$$

Conditions (21) with (24) lead to functional equations of the type

$$\left.\begin{aligned} &\sum_{n=0}^{\infty} B_n \frac{2n+1}{n+1} P_n(\cos\theta) = -\frac{3}{2} P_1(\cos\theta), \quad 0 \leqslant \theta \leqslant \theta_0, \\ &\sum_{n=1}^{\infty} B_n n P_n(\cos\theta) = 0, \quad \theta_0 \leqslant \theta \leqslant \pi. \end{aligned}\right\} \tag{25}$$

Using the integral Mehler–Dirichlet representation[8] for the Legendre polynomials, we can simplify Eqs. (25) (ref. 9):

$$\left.\begin{aligned} &\sum_{n=0}^{\infty} B_n \frac{2n+1}{n+1} \cos\left[\left(n+\frac{1}{2}\right)\theta\right] = -\frac{3}{2} \cos\frac{3\theta}{2}, \quad 0 \leqslant \theta \leqslant \theta_0, \\ &\sum_{n=1}^{\infty} B_n n \sin\left[\left(n+\frac{1}{2}\right)\theta\right] = 0, \quad \theta_0 \leqslant \theta \leqslant \pi. \end{aligned}\right\} \tag{26}$$

From (26) we find an infinite system of linear, homogeneous equations for the B_m:

$$\begin{aligned} mB_m = &-\frac{9}{8\pi}\left\{\frac{\sin[(m-1)\theta_0]}{m-1} - \frac{\sin[(m+2)\theta_0]}{m+2}\right\} \\ &-\frac{1}{4\pi}\sum_{n=0}^{\infty} B_n \left\{\frac{\sin[(n-m)\theta_0]}{n-m} - \frac{\sin[(n+m+1)\theta_0]}{n+m+1}\right\}\frac{1}{n+1}. \end{aligned} \tag{27}$$

Since we are interested only in the shielding coefficient and not the details of the magnetic field distribution around a superconducting sphere, we use (27) to find only the first expansion coefficient, B_1; this coefficient governs the magnetic field at the center of the sphere. The curve in Fig. 5 shows the ratio of the field at the center of the sphere to the external homogeneous field H_0 as a function of the angle θ_0.

EXPERIMENTAL STUDY OF SUPERCONDUCTING SHIELDS

Since this analysis shows axisymmetric shields to be more effective than planar shields, we have carried out an experimental study of the shielding properties of a spherical shield (with a circular aperture) and a cylindrical shield with a bottom.

The apparatus, shown in Fig. 6, consists of a helium cryostat 1 with superconducting shield 2 and a system of Helmholtz coils 5, 100 cm in diameter, used to produce the desired external field (with transverse and longitudinal components). The magnetic field is measured by ferroprobe magnetometer 8, which has a sensitivity of $3 \cdot 10^{-5}$ Oe at liquid-helium temperature. The shields are fabricated by cold compression from 99.995%-pure lead; the lead sphere is made from two hemispheres fabricated in this manner and then welded together. The sphere is 13 cm in diameter, with a wall 0.3 cm thick. The cylindrical shield, having a hemispherical bottom, is 11 cm in diameter and 22 cm long and has a wall 0.2 cm thick. In the measurements, a known external field is applied in two directions to the cylindrical shield: along the axis of the shield and along the normal to this axis. The changes in the magnetic field (for the two components) are measured along the axis within the shield. The shielding coefficient is evaluated from the results of the measurements.

In the case of the spherical shield with an aperture the external field is also imposed in two directions: perpendicular and parallel to the plane of the aperture. The penetrating field is measured along the radial direction through the center of the aperture. The maximum field imposed is 1.5-2 Oe.

Table 1 shows the data found on the shield of the longitudinal and transverse components by the superconducting sphere with an aperture, for various diameters of this aperture. The experimental points are also shown in Fig.

5, by the crosses. We see that the calculated data agree well with the experimental data.

The shielding properties of the cylindrical shield are studied for an untreated shield, i.e., one which is not annealed and whose surface is not etched, fabricated by mechanical compression. In this case the shielding coefficient for the transverse component is 30, while that for the longitudinal component is 1100. Etching the surface of the shield for 1 min in a solution of 20% hydrogen peroxide (30% concentration) and 80% glacial acetic acid causes no perceptible change in the shielding coefficients.

When the shield is annealed at + 170°C for 20 h, the shielding properties are affected: The shielding coefficient for the longitudinal field component increases to 1200, and that for the transverse component increases to 37. In the latter case there is a good order-of-magnitude agreement between theory and experiment. For the longitudinal component the discrepancy between the theoretical and experimental shielding coefficients is larger.

---

1) The distribution of the "frozen" magnetic flux and its homogeneity in doubly connected superconductors have been studied by several groups of investigators[1-3] working on the basis of the ideal Meissner effect, and the results have agreed satisfactorily with experiment.

2) The unknown constant is determined from the condition $\lim_{x \to \infty} H_x = H$.

3) Strictly speaking, this definition holds for an exponential decay of the field with distance into the shielded volume. We evaluate K_s for the configuration of this problem only for comparison with other shield configurations.

4) For consistency, a shield of finite dimensions should be treated.

[1] A. F. Hildebrandt, H. Wahlquist, and D. D. Elleman, J. Appl. Phys., 33, 1798 (1962).

[2] W. L. Williams, M. J. Stephen, and C. T. Lane, Phys. Lett., 9, 102 (1964).

[3] S. I. Bondarenko, S. S. Vinogradov, G. A. Gogadze, and V. I. Sheremet, Report to the 17th All-Union Conference on Low-Temperature Physics, Donetsk, 1972.

[4] G. A. Gogadze and S. S. Perepelkin, Report to the Second All-Union Conference on the Physical Bases of Quantum Magnetometry, Saransk, 1973.

[5] S. I. Bondarenko, V. I. Sheremet, and S. S. Vinogradov, Report to the Second All-Union Conference on the Physical Bases of Quantum Magnetometry, Saransk, 1973.

[6] P. M. Morse and H. Feshbach, Methods of Theoretical Physics, Vol. 1, McGraw-Hill, New York (1953).

[7] S. G. Mikhlin, Course in Mathematical Physics [in Russian], Izd. Nauka, Moscow (1958).

[8] A. Erdélyi (ed.), Higher Transcendental Functions, McGraw-Hill, New York (1953).

[9] A. M. Radin and V. P. Shestopalov, Dokl. Akad. Nauk SSSR, 212, 838 (1973) [Sov. Phys. – Dokl., 18, 642 (1974)].

Brief communications

Sign of the change in optical path length in a laser interferometer with feedback

I. M. Belousova and A. F. Zapryagaev

(Submitted April 24, 1973)
Zh. Tekh. Fiz., 44, 1321-1323 (June 1974)

An experimental investigation is made of the possibility of determining the sign of the change in optical path length in a passive (empty) resonator which is a part of a composite resonator of a He−Ne laser. A laser with coupled resonators has been considered as an interferometer by several authors. The experiments are carried out for different parameters of a composite resonator which is constructed from three or five mirrors. Under certain conditions the exit laser beam carries information about the sign of the change in optical path length in the resonator of a laser interferometer.

In a number of papers (in particular refs. 1-4) a laser with two coupled resonator cavities is considered as a system for interferometer measurements. A change in n, the refractive index of the medium between the mirrors in a passive (empty) resonator, or in L_p, the geometric length of this resonator, causes amplitude modulation of the laser output. By detecting and recording the laser output information is obtained about the time dependence of the magnitude of n or L_p.

In ref. 5 special conditions are determined under which the output laser beam from two coupled resonators carries information on ΔL_p, the sign of the change in optical path length of the passive resonator. This paper presents several experimental results on the possibility of determining the sign of ΔL_p for various passive resonator parameters. The following parameters of the passive resonator are varied: the number of mirrors forming the resonator, the mirror geometry and resonator length, and the position of the optical axis of the external spherical mirror (Z_3) with respect to the optical axis of the active resonator (containing the active medium).

In a He−Ne laser several longitudinal modes are excited. Higher transverse modes are suppressed by an iris. The wavelength of the laser emission is $\lambda = 0.63\ \mu$.

We consider the results of experiments with a three-mirror system $Z_1-Z_2-Z_3$, in which the lengths of the active, Z_1-Z_2, and the passive, Z_2-Z_3, resonators are the same ($L_{12} = L_{23} = 1$ m). The central mirror of the system is a plane. The laser beam, upon passing mirror Z_1, enters a photomultiplier tube, whose output signal is fed to an oscilloscope. The mirror Z_3 is translated along the system axis over a distance of 2 mm.

In the first group of experiments the degree of mismatch between the curvature of mirror Z_3 and of the incident TEM_{00} wave front from the active resonator is changed. The values of the radius of curvature r_3 of the exchangeable mirror Z_3 are given here (m):

r_3, m	1	2	3.4	10	20	34	∞

The coefficient of (energy) reflection of Z_3 is approximately 0.99. For $r_3 = 2$ m, the geometric parameters[6] of the characteristic TEM_{00} waves of the two coupled cavities are matched.

The sign of ΔL_p, the change in optical path length of the passive resonator of this system, can be measured if the function describing the periodic amplitude modulation of the laser emission is not symmetric. We have established experimentally that this is the case if systems are used in which the coupled coaxial resonators with spherical mirror Z_3 are mismatched, or the optical axes of coupled mismatched resonators are displaced by a distance on the order of 10^{-1} mm, or coupled resonators with a plane mirror Z_3 are mismatched.

We show that if L_p the length of the passive resonator

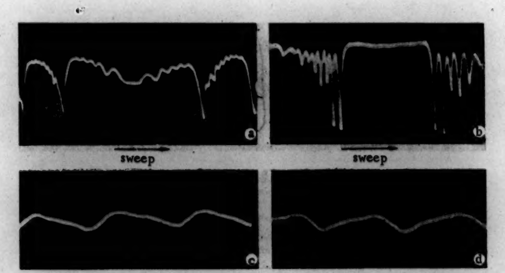

Fig. 1. Oscilloscope traces of photomultiplier current illustrating the possibility of determining the sign of ΔL_p. (a) Mismatched coupled coaxial resonators; (b) optical axes of mismatched resonators shifted approximately 10^{-1} mm; (c) and (d) a screen placed in the passive resonator of a matched system.

Z_2-Z_3 is changed in one direction with velocity V and then returned to its earlier value L_p at the same velocity, then each of the two traces of the time dependence of the photomultiplier current will be a mirror image of the other (see the oscilloscope traces of PM current in Fig. 1, a and b). In both traces 1a and 1b one can see two symmetrically located groups of signal. The first (after start of sweep) group corresponds to a reduction in length of the Z_2-Z_3 resonator; the second, to an increase. The forms of amplitude modulation of the laser output illustrated in Figs. 1a and 1b correspond, respectively, to the following cases: 1) mismatched coaxial resonators with spherical mirrors; 2) optical axes of mismatched resonators shifted on the order of 10^{-1} mm.

It is impossible to determine the sign of ΔL_p for matched optical parameters of the characteristic TEM_{00} modes of two coupled resonators. However, if the laser field is partially screened at the outer mirror of the passive resonator while the geometry of the coupled resonators is not changed, then, due to diffraction of light at the edge of the screen, information about the sign of ΔL_p may be obtained (see Fig. 1, c and d).

For the above described geometry of matched coupled resonators a shift of the optical axes of the resonators by a few millimeters, with all other conditions remaining fixed, causes an increase in the amplitude modulation frequency of the laser by a factor of 4. This effect arises because the light beam completes four double passes between the mirrors of the passive resonator before it falls into the exit point of the active resonator. In this case it is also necessary to partly screen the field of the external mirror of the passive resonator to determine the sign of ΔL_p. The result of inserting a screen in the passive resonator is shown in the oscilloscope traces of Fig. 1, c and d.

In addition to the experiments with a three-mirror system, we have conducted experiments with a five-mirror system, $Z_1-Z_2-Z_3-Z_4-Z_5$, which is of practical interest. For a given five-mirror geometry, periodic focusing of the light beam in the passive resonator Z_2-Z_3 occurs in the case where it is excited off-axis. For off-axis excitation of the passive resonator the axes of light beams falling on the external mirror of the given resonator and reflected from it do not coincide.

We point out two basic results of our experiments involving five-mirror laser resonators of differing geometries. In Fig. 2a an oscilloscope trace of photomultiplier current is shown which illustrates the unique form of the periodic amplitude modulation of the laser emission. This periodic amplitude modulation (of period T) is described by a nonsymmetric function. In this case it is possible to determine the sign of ΔL_p if $\Delta L_p \geq \lambda/14$. One cycle of amplitude modulation with period T (Fig. 2a) is completed as a result of a change in passive resonator lenght by $\Delta L_p = \lambda/2$. During the period T, seven modulation cycles with period $T' = T/7$ are completed. For another five-mirror geometry, with which we have experimented, 40 modulation cycles with period $T'' = T/40$ are completed during a change in passive resonator length $\Delta L_p = \lambda/2$. An oscilloscope trace of photomultiplier current for this experiment is shown in Fig. 2b. It is necessary to point out that during the experiment the speed at which the external mirror of the passive resonator moved is not strictly constant.

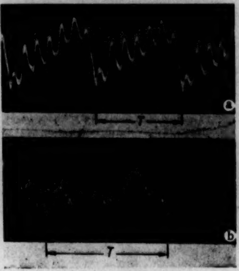

Fig. 2. Oscilloscope traces of photomultiplier current illustrating the form of periodic (period T) amplitude modulations of emission from a laser with a five-mirror resonator. The sign of ΔL_p may be determined (a) if $\Delta L_p \geq \lambda/14$; (b) if $\Delta L_p \geq \lambda/5$.

Using the system from which data are recorded in Fig. 2b, it is possible to measure an absolute value of $\Delta L_p \geq \lambda/80$. However, the sign of ΔL_p can be measured with confidence only for $\Delta L_p \geq \lambda/5$.

---

[1] D. E. T. F. Ashby and D. F. Jephcott, Appl. Phys. Lett., 3, 13 (1963).

[2] J. B. Gerardo and J. T. Verdeyen, Proc. IEEE, 52, 690 (1964).

[3] V. V. Tatarinov, Zh. Prikl. Spektrosk., 9, 369 (1968).

[4] S. V. Sikora and G. S. Simkin, Proc. Khar'kov Scientific Research Institute for Metrology, No. 2, 104 (1969) [in Russian].

[5] I. M. Belousova, O. B. Danilov, and A. F. Zapryagaev, Zh. Tekh. Fiz., 41, 1028 (1971) [Sov. Phys.-Tech. Phys. 16, 807 (1971)].

[6] Kh. Kogel'nik, in: Quasioptics [in Russian], p. 210, Izd. Mir, Moscow (1966).

Spontaneous mode locking in a laser with a multifaceted element

E. I. Kamenskii and V. V. Kozlov

M. V. Lomonosov Moscow State University

(Submitted July 20, 1973)
Zh. Tekh. Fiz., 44, 1323-1326 (June 1974)

A laser with a multifaceted element operating in the mode-locked regime is investigated experimentally. A stable train of equally spaced pulses is obtained with an individual pulsewidth of ~ 2 nsec, a pulse separation of 13 nsec, and a peak power of ~ 15 MW. The reproducibility of the time trace and modulation character of the giant pulses is 95%. The investigated laser has the advantages of small physical size (~ 18 cm) combined with large optical length for the cavity (~ 200 cm).

A method widely used to enhance the output power of present-day lasers is mode locking by means of a bleachable filter in the cavity.[1,2] The time trace of the laser output in this case is a periodic train of pulses with repetition frequency equal to the frequency difference c/2L between adjacent modes, where L is the optical length of the cavity and c is the speed of light.

In certain cases it is necessary to have a single pulse rather than a pulse train. The isolation of an ultrashort pulse can be greatly facilitated by using a low duty-cycle factor for the pulse train. Since the time interval between consecutive pulses is 2L/c, increasing the pulse separation means an increase in the optical length of the cavity.

We have observed spontaneous mode locking in a PGLS-1 laser with a multifaceted neodymium-glass element.[3] The virtue of this laser is the fact that the physical length of the system on the optical bench is less than 18 cm, while the optical length of the cavity L = 200 cm (nl = 188 cm, where l is the length of the active element and n is the refractive index of the laser material).

A solution of No. 3955 polymethine dye in nitrobenzene is used for Q switching. The initial transmissivity T_f of the filter per unit wavelength $\lambda = 1.06\ \mu$ is varied from 0.55 to 0.9. The thickness of the cell containing the dye solution is 3 mm. A time trace of the output is made with an FÉK-09 detector and an I2-7 oscilloscope with a resolution of 1.5 nsec or better. The width of the pump at the half-power points is about 450 μsec.

The cell with the bleachable dye is set up at an angle of 30' to 40' with respect to the cavity axis. The active element is tilted 20' to 25' with respect to the cavity axis to eliminate the discriminating action of the end of the active element on the Q of closely spaced modes.

A train of short pulses is observed when the cell is placed near the exit mirror ($s \approx 4$ cm, where s is the distance between the cell and the mirror). For initial filter transmissivities T_f = 0.8 to 0.9 the intensity of 40% of the giant pulses is modulated at the frequency c/2L, the percentage modulation m_0 reaching 50%. The nature of the modulation is invariant from one burst to the next, remaining sinusoidal (Fig. 1a). The other pulses exhibit 100% modulation (Fig. 1b). For the time resolution of the instrumentation, ~ 1.5 nsec, an isolated light pulse is observed in one axial period. The width of the pulse is 2 or 3 nsec, and the repetition period t_r = 13 nsec ≈ 2L/c. The peak power attains 2 or 3 MW in this case. The total giant-pulse envelope width τ is 750 to 800 nsec for T_f = 0.8.

Stable time traces (from burst to burst) with a percentage modulation of about 100% (Fig. 1b) are observed when the initial transmissivity is decreased to T_f = 0.6. In this case a pulse train with close to 95% reproducibility is generated near the threshold (pump energy no more than 15% above threshold, which is interpreted as the self-excitation threshold of the laser and filter cell). The peak power is increased to 10-12 MW because of a reduction in the number of pulses and an increase in the lasing energy.

It is well known that at higher pump energy a passive switch can be bleached several times in one pump pulse, i.e., the generation of several giant pulses with a decaying amplitude is observed (Fig. 2). The position in time and the number of giant pulses are recorded with an F-5 detector and an S1-29 oscilloscope with a resolution of ~ 3 μsec.

To study the time variation of each of the giant pulses we have conducted an experiment using an I2-7 oscilloscope in the periodic regime. Inasmuch as the minimum spacing (with ~ 98% probability) between adjacent pulses is about 50 μsec, the instrumentation is capable of recording the time variation of all the pulses.

In the generation of two giant pulses the time variation of the first has the usual smooth shape, whereas the intensity of the second pulse is modulated with m_0 = 60 to 70% (Fig. 3a). The second pulse has $m_0 \approx 100\%$ in 40% of the cases (Fig. 3b). For T_f = 0.65 the total width τ of the giant pulse is 400 to 450 nsec.

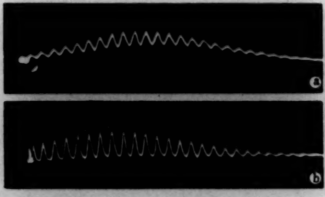

Fig. 1. Oscillograms of the giant-pulse output of a laser with a multifaceted neodymium-glass element. L = 200 cm; s = 4 cm.

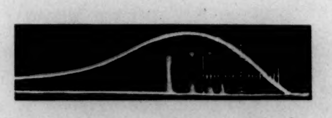

Fig. 2. Time trace of the pump intensity (upper curve) and output intensity (lower curve) of a laser with a multifaceted element and a passive Q-switch. One large division = 100 μsec.

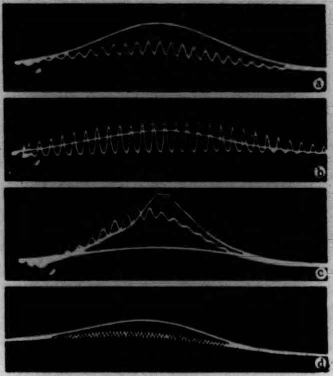

Fig. 3. Oscillograms of the giant-pulse output of a laser with a multifaceted element. The pump energy is more than 70% above threshold.

A further increase in the pump energy leads to the generation of three giant pulses (Fig. 3c). The time variation of each pulse is generally different. For certain bursts the first (and most powerful) pulse has a flattened pyramidal shape, obviously as the result of vibrational–rotational relaxation in the passive switch. A pulse train with $m_0 \approx 100\%$ is not observed in this case. The different time variations of two or more giant pulses is attributable to the fact that a very large part of the energy stored in the cavity is emitted during the first pulse; for the second pulse near-threshold conditions are established in the cavity, increasing the probability of excitation of a train of short pulses with a repetition rate c/2L. For $s \approx 50$ cm the pulse repetition rate is 3(c/2L), i.e., a displacement of the exit mirror for a constant position of the passive switch changes the pulse repetition rate. In this case, m_0 is not greater than 50% (Fig. 3d).

The width of the emission spectrum in the case of a tilted rod is investigated by means of a Fabry – Perot etalon with a resolution of $\sim 2 \cdot 10^{-3}$ cm^{-1}. Near threshold pump intensities, where mode locking of the laser is observed, the width of the spectrum is $\Delta\gamma_0 \approx 0.015$ cm^{-1}. The spectrum in this case consists of several components (five or six) separated by a distance ~ 1/2L. We have observed this effect in a free-running laser.[4]

According to refs. 5 and 6, the width of a single pulse at the 0.5 level in the case of N_j locked modes is

$$t_{0.5} = \frac{2.78 \cdot 2L}{\pi c N_j} \approx \frac{1}{c\Delta\lambda_0}.$$

For $\Delta\lambda_0 \approx 0.015$ cm^{-1} pulses of width $t_{0.5} \approx 2 \cdot 10^{-9}$ sec must be formed; this result is consistent with the experimental data.

The authors are grateful to R. V. Khokhlov for useful discussion.

---

[1] A. I. DeMaria, D. A. Stetser, and H. Heynau, Appl. Phys. Lett., 8, 174 (1966).

[2] V. I. Malyshev and A. S. Markin, Zh. Eksp. Teor. Fiz., 50, 339 (1966) [Sov. Phys. – JETP, 23, 225 (1966)].

[3] E. I. Kamenskii and V. V. Kozlov, Kvant. Elektron. (Mosc.), No. 4, 77 (1971) [Sov. J. Quant. Electron., 1, 369 (1972)].

[4] V. V. Kozlov, Kvant. Elektron. (Mosc.), No. 2(8), 30 (1972) [Sov. J. Quant. Electron., 2, 111 (1972)].

[5] M. DiDomenico, Jr., J. Appl. Phys., 35, 2870 (1964).

[6] S. Yariv, J. Appl. Phys., 36, 388 (1965).

Optical simulation of a radiator aperture with arbitrary amplitude – phase distribution

M. M. Butusov and Sh. V. Yurevichyus
M. I. Kalinin Leningrad Polytechnical Institute

(Submitted April 19, 1973; resubmitted August 13, 1973)
Zh. Tekh. Fiz., 44, 1326-1328 (June 1974)

A description is given of a method for producing transparencies for Fourier analyzers for arbitrary two-dimensional complex functions. The method is employed for simulation of an acoustic radiator with a complex amplitude–phase aperture distribution.

1. The wide-spread application of the fruitful idea[1,2] of coherent-optical simulation of the directivity patterns of radio and acoustic radiators has been hindered for a long time by the difficulties encountered in fabricating an input transparency which can simulate an arbitrary two-dimensional amplitude–phase distribution at the radiation aperture.

Simulation of amplitude distribution requires an exact evaluation of the nonlinear properties of the photographic film so that the amplitude transmittance of the transparency corresponds, on some scale, to the amplitude distribution of the field. However, linearization of the characteristic curve of the film is a complicated problem[3] even if a device is constructed in which the two-dimensional distribution of the light flux follows the required relation. In holography, preliminary exposure of film is often used to obtain the output for the quasilinear segment of the characteristic curve. This method is not applicable to Fourier analyzers since the output signal is the sum, with weighted coefficients, of the Fourier transform of the aperture, for which the input function is given and the desired output signal; unavoidable distortion is the result.

In simulation of two-dimensional arbitrary distributions it is inconvenient, and even impossible, to use the previously proposed methods (see refs. 4 and 5 for example) for inserting the appropriate phase plates or providing controlled bleaching of the transparency emulsion.

2. The present paper describes an experiment involving the idea proposed in refs. 6 and 7 for simulating amplitude distribution by a binary structure and phase distribution using a spatial carrier imprinted on a transparency by a holographic method. The advantages of using two-dimensional binary transparencies are described in ref. 8; the basic elements selected for the transparencies are circles located at the lattice points.

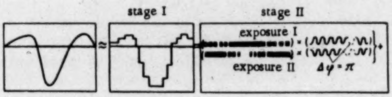

Fig. 1. Principle of transparency recording for a one-dimensional function. The initial function is on the left, next is a step approximation, and then binary masks for each of the inphase regions and the corresponding spatial carrier with a π phase shift.

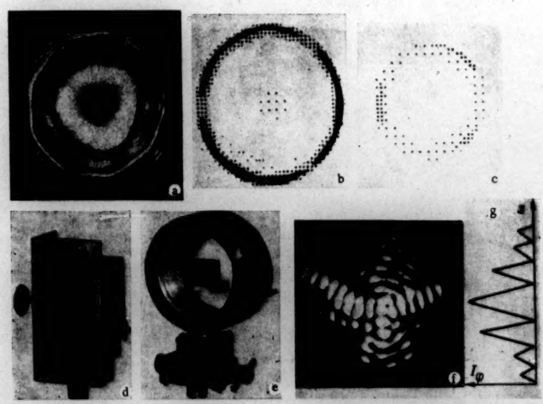

Fig. 2. Simulation of an acoustic radiator: interferogram of the surface (a), transparency masks for each of the two inphase regions (b, c), device for masking the holograph transparency in a system with a movable mirror (d), holograph transparency in the immersion cell (e), distribution of light near the central maxima of the pattern (g), and photometer cross section of this distribution (f).

We recall that the main advantage of using such elements is that the amplitude transmittance of the structure is proportional to the radius of the circles, which makes it easier to implement the transparency.

A holograph system is used to regulate the phase input from the spatial carrier. One of its mirrors is mounted on a piezoceramic column and the voltage across the column is used to vary linearly the phase of the diffraction grating recorded on the holograph transparency.

The basic idea of the method is shown in Fig. 1: Represented on the left is an arbitrary one-dimensional function whose phase assumes two values $(0, \pi)$ and whose amplitude varies arbitrarily. The amplitude is simulated in two stages, shown in Fig. 1 on the right: First, the function is broken down into several gradation regions whose number depends on the desired experimental accuracy. Then within each region a constant value of the function is simulated by the transmittance of the binary transparency. The spatial carrier (diffraction grating) is recorded on the binary transparency mask prepared in the above manner; only region I is exposed during the first exposure, and then the spatial carrier undergoes a phase shift and region II is exposed.

3. The results obtained from the method for simulation of the directivity pattern of an acoustic radiator are shown in Fig. 2. Shown on the left is an interferogram of the radiator surface obtained by a time-averaging holograph method. The interference bands represent lines of equal amplitude at each point on the surface. It can also be seen that the surface has two inphase regions: Central and peripheral regions oscillate in the same phase, and the average fringe region oscillates in the opposite phase. Further to the right there are two binary transparency masks corresponding to each of the two inphase regions. Then there is the device in which the diffraction grating in imprinted on the holographic transparency. The photograph on the extreme right shows the light intensity distribution at the output plane written in first-order diffraction on the spatial carrier of the holograph transparency and representing the directivity pattern of the radiator. The photometer cross section of this diagram is along the horizontal axis. The shape of this cross section agrees with the results of acoustic measurements.

Special attention should be given to two aspects of the experiment. First, the quality of the optics used to record the diffraction grating should not be worse than the quality of the Fourier objective. Otherwise, unavoidable aberrations appear and the transmission function of the Fourier transformer is distorted. Second, to increase the diffraction efficiency of the holograph carrier the transparency must be bleached and placed in an immersion cell. The very small decrease in diffraction efficiency after the transparency is submerged in the cell again convinces us that the primary reason for the diffraction of light in bleached holograms with a high frequency of the spatial carrier is the difference between the refractive coefficients of the gelatin and the silver salts arising after bleaching. The view that the decisive factor is the surface relief[9] is erroneous in this case.

---

[1] K. Cutrona, Optical Data Processing, MIT Press (1966).

[2] L. D. Bakhrakh and A. P. Kurochkin, Antennas [in Russian], Svyaz, Moscow (1967), No. 2.

[3] A. R. Shulman, Optical Data Processing, Wiley, New York (1970).

[4] G. S. Kondratenkov, Data Processing by Coherent-Optical Systems [in Russian], Sovetskoe Radio, Moscow (1972).

[5] L. S. Gibin, A. G . Kazachok, E. S. Nezhevenko, Yu. N. Solodkin, and Yu. V. Chugui, Avtometriya, 7, No. 1 (1971).

[6] A. P. Kurochkin and V. I. Troitskii, Radiotekh. Elektron., 14, 710 (1969).

[7] E. B. Felstead, Appl. Opt. 10, 2468 (1971).

[8] M. M. Butusov, B. A. Belogorodskii, and Yu. G. Turkevich, Proc. First All-Union Conf. on Holography [in Russian], Tbilisi (1972).

[9] V. A. Zverev and E. F. Orlov, Optical Transformers [in Russian], Sovet-skoe Radio, Moscow (1971).

Lasing properties of Yb^{3+} and Er^{3+} glass laser pumped by a laser

V. N. Kalinin, A. A. Mak, D. S. Prilezhaev, and V. A. Fromzel'

(Submitted September 14, 1973)
Zh. Tekh. Fiz., 44, 1328-1331 (June 1974)

Lasing at 1.54 μ is obtained in silicate and phosphate glasses activated by Yb^{3+} and Er^{3+} and pumped by a neodymium laser at 1.06 μ. Induced absorption of pump radiation resulting from the excitation of the $^4I_{13/2}$ level in Er^{3+} ions is investigated. When the Yb–Er glass specimens are placed in the pump cavity the pump spectrum shifts towards long wavelengths. These effects reduce the efficiency of the laser.

Lasing at λ = 1.54 μ by silicate and phosphate glasses activated by Yb^{3+} and Er^{3+} and pumped by flash lamps was first obtained by Snitzer.[1,2] However, the use of flash lamps to pump media activated by these ions is not very efficient since these do not produce the appropriate pumping spectrum of intense and broad absorption bands; therefore, such lasers have a comparatively low energy output and high pump thresholds.

We have investigated the possibility of lasing by Yb^{3+} and Er^{3+} glasses pumped by a neodymium laser to obtain efficient pump radiation (theoretically, the conversion factor can reach ~ 70%) and reduce thermal losses in the active medium.

Radiation of the neodymium laser is absorbed by the edge of the Yb^{3+} resonance absorption band (in the $^2F_{7/2}-{}^2F_{5/2}$ transition). Because of rapid radiationless transfer, excitation energy is transferred from Yb^{3+} ions to Er^{3+} ions (to the $^4I_{11/2}$ level), which relax in the metastable $^4I_{13/2}$ state. Three-level lasing occurs in the $^4I_{13/2}-{}^4I_{15/2}$ transition of Er^{3+}. Thus, direct excition of Er^{3+} does not occur with laser pumping.

Silicate and phosphate glasses with different $Yb^{3+}-Er^{3+}$ ratios are investigated in the present paper. Certain spectroscopic parameters of the glasses are shown in Table 1.

N_{Yb} and N_{Er} are the activator concentrations, τ_{Er} and τ_{Yb} are the the lifetimes of the $^4I_{13/2}$ level of Er^{3+} and the $^2F_{7/2}$ level of Yb^{3+}, k_λ are the absorption coefficients of the glasses at the appropriate wavelength (absorption of the glass base is shown for λ = 1.54 μ), σ is the cross section for the stimulated transition $^4I_{13/2}-{}^4I_{15/2}$, α is the energy transfer rate from Yb^{3+} to Er^{3+} ($\alpha = 1/\tau_{Yb} - 1/\tau^0_{Yb}$ where τ^0_{Yb} is the Yb^{3+} lifetime in a glass without Er^{3+}).

Lasing by Yb–Er glasses is investigated using the optical system shown in Fig. 1. The specimen is a parallelepiped placed in the cavity of the pumping laser. Since it is an efficient load for the neodymium laser, the pumping radiation is used with the greatest possible efficiency. The pump energy absorbed by the specimen is determined from the well-known absorption coefficient of the specimen at the pump wavelength and from the energy exiting from the pump cavity through one of the opaque mirrors.

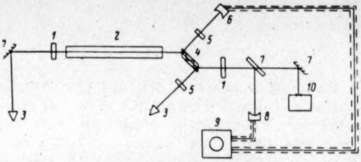

Fig. 1. Schematic diagram of the apparatus. 1) Cavity mirrors with transmission τ <0.5% for λ = 1.06 μ; 2) active medium of GLS-1 glass; 3) calorimeters; 4) Yb–Er glass samples; 5) cavity mirrors for radiation at λ ≈ 1.54 μ; 6) FD9E111 photodiode; 7) plane-parallel glass plate; 8) FÉU-22 photomultiplier; 9) S-1-17 oscilloscope; 10) spectrograph (9 Å/mm dispersion).

The cavity is formed by two planar dielectric mirrors for radiation at λ ≅ 1.54 μ, and the lasing radiation is propagated in the specimen at an angle of 45° to the direction of propagation of the pumping radiation.

Table 2 gives the measured values of the specific threshold pump energy W_{thr-V} and efficiency η for various glass specimens. The parentheses contain theoretical values corresponding to experiment, which are calculated according to the following relations:[1]

$$W_{thr-v} = \frac{h\nu_p}{2}(N_{Er}+\delta)\left[1+\frac{2N_{Er}}{\tau^0_{Yb}\alpha(N_{Er}-\delta)}\right] \times\left[1-\frac{(N_{Er}+\delta)N_{Er}}{\tau_{Er}N_{Yb}(N_{Er}-\delta)\alpha}\right],$$

$$\eta = \frac{\nu_l}{\nu_p}\frac{\ln\frac{1}{R}}{\ln 1/R+G}\left(1-\frac{1}{n_W}\right),$$

TABLE 1

Glass base	$N_{Yb}\cdot 10^{-20}$, cm^{-3}	$N_{Er}\cdot 10^{-20}$, cm^{-3}	$\tau_{Yb}\cdot 10^3$, sec	$\tau_{Er}\cdot 10^3$, sec	k_λ, cm^{-1}		$\sigma\cdot 10^{20}$, cm^2	$\alpha\cdot 10^{3}$, sec^{-1}
					λ = 1.06 μ	λ = 1.54 μ		
Silicate	1.84	4.7	20	13	0.034	0.007	0.4	5
Phosphate	1.43	3	11	5.9	0.036	0.016	0.85	7
Phosphate	1.45	4.24	2.5	5.9	0.043	0.013	0.85	40
Phosphate	2.2	6.6	1.8	5	0.06	—	0.85	53

TABLE 2

Glass base	W_{thr-V}, J/cm³			η, %	Δk_λ per 1 J/cm³ of absorbed energy, cm⁻¹
	$R = 0.96$	$R = 0.8$	$R = 0.5$		
Silicate	7.1 (4.4)	7.1	—	0.35 (20)	0.018 ($\lambda_{av} = 1.064\ \mu$)
Phosphate	4.6 (2.8)	5.8	8.2	3 (16)	0.013 ($\lambda_{av} = 1.068\ \mu$)
Phosphate	5.8 (3.9)	6.5	8.0	2 (16)	0.013 ($\lambda_{av} = 1.068\ \mu$)
Phosphate	9.3 (6.1)	10.5	12	0.4 (16)	—

where

$$\delta = \frac{c\left(G + \ln\frac{1}{R}\right)}{2\varkappa h\nu_1 B_1 l}$$

is the threshold inversion, G are the nonactive and diffraction losses, R is the reflectance of the cavity mirrors, $\varkappa l$ is the optical length of the active medium, ν_p and ν_l are the pumping and lasing frequencies, respectively, and n_W is the excess of pumping energy over the threshold.

We note that the comparatively high G of the glasses investigated here, in particular the phosphate glasses, is due to the appreciable nonactive absorption at 1.54 μ caused by the presence of water traces in the glass matrix

It can seen from Table 2 that there are appreciable discrepancies between the calculated and experimental data. We have established that one of the reasons for these discrepancies is the additional (stimulated) absorption of pumping radiation by the specimens. To determine the magnitude and nature of this stimulated absorption we use probing pulses from a nonspiking laser with a narrow radiation spectrum which is tuned between 1.05–1.07 μ. The stimulated absorption occurring in the pumped specimen produces a substantial change in the shape of the probing pulse (Fig. 2). It is established that the magnitude of the stimulated absorption increases with the wavelength, and the duration of this absorption corresponds to τ_{Er}. From the above data and from an analysis of the Er^{3+} energy level diagram,[3] one can conclude that the stimulated absorption is related to the short wavelength edge of the $^4I_{13/2} - {}^4I_{9/2}$ absorption band, which is produced by excitation of the metastable $^4I_{13/2}$ level of Er^{3+}.

The measured values Δk_λ of the stimulated absorption are shown in Table 2 for different glasses activated by Yb^{3+} and Er^{3+}. The stimulated absorption is higher in the silicate glasses than in the phosphate glasses. This evidently is the main reason they have a low efficiency and a high pump threshold.

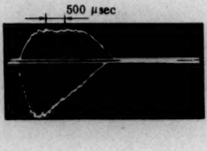

Fig. 2. Variation in the shape of the probing signal whose spectrum coincides with the pump spectrum when it passes through the pumped Yb–Er glass specimen as shown by the data of Tables 1 and 2.

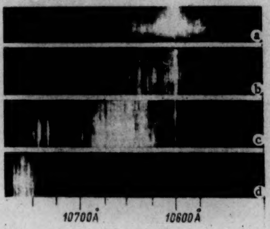

Fig. 3. Laser pumping spectrum with a GLS-1 glass active medium. a) Without Yb–Er glass in the cavity; b) with Yb–Er silicate glass; c and d) with Yb–Er phosphate glasses corresponding to the data of Table 1.

In our case, the discrepancy between the calculated and measured efficiencies and W_{thr-V} is also due to a certain degree to the properties of the intracavity pumping of the Yb–Er glasses by the neodymium laser. The neodymium lasing band coincides with the long-wavelength absorption edge of Yb^{3+}; therefore, the introduction of Yb–Er glass into the cavity is equivalent to the introduction of a spectral selector into the neodymium laser cavity. As a result, the pump radiation spectrum shifts towards long wavelengths (Fig. 3). In our case this shift leads to a number of undesirable effects: The pump laser efficiency is reduced by the reduction in the load efficiency, pumping efficiency falls so that Yb^{3+} absorption is reduced, and furthermore the losses increase due to the increase in stimulated absorption.

These considerations are evidently the cause of the anomalously strong dependence, for a three-level laser, of the laser pumping threshold on cavity Q.

The removal of the above-mentioned undesirable effects, which lower the lasing efficiency of Yb–Er glasses subjected to laser pumping, may be obtained by pumping at ≤ 1.05 μ.

In conclusion, the authors thank E. I. Galant, S. G. Lunter, and M. N. Tolstoi for preparing the Yb–Er glass specimens.

---

1) These relations are obtained from the balance equations. A more detailed account of the computational technique will be given in a separate paper.

[1] E. Snitzer and R. F. Woodcock, Appl. Phys. Lett., 6, 45 (1965).

[2] E. Snitzer, R. F. Woodcock, and J. Segre, IEEE J. Quantum Electron., QE-4, 360 (1968).

[3] G. H. Dieke, Adv. Quant. Electron., J. R. Singer (ed.), Columbia Univ. Press, New York (1961).

Characteristics of diffraction gratings obtained by photoetching of semiconductor surfaces

L. V. Belyakov, D. N. Goryachev, M. N. Mizerov, and E. L. Portnoi

A. F. Ioffe Physicotechnical Institute, Academy of Sciences of the USSR, Leningrad

(Submitted July 17, 1973)
Zh. Tekh. Fiz., 44, 1331-1333 (June 1974)

The present note reports on certain characteristics of diffraction gratings produced by selective photoetching of semiconductor surfaces. The method can be used to obtain relief-type diffraction gratings on the surface of semiconductors with a grating constant exceeding 2500 mm^{-1}. The diffraction efficiency of these gratings is high. The method can be employed to produce periodic inhomogeneities in various optical components.

Because of the recent rapid development of lasers, quantum electronics, and nonlinear optics, it is now frequently necessary to fabricate optical waveguides for the transmission between individual quantum-electronic components at optical frequencies. Simple to build and very convenient for optical solid-state devices is the plane, asymmetric waveguide in the form of a thin dielectric film deposited on a substrate. Optical waveguides with a transmission layer made of semiconducting material are of great importance for certain applications. Structures with heterogeneous junctions are very promising in this respect. The discontinuity in the refractive index at the boundary and the excellent optical properties of epitaxial layers mean that these structures can be used for optical thin-film waveguides. When special devices such as relief-type diffraction gratings on the surface of the waveguide are employed, it becomes possible to solve problems of coupling radiation in and out of the thin-film waveguides,[1] to achieve phase matching,[2] and to produce lasers with distributed feedback.[3] Selective photoetching without use of a photoresistive layer[4] is one of the possible techniques of producing such gratings on the surface of semiconductors. We have used this method to produce diffraction gratings on single crystals of both n- and p-gallium arsenide and on epitaxial AlGaAs layers. A two-beam interference pattern obtained from an LG-38 helium–neon laser is projected onto the semiconductor surface. The surface is etched at the same time with an aqueous solution of an oxidizing agent. When the oxidizing agent is selected, particular attention is paid to the transparency of the solution for the laser beam. Furthermore, no gas can be generated during the etching reaction with the semiconductor material. The optimum etching time depends both on the composition and concentration of the solution and amounts to several minutes. The etching conditions are selected with small spatial frequencies directly during the exposure process. The etching conditions are selected on the basis of the intensity of reflected first-order diffraction maxima. After the exposure, the sample surface is rinsed with distilled water.

Figure 1a shows the surface of a diffraction grating obtained with our method on n-type gallium arsenide; Fig. 1b is the profile of the grating. The cut runs along the crystallographic sample surface perpendicularly to the grating lines. The spatial frequency of the grating is 200 mm^{-1}.

Figure 2 shows a typical distribution of the intensity of diffraction maxima of various orders in normal incidence of a ray upon the grating (λ = 6328 Å).

Figure 3 shows the dependence of the relative intensity of the first-order maxima on the spatial frequency of the grating. The intensity of the beam which is reflected in mirror fashion from the polished crystal surface is taken as 100 %.

Our method makes it possible to obtain relief-type diffraction gratings on the surface of semiconductors; the gratings have a spatial frequency exceeding 2500 mm^{-1} and a rather high diffracting efficiency. The method is distinguished by simplicity and high reproducibility.

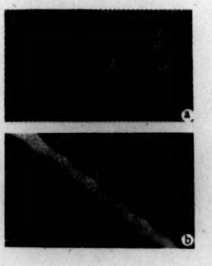

Fig. 1. Photographs of the diffraction grating produced on the semiconductor surface.

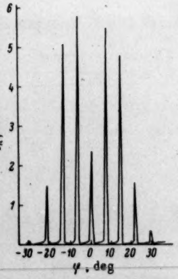

Fig. 2. Angular distribution of the intensities of the diffraction maxima.

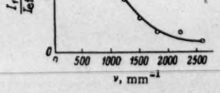

Fig. 3. Dependence of the intensity of the first-order maxima upon the grating constant.

The authors thank S. G. Konnikov for the photographs which were obtained on an electronic microanalyzer and Zh. I. Alferov for his interest.

---

[1] M. L. Dakss, L. Kuhn, P. F. Heidrich, and B. A. Scott, Appl. Phys. Lett., 16, 523 (1970).

[2] N. Bloembergen and A. J. Sievers, Appl. Phys. Lett., 17, 483 (1970).

[3] D. P. Shank, P. G. Smith, E. C. Spencer, and M. F. Calvin, Appl. Phys. Lett., 21, 494 (1972).

[4] L. V. Belyakov, D. N. Goryachev, Yu. I. Ostrovskii, and L. G. Paritskii, in: Reports of the Scientific-Technical Conference on Use of Optical Lasers in Modern Science and Technology [in Russian], Leningrad (1973).

Ion emission into vacuum from a discharge in crossed electric and magnetic fields

V. A. Nikitinskii and A. S. Zakharov

Rubezhnoe Branch, V. I. Lenin Khar'kov Polytechnical Institute

(Submitted April 16, 1973)
Zh. Tekh. Fiz., 44, 1333-1334 (June 1974)

The ion emission has been studied in a low-pressure discharge constricted by a slit between coaxial ferromagnetic electrodes in a transverse magnetic field. Change of the discharge constriction approximately doubles the emission into vacuum, and the application of a transverse magnetic field increases this emission by a factor of tens.

The electrostatic double sheath which forms on the cathode side of the constriction in a constricted discharge produces oppositely directed electron and ion fluxes.[1,2] Dallenbach has suggested that the directional ion flux can be exploited to draw the ions off into vacuum from the cathode side of the constriction. However, a quantitative comparison on the basis of the extraction of ions from the cathode and anode sides of the constriction at accelerating voltages up to 10 kV has shown that for fixed constricting and emission apertures the efficiency of the ion extraction is roughly the same in both cases. The explanation lies in the fact that the electrostatic double sheath is convex toward the cathode and thus defocuses the ions, so that only a fraction of the ions accelerated by the sheath passes through the emission aperture into vacuum. The advantages of extracting ions from the cathode side of the constriction can be realized by shaping the sheath in an appropriate manner and by increasing the directed velocity of the ions.

In our experiments, the shape of the electrostatic double sheath is altered by inserting a cylindrical rod 2 along the axis of the aperture in intermediate electrode 1 (Fig. 1). The rod is maintained at the same potential as electrode 1. The directed velocity of the ions is increased by changing the discharge voltage by means of a transverse magnetic field. The magnetic field is produced in the annular gap (having an outside diameter of 8 mm and a width of 1 mm) between ferromagnetic electrodes 1 and 2 by means of coil 3 and magnetic guide 4. The electron emitter is a thermionic cathode 5, a tungsten-wire ring, and the anode is a hollow copper cylinder 6. The emission electrode 7, with an 8-mm exit aperture, is located 8 mm from intermediate electrode 1 and held at the potential of one of the cathode leads. It separates the discharge region from the high-vacuum volume, in which a pressure of $\sim 10^{-5}$ torr is maintained. The working gas, argon, is injected from the anode side of the slit. The current of ions which escape from the discharge into vacuum is measured by Faraday cup 8, connected electrically with electrode 7. When a discharge is initiated through the slit from the cathode side, an electrostatic double sheath in the form of an unterminated toroid is produced. This sheath shape permits an increase in the ion emission current because of a change in the ratio $k = S_e/S$ (where S is the total surface area of the double sheath and S_e is the part of the sheath surface from which ions reach the emission aperture). The quantity k is evaluated under the assumption that the toroid axis is the center line of the slit, while the center of the spherical double sheath produced in the same discharge system when the central rod 2 is removed lies at the center of the constricting aperture. Calculation shows that k is doubled, while experiments show that the ion emission current is increased by a factor of 1.8.

When the electromagnet coil is turned on, a radial magnetic field appears in the slit, increasing the discharge voltage. Under the influence of the crossed fields, the electrons drift in the constricting slit in the tangential direction. Unfolding the cylindrical surface over which an electron moves gives the electron trajectory in the form of a trochoid. Electrons can move in the axial direction toward the anode over a distance larger than the Larmor radius only as a result of collisions with gas atoms. By increasing the electron energy and the path which the electrons travel in the constricting slit, the magnetic field intensifies the gas ionization in the immediate vicinity of the exit aperture of the discharge chamber and leads to an order-of-magnitude increase in the current of ions which escape from the chamber into vacuum. Figure 2 shows the discharge voltage U_d and the ion current I_i as functions of the current in the electromagnet coil, I_c, for fixed values of the discharge current I (sic) and the gas flow rate (70 cm^3/h). The steepness of the functional dependence $U_d = f(I_c)$ increases due to a reduction of the gas density at the constriction, itself due to the removal of atoms in the form of ions by the electric field of the discharge. Increasing I_c beyond a certain critical value

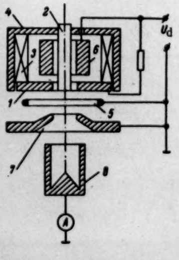

Fig. 1. The experimental apparatus.

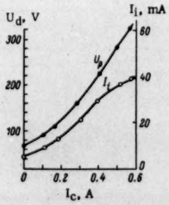

Fig. 2. Discharge voltage U_d and ion emission current I_i as functions of the current in the coil, I_c.

leads to oscillations and a cutoff of the discharge current. The gas flow rate must be increased to suppress these oscillations and to prevent the current cutoff. Bringing the emission electrode closer to the constricting slit results in a more efficient use of the directional ion flux; in particular, when the separation between the emission and intermediate electrodes is d = 3 mm, the current to the Faraday cup reaches 70 mA. When d is reduced further, it becomes difficult to initiate or maintain the discharge without increasing the gas flow rate.

A change in the potential of the emission electrode, with the potentials of the cathode and the Faraday cup held constant, does not appreciably affect the value of I_i.

---

[1] I. I. Andrews and R. H. Verey, Nature, 225, 270 (1970).

[2] Yu. E. Kreindel' and V. A. Nikitinskii, Zh. Tekh. Fiz., 41, 323 (1971) [Sov. Phys. – Tech. Phys., 16, 242 (1971)].

[3] W. Dällenbach, Z. Naturforsch., 10, 803 (1955).

Angular aberration corrector in a cylindrical mirror analyzer

V. V. Zashkavara and V. F. Tarasov

Nuclear Physics Institute,
Academy of Sciences of the Kazakhstan SSR, Alma-Ata

(Submitted June 18, 1973)
Zh. Tekh. Fiz., 44, 1134-1137 (June 1974)

A calculation is given for correction of third- and fourth-order angular aberrations in a cylindrical-mirror electrostatic analyzer. The correction is based on the refracting property of the potential of a double layer produced by two axially symmetric grid electrodes placed in the focal region of a charged particle beam on the axis of the cylindrical mirror.

The angular aberration in the direction of dispersion for a cylindrical mirror which focuses charged particles on the axis of symmetry can be of higher than second order.[1,2] The exact equations for plane trajectories in a cylindrical field can be used to show that for beam divergences up to 20° the spherical aberration can be closely approximated by the sum of third- and fourth-order angular aberrations; the cubic aberration makes the largest contribution and is of the order of 10-15% of the radius of the inner cylindrical electrode for an angular divergence of 20°. In cases where it is necessary to increase the aperture ratio of the cylindrical mirror by increasing the angular divergence of the beam without any serious loss of resolving power it becomes necessary to correct or at least partially compensate for these aberrations.

In this paper we give the design of a corrector for third- and fourth-order aberrations in a cylindrical mirror; the principle is based on the refracting property of the potential of a double layer produced by means of two axially symmetric grid electrodes of special shape, placed at the output of the analyzed beam from the cylindrical field. Figure 1 shows the focusing region of the charged particles, which have passed through the field of the cylindrical mirror. We discuss the arrangement of the electrodes at the end of the paper. Electrode 1 is at the same potential as the inner cylinder 3, while electrode 2 is connected to an accelerating potential U. Three rays are shown in Fig. 1: the central ray, which is at an angle α_0 to the axis of symmetry and for which the second-order angular focusing condition is satisfied, and two limiting rays in the beam. The central ray passes through the corrector normal to the surface; it does not suffer any refraction so it crosses the z axis of the mirror at the point 0, corresponding to the position of the second-order focus. If there is no corrector, or if U = 0, the limiting rays (denoted by the dashed lines) would cut the axis of symmetry at points separated from 0 by a distance l, as determined in our approximation by the amount of spherical aberration

$$l = r_1 \left[A_{III}\,(\alpha-\alpha_0)^3 + A_{IV}\,(\alpha-\alpha_0)^4\right], \tag{1}$$

where A_{III} and A_{IV} are the third- and fourth-order aberration coefficients of the cylindrical mirror.[3,4] In what follows we put $r_1 = 1$. The shape of the corrector electrodes in the approximation (1) must be calculated so that for a given double-layer potential U, all the particles in the analyzed beam are directed after refraction towards the point 0 with a kinetic energy W + qU, where q is the particle charge and W is the potential energy before passing through the corrector.

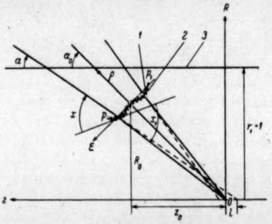

Fig. 1

We ignore the size of the interelectrode gap and consider the surface on which the charged-particle trajectories are refracted in accordance with Snell's law (Fig. 1):

$$\cos\chi_1 = \frac{\cos\chi}{\sqrt{1+u}}, \tag{2}$$

where u = qU/W. A line of refraction (pp' in Fig. 1) is formed on a section of the surface of the axial plane.

The differential equation of the refraction line in the R, z system of coordinates can be obtained from the law of refraction (2) and the condition that after refraction an arbitrary ray must pass through the focus 0:

$$(z + RR')\left[(1 - xR')^2 + u\,(1 + x^2)\,(1 + R'^2)\right]^{1/2} - (x + R')\,(R - zR') = 0, \tag{3}$$

where $R' = dR/dz$, $z = Rx - l(x)$, and $x = \cot\alpha$. The boundary condition is as follows: The central ray of the focused beam intersects the refraction line at the point R_0, z_0 at a right angle and at this point $R' = -\cot\alpha_0 = -x_0$, $z_0 = R_0x_0$. Equation (3) is a first-order nonlinear differential equation, which cannot be integrated in terms of elementary functions. The solution has been obtained by the power series method. The following equation has been found up to the seventh order in the small expansion parameter $x - x_0$ for the derivative which defines the slope of the tangent to the refraction line in the coordinate system ρ and ξ (Fig. 1):

$$\rho' = \frac{d\rho}{d\xi} = -\frac{x - x_0}{1 + xx_0} - \frac{\gamma}{\gamma - 1}\,\frac{(x - x_0)^3}{1 + x_0^2}\Bigg\{-\beta_3 + \left[\frac{x_0}{1 + x_0^2}\beta_3 - \beta_4\right](x - x_0)$$
$$+ \left[-\frac{x_0^2 + \frac{1}{2}}{(1 + x_0^2)^2}\beta_3 + \frac{x_0}{1 + x_0^2}\beta_4 - \beta_5\right](x - x_0)^2$$
$$+ \Bigg[\frac{x_0\left(x_0^2 + \frac{3}{2}\right)}{(1 + x_0^2)^3}\beta_3 - \frac{x_0^2 + \frac{1}{2}}{(1 + x_0^2)^2}\beta_4$$
$$+ \frac{x_0}{1 + x_0^2}\beta_5 - \beta_6\Bigg](x - x_0)^3$$

$$+\left[-\frac{x_0^4+3x_0^2-\frac{1}{8}}{(1+x_0^2)^4}\beta_3-\frac{1}{4}\frac{\beta_3^2}{(1+x_0^2)^2}+\frac{x_0\left(x_0^2+\frac{3}{2}\right)}{(1+x_0^2)^3}\beta_4\right.$$
$$\left.-\frac{x_0^2+\frac{1}{2}}{(1+x_0^2)^2}\beta_5+\frac{x_0}{1+x_0^2}\beta_6-\beta_7\right](x-x_0)^4\Bigg\},$$

where $\gamma = \sqrt{1+u}$ and the β_n are the expansion coefficients for the series in $x - x_0$ of the function (1), $l(x) = R_0 \sum_{n=3}^{\infty} \beta_n (x-x_0)^n$, and

$$\beta_3=-\frac{A_{III}}{R_0(1+x_0^2)^3},\quad \beta_4=\frac{3x_0A_{III}+A_{IV}}{R_0(1+x_0^2)^4},$$
$$\beta_5=-\frac{(6x_0^2-1)A_{III}+4x_0A_{IV}}{R_0(1+x_0^2)^5},$$
$$\beta_6=\frac{x_0(10x_0^2-5)A_{III}+\left(10x_0^2-\frac{4}{3}\right)A_{IV}}{R_0(1+x_0^2)^6},$$
$$\beta_7=-\frac{\left(15x_0^4-15x_0^2+\frac{14}{15}\right)A_{III}+x_0(20x_0^2-8)A_{IV}}{R_0(1+x_0^2)^7}\quad \text{etc.} \tag{6}$$

The first term in (4) is the tangent of the slope of the line which is orthogonal to the rays in the focused beam. We now use (4) to calculate and construct the refraction line. In the coordinate system ρ, ξ, the equation of any ray incident on the corrector can be written as

$$\rho=\frac{xx_0+1}{x-x_0}\xi-R_0\sqrt{1+x_0^2}\,\lambda(x),$$

where

$$\lambda(x)=1-\beta_3(x-x_0)^2-\beta_4(x-x_0)^3$$
$$-\beta_5(x-x_0)^4-\beta_6(x-x_0)^5-\beta_7(x-x_0)^6.$$

Assume that we have chosen the set of inclination angles α_i or $x_i = \cot\alpha_i$, which determines the bundle of rays in the beam incident on the corrector. If the bundle is sufficiently dense, a small section of the refraction line between the neighboring intersections with rays can be approximated by the straight-line section

$$\rho_{i+1}=\rho_i'(\xi_{i+1}-\xi_i)+\rho_i, \tag{7}$$

where ρ_i' is determined by (4) with $x = x_i$. At the point of intersection of the straight lines where $x = x_{i+1}$ we get from (6) and (7) that

$$\xi_{i+1}=\frac{\rho_i'\xi_i-\rho_i-R_0\sqrt{1+x_0^2}\,\lambda_{i+1}}{\rho_i'-\frac{x_{i+1}x_0+1}{x_{i+1}-x_0}}. \tag{8}$$

Equations (8) and (7), together with (4) for the initial data $\rho_0 = 0$, $\xi_0 = 0$ for $x = x_0$ (normal ray), enable the line of refraction to be calculated along the points corresponding to the set of α_i. The results of such a calculation for a cylindrical mirror which focuses a beam of charged particles in an ion-optical arrangement with a point source[1] is shown in Fig. 2. In this case $A_{III} = -15.5292$, $A_{IV} = 4.0532$, $\alpha_0 = 42°18'$, $x_0 = 1.0987$. The family of lines of refraction corresponding to values of u = 0.02, 0.06, 0.1, 0.2, 0.5, 0.7, 1.0, and 10.0 and the line orthogonal to the rays (the lower curve u = −1) are constructed in the ρ, ξ coordinate system with the origin on the central ray at the point $R_0 = 0.7$. Each line is calculated for the set of α_i in the interval 32-52° at 1° steps. Owing to the fourth-order aberration effect, the curves are all clearly asymmetric about the ρ axis. At the point $\rho = 0$, $\xi = 0$, the orthogonal line touches the family of refraction lines and the order of contact, from (4), is equal to 3. The error in ρ' due to the approximate nature of (4) increases with $x - x_0$ and for the limiting rays with α = 32 and 52° is a few percent in this particular case.

The corrector electrodes must be made of high-transparency metal grids parallel to the calculated surface of refraction and separated by a small gap. It is necessary to allow for the electron-optical action of the individual cells of the grid. In order to eliminate any focusing effect of the cells in the direction of the symmetric axis of the cylindrical mirror, each electrode must be made only of a set of wires placed uniformly in the axial planes at a small angular interval. Then, when the additional accelerating potential U is applied to the corrector, each cell of two pairs of wires will form an immersion cylindrical lens, which focuses an elementary beam only in the direction perpendicular to the symmetry axis of the mirror. A very approximate calculation made on the basis of the results in ref. 5 shows that the optical power when the interelectrode gap is twice the distance between the neighboring wires can be much less than $1/r_1$, if $u \leq 0.3$.

It should be noted that a grid-type electrostatic corrector for spherical aberration was earlier sucessfully used by Bergkvist in a $\pi\sqrt{2}$ type magnetic spectrometer[6] and increased the brightness of the instrument significantly. It is to be hoped that an electrostatic angular-aberration corrector for a cylindrical mirror will prove just as useful, in spite of the difficulties involved in its construction.

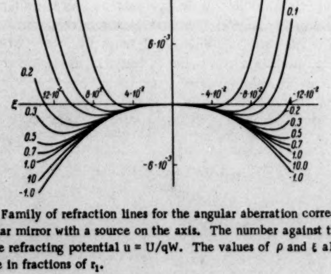

Fig. 2. Family of refraction lines for the angular aberration corrector in a circular mirror with a source on the axis. The number against the curves show the refracting potential u = U/qW. The values of ρ and ξ along the axes are in fractions of r_1.

---

[1] V. V. Zashkvara, M. I. Korsunskii and O. S. Kosmachev, Zh. Tekh. Fiz., 36, 132 (1966) [Sov. Phys.—Tech. Phys., 11, 96 (1966)].

[2] V. V. Zashkvara and V. S. Red'kin, Zh. Tekh. Fiz., 39, 1452 (1969) [Sov. Phys.—Tech. Phys., 14, 1089 (1970)].

[3] V. V. Zashkvara, Zh. Tekh. Fiz., 41, 193 (1971) [Sov. Phys.—Tech. Phys., 16, 146 (1971)].

[4] V. V. Zashkvara, Zh. Tekh. Fiz., 41, 829 (1971) [Sov. Phys.—Tech. Phys., 16, 651 (1971)].

[5] L. G. Glikman, V. M. Kel'man, and E. M. Yakushev, Zh. Tekh. Fiz., 37, 1028 (1967) [Sov. Phys.—Tech. Phys., 12, 740 (1967)].

[6] K. E. Bergkvist, Ark. Fysik., 13, 256 (1958).

Resonant amplification of an image potential by an electromagnetic wave

Yu. I. Balkarei É. M. Épshtein
Institute of Radio Engineering and Electronics,
Academy of Sciences of the USSR, Moscow
(Submitted June 18, 1973)
Zh. Tekh. Fiz., 44, 1337-1339 (June 1974)

The image potential is calculated for an electron above the surface of a conducting medium in the presence of an rf field parallel to the surface. The image potential can be amplified when the frequency of this field is close to a surface-plasmon frequency.

The image force which acts between the surface of a conductor and a nearby charge plays an important role in adsorption and desorption as particles move across various types of potential barriers at interfaces (in particular, in emission phenomena), etc. It was shown recently[1] that an electronic phase transition can be caused by image forces, so that it is extremely interesting to examine the possibility of influencing image forces. Below we show that it is in fact possible to influence the image force by imposing a sufficiently strong electromagnetic wave $\mathbf{E} = \mathbf{E}_0 \sin \Omega t$ on a charge (an electron).

The most convenient approach, developed in refs. 2-4, is that which the appearance of an image potential is treated as the result of an interaction between the charge and surface plasmons of the conductor. In particular, this approach makes it possible to incorporate dynamic corrections to the image potential.[4,5]

We begin from the Hamiltonian describing a system of surface plasmons which interact with a charge above the surface of the medium:[3]

$$H = \sum_{\mathbf{k}} \omega_{\mathbf{k}} \left(a_{\mathbf{k}}^{+} a_{\mathbf{k}} + \frac{1}{2} \right) + \Gamma_{\mathbf{k}}(\rho, z)\,(a_{\mathbf{k}} + a_{-\mathbf{k}}^{+}), \tag{1}$$

$$\Gamma_{\mathbf{k}}(\rho, z) = \left(\frac{\pi e^2 \omega_p^2}{2 A_0 k \omega_{\mathbf{k}}} \right)^{1/2} \exp(-kz + i\mathbf{k}\rho), \tag{2}$$

where $\omega_{\mathbf{k}}$ is the frequency of a surface plasmon having a (two-dimensional) wave vector $\mathbf{k}$, ω_p is the plasma frequency, $a_{\mathbf{k}}^{+}$ and $a_{\mathbf{k}}$ are the creation and annihilation operators for the surface plasmon, (ρ, z) are the cylindrical coordinates of the charge (the z axis is measured from the surface), A_0 is a normalization area, and we have set $\hbar = 1$.

The equation for the plasmon-annihilation operator,

$$\frac{da_{\mathbf{k}}}{dt} + i\omega_{\mathbf{k}} a_{\mathbf{k}} = -i\Gamma_{-\mathbf{k}}(\rho, z) \tag{3}$$

found from Hamiltonian (1), has the form of the equation of motion of an oscillator subject to an external force;[6] here the external force is the perturbing effect of the charge on the plasmon system. The image force is the reaction of the plasmon system to this perturbation, so that the image potential W must be equal in magnitude and opposite in sign to the work performed by the charge on the plasmon system:[6]

$$W = -\sum_{\mathbf{k}} \omega_{\mathbf{k}} \left| \int_{-\infty}^{t} \Gamma_{-\mathbf{k}}(\rho(\tau), z(\tau))\, e^{i\omega_{\mathbf{k}}\tau}\, d\tau \right|^2. \tag{4}$$

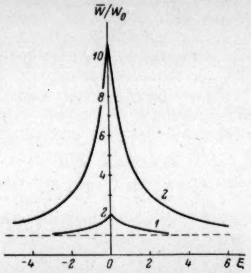

Fig. 1. Shape of the resonance line (the functional dependence of $\bar{W}/W_0$ on ξ). 1) A = 1; 2) A = 10.

We assume that a charge above the surface of a conductor is subject to the electric field of an electromagnetic wave propagating parallel to the surface, so that $\rho(t) = \rho_0 \sin \Omega t$, where $\rho_0 = (e\mathbf{E}_0)/(m\Omega^2)$ and m is the effective mass of the electron; we also assume that the charge moves parallel to the z axis at a constant velocity v. We are interested in the image potential average of a period of the wave $(T = 2\pi/\Omega)$, $\bar{W}$. Substituting $\rho(t)$ and $z(t)$ into (4) we find

$$\bar{W}(z) = -\frac{e^2\omega_s^2}{4\pi} \int_0^{2\pi} d\varphi \int_0^{\infty} dk\, e^{-2kz} \sum_{n=-\infty}^{\infty} \frac{J_n^2(k\rho_0 \cos\varphi)}{k^2 v^2 + (\omega_s - n\Omega)^2}, \tag{5}$$

where $J_n(x)$ is the Bessel function of real argument, $z = z(t) > 0$, and $\omega_s = \omega_p/\sqrt{2}$ is the frequency of a surface plasmon in the absence of dispersion; in deriving (5) we have assumed $z \gg R$, where R is the shielding length for the conductor.

It follows from (5) that with $v/z \ll \omega_s$ the functional dependence of the image potential on the wave frequency contains resonant peaks at $\Omega = \omega_s/n$; the widths of these peaks are governed by the velocity v. With $z \gg \rho_0$ and $z \gg v/\omega_s$, Eq. (5) becomes

$$\bar{W} = W_0[1 + AF(\xi)], \tag{6}$$

$$F(\xi) = 1 - \xi\,[\mathrm{ci}(\xi)\sin\xi - \mathrm{si}(\xi)\cos\xi], \tag{7}$$

where

$$A = \frac{1}{8}\left(\frac{\rho_0\omega_s}{v}\right)^2,\quad \xi = \frac{2z(\omega_s - \Omega)}{v},\quad W_0 = -\frac{e^2}{4z}$$

is the image potential in the absence of the wave field, and si(ξ) and ci(ξ) are the sine and cosine integrals. The amplitude of the first resonant peak ($\Omega = \omega_s$), A, can, in principle, become very large, since it is proportional to the product of the small expansion parameter $(\rho_0/z)^2$ and the large parameter $(z\omega_s/v)^2$. The height of each of the succeeding peaks ($n\Omega = \omega_s$, n = 2, 3, ...) is smaller than the height of the preceding peak by a factor $(\rho_0/z)^{-2}$. Figure 1 shows $\bar{W}/W_0$ as a function of ξ.

Result (6) can also be derived from the equations of electrodynamics. The field in the medium in which the charge is located consists of the field of the charge itself and the field which is the solution of the homogeneous system of Maxwell equations. The only field in the second medium is the solution of this homogeneous system. The matching of the fields at the interface ensures that the dynamic image potential is established as a result of the excitation of all types of surface waves.

For the case of an electron above the surface of a semiconductor ($\omega_s \sim 10^{14}$ sec^{-1}) and with $v \sim 10^7$ cm/sec, the value A = 1 is reached at $E_0 \sim 10^6$ V/cm (at $\Omega \sim 10^{14}$ sec^{-1}). If the electron is in another semiconductor (e.g., in the case of a heterojunction or tunnel contact), rather than in vacuum, the field required to reach A = 1 can be weaker by one or two orders of magnitude if the effective electron mass is small.

The height of the resonant peak is governed by factors such as the dispersion and damping of surface plasmons as well as by the motion of the charge normal to the surface; at typical parameter values these other factors make contributions on the same order as that of the charge motion, evaluated above.

An analogous resonant amplification of the image potential will occur if the charge is in a strong magnetic field normal to the surface; in this case the motion of the electron along its Larmor orbit plays a role analogous to that of the oscillations of the electron in the electric field of the electromagnetic wave.

---

[1] V. M. Agranovich and Yu. E. Lozovik, ZhETF Pis. Red., 17, 209 (1973) [JETP Lett., 17, 148 (1973)].

[2] A. A. Lucas and M. Sunjić, J. Vac. Sci. Technol., 9, 725 (1972).

[3] A. A. Lucas and M. Sunjić, Surf. Sci., 32, 439 (1972).

[4] M. Sunjić, G. Toulouse, and A. A. Lucas, Solid State Commun., 11, 1629 (1972).

[5] R. Ray and G. D. Mahan, Phys. Lett., A42, 301 (1972).

[6] L. D. Landau and E. M. Lifshitz, Mechanics, Addison-Wesley, Reading, Mass. (1960).

Thermoacoustic waves in conducting gases and liquids

P. A. Andreev

Zh. Tekh. Fiz., 44, 1339-1342 (June 1974)

Instabilities occurring in the absorption of an acoustic wave which couples to temperature fluctuations in a medium are investigated.

It has been shown[1,2] that the transmission of sound through a conducting medium can generate waves and the nature of the resulting instabilities has been studied. Oscillations for which a variation of the temperature T does not occur were considered in this earlier work. In the present work we consider instabilities produced by an acoustic flux which couples to temperature deviations $\Theta \neq 0$. We call these instabilities thermo-acoustic instabilities.

As in the earlier work,[1,2] we write the expression for the acousto-electric field $\mathbf{E}^{ae}$:

$$\mathbf{E}^{ae} = \chi \mathbf{J} + \chi_1 [\mathbf{J},\ \mathbf{H}_0] + \chi_2 \mathbf{H}_0 (\mathbf{J},\ \mathbf{H}_0), \tag{1}$$

in which **J** is the acoustic energy flux ($J = J_x$) and H_0 is the external magnetic field.

The heat flux produced by absorption of the acoustic wave in the medium can be written

$$\mathbf{q} = \beta \mathbf{J} + \beta_1 [\mathbf{J},\ \mathbf{H}_0] + \beta_2 \mathbf{H}_0 (\mathbf{J},\ \mathbf{H}_0), \tag{2}$$

where the coefficients β, β_1, and β_2 are proportional to χ, χ_1, and χ_2, respectively, and are of order $\beta_i \sim \chi_i T/e$.

Assuming that the external magnetic field $H_0 = H_{0y}$, we write the following linearized system of equations for small deviations of the electric field $\mathbf{E}'$, magnetic field $\mathbf{H}'$, current $\mathbf{j}'$, and temperature Θ:

$$\left.\begin{aligned}
&\operatorname{curl} \mathbf{H}' = \frac{4\pi}{c}\mathbf{j}', \operatorname{curl} \mathbf{E}' = -\frac{1}{c}\frac{\partial \mathbf{H}'}{\partial t},\\
&\mathbf{E}' = \alpha \nabla\Theta + \alpha_1 [\nabla\Theta,\ \mathbf{H}_0] + \alpha_2 \mathbf{H}_0 (\nabla\Theta,\ \mathbf{H}_0)\\
&\quad + \rho \mathbf{j}' + \rho_1 [\mathbf{j}',\ \mathbf{H}_0] + \rho_2 \mathbf{H}_0 (\mathbf{j}',\ \mathbf{H}_0)\\
&+ \frac{\partial \chi}{\partial T}\Theta \mathbf{J} + \frac{2\chi}{H_0^2}(\mathbf{H}',\ \mathbf{H}_0)\mathbf{J} + \frac{\partial \chi_1}{\partial T}\Theta [\mathbf{J}, \mathbf{H}_0] + \chi_1 [\mathbf{J},\ \mathbf{H}'] + \chi_2 \mathbf{H}_0 (\mathbf{J},\ \mathbf{H}'),\\
&c_T \rho_0 \frac{\partial \Theta}{\partial t} = \operatorname{div}\Big\{\varkappa \nabla\Theta + \frac{\partial \beta}{\partial T}\Theta \mathbf{J} + \beta_1 [\mathbf{J},\ \mathbf{H}'] + \frac{\partial \beta_1}{\partial T}\Theta [\mathbf{J},\ \mathbf{H}_0]\\
&\quad + \beta_2 \mathbf{H}_0 (\mathbf{J},\ \mathbf{H}') + \frac{2\beta}{H_0^2}(\mathbf{H}',\ \mathbf{H}_0)\mathbf{J}\Big\},
\end{aligned}\right\} \tag{3}$$

where α, α_1, α_2 are the thermoelectric coefficients, ρ, ρ_1, ρ_2 are the normal, Hall, and focusing resistivities, c_T is the specific heat of the medium, ρ_0 is the density of the medium, and $\varkappa$ is the thermal conductivity of the medium.

Assuming that all the unknowns in (3) are proportional to $\exp i(\mathbf{kr} - \omega t)$, we obtain a dispersion relation, which (because of its intricacy we analyze only in special cases.

In the case $k = k_x$ the dispersion relation has the form

$$\omega^2 + \left[(\nu_m + a)ik + c\chi_1 J + \frac{\partial \beta}{\partial T}\frac{J}{c_T \rho_0}\right]k\omega$$
$$+ \left(aik + \frac{\partial \beta}{\partial T}\frac{J}{c_T \rho_0}\right)(\nu_m ik + c\chi_1 J)k^2 - \frac{2ck^2\beta J}{c_T \rho_0}\left(\frac{\partial \chi_1}{\partial T}J + i\alpha_1 k\right) = 0, \tag{4}$$

where $\nu_m = c^2\rho/4\pi$, $a = \varkappa/c_T\rho_0$.

For large acoustic fluxes $c\chi_1 J/k\nu_m \gg 1$ and for $c_T\rho_0 c\chi_1/(\partial\beta/\partial T) \gg 1$ we obtain the frequency of the resulting instability:

$$\omega = ck|\chi_1|J + ik^2\left(\frac{2c\beta\alpha_1}{c_T\rho_0|\chi_1|} - a\right). \tag{5}$$

Note that $\chi_1 < 0$ (see ref. 1). The ratio $\Lambda = (\Theta/T)/(H'/H_0)$, in which $H' = H'_y$, is of order unity for $\beta J/\varkappa k H_0 \gg 1$ and $\Lambda \ll 1$ for $\beta J/\varkappa k H_0 \ll 1$. An investigation[3] of the character of the instability (5) shows that this instability is of the convective type.

In the case $k = k_y$ the dispersion relation assumes the form

$$\omega^3 + (2\nu_m + a)ik^2\omega^2 + \left[\frac{J^2}{c_T\rho_0}\left(\beta_2 \frac{\partial \chi_1}{\partial T}H_0^2 + \beta_1 \frac{\partial \chi}{\partial T}\right) + k^2(\nu_m^2 + \nu_{m_1}^2 + 2a\nu_m)\right]k^2\omega$$
$$- ia(\nu_m^2 + \nu_{m_1}^2)k^6 + \frac{ik^4J^2}{c_T\rho_0}\left[\nu_{m_1}H_0\left(\beta_1\frac{\partial \chi_1}{\partial T} - \beta_2\frac{\partial \chi}{\partial T}\right)\right. \tag{6}$$
$$\left. + \nu_m\left(\beta_2 H_0^2 \frac{\partial \chi_1}{\partial T} + \beta_1 \frac{d\varkappa}{\partial T}\right)\right] = 0,$$

where $\nu_{m_1} = c^2\rho_1 H_0/4\pi$.

We assume that the acoustic flux is large, i.e., that the following relation holds:

$$\frac{J^2}{c_T\rho_0\nu_m k^2}\left(\beta_2 H_0^2 \frac{\partial \chi_1}{\partial T} + \beta_1 \frac{\partial \chi}{\partial T}\right) \gg 1. \tag{7}$$

The solution for Eq. (6), i.e., a solution with $\operatorname{Im}\omega > 0$, is given by the expression

$$\omega = -ik^2\left(\nu_m + \nu_{m_1}H_0 \frac{\beta_1 \frac{\partial \chi_1}{\partial T} - \beta_2 \frac{\partial \chi}{\partial T}}{\beta_2 \frac{\partial \chi_1}{\partial T}H_0^2 + \beta_1 \frac{\partial \chi}{\partial T}}\right). \tag{8}$$

Equation (8) describes a periodic structure if the following relation holds:

$$\frac{\rho_1 H_0^2}{\rho}\,\frac{\beta_1 \frac{\partial \chi_1}{\partial T} - \beta_2 \frac{\partial \chi}{\partial T}}{\beta_2 \frac{\partial \chi_1}{\partial T}H_0^2 + \beta_1 \frac{\partial \chi}{\partial T}} > 1. \tag{9}$$

In the case $k = k_z$ the dispersion relation has the form

$$\omega^2 + \left[(\nu_m + a)ik - 2_e\frac{\chi}{H_0}J + \frac{\partial \beta_1}{\partial T}\frac{JH_0}{c_T\rho_0}\right]k\omega$$
$$+ \left(aik + \frac{\partial \beta_1}{\partial T}\frac{JH_0}{c_T\rho_0}\right)\left(\nu_m ik - 2_e\frac{\chi}{H_0}J\right)k^2 + \frac{ck^2\beta_1 J}{c_T\rho_0}\left(\frac{\partial \chi}{\partial T}J - i\alpha_1 H_0 k\right) = 0.$$

For large acoustic fluxes

$$\frac{J}{kv_m}\left(\frac{2\chi}{H_0}c+\frac{H_0}{c_T\rho_0}\frac{\partial\beta_1}{\partial T}\right)\gg 1,\quad \frac{J}{k}\,\frac{\left(\frac{2\chi}{H_0}c+\frac{H_0}{c_T\rho_0}\frac{\partial\beta_1}{\partial T}\right)^2}{\frac{v_m H_0}{c_T\rho_0}\frac{\partial\beta_1}{\partial T}-\frac{\chi}{H_0}cv_m+\frac{ca_1\beta_1 H_0}{c_T\rho_0}}\gg 1 \qquad (11)$$

we find that a nonstationary distribution of the field and temperature is established in the medium:

$$\omega=\frac{2\chi}{H_0}ckJ+i\left(\frac{ca_1\beta_1 H_0}{c_T\rho_0}\,\frac{1}{\frac{2\chi}{H_0}c+\frac{H_0}{c_T\rho_0}\frac{\partial\beta_1}{\partial T}}-a\right)k^2 \qquad (12)$$

for

$$\left(\frac{2\chi}{H_0}c+\frac{H_0}{c_T\rho_0}\frac{\partial\beta_1}{\partial T}\right)^2\gg\frac{c}{c_T\rho_0}\beta_1\frac{\partial\chi}{\partial T},$$

and

$$\omega=J_k\left(\frac{\chi}{H_0}c-\frac{H_0}{2c_T\rho_0}\frac{\partial\beta_1}{\partial T}+i\sqrt{\frac{c}{c_T\rho_0}\beta_1\frac{\partial\chi}{\partial T}}\right) \qquad (13)$$

for

$$\left(\frac{2\chi}{H_0}c+\frac{H_0}{c_T\rho_0}\frac{\partial\beta_1}{\partial T}\right)^2\ll\frac{c}{c_T\rho_0}\beta_1\frac{\partial\chi}{\partial T}.$$

The instability described by (12) and (13) is of the convective type.

To find the conditions for the onset of instability in the conducting medium we use the system of magnetohydrodynamic equations,[4] which must be solved simultaneously with the system (3); in the latter it is necessary to replace **E'** by **E'** + (1/c)[**v**, H_0], where **v** is a small velocity perturbation in the medium. The resulting dispersion relation is analyzed in special cases.

Inasmuch as $v_A/u_0 \ll 1$ in real situations, where v_A is the Alfvén velocity and u_0 is the velocity of sound, the dispersion relation has the same form as (4) for $k = k_x$.

For the case $k = k_z$ the dispersion relation has the form

$$[\omega^2-(u_0^2-i\nu\omega)k^2]\left(\omega+iv_mk^2+\frac{2\chi}{H_0}ckJ\right)\left(\omega+iak^2+\frac{\partial\beta_1}{\partial T}k\frac{JH_0}{c_T\rho_0}\right)+ck^2\frac{\beta_1 J}{c_T\rho_0}$$
$$\times\left(J\frac{\partial\chi}{\partial T}-ia_1H_0k\right)[\omega^2-(u_0^2-i\nu\omega)k^2]$$
$$-\frac{H_0^2}{4\pi\rho_0}\omega k^2\left(\omega+iak^2+\frac{\partial\beta_1}{\partial T}k\frac{JH_0}{c_T\rho_0}\right)=0. \qquad (14)$$

If we assume that $\omega = \omega_0(1+\delta+i\delta_1)$, where $\omega_0 = \pm k\cdot\sqrt{u_0^2 + H_0^2/4\pi\rho_0}$, we can linearize (14) with respect to δ and δ_1 to obtain

$$\omega=\omega_0\left[1+\frac{J}{2}\left(\frac{k}{\omega_0}\right)^3\frac{H_0}{c_T\rho_0}\left(\frac{H_0^2}{4\pi\rho_0}\frac{\partial\beta_1}{\partial T}-\nu a_1c\right)+\frac{J\nu}{2}\left(\frac{k}{\omega_0}\right)^3\left(\frac{2\chi c}{H_0}a+\frac{H_0}{c_T\rho_0}\frac{\partial\beta_1}{\partial T}v_m\right)k^2\right.$$
$$\left.-i\frac{\nu J}{2}\left(\frac{k}{\omega_0}\right)^2\left(\frac{2\chi}{H_0}c+\frac{H_0}{c_T\rho_0}\frac{\partial\beta_1}{\partial T}\right)k-i\frac{\nu J^2}{2}\left(\frac{k}{\omega_0}\right)^3\frac{c}{\beta_1}\frac{\partial}{\partial T}(\chi\beta_1^2)\,k\right]. \qquad (15)$$

Growth of the excited fluctuation requires that the following relation be satisfied:

$$J\gg\omega_0\frac{\frac{2|\chi|}{H_0}c-\frac{H_0}{c_T\rho_0}\frac{\partial\beta_1}{\partial T}}{k\frac{\partial}{\partial T}(\chi\beta_1^2)}. \qquad (16)$$

The following ratios are determined from the system of fundamental equations for the given case:

$$\frac{w}{u_0}\Big/\frac{H'_y}{H_0}=\frac{\omega}{u_0k},\quad \frac{\theta}{T}\Big/\frac{H'_y}{H_0}=\frac{\beta_1}{T}\Big/\frac{\partial\beta_1}{\partial T}, \qquad (17)$$

where w is the x component of the velocity. The ratios (17) are of order unity.

It is instructive to compare the critical acoustic fluxes J_{kR_1} and J_{kR_2} for the excitation of acoustomagnetic waves [see ref. 2, Eq. (4)] and thermo-acoustic waves [Eq. (9) above], respectively.

The ratio $J_{kR_1}/J_{kR_2} \approx k|\chi|/\gamma|\chi_1|H_0 = k\Omega\tau/\gamma$, where γ is the acoustic damping factor and k is the excited wave vector. Thus, thermo-acoustic waves are more readily excited in the short-wave range, and acoustomagnetic waves in the long-wave range.

I am grateful to I. V. Ioffe for discussion.

---

[1] P. A. Andreev, Zh. Tekh. Fiz., 43, 1756 (1973) [Sov. Phys.—Tech. Phys., 18, 1108 (1974)].

[2] P. A. Andreev, Zh. Tekh. Fiz., 44 (1974) [Sov. Phys.—Tech. Phys., 19, (in press)].

[3] A. I. Akhiezer and R. V. Polovin, Usp. Fiz. Nauk, 104, 186 (1971) [Sov. Phys.—Usp., 14, 278 (1971)].

[4] S. I. Syrovatskii, Usp. Fiz. Nauk, 62, 247 (1957).

Hologram interferometry for vibration analysis (review)

V. S. Listovets and Yu. I. Ostrovskii

A. F. Ioffe Physicotechnical Institute,
Academy of Sciences of the USSR, Leningrad

(Submitted July 26, 1973)
Zh. Tekh. Fiz., 44, 1345-1372 (July 1974)

The application of hologram interferometry to vibration analysis is reviewed. The Powell–Stetson (time-averaging) method, the hologram strobe method, and the phase modulation of a reference beam are considered. The merits and limitations of these methods are discussed. Experimental results are provided on vibration analysis of industrial products by hologram methods.

INTRODUCTION

As early as 1932 the American scientist Osterberg[1] used time averaging of light waves, reflected by a vibrating surface, for interferometer vibration analysis of piezoelectric crystals. He showed that the luminosity distribution over the investigated surface, observed at the interferometer output, is given by the function

$$I=I_0\left[1+J_0\left(\frac{4\pi A}{\lambda}\right)\right],$$

where J_0 is the zeroth-order Bessel function, A is the vibration amplitude, and λ is the wavelength of the light.

Osterberg used a Michelson interferometer, replacing one of the mirrors by the investigated crystal with a polished surface. Osterberg's method is restricted by the fact that the investigated object must be a planar, mirror-finished surface.

In 1965, in one of the first papers on hologram interferometry,[2] Powell and Stetson suggested a more powerful method of vibration analysis, which is based on Osterberg's principle, but uses the hologram scheme of Leith and Upatnieks[3] for recording the light scattered by the vibrating object.

The hologram technique widened the possibilities of Osterberg's method, allowing interferometer analysis of opaque objects of any shape with any surface state. Polishing of the investigated surface or deposition of a mirror coating is not required.

In the same year, 1965, Stetson and Powell suggested a real-time variation of their own method,[4] in which the interference pattern formed by the waves, recovered from the hologram of the unperturbed object and scattered by the vibrating object (the hologram occurs at the same place or is recovered after occurrence at the previous place), is observed directly or photographed.

The idea of the time-averaging method is simple. If the object vibrates during an exposure time significantly longer than the period of vibration the waves scattered by this object in all states which it traverses will be recorded on the hologram.

The waves restored by the hologram form an interference pattern, which provides information on the motion of the various portions of the object.

The contributions of the various object positions to the total exposure is determined by the velocity with which the object passes through these positions. The higher the velocity, the shorter the time spent by the object at this position, and the smaller the contribution of this state to the exposure. Since the object stops at the extreme positions and its velocity is low close to these positions, the contribution of these two object states to the exposure is very large and we can assume that the hologram is due to the two corresponding positions of the object, i.e., a hologram obtained by two exposures. The recovered image of the object is the intersection of interfering fields of equal vibrational amplitudes. The nonmoving object portions (node lines) exhibit the maximum luminosity, since these object points are in the same position during the total exposures. The points for which the path difference between the waves scattered by the object consists of an odd number of half-wavelengths provide minimum intensity and correspond to dark bands.

The points for which this path difference is an even number of half-wavelengths form the maxima of the light bands. These maximum intensities, however, decrease for increasing vibrational amplitudes since then the time which the object spends around the extremum is reduced (Fig. 1).

A more rigorous analysis verifies these qualitative considerations.

Thus, due to the capability of recording the complex amplitude of light waves in the Powell–Stetson method, we do not deal with an intensity average (as in the Osterberg method), but with the actual complex amplitude.

EFFECT OF VARIOUS OBJECT MOTIONS ON IMAGE LUMINOSITY

We perform this analysis for general motion. The complex amplitude of the wave, scattered by some point of a fixed object, can be represented in the form

$$ae^{-i\psi_0},$$

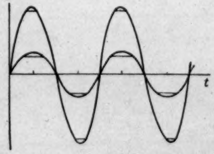

Fig. 1. With increasing vibrational amplitudes the time which the object spends near the extremum position is reduced.

where

$$\psi_0 = \frac{2\pi x \sin\theta}{\lambda}.$$

If this point moves in direction v (Fig. 2), the time dependence of the phase of the wave scattered into the same hologram point is

$$\psi = \psi_0 + \frac{2\pi}{\lambda}\int_0^t (\cos\varphi_1 + \cos\varphi_2)\,v\,dt. \tag{1}$$

The notation for the angles φ_1 and φ_2 is clear from Fig. 2.

The complex amplitude is

$$ae^{-i\left[\psi_0 + \frac{2\pi}{\lambda}\int_0^t (\cos\varphi_1 + \cos\varphi_2)\,v\,dt\right]}, \tag{2}$$

and its average over the exposure time T determines the luminosity of point 0 in the restored object image:[1)]

$$I \sim \left|\frac{a}{2}\int_0^T e^{-i\left[\psi_0 + \frac{2\pi}{\lambda}\int_0^t (\cos\varphi_1 + \cos\varphi_2)\,v\,dt\right]}\,dt\right|^2. \tag{3}$$

Equation (3) is very general and covers different motions of the point 0. For a nonmoving object (v = 0) we obtain the obvious equation $I \sim a^2$.

Constant velocity. In case of rectilinear uniform motion (v = const) we have

$$I \sim \left|\frac{a}{2}\int_0^T e^{-i\left[\psi_0 + \frac{2\pi}{\lambda}(\cos\varphi_1 + \cos\varphi_2)\,v\,t\right]}\,dt\right|^2. \tag{4}$$

Integration of this expression leads to

$$I \sim a^2 \frac{\sin^2\left[\frac{\pi}{\lambda}(\cos\varphi_1 + \cos\varphi_2)\,vT\right]}{\left[\frac{\pi}{\lambda}(\cos\varphi_1 + \cos\varphi_2)\,vT\right]^2}. \tag{5}$$

In the special case $\varphi_1 = \varphi_2 = 0$ (the object illuminated from the hologram side and moving in that direction) we obtain

$$I \sim a^2 \frac{\sin^2\frac{2\pi vT}{\lambda}}{\left(\frac{2\pi vT}{\lambda}\right)^2} = a^2 \frac{\sin^2\frac{2\pi r}{\lambda}}{\left(\frac{2\pi r}{\lambda}\right)^2}. \tag{6}$$

This function is plotted in Fig. 3.

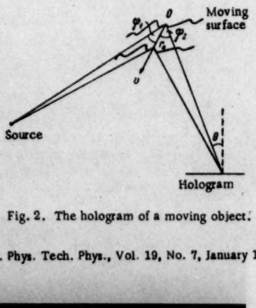

Fig. 2. The hologram of a moving object.

The time-averaging method of recording a hologram of a uniformly moving object was investigated independently by several authors from various points of view.

Considering the hologram as a linear time filter acting on the time-varying light wave propagating away from the object during the exposure time, Goodman[5] shows, using the example of an object rotating with constant angular velocity, that the luminosity of the restored image is described by Eq. (5).

Constructing a mathematical model for recording two plane waves with constant amplitudes on a hologram, but with one of the phases linearly varying during the exposure time, Redman[6] obtained the same result for the luminosity of the restored image. He suggested the use of the hologram time-averaging method to study very slowly moving surfaces, such as the surface of an evaporating liquid; for shorter exposure times, he suggested the study of isotachs (equal velocity lines used to investigate liquid flow).

The function in Eq. (5) was obtained by Lurie,[7,8] starting from an estimate of the luminosity dependence of the restored image on the degree of coherence between the reference wave and that reflected on the hologram by an object uniformly moving during the exposure time, and by Neumann,[9] who showed that the effect of motion of the object appears in the spatial modulation of the contrast of bands forming the hologram. This modulation causes a smearing of the restored image, similar to the diffuse image obtained in ordinary photography of a moving object, and a luminosity loss in the restored image, corresponding to Eq. (5).

Step motion of the object. Consider another special case of a displaced object, which is located at one place during half the exposure time and is displaced by r during the other half. This case corresponds to the two-exposures method.

In this case the integral (3) is split into two parts, corresponding to the first and second exposures:

$$I \sim \left|\frac{a}{T}\left\{\int_0^{\frac{T}{2}} e^{-i\frac{2\pi}{\lambda}\int_0^t (\cos\varphi_1 + \cos\varphi_2)\,v\,dt}\,dt + \int_{\frac{T}{2}}^{T} e^{-i\frac{2\pi}{\lambda}\left[\Delta + \int_0^t (\cos\varphi_1 + \cos\varphi_2)\,v\,dt\right]}\,dt\right\}\right|^2, \tag{7}$$

where $\Delta = r(\cos\varphi_1 + \cos\varphi_2)$ is the resulting path difference for the wave scattered by the points during motion (Fig. 2). Since v = 0, we transform (7) to the form

$$I \sim \left|\frac{a}{T}\left\{\frac{T}{2}\left[1 + e^{-i\frac{2\pi}{\lambda}\Delta}\right]\right\}\right|^2, \tag{8}$$

whence, after simple transformations,

$$I \sim a^2\cos^2\frac{\pi}{\lambda}r(\cos\varphi_1 + \cos\varphi_2). \tag{9}$$

In the special case of an object illuminated on the hologram side and moving in the same direction, when $\varphi_1 = \varphi_2 = 0$, we have

$$I \sim a^2\cos^2\frac{2\pi r}{\lambda}. \tag{10}$$

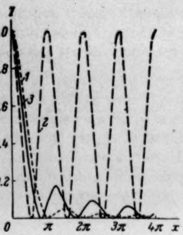

Fig. 3. Intensity distribution in the restored image of an object, moving during the exposure time. 1) Rectilinear uniform motion ($I \sim \sin^2 x/x^2$); 2) step motion [two-exposures method ($I \sim \cos^2 x$)]; 3) harmonic vibration [$I \sim J_0^2(x)$]; the abscissa is $x = 2\pi r/\lambda$ for curves 1 and 2, and $x = 4\pi A/\lambda$ for curve 3.

This function is also shown in Fig. 3. In this case we obtain band interference with nondecreasing intensity maxima.

A harmonically vibrating object. Finally, consider harmonically vibrating points of an object, i.e.,

$$\int_0^t (\cos\varphi_1 + \cos\varphi_2)\, v\, dt = A(\cos\varphi_1 + \cos\varphi_2)\sin\omega t,$$

where A is the vibrational amplitude. The general expression (3) becomes

$$I \sim \left| \frac{a}{T} \int_0^T e^{-i\left[\frac{2\pi A}{\lambda}(\cos\varphi_1+\cos\varphi_2)\sin\omega t\right]} dt \right|^2. \tag{11}$$

Since

$$e^{-i\frac{2\pi A}{\lambda}(\cos\varphi_1+\cos\varphi_2)\sin\omega t} = \sum_{n=-\infty}^{\infty} J_n\left[\frac{2\pi A}{\lambda}(\cos\varphi_1+\cos\varphi_2)\right] e^{in\omega t}, \tag{12}$$

where J_n is the n-th order Bessel function, we obtain

$$I \sim \left| \frac{a}{T} \sum_{n=-\infty}^{\infty} \left\{ J_n\left[\frac{2\pi A}{\lambda}(\cos\varphi_1+\cos\varphi_2)\right] \int_0^T e^{in\omega t} dt \right\} \right|^2. \tag{13}$$

Following integration, we have

$$I \sim \left| a \sum_{n=-\infty}^{\infty} \left\{ J_n\left[\frac{2\pi A}{\lambda}(\cos\varphi_1+\cos\varphi_2)\right] \frac{e^{in\omega T}-1}{in\omega T} \right\} \right|^2. \tag{14}$$

If the exposure time is an integral number of the vibrational periods of the object, i.e., $T = 2k\pi/\omega$, all terms except $n = 0$ vanish and we have

$$I \sim a^2 J_0^2\left[\frac{2\pi A}{\lambda}(\cos\varphi_1+\cos\varphi_2)\right]. \tag{15}$$

For $T \gg 2\pi/\omega$ the role of the zeroth term in the sum (14) is again dominant, since the factor $(e^{in\omega T} - 1)/in\omega T$ tends to zero with increasing ωT, and the intensity distribution over the surface of the object is also expressed by Eq. (15). Physically it is clear that the transition from the exposure time $T_1 = 2k\pi/\omega$ to $T_2 = 2(k + \delta)\pi/\omega$, where k is a large integer and $\delta < 1$ is a small correction to k, does not change the hologram substantially; consequently, it does not change the luminosity of the restored image.

When $\varphi_1 = \varphi_2 = 0$ Eq. (15) becomes

$$I \sim a^2 J_0^2\left(\frac{4\pi A}{\lambda}\right). \tag{16}$$

The function in (16), like the preceding equations (5) and (10), is oscillatory and modulates the luminosity of the restored image, thus forming interference bands. This function is also shown in Fig. 3. We note that the positions of maxima and minima of the functions (10) and (16) are insignificantly displaced with respect to each other (less than a quarter of a band). Therefore the calculation of vibrational amplitudes by time averaging the interferogram, based on the simplified idea of regarding the Powell–Stetson method as a variant of the two-exposures method, does not lead to significant errors.

EXPERIMENTS IN VIBRATION ANALYSIS BY THE POWELL–STETSON METHOD

The vibration of a long, narrow steel pole, rigidly fixed at the ends, has been investigated[10] by the Powell–Stetson method. To reduce the sensitivity it was proposed to use large illumination and observation angles, since the number of bands in the interference pattern of the restored image is proportional to the sum of cosines of these angles; for high-order band resolution at large vibrational amplitudes of the object it was proposed to scan photometrically the interference pattern recovered together with the hologram.

Hologram measurements of sinusoidal vibrations of a film have been performed[11] by independent interferometer determinations of the vibrational amplitudes of this film using a Twyman–Green interferometer. A small mirror, used as an interferometer mirror, is attached to the opposite side of the film. At the interferometer output the vibrational amplitude of the mirror is measured photoelectrically with an accuracy of ± 0.04 λ.

The hologram and interferometer measurements are performed simultaneously. Comparison of the experimental data shows agreement for the vibrational amplitudes of the film by both methods.

Three types of motion of a thin steel film, sinusoidal vibration, motion with constant velocity, and their superposition have been studied experimentally[12] by the Powell–Stetson method. From the experimental results it was concluded that in studying sinusoidal vibrations one must apply careful procedures to eliminate drifting of the object during the exposure; otherwise the interpretation of the interference band pattern is difficult.

The Powell-Stetson method, however, is applicable[13] to the analysis of sinusoidal vibrations if the object as a whole exhibits significant piston-like vibrations (of several microns), of the same frequency as the sinusoidal vibrations of the surface of the object. Moreover, in this case the band intensity falls off slower with increasing band number since the band intensity is determined by the higher-order maxima of the function J_0^2.

Another method in which, on the other hand, piston components of vibration are excluded[14] is described below.

The time-averaging method has been used to study vibrations of circular membranes[15,16] oscillating in two modes simultaneously. Cases of two simultaneous vibrations at the same frequency, but with different phases, and of two vibrations at different frequencies have been treated.

The Powell–Stetson method has been applied[17,18] to the study of high-frequency sinusoidal vibrations. The vibrational modes of a cantilever have been studied[17] from the fifth to the 34th mode in the frequency regime from 500 Hz to 25.665 kHz and a hologram of the vibrating cantilever has been obtained in the 77th mode at a frequency of 99.395 kHz.

A similar study has been performed[18] for a rectangular plate up to a frequency of 76.8 kHz.

In both papers the experimental results on the resonance frequencies and modes are in agreement with the classical theory of cantilever and rectangular plate vibrations. We note that the time-averaging method is applicable only to vibrations of relatively small amplitudes.

Vibrations of simple objects, thin membranes, diaphragms, films, and beams have been studied[2,4,10–13,15–18] by the time-averaging method.

The papers of Waddell and Kennedy[19,20] were the first in which the averaging method was applied to vibration analysis of actual industrial machines, turbine blades.

In addition to determining the frequency characteristic of turbine blades, a study has been made[21] of the effect of various design factors on the vibrational distribution in an aircraft thrust reverser. The time-averaging method has been used to study fin resonances in the Concorde aircraft.[22]

Similar experiments have been performed[23–25] by the Powell–Stetson method to determine the vibrational characteristics of aircraft elements, turbine blades, and disks with hollow blade sections. A compact hologram setup is described in these papers; it is built by Rolls-Royce and can be used to study objects with transverse dimensions up to 60 cm. The setup is simple enough so that an operator without special training can operate it.

The vibrations of turbine blades and stacks of 10 turbine blades have been studied[26] by a real-time-averaging method, following the work in refs. 19 and 20. A special dye, containing minute glass globules, is used in this work to enhance the reflectivity of objects. The light reflected from the object is not depolarized so that the light diffracted by the hologram and reflected by the object has a unique direction of polarization. This enhances the band contrast, which is essential in hologram interferometry in real time. The high reflectivity allows shorter exposure times and the use of a low-power laser. The authors estimate a hologram of an object with an area of 0.3 m^2 with a 5-mW laser requires an exposure time of 0.25-0.5 sec (the "Ilford He–Ne I" plate with sensitivity 5 erg/cm^2 is used).

An original application of holography[27,28] uses the real-time-averaging method to study the vibrational characteristics of the frame of a violin.

The method of time averaging has been used[29] to determine the vibrational fields of cylinders with cone tops.

A study of the sound fields of an ultrasound transmitter in a transparent cell filled with water has been performed[30] by the time-averaging method. Equal amplitude lines of sound pressure formed by the phase modulation of the light passing through the transparent cell are obtained in the hologram image.

Limitation of the Powell – Stetson method. As follows from the analysis given above and from the short review of the experimental work, the Powell–Stetson method is experimentally very simple and convenient, and is applicable in a wide variety of problems in vibration analysis. There are, however, a number of limitations.

1. The band luminosity falls off quickly with increasing amplitude, the 10th band has a luminosity 2% of that of the node line, and the 20th, 1%. Therefore it is impossible to study objects whose vibrational amplitude[2)] exceeds 5λ.

2. In principle the Powell–Stetson method can be used to study vibrations in real time; in actuality such studies give node lines only.[4]

3. The time-averaging method does not provide objective information about the relative vibrational phases of different points of the surface of the object.

4. The time-averaging method cannot be used to analyze vibrations with very small amplitudes ($A < \lambda/4$).

The first three limitations can be removed by a hologram strobe method of vibration analysis. The fourth limitation can be overcome by phase modulation of the reference beam and by a "hologram subtraction" method, both of which are dicussed below.

HOLOGRAM STROBE METHOD

This name is given to hologram methods using repeated synchronized light pulses. The hologram strobe method was first developed in[32] 1967 to study a plasma fed by a varying current. The apparatus is presented in Fig. 4. A drum-chopper, through which a mercury–argon discharge lamp (PRK-4) is fed, is mounted on the axis of an electric motor. A disk with apertures, through which a helium–neon laser beam passes, rotates on the same axis. The disk is arranged so that the light pulses correspond alternately to breaks and to maxima of the current through the lamp. This method is thus equivalent to the two-exposures method, with two waves corresponding to two states of the lamp being recorded on the hologram. The purpose of the study was to explain the variations of the radial density distribution of the gas, which is due to the current through the lamp. The present authors did not succeed in observing variations of this type in the lamps, as those border on the sensitivity limits of the interferometer method. This very idea of strobe holography, however, is very fruitful in vibration analysis.

Hologram strobe vibration analysis. In one of the first papers devoted to hologram strobe vibration analysis[33] an approximate analysis of the possibilities of this technique was given. We start with the Powell–Stetson method. We assume that it is a two-exposures method and that an interference structure is created on the hologram due to the object stopping at the extreme positions. The restored light waves scattered by the ob-

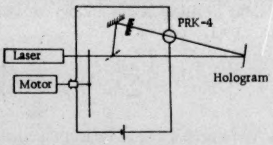

Fig. 4. Schematic of arrangement for hologram strobe investigation of a plasma.

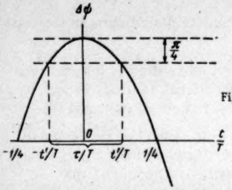

Fig. 5. For the derivation of Eq. (17).

ject interfere with each other at the extreme positions. The band luminosity is determined by the dwell time at the extreme positions τ. This dwell time is the interval during which the phase of the wave, scattered by the object in the hologram direction, changes by less than $\pi/4$, i.e., the time during which the quantity

$$\Delta\psi=\frac{2\pi}{\lambda}A\,(\cos\varphi_1+\cos\varphi_2)-\frac{2\pi}{\lambda}A\,(\cos\varphi_1+\cos\varphi_2)\cos\frac{2\pi t'}{T}\tag{17}$$

remains smaller in absolute value than $\pi/4$ (Fig. 5). Denoting by t' the time at which $\Delta\psi = \pi/4$, and taking account of $\tau = 2t'$, we have

$$\cos\frac{2\pi t'}{T}=1-\frac{\lambda}{8A\,(\cos\varphi_1+\cos\varphi_2)}\tag{18}$$

where

$$p=\frac{2\tau}{T}=\frac{2}{\pi}=\text{arc}\cos\left[1-\frac{\lambda}{8A\,(\cos\varphi_1+\cos\varphi_2)}\right].\tag{19}$$

The quantity p, defined by the last equality, is the "efficiency" of the Powell–Stetson method. It is that portion of the whole exposure which is the "duty" cycle of the exposure (the time during which the object is fixed in the sense discussed above). Since the largest number of bands observed in the Powell–Stetson method does not usually exceed 10, we have

$$2A\,(\cos\varphi_1+\cos\varphi_2)\leqslant 10\lambda;\tag{20}$$

using (19) we have $P_{\min} \simeq 0.15$. Thus, in the time-averaging method the effective exposure is at least 0.15 of the total exposure. The point luminosity of the restored object image, for which this quantity is less than 0.15, is usually insufficient to be observed. As noted above, the quantity J_0^2 for the 10th maximum of this function is equal to 0.02. Under ideal conditions one can observe even higher-order bands; this requires image restoration with a large-area hologram, so as to decrease the effect of spot noise. High stability of all components is also required. The values we use for a maximum observed number of bands (10), and the corresponding value $p_{\min} = 2\tau/T = 0.15$, correspond to ordinary conditions in obtaining holograms of vibrating objects.

By stroboscopic hologram illumination we can control the time and length of the hologram exposure. If the length of the illuminating pulse is a k-th part of a half-cycle (k is the pulse duty cycle), this causes a corresponding reduction of the total exposure without reduction of its useful part. The quantity p thus increases by a factor k, which widens the range of amplitudes that can be studied or, for a given amplitude, enhances the band luminosity

$$p=\frac{2k}{\pi}\text{arc}\cos\left[1-\frac{\lambda}{8A\,(\cos\varphi_1+\cos\varphi_2)}\right].\tag{21}$$

or

$$\frac{A\,(\cos\varphi_1+\cos\varphi_2)}{\lambda}=\frac{1}{8\left(1-\cos\frac{p\pi}{2k}\right)}.\tag{22}$$

When $\varphi_1 = \varphi_2 = 0$

$$\frac{A}{\lambda}=\frac{1}{16\left(1-\cos\frac{p\pi}{2k}\right)}=\frac{1}{32\sin^2\frac{p\pi}{4k}}.\tag{23}$$

This equation allows one to estimate the maximum value of vibrational amplitude for a given duty cycle k. For p = 0.15, which corresponds to the limiting characteristics of the Powell–Stetson method, we have

$$\left(\frac{A}{\lambda}\right)_{\max}=\frac{1}{32\sin^2\frac{0.15\pi}{4k}}\approx 2.5k^2.\tag{24}$$

Thus the hologram strobe method provides a quadratic increase in the limiting vibrational amplitude, while reducing the pulse length.

We consider more rigorously the intensity distribution over the restored image of the vibrating object.

Let the complex amplitude of the object wave incident on the hologram from some object point vibrating with amplitude A be $a\cdot\exp\{i[\varphi_0 + (4\pi A/\lambda)\sin\omega t]\}$.

The intensity of the restored image is proportional to the square of the absolute value averaged over the exposure time τ:

$$I=\left|\frac{ae^{-i\varphi_0}}{\tau}\int\limits_0^{\tau}e^{i\frac{4\pi A}{\lambda}\sin\omega t}\,dt\right|^2.\tag{25}$$

We expand the integrand in a Bessel function series

$$I=\left|\frac{a}{\tau}\sum_{n=-\infty}^{\infty}J_n\left(\frac{4\pi A}{\lambda}\right)\int\limits_0^{\tau}e^{in\omega t}\,dt\right|^2.\tag{26}$$

Taking the strobe pulse length to be equal to the k-th part of the vibrational period T, i.e., $2\pi/\omega k = T/k$, and synchronizing it with an extremum of the object positions, we obtain

$$I=a^2\left|\frac{k}{T}\sum_{n=-\infty}^{\infty}J_n\left(\frac{4\pi A}{\lambda}\right)\int\limits_{\frac{T}{4}-\frac{T}{2k}}^{\frac{T}{4}+\frac{T}{2k}}e^{in\frac{2\pi t}{T}}dt\right|^2. \qquad (27)$$

The integral inside the summation sign is exp(in π/2) · (T/k)[(sin nπ/k)/(nπ/k)], and we have

$$I=a^2\left|\sum_{n=-\infty}^{\infty}J_n\left(\frac{4\pi A}{\lambda}\right)\left(\frac{\sin\frac{n\pi}{k}}{\frac{n\pi}{k}}\right)e^{in\frac{\pi}{2}}\right|^2. \qquad (28)$$

Since $J_{-n} = (-1)^n J_n$, and $\exp(in\pi/2) = i^n$, we have $J_n \exp(in\pi/2) = J_{-n}\exp(-in\pi/2)$ and

$$I=a^2\left|J_0\left(\frac{4\pi A}{\lambda}\right)+2\sum_{n=1}^{\infty}J_n\left(\frac{4\pi A}{\lambda}\right)\left(\frac{\sin\frac{n\pi}{k}}{\frac{n\pi}{k}}\right)i^n\right|^2. \qquad (29)$$

Considering such illumination of an object restored with a hologram and exposed by pulses of the same duration T/k, but synchronized with another position extremum of the vibrating object, we obtain

$$I=a^2\left|\frac{k}{2T}\sum_{n=-\infty}^{\infty}J_n\left(\frac{4\pi A}{\lambda}\right)\int\limits_{\frac{3T}{4}-\frac{T}{2k}}^{\frac{3T}{4}+\frac{T}{2k}}e^{in\frac{2\pi t}{T}}dt\right|^2$$
$$=a^2\left|J_0\left(\frac{4\pi A}{\lambda}\right)+2\sum_{n=1}^{\infty}J_n\left(\frac{4\pi A}{\lambda}\right)\left(\frac{\sin\frac{n\pi}{k}}{\frac{n\pi}{k}}\right)(-i)^n\right|^2. \qquad (30)$$

If the hologram is illuminated when the images (29) and (30) are restored, we observe the interference pattern formed by their superposition with the following intensity distribution:

$$I=a^2\left|\frac{k}{T}\sum_{n=-\infty}^{\infty}J_n\left(\frac{4\pi A}{\lambda}\right)\left\{\int\limits_{\frac{T}{4}-\frac{T}{2k}}^{\frac{T}{4}+\frac{T}{2k}}e^{in\frac{2\pi t}{T}}dt+\int\limits_{\frac{3T}{4}-\frac{T}{2k}}^{\frac{3T}{4}+\frac{T}{2k}}e^{in\frac{2\pi t}{T}}dt\right\}\right|^2$$
$$=a^2\left|J_0\left(\frac{4\pi A}{\lambda}\right)+\sum_{n=1}^{\infty}J_n\left(\frac{4\pi A}{\lambda}\right)\left(\frac{\sin\frac{n\pi}{k}}{\frac{n\pi}{k}}\right)[i^n+(-i)^n]\right|^2. \qquad (31)$$

The quantity in the square brackets inside the summation sign is $2i^n$ for even n and vanishes for odd n. As a result all terms with odd indices drop out of the summation, and the interference pattern has the following intensity distribution:

$$I=a^2\left|J_0\left(\frac{4\pi A}{\lambda}\right)+2\sum_{p=1}^{\infty}J_{2p}\left(\frac{4\pi A}{\lambda}\right)\left(\frac{\sin\frac{2p\pi}{k}}{\frac{2p\pi}{k}}\right)(-1)^p\right|^2. \qquad (32)$$

It is easily shown that in the particular case k = 2, corresponding to a continuously exposed object, sin (2pπ/k) = 0 for all p and we have the Powell–Stetson equation

$$I=a^2J_0^2\left(\frac{4\pi A}{\lambda}\right). \qquad (33)$$

The exposures method corresponds to the limit k → ∞. Indeed, replacing $(-1)^p$ by cos pπ in (32) and putting [sin (2pπ/k)]/(2pπ/k) = 1, we have

$$I=a^2\left|J_0\left(\frac{4\pi A}{\lambda}\right)+2\sum_{p=1}^{\infty}J_{2p}\left(\frac{4\pi A}{\lambda}\right)\cos 2p\frac{\pi}{2}\right|^2. \qquad (34)$$

By the well-known properties of Bessel functions of even index[3)] we have

$$I=a^2\cos^2\left(\frac{4\pi A}{\lambda}\right), \qquad (35)$$

which corresponds to the intensity distribution in the two-exposure method (Eq. 10).

Figure 6 shows maximum intensities of interference bands as a function of the vibrational amplitude (Eq. 29 for various k), calculated[4)] by Eqs. (29), (33), and (35).

We now consider the case in which the strobe pulse is not synchronized with an extremum of the object position but with an arbitrary position. Obviously, the requirement of a short pulse length is least serious in the case already considered, in which the object hologram is taken when it is almost at rest. If, however, the vibrational amplitude of the object is so large that the number of bands on the restored image is too large and they become unresolved, it is of interest to use a time-gated pulse so as to reduce the sensitivity of the method. Such attempts have been undertaken[33] (Fig. 10).

Let the duration of the gating pulse be T/k, as before, but assume that its mean is not reached at a time T/4 (and 3T/4), but at an arbitrary time αT (and αT + T/2). This case should reduce to that already considered if α = 1/4. The problem thus reduces to deriving the function (27) for new limits of integration: from αT−T/2k to αT + T/2k, i.e.,

$$I=a^2\left|\frac{k}{T}\sum_{n=-\infty}^{\infty}J_n\left(\frac{4\pi}{\lambda}A\right)\int\limits_{\alpha T-\frac{T}{2k}}^{\alpha T+\frac{T}{2k}}e^{in\frac{2\pi t}{T}}dt\right|^2. \qquad (36)$$

Integrating, we obtain

$$I=a^2\left|\sum_{n=-\infty}^{\infty}J_n\left(\frac{4\pi A}{\lambda}\right)\left(\frac{\sin\frac{n\pi}{k}}{\frac{n\pi}{k}}\right)e^{i\alpha 2\pi n}\right|^2. \qquad (37)$$

The function (37) is shown in Figs. 7 and 8 for k = 100, 200 and various α.

As seen from the figures, a shift of the gating phase from the vibrational period by a few percent only causes a sharp decrease of the band luminosity, particularly in the higher orders. If, however, the duty cycle is large enough, the gating pulse shift can be applied effectively to vibration analysis.

EXPERIMENTS IN HOLOGRAM STROBE VIBRATION ANALYSIS

In 1968 it was suggested independently and simultaneously in a number of papers[33-36] that the hologram strobe method could be used to study periodic processes

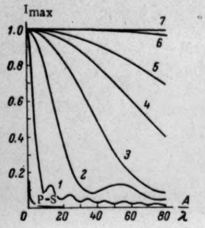

Fig. 6. Maximum intensity of interference bands as a function of the vibrational amplitude for the Powell–Stetson method (P–S) and for the hologram strobe method for various duty cycles of the strobing pulse k: 1) 10; 2) 20; 3) 30; 4) 40; 5) 50; 6) 100; 7) ∞.

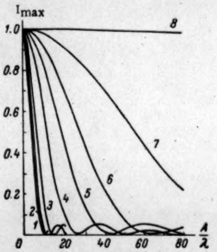

Fig. 7. Maximum intensity of interference bands as a function of vibrational amplitudes, displacing the gating pulse by αT from the passage moment of the vibrating body through the stationary position. Curves are given for different values of α. α = 0.25 corresponds to an extreme position of the object amplitude. The strobe duty cycle k = 100. α: 1) 0.05; 2) 0.10; 3) 0.15; 4) 0.20; 5) 0.22; 6) 0.23; 7) 0.24; 8) 0.25.

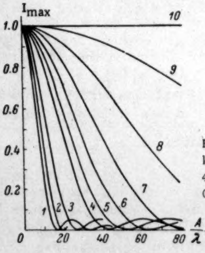

Fig. 8. Same as Fig. 7 for a duty cycle k = 200. α: 1) 0.05; 2) 0.10; 3) 0.15; 4) 0.19; 5) 0.20; 6) 0.21; 7) 0.22; 8) 0.23; 9) 0.24; 10) 0.25.

in solid transparent objects[33] and in diffuse light-scattering opaque[33–36] objects.

The scheme in Fig. 9 is used in ref. 33. A light beam from a helium–neon laser is chopped by a disk with apertures. The disk is attached to the axis of a motor–generator. The ac current generated by the latter is passed through a light coil in a constant magnetic field. The coil vibrations excite vibrations of the object under investigation, a disk of Plexiglas, in which the internal stresses arising near contractions during vibration are studied. The disk is illuminated by transmitted light (Fig. 9a) without a scatterer. Examples of the images are shown in Fig. 10a. Vibrating brass disks are also recorded by the hologram strobe (Fig. 10b). The modulator disk is attached to the axis of the motor–generator, so that the slits transmit light at specified phases. Control is achieved by the optical scheme shown by dashes in Fig. 9b. A small galvanometer mirror is glued to the vibrating object.

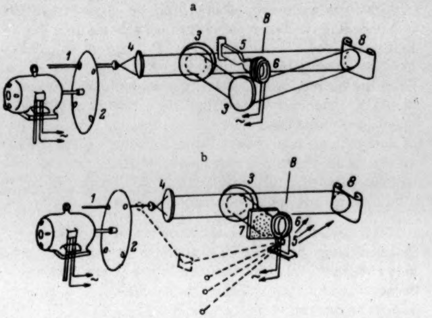

Fig. 9. Diagram of arrangement for hologram strobe vibration analysis. a) For the study of transparent objects; b) reflecting objects. 1) Laser beam; 2) modulator disk; 3) mirror; 4) telescopic system; 5) vibrating object; 6) coil placed in a magnetic field B; 7) scatterer; 8) photosensitive layer. The dashes indicate units for synchronization of the vibrational phase and light modulation.

Attempts at observing the restored images in real time are also performed on this design. In this case the hologram of an immobile object appears in place, and the vibrating object is observed through it with pulsed illumination (Fig. 11).

With this scheme the oscillation frequency of the object is determined by the motor frequency, which is 100 Hz.

The possibilities of the hologram strobe method have been demonstrated[34] in the vibration analysis of a diffusely reflecting disk, illuminated by laser light pulses obtained, as in ref. 33, with a rotating disk. The disk is driven by an electric motor which is driven by the same generator which supplies the acoustic excitation of the object. The hologram is exposed at maximum displacement. It has been shown[34] that the interpretation of the hologram strobe bands is simpler than that of bands obtained by the Powell–Stetson method. The bands are related directly to displacements and, consequently, to the vibrational amplitude of the object, as in the two-exposure method, the deformation analysis for which is given in refs. 37 and 38. The conclusions of these papers also apply to the band pattern obtained by the hologram strobe method.

A bar-shaped stroboscope with an aperture drilled in it perpendicular to its axis, through which a focused laser light beam is passed, was used in ref. 35. The bar is on the axis of a turbine driven by compressed air. The rotational velocity of the turbine can be controlled.

To eliminate one limitation of the strobe scheme,[33] the fact that the vibrational frequency cannot be varied, one can use another scheme (Fig. 12), which provides analysis at different frequencies up to $1.2 \cdot 10^4$ Hz.

The basic element controlling the object vibrations and chopping the laser pulse in this scheme is a disk with several series of apertures (Fig. 13), one of which chops the laser beam, and the other chops the light flux incident from the incandescent bulb on the photodiode. The fundamental frequency at the photodiode output is amplified and drives the membrane under investigation. The simplicity of this scheme is a considerable advantage. The disk is driven by an electric motor up to 200 Hz; since the disk has 60 apertures, this corresponds to a frequency of 12 kHz. The motor speed is controlled by a rheostat.

If a series with twice the number of apertures as those exciting the vibrations is used to chop the laser beam, thus obtaining two strobe pulses in one period of the membrane vibration, the hologram is equivalent to a two-exposure hologram.

This apparatus[39] also allows one to observe vibrations in real time. In this case the hologram of the fixed membrane is first exposed with the disk at rest; then when the disk rotates through the rest position the vibrating membrane is observed. By smoothly increasing the speed of the motor it becomes possible to follow the dynamic evolution of the vibrations. To chop the laser beam we use a series with the same number of apertures as that used to excite the current that drives the membrane (one strobe pulse per vibrational period). The strobe phase can also be changed smoothly by rotating the bulb–photodiode system around the disk axis.

The main limitations of the system are the difficulty of establishing a definite frequency, the instability of the rotating disk frequency, the restricted frequency range, and the impossibility of smoothly controlling the strobe pulse.

The hologram strobe method with a disk stroboscope has been used[40–42] for vibration analysis of circular membranes[40,41] and of a cantilever.[42]

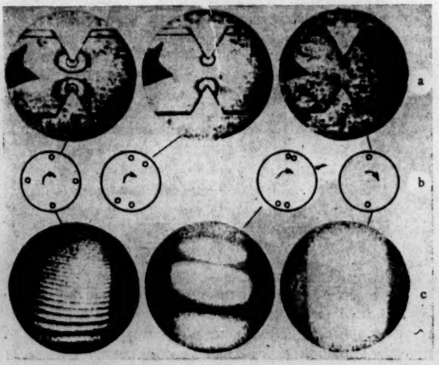

Fig. 10. Images of vibrating objects. a) Disk of Plexiglas; b) brass disk; c) corresponding aperture position in the modulator disk. (Two periods of the varying current and, consequently, two periods of the object vibration, correspond to one disk revolution.)

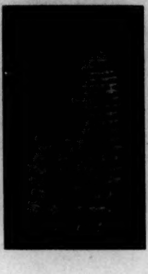

Fig. 11. Interferogram of a vibrating brass disk obtained in real time.

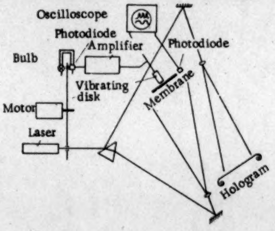

Fig. 12. Apparatus for hologram strobe vibration analysis.

The strobe capabilities described in refs. 33-35, 39-42 are not recommended for practical applications due to inherent limitations: inconvenient synchronization, limited frequency range, complexity, and inertia. An electrooptic strobe scheme eliminates these limitations completely.

Electrooptic light modulators are convenient in many respects; they are inertialess, have a wide range of frequencies (from several Hz to several hundred MHz), are of small size, weigh little, and can be synchronized easily.

Detailed information on electrooptic modulators can be found in refs. 43 and 44.

A stroboscope was first used in ref. 36; in this case, an electrooptic light modulator using a Pockels cell was employed. A thin circular disk, clamped at the periphery, is excited by a sine wave generator. A pulse generator gives rectangular voltage pulses to drive the Pockels cell with a half-wave voltage of 1300 V. Means for varying the pulse length and synchronizing pulses are provided. In the open state the cell transmits about 90% of the laser light.

It is shown in ref. 36 that in vibration analysis of an object with a large amplitude the hologram strobe method is restricted only by the hologram resolution and the quality of the photographic recording.

To analyze very large amplitudes it is suggested in that paper, as well as in refs. 33 and 34, that several holograms be recorded with strobe pulses synchronized with different phases of the object vibrational period, starting from one position of maximum displacement to another, thus spanning the total excursion.

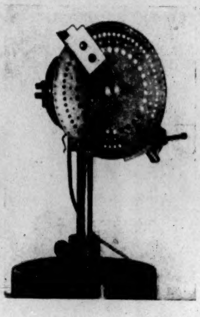

Fig. 13. Rotating disk.

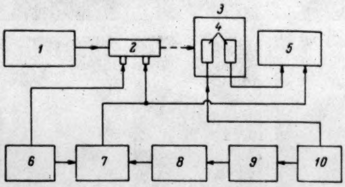

Fig. 14. Block diagram of the hologram strobe apparatus with the electrooptic chopper. 1) He–Ne; 2) modulator; 3) sample; 4) piezocrystal; 5) double-beam oscilloscope; 6) power source; 7) amplifier; 8) pulse generator; 9) phase-shift control; 10) sound generator.

This method is particularly important in nondestructive hologram testing, in which disturbances in machine parts or deviations from standard construction appear more clearly at high amplitudes.

The hologram strobe method has been used[45–47] with an electrooptic light modulator using a KDP crystal. In refs. 45 and 46 the vibration analysis is performed in real time, and in ref. 47 the holograms are exposed twice. The first exposure is in one position of the maximum displacement, and the second exposure is in the other. Another variant of this two-exposure hologram strobe method is also used, with half the sensitivity: During the first exposure the object is in a stationary state (with the modulator disconnected), and during the second exposure in one of the maximum displacement positions.

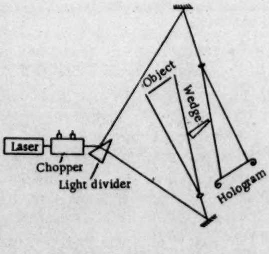

Fig. 15. Optical arrangement of apparatus with electrooptic chopper.

A schematic diagram of the apparatus with the electrooptic modulator[46,47] is given in Fig. 14. The frequency is determined by an audio generator, which drives a piezoelectric vibrator or an electromagnetic element. A rectangular pulse generator is also driven by this audio generator through a phase shifter and provides 100 V pulses.

An ML-3 electrooptic light modulator is used as the stroboscope.

Since the half-wave required by the voltage modulator is about 600 V, the pulses from the modulator are first amplified to this level.

Synchronization control of the strobe pulses is realized by a shielded double-beam oscilloscope, on one of whose channels is placed a pulse going to the modulator, and on the other a signal with a piezoelectric transducer glued to the sample.

A phase-shift control and a delay-line pulse generator are used for synchronization.

The light source is a 40 mW helium–neon LG-36 A laser power.

The intensity ratio of the reference and the object beam is 3-5. The exposure time for obtaining a good quality high-resolution (more than 2000 lines/mm) film for holograms (developed at the Kasan NIIKhim photoproject) is 10 sec in the time-averaging method. Using a strobe, the half-time exposure time (for a vibrating object) is 3 min 40 sec with a duty cycle of 20, and, correspondingly, 7 min 20 sec for a factor of 40.

The optical arrangement of the apparatus is shown is Fig. 15. The apparatus is mounted on a reinforced concrete slab weighing 1.5 ton resting on inflated self-powered chambers. Examples of interferograms of vibrating objects obtained by this object are given in Figs. 16-22.

Interferograms of a turbine blade, obtained by the Powell–Stetson method (without a chopper), are shown in Fig. 16. The same blade is also studied by the hologram strobe method, as shown in Figs. 17 and 18 (for comparison we also show the interferogram obtained under the same conditions by the Powell–Stetson method). Interferograms of a vibrating piezoelectric ceramic have also been obtained. Very small cracks (Fig. 19) are clear in some of them. An interferogram survey of vacuum tubes was performed with the purpose of explaining sites at which high voltages occur in vibrations of these tubes (Figs. 20, 21).

PHASE MODULATION OF THE REFERENCE BEAM

To increase the scope of the Powell–Stetson method it has been suggested[48–51] that the reference beam be phase-modulated while the hologram is recorded.

We consider analytically what this means. In the time-averaging method the light wave scattered by some point 0 undergoing harmonic vibrations seems to be phase-modulated with a modulation depth proportional to the vibrational amplitude of this point.

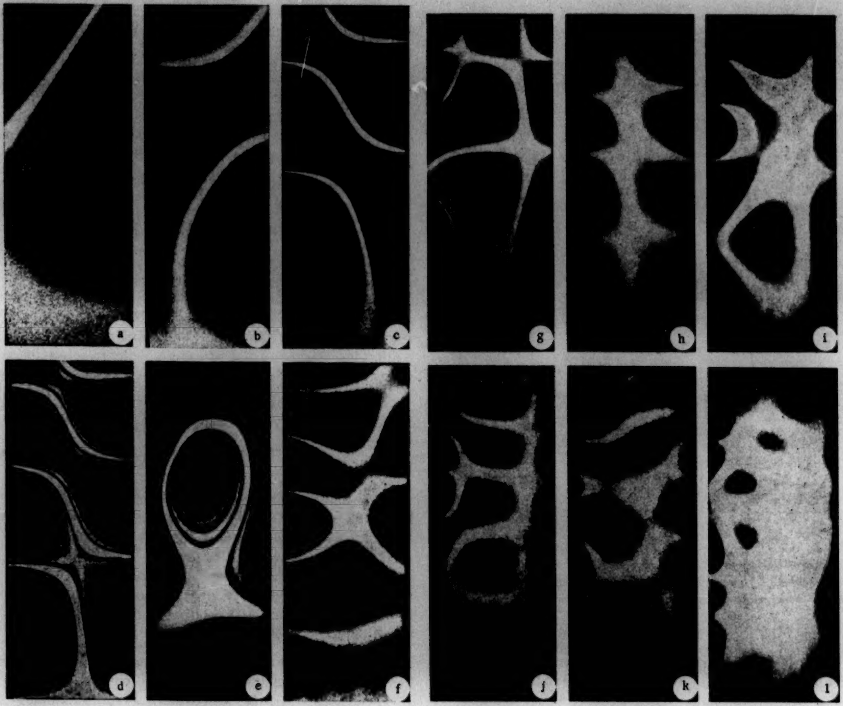

Fig. 16. Interferograms of a turbine blade vibrating at different frequencies, obtained by the Powell–Stetson method (without a chopper). ω, Hz: a) 820; b) 2720; c) 3800; d) 5650; e) 7360; f) 8800; g) 9650; h) 10,500; i) 11,250; j) 16,500; k) 18,900; l) 20,000.

The complex amplitude of the wave reaching the hologram from the vibrating object is, by Eq. (2),

$$ae^{-i\left[\psi_0+\frac{2\pi}{\lambda}\int\limits_0^t(\cos\varphi_1+\cos\varphi_2)A\sin\omega t\,dt\right]}, \tag{38}$$

where A is the vibration amplitude, which determines the phase-modulation depth of the object wave, and ψ_0 is the initial phase of the object wave.

If the reference beam is phase-modulated (for example, by displacing its source) with a frequency equal to the object vibrational frequency, its complex amplitude is written in the form

$$a_r e^{-i\left[\theta_r+\frac{2\pi}{\lambda}\int\limits_0^t M\sin\omega t\,dt\right]}, \tag{39}$$

where M is the displacement amplitude of the reference source, which determines the phase modulation depth of the reference wave, and θ_r is the initial phase of the reference wave.

As in Eq. (3), the illumination of point 0 in the restored image is determined by the equation

$$I=\left|\frac{a}{T}\int\limits_0^T e^{-i\left\{\left[\frac{2\pi}{\lambda}(\cos\varphi_1+\cos\varphi_2)A-\frac{2\pi}{\lambda}M\right]\sin\omega t+(\psi_0-\theta_r)\right\}}dt\right|^2. \tag{40}$$

When $\varphi_1=\varphi_2=0$, putting $\psi_0=\theta_r$ we have

$$I=\left|\frac{a}{T}\int\limits_0^T e^{-i\left[\frac{4\pi}{\lambda}(A-B)\sin\omega t\right]}dt\right|^2, \tag{41}$$

where we write B = M/2.

Expanding the exponent in the integrand in a series similar to Eq. (12), we have, corresponding to Eqs. (13) and (14),

$$I=a^2J_0^2\left[\frac{4\pi}{\lambda}(A-B)\right]. \tag{42}$$

This expression is similar to Eq. (15) for the Powell–Stetson method with the only difference that the argument of the zeroth-order Bessel function depends on the phase modulation depth B of the reference beam. This fact reveals the following possibilities of phase modulation of the reference beam.

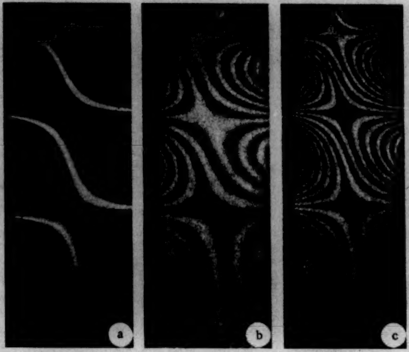

Fig. 17. Interferograms of a turbine blade, vibrating at 5650 Hz. a) The Powell–Stetson method; b) the hologram strobe method: two exposures; for the first the blade is fixed, for the second it vibrates, with the strobe activated in one of the extrema of the blade positions; c) the hologram strobe method, with the strobe activated in both extrema of the blade positions.

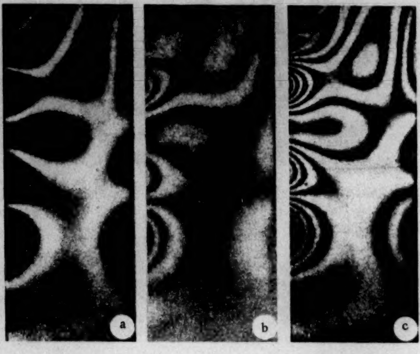

Fig. 18. Same as Fig. 17, but at a vibrational frequency of 13,000 Hz.

Determination of larger vibrational amplitudes. As seen from Eq. (42), by a suitable selection of the phase modulation phase of the reference beam one can compensate for part of the vibrating body amplitude; in the image the maximum luminosity is not that of interference bands with A = 0, as in the Powell–Stetson method, but A – B = 0; each band is the set of points of identical difference A – B.

This result was first illustrated experimentally by Aleksoff[48] in observing structural modes of an ADP crystal under zero shear stress in which standing shear waves are excited electrically.

Using phase modulation of the reference beam,[51] Aleksoff successfully investigated loudspeaker oscillations with an amplitude exceeding 6λ.

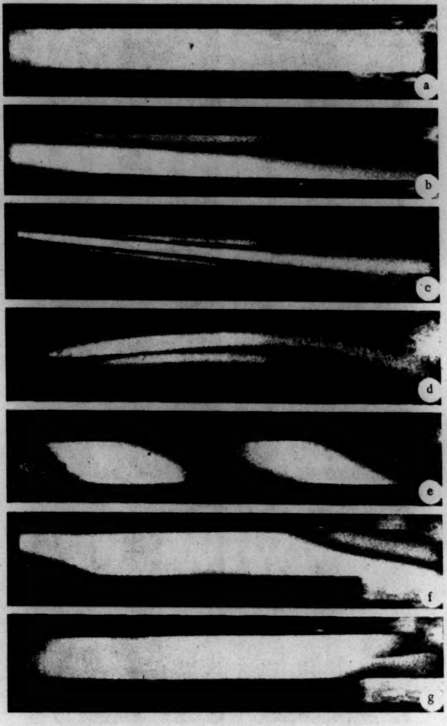

Fig. 19. Interferograms of a piezoelectric crystal vibrating with different frequencies, obtained by the Powell–Stetson method. a) At rest; ω, Hz; b)1780; c) 3660; d) 4500; e) 6760; f) 9320; g) 21,300. A sample defect (a crack) is observed at frequency 21,300 Hz.

It has been shown[55] that reference beam modulation allows one to study inhomogeneity of object vibrations in the presence of large reciprocating (piston) components in these oscillations. The surface vibrations of a piezoceramic electromechanical transformer with an amplitude exceeding 10λ have been analyzed.

Mottier[49,50] has suggested the use of automatic phase modulation of the reference beam by means of a small mirror attached to the moving object.

As shown by Caulfield,[52] Mottier's suggestion[49] is a special case of the use of a local reference beam.[53,54] This unifies all methods in which a reference beam, starting from part of the object beam, is used. A small motion of the object, illuminated by laser light, is accompanied by a phase change of the optic field of the reference beam. Mottier obtained a hologram of a sliding helix structure, in one of whose cavities a small mirror is attached, forming the reference beam when the helix is illuminated.

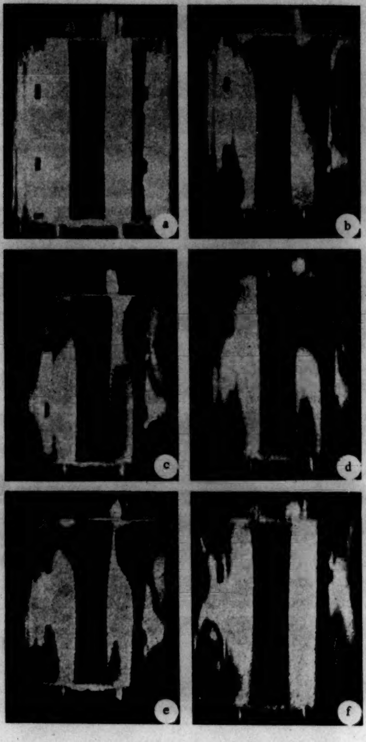

Fig. 20. Interferograms of a 6N9S vacuum tube vibrating at different frequencies, taken by the Powell–Stetson method. a) At rest; ω, Hz: b) 8350; c) 8960; d) 9140; e) 9290; f) 19,500.

In a following paper[50] Mottier proposed to synchronize the phase modulation of the reference beam by means of a mirror attached to a separate vibrating piezocrystal. The second piezoelectric vibrator was attached to a cantilever, whose vibrations were studied. This property of reference beam phase modulation was also used in ref. 55.

Determination of small vibrational amplitudes. If the modulation depth B in Eq. (42) is taken as the first root of the function $J_0^2(B)$, the possibility arises of observing the region of smallest vibrational amplitudes in the form of light spots on a general dark background of the object image.[55]

By Eq. (42), for small values of B the function $J_0[(4\pi/\lambda)(A-B)]$ can be expanded in a Taylor series

$$J_0\left[\frac{4\pi}{\lambda}(A-B)\right]=J_0\left(\frac{4\pi}{\lambda}B\right)+\frac{4\pi}{\lambda}(A-B)\,J_0'\left(\frac{4\pi}{\lambda}B\right)+\left(\frac{4\pi}{\lambda}\right)^2\frac{(A-B)^2}{2}\,J_0''\left(\frac{4\pi}{\lambda}B\right)+\dots \qquad (43)$$

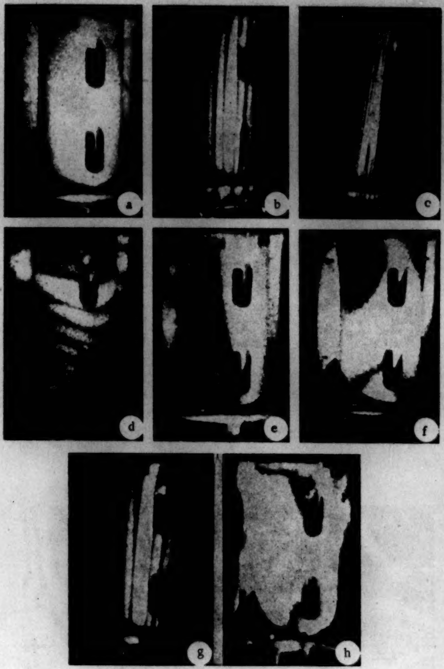

Fig. 21. Interferograms of a 6P1P vacuum tube, taken by the Powell–Stetson method. a) At rest; ω, Hz: b) 530; c) 534; d) 563; e) 595; f) 3700; g) 13,700; h) 14,200.

Restricting the discussion to the first two expansion terms and realizing that for the value of B chosen here the first expansion term vanishes, and using $J_0'(z) = -J_1(z)$, we can write for the brightness distribution in the restored object image

$$I=a^2\left[\frac{4\pi}{\lambda}(A-B)\right]^2 J_1^2\left(\frac{4\pi}{\lambda}B\right), \qquad (44)$$

i.e., in this case the intensity distribution in the restored object image is proportional to the square of the first order, rather than the zeroth-order, Bessel function.

The "dark-field" method allows one to determine[51,55] vibrational amplitudes of order 0.01λ.

Thus, to record very small vibrational amplitudes the sensitivity of the time-averaging method can be enhanced by phase modulation of the reference beam during exposure. Experimentally, however, realization of this property requires a complicated experimental procedure.

An alternative property of reference beam phase modulation for the determination of small vibrational amplitude is the relatively simple "hologram subtraction" method, suggested in ref. 56 and first experimentally carried out in ref. 57. In this method two object holograms are successively recorded on one photolayer, but with a phase shift of one beam by 180° between the exposures. The object portions not varying between exposures vanish in the restoration, and only those portions undergoing a change between exposures or during one of them are visible.[57]

To obtain a phase shift of 180° in the object beam it has been suggested[58] to superpose the object hologram in a state of rest on a vibrating object hologram taken by the Powell–Stetson method.

A similar method has been suggested[59] to observe the band pattern in real time.

Phase shifts of 180° in the reference beam have been obtained between exposures[60,61] by means of half-wave films.

In addition to the experimental complications, similar to those of the hologram strobe method, the reference beam phase modulation method also suffers from the limitation that the interpretation of band patterns and the calculational labor are quite complicated.

PHASE DETERMINATION OF A VIBRATING OBJECT

Obtaining information on the relative vibrational phases of various object points is of interest in vibration analysis in various technical areas. It has been shown[48,50,51] that reference beam phase modulation enables one to determine the vibrational phase of an object.

A method of determining vibrational phases of various object points has been suggested,[62] using the time-averaging method or its variant in real time, but with phase modulation of the reference beam, in whose arm a mirror vibrating with the object frequency is placed. The interference pattern depends on the amplitude and phase of the mirror vibrations with respect to the object vibrations. Regulating the amplitude and phase of the vibrating mirror, one can displace the node lines at any point of the object surface. The vibrational phase of object points is determined by the phase of the vibrating mirror, whose value is referred to the scale of a sinusoidal vibration generator, excited by the mirror vibrations.

To determine the vibrational phases of an object it has been suggested[63] that stroboscopic illumination be used in a hologram rotated by a small angle between exposures. If the object does not vibrate, a system of equidistant parallel bands is formed on its image. If the object vibrates during one of the exposures the parallel band pattern will be bent according to the field displacement of the vibrating object in the image restored with the hologram. Since the band system consists of lines of equal object displacements relative to the hologram with a known sign of phase variation of rotation of the hologram, the sign of vibrational phases of the different object portions is determined by the local bending of the resulting band pattern. A similar approach has been used[40] for the real-time method.

To create a system of parallel equidistant bands a simple and convenient wedge method[64] has been used,[47] allowing one to calculate uniquely the phase signs of points of the vibrating object from the bending of the band pattern in the restored image.

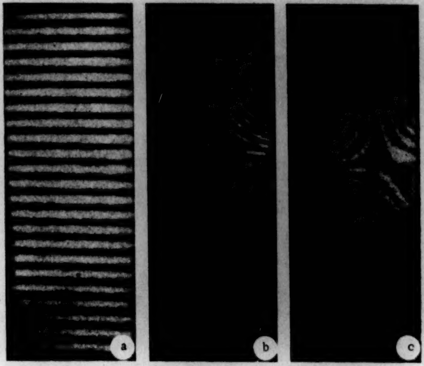

Fig. 22. Hologram strobe interferograms, obtained with a wedge. a) Interferogram of a fixed blade, obtained by the two-exposure method. The wedge is rotated before the second exposure; b) interferogram of a vibrating blade, obtained by the hologram strobe two-exposure method. Before the second exposure the strobe phase is changed by 180°, and the wedge remains fixed; c) interferogram of the vibrating blade, obtained as in case b, but with the wedge rotated before the second exposure. The vibrational frequency is 3800 Hz.

Interferograms of a vibrating turbine blade,[47] obtained with a wedge, are given in Fig. 22. Two exposures were performed to obtain this interferogram: During the first exposure the blade was stationary, and the second exposure was performed with a vibrating blade and stroboscopic hologram illumination. Before the second exposure the wedge (Fig. 15) is rotated and inclined to the object wave.

---

1) We consider idealized linear hologram recording.

2) It is shown[31] that some luminosity enhancement of high-order bands can be achieved by increasing the intensity ratio of the object and reference beams.

3) See, for example, V. I. Smirnov, A Course in Higher Mathematics, Vol. 3, Chap. 2, 5th ed., Moscow (1951), p. 531.

4) The authors are grateful to their colleagues in the computing center of the A. F. Ioffe Physicotechnical Institute, Ya. S. Uflyand, I. G. Dymnikov, and E. V. Galaktionov, for setting up the program and performing the calculations on a computer.

---

[1] H. Osterberg, J. Opt. Soc. Am., 22, 19 (1932).
[2] R. L. Powell and K. A. Stetson, J. Opt. Soc. Am., 55, 1593 (1965).
[3] E. N. Leith and J. Upatnieks, J. Opt. Soc. Am., 53, 1377 (1965).
[4] K. A. Stetson and R. L. Powell, J. Opt. Soc. Am., 55, 1694 (1965).
[5] J. W. Goodman, Appl. Opt., 6, 857 (1967).
[6] J. D. Redman, J. Sci. Instrum., 44, 1032 (1967).
[7] M. Lurie, J. Opt. Soc. Am., 57, 573 A (1967).
[8] M. Lurie, J. Opt. Soc. Am., 58, 614 (1968).
[9] D. B. Neumann, J. Opt. Soc. Am., 58, 1003 (1968).
[10] M. R. Wall, Symp. on Engineering Uses of Holography, Glasgow, September 1968, Cambridge Univ. Press (1970).
[11] M. Lurie and M. Zambuto, Appl. Opt., 7, 2323 (1968).
[12] M. Zambuto and M. Lurie, Appl. Opt., 9, 2066 (1970).

[13] M. O. Fein and E. L. Green, Appl. Opt., 7, 1864 (1968).

[14] B. A. Belogorodskii, M. M. Butusov, and Yu. G. Turkevich, Akust. Zh. 17, 455 (1971) [Sov. Phys.-Acoust., 17, 378 (1972)].

[15] N. E. Molin and K. A. Stetson, J. Sci. Instrum., 2, Ser. 2, 609 (1969).

[16] A. D. Wilson and D. H. Strope, J. Opt. Soc. Am., 60, 1162 (1970).

[17] R. Aprahamian and D. A. Evensen, J. Appl. Mech., 37, Ser. E, No. 2, June (1970).

[18] R. Aprahamian, D. A. Evensen, J. S. Mixon, and J. E. Wright, J. Appl. Mech., 37, Ser. E, No. 4, December (1970).

[19] P. Waddell and W. Kennedy, Symp. on Engineering Uses of Holography, Glasgow, September 1968, Cambridge Univ. Press (1970).

[20] P. Waddell and W. Kennedy, New Scientist, 633, June (1968).

[21] W. G. Alwang, R. Burr, and L. A. Cowanaugh, SAE preprint, No. 265, 1 (1969).

[22] P. Spicer, J. W. Langworthy, and D. Holt, Flight, 95, No. 3126, 253 (1969).

[23] B. S. Hockley and R. S. Hill, Aircraft Engineering, 41, No. 8, 6 (1969).

[24] B. S. Hockley and J. N. Butters, J. Photogr. Sci., 18, 16 (1970).

[25] B. S. Hockley and J. N. Butters, J. Mech. Eng. Sci., 12, No. 1 (1970).

[26] W. F. Fagan, P. Waddell, and W. McCracken, Opt. Laser Tech., 167 August (1970).

[27] E. Jansson, N. E. Molin, and H. Sundin, Physica Scripta, 2, 243 (1970).

[28] C. H. Ågren and K. A. Stetson, J. Acoust. Soc. Am., 51, No. 6 (pt. 2), 1971 (1972).

[29] M. Lashkari and V. I. Weingarten, Exper. Mech., 120, March (1973).

[30] B. A. Belogorodskii, E. P. Smirnov, Yu. G. Turkevich, and E. I. Kheifets, Akust. Zh., 17, 303 (1971)[Sov. Phys. - Acoust., 17, 256 (1971)].

[31] B. A. Belogorodskii and M. M. Butusov, Proc. Conf. "Use of Lasers in Contemporary Science and Technology," LDNTP (1973).

[32] A. N. Zaidel' (Zaidel) and Yu. I. Ostrovskii (Ostrovsky), Proc. Eighth Intern. Conf. on Phenomena in Ionized Gases, Vienna (1967).

[33] A. N. Zaidel', L. G. Malkhasyan, G. V. Markova, and Yu. I. Ostrovskii, Zh. Tekh. Fiz., 38, 1824 (1968)[Sov. Phys.-Tech. Phys., 13, 1470 (1969)].

[34] B. M. Watrasiewicz and P. Spicer, Nature, 217, 1442 (1968).

[35] E. Archbold and A. E. Ennos, Nature, 217, 842 (1968).

[36] P. Shajenko and C. D. Johnson, Appl. Phys. Lett., 13, 44 (1968).

[37] K. A. Haines and B. P. Hildebrand, Appl. Opt., 5, 595 (1966).

[38] E. B. Aleksandrov and A. M. Bonch-Bruevich, Zh. Tekh. Fiz., 37, 360 (1967)[Sov. Phys.-Tech. Phys., 12, 258 (1967)].

[39] V. I. Gerasev and Yu. I. Ostrovskii, Proc. All-Union Conference, Novosibirsk (1970), p. 37.

[40] C. R. Hazell and C. D. Liem, Proc. Intern. Symp. on the Appl. of Holography, Besançon, France (1970).

[41] H. Saito, I. Yamaguchi, and T. Nakajima, Appl. Holography (ed. by Barrekette, Koch, Ose, Tsujichi, and Stroke), Plenum, New York (1971).

[42] C. T. Moffat and B. M. Watrasiewicz, Proc. Intern. Symp. on the Appl. of Holography, Besançon, France (1970).

[43] D. F. Nelson, Scientific American, 218, 17 (1968).

[44] F. S. Chen, Proc. IEEE, 58, 1440 (1970).

[45] A. J. Waddell, W. Kennedy, and P. Waddell, Proc. Intern. Symp. on the Appl. of Holography, Besançon, France (1970).

[46] V. I. Gerasev, V. S. Listovets, and Yu. I. Ostrovskii, Proc. Conf. "Use of Lasers in Contemporary Technology," LDNTP, Leningrad (1971), p. 24.

[47] V. S. Listovets and Yu. I. Ostrovskii, Proc. Conf. "Automatization of Scientific Studies on Computers," Novosibirsk (1972), p. 81.

[48] C. C. Aleksoff, Appl. Phys. Lett., 14, 23 (1969).

[49] F. M. Mottier, Appl. Phys. Lett., 15, 44 (1969).

[50] F. M. Mottier, Appl. Phys. Lett., 15, 285 (1969).

[51] C. C. Aleksoff, Appl. Opt., 10, 1329 (1971).

[52] H. S. Caulfield, Appl. Phys. Lett., 16, 234 (1970).

[53] H. S. Caulfield, J. L. Harris, H. W. Hemstreet, and J. G. Cobb, Proc. IEEE, 55, 1758 (1967).

[54] W. T. Cathey, US Patent, 3, 415, 587 (1968).

[55] B. A. Belogorodskii, M. M. Butusov, and Yu. G. Turkevich, Avtometriya, No. 1, 47 (1972).

[56] D. Gabor, G. W. Stroke, R. Restrick, A. Funkhouser, and B. Brumm, Phys. Lett., 18, 116 (1965).

[57] L. F. Gollins, Appl. Opt., 7, 203 (1968).

[58] M. R. Wall, Opt. Tech., 1, 266 (1969).

[59] K. Biedermann and N. E. Molin, J. Phys. E, 3, 669 (1970).

[60] P. Hariharan and B. S. Ramprasad, J. Phys. E, 5, 976 (1972).

[61] P. Hariharan, Appl. Opt., 12, 143 (1973).

[62] D. B. Neumann, C. F. Jacobson, and G. M. Brown, Appl. Opt., 9, 1957 (1970).

[63] G. M. Mayer, J. Appl. Phys., 40, 2863 (1969).

[64] A. Kakos, G. V. Ostrovskaya, Yu. I. Ostrovskii (Ostrovsky), and A. N. Zaidel' (Zaidel), Phys. Lett., 23, 31 (1966).

Stability of ball lightning

I. P. Stakhanov

(Submitted January 7, 1974)
Zh. Tekh. Fiz., 44, 1373-1379 (July 1974)

It is suggested that ball lightning consists of positive and negative ions surrounded by solvate shells of water molecules. These shells prevent the ions from approaching each other during collisions and greatly reduce the recombination rate. An attempt is made to estimate the value of the surface tensions of liquid metals and strong electrolytes. The stability of spherical lightning against the excitation of surface capillary gravity waves is calculated. The solution to this problem is used to derive conclusions about the possible size of ball lightning and about breakup.

1. One of the most astonishing properties of ball lightning is that it does not disappear as a result of recombination but can exist for a considerable period of time (1-100 sec). We may recall that in an ordinary lightning channel, which is subject to almost the same conditions, the recombination is complete a few milliseconds after the end of the discharge.[1] The radiation from ball lightning is not apparently related to a high temperature in the component material. It is well known that the intensity of this radiation undergoes sudden changes[2] and may increase or decrease by several orders of magnitude in a time of about one second. If the radiation were thermal, the temperature and volume of the lightning would also have to undergo significant changes during these pulsations. The lightning would then be unlikely to maintain stability.

Moreover, it has been shown in ref. 1 from an analysis of photographs that the radiation comes from the entire volume of the lightning. This is confirmed by the evidence of eye witnesses that it is possible to see surrounding objects through ball lightning. If the temperature of the lightning was high enough to maintain a significant degree of ionization, the lightning would radiate as a blackbody and would therefore not transmit radiation. The transparency of the lightning to both external radiation and to its own radiation shows that the temperature is not very high and that there cannot be any significant number of free electrons.

On the other hand, the lightning contains a considerable reserve of energy, which the available estimates[1,3] put as comparable with the ionization energy of a gas occupying the same volume. Thus the number of ions in 1 cm^3 of lightning must be about 10^{19}. If we take account of the low density of the material involved (which must be of the same order as that of the surrounding air), we come to the conclusion that the lightning cannot consist of charged, finely dispersed dust particles, unless the mass of these particles is comparable with atomic or molecular masses.

The suggestion is made in ref. 4 that ball lightning consists of positive and negative ions surrounded by solvate shells of water molecules. Such a shell would have a considerable bonding energy and would not be broken by collisions if the temperature were not very high. They would prevent direct contact between ions during collision and hinder recombination. It is well known that in the gas phase recombination usually takes place through highly excited atomic states.[5] The presence of water molecules around the ions disturbs the higher energy levels and makes the normal recombination mechanism ineffective. It is suggested in ref. 4 that recombination in the lightning material takes place through the fusion of two solvated ions of different sign into a single "molecule." Because the stability of such molecules is small at the temperature of lightning, we may expect that this process would be considerably slower than the usual recombination in the gas phase.

It is well known that ions surrounded by solvate shells have been found in solutions. It is natural to ask whether such a situation could be observed in gases. Positive and negative ions joined with one or more molecules of water (the so-called "ionic connections" or "clusters") have recently been discovered in rocket studies of the composition of the ionospheric D layer.[6,7] The discovery of solvated ions behind the shock front which always accompanies the rocket and at heights where the water vapor content is negligible shows the high stability of the solvate shells of these ions.

It is shown in ref. 4 that under certain circumstances slow recombination is replaced by a chain reaction of disintegration of the solvate shells ending in explosion. In the present paper we consider only quiescent recombination, which leads to a gradual "burn up" of the lightning material. We might note that the hypothesis explains why ball lightning does not rise through the surrounding cold air. This is because of the high molecular weight of the solvated ions. The reduction in density due to the rise in temperature is compensated by an increase in density due to the high molecular weight of the particles which form the lightning. It is still necessary, however, to explain why ball lightning is a rather rare phenomenon despite the fact water frequently occurs in the air and the formation of large quantities of solvated ions (clusters) should not be a rare event during the decay of a linear lightning channel.

2. Another surprising property of ball lightning is that it does not disintegrate as a result of hydrodynamic instabilities. It is easy to show that normal molecular diffusion is insignificant for the characteristic dimensions and lifetimes we are concerned with here. However, even a small difference in densities is sufficient to ensure that the development of a convective instability over a period of fractions of a second would lead to the dispersion of the lightning material into the surrounding medium. In fact, the lightning not only does not disintegrate but actually moves through the air with a velocity of the order[8] of 1 m/sec. The motion produces a tangential discontinuity in velocity at its surface, which is also absolutely unstable and this is another reason why the lightning should disappear rapidly.

The spherical shape of the lightning indicates that it must possess a considerable surface energy. Cases are known in which the lightning has disintegrated into several smaller pieces, which are also spherical.[9] It sometimes penetrates buildings through small openings or cracks but regains its shape completely after doing so.[1] We might expect the surface tension of plasma media to be anomalously high because of the large range of interaction of Coulomb forces. In fact the surface tension σ of the majority of liquid metals lies between 500 and 1000 erg/cm^2 as compared to a value of 20-30 erg/cm^2 for most organic liquids. We can assume that if the nature of the molecular forces remains the same, the value of σ should be proportional to the number of particles per unit area, i.e, to $n^{2/3}$, where n is the volume number density of the particles. Since the particle density in lightning, as in a normal gas, is about three orders of magnitude smaller than that of liquid metals, the value of σ should be 5-10 erg/cm^2.

Strong electrolytes represent another type of medium which contains ions. Despite the fact that the surface tension of water is rather high (about 80 erg/cm^2), the value of σ for all strong electrolytes except HCl increases linearly with the solute concentration. It is natural to assume that the surface tension of electrolyte σ_S is made up of the surface tension of water σ' and that of the ions into which the solute material decomposes σ''. The coefficients of σ' and σ'' in the total sum must be equal to the ratio of the number of particles of the given kind to the total number of particles per unit area of surface, i.e.,

$$\sigma_s = \sigma' \frac{N'}{N' + N''} + \sigma'' \frac{N''}{N' + N''}, \tag{1}$$

where N' and N" are the number of molecules and ions per square centimeter. We assume that the density of the solute at the surface does not differ from that in the main volume and that the dissolved molecules are fully dissociated into ions. Thus N' ~ c' and N" ~ c", where c' and c" are the molar densities of water and of the solute and α is the number of ions into which a molecule decomposes. In order that the degree of dissociation be close to 100%, we consider only very dilute solutions, i.e., c" ≪ c'. It then follows from (1) that

$$\sigma'' = \sigma' + \Delta\sigma \frac{c'}{\alpha c''}, \tag{2}$$

where $\Delta\sigma = \sigma_S - \sigma'$. Table 1 gives values of the surface energy of ions σ'', calculated from (2); the values of $\Delta\sigma$ are taken from the Handbook of Chemistry and Physics.[10] It has been assumed that $CaCl_2$ and Na_2SO_4 are fully dissociated into three ions, and the remaining molecules into two ions. The assumption of 100% dissociation, which is not completely true even for strong electrolytes, means that the values of σ'' given in Table 1 are rather too low. The same conclusion follows from the assumption that the ion density is the same in the volume and at the surface. The increase in surface energy on solution must in fact create a tendency for the density of ions to decrease at the surface. Thus the true values of the ion surface tensions must be slightly greater than in Table 1. After allowance for the $n^{2/3}$ factor, we get the surface tension of the lightning material to be about 2 erg/cm^2 and this is in order of magnitude agreement with the results obtained from the data on liquid metals. We can thus expect that the surface tension σ of lightning lies in the range 1-10 erg/cm^2.

TABLE 1

	KOH	NaOH	$MgSO_4$	NaCl	KCl	HCl	$CaCl_2$	Na_2SO_4
σ''	123	151	145	120	112	75	143	123

A result of the same order of magnitude for the surface tension follows from an estimate of the stability condition for the tangential discontinuity which arises when the lightning moves. In making this estimate we can use the dispersion relationship for waves at an infinite plane interface between two media.[11] Assuming the densities of the lightning ρ_1 and of the ambient air ρ_2 to be identical, we find that

$$\omega = \frac{ku}{2} \pm \sqrt{\frac{\sigma k^3}{2\rho_1} - \frac{k^2 u^2}{4}}, \tag{3}$$

where ω and k are the frequency and wave number of the wave and u is the velocity of movement of the lightning. The boundary of the stability region is given by the condition

$$u \leqslant \sqrt{\frac{2\sigma}{\rho_1} k}. \tag{4}$$

If the lightning has a radius R_0, then $k \gtrsim 2\pi/R_0$. Putting $\rho_1 \simeq 10^{-3}$ g/cm^3, $R_0 \simeq 10$ cm, we find that for stability at a velocity $u \approx 10^2$ cm/sec, it is necessary that $\sigma \simeq 10$ erg/cm^2. This estimate can only give an order of magnitude for σ because (3) and (4) are valid only for a plane interface.

3. We now consider the stability of lightning in more detail, assuming that the density of its material ρ_1 and that of the ambient air ρ_2 are different. For simplicity we take the lightning to be at rest. For a plane boundary the result of the problem is well known: The system is stable if the medium with the greater density is on the bottom. If not, capillary waves with long wavelengths become unstable. This criterion is not applicable to a spherical body because the difference $\rho_1 - \rho_2$ changes sign on the surface. We therefore consider the stability of capillary waves on a spherical surface.

The pressure difference on the boundary, equal to the sum of the inverse radii of curvature, gives the following expression for an incompressible liquid:[1]

$$p_1 - p_2 = -\rho_1 \frac{\partial \psi_1}{\partial t} + \rho_2 \frac{\partial \psi_2}{\partial t} - (\rho_1 - \rho_2) g z = \frac{2\xi}{R_0^2}\sigma - \frac{\sigma}{R_0^2}\hat{M}\xi, \tag{5}$$

where $\xi = R - R_0 \ll R_0$ is the deviation of the actual radius at a given point on the surface from the radius in the unperturbed state R_0; ψ_1 and ψ_2 are the velocity potentials; p_1 and p_2 are the pressures of the lightning material (subscript "1") and of the surrounding air (subscript "2"); g is the acceleration due to gravity. The operator $\hat{M}$ is defined as

$$\hat{M} = \frac{1}{\sin\theta} \frac{\partial}{\partial\theta}\left(\sin\theta \frac{\partial}{\partial\theta}\right) + \frac{1}{\sin^2\theta} \frac{\partial^2}{\partial\varphi^2}, \tag{6}$$

where θ and φ are the angles in a spherical coordinate system and the z axis is taken vertically upwards. On the boundary we must have

$$\frac{\partial\psi_2}{\partial r}=\frac{\partial\psi_1}{\partial r}\equiv\frac{\partial\psi}{\partial r}. \tag{7}$$

Since $\psi_1, \psi_2 \sim e^{-i\omega t}$ and $z = (R_0 + \xi) \cos\theta$, on differentiating (5) with respect to t with constant R_0, θ, φ and remembering that $(\partial\xi/\partial t)_{\theta,\varphi} = v_r = \partial\psi/\partial r$, we find

$$(\rho_1\psi_1-\rho_2\psi_2)\,\omega^2-(\rho_1-\rho_2)\,g\cos\theta\,\frac{\partial\psi}{\partial r}+\frac{\sigma}{R_0^2}(\hat{M}+2)\frac{\partial\psi}{\partial r}=0. \tag{8}$$

In order to determine ψ_1 and ψ_2 we require solutions of the Poisson equation which are bounded as $r \to 0$ and $r \to \infty$ respectively (r is the radius of any point in space). These have the form

$$\psi_1=\sum_{l=1}^{\infty}\sum_{m=-l}^{m=l}A_l^{(m)}r^lY_l^{(m)}(\theta,\varphi),\quad \psi_2=\sum_{l=0}^{\infty}\sum_{m=-l}^{l}B_l^{(m)}r^{-l-1}Y_l^{(m)}(\theta,\varphi), \tag{9}$$

where the $Y_l^{(m)}$ are spherical functions. Since condition (7) must hold when $r = R_0$, we find that

$$B_0=0,\quad B_l^{(m)}=-\frac{l}{l+1}R_0^{2l+1}A_l^{(m)},\quad l\geqslant 1. \tag{10}$$

Using (10) and (9) in (8) we get

$$\sum_{l=1}^{\infty}\sum_{m=-l}^{l}C_l^{(m)}Y_l^{(m)}\left\{\left(1+\frac{l}{l+1}\frac{\rho_2}{\rho_1}\right)\Omega^2-l(l-1)(l+2)\right\}
=2\eta\sum_{l=1}^{\infty}\sum_{m=-l}^{l}C_l^{(m)}l\cos\theta\,Y_l^{(m)}, \tag{11}$$

where

$$C_l^{(m)}=A_l^{(m)}R_0^l,\quad \eta=\frac{\rho_1-\rho_2}{2\sigma}gR_0^2,\quad \Omega^2=\omega^2\frac{\rho_1R_0^3}{\sigma}. \tag{12}$$

Multiplying (11) by $Y_n^{(s)*}$ and integrating over the angles, we obtain the following system of equations:

$$C_l^{(m)}(\Omega^2-E_l)=2\eta\left(\mu_l^{(m)}C_{l-1}^{(m)}+\lambda_l^{(m)}C_{l+1}^{(m)}\right), \tag{13}$$

where

$$E_l=\frac{l(l-1)(l+2)}{1+\frac{l}{l+1}\nu}, \tag{14}$$

$$\mu_l^{(m)}=\frac{l-1}{1+\frac{l}{l+1}\nu}\sqrt{\frac{l^2-m^2}{4l^2-1}},\quad \lambda_l^{(m)}=\frac{l+1}{1+\frac{l}{l+1}\nu}\times\sqrt{\frac{(l+1)^2-m^2}{4(l+1)^2-1}},\quad \nu=\frac{\rho_2}{\rho_1}. \tag{15}$$

The system (13) can be solved approximately by considering the right side as a perturbation. The unperturbed spectrum of eigenvalues is defined by the expression $\Omega^2 = E_l$. The corrections to the unperturbed values $\Delta_l^{(m)}$ appear in second-order perturbation theory[12] and are given by the expressions

$$\Delta_l^{(m)}=-4\eta^2\left(N_{l+1}^{(m)}-N_l^{(m)}\right), \tag{16}$$

where

$$N_l^{(m)}=\frac{l^2-m^2}{4l^2-1}\,\frac{l}{l(l+2)\left(1+\frac{l-1}{l}\nu\right)-(l+1)(l-2)\left(1+\frac{l}{l+1}\nu\right)}. \tag{17}$$

The eigenfrequencies of the capillary oscillations with the surface tension perturbation included and $\rho_1 \neq \rho_2$ are

$$\Omega^2=E_l+\Delta_l^{(m)}, \tag{18}$$

and the E_l are defined by (14) with $l = 2, 3, 4 \ldots$ ($l = 1$ corresponds to movement of the sphere as a whole and not to a surface wave mode). The imposition of the perturbations leads to the removal of the degeneracy; the eigenfrequencies become dependent on m. As in the quadratic Stark effect, the change in the eigenfrequencies does not depend on the direction of the forces, i.e., on the sign of $\rho_1 - \rho_2$.

Let us consider two important cases. If the densities of the lightning and of the surrounding air are not very different we can put $\nu \simeq 1$. We are mainly interested in corrections to the lowest eigenfrequency, i.e., for $l = 2$. These are equal to

$$\Delta_2^{(0)}=\frac{2}{315}\eta^2,\quad \Delta_2^{(1)}=-\frac{2}{105}\eta^2,\quad \Delta_2^{(2)}=-\frac{2}{21}\eta^2. \tag{19}$$

The boundary of stability is defined by the condition $E_2 + \Delta_2^{(2)} = 0$, at which the corresponding eigenfrequency goes to zero. Thus the first unstable oscillation mode occurs for $\eta \geq \eta_0 = 7$. Although the perturbation method is strictly speaking, not applicable to such large changes in the eigenfrequencies, we assume that this result is correct in order of magnitude.

If a sufficiently thick layer of air around the lightning is heated to a temperature close to that of the lightning material, then $\rho_2 \ll \rho_1$, and we can put $\nu = 0$. This gives

$$\Delta_2^{(0)}=-1.4\cdot10^{-3}\,\eta^2,\quad \Delta_2^{(1)}=-0.05\,\eta^2,\quad \Delta_2^{(2)}=-0.156\,\eta^2. \tag{20}$$

Using the expression for E_2 with $\nu = 0$ we find that the critical value of the parameter remains about the same in this case as well ($\eta_0 \simeq 7$).

4. It follows from our solution that the lightning is stable if

$$\sqrt{g\frac{|\rho_1-\rho_2|}{2\sigma}}\,R_0<\sqrt{\eta_0}\simeq 2.5. \tag{21}$$

The left side of the inequality (21) represents the ratio of the lightning radius to the capillary constant of its material. It is known that this ratio must be of the order of or less than unity in order for the body to have the shape of a sphere.[11] We still have to establishd what happens when (21) is violated. The aperiodic instability which is produced could lead to the development of turbulence and the disintegration of the lightning. However, in principle the possibility is not excluded that there might be a transformation to a new, nonspherical, equilibrium shape. A final solution to this problem is not possible without further studies. It nevertheless seems probable that ball lightning cannot exist if condition (21) or some closely related condition is violated.

Equation (21) also explains both the observed sizes and lifetimes of ball lightning. It follows from this equation that the lightning is only stable if its density is nearly the same as that of the surrounding air. In fact, putting $\sigma \simeq 2$ erg/cm^2, we get

$$\Delta\rho \equiv |\rho_1 - \rho_2| \leqslant \frac{24 \cdot 10^{-3}}{R_0^2}. \quad (22)$$

When $R_0 = 15$ cm, the relative deviation $\Delta\rho/\rho_2$ must be less than 10%, i.e., we are not talking about an order of magnitude agreement but an almost exact equality of densities. This explains why the lightning often hovers in the air. It also follows that lightning with a diameter of the order of one meter or greater must be a very rare phenomenon. It can easily be seen from (22) that for $R_0 = 50$ cm, the difference between the density of the lightning and that of air must not exceed 1%. Such lightning requires very special initial conditions, which would rarely be realized in practice. This answers the question which was posed above as to why ball lightning is comparatively rarely observed although the formation of ions with a solvate shell of water molecules during lightning discharges can hardly be a rare event. In the majority of cases the clusters which are formed become scattered as a result of instability in the surrounding air and gradually recombine.

Condition (22) is not very restrictive for ball lightning with a diameter of about 10-20 cm and in fact such lightning is particularly often observed.[8] However, estimates which are not given here show that it is also difficult to observe lightning balls with diameter less than 1 cm because they burn up in less than 1 sec. We thus agree with the opinion expressed in refs. 8 and 13 that ball lightning occurs during practically every normal lightning discharge but only in comparatively rare cases does it last for any length of time (more than 1 sec). The observed diameters of ball lightning[8] do in fact lie between 1 and 100 cm.

The other result which follows from (21) is that in the majority of cases quiescent burning (without explosion) would not be expected to end in total recombination of all the ions, but in disintegration of the lightning as a result of the development of instability. This explains the short lifetimes[8,13] (average of 2-10 sec). Estimates show that in this time only a small fraction of the overall energy contained in the lightning can be disposed of (for diameters greater than 5-10 cm). The recombination of each pair of ions is accompanied by the production of a considerable number (6-10) of water molecules, whose diffusion can be neglected during the lifetime of the lightning. If the solvate shells are not completely filled, these molecules will be trapped by ions. The molecular weight and density of the material therefore increase. If the shells are filled, on the other hand, the light decay products will gradually accumulate in the lightning and lead to a reduction in the molecular weight and density. In both cases, the stability condition (21) or (22) is violated by the change in density long before a considerable fraction of the energy has been expended. This situation refers especially to lightning with a fairly large diameter (5-10 cm).

Observers confirm[9,14] that the quiet disappearance of the lightning is preceded by "sparkling" or "boiling". Every time a "spark" is emitted, the lightning recoils in the opposite direction.[14] We are obviously talking here not about an electrical discharge but about an ejection of material from the lightning as a result of instability development, which produces a recoil because of the conservation of momentum.

It is natural to consider the production of ball lightning under laboratory conditions. This might be attempted by introducing a large drop of water of about 1 cm in diameter into the channel of a high-current pulse discharge. Such a drop could produce ball lightning of 10 cm diameter. As we have shown, with a large drop of water the growth of instabilities could hinder the formation of the lightning. Lightning arising from smaller drops (a few millimeters in diameter) would probably burn up quickly but it is possible that it could be recorded by fast motion-picture film. The discharge should be short enough so that the water in the drop does not move in the surrounding air during the period of the pulse. Water drops of diameter 1 cm are unstable against motion and should probably therefore be found on the electrode; small drops (less than 3 mm) retain their stability under free fall.

---

[1] E. L. Hill, J. Geophys. Res., 65, 1947 (1960).

[2] M. T. Dmitriev, V. M. Deryugin, and G. A. Kalinkevich, Zh. Tekh. Fiz., 42, 2187 (1972) [Sov. Phys.—Tech. Phys., 17, 1724 (1973)].

[3] P. D. Zimmerman, Nature, 228, 853 (1970).

[4] I. P. Stakhanov, ZhETF Pis. Red., 18, 193 (1973) [JETP Lett., 18, 114 (1973)].

[5] A. V. Gurevich and L. P. Pitaevskii, Zh. Eksp. Teor. Fiz., 46, 1281 (1964) [Sov. Phys.—JETP, 19, 870 (1964)].

[6] G. S. Ivanov-Kholodnyi and G. M. Nikol'skii, Sun and Ionosphere [in Russian], Nauka, Moscow (1969), p. 160.

[7] M. N. Fatkullin, in: Geomagnetism and the Upper Layers of the Atmosphere [in Russian], ed. by N. P. Ben'kova and L. P. Danilin, VINITI, Moscow, (1972).

[8] M. A. Uman, Lightning, McGraw-Hill, New York (1969).

[9] B. L. Goodlet, J. Inst. Elect. Eng., 81, I (1937).

[10] Handbook of Chemistry and Physics (ed. C. D. Hodyman), Cleveland, Ohio (1951).

[11] L. D. Landau and E. M. Lifshitz, Mechanis of Continuous Media [in Russian], Moscow (1953).

[12] L. D. Landau and E. M. Lifshitz, Quantum Mechanics, Pergamon Press, Oxford—New York (1965).

[13] W. D. Rayle, NASA Technical Note, D-3188, Washington, D. C. (1966).

[14] M. T. Dmitriev, Priroda, No. 6 (1967).

Radiation from a charged particle moving close to an anisotropic dielectric

A. I. Plis and N. M. Safikhodzhaev
Moscow Power Engineering Institute
Andizhan State Pedagogical Institute
(Submitted October 11, 1973)
Zh. Tekh. Fiz., 44, 1380–1384 (July 1974)

The radiation from a charged particle moving along a uniaxial crystal cut perpendicularly to its optic axis is discussed. The problem is solved by expanding the fields in terms of the polarizations and using the Fresnel coefficients.

1. In connection with recent discussions of the possibilities of obtaining high-current relativistic beams it is of interest to consider the interaction of a beam with a dielectric. The interactions of moving line and point sources with isotropic slabs are discussed in refs. 1–3, and the interaction of line sources with an anisotropic slab is treated in ref. 4. In the present paper we discuss the radiation from a point charge moving along a plane-parallel slab of a uniaxial crystal cut perpendicularly to its optic axis.

2. Ordinarily, problems involving radiation from sources moving near interfaces are solved by matching fields or by the method of images. Both methods are well known and typical examples can be found, for example, in refs. 5 and 6.

Here we solve the Cerenkov radiation boundary-value problem by what we shall call the Fresnel-coefficient method. The Fresnel coefficients relate the amplitudes of the incident, reflected, and refracted waves in the case of a plane monochromatic wave incident on the plane interface between two media. Use of the Fresnel coefficients yields an efficient solution of boundary-value problems. The self-field of the moving charge can be expanded in plane waves by a Fourier integral. The amplitudes in the plane-wave expansion of the free fields can be found by multiplying the Fourier amplitudes of the self-field by the appropriate Fresnel coefficients. Thus, the most laborious part of the calculation involved in using Fresnel coefficients – the expansion of the field of the particle in terms of the polarizations – is much simpler than solving the system of equations in the method of matching fields or constructing dipoles in using the method of images.

3. We choose a rectangular coordinate system such that the anisotropic layer with the permittivity tensor $\hat{\varepsilon}_{ik}$ occupies the region $a > x > 0$, and the regions $x > a$ and $x < 0$ are filled with an isotropic dielectric. A charge q moves with a uniform velocity v at a distance d from the layer, so that the equations of motion can be written in the form

$$x = -d, \quad y = 0, \quad z = vt. \tag{1}$$

Thus the x axis is normal to the interface and parallel to the optic axis of the crystal. In this coordinate system the permittivity tensor has the form

$$\varepsilon_{ik} = \begin{bmatrix} \varepsilon_e & & \\ & \varepsilon_0 & \\ & & \varepsilon_0 \end{bmatrix}. \tag{2}$$

We assume that the media are nonmagnetic ($\mu_1 = \mu_2 = 1$), and denote the permittivity of the isotropic medium by ε_1.

Solving the problem by the method of Fresnel coefficients requires an expression for the self-field of a particle moving in an isotropic medium in the form of an expansion in plane inhomogeneous waves polarized in and perpendicular to the plane of incidence. By using Eqs. (A16)-(A19) of ref. 7 this expansion is easily found to be

$$\left.\begin{aligned} H_{y\parallel}^{(0)} &= -\frac{q}{2\pi v}\int\int dk_y d\omega \frac{\omega^2}{vc\varkappa^2} e^{i\nu}\,\mathrm{sign}\,(x+d), \\ H_{z\parallel}^{(0)} &= \frac{q}{2\pi v}\int\int dk_y d\omega \frac{k_y\omega}{c\varkappa^2} e^{i\nu}\,\mathrm{sign}\,(x+d); \end{aligned}\right\} \tag{3}$$

$$\left.\begin{aligned} E_{y\perp}^{(0)} &= \frac{q}{2\pi v}\int\int dk_y d\omega \frac{\omega^2 k_y}{c^2\varkappa^2\lambda_1} e^{i\nu}, \\ E_{z\perp}^{(0)} &= \frac{q}{2\pi v}\int\int dk_y d\omega \frac{v\omega k_y^2}{c^2\varkappa^2\lambda_1} e^{i\nu}, \end{aligned}\right\} \tag{4}$$

where

$$\nu = \lambda_1 |x+d| + k_y y + \frac{\omega}{v} z - \omega t,$$

$$\lambda_1 = \sqrt{\Sigma_1 \frac{\omega^2}{c^2} - \varkappa^2}, \quad \varkappa^2 = k_y^2 + \frac{\omega^2}{v^2}.$$

The superscript (0) denotes the self-field of the particle and the symbols ∥ and ⊥ refer to waves polarized in and perpendicular to the plane of incidence.

4. The Fresnel coefficients for an isotropic dielectric slab are given, for example, in ref. 8, p. 352, problem 4. Because of the choice of the orientation of the optic axis of the crystal these coefficients are easily modified for an anisotropic uniaxial crystal. Since our basic problem is the determination of the radiation loss, we need expressions only for the fields in the half-space in which the particle moves. Thus we only need the values of the reflection coefficients for waves of both polarizations. The expressions for these coefficients, taking account of the anisotropy of the slab, are

$$r_{\perp} = \frac{2i(\lambda_0^2 - \lambda_1^2)\sin\lambda_0 a}{(\lambda_1 + \lambda_0)^2 e^{-i\lambda_0 a} - (\lambda_1 - \lambda_0)^2 e^{i\lambda_0 a}}, \tag{5}$$

$$r_{\parallel} = \frac{2i[\varepsilon_1^2\lambda_e^2 - \varepsilon_0^2\lambda_1^2]\sin\lambda_e a}{(\varepsilon_0\lambda_1 + \varepsilon_1\lambda_e)^2 e^{-i\lambda_e a} - (\varepsilon_0\lambda_1 - \varepsilon_1\lambda_e)^2 e^{i\lambda_e a}}. \tag{6}$$

Here

$$\lambda_0 = \sqrt{\frac{\omega^2}{c^2}\varepsilon_0 - \varkappa^2}, \quad \lambda_e = \sqrt{\frac{\omega^2}{c^2}\varepsilon_0 - \frac{\varepsilon_0}{\varepsilon_e}\varkappa^2}.$$

It should be noted that these values of the Fresnel coefficients apply for pure transverse fields. The plane-wave expansion of the self-field of a particle also contains longitudinal field components and when these are taken into account the coefficient $r_{\parallel}$ is changed. Equations (5) and (6) can be used in our problem, however, since the correction term in $r_{\parallel}$ describes the Coulomb field of the charge in the first medium, and this does not contribute to the radiative energy loss.

The values of the Fresnel coefficients enable us to write the expressions for the free fields in the region x < 0:

$$\left.\begin{aligned}E_{y\perp}^{(1)}&=\frac{q}{2\pi v}\iint dk_y d\omega\frac{2i(\lambda_0^2-\lambda_1^2)\sin\lambda_0 a}{(\lambda_1+\lambda_0)^2e^{-i\lambda_0 a}-(\lambda_1-\lambda_0)^2e^{i\lambda_0 a}}\frac{\omega^2k_y}{c^2\varkappa^2\lambda_1}e^{i\nu_1},\\E_{z\perp}^{(1)}&=-\frac{q}{2\pi v}\iint dk_y d\omega\frac{2i(\lambda_0^2-\lambda_1^2)\sin\lambda_0 a}{(\lambda_1+\lambda_0)^2e^{-i\lambda_0 a}-(\lambda_1-\lambda_0)^2e^{i\lambda_0 a}}\frac{v\omega k_y^2}{c^2\varkappa^2\lambda_1}e^{i\nu_1},\end{aligned}\right\}\quad(7)$$

$$\left.\begin{aligned}H_{y\parallel}^{(1)}&=-\frac{q}{2\pi v}\\&\times\iint dk_y d\omega\frac{2i[\varepsilon_1^2\lambda_e^2-\varepsilon_0^2\lambda_1^2]\sin\lambda_e a}{(\varepsilon_0\lambda_1+\varepsilon_1\lambda_e)^2e^{-i\lambda_e a}-(\varepsilon_0\lambda_1-\varepsilon_1\lambda_e)^2e^{i\lambda_e a}}\frac{\omega^2}{v\varkappa^2c}e^{i\nu_1},\\H_{z\parallel}^{(1)}&=\frac{q}{2\pi v}\iint dk_y d\omega\frac{2i[\varepsilon_1^2\lambda_e^2-\varepsilon_0^2\lambda_1^2]\sin\lambda_e a}{(\varepsilon_0\lambda_1+\varepsilon_1\lambda_e)^2e^{-i\lambda_e a}-(\varepsilon_0\lambda_1-\varepsilon_1\lambda_e)^2e^{i\lambda_e a}}\frac{k_y\omega}{c\varkappa^2}e^{i\nu_1},\end{aligned}\right\}\quad(8)$$

where $\nu_1=-\lambda_1(x-d)+k_y y+(\omega/v)z-\omega t$.

5. We calculate the total radiative energy loss of a particle as the work done per unit displacement by the retarding force on the charge due to the radiation field, using the usual equation:

$$\frac{dw}{dz}=qE_z\Big|_{\substack{x=-d\\y=0\\z=vt}}=q\left(E_{z\perp}^{(0)}+E_{z\perp}^{(1)}+E_{z\parallel}^{(0)}+E_{z\parallel}^{(1)}\right)\Big|_{\substack{x=-d\\y=0\\z=vt}}.\quad(9)$$

The expressions for the fields $E_{z\parallel}^{(0)}$ and $E_{z\parallel}^{(1)}$ are found from (3) and (8) by using Maxwell's equations:

$$E_{z\parallel}^{(0)}=-\frac{q}{2\pi v}\iint dk_y d\omega\frac{\omega\left(\varepsilon_1\frac{\omega^2}{c^2}-\varkappa^2\right)}{v\varepsilon_1\lambda_1\varkappa^2}e^{i\nu},\quad(10)$$

$$E_{z\parallel}^{(1)}=\frac{q}{2\pi v}\iint dk_y d\omega\frac{2i[\varepsilon_1^2\lambda_e^2-\varepsilon_0^2\lambda_1^2]\sin\lambda_e a}{(\varepsilon_0\lambda_1+\varepsilon_1\lambda_e)^2e^{-i\lambda_e a}-(\varepsilon_0\lambda_1-\varepsilon_1\lambda_e)^2e^{i\lambda_e a}}\frac{\lambda_1\omega}{v\varepsilon_1\varkappa^2}e^{i\nu_1}.\quad(11)$$

Substituting the values of $E_{z\perp}^{(0)}$, $E_{z\perp}^{(1)}$, $E_{z\parallel}^{(0)}$, and $E_{z\parallel}^{(1)}$ from (4), (7), and (10), (11) into (9) we obtain the total energy loss:

$$\begin{aligned}\frac{dw}{dz}&=-\frac{q^2}{2\pi v}\operatorname{Re}\iint dk_y d\omega\\&\times\left\{\frac{v\omega k_y^2}{c^2\lambda_1\varkappa^2}\left[1+\frac{2i[\lambda_0^2-\lambda_1^2]\sin\lambda_0 a}{(\lambda_1+\lambda_0)^2e^{-i\lambda_0 a}-(\lambda_1-\lambda_0)^2e^{i\lambda_0 a}}e^{2i\lambda_1 d}\right]\right.\\&\left.+\frac{\lambda_1\omega}{v\varepsilon_1\varkappa^2}\left[1-\frac{2i[\varepsilon_1^2\lambda_e^2-\varepsilon_0^2\lambda_1^2]\sin\lambda_e a}{(\varepsilon_0\lambda_1+\varepsilon_1\lambda_e)^2e^{-i\lambda_e a}-(\varepsilon_0\lambda_1-\varepsilon_1\lambda_e)^2e^{i\lambda_e a}}e^{2i\lambda_1 d}\right]\right\}.\end{aligned}\quad(12)$$

Equation (12) is obtained under the assumption that the Cerenkov condition is satisfied everywhere.

6. If the isotropic medium in which the particle moves is replaced by vacuum ($\varepsilon_1=1$), and the uniaxial crystal by an isotropic dielectric ($\varepsilon_0=\varepsilon_2=\varepsilon$), this equation goes over into Eq. (7) of ref. 3. However, Eq. (7) is obtained in ref. 3 by a cumbersome calculation.

We now examine certain special cases. First we consider a frequency range such that the Cerenkov condition is not satisfied in the isotropic medium but is satisfied in the slab. This is the most interesting case for the production of radio waves by Cerenkov radiation. Clearly, in the isotropic medium in which the particle moves

$$\beta^2\varepsilon_1-1<0.\quad(13)$$

Consequently λ_1 becomes pure imaginary:

$$\begin{aligned}\lambda_1&=ig_1,\\g_1&=\sqrt{\frac{\omega^2}{v^2}(1-\varepsilon_1\beta^2)+k_y^2}.\end{aligned}\quad(14)$$

Substituting the value of λ_1 into (12) and performing some simple transformations we obtain

$$\begin{aligned}-\frac{dw}{dz}&=\frac{q^2}{\pi v^2}\operatorname{Re}i\int_{\beta^2\varepsilon_1<1}\frac{\omega d\omega}{\varepsilon_1}\int\frac{g_1}{\left(\frac{\omega^2}{v^2}+k_y^2\right)}\\&\times\left\{\left[1+\frac{(\varepsilon_1^2\lambda_e^2+\varepsilon_0^2g_1^2)\sin(\lambda_e a)e^{-2g_1 d}}{(\varepsilon_1^2\lambda_e^2-\varepsilon_0^2g_1^2)\sin(\lambda_e a)-2\varepsilon_0\varepsilon_1g_1\lambda_e\cos\lambda_e a)}\right]\right.\\&\left.-\frac{\beta^2k_y^2}{g_1^2}\left[1-\frac{(\lambda_0^2+g_1^2)\sin(\lambda_0 a)e^{-2g_1 d}}{(\lambda_0^2-g_1^2)\sin(\lambda_0 a)-2g_1\lambda_0\cos(\lambda_0 a)}\right]\right\}dk_y.\end{aligned}\quad(15)$$

Equation (15) can be integrated over k_y by using the theory of residues. In integrating (15) the first terms in the square brackets can be eliminated since they do not have poles within the path of integration and do not contribute to the energy loss. From the physical point of view these terms describe the energy lost by a charge in an infinite medium in which the Cerenkov radiation conditions are not satisfied, i.e. these terms are actually zero.

As a result of integrating (15) we obtain

$$\begin{aligned}\frac{dw}{dz}&=\frac{2q^2}{v^2}\int_{\varepsilon_1\beta^2-1<0}\frac{\omega d\omega}{\varepsilon_1}\sum_m\frac{1}{a}\left[\operatorname{sign}(\sin x_{lm})\frac{\varepsilon_0\varepsilon_1x_{em}\left[p^2(\varepsilon_e-\varepsilon_1)-\frac{\varepsilon_e}{\varepsilon_0}x_{em}^2\right]}{\left(p^2\varepsilon_e-\frac{\varepsilon_e}{\varepsilon_0}x_{em}^2\right)\Phi'_{em}}\right.\\&\times\exp\left(-\frac{2d}{a}\sqrt{p^2(\varepsilon_e-\varepsilon_1)-\frac{\varepsilon_e}{\varepsilon_0}x_{em}^2}\right)+\operatorname{sign}(\sin x_{0m})\\&\left.\times\frac{x_{0m}[p^2(\varepsilon_0\beta^2-1)-\beta^2x_{0m}^2]}{(p^2\varepsilon_0-x_{0m}^2)\Phi'_{0m}}\exp\left(-\frac{2d}{a}\sqrt{p^2(\varepsilon_0-\varepsilon_1)-x_{0m}^2}\right)\right],\end{aligned}\quad(16)$$

where x_{lm} and x_{0m} are roots of the equations

$$\operatorname{tg}x_e=\frac{2\varepsilon_0\varepsilon_1x_e\sqrt{p^2(\varepsilon_e-\varepsilon_1)-\frac{\varepsilon_e}{\varepsilon_0}x_e^2}}{x_e^2(\varepsilon_0\varepsilon_e+\varepsilon_1^2)-\varepsilon_0^2(\varepsilon_e-\varepsilon_1)p^2},\quad(17)$$

$$\operatorname{tg}x_0=\frac{2x_0\sqrt{p^2(\varepsilon_0-\varepsilon_1)-x_0^2}}{2x_0^2-p^2(\varepsilon_0-\varepsilon_1)},\quad(18)$$

and in addition the following notation is used:

$$x_e=\lambda_e a,\quad x_0=\lambda_0 a,\quad p=\frac{\omega}{c}a,\quad(19)$$

$$\Phi'_{em}=\frac{d}{dk_y}\left[(\varepsilon_1^2\lambda_e^2-\varepsilon_0^2g_1^2)\sin(\lambda_e a)-2\varepsilon_0\varepsilon_1g_1\lambda_e\cos(\lambda_e a)\right]_{x_e=x_{em}},\quad(20)$$

$$\Phi'_{0m}=\frac{d}{dk_y}\left[(\lambda_0^2-g_1^2)\sin(\lambda_0 a)-2g_1\lambda_0\cos(\lambda_0 a)\right]_{x_0=x_{0m}}.\quad(21)$$

The number of roots of Eqs. (17) and (18) depends on the frequency ω and the layer thickness a.

It is easy to see that the first term in the square brackets in (16) gives the energy loss due to the excitation of extraordinary waves in the slab, and the second term the energy loss due to ordinary waves.

It should be noted that in the limiting case of vanishing anisotropy and for $\varepsilon_1=1$, Eq. (16) agrees[1)] with Eq. (8) of ref. 3. In addition, formally writing in Eq. (16)

$$q^2=2\pi p\delta(k_y),$$

gives an expression for the energy loss of an infinite charged

filament carrying a charge density ρ which agrees with the corresponding equation of ref. 4.

The use of Fresnel coefficients also significantly simplifies the solution of transition radiation problems, as is seen, for example, in refs. 9 and 10.

In conclusion the authors thank B. M. Bolotovskii for discussion.

---

1) A factor $1/h$ is missing in Eq. (8) of ref. 3.

---

[1] A. I. Morozov, Vestn. MGU, Ser. Fiz.-Mat., 1, 72 (1957).

[2] L. G. Naryshkina and P. M. Yurkov, Zh. Tekh. Fiz., 39, 1810 (1969) [Sov. Phys. – Tech. Phys., 14, 1360 (1970)].

[3] L. G. Naryshkina and P. M. Yurkov, Zh. Tekh. Fiz., 41, 1096 (1971) [Sov. Phys. – Tech. Phys., 16, 867 (1971)].

[4] O. S. Mergelyan and N. M. Safikhodzhaev, Izv. AN ArmSSR, Fizika, 5, 237 (1970).

[5] G. M. Garibyan, Zh. Eksp. Teor. Fiz., 33, 1403 (1957).

[6] V. E. Pafomov, Tr. FIAN, 44, 28 (1969).

[7] B. M. Bolotovskii, Usp. Fiz. Nauk, 62, 201 (1967).

[8] L. D. Landau and E. M. Lifshitz, Electrodynamics of Continuous Media, Addison-Wesley (1960).

[9] B. M. Bolotovskii and A. I. Plis, Preprint FIAN, No. 76 (1973).

[10] S.-Y. Shieh, Phys. Rev., 172, 1310 (1968).

Estimate of the angular divergence in intense electron beams

V. S. Kuznetsov, Yu. P. Vakhrushin, O. L. Komarov, and R. P. Fidel'skaya

(Submitted August 15, 1973)
Zh. Tekh. Fiz., 44, 1385-1388 (July 1974)

The focusing of intense electron beams in a longitudinal magnetic field is discussed. Analytical expressions are derived for the maximum angular divergence arising from nonlinear Coulomb forces. A comparative analysis is given of the angular divergence as a function of the method used to shape the electron beam.

In many problems, for example collective acceleration,[1] a limitation is imposed on the angular divergence of the particles in an intense electron beam. An accurate determination of the value of the angular divergence involves the numerical integration of the self-consistent field equations. It is shown in ref. 2 that in the focusing of intense electron beams by longitudinal magnetic fields the angular divergence of the beam electrons is determined mainly by the effect of nonlinear Coulomb forces.

We derive below some simple equations for estimating the maximum angular divergence due to nonlinear Coulomb forces in intense beams. A comparative analysis is made of the angular divergence as a function of the method of shaping the electron beam.

We first consider the focusing of a beam in a magnetic field in which the cathode is completely shielded from the magnetic field. The equation of motion of the electrons in an intense beam focused by a longitudinal field B has the form

$$\ddot{r}=\frac{\eta I}{2\pi\varepsilon c\beta\gamma^3 r}-\frac{\eta^2 B^2}{4\gamma^2}r. \qquad (1)$$

Here, r is the radial coordinate of an electron, I is the beam current inside a cylinder of radius r, $\eta = e/m_0$ is the ratio of charge to rest mass of the electron, $\gamma = m/m_0$, and $\beta = v_z/c$ is the relative longitudinal velocity of the electrons. When the current density is not uniform over the cross section of the beam the repulsive Coulomb forces and the focusing forces of the external magnetic field are not in equilibrium for all beam particles. Numerical experiments[2] show that ordinarily the maximum angles are

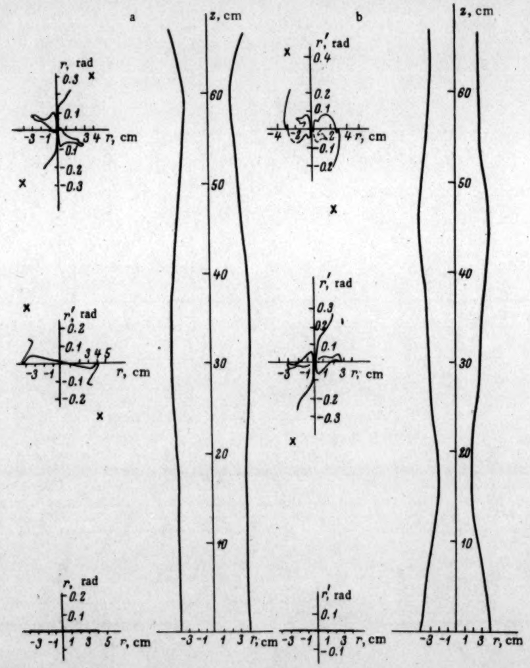

Fig. 1. A beam in a longitudinal magnetic field. $B_k = 0$, I = 5kA, W = 0.7 MeV, $r_0 = 4$ cm, B: a) $5\cdot10^{-2}$; b) $7.5\cdot10^{-2}$ Wb/m².

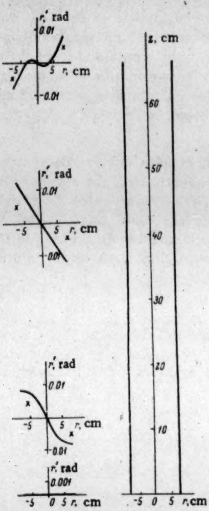

Fig. 2. A beam in a longitudinal magnetic field. $B_k = B$, $I = 10$ kA, $W = 1$ MeV, $r_0 = 7$ cm, $N = 0.73$ Wb/m².

acquired by particles which are initially at the periphery of the beam. For these particles the magnetic focusing forces are appreciably larger than the repulsive Coulomb forces. These particles cross the beam in the radial direction almost as though the beam current were zero. Thus, the maximum transverse velocities which the electrons can acquire can be obtained from Eq. (1) by setting $I = 0$:

$$\ddot{r}+\omega^2 r=0, \tag{2}$$

where

$$\omega=\frac{\eta B}{2\gamma}.$$

Using the initial conditions $r|_{t=0} = r_0$; $\dot{r}|_{t=0} = 0$ we obtain the solution of Eq. (2) in the form

$$r=r_0\cos\omega t. \tag{3}$$

From this we find an approximate equation for the maximum angular divergence of the beam particles $r_1' = \dot{r}_{max}/v_z$:

$$r_1'=\frac{\eta r_0 B}{2c\beta\gamma}. \tag{4}$$

Equation (4) essentially determines the maximum slope of the trajectory of a peripheral particle of a linear beam for zero initial divergence and zero beam current. In addition, this value determines approximately the maximum beam spread for a nonlinear distribution of Coulomb forces.

Thus the maximum angular divergence of the particles is proportional to B, or, as follows from the relation between the field and the beam current for Brillouin flow, $r_1' \sim I^{1/2}$.

The degree of reliability of (4) can be established by comparing the angular divergence calculated from (4) with numerical or experimental results. Figure 1 shows the results of a numerical solution of the equations of motion of a nonlaminar electron beam by the method described in ref. 2. The crosses show values of r_1' obtained from Eq. (4). The agreement is satisfactory.

Let us now consider the focusing of a beam when the cathode is in a magnetic field B_k.

To simplify the analysis we consider the special case $B_k = B$.

In this case the equation of motion of the electrons has the form

$$\ddot{r}=\frac{\eta I}{2\pi\varepsilon c\beta\gamma^3 r}-\frac{\eta^2 B^2}{4\gamma^2}r\left(1-\frac{r_k^4}{r^4}\right), \tag{5}$$

where r_k is the radius of the cathode.

From the condition for equilibrium between the Coulomb force and the magnetic force the equilibrium radius r_p is

$$r_p=r_k\sqrt{\frac{1}{2b^2}+\sqrt{\frac{1}{4b^4}+1}}, \tag{6}$$

where $b = B/B_B$, and B_B is the value of the Brillouin magnetic field for $r = r_k$:

$$B_B=\frac{1}{r_k}\sqrt{\frac{2I}{\pi\varepsilon\eta c\beta\gamma}}. \tag{7}$$

For values of the magnetic field $B \geq B_B$ and initial particle radii close to the equilibrium value, r is close to r_p. Therefore we take

$$r=r_p+x. \tag{8}$$

Substituting (8) into (5) we obtain the equation for x in the linear approximation:

$$\ddot{x}+\left[\frac{\eta I}{2\pi\varepsilon c\beta\gamma^3 r_p^2}+\frac{\eta^2 B^2}{\gamma^2}\left(1+3\frac{r_k^4}{r_p^4}\right)\right]x=0. \tag{9}$$

By using (7) we obtain

$$\ddot{x}+\omega^2 x=0, \tag{10}$$

where

$$\omega^2=\frac{\eta^2 B^2}{\gamma^2}\left[1-\frac{1}{4b^2}\left(\frac{r_k}{r_p}\right)^2\right].$$

The solution of Eq. (10) for the initial values $x|_{t=0} = x_0 = r_k - r_p$ and $\mathring{x}|_{t=0}$ has the form

$$x=x_0\cos\omega t. \tag{11}$$

Hence the maximum angular divergence of the beam particles $r_2' = \dot{x}_{max}/v_z$ is

$$r_2'=\frac{x_0\omega}{c\beta}. \tag{12}$$

Let us express the amplitude of the oscillations x_0 in terms of the magnetic field B. For equilibrium it follows from (5) that

$$1-\frac{r_k^4}{r_p^4}=\frac{1}{b^2}\frac{r_k^2}{r_p^2}. \tag{13}$$

Substituting into (13) $r_p = r_k - x_0$ and expanding $1/r_p^4$ in a series we obtain

$$x_0 \simeq \frac{r_k}{4b^2}. \tag{14}$$

Taking account of (7) and (14) we obtain an expression for r_2':

$$r_2' = \frac{I}{2\pi\varepsilon\,(c\beta\gamma)^2 r_k B}\sqrt{1 - \frac{1}{4b^2}\frac{r_k^2}{r_p^2}}. \tag{15}$$

When b ≫ 1 Eq. (15) becomes

$$r_2' = \frac{I}{2\pi\varepsilon\,(c\beta\gamma)^2 r_k B}. \tag{16}$$

Equation (15) can also be obtained by considering the azimuthal motion of a peripheral particle in a magnetic field. By calculating the maximum azimuthal component of the velocity of a peripheral particle it is easy to obtain Eq. (15) for r_2'.

It is clear from (16) that when $B_k \neq 0$ the maximum divergence of the beam electrons is inversely proportional to B.

The degree of reliability of Eq. (15) can be determined by comparing the values of the angular divergence found from (15) with the values obtained from the numerical solution of the equations of motion of a nonlaminar beam. Figure 2 shows the calculated results and the crosses give the values of r_2' obtained from Eq. (15). The agreement is satisfactory.

The following conclusions can be drawn. When the cathode is in a magnetic field the angular divergence of the beam decreases with increasing B, and in the absence of a magnetic field it increases [Eqs. (4) and (16)]. Therefore to decrease the angular divergence of the particles it is advantageous to place the cathode in a magnetic field.

---

[1] Yu. G. Globenko and D. G. Koshkarev, OIYaI, D9-6707, 68, Dubna (1972).

[2] V. S. Kuznetsov, V. I. Bogdanova, and O. L. Komarov, Radiotekh. Elektron., 16, 1476 (1971).

Parametric instability of a spatially moderated electron beam in a magnetic field

N. S. Repalov and V. F. Tyrnov

(Submitted September 9, 1973; resubmitted December 10, 1973)
Zh. Tekh. Fiz., 44, 1389-1394 (July 1974)

The parametric instability of an electron beam modulated by a spatially periodic electric field and focused by a uniform magnetic field is studied. It is shown that the development of a longitudinal instability characteristic of a beam in a magnetic field broadens the range of frequencies for which parametric amplification is possible and lowers the requirements imposed on the perveance of the beam.

The instability of an electron beam arising from its spatial modulation by an external electrostatic field is studied in refs. 1-3. The theoretical model used in these paper assumes either that the electron beam is focused by a strong enough magnetic field so that the particles move strictly along the lines of force,[1-2] or that there is no magnetic field at all.[3] Under these conditions an interaction leading to the development of an instability always involves the participation of the electron plasma wave. Although the parametric instability due to the electron plasma wave is rather effective and easily controlled, there is a limitation on the frequency range because of the interaction of the waves with the beam particles. Under actual conditions, in which the electron beam is produced by emission from a hot cathode, the upper limit of the instability[4] is about 500 MHz. In addition, the conditions for parametric resonance involving plasma waves ($k_0v_0 = 2\omega_0$) are equivalent to requiring a certain perveance of the beam, and this cannot always be achieved. There are two ways to extend the range of frequencies which can be amplified by the transfer of energy from the electrostatic field to the electromagnetic wave: reducing the energy spread of the beam particles or using a different instability.

In the present paper we study a parametric instability in an electron beam involving waves associated with the magnetic field and the transverse motion of the particles. This instability is less sensitive to the thermal motion of the particles and the perveance of the beam.

Assuming that the perturbations are electrostatic we start from the kinetic equation

$$\frac{df}{\partial t}+\mathbf{v}\frac{\partial f}{\partial \mathbf{r}}+\frac{e}{m}\mathbf{E}_{\text{st}}\frac{\partial f}{\partial \mathbf{v}}-\omega_H\frac{\partial f}{\partial \theta}=\frac{e}{m}\nabla\varphi\frac{\partial F^{(0)}(\mathbf{v};\,\mathbf{r})}{\partial \mathbf{v}}, \tag{1}$$

where $\mathbf{E}_{\text{st}}$ is the stationary field, described by the potential $\varphi_{\text{st}} = \varphi_0 \cos k_0 z$, θ is the polar angle in velocity space, and ω_H is the cyclotron frequency. If all the beam particles in velocity space are far from the region of trapping by the stationary field ($|\xi| = e\varphi_0/mv_0^2 \ll 1$, where v_0 is the average velocity of the beam in the direction of the magnetic field along the z axis), the steady-state distribution function of the particles depends only on the energy integral, i.e., $[\mathbf{v}-\mathbf{v}_0(1+2\xi\cos k_0 z)^{1/2}]^2$, and, to terms of order ξ, can be written

$$F^{(0)}(\mathbf{v};\,z)=f_0(\mathbf{v})+\xi\sigma(\mathbf{v})\cos k_0 z, \tag{2}$$

where $f_0(\mathbf{v})$ and $\sigma(\mathbf{v})$ are the first coefficients in the expansion of the steady-state distribution function in the Taylor's series in ξ. Taking the Fourier transforms of Eq. (1) with respect to time and coordinates we obtain

$$\frac{a_0\xi}{\gamma}\frac{\partial f(\mathbf{k}_{-1})}{\partial v_z}+f(\mathbf{k})-\frac{a_0\xi}{\gamma}\frac{\partial f(\mathbf{k}_1)}{\partial v_z}+\frac{i\omega_H}{\gamma}\frac{\partial f(\mathbf{k})}{\partial \theta}$$

$$=\frac{e}{m}\left\{\xi\frac{\mathbf{k}_{-1}}{2\gamma}\frac{\partial\sigma}{\partial\mathbf{v}}\varphi(\mathbf{k}_{-1})-\frac{\mathbf{k}}{\gamma}\frac{\partial f_0}{\partial\mathbf{v}}\varphi(k)+\xi\frac{\mathbf{k}_1}{2\gamma}\frac{\partial\sigma}{\partial\mathbf{v}}\varphi(\mathbf{k}_1)\right\}. \tag{3}$$

In Eq. (3) $a_0 = k_0v_0^2/2$, $\gamma = \omega - \mathbf{kv}$, and $\mathbf{k}_m = \mathbf{k} + m\mathbf{k}_0$. We solve Eq. (3) by successive approximations. In the zeroth approximation ($\xi = 0$), writing all the vectors in the form $\mathbf{R} = \mathbf{e}_z R_\parallel + \mathbf{R}_\perp$, we find[5-6]

$$f(\mathbf{k})=-\frac{e\varphi(\mathbf{k})}{m\omega_H}\sum_{ll'=-\infty}^{\infty}\frac{J_l(a)J_{l'}(a)}{b-l}\left[k_\parallel\frac{\partial f_0}{\partial v_\parallel}+\frac{l\omega_H}{v_\perp}\frac{\partial f_0}{\partial v_\perp}\right]e^{i(l-l')\theta}, \tag{4}$$

where

$$b=\frac{\omega-k_\parallel v_\parallel}{|\omega_H|};\quad a=\frac{k_\perp v_\perp}{|\omega_H|};$$

and J_l is the Bessel function. Assuming that the true value of $f(\mathbf{k})$ differs from the value calculated by Eq. (4) by a small correction $f^{(1)}$ of order ξ, and substituting Eq. (4) into the terms proportional to ξ, we obtain the first-approximation equation

$$\frac{i\gamma}{\omega_H}f^{(1)}(\mathbf{k})-\frac{\partial f^{(1)}}{\partial\theta}=i\left\{\xi\left[\frac{e\mathbf{k}_{-1}}{2m\omega_H}\frac{\partial\sigma}{\partial\mathbf{v}}\varphi(\mathbf{k}_{-1})-\frac{a_0}{\omega_H}\frac{\partial f(\mathbf{k}_{-1})}{\partial v_\parallel}\right]\right.$$

$$\left.-\frac{e\mathbf{k}}{m\omega_H}\frac{\partial f_0}{\partial\mathbf{v}}\varphi(\mathbf{k})+\xi\left[\frac{e\mathbf{k}_1}{2m\omega_H}\frac{\partial\sigma}{\partial\mathbf{v}}\varphi(\mathbf{k}_1)+\frac{a_0}{\omega_H}\frac{\partial f(\mathbf{k}_1)}{\partial v_\parallel}\right]\right\}. \tag{5}$$

Solving this equation for $f^{(1)}$ and performing the angle integration of $f^{(1)}$ in velocity space we find

$$f^{(1)}(\mathbf{k};\,v_\parallel;\,v_\perp)=\frac{2\pi e}{m\omega_H}\xi\sum_{l,l',p}\left\{\frac{1}{2}\psi_l(\mathbf{k})S_l(\mathbf{k}_{-1};\,\sigma)\right.$$

$$\left.+\frac{a_0}{\omega_H}\psi_{ll'p}(\mathbf{k};\,\mathbf{k}_{-1})S_l(\mathbf{k}_1;\,f_0)\right\}\varphi(\mathbf{k}_{-1})+\frac{2\pi e}{m\omega_H}\xi\sum_{ll'p}\left\{\frac{1}{2}\psi_l(\mathbf{k})S_l(\mathbf{k}_1;\,\sigma)\right.$$

$$\left.-\frac{a_0}{\omega_H}\psi_{ll'p}(\mathbf{k};\,\mathbf{k}_1)S_l(\mathbf{k}_1;\,f_0)\right\}\varphi(\mathbf{k}_1), \tag{6}$$

where

$$\psi_l(\mathbf{k})=\frac{J_l^2(a)}{b-l};\quad S_l(\mathbf{k}_m;\,q)=k_{\parallel m}\frac{\partial q}{\partial v_\parallel}+\frac{l\omega_H}{v_\perp}\frac{\partial q}{\partial v_\perp},$$

$$\psi_{ll'p}(\mathbf{k};\,\mathbf{k}_m)=\frac{J_p(a)J_{l-l'+p}(a)}{b-(l-l'+p)}\frac{\partial}{\partial v_\parallel}\frac{J_l(a)J_{l'}(a)}{b_m-l}.$$

In our case the transverse component of the wave vector is conserved, and therefore the subscript on $k_\perp$ is omitted. Knowing the distribution function, which is the sum of the expressions in Eqs. (4) and (6), we find the Fourier component of the electron density:

$$n(\mathbf{k})=\frac{2\pi e}{m\omega_H}\xi\sum_{ll'p}\int\left\{\frac{1}{2}\psi_l(\mathbf{k})S_l(\mathbf{k}_{-1};\,\sigma)\right.$$

$$\left.+\frac{a_0}{\omega_H}\psi_{ll'p}(\mathbf{k};\,\mathbf{k}_{-1})S_l(\mathbf{k}_{-1};\,f_0)\right\}\varphi(\mathbf{k}_{-1})v_\perp dv_\perp dv_\parallel$$

$$-\frac{2\pi e}{m\omega_H}\sum_l\int\psi_l(\mathbf{k})S_l(k;\,f_0)\varphi(\mathbf{k})v_\perp dv_\perp dv_\parallel+$$

$$+\frac{2\pi e}{m\omega_H}\xi\sum_{ll'p}\int\left\{\frac{1}{2}\psi_l(\mathbf{k}_1)S_l(\mathbf{k}_1;\ \sigma)\right.$$
$$\left.-\frac{a_0}{\omega_H}\psi_{ll'p}(\mathbf{k};\ \mathbf{k}_1)S_l(\mathbf{k}_1;\ f_0)\right\}\varphi(\mathbf{k}_1)v_\perp dv_\perp dv_\parallel.$$

Substituting ... n($\mathbf{k}_{-m}$) ... n($\mathbf{k}$) ... n($\mathbf{k}_m$) ... into Poisson's equation we obtain an infinite set of equations relating the amplitudes of the interacting waves. We consider the stability of a modulated beam with respect to two waves satisfying the conservation law for wave number $\mathbf{k}_1 = \mathbf{k} + \mathbf{k}_0$ (the law of conservation of frequency is satisfied automatically), assuming that other waves are not excited. Mathematically this means that only $\varphi(\mathbf{k})$ and $\varphi(\mathbf{k}_1)$ are different from zero. The set of equations relating $\varphi(\mathbf{k})$ and $\varphi(\mathbf{k}_1)$ has the form

$$\left.\begin{aligned}&\varepsilon(\mathbf{k};\ \omega)\varphi(\mathbf{k})-\frac{8\pi^2e^2}{k^2\omega_H}\xi\sum_{ll'p}\int\left\{\frac{1}{2}\psi_l(\mathbf{k})S_l(\mathbf{k}_1;\ \sigma)\right.\\&\left.-\frac{a_0}{\omega_H}\psi_{ll'p}(\mathbf{k};\ \mathbf{k}_1)S_l(\mathbf{k}_1;\ f_0)\right\}\varphi(\mathbf{k}_1)v_\perp dv_\perp dv_\parallel=0,\\&\frac{8\pi^2e^2}{k_1^2\omega_H}\xi\sum_{ll'p}\int\left\{\frac{1}{2}\psi_l(\mathbf{k}_1)S_l(k;\ \sigma)\right.\\&\left.+\frac{a_0}{\omega_H}\psi_{ll'p}(\mathbf{k}_1;\ \mathbf{k})S_l(\mathbf{k};\ f_0)\right\}\varphi(\mathbf{k})v_\perp dv_\perp dv_\parallel\\&-\varepsilon(\mathbf{k}_1;\ \omega)\varphi(k_1)=0,\end{aligned}\right|\quad(7)$$

where

$$\varepsilon(\mathbf{k};\omega)=1+\frac{8\pi^2e^2}{k^2\omega_H}\sum_l\int\frac{J_l^2(a)}{b-l}\left[k_\parallel\frac{\partial f_0}{\partial v_\parallel}+\frac{l\omega_H}{v_\perp}\frac{\partial f_0}{\partial v_\perp}\right]v_\perp dv_\perp dv_\parallel.\quad(8)$$

The condition for the solvability of Eqs. (7) leads to the dispersion relation

$$\frac{64\pi^4e^4}{k^2k_1^2\omega_H^2}\xi^2\left\{\sum_{ll'p}\int\left[\frac{1}{2}\psi_l(\mathbf{k})S_l(\mathbf{k}_1;\ \sigma)\right.\right.$$
$$\left.\left.-\frac{a_0}{\omega_H}\psi_{ll'p}(\mathbf{k};\ \mathbf{k}_1)S_l(\mathbf{k}_1;\ f_0)\right]v_\perp dv_\perp dv_\parallel\right\}$$
$$\times\left\{\sum_{ll'p}\int\left[\frac{1}{2}\psi_l(\mathbf{k}_1)S_l(\mathbf{k};\ \sigma)+\frac{a_0}{\omega_H}\psi_{ll'p}(\mathbf{k}_1;\ \mathbf{k})S_l(\mathbf{k};\ f_0)\right]v_\perp dv_\perp dv_\parallel\right\}$$
$$=\varepsilon(\mathbf{k})\varepsilon(\mathbf{k}_1).\quad(9)$$

Equation (9) contains an arbitrary steady-state distribution function. The simplest distribution function which can be used to describe effects related to transverse motion in an electron beam in an external magnetic field is[7]

$$f_0=\frac{n_0}{2\pi v_{0\perp}}\delta(v_\perp-v_{0\perp})\delta(v_\parallel-v_0).\quad(10)$$

It is easy to show that

$$\sigma=-\frac{n_0v_0^2}{2\pi v_{0\perp}v_\parallel}\delta(v_\perp-v_{0\perp})\frac{d}{dv_\parallel}\delta(v_\parallel-v_0).\quad(11)$$

Substituting (10) into the expression for ε we obtain

$$\varepsilon(\mathbf{k};\ \omega)=1-\frac{\omega_0^2}{k^2\omega_H^2}\sum_l\left\{\frac{k_\parallel^2J_l^2(a)}{(b-l)^2}+\frac{k_\perp^2\,[J_{l-1}^2(a)-J_{l+1}^2(a)]}{2(b-l)}\right\},$$

and the zero-order dispersion relation ($\xi = 0$) takes the form $\varepsilon(\mathbf{k};\ \omega) = 0$. This equation cannot be solved in analytic form. The case $k_\parallel \gg k_\perp$ is the simplest to investigate. In this case the zero-order dispersion relation is simplified close to its root:

$$1-\frac{\omega_0^2J_l^2(a)}{(\omega-k_\parallel v_0-l\omega_H)^2}=0.$$

Solving this equation for $k_\parallel$ we find

$$k_\parallel^l=\frac{\omega-l\omega_H-\omega_0J_l(a)}{v_0};\ k_{\parallel 1}^l=\frac{\omega-l\omega_H+\omega_0J_l(a)}{v_0}.\quad(12)$$

Since $\omega_H \gg \omega_0$ it is clear from Eq. (12) that the relative phase velocities of the waves ($|v_\varphi - v_0|$) for $l \neq 0$ is much larger than the relative phase velocities of the plasma waves. The boundary for parametric complication is found by setting the relative phase velocity of the wave equal to the thermal velocity of the beam particles. When this equality is satisfied the particles interact effectively with the electric field of the wave, and the parametric instability is suppressed.[3] Consequently, use of an instability associated with a longitudinal wave in a magnetic field extends to the frequency range for parametric amplification.

Conservation of wave number, the condition for parametric resonance, can be ensured by the choice of the distance between the branches of the dispersion diagram corresponding to the same l and different l, say l and l'. We consider these two possibilities separately.

In the first case the resonance condition has the form $k_0v_0 = 2\omega_0J_l(a)$. In evaluating the left-hand side of Eq. (9) we retain only those terms which contain the resonance denominator $b \approx l$. By using the resonance condition, the identity $\sum_p J_p^2(a) = 1$, and the inequality $k_\parallel \gg k_\perp$ it is easy to write Eq. (9) in the form

$$\varepsilon(\mathbf{k})\varepsilon(\mathbf{k}_1)=\frac{9}{4}\xi^2.\quad(13)$$

Let ω be the frequency of excitable waves in the absence of modulation. We seek the solution of Eq. (13) in the form $\omega + i\gamma_l$, where $\gamma_l \ll \omega$. Then when the resonance condition is satisfied exactly we obtain the parametric instability growth rate γ_l:

$$\gamma_l=\frac{3}{4}\xi\omega_0J_l(a).$$

It is clear that γ_l decreases rapidly with increasing l and oscillates for a monotonic change in the parameter a. The value of a corresponding to optimum amplification is given by the first root of the equation $J'_l(a) = 0$. It is also clear that in this case a broad amplification band imposes rigid requirements on the perveance of the beam.

We turn to the investigation of the second case $l \neq l'$. These instabilities are ensured by satisfying the conservation laws

$$k_\parallel^l+k_0=k_\parallel^{l'}\text{ and }k_\parallel^l+k_0=k_{\parallel 1}^{l'}.\quad(14)$$

The corresponding resonance conditions are

$$k_0v_0=(l-l')\omega_H+\omega_0[J_l(a)-J_{l'}(a)],\quad(14a)$$

$$k_0v_0=(l-l')\omega_H+\omega_0[J_l(a)+J_{l'}(a)].\quad(14b)$$

Since $l \neq l'$, $(l - l')\omega_H \gg \omega_0J_l(a)$. Hence it follows that the resonance conditions (14) are weakly dependent on the plasma frequency and, consequently, on the perveance of the beam. This condition permits the use of low-perveance beams.

Using the latter inequality and assuming, as before, that $k_\parallel \gg k_\perp$ and $b \approx l$, Eq. (9) determining the growth rate of the instability when resonance condition (14a) is satisfied can easily be put in the simple form

$$\varepsilon(k^{l})\,\varepsilon(k^{l'})=\frac{\xi^2}{4}\left[1-\frac{\omega-l'\omega_H}{(l-l')\,\omega_H}\right]\left[1+\frac{\omega-l\omega_H}{(l-l')\,\omega_H}\right]. \qquad (15)$$

Solving Eq. (15) in the same way as Eq. (13) we obtain the frequency correction

$$\Upsilon_{ll'}=\frac{\xi}{2}\left\{\left[1-\frac{\omega-l'\omega_H}{(l-l')\,\omega_H}\right]\left[1+\frac{\omega-l\omega_H}{(l-l')\,\omega_H}\right]\left(\frac{\partial\varepsilon(k^{l})}{\partial\omega}\,\frac{\partial\varepsilon(k^{l'})}{\partial\omega}\right)^{-1}\right\}^{1/2}.$$

Since

$$\left.\frac{\partial\varepsilon}{\partial\omega}\right|_{k=k^{l}}\left.\frac{\partial\varepsilon}{\partial\omega}\right|_{k=k^{l'}}=\frac{4}{\omega_0^2 J_l(a)\,J_{l'}(a)},$$

we obtain

$$\Upsilon_{ll'}=\frac{\xi\omega_0}{4}\left\{\left[1-\frac{\omega-l'\omega_H}{(l-l')\,\omega_H}\right]\left[1-\frac{\omega-l\omega_H}{(l-l')\,\omega_H}\right]\right\}^{1/2}\sqrt{J_l(a)\,J_{l'}(a)}. \qquad (16)$$

This expression can be either real or imaginary. In the latter case there is an instability. The expression in curly brackets is positive if the frequency ω satisfies the inequalities

$$l'\omega_H<\omega<l\omega_H, \qquad (17)$$

and the product of the Bessel functions is positive if the value lies between the n-th roots of the Bessel functions of order l and l', which we denote by $\varkappa_n^{l}$ and $\varkappa_n^{l'}$:

$$\varkappa_n^{l'}<a<\varkappa_n^{l}. \qquad (18)$$

The simultaneous satisfaction or violation of inequalities (17) and (18) determines the regimes under which the electron beam is stable. If only one of the indicated inequalities is violated, a parametric instability develops with a growth rate given by Eq. (16).

If resonance condition (14b) is satisfied the product of the derivatives of the permittivity with respect to frequency changes sign. The expression for the growth rate remains the same (16) but the simultaneous satisfaction or violation of (17) and (18) now determines the instability modes of the beam.

Although we have used a model distribution function, it is adequate to describe the physical processes occurring in a plasma in a magnetic field[7] if the relative phase velocities of the excited waves differ appreciably from the thermal velocity of the particles. Taking account of the finite width of the distribution function must lead to a threshold for the parametric instability[3] due to the resonance interaction of beam particles with the electric field of the excited waves.

Thus it has been shown that a parametric instability can be excited which is associated with plasma modes in a magnetic field. This result relaxes many of the rigid limitations characteristic of a parametric instability based on electron plasma waves: The range of useful frequencies is broadened, and the requirements imposed on the perveance of the beam are significantly reduced. The development of a parametric instability leads to the formation of intense charge density waves which may have many important practical applications such as the generation and amplification of microwaves and the collective acceleration of heavy ions.

---

[1] N. S. Repalov and N. A. Khizhnyak, Zh. Tekh. Fiz., 36, 219 (1966) [Sov. Phys. – Tech. Phys., 11, 162 (1966)].

[2] N. S. Repalov and V. F. Tyrnov, Zh. Tekh. Fiz., 42, 905 (1972) [Sov. Phys. – Tech. Phys., 17, 719 (1972)].

[3] N. S. Repalov and V. F. Tyrnov, Zh. Tekh. Fiz., 43, 1588 (1973) [Sov. Phys. – Tech. Phys., 18, 1003 (1973)].

[4] G. G. Aseev, G. G. Kuznetsova, N. S. Repalov, and N. A. Khizhnyak, Zh. Tekh. Fiz., 42, 2264 (1972) [Sov. Phys. – Tech. Phys., 17, 1777 (1973)].

[5] E. G. Harris, Phys. Rev. Lett., 2, 34 (1959); E. G. Harris, Plasma Phys., (J. Nucl. Energy C) 2, 138 (1961).

[6] A. I. Akhiezer, I. A. Akhiezer, R. V. Polovin, A. G. Sitenko, and K. N. Stepanov, Collective Oscillations in a Plasma [in Russian], Atomizdat, Moscow (1964).

[7] G. Bekefi, Radiation Processes in Plasmas, Wiley, New York (1966).

Magnetohydrodynamic channel flow in a tapered magnetic field

S. A. Regirer

Institute of Mechanics, M. V. Lomonosov Moscow State University

(Submitted September 12, 1973)
Zh. Tekh. Fiz., 44, 1395-1400 (July 1974)

Fully developed flows of a viscous incompressible isotropically conducting fluid are investigated in a rectangular channel in the presence of a transverse magnetic field $\mathbf{B} = (B_0/a)(-\mathbf{e}_y y + \mathbf{e}_z z)$. An exact solution of the problem is obtained in general form and for the limiting case corresponding to a flow in a plane slit. It is shown that at high Hartmann numbers a region of elevated velocities can form near the axis of the channel. In this regard, a flow in a plane slit exhibits a paradox: The reason is that the limiting case "carries" the region with an infinitely large emf to infinity; in the region considered the flow acts as a pump. In conclusion, some other flows in inhomogeneous fields with tapered geometry are considered.

1. Developed flows of a conducting fluid in channels have been studied in great detail,[1] and the possibilities of obtaining new exact analytic solutions are extremely limited. The possibilities exist nevertheless and it is possible, as will be shown below, to find even simple new solutions which have fairly interesting qualitative properties as well.

Let a plane slit bounded by infinite nonconducting planes $z = \pm a$ (Fig. 1) contain a totally developed flow of an incompressible viscous conducting fluid with constant and isotropic properties; the flow velocity **v** is coplanar with the boundaries and depends only on z: $\mathbf{v} = [u(z), v(z), 0]$. The external (independent of motion) magnetic field is

$$\mathbf{B}^e = \left(0, -\frac{B_0 y}{a}, \frac{B_0 z}{a}\right), \tag{1}$$

where $B_0 = \text{const}$. For the geometry of the induced magnetic field we take the same hypotheses used for the velocity, setting $\mathbf{B}^i = [b(z), b_1(z), 0]$. Thus, the total field is

$$\mathbf{B} = \left(b(z), b_1(z) - \frac{B_0 y}{a}, \frac{B_0 z}{a}\right). \tag{2}$$

Finally, we assume that the effective pressure $p^* = p + B^2/8\pi$ depends on all three coordinates

$$p^* = \frac{B_0^2}{8\pi a^2}(y^2 + z^2) - Px - P_1 y + \text{const},$$

where P and P_1 are constants either given or dependent on given flow rates Q and Q_1 in the x and y directions, respectively.

Considering the general equations of magnetohydrodynamics, we can easily be convinced that the above assumptions are not contradictory[1)] and lead to the following boundary problem in u, v, b, and b_1:

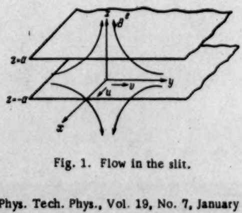

Fig. 1. Flow in the slit.

$$\left.\begin{aligned} &\mu v'' + \frac{B_0 z}{4\pi a} b_1' - \frac{B_0}{4\pi a} b_1 + P_1 = 0, \\ &\frac{B_0 z}{a} v' + \nu_m b_1'' = -\frac{B_0}{a} v, \ v(\pm a) = 0, \ b_1(\pm a) = 0; \end{aligned}\right\} \tag{3}$$

$$\left.\begin{aligned} &\mu u'' + \frac{B_0 z}{4\pi a} b' + P = 0, \\ &\frac{B_0 z}{a} u' + \nu_m b'' = 0, \ u(\pm a) = 0, \ b(\pm a) = 0. \end{aligned}\right\} \tag{4}$$

Obviously, flows in the x and y directions are hydrodynamically independent. The flow along the y axis is governed by Eq. (3) and was analyzed in ref. 1. It is a plane analog of an axially symmetric flow in a tube of radius *a* for $\mathbf{v} = u(r)\mathbf{e}_x$ and

$$\mathbf{B}^e = \frac{B_0 r}{a}\mathbf{e}_r - \frac{2B_0 x}{a}\mathbf{e}_x. \tag{5}$$

This axially symmetric problem was first solved by S. I. Pai prior to the renewed interest in magnetohydrodynamics;[2] the solution was derived twice later.[3,4]

Problem (4), which describes the flow along the x axis, i.e., parallel to the zero magnetic field line, is studied below.

2. We now consider the dimensionless variables, choosing as the length, velocity, and induced field scales the quantities

$$l_* = a, \ u_* = \frac{Pa^2}{\mu}, \ b_* = \frac{4\pi P a^2}{c}\sqrt{\frac{\sigma}{\mu}}, \tag{6}$$

and introducing the Hartmann number $H = (B_0 a/c)\sqrt{\sigma/\mu}$. Then, from (4)

$$\left.\begin{aligned} &u'' + Hzb' = -1, \ b'' + Hzu' = 0, \\ &u(\pm 1) = 0, \ b(\pm 1) = 0, \end{aligned}\right\} \tag{7}$$

or, in symmetric variables,

$$\left.\begin{aligned} &w_1'' + Hzw_1' = -1, \ w_2'' - Hzw_2' = -1, \\ &w_1(\pm 1) = 0, \ w_2(\pm 1) = 0, \end{aligned}\right\} \tag{8}$$

where

$$w_1 = u + b, \ w_2 = u - b. \tag{9}$$

The solution of the problem is symmetric in u, b, and w_i – even functions of z. From (8) we find

$$w_1=\int_z^1 e^{-\frac{Ht^2}{2}}\int_0^t e^{\frac{Hs^2}{2}}ds\,dt,\quad w_2=\int_z^1 e^{\frac{Ht^2}{2}}\int_0^t e^{-\frac{Hs^2}{2}}ds\,dt. \tag{10}$$

Then, the velocity and the dimensionless y component of the current density $j_y = 1/2(w_1-w_2)'$ are

$$u=\int_z^1\int_0^t \operatorname{ch}\frac{H}{2}(t^2-s^2)\,ds\,dt,\quad j_y=\int_0^z \operatorname{sh}\frac{H}{2}(z^2-s^2)\,ds. \tag{11}$$

The total current across the system is zero, and the flow rate (per unit width of the channel in the y direction) is

$$Q=\frac{1}{H}\int_0^1 \operatorname{sh}\frac{H}{2}(1-s^2)\,ds. \tag{12}$$

When H ≫ 1 we find from (11) and (12)

$$u(0)\sim\sqrt{\frac{\pi}{8H^3}}\,e^{\frac{H}{2}},\quad Q\sim\sqrt{\frac{\pi}{8H^3}}\,e^{\frac{H}{2}}. \tag{13}$$

Equations (11) - (13) lead to conclusions directly opposite to those that are well known for Hartmann and similar-type flows: a) for $z > 0$ ($z < 0$) the current j_y has a positive (negative) direction, i.e., everywhere the opposite electromotive force $(\mathbf{v}\times\mathbf{B})_y$; b) the Lorentz force is everywhere in the same direction as the velocity, i.e., it accelerates rather than retards the stream; c) the current, the Lorentz force, and the velocity increase exponentially everywhere with increasing Hartmann number H.

3. The proposed explanation for these paradoxical facts is the following. Consider a channel of finite, but greatly extended, rectangular cross section (Fig. 2) with insulated walls $y = \pm h$, $z = \pm 1$, $h \gg 1$. Near the remote walls $y = \pm h$ the dimensional emf is of the order of $h(B_0u/c)$ and is h times greater than in the middle of the channel. One can expect, therefore, that the emf in the distant lateral regions determines the direction of the current in the middle part, i.e., the distant regions operate as generators, and the middle section acts as a pump fed by the voltage from the "generator section." For increasing Hartmann number in a certain range (probably broadened with increasing h), the work of the "pump section" intensifies. The solution constructed above corresponds to the case h → ∞ for a fixed H, and describes the "pump section" with a voltage source at infinity.

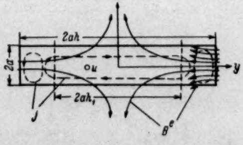

Fig. 2. Pattern of currents in a transverse channel cross section. $|y| < ah_1$ is the "pump" section, $ah_1 < |y| < ah$ is the "generator" section. In the $|y| = ah_1$ cross sections, roughly $j_z = 0$ and $E_z = -uB_y/c$ (all quantities are dimensional).

The equations for a fully developed flow in a rectangular channel with insulated walls have the form, in the variables of Sec. 2,

$$\left.\begin{aligned}&\Delta w_{1,2}\pm H\left(-y\frac{\partial w_{1,2}}{\partial y}+z\frac{\partial w_{1,2}}{\partial z}\right)=-1,\\ &w_{1,2}=0\ \text{when}\ \begin{cases}y=\pm h, & |z|\leqslant 1,\\ |y|\leqslant h, & z=\pm 1.\end{cases}\end{aligned}\right\} \tag{14}$$

Assume that in the region $|y| < h_1 < h$ (Fig. 2) the solution of this problem varies slowly with y; this requires that $\partial w_{1,2}/\partial y$, $\partial u/\partial y$, $j_z \sim \partial b/\partial y$ be close to zero for $|y| = h_1$. On a purely theoretical basis, this condition can probably be obtained by decreasing the viscosity and by arranging the electric field $E_z \approx uB_y/c$ in the region $|y| \approx h_1$. For a "pump section" $|y| < h_1$ this field is the external field. Since here $E_z(-h_1, z) = -E_z(h_1, z)$ an external potential difference appears between the points $(-h_1, z)$ and (h_1, z).

Partial confirmation of these considerations is obtained from an analysis of the exact solution of problem (14), which is constructed in the following manner.

Let $V_n(z, q)$ and $\gamma_n = \gamma_n(q)$ be eigenelements of the Sturm–Liouville equation

$$\frac{d}{dz}e^{\frac{qz^2}{2}}\frac{dV}{dz}+\gamma e^{\frac{qz^2}{2}}V=0,\quad V(\pm1)=0. \tag{15}$$

The normalized eigenfunctions V_n are expressed in terms of the Whittaker function

$$V_n=\frac{1}{a_n\sqrt{z}}\,e^{-\frac{qz^2}{4}}M_{k_n,-\frac{1}{4}}\left(\frac{qz^2}{2}\right),$$
$$a_n(q)=\left[\int_{-1}^{1}\frac{1}{z}M^2_{k_n,-\frac{1}{4}}\left(\frac{qz^2}{2}\right)dz\right]^{1/2},$$

where $k_n = k_n(q)$ are successive roots of $M_{k,-1/4}(q/2) = 0$. The eigenvalues γ_n are related to k_n by $\gamma_n = 2qk_n$. Changing in (15) to the variable $U = V\exp(qz^2/4)$ it is easy to show that $\gamma_n > q/2$ and thus $k_n > 1/4$ for $q > 0$. One can also show that $k_1 \to 1/4$ as $q \to \infty$. The following equations hold:

$$\int_{-1}^{1}e^{\frac{qz^2}{2}}V_k(z,q)\,V_l(z,q)\,dz=\delta_{kl},$$

$$a_n(-q)=a_n(q),\quad \gamma_n(-q)=\gamma_n(q),\quad k_n(-q)=-k_n(q),$$
$$e^{-\frac{qz^2}{4}}V_n(z,-q)=e^{\frac{qz^2}{4}}V_n(z,q).$$

The solutions of problem (14) can be represented in the form of expansions

$$w_1=\sum_{n=1}^{\infty}w_{1n}(y)\,V_n(z,H),\quad w_2=\sum_{n=1}^{\infty}w_{2n}(y)\,V_n(z,-H). \tag{16}$$

The coefficients

$$w_{in}(y)=\int_{-1}^{1}w_i e^{\pm\frac{Hz^2}{2}}V_n(z,\pm H)\,dz\quad (i=1,\ 2),$$

indicate direct calculations and are also expressed in terms of the Whittaker function

$$w_{in}=\frac{\alpha_{in}}{\gamma_n(H)}\left[1-\sqrt{\frac{h}{y}}\,e^{\pm\frac{H}{4}(y^2-h^2)}M_{s_n,-\frac{1}{4}}\left(\frac{Hy^2}{2}\right)M^{-1}_{s_n,-\frac{1}{4}}\left(\frac{Hh^2}{2}\right)\right]. \quad (17)$$

Here,

$$\alpha_{in}=\int_{-1}^{1}e^{\pm\frac{Hz^2}{2}}V_n(z,\ \pm H)\,dz,\ \ s_n(H)=-\frac{\gamma_n(H)}{2H}=-k_n(H).$$

Equations (16) and (17) give a formal solution to problem (14). We note that it is not difficult to write another expansion, equivalent to that given, in eigenfunctions dependent on y and with coefficients dependent on z. Therefore, conclusions unrelated to h as to the behavior of the solution for one coordinate are also valid for the other coordinate.

The solution of problem (8) can also be represented in the form of expansions in V_n; it is easy show that they are

$$w_i=\sum_{n=1}^{\infty}\frac{\alpha_{in}}{\gamma_n}V_n(z,\ \pm H). \quad (18)$$

For large $h(Hh^2 \gg 1)$

$$M_{s_n,-\frac{1}{4}}\left(\frac{Hh^2}{2}\right)\sim\frac{\Gamma\left(\frac{1}{2}\right)}{\Gamma\left(\frac{1}{4}+k_n\right)}e^{\frac{Hh^2}{4}}\left(\frac{Hh^2}{2}\right)^{k_n},$$

and thus

$$w_{in}\sim\frac{\alpha_{in}}{\gamma_n}\left[1-\frac{1}{\sqrt{y}}\frac{\Gamma\left(\frac{1}{4}+k_n\right)}{\Gamma\left(\frac{1}{2}\right)}e^{\frac{H}{4}(\pm y^2-h^2\pm h^2)}\right.$$

$$\left.\times\left(\frac{H}{2}\right)^{-k_n}h^{\frac{1}{2}-2k_n}M_{s_n,-\frac{1}{4}}\left(\frac{Hy^2}{2}\right)\right].$$

Since α_{in}, γ_n, S_n are independent of h and $k_n > 1/4$, then as $h \to \infty$, and H = const, y = const ≠ 0,

$$w_{in}\to\frac{\alpha_{in}}{\gamma_n}. \quad (19)$$

This ratio is valid for y = 0 also, since

$$M_{s_n,-\frac{1}{4}}\left(\frac{Hy^2}{2}\right)\sim\left(\frac{Hy^2}{2}\right)^{1/4}\ \ \text{as}\ \ y\to 0.$$

However, the larger H is, the closer k_1 comes to 1/4 and, thus, the larger h must be for some $w_{in} \approx \alpha_{in}\gamma_n^{-1}$ in a certain range $|y| \ll h$. The size of this range obviously decreases with an increasing Hartmann number, since for it

$$\left(\frac{y}{h}\right)^{2k_1-\frac{1}{2}}\ll 1.$$

Thus, the limiting case $h \to \infty$, as can be seen by comparing (18) to (16) and (19), actually leads to the solution in Sec. 2, which is independent of y.

This solution is a satisfactory approximation of the exact solution with $h \gg 1$ only for a certain range $|y| \ll h$ whose size decreases with an increasing Hartmann number, only if h does not increase fast enough with H.

A rigorous investigation of the asymptotic behavior of the solution of (16) and (17) for fixed h and $H \to \infty$ represents a fairly difficult task since a termwise analysis of the series does not produce the desired result and evidently indicates only the existence of a difference in asymptotic behavior for the wall boundary layers, for free boundary layers[2)] along the y = 0 and z = 0 lines, for the region near the zero point y = 0, z = 0, and finally for four cores of the flow.

4. The distribution of the external magnetic field expressed by Eq. (1) is a particular case of the more general solution of Maxwell's equations

$$\mathbf{B}^e=\left(0,\ -B_0\frac{r^n}{a^n}\sin n\vartheta,\ B_0\frac{r^n}{a^n}\cos n\vartheta\right) \quad (20)$$

for n = 1. When n = 0, we obtain a homogeneous field $\mathbf{B}^e = (0, 0, B_0)$. If, as proposed by Yakubenko,[5] we introduce new independent variables ζ and η related to $\mathbf{B}^e$ by $\mathbf{B}^e = \nabla\zeta$ and $\mathbf{B}^e = \mathbf{e}_x\cdot\nabla\eta$ then the r = const and ϑ = const lines in the plane (y, z) will correspond to the arcs of the circles and the radii in the plane (ζ, η). This allows the solution for the problem of the flow in a circular tube for the field (20) with arbitrary n to be written comparatively simply as a series, by analogy[3)] with the solutions of Uflyand and Yakubenko.[5,6]

An exact solution can also be obtained for the problem of the flow in an annular tube in the presence of an external magnetic field of type (20) with positive or negative integers n. For n = −1 the solution is well known (an annular tube with a purely radial magnetic field).

We note in conclusion that the Pai problem[2] for a circular pipe mentioned at the beginning of this paper admits several generalizations when the solution is found in finite form, or reduces to integration of ordinary differential equations. In particular, if the magnetic field has the form (5) and the stream becomes helical due to the longitudinal current J, then

$$\left.\begin{array}{c}\mathbf{v}=(0,\ v_\vartheta(r),\ v_x(r)),\quad \mathbf{B}=\mathbf{B}^e+\mathbf{B}^i,\\ \mathbf{B}^i=(0,\ b_\vartheta(r),\ b_x(r)),\quad \mathbf{j}=(0,\ j_\vartheta(r),\ j_x(r)),\\ p=p\,(r,\ x).\end{array}\right\} \quad (21)$$

Cylindrical coordinates and dimensional variables are used above. Omitting the calculations, we show that the problems in which v_x, b_x, j_ϑ and v_ϑ are to be found are separate; the first term has been solved in ref. 2 and the solution of the second has the form

$$v_\vartheta=\frac{Jr}{2\pi a^2\theta\sqrt{\sigma\mu}}\int_{\rho}^{1}\frac{1}{t}I_1\left(\frac{Ht^2}{2}\right)dt,$$

$$b_\vartheta=\frac{2J}{r}\left[1-\frac{1}{\theta}\int_{\rho}^{1}tI_0\left(\frac{Ht^2}{2}\right)dt\right],\ \ j_x=\frac{J}{2\pi a^2\theta}I_0\left(\frac{H\rho^2}{2}\right),$$

$$\theta=\int_{0}^{1}tI_0\left(\frac{Ht^2}{2}\right)dt,\ \ \rho=\frac{r}{a},$$

where a is the tube radius. It is interesting that the electric current has a cross-sectional distribution that is essentially nonuniform by comparison to the case of the absence of a magnetic field or a rigid conductor $(\mu \to \infty)$. With an increasing Hartmann number the current tends to concentrate near the axis of the tube.

If we consider anisotropic conductivity (Hall effect), then the solution retains the structure of (21), but the longitudinal and rotational motions are interrelated. The problem again reduces to ordinary linear equations, but the solution cannot be obtained in closed form.

---

1) The considerations on which they are based are closely related to the conditions for the existence of fully developed flows.[1]

2) Proof of the existence of these layers and some estimates of them are given by Todd, to whom the author is indebted for making available the results of his unpublished work.

3) This transformation was also proposed by Todd,[7] who used it for the case $n \geq 1$ and $H \gg 1$ to obtain a direct estimate of the asymptotic behavior of a flow in a channel of arbitrary cross section having roughly the same characteristic dimensions along the y and z axes (see the second footnote).

[1] A. B. Vatazhin, G. A. Lyubimov, and S. A. Regirer, Magnetohydrodynamic Flows in Channels [in Russian], Nauka, Moscow (1970).

[2] S.-I. Pai, J. Appl. Phys., 25, 1205 (1954).

[3] A. Demetriades, J. Aerospace Sci., 27, 388 (1960).

[4] P. Kh. Derkach and N. P. Busoverya, in: Hydrodynamics and the Theory of Elasticity [in Russian], (1970), No. 2 (1970), p. 33.

[5] A. E. Yakubenko, Izv. Akad. Nauk SSSR Otd. Tekh. Nauk Mekh. Mashinostr., No. 1, 90 (1961).

[6] Ya. S. Uflyand, Zh. Tekh. Fiz., 30, 1258 (1960) [Sov. Phys.–Tech. Phys., 5, 1194 (1961)].

[7] L. Todd, J. Fluid Mech., 31, 321 (1968).

Nonstationary magnetohydrodynamic flow and wave propagation

M. Ya. Antimirov and Yu. Ya. Boguslavskii

(Submitted July 16, 1973; resubmitted November 19, 1973)
Zh. Tekh. Fiz., 44, 1401-1404 (July 1974)

It is well known that propagation of waves in an absorbing medium is accompanied by a unidirectional motion of this medium – a flow that arises because the wave loses momentum as well as energy. In accordance with momentum conservation these losses are compensated by the flow. The present paper considers a system of equations describing nonstationary flow in a conducting medium in a magnetic field. The nonstationary solutions obtained relax after a time to the steady state. It is shown that the transition to the steady state depends on the Hartmann number and that it can be oscillatory or monotonic.

The motion of a conducting fluid in a magnetic field is described by the magnetohydrodynamic equations[1]

$$\left.\begin{array}{c}\operatorname{div}\mathbf{H}=0,\\ \frac{\partial\rho}{\partial t}+\operatorname{div}\rho\mathbf{V}=0,\\ \frac{\partial\mathbf{H}}{\partial t}=\operatorname{curl}(\mathbf{V}\times\mathbf{H})+\frac{c^2}{4\pi\sigma}\Delta\mathbf{H},\\ \frac{\partial\mathbf{V}}{\partial t}+(\mathbf{V}\nabla)\mathbf{V}=-\frac{\nabla P}{\rho}-\frac{1}{4\pi\rho}\mathbf{H}\times\operatorname{curl}\mathbf{H}\\ +\frac{\eta}{\rho}\Delta\mathbf{V}+\frac{1}{\rho}\left(\xi+\frac{\eta}{3}\right)\operatorname{grad}\operatorname{div}\mathbf{V},\\ P=P(\rho,\ T),\\ \rho T\left(\frac{\partial S}{\partial t}+\mathbf{V}\nabla S\right)=\sigma'_{ik}\frac{\partial V_i}{\partial x_k}\\ +\operatorname{div}(\varkappa\nabla T)+\frac{c^2}{16\pi^2\sigma}(\operatorname{curl}\mathbf{H})^2\end{array}\right\} \quad (1)$$

where V is the velocity, ρ is the fluid density, η and ξ are two viscosity coefficients of the fluid, P is the pressure, H is the magnetic field, T_1 is the temperature, σ'_{ik} is the viscous stress tensor,[1] σ is the conductivity of the fluid, and c is the speed of light. We consider an infinite plane layer of thickness $2a$ bounded by plane solid walls and filled with a conducting fluid. A beam of waves of width 2b propagates along the axis of the layer. The ends of the layer are filled with films that are transparent to the waves. An external perpendicular magnetic field H_0 is applied to the planes that bound the layer. The flow generated in the system is to be determined.

We consider a wave of the form

$$v=v_0\cos(\omega t-\mathbf{kx})e^{-\alpha x}, \quad (2)$$

where v_0 is the velocity, ω is the frequency, k is the wave vector, and α is the absorption coefficient (see ref. 2). The value of α is assumed to be small $\alpha L \ll 1$ where L is the length of the layer.

A system of equations for a nonstationary magnetohydrodynamic flow can be obtained, as in ref. 2, by considering system (1) in the second approximation, taking expressions of type (2) for the magnetohydrodynamic waves as the first approximation. In the present case, in contrast to ref. 2, it is necessary to average the equations obtained over a time interval larger than $T=2\pi/\omega$ but much smaller than the time for generating the flow.

We are interested in the flow generated by wave absorption only in the middle section of the layer; end effects are neglected.

We assume further that the velocity of the flow U is everywhere in the direction of the x axis and depends only on the y coordinate in the direction perpendicular to the planes.

Then, the continuity equation is satisfied automatically, and the problem reduces to integration of the following system of equations:

$$\left.\begin{array}{c}D\frac{\partial^2 h}{\partial y^2}+H_0\frac{\partial U}{\partial y}=\frac{\partial h}{\partial t},\\ \nu\frac{\partial^2 U}{\partial y^2}+\frac{H_0}{4\pi\rho}\frac{\partial h}{\partial y}+C(t)=\frac{\partial U}{\partial t}-F\end{array}\right\} \quad (3)$$

with the boundary condition and initial conditions

$$\left.\begin{array}{c}h|_{y=0}=\left.\frac{\partial U}{\partial y}\right|_{y=0}=h|_{y=a}=U|_{y=a}=0,\\ h|_{t=0}=U|_{t=0}=0.\end{array}\right\} \quad (4)$$

The condition that the total flow of the fluid be zero over the cross section of the layer must be satisfied:

$$\int_0^a U dy=0. \quad (5)$$

In system (3), $F=\alpha(v_0^2/2)\theta(b-y)$ is the force that generates the flow

$$\theta(b-y)=\begin{cases}1\,\text{when}\,0\leqslant|y|\leqslant b,\\ 0\,\text{when}\,b<|y|\leqslant a,\end{cases}$$

$C(t)=(-1/\rho_0)(\partial P/\partial x)$ is an unknown pressure gradient, and h is the magnetic field induced by the flow.

When y = 0, condition (4) applies because U(y, t) is even and h (y, t) is odd in the range $-a\leq y\leq a$.

The solution of the problem (3)-(5) is obtained by using the Laplace transform:

$$U(\bar{y},t)=U_e(\bar{y})+\sum_{n=1}^{\infty}\frac{D\varphi_1(p_n)}{aH_0\varphi_2'(p_n)}\left\{(k_{1n}-\mu k_{2n})\frac{\operatorname{ch}k_{1n}-\operatorname{ch}k_{1n}\bar{y}}{\operatorname{sh}k_{1n}}\right.$$
$$\left.-(k_{2n}-\mu k_{1n})\frac{\operatorname{ch}k_{2n}-\operatorname{ch}k_{2n}\bar{y}}{\operatorname{sh}k_{2n}}\right\}e^{p_n t}, \quad (6)$$

$$h(\bar{y},\ t)=h_e(\bar{y})+\sum_{n=1}^{\infty}\frac{\varphi_1(p_n)}{\varphi_2'(p_n)}\left(\frac{\operatorname{sh}k_{1n}\bar{y}}{\operatorname{sh}k_{1n}}-\frac{\operatorname{sh}k_{2n}\bar{y}}{\operatorname{sh}k_{2n}}\right)e^{p_n t},$$

$$C(t)=\frac{\alpha}{2}v_0^2a_1+\sum_{n=1}^{\infty}\frac{\alpha D}{a^3H_0}\frac{\varphi_1(p_n)}{\varphi_2'(p_n)}$$
$$\times\sqrt{(\mu+1)^2\frac{a^2p_n}{a}+H_a^2}\sqrt{(\mu-1)^2\frac{a^2p_n}{a}+H_a^2}e^{p_n t},$$

where[1]

$$U_e(\bar{y})=\begin{cases}\frac{\alpha v_0^2a^2}{2\alpha H_a^2}\left\{a_1+1-\frac{1}{\operatorname{ch}H_a}\left(a_1+\operatorname{ch}\left(1-\frac{b}{a}\right)H_a\right]\operatorname{ch}H_a\bar{y}\right\}\\ \qquad\text{when }0<\bar{y}<\frac{b}{a},\\ \frac{\alpha v_0^2a^2}{2\lambda H_a^2\operatorname{ch}H_a}\left\{a_1[\operatorname{ch}H_a-\operatorname{ch}H_a\bar{y}]+\operatorname{sh}\frac{b}{a}H_a\operatorname{ch}H_a(1-\bar{y})\right\}\\ \qquad\text{when }\frac{b}{a}<\bar{y}<1,\end{cases} \quad (7)$$

$$h_e(\bar{y}) = \left\{ \begin{array}{c} \frac{\alpha a^2 v_0^2 H_0}{2\nu D H_a^2} \left\{ \left[a_2 + \frac{a \operatorname{sh}\left(1-\frac{b}{a}\right) H_a}{H_a} \right] \frac{\operatorname{sh} H_a \bar{y}}{\operatorname{sh} H_a} \right. \\ \left. -(1+a_1) a \bar{y} \right\} \\ \text{when } 0 < \bar{y} < \frac{b}{a}, \\ \frac{\alpha v_0^2 a^2 H_0}{2\nu D H_a^2} \left\{ \frac{a_2 H_a \operatorname{sh} H_a \bar{y} + a \operatorname{sh} H_a \frac{b}{a} \operatorname{sh} H_a (1-\bar{y})}{H_a \operatorname{sh} H_a} \right. \\ \left. -(a a_1 \bar{y} + b) \right\} \\ \text{when } \frac{b}{a} < \bar{y} < 1, \end{array} \right\} \qquad (8)$$

$$\phi_1(p_n) = \alpha \frac{v_0^2 a H_0}{\mu D \sqrt{A_n B_n}} \Big[k_{2n}(k_{1n} - \mu k_{2n}) \operatorname{sh} k_{1n} \frac{b}{a} \operatorname{sh} k_{2n} - k_{1n}(k_{2n} - \mu k_{1n})$$

$$\times \operatorname{sh} k_{2n} \frac{b}{a} \operatorname{sh} k_{1n} - \mu \frac{b}{a} \sqrt{A_n B_n} \operatorname{sh} k_{1n} \operatorname{sh} k_{2n} \Big],$$

$$A_n = (\mu+1)^2 \frac{a^2 p_n}{\nu} + H_a^2; \quad B_n = (\mu-1)^2 \frac{a^2 p_n}{\nu} + H_a^2;$$

$H_a = \frac{a H_0}{c} \sqrt{\frac{\sigma}{\rho \nu}}$ is the Hartmann number.

$$\mu = \sqrt{\frac{\nu}{D}}; \; D = \frac{c^2}{4\pi\sigma}; \; \bar{y} = \frac{y}{a}; \; k_{1n} = \frac{1}{2}(\sqrt{A_n} + \sqrt{B_n});$$

$$K_{2n} = \frac{1}{2}(\sqrt{A_n} - \sqrt{B_n}); \; n = 1,\ 2,\ 3\ldots$$

$$a_1 = \frac{\operatorname{sh} \frac{b}{a} H_a - \frac{b}{a} H_a \operatorname{ch} H_a}{H_a \operatorname{ch} H_a - \operatorname{sh} H_a}; \quad a_2 = \frac{a \operatorname{sh} \frac{b}{a} H_a - b \operatorname{sh} H_a}{H_a \operatorname{ch} H_a - \operatorname{sh} H_a};$$

the p_n are the roots of the equation

$$\varphi_2(p) = p^2 \Big[(\mu-1)\sqrt{A} \operatorname{sh} \sqrt{B} + (\mu+1)\sqrt{B} \operatorname{sh} \sqrt{A}$$

$$- \frac{\nu}{a^2 p} \sqrt{AB} (\operatorname{ch} \sqrt{A} - \operatorname{ch} \sqrt{B}) \Big] = 0. \qquad (9)$$

Here,

$$A = (\mu+1)^2 \frac{a^2 p}{\nu} + H_a^2; \quad B = (\mu-1)^2 \frac{a^2 p}{\nu} + H_a^2.$$

Equation (9) differs from the corresponding equation for a nonstationary Hartmann flow[3] by the last term in the left-hand side.

In the general case the roots of Eq. (9) can be calculated only by numerical methods. However, for $\mu \ll 1$ simple approximations can be obtained.

1. Let $\mu = \sqrt{\nu/D} \ll 1$ and let $\mu H_a^2 \ll 1$; then

$$p_n \simeq -\frac{\nu}{a^2} \Big[x_n^2 + H_a^2 + \Big(\frac{5}{3} - \frac{x_n^2}{6} \Big) \mu^2 H_a^2 + 0(\mu^2 H_a^4) \Big], \qquad (10)$$

where x_n are the roots of the equation

$$\operatorname{tg} x = x.$$

It follows from (10) that the transition to the steady state is monotonic.

2. Let $\mu \ll 1$ and let $H_a^2 \sim 0(1/\mu^2)$; then

$$p_n \simeq -\frac{\nu n \pi}{2a^2\mu^2} \Big[\frac{n\pi}{2} \pm i \sqrt{4H_a^2\mu^2 - n^2\pi^2} \Big] + 0(\mu). \qquad (11)$$

It can then be seen that in the given case the transition to the steady state is oscillatory. It is interesting to note that (11) coincides with the similar value for a nonstationary Hartmann flow. There is a difference only in the terms $0(\mu)$. When $\mu = 1$, Eq. (9) only has real roots.

---

1) We note that an error was made for $\langle v_{2x} \rangle$ in Eq. (17) in ref. 2. The true value of $\langle v_{2x} \rangle$ is determined from Eq. (7) for $U_c(\bar{Y})$.

---

[1] L. D. Landau and E. M. Lifshitz, Electrodynamics of Continuous Media, Addison-Wesley, New York (1960).

[2] Yu. Ya. Boguslavskii, A. I. Ioffe, and Yu. G. Statnikov, Prikl. Mekh. Tekh. Fiz., No. 4, 30 (1970).

[3] S. A. Regirer, Inzh.-Phys. Zh., No. 8, 43 (1959).

Propagation and stability of large amplitude ionization waves

M. S. Gorelik and L. D. Tsendin
M. I. Kalinin Leningrad Polytechnic Institute
(Submitted October 5, 1973)
Zh. Tekh. Fiz., 44, 1405-1409 (July 1974)

Nonlinear ionization waves are investigated in a weakly ionized plasma which carries a current. Stationary and nonstationary waves with parameters which vary slowly in space and time are considered for various cases with weak dissipation. The stability regions for self-modulation and the propagation velocities of amplitude and frequency perturbations are found. The influence of dissipative effects on stability is considered.

INTRODUCTION

The linear theory of ionization waves in a plasma has been developed in refs. 1-3. Nonlinear periodic ionization waves with strong temperature or density nonlinearities have been considered in ref. 4. For a number of reasons ionization waves are a convenient medium for studying the properties of large-amplitude wave motion. It is therefore interesting to consider the evolution of slow changes (in comparison with the wavelength and period) in amplitude and frequency. In this paper we use the asymptotic method of Whitham[5] to investigate nonlinear waves with slowly varying amplitude frequency and wave number. Since the medium exhibits competing dissipative mechanisms which are analogous to positive and negative friction in mechanical systems, the method can be generalized to cover nonconservative systems. The boundaries of the instability regions against self-modulation are defined as functions of the amplitude and wave velocity. The propagation of small amplitude and velocity perturbations is analyzed for the case of a stable wave. In contrast to small amplitude waves, for which such perturbations propagate with the group velocity, nonlinear wave perturbations have two velocities[5] and the difference between them increases with amplitude.

BASIC EQUATIONS

We write the basic equations in the form[4] ($n_e = n_p = n$)

$$\left.\begin{aligned}&\frac{\partial n}{\partial x}+\frac{\partial}{\partial x}nv_p=Z(n,\ T_e)n-\frac{n}{\tau_0},\\&v_p=b_pE,\\&v_e=-b_e(T_e)\left(E+\frac{T_e}{en}\frac{\partial n}{\partial x}+\frac{\gamma}{e}\frac{\partial T_e}{\partial x}\right),\\&\frac{\partial}{\partial x}n(v_e-v_p)=0,\\&\left(\frac{3}{2}+\gamma\right)nv_e\frac{\partial T_e}{\partial x}-\frac{\partial}{\partial x}\frac{anb_e}{e}\frac{\partial T_e}{\partial x}+enEv_e+nH(T_e)=0.\end{aligned}\right\}\qquad(1)$$

Here, H is the energy interchange between electrons and neutrals, Z is the number of ionization events per electron per unit time, b_e and b_p are the electron and ion mobilities, v_e and v_p are the drift velocities, $\gamma \sim 1$ is the thermal diffusion, a is the dimensionless electron thermal conductivity and τ_0 is the lifetime of the plasma particles. The conditions for which (1) is valid are discussed in ref. 4. For the ionization rate we take the model expression

$$Z=\frac{1}{\tau_0}[1+\zeta(n)]\exp\frac{\varepsilon_1(T-T_0)}{TT_0};\quad \zeta(n)\ll 1;\quad \frac{\varepsilon_1}{T}\gg 1,$$

where ε_1 is the ionization energy and T_0 is the unperturbed electron temperature. The system (1) has homogeneous stationary solutions n_0, E_0, T_0. If we assume that all quantities vary as $(x-Vt) \sim (\eta-b\theta) = \eta'$ and introduce the notation

$$\eta=\frac{eE_0\varepsilon_1}{aT_0^2}x,\quad \theta=\frac{t}{\tau_0},\quad b=\frac{eE\varepsilon_1\tau_0}{aT_0^2}V,$$

$$q=\ln\frac{n}{n_0},\quad \tau=1-\exp\frac{\varepsilon_1(T-T_0)}{T_0^2},$$

we obtain a system equivalent to the equations for an anharmonic oscillator

$$-\frac{\partial q}{\partial\theta}=b\frac{dq}{d\eta'}=\tau+F_1,\quad \frac{e^q}{1-\tau}\frac{d\tau}{d\eta'}+q=Q+F_2\qquad(2)$$

together with the additional condition

$$\oint(e^q-e^{-q})\frac{dq}{q'}=0,\qquad(3)$$

F_1 and F_2 are small terms corresponding to the damping and buildup of the oscillations. When F_1, $F_2 = 0$, the system (2) has the energy integral

$$-\tau-\ln(1-\tau)+be^{-Q}+be^{-q}(Q-q-1)=T(\tau)+U(q)=A;\qquad(4)$$

Q is the dimensionless electron heat flux along the x axis. Condition (3) follows from the balance between ohmic heating and thermal losses in collisions with neutrals. It defines the connection between the amplitude of the oscillations and Q. A property of the equivalent mechanical problem is therefore that the shape of the "potential well" depends, through Q(A, b), on the amplitude of the oscillations; this leads, in particular, to the absence of soliton type solutions in the system. The shape of a progressive periodic wave in the limiting cases $A \ll 1$ ($A/b \ll 1$ is a small nonlinearity; $A \gg 1$, $A/b \ll 1$ is temperature nonlinearity and $A \ll 1$, $A/b \gg 1$ is density nonlinearity) has been analyzed in ref. 4. The system (2) without F_1 and F_2 describes stationary progressive waves. We now obtain equations which will enable us to describe nonstationary effects in a locally progressive wave caused by dispersion and dissipation. In the general case it follows from (1) that

$$\left.\begin{aligned}&-\frac{\partial q}{\partial\theta}=\tau+F_1,\\&\frac{e^q}{1-\tau}\frac{\partial\tau}{\partial\eta}+q=Q+F_2.\end{aligned}\right\}\qquad(2a)$$

Here, $\theta = t/\tau_0$. Multiplying the second equation of (2a) by

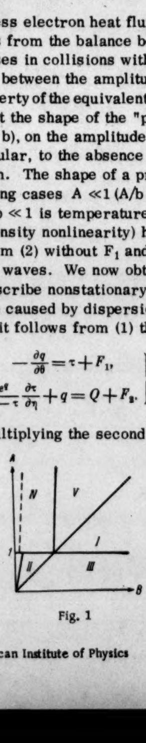

Fig. 1

dq/dθ, using the first equation of the system and averaging over a wavelength, we get

$$\frac{\partial}{\partial\eta}\langle T\rangle-\frac{\partial}{\partial\theta}\frac{\langle U\rangle}{b}=\langle R\rangle. \tag{5}$$

The kinetic and potential energies T and U are defined in (4) and an explicit expression for the dissipative term R is given in ref. 4. Averaging means, for example,

$$\langle T\rangle=\frac{1}{\lambda}\oint\frac{T\,dq}{dq/d\eta'}, \tag{6}$$

where the integrals are calculated using the unperturbed solution of (2). The function R is linear in the dissipative coefficients so that the given approximation corresponds to the inclusion of the first two terms of the iterative series in these coefficients.[6] Equation (5) together with the condition for wave conservation

$$\frac{\partial\omega(A,\,b)}{\partial\eta}+\frac{\partial k(A,\,b)}{\partial\theta}=0 \tag{7}$$

defines the A(η, θ) b(η, θ) relationship. We first take the dissipation to be small and put ⟨R⟩ = 0.

TEMPERATURE NONLINEARITY

In this case (region I in Fig. 1) it follows from (4) that the τ oscillations in a periodic wave are large, while $|q| \ll 1$. In (3) we can limit ourselves to terms which are linear in q and we then get $\oint 2q(dq/q') = \lambda\langle q\rangle = 0$. For small oscillations $Q \sim \langle q\rangle$; in this case Q = 0 and $U(q) = bq^2/2$. The energy integral (4) has the form

$$-\tau-\ln(1-\tau)+\frac{bq^2}{2}=A. \tag{4a}$$

For any values of A the quantity $\tau < 1$. It follows from (4a) that the main contribution to the integral (6), which defines the wavelength, comes from the motion of a "particle" from left to right (with $\tau > 0$); then $1-\tau \ll 1$, $q' \sim 1/b \ll 1$. This condition breaks down in a narrow region $[\Delta q = (2Ab)^{-1/2} \ll 1]$ near the right turning point, which gives a small contribution to (6). We can therefore put q' = 1/b. The contribution from the small neighborhood of the point $q_0 = \sqrt{2A/b}$, where τ is much less than unity, to the value of ⟨V⟩ is also small, so that

$$\lambda\approx\int_{-q_0}^{q_0} b\,dq=2\sqrt{2Ab},$$

$$\langle U\rangle\simeq\frac{1}{\lambda}b\int_{-q_0}^{q_0}\frac{bq^2}{2}dq=\frac{A}{3}, \tag{8}$$

Thus ⟨T⟩ = A − ⟨U⟩ = 2A/3.

Linearizing (5) and (7) over small perturbations A and b, we can get expressions for the velocities of the wave envelopes:[7]

$$W_{1,2}=-\frac{b}{2}\pm i\,\frac{b\sqrt{3}}{2}. \tag{9}$$

Thus a stationary wave in this case is unstable against buildups in the small envelope wave, i.e., against self-modulation.

DENSITY NONLINEARITY

When $b \ll A \ll 1$, the q oscillations are large while $|\tau| \ll 1$. Condition (4) takes the form

$$\frac{b(q')^2}{2}+be^{-Q}+be^{-q}(Q-q-1)=A. \tag{4b}$$

It is easy to show that $\langle T\rangle \ll A$ so that ⟨U⟩ = A. The wavelength $\lambda \approx b^{1/3}A^{1/6}$.

Averaging, we get

$$\langle T\rangle=\alpha A\left(\frac{b}{A}\right)^{2/3}, \tag{10}$$

where $\alpha \cong 8\sqrt{e}(\sqrt{\pi}/4-1/6\sqrt{2})$. The velocities of the envelope waves are

$$W_{1,2}=-\frac{b}{2}\pm b\sqrt{\frac{1}{4}-\frac{2\alpha}{3}\left(\frac{b}{A}\right)^{2/3}}. \tag{11}$$

The wave is unstable when $A/b < (8\alpha/3)^{3/2}$ (region II in Fig. 1). This is fully compatible with the original inequality $A/b \gg 1$ (it should be noted that density nonlinearity becomes significant as early as $A/b \leqslant 1$).

NONLINEARITY IN BOTH VARIABLES

The oscillations in both electron temperature and plasma density are large. When $b \ll 1$ (region IV) we find from (3) that

$$\frac{\sqrt{b}\,e^{3/2\,q_2}}{\sqrt{q_2+|Q|}}=be^{|Q|}. \tag{12}$$

Here, q_2 is the right turning point. Thus $q_2 = |Q|/3$ as in the case of density nonlinearity.[4] Therefore $be^{|Q|} - A \ll 1$ and the main contribution to (6) comes from the region near q_2. In this region $\tau \ll 1$ and $T(\tau) = \tau^2/2$:

$$\lambda\sim\int_{Q}^{q_2}\frac{b\,dq}{\sqrt{2[A-be^{|Q|}-be^{-q}(Q-q-1)]}}\sim b^{1/3}A^{1/6}. \tag{13}$$

In order to calculate ⟨T⟩ we recall that the basic "time" of a particle moves to the right ($|\tau_{\max}/\tau_{\min}| \sim A^{-1}$). In the region where T is nonzero, $\tau \cong 1$. Thus

$$\langle T\rangle\approx\frac{b}{\lambda}\int_{Q}^{q_2}[A-be^{|Q|}-be^{-q}(Q-q-1)]\,dq=2b^{2/3}A^{5/6}\ll A. \tag{14}$$

The phase velocities of the envelopes waves are

$$W_{1,2}=-\frac{b}{2}-\frac{b^{2/3}}{3A^{1/6}}\pm b\sqrt{\frac{1}{4}+\frac{b^{4/3}}{9A^{1/3}}\frac{7b^{2/3}}{3A^{1/6}}}. \tag{15}$$

These correspond to instability when $21b^{2/3}A^{-1/6} > 1$.

In region V with $A/b^2 < 1$, it can be shown by using $A/b \gg 1$, $b \gg 1$ that the section where $|\tau| \ll 1$ and $T = \tau^2/2$ is close to q_2, i.e., the principal time of the equivalent oscillator moves to the right with a "velocity" $\tau \cong 1$, and only in a narrow neighborhood ($\sim A/b^2$) of the point q_2 does this velocity fall to zero. Proceeding as before, we get

$$q_2\approx|Q|=\ln\frac{A}{b}; \tag{16}$$

$$\lambda=2b\ln\frac{A}{b}; \tag{17}$$

$$\langle T\rangle=\frac{A}{\ln\frac{A}{b}}\ll A;\quad\langle U\rangle=A. \tag{18}$$

In this region the wave is stable

$$\left.\begin{aligned} W_1 &= -\left(\ln\frac{A}{b}-1\right)^{-1}, \\ W_2 &= -b\left(\ln\frac{A}{b}-1\right)^{-1}. \end{aligned}\right\} \qquad (19)$$

The connection between A and b in progressive envelope waves (the Riemann invariants) is of the form

$$\left.\begin{aligned} dI_1 &= dA\left(\frac{1}{z}-\frac{1}{Az^2}-\frac{1}{z-1}\right)+\frac{db}{bz^2}=0, \\ dI_2 &= dA\left(\frac{1}{z}-\frac{1}{Az^2}-\frac{b}{z-1}\right)+\frac{db}{bz^2}=0, \end{aligned}\right\} \qquad (20)$$

where z = ln(A/b).

Expressions (19) represent the nonlinear generalization of the group velocity.

THE EFFECT OF DISSIPATION

So far we have neglected dissipative effects. When we include these we find that the wave amplitude increases for $\langle R \rangle > 0$ and decreases for $\langle R \rangle < 0$. It is therefore of interest to consider the stability of a stationary wave for which the nonlinear dissipation reduces to zero (like the limit cycle in the theory of nonlinear oscillations[8]). For small perturbations of this wave

$$\langle R \rangle = (\alpha A' + \beta b')\, e^{i(\varkappa\eta-\Omega\theta)}.$$

For temperature nonlinearity, in place of (9) we have

$$\frac{W}{b}=\frac{1}{2}\left[-1-\frac{i\alpha}{2\varkappa}+\frac{i\beta}{2\varkappa A}\pm\sqrt{-3-\frac{\alpha^2}{4\varkappa^2}-\frac{\beta^2}{4\varkappa^2A^2}-2\frac{i\beta b}{A\varkappa}}\right], \qquad (9a)$$

while for the density mechanism

$$\frac{W}{b}=-\frac{1}{2}+\frac{i\beta b}{6A\varkappa}-\frac{i\alpha}{3\varkappa}$$
$$\pm\frac{1}{6}\sqrt{9-24\left(\frac{b}{A}\right)^{1/3}-\frac{i\beta b73}{6A\varkappa}-\frac{i143\alpha}{3\varkappa}-\frac{\beta^2b^2}{36A^2\varkappa}-\frac{\alpha^2}{9\varkappa^2}+\frac{\beta\alpha b}{9A\varkappa^2}}. \qquad (11a)$$

When dissipation is taken into account the wave can be unstable in a case where it would be stable without dissipation or with the inclusion of only one dissipative effect.

---

[1] A. V. Nedospasov, Usp. Fiz. Nauk, 94, 439 (1968) [Sov. Phys. – Usp., 11, 174 (1968)].

[2] K. Wojaczeck, Beitr. Plasmaphys., 6, 319 (1966).

[3] L. D. Tsendin, Zh. Tekh. Fiz., 39, 1341 (1969) [Sov. Phys. – Tech. Phys., 14, 1013 (1970)].

[4] M. S. Gorelik and L. D. Tsendin, Zh. Tekh. Fiz., 43, 760 (1973) [Sov. Phys. – Tech. Phys., 18, 478 (1973)].

[5] G. B. Whitham, Proc. R. Soc. A, 283, 238 (1965).

[6] L. A. Ostrovskii and E. N. Pelinovskii, Prikl. Matem. Mekhan., 36, 71 (1972).

[7] V. I. Karpman, Nonlinear Waves in Dispersive Media [in Russian], Novosibirsk State University (1968).

[8] A. A. Andronov, A. A. Vitt, and S. É. Khaikin, The Theory of Oscillations [in Russian], State Publishing House for Physics and Mathematics, Moscow (1959).

Surface waves in periodic plasma systems

V. F. Dryakhlushin and Yu. A. Romanov

Gor'kovskii Physicotechnical Research Institute

(Submitted July 13, 1973)
Zh. Tekh. Fiz., 44, 1410-1417 (July 1974)

Surface waves in periodic plasma systems with finite periodicity are investigated. The spectrum is similar to the Tamm electronic levels in bounded crystals.

Plasma waves in unbounded periodic systems are considered in refs. 1 and 2. In the present paper we consider the spectrum of plasma waves in a stratified periodic structure of finite thickness. Particular attention is given to surface waves; like Tamm electronic levels, these appear in systems with a terminated periodicity in the bands which are forbidden for volume waves.

GENERAL RELATIONSHIPS

We consider a periodic structure of finite thickness L which consists of 2N alternating layers 1 and 2. We denote the thicknesses of the layers by d_1 and d_2 so that the structure period $d = d_1 + d_2$. The edge layers (zeroth and 2N + 1-th) are taken to be infinitely thick. We choose a Cartesian coordinate system such that the xy plane is parallel to the layer boundaries and the z axis is perpendicular. The x axis coincides with the direction of the wave vector k_1 of a wave propagating in the multilayer waveguide. The coordinates of the lower and upper boundaries of the ν-th layer are denoted by a_ν and $a_{\nu+1}$. We take the coordinate and time variation of the field in the form $f(z)\exp[i(k_1x-\omega t)]$.

We limit the analysis to an E wave with nonzero components E_x, E_z and H_y. We assume for simplicity that the layer boundaries cannot be penetrated by electrons. The electromagnetic fields inside each layer are then uniquely defined (when the interaction mechanism between the particles and the boundary is given) by the boundary values of the tangential magnetic field components. We can therefore write

$$\left.\begin{aligned} E_x^\nu(z) &= \sigma_\nu^-(z)\,H_y^\nu(a_\nu) - \sigma_\nu^+(z)\,H_y^\nu(a_{\nu+1}),\\ E_z^\nu(z) &= \bar{\sigma}_\nu^-(z)\,H_y^\nu(a_\nu) - \bar{\sigma}_\nu^+(z)\,H_y^\nu(a_{\nu+1}). \end{aligned}\right\} \tag{1}$$

We assume that there are no surface currents in the boundaries; therefore, the tangential components of the E and H fields are continuous. These conditions lead to the following system of homogeneous equations:

$$T_1(\nu)\begin{pmatrix} H_y^\nu(a_\nu) \\ H_y^\nu(a_{\nu+1}) \end{pmatrix} = T_2(\nu-1)\begin{pmatrix} H_y^{\nu-1}(a_{\nu-1}) \\ H_y^{\nu-1}(a_\nu) \end{pmatrix}, \tag{2}$$

where

$$T_1(\nu) = \begin{pmatrix} \sigma_\nu^-(a_\nu), & -\sigma_\nu^+(a_\nu) \\ 1, & 0 \end{pmatrix}, \quad T_2(\nu) = \begin{pmatrix} \sigma_\nu^-(a_{\nu+1}), & -\sigma_\nu^+(a_{\nu+1}) \\ 0, & 1 \end{pmatrix}. \tag{3}$$

By means of (2) we can express $H_y^m(a_{m,m+1})$ in terms of the values of the magnetic field on the boundaries of the l-th layer

$$\begin{pmatrix} H_y^m(a_m) \\ H_y^m(a_{m+1}) \end{pmatrix} = \prod_{\nu=l}^{m-1} T_1^{-1}(\nu+1)\,T_2(\nu)\begin{pmatrix} H_y^l(a_l) \\ H_y^l(a_{l+1}) \end{pmatrix}. \tag{4}$$

Putting $m = 2N + 1$, $l = 0$ in (4) and remembering that $H_y^0(a_0) = H_y^{2N+1}(a_{2N+2}) = 0$, we obtain the dispersion equation for electromagnetic waves propagating in the plane multilayer waveguide:

$$\mathrm{Tr}(L\bar{M}^{(N)}(1)) = 0, \tag{5}$$

where

$$L = \begin{pmatrix} \sigma_0^+(a_1), & -\sigma_0^+(a_1)\,\sigma_{2N+1}^-(a_{2N+1}) \\ -1, & \sigma_{2N+1}^-(a_{2N+1}) \end{pmatrix}, \tag{6}$$

$$\bar{M}(m) = T_2(m+1)\,T_1^{-1}(m+1)\,T_2(m)\,T_1^{-1}(m). \tag{7}$$

The matrix $\bar{M}$ is related to the M derived in ref. 1 by the equation

$$\bar{M}(m) = T_1(m)\,M(m)\,T_1^{-1}(m). \tag{8}$$

It is easy to see that

$$\det\bar{M} = \det M, \quad \mathrm{Tr}\,\bar{M} = \mathrm{Tr}\,M. \tag{9}$$

For convenience in the following calculations we reduce $\bar{M}$ to diagonal form by means of the transformation (which in general, is not unitary)

$$A\bar{M}A^{-1} = \sqrt{\det\bar{M}}\begin{pmatrix} \lambda, & 0 \\ 0, & \lambda^{-1} \end{pmatrix}, \tag{10}$$

where

$$\lambda = \frac{1}{2\sqrt{\det\bar{M}}}\left[\mathrm{Tr}\,\bar{M} - \sqrt{(\mathrm{Tr}\,\bar{M})^2 - 4\det\bar{M}}\right]. \tag{11}$$

We can choose either branch for the square root. The above transformation does not affect the values of Tr $\bar{M}$ and det $\bar{M}$.

Putting $\bar{M}$ in the form

$$\bar{M} = \begin{pmatrix} \bar{a}, & \bar{b} \\ \bar{c}, & \bar{d} \end{pmatrix}, \tag{12}$$

from (10) we have

$$\left.\begin{gathered} A = \begin{pmatrix} \alpha, & 1 \\ 1, & \delta \end{pmatrix}, \\ \alpha = \frac{\lambda\sqrt{\det\bar{M}} - \bar{d}}{\bar{b}}, \quad \delta = \frac{\bar{b}}{\lambda^{-1}\sqrt{\det\bar{M}} - \bar{d}}. \end{gathered}\right\} \tag{13}$$

The Floquet theorem is valid for a periodic medium. Thus for the particular solutions of the Maxwell equations we can choose functions corresponding to

$$\begin{pmatrix} H_y^m(a_m) \\ H_y^m(a_{m+1}) \end{pmatrix} = M(m)\begin{pmatrix} H_y^{m-2}(a_{m-2}) \\ H_y^{m-2}(a_{m-1}) \end{pmatrix} = e^{iqd}\begin{pmatrix} H_y^{m-2}(a_{m-2}) \\ H_y^{m-2}(a_{m-1}) \end{pmatrix}, \tag{14}$$

where q is the wave vector of the Bloch wave. From (14) we get the dispersion relationship

$$\det(M - e^{iqd}) = 0. \tag{15}$$

A comparison of (15) with (11) shows that we can put

$$\lambda = \frac{1}{\sqrt{\det\bar{M}}}e^{iqd}, \tag{16}$$

and the meaning of the quantity λ thus becomes clear.

Using the transformation (10), we can write the dispersion equation (5) in the form

$$\mathrm{Sp}\left[ALA^{-1}\begin{pmatrix}\lambda^{N}, & 0\\ 0, & \lambda^{-N}\end{pmatrix}\right]=0 \tag{17}$$

or

$$[a\sigma_0^+(a_1)-1][\delta+\sigma_{2N+1}^-(a_{2N+1})]\lambda^N + [\delta-\sigma_0^+(a_1)][1+a\sigma_{2N+1}^-(a_{2N+1})]\lambda^{-N}=0. \tag{18}$$

We consider a structure with a large number of periods. Putting N → ∞ in (18) and taking $|\lambda|<1$, we get two dispersion equations which describe the propagation of surface waves along the boundary of a semiinfinite periodic system with edge layers of type "1" or "2":

$$\delta-\sigma_0^+(a_1)=0, \tag{19}$$

$$1+a\sigma_{2N+1}^-(a_{2N+1})=0. \tag{20}$$

Substituting (19) into (3), (8), (11), and (13) we get

$$\sigma_1^-(a_2)[\sigma_2^+(a_3)+\sigma_1^-(a_1)]-\frac{\sigma_0^+(a_1)+\sigma_1^-(a_1)}{\sigma_1^+(a_1)}\{[\sigma_2^+(a_3)-\sigma_0^+(a_1)] \times[\sigma_1^+(a_2)+\sigma_2^-(a_2)]-\sigma_2^-(a_3)\sigma_2^+(a_2)+\sigma_1^-(a_2)\sigma_1^+(a_1)\}=0. \tag{19'}$$

After solving (19') we have to verify that $|\lambda|<1$ by using the relationship

$$\lambda=\frac{\sqrt{\det M}}{\frac{\delta}{\sigma_0^+(a_1)}+d}, \tag{21}$$

which follows from (13) and (19).

The supposition that $|\lambda|>1$ leads to a valid system of equations. The parameter region where $|\lambda|=1$ is singular and this means in fact that the surface wave disappears; it becomes a volume wave.

In order to study the dispersion equations we need explicit expressions for $\sigma^\pm$. For homogeneous layers in the kinetic approximation with the plasma particles undergoing mirror reflection from the boundaries these quantities have the form[1]

$$\sigma^-(z)=\sigma^+(d_\nu-z)=\frac{ic}{\omega d_\nu}\sum\left[\frac{k_1^2}{k^2\varepsilon^l}+\frac{k_3^2}{k^2\left(\varepsilon^{t_\nu}-\frac{c^2k^2}{\omega^2}\right)}\right]\exp(ik_3z), \tag{22}$$

where $k^2 = k_1^2 + k_3^2$, $k_3 = n\pi/d_\nu$, $n = 0, \pm1, \pm2, \ldots$, ε^l and ε^{t_2} are the longitudinal and transverse permittivities of the material forming the ν-th layer. The origin for z is chosen to be at the left-hand boundary of the ν-th layer.

We now investigate the dispersion equations (18)-(20); we first use the approximations of elementary theory and then take thermal effects into account for a particular case.

ELEMENTARY THEORY

In (22) we write

$$\varepsilon_{1,2}^l=\varepsilon_{1,2}^{tr}=\varepsilon_{1,2}(\omega)=\varepsilon_{01,2}\left(1-\frac{\omega_{01,2}^2}{\omega(\omega+i\nu_{1,2})}\right), \tag{23}$$

whence

$$\sigma^+(z)=\frac{ic}{\varepsilon\omega}\varkappa\frac{\mathrm{ch}(\varkappa z)}{\mathrm{sh}(\varkappa d)}, \tag{24}$$

where

$$\varkappa=\sqrt{k_1^2-\varepsilon\frac{\omega^2}{c^2}}. \tag{25}$$

Before going on to surface waves we give some results for waves in an unbounded periodic system. The appropriate dispersion solution, which follows from (15) and (24), has the form

$$\cos(qd)=\frac{1}{2}\left(\frac{\varkappa_1\varepsilon_2}{\varkappa_2\varepsilon_1}+\frac{\varkappa_2\varepsilon_1}{\varkappa_1\varepsilon_2}\right)\mathrm{sh}(\varkappa_1d_1)\,\mathrm{sh}(\varkappa_2d_2)+\mathrm{ch}(\varkappa_1d_1)\,\mathrm{ch}(\varkappa_2d_2). \tag{26}$$

This equation is studied, in the quasistatic approximation, in ref. 1. For long waves, more precisely

$$\varkappa_{1,2}d_{1,2}\ll 1,\quad qd\ll 1, \tag{27}$$

Equation (25) simplifies in accordance with the equivalence of a periodic system in a quasihomogeneous anisotropic medium[3-5] and takes the form

$$q^2\varepsilon_\parallel+k_1^2\varepsilon_\perp=\frac{\omega^2}{c^2}\varepsilon_\parallel\varepsilon_\perp, \tag{28}$$

where

$$\varepsilon_\perp=\frac{1}{d}\int\varepsilon(z)\,dz,\quad \varepsilon_\parallel=\frac{1}{d}\int\frac{dz}{\varepsilon(z)}. \tag{29}$$

In the general case, Eq. (26) describes an infinite set of E-wave frequency zones in a periodic system. A qualitative picture of the first three zones is given in Fig. 1. The corresponding isofrequency surfaces are shown in Fig. 2. The difference between Figs. 1 and 2 and the results in ref. 1 is due to the fact that we have here allowed for electrodynamic retardation.

As with Tamm electronic levels, surface electromagnetic waves can appear in the forbidden bands of a semibounded periodic system. The appropriate dispersion equation in the elementary theory follows from (19') and (24)

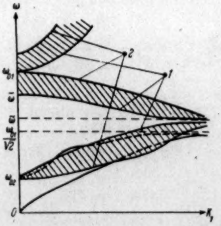

Fig. 1. Relative positions of the volume wave (shaded regions) and surface wave (continuous lines) regions. The dashed curves are the solutions of $\bar{\omega}^2 = (\omega_{01}^2+\omega_{02}^2)/2$, $\bar{\bar{\omega}}^2 = (d_1\omega_{01}^2+d_2\omega_{02}^2)/d$; q: 1) 0; 2) π/d.

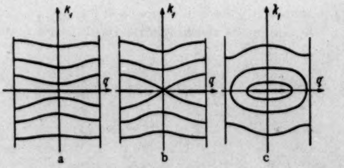

Fig. 2. Isofrequency surfaces of the first three zones of volume plasmons.

and has the form

$$\left(\frac{\varkappa_0}{\varepsilon_0}\right)^2\left[\frac{\varkappa_2}{\varepsilon_2}\operatorname{sh}(\varkappa_1 d_1)\operatorname{ch}(\varkappa_2 d_2)+\frac{\varkappa_1}{\varepsilon_1}\operatorname{ch}(\varkappa_1 d_1)\operatorname{sh}(\varkappa_2 d_2)\right]$$
$$+\frac{\varkappa_0}{\varepsilon_0}\left[\left(\frac{\varkappa_1}{\varepsilon_1}\right)^2-\left(\frac{\varkappa_2}{\varepsilon_2}\right)^2\right]\operatorname{sh}(\varkappa_1 d_1)\operatorname{sh}(\varkappa_2 d_2)$$
$$-\frac{\varkappa_1\varkappa_2}{\varepsilon_1\varepsilon_2}\left[\frac{\varkappa_1}{\varepsilon_1}\operatorname{sh}(\varkappa_1 d_1)\operatorname{ch}(\varkappa_2 d_2)+\frac{\varkappa_2}{\varepsilon_2}\operatorname{ch}(\varkappa_1 d_1)\operatorname{sh}(\varkappa_2 d_2)\right]=0, \qquad (30)$$
$$\varkappa_0=\sqrt{k_1^2-\varepsilon_0\frac{\omega^2}{c^2}}, \quad \operatorname{Re}\varkappa_0>0, \ |\lambda|<1.$$

For long waves [see (27)] it follows from (30) that

$$\frac{\varkappa_0}{\varepsilon_0}=-\frac{\varkappa}{\varepsilon_\perp}, \qquad (31)$$

where

$$\varkappa=\sqrt{k_1^2\frac{\varepsilon_\perp}{\varepsilon_\parallel}-\frac{\omega^2}{c^2}\varepsilon_\perp}, \ \operatorname{Re}\varkappa>0. \qquad (32)$$

As expected, Eq. (31) is identical in form with the dispersion equation for surface waves in a semibounded anisotropic medium.

Solving (31) for k_1 we get

$$k_1=\frac{\omega}{c}\left\{\frac{\varepsilon_0\varepsilon_1\varepsilon_2[d_1(\varepsilon_1-\varepsilon_0)+d_2(\varepsilon_2-\varepsilon_0)]}{d_1\varepsilon_2(\varepsilon_1^2-\varepsilon_0^2)+d_2\varepsilon_1(\varepsilon_2^2-\varepsilon_0^2)}\right\}^{1/2}. \qquad (33)$$

We now consider the quasistatic region, i.e.,

$$\varepsilon_{1,2}\frac{\omega^2}{c^2}\ll k_1^2. \qquad (34)$$

Equation (30) now takes the form

$$\varepsilon_2(\varepsilon_1^2-\varepsilon_0^2)\operatorname{th}(k_1d_1)+\varepsilon_1(\varepsilon_2^2-\varepsilon_0^2)\operatorname{th}(k_1d_2)$$
$$-\varepsilon_0(\varepsilon_1^2-\varepsilon_2^2)\operatorname{th}(k_1d_1)\operatorname{th}(k_1d_2)=0. \qquad (35)$$

In particular, when $d_1 = d_2$ we get the two solutions:

$$\varepsilon_1+\varepsilon_2=0, \qquad (36)$$
$$\operatorname{th}(k_1d_1)=\frac{\varepsilon_1\varepsilon_2-\varepsilon_0^2}{\varepsilon_0(\varepsilon_1-\varepsilon_2)}. \qquad (37)$$

The qualitative shape of the solutions of (30) for various relations between the parameters ω_{01}, ω_{02}, d_1, and d_2 for $\nu_{1,2} = 0$ is shown in Fig. 3.

For certain parameter values the solutions are spurious, i.e., there are windows in which the surface wave does not exist if the radiation conditions

$$\operatorname{Re}\varkappa_0>0, \qquad (38)$$
$$\operatorname{Im}q>0. \qquad (39)$$

are not satisfied.

We consider this problem for long waves in the quasistatic region. For long waves, from (21) we find

$$\lambda\simeq 1+\frac{\varkappa_0}{\varepsilon_0}(\varepsilon_1d_1+\varepsilon_2d_2). \qquad (40)$$

Since $\operatorname{Re}\varkappa_0 > 0$, from (40) we find

$$\varepsilon_1d_1+\varepsilon_2d_2<0. \qquad (41)$$

Using (23) with $\varepsilon_{01} = \varepsilon_{02}$ for $\varepsilon_{1,2}$, we find that for long waves the surface states exist only in the band

$$\omega^+<\omega<\bar{\omega}, \qquad (42)$$

where

$$\bar{\omega}^2=\frac{d_1\omega_{01}^2+d_2\omega_{02}^2}{d}, \qquad (43)$$

$$\omega^{+2}=\frac{d\omega_{01}^2\omega_{02}^2}{d_1\omega_{01}^2+d_2\omega_{02}^2}.$$

The conditions (41) only impose restrictions on the upper branch. We now consider the quasistatic region. For simplicity we put $d_1 = d_2$. Substituting (24) and (37) into (21), we get

$$e^{iqd}=\frac{(\varepsilon_1^2-\varepsilon_0^2)\varepsilon_2}{(\varepsilon_0^2-\varepsilon_2^2)\varepsilon_1}. \qquad (44)$$

Using (23) for $\varepsilon_{1,2}$ and putting $\varepsilon_{01} = \varepsilon_{02} = \varepsilon_0$, we find that the surface wave does not exist in the region

$$\left.\begin{array}{c}\dfrac{\omega_{01}^2+\omega_{02}^2-\sqrt{\omega_{01}^4+\omega_{02}^4-6\omega_{01}^2\omega_{02}^2}}{4}\leqslant\omega^2\\ \leqslant\dfrac{\omega_{01}^2+\omega_{02}^2+\sqrt{\omega_{01}^4+\omega_{02}^4-6\omega_{01}^2\omega_{02}^2}}{4},\\ \omega_{01}>\omega_{02}.\end{array}\right\} \qquad (45)$$

Condition (45) leads to the appearance of windows in the lower dispersion curve for $\omega_{01} \geq (1 + \sqrt{2})\omega_{02}$. For the entire upper curve, $\operatorname{Im} q = 0$.

The case where d_1 and d_2 are different can only be investigated by numerical methods. Surface waves do not exist for particular values of the parameters in the dispersion curves. In all cases where windows are formed the surface wave dispersion curves break away from the boundaries of the volume wave zones. Figure 1 shows one possible picture for the surface and volume waves.

What we have said above refers to a semiinfinite system. The transition to a periodic structure with finite thickness leads to a discrete spectrum for the volume waves and to some change in the surface states. In thin layers [see (27)], for example, the E-wave spectrum is described by the dispersion equation

$$\frac{\varkappa_0}{\varepsilon_0}=-\frac{1\pm e^{-\varkappa L}}{1\mp e^{-\varkappa L}}\frac{\varkappa}{\varepsilon_\perp}, \qquad (46)$$

where the upper sign refers to symmetric waves (tangential plasmons) and the lower sign to asymmetric waves (normal plasmons).

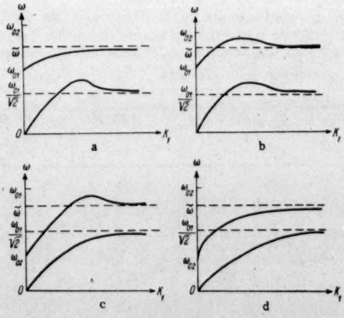

Fig. 3. Dispersion curves of surface waves for various relations between the structure parameters. a) $\omega_{01} < \omega_{02}$, $d_1 < d_2$; b) $\omega_{01} < \omega_{02}$, $d_1 > d_2$; c) $\omega_{01} > \omega_{02}$, $d_1 < d_2$; d) $\omega_{01} > \omega_{02}$, $d_1 > d_2$.

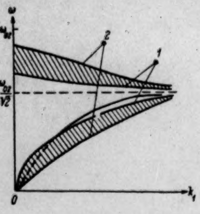

Fig. 4. Zones for volume waves (shaded regions) and surface waves (continuous curves) for structures with layers at different temperatures. q: 1) 0; 2) π/d.

In the quasistatic approximation the solutions of (46) can be written as

$$\frac{k_1 L}{2}=\frac{in\pi-\operatorname{arc\,th}\left(\varepsilon_{\parallel}\sqrt{\frac{\varepsilon_{\perp}}{\varepsilon_{\parallel}}}\right)}{\sqrt{\frac{\varepsilon_{\perp}}{\varepsilon_{\parallel}}}}\tag{47}$$

for normal plasmons and

$$\frac{k_1 L}{2}=\frac{in\pi-\operatorname{arc\,th}\left(\varepsilon_{\parallel}\sqrt{\frac{\varepsilon_{\perp}}{\varepsilon_{\parallel}}}\right)}{\sqrt{\frac{\varepsilon_{\perp}}{\varepsilon_{\parallel}}}}\tag{47'}$$

for tangential plasmons.

THERMAL EFFECTS

As a second example, we consider a semiinfinite periodic structure consisting of layers at different temperatures; in one layer we neglect the time dispersion (layer 1) and in the other the spatial dispersion (layer 2) in the dielectric permittivity. In the quasistatic approximation, using (22) we find

$$\sigma_1^{+}(z)=\frac{ic}{\varepsilon_{01}\omega}\frac{k_1^2}{\varkappa_1^l}\frac{\operatorname{ch}(\varkappa_1^l z)}{\operatorname{sh}(\varkappa_1^l d)},\tag{48}$$

where

$$\varkappa_1^l=\sqrt{k_1^2+\frac{2\omega_{01}^2}{v_{T1}^2}},$$

and $\sigma^{\pm}(z)$ is defined by (24).

From (19'), (24), and (48) we get the dispersion equation

$$\left.\begin{aligned}&\varepsilon_2\left[\left(\frac{\varepsilon_{01}\varkappa_1^l}{k_1}\right)^2-\varepsilon_0^2\right]\operatorname{th}(\varkappa_1^l d_1)+\frac{\varepsilon_{01}\varkappa_1^l}{k_1}(\varepsilon_2^2-\varepsilon_0^2)\operatorname{th}(k_1 d_2)\\&\quad-\varepsilon_0\left[\left(\frac{\varepsilon_{01}\varkappa_1^l}{k_1}\right)^2-\varepsilon_2^2\right]\operatorname{th}(\varkappa_1^l d_1)\operatorname{th}(k_1 d_2)=0,\\&\qquad|\lambda|<1.\end{aligned}\right\}\tag{49}$$

If there is no spatial dispersion in layer 1 and no time dispersion in layer 2 (i.e., a layer in which only time dispersion is significant is bounded by a vacuum), (49) is replaced by

$$\left.\begin{aligned}&\frac{\varepsilon_{02}\varkappa_2^l}{k_1}(\varepsilon_1^2-\varepsilon_0^2)\operatorname{th}(k_1 d_1)+\varepsilon_1\left[\left(\frac{\varepsilon_{02}\varkappa_2^l}{k_1}\right)^2-\varepsilon_0^2\right]\operatorname{th}(\varkappa_2^l d_2)\\&\quad-\varepsilon_0\left[\varepsilon_1^2-\left(\frac{\varepsilon_{02}\varkappa_2^l}{k_1}\right)^2\right]\operatorname{th}(k_1 d_1)\operatorname{th}(\varkappa_2^l d_2)=0,\\&\qquad|\lambda|<1,\end{aligned}\right\}\tag{50}$$

where

$$\varkappa_2^l=\sqrt{k_1^2+\frac{2\omega_{02}^2}{v_{T2}^2}}.$$

Solving (49) and (50) for ω with $\varepsilon_{01} = \varepsilon_{02} = \varepsilon_0$ we find

$$\begin{aligned}\omega(\omega+i\nu_2)=\omega_{02}^2\Biggl\{&\frac{\varkappa_1^l}{k_1}\operatorname{cth}(\varkappa_1^l d_1)+1+\frac{1}{2}\left[\left(\frac{\varkappa_1^l}{k_1}\right)^2-1\right]\operatorname{cth}(k_1 d_2)\\&-\sqrt{\frac{1}{4}\left[\left(\frac{\varkappa_1^l}{k_1}\right)^2-1\right]^2\operatorname{cth}^2(k_1 d_2)+\frac{\varkappa_1^l}{k_1}\left[\frac{\varkappa_1^l}{k_1}\operatorname{cth}(\varkappa_1^l d_1)+1\right]\left[\operatorname{cth}(\varkappa_1^l d_1)+\frac{\varkappa_1^l}{k_1}\right]}\Biggr\}\left[\left(\frac{\varkappa_1^l}{k_1}\right)^2-1\right]^{-1}[\operatorname{cth}(k_1 d_2)-1]^{-1},\end{aligned}\tag{51}$$

$$\begin{aligned}\omega(\omega+i\nu_1)=\omega_{01}^2\Biggl\{&\frac{\varkappa_2^l}{k_1}\operatorname{cth}(\varkappa_2^l d_2)-1+\frac{1}{2}\left[\left(\frac{\varkappa_2^l}{k_1}\right)^2-1\right]\operatorname{cth}(k_1 d_1)\\&-\sqrt{\frac{1}{4}\left[\left(\frac{\varkappa_2^l}{k_1}\right)^2-1\right]^2\operatorname{cth}^2(k_1 d_1)+\frac{\varkappa_2^l}{k_1}\left[\operatorname{cth}(\varkappa_2^l d_2)-\frac{\varkappa_2^l}{k_1}\right]\left[\frac{\varkappa_2^l}{k_1}\operatorname{cth}(\varkappa_2^l d_2)-1\right]}\Biggr\}\left[\left(\frac{\varkappa_2^l}{k_1}\right)^2-1\right]^{-1}[\operatorname{cth}(k_1 d_1)+1]^{-1}.\end{aligned}\tag{52}$$

The qualitative shape of the dispersion curve defined by (51) with $\nu_2 = 0$ and the corresponding zones for volume plasmons are shown in Fig. 4. The dashed line corresponds to the spurious solution.

---

[1] Yu. A. Romanov, Zh. Tekh. Fiz., 42, 1804 (1972) [Sov. Phys. – Tech. Phys., 17, 1447 (1973)].

[2] E. N. Economou, Phys. Rev., 182, 539 (1969).

[3] L. M. Brekhovskikh, Waves in Layered Media [in Russian], Academy of Sciences of the USSR, Moscow (1957).

[4] S. M. Rytov, Zh. Eksp. Teor. Fiz., 29, 605 (1955) [Sov. Phys. – JETP, 2, 466 (1956)].

[5] Ya. B. Fainberg and N. A. Khiznyak, Zh. Tekh. Fiz., 25, 711 (1955).

Solitary waves in anisotropic plasma waveguide

V. I. Kurilko and A. P. Tolstoluzhskii

Physicotechnical Institute,
Academy of Sciences of the Ukrainian SSR, Khar'kov

(Submitted August 17, 1973)
Zh. Tekh. Fiz., 44, 1418-1423 (July 1974)

An analytical and numerical study is made of the field configuration and dispersion of solitary waves of finite amplitude propagating along the axis of a cylindrical plasma waveguide with conducting walls in a strong external magnetic field. Curves are given which show the potential distribution on the waveguide axis and the phase velocity of the solitary waves as a function of amplitude. Even when the amplitudes of the fields are comparable with the maximum permissible amplitude, when effects associated with the intersection of the trajectories of the plasma electrons become significant the main contribution to the field configuration and the dispersion comes from a single radial harmonic of the field. The dependence of the characteristics of a solitary wave on the linear density of the plasma is investigated.

1. Theoretical studies on the dispersion and the field configuration of regular waves of finite amplitude propagating in bounded plasma waveguide systems are important in connection with the development of collective methods of accelerating charged particles[1,2] and methods of controlling convective instabilities that utilize the nonlinear properties of a plasma.[3,4] Special interest attaches to solitary waves, the energy of which is concentrated in a bounded region of coordinate space. One-dimensional low-frequency solitary waves in a plasma have been studied in detail (see refs. 5 and 6, for example). That solitary waves can exist in a bounded anisotropic plasma was first shown in refs. 7 and 8 for waveguides with cylindrical and planar geometries respectively. In these papers the dispersion characteristics and field configuration of nonrelativistic ($V \ll c$) solitary waves were investigated analytically assuming weak nonlinearity. However, in order to assess the practical usefulness of these waves it is necessary to know the parameters (phase velocity, half-width, and so on) in the region in which the potential reaches its maximum value. For example, the possibility of increasing the amplitude of a soliton is restricted by effects associated with the intersection of the trajectories of the plasma electrons and capture by the wave field.[9-11] It is these effects that set an upper limit on the acceleration of a soliton by an electron beam.[10,11] A weak-signal theory[7] gives a value of about 1.18 for the maximum Mach number of a nonrelativistic soliton in a waveguide with cylindrical geometry and conducting walls. This means that in a homogeneous plasma waveguide it is not possible to obtain a solitary wave with a phase velocity more than 18% above the value for an infinitesimal amplitude. The question as to what extent this estimate is true can be answered only by a theory of solitary waves of finite amplitude. Of no less interest for applications is the question of the existence and characteristics of solitary waves with phase velocities close to the velocity of light.

In the present paper we make a theoretical study of the dispersion and field configuration of solitary waves of finite amplitude propagating along the axis of an anisotropic plasma waveguide.

2. Consider a cylindrical waveguide with conducting walls of radius a filled with a homogeneous plasma of density n_p in a strong external magnetic field ($H_0^2 \gg 4\pi n_p m_0 c^2$). The self-consistent set of equations describing the propagation of regular waves in such a waveguide consists of Maxwell's equations for the fields and the equations of motion of the plasma particles in these fields. In the axially symmetric case these equations are

$$\left.\begin{aligned} &\frac{dp}{dt} = eE_\parallel; \quad \frac{\partial\rho}{\partial t} + \frac{\partial}{\partial z}(\rho v) = 0,\\ &\frac{\partial H_\perp}{\partial z} + \frac{1}{c}\frac{\partial E_\perp}{\partial t} = 0,\\ &\frac{1}{c}\frac{\partial H_\perp}{\partial t} + \frac{\partial}{\partial z}E_\perp - \frac{\partial E_\parallel}{\partial r} = 0,\\ &\frac{1}{r}\frac{\partial}{\partial r} rH_\perp - \frac{1}{c}\frac{\partial E_\parallel}{\partial t} = \frac{4\pi}{c} e\rho v. \end{aligned}\right\} \tag{1}$$

The solutions of solitary-wave type in which we are interested contain a broad spectrum of wave numbers and can exist in the frequency range in which dispersion is insignificant.[6] In the present case the phase velocity of a linear axially symmetric periodic TM wave depends on frequency as follows:

$$\left.\begin{aligned} &V_m^2(\omega) = \frac{c^2}{1 + \dfrac{\lambda_m^2 c^2}{(\omega_p^2 - \omega^2)a^2}},\\ &\omega_p^2 \equiv \frac{4\pi n_p e^2}{m_0}, \quad J_0(\lambda_m) = 0, \; m = 1, 2, 3 \ldots, \end{aligned}\right\} \tag{2}$$

from which it can be seen that there is no dispersion at frequencies $\omega \ll \omega_p$ ($\omega^2 \gg \omega_{cl}\omega_{ci}$). This means that waves in the form of a superposition of space harmonics moving with the same velocity $V \sim V_s(0)$ can propagate in the waveguide.

Axially symmetric solutions of this type can be determined by introducing the new variables: $\xi \equiv (\omega_p/V)(z - Vt)$; $\eta \equiv r/a$ in Eq. (1). In these variables Eq. (1) exhibits three first integrals

$$\rho(\eta, \xi)u(\eta, \xi) = \beta[\rho(\eta, \xi) - \rho_+], \tag{3a}$$

$$\frac{1 - \beta u}{(1 - u^2)^{1/2}} + \frac{e\varphi}{m_0 c^2} = 1, \quad \beta \equiv V/c, \tag{3b}$$

$$H_\perp(\eta, \xi) - \beta E_\perp(\eta, \xi) = 0, \quad u \equiv v/c, \tag{3c}$$

$$E_\perp \equiv -\gamma^2 \frac{1}{a}\frac{\partial\varphi}{\partial\eta}, \quad E_\parallel \equiv -\frac{\omega_p}{V}\frac{\partial\varphi}{\partial\xi}, \quad \gamma \equiv (1 - \beta^2)^{-1/2},$$

in which the constants of integration are determined from the conditions at infinity, where the potential φ and the particle velocities vanish: $\varphi(\pm\infty, \eta) = v(\pm\infty, \eta) = 0$.

Using (3) in (1) and transforming to the dimensionless potential $\Phi \equiv e\varphi/(m_0 V^2)$, we find that the problem of finding the function $\Phi(\eta, \xi)$ reduces to solving the following quasilinear equation of elliptic type:[12]

$$\left.\begin{aligned}&M_0^2\frac{1}{\eta}\frac{\partial}{\partial\eta}\eta\frac{\partial\Phi}{\partial\eta}+\frac{\partial^2\Phi}{\partial\xi^2}+R(\Phi)=0,\\&R(\Phi)\equiv\frac{w(\Phi)}{1-w(\Phi)},\\&w(\Phi)\equiv\frac{u(\Phi)}{\beta}=\frac{1-(1-\beta^2\Phi)\sqrt{1-2\Phi+\beta^2\Phi^2}}{(1-\beta^2\Phi)^2+\beta^2},\\&\Phi_{\max}=\frac{\gamma}{\gamma+1},\quad M_0^2\equiv\frac{V^2\gamma^2}{\omega_p^2a^2},\quad\omega_p^2\equiv\frac{4\pi e^2n_+}{m_0}.\end{aligned}\right\}\qquad(4)$$

We now find the solution to this equation which satisfies the condition that the potential Φ vanish at infinity and at the waveguide walls and the condition that the derivatives of the potential vanish on the axis of the waveguide, i.e.,

$$\Phi(\eta,\ \pm\infty)=\Phi'_\xi(\eta,\ \pm\infty)=\Phi'_\eta(0,\ \xi)=\Phi'_\xi(1,\ \xi)=0. \qquad (5)$$

3. In a frame of reference in which the soliton is at rest, its amplitude decreases (increases) exponentially at large distances from the maximum of potential. A similar dependence holds for time in a laboratory frame of reference. This means that the equivalent soliton frequencies are purely imaginary, so that their phase velocities at small amplitudes are given by expression (2) with the substitution $\omega^2 \to -\Omega^2(\Omega^2 > 0)$. Evidently the phase velocity of an s-type soliton is always greater than the threshold phase velocity $V_m(0)$ of a linear wave with a corresponding radial-harmonic index ($V_c > V_m(0)$). Thus, in order-of-magnitude terms the phase velocity of a solitary wave is determined by the linear density of the plasma and increases monotonically with the latter.

By inserting the constant $V_m(0)$ into Eq. (4) it can be shown that in general this equation does not contain a small parameter. An exception is the case of small amplitudes ($\Phi \ll 1$) considered by Ikezi et al.[7] In this case, for the fundamental solitary wave (with minimum variation of the potential along the radius), it is possible to find analytic expressions for the dependence of the field configuration and dispersion of the wave on its amplitude.

We shall show below that the problem of finding the field configuration and the phase velocity of solitary waves of finite amplitude can be reduced to solving a set of integrodifferential equations. These equations can be used to carry out a semianalytic study up to amplitudes comparable with the maximum possible value.

We represent the potential $\Phi(\eta, \xi)$ as a superposition of waves satisfying boundary conditions (5) on the axis and walls of the waveguide in the linear theory:

$$\Phi(\eta,\ \xi)=\sum_{s=1}^{\infty}J_0(\lambda_s\eta)Z_s(\xi). \qquad (6)$$

Inserting this expression into the initial equation (4) gives a set of coupled nonlinear differential equations[12] for the amplitudes $Z_m(\xi)$:

$$\left(\frac{d^2}{d\xi^2}-M_m^2\right)Z_m(\xi)=-\langle R[\Phi(\eta,\ \xi)]\rangle_\eta^{(m)},\quad M_m^2\equiv\lambda_m^2M_0^2, \qquad (7)$$

where the angular brackets denote an average taken over the cross section of the waveguide with the weight of the harmonic with index s:

$$\langle f(\eta,\ \xi)\rangle_\eta^{(m)}\equiv\frac{\int\limits_0^1 f(\eta,\ \xi)J_0(\lambda_m\eta)\,\eta d\eta}{\int\limits_0^1 J_0^2(\lambda_m\eta)\,\eta d\eta}. \qquad (7a)$$

4. The fundamental mode (m = 1) is the one of most interest for applications, and the rest of the paper will be concerned with it. It is necessary to discuss separately the cases of a low and high linear density of the plasma in the waveguide, which correspond to nonrelativistic and relativistic soliton phase velocities.

Nonrelativistic solitons ($\beta^2 \ll 1$). By neglecting terms of order β^2 in the right sides of (7) and estimating the ratio of the amplitudes of higher ($m \geq 2$) radial harmonics to the amplitude of the fundamental ($m = 1$), it is not hard to see that, even for amplitudes of potential comparable with the maximum permissible for this case [$\Phi_{\max} = 1/2 + 0(\beta^2)$], the contribution of higher radial harmonics is comparatively small.

Remembering that the potential is a slowly varying function of the coordinate (for reasonable amplitudes), the second derivative in the left sides of (7) can be neglected for $m \geq 2$. The problem of finding the dependence of the amplitude of the potential Z_1 on the axial coordinate thus reduces to solving the equation of motion of a particle with coordinate Z_1 in a potential field of force

$$\left(\frac{d^2}{d\xi^2}-M_1^2\right)Z_1=\left\langle\left[1-2\sum_{m=1}^{\infty}J_0(\lambda_m\eta)Z_m(\xi)\right]^{-1/2}-1\right\rangle_\eta^{(1)}, \qquad (8a)$$

$$Z_m(\xi)=\frac{1}{M_m^2}\langle 1-[1-2Z_1J_0(\lambda_1\eta)]^{-1/2}\rangle_\eta^{(m)},\quad m\geqslant 2. \qquad (8b)$$

A numerical solution of (8) shows that these relationships can be used to find the form of the potential and its phase velocity up to $\Phi \simeq 0.8\Phi_{\max}$. At the upper end of this interval the contribution to (8a) resulting from the incorporation of (8b) does not exceed 10% of the total potential. These terms can thus be neglected in the region $\Phi \leq (0.5\text{-}0.6)\Phi_{\max}$, and we obtain an explicit expression for the first integral of (8a):

$$\left(\frac{dZ_1}{d\xi}\right)^2-M_1^2Z_1^2=\frac{4Z_1}{J_1(\lambda_1)\lambda_1}+\frac{2}{N_1}\int\limits_0^1\{[1-2Z_1J_0(\lambda_1\eta)]^{1/2}-1\}\,\eta d\eta, \qquad (9)$$

$$N_1\equiv\int\limits_0^1 J_0^2(\lambda_1\eta)\,\eta d\eta=\frac{1}{2}J_1^2(\lambda_1),$$

in which the constant of integration and the relative phase velocity of the wave M_1 (the Mach number of this wave) are expressed through the amplitude A:

$$M_1^2\equiv\frac{1}{N_1A^2}\left\{1-2\int\limits_0^1\eta d\eta\left[\sqrt{1-2AJ_0(\lambda_1\eta)}-AJ_0(\lambda_1\eta)\right]\right\}. \qquad (10)$$

For $A \ll 1$, (9) and (10) give the dispersion and field configuration of the small-amplitude nonrelativistic solitary wave investigated by Ikezi et al.[7]

Equations (8)-(10) are used to calculate the potential on the waveguide axis ($\eta = 0$) as a function of the axial coordinate and the phase velocity of the wave M_1 as a function of amplitude A. The results of the calculation are shown

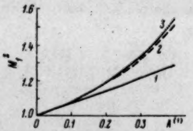

Fig. 1. Phase velocity of nonrelativistic soliton vs amplitude $A^{(1)}$ of first harmonic of potential. 1) Ikezi et al.[7] theory of weakly nonlinear soliton; 2) single-mode approximation ($Z_m = 0$, $m \geq 2$); 3) dispersion allowing for second harmonic ($m = 2$).

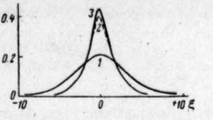

Fig. 2. Potential of nonrelativistic soliton on waveguide axis ($\eta = 0$) vs axial coordinate. $A^{(1)}$: 1) 0.2; 2) 0.4 (ignoring second harmonic); 3) 0.4 (allowing for second harmonic).

in Figs. 1 and 2. With increasing amplitude the soliton phase velocity increases more rapidly than the linear law predicted by the weakly nonlinear theory.[7] However, even for A = 0.4 this velocity of the soliton exceeds the threshold value $[V_1(0)]$ by no more than 25% ($M_1 = 1.25$). Allowing for terms (8b) gives a correction to the phase velocity which is less than 1.5%.

Physically, the relatively small contribution made by the harmonics to the field configuration and the dispersion of the fundamental wave (m = 1) comes about because the potential of this wave reaches a maximum only in a restricted (with respect to ξ and η) region near the waveguide axis. Only in this region of coordinates is the dependence of the dimensionless plasma density R on the potential Φ essentially nonlinear [see (4)]. The phase velocity of the wave and the amplitude of the harmonics of the potential [see (8)] are, however, determined by integrals over the entire cross section of the waveguide, in which the region of strong nonlinearity ($\eta < 1$) gives a relatively small contribution.

It can be seen from Fig. 1 that even for the maximum of the considered values of A the half-width of the pulse is quite large, $\Delta(A = 0.4) = 3.0$. Neglecting terms $\sim d^2/d\xi^2$ in the left sides of (8b) is thus justified. These terms begin to play a significant role when $\Phi \sim \Phi_{\max}$. However, in this region of soliton amplitudes the solution of the present problem in the hydrodynamic approximation probably has no physical significance, since one must allow for the thermal spread of the plasma particles and the damping of the solitary wave resulting from trapping of these particles.[9-11] The maximum plasma temperature for which it is permissible to neglect this damping is given by the inequality $T_{\max} \ll mV^2(1-2A_{\max})$, where $A_{\max}$ is the amplitude of the potential at the maximum.

Relativistic soliton ($\gamma^2 \gg 1$). Equation (2) implies that the phase velocity of the regular waves of an anisotropic plasma waveguide increases linearly with increasing linear density of the plasma at small values of the latter ($\omega_p^2 a^2 < \lambda_1^2 c^2$), approaching the velocity of light when $\omega_p^2 a^2 > \lambda_1^2 c^2$. It is clear that in the latter case the solitary waves can have relativistic phase velocities. There are no solitary waves, however, in a one-dimensional plasma and so one would expect that with subsequent increase of the linear density of the plasma effects would arise preventing such waves from existing. The physical nature of one such effect can be elucidated from an investigation of the initial equation for the potential (4). It can be seen from this equation that for a two-dimensional soliton, unlike the one-dimensional, the average (over the axial coordinate) value of the charge density and so also the electron current [see (3a)] is nonzero:

$$\left.\begin{aligned}\langle R(\Phi)\rangle_\xi &= -M_0^2 \frac{1}{\eta}\frac{d}{d\eta}\left(\eta \frac{d}{d\eta}\langle\Phi\rangle_\xi\right) \neq 0,\\ \langle\rho u\rangle_\xi &= \beta\rho_+ \langle R(\Phi)\rangle_\xi.\end{aligned}\right\} \tag{11}$$

Thus, increasing the linear density of the plasma leads to an increase in the current of electrons in the wave and to an increase in the transverse electric and magnetic fields of this wave:

$$E_\perp \sim \gamma^2 \frac{m_0 c^2}{|e|a}\frac{\partial\Phi}{\partial\eta} \sim 4\pi|e|n_p a, \quad H_\perp \sim E_\perp.$$

The collective properties of the plasma can be conserved only so long as the energy density of the field of the wave propagating in it does not greatly exceed the rest energy density of the plasma particles (the opposite limiting case corresponds to the motion of a rarefied plasma in external fields). This leads to the following estimate for the upper bound on the permissible values of the linear density of the plasma:

$$E_\perp^2 \simeq 4\pi n_p m_0 c^2 \frac{\omega_p^2 a^2}{c^2} \leqslant n_p m_0 c^2 \ll H_0^2. \tag{12a}$$

A second constraint follows from the requirement that the transverse velocity of the plasma particles in the wave ($\nu_\perp \sim cE_\perp/H_0$) be small compared with the axial velocity ($\nu_\parallel \sim c$):

$$4\pi|e|n_p a^2 \ll H_0 a. \tag{12b}$$

The latter inequality is the weaker, and can be satisfied by increasing the external magnetic field.

Solitary waves with amplitudes of the order of the maximum possible value thus cannot exist in plasma waveguides with large values of the plasma linear density; accordingly the phase velocities cannot be arbitrarily close to the velocity of light c.

The dispersion and field configuration of solitary waves for $\beta \sim 1$ can be calculated by the method described above by utilizing Eqs. (6) and (7a) transformed to relationships of form (8):

$$\left(\frac{d^2}{d\xi^2} - M_1^2\right) Z_1 = -\langle R(\Phi)\rangle_\eta^{(1)}, \tag{13a}$$

$$Z_s = \frac{\lambda_1^2}{\lambda_s^2 M_1^2}\langle R[Z_1 J_0(\lambda_1\eta)]\rangle_\eta^{(s)}, \quad s \geqslant 2. \tag{13b}$$

The results of such a calculation show that the characteristics of solitary waves in the region $\beta \sim 1$ (the calculations were performed up to $\gamma_{\max} = 3$) are weakly dependent on the parameter γ: The dispersion and the field configuration of the potential on the waveguide axis in the above-adopted dimensionless variables coincide to within

10% with the results of Figs. 1 and 2 (the absolute values of the potential and the square of the phase velocity of the wave increase in proportion to β^2).

5. The main results of the above analysis can be summarized as follows.

A study has been made of the dispersion and the pulse shape of a solitary wave of finite amplitude propagating along the axis of an anisotropic plasma waveguide with conducting walls. It is shown that up to amplitudes comparable with the maximum permissible value the main contribution to the field configuration of these waves and their phase velocities comes from a single radial harmonic of the field. It is also shown that, under the investigated conditions (a conducting wall), the phase velocity increases monotonically as the potential increases in amplitude. However, even at the maximum possible potential the Mach number for the first radial harmonic (m = 1) does not exceed 1.25. The growth of the amplitude of the transverse electric field with increasing linear density of the plasma keeps the phase velocity from rising to values of the order of c.

---

[1] V. I. Veksler, Proc. Symp. CERN, 1, 80 (1956); At. Energ., 2, 427 (1957).

[2] Ya. B. Fainberg, Proc. Symp. CERN, 1, 84 (1956); At. Energ., 6, 431 (1959); Usp. Fiz. Nauk, 93, 617 (1967) [Sov. Phys. – Usp., 10, 750 (1968)].

[3] Ya. B. Fainberg, At. Energ., 11, 313 (1961).

[4] Ya. B. Fainberg, Survey of Phenomena in Ionized Gases (Vienna, 1967), IAEA, Vienna (1969), p. 149.

[5] A. A. Vedenov, E. P. Velikhov, and R. Z. Sagdeev, Usp. Fiz. Nauk, 73, 701 (1961) [Sov. Phys. – Usp., 4, 332 (1961)].

[6] B. B. Kadomtsev and V. I. Karpman, Usp. Fiz. Nauk, 103, 193 (1971) [Sov. Phys. – Usp., 14, 40 (1971)].

[7] H. Ikezi, P. J. Barret, R. B. White, and A. Y. Wong, Phys. Fluids, 14, 1997 (1971).

[8] B. N. Rutkevich, V. A. Panchenko, V. D. Fedorchenko, and V. N. Muratov, Zh. Tekh. Fiz., 42, 931 (1972).

[9] R. N. Sudan and E. Ott, Phys. Fluids, 12, 2388 (1969).

[10] V. D. Shapiro and V. I. Shevchenko, ZhETF Pis. Red., 16, 487 (1972) [JETP Lett., 16, 347 (1972)].

[11] S. M. Krivoruchko, Ya. B. Fainberg, V. D. Shapiro, and V. I. Shevchenko, ZhETF Pis. Red., 17, 344 (1973) [JETP Lett., 17, 244 (1973)].

[12] V. I. Kurilko and A. P. Tolstoluzhskii, Symp. on Collective Methods of Acceleration (Dubna, 1972) [in Russian], Izd. OIYaI, Dubna (1972), p. 111.

Low pressure discharge with high-energy electrons

R. A. Demirkhanov, Yu. V. Kursanov, and L. P. Skripal'

(Submitted May 29, 1973; resubmitted October 20, 1973)
Zh. Tekh. Fiz., 44, 1424-1431 (July 1974)

The potential distribution current and ion energy are found in a plasma with a non-Maxwellian electron distribution. If the density of high-energy electrons is above a critical value, the potential and ion energy at the boundary of the plasma are of the same order as the electron energy. Depending on the form of the electron distribution, the potential is either continuous or undergoes a jump across a space-charge double layer.

The theory of low-pressure discharges initiated by Tonks and Langmuir[1] and developed by others,[2-6] makes use of an equilibrium electron velocity distribution function; the resulting solutions are determined to a large extent by the choice of the distribution. This theory is widely used to explain the physical phenomena occurring in various gaseous discharge devices, in particular the emission properties of plasma ion sources, the interpretation of the results of probe measurements, etc.

In a number of cases the electron velocity distribution may deviate strongly from equilibrium and the results of the theory[1-6] may not be directly applicable. Two examples are reflex and plasma-beam discharges in which, at low pressures, two groups of electrons with differing energies are observed.[7-9] In these cases a theory of the discharge must be based on the kinetic equation; however, the electron velocity distribution often is only known approximately (from experiments). Then, results can be obtained from the theory mentioned above,[1-6] with changes due to the non-Maxwellian electron distribution.

In the present paper, the potential distribution, ion current, and energy spectrum are found for a discharge with plane geometry and an electron velocity distribution in the form of two Maxwellian distributions, and a Maxwellian distribution and a beam. These approximations are often used to describe the electron distributions observed in experiments.[7-9]

We consider a plasma enclosed between two plane electrodes. The potential of the electrons with respect to the plasma is kept negative. As in refs. 1-6 we assume the plasma to consist of electrons, positive ions, and neutral gas at sufficiently low densities that scattering of the ions can be neglected. The ion velocity is taken to be zero when the plasma is produced. We write the Poisson equation for the dimensionless potential, $\eta = -e\varphi/T_1$, in the form of the Tonks–Langmuir equation,[1] taking the z coordinate from the plane of symmetry and taking $\eta(0) = 0$:

$$\left(\frac{T_1}{4\pi e^2}\right)\frac{d^2\eta}{dz^2}=\left(\frac{M}{2T_1}\right)^{1/2}\int\limits_0^{\eta}\frac{g(u)\,du}{\frac{du}{ds}(\eta-u)^{1/2}}-n_e(\eta). \tag{1}$$

Here, $g(u) = n_e(u)n_0(u)\langle\sigma_i\nu_e\rangle$ is the number of ions formed in 1 cm^3/sec; $n_e(u)$ is the electron density; $n_0(u)$ is the neutral gas density; $\langle\sigma_i\nu_e\rangle$ is the average of the product of the effective ionization cross section and the electron velocity; e is the charge of the electron; and T_1 is the temperature (in energy units) of one of the groups of electrons. The integration is carried out with respect to the dimensionless potential $u = -e\varphi/T_1$ from $u = 0$ to $u = \eta$, and S is the coordinate corresponding to potential u.

We limit ourselves to consideration of the region of plasma in which Eq. (1) yields the neutrality condition

$$\left(\frac{M}{2T_1}\right)^{1/2}\int\limits_0^{\eta}\frac{g(u)\,du}{\frac{du}{ds}(\eta-u)^{1/2}}=n_e(\eta). \tag{2}$$

We take the electron distribution $n_e(\eta)$ as follows: 1) two Boltzmann distributions and 2) a Boltzmann distribution and a beam.

1. TWO BOLTZMANN DISTRIBUTIONS

In this case Eq. (2) becomes

$$\left(\frac{M}{2T_1}\right)^{1/2}\int\limits_0^{\eta}\frac{g(u)\,du}{\frac{du}{ds}(\eta-u)^{1/2}}=n_{0e}\left[(1-\lambda)e^{-\eta}+\lambda e^{-\beta\eta}\right], \tag{3}$$

where $\beta = T_1/T_2$ and n_{0e} and λ are, respectively, the total electron density and the relative portion of electrons with temperature T_2 at the coordinate origin ($\eta = 0$).

Applying the Laplace transform[10] to Eq. (3), we obtain the following differential equation for the potential:

$$g(\eta)\frac{dz}{d\eta}=\left(\frac{2T_1}{M}\right)^{1/2}\frac{n_{0e}}{\pi}\left[\frac{1}{\sqrt{\eta}}-(1-\lambda)\,2e^{-\eta}D(\sqrt{\eta})-2\lambda\sqrt{\beta}\,e^{-\beta\eta}D(\sqrt{\beta\eta})\right], \tag{4}$$

where $e^{-\eta}D(\sqrt{\eta}) = e^{-\eta}\int\limits_0^{\sqrt{\eta}} e^{x^2}dx$ is a tabulated function.[11]

We first use Eq. (4) to determine the potential at the boundary at which there is a transition from plasma to a space-charge electrode sheath.

Since the electric field in the sheath is much larger than in the plasma, Tonks and Langmuir,[1] as well as the authors of refs. 2-6, define the plasma boundary by formally assuming the electric field at the boundary to be infinite. Thus, equating the right-hand side of Eq. (4) to zero, we obtain a relationship between the boundary potential η_a and the parameters of the electron distribution, λ and β, [for an arbitrary ion generation distribution $g(\eta)$]:

$$\frac{\lambda}{1-\lambda}=\frac{2\sqrt{\eta_a}e^{-\eta_a}D(\sqrt{\eta_a})-1}{1-2\sqrt{\beta\eta_a}e^{-\beta\eta_a}D(\sqrt{\beta\eta_a})}. \tag{5}$$

For a single Boltzmann distribution η_a is defined from Eq. (5) as a special case with $\lambda = 0$ (absence of electrons with temperature T_2) or with $\lambda = 1$ (absence of electrons with temperature T_1). In these cases Eq. (5) breaks up into two equations

$$\left.\begin{aligned}2\sqrt{\eta_a}e^{-\eta_a}D(\sqrt{\eta_a})&=1,\\2\sqrt{\beta\eta_a}\,e^{-\beta\eta_a}D(\sqrt{\beta\eta_a})&=1,\end{aligned}\right\} \tag{6}$$

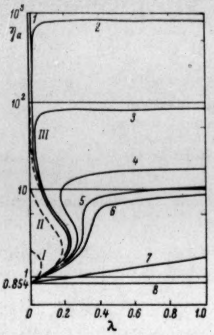

Fig. 1. Dependence of the boundary potential η_a on the parameters of the electron distribution λ, β, and γ. The solid curves refer to the case of two Maxwellian distributions. β: 1) 0; 2) 10^{-3}; 3) 10^{-2}; 4) $5\cdot10^{-2}$; 5) $8.5\cdot10^{-2}$; 6) 10^{-1}; 7) 0.5; 8) 1. Dotted curves refer to the case of a Maxwellian distribution with a beam. γ: I) 2; II) 10; III) 10^2.

to which correspond[3] the known solutions $\eta_a = 0.854$ and $\eta_a = 0.854/\beta$.

The dependence of η_a on arbitrary λ and $\beta \leq 1$ is shown in Fig. 1 (solid curves) and is characterized by the following properties.

1. For variation of λ and β within the limits $0 \leq \lambda \leq 1$ and $0 \leq \beta \leq 1$ the boundary potential η_a may assume any value within $0.854 \leq \eta_a \leq 0.854/\beta$.

2. For $\beta \leq 0.085$ there is a definite minimum $\lambda_1(\beta)$ such that for $\lambda < \lambda_1(\beta)$ the potential of the exterior boundary of the plasma is approximately established at the lower temperature T_1, and for $\lambda > \lambda_1(\beta)$ at the higher temperature T_2. $\lambda_1(\beta)$ decreases with decreasing β, being ~ 0.3 for $\beta = 0.085$ and ~ 0.035 for $\beta = 10^{-2}$. For $\beta > 0.085$ the boundary potential increases monotonically with λ.

3. For $\lambda_1 < \lambda < 0.3$ and $0 \leq \beta < 0.085$ there are three successively increasing values of η_a. The first two correspond to the boundaries of a space-charge double layer which arises in the plasma volume due to a mismatch in the ion and electron densities. The third value of η_a corresponds to the exterior boundary of the plasma adjacent to the electrode positive sheath.

4. If $\lambda > 0.3$ or $\beta > 0.085$, the interior sheath and potential jump are not formed inside the plasma. The boundary potential has a unique value in this case and corresponds to the exterior plasma boundary.

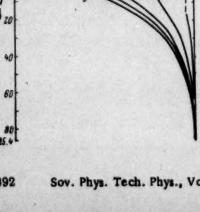

Fig. 2. Potential distributions, η. Here and in Fig. 3 the high-energy electrons have Maxwellian velocity distributions. $\beta = 10^{-2}$, $\alpha = 0$. λ: 1) 0.03; 2) 0.05; 3) 0.1; 4) 0.2; 5) 0.3; 6) 1.

In order to determine the potential distribution it is necessary to prescribe the neutral gas distribution $n_0(z)$ or $n_0(\eta)$ in Eq. (4). In this case only a numerical solution is possible. Thus, we prescribe the ion generation distribution, for example, in the form of the function $g(z) = g_0e^{\alpha z}$, which can always be accomplished by appropriate choice of the (neutral) gas distribution. In this case Eq. (4) has the integral

$$\left.\begin{aligned} &z=\frac{1}{\alpha}\ln[1+\alpha F(\eta)];\\ &F(\eta)=\left|\begin{aligned}&\frac{2I_0}{g_0}\left\{(1-\lambda)e^{-\eta}D(\sqrt{\eta})+\frac{\lambda}{\sqrt{\beta}}e^{-\beta\eta}D(\sqrt{\beta\eta})\right\} \quad \text{for} \quad \eta\leqslant\eta_1,\\ &F(\eta_1)+\frac{2I_0}{g_0}\left\{(1-\lambda)[e^{-\eta}D(\sqrt{\eta})-e^{-\eta_2}D(\sqrt{\eta_2})]\right.\\ &\left.+\frac{\lambda}{\sqrt{\beta}}[e^{-\beta\eta}D\sqrt{\beta\eta})-e^{-\beta\eta_2}D(\sqrt{\beta\eta_2})]\right\} \quad \text{for} \quad \eta_2\leqslant\eta\leqslant\eta_3,\end{aligned}\right.\end{aligned}\right\} \quad (7)$$

where $I_0 = n_{0_e}(2T/M)^{1/2}/\pi$; and η_1, η_2, η_3 are the values of the boundary potential as determined from Eq. (7) or Fig. 1. The quantity $F(\eta)$ is calculated neglecting the thickness of the inner space-charge sheath (if it exists); hence, when $\eta > \eta_2$ the z coordinate is determined using Eq. (7) to an accuracy of the order of the sheath thickness (with a reduction of the value). Calculation of the sheath thickness requires the solution of Eq. (1).

Taking this remark into account, the potential distribution between the origin (of the coordinates) and the exterior plasma boundary, whose coordinate we denote by L, can be written in the form

$$\frac{z}{L}=\frac{\ln[1+\alpha F(\eta)]}{\ln[1+\alpha F(\eta_a)]}, \quad (8)$$

where $\eta_a = \eta_3$, if there is an interior sheath, and $\eta_a = \eta_1$, if there is no interior sheath. This distribution is shown in Fig. 2 for $\alpha = 0$ (uniform ion generation), $\beta = 10^{-2}$, and several values of λ. From the figure it is clear that for sufficiently high densities of hot (T_2) electrons the potential distribution is monotonic with a boundary potential of the order of the temperature T_2. With a reduction in λ a discontinuity in the potential (a space-charge double layer), which divides the plasma into two parts, arises within the plasma volume: an anode part with low potential (on the order of T_1) and a cathode part with a high boundary potential (on the order of T_2). Depending on the reduction in λ the interior sheath is shifted in the direction of the exterior boundary of the plasma. For very small λ (e.g., $\lambda = 0.03$) the interior sheath and the cathode plasma do not develop. For $\beta > 0.085$ the potential distribution is monotonic for any λ.

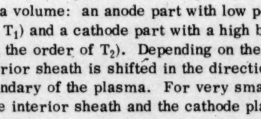

Fig. 3. Density distribution. λ: 1) 0.05; 2) 0.1; 3) 0.2; 4) 0.3; 5) 0.4; 6) 0.5; 7) 0.6; 8) 0.8; 9) 1.

In Fig. 3 the spatial electron density distribution is shown as calculated using Eq. (8) and the known function $n_e(\eta)$ for the case $\alpha = 0$. For $\alpha > 0$ (ion generation increases with z) the curves for the potential and density distributions will lie above the curves for $\alpha = 0$; while for $\alpha < 0$ (generation decreases with z) they will lie below these curves.

We now find the local ion current density

$$I(\eta) = \int_0^{\sqrt{\frac{2T_1}{M}\eta}} v_i f_i(v_i)\, dv_i.$$

Here, $f_i(v_i)$ is the ion velocity distribution and $v_i = (2T_1/M)^{1/2} \cdot (\eta - u)^{1/2}$ is the velocity of ions with energies $W = T_1(\eta - u)$ (in the z direction). Assuming that $f_i(v_i)dv_i$ corresponds to the expression under the integral of Eq. (1), we obtain

$$I(\eta) = \int_0^{\eta} g(u) \frac{dz}{du}\, du = g_0 F(\eta), \tag{9}$$

where $F(\eta)$ is defined in Eq. (7). Thus the ion current density at any point is independent of the ion generation distribution and is completely determined by the electron density distribution. In the case of a single Boltzmann distribution ($\lambda = 0$) the ion current density at the plasma boundary ($\eta = \eta_1$) is obtained from Eqs. (9) and (7),[3]

$$I(\eta_1) = \frac{2n_{0e}}{\pi}\left(\frac{2T}{M}\right)^{1/2} e^{-\eta_1} D(\sqrt{\eta_1}) = 0.344 n_{0e} \left(\frac{2T}{M}\right)^{1/2}. \tag{10}$$

As λ increases the ion current at the exterior boundary increases monotonically from the minimum given in Eq. (10) for $\lambda = 0$ to a maximum value of

$$I(\eta_3) = 0.344 \frac{n_{0e}}{\sqrt{3}} \left(\frac{2T_1}{M}\right)^{1/2}.$$

For fixed λ and β the function $I(\eta)$ is the integrated distribution of ion current over energy (the current of ions with energies from $W = 0$ to $T_1\eta$). Expressions for the differential current distribution and density of the ions at the point with potential η follow from Eq. (9):

$$\left.\begin{aligned} \frac{dI(W)}{dW} &= \frac{1}{T_1} g\left(\eta - \frac{W}{T_1}\right) \frac{dz}{d\eta}\left(\eta - \frac{W}{T_1}\right), \\ \frac{dn_i(W)}{dW} &= \frac{1}{T_1}\left(\frac{M}{2W}\right)^{1/2} g\left(\eta - \frac{W}{T_1}\right) \frac{dz}{d\eta}\left(\eta - \frac{W}{T_1}\right), \end{aligned}\right\} \tag{11}$$

where

$$g\left(\eta - \frac{W}{T_1}\right) \frac{dz}{d\eta}\left(\eta - \frac{W}{T_1}\right)$$

is defined by Eq. (4).

2. BOLTZMANN DISTRIBUTION AND MONOENERGETIC BEAM

In this case Eq. (2) has the form

$$\left(\frac{M}{2T}\right)^{1/2} \int_0^{\eta} \frac{g(\gamma)\, du}{\frac{du}{dz}(\eta - u)^{1/2}} = n_{0e}\left[(1-\lambda)e^{-\eta} + \frac{\lambda\sqrt{\gamma}}{(\gamma - \eta)^{1/2}}\right]. \tag{12}$$

Here, $\gamma = W_e/T$ and λ and W_e are the relative density and energy of the electron beam at $\eta = 0$. For $0 \le \eta \le \gamma$ Eq. (12) has a solution analogous to Eq. (4):

$$g(\eta)\frac{dz}{d\eta} = \frac{n_{0e}}{\pi}\left(\frac{2T}{M}\right)^{1/2}\left[\frac{1}{\sqrt{\eta}} - (1-\lambda)\, 2e^{-\eta} D(\sqrt{\eta}) + \lambda \frac{\sqrt{\eta}}{\gamma - \eta}\right]. \tag{13}$$

From Eq. (13) there follows an equation for the boundary potential η_a:

$$\frac{\lambda}{1-\lambda} = \frac{2\sqrt{\eta_a}\, e^{-\eta_a} D(\sqrt{\eta_a}) - 1}{1 + \frac{\eta_a}{\gamma - \eta_a}}. \tag{14}$$

The dependence of η_a on the parameters of the electron distributions, γ and λ, is shown in the dotted curves of Fig. 1. As in the preceding case, for relative electron beam densities below some critical value $\lambda_1(\gamma)$ an internal space-charge sheath is formed in the plasma whose boundary potentials are η_1 and η_2. For $\lambda > 0.22$ the interior sheath is not formed. A feature of this case is the absence of a solution for a third value of the boundary potential for arbitrary λ and γ.

The potential distribution between the origin of the coordinates and the point $z = L$ with a fixed potential $\eta_L < \gamma$ for the above generation distribution has the form

$$\frac{z}{L} = \frac{\ln|1 + \alpha F_1(\eta)|}{\ln|1 + \alpha F_1(\eta_1)|}; \tag{15}$$

where

$$F_1(\eta) = \left|\begin{aligned} &\frac{I_0}{g_0}\left\{2(1-\lambda)e^{-\eta} D(\sqrt{\eta}) + \lambda\sqrt{\gamma}\ln\left(\frac{\sqrt{\gamma}+\sqrt{\eta}}{\sqrt{\gamma}-\sqrt{\eta}}\right)\right\} \quad \text{for} \quad \eta \leqslant \eta_1, \\ &F_1(\eta_1) + \frac{I_0}{g_0}\left\{2(1-\lambda)\left[e^{-\eta} D(\sqrt{\eta}) - e^{-\eta_2} D(\sqrt{\eta_2})\right]\right. \\ &\left. + \lambda\sqrt{\gamma}\ln\frac{(\sqrt{\gamma}+\sqrt{\eta})(\sqrt{\gamma}-\sqrt{\eta_2})}{(\sqrt{\gamma}-\sqrt{\eta})(\sqrt{\gamma}+\sqrt{\eta_2})}\right\} \quad \text{for} \quad \eta_2 \leqslant \eta \leqslant \eta_L. \end{aligned}\right.$$

This distribution is shown in Fig. 4 for the case $\alpha = 0$, $\gamma = 10^2$ and several values of λ and η_L. The ion current density at the point with potential η is determined by Eq. (9) upon substitution of $F_1(\eta)$ for $F(\eta)$. The distributions of ion current and density (as functions of energy) are determined by Eqs. (11), where

$$g\left(\eta - \frac{W}{T_1}\right) \frac{dz}{d\eta}\left(\eta - \frac{W}{T_1}\right)$$

is determined by Eq. (13).

3. STABILITY OF THE ION CURRENT

It has been assumed above that the potential η increases monotonically from the origin of coordinates to the plasma boundary. In this case there are no trapped

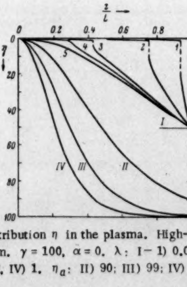

Fig. 4. Potential distribution η in the plasma. High-energy electrons in the form of a beam. γ = 100, α = 0. λ: I – 1) 0.02, 2) 0.05, 3) 0.15, 4) 0.23, 5) 1; II, III, IV) 1. η_a: II) 90; III) 99; IV) 99.9.

ions and all the ions which are generated move to the exterior boundary. The conditions for monotonic variation of the potential as found from Eq. (1) in the linear approximation are

$$\left\langle \frac{1}{W} \right\rangle_{\eta} \leqslant \left(\frac{2}{T_1}\right) \frac{n_{0e}\left[(1-\lambda)e^{-\eta}+\lambda\beta e^{-\beta\eta}\right]+\left(\frac{M}{2T_1}\right)^{1/2} g(\eta)\frac{dz}{d\eta}\frac{1}{\sqrt{\eta}}}{n_{0e}\left[(1-\lambda)e^{-\eta}+\lambda e^{-\beta\eta}\right]} \tag{16}$$

for two Boltzmann electron distributions and

$$\left\langle \frac{1}{W} \right\rangle_{\eta} \leqslant \left(\frac{2}{T}\right) \frac{n_{0e}\left[(1-\lambda)e^{-\eta}-\frac{\lambda\sqrt{\gamma}}{2(\gamma-\eta)^{3/2}}\right]+\left(\frac{M}{2T}\right)^{1/2} g(\eta)\frac{dz}{d\eta}\frac{1}{\sqrt{\eta}}}{n_{0e}\left[(1-\lambda)e^{-\eta}+\frac{\lambda\sqrt{\gamma}}{(\gamma-\eta)^{1/2}}\right]} \tag{16a}$$

for a Boltzmann distribution and a beam, where $\langle 1/W \rangle_{\eta}$ is the mean value of the reciprocal of the ion energy at an arbitrary point $\eta > 0$. These conditions are clearly satisfied for any $\eta < \eta_a$ if they are satisfied on the plasma boundary ($dz/d\eta \to 0$):

$$\left\langle \frac{1}{W} \right\rangle_{\eta_a} \leqslant \left(\frac{2}{T_1}\right) \frac{(1-\lambda)e^{-\eta_a}+\lambda\beta e^{-\beta\eta_a}}{(1-\lambda)e^{-\eta_a}+\lambda e^{-\beta\eta_a}}, \tag{17}$$

and

$$\left\langle \frac{1}{W} \right\rangle_{\eta_a} \leqslant \left(\frac{2}{T}\right) \frac{(1-\lambda)e^{-\eta_a}-\frac{\lambda\sqrt{\gamma}}{2(\gamma-\eta_a)^{3/2}}}{(1-\lambda)e^{-\eta_a}+\frac{\lambda\sqrt{\gamma}}{(\gamma-\eta_a)^{1/2}}}. \tag{17a}$$

Thus, the inequalities in Eq. (17) represent a condition for a monotonic potential distribution as a whole, including the plasma boundary. For $\lambda = 0$ the well-known "instability criterion" follows from Eq. (17) for the case of a single Boltzmann distribution:[3]

$$\left\langle \frac{1}{W} \right\rangle_{\eta_a} \leqslant \frac{2}{T}. \tag{18}$$

The inequalities (17) must be supplemented by conditions for the existence of solutions to Eq. (1) which satisfy the boundary values $\eta(0) = 0$ and $(d\eta/dz)_{z=0} = 0$. These additional conditions are obtained from the expression for the first integral of Eq. (1) in the range from $\eta = 0$ to arbitrary η and may be written in the form

$$\langle W(\eta) \rangle \geqslant \frac{T_1}{2} \frac{(1-\lambda)(1-e^{-\eta})+\frac{\lambda}{\beta}(1-e^{-\beta\eta})}{(1-\lambda)e^{-\eta}+\lambda e^{-\beta\eta}} \tag{19}$$

for two Boltzmann electron distributions and

$$\langle W(\eta) \rangle \geqslant \frac{T}{2} \frac{(1-\lambda)(1-e^{-\eta})+\lambda\gamma 2\left[\left(1-\frac{\eta}{\gamma}\right)^{1/2}-1\right]}{(1-\lambda)e^{-\eta}+\frac{\lambda\sqrt{\gamma}}{(\gamma-\eta)^{1/2}}} \tag{19a}$$

for a Boltzmann distribution and a beam, where $\langle W(\eta) \rangle$ is the mean energy of the ions at the point η. Equalities in Eqs. (17) and (19) correspond to solutions of Eq. (2).

The conditions Eqs. (17) and (19) are necessary for the existence of the preceding stationary solutions (but not sufficient). If either of them is not satisfied there is either no solution for Eq. (1) and the given boundary conditions, or the potential distribution is oscillatory. In the latter case, due to buildup of the generated ions in potential wells the positive charge increases with time for constant electron density and a stationary solution becomes impossible.

CONCLUSION

It follows from the above solutions that the presence of a group of high-energy electrons with a Maxwellian velocity distribution or in the form of a beam, and with a relative density higher than a few percent, leads to a drop in the plasma potential of the order of the temperature of these electrons. Depending on the relative densities and energies of the high- and low-energy electrons the potential distribution may either be continuous or undergo jumps corresponding to the formation of a space-charge double layer. The current and energy spectrum of the ions at any point of the discharge are determined only by the electron velocity distribution, being independent of the potential distribution and the ion generation distribution in the plasma.

These results explain the mechanism by which ions are accelerated to high energies in discharges which have high-energy electrons.[7,12] More accurate solutions require that the initial ion velocities, the spread in velocity of the electron beam, and the recombination of ions with neutral atoms be taken into account.

---

[1] L. Tonks and I. Langmuir, Phys. Rev., 34, 876 (1929).

[2] O. B. Firsov, Zh. Tekh. Fiz., 26, 445 (1956) [Sov. Phys. – Tech. Phys., 1, 431 (1956)].

[3] E. R. Harrison and W. B. Thompson, Proc. Phys. Soc., 74, 145 (1959).

[4] P. L. Auer, Nuovo Cimento, 22, 548 (1961).

[5] A. Caruso and A. Cavaliere, Nuovo Cimento, 26, 1389 (1962).

[6] S. Self, J. Appl. Phys., 36, 456 (1965).

[7] R. A. Demirkhanov, Yu. V. Kursanov, and L. P. Skripal', Zh. Tekh. Fiz., 40, 1351 (1970); 39, 666 (1969) [Sov. Phys.–Tech. Phys., 15, 1047 (1971); 14, 500 (1969)].

[8] L. Ševarac, Nucl. Instr. Meth., 38, 12 (1965).

[9] A. I. Karchevskii, V. G. Averin, and V. N. Bezmel'nitsyn, Zh. Eksp. Teor. Fiz., 58, 1131 (1970) [Sov. Phys. – JETP, 31, 605 (1970)].

[10] T. Dech, Manual on the Practical Application of the Laplace Transform [in Russian], Fizmatgiz, Moscow (1960).

[11] K. A. Karpov, Tables [in Russian], Izd. Akad. Nauk SSSR, Moscow (1954).

[12] R. A. Demirkhanov, Yu. V. Kursanov, L. P. Skripal', and G. B. Kharin, in: Plasma Accelerators [in Russian], Mashinostroenie, Moscow (1972), p. 99.

Stabilization of the major radius of toroidal pinch by a feedback system

V. V. Arsenin

(Submitted June 4, 1973)
Zh. Tekh. Fiz., 44, 1432-1436 (July 1974)

The stabilization of the major radius of a toroidal current-carrying pinch by a feedback system is considered. The case in which the control field is homogeneous over the torus has been studied earlier. In the present work the more general case of an inhomogeneous winding density is considered. In particular, the winding can be local. A dispersion equation of the oscillations is obtained taking account of the mode coupling resulting from the breakdown of axial symmetry. When the frequency (growth rate) of oscillations of the major radius in the absence of stabilization is much less than the frequencies of the helical modes the coupling is weak. In the stable state the control field appears in the form of an average taken over a circuit around the torus.

The elongation of a toroidal current-carrying pinch can be balanced by a Lorentz force due to a magnetic field perpendicular to the plane of the torus. Such a field arises, for example, if the plasma is surrounded by a metal wall.[1] Stable equilibrium in the absence of a wall can be attained by using a feedback system, which controls the value of the transverse field. The efficiency of such a system has been demonstrated in experiments on a Tokamak[2]. In these experiments the control field generated by a special winding is constant over the torus (the case considered theoretically in ref. 3). This kind of stabilizing field corresponds to the perturbation which it is desired to quench. However, it is convenient to achieve stabilization of the major radius using an inhomogeneous control winding (such a system simplifies access to the plasma for diagnostics). In the present work we analyze a stabilizing system of the type of ref. 2 with an inhomogeneous winding density. We obtain a dispersion equation taking account of the mode coupling arising as a result of the breakdown in axial symmetry. When the frequency (growth rate) of the oscillations of the major radius in the absence of stabilization is much lower than the frequencies of the helical modes, the coupling is weak (the pinch is not deflected). The oscillations of the major radius prove to be affected only by the value of the control field averaged over the torus.

We consider a toroidal pinch of an ideally conducting incompressible fluid of density ρ with longitudinal current J uniformly distributed over the cross section in a longitudinal field $B_{\parallel}$. Let the major radius of the pinch be R, and the minor radius be a. We introduce a radial coordinate r, measured from the circular axis, and two angular coordinates: θ – along the small circuit, and φ – along the large circuit. We consider the stability of a pinch with respect to displacements

$$\xi_r = \sum_{m,n} \xi_{m,n} \exp(im\theta - in\varphi - i\omega t),$$

where $m = \pm 1$, $n \ll R/a$. In the absence of external ("stabilizing") currents, the oscillations of particular harmonics m and n are independent (neglecting weak toroidal effects).

We assume that the longitudinal field $B_{\parallel}$ is much greater than the field of the current $B_J = 2J/(ca)$, so that $q = aB_{\parallel}/(RB_J) > 1$, and perturbations with $n \neq 0$ (helical modes), satisfying (neglecting toroidal effects) the equations

$$\xi_{m,n} + \omega^2_{m,n}\xi_{m,n} = 0, \tag{1}$$

where

$$\omega^2_{m,n} = 2\Omega_A^2[(m - nq)^2 - m(m - nq)], \quad \Omega_A = \frac{B_J}{\sqrt{4\pi\rho}\, a}$$

is the Alfvén frequency, are stable.

We assume that the pinch is unstable (with growth rate γ) with respect to variations in the major radius ($n = 0$, $\xi_{1,0} = \xi_{-1,0}$), and the oscillations are described by the equation

$$\xi_{\pm 1,0} - \gamma^2\xi_{\pm 1,0} = 0. \tag{2}$$

These perturbations can be stabilized by applying to the fluid perpendicular to the plane of the torus a magnetic field B_Z, proportional to the displacement δR, $B_Z = \alpha \cdot (ca^2)^{-1}[J \cdot \delta R]$. Taking account of the force $(1/c)[JB_Z]$, we have

$$\xi_{\pm 1,0} - \gamma^2\xi_{\pm 1,0} + \alpha\Omega_A^2\xi_{\pm 1,0} = 0. \tag{3}$$

For stability it is sufficient that

$$\alpha > \left(\frac{\gamma}{\Omega_A}\right)^2. \tag{4}$$

The required field B_Z is produced by the winding $r = d$, $a < d \ll R$, which is homogeneous with respect to φ. The current excited in the winding by the "primary" magnetic perturbation field (i.e., the field that would exist outside the plasma in the absence of the winding), and the coefficient α, depend on the impedance of the winding and the spatial structure of the primary field. Because of the φ homogeneity the winding affects only the perturbation field, as averaged over the torus. Thus, a homogeneous winding automatically acts on spatial modes for which $n = 0$.

The problem of finding the frequency spectrum of the plasma + winding system is complicated in the case of interest to us, in which the current in the winding depends on φ. The eigenfunctions are not the separate Fourier harmonics $\exp(in\varphi)$, but are coupled. Below we introduce the dispersion equation for this case.

We represent the density of the surface current $j_\varphi = j(\varphi)\cos\theta\exp(-i\omega t)$, $\operatorname{div} \mathbf{j} = 0$, produced by the winding $r = d$, by the Fourier series

$$\left.\begin{aligned} j_\varphi &= \sum_{m=\pm 1}\sum_n j_{m,n}\exp(im\theta - in\varphi), \\ j_{m,n} &= \frac{1}{4\pi}\int_0^{2\pi} j(\varphi)\exp(in\varphi)\,d\varphi. \end{aligned}\right\} \tag{5}$$

The constant component of current (n = 0) produces in the region r < d a homogeneous (neglecting the toroidality) magnetic field $B_z = (2\pi/c)(j_{1,0} + j_{-1,0})$. Thus, the equation of oscillations of the major radius of the pinch is

$$(\omega^2 + \gamma^2)\xi_{\pm 1,0} + 2\pi\Omega_A^2 \frac{j_{\pm 1,0}a^2}{J} = 0. \tag{6}$$

The harmonics n ≠ 0 in the expansion of the current affect the helical modes. These modes are described by the equation

$$(\omega^2 - \omega_{m,n}^2)\xi_{m,n} + 2\pi m(m - nq)\Omega_A^2 \frac{j_{m,n}a^2}{J} = 0. \tag{7}$$

For j = 0, Eqs. (6) and (7) are transformed, respectively, into (2) and (1).

The density of the current induced in the winding, which appears in Eqs. (6) and (7), depends, in turn, on the displacement of the pinch. We find this density under the assumption that the winding consists of N series-connected loops with angular dimensions $\Delta\theta \ll 1$ and $\Delta\varphi$ (see Fig. 1), the centers of which are distributed over the surface r = d with angular density $(N/4)\, n(\varphi) \sin\theta$ (the variation in sign indicates a difference in orientation). The $n(\varphi)$ distribution is normalized to unity. The flux of the perturbation magnetic field $B_r' = \sum_{m,n} B_{m,n} \exp(im\theta - in\varphi)$, in terms of a single loop, is

$$\Phi = Rd\Delta\theta \sum_n \frac{2}{n} \sin\frac{n\Delta\varphi}{2} \sum_m B_{m,n} \exp(im\theta_0 - in\varphi_0), \tag{8}$$

where θ_0 and φ_0 are the angular coordinates of the center of the loop. The flux through the entire winding is

$$\Phi = i\frac{\pi}{4} NRd\Delta\theta \sum_n \frac{2}{n} \sin\frac{n\Delta\varphi}{2} C_n \sum_{m=\pm 1} mB_{m,n}, \tag{9}$$

where

$$C_n = \frac{1}{2\pi}\int_0^{2\pi} n(\varphi) \exp(-in\varphi)\, d\varphi \tag{10}$$

(for the assumed normalization, $C_0 = 1$).

A current

$$I = -\frac{i\omega}{cZ}\Phi \tag{11}$$

is excited in the winding, where Z is the impedance of the winding. If the inductive component of the impedance is calculated[1] under the assumption that the volume of the plasma is occupied by a solid ideal conductor, then the $B_{m,n}$ in (9) are the harmonics of the primary perturbation field

$$B_{m,n} = i(m - nq) B_J \frac{\xi_{m,n}}{d} \tag{12}$$

(see, e.g., ref. 4).

As a result we have

$$I = \frac{i\omega\pi NR\Delta\theta B_J}{4cZ} \sum_n \frac{2}{n} \sin\frac{n\Delta\varphi}{2} C_n \sum_{m=\pm 1} m(m - nq)\xi_{m,n}. \tag{13}$$

We calculate the surface current density. The density produced by a single winding is

$$j_\varphi = \frac{I}{d} f(\varphi - \varphi_0)\left[\delta\left(\theta - \theta_0 - \frac{\Delta\theta}{2}\right) - \delta\left(\theta - \theta_0 + \frac{\Delta\theta}{2}\right)\right], \tag{14}$$

where

$$f = \begin{cases} 1, & |\varphi - \varphi_0| < \frac{\Delta\varphi}{2}, \\ 0, & |\varphi - \varphi_0| > \frac{\Delta\varphi}{2}. \end{cases}$$

The total current density is obtained by integrating (14) over θ_0, φ_0 with weight factor $(N/4) \sin\theta_0 n(\varphi_0)$. The Fourier harmonics of the current density of interest to us will be (since $\Delta\theta \ll 1$)

$$j_{m,n} = \frac{IN\Delta\theta}{8d} \frac{2}{n} \sin\frac{n\Delta\varphi}{2} C_n^* \tag{15}$$

(the asterisk denotes the complex conjugate).

In order to obtain the dispersion equation we express $\xi_{m,n}$ from (6), (7), and (15) in terms of I, and we substitute in (13). We obtain

$$1 = -\frac{i\omega}{c^2 Z}(\pi N\Delta\theta)^2 \frac{Ra}{d} \Omega_A^2 \left[\frac{(\Delta\varphi)^2}{\omega^2 + \gamma^2} + \frac{1}{2}\sum_{n\neq 0}\left(\frac{2}{n}\sin\frac{n\Delta\varphi}{2}\right)^2 |C_n|^2 \sum_{m=\pm 1} \frac{(m - nq)^2}{\omega^2 + \omega_{m,n}^2}\right]. \tag{16}$$

For $N\Delta\theta \to 0$ or $\Delta\varphi = 0$ this equation breaks up into an equation for the separate harmonics (1) and (2). When one loop occupies the entire major circumference of the torus ($\Delta\varphi = 2\pi$), Eq. (16) contains only the term with the mean field

$$1 = -\frac{i\omega}{c^2 Z}(2\pi^2 N\Delta\theta)^2 \frac{Ra}{d} \frac{\Omega_A^2}{\omega^2 + \gamma^2}. \tag{17}$$

The helical modes also drop out of Eq. (16) when the loops (with arbitrary $\Delta\varphi$) are distributed uniformly over the large circuit of the torus ($C_n = 0$ for n ≠ 0).

In the absence of current in the winding ($|Z| \to \infty$), Eq. (17) has the unstable root $\omega = i\gamma$. Stabilization holds if the impedance Z is purely inductive ($Z = -i\omega L/c^2$) and

$$0 < L < (2\pi^2 N\Delta\theta)^2 \frac{Ra}{d} \frac{\Omega_A^2}{\gamma^2}. \tag{18}$$

The required impedance with small inductance is

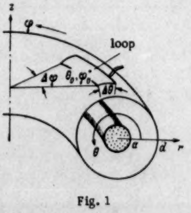

Fig. 1

achieved by connecting the winding to an external two-terminal network with negative resistance, which compensates the resistance of the winding, and a negative inductance.[3]

For $\Delta\varphi < 2\pi$ and arbitrary density of the winding, the dispersion equation (16) is unwieldy. We consider the interesting case in which the instability growth rate of the major radius γ is much smaller than the frequencies of the helical modes $\omega_{m,n}$ (order of the Alfvén frequency Ω_A). In the frequency region $|\omega| \lesssim \gamma$ the sum of terms with $n \neq 0$ in (16) is small. The equation of the low-frequency oscillations takes the form

$$1 = \frac{i\omega}{c^2 Z} (\pi N \Delta\theta\Delta\varphi)^2 \frac{Ra}{d} \frac{\Omega_A^2}{\omega^2 + \gamma^2}, \tag{19}$$

and the stability condition for inductive impedance is

$$0 < L < (\pi N \Delta\theta\Delta\varphi)^2 \frac{Ra}{d} \frac{\Omega_A^2}{\gamma^2}. \tag{20}$$

As can be seen from (19), for given $\Delta\varphi$, $\Delta\Theta$ the motion of the pinch depends on the total number of loops N. The distribution of loops over the surface $r = d$ appears in (19) only in terms of the inductance of the winding. For a given N the total impedance Z is fixed (by the choice of the inductance of the external two-terminal network); the motion of the pinch does not depend, in particular, on whether or not the loops are distributed about the torus uniformly, or the winding is local.

The terms with $n \neq 0$ in (16) are important for $\omega \approx \omega_{m,n}$. If the inductance L is not too small, so that $(\pi N \Delta\theta\Delta\varphi)^2 (Ra/d) \sim \gamma^2/\Omega_A^2$, they give stable natural oscillations with frequencies close to the frequencies of the helical modes $\omega_{m,n}$ in the absence of feedback.

We give an expression for the variation in major radius when the given current I(t) is fed into the control winding for a time much less than $1/\gamma$ (programmed control by the position of the pinch)

$$\delta R = \frac{\pi}{2} N \Delta\theta\Delta\varphi \frac{a^2}{d} \Omega_A^2 \int_0^t d\tau \int_0^\tau \frac{I(\alpha)}{J} d\alpha. \tag{21}$$

We thank L. I. Artemenkov for discussion.

---

1) Or is measured directly.

---

[1] L. A. Artsimovich, Closed Plasma Configurations [in Russian], Izd. Nauka, Moscow (1969).

[2] L. I. Artemenkov, V. K. Butenko, I. N. Golovin, V. F. Gubarev, P. I. Kozlov, A. I. Kukhtenko, Yu. P. Ladikov-Roev, P. I. Melikhov, Yu. I. Samoilenko, and N. N. Shvindt, Plasma Physics and Controlled Nuclear Fusion Research (Fourth Conf. Proc., Madison, Wisconsin, U.S.A., June, 1971), Vol. 1, IAEA, Vienna (1971), p. 359.

[3] V. K. Butenko, Yu. P. Ladikov-Roev, and Yu. I. Samoilenko, in: Cybernetics and Computer Technology, No. 8 [in Russian], Izd. Naukova Dumka, Kiev (1971), p. 80.

[4] V. D. Shafranov, in: Plasma Physics and the Problem of Controlled Thermonuclear Reactions, Vol. 4, Pergamon (1960), p. 71.

High-frequency discharge in a mercury – helium mixture

S. D. Vagner, Yu. M. Kagan, A. I. Konstantinov, and I. S. Niskonen

Karelskii Pedagogical Institute, Petrozavodsk

(Submitted September 21, 1973)
Zh. Tekh. Fiz., 44, 1437-1441 (July 1974)

The radial electron distribution function, the ion densities, the densities of atoms in the lower excited levels, and the absolute intensities of certain helium and mercury lines are measured in a high-frequency discharge. The spatial characteristics of the helium and mercury line intensities and the densities of atomic mercury are calculated, allowing for the radial densities of electrons and mercury atoms, and the densities of atoms in the lower excited states.

INTRODUCTION

The properties of discharges in gas – vapor mixtures are closely related to the phenomenon of electrophoresis.[1] Spatial separation of the components of the mixture can occur in both the longitudinal and radial directions. There is essentially no experimental literature on radial electrophoresis, although this phenomenon is of considerable interest in regard to the development of gas discharges in mixtures. Radial electrophoresis and related phenomena can be studied most conveniently in the central part of a high-frequency discharge in which there is no constant longitudinal electric field. Longitudinal electrophoresis does not occur under these conditions.

In the present paper the electrical and optical properties of a high-frequency discharge are investigated in the central part of a cylindrical tube. The radial characteristics of the electron distribution function, the ion densities, the densities of atoms in the lower excited states, and the absolute intensities of some helium and mercury lines are measured.

The measured electron distribution functions and the densities of atoms in the lower excited states are used to calculate the radial densities of the mercury atoms and mercury ions, and the radial characteristics of helium and mercury line intensities. The calculated characteristics are compared with the experimental data.

EXPERIMENTAL TECHNIQUE

The measurements are performed in a tube 34 mm in diameter and 300 mm long. The discharge is excited by a high-frequency oscillator with a balanced output at 28 MHz by means of cylindrical electrodes. The discharge current is measured by two T-22 thermoelectric milliammeters connected directly to the electrodes.

A cylindrical probe 5 mm long and 0.03 mm in radius is placed in the center of the tube and is perpendicular to the tube axis. The probe is moved in the radial direction by means of a magnetic system. Two nickel counterprobes, with an area of 7.6 cm^2 each, are placed symmetrically on the walls. The procedure described in refs. 2 and 3 is used to measure the electron distribution function by the second derivative method.

The ends of the discharge tube contain glass windows, and end-on measurements are made of the radial emission distribution. A micrometer screw is used for radial scans of the discharge tube. The optical system includes a DMR-4 monochromator with a photoelectric recorder. The densities of atoms in the lower excited levels were determined by the reabsorption method with the aid of a planar mirror.[4] The absolute line intensities are obtained from an SI-300 temperature-calibrated lamp.

The basic measurements are carried out at a current of 200 mA, a helium pressure of 0.5 torr, and a mercury vapor pressure of $2 \cdot 10^{-4}$ torr. The mercury vapor pressure is determined by a temperature sidearm with mercury mounted at the center of the tube.

EXPERIMENTAL RESULTS

In Fig. 1, the electron energy distribution function, normalized for the same area, is given for three points along the radius. The shape of the distribution does not vary along the radius and differs from a Maxwellian distribution for potentials larger than the mercury ionization potential. The radial electron density shown in Fig. 2 differs negligibly from the Bessel function. The electron density is determined from the electron current at the space potential. The space potential is taken to be the potential at which the second derivative of the probe current is zero. The average electron velocity is determined from the measured electron distribution function. Figure 2 also gives the radial distributions of the total population of the lower excited mercury levels 6^1P_1 and 6^3P_{012} and the lower excited helium levels 2^3S_1, 2^3P_{012}, 2^1S_0, and 2^1P_1. In interpreting the results it is assumed that the line profiles have a Doppler shape corresponding to room temperature, 300°K. At the $k_0 l$ values occurring in our experiments the fine structure and edge effects can be neglected. It can be seen that the density of atoms in the lower excited states declines more slowly along the radius for mercury than for helium. The distribution of the latter coincides with the Bessel function. The ion parts of the probe characteristic curves are determined simultaneously with the second derivative of the probe current. The simultaneous use of the electron and ion parts of the characteristic curves, as shown in ref. 5, allows the ion densities of the components in the case of a binary mixture to be estimated. The experimental values of the mercury ion density are shown in Fig. 3.

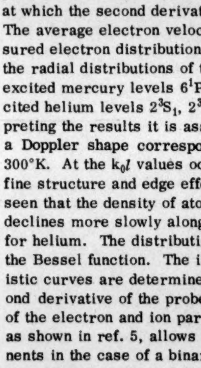

Fig. 1. Electron energy distribution functions normalized to the same area. 1) Maxwellian distribution; 2) distribution for r/R: 2) 0; 3) 0.4; 4) 0.8.

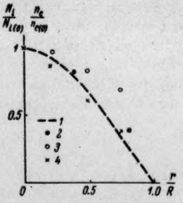

Fig. 2. Radial distribution of electron density and densities of mercury and helium atoms in lower excited levels. 1) Bessel function; 2) distribution of electron density $n_e(0) = 3.4 \cdot 10^{10}\ \mathrm{cm}^{-3}$; 3) distribution of the total population of mercury levels 6^1P_1 and 6^3P_{012}, $N_i(O) = 1.1 \cdot 10^{11}\ \mathrm{cm}^{-3}$; 4) distribution of the total population of helium levels 2^1S_0, 2^1P_1, 2^3S_1, 2^3P_{012}, $N_i(O) = 6 \cdot 10^{11}\ \mathrm{cm}^{-3}$.

The absolute values of the measured parameters at the tube axis are given under the captions to the figures.

The radial distribution of mercury neutrals and ions can be estimated by solving the balance equations for the neutral and charged particles[6,7]

$$\operatorname{div}\left(-D_a \frac{dn}{dr}\right) = (z_1 + z_2) n_e + \alpha, \tag{1}$$

$$-D_a \frac{dn}{dr} = D \frac{dN}{dr}, \tag{2}$$

where n_e, n, and N are the densities of the electrons, mercury ions, and neutral mercury atoms, respectively, z_1 and z_2 are the frequencies of direct and cascade ionization, α is the number of ionizations per unit volume per unit time due to the Penning effect, D_a is the ambipolar diffusion coefficient of mercury ions, and D is the diffusion coefficient of neutral mercury atoms. The flux of metastable mercury atoms can be neglected in Eq. (2) since the diffusion coefficient of metastable mercury atoms is much smaller than the ambipolar diffusion coefficient of mercury ions, and the density gradients of these particles differ negligibly (see Figs. 2 and 3). After substitution of (2) into (1), in the case of cylindrical geometry for the radial component, Eq. (1) transforms to

$$\frac{d^2N}{dr^2} + \frac{1}{r}\frac{dN}{dr} = \frac{z_1 + z_2}{D} n_e + \frac{\alpha}{D}. \tag{3}$$

The radial density N is approximated by

$$N(r) = N(R) - \Delta N J_0\left(2.4 \frac{r}{R}\right), \tag{4}$$

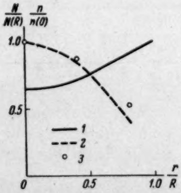

Fig. 3. Radial distribution of densities of neutral mercury atoms and ions. 1) Calculated density of neutral mercury atoms $N(O) = 4.5 \cdot 10^{12}\ \mathrm{cm}^{-3}$; 2) calculated density of mercury ions; 3) experimental values of mercury ion density $n(0) = 1.9 \cdot 10^{10}\ \mathrm{cm}^{-3}$.

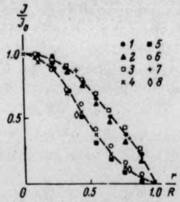

Fig. 4. Radial distribution of radiation intensity of mercury and helium. Mercury: 1) 4047; 2) 4358; 3) 5461 Å; 7) calculated excitation of the 7^3S_1 level. Helium: 4) 5015; 5) 5876; 6) 3888 Å; 8) calculated excitation of 3^1P_1 level.

where N(R) is the density of atomic mercury at the wall determined from the mercury temperature in the sidearm, ΔN is the difference in the densities of atomic mercury at the wall and at the axis of the tube, and $J_0\,(2.4\ r/R)$ is the zeroth-order Bessel function. Substitution of (4) into (3) gives for r = 0

$$\Delta N = \frac{R^2}{5.8}\left[\frac{(z_1 + z_2) n_e + \alpha}{D}\right]. \tag{5}$$

Thus, if the values of z_1, z_2, α, n_e, and D are known at the center of the tube, the value of ΔN can be estimated.

The first calculation of z_1 and α does not allow for the decreased density of atomic mercury at the axis of the tube. Then, the method of successive approximations is used to refine the values of z_1 and α, and thus of ΔN.

The ionization rates of z_1 and z_2 are calculated from the measured electron distribution functions. To calculate direct ionization the experimental value of the cross section of the process is used.[8] Cascade ionization is calculated from the experimental values of the populations of the lower excited levels. The cross section of this process is approximated by an expression taken from ref. 9.

The value of the diffusion coefficient of atomic mercury and helium is not known to us. The data[10] indicate that the diffusion coefficients for atoms of different elements in helium, in the cases where they are known, are close to the corresponding values for the diffusion coefficients in hydrogen. To estimate ΔN, therefore, D was taken to be the value of the diffusion coefficient of atomic mercury in hydrogen given in ref. 10.

The density of atomic mercury obtained is shown in Fig. 3. The density at the axis is roughly 35% smaller than at the wall.

The corresponding calculation for helium gives a value of the order of 0.02%. The possible radial gradients of the gas temperature produce effects that considerably exceed the indicated value. Therefore, a calculation of the radial density of atomic helium must allow for the gas temperature gradient.

Using Eqs. (2) and (4), and the relationship between the fluxes and the corresponding diffusion coefficients, the following expression can be obtained for the radial distribution of atomic mercury:

$$n(r) = n(0) - \frac{D\Delta N}{D_a}\left[1 - J_0\left(2.4 \frac{r}{R}\right)\right]. \tag{6}$$

To calculate D_a the mobility of mercury ions in helium is used.[8] An equation similar to (6) is not used to calculate the radial distribution of helium ions due to the lack of sufficiently precise values for the difference between the densities of atomic helium at the axis and the wall of the tube.

Figure 3 gives the radial density of mercury ions calculated from Eq. (6). Good agreement with experiment is shown.

The measured radial radiation intensities of some helium and mercury lines are shown in Fig. 4. This figure also gives the calculated excitation frequencies of the emitting levels for mercury at 4046, 4358, and 5461 Å and for helium at 5015 Å. The excitation calculations for mercury include both direct and cascade processes. The Fabrikant approximation and experimental values of the cross sections[12] are used to calculate direct excitation. Cascade excitation is calculated using the cross section approximation given in ref. 9. Only cascade processes are included in the calculation of helium excitation, which employs the tables given in ref. 13.

The agreement between the experimental and calculated values makes it possible to conclude that the assumptions as to the nature of the excitation processes are valid.

Thus, the differences in the radial distribution of emission by helium and mercury lines are due to the difference in the excitation processes, the radial densities of lower excited atoms of helium and mercury, and to the decrease in the density of normal mercury atoms at the axis of the tube resulting from electrophoresis.

---

[1] V. L. Granovskii, Electric Current in a Gas. Steady-State Current [in Russian], Nauka, Moscow (1971).

[2] S. D. Vagner, V. A. Virolainen, and Yu. M. Kagan, Zh. Tekh. Fiz., 39, 669 (1969) [Sov. Phys. – Tech. Phys., 14, 502 (1969)].

[3] S. D. Vagner, V. A. Virolainen, Yu. M. Kagan, and T. A. Kalmykova, Zh. Tekh. Fiz., 44, 468 (1974) [Sov. Phys. – Tech. Phys., 19, 000 (1974)].

[4] S. É. Frish and O. P. Bochkova, Vestn. Leningr. Univ., No. 16, 40 (1961).

[5] S. D. Vagner, Uchen. Zap. Petrozavod. Univ., 5, 129 (1957).

[6] M. J. Druyvestyn (Druyvestein), Physica, 2, 255 (1935).

[7] Yu. A. Pekar, Zh. Tekh. Fiz., 36, 1372 (1966) [Sov. Phys. – Tech. Phys., 11, 1024 (1967)].

[8] S. C. Brown, Basic Data of Plasma Physics, MIT Press, Cambridge (1961).

[9] H. W. Drawin, Z. Phys., 164, 513 (1961).

[10] W. Jost, Diffusion in Solids, Liquids, and Gases, Academic Press, New York (1960).

[11] J. B. Hasted, Physics of Atomic Collisions, Butterworth (1964).

[12] V. L. Granovskii, Electric Current in Gases [in Russian], GITTL, Moscow (1952).

[13] L. A. Vainshtein and I. I. Sobelman, J. Quant. Spectrosc. Radiat. Transfer, 8, 1491 (1968).

Effect of ionization and excitation on the penetration of an electromagnetic wave into a weakly ionized plasma

A. G. Boev and A. V. Prokopov
Institute of Radiophysics and Electronics,
Academy of Sciences of the Ukrainian SSR, Khar'kov
(Submitted July 17, 1973)
Zh. Tekh. Fiz., 44, 1442-1447 (July 1974)

The effect of excitation and ionization on the spatial structure of a low-frequency electromagnetic field ($\omega \ll \nu$) in a plasma is analyzed. It is shown that consideration of these processes leads to a qualitatively different dependence of skin depth (a decrease rather than an increase) on the amplitude of the incident field as compared with the case in which only elastic processes are considered. Calculated results for the skin depth and the dependence on amplitude are given for a discharge in argon excited by an electromagnetic field with λ = 10 cm.

Although the electron temperature and density are important characteristics in the case of a discharge excited by an electromagnetic field, the depth of penetration is also very important, as is its dependence on field strength. These quantities figure in practical problems such as the determination of the volume of a plasma chemical microwave reactor,[1] the selection of channel diameter for a magnetohydrodynamic generator with microwave ionization,[2] the calculation of the specific power dissipated in a discharge, etc.

The calculation of the depth of field penetration into a plasma (skin depth) is based on solutions of the self-consistent boundary value problem for Maxwell's equations and the balance equations for temperature and density with consideration of such inelastic atomic processes as excitation and ionization being necessary from the very definition of a self-sustaining discharge.

The problem of field penetration into plasma including only elastic atomic processes has been considered;[3,4] the problem has also been considered[5,6] with ionization taken into account (atomic excitation was not considered) with the dependence of the ionization rate ν_i on the electron temperature T_e being taken as

$$\nu_i \sim \exp\left(-\frac{I}{\varkappa T_e}\right). \qquad (1)$$

In calculating the parameters of a microwave discharge in which the electron–neutral collision frequency is much greater than the field frequency, $\nu \gg \omega$, one can exploit the analogy between a microwave discharge and a dc discharge; in the latter the ionization rate is

$$\nu_i = \alpha\left(\frac{E}{p}\right)(\mu p)\frac{E}{p}, \qquad (2)$$

where α(E/p) is the first Townsend coefficient, μ is the electron mobility, and p is pressure.

In this connection, in the present work the effect of excitation and ionization on the spatial structure of a low-frequency electromagnetic field $\omega \ll \nu$ in a plasma is carried out below using the dc description.

1. Consider a half-space x ≥ 0 filled with an atomic gas at pressure p. On the boundary of this half-space there is incident along the normal to the surface a plane, linearly polarized electromagnetic wave

$$E = E_0 e^{i(kx-\omega t)}$$

with amplitude E_0 sufficient to ionize the gas.

The behavior of this wave in the plasma is described by the equation

$$\frac{d^2E}{dx^2} + k^2\varepsilon' E = 0 \qquad (1.1)$$

with the boundary conditions

$$E_{x=+0} = E_{x=-0}, \quad \left.\frac{dE}{dx}\right|_{x=+0} = \left.\frac{dE}{dx}\right|_{x=-0}, \qquad (1.2)$$

which express the continuity of the tangential components of the electric and magnetic fields at the plasma boundary. We assume that the plasma is weakly ionized and neglect electron–electron collisions.

The complex dielectric constant

$$\varepsilon' = 1 - \frac{\omega_0^2}{\omega^2+\nu^2}\left(1 + i\frac{\nu}{\omega}\right) \qquad (1.3)$$

is related to the electron density n through the plasma frequency $\omega_0 = (4\pi e^2 n m^{-1})^{1/2}$ and to the electron temperature T_e through the electron–neutral collision frequency[3]

$$\nu = \nu_0\left(\frac{T_e}{T}\right)^{1/2} \qquad (1.4)$$

(T is the gas temperature). Because of this, Eq. (1.1) must be solved simultaneously with the balance equations for electron temperature

$$\frac{e^2|E|^2}{m(\omega^2+\nu^2)} = 3\varkappa\delta(T_e - T) \qquad (1.5)$$

and electron density

$$\rho n = \nu_i(|E|), \qquad (1.6)$$

where ν_i is the ionization rate, ρ is the coefficient of volume recombination, δ is the average fractional energy transferred to an atom by an electron in a single collision, and $\varkappa$ is the Boltzmann constant.

Equations (1.5) and (1.6) do not contain terms with spatial derivatives and consequently do not take account of such processes as thermal conductivity, diffusion, and redistribution of electron density because of plasma heating in a nonuniform field, i.e., they determine the local dependence of temperature and density on the field. Thus, they are valid only when

$$l\delta^{-1/2} \ll L, \quad \left(\frac{D_a}{\rho n}\right)^{1/2} \ll L, \qquad (1.7)$$

where l is the mean free path, D_a is the coefficient of ambipolar diffusion, and L is the characteristic scale length

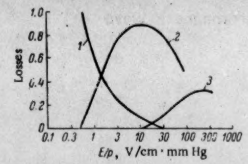

Fig. 1. Distribution of energy losses in an argon discharge.[9]

for field variation in the plasma.

In the following we shall be interested in the behavior of an electromagnetic wave with a frequency ω satisfying the inequality

$$\omega \ll \nu \leqslant \omega_0,$$

which is equivalent to the consideration of a highly damped wave.

2. Consideration of inelastic collisions in the equation for temperature balance (1.5) can be achieved by the introduction of a certain effective parameter

$$\delta = \delta_e + \delta_{in}, \tag{2.1}$$

which can characterize the average fractional electron energy transferred to a heavy neutral[3] in both elastic collisions, δ_e, and inelastic collisions, δ_{in}. The calculation of δ implies a knowledge of the detailed picture of the distribution of the energy supplied to the discharge among the various processes (elastic and inelastic) and generally requires the solution of the kinetic equation.

The energy distribution per unit volume among the various processes was determined by Druyvestyn and Penning[9] as a function of electric field for a dc discharge in certain gases (Ar, Ne, N_2). Figure 1 shows a diagram of the energy distribution for a discharge in argon. Curve 1 characterizes energy losses in elastic collisions, curve 2 losses in excitation, and curve 3 losses in ionization of atoms. The presence of maxima in curves 2 and 3 is associated with the existence of maxima in the cross sections for atomic excitation and ionization.

A picture similar to that shown in Fig. 1 occurs for any atomic gas; the effect of the kind of gas and of the electron energy distribution function appears only in the height and width of the maxima and in a shift of the excitation and ionization regions along the E/p axis.

According to the dc analogy,[8] this feature is also true of a discharge excited by a varying electromagnetic field with frequency ω below the collision frequency ν, with the sole difference that the quantity $E_* = E/\sqrt{2}$ now plays the part of the field E.

Using these results we can approximate the effective parameter δ in the region where the losses in elastic collisions are nonzero by the equation

$$\delta = \delta_e \left\{ 1 + \left(\frac{E_*}{pV_m} \right)^q \right\}, \tag{2.2}$$

where $\delta_e = 2m/M$ is twice the ratio of electron mass to atomic mass; the quantity $V_m = (E_*/p)_m$ characterizes the minimum electron energy for which the losses in inelastic collisions are comparable to the losses in elastic collisions. This quantity and the exponent q depend on the kind of gas.

Since the role of inelastic processes increases as the field increases, the average fractional energy δ transferred to an atom by an electron must also rise, and therefore the exponent q must be positive:

$$q > 0. \tag{2.3}$$

A solution of Eq. (1.5) can easily be found with δ from Eq. (2.2); for the case $E \gg pV_m$, the electron temperature is a power function of the electric field

$$T_e = A \, |E|^{1-q/2}, \tag{2.4}$$

where

$$A = \left[\frac{e^2 T (\sqrt{2} p V_m)^q}{3 \varkappa \delta_e m \nu_0^2} \right]^{1/2}.$$

As is well known,[3] the electron temperature for the case $\omega \ll \nu$ with only elastic collisions considered increases linearly as the electric field increases, $T_e \sim |E|$. As expected, consideration of inelastic collisions leads to a slower rise in temperature $T_e \sim |E|^{1-q/2}$.

3. The electron density n must be determined from Eq. (1.6) for a given ionization rate ν_i and recombination coefficient ρ:

$$n = \frac{\nu_i(|E|)}{\rho}. \tag{3.1}$$

Generally speaking, the recombination coefficient ρ depends on the value of the field E; however, following refs. 5 and 6, we shall assume it to be constant in the subsequent development; to determine the dependence of ionization coefficient on field amplitude we use the analogy of a low frequency discharge with $\omega \ll \nu$ to a dc discharge.

In the theory of a dc discharge the following equation is used for the ionization rate:[9]

$$\nu_i = \alpha \left(\frac{|E|}{p} \right) (\mu p) \frac{|E|}{p}, \tag{3.2}$$

where $\alpha(|E|/p)$ is the so-called first Townsend ionization coefficient and μ is the electron mobility. Experimental measurements[10] of ν_i and theoretical calculations[11] make it possible to represent the ionization coefficient in the form of a power function:

$$\nu_i = B \left(\frac{|E|}{p} \right)^r, \tag{3.3}$$

where B and the exponent r depend on the kind of gas.

The dependence of the Townsend coefficient α on field is determined by the dependence of the ionization cross section on electron energy and is an increasing function of E/p in the region of all achievable electric fields. When $\omega \ll \nu$ the electron mobility cannot decrease more rapidly than $E^{-1/2}$ as the field increases. This means that the exponent r in Eq. (3.3) is greater than 1/2:

$$r > \frac{1}{2}. \tag{3.4}$$

Thus the dependence of density on electric field, which we shall use subsequently, can be written in the form

$$n = \frac{B}{\rho}\left(\frac{|E|}{\sqrt{2}\,p}\right)^r. \qquad (3.5)$$

4. Using Eq. (2.4) for the electron temperature and Eq. (3.5) for the electron density, the equation for the determination of the electric field in the plasma can be brought to the following form:

$$\frac{d^2E}{dx^2} - iQ\,|E|^{\gamma} E = 0, \qquad (4.1)$$

where $\gamma = r-(1/2) + (q/4)$,

$$Q = \frac{4\pi k e^2 B}{mc\rho\,(\sqrt{2}\,p)^r}\left\{\frac{e^2\nu_0^2\,(\sqrt{2}\,p\,V_m)^q}{3\varkappa\delta_y mT}\right\}^{-1/4}.$$

A nonlinear equation of this type has been investigated;[4] its solution can be written in the form

$$E(x) = E(0)\left(1+\frac{x}{L}\right)^{-(\alpha+i\beta)}, \qquad (4.2)$$

where E(0) is the value of the field at the point x = + 0. By substituting Eq. (4.2) into Eq. (4.1), equating powers of 1 + (x/L), and then eliminating α, β, and L, the value of E(0) is determined by the boundary conditions (1.2). In our case, the dependence of the electric field on the coordinate has the form

$$E(x)| = 2|\zeta|\,E_0\left\{1+\frac{\gamma}{[8+2\gamma]^{1/2}}\frac{\omega}{\quad}x\right\}^{-2/\gamma}, \qquad (4.3)$$

where

$$L = E_0^{-\frac{\gamma}{2+\gamma}}\,\frac{[8+2\gamma]^{1/2}}{\gamma k}\left\{\frac{k^2}{2^{\gamma}Q}\left[1+\frac{\gamma}{2}\right]^{1/2}\right\}^{\frac{1}{2+\gamma}} \qquad (4.4)$$

is a typical scale factor for the variation of field amplitude in the plasma, and

$$|\zeta| = E_0^{-\frac{\gamma}{2+\gamma}}\left\{\frac{k^2}{2^{\gamma}Q}\left[1+\frac{\gamma}{2}\right]^{1/2}\right\}^{\frac{1}{2+\gamma}}$$

is the absolute value of the surface impedance ζ. The region of applicability of solutions of the form (4.2) is discussed in ref. 4.

It is clear from Eqs. (4.3) and (4.4) that the change in plasma properties under the influence of the field leads to qualitatively new results in comparison with linear theory: a slower fall-off of the field within the plasma and of a dependence of the penetration depth L on the amplitude of the incident field E_0. Furthermore, the sign of the derivative dL/dE_0, which characterizes the variation of the depth of penetration with amplitude of the incident field E_0, is determined by the value of the exponent γ.

To clarify the role of inelastic atomic processes on the nature of field penetration into a plasma we discuss Eqs. (4.3) and (4.4) for the following cases.

a) Plasma properties determined by elastic collisions only. In this case

$$\gamma = -\frac{1}{2}, \quad Q = \frac{4\pi k e^2 n}{mc}\left\{\frac{3\varkappa\delta_y mT}{\nu_0^2 e^2}\right\}^{1/4}$$

and

$$|E(x)| \sim E_0^{1/3}\left(1-\frac{x}{|L|}\right)^4, \quad L \sim E_0^{1/3},$$

which agrees with previous results[4] for strong damping. In this case, an increase in the amplitude of the incident field leads to a reduction in plasma conductivity and consequently to an increase in the depth of field penetration $[dL/(dE_0) > 0]$.

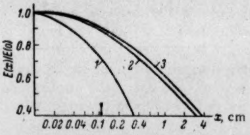

Fig. 2. Spatial distribution of field in plasma.

b) Plasma properties determined by both elastic and inelastic atomic processes.

According to Eqs. (2.3) and (3.4), q > 0 and r > ½ and consequently $\gamma > 0$. Thus, consideration of inelastic processes leads to a change in the sign of the derivative

$$\frac{\partial L}{\partial E_0} < 0$$

and consequently not to an increase as in a) but to a decrease in the depth of penetration L with increasing E_0.

5. We can carry out a further analysis of the effect of inelastic collisions on the nature of electromagnetic field penetration into a plasma by considering a discharge in argon excited by an electromagnetic field with λ = 10 cm and a field E_0 = 500 V/cm, which corresponds to an input power W ~ 3 kW.

The recombination rate is taken to be

$$\rho = 10^{-13}\ \mathrm{cm}^{-3}\cdot\mathrm{sec}^{-1},$$

which is typical for collisional radiative recombination at an electron temperature characteristic of a microwave discharge.[12] For definiteness we assume a gas temperature $T = 10^3$ °K and a pressure of 100 mm Hg. The value of the electron density created by the incident field at the plasma boundary is $n = 10^{13}$ cm^{-3}. Under these conditions, all the assumptions made above are satisfied, as is easily verified.

The dependence of the electric field amplitude normalized to E(0) on the coordinate x measured into the plasma is shown in Fig. 2 for elastic atomic processes only (curve 1), for ionization and elastic processes (curve 2), and for ionization, excitation, and elastic processes (curve 3). The coordinates of the points at which the curves intersect the x axis characterize the distances at which the field amplitude decreases by a factor of e. The arrow on the x axis indicates the depth of the skin layer calculated from linear theory for a constant electron density and temperature $T_e = T$.

It is clear that the failure to consider the effect of in-

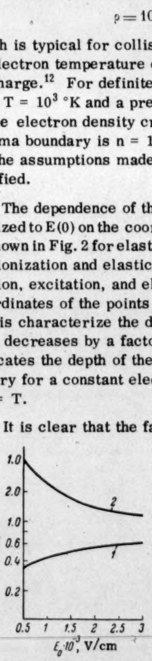

Fig. 3. Depth of field penetration into plasma as a function of incident field amplitude.

elastic processes leads to an error of an order of magnitude in the estimate of the depth of the skin layer; complete neglect of the effect of the field on plasma properties leads to an error of almost two orders of magnitude. At the same time, neglect of the effect of excitation with ionization taken into account is completely valid; this is due to the large difference of the exponents r and $q/4$ (for argon $r = 4.5$ and $q = 1.4$). Physically, this means that atomic excitation influences the optical properties of a discharge rather than the electrical properties. The error in the estimate of skin depth when ionization is not included is due to the neglect of the large drop in conductivity within the plasma.

Figure 3 illustrates the dependence of depth of penetration on E_0 for electron heating alone (curve 1) and for electron heating plus atomic excitation and ionization (curve 2). The difference in the curves is due to the difference in the effect of collision frequency and electron density on plasma conductivity.

The authors thank A. P. Motornenko and Yu. G. Gurevich for discussion and F. G. Bass for his interest.

---

[1] L. S. Polak (ed.), Outline of the Physics and Chemistry of a Low-Temperature Plasma [in Russian], Izd. Nauka, Moscow (1971).

[2] A. Ya. Usikov, I. D. Truten', A. P. Motornenko, and E. V. Belousov, Ukr. Fiz. Zh., 16, 705 (1971).

[3] V. L. Ginzburg and A. V. Gurevich, Usp. Fiz. Nauk, 70, 201, 393 (1960) [Sov. Phys. – Usp., 3, 115, 175 (1960)].

[4] F. G. Bass and Yu. G. Gurevich, Usp. Fiz. Nauk, 103, 447 (1971) [Sov. Phys. – Usp., 14, 113 (1971)].

[5] M. A. Liberman and A. T. Rakhimov, Zh. Eksp. Teor. Fiz., 61, 1047 (1971) [Sov. Phys. – JETP, 34, 559 (1972)].

[6] M. A. Liberman and A. T. Rakhimov, Zh. Tekh. Fiz., 42, 1799 (1972) [Sov. Phys. – Tech. Phys., 17, 1443 (1973)].

[7] L. M. Blinov, V. V. Volod'ko, G. G. Gontarev, G. V. Lysov, and L. S. Polak, Generators of Low-Temperature Plasma [in Russian], Izd. Energiya, Moscow (1969).

[8] V. E. Golant, Usp. Fiz. Nauk, 65, 39 (1959).

[9] M. J. Druyvestyn (Druyvestein) and F. M. Penning, Rev. Mod. Phys., 12, 87 (1940).

[10] S. C. Brown, Elementary Processes in Gas Discharges, Wiley, New York (1961).

[11] V. E. Golant, Zh. Tekh. Fiz., 29, 756 (1959) [Sov. Phys. – Tech. Phys., 4, 680 (1959)].

[12] L. M. Biberman, V. S. Vorob'ev, and I. T. Yakubov, Usp. Fiz. Nauk, 107, 353 (1972) [Sov. Phys. – Usp., 15, 375 (1973)].

Optical investigation of a turbulent plasma

Ya. F. Volkov, V. G. Dyatlov, and N. I. Mitina

(Submitted September 24, 1973)
Zh. Tekh. Fiz., 44, 1448-1454 (July 1974)

Θ-pinch plasma is investigated. For a density $n \geq 5 \cdot 10^{14}$ cm^{-3} and ion temperature $T_i \sim 30$ eV there are intense oscillations with electric fields up to 25 kV/cm. These are low-frequency ($\omega \gg \omega_{pe}$) oscillations with vector directed predominantly along the azimuthal plasma current. The plasma turbulence level is of the order of 10^{-3}.

There is a good deal of interest in plasma systems in which a closed confinement magnetic field depends on the plasma currents. These systems are like Tokamaks, in a certain sense but have special features.

One such system is the Θ pinch with a superimposed azimuthal magnetic field and a reverse axial field. This system has been investigated by several authors (refs. 1, 2), from the viewpoint of plasma heating and confinement. A high-power facility (~ 1 MJ) was used in ref. 2 to investigate a dense plasma ($n \sim 10^{16}$ cm^{-3}) formed at initial gas pressures $P \geq 0.1$ torr.

The same authors had investigated a discharge with initial pressure $P \leq 0.01$ torr. For these conditions ($n \sim 10^{14}$ cm^{-3}) the induction electric field generates directed velocities of the order of electron and ion thermal velocities. In this case the plasma can contain runaway electrons which can be accelerated to large energies (ref. 3) when the magnetic configuration favors containment. The interaction of the electron beam with the plasma can excite various instabilities, leading to turbulent heating if the fluctuations are large enough. A turbulent plasma has an anomalously large resistance, leading to accelerated diffusion of the fields into the plasma. This can limit the lifetime of the Θ pinch with an aximuthal magnetic field, since these require that the plasma ring contain a trapped axial field opposite to the external field. The present paper discusses turbulent heating and certain plasma containment processes in such systems in which the plasma parameters are measured by optical methods.

APPARATUS AND METHODS OF MEASUREMENT

The experiments are carried out on an apparatus which differs in size from those described in refs. 1 and 3 (discharge tube diameter D = 22 cm, distance between coils 20 cm) and in the capacitor bank energy (c = 65 μF, V = 20 kV; T = 33 μsec). The discharge is in flowing helium at pressure $P = 5 \cdot 10^{-4}$ to 10^{-2} torr. The optical measurements are similar to those described in refs. 4 and 5. An image of the plasma volume to be investigated is projected on the entrance slit of a type ISP-51 spectrograph employing a five-stage image-converter tube operating in the continuous scan mode. When the system induces a Fabry–Perot etalon the latter is mounted behind the collimating objective of the spectrograph.

The plasma density is measured using the cutoff of a microwave signal at λ = 2, 4, and 8 mm.

The radial electron and ion distributions are determined at different times by taking integral transforms of high-speed scans of the discharge in continuum light or in light from ion lines. The continuum is studied in the wavelength region 4980 Å with a bandwidth of ± 10 Å. There are no spectral lines in this region. The relative ion density distribution is investigated by measuring the light in the He II 4686 Å and C II 4627 Å lines. Since the plasma electron temperature is high ($T_e > 100$ eV), one can assume that the intensities of the continuum and of the C II and He II spectral lines depend only slightly on T_e. In reducing the data of the high-speed scans in continuum light we assume that multiply charged impurity ions have the same distribution as He^{++} ions, i.e., that the effective ion charge is independent of the radius. Then more than 90% of the positively charged plasma component consists of He^{++} ions.

The electron temperature is evaluated from the absorption of the soft x radiation in beryllium. Under the conditions of greatest interest, from the viewpoint of interaction of the electron flux with the plasma ($P \leq 7 \cdot 10^{-3}$ torr), the hard x radiation makes it impossible to measure T_e.

The ion temperature is measured from the Doppler broadening of the C II and O II lines. The instrumental width of the system does not exceed 0.25 Å for the He II 4886 Å and 0.35 Å for C II and O II 4103 Å lines. The instrumental line shape is close to a Lorentzian; therefore the Doppler width of the C II and O II lines is computed from tables for the Voigt profile.

The mean intensity of the turbulent electric fields is calculated from the width of the He II 4686 Å line. This line profile is the sum of the instrumental and Doppler profiles and that due to Stark broadening in the turbulent electric fields. The Stark broadening due to the Coulomb fields of the electrons and ions is negligibly small for $n < 10^{15}$ cm^{-3}. The total width due to instrumental and Doppler broadening is calculated from tables for the Voigt profile. Assuming that the turbulent field intensity distribution is Gaussian, and that the Doppler broadening is much greater than the instrumental width, we compute the linewidth due to the turbulent fields to be

$$\Delta\lambda_s = (\Delta\lambda^2_{\text{mea}} - \Delta\lambda^2_{\text{d.i.}})^{1/2},$$

where $\Delta\lambda_{\text{meas}}$ is the measured linewidth; $\Delta\lambda_{\text{d.i.}}$ is the linewidth due to the Doppler effect and the instrument. With this assumption the width of the He II 468.6 nm line is related to the mean turbulent field intensity $\overline{E}$, according to ref. 6, by the expression $\Delta\lambda_s = 4 \cdot 10^{-2}\,\overline{E}$ (Å, kV/cm).

One probable cause of the appearance of turbulent fields is the ion-acoustic instability. The electrical field of these waves is predominantly directed along the current created by the instability. In the experiment an attempt is made to determine the degree of anisotropy of the electric fields by the method described in ref. 7. The most suitable line for this purpose is Hα, used by the authors of ref. 7. However, in our discharge this hydrogen line does not emit at the times of interest to us, because of the high electron temperature. We therefore use the He II 4686 Å line to evaluate the degree of anisotropy of the fields. Computed values of the σ- and π-component intensities of this line are taken from ref. 8, and difference profiles for the He II line are constructed for two positions of the polaroid filter; 1) with the polaroid transmission axis along the facility axis (y polarization), and 2) with the polaroid axis in a plane perpendicular to the facility axis (z polarization). The degree of anisotropy is given by the ratio E_z/E_y. A series of computed curves is constructed for different values of E_z/E_y and for the specific value of E_z found from the linewidth $\Delta\lambda_s$.

It turns out there is a noticeable difference in the profiles even for an insignificant degree of anisotropy. However, we have not found an accurate value of the anisotropy when the Doppler width of each component is more than 0.5 Å. In our case, therefore, ($\Delta\lambda_{Dop} \sim 1$ Å) we can only indicate the presence of anisotropy.

We have also determined the density of the azimuthal plasma current by magnetic probe measurements.

RESULTS AND DISCUSSION

All the measured results presented here refer to the third half-cycle of the discharge. In this half-cycle closed magnetic configurations and beams of accelerated electrons appear for pressures $5 \cdot 10^{-4}$ torr $\leq P \leq 6 \cdot 10^{-3}$ torr.

Figure 1a shows the dependence of maximum plasma density on the initial gas pressure, obtained with different discharge tube volumes [D_1 = 11 cm (ref. 3), and D_2 = 22 cm] at essentially the same magnetic field parameters. It can be seen that the density is greater by a factor of 3 or 4, in the larger facility, which can be explained as follows. The minimum, i.e., limiting size of the plasma tube, is determined mainly by the ratio between the trapped opposed magnetic field and the external compression field. Since the field intensities are the same, the limiting size of the plasma tube will not differ in the two cases, when the gas-kinetic pressure of the plasma is less than the magnetic pressure ($\beta < 1$). When the "snowplow" model holds, as it does in most Θ pinch cases, the limiting density increases with the volume from which the plasma is collected.

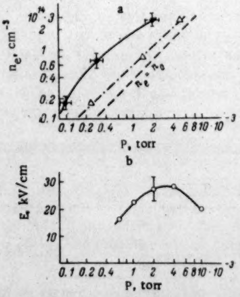

Fig. 1. a) Plasma density as a function of initial pressure: solid line – in an apparatus of tube diameter 22 cm; dot-dash line – in an apparatus whose linear dimensions are less by a factor of 2; broken line – for a plasma density equal to the initial density of the neutral gas ($n_e = n_0$). (b) Turbulent electric field as a function of pressure.

Intense hard γ radiation is observed in ref. 3, due to the flux of accelerated electrons for initial gas pressures $P \leq 3 \cdot 10^{-3}$ torr, which corresponds to a maximum plasma density of $n \leq 1 \cdot 10^{14}$ cm^{-3}. It is interesting that this radiation is observed in the present system at pressures $P \leq 6 \cdot 10^{-13}$ torr, when the density can reach $6 \cdot 10^{14}$ cm^{-3}, although the induction electric field remains the same. This is evidence that a particularly important requisite for the existence of beams of accelerated electrons is that runaway conditions prevail for some of the plasma electrons in the initial phases of the discharge. Following preliminary acceleration at the very beginning of the compression phase, when the plasma density favors runaway, the electrons becomes less sensitive to increased density at later times, i.e., they possess enough initial velocity to escape, even at high densities. Thus, a larger system makes it possible to have large beams of relativistic electrons in a high-density plasma.

When the electron temperature is high enough ($T_e >$ 100 eV) the intensity of the He II line can be expressed as $I_{He\,II} \sim n_e n^+_{He}$, where $n_e n^+_{He}$ are the density of electrons and singly charged ions, respectively, and the continuum intensity can be expressed as $I_c \sim n_e^2$. Then the radial distribution of I_c can be used to determine the radial distribution of the electron density, and the ratio $I_{He\,II}/\sqrt{I_c}$ can be used to determine the radial density distribution of the He$^+$ ions since $I_{He\,II}/\sqrt{I_c} \sim n^+_{He}$. Figure 2 shows the experimental radial distributions of n_e and n^+_{He} at various times during the discharge. Evidently the maximum of the He$^+$ ion density is displaced relative to the maximum electron density. A possible reason is that the ions are formed in the plasma ring from neutrals which come in from the periphery and are heated as they penetrate more into the plasma ring.

Measurements show that the ion temperature depends very little on the neutral gas pressure in this range (0.5 to $10 \cdot 10^{-3}$ torr). After a time $\tau \sim \mu$sec, the ion temperature increases to 30 eV, and then remains essentially constant during the time in which the containment field exists. After the collapse of the magnetic configuration the temperature falls rapidly.

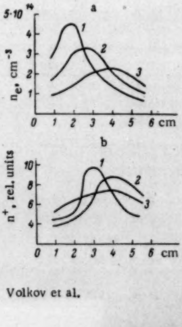

Fig. 2. Radial density distributions for electrons (a) and He$^+$ ions (b). t is in μsec; 1) 1.5 after the start of the magnetic field subperiod; 2 and 3) 3 to 5.

One can attribute the heating of the ions both to adiabatic compression and to turbulent heating. It can be seen from the high-speed scans of the discharge that the first stage of compression down to a radius of ~ 4 cm occurs in approximately 1 μsec; then there is a slow compression down to a radius of 2 to 2.5 cm in a time of 4 to 5 μsec.

The large intensity of the turbulent electric fields in the plasma indicates turbulent heating. The electric field (Fig. 1b) increases with pressure up to $P \sim 1 \cdot 10^{-3}$ torr, reaching a value of 25 kV/cm; it then remains almost constant for pressures up to 5 to $6 \cdot 10^{-3}$ torr. It is difficult to measure the electric field for higher initial pressures because of line broadening due to Holtsmark fields. The observed level of the electric oscillations (25 kV/cm) is reached in a time $\tau \sim 1$ μsec, and remains essentially constant until the breakdown of the plasma formation, for initial pressure $P > 10^{-3}$ torr. For $P < 10^{-3}$ torr the linewidth (which means the electric field also) increases monotonically from the beginning of the half-cycle until the decay of the plasma. Figure 3 shows image-converter tube pictures of the He II line shape for three values of pressure; and these bear out the analysis above.

From the nature and magnitude of the spectral line broadening one can evaluate the frequency range of the electric fluctuations which excite the broadening. A current-carrying plasma containing beams of accelerated electrons can show instabilities at frequencies in the region of the electron frequencies ω_{pe} and the ion plasma frequency ω_{pi}. If we assume that the line broadening results from high-frequency fields (ω_{pe}), then the linewidth $\Delta\lambda_{hf}$ at the maximum plasma density cannot exceed 0.5 Å since $\Delta\lambda_{hf} = \lambda^2(\omega_{pe}/2\pi c)$ (where λ is the wavelength of the spectral line), while the observed widths are as large as 1 Å. This is evidence that strong low-frequency fluctuations are present and, that if there are high-frequency fluctuations, their contribution is small. Moreover, broadening in a field of frequency of the order of ω_{pe} is similar to shock broadening; therefore the radiated light is not polarized. In low-frequency fields, e.g., ion-acoustic fields, the broadening resembles that in a static field, and the light wave is polarized. It is known that the electric vector in ion-acoustic oscillations is directed along the current which has caused the oscillations. The He II 4686 Å line profile radiation in polarized light (Fig. 4) confirms the presence of anisotropy in the electric fluctuations of the plasma in that the electric vector has a predominant direction coinciding with that of the plasma current. This once again confirms the presence of low-frequency oscillations.

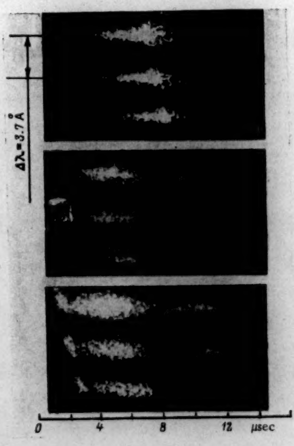

Fig. 3. Image-converter tube photographs of the 4686 Å He II line for different pressures. P, torr: 1) $6 \cdot 10^{-4}$; 2) 10^{-3}; 3) $4 \cdot 10^{-3}$.

The discharge has all the conditions necessary for the excitation of an ion-acoustic instability. Estimates of the current velocity from the measured plasma density ($n \approx 6 \cdot 10^{14}$ cm^{-3}) and the azimuthal current density ($j \approx 10$ kA/cm^2 give

$$u = \frac{j}{en} \approx 10^8 \text{ cm/sec}.$$

Here the thermal velocity of the ions and electrons in $4 \cdot 10^6$ cm/sec, and $V_{Te} \geq 6 \cdot 10^8$ cm/sec, while the acoustic velocity $C_s = 10^7$ cm/sec.

Estimates of the plasma conductivity $\sigma = j/E_\varphi$, where E_φ is the strength of the vortical electric field, give $\sigma \approx 2 \cdot 10^2/\Omega^{-1} \cdot \text{cm}^{-1}$, which corresponds to an effective collision frequency of $\nu_{eff} = 8 \cdot 10^8$ sec^{-1}. We note that this is two orders higher than the Coulomb collision frequency. From the well-known relation (ref. 9) $\nu_{eff} = \alpha\omega_{pe}(w/nT)$, where w is the energy density of the fluctuations, α is a coefficient, and $\alpha \sim 1$, we can find the turbulence level of the fluctuations:

$$\frac{w}{nT} = \frac{\nu_{eff}}{\alpha\omega_{pe}} \approx 6 \cdot 10^{-4}.$$

A comparison of the energy density of the fluctuations $\overline{E}^2/8\pi$ ($\overline{E}^2$ was obtained from the optical measurements) with the density of thermal energy in the plasma gives a turbulence level of $3 \cdot 10^{-3}$. Bearing in mind the tentative nature of the calculations, one can conclude that the agreement is satisfactory.

Thus, the plasma investigated is highly turbulent. The conductivity of such a plasma can be much smaller than the classical value. Therefore, because of the accelerated penetration of the magnetic field into the plasma, the life-

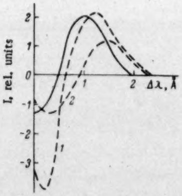

Fig. 4. Difference in the He II λ = 4686 Å line shape with z and y polarization. The solid curve is experimental; the broken lines are theoretical, for $E_z = 30$ kV/cm and level of anisotropy E_z/E_y = 1) 5; 2) 1.5. In the calculations the shape of each individual component is assumed to be gaussian, with $\Delta\lambda_{1/2} = 1$ Å.

time of the trapped magnetic field and, therefore, the lifetime of the closed magnetic configurations in a Θ-pinch system with an azimuthal magnetic field cannot exceed 25 μsec in our case. The fact is that the turbulence produces rapid heating, leading to the undesired limtation on the lifetime of the confinement configuration. It is known that the conductivity of a turbulent plasma increases with density; therefore one can increase the lifetime of the containment configuration by increasing the density. But if we increase the density by increasing the initial gas pressure, it is difficult to obtain a turbulent discharge regime, because of the lighter electric fields that are required. It is therefore desirable to increase the final density by increasing the size of the system. It is then easy to reach critical velocities with a comparatively small electron density, and some of the electrons, being accelerated, can remain runaway electrons during the subsequent density increase due to compression. In this way one can reach the requisite degree of turbulence when the plasma conductivity is large enough.

CONCLUSIONS

It has been shown that in a plasma with density $n \geq 5 \cdot 10^{14}$ cm^{-3} and ion temperature $T_i \sim 30$ eV there are intense fluctuations with electric fields, up to 25 kV/cm. These fluctuations are low-frequency ($\omega \ll \omega_{pe}$), and their electric vector has a predominant direction along the plasma azimuthal current. The plasma level of turbulence is 10^{-3}. Because of the anomalously high resistance of a turbulent plasma, which limits the lifetime of the closed magnetic configurations, it is proposed to increase the plasma conductivity by increasing the density without changing the conditions for excitation of instability; this can be done by increasing the discharge volume.

---

[1] Ya. F. Volkov, V. T. Tolok, and K. D. Sinel'nikov, Zh. Tekh. Fiz., 32, 811 (1962) [Sov. Phys. – Tech. Phys., 7, 593 (1963)].

[2] A. S. Kolb, R. H. Dixon, D. Duchs, R. C. Elton, and M. P. Young, Plasma Physics and Controlled Nuclear Fusion Research Conf. Proc., 2, Novosibirsk (1968), p. 567.

[3] T. A. El-Khalafawy, A. M. Youssef, V. G. Diatlov, and Ya. F. Volkov, Plasma Phys., 14, 103 (1972).

[4] Ya. F. Volkov, V. G. Dyatlov, and N. I. Mitina, Ukr. Fiz. Zh., 17, 916 (1972).

[5] S. P. Zagoradnikov, G. E. Smolkin, and G. V. Sholin, in: Plasma Diagnostics [in Russian], Atomizdat, Moscow (1968), p. 168.

[6] H. R. Griem and H. J. Kunze, Phys. Rev. Lett., 23, 1279 (1969).

[7] E. K. Zavoiskii, Yu. G. Kalinin, V. A. Skopyupin, V. V. Shapkin, and G. V. Sholin, ZhETF Pis. Red., 13, 19 (1971) [JETP Lett., 13, 12 (1971)].

[8] W. Steubing, and R. Gunter, Ann. Physik., Bd. 15, 345 (1955).

[9] A. A. Vvedenov and D. D. Ryutov, in: Reviews of Plasma Physics, No. 6 [in Russian], Atomizdat, Moscow (1972), p. 3.

Electron temperature in a high-frequency helium discharge

V. S. Voitsenya, A. Yu. Voloshko, V. G. Konovalov, and S. I. Solodovchenko

(Submitted September 24, 1973; resubmitted December 20, 1973)
Zh. Tekh. Fiz., 44, 1455-1457 (July 1974)

Spectroscopic measurements of the electron temperature in a high-frequency discharge plasma ($T_e \sim 10$ eV, $n_e \sim 2 \cdot 10^{11}$ cm^{-3}) in a toroidal stellarator are described. As the density of neutrals in the discharge increases one must take account of radiation trapping resonance lines.

The "helium thermometer" method is widely used for nocontact measurement of the electron temperature of a plasma. Many theoretical and experimental papers have been published on the possibilities and the conditions for application of this method. It has been shown (refs. 1, 2) that although the method is experimentally simple, there are serious limitations on its applicability. The experimental conditions in a plasma very often do not admit of the simplest model for level populations, i.e., the corona model, and one must take account of processes which give additional populations (e.g., multistage excitation, cascade, transitions, etc.). The almost complete absence of experimental level excitation cross sections requires rather complex calculations when the corona model cannot be applied.

In addition, in the case of incomplete helium ionization (and in the corresponding pressure range) the population of some levels can be appreciably affected by absorption of radiation in resonance lines.

The present paper compares experimental results of measurement of T_e from various pairs of singlet and triplet helium lines in a weakly ionized high-frequency discharge.

The discharge is produced in the metal chamber of the "Saturn" toroidal stellarator (ref. 3) using the electron cyclotron resonance. The microwave power at f = 10 GHz is 12 W. The helium pressure in the chamber is varied from $3 \cdot 10^{-5}$ to $6 \cdot 10^{-4}$ torr. The major and minor radii of the vacuum chamber are R = 36 and r = 8.7 cm, and the plasma volume is a little more than 20 liters.

The plasma parameters are investigated by means of single and double electrostatic probes, a microwave interferometer (λ = 8 mm and λ = 16 mm), and a type MDR-2 monochromator with an FÉU-39 photomultiplier.

The monochromator is used to determine the ratio of intensities of the following pairs of neutral helium lines: 4713 and 4922 Å, 5016 and 4713 Å, 5047 and 4713 Å. In determining the electron temperature we use the results of calculations of refs. 4-6, based on the corona model.

An error estimate of the intensity determination, (taking account of the spectral sensitivity of the photomultiplier) gives ±15%, which corresponds to a relative error in the T_e measurement below ±25% for all pairs of lines.

Measurement shows that the plasma density (an average through the plasma cylinder with radius r_{pl} = 6 cm) is $\sim 2 \cdot 10^{11}$ cm^{-3} and varies very little as the helium pressure is varied.

Figure 1 shows the dependence of electron temperature on pressure. As expected (ref. 7), at increased pressures the electron temperature, determined from the I_{5016}/I_{4713} ratio, is appreciably higher than values found for the other line pairs and by means of the electrostatic probes. The observed difference can be accounted for numerically in a satisfactory manner if one takes account of the additional increase of 3^1P level population due to absorption of radiation by the resonance line He I at λ = 537 Å.

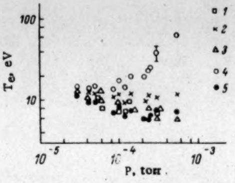

Fig. 1. Pressure dependence of the electron temperature as measured by probes (1) and from the intensity ratios of He I lines. 2) I_{4713}/I_{4922}; 3) I_{5047}/I_{4713}; 4) I_{5016}/I_{4713} without accounting for absorption at λ = 537 Å; 5) I_{5016}/I_{4713} allowing for absorption at λ = 537 Å.

Figure 2 shows the results of calculations of the effective excitation cross section for the 5016 Å line from ref. 7, taking the vacuum chamber radius (8.7 cm) to be the radius of the absorbing region. It follows from this relation that in these experiments (10^{12} cm$^{-3} \le n_0 \le 1.9 \cdot 10^{13}$ cm^{-3}) the value of Q_{eff}^{5016} can differ by roughly a factor of 10 from the value for the fully ionized plasma.

Figure 1 also shows the electron temperature, determined from the I_{5016}/I_{4713} ratio, taking account of the results of ref. 7. There is good agreement between the results from the 5016 and 4713 Å pairs, the probe measurements, and the I_{5047}/I_{4713} ratio results. The difference does not exceed 20% over the entire range of pressure variation. However, the electron temperature, determined from the intensity ratio for the 4922 and 4713 Å lines, is systematically higher than the values from the other methods. A possible cause of this discrepancy is the additional popu-

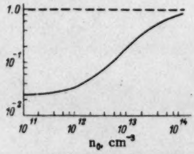

Fig. 2. Calculated dependence of the effective cross section for excitation of the He I 5016 Å line on helium atom density in the discharge. The broken line shows the total absorption of the λ = 537 Å line.

lation of the upper level of the 4922 Å line (4^1D), not accounted for in ref. 4, due to absorption at the resonance line 522 Å (1s−4p transition) and to collisional transitions between 4p−4d levels.

Thus, the present paper has shown that for plasma density ~ $2 \cdot 10^{11}$ cm^{-3} and higher a comparatively wide range of neutral helium density (10^{12} cm$^{-3} \leq n_0 \leq 1.9 \cdot 10^{13}$ cm^{-3}), the helium thermometer method gives results in good agreement when one uses the line pairs 5016 and 4713 Å, and 5047 and 4713 Å.

In conclusion the authors thank V. I. Kononenko, I. Yu. Adamov, and V. L. Berezhnyi for the microwave measurements, and O. S. Pavlichenko for useful discussion.

---

[1] I. M. Padgomyi and G. V. Sholin, Dokl. Akad. Nauk SSSR, 160, 575 (1965) [Sov. Phys. – Dokl., 10, 48 (1965)].

[2] V. M. Strunnikov, Opt. Spektrosk., 20, 3 (1966).

[3] V. S. Voitsenya, A. V. Georgievskii, V. E. Ziser, D. P. Pogozhev, A. I. Skibenko, S. I. Solodovchenko, V. A. Suprenenko, V. T. Tolok, I. P. Fomin, and L. A. Dushin, IAEA, Vienna, 3, 131 (1971).

[4] Collection: Plasma Diagnostics (ed. by R. Huddlestone and S. Leonard), Academic Press, New York.

[5] V. G. Konovalov, G. P. Pavlova, and O. S. Pavlichenko, Zh. Tekh. Fiz., 42, 1854 (1972) [Sov. Phys. – Tech. Phys., 9, 1486 (1973)].

[6] R. J. Sovie, Phys. Fluids, 7, 613 (1964).

[7] A. V. Phelps, Phys. Rev., 110, 1362 (1958).

Effect of molecular hydrogen on a cesium discharge. I

N. D. Morgulis and V. I. Klapchenko

T. G. Shevchenko Kiev University

(Submitted July 30, 1973)
Zh. Tekh. Fiz., 44, 1458-1462 (July 1974)

The effect of neutral molecular hydrogen at pressures of 0.003–0.2 mm Hg on a cesium discharge at 0.01 0.1 mm Hg is considered. It is shown that the addition of such a gas causes: 1) a marked increase in both the electric field E in the plasma and in the energy $\omega = jE$ needed to maintain it, and 2) a deficit of electrons with energies $\gtrsim$ 1 eV in the Maxwellian distribution. The reason is that under these conditions additional energy losses occur due to: a) impact excitation of the rotational–vibrational spectrum of molecular hydrogen, and b) partial quenching by these molecules of the resonance excitation of atomic cesium which is important for generation of the plasma. Experimental results are compared with the conclusions following from a) and b), and good agreement is found.

Cesium discharges, either pure or in a mixture with neutral inert gases, have been subjected to detailed analysis in recent years. The basic stimulus for this interest comes from the importance of such systems in energy conversion – in thermionic converters and closed-cycle MHD generators. At the present time, new applications have been found for cesium plasmas – but of a different type, in mixtures with different molecular gases – primarily in the physics of open-cycle MHD generators, high-power gas lasers, etc. Undoubtedly, the molecular gas, even in neutral form, can have a considerable effect on the properties and parameters of the cesium plasma, causing for example: 1) appreciable impact deexcitation quenching of the cesium atoms[1] in the 6P resonance level, which is very important for ionization–recombination processes;[2] 2) additional marked energy losses due to impact excitation of the rotational–vibrational spectrum in this mixture;[3] 3) numerous ion–molecular processes that are much more complicated and diverse than in a pure cesium plasma;[4] etc. The experimental material on this interesting problem is very limited,[5–7] basically involving a general description of the phenomena without a detailed analysis of the elementary processes and parameters of the plasma. This situation makes it very difficult to analyze the processes occurring in such plasmas,[8,9] and is the reason that the present work has been undertaken.

In the first part of this paper, pure molecular hydrogen is used as the neutral and passive un-ionized gas added to the cesium discharge plasma with a comparatively low electron temperature. The hydrogen is easily and conveniently admitted to the experimental apparatus using the familiar titanium leak. The useful nature of the gas is also seen from the fact that the usually bright Hγ line at $\lambda = 4340$ Å is difficult to observe in the background of the cesium recombination spectrum. In this sense, our work differs considerably from, for example, ref. 10, in which a sodium–hydrogen pulsed discharge laser is investigated.

A schematic diagram of the apparatus is shown in Fig. 1, where the middle plasma section has a radius R = 1 cm and a length l = 12 cm ≫ R. In addition to a hot cathode 1, an anode 2, two axial probes 3, and a sidearm with the cesium 4, which are conventional, the apparatus also has a hydrogen source 5 and a thermocouple manometer 6 to measure the pressure P. The probes are used to determine the axial temperature T_e and density n_e of the plasma electrons, their energy distribution function $f(v_e)$, and the electric field E in the plasma. The function $f(v_e)$ is determined by double differentiation of the probe characteristic curve. In certain cases the T_e is also determined from the cesium recombination spectrum. Other required quantities are: 1) the axial density of cesium atoms n_a^* excited to the 6P resonance level, which is determined from the reversal temperature in a similar device with end windows, and 2) the axial current density j_0, which is roughly determined from the discharge current I_d and the radial distribution of the radiation intensity of the plasma column Q = f(r), which is determined using an antinomy–cesium photoelectric sensor with a subsequent Abel inversion procedure.

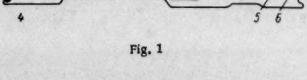

Fig. 1

In the initial stage the hydrogen source is not connected to the apparatus, and control measurements are performed in the pure cesium plasma. Then the connection between them is broken; the hydrogen flows into the apparatus until the required pressure P is reached, and the corresponding measurements are made largely at only one cesium pressure p = 0.1 mm Hg and at one n_e value $n_e = 2.5 \cdot 10^{13}$ cm^{-3}. The latter condition (n_e = const) greatly facilitates the subsequent analysis of the experimental data. We note also that when the hydrogen is admitted into the apparatus a sharp increase occurs in both the potential drop and in the discharge current necessary to maintain n_e = const, i.e., in the power required by the apparatus; simultaneously, a marked contraction of the plasma column occurs.

Thus, the standard we use is a pure cesium plasma (P = 0) with the following axial parameters: T_e = 2700°K, $n_e = 2.5 \cdot 10^{13}$ cm^{-3}, E = 0.3 V/cm, $n_a^* \approx 3 \cdot 10^{12}$ cm^{-3}, conductivity $\sigma_0 = j_0/E = 1.8\ \Omega^{-1} \cdot$ cm^{-1} and power $\omega_0 = j_0 E$ = 0.16 W/cm^3 with a purely Maxwellian electron energy distribution $f(v_e)$ and the usual radial distribution of the electron density, similar to the curve Q = f(r). With the subsequent admission of the hydrogen gas, p and n_e remain constant, but all the other parameters can change. This feature is shown in Figs. 2 and 3 on a semilogarithmic scale for the point P = 0, and then for P = 0.003-0.2 mm Hg, where the following quantities are given: T_e(I), E(II), σ (III), and ω (IV). Examination of the figures leads to the following conclusions.

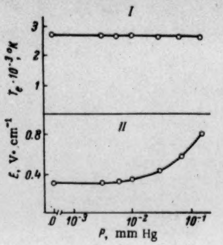

Fig. 2

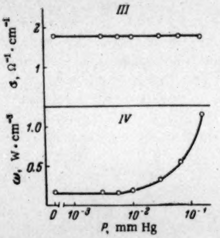

Fig. 3

1. We find n_e = const, and T_e remains constant and independent of P. This means that n_a^* remains constant along with the equilibrium ionization rate of the cesium $dn_e/dt = f(T_e) = n_e/\tau_p$, i.e., the charge recombination rate in the plasma $1/\tau_p$. Consequently, the introduction of the hydrogen gas (up to P = 0.2 mm Hg) does not change the existing significant volume recombination in the plasma, which is very sensitive to a change in plasma density. Thus, there are no new phenomena in the plasma due to the hydrogen: This results from the fairly high critical potentials for a plasma with T_e = 2700°K and to their low effective cross sections.[3]

2. The conductivity $\sigma = e\mu_e n_e$, i.e., the electron mobility $\mu_e = e/mu_e\,\Sigma nq$, is constant in our case, along with n_e and T_e. This indicates that the additional scattering of plasma electrons by hydrogen molecules ($q_1 \approx 1\cdot10^{-15}\,cm^2$) is significantly smaller than the total scattering by cesium atoms ($q_a \approx 2\cdot10^{-14}\,cm^2$) and the Coulomb scattering ($q_k \approx 5\cdot10^{-12}\,cm^2$ at T_e = 2700°K). This same situation (μ_e = const) can also be observed in Fig. 4, I, which shows the variation with increasing P of n_e and σ under different conditions, where a constant discharge current $I_d \sim \sigma E$ = const is maintained and where an increase in energy losses leads inevitably to an increase in E, i.e., to a decrease in σ.

3. The values of E and ω exhibit a very strong increase, especially starting near P > 0.01 mm Hg and above. The reason for the increase is the necessity for compensation of the additional energy losses $\Delta\omega = (\omega - \omega_0)$ primarily due to 1) excitation of the rotational–vibrational spectrum of molecular hydrogen due to electron impact, and 2) partial quenching of the 6P resonance level of the cesium atoms through collisions with these same molecules; for example, when P = 0.2 mm Hg, we obtain $\Delta\omega/\omega_0 \approx 6$.

Actually, for $\Delta\omega = (\Delta\omega_1 + \Delta\omega_2)$ we can write

$$\Delta\omega = q_1 u_e n_e n_{H_2} \alpha \mathcal{E}_e + q_2 u_a n_a^* n_{H_2} \mathcal{E}_a^*$$

or

$$\beta = \frac{d\Delta\omega}{dn_{H_2}} = q_1 u_e n_e \alpha \mathcal{E}_e + q_2 u_a n_a^* \mathcal{E}_a^* = \beta_1 + \beta_2.$$

To check this expression and the estimates of the contributions of $\Delta\omega_1$ and $\Delta\omega_2$ to the additional energy losses due to the hydrogen gas. Fig. 4, II, gives $\Delta\omega = f(n_{H_2})$ replotted from the data of Fig. 3, IV, for P > 0.01 mm Hg. This dependence actually has a linear character, with slope $\beta = 3.6\cdot10^{-16}$ W. On the other hand, reliable values[11] of q_2, which are the same for the $6P_{3/2}$ and $6P_{1/2}$ cesium sublevels ($8\cdot10^{-16}\,cm^2$ on the average), make it possible to obtain a reliable estimate $\beta_2 = 1.2\cdot10^{-16}$ W; thus $\beta_1 = (\beta - \beta_2) = 2.4\cdot10^{-16}$ W, i.e., $\beta_1/\beta_2 \approx 2$. The latter estimate for β_1 also gives – for our electrons at T_e = 2700°K, i.e., $\mathcal{E}_e$ = 0.35 eV, and with a rough use of the not very reliable value given in the literature[3] for the transport cross section $q_1 \approx 1\cdot10^{-15}\,cm^2$ – the effective accommodation coefficient $\alpha = 5\cdot10^{-3}$. For comparison, we point out that the calculated value for molecular hydrogen is $\alpha_0 = 2m/M = 5.5\cdot10^{-4}$, i.e., a loss coefficient $\delta = \alpha/\alpha_0 = 10$. These values for α and δ are in good agreement with those in the literature,[3] i.e., there is a good correlation between the experimental data given here and the general picture of the physical processes occurring in the plasma. We note also that the two-way transitions between the cesium sublevels $6P_{3/2}-6P_{1/2}$, which often occur along with the quenching, have little effect on the energy balance in the plasma.

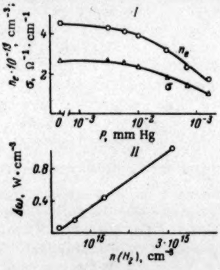

Fig. 4

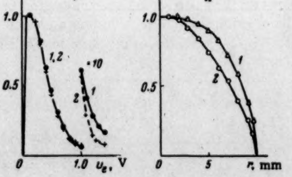

Fig. 5

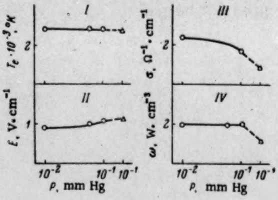

Fig. 6

The effect of the hydrogen gas on the energy spectrum of the plasma electrons $f(v_e)$ is shown in Fig. 5, I, for the following two cases: 1) P = 0, and 2) P = 0.2 mm Hg. In this figure: a) The origin is at the maximum of the second derivative of the probe characteristic curve, and b) the tail of this curve is shown on a 10× scale for clarity. It can be seen from the figure that in the first case $f(v_e)$ always has a purely Maxwellian shape at $T_e = 2700$°K (solid curve). In the second case with the gas present, it retains this shape only for $0 < v_e < 1$ eV; then, a certain deficit of fast ($v_e \gtrsim 1$ eV) electrons occurs. The reason is obviously that in this range there is a sharp increase in the effective cross section for impact excitation of the vibrational spectrum of molecular hydrogen.[3] Thus, the rate of decay of the Maxwellian distribution under these conditions is comparable to its rate of regeneration by the Coulomb interaction.

On the other hand, Fig. 5, II, gives the curves after Abel inversion of the radial distribution of radiation intensity $Q = f(r)$ for these same two cases, and it can be seen that the introduction of the hydrogen gas produces a marked contraction of the cesium plasma column.

Finally, we point out that, as mentioned above, some measurements have been performed for I_d = const and the same pressure p = 0.1 mm Hg. The data obtained in this case for n_e and σ are shown in Fig. 4, I. The general pattern of results obtained in this case is similar to those obtained in the first case n_e = const; therefore, they have not been subjected to additional quantitative analysis.

Up to this point, we have considered the case $P \leq p$. It is therefore of interest to include some preliminary data for the inverse case $p \leq P$ but with the same conditions of a cesium plasma with neutral hydrogen. For example, we consider the case P = 0.2 mm Hg = constant and a range of cesium vapor pressures p = 0.01–0.1 mm Hg, but a somewhat larger electron density $n_e = 5 \cdot 10^{13}$ cm^{-3}. The results obtained are shown in Fig. 6 for T_e (I), E (II), σ (III), and ω (IV); for comparison, the points on the extreme right give the values of these parameters for the previous case: P = 0.2, p = 0.1 mm Hg, and $n_e = 2.5 \cdot 10^{13}$ cm^{-3}. It can be seen from the figure that variation in p for the given limits has a comparatively small effect on these parameters, about equal to its effect on $f(v_e)$, which continues to exhibit the above-mentioned small deficit of fast electrons. Nevertheless, the variations in these parameters (dashed curve) between the new and old n_e values looks reasonable. These data are limited and require further analysis.

In conclusion, the authors thank A. M. Przhonskii for his help.

---

[1] A. C. Mitchell and M. W. Zemansky, Resonance Radiation and Excited Atoms, Macmillan, New York (1934), Ch. IV.

[2] L. Biberman, V. Vorob'ev, and I. Yakubov, Usp. Fiz. Nauk, 107, 353 (1972) [Sov. Phys. – Usp., 15, 375 (1973)].

[3] H. S. W. Massey, E. H. S. Burhop, and H. B. Gilbody, Electronic and Ionic Impact Phenomena, Clarendon Press, Oxford (1969), Vol. 2, Parts 10–13; B. Smirnov, Atomic Collisions and Elementary Processes in Plasmas [in Russian], Atomizdat, Moscow (1968), Ch. 6; A. Phelps, Rev. Mod. Phys., 40, 399 (1968).

[4] N. Morgulis and Yu. Korchevoi, ZhETF Pis. Red., 8, 313 (1968) [JETP Lett., 8, 192 (1968)]; A. Przhonskii, Zh. Tekh. Fiz., 43, 1516 (1973) [Sov. Phys.–Tech. Phys., 18, 960 (1974)].

[5] V. Zhibritskii, Teplofiz. Vys. Temp., 2, 945 (1964).

[6] J. Bernard and E. Labois, Plasma Phys., 9, 193 (1967); in: Proceedings of the Eighth Intern. Conf. on Ionization Phenomena in Gases (Vienna, 1967), p. 312; Inf. Byull. VINITI, No. 1, 37 (1969).

[7] G. Kasabov and V. Konakh, in: MHD Generators [in Russian], INI AN SSSR (1967), Vol. 1, p. 21.

[8] A. Mnatsakanyan, Teplofiz. Vys. Temp., 7, 385 (1969); 8, 1149 (1970).

[9] D. Bender, M. Mitchner, and S. Kruger, Inf. Byull. VINITI, No. 1, 3 (1972); I. Draper and J. L. Kerrebrock, Inf. Byull. VINITI, No. 2, 65 (1972).

[10] A. Tibilov and A. Shukhtin, Opt. Spektrosk., 25, 409 (1968); V. Pogorelyi and A. Tibilov, Opt. Spektrosk., 25, 542 (1968).

[11] D. McGillis and L. Krause, Phys. Rev., 153, 44 (1967); Can. J. Phys., 46, 1051 (1968).

Mass and energy analysis of ions in the cathode of an anomalous glow discharge. II. Binary gas mixtures Ne + Ar and N_2 + Ar

A. V. Bondarenko
M. V. Lomonosov Moscow State University

(Submitted June 26, 1973)
Zh. Tekh. Fiz., 44, 1463-1471 (July 1974)

Detailed mass-energy spectra have been obtained with a double-focusing mass spectrometer for the ions from discharges in various mixtures. The transformation of the energy spectra and the change in the total relative abundances of the various ion species are studied as a function of the mixture composition. For the mixture N_2 + Ar the production of nitrogen ions (N_2^+ and N^+) and argon ions obeys an additivity rule. The N^+ ions are produced predominantly in the cathode fall as a result of secondary processes involving N_2^+ ions which drift away from the negative glow. The most probable elementary processes resulting in the production of N^+ ions are discussed. For the Ne + Ar mixture the additivity rule is not obeyed in the production of the principal ions of the components, perhaps because of a difference between the cross sections for ionization by electrons and because of the supplementary ionization of Ar due to the Penning effects. The transformation of the Ne^+ and Ar^+ spectra resulting from a change in the mixture composition is interpreted on the basis of secondary processes. It is concluded that the point near the cathode at which the ions are produced depends on the nature of the medium and can vary as a function of the mixture composition.

On the basis of general considerations, the energy spectra of the various ion species in the cathode fall of a glow discharge should be governed by the electric field distribution, the distribution and intensity of the primary ion production, and the efficiency of secondary processes of energy and charge exchange between particles in the cathode fall.[2] As is shown in the first part of this work,[1] the majority of the principal ions (Ne^+, Ar^+, N_2^+, etc.) in an anomalous discharge in an individual gas form in the negative glow; as they move through the cathode fall they undergo a rapid charge exchange and acquire an exponential energy spectrum. The nature of the low-energy peak in the experimental spectrum requires special study.[1]

An elementary theory for the energy spectrum of the ions near the cathode is proposed in ref. 3 on the basis of simplified arguments regarding the linearity of the field in the cathode fall; it is assumed that all the ions are produced in the glow and that the predominant interaction of these ions with neutrals is charge exchange, for which the cross section is not a function of the energy. Analysis of the experimental data on slightly anomalous discharges in various gases has given the charge-exchange cross sections for He, Ne, Ar, and hydrogen ions for charge exchange with neutrals of the same atomic species.[3]

In a discharge in a gaseous mixture the situation is complicated because of the additional interactions between the various particles. Nevertheless, the corresponding experimental results can be used to evaluate the relative importance of a particular elementary process in a gas discharge.

There are well-known cases in the development and application of gas-discharge devices in which a slight impurity has a strong effect on the operation and in the characteristics of these devices. There has been essentially no study of the effect of the composition of the medium on the mass-energy spectra. Cumme[4] has reported, along with the mass-energy spectra of the principal ions from anomalous discharges in He and Ne, data on the ion distribution for mixtures of Ne with small amounts of He and Ar of fixed compositions. Bashirova[5] reported the mass spectra of channeled ions in a narrow energy range (near the high-energy peak) from discharges in binary mixtures of Ne + Ar, N_2 + Ar, O_2 + Ar, and N_2 + O_2 of various compositions. Obviously, these results do not give a complete picture of the situation, since the high-energy peak contains only a negligibly small fraction of the ions of the principal gases.[1]

TABLE 1

Mixture comp., %		Pressure p, torr	Current I_r, mA	Ion abundance in beam, %	
Ne	Ar			Ne^+	Ar^+
99	1	0.07	0.2	85	15
95	5	0.7	0.6	54	46
80	20	0.7	0.6	31	69
50	50	0.7	1.2	15	85
20	80	0.7	2.9	5.6	94.4
10	90	0.1	7.0	3.3	96.7

We have now obtained and analyzed detailed mass-energy spectra for the principal channeled ions from anomalous low-pressure glow discharges in mixtures of Ne + Ar and N_2 + Ar for various ratios of the components.

EXPERIMENTAL PROCEDURE

The mass-energy analysis of the channeled ions is carried out in the experimental apparatus described in detail previously,[1] under the following conditions: a voltage of V_r = 3000 V (±1%) across the electrodes and a pressure of p = 0.05-0.1 torr (±10%) in the gas-discharge medium. A thermocouple gauge calibrated for air is used to measure the pressures of Ne, Ar, and their mixtures; conversion coefficients are used for this purpose.[6] The reduced current density j/p^2 is $(5-80) \cdot 10^{-3}$ A/(cm^2 · torr^2), corresponding to the anomalous regime of the glow discharge.

The functional dependence of the photomultiplier gain

TABLE 2

Mixture comp., %		Pressure p, torr	Current I_r, mA	Ion abundance in beam, %		
Ne	Ar			N_2^+	N^+	Ar^+
95	5	0.05	0.5	40	55	5
80	20	0.05	0.5	32	47	21
50	50	0.05	0.5	14	38	48
			0.7	17	37	46
20	80	0.05	0.8	4.2	9.8	86
5	95	0.05	1.0	0.8	3.2	96

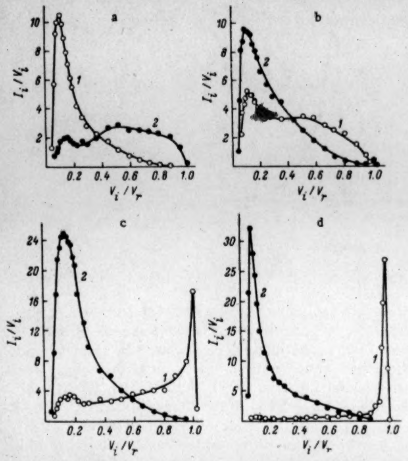

Fig. 1. Discharge in a mixture of neon with argon; energy spectra of the principal ions. a: 99% Ne + 1% Ar. 1) Ne^+; 2) Ar^+ (×5). b: 50% Ne + 50% Ar. 1) Ne^+ (×5); 2) Ar^+. c: 20% Ne + 80% Ar. 1) Ne^+ (×10); 2) Ar^+. d: 10% Ne + 90% Ar. 1) Ne^+ (×10); 2) Ar^+. Here and in Fig. 2 the "×" indicates that the ordinates of these curves are multiplied by the corresponding number.

on the mass and nature of the ion species is incorporated in the analysis of the results.[1] For this purpose the argon-ion current is multiplied by a factor of 1.4 (with respect to Ne^+). In the case of the N_2 + Ar mixture the ion currents are normalized to the N^+ current, i.e., the N_2^+ current is divided by 1.2, while the current of Ar^+ and Ar^{2+} ions is multiplied by 1.7. For each of the mixtures, differential energy spectra are plotted for the current of the principal ions,[1] and the contribution of ions of each species to the total ion current is determined graphically. For the N_2 + Ar mixtures the ratio between the currents of N_2^+ and N^+ ions is also calculated.

EXPERIMENTAL RESULTS

We have studied six different Ne + Ar mixtures and five different N_2 + Ar mixtures; the results for the individual components are reported in ref. 1. The mixture composition, the experimental conditions, and certain results are shown in Tables 1 and 2.

The mixture Ne + Ar. As the amount of Ar in this mixture is increased the total discharge current I_r increases along a hyperbolic curve. The principal ions of the channeled beam are $^{40}Ar^+$, $^{20}Ne^+$, and $^{22}Ne^+$. At energies near eV_r we detect a few (1%-3%) foreign ions,[1] not included in the overall balance. The hydride ions NeH^+ and ArH^+, whose numbers are about 1% and 2%-3%, respectively, of the numbers of the numbers of Ne^+ and Ar^+ ions, are added to the total current of principal ions. Doubly charged Ne^{2+} ions (amounting to about 2% of the number of Ne^+ ions) and Ar^{2+} ions (up to 3% of the number of Ar^+ ions) are taken into account in a similar manner. Appreciable numbers of these additional components are found in the case of Ne only in mixtures containing 80% or more Ne; for the case of Ar, these amounts are appreciable when there is only 5% Ar.

Direct measurement of the $^{40}Ar^{2+}$ current in the Ne + Ar mixtures is complicated by the circumstance that the mass line of this ion coincides with the $^{20}Ne^+$ line. We deal with this difficulty by multiplying the measured $^{22}Ne^+$ current by 9.3, corresponding to the natural abundance of neon isotopes.[1] In the same manner we determine the correct current of $^{20}Ne^+$ ions and attribute its difference from the current measured for m = 20 to $^{40}Ar^{2+}$.

Figure 1 shows the most characteristic energy spectra of the principal ions in several Ne + Ar mixtures. For Ne the total current of the ions of the isotopes is shown. The Ne^+ and Ar^+ spectra for a mixture of a given composition are markedly different in shape. As the composition is changed, these spectra undergo a gradual transformation, which can be described qualitatively as follows: The low-energy peak on the Ne^+ curve for (0.11-0.12) eV_r broadens slightly and fades rapidly. A step appears on the monotonically decaying branch of the curve at about 80% Ne; this step is clearly defined for the mixture with 50% Ne. The curvature of the subsequent part of this curve changes (Fig. 1b). As the amount of Ne in the mixture is reduced further, the low-energy peak is flattened out almost completely; at higher energies the amount of Ne^+ does not fall off, but instead gradually increases. For the mixture with 10% Ne most of the Ne^+ ions have energies in the range (0.9-1.0)eV_r, i.e., form a sharp high-energy peak (Fig. 1d).

The Ar^+ curve, with a low-energy peak at (0.08-0.12) eV_r, retains its shape as the amount of Ar in the mixture is reduced to 50% and below; only at 20% Ar does the descending branch display a step and a change in the nature of the curvature. Subsequently (at 5% and 1% Ar) a broad peak forms in the center of the energy range, and the low-energy peak fades markedly. The relative number of high-energy Ar^+ ions increases, as in the case of Ne. However, the mixture components do not behave in a completely symmetric manner: Down to 1% Ar, the Ar^+ ions are distributed more uniformly over the energy range, and the high-energy peak at V_r is not found in this case. A further deviation from the symmetry is evident in the circumstance that even a slight addition of argon (1%-5%) to the Ne leads to a disproportionately high yield of Ar^+ ions and a rapid decrease in the number of Ne^+ ions, while the addition of up to 20% neon to the Ar has little effect on the abundance of Ar^+ ions.

The mixture N_2 + Ar. As the amount of Ar in this mixture is increased, the discharge current increases nearly linearly. The principal channeled ions in this case are $^{40}Ar^+$, N_2^+, and N^+. In the nitrogen-rich mixtures, some N_2^{2+} ions can form; their mass line coincides with that of N^+ (ref. 1). In the argon-rich mixtures (80% and 95% Ar), there are an appreciable number of Ar^{2+} ions (amounting to about 3% of the number of Ar^+ ions) as well as ArH^+ ions. In the overall calculations, the number of these ions was combined with that of Ar^+ ions.

Figure 2 shows the energy spectrum of the principal ions for several N_2 + Ar mixtures. The shape of the curves for the Ar^+ and N_2^+ ions is essentially unaffected by the mixture composition, remaining similar to the

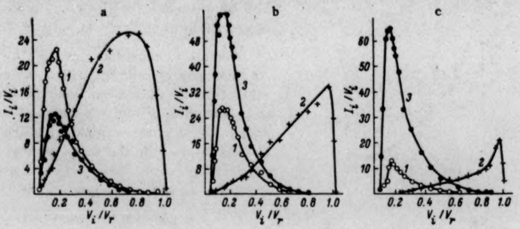

Fig. 2. Discharge in mixtures of nitrogen with argon; energy spectra of the principal ions. a: 95% N_2 + 5% Ar. 1) N_2^+; 2) N^+ (×2); 3) Ar^+ (×5). b: 20% N_2 + 80% Ar. 1) N_2^+ (×10); 2) N^+ (×10); 3) Ar^+. c: 5% N_2 + 95% Ar. 1) N_2^+ (×20); 2) N^+ (×10); 3) Ar^+.

curves for the individual gases.[1] The height of the peaks and the relative ion abundances are functions of the composition. The Ar^+ abundance is essentially proportional to the Ar concentration, while the N_2^+ abundance falls off slightly more rapidly than the amount of neutral N_2 in the mixture.

The curves for N^+ undergo an appreciable transformation as the composition is changed. The broad peak characteristic of a discharge in pure nitrogen[1] gradually vanishes as the amount of N_2 is reduced, the relative abundance of low-energy ions decreases, and a sharp peak forms at high energies. For the mixture with 5% N_2 an appreciable fraction of the N^+ ions have energies approximately equal to eV_r. In contrast with the case of N_2^+, the relative abundance of N^+ ions falls off more slowly than the concentration of neutral N_2.

The results are summarized in Fig. 3, which shows the total relative contribution of the principal ions as a function of the mixture composition. For the N_2 + Ar system we analyzed the contribution of the Ar^+ ions and the nitrogen ions, $N_2^+ + N^+$. In Fig. 3, points 1 show the abundance of argon ions, while the straight line corresponds to the additive rule for the production of ions of both components of the mixture. The positions of the experimental points show that argon ions and, correspondingly, nitrogen ions are produced and exist in a number proportional to the abundance of the neutral components. However, the relative abundances of the different nitrogen-ion species do not display the same functional dependence on the mixture composition. Points 2 in Fig. 3 show the N^+ contribution to the total current of nitrogen ions. The tendency for the relative N^+ abundance to increase approximately linearly (and, correspondingly, for the relative N_2^+ abundance to decrease approximately linearly) as a function of the argon concentration is evidence that argon affects the production of both molecular and atomic nitrogen ions.

Curve 3 in Fig. 3 shows the Ar^+ contribution to the total ion current for the Ne + Ar mixture. The hyperbolic shape of this curve implies a nonadditive production of ions in this mixture.

DISCUSSION OF RESULTS

The immediate problem of a study of binary mixtures is to determine the reasons for the change in the total relative abundance of the ions of the various species and in the shape of their spectral curves as functions of the composition. An analysis of the experimental results should incorporate: 1) the difference between the cross sections for ionization of the mixture components by electrons, 2) the difference between the cross sections for charge exchange of the component ions with their own neutrals, 3) the functional dependence of the charge-exchange efficiency on the partial pressures of the components, 4) the functional dependence of this efficiency on the length of the cathode fall, which is itself a function of the composition, and 5) cross interactions of ions and neutrals of different atomic species, taking account of the cross sections, partial abundances, etc.

When we take these circumstances into account we find that the nonadditive nature of the functional dependence of the relative ion abundance on the composition of the Ne + Ar mixture (Fig. 3) is due largely to the difference between the ionization cross sections of the mixture components. The ratio of the cross sections σ_{Ar} and σ_{Ne} for electron energies of 300-3000 eV is 3-4. When we take account of ionization by secondary electrons, which have lower energies and thus higher cross sections, we conclude that the value 4 is preferable. Calculation of the relative Ar^+ abundance on the basis of this assumption yields hyperbolic curve 4 (Fig. 3), which approximately coincides with the experimental curve for mixtures having > 50% Ar. In mixtures with less Ar, the measured fractions of Ar ions are much higher than the calculated fractions, apparently because of an additional mechanism for the production of Ar^+ ions. As this additional mechanism we can suggest the secondary charge exchange

$$Ne^+ + Ar \rightarrow Ne + Ar^+, \tag{1}$$

whose cross section over the energy range 20-200 eV is 7-8 cm^2/cm^3 (ref. 7) or five to six times lower than the cross section for charge exchange of Ne^+ with Ne known for this energy range.[8] In neon-rich mixtures the contribution of process (1) would be appreciable. However, it is necessary to keep in mind the opposing process,

$$Ar^+ + Ne \rightarrow Ar + Ne^+, \tag{2}$$

for which the cross section is one third that for process (1) (ref. 7). Nevertheless, a straightforward calculation shows that in a mixture of any composition the contributions of processes (1) and (2) essentially cancel out because of the simultaneous changes in the ratio of both the neutral components and the abundance of both ion species, although these contributions are also functions of the absolute composition.

Another mechanism leading to the formation of more Ar^+ ions is the Penning effect:

$$Ne^* + Ar \rightarrow Ne + Ar^+ + e, \qquad (3)$$

where Ne^* is metastably excited neon (16.5 V). The reverse process does not occur. The cross section for process (3) is approximately equal to the gas-kinetic cross section, i.e., can exceed the cross section for ionization of Ar by electrons. Also assuming that the additional contribution of process (3) is proportional to the product of the Ne and Ar abundances, we can show that the Ar^+ abundance due to this process in neon-rich mixtures increases significantly, approaching the experimental values.

Rapid charge exchange of one or another of the ion species produced does not affect the number of these ions but does strongly affect the shape of the spectral curves. Then we can offer a qualitative explanation for the transformation of the experimental curves which occurs as the composition of the Ne + Ar mixture is changed. In the mixture 10% Ne + 90% Ar (Fig. 1d) the efficiency of the resonance Ne^+ charge exchange is low because of the low abundance of Ne. A large fraction of the Ne^+ (~50%) from the negative glow pass through the cathode fall without losing energy, explaining the high-energy neon peak (Fig. 1d). The decaying branch of the curve to the left of the peak is characteristic of inefficient charge exchange.[3] Charge exchange of Ar^+ with Ar is much more efficient because the cross section for this process is higher (by a factor of ~ 3) than for Ne^+ and because of the large Ar abundance. Therefore, the Ar^+ spectrum is an exponential branch at low energies. As the abundance of Ne in the mixture is increased to (20%), the probability for charge exchange of Ne^+ increases, so that the high-energy peak fades and a low-energy branch of the curve begins to form (Fig. 1c). Nonresonance charge-exchange processes (1) and (2), although they do not alter the total abundance of the various ion species, do affect the shapes of the curves. For example, a calculation shows that process (2) in neon-poor mixtures produces Ne^+ in an amount comparable to that formed in the primary process. The subsequent fate of the ions produced in both processes is the same: charge exchange at a relatively low efficiency. However, since process (2) is distributed along the cathode fall, the resulting Ne^+ ions begin their motion from different energy levels and produce a continuous "background" in the cathode fall. As the mixture is enriched with neon this background intensifies, to the point at which a convex region appears in the curve for 50% Ne (Fig. 1b). Process (1) which produces Ar^+ ions, simply offsets their loss due to process (2) and does not affect the shape of the curve for Ar^+ because of the intense charge exchange of Ar^+ with Ar. An increase in the Ne abundance to 80% leads to a situation in which the efficiency of the resonance charge exchange of Ne^+ becomes higher than that of Ar^+. The Ne^+ ions produced in process (2) reach the low-energy region more rapidly than the Ar^+ ions, and the distribution of the latter ions becomes distorted by process (1). The curve for Ne^+ converts into an exponential branch in the low-energy region, and a step is observed on the decaying curve for Ar^+, i.e., these curves in a sense begin to interchange.

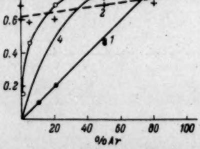

Fig. 3. Relative contributions of various ions as functions of the amount of Ar in the mixture. 1) Fraction of argon ions in the total ion current of the discharge in N_2 + Ar; 2) fraction of N^+ ions in the total current of nitrogen ions; 3) fraction of argon ions in the total current for Ne + Ar; 4) fraction of Ar^+ ions in the total current (the difference between the Ne and Ar ionization cross sections is taken into account).

A further reduction of the Ar concentration causes a further reduction in the efficiency of the Ar^+ charge exchange, leads to an increasingly pronounced accumulation of Ar^+ at intermediate energies because of processes (1) and (3), and leads to convex areas on the curves for the mixtures with 5% and 1% Ar (Fig. 1a). Although we cannot expect a completely analogous behavior of the mixture components, we do not understand why the argon-poor mixtures do not display a high-energy Ar^+ peak analogous to the Ne^+ peak (Fig. 1d). It may be that this peak appears at an even lower Ar content, on the order of some tenths of 1%, at which the efficiency of the charge exchange of Ar^+ with Ar is extremely low. It should also be noted that the relative number of high-energy Ar^+ $[E \geq 0.5\ (V_i/V_r)]$ in the Ar-poor mixtures is much higher (amounting to 10% of the total ion current) than the relative number of such Ne^+ (~2%) in the mixture with 10% Ne.

These results should be examined in light of the known separation of a gaseous mixture in a discharge, which results in the concentration of the component having the lower ionization potential (Ar) near the cathode. As a result of this separation, the current of Ar^+ ions might increase disproportionately. However, as is shown in ref. 9, this separation is observed only at pressures of ~ 0.4 torr and above, at discharge currents mA, and at a length-to-diameter ratio of > 20 for the discharge tube. In our experiments these conditions are not satisfied, so that this separation can not have affected our results.

In the other gaseous system, N_2 + Ar, the experiments revealed a simple proportionality between the relative Ar^+ contribution and the total number of ionized nitrogen particles, on the one hand, and the abundance of the corresponding neutral components, on the other. This result is primarily a consequence of the circumstance that the cross sections for the ionization of N_2 and Ar are essentially equal in the energy range 300–3000 eV. The cross sections for the resonance charge exchange of Ar^+ with Ar and of N_2^+ with N_2 are large and also approximately equal.[8–10] Finally, the cross sections for the cross charge-exchange processes

$$Ar^+ \text{ with } N_2 \qquad (4)$$

and

$$N_2^+ \text{ with} Ar \qquad (5)$$

are not very small and apparently only slightly different, i.e., these processes cancel each other out. These circumstances also furnish an explanation for the fact that the shapes of the N_2^+ and Ar^+ distributions are essentially independent of the composition, and the exponential shapes of these curves at low energies imply a high efficiency for resonance and cross charge exchange and the absence of a distorting effect of the latter process, as in the case of Ne + Ar.

This simplification of the situation in the $N_2 + Ar$ case permits an almost trivial interpretation of the results, except for the question regarding the production and behavior of the N^+ ions, which display an unusual distribution. The N^+ ions can be produced in the primary ionization and dissociation of N_2

$$N_2 + e \rightarrow N^+ + N + 2e, \tag{6}$$

as well as in certain secondary processes. Lacking reliable data on the cross section for process (6) for electrons having energies on the order of 1 keV, we cannot determine how this contribution compares with that of ordinary ionization of N_2. However, direct mass-spectrum observations of ions in the negative glow of discharges in N_2 (ref. 12) show that in this case the number of N^+ ions is much lower than the number of N_2^+ ions. The distribution of N^+ ions (Fig. 2) shows that most of them have high energies [above $0.6\,(V_iV_T)$], so that they move from the part of the cathode fall nearer the negative glow, where apparently most of them are produced. In interactions with neutrals,

$$N^+ + N_2 \rightarrow N_2^+ + N, \tag{7}$$

$$N^+ + Ar \rightarrow Ar^+ + N \tag{8}$$

some of the N^+ ions can be consumed. The cross section for process (7), however, is known to be low:[13] 2-3 $cm^2 \cdot cm^{-3}$. The cross section for process (8) is not known, but we would believe that it is inefficient because in Ar-rich mixtures there are a large number of high-energy N^+ ions, which would be consumed if the efficiency for this process were high. The same can be said of process (7) in N_2-rich mixtures.

Accordingly, the low-energy descending branch of the curve for N^+ ions must primarily reflect a decrease in the production of these ions. Since the additivity rule for the numbers of Ar^+ and nitrogen ions holds only for the total number of N_2^+ + N particles, it is extremely likely that N^+ is produced primarily in the cathode fall in secondary processes involving N_2^+ ions which have drifted from the negative glow. In pure nitrogen this could be the process

$$N_2^+ + N_2 \rightarrow N^+ + N + N_2, \tag{9}$$

postulated in ref. 14. In a mixture with Ar we could also have

$$N_2^+ + Ar \rightarrow N^+ + Ar + N \tag{10}$$

or

$$Ar^+ + N_2 \rightarrow N^+ + N + Ar. \tag{11}$$

Processes (10) and (11) are variants of processes (5) and (4) and must compete with them. Process (9) competes with the resonance charge exchange of N_2^+.

The cross section for process (9) at ion energies ~ 50 eV has been found[15] to be on the order of 3 cm^2/cm^3 or 30-40 times smaller than the cross section for charge exchange of N_2^+ with N_2. Accordingly, charge exchange must be predominant here. The same conclusion can apparently be drawn regarding processes (10) and (11), i.e., all these processes together could not produce the high relative abundance of N^+ ions in the cathode fall which is observed experimentally. However, it should be kept in mind that the cross section for process (9) can be a function of the excitation state of the N_2^+ ions. There are several known excited electronic and vibrational states $(N_2^+)^*$, e.g., $A^2\Pi_u$, having excitation energies of a few electron volts and lifetimes of 10^{-6}-10^{-7} sec (ref. 15). The cross sections for processes (9) and (10) involving $(N_2^+)^*$ states can be much larger than 3 cm^2/cm^3. The appearance of such N_2^+ states in the negative glow is quite possible. The mean free path for resonance charge exchange of N_2^+ is approximately equal to the gas-kinetic value, while the time between collisions of N_2^+ with neutrals under our experimental conditions is on the same order of magnitude as the $(N_2^+)^*$ lifetime. Accordingly, processes (9) and (10) can compete with resonance charge exchange to such a degree that the abundances of N^+ and N_2^+ in the cathode fall and become comparable. The reduced production of N^+ ions at a point far from the negative glow can be attributed to the circumstance that most of the excited N_2^+ ions have vanished by the time this point is reached.

According to this scheme, when there is a change in the relative concentration of N_2 in the mixture the ratio of the abundances of N^+ and N_2^+ should remain constant, since we have $N^+ \sim (N_2)^* \sim N_2$ and $N_2^+ \sim N_2$. Actually, the ratio between the N^+ and N_2^+ abundances changes slightly, with an increase in the N^+ abundance and a decrease in the N_2^+ abundance, as argon is added (curve 2 in Fig. 3). Processes (10) and (11) may be responsible for a similar effect in the case of Ar.

On the whole, the experimental results with binary mixtures confirm the conclusion[1] that the point at which the ions are predominantly produced in the cathode region of an anomalous discharge is a function of the nature of the gas-discharge medium and can be different not only for ions of different species, but also for ions of a given species for different ratios of the mixture components.

Yu. A. Lamakin and E. V. Ilyukin participated in these experiments.

---

[1] A. V. Bondarenko, Zh. Tekh. Fiz., 43, 821 (1973) [Sov. Phys.–Tech. Phys., 18, 515 (1973)].
[2] R. Döpel and M. Lüsch, Wiss. Zs. T. H. Ilmenau, 15, 77 (1969).
[3] W. D. Davis and T. A. Vanderslise, Phys. Rev., 131, 219 (1963).
[4] G. Cumme, Wiss. Zs. T. H. Ilmenau, 13, 29 (1967).
[5] R. M. Bashirova, Izv. VUZ. Fiz., No. 5, 99 (1967).
[6] L. P. Khavkin, Zh. Tekh. Fiz., 25, 726 (1955).
[7] H. Schlumbohn, Z. Naturforsch., 24a, 1716 (1969).
[8] A. von Engel, Ionized Gases, Oxford Univ. Press, London (1965).
[9] N. A. Matveeva, Vestn. LGU, No. 4, 11 (1959).
[10] J. Klein, Wiss. Zh. T. H. Ilmenau, 14, 127 (1968).
[11] K. R. Ryan, Phys. Rev., 171, 107 (1968).
[12] P. F. Knewstubb and A. W. Tickner, J. Chem. Phys., 37, 2941 (1962).
[13] W. B. Maier and E. Murad, J. Chem. Phys., 55, 2307 (1971).
[14] M. M. Shahin, J. Chem. Phys., 43, 1798 (1965).
[15] W. B. Maier, J. Chem. Phys., 55, 2699 (1971).

Electromagnetic fields outside a synthesized plasma jet

E. V. Bogdanov, G. M. Mantrova, and M. N. Yakovleva
Institute of Radio Engineering and Electronics,
Academy of Sciences of the USSR, Moscow

(Submitted July 11, 1973)
Zh. Tekh. Fiz., 44, 1472-1476 (July 1974)

An experimental study is made of the high-frequency oscillations of argon plasma in a synthesized jet in the range 20-200 MHz at distances $r \leq \lambda$ from the axis of the jet. At distances $r/\lambda < 0.3$ the field from the jet is similar to the field in the near-field region of a dipole. The possibility of increasing the radiation from the jet by inserting a conductor in the jet or placing a dielectric plate across it is demonstrated experimentally. The coefficient for conversion of the longitudinal wave into an electromagnetic wave is estimated for the case of an immersed conductor-antenna. The increase in the radiation in the case of the dielectric plate is due mainly to an increase in the amplitude of the field of the high-frequency oscillations in the jet as the result of a reflected electron stream.

Oscillations at the characteristic electron frequencies of plasma have been observed in a synthesized plasma in the presence of streams of fast electrons.[1-3] In a previous paper[4] study was made of the spatial distribution of the amplitude of the high-frequency oscillations in a synthesized argon plasma and the relation of the intensity and spectrum of the oscillations to the parameters of the jet was investigated. The paresent paper is a continuation of ref. 4. It is devoted to a study of characteristic oscillations in the range 20-200 MHz and to methods of increasing the radiated intensity of these oscillations outside the jet.

A schematic diagram of the experimental arrangement is shown in Fig. 1. The synthesized plasma is produced by the source described previously.[4] The fields of the jet outside the experimental volume (at plasma densities 10^8-10^9, electron-beam energies 80-250 eV, electron-beam currents 150-250 mA) are investigated by means of a ferrite antenna and P5-1 and P5-2 receivers.

The experiments have established the following.

1. The magnitude of the alternating magnetic field and its spatial distribution outside the jet are determined by the motion of the fast electrons, which interact with the plasma, since a forced distortion of the electron trajectories by a dc magnetic field of the order of a few gauss results in a change in the magnitude and orientation of the alternating magnetic field. The motion of the ions is perturbed weakly since the ion Larmor radius is much greater than the dimensions of the jet.

As the distance increases from the experimental volume in a direction perpendicular to the axis, the alternating magnetic field varies with radius approximately as $1/r^2$ for distances r such that $r/\lambda < 0.3$, indicating the similarity of the field distribution outside the jet to the near field of a dipole (Fig. 2).

It has been shown previously[4] that in a synthesized plasma jet the intensity of the high-frequency oscillations is strongest at a short distance (a few retarded wavelengths) from the source, the intensity thereafter decreasing as a result of the divergence of the jet. Since the radial dimensions of the jet are finite, one can assume that some of the force lines induced by the alternating space charge close, from the region in which its density is greatest, on the source and on the metal part of the experimental volume. The field configuration is then similar to that of a dipole.

As expected, for $r/\lambda > 0.3$ the magnetic field varies with radius less sharply than $1/r^2$. One should keep in mind, however, that under laboratory conditions the field distribution can be distorted by metal objects even at these distances from the jet, and more so when $r/\lambda > 1$, as the field of the jet becomes comparable with the fringing field.

The electric field at 103 MHz is 60 mV/m for $r \simeq \lambda$.

2. The field outside the jet can be increased by placing a dielectric plate in the jet. The field enhancement in this case is due mainly to an increase in the intensity of the oscillations of the jet as a result of the formation of a counterstreaming electron beam which is reflected from the plate.

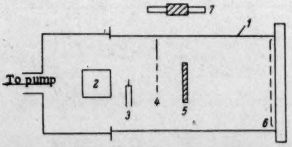

Fig. 1. Schematic diagram of the experimental arrangement. 1) Cavity with ceramic walls; 2) plasma source; 3) high-frequency probe; 4) conductor-antenna; 5) dielectric plate; 6) collector; 7) ferrite antenna.

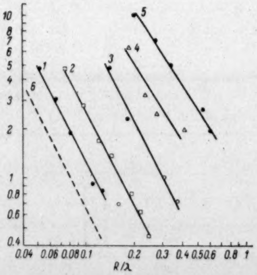

Fig. 2. Experimental plots of alternating magnetic field as a function of radius (relative units) for various frequencies. ω, MHz: 1) 24, 2) 36, 3) 68.5, 4) 80.5, 5) 103, 6) $1/R^2$.

Conversion of longitudinal waves reflected from the dielectric plate into electromagnetic radiation can occur at the plasma–dielectric boundary. The conversion efficiency depends strongly on the angle at which the longitudinal wave is incident upon this boundary.[5] Under the experimental conditions it is difficult to achieve the conditions required for efficient conversion, as the electron flow in the jet is an unfocused divergent flow and the plasma boundary near the dielectric can have an arbitrary curvature because of the inhomogeneity of the charge distribution over the dielectric surface.

Placing a plate of mica across the stream (dimensions of mica plate 20 × 30 cm) increases the amplitude of the oscillations in the stream by a factor of 5-7 (f = 150-200 MHz), and a capacitive probe picks up oscillations in the second-harmonic range of frequencies (300-400 MHz), indicating the nonlinear character of the interaction of the plasma and the electron stream. The amplitude of the oscillations detected in the frequency range 150-200 MHz by an antenna located 2 m from the experimental volume increases by a factor of 4-5 when the mica plate is introduced. The optimum orientation of the mica plate in the jet is perpendicular to the axis in the region of maximum oscillation intensity.

3. Experiments have shown that the field outside the jet can be increased by partially immersing a conductor (conductor–antenna) in the jet in a plane perpendicular to the direction of propagation of the longitudinal wave. In the jet a layer of positive space charge is formed around the insulated conductor. The boundary of the plasma and the surface of the conductor constitute a capacitor; as a result an alternating charge is induced on the conductor by the longutidinal waves of the jet. Clearly, when the conductor is oriented along the direction of propagation of the longitudinal wave and the length of the conductor extends over a few retarded wavelengths, the total induced charge will not be large.

In the first approximation the alternating electromagnetic fields near the part of the conductor–antenna jutting out from the plasma are distributed like the fields of an asymmetric dipole.

The longitudinal wave incident upon the surface of the plasma–conductor layer can be regarded as a certain line with distributed parameters loaded by a complex impedance determined by the parameters of the conductor and the plasma. The equivalent circuit of the load is shown in Fig. 3.

The power flux for a plane wave is $P_n = \varepsilon_0 k^2 U_0 v_g$ is the wave number, ω_p is the electron plasma frequency, U_0 is the potential of the longitudinal wave, S is the cross-sectional area of the flux, v_g is the group velocity of the wave, close to the velocity of the electron stream v_e, and ε_0 is the dielectric constant. We represent the power flux in the form $P_n = (1/2)(U_0^2/\rho)$ and regard $\rho = 2/(\varepsilon_0 k^2 S v_g)$ as a certain equivalent wave impedance of the longitudinal wave.

The power radiated by the conductor–antenna can be expressed as

$$P_r = \frac{1}{2}\frac{(1-p)^2 U_0^2 R_r}{\rho^2},$$

where

$$p = \sqrt{\frac{(R_{in}-\rho)^2 + \left(X + \frac{1}{\omega C}\right)^2}{(R_{in}+\rho)^2 + \left(X + \frac{1}{\omega C}\right)^2}}$$

is the reflection coefficient,

$$R_{in} = \frac{R_r}{\sin^2\frac{2\pi l}{\lambda}}.$$

If the reflected wave is assumed to have no effect on the processes in the plasma, the conversion coefficient is given by

$$\frac{P_r}{P_n} = \frac{(1-p)^2 R_r}{\rho}.$$

By suitably choosing the length of the external radiating portion of the conductor–antenna l it is possible to balance out the capacitive reactance of a layer for $0.25 < l/\lambda < 0.5$. The required length l is found from the relationship

$$-60\left(\ln\frac{l}{r_1} - 1\right)\operatorname{ctg}\frac{2\pi l}{\lambda} = \frac{1}{\omega_p C}$$

where r_1 is the radius of the conductor. The results of a calculation of the conversion coefficient as a function of ρ for zero load reactance are shown in Fig. 4 along with the values of l/λ required to achieve this condition. In the calculations the thickness of the plasma–conductor layer is estimated through the equation for a planar layer near an electrode having a negative potential relative to the plasma, the space charge of the fast electron beam being ignored. In this approximation

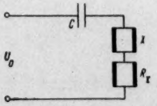

Fig. 3. Equivalent circuit of radiating conductor. U_0) Amplitude of potential of longitudinal wave; C) capacitance of conductor–plasma layer; R_r) radiation resistance of asymmetric dipole; X) reactance of asymmetric dipole.

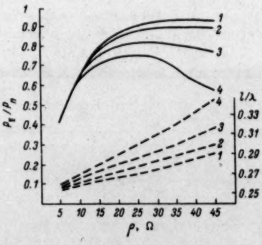

Fig. 4. Coefficient of conversion of longitudinal wave into electromagnetic wave by conductor–antenna (solid curves) and l/λ (dashed curves) vs equivalent wave impedance of longitudinal wave under condition $1/\omega_p C + X = 0$. U/T_e: 1) 50, 2) 150, 3) 500, 4) 1500.

$$\frac{\frac{1}{\omega_p C}}{\rho} = 0.37\sqrt[4]{\frac{U}{T_e}},$$

where U is the potential determining the energy of the fast electron beam and T_e is the temperature of the plasma electrons (in eV).

Figure 5 shows plots of conversion coefficient vs ρ for $l/\lambda = 0.25$ and $X = 0$, $R_r = 36.5\ \Omega$.

The conversion coefficient is somewhat lower here on account of the large reflection coefficient. Since

$$\rho = \frac{12 \cdot 10^3 U^{1/2}}{\varepsilon_0 \omega_p^2 S},$$

we can use Figs. 4 and 5 to determine the optimum geometrical dimensions of the radiative part of the conductor–antenna and the part of it immersed in the plasma.

It is found experimentally that a molybdenum wire 1 mm in diameter and 30 cm long immersed to one half its length in a plasma jet in the transverse direction to the jet in the region where the oscillations are most intense gives a fivefold increase in the intrinsic noise at 170 MHz. The receiving antenna is located 2 m from the experimental volume. Replacing the wire with a grid of dimensions 15×15 cm and cell size 1.5×1.5 mm increases the field amplitude by a further factor of 20.

Estimates imply that this corresponds to an increase in the surface area of the layer by a factor of 10-15. The ratio of the amplitude for the grid to the amplitude for the wire calculated allowing for the experimental parameters of the jet amounts to 15-22, in good agreement with experiment.

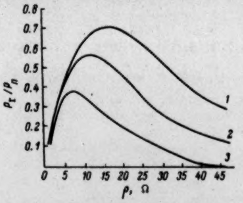

Fig. 5. Coefficient of conversion of longitudinal wave into electromagnetic wave by conductor–antenna vs equivalent wave impedance of longitudinal wave under condition $l/\lambda = 0.25$. U/T_e: 1) 15, 2) 150, 3) 1500.

---

[1] S. Ya. Lebedev, Yu. Ya. Stavisskii, L. I. Bondarenko, S. A. Maev, I. P. Stakhanov, and É. A. Stambur, Zh. Tekh. Fiz., 31, 1202 (1961) [Sov. Phys. – Tech. Phys., 6, 878 (1962)].

[2] W. Bernstein and I. M. Sellen, Phys. Fluids, 6, 1032 (1963).

[3] K. S. Golovanivskii and A. I. Lushchik, Zh. Tekh. Fiz., 37, 2234 (1967); 40, 1497 (1970) [Sov. Phys. – Tech. Phys., 12, 1647 (1968); 15, 1155 (1971)].

[4] M. N. Yakovleva, G. M. Mantrova, and T. A. Novskova, Zh. Tekh. Fiz., 42, 2472 (1972) [Sov. Phys. – Tech. Phys., 17, 1926 (1973)].

[5] A. M. Fedorchenko, Ukr. Fiz. Zh., 13, 1032 (1968) [Ukr. Phys., 13, 737 (1968)].

Accelerators

Efficiency of internal targets in the accelerator at the Institute of High-Energy Physics

V. I. Gridasov, K. P. Myznikov, and V. N. Chepegin

(Submitted September 18, 1973)
Zh. Tekh. Fiz., 44, 1477-1483 (July 1974)

The accelerator at the Institute of High-Energy Physics has been studied in an attempt to maximize the efficiency of the beam—target interaction. An efficiency higher than 90% can be achieved if the beam is brought onto the target slowly; an efficiency of 30%-50% can still be achieved if the beam is brought onto the target rapidly, in a time as short as 1 msec.

Most of the physical experiments carried out with the accelerator at the Institute of High-Energy Physics use particle beams produced on internal targets. Methods for producing these secondary-particle beams have been described elsewhere.[1,2] The target position in the accelerator chamber is chosen so that the desired secondary-particle species at the desired momentum can be extracted from the accelerator at a very small angle. Intense beams can be extracted in this manner. On the other hand, since it is desirable to extract beams as intense as possible containing particles with various momenta in a specified direction, it is necessary to vary the radial and azimuthal positions of the target. Figure 1 shows a cross section of the vacuum chamber in the radial-focusing unit and the extreme radial positions of the target. The proton beam is held at the central orbit throughout the acceleration cycle. With the beam in this position, a dynamic gradient-correction system provides conditions such that the working point as far as synchrotron-oscillation frequencies are concerned is far from any nonlinear-resonance lines.[3] This measure makes it possible to avoid anomalous beam broadening; the beam dimensions at the end of the acceleration cycle do not exceed 10 mm horizontally and 7 mm vertically in the focusing unit. The practical range of target radial positions is ± 4 cm from the central orbit. In the vertical direction the center of the target coincides with that of the accelerated beam at the given azimuth. The target is brought to the specified position by an actuating mechanism which positions the target in both the outer and inner parts of the chamber with respect to the beam. The beam is brought onto the target by systems which excite a local distortion of the orbit at the target position. Long secondary-particle pulses (up to 2 sec long) are produced by slowly increasing this local distortion.[4] When the beam is shifted to the target rapidly a rapidly increasing perturbation results.[5]

The structural elements of the internal target are shown at the top of Fig. 1. The target proper, i.e., the part which interacts with the beam, is attached to the target holder by a brace. The holder is quite massive, since it supplies the rigidity for the structure. The brace length is limited by the operating conditions within the radial-focusing units, in which the vertical dimension of the gap at the edge of the open part is 80 mm (Fig. 1). The brace itself is limited to a length of 15 mm. The target dimensions are governed largely by the operating conditions in the channel which guides the extracted beam to the experimental apparatus. The transverse dimensions of the target must satisfy the conditions imposed by the specified momentum resolution and the specified dimensions of the particle beam incident on the experimental apparatus; in most cases the target diameter cannot exceed 3 mm. The mass of the target along the beam direction must be much larger than that of the brace and holder so that the latter do not make important contributions to the secondary beam. The brace and the part of the holder near the target are therefore as light as possible. The material and maximum dimension of the target are chosen to maximize the efficiency of the beam-target interaction, i.e., to maximize the fraction of the accelerated particles which undergo nuclear interactions in the target itself. Below we report work carried out to determine the conditions maximizing this efficiency for operation of internal targets in the accelerator at the Institute of High-Energy Physics at an accelerator energy of 70 GeV.

Numerical calculations have been carried out on a BÉSM-6 computer to study the mechanism for the beam—target interaction. In these calculations the beam of accelerated protons is described as a set of particles differing in initial amplitudes and phases of synchrotron oscillation. The calculation procedure itself is described in detail elsewhere.[6] We have modified this procedure by calculating the trajectory of each particle through an integration of the equations of motion (not linearized) in the magnetic field, determined from magnetic measurements, taking nonlinear terms up to the fifth power, inclusively, into account.[1] In several cases it is possible to incorporate the effects of the nonlinearities of the accelerator magnetic field. The instantaneous coordinates of the particle trajectory near the target are compared with the specified coordinates of the volumes occupied by the target, brace, and holder for each orbit. When a particle with specified initial conditions is incident on

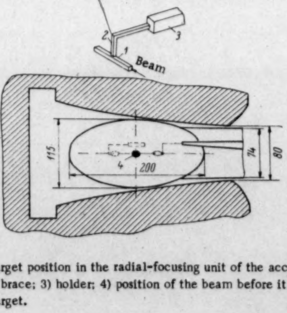

Fig. 1. Target position in the radial-focusing unit of the accelerator. 1) Target; 2) brace; 3) holder; 4) position of the beam before it is brought onto the target.

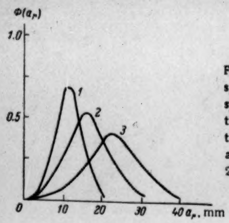

Fig. 2. Particle distribution with respect to the amplitudes of the radial synchrotron oscillations after 80% of the particles initially incident on the target have undergone nuclear interactions with it. 1) Beryllium target; 2) aluminum; 3) copper.

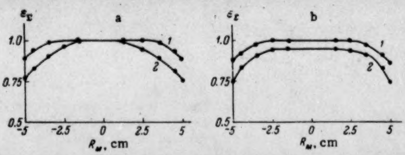

Fig. 3. Relative efficiencies of beryllium (1) and aluminum (2) targets as functions of the radial position of the target in the radial-focusing (a) and radial-defocusing (b) units of the accelerator.

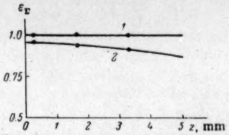

Fig. 4. Relative efficiencies of beryllium (1) and aluminum (2) targets in the radial-defocusing unit as functions of the amplitude of the vertical orbit distortion.

one of these volumes the relative number of particles which undergo nuclear interactions with the absorber is calculated; the particle energy is modified by the magnitude of the ionization loss; the multiple-scattering angle is calculated by a standard random-number program. A definite intensity is assigned to particles with specified initial conditions and the calculation is continued until all the particles undergo nuclear interactions with the target, the supporting structures, or the walls of the vacuum chamber. The choice of initial conditions incorporates the experimental distributions of the beam particles with respect to free-oscillation amplitudes.[7]

Figure 2 shows the particle distributions with respect to oscillation amplitude for multiple interactions of the beam with copper, aluminum, and beryllium targets according to numerical calculations carried out for 100 particles with various initial conditions. The beam dimensions increase rapidly with the number of passes through the target; this increase is more pronounced, the heavier the target material. Calculations of this type show that the interaction efficiency for heavy targets is reduced significantly by particles which strike the chamber walls. The interactions with the walls can be avoided when beryllium and aluminum targets are used in a restricted radial interval.

In practice, the amplitudes of the synchrotron oscillations can also increase because of resonances as well as multiple scattering. Experiments have been carried out to determine the relative efficiency of the beam–target interaction as a function of the radial position of the target. In these experiments a scintillation detector monitoring the target measures a signal proportional to the integrated number of particles which have interacted with the target. The resultant effect due to interactions with the target, brace, and holder is recorded in this manner. To reduce the spread in working-point positions on the diagram of synchrotron-oscillation frequencies, as the radial target position is varied the beam is brought onto the target through a local distortion of the orbit; this procedure minimizes the frequency shift which occurs as the distortion amplitude is raised.[1] For changes of ± 5 cm in the radial position of the target, the frequency shift is about ± 0.02. Figure 3a shows the measured relative efficiency for various positions of beryllium and aluminum targets with respect to the central orbit in the radial-focusing unit; the analogous curves for the radial-defocusing unit are shown in Fig. 3b. The efficiency falls off considerably more rapidly for aluminum targets than for beryllium targets as the target is withdrawn from the center of the chamber. The reason for this efficiency reduction is the incidence of the beam on the chamber walls, which occurs because of the increase in the beam dimensions due to the interaction with the target. Since the dimensions of the part of the beam in a strong-focusing accelerator which interacts with the target are functions of the azimuthal position of the target, these functional dependences of the efficiency on the target position are quite different for the focusing and defocusing units.

We carry out additional measurements to study this question in more detail. With the target in the radial-defocusing unit, corresponding to the maximum vertical dimension of the beam envelope, we cause an artificial vertical distortion of the orbit; the peak of this distortion also coincides with the defocusing unit. Figure 4 shows the relative efficiences of Al and Be targets as functions of the amplitude of this vertical distortion. We see that when a Be target is used there is a gap between the edge of the beam and the vertical chamber wall, but there is no such gap in the case of an Al target; in this latter case the beam strikes the vertical walls even when the target is near the center of the chamber (Fig. 3b). When the target is in the radial-focusing unit there is no beam loss at the vertical walls, so that the curves in Fig. 3a for Al and Be coincide for the central part of the chamber.

The horizontal dimensions of the beam interacting with the target are determined with probe targets. For this purpose the beam is brought onto the target slowly. Two targets, used as probes, are placed in the accelerator unit through which the beam passes before it reaches the unit under study. One of these probes is inserted from the outer chamber wall, and the other is inserted from the inner wall. A detector monitoring the probe records the coordinate at which the probe becomes tangent to the edge of the beam. The positions of the inner and outer edges of the beam interacting with the target are determined. From these results and from the previously measured position of the beam, unperturbed by the target, the amplitude of the envelope of horizontal

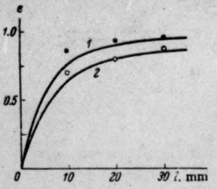

Fig. 5. Absolute efficiences of beryllium (1) and aluminum (2) targets as functions of their length.

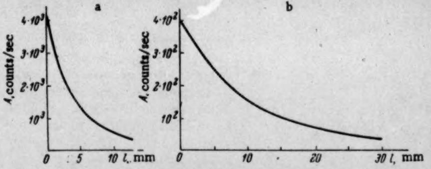

Fig. 6. Induced activity along the length of the brace (a) and along the length of the holder (b).

synchrotron oscillation, a_r, and the maximum momentum spread of the particles after interacting with the target, $(\Delta p/p)_{max}$, are determined. Table 1 shows the results for Be and Al targets 30 mm long and 3 mm in diameter, corresponding to a 95% efficiency.

We can explain the curves in Fig. 3 on the basis of these results. When an Al target is in the radial-focusing unit, with the beam envelope at a maximum, the efficiency reduction due to particle loss at the walls occurs relatively rapidly as the target is withdrawn from the center of the chamber. There is a corresponding contraction of the range of radial target positions in which the efficiency is a maximum.

When the beam is prevented from reaching the chamber walls, and the efficiency is a maximum, the particles can undergo nuclear interaction only with the target holder and brace in addition to the target proper. Numerical calculations show that the fraction of particles interacting with the target increases directly as the target volume is increased (Fig. 5). In an experimental check of these results, aluminum and beryllium targets of various length, all 3 mm in diameter, are irradiated by a 70-GeV proton beam. This irradiation is carried out in a radial-focusing unit with the target 12 mm outside the equilibrium orbit, at a position at which the efficiency is a maximum for Be and Al targets (Fig. 3). In each irradiation care is taken to prevent the beam from striking the chamber walls. The holder and brace are made of aluminum. In the case of the aluminum targets the fraction of particles undergoing nuclear interactions with the target, brace, and holder is determined through relative measurements of the activity of Na^{22} nuclei formed in these structural elements. In the irradiation of the Be targets, an absolute measurement is made of the number of Na^{22} nuclei formed in the holder and brace. The relative number of particles undergoing nuclear interactions with the beryllium target is determined from the results of the measurements and the measured intensity of protons incident on the target. The experimental points are shown along with the calculated curves in Fig. 5. Figure 6 shows the measured distributions of induced activity over the lengths of the holder and brace for the irradiation of a beryllium target 3 mm in diameter and 30 mm long. Using these results, we select a length for the irradiated part of the target holder.

Comparing the calculated and experimental results we conclude that under the optimum working conditions of the accelerator at the Institute of High-Energy Physics, with the beam brought onto the internal targets slowly, the efficiency of these targets can exceed 90%. Beryllium is the best target material. When beryllium is used the efficiency reaches a maximum over the entire range of radial target positions, within ± 40 mm from the central orbit. Measurements have shown that the effects of nonlinear resonances can cause an additional broadening of the beam during its interaction with targets and can significantly reduce the efficiency. The corresponding results will be published and discussed in a separate paper; here we simply note that the results given here correspond to the case in which the effects of these nonlinear resonances are minimized.

TABLE 1

Target position	Target material	Δr_{max}, mm	$\left(\frac{\Delta p}{p}\right)_{max}$
Radial-focusing unit	Be	50	$5\cdot10^{-3}$
	Al	74	$7\cdot10^{-3}$
Radial-defocusing unit	Be	32	$5\cdot10^{-3}$
	Al	55	$7\cdot10^{-3}$

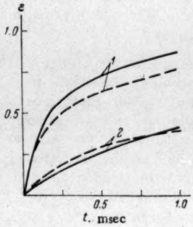

Fig. 7. Efficiency as a function of the duration of the interaction of the beam with Be targets having volumes of 180 mm³ (1) and 1000 mm³ (2). The dashed curves are the analogous curves for Al.

The efficiency is significantly reduced when the accelerated beam is brought onto the target rapidly, due to the reduction in the number of times the particles pass throught the target over the interaction time. Nevertheless in certain physics experiments it is important to hold the beam–target interaction time to a few hundred microseconds, and the efficiency must be maximized under this constraint. Numerical calculations show that if the beam–target interaction is not deliberately interrupted the particles which are incident on the target and undergo repeated interactions with it can continue to interact with the target for some tens of milliseconds, the precise duration depending on the target material, size, and shape and on the method used to bring the beam onto the target. The upper limit on the efficiency can be found

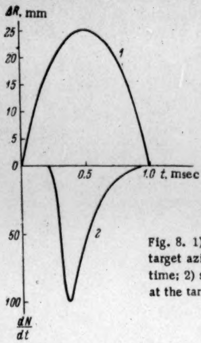

Fig. 8. 1) Distortion of the orbit at the target azimuth as a function of the time; 2) shape of the particle pulse at the target.

by instantaneously shifting the beam to the target, holding it there for a specified time, and then instantaneously removing it. From the curves calculated for this situation (Fig. 7) we see the functional dependence of the efficiency on the beam−target interaction time for targets of various materials and volumes. For maximum efficiency at a limited interaction time the target should be made of a light material and should have as large a volume as possible.

In practice it is extremely difficult to move the beam onto the target "instantaneously," so we have carried out calculations for the fast-deflection system used in the accelerator at the Institute of High-Energy Physics.[5] Figure 8 shows the orbital deflection at the target azimuth as a function of the time for this system. We calculated the efficiency for the interaction with a beryllium target under 50 sets of initial conditions. Figure 8 shows the shape of the particle pulse (current pulse) incident on a beryllium target 3 × 3 × 30 mm in size. The efficiency varies from 0.3 to 0.5 for this target, depending on the initial conditions.

In conclusion the authors thank Yu. S. Fedotov for assistance in the calculations, and G. I. Britvich and V. S. Lukanin for participating in measurements of the absolute target efficiency.

---

[1] V. I. Gridasov and K. P. Myznikov, Preprint 68-60, Institute of High-Energy Physics, Serpukhov (1968).

[2] V. I. Gridasov, A. A. Kardash, O. V. Kurnaev, É. A. Merker, L. L. Moizhes, K. P. Myzikov, and N. M. Tarakanov, Proceedings of the Seventh International Conference on Accelerators [in Russian], Vol. 1, Erevan (1970), p. 509.

[3] V. I. Gridasov, K. P. Myznikov and V. N. Chepegin, Preprint 70-90, Institute of High-Energy Physics, Serpukhov (1970); At. Energ., 32, 1 (1972).

[4] V. I. Gridasov, A. A. Kardash, K. M. Kozlov, O. V. Kurnaev, V. V. Lapin, S. V. Lobanov, L. L. Moizhes, K. P. Myznikov, and A. A. Naumov, Preprint 70-57, Institute of High-Energy Physics, Serpukhov (1970); At. Energ., 30, 520 (1972).

[5] V. I. Gridasov, B. A. Zelenov, O. V. Kurnaev, É. A. Merker, K. P. Myznikov, and N. M. Tarakanov, Proceedings of the Second All-Union Conference on High-Energy Accelerators [in Russian], Vol. 11, Moscow (1972), p. 184.

[6] H. G. Hereward, J. Ranft, and W. Richter, CERN, 65-1, 1965.

[7] V. I. Gridasov, B. A. Zelenov, V. A. Zenin, and K. P. Myznikov, Preprint 70-58, Institute of High-Energy Physics, Serpukhov (1970); At. Energ., 30, 3 (1971).

Phase motion of particles in an accelerator with an azimuthally varying electric field

M. F. Vorogushin and V. I. Petrunin

(Submitted May 22, 1973; resubmitted October 19, 1973)
Zh. Tekh. Fiz., 44, 1484-1489 (July 1974)

The slow phase motion of particles in an accelerator with an azimuthally varying electric field is analyzed by averaging the dynamic equations. Phase focusing is caused by the rf field components.

In the elementary analysis of an accelerator with an azimuthally varying electric field[1] the nonrelativistic dynamic equations are used for a quasistatic approximation of the single-harmonic field in the gap.

In this note we give the complete system of dynamic equations in the electromagnetic fields of a resonator with azimuthally varying gap;[2] in this system of equations it is possible to incorporate the irregularities in the particle motion due to the high acceleration rate. We also analyze slow phase motion.

We use the Lorentz equation

$$\frac{d\mathbf{V}}{dt}=\frac{e}{m}\left[\mathbf{E}+\mathbf{V}\times\mathbf{B}-\frac{1}{c^2}\mathbf{V}(\mathbf{VE})\right], \tag{1}$$

where **V** and c are the particle velocity and the speed of light, **E** and **B** are the electric field and the magnetic field, and e and $m = m_0/\sqrt{1-(V/c)^2}$ are the charge and relativistic mass of the particle.

The last term in the brackets is due to the mass change during acceleration:

$$\frac{e}{c^2}\mathbf{V}(\mathbf{VE})=e\mathbf{V}\frac{dm}{dt}.$$

Denoting the particle gyrofrequency by $\omega_0 = -eB_0/m_0$, in the usual manner, and denoting the decay rate of the isochronous magnetic field by

$$n_n=-\frac{\omega_0^2r^2}{c^2}, \tag{2}$$

we write the static and rf components of the magnetic field in the cylindrical coordinate system r, φ, z as follows

$$\left.\begin{aligned}B_z&=B_0\left(1+\frac{\omega_0^2r^2}{2c^2}\right)+B_z(t),\\B_r&=B_0\frac{\omega_0^2rz}{c^2}+B_r(t),\\B_\varphi&=B_{\varphi\,\mathrm{st}}+B_\varphi(t).\end{aligned}\right\} \tag{3}$$

Substituting (3) and

$$(\bar{V}E)=\omega_0(r'E_r+r\varphi'E_\varphi+z'E_z) \tag{4}$$

into (1), and transforming to the new variable $\theta = \omega_0 t$, we find a system of equations for all fields in the accelerating structure:

$$\begin{aligned}r''=r\varphi'\left(\varphi'-\frac{\omega}{\omega_0}\right)+\frac{e}{m_0\gamma\omega_0^2}\Big[&E_r\left(1-\frac{\omega_0^2r'^2}{c^2}\right)-\omega_0z'\left(B_\varphi+\frac{\omega_0r'}{c^2}E_z\right)\\&-\frac{\omega_0^2rr'\varphi'}{c^2}E_\varphi+\omega_0r\varphi'B_z(t)\Big],\end{aligned} \tag{5}$$

$$\begin{aligned}\varphi''=-\frac{r'}{r}\left(2\varphi'-\frac{\omega}{\omega_0}\right)+\frac{e}{m_0\gamma\omega_0^2r}\Big[&E_\varphi\left(1-\frac{\omega_0^2r^2\varphi'^2}{c^2}\right)\\&+\omega_0z'\left(B_r-\frac{\omega_0r\varphi'}{c^2}E_z\right)-\frac{\omega_0^2rr'}{c^2}E_r-\omega_0r'B_z(t)\Big],\end{aligned} \tag{6}$$

$$\begin{aligned}z''=\frac{e}{m_0\gamma\omega_0^2}\Big[&E_z\left(1-\frac{\omega_0^2z'^2}{c^2}\right)+\omega_0r'\left(B_\varphi-\frac{\omega_0z'}{c^2}E_r\right)\\&-\omega_0r\varphi'\left(B_r+\frac{\omega_0z'}{c^2}E_\varphi\right)\Big],\end{aligned} \tag{7}$$

where

$$\frac{\omega}{\omega_0}=\frac{1}{\gamma}\left(1+\frac{\omega_0^2r^2}{2c^2}\right),$$

and $\gamma \cong 1+\omega_0^2r^2\varphi'^2/2c^2$ is the relativistic factor.

The field components in Eqs. (5)-(7) were determined previously[2] for an accelerating structure with azimuthally varying boundaries. Using these components, we can integrate the dynamic equations on a computer.

In an analytic approach we evaluate the terms in Eqs. (5)-(7) using several characteristic parameters, usually known in order of magnitude:[1] the energy increment per revolution and the kinetic energy of the particle (both in volts),

$$U_{\mathrm{rv}}=\frac{\pi}{2}U_0\delta\nu f(r)\cos\psi_\theta=|U_{\mathrm{rv}}|\cos\psi_\theta, \tag{8}$$

$$U_m=\frac{m\omega_0^2r^2}{2e}; \tag{9}$$

the electric-focusing index,

$$n_{\mathrm{el}}=\frac{U_0\nu^2\delta f(r)}{8U_m}\sin\psi_\theta=|n_{\mathrm{el}}|\sin\psi_\theta; \tag{10}$$

and the instantaneous particle phase,

$$\psi_\theta=\psi-\nu(\varphi-\theta).$$

Here

$$\delta=\left(1-\frac{2z_0}{d}\right)\frac{\mathrm{ch}\,\frac{\nu z}{r}}{\mathrm{ch}\,\frac{\nu z_0}{r}}.$$

Let us consider the equation for the vertical motion, Eq. (7). Using the obvious inequalities $r\varphi' \gg r'$, $r\varphi' \gg z'$ we simplify Eq. (4)

$$(\bar{V}E)\cong r\varphi'E_\varphi\omega_0. \tag{11}$$

Then, using (8)-(11) and the approximation $r' \cong [e/(m_0\cdot\omega_0^2)]E_\varphi$ of ref. 1, and averaging the terms of the equation over the period of the structure $(2\pi/\nu)$, we find the following equation, which holds near the median plane $(z < z_0)$:

$$z''+\frac{U_{\mathrm{rv}}\delta^2}{4\pi U_m}z'+\left[n_{\mathrm{el}}+n_n-\frac{df}{dr}\frac{|U_{\mathrm{rv}}|^2r\cos 2\psi_\theta}{(4\pi U_m)^2 2f}\right]z=0. \tag{12}$$

This equation, with slowly varying coefficients, has an oscillatory solution with a damping constant

$$\sigma=\frac{U_{\mathrm{rv}}\delta^2}{8\pi U_m}=\omega_0\frac{m'}{m},$$

which is negligibly small – a typical situation for a cyclotron.[3] The frequency of the vertical oscillations of a particle is governed by the three terms in the coefficient of z; the first is related to E_z, a component of the rf electric field;[1)] the second is due to the defocusing effect of the isochronous magnetic field; and the third is due to the interaction of r' and B_φ, a component of the rf magnetic field. This last term is defocusing in the case $\cos 2\psi_0 > 0$ and focusing in the case $df/dr > 0$, but in practice it is difficult to use it because it is small in comparison with the preceding terms.

Taking these assumptions into account, we write the averaged equation of the vertical oscillations in the standard form,[4]

$$z'' + (n_{el} + n_M) z = 0. \tag{13}$$

In our case, however, in contrast with the case of slit focusing, the vertical stability of a particle is governed by the aperture coefficient δ, which incorporates the electric field configuration in the median plane, and the function $f(r)$, which governs the radial distribution of the rf field. In addition, the quantity n_{el} is typically a quadratic function of the number of azimuthal field cycles. In particular, for a two-dee accelerating structure $\nu = 1$, $f(r) \equiv 1$, $\delta = 1$ and the equations for n_{el} are the same.

We now consider the radial-phase motion. In accelerating structures in which the electric field varies in the azimuthal direction the rapid acceleration rate causes the term r" to become important. This term causes both the "fast" radial-phase oscillations, which (in contrast with synchrotron oscillations) are related to energy oscillations, and a "slow" phase drift. Since the characteristic times for these types of motion are of different orders of magnitude, a separate analysis is possible.

Equation (13) is solved by the WKB method[1] for the slow phase motion ($\varphi' \cong 1$; $r\varphi'' \ll r'$), and Eqs. (5) and (6) can be solved jointly. In this case, with an isochronous magnetic field ($\omega/\omega_0 \cong 1$), the quantity $2\varphi' - \omega/\omega_0$ is approximately equal to unity; thus, neglecting the term containing the product of small quantities zz' in Eq. (6), we find

$$r' = \frac{eE_\varphi}{m_0\gamma\omega_0^2\left[1 + \frac{2|n_{el}|rf'_r}{\nu^2 f}\sin\nu\varphi\cos(\nu\theta + \psi)\right]}.$$

An estimate of the last term in brackets by averaging shows that the effect of the H_z component of the rf magnetic field on the radial motion is negligible $[n_{el}\, rf'_r \cdot (\nu^2 f)^{-1} \ll 1]$:

$$r' \cong \frac{eE_\varphi}{m_0\gamma\omega_0^2}. \tag{14}$$

Evaluating the total derivative

$$r'' = \frac{e}{m\omega_0^2}\left(\frac{\partial E_\varphi}{\partial\theta} + r'\frac{\partial E_\varphi}{\partial r} + \varphi'\frac{\partial E_\varphi}{\partial\varphi}\right) \tag{15}$$

and substituting into Eq. (5), we average this equation over the period of the structure, using Eqs. (8) and (10):

$$\varphi' = \frac{1 - n_{el} - \frac{n_{el}z_0}{\nu r}\operatorname{th}\frac{\nu z_0}{r} + \frac{e^2U_0^2 ff'_r}{2m^2\omega_0^4\nu^2 d^2 r} + \frac{|n_{el}|^2}{\nu^2}\left[\frac{rf'_r}{f} - 1 - \frac{\nu z_0}{r}\operatorname{th}\frac{\nu z_0}{r}\right]\left(\frac{1}{2} + \cos^2\psi_\theta\right)}{1 - n_{el} - \frac{rf'_r}{\nu^2 f}n_{el} - \frac{\omega_0^2 r^2}{\nu^2 c^2}|n_{el}|^2\left(\frac{1}{2} + \cos^2\psi_\theta\right)}.$$

Differentiating the equation for the instantaneous phase $\psi'_\theta = -\nu(\varphi' - 1)$ and substituting into (16), we find

$$\psi'_\theta = -\frac{1}{\nu}\,\frac{|n_{el}|^2\left[\frac{rf'_r}{f} - 1 + \frac{\nu z_0}{r}\operatorname{th}\frac{\nu z_0}{r}\right]\left(\frac{1}{2} + \cos^2\psi_\theta\right) + n_{el}\left(\frac{rf'_r}{f} + \frac{\nu z_0}{r}\operatorname{th}\frac{\nu z_0}{r}\right)}{1 - n_{el} - n_{el}\frac{rf'_r}{\nu^2 f} - |n_{el}|^2\frac{\omega_0^2 r^2}{\nu^2 c^2}\left(\frac{1}{2} + \cos^2\psi_\theta\right)}. \tag{17}$$

The smallness of the quantities $(\omega_0 r/c)^2 \ll 1$ and $2 \cdot (2r/\delta d\nu^2)^2 \ll 1$, is taken into account here; physically, this smallness means that the contribution of the azimuthal component of the rf magnetic field and of scalar product (4) to the phase motion of the particles is negligible.

Accordingly, in this case the dynamics of the particles in an accelerator with an azimuthally varying electric field is described by the system of averaged equations (13), (14), (17).

For estimate purposes we neglect the terms small in comparison with one in the denominator in (17); it can be shown that this simplification has only a quantitative effect and does not alter the nature of the phase motion. Then, using $\psi'_\theta = (d\psi_\theta/dr)r'$, we convert Eq. (17) to a Riccati equation through the substitution $y = \sin\psi_\theta$:

$$\frac{dy}{dr} = \frac{|n_{el}|}{r}\left(\frac{rf'_r}{f} - 1 + \frac{\nu z_0}{r}\operatorname{th}\frac{\nu z_0}{r}\right)\left(y^2 - \frac{3}{2}\right) - y\left(\frac{f'_r}{f} + \frac{\nu z_0}{r}\operatorname{th}\frac{\nu z_0}{r}\right) \tag{18}$$

For phases satisfying $\sin^2\psi_\theta \ll 3/2$ the solution can be found by quadratures:

$$y = \frac{\operatorname{ch}\frac{\nu z_0}{r}}{f}\left[C - \frac{3}{2}\int\frac{|n_{el}|f}{r\operatorname{ch}\frac{\nu z_0}{r}}\left(\frac{rf'_r}{f} + \frac{\nu z_0}{r}\operatorname{th}\frac{\nu z_0}{r}\right)dr\right].$$

Using (10) and the initial conditions at $\theta = 0$,

$$f = f(0),\ |n_{el}| = |n_{el}(0)|,\ \psi_\theta = \psi,$$

we can evaluate the integral:

$$\sin\psi_\theta = \sin\psi\,\frac{f(0)}{f}\,\frac{\operatorname{ch}\frac{\nu z_0}{r}}{\operatorname{ch}\frac{\nu z_0}{r(0)}} - \frac{3}{4}|n_{el}|\left[1 - \left(\frac{rf(0)\operatorname{ch}\frac{\nu z_0}{r}}{r(0)f\operatorname{ch}\frac{\nu z_0}{r(0)}}\right)^2\right]. \tag{19}$$

The slow phase motion is governed by two terms. In the first term the factors $f(0)/f$ and $\cosh(\nu z_0/r)/\cosh[\nu z_0/r(0)]$

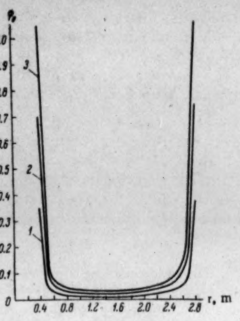

Fig. 1. Phase focusing of the particles. ψ, deg: 1) 20; 2) 40; 3) 60.

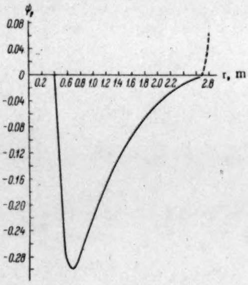

Fig. 2. Phase drift due to the quantity $\langle E_\varphi(\partial E_\varphi/\partial r)\rangle$.

are due to the H_z and E_r components of the rf field, which cause a rapid phase focusing of the particles[2] (Fig. 1); the result of this focusing (the small phase spread of the bunch of particles) is retained essentially to the final acceleration radius r_k. Outside the working region ($r > r_k$), the H_z component causes a phase defocusing. The maximum "phase-contraction" coefficient is

$$k_p = \left.\frac{\sin\psi}{\sin\psi_0}\right|_{\substack{f=1\\ \operatorname{ch}\frac{\nu z_0}{r}\cong 1}} = \frac{\operatorname{ch}\frac{\nu z_0}{r_0}}{f(0)} \cong 20. \tag{20}$$

The second term, governed by the component E_φ and its radial variation, $\langle E_\varphi(\partial E_\varphi/\partial r)\rangle$, is independent of ψ and leads to a phase drift of all the particles as a unit (Fig. 2). Hence this term can be balanced by an appropriate radial variation of the static magnetic field.

Since phase drift (17) is equivalent to a change in the revolution frequency, we can introduce an additional correction into the functional dependence of the magnetic field on the radius, $B_z/B_0 = \gamma(\omega/\omega_0)$; this correction, which is numerically equal to φ'_{dr}, taken with a negative sign, cancels out the undesirable change in the revolution frequency. If this phase-drift compensation is provided for a particle with $\psi = 0$, the corresponding change in the static magnetic field is

$$\frac{B_z}{B_0} = 1 + \frac{\omega_0^2 r^2}{2c^2} - \varphi'_{dr} = 1 + \frac{\omega_0^2 r^2}{2c^2} - \frac{3}{2}\frac{|n_{el}|^2}{\nu^2}\left(\frac{rf'_r}{f} - 1 + \frac{\nu z_0}{r}\operatorname{th}\frac{\nu z_0}{r}\right). \tag{21}$$

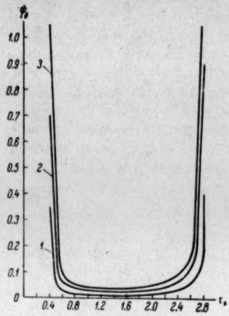

Fig. 3. Slow phase motion with balancing taken into account. ψ, deg: 1) 20; 2) 40; 3) 60.

The condition $\sin^2\psi_\theta \ll 3/2$ is satisfied automatically and is not used below. We also note that the change in the decay rate of the magnetic field caused by the term φ'_{dr} in Eq. (21) is negligible at all radii (it is on the order of 10^{-3}), so the corresponding change in the vertical motion can be neglected. Using (21), we transform Eq. (18) to the Bernoulli form:

$$\frac{dy}{dr} + \left(\frac{rf'_r}{f} + \frac{\nu z_0}{r^2}\operatorname{th}\frac{\nu z_0}{r}\right)y = \frac{|n_{el}|}{r}\left(\frac{rf'_r}{f} - 1 + \frac{\nu z_0}{r}\operatorname{th}\frac{\nu z_0}{r}\right)y^2,$$

for which the solution is

$$y = \frac{\operatorname{ch}\frac{\nu z_0}{r}}{f}\left[C - \int |n_{el}|\frac{d}{dr}\left(\ln\frac{f}{r\operatorname{ch}\frac{\nu z_0}{r}}\right)\frac{\operatorname{ch}\frac{\nu z_0}{r}}{f}\,dr\right]^{-1}.$$

Integrating by parts and using (10) we find, for the previous initial conditions,

$$\sin\psi_0 = \frac{\sin\psi\,\frac{f(0)}{f}\,\frac{\operatorname{ch}\frac{\nu z_0}{r}}{\operatorname{ch}\frac{\nu z_0}{r(0)}}}{1 - |n_{el}|\frac{r^2 f(0)\operatorname{ch}\frac{\nu z_0}{r}}{f\operatorname{ch}\frac{\nu z_0}{r(0)}}\sin\psi\int\limits_{r(0)}^{r}\left(\frac{rf'_r}{f} - 1 + \frac{\nu z_0}{r}\operatorname{th}\frac{\nu z_0}{r}\right)\frac{dr}{r^3}}. \tag{22}$$

Figure 3 shows the particle phase as a function of the radius with the compensation taken into account. We note that the phase drift due to the high acceleration rate is compensated completely only for $\psi = 0$, but even for $\psi \neq 0$ we see that the phase motion is still satisfactory. This circumstance justifies the use of approximate solution (19).

Accordingly, in magnetic field (21) the phase drift due to the acceleration rate is compensated, while the useful effect of the phase focusing is retained [the first term in (19)]. Furthermore, by varying the amount of compensation [e.g., through the coefficient $\alpha \sim 1$ of the term with φ'_{dr} in (21)], we can control the phases of all particles being accelerated as a unit and thus control the relation between the acceleration rate and the degree of focusing.

---

[1] It can be shown that in the general case of an azimuthally periodic field with a potential $U(r, \varphi, z, t)$ the electric-focusing index is

$$n_{el} = -\left\langle \frac{1}{2U_m} \frac{\partial^2 U}{\partial \varphi^2} \Big|_{z=0} \right\rangle,$$

where the averaging is carried out over the period of the structure.

[2] Here and below the numerical calculations are carried out for U^{20}_{238} ions with the following parameters (International Units): $\omega_0 = 16.08 \cdot 10^6$, $U_0 = 10^5$, $z_0 = 10^{-2}$, $d = 0.12$, $\nu = 23$. The radial profile of the rf field in a resonator having a central rod is $f = 0.77\, J_0(k_0 r) + 1.534\, N_0(k_0 r)$. The particles are accelerated from radius $r(0) = 0.403$ to $r_k = 2.1$.

---

[1] V. I. Petrunin, Zh. Tekh. Fiz., 43, 782 (1973)[Sov. Phys.—Tech. Phys., 18, 491 (1973)].

[2] M. V. Vorogushin and V. I. Petrunin, Zh. Tekh. Fiz., 44, 1218 (1974)[Sov. Phys.—Tech. Phys., 19, 767 (1974)].

[3] J. J. Livingood, Principles of Cyclic Particle Accelerators, Van Nostrand, Princeton, N. J. (1961).

[4] A. A. Kolomenskii and A. N. Lebedev, Theory of Cyclic Accelerators [in Russian], Fizmatgiz, Moscow (1962).

Multiple-section linear electron accelerator with synchronized oscillators

V. F. Vikulov, V. A. Volodin, and O. S. Milovanov

(Submitted October 5, 1973)
Zh. Tekh. Fiz., 44, 1490-1493 (July 1974)

The control and frequency characteristics of multisection linear electron accelerators supplied with rf power from synchronized oscillators are found as functions of the parameters of the synchronous, regime for the particular case of a two-section 10-MeV accelerator driven by two synchronized magnetrons. The calculated and experimental characteristics are compared.

The operating characteristics of a linear electron accelerator in which the rf power is supplied from synchronized oscillators are different from the characteristics of a multiple-section linear electron accelerator with other rf-supply systems. Examples of other systems are the parallel and series supply with rf power from a single oscillator or parallel supply from oscillators synchronized by a master oscillator. These distinguishing features are due to changes in the synchronous frequency, power, and phase in a system with synchronized self-excited oscillators caused by changes in the coupling parameters or in the resonant frequency and power of one or more of the oscillators.

A change in the phase difference between oscillators leads to a change in the phase at which the particles enter the accelerating systems; this phase change leads, in turn, to changes in the energy and energy spectrum of the particles. The effects of a change in the synchronous frequency or power of the oscillators on the particle dynamics in the accelerator are obvious and do not require special analysis.

As an example we analyze the control and frequency characteristics of a two-section, 10-MeV linear electron accelerator in which the sections are supplied rf power separately by two synchronized magnetrons. By "control characteristics" here we mean the functional dependence of the electron energy on the phase with which the particles enter the second section.

Figure 1 shows a block diagram of the accelerator. The first section is a waveguide buncher with slowly varying dimensions. The second is an accelerating waveguide with uniform structure and phase velocity equal to the speed of light. Each section is 2 m long. The oscillator power is 1.3-1.5 MW. The coupler between the oscillators, Co (a narrow-wall directional coupler), and the phase shifters Φ_1 and Φ_2 are used to control the synchronization of magnetrons M_1 and M_2. Ferrite isolaters FR_1 and FR_2 serve as isolators between the oscillators and the accelerator sections. Phase shifter Φ_3 changes the phase with which the particles enter the second section and thus provides control of the particle energy. Two such (U-13) accelerators, constructed at the Moscow Engineering Physics Institute, were put into service in 1968 and 1969; the accelerator design and characteristics are described in detail elsewhere.[1-4] The operation of two synchronized self-excited oscillators (magnetrons) has been analyzed in the a weak-coupling approximation assuming identical magnetron characteristics, a wide-band coupler, and ideal matching of the rf system.[6-9]

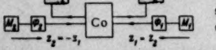

Fig. 1. Block diagram of the accelerator. I_C, II_C) Accelerator sections; M_1, M_2) magnetrons; Φ_1, Φ_2, Φ_3) phase shifters; FR_1, FR_2) ferrite isolators Co) coupler.

The frequency f_C; the power levels P_1 and P_2; the phases of the reflection coefficients at the oscillator flanges, ψ_1 and ψ_2; the phase difference of the rf oscillations at the oscillator flanges, $\varphi_{22}-\varphi_{11}$; and that of the oscillations in the loads, $\varphi_{2C}-\varphi_{1C}$, in the stable-operation regime of the oscillators satisfy the following equations:

$$f_c=\frac{f_{01}+f_{02}}{2}-\frac{12}{5}F_0\Gamma_0\,\mathrm{tg}\,\theta\sqrt{\cos^2\theta-\left(\frac{f_{01}-f_{02}}{\frac{24}{5}F_0\Gamma_0}\right)^2}, \tag{1}$$

$$P_1=P_0\left[1+2\Gamma_0\left(\sqrt{\cos^2\theta-\left(\frac{f_{01}-f_{02}}{\frac{24}{5}F_0\Gamma_0}\right)^2}-\frac{f_{01}-f_{02}}{\frac{24}{5}F_0\Gamma_0}\,\mathrm{tg}\,\theta\right)\right]^{-1}, \tag{2}$$

$$P_2=P_0\left[1+2\Gamma_0\left(\sqrt{\cos^2\theta-\left(\frac{f_{01}-f_{02}}{\frac{24}{5}F_0\Gamma_0}\right)^2}+\frac{f_{01}-f_{02}}{\frac{24}{5}F_0\Gamma_0}\,\mathrm{tg}\,\theta\right)\right]^{-1}, \tag{3}$$

$$\psi_1=\theta+\arcsin\frac{f_{01}-f_{02}}{\frac{24}{5}F_0\Gamma_0\cos\theta}, \tag{4}$$

$$\psi_2=\theta-\arcsin\frac{f_{01}-f_{02}}{\frac{24}{5}F_0\Gamma_0\cos\theta}, \tag{5}$$

$$\varphi_{22}-\varphi_{11}=\frac{1}{2}(\psi_1-\psi_2)=\arcsin\frac{f_{01}-f_{02}}{\frac{24}{5}F_0\Gamma_0\cos\theta}, \tag{6}$$

$$\varphi_{2c}-\varphi_{1c}=\beta(l_2-l_1)+\Phi_3+\arcsin\frac{f_{01}-f_{02}}{\frac{24}{5}F_0\Gamma_0\cos\theta}, \tag{7}$$

where f_{01} and f_{02} are the resonant frequencies of the oscillators; $\theta=(2\pi/\Lambda)l_0$ is the electrical length of the transmission line between the oscillators; F_0 is the pulling factor for the magnetron; $\Gamma_0 \ll 1$ is the coupling between the oscillators, since $P_{01}=P_{02}$; $P_{01}=P_{02}=P_0$ is the power level of the oscillators for operation with a matched load; Λ is the wavelength in the waveguides of the rf transmission line; β is the phase constant; $\beta=(2\pi/\Lambda)$ is the geometric length of the rf transmission lines between the oscillators and the sections; and Φ_3 is the phase shift of the wave in phase shifter Φ_3.

The criterion for operating stability of the synchronized oscillators is

$$-\arccos \frac{|f_{01}-f_{02}|}{\frac{24}{5} F_0\Gamma_0} < \theta < \arccos \frac{|f_{01}-f_{02}|}{\frac{24}{5} F_0\Gamma_0}. \tag{8}$$

Experimental study of the this type of synchronized operation of self-excited oscillators has verified (1)-(8).

When the parameters of the synchronous operation are changed, and provided that the changes in the synchronous frequency and the relative particle velocity are small ($\Delta f_c/f_c \leq 10^{-3}$; $\Delta\beta_e/\beta_e \leq 10^{-3}$ at a particle energy of 5 MeV) and that the gap between the sections is no longer than 1 m, the increment in the phase with which the particles enter the second section can be written

$$\Delta\varphi_{in} = \arcsin\left(\frac{f_{01}-f_{02}}{\frac{24}{5} F_0\Gamma_0 \cos\theta}\right)_2 - \arcsin\left(\frac{f_{01}-f_{02}}{\frac{24}{5} F_0\Gamma_0 \cos\theta}\right)_1 + (\beta_2-\beta_1)(l_2-l_1). \tag{9}$$

We see from Eqs. (1)-(7) that the oscillators operate at the same synchronous frequency at different combinations of resonant frequencies and electrical lengths of the transmission line between the oscillators; on the other hand, various methods can be used to tune the synchronous frequency, i.e., the frequency of the rf power supply of the accelerator. For example, one or both of the resonant frequencies of the oscillators can be changed, or the electrical length of the transmission line between the oscillators can be changed. In the former case, however, the power, the phase difference between the oscillations of the oscillators, and the phases of the reflection coefficients are different; in the latter case these quantities are functions of the method used to adjust the synchronism frequency. According to (9), there is an analogous change in the phase with which the particles enter the second section. The net result is a change in the energy of the accelerated electrons.

The nature of the frequency characteristics is thus a function of the method used to adjust the synchronous frequency, while the nature of the control characteristics is a function of the parameters of the synchronous regime in which the characteristics are studied.

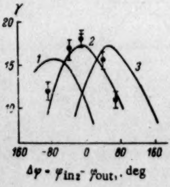

Fig. 2. Control characteristics. P = 11 MW, I = 50 nA/pulse. Solid curves) calculated. 1) f_{c0} + 1 MHz; 2) f_{c0}; 3) f_{c0} − 1 MHz. The experimental points correspond to $f_c = f_{c0}$.

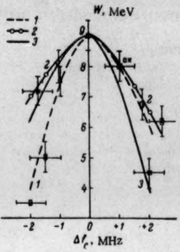

Fig. 3. Frequency characteristics of the accelerator. The solid and dashed curves are calculated. $\theta_{ini} = \Delta f_{0ini} = 0$, $\Gamma_0 = 0.1$, P = 1.2 MW, I = 50 mA/pulse. 1) f_{01} = var, f_{02} = const; 2) $f_{01} = f_{02}$ = var; 3) f_{02} = var; f_{01} = const.

In Figs. 2 and 3 the calculated and experimental characteristics of the U-13 accelerator are shown. The calculations carried out for the particle dynamics in the accelerator incorporate the effect of the coupler on the longitudinal motion of the electrons. The distribution of the phase velocity of the wave along the length of the accelerator has been found experimentally by a nonresonant-perturbation method.[5] The nominal operating parameters of the synchronized magnetrons are taken to be $f_{01} = f_{02} = f_c$, $\theta = 0$, $\Gamma_0 = 0.1$-0.2, and $P_{01} = P_{02}$. Theory and experiment show that these conditions optimize the stability of the frequency, the power, the phase difference between the oscillators, and the phase with which the particles enter the second section. From the data in Figs. 2 and 3 we see that the calculated results agree with experiment, implying that the assumptions used in the analysis are valid.

In conclusion the authors thank V. N. Gusarov for assistance in the calculations and L. I. Kudinov for assistance in the accelerator experiments.

---

[1] O. A. Val'dner, V. F. Vikulov, O. S. Milovanov, E. G. Pyatnov, and I. A. Smirnov, in: Accelerators [in Russian], No. XI, Atomizdat, Moscow (1969), p. 16.

[2] O. A. Val'dner, O. S. Milovanov, V. A. Ostanin, V. F. Vikulov, V. M. Svetlov, and I. S. Shchedrin, in: Accelerators [in Russian], No. XII, Atomizdat, Moscow (1970), p. 83.

[3] E. A. Kistanov, N. N. Nechaev, V. A. Pavlovskii, and V. N. Podshivalov, in: Accelerators [in Russian], No. XII, Atomizdat, Moscow (1970), p. 89.

[4] O. A. Val'dner, O. S. Milovanov, V. A. Ostanin, E. G. Pyatnov, I. A. Smirnov, and I. S. Shchedrin, At. Energ., 29, 140 (1970).

[5] V. F. Vikulov and V. N. Podshivalov, in: Accelerators [in Russian], No. XI, Atomizdat, Moscow (1969), p. 123.

[6] Crossed-Field Microwave Devices [Russian translation], ed. M. M. Fedorov, Vol. 2, IL, Moscow (1961), p. 327.

[7] V. F. Vikulov, O. S. Milovanov, and Yu. M. Pashkin, in: Accelerators [in Russian], No. IX, Atomizdat, Moscow (1967), p. 66.

[8] V. F. Vikulov, K. A. Vinogradov, and O. S. Milovanov, in: Accelerators [in Russian], No. X, Atomizdat, Moscow (1968), p. 181.

[9] K. A. Vinogradov and O. S. Milovanov, in: Accelerators [in Russian], No. XI, Atomizdat, Moscow (1969), p. 61.

Control of output energy in linear electron accelerators

V. N. Golovin and N. P. Sobenin

(Submitted September 27, 1972; resubmitted October 1, 1973)
Zh. Tekh. Fiz., 44, 1494-1498 (July 1974)

A method of control of beam output energy in a linear electron accelerator is described. The method lies in injecting bunches of small phase width (~ 60-90°) whose phase relative to the high-frequency wave is determined by a phase shifter; these are injected into a waveguide buncher with an equilibrium phase of $\pi/2$. With this method the beam output energy can be controlled up to energies approaching the rest energy. The mean beam output energy and the energy spread are determined. Possible implementation schemes are suggested.

The range of applications of linear electron accelerators can be greatly extended if the output energy of the beam can be made adjustable. Various methods for varying the output energy of the beam are employed, depending on the range of variation of electron energy that is required. Thus, methods of regulating the energy by varying the frequency of the supply source or its power have been developed.[1] Methods of regulating the energy in systems consisting of two or more sections are known.[2] In this case the energy can be varied over a wide range by varying the phase of the accelerating wave at the input to the second or following sections. However, these methods do not lend themselves to regulation of the energy up to levels approaching the electron rest energy. The method described below is free from this shortcoming, and can be used to vary the output energy over a wide range, almost to the rest energy.

The method uses a waveguide section with a constant equilibrium phase, equal to $\pi/2$, in which bunches of a small phase width are accelerated. This system has advantages over other methods of varying the output energy. Thus, for a given intensity parameter function and a given accelerator length, it is possible to obtain a mean beam output energy close to the maximum possible value. Moreover, output energies close to the rest energy can be obtained.

To bring out the physical principles involved, we consider the axial motion of particles in such a system. The following equations describe the axial dynamics of particles in a linear electron accelerator:

$$\left.\begin{aligned}\frac{d\gamma}{d\zeta} &= A(\zeta)\sin\varphi,\\ \frac{d\varphi}{d\zeta} &= 2\pi\left[\frac{1}{\beta_{ph}(\zeta)} - \frac{\gamma}{\sqrt{\gamma^2-1}}\right],\end{aligned}\right\}$$

where γ is the particle energy (in units of the rest energy); $A(\zeta)$ is the intensity parameter function (in dimensionless units); φ is the phase of the particles; $\beta_{ph}(\zeta)$ is the wave phase velocity function (in units of the velocity of light); and ζ is the accelerator length (in dimensionless units).

In an accelerator with a constant equilibrium phase equal to $\pi/2$ the wave phase velocity function is chosen from the requirement of synchronism with particles at a maximum of the accelerating field.

Assume that electron bunches of small phase width are injected into such a system, and that their position relative to the high-frequency field can be varied by a phase shifter. It follows from the equations above that no particle with an initial phase different from $\pi/2$ can acquire an energy greater than or equal to the energy of an equilibrium particle; accordingly, particles can "slip" relative to the high-frequency wave. The magnitude of the phase slip is determined by the distance from the maximum of the accelerating field: The further the particle is from the maximum, the greater its slip relative to the wave. Certain particles, injected in a decelerating field, lose a considerable fraction of their energy in the initial section of the accelerator, and drop out of the stable acceleration made for the fundamental wave. The subsequent phase motion of such particles reduces to a strong slip relative to the high-frequency waves. It is the presence of this physical mechanism in accelerators with $\varphi_{equ} = \pi/2$ that enables the output energy of the beam to be regulated over wide limits.

Let us consider an example of the use of an accelerator with $\varphi_{equ} = \pi/2$ to regulate the beam output energy. In the calculations the accelerator length ξ (in dimensionless units) is taken to be $\xi_k = 13.62$; the intensity parameter function has the following form:

$$A(\xi) = a_0 + a_1\xi + a_2\xi^2 + a_3\xi^3,$$

where $a_0 = 0.6$, $a_1 = 180$, $a_2 = 0.0556$, $a_3 = -0.00391$. The injection energy of the electrons is 120 keV ($\gamma_{in} = 1.236$).

The intensity parameter function and the wave phase-velocity function along the length of the accelerator are shown in Fig. 1. In the calculations the input phase width of the beam is given the values $\Delta_{in} = 60, 90, 120, 180°$. The mean beam energy is determined using the following equation:

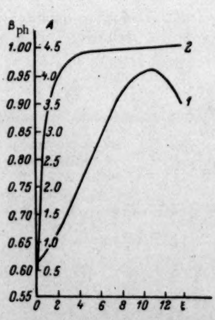

Fig. 1. Intensity parameter function $A(\xi)$ (1) and wave phase velocity function $\beta_{ph}(\xi)$ (2) along length of waveguide buncher with constant equilibrium phase $\varphi_{equ} = \pi/2$.

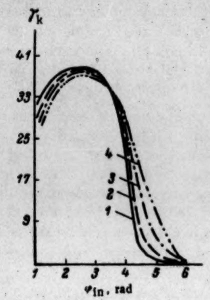

Fig. 2. Dependence of beam output energy on mean input phase of bunch for various values of the input phase width of bunch. Δ_{in_1} = 60°, Δ_{in_2} = 90 (2), Δ_{in_3} = 120 (3), Δ_{in_4} = 180° (4).

$$\gamma_{k_m} = \frac{\sum\limits_{i=1}^{N} \gamma_i}{N},$$

where N is the number of particles for a beam of given phase width. The number of particles is taken from 30 to 90.

Figure 2 shows the output energy vs the mean input phase of the bunch for various values of the phase width of the bunch at the input. For small phase widths (60–90°) and φ_{in} = 2–3 the beam has a maximum energy $\gamma_{k_{mn}}$ = 38.08. This is close to the maximum possible, which, for the intensity function in Fig. 1, is equal to

$$\gamma_{k_{max}} = \gamma_{in} + \xi_k\left(a_0 + \frac{1}{2}a_1\xi_k + \frac{1}{3}a_2\xi_k^2 + \frac{1}{4}a_3\xi_k^3\right) = 39.26.$$

When the mean phase of the beam is varied in the direction of a decelerating wave the mean energy decreases and, in the limit, tends to a value close to unity. Increasing the phase width of the beam to 120–180° is inexpedient, since the region in which low energies are achieved is reduced sharply. The input phase width is also determined by the requirements on the output energy spread. Figure 3a shows the output energy spread (over the basis) as a function of the phase position of the bunch at the input to the section for various values of Δ_{in}. It follows from this figure that minimum energy spreads are obtained for maximum and minimum beam energies, at intermediate values. The energy spread increases. However, if the energy is estimated over 70% of the trapped particles, a reduced energy spread is obtained (Fig. 3b). When the phase of the beam is varied the main portion of the electrons have the same energy on the average; only a few particles have very different energy. If stringent demands are imposed on the energy spectrum in the variation of the output energy, these particles determine the input phase width of the bunch.

In order to compare the different methods of energy control we introduce the output-energy regulation coefficient, defined as the ratio of the maximum bean output energy to the minimum: $r = \gamma_{k_{max}}/\gamma_{k_{min}}$. In any method of control the value of this coefficient cannot be greater than $r_{max} = \gamma_{k_{max\ poss}}$, where $\gamma_{k_{max\,poss}}$ is the maximum possible energy for a given intensity function $A(\xi)$.

The value of the control factor for the present method works out to be r = 38.08/1.2 = 32 in the given example for a bunch phase width of 60°. This is not far from the maximum possible value r_{max} = 39.26.

In a number of cases it is important to know the reduction of the absolute energy spread for low mean output energies of the beam. Let us estimate how the basic parameters of the accelerator affect the output energy spread at low energy levels. It turns out that in an accelerator with $\varphi_{equ} = \pi/2$ low energy levels are achieved with a strong phase slip of the bunch relative to the high-frequency field. With an accuracy sufficient for qualitative calculations the phase slip can be regarded as a linear function of the length of the section since β_{ph} is close to unity over a large part of the accelerator and the particle energy is close to unity. The energy spread in the case of strong phase slip relative to the high-frequency wave is given by the difference in the energies which the particle acquires when it is in an accelerating half-wave and which it loses when it is in a decelerating half-wave, i.e., the energy spread depends on the value of the intensity parameter.

In a structure with a constant gradient the maximum possible energy spread of low-energy particles can be estimated using the equation

$$\Delta\gamma_{k_{max\ poss}} = \frac{A_0}{\pi} = \frac{eE\lambda}{\pi m_0 c^2},$$

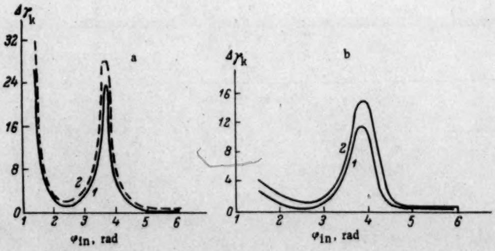

Fig. 3. Output energy spread over total number (a) and over 70% of trapped particles (b) vs phase position of bunch for different input phase widths. Δ_{in_1} = 60°, Δ_{in_2} = 90° (2).

Thus, the maximum energy spread at low output energies decreases linearly with decreasing intensity parameter A_0 (or E). Accordingly, in accelerators with $\varphi_{equ} = \pi/2$ designed for regulating the beam output energy over wide limits, the energy spread at low energy levels can be reduced by decreasing the value of the intensity parameter towards the end of the accelerator.

We note that the energy spread is also reduced by increasing the supply frequency.

Let us consider ways of putting the proposed method into effect. Two schemes are possible; these differ in the method of obtaining bunches of small phase width. The first scheme consists of a microwave generator, an injector, a chopping device, and a waveguide section with $\varphi_{equ} = \pi/2$. Bunches with phase width 60-90° are obtained with the aid of the chopper and the output energy is controlled by locating the bunches into different phases of the high-frequency wave. In the second scheme, consisting of a microwave generator, an injector, a bunching section, an attenuator, a phase shifter, and a waveguide section with $\varphi_{equ} = \pi/2$, bunches of phase width 60-90° are produced by the bunching section. The use of a bunching waveguide section means that this scheme has an increased trapping coefficient. The bunches are injected into the section with $\varphi_{equ} = \pi/2$ where, in order to reduce the energy spread, the high-frequency field is made to fall off at the end or over a large part of the section.

The example of output energy regulation considered above is very specific. It is distinguished by an intense accelerating field ($A_{max} \simeq 4$), and, accordingly, by a sharp rise in the phase velocity function. Smaller values of the intensity parameter result in a reduction of the maximum beam output energy and thus also of the regulation coefficient. However, it is easier to realize the phase velocity function of the wave when the intensity parameter is small.

Thus, by using accelerators with a constant equilibrium phase of $\pi/2$, it is possible to effect strong control of the beam output energy with high control factors.

---

[1] O. A. Val'dner, A. A. Glazkov, E. G. Pyatnov, and V. D. Seleznev, in: Accelerators [in Russian], Vol. (5), Atomizdat, Moscow (1963), p. 108.

[2] O. A. Val'dner and V. D. Seleznev, in: Accelerators [in Russian], Vol. 8, Atomizdat, Moscow (1966), p. 5.

Quantum electronics

Crystal defects of heterostructures of AlAs-GaAs solid solutions and effect on the characteristics of injection lasers

L. V. Druzhinina, V. T. Bublik, L. M. Dolginov, P. G. Eliseev,

M. P. Kerbelev, V. B. Osvenskii, I. Z. Pinsker, and M. G. Shumskii

P. N. Lebedev Physics Institute, Academy of Sciences of the USSR, Moscow

(Submitted July 26, 1973)
Zh. Tekh. Fiz., 44, 1499-1506 (July 1974)

X-ray structural studies have been carried out on epitaxial films of $Al_xGa_{1-x}As$ solid solutions and two-sided heterostructures prepared from them and used in injection lasers. The lattice constant of the $Al_xGa_{1-x}As$ solid solutions is measured as a function of the concentration and found to deviate significantly from the Vegard law. The AlAs lattice constant is found to be 5.6675 ± 0.0005 Å. Rocking curves recorded for multilayer structures reveal a degradation of the crystal structure near heteroepitaxial boundaries. X-ray topography reveals defects in these regions, which are apparently due to a discontinuity in the lattice constant at the heteroepitaxial boundary. A study is made of the effect of the dislocation density in the GaAs substrate and in the structure itself on the characteristics of injection lasers prepared from two-sided heterostructures. Dislocations significantly degrade the laser characteristics (the threshold and efficiency) only at densities $N_d \gtrsim 10^5$ cm^{-2}. A study is made of the effects of structural defects, the thickness of the active layer, and the doping level on the rate of the progressive degradation of injection lasers using two-sided heterostructures. The rate of increase in the threshold current due to the degradation increases in diodes with a thin active layer (thinner than 1 μ). Doping has essentially no effect on the degradation rate.

INTRODUCTION

Two-sided heterostructures of the $Al_xGa_{1-x}As-GaAs-Al_xGa_{1-x}As$ type are widely used in injection lasers because they permit significant improvements in the characteristics of lasers that operate at room temperature.[1-5] Important current problems are an increase in the reproducibility of the characteristics and an increase in the reliability of injection lasers. It has been shown that heterojunctions in the AlAs−GaAs system are of high quality in terms of both their optical and recombination properties.[6] It must be noted that in ordinary heterojunctions, in which the variations of x is 0.2-0.3, there is a jump in the lattice constant, Δa, many times the characteristic value for homojunctions in GaAs, where this jump is due to a gradient in the impurity concentrations. It is known that the defects associated with impurity-concentration gradients in GaAs can influence the characteristics of lasers.[7-9] We have therefore felt it useful to study the extent to which heterojunctions affect the defect properties of crystals and the basic properties of lasers. We report here on a study of the crystal defects of two-sided heterostructures in several series of samples, among which the lowest-threshold lasers operate continuously at 300°K (ref. 4); characteristic values for the better diodes are a threshold near 1 kA/cm^2 (the lowest value is 940 A/cm^2 with a resonator 500μ long) and a differential efficiency of about 40% (up to 80% at 77°K).

METHODOLOGICAL QUESTIONS

The two-sided heterostructures are grown by liquid epitaxy from molten gallium−aluminum−arsenic solutions on n-type GaAs substrates in the (100) orientation. The active region is doped with impurities such as Ge, Si, Zn, and Te (to a concentration of about 10^{17} cm^{-3}); the n-type and p-type layers of the $Al_xGa_{1-x}As$ are doped with tin and germanium, respectively (the concentrations are $\sim 1 \cdot 10^{18}$ and $5 \cdot 10^{18}$ cm^{-3}). The substrates are doped with Te or Sn [concentration of $(1\text{-}3) \cdot 10^{18}$ cm^{-3}]. The dislocation density in the substrate is varied from $N_d \leq 10^2$ cm^{-2} to 10^5 cm^{-2}. Furthermore, dislocations at a density of $N_d \sim 10^7$ cm^{-2} are introduced into the substrate and into other parts of the heterostructure by deformation in a three-point bending setup at 450°C.

To measure the lattice constants of the solid solutions we prepare undoped-crystal films (having an electron density of $\sim 2 \cdot 10^{16}$ cm^{-3}) 5-15 μ thick. A JXA-3A x-ray microanalyzer is used to monitor the compositional homogeneity along the thickness of the samples. The x-ray structural analysis includes (1) determination of the lattice constant a as a function of the composition of the solid solution, (2) measurement of the width of the rocking lines ($B_{H/2}$), recorded by means of a two-crystal spectrometer at various parts of the heterostructure, and (3) x-ray topography of the heterostructures by the Berg−Barrett method.

The x-ray structural analysis of the two-sided heterostructures is carried out with oblique sections, and the rocking curves are measured at characteristic structural points (Fig. 3a). The sample surfaces are chemically polished in a $H_2SO_4 : H_2O_2$ (3 : 1) mixture. The Cu $K_{\alpha 1}$ line is monochromatized by a dislocation-free germanium crystal.

Luminescent diodes and injection lasers are synthesized in the standard manner by splitting along cleavage planes. The resonator length is in the range 400-600 μ. The laser characteristics are measured at 300°K in pulses 0.1-0.2 μsec long at a repetition frequency of 1-2 kHz.

LATTICE CONSTANT OF THE SOLID SOLUTION

The x-ray structure studies of typical heterojunctions with x ∼ 0.2 reveal a lattice-constant discontinuity Δa of about $3.5 \cdot 10^{-3}$ Å, i.e., at least twice that expected on the basis of a linear interpolation of the lattice constants of AlAs and GaAs according to refs. 10 and 14. In this connection we have performed more detailed measurement of the lattice constant of solid solutions of the $Al_xGa_{1-x}As$ system over a broad range of compositions; the results are shown in Fig. 1. The sample with the most AlAs has

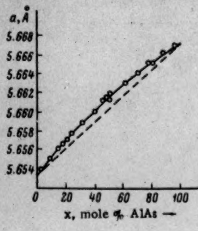

Fig. 1. Lattice constant in the GaAs–AlAs system as a function of the concentration.

TABLE 1

Lattice	a, Å	Reference	Thermal expansion coefficient, $\alpha \cdot 10^6$ deg^{-1}	Reference
GaAs	5.6534 (273° K)	[10]	5.8	[11]
AlAs	5.6622 (300° K)	[13]	6.63	[12]
	5.6605 (273° K)	[14]	5.2	[14]
	5.6675*(300° K)			

*Found through extrapolation of the present data.

a composition of $Al_{0.96}Ga_{0.04}As$ and is grown by liquid epitaxy from a molten aluminum–arsenic alloy on a GaAs substrate. Extrapolation of the functional dependence of the lattice constant on the concentration to x = 1 yields $a(AlAs) = 5.6675 \pm 0.0005$ Å, significantly different from the values given in the literature (Table 1).

A possible explanation for this discrepancy is that the previous measurements of a(AlAs) were carried out with AlAs powders containing certain impurities. Furthermore, AlAs is susceptible to corrosion, and this susceptibility can be even more important when a powdered material is used.

The functional dependence of the lattice constant on the $Al_xGa_{1-x}As$ composition (Fig. 1) displays a positive deviation from the Vegard law, i.e., from a linear $a(x)$ functional dependence. This deviation reaches a broad maximum in the center of the composition range. This deviation in the GaAs–AlAs system apparently cannot be described by geometric models of elastic spheres. The relative excess displacement volume ($\Delta V_{di}/\Delta V$) for this system can be described by the empirical equation

$$\frac{\Delta V_{\text{di}}}{\Delta V} \cong 0.308x(1-x). \tag{1}$$

The positive value of ΔV_{di} means that the activity coefficients of GaAs and AlAs in the $Al_xGa_{1-x}As$ solid solution are larger than unity, i.e., the components of the real solution have higher activities than in the ideal solution of the same composition. This circumstance in turn affects the mutual repulsion of the components in the solid solution and indicates a short-range order of the stratification type.

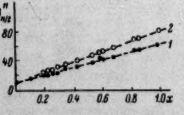

Fig. 2. Structural defect properties of a $Al_xGa_{1-x}As$ film and adjacent regions of the GaAs substrate as a function of the composition of the epitaxial film. 1) Reflections from GaAs; 2) from AlAs.

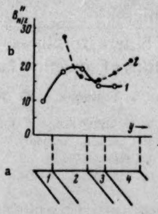

Fig. 3. Structural defect properties along the thickness of the two-sided heterostructure. a: Arrangement of the oblique section for recording the rocking curve and topograms. 1) GaAs substrate; 2) n-$Al_xGa_{1-x}As$; 3) GaAs; 4) p-type $Al_xGa_{1-x}As$. b: Halfwidth of the rocking curve, $B_{H/2}$, as a function of the position of the x-ray beam on the oblique section. 1) GaAs reflections; 2) AlAs reflections.

CRYSTAL DEFECTS OF THE HETEROSTRUCTURES

Figure 2 shows the measured values of $B_{H/2}(x)$ for films of the solid solution $Al_xGa_{1-x}As$ and the adjacent regions of the GaAs substrates. As mentioned previously, the epitaxial films are 5-15 μ thick. The film apparently affects the substrate because of the appearance of stress in the heterojunction. Because of the different thermal expansion coefficients of GaAs and AlAs (Table 1) the value of Δa at the heterojunction boundary is lower at the crystallization temperature of the epitaxial film than at room temperature. Accordingly, after cooling to room temperature the heterojunction is in a stressed state. Figure 3b shows the profile of $B_{H/2}$ along the thickness of one of the heterostructures; these measurements are carried out at characteristic points on oblique sections (Fig. 3a). We see that the heterojunction causes an appreciable broadening of the rocking curves; in addition to the broadening caused by the structural defects there is some additional broadening of the rocking curves from the epitaxial films of the solid solution due to fluctuations in the solution composition. We note that since the cor-

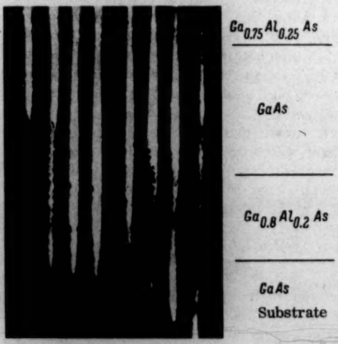

Fig. 4. X-ray topograms of an oblique section of a two-sided heterostructure (the GaAs active layer is about 7 μ thick). The seven successive topograms are recorded for various positions of the monochromator crystal in order to emphasize the reflections from all the layers forming the heterostructure. Reflection inhomogeneities are evident in the transition regions near the heterojunctions.

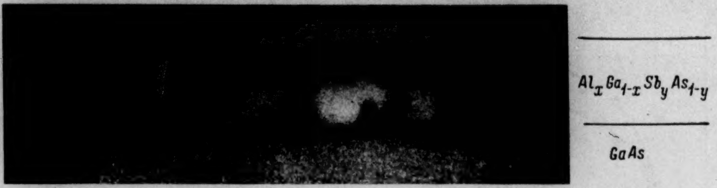

Fig. 5. Photomicrograph of a GaAs$-Al_xGa_{1-x}Sb_yAs_{1-y}$($x = 0.2, y = 0.1$) heterojunction in transmitted IR light.

responding reflection is superimposed on a reflection from the substrate we can only argue that the defectiveness of the active layer (GaAs) of the heterostructure is no worse than that of the boundary layer of the substrate.

X-ray topograms are recorded from samples (Fig. 3a) for which rocking curves were recorded in a scan over an oblique section. To obtain spatial resolution of the active region (GaAs) on the topograms we choose different compositions for the solid solutions at the heterojunctions with the active region (the usual difference was $\Delta x \sim 0.05$). In inspecting the region of homogeneous contrast at the reflection corresponding to the $Al_xGa_{1-x}As$ solid solution or GaAs on the resulting topograms (Fig. 4) we always observe regions 0.5-1 μ in size having a contrast different from that of the crystal matrix, extending in both directions from the heterojunction. The average size of these spots increases with increasing discontinuity in the lattice constant at the heterojunction.

Apparently, the most logical way to explain the regions observed on the topograms displaying a contrast different from that of the crystal matrix is to identify these regions as structural defects at the heterojunctions of the epitaxial films due to the difference in lattice constants. Similar defects have been observed at homojunctions in GaAs with a large jump in the impurity concentration ("planar" defects),[15] but the precise nature of these defects is not known. In two-sided heterostructures with a thin active layer such defects occupy a large part of the active volume and can cross the entire thickness of this volume if this thickness is less than 1 μ.

OPTICAL AND LASER CHARACTERISTICS OF THE HETEROSTRUCTURES

Observations of the heterostructures in transmitted light with an MIK-4 IR microscope reveal that in the overwhelming majority of cases the heterostructures contain no defects visible in IR light. At the same time, an increase in the discontinuity Δa beyond the values characteristic of this type of heterojunction rapidly leads to the appearance of large defects and then to the formation of a dark defect layer. Figure 5 shows an IR photomicrograph of a heterostructure with a GaAs$-Al_xGa_{1-x}Sb_yAs_{1-y}$ junction in which a lattice-constant discontinuity of $\Delta a \cdot a^{-1} > 1\%$ is achieved through the introduction of Sb. Dark regions are visible, extending 10-15 μ into the epitaxial film.

It is sometimes possible to use an IR polariscope to visualize the stress in heterostructures based on GaAs and $Al_xGa_{1-x}As$; estimates of the elastic-stress level near a heterojunction on the basis of calculations using the photoelastic constants[16] yield values below 200 kgf/cm^2. However, such stresses are capable of affecting the local value and ratio of the thresholds for TE and TM waves in lasers using two-sided heterostructures.

Observation of the near-zone pattern of the laser reveals that the inhomogeneities in the emission are frequently correlated with the stress distribution, although in most cases we are not able to identify the reason for the inhomogeneities. We have detected a certain correlation, however, with the defectiveness of the substrate, inferred from the dislocation density. The near-zone homogeneity and efficiency of the lasers are degraded significantly when the dislocation density in the substrate exceeds 10^5 cm^{-2} (Fig. 6), while the difference is negligible at lower densities. We can get some idea of the effect of the dislocation density in the substrate on the threshold characteristics of injection lasers from Fig. 7, which shows the integral distribution of samples with respect to the threshold current density, corrected to an active layer thickness of 1μ (over the thickness range studied, $0.8 < d < 2\,\mu$, the threshold current density in a two-sided heterostructure increases in proportion to the thickness).

Our study of the effect of the structural defectiveness on the degradation characteristics has included measure-

Fig. 6. Near field of laser diodes operating at 1 kHz and 0.2 μsec; the threshold is exceeded by a factor of $p_0 = 3$. a) $N_d = 10^4$ cm^{-2}; b) on a structure deformed by bending.

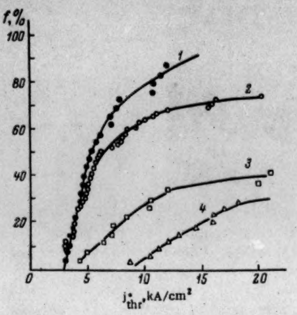

Fig. 7. Distribution of samples in series differing in the dislocation density in the GaAs substrate with respect to the reduced threshold current density j_{thr}/d at 300°K. 1) 10^2 cm^{-2}; 2) 10^4 cm^{-2}; 3) quenched substrate; 4) bending of structure.

ments of the initial rate of increase in the threshold current density under working conditions (pulse length of 0.2 μsec repetition frequency of 2 kHz, and temperature of 300°K) at a level above the threshold by a factor of 1.4-1.5. The threshold current is determined by extrapolating the linear region of the output characteristic P(I) to the abscissa. In operating over 3-6 h we determine the change in the threshold current due to the gradual degradation (aging) of the diodes. The better samples display a relative rate of increase in the threshold lower than the experimental error, corresponding to 10^{-3} sec^{-1}. We find that the thickness of the active layer of the two-sided heterostructure and the dislocation density in the substrate (provided that it is above 10^5 cm^{-2}) are among the factors affecting the degradation rate. Figure 8 shows the effect of d on dj_{n}/dt for various types of doping of the active layer; we see that at d ≈ 0.5 μ the degradation rate increases rapidly, while the effect of doping is slight.

The most rapid degradation is observed in diodes in which inhomogeneities are observed in the distribution of elastic stress near the heterojunction and near large defects.

Observation of the evolution of the laser near zone during accelerated degradation shows that this degradation is usually of an inhomogeneous nature. Figure 9 shows scan curves of the near zone recorded before and after tests as well as at intermediate times. The changes in the near zone resulting from degradation in this case cannot be offset by an increase in the pumping current, since certain parts of the near zone, which become degraded several times more rapidly than other spots of the near zone, suffer irreversible failure. This is particularly true of a region about 30 μ long to the right of the center of the end. Since this region does not display an unusual brightness at the beginning of the tests, and since self-destruction defects are not found at the ends of the diode after the tests, we can assume that the local degradation is due to internal defects in the crystal, which sharply reduce the efficiency of radiative recombination in a limited part of the active region. It is natural to assume that this process is initiated by the defects described above.

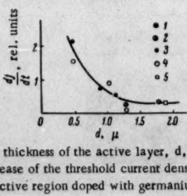

Fig. 8. Effect of the thickness of the active layer, d, on the degradation rate (the rate of increase of the threshold current density) dj_{thr}/dt for various situations: 1) Active region doped with germanium; 2) with tellurium; 3) with silicon; 4) undoped; 5) one-sided heterostructure.

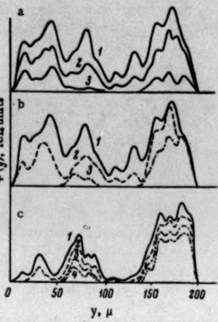

Fig. 9. Distribution of the radiation intensity in the near zone of the sample along the p–n junction. The initial parameters are a threshold current of 4.5 A and a differential efficiency of 16%. The sample gradually undergoes degradation over 20 h during operation at 1 kHz, 0.2 μsec, and a current of 20 A. a: Initial distribution during the aging period. 1) Initial distribution at 10 A; 2) after 2 h; 3) 6h. c: Final distribution. 1) 14; 2) 13; 3) 12; 4) 11 A.

The degrading of the reliability due to the defectiveness of the heteroepitaxial junctions poses a serious problem for the development of lasers using heterojunctions with a large relative jump in the lattice constant.

CONCLUSION AND RESULTS

The quality of a heterojunction and the characteristics of a laser in which it is used depend on the jump in the lattice constant at the chemical boundary. In this regard the GaAs–$Al_xGa_{1-x}As$ heterojunctions have a clear advantage over other heterojunctions because of the smallness of the value of Δa, although we have shown that the value of Δa in this case is roughly twice that assumed previously. The advantages of this system have been demonstrated by its practical use in heterojunction lasers. Nevertheless, x-ray structural studies of two-sided heterostructures and study of the laser degradation show that the heterojunctions cause a certain increase in the crystal defectiveness, which in turn affects the reliability of diodes having a thin active layer. In the latter diodes the heterojunction defects apparently span the entire layer.

The thickness of the defective region extending from the heterojunction increases rapidly with increasing Δa, reaching ~10-15 μ at $\Delta a/a$ ~1% (Fig. 5).

In GaAs–$Al_xGa_{1-x}As$ heterostructures with small jumps in the lattice constant at the junction ($\Delta a \leq 4 \cdot 10^{-3}$ Å with $\Delta x \leq 0.25$), impurities from groups III and V or other impurities can be used to compensate for this jump.

By reducing Δa in this manner it would be possible to improve the characteristics of lasers with a thin active region.

We can summarize our results as follows:

1. We have plotted the lattice constant of the $Al_x \cdot Ga_{1-x}As$ solid solutions as a function of the concentration. We find the lattice constant of AlAs to be 5.6675 ± 0.0005 Å.

2. We have used x-ray structural analysis to study the defectiveness of the heterostructures; we found that the $GaAs-Al_xGa_{1-x}As$ heterojunctions, by virtue of the jump in the lattice constant at the junction, are the source of the defects detected by the x-ray methods.

3. We have studied the correlation of the structural defectiveness of the two-sided heterostructures with the laser characteristics. We find that the characteristics of injection lasers are essentially independent of the nature of the dopant in the active region of the diodes. We find a rapid increase in the degradation rate in two-sided heterostructures having a thin active layer.

---

[1] Zh. I. Alferov, V. M. Andreev, V. I. Korol'kov, E. L. Portnoi, and D. N. Tret'yakov, Fiz. Tekh. Poluprovodn., 2, 1545 (1968) [Sov. Phys.−Semicond., 2, 1289 (1969)].

[2] Zh. I. Alferov, V. M. Andreev, P. G. Eliseev, I. Z. Pinsker, and E. L. Portnoi, Fiz. Tekh. Poluprovodn., 4, 2388 (1970) [Sov. Phys.−Semicond., 4, 2057 (1971)].

[3] L. M. Dolginov, L. V. Druzhinina, P. G. Eliseev, I. V. Krasavin, and L. D. Libov, Krat. Soobshch. Fiz., FIAN, 2, 57 (1971).

[4] A. P. Bogatov, L. M. Dolginov, P. G. Eliseev, L. D. Libov, and L. V. Druzhinina, Fiz. Tekh. Poluprovodn., 6, 43 (1972) [Sov. Phys.−Semicond., 6, 34 (1972)].

[5] Zh. I. Alferov, V. M. Andreev, V. I. Borodulin, D. Z. Garbuzov, E. P. Morozov, G. T. Pak, A. I. Petrov, E. L. Portnoi, N. P. Chernousov, V. I. Shveikin, and I. V. Yashumov, Fiz. Tekh. Poluprovod., 5, 972 (1971) [Sov. Phys.−Semicond., 5, 858 (1971)].

[6] I. Hayashi and M. B. Panish, J. Appl. Phys., 41, 150 (1970).

[7] M. S. Abrahams and J. I. Pankove, J. Appl. Phys., 37, 2596 (1966); M. S. Abrahams and C. J. Buiocchi, J. Appl. Phys., 37, 1973 (1966).

[8] H. Kressel, H. Nelson, S. H. McFarlane, M. S. Abrahams, P. LeFur, and C. J. Buicchi, J. Appl. Phys., 40, 3587 (1969).

[9] J. Hatz, Phys. Status Solidi, 28, 233 (1968).

[10] G. Giesecke and H. Pfister, Acta Crystallogr., 11, 369 (1958).

[11] H. Welker and H. Weiss, in: New Semiconducting Materials [Russian translation], IL, Moscow (1958), p. 9.

[12] I. Kudman and R. J. Paff, J. Appl. Phys., 43, 3760 (1972).

[13] N. A. Goryunova, Chemistry of Diamond-Like Semiconductors [in Russian], Izd. LGU, Leningrad (1963), p. 92.

[14] M. Ettenberg and R. J. Paff, J. Appl. Phys., 41, 3926 (1970).

[15] S. Kishino and S. Lida, J. Electrochem. Soc., 119, 1113 (1972).

[16] R. W. Dixon, J. Appl. Phys., 38, 5149 (1967).

Determination of ionization potentials and electron affinities of certain elements by extrapolation

A. G. Kamenev, É. Ya. Zandberg, and V. I. Paleev
A. F. Ioffe Physicotechnical Institute,
Academy of Sciences of the USSR, Leningrad
(Submitted December 28, 1973)
Zh. Tekh. Fiz., 44, 1507-1510 (July 1974)

Changes in the ionization potentials of elements in subgroups of the periodic table are proportional to changes in the next ionization potentials of adjacent elements of different subgroups because of the identical structure of the outer electronic shells. The proportionality factors differ, depending on the subgroups involved. This regularity is observed for elements beginning in the third row of the periodic table, provided that the outer electronic shell is filled in a regular manner in the transition of an atom of one subgroup to a neighboring atom of a different subgroup. Extrapolation on the basis of these regularities yields the following values (in volts): the first ionization potential V_1 for Fr (3.95); the second ionization potentials V_2 for Po (13.2), At (17.0) and Rn (18); and the electron affinities S of Rb (0.49), Cs (0.48), Fr (0.48), P (0.3), As (0.6), Te (1.96), Po (1.90), and At (2.90). The values of S(P) and S(As) are subsequently refined on the basis of the more accurate experimental determination of the values of S for reference elements in this subgroup.

The ionization potentials V (the first, second, and higher ionization potentials) and the electron affinities S are the most important properties of atoms, molecules, and radicals; however, experimental difficulties have prevented measurements of V_2 for certain elements and S for most elements. Calculations of S for many-electron atoms are carried-out by various approximate methods and lead to different results for certain elements. Various extrapolation approaches, e.g., those of refs. 1-3, are therefore used to evaluate S, and there has been much interest in establishing regularities in the behavior of S and V from element to element within the rows or subgroups of the periodic table. When such regularities are found it may become possible to predict the values of S and V for those atoms for which measurements of these properties have not yet been carried out.

To evaluate S and V here we use the extrapolation approach proposed in ref. 3, based on a comparison of the changes in the electron affinity in the alkali-metal subgroup with the changes in the ionization potentials in the subgroup of the adjacent alkaline earths. The comparison is based on the identical structure of the outer electronic shells of negative alkali ions and the atoms of the alkaline earths. It is assumed that the extent to which the electron affinity changes from element to element within the alkali-metal subgroup is the same as that for the change in the ionization potentials of the adjacent alkaline earth atoms. Hydrogen has been adopted as a reference element for which the value of S is known. The available experimental results on the electron affinities permit more general comparisons for elements of several subgroups.

Let us consider the sequences of values of V_1 and V_2 and those of the values of S and V_1 for those atoms in the subgroups which form isoelectronic series within rows with the correct filling of the outer electronic shell. In the determinations of S the first term of an isoelectronic series is the negative ion of the element whose affinity is to be determined. The value of S for this element is treated as the ionization potential of the negative ion.

Figure 1 shows the ionization potentials V of sequential numbers of isoelectronic series beginning with the negative halogen ions; the elements are ordered according to their atomic number N, and the dashed lines connect identically charged atoms forming the subgroups of elements in the periodic table.

From Fig. 1, we see that except for the first elements in the subgroups (F^-, Ne, Na^+, and Mg^{++}) the ionization potentials of the atoms within subgroups vary linearly, in a first approximation, from element to element. The deviation from this linearity for elements of the first and second rows can be attributed to the reduced shielding of the nuclear charge of these elements by electrons of the outer shells. It can be shown that the sequences of elements constituting the other subgroups in the periodic table display the same regularities.

On the basis of this essentially linear variation of the values of V within the subgroups for elements in the third and higher rows, we can assume the following proportionality:

$$\frac{V_q(N)}{V_{q+1}(N+1)}=\frac{V_q(N+Z)}{V_{q+1}(N+1+Z)}=K(q). \tag{1}$$

Here, Z is the change in the atomic number of the element in a subgroup corresponding to a change in the number of the row, q is the final charge state of the ionized particle (q = 0 for negative ions), and K(q) is a constant for the subgroups being compared.

Now let us compare the first ionization potentials $V_1(N)$ with the second ionization potentials $V_2(N+1)$ of neighboring atoms. The values of V_1 and V_2 are known accurately[4] for many atoms. The linear relationship between $V_1(N)$ and $V_2(N+1)$ which follows from Eq. (1) is illustrated well in Fig. 2 for several subgroups. In this figure the position of each given element of a subgroup

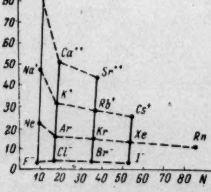

Fig. 1. Ionization potentials V_q of sequential members of isoelectric series beginning from the negative halogen ions. Here N is the atomic number of the element.

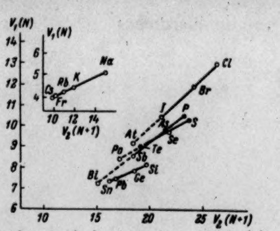

Fig. 2. Relation between the first ionization potentials of the elements and the second ionization potentials of the neighboring elements in different subgroups.

is governed by its first ionization potential $V_1(N)$ and by the second ionization potential of the neighboring element, $V_2(N + 1)$. The solid lines connect points within these subgroups corresponding to known values of $V_1(N)$ and $V_2(N + 1)$, taken from refs. 4 and 5. We see that the coefficient K(q) is in fact constant for the elements within a subgroup, and that it varies from one subgroup to another.

On the basis of these linear functional dependences $V_1(N) = f[V_2(N + 1)]$ we can use a linear extrapolation (dashed lines in Fig. 2) to evaluate the unknown values of V_1 or V_2 within the various subgroups, provided that one of these values is known (we emphasize that this procedure is possible only if the outer electronic shells in the isoelectronic sequence of neighboring elements are filled regularly, and we are not considering the elements in the first two rows of the periodic table). Through extrapolation we find the ionization potentials of the following elements: $V_1(\mathrm{Fr}) = 3.95$ V, $V_2(\mathrm{Po}) = 13.2$ V, $V_2(\mathrm{At}) = 17.0$ V, and $V_2(\mathrm{Rn}) = 18 \pm 1$ V. The error specified with the value of $V_2(\mathrm{Rn})$ is governed by the error assigned the value of $V_1(\mathrm{At})$ in ref. 5.

Similarly, we can trace the regularities in the values of S for atoms in several subgroups. For this purpose we use the values of S determined by surface ionization (SI), photodetachment of electrons from negative ions (PD) and spectroscopy (S).

Figure 3 shows the functional dependence between S(N) and $V_1(N + 1)$ for elements of several subgroups. Here the position of each element of a subgroups is governed by its electron affinity and by the first ionization potential of the neighboring element. The values of S(N) used and the method used to determine them experimentally are given in Table 1.

Figure 3 shows that in the functional dependence $S(N) = f[V(N + 1)]$ for elements of subgroups IVA and VIIA there is the regular behavior predicted by Eq. (1). In the other subgroups shown, the values of S are known for only two elements, but this information is a sufficient basis for determining the values of K(q) and, by extrapolation, the values of S for the other elements in the subgroups. The results are (in volts): S(Rb) = 0.49, S(Cs) = 0.48, S(Fr) = 0.48, S(P) = 0.3, S(As) = 0.6, S(Te) = 1.96, S(Po) = 1.90, and S(At) = 2.90. It should be noted that there can be errors in the values found for S(P) and S(As) because of the relatively poor accuracy with which S(Bi) and S(Sb) were determined.

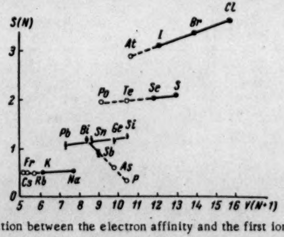

Fig. 3. Relation between the electron affinity and the first ionization potential of the neighboring element in various subgroups.

TABLE 1

Element	S(V)	Method	Reference
Na	0.542 ± 0.010	PD	[6]
K	0.501 ± 0.010	PD	
Si	1.24 ± 0.02	SI	[7, 13]
Ge	1.14 ± 0.03	SI	
Sn	1.16 ± 0.06	SI	[8, 13]
Pb	1.05 ± 0.08	SI	
Sb	0.90 ± 0.07	SI	[9, 13]
Bi	1.16 ± 0.06	SI	
S	2.0772 ± 0.0005	PD	[10]
Se	2.0201 ± 0.0003	PD	[11]
Cl	3.613 ± 0.003	S	[12]
Br	3.363 ± 0.003	S	
I	3.063 ± 0.003	S	

The values of S for the alkali metal atoms are evaluated in ref. 3 through the use of elements of the first row as reference elements. Furthermore, it is assumed there that the values of S in the alkali metal subgroup change from element to element to the same extent as the values of V_1 for the neighboring alkaline earths [equivalently, K(q) = 1]. This procedure leads to the low values of S for the alkali metal atoms.

We note in conclusion that this extrapolation method can be used to determine higher-order ionization potentials of certain elements. We have not studied the question of the values of K(q) or of the changes in these values from subgroup to subgroup; this question is of independent interest.

---

[1] R. J. Zollweg, J. Chem. Phys., 50, 4251 (1969).

[2] P. Politzer, Trans. Faraday Soc., 64, 2241 (1968).

[3] V. M. Dukel'skii, in: Collection Dedicated to the 70th Birthday of Academician A. F. Ioffe [in Russian], Izd. Akad. Nauk SSSR, Moscow (1950).

[4] C. E. Moore, NSRDS-NBS, 34, (Sept. 1970).

[5] M. Von Ardenne, Tables of Electron Physics, Ion Physics and Ultramicroscopy [in German], Vol. 1, Veb Deutscher Verlag der Wissenschaften, Berlin (1956).

[6] T. A. Patterson, H. Hotop, and W. C. Lineberger, in: Electronic and Atomic Collisions, Abstracts of Papers, VIII ICPEAC (ed. B. C. Cobic and M. V. Kurepa), Vol. 2, Beograd (1973), p. 597.

[7] É. Ya. Zandberg, A. G. Kamenev, and V. I. Paleev, Zh. Tekh. Fiz., 41, 1983 (1971) [Sov. Phys. – Tech. Phys., 16, 1567 (1972)].

[8] É. Ya. Zandberg, A. G. Kamenev, and V. I. Paleev, Zh. Tekh. Fiz., 41, 1057 (1971) [Sov. Phys. – Tech. Phys., 16, 832 (1971)].

[9] É. Ya. Zandberg and V. I. Paleev, Dokl. Akad. Nauk SSSR, 190, 562 (1970) [Sov. Phys. – Dokl., 15, 52 (1970)].

[10] W. C. Lineberger and B. W. Woodward, Phys. Rev. Lett., 25, 424 (1970).

[11] H. Hotop, T. A. Patterson, and W. C. Lineberger, Bull. Am. Phys. Soc., 17, 150 (1972).

[12] R. S. Berry and C. W. Reimann, J. Chem. Phys., 38, 1540 (1963).

[13] É. Ya. Zandberg, A. G. Kamenev, and V. I. Paleev, Zh. Tekh. Fiz., 44, 617 (1974) [Sov. Phys. – Tech. Phys., 19, 385 (1974)].

Evaluation of charge distribution in a crossed-field device from ion bombardment of the cathode

V. I. Malyugin and G. G. Sominskii
M. I. Kalinin Leningrad Polytechnic Institute

(Submitted July 5, 1973)
Zh. Tekh. Fiz., 44, 1511-1516 (July 1974)

A method is described for measuring the charge distribution in high-power crossed-field devices. The energy distribution of ions bombarding the cathode in a pulsed Amplitron with a cold secondary-emission cathode is investigated. The space-charge distribution in the Amplitron is determined from the ion bombardment data.

Although space charge plays an important role in the operation of crossed-field devices, there is little information available on the distribution of the electron cloud in actual amplifiers or magnetrons. This lack is explained primarily by the absence of simple and reliable methods for studying space-charge characteristics in crossed fields. Methods developed for studying space-charge characteristics in magnetron diodes[1–6] have certain shortcomings. A method suitable for analyzing the space-charge characteristics in M-type amplifiers and oscillators is proposed in ref. 7. An analysis of the end current (electron flow along the magnetic field) yields data on the radial space-charge distribution in a magnetron oscillator. However, because of difficulties associated with fringing fields, the most accurate data are obtained only for the electron-cloud regions near the cathode.

As follows from ref. 8, useful information on the space-charge distribution in crossed fields can be obtained from an analysis of the bombardment of the cathode by ions generated in ionization of residual gas by the electrons.

In this note we consider the relation between ion bombardment and the space-charge distribution.

ION CURRENT AND THE SPACE-CHARGE DISTRIBUTION

The ions that are formed in the interaction space of an M-type device under the action of an electric field move toward the cathode along trajectories that are essentially straight lines. Since the action of the microwave field on the ion motion is insignificant, the energy of the ions at the cathode is equal to the potential difference between their point of formation and the cathode surface eU. The current density of the ions striking the cathode with energies from eU to eU_a is

$$j_+ = -\int_U^{U_a} n\rho\sigma_{\text{eff}} \frac{r}{r_c}\frac{dr}{dU}\,dU. \qquad (1)$$

Here, ρ is the electron-charge density at a distance r from the axis of the system, U_a is the anode potential, r_c is the cathode radius, n is the residual-gas density, and σ_{eff} is the effective electron-impact ionization cross section of the gas. The value of n can be found from the pressure p in the device, $n = p/kT$ (k is the Boltzmann constant and T is the temperature). The effective cross section is generally determined as follows:

$$\sigma_{\text{eff}} = \int_{v_i}^{\infty} v^3 S(v)\,dv \int_0^{\pi} \sin\theta\,d\theta \int_0^{2\pi} f(v,\ \theta,\ \varphi)\,d\varphi. \qquad (2)$$

The integration is carried out from velocity v_i corresponding to ionization potential U_i, $v_i = \sqrt{2eU_i/m}$, e and m are the electron charge and mass, S(v) is the dependence of the ionization cross section on the total electron velocity v and $f(v,\ \theta,\ \varphi)$ is the electron velocity distribution function. Introduction of the electron velocity distribution function into the expression for σ_{eff} indicates that the electron motion can be randomized in the interaction space.[7,9–13] The electron velocity spread is given by an electron temperature T_e. Investigations[7,13] in high-power crossed-field devices show that T_e does not exceed $\sim 10^6$°K. In magnetron systems operating at anode voltages $U_a \sim 10^4$ V, the electron energy W is much greater then kT_e in a large part of the interaction space. Therefore, the randomization of the space charge is important in the effective ionization cross section σ_{eff} only near the cathode, where $W \leqslant kT_e$. The dimension of this region can be estimated on the basis of the results of ref. 13, where the electron velocity and temperature T_e are calculated. Figure 1 shows the ratio of kT_e to the electron energy $mv^2/2$ (curve 1) as a function of the radial coordinate r, as obtained from the data of ref. 13 for the magnetron amplifier described in refs. 8 and 14. Evidently $2kT_e/mv^2$ can approach unity only for $r - r_c \leqslant 0.2$ mm. This example indicates that in high-power magnetron devices operated at high anode voltages the effective ionization cross section σ_{eff} in Eq. (1) can be calculated in a large part of the interaction space without taking account of the electron velocity spread.

Differentiating both sides of Eq. (1) with respect to U, we obtain

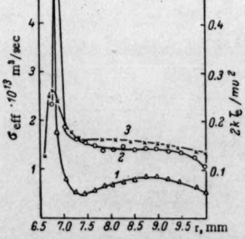

Fig. 1. 1) Dependence of $2kT_e/mv^2$ on the radial coordinate r; 2) characteristics $\sigma_{1\text{eff}} = \sigma_{1\text{eff}}(r)$, calculated on the basis of data of ref. 13; 3) characteristics $\sigma_{2\text{eff}} = \sigma_{2\text{eff}}(r)$, obtained for B = 0.215 T.

$$\frac{dj_+}{dU} = n\rho\sigma_{\text{eff}} \frac{r}{r_c} \frac{dr}{dU}. \tag{3}$$

Solving Eq. (3) together with the Poisson equation

$$\frac{1}{r}\frac{d}{dr}\left(r\frac{dU}{dr}\right) = -\frac{\rho}{\varepsilon_0}, \tag{4}$$

we can obtain the density distribution of the space charge ρ over the radius for a known form of the dependence of dj_+/dU on U. The form of this dependence is determined experimentally in the present article on the basis of an analysis of the energy distribution of the ions bombarding the cathode.

METHOD OF MEASUREMENT AND APPARATUS

The measurements are carried out with the Amplitron described in refs. 8 and 14, which has cold, secondary-emission platinum cathodes. The Amplitron is started by a magnetron oscillator. The pulse length τ of the anode current I_a and the repetition frequency can be varied over wide limits. The device is pumped continuously. The pressure of the residual gas is below $5 \cdot 10^{-6}$ torr. Ion bombardment is investigated by admission of argon; the pressure is controlled by a needle valve.

To determine the form of the function $dj_+/dU = f(U)$ we use the system in Fig. 2. A metal cylinder 3 with a longitudinal 1-mm-wide slit 4 is placed inside a hollow cathode 1 with a diameter[1)] of 13 mm with a transverse slit 2 1.5 mm wide. The ions from the working space enter the system at the point of intersection of the longitudinal and transverse slits. By rotating cylinder 3 we can isolate ion beams from various sections of the interaction space with respect to the azimuth. Only the region that is covered by a diaphragm on the 4-mm-wide cathode 5 remains inaccessible. The ions passing inside the analyzing system must pass through the grids 6 and 7 before they reach the collector 8.

In studying the ion bombardment of the cathode it is important to keep the electrons that bombard the cathode from striking the collector. The electrons passing into the analyzing system are shielded out in the drift space (~4 mm side) between the inner surface of the cylinder 3 and the grid 6. The ion energy distribution is analyzed by the retarding-field method in the space between the grids 6 and 7 by applying a pulsed voltage U. The pulses U are synchronized with the pulses U_a, and the pulse length is selected so that they completely overlap the pulse of the anode-current I_a. The drift space between grid 7 and collector 8(~2 mm) is a barrier for the electrons that result from ionization in the region between grids 6 and 7. Drift of secondary electrons from the collector along the magnetic field is eliminated by choosing a collector in the shape of a small box with folded edges. The analyzing system is rigidly fixed in cylinder 3, which is rotated in vacuum by a special magnet device.

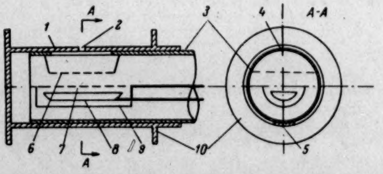

Fig. 2. Schematic representation of cathode with analyzing system, used for studying ion bombardment. 1) Cathode with transverse slit 2; 3) cylinder with longitudinal slit 4; 5) iris on cathode; 6, 7) grids; 8) ion collector; 9) guard electrode; 10) end shield.

The lower limit of the ion energy to be analyzed is determined by the distance between the collector 8 and the cathode surface, which is ~8 mm. In the investigated range of magnetic fields (B ≤ 0.235T) the minimum energy needed by an argon ion to reach the collector is less than 1 eV. Thus, for U = 0 essentially the total ion current incident on the cathode reaches the collector. When U > 0, only those ions formed in the working space of the Amplitron at distances at which the potential exceeds the value U reach the collector.

ENERGY DISTRIBUTION OF IONS BOMBARDING THE CATHODE

The analyzing system allows us to investigate the azimuthal distribution of ions over the cathode surface and the energy distribution of ions bombarding the cathode at different azimuthal angles. The dependence of the ion current I_+ on the azimuthal coordinate φ is measured for different values of retarding ion voltage. It turns out that there is a marked azimuthal variation of the ion current[2)] which does not change with increasing U. The fact that the variation is observed for retarding voltages up to U = 13 kV indicates that the azimuthal inhomogeneities of the space charge are preserved at large distances from the cathode and that they extend over large radial distances. The $I_+ = I_+(\varphi)$ characteristics are qualitatively similar over the entire investigated range of variation of magnetic field (0.15 ≤ B ≤ 0.235 T) and anode voltage (up to 25 kV).

A more complete representation of the energy spectrum of the ions bombarding the cathode is obtained by analysis of the retardation curves $I_+ = I_+(U)$, which are plotted for different values of the coordinate φ. Figure 3 shows typical $I_+/I_{+m} = f(U)$ characteristics, obtained for

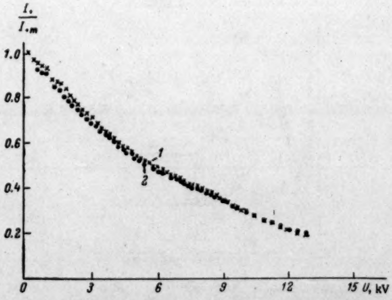

Fig. 3. The ratio I_+/I_{+m} as a function of the retarding voltage U (I_{+m} is the ion current for U = 0), measured at the maximum (curve 1) and the minimum (curve 2) azimuthal distributions of ion current; B = 0.215 Te, U_a = 19.4 kV.

magnetic field B = 0.215 T and anode voltage U_a = 19.4 kV for the maximum (curve 1) and the minimum (curve 2) azimuthal distributions of ion current. The quantity I_{+m} is the maximum value of the ion current for U = 0. As follows from the figure the form of the ion-current distribution varies insignificantly over azimuth.

CALCULATION OF RADIAL SPACE-CHARGE DENSITY DISTRIBUTION IN AN AMPLITRON

The value of dj_+/du necessary for calculating the density of the space charge ρ is obtained by differentiating the experimentally measured retardation curves. The $j_+ = j_+(U)$ characteristics are processed by regression analysis using a computer.

The value of the effective ionization cross section is determined neglecting the randomization of the space charge. The dependence of σ_{eff} on r is calculated for two types of electron velocity distributions in the interaction space, known from literature. Curve 2 of Fig. 1 represents the function $\sigma_{eff} = \sigma_{eff}$ (r), obtained on the basis of the data of ref. 13. Curve 3 $[\sigma_{eff} = \sigma_{eff}(r)]$ is obtained under the assumption that there is a Brillouin velocity distribution $v = (eB/2m)r \times (1 - r_c^2/r^2)$ up to the synchronization radius r_{syn}; for $r > r_{syn}$ it is assumed that the electrons are synchronized with the high-frequency wave. With different electron velocity distributions we obtain similar values of σ_{eff}, which indicates that the values of σ_{eff} do not depend critically on the particular electron velocity distribution.

In solving the system of equations (3) and (4) we use the data on the value of the ionization cross section S(v) of argon from ref. 15. In calculating the gas density ion we take the gas temperature T equal to the cathode temperature. The argon pressure in the working space of the Amplitron is determined directly from the ion current[14] assuming that I_+ depends linearly on p. The radial space-charge density distribution is calculated by numerical methods using a computer. Figure 4 shows the family of characteristics $\rho = \rho(r)$, obtained for B = 0.215 T, anode voltage U_a = 19.4 kV, and various values of φ. The functions 1 and 2 characterize the space-charge density distribution at the maxima of the azimuthal ion-current distribution at the cathode. Curves 3 and 4 are obtained at the minima of the $I_+ = I_+(\varphi)$ function. The characteristics $\rho = \rho(r)$, obtained when the effective ionization cross section is set equal to σ_{2eff} (solid lines) and calculated for the case $\sigma_{eff} = \sigma_{1eff}$ (dashed curves), differ insignificantly over a large part of the interaction space, except for the cathode region. According to these data, the form of the radial space-charge density distribution does not vary qualitatively with the azimuthal coordinate: There are two space-charge density peaks, one of which is near the cathode surface; the position of the second varies with φ. Near the maxima of the azimuthal ion-current distribution, located opposite the slit of the retarding system,[14] the extremal values of the space-charge density are attained at greater distances from the cathode than under the vanes [at the minima of the $I_+ = I_+(\varphi)$ curve]. After the second maximum of the $\rho = \rho$ (r) curve the change in space-charge density is insignificant.

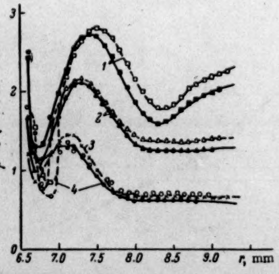

Fig. 4. Dependence of space-charge density ρ on radial coordinate r obtained with the effective ionization cross section set equal to σ_{2eff} (solid lines) and calculated for the case $\sigma_{eff} = \sigma_{1eff}$ (dashed curves). 1, 2) Characteristics $\rho = \rho(r)$ at the maximum (respectively, φ = 70° and φ = 340°) of the azimuthal ion-current distribution; 3, 4) the function $\rho = \rho(r)$ at the minima of the $I_+ = I_+(\varphi)$ (for φ = 240° and φ = 90°).

The form of the characteristics $\rho = \rho$ (r) does not vary qualitatively with changes in the mode of operation of the device. Data on the space-charge distribution near the cathode agree with data obtained earlier, in a study of the end current, on the form of the characteristics $\rho = \rho$ (r) in a magnetron oscillator.[7]

Summing up our study we note the following:

1. The method developed here enables us to measure the radial space-charge distribution in crossed-field devices. The proposed method is relatively simple, it does not disturb the electron cloud, and can be recommended for analyzing the high-density space charge in high-power M-type devices.

2. The energy distribution of ions bombarding the cathode in a pulsed Amplitron with a cold secondary-emission cathode has been investigated.

3. On the basis of the data on the ion bombardment of the cathode we have calculated the $\rho = \rho(r)$ curves for various sections of the interaction space of an experimental Amplitron the $\rho = \rho$ (r) characteristics have two maxima. We observe a radial displacement in the space-charge-density peak that is not at the cathode with a variation in the coordinate φ.

The authors are grateful to E. A. Nefed'evoi, who participated in the measurement, to V. P. Balabin for help with the numerical calculations, and to S. A. Frdirikhov for his interest.

---

1) Anode diameter D_a = 20 mm.

2) These data agree with the results published earlier in a study of the azimuthal distribution of ion current.[8]

[1] W. Engbert, H. F. T. u. Elek., 51, 47 (1938).
[2] D. L. Reverdin, J. Appl. Phys., 22, 257 (1951).
[3] H. C. Nedderman, J. Appl. Phys., 26, 1420 (1955).
[4] L. E. Matias, J. Electron. Control, 1, 8 (1955).
[5] M. I. Kuznetsov and L. M. Groshkov, Izv. VUZ. Radiofiz., 1, 1104 (1961).
[6] L. M. Groshkov, Izv. VUZ. Radiofiz., 9, 1 (1966).
[7] G. G. Sominskii, Zh. Tekh. Fiz., 38, 663 (1968) [Sov. Phys.-Tech. Phys., 13, 497 (1968)].
[8] V. I. Malyugin, G. G. Sominskii, and L. M. Gorshkova, Elektron. Tekh., Ser. 1, Elektronika SVch, No. 7 (1972).

[9] E. G. Linder, Proc. IRE, 26, 346 (1938).
[10] I. M. Vigdorchik, Zh. Tekh. Fiz., 6, 1657 (1936).
[11] G. Hok, Electronic Microwave Devices with Crossed Fields [Russian translation], ed. by M. M. Federov, IL, Moscow (1961), p. 204.
[12] S. P. Yu, G. P. Cooyers, and O. Buneman, J. Appl. Phys., 36, 2550 (1965).
[13] A. S. Roshal' and P. V. Romanov, Zh. Tekh. Fiz., 42, 2501 (1972) [Sov. Phys.—Tech. Phys., 17, 1948 (1973)].
[14] V. I. Malyugin and G. G. Sominskii, Elektron. Tekh., Ser. 1, Elektronika SVCh, No. 10 (1970).
[15] L. J. Kieffer and G. H. Dunn, Rev. Mod. Phys., 38, No. 1 (1966).

Thermal conditions for a sandwich cold cathode

F. M. Benson, P. E. Troyan, and Yu. B. Yankelevich
Tomsk Institute of Automatic Control Systems and Radio Electronics
(Submitted February 18, 1973; resubmitted July 31, 1973)
Zh. Tekh. Fiz., 44, 1517-1520 (July 1974)

The thermal operating conditions of a metal–dielectric–metal system used as a cold electron source are analyzed. In the steady state the system reaches + 100°C. The temperature distribution in the sandwich is governed by the substrate properties. A thermal analysis is made of the operation of a thin-film cathode under pulsed conditions.

Thin-film metal–dielectric–metal systems have found extensive application in modern microelectronics as capacitors, diodes, switches, etc.

One recent application of the system is as a nonincandescent or cold electron source (a sandwich cold cathode)[1] (Fig. 1).

Extremely strong electric fields arise in a thin-film metal–dielectric–metal system, even at low voltages, causing intense field emission from the lower electrode into the dielectric. Some of the electrons accelerated in the dielectric film pass through the upper metal film and, after overcoming the potential barrier at the metal–vacuum interface, leave the system. The transfer coefficient of such a system (the ratio of the electron current into vacuum to the total current through the metal–dielectric–metal system) is usually in the range 10^{-7}-10^{-2}, since most of the electrons are absorbed in the upper metal electrode. The energy of the electrons accelerated in the field is dissipated nearly completely in the upper metal film, causing heating of the latter. The electron acceleration itself is accompanied by the scattering of electrons in the dielectric, which also tends to heat the system.

This heating can cause important changes in the structural properties of the upper metal electrode and can even melt it; the system can crack as a result of the thermoelastic stress arising because of the different expansion coefficients of the components of the system, the conductivities of the metal electrodes can change, etc.

In the systems which we have studied, based on the $Al-Si_3N_4-Al$ structure, the through current reaches a density of 5-10 A/cm^2 at a voltage drop of 10-15 V across the dielectric film. Sandwich cathodes made from this system, on glass substrates, usually fail rapidly (parts of the cathode burn, and the glass substrate cracks). Accordingly, it is very important to analyze the thermal conditions of a thin-film metal–dielectric–metal system in order to determine the optimum operating conditions and the optimum choice of structural components.

We turn now to an analysis of the temperature fields in a metal–dielectric–metal system in vacuum operating under steady-state or pulsed conditions. The structure is shown schematically in Fig. 1, where d_1, d_2, and d_3 are the thicknesses of the sandwich components, and D is the substrate thickness.

1. THE HEAT-SOURCE APPROXIMATION

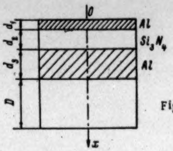

Fig. 1. Construction of a "sandwich" cathode.

Heat is evolved in the dielectric and the upper metal electrode in accordance with the distribution of absorbed energy resulting from the scattering and absorption of hot electrons. In view of the complexity of the analytic distribution function for the energy absorbed in the dielectric film, we assume that all the heat is evolved in the upper metal electrode; we do not introduce any simplifications regarding the conditions for heat transfer from the sandwich. Scattering of hot electrons in the upper metal electrode of a sandwich has been studied experimentally in detail.[2,3]

The number of electrons leaving the upper electrode is given by $n_0 S \exp(-d_1/l)$, where n_0 is the number of electrons incident per unit time on a unit area of the upper electrode; S is the area of this upper electrode; l is the "attenuation length" for the hot electrons, a function of their energies, which are in turn governed by the acceleration and scattering in the dielectric and by the properties of the upper-electrode material;[4] and d_1 is the thickness of the upper electrode. The number of electrons absorbed in the upper electrode is then equal to $n_0 S[1-\exp(-d_1/l)]$. Writing the through current of the system as $i_S = q/t = n_0 S_0 l$, and denoting the voltage applied to the electrodes by U_0, we find that the heat evolved in a unit volume of the upper electrode is

$$Q=\frac{i_S U_0}{S d_1}\left[1-\exp\left(-\frac{d_1}{l}\right)\right]. \qquad (1)$$

In sandwich cathodes the condition $d_1 \approx 2l$ is usually arranged in order to provide the necessary conductivity of the upper electrode and the necessary conditions for the scattering of hot electrons in it. Then we can approximate the heat source by

$$Q(x)=\frac{i_S U_0}{S d_1}, \qquad (1a)$$

which is constant for given values of i_S and U_0.

2. STEADY-STATE TEMPERATURE FIELD IN THE METAL–DIELECTRIC–METAL SYSTEM

We assume that heat is removed from the upper electrode by thermal conductivity. The heat loss due to IR radiation of the free surface of the upper electrode is very small (2%) because of the small area of this electrode and its mirror finish. Convective heat transfer from the surface of the upper electrode, due to collisions with residual gas molecules, is also negligible (on the order of a fraction of 1%). In sandwich cathodes the linear dimensions of the emitting surface are much larger than the thickness of the thin-film metal electrodes, so that it is difficult to remove heat from the lateral surfaces through conducting contacts unless special measures are taken. We can therefore take the one-dimensional approach to determine the steady-state temperature field T(x) in the system (Fig. 2); this field is found from the solutions of the following four heat-conduction equations:

$$\frac{d^2T_1(x)}{dx^2} = -\frac{1}{\lambda_1}Q;\quad \frac{d^2T_i(x)}{dx^2} = 0\ (i = 2, 3, 4)\,, \tag{2}$$

with the adiabatic boundary condition at the free surface of the upper electrode and the isothermal boundary condition at the lower free surface of the substrate. Since the values of d_i (i = 1, 2, 3) are negligibly small, and since $d_i \ll D$, we can omit all terms in the solutions of system (2) containing d_i^2 or $d_i d_j$ $(i \neq j)$. We then find that the temperatures in all the thin-film components of the sandwich are equal:

$$T_1(x) = T_2(x) = T_3(x) = T_S(x), \tag{3}$$

and equal to the temperature at the substrate surface, T_S, with $x = d_1 + d_2 + d_3$. It follows that the thermal situation in a thin-film sandwich (Fig. 2) is governed completely by the comparatively thick substrate, which is described by

$$T_S = \frac{U_0 i_S}{S\lambda}\left[1 - \exp\left(-\frac{d_1}{l}\right)\right]D, \tag{4}$$

where λ is the thermal conductivity of the substrate.

It follows from (4) that the sandwich can be cooled most efficiently if the substrate is a good heat conductor.

Study of the operation of sandwich cathodes over a broad temperature range has shown that the emission current is stable up to 100°C. When the heat evolution corresponds to ~ 150 W/cm², Eq. (4) predicts a temperature reaching 600°C for a sandwich on a glass substrate. Cathodes on a sapphire substrate [λ = 4.2 W/cm · deg)] operate reliably and stably ($T_S \simeq 100°C$).

3. PULSED OPERATION

Since the response time of cold cathodes is extremely short, they can be used to produce high current densities in pulsed operation.

Since the temperature distribution in a thin-film sandwich is governed by the temperature field of the massive substrate, in an analysis of the thermal regime under pulsed conditions we can treat sandwich and substrate as a unit and describe them by means of simply the heat-conduction equation for the substrate:

$$\frac{\partial T}{\partial t} = \varkappa\frac{\partial^2 T}{\partial x^2} + \frac{Q}{cp}, \tag{5}$$

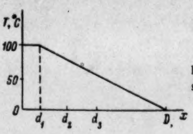

Fig. 2. Topological thermogram of a sandwich cathode in the steady-state.

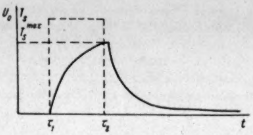

Fig. 3. Applied-voltage pulse (dashed lines) and chronological heating thermogram for a sandwich cathode (solid curve).

where ϰ = λ/cp, where λ is the thermal conductivity, c is the specific heat, and p is the density.

We restrict the analysis to finding the effect of a single rectangular heat pulse produced in the plane of the upper metal electrode with an abscissa equal to zero and which spans the entire thickness of the system, D. Between time τ_1 and τ_2 the rectangular heat pulse is described by an equation found from Eq. (5) (ref. 5):

$$T_S = \frac{i_S U_0}{S\lambda}\left[1 - \exp\left(-\frac{d_1}{l}\right)\right]D \times \sum_{m=0}^{\infty}\frac{8}{(2m+1)^2\pi^2}\left\{\exp\left[-\frac{(2m+1)^2}{4D^2}\pi^2\varkappa(t-\tau_2)\right] - \exp\left[-\frac{(2m+1)^2}{4D^2}\pi^2\varkappa(t-\tau_1)\right]\right\}, \tag{6}$$

which is a series which converges quite rapidly. Assuming m = 0, we find a simplified equation, from which we can easily find numerical values, describing the heating between $\tau_1 = 0$ and τ_2:

$$T_S = \frac{i_S U_0}{S\lambda}\left[1 - \exp\left(-\frac{d_1}{l}\right)\right]D \times \left\{\exp\left[-\frac{2.5}{D^2}\varkappa(t-\tau_2)\right] - \exp\left(-\frac{2.5}{D^2}\varkappa t\right)\right\}. \tag{7}$$

Figure 3 shows the applied-voltage pulse (the dashed lines) and a chronological heating thermogram for a sandwich cathode (solid curve). Evaluation of the pulsed operation on the basis of (7) shows that a sandwich cold cathode on a glass substrate having λ = 0.7 W/(m · deg) can operate reliably at 50 Hz at a length of up to $5 \cdot 10^{-4}$ sec of the voltage pulse; the heat evolution during the pulse is ~ 150 W/cm².

---

[1] C. Mead, J. Appl. Phys., 32, 646 (1961).

[2] L. Eckertova, J. Vac. Sci. Tech., 6, 508 (1969).

[3] C. Mead, Phys. Rev. Lett., 8, 56 (1962).

[4] S. M. Sze, J. L. Mool, and T. Sugano, Solid State Electron., 7, 509 (1964).

[5] F. M. Kam'ya, Pulsed Theory of Heat Conduction [in Russian], Izd. Energiya, Moscow (1972).

Nanosecond x-ray pulses

G. A. Mesyats
Atmospheric Optics Institute, Siberian Branch,
Academy of Sciences of the USSR, Tomsk
(Submitted July 16, 1973)
Zh. Tekh. Fiz., 44, 1521-1527 (July 1974)

Nanosecond x-ray pulse generators are used both in the study of rapid processes and for normal radiography. The generator tubes contain either field emission cathodes or cathodes that use explosive emission of electrons. Explosive emission occurs as a result of the interaction with the cathode of a dense plasma formed by the explosion of needles on the cathode. The heating and explosion processes of these needles are considered. The voltage—current characteristics of nanosecond x-ray tubes with this type of emission are subject under certain conditions, to the "three-halves" law. A calculation of these characteristics must take account of the configuration of the cathode plasma. A calculation is made of the parameters of nanosecond x-ray pulses in generators operating by the discharge of a storage capacitor and of a line through the tube which has a large or small number of emission centers. Satisfactory agreement is obtained with the available experimental results.

1. INTRODUCTION

Nanosecond x-ray pulse generators are used in the study of rapid processes and also in normal radiography.[1] The electrons in the generator tubes are obtained either by field emission or by means of an electric discharge in a high vacuum.[2] While the operating mechanism of field-emission x-ray tubes is well understood, the operations of discharge tubes is not clear.

A very fertile concept in the explanation of the operation of these tubes is that the electrons are emitted during the explosive destruction of cathode microneedles as a result of the field emission current.[3] This phenomenon has been called explosive electron emission.[4] The presence of microscopic projections on the cathode surface means that the electric field at these projections is several times greater than the average electric field in the vacuum gap. This produces a greater field emission current from the projections so that they heat up and explode. The same effect of course occurs if metal needles are used for the cathode. The metal vapor from the cathode diffuses into the vacuum and is ionized by the electrons from the cathode; the resulting plasma is known as the cathode flare. The formation of a dense plasma at the cathode surface produces an amplification of the electron current from the cathode. These electrons will be extracted by means of the electric field at the cathode which is formed, apparently, by charge separation in the plasma.[5] The electron current flow in the vacuum gap depends on the rate of expansion and the number of cathode flares, the length of the gap, the applied potential, and the electrodes configuration. The aim of this paper is to calculate the principal parameters of nanosecond x-ray pulses from discharge tubes from the relations governing the explosive electron emission.

2. HEATING AND EXPLOSION OF MICRONEEDLES ON THE CATHODE OF AN X-RAY TUBE

We consider the simplified problem of a cylindrically shaped microscopic emitter under the action of a current of density j (Fig. 1a). If the height of the emitter $h \gg r$ and $h \gg \sqrt{at}$, where t is time and a is the thermal conductivity, we can neglect heat losses due to conductivity and get

$$\rho c \frac{\partial T}{\partial t} \simeq j^2 \varkappa_0 T, \qquad (1)$$

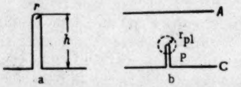

Fig. 1. a) Heating of a microprojection; b) Voltage —current characteristics of a diode with a projection (P) on the cathode (C); A is the anode and r_{pl} = vt is the radius of the cathode flame plasma.

where ρ, c and $\varkappa = \varkappa_0 T$ are the density, specific heat and resistivity of the cathode material, and T is the absolute temperature. It follows from (1) that

$$\int_0^{t_d} j^2 dt = \frac{\rho}{\varkappa_0} \int_{T_0}^{T_k} \frac{c}{T} dT. \qquad (2)$$

If we take $j(t) \simeq \text{const}$ and $c(T) = \text{const}$, we can use (2) to calculate the time t_d required to reach some critical temperature T_{cr}, at which the explosion occurs:

$$j^2 t_d \approx \frac{\rho c}{\varkappa_0} \ln \frac{T_{cr}}{T_0}. \qquad (3)$$

A more rigorous analysis of the emitter heating requires allowance for the fact that the average energy with which the conduction electrons move from inside the metal to the emission boundary is different from the average energy after emission. This leads to heating of the cathode at low temperatures and cooling at high temperatures (the Nottingham effect). In addition, the density of the electron current emitted by the cathode depends on temperature (thermofield emission). When these effects are taken into account, the nature of the relationship between t_d and j remains the same as in (3) but the coefficient of $\rho c/\varkappa_0$ changes. For tungsten, in particular, this coefficient is equal[6] to ~ 55. The $j^2 t_3$ = const relationship is in good agreement with experimental results on the delay time for explosion of tungsten microneedles.[7]

The metal vapor formed after the explosion of needles is ionized by the electrons from the cathode which flow through it. The movement of the plasma (cathode flare) can be represented as the dispersion of a gaseous sphere in space.[8,9] The relevant equations to describe this contain the inertial characteristics of the ions and the total kinetic parameters (pressure, for example) of the electrons and ions. In the self-similar limit, in particular, when the size of the cathode flare becomes much greater than its initial value (transit time t ≫ 10^{-9} sec), we can write the expansion velocity as

$$v \approx \sqrt{\frac{4\gamma}{\gamma-1}(\varepsilon_{i0}+z\varepsilon_{e0})}, \tag{4}$$

where γ is the effective adiabatic coefficient for the plasma, z is the average charge number of the ions and ε_{i0} and ε_{e0} are certain initial specific energies for the electron and ion components.

If we take[8,9] $\gamma = 5/3$ and z = 3, with ε_{i0} as the specific sublimation energy and ε_{e0} corresponding to the Fermi energy in the cathode metal, we get the expansion velocity as v = (2-3) · 10^6 cm/sec (Al, Mo, Cu) and v = 10^6 cm/sec (Pb). These figures are in good agreement with the experimental data,[10] and the model we have used explains the fact that v is a constant (i.e., it does not depend on the interelectrode gap or the applied potential difference).

3. VOLTAGE–CURRENT CHARACTERISTICS FOR NANOSECOND X-RAY TUBES

Flynn's idea that the current is limited by the space charge in the plasma front–anode electrode system[11] has been used to calculate the voltage–current characteristics of a tube with explosive electron emission. However, the plasma electrons in explosive emission are not formed by auxilliary sources (as in ref. 11), but from the explosion of the needles. We first consider the characteristics of a diode in which one needle explodes. Suppose that the emitted plasma sphere has a radius vt (Fig. 1b). We assume that the conductivity of the cathode flare plasma is much greater than that of the diode. An exact solution of the system of partial differential equations which describe the movement of the electrons under space-charge-limited conditions is difficult for the case of an arbitrary electrode geometry. We therefore make use of the approximate methods suggested in the review by Ivy[12] who gives preference to the Matrikon and Truve method as being the most universal. In this method the electrostatic capacity of an arbitrary system of electrodes is equated to the capacity of a plane cylindrical or spherical condenser for which the usual "three-halves" power law is known to hold. The dimensions of the equivalent system are found by simple geometric considerations. These dimensions are then used to calculate the current. A large number of examples of the use of this method is given in refs. 12 and 13.

We first assume that the shape of the cathode flare is not spherical, but cylindrical. For a plane infinite anode the electron current

$$i = 2.33 \cdot 10^{-6} U^{3/2} \frac{2\pi r_a l}{(r_a - r_c)^2} \beta\left(\frac{r_a}{r_c}\right), \tag{5}$$

where $\beta(r_a/r_c) = (1 - r_a/r_c)^2 \theta^2 (r_a/r_c)$ and the function $\theta(r_a/r_c)$ is defined and tabulated in ref. 13. Assuming that the length of the cylinder $l = \pi vt$, the radius of the cathode $r_c = vt$, and the radius of the equivalent anode

$$r_a = r_c \left\{\frac{d}{r_c} + \left[\left(\frac{d}{r_c}\right)^2 - 1\right]^{1/2}\right\}$$

with vt ≪ d, we get

$$i = A_1 U^{3/2} \frac{vt}{d - vt}, \tag{6}$$

where d is the interelectrode distance and $A_1 = 2.2 \cdot 10^{-5}$ A · $V^{-3/2}$. A calculation of $i = f(U, t)$ by the method in which the specific capacities of the real and fictitious condensers are equated leads to a coefficient $A_1 = 3.7 \cdot 10^{-5}$ A · $V^{-3/2}$. An experimental study of the relationship[4] has shown that in fact $i/U^{3/2} \sim vt/(d - vt)$ and the coefficient of proportionality $A_1 = 3 \cdot 10^{-5}$ A · $V^{-3/2}$.

Equation (6) is valid for vt ≪ d. When vt ≥ d/2 the diameter of the sphere begins to exceed the interelectrode distance and a more correct equation is

$$i = 2.33 \cdot 10^{-6} U^{3/2} \frac{\pi (vt)^2}{(d - vt)^2}, \tag{7}$$

which expresses the three-halves power law for a plane diode. In order to calculate the parameters of x-ray pulses with $t_{\text{pul}} \geq d/2v$ it is best to use (7). This is the equation used by Flynn[11] for the calculation of microsecond x-ray pulses. If the cathode has more than one emission center and the distance between the centers is comparable to the interelectrode distance d, the current in the diode is given by

$$i = A_1 n U^{3/2} \frac{vt}{d - vt}, \tag{8}$$

where n is the number of centers. If the distance between the centers a ≪d, the current is found from experimental studies[14] to be

$$i = A_2 U^{3/2} \frac{s}{(d - vt)^2}, \tag{9}$$

where s is the area of the cathode and $A_2 = 2.33 \cdot 10^{-6}$ A · $V^{3/2}$.

In order to calculate the voltage–current relationships in systems with more complicated geometries we have to make direct use of the Matrikon–Truve method mentioned above. The capacity of the entire system can be determined by the usual conformal mapping technique. It is assumed that the characteristics of the real diode are similar to those of the fictitious diode. We may recall that the main assumption in this method is that the shape of the equipotential surfaces is the same with and without the space charge and they differ only in their potential values.

We have assumed above, in agreement with the experimental results of refs. 4 and 14, that a plasma cathode of arbitrary shape can, under certain conditions, be considered as an ordinary metal cathode. In this case we can use the methods developed for normal indirectly heated diodes to determine the voltage–current characteristics of diodes with explosive emission. However, this approach is only valid within certain definite limits. First, the current in the diode in a low vacuum might be greater than that given by the three-halves law because of neutralization by the electron space-charge current. Second, the current can be increased by the formation of a plasma at the cathode before the arrival of the main voltage pulse because of the explosion of needles from prepulses. The current can be amplified by factors of 10 or so in this way.[4] Third, deviations from (6) are observed when a single needle is used with a high average field in the diode because the explosion occurs at the side surfaces not only at the end of the emitter. The three-halves power law is then violated because a higher applied voltage means that a larger surface area emits electrons. Fourth, the power law is also violated at very high currents when the emission power of the plasma itself reaches saturation. This occurs when

$$n_e\sqrt{T_e}<A_1\sqrt{\frac{2\pi m}{ke^2}}\,U^{3/2}\frac{vt}{d}, \tag{10}$$

where n_e and T_e are the density and temperature of the plasma electrons, m and e are the mass and charge of the electron and k is the Boltzmann constant.

4. X-RAY PULSE PARAMETERS

The most widespread method of obtaining nanosecond x-ray pulses is to use the discharge of a condenser across the x-ray tube through a switching spark gap (S) in a compressed gas (Fig. 2). The switch is necessary[15] in order to connect the condenser to the tube in a time less than 10^{-9} sec. If the cathode has one or more independent emission centers and the anode is plane we get the following equation for the current and voltage if we neglect the inductance of the circuit and the resistance of the spark gap:

$$i+C\frac{dU}{dt}=0 \tag{11}$$

together with Eq. (8) and the initial conditions t = 0, $U = U_0$ and i = 0.

We can combine (8) and (11) into a single equation

$$\frac{dy}{dt}+By^{3/2}\frac{\tau}{1-\tau}=0, \tag{12}$$

where

$$x=\frac{id}{CU_0v},\quad y=\frac{U}{U_0},\quad \tau=\frac{vt}{d},\quad B=\frac{A_1ndU_0^{1/2}}{Cv}.$$

The length of the nanosecond x-ray pulses is usually such that $t_{\text{xpul}} \ll d/v$ and $\tau \ll 1$. The tube current and voltage are then

$$x=\frac{64B\tau}{(4+B\tau^2)^3},\quad y=\frac{16}{(4+B\tau^2)^2}. \tag{13}$$

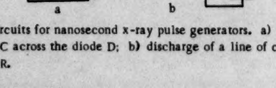

Fig. 2. Circuits for nanosecond x-ray pulse generators. a) Discharge of condenser C across the diode D; b) discharge of a line of characteristic resistance R.

The time to acheive maximum current and the value of this current are defined by the equations

$$t_{im}=\frac{2\sqrt{dC}}{\sqrt{5A_1nvU_0^{1/2}}}, \tag{14}$$

$$i_m=0.52\frac{U_0^{5/4}(CA_1nv)^{1/2}}{d^{1/2}}. \tag{15}$$

The intensity of the x radiation

$$P\sim iU^2. \tag{15'}$$

The time to the maximum intensity and the value of this intensity are defined by

$$t_m=\frac{2\sqrt{dC}}{\sqrt{13A_1nvU_0^{1/2}}}, \tag{16}$$

$$P_m\sim U_0^{13/4}\sqrt{\frac{A_1nvC}{d}}. \tag{16'}$$

The length of the x-ray pulse at the half-power points is

$$t_{\text{x pul}}=\frac{0.88\sqrt{Cd}}{\sqrt{A_1U^{1/2}nv}}. \tag{17}$$

If the condition $t_{\text{xpul}} \ll d/v$ is written in the form $t_{\text{xpul}} \le 0.3\ d/v$, then the above relationships are valid for $B \ge 12$.

For a cathode with a large number of emission centers the average distance between which $a \ll d$ and the emission area of which $s > d^2$, the current and voltage are calculated by solving (9) and (11). If the length of the pulse $t_{\text{xpul}} \ll d/v$, we get

$$U=\frac{U_0}{(1+\tau)^2},\quad i=\frac{2.33\cdot10^{-6}\,sU_0^{3/2}}{d^2(1+\tau)^3},\quad P\sim\frac{U_0^{7/2}s}{d^2(1+\tau)^7}, \tag{18}$$

where

$$\tau=\frac{t}{\theta},\quad \theta=\frac{8.7\cdot10^5\,Cd^2}{s\sqrt{U_0}}.$$

The length of the pulse at the half-power points is

$$t_{\text{x pul}}=5.6\cdot10^4\frac{Cd^2}{sU_0^{1/2}}. \tag{19}$$

Some nanosecond x-ray pulse generators use lines rather than condensers as storage devices. If the line is discharged across a tube with one or more emission centers, the current and voltage are described by a system of equations consisting of (8) together with

$$iR+U=U_0, \tag{20}$$

where R is the characteristic resistance of the line and U_0 is the charged potential of the line.

The time variation of the current and radiation intensity are given by

$$\frac{vt}{d-vt}=\frac{i}{A_1 n\,(U_0-iR)^{3/2}},\qquad (21)$$

$$P \sim i\,(U_0-iR)^2.\qquad (22)$$

The maximum radiation intensity

$$P_м \sim \frac{U_0^3}{R}\qquad (22')$$

is reached for a current $i_{xM} = U_0/3R$.

The time for maximum intensity

$$t_{xM}=\frac{d}{v}\,\frac{1}{1+\sqrt{\frac{8}{3}B_1}},\qquad (23)$$

where $B_1 = A_1 nRU_0^{1/2}$.

We define the length of the x-ray pulse as the time $t_{xpul} = 2t_{xm}$. To the accuracy of a constant coefficient, the total radiation dose can be determined from the equation $D \approx P_m t_{pul}$, and so

$$D \sim \frac{U_0^3}{Rv}\,\frac{1}{1+\sqrt{\frac{8}{3}A_1 nRU_0^{1/2}}}.\qquad (24)$$

It follows from (22)-(24) that the maximum intensity does not depend on the length of the gap, that the dose $D \sim d$, and that the pulse length $t_{xpul} \sim d$.

5. COMPARISON WITH EXPERIMENTAL RESULTS

The length of the x-ray pulse produced by the discharge of a long line across a vacuum gap was measured in ref. 16. The pulse has a square shape of length 300 nsec and an amplitude up to 200 keV; the characteristic impedance of the line is 66 Ω. The x-rays are recorded by a scintillation counter with an FÉU-36 photomultiplier and an n-terphenyl scintillator. The signal from the photomultiplier is recorded by means of a I2-7 oscilloscope and a UZ-5A amplifier with a bandwidth of 150 MHz. The cathode is a plane copper electrode on which several cathode flares were produced.

Figure 3 shows how the length of the x-ray pulse (at 0.1 of the amplitude) depends on the gap length d. Also shown is the relationship between the integrated radiation dose in the pulse and the value of d. These results confirm the principal theoretical conclusions that for a line discharge $D \sim d$ and $t_{xpul} \sim d$.

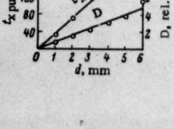

Fig. 3. Relationship[16] of the length of the x-ray pulse and the relative radiation dose D on the gap length d.

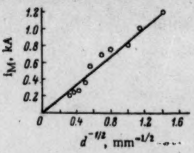

Fig. 4. Relationship between the amplitude of the electron current pulse i_M and the quantity $d^{-1/2}$ for an x-ray tube with a needle cathode and a plane anode for discharge through this tube of a condenser through a spark gap in compressed nitrogen (P = 10 atm).

The $t_{xpul} \sim d$ prediction is also in agreement with results which can be obtained by analyzing the oscillograms of Freytag,[17] who studied the x-ray radiation produced by the discharge of a line across a tube with a needle cathode.

We can use the experimental results of Vavilov[18] to verify Eq. (15). Figure 4 shows the relationship between the amplitude of the electron current pulse in the tube and the inverse square root of the gap length, i.e., $d^{-1/2}$; this relationship from (15) is a linear one (C = 30 pF and U_0 = 180 kV). The dipole of the x-ray tube used in ref. 18 contained a needle cathode and a plane anode. The value of t_{xpul}, calculated from (19) can be compared with the experimental value[19] for U_0 = 100 kV and C = 30 pF. If the ratio d^2/s = 1-2, the calculated value is 5-10 nsec and the experimental value ~ 10 nsec.

Thus the available experimental data on the x-ray pulse parameters do not contradict the above calculations.

---

[1] V. A. Tsukerman, L. V. Tarasova, and S. I. Lobov, Usp. Fiz. Nauk, 103, 319 (1971) [Sov. Phys. – Usp., 14, 61 (1971)].

[2] G. Tomer, in: The Physics of Rapid Processes [Russian translation], Vol. 1, Mir, Moscow (1971), p. 336.

[3] G. A. Mesyats and D. I. Proskurovskii, Izv. VUZ., Fiz., No. 1, 81 (1968).

[4] G. A. Mesyats and D. I. Proskurovskii, ZhETF Pis. Red., 13, 7 (1971)[JETP Lett., 13, 4 (1971)].

[5] G. P. Fursei and P. N. Vorontsov-Vel'yaminov, Zh. Tekh. Fiz., 37, 1870 (1967) [Sov. Phys. – Tech. Phys., 12, 1370 (1968)].

[6] E. A. Litvinov, G. A. Mesyats, and A. F. Shubin, Izv. VUZ. Fiz. No. 4, 147 (1970).

[7] G. K. Karptsev, G. A. Mesyats, D. I. Proskurovskii, V. P. Rotshtein, and G. P. Fursei, Dokl. Akad. Nauk SSSR, 192, 309 (1970) [Sov. Phys. – Dokl., 15, 475 (1970)].

[8] G. A. Mesyats, E. A. Litvinov, and D. I. Proskurovskii, Proc. Fourth Intern. Symp., Waterloo, Canada (September 1970), p. 82.

[9] R. B. Baksht, S. P. Vavilov, A. P. Kudinov, E. A. Litvinov, and V. I. Manilov, Proc. Fifth Intern. Symp., Poznan, Poland (1972), p. 139.

[10] S. P. Bugaev, G. A. Mesyats and D. I. Proskurovskii, Dokl. Akad. Nauk, SSSR, 186, 1067 (1969) [Sov. Phys. – Dokl., 14, 605 (1969)].

[11] P. T. G. Flynn, Proc. Phys. Soc., 69, 748 (1956).

[12] G. Ivy, Problems in Modern Physics [Russian translation], Izd. IL, Moscow (1956).

[13] B. M. Tsarev, Design and Construction of Electronic Valves [in Russian], Gosenergoizdat, Moscow (1961).

[14] S. P. Bugaev, F. Ya. Zagulov, E. A. Litvinov, and G. A. Mesyats, Zh. Tekh. Fiz., 43, 611 (1973) [Sov. Phys. – Tech. Phys., 18, 384 (1973)].

[15] G. A. Mesyats, Generation of Powerful Nanosecond Pulses [in Russian], Sovetskoe Radio, Moscow (1974).

[16] R. B. Baksht, S. P. Vavilov, and M. N. Urbazaev, Izv. VUZ. Fiz., 3, 140 (1973).

[17] I. P. Freytag, Extrait de la Revue Tech., Thomson CSF, 1, 553 (1969).

[18] S. P. Vavilov, Thesis, Tomsk (1973).

[19] N. V. Belkin and G. V. Aleksandrovich, Prib. Tekh. Eksp., No. 2 (1972).

Superconducting magnetic shields

S. I. Bondarenko and V. I. Sheremet

Physicotechnical Institute of Low Temperatures,
Academy of Sciences of the USSR, Khar'kov

(Submitted December 18, 1972; resubmitted August 28, 1973)
Zh. Tekh. Fiz., 44, 1528-1533 (July 1974)

An experimental study has been made of superconducting magnetic shields of various shapes and sizes in external fields from $1 \cdot 10^{-3}$ to 350 Oe. The possibility of creating a magnetic "vacuum" by means of superconducting shields is considered. A vacuum of less than $3 \cdot 10^{-6}$ Oe has been obtained in a volume of 0.6 liters in an external field of $5 \cdot 10^{-2}$ Oe. The stability of the vacuum, measured with a superconducting quantum magnetometer, is better than $1 \cdot 10^{-8}$ Oe.

INTRODUCTION

Work has been carried out during the last few years on the properties of superconducting magnetic shields and the creation by means of such shields of a magnetic "vacuum" (magnetic field smaller than that of the earth).[1-5]

The interest in these problems is due to a series of new physical ideas on ways of testing the validity of the general theory of relativity, on field theory, and in biophysics.[1,6] The use of superconductors for shielding is also of importance in the development of some fundamentally new instruments, in particular, high-sensitivity superconducting quantum magnetometers.

We report here on an experimental study of the shielding possibilities of stationary superconducting shields in the form of thin-walled cylindrical shells with a) open ends and b) a hemispherical bottom. We impose an external magnetic field H_e of known magnitude and measure the increase of the field H_i inside the shield.

The same shields are used to obtain a magnetic vacuum. A method has been devised to bring a superconducting shield in a magnetic field H_{e0} into the superconducting state so that the field, or part of it, is expelled from the shield cavity. A magnetic vacuum H_{i0} is thus created. It is of interest, in studying these properties of superconducting shields, to consider the effect of the magnitude of the external field, the shape and size of the shield, the material and its state of purity, and the method of bringing the shield into the superconducting state.

EXPERIMENTAL APPARATUS

The apparatus for studying the shielding properties of superconducting shields and for obtaining a magnetic vacuum (Fig. 1) consists of a metal helium cryostat 1 with the superconducting shield 2, a system for introducing liquid-helium 3, and an auxiliary isolating helium cryostat 4 placed in the superconducting shield inside of which the temperature can be set to any value from liquid-helium temperature to room temperatures. The apparatus also contains a system 5 for cancelling the earth's magnetic field, a solenoid 6 for producing an external field up to 300 Oe and a magnetometer unit 7. The Kh18H10T stainless steel helium cryostat has the same diameter as the neck of the helium bath – 150 mm – and a height of 1000 mm. The preliminary cooling of the cryostat and fittings is achieved by means of liquid-nitrogen.

Two types of isolating cryostat are used: a glass, double-walled nitrogen Dewar with an internal insulated volume diameter of 78 mm and a length of 900 mm and a

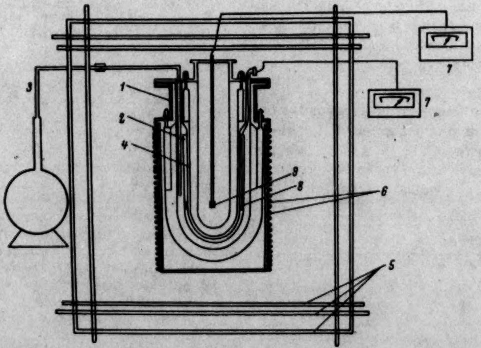

Fig. 1. Cryogenic magnetic apparatus. 1) Metal-helium cryostat; 2) superconducting magnetic shield; 3) system for supplying liquid-helium; 4) auxilliary isolating helium cryostat; 5) system for cancelling the earth's magnetic field; 6) solenoid; 7) magnetometer unit; 8) superconducting quantum magnetometer head; 9) ferroprobe head.

metal triple-walled unit using nitrogen shielding with an inside diameter (for the insulated volume) of 65 mm and a length of 900 mm. After the introduction of helium into the cryostat the temperature is $-30°C$ in the first unit and $+13$ to $+15°C$ in the second.

The support for the superconducting shields, which are in the form of thin-walled shells (usually of lead), is fixed to the flange of the isolating cryostat. The flange also carriers the lines for supplying the helium and a hermetic feed-through with the electric wires to the thermometers (germanium and Allen-Bradley types), the level indicator, heater, and a superconducting quantum magnetometer which has been developed by the Physicotechnical Institute of Low Temperatures of the Academy of Sciences of the USSR.[7,8] The solenoid is 1000 mm long and has an inside diameter of 260 mm and a solenoid constant of 64 Oe/A. Two different compensation systems can be used: 1) circular Helmholtz coils 1000 mm in diameter along three orthogonal axes; 2) squared Fanzelau rings 2000 mm on a side. The first system can create a homogeneous field (gradient $5 \cdot 10^{-5}$ Oe/cm) in a sphere 150 mm in diameter and the second in a sphere 400 mm in diameter. The same ring systems are used to create an increment ΔH_e in the external field.

The preliminary attenuation of the magnetic field, and specially of its time variations, is achieved by means of a triple-layer ferromagnetic cylindrical shield with a plane bottom made of 79 nm Permalloy 1.5 mm thick, 450 mm in diameter and 1200 mm high. This shield attenuates the external field of the earth by a factor of 440 in the longitudinal direction and a factor of 600 in the transverse direction; the attenuation of variations is 30 and 50 times respectively. The normal level of variations in our laboratory varies up to 200 $\gamma (\gamma = 10^{-5}$ Oe).

The magnetometer unit contains a superconducting quantum magnetometer 8 and a ferroprobe system with a block of small ($l = 10$ mm) ferroprobes 9 which allow the longitudinal and transverse components of the magnetic field in the superconducting shield to be measured simultaneously. The smallest field which can be detected by the ferroprobe unit is $3 \cdot 10^{-6}$ Oe. The zero drift of the magnetometer is less than $1 \cdot 10^{-5}$ Oe in 8 h. The ferroprobe block is placed on a movable calibrated rod by means of which the probes can be either rotated about the longitudinal axis of the superconducting shield or moved in the vertical direction along the axis of the shield.

A superconducting quantum magnetometer is used to measure the stability of the magnetic vacuum obtained in the superconducting shield. The sensitivity of the magnetometer is $1 \cdot 10^{-8}$ Oe. The ring of the magnetometer head is 100 mm in diameter and is made from 0.05 mm diameter niobium wire with Clark contacts; it is placed 80 mm from the bottom of the shield.

The shields are made from: 1) 99.99% pure lead by cold pressure and galvanic deposition on to a copper base followed by etching; 2) from 99.9% pure niobium by electric deposition from a melt of the salts on to a copper base, again followed by etching.

Characteristic sizes of the shields are: internal diameter from 65 to 140 mm, length from 200 to 550 mm, and wall thickness from 0.5 to 2.5 mm.

In the shielding experiments the magnetic field which penetrates through the hole in the superconducting shield into the inside cavity is measured in two directions: parallel and perpendicular to the axis. The ratio of the components of the applied external field to the components in the cavity of the superconducting shield gives the shielding coefficient.

There is no penetration of the field through the walls of the shield until the critical values are reached (hundreds of Oe).

An analysis of the possible methods of creating a magnetic vacuum by means of superconductors and of the methods which have already been suggested shows that the simplest technique, and one which is quite effective, is the use of the Meissner effect, which occurs when the superconductor goes over into the superconducting state. This process takes place in a definite sequence, starting at the lowest point of the shield in the cryostat. In the shield with a hemispherical bottom the dynamics of the magnetic field expulsion process as the shield goes over into the superconducting state can be illustrated as in Fig. 2.

As soon as the lowest part of the hemisphere becomes superconducting the magnetic field lines pass around this section as a result of the Meissner effect. As the boundary between the normal and superconducting phases moves upwards, a greater part of the material and, as can be seen from Fig. 2, of the cavity inside (because of the particular shape chosen) becomes free of any magnetic field or at least carriers a weaker field.

A higher vacuum can, of course, be obtained by the successive transition of a number of coaxial shields into the superconducting state. Each shield gives a certain attenuation K and for a total of n shields we may expect an overall attenuation equal to the product of the individual K_n ($n = 1, 2, 3, \ldots$).

We have studied both one- and two-step field attenuation by this method. In the latter case the two shields are thermally isolated by means of plastic foam shells with wall thicknesses of 10 mm.

DISCUSSION OF EXPERIMENTAL RESULTS

The shielding is tested by applying fields from $H_e = 10^{-3}$ to $H_e = 350$ Oe. For a hollow lead cylindrical shield with open ends, made by extrusion or electrodeposition, the degree of shielding S (attenuation of the external field in the shield along its axis at a distance equal to the inside diameter) is $S_{long} = 900$ for the longitudinal component and $S_{tran} = 30$ for the transverse component. The values remain the same to within ± 15% for all the sizes tried (length l, diameter ϕ, and wall thickness t) for shields prepared by this method.

The method of fabricating the lead shield is found to affect the degree of shielding of the transverse and particularly of the longitudinal component. Thus for shields prepared by turning a lead sheet and welding along the generator of the cylinder, we find $S_{long} = 160$ and $S_{tran} = 25$ (for the same dimensions). It can be seen that the lon-

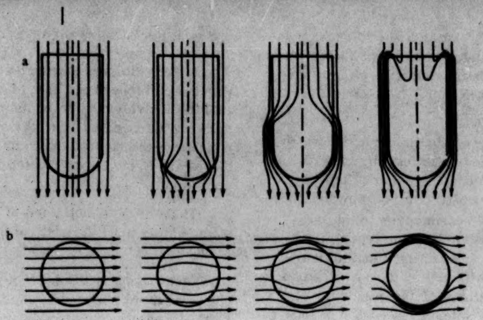

Fig. 2. Ejection of the magnetic field as the shield goes over the superconducting state. a) Longitudinal component of the magnetic field; b) transverse component.

gitudinal component is attenuated only 160 times in comparison with 900 in the previous case.

Shields in the form of a lead shell with a hemispherical bottom, made by extrusion or electrodeposition, have $S_{long} = 1500$ and $S_{tran} = 40$ with a maximum scatter of ± 15% between one shield and another.

A shield of the same shape made from niobium ($\varnothing$ 70 mm, $l = 230$ mm, $t = 1.5$ mm) has $S_{long} = 1200$ and $S_{tran} = 40$. In all cases the measurements are made at a temperature $T = 4.2°K$.

Measurements of the maximum shielded field are made on an extruded lead shield with a hemispherical bottom ($\varnothing$ 85 mm, $l = 440$ mm, $t = 1.5$ mm). A ferroprobe is placed at the lowest point of the isolating cryostat at a distance of 25 mm from the bottom of the shield. The longitudinal field at which the material begins to go over to the intermediate state and the field to penetrate the shield is found to be 252 Oe. The penetrating field H_l increases smoothly but if H_e goes even slightly above 252 Oe H_l begins to rise more rapidly and the shield ceases to screen at all at $H_e = 270$ Oe.

We are now preparing to carry out measurements on the maximum transverse component of a magnetic field which can be shielded. The degree of shielding remains independent of the frozen-in field in the shield right up to the point at which the superconductivity begins to be destroyed.

The frozen-in field has a high stability. In order to verify this, it is first necessary to choose the shield dimensions so that the variations in the external field are attenuated by a sufficiently high factor at the point where the recording head is placed. The value is usually chosen so that for known S_{long} and S_{tran} the expected variations in H_l for given variations in H_e are much smaller than the sensitivity of the recording head. Measurements of the stability of a 0.4 Oe frozen-in field by a ferroprobe showed that any variations were smaller than the sensitivity of the magnetometer.

We have now begun measurements of the stability of the frozen-in fields in superconducting shields with open ends by means of a high-sensitivity superconducting quantum magnetometer. The results will be published elsewhere.

We now turn to the results on the creation of a magnetic vacuum by means of superconducting shields with a hemispherical bottom. Because of the Meissner effect, these shields produce an attenuation of the frozen-in field in the shell cavity.

It is found that in order to achieve the maximum magnetic vacuum it is necessary that two important conditions be satisfied: a) There should be a sufficiently high temperature gradient along the shield during the transition to the superconducting state; b) the cooling should be sufficiently slow.

A high temperature gradient along the shield is necessary in order that the initial annular superconducting zone which forms at the apex of the hemisphere should be of minimal size. The magnetic flux trapped by this annulus in fact determines the maximum possible level of the magnetic vacuum in the superconducting shield. Moreover, with a high temperature gradient it is much easier to ensure a slow propagation of the superconducting phase.

A slow supply of helium into the cryostat and thermal isolation of the shields from the cold helium vapor by means of plastic foam sleeves enables us to get a gradient of $dT/dl \simeq -0.5$ deg/cm during the transition into the superconducting state and a boundary propagation rate of $dl/dt \simeq 0.5$ cm/sec.

It can be seen from this that the prediction by this method of the transition process into the superconducting state is a rather complicated thermomagnetic problem which still awaits analysis and theoretical solution. The total Meissner effect probably depends on the mechanical stressing of the material, its chemical purity and the type of inclusions, the surface state and the kind of superconductor.

Our extruded lead shields are tested after preparation in both annealed and nonannealed states. The annealing is carried out for 6–10 h in a vacuum of 10^{-3} torr at $t = 200°C$. The experiments show that this treatment and the use of lead with an initial industrial purity and a final purity of 99.99% do not essentially alter the maximum attainable magnetic vacuum (for a given method of bringing

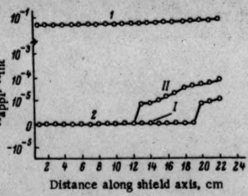

Fig. 3. Distribution of the external magnetic field along a two-layer shield before the transition to the superconducting state (1) and of the frozen-in magnetic field after the transition of both shields (2). I, II) Distributions of the longitudinal and transverse components of the frozen-in field respectively.

the shield into the superconducting state and for a particular surface quality).

For one lead shield with $\varnothing = 140$ mm, $l = 550$ mm, $t = 2$ mm in an external field $H_{e0\,long} = H_{e0\,tran} = 1 \cdot 10^{-3}$ Oe, a magnetic vacuum lower than the limit of sensitivity of the ferroprobe ($3 \cdot 10^{-6}$ Oe) is obtained throughout the entire volume of the shield at 14-15 cm from the bottom. In an external field $H_{e0} = 5 \cdot 10^{-2}$ Oe a field of $H_{i0\,long} = 2 \cdot 10^{-4}$ Oe and $H_{i0\,tran} = 4 \cdot 10^{-5}$ Oe is recorded at a height of 14 cm from the bottom, i.e., the attenuation in this volume for an external field of $1 \cdot 10^{-3}$-$5 \cdot 10^{-2}$ Oe is not less than $K_{long} = 250$ for the longitudinal component and not less than $K_{tran} = 1250$ for the transverse component.

In the case of two shields, brought successively into the superconducting state with a time interval of about 200 sec, a magnetic field of less than $3 \cdot 10^{-6}$ Oe is obtained in the lower part of the inner shield at a length of 11 cm from the bottom for an external field of $5 \cdot 10^{-2}$ Oe; the dimensions are $\varnothing_1 = 140$ mm, $l_1 = 550$ mm, $t_1 = 2$ mm, $\varnothing_2 = 110$ mm, $l_2 = 500$ mm, $t_2 = 2$ mm.

Figure 3 shows the external field distribution along the axis of the shield (1), and the distribution of the frozen-in field after the two shields have gone over into the superconducting state (2). The curves with the Roman numerals I and II indicate the distributions of the longitudinal and transverse components respectively.

The stability of the magnetic vacuum is measured at a height of 8 cm from the bottom of the shield by means of a quantum magnetometer with a sensitivity to change in magnetic flux of $3.9 \cdot 10^{-6}$ mks which, for a uniform field across the head, corresponds to a change in the magnetic field of $1 \cdot 10^{-8}$ Oe. The time constants of the instrument is ~ 5 sec. It turns out that the stability of the vacuum is never worse than $1 \cdot 10^{-8}$ Oe. A further increase in the sensitivity of the magnetometer will enable the stability of the field in the shield to be measured more accurately.

The results of the experiments carried out on the apparatus we have developed for cryogenic magnetic measurements are therefore as follows: 1) The degree of shielding of superconducting lead and niobium shields of various shapes and sizes, prepared by cold pressure working and electrodeposition has been determined at a temperature of 4.2 K; 2) a method has been investigated for obtaining a magnetic vacuum by using the Meissner effect in lead cold-drawn shields with a hemispherical bottom, and the attenuation coefficients for the longitudinal and transverse magnetic fields have been obtained; the great possibilities for this type of superconducting shield and this method of obtaining a stable magnetic vacuum have been shown; 3) the stability of the frozen-in field has been measured in cylindrical superconducting shields with open ends and the stability of the magnetic vacuum in a shield with a hemispherical bottom has been determined.

The authors are grateful to I. M. Dmitrenko for useful discussions.

---

[1] W. M. Fairbank and W. O. Hamilton, Proc. of 10th Intern. Conf. on Low-Temperature Physics, Vol. 2, Moscow (1966), p. 327.
[2] B. S. Deaver, and W. S. Goree, Rev. Sci. Instrum., 38, 311 (1967).
[3] R. E. Brown, Rev. Sci. Instrum., 39, 547 (1968).
[4] W. O. Hamilton, Rev. Phys. Appl., 5, 41 (1970).
[5] A. F. Hildebrandt, Rev. Phys. Appl., 5, 49 (1970).
[6] D. Cohen, E. A. Edelsack, and J. E. Zimmerman, Appl. Phys. Lett., 16, 278 (1968); J. E. Zimmerman, J. Appl. Phys., 42, 30 (1971).
[7] S. I. Bondarenko and I. M. Dmitrenko, Fiz. Kondens. Sost., 3, 79 (1968).
[8] I. M. Dmitrenko and S. I. Bondarenko, Zh. Eksp. Teor. Fiz., 57, 1513 (1969) [Sov. Phys. – JETP, 30, 817 (1970)].

Effect of the adsorption rate on the diffusion of deuterium through nickel

Yu. I. Belyakov, Yu. I. Zvezdin, A. A.Kurdyumov, and G. G. Nevdakha

A. A. Zhdanov Leningrad State University

(Submitted July 17, 1973)
Zh. Tekh. Fiz., 44, 1534-1538 (July 1974)

A procedure described previously is used to study the penetrability of nickel membranes with respect to deuterium from the molecular phase (P_m), from a gas discharge (P_c), and atomized on incandescent tungsten (P_{at}). The functional dependences of P_m and P_{at} on temperature display slope changes; these are attributed to an effect of the rate at which deuterium is adsorbed from the molecular phase onto the nickel surface.

There is currently much interest in the effect of the rates of interfacial processes on the penetration of hydrogen isotopes through metals.[1-3]

Kunin et al.[1] have solved the diffusion problem, assuming the interfacial reactions to occur much more slowly than diffusive mass transport in the bulk metal. These authors give the following equation for the gas flow through a membrane on one of whose sides a relatively slow interfacial reaction is occurring with a rate constant K and on whose other side all reactions occur rapidly:

$$P=\frac{\Gamma p}{\frac{1}{K}+\frac{d}{D}}, \tag{1}$$

where Γ is the Henry constant, p is the gas pressure, d is the membrane thickness, and D is the diffusion coefficient of the gas in the metal.

Generally speaking, Eq. (1) is derived for the case in which a monatomic gas penetrates a membrane; nevertheless, it is valid for the penetration of a diatomic gas dissociating at the metal surface if the gas pressure is held constant.

The penetrability of nickel membranes of various thicknesses with respect to hydrogen has been studied experimentally[3] over the temperature range 250-800°C. It follows from these results that the classical functional dependence $P_m \sim 1/d$ yields to a situation in which the penetrability is independent of the membrane thickness as the thickness is reduced. On the basis of these experiments and Eq. (1) Kunin et al. derived the following equation for the functional dependence of K on the temperature:

$$K=4.1\cdot 10^{-2}\exp\left[-\frac{2700}{RT}\right], \tag{2}$$

where R is the universal gas constant (in calories per mole per degree), and T is the Kelvin temperature.

However, it is unclear whether Eq. (2) describes some single process or the resultant effect of several interfacial reactions characterized by approximately equal activation energies. It is this question which we are concerned with here.

To distinguish between reactions occurring on the entrance and exit sides of the membrane, we use the method described in ref. 4 for studying penetrability in cathode absorption of deuterium from a glow discharge.

We have also carried out experiments on the penetration of deuterium atomized on an incandescent tungsten filament located near the entrance surface of the sample.

Studying the penetrability P_m of nickel membranes of various thicknesses as a function of the temperature for the direct interaction with molecular deuterium (p = 3 torr), we find slope changes at d < 0.3 mm (Fig. 1). The slope of the linear parts of the curves in the low-temperature region corresponds to an activation energy of 14.6 kcal/g-at. i.e., a value which agrees with the known activation energies for the penetrability of nickel with respect to deuterium.[5] Over this temperature range the proportionality $P_m \sim 1/d$ is satisfied (Fig. 2), implying that the rates of all the interfacial reactions are large in comparison with that of diffusive transport in the interior of the membrane.

As the temperature is raised the activation energy for the penetrability of sufficiently thin samples (d < 0.3 mm) (Fig. 1) decreases and the proportionality $P_m \sim 1/d$ is disrupted (Fig. 2). These results constitute evidence that the penetration is limited by the rate of interfacial reactions under these conditions. From Eq. (1) we calculate

$$K=7\cdot 10^{-3}\exp\left[-\frac{2500}{RT}\right], \tag{3}$$

in good agreement with the functional dependence found in ref. 3 [see (2)].

To determine the diffusion coefficient for deuterium in nickel, D, which is required for the calculation of K, we use the buildup method to measure the steady-state gas flow through a sample 0.6 mm thick. Curve 5 in Fig. 1 shows the functional dependence log D = $f(10^3/T)$. The discontinuities in the functional dependences of P_m and D on the temperature are due to the change in the diffusion coefficient and the solubility of deuterium in nickel at the Curie point (≈ 360°C) (ref. 5). These discontinuities are not observed in very thin samples, apparently because the interfacial reactions are less sensitive than diffusion or dissolution to structural changes.

Under the conditions prevailing in a gas discharge

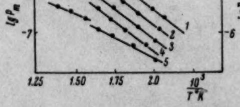

Fig. 1. Penetrability P_m of nickel membranes of various thicknesses as a function of the temperature. d, mm: 1) 0.05; 2) 0.12; 3) 0.3; 4) 0.6; 5) diffusion coefficient of deuterium in nickel as a function of the temperature.

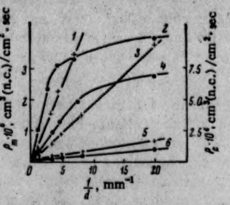

Fig. 2. The functional dependences $P_m(d)$ (curves 2, 4, 6) and $P_c(d)$ (1, 3, 5) for various temperatures. T, °K: 1, 2) 645; 3, 4) 600; 5, 6) 500.

the deuterium concentration in the surface layers of the nickel is governed by penetration and cathode sputtering,[4] rather than by activated interfacial reactions. Accordingly, the concentration is not a function of the temperature or the membrane thickness, i.e., of the rate of diffusive removal. We can therefore distinguish between slow interfacial reactions at the entrance and exit surfaces of the membrane: If the penetration rate is limited by a reaction at the exit surface, the $P_c \sim 1/d$ functional dependence is not satisfied, even under gas-discharge conditions;[6] if, on the other hand, some reaction at the entrance side is the slowest step, the functional dependence $P_c \sim 1/d$ is retained at small d during cathode absorption of deuterium from the glow discharge, in contrast with the case of penetration from the molecular phase; this behavior is in fact observed in our experiments (Fig. 2).

At the entrance side of the membrane two processes occur, whose activation energies can turn out to be approximately equal to the value of 2.5 kcal/g-at, which appears in (3): activated chemisorption and migration of atoms over the surface. A third interfacial reaction on the entrance side – dissolution (i.e., the conversion of atoms from an adsorbed to an absorbed state) – has a much higher activation energy (~25 kcal/g-at) (ref. 2, 5, 7).

Migration can play a role if we assume that the number of possible dissolution paths is limited and that the chemisorbed deuterium atoms must spend a certain time in motion over the surface in order to reach an absorbed state. However, it is difficult to believe that this process could be manifest in some manner at coverages Θ near a monolayer. It is apparently just such coverages with which we are dealing, since the deuterium pressure is ≥ 3 torr. Furthermore, this process is not due to recombination or dissociation, so its rate must be proportional to the surface concentration of deuterium atoms, C_{ads}, and must be a weak function of the pressure at $\Theta \approx 1$ ($C_{ads} \sim p^n$, where $n < 0.5$) (ref. 7).

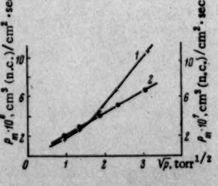

Fig. 3. The penetrability P_m as a function of the deuterium pressure p. T, °K: 1) 645; 2) 500.

Analysis of our isotherms for the penetrability of nickel membranes (d = 0.05 mm thick) with respect to molecular deuterium shows that at $T < T_0$, at which the proportionality $P_m \sim 1/d$ holds, the proportionality $P_m \sim p^{1/2}$ also holds (Fig. 3). In this case the proportionality holds because all the surface processes occurring on the entrance side of the sample occur so rapidly that a deuterium concentration equal to the solubility under the given conditions is established in a surface layer of the metal, and the solubility of deuterium in a metal is known[8] to be proportional to $p^{1/2}$.

At $T > T_0$, with an appreciably stronger influence of surface reactions, we find $P \sim p^n$, where n is approximately equal to unity (Fig. 3). According to current ideas,[7,9] such a functional dependence on the pressure holds when the step limiting the penetration is chemisorption at the entrance side of the membrane.

We have carried out experiments on the penetration of deuterium atomized on incandescent tungsten; the results of these experiments are shown in Fig. 4. Curves 1 and 2 in this figure show the functional dependence on the temperature of the penetrability P_{at} of nickel membranes 0.05 mm thick with respect to deuterium partially atomized on a tungsten filament heated to 2300°K. The filament temperature is measured by means of a pyrometer. Curves 4 and 3 in this figure show the same functional dependences with the atomizer turned off.

Curves 1 and 2 display two linear regions (I and II), whose slopes are markedly different. In temperature range II the deuterium flux through the membrane is a weak function of the temperature. At a certain temperature T_0, which varies with the deuterium pressure, there is a slope change coinciding with the slope change on the curve showing the penetration of deuterium from the molecular phase as a function of the temperature. At $T > T_0$ there is an appreciable increase in the flux with increasing temperature; the slope of region I is approximately equal to that of the functional dependence on the temperature of the penetrability from the molecular phase, in which case this penetrability is governed by the adsorption rate.

It should also be pointed out that P_m always increases with increasing pressure. The functional dependence of the flux on the pressure of molecular deuterium displays a different behavior when the atomizer is turned off: As the pressure of molecular deuterium is raised, the flux decreases rather than increases.

We believe that these results can be explained in the following manner.

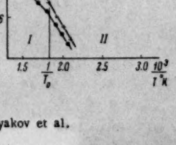

Fig. 4. P_m and P_{at} as functions of the temperature. p, torr: 1, 4) 3; 2, 3) 10.

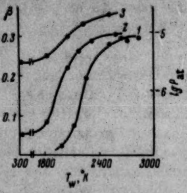

Fig. 5. Atomization coefficient β (1) and penetrability P_{at}. T, °K: 2) 500; 3) 645.

The increase in the deuterium flux through the membrane with the atomizer turned off over the entire temperature range studied undoubtedly results from the atomic deuterium. Evidence in favor of this conclusion is the strong similarity of the functional dependences of the penetrability and the atomization coefficient[10] on the temperature of the tungsten filament (Fig. 5). There is some difference between these curves, probably due to errors in the pyrometric measurement of the filament temperature and the distortion of the penetrability curves at low atomization coefficients because of the penetration of the deuterium from the molecular phase.

In our case the partial pressure of molecular deuterium is much higher than that of atomic deuterium, so that the metal surface is largely covered by chemisorbed deuterium atoms, formed in the dissociation of deuterium molecules on the nickel surface. The penetration of these atoms into the metal is hindered somewhat, since the energy evolved in the chemisorption is less than the activation energy for dissolution. As a result, some of the chemisorbed atoms are at thermal equilibrium with the metal surface, so that the probability for their dissolution is reduced even further.

The energy levels of the deuterium atoms and molecules in the gas phase differ by the dissociation energy (~ 50 kcal/g-at), so that sorption of atomic deuterium on the nickel is not an activated process, and the probability for the dissolution of atomic deuterium is much higher than that for atoms produced in the dissociation of deuterium molecules on the nickel surface and which have arrived at a thermal equilibrium with the surface. However, the chemisorption of the atomized deuterium can occur only on that part of the surface $(1-\Theta)$ not covered by atoms chemisorbed from the molecular phase.

We note that the small surface area capable of chemisorbing atomic deuterium from the gas phase and the rapid diffusive removal lead to a situation in which the deuterium concentration in the metal C is much lower than the equilibrium solubility S which can be achieved through the interaction of atomic deuterium with nickel under the given conditions. For this reason the reactions at the interface between the metal volume and surface are displaced toward absorption for the case of previously atomized deuterium, and the absorption rate is known[9] to be proportional to $1-C/S$.

Assuming that the accommodation coefficient for atomic deuterium and the rate at which atomic deuterium is chemisorbed by the metal surface are quite large, we can assume that the flux measured in our experiments with an atomizer is approximately equal to the rate at which atomic deuterium is absorbed from the gas phase, W:

$$P_{at} \approx W = N(p)\,\alpha(p)\left(1-\frac{C}{S}\right)(1-\Theta), \tag{4}$$

where N(p) is the efficiency of the atomizer, governed by the number of deuterium atoms produced per unit time, and $\alpha(p)$ is a coefficient taking into account the recombination of deuterium atoms in the interior and at the walls of the diffusion cell.

Accordingly, at sufficiently low temperatures, for which Θ is approximately equal to unity and is relatively independent of the temperature (II in Fig. 4), the deuterium flux at constant pressure is also a weak function of the membrane temperature.

At $T > T_0$ (I, Fig. 4), the penetration is limited by the adsorption rate, as was shown above. According to Barrer,[8] the result is a reduction of Θ and thus an increase of P_{at} [see (4)].

An increase in the pressure of the molecular deuterium at a fixed temperature causes an increase in the atomizer efficiency N(p); on the other hand it causes an increase in Θ and in the scattering of deuterium atoms by molecules. This scattering results in additional recombination of particles. These latter two factors very probably play an important role in these pressure and temperature ranges, so that P_{at} decreases as P increases.

---

[1] L. L. Kunin, A. M. Golovin, Yu. N. Surovoi, and V. M. Khokhrin, Problems of the Degassing of Metals [in Russian], Izd. Nauka, Moscow (1972).

[2] R. E. Sticknay, T. L. Bradley, and R. L. Levin, Proceedings of the Conference on Instruments for Nuclear Research, Vol. 1, Jülich (1972), p. 231.

[3] D. M. Kazakov, L. L. Kunin, and N. F. Litvinova, Izv. Akad. Nauk SSSR, Metally, No. 2, 91 (1973).

[4] A. A. Kurdyumov, Yu. I. Belyakov, and Yu. I. Zvezdin, Zh. Tekh. Fiz., 43, 164 (1973) [Sov. Phys. – Tech. Phys., 18, 106 (1973)].

[5] Yu. I. Belyakov and N. I. Ionov, Zh. Tekh. Fiz., 31, 204 (1961) [Sov. Phys. – Tech. Phys., 6, 146 (1961)].

[6] A. A. Kurdyumov, Yu. I. Belyakov, and Yu. I. Zvezdin, Zh. Tekh. Fiz., 43, 1280 (1973) [Sov. Phys. – Tech. Phys., 18, 810 (1973)].

[7] B. M. W. Trapnell, Chemisorption, Butterworths, London (1955).

[8] R. M. Barrer, Diffusion in and Through Solids, Mac Millan, Cambridge (1941).

[9] R. Ash and R. Barrer, Phil. Mag., 4, 1197 (1959).

[10] J. N. Smith, Jr., and W. L. Fite, In: Interaction of Gases with Surfaces [Russian translation], Izd. Nauka, Moscow (1965), p. 194.

Brief communications

Ion-acoustic instability of a fully ionized ultrarelativistic plasma in an electric field

D. I. Dzhavakhishvili

Tbilisi State University

(Submitted February 5, 1974)
Zh. Tekh. Fiz., 44, 1539-1541 (July 1974)

The stability of an ion-acoustic wave propagating in a collision-dominated, fully ionized hot-electron plasma is considered; the electron thermal energy considerably exceeds the electron rest energy. The growth rate is compared with the corresponding expression in nonrelativistic theory. It is shown that the growth rate is much smaller in a plasma with ultrarelativistic electrons.

When a fixed electric field $\mathbf{E}_0$ acts in a collision-dominated plasma to produce motion of the electrons relative to the ions the ion-acoustic wave becomes unstable if the steady velocity of the electrons V_{0e} is several times greater than the thermal speed of the ions.[1,2] These results, however, are valid only for a nonrelativistic plasma: $T_a \ll m_a c^2$, where T_a and m_a are the temperature (in energy units) and the rest mass of the electrons or ions.

Recently, a closed system of hydrodynamic equations has been obtained[3] for a fully ionized, collision-dominated plasma in which the ions remain nonrelativistic ($T_i \ll m_i c^2$) but the electrons are at a very high temperature ($T_e \gg m_e c^2$); it is assumed that the average speeds of motion of the plasma components are small ($V_a^2/c^2 \ll 1$). It has been shown that under these conditions the transport coefficients of the plasma are modified drastically and that in fact the actual system of hydrodynamic equations is quite different from the nonrelativistic transport equations obtained by Braginskii.[4]

It might be expected that the growth rates of the various collisional instabilities might be quite different for such a hot plasma and it is of particular interest to consider the case of ion-acoustic oscillations.

Assume that the external electric field and the wave vector **k** are directed along the z axis and that $V_{i0} = 0$. The system of transport equations for the one-dimensional case then has the form[3]

$$\left.\begin{aligned}
&\frac{\partial n_e}{\partial t}+\frac{\partial}{\partial z}(n_e V_e)=0,\\
&\frac{4n_e}{c^2}\left(\frac{\partial}{\partial t}+V_e\frac{\partial}{\partial z}\right)(T_e V_e)=-\frac{\partial}{\partial z}(n_e T_e)+\frac{4}{3}\frac{\partial}{\partial z}\left(\eta_e\frac{\partial V_e}{\partial z}\right)-n_e eE+R_e\\
&\quad+\frac{V_e}{c^2}Q_e+\frac{4}{3}\frac{1}{c^2}\frac{\partial}{\partial t}\left(V_e\eta_e\frac{\partial V_e}{\partial z}\right)-\frac{1}{c^2}\frac{\partial q_e}{\partial t}-\frac{2}{c^2}\frac{\partial}{\partial z}(q_e V_e),\\
&3n_e\left(\frac{\partial}{\partial t}+V_e\frac{\partial}{\partial z}\right)T_e+T_e n_e\frac{\partial V_e}{\partial z}=-\frac{\partial q_e}{\partial z}+\frac{4}{3}\eta_e\left(\frac{\partial V_e}{\partial z}\right)^2+Q_e\\
&\quad+\frac{4}{3}\frac{1}{c^2}V_e\eta_e\frac{\partial V_e}{\partial t}\frac{\partial V_e}{\partial z}-\frac{1}{c^2}V_e\frac{\partial q_e}{\partial t}-\frac{2}{c^2}q_e\frac{\partial V_e}{\partial t}-\frac{2}{c^2}V_e q_e\frac{\partial V_e}{\partial z},\\
&\frac{\partial n_i}{\partial t}+\frac{\partial}{\partial z}(n_i V_i)=0,\\
&m_i n_i\left(\frac{\partial}{\partial t}+V_i\frac{\partial}{\partial z}\right)V_i=-\frac{\partial}{\partial z}(n_i T_i)+\frac{4}{3}\frac{\partial}{\partial z}\left(\eta_i\frac{\partial V_i}{\partial z}\right)+n_i eE+R_i\\
&\frac{3}{2}n_i\left(\frac{\partial}{\partial t}+V_i\frac{\partial}{\partial z}\right)T_i+n_i T_i\frac{\partial V_i}{\partial z}=-\frac{\partial q_i}{\partial z}+\frac{4}{3}\eta_i\left(\frac{\partial V_i}{\partial z}\right)^2+Q_i.
\end{aligned}\right\}\quad(1)$$

Here, we have introduced the quantities

$$\left.\begin{aligned}
&R_e=-0.87\frac{m_e^* n_e}{\tau_e^*}(V_e-V_i)-0.17n_e\frac{\partial T_e}{\partial z}\\
&\quad+\frac{1}{3}0.17T_e\frac{\partial n_e}{\partial_z}+\frac{1}{3}0.17en_eE,\\
&q_e=0.46n_eT_e(V_e-V_i)-\varkappa_e\frac{\partial T_e}{\partial z}+\frac{1}{3}\frac{T_e\varkappa_e}{n_e}\frac{\partial n_e}{\partial z}+\frac{1}{3}e\varkappa_eE,\\
&Q_e=-R_e(V_e-V_i)-Q_i,\\
&R_i=-R_e-\frac{V_e}{c^2}Q_e,\ q_i=-\varkappa_i\frac{\partial T_i}{\partial z},\ Q_i=\frac{3m_e^* n_e}{m_i\tau_e^*}(T_e-T_i).
\end{aligned}\right\}\quad(2)$$

The thermal conductivities and viscosities of the electrons and ions in (2) are

$$\left.\begin{aligned}
&\varkappa_e=0.72\frac{n_eT_e\tau_e^*}{m_e^*},\ \varkappa_i=3.9\frac{n_iT_i\tau_i}{m_i},\\
&\eta_e=0.21n_eT_e\tau_e^*,\ \eta_i=0.96n_iT_i\tau_i,
\end{aligned}\right\}\quad(3)$$

where n_e and n_i are the electron and ion densities respectively,[3] the electron "mass" $m_e^* = 4\,T_e/c^2$, and the scattering time τ_e^* for electrons at ions is different from the expression obtained in nonrelativistic theory, whereas the scattering time of ions by ions remains unchanged:

$$\tau_e^*=\frac{3T_e^2}{\pi e^4 L n_i c},\quad \tau_i=\frac{3m_i^{1/2}T_i^{3/2}}{4\pi^{1/2}Le^4n_i}\quad(4)$$

(L is the Coulomb logarithm).

Knowing the collisional transfer of momentum from ions to electrons R_e, we can easily find the velocity of the electrons relative to the ions:

$$\mathrm{V}_{e0}=-1.08\frac{e\tau_{e0}^*}{m_{0e}^*}\mathrm{E}_0.\quad(5)$$

If we consider long wavelengths, $kd \ll 1$ [$d=(T/4\pi e^2 n)^{1/2}$ is the Debye radius], we can neglect div E in Poisson's equation and we then assume plasma neutrality, $n_e = n_i \equiv n$. After linearization the continuity equations for electrons and ions give

$$n'=\frac{kV_i'}{\omega}n_0=\frac{V_i'-V_e'}{V_{0e}}n_0,\quad(6)$$

where n_0 is the equilibrium density of electrons and ions and ω is the frequency [we look for small perturbations in the hydrodynamic quantities n', V_e', V_i', and T_e'' and T_i' in the form $\exp(-i\omega t + ikz)$]. By means of (6) we can linearize the equations of motion and of thermal balance for electrons and ions but the resultant system is rather complicated even if we neglect the electron inertia, which is of order $(\omega/kc)^2$, as is usually done in considering low-frequency ion-acoustic oscillations. However, we can simplify the problem if we consider a plasma with a high electron thermal conductivity but a low ion conductivity so that $\tau_{e0}k^2c^2 \gg \omega \gg \tau_{i0}(k^2T_0/m_i)$ ($T_{0e} = T_{0i} \equiv T_0$ is the equilibrium value of the electron and ion temperature in the plasma). In this case the linearized hydrodynamic equations become

$$\left.\begin{aligned}
&\frac{T_e'}{T_0}=-i\frac{\omega-kV_{0e}}{0.25k^2c^2\tau_{e0}}\frac{n'}{n_0},\\
&\frac{T_i'}{T_0}=\frac{2}{3}\left(1-i2.6k^2\frac{T_0}{m_i}\frac{\tau_{0i}}{\omega}-i8\frac{T_0}{m_ic^2}\frac{1}{\tau_{e0}\omega}\right)\frac{n'}{n_0},\\
&\left(\omega^2-2k^2\frac{T_0}{m_i}+i1.28k^2\frac{T_0}{m_i}\tau_{i0}\omega\right)\frac{n'}{n_0}-k^2\frac{T_0}{m_i}\frac{T_e'}{T_0}-ik^2\frac{T_0}{m_i}\frac{T_i'}{T_0}=0.
\end{aligned}\right\}\quad(7)$$

Setting up the dispersion equation and introducing the real and imaginary parts of $\omega(\omega = \omega_0 + i\gamma)$, we have

$$\left.\begin{aligned}\omega_0 &= k\left(\frac{8}{3}\frac{T_0}{m_i}\right)^{1/2},\\ \gamma &= -\frac{T_0}{m_i c^2 \tau_{e0}}\left(1-\frac{2kV_{0e}}{\omega_0}\right) - 0.96k^2\frac{T_0}{m_i}\tau_{i0}.\end{aligned}\right\} \quad (8)$$

It is evident from (8) that the ion-acoustic mode becomes unstable when $V_{0e} > V_{cr}$, where

$$V_{cr} = \left(\frac{8}{3}\frac{T_0}{m_i}\right)^{1/2}(0.50 + 0.48k^2c^2\tau_{e0}\tau_{i0}). \quad (9)$$

In comparison with the nonrelativistic expressions,[2] V_{cr} is much higher and the growth rate γ is reduced by a factor $(T_1/m_ec^2)^{1/2}$ (T_1 is the equilibrium temperature of the electrons and ions in nonrelativistic theory).

In conclusion the author wishes to thank N. L. Tsintsadze for his interest.

---

[1] A. Kuckes, Phys. Fluids, 7, 511 (1964).

[2] A. B. Mikhailovskii, Theory of Plasma Instabilities, Vol. 1, Consultants Bureau, New York (1973).

[3] D. I. Dzhavakhisvili and N. L. Tsintsadze, Zh. Eksp. Teor. Fiz., 64, 1314 (1973).

[4] S. I. Braginskii, Zh. Eksp. Teor. Fiz., 33, 459 (1957).[Sov. Phys. – JETP, 6, 358 (1958)].

Correction of third-order angular aberration in a system with two electrostatic mirrors

V. V. Zashkvara
Institute of Nuclear Physics,
Academy of Sciences of the Kazakh SSR, Alma-Ata

(Submitted July 9, 1973)
Zh. Tekh. Fiz., 44, 1541-1543 (July 1974)

The ion-optical configuration of a two-stage electrostatic energy analyzer is discussed. The analyzer consists of two electrostatic electron mirrors, one hyperbolic and one cylindrical, matched in such a way that the total spherical aberration of the system in the direction of the dispersion is proportional to the fourth power of the divergence half-angle in the plane of the axial trajectory.

The analyzer with a hyperbolic mirror proposed by Bredov[1] exhibits second-order angular focusing in the plane of symmetry of the field and first-order focusing in the transverse plane. In an analyzer with a cylindrical mirror[2] there is second-order focusing with respect to the angle of divergence of the beam in the axial plane and exact angular focusing with respect to the angle of divergence in the plane of the azimuthal cross section. The corresponding ion-optical diagrams are the same: In both cases point sources of charged particles and foci which are nearly points are located outside the analyzing fields on the axes of symmetry parallel to the generation of the deflecting electrodes. Spherical aberrations, which determine the longitudinal broadening of the images, are proportional to the cube of the half-angle of divergence of the beam $\Delta\alpha$ in the plane of the axial trajectory. The third-order aberrations are of opposite sign in hyperbolic and cylindrical electrostatic mirrors, making possible a system of two electron mirrors, in which the third-order angular aberration in the direction of the dispersion is corrected completely. The ion-optical diagram of such a two-stage analyzer consisting of matched hyperbolic 1 and cylindrical 2 electron mirrors is shown in Fig. 1. A point source of charged particles 0 is located on the z axis in the plane of symmetry of the deflecting electrodes of the hyperbolic mirror. Point 0 is a distance H from the surface of the inner hyperbolic electrode, the angle of entrance of the central ray $\alpha_h = 51°55'$, and the focal length $L_h = 7.092$ H (ref. 1). For second-order focusing in a cylindrical mirror[2] the entrance angle $\alpha_c = 42°18'$, and the focal length $L_c = 6.1298\ r_1$, where r_1 is the radius of the inner cylindrical electrode. At point f the Gaussian foci of the two mirrors are superposed, and the axis of the cylindrical mirror z' passes through point f and is inclined to the axis of the hyperbolic mirror at an angle $\alpha_h - \alpha_c = 9°37'$. The geometry of the beam being analyzed is shown in Fig. 2 for the vicinity of the intermediate focus f. The axial ray is labelled 00', and the peripheral rays 11' and 22' bounding the beam have an angular spread $\pm\Delta\alpha$. Rays 33' and 44' make small angles with the axial trajectory. The dashed line is the caustic curve, which is the envelope of the family of rays. The segments a_h and a_c characterize the third-order angular aberrational broadening of the images of the hyperbolic and cylindrical mirrors in the axial directions along the z and z' axes respectively.

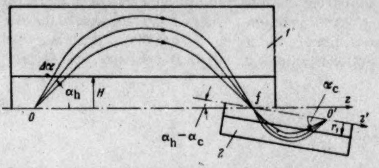

Fig. 1. Two-stage electrostatic energy analyzer. 1) Hyperbolic electron mirror; 2) cylindrical mirror.

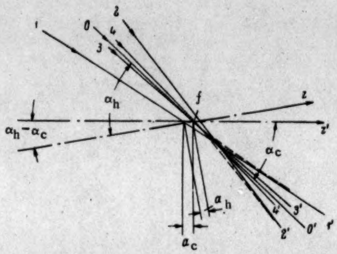

Fig. 2. Beam geometry in the vicinity of the intermediate focus.

To correct the angular aberration at the system exit, point 0' in Fig. 1, under the conditions considered, the characteristic dimensions H and r_1 must satisfy a relation obtained by requiring the equality of the third-order angular aberrations in the vicinity of the intermediate focus:

$$|a_c| \sin\alpha_c = |a_h| \sin\alpha_h, \tag{1}$$

where $|a_c|$ and $|a_h|$ are the absolute values of the third-order aberrations. The expression for a_c is[2]

$$a_c = -15.529 r_1 (\Delta\alpha)^3. \tag{2}$$

The third-order angular aberration of a hyperbolic mirror is not calculated in ref. 1. It must be determined from the expression[1] for L_h by finding $\partial^3 L_h/\partial\alpha^3$ when $\partial^2 L_h/\partial\alpha^2 = \partial L_h/\partial\alpha = 0$.

Thus,

$$a_h = \frac{1}{3!}\frac{\partial^3 L_h}{\partial\alpha^3}(\Delta\alpha)^3 = \frac{1}{3}\frac{H}{\varepsilon}\operatorname{ctg}^2\alpha_h\left[\frac{\beta^2(7+3\beta^2)}{(1-\beta^2)^2}\right.$$
$$\left. + 4\operatorname{ctg}^2\alpha_h\beta^2\frac{1-3\beta^2}{(1-\beta^2)^3} - 3\beta\,\operatorname{Arth}\beta\right](\Delta\alpha)^3. \tag{3}$$

It is established in ref. 1 that for double angular focusing of a beam in a hyperbolic mirror $\beta = -0.8438$ and $\varepsilon = -0.2957$. Substituting these values into Eq. (3) gives

$$a_{\mathrm{h}} = 5.4628H\,(\Delta\alpha)^3. \tag{4}$$

Now, substituting a_{c} and a_{h} into the condition for the compensation of the third-order aberration (1) we obtain the required relation between H and r_1:

$$r_1 = 0.4115H. \tag{5}$$

The ion-optical diagram in Fig. 1 is drawn by taking account of this relation. The fact that the axes of the electrostatic mirrors in the ion-optical diagram shown do not coincide leads only to an insignificant extra broadening of the intermediate image in the transverse plane by an amount $a_{\mathrm{h}}\gamma \sin(\alpha_{\mathrm{h}} - \alpha_{\mathrm{c}})$, where γ is the angular divergence of the beam of charged particles in the transverse plane, and there is first-order focusing with respect to the angle γ for the system as a whole, as for a hyperbolic mirror alone. On the basis of data in refs. 1 and 2 and Eq. (5) the energy dispersion of the mirror system is

$$\Delta L = 9.3118H\,\frac{\Delta u}{u} + 5.6038r_1\,\frac{\Delta u}{u} = 11.6178H\,\frac{\Delta u}{u}. \tag{6}$$

---

[1] M. M. Bredov, Zh. Tekh. Fiz., 29, 1032 (1959) [Sov. Phys. – Tech. Phys., 4, 940 (1960)].

[2] V. V. Zashkvara, M. I. Korsunskii, and O. S. Kosmachev, Zh. Tekh. Fiz., 36, 132 (1966) [Sov. Phys. – Tech. Phys., 11, 96 (1966)].

Linear transient response of a fully ionized plasma in a pulsed electric field

V. V. Istomin, S. P. Sher, and S. P. Dovgopol

S. M. Kirov Ural Polytechnical Institute,

(Submitted May 25, 1973; resubmitted December 4, 1973)
Zh. Tekh. Fiz., 44, 1543-1545 (July 1974)

A kinetic equation for the one-particle distribution function with a Landau collision integral is used to investigate the linear transient response of a fully ionized plasma in a pulsed electric field. General expressions are obtained for the electric current as a function of time and the energy absorbed by the plasma. Computer calculations are presented in the form of curves of the current and energy; these lead to the conclusion that the transition to the steady state is slower than in a weakly ionized plasma. For this reason, measurements of the electrical conductivity of a plasma can be lower than the Spitzer value if the measurements are not performed in the steady state.

An investigation of transient processes in a plasma in a pulsed electric field is of interest with regard to plasma heating. In ref. 1 this problem is considered for a weakly ionized plasma, where only electron–neutral collisions are considered; it is assumed that the electron velocity dependence of the collision frequency is proportional to v^s and s = 0,1 or 2. It is found that the parameters of the steady state are not appreciably affected by s.

In the present paper the transient process is considered in a fully ionized homogeneous plasma and it is shown that the velocity dependence of the collision frequency is very important.

We start with the kinetic equation for the single particle distribution function $f_e(\mathbf{v})$ with the Landau collision integral[2] linearized for an ideal Lorentzian gas:[3]

$$\left.\begin{aligned}\left(\frac{\partial}{\partial t}-\frac{e}{m}\mathbf{E}(t)\frac{\partial}{\partial \mathbf{v}}\right)f_e(\mathbf{v},t)=A\partial_r v^{-3}(v^2\delta_{rs}-v_r v_s)\partial_s f_e(\mathbf{v},t),\\ A=\frac{2\pi e^2 e_i^2 n_i L}{m^2},\end{aligned}\right\}\qquad(1)$$

where E(t) is a time-dependent electric field, $\partial_j = \partial/\partial v_j$, (j = x, y, z), n_i is the ion density, e and e_i are the electron and ion charge, respectively, and L is the Coulomb logarithm.[2] The contribution of electron–electron collisions is neglected in (1); this is justified by the small electron–ion mass ratio.[3] This procedure also allows us to use the Lorentzian model,[3] assuming the ion distribution function to be a delta function if the field frequencies are not too low.[1]

Assuming the field to be in the direction of the x axis, we use the linear approximation

$$f_e(\mathbf{v})=f^0(v)+\frac{v_x}{v}F(v,t),\quad f^0(v)=\left(\frac{m}{2\pi kT_e}\right)^{3/2}\exp\left(-\frac{mv^2}{2kT_e}\right).\qquad(2)$$

Solving Eq. (1) to the same approximation, we obtain

$$F(v,t)=\frac{e}{m}\frac{\partial f_0(v)}{\partial v}\Phi(v,t),\quad \Phi(v,t)=e^{-\frac{2At}{v^3}\int\limits_1^t dt' e^{\frac{2At'}{v^3}}E(t')}.\qquad(3)$$

The current $I(t) = -en_e\int d\mathbf{v}u_x f_e(\mathbf{v})$ (n_e is the electron density) is

$$I(t)=\frac{8n_e e^2}{3\sqrt{\pi}\,m}\int\limits_0^\infty dW W^4\Phi'(W,t)e^{-W^2},\qquad(4)$$

where Φ' is obtained from Φ by replacing $2A/v^3$ by ν(W),

$$\nu(W)=\frac{4\pi e^2 e_i^2 n_i L}{m^{1/2}(2kT_e)^{3/2}}W^{-3},\quad W\equiv\left(\frac{m}{2kT_e}\right)^{1/2}v.\qquad(5)$$

Further, we calculate the energy absorbed by the plasma in time τ:

$$\varepsilon(\tau)=\frac{1}{\tau}\int\limits_0^\tau dt I(t)E(t).\qquad(6)$$

We consider two cases separately: $E(t) = E_0$ = const and $E(t) = E_0 \cos \omega t$. In the first case

$$I_1(t)=I_0[3-\rho_1(at)],\quad a=\frac{4\pi e^2 e_i^2 n_i L}{m^{1/2}(2kT_e)^{3/2}},\qquad(7)$$

where I_0 is the steady-state current, $I_0 = I_1(\infty) = 8n_e e^2 E_0\cdot(3\sqrt{\pi m a})^{-1}$, and

$$\rho_{1'}(x)\equiv\int\limits_0^\infty dW W^7\exp(-W^2-xW^{-3}).\qquad(8)$$

Correspondingly,

$$\varepsilon_{1'}(\tau)=\varepsilon_0\left[3-\frac{945\sqrt{\pi}}{64a\tau}+\frac{\rho_1(a\tau)}{a\tau}\right],\qquad(9)$$

where $\varepsilon_0 = I_0E_0$. In the second case

$$I_2(t)=I_0\left[\cos\omega t\rho_2\left(\frac{\omega}{a}\right)+\frac{\omega}{a}\sin\omega t\rho_3\left(\frac{\omega}{a}-\lambda_1\left(\frac{\omega}{a},at\right)\right)\right],\qquad(10)$$

where

$$\begin{Bmatrix}\rho_2(\alpha)\\ \rho_3(\alpha)\end{Bmatrix}=\int\limits_0^\infty dW\begin{Bmatrix}W^7\\ W^{10}\end{Bmatrix}e^{-W^2}(1+\alpha^2W^6)^{-1},\qquad(11)$$

$$\lambda_1(\alpha,x)=\int\limits_0^\infty dW W^7(1+\alpha^2W^6)^{-1}\exp(-W^2-xW^{-3}).\qquad(12)$$

Further, in the second case we have for the energy

$$\begin{aligned}\varepsilon_{2'}(\tau)=\varepsilon_0\Big[&\frac{1}{2}\left(1+\frac{\sin 2\omega\tau}{2\omega\tau}\right)\rho_2\left(\frac{\omega}{a}\right)+\frac{\sin^2\omega\tau}{2a\tau}\rho_3\left(\frac{\omega}{a}\right)\\ &+\frac{\cos\omega\tau}{a\tau}\lambda_2\left(\frac{\omega}{a},a\tau\right)-\frac{\omega\sin\omega\tau}{a^2\tau}\lambda_3\left(\frac{\omega}{a},a\tau\right)-\frac{1}{a\tau}\rho_4\left(\frac{\omega}{a}\right)\Big],\end{aligned}\qquad(13)$$

where

$$\rho_4(\alpha)=\int\limits_0^\infty dW W^{10}(1+\alpha^2W^6)^{-2}e^{-W^2},\qquad(14)$$

$$\begin{Bmatrix}\lambda_2(\alpha,x)\\ \lambda_3(\alpha,x)\end{Bmatrix}=\int\limits_0^\infty dW\begin{Bmatrix}W^{10}\\ W^{13}\end{Bmatrix}(1+\alpha^2W^6)^{-2}\exp(-W^2-xW^{-3}).\qquad(15)$$

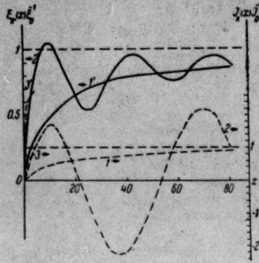

Fig. 1. Transient process for the current and the energy absorbed by the plasma during the pulse.

The integrals for ρ_i and λ_i are not expressed in elementary or special functions: They were calculated on a computer for $x \in [0.85]$ and $\alpha = 0.1$. The values obtained are $\rho_2(0.1) = 1.899$, $\rho_3(0.1) = 11.768$, and $\rho_4(0.1) = 6.990$. Curves of the functions $I_k(at)\ J_0^{-1}$ and $\varepsilon_k(a\tau)\ \varepsilon_0^{-1}$ have been plotted from the results of these calculations (see Fig. 1). Curves 1 and 1' correspond to k and k', curves 2 and 2' correspond to k and k'. For comparison, we give curves 3 and 3' from ref. 1 which describe the functions $I_1(at)\ I_0^{-1}$ and $\varepsilon_1(a\tau)\ \varepsilon_0^{-1}$ for a weakly ionized plasma with a constant (not dependent on velocity) collision frequency.

Comparison of curves 1 and 3 (1' and 3') clearly indicates that in a fully ionized plasma the transition to the steady state is much slower than in a weakly ionized plasma. This fact can be explained as due to the predominance, in a weakly ionized plasma, of short-range collisions with neutrals; in a fully ionized plasma there is a long-range Coulomb interaction between particles. In the case of an ac field, a slower transition to the steady-state occurs (curves 2 and 2') with the presence of characteristic oscillations.

In conclusion we note, first, that the slow transition to the steady state in a fully ionized plasma can evidently cause a discrepancy (toward smaller) between the electrical conductivity measured experimentally and that calculated according to the Spitzer equation[4] if the experiment is not carried out under rigorous steady-state conditions. This fact is mentioned in ref. 5.

Second, it is clear that although the conditions for absorption (and thus heating) are favorable in a weakly ionized plasma, periodic modulation of the pulse provides fairly intense absorption in a fully ionized plasma up to the transition to the steady state.

---

[1] M. S. Sodha and A. K. Ghatck, J. Appl. Phys., 43, 1529 (1972).

[2] L. D. Landau, Zh. Eksp. Teor. Fiz., 7, 203 (1936).

[3] R. Balescu, Statistical Mechanics of Charged Particles, Interscience, New York (1963).

[4] L. Spitzer, Physics of Fully Ionized Gases, Interscience, New York (1956).

[5] R. E. Rovinskii, Teplofiz. Vys. Temp., 10, No. 1 (1972)

7

Capillary gravitational waves and the mechanogalvanic effect

E. D. Korlyakov
S. O. Makarov Leningrad College of Marine Studies
(Submitted September 25, 1973; resubmitted December 25, 1973)
Zh. Tekh. Fiz., 44, 1545-1546 (July 1974)

The movement of aqueous solutions of electrolytes relative to a continuous interface with a solid medium produces a potential gradient along the tangent to the interface. This phenomenon (the mechanogalvanic effect) is of an electrodynamic nature. A theoretical and experimental analysis for an interface between an electrolyte and a solid is given in the review of ref. 1. The quantitative explanation of the effect for this case is based on the Helmholtz–Smolukhov theory of the double electric layer and the theory of motion in a viscous liquid. The assumptions made below suggest that the mechanogalvanic effect should also be observed in relative motion between a liquid and a gas phase.

It was established as early as 1915 that the surface of a liquid at an interphase boundary with a gas is covered by a double electric layer, which is entirely inside the liquid and is not caused by the contact with the gas.[2] Frenkel[3] analyzed the orientation of molecules at a free liquid surface and showed that if the quadrupole moment of the molecules is taken into account, as in the case of water, the surface would be covered by a double electric layer; the presence of absorbed molecules with active dipole groups produces double layers with a considerably higher jump in potential than in pure liquids.

It has been shown experimentally[4] that if a stream of air whose density is ρ(kg/m^3) moves at a velocity v(m/sec), then a tangential frictional force of

$$F = 2 \cdot 10^{-4} \rho v^2 \text{ N},$$

acts on each square meter of water.

If we carry out calculations similar to those for the mechanogalvanic effect at an electrolyte/solid interface,[1] we find that for a boundary between an aqueous solution of electrolyte and air the potential gradient that is produced by relative motion is given by the expression

$$E = 2 \cdot 10^{-4} \frac{\delta}{\zeta \varepsilon_0 \varepsilon} \rho v^2,$$

where ρ is the density of air, v is its velocity relative to the solution, ζ is the zeta potential (electrokinetic potential), and δ is the effective thickness of the surface layer. This equation shows, for example, that at an air speed of about 2 m/sec a field strength of around 0.5 mV/m is to be expected. Since a stream of air generates surface waves at a liquid interface, the production of these waves and the appearance of the electric field are interrelated.

An experimental study of the mechanogalvanic effect at the interface between an aqueous solution and air has been performed with the method and apparatus described in the review of ref. 1. It might be noted that in the present case the investigation is made more difficult by the fact that the effect also occurs at the measuring electrodes when a wave motion is produced; the noise thus measured is known as wave noise.[5] In the laboratory, investigations are made below the point at which the wave noise becomes distinctly observable. For air speeds up to 3 m/sec, the experimental data agree, in order of magnitude, with the theoretical calculations. Thus, for example, an air speed of 2 m/sec over sea water (the most widely occurring natural electrolyte) produces an alternating field of from 0.5 to 1 mV/m. Thus an air stream produces both surface waves and an alternating current at the interface.

General electrodynamic principles suggest that the alternating currents must set up alternating magnetic fields. It is interesting to note in this connection that studies of sea waves under natural conditions by means of a cesium magnetometer have shown the presence of magnetic fields accompanying wave motion.[6] It also follows from geophysical data that there is a close connection between the characteristics of wave motion and the induced magnetic fields.[7]

We might note that an experimental study has established that surface waves are produced when an alternating current is passed through an electrolyte in an external magnetic field;[8] this is the inverse effect to the generation of surface waves and electromagnetic fields by the mechanogalvanic effect at an electrolyte–air interface. Further studies of this effect are needed and would be useful in understanding processes occurring in diffusion and mixed kinetics.

---

[1] E. D. Korlyakov, Izv. VUZ. Fizika, No. 11, 159 (1970).

[2] O. D. Khvol'son (sic), Course in Physics, Vol. 4, Berlin (1925), p. 210.

[3] J. Frenkel, Kinetic Theory of Liquids, Dover, New York (1955).

[4] V. V. Shuleikin, Physics of the Sea [in Russian], Nauka, Moscow (1968), p. 7.

[5] G. A. Fonarev, Geomag. Aeronom., 1, 459 (1961).

[6] A. N. Kozlov, G. A. Fonarev, and L. A. Shumov, Geomag. Aeronom., No. 4, 741 (1971).

[7] A. G. Kravtsov and G. V. Sokolov, Geomag. Aeronom., No. 5, 927 (1971).

[8] M. Z. Gak and E. Z. Gak, Zh. Tekh. Fiz., 42, No. 9, 1992 (1972) [Sov. Phys. – Tech. Phys., 17, 1595 (1973)].

Elimination of spherical aberration in an axial plasma lens

S. V. Lebedev and A. I. Morozov

(Submitted July 23, 1973)
Zh. Tekh. Fiz., 44, 1547-1548 (July 1974)

The conditions under which spherical aberration can be eliminated from an axial plasma lens are analyzed. A necessary condition for this elimination is a parabolic potential profile along the magnetic lines of force.

The focusing properties of an axial plasma lens used to focus dense, neutral ion beams are analyzed in ref. 1. The lens under consideration here is a ring carrying a current R_0; a potential difference U_0 is applied betweeen the ring and the source.

In an experimental study of a lens of this type,[2] it has been shown that the focal length of the lens agrees with that calculated in the thin-lens approximation.[3] It has also been found that when a system of electrodes is used to vary the profile of the electric potential along the magnetic lines of force changes occur in the magnitude of the spherical aberration; this aberration is minimized in the case of a parabolic $\Phi(\Psi)$ profile,

$$\Phi = K_1\Psi + K_2\Psi^2, \tag{1}$$

where K_1 and K_2 are constants, Ψ is the magnetic flux function, and $\Phi(\Psi)$ is the scalar potential of the electric field.

We can show that functional dependence (1) is a necessary condition for the elimination of spherical aberration for the case of an arbitrary magnetic field configuration in the lens. We write the flux $\Psi(r, z)$ as a power series in r, retaining only the first two terms:

$$\Psi = \frac{r^2}{2} H - \frac{r^4}{4!} H'', \tag{2}$$

where H(z) is the magnetic field at the axis, and the primes denote differentiation with respect to the z coordinate. In the same approximation the generalized potential[4] $V = (e^2/Mc^2)(\Psi^2/2r^2) + e\Phi(\Psi)$, which governs the motion of a particle in a plane, can be written

$$V = \frac{r^2}{2}\left[\frac{e^2}{Mc^2}\frac{H^2}{4} + e\frac{d\Phi}{d\Psi}H\right] + \frac{r^4}{4}\left[-\frac{e^2}{Mc^2}\frac{1}{12}HH' - e\frac{d\Phi}{d\Psi}\frac{H''}{3!} + e\frac{d^2\Phi}{d\Psi^2}\frac{H^2}{2}\right]. \tag{3}$$

Substituting (3) into the equation of motion

$$\ddot{r} = -\frac{1}{M}\frac{\partial V}{\partial r}, \quad \ddot{z} = -\frac{1}{M}\frac{\partial V}{\partial z}, \tag{4}$$

and assuming the velocity $\dot{z}$ to be constant along the axis of the lens, we find the angle through which the ion trajectory is refracted in passage through the lens:

$$r' = -\frac{1}{M}\frac{1}{\dot{z}}\int_{-\infty}^{0}\frac{\partial V}{\partial r}\frac{1}{\dot{z}}\,dz = -\frac{1}{M}\frac{1}{\dot{z}_0}\int_{-\infty}^{z}\left\{r\left[\frac{e^2}{Mc^2}\frac{H^2}{4} + e\frac{d\Phi}{d\Psi}\right] + r^3\left[-\frac{e^2}{M^2c^2}\frac{1}{12}HH'' - e\frac{d\Phi}{d\Psi}\frac{H''}{3!} + \frac{e}{M}\frac{d^2\Phi}{d\Psi^2}\frac{H^2}{2}\right]\right\}dz. \tag{5}$$

From Eq. (5), using the thin-lens approximation, we find the focal length taking spherical aberration into account:

$$\frac{1}{F} = \frac{1}{v_0^2}\int_{-\infty}^{+\infty}\left[\frac{e^2}{M^2c^2}\frac{H^2}{4} + \frac{e}{M}\frac{d\Phi}{d\Psi}H\right]dz - \frac{r_0^2}{v^2}\int_{-\infty}^{+\infty}\left[\frac{e^2}{Mc^2}\frac{1}{12}HH'' - \frac{e}{M}\frac{d\Phi}{d\Psi}\frac{H}{3!} + \frac{e''}{M}\frac{d^2\Phi}{d\Psi^2}\frac{H^2}{2}\right]dz. \tag{6}$$

The second term in (6) gives the spherical aberration, v_0 is the total ion velocity, and r_0 is the beam width. Clearly, if the spherical aberration is to be eliminated, the second term in (6) must vanish. Substituting (1) into (6), and taking account of the spatial confinement of the fields in the lens, we find that the spherical aberration is suppressed under the condition

$$\frac{1}{12}\frac{e^2}{M^2c^2}\int_{-\infty}^{+\infty}(H')\,dz + \frac{e}{M}k_2\int_{-\infty}^{+\infty}H^2dz = 0, \tag{7}$$

and from this condition we find

$$k_2 = -\frac{1}{12}\frac{e^2}{Mc^2}\frac{\int_{-\infty}^{+\infty}(H')^2\,dz}{\int_{-\infty}^{+\infty}H^2dz}. \tag{8}$$

For the magnetic field of the plasma lens analyzed in ref. 1,

$$H = \frac{2I_0R^2}{(z^2 + R^2)^{3/2}}, \tag{9}$$

where R is the ring radius, the value of k_2 is

$$k_2 = -3\cdot 10^{-2}\frac{1}{R^2}\frac{e}{Mc^2}. \tag{10}$$

We can conclude that in contrast with ordinary axial lenses used in ion optics, spherical aberration can be eliminated in a plasma lens if the electric field is specified in form (1). We note that the focal length is independent of k_2.

---

[1] S. V. Lebedev and A. I. Morozov, Zh. Tekh. Fiz., 36, 960 (1966) [Sov. Phys. – Tech. Phys., 11, 707 (1966)].

[2] V. V. Zhukov, A. I. Morozov, and G. Ya. Shchepkin, ZhETF Pis. Red., 9, 24 (1969) [JETP Lett., 9, 14 (1969)].

[3] V. N. Kel'man and S. Ya. Yavor, Electron Optics [in Russian], Izd. Akad. Nauk SSSR, Moscow – Leningrad (1963).

[4] A. I. Morozov and L. S. Solov'ev, Reviews of Plasma Physics, Vol. 3, Consultants Bureau, New York (1967).

Achromatic plasma–lens system

A. I. Morozov and S. V. Lebedev

(Submitted August 15, 1973)
Zh. Tekh. Fiz., 44, 1548-1549 (July 1974)

Annular plasma lenses with axisymmetric focusing fields differ markedly from their vacuum analogs (which focus low-density electron and ion beams). In particular, plasma lenses can display a different velocity dispersion and can be either converging or diverging lenses. Because of these properties systems of plasma lenses without chromatic aberration can be designed, by analogy with ordinary (visible-light) optics.

Plasma lenses are designed for use in focusing neutral ion beams; their basic properties and methods for designing them are given in ref. 1. When the axisymmetric focusing electromagnetic fields are chosen appropriately, annular plasma lenses (i.e., lenses which focus tubular ion beams) can be constructed which have various velocity dispersions. Furthermore, such lenses can be either converging or diverging. These properties make it possible to stabilize the focal point (to eliminate longitudinal chromatic aberration) by analogy with ordinary (visible-light) optics. In light optics achromatic lenses are obtained by cementing together two lenses, one converging and the other diverging, with a relatively pronounced dispersion. Accordingly, by replacing these lenses by their plasma-optics analogs, we can reproduce an optical system.

Let us assume that the focal lengths of the two lenses are

$$F_1 = F_{10}\left(\frac{v}{v_0}\right)^{n_1}, \quad F_2 = F_{20}\left(\frac{v}{v_0}\right)^{n_2}. \tag{1}$$

Here v_0 is the characteristic ion velocity, n_1 and n_2 are positive definite numbers, and F_{10} and F_{20} are the focal lengths of the lenses at velocity v_0.

If the characteristic distance between the lenses is L, and if the source is a distance a_1 from the first lens (Fig. 1), the focal point is found from the familiar equations

$$\frac{1}{a_1} + \frac{1}{b_1} = \frac{1}{F_1}, \quad \frac{1}{a_2} + \frac{1}{b_2} = \frac{1}{F_2}, \quad a_2 = L - b_1. \tag{2}$$

Introducing the auxiliary variables

$$\alpha = \frac{1}{a_1}, \quad \beta = \frac{1}{b_2}, \quad \omega_1 = \frac{1}{F_1}, \quad \omega_2 = \frac{1}{F_2}, \tag{3}$$

we can rewrite (2), incorporating the stabilization condition

$$\frac{\partial b_2}{\partial v} = 0 \tag{4}$$

as

$$\frac{1}{\omega_1 - \alpha} + \frac{1}{\omega_2 - \beta} = L, \quad \left(\frac{\omega_1 - \alpha}{\omega_2 - \beta}\right)^2 = -\frac{n_1}{n_2}\frac{\omega_1}{\omega_2}. \tag{5}$$

It follows that with $n_1 > 0$ and $n_2 > 0$ stabilization of the focus requires that one lens be converging and the other diverging (e.g., $\omega_1 > 0$, $\omega_2 < 0$).

System (5) can be written in a more compact form if we introduce

$$\frac{1}{\omega_1 - \alpha} = \xi, \quad \frac{1}{\omega_2 - \beta} = \eta, \quad \frac{n_1}{n_2} = \theta$$

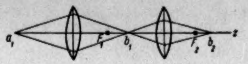

Fig. 1

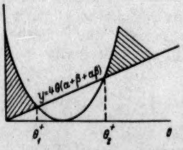

Fig. 2

and set L = 1.

Then we replace (5) by

$$\xi + \eta = 1, \quad \frac{\eta}{\xi} = -\theta\frac{1 + \xi\alpha}{1 + \eta\beta}. \tag{6}$$

Then

$$\eta = \frac{-1 + \theta(1 + 2\alpha) \pm \sqrt{(1-\theta)^2 - 4\theta(\alpha + \beta + \alpha\beta)}}{2(\beta + \alpha\theta)}. \tag{7}$$

From the condition for the positive definiteness of the discriminant

$$D = (1-\theta)^2 - 4\theta(\alpha + \beta + \alpha\beta) \geqslant 0, \tag{8}$$

we find the ratio $n_1/n_2 = \theta$ at which stabilization is possible.

Figure 2 shows regions with $D \geq 0$. The slope of the line $y = 4\theta(\alpha + \beta + \alpha\beta)$ is a function of the optic power of the lenses. We see that stabilization is possible under the conditions $\theta < \theta_1^*$ and $\theta_1^* > \theta_2$. We note that these regions correspond to the visible-light system. Under the condition $\theta < \theta_1^*$ the first lens must be converging ($\omega_1 > 0$) and the second must be diverging ($\omega_2 < 0$); if a real image is to be obtained we must arrange $\omega_1 > |\omega_2|$. In the region $\theta > \theta_2^*$ we must use lenses satisfying $\omega_1 < 0$, $\omega_2 > 0$, and $|\omega_1| < \omega_2$.

We can superpose the converging and diverging lenses, i.e., we can arrange L = 0. Now the stabilization condition is $\omega_1 = -\theta\omega_2$. A real image is obtained if $\theta < 0$. This result follows from the focal length of this "superposed" system:

$$\beta = \omega_2(1 - \theta), \quad \alpha = 0. \tag{9}$$

---

[1] A. I. Morozov and S. V. Lebedev, in: Problems of Plasma Theory [in Russian], Atomizdat, Moscow (1974).

Multiple-aperture ion source for electromagnetic mass separator

S. V. Lebedev

(Submitted October 5, 1973)
Zh. Tekh. Fiz., 44, 1550 (July 1974)

From the ion-optics standpoint, multiple-aperture sources are "broad" sources; in their current form they are unsuitable for use in mass separators since the source width affects the resolution of the separator.

This shortcoming of multiple-aperture sources can be avoided by choosing appropriately the potential distribution on the extracting electrodes. As an example we consider the use of a multiple-aperture source for an electromagnetic separator with a fixed magnetic field (Fig. 1). We assume that two source slits are a distance δR apart and that the potentials on the extracting electrodes are different, equal to Φ_1 and Φ_2, respectively ($\Phi_2 > \Phi_1$). For ions of mass M_0 the velocities of the ions emerging from the first and second slits are

$$v_1 = \sqrt{-\frac{2e}{M_0}\Phi_1}, \quad v_2 = \sqrt{-\frac{2e}{M_0}\Phi_2}. \tag{1}$$

Since the magnetic field is fixed, the Larmor radii of the ions moving at the velocities v_1 and v_2 are constant and equal to

$$R_1 = \frac{v_1}{\omega_H}, \quad R_2 = \frac{v_2}{\omega_H}, \tag{2}$$

where $\omega_H = eH_0/(M_0c)$ and H_0 is the magnetic field of the separator. The beams emerging from these slits are focused (for masses M_0) at a distance

$$\delta l = 2(R_2 - R_1) - \delta R \tag{3}$$

apart.

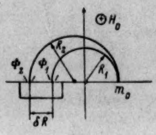

Fig. 1

We see that the focal points coincide if the potentials on the electrodes are chosen to satisfy

$$\delta R = 2(R_2 - R_1) = 2\frac{\Delta v}{v_1}R_1, \tag{4}$$

where $\Delta v = v_2 - v_1$.

Accordingly, the source "width" can be compensated through an appropriate choice of potentials. The mass dispersions for the beams emerging from the first and second slits are, respectively,

$$\delta_1 = 2\frac{\delta M}{M_0}\frac{v_1}{\omega_H}, \quad \delta_2 = 2\frac{\delta M}{M_0}\frac{v_1}{\omega_H} + 2\frac{\delta M}{M_0}\frac{\Delta v}{\omega_H}, \tag{5}$$

where δM is the mass spread.

It follows from (5) that if $\Delta v/\omega_H \ll R_1$ (e.g., with $\delta R/R \sim 0.08$ and $\Delta v/v_1 \sim 0.04$), the blurring of the focal point for mass $M_0 + \delta M$ is a quantity of second order for the case in which two slits are used.

Viscous momentum transport in a gaseous mixture

B. M. Markeev

Institute of Problems of Mechanics,
Academy of Sciences of the USSR, Moscow

(Submitted September 24, 1973; resubmitted January 7, 1974)
Zh. Tekh. Fiz., 44, 1550-1553 (July 1974)

The transport equations for a gaseous mixture are analyzed on the basis of the 13-moment approximation through an expansion of the distribution function about the Maxwellian values for the average partial velocity of the component. The transport equations contain an additional viscous force in the second approximation in the small Knudsen number. This latter circumstance leads to a finite mean mass velocity under the condition Δp = 0 in the motion of a binary mixture between plates in the field of partial pressure gradients tangential to the plates.

Transport-equation theory for a gaseous mixture is derived on the basis of the 13-moment approximation in refs. 1-3. The distribution function is expanded about the Maxwellian values in the mean mass velocity in order to obtain transport equations.

Below we analyze viscous momentum transport in a multicomponent gaseous mixture on the basis of an expansion of the distribution function about the Maxwellian values in the mean partial velocity of the component. We include the gradient of the heat flux together with the gradient in the partial velocity in solving the equation for the viscous-stress tensor in the first approximation in the small Knudsen number. We show that this approximation of the distribution function provides a more detailed description of the behavior of the mixture than the approximation in refs. 1-3; in particular, it leads to the appearance of additional viscous forces in the equations of motion for the components. We consider the problem of gas flow between parallel plates in the field of partial pressure gradients tangential to the plates.

We show that under the influence of these partial gradients the gas moves with a finite mean mass velocity even if the gradient in the total pressure vanishes.

1. The transport equation for the quantities ψ_α can be obtained by multiplying the left and right sides of the kinetic equation by the given quantity and then integrating over velocities. Successively setting $\psi_\alpha = 1$, $m_\alpha v_\alpha$, and $(m_\alpha/2)(v_\alpha - u_\alpha)$, and expanding the distribution function about the Maxwellian values for the mean partial velocity of the components, we find the continuity equation, the momentum-conservation equation, and the energy-conservation equation:

$$\frac{\partial n_\alpha}{\partial t} + \operatorname{div} n_\alpha u_\alpha = 0, \tag{1.1}$$

$$n_\alpha m_\alpha\left[\frac{\partial u_\alpha}{\partial t} + (\mathbf{u}_\alpha\nabla)\,\mathbf{u}_\alpha\right]_k + \nabla_k n_\alpha T_\alpha - \nabla_j\sigma_{\alpha kj} = R_{\alpha k}, \tag{1.2}$$

$$\frac{3}{2}n_\alpha\left[\frac{\partial}{\partial t} + (\mathbf{u}_\alpha\nabla)\right]T_\alpha + n_\alpha T_\alpha(\nabla u_\alpha) + (\nabla\mathbf{q}_\alpha) - \sigma_{\alpha ks}(\nabla_k u_{\alpha s}) = Q_\alpha, \tag{1.3}$$

where n_α, u_α, $\sigma_{\alpha ij}$, and q_α are the number density of the particles, the mean velocity, the viscous-stress tensor, and the heat-flux vector for particles of species α.

Multiplying the kinetic equation by $\psi_\alpha = m_\alpha(v_\alpha - u_\alpha)_k(v_\alpha - u_\alpha)_s$, $(m_\alpha/2)(v_\alpha - u_\alpha)^2(v_\alpha - u_\alpha)_k$, and integrating over velocities, we find the transport equations

$$\frac{\partial}{\partial t}\sigma_{\alpha kl} + \nabla_s(u_{\alpha s}\sigma_{\alpha kl}) + \sigma_{\alpha ks}(\nabla_s u_{\alpha l}) + \sigma_{\alpha sl}(\nabla_s u_{\alpha k})$$
$$-\frac{2}{3}\delta_{kl}\sigma_{\alpha sp}(\nabla_s u_{\alpha p}) - \frac{2}{5}(\nabla q_\alpha)_{kl} - n_\alpha T_\alpha(\nabla u_\alpha)_{kl} = -R_{\alpha kl}, \tag{1.4}$$

$$\frac{\partial}{\partial t}q_{\alpha k} + (\mathbf{u}_\alpha\nabla)q_{\alpha k} + \frac{7}{5}q_{\alpha k}(\nabla_s u_{\alpha s}) + \frac{2}{5}q_{\alpha s}(\nabla_k u_{\alpha s})$$
$$+\frac{5}{2}\left(\frac{n_\alpha T_\alpha}{m_\alpha}\right)\nabla_k T_\alpha - \left(\frac{T_\alpha}{m_\alpha}\right)\nabla_s\sigma_{\alpha ks} + \frac{7}{5}(q_{\alpha s}\nabla_s)u_{\alpha k}$$
$$-\frac{7}{2}\left(\frac{\sigma_{\alpha ks}}{m_\alpha}\right)\nabla_s T_\alpha + \left(\frac{\sigma_{\alpha ks}}{n_\alpha m_\alpha}\right)(\nabla_s n_\alpha T_\alpha - \nabla_l\sigma_{\alpha sl})$$
$$= R_{\alpha kss} - m_\alpha^{-1}\left[\frac{5}{2}T_\alpha\delta_{kl} - \left(\frac{\sigma_{\alpha kl}}{n_\alpha}\right)R_{\alpha l}\right], \tag{1.5}$$

where $(A, B)_{kj} = A_k B_j + A_j B_k - (2/3)\delta_{kj}(A_s B_s)$.

2. The right sides of the transport equations can be written as follows:

$$R_{\alpha i} = -\sum_\beta\left(\frac{n_\alpha n_\beta T}{n\,[D_{\alpha\beta}]_1}\right)u_{\alpha\beta} - \sum_\beta\zeta_{\alpha\beta}\left(\frac{q_{\alpha i}}{m_\alpha n_\alpha} - \frac{q_{\beta i}}{m_\beta n_\beta}\right), \tag{2.1}$$

$$R_{\alpha ik} = \frac{p^2\sum\limits_\beta a_{\alpha\beta}\sigma_{\beta ik}/p_\beta}{p_\beta}, \tag{2.2}$$

$$\left[R^{(3)}_{\alpha kss} - \frac{5}{2}\frac{T_\alpha}{m_\alpha}R_{\alpha k}\right] = \frac{5}{2}\frac{T_\alpha}{m_\alpha}\left[-\frac{p^2}{T_\alpha}\sum_\beta b_{\alpha\beta}\left(\frac{q_{\beta k}}{p_\beta}\right) - \sum_\beta\left(\frac{T_\alpha}{m_\alpha}\right)\zeta_{\alpha\beta}u_{\alpha\beta k}\right], \tag{2.3}$$

$$Q_\alpha = \left(\frac{m_{\alpha\beta}}{m_\alpha}\right)\left\{\sum_\beta\left(\frac{n_\alpha n_\beta T}{n\,[D_{\alpha\beta}]_1}\right)u^2_{\alpha\beta} + \sum_\beta\zeta_{\alpha\beta}u_{\alpha\beta i}\left(\frac{q_{\alpha i}}{m_\alpha n_\alpha} - \frac{q_{\beta i}}{m_\beta n_\beta}\right)\right., \tag{2.4}$$

where $u_{\alpha\beta} = u_\alpha - u_\beta$; $y_\alpha = n_\alpha/n$; $n = \sum\limits_\alpha n_\alpha$, and equations for $[D_{\alpha\beta}]_1$, $\zeta_{\alpha\beta}$, $a_{\alpha\beta}$, and $b_{\alpha\beta}$ are given, e.g., in ref. 3.

3. The values of $\sigma_{\alpha kl}$ and q_α are determined from system (1.4), (1.5). In the first approximation in the small Knudsen number we find

$$q^{(1)}_{\alpha i} = -\eta_\alpha\nabla_i T - \left(\frac{T}{p}\right)\sum_{\delta,\nu}y_\alpha\left(\frac{T}{m_\delta}\right)\zeta_{\delta\nu}\left(\frac{|b|_{\delta\nu}}{|b|}\right)u_{\delta\nu i}, \tag{3.1}$$

$$\sigma^{(1)}_{\alpha kl} = \left(\frac{2}{5}\right)p^{-1}\sum_\delta\left(\frac{|a|_{\delta\alpha}}{|a|}\right)y_\alpha(\nabla q_\delta)_{kl} + \sum_\delta\left(\frac{|a|_{\delta\alpha}}{|a|}\right)y_\alpha y_\delta(\nabla u_\delta)_{kl}, \tag{3.2}$$

where $\eta_\alpha = \sum\limits_\delta y_\alpha y_\delta(|b|\delta_\alpha/|b|)$ is the partial thermal conductivity, $|a|$ and $|b|$ are the determinants of systems (1.4) and (1.5), and $|a|_{\alpha\beta}$ and $|b|_{\alpha\beta}$ are the corresponding signed minors of element $\alpha\beta$. The heat-flux gradient is incorporated in (3.2) (cf. ref. 2). This gradient becomes important when the mixture moves at small Reynolds numbers.

In the second approximation in the small Knudsen number, the quantities $\sigma_{\alpha kl}$ and q_α are found from

$$-\frac{2}{5}(\nabla q^{(1)}_\alpha)_{kl} = -p^2\sum_\beta a_{\alpha\beta}\left(\frac{\sigma^{(2)}_{\beta kl}}{p_\beta}\right), \tag{3.3}$$

$$-\left(\frac{T}{m_\alpha}\right)\nabla_s\sigma^{(1)}_{\alpha ks}-\left(\frac{7}{2}\right)\left(\frac{\sigma^{(1)}_{\alpha ks}}{m_\alpha}\right)\nabla_s T+\left(\frac{\sigma^{(1)}_{\alpha ks}}{m_\alpha n_\alpha}\right)\nabla_s p_\alpha=-\frac{5}{2}\frac{p^2}{m_\alpha}\sum_\beta b_{\alpha\beta}\left(\frac{q^{(2)}_{\beta k}}{p_\beta}\right). \tag{3.4}$$

It follows from (3.3) and (3.4) that $\sigma^{(2)}_{\beta kl}$ and $q^{(2)}_\beta$ are of order Kn M (where $M = u/T^{1/2}m^{-1/2}$) if the second term in (3.2) is small in comparison with the first but larger than all others.

4. We consider the motion of a binary mixture between two planes in a field of partial pressure gradients. We locate the origin of the coordinate system halfway between the planes, which are separated by a distance 2L; the X axis is perpendicular to the planes, and the Z axis is parallel. System (1.1)-(1.5) with the sticking boundary conditions[1)] has the solution

$$\mathbf{u}_0=\left(\frac{\rho_1}{\rho}\right)\mathbf{u}_1+\left(\frac{\rho_2}{\rho}\right)\mathbf{u}_2=\left(\frac{p}{\mu}\right)(\nabla\ln p)\frac{1}{2}(x^2-L^2)-a(\mathbf{u}_1-\mathbf{u}_2), \tag{4.1}$$

$$\mathbf{u}_\alpha-\mathbf{u}_\beta=-\left(\frac{D_{\alpha\beta}}{y_\alpha y_\beta}\right)[\nabla y_\alpha+[a_p]_1\,y_\alpha y_\beta\nabla\ln p+[a_{T\alpha}]_1\,y_\alpha y_\beta\nabla\ln T]\left\{1-\frac{(\operatorname{ch}p^*x)}{\operatorname{ch}p^*L}\right\}. \tag{4.2}$$

Equations for $[a_p]_1$ and $[a_{T\alpha}]_1$ are given in refs. 3, 4; the constant a is given by

$$a=\left[\frac{n(m_\alpha+m_\beta)}{2\rho}\right]\left\{y_\alpha y_\beta[a_p]_1-\left[\left(\frac{\mu_\alpha}{\mu}\right)y_\beta+\left(\frac{\mu_\beta}{\mu}\right)y_\alpha\right]\frac{m_\beta-m_\alpha}{m_\alpha+m_\beta}\right\}+\frac{(\omega_\alpha-\omega_\beta)}{\mu},$$

where

$$p^{*-2}=\frac{(p^2_{11}+p^2_{22}+p^2_{12}+p^2_{21})}{(p^2_{11}p^2_{22}-p^2_{12}p^2_{21})},$$

$$\omega_\alpha=\left(\frac{2}{5}\right)\left(\frac{T}{p}\right)^2\sum_\beta\mu_{\alpha\beta}\left\{\left(\frac{\zeta_{\alpha\beta}}{m_\alpha}\right)\left(\frac{|b|_{\alpha\beta}}{|b|}\right)-\left(\frac{\zeta_{\beta\alpha}}{m_\beta}\right)\left(\frac{|b|_{\beta\beta}}{|b|}\right)\right\},$$

$$p^2_{\alpha\alpha}=(-\omega^*+\mu_{\alpha\alpha})\left(\frac{nD_{\alpha\beta}}{n_\alpha n_\beta T}\right),$$

$$p^2_\alpha=(\omega_\alpha+\mu_{\alpha\beta})\left(\frac{nD_{\alpha\beta}}{n_\alpha n_\beta T}\right),$$

and

$$\mu_{\alpha\beta}=\left(\frac{|a|_{\beta\alpha}}{|a|}\right)y_\alpha y_\beta.$$

In the first approximation of the Chapman–Enskog method[4] the mixture is described by a mean mass velocity, which is determined from the Navier–Stokes equation. The diffusion rates appear in the second approximation. Equation (4.1) for u_0 differs from the corresponding equation derived on the basis of the method of ref. 4 by the second term, which is the next term in the expansion in the parameter $Kn \ll 1$. In the case $\nabla p = 0$, the second term is of the first order of magnitude and governs the motion of a mixture with nonvanishing mean mass velocity.

In a binary gaseous mixture, by analogy with a single-component gas, steady-state flow is established because the "ideal" momentum flux due to the total pressure gradients is balanced by the total viscous momentum flux, which is directed from points characterized by a high velocity toward points characterized by a low velocity, and which is absorbed at the boundary. Since the distribution function is expanded about the Maxwellian values for the partial component velocity, the total viscous-stress tensor can be divided into two parts (for simplicity we neglect the Dufour effect):

$$\sigma_{kl}=\mu\,[(\nabla u_0)_{kl}+(\mu\rho)^{-1}(\mu_{\alpha\beta}-\mu_{\beta\alpha})(\nabla u_{\alpha\beta})_{kl}]. \tag{4.3}$$

These terms describe viscous momentum transport due to the mean mass and diffusion velocities. With $\nabla p = 0$ the condition $\sigma_{xy} = 0$ must be satisfied for steady-state flow. However, in contrast with a single-component gas, this latter condition is not satisfied with $u_0 = 0$, since, according to (4.3), there is an additional viscous momentum due to diffusion. Roughly speaking, we can say that this additional viscous momentum transport due to diffusion is also responsible for the finite mean mass velocity of the gaseous mixture in the case $\nabla p = 0$.

The author thanks A. A. Rukhadze for discussion.

[1)] Any creep velocity can be added to the right side of Eq. (4.1).

[1] I. Kolodner, N 40-7980, Courant Institute of Math. Sci., New York University (1957).

[2] R. Herdan and B. S. Liley, Rev. Mod. Phys., 32, 731 (1960).

[3] V. Zhdanov, Yu. Kogan, and A. Sazykin, Zh. Eksp. Teor. Fiz., 42, 857 (1962) [Sov. Phys. – JETP, 15, 596 (1962)].

[4] S. Chapman and T. G. Cowling, Mathematical Theory of Non-Uniform Gases, Cambridge Univ. Press, London (1953).

Atomic diffusion from a finite film over a solid surface

Yu. D. Kornyushkin

Leningrad Institute of Precision Mechanics and Optics

(Submitted June 29, 1973; resubmitted January 2, 1974)
Zh. Tekh. Fiz., 44 1553-1555 (July 1974)

An equation is derived describing the functional dependence on time of the concentration of atoms of a film on a solid surface taking account of surface diffusion. Equations are given for the concentration and the surface diffusion coefficient. An equation is derived for the total number of atoms in a finite region of the surface layer.

The physical properties of films are currently being exploited in various devices which find widespread use in microelectronics.[1] Diffusion processes,[2] including surface diffusion, should be taken into account in an explanation of the growth mechanism and properties of films. In particular, surface diffusion is responsible for the formation of islands in thin metal films.[3] For this reason, knowledge of the surface diffusion coefficient, or the law governing the distribution of the atomic concentration over the surface, is as important as knowledge of the corresponding coefficients for bulk diffusion.

The literature reveals several papers on the dynamics of surface diffusion, e.g., Drechsler[4] measured the surface diffusion coefficient of barium on the surface of a tungsten single-crystal and discussed this phenomenon. However, these experiments do not correspond to the basic theoretical conditions. Abramenkov et al.[5] examined surface diffusion, but the functional dependence which they derive is valid only for short periods of time and is thus of a highly specialized nature.

In this note we analyze the surface diffusion of atoms of a finite film, develop a method for calculating the surface diffusion coefficient from experimental data in the most general case, and find the functional dependence on the time of the atomic concentration at any point in the one-dimensional space.

We assume that there is initially a film of infinite length, of width $2x_0$ along the OX axis, and of thickness h on a solid surface. Bulk diffusion into the interior of the solid is very weak, so that the film atoms essentially diffuse only over the surface. The surface area of the solid is infinite. This formulation of the problem is essentially the same as that for the diffusion of atoms from a film of finite thickness into an infinite medium,[6] so that we can use the earlier results.

If we assume that some method is available for measuring the concentration of atoms which have diffused over the surface at various times and at a distance x from the center of the film, we can determine the law governing the concentration for any spatial point from

$$n_1=\frac{n_0}{2}\left[\Phi\left(\frac{x_0+x}{\sqrt{2Dt}}\right)+\Phi\left(\frac{x_0-x}{\sqrt{2Dt}}\right)\right](0\leqslant x\leqslant x_0), \qquad (1)$$

$$n_2=\frac{n_0}{2}\left[\Phi\left(\frac{x+x_0}{\sqrt{2Dt}}\right)-\Phi\left(\frac{x-x_0}{\sqrt{2Dt}}\right)\ (x_0\leqslant x\leqslant\infty)\right], \qquad (2)$$

where

$$\Phi(y)=\frac{2}{\sqrt{2\pi}}\int\limits_0^y e^{-u^2/2}\,du,$$

n_0 is the initial number of atoms per unit length in the film region, n_1 is the number of atoms per unit length within the original geometric boundary of the film at time t, n_2 is the number of atoms per unit length outside this original boundary at time t, x_0 is the distance from the center of the film to the observation point x_0 is the distance from the center of the film to its original geometric boundary, and D is the surface diffusion coefficient of the film atoms.

It follows from the form of Eqs. (1) and (2) that the function $n_1 = n_1(t)$ has no singularities, decreasing monotonically as time elapses; with regard to the function $n_2 = n_2(t)$, we note that at $t = t_m$ it reaches its maximum $n_{2\max} = n_2(t_m)$. From the condition for the extremum we find

$$t_m=\frac{xx_0}{D\ln\dfrac{x+x_0}{x-x_0}}. \qquad (3)$$

If we use the quantity t_m given by (3) as the unit of time in Eq. (2), we find

$$n_2=\frac{n_0}{2}\left[\Phi\left(\frac{z+1}{\sqrt{\dfrac{2z}{\ln\dfrac{z+1}{z-1}}\dfrac{t}{t_m}}}\right)-\Phi\left(\frac{z-1}{\sqrt{\dfrac{2z}{\ln\dfrac{z+1}{z-1}}\dfrac{t}{t_m}}}\right)\right], \qquad (4)$$

where $z = x/x_0 > 1$.

Figure 1 shows $n_2 = n_2(t/t_m)$ curves for z = 1.1, 1.4, and 2.0. It follows from this family of curves that the function $n_2(t/t_m)$ initially increases rapidly, with this increase being larger the smaller the value of z. In the region $t/t_m \approx 1.0$ the function varies weakly; at $t/t_m \geq 1.5$ the concentration $n_2(t/t_m)$ falls off linearly at an essentially constant rate.

Equations (1), (2), and (4) are valid if the concentration is measured over a surface region whose dimension along the OX axis is infinitesimally small. However, they are also valid for a finite part of the substrate surface, from $x - a$ to $x + a (x > x_0)$, to which the film atoms diffuse as a result of surface diffusion, provided that the

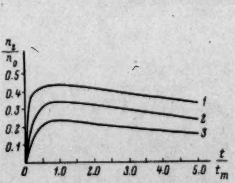

Fig. 1. Concentration at various times. z: 1) 1.1; 2) 1.4; 3) 2.

inequality

$$a \ll x - x_0. \tag{5}$$

is satisfied.

We now compare Eq. (2) with the experimental results, e.g., those of ref. 5. It follows from the data of refs. 5 and 7 that under these experimental conditions $x_0 = 2.5$ mm, $x = 3.5$ mm, $z = 1.4$, and $a \ll x - x_0$. With $D = 2.2 \cdot 10^{-6}$ cm/sec the experimental and theoretical functions $n_2(t)$ agree and the surface diffusion coefficient which we find by superimposing the experimental and theoretical curves corresponds to the surface diffusion coefficient given in ref. 5. Figure 2 shows the results calculated from Eq. (2) with the value found for D; also shown, with the same scale, are the experimental points from ref. 5. Comparison of these data reveals that the theoretical and experimental points agree within 15% over the entire range of t.

If, on the other hand, the substrate region within which the concentration $n_2(t)$ is determined has a finite width $2a$, so that inequality (5) does not hold, we must calculate the surface diffusion coefficient from

$$N_2 = \frac{n_0}{2}\left\{\int_{x-a}^{x+a}\left[\Phi\left(\frac{\xi + x_0}{\sqrt{2Dt}}\right) - \Phi\left(\frac{\xi - x_0}{\sqrt{2Dt}}\right)\right]d\xi\right\}, \tag{6}$$

where N_2 is the total number of film atoms which have diffused to the surface region between $x-a$ and $x+a$ by time t, and t, $\Phi(x)$ is the probability integral.

Evaluation of integral (6) through the use of

$$\Phi(z\sqrt{2}) = 1 - \operatorname{erf} cz, \quad \int_z^\infty \operatorname{erf} cy\,dy = \frac{1}{\sqrt{\pi}}e^{-z^2} - z \operatorname{erf} cz,$$

where

$$\operatorname{erf} cz = \frac{2}{\sqrt{\pi}}\int_z^\infty e^{-x^2}dx,$$

leads to

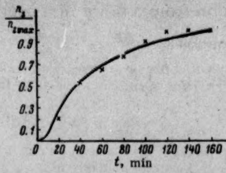

Fig. 2. Comparison of experimental and theoretical data. Solid curve) theoretical, according to Eq. (2) of the present work; points) experimental data of ref. 4.

$$\begin{aligned}\frac{N_2}{n_0} = \sqrt{\frac{Dt}{\pi}}\Bigg(&e^{-\frac{(x+a+x_0)^2}{4Dt}} - e^{-\frac{(x-a-x_0)^2}{4Dt}} + e^{-\frac{(x+a-x_0)^2}{4Dt}} - e^{-\frac{(x+a-x_0)^2}{4Dt}}\Bigg)\\ &+ \frac{1}{2}\Bigg[(x+a+x_0)\,\Phi\left(\frac{x+a+x_0}{\sqrt{2Dt}}\right)\\ &- (x-a+x_0)\,\Phi\left(\frac{x-a+x_0}{\sqrt{2Dt}}\right) + (x-a-x_0)\,\Phi\left(\frac{x-a-x_0}{\sqrt{2Dt}}\right)\\ &- (x+a-x_0)\,\Phi\left(\frac{x+a-x_0}{\sqrt{2Dt}}\right)\Bigg]\cdots\end{aligned} \tag{7}$$

Calculations show that when the values from ref. 5 ($x = 3.5$ mm, $x_0 = 2.5$ mm, $a = 0.2$ mm, and $D = 2.2 \cdot 10^{-6}$ cm^2/sec) are substituted into Eq. (7), the results agree with the results calculated from Eq. (2) within 1.0%.

We have thus shown that Eqs. (1) and (2) give an accurate description of the change in the concentration of film atoms due to surface diffusion. If the observation time is long the $n_2 = n_2(t)$ curve should display a maximum; in this case the surface diffusion coefficient can be determined from Eq. (3).

---

[1] V. V. Novikov, Basic Theory of Microelectronics [in Russian], Izd. Vysshaya Shkola, Moscow (1972).

[2] N. T. Gladkikh and V. I. Khotevich, in: First All-Union Symposium on Disperse Metal Films [in Russian], Kiev (1972), p. 5.

[3] G. S. Zhdanov and V. N. Vertsner, in: First All-Union Symposium on Disperse Metal Films [in Russian], Kiev (1972), p. 72.

[4] M. Drechsler, Zs. Elektrochem., 58, 340 (1954).

[5] A. D. Abramenkov, V. V. Slezov, L. V. Tanatarov, and Ya. M. Fogel', Fiz. Tverd. Tela, 12, 2928 (1970) [Sov. Phys. – Solid State, 12, 2365 (1971)].

[6] B. I. Boltaks, Diffusion in Semiconductors [in Russian], Moscow (1961).

[7] A. D. Abramenkov, V. M. Azhazha, Ya. M. Fogel' and V. I. Shvachko, Fiz. Met. Metalloved, 29, 519 (1970).

Ion focusing of an electron beam in deep melting of a metal

M. D. Gabovich, V. P. Kovalenko, O. A. Metallov,

O. K. Nazarenko, and S. K. Pats'ora

E. O. Paton Institute of Electric Welding,
Academy of Sciences of the Ukrainian SSR, Kiev

(Submitted December 24, 1973)
Zh. Tekh. Fiz., 44, 1556-1557 (July 1974)

Experiments with a model show that, the high-density electron beam in a welding channel cannot be attributed to ion focusing; this result is in disagreement with several explanations.

In several analyses[1-3] of the welding channel formed by an electron beam in a situation characterized by a dagger-shaped melting zone, it has been suggested that the electron beam experiences an additional compression due to ion focusing. In particular, it has been asserted[2] that the ion focusing reduces the beam diameter by an order of magnitude or more.

An attempt has been made to support this assumption by using the familiar theory of Davydov and Braginskii[4] and experimental data indicating the existence of a dense plasma in the welding channel.[3] However, this latter circumstance in fact renders the results of ref. 4 invalid for the case of electron-beam welding.

Estimates show that pronounced compression of an electron beam over some length L requires a field $E \approx 2dU_0/L^2$, where d is the initial beam diameter and U_0 is the accelerating voltage. With d = 0.1 cm, L = 1 cm, and $u_0 = 20$ keV, the field E should be $\approx 4 \cdot 10^3$ V/cm. Strong static fields of this magnitude would not be expected in the plasma formed by an electron welding beam. On the contrary, the experiments of ref. 3 indicate that these fields are weak.

Accordingly, the assumption that the beam compression in the welding channel results from ion focusing is open to question and would benefit from an experimental test.

We have therefore carried out an experimental study with a model in which the conditions correspond to those for an electron beam in a welding channel (Fig. 1). The electron beam 6 moving in a high vacuum is aligned along channel 7, drilled in a massive copper block 8. Channel 7 consists of two parts: a broad part (~ 1 mm in diameter, 2 cm long) and a narrow part (~ 0.3 mm in diameter and 1.2 cm long). Before the beam enters the channel its diameter is much larger than that of the narrow part of the channel; thus, in the absence of compression only a negligible part of the beam can reach collector 9. The air pressure in the channel can be adjusted over a broad range. The beam is deflected at a frequency of 50 Hz in order to prevent the channel walls from metlting in experiments in which the beam density is high. The beam passes through the channel in pulses much longer than the characteristic time for the plasma formation.

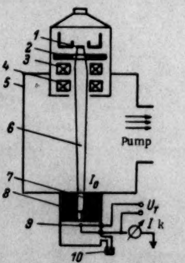

Fig. 1. The model apparatus. 1) Gun cathode; 2) anode; 3) focusing system; 4) deflecting system; 5) vacuum chamber; 6) electron welding beam; 7) channel; 8) water-cooled target; 9) collector-thermocouple; 10) gas heater.

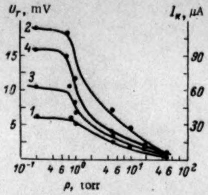

Fig. 2. Thermocouple emf and collector current as functions of the channel pressure. 1, 2) 20 keV, 70 mA; 3, 4) 10 keV, 3 mA. 1, 3) I_k; 2, 4) U_T.

Most of the measurements involved the determination of the electron-beam current to grounded collector 9 as a function of the channel pressure. If the beam were compressed at some pressure, there would be a corresponding increase in the collector current. To get more reliable measurement of the electron current reaching the collector we use a thermocouple to measure the relative power generated at the collector in addition to measuring the current in the collector circuit.

Figure 2 shows the results. If we assume that heat exchange between the collector and the chamber walls is not strongly influenced by the pressure under these experimental conditions (we check this point experimentally) we conclude that the current of the electron reaching the collector falls off monotonically with increasing pressure. No significant beam compression occurs. The current decrease can be explained on the basis of the scattering of the beam in the vapor–gas channel.

That this model is adequate for determining the role of ion focusing under the conditions actually prevailing in electron-beam melting is clear from the following considerations: The vapor pressure in the welding channel is known to reach 10^2-10^3 torr at a temperature of several thousand degrees.[1-5] The atomic density under these conditions should be roughly the same as in our experiments, in which the pressure and temperature are an order of magnitude lower. The lower gas temperature in the phototype apparatus and the relatively low beam velocity (in comparison with that under conditions of deeper melting) could only intensify the compression of the electron beam if ion focusing actually occurred under these conditions.

Accordingly, this direct experimental check with a model and the discussion show that ion focusing is not important for electron-beam welding.

---

[1] H. Schwartz, in: Electron and Ion Beam Science and Technology, ed. by R. Bakish, Wiley, New York (1965).
[2] V. P. Ledovskoi and G. M. Mladenov, Zh. Tekh. Fiz., 40, 260 (1970).
[3] V. P. Ledovskoi and G. M. Mladenov, Izv. LETI, 126, 96 (1972).
[4] B. I. Davydov and S. I. Braginskii, in: Collection Dedicated to the 70th Birthday of Academician A. F. Ioffe [in Russian], Izd. Akad. Nauk SSSR, Moscow (1950), p. 72.
[5] K. S. Akop'yants, Yu. V. Zubchenko, V. E. Lokshin, and O. K. Nazarenko, Avtomaticheskaya Svarka, 11, 11 (1972).

N_2O-N_2 –He gasdynamic laser

Yu. I. Grin' and V. G. Testov
Institute of Radio Engineering and Electronics,
Academy of Sciences of the USSR, Moscow

(Submitted December 25, 1973)
Zh. Tekh. Fiz., 44, 1557-1558 (July 1974)

Lasing is observed in a shock-heated mixture of N_2O, N_2, and He issuing through a nozzle into vacuum. The optimum composition of the mixture is 10% N_2O, 20% N_2, and 70% He.

The onset of population inversion has been observed experimentally[1] in a ternary gas mixture of nitrous oxide, nitrogen, and helium preheated by a shock wave and subjected to adiabatic expansion through a wedge-shaped nozzle. Inversion takes place between the 00^01 and 10^00 levels of the N_2O molecule.

We have determined the optimum partial composition of the mixture for maximum amplification and observed lasing by placing mirrors that form an optical cavity at the nozzle exit.

The amplification of a weak signal is measured by means of the arrangement described in ref. 1. The results of the experiments show that the maximum inversion is realized in a mixture with the following composition: 10% N_2O, 20% N_2, and 70% He, at an incident-wave Mach number M = 2.8 (stagnation parameters: $T_0 \sim 1680°K$; $p_0 \sim 8$ atm). As Fig. 1 indicates, the gain for the given mixture is twice the value for a maixture[1] of 20% N_2O, 10% N_2, and 70% He. The position of the optical cavity is determined by measuring the gain along the flow; these measurements show that the gain decreases monotonically as the distance from the nozzle orifice is increased.

The cavity is placed at a distance of 15 mm from the nozzle orifice. The cavity consists of two mirrors with a diameter of 45 mm: one plane mirror 3 with an aperture diameter of 1 mm in the center (Fig. 2) and one concave mirror 2 with a radius of curvature of 990 mm. The reflecting surfaces of the mirrors are coated with an aluminum layer. The spacing of the mirrors is 27.1 cm. The cavity is located inside a supersonic chamber, from which the radiation is emitted through a KCl window 4.

Lasing is observed both independently of and simultaneously with the amplification measurement, making it possible to determine the temporal correlation between the amplification and lasing curves (Fig. 3). The arrangement for simultaneous measurement of amplification and lasing in a supersonic chamber equipped with four windows spaced at 90° angles is shown in Fig. 2.

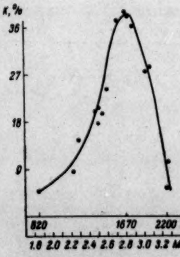

Fig. 1

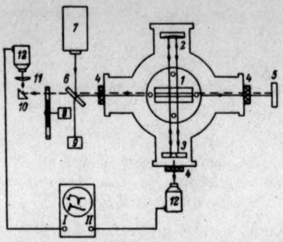

Fig. 2. Experimental arrangement. 1) Nozzle; 2) concave mirror; 3) plane mirror; 4) KCl mirror; 5) rotatable plane mirror; 6) opaque silicon mirror; 7) N_2O laser; 8) shutter; 9) thermocouple; 10) rotatable mirror; 11) lens; 12) detector (Ge–Au).

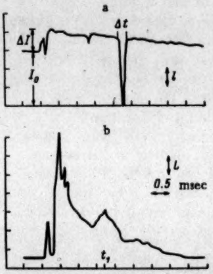

Fig. 3. Amplification (2) and lasing (b) oscillograms. I_0 and Δt are the amplitude and width of the calibration pulse.

Typical oscillograms of amplification and lasing signals are given in Fig. 3. The amplitude scale of the lasing and amplification signals is $L/l = 50$. It is seen that temporal correlation exists between the amplification and lasing signals. The lasing pulse is somewhat shorter than the amplification pulse. This is caused by the fact that the cavity losses at that time exceed the gain. the fact that the secondary maximum in the lasing pulse (time t_1) is possibly due to the dissociation process $N_2O \rightarrow N_2 + O$ and the resulting formation of vibrationally excited N_2 molecules, which transfer their energy to the N_2O molecules.[2,3]

---

[1] Yu. I. Grin', V. M. Polyakov, and V. G. Testov, ZhETF Pis. Red., 18, 260 (1973) [JETP Lett., 18, 155 (1973)].

[2] I. S. Zaslonko, S. M. Kogarko, E. V. Mozzhukhin, and A. I. Demin, Dokl. Akad. Nauk SSSR, 202, 1121 (1972).

[3] A. I. Demin, E. M. Kudryavtsev, Yu. A. Kulagin, and N. N. Sobolev, ZhETF Pis. Red., 18, 249 (1973) [JETP Lett., 18, 149 (1973)].

Scattering of He^+ ions by the core of the He atom

Z. Z. Latypov and A. A. Shaporenko

A. F. Ioffe Physicotechnical Institute,
Academy of Sciences of the USSR, Leningrad

(Submitted January 8, 1974)
Zh. Tekh. Fiz., 44, 1559-1560 (July 1974)

The total cross sections for the following resonant processes involving electron capture and transfer of excitation energy are discussed as function of the collision energy: $He^+ + He \rightarrow He + He^+$, $He^*(2^1S) + He \rightarrow He + He^*(2^1S)$, and $He^*(2^3S) + He \rightarrow He + He^*(2^3S)$. The similar structures of these cross sections are explained on the basis of the scattering of the projectile particles by the core of the target atom.

We previously[1] detected a slight oscillation in the effective cross section for the resonant charge exchange

$$He^+ + He \rightarrow He + He^+ \tag{1}$$

over the collision-energy range 200-3200 eV. We attributed this structure to scattering of incident ions by the core of the target atom, predicted by theory.

According to the theory of ref. 2, the cross section for resonant electron transfer is

$$\sigma = 2\pi \int_0^\infty b \sin^2(\eta_g - \eta_u)\, db, \tag{2}$$

where b is the impact parameter and $\eta_g - \eta_u$ is the difference between the phase changes of the odd and even states. The functional dependence $\sigma(v)$ of cross section (2) on the collision velocity v is oscillatory if $\eta_g - \eta_u$ is independent of b. Two situations could be responsible for such a stationarity of the difference between the phase changes: a) the existence of an extremum in the difference $V_g - V_u$ between the levels of the even and odd states of the quasimolecule; b) scattering of the projectile by the core of the target ions. In this latter effect, the position of the classical turning point varies slowly as a function of the impact parameter when this parameter is small, giving rise to a weak functional dependence $\eta_g - \eta_u$ on b.

The He_2^+ quasimolecule has a series of pseudointersections between the ground-state $^2\Sigma g$ level, which dissociates into $He^+ + He(1s^2)$, and the excited-state $^2\Sigma g$ levels, which dissociate into $He^+ + He(1s, nl)$. Calculations[3] give R = 1.4 atomic units for the position of the lowest-lying pseudointersection, in agreement with the data from other sources. Accordingly, the difference $V_g - V_u$ for the He_2^+ ground states has an extremum if the even level of the ground state is adiabatic. Here the position of the extremum is given by R = 1.4 atomic units. However, it follows from ref. 3 that the parameters of the pseudointeractions of the $^2\Sigma_g$ levels are such that the He_2^+ system follows adiabatic levels at sufficiently high collision energies.

Using the method of ref. 4 to determine the difference $V_g - V_u$ from the experimental cross sections for resonant charge exchange, we analyzed the cross section for process (1). We assumed that the structure which we observed in this cross section is a regular oscillation. The results of this analysis show that the observed structure of cross section (1) could be due to a maximum in the difference $V_g - V_u$ at 1.5 eV with an internuclear distance of R = 5.8 atomic units. However, there is no such extremum in the difference between the levels of the He_2^+ ground states, so that this first possible explanation for the oscillation in the cross section must be discarded.

Hollstein et al.[5] have carried out an experimental study of the cross section for the resonant transfer of excitation energy in the collision of metastable He atoms with normal atoms,

$$He^*(2^1S) + He \rightarrow He + He^*(2^1S), \tag{3}$$
$$He^*(2^3S) + He \rightarrow He + He^*(2^3S) \tag{4}$$

over the energy range 150-2200 eV. They suggest that the structure which they have observed in the cross sections for processes (3) and (4) is probably due to an extremum in the difference $V_g - V_u$. Evans and Lane[6] have calculated the cross section for process (3) over the energy range $2 \cdot 10^{-2}$-10^3 eV in two manners: a) in the approximation of perturbed stationary states, making use of the most accurate adiabatic levels $^3\Sigma_u^+$ and $^3\Sigma_g^+$, which are given in the literature for He_2 for R > 1.3 atomic units; b) through the use of the adiabatic collisional $^3\Sigma_g^+$ level, constructed in the appropriate manner. The calculated cross sections are approximately equal to the experimental cross sections in magnitude, but the structures are markedly different. It follows that either the structures of experimental cross sections (3) are independent of the level difference $V_g - V_u$ at R > 1.3 atomic units, or the levels used in the calculations in ref. 6 are not sufficiently accurate.

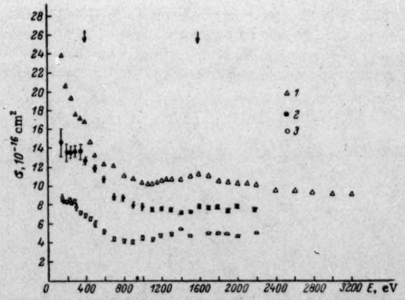

Fig. 1. Effective cross sections as functions of the collision energy. 1) Cross section for process (1) from ref. 1; 2) cross section for process (3) from ref. 5; 3) cross section for process (4) from ref. 5. The arrows show the maxima in the oscillatory components of the cross section for process (1).

Figure 1 shows the cross sections for process (1) according to ref. 1 and the cross sections for processes (3) and (4) according to ref. 5. The similarity observed among the cross-section structes for the three different processes implies a common origin of these structures. We believe that the structures observed in the cross sections for processes (1), (3), and (4) are due to scattering of the projectile particles by the cores of the target atoms, since it seems reasonable to assume a similarity between the scattering of He$^+$ ions and excited He* atoms by He atoms at small impact parameters. It follows from the amplitudes of the oscillation in the cross section for process (1) that, at the collision energies studied, the range in which the phase difference is stationary is governed by the values of the impact parameter: $0 < b \leqslant 1$ atomic unit. Accordingly, the levels of the He$^+$–He, He* (2^{1}S)–He, and He* (2^{3}S) systems must be similar for internuclear distances $R \leqslant 1$ atomic unit.

The authors thank V. V. Afrosimov and V. K. Nikulin for useful discussion.

---

[1] Z. Z. Latypov, N. V. Fedorenko, I. P. Flaks, and A. A. Shaporenko, ZhETF Pis. Red., 11, 189 (1970) [JETP Lett., 11, 116 (1970)].

[2] F. J. Smith, Phys. Lett., 20, 271 (1966); Planet. Space Sci., 11, 1126 (1963); VI ICPEAC, Leningrad (1967), p. 177; VI ICPEAC, Cambridge (1969).

[3] J. N. Bardsley, Phys. Rev., A3, 1317 (1971).

[4] R. E. Olson, Phys. Rev., 187, 153 (1969).

[5] M. Hollstein, J. Sheridan, J. Peterson, and D. Lorents, Phys. Rev., 187, 118 (1969).

[6] S. Evans and N. Lane, Phys. Rev., 188, 268 (1969).

Energy spectra of scattered particles in proton bombardment of a metal target

G. I. Zhabrev, V.A. Kurnaev, and V. G. Tel'kovskii

Moscow Engineering Physics Institute

(Submitted May 7, 1973; resubmitted January 2, 1974)
Zh. Tekh. Fiz., 44, 1560-1562 (July, 1974)

By measuring the fraction of neutrals in the scattered beam and the energy spectra of the ion components, the energy distributions of the total flux of reflected atomic particles can be obtained without dependence on charge. Spectra are found for bombardment of a Ni target at a glancing angle $\alpha = 15°$ by 20 keV protons. At a small scattering angle (20°) the spectral shape is in qualitative agreement with that calculated from multiple-scattering theory. At larger angles (55°) the spectral shape is characteristic of the single-scattering model.

In experiments on the reflection of medium energy light ions from a solid surface the charged components of the scattered beam have received the most attention. However, most of the particles leave the target surface as neutrals.[1] Various models of the scattering of light ions from a continuous medium[2,3] do not take account of electron exchange, which is responsible for the charge distribution of the reflected particles. Therefore, to make comparisons with experiment these theories require data on the total flux of the various charged components of the scattered beam.

For fixed angles of incidence and detection the energy distribution of the total flux of reflected particles $J^\Sigma(E)$ can be found from the spectrum of the i-th ion component $J^i(E)$ if $W^i(E)$ the probability of scattering of a particle of charge i from the target is known over the whole energy range of the spectrum for these angles. In this case

$$J^\Sigma(E) = \frac{J^i(E)}{W^i(E)}, \quad \sum_i W^i(E) = 1. \tag{1}$$

The fraction of neutrals in the scattered beam B_K can be determined by subtracting the charged components from the total flux. By using an integrating detector with counting efficiency K(E) independent of the charge of the particles the values obtained for various initial energies can be related to the probability $W^i(E)$ by the expression

$$B_K = 1 - \frac{\sum\limits_{i \neq 0} \int\limits_0^{E_K} J^i(E)\,K(E)\,dE}{\int\limits_0^{E_K} \frac{J^i(E)\,K(E)\,dE}{W^i(E)}}, \tag{2}$$

where E_K is the energy of the bombarding ions.

By measuring B_K and the energy spectra $J^i(E)$ for a sufficiently broad range of values of E_K and knowing K(E), $W^i(E)$ can be found by assuming that it is a smooth function. To do this we use successive approximations to find a $W^i(E)$ which satisfies Eq. (2) within the limits of accuracy of the experiment. Knowing $J^i(E)$ and $W^i(E)$ we use Eq. (1) to find the energy distribution of the total flux of reflected ions and atoms.

The method described has been used to study the small-angle scattering of hydrogen ions from a nickel target.[1] The energy spectra of the protons and negative hydrogen ions are determined by an electrostatic analyzer. A secondary emission detector with its entrance window covered with thin foil is used to determine the approximate fraction of neutrals in the scattered beam. The neutral and charged components of the beam are thus measured with the same efficiency. The instrument and the experimental procedure are described in detail in ref. 1, where data on the charge composition of the scattered beam are given.

Figure 1 shows the normalized proton energy spectra and the total flux of particles scattered at various angles φ relative to the initial direction of the beam. The spectra are obtained by bombarding a nickel target with 20 keV protons at a glancing angle $\alpha = 15°$. The figure also shows $W^{i=+1}$ found by the method described above for a scattering angle $\varphi = 20°$. The accuracy in finding $W^+(E)$ does not exceed 10% in the energy range from 5 to 30 keV. To this accuracy $W^+(E)$ for other values of φ does not differ from the curve given for $E/E_0 > 0.3$.

Figure 2 compares our spectra of $J^\Sigma(E)$ with those calculated by the single-scattering model, generalized to the case of oblique incidence of the particles on the target,[2] and by a theory[3] which treats the motion of particles in the medium by using the diffusion approximation in

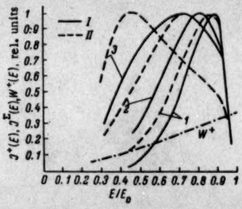

Fig. 1. Energy spectra of H^+ ions $J^+(E)$ and the total flux of particles $J^\Sigma(E)$ scattered at various angles in the proton bombardment of a nickel target at a glancing angle $\alpha = 15°$. W^+ is the probability of scattering particles in the form of protons. I) $J^+(E)$; II) $J^\Sigma(E)$; φ, deg: I) 20; II) 30; III) 55.

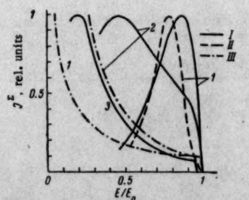

Fig. 2. Energy spectra of the total flux of scattered particles. I) experiment; II) multiple-scattering theory;[3] III) single-scattering theory;[2] α and φ in deg are respectively: 1) 15, 20; 2) 15, 55; 3) 45, 135 from data in ref. 5 for the bombardment of a nickel target by deuterons.

velocity space. In both cases a Coulomb interaction potential is assumed. Data on the slowing down power of Ni for protons obtained earlier in experiments with foils[4] are used in the calculations. For comparison the figure also shows a similar spectrum corresponding to the results of ref. 5 on the back scattering of deuterons.

While the single-scattering theory leads to an energy spectrum whose shape differs sharply from experiment at small angles, the spectrum corresponds more and more closely to this model at larger angles. For glancing angles, the shape of the distribution is adequately described by diffusion theory for the motion of the particles.[3] This confirms that multiple collisions have a definite effect in forming the beam scattered at small angles.

In conclusion the authors thank O. B. Firsov and V. M. Smirnov for helpful discussion.

---

[1] G. I. Zhabrev, V. A. Kurnaev, and V. G. Tel'kovskii, Proceedings of the Second All-Union Symposium on the Interaction of Atomic Particles with a Solid [in Russian], Moscow (1972), p. 112.

[2] T. Ishitani and R. Shimizu, Japan. J. Appl. Phys., 10, 821 (1971).

[3] O. B. Firsov, Zh. Eksp. Teor. Fiz., 61, 1452 (1971) [Sov. Phys. – JETP, 34, 773 (1972)].

[4] V. A. Kurnaev, A. S. Savelov, V. M. Sotnikov, and V. G. Tel'kovskii, in: Plasma Physics [in Russian], Vol. 2, Atomizdat, Moscow (1969), p. 65.

[5] G. M. McCracken and N. J. Freeman, J. Phys. B: Atom. Molec. Phys., 2, 661 (1969).

Mode coupling in a double-anode discharge

Yu. G. Zakharenko and V. E. Privalov

D. I. Mendeleev All-Union Scientific-Research Institute of Metrology; Leningrad

(Submitted August 13, 1973; resubmitted October 25, 1973)
Zh. Tekh. Fiz., 44, 1562-1565 (July 1974)

Mode coupling is studied in a discharge with a common cathode and two anodes. The interaction of the fields generated by the striations in the two positive columns is investigated in detail. Within the locking range the system has features characteristic of any coupled oscillators. Field cancellation is observed. Striations appear in the cathode region as a result of interaction of the striations in the positive column.

Mode coupling in a glow discharge can lead to frequency pulling and locking and mode suppression.[1,2] It is of interest to investigate the interaction between modes in a coupled discharge establishing the possibility of controlling the mode parameters. We have investigated a discharge with a common cathode and two anodes. The discharge is produced in a T-shaped tube comprising a capillary (diameter 2.5 mm, length 200 mm) terminating at each end in a ring anode and a branch tube (diameter 6 mm, length 60 mm) perpendicular to the capillary, with an indirectly heated oxide cathode. To increase the reliability the measurements are performed on a series of such tubes with approximately the same parameters. The discharges are produced in inert gases and mixtures at pressures 1.5-2 torr and currents in the range 0.5-60 mA. The experimental method is described in detail in a previous paper.[3]

1. The results of measurements obtained with a discharge in one arm of the tube (voltage applied only to one anode) are similar to those observed previously.[1-3] Feedback oscillations at optimum ballast resistance (160 kΩ) disappear at currents above 1.3-1.5 mA. (Numerical values relate to a He — He mixture at a pressure 1.6 torr, ratio He : Ne = 7 : 1.) The frequency of the feedback mode in the initial stage[4] is 300 kHz. The depth of modulation of the discharge current increases with decreasing discharge current, and can reach 10% at appearance of the second harmonic. Striations appear in the positive column at currents 12-14 mA. The frequency generated by the traveling striations falls from 700 to 400 kHz when the discharge current is increased from 12 to 44 mA. The depth of modulation of the discharge current is about 1% and the amplitude of the striations increases with increasing discharge current (in the stated range). The striations are about 9 mm long and become several times more intense the closer they move to the anode. With increasing temperature, especially as the tube is warming up, the frequency at which the current is modulated by the striations increases and the region of existence of the striations is shifted towards higher currents.[5] Cathode oscillations appear when the discharge current is equal to the cathode current, but these are easily suppressed by controlling the cathode heating. No other modes are detected in this tube in operation with a single anode.

2. With discharges simultaneously in both arms of the tube, the current range corresponding to quenched contacts and the modes of the same type in the two discharges interact, with an effect on amplitudes, frequencies and phases. Feedback oscillations affect up to 1.8 mA; increasing the current in one of the arms by an order of magnitude or more does not affect the current at which these oscillations are suppressed; the frequency of the oscillations first increases slightly and then remains unchanged with increasing current. When the currents in both arms are equal the amplitude of the feedback oscillations is smallest. The initial-stage region of feedback oscillations in this tube is small, and the appearance of higher harmonics makes it difficult to investigate the interaction between these oscillations. The striations in the positive column interact over the entire range of currents. Measurements are simultaneously made with two shielded photomultipliers movable along the discharge and with antennas.[1-3] A signal is taken from a resistor connected to the cathode of the discharge tube and led to an SCh-8 spectrum analyzer and an S1-19 oscilloscope. Signals are also taken from both anodes through capacitors and fed to the inputs of an S1-18 dual-beam oscilloscope.

These results can be generalized in the following manner. It is known that traveling striations generate an electromagnetic field and modulate the discharge current. The striations can interact with the field that they themselves produce. The closer the currents in two arms, the more nearly identical become the parameters of the striations in both discharges. This results in a mutual pulling of the

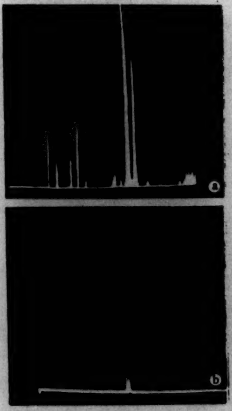

Fig. 1. Spectrum of interacting striations in a tube with two anodes. a) Interaction of striations outside pull-in zone; the two large-amplitude signals (on the right) correspond to striations in separate capillaries, signals of small amplitude are combination frequencies. b) Locking mode; oscillations of discharge current in separate capillaries in antiphase, 100-fold reduction of resultant field.

frequencies and locking (entrainment). When the radiation frequencies are not the same, combination frequencies are observed (Fig. 1a) and the amplitudes vary with varying frequency. In frequency locking the most stable state is one in which the currents in both arms are modulated in antiphase. In this case the amplitude of the restultant field falls sharply by two orders of magnitude compared with the field generated by the striations in a single discharge (Fig. 1b). It is found that the mode amplitudes are not governed by the expression

$$|\mathbf{A}_1+\mathbf{A}_2|=\sqrt{A_1^2+A_2^2+2A_1A_2\cos\varphi} \tag{1}$$

[A_i (i = 1, 2) denote the amplitudes, φ is the phase difference]. Varying the phase by means of the current causes the system to operate in the unstable region adjacent to the locking regime.[6]

In electronic oscillators[6,7] and ring lasers[8,9] the frequencies and amplitudes in the locking zone are described by the following expressions:

$$(\nu^2-\nu_1^2)(\nu_2^2-\nu^2)=\alpha\nu^4\sin\varphi, \tag{2}$$

$$A_1^2-A_2^2=B(\nu_2-\nu_1)+C, \tag{3}$$

where ν_i (i = 1, 2) are the frequencies of the oscillators, ν is the locking frequency, and α, B, and C are parameters.

Regarding our two discharges with traveling striations as two coupled oscillators, we find that their behavior is satisfactorily described by Eqs. (1) and (2). Figure 2 shows the results. The situation is similar to the case in which the difference between the intensities of the oppositely directed waves in a ring laser within the pull-in zone varies linearly with the current through the solenoid of the nonreciprocal element.[10]

As far as we are aware[6-9] locking occurs in the range of phase differences: $\pi/2 \le \varphi \le \pi/2$; the $\varphi = 0$ mode is stable. In the case of the interaction of the fields generated by traveling striations, the phase difference $\varphi = \pi$ is stable, as already mentioned. Symmetry about the stable value of φ is lost. For example, with 15 mA in each arm of the discharge, locking is observed in the phase interval $-0.3\pi \le \varphi \le 0.7\pi$. With increasing current the range of variation of phase within the pull-in zone is reduced. The amplitudes of the striations themselves vary much less when the fields interact in the pull-in zone. As a rule, minimum amplitude of the resultant field corresponds to maximum amplitude of the striations. With striations in a discharge in one arm, striking a discharge in the other arm produces striations at a current below the threshold value required for one arm alone. These striations are induced by the first striations, are phase-shifted relative to the first, are several times smaller in amplitude, and do not exhibit any signs of interaction.

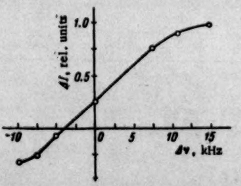

Fig. 2. Variation of intensity difference between fields generated by striations vs detuning ($\nu_1-\nu_2$) within limits of locking zone. Frequency is varied by varying the discharge current, ν_1 and ν_2 denote the frequencies of the radiation of the striations in each discharge separately.

We are unable to say very much concerning how the striations interact. The following can be said concerning the interaction of the fields generated by the traveling striations. Combination frequencies exist, the interaction becomes stronger the more the frequencies approach, and frequency pulling is observed. In the pull-in zone the interaction is determined by the relationships of the amplitudes and phases characteristic for locking. A stable reduction of the resultant amplitude in accordance with (1) is observed for $\varphi = \pi$. Clearly, the incomplete compensation of the fields is determined by the extent to which they are coherent, by the phase relationships, and by the amplitude difference (it should be remembered that the wavelength of this radiation is of the order of hundreds of meters).

Striations (of length 16 mm) appear in the cathode tube only with simultaneous discharges in both arms. This corresponds to a total current in the cathode tube of 30 mA and higher. The frequency is 150-180 kHz; the depth of modulation of the discharge current if 5-10%. The amplitude of the striations in the positive column decreases sharply. The striations in the cathode branch tube can be quenched by varying the heater current and applying a local magnetic field in the cathode region. We propose the following mechanism for the striations. The interaction of the striations in the positive column increases the instability of the discharge and oscillations of the head of the positive column result,[11] which stimulate striations in the branch tube. We note that striations do not appear in the branch tube at a definite total current, but for a definite combination of currents in the arms.

The present work leads to the following conclusions.

1. Modes of the same type interact in a discharge with two anodes (striations interact with striations, feedback oscillations with oscillations).

2. The interaction of the fields generated by the striations in the positive column in the locking zone can lead to the mutual compensation of the fields; it is difficult for the fields to add due to the character of the phase relationships in the locking zone; combination frequencies fixed in the discharge current and in the surrounding space are observed outside the limits of the locking zone.

3. The interaction of the striations in the positive column helps to suppress the striations in the cathode branch tube.

We thank A. A. Zaitsev, L. A. Sen, and L. D. Tsendin for useful discussion.

---

[1] V. E. Privalov, Zh. Tekh. Fiz., 41, 1682 (1971) [Sov. Phys. – Tech. Phys., 16, 1324 (1972)].

[2] Yu. G. Zakharenko and V. E. Privalov, Opt. Spektrosk., 35, No. 4 (1973).

[3] Yu. G. Zakharenko and V. E. Privalov, Zh. Tekh. Fiz., 41, 553 (1971) [Sov. Phys. – Tech. Phys., 16, 429 (1971)].

[4] Yu. G. Zakharenko and V. E. Privaloz, Zh. Tekh. Fiz., 42, 1899 (1972)

[Sov. Phys. – Tech. Phys., 17, 1522 (1972)].

[5] D. V. Gordeev, A. A. Zaitsev, V. F. Makhrov, I. A. Savchenko, and B. N. Shvilkin, Proc. Conf. on Electronic Technology [in Russian], 2(18), 32, Moscow (1970).

[6] K. F. Teodorchik, Self-Oscillating Systems [in Russian], Gostekhizdat, Moscow–Leningrad (1948).

[7] I. S. Gonorovskii, Radio Engineering Circuits and Signals [in Russian], Izd. Sovetskoe Radio, Moscow (1963).

[8] G. S. Kruglik, The Theory of Beats in Ring Lasers [in Russian], Inst. Phys., Academy of Sciences of the Belorussian SSR, Minsk (1967).

[9] N. N. Rozanov, G. V. Vinokurov, and O. B. Danilov, Opt. Spektrosk., 23, 624 (1967).

[10] B. A. Blazhnov and G. S. Kruglik, Zh. Prikl. Spektrosk., 13, 996 (1970).

[11] A. A. Zaitsev, Dokl. Akad. Nauk SSSR, 79, 779 (1951).

Theoretical and mathematical physics

Fundamentals of heat-pipe theory and design

M. M. Levitan and T. L. Perel'man
Institute of Heat and Mass Transfer,
Academy of Sciences of the Belorussian SSR, Minsk

(Submitted July 18, 1973; resubmitted November 15, 1973)
Zh. Tekh. Fiz., 44, 1569-1591 (August 1974)

The problem of heat-pipe design is treated rigorously. Heat and mass transfer in the jacket and cavity of a heat pipe are considered. Coupling conditions at the internal surface of the jacket are analyzed in detail. As applied to high-temperature heat pipes in which alkali metals are used as the heat-transfer agent the problem is formulated with the inclusion of chemical transformations of the vapors of those transfer agents. For proper heat-pipe optimization operating conditions are set up which include the reaction of the fluxes of vaporizing and condensing materials at the phase-transition surface.

Many problems of heat transfer which arise in modern technological fields such as atomic power, space technology, etc., cannot be solved without using design principles based on new, high-efficiency structural elements for power systems. One such element is the heat pipe – a device for the transfer of large amounts of thermal energy with minimal temperature drop.[1] Devised in 1963[1)] in connection with certain problems in space power, heat pipes have since attracted the attention of many designers in heat transfer because of their unique properties. For example, a heat pipe can transfer a very large amount of thermal energy with an insignificant drop in temperature over its length, it can bring about the conversion of thermal fluxes, it can create isothermal conditions over relatively large areas, and it can operate under conditions of weightlessness; per unit weight a heat pipe has a thermal conductivity several times greater than any solid heat conductor; depending on the heat-transfer agent, a heat pipe can operate from cryogenic temperatures to 2000°C These properties, in combination with structural simplicity, insignificant weight, absence of moving parts, and total self-regulation, ensure diverse application of heat pipes in atomic power, space technology, experimental technology, etc.

Past experimental and theoretical studies of heat pipes have been directed chiefly toward optimal designs for heat pipes and an explanation of their basic characteristics; successful application of heat pipes is impossible without information about the maximum value of thermal power at the ends of the pipe which is transportable along the pipe, about the temperature drop, and about operating resources.

The problem of heat-pipe theory and design is presently the subject of a considerable number of publications. In the main, however, these papers are qualitative in nature. This fact is evident from the limited assumptions that are used and the resulting incomplete formulation of the problem. Suffice it to say that thus far all results of heat-pipe calculations refer only to long pipes and only to a single kind of condition at the external surface of the heat pipe, where the heat fluxes in the vaporization and condensation zones are constant.

There are two papers[3,4] which are highly important for the clarification of the fundamental principles of heat-pipe design. In the first, an outline of the problem and a method for heat-pipe design are given in general terms; in the second, the operating conditions are given in comparatively clear form. Even in these papers, however, the formulation of the problem is approximate and leaves out a number of real effects, is based on intuitive considerations, and does not yield even in principle an accurate calculation for a heat pipe over a broad range of parameter values and for various modes of operation. This is not to say that individual design elements, for example the calculation of laminar motion of an incompressible vapor in long heat pipes[5] and the calculation of condensate motion along certain types of capillary structures,[6–9] are not useful; the results can indeed be used in calculations within a systematic theory for heat pipes.

Recent experimental data have show that in certain modes of operation heat pipes can have a significant thermal resistance, which cannot be attributed to vapor compressibility. The results of vapor temperature measurements in the cavity of a sodium heat pipe represent a particular case.[10]

To construct a theory that can be used to determine the thermal resistance of a pipe, including short heat pipes, and to describe the heat exchange between a pipe and an external medium with a strong nonuniformity in the longitudinal direction, it is necessary to carry out an analysis in which all the basic processes of heat and mass transfer in the jacket and in the cavity of the pipe are considered together, i.e., a formulation of the "combined" problem in the sense of ref. 11. The construction of a systematic theory for heat pipes and the development of design methods are the subjects of the present paper.

COMBINED DESIGN PROBLEM FOR HEAT PIPES

1. The different modes of heat-pipe operation complicate the construction of a systematic theory for these devices. A change in the operating conditions of a heat pipe can change the nature of the transport processes. For example, depending on thermal load and operating temperature, the vapor motion in the pipe cavity can be laminar or turbulent, and the vapor itself can be compressible or incompressible. Transport in the jacket can be complicated by boiling of the heat-transfer agent in the wick and partial drying of the latter. Hence, it is necessary to delineate the conditions that pertain to a given mode of operation of a heat pipe.

As is well known, the nature of the vapor flow depends on the values of the Reynolds number Re and the Mach number M (Fig. 1). We define these parameters on the basis of the average vapor velocity in the adiabatic zone:

$$\mathrm{Re}=\frac{Q}{\pi R^2}\frac{R}{L\eta_{\mathrm{v}}};\quad \mathrm{M}=\frac{Q}{\pi R^2}\frac{1}{LP_{\mathrm{v}}}\sqrt{\frac{c_{\mathrm{v}}}{c_p}\frac{R^*}{\mu}T_{\mathrm{v}}}, \tag{1}$$

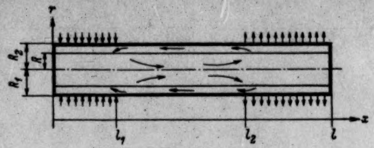

Fig. 1. Diagram of a heat pipe.

where Q is the heat flux transported along the pipe; L is the latent heat of vaporization; η_V is the vapor viscosity; μ is the molecular weight of the vapor; R^* is the universal gas constant; c_p and c_V are the specific heats of the vapor at constant pressure and constant volume; p_V and T_V are the pressure and temperature of the vapor at the end of the vaporization zone. Unfortunately, there is no reliable experimental information in the literature concerning the critical Reynolds number Re_{cr}, for which the transition from laminar flow to turbulent flow occurs in pipes with an inlet and outlet. For this reason, we take Re_{cr} to be the value for flow in an infinitely long pipe, $Re_{cr} = 1250$. With compressibility, matters are somewhat simpler. Since the fundamental quantity needed for heat-pipe calculations is the vapor pressure (see Sec. 3, below) and the ratio between the pressure drop resulting from the motion and the total vapor pressure is proportional to the square of the Mach number M, one can construct some arbitrary boundary by assuming, for example, that motion with $M < 0.1$ is motion of an incompressible vapor.

Using Eq. (1) and the remarks made above with respect to the critical values of Re and M, one can distinguish regions in the thermal-load, temperature plane for a given heat pipe, in which definite modes of vapor flow are realized (Fig. 2).

2. The structure of the combined problem in heat-pipe design does not depend on the mode of operation. The differences appear only in the individual equations, which describe transport processes that undergo a change in the transition to a new mode of operation. We shall discuss the formulation of the combined design problem for heat pipes operating with laminar flow of an incompressible vapor. The generalization of this problem to other modes of operation will be discussed in the second part of this paper.

Thus, the motion of the vapor is described by the system

$$\frac{\partial r v_x}{\partial x}+\frac{\partial r v_r}{\partial r}=0, \tag{2}$$

$$\rho_V v_x \frac{\partial v_x}{\partial x}+\rho_V v_r \frac{\partial v_x}{\partial r}=-\frac{\partial P_V}{\partial x}+\eta_V\left(\frac{\partial^2 v_x}{\partial x^2}+\frac{\partial^2 v_x}{\partial r^2}+\frac{1}{r}\frac{\partial v_x}{\partial r}\right), \tag{3}$$

$$\rho_V v_x \frac{\partial v_r}{\partial x}+\rho_V v_r \frac{\partial v_r}{\partial r}=-\frac{\partial P_V}{\partial r}+\eta_V\left(\frac{\partial^2 v_r}{\partial x^2}+\frac{\partial^2 v_r}{\partial r^2}+\frac{1}{r}\frac{\partial v_r}{\partial r}-\frac{v_r}{r^2}\right), \tag{4}$$

$$\rho_V c_{pV} v_x \frac{\partial T_V}{\partial x}+\rho_V c_{pV} v_r \frac{\partial T_V}{\partial r}=\lambda_V\left(\frac{\partial^2 T_V}{\partial x^2}+\frac{\partial^2 T_V}{\partial r^2}+\frac{1}{r}\frac{\partial T_V}{\partial r}\right), \tag{5}$$

where λ_V is the coefficient of thermal conductivity of the vapor; T_V is the vapor temperature v_x and v_r are the components of the vapor velocity, and ρ_V is the vapor density.

Transport processes in the pipe jacket include heat transport and filtration of the heat-transfer agent through the capillary structure. The pipe jacket consists of two layers: the casing and the capillary structure saturated with the heat-transfer agent. The propagation of heat along the casing of a heat pipe is given by

$$\frac{\partial^2 T}{\partial x^2}+\frac{\partial^2 T}{\partial r^2}+\frac{1}{r}\frac{\partial T}{\partial r}=0, \tag{6}$$

where T is the jacket temperature.

Matters are considerably more complicated for the energy transport equation in the capillary structure. This is the case because the temperature of the heat-transfer agent flowing through the pores of the wick can be different from the temperature of the skeleton of the capillary structure; the description of energy transport for this case requires a system of two coupled equations, one for the heat-transfer agent and the other for the skeleton of the capillary structure. However, if the coefficients of thermal conductivity of the heat-transfer agent and the skeleton material are similar, as happens in high-temperature heat pipes, the temperature of the heat-transfer agent is almost the same as the temperature of the skeleton, and the equation for energy transport in the capillary structure can be written

$$\frac{\partial}{\partial x}\left[r\left(\tau_{l_x} h_l-\lambda'_x\frac{\partial T}{\partial x}\right)\right]+\frac{\partial}{\partial r}\left[r\left(\tau_{l_r} h_l-\lambda'_r\frac{\partial T}{\partial r}\right)\right]=0, \tag{7}$$

where λ'_x and λ'_r are the coefficients of thermal conductivity for the capillary structure skeleton and heat-transfer agent system; τ_{l_x} and τ_{l_r} are the components of the flux density vector for the liquid; h_l is the enthalpy of the liquid.

It is convenient to take as a base line for measuring the enthalpy the enthalpy of the condensed heat-transfer agent in the state in which its temperature is equal to the characteristic heat-pipe temperature T_p and its pressure is equal to the pressure of the saturated vapor at the temperature T_p. Then the enthalpies of the vapor and liquid are

$$\left.\begin{aligned} h_V &= L+c_{pV}(T_V-T_p), \\ h_l &= c_{pV}(T-T_p), \end{aligned}\right\} \tag{8}$$

where L is the latent heat of vaporization at the temperature T_p.

The specific form of the filtration equation for the

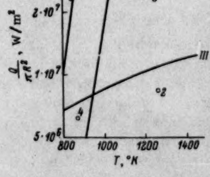

Fig. 2. Regions with various modes of vapor flow in the cavity of a heat pipe (Na, R = 1 cm). 1, 3) Regions of turbulent vapor flow; 2, 4) regions of laminar vapor flow; 1, 2) regions of incompressible vapor; 3, 4) regions of compressible vapor; 5) ultrasonic region. I) M = 1; II) M = 0.1; III) R = 1 cm.

heat-transfer agent depends on the type of capillary structure used in the heat pipe and will be discussed in the second part.

Formulation of the combined problem also implies the formulation of boundary conditions and coupling conditions. The boundary conditions at the external surface of a heat pipe are determined by the specific conditions for heat exchange between the heat pipe and the environment. For definiteness we consider the case in which these reduce to a given heat flux through this surface. If necessary, the formulation of the problem can easily be extended to other conditions. We also assume there is no heat exchange through the ends of the pipe. We denote the heat flux density through the external surface of the heat pipe at $r = R_2$ by $q_2(x)$. With these assumptions a stationary mode of heat pipe operation is possible only when $\int_0^l q_2(x)dx = 0$.

As a rule the thickness of the casing of a heat pipe is considerably smaller than the thickness of the capillary structure, and redistribution of heat along the former can be neglected. In this case, the equation for thermal conductivity in the casing is easily integrated and one obtains the following relation between the thermal fluxes through the external and internal surfaces of the pipe casing, $q_1 = q_2R_2/R_1$. If it is impossible to neglect redistribution of heat along the casing Eqs. (6) and (7) must be solved simultaneously and matched at $r = R_1$.

We now consider conditions at the internal surface of the capillary structure at $r = R$. One can show that for all types of capillary structure the effect of condensate motion at the vapor–liquid interface on vapor motion can be neglected; it can be assumed the vapor velocity component tangential to the surface is zero on the entire surface of the cavity of the heat pipe. Furthermore, conditions must be written for this surface which couple the equations of thermal conductivity in the vapor and in the capillary structure as well as an expression for the vapor velocity component normal to the surface.

It should be noted that at high loading phase transitions in a heat pipe are of a nonequilibrium nature. This is expressed by the fact that the vapor temperature and pressure at the phase transition surface are different from the temperature of the liquid surface and the pressure of saturated vapor at that temperature. The conditions which relate the vapor and liquid parameters in this case are obtained by formulation of the balance equations at the phase transition surface for various moments of the vapor molecule distribution function.[12] For example, by balancing the first moments of the distribution function we obtain an expression for the vaporization rate:

$$\tau = \frac{2\alpha}{2-\alpha}\sqrt{\frac{\mu}{2\pi R^*}}\left[\frac{P_V}{\sqrt{T_V}} - \frac{P(T_0)}{\sqrt{T_0}}\right], \tag{9}$$

where α is the condensation coefficient; T_0 is the temperature of the surface of the liquid; $P(T_0)$ is the saturated vapor pressure at temperature T_0. If a phase transition exists we neglect the transport of energy between the vapor and liquid because of the low-thermal conductivity of the vapor, i.e., we say

$$\left.\frac{\partial T_V}{\partial r}\right|_{r=R} = 0, \tag{10}$$

then the condition for continuity of energy flow through the phase transition surface can then be written as

$$\tau L = -\lambda_r' \left.\frac{\partial T}{\partial r}\right|_{r=R}. \tag{11}$$

Equations (9)-(11) are also the desired conditions for regions of the surface $r = R$, where condensation occurs. Where vaporization occurs Eq. (10) is replaced by a relation which, being a consequence of energy balance and the condition (10), relate directly the temperatures of the vapor and liquid at the vaporization surface. Thus we can take account of the variation along the vaporization zone of the temperature of vapor injected into the cavity of the pipe; this is associated with variation along this zone of the temperature of the surface $r = R$ or of the rate of vaporization. This condition is obtained from the balance for second moments of the distribution function and has the form

$$T_V = T_0\left[1 + \sqrt{\frac{2\pi R^* T_0}{\mu}}\frac{\tau}{8P(T_0)[\alpha + \beta(1-\alpha)]}, \tag{12}$$

where β is the accommodation coefficient.

Although Eq. (12) indicates that $(T_V - T_0)/T_0$ is of the order of the ratio between the vaporization rate and the velocity of sound it should be noted that nevertheless the absolute value of the temperature discontinuity at the phase transition surface, $T_V - T_0$, can amount to a significant part, if not the main part, of the temperature drop between the vaporization and condensation zones of a heat pipe.

Equations (9) and (12) must be refined to apply to phase transitions in heat pipes. Phase transitions do not occur over the entire surface $r = R$, but only over a portion of it equal to the total area of the menisci. We pick out some element of the channel surface. We designate its area by s and the total area of the menisci in this element at which phase transition occurs by s_{tr}; we then introduce the dimensionless quantity $\varepsilon = s_{tr}/s$. Using this definition we can write a complete set of boundary conditions and coupling conditions for (2)-(5) and (7):

$$v_x|_{x=0} = v_r|_{x=0} = v_x|_{x=l} = v_r|_{x=l} = v_x|_{r=R} = 0, \tag{13}$$

$$\left.\frac{\partial T_V}{\partial x}\right|_{x=0} = \left.\frac{\partial T_V}{\partial x}\right|_{x=l} = 0;\ \left.\frac{\partial T}{\partial x}\right|_{x=0} = \left.\frac{\partial T}{\partial x}\right|_{x=l} = 0, \tag{14}$$

$$-\lambda_r' \left.\frac{\partial T}{\partial r}\right|_{r=R_1} = q_1, \tag{15}$$

$$L\tau|_{r=R} = -\lambda_r' \left.\frac{\partial T}{\partial r}\right|_{r=R};\ \tau|_{r=R} = \frac{2\alpha\varepsilon}{2-\alpha}\sqrt{\frac{\mu}{2\pi R^*}}\left[\frac{P_V}{\sqrt{T_V}} - \frac{P(T_0)}{\sqrt{T_0}}\right]_{r=R}, \tag{16}$$

$$T_V|_{r=R} = T_0\left[1 + \sqrt{\frac{2\pi R^* T_0}{\mu}}\frac{\tau}{8\varepsilon P(T_0)[\alpha + \beta(1-\alpha)]} \text{ for } \tau|_{r=R} < 0, \tag{17}$$

$$\left.\frac{\partial T_V}{\partial r}\right|_{r=R} = 0 \qquad \text{for } \tau_{r=R} > 0, \tag{18}$$

$$\lambda_r' \left.\frac{\partial T}{r}\right|_{r=R} = \lambda_V \left.\frac{\partial T_V}{\partial r}\right|_{r=R} \text{ for } \tau|_{r=R} = 0. \tag{19}$$

In this formulation, there is no characteristic value of the temperature and therefore the solution of the problem will be determined except for the value of the temperature at any point of the heat pipe.

We now consider certain limiting cases. If the following two conditions are satisfied: a) the temperature drop along the wick of the thermal pipe is of the same order of magnitude as the drop across it, and b) $R_1 - R \ll l$, heat transport through the heat-pipe jacket can be neglected along the x axis. Then $q_0 = q_2R_2/R$ and the problem reduces to the equation system (2)-(5) with the conditions (13), (14), (16)-(18), where it is assumed, however, that

$$-\lambda_r' \frac{\partial T}{\partial r}\Big|_{r=R} = q_0. \tag{20}$$

For small thermal loading, for which we can neglect the temperature jumps in vaporization and condensation, the problem allows further simplification; Eq. (5) for the thermal conductivity in the vapor need not be included. In this case the problem reduces to the equation system (2)-(4), with the boundary conditions (13) and

$$\tau|_{r=R} = \frac{q_0}{L}. \tag{21}$$

We note that all attempts to calculate vapor motion to date have applied to this problem.

The value of the parameter ε is determined by such factors as the surface porosity of the wick, ε_W, the extent to which it is filled with condensate, the type of capillary structure, etc. In addition, ε can depend on the thermal loading since partial drying of the wick can occur at high loading.[10] Because the phase transition occurs over the entire surface of the channel at r = R in the condensation zone, ε = 1 there. In the vaporization zone, when the capillary structure is completely filled, $\varepsilon = \varepsilon_W$. We note further that with partial drying of the wick, ε in the vaporization zone will be a function of distance along the heat pipe.

3. An arbitrary solution of the combined problem of heat-pipe design formulated in the preceding section is not actually realized in a heat pipe, nor is an exact solution with specific boundary conditions realized. Only that solution is realized which satisfies the operating condition for the heat pipe. By selecting from the multiplicity of all solutions those which are actually realized in the heat pipe the operating condition for heat pipes becomes a fundamental relation for determining the limiting characteristics of heat pipes and for solving the optimization problem. Various versions are encountered[3,4,13] but all are of a qualitative nature. This is evidenced by the fact that while there is a limit on the magnitude of the total pressure drop in the heat pipe, these solutions do not indicate between what points on the phase interface this pressure drop must be determined.

A rigorous operating condition for a heat pipe, free of this deficiency, has been obtained by the present authors[14] in the following manner. The condition for the conservation of the momentum component normal to the vapor–liquid interface with a phase transition present has the form

$$P_v - P_l + \rho_v v_r^2 - \rho_l u_r^2 = \sigma K, \tag{22}$$

where u is the velocity of the liquid; σ is the coefficient of surface tension; K is twice the average curvature of the liquid surface. With the help of Eq. (22), for any two points x_1 and x_2 on the surface of the liquid in the vaporization and condensation zones we can write

$$(P_{v1} - P_{v2}) - (P_{l1} - P_{l2}) + (\rho_{v1}v_{r1}^2 - \rho_{l1}u_{r1}^2) - (\rho_{v2}v_{r2}^2 - \rho_{l2}u_{r2}^2) = \sigma_1 K_1 - \sigma_2 K_2. \tag{23}$$

This relation determines the value of the capillary pressure between the two points needed for the realization of given modes of vapor and liquid flow. It is analogous to a condition given previously.[4]

Normal operation of a heat pipe is possible only when the capillary pressure given by Eq. (23) does not exceed the maximum value of capillary pressure, $P_{K\max}$ created by the heat-pipe wick. Since this requirement must be satisfied for any two points in the vaporization and condensation zones, it must be satisfied for the points at which the left side of Eq. (23) has a maximum. As a result, the operating condition for a heat pipe takes the form

$$\max_{\substack{0\leqslant x_1\leqslant l\\ 0\leqslant x_2\leqslant l}} [(P_{v1} - P_{v2}) - (P_{l1} - P_{l2}) + (\rho_{v1}v_{r1}^2 - \rho_{l1}u_{r1}^2) - (\rho_{v2}v_{r2}^2 - \rho_{l2}u_{r2}^2)] \leqslant P_{K\max}. \tag{24}$$

The points corresponding to the maximum of the left side of inequality (24) considered as a function of the two variables x_1 and x_2 are also points of greatest and least curvature of menisci in the vaporization and condensation zones. Thus, the condition (24) clearly denotes the points for which a pressure balance must be formulated and indicates a procedure for determining their location. It is thus significantly different from the operating condition for a heat-pipe proposed previously[3,4,13] and which resembles Eq. (23). A second property of the condition (24) is that the reaction between the flows of vaporizing and condensing material at the phase transition surface is taken into account. This phenomenon is only significant at very high phase transition rates and for significant transformation of the thermal fluxes through the jacket of the heat pipe in the vaporization and condensation zones. As a rule this effect can be neglected in heat-pipe design. The condition (24) then takes the simpler form

$$\max_{\substack{0\leqslant x_1\leqslant l\\ 0\leqslant x_2\leqslant l}} [(P_{v1} - P_{v2}) - (P_{l1} - P_{l2})] \leqslant P_{K\max}. \tag{25}$$

A first attempt has been made to include the reaction of vaporizing material at the phase transition surface in the analysis of heat-pipe start-up.[15]

The maximum capillary pressure $P_{K\max}$ in condition (24) is determined primarily by the capillary structure and can be determined easily for a given type of structure. For example, in the case of a wick with cylindrical pores of radius *a*, the pressure $P_{K\max}$ is given by (σ is the wetting angle of the edge)

$$P_{K\max} = \frac{2\sigma}{a}\cos\delta - \frac{\sigma}{R}, \tag{26}$$

and for a wick in the form of open channels of width *a* on the internal surface of the casing of the heat pipe, it is given by

$$P_{K\max} = \frac{\sigma}{a}\cos\delta - \frac{\sigma}{R}. \tag{27}$$

NUMERICAL SOLUTION OF THE HEAT-PIPE DESIGN PROBLEM

1. Because of the complicated nonlinear nature of the problem it is necessary to set up an iterative procedure for the numerical solution. The most reasonable iterative procedure would be numerical simulation of the output of a heat pipe in a stationary operating mode. A necessary, but not sufficient, condition for the convergence of this process is the requirement of spatial stability in each iteration. As shown in the course of the calculations, satisfaction of this requirement for simultaneous solution of the entire system of equations describing the processes occurring in a heat pipe is difficult because of the nonlinear coupling conditions.

However, spatial stability can be achieved if the iteration is set up on the principle of sequential solution of the problems of vapor motion in the cavity, heat transport through the heat-pipe jacket, and motion of the heat-transfer agent along the capillary structure. Since all these problems are interrelated, in the solution of each all quantities related to the other problems are taken from their solutions in a previous iteration. Thus, in the solution of the problem of vapor motion in the channel the surface temperature T_0 and the energy flux τh_V through this surface must be taken from the solution in the previous iteraction of the problem of thermal conductivity in the heat-pipe jacket. By sequential solution of the specified problems the demands on the core storage of the computer are reduced considerably and spatial stability is achieved. Further, it is possible to make maximum use of previously published results in solving the problem. We now discuss methods of solution in greater detail. We also describe variations of the problems associated with different modes of heat-pipe operation.

2. Problem of vapor motion in a heat-pipe cavity. For given q_0 and T_0, Eqs. (2)-(4) do not depend on Eq. (5); therefore they can be solved individually. We designate by v_{r_0} a characteristic value for the velocity component v_r in the heat pipe. One can take the quantity $Q/2\pi R l_1 \rho_V$ as v_{r_0}. If we take as a characteristic value of the velocity component $v_{x_0} = v_{r_0} l/R$, the system of equations of motion in the dimensionless variables

$$v'_r=\frac{v_r}{v_{r_0}};\quad v'_x=\frac{v_x}{v_{x_0}};\quad P'=\frac{P}{\rho_V v^2_{x_0}};\quad x'=\frac{x}{l};\quad r'=\frac{r}{R} \tag{28}$$

reduces to the form (primes omitted)

$$\left.\begin{gathered}\frac{\partial r v_x}{\partial x}+\frac{\partial r v_r}{\partial r}=0,\\ v_x\frac{\partial v_x}{\partial r}+v_r\frac{\partial v_x}{\partial r}=-\frac{\partial P}{\partial x}+\frac{\mathrm{Re}_{r_0}}{\mathrm{Re}_0^2}\frac{\partial^2 v_x}{\partial x^2}+\frac{1}{\mathrm{Re}_{r_0}}\left(\frac{\partial^2 v_x}{\partial r^2}+\frac{1}{r}\frac{\partial v_x}{\partial r}\right),\\ \frac{\mathrm{Re}^2_{r_0}}{\mathrm{Re}_0^2}\left(v_x\frac{\partial v_r}{\partial x}+v_r\frac{\partial v_r}{\partial r}\right)=-\frac{\partial P}{\partial r}+\frac{\mathrm{Re}^3_{r_0}}{\mathrm{Re}_0^4}\frac{\partial^2 v_r}{\partial x^2}\\ +\frac{\mathrm{Re}_{r_0}}{\mathrm{Re}_0^2}\left(\frac{\partial^2 v_r}{\partial r^2}+\frac{1}{r}\frac{\partial v_r}{\partial r}-\frac{v_r}{r^2}\right),\end{gathered}\right\} \tag{29}$$

where

$$\mathrm{Re}_0=\frac{v_{x_0}R}{\nu_V},\quad \mathrm{Re}_{r_0}=\frac{v_{r_0}R}{\nu_V}.$$

The boundary conditions for this equation system are

$$v_x|_{x=0}=v_r|_{x=0}=v_x|_{x=1}=v_r|_{x=1}=0, \tag{30}$$

$$v_x|_{r=1}=0;\quad v_r|_{r=1}=\frac{q_0}{L\rho_V v_{r_0}}=\varphi(x). \tag{31}$$

In addition, from symmetry considerations we have

$$\left.\frac{\partial v_x}{\partial r}\right|_{r=0}=0;\quad v_r|_{r=0}=0. \tag{32}$$

The most suitable numerical method for solving the problem (28)-(32) is the method of finite differences. Up until now, it has received rather wide acceptance for the calculation of viscous fluid flow. In the main two-dimensional problems in plane geometry have been solved by this method thus far. The algorithms developed for the solution of these problems can be modified for the solution of problems with cylindrical symmetry. In particular, an algorithm for the solution of the problem (28)-(32) by finite differences has been developed by the present authors. The economy of this algorithm, based on an implicit scheme of variable directions, makes it realizable on the Minsk-22 computer. We cannot discuss this algorithm here in detail because of the lack of space. We only point out that the scheme for solution is similar in many respects to the scheme for the case of Cartesian coordinates.[16] The equation system (29) is written in the form of a system of two equations with respect to the flow function ψ and the vorticity function ξ. The equations for ψ and ξ are solved alternately using approximate boundary conditions[17] for ξ. The equation for ξ is approximated in accordance with the scheme of Allen.[18]

The solution of the problem of vapor motion in long heat pipes by finite differences is difficult because of computational instabilities at large values of 1/R. In addition, to obtain the required accuracy as the length of the heat pipe increases it is necessary to reduce the spatial steps along the x axis and, to a lesser extent, along the r axis. The resulting increase in the number of mesh points is limited by the capacity of computer memory core, the computational labor, and the computing time. Therefore, a need arises for another method of solution of the problem (28)-(32) for the case of long heat pipes.

The entire region of vapor flow in a long pipe can be subdivided into several parts in accordance with the rate of change of the flow characteristics in the x direction. Portions of the cavity near the ends of the pipe, and also near the boundaries l_1, l_2 between zones, are distinguished by a rapid readjustment of the flow. The length of each of these sections is of the order of several radii and the flow in these can be investigated with (29). In other sections of the pipe cavity the nature of the flow varies slowly in the direction of the x axis; in these cases, the vapor flow can be calculated on the basis of the simpler system of equations for a boundary layer. This system is obtained by taking the limit $\mathrm{Re}_0/\mathrm{Re}_{r_0} \to \infty$ in (29) and has the form

$$\frac{\partial r v_x}{\partial x}+\frac{\partial r v_r}{\partial r}=0, \tag{33}$$

$$v_x\frac{\partial v_x}{\partial x}+v_r\frac{\partial v_x}{\partial r}=-\frac{\partial P}{\partial x}+\frac{1}{\mathrm{Re}_{r_0}}\frac{1}{r}\frac{\partial}{\partial r}\left(r\frac{\partial v_x}{\partial r}\right), \tag{34}$$

$$\frac{\partial P}{\partial r}=0. \tag{35}$$

Solutions of the system of Navier–Stokes equations in the transition sections of the heat pipe are then matched to solutions of Eqs. (33)-(35) in the other sections of the cavity. As in the case of short heat pipes, the former can be obtained by finite differences. The matching boundary conditions for Eqs. (29) and the boundary-layer equations have been investigated.[19]

An approximate solution of Eqs. (33)-(35) with boundary conditions (31) and (32) can be found through the Karman–Polhausen integral relations. Assuming $v_r|_{r=1} =$ const in Eq. (31), Busse made the first such calculation as applied to heat pipes.[5] Of the earlier work on the calculation of fluid flow in a permeable pipe based on Eqs. (33)-(35), one paper is of particular interest.[20] We extend the results of this work to the case $v_r|_{r=1} = \varphi(x) \neq \text{const}$.

From a comparison of earlier results,[5,20] it follows that in solving Eqs. (33)-(35) by the Karman–Polhausen method the velocity profile v_x must be approximated by a polynomial of at least the sixth power in r. Symmetry considerations dictate that it can only contain even powers of r:

$$v_x(x,\ r) = a_0(x) + a_2(x) r^2 + a_4(x) r^4 + a_6(x) r^6. \tag{36}$$

Since it is impossible to satisfy Eqs. (33)-(35) exactly with the polynomial (36), we only require exact satisfaction of the boundary conditions (31) and (32), of Eqs. (33) and (34) averaged over the cross section of the pipe cavity, and of the relations

$$\left.\frac{\partial P}{\partial x}\right|_{r=0} = \left.\frac{\partial P}{\partial x}\right|_{r=1} = \frac{d\bar{P}}{dx} \tag{37}$$

because of (35), where the derivatives at r = 0 and r = 1 are determined with the help of Eq. (34) and the bar denotes the average:

$$\bar{P} = 2\int_0^1 Pr dr.$$

After some simple transformations we obtain the following system of equations for the coefficients of the polynomial and for P:

$$\left.\begin{aligned}
&a_0 + a_2 + a_4 + a_6 = 0,\\
&\frac{d}{dx}\left(a_0 + \frac{a_2}{2} + \frac{a_4}{3} + \frac{a_6}{4}\right) = -2\varphi(x),\\
&\frac{d}{dx} a_0^2 = 4\varphi(x)(a_2 + 2a_4 + 3a_6) - \frac{8}{\mathrm{Re}_{r_0}}(4a_4 + 9a_6),\\
&\frac{d}{dx}\left[\frac{a_0^2 + 2a_0a_2 + a_0a_6 + a_2a_4}{2} + \frac{2a_0a_4 + a_2^2 + a_4a_6}{3}\right.\\
&\left. + \frac{2a_2a_6 + a_4^2}{5} + \frac{a_6^2}{7}\right] = \frac{4}{\mathrm{Re}_{r_0}}(2a_4 + 3a_6),\\
&\frac{d}{dx}\left[P + \frac{2a_0^2 + 2a_0a_2 + a_0a_6 + a_2a_4}{2}\right.\\
&\left. + \frac{2a_0a_4 + a_2^2 + a_4a_6}{3} + \frac{2a_2a_6 + a_4^2}{5} + \frac{a_6^2}{7}\right] = \frac{4}{\mathrm{Re}_{r_0}}(a_2 + 2a_4 + 3a_6),
\end{aligned}\right\} \tag{38}$$

which makes it possible to calculate the motion of the vapor in the portion of the pipe where the motion is described by the equation system (33)-(35) from the velocity profile, i.e., from the values of the coefficients in the polynomial (36) and from the pressure at the entrance to that portion of the pipe. The initial values of a_i (i = 0, 2, 4, 6) and $\bar{P}$ must be determined from the solution of the complete system of Navier–Stokes equations in the preceding transition section.

With this scheme for the calculation of vapor motion in the cavity of a long heat pipe the demands on the core storage of the computer are reduced sharply since the equations are solved by finite differences only in the transition sections, and they make up a small part of the total cavity of the pipe. We note that sometimes reorganization of vapor flow in the transition sections is generally neglected and the solutions of Eqs. (33)-(35) are matched directly at $x = l_1$ and $x = l_2$ in each of the zones of the heat pipe.[5]

Because of the identical structure of the equations the methods for solving Eqs. (28)-(32) can also be applied to the solution of Eq. (5).

If an increase in the longitudinal vapor velocity in the vaporization zone causes the local Reynolds number to exceed $\mathrm{Re}_{\mathrm{cr}}$ the vapor flow can become turbulent. The transition from laminar flow to turbulent flow takes place over a distance of several channel diameters. The turbulent flow maintains its nature over the extent of the adiabatic zone and into the beginning of the condensation zone. Some stabilization of the flow must occur at the end of the condensation zone, where the vapor motion is decelerated, but the entire flow obviously does not become completely laminar. Analysis of vapor motion in the transition zones of the vaporization and condensation regions is extremely difficult. In the following, therefore, we neglect those zones, assuming that turbulence in the flow occurs immediately at the point in the vaporization zone where $\mathrm{Re} = \mathrm{Re}_{\mathrm{cr}}$ and that the region of turbulent flow extends over the entire condensation zone.

It should be noted that turbulent vapor motion is only possible in long heat pipes. In short heat pipes with high thermal loading a situation can occur in which the Reynolds number reaches $\mathrm{Re}_{\mathrm{cr}}$; however, the laminar flow cannot become turbulent before the beginning of the condensation zone. This circumstance greatly facilitates the analysis of vapor motion, making it possible to use the approximation of a turbulent boundary layer.

If one proceeds on the basis of the requirements of heat-pipe design, one can limit oneself to the determination of flow characteristics averaged over the cross section of the channel. Because of very intense turbulent displacement and the relation $R \ll l$, such vapor parameters as ρ_V and T_V are only weakly dependent on the transverse coordinate r. Assuming them independent of r, we average the equations for a turbulent boundary layer[21] over the cross section of the channel. The averaged equations have the form

$$\left.\begin{aligned}
&\frac{d\rho_V v}{dx} = -\frac{2l}{R}\tau|_{r=R},\\
&\frac{d}{dx}[P_V + \beta\rho_V v^2] = -\frac{2l}{R}\tau_w,\\
&\frac{d}{dx}\left[\rho_V v\left(h_V + \frac{\alpha v^2}{2}\right)\right] = -\frac{2l}{R}(\tau h_V)_{r=R},\\
&P_V = \frac{\rho_V R^* T_V}{\mu_V}.
\end{aligned}\right\} \tag{39}$$

Here a conversion has been made to the dimensionless coordinate x' = x/l (primes omitted) and the notation

$$v=\frac{2}{R^2}\int_0^R v_x r\,dr;\ \beta=\frac{2}{v^2R^2}\int_0^R v_x^2 r\,dr;\ \alpha=\frac{2}{v^3R^2}\int_0^R v_x^3 r\,dr. \tag{40}$$

has been introduced.

Note that the equation system (39) is written with vapor compressibility included.

The equation system (39) is an open system. To solve it, information is needed about the coefficient of momentum flow β, the frictional force τ_ω acting on a unit lateral surface of the channel, and the coefficient α. In the general case the coefficient of friction ζ, which is associated with τ_ω through the relation $\zeta = 8\tau_\omega/\rho_V v^2$, and α and β are functions of the local criteria Re = vR/ν_V and $\mathrm{Re}_r = (v_r(x)|_{r=R}R)/\nu_V$. Experimental data for these coefficients are still very sparse at the present time. Some information about β and ζ is given for the case of uniform injection[22] and extraction.[23] According to this data, starting at a distance of the order of four channel diameters from the entrance to the injection or extraction sections the coefficient β depends very slightly on x and can be assumed to be constant. Obviously, this also holds for a rate of injection or extraction which is a slowly varying quantity along the pipe. Under extraction, the coefficient β is the same as in an impermeable pipe, i.e., close to unity.

Experimental data on the coefficient of friction are very scarce. For injection, it is very small[22] and the inertial term $\beta\rho_V v^2$ in the equation of motion plays the principal role in the distribution of pressure along the flow. Because of this and also because of the absence of reliable experimental data for the coefficient ζ, one can use in the calculations the known laws for resistance to the motion of a fluid in a pipe assuming that they are also satisfied locally with injection. Since the Reynolds number for vapor motion does not exceed 10^5 as a rule, the Blausius equation with local Reynolds number

$$\zeta=\frac{0.3164}{\mathrm{Re}^{1/4}}$$

is suitable for this purpose.

With extraction, the friction force is significant and has a strong effect on the pressure distribution in the pipe. In particular, according to ref. 23, the coefficient of friction when there is extraction is an order of magnitude higher than the coefficient given by the Blasius equation. It turns out in this case that it depends strongly on the extraction coefficient $K_\perp = v_r|_{r=R}/v$ and for the region $0.006 < K_\perp < 0.022$ is given by

$$\zeta=17.5K_\perp.$$

This formula has been checked for two values of Re at the entrance to a porous section: $3.7\cdot10^4$ and $7.9\cdot10^4$.

3. Problem of heat propagation through a capillary structure totally saturated by a heat-transfer agent. Because of the sequence of iterations specified in Sec. 1 for the calculation of a heat-pipe design, the quantities τ_{l_x} and τ_{l_r} as well as $P_V|_{r=R}$ and $T_V|_{r=R}$ are assumed to be known and taken from the solutions of the appropriate problems in the preceding iteration. The propagation of heat through the capillary structure is described by Eq. (7). The boundary conditions take the form

$$\left.\begin{aligned}(\tau h_l)_{r=R}-\left(\lambda'_r\frac{\partial T}{\partial r}\right)_{r=R}&=(\tau h_V)_{r=R},\\ \tau_{l_r}|_{r=R}=\tau_{V_r}|_{r=R}&\equiv\tau,\\ -\left(\lambda'_r\frac{\partial T}{\partial r}\right)_{r=R_1}&=q_1,\end{aligned}\right\} \tag{41}$$

$$\left.\frac{\partial T}{\partial x}\right|_{x=0}=\left.\frac{\partial T}{\partial x}\right|_{x=l}=0. \tag{42}$$

The solution of Eq. (7) under the conditions (41) and (42) is a rather complicated problem because of the nonlinearity of the first of the conditions (41); therefore it is solved approximately. We look for a solution T(x, r) in the form of a polynomial in r requiring satisfaction of the boundary conditions and of the energy equation (7) averaged over the cross section of the capillary structure. For a liquid filtering through the capillary structure, the equation of continuity

$$\frac{\partial r\tau_{l_x}}{\partial x}+\frac{\partial r\tau_{l_r}}{\partial r}=0. \tag{43}$$

must be satisfied.

Taking account of Eq. (43) and the boundary conditions (41) and (42), we write the averaged equation (7) in the form

$$\int_R^{R_1}\tau_{l_x}\frac{\partial rh_l}{\partial x}dr-\lambda'_x\frac{d^2}{dx^2}\int_R^{R_1}Tr\,dr=R\tau(h_V-h_l)_{r=R}$$
$$-R_1q_1-\int_R^{R_1}r\tau_l\frac{\partial h_l}{\partial r}dr. \tag{44}$$

Because of the approximate nature of the solution of the problem of thermal conductivity in the capillary structure of a heat pipe, we assume in Eq. (44) that τ_l does not depend on r but that it is an average of the true value over the cross section of the wick. This assumption is not necessary; however, while having no marked effect on the accuracy of the solution, it permits unification of the calculation for different types of capillary structures and simplifies subsequent calculations significantly. The replacement of τ_{l_x} by $\bar{\tau}_{l_x}$ is justified for wicks of irregular structure, in which the velocity profile of the liquid is almost planar. Using this simplification we write Eq. (44) in the form

$$\frac{d^2\bar{T}}{dx^2}-\frac{\bar{\tau}_{l_x}}{\lambda'_x}\frac{d\bar{h}_l}{dx}=\frac{2R_1q_1}{\lambda'_x(R_1^2-R^2)}-\frac{2R\tau}{\lambda'_x(R_1^2-R^2)}$$
$$\times\left[(h_V-h_l)_{r=R}-\int_R^{R_1}\frac{R_1^2-r^2}{R_1^2-R^2}\frac{\partial h_l}{\partial r}dr\right], \tag{45}$$

where the bar indicates an average over the cross section of the wick.

$$\bar{T}=\frac{2}{R_1^2-R^2}\int_R^{R_1}Tr\,dr.$$

We assume a dependence of the temperature T(x, r) on r in the form of the following polynomial of second degree:

$$T(x, r) = T_0(x) + a_1(x)(r - R) + a_2(x)(r - R)^2. \qquad (46)$$

We determine the coefficients a_1 and a_2 by requiring satisfaction of the boundary conditions (41):

$$a_1(x) = -\frac{1}{\lambda'_r}\tau(h_v - h_l)_{r=R}; \quad a_2(x) = -\frac{q_1 + \lambda'_r a_1(x)}{2\lambda'_r(R_1 - R)}. \qquad (47)$$

We use Eq. (45) to determine the coefficient $T_0(x) \equiv T(x, R)$. After substitution of Eqs. (46) and (47) in Eq. (45), replacement of the variable x by the dimensionless variable $x' = x/l$ (the primes are omitted in the following), and simple transformations, we obtain a nonlinear differential equation with respect to T_0:

$$\frac{d^2\bar{T}}{dx} - \frac{\tau l_x c_{pl} l}{\lambda'_x}\frac{d\bar{T}}{dx} = \frac{2R_1 l^2 q_1}{\lambda'_x(R_1^2 - R^2)} - \frac{2Rl^2\tau}{\lambda'_x(R_1^2 - R^2)}$$
$$\times [L + c_{pv}(T_v - T_p) - c_{pl}(T_0 - T_p) - c_{pl}(a_1 A + B)], \qquad (48)$$

where

$$\bar{T} = T_0 + Aa_1 + B; \quad A = \frac{R_1 - R}{R_1 + R}\left(\frac{5}{12}R_1 + \frac{R}{4}\right);$$

$$B = -\frac{q_1}{4\lambda'_r}\frac{R_1 - R}{R_1 + R}\left(R_1 + \frac{R}{3}\right).$$

We recall that τ is related to T_0 by Eq. (16), and that the enthalpy h_l of the heat-transfer agent and the enthalpy h_v of the vapor at r = R are given by Eq. (8). If $T_v|_{r=R}$ is taken as the vapor temperature in the region of the surface r = R, where condensation occurs, in the calculation of $h_v|_{r=R}$, then the temperature of the vapor at the vaporization surface $T_v|_{r=R}$ must be calculated from Eq. (17) in regions where vaporization occurs.

It is impossible to satisfy (42) exactly with the polynomial (46). Therefore we weaken this condition, requiring only that

$$\left.\frac{\partial\bar{T}}{\partial x}\right|_{x=0} = \left.\frac{\partial\bar{T}}{\partial x}\right|_{x=1} = 0. \qquad (49)$$

Equation (48) with the condition (49) can be solved by the Newton–Kantorovich method. In this case it is not convenient to determine $T_0(x)$ directly from Eq. (48); rather we find the energy flux density through the surface r = R. We designate it by z. Then we determine $T_0(x)$ from

$$\tau h_v|_{r=R} = z \qquad (50)$$

and τ from Eq. (16).

Let the functions $z^n(x)$ and $T_0^n(x)$, which are related through Eq. (50), be the n-th approximation to the desired solution of Eq. (48). We obtain an equation for the correction δz to this approximation by variation of Eq. (48) in the neighborhood of $z^n(x)$. We write each of the expressions in Eq. (48) which depend on z correctly to the linear term in δz in the neighborhood of z^n; T_0^n. For example, $\bar{T}$ can be written in the form $\bar{T} = \bar{T}|_{T_0^n} + F\delta z$, where $F = \partial\bar{T}/\partial z|_{F_0^n, z^n} = \partial\bar{T}/\partial T_0|_{T_0^n}\,\partial T_0/\partial z|_{T_0^n}$. Proceeding in the same way in the other expressions in Eq. (48) and keeping only first-order terms, we obtain the following equation for the correction δz:

$$\frac{d^2F\delta z}{dx^2} - \frac{\tau l_x c_{pl} l}{\lambda'_x}\frac{dF\delta z}{dx} + \frac{2Rl^2\delta z}{\lambda'_x(R_1^2 - R^2)} = -\frac{d^2\bar{T}}{dx^2} + \frac{\tau l_x c_{pl} l}{\lambda'_x}\frac{d\bar{T}}{dx}$$
$$+ \frac{2R_1 q_1 l^2}{\lambda'_x(R_1^2 - R^2)} - \frac{2Rl^2}{\lambda'_x(R_1^2 - R^2)}[z - \tau c_{pl}(T_0 - T_p + a_1 A + B)], \qquad (51)$$

the coefficients and right side of which are calculated for the values $T_0(x) = T_0^n(x)$ and $z(x) = z^n(x)$. The boundary conditions for Eq. (51) are obtained from Eq. (49):

$$\left.\frac{dF\delta z}{dx}\right|_{x=0} = -\left.\frac{d\bar{T}}{dx}\right|_{x=0}; \quad \left.\frac{dF\delta z}{dx}\right|_{x=1} = -\left.\frac{d\bar{T}}{dx}\right|_{x=1}. \qquad (52)$$

A single iteration in the solution of Eq. (48) as the result of which the (n + 1)-th approximations T_0^{n+1}, z^{n+1} are determined from the n-th approximations T_0^n and z^n includes solution of Eq. (51) with respect to δz with the boundary conditions (52), the calculation of the (n + 1)-th approximation z^{n+1} from the expression $z^{n+1} = z^n + \delta z$, and the determination of T_0^{n+1} from Eq. (50) in which we set $z = z^{n+1}$. With the proper choice of the first approximation, this iteration process converges very rapidly. As a rule a few iterations are sufficient. Equation (51) can be solved numerically by finite differences.

4. The calculation of the filtration of the heat-transfer agent depends on the capillary structure and cannot be formulated in a universal fashion. In contrast to the vapor, the great influence exerted by gravity must be taken into account in the calculation of condensate motion. This is comparatively simple. Since gravity represents a potential energy, it is then sufficient to subtract from the pressure of the liquid which is obtained by solving the problem without including gravity a quantity $\rho_l gx\sin\gamma$, where g is the gravitational acceleration and γ is the slope of the heat pipe with respect to the horizontal.

We now consider the filtration of the heat-transfer agent under conditions of weightlessness for three types of capillary structures: a coaxial gap formed by a fine porous screen and the pipe casing, a system of longitudinal grooves on the internal surface of the casing covered by a finely porous screen, and a wick of irregular structure (made of several layers of mesh, dried powder, porous capillary material, etc).

With sufficiently high screen porosity the pressure of the liquid in the gap is due mainly to the average characteristics of the flow and depends only to a limited extent on the details of influx of liquid into the gap and efflux through openings in the screen. We therefore assume that the influx and efflux of liquid does not occur through individual openings in the screen but over the entire surface.

An estimate of the Reynolds number Re_{r_1} for filtration of a heat-transfer agent in a heat pipe yields a value less than unity for alkali metals. This makes it possible to neglect convective terms in the equations of motion and the Stokes approximation is used for calculation of liquid motion along the capillary structure. In this approximation the motion of the liquid along a coaxial gap is described by the system

$$\left.\begin{aligned}&\frac{dru_x}{\partial x}+\frac{l}{R_1}\frac{\partial ru_r}{\partial r}=0,\\&\frac{\eta_l l}{R_1^2}\frac{1}{r}\frac{\partial}{\partial r}\left(r\frac{\partial u_x}{\partial r}\right)=\frac{\partial P_l}{\partial x},\\&\frac{\partial P_l}{\partial r}=0\end{aligned}\right\}\qquad(53)$$

with the boundary conditions

$$u_x|_{r=\alpha}=u_x|_{r=1}=u_r|_{r=1}=0,\qquad(54)$$

$$u_r|_{r=\alpha}=\frac{\tau}{\rho_l}\equiv u_r^*.\qquad(55)$$

Here, we have introduced the dimensionless variables $x' = x/l$, $r' = r/R_1$, and the notation $\alpha = R/R_1$. The primes on the new variables are omitted. The quantity τ in Eq. (55) is determined from a solution of the problem of heat propagation through a capillary structure, Eq. (41).

Integrating Eq. (53), we obtain the following expressions for the velocities u_x and u_y subject to (54):

$$u_x=\frac{R_1^2}{4\eta_l l}\frac{dP_l}{dx}\left[r^2+\frac{1-\alpha^2}{\ln\alpha}\ln r-1\right],\qquad(56)$$

$$u_r=-\frac{R_1^2}{4\eta_l l^2}\frac{d^2P_l}{dx^2}$$

$$\times\left[\frac{r^3}{4}-r\left(\frac{1-\alpha^2}{4\ln\alpha}+\frac{1}{2}\right)+\frac{1-\alpha^2}{2\ln\alpha}r\ln r+\left(\frac{1-\alpha^2}{4\ln\alpha}+\frac{1}{4}\right)\frac{1}{r}\right].\qquad(57)$$

Assuming $r = \alpha$ in Eq. (57) and using Eq. (55), we obtain an equation for the pressure,

$$\frac{d^2P_l}{dx^2}=-\frac{4\eta_l l^2Ru_r^*}{R_1^4\left[\frac{1-\alpha^4}{4}+\frac{(1-\alpha^2)^2}{4\ln\alpha}\right]}.\qquad(58)$$

From Eq. (56) and the requirement that the liquid velocity u_x must vanish at $x = 0$, we obtain a condition for Eq. (58),

$$\left.\frac{dP_l}{dx}\right|_{x=0}=0.\qquad(59)$$

This relation determines the solution of Eq. (58) except for an arbitrary term. However, this ambiguity is unimportant for the heat pipe since the pressure difference between two points in the gap, which is determined unambiguously, appears in the operating condition (24).

The solution of Eq. (58) with condition (59) has the form

$$P_l(x)=P_l(0)-\frac{\nu l}{K}dl^2\int_0^x dx\int_0^x\tau dx,\qquad(60)$$

where

$$K=\frac{R_1^2}{2}\left[\frac{1+\alpha^2}{4}+\frac{1-\alpha^2}{4\ln\alpha}\right],\quad d=\frac{2R}{R_1^2-R^2}.\qquad(61)$$

In Eq. (60) the actual specifications of the capillary structure are taken into account through the coefficients K and d. One can show that the pressure of the liquid along the wick can also be represented in the form (60) for other capillary structures in the Stokes approximation but with different coefficients K and d. In the case of a wick of irregular structure K is determined by the permeability of the wick and d is given by Eq. (61). For a wick in the form of a system of longitudinal grooves covered by a finely porous screen K and d are given by

$$d=\frac{a+b}{ah};\quad K=-\frac{16a^3}{\pi^5h}\sum_{i=0}^{\infty}\frac{1}{(2i+1)^5}\frac{\operatorname{ch}\frac{(2i+1)\pi h}{a}-1}{\operatorname{sh}\frac{(2i+1)\pi h}{a}}$$

$$+\frac{8a^2}{\pi^4}\sum_{i=0}^{\infty}\frac{1}{(2i+1)^4},\qquad(62)$$

where a is the width of a groove, h its depth, and b the spacing between grooves.

5. The capillary pressure created by menisci located in the pores of a wick depends on the radius of the pore and the location of the meniscus. If the capillary structure is such that there are pores of different diameters a situation is possible in which the capillary pressure created by menisci in large pores does not provide transport of the heat-transfer agent while motion of heat-transfer agent along small pores is still possible. In this case, complete or partial drying of the large pores occurs when the condensate does not occupy the entire cross section of a pore. This takes place not over the entire length of a capillary but starting at the point where the difference in vapor and liquid pressures is equal to the maximum surface pressure of the meniscus at this point of the pore. Thus, in operation of a heat pipe under conditions of drying of the capillary structure the extent to which the wick is filled by the heat-transfer agent varies along the pipe. It is completely filled in the condensation zone and is partially dry somewhere at the beginning of the vaporization zone.

Resistance to the motion of the heat-transfer agent, which is characterized by the coefficient of permeability, depends on the degree to which the wick is filled with condensate. Consequently, filtration of the heat-transfer agent is accomplished in this situation under conditions of a varying coefficient of permeability along the pipe, which, in turn, becomes a function of the process of filtration.

With partial drying of the capillary structure vaporization of the condensate takes place within the wick, and the vapor formed in large pores is transported to the surface of the capillary structure and thus arrives in the cavity of the heat pipe. The vapor is heated as the result of heat exchange with the skeleton of the wick in proportion to the amount of travel along large pores. In order to include these processes in the formulation of the problem it is necessary to take as a basis some model of the capillary structure and of the filtration of the condensate through it under conditions of partial drying.[24]

As an assumption with respect to vapor and condensate filtration we may say that the vapor is propagated only across the wick in the r direction and the liquid is propagated along the wick in the x direction. Then we have

$$\tau_{v_x}=\tau_{l_r}=0;\quad\tau_x=\tau_{l_x};\quad\tau_r=\tau_{v_r},$$

$$q_x=\tau_{l_x}h_l-\lambda_x'\frac{\partial T}{\partial x};\quad q_r=\tau_{v_r}h_v-\lambda_r'\frac{\partial T}{\partial r},$$

and the energy and continuity equations become

$$\frac{\partial r\tau_{l_x}}{\partial x}+\frac{\partial r\tau_{v_r}}{\partial r}=0, \tag{63}$$

$$\frac{\partial}{\partial x}\left[r\left(\tau_{l_x}h_l-\lambda'_x\frac{\partial T}{\partial x}\right)\right]+\frac{\partial}{\partial r}\left[r\left(\tau_{l_r}h_l-\lambda'_r\frac{\partial T}{\partial r}\right)\right]=0. \tag{64}$$

As before, the coefficients of thermal conductivity for the heat-transfer agent and the wick skeleton are assumed to be similar and sufficiently large to justify the introduction of the same temperature for them. Taking account of the physical meaning of each of the terms in Eq. (64), it can be rewritten as

$$\tau_{l_x}\frac{\partial h_l}{\partial x}-\frac{\partial}{\partial x}\left(\lambda'_x\frac{\partial T}{\partial x}\right)=-(h_v^{ev}-h_l)\frac{1}{r}\frac{\partial r\tau_{v_r}}{\partial r}+\frac{1}{r}\frac{\partial}{\partial r}\left(r\lambda'_r\frac{\partial T}{\partial r}\right)-\tau_{v_r}\frac{\partial h_v}{\partial r}, \tag{65}$$

where the enthalpy h_v^{ev} created through evaporation of the vapor is taken at the temperature

$$T_v^{ev}=T+\frac{T^{3/2}}{4P(T)}\frac{\alpha}{(2-\alpha)[\alpha+\beta(1-\alpha)]}\left[\frac{P_v}{\sqrt{T_v}}-\frac{P(T)}{\sqrt{T}}\right]. \tag{66}$$

The variation in vapor flow along the r axis, which is reflected by the expression $\partial r\tau_{v,r}/\partial r$ in Eq. (65), is associated with vaporization within the wick. If we designate by ε_1 the total area of the free surface of the liquid per unit volume of the wick, then with the help of Eq. (16) we can write an expression for the rate of vaporization

$$\frac{\partial r\tau_{v_r}}{\partial r}=-\frac{2\alpha}{2-\alpha}\sqrt{\frac{\mu}{2\pi R^*}}\left[\frac{P_v}{\sqrt{T_v}}-\frac{P(T)}{\sqrt{T}}\right]r\varepsilon_1. \tag{67}$$

We take account of heat exchange between the vapor and the skeleton of the capillary structure by means of the coefficient of heat exchange. Then, introducing the porosity ε_r^{dry} of dry pores in a section of the wick normal to the r axis, we write

$$\tau_{v_r}\frac{\partial h_v}{\partial r}=\frac{2\lambda_v \mathrm{Nu} f_1}{a^2}(T-T_v)\varepsilon_r^{dry}, \tag{68}$$

where *a* is the pore radius and f_1 is the sinuosity factor for the pore. Equations (65)-(68) describe the propagation of heat through a capillary structure in regions of partial drying. In those locations where the wick is completely filled with heat-transfer agent the propagation of heat is described by Eq. (7).

To determine the pressure p_l of the liquid and also the quantities ε_1 and ε_r^{dry} appearing in Eqs. (67) and (68), we turn to a wick previously used[10] made of several layers of woven wire mesh. During drying the liquid moves along channels of wedge-shaped cross section formed by the warp wires and the densely packed woof wires,[10] i.e., in a wick of such structure, the number of channels along which the liquid moves and their cross section occupied by heat-transfer agent vary in proportion to the drying. In the case of partial drying the wick under discussion reduces to a stack of capillaries located along the pipe. The permeability of a stack of capillaries is related in the following manner to the average cross sections of the liquid-filled capillaries and their density n:

$$K=fs^2n,$$

where f is a coefficient which is determined by the geometry of the capillaries – the sinuosity and cross-sectional shape.

Using the simple geometric concepts in Fig. 3 we obtain the following approximate expression for the cross section of a wedge-shaped channel: $s=2r_k^2\sqrt{R_{warp}/r_k}$. The permeability of the wick is then

$$K(x)=\begin{cases} f4r_k^3R_{warp}n, & 0\leqslant x\leqslant x_{dry},\\ K_w, & x_{dry}\leqslant x\leqslant l, \end{cases} \tag{69}$$

where K_w is the permeability of a wick completely saturated with liquid; x_{dry} is the point at which drying begins, which is determined from the condition

$$(P_v-P_l)_{x=x_{dry}}=\frac{2\sigma\cos\delta}{a}. \tag{70}$$

The half-width r_k of the channel is determined from the pressure difference p_v-p_l along both sides of the free surface of the liquid:

$$r_k=\frac{\sigma\cos\delta}{P_v-P_l}. \tag{71}$$

Note that Eqs. (70) and (71) are written without inclusion, unimportant as a rule, of the phenomenon of recoil in phase transitions. Thus filtration of the heat-transfer agent is described by the Darcy equation

$$\frac{dP_l}{dx}=-\frac{\nu_l}{K}\tau_{l_x}, \tag{72}$$

in which the permeability of the wick is given by Eqs. (69) and (71). To determine the pressure of the liquid along the wick of a heat pipe by means of Eqs. (69)-(72) it is necessary to give its value at some point in the capillary structure. When the wick dries an excess of heat-transfer agent appears, which is driven back into the condensation zone by vapor flow. Therefore, at the point of minimum curvature of the free surface of the liquid, x_{min}, the latter coincides with the surface of the cavity of the heat pipe, and consequently

$$P_l|_{x_{min}}=P_v|_{x_{min}}-\frac{\sigma}{R}. \tag{73}$$

We determine x_{min} from the condition

$$\frac{d}{dx}[P_v-P_l]_{x_{min}}=0, \tag{74}$$

where dP_l/dx is given by Eq. (72). If there is no root of Eq. (74) in the condensation zone, x_{min} is equal to unity.

Finally, we discuss the quantities ε_1 and ε_r^{dry}. On the basis of the above ideas concerning the heat-transfer agent and the structure of a wick made of woven wire mesh, one can set $\varepsilon_1=2r_kn$ and ε_r^{dry} equal to the porosity

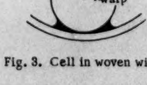

Fig. 3. Cell in woven wire mesh.

of the wick, ε_{WT}. The coefficients of thermal conductivity λ'_x and λ'_r are given approximately by

$$\lambda'_x = \lambda_{TB}(1-\varepsilon_{W.x}); \quad \lambda'_r = \lambda_{TB}(1-\varepsilon_{WT}).$$

With insignificant changes we also apply the method discussed above for approximate solution of Eq. (7) to the present problem of heat propagation through the jacket of a pipe with partial drying of the capillary structure.

SOME RESULTS OF HEAT-PIPE CALCULATIONS

To carry out specific heat-pipe calculations and to compare the results of these calculations with existing experimental data a final development of the computational method at the level of an algorithm and its realization in the form of a computer program has been accomplished. Some of the results obtained in two sets of calculations are discussed below. By mathematical simulation of the appropriate operating conditions for a heat pipe, the nature of the observed significant variations of vapor temperature in the cavity of a heat pipe[10] is clarified in the first set of calculations. The second set is concerned with the question of heat-pipe optimization.

1. The considerable variation in vapor temperature (up to 40°C) observed along the cavity of a heat pipe[10] cannot be interpreted as a manifestation of the effect of vapor compressibility since the Mach number is considerably less than unity under the experimental conditions. Several probable causes for such behavior of vapor temperature have been suggested.

The first possible mechanism is a strong nonuniformity in the jacket temperture created by heat propagation. However, calculations performed on the basis of the combined formulation of the problem of heat-pipe design, in which this phenomenon is automatically included, show that heat propagation along the jacket of the pipe studied[10] is insignificant and does not lead to a change in vapor temperature along the pipe.

Another possible mechanism for the variation in vapor temperature is any process occurring directly in the cavity of the pipe and associated with the fact that vapors of alkali metals are a mixture of chemically reacting molecules with different structures (A_1, A_2, A_3, etc., where A is the designation for a chemical element). The chief chemical reaction is the dimerization reaction

$$A_2 \rightleftarrows 2A_1 \tag{75}$$

with a rather low value for the heat of reaction. Estimates of the rate constant for this reaction in the region of heat-pipe operating temperatures give a value of 10^{10} from the Arrhenius equation. This high value for the rate constant indicates the equilibrium nature of the reaction (75). The existence of an equilibrium chemical reaction in the vapor shows up in its heat capacity. This quantity increases severalfold in comparison with the vapor heat capacity for the freezing reaction. The high value of the vapor heat capacity should prevent a drop in the vapor temperature. However, this tendency can be disturbed by the vaporization process. If conditions are created such that the ratio between the fluxes of vaporizing monatomic and diatomic molecules changes along the vaporization zone, if the phase transition occurs in this case with molecules of different atomicities involved, and if this ratio is different from the molecular ratio in the pipe cavity, then a chemical reaction can occur in the cavity and can cause a drop in vapor temperature. Nonuniformity of conditions along the vaporization zone can be associated with variation in vapor pressure and with the dependence of ε on x.

To check this supposition a combined problem of heat-pipe design has been treated and includes chemical transformations of heat-transfer agent vapors as described by (75). A solution of this problem for various linear functions $\varepsilon(x)$ in the vaporization zone shows that nonuniformity of conditions along the vaporization zone created by variation in vapor pressure and by the $\varepsilon(x)$ dependence has an insignificant effect on the ratio between vaporizing monatomic and diatomic molecules along the vaporization zone and does not lead to a drop in vapor temperature. This calculation also indicates that the vapor produced by vaporization has almost the same composition as the vapor moving along the pipe cavity. As a result, it becomes possible to simplify significantly the calculation for a heat pipe in which alkali metals are used as a heat-transfer agent by eliminating the calculation for chemical transformations of vapors of the heat-transfer agent and by including this phenomenon effectively through a coefficient of heat capacity for the vapor which takes into account chemical reactions.

The consequences of partial drying of the capillary structure have been subsequently studied with this result included on the basis of the model discussed above. The solution of the problem shows that in this case a considerable variation in vapor temperature along the vaporization zone of the heat pipe actually occurs (Fig. 4). It should be noted that there is considerable arbitrariness in the selection of values for the parameters f, f_1, Nu, n, β, and a. One can achieve agreement between the vapor temperature curve and the experimental data[10] by appropriate choice of these parameter values, particularly for the function n(x) in the region of partial drying.

Thus, on the basis of the calculations intended to explain the nature of the observed drop in vapor temperature,[10] one can assert that the drop is caused by partial drying of the capillary structure.

2. With the help of the operating condition (25) for heat pipes, calculations have also been performed to optimize the geometric parameters of heat pipes and to determine the limiting characteristics.

The left side of inequality (25) (denoted by ΔP_{max}) depends on geometric parameters of heat pipes (l, l_1, l_2, R, R_1), the thermal flux Q along the pipe, the operating temperature, and the properties of the capillary struc-

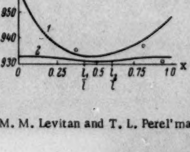

Fig. 4. Variation of vapor temperature along a heat pipe. 1) With partial drying of the capillary structure; 2) with a completely saturated wick; the points are experimental data.[10]

ture and heat-transfer agent. When Q increases $\Delta P_{\max}$ increases monotonically. Therefore the thermal loading for which the equality in (25) is satisfied is the maximum for a given heat pipe. It is obvious that for a given R_1 and with other conditions remaining the same, there is an optimum value for the radius of the heat-pipe cavity R at which the minimum pressure drop must be overcome by the capillary structure. Equating this drop to the maximum value of the capillary pressure $P_{k\max}$ we obtain the following expression for the maximum heat flux $Q_{\max}$ along a pipe:

$$\min_{0<R<R_1} [\Delta P_{\max}(Q_{\max})] = P_{k\max}. \tag{76}$$

Here one should immediately stipulate that Eq. (76) represents a limitation imposed on the quantity Q by the capabilities of the capillary structure. The true value of $Q_{\max}$ can be much smaller because of limitations on the thermal flux density through the pipe jacket in the vaporization zone associated with boiling of the heat-transfer agent and perturbations caused by this type of wick operation.

Shown below are some results for optimization by means of Eq. (76) for heat pipes with a capillary structure in the form of a coaxial gap formed by the pipe casing and a perforated screen. With transfer of maximum heat fluxes along high-temperature heat pipes, the mode of vapor flow is turbulent. Therefore the calculation of the vapor motion is based on the equation system (39). The radius of the screen openings is assumed to be $a = 0.1$ mm, the screen porosity $\varepsilon = 0.5$, and the coefficient of accommodation $\beta = 0.1$. Values for the condensation coefficient are taken from ref. 25.

Shown in Fig. 5 for three pipe lengths with proportional changes in each of the zones ($l_1/l = 0.36$, $l_2/l = 0.5$, $R_1 = 1$ cm) is the temperature dependence of the maximum heat flux density along the pipe for sodium and potassium heat pipes. As is clear from the curves, sodium heat pipes are able to transfer greater heat fluxes than potassium heat pipes at the same temperature, with the difference increasing as the temperature rises.

The dependence of maximum heat load on pipe length for sodium heat pipes at T = 973°K is also shown in Fig. 6. Curves 1, 5, and 6 correspond to a proportional variation of the length of each of the heat-pipe zones. With pipe operation in the vertical position (curve 6), where the vaporization zone is below, $Q_{\max}$ increases very little in comparison with the horizontal case (curve 5). For l somewhat greater than 1 m and T = 973°K, the heat-transfer agent generally cannot be maintained in the gap because of the effect of gravity and the gap dries. In this case return of the heat-transfer agent to the vaporization zone is not accomplished with the help of a capillary structure, as in wickless pipes, but as the result of a flow of condensate film along the internal surface of the pipe casing. It should be pointed out that if there are no differences in vapor pressure between the vaporization and condensation zones to oppose the gravitational force, then the coaxial gap will dry out when $l = 0.5$ m. The thermal pipe being discussed with a screen opening radius $a = 0.1$ mm and a length greater than 0.5 m cannot operate against the force of gravity. The same figure (curve 4) shows the dependence of maximum loading on l when only the length of the adiabatic zone is changed and the vaporization and condensation zones remain fixed. In this case $Q_{\max}$ falls considerably more rapidly with increasing l than with proportional changes in each of the pipe zones. A reduction in heat-pipe radius (curve 1) also leads to a reduction in maximum heat load.

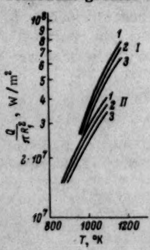

Fig. 5. Temperature dependence of maximum heat load transported along a heat pipe for sodium (I) and potassium (II) heat pipes. $R_1 = 1$ cm, $a = 0.1$ mm, $l_1/l = 0.36$, $l_2/l = 0.5$. l: 1) 0.5; 2) 1; 3) 2 m.

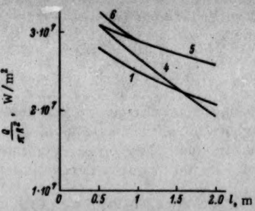

Fig. 6. Dependence of maximum heat load on pipe length for sodium heat pipes at 973°K. 1) $R_1 = 0.5$ cm, $\gamma = 0$; 4) $R_1 = 1$ cm, $\gamma = 0$; 5) $R_1 = 1$ cm, $\gamma = 0$; 6) $R_1 = 1$ cm, $\gamma = \pi/2$.

The optimum width of a coaxial gap for the maximum heat fluxes $Q_{\max}$ along the pipes in Figs. 5 and 6 is plotted in Fig. 7.

Typical distributions of vapor and liquid pressures as well as distributions of vapor temperature T_v, internal surface temperature T_0, and outer surface temperature T_1 of the coaxial gap are shown in Figs. 8 and 9 for maximum heat loads along sodium heat pipes. As is clear from the data, the thermal resistance of heat pipes is made up principally of the thermal resistance of the phase transitions in the vaporization and condensation zones

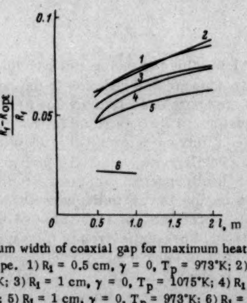

Fig. 7. Optimum width of coaxial gap for maximum heat flux along a sodium heat pipe. 1) $R_1 = 0.5$ cm, $\gamma = 0$, $T_p = 973$°K; 2) $R_1 = 1$ cm, $\gamma = 0$, $T_p = 1175$°K; 3) $R_1 = 1$ cm, $\gamma = 0$, $T_p = 1075$°K; 4) $R_1 = 1$ cm, $\gamma = 0$, $T_p = 973$°K; 5) $R_1 = 1$ cm, $\gamma = 0$, $T_p = 973$°K; 6) $R_1 = 1$ cm, $\gamma = \pi/2$, $T_p = 973$°K.

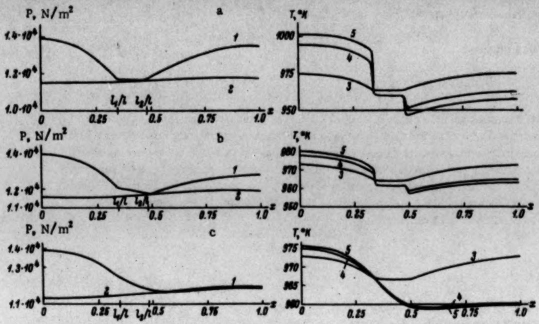

Fig. 8. Variation of vapor pressure P_v (1), liquid pressure P_l(2), vapor temperature T_v (3), internal surface temperature T_0 (4), and external surface temperature T_1 (5) of the coaxial gap along a pipe for transfer of maximum heat loads with Na. T_p = 973°K, $\gamma = 0$; a) R_1 = 1 cm, l = 0.5 m; b) R_1 = 1 cm, l = 2 m; c) R_1 = 0.5 cm, l = 2 m. a, b) x_{min} = 0.48331, x_{max} = 0; c) x_{min} = 0.68331, x_{max} = 0.

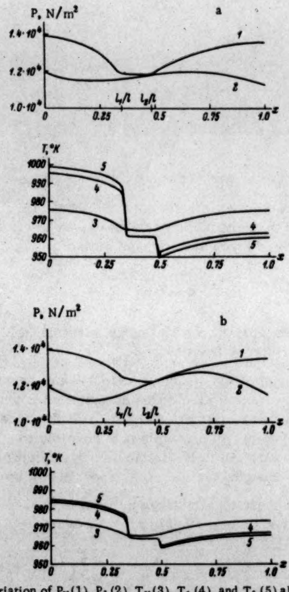

Fig. 9. Variation of P_v(1), P_l (2), T_v(3), T_0 (4), and T_1 (5) along a vertical pipe for transfer of maximum heat loads by Na at 973°K. a) R_1 = 1 cm, l = 0.5 m, x_{min} = 0.48331, x_{max} = 1.0; b) R_1 = 1 cm, l = 1 m, x_{min} = 0.5, x_{max} = 0.13333.

and the thermal resistance of the pipe jacket in the same zones in heat pipe operation at maximum heat loads. In all the cases shown, the points of maximum meniscus curvature, x_{max}, and of minimum meniscus curvature, x_{min}, occupy very different locations; this result confirms the need to use the heat-pipe operating condition in the form (24) or (25) in the calculations.

---

1) The operational principles of heat pipes were patented considerably earlier,[2] in 1944.

[1] G. M. Grover, T. P. Cotter, and T. F. Erickson, J. Appl. Phys., 35, 1990 (1964).
[2] R. S. Gaugler, US Patent 2,350,348, June 6, 1944.
[3] T. P. Cotter, Theory of Heat Pipes, LA-3246-MS (1965).
[4] E. Van Andel, Proc. Second Int. Conf. Thermionic Electrical Power Generation, Stresa (1968).
[5] C. A. Busse, "Pressure drop in the vapor phase of long heat pipes," Proc. Thermionic Conversion Specialist Conf., Palo Alto (1967).
[6] Yu. F. Potapov, Uch. Zap., TsAGI, 1, 126 (1970).
[7] I. M. Blinchevskii and B. F. Aptekar', Teplofiz. Vys. Temp., 9, 1089 (1971).
[8] Yu. F. Potapov, Uch. Zap. TsAGI, 2, 117 (1971).
[9] W. Hufschmidt, E. Burke, G. Kola, and H. Hoffman, in: Heat Pipes (E. E. Shpilrein, ed.) [Russian translation], Izd. Mir, Moscow (1972), p. 203.
[10] M. N. Ivanovskii, V. P. Sorokin, V. I. Subbotin, and M. V. Shustov, Teplofiz. Vys. Temp., 8, 319 (1970).
[11] T. L. Perelman, Int. J. Heat Mass Transfer, 3, 293 (1961).
[12] R. Ya. Kucherov and L. E. Rikenglaz, Dokl. Akad. Nauk SSSR, 133, 1130 (1960).
[13] Yu. V. Moskvin and Yu. N. Fillipov, Teplofiz. Vys. Temp., 7, 766 (1969).
[14] M. M. Levitan and T. L. Perel'man, Teplo- i Massoperenos, 2, 42 (1972) Minsk.
[15] F. Reiss and K. Schretzman, Proc. Second Int. Conf. Thermionic Electrical Power Generation, Stresa (1968).
[16] T. V. Kuskova, Computational Methods and Programming, No. 7 [in Russian], Izd. MGU (1967).
[17] T. V. Kuskova and L. A. Chudov, Computational Methods and Programming, No. 11 [in Russian], Izd. MGU (1968).
[18] N. I. Buleev and G. I. Timukhin, Izv. SO Akad. Nauk SSSR, Ser. Tekhn. Nauk, No. 1, 14 (1969).
[19] V. N. Varapaev, Izv. Akad. Nauk SSSR, MZhG, No. 4, 178 (1969).
[20] H. L. Weissberg, Phys. Fluids, 2, 510 (1959).
[21] I. P. Ginzburg, Teplo- i Massoperenos, 2 (1965) Minsk.
[22] R. M. Olson and E. P. D. Eckert, Applied Mechanics, Series E, 88, No. 1, 7 (1966).
[23] V. S. Mikhailov, A. M. Krapivin, P. I. Bystrov, G. I. Anofriev, and A. A. Volovik, Teplofiz. Vys. Temp., 10, 1256 (1972).
[24] T. L. Perel'man and M. M. Levitan, Inzh. Fiz. Zh., 25, 816 (1973).
[25] I. T. Alad'ev, N. S. Kondrat'ev, V. A. Mukhin, M. E. Kipshidze, I. F. Parfent'eva, and V. V. Kisilev, Heat Exchange, Hydrodynamics, and Thermophysical Properties of Matter [in Russian], Izd. Nauka, Moscow (1968), p. 32.

Design of axisymmetric plasma lenses

A. I. Morozov and S. V. Lebedev

(Submitted August 15, 1973)
Zh. Tekh. Fiz., 44, 1592-1600 (August 1974)

The focusing properties of plasma lenses differ significantly from those of ordinary electromagnetic lenses in the additional focusing or defocusing by the electric fields arising from the space charge in the plasma beam in the lens. For a very low electron temperature ($T_e \to 0$) Laplace's equation ($\Delta\Phi = 0$) for the scalar electric potential is replaced by the equation $\Phi = \Phi(rA_\theta)$, where A_θ is the azimuthal component of the vector potential of the magnetic field. We discuss the focusing properties and methods of designing axisymmetric plasma lenses when $\Phi = \Phi(rA_\theta)$. We calculate focal lengths of plasma lenses for shaping beams close to the axis of symmetry and hollow cylindrical plasma beams.

INTRODUCTION

Plasma lenses are used to focus dense neutralized ion beams. Plasma lenses differ from vacuum lenses[1)] in their ability to focus not only by external electromagnetic fields, but also by the electric field due to the space charge of the beam. Morozov[3] showed the possibility of producing plasma systems with focusing by E and H fields, and experimental confirmation is reported in refs. 4-6. Depending on the beam geometry we can distinguish two types of axisymmetric plasma lenses: axial and annular. Axial lenses focus plasma beams passing close to the axis symmetry. The axis of symmetry in these lenses is the optical axis, and the H field has no azimuthal component $H\varphi$. An example of such an axial plasma lens is given in refs. 4 and 7. Annular lenses operate with hollow cylindrical beams passing close to a certain cylindrical surface r = R, which we call the initial surface. The analog of the optical axis in such lenses is a cylindrical surface, whose generators can have a rather complicated form. We call this the fundamental surface and determine its actual shape later.

For simplicity we limit ourselves to a discussion of paraxial beams. In annular lenses we take the condition for a beam to be paraxial as

$$a \ll R, \tag{1}$$

where R is the radius of the initial surface and *a* is the characteristic width of the beam.

SPECIFICATION OF THE ELECTRIC AND MAGNETIC FIELDS

We specify the magnetic field by using the magnetic flux function ψ, which is related to the magnetic field components by the equations

$$H_r = -\frac{1}{r}\frac{\partial\psi}{\partial z}, \quad H_z = \frac{1}{r}\frac{\partial\psi}{\partial r}. \tag{2}$$

The function ψ satisfies the equation

$$\Delta^*\psi = r\frac{\lambda}{\partial r}\frac{1}{r}\frac{\partial\psi}{\partial r} + \frac{\partial^2\psi}{\partial z^2} = 0, \tag{3}$$

and the line ψ = const is the equation of the projection of the lines of force on the meridian (r, z) planes.

For paraxial beams we can expand ψ in powers of y = r − R (R = 0 for axial lenses), keeping the first terms of the expansion. By taking account of the symmetry about the z axis, for axial lenses we have

$$\psi = \frac{r^2}{2}H_0(z) - \frac{3}{2}\frac{r^4}{4!}H_0(z) + \frac{3\cdot5}{2\cdot4}\frac{r^6}{6!}H_0^{(\mathrm{IV})} + \ldots, \tag{4}$$

where $H_0(z)$ is the magnetic field H_z at r = 0, and the primes denote differentiation with respect to z.

For annular lenses we have

$$\psi = \psi_0(z) + \psi_1(z)\,y + \psi_2(z)\frac{y^2}{2} + \psi_3(z)\frac{y^3}{3!} + \ldots, \tag{5}$$

where by Eqs. (2) and (3)

$$\left.\begin{aligned} &\psi_0 = -R\int_{-\infty}^{z} H_r^0 dz, \quad \psi_1 = RH_z^0, \\ &\psi_2 = -\psi_0'' - \frac{\psi_1}{R}, \quad \psi_3 = -\psi_1'' - \frac{1}{R}\psi_0'', \end{aligned}\right\} \tag{6}$$

H_r^0 and H_z^0 are the projections of H on the initial surface.

For a plasma beam with cold electrons ($T_e \to 0$) the electric and magnetic fields are related by the condition that the lines of force are equipotentials:[3]

$$\Phi = \Phi(\psi). \tag{7}$$

Here, Φ is the scalar potential of the electric field, and $\Phi(\psi)$ is an arbitrary function of ψ.

The electric field distribution in a beam is established either by a system of electrodes at specified potentials,[4] or by conduction mechanisms characteristic of the given particular system. In principle it is possible to produce an arbitrary electric field distribution by a sytem of electrodes, thus changing the focusing properties of the lens.

If the expansions of ψ given by Eqs. (4) and (5) are known, $\Phi(\psi)$ can be expanded in a power series

$$\Phi(\psi) = \Phi(\psi_0) + \left.\frac{d\Phi}{d\psi}\right|_{\psi_0}\psi_1 y + \left(\left.\frac{d\Phi}{d\psi}\right|_{\psi_0}\psi_2 + \left.\frac{d^2\Phi}{d\psi^2}\right|_{\psi_0}\psi_1^2\right)\frac{y^2}{2} + \cdots \tag{8}$$

For axial lenses the coefficients Φ_{2n+1} (n = 0, 1, 2,...) are zero.

EQUATIONS OF MOTION

Taking account of the cyclic nature of the coordinate φ we write the equations of motion in the form[8]

$$M\ddot{r} = -\frac{\partial v}{\partial r} - \frac{l}{c}\dot{z}H_\varphi, \tag{9a}$$

$$M\ddot{z} = -\frac{\partial v}{\partial z} + \frac{l}{c}\dot{r}H_{\varphi}, \tag{9b}$$

$$Mr^2\dot{\varphi} + \frac{e}{c}\psi = D = \text{const}, \tag{9c}$$

where v is the generalized potential

$$v = \frac{\left(D - \frac{l}{c}\psi\right)^2}{2Mr^2} + l\Phi(\psi), \tag{10}$$

and D is the generalized momentum.

Since we are interested in the geometry of ion trajectories it is expedient to change from the variable t to z. As a result, (9a) and (9b) are replaced by

$$r'' + r'\frac{\ddot{z}}{\dot{z}^2} = -\frac{1}{M\dot{z}^2}\frac{\partial v}{\partial r} - \frac{l}{M_e}\frac{H_{\varphi}}{\dot{z}}. \tag{11}$$

The equation for $\dot{z}$ can be obtained from the conservation of energy:

$$\frac{M}{2}\dot{z}^2(1 + r'^2) = -u, \tag{12}$$

where u ≡ v − ε, and ε is the total ion energy.

Eliminating $\ddot{z}$ and $\dot{z}^2$ by using (9b) and (12) we obtain

$$r'' = -\frac{1 + r'^2}{(-2u)}\left(\frac{\partial v}{\partial r} + r'\frac{\partial v}{\partial z}\right) - \left(\frac{eH_{\varphi}}{M_e}\right)^2 \frac{(1 + r'^2)^{3/2}}{\left(-\frac{2u}{M}\right)^{1/2}}. \tag{13}$$

In order to obtain the equation of motion in the paraxial approximation we expand the generalized potential v in a series, substitute it into (13), and retain terms linear in y. For axial systems we obtain

$$u = -\varepsilon + \frac{r^2}{2}v_2 + 0(r^4), \tag{14}$$

where

$$v_2 = \frac{e^2}{M_e^2}\frac{\psi_2^2}{4}, \tag{14a}$$

while for annular systems we have

$$u = -\varepsilon + v_0 + yv_1 + \frac{y^2}{2}v_2, \tag{15}$$

$$v_0 = \frac{\left(D - \frac{l}{c}\psi_0\right)^2}{2MR^2} + e\Phi(\psi_0), \tag{15a}$$

$$v_1 = \frac{\left(D\frac{l}{c}\psi_0\right)^2}{2MR^2} + \frac{l}{M_e}\frac{\psi_1\left(D - \frac{l}{c}\psi_0\right)}{R^2} + e\frac{d\Phi}{d\psi}\Big|_{\psi_1}, \tag{15b}$$

$$v_2 = 3\frac{\left(D - \frac{l}{c}\psi_0\right)^2}{MR^4} + \frac{1}{MR^2}\frac{l^2}{c^2}\psi_1^2 + \frac{l}{c}\frac{D\frac{l}{c}\psi_0}{MR^2}\left(\frac{4\psi_1}{R} - \psi_2\right)$$
$$+ e\left(\frac{d\Phi}{d\psi}\Big|_{\psi_0}\psi_2 + \frac{d^2\Phi}{d\psi^2}\Big|_{\psi_0}\psi_1^2\right). \tag{15c}$$

Substituting Eqs. (15) into (13) and linearizing, we obtain the equation in the paraxial approximation:

$$y'' + ay' + by + c = 0. \tag{16}$$

For annular lenses

$$a = -\frac{1}{M}\frac{v_0'}{\left(-\frac{2}{M}u_0\right)}, \quad b = \frac{1}{M}\frac{1}{\left(-\frac{2}{M}u_0\right)}\left(v_2 - \frac{v_1^2}{u_0}\right)$$
$$+ \left(\frac{eH_{\varphi 0}}{M_e}\right)^2 \frac{1}{\left(-\frac{2u_0}{M}\right)^{1/2}}\left(-\frac{2}{R}\frac{1}{2}\frac{v_1}{u_0}\right); \quad c = \frac{1}{M}\frac{v'}{\left(-\frac{2}{M}u_0\right)} + \frac{\left(\frac{eH_{\varphi 0}}{Mc}\right)^2}{\left(-\frac{2u_0}{M}\right)^{1/2}}, \tag{17}$$

$u_0 = v_0 - \varepsilon$, $H_{\varphi 0} = H_{\varphi}|_{r = R}$. If the lenses are axial, $v_0 = v_1 = 0$, $H_{\varphi} = 0$, $a = 0$, $c = 0$.

GAUSSIAN DIOPTRICS

We consider plasma lenses as analogs of thick optical lenses and describe them from the point of view of Gaussian dioptrics, introducing the cardinal elements – the focal lengths, nodal points etc. For generality we keep annular lenses in mind. The transition to axial lenses is made by letting R → 0.

We write the solution of Eq. (16) in the form

$$y = A_{q_1}(z) + B_{q_2}(z) + y_{\text{med}}, \tag{18}$$

where y_{med} is a particular solution of the inhomogeneous equation in (16), q_1 and q_2 are linearly independent solutions of the homogeneous equation in (16) for c = 0, and A and B are arbitrary constants that depend on the initial conditions.

We choose the boundary conditions of the function y_{med} as follows:

$$y'_{\text{med}}(-\infty) = y'_{\text{med}}(+\infty) = 0. \tag{19a}$$

Then the surface determined by the set of lines y_{med} will be the analog of the optical axis – the fundamental surface.

It is convenient to choose the functions $q_1(z)$ and $q_2(z)$ as basis functions relative to the fundamental surface, setting the boundary conditions equal to

$$q_1(-\infty) = 1, \; q_1'(-\infty) = 0, \; q_2(+\infty) = 1, \; q_2'(+\infty) = 0. \tag{19b}$$

The optical properties of a thick lens are completely determined by the asymptotic forms of the function q_1, q_2, and y_{med}. The starting and focal points in this case are conjugate points in the Gaussian sense, as follows from the linearity of Eq. (16).

If we introduce the focal lengths F_1 and F_2 (Fig. 1) the asymptotic forms of the functions $q_1(z)$ and $q_2(z)$ are

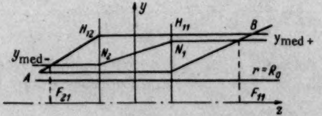

Fig. 1

$$q_1=\begin{cases}1, \\ \alpha_1\left(1-\frac{z}{F_1}\right),\end{cases} \quad q_2=\begin{cases}\beta_1\left(1+\frac{z}{F_2}\right) & (z\ll-\Lambda), \\ 1 & (z\gg\Lambda),\end{cases} \tag{20}$$

Λ is a characteristic dimension of the focusing fields along the initial surface, and F_1 and F_2 are measured from the plane z = 0. If we find d_1, β_1, F_1, and F_2 from (18) it is easy to determine the remaining cardinal elements of the lens. For example, the coordinates of the fundamental planes H_1 and H_2 are

$$H_1(z)=(d_1-1)\frac{F_1}{d_1}, \quad H_2(z)=-(\beta_1-1)\frac{F_2}{\beta_1}. \tag{21}$$

The principal points lie on the intersections of the fundamental planes with the "lines" $y_{\text{med}}(-\infty)$ and $y_{\text{med}}(+\infty)$. The construction of the image in a thick lens using the cardinal elements is shown in Fig. 1. It is frequently more convenient to find the asymptotic forms of the functions $q_1(z)$, $q_2(z)$, and y_{med} rather than F_1, F_2, d_1, and β_1. Then d_1 and β_1 are found by the points of intersection of the lines $q_1(-\infty)$, $q_1(+\infty)$, and $q_2(-\infty)$, $q_2(+\infty)$, and the focal lengths are

$$\frac{1}{F_1}=-\frac{q_1'(-\infty)}{\alpha_1}, \quad \frac{1}{F_2}=-\frac{q_2'(-\infty)}{\beta_1}. \tag{22}$$

WEAK FIELD APPROXIMATION

Since an exact analytic solution of Eq. (18) generally cannot be found, we present a method for finding the approximate form of the functions q_1, q_2, and y_{med}. In this method, the ratio of the change in particle velocity in the lens δv to the total velocity v_0 appears as a small parameter

$$\mu=\frac{\delta v}{v_0}\ll 1. \tag{23}$$

Thus we can seek a solution of Eq. (18) in the form of a series in inverse powers of v_0. For example

$$y=y_0+\frac{1}{v_0}y_1+\frac{1}{v_0^2}y_2+\ldots. \tag{24}$$

We apply the weak field method to determine the functions q_1, q_2, and y_{med}, assuming for simplicity that $H_\varphi = 0$. To do this we expand the coefficients *a*, b, and c in Eq. (17) in powers of v_0^{-2}. Taking account of the fact that

$$\frac{1}{\left(-\frac{2}{M}u\right)}=\frac{1}{v_0^2-\frac{2}{M}v}=\frac{1}{v_0^2}\left(1+\frac{2v}{Mv_0^2}+\cdots\right), \tag{25}$$

we obtain

$$a=\frac{a_1}{v_0^2}+\frac{a_2}{v_0^4}+\cdots=\frac{1}{v_0^2}\left(-\frac{1}{M}\frac{dv_0}{dz}\right)+\frac{1}{v_0^4}\left(-\frac{2v_0}{M^2}v_0'\right)+\ldots, \tag{26a}$$

$$b=\frac{b_1}{v_0^2}+\frac{b_2}{v_0^4}+\ldots+\frac{1}{v_0^2}\left(\frac{v^2}{M}\right)+\frac{1}{v_0^4}\left(\frac{2}{M}(v_1^2+v_0v_2)\right)+\ldots, \tag{26b}$$

$$c=\frac{c_1}{v_0^2}+\frac{c_2}{v_0^4}+\ldots=\frac{1}{v_0^2}\left(\frac{1}{M}v_1\right)+\frac{1}{v_0^4}\left(\frac{2}{M^2}v_1v_0\right)+\ldots. \tag{26c}$$

The functions q_1 and q_2 satisfy the homogeneous equation (18) for c = 0 with boundary conditions (19b):

$$q''+aq'+bq=0. \tag{27}$$

In order to use Eqs. (26) we write (27) in the form

$$q_1=1-\int_{-\infty}^{z}dz_1\int_{-\infty}^{z_1}dz_2\left[\left(\frac{a_1}{v_0^2}+\frac{a^2}{v_0^4}+\ldots\right)q_1'+\left(\frac{b_1}{v_0^2}+\frac{b_2}{v_0^4}+\ldots\right)q_1\right]. \tag{28a}$$

The expression for q_2 is similar except for the limits of integration :

$$q_2=1-\int_{+\infty}^{z}dz_1\int_{+\infty}^{z_1}dz_2\left[\left(\frac{a_1}{v_0^2}+\frac{a}{v_0^4}+\ldots\right)q_2'+\left(\frac{b_1}{v_0^2}+\frac{b_2}{v_0^4}+\ldots\right)q_2\right]. \tag{28b}$$

We seek the solution of (28a) in the form

$$q_1=q_{10}+q_{11}+q_{12}+\ldots. \tag{29}$$

Substituting (29) into (28a) we obtain

$$q_{10}=1, \tag{30a}$$

$$q_{11}=-\frac{1}{v_0^2}\int_{-\infty}^{z}dz\int_{-\infty}^{z}dz_2b_1, \tag{30b}$$

$$q_{12}=-\frac{1}{v_0^4}\left[\int_{-\infty}^{z}dz_1\int_{-\infty}^{z_1}dz_2b_2-\int_{-\infty}^{z}dz_1\int_{-\infty}^{z_1}dz_2a_1\int_{-\infty}^{z_2}dz_3b_1\right.$$
$$\left.-\int_{-\infty}^{z}dz_1\int_{-\infty}^{z_1}dz_2b_1\int_{-\infty}^{z_2}dz_3\int_{-\infty}^{z_3}dz_4b_1\right]. \tag{30c}$$

The expression for q_2 is similar. The function y_{med} differs from q_1 and q_2 by the boundary condition (19a) and therefore cannot be calculated by the Cauchy method, i.e., solution (28) is useless in this case. However, as before this function can be sought in the form of a series

$$y_{\text{med}}=y_{\text{med}\,0}+\varepsilon y_{\text{med}\,1}+\cdots+\varepsilon\sim\frac{1}{v_0^2}, \tag{31}$$

where successive terms of the series decrease rapidly with increasing v_0, and the first term y_{med} can be considered constant.

We again write Eq. (18) in integral form but now take account of the free term c(z). For condition (19a) we obtain

$$y_{\text{med}}=y_{\text{med}}(-\infty)-\int_{-\infty}^{z}dz_1\int_{-\infty}^{z_1}dz_2(ay'_{\text{med}}+by_{\text{med}}+c). \tag{32a}$$

$$y'_{\text{med}}(z)=-\int_{-\infty}^{z}dz_1(ay'_{\text{med}}+by_{\text{med}}+c). \tag{32b}$$

The equation for y'_{med} is obtained by taking account of the fact that a second boundary condition is imposed on this function at $z = -\infty$.

Substituting expansion (31) into (32) and using the fact that[2] y_{med} = const we obtain the equation for this quantity:

$$0=\int_{-\infty}^{+\infty}(b_1y_{\text{med}\,0}+c_1)\,dz. \tag{33a}$$

Hence using (26) we obtain

$$y_{\text{med}} = -\frac{\int\limits_{-\infty}^{+\infty} c_1 dz}{\int\limits_{-\infty}^{+\infty} b_1 dz} = -\frac{\int\limits_{-\infty}^{+\infty}}{\int\limits_{-\infty}^{+\infty} v_2 dz}. \tag{33b}$$

It follows from (33b) that $y_{\text{med}0}$ for $H_\varphi = 0$ does not depend on the mass or the velocity of the particles, i.e., the fundamental surface for a thin lens is an exact analog of the optical axis.

Knowing $y_{\text{med}0}$ and substituting it into (32a) we find the more accurate value $y_{\text{med}1}$:

$$y_{\text{med}\,1} = y_{\text{med}\,1}(-\infty) - \frac{1}{v_0^2}\int\limits_{-\infty}^{z} dz_1 \int\limits_{-\infty}^{z_1} dz_2 (b_1 y_{\text{med}\,0} + c_1)$$

$$\equiv y_{\text{med}\,1}(-\infty) + \tilde{y}_{\text{med}}. \tag{34a}$$

Here $y_{\text{med}1}(-\infty)$ must be determined from the condition

$$y'_{\text{med}\,1}(+\infty) = 0. \tag{35}$$

It is convenient to write $y_{\text{med}1}(-\infty)$ in the form

$$y_{\text{med}\,1}(-\infty) = y_{\text{med}\,0} - \delta y_1. \tag{34b}$$

Substituting (34b) into (32b) and using (35) we obtain

$$\delta y_1 = -\frac{\int\limits_{-\infty}^{+\infty} dz\,(a_1 \tilde{y}'_{\text{med}\,1} + b_1 \tilde{y}_{\text{med}\,1} + c)}{\int\limits_{-\infty}^{+\infty} b_1 dz}. \tag{36}$$

The expressions are simplified for axial lenses since $v_0(z)$ and $v_1(z)$ are identically zero. Therefore in the present case we obtain

$$q_1 = 1 - \frac{1}{Mv_0^2}\int\limits_{-\infty}^{z} dz_1 \int\limits_{-\infty}^{z_1} dz_2 v_2$$

$$-\frac{1}{(Mv_0^2)^2}\int\limits_{-\infty}^{z} dz_1 \int\limits_{-\infty}^{z_1} dz_2 v_2 \int\limits_{-\infty}^{z_2} dz_3 \int\limits_{-\infty}^{z_3} dz_4 v_2, \tag{37a}$$

$$y_{\text{med}0} = 0. \tag{37b}$$

FOCAL LENGTH OF LENSES

The focal length is determined by Eqs. (22), where, in the weak field approximation, the functions $q_1(z)$ and $q_2(z)$ can be found from Eqs. (30). Taking the right-hand focus F_1 for definiteness we find the value of a in this approximation. The equation for a follows from (20) and can be written as

$$a = \lim (q_1 - zq_1'), \quad z \to \infty. \tag{38}$$

Substituting (28a) into (38) we obtain

$$a = 1 + \int\limits_{-\infty}^{0} dz_1 \int\limits_{-\infty}^{z_1} dz_2 f(z_2, q_1) - \int\limits_{0}^{\infty} dz_1 \int\limits_{z_1}^{\infty} dz_2 f(z_2, q_1), \tag{39}$$

where

$$f(z_2, q_1) = \left(\frac{a_1}{v_0^2} + \frac{a_2}{v_0^4} + \dots\right) q_1' + \left(\frac{b_1}{v_0^2} + \frac{b_2}{v_0^4} + \dots\right) q_1.$$

Thus the required quantity F_1 is

$$\frac{1}{F_1} = -\frac{q_1'(+\infty)}{a} =$$

$$-\frac{\int\limits_{-\infty}^{+\infty} dz f(z_1, q_1)}{1 + \int\limits_{-\infty}^{0} dz_1 \int\limits_{-\infty}^{z_1} dz_2 f(z_2, q_1) - \int\limits_{0}^{\infty} dz_1 \int\limits_{z_1}^{\infty} dz_2 f(z_2, q_1)}. \tag{40a}$$

The equation for F_2^0 is similar:

$$\frac{1}{F} = -\frac{q_2'(-\infty)}{b} =$$

$$-\frac{\int\limits_{-\infty}^{+\infty} dz_1 f(z_1, q_2)}{1 + \int\limits_{\infty}^{0} dz_1 \int\limits_{\infty}^{z_1} dz_2 f(z_2, q_2) - \int\limits_{0}^{\infty} dz_1 \int\limits_{\infty}^{0} dz_2 f(z_2, q_2)}. \tag{40b}$$

Substituting into these expressions the explicit form of $f(z, q)$ and collecting terms with the same powers of v_0^2, we obtain expressions for the focal lengths as power series in v_0^2. Thus F_1 has the form

$$\frac{1}{F_1} = \frac{1}{Mv_0^2} W\Big|_{-\infty}^{+\infty} + \frac{1}{(Mv_0^2)^2} A + 0\left(\frac{1}{(Mv_0^2)^3}\right), \tag{41}$$

where

$$W = \int\limits_{-\infty}^{z} v_2 dz, \tag{42a}$$

$$A = 2\int\limits_{-\infty}^{+\infty} v_1^2 dz + 2\,[v_0 W]_{-\infty}^{+\infty} - W\Big|_{-\infty}^{+\infty} \int\limits_{-\infty}^{+\infty} W dz + \int\limits_{-\infty}^{+\infty} W^2 dz$$

$$-\int\limits_{-\infty}^{+\infty} W v_0' dz - W\Big|_{-\infty}^{+\infty}\left[\int\limits_{-\infty}^{0} W dz + \int\limits_{0}^{\infty} dz_1 \int\limits_{z_1}^{\infty} v_2 dz\right]. \tag{42b}$$

For axial lenses F_1 is given by

$$\frac{1}{F} = \frac{1}{Mv_0^2} W\Big|_{-\infty}^{+\infty} - \frac{1}{(Mv_0^2)^2} A_1 + 0\left(\frac{1}{Mv_0^2}\right)^3, \tag{43}$$

where

$$A = \int\limits_{-\infty}^{+\infty} W^2 dz + W\Big|_{-\infty}^{+\infty}\left(\int\limits_{-\infty}^{+\infty} W dz - \int\limits_{-\infty}^{0} W dz + \int\limits_{0}^{\infty} dz_1 \int\limits_{z_1}^{\infty} v_2 dz_2\right). \tag{44}$$

THIN ANNULAR BILENSES

1. Example of a magnetic bilens. As an example we find the focal length and position of the fundamental surface for an annular magnetic bilens. We specify the magnetic field of the bilens in the form

$$\psi_0 = H_0 R \Lambda \sqrt{\frac{e}{2}}\, e^{-z^2/\Lambda^2}, \quad \psi_1 = 0. \tag{45}$$

Here H_0 is a characteristic value of the magnetic field intensity on the initial surface, and Λ is a characteristic length of the field over the initial surface.

We assume that the electric field is zero. We assume that the bilens is thin, i.e., we retain only the first term in expansion (41). Substituting the expression for the magnetic field (45) into Eq. (41) for the focal length and integrating, we find

$$\frac{1}{F_1}=\frac{H_0^2 e_0^2 \Lambda^3}{c^2 (Mv_0)^2 R^3}\frac{e}{2}\sqrt{\frac{\pi}{2}}1+3\frac{\Lambda^2}{R^2}. \tag{46}$$

The position of the fundamental surface is given by Eq. (33b). We obtain

$$y_{\text{med}\,0}=\frac{\Lambda^2}{R}\frac{1}{1+\frac{3\Lambda^2}{R^2}}. \tag{47}$$

The paraxial condition (1) leads to a bound on the value of $y_{\text{med}0}$:

$$y_{\text{med}\,0}\ll R. \tag{48}$$

It follows from this that R must satisfy the inequality

$$\left(\frac{\Lambda}{R}\right)^2\ll 1. \tag{49}$$

As R increases $y_{\text{med}0} \to 0$ and the fundamental surface coincides with the initial surface. It is easy to see that for $\psi_1 = 0$ this is true for any field distribution H_r on the initial surface. Setting $\psi_1 = 0$ and integrating by parts we find for any ψ_0 we have

$$y_{\text{med}\,0}=\frac{\Lambda^2}{R}\frac{\int\limits_{-\infty}^{+\infty}\psi_0^2\,dz}{\int\limits_{-\infty}^{+\infty}\left(\psi_0'^2+3\frac{\Lambda^2}{R^2}\psi_0^2\right)dz}. \tag{50}$$

We note that in such lenses the fundamental surface is always above the initial surface ($y_{\text{med}0} > 0$).

2. Example of an electrostatic bilens. We assume that $H \to 0$ but is large enough to confine the space charge. Then the focusing will be determined by the magnitude and distribution of the electric field, i.e., the lens will be electrostatic. Retaining the shape of the magnetic field as given by (45) we specify the electric field distribution on the initial surface as[3)]

$$E_z=2E_0\frac{z^2}{\Lambda^2}e^{1-2z^2/\Lambda^2}. \tag{51}$$

Then substituting (51) into (42a) we find

$$W=e_0\int\limits_{-\infty}^{z}E_z\frac{1}{H_r}\frac{dH_r}{dz}dz=\frac{e_0E_z}{2}. \tag{52}$$

Since $E_z \big|_{-\infty}^{+\infty} = 0$, Eq. (43) shows that the focal length of the bilens $F_1 \sim v_0^4$. Substituting (52) into (43) we find that

$$\frac{1}{F_1}=\frac{3\sqrt{\pi}}{512}\frac{1}{\left(\frac{Mv_0^2}{2l_0}\right)^2}\frac{e_0^2\Phi_0^2}{\Lambda}, \tag{53}$$

where Φ_0 denotes the value of $E_0\Lambda$.

In order to make an electrostatic plasma bilens with a focal length $F \sim v_0^2$ the electric field must be eliminated from the defocusing parts of the magnetic bilens, e.g., by shortening the electrodes determining the electric field distribution. Thus taking the electric field distribution in the form

$$E_z=\sqrt{2e}E_0\frac{z}{\Lambda}e^{-z^2/\Lambda^2},\quad -\frac{\Lambda}{\sqrt{2}}>z,\quad z>\frac{\Lambda}{\sqrt{2}}, \tag{54a}$$

$$E_z=0,\quad -\frac{\Lambda}{\sqrt{2}}<z<\frac{\Lambda}{\sqrt{2}} \tag{54b}$$

and substituting (54) into (43) we obtain after integrating

$$\frac{1}{F}=\frac{\sqrt{2}}{(Mv_0^2)\,12e_0}\frac{\Phi_0}{\Lambda}. \tag{55}$$

It follows from Eqs. (53) and (55) that by changing the electric field distribution with respect to the magnetic lines of force it is possible to change the velocity dispersion as well as the focal length. We note also that an electrostatic bilens with fields (45) and (54) can be either converging or diverging.

[1)] Lenses which focus tenuous unneutralized charged-particle beams are called vacuum lenses.

[2)] Clearly $y_{\text{med}} = y_{\text{med}0}$ at $\varepsilon = 0$, but in this case $v_0 \to \infty$ and the trajectory is not perturbed.

[3)] Because of condition (7) the electric field distribution is generally arbitrary with respect to the lines of force.

---

[1] V. M. Kel'man and S. Ya. Yavor, Electron Optics [in Russian], AN SSSR, Moscow–Leningrad (1963).

[2] L. Ya. Artsimovich and S. Yu. Luk'yanov, The Motion of Charged Particles in Electric and Magnetic Fields [in Russian], Nauka, Moscow (1972).

[3] A. I. Morozov, Dokl. Akad. Nauk SSSR, 163, 1363 (1965) [Sov. Phys.–Dokl., 10, 775 (1966)].

[4] V. V. Zhukov, A. I. Morozov, and G. Ya. Shchepkin, ZhETF Pis. Red., 9, 24 (1969) [JETP Lett., 9, 14 (1969)].

[5] A. I. Morozov, Yu. V. Esipchuk, G. N. Talinin, A. V. Trofimov, Yu. A. Sharov, and G. Ya. Shchepkin, Zh. Tekh. Fiz., 42, 54 (1972) [Sov. Phys.–Tech. Phys., 17, 38 (1972)].

[6] I. P. Zubkov, A. Ya. Kislov, S. V. Lebedev, and A. I. Morozov, Zh. Tekh. Fiz., 41, 526 (1971) [Sov. Phys.–Tech. Phys., 16, 409 (1971)].

[7] S. V. Lebedev and A. I. Morozov, Zh. Tekh. Fiz., 36, 960 (1966) [Sov. Phys.–Tech. Phys., 11, 707 (1966)].

[8] A. I. Morozov and L. S. Solov'ev, Reviews of Plasma Physics, Vol. 3, Consultants Bureau, New York (1967).

Acousto-electric waves in conducting media

P. A. Andreev

M. I. Kalinin Leningrad Polytechnic Institute

(Submitted September 21, 1973)
Zh. Tekh. Fiz., 44, 1601-1607 (August 1974)

The instability excited by the transmission of an acoustic wave through a conducting medium is investigated. The critical values of the acoustic flux density at which the instability becomes absolute or convective are determined.

An acoustic wave propagating in a medium entrains charge carriers and produces a constant acousto-electric current $\mathbf{j}^{ae}$ or, in the case of an open circuit, a constant acousto-electric field $\mathbf{E}^{ae}$. The acousto-electric field can be represented in the form

$$\mathbf{E}^{ae} = \chi\mathbf{J} + \chi_1[\mathbf{J},\ \mathbf{H}_0] + \chi_2\mathbf{H}_0(\mathbf{J},\ \mathbf{H}_0), \qquad (1)$$

where $\mathbf{J}$ is the energy flux density of the acoustic wave and $\mathbf{H}_0$ is the external magnetic field.

A magnetohydrodynamic (MHD) theory of the acoustic electric effect has been formulated in the single-fluid and two-fluid MHD approximations.[1,2] Expressions have been derived for the coefficients $\varkappa$, $\varkappa_1$, and $\varkappa_2$ in these approximations. It has been shown[2] that acoustic streaming can generate waves and magnetic field structures. In the present paper we investigate the stabilities of the magnetic field (Sec. 1). We also show that an acoustic flux can produce instability in a conducting medium (Sec. 2).

1. ANALYSIS OF INSTABILITIES

We assume that an acoustic wave with an energy flux density J propagates in a conducting medium in the x direction. The external magnetic field $\mathbf{H}_0$ is directed along the y axis. We have previously[2] derived a dispersion relation from the linearized equations for small deviations of the magnetic field $\mathbf{H}'$, the electric field $\acute{E}$, and the current $\mathbf{j}'$ under the stated assumptions. It is assumed that $|\mathbf{k}_H| \ll |\mathbf{k}|$, $\omega_H \ll \omega$ (where $\mathbf{k}_H$ is the wave vector for the generated wave, $\mathbf{k}$ is the wave vector for the transmitted wave, and ω_H, ω are the corresponding wave frequencies). This dispersion relation is extremely cumbersome, so that the nature of the instability is investigated in the same special cases as in ref. 2.

1. $k_H \equiv k_x$. In this case the dispersion relations obtained in ref. 2 can be written in the form

$$\omega_H = c|\chi_1|Jk_H - i\left(\frac{c^2\rho}{4\pi}k_H^2 - 2c\gamma|\chi_1|J\right), \qquad (2)$$

$$\omega_H = c|\chi_1|Jk_H - i\left[\frac{c^2k_H^2}{4\pi}(\rho + \rho_2H_0^2) - 2c\gamma|\chi_1|J\right], \qquad (3)$$

where ρ and ρ_2 are the ordinary and the focused resistivities, γ is the attenuation of the transmitted wave, and $\chi_1 < 0$.

We assume the external magnetic field to be weak, i.e., $\rho/\rho_2H_0^2 \gg 1$. We can then limit the analysis to an instability with the dispersion relation (2). For an acoustic flux density

$$J > \frac{c\rho k_H^2}{8\pi\gamma|\chi_1|} \qquad (4)$$

the frequency ω has a positive imaginary part, indicating an instability. To calculate the character of that instability, following ref. 3, we find the inverse function

$$k_{H_{1,2}}(\omega_H) = -\frac{2\pi|\chi_1|J}{c\rho}i \pm \sqrt{\frac{4\pi}{c\rho}\left(\frac{i\omega}{c} + 2\gamma|\chi_1|J\right) - \left(\frac{2\pi|\chi_1|J}{c\rho}\right)^2}. \qquad (5)$$

The function $k_H(\omega_H)$ has a branch point at the frequency

$$\omega_H = iJ|\chi_1|c\left(2\gamma - \frac{\pi|\chi_1|J}{c\rho}\right). \qquad (6)$$

We consider the contour Ω described by the point ω_H in the complex plane given by Eq. (2) as the real variable k_H varies over the interval $-\infty \leq k_H \leq +\infty$. Putting $\omega_H = \alpha + i\beta$, we obtain the following equation for the portion of Ω that lies in the upper half-plane:

$$\beta = 2\gamma c|\chi_1|J - \frac{\rho}{4\pi}\left(\frac{\alpha}{|\chi_1|J}\right)^2. \qquad (7)$$

At the branch point $\omega_0 = \alpha_0 + i\beta_0$

$$\alpha_0 = 0,\quad \beta_0 = 2\gamma c|\chi_1|J - \frac{\pi}{\rho}(|\chi_1|J)^2, \qquad (8)$$

i.e., in accordance with ref. 3, the instability is convective for $J \geq 2\gamma c\rho/\pi|\chi_1|$ and absolute for $J < 2\gamma c\rho/\pi|\chi_1|$. We note that for (4) to be satisfied it is necessary that $\gamma/k_H > 0.25$ in the case of absolute instability (in the case of convective instability there are no constraints on the ratio γ/k_H). The range corresponding to the absolute instability is very narrow because the analysis is valid for $\gamma/k_H < 1$.

It is evident from an examination of (5) that the following inequalities hold for two waves with wave vectors $k_{H_1}(\omega_H)$ and $k_{H_2}(\omega_H)$ for $\mathrm{Im}\,\omega_H = 0$:

$$\mathrm{Im}\,k_{H_1}(\omega_H) < 0,\quad \mathrm{Im}\,k_{H_2}(\omega_H) < 0,$$

for waves where $\mathrm{Im}\,\omega_H \to \infty$ the appropriate inequalities are

$$\mathrm{Im}\,k_{H_1}(\omega_H) > 0,\quad \mathrm{Im}\,k_{H_2}(\omega_H) < 0.$$

Therefore, according to ref. 3, the solution $k_{H_1}(\omega_H)$ corresponds to wave amplification, and the solution $k_{H_2}(\omega_H)$ to cutoff.

2. $k_H \equiv k_z$ (for $k_H \equiv k_y$, as is shown in ref. 2, periodic field structures are excited). The dispersion relation for this case has the form

$$\omega_H = -2c\frac{|\chi|}{H_0}Jk_H - i\left(\frac{c^2\rho}{4\pi}k_H^2 - 2c\gamma|\chi_1|J\right). \qquad (9)$$

The value of the critical acoustic flux density at which the instability sets in is given by Eq. (2). The only difference is in the frequency of the waves. The instability is analyzed as in case 1. For

$$J < \frac{c\rho\gamma|\chi_1|}{2\pi}\left(\frac{H_0}{|\chi|}\right)^2, \quad \frac{\gamma}{k_H} > \frac{1}{4}\frac{|\chi|}{H_0|\chi_1|}$$

the instability is absolute, and for

$$J \geqslant \frac{c\rho\gamma|\chi_1|}{2\pi}\left(\frac{H_0}{|\chi|}\right)^2$$

it is convective. Note[2] that $|\chi|/H_0|\chi_1| \ll 1$, so that the range corresponding to the absolute instability is now much broader than in case 1.

The inverse of the function (9) has the form

$$k_{H_{1,2}}(\omega_H) = \frac{2\pi|\chi|J}{c\rho H_0}i \pm \sqrt{\frac{4\pi}{c\rho}\left(\frac{i\omega}{c} + 2\gamma|\chi_1|J\right) - \left(\frac{2\pi|\chi|J}{c\rho H_0}\right)^2}. \tag{10}$$

It is evident from an investigation of (10) that the solution $k_{H_1}(\omega_H)$ corresponds to cutoff, and the solution $k_{H_2}(\omega_H)$ to wave amplification.

3. We now consider the case in which the wave vector of the generated wave has two components. The simplest dispersion relations are obtained for $\mathbf{k}_H = (k_x, 0, k_z)$. Hereinafter, so as not to encumber the notation with subscripts, we write k instead of k_H. The dispersion relations now have the form

$$\omega = c|\chi_1|Jk_x - i\left[\frac{c^2k^2}{4\pi}(\rho + \rho_2H_0^2) - 2\gamma c|\chi_1|J\right], \tag{11}$$

$$\omega = cJ\left(|\chi_1|k_x - \frac{2|\chi|}{H_0}k_z\right) - i\left(\frac{c^2\rho}{4\pi}k^2 - 2\gamma c|\chi_1|J\right). \tag{12}$$

An instability arises when

$$J > \frac{ck^2(\rho + \rho_2H_0^2)}{8\pi\gamma|\chi_1|}$$

for the dispersion relation (11) and when

$$J > \frac{c\rho k^2}{8\pi\gamma|\chi_1|}$$

for the dispersion relation (12). Following ref. 4, we determine the character of the resulting instability as follows. If a magnetic field fluctuation occurs at time t = 0, being represented in the form

$$H'(r, 0) = \frac{1}{(2\pi)^3}\int H'(k)e^{i\mathbf{kr}}d^3k, \tag{13}$$

the magnetic field at time t is equal to

$$H'(r, t) = \frac{1}{(2\pi)^3}\int H'(k)e^{i\mathbf{kr} - i\omega(k)t}d^3k. \tag{14}$$

The initial fluctuation is finite in space; therefore the integral in (14) converges. We substitute the frequency given by (11) into (14):

$$H'(r, t) \sim \int H'(k)e^{i\left\{k_x x + k_z z - c|\chi_1|Jk_x t + it\left[\frac{c^2k^2}{4\pi}(\rho+\rho_2H_0^2) - 2c\gamma|\chi_1|J\right]\right\}}dk_x dk_z$$

$$\sim e^{2\gamma c|\chi_1|t - \frac{\pi(c|\chi_1|Jt - x)^2}{c^2(\rho+\rho_2H_0^2)t} - \frac{\pi z^2}{c^2(\rho+\rho_2H_0^2)t}}\int_{-\infty}^{+\infty}H'(\tilde{k})e^{-(\tilde{k}_x^2+\tilde{k}_z^2)}d\tilde{k}_x d\tilde{k}_z, \tag{15}$$

where $\tilde{k}_x$ and $\tilde{k}_z$ depend linearly on k_x and k_z, respectively. The integral in (15) converges. If the magnetic field fluctuation is not to be attenuated it is necessary that the exponent of the exponential function preceding the integral in (15) be nonnegative. This condition is satisfied by points inside the conic surface described by the equation

$$\frac{c^2(\rho + \rho_2H_0^2)}{\pi}\left[2\gamma c|\chi_1|J - \frac{(\pi c|\chi_1|J)^2}{c^2(\rho + \rho_2H_0^2)}\right] - z^2 - x^2 + 2c|\chi_1|Jtx \geqslant 0. \tag{16}$$

We consider the intersection of this cone with the plane z = 0 (Fig. 1). Two cases are possible, depending on the magnitude of J; in the first case (Fig. 1a) condition (16) is satisfied for a particular $x = x_0$ only in a definite time interval, i.e., the resulting magnetic field fluctuation exists at the given point only for a certain time; in the second case (Fig. 1b) condition (16) is satisfied for a particular $x = x_0$ after a time $t = t_1$, i.e., the fluctuation grows at its place of origin. Consequently, in the first case the system is convectively unstable, and in the second case it is absolutely unstable. It is inferred from (16) that the regions in which perturbations can propagate in the case of convective instability correspond to the points

$$|z| \leqslant ct\sqrt{\frac{2\gamma c|\chi_1|J(\rho + \rho_2H_0^2)}{\pi}}.$$

The existence of a convective instability requires that $J > 2c\gamma(\rho + \rho_2H_0^2)/\pi|\chi_1|$, and an absolute instability requires that $J \leq 2c\gamma(\rho + \rho_2H_0^2)/\pi|\chi_1|$ (here, as before, $\gamma/k > 0.25$). To investigate the possibility of wave amplification we find the inverse of the function (11). Inasmuch as $\omega = \omega(k_x, k_z)$, we consider the two inverse functions $k_z = k_z(\omega, k_x)$ and $k_x = k_x(\omega, k_z)$, treating the wave vector component entering into the right-hand sides of the equations as a parameter. The first equation has the form

$$k_{z_{1,2}} = \pm\sqrt{\frac{4\pi(i\omega - ic|\chi_1|Jk_x + 2\gamma c|\chi_1|J)}{c^2(\rho + \rho_2H_0^2)} - k_x^2}. \tag{17}$$

For any k_x we find that the following inequalities hold for two waves with wave vectors $k_{z_1}(\omega, k_x)$ and $k_{z_2}(\omega, k_x)$ when $\operatorname{Im}\omega = 0$ and $\operatorname{Im}\omega \to +\infty$:

$$\operatorname{Im}k_{z_1}(\omega, k_x) > 0, \quad \operatorname{Im}k_{z_2}(\omega, k_x) < 0.$$

Consequently, the system does not transmit waves along the z axis. The second equation is written in the form

$$k_{x_{1,2}} = -\frac{2\pi|\chi_1|i}{c(\rho + \rho_2H_0^2)} \pm$$

$$\pm\sqrt{\frac{4\pi}{c^2(\rho + \rho_2H_0^2)}\left(i\omega + 2\gamma c|\chi_1|J - \frac{\pi|\chi_1|}{\rho + \rho_2H_0^2}\right) - k_z^2}. \tag{18}$$

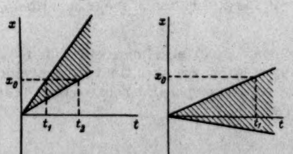

Fig. 1. a) Convective instability; b) absolute instability.

For any k_z, in the limit $\operatorname{Im}\omega \to +\infty$

$$\operatorname{Im} k_{x_1}(\omega, k_z) > 0, \quad \operatorname{Im} k_{x_2}(\omega, k_z) < 0.$$

If k_z is a real number, for $\operatorname{Im}\omega = 0$ we obtain $\operatorname{Im} k_{x_1} \cdot (\omega, k_z) < 0$ $\operatorname{Im} k_{x_2}(\omega, k_z) < 0$ for $k_z^2 < 8\pi\gamma|\chi_1| J/c(\rho + \rho_2 H_0^2)$ and $\operatorname{Im} k_{x_1}(\omega, k_z) > 0$, $\operatorname{Im} k_{x_2}(\omega, k_z) < 0$ for $k_z^2 > 8\pi\gamma|\chi_1| \cdot J/c(\rho + \rho_2 H_0^2)$.

Consequently, for $k_z^2 < 8\pi\gamma|\chi_1|J/c(\rho + \rho_2 H_0^2)$ the solution $k_{x_1}(\omega, k_z)$ corresponds to wave amplification, and the solution $k_{x_2}(\omega, k_z)$ to cutoff; for $k_z^2 > 8\pi\gamma|\chi_1|J/c(\rho + \rho_2 H_0^2)$ the system does not transmit waves along the x axis.

If k_z is imaginary, then for $\operatorname{Im}\omega = 0$

$$\operatorname{Im} k_{x_1}(\omega, k_z) < 0, \quad \operatorname{Im} k_{x_2}(\omega, k_z) < 0.$$

Consequently, the solution $k_{x_1}(\omega, k_z)$ corresponds to amplification, and the solution $k_{x_2}(\omega, k_z)$ to cutoff.

We investigate the character of the instability given by the dispersion relation (12) by the same procedure. The condition for the onset of instability is $J > c\rho k^2/8\pi\gamma \cdot |\chi_1|$.

For the magnetic field fluctuation we obtain the expression

$$H'(r, t) \sim e^{2\gamma c|\chi_1|Jt - \frac{\pi t}{\rho c^3}\left[\left(cJ|\chi_1| - \frac{x}{t}\right)^2 + \left(2cJ\frac{|\chi|}{H_0} + \frac{z}{t}\right)\right]^2} \times \int_0^\infty H'(\bar{k}) e^{-\bar{k}_x^2 - \bar{k}_z^2} d\bar{k}_x d\bar{k}_z. \tag{19}$$

The magnetic field fluctuation is unattenuated for points inside the conic surface (Fig. 2)

$$(x - cJ|\chi_1|t)^2 + \left(z + 2cJ\frac{|\chi|}{H_0}t\right)^2 - \frac{2\gamma c^3|\chi_1|\rho t^2}{\pi} \leqslant 0. \tag{20}$$

The axis of this cone is the line of interaction of the two planes $x = cJ|\chi_1|t$ and $z = -2cJ|\chi|t/H_0$. It is clear that an absolute instability occurs only when the onset conditions along the x axis and along the z axis are satisfied. Considering the intersections of the cone (20) with those planes we obtain the following conditions for the onset of the absolute instability: $J \leq 2\gamma c\rho/\pi|\chi_1|$, $\gamma/k > 0.25$, and for the onset of convective instability: $J > 2\gamma c\rho/\pi|\chi_1|$. The complexity of the dispersion relation (12) prevents us from carrying out a complete instability analysis. We merely note that this dispersion relation implies the existence of waves that are amplified in propagation.

2. EXCITATION OF INSTABILITY OF A MEDIUM

To find the condition for the onset of instability of a conducting medium we use the linearized system of equations for the perturbations of the velocity v', density of the medium ρ', pressure p', current, and magnetic and electric fields:

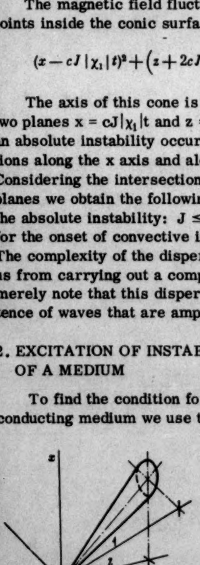

Fig. 2. Cone of instability in a conducting medium. 1) $x = cJ|\chi|t$; 2) $z = -2cJ(|\chi|/H_0)t$.

$$\left.\begin{aligned}
&\operatorname{curl}\mathbf{H}' = \frac{4\pi}{c}\mathbf{j}', \operatorname{curl}\mathbf{E}' = -\frac{1}{c}\frac{\partial\mathbf{H}'}{\partial t},\\
&\frac{\partial\rho'}{\partial t} = -\rho_0 \operatorname{div} v', \ \nabla p = u_0^2\nabla\rho',\\
&\frac{\partial\mathbf{v}'}{\partial t} = -\frac{\nabla p'}{\rho_0} - \frac{1}{4\pi\rho_0}[\mathbf{H}_0, \operatorname{curl}\mathbf{H}'] + \nu\nabla\mathbf{v}',\\
&\sigma\left(\mathbf{E} + \frac{1}{c}[\mathbf{v}', \mathbf{H}_0]\right) = \rho\mathbf{j}' + \rho_1[\mathbf{j}', \mathbf{H}_0] + \rho_2\mathbf{H}_0(\mathbf{j}', \mathbf{H}_0)\\
&\quad + \rho\lambda[\mathbf{J}, \mathbf{H}'] + 2\rho_1\lambda(\mathbf{H}', \mathbf{H}_0)\mathbf{J} - \rho_1\lambda\mathbf{H}_0(\mathbf{H}', \mathbf{J}),
\end{aligned}\right\} \tag{21}$$

where u_0 is the usual acoustic velocity in the medium, ρ_0 is the unperturbed density of the medium, ν is the kinematic viscosity, σ is the conductivity of the medium, and λ is the coefficient in the relation[2] $\mathbf{j}^{ae} = \lambda[\mathbf{J}, \mathbf{H}_0]$. The external magnetic field is perpendicular to the direction of propagation of the acoustic wave. We confine the analysis of the dispersion relation to special cases.

1. $k \equiv k_x$. In addition to the instabilities indicated in Sec. 1 an instability occurs in the medium with the dispersion relation

$$\begin{aligned}
&\omega^3 + [ik^2\nu_m - cJ|\chi_1|(k + 2i\gamma)]\omega^2\\
&- \left[\frac{H_0^2}{4\pi\rho_0} + u_0^2 + \nu\nu_m k^2 + \nu cJ|\chi_1|(2\gamma\right.\\
&\left. - ik)\right]k^2\omega - (i\nu_m k - cJ|\chi_1|)u_0^2 k^3 = 0,
\end{aligned} \tag{22}$$

in which ν_m is the magnetic viscosity. Requiring that $H_0^2/4\pi\rho_0 u_0^2 \ll 1$ and $\nu cJ|\chi_1|k/u_0^2 \ll 1$, we solve (22) by an iteration method.

For the roots $\omega_0 = \pm ku_0$, putting $\omega = \omega_0(1 + \alpha + i\beta)$, we obtain

$$\left.\begin{aligned}
&\alpha = \frac{1}{2(u_0^2 + k^2\nu_m^2)}\left[\frac{H_0^2}{4\pi\rho_0} + cJ|\chi_1|\nu\left(\frac{\nu_m k^3}{\omega_0} - 2\gamma\right)\right],\\
&\beta = \frac{\omega_0}{2(u_0^2 + k^2\nu_m^2)}\left[\nu\frac{cJ|\chi_1|k}{\omega_0}\left(1 + 2\gamma\frac{\nu_m k}{\omega_0}\right)\right.\\
&\qquad \left. - \nu\left(1 + \frac{\nu_m^2 k^4}{\omega_0^2}\right) - \frac{\nu_m k^2 H_0^2}{\omega_0^2 4\pi\rho_0}\right].
\end{aligned}\right\} \tag{23}$$

From (23) we find the following condition for the onset of instability:

$$J > \frac{\nu\left(1 + \frac{\nu_m^2 k^2}{u_0^2}\right) - \frac{\nu_m}{u_0^2}\frac{H_0^2}{4\pi\rho_0}}{\frac{\nu c|\chi_1|}{u_0}\left(1 + 2\gamma\frac{\nu_m}{u_0}\right)}. \tag{24}$$

If $\omega_0 = -u_0 k$, the instability condition assumes the form

$$J > \frac{\nu\left(1 + \frac{\nu_m^2 k^2}{u_0^2}\right) - \frac{\nu_m}{u_0^2}\frac{H_0^2}{4\pi\rho_0}}{\frac{\nu c|\chi_1|}{u_0}\left(2\gamma\frac{\nu_m}{u_0} - 1\right)}. \tag{25}$$

These conditions are compatible with the indicated constraints.

Using the system of equations (21), we can also obtain the ratio of the kinetic energy of the excited medium to the energy of the electromagnetic field:

$$\Gamma = \frac{\rho_0|\mathbf{v}'|^2/2}{|\mathbf{H}'|^2/8\pi} = \frac{1}{4\pi\rho_0}\left(\frac{H_0}{k\nu}\right)^2. \tag{26}$$

An estimate of the ratio Γ shows that in strong fields

$\Gamma \gg 1$, i.e., in transmitting an acoustic wave through a conducting medium we "drive" the medium and not the field.

2. $k \equiv k_y$. The dispersion relation for this case has the form

$$\omega\left(\omega + i\nu_m k^2 - \frac{H_0}{\sqrt{4\pi\rho_0}}k\right)\left(\omega + i\nu_m k^2 - \frac{H_0}{\sqrt{4\pi\rho_0}}k - 2\gamma c|\chi_1| J_i\right) + \frac{c^2\rho_1 H_0}{4\pi}k^2\left(2\gamma\frac{|\chi|}{H_0}J - \frac{c^2\rho_1 H_0}{4\pi}k^2\right) = 0. \tag{27}$$

A simple approximate solution is possible if we let $\omega = \omega_0(1 + \alpha + i\beta)$, where $\omega_0 = \pm H_0 k/\sqrt{4\pi\rho_0}$ is the magnetodynamic wave frequency (the relation $\sqrt{4\pi\rho_0}\,\nu_m k/H_0 \ll 1$ must also be satisfied). Under this assumption we obtain

$$\omega| = \left[\nu_m(\nu_m k^2 - 2\gamma|\chi_1|cJ) - \frac{c^2\rho_1 H_0}{4\pi}\left(\frac{c^2\rho_1 H_0}{4\pi}k^2 - \frac{|\chi|}{H_0}2\gamma cJ\right)\right] \times \frac{k^2}{2}\left(\frac{1}{2\omega_0} + i\frac{k^2}{\omega_0^2}\nu\right). \tag{28}$$

From (28) we obtain the following condition for the onset of instability:

$$J > \frac{ck^2}{8\pi\gamma}\,\frac{\rho_1^2 H_0^2 - \rho^2}{|\chi|\rho_1 - |\chi_1|\rho}. \tag{29}$$

From the system of equations (21) we find the following ratios for the given case:

$$\frac{u'}{w'} = \frac{\rho_1 k c^2}{2}\sqrt{\frac{\rho_0}{4\pi}},\quad \frac{H_z'}{H_x'} = \frac{\rho}{\rho_1 H_0},\quad \frac{v'}{w'} = \frac{H_y'}{H_x'} = 0,\qquad \Gamma = \frac{(H_x'^2 + H_z'^2)/8\pi}{\rho_0(u'^2 + w'^2)/2} = \left(\frac{\rho}{\rho_1 H_0}\right)^2, \tag{30}$$

where u', v', and w' are the velocity components along the x, y, and z axes, respectively. The ratios (30) have orders of magnitude far greater than unity.

3. $k \equiv k_z$. In this case we have the dispersion relation

$$\omega^3 + i\left[\nu_m k^2 - cJ\left(2\gamma|\chi_1| + ik\frac{|\chi|}{H_0}\right)\right]\omega^2 - \left\{\frac{H_0^2}{4\pi\rho_0} + u_0^2 + \nu\left[\nu_m k^2 - cJ\left(2\gamma|\chi_1| + ik\frac{|\chi|}{H_0}\right)\right]\right\}k^2\omega - iu_0^2 k^2\left[\nu_m k^2 - cJ\left(2\gamma|\chi_1| + ik\frac{|\chi|}{H_0}\right)\right] = 0. \tag{31}$$

As in case 1 of this section, we use the iteration method (assuming $\omega_0 = \pm u_0 k$) to obtain

$$\left.\begin{aligned}\alpha &= \frac{1}{2(u_0^2 + k^2\nu_m^2)}\left[\frac{H_0^2}{4\pi\rho_0} - \nu cJ\left(2\gamma|\chi_1| + \frac{\nu_m k^3}{\omega_0}\frac{|\chi|}{H_0}\right)\right],\\ \beta &= \frac{\omega_0}{2(u_0^2 + k^2\nu_m^2)}\left[\nu\frac{k}{\omega_0}cJ\left(\frac{2\gamma k\nu_m}{\omega_0}|\chi_1| - \frac{|\chi|}{H_0}\right) - \nu_m\frac{H_0^2}{4\pi\rho_0 u_0^2} - \nu\left(1 + \frac{\nu_m^2 k^2}{u_0^2}\right)\right].\end{aligned}\right\} \tag{32}$$

From (32) we find the instability condition

$$J > \frac{\nu\left(1 + \frac{\nu_m^2 k^2}{u_0^2}\right) + \frac{\nu_m}{u_0^2}\frac{H_0^2}{4\pi\rho_0}}{\frac{\nu ck}{\omega_0}\left(\frac{\nu_m k}{\omega_0}2\gamma|\chi_1| - \frac{|\chi|}{H_0}\right)}. \tag{33}$$

From (21) we obtain Γ, which turns out to be equal to the ratio (26).

I wish to thank I. V. Ioffe for valuable comments.

---

[1] P. A. Andreev and I. V. Ioffe, Zh. Tekh. Fiz., 43, 849 (1973) [Sov. Phys.—Tech. Phys., 18, 534 (1973)].
[2] P. A. Andreev, Zh. Tekh. Fiz., 43, 1756 (1973) [Sov. Phys.—Tech. Phys., 18, 1108 (1974)].
[3] A. I. Akhiezer and R. V. Polovin, Usp. Fiz. Nauk, 104, 186 (1971) [Sov. Phys.—Usp., 14, 278 (1971)].
[4] L. É. Gurevich and B. L. Gel'mont, Zh. Eksp. Teor. Fiz., 46, 884 (1964) [Sov. Phys.—JETP, 19, 604 (1964)].

Equilibrium in a tokamak with noncircular cross section

L. E. Zakharov

(Submitted November 19, 1973)
Zh. Tekh. Fiz., 44, 1608-1613 (August 1974)

A general method is proposed for calculating the equilibrium in a toroidal configuration with noncircular cross section. Illustrative calculations are carried out for the equilibrium of a plasma in a chamber with cross section extended along the symmetry axis and in external fields.

In this work we describe a numerical method for solving problems dealing with the equilibrium of a plasma in an axisymmetric toroidal configuration. Interest in such problems has been revived because of experimental studies of plasma confinement in systems in which the plasma has a noncircular cross section (e.g., the "napkin ring" tokamak[1] in the USSR, the Ohkawa doublet[2] in the USA, and the belt-pinch[3] in the German Federal Republic) and because of the development of various axisymmetric diverters.[4] In the course of these studies problems related to the plasma equilibrium have arisen: producing a plasma with a specified cross section by means of a conducting wall or by a system of control windings and monitoring this cross section during the discharge.

Several numerical methods for analyzing plasma equilibrium in configurations in which the plasma has a noncircular cross section have now been reported. The most versatile of these methods appears to be that proposed by Hagenov and Lackner,[5] in which a solution is sought for the (generally nonlinear) equilibrium equation as an expansion in orthogonal polynomials. The simple iterative procedure used by Hagenov and Lackner converges well. This method can be used to analyze the equilibrium of a plasma both in a conducting wall and in an external field, without any restrictions on the cross-sectional shape of the plasma, the current distribution, or the pressure distribution.

Dnestrovskii et al.[6] based their analysis of the equilibrium in an ideally conducting wall on the time-dependent MHD equations incorporating an artificial dissipation. Their method has yielded several solutions for a toroidal plasma with elliptical cross section. However, this method is restricted to a certain class of analytically selected initial conditions, so that it cannot be used to solve equilibrium problems of a general nature.

We have developed a different method for studying the equilibrium in a tokamak with noncircular cross section; the method is based on the equilibrium equation written in integral form. An interative procedure which converges rapidly is used to solve this equation; on the BÉSM-6 computer a typical calculation requires only a few seconds. This integral-equation method is a general method and, in practice, is much simpler than the method of ref. 6. It does not seem to have any advantages over the method of ref. 5, but since it is an independent method and has already been used to study the equilibrium in a tokamak with noncircular cross section[7] we felt it worthwhile to report it.

1. EQUILIBRIUM EQUATIONS IN INTEGRAL FORM

We recall that the equilibrium equations for a plasma in an axisymmetric configuration reduce to a single equation for the flux function $\Psi(r, z)$, which is associated with the equilibrium poloidal field $\mathbf{B}(r, z)$ (ref. 8) (r, z, φ are the cylindrical coordinates; $\partial/\partial\varphi = 0$, $\mathbf{B} = (1/2\pi r)[\nabla\Psi \mathbf{e}_\varphi]$):

$$L\Psi = \frac{1}{r}\frac{\partial^2\Psi}{\partial r^2} - \frac{1}{r^2}\frac{\partial\Psi}{\partial r} + \frac{1}{r}\frac{\partial^2\Psi}{\partial z^2} = -\frac{8\pi^2}{c} j_\varphi$$

$$= -\frac{8\pi^2}{c}\left[A(\Psi) r + B(\Psi)\frac{1}{r}\right],$$

$$j_\varphi = j_\varphi(\Psi, r) = A(\Psi) r + B(\Psi)\frac{1}{r}. \tag{1}$$

The functions $A(\Psi)$ and $B(\Psi)$ are related to the pressure distribution $p(\Psi)$ and the distribution of the poloidal field, $I(\Psi)$, over the magnetic surfaces:

$$A(\Psi) = 2\pi c\frac{dp}{d\Psi}, \quad B(\Psi) = \frac{1}{c}\frac{dI^2}{d\Psi}. \tag{2}$$

We denote by $\Psi_0(r, z; r', z')$ and $b(r, z; r', z')$ the flux function and the magnetic field of a unit ring current at point (r', z') (we will use these functions below):

$$\left.\begin{aligned}
\Psi_0(r, z; r', z') &= \frac{8\pi}{c}\sqrt{\frac{rr'}{k^2}}\left[\left(1 - \frac{k^2}{2}\right)K(k) - E(k)\right],\\
b_r(r, z; r', z') &= \frac{2}{c}\frac{z}{\sqrt{(r + r')^2 + (z - z')^2}}\Big[-K(k)\\
&\quad + \frac{r'^2 + r^2 + (z - z')^2}{(r - r')^2 + (z - z')^2}E(k)\Big],\\
b_z(r, z; r', z') &= \frac{2}{c}\frac{1}{\sqrt{(r + r')^2 + (z - z')^2}}\Big[K(k)\\
&\quad + \frac{r'^2 - r^2 - (z - z')^2}{(r - r')^2 + (z - z')^2}E(k)\Big],\\
k^2 &= \frac{4rr'}{(r + r')^2 + (z - z')^2}.
\end{aligned}\right\} \tag{3}$$

Here and below the semicolon separates the coordinates of the observation point from the current coordinates.

a) Integral equation for the problem with an external field. We denote by Ψ_e the specified flux function of the external (confining) field, and we denote by Ψ_c the flux of the field produced by the plasma current j_φ. Then we have

$$\Psi_c(r, z) = \iint\limits_S \Psi_0(r, z; r', z')\, j_\varphi(\Psi_e + \Psi_c, r')\, dr'dz', \tag{4}$$

where j_φ is given by Eq. (1). Here, the integral is evaluated over the plasma cross section. The current density outside some magnetic surface Ψ_p corresponding to the plasma boundary must vanish:

$$j_\varphi(\Psi_e + \Psi_c, r) = 0 \text{ for } \Psi_e + \Psi_c \leqslant \Psi_p. \tag{5}$$

b) Integral equation for the equilibrium problem of a plasma in an ideally conducting wall. In this case the wall is a magnetic surface, and we can use $\Psi|_\Gamma = 0$ as a boundary condition (Γ is the contour of the wall cross section).

We denote by $\Psi_f(r, z; r', z')$ the fundamental solution of the problem

$$L_{r,z}\Psi_f(r,\ z;\ r',\ z') = -\frac{8\pi^2}{c}\delta(r-r')\delta(z-z'), \tag{6}$$

$$\Psi_f|_\Gamma = 0.$$

Then we can write the equilibrium equation for a plasma in a conducting wall as the nonlinear integral equation

$$\Psi(r,\ z) = \iint_S \Psi_f(r,\ z;\ r',\ z')\, j_\varphi(\Psi,\ r')\, dr'dz'. \tag{7}$$

Below we offer a different derivation of this equation, which yields an algorithm for calculating the kernel Ψ_f.

At the equilibrium of a plasma in an ideally conducting wall, the confining field is produced by the surface current of the wall i_φ, so that the flux function of the equilibrium field is the sum

$$\Psi = \Psi_c + \Psi_e, \tag{8}$$

where Ψ_c is given by (4) and where

$$\Psi_e(r,\ z) = \oint_\Gamma \Psi_0(r,\ z;\ l)\, i_\varphi(l)\, dl. \tag{9}$$

The current i_φ satisfies

$$\frac{2\pi}{c} i_\varphi(l) + \oint_\Gamma b_\tau(l;\ l')\, i_\varphi(l')\, dl' = -\iint_S b_\tau(l;\ r',\ z')\, j_\varphi(r',\ z')\, dr'dz', \tag{10}$$

$$b_\tau(l;\ r',\ z') = \mathbf{b}(l;\ r',\ z')[\mathbf{e}_\varphi \cdot \mathbf{n}(l)]$$

(**n** is the outward unit vector normal to the wall). Here, the left-hand side is the tangential component of the field of surface current i_φ at the outer side of Γ, and the right-hand side is equal in magnitude but opposite in sign to the tangential component of the field of the plasma current j_φ. Equation (10) must hold since there is no magnetic field outside the wall.

We denote by $\oint_\Gamma dl'K(l,\ l')$ the operator which is the inverse of that on the left-hand side of Eq. (10). It can be calculated on a computer by a standard method. Using this operator we find a linear relationship between the currents i_φ and j_φ:

$$i_\varphi(l) = -\oint_\Gamma dl'K(l,\ l') \iint_S b_\tau(l';\ r',\ z')\, j_\varphi(r',\ z')\, dr'dz'. \tag{11}$$

Equation (8) can be rewritten as

$$\Psi(r,\ z) = \iint_S \Psi_0(r,\ z;\ r',\ z')\, j_\varphi(\Psi,\ r')\, dr'dz'$$

$$-\oint_\Gamma dl\Psi_0(r,\ z;\ l) \oint_\Gamma dl'K(l,\ l') \iint_S b_\tau(l';\ r',\ z')\, j_\varphi(\Psi,\ r')\, dr'dz'. \tag{12}$$

Comparing with Eq. (7), we find an explicit equation for the kernel Ψ_f:

$$\Psi_f(r,\ z;\ r',\ z') = \Psi_0(r,\ z;\ r',\ z') - \oint_\Gamma\oint_\Gamma dl\,dl'\Psi_0(r,\ z;\ l)\, K(l,\ l')\, b_\tau(l';\ r',\ z'). \tag{13}$$

Since the magnetic field vanishes outside the wall, the boundary condition $\Psi_f|_\Gamma = 0$ is satisfied automatically.

We note that the kernel of Eq. (8), like that of (4), is a function of the geometry alone, so that once it is calculated for a specific geometry it can be used to analyze equilibrium situations with various current and pressure distributions. Despite the singularities of the kernels Ψ_f and Ψ_0 at r = r' and z = z', there is no difficulty in computer evaluation since these singularities are integrable. For a mesh containing ~ 120 internal mesh points and ~ 50 mesh points at the jacket surface, the calculation of Ψ_f requires 1.5 min on a BÉSM-6 computer.

c) Iteration scheme. In Secs. 2 and 3 below we illustrate the equilibrium calculations for a plasma in a jacket and in an external field. We describe the method for solving Eq. (8); with the obvious changes, this method can also be applied to Eq. (4).

We write the functional dependence of the current on Ψ in the form

$$j_\varphi(\Psi,\ r) = A\left(\frac{\Psi}{\Psi_{\max}}\right) r + B\left(\frac{\Psi}{\Psi_{\max}}\right)\frac{1}{r}. \tag{14}$$

where $\Psi_{\max}$ is the value of Ψ at the elliptical magnetic axis.

To solve Eq. (8) we use two iterative procedures,

$$1.\ \Psi_{n+1} = \iint \Psi_f j_\varphi(\Psi_n,\ r')\, dr'dz',$$

$$2.\ \Psi_{n+1} = \Psi_n + \delta\Psi,$$

determining δΨ from

$$\delta\Psi - \iint \Psi_f \frac{\partial j_\varphi}{\partial \Psi}\delta\Psi\, dr'dz' = \iint \Psi_f j_\varphi(\Psi_n,\ r')\, dr'dz' - \Psi_n.$$

In the course of the iteration the functions A and B can be assumed fixed or normalized in such a manner that the total current is conserved. The quantity $\Psi_{\max}$ serves as an eigenvalue. The initial current distribution is taken to be a homogeneous distribution or a distribution concentrated at a single point.

Procedure 1 requires ~ 30 iterations instead of the 2-10 iterations required in procedure 2, but less computer time is required.

2. Plasma equilibrium in an ideally conducting jacket.

As an example we consider the equilibrium of a force-free (∇p = 0) plasma in a wall with a racetrack cross section. Then the function A(Ψ) in Eq. (14) vanishes, and we choose the function B(Ψ) as follows (Fig. 1): for $\Psi < \Psi_p$ we have B(Ψ) = 0, and elsewhere this function is part of a parabola. We recall that the magnetic surface Ψ = 0 coincides with the wall, while the surface $\Psi = \Psi_{\max}$ coincides with the magnetic axis. The surface $\Psi = \Psi_p$ is the plasma boundary.

Figure 2 shows the results of the equilibrium calculation corresponding to three functions B(Ψ). In the first case the current fills the entire cross section of the wall, but in the second and third cases (Fig. 2a) there is a current-free region between the plasma and the wall. Figures

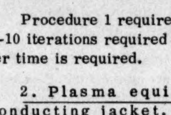

Fig. 1. Functional dependence of the current, $j_\varphi = B(\Psi)(1/r)$.

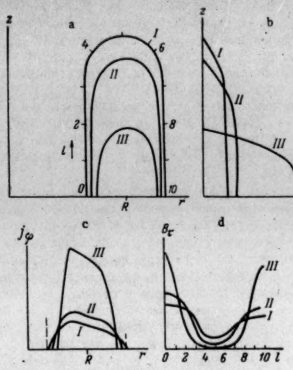

Fig. 2. Equilibrium in a conducting wall. a) Plasma cross sections; b) current distribution along z at r = R; c) current distribution along r at z = 0; d) distribution of the poloidal field at the inner surface of the wall.

2b and 2c show the current distributions j_ψ along z at r = R and along r at z = 0 corresponding to these cases. When the current is concentrated near the magnetic axis the ratio of the vertical dimension to the horizontal dimension decreases.

The problem of determining the characteristic parameters of a plasma cross section from measurements of the magnetic field outside the plasma has been discussed previously.[9] Figure 2d shows the distribution of the equilibrium field at the inner surface of the wall corresponding to the three cases under consideration here (the total current is the same in each case). The explicit functional dependence of the field distribution on the dimensions of the region through which the current flows is available so that we can determine the basic dimensions of the plasma for systems having an extended plasma cross section by means of simple probe measurements.

3. Equilibrium of a plasma in an external field. In systems designed for prolonged plasma confinement the equilibrium must be maintained by a system of control windings. Even in systems with walls these coils are required to maintain the extended shape of the plasma cross section.

The first question which arises in connection with the confinement of a plasma by external fields is that of the magnitudes of the currents in the control windings. Figure 3 shows the equilibrium force-free configuration in the field of three coils calculated on the basis of Eq. (4). In this calculation we assume a parabolic functional dependence $B(\Psi)$ and choose Ψ_p so that the plasma has the specified height. The current distribution in the plasma is shown in the same figure.

We see from these results that the currents in the coils used to extend the plasma cross section are no higher than the plasma current in this arrangement.

Figure 4 also shows a configuration which is not force-free, but with $\beta_p = 1$ (there are no poloidal currents in the plasma). Here we have $B(\Psi) = 0$, and $A(\Psi)$ is chosen to be parabolic. We choose the function Ψ_p so that the plasma has the same vertical dimension as in the preceding case. To balance the forces due to the pressure we are forced to increase the current in the third coil. Under these conditions both the position and shape of the plasma remain essentially unchanged. The current-density maximum in the case of a plasma with pressure is displaced outward from the symmetry axis.

This calculation shows that comparatively low currents are required to compensate for the plasma extension due to the pressure change; with $\beta_p \sim 1$, the currents required are of the order of 10% of the plasma current.

CONCLUSION

We have outlined a general method for solving fundamental problems dealing with plasma equilibrium in ax-

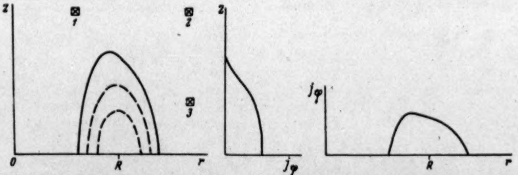

Fig. 3. Equilibrium of a force-free plasma in the field produced by three turns. $I_p = 1$, $I_1 = 0.75$, $I_2 = -0.15$, $I_3 = -0.175$, $\beta_p = 0$.

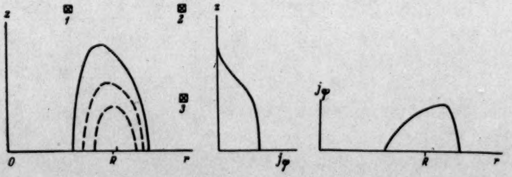

Fig. 4. Equilibrium of a plasma with $\beta_p = 1$ in the field produced by three turns. $I_p = 1$, $I_1 = 0.75$, $I_2 = -0.15$, $I_3 = -0.25$.

isymmetric toroidal configurations. By comparing the results found in equilibrium calculations for specific systems such as the tokamak with noncircular cross section with the experimental distribution of the magnetic field outside the plasma we can determine the dimensions of the region in which the current is concentrated. A comparison of this kind is reported in ref. 7. Calculations show that the functional dependence of the distribution of the poloidal field on the pressure is weak in the case $\beta_p \lesssim 1$. This functional dependence is evidently not a suitable basis for determining parameters such as β_J and β_p.

This method can be used to find the currents required in the control windings in order to produce a plasma cross section of the specified shape. We have shown that, for a particular arrangement, the currents in the windings required are no higher than the plasma current.

The author thanks V. D. Shafranov for his interest.

---

[1] A. V. Bortnikov, Yu. T. Baiborodov, N. N. Brevnov, V. G. Zhukovskii, L. E. Zakharov, D. V. Orlinskii, V. I. Pergament, M. K. Romanovskii, N. I. Sokolov, and A. M. Us, Paper B-5, Third International Symposium on Toroidal Plasma Confinement (Garching, March 26-30, 1973).

[2] T. Ohkawa, M. Chu, R. Fisher, C. L. Hsieh, and T. Jensen, Paper B-17-1, Third International Symposium on Toroidal Plasma Confinement (Garching, March 26-30, 1973).

[3] R. Wilhelm and H. Zwicker, Paper G-6, Third International Symposium on Toroidal Plasma Confinement (Garching, March 26-30, 1973).

[4] A. Kitsunezaki, H. Maeda, Y. Shimomura, and M. Yoshikawa, Paper G-2, Third International Symposium of Toroidal Plasma Confinement (Garching, March 26-30, 1973).

[5] K. V. Hagenov and K. Lackner, Paper F-7, Third International Symposium on Toroidal Plasma Confinement (Garching, March 26-30, 1973).

[6] Yu. N. Dnestrovskii, D. P. Kostomarov, and A. M. Popov. Zh. Tekh. Fiz., 42, 2255 (1972) [Sov. Phys. – Tech. Phys., 17, 1771 (1973)].

[7] A. V. Bortnikov, Yu. T. Baiborodov, N. N. Brevnov, V. G. Zhukovskii, L. E. Zakharov, D. V. Orlinskii, V. I. Pergament, M. K. Romanovskii, N. I. Sokolov, and A. M. Us, Sixth European Conference on Controlled Fusion and Plasma Physics (Moscow, 1973), Vol. 1, 165.

[8] V. D. Shafranov, Zh. Eksp. Teor. Fiz., 33, 710 (1957).

[9] L. E. Zakharov and V. D. Shafranov, Zh. Tekh. Fiz., 43, 225 (1973) [Sov. Phys. – Tech. Phys., 18, 151 (1973)].

Lagrange problem in magnetohydrodynamics

P. V. Zagorskii and Yu. P. Lun'kin
A. F. Ioffe Physicotechnical Institute,
Academy of Sciences of the USSR, Leningrad

(Submitted September 19, 1973)
Zh. Tekh. Fiz., 44, 1614-1618 (August 1974)

The acceleration of a piston in a semiinfinite tube filled with a conducting gas is investigated in the presence of crossed electric and magnetic fields. The effects of the initial conditions on the distribution of the gas dynamic parameters behind the piston and on piston acceleration have been investigated. It is shown that the electromagnetic forces increase the piston velocity by a factor of one and a half as compared with the case of a nonconducting gas.

1. FORMULATION OF PROBLEM AND INITIAL EQUATIONS

The Lagrange problem in magnetohydrodynamics is formulated as follows: There is a semiinfinite tube in which a piston of mass M is placed at a distance L from the back wall. The space between the back wall and the piston is filled with a gas of mass m at pressure p_0, density ρ_0, temperature T_0, and conductivity σ_0. We assume that there is a vacuum to the right of the piston. If we take the x axis along the tube axis, and the external electric field E_0 (initially the current is distributed uniformly with density j_0) and the magnetic field H_0, respectively, along the y and z axes, then as a result of the pressure differential and the action of the electromagnetic forces the gas will move with velocity V and the piston will accelerate in the tube.

This problem is considered in ref. 1 for the case $\sigma = \infty$, and in refs. 2-4 for the case $\sigma = \text{const}$. The most interesting results based on the distribution of gasdynamic parameters and magnetic field in the space behind the piston are obtained in ref. 4. However, the functional dependence of the piston velocity is not treated. Moreover, the effect of a number of initial parameters on the acceleration of the piston, in particular the parameter $\mu = m/M$, has not been investigated.

In the present work we consider the case of variable gas conductivity and investigate the effect of all initial parameters.

We introduce the Lagrangians for the coordinate t and $\xi = \rho_0 x_0$ (x_0 is the initial coordinate of a particle) and the dimensionless variables

$$\left.\begin{aligned}&\mu=\frac{m}{M},\ t=\frac{a_0 t}{M}\left(a_0^2=\gamma\frac{p_0}{\rho_0}\right),\ x=\frac{\xi}{L\rho},\\ &V=\frac{U}{a_0},\ d=\frac{p}{\gamma p_0},\ D=\frac{1}{\gamma p_0}\left(p+\frac{H^2}{8\pi}\right)=d+\frac{h^2}{2},\\ &\nu=\frac{c^2}{4\pi\sigma a_0 L},\ r=\frac{\rho}{\rho_0},\ h^2=\frac{H^2}{4\pi\rho_0 a_0^2},\\ &h_0^2=\frac{H_0^2}{4\pi\rho_0 a_0^2},\ i=\sqrt{\frac{4\pi}{\rho_0}}\frac{L}{ca_0}j.\end{aligned}\right\} \tag{1.1}$$

Then, according to refs. 4 and 5, the initial equations, and the initial and boundary conditions, are written (dropping the bars over the dimensionless quantities):

$$\frac{\partial V}{\partial t}+\frac{\partial D}{\partial x}=0, \tag{1.2}$$

$$\frac{\partial}{\partial t}\left(\frac{1}{r}\right)=\frac{\partial V}{\partial x}, \tag{1.3}$$

$$\frac{\partial}{\partial t}(r^{-\gamma}d)=(\gamma-1)r^{2-\gamma}\nu i^2,\ i=-r\frac{\partial h}{\partial x}, \tag{1.4}$$

$$\frac{\partial}{\partial t}\left(\frac{h}{r}\right)=\frac{\partial}{\partial x}\left(\nu r\frac{\partial h}{\partial x}\right). \tag{1.5}$$

For t = 0, 0 ≤ x ≤ 1

$$h(0,\ x)=h_0+i_0(1-x),\ d=\frac{1}{\gamma},\ r=1,\ V=0. \tag{1.6}$$

For t > 0, x = 0

$$h-\frac{a_0 r\nu}{c}\frac{\partial h}{\partial x}=h_0-\frac{a_0\nu}{c}i_0,\ V=0, \tag{1.7}$$

for x = 1

$$\left(1-\frac{a_0\nu}{c}\right)h+\frac{a_0 r\nu}{c}\frac{\partial h}{\partial x}=h_0-\frac{a_0\nu}{c}i_0,\ \frac{\partial V}{\partial t}=\mu d. \tag{1.8}$$

Thus, the problem reduces to the solution of the system (1.2)-(1.8), in which the gas conductivity is a function of temperature and pressure (or density).

2. DETERMINATION OF GAS CONDUCTIVITY

The exact calculation of the conductivity of a partially ionized gas is rather complicated; therefore, we use the approximate relation[6]

$$\frac{1}{\sigma}=\frac{1}{\sigma_p}+\frac{1}{\sigma_s}, \tag{2.1}$$

where σ_p is the conductivity of a fully ionized plasma with singly charged ions[7]

$$\sigma_p=\frac{0.591\,(\pi\varepsilon)^2(kT)^{3/2}}{m^{1/2}e^2\ln\left[\frac{12\,\pi\varepsilon kT}{e^2}\sqrt{\frac{\varepsilon kT}{n_e e^2}}\right]}\ (\Omega\cdot\text{m}^{-1}), \tag{2.2}$$

and σ_s is the conductivity of a weakly ionized plasma[8]

$$\sigma_s=\frac{3\sqrt{2}}{2}\sqrt{\frac{kT}{\pi m_e}}\frac{e^2}{(n_e Q_e+n_a Q_{en})}. \tag{2.3}$$

Here, ε is the dielectric constant of the plasma; m_e and n_e are the mass and density of electrons, respectively; k is the Boltzmann constant; Q_e is the Coulomb cross section for the interaction of charged particles

$$Q_e=0.8\left(\frac{e^2}{4\pi\varepsilon kT}\right)^2\ln\left[\frac{12\pi\varepsilon kT}{e^2}\sqrt{\frac{\varepsilon kT}{n_e e^2}}\right], \tag{2.4}$$

Q_{en} is the cross section for the interaction of electrons

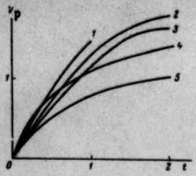

Fig. 1. Profiles of dimensionless piston velocities V_p as a function of dimensionless time t for given current i_0 ($i_0 = 1.0$, $\mu = 3$) and different initial magnetic fields. h_0: 1) 1.1, 2) 0.22, 3) 0; 4) $\sigma = \infty$, 5) $\sigma = 0$.

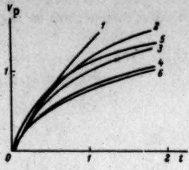

Fig. 2. Profiles of dimensionless piston velocities V_p as a function of dimensionless time t for given magnetic field h_0 ($h_0 = 0.8$, $\mu = 3$) and different initial currents. i_0: 1) 1.0, 2) 0.8, 3) 0.5, 4) 0.2; 5) $\sigma = \infty$, 6) $\sigma = 0$.

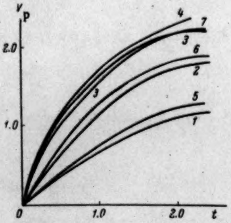

Fig. 3. Profiles of dimensionless piston velocities V_p as a function of dimensionless time t for given current i_0 ($i_0 = 1.0$) and different initial magnetic fields h_0 ($h_0 = 0.22$ and 0.55) and ratio of mass of gas to mass of piston. μ: 1, 5) 1; 2, 6) 3; 3, 7) 7; 4) 10. 1-4) $h_0 = 0.22$, 5-7) $h_0 = 0.55$.

with neutrals. The values of Q_{en} for different gases are given, e.g., in ref. 9. In particular, for helium, which is widely used in light-gas guns, in the range $5.5 \cdot 10^3 \le T \le 2.2 \cdot 10^4$, the quantity Q_{en} is well approximated by a polynomial[10] of third degree in T.

3. CALCULATION RESULTS

Several schemes have been developed[4,11-13] for the numerical solution of one-dimensional nonstationary problems of magnetohydrodynamics. In the calculations we have approximated the "gasdynamic" equations according to the scheme of Courant, Isaacson, and Rees[11] with first-order accuracy, and we have approximated the equations of magnetic induction by an implicit scheme of second-order accuracy, and solved them by a pivotal method.[4] The corresponding boundary conditions were also approximated with the same order of accuracy. All the calculations are carried out on a BÉSM-4 computer for helium for $L = 10^2$ cm, $T_0 = 10^4$°K, and $p_0 = 10^3$ atm.

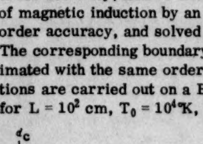

Fig. 4. Profiles of dimensionless values of pressure of gas on bottom of chamber d_c as a function of dimensionless time t for given current i_0 ($i_0 = 1.0$, $\mu = 3$) and different initial magnetic fields. h_0: 1) 1.1, 2) 0.22, 3) 0.

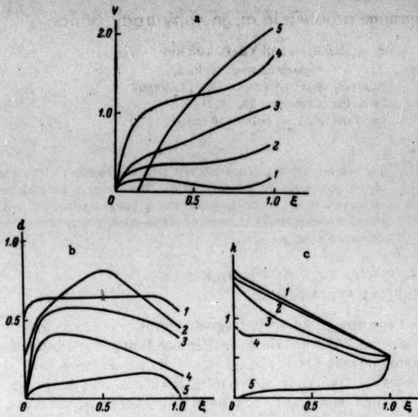

Fig. 5. Profiles of dimensionless values of velocity $V(\xi)$ (a) in the space behind the piston ($0 \le \xi \le 1$) at different dimensionless time t for given current i_0 and magnetic field h_0 ($i_0 = 1.0$, $h_0 = 0.55$), gas pressure $d(\xi)$(b), magnetic field $h(\xi)$ (c). t: 1) 0, 2) 0.4, 3) 0.8, 4) 1.6, 5) 3.2.

In order to investigate the effect of the initial parameters on the flow picture we carry out three series of calculations. In the first series we determine the effect of the initial magnetic field h_0 ($0.22 \le h_0 \le 1.1$; $3.15 \cdot 10^4$ Oe $\le H_0 \le 1.57 \cdot 10^5$ Oe; $0.04\, p_0 \le H_0^2/8\pi \le p_0$) for $\mu = 3$, $i_0 = 1.0$ ($j_0 = 3.44 \cdot 10^{12}\, 2^{1/2}$ cm$^{-1/2}$ sec^{-1}). In the second series we consider the dependence of the parameters on the initial current i_0($0.2 \le i_0 \le 1.0$) for $h_0 = 0.8$, $\mu = 3$. In the third series we study the effect of the quantity μ (μ = 1-10) for $h_0 = 0.22$, 0.55, and $i_0 = 1$. The principal results of the calculations are given in Figs. 1-5.

Figures 1-3 represent profiles of dimensionless piston velocities V_p as a function of time. For comparison we give the $V_p(t)$ profiles for $\sigma = \infty$($h_0 = 0.5$) and $\sigma = 0$.

Figure 4 gives profiles of dimensionless values of gas pressure on the bottom of the chamber $d_c(t)$ for different h_0 (for fixed i_0). Similar $d_c(t)$ profiles are obtained for different i_0 and fixed h_0.

Figure 5 represents the distributions of dimensionless velocities $V(\xi)$, gas pressure $d(\xi)$, and magnetic field $h(\xi)$ in the space behind the piston at different times for $h_0 = 0.55$ and $i_0 = 1$. Similar profiles of $V(\xi)$, $d(\xi)$, and $h(\xi)$ hold also for other values of h_0 and i_0.

The calculation results show that for a conducting gas we can obtain a piston velocity 1.5 times greater than for a nonconducting gas.

It is interesting to note that for the case $\sigma = \infty$ the piston velocity first increases more rapidly than for the case of finite conductivity, but then, more slowly (Figs. 1 and 2). This is explained as follows: With $\sigma = \infty$ the piston is first subject to a pressure $p_0 + H_0^2/8\pi$, and it is greater than for $\sigma = \infty$. With time, however, as the piston moves, the gas expands, and the gas pressure and magnetic field fall, (since the field is frozen in), and this fall occurs more strongly than for the case of finite conductivity; in the latter case the gas is still heated owing to the generation of Joule heat.

The dependence of $V_p(t)$ on μ, falls with increasing μ (Fig. 3) as for a nonconducting gas. Therefore, for practical purposes it is sufficient to take $\mu = 6$–7. Any further increase in μ leads to a small increase in piston velocity, but requires an expenditure of energy proportional to μ for the heating.

It follows from Fig. 5, a and b, that the distribution of velocity and pressure in the space behind the piston (unlike the case of a nonconducting gas) has a clearly nonmonotonic character. In time the magnetic field and velocity can change sign; reverse flows arise in the gas due to the retarding effect of the magnetic field and the generation of Joule heat. In a certain sense, a similar result (the presence of a zone with negative velocity on the bottom of the chamber) is obtained in ref. 14, where the acceleration of a piston by a nonconducting gas is considered, but with the introduction of heat. The profile of pressure has a maximum, the position and shape of which varies with time: At first, it is smeared out; then it becomes more sharply defined, and then it is displaced from the bottom of the chamber to the bottom of the piston.

---

[1] A. I. Loshkarev, Vest. MGU, Ser. Matem.-Mekh., No. 4, 75 (1962).

[2] N. N. Popov, Vest. MGU, Ser. Matem.-Mekh., No. 4, 69 (1962).

[3] N. N. Kusnetsov, in: Calculating Methods and Programming, No. 7 [in Russian], Izd. Moscow State University, Moscow (1967), p. 242.

[4] N. N. Kuznetsov and E. A. Starova, in: Calculating Methods and Programming, No. 7 [in Russian], Izd. Moscow State University, Moscow (1967), p. 247

[5] A. Ron, in: Moving Plasmas [Russian translation], IL, Moscow (1961), p. 285.

[6] L. E. Kalikhman, Elements of Magnetohydrodynamics [in Russian], Atomizdat, Moscow (1964).

[7] L. Spitzer, Physics of Fully Ionized Gases, Interscience (1962).

[8] S. Chapman and T. G. Cowling, Mathematical Theory of Nonuniform Gases, Cambridge Univ. Press (1952).

[9] B. S. Smirnov, Atomic Collisons and Elementary Processes in Plasma [in Russian], Atomizdat, Moscow (1968).

[10] R. W. LaBahn and J. Callaway, Phys. Rev., 135A, 1539 (1964).

[11] G. E. Forsythe and W. R. Wasow, Finite Difference Methods for Partial Differential Equations, Wiley (1960).

[12] A. A. Samarskii, P. P. Volosevich, M. I. Volginskaya, and S. P. Kurdyumov, Zh. Vychislit. Matem. Matem. Fiz., 8, 1025 (1968).

[13] E. Levi and M. Sandler, Teplofiz. Vys. Temp., 2, 351 (1964).

[14] L. V. Komarovskii, Trans. First Republic Conference on Aerohydromechanics, Heat Transfer, and Mass Transfer, Izd. KGU, Kiev (1969), p. 79.

Liquid crystals in external fields

I. V. Ioffe

A. F. Ioffe Physicotechnical Institute,
Academy of Sciences of the USSR, Leningrad

(Submitted June 1, 1973)
Zh. Tekh. Fiz., 44, 1619-1624 (August 1974)

The electrohydrodynamic effect is considered for nematic crystals in parallel electric and magnetic fields, for piezoelectric nematic crystals, and for type C smectic crystals in an electric field. The critical fields are determined. It is shown that the effect is oscillational in piezoelectric crystals.

I. In this paper the electrohydrodynamic effect (EHDE) is investigated in nematic crystals in parallel electric and magnetic fields $\mathbf{E}_0$ and $\mathbf{H}_0$, and in piezoelectric nematic crystals and type C smectic crystals[1] in an electric field. The author knows of no other work concerned with EHDE in these cases. We present the results before turning to the calculations.

1. It is well known[2] that a homogeneous magnetic field exceeding a critical value H_c gives rise to the formation of domains in nematic crystals. A field $H_0 \leq H_c$ is considered here. It turns out that the critical electric field E_c for which the EHDE arises can be written in the form

$$E_c = E_c^0 \left[1 - \frac{H_0^2}{H_c^2}\right]^{1/2}, \tag{1}$$

when $\mathbf{E}_0 \parallel \mathbf{H}_0$, where E_c^0 is the field which gives rise to EHDE when $H_0 = 0$ and which is determined, for example in ref. 3. If we neglect the drift velocity of current carriers,[3,4] the EHDE also develops aperiodically when $H_0 \neq 0$. The amplitude of the hydrodynamic velocity $\mathbf{v}$ decreases as H_0 increases from zero to H_c with $\mathbf{v} = 0$ when $H_0 = H_c$. An EHDE is also not possible in nonconducting crystals when $H_0 = 0$; only the formation of "electric" domains similar to the magnetic domains[2] is possible. The critical fields required for the formation of electric domains when $H_0 = 0$ and $H_0 \neq 0$ are also related through Eq. (1).

2. In piezoelectric nematic crystals, one ordinarily assumes[5,6] a dependence on a single coordinate for the components of the vector $\mathbf{n}$, which leads to the appearance of piezoelectric domains. If $\mathbf{n}$ depends on two coordinates and the electric field is greater than some critical field, the EHDE is possible. It is significant that the EHDE is possible in piezoelectric crystals in the absence of a conductivity even with an isotropic dielectric constant. The point is that even for the approximation used in refs. 5 and 6, when it is assumed that the relation $\beta_2 = -\beta_1 = \beta$ holds between the coefficients in the piezoelectric portion of the free energy density

$$F_\beta = -\beta_1 (\mathbf{E}\mathbf{n}) \operatorname{div} \mathbf{n} - \beta_2 (\mathbf{E}(\mathbf{n}\nabla)\mathbf{n}), \tag{2}$$

the curl of the piezoelectric force acting on the crystal is nonzero when $\mathbf{n} \neq \text{const}$. Therefore, for zero conductivity and, consequently, zero charge q, and with an isotropic dielectric constant with consequent absence of a fluctuation potential of the electric field φ, the creation of a fluctuation angle of rotation θ in the vector leads to motion of the liquid. This motion creates a frictional moment which gives rise, in turn, to the appearance of an angular moment proportional to θ. Since the piezoelectric force increases as the field increases, the fluctuation deflection is not damped for some field.

The critical electric field is

$$E_1 = \sqrt{\frac{K}{\rho}} \frac{\alpha}{\beta} k, \tag{3}$$

where K is the value of the elastic constant in the usual expansion of the free energy density in the Oseen–Frank approximation;[7,8] ρ is the density; α is a characteristic value for the coefficients of viscosity in the Navier–Stokes equation and the moment equations (the viscosity coefficients are much the same[3,9,10]); k is the wave vector for the fluctuation.

In piezoelectric crystals the EHDE is oscillational. The frequency of the oscillations is

$$\omega = \omega_0 = \frac{\beta k E_0}{\alpha}. \tag{4}$$

Assume that in the dielectric constant,

$$\varepsilon_{ik} = \varepsilon_\perp \delta_{ik} + (\varepsilon_\parallel - \varepsilon_\perp) n_i n_k \tag{5}$$

the anisotropic part $\varepsilon_a = \varepsilon_\parallel - \varepsilon_\perp \neq 0$; then Eq. (3) holds for the critical field only when $\beta > \alpha \sqrt{\varepsilon_a / 4\pi\rho}$. In the other limit ($E_c \simeq E_c^0$) the oscillatory EHDE arises at a frequency ω_0 given by Eq. (4).

When $\beta_+ = \beta_1 + \beta_2 \neq 0$, the EHDE is also possible in nonconducting crystals.[10]

Three cases should be distinguished. If $\beta_+ < \alpha/\sqrt{\rho}$, the EHDE is oscillatory at a frequency ω_0. The critical field is equal to E_c^0 when $\beta_2 < \alpha\sqrt{\varepsilon_a/4\pi\rho}$ and is

$$E_c \simeq \frac{\alpha k}{\sqrt{\rho}} \frac{\sqrt{K + \beta_+^2}}{\beta_2}$$

when $\beta_2 > \alpha\sqrt{\varepsilon_a/4\pi\rho}$.

If $\beta_2, \beta_+ > \alpha/\sqrt{\rho}$, the frequency is $\alpha k^2/\rho$ and

$$E_c \simeq \frac{\alpha k}{\sqrt{\rho}}.$$

In conducting piezoelectric crystals we confine ourselves to the cases in which the conductivity σ is considerably greater than all frequencies encountered in the problem. Then the results given above remain valid.

3. In type C smectic crystals the EHDE occurs only for finite conductivity. As usual,[11,12] we assume the free energy density is a function of the variation along the k axis of the angle of rotation Ω_i around the i axis: $d\Omega_i/dx_k$. Similarly, we expand the dielectric constant (conductivity) in a series[12] Ω_i:

$$\varepsilon_{ik}=\varepsilon_{ik}^0+\varepsilon_{ikl}\Omega_l+\varepsilon_{iklm}\Omega_l\Omega_m. \qquad (6)$$

The appearance of Ω_l leads to a change in ε_{ik} and σ_{ik} which leads to the appearance, in an external electric field, of a charge and fluctuation field in the same way that ε_a, $\sigma_a=\sigma_\parallel-\sigma_\perp$ leads to q, $\psi\neq 0$ in nematic crystals. The EHDE is therefore possible in this case also. It is aperiodic and the critical field is $\sqrt{a/\varepsilon k}$, where a is the constant in the expansion of the free energy density over $\Omega_{i,k}=\partial\Omega_i/\partial x_k$.

Only the linear theory in constant homogeneous fields is considered here. Everywhere in the calculations the problem is discussed without consideration of boundary conditions; all fluctuation quantities are taken as $\sim\exp[i\cdot(kr-\omega t)]$. The values of the components of the wave vector k are taken to be of the same order of magnitude except where specifically stated otherwise.

II. Let $E_0\parallel H_0\parallel Ox$. Assuming $k=k_x, 0, k_n$, we write a linearized system of equations for the EHDE. Since the effect is aperiodic, $\partial/\partial t\equiv 0$ and for

$$\sigma_{ik}=\sigma_\perp\delta_{ik}+\sigma_a n_i n_k, \qquad (7)$$

$$n_x=\sin\theta\simeq\theta,\ n_z=\cos\theta\simeq 1 \qquad (8)$$

we have the continuity equation for the current

$$\sigma_a(\mathbf{E}_0\nabla)\theta-\sigma_\parallel\frac{\partial^2\varphi}{\partial x^2}=\sigma_\perp\frac{\partial^2\varphi}{\partial z^2}=0, \qquad (9)$$

the Poisson equation

$$\varepsilon_a(\mathbf{E}_0\nabla)\theta-\varepsilon_\parallel\frac{\partial^2\varphi}{\partial x^2}-\varepsilon_\perp\frac{\partial^2\varphi}{\partial z^2}=4\pi q, \qquad (10)$$

the incompressibility equation

$$\frac{\partial v_x}{\partial x}+\frac{\partial v_z}{\partial z}=0, \qquad (11)$$

the equation for moment equilibrium

$$\frac{\varepsilon_a E_0\left(E_0\theta-\frac{\partial\varphi}{\partial x}\right)+\chi_a H_0[H_0\theta+H'_x]}{4\pi}-K\Delta\theta+\alpha_1\frac{\partial v_x}{\partial z}+\alpha_2\frac{\partial v_z}{\partial x}=0, \qquad (12)$$

the projection of the curl of the Navier–Stokes equation

$$E_0\frac{\partial q}{\partial z}+\sigma_\perp\left[\frac{H_0^2}{c^2}\frac{\partial v_x}{\partial z}-\frac{j_0H_0}{Nec^2}\frac{\partial H'_x}{\partial z}\right]+\alpha_3\frac{\partial^3 v_x}{\partial z^3}$$

$$+\alpha_4\frac{\partial^3 v_k}{\partial z\partial x^2}+\alpha_5\frac{\partial^3 v_z}{\partial x^3}+\alpha_6\frac{\partial^3 v_r}{\partial x\partial z^2}=0, \qquad (13)$$

$$E_0H_0\sigma_a\frac{\partial\theta}{\partial z}-H_0\sigma_\parallel\frac{\partial^2\varphi}{\partial x\partial z}-j_0\frac{\partial H'_x}{\partial z}=0 \qquad (14)$$

and the equation

$$\chi_\perp\frac{\partial H'_z}{\partial z}+\chi_\parallel\frac{\partial H'_x}{\partial x}+\chi_a H_0\frac{\partial\theta}{\partial x}=0. \qquad (15)$$

Here, j_0 is the stationary current; $\chi_a=\chi_\parallel-\chi_\perp$; $\sigma H_0/Nec\ll 1$,

$$\chi_{ik}=\chi_\perp\delta_{ik}+\chi_a n_i n_k \qquad (16)$$

is the magnetic susceptibility; N is the number of carriers.

It is clear from Eqs. (9)-(15) that when $\sigma_{ik}=0$ and $E_0=0$, it is possible that $\theta\neq 0$ for

$$H_0=H_c=\sqrt{\frac{4\pi K}{\chi_a}}\,k. \qquad (17)$$

Furthermore $H'_x=H'_z=v_x=v_z=\varphi=0$. Electric domains are possible if $H_0=0$, $E_0\neq 0$. For $\sigma_{ik}\neq 0$, we set $\mathbf{v}$, φ, θ, and $H'\sim\exp i(k_x x+k_z z)$, $k_x\simeq k_z\simeq k$, and assume that the quantity $K\sigma/\alpha c^2\ll 1$. Then, setting the determinant of the system (9)-(15) equal to zero, we obtain Eq. (1). When $E=E_c$

$$\frac{H'_x}{H_0}=-\frac{\sigma_a}{\sigma}\theta;\quad \frac{H'_z}{H_0}=\left(\frac{\chi_\parallel}{\chi_\perp}\frac{\sigma_a}{\sigma}-\frac{\chi_a}{\chi_\perp}\right)\theta$$

(everywhere, except for ε_a, σ_a, and χ_a, it is assumed $\varepsilon_\parallel=\varepsilon_\perp=\varepsilon$ etc.). The ratio $|H'/H_0|/|E'/E_0|\simeq|(\chi_a/\chi)(\varepsilon/\varepsilon_a)|\simeq 1$. Thus a magnetic field parallel to the electric field does not change the possibilities of the planar EHDE (depending only on x and z) or its aperiodic nature.

III. Using Eq. (2) in a piezoelectric crystal we find that the linearized system of equations consists of

$$\varepsilon_a(\mathbf{E}_0\nabla)\theta-\varepsilon_\parallel\frac{\partial^2\varphi}{\partial x^2}-\varepsilon_\perp\frac{\partial^2\varphi}{\partial z^2}+4\pi(\beta_1+\beta_2)\frac{\partial^2\theta}{\partial x\partial z}=4\pi q, \qquad (18)$$

$$\frac{\partial q}{\partial t}+\sigma_a(\mathbf{E}_0\nabla)\theta-\sigma_\parallel\frac{\partial^2\varphi}{\partial x^2}-\sigma_\perp\frac{\partial^2\varphi}{\partial z^2}=0, \qquad (19)$$

$$J\frac{\partial^2\theta}{\partial t^2}+\alpha_0\frac{\partial\theta}{\partial t}-K\Delta\theta+\alpha_1\frac{\partial v_x}{\partial z}+\alpha_2\frac{\partial v_z}{\partial x}+\frac{\varepsilon_a E_0}{4\pi}\left(E_0\theta-\frac{\partial\varphi}{\partial x}\right)$$

$$+(\beta_1+\beta_2)\left(E_0\frac{\partial\theta}{\partial z}-\frac{\partial^2\varphi}{\partial x\partial z}\right)=0, \qquad (20)$$

$$\frac{\partial^2 v_x}{\partial t\partial z}-\frac{\partial^2 v_z}{\partial t\partial x}+\alpha_3\frac{\partial^3 v_x}{\partial z^3}+\alpha_4\frac{\partial^3 v_x}{\partial z\partial x^2}+\alpha_5\frac{\partial^3 v_z}{\partial x^3}$$

$$+\alpha_6\frac{\partial^3 v_z}{\partial x\partial z^2}+E_0\frac{\partial q}{\partial z}+\beta_2E_0\frac{\partial^3\theta}{\partial x\partial z^2}=0 \qquad (21)$$

and the incompressibility equation (11).

We set $\mathbf{v}$, φ, θ, and $q\sim\exp i(k_x x+k_z z-\omega t)$. We are interested only in $\mathrm{Re}\,\omega$ and E_c, for which $\mathrm{Im}\,\omega=0$. Using the same approximations as in Sec. II we find an equation for the determination of the frequency in the case $\beta_+=\beta_1+\beta_2=0$ and $\sigma_{ik}=0$,

$$\omega^3-\left[\frac{\alpha^2k^2}{J\rho}+\frac{Kk^2}{J}-\frac{\varepsilon_a\varepsilon_\perp k^2E_0^2}{4\pi(\varepsilon_\parallel k_x^2+\varepsilon_\perp k_z^2)}\right]\omega-\frac{\beta_2\alpha E_0k^3}{J\rho}=0. \qquad (22)$$

We assume $k^2J/\rho\simeq(kl)^2\ll 1$ (l is the length of a molecule of the nematic crystal material), $\alpha^2\gg K\rho$, $\alpha k>E_0\sqrt{\rho}$ up to fields of the order of 3 kV/cm. Then the only real root of Eq. (22) is

$$\omega=\omega_0=\beta_2\frac{kE_0}{\alpha}.$$

Substituting this frequency value into the equation for the determination of E_c we have

$$\rho\omega^2-Kk^4+\frac{\varepsilon_a\varepsilon_\perp k^4E_0^2}{4\pi(\varepsilon_\parallel k_x^2+\varepsilon_\perp k_z^2)}=0. \qquad (23)$$

It is clear that for

$$\beta_2<\alpha\sqrt{\frac{\varepsilon_a\varepsilon_\perp k^2}{4\pi\rho\,[\varepsilon_\parallel k_x^2+\varepsilon_\perp k_z^2]}}\equiv\beta$$

one can neglect the term $\sim\omega^2$ and $E_c \simeq E_c^0$. For the opposite sign in the inequality

$$E_c=E_1=\frac{\beta}{\beta_2}E_c^0<E_c^0.$$

When $E_c = E_1$, $\omega \simeq \sqrt{K/\rho}\,k$. If $K \simeq 10^{-6}$ erg/cm and $k \simeq 10^3$ cm^{-1}, $\omega \simeq 1$ Hz. Note that if $\beta = 0$ but $\varepsilon_a \neq 0$, domains develop when $E = E_c^0$ in which θ and φ are nonzero but $\mathbf{v} \equiv 0$. When $\beta_2 < \bar{\beta}$ and $E \simeq E_c^0$, $\mathbf{v} \neq 0$ and EHDE occurs.

We turn to the case where $|\beta_+| \simeq |\beta_2|$.

The equation analogous to Eq. (22) is

$$\omega^3-\left[\frac{\alpha^2k^2}{J\rho}+\frac{Kk^2}{J}+\frac{\beta^2+k^2}{J}-\frac{\varepsilon_a\varepsilon_\perp k^2E_0^2}{4\pi(\varepsilon_\parallel k_x^2+\varepsilon_\perp k_z^2)}\right]\omega-\frac{\alpha\beta_2E_0k^3}{J\rho}=0. \qquad (24)$$

The ratio $\beta_+\sqrt{\rho}/\alpha$ is important. If it is smaller than unity and $\beta_2 > \alpha\sqrt{\varepsilon_a/4\pi\rho}$, then $\omega = \omega_0$ and

$$E_c\simeq\frac{\alpha k}{\beta_2}\sqrt{\frac{K+\beta_+^2}{\rho}}.$$

When $\beta_2 < \alpha\sqrt{\varepsilon_a/4\pi\rho}$, $\omega = \omega_0$ and

$$E_c=E_c^0\sqrt{\frac{K+\beta_+^2}{K}}.$$

For the case $\beta_+ > \alpha/\sqrt{\rho}$ we find a real root of Eq. (24),

$$\omega=\frac{\alpha k}{\rho}\frac{\beta_2}{\beta_+^2}E_0.$$

Substituting this value in the equation

$$\omega^2-\frac{(K+\beta_+^2)k^4}{J\rho}+\frac{\varepsilon_a\varepsilon_\perp k^2E_0^2}{4\pi(\varepsilon_\parallel k_x^2+\varepsilon_\perp k_z^2)}\frac{1}{J\rho}+\frac{\beta kE\omega}{\alpha}=0, \qquad (25)$$

we find that the EHDE at a frequency $\omega = \alpha k^2/\rho$ is possible when $E_0 > k\beta_+^2/\beta_2$. Since $|\beta_+| \simeq |\beta_2|$ by assumption and $\beta > \alpha/\sqrt{\rho}$, the required $E_0 > \alpha k/\sqrt{\rho}$. In this case, the frequency $\omega \simeq \alpha k^2/\rho$. If $\alpha \simeq 10^{-2}$ g/cm · sec and $k \simeq 10^3$ cm^{-1} $E_c \simeq$ kV/cm [sic] $\omega \simeq 10^4$ sec^{-1}. The inhibition of the EHDE with increasing β_+ is reasonable if one recalls that piezoelectric domains form more easily when $\beta_+ = 0$ (generally, there are no domains when $\beta_1 = \beta_2$). When $\sigma \neq 0$ we limit our considerations to $\sigma \gg \alpha/J$, $E/\sqrt{J}$, $k\beta/\sqrt{J}$; then $\sigma \gg \omega$, as shown by calculation.

In this case we find that the equations for the determination of frequency and E_c agree with Eqs. (22)-(25) when ε_a is replaced by $(\varepsilon_\parallel\sigma_\perp - \varepsilon_\perp\sigma_\parallel)(k^2)/(\sigma_\parallel k_x^2 + \sigma_\perp k_z^2)$. Therefore the results obtained above are also valid for this case.

IV. In smectic type C crystals, we use the usual axial directions.[11,12] Then the nonzero coefficients a_{iklm} in the expression for the elastic portion of the free energy density,

$$F_{el}=\frac{a_{iklm}}{2}\Omega_{i,k}\Omega_{e,m} \qquad (26)$$

are known.[11,12] Assuming that $\sigma_{xy}^0 = \sigma_{zy}^0 = \varepsilon_{xy}^0 = \varepsilon_{zy}^0 = 0$, we determine the nonzero values of $\varepsilon_{ikl}(\sigma_{ikl})$ and ε_{iklm} · (σ_{iklm}) which appear in Eq. (6) and in the electric portion of the free energy density,

$$F_E=\frac{1}{8\pi}\left\{\varepsilon_{iklm}E_iE_k\Omega_l\Omega_m-\varepsilon_{ikl}\left(E_i\frac{\partial\varphi}{\partial x_k}+E_k\frac{\partial\varphi}{\partial x_i}\right)\Omega_l\right\}, \qquad (27)$$

$$\begin{gathered}
\varepsilon_{zxy}=-\varepsilon_{xzy}=-2\varepsilon_{xz}^0;\ \varepsilon_{xyx}=\varepsilon_{yxx}=-\varepsilon_{xz}^0,\\
\varepsilon_{xyz}=\varepsilon_{yxz}=\varepsilon_{xx}^0-\varepsilon_{yy}^0;\ \varepsilon_{zzy}=\varepsilon_{zxy}=\varepsilon_{xx}^0-\varepsilon_{zz}^0,\\
\varepsilon_{yxz}=\varepsilon_{zyx}=\varepsilon_{yy}^0-\varepsilon_{zz}^0;\ \varepsilon_{zyz}=\varepsilon_{yzz}=\varepsilon_{xz}^0,\\
\varepsilon_{xxxz}=-\varepsilon_{xx}^0;\ \varepsilon_{yyxz}=-\varepsilon_{yy}^0;\ \varepsilon_{zzxz}=-\varepsilon_{zz}^0,\\
\varepsilon_{xxzz}=\varepsilon_{yyxz}=\varepsilon_{zz}^0-\varepsilon_{yy}^0,\\
\varepsilon_{xxyy}=-\varepsilon_{zzxx}=\varepsilon_{zz}^0-\varepsilon_{xx}^0,\\
\varepsilon_{zxxz}=\varepsilon_{xxzx}=\varepsilon_{yyzz}=\varepsilon_{yyzx}=\varepsilon_{zzxz}=\varepsilon_{zzzx}=2\varepsilon_{xz}^0,\\
\varepsilon_{xzxz}=\varepsilon_{xzzx}=\varepsilon_{zxxz}=\varepsilon_{zxzx}=\varepsilon_{xyxy}=\varepsilon_{xyyx}\\
=\varepsilon_{yxyx}=\varepsilon_{yxxy}=\varepsilon_{yzyz}=\varepsilon_{yzzy}\\
=\varepsilon_{zyzy}=\varepsilon_{zyyz}=\varepsilon_{xx}^0+\varepsilon_{yy}^0+\varepsilon_{zz}^0,\\
\varepsilon_{yzyx}=\varepsilon_{zyyx}=\varepsilon_{yzxy}=\varepsilon_{zyxy}=\varepsilon_{xz}^0,\\
\varepsilon_{yzxz}=\varepsilon_{zyxz}=\varepsilon_{yzzx}=\varepsilon_{zyzx}=\varepsilon_{xx}^0.
\end{gathered} \qquad (28)$$

The calculation shows that the EHDE is aperiodic in smectic type C crystals. Then, following refs. 9-12, we write the moment of the viscous stresses and the moment of the viscous forces in the forms

$$\pi_{ik}=\alpha_{iklm}^{(1)}\left[\frac{\partial v_l}{\partial x_m}+\frac{\partial v_m}{\partial x_l}\right]+\alpha_{iklm}^{(2)}e_l[\operatorname{curl}\mathbf{v}\cdot\mathbf{e}]_m+\alpha_{iklm}^{(3)}e_m[\operatorname{curl}\mathbf{v}\cdot\mathbf{e}]_l, \qquad (29)$$

$$\Gamma_i=\alpha_1\operatorname{curl}\mathbf{v}+\alpha_2e_{i\,np}e_k\left(e_m,\frac{\partial v_m}{\partial x_p}+\frac{\partial v_p}{\partial x_m}\right)+\alpha_3e_i(\mathbf{e}\operatorname{curl}\mathbf{v}) \qquad (30)$$

(e_i is a unit vector along the i axis; $e_{i\,cr}$ is a unit antisymmetric tensor).

Considering Eqs. (26)-(30), the system of equations describing EHDE in smectic type C crystals consists of the equation for moment equilibrium

$$-\frac{\partial}{\partial\Omega_i}(F_{el}+F_E)+\Gamma_i=0, \qquad (31)$$

the equation of continuity

$$\sigma_{ik}\frac{\partial^2\varphi}{\partial x_i\partial x_k}-\sigma_{i\,cr}E_k\Omega_{p,i}=0, \qquad (32)$$

the Poisson equation

$$\varepsilon_{ik}\frac{\partial^2\varphi}{\partial x_i\partial x_k}-\varepsilon_{i\,cr}E_k^0\Omega_{p,i}+4\pi q=0, \qquad (33)$$

the incompressibility equation

$$\operatorname{div}\mathbf{v}=0 \qquad (34)$$

and the curl of the Navier–Stokes equation

$$[E_i\nabla q] + \operatorname{curl}\frac{\partial \pi_{ik}}{\partial x_k} = 0. \tag{35}$$

Assuming φ, Ω_i, v, and $q \sim e^{ikr}$ and equating the determinant of the system (31)-(35) to zero, we obtain an equation for the determination of the critical field,

$$(ak^2)^3 + b_1 (ak^2)^2 E_c^2 + b_2 ak^2 E_c^4 + b_3 E_c^6 = 0, \tag{36}$$

where a is a quantity of the order of a_{iklm} and $b_{1,2,3}$ are complicated quantities which are determined by the coefficients of viscosity and by the quantities $\varepsilon_{ik}(\sigma_{ik})$, $\varepsilon_{ikl}\cdot(\sigma_{ikl})$, and $\varepsilon_{iklm}(\sigma_{iklm})$. In order of magnitude, the quantities $b_{1,2,3} \simeq 1$. A solution of Eq. (36), if it exists, is of the form $E_c^2 \simeq ak^2b$. We shall show that a solution exists; for this, we consider the case $E^0 = E_z^0$, $k = k_x$, $v = v$, $\Omega_z = \Omega_y$. Then for $\varepsilon_{xx}, \varepsilon_{zz} \gg \varepsilon_{xz}$ and $\sigma_{xx}, \sigma_{zz} > \sigma_{xz}$, we find from Eqs, (26)-(35)

$$E_c^2 = a_{yxyx} k^2 \frac{\sigma_{xx}}{(\varepsilon_{xx}^0 - \varepsilon_{zz}^0)(\sigma_{zz}^0 - \sigma_{xx}^0)}$$

and EHDE is possible when $(\varepsilon_{xx}^0 - \varepsilon_{zz}^0)(\sigma_{zz}^0 - \sigma_{xx}^0) > 0$.

Assuming $a \simeq 10^{-6}$ erg · cm^{-1} and $k \simeq 10^3$ cm^{-1}, we find $E_c \simeq 10^2$ V/cm.

---

[1] H. Sackman and D. Demus, Proc. Intern. Conf. Liquid Crystals, Kent (1965), p. 361.

[2] J. L. Ericksen, Quart. J. Mech. Appl. Math., 21, 463 (1963).

[3] S. A. Pikin, Zh. Eksp. Teor. Fiz., 60, 1185 (1971) [Sov. Phys.–JETP, 33, 641 (1971)].

[4] E. Dubois-Violette, P. G. de Gennes, and O. Parodi, J. Phys., 32, 305 (1971).

[5] S. G. Dmitriev, Zh. Eksp. Teor, Fiz., 61, 2049 (1971) [Sov. Phys.–JETP, 34, 1093 (1972)].

[6] W. Meyer, Phys. Rev. Lett., 22, 918 (1969).

[7] G. W. Oseen, Trans. Faraday Soc., 29, 882 (1938).

[8] F. G. Frank, Disc. Faraday Soc., 25, 1 (1958).

[9] Groupe de Etude des Cristoux Liquides (Orsay), J. Chem. Phys., 51, 816 (1969).

[10] P. de Gennes, J. Phys., 30, Suppl 11/12, Col. C, 65 (1969).

[11] Orsay Group Liquid Crystals, Solid State Commun., 9, 653 (1971).

[12] A. Rapini, J. Phys., 33, 237 (1972).

Effect of temperature-dependent conductivity on electromagnetic field, current, temperature, and impedance in a plane conductor. I

R. S. Kuznetskii

(Submitted May 10, 1973; resubmitted August 6, 1973)
Zh. Tekh. Fiz., 44, 1625-1632 (August 1974)

First-order corrections to the monochromatic electromagnetic field, the current density, and the distribution of the steady-state temperature in a plane conductor due to a linear temperature dependence of the conductivity are obtained in analytic form. The corrections are analyzed in detail, and curves are given.

INITIAL EQUATIONS

A monochromatic high-frequency electromagnetic field $\mathbf{E} = \mathbf{e}(z)\exp(i\omega\tau)$, $\mathbf{H} = \mathbf{h}(z)\exp(i\omega\tau)$, and the steady-state temperature t(z) due to the surface outflow of heat in a conducting plane layer (a slab) $|z| \leq a$, on the surface of which the tangential electric field $\mathbf{e}^0\exp(i\omega\tau)$ ($\mathbf{e}^0 = \mathrm{const}$, $\mathrm{Im}\,\mathbf{e}^0 = 0$) and the constant temperature [from which we calculate t(z)] are given, satisfy the following equations:[1,2]

$$e'' = i\mu\omega\sigma e, \quad t'' = -\frac{\sigma}{2\lambda}|e|^2, \tag{1}$$

where $h = i/\mu\omega e'$, and the current density $j = \sigma e = -h'$. The boundary conditions are $e(a) = e^0$, $t(a) = 0$, $e'(0) = 0$, $t'(0) = 0$. Here and below the monochromatically varying quantities are represented by their complex amplitudes: μ, λ and σ are the magnetic permeability, the thermal conductivity, and the conductivity of the conductor, respectively. The electric field (and the current density) are parallel to $\mathbf{e}^0$, and the magnetic field is perpendicular to $\mathbf{e}^0$ and parallel to the surfaces of the layer.[2,3]

We consider an extended conductor, one of the dimensions of which is small compared with the two others. If the formulation of the problem is physically associated with electromagnetic waves incident on a conductor we assume two plane waves with the same linearly polarized electric vector normally incident (the electric field, current, and temperature distribution in the conductor are symmetric, while the magnetic field distribution is asymmetric with respect to the central plane z = 0); $\mathbf{e}^0$ represents the total electric vector at the boundary. It should be noted, however, that there is generally no dependence on $\mathbf{e}^0$ in the above distributions (i.e., in the components of the complex surface impedance). The assumed constancy with time of the steady-state temperature of the conductor for high-frequency currents is provided by thermal inertia. The absolute temperature of the conductor surface can be found first by using the equation for heat balance between the conductor and the external medium (or by direct experimental measurement); it depends on the nature of the external surface heat exchange. This procedure does not present any difficulties, and will not be specifically considered in this communication, which is devoted purely to the internal problem.

We assume that the conductivity $\sigma(t)$ always depends on temperature with constant thermal conductivity $\lambda = \mathrm{const}$ (the case in which there is also a temperature dependence of thermal conductivity can, in principle, be reduced to the case considered in refs. 4 and 5). In this case Eq. (1) is nonlinear. We then have the problem of nonlinear macroscopic electrodynamics of a conducting solid,[6] which has not been considered in general form. The corresponding microscopic equations with a self-consistent $\sigma(t)$ have been studied in semiconductors.[7]

Equation (1) is solved in quadratures[8] for a steady-state boundary field ($\omega = 0$), and in finite analytic form for a constant conductivity ($\sigma = \mathrm{const}$, the "degenerate" linear case).[3] In more general cases Eq. (1) cannot be solved in quadratures. An approximate analytic solution (the first correction to the solution for $\sigma = \mathrm{const}$), similar to that given below, has been obtained for a semiinfinite conductor with plane boundaries ($a \to \infty$ with one of its surfaces fixed).[2] A similar problem has also been solved for a cylindrical conductor with constant[9] and monochromatic[10,11] boundary fields.

We introduce the following dimensionless quantities:

$$\left.\begin{aligned} z_* = \frac{z}{a}, \quad e_* = \frac{e}{e^0}, \quad h_* = \frac{a\mu\omega}{e^0}h, \quad j_* = \frac{j}{\sigma^0 e^0}, \\ t_* = \frac{2\lambda}{\sigma^0 (ae^0)^2}, \quad \sigma_* = \frac{\sigma}{\sigma^0}, \quad l^2 = a^2\frac{\sigma^0\mu\omega}{2}, \end{aligned}\right\} \tag{2}$$

where $\sigma^0 \equiv \sigma(0)$ and l is the ratio of a to the skin depth of the conductor $z \leq a$ for $\sigma \equiv \sigma^0$. The asterisks will be omitted below.

Equation (1) and the boundary conditions now take the form

$$e'' = 2il^2\sigma e, \quad t'' = -\sigma|e|^2, \tag{3}$$

$$e(1) = 1, \quad t(1) = e'(0) = t'(0) = 0, \quad 0 \leqslant z \leqslant 1, \tag{4}$$

where $h = ie'$, $h(0) = 0$; $j = \sigma e = -h'/2l^2$, $j(1) = 1$, $j'(0) = 0$. The dimensionless distributions of the electric and magnetic fields, the current, and the temperature in a plane conductor are determined below.

EXPRESSIONS FOR THE FIELDS AND THE TEMPERATURE IN THE FORM OF SERIES

We consider the linear dependence of the conductivity on temperature

$$\sigma = 1 - kt, \quad k \equiv \frac{\sigma^0 (ae^0)^2}{2\lambda}\alpha, \tag{5}$$

where $\alpha > 0$ is the temperature coefficient of conductivity. Hence, the frequency factor l and the dimensionless temperature coefficient of conductivity k [a measure of the degree of nonlinearity of the system of Eqs. (1) or (3)] are defining parameters in terms of the theory of similitude.

Assuming k to be a small parameter, and representing the solutions of Eqs. (3), h, and j in the form of series

$$e=\sum_{\rho=0} k^{\rho} e_{\rho}, \quad h=\sum_{\rho=0} k^{\rho} h_{\rho}, \quad j=\sum_{\rho=0} k^{\rho} j_{\rho}, \quad t=\sum_{\rho=0} k^{\rho} t_{\rho}, \tag{6}$$

we obtain the following linear differential equations for the coefficients:

$$\frac{i}{2l^2} e_s'' + e_s = p_s(z), \quad t_s'' = q_s(z) \tag{7}$$

(where $h_s = ie_s'$, $j_s = -h_s'/2l^2$), the right side of which,

$$p_s(z)=\sum_{\rho=0}^{s-1} t_\rho e_{s-\rho-1}, \quad q_s(z)=\sum_{m=0}^{s} e_m^* \left(\sum_{\rho=0}^{s} e_\rho t_{s-\rho-m-1} - e_{s-m}\right) \tag{8}$$

are defined by recursion relations in terms of the preceding coéfficients. The boundary conditions for e_s and t_s, which are identical with Eq. (4) for s = 0, vanish for s ≥ 1.

The solution of Eq. (7) is

$$e_s = C_s \operatorname{ch}(1+i) lz + \int_{\zeta=0}^{\zeta=z} p_s(\zeta)\, d \operatorname{ch}(1+i) l (\zeta - z), \quad j_s = p_s(z) + e_s, \tag{9}$$

$$h_s = (i-1) l \left[C_s \operatorname{sh}(1+i) lz + \int_{\zeta=0}^{\zeta=z} p_s(\zeta)\, d \operatorname{sh}(1+i) l (z-\zeta) \right], \tag{10}$$

$$t_s = \int_1^z d\zeta \int_0^{\zeta} q_s(\xi)\, d\xi, \tag{11}$$

the constant of integration being determined by the value of $e_s(1) = \delta_{0s}$:

$$C_s = \operatorname{ch}^{-1}(1+i) l \left[\delta_{0s} + \int_{\zeta=0}^{\zeta=1} p_s(1-\zeta)\, d \operatorname{ch}(1+i) l\zeta \right]. \tag{12}$$

In the zeroth approximation (s = 0) the quantities (9)–(11) take the well-known form[3]

$$e_0 = j_0 = \frac{\operatorname{ch}(1+i) lz}{\operatorname{ch}(1+i) l}, \quad h_0 = (i-1) l \frac{\operatorname{sh}(1+i) lz}{\operatorname{ch}(1+i) l},$$
$$t_0 = \frac{c_2(n) - c_2(nz)}{n^2 c_1(n)}. \tag{13}$$

In the same way[3] we have

$$n \equiv 2l, \quad c_{1,2}(\xi) = \operatorname{ch}\xi \pm \cos\xi, \quad s_{1,2}(\xi) = \operatorname{sh}\xi \pm \sin\xi. \tag{14}$$

For s ≥ 1 (9) and (10) take the form

$$e_s = \int_{\zeta=0}^{\zeta=z} p_s(\zeta)\, d \operatorname{ch}(1+i) l(\zeta - z)$$
$$+ \frac{\operatorname{ch}(1+i) lz}{\operatorname{ch}(1+i) l} \int_{\zeta=0}^{\zeta=1} p_s(1-\zeta)\, d \operatorname{ch}(1+i) l\zeta, \tag{15}$$

$$h_s = 2l^2 \left[\int_0^z p_s(\zeta) \operatorname{ch}(1+i) l(z-\zeta)\, d\zeta \right.$$
$$\left. - \frac{\operatorname{sh}(1+i) lz}{\operatorname{ch}(1+i) l} \int_0^1 p_s(1-\zeta) \operatorname{sh}(1+i) l\zeta\, d\zeta \right]. \tag{16}$$

In particular, in the median plane and on the surfaces of the plane layer we have

$$e_s(0) = \operatorname{ch}^{-1}(1+i) l \int_{\zeta=0}^{\zeta=1} p_s(1-\zeta)\, d \operatorname{ch}(1+i) l\zeta,$$
$$j_s(0) = p_s(0) + e_s(0), \tag{17}$$

$$h_s(0) = e_s(1) = j_s(1) = 0,$$
$$h_s(1) = 2l^2 \operatorname{ch}(1+i) l \int_0^1 p_s(\zeta) \operatorname{ch}(1+i) l\zeta\, d\zeta. \tag{18}$$

FIRST-ORDER CORRECTIONS TO THE FIELD, CURRENT, AND TEMPERATURE

We now obtain the first correction $(s = 1)$ to the zeroth approximation (13), proportional to k. Using the Puzyrevskii–Krylov functions

$$f_1(\xi) = \operatorname{ch}\xi \cos\xi, \quad f_{2,4}(\xi) = \operatorname{ch}\xi \sin\xi \pm \operatorname{sh}\xi \cos\xi, \quad f_3(\xi) = \operatorname{sh}\xi \sin\xi \tag{19}$$

and bilinear combinations

$$f^{\pm}_{abcd} \equiv f^{\pm}_{abcd}(l, z) = f_a(l) f_b(lz) \pm f_c(l) f_d(lz) \quad (f^{\pm}_{abcd} = \pm f^{\pm}_{cdab}) \tag{20}$$

from Eqs. (15), (16), and (11), we have

$$2n^2 c_1^2(n) \operatorname{Re} e_1 = [c_2(n) nz - s_2(nz)] f^-_{1433}$$
$$+ \frac{nc_2(n) - s_2(n)}{c_1(n)} \{f_3(n) f^-_{2143} - [f_1(n) + 1] f^+_{2341}\}$$
$$+ \frac{1}{5} \left\{ \left[12 \frac{f_1(n)+1}{c_1(n)} - c_1(n) + c_1(nz) \right] f^-_{1331} + 3 [c_2(n) - c_2(nz)] f^+_{1133} \right\},$$
$$2n^2 c_1^2(n) \operatorname{Im} e_1 = -[c_2(n) nz - s_2(nz)] f^+_{1234} \tag{21}$$

$$+ \frac{nc_2(n) - s_2(n)}{c_1(n)} \{f_3(n) f^+_{2341} + [f_1(n) + 1] f^-_{2143}\}$$
$$+ \frac{1}{5} \left\{ 3 \left[c_2(n) - c_2(nz) - 4 \frac{f_3(n)}{c_1(n)} \right] f^-_{1331} + [c_1(n) - c_1(nz)] f^+_{1133} \right\}, \tag{22}$$

$$4nc_1^2(n) \operatorname{Re} h_1 = 2 \left[c_2(n) nz - \frac{4}{5} s_2(nz) \right] f^+_{1133}$$
$$+ \frac{nc_2(n) - s_2(n)}{c_1(n)} \{[f_1(n) + 1] f^+_{2442} + f_3(n) f^-_{4422}\}$$
$$+ \frac{1}{5} \left\{ [c_1(n) - c_1(nz)] f^-_{1432} + 6 s_1(nz) f^-_{1331} \right.$$
$$\left. + \left\{ 12 \frac{f_3(n)}{c_1(n)} + 7 [c_2(n) - c_2(nz)] \right\} f^+_{1234} \right\}, \tag{23}$$

$$4nc_1^2(n) \operatorname{Im} h_1 = 2 \left[c_2(n) nz - \frac{4}{5} s_2(nz) \right] f^-_{1331}$$
$$+ \frac{nc_2(n) - s_2(n)}{c_1(n)} \{[f_1(n) + 1] f^-_{4422} - f_3(n) f^+_{2442}\}$$
$$+ \frac{1}{5} \left\{ 7 [c_2(n) - c_2(nz)] f^-_{1432} \right.$$
$$\left. + \left[12 \frac{f_1(n)+1}{c_1(n)} - c_1(n) + c_1(nz) \right] f^+_{1234} - 6 s_1(nz) f^+_{1133} \right\}, \tag{24}$$

$$j_1 = e_1 - e_0 t_0 = e_1 - \frac{c_2(n) - c_2(nz)}{2l^2 c_1^2(n)} (f^+_{1133} + i f^-_{1331}), \tag{25}$$

$$2n^4 c_1^2(n) t_1 = \left\{ \frac{nc_2(n) - s_2(n)}{2c_1^2(n)} [s_2(2n) - 2f_4(n)] \right.$$
$$\left. - \frac{1}{5} \left[6 \frac{f_3(n)}{c_1(n)} + 7c_2(n) \right] + 2c_2(n) \right\} [c_2(n) - c_2(nz)]$$
$$+ \frac{1}{10} \{4 [f_1(n) - f_1(nz)] + 3 [c_1(2n) - c_1(2nz)]\}$$
$$- nc_2(n) [s_1(n) - zs_1(nz)]. \tag{26}$$

The moduli $|e_1|$, $|h_1|$, $|j_1|$ and phases $\varphi_e = \arg e_1$, $\varphi_h = \arg h_1$, $\varphi_j = \arg j_1$ of the quantities e_1, h_1, j_1, and the temperature t_1 are shown in Fig. 1 for various values of the parameter l. In particular, on the surfaces of the plane layer of the quantities in Eqs. (21)-(26) only h_1 is nonzero:

$$4nc_1^2(n)\operatorname{Re}h_1(1)=[nc_2(n)-s_2(n)]\left[c_1(n)+\frac{5-3c_1(2n)+f_1(2n)}{8c_1(n)}\right]$$
$$+\frac{1}{5}\left[c_1(n)\,s_2(n)+6f_3(n)\frac{s_1(n)}{c_1(n)}\right], \tag{27}$$

$$4nc_1^2(n)\operatorname{Im}h_1(1)=\frac{3}{5}s_1(n)\left[2\frac{f_1(n)+1}{c_1(n)}-c_1(n)\right]$$
$$-\frac{nc_2(n)-s_2(n)}{2c_1(n)}f_3(n)[f_1(n)+3]. \tag{28}$$

For $l \ll 1$ (a thin layer, at low frequencies) we have

$$|e_1|\simeq\operatorname{Im}e_1\simeq\frac{l^2}{12}(1-z^2)(5-z^2),\quad \varphi_e\simeq\frac{\pi}{2}-\frac{l^2}{15}\frac{127-38z^2+7z^4}{5-z^2}, \tag{29}$$

$$|h_1|\simeq\operatorname{Re}h_1\simeq\frac{l^2}{3}z(3-z^2),\quad \varphi_h\simeq-\frac{l^2}{10}\frac{55-30z^2+7z^4}{3-z^2}, \tag{30}$$

$$|j_1|\simeq-\operatorname{Re}j_1\simeq t_0\operatorname{Re}e_0\simeq\frac{1}{2}(1-z^2),\quad \varphi_j\simeq\pi-\frac{l^2}{6}(11-7z^2), \tag{31}$$

$$t_1\simeq-\frac{1}{24}(1-z^2)\left[5-z^2-\frac{4}{525}l^4(1717-208z^2-33z^4+72z^6)\right]. \tag{32}$$

The ratios of the corrections to the corresponding quantities in the zeroth approximation, i.e.,[3]

$$|e_0|=|j_0|\simeq1,\quad |h_0|\simeq2l^2z,\quad t_0\simeq\frac{1}{2}(1-z^2), \tag{33}$$

are

$$\left|\frac{e_1}{e_0}\right|\simeq\left|\frac{j_1}{j_0}\right|\simeq|e_1|\simeq|j_1|,\quad \left|\frac{h_1}{h_0}\right|\simeq\frac{1}{6}(3-z^2),$$
$$\frac{t_1}{t_0}\simeq-\frac{1}{12}(5-z^2). \tag{34}$$

The limiting values of the corrections and their phases are

$$\lim_{l\to0}e_1=\lim_{l\to0}h_1=0,\quad \lim_{l\to0}\varphi_e=\frac{\pi}{2},\quad \lim_{l\to0}\varphi_h=0,\quad \lim_{l\to0}\varphi_j=\pi.$$

For $l \gg 1$ for a large part of the cross section of the lay-

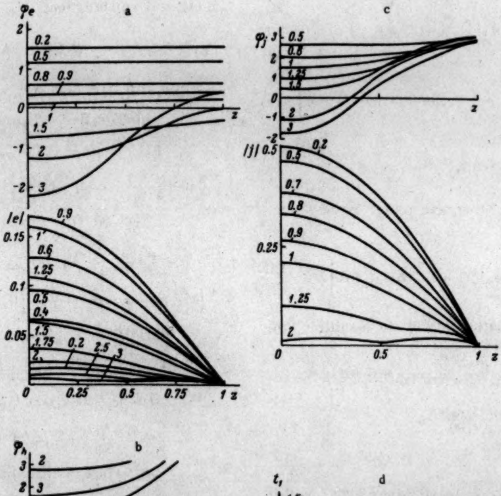

Fig. 1. Moduli and phases of e_1 (a), h_1 (b), j_1 (c), and t_1 (d) as a function of z, for various values of l.

er, for which $l \min(z, 1-z) \gg 1$, we have

$$\operatorname{Re} e_1 \simeq \operatorname{Re} j_1 \simeq \frac{\exp[-l(1-z)]}{4l}\left\{\sin\left(n-\frac{\pi}{4}\right)\sin\left[l(1-z)-\frac{\pi}{4}\right] - \frac{z}{\sqrt{2}}\sin\left[l(1-z)+\frac{\pi}{4}\right]\right\}, \tag{36}$$

$$\operatorname{Im} e_1 \simeq \operatorname{Im} j_1 \simeq \frac{\exp[-l(1-z)]}{4l}\left\{\sin\left(n+\frac{\pi}{4}\right)\sin\left[l(1+z)-\frac{\pi}{4}\right] + \frac{z}{\sqrt{2}}\sin\left[l(1-z)-\frac{\pi}{4}\right]\right\}, \tag{37}$$

$$\operatorname{Re} h_1 \simeq \frac{1}{4}\exp[-l(1-z)]\left\{\cos n \sin\left[l(1+z)-\frac{\pi}{4}\right] - \sin n \sin l(1+z) + z\cos l(1-z)\right\}, \tag{38}$$

$$\operatorname{Im} h_1 \simeq \frac{1}{4}\exp[-l(1-z)](1-z)\sin l(1-z), \tag{39}$$

$$t_1 \simeq \frac{3}{80 l^4}. \tag{40}$$

For the field and the current the main, exponentially small factor, which determines the order of e_1, j_1, and h_1, is the same as in the zeroth approximation, (30), i.e., of the quantities[3]

$$|e_0| = |j_0| \simeq \exp[-l(1-z)], \quad |h_0| \simeq l\sqrt{2}\exp[-l(1-z)] \tag{41}$$

$|e_1|$, $|j_1|$, and $|h_1|$ are approximately damped oscillations (and their ratios to $|e_0|$ and $|h_0|$ are approximately undamped oscillations) with period $\Delta z = 2\pi/l$. The correction to the temperature is positive; everywhere, in addition to a small region near the surface, it is constant and proportional to l^{-4}; its ratio to $t_0 = 1/(4l^2)$ is $t_1/t_0 \simeq 3/(20 l^2)$ (see ref. 3). The limiting values are

$$\left.\begin{aligned} &\lim_{l\to\infty} e_1 = \lim_{l\to\infty} h_1 = \lim_{l\to\infty} j_1 = \lim_{l\to\infty} t_1 = 0,\\ &\lim_{l\to\infty}\frac{e_1}{e_0} = \lim_{l\to\infty}\frac{h_1}{h_0} = \lim_{l\to\infty}\frac{j_1}{j_0} = \lim_{l\to\infty}\frac{t_1}{t_0} = 0. \end{aligned}\right\} \tag{42}$$

The quantities $|e_1|$, $|h_1|$, and $|j_1|$ are functions which decrease for $l \leq \pi$ with a maximum at $z = 0$, increase for $l \leq 1$ with a maximum at $z = 1$, and decrease for $l < \pi/2$, with a maximum at $z = 0$. For large l they have additional extrema, the first of which is reached for smaller values of z, the larger the value of l; $|e_1|$ and $|h_1|$ as functions of l have maxima for $l \simeq 0.9008$ and 0.8045 respectively; $|j_1|$ decreases monotonically as a function of l.

The phases φ_e, φ_h, and φ_j $(-\pi < \varphi \leq \pi)$ are increasing functions of $z = 0$ and a maximum at $z = 1$. For $l < \pi$, $l < \pi/2$, and $l < \pi$ respectively they are continuous; in the opposite case, for values which are multiples of π, the phases have discontinuities with jumps of -2π (the number of which for φ_e, in particular, is $[l/\pi]$). The range of variation of the phases and their closeness to a linear relationship is the greater the smaller the value of l.

The value of t_1 for small values of l is negative and decreases in absolute value as l increases, and for $l \simeq 1.198$ becomes zero (for smaller values of l, t_1 is an increasing function of z with a minimum at $z = 0$, and for larger values of l is a decreasing function with a maximum at $z = 0$). When l is increased further, t_1, while remaining positive, continues to increase, and for $l \simeq 1.381$ reaches a maximum and then tends to zero monotonically in accordance with the asymptotic equation (40).

For $t_1 < 0$ the overall temperature profile in the conductor is less convex and flatter than for constant conductivity ($k = 0$), and for $t_1 > 0$ the reverse is true.

CONDITION UNDER WHICH THE APPROXIMATION IS VALID

The above approximation [beginning with Eqs. (6) and (7)] is valid when the initial set of equations (3) are weakly nonlinear, i.e., when

$$k t_0(0) \ll 1 \quad \text{or} \quad k \ll n^2 \frac{c_1(n)}{c_2(n)}. \tag{43}$$

In addition to this an essential physical requirement is the condition that the maximum absolute temperature of the conductor (for $z = 0$) must remain below the melting point. Together with Eq. (43), this requirement leads to a system of two equalities of the same sense:

$$\frac{(e^0)^2}{4\lambda\mu\omega}\frac{c_2(n)}{c_1(n)}\begin{cases} < \delta t,\\ \ll \alpha^{-1}\end{cases} \tag{44}$$

(δt is the difference between the melting point and the temperature of the surface of the conductor), which answers the question of the condition of applicability of the approximation considered. The system (44) can be regarded as a limitation on the allowed amplitude of the electric field at the boundary.

In the limiting cases with respect to n, condition (44) can be written in a form which does not contain transcendental functions and which is thus more suitable from the practical point of view. For a weak skin effect ($n \ll 2$) Eq. (44) is replaced by

$$\sigma^0 a^2\begin{cases} < \dfrac{4\lambda}{(e^0)^2}\delta t,\\ \ll \min\left[\dfrac{4\lambda}{(e^0)^2\alpha}, \ \dfrac{1}{2\mu\omega}\right],\end{cases} \tag{45}$$

and for a strong skin effect ($n \gg 2$),

$$\mu\omega\begin{cases} > \dfrac{(e^0)^2}{4\lambda\delta t},\\ \gg \max\left[\dfrac{(e^0)^2}{4\lambda}\alpha, \ \dfrac{1}{2\sigma^0 a^2}\right].\end{cases} \tag{46}$$

---

[1] L. D. Landau and E. M Lifshits, Electrodynamics of Continuous Media, Addison-Wesley (1960).

[2] R. S. Kuznetskii and M. K. Likht, Izv. AN SSSR, Energetika i Transport, No. 3, 128 (1969).

[3] R. S. Kuznetskii, Ukr. Fiz. Zh., 13, 1314 (1968) [Ukr. Phys. J., 13, 939 (1969)].

[4] G. A. Varshavskii, Zh. Eksp. Teor. Fiz., 6, 282 (1936).

[5] G. A. Varshavskii, Prikl. Mekh. Tekh. Fiz., No. 3 (1960).

[6] P. M. Kolesnikov, Introduction to Nonlinear Electrodynamics [in Russian], Nauka i Tekhnika, Minsk (1971).

[7] Yu. G. Gurevich and O. N. Chavchanidze, Fiz. Tverd. Tela, 13, 1091 (1971) [Sov. Phys.-Solid State, 13, 906 (1971)].

[8] R. S. Kuznetskii, Ukr. Fiz. Zh., 12, 697 (1967).

[9] R. S. Kuznetskii, Ukr. Fiz. Zh., 13, 1028 (1968) [Ukr. Phys. J., 13, 733 (1968)].

[10] R. S. Kuznetskii, Ing. Fiz. Zh., 17, 1132 (1969).

[11] R. S. Kuznetskii, Izv. AN SSSR, Energetika i Transport, No. 4, 163 (1970).

Parametric interaction of a charged particle beam with a periodic system

V. I. Koroza and E. S. Sukhovskii

Moscow Engineering Physics Institute

(Submitted July 25, 1973; resubmitted November 22, 1973)
Zh. Tekh. Fiz., 44, 1633-1640 (August 1974)

A method is proposed for the exact numerical calculation, in the hydrodynamic approximation, of the interaction of a charged particle beam with a periodic waveguide. Typical numerical calculations are given and the results are compared with approximate calculations based on conventional methods. It is shown that there are significant discrepancies in certain cases.

INTRODUCTION

The study of plasma instabilities (space-charge) waves in periodic structures is of both practical and theoretical interest. Examples of periodic structures might be: a waveguide with a periodically modulated conducting surface;[1] a waveguide filled with a stratified medium;[1-3] a uniform waveguide with a premodulated current density.[4] Another example of a periodic system is a waveguide with a plasma whose density is acoustically modulated so that in a coordinate system moving with the phase velocity of the sound wave the plasma can be regarded as a dielectric medium with a permittivity $\varepsilon(z) = [1-\omega_p^2(z)/\omega^2]$, $\mu \equiv 1$ with $\varepsilon(z+\lambda) \equiv \varepsilon(z)$, where λ is the acoustic wavelength. A plasma with a density of 10^8-10^{14} cm^{-3} is transparent to a beam of particles but would at the same time cause retardation of electromagnetic waves[5,6] in the range 3m to 3 mm.

We consider here an exact method of investigating the behavior of a beam of charged particles in periodic systems, using a linearized hydrodynamic model. It is shown below that this method leads to quantitative, and in some cases, qualitative differences from approximate methods. Our method is based on the formulation of the problem in the equivalent variational statement and the subsequent reduction to a system of normal differential equations in the auxiliary unknowns which characterize the self-consistent distribution of the wave field and beam current density.

FORMULATION OF THE PROBLEM[1)]

We assume that the system has axial symmetry and is bounded by the conducting surface of the waveguide $r = \Pi(z)$. Assume that a beam of charged particles with radius r_e moves along the z axis of the system. We assume that the velocity of all the particles in the beam is directed along the z axis. We use the hydrodynamic approximation and introduce the following notation: $e(n_0+n)$ is the spatial charge density, $(v_0 = v)\mathbf{e}_z$ is the velocity of the particles and $(j_0 + j)\mathbf{e}_z$ is the current density. Here, n_0, v_0 and $j_0 = en_0v_0$ are constant in time and space and the terms n, v and j are small and vary with time as $\sim e^{-i\omega t}$.

From the linearized equations of motion $(e/m)\mathcal{E}_z = \partial v/\partial t + v_0(\partial v/\partial z)$, the equation of continuity $\partial j/\partial z = -e(\partial n \cdot dt^{-1})$, the relationship $j = e(n_0v + nv_0)$, the Maxwell equation $-i\omega\mathcal{E} = \operatorname{curl}\mathcal{H} - (4\pi/c)\mathbf{j}$ and the fact that only axially symmetric TM waves (for which $\mathcal{H} = \mathcal{H}\mathbf{e}_\varphi$) are excited, we get

$$\left[\frac{\partial^2}{\partial z^2} - 2i\beta_e\frac{\partial}{\partial z} - (\beta_e^2 - \beta_p^2)\right]j = \frac{c}{4\pi}\beta_p^2\left[\frac{\partial}{\partial r} + \frac{1}{r}\right]\mathcal{H}. \tag{1}$$

Here, we have introduced the notation:

$$\beta_e = \frac{\omega}{v_0} = \frac{k}{\beta}, \quad k = \frac{\omega}{c}, \quad \beta = \frac{v_0}{c}; \quad \beta_p = \frac{\omega_p}{v_0}, \quad \omega_p = \left(\frac{4\pi}{\varepsilon}\frac{e^2}{m}n_0\right)^{1/2}.$$

Equation (1) relates the complex amplitudes of the field $\mathcal{H} = \mu^{-1}B$ excited in the system to the varying component of the beam current density j.

We can get a second equation relating $\mathcal{H}$ and j from the condition

$$\delta_{\mathcal{H}_0} J(\mathcal{H}, \mathcal{H}_0, \mathbf{j}) = 0 \quad \text{for} \quad \delta\mathcal{H}_0[S(z_{1,2})] = 0. \tag{2}$$

Here

$$J(\mathcal{H}, \mathcal{H}_0, \mathbf{j}) = \iiint\limits_W \Big[\varepsilon^{-1}(\operatorname{curl}\mathcal{H}, \operatorname{curl}\mathcal{H}_0) - k^2\mu(\mathcal{H}, \mathcal{H}_0) - \frac{4\pi}{c}(\operatorname{curl}\varepsilon^{-1}\mathbf{j}, \mathcal{H}_0)\Big]dv - ik\iint\limits_\Pi w(\mathcal{H}_\tau, \mathcal{H}_{0\tau})\,d\sigma,$$

W is the region bounded by the conducting surface Π and the cross section planes S(z) normal to the z axis at $z = z_1$, and $z = z_2$ $(z_1 < z_2)$; $\mathbf{n}$ is the external normal to Π. It is evident that the stationarity condition (2) is equivalent, inside the region W, to the equation

$$\operatorname{curl}[\varepsilon^{-1}\operatorname{curl}\mathcal{H}] - k^2\mu\mathcal{H} = \frac{4\pi}{c}\operatorname{curl}\varepsilon^{-1}\mathbf{j},$$

and on the conducting boundary Π to the Leontovich boundary condition

$$\{(\operatorname{curl}\mathcal{H})_\tau + ikw[\varepsilon\mathcal{H}, \mathbf{n}]\}_\Pi = 0.$$

Remembering that $= \mathcal{H}\mathbf{e}_\varphi$, $\mathbf{j} = j\mathbf{e}_z$ and taking $\mathcal{H}_0 = \mathcal{H}_0\mathbf{e}_\varphi$, we can put

$$\mathcal{H} = \sum_n e_n(r, z)f_n(z); \quad \mathcal{H}_0 = \sum_n e_n(r, z)v_n(z); \quad j = \sum_k \eta_k(r)j_k(z). \tag{3}$$

Here $\{e_n\}$ and $\{\eta_k\}$ are systems of basis functions. In the approximation of order (N, N_1) we assume that the sum over n in (3) contains N terms $(n = 1, 2, \ldots, N)$ and the sum over k has N_1 terms $(k = 1, 2, \ldots, N_1)$.

Substituting (3) first into (1) with the application of the Galerkin method and then into (2) where we use $\delta v_n(z_1) = \delta v_n(z_2) = 0$, we obtain the following two systems of equations:

$$T\left[\frac{d^2}{dz^2}\mathbf{f}_1 - 2i\beta_e\frac{d}{dz}\mathbf{f}_1 - (\beta_e^2 - \beta_p^2)\mathbf{f}_1\right] = \frac{c}{4\pi}\beta_p^2\Phi\mathbf{f}_0,$$

$$\frac{d}{dz}\left[G(z)\frac{d\mathbf{f}_0}{dz} + Q(z)\mathbf{f}_0\right] - Q^\tau(z)\frac{d\mathbf{f}_0}{dz} + P(z)\mathbf{f}_0 = \frac{4\pi}{c}\mathcal{T}\mathbf{f}_1,$$

in which $\mathbf{f}_0 = (f_1, \ldots, f_N)^T$, $\mathbf{f}_1 = (j_1, \ldots, j_{N_1})^T$ and the elements of the matrices T, Φ, $\mathscr{F}$, G, Q, and P are the following integrals:

$$T_{ns} = \iint\limits_{S(z)} \eta_s \eta_n dS; \quad \Phi_{ns} = \iint\limits_{S(z)} \left(\frac{\partial e_s}{\partial r} + \frac{1}{r} e_s\right) \eta_n dS;$$

$$\mathscr{F}_{ns} = \iint\limits_{S(z)} \frac{\partial}{\partial r} (\varepsilon^{-1} \eta_s) \bar{e}_n dS,$$

$$G_{ns} = \iint\limits_{S(z)} \varepsilon^{-1} e_s \bar{e}_n dS; \quad Q_{ns} = \iint\limits_{S(z)} \varepsilon^{-1} \frac{\partial e_s}{\partial z} \bar{e}_n dS,$$

$$P_{ns} = k^2 \iint\limits_{S(z)} \mu e_s \bar{e}_n dS - \iint\limits_{S(z)} \varepsilon^{-1} \left[\frac{\partial e_s}{\partial z} \frac{\partial \bar{e}_n}{\partial z} + \frac{1}{r^2} \frac{\partial (r e_s)}{\partial r} \frac{\partial (r \bar{e}_n)}{\partial r}\right] dS$$

$$+ ik\Pi \sqrt{1 + \left(\frac{d\Pi}{dz}\right)^2} \int\limits_0^{2\pi} w e_s \bar{e}_n d\varphi.$$

This system of two vector equations (in the unknowns $\mathbf{f}_0$ and $\mathbf{f}_1$) describes in a self-consistent way the interaction of a cylindrical plasma beam with a nonuniform system and can be written as the single vector equation

$$\frac{d}{dz}\left[\tilde{G} \frac{d\mathbf{f}}{dz} + \tilde{Q}\mathbf{f}\right] - \tilde{R} \frac{d\mathbf{f}}{dz} + \tilde{P}\mathbf{f} = 0, \qquad (4)$$

in which

$$\mathbf{f} = \begin{pmatrix} \mathbf{f}_0 \\ \mathbf{f}_1 \end{pmatrix}, \quad \tilde{G} = \left(\begin{array}{c|c} G & 0 \\ \hline 0 & T \end{array}\right), \quad \tilde{Q} = \left(\begin{array}{c|c} Q & 0 \\ \hline 0 & -i\beta_e T \end{array}\right), \quad \tilde{R} = \left(\begin{array}{c|c} Q^* & 0 \\ \hline 0 & i\beta_e T \end{array}\right)$$

$$\tilde{P} = \left(\begin{array}{c|c} P & -\frac{4\pi}{c} F \\ \hline -\frac{c}{4\pi} \beta_p^2 \Phi & (\beta_p^2 - \beta_e^2) T \end{array}\right).$$

Taking

$$\tilde{\mathbf{f}}(z) = \tilde{G} \frac{d\mathbf{f}}{dz} + \tilde{Q}\mathbf{f} = \begin{pmatrix} \tilde{\mathbf{f}}_0 \\ \tilde{\mathbf{f}}_1 \end{pmatrix} \text{ and } \mathbf{g}(z) = \begin{pmatrix} \mathbf{f} \\ \tilde{\mathbf{f}} \end{pmatrix},$$

we write (4) in the form of a first-order vector differential equation

$$\frac{d\mathbf{g}}{dz} = A(z)\mathbf{g}, \quad A(z) = \left(\begin{array}{c|c} -\tilde{G}^{-1}\tilde{Q} & \tilde{G}^{-1} \\ \hline -\tilde{P} - \tilde{R}\tilde{G}^{-1}\tilde{Q} & \tilde{R}\tilde{G}^{-1} \end{array}\right). \qquad (5)$$

In the following calculations we take the basis functions appearing in (3) as:

$$e_n(r, z) = \frac{J_0'\left(\nu_n \frac{r}{\Pi(z)}\right)}{\sqrt{\pi} J_1(\nu_n)}, \quad \eta_k(r) = \frac{J_0\left(\mu_{k-1} \frac{r}{r_e}\right)}{\sqrt{\pi} r_e J_0(\mu_{k-1})} \theta(r_e - r). \qquad (6)$$

Here ν_n and μ_n are the positive roots of the Bessel function $J_0(x)$ and its derivative $J_0'(x)$ respectively (n = 1, 2, ...), $\mu_0 = 0$, $\theta(x) = 1$ for $x \geq 0$ and 0 for $x < 0$. Physically this choice of $\{e_n\}$ means that we represent the field at each cross section by the superposition of the TM_0 modes of a cylindrical waveguide of the same cross section. With this choice of $\{\eta_k\}$ the first term of the sum for j in (3) corresponds to the approximation of a current density uniformly distributed over the cross section of the beam.

The expressions for the matrix elements in (4) are given in Appendix (1) for the basis defined by (6).

In the statement of the problem we have given there is no unique solution if only because under the stationarity condition (2) no restrictions are placed on the values of the unknown field $\mathscr{H}$ in the cross sections $S(z_1)$ and $S(z_2)$. Therefore Eq. (4) or the equivalent form (5) must be considered with auxiliary initial or boundary conditions depending on which process is in fact modulated. Putting, for example,

$$\mathbf{g}(z_1) = (\mathbf{f}_0^{\tau}(z_1),\ \mathbf{0}_{N_1}^{\tau},\ \tilde{\mathbf{f}}_0^{\tau}(z_1),\ \mathbf{0}_{N_1}^{\tau})^{\tau}, \qquad (7)$$

we get a model of a traveling-wave tube where there is no velocity or current density modulation at the input ($z = z_1$). Problem (5), (7) is a normal initial value problem and a numerical solution does not present any difficulties. It is just as simple to construct a model for a backward-wave tube; here it is necessary to use two-point type conditions $\mathbf{f}_1(z_1) = \tilde{\mathbf{f}}_1(z_1) = \mathbf{0}_{N_1}$, $\mathbf{f}_0(z) = \tilde{\mathbf{f}}_0(z_2) = \mathbf{0}_N$, which denote the absence of density and velocity modulation of the beam at the input ($z = z_1$) and the fact that the transverse field components are zero at the output ($z = z$).

PERIODIC SYSTEMS

We consider the particularly interesting case of a beam in a periodic waveguide where the shape of the boundary and the medium filling the waveguide vary periodically (period D) with the z coordinate along the axis [$\Pi(z + D) \equiv \Pi(z)$, $\varepsilon(z + D) \equiv \varepsilon(z)$ and $\mu(z + D) \equiv \mu(z)$]. The matrix coefficient A(z) in (5) is then periodic in z with period D and we may therefore consider solutions (5) which satisfy the Floquet boundary condition

$$\mathbf{g}(z) = e^{ihz}\mathbf{u}(z), \ \mathbf{u}(z + D) \equiv \mathbf{u}(z). \qquad (8)$$

Solutions of type (8) always exist and in many cases have the property of completeness. The set of solutions of type (8) (normal modes[7]) is conveniently divided into two groups: One is the group of normal modes of a periodic waveguide, excited as it were by the particle beam, and the other represents space-charge waves.[8]

We note that in certain cases the set of normal modes (5), (8) does not possess the property of completeness (points of nondiagonalizable multiplicity of the cell operator); in order to maintain completeness in this case we have to consider in addition to the normal modes the adjoint modes[9] which differ from (8) in the presence of a secular factor (polynomials in z). This general case is covered by the matrix formulation of the Floquet theorem on the structure of the fundamental matrix Y(z) of the system (5) with $A(z + D) \equiv A(z)$

$$Y(z) = U(z)e^{iBz}.$$

Here, U(z) is a matrix function which is periodic with the period D, and B is a constant matrix. The propagation constants h in (8) are the eigenvalues of B to an accuracy of $2\pi n/D$ ($n = 0, \pm 1, \ldots$). If to some h_j in the Jordan form $\tilde{B}$ of the matrix B ($B = C^{-1}\tilde{B}C$) there corresponds some cell of dimension $n_j \geq 1$, then to this cell there corresponds n_j columns of the fundamental matrix $\tilde{Y}(z) =$

$CY(z)C^{-1}$, one of which is the normal wave and the remaining $(n_j - 1)$ are the adjoint waves.

We limit ourselves to a consideration of the normal modes. We seek the approximate solutions of (4) which satisfy the Floquet condition (8) in the form of a finite sum of $(2q+1)$ terms $(q = 0, 1, 2, \ldots)$

$$\mathbf{f}(z) \simeq \mathbf{f}_q(z) = \sum_{m=-q}^{q} e^{ih_{(m)}z}\mathbf{c}^{(m)}, \quad h_{(m)} = h + \frac{2\pi}{D}m. \qquad (9)$$

After substitution of (9) into (4), multiplication of the resultant equation by $e^{-ih_{(p)}z}$ $(p = 0, \pm 1, \ldots, \pm q)$ and integration with respect to z over the period D we obtain a system of $(2q+1)$ equations in the unknown vectors $\mathbf{c}^{(m)}$

$$\sum_{m=-q}^{q} [-h_{(m)}h_{(p)}\tilde{G}^{(p-m)} + ih_{(p)}\tilde{Q}^{(p-m)} - ih_{(m)}\tilde{R}^{(p-m)} + \tilde{P}^{(p-m)}]\mathbf{c}^{(m)} = 0. \qquad (10)$$

Here, $A^{(m)}$ is the matrix coefficient of the Fourier series

$$A(z) = \sum_{m} A^{(m)} \exp\left(i\frac{2\pi m}{D}z\right),$$

where A(z) is any of the matrices $\tilde{G}$, $\tilde{Q}$, $\tilde{R}$ and $\tilde{P}$. The unknown vectors $\mathbf{c}^{(m)} = \begin{pmatrix}\mathbf{f}_0^{(m)}\\ \mathbf{f}_1^{(m)}\end{pmatrix}$ have dimension $(N + N_1)$ so that the system (10) contains $(N+N_1)(2q+1)$ unknowns $c_n^{(m)} = f_n^{(m)}$ for $1 \le n \le N$ and $j_n^{(m)}$ for $N+1 \le n \le N+N_1$.

After introducing new notation and eliminating $\mathbf{J}_1 = -\beta_p^2 K^{-1}(h)M\mathbf{J}_0$, we can write (10) in the form

$$[B(h) - \beta_p^2 FK^{-1}(h)M]\mathbf{J}_0 = 0, \qquad (11)$$

where B, K, M and F are block matrices with elements

$$B^{lm} = -h_{(m)}h_{(l)}G^{(l-m)} + ih_{(l)}Q^{(l-m)} - ih_{(m)}Q^{*(l-m)} + P^{(l-m)},$$
$$K^{lm} = [\beta_p^2 - (h_{(m)} - \beta_l)^2] I_{N_1}\delta_{lm},$$
$$M^{lm} = \Phi^{(l-m)}, \quad F^{lm} = F^{(l-m)} = -\frac{1}{\varepsilon}\Phi^{*(l-m)},$$

and the matrices G, Q, P and Φ are given in the Appendix (1).

The condition

$$\det[B(h) - \beta_p^2 FK^{-1}(h)M] = 0 \qquad (12)$$

is the dispersion equation. This equation can be expanded in powers of a small parameter (the amplitude of the periodic modulation, for example) and if terms of second order are neglected we get approximate dispersion equations[1,4] which give a useful qualitative picture. Here, however, we consider exact solutions of the dispersion equation (12) obtained by means of a computer.

SOLUTION OF THE DISPERSION EQUATION

We now give the results of calculations for a waveguide bounded by the surface $\Pi(z) = a[1 + \varkappa\cos(2\pi/D)z]$, with $\varepsilon = \mu = 1$ and a perfectly conducting boundary $(w = 0)$. The greatest interest is in the cases where the phase constants of the lower-type space-charge waves[8] are close to the phase constants of the waveguide waves.

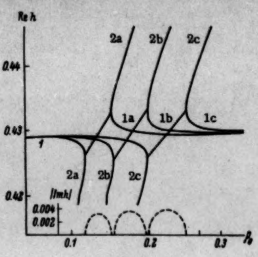

Fig. 1

The following parameter values are chosen for the calculations: $a = 4.315$ cm, $D = 3.333$ cm, $r_e = 0.500$ cm. The calculations apply for an electron beam.

Figure 1 shows the way the phase constant h (8) depends on the density of the space charge $\rho_0 = en_0$ in cgs esu near the resonance of the direct wave of the system with the slow space-charge wave ($\varkappa = 0.25$, $k_0 = \omega/c = 0.660\ \mathrm{cm}^{-1}$) for various values of the relative particle velocity $\beta = v_0/c$ (c is the velocity of light in vacuum). The indices a, b and c correspond respectively to the values $\beta = 0.298$, 0.300 and 0.302. The numbers in Fig. 1 denote: 1) the direct waveguide wave (i.e., the direct wave of the periodic system excited by the particle beam); 2) the slow space-charge wave. This division of the waves is arbitrary and loses its meaning very close to the resonance parameter values where the dispersion curve 1 goes over to curve 2. The continuous lines in Fig. 1 (and also in Fig. 2) give the values of $|\mathrm{Re}\,h|$ (cm^{-1}) and the dashed lines the values of $|\mathrm{Im}\,h|$ (cm^{-1}) in the complex h region. It can be seen from Fig. 1 that there is a region of values of ρ_0 for which h is complex. It can be established from refs. 10 and 11 that convective instability exists and one of the system waves is amplified. It is evident from the dispersion curves that as β is increased the region of complex h moves towards higher space charge densities and the width of the instability region increases together with the value of max $|\mathrm{Im}\,h|$.

Figure 2 shows the way that the propagation constant h in (8) depends on $\beta = v_0/c$ for $\varkappa = 0.5$ and $k_0 = \omega/c = 0.6131\ \mathrm{cm}^{-1}$ near the same resonance (the direct waveguide wave corresponds to 1 and the slow space-charge wave to 2) for space-charge density values $\rho_0 = 0.09$ cgs esu

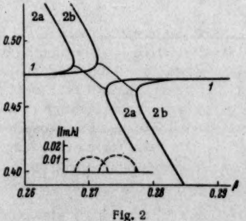

Fig. 2

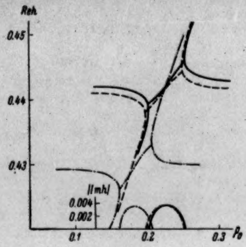

Fig. 3

(letter a) and $\rho_0 = 0.18$ cgs esu (letter b). The beam instability shown in Fig. 2 is convective as in Fig. 1. The results given in Figs. 1 and 2 correspond to the approximation $N = N_1 = 3$, $q = 1$.

We have made a numerical study of the rate at which this method of calculation converges. The nature of the approximations is defined by the choice of the values of the three indices N, N_1, and q. The convergence over N is similar to that of the normal method of calculating nonregular waveguides without particle beams according to the Galerkin technique studied in ref. 12. From physical considerations the convergence over N_1 must be similar to that over N. It is therefore of most interest to consider the convergence over q. The results of some calculations are given in Fig. 3 for $\varkappa = 0.25$, $k_0 = \omega/c = 0.6600$ cm^{-1}, $\beta = v_0/c = 0.300$; the axes represent the values of h (cm^{-1}) and ρ_0 in cgs esu. The calculations are for $N = N_1 = 3$ and $q = 1$ (dashed dotted lines), $q = 2$ (dashed lines) and $q = 3$ (continuous lines).

For the system we have considered here the dispersion equation is known but it is difficult to use it for actual calculations because it contains the unknown amplitude distributions of the spatial harmonics (see, for example, refs. 13 and 14). This equation reduces approximately to a fourth-order algebraic equation with coefficients K_c (coupling factor) and T (depression coefficient) which depend on the unknown propagation constant and the unknown field distribution in a cross section. In the calculation of these coefficients approximate use is made of the values of the high-frequency characteristics of the system in the absence of a beam and it is assumed that the effect of the beam is small. It has been noted in refs. 13 and 14 that even in this approximation the determination of the system characteristics in the absence of a beam is in itself a rather difficult problem, especially in a structure with a complex geometry. We also note that this approach, which is based on the use of a characteristic fourth-order equation with coefficients which are calculated only approximately without beam effects taken into account, leads to large errors near the boundary between the real and significantly complex values of h. The reason is that the coefficients of the characteristic equation contain in the energy flux the denominator; in the absence of a beam this quantity vanishes at the edge of the passband. This was in fact used in ref. 15 as the basis of the idea that the transverse instability would be suppressed in the high intensity beam of a linear accelerator under conditions where the parasitic wave responsible for the growth of the instability was excited near the edge of the passband of a system without a beam. This idea, which is based on the use of the above-mentioned characteristic equation, is not valid, as has been shown experimentally[16] and theoretically.[17,18]

We now give a comparison of the results of calculations of the growth rate Im h near resonance for the direct waveguide wave and the slow space-charge wave; we use the example described above with $\varkappa = 0.25$, $k_0 = 0.660$ cm^{-1}, $\beta = 0.300$ and $\rho_0 = 0.2295$ cgs esu. From the fourth-order characteristic equation we get $|\mathrm{Im}\, h| = 0.448 \cdot 10^{-2}$ cm^{-1}. For the model used in ref. 19, an approximate calculation[13] gives $\Gamma = 1$ and in our notation we have for k_c that

$$k_c = \frac{c}{8\pi\mathscr{P}} \frac{[\beta_p^2 - (h_s - \beta_e)^2]^2}{h_s k} \frac{(FK^{-1}M\mathbf{j}_0, \mathbf{j}_0)^2}{\left|\sum\limits_m \Phi^{(s-m)} \mathbf{f}^{(m)}\right|^2},$$

where $h_{(s)}$, $\mathbf{j}_0$, and $\mathscr{P}$ are the values calculated in the absence of a beam for the propagation constant of the spatial harmonic which is synchronous with the beam ($s = 1$ here), of the vector $\mathbf{j}_0$ from (11) and the energy flux $\mathscr{P}$ through a cross section. The expression for $\mathscr{P}$ in given in the Appendix (2).

A numerical calculation from the dispersion equation (12) in the approximation $N = N_1 = q = 3$, which produces results to three significant figures, gives $|\mathrm{Im}\, h| = 0.368 \cdot 10^{-2}$ cm^{-1}. The discrepancy might be a result of the fact that the effect of the higher modes and of the nonresonant spatial harmonics ($\Gamma = 1$) has not been taken into account and also of the approximate nature of the calculation of k_c which has used the values of h_s, J_0 and $\mathscr{P}$ for a "cold" system.

The authors are grateful to A. A. Rukhadze for discussion.

APPENDIX

1. We give the expressions for the elements of the matrices G, Q, P, T, and Φ in the basis (6)

$$G_{ns} = \varepsilon^{-1}\Pi^2(z)\delta_{ns};\ Q_{ns} = \varepsilon^{-1} q_{ns} \frac{d}{dz}(\Pi^2),$$

$$q_{ns} = \frac{\nu_s^2}{\nu_n^2 - \nu_s^2} \text{ for } n \neq s,\ q_{nn} = 0,$$

$$P_{ns} = \left\{\mu [k\Pi]^2 - \frac{\nu_n^2}{\varepsilon}\right\}\delta_{ns} + \varepsilon^{-1}\left(\frac{d\Pi}{dz}\right)^2 p_{ns} + 2ik\omega\Pi\sqrt{1 + \left(\frac{d\Pi}{dz}\right)^2},$$

$$p_{ns} = 2 - \frac{8\nu_n^2\nu_s^2}{(\nu_n^2 - \nu_s^2)^2} \text{ for } n \neq s,\ p_{nn} = \frac{5 - \nu_n^2}{3},$$

$$T_{ns} = \delta_{ns};\ \Phi_{ns}' = -\frac{2(\nu_s r_e)^2}{J_1(\nu_s)} \frac{J_1\left(\nu_s \frac{r_l}{\Pi(z)}\right)}{(\nu_s r_e)^2 - [\mu_{n-1}\Pi(z)]^2}.$$

2. The electromagnetic energy flux through a cross section averaged over the hf period is defined for $\mathbf{j} = 0$ by

$$\mathscr{P}(z) = \frac{c}{8\pi k} \mathrm{Im} \iint\limits_{S(z)} \varepsilon^{-1}([\mathbf{e}_z, \mathrm{curl}\,\mathscr{H}], \mathscr{H})\, dS.$$

Using (3), we get

$$\mathscr{P}(z)=\frac{c}{8\pi k}\operatorname{Im}\left(G\frac{d\mathbf{f}}{dz}+Q\mathbf{f},\ \mathbf{f}\right).$$

Since in the absence of losses and for a system without a beam $\mathscr{P}(z) = \text{const}$, then $\mathscr{P} = 1/D\int\limits_{-D/2}^{D/2}\mathscr{P}dz$.

Remembering that $\mathbf{f} = \sum\limits_{m} e^{ih(m)z}\mathbf{f}(m)$, we get

$$\mathscr{P}=\frac{c}{8\pi kD}\operatorname{Im}\sum_{p,\,m=-q}^{q}\left([ih_{(m)}G^{(p-m)}+Q^{(p-m)}]\mathbf{f}^{(m)},\ \mathbf{f}^{(p)}\right).$$

[1)] In this section the structure is not assumed to be periodic and the problem is formulated for the general case.

[1] V. I. Koroza and V. M. Starzkinskii, Vestn. MGU, Ser. Matem.–Mekhan., No. 6, 117 (1970).
[2] C. Yeh, K. F. Casey, and Z. A. Kaprielian, IEEE Trans. MTT-13, 297 (1965).
[3] T. Tamir, H. C. Wang, and A. A. Oliner, IEEE Trans., MTT-12, 323 (1964).
[4] A. I. Pasynok, N. S. Repalov, and N. A. Khizhnyak, Zh. Tekh. Fiz., 42, 2452 (1972) [Sov. Phys.–Tech. Phys., 17, 1913 (1973)].
[5] Ya. B. Fainberg, Atom. Energ., 6, 431 (1959).
[6] S. S. Kalmykova, Zh. Tekh. Fiz., 31, 1374 (1961) [Sov. Phys.–Tech. Phys., 6, 1001 (1962)].
[7] P. E. Krasnushkin, Zh. Tekh. Fiz., 20, 1065 (1950).
[8] V. N. Shevchik, G. N. Shvedov, and A. V. Soboleva, Wave and Oscillation Phenomena in Electron Beams at Very High Frequencies [in Russian], Saratov University (1962).
[9] I. I. Golichev and P. E. Krasnushkin, Teor. Matem. Fiz., 10, 370 (1972).
[10] P. A. Sturrock, Phys. Rev., 112, 1488 (1958).
[11] R. V. Polovin, Zh. Tekh. Fiz., 31, 1220 (1961) [Sov. Phys.–Tech. Phys., 6, 889 (1962)].
[12] A. S. Il'inskii and A. G. Sveshnikov, Zh. Vyssh. Matem. Matem. Fiz., 8, 363 (1968).
[13] Yu. N. Pchel'nikov, Proc. of Conf. on Electronic Engineering, No. 1 (27), 78 (1971).
[14] L. A. Vainshtein, Zh. Tekh. Fiz., 27, 2340 (1957) [Sov. Phys.–Tech. Phys., 2, 2176 (1958)].
[15] H. Hirakawa, Japan. J. Appl. Phys., 3, 27 (1964).
[16] V. A. Vishnyakov, A. I. Zykov. V. M. Grizhko, and I. A. Grishaev, Zh. Tekh. Fiz., 38, 129 (1968) [Sov. Phys.–Tech. Phys., 13, 89 (1968)].
[17] G. V. Voskresenskii (Voskressensky), and V. I. Koroza, Proc. Fifth Intern. Conf. on High Energy Accelerators, Rome (1966), p. 645.
[18] G. V. Voskresenskii, V. I. Koroza, and Yu. N. Serebryakov, Atom. Energ. 20, 3 (1966).
[19] V. A. Solntsev, Zh. Tekh. Fiz., 38, 109 (1968) [Sov. Phys.–Tech. Phys., 13, 76 (1968)].

Computer calculation of quasistationary pulsed magnetic fields

V. I. Yurchenko

Institute of Nuclear Physics, Siberian Branch,
Academy of Sciences of the USSR, Novosibirsk

(Submitted March 17, 1973)
Zh. Tekh. Fiz., 44, 1641-1649 (August 1974)

A procedure for calculating two-dimensional magnetic fields (plane-parallel or with rotational symmetry) is described. The skin effect is taken into account. The procedure is based on the replacement of a differential equation by a system of difference equations relating the values of the vector potential at different points of a rectangular grid at two different times. Two iteration methods, a longitudinal—transverse method and an upper-relaxation method, are used to solve the difference equations. The calculation procedure is illustrated for the case of a pulsed magnet. The calculation is carried out for a δ-function excitation. In this form, the results can be used in a simple manner to determine the field for any functional dependence of the excitation on time. The procedure for calculating the field is described for the case in which a capacitor discharges into a magnet of unit length.

Various physics research experiments use pulsed magnets, in which the skin effect is important. Such magnets are used, e.g., in the production of ultrastrong fields[1] and, with a thin skin, in the production of the desired field configuration in a gap.[2,3] Optimization of the parameters of these magnets requires an effective method for calculating magnetic fields with the skin effect taken into account.

Appropriate calculations have been carried out on the basis of the integral form of the field equations.[4-7] This is not the only possible approach; in the magnetostatic case, e.g., the equation for the vector potential can be solved by a difference method.[8,9] The same method can be used to solve the quasisteady-state problem. The difference method has the advantage of simplicity; also, it can be used in nonlinear problems, in which the relative permeability of the magnet, μ, is a function of the induction, or in problems in which the conductivity varies as a function of the time because the conductors are heated. The latter case is important, e.g., in producing ultrastrong fields.[1]

Our purpose here is to examine the practical usefulness of the difference method for solving the two-dimensional problem (in which the field is plane-parallel or has rotational symmetry) in the linear, quasistationary case. The use of this method is illustrated by the calculation of the field in an iron-free magnet with zero gradient in which the ratio of the height of the conductors to separation is 2 : 1.

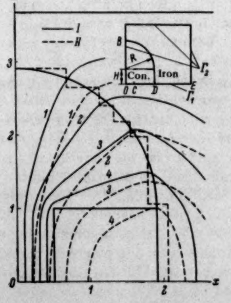

Fig. 1. H = 1, R = 1.91, δ-shaped voltage pulse. I) Lines of force at t = 0; II) at t = 5000 μsec. A: 1) 0.1; 2) 0.2; 3) 0.3; 4) 0.4.

NUMERICAL CALCULATION

Figure 1 shows one quadrant of the cross section of the iron-free magnet. The aperture dimension is adopted as the unit of length along the x and z axes. We are treating a relatively simple configuration of conductors and iron polepiece, characterized by the parameters H and R. The parameter R is chosen so that the induction in the polepiece is roughly one sixth that at the center of the aperture; hence the iron in the magnetic circuit is not saturated when the induction at the center is ~10 T. The aperture dimension is 2 cm and the conductor metal has a conductivity $5.9 \cdot 10^7 \Omega^{-1} \cdot m^{-1}$ (corresponding to copper). The calculated results can be extended to the cases of other conductivities and apertures through the use of a similarity transformation for the heat-conduction equation. The magnet length L = 1 m.

The iron of the magnetic circuit is assumed to have a relative permeability $\mu = 100$. Calculations show that the characteristics of the field in the aperture of this magnet are weak functions of μ (as well as of the shape of the magnetic-circuit pole) and are essentially the same in the case $\mu = 100$ as in the case $\mu = \infty$.

We assume that the length of the magnet along the y axis is much larger than its transverse dimension. We are to find the solution of the equation for a certain potential in the plane-parallel case:

$$\gamma \frac{\partial A}{\partial t} = \frac{\partial}{\partial x} \frac{1}{\mu} \frac{\partial A}{\partial x} + \frac{\partial}{\partial z} \frac{1}{\mu} \frac{\partial A}{\partial z} + \gamma E^{g}, \qquad (1)$$

where A and E^g are the y components of the vector potential and the electric field gradient. The coefficient γ has the constant value $a^2 \sigma \mu_0$ (where σ is the conductivity of the medium) within the conductor and vanishes elsewhere. The electric field gradient is constant over the cross section of the conductor (by virtue of the condition curl $E^g = 0$). The circulation integral of this vector along the contour of the turn formed by the conductors is equal to the potential difference between the leads of the conductors, i.e., is equal to the applied voltage, u(t). By virtue of the symmetry of the problem, the values of E^g in the two conductors are the same in magnitude but opposite in sign. We assume that the voltage u(t) is applied to the right-hand conductor with respect to the left-hand conductor; then in the right-hand conductor we have

$$E^{g}=\frac{u(t)}{2L}.$$

Equation (1) with this value of E^g is calculated by a difference method in the rectangular region shown in Fig. 1 with the initial condition

$$A|_{t=0}=0$$

and the boundary conditions

$$\left.\frac{\partial A}{\partial z}\right|_{\Gamma 1}=0,\quad A|_{\Gamma 2}=0. \tag{2}$$

The coordinate grid is constructed so that the intersections of the grid lines with the contour of the conductor are grid points, for improved accuracy. In the lower left-hand corner the grid is uniform in each direction. The grid is uniform along the x axis out to x = 0.75, with the specified spacing h; along the z axis it is uniform up to z = H, with approximately the same spacing. Thus, each unit of the grid is about 10% larger than the preceding unit, in both directions. The increase in the spacing is chosen so that the x = R line coincides with a grid line. To simplify the program the contour of the iron polepiece is chosen to be different from that specified (the dashed lines), but the difference is less than half a spacing. In Fig. 1, with a 19×22 grid (the first number is the number of spacings in the horizontal direction, and the second number is that in the vertical direction), we have h˙ = 0.5/4; the modified contour is shown by the dashed lines.

The difference equations, as in the case of the heat-conduction equation with variable coefficients, are obtained from the balance equation written for each grid cell.[10] In our case the balance equation is the equation giving the total current through the area bounded by the dashed lines in Fig. 2, S, averaged over the time from t_{l-1} to t_l. The vector potential in the l-th time layer A^l is given by the difference equation

$$-\bar{\gamma}\,\frac{A^{l}-A^{l-1}}{\tau_l}+\sigma_l\lambda A^{l}+(1-\sigma_l)\,\lambda A^{l-1}+\bar{\gamma}\,\frac{u^{l-1/2}}{2L}=0, \tag{3}$$

where τ_l is the time spacing and σ_l is the weight of the upper layer, $t = t_l$.

At point i, j we have

$$\bar{\gamma}_{i,j}=\frac{1}{\hbar_{x,i}\hbar_{z,j}}\int\limits_{S}\gamma(x,\ z)\,dx\,dz,$$

$$\hbar_{x,i}=\frac{h_{x,i}+h_{x,i+1}}{2};\quad \hbar_{z,j}=\frac{h_{z,j}+h_{z,j+1}}{2},$$

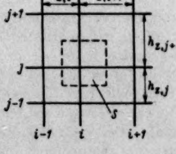

Fig. 2.

where

$$\lambda=\lambda_1+\lambda_2$$

is the difference operator corresponding to the differential on the right-hand side of Eq. (1). The operator λ_1 acts along the lines:

$$\lambda_1 A=a_i A_{i-1,j}-(a_i+b_i)\,A_{i,j}+b_i A_{i+1,j},$$
$$a_i=\frac{1}{\mu_{i-1/2}\hbar_{x,i}h_{x,i}}\quad b_i=\frac{1}{\mu_{i+1/2}\hbar_{x,i}h_{x,i+1}},$$

where $\mu_{i\pm 1/2}$ is the half-sum of the limiting values of μ to the left and right of the line i ± 1/2 at $z = z_j$. The operator λ_2, which acts along the columns, is analogous.

Equation (3) and boundary conditions (2) give a system of difference equations for determining A^l. To calculate the vector potential in the l-th time layer we must hold the values of the vector potential in the preceding layer, in the conductor region, in the computer memory. Elsewhere we have $\bar{\gamma} = 0$ and $\lambda A^{l-1} = 0$, and the values of the vector potential need not be stored.

An iteration method is used to solve the difference equations in each time layer. We have tried two such methods; one, for the Poisson equation, involves a time integration of the heat-conduction equation

$$\frac{\partial\varphi}{\partial t}=\Delta\varphi+\rho \tag{4}$$

until the solution reaches a steady state, with $\partial\varphi/\partial t = 0$ (ref. 10). Here we use the same approach; to determine A^l we write the longitudinal–transverse iteration scheme

$$\left.\begin{aligned}
&A^{l,s+1/2}+\mu\tau^{s}\left(\frac{\bar{\gamma}}{\sigma_l\tau_l}A^{l,s+1/2}-\lambda_1 A^{l,s+1/2}\right)=F^{s},\\
&A^{l,s+1}+\mu\tau^{s}\left(\frac{\bar{\gamma}}{\sigma_l\tau_l}A^{l,s+1}-\lambda_2 A^{l,s+1}\right)=F^{s+1/2},\\
&F^{s}=A^{l,s}+\mu\tau^{s}\left(\lambda_2 A^{l,s}+f^{l}\right),\\
&F^{s+1/2}=A^{l,s+1/2}+\mu\tau^{s}\left(\lambda_1 A^{l,s+1/2}+f^{l}\right),\\
&f^{l}=\begin{cases}\dfrac{\bar{\gamma}}{\sigma_l\tau_l}A^{l-1}+\dfrac{1-\sigma_l}{\sigma_l}\lambda A^{l-1}+\dfrac{\bar{\gamma}}{2L\sigma_l}u^{l-1/2}, & \text{if}\quad \bar{\gamma}\neq 0,\\ 0, & \text{if}\quad \bar{\gamma}=0.\end{cases}
\end{aligned}\right\} \tag{5}$$

Here s is the iteration number. To find $A^{l,s+1/2}$ we use the pivotal condensation method, working along the rows, while to find $A^{l,s}$ we work along the columns. The coefficient of the iteration parameter τ^s is the relative permeability at the given point of the grid, i.e., we are essentially solving an equation like (4) ($\rho = 0$) in the iron-filled region. Without this coefficient we would have the equation $\mu(\partial\varphi/\partial t) = \Delta\varphi$; we thus see that the introduction of the factor of μ in the iteration scheme makes the process of the signal propagation in the iron-filled region identical to that in the region outside the iron (where $\mu = 1$). This approach significantly reduces the number of iterations required. To accelerate the convergence we use a cyclic choice of parameters τ^s, determined in the same manner as for the Direchlet problem in a square of side b and with a quadratic grid of spacing h. The value of b in the equations for τ^s (ref. 11) is assumed to be equal to the transverse dimension of the magnetic circuit, DE (in units of the aperture b = 3). The iterations according to scheme (5) are stopped when

$$\frac{\Delta A}{A_m}\leqslant 10^{-6}, \tag{6}$$

where ΔA is the maximum magnitude of the correction to the vector potential during a cycle of the pivotal condensation method along rows or columns, and A_m is the maximum magnitude of the vector potential. The adequacy of condition (6) is checked in a large number of calculations; it is found that this iteration method converges reliably in practice and can be used to solve problem (3). We have also tested the upper-relaxation method.[8] This method is simpler to use, but it requires some two or three times as much computer time.

In the case of a linear problem, like that treated here (in which μ is not a function of the induction and the conductivity of the conductor is not a function of the temperature), it is sufficient to calculate the field for a δ-function or step-function dependence of the voltage on time. In this form the calculated results are universal, since they can be used in a simple manner to determine the field for any functional dependence of u on t. Below we consider the case of a δ-function voltage. Any linear combination of the vector potential and its derivatives, β, is given by the following expression for an arbitrary functional dependence of u on t:

$$\beta(t)=\int_0^t \beta_0(t-\tau)\,u(\tau)\,d\tau, \qquad (7)$$

where β_0 is the same linear combination for the case of a δ-function voltage.

The field is calculated in the electrostatic approximation (corresponding to an infinitesimally thin skin) for time zero ($l = 0$). For this calculation we use scheme (5), with $\sigma_0 = 0.5$, $\tau_0 = 10^{-8}$ sec, $f^0 = \bar{\gamma}/2L\sigma_0\tau_0$, and $A^{0,1} = 0$. The resulting calculated values of the vector potential A^0 correspond to the field which arises with the zero initial condition under the influence of a rectangular voltage pulse with base τ_0 and unit area. The parameter τ_0 is small enough for us to consider this pulse to be a δ function.

For $l \geq 1$ the calculated values of the vector potential describe the field relaxation; here the voltage is assumed to vanish in the equations; the first approximation, $A^{l,1}$, is assumed equal to A^{l-1}, and the parameters τ_l and σ_l are functions of l. Since the field changes most rapidly as a function of the time during the relaxation at small t, the time spacing is initially small, increasing with increasing l, to improve the accuracy. The quantities τ_l and σ_l are found as functions of l on the basis of the following considerations: The field relaxation in the aperture is described by

$$B(t)\approx B^0\frac{a}{a+2\delta(t)}\approx B^0\left(1-\frac{2\delta(t)}{a}\right),$$

where B^0 is the induction at the center of the aperture at zero time, and δ is the skin thickness. Since $\delta \sim \sqrt{t}$, the integration is not carried out over the coordinate t, but over the coordinate $\theta = \sqrt{t/T}$, where T is the time at which the integration is ended in the balance equation. The functional dependence of the field on θ at small θ is nearly linear, and better accuracy can be achieved through integration over this coordinate. In fact, the quantity $\sigma_l\lambda A^l + (1-\sigma_l)\lambda A^{l-1}$ in Eq. (3) is an approximation of the integral

$$\frac{1}{\tau_l}\int_{t_{l-1}}^{t_l}\lambda A\,dt=\frac{1}{\tau_l}\int_{\theta_{l-1}}^{\theta_l}\lambda A 2T\theta\,d\theta.$$

Since $\lambda A \approx \gamma(\partial A/\partial t)$ and since $\partial A/\partial t \sim t^{-1/2}$ in the skin, the integrand on the right is a weak function of θ. We approximate the integral by means of the trapezoid equation:

$$\frac{1}{\tau_l}\int_{\theta_{l-1}}^{\theta_l}\lambda A 2T\theta\,d\theta\simeq\frac{T(\theta_l-\theta_{l-1})}{\tau_l}(\Lambda A^l\theta_l+\Lambda A^{l-1}\theta_{l-1}).$$

Since $\theta_l - \theta_{l-1} = \tau_l/T(\theta_l + \theta_{l-1})$, this expression can be rewritten as

$$\sigma_l\lambda A^l+(1-\sigma_l)\lambda A^{l-1},$$

where $\sigma_l = \theta_l/(\theta_l+\theta_{l-1})$. In the calculations T is set equal to 5 msec, and the step in the coordinate θ is uniform ($l \geq 1$):

$$\theta_l=\frac{l}{N},\quad t_l=T\theta_l^2,$$

$$\tau_l=\frac{T(2l-1)}{N^2},\quad \sigma_l=\frac{l}{2l-1},$$

where N is the number of steps in the coordinate θ. For all $l \geq 1$ we have $\sigma > 1/2$, a necessary condition for the stability of the scheme.

In the course of the calculations we found, by increasing the number of grid points and by increasing N, that the difference problem described above is stable and converges.

ACCURACY OF THE CALCULATIONS; RESULTS

The errors in the calculation result from the conversion of the problem to discrete steps in the time and the space variables as well as from the approximate nature of the solution of the difference equations. Condition (6) provides a number of iterations sufficient for us to neglect errors of this latter type. The error due to the discrete nature of the time steps is a function of l. Table 1 shows the calculated values of the induction at the cen-

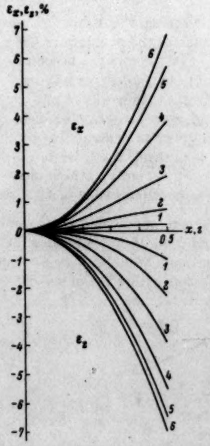

Fig. 3. Field inhomogeneity in the horizontal and vertical directions for the case of a δ-shaped pulse. θ: 1) 0; 2) 0.2; 3) 0.4; 4) 0.6; 5) 0.8; 6) 1.0.

TABLE 1

N	θ								
	0	0.125	0.250	0.375	0.500	0.625	0.750	0.875	1.000
2	$l=0$, 49.95	—	—	—	$l=1$, 35.01	—	—	—	$l=2$, 22.18
4	$l=0$, 49.95	—	$l=1$, 41.58	—	$l=2$, 32.69	—	$l=3$, 27.22	—	$l=4$, 22.235
8	$l=0$, 49.95	$l=1$, 45.86	$l=2$, 40.19	$l=3$, 36.32	$l=4$, 32.73	$l=5$, 29.72	$l=6$, 26.93	$l=7$, 24.49	$l=8$, 22.244

ter of the aperture found for various values of N with a 31×36 grid with $h = 0.5/8$. Comparison of these results shows that with even l ($\theta = 0.5$ with $N = 4$, 8 and $\theta = 1$ with $N = 2$, 4, 8) the calculation error is much smaller than with odd l. The number of steps, N, is thus chosen even, and the necessary quantities are stored and printed for even l.

Table 2 shows some calculated values of the field parameters on a 42×47 grid with $h = 0.5/12$ in the case $N = 10$.

In Table 2, δ is the skin thickness, which is calculated, as in the case of an infinitely thick conductor, from

$$\delta=\frac{\Phi(t)}{B(t)},$$

where $\Phi(t) = \int_0^t E^g dt - A_g(t)$ is the magnetic flux in the conductor at time t, $A_g(t)$ and $B(t)$ are the vector potential and the induction at the surface of the conductor (at the point $x = 0.5$, $z = 0$), B_0 is the induction at the center of the aperture, I is the current in the conductors (twice the value of the integral of the field over the segment OB), F is the force per unit length exerted on the conductor (twice the value of the integral of $B^2/2\mu_0$ over the same segment) calculated for $B_0 = 10$ T, and

$$\varepsilon_x(x)=\frac{B_z(x,\,0)-B_0}{B_0}\,100\%, \qquad \varepsilon_z(z)=\frac{B_z(0,\,z)-B_0}{B_0}\,100\%.$$

are the field inhomogeneities in the horizontal and vertical directions (Fig. 3).

The calculation error for the data in Table 2 is due primarily to the discrete nature of the problem in the spatial variables. The size of this error can be determined by comparing the results in Table 2 with the results calculated for a 31×36 grid with $h = 0.5/8$ and a 19×22 grid with $h = 0.5/4$, i.e., with large values of h. It is found that the maximum error in determining the field B_0 and the current I is less than[1)] 0.4%, while the maximum error in the values of ε_x and ε_z, which characterize the field distribution, is of the order of 1%.

The error due to the discrete nature of the step in θ is lower by a factor of about 5 to 10 for the data in Table 2. In this case the minimum value of N is governed primarily by the error in the approximation of the calculated values of the vector potential for a δ-shaped voltage at other values of t. This procedure is required in order to determine the field from Eq. (7) for an arbitrary functional dependence of the voltage on the time. For better accuracy the approximation by polynomials should be carried out with respect to the coordinate θ rather than t. Calculation of the field during the discharge of a capacitor shows (see below) that the value $N = 10$ is sufficient to keep the error of the approximation below the calculation errors specified above.

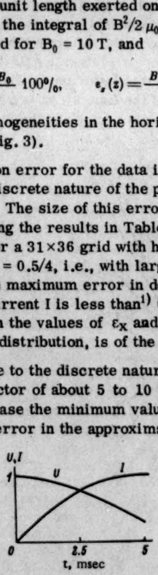

Fig. 4.

An important characteristic of an iron-free magnet is the energy required to produce a given field in the aperture for a specific rise time of the field. Pulsed magnets are usually supplied power from capacitor banks. We illustrate the calculation method for the discharge of a capacitor into a magnet 1 m long; this calculation is straightforward when the solution is known for the case of a δ-function voltage. The current in the circuit is given by

$$I(t)=\int_0^t u(\tau)\,I^{(0)}(t-\tau)\,d\tau, \tag{8}$$

where $I^{(0)}(t)$ is the current corresponding to a δ-function voltage, and $u(t)$ is the voltage on the capacitor. We also write

$$\frac{du(t)}{dt}=-\frac{1}{C}I(t), \tag{9}$$

where C is the capacitance of the capacitor.

We partition the integration range in (8) into equal segments of length τ and denote the value of the functions at time $t = m\tau$ by the subscript "m." We write the integral in (8) by means of the trapezoid equation, and we write Eq. (9) in difference form:

$$\left.\begin{aligned} I_m&=S_{m-1}+\frac{\tau I_0^{(0)}u_m}{2},\\ S_{m-1}&=\tau\left(\frac{I_m^{(0)}u_0}{2}+\sum_{i=1}^{m-1}u_iI_{m-i}^{(0)}\right),\\ \frac{u_m-u_{m-1}}{\tau}&=-\frac{1}{C}\,\frac{I_m+I_{m-1}}{2}.\end{aligned}\right\} \tag{10}$$

The sum in the expression for S_{m-1} with $m = 1$ should be set equal to zero. Eliminating I_m from these equations, we find

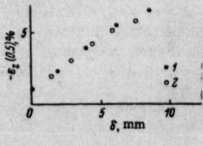

Fig. 5. The quantity ε_z as a function of the skin thickness for two functional dependences of the voltage on the time, u(t). 1) A δ-function pulse; 2) a capacitor discharge ($t = t_r$).

TABLE 2

θ	t, μsec	δ, mm	B_0, T	I, kA	$\varepsilon_x(0.5)$, %	$\varepsilon_y(0.5)$, %	F, tons/cm $B_0 = 10$ T	A_s, Wb/m
0	0	0	49.95	2650	0.201	−1.00	2.06	0.5
0.2	200	1.9	41.87	2205	0.753	−2.30	1.99	0.4201
0.4	800	4.0	35.43	1862	1.92	−3.94	1.94	0.3569
0.6	1800	6.2	30.23	1591	3.83	−5.50	1.92	0.3066
0.8	3200	8.6	25.90	1372	5.73	−6.55	1.91	0.2641
1.0	5000	11.5	22.24	1190	6.82	−7.01	1.93	0.2275

TABLE 3

t_r, μsec	C, F	U_0, V	W, kJ	δ, mm	I, kA	$\varepsilon_x(0.5)$, %	$\varepsilon_y(0.5)$, %
200	$4.2 \cdot 10^{-2}$	1736	64.0	1.4	527.5	0.582	−1.97
800	$6.7 \cdot 10^{-1}$	477	76.3	2.9	526.0	1.29	−3.12
1800	3.3	232	90.3	4.4	525.8	2.38	−4.24
3200	10.5	142	106	5.9	526.8	3.64	−5.17
5000	25.5	98.9	125	7.6	529.0	4.70	−5.80

$$u_m = \frac{u_{m-1} - \frac{\tau}{2C}(I_{m-1} + S_{m-1})}{1 + \frac{\tau^2}{4C} I_0^{(0)}}. \tag{11}$$

Setting $I_0 = 0$ and $u_0 = u(0)$, we can use recursion relations (10) and (11) to find I_m and u_m; then we can determine any linear combination of the vector potential and its derivatives from Eq. (7).

Table 3 shows the calculated results; here t_r is the specified time required for the field to rise from zero to $B_{max} = 10$ T, and C, u_0, and W are the necessary capacitance, initial voltage, and energy $(Cu_0^2/2)$ of the capacitor. The other parameters have the same meaning as in Table 2. Their values correspond to a time $t = t_r$. Figure 4 shows the circuit voltage and current, normalized to their maximum values, which occur at $t_r = 5$ msec. The data in Table 2 are used in the calculations.

The force acting on a conductor cannot be found from Eq. (7); it is necessary to use the field distribution on segment OB for various values of θ in a δ-function pulse. We see from Table 2 that the change in the force as a function of the skin thickness, which is related to the change in the field geometry in the gap (Fig. 1), is small, and for Table 3 we can assume $F \simeq 2$ metric tons/cm. A more accurate value can be found if some skin thickness in Table 3 can be associated with the force in Table 2 for the same thickness. This procedure can also be used to determine other parameters. As long as the skin thickness is small in comparison with the aperture, the field parameters for various u(t) but for the same skin thickness differ very little (Fig. 5). The skin thickness, on the other hand, can be determined easily for a given u(t).

All these calculations have been carried out on the BÉSM-6 computer of the Computation Center, Siberian Branch, Academy of Sciences of the USSR. The program is written[12] in ALPHA. The time required to calculate the data in Table 2 is 6 min.

CONCLUSION

These calculations have shown that the solution of the equation for the vector potential by the net-point method in the quasisteady-state case reduces to a simple and efficient calculation scheme. In the case of iron-free magnets this method can be used for a numerical search for the optimum conductor geometry and the polepiece of the magnetic circuit. The method is easily generalized to systems with rotational symmetry.

Solution of the problem for a δ-function voltage yields a universal characteristic of the system of conductors and considerably reduces the expenditure of computer time. The calculation for an arbitrary u(t) is carried out in a simple manner. Furthermore, as is shown by a calculation of the field for the case of the discharge of a capacitor, this solution permits the system to be matched with various loads in a simple manner.

Calculation methods not involving iteration can be used in the case of the two-dimensional problem in a region in which the conductivity is nonvanishing everywhere or in the case of the one-dimensional problem. In the one-dimensional problem, the pivotal condensation method can be used, while in the two-dimensional problem the method of variable directions can be used. In these cases it is particularly efficient to use the difference method.

Above we have treated the case of conductors in a symmetric arrangement, with E^g known in each conductor. For symmetric conductors, as in the case of a multiturn system, the value of E^g in each conductor must be determined in the course of the calculation. The formulation of the problem for such cases will be treated in a separate paper.

Here we have assumed a relatively simple geometry for the conductors, and we have used a simple rectangular grid. Accurate results can be calculated by placing grid points on the contour of the conductor. In general, this procedure requires the construction of a special grid, e.g., as in certain programs used in calculations for fixed-field magnets.[9]

The authors thanks V. L. Auslender, Yu. B. Glagolev, A. A. Livshits, B. L. Faktorovich, and B. V. Chirikov for discussion.

---

[1] Doubling the integral of the field over the segment OB yields a current too low by about 0.3% because of the incomplete integration contour. The ac-

curacy stated in the test actually holds for this integral, rather than for the current.

---

[1] H. E. Knoepfel, Pulsed High Magnetic Fields, North-Holland, Amsterdam (1970).

[2] T. A. Vsevolozhskaya, L. L. Danilov, G. I. Sil'vestrov, and N. F. Sokolova, Prib. Tekh. Eksp. No. 6, 32 (1968).

[3] T. A. Vsevolozhskaya, V. N. Pakin, and G. I. Sil'vestrov, At. Energ., 22, 210 (1967).

[4] O. V. Tozoni, Computer Calculations of Electromagnetic Fields [in Russian], Izd. Tekhnika, Kiev (1967).

[5] É. V. Kolesnikov and D. D. Savvin, Izv. VUZ. Elektromekhanika, No. 8, 827 (1968).

[6] É. V. Kolesnikov, Izv. VUZ. Elektromekhanika, No. 12, 1294 (1970).

[7] É. V. Kolesnikov, Izv. VUZ. Electromekhanika, No. 1, 3 (1971).

[8] N. I. Doinikov and A. S. Simakov, Zh. Tekh. Fiz., 39, 1463 (1969) [Sov. Phys.—Tech. Phys., 14, 1097 (1970)].

[9] L. Rezegotti, Proceedings of the Second All-Union Conference on Charged-Particle Accelerators (1970) [Russian translation], Vol. 1, Izd. Nauka, Moscow (1972), p. 133.

[10] A. N. Tikhonov and A. A. Samarskii, Equations of Mathematical Physics [in Russian], Izd. Nauka, Moscow (1966).

[11] A. A. Samarskii, Introduction to the Theory of Difference Schemes [in Russian], Izd. Nauka, Moscow (1971).

[12] A. P. Ershov, G. I. Kozhukhin, and N. V. Pottosin, Manual on the Use of the ALPHA System [in Russian], SO Izd. Nauka, Novosibirsk (1968).

Flux loss in the production of ultrastrong fields by rapid compression of conducting shells

V. I. Yurchenko

Institute of Nuclear Physics, Siberian Branch,
Academy of Sciences of the USSR, Novosibirsk

(Submitted May 10, 1973; resubmitted November 19, 1973)
Zh. Tekh. Fiz., 44, 1650-1655 (August 1974)

The flux-loss problem is written as a system of two equations under the assumption that the shell compressing the flux is solid and that certain parameters, which are functions of the shell geometry alone, are specified. These equations are solved for certain particular cases of compression. Despite the loss through the sliding contact, the field amplification is much higher in systems in which the shell contour decreases in length during the compression.

The explosion method of producing strong magnetic fields, proposed and investigated in 1951 (ref. 1), is currently used in various research projects. In devices operating on the basis of this method, there is always some flux loss because of the finite conductivity of the shell material: The flux through the area subtended by the shell is lower at the end of the compression than at the beginning. In practice, this effect reduces significantly the field amplification[2] and must be taken into account in the design of explosion generators.

The only exact flux calculation which has been reported is that for parallel plates with constant conductivity moving toward each other at a constant speed.[3-5] Various approximate methods are used for such calculations. Below, by assuming the shell material to be solid and by assuming that certain parameters which are functions of the shell geometry alone are specified, we write the flux-loss problem as a system of equations which can be solved numerically; for certain particular cases different from those treated in refs. 3-5, we are able to give exact solutions of these equations.

THE INITIAL EQUATIONS

A cross section of a shell compressing the flux in region G is shown schematically in Fig. 1. The contour F(t), a function of the time, is chosen so that the current-density vector is parallel to the contour at each point s. We assume that there is no flux loss through contact C due to surface inhomogeneities, that the flux compression begins at time t = t_b, and that the initial flux is produced in the interval 0 ≤ t ≤ t_b. To calculate the current in this system we use the flux-balance equation. Taking account of the penetration of some part of the flux into the conductor and the flux loss through the sliding contact,[2] we can write this equation as

$$\Phi(t)+\int\limits_{F(t)}\varphi(s,\ t)\,ds+\int\limits_{t_b}^{t}v(\tau)\left[\varphi_k^+(\tau)+\varphi_k^-(\tau)\right]d\tau =\Phi(t_b)+\int\limits_{F(t_b)}\varphi(s,\ t_b)\,ds, \tag{1}$$

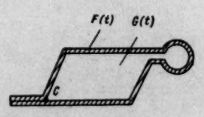

Fig. 1

where $\Phi(t)$ is the flux through the area subtended by contour F, $\varphi(s, t)$ is the shell per unit length of F at point s, v(t) > 0 is the velocity at which contact C moves along contour F(t), and $\varphi_k^+(t)$ and $\varphi_k^-(t)$ are the values of $\varphi(s, t)$ on the two sides of C.

When there are several contacts, a sum of integrals over all the contacts should stand on the left-hand side of (1). To calculate the current I(t) we must write $\Phi(t)$ and $\varphi(s, t)$ in terms of it.

We assume that the skin thickness is much smaller than the radius of curvature of the shell and we assume that the penetration of the field into the metal is described by the one-dimensional problem for the field in a conductor filling the half-space x > 0. The vector potential is measured from infinity:

$$A\, x,\ t)=-\int\limits_{x}^{\infty}B(x,\ t)\,dx,$$

where B(x, t) is the induction. Then in the electric-field equation

$$\mathbf{E}=-\frac{\partial\mathbf{A}}{\partial t}-\nabla\varphi$$

we are left with only the first term [in this case we have $\nabla\varphi$ = const by virtue of the condition curl$(\nabla\varphi)$ = 0]; assuming that **A**, **E** = 0 at x = ∞, we find from the electric-field equation that $\nabla\varphi = 0$. We can now write the following equation for the vector potential for x > 0:

$$\sigma_s\mu_0\frac{\partial A_s}{\partial t}=\frac{\partial^2 A_s}{\partial x^2}, \tag{2}$$

where $\sigma_s(x, t)$ is the conductivity of the shell material. The detailed equation for the case of nonlinear diffusion is treated in ref. 6. Here, the subscript "s" implies that we are considering the situation at point s; at this point we can write

$$\varphi(s,\ t)=-A_s(0,\ t). \tag{3}$$

The boundary condition for Eq. (2) can be written as

$$\frac{\partial}{\partial x}A_s\Big|_{x=0}=\mu_0\frac{I(t)}{b(s,\ t)}. \tag{4}$$

Here, b(s, t) is the average length of a line of force at the given point of the contour. We assume b (s, t) to be known. In cases of practical interest it is only a weak function of the skin thickness, being governed only by the instantaneous conductor configuration. The quantity b(s, t) can be set equal to the height of the plates forming the generator, provided that this height is greater than the plate separation. When the fringing fields are taken into account, b(s, t) is found to be larger by an amount roughly equal to this distance. The value of b(s, t) can be measured in a prototype apparatus.

We assume that L(t), the inductance of a turn enveloping the region G in the case of an infinitesimally thin skin, is also known. The value of L(t) is a function only of the instantaneous conductor configuration; it, too, can be measured in a prototype apparatus. Then we can write the flux through the area enveloped by contour F as

$$\Phi(t)=L(t)\,I(t). \tag{5}$$

To determine I(t) from Eqs. (1)-(5) we must specify the functional dependence on the time in the interval $0 \le t \le t_b$, during which the initial field is produced. Only Eq. (2) is solved for this interval.$^{1)}$

Then the functional dependence of the current on the time can be determined from the solution of Eqs. (1) and (2).

For fields of $\leqslant$ 0.5 MOe, for which we can neglect thermal effects[2] and assume $\sigma_g(x,\,t)=\sigma=\mathrm{const}$, the problem is simplified. From Eq. (2) and (4) for this case we find

$$\varphi(s,\,t)=\sqrt{\frac{\mu_0}{\sigma\pi}}\int_0^t\frac{I(\tau)\,d\tau}{b(s,\,\tau)\sqrt{t-\tau}}, \tag{6}$$

and the problem reduces to the solution of Eq. (1) alone.

ANALYSIS OF CERTAIN SIMPLE CASES

We turn to certain simple cases of flux compression with $\sigma_g(x,\,t)=\sigma=\mathrm{const}$. We assume that in each case the shell height is uniform [b(s, t) = const] and that the field within the shell is homogeneous, equal to H(t). We assume for simplicity that the initial field is produced instantaneously at time t = 0. From Eqs. (1) and (6) we find the following equation for H(t):

$$H(t)\,S(t)+\frac{1}{\sqrt{\sigma\mu_0\pi}}\int_0^t\left(\mathscr{L}(\tau)\frac{d}{d\tau}\int_0^\tau\frac{H(\eta)\,d\eta}{\sqrt{\tau-\eta}}\right)d\tau=H(0)\,S(0), \tag{7}$$

where S(t) is the area enveloped by contour F, and $\mathscr{L}(t)$ is the length of this contour. Taking the time derivative of (7), dividing the result by $\mathscr{L}(t)$, and integrating the resulting equation from 0 to t, we find

$$\frac{H(t)\,S(t)}{\mathscr{L}(t)}+\frac{1}{\sqrt{\sigma\mu_0\pi}}\int_0^t\frac{H(\eta)\,d\eta}{\sqrt{t-\eta}}=\frac{H(0)\,S(0)}{\mathscr{L}(0)}-\int_0^t\frac{H(t)\,S(t)}{\mathscr{L}^2(t)}\frac{d}{dt}\mathscr{L}(t)\,dt. \tag{8}$$

Written in this form, the initial equation is more convenient in the calculations for the cases considered below.

Let us compare three cases of the compression of a generator shell consisting of two parallel plates (Fig. 2), initially a distance a_0 apart. We introduce the notation

$$\tau=\frac{t}{t_0};\quad h(\tau)=\frac{H(\tau)}{H(0)};\quad \varepsilon=\frac{2}{a_0}\sqrt{\frac{t_0}{\sigma\mu_0}}.$$

We are also to determine the value of t_0 for each case.

a. For the case illustrated in Fig. 2a the contact C begins to move from point x = 0 along the x axis at a constant velocity v_x. Here we have $a=a_0=\mathrm{const}$, $t_0=l/v_x$, and the end of compression at time $\tau_k=l_k/(v_x t_0)$. We consider the case $l-l_k\gg a_0$; here $\mathscr{L}(t)\approx 2(l-v_x t)$ and $S(t)=a_0(l-v_x t)$. Equation (8) becomes

$$h(\tau)+\frac{\varepsilon}{\sqrt{\pi}}\int_0^\tau\frac{h(\eta)\,d\eta}{\sqrt{\tau-\eta}}=1+\int_0^\tau\frac{h(\eta)\,d\eta}{1-\eta}. \tag{9}$$

The solution of this equation is (see the Appendix)

$$h(\tau)=e^{\varepsilon^2\tau}\mathit{Erf}(\varepsilon\tau^{1/2})+g(\tau)+\varepsilon\pi^{-1/2}\int_0^\tau\frac{g(\xi)}{\sqrt{\tau-\xi}}\,d\xi, \tag{10}$$

where

$$g(\tau)=\frac{\tau}{1-\tau}\left[(1+2\varepsilon^4\tau^2)\,e^{\varepsilon^2\tau}\mathit{Erf}(\varepsilon\tau^{1/2})-2\pi^{-1/2}\varepsilon\tau^{1/2}\right]. \tag{11}$$

We introduce the quantity $K_0=1/(1-\tau_k)=S(0)/S_L$ (S_L is the area of the load turn), which is equal to the field amplification in the case of superconducting conductors. With $K_0\gg 1$ and rapid compression ($\varepsilon\ll 1$), we find from (10) and (11)

$$K=h(\tau_k)\approx K_0\left[1-\frac{4\varepsilon}{\sqrt{\pi}}\left(1-\frac{\pi K_0^{-1/2}}{4}\right)\right]. \tag{12}$$

As long as the approximation $l-v_x t\gg a$ is valid, with sufficiently rapid compression the functional dependence of the field on the time is described by $1/(1-\tau)$.

b. The case of Fig. 2b is analogous to that treated in refs. 3-5, differing only in the presence of a load turn. The generator plates approach each other at a constant speed v_y over the range $0\le x\le l$. In Eq. (8) we have

$$S(t)=la_0\left(1-\frac{t}{t_k}\right)+S_L,$$
$$\mathscr{L}=2l+\mathscr{L}_L=\mathrm{const},$$

where $t_k=a_0/v_y$; S_L is the area of the load turn, and $\mathscr{L}_L$ is its length. In this case we use

$$t_0=\left(a_0+\frac{S_L}{l}\right)\frac{1}{v_y},\quad \varepsilon=\frac{\mathscr{L}(0)}{S(0)}\sqrt{\frac{t_0}{\sigma\mu_0}}$$

[for cases of practical interest $\varepsilon\approx(2/a_0)\sqrt{t_0/\sigma\mu_0}$].

For $h(\tau)$ we find the equation

$$h(\tau)(1-\tau)+\frac{\varepsilon}{\sqrt{\pi}}\int_0^\tau\frac{h(\eta)}{\sqrt{\tau-\eta}}\,d\eta=1.$$

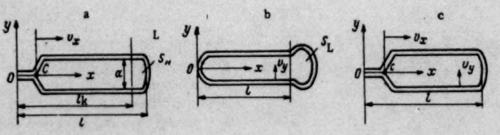

Fig. 2

This equation is solved in ref. 5; the solution for time $\tau_k = t_k/t_0$ can be written as

$$h(\tau_k)=\frac{1}{2}K_0^{3/2}e^{\varepsilon^2 K_0}\int\limits_{K_0}^{\infty}\left(1+\frac{2\varepsilon}{\sqrt{\pi}}\sqrt{\frac{\eta}{\eta-1}}\right)e^{-\varepsilon^2\eta}\eta^{-5/2}d\eta,$$

where $k_0 = 1/(1-\tau_k) = S(0)/S_L$.

For large values of K_0 the quantity within the parentheses in the integrand can be replaced by $1+2\varepsilon/\sqrt{\pi}$, so that the field amplification becomes

$$K\approx\left(1+\frac{2\varepsilon}{\sqrt{\pi}}\right)K_0\left[1-\sqrt{\pi}\,\varepsilon\sqrt{K_0}\,e^{\varepsilon^2 K_0}\,\mathrm{Erf}\left(\varepsilon\sqrt{K_0}\right)\right].$$

In the case of rapid compression, with $\varepsilon^2 K_0 \ll 1$, this expression yields

$$K\approx K_0\left(1-\sqrt{\pi}\,\varepsilon\sqrt{K_0}\right), \tag{13}$$

while with $\varepsilon^2 K_0 \gg 1$

$$K\approx K_{\lim}\left(1-\frac{3}{2\varepsilon^2 K_0}\right),$$

where

$$K_{\lim}=\frac{1}{2\varepsilon^2}+\frac{1}{\sqrt{\pi}\,\varepsilon}, \tag{14}$$

which is the limiting value of K in the absence of a load ($K_0 = \infty$) (refs. 3-5).

c. In this case (Fig. 2c) contact C moves at a constant speed v_x, and the plates come together at a relative velocity v_y. There is no load turn. The relation between v_x and v_y is such that when contact reaches the point $x = l$ the distance between the plates vanishes. In the case $l \gg a_0$, we have

$$\mathscr{L}\approx 2l(1-\tau),\ S=a_0 l(1-\tau)^2,\ t_0=\frac{l}{v_x}=\frac{a_0}{v_y}.$$

For $h(\tau)$ we find

$$h(\tau)(1-\tau)+\frac{\varepsilon}{\sqrt{\pi}}\int\limits_0^{\tau}\frac{h(\xi)\,d\xi}{\sqrt{\tau-\xi}}=1+\int\limits_0^{\tau}h(\xi)\,d\xi.$$

We use the notation $f(\tau)=\int\limits_0^{\tau}h(\eta)d\eta$. For the transform $F(p) \doteqdot f(\tau)$ we find

$$\frac{dF}{dp}+(1+\varepsilon p^{-1/2})F=p^{-2}.$$

The inverse of the transform which obeys this equation is calculated in ref. 3. We find

$$h(\tau)=\frac{\varepsilon}{\sqrt{\pi}}\int\limits_{1-\tau}^{1}\frac{\xi^{-2}(1-\xi^{1/2})}{(\xi-1+\tau)^{3/2}}\exp\left(-\frac{\varepsilon^2(1-\xi^{1/2})^2}{\xi-1+\tau}\right)d\xi.$$

Hence the field at the end of compression is

$$h(1)=\frac{3}{4}\varepsilon^{-4}+\frac{3}{\sqrt{\pi}}\varepsilon^{-3}+\frac{3}{2}\varepsilon^{-2}+\frac{1}{\sqrt{\pi}}\varepsilon^{-1}.$$

Comparison of these cases shows that despite the loss through the contact the best compression method is that in which the length of the contour F over which the loss occurs decreases during the compression. For a given value of ε the flux loss is strongly influenced by the compression method. It follows from (12) and (13) that, for a given value of K_0, the flux loss in case b is larger than that in case a by a factor of $\pi\sqrt{K_0/4}$. The limiting field in case c with $\varepsilon \ll 1$ is larger by a factor of $(3/2)\varepsilon^{-2}$ than that in case b [Eq. (14)]. The difference is important, since $K_0 \gg 1$ and $\varepsilon \ll 1$.

The area enveloped by contour F has different functional dependences on the time in cases b and c, but this difference does not affect our comments. If we adopt for case b the behavior of the area corresponding to case c, i.e., $S = la_0(1-\tau)^2$ ($S_L = 0$, $\mathscr{L}_L = 0$), we find that the plates begin to move toward each other at a speed $2v_y$ at the same t_0; decelerating uniformly, they reach zero velocity at the end of compression. In this case the limiting field is obviously even weaker than predicted by Eq. (14).

APPENDIX

In Eq. (9) we use the replacement

$$h(\tau)=(1-\tau)f(\tau). \tag{A.1}$$

We apply a Laplace transform to the equation for $f(\tau)$:

$$(1-\tau)f(\tau)+\frac{\varepsilon}{\sqrt{\pi}}\int\limits_0^{\tau}\frac{(1-\eta)f(\eta)}{\sqrt{\tau-\eta}}d\eta=1+\int\limits_0^{\tau}f(\eta)\,d\eta.$$

We find the transform $F(p) \doteqdot f(\tau)$ to satisfy

$$\frac{dF}{dp}+\left(1-\frac{1}{p+\varepsilon\sqrt{p}}\right)F=\frac{1}{p+\varepsilon\sqrt{p}}. \tag{A.2}$$

We introduce the auxiliary transform

$$G(p)=\frac{F(p)}{(\varepsilon+\sqrt{p})^2}.$$

We denote the corresponding inverse transform by $g(\tau)$; then it follows from Eqs. (A.1) and (A.2) that

$$(1-\tau)g(\tau)\doteqdot\frac{d}{dp}G(p)+G(p)=\frac{1}{\sqrt{p}\,(\varepsilon+\sqrt{p})^3},$$

$$h(\tau)\doteqdot\frac{1}{p+\varepsilon\sqrt{p}}+\left(1+\frac{\varepsilon}{\sqrt{p}}\right)G(p).$$

Then we find Eqs. (10) and (11) for $h(\tau)$ and $g(\tau)$.

---

1) If the initial field is produced by the discharge of a capacitor we can use the results for a turn of two parallel conductors,[7] assuming that the inductance of the gap between the conductors is L(0) and that the gap width is

$$d=\frac{2L(0)}{\mu_0}\left(\int\limits_F\frac{ds}{b(s,0)}\right)^{-1}.$$

---

[1] A. D. Sakharov, R. Z. Lyudaev, E. N. Smirnov, Yu. I. Plyushchev, A. N. Pavlovskii, V. K. Chernyshev, E. A. Feoktistova, E. I. Zharinov, and Yu. A. Zysin, Dokl. Akad. Nauk SSSR, 165, 65 (1965) [Sov. Phys. – Dokl., 10, 1045 (1966)].
[2] H. E. Knoepfel, Pulsed High Magnetic Fields, North-Holland, Amsterdam (1970).
[3] A. Paton and W. Millar, J. Appl. Phys., 35, 1141 (1964).
[4] G. Lehner, J. G. Linhart, and J. P. Somon, Nucl. Fusion, 4, 362 (1964).
[5] E. N. Bichenkov, Zh. Prikl. Mekh. Tekh. Fiz., No. 6, 3 (1964).
[6] G. A. Shneerson, Zh. Tekh. Fiz., 37, 513 (1967) [Sov. Phys. – Tech. Phys., 12, 368 (1967)].
[7] V. I. Yurchenko, Zh. Tekh. Fiz., 43, 1866 (1973) [Sov. Phys. – Tech. Phys., 18, 1180 (1974)].

Stability of the diode

V. A. Buts

(Submitted September 28, 1973; resubmitted January 14, 1974).
Zh. Tekh. Fiz. 44, 1656-1661 (August 1974)

The stability of an electron beam in a diode and the effect of an external electric field on the Pierce stability criterion are considered. It is shown that the instability arises when the beam is slowed down; an accelerated beam is stable. It is also shown that an external electric field changes the Pierce threshold and causes new instabilities. The mechanism by which the threshold is increased for an accelerated beam is explained.

Electron beams are used to generate and amplify electromagnetic waves, to heat plasmas and for many other purposes. In most cases the beams are formed in diodes. Hence it is desirable to know whether it is possible to excite a required oscillation spectrum directly as the beam is being formed or what is necessary in order to produce a beam with a given modulation.

In this note we consider the stability of a uniform electron beam which is infinite in the transverse direction and which moves with a variable velocity $v_0 = f(z)$ from the cathode ($z = 0$) to the anode ($z = L$). The solution of this problem will provide an answer to some of the questions listed above.

1. GENERAL DISPERSION EQUATION

To describe the development of a perturbation in the system we use the following set of equations:

$$\frac{d\mathbf{P}}{dt} = e\mathbf{E};\quad \frac{\partial\rho}{\partial t} + \operatorname{div}\mathbf{j} = 0;\ \operatorname{div}\mathbf{E} = 4\pi\rho. \tag{1}$$

We linearize this system and take the time dependence in the form $e^{-i\omega t}$. Eliminating $\tilde{p}$ and $\tilde{v}$ from the linearized equations we obtain the following equation for $\tilde{E}$:

$$\mathcal{E}'' + Q^2\mathcal{E} = F, \tag{2}$$

where

$$\mathcal{E} \equiv \tilde{E}\exp\left[\frac{1}{2}\int_0^z X(z_1)\,dz_1\right],\quad \mathcal{E}' \equiv \frac{d\mathcal{E}}{dz},$$

$$X \equiv -\frac{2i\omega\gamma_0}{c\sqrt{\gamma_0^2-1}} + 3\frac{\gamma_0'}{\gamma_0}\left[1-\frac{1}{\gamma_0^2-1}\right],\quad \gamma_0 \equiv (1-\beta_0^2)^{-1/2},$$

$$\beta_0 \equiv \frac{v_0}{c},\quad Q^2 \equiv \left[\frac{\omega_b^2}{c^2}\frac{\beta_0}{(\gamma_0^2-1)^{3/2}} + \frac{5(\gamma_0')^2}{(\gamma_0^2-1)^2} + \frac{9}{4}\left(\frac{\gamma_0'}{\gamma_0}\right)^2\right]$$
$$-\frac{3}{2}\frac{\gamma_0''\gamma_0}{(\gamma_0^2-1)} - \left(\frac{\gamma_0'}{\gamma_0}\right)^2\left[3+\frac{5}{\gamma_0^2-1}+\frac{17}{4}\frac{1}{(\gamma_0^2-1)^2}\right],$$

$\omega_b^2 \equiv 4\pi e\rho_0/m$; m is the rest mass,

$$F \equiv -A\frac{\gamma_0}{c\sqrt{\gamma_0^2-1}}\left[\frac{i\omega\gamma_0}{c\sqrt{\gamma_0^2-1}} - \frac{2\gamma_0'}{\gamma_0(\gamma_0^2-1)} - \frac{3\gamma_0'}{\gamma_0}\right]\exp\left[\frac{1}{2}\int_0^z X\,dz_1\right],$$

and A is an arbitrary constant, which appears when the equation of continuity and Poisson's equations $\operatorname{div}(-i\omega\tilde{E} + 4\pi\tilde{j}) = 0$ are solved simultaneously. The expressions for Q^2, X, and F are simplified considerably in the nonrelativistic case ($\beta_0^2 \ll 1$), and for high beam velocities ($\gamma_0^2 \gg 1$). In ref. 1 the stability of a nonrelativistic beam whose velocity varies with coordinate is considered. Since the beam is infinite, $A = 0$. In the case of a bounded beam (in the longitudinal direction) it is necessary to take this constant into account. In the nonrelativistic case Eq. (2) without the right side is the same as the equation obtained in ref. 1.

We use the following boundary conditions to obtain the dispersion equation for the perturbed quantities:[2]

$$\tilde{\rho}(0) = \tilde{v}(0) = \tilde{\varphi}(0) = \tilde{\varphi}(L) = 0, \tag{3}$$

where

$$\tilde{E} = -\nabla\tilde{\varphi}.$$

Solving Eq. (2) and substituting the solution into the boundary conditions (3), we obtain the following dispersion equation for the frequency ω:

$$\int_0^L dz\exp\left[-\frac{1}{2}\int_0^z X\,dz_1\right]\left\{\frac{i\omega}{4\pi A}\left[\mathcal{E}_{01}\int_0^z \mathcal{E}_{02}F\,dz_1 - \mathcal{E}_{02}\int_0^z \mathcal{E}_{01}F\,dz_1\right]\right.$$
$$\left. + [\mathcal{E}_{01}\mathcal{E}_{02}'(0) - \mathcal{E}_{02}\mathcal{E}_{01}'(0)] - \frac{1}{2}X[\mathcal{E}_{01} - \mathcal{E}_{02}(0)\mathcal{E}_{02}\mathcal{E}_{01}(0)]\right\} = 0, \tag{4}$$

where $\mathcal{E}_{0s}$ is the particular solution of the homogeneous equation (2).

Equation (4) is valid for both a neutralized beam and a nonneutral beam, and for any dependence of the unperturbed velocity $v_0(z)$ on the z coordinate. We consider the case of a diode in which the unperturbed beam velocity $v_0(z)$ is determined both by the electrode potentials and by the space charge of the beam itself (2), and the case in which the space charge of the beam is neutralized and the dependence of the velocity $v_0(z)$ on z is determined solely by the external fields (3).

2. STABILITY OF THE BEAM
IN THE DIODE

Solving the unperturbed set of equations (1) in the nonrelativistic case with the boundary conditions $\varphi_0(0) = U_k$, $\varphi_0(L) = U_A$ [where U_k (U_A) is the constant potential applied to the cathode (anode)], we find the unperturbed velocity in the diode:

$$v_0 = (\psi \pm \eta z)^{2/3}, \tag{5}$$

where

$$\psi \equiv \left(U_k\frac{2e}{m}\right)^{3/4};\ \eta \equiv \sqrt{18\pi j_0\frac{e}{m}};\ j_0 = \rho_0 v_0 = \text{const}.$$

The minus sign describes the case in which the beam is retarded in the diode.

Substituting Eq. (5) into Eq. (2) and making the substitution $x = \psi + \eta z$, we obtain

$$\frac{d^2\mathscr{E}}{dx^2} + \frac{2}{9x^2}\mathscr{E} = F_1, \tag{6}$$

where $F_1 \equiv F/\eta^2$.

The following functions are solutions of the homogeneous equation (6):

$$\mathscr{E}_{01} = x^{2/3}, \quad \mathscr{E}_{02} = x^{1/3}. \tag{7}$$

Substituting these functions in Eq. (4) and introducing the quantity $\xi \equiv (\omega/\eta)\sqrt[3]{x}$, for $\xi \gg 1$ we obtain the following dispersion equation:

$$e^{-3i(\xi_L - \xi_0)} = -\frac{\xi_0}{3}\frac{1}{(\xi_L^3 - \xi_0^3)}\left(\frac{\xi_L}{\xi_0}\right)^{5/4} \times \left\{\left[10 - 14\left(\frac{\xi_0}{\xi_L}\right)^{1/3}\right] + i\left[3 - 7\left(\frac{\xi_0}{\xi_L}\right)^{1/3}\right]\right\}. \tag{8}$$

It is evident from Eq. (8) that instability is possible only when $\xi_0 > \xi_L$, i.e., only when the beam is slowed down. Taking $U_k \gg U_A$ and using Eq. (8) we get the following simple expressions for the frequency and growth rate:

$$\left.\begin{aligned} \operatorname{Re}\omega &= \frac{2\pi n}{3}\sqrt{\frac{2e}{m}U_k} = \frac{2\pi n}{3}\frac{v_k}{L}, \\ \operatorname{Im}\omega &= \frac{2}{3}\frac{v_k}{L}\ln\left(\frac{2\pi n}{3}\right), \end{aligned}\right\} \tag{9}$$

where n is an integer ($n \gg 1$), and v_k is the velocity of the beam at the cathode.

Since the growth rate of the oscillation increases (slowly) as n increases, a question arises regarding the maximum value of n. In order to determine this quantity, and correspondingly, the maximum frequency generated by the beam in the diode, it is necessary to take the thermal motion into account. To do this we must add the following term to the right side of the linearized first equation (the equation of motion) of system (1) (see, for example, ref. 1):

$$m\left[\frac{\rho}{\rho_0}\frac{\partial\rho_0}{\partial t} - \frac{\partial\rho}{\partial z}\right]\frac{v_T^2}{\rho_0}. \tag{10}$$

Taking this term into account leads to the following inequality:

$$2\pi n < \sqrt{\frac{v_k v_A}{v_T^2}}, \tag{11}$$

where v_A is the velocity of the beam at the anode, and v_T is the thermal velocity.

This limitation leads to the following value of the maximum frequency generated by the beam:

$$\operatorname{Re}\omega_{\max} = \frac{v_k}{L}\frac{\sqrt{v_k v_A}}{3v_T}, \quad \operatorname{Im}\omega_{\max} = \frac{2}{3}\frac{v_k}{L}\ln\left(\frac{\sqrt{v_k v_A}}{3v_T}\right). \tag{12}$$

As an example we substitute the following values of the velocities in Eq. (12): $v_k = 3 \cdot 10^9$, $v_A = 3 \cdot 10^8$, and $v_T = 3 \cdot 10^7$. Then for L = 1 cm the beam in the diode will generate a frequency $\omega_{\max} = 5.5 \cdot 10^{10}$ with a growth rate $\operatorname{Im}\omega_m = 4.9 \cdot 10^9$.

A device in which the beam is slowed down at the anode is a triode with an accelerating grid and a retarding anode. The instability in such a system has been observed experimentally in refs. 3 and 4 (see also ref. 5). In this case it is assumed that the generation of oscillations in such a triode is due to oscillations of electrons about the positive grid and that the frequency is determined either by external circuits,[4] or by the frequency of oscillation of the electrons around the grid.[3] The analysis above shows that another instability mechanism is possible in a triode with a positive grid. In this case it is clear that the maximum oscillation efficiency will obtain when the frequency of the external circuit (with respect to the electron beam) coincides with one of the frequencies generated by the beam.

3. EFFECT OF AN EXTERNAL ELECTRIC FIELD ON THE PIERCE CRITERION

We consider the effect of an external electric field on the stability of an electron beam traveling with constant velocity v_0 through a system with two electrodes. As is well known,[2,6] such a beam is unstable with respect to the excitation of aperiodic oscillations $\operatorname{Re}\omega \ll \operatorname{Im}\omega$ (Pierce instability). The ion background neutralizes the electron-beam charge ($n_i = n_{0e}$). Equation (2) describes the behavior of a perturbation in such a system.

We assume that the external electric field and the time during which it acts are fairly small so that we can neglect the motion of the ions and use the WKB approximation in solving Eq. (2), i.e., we assume that the distance L over which the beam velocity changes appreciably (by a factor of 2) is much greater than the characteristic wavelength $\lambda \sim 1/Q$ ($L \gg \lambda$). Solving the homogeneous equation (2) in this approximation we obtain

$$\mathscr{E}_{01} = \frac{1}{\sqrt{Q}}\exp\left[i\int_0^z Q\,dz_1\right], \quad \mathscr{E}_{02} = \frac{1}{\sqrt{Q}}\exp\left[-i\int_0^z Q\,dz_1\right]. \tag{13}$$

To solve the dispersion equation (4) with the solutions (13) we consider the relativistic and nonrelativistic cases separately.

The nonrelativistic case ($\beta_0^2 \ll 1$). The dependence of the velocity on the coordinate can be chosen in the following form:

$$v_0 = V(1 + \zeta z), \tag{14}$$

where $\zeta = eE_0/mV^2$, $\zeta L \ll 1$, and E_0 is the external field. The WKB approximation holds when $\zeta \ll 2/3\,(\omega_b/V)$. The dispersion equation (4) becomes

$$\Delta = \zeta L \Phi, \tag{15}$$

where

$$\Delta \equiv 2\alpha\xi[1 - e^{i\xi_1}\cos\alpha_1] + ie^{i\xi_1}(\xi^2 + \alpha^2)\sin\alpha_1 + i\frac{\xi^2}{\alpha}(\xi^2 - \alpha^2),$$

$$\alpha \equiv \frac{\omega_b}{V}L, \quad \xi \equiv \frac{\omega}{V}L, \quad \alpha_1 \equiv \alpha\left(1 - \frac{3}{4}\zeta L\right), \quad \xi_1 \equiv \xi(1 - \zeta L),$$

Φ is an unwieldy expression, so that we will write it in explicit form for the special cases considered below.

Assuming $\xi \ll 1$ we substitute $\alpha = \pi n + \delta$ in Eq. (15), where $n = 1, 3, 5, \ldots$, and $\zeta L < \delta \ll 1$; we find $\Phi \to 0\,(\xi, \delta)$ and

$$\xi = i\frac{\pi n}{4}\left[\delta - \frac{3}{4}\pi n\zeta L\right]. \tag{16}$$

For $\zeta = 0$, Eq. (16) gives the growth rate for the Pierce instability.[6]

It can be seen from Eq. (16) that an external electric field which accelerates the electron beam leads to a threshold for the Pierce instability, while a retarding electric field increases the growth rate.

We will now show that an external electric field not only can quench the Pierce instability but also can cause new instabilities. To show this we put $\xi = \alpha + \mu$, where $\zeta L \ll \mu \ll 1$. From Eq. (15) we have

$$\Phi = \frac{1}{\mu}\alpha^3;\ \mu^3 = \frac{\zeta L\alpha^3}{2i\alpha + 2\alpha^2 + ie^{i\alpha}\sin\alpha}. \tag{17}$$

Hence, when $\alpha \gg 1$

$$\left.\begin{aligned} \operatorname{Re}\omega &= \omega_b - \frac{V}{L}\frac{1}{(2)^{1/3}}(\zeta L\alpha)^{1/3}, \\ \operatorname{Im}\omega &= \frac{V}{L}\frac{\sqrt{3}}{(2)^{1/3}}(\zeta L\alpha)^{1/3} \end{aligned}\right\} \tag{18}$$

and when $\alpha \ll 1$

$$\operatorname{Re}\omega = \omega_b,\ \operatorname{Im}\omega = \frac{V}{L}\left[\frac{1}{3}\zeta L\alpha^2\right]^{1/3}. \tag{19}$$

The relativistic case ($\gamma_0^2 \gg 1$). We assume that γ_0 varies as

$$\gamma_0 = \gamma(1 + \zeta z). \tag{20}$$

To satisfy the WKB approximation we require

$$\zeta \ll \frac{2}{3}\frac{\omega_{b1}}{c},\ \text{where}\ \omega_{b1}^2 \equiv \frac{4\pi e^2 n}{m\gamma^3}.$$

Substituting into the expressions for Q^2, X and F, from Eq. (4) we obtain the dispersion equation

$$\Delta_1 = \zeta L\Phi_1, \tag{21}$$

where

$$\Delta_1 \equiv 2\alpha\xi[1 - e^{i\xi}\cos\alpha_1] + ie^{i\xi}(\xi^2 + \alpha^2)\sin\alpha_1 + i\frac{\xi^2}{\alpha}(\xi^2 - \alpha^2),\ \xi \equiv \frac{\omega}{c}L,\ \alpha \equiv \frac{\omega_{b1}}{c}L,\ \alpha_1 \equiv \alpha\left(1 - \frac{3}{4}\zeta L\right).$$

The expressions for Φ_1, as in the nonrelativistic case, will be written for some special cases.

For $\xi \ll 1$ we substitute $\alpha = \pi n + \delta$ in Eq. (21), where $\delta \ll 1$. Then $\Phi_1 \to 0\,(\xi, \delta)$, and we obtain (16) for ξ, i.e., as in the nonrelativistic case, an external electric field which accelerates the beam increases the Pierce instability threshold.

Putting $\xi = \alpha + \mu$, we obtain the following values of the frequency and growth rate

$$\left.\begin{aligned} \operatorname{Re}\omega &= \omega_{b1} - \frac{1}{2}\frac{V}{L}\left(\frac{3}{4}\zeta L\alpha\right)^{1/3} \\ \operatorname{Im}\omega &= \frac{\sqrt{3}}{2}\frac{V}{L}\left(\frac{3}{4}\zeta L\alpha\right)^{1/3} \end{aligned}\right\} \tag{22}$$

for $\alpha \gg 1$, and

$$\operatorname{Re}\omega = \omega_{b1};\ \operatorname{Im}\omega = \frac{V}{L}\left(\frac{1}{2}\zeta L\alpha^2\right)^{1/3} \tag{23}$$

for $\alpha \ll 1$.

Hence, both in the relativistic and in the nonrelativistic cases an accelerating external electric field increases the Pierce instability threshold, and generates new instabilities.

4. THE MECHANISM BY WHICH THE OSCILLATION THRESHOLD IS INCREASED

It is of interest to understand why the Pierce instability threshold is increased when the beam is accelerated to understand why the instability develops when the beam is slowed down in a diode, and why it is quenched when the beam is accelerated.

As is well known,[7-9] for a collective instability to develop it is necessary that each particle of the beam should radiate (i.e., an elementary radiation mechanism is necessary) so that the radiating particles form coherent bunches, and that there should be coherence between the bunches. The instability develops in the following way. The perturbation groups the particles into bunches: They begin to radiate coherently, increasing the amplitude of the perturbation, etc. It follows from this, that for the instability to be quenched it is necessary to reduce the radiating capacity of the particles, or the number coherently radiating particles, in order to compensate the increase in the perturbation. Since the perturbations usually grow from the thermal noise level, one might expect that this interference requirement will not be very severe.

The increase in the Pierce instability threshold occurs due to a reduction in the number of coherently radiating particles in a bunch. A change in the number of coherently radiating bunches plays no part in this case. It can be shown that for any instabilities for which $\operatorname{Re}\omega \gg \operatorname{Im}\omega$, a change in the number of particles in the bunches will play the main part. This can be seen from the fact that in determining $\operatorname{Im}\omega$ we use the unperturbed value of $\operatorname{Re}\omega$, i.e., we neglect the change in the wavelength in determining the growth rate to a first approximation. In the general case, for the instability to be quenched, it is necessary to accelerate the beam; in this case the number of coherent bunches and the number of particles in a bunches are both reduced. This can be clearly seen in the above example of the instability of a beam in a diode.

To summarize, we have obtained the following results.

1. A retarded electron beam in a diode is unstable with respect to the excitation of longitudinal oscillations at frequency $\omega = (v_k/L)2\pi n/3$ with growth rate $\operatorname{Im}\omega =$

$(^2/_3)v_k/L\ln(2\pi n/3)$. An accelerated beam in a diode is stable.

2. Thermal motion sets an upper limit to the frequency of the oscillations generated by the beam in the diode

$$\omega_{\max}=\frac{v_k}{L}\frac{\sqrt{v_k v_A}}{3v_T}; \quad \operatorname{Im}\omega_{\max}=\frac{3}{2}\frac{v_k}{L}\ln\left(\frac{\sqrt{v_k v_A}}{3v_T}\right).$$

3. An accelerating external electric field leads to an increase in the Pierce instability threshold, while a retarding field increases the growth rate of this instability.

4. An external electric field leads to new instabilities.

5. The mechanism by which the oscillation threshold increases when the electron beam is accelerated has been determined.

In conclusion I wish to thank V. I. Kurilko for drawing my attention to the problem.

---

[1] P. V. Bliokh and Ya. B. Fainberg, Zh. Tekh. Fiz., 26, 530 (1956) [Sov. Phys.—Tech. Phys., 1, 510 (1956)].

[2] J. Pierce, J. Appl. Phys. 15, 721 (1944).

[3] H. Barkhausen and K. Kurtz, Phys. Zs., 21, 1 (1920).

[4] E. W. B. Gill and J. M. Morel, Phil. Mag., 44, 161 (1922).

[5] R. G. Mirimanov (ed.) Millimeter and Submillimeter Waves, IL, Moscow (1959).

[6] A. B. Mikhailovskii, Theory of Plasma Instabilities, Vol. 1, Consultants Bureau, New York (1973).

[7] V. I. Kurilko, Dissertation, Khar'kov (1970).

[8] V. A. Buts, ZhETF, Pis. Red., 15, 52, (1972)[JETP Lett., 15, 36 (1972)]; Zh. Tekh. Fiz., 42, 710 (1972); 43, 456 (1973) [Sov. Phys.—Tech. Phys., 17, 559 (1972); 18, 293 (1973)].

[9] V. I. Kurilko, Dokl. Akad. Nauk SSSR, 208, 1059 (1973) [Sov. Phys.—Dokl., 18, 132 (1973)].

Low-frequency oscillations in counter-streaming high-current electron beams

A. F. Timoshenko, D. V. Iremashvili, and Yu. K. Udovichenko

(Submitted March 26, 1973; resubmitted February 4, 1974)
Zh. Tekh. Fiz., 44, 1662-1668 (August 1974)

Low-frequency (lf) oscillations are investigated experimentally in counterstreaming beams in a background plasma in a homogeneous magnetic field. The current is 3 A, the electron beam energy is 25 keV, and the magnetic field varies from 250 to 1000 Oe. The counterstreaming beams are produced by reflection of the electron beam from a negative electrode. The oscillation frequency is close to the ion plasma frequency; the oscillations are radial oscillations of the density. These oscillations cause periodic excitation of high-frequency (hf) oscillations at half the electron cyclotron frequency and its harmonics $n\omega_H/2$ ($n = 1, 2, 3, \ldots$). The lf oscillations can result from the interaction of drift instabilities in the counterstreaming beams. The current cutoff due to the lf oscillations limits the amplitude of the hf oscillations.

As reported earlier,[1] the interaction between counterstreaming electron beams in a system in which the magnetic field increases at the imput leads to hf oscillations at half the electron cyclotron frequency, and its harmonics $n\omega/2$, which are strongly modulated at low frequencies under certain conditions.

In the present paper we study lf oscillations and the effect on the hf oscillations excited in counterstreaming electron beams.

The investigation is carried out on the apparatus described in ref. 1. The beam parameters are as follows: current I 3 A, electron energy eV 25 keV, and pulse length 10-40 μsec. The glass test chamber, 4 cm in diameter and L = 40 cm long, with a movable electrode (collector), is located with the electron gun in a constant homogenous magnetic field H = 250-1000 Oe. Counterstreaming beams are produced by reflection of the beam injected into the test chamber; the beam originates from an electrode at a negative potential equal to the cathode potential. The beam is 1 cm in diameter at the entrance to the system. The lf and hf oscillations are detected by coaxial probes. A system of probes that can move along the length and radius enables us to measure the intensity and to observe the phase shift of the lf oscillations in space. The lf oscillations can also be detected from the envelope of the oscillations at frequencies $n\omega_H/2$. The diameters of the injected and oscillating beams are measured in cross section by using a current-detecting spherical probe which is rotated about its own axis, which is asymmetric to the axis of the system. The probe can be moved along the chamber. This probe is used to measure the amplitude of the lf oscillations of the density. The current in the cathode and electrode (collector) circuits is recorded by a Rogowski loop. A probe is used to determine the density n_p and electron temperature T_e. The longitudinal electron distribution function of the injected beam is measured by a multigrid analyzer located behind the collector. The particles enter the analyzer through an aperture 0.03 cm in diameter. Similar apertures placed along the diameter are used to obtain radial and azimuthal measurements of the phase and amplitude of electron density oscillations in the injected beam with the aid of a system of microcollectors. Segmented collectors (two segments, a disk and a diaphragm) are also used to investigate the phase of density oscillations.

The pressure in the gun region is $\sim 10^{-6}$ mm Hg. The pressure in the test chamber can be varied from $5 \cdot 10^{-6}$–1.10^{-3} mm Hg. Nitrogen is usually the working gas; hydrogen, helium, argon, and krypton are used in certain experiments.

The investigation indicates that (as for high-current counterstreaming electron beams in an inhomogeneous magnetic field) in a system with a homogeneous magnetic field intense oscillations are excited at frequency $n\omega_H/2$. The dependence of the intensity and frequency of lf oscillations on different parameters is similar to that studied in ref. 1. A general characteristic of these systems is the strong modulation of the hf oscillations by lf oscillations.

The lf oscillations under study appear in the system after the electrons in the oscillating beam are neutralized. The oscillations develop faster if the current and pressure are increased; they disappear when conditions for the development of a beam–plasma discharge occur in the system. The density n_p is measured by two electric probes in the pressure range $p = (2\text{-}4) \cdot 10^{-4}$ mm Hg preceding the beam–plasma discharge, when the lf oscillations have almost disappeared, and the density is 10^8–10^9 cm^{-3}, $T_e \simeq 20$–40 eV for I = 0.2–1.5 A, eV = 5–15 keV. The measurements show lf oscillations for plasma densities from $n_p \ll n_b$ to $n_p \sim n_b$ (n_b is the density of beam electrons); in the calculations we assume $n_i \simeq n_b$.

In Fig. 1, the frequency (curve 1) and amplitude (curve 2) of the lf oscillations and the beam diameter $2a$ (curve 3) are given as functions of the current. The beam radius a is estimated at 1/3 the height of the time-averaged radial distribution of the current density.

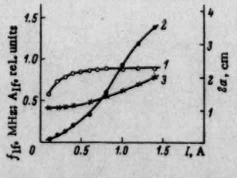

Fig. 1. Frequency (1) and amplitude (2) of the lf oscillations, and diameter of the beam (3) as functions of current. eU = 15 keV, H = 750 Oe, L = 30 cm, p = $1 \cdot 10^{-4}$ mm Hg.

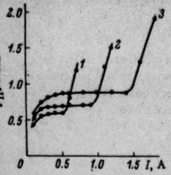

Fig. 2. Frequency of the lf oscillations as a function of beam current for different energies. 1) 5; 2) 7.5; 3) 15 keV. The other parameters are the same as in Fig. 1.

It is evident from the figure that the frequency at I = 0.1-0.4 A increases for a small change in the beam diameter. With a further increase in the current the frequency becomes saturated and the beam diameter increases noticeably. With an increase in current the amplitude of the lf oscillations increases considerably. Figure 1 shows the maximum amplitude of the oscillations over the beam cross section.

In Fig. 2, the frequency of the lf oscillations in counterstreaming beams is shown as a function of current for different energies of the injected beam. The frequency increases as the injected energy increases. As the measurements indicate, the radius of the beam changes. For example, with I = 0.5 A in curves 1, 2, and 3 the beam radius is 7.5, 6.5, and 5 mm, respectively. As the current changes, the beam radius in curves 1, 2, and 3 changes in a fashion similar to curve 3 in Fig. 1. At a certain current I', the frequency of lf oscillations increases significantly. This result is discussed below. When I < I' the oscillations are regular.

The diameter of the beam also depends on the length of the test chamber. If the length of the system is increased the beam diameter increases and the frequency of the lf oscillations decreases. The oscillation frequency is roughly inversely proportional to the square root of the gas mass M, is independent of the pressure ($p = 2 \cdot 10^{-5} - 2 \cdot 10^{-4}$ mm Hg), and varies slowly with the magnetic field.

With H = 800-1000 Oe, eV = 10-25 keV, and a negligible change in a, the intensity of the lf oscillations decreases as the injection energy increases for a constant current and does not vary for a constant beam density n_b for an increasing electron energy. In other words, the intensity of the lf oscillations is determined by the density n_b of the beam and not by the energy eU.

In view of the dependence of frequency and amplitude on the system parameters (eU, I, p, M) and the conditions for onset ($n_p < n_b$) we conclude that the lf oscillations are determined by the density of the ions n_i which neutralize the beam.

Measurements and estimates that include the beam diameter indicate that the frequency of the lf oscillations coincides with ion plasma frequency ($\omega \simeq \omega_i$). Investigations employing probes that move along the radius of the chamber and located 180° apart indicate that the phase of the lf oscillations changes along the radius but not in azimuth. The oscillations are concentrated in the beam region. The intensity distribution of the lf oscillations along the beam is such that the maximum amplitude occurs at the center of the chamber, i.e., a standing half-wave is formed.

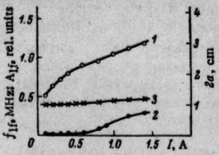

Fig. 3. Frequency (1) and amplitude (2) of the lf oscillations, and diameter of the injected beam (3) as functions of the current. $p = 6 \cdot 10^{-5}$ mm Hg. The other parameters are the same as in Fig. 1.

The experimental results indicate that the lf oscillations are radial oscillations of the density of the beam.

It is well known from the experiments in ref. 2 that an electron beam injected into a chamber in the presence of a background plasma, can exhibit a drift instability at the frequency described by (1), with wave vector $k = (k_z^2 + k_\varphi^2 + k_r^2)^{1/2}$ ($k_z \sim 1/L$ and $k_r \simeq k_\varphi \sim 1/r$ are the longitudinal, radial, and azimuthal components of the wave vector). If we assume that the same instability develops in a reflected beam, then the azimuthal component can be cancelled in a system of counterstreaming beams. Since $k_z \ll k_r$ the lf oscillations are radial. Since the experimental conditions of the present paper differ from those of ref. 2, additional experiments on lf oscillations have been performed with a straight-through beam (the collector at ground potential). Figure 3 gives the frequency (curve 1), the amplitude (curve 2), and the beam diameter (curve 3) as functions of the current. The oscillation frequency increases with the current. The beam diameter varies comparatively slowly (curve 3, Fig. 3). The oscillation amplitude increases slowly as the current increases. A marked increase in the amplitude occurs at I = 0.6 A. Figures 1 and 3 give values of the amplitude in the same relative units. Evidently the amplitude for straight through conditions (for the same injection current) is appreciably smaller than for a reflected beam. This situation can be caused by the strong feedback associated with the reflected electron beam.

In the present paper all the experimental results are given for the case of a negligible space charge in the cathode region of the gun. In the presence of a large space charge near the cathode, obtained by increasing the cathode–anode spacing for the same electrical parameters of the gun, frequency saturation of the lf oscillations with a corresponding change in the beam diameter) is also observed under straight-through conditions with I ≃ 0.2 A (eU = 15 keV and H = 700 Oe). An appreciable increase in the oscillation amplitude is also observed at I ≃ 0.2 A; this may be due to the amplification coming from the feedback as a result of the large space charge in the cathode region of the gun, similar to that discussed in detail in ref. 3.

These and several other investigations of the dependence of the frequency of the lf oscillations on the parameters eU, L, p, H, and M, with the change in beam diameter included, have shown that under straight-through conditions oscillations can develop in the system with a frequency close to the ion plasma frequency ($\omega \simeq \omega_i$).

Investigations of space phase correlations employing probes and microcollectors indicate that the phase of lf oscillations varies in both azimuth and radius. A half-wave fits into the length of the system. The currents to the 0.5 cm diameter disk (admitting the central portion of the beam) and the diaphragm (admitting the peripheral portion of the beam) are modulated by the lf oscillations. The current oscillations are in opposite phase. The same pattern is observed when two segments are used which divided the injected beam into two equal parts. The total current to the collector (two segments, a disk and a diaphragm) shows no lf modulation.

The experimental results and estimates indicate that under straight-through conditions the drift instability that is thoroughly studied in refs. 2 and 4 develops in the system. We consider the well-known dispersion relation

$$\omega^2 = \frac{\omega_i^2}{1 + \frac{1}{k^2 d^2}}, \tag{1}$$

where d is the electron Debye radius.

With the instability $n_p \ll n_b$ and $T_e \simeq 20\text{-}40$ eV and thus the current is neutralized by the ions. For example, with the parameters of Fig. 3 at a current $I \simeq 1A$, a density $n_b \simeq 1 \cdot 10^9$ cm^{-3}, setting $T_e = 40$ eV and $n_p \simeq 1 \cdot 10^8$ cm^{-3}, we have $1/k^2d^2 \simeq 0.2$. According to (1), when $1/k^2d^2 \ll 1$ the oscillation frequency is $f = f_i = 1.18$ MHz, which is close to the experimental value. When $1/k^2d^2 \gg 1$, the drift instability should change to an ion-acoustic instability for a density $n_p \simeq 3 \cdot 10^9$ cm^{-3} and with these parameters, the lf oscillations are quenched.

It follows from the experimental results that an appreciable increase in the intensity of lf oscillations is always accompanied by a broadening of the beam diameter under both beam conditions.

Under straight-through conditions, broadening of the beam due to an appreciable increase in the amplitude of lf oscillations is observed at I = 0.2–0.6 A. These currents are of the same order as the calculated value of the critical current $I_{cr} \simeq 0.6$ A. The value of I_{cr} is determined from[2]

$$I_{cr} = \frac{ma^2}{4e} \frac{k^2 v^3}{\left[1 + 2k_\varphi \frac{v}{a\omega_H k_z}\right]}, \tag{2}$$

where v is the beam velocity.

Analysis of the results obtained leads to the conclusion that radial lf oscillations in counterstreaming beams are generated by the interaction with drift instabilities developed in the injected and reflected beams. The azimuthal component of the electric field of the lf oscillations is cancelled. Evidently, this is due to the qualitative difference in the radial distribution of the amplitude of lf oscillations under straight-through (curve 1) and reflected-beam (curve 2) conditions (Fig. 4).

The amplitude of the lf oscillations under reflected-beam conditions varies slowly at chamber pressures of $p = 2.10^{-5}\text{-}2.10^{-4}$ mm Hg; under straight-through conditions this occurs for $p = 1.5 \cdot 10^{-5}\text{-}1.10^{-4}$ mm Hg (eU = 15 keV, $I \simeq 1$ A, H = 500 Oe). A further increase in pressure leads to a decrease in the amplitude. Under straight-through conditions the amplitude decreases sharply at $p = (1\text{-}2) \cdot 10^{-4}$ mm Hg; under reflected-beam conditions at $p = (2\text{-}4) \cdot 10^{-4}$ mm Hg. The decrease in the amplitude of the oscillations for an increasing pressure up to the time they disappear under both conditions is ascribed, as in ref. 2, to the destruction of the conditions for excitation of drift instability as the plasma density increases.[4]

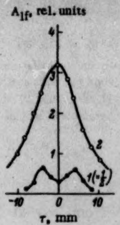

Fig. 4. Radial distribution of the amplitude of lf oscillations of beam density under direct-beam (1) and reflected-beam (2) conditions. I = 0.6 A, eU = 15 keV, H = 500 Oe, L = 35 cm, $p = 8 \cdot 10^{-5}$ mm Hg.

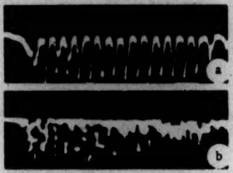

Fig. 5. Oscilloscope traces of hf oscillations. eU = 15 keV, H = 600 Oe, $p = 1 \cdot 10^{-4}$ mm Hg, L = 40 cm; I in A: a) 0.5; b) 1.4. 18 μsec scans.

The difference in the pressures at which lf oscillations disappear from the system under both conditions is explained on the basis that under straight-through conditions a substantial contribution to the generation of the plasma is made by secondary low-energy electrons. Under reflected-beam conditions the plasma density can drop sharply due to the loss of ions from the system resulting from more intense lf oscillations than in the reflected-beam mode, and the extraction of ions by the electrode.

Similar dependences of lf oscillations on I, eU, L, and M under reflected-beam conditions are obtained using a magnetically shielded gun placed at the exit to the test chamber with an increasing magnetic field.[1] The experimental results are in qualitative agreement with those given above. Quantitative estimates are complicated due to the presence of a large transverse velocity component $v_\perp$ of the beam electrons.

It can also be seen in Fig. 2 that there is a sharp increase in the oscillation frequency as well as saturation at large beam currents. The oscillations exhibit an irregular random nature which appears simultaneously in the random excitation of half-cyclotron oscillations (Fig. 5b). In Fig. 5a, hf oscillations modulated by regular lf oscillations are shown.

When intense lf oscillations develop at high currents under straight-through conditions, a cutoff (a sharp drop in the current to the collector) is observed similar to that in ref. 4. In this case the value of the current at which the cutoff occurs should be considered the limiting current I_{l_1}. A similar characteristic is observed under reflected-beam conditions. The cutoff could be estimated from the sharp decrease in current to the spherical probe 0.03 cm in diameter which is placed in the os-

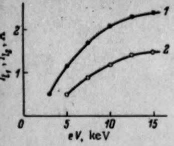

Fig. 6. Cutoff current under direct-beam I_{l_1} (1) and reflected beam I_{l_2} (2) conditions as a function of electron beam energy. H = 500 Oe, L = 35 cm, p = $2\cdot 10^{-5}$ mm Hg.

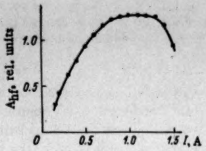

Fig. 7. Amplitude of integral hf signal as a function of beam current. eU = 15 keV, p = $1\cdot 10^{-4}$ mm Hg, L = 30 cm.

cillating beam at the axis of the test chamber. With counterstreaming beams there is no current in the circuit of the reflecting electrode; therefore, the value corresponding to the cutoff current should be considered spurious. The current is recorded under counterstreaming conditions by a Rogowski loop from the total current in the cathode circuit with the current transmission coefficient taken into account. Current cutoff under both beam conditions is accompanied by an increase in the frequency of the lf oscillations. Figure 6 gives the cutoff current as a function of electron beam energy for straight-through I_{l_1} (curve 1) and reflected-beam I_{l_2} (curve 2) conditions.

The measurements indicate that the value of I_l increases with an increasing magnetic field H. The increase in I_{l_1} with increasing H and eU under straight-through conditions agrees with the results of ref. 4. Under reflected-beam conditions the increase in I_{l_2} with increasing H and eU indicates a similar mechanism for current cutoff resulting from the development of drift instabilities in counterstreaming beams. As expected, under reflected-beam conditions $I_{l_2} \simeq I_{l_1}/2$.

The values of I_{l_2} under reflected-beam conditions coincide with the currents at which a sharp increase in the frequency of the lf oscillations is observed in the system (Fig. 2). This phenomenon allows us to understand the observed decrease in the amplitude of the integral hf oscillations at frequencies $n\omega_H/2$ for a beam current $I \simeq 1.3$–1.5 A (Fig. 7). At first, the amplitude of hf oscillations increases with the increase in the current (in the density n_b, and thus in the growth rate[6] $\gamma \sim \omega_b$, where ω_b is the electron plasma frequency). With a further increase in current, saturation occurs which can be ascribed to nonlinearities broadening the oscillation spectrum. For $I \simeq 1.3$–1.4 A the amplitude of hf oscillations drops considerably. This decrease is related to the current cutoff. The phenomenon of current cutoff is a significant obstacle to the possible increase in oscillation intensities at $n\omega_H/2$ when a system of counterstreaming beams is used to generate hf oscillations.

The presence of strong radial modulation of beam density over time is due to the periodic nature of the excitation of oscillations at $n\omega_H/2$ (Figs. 5a and 5b in Ref. 1). Actually, with a given magnetic field H and a thermal velocity spread v_T (a measured value $v_T \sim 1\% v$), hf oscillations will develop at a density n_{b_1} determined by[7]

$$n_{b_1} \simeq \frac{1}{2mc^2}\left(\frac{v_T}{v} H\right)^2. \tag{3}$$

On the other hand, hf oscillations will develop for a density n_{b_2} at which the growth rate of hf oscillations ($\gamma \sim \omega_{b_2}$) is larger than the inverse time of flight of beam electrons in the test chamber ($\gamma > v/L$). Thus, for a mononenergetic beam $v_T \sim 1\% v$, with $v = 7.10^9$ cm/sec, H = 700 Oe, and L = 35 cm, $n_{b_1} \ll n_{b_2}$; when $v_T \sim 5\% v$, $n_{b_1} \gg n_{b_2}$. The threshold beam density at which hf oscillations are generated is determined by the largest values of n_{b_1} and n_{b_2}. And since the beam density is strongly modulated (up to 80–90%) by lf oscillations, the conditions for development of oscillations at frequencies $n\omega_H/2$ occur periodically and their intensity agrees with the variation in n_b.

---

[1] D. V. Iremashvili, A. P. Timoshenko, and Yu. K. Udovichenko, Zh. Tekh. Fiz., 43, 550 (1973) [Sov. Phys.–Tech. Phys., 18, 348 (1973)].

[2] M. V. Nezlin, M. I. Taktakishvili, and A. S. Trubnikov, Zh. Eksp. Teor. Fiz., 55, 397 (1968) [Sov. Phys.–JETP, 28, 208 (1969)].

[3] Yu. K. Udovichenko, N. I. Leont'ev, and A. P. Timoshenko, Zh. Tekh. Fiz., 42, 605 (1972) [Sov. Phys.–Tech. Phys., 17, 477 (1972)].

[4] M. V. Nezlin, M. I. Taktakishvili, and A. S. Trubnikov, Zh. Eksp. Teor. Fiz., 60, 1012 (1971) [Sov. Phys.–JETP, 33, 548 (1971)].

[5] A. B. Mikhailovskii, Zh. Tekh. Fiz., 35, 1945 (1965) [Sov. Phys.–Tech. Phys., 10, 1498 (1966)].

[6] I. Olwain, Rapport CEA-R-3075, Fortanay aux Roses (1966).

[7] D. H. Handel and G. Muller, Plasma Physics and Controlled Nuclear Fusion, Vienna (1969), Vol. 2, p. 793.

Cell for forming electron beams of arbitrary shape in a high-voltage gaseous discharge

I. V. Vagner, É. I. Bolgov, V. F. Grakun, V. L. Gokhfel'd, and V. A. Kudlai

E. O. Paton Electrical Welding Institute,
Academy of Sciences of the Ukrainian SSR, Kiev

(Submitted June 25 1973; resubmitted November 22, 1973)
Zh. Tekh. Fiz., 44, 1669-1674 (August 1974)

Electron beams with various cross sections from high-voltage discharges find wide use in engineering, particularly for welding purposes (refs. 1-3). Therefore, the physical processes occurring in systems used to produce such beams are of special interest. This paper presents results of an investigation of the discharge process and the formation of a fine pencil beam of circular cross section with a very simple electrode system called a cell. A discussion is given of methods for the design of electrode systems to form beams of arbitrary shape using the cell.

INTRODUCTION

In the cathode fall of a glow discharge one typically finds directed motion of the charges, as opposed to random motion in the positive column. In a high-voltage discharge, which corresponds to the left branch of the Paschen curve, near the ignition potential the cathode fall fills the entire interelectrode space. The high field gradients, especially at the cathode, and the low gas pressure enhance the directed motion. This feature holds in both homogeneous and inhomogeneous electric fields.

One consequence of this directed motion of the charges is the development of a high-voltage discharge in homogeneous fields along specific trajectories, as has been pointed out by Gusev.[4] In this case most of the electrons ejected from the cathode and of the ions formed in the discharge gap move along definite trajectories, as they do in vacuum.

Because of the directed motion of the charges each cathode point is related to a specific trajectory for the electrons leaving the point. For a trajectory along which Q_i ions are formed on the average and arrive at the cathode at the point of liberation of the electron, one finds that the discharge ignites along the trajectory when the charge conservation relation is satisfied:

$$Q_i\gamma = 1 \tag{1}$$

(where γ is the average number of electrons liberated by one ion from the cathode). The motion of the electrons and the ions along the trajectory is a necessary condition for the ignition of a high-voltage discharge along the trajectory.

All field lines of force near the cathode are straight in a certain region L_m. In some cases this section is of negligible extent; in other cases it is large, and can even occupy the entire space up to the anode. If the field gradient near the cathode is large enough each electron emerging from the cathode moves along the rectilinear section of the appropriate line of force. It is only after the line of force has begun to deviate from a rectilinear path that the electron trajectory can begin to curve. All the ions formed in this rectilinear cathode section will move along the same line of force, and will reach the cathode, because of their mass, at the point where the electron emerges i.e., the above-mentioned necessary discharge ignition condition will be satisfied along these lines of force.

The number of ions formed in a rectilinear cathode section of length L_m depends on the length, the gas pressure p, and the field distribution in the section. The number of ions increases as the pressure increases. However, not all the ions formed in the rectilinear section will move towards the cathode along the line of force. Only ions formed at places with sufficient field gradient to direct them towards the cathode will move to the cathode. Let L0 be the length of the rectilinear section within which all ions are directed by the field towards the cathode ($L_0 \leq L_m$).

A proportional increase in the electrode potentials does not alter the electric field configuration (in the absence of space charge), and therefore does not change the value of L_m. The field gradients will change, and L_0 along with them, and there will therefore be a change in the number of ions directed towards the cathode, for the same gas pressure. Thus, Eq. (1) can be satisfied by a choice of the values of the potentials and the pressure. Then the discharge will ignite along the rectilinear section.

CELL

Our analysis of existing gas-discharge electron beams and our experimental experience have led to the evolution of a so-called beam element, the cell (ref. 3), which generates a pencil beam of electrons (a small-diameter, cylindrical beam of circular cross section). This cell can be used to generate beams of arbitrary shape.

The electrode system comprising the cell element is shown in Fig. 1a. The cell consists of a planar cathode K, a planar anode A, and a planar diaphragm D with a circular aperture of diameter d_D; V_a and V_D are the potentials of the anode and the diaphragm relative to the cathode ($V_a = V_D$). The distance h between K and D is such that no discharge ignites outside the aperture in the diaphragm at the working gas pressures $p = 10^{-2}$ to 10^{-1} torr and voltages $V_a \leq 50$ kV. The quantity H is the distance between the cathode and the anode. The cell field is axisymmetric about axis OZ. Figure 1b shows the field distribution in an axial section for h = 10 mm, d_D = 10 mm, and H = 100 mm. Figure 1c shows the variation of the potential along the cell axis.

The rectilinear line of force of maximum length L_m = H is located along the cell axis. The value of L_m drops as one moves away from the axis.

For specific values of V_a and p the discharge ignites along the cell axis in the form of a thin pencil beam of

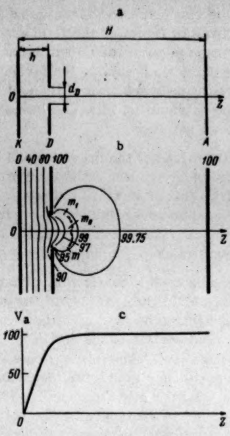

Fig. 1. a) Diagram of the cell; b) field distribution in an axial section of the cell; c) variation of the potential along the cell axis.

circular cross section. The beam diameter is much smaller than that of the diaphragm aperture (see Fig. 7). Figure 2 shows the dependence of the ignition potential on the pressure, $V_i = f(p)$, for H = 100 mm, h = 10 mm, d_D = 20 mm, He gas filling, and cathodes of Ti, Cu, and duralumin D-16. The current in the cell does not exceed 1 μA at ignition.

To check the proposition that only a small axial zone of the cathode surface where the rectilinear lines of force begin takes part in forming the discharge, we carry out the following experiment. The surfaces of cathodes of Ti and D-16 are covered by a thin layer of electrically deposited copper. For these cathodes the ignition curves first obtained coincide with the analogous curve for Cu (Fig. 2). After the cell has been operated for a certain time the ignition curves change and coincide with the corresponding curves for Ti and D-16. Inspection shows that the copper layer has been removed from the cathode in the axial region as a result of ion bombardment. The diameter of the affected spot is less than 0.8 mm. The rest of the cathode remains covered with copper. The fact that the appropriate ignition curves coincide, when the entire cathode surface is of Ti or D-16, when it is completely covered with copper, and when only the central part has exposed the Ti or D-16, is evidence that only the central part of the cathode takes part in sustaining the discharge. The nonaxial parts of the cathode only take part in generating the electric field. Figure 3 shows discharge ignition curves in the cell with a cathode of dural D-16, and Al anode, with cell parameters h = 5, 10, and 15 mm, d_D = 14 and 20 mm, H = 100 mm, and with air filling. Here the ignition potentials fall in the range 0.5 to 5 kV, while the ignition potentials outside the diaphragm aperture exceed 25 kV for values of h ≤ 15 mm and pressures $p = 5 \cdot 10^{-2}$ torr. At lower h the ignition potentials along the cell axis decrease (Fig. 3), while the ignition potentials outside the aperture increase. Even for h = 5 mm the latter exceed 10^5 in refs. 5 and 6. These facts enable us to increase the voltage V_a at the anode appreciably, in comparison with the ignition potential, without disturbing the conditions favoring the formation of a thin pencil beam. The value of V_a reaches 50 kV in these experiments.

As V_a increases the ionization processes in the discharge gap become more intense, leading to the formation of a plasma toward the anode and a dark space at the cathode. The dark space penetrates through the aperture in the diaphragm in the region between D and A. The broken line mm_0m_1 in Fig. 1b shows the interface between the dark space and the plasma.

The electron beam intersects the dark-space boundary at the point m_0. A flux of ions is directed from the vicinity of m_0 towards the cathode, thus increasing the flux of electrons in the beam. Experiment shows that an increase or decrease in the plasma density in the vicinity of m_0 leads to a corresponding increase or decrease in the beam. As the gas pressure is increased the mm_0m_1 boundary approaches the cathode and increases the charge density in the vicinity of m_0, thus increasing the current in the beam.

The field structure at the cathode is determined both by the geometry of the cell electrode system and by the space charge in the discharge. Therefore the length of the axial section where the necessary condition for sustaining the discharge is met (section L_0) may be smaller than H. The section $0 \le Z \le L_0$ is the beam generation zone. The section $L_0 \le Z \le H$ is the beam drift region. Departure from the rectilinear condition is not allowable in the formation region, since it perturbs the necessary discharge ignition condition. Beam bending in the drift region does not perturb the ignition condition, on the other hand. In order to check that the above-mentioned zones are present, we pass the beam formed in the cell through a magnetic or electrostatic deflection system. When the deflection system is positioned in the drift region one observes the normal deflection for such cases. But with the deflection system positioned in the formation zone, where

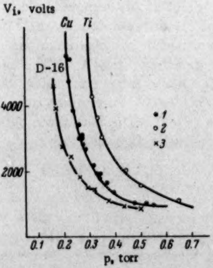

Fig. 2. Discharge ignition potential in the cell as a function of the pressure. d_D = 10 mm, h = 10 mm, H = 100 mm; He gas. The solid lines are for cathodes of Ti, Cu, and D-16. 1) Ignition potentials with cathodes of Ti and D-16, covered with a film of Cu; 2) ignition potentials with a cathode of Ti, covered with a copper layer, after removal of the copper layer at the center; 3) ignition potentials with a D-16 cathode, covered with a copper layer, and after removal of the copper layer at the center.

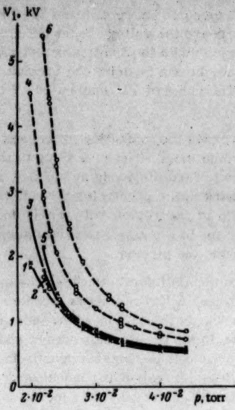

Fig. 3. Discharge ignition potential in the cell element, as a function of pressure. h, mm: 1, 2) 5; 3, 4) 10; 5, 6) 15. d_D, mm: 1, 3, 5) 20; 2, 4, 6) 14; H = 100 mm; D-16 cathode, Al anode, air filling.

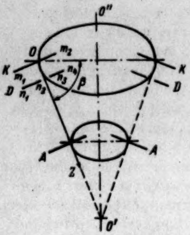

Fig. 4. Method of generating an electrode system to form a conical electron beam.

one must not perturb the rectilinearity of the beam, attempts to deflect the beam quench the beam.

The characteristics of the pencil electron beam (the total current and the current density distribution in the beam) are determined by the cell parameters: h and d_D, the gas density, and the voltage V_a. The current density distribution in the beam is approximately Gaussian. For $d_D = 10$, h = 10, $p = 7\cdot10^{-2}$ torr, and V_a = 25 kV, the total beam current is 48 mA. The maximum current is then $j(r = 0) = 41$ mA/mm² with half-width $d_{0.5} = 0.9$ mm.

PRODUCTION OF ELECTRON BEAMS OF ARBITRARY SHAPE

The cell can be used with electrode systems to form electric fields which will produce cylindrical and conical beams with an arbitrary directrix. For example, to form a cylindrical beam with directrix $y = \varphi(x)$ and given direction of generators, one needs to form an electric field with a set of rectilinear lines of force near the cathode coincident with the generators of the cylinder. The field distributions along these lines of force must be identical, to ensure that L_0 is equal to the length of the formation zone along each generator. In addition, the main part of the field must be concentrated within the rectilinear sections of these lines of force. If the field gradients are small outside these sections there will be no forces to perturb the electron beam outside the formation zone. All the other rectilinear sections of lines of force at the cathode must be so small that the self-sustaining condition (ref. 1) is not satisfied.

For specific values of the pressure and the supply voltage, our discharge ignites in the field produced, and forms an electron flux or beam of cylindrical shape on the anode side, and an equal flux of ions on the cathode side. Outside the formation zone we have a beam of electrons of the required shape, moving through the gas.

The cell can be used to produce electrode systems to form the above fields. The surfaces of the desired electrodes can be generated by motion of the straight lines, which form an axial section of the cell (Fig. 1a). If the plane of the section is displaced in such a way that the cell axis, considered as a generator, describes a cylinder with directrix $y = \varphi(x)$ while the plane itself always remains perpendicular to the tangent at the point of its intersection with the directrix, then a cylindrical beam with directrix $y = \varphi(x)$ will be formed in the electrode system. The system thus formed consists of a planar cathode, a planar anode, and a diaphragm with an aperture in the

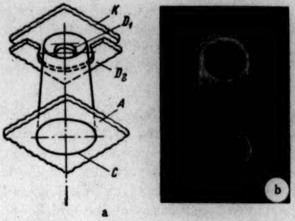

Fig. 5. Cylindrical electron beam, V_a = 25 kV, beam current 400 mA. The rear view shows the hot glowing ring formed by the beam.

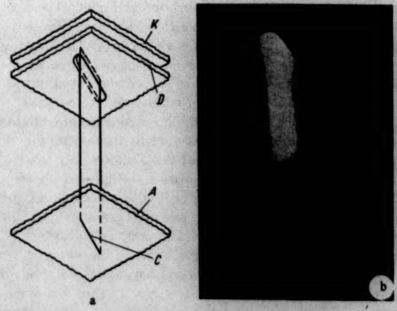

Fig. 6. Line-shaped or ribbon-type electron beam, V_a = 17 kV, beam current 600 mA. On the back side the glowing trace of the beam is visible.

Fig. 7. A multipencil electron beam. V_a = 25 kV, beam current 3× 45 mA. On the rear side of the anode one can see glowing spots generated by the electron beams.

form of a slot, whose average length is given by the equation $y = \varphi(x)$. Similarly one can form electrode systems to obtain conical beams. Here one must assign the directrix of the cone vertex and displace the axial section of the cell in an analogous way.

Figure 4 shows a method of forming an electrode system to generate a conical annular beam. The lines of the cathode K, the diaphragm D, and the OZ axis determine the plane of the section of the cell element. When this plane is rotated about the axis 0'0", the straight lines m_1–m_2, n_1–n_2, and n_3–n_4 draw out the surface of the required electrode system which will form the electron beam along the set of OZ axes. Depending on the angle β, the electron beam will either converge, $0 \leq \beta \leq \pi/2$, have a concentration of power at the anode A and a deconcentration of power liberated at the cathode, or will diverge, $\pi/2 \leq \beta \leq \pi$ and have a concentration of ion beam power at the cathode.

Figures 5 and 6 are photographs of ring-shaped and line-shaped or ribbon-type electron beams. In the upper parts of the pictures one can see the annular and rectangular slots, respectively, in the diaphragm. At the cathode (in Fig. 5) one can clearly see a bright ring where there is ion bombardment of the cathode surface. The lower parts of the pictures show the anodes A, which are stainless steel plates of thickness 1.5 mm. As a result of bombardment by a beam of 25 keV electrons the anode shows, respectively, a glowing ring and a glowing rectangle, visible on the back side of the anode.

When there are several circular apertures in the diaphragm a multipencil beam is formed, as shown in the photograph of Fig. 7. In actual fact this case has three cell elements combined into a single diaphragm. Again, on the back side of the anode one can see three glowing spots formed by the three beams.

---

[1] G. G. Isaacs, Electron. Lett., 4, 405 (1968).

[2] I. V. Vagner, V. F. Grakun, and V. A. Gokhfel'd, Avtomat. Svarka, No. 12, 15 (1971).

[3] I. V. Vagner, E. I. Bolgov, V. F. Grakun, V. L. Gokhfel'd, and V. A. Kudlai, Avtomat. Svarka, No. 12, 27 (1972).

[4] L. G. Guseva, Tr. VÉI, No. 63, 17 (1958).

[5] J. Meek and J. Craggs, Electrical Breakdown in Gases [Russian translation], IL, Moscow (1960).

[6] I. N. Slivkov, V. I. Mikhailov, M. I. Sidorov, and A. I. Nastyukha, Electrical Breakdown Discharge in Vacuum [in Russian], Atomizdat, Moscow (1966).

Scattering of an electron beam in a straight dc turbulent plasma

Yu. P. Golovanov, L. P. Zakatov, A. S. Kingsep, and A. G. Plakhov

(Submitted July 7, 1973)
Zh. Tekh. Fiz., 44, 1675-1681 (August 1974)

A sharp reduction is observed in the current density of an external electron beam that moves through a turbulent straight dc discharge. It is established that the reduction in beam current density is correlated with radiation at twice the plasma frequency and with x-ray radiation bursts. The sharp reduction in current density is due to scattering of beam electrons by turbulent plasma fluctuations in localized regions. On the basis of theoretical estimates and controlled experiments the electron scattering is related to fluctuations associated with electron plasma oscillations.

A great deal of experimental work has been done on the transmission of electron beams through plasmas. Usually, plasma heating and beam retardation due to fluctuations excited by the beam itself are investigated. However, there is great interest, both for the physics of turbulent plasmas and for diagnostic purposes, in investigating the passage of a beam through a plasma with a high level of turbulence produced by some additional source of noise.

In the present paper we investigate the interaction between an external electron beam[6] and the plasma in a straight discharge, in which, as is well known,[1,2] the turbulence W/nT can reach 10^{-2}.

DESCRIPTION OF THE APPARATUS

A schematic diagram of the apparatus is given in Fig. 1. A fixed mirror field is produced by a system of coils 1 with a maximum field of 1 kOe at the center and 5 kOe at the mirrors. The mirror separation is 85 cm. A metal vacuum chamber 2 is evacuated to a residual pressure 10^{-6} torr. A plasma injector 3, set up at the axis of the apparatus near one of the mirrors, fills the trap with a plasma with a density up to $(1\text{-}2)\cdot 10^{12}$ cm^{-3}.

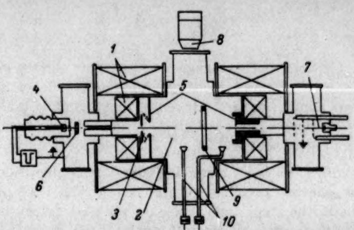

Fig. 1. Experimental arrangement. 1) Magnet coils; 2) vacuum chamber; 3) plasma injector; 4) electron gun; 5) discharge gap electrodes; 6) Rogowski loop; 7) multigrid analyzer; 8) x-ray detector; 9) diamagnetic probe; 10) microwave detector.

The plasma injector has an aperture on the axis for admitting the external electron beam produced by the electron gun 4. The beam parameters are as follows: current up to 10 A, energy 20-40 keV, and pulse length 130 μsec. The direct current is generated by a 0.5 μF capacitor bank, charged to 5-7 kV, and applied to a column of previously prepared plasma. The electrodes 5 are 55 cm apart, and the electrode diameter is 4.5 cm. Under typical conditions the discharge current is 500-800 A with a pulse length of 4-5 μsec. The electron beam and the plasma injector operate simultaneously, and the start of the dc discharge is delayed for 50-70 μsec. The electron beam current at the entrance to the trap is measured by a Rogowski loop 6 placed between the gun anode and the drift channel.

A high-voltage electrode 5 has a 1-mm diameter aperture, through which the central portion of the electron beam falls on a multigrid probe 7 set up behind the mirror. The x-ray bremsstrahlung from targets located a certain distance from the beam is recorded by scintillation counters 8. The counters are enclosed in lead containers, and the radiation from the tungsten-needle targets is incident on the crystals only through narrow, long channels in the lead collimators. The intensity of radiation from the plasma volume is several orders of magnitude smaller, and therefore is not recorded. If a needle is removed from the field of view of a collimator the signal from the corresponding counter disappears completely. The plasma energy is measured by a diamagnetic probe 9. High-frequency electromagnetic oscillations excited in the plasma are picked up by two horns, one set up at the center of the chamber and the other to the side, 20 cm from the center. The dc current is recorded by the Rogowski loop, and the voltage across the discharge is measured by a low-inductance resistance divider.

EXPERIMENTAL RESULTS

Both transmission of current and passage of an external electron beam through a cold plasma heat the plasma. The heating is observed by noting the increase in plasma diamagnetism due to the separate and combined effect of the electron beam and the discharge current. An oscilloscope trace of the diamagnetic signal is given in Fig. 2a for the case of plasma heating by a direct current. The magnitude of this signal when the current is terminated, when there is no paramagnetic effect, indicates that the plasma pressure is ~ 10^{15} eV/cm^3. An oscilloscope trace of the signal from the diamagnetic probe is given in Fig.

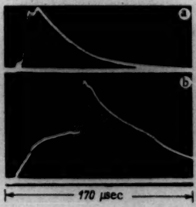

Fig. 2. Oscilloscope traces of diamagnetic signals. a) Direct discharge alone; b) electron beam and direct discharge.

2b for the case of combined heating by an electron beam and dc current. The cold plasma and the electron beam are injected simultaneously. The plasma is heated by the beam to a certain steady-state level; then the dc discharge is switched on, and the thermal energy of the plasma increases rapidly due to transmission of the current. The increase in the diamagnetic signal is roughly on the same scale as for one electron beam. The results given below refer to these operating conditions, when plasma turbulence increases greatly due to transmission of the dc current through the plasma. The increase in turbulence above the level produced by the beam itself sharply modifies the transmission of the electron beam through the plasma. Numerous experiments on the passage of monochromatic electron beams through a cold plasma in a magnetic field indicate that the longitudinal velocities of the beams are greatly spread out and the beams lose a significant portion (up to 70%) of their energy in generation of oscillations and heating the plasma. Also, longitudinal beam energy is effectively connected to transverse energy. However, the radius of the beam at exit from the plasma increases by very little (by a Larmor radius), and the beam current density at the entrance of the analyzer undergoes essentially no change.[3,4]

An electron beam injected into a turbulent plasma does not penetrate the plasma during certain stages of the discharge. Experimentally, this is observed from the sharp decrease in beam current density at the entrance to the multigrid analyzer as compared with the density at times corresponding to beam transmission. The nature of the phenomenon is illustrated in Fig. 3, which gives oscilloscope traces of a direct-discharge and beam current. The number of dips in the beam current (current cutoffs) depends, to a considerable degree, on the nature of the discharge current, but the dips themselves are observed under any discharge conditions and are independent of polarity at the electrodes. It is quite clear that under strongly oscillatory (inductive) conditions (Fig. 3) the current cutoffs are correlated with points at which the discharge-current goes through zero (voltage peaks across the electrodes) and thus, with electric fields in the plasma. The observed beam cutoffs are due either to scattering of beam particles by fluctuations in the turbulent plasma or deflection of the beam as a whole in the azimuthal electric fields associated with the current-convective instability.

Different stages of the electron beam in the turbulent discharge can be investigated using x-ray analysis. For this purpose a tungsten needle is placed in the center of the apparatus along the radius of the vacuum chamber; the distance of the point of the needle from the boundary of the beam is roughly equal to the beam radius. Control experiments indicate that bremsstrahlung from the needle is absent if only the electron beam or only the discharge current is transmitted through the plasma. With combined beam and discharge-current transmission, intense surges of x-ray radiation are observed from the needle with the same instrumental sensitivity. The radiation bursts occur at times that are correlated with current cutoffs (Fig. 4). The x-ray bursts are due to electrons scattered from the beam by turbulent fields excited in the plasma by the direct current. Proof that scattering of beam electrons occurs rather than deflection of the beam as a whole is provided by experiments which simultaneously record x-ray radiation from two needle targets set up around the beam at a distance from each other that is more than twice the beam diameter. Figure 5 illustrates the good correlation between the x-ray radiation from both targets. It is clear from the traces in Fig. 4 that every cutoff of the beam current is not accompanied by an x-ray burst. The discrepancy between the number of current cutoffs and the number of bursts can be explained if it is assumed that the beam is scattered in local regions with a potential jump whose length is less than the length of the apparatus. The electron beam penetrates through the entire length of the apparatus and unavoidably passes through all the regions where scattering occurs; therefore, the number of current cutoffs is always determined by the stages of the transmission of the discharge current. The number of x-ray bursts recorded only from the center of the apparatus is two times smaller on the average since the bursts from the localized

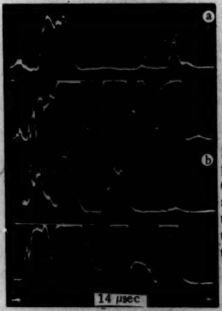

Fig. 4. Traces of x-ray radiation (upper curves and trace of beam current (lower curves) for two typical experiments, (a) and (b). The disparity between the number of x-ray bursts and the number of current cutoffs indicates the presence of local regions.

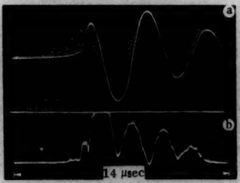

Fig. 3. a) Trace of a direct-discharge current; b) electron beam current. Cutoffs of the beam current correspond to certain stages of current transmission.

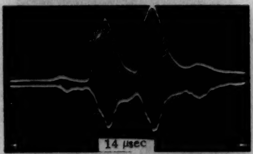

Fig. 5. Traces of x-ray radiation from two targets set up around the beam at different azimuths. The distance between the targets is greater than twice the beam diameter.

noise regions to the right of the center along the beam path will not be recorded since back-scattering of electrons has a low probability, and obviously does not occur.

Microwave radiation at twice the plasma frequency ($2\omega_{pe}$) is recorded to enable us to understand the nature of the fluctuations which scatter the beam electrons. It turns out that radiation at frequency $2\omega_{pe}$ occurs only at times of beam current cutoff, and its intensity is more than an order of magnitude higher than the radiation due to the electron beam itself. Radiation at twice the plasma frequency indicates electron plasma oscillations are excited during certain stages of the direct current flow. The traces in Fig. 6 are taken from two different experiments and indicate that the peaks of microwave radiation actually are correlated with dips in the beam current. As in the x-ray experiments, the number of peaks observed in the microwave radiation picked up by the horn at the center of the apparatus is always smaller than the number of beam current cutoffs. This is an indication that the beam is not scattered along the entire length of the apparatus, but in fairly narrow regions, where the noise is localized. To check the existence of such localized regions the microwave radiation is measured by two horns placed 20 cm apart along the length of the apparatus. In Fig. 7, the traces of microwave radiation are obtained by simultaneous pickups of the two antennas in two different experiments. In Fig. 7 a, the upper trace shows the radiation peaks obtained from the center antenna, and the lower trace is from the side antenna. The peaks in both traces are correlated well and correspond to radiation from regions in the field of view of both antennas. In the upper trace in Fig. 7b, the radiation peaks are farther apart in time, and in the lower trace only one peak is observed. This is possible only when the localized noise regions occur at random points along the length of the apparatus; these points are not always in the field of view of one horn or the other and are even less likely to be in the field of view of both horns simultaneously.

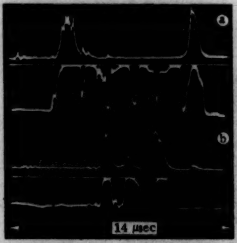

Fig. 6. Radiation from the plasma at twice the plasma frequency (upper traces) and beam current (lower traces) for two typical experiments (a) and (b).

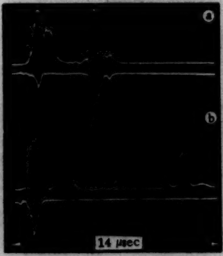

Fig. 7. Radiation signals at twice the plasma frequency from different places in the apparatus for two typical experiments (a) and (b), demonstrating the local nature of the scattering effect.

Intense beams of runaway electrons are not observed in these experiments. However, electron beams with negligible density (below 0.5 A/cm^2) escape from the turbulent plasma with the appropriate electrode when the external electron beam passes through the plasma without scattering. When the external beam is effectively scattered the current of runaway electrons vanishes.

DISCUSSION OF RESULTS

The scattering of beam electrons observed in this dc-discharge can be ascribed to interactions either with ion-acoustic fluctuations or with electron plasma oscillations, which are generated during certain stages of the development of current instability.[5] In both cases the particle velocity of the probe beam is much larger than the characteristic phase velocity of the fluctuations. For ion acoustic waves this is obvious; in regard to electron plasma oscillations the energy of the exciting particles in the discharge cannot exceed the voltage applied to the discharge gap, so that we obtain

$$\left(\frac{\omega}{kv_b}\right)^2 \leqslant \frac{eU}{\varepsilon} \ll 1, \tag{1}$$

where v_b is the velocity, ε is the beam energy, and U is the voltage across the electrodes.

Under condition (1), relaxation of the beam only leads to a spread with respect to the transverse velocities,[6] which are governed by

$$\left.\begin{aligned} &\langle v_\perp^2\rangle \sim D(v_b)t,\\ &D(v_b) = 4\pi^2\frac{e^2}{m^2v_b}\int W_k\delta(\omega - kv)v\,dk \simeq \omega_{pe}\frac{W}{nT_e}\frac{v_b^2}{\langle k\rangle r_D}\left(\frac{v_{Te}}{v_b}\right)^3, \end{aligned}\right\} \tag{2}$$

where W is the integrated fluctuation density, $\langle k\rangle$ is the characteristic wave number, and r_D is the Debye radius. Accordingly, the Langmuir radius of the beam particles is changed at the exit from the discharge gap:

$$\rho_b^2 \sim \rho_0^2\frac{W}{nT_e\langle k\rangle r_D}\left(\frac{v_{Te}}{v_b}\right)^3\frac{L}{v_b}\omega_{pe}, \tag{3}$$

where L is the length of the region in which the noise is localized (in particular, this can be the length of the apparatus), and $\rho_0 = v_b/\omega_{He}$ is of the order of 1 cm under our conditions. Since the beam diameter is of the same order of magnitude, it can be seen that the current density of the beam (and, thus, the current to the analyzer) decreases by one order of magnitude if the transverse energy of the beam particles is the same order of magnitude as the longitudinal energy.

It is reasonable to assume that the scattering of the beam particles is the result of electron plasma noise, which, as we have shown, is localized in regions with dimensions smaller than the length of the apparatus. Earlier,[4] we have established that the relaxation of the beam becomes essentially non-one-dimensional (an angular spread appears) along the length of the apparatus even for an increase in the beam current from 10 to 20 A, i.e., roughly at double the noise energy.

In experiments on turbulent heating of a plasma, the level of electron plasma oscillations is an order of magnitude higher than the level generated by a beam with our parameters (under our conditions this is controlled by the power radiated at frequency $2\omega_{pe}$). This noise level is adequate for beam retardation in a length much smaller than the length of the apparatus.

It can be seen from (3), however, that with sufficient intensity, the ion-acoustic waves effectively retard the beam (it is true that in this case $\langle kr_D \rangle \sim 1$, thus increasing the scattering length). As a result, we estimate that under such conditions $\langle v_\perp^2 \rangle \sim v_b^2$. This can be done if we take into account that the effective scattering frequency of thermal plasma electrons by ion-acoustic noise is

$$\nu_{\text{eff}} \sim \omega_{pe} \frac{W_s}{nT_e} \frac{1}{\langle k \rangle r_D}. \tag{4}$$

On the other hand, we have

$$eE = m\nu_{\text{eff}} \frac{j}{ne}; \quad \nu_{\text{eff}} \leqslant \frac{eE}{mc_s} \sim \frac{eU}{mc_s L}. \tag{5}$$

It is evident from Eqs. (3)-(5) that

$$\frac{\langle v_\perp^2 \rangle}{v_b^2} \sim \frac{T_e}{\varepsilon} \frac{eU}{\varepsilon} \sqrt{\frac{M}{m}}. \tag{6}$$

In order to exclude scattering by ion-acoustic waves a control experiment has been carried out with 40-keV beam energies and a 2 kV direct discharge. We estimate the upper limit of the electron temperature in the direct discharge is eU. Then the retardation length for ion-acoustic waves is 10 times larger than the dimensions of the potential drop region of the direct discharge [on the right side of (6), this is of the order of 1/10]. Nevertheless, oscilloscope traces of the beam current in this case do not differ significantly from those of Fig. 3. This result indicates that the beam retardation in the turbulent plasma is due to electron plasma oscillations.

Thus, our experiments have established that an energetic beam of electrons is effectively scattered in a turbulent direct-discharge plasma. Retardation of the beam is the result of the interaction with electron plasma oscillations in localized regions.

The authors thank L. I. Rudakov for valuable discussions.

---

[1] Yu. G. Kalinin, D. N. Lin, V. D. Pyutov, and V. A. Skoryupin, Zh. Eksp. Teor. Fiz., 55, 115 (1968) [Sov. Phys. – JETP, 28, 61 (1969)].

[2] E. K. Zavoiskii, Yu. G. Kalinin, V. A. Skoryupin, V. V. Shapkin, and G. V. Sholin, Dokl. Akad. Nauk SSSR, 194, 55 (1970) [Sov. Phys. – Dokl., 15, 823 (1971)].

[3] I. Cabral, H. I. Hopman, F. G. Insinger, and W. Ott, Third Conference on Plasma Physics and Controlled Nuclear Fusion, Novosibirsk, August, 1968.

[4] L. P. Zakatov and A. G. Plakhov, Zh. Eksp. Teor. Fiz., 60, 588 (1971) [Sov. Phys. – JETP, 33, 320 (1971)].

[5] Yu. G. Kalinin, D. N. Lin, L. I. Rudakov, V. D. Ryutov, and V. A. Skoryupin, Zh. Eksp. Teor. Fiz., 59, 1056 (1970) [Sov. Phys. – JETP, 32, 573 (1971)].

[6] L. I. Rudakov and L. V. Korablev, Zh. Eksp. Teor. Fiz., 50, 220 (1966) [Sov. Phys. – JETP, 23, 145 (1966)].

Effect of loss on electron avalanches in optical breakdown

V. I. Fisher

I. I. Mechnikov Odessa State University

(Submitted May 15, 1973; resubmitted January 17, 1974)
Zh. Tekh. Fiz., 44, 1682-1686 (August 1974)

The experimental functional dependence of the threshold for optical breakdown of inert gases on the pressure and characteristic dimensions of the focal region can be explained by an avalanche-ionization mechanism that takes elastic loss and diffusion loss into account.

The threshold for optical breakdown is a function of the parameters of the laser beam (the divergence and frequency of the radiation, the pulse length, and the diameter of the focal spot) and of the gas pressure and impurity concentration. The mass and excitation energy of the gas atoms are of great importance. Excitation of electronic levels can retard or accelerate the breakdown, depending on the level structure of the particular gas and on the radiation intensity. Optical breakdown has been studied in many previous experiments, but the results are compatible only to an order of magnitude because of the differences among the radiation parameters and because of the inadequate methods used to determine the dimensions of the breakdown region.

In this note we describe the processes which occur in the focal region as the degree of ionization increases from the initiating level to the breakdown level; the latter, according to the results of ref. 1, is 10^{-3} for helium and argon.

The electron temperature in the avalanche is described by

$$\frac{3}{2}n(\mathbf{r},t)\frac{\partial T(\mathbf{r},t)}{\partial t}=\frac{4\pi e^2}{mc}n(\mathbf{r},t)\frac{\nu}{\omega^2+\nu^2}q(\mathbf{r},t)-\frac{3m}{M}\nu n(\mathbf{r},t)T(\mathbf{r},t)-I\left(\frac{\partial n(\mathbf{r},t)}{\partial t}\right)_i. \tag{1}$$

Here, e and m are the charge and mass of the electron, n and N are the densities of electrons and atoms, c is the speed of light, ω and $q(r, t)$ are the frequency and intensity of the radiation, I and M are the first excitation energy and mass of the atom, $\nu = \langle\sigma^y v\rangle N$ is the frequency of elastic electron–atom collisions, v is the electron velocity, and σ^y is the cross section for elastic collisions. In the calculation of $\langle\sigma^y v\rangle$ we use the experimental cross sections $\sigma^y(v)$ of ref. 2. The light-absorption coefficient is corrected for stimulated emission.[3] Elastic energy loss, which becomes important at high pressures, is taken into account. The ionization rate $(\partial n/\partial t)_i$ is assumed to be equal to the rate at which the lower-lying atomic levels are excited by electron impact. Instantaneous photoionization of the excited levels is assumed for helium on the basis of the results of ref. 4. This ionization mechanism is also adopted for the argon calculations. In this case we can write the ionization rate as

$$\left(\frac{\partial n}{\partial t}\right)_i=\langle\sigma^*(v)v\rangle Nn.$$

In averaging we use the excitation cross sections for the lower-lying levels, $\sigma^*(v)$, given in ref. 3.

When the electron avalanche in the radiation field is initiated the temperature rise is terminated, since the absorbed radiation energy is expended completely in ionization and in the replenishment of elastic loss. This situation obtains until Coulomb collisons increase ν considerably, i.e., up to a burst. We can then determine the electron temperature during the avalanche by setting the right-side of Eq. (1) equal to zero. The temperature turns out to be a weak function of the radiation intensity. Over the range of threshold intensities which have been observed experimentally we can assume the electron temperature to be 4 eV in helium and 3 eV in argon.

Electron diffusion from the focal region reduces the growth rate of the electron density:

$$\frac{\partial n}{\partial t}=\left(\frac{\partial n}{\partial t}\right)_i+D\Delta n. \tag{2}$$

Here, D is the free-diffusion coefficient of the electrons. By "focal region" we mean the volume of a cylinder whose diameter is $d = f\alpha$ and whose height is $l = (\sqrt{2}-1)f^2\alpha/A$, where f is the focal length of the lens, α is the divergence of the radiation, and A is the diameter of the laser beam. In this case the characteristic diffusion length Λ satisfies

$$\frac{1}{\Lambda^2}=\left(\frac{4.8}{d}\right)^2+\left(\frac{\pi}{l}\right)^2.$$

Recombination is neglected since the breakdown sets in at a small degree of ionization, in which case

$$\left(\frac{\partial n}{\partial t}\right)_i\gg\left(\frac{\partial n}{\partial t}\right)_{\text{recomb}}\sim n^2.$$

The radiation of a single-mode laser has a Gaussian intensity distribution in the focal plane:

$$q(r,t)=q(0,t)\exp\left(-\frac{r^2}{r_0^2}\right).$$

Here, r_0 is the characteristic Gaussian radius, which governs the diameter of the focal region. We neglect the intensity distribution along the beam axis, a simplification which is valid when the loss due to diffusion along the axis is much smaller than that in the transverse direction:

$$\left(\frac{4.8l}{\pi d}\right)^2=\left[\frac{4.8(\sqrt{2}-1)f}{\pi A}\right]^2\gg1,$$

i.e., for $f \gg 3$. Using (1) and the constancy of the temperature in the avalanche, we can write the electron-

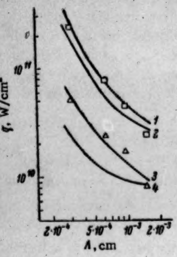

Fig. 1. Threshold intensity for breakdown in argon as a function of the diffusion length. Pressure p, atm: 1, 2) 3.7; 3,4) 11.7. A single-mode ruby laser is used. 1,3) Equation (3); 2,4) Eq. (4b).

diffusion equation for the case of a Gaussian intensity distribution as

$$\frac{\partial n(r,\ t)}{\partial t}=D\Delta n(r,\ t)+\frac{4\pi e^2}{mcI}\frac{\nu n(r,\ t)}{\omega^2+\nu^2}q(0,\ t)\exp\left(-\frac{r^2}{r_0^2}\right)-\frac{3mT\nu}{MI}n(r,\ t). \tag{3}$$

We seek a solution in the form

$$n(r,\ t)=e^{t/\tau}\varphi(r).$$

Substitution into (3) yields an equation for $\varphi(r)$:

$$D\Delta\varphi(r)+\left(\frac{4\pi e^2}{mcI}\frac{\nu}{\omega^2+\nu^2}q(0,\ t)\exp\left(-\frac{r^2}{r_0^2}\right)-\frac{3mT}{MI}\nu-\tau^{-1}\right)\varphi(r)=0,$$

which is solved numerically by a variational method with the test function

$$\varphi(r)=2e^{-\gamma r}-e^{-2\gamma r},$$

which displays the correct behavior at large r and has a vanishing derivative at r = 0.

Figure 1 compares the results of the numerical calculation with experimental results.[5] The threshold intensity is seen to be a function of the diffusion length in argon. In the corresponding experiments a single-mode ruby laser with a pulse half-width of 10^{-8} sec is used.

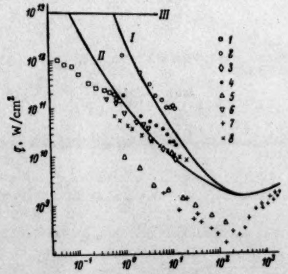

Fig. 2. Threshold intensity for breakdown in argon as a function of the pressure. I,II) Equation (4b) $\tau = 10^{-9}$ Λ, cm: I) $2.5\cdot10^{-4}$; II) $2\cdot10^{-3}$; III) threshold for multiphoton breakdown.[10] Singlemode lasers: 1) ref. 1; 2,3) ref. 5. Multimode lasers: 4) ref. 5; 5) ref. 6; 6) ref. 7; 7) ref. 8; 8) ref. 9. Λ, cm: 1) $\sim 2\cdot10^{-3}$; 2) $2.5\cdot10^{-4}$; 3) $1.5\cdot10^{-3}$; 4) $1.58\cdot10^{-3}$; 5) $2.4\cdot10^{-3}$; 6) $\sim 10^{-3}$; 8) $\approx 2\cdot10^{-3}$; 7) d $\sim 10^{-2}$.

If the electron density in the focal region, $\alpha_e = n/N$ increases from the seed value $\alpha_e^0 \le 10^{-7}$ to the breakdown value $\alpha^* \sim 10^{-3}$ in the pulse length τ, the characteristic time for avalanche development, τ_l, can be determined from the breakdown condition

$$\tau^{-1}=\tau_l^{-1}\ln\frac{n^*}{n^0}.$$

For a rectangular pulse, τ_l is the pulse length; for a triangular pulse, it is the half-width. In the latter case the radiation intensity near the maximum must be a slowly varying function of the time:

$$\sqrt{\frac{\partial^2 q(0,\ t_{\max})}{\partial t^2}\Big/q(0,\ t_{\max})}\leqslant\tau^{-1}.$$

Here, $q(0, t_{\max}) = q_{\max}$ is the maximum value of q(r, t).

The radiation intensity has a complicated spatial profile and is characterized by the quantity $\bar{q}$ averaged over the area. We assume the intensity to be equal to $\bar{q}$ within the focal region and negligibly small elsewhere.

Since the results of the various experiments[1,5-9] agree only in order of magnitude, for simplicity we replace Δn by $-n/\Lambda^2$ in Eq. (3) [the satisfactory agreement between the results found in this manner with the experimental results and with the results of the numerical solution of Eq. (3) (Fig. 1) is evidence in favor of this simplification]:

$$\frac{n(r,\ t)}{\tau}=-\frac{D}{\Lambda^2}n(r,\ t)+\frac{4\pi e^2}{mcI}\frac{\nu n(r,\ t)}{\omega^2+\nu^2}\bar{q}-\frac{3m}{MI}\nu Tn(r,\ t).$$

In the analysis it is more convenient to rewrite this equation as

$$\bar{q}=\frac{mc\omega^2I}{4\pi e^2\nu}\left(1+\frac{\nu^2}{\omega^2}\right)\left(\tau^{-1}+\frac{3m}{M}\frac{T}{I}\nu+\frac{D}{\Lambda^2}\right). \tag{4}$$

Substitution of the numerical values into Eq. (4) yields

$$\bar{q}=\frac{112}{p}(1+5.4\cdot10^{-7}p^2)\left(\tau^{-1}+1.64\cdot10^8p+\frac{3\cdot10^3}{p\Lambda^2}\right)\text{W/cm}^2 \tag{4a}$$

for helium and

$$\bar{q}=\frac{74.4}{p}(1+4.06\cdot10^{-7}p^2)\left(\tau^{-1}+1.85\cdot10^7p+\frac{2.6\cdot10^3}{p\Lambda^2}\right)\text{W/cm}^2 \tag{4b}$$

for argon. The pressure is measured in atmospheres and the diffusion length in centimeters.

Figures 2 and 3 compare the functional dependence of the threshold intensity on pressure with the experimental results of refs. 1,5-9. A single-mode ruby laser was used in certain experiments,[1,5] and a multimode laser in others.[6-9] The pulse shapes and half-widths, the impurity concentrations, the focal volumes, and the methods used to determine them differ in these experiments. In ref.

8 the diameter of the focal volume is determined by burning holes in a thin foil, but the length is not measured. These holes result from evaporation, which is a linear effect in q(r), while optical breakdown, a nonlinear effect, is more sensitive to the decrease in q(r) with distance from the center, so that the diameter of the breakdown region is lower. If we assume the error to be a factor of 2, we conclude that the intensity is lower by a factor of 4 and that its corrected values would agree with the theoretical values for argon, since the curves are identical over the entire pressure range. Surprisingly, the results of ref. 6, which, in the case of helium, agree with the results of refs. 1,5, 7, and 9 and with the theoretical results, are severalfold different from the results for argon in the work cited. The results of ref. 8 for helium are also too low.

At high pressures the threshold is governed by elastic energy loss alone and is independent of the diffusion length. The corresponding pressure range for helium is $p \geqslant 100$ atm, and that for argon, whose atoms are 10 times as heavy, is $p \geqslant 1000$ atm. As the pressure is reduced the curves corresponding to different values of Λ diverge more markedly, implying an increased role for diffusion loss. At comparatively large values of $p \leqslant 1$ for argon in the range 1-10 atm the threshold is governed primarily by the ionization rate, but for the more typical values of Λ and in the center of the pressure range all loss channels must be taken into account.

Multiphoton ionization by a picosecond pulse occurs at a radiation intensity of 10^{13} W/cm^2 in argon and $6 \cdot 10^{13}$ W/cm^2 in helium,[10] so an avalanche cannot occur for small values of Λ at low pressures. For example, with $\Lambda = 2.5 \cdot 10^{-4}$ cm and at a pressure of 0.7 atm, an intensity of 10^{13} W/cm^2 is required for avalanche breakdown in argon, but this intensity causes multiphoton ionization, rather than avalanche ionization. Accordingly, large focal volumes, i.e., long-focal length lenses, are required to study electron avalanches at low pressures. Otherwise, the breakdown threshold can be a multiphoton threshold.

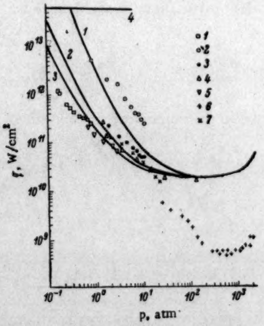

Fig. 3. Threshold intensity for breakdown in helium as a function of the pressure. I-III) Equation (4a). $\tau = 10^{-9}$, Λ, cm: I) $2.5 \cdot 10^{-4}$; II) 10^{-3}; III) $2 \cdot 10^{-3}$; IV) threshold for multiphoton breakdown.[10] Single-mode lasers: 1) ref. 1; 2) ref. 5. Multimode lasers: 3) ref. 5; 4) ref. 6; 5) ref. 7; 6) ref. 8; 7) ref. 9. Λ, cm: 1) $\sim 2 \cdot 10^{-3}$; 2) $2.5 \cdot 10^{-4}$; 3) $1.58 \cdot 10^{-3}$; 4) $2.4 \cdot 10^{-3}$; 5) $\sim 10^{-3}$; 7) $\approx 2 \cdot 10^{-3}$; 6) d $\sim 10^{-2}$.

Figure 1 shows the breakdown threshold as a function of the diffusion length according to Eq. (4b). The agreement with experiment is satisfactory, but poorer than that found when the pulse shape is taken into account [Eq. (3)].

The functional dependence for the breakdown threshold on the diffusion length at a pressure of 8.15 atm observed in ref. 6 cannot be attributed to free electron diffusion from the over-all focal volume. A multimode neodymium-glass laser is used in these experiments and the spatial structure of the radiation has not been studied. It is reasonable to assume that there are local radiation inhomogeneities a few microns in size with an intensity greater than the average intensity by a factor of 10 or more in the focal plane; such inhomogeneities have been observed in ruby.[11] If the avalanche develops experimentally in a cylindrical volume with a diameter equal to 0.6–0.8 of the diameter of the focal spot, and if the intensity exceeds the average intensity by a factor of 5-10, Eq. (4) can explain the functional dependence of the breakdown threshold on the diffusion length observed in ref. 6 for helium and argon. It should be noted that the actual shape of the local inhomogeneity is not cylindrical, and we can only state that the assumption of a local nature for the breakdown caused by the radiation of a multimode laser yields plausible estimates of the threshold. In the case of the single-mode laser[5] taking account of free electron diffusion from the focal volume leads to good agreement with the experimental results.

The author thanks S. I. Anisimov for useful discussion; D. I. Polishchuk for assistance, and É. I. Vitkin for the numerical calculations.

---

[1] M. Young and M. Hercher, J. Appl. Phys., 38, 4393 (1967).

[2] D. E. Golden and H. W. Bandel, Phys. Rev., 138, 14 (1965); Phys. Rev., 149, 58 (1966).

[3] Ya. B. Zel'dovich and Yu. P. Raizer, Physics of Shock Waves [in Russian], Izd. Nauka, Moscow (1966).

[4] J. Bakos, J. Kantor, and A. Kiss, ZhETF Pis. Red., 12, 371 (1970) [JETP Lett., 12, 255 (1970)].

[5] A. I. Alcock, C. DeMichelis, and M. C. Richardson, IEEE J. Quant. Electron., 6, 622 (1970).

[6] A. G. Haught, R. G. Meyer, and D. S. Smith, Physics of Quantum Electronics, P. L. Kelley, et al., (eds.), McGraw-Hill, New York (1966), p. 509.

[7] R. G. Tomlinson, E. K. Damon, and H. T. Buscher, Physics of Quantum Electronics, P. L. Kelley, et al. (eds.), McGraw-Hill, New York (1966), p. 520.

[8] D. H. Gill and A. A. Dougal, Phys. Rev. Lett., 15, 845 (1965).

[9] F. Morgan, L. R. Evans, and C. Grey Morgan, J. Phys. D: Appl. Phys., 4, 225 (1971).

[10] L. K. Krasyuk, P. P. Pashinin, and A. M. Prokhorov, Zh. Eksp. Teor. Fiz., 58, 1606 (1970) [Sov. Phys.-JETP, 31, 860 (1970)].

[11] T. M. Barkhudarova, G. S. Voronov, V. M. Gorbunkov, and N. B. Delone, Zh. Eksp. Teor. Fiz., 49, 386 (1965) [Sov. Phys.-JETP, 22, 269 (1966)].

Power spectrum of potential fluctuations in a moving magnetoactive plasma

V. M. Kostin

Institute of Terrestrial Magnetism, Ionosphere, and Radiowave Propagation,
Academy of Sciences of the USSR, Moscow

(Submitted July 2, 1973; resubmitted February 11, 1974)
Zh. Tekh. Fiz., 44, 1687-1692 (August 1974)

The thermal fluctuations of the potential between two moving points in a plasma are studied. The singularities of the power spectrum at the lower and upper hybrid frequencies are analyzed in detail.

There is interest at the present time in measuring such parameters of the near-earth plasma as the ion and electron temperatures and densities by means of a correlation analysis of the signals from two probes located at two different points in space.[1] To this end Grabowski[1,2] has calculated the spectral density of the square of the potential difference between two spatially-separated points in a plasma in the absence of an external magnetic field. A calculation of this kind has been carried out by the present author[3] for the case of a magnetoactive plasma. However, in the analysis of experiments performed in near-earth plasma, allowance sometimes has to be made for the relative motion of the plasma.[4] In the present paper the potential correlation function in a uniformly moving magnetoactive plasma is calculated for the case $V \ll v_e$, which is usually satisfied in near-earth plasma.[4] The plasma is considered in the collisionless approximation, and the particles are assumed to have a Maxwellian distribution.

The fluctuation field of the charges in the plasma creates between two points a potential difference given by

$$U(t)=\int_0^l E_\parallel dx,$$

where $E_\parallel$ is the longitudinal component of the electric field. Since the integral is independent of the path, the integration in this expression can be taken along the straight line l joining these points. The mean value of U(t) is zero, and the spectral density over positive frequencies of the potential-difference correlation function is calculated from the expression

$$\langle U^2\rangle_\omega=2\int_0^l dx_1\int_0^l dx_2\int d\mathbf{k}\,\langle E_\parallel^{(1)}E_\parallel^{*(2)}\rangle_{\omega,\mathbf{k}}\exp i\mathbf{k}(\mathbf{x}_1-\mathbf{x}_2). \quad (1)$$

Here, the angle brackets ⟨⟩ signify statistical averaging and the indices ω and k denote, respectively, time and space Fourier components. Below the angle brackets will be omitted from $\langle U^2\rangle_\omega$. We note that expressions similar to (1) arise in the calculation of the spectral density of the noise emf of an antenna immersed in a plasma.[5-7] The spectral density of the correlation function $\langle E_\parallel E_\parallel^*\rangle_{\omega,\mathbf{k}}$ is given by

$$\langle E_\parallel E_\parallel^*\rangle_{\omega,\mathbf{k}}=\frac{1}{2\pi^3}\frac{k_z^2}{k^2}\frac{T}{\omega-\mathbf{kV}}\operatorname{Im}\frac{1}{\varepsilon^*(\omega-\mathbf{kV},\ \mathbf{k})}. \quad (2)$$

Expression (2) represents the correlation function for potential fields in a plasma with a Doppler frequency shift.[8] As is well known, the dielectric constant has the following form in the general case:

$$\varepsilon(\omega-\mathbf{kV},\ \mathbf{k})=1+\sum_{j,n}\frac{\exp\left(-\frac{k_\perp^2\rho_j^2}{2}\right)I_n\left(\frac{k_\perp^2\rho_j^2}{2}\right)}{k^2D^2}\times\left(1+i\sqrt{\pi}\frac{\omega-\mathbf{kV}}{k_zv_j}W\left(\frac{\omega-\mathbf{kV}-n\omega_{Bj}}{k_zv_j}\right)\right), \quad (3)$$

where W(x) is the Cramp function, V is the relative velocity of the plasma, $D=\sqrt{T/4\pi e^2N}$ is the Debye radius, N is the particle density, $\rho_j=v_j/\omega_{Bj}$ is the Larmor radius, $v_j=\sqrt{2T/m_j}$ is the thermal velocity, ω_{Bj} is the cyclotron frequency, $\omega_{0j}=\sqrt{4\pi Ne^2/m_j}$ is the plasma frequency, and $k_{\perp,z}$ denote the components of the wave vector transverse and parallel to the external magnetic field B. In (3) the summation extends over the species of particles j and over the index n.

It is readily shown, following ref. 3, that for points uniformly moving relative to the plasma the mean square of the potential difference, i.e., the integral of expression (1), does not vary over frequency. In a similar manner as for stationary points,[3] we obtain

$$U^2=\frac{2\sqrt{2}T}{D}\left\{1-\frac{D}{\sqrt{2}l}\left[1-\exp\left(-\frac{\sqrt{2}l}{D}\right)\right]\right\}.$$

This means that the motion has the effect of redistributing the spectral density U_ω^2 over the frequency spectrum. Clearly, in the evaluation of (1) the Doppler frequency shift in (2) must lead to a smoothing of the singularities of U_ω^2 occurring in the case of stationary points[3] which are caused by fluctuations at the characteristic frequencies of oscillation of the plasma. The imaginary part of the dielectric constant is negligibly small, and the following relationship[8] can be used in the integration of (1):

$$\operatorname{Im}\frac{1}{\varepsilon(\omega,\ \mathbf{k})}=\pi\delta(\varepsilon(\omega,\ \mathbf{k})).$$

Performing the double integration in (1) with respect to x_1 and x_2 utilizing this expression, we obtain the contribution to the spectral density U_ω^2 from the fluctuating fields of the potential oscillations in an unperturbed plasma:

$$U_\omega^2=\frac{2T}{\pi^2}\int\frac{1-\cos(k_zl\cos\theta+k_\perp l\sin\theta\cos\psi)}{\omega-\mathbf{kV}}\delta(k^2\varepsilon(\omega-\mathbf{kV},\ \mathbf{k}))\,d\mathbf{k}, \quad (4)$$

where θ is the angle between the vector l and the magnetic field B, and ψ is the angle between the projections of k and l on a plane perpendicular to B. Let us now examine how the motion affects the spectrum U_ω^2.

Slow extraordinary wave. The power spectrum of the potential[3] has a sharp maximum at the upper hybrid frequency $\omega_u = \sqrt{\omega_{0e}^2 + \omega_{Be}^2}$. The dielectric constant (3) can be taken in the cold-plasma approximation. The condition $V \ll v_e$ usually holds[4] in the near-earth plasma. Accordingly, the validity of the expansion of (3) in $\omega/k_z v_e < 1$ and $k_\perp \rho_{e,i} < 1$, in which the approximation used below for $\varepsilon(\omega, k)$ is obtained, is not violated by the motion of the body. Near ω_u we have

$$\varepsilon(\omega - \mathbf{kV}, \mathbf{k}) = \frac{k_z^2}{k^2}\frac{\omega_{Be}^2}{\omega_u^2} - \frac{k_\perp^2}{k^2}\frac{2\omega_u(\mathbf{kV} - \Delta\omega)}{\omega_{0e}^2}, \tag{5}$$

where $\Delta\omega = \omega - \omega_u$. With this value of $\varepsilon(\omega, k)$ expression (4) is readily integrated with respect to k_z, and

$$U_\omega^2 = \frac{2T}{\pi^2}\frac{\omega_u}{\omega_{Be}^2}\int \frac{1 - \cos(k_\perp^2 a l V_z \cos\theta + k_\perp l \sin\theta\cos\psi)\ \cos\left(l\cos\theta\sqrt{(k_\perp^2 a V_z)^2 + 2k_\perp^2 a(k_\perp V_\perp\cos\varphi - \Delta\omega)}\right)}{\sqrt{(k_\perp^2 a V_z)^2 + 2k_\perp^2 a(k_\perp V_\perp \cos\varphi - \Delta\omega)}}\, k_\perp dk_\perp d\varphi. \tag{6}$$

Here, φ is the angle between the projections of k and V on a plane perpendicular to B. For convenience we use the notation $a = \omega_u^3/\omega_{0e}^2\omega_{Be}^2$.

The oscillating term in the numerator of (6) is important under certain conditions. The case $l \gg \rho_e$ is of most interest for the ionospheric plasma.[4] The characteristic range of integration in (6) with respect to $k_\perp$ will be ρ_e^{-1}. In this case the second term in the numerator of (6) must be taken into account only if $\theta < \rho_e/l$ and at frequencies $\Delta\omega_{\text{eff}}/\omega_u < \rho_e^2/l^2$. The sharp reduction of U_ω^2 in this case is due to the fact that the oscillations at frequency ω_u are transverse to the magnetic field while the vector distance between the points l is along B. The field associated with these oscillations is therefore not important. The effective Doppler frequency shift cannot be large either since oscillations with frequencies $\omega < \omega_u$ are not transverse to l and B.

Let us consider the evaluation of the main term in (6). We integrate with respect to $k_\perp$ from 0 to ρ_e^{-1} in the region in which oscillations exist, i.e., where the expression under the radical in the denominator of (6) is positive:

$$k_\perp \leqslant k_{\perp 1} = \frac{1}{aV_z^2}\left(V_\perp\cos\varphi - \sqrt{V_\perp^2\cos^2\varphi + 2a\Delta\omega V_z^2}\right);$$

$$k_\perp \geqslant k_{\perp 2} = \frac{1}{aV_z^2}\left(V_\perp\cos\varphi + \sqrt{V_\perp^2\cos^2\varphi + 2a\Delta\omega V_z^2}\right).$$

The limitations on the range of integration are connected with the transverse wave vectors: Near the hybrid frequency ω_u, the waves are almost perpendicular to B. Performing the integration with respect to $k_\perp$ we obtain

$$U_\omega^2 = \frac{4T}{\pi^2}\frac{\omega_u}{aV_z\omega_{Be}^2}$$

$$\times \int_0^{\arccos\max\left\{-1,\ \frac{\Delta\omega\rho_e}{V_\perp} - \frac{aV_z^2}{2\rho_e V_\perp}\right\}} d\varphi \ln\frac{aV_z^2 + \rho_e V_\perp\cos\varphi + V_z\sqrt{(aV_z)^2 + 2a\rho_e V_\perp\cos\varphi - 2a\rho_e^2\Delta\omega}}{\sqrt{V_\perp^2\cos^2\varphi + 2a\Delta\omega V_z^2}}. \tag{7}$$

The integrand in (7) is weakly dependent on the parameter of integration; accordingly it is useful to consider the two cases $V_z \gg V_\perp$ and $V_z \ll V_\perp$ for which the integral can be evaluated. More precisely, the criterion

$$\frac{aV_z^2}{\rho_e V_\perp} > 1 \tag{8}$$

signifies that the mean Doppler frequency shift in (5) due to the longitudinal motion is greater than the corresponding shift due to the transverse motion.

We expand the radical in the numerator of the logarithm in (7) in the parameter (8) and retain two terms. The integral with respect to φ is then readily evaluated by integration in the complex plane.

For frequencies satisfying the condition

$$\Delta\omega = \omega - \omega_u \leqslant -\frac{V_\perp^2}{2aV_z^2}, \tag{9}$$

the power spectrum of the potential between two points is given by

$$U_\omega^2 = \frac{4T\omega_u}{\pi a V_z \omega_{Be}^2}\ln\frac{2aV_z^2\left(1 + \sqrt{1 - \frac{2\rho_e^2\Delta\omega}{aV_z^2}}\right)}{\rho_e V_\perp\left(\frac{V_z}{V_\perp}\sqrt{-2a\Delta\omega} + \sqrt{-\frac{2a\Delta\omega V_z^2}{V_\perp^2} - 1}\right)}. \tag{10}$$

At the point where the equality sign in (9) is satisfied the function U_ω^2 has a discontinuous change of slope (break) and, for large $\Delta\omega$, is given by (10) without the bracketed expression in the denominator of the logarithm, which has a singularity.

This behavior is explained by the fact that for frequencies that do not satisfy criterion (9) wave vector k in (5) becomes discontinuous at $\varphi = \pi$.

For $\Delta\omega \geq 0$ there remains of this region only the part corresponding to short wavelengths. As a result U_ω^2 has a kink at the point $\Delta\omega = 0$, where $\omega = \omega_u$, and its behavior is given by the following expression:

$$U_\omega^2 = \frac{4T\omega_u}{\pi\omega_{Be}^2 a V_z}\ln\frac{2aV_z^2\left(1 + \sqrt{1 - \frac{2a\omega\rho e_z^2}{aV_z^2}}\right)}{\rho_e V_\perp\sqrt{1 + \frac{4V_z^2 a\Delta\omega}{V_\perp^2} + \sqrt{\left(1 + \frac{4aV_z^2\Delta\omega}{V_\perp^2}\right)^2 - 1}}}, \tag{11}$$

which is valid up to

$$\Delta\omega = \frac{aV_z^2}{2\rho_e^2} - \frac{V_\perp}{\rho_e}. \tag{12}$$

Starting at this value of $\Delta\omega$ there is a break in the wave vector space of the upper limit of integration and U_ω^2 begins to fall sharply. It can be shown by direct differentiation of (7) that at this point U_ω^2 exhibits a discontinuity in the first derivative.

Unlike the two breaks in U_ω^2 described above, which have a clear physical significance, the present one is connected with the approximate character of extrapolation (5) at the upper limit of integration in (7) and with terminating the integration over $k_\perp$ at the value ρ_e^{-1}.

The spectrum U_ω^2 is cut off at frequencies satisfying the equality

$$\Delta\omega = \frac{aV_z^2}{2\rho_e} + \frac{V_\perp}{\rho_e}. \qquad (13)$$

The contribution to the spectral density U_ω^2 from the natural longitudinal oscillations of the slow extraordinary wave is zero. It can be shown, in the same manner as in ref. 3, that $U_\omega^2 \approx T/v_e$ is determined by the fluctuating motion of individual electrons in the vicinity of a Debye radius about the point under consideration.

We shall show that similar results obtain in the limiting case opposite to condition (8). Expression (7) reduces to the following form in the limit $V_z \to 0$:

$$U_2^\omega = \frac{4\sqrt{2}\,T\omega_u}{\pi^2\omega_{Be}^2\sqrt{a\rho_e V_\perp}} \int\limits_0^{\operatorname{ars\,cos\,max}\left\{-1,\ \frac{\Delta\omega\rho_e}{V_\perp}\right\}} d\varphi\, \frac{\sqrt{\cos\varphi - \frac{\Delta\omega\rho_e}{V_\perp}}}{\cos\varphi}.$$

This integral can be expressed through the complete elliptic integrals of the first and third kinds. If $\Delta\omega\rho_e/V_\perp < -1$ we find that

$$U_\omega^2 = \frac{8T\omega_u\sqrt{\varkappa_1}}{\pi^2\omega_{Be}^2\sqrt{a\rho_e V_\perp}}\left[2K(\varkappa_1) - \Pi_1\left(\frac{\varkappa_1 V_\perp}{2\Delta\omega\rho_e},\ \varkappa_1\right)\right], \qquad (14a)$$

where $\varkappa_1 = V_\perp/[-\rho_e\Delta\omega + \sqrt{(\rho_e\Delta\omega)^2 - V_\perp^2}]$. If $\Delta\omega\rho_e/V_\perp > -1$ we obtain the following expression:

$$U_\omega^2 = \frac{8T\omega_u}{\pi^2\omega_{Be}^2\sqrt{a\rho_e V_\perp}}\left[K(\varkappa_2) - \frac{\Delta\omega\rho_e}{V_\perp}\Pi_1(-2\varkappa_2^2,\ \varkappa_2)\right], \qquad (14b)$$

where $\varkappa_2 = \sqrt{(V_\perp - \rho_e\Delta\omega)/2V_\perp}$.

Plots of the power spectrum U_ω^2 in the vicinity of the upper hybrid frequency are shown in Fig. 1 for three values of the parameter $\alpha = aV_z^2/\rho_e V_\perp = 10,\ 1,\ 0$. The first is constructed through Eqs. (10) and (11); the second is obtained by numerical calculation of (7); the third is obtained through Eq. (14). In the latter case the values of the elliptic integrals are taken from ref. 9, and the complete elliptic integrals of the third kind $\Pi_1(\nu, \varkappa)$ for the interval $\nu < -1$ are expressed in terms of the incomplete elliptic integrals of the first and second kinds through the equation[10]

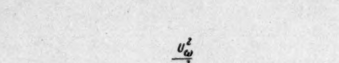

Fig. 1. Contribution to function U_ω^2 from fluctuating fields due to characteristic plasma oscillations near the upper hybrid resonance frequency.

$$\operatorname{ctg}\beta\Delta(\beta,\ \varkappa)\,\Pi_1\left(-\frac{1}{\sin^2\beta},\ \varkappa\right) = E(\varkappa)F(\beta,\ \varkappa) - K(\varkappa)E(\beta,\ \varkappa).$$

A comparison of the curves shows that when the parameter $aV_z^2/\rho_e V_\perp \le 10$ the quantity max U_ω^2 shows little variation, being equal to

$$U_0^2 = \frac{16G\omega_u}{\pi^2\omega_{Be}^2\sqrt{aV_\perp\rho_e}}, \qquad (15)$$

where G = 0.916 is the Katalan constant. For $aV_z^2/\rho_e V_\perp > 1$ the maximum proper is shifted to the point $\Delta\omega = -V_\perp^2/2aV_z^2$, but up to values $\omega = \omega_u$ the spectral density U_ω^2 falls so slowly that the plateau approximation can be used. The following asymptotic expression can be used in place of (14) for frequencies for which $U_\omega^2 \ll U_0^2$:

$$U_\omega^2 = \frac{4T}{\pi}\,\frac{\omega_u}{aV_z\omega_{Be}^2}\ln\left(1 + \frac{V_z}{\rho_e}\sqrt{-\frac{a}{2\Delta\omega}}\right). \qquad (16)$$

It is readily seen that in the limit $V_z \to 0$ this expression coincides with Eq. (13) of ref. 3.

We note that max U_ω^2 begins to fall slowly with increasing value of the parameter (8). Thus, for $aV_z^2/\rho_e V_\perp = 100$, max U_ω^2 is smaller than (15) by a factor of 2, as is readily seen from Eq. (10) or (11).

Fast magnetoacoustic wave. At the lower hybrid frequency $\omega_L = [\omega_{Bi}\omega_{Be}(\omega_{0i}^2 + \omega_{Bi}^2)/(\omega_{Bi}\omega_{Be} + \omega_{0i}^2)]^{1/2}$ these oscillations are electrostatic, and the noise intensity U(t) also has a sharp maximum.[3] The situation here is similar to that at the upper hybrid frequency.

The dielectric constant in the cold-plasma approximation also applies here:

$$\varepsilon(\omega - \mathbf{kV},\ \mathbf{k}) = 1 - \frac{\omega_{0i}^2}{(\omega - \mathbf{kV})^2} + \frac{k_\perp^2}{k^2}\,\frac{\omega_{0e}^2}{\omega_{Be}^2 - (\omega - \mathbf{kV})^2} - \frac{k_z^2}{k^2}\,\frac{\omega_{0e}^2}{(\omega - \mathbf{kV})^2}.$$

Expansion (17) at the frequency ω_L has the form

$$\varepsilon(\omega - \mathbf{kV},\ \mathbf{k}) = \frac{2k_\perp^2}{k^2}\,\frac{(\omega_{Be}^2 + \omega_{0e}^2)(\omega - \omega_L - \mathbf{kV})}{\omega_L\omega_{Be}^2} - \frac{k_z^2}{k^2}\,\frac{\omega_{0e}^2}{\omega_L^2},$$

which is completely analogous to (5). As a result, all the equations for U_ω^2 in the vicinity of the lower hybrid frequency can be obtained from expressions (6)-(16) by making the simple substitutions ω_L/ω_{0e}^2 for ω_u/ω_{Be}^2, ρ_i for ρ_e, $\omega_L - \omega$ for $\Delta\omega$, and by setting $a = \omega_L(\omega_{Be}^2 + \omega_{0e}^2)/\omega_{0e}^2\omega_{Be}^2$.

For the ionosphere plasma[4], in which frequently $\omega_{0e} > \omega_{Be}$, max $U_{\omega_u}^2$/max $U_{\omega L}^2 = (\omega_{0i}/\omega_{Bi})^3$, where max U_ω^2 is given by expression (15). The less sharply expressed maximum at the lower hybrid frequency is due to the fact that the collective oscillations of the plasma occupy a smaller phase volume in k space than near ω_u.

At frequencies where there are no potential oscillations of the plasma it can be shown, as in ref. 3, that $U_\omega^2 \approx T/v_1$ and the main contribution comes from the fluctuating motions of individual ions in the neighborhood of a Debye radius about the points under consideration.

The conclusions of the present work can be summarized as follows.

1. The mean square of the potential difference between two points does not vary as a result of relative motion of the plasma. A redistribution of the spectral density occurs.

2. The effect of the relative motion of the plasma is to smooth the maxima of the power spectra U_ω^2 at the hybrid frequencies. If criterion (8) is obeyed, then max U_ω^2 is shifted towards lower frequencies in the region of the upper hybrid frequency, and towards higher frequencies in the region of the lower hybrid frequency. Starting at a frequency defined by expression (9), the spectral density U_ω^2 is approximately constant up to the hybrid frequency.

3. At the frequencies $\omega_{u,L}$ and at the frequency defined by (9), breaks occur in the curve of U_ω^2.

I should like to thank Ya. L. Al'perta for discussion and A. A. Andronov and Yu. V. Chugunov for a number of useful remarks.

---

[1] R. Grabowski, Space Res. 13, Proc. Open Meet. Working Groups Phys. Sci., 15th Plenary Meet. (COSPAR, Madrid, 1972), 1, 593, Berlin (1973).

[2] R. Grabowski, Planet. Space Sci., 20, 573 (1972).

[3] V. M. Kostin, Izv. VUZ. Radiofiz. (in press).

[4] Ya. L. Al'perta, A. V. Gurevich, and L. P. Pitaevskii, Artificial Satellites in a Rarefied Plasma [in Russian], Izd. Nauka, Moscow (1964).

[5] A. A. Andronov, Kosmich. Issled., 4, 558 (1966).

[6] Yu. V. Chugunov, Izv. VUZ Radiofiz., 14, 44 (1971).

[7] A. A. Andronov and V. Ya. Éidman, Zh. Tekh. Fiz., 39, 365 (1969) [Sov. Phys.—Tech. Phys., 14, 267 (1969)].

[8] V. D. Shafranov, Reviews of Plasma Physics, Vol. 3, Consultants Bureau, New York (1967).

[9] V. M. Belyakov, R. M. Kravtsova, and M. G. Rappoport, Tables of Elliptic Integrals [in Russian], Vol. 1, Izd. AN SSSR, Moscow (1962).

[10] A. Erdélyi, Higher Transcendental Functions (Elliptical and Automorphic Functions, Lamé and Mathieu Functions) (Bateman Manuscript Project) [Russsian translation], Izd. Nauka, Moscow (1967).

Radiation emitted by charged particles trapped by plane electromagnetic waves

V. Ya. Davydovskii and A. S. Ukolov

Taganrog Radio Engineering Institute

(Submitted September 11, 1973; resubmitted January 11, 1974)
Zh. Tekh. Fiz., 44, 1693-1698 (August 1974)

Radiation emitted by a charged particle trapped by a plane monochromatic circularly polarized wave with slowly varying propagation and amplitude is considered. With radiative reactions neglected expressions are obtained for the energy emitted in a period of the phase oscillations, the average radiated power, and the time in which the phase oscillation energy varies significantly. The spectral composition of the radiation is investigated and it is shown that the trapped particles radiate primarily at the phase oscillation frequency, which can be very different from the wave frequency.

The motion of a charged particle trapped by a plane electromagnetic wave consists of two motions: a uniform motion together with the wave (plane motion), and oscillatory motion about some phase of the wave (phase oscillations). The latter motion should be accompanied by radiation that damps the oscillations. Investigation of this radiation is of interest for the following reasons. First, damping of the phase oscillations enhanches the confinement of the particle by the wave which, in turn, can increase the particle energy if the propagation velocity increases.[1-4] Second, the trapped particles radiate at the phase oscillation frequency, which is different from the wave frequency; this may be one of the mechanisms responsible for generation of astrophysical radio emission.

The energy emitted during a period T of a phase oscillation for particles moving in an electromagnetic field **E** and **B** can be written[5]

$$\Delta\varepsilon = \frac{2e^4}{3m^2c^3}\int_0^T \frac{\left(\mathbf{E}+\frac{1}{c}[\mathbf{vB}]\right)^2 - \frac{1}{c^2}(\mathbf{Ev})^2}{1-\frac{v^2}{c^2}}\,dt. \tag{1}$$

In Eq. (1) it is assumed that the variation in the parameters due to radiation can be neglected for the period of particle motion. Introducing the dimensionless velocity **u** and energy β of the particle, normalized, respectively, to the speed of light c in vacuum and the rest energy mc^2, and also the momentum **p** divided by mc, and remembering that

$$\frac{d\mathbf{p}}{dt} = \frac{e}{mc}(\mathbf{E}+[\mathbf{uB}]),\quad \frac{d\beta}{dt} = \frac{e}{mc}\mathbf{Eu}, \tag{2}$$

we rewrite (1) as

$$\Delta\varepsilon = \frac{2e^2}{3c}\int_0^T \left\{\left(\frac{dp}{dt}\right)^2 - \left(\frac{d\beta}{dt}\right)^2\right\}\beta^2 dt. \tag{3}$$

It is also convenient to introduce the phase θ on which the field depends:

$$\theta = t - \int_0^z n(z)\,dz. \tag{4}$$

Above, n(z) is the refractive index, which is assumed to remain essentially fixed during the period T. Replacing the time t by θ in Eq. (3), we obtain

$$\Delta\varepsilon = \frac{2e^2}{3c}\oint \left\{\left(\frac{dp}{d\theta}\right)^2 - \left(\frac{d\beta}{d\theta}\right)^2\right\}\beta(\beta - np_z)\,d\theta, \tag{5}$$

where it is assumed that $d\theta/dt = 1 - nu_z = 1 - np_z/\beta$. The integration in (5) is carried out over one period of θ.

We assume further that the electromagnetic field is a plane circularly polarized wave with potential A determined by

$$A_x = \frac{c}{\omega}\mathscr{E}(z)\cos\omega\theta,\quad A_y = -\frac{c}{\omega}\mathscr{E}(z)\sin\omega\theta,\quad A_z = 0, \tag{6}$$

where the amplitude $\mathscr{E}$ (z) is assumed to be a slowly varying function and ω = const. The motion of a particle trapped by a wave (6) has been thoroughly studied.[1,6] In particular, the expressions for the energy and momentum, assuming that the wave parameters do not vary, are

$$\left.\begin{aligned} \beta &= \frac{Yn}{n^2-1} + 2\sigma\sqrt{\frac{\lambda C}{n^2-1}\left(\tau - \sin^2\omega\frac{\theta-\theta_0}{2}\right)},\\ p_z &= \frac{Y}{n^2-1} + 2\sigma n\sqrt{\frac{\lambda C}{n^2-1}\left(\tau - \sin^2\omega\frac{\theta-\theta_0}{2}\right)}, \end{aligned}\right\} \tag{7}$$

$$\left.\begin{aligned} &\mathbf{p}_\perp = \mathbf{C} - \frac{e}{mc^2}\mathbf{A},\quad \lambda = \frac{e\mathscr{E}}{mc\omega},\quad \sigma = \frac{u_z n - 1}{|u_z n - 1|},\\ &Y = n\beta - p_z,\quad \tau = \frac{Y^2 - [(C-\lambda)^2+1](n^2-1)}{4C\lambda(n^2-1)},\quad \mathrm{tg}\,\omega\theta_0 = -\frac{C_y}{C_x}. \end{aligned}\right\} \tag{7a}$$

Here, $\mathbf{C} = \mathbf{i}C_x + \mathbf{j}C_y$ is the generalized transverse momentum, which remains constant since the field is independent of the x and y coordinates, Y for constant n is an integral of motion equivalent to the particle energy conserved in the wave coordinate system, and index $\perp$ denotes projection of the vectors onto the xy plane. We assume further that while the particle moves the refractive index n and the parameter λ (which is proportional to the amplitude of the wave), and thus Y and τ, vary negligibly.

Substituting (7) into (5) and integrating, we obtain the energy emitted by a trapped particle in one period normalized to mc^2

$$\Delta\beta = \frac{32e^2\lambda^{3/2}C^{1/2}\omega n}{9mc^3}\sqrt{1+4C\lambda\tau+(C-\lambda)^2}\left\{\left[\frac{C}{2} - 3\lambda(1-\tau)\right]K(\tau) + \left[3\lambda + C\left(\tau - \frac{1}{2}\right)\right]E(\tau)\right\}. \tag{8}$$

Here, K and E are complete elliptical integrals of the first and second kind, respectively.

The parameter τ characterizes the phase oscillation amplitude[1]; more precisely the range of variation of the phase θ for the particle motion is determined by

$$\theta_0-\frac{2}{\omega}\arcsin\sqrt{\tau}\leqslant\theta\leqslant\theta_0+\frac{2}{\omega}\arcsin\sqrt{\tau}. \tag{9}$$

The expression for $\Delta\beta$ in the limit $\tau \to 0$ is

$$\Delta\beta=\frac{4\pi e^2\lambda^{3/2}C^{1/2}\omega n}{9mc^3}\sqrt{1+(C-\lambda)^2}\,(5C+6\lambda)\,\tau. \tag{10}$$

In the opposite case of large phase oscillation amplitudes $\tau \to 0$ that are extremely large for captured particles, using the asymptotic behavior of the complete elliptical integrals we obtain,

$$\Delta\beta=\frac{16e^2\lambda^{3/2}C^{1/2}\omega n}{9mc^3}\sqrt{1+(C+\lambda)^2}\ln\frac{4}{\sqrt{1-\tau}}. \tag{11}$$

We note that Eq. (8) does not contain the factor n^2-1; consequently, the energy emitted during a period tends to a finite value for $n \to 1$. This cannot be said of the radiated power. Actually, the period of phase oscillation of the particle[1] is

$$T=\frac{8nK(\tau)}{\omega(n^2-1)}\left[\tau+\frac{1+(C-\lambda)^2}{4C\lambda}\right]^{1/2}, \tag{12}$$

and the average power radiated by the particle is

$$I=\frac{\Delta\beta}{T}=\frac{8e^4\mathcal{E}^2C(n^2-1)}{9m^3c^5}\left\{\frac{C}{2}-3\lambda(1-\tau)+\left[3\lambda+C\left(\tau-\frac{1}{2}\right)\right]\frac{E(\tau)}{K(\tau)}\right\}. \tag{13}$$

We note that the average radiated power has only a very weak (through the parameter λ) dependence on the frequency, but is proportional to the square of the wave amplitude and falls sharply in the limit $n \to 1$. For small τ this quantity becomes

$$I=\frac{2e^4\mathcal{E}^2C(n^2-1)}{9m^3c^5}(6\lambda+5C)\,\tau, \tag{14}$$

and for $\tau \to 1$

$$I=\frac{4e^4\mathcal{E}^2C^2(n^2-1)}{9m^3c^5}. \tag{15}$$

We obtain the expression for the emission time, i.e., the time in which there is substantial variation of the phase oscillation amplitude. The oscillation amplitude of the energy is obtained from (7) if we set $\sin\omega(\theta-\theta_0)/2 = 0$,

$$\delta\beta=2\sqrt{\frac{\lambda C\tau}{n^2-1}}. \tag{16}$$

Differentiating this expression with respect to time and equating the result to the average radiated power (13), we obtain

$$\frac{d\tau}{dt}=\frac{8}{9}\sqrt{\frac{e^7\mathcal{E}^3C(n^2-1)^3\omega\tau}{m^5c^9}}$$

$$\times\left\{\frac{C}{2}-3\lambda(1-\tau)+\left[3\lambda+C\left(\tau-\frac{1}{2}\right)\frac{E(\tau)}{K(\tau)}\right\}. \tag{17}$$

The solution of (17) is not expressed in terms of known functions. Therefore, we are limited to the case of small τ

$$\tau=\frac{\tau_0}{(At\sqrt{\tau_0}+1)^2}, \tag{18}$$

where τ_0 is the value of τ at $t = 0$, and

$$A=\frac{1}{9}\sqrt{\frac{e^7\mathcal{E}^3C(n^2-1)^3\omega}{m^5c^9}}(6\lambda+5C). \tag{19}$$

The time of the decrease in τ is twice

$$t_0=\frac{\sqrt{2}-1}{A\sqrt{\tau_0}}. \tag{20}$$

It is easy to see that this time is very large for realistic values $\lambda_0 = 2\pi c/\omega \sim 1$ m, $\mathcal{E} \sim 1$ V/cm, and $C \sim 1$. Emission cannot occur in processes that take place inside the solar system; it may occur in such interstellar phenomena as the flare-up of new stars and supernovae.

We now consider the frequency composition of the radiation. We do not find the radiation field of the trapped particle since this field depends on the properties of the medium (the effect of the medium is essential: In vacuum the wave velocity is equal to c and there is no trapped particle of finite rest mass); we are interested in the relative magnitudes of the harmonic amplitudes. Under the above assumptions with respect to n and λ the instantaneous radiated power is a quasiperiodic function of time whose parameters are constant during time intervals comparable to the phase oscillation period of the particle. Therefore, to find the frequency composition of the radiation we expand the instantaneous radiated power in a Fourier series with fundamental frequency Ω equal to the phase oscillation frequency. In the coordinate system in which the wave is at rest the corresponding expressions are

$$I'=\frac{8e^2\lambda^2\omega^2(n^2-1)C}{3mc^2}\left\{\lambda\left(\tau-\sin^2\frac{k}{2}(z'-z_0')\right)+\frac{C}{4}\sin^2k(z'-z_0')\right\}, \tag{21}$$

$$\Omega'=\frac{2\pi\omega\sqrt{C\lambda(n^2-1)}}{4\beta'K(\tau)},\quad C_x=C\cos kz_0',\quad C_y=-C\sin kz_0', \tag{22}$$

and $k = \omega\sqrt{n^2-1}$; the primes denote values in the wave coordinate system.

If the average radiated power is to be an additive function of the harmonic number, one must expand the quantity $R = \sqrt{I'}$ in a Fourier series; this quantity is proportional to the field that the particle would radiate in vacuum

$$R=\sum_{j=0}^{\infty}(a_j\cos j\Omega't'+b_j\sin j\Omega't'), \tag{23}$$

Since t' and z' are related by

$$\frac{dz'}{dt'}=u_z'=\frac{p_z'}{\beta'}=\frac{\sqrt{\beta'^2-p_\perp'^2-1}}{\beta'}=\frac{2a}{\beta'}\sqrt{C\lambda\left(\tau-\sin^2k\frac{z'-z_0'}{2}\right)}, \tag{24}$$

for the wave in (6) we have

$$a_{2j}=(-1)^j\frac{4\beta'}{T'\sqrt{C\lambda}}\int_{z_0'}^{z_1'}R\cos\left[j\pi\frac{F(\tau,\varphi)}{K(\tau)}\right]\frac{dz'}{\sqrt{\tau-\sin^2k\frac{z'-z_0'}{2}}},\qquad(25)$$

$$b_{2j+1}=(-1)^j\frac{4\beta'}{T'\sqrt{C\lambda}}\int_{z_0'}^{z_1'}R\cos\left[\frac{2j+1}{2}\pi\frac{F(\tau,\varphi)}{K(\tau)}\right]\frac{dz'}{\sqrt{\tau-\sin^2k\frac{z'-z_0'}{2}}},\qquad(26)$$

where $F(\tau, \varphi)$ is an incomplete elliptical integral of the first kind, and

$$\left.\begin{aligned}\varphi&=\arcsin\left(\frac{1}{\sqrt{\tau}}\sin k\frac{z'-z_0'}{2}\right),\\ z_1'&=z_0'+\frac{2}{k}\arcsin\sqrt{\tau}.\end{aligned}\right\}\qquad(27)$$

All odd a_j and even b_j vanish indentically. Combining (25) and (26) and eliminating terms that do not occur in the calculation of the strengths, we obtain

$$a_j=\frac{4\beta'}{T'\sqrt{C\lambda}}\int_{z_0'}^{z_1'}R\cos\left[\frac{j}{2}\pi\frac{F(\tau,\varphi)}{K(\tau)}\right]\frac{dz'}{\sqrt{\tau-\sin^2k\frac{z'-z_0'}{2}}}.\qquad(28)$$

Changing to integration over φ and taking account of

$$\beta'=\frac{Y}{\sqrt{n^2-1}},$$

and substituting T' and i' from (21) and (22), we rewrite (28)

$$a_j=\frac{4e\lambda k}{K(\tau)}\sqrt{\frac{2C\tau}{3mc^3}}\int_0^{\pi/2}\sqrt{\frac{\lambda\cos^2\varphi}{1-\tau\sin^2\varphi}+\frac{C}{2}\sin^2\varphi}\,\cos\left[j\frac{\pi}{2}\frac{F(\tau,\varphi)}{K(\tau)}\right]d\varphi.\qquad(29)$$

The integral in (29) is not expressed in terms of known functions. However, in the limiting case of small oscillations and a weak wave

$$\tau\ll 1,\quad \lambda\ll C\qquad(30)$$

one can assume that $F(\tau, \varphi) \approx \varphi$ and $K(\tau) \approx \pi/2$. Then,

$$a_j=\frac{2e\lambda kC}{K(\tau)}\sqrt{\frac{\tau}{3mc^3}}\left[\frac{1-\cos(j+1)\frac{\pi}{2}}{j+1}-\frac{1-\cos(j-1)\frac{\pi}{2}}{j-1}\right]\qquad(31)$$

for $j \neq 1$, and

$$a_1=\frac{e\lambda kC}{K(\tau)}\sqrt{\frac{\tau}{3mc^3}}.$$

Thus, in this limiting case the coefficients a_j decrease as j increases, and the odd a_j are proportional to $1/(j^2 - 1)$ and the even a_j are proportional to the factor

$$\frac{j(-1)^{\frac{j+1}{2}}+1}{j^2-1}.$$

When the inequality (30) does not hold, the coefficients are calculated for different values of λ, C, and τ. The results of the calculations are shown in Table 1, which gives the values for $a_j/a_0 = a_j$.

Examination of Table 1 indicates that the radiation intensity, which is proportional to a_j^2, declines rapidly with increasing j, i.e., a significant portion of the energy is emitted by the particle at the fundamental and the first few harmonics.

In regard to the dependence of a_j on τ we note that the radiation intensity increases in the region $0.5 \leqslant \tau \leqslant 0.75$. It is understandable physically that there is a maximum of radiation intensity for the charged particles. When $\tau \to 0$, the phase oscillation amplitude, as well as the radiation intensity, tend to zero. When $\tau \to 1$ the period of the phase oscillation (12) increases infinitely, and the average power emitted by the particle also tends to zero. Consequently, in the region of variation of τ, $0 \leq \tau \leq 1$ the radiation intensity reaches a maximum.

This effect can lead to reradiation of the wave energy by particles trapped by this wave at frequencies different than the wave frequency. It can be seen from (12) that for a phase period that is the same as the period of the fundamental emitted harmonic, the latter can differ considerably from the period of the wave $2\pi/\omega$. Reradiation occurs largely at low frequencies, and the frequency decreases with increasing phase oscillation amplitude when τ increases. For small oscillations the period does not depend on τ.

$$T=\frac{2\pi}{\omega}\frac{n}{n^2-1}\sqrt{\frac{1+(C-\lambda)^2}{C\lambda}}.$$

In this case, however, since $n \gg 1$, and λ and C are small, $T > 2\pi/\omega$. The latter expression, like (12), is val-

TABLE 1

	$C=1,\ \lambda=0.01$					$C=1,\ \tau=0.5$			$\lambda=0.1,\ \tau=0.5$	
	$\tau=0.05$	$\tau=0.25$	$\tau=0.50$	$\tau=0.75$	$\tau=0.99$	$\lambda=0.1$	$\lambda=0.5$	$\lambda=1.0$	$C=10$	$C=100$
a_0	1.000	1.000	1.000	1.000	1.000	1.000	1.000	1.000	1.000	1.000
a_1	0.512	0.516	0.530	0.564	0.735	0.580	0.652	0.686	0.530	0.520
a_2	0.302	0.294	0.264	0.190	0.214	0.141	0.033	0.110	0.264	0.290
a_3	0.469	0.465	0.450	0.409	0.109	0.338	0.197	0.141	0.450	0.476
a_4	0.052	0.057	0.072	0.104	0.136	0.035	0.019	0.023	0.072	0.085
a_5	0.172	0.166	0.144	0.092	0.098	0.142	0.105	0.080	0.144	0.138
a_6	0.019	0.020	0.024	0.037	0.129	0.006	0.001	0.004	0.024	0.032
a_7	0.154	0.152	0.146	0.135	0.142	0.114	0.079	0.061	0.146	0.156
a_8	0.009	0.009	0.011	0.017	0.080	0.002	0.000	0.001	0.011	0.017

id for slowly varying wave parameters, when n and λ are functions of z whose variation during a period of phase oscillations of the particle can be neglected. Therefore, the radiation frequency of the trapped particles can vary due to the gradient of the refractive index n, and also due to the variation in the wave amplitude, for example as a result of damping.

---

[1] V. Ya. Davydovskii and E. M. Yakushev, Zh. Eksp. Teor. Fiz., 52, 1068 (1967)[Sov. Phys.-JETP, 25, 709 (1967)].

[2] V. Ya. Davydovskii and E. M. Yakushev, Zh. Tekh. Fiz., 38, 2236 (1968).

[3] V. Ya. Davydovskii and E. M. Yakushev, Izv. Akad. Nauk SSSR Ser. Fiz., 32, 1796 (1968).

[4] N. A. Davydovskaya, V. Ya. Davydovskii, and A. S. Ukolov, Zh. Tekh. Fiz., 43, 1132 (1973)[Sov. Phys.-Tech. Phys., 18, 725 (1973)].

[5] L. D. Landau and E. M. Lifshitz, Classical Field Theory, Pergamon, New York (1971).

[6] V. Ya. Davydovskii and E. M. Yakushev, Zh. Tekh. Fiz., 41, 2259 (1971) [Sov. Phys.-Tech. Phys., 16, 1796 (1972)].

Investigation of a plasma focus with a time-resolved laser interferometer

I. M. Zolototrubov, I. P. Skoblik,

A. G. Tolstolutskii, and V. I. Privezentsev

(Submitted September 4, 1972; resubmitted January 7, 1974)
Zh. Tekh. Fiz., 44, 1699-1702 (August 1974)

A modified Mach–Zender interferometer with a He–Ne laser as light source and an SFR rotating mirror camera for time resolution is described. By sweeping the sharply focused laser beam a time resolution of to $3 \cdot 10^{-8}$ sec is achieved. The interferometer is used to observe plasma density fluctuations and to determine the geometrical size of a plasma focus.

A Mach–Zender interferometer with a laser light source and a rotating-mirror camera has been used to investigate the electron density in a plasma focus.

The optical system is chosen to give the best spatial and temporal resolution for the interferometer. Therefore a system is used which focuses the light beam in a region of the plasma. The light source is a He–Ne laser which gives the least spreading of the beam[1] when operating in the TEM_{00q} mode.

Figure 1 shows the arrangement. A light beam is formed by means of a telescopic lens system. The short focal length cylindrical lens 2 expands the beam to ~ 8 cm in the yz plane. Lens 3 forms a parallel beam in the yz plane and simultaneously focuses in the xy plane down to a size $2\delta = 5 \cdot 10^{-2}$ cm. The focal length of lens 3 is 70 cm, so that the minimum beam width δ coincides with the plasma focus region with the lens outside the vacuum chamber 6.

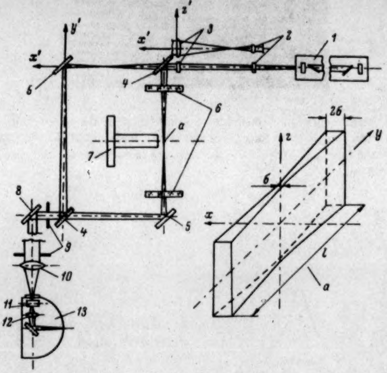

Fig. 1. The optical arrangement of the interferometer. 1) LG-36A He–Ne laser; 2) cylindrical lens; 3) lens forming the laser light beam; 4) beam-splitter mirror; 5) mirror blanks; 6) glass windows of the vacuum chamber; 7) coaxial plasma accelerator; 8) rotating mirror; 9) masking stops; 10) I-38 objective; 11) shutter; 12) RO2-2M objective; 13) SFR-2M camera. a) shape of the light beam in the probed region; l = 8 cm is the distance at which the minimum laser beam width is doubled.

The time sweep is accomplished by means of the SFR-2M camera (13), operating in the scan mode. An image of the test object and the interference bands is formed on the film by means of the objectives I-37 (10) and RO2-2M (12). In the focal plane of the objective 10 there is a shutter 11, adapted from the measuring device of a magnetoelectric system (ref. 2), with an opening time of ~ 1 μsec, which is equal to the time for one revolution of the SRF mirror when its speed is $n = 6 \cdot 10^4$ rev/min. Objective 12 focuses the laser beam sharply on the sensitive layer of the film in the form of a narrow light strip of width as large as $\delta' \approx 10^{-2}$ cm. Hence the time resolution of the interferometer, defined as

$$\Delta t = \frac{\delta'}{v_p},$$

is $3 \cdot 10^{-8}$ sec. Here v_p is the linear speed of the sweep, $3 \cdot 10^5$ cm/sec.

The spatial resolution of the interferometer in the direction perpendicular to the probe beam is determined by the width of the interference fringe related to the plasma probe region, and is about 2 mm.

Because of the small angular spreading of the laser beam it is easy to eliminate the plasma light by means of the stops 9 mounted in the path of the beam and by withdrawing the SFR camera to a distance of 3.5 m from the plasma source.

The coaxial gun used for the experiment is described in ref. 3. The capacitor bank is charged to 25 kV. The discharge period is ~ 12 μsec. About 1.2 cm³ of hydrogen is injected into the interelectrode gap of the coaxial accelerator. The delay time τ_d between the gas injection pulse and the voltage pulse to the electrodes is varied from 100 to 250 μsec. The plasma is probed at distances of 1.5, 4.5, and 6.5 cm from the end of the accelerator.

Figure 2 shows typical interferograms. Figure 2a illustrates the case in which the spatial resolution of the interferometer is inadequate: the spherical lens 3 in the experimental arrangement (Fig. 1) is replaced by a cylindrical lens, which increases the size of the probe beam in the plasma region to 0.5 cm. The temporal resolution of the interferometer remains unchanged. A possible reason for blurring of the interference fringes is substantial spatial variations of the plasma refractive index perpendicular to the direction of propagation of the probe beam. To observe the time variations of the refractive index by themselves (ref. 4), the beam width in the probe region must be smaller than the size of the inhomogeneity in the plasma.

Figures 2b and 2c are obtained with the probe beam focused in the plasma region with width $5 \cdot 10^{-2}$ cm. The interferograms give a good picture of the time variation

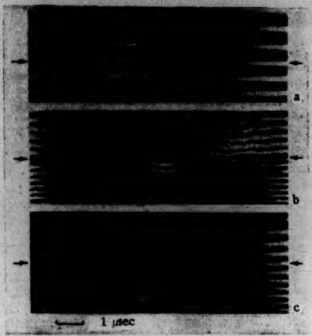

Fig. 2. Interferograms obtained 4.5 cm from the end of the accelerator. a) τ_d = 130 μsec, with no focusing of the probe beam, when δ = 0.5 cm; b) τ_d = 130 μsec, and c) τ_d = 250 μsec, with the probe beam focused, when 2δ = 0.05 cm.

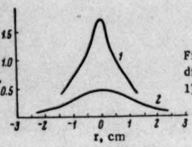

Fig. 3. Variation of $\bar{n}_e$ along the radius of the plasma filament. τ_d, μsec: 1) 130; 2) 250.

of the plasma refractive index, averaged over the plasma in the direction of propagation of the probe beam.

Figure 3 shows the average electron density $\bar{n}_e$ at various distances from the accelerator axis, as obtained by processing the interferograms of Figs. 2b and 2c, and with the values referred to the time of maximum fringe shift. The diameter of the plasma cylinder is determined separately for each accelerator operating condition from the position of the undisturbed edge fringes. It follows from Fig. 2 that with a 130 μsec delay a dense plasma is concentrated on the accelerator axis; the maximum average electron density reaches $1.6 \cdot 10^{17}$ cm^{-3}. When the delay time is increased to 250 μsec the plasma increases to the dimension of the central electrode of the coaxial accelerator (≈ 3 cm), while the average density diminishes by a large factor (curve 2).

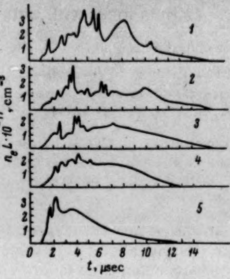

Fig. 4. The variation of n_eL with time near the accelerator axis. τ_d, μsec: 1) 100; 2) 130; 3) 150; 4) 200; 5) 250.

Figure 4 shows the variation of plasma density with time for various delay times. The curves are obtained from the deflections of the interference fringes, whose position in space corresponds to that of the accelerator axis. Density fluctuations with maximum frequency up to 5 MHz can be seen. These fluctuations are observed on more than one fringe. In Fig. 2b one can clearly see synchronous fluctuations of several fringes, which is evidence of the displacement of the plasma as a whole in the plane of the figure.

When the plasma probe plane is displaced along the axis of the accelerator the nature of the density variations remains much the same. However, at a distance of about 6.5 cm from the face of the accelerator one sees a displacement of the peripheral fringes in the opposite direction, indicating the appearance of a neutral "sleeve" of considerable density around the plasma cluster.

Thus, the interferometer measurements show that a dense plasma is concentrated at the exit, near the accelerator axis, with a maximum average density of $1.6 \cdot 10^{17}$ cm^{-3}, and that density fluctuations with frequencies up to 5 MHz are generated.

---

[1] E. F. Ishchenko and Yu. M. Klimkov, Lasers [in Russian], Izd. Sov. Radio, Moscow (1968).

[2] A. S. Dubovik, Photography of High-Speed Processes [Russian translation], Izd. Nauka, Moscow (1964).

[3] I. P. Skoblik, I. M. Zolototrubov, and Yu. M. Novikov, Zh. Tekh. Fiz., 43, 281 (1973) [Sov. Phys.—Tech. Phys., 18, 184 (1973)].

[4] Rouli, Pribory dlya Nauch. Issled., 41, 3 (1970).

Plasma equilibrium and confinement in a poloidal heliotron configuration. I

V. G. Zykov, V. I. Karpukhin, Yu. F. Lonin, N. N. Podteregera, N. I. Rudnev, and V. T. Tolok

(Submitted July 4, 1973; resubmitted January 7, 1974)
Zh. Tekh. Fiz., 44, 1703-1712 (August 1974)

The equilibrium and confinement of an injected plasma [$n \sim 10^{12}$ cm^{-3}, $T_e \sim 10$ eV, $T_i \sim 5$-50 eV] have been studied in a toroidal trap with a poloidal heliotron field. The plasma reaches a stable equilibrium in the heliotron field with decay governed by the charged-particle loss at the supports of the opposed-field coils which produce the heliotron configuration.

INTRODUCTION

Toroidal drift of plasma particles can be suppressed in systems other than those having a rotational transform[1-3] e.g., bumpy torus.[3] Although this latter system provides single-frequency confinement, it does not satisfy the condition for MHD stability of the plasma. Theory[4] and experiment[5-7] have drawn attention to the heliotron configuration, which is essentially a modification of the bumpy-torus systems. These configurations are produced by a series of coils carrying a current whose magnitude and direction differ from those of the current in the coils of the main confining field. The bumpiness and the superposition of the main and opposed fields produce a min-B configuration, which suppresses the MHD flute instabilities locally, near the opposed-field coils.[4] Wiley[8] has predicted that, in addition to the local MHD stability, the average min B produced by the heliotron cells can exert a stabilizing influence on the flute and ballooning instabilities, which arise in regions with unfavorable curvature. In stellarators with low shear and rotational transform, one or more heliotron cells can increase the critical gas-kinetic pressure for the excitation of the ballooning instability. Experiments[9] with a potassium plasma in a straight Q machine with a heliotron configuration have demonstrated that the amplitude of the drift instabilities can be significantly limited through the imposition of an average min B or "connection length." Because of their stabilizing properties with respect to the most dangerous plasma instabilities and because of their simplicity, heliotron configurations are of interest for possible use in confining plasmas in closed toroidal traps. Below we report an experimental study of the plasma equilibrium and the stability of heliotron configurations displaying min-B properties in a toroidal field.

EXPERIMENTAL

The Pluton toroidal trap with a heliotron configuration is shown schematically in Fig. 1.

The basic parameters of the configuration are as follows: The toroidal field H_{tor} = 0-5 kOe; the radius of curvature R = 41 cm; the diameter of the toroidal vacuum chamber d = 14.7 cm; the axial circumference of the system L = 370 cm; the distance along the perimeter between the opposed-field coils, which produce the poloidal heliotron

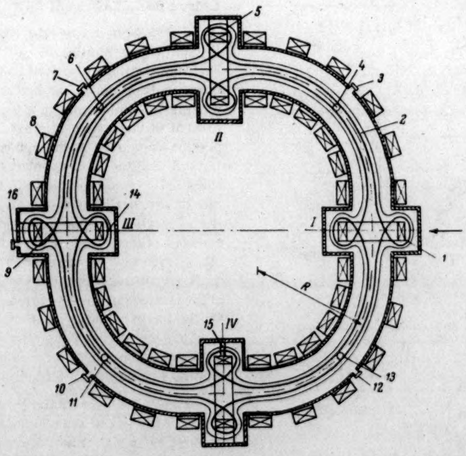

Fig. 1. The experimental apparatus. 1) Opposed-field coils; 2) $\psi = 0$ surface; 5) current conductors for the opposed field; 8) coils of the toroidal field; 9) regions of null magnetic field; 14) "plasma-bridge" regions; 15) supports for the opposed field coils; 3, 4, 6, 7, 10-13, 16) diagnostic ports. The arrow shows the injection direction.

configuration, is $L_{co} = L/4 = 92.5$ cm; the field at the magnetic axis in the cross sections corresponding to the positions of the opposed coils is $H_0 = H_{tor}/8$; the poloidal field in the magnetic flux linking the opposed-field coils (region 14 in Fig. 1) is $H_{pol} = 0.56\ H_{tor}$; the diameter of the field null near the opposed-field coils (region 9 in Fig. 1) is $d_0 = 9$ cm; and the magnetic surface intersecting the null-field regions, which is the separatrix for the lines of force closed within the confinement volume from those which link the opposed-field coils (the $\psi = 0$ surface in Fig. 1), has a diameter of $d_{\psi=0} = 4$ cm.

The opposed-field coils, which produce the poloidal heliotron configuration, are in the evacuated volume, mounted on the current conductors and held by supports (Fig. 1). The coils have an inside diameter of 21 cm, an outside diameter of 27 cm, and a width of 5 cm. The magnet system is driven by current from the discharge of a capacitor, which is common to the coils for the opposed and toroidal fields; this magnet system can produce a poloidal-heliotron configuration near the opposed-field coils.[6,7] An important parameter from the particle-confinement standpoint is the distance between the $\psi = 0$ surface and the housing of the opposed-field coils, Δr. The minimum value of Δr [(the distance between the $\psi = 0$ surface and the coil edge (Fig. 1)] is 0.41 cm, and the average value is $(\Delta r)_{av} = 1$ cm, so that the distance between the $\psi = 0$ surface and the coil housing corresponds, on the average, to 1 to 6 or 7 Larmor radii of 5-eV ions at a field of $H_{tor} = (0.6-4)$ kOe. In principle, the value of Δr can be raised by increasing the current through the opposed-field coils, but the power supply for the opposed-field coils used in these experiments (these coils are in series with the coils of the toroidal field) does not permit an adjustment of the opposed field, and the $\psi = 0$ surface occurs at only one position.

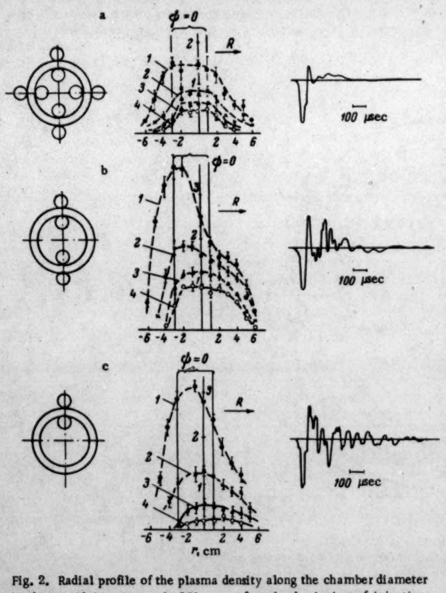

Fig. 2. Radial profile of the plasma density along the chamber diameter in the toroidal regions. 1) 250 μsec after the beginning of injection; 2) after 500 μsec; 3) after 750 μsec; 4) after 1000 μsec.

The plasma is injected across the magnetic flux linking one of the opposed-field coils from a coaxial plasma accelerator with pulsed gas injection. The plasma source is located 150 cm from the chamber since locating it in the immediate vicinity of the confinement volume causes rapid filling of the trap with neutral gas and undesirable particle loss due to recombination and charge exchange. The residual gas pressure in the chamber is $p_0 = 10^{-6}$ torr, so that these processes are not important. The neutral gas from the accelerator arrives at the trap chamber after a delay of about 1.5 msec, and this delay is usually longer than the plasma-confinement time.

Electrostatic (Langmuir) probes are used to measure the velocity and density of the injected plasma and the electron temperature and lifetime. In the measurements of the absolute densities and temperatures the probes are placed at a field null, under the opposed-field coils, in order to avoid the effect of the magnetic field on the probe readings. In certain cases the probes are calibrated against an 8-mm microwave diagnostic signal.

The average energy of the plasma ion component is determined from the transit time of the plasmoid between two probes. Typical parameters of the trapped plasma are an initial density of $n = 3-5 \cdot 10^{12}$ cm^{-3}, an electron temperature of $T_e \sim 5-10$ eV, and an average ion energy of 5 to 50 eV, depending on the operating conditions of the coaxial injector. In most of the experiments, this energy is $W_i \sim 5-7$ eV.

EXPERIMENTAL RESULTS

It has been shown previously[10,11] that a plasma equilibrium can be maintained in a toroidal magnetic field by "plasma limiters" formed in the min-B regions under the opposed-field coils. In analyzing the confinement of a plasma in equilibrium in a toroidal field with plasma limiters it is necessary to start from two conditions: The plasma-loss area at the opposed-field coils must be minimized, and the plasma must be stabilized. These conditions are mutually exclusive, since an improvement of the min-B properties of the configuration through an increase in the number of opposed-field coils would result in increased plasma loss at the coils and their supports. Another important parameter in connection with the flute and drift instabilities is the distance along the magnetic lines of force between min-B regions, i.e., the connection length.[8,9] On the basis of these considerations, we feel it worthwhile to study the effect of the number of plasma limiters and the connection length on the equilibrium and stability of a plasma in a toroidal field with a heliotron configuration.

Figure 2 shows radial profiles of the plasma density, obtained from a probe which is inserted through diagnostic port 10 in Fig. 1 and moved along the radius of curvature of the toroidal field. The radial profiles shown in the three parts of Fig. 2 are obtained with different numbers of poloidal heliotron configurations in operation: four, two, and one (through which the plasma is injected). The configuration is shown at the left in each part of the figure, and typical oscillograms of the fluctuations in the ion probe current are shown at the right. In these measurements the probe is placed at the maximum of the radial density profile. The observed density fluctuations are attributed to the flute instability on the basis of the frequencies and other characteristic features.

We see from the radial profiles that the plasma is detached from the walls and is located near the $\psi = 0$ surface. Because of the toroidal nature of the system, this surface is displaced inward from the geometric axis of the chamber. However, on the basis of a) the plasma-density fluctuations (which do not decay as a function of the time) observed when one or two of the opposed-field coils are turned on, b) the displacement of the radial-profile maximum from the region bounded by the $\psi = 0$ surface along the radius of curvature, and c) the decrease in the magnitude of grad n as a function of the time, we conclude that the equilibrium established by one or two plasma limiters is not stable. The constancy of the density profile over time and the damping of the density fluctuations within the confinement volume (within the $\psi = 0$ surface) show that the plasma is in equilibrium and stable when four plasma limiters are in operation (or with a connection length equal to one-fourth the circumference of the system).

Figure 3a shows the radial profiles of the relative plasma-fluctuation levels $\tilde{n}/n$ for one, two, and four (curves 1-3, respectively) plasma limiters; Fig. 3b shows the decay constant of the plasma density as a function of the connection length (this length is inversely proportional to the number of opposed-field coils which are activated; it is defined as $L_{co} = L/n$, where L is the circumference of the system, and n = 1, 2, 4 is the number of coils in operation). From these curves and Fig. 2, which show the radial density profiles as a function of the time, we can determine the relationship between the plasma lifetime and the observed instabilities. We see from Fig. 3a that with $L_{co} = L$ (one opposed-field coil activated) the plasma is stable essentially only in the region in which the curvature is favorable, and where grad n and grad H are antiparallel; in the case $L_{co} = L/2$ the boundary of the stability region is displaced outward, along the radius of curvature, and with $L_{co} = L/4$ the density fluctuations exist only in the density-gradient region beyond the $\psi = 0$ surface near the outer wall of the toroidal chamber. On the other hand, in Figs. 2b and 2c we observe a displacement of the plasma along the radius of curvature in the cases $L_{co} = L$, L/2, and in Fig. 3b we see a decrease in the density-decay time at the position of the initial density maximum for $L_{co} = L$, L/2. If the density decay were due solely to the charge-particle loss to the opposed-field coils and supports we would expect τ to decrease with increasing L/L_{co}, since the plasma loss would increase in proportion to the number of opposed-field coils in operation. Accordingly, the observed decrease in the density-decay constant in the cases $L_{co} = L$, L/2 can apparently be attributed to a situation in which the plasma departs from equilibrium because of the plasma instabilities within the entire confinement region (in the region bounded by the $\psi = 0$ surface). In the case $L_{co} = L/2$ the loss of equilibrium due to the instabilities is less important, and in the case $L_{co} = L/4$ it is essentially negligible. The $\tau = f(L/L_{co})$ curve apparently reaches saturation because the plasma loss at the coils and at their supports becomes significant when four opposed-field coils are activated although the plasma is in stable equilibrium. Further evidence for this suggestion is the observation that when four opposed-field coils are activated the initial plasma-density level in the trap is roughly half that for the case in which fewer coils are turned on.

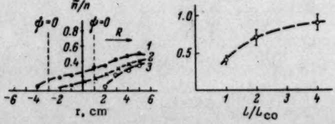

Fig. 3. a: Density-fluctuation level as a function of the radius: 1) $L_{co} = L$; 2) $L_{co} = L/2$; 3) $L_{co} = L/4$; b: Lifetime as a function of L_{co}/L.

Figure 4 shows the plasma stability in the toroidal field as a function of the connection length. The oscillograms in Fig. 4 are obtained during a single pulse by two probes at the same point in the plasma cross section but in diametrically opposite cross sections of the torus. The corresponding field configurations and probe arrangements are shown at the left of each of the oscillograms. If a given connection length ($L_{co} = L/4$; Fig. 4a) is imposed on the plasma at the probe positions, the probe signals are nearly identical, displaying no fluctuations. If the connection length is increased at the position of one of the probes ($L_{co} = 3L/4$; probes II and I; Figs. 4b and 4c, respectively), the plasma becomes unstable in these regions, while a local plasma stability is observed in regions with a shorter connection length ($L_{co} = \frac{1}{4}L$; probes I and II; Figs. 4b and 4c, respectively). The connection length is thus the decisive parameter governing the plasma stability in a toroidal field with a heliotron configuration.

Figure 5a shows density profiles of the plasma in the cross section corresponding to the position of one of the

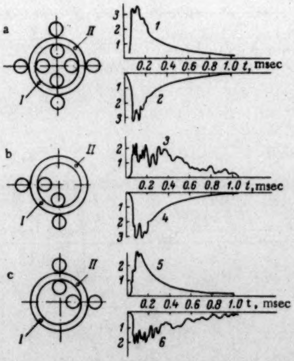

Fig. 4. Oscillograms illustrating the suppression of the flute instability as a function of connection length. 1) Probe II ($L_{co} = L/4$); 2) probe I ($L_{co} = L/4$); 3) probe II ($L_{co} = 3L/4$); 4) probe I ($L_{co} = L/4$); 5) probe II ($L_{co} = 3L/4$); 6) probe I ($L_{co} = 3L/4$).

opposed-field coils; these profiles are obtained by a probe inserted into the plasma through diagnostic part 16 in Fig. 1. This cross section corresponds to the position of the magnetic well, which is formed by the superposition of the toroidal confining field and the field of the opposed-field coil. The vertical lines show the positions of the $\psi = 0$ surface in this cross section. The arrow shows the direction of the radius of curvature of the torus.

This density profile is a typical equilibrium profile for a poloidal heliotron configuration, for which the quantity $U = -\int(dl/B)$ reaches a minimum at the $\psi = 0$ surface.[4] The oscillograms in Fig. 5b (1-3) illustrate the plasma decay at various points of the equilibrium radial profile. Oscillogram 1, obtained at point I (Fig. 5a), illustrates the absolute local stability of the plasma in the min-B region. Oscillograms 2 and 3 are obtained in the plasma bridge, in the magnetic flux linking the opposed-field coil (points 2 and 3 in Fig. 5a). A probe placed at the $\psi = 0$ surface in the bridge region reveals a plasma density equal to half the density at the same surface in the region of the absolute min B (as is evident from the radial distributions in Fig. 5a) and reveals fluctuations in the plasma density in the bridge region. However, these measurements are not correct, since the plasma dimension is comparable to the plasma thickness in the bridge, so that there could be a local decrease in the plasma density due to plasma loss at the probe. Local density perturbations caused by the probe can also cause fluctuations. However, we do not rule out the existence of plasma instabilities in the bridge region, even in the absence of density perturbations caused by the probe. The observed fluctuations in the bridge can be explained in the following manner: The plasma sheath is very thin in this region, and the plasma can be stable only on the $\psi = 0$ surface, whose width is of the order of the Larmor diameter. Accordingly, there are high density gradients ($\nabla n/n \sim \rho_i^{-1}$), which cause instabilities with a typical scale length $\gtrsim \rho_i$. Accordingly, even if the instabilities arise outside the $\psi = 0$ surface, they can fill the entire plasma volume in the bridge. A probe moved beyond the $\psi = 0$ surface from the plasma displays characteristic density spikes (oscillogram 3 in Fig. 5), which can be interpreted as corresponding to plasma ejection from the confinement region across the magnetic lines of force. The effect of plasma instabilities in the bridge on the plasma lifetime requires further study and will not be discussed here.

In other experiments we study the plasma lifetime in the field formed with four opposed-field coils; under these conditions the plasma is both in equilibrium and stable in the toroidal regions. We find the density decay constant as a function of the average ion energy and the field. These experiments are carried out with an initial plasma density $n \sim (2-4)\cdot 10^{12}$ cm^{-3}, at ion energies $W_i = (5-50)$ eV, and fields $H_{tor} = (0.6-4)$ kOe.

The plasma lifetime in this system, governed by the charged-particle loss at the supports of the opposed-field coils, can be evaluated on the basis of the following assumptions.

We assume that the plasma loss from the trap is due solely to the presence of holes in the null magnetic field (region 9 in Fig. 1), through which the plasma particles impinge on the magnetic flux linking the opposed-field coils (in the bridge region), where they can interact with the supports.

The particle behavior at the magnetic nulls is assumed to be nonadiabatic. Particle scattering by a magnetic null leads to equiprobable departure from the null along lines of force of the linking magnetic flux and along lines of flux of the basic confining field. Since the plasma in the cross sections under the opposed-field coils is localized near the field nulls, the probability for motion to a bridge after a single collision with a field null is $p_1 = 1/3$ for each individual charged particle of the confined plasma.

The particles moving along a bridge return to the field null and are not lost if they meet an obstacle, such as a coil support, along their trajectory in the bridge. The probability for the loss of a single particle after a single trip along the magnetic flux around the opposed-field coil (p_2) can be defined as the ratio of the azimuthal width of the bridge subtended by the supports to the total azimuthal dimension of the bridge. The resultant probability for the loss of a single charged particle after it has been scattered once by a field null is the product of probabilities p_1 and p_2.

We now assume that the plasma-loss rate is proportional to $p_0\nu_{i0}$, where $p_0 = p_1p_2$ and ν_{i0} is the rate with

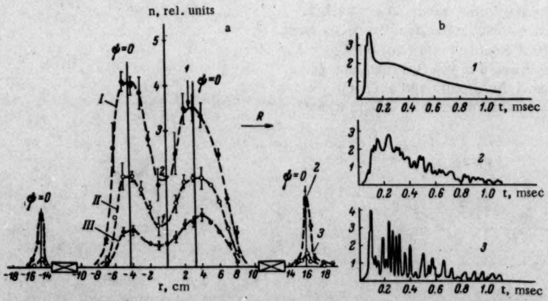

Fig. 5. a: Radial density profiles above an opposed-field coil. I) 200 μsec after the beginning of injection; II) after 400 μsec; III) after 600 μsec. b: Oscillograms of the ion probe current.

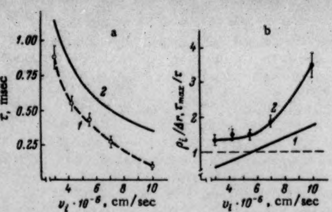

Fig. 6. a: Plasma lifetime as a function of the ion velocity. 1) Experimental; 2) calculated. b: 1) The quantity $\rho_i/\Delta r$ as a function of the ion velocity; 2) τ_{max}/τ as a function of the ion velocity.

which ions interact with the field nulls. We define ν_{i0} as $\nu_{i0} = v_i/L_{co}$, where v_i is the ion velocity and L_{co} is the distance between the opposed-field coils (or the distance between the field nulls). The plasma lifetime governed by the loss at the supports of the opposed-field coils and evaluated on the basis of these arguments is

$$\tau_{\max} = \frac{L_{co}}{v_i p_0}. \quad (1)$$

Curve 1 in Fig. 6a shows the experimental functional dependence $\tau = f(v_i)$; curve 2 shows the lifetime corresponding to loss at the supports of the opposed-field coils as a function of the ion velocity calculated from Eq. (1). Figure 6b shows two curves: Curve 1 is the ratio of the ion Larmor radius ρ in the bridge to the minimum distance from the $\psi = 0$ surface to the housing of the opposed-field coil, Δr; curve 2 shows the ratio of the calculated lifetime τ_{max} (which is apparently the maximum possible lifetime for the given system) to the experimental lifetime τ. From the curves in Fig. 6 we see that τ approaches τ_{max} when the Larmor radius does not exceed Δr. The maximum plasma lifetime determined from the geometric parameters of the system and Eq. (1) is not reached. The slight discrepancy between τ and τ_{max} at $\rho_i < \Delta r$ implies additional loss, not associated with the loss at the supports; however, this additional loss is much less important than that at the supports (an evaluation of this loss yields a plasma lifetime, calculated from the known values of τ and τ_{max}, on the order of 3.5 msec at an ion energy of 5-7 eV). Accordingly, the plasma loss from the trap at low ion energies is governed by the loss of charged particles to the supports of the opposed-field coils; at high ion energies, in which case the ion Larmor radius is comparable to or greater than the distance from the $\psi = 0$ surface in the bridge to the opposed-field coils, the plasma loss increases because of the ion loss at the coils.

This latter conclusion is also supported by the functional dependence of the decay constant on the field in the system. Figure 7 shows the $\tau \sim f(H_{tor})$ functional dependences obtained at various times: Curve 1 corresponds to 500 μsec after the beginning of injection, while curve 2 corresponds to 1500 μsec after the beginning of injection. These functional dependences are obtained with an initial plasma density of $n \sim 10^{12}$ cm^{-3} and with an average ion energy of $W_i \sim 7$ eV. We see that τ is noticeably a function of H in weak fields and that the functional dependence $\tau \sim f(H_{tor})$ becomes less pronounced in the strong fields (with $\rho_i < \Delta r$) or at later times. The increasing functional dependence in the earlier stages and in the case of weak fields can be attributed to a reduction of the particle loss at the opposed-field coils because of the reduction in the particle Larmor radius. The functional dependence of τ on time in the case of weak fields apparently results from the decrease in the average energy of the plasma ions as time elapses because the most energetic ions (for which $\rho_i \gg \Delta r$) are lost from the plasma first, at the coils and at their supports. The weak functional dependence $\tau \sim f(H)$ at later times is apparently due to a spread of the particles with respect to Larmor radius or to a reduction in the size of the magnetic hole through which the particles enter the bridge.

CONCLUSION

On the basis of these experiments we can draw the following conclusions.

1. A plasma equilibrium can be established in a toroidal magnetic field without a rotational transform if the field has a heliotron configuration.

2. The parameter governing the stability of an equilibrium plasma in a toroidal heliotron field is the connection length.

3. Suppression of the flute instability within the $\psi = 0$ surface in the toroidal regions requires a connection length no longer than one fourth the length of the system.

4. If the plasma is in a stable equilibrium within the $\psi = 0$ surface, its confinement is governed by the loss of charged particles at the supports of the opposed-field coils, which produce the heliotron configuration, provided that the average Larmor radius of the confined particles is smaller than the distance from the $\psi = 0$ surface to these coils. Otherwise (with $\rho_i \gg \Delta r$), ion loss at these cells can become significant.

5. In all the situations studied here, including that in which the ion Larmor radius is much smaller than the distance from the $\psi = 0$ surface to the coils, the maximum possible plasma lifetime for the given system is not achieved. This result implies an additional loss of charged particles (other than the loss at the supports). There are various possible mechanisms for this additional loss: First, there are the plasma instabilities observed at the boundary of the $\psi = 0$ surface, which are clearest in the plasma bridge, in the magnetic flux linking the opposed-field coils. Second, there can be particle collisions in the bridge, where the thickness of the plasma sheath is of the order of the ion Larmor diameter, and a single ion–ion collision can displace an ion from the $\psi = 0$ surface by a distance of the

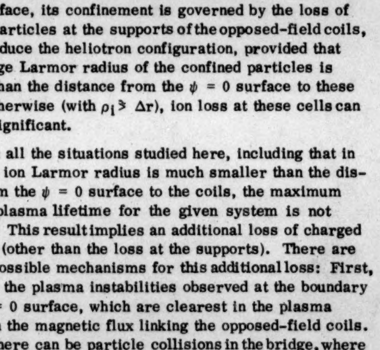

Fig. 7. Plasma lifetime as a function of the intensity of the confining field. 1) 500 μsec after the beginning of injection; 2) 1500 μsec.

order of the Larmor radius, causing it to strike an opposed-field coil.

If an effective method is found for suppressing the effect of the supports on the plasma lifetime in systems with internal conductors (e.g., through the use of magnetically shielded supports[12] or through the compensation of the loss at the supports by repeated injections[6,7]), the plasma loss due to the observed instabilities will dominate the situation. A study of the mechanisms responsible for the additional loss and quantitative estimates for these loss mechanisms are an important and necessary future step in the study of plasma confinement in a heliotron magnetic field.

---

[1] S. Yoshikawa, R. M. Sinclair, J. O. Keseler, and W. L. Harries, Phys. Fluds, 6, 932 (1963).

[2] J. Colomes and D. Veron, Phys. Fluds, 12, 1717 (1969).

[3] G. Gibson, W. C. Jordan, and E. J. Lauer, Phys. Rev. Lett., 4, 217 (1960).

[4] B. B. Kadomtsev, in: Plasma Physics and Problems of Controlled Thermonuclear Reactions [in Russian], Vol. 4, Izd. Akad. Nauk SSSR, Moscow (1958), p. 353.

[5] K. Uo, A. Mohri, H. Oshiyama, R. Kato, and K. Ishii, Phys. Fluids, 5, 1293 (1962).

[6] A. Mohri, S. Matsuda, and K. Uo, Karyugo-KenKyu, 22, 245 (1969).

[7] A. Mohri, S. Matsuda, and K. Uo, Karyugo-KenKyu, 62, 277 (1969).

[8] D. S. Wiley, Phys. Fluids, 12, 2434 (1969).

[9] F. F. Chen and K. C. Rodgers, Plasma Phys., 12, 253 (1970).

[10] V. G. Zykov, V. I. Karpukhin, N. I. Rudnev, and V. T. Tolok, Zh. Tekh. Fiz., 40, 1602 (1970).

[11] V. G. Zykov, V. I. Karpukhin, Yu. F. Lonin, N. I. Rudnev, and V. T. Tolok, Zh. Tekh. Fiz., 42, 939 (1972) [Sov. Phys. – Tech. Phys., 17, 744 (1972)].

[12] M. G. Rusbridge, Plasma Phys., 13, 33 (1971).

Plasma equilibrium and confinement in a poloidal heliotron configuration. II

V. G. Zykov, V. I. Karpukhin, Yu. F. Lonin, N. N. Podteregera, N. I. Rudnev,
A. Y. Skibenko, V. T. Tolok, and I. P. Fomin

(Submitted September 24, 1973; resubmitted January 7, 1974)
Zh. Tekh. Fiz., 44, 1713-1718 (August 1974)

The decay of an injected plasma [$n \geq 2 \cdot 10^{13}$ cm^{-3}, $n(T_e + T_i) \simeq 5 \cdot 10^{14}$ eV/cm^3] has been studied in a toridal trap with a poloidal heliotron configuration. The decay constant is found to be a function of the magnetic field H, the plasma density n, and the size of the regions in which the lines of force have an unfavorable curvature, L_{co}. This functional dependence, which can be written as $\tau \sim H/nl_{co}$, is attributed to the stabilizing effect of the poloidal heliotron configuration on the instabilities due to the toroidal nature of the system. The decay constant for the plasma density is τ = 0.5-1 msec and, in the case $L_{co} = L/4$ is in order-of-magnitude agreement with the lifetime calculated from the measured flux of ions to the supports and coils of the opposed magnetic field, which are not completely shielded magnetically.

The Pluton toroidal system is described and experimental results on the confinement of an injected plasma with the parameters $nT \sim 5 \cdot 10^{12}$ eV/cm^3 and $n \sim 10^{11}$ cm^{-3} are reported in ref. 1. Below we report experimental results on plasma confinement in the Pluton poloidal heliotron with the different initial parameters $nT \sim 5 \cdot 10^{14}$ eV/cm^3 and $n \sim 2 \cdot 10^{13}$ cm^{-3} but with the same confining field (H = 5 kOe). The parameters n and T and thus the parameter $\beta = 8\pi nkT/H^2$ of the confined plasma are increased by applying a guiding magnetic field along the plasma guide section connecting the plasma accelerator with the chamber; this magnetic field significantly reduces the loss at the guide-section walls. Because of the higher density of the confined plasma we are able to use microwave methods to study it; these methods are more accurate and more reliable than probe methods for diagnosing a decaying plasma.

The density of the trapped plasma and its functional dependence on the time are measured by means of microwave interferometers at λ = 4, 8, and 14 mm; the electric vector of the microwave signals is parallel to the external magnetic field. Since the phase shift of the wave transmitted by the plasma is

$$\Delta\varphi \sim \bar{n}l,$$

where $\bar{n}$ is the average density and l is the distance which the wave travels through the plasma, the wave is passed through the plasma twice in order to expand the range of measurable densities. In situations in which the plasma in the trap is opaque to the microwave signals (i.e., λ = 4 and 8 cm^{-3}, respectively), we measure the phase of the wave reflected from the plasma. The microwave signal is directed onto the plasma in cross sections corresponding to diagnostic ports 12 and 10 in Fig. 1 of ref. 1.

EXPERIMENTAL RESULTS

The imposition of an average min B or a connection length is the decisive factor for the plasma stabilization in the toroidal parts of the system. Accordingly, in these experiments we are primarily interested in the plasma decay as a function of connection length.

Figure 1 shows n = n(t) curves obtained for various cross sections of the chamber and for various connection lengths. The curves in Fig. 1a are obtained in a cross section near the injection point (in the cross section corresponding to the position of diagnostic port 12 in Fig. 1 of ref. 1), while the curves in Fig. 1b correspond to a remote cross section (corresponding to diagnostic port 10 in Fig. 1 of ref. 1). Curves 1 and 4 in these figures are obtained in configurations with L_{co} = L/4 and L, respectively. Curves 2 and 3 correspond to configurations with L_{co} = L/2, obtained by turning off poloidal heliotron cells IV and III, respectively (see Fig. 1 of ref. 1). We see that the slope of the curves, which is proportional to the decay constant of the plasma density, is a strong function of L_{co} in the remote cross section but independent of it in the near cross section. The decay constant for the plasma density in the near cross section is lower than that in the remote cross section for any value of L_{co}.

This difference is not due to the initial density of the plasma which fills the toroidal regions corresponding to these cross sections. The difference in the plasma decay is most clearly observed in the configuration with L_{co} = L/4, in which case heliotron cell IV, which lies between the near and remote cross sections, is activated, and the plasma density in the remote cross section falls off be-

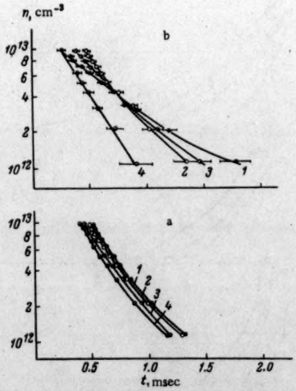

Fig. 1. The functional dependence n = n(t) for various connection lengths 1) L_{co} = L/4; 2) L_{co} = L/2 (poloidal heliotron configuration IV in Fig. 1 of ref. 1 is turned off); part b, curve 3) L_{co} = L/2 (poloidal heliotron configuration III in Fig. 1 of ref. 1 is turned off); part a, curve 3) L_{co} = L/4; 4) L_{co} = L.

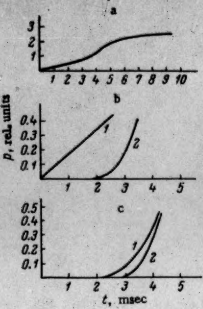

Fig. 2. Neutral-gas pressure as a function of the time. a,b) In the cross section corresponding to the position of diagnostic port 12 in Fig. 1 of ref. 1; c) in the cross section corresponding to diagnostic port 10 in that figure. In parts b and c, curves 1 correspond to the situation during plasma injection, while curves 2 correspond to the situation when only the gas-injection valve operates.

cause of scattering of the plasma by the cell. However, this difference does not vanish when heliotron cell IV is turned off, and the corresponding toroidal regions are filled with plasma of the same density.

The most probable assumption which we can make regarding the observed difference in the decay behavior is that there is an inhomogeneous distribution of the neutral gas which enters the plasma volume from the plasma accelerator and which reduces the plasma decay constant because of recombination or charge exchange. Using a pulsed gauge, whose operation is described elsewhere,[2] we evaluate the neutral gas pressure in various cross sections of the trap. This gauge is removed from the magnetic field to avoid an effect of the plasma particles on the gauge indications. Figure 2 shows the neutral gas pressure as a function of the time in the near (Fig. 2, a and b) and remote (Fig. 2c) cross sections.

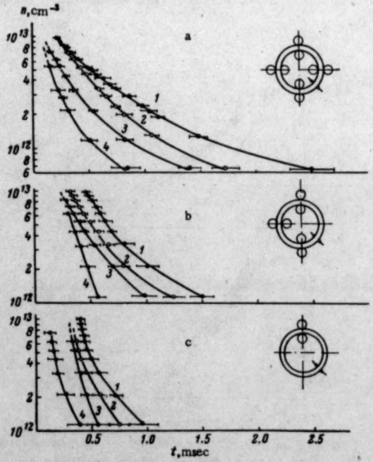

Fig. 3. The function n = n(t) for various values of L_{co} and for various values of the toroidal field. a, b, c) L_{co} = L/4, L/2, and L, respectively. H, kOe: 1) 5.0; 2) 3.0; 3) 2.0; 4) 1.0.

Figure 2a illustrates the behavior of the neutral gas pressure in the near cross section during injection of plasma into the trap. We see that the pressure in the near cross section begins to increase at the time corresponding to that at which the injected plasma arrives at the trap. Figures 2b and 2c show the pressure in the near and remote cross sections, respectively, over a shorter time interval. Curves 2 in Figs. 2b and 2c show the pressure as a function of the time for the case in which only a single pulsed valve of the accelerator is in operation, while curves 1 correspond to plasma injection from the accelerator. The difference between the behavior of the pressure during injection of the plasma and that when only the gas-injection valve operates can be attributed to the contribution of the neutral gas ejected from the chamber walls by high-energy plasma particles in the region in which the plasma enters the system. It is difficult to evaluate the absolute neutral gas pressure since we do not know the nature of the gas ejected from the chamber walls. Because of the delay in the arrival of the neutral gas in the remote cross section, the influence of this gas on the plasma decay there is apparently weak so we assume that n = n(t) obtained in the remote cross section give a correct qualitative idea of the confining properties of the poloidal heliotron configuration.

Figure 3 shows n = n (t) curves for various fields and various field configurations, characterized by different connection lengths. Comparison of Figs. 3a, 3b, and 3c clearly reveals a decrease in the confinement time with increasing connection length. We also see that the decay rate is a function of the intensity of the toroidal field and of the plasma density for a given value of L_{co}. Figure 4 shows the decay constant τ for various values of L_{co} which were calculated from these curves. For L_{co} = L/4, Fig. 4 shows two functional dependences: curve 1, for the density decay from $5.5 \cdot 10^{12}$ to $1.7 \cdot 10^{12}$ cm^{-3}; and curve 5, for that from 10^{12} to $6 \cdot 10^{11}$ cm^{-3}. To summarize these results we can write the decay constant of a dense plasma ($n \geqslant 2 \cdot 10^{12}$ cm^{-3}) as a function of n, H, and L_{co} as

$$\tau \sim \frac{H}{nL_{co}}$$

and attribute the decay to the gravitational-dissipative instability[3] of a collisional plasma for which $\lambda_{ei} \leqslant L_{co}$; the growth rate of this instability,

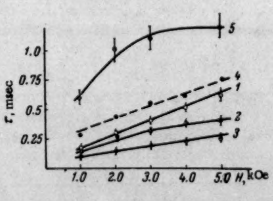

Fig. 4. Decay constant as a function of the value of the toroidal field. 1-3) L_{co} = L/4, L/2, L, respectively; 4) calculated from the measured particle flux to the opposed-field coil; 5) L_{co} = L/4 for decay over the range $6 \cdot 10^{11}$ cm^{-3} $\leq n \leq 10^{12}$ cm^{-3};

$$\mathrm{Im}\left(\frac{\omega_{bo}}{\omega_{Bi}}\right)=\left(\frac{en}{aB}\right)\left(\frac{k_{\perp}}{k_{\parallel}}\right)^{2}\frac{\rho_i^2}{R}\frac{n'}{n}, \qquad (1)$$

is proportional to L_{co}^2/H if the wavelength of the perturbation in the longitudinal direction is governed by the connection length ($\lambda_{\parallel} = 2L_{co}$).

However, as L_{co} is reduced we see from (1) that the plasma lifetime against the gravitational-dissipative instability increases in proportion to L_{co}^{-2}. The plasma loss at the opposed-field coils (which produce the heliotron configuration) and at the supports for these coils increases linearly with decreasing L_{co} (the connection length is inversely proportional to the number of opposed-field coils in operation and is defined by $L_{co} = L/k$, where L is the circumference of the system and k is the number of opposed-field coils in operation). Accordingly, with $L_{co} = L/4$ we would expect a significant decrease in the contribution of the gravitational-dissipative instability, so that the plasma decay would be governed primarily by particle loss at the opposed-field coils and their supports.

We measure the ion flux to the frame of one of the opposed-field coils; curve 2 in Fig. 5 shows the flux to the coil frame along with that to the conductor and the supports as a function of the field intensity. Curve 1 shows the ion flux to the coils without the conductor and supports (which are insulated from the plasma). We see that the particle flux to the coil in the case of the insulated conductor and supports is essentially the same as that in the absence of insulation. This result is evidence that the plasma particles are lost at the coil along its entire perimeter and that only a slight fraction of the plasma particles are lost at the conductor and supports (the fraction is proportional to the part of the coil perimeter occupied by the conductor and supports). Accordingly, under these experimental conditions the opposed-field coils are not completely shielded magnetically from contact with the plasma. The inverse proportionality between the ion current to the coil frame and the field intensity can be explained in the following manner: Because of the small distance between the $\psi = 0$ surface in the plasma "bridge" (in the magnetic flux linking the opposed-field coil) to the coil housing, and because of the low field intensity in the plasma bridge, the plasma ions can strike the coils as they move along lines of force in the bridge. The thickness of the plasma sheath in the bridge is on the order of two Larmor diameters, falling off with increasing field intensity. The number of ions whose Larmor diameter is comparable to or greater than the distance from the $\psi = 0$ surface to the coil housing decreases in proportion to the change in the Larmor diameter. The linear functional dependence $\tau \sim f(H)$ can be attributed on the basis of these measurements of the ion flux to the coil in the case $L_{co} = L/4$ to plasma loss at the opposed-field coils. However, the presence of neutral gas in this system and the inhomogeneity of the profiles of the plasma and neutral-gas densities along the perimeter of this system prevent final conclusions regarding the contribution of particle loss at the coils and that of loss due to the toroidal nature of the system. Estimates show a correspondence between the experimental lifetime and the lifetime calculated from the measured flux and an average plasma density assumed equal to the density in the remote cross section, where the measurements were carried out (curve 4 in Fig. 4). On the other hand, the probe measurements show that the plasma is not unstable in the toroidal regions within the $\psi = 0$ surface if $L_{co} = L/4$. We can therefore assume that the functional and quantitative dependence $\tau \sim f(H)$ in the configuration with $L_{co} = L/4$ is governed primarily by the loss of plasma particles at the opposed-field coils and its supports, which are not completely magnetically shielded under the given experimental conditions.

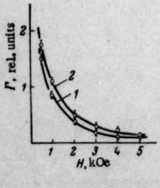

Fig. 5. Ion flux to the opposed-field coil. 1) Insulated current conductor and coil supports; 2) no insulation.

As was mentioned above, the weak magnetic shielding of the opposed-field coils is due to the weakness of the opposed field and the correspondingly small distance from the $\psi = 0$ surface to the opposed-field coil. In addition, the magnetic insulation of the opposed-field coils could be disrupted by neoclassical plasma diffusion to the coils in the plasma bridge. If the plasma dimensions in the bridge is $2\rho_i$ and if $T_e \sim T_i$, the particle flux to the coils due to neoclassical diffusion is

$$nv_r = D_{ei}\frac{du}{dr} \simeq \rho_e^2\nu_{ei}\frac{n}{2\rho_i} = \frac{1}{2}\sqrt{\frac{M}{m}}\rho_e\nu_{ei}n.$$

The particle flux to the coil due to neoclassical diffusion also corresponds in magnitude to the experimental flux; this flux turns out to be proportional to H^{-1} and to the plasma density n. Then we can attribute the functional dependences $\tau \sim f(H)$ and $\tau \sim f(1/n)$ to neoclassical diffusion in the bridge.

CONCLUSIONS

On the basis of these experiments we draw the following conclusions:

1. The decay constant of a plasma held in equilibrium by plasma limiters of a poloidal heliotron magnetic configuration is governed by the connection length; this result is quantitative evidence that toroidal drift and the plasma instabilities due to the toroidal nature of the system are stabilized efficiently by the poloidal heliotron configuration.

2. At all connection lengths we find the decay constant to be a function of the field intensity and the plasma density. This functional dependence, which can be written qualitatively as $\tau \sim H/nL_{co}$ can be attributed to the gravitational-dissipative instability of the plasma in the field regions with an unfavorable curvature of the magnetic lines of force if the dimensions of these regions, L_{co}, are large enough.

3. If the connection lengths are short so that the relative contribution of the gravitational-dissipative

instability to the plasma decay must be significantly reduced (because of $\mathrm{Im}\,\omega_p \sim L_{co}^2$), no significant plasma instabilities are observed in the toroidal regions, and we assume that the observed decay is due to plasma loss at the opposed-field coils, which are weakly shielded magnetically in these experiments.

4. The weak magnetic shielding of the opposed-field coils is due to the weakness of the opposed field and the short distance from the $\psi = 0$ surface (in the plasma bridge in the magnetic flux linking the opposed-field coils) to the coil housing. The magnetic shielding of the opposed-field coils can also be disturbed because of neoclassical plasma diffusion in the narrow sheath of the plasma bridge.

5. Since the plasma volume contains neutral gas ejected from the chamber walls and coils, and since the opposed-field coils are not completely shielded magnetically, we cannot find quantitative estimates of the relative contributions of these processes to the quality of the confinement of a dense plasma in a poloidal heliotron field. Further experiments should be carried out with stronger opposed fields and with a different method for producing the plasma.

---

[1] V. G. Zykov, V. I. Karpukhin, Yu. F. Lopin, N. I. Rudnev, and V. T. Tolok, Zh. Tekh. Fiz., 44, in press.

[2] V. B. Yuferov, E. I. Skibenko, A. M. Il'chenko, Yu. F. Kholod, A. I. Maslov, and M. Yu. Bredikhin, Zh. Tekh. Fiz., 41, 1708 (1971).

[3] F. F. Chen, Phys. Fluids, 8, No. 5 (1965).

Nonequilibrium ionization in the cathode region of a high-pressure arc

S. P. Reshenov

Moscow Energy Institute

(Submitted April 26, 1973; resubmitted December 18, 1973)
Zh. Tekh. Fiz., 44, 1719-1723 (August 1974)

The electron energy and velocity distribution and the rates of nonequilibrium ionization are calculated in the cathode region of a high-pressure arc. If the plasma temperature is low or if the sheath cooled by the cathode is large nonequilibrium ionization can make an important contribution to the ion current to the cathode.

1. To determine the ion current density to the cathode in the present models of the cathode spot of a high-pressure arc discharge[1,2] it is usually assumed that the ions are emitted by a hot plasma located some distance from the cathode, local thermodynamic equilibrium obtaining. It is noted in ref. 3 that electrons emitted by the cathode and accelerated in the Langmuir sheath can participate in the ionization near the cathode, but the quantitative contribution of this mechanism is still unclear. In the present paper, we estimate the contribution of nonequilibrium ionization of the gas near the cathode in a high-pressure arc with a refractory cathode.

The electron distribution function is usually determined before the rate of nonequilibrium ionization is calculated. Since, according to ref. 3, the ion portion of the current to the cathode is several tens of percent, calculation of the electron distribution function should allow for its energy relaxation due not only to Coulomb interaction between fast and plasma electrons, but also due to inelastic collisions between electrons and neutrals. A similar problem is solved in ref. 4 for the case of a low-voltage arc, where the cathode potential drop is smaller than the first excitation potential. The opposite relationship[3] holds more often in a high-pressure arc and is assumed below.

The electron distribution function in the plasma near the cathode is represented in the form[5]

$$f(\eta,\ \xi)=f_0(\eta)\left[1+\psi(\eta,\ \xi)-\cos\alpha\,\frac{\lambda_y}{L}\,\frac{\partial\psi}{\partial\xi}\right], \tag{1}$$

where

$$\xi=\frac{x}{L};\quad L=\sqrt{\frac{\eta_k\lambda_k\lambda_y}{3}};\quad \eta=\frac{eU}{T_e};\quad \eta_k=\frac{eU_k}{T_e},$$

x is the distance to the cathode; λ_y and λ_k are the electron mean free paths for scattering by atoms and electrons; α is the angle between the normal to the cathode and the electron velocity vector; eU is the electron energy; U_k is the potential drop in the sheath near the cathode, and

$$f_0(\eta)=n_e\left(\frac{m_e}{2\pi T_e}\right)^{3/2}e^{-\eta}.$$

The correction $\psi(\eta,\ \xi)$ is determined by the solution of the equation[4]

$$\frac{\partial^2u}{\partial\xi^2}+\frac{\partial^2u}{\partial\varepsilon^2}-\left[\theta(E)\delta+\frac{1}{4}\right]u-\delta(1-\nu_1)e^{-\varepsilon/2}\theta(\varepsilon)=0 \tag{2}$$

with the boundary conditions

$$\left.\begin{aligned}\xi=0,\quad &\frac{\partial u}{\partial\xi}=0; && \varepsilon<\varepsilon_k,\\ &-a(\varepsilon)\frac{\partial u}{\partial\xi}=\varphi(\varepsilon), && \varepsilon>\varepsilon_k,\\ &\xi=\infty,\ u=0, &&\end{aligned}\right\} \tag{3}$$

where $u=\psi e^{-\varepsilon/2}$; $\varepsilon=\eta-\eta_b$; $\eta_b=eU_b/T_e$; $\delta=\eta_k\lambda_k n_a\sigma(\eta_k)$; U_b is the excitation potential of the first excited atomic level; $\nu_1=n_1/n_{1p}$; $n_{1p}=(g_1/g_0)n_a e^{-eUb/Te}$; n_a and n_1 are the densities of the normal and excited atoms; $\sigma(\eta_k)$ is the excitation cross section of the first excited atomic state for an electron energy equal to eU_k;

$$\theta(\varepsilon)=\begin{cases}1 & \text{for}\quad \varepsilon>0,\\ 0 & \text{for}\quad \varepsilon<0;\end{cases}$$

$$\varepsilon_k=\eta_k-\eta_b;\quad a(\varepsilon)=\frac{4\eta\lambda_y e^{\varepsilon/2}}{3L(\varepsilon-\varepsilon_k)},$$

$$\varphi(\varepsilon)=\Theta\exp[-(\beta-1)(\varepsilon-\varepsilon_k)];\quad \Theta=\frac{4j_{ek}\beta^{3/2}}{en_e v_e}e^{\eta_k},$$

$$\beta=\frac{T_e}{T_k};\quad v_e=\sqrt{\frac{8T_e}{\pi m_e}},$$

j_{ek} is the electron current density to the cathode; T_e and T_k are the temperatures of the plasma electrons and the cathode.

The boundary condition for $\xi=0$ and $\varepsilon>\varepsilon_k$ is approximate. It is obtained from an exact expression[5] if the following inequalities are satisfied: $(\varepsilon-\varepsilon_k)\ll\eta_k$, $a(\varepsilon)\gg1$ and $\varphi(\varepsilon)\gg1$; this is usually true in the neighborhood of the point $\varepsilon=\varepsilon_k$ for small ξ for gases with large U_b.

In the right-hand side of Eq. (2) the last term in the first approximation can be neglected since the energy range $\psi\gg1$ is of interest in practical problems. From the physical point of view this means that processes involving production and loss of fast electrons are not included in the interactions between plasma electrons and excited and normal atoms.

The solution of Eq. (2) with boundary conditions (3) is found by dividing the entire energy range into three intervals: 1) $\varepsilon<0$, 2) $0<\varepsilon<\varepsilon_k$, 3) $\varepsilon>\varepsilon_k$; and by using the Fourier cosine transform in the variable ξ. As a result, we have

$$\varepsilon<0;\quad \frac{\partial^2\Phi_1}{\partial\varepsilon^2}-p\Phi_1=0, \tag{4}$$

$$0<\varepsilon<\varepsilon_k;\quad \frac{\partial^2\Phi_2}{\partial\varepsilon^2}-p_1\Phi_2=0, \tag{5}$$

$$\varepsilon>\varepsilon_k;\quad \frac{\partial^2\Phi_3}{\partial\varepsilon^2}-p_1\Phi_3-\sqrt{\frac{2}{\pi}}\left.\frac{\partial u}{\partial\xi}\right|_{\xi=0}=0, \tag{6}$$

whose solutions under the continuity condition $\psi(\eta,\ \xi)$ and its first energy derivative at the limits of the intervals are

$$\Phi_1(\varepsilon,\ k)=\frac{Me^{-p_1\varepsilon_k+p\varepsilon}}{(p_1+p)(\gamma+p_1)^2}, \tag{7}$$

$$\Phi_2(\varepsilon,\ k)=\frac{Me^{-p_1(\varepsilon_k-\varepsilon)}}{2p_1(\gamma+p_1)^2}\left(1+\frac{p_1-p}{p_1+p}e^{-2p_1\varepsilon}\right), \tag{8}$$

$$\Phi_3(\varepsilon_1,\ k)=M\left[\frac{e^{-p_1\varepsilon_1}}{2p_1(\gamma+p_1)^2}\left(1+\frac{p_1-p}{p_1+p}e^{-2p_1\varepsilon_k}\right)\right. +$$

$$+\frac{2\gamma e^{-p_1\varepsilon_1}}{(\gamma^2-p_1^2)^2}\left(1-e^{-\varepsilon_1(\gamma-p_1)}\right)-\varepsilon_1\frac{e^{-\gamma\varepsilon_1}}{\gamma^2-p_1^2}\Bigg], \qquad (9)$$

where

$$p=\sqrt{k^2+\frac{1}{4}},\quad p_1=\sqrt{p^2+\delta}+\frac{1}{4},\quad \gamma=\beta-\frac{1}{2},$$

$$M=\sqrt{\frac{2}{\pi}}\frac{3L\Theta}{4\lambda_y\eta}e^{-\varepsilon_k/2};\quad \varepsilon_1=\varepsilon-\varepsilon_k.$$

In determining the Fourier cosine transforms Φ_1, Φ_2, and Φ_3, the terms η and M are assumed to be constant. This procedure corresponds to neglecting terms of the order of T_k/eU_k compared to unity.

2. The excitation rate of the lower excited state is found from

$$z(\xi)=\frac{n_e v_e}{\lambda_n}e^{-\eta\delta}\int_0^\infty e^{-\varepsilon/2}\varepsilon\eta u(\varepsilon,\xi)\,d\varepsilon, \qquad (10)$$

where λ_n is the electron mean free path for an exciting collision at an electron energy $eU = eU_k + T_e$. The integral excitation rate in the range $0 < x < L\xi$ is determined from

$$Z(\xi)=\frac{eL}{j_{ek}}\int_0^\xi z(\xi)\,d\xi. \qquad (11)$$

With allowance for (8)-(10), the expression for $Z(\xi)$ becomes

$$Z(\xi)=\frac{2\lambda_k}{\pi\lambda_n}\eta_k\int_0^\infty R(k,\varepsilon_k,\beta,\delta)\frac{\sin k\xi}{k}\,dk, \qquad (12)$$

where

$$R(k,\varepsilon_k,\beta,\delta)=\frac{\beta^2}{2p_1(p_1+\gamma)^2}\Bigg\{\frac{\varepsilon_k}{p_1-\frac{1}{2}}\left[1-\frac{1-e^{-\left(p_1-\frac{1}{2}\right)\varepsilon_k}}{\varepsilon_k\left(p_1-\frac{1}{2}\right)}\right]$$
$$+\frac{p_1-p}{\left(p_1+\frac{1}{2}\right)(p_1+p)}e^{-p_1\varepsilon_k}\left[\frac{1}{p_1+\frac{1}{2}}-\left(\varepsilon_k+\frac{1}{p_1+\frac{1}{2}}\right)e^{-\varepsilon_k\left(p_1+\frac{1}{2}\right)}\right]$$
$$+\frac{4p_1\gamma}{(\gamma-p_1)^2}\left[\varepsilon_k\left(\frac{1}{p_1+\frac{1}{2}}-\frac{1}{\beta}\right)+\frac{1}{\left(p_1+\frac{1}{2}\right)^2}-\frac{1}{\beta^2}\right]$$
$$+\left(1+\frac{p_1-p}{p_1+p}e^{-2p_1\varepsilon_k}\right)\frac{\varepsilon_k}{p_1+\frac{1}{2}}\left[1+\frac{1}{\varepsilon_k\left(p_1+\frac{1}{2}\right)}\right]$$
$$-\frac{2p_1(\gamma+p_1)}{(\gamma-p_1)\beta^2}\left(\varepsilon_k+\frac{2}{\beta}\right)\Bigg\}.$$

If the ionization is predominantly cascade in nature, and the redistribution of atoms between the upper excited states and ionization from excited states are due to plasma electrons, then the relation found for $Z(\xi)$ can be used to estimate the upper limit of the ionization rate.

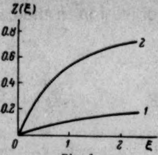

Fig. 1

Figure 1 gives $Z(\xi)$ for two values of δ with $\varepsilon_k = 1$ and indicates that with increasing δ the ionization rate increases and the ionization region as a whole moves toward the cathode. When $\delta > 1$, the linear dimension of the nonequilibrium ionization region in the direction perpendicular to the cathode becomes almost $L' = \sqrt{\lambda_y/3n_a\sigma(\eta k)}$. Figures 2 and 3 give the total excitation rate1) (Z_∞) as a function of δ for $\varepsilon_k = 1$ and as a function of ε_k for $\delta = 0.1$, 1.0. In all cases the maximum value of Z_∞ is of order unity; for a cathode fall of the order of the first excitation potential each electron exiting from the cathode cannot experience more than one excitation event.2)

Table 1 illustrates the contribution of nonequilibrium ionization to the ion current to the cathode for different temperatures of the plasma near the electrode. The calculations have been performed for argon at an initial atomic density of $2.69 \cdot 10^{19}$ cm^{-3}, corresponding to a cold pressure of 1 atm, with $\varepsilon_k = 1$. The equilibrium electron density is determined from the Saha equation

$$\frac{n_e n_i}{n_a}=\frac{2g_i}{g_a}3\cdot10^{21}T_e^{3/2}e^{-\frac{eU_i}{T_e}}, \qquad (13)$$

where n_e and n_i are the electron and ion densities, g_a and g_i are the statistical atomic and ionic weights, and U_i is the ionization potential. The limiting value of the fraction of ion current to the cathode provided by nonequilibrium ionization was determined, as in ref. 6, by

$$\frac{\mu_n}{1-\mu_n}=Z_\infty, \qquad (14)$$

where $\mu_n = j_i/j_p$; j_i and j_p are the ion and discharge cur-

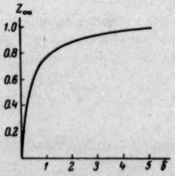

Fig. 2

TABLE 1

	T_e, eV				
	0.50	0.75	1.0	1.5	2.0
n_e, cm^{-3}	$5.19\cdot10^{13}$	$1.29\cdot10^{16}$	$2.22\cdot10^{17}$	$3.80\cdot10^{18}$	$1.05\cdot10^{19}$
λ_k, cm	$0.66\cdot10^{-3}$	$0.80\cdot10^{-4}$	$0.98\cdot10^{-5}$	$1.52\cdot10^{-6}$	$1.00\cdot10^{-6}$
λ_n, cm	$6.6\cdot10^{-3}$	$4.4\cdot10^{-3}$	$3.3\cdot10^{-3}$	$2.2\cdot10^{-3}$	$1.65\cdot10^{-3}$
δ	24.3	0.30	$3.8\cdot10^{-2}$	$6.1\cdot10^{-3}$	$4.1\cdot10^{-3}$
Z_∞	~1	0.48	0.11	0.018	0.012
μ_n	0.50	0.32	0.099	0.018	0.012
μ_p	$2.4\cdot10^{-6}$	$7.2\cdot10^{-4}$	$1.43\cdot10^{-2}$	0.30	0.96

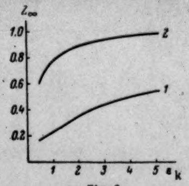

Fig. 3

rent densities to the cathode.

The flux of ions to the cathode in the case of equilibrium ionization and the corresponding value of the ion fraction of the current μ_p are determined from

$$j_i = \frac{en_i}{4}\sqrt{\frac{8T_e}{\pi m_i}}, \tag{15}$$

where m_i is the ionic mass.[3)]

According to the results of the calculation shown in the table, if the temperature of the hot plasma near the cathode does not exceed 1 eV or the longitudinal dimension of the plasma region cooled by the cathode and located between it and the hot plasma is of the order of L', then nonequilibrium ionization can make an important contribution to the ion current to the cathode. It should be noted that at low plasma temperatures, due to the small density of plasma electrons, ionization of the excited state is provided by fast (emission) electrons. It is not difficult to show that in this case the limiting value of Z_∞ is 0.5 and that of μ_n corresponds to 1/3. In this case, however, the contribution of nonequilibrium ionization near the cathode to the thermal plasma is comparatively large. We note also that with intense nonequilibrium ionization near the cathode and a low plasma temperature the density of plasma electrons can appreciably exceed the value obtained from the Saha equation. However, this cannot lead to a substantial decrease in the nonequilibrium ionization rate since it is the primary cause of the increase in the concentration of plasma electrons. In conclusion, it should be noted that the above considerations as to the contribution of nonequilibrium ionization near the cathode to a thermal plasma are preliminary in nature. Further refinement of the situation requires that one take into account the effect of transitions between excited atomic states on the ionization rate and on relaxation of the electron distribution function, and also determine the temperature distribution and plasma electron density in the cathode region.

[1)] The value of Z_∞ is determined from (11) for $\xi \to \infty$.

[2)] In individual cases, Z_∞ exceeds unity by an amount T_k/T_e. This occurs because $\sigma(\eta_k)$ is assumed constant when determining $\psi(\eta, \xi)$, while the linear dependence of the cross section above the excitation threshold is used to obtain Eq. (12).

[3)] When calculating μ_p, the characteristic discharge current density in the cathode spot is taken[3] to be $j_p = 5 \cdot 10^4$ A/cm^2.

[1] J. Slepian, Phys. Rev., 27, 407 (1926).
[2] B. Ya. Moizhes and V. A. Nemchinskii, Zh. Tekh. Fiz., 42, 1001 (1972) [Sov. Phys.-Tech. Phys., 17, 793 (1972)].
[3] V. L. Granovskii, Electric Current in Gases. Steady-State Current [in Russian], Nauka, Moscow (1971).
[4] L. P. Stakhanov and V. E. Cherkovets, Zh. Tekh. Fiz., 41, 1400 (1971) [Sov. Phys.-Tech. Phys., 16, 1102 (1972)].
[5] I. P. Stakhanov, Zh. Tekh. Fiz., 37, 1277 (1967) [Sov. Phys.-Tech. Phys., 12, 929 (1968)].
[6] S. P. Reshenov, Svetotekhnika, No. 4, 7 (1972).

Quantum electronics

Plasma dynamic lasers

S. A. Reshetnyak and L. A. Shelepin

(Submitted September 4, 1973)
Zh. Tekh. Fiz., 44, 1724-1732

In the rapid expansion of a dense, highly ionized plasma in the plasma laser, the electron gas is cooled, the plasma recombines, and lasing occurs on atomic transitions. A method of calculating these is developed using quasistationary analytic population distribution functions over discrete levels. A quenching effect is considered for a hydrogen plasma and a radiative mechanism for emptying the lower laser level is analyzed. The possibility of an effective collision mechanism for lithium, helium, and beryllium plasmas is pointed out which would permit the use of large plasma volumes for generation. The dependence of population inversion on a number of parameters is studied.

1. INTRODUCTION

There has been a rapid growth in research on gasdynamic lasers, in which lasing occurs by virtue of vibrational–rotational transitions in molecules (primarily CO_2). Several such lasers have been developed; among them is the electrogasdynamic laser, in which a discharge is used to increase the efficiency. High powers have been obtained in the continuum regime.

Plasma dynamic lasers, in which a population inversion is created on atomic transition in plasma expansion, have not been developed to as great a degree. The plasma dynamic laser is evaluated in ref. 1, where the possibility of creating a population inversion as a result of recombination in adiabatic expansion of a highly ionized plasma (field free or magnetized) is considered.

Experimentally, a population inversion has been observed[2] in a plasma jet expanding through a nozzle in argon, between the lower 5p levels and 4p levels, and in helium, between levels with n = 4 and n = 3 (n is the principal quantum number). Spectroscopic measurements[3] in a hot high-pressure arc in mixtures of helium and methane or argon and methane which expand in a nozzle yield observation of a population inversion in the neutral carbon line corresponding to the transition $2p^{21}S_0 \rightarrow 2p3s\,{}^1P_1^0$ (λ = 2478.6 Å). In addition population inversion is observed in neon[4] and in regions of low electron density in hydrogen.[5,6]

A theoretical treatment of the relaxation processes in plasma expansion is carried out in refs. 7-10. The numerical calculations of refs. 9 and 10 show the possibility of obtaining a population inversion on a neutral nitrogen line (λ = 1745 Å) and in lines of neutral xenon (7p–5d, 4*f*–5d).

The significance of plasma dynamic lasers (compared with usual gasdynamic lasers) lies, first of all, in the possibility of extending the wavelength to the visible and ultraviolet regions of the spectrum. However, there are important difficulties, connected with the rate of relaxation of atomic systems, the complexity of analysis of inversion in plasma jets, and the choice of optimal conditions and materials.

The purpose of the present paper is to present a computational design method for plasma dynamic lasers based on quasistationary analytic population distribution functions, and, to show that in such lasers a collisional mechanism for emptying the lower level can work efficiently, permitting the use of large volumes for efficient lasers.

2. POPULATION OF ATOMIC LEVELS IN PLASMA EXPANSION. COMPUTATIONAL METHOD

We consider electron–ion recombination due to cooling of the electrons as a plasma expands. It is assumed that the plasma is initially in thermodynamic equilibrium at an electron temperature, T_e. At some point the ionization of the plasma begins to deviate from the equilibrium value. In the flow a population inversion can develop between the discrete atomic (ionic) levels in the recombining plasma.

In a general analysis of inversion in expansion of a plasma it is necessary to solve simultaneously the equations for population relaxation, electron temperature, and gas dynamics. We shall assume that the characteristic time for changes in the electron temperature, T_e, is much greater than the time for establishment of a quasistationary distribution.[9] Thus, a quasistationary distribution of excited atomic states exists.

In order to present the clearest explanation of this new computional method for plasma dynamic lasers, we have not considered in any detail the questions of gas dynamics and recombination heating of electrons; rather, we have assumed T_e and N_e to be given functions of time. (The calculation of T_e and N_e is similar to that for ordinary gasdynamic lasers.) Emphasis is placed on the quasistationary population distribution functions.

We consider the system of equations for population balance over the discrete levels of an atom:

$$\left.\begin{aligned} \frac{dN_{nl}}{dt} + N_{nl}\operatorname{div}\mathbf{v} = N_e \sum_{n'l' \neq nl} [V(n'l',\, nl)\, N_{n'l'} \\ - V(nl,\, n'l')\, N_{nl}] \\ + \sum_{E_{n'l'} > E_{nl}} A(n'l',\, nl)\, N_{n'l'} - \sum_{E_{n'l'} < E_{nl}} A(nl,\, n'l')\, N_{nl}, \\ \frac{dN}{dt} + N\operatorname{div}\mathbf{v} = 0, \end{aligned}\right\} \quad (2.1)$$

where N_{nl} and E_{nl} are the population and energy of the nl-th energy level (n is the principal quantum number, and l is the orbital quantum number), $V(nl,\, n'l')$ is the transition probability from states nl to $n'l'$ due to atomic collisions with electrons as averaged over a Maxwellian electron distribution, $A(nl,\, n'l')$ is the radiative transition probability from nl to $n'l'$ per unit time, N_e is the electron density, and v is the hydrodynamic expansion velocity of the plasma.

Substituting

$$N_{nl} = N g_{nl} \exp\left(-\frac{E_{nl}}{kT_e}\right) f_{nl} \qquad (2.2)$$

(where g_{nl} is the statistical weight of the level nl and k is Boltzmann's constant) and using the relation between forward and reverse transitions, we obtain

$$f_{nl}^{(1)} = \frac{1}{N_e}\frac{df_{nl}}{dt} = \sum_{n'l' \neq nl} V(nl,\ n'l')(f_{n'l'} - f_{nl}) \qquad (2.3)$$

for the case of a dense plasma, in which radiative decay can be neglected.

The system of Eqs. (2.3) is formally identical to the system of equations considered in ref. 11, where the distribution function, N_{nl}, is obtained for constant N and T_e in the "single-photon approximation" for n, including optically allowed transitions, and assuming a Boltzmann distribution in l. Using the results of ref. 11 and considering the energy levels of lithium, we have

$$N_{nl} = N_{2s} g_{nl} \exp\left(-\frac{E_{nl}}{kT_e}\right)(1 + \beta_{ns}^1 \varkappa), \qquad (2.4)$$

$$\beta_{ns}^1 = \sum_{m=2}^{n-1} \frac{1}{V^*(ms,\ m+1p)}\left(1 + \sum_{i=3}^{m}\prod_{k=i}^{m} \frac{V(ks,\ k-1p)}{V^*(k-1s,\ kp)}\right), \qquad (2.5)$$

and

$$\varkappa = \frac{1}{N_e}\frac{d}{dt}\ln\frac{N_{2s}}{N} = \frac{f_{2s}^{(1)}}{f_{2s}}; \quad (E_{2s} = 0,\ g_{nl} = 2l+1). \qquad (2.6)$$

Here,

$$V^*(ms,\ m+1p) = V(ms,\ m+1p)\exp\left(\frac{E_{m+1p} - E_{m+1s}}{kT_e}\right)$$

are the effective ionization probabilities for the transition [ms → (m + 1) s], and s, p, d, . . . are the spectroscopic notation for the orbital quantum number l.

The terms with second, third, etc., derivatives can be neglected if

$$\left|\frac{f_{2s}^{(2)}}{f_{2s}^{(1)}}\right| \ll \frac{\exp\left(\frac{E_{ns}}{kT_e}\right)}{g_{ns}\beta_{ns}^1} \quad (n = 3,\ 4,\ \ldots). \qquad (2.7)$$

We consider recombination for $N_i = N_e$ and for times beginning at which the population distribution function, Eq. (2.4), deviates from the Boltzmann case ($\beta_{ns}^1 \varkappa \gg 1$) while the population of the ground state of lithium, N_{2s}, exceeds significantly the population of the excited states, being equal to the neutral density ($N_{2s} = N_0 = N - N_e$). That is, we assume the following inequalities:

$$\frac{1}{\beta_{ns}^1} \ll \varkappa \ll \frac{\exp\left(\frac{E_{ns}}{kT_e}\right)}{g_{ns}\beta_{ns}^1} \ (n = 3,\ 4,\ \ldots). \qquad (2.8)$$

Introducing the ionization, $x = N_e/N$, and combining the distribution function obtained in Eq. (2.4) and the Saha distribution for upper levels ($n \geq n_0$), we obtain the following equation for the ionization:

$$N_{2s}\varkappa = \frac{K(T_e)}{\beta_{n_0s}^1(T_e)} N_e^2 \ \text{or} \ \frac{dx}{dt} = -\frac{K(T_e)}{\beta_{n_0s}^1(T_e)} N^2 x^3, \qquad (2.9)$$

where

$$K(T_e) = \frac{1}{Z_1}\left(\frac{2\pi\hbar^2}{mkT_e}\right)^{3/2}\exp\left(\frac{I}{kT_e}\right)$$

is the ionization equilibrium constant, z is the statistical sum for the lithium ion, I is the ionization potential of lithium, m is the mass of the electron, and ħ is Planck's constant.

3. RECOMBINATION OF A HYDROGEN PLASMA. RADIATIVE MECHANISM FOR POPULATION INVERSION

A number of simple features in the change of the population distribution function in expansion are evident in a hydrogen plasma. The expression for the relaxation factor, Eq. (2.5), for hydrogen can be written in the form

$$\beta_{n_0}^1 = \sum_{m=2}^{n_0} \frac{\exp\left(\frac{E_m}{kT_e}\right)}{g_m V(m,\ m-1)} \sum_{k=1}^{m-1} g_k \exp\left(-\frac{E_k}{kT_e}\right). \qquad (3.1)$$

Substituting in Eq. (3.1), using the equation for the probabilities V (m, m − 1) (cf. ref. 12), and limiting discussion to low recombination temperatures (such that $\sum_{k=1}^{m-1} g_k \exp(-E_k/kT_e) \simeq 1$, we have

$$\beta_{n_0}^1 = \frac{10^7}{1.73}\left(\frac{kT_e}{R}\right)^{1/2}\exp\left(\frac{R}{kT_e}\right)\sum_{m=2}^{n_0}\frac{(2m-1)^4}{[m(m-1)]^5}\,\frac{\exp\left(-\frac{R}{kT_e m^2}\right)}{U\left(\frac{E_{m,\,m-1}}{kT_e}\right)}, \qquad (3.2)$$

where R is the Rydberg constant, $U(x) = 1 + x\,\mathrm{Ei}(-x)\exp x$, and $\mathrm{Ei}(-x)$ is the exponential integral.

The summation in Eq. (3.2) has a sharp maximum in m: for small m the first terms in the summation are small because of the smallness of the exponential factor, resulting from the large distance between neighboring energy levels; for large m these are small because of the higher transition probabilities, V (m, m − 1). The term with $m = m^*$, which makes the basic contribution to the sum Eq. (3.2), corresponds to the so-called "bottleneck" in the energy level spectrum of the hydrogen atom. This bottleneck has an important effect on the entire recombination process.

By finding the extremum in m in the term following the summation in Eq. (3.2) it is possible to find the location of the bottleneck in the spectrum of energy levels of hydrogen for two limiting cases of the function U (x). For $x \ll 1$, U (x) = 1, and m^* is the root of the equation

$$\frac{R}{kT_e} = \frac{m^2}{2(2m-1)(m-1)}[18m^2 - 18m + 7], \quad m^* \simeq \frac{1}{3}\sqrt{\frac{2R}{kT_e}}.$$

For $x \gg 1$, U (x) = 1/x, and m^* is a root of the equation.

Evaluation of the sum in Eq. (3.2) by means of an electronic computer shows that for temperatures in the interval 0.1 eV ≤ kT_e ≤ 1.2 eV the factor $\beta_{n_0}^1$ is well approximated by an analytic expression of the form

$$\beta_{n_0}^1 = (1.4 \pm 0.2) \cdot 10^8 T_e^4(\mathrm{eV}) \exp\left(\frac{R}{kT_e}\right). \quad (3.3)$$

The lower the electron temperature, the higher the bottleneck. The bottleneck m = m* divides the energy level spectrum into two parts. The population distribution function for energy levels which lie below the bottleneck $[\beta_n^1 \simeq \exp(E_n/kT_e)/g_n V(n, n-1)]$ deviates strongly from equilibrium. For energy levels above the bottleneck $(\beta_n^1 \simeq \beta_{n_0}^1)$ we have almost a Boltzmann distribution in equilibrium with the continuous spectrum. Thus, the boundary level n_0 must be chosen to be higher than the bottleneck so that the magnitude of n_0 will not affect the results of the calculation.

Substituting Eq. (3.3) in Eq. (2.9) we obtain the following equation for ionization:

$$\frac{dx}{dt} = -bN^2 T_e^{-11/2}(\mathrm{eV}) x^3, \quad b = 2.4 \cdot 10^{-28}. \quad (3.4)$$

We assume that the density of heavy plasma particles N and the electron temperature T_e change according to the law

$$\left.\begin{aligned} N &= N_0\left(\frac{t_0}{t}\right)^\alpha, \\ T_e &= T_{e0}\left(\frac{t_0}{t}\right)^\beta \; (\alpha, \beta > 0, \; t > t_0) \end{aligned}\right\} \quad (3.5)$$

during expansion, where N_0 is the initial plasma density, T_{e_0} is the initial electron temperature, α and β are given parameters, and t_0 is the time scale for changes in N and T_e.

Integrating Eq. (3.4) and taking Eq. (3.5) into account yields

$$x^2 = \frac{x_0^2}{1 + \frac{\xi}{\varepsilon}\left[\left(\frac{t}{t_0}\right)^\varepsilon - 1\right]}, \quad \xi = \frac{2bt_0 N_0^2 x_0^2}{T_{e0}^{11/2}}, \quad (3.6)$$

where x_0 is the initial ionization level of the plasma and $\varepsilon = (11/2)\beta - 2\alpha + 1 \neq 0$.

It is clear from Eq. (3.6) that for $\varepsilon > 0$ the ionization of the plasma approaches zero as $t \to \infty$, and that for $\varepsilon < 0$, the plasma expands to infinity (partially ionized i.e., quenching) with a residual degree of ionization given by the equation

$$x_\infty = \frac{x_0}{\sqrt{1 + \frac{\xi}{\varepsilon}}}. \quad (3.7)$$

It is clear that the residual ionization is greater for a higher initial electron temperature and smaller for a higher initial plasma density and characteristic scale change in density and electrom temperature.

For spherical $(N \sim t^{-3})$, cylindrical $(N \sim t^{-2})$, and plane $(N \sim t^{-1})$ adiabatic expansion of gas into a vacuum with equal electron and ion temperatures $T \sim N^{\gamma-1}$ (γ is the adiabatic index), quenching will be observed in spherical expansion for $\gamma < 1\ 10/33$, cylindrical for $\gamma < 1\ 3/22$, and finally, planar, for $\gamma < 1\ 2/11$.

The ionization equation [Eq. (2.5)] then yields an expression for the recombination coefficient with constant N and T_e:

$$\gamma = -\frac{1}{N_e^2}\frac{dN_e}{dt} = bT_e^{-11/2}(\mathrm{eV}) N_e. \quad (3.8)$$

Within the given range of temperatures T_e and for electron densities $10^{13} \leq N_e \leq 10^{16}$, the recombination coefficients evaluated according to Eq. (3.8) are only two or three times smaller than those obtained by numerical calculation in ref. 13. In addition, Eq. (3.8) is exactly the same as the expression for the recombination coefficient obtained by numerical calculations of relaxation in a lithium plasma in ref. 14.

In recombination of an arbitrary atomic plasma, Eq. (3.4) and Eq. (3.8) can be used provided the bottleneck in the energy level spectrum which defines the recombination rate is located in a region of hydrogen-like levels. The more the energy spectrum of the atom is hydrogen-like, the better Eq. (3.4) represents the recombination process. As T_e is decreased the bottleneck shifts to the region of hydrogen-like levels. Thus, for small T_e the conditions for applicability of Eq. (2.5) improve. If the spectrum differs strongly from that of hydrogen, then the sum in Eq. (2.5) must be analyzed as a function of T_e.

In investigating the possibility of obtaining an inverted population, we now consider radiative decay in expansion of an optically thin hydrogen plasma. In such a plasma, as has been shown theoretically[12] and confirmed experimentally,[5,6] a population inversion can arise by virtue of a rapid depletion of the lower laser levels caused by the high probability of radiative decay.

Carrying out calculations analogous to those in ref. 11, we obtain the following expression for the distribution function with radiative decay taken into account:

$$N_n = N_1 g_n \exp\left(-\frac{E_n}{kT_e}\right)(Q_1^n + \delta_n^1 x), \quad (3.9)$$

$$Q_m^n = \prod_{k=m}^{n-1}\left(1 + \frac{A(k+1, k)}{N_e V(k+1, k)}\right)^{-1} \; (Q_1^1 = 1), \quad (3.10)$$

$$\delta_n^1 = \sum_{m=2}^{n} \frac{\exp\left(\frac{E_m}{kT_e}\right)}{g_m V(m, m-1)} Q_{m-1}^n \sum_{k=1}^{m-1} g_k \exp\left(-\frac{E_k}{kT_e}\right). \quad (3.11)$$

The radiative decay of the levels has been considered subjected to

$$\sum_{k=n}^{n_0} \sum_{m=1}^{n-1} A(k, m) N_k \simeq \sum_{m=1}^{n-1} A(n, m) N_n = A(n) N_n,$$

where A (k, m) is the probability of radiative decay of level k to level m per unit time. The expression for A(n) can be found, for example, in ref. 12.

For reasonably large electron densities, $N_e \gg A \cdot [m^*/V(m^*, m^*-1)]$, the location of the bottleneck in the energy level spectrum of hydrogen and Eq. (3.4) (for the degree of ionization) are unchanged. For the population of levels below the bottleneck the sum in Eq. (3.11) can, as before, be terminated by the last term with m = n. At temperature of recombination $\sum_{k=1}^{m-1} g_k \exp(-E_k/kT_e) \approx 1$ we obtain an expression for the inversion of population between neighboring levels of the hydrogen atom; then

$$\frac{N_{n+1}}{g_{n+1}}-\frac{N_n}{g_n}=\varkappa N_1\left(\frac{Q_n^{n+1}}{g_{n+1}V(n+1,\ n)}-\frac{Q_{n-1}^{n}}{g_nV(n,\ n-1)}\right),\ n=2,\ 3,\ \ldots. \tag{3.12}$$

It follows from Eq. (3.12) that a population inversion can be realized in a hydrogen plasma by radiative emptying of the lower level alone if

$$N_e<\frac{g_nA(n)-g_{n+1}A(n+1)}{g_{n+1}V(n+1,\ n)-g_nV(n,\ n-1)}. \tag{3.13}$$

The upper limit on the electron density and the requirement that the optical thickness of the plasma be small indicate that the use of a hydrogen plasma in a plasma dynamic laser is not promising.

4. COLLISIONAL MECHANISM FOR POPULATION INVERSION

In contrast with hydrogen, in which population inversion occurs by a radiative mechanism, a collisional mechanism due to recombination branching can occur in more complex atoms (ions).

We consider population inversion between the 4p and 3s levels of a lithium plasma based on the population distribution function, Eqs. (2.4)-(2.6), obtained earlier.

Noting that the probability of ionization of the ground state of the lithium atom $V^*(2s, 3p) \ll V(3s, 2p)$, from Eqs. (2.4) and (2.5) we have

$$\frac{\Delta N}{g}=\frac{N_{4s}}{g_{4s}}-\frac{N_{3p}}{g_{3p}}=\varkappa N_{2s}G(T_e), \tag{4.1}$$

where

$$G(T_e)=[3V(3p,\ 2s)]^{-1}\left[\frac{V(3s,\ 2p)}{3V(4p,\ 3s)}-\exp\left(-\frac{E_{3p}-E_{3s}}{kT_e}\right)+\exp\left(-\frac{E_{4s}-E_{3s}}{kT_e}\right)\right].$$

The function $G(T_e)$ depends on the energy spectrum of the atom and the associated transition probabilities. Using the cross section for inelastic collisions between atoms and electrons calculated in ref. 15, it can be shown that for low recombination temperatures $G(T_e)$ is essentially constant and that the inverted population as a function of time, initial electron temperature, and plasma density is determined by the factor $\varkappa N_{2s}$.

If the bottleneck in the energy level spectrum of the lithium atom lies in the region of hydrogen-like levels, then the factor $\varkappa N_{2s}$ can be calculated using Eqs. (2.6) and (3.4):

$$\varkappa N_{2s}=\frac{\xi}{2t_0}f\left(\frac{t}{t_0}\right),\quad f(z)=\frac{z^{\varepsilon-1}}{1+\xi\varepsilon^{-1}(z^{\varepsilon}-1)}\ (\varepsilon\neq 0). \tag{4.2}$$

Analysis of the behavior of $f(z)$ leads to the conclusion that the inverted population at the start of plasma expansion increases with time if $\xi < \varepsilon - 1$. The time $t = t^*$ at which the inverted population reaches a maximum value is given by

$$\frac{t^*}{t_0}=[(\varepsilon-1)(\varepsilon-\xi)\xi^{-1}]^{1/\varepsilon}, \tag{4.3}$$

and the corresponding maximum inverted population is given by

$$\left(\frac{\Delta N}{g}\right)_{\max}=\left(\frac{\varepsilon-1}{2t_0}\right)^{\varepsilon-1/\varepsilon}\left(\frac{\xi}{\varepsilon-\xi}\right)^{1/\varepsilon}G(T_e). \tag{4.4}$$

Thus, the larger the initial plasma density, the more rapidly the inverted population reaches its maximum and the larger the maximum value.

The dependence of $\Delta N/g$ on time is shown in Fig. 1. The expansion of the plasma is modelled using a cylindrical ($\alpha = 2$) expansion with an adiabatic index, $\gamma = 16/11$, $N_0 = 4 \cdot 10^{14}$ cm^{-3}, $T_{e0} = 0.4$ eV, and $t_0 = 2.5 \cdot 10^{-5}$ sec. The initial growth in $\Delta N/g$ is explained by an increase in the recombination flux to discrete levels due to cooling of the electrons. The fall in inverted population occurs because of the decrease in recombination flux and the decrease in density as the plasma expands.

An examination of the dependence of $(\Delta N/g)_{\max}$ on T_{e0} shows that there are optimum initial electron temperatures, T_{e0}^{opt}. The existence of these T_{e0}^{opt} can be explained as follows: as T_{e0} becomes larger, the initial degree of ionization of the plasma and the electron density become greater; however, the recombination flux which populates the higher discrete levels decreases at higher T_{e0}. The optimum electron temperature can be found using the condition $\partial\xi/\partial T_{e0} = 0$ or $11/4T_{e0} = \partial(\ln x_0)/\partial T_{e0}$. Taking $(1 - x_0)/x_0^2 = K(T_{e0})N_0$, we have

$$\frac{2}{11}\left(\frac{I}{kT_{e0}}-\frac{5}{4}\right)=\frac{y}{1+2y-\sqrt{1+4y}},\quad y=K(T_{e0})N_0. \tag{4.5}$$

Here, I is the ionization potential of the atom and $K(T_{e0})$ is the ionization equilibrium constant.

The results of a calculation of optimum initial electron temperatures as a function of the initial density of a lithium plasma are shown in Fig. 2. It is clear that these T_{e0}^{opt} values lie within a relatively narrow range of electron temperatures and increase as N_0 increases.

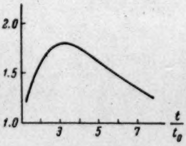

Fig. 1. Time variation of the inverted population during expansion of a lithium plasma. $N_0 = 4 \cdot 10^{14}$ cm^{-3}, T_{e0} = 0.4 eV, $t_0 = 2.5 \cdot 10^{-5}$ sec, α = 2, γ = 16/11.

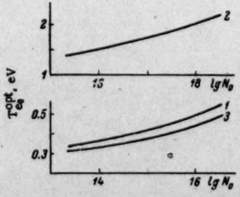

Fig. 2. Dependence of optimum initial electron temperatures on the initial density of lithium (1), Be II (2), and orthohelium (3) plasmas.

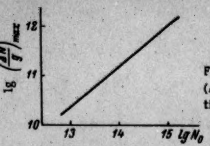

Fig. 3. Maximum inverted population, $(\Delta N/g)_{max}$, as a function of the initial density (for lithium).

Taking the dependence of $T_{e_0}^{opt}$ on N_0 into account we also obtain the inverted population, $\Delta N/g$, as a function of N_0. This function is shown in Fig. 3 on a logarithmic scale and is almost a straight line. Thus, as the initial plasma density increases the inverted population, $\Delta N/g$, increases according to a power law, $\Delta N/g \propto N_0^q$, where q is the slope of the curve (for lithium q = 0.87), to the limits of applicability of this theory, which are defined by Eq. (2.8).

Similar calculations can be carried out in the second ionization region of the atom if the plasma consists of singly and doubly charged ions. Estimates for Be II (a lithium-like ion) show that at $t^* = 2.6\, t_0$, $(\Delta N/g)_{max} = 4.6 \cdot 10^{11}$ cm^{-3} for $N_0 = 3.6 \cdot 10^{16}$ cm^{-3}, $T_{e0} = 1.6$ eV, and $t_0 = 10^{-5}$ sec. The optimum electron temperatures as a function of initial density, N_0, are given in Fig. 2.

The optimum electron temperatures for He I (Fig. 2) have been calculated using the metastable 2^3S state of orthohelium as a ground state. For $N_0 = 2.2 \cdot 10^{14}$ cm^{-3}, $T_{e0} = 0.35$ eV, and $t_0 = 10^{-5}$ sec, the maximum population inversion between the 4^3S and 3^3P levels is reached when $t^* = 6t_0$, and $(\Delta N/g)_{max} \simeq 7 \cdot 10^{11}$ cm^{-3}.

Analysis of the population distribution function for parahelium shows that inversion between the 3^1S and 2^1P, and 4^1S and 3^1P levels is not observed. This is connected with the presence of the highly excited metastable 2^1S state in parahelium. During recombination the 2^1S state is repopulated while the population of the lower laser levels, 2^1P and 3^1P, increases.

If the plasma expands from an orifice (slit or nozzle) with characteristic dimension *a*, then the scale of change in the density and electron temperature, t_0, is of order *a*/v, where v is the plasma flow velocity from the orifice. Then the distance from the orifice at which the inverted population reaches a maximum is approximately equal to $a(t^*/t_0)$, i.e., the greater the plasma flow velocity from the orifice, the greater the inverted population and the earlier it reaches its maximum value.

Hence, on the basis of examples using lithium, beryllium, and helium plasmas, we see a distinct possibility of realization of a collisional mechanism and of the use of large plasma volumes for lasing. This suggests a promising outlook for plasma dynamic lasers. The method developed here can be used for further analysis of optimum regimes in plasma jets and calculations of specific systems with different plasma compositions.

---

[1] L. I. Gudzenko, S. S. Filippov, and L. A. Shelepin, Zh. Eksp. Teor. Fiz., 51, 1115 (1966) [Sov. Phys.–JETP, 24, 745 (1967)].

[2] V. M. Gol'dfarb, E. V. Il'ina, I. E. Kostygova, and G. A. Luk'yanov, Opt. Spektrosk., 27, 204 (1969).

[3] S. W. Bowen and C. Park, AIAA J., 10, 522 (1972).

[4] A. Czernichwski, J. Chapelle, and F. Cbanennes, Comp. Rend. Acad. Sci. Paris, Sér. B, 270, 54 (1970).

[5] V. M. Gol'dfarb, E. V. Il'ina, I. E. Kostygova, G. A. Luk'yanov, and V. A Silant'ev, Opt. Spektrosk., 20, 1085 (1966).

[6] W. L. Bohn and P. Hoffmann, Z. Naturforsch, A27, 878 (1972).

[7] N. M. Kuznetsov and Yu. P. Raizer, Prikl. Mekh. Tekh. Fiz., No. 4, 10 (1965).

[8] L. I. Gudzenko, S. S. Filipov, and S. I. Yakovlenko, ZhPS, 13, 357 (1970).

[9] S. W. Bowen and C. Park, AIAA J., 9, 183 (1971).

[10] E. L. Stupitskii and G. I. Kozlov, Preprint No. 13, IPM AN SSSR (1972).

[11] S. A. Reshetnyak and L. A. Shelepin, Prikl. Mekh. Tekh. Fiz., No. 4, 18 (1972).

[12] B. F. Gordiets, L. I. Gudzenko, and L. A. Shelepin, JQSRT, 8, 791 (1968).

[13] D. R. Bates, A. E. Kingston, and R. W. P. McWhirter, Proc. R. Soc., A, 267, 297 (1962).

[14] B. F. Gordiets, L. I. Gudzenko, and L. A. Shelepin, Zh. Eksp. Teor. Fiz., 55, 942 (1968) [Sov. Phys.–JETP, 28, 489 (1969)].

[15] L. A. Vainshtein, I. I. Sobel'man, and E. A. Yukov, Cross Sections for Electronic Excitation of Atoms and Ions [in Russian], Izd. Nauka, Moscow (1973).

Effect of plasma parameters on emission in an ion laser

I. E. Sakharov, V. V. Ermolin, and S. V. Shatalin

M. I. Kalinin Leningrad Polytechnic Institute

(Submitted July 13, 1973)
Zh. Tekh. Fiz., 44, 1733-1739 (August 1974)

The plasma parameters (electron temperature, density) and the laser emission in a discharge in argon are studied experimentally. The parameter range studied includes a region in which the degree of ionization is near unity. The discharge is produced in a tube 6 mm in diameter and 1 m long in a long-pulse regime (100 μsec) at currents up to 600 A at pressures $2 \cdot 10^{-2}$ to 10^{-1} torr. The high degree of ionization permits observations up to electron temperatures of ~ 20 eV. The pressure range varies from $3 \cdot 10^{14}$ to $1 \cdot 10^{15}$ cm^{-3}. The data yield the optimum values of plasma parameters from the standpoint of laser emission. It is proposed that one of the mechanisms which limits the growth of laser emission with discharge current is an instability observed in these experiments.

INTRODUCTION

In recent years considerable success has been achieved in increasing the power of ion lasers. In particular, a power of 175 W has been obtained from an argon laser in the cw mode.[1] Analysis of the operation of ion lasers shows that in the discharge regimes characteristic of maximum output power the degree of ionization of the gas is rather high. Thus, in ref. 2 the degree of ionization is 0.2 to 0.3 at a current density of 500 A/cm^2. That the degree of ionization of the gas in the discharge region near the axis can be very high is also shown by the authors of refs. 1 and 3.

The transition to a high degree of ionization ($\alpha \sim 1$) changes significantly the properties of the discharge.[4] In particular, the electron temperature is not determined by the balance of charged particles and can increase rapidly as the discharge current is increased. This implies a possible extension of the range of electron temperatures over which lasers operate to very much higher values. Nevertheless, in the literature, investigations of the dependence of laser emission properties on the mean electron energy are limited to values $T_e \leq 10$ eV, i.e., to values close to the temperature determined by the charged particle balance. Hence, it is of interest to relate the properties of laser emission to the parameters of a plasma which is fully ionized.

In the present paper the dependence of the emission from an argon ion laser on the discharge parameters (current density and gas pressure) and on the plasma parameters (the density and average electron energy) is studied. The experiments are carried out in a quasistationary regime (long current pulses) in a weakly ionized plasma and a highly ionized plasma. This means the electron temperature varies from 3-4 eV to ~20 eV.

EXPERIMENTAL ARRANGEMENT

The experimental arrangement consists of a modification of an earlier apparatus.[4] The present apparatus differs from the earlier one in that it has plane-parallel quartz plates mounted at the Brewster angle at its ends and is located within an optical resonator. A circuit to measure the laser output power and apparatus for optical spectrum analysis are added.

The subject of this investigation is the laser emission from a plasma column produced in a quartz tube 6 mm in diameter and approximately 1 m long by means of a pulsed current whose magnitude is variable between 50 and 600 A. The minimum pressure of argon fill gas at which it is possible to obtain stable pulses for all values of discharge current is $2 \cdot 10^{-2}$ torr. The pulse source is a modulator with an artificial delay line, which delivers a pulse up to 12.5 kV 100 μsec long to a matched load. The discharge current is controlled by simultaneous variation of the load and matching impedances.

The long pulse regime is chosen for the following reasons. On one hand, the discharge must last significantly longer than the characteristic time required to establish the plasma parameters, which, under the present experimental conditions, is of the order of 10 μsec. On the other hand, the change in volume density of heavy particles (total density of ions plus atoms) due to gas breakup must be insignificant during the discharge. If this is so, then it is possible to use an easily measured quantity, the initial gas density, to calculate the degree of ionization. The characteristic breakup time, estimated from the speed of sound in the apparatus and the plasma parameters, is of the order of 1 msec. Thus the current pulse length is taken to be 100 μsec.

The basic plasma parameter measurements are carried out using a double probe (electron temperature from the slope of the curve and density from the ion saturation current); when a bias magnetic field is used a diamagnetic signal probe (product of electron density and temperature) is used. In addition, there are antennas and horns to detect low-frequency noise and microwave emission. Optical spectra are observed using an STÉ-1 spectrograph, and the laser output power is measured using a system of calibrated absorbers with a calibrated photodetector.

DEPENDENCE OF OUTPUT POWER ON DISCHARGE PARAMETERS

Analysis of oscilloscope traces shows that the relaxation times are less than 15-20 μsec, after which such variables as the discharge current, longitudinal field, potential drop across the discharge, diamagnetic signal, and probe current remain essentially constant over the remainder of the pulse. Nevertheless, the experiments show that the laser output is not stationary. The laser output as a function of time is a curve with several maxima. The first maximum corresponds to the time at which the discharge is initiated and has the form of a narrow peak. Its appearance is associated with the excitation of

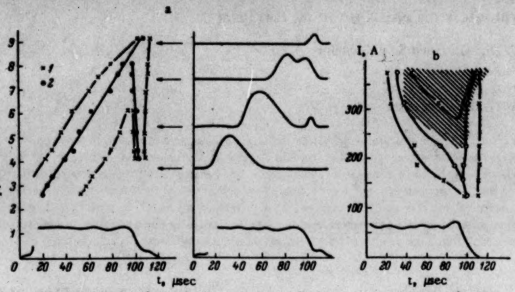

Fig. 1. Variation in time of output pulses relative to discharge current pulse as a function of a) pressure, p (discharge current I = 310 A), and b) discharge current (pressure p = 4.5 · 10^{-2} torr). The points 1 correspond to edges of pulses, and points 2 to maxima of pulses.

ionic levels in the unformed discharge. Since information on the plasma parameters at these times is lacking, this peak is not discussed. The second maximum is observed when the discharge current is essentially constant (current plateau). Its height and displacement in time relative to the beginning of the discharge depend on the discharge current and argon pressure. The third maximum corresponds to the time interval during which the discharge current is falling (the current fall time is approximately 10 μsec). Sometimes it is possible to see these maxima even when there is no plateau pulse. Below we call this the "fall" pulse. When this pulse follows a plateau pulse we call it the secondary fall pulse.

The output characteristics and location of the maxima as functions of gas pressure are shown in Fig. 1a. To the right of the figure is a schematic representation of the oscilloscope traces obtained for a single value of the discharge current (I = 310 A, which corresponds to a current density of 1100 A/cm^2) but different pressures. The lower curve represents the time variation of the discharge current. A more detailed picture of the change in the time of the edges of the observed pulses (experimental values denoted by crosses)and of the maxima (dots) as the pressure is changed are shown in the left half of Fig. 1a. It is clear that at high pressures only a single fall pulse is observed. Then, depending on the reduction in pressure, the plateau pulse blends with a secondary fall pulse. Later, the two pulses occur separately, and at low pressures only a plateau pulse, strongly shifted to the beginning of the current pulse, occurs. We note that small shifts in the fall peak correspond to large changes in the optimum current, i.e., the instantaneous value of the current at maximum (laser) output power. Diagrams similar to Fig. 1a are obtained for different values of the current, but the absolute value of the shift in the output pulse on the plateau relative to the beginning of the current pulse depends on the current.

A diagram which shows the change in the time of the output peaks as a function of the current is shown in Fig. 1b. A single fall pulse occurs at low currents and a plateau pulse shifted toward the beginning of the current pulse is observed at higher discharge current.

In addition to observing the time of occurrence of the peaks, we also study the spectral composition and power of the laser emission at the maxima. It should be noted that the Q factor of the optical resonator is very low (because of the construction of the experimental apparatus). Thus, the output power data should be considered only as an indication of optimum discharge and plasma parameter regimes. More than 98% of the power is in the λ = 4880 Å line. Emission at λ = 5145 Å is observed at several currents (~ 100 A) and pressures (2.5-4 · 10^{-2} torr). Emission at λ = 4765 Å is recorded when the discharge is initiated. The experimental data are sufficient to determine the maximum plateau output power and fall power as functions of discharge current and pressure. Emission is observed for pressures from the minimum possible (2 · 10^{-2} torr) up to 10^{-1} torr and for currents from 50 to ~ 400 A. In each case the dependence on current is obtained for 10 values of the pressure, and the dependence on pressure for eight values of current. The results of such experiments averaged over three series are shown in Fig. 2 as equal power contours with pressure and discharge current as coordinates. The diagram corresponds to plateau emission. The diagram for fall emission is similar. It is shown here because its interpretation is unreliable due to the difficulty of comparing the instantaneous discharge parameters with the plasma parameters in an unstable portion of the current pulse.

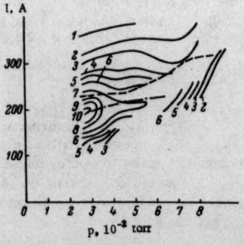

Fig. 2. Contours of equal laser output power with pressure p and discharge current I coordinates. Power, mW: 1) 100; 2) 200; 3) 300; 4) 400; 5) 450; 6) 500; 7) 550; 8) 600; 9) 620; 10) 640.

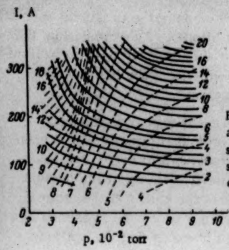

Fig. 3. Lines of equal electron temperature (eV) and charged particle density (in units of 10^{14} cm^{-3}) with pressure p and discharge current I as coordinates.

DEPENDENCE OF OUTPUT POWER ON PLASMA PARAMETERS

In order to study the dependence of laser output power on electron temperature and density it is necessary to establish the relation of these parameters to the discharge current and filling pressure. As has been indicated earlier, double probes and the diamagnetic signal are used for this purpose. It should be noted that it is not possible to obtain information about the plasma parameters for all discharge parameter ranges over which coherent emission is observed. In particular, noise appears at very high currents, making measurement difficult.

The electron temperature is determined from the slope of the probe volt–ampere characteristic. The error is ~30%. The electron temperature and saturation currents are used to find the density. The errors connected with the assumptions made in treating the data (in particular, the assumption concerning the form of the radial density distribution and the method of averaging the current along the length of the probe) can be significant. Estimates show that these errors have a systematic character and lead to the conclusion that a constant coefficient (which lies between 0.5 and 2) must be introduced into each value of the density. In experiments with a weak magnetic field (when the probe measurements are still accurate but a diamagnetic signal can be obtained) the results of probe and diamagnetic measurements agree within the limits of error.

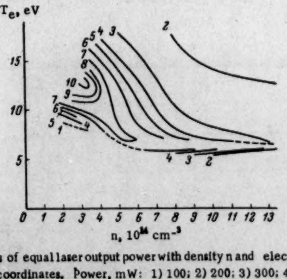

Fig. 4. Lines of equal laser output power with density n and electron temperature T_e as coordinates. Power, mW: 1) 100; 2) 200; 3) 300; 4) 400; 5) 450; 6) 500; 7) 550; 8) 600; 9) 620; 10) 640. The dotted curves correspond to unreliable experimental data.

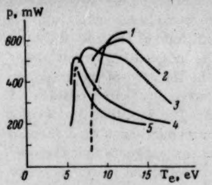

Fig. 5. Dependence of laser output power P on electron temperature T_e for various densities n. n · 10^{14} cm^{-3}: 1) 3; 2) 4; 3) 5; 4) 8; 5) 10. The dotted portions of the curves are those for which experimental data are unreliable.

The results of measurements of electron temperature and charged particle density as a function of discharge current and pressure are shown in Fig. 3 in the form of a diagram constructed by interpolation of experimental data. In this figure the numbers on the left next to the dotted lines correspond to T_e, and the numbers to the right (solid lines), to the electron density. The rapid growth in electron temperature as the current increases at low pressures is due to the transition to a high degree of ionization. These measurements provide information about the direct dependence of output power on the plasma parameters. In Fig. 4 equal power contours are shown in the output power as a function of electron temperature for various densities. As the density is decreased the optimum electron temperature is shifted to larger values. As this occurs the laser output power increases.

The dependence of power on density at constant temperature (obtained, as are the curves of Fig. 5, from the intercepts of the contours of Fig. 4) is shown in Fig. 6. The optimum density is lower for a higher electron temperature. For $T_e \geq 13$ eV the output maximum apparently occurs at densities lower than the minimum density obtained in these experiments.

PLASMA OSCILLATIONS

In the experiments, under certain conditions low- ($\omega \sim 1$ -10 MHz) and high- ($\omega \sim 10^{11}$ Hz) frequency oscillations are observed simultaneously. The low-frequency noise is picked up by probes in the plasma and by external antennas in the shape of spiral sections enclosing the apparatus or of bulk sensors (small plates) located on the outside wall of the discharge tube. Microwave oscillations are detected by a horn with a two-millimeter detector. In all cases the signal is fed directly to the input of an oscilloscope without preamplification.

The oscillations are observed immediately following the plateau laser pulse. A growth in the amplitude of the oscillations coincides with a decrease in laser output power. During the time interval in which high-amplitude

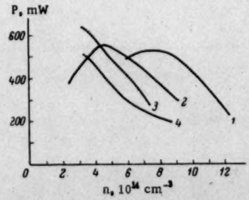

Fig. 6. Dependence of laser output power P on density n for various values of electron temperature, T_e. T_e, eV: 1) 6; 2) 9; 3) 13; 4) 16.

oscillations are observed there is no laser emission. The reduction in the oscillation amplitude at the end of the current pulse coincides with the increase in output power associated with "fall" peak. The location of the noise on the time axis for various discharge currents is indicated in Fig. 1b by the shaded region. The fact that the development of an instability leads to a reduction in or disappearance of laser emission in all cases suggests that the oscillations represent a limitation on output power at large discharge currents.

Apparently, the observed bell-shaped form of the plateau output pulse (absence of a step) is associated with the fact that the oscillations of the plasma damp out the laser emission before it reaches the level which might be expected for a given electron temperature and density in the absence of oscillations. From this standpoint the reduction in output power for large T_e and n (Fig. 4) or large currents (Fig. 2) can be explained by an increase in the amplitude of the oscillations and a corresponding earlier quenching of the output pulse.

The dotted line of Fig. 2 denotes the lower boundary of the currents at which intense oscillations are observed. From this figure it is clear that the oscillation regime coincides approximately with the region in which the output power decreases with increasing current.

There is another (circumstantial) argument to indicate that the oscillations tend to inhibit the laser action.

Measurements of the density for various argon pressures suggest constructing lines of equal degrees of ionization on diagrams analogous to Figs. 2 and 4. One such line (for a degree of ionization equal to 0.3) is shown in Fig. 2 by a dot–dash line. Clearly, it coincides with the location on the diagram of the optimum values of the current. In other words, for all pressures the output begins to decrease with increasing current until a given, fairly high degree of ionization is attained. It should be noted that this value, as well as the density, is known to within a factor of 2: It also characterizes the degree of ionization averaged over the cross section. Thus, near the axis of the apparatus the degree of ionization can exceed 0.3.

Neither the absorption of radiation nor the destruction of the inverted population by electron impact is related unambiguously to the degree of ionization; on the other hand several plasma instabilities (such as the two-stream instability due to runaway electrons) require nearly complete ionization (which can occur near the tube axis under the present experimental conditions). An explanation of the nature of the observed instabilities and the mechanism by which the plasma oscillations affect the laser output power awaits further investigation.

We note that under the present experimental conditions the limitation on and drop in laser power with current cannot be due to the causes discussed in ref. 1, but are due specifically to the reduction in density of the heavy particles due to displacement of the gas. On the other hand, in the same work, the author noted the presence of instabilities (at currents slightly exceeding the optimum value). Intense oscillations and their effect on laser output power in the cw mode were observed in ref. 3.

CONCLUSION

An experimental study of laser emission from a highly ionized argon plasma with density $3 \cdot 10^{14}$–$1 \cdot 10^{15}$ cm^{-3} and temperature 3 to 20 eV shows that the optimum value of the mean electron energy depends on the density and that this optimum value shifts to larger values as n decreases. When n changes from $\sim 1 \cdot 10^{15}$ to $3 \cdot 10^{14}$ cm^{-3}, $T_{e\,opt}$ increases from 6 to 12-13 eV.

As the density increases the output power (corresponding to the optimum T_e in the observed parameter range) increases monotonically. Hence, the optimum density value is apparently less than $3 \cdot 10^{14}$ cm^{-3} and the corresponding $T_{e\,opt}$ exceeds 13 eV.

It is observed that the optimum value (with respect to emission) of the discharge current for various pressures corresponds to a constant value of the degree of ionization averaged over the cross section. The probable reason for the reduction in output power as the current exceeds the optimum value is the oscillation of the plasma observed in these experiments.

The authors thank V. E. Golant, A. P. Zhilinskii, and A. É. Fotiadi for valuable comments.

---

[1] V. I. Donin, Zh. Eksp. Teor. Fiz., 62, 1648 (1972) [Sov. Phys.–JETP, 35, 858 (1972)].

[2] T. Fujimoto, Y. Ogata, and K. Fukuda, Mem. Fac. Eng. Kyoto Univ., 32, 236 (1970).

[3] A. É. Fotiadi and S. A. Fridrikhov, Zh. Tekh. Fiz., 43, 2010 (1973) [Sov. Phys.–Tech. Phys., 18, 1271 (1974)].

[4] I. E. Sakharov and L. D. Tsendin, Zh. Tekh. Fiz., 42, 916 (1972) [Sov. Phys.–Tech. Phys., 17, 727 (1972)].

Self-excited waveguide buncher

N. M. Gavrilov and A. V. Nesterovich

(Submitted May 14, 1973; resubmitted December 28, 1973)
Zh. Tekh. Fiz., 44, 1740-1742 (August 1974)

The possible use of longitudinal beam instability in a slow wave system for a phase bunching before injection into a linear accelerator is analyzed.

The acceleration efficiency of linear particle accelerators can be increased by preliminary phase bunching by means of klystron and waveguide bunchers with constant or varying phase velocity in the beam direction equal to or higher than the particle velocity.[1]

The use of such bunchers assumes the use of separate power supplies that are synchronized with the power supplies of the accelerator sections.

We propose here and analyze the possibility of bunching based on the interaction of particles with the backward wave excited in a slow-wave system by a beam moving at a velocity higher than the phase velocity of the wave, by analogy with backward-wave tubes. A backward-wave tube is known to produce a bunched beam at the exit from the structure. Such a buncher does not require a separate power supply, since the bunching results from power drawn from the beam.

The buncher and accelerator sections can be synchronized by supplying a signal from a stable master oscillator to the input of the "backward-wave" tube. The signal from such an oscillator can be used for a number of accelerator stages. Systems are available for increasing the frequency stability and the output power.[2]

The efficiency of this bunching method is analyzed on the basis of the theory of nonlinear interactions,[3] which gives the most complete information about the phase and energy characteristics of the beam. A unique feature of this system, which distinguishes it from backward-wave tubes, is the existence of high currents and voltages, characteristic of the injectors for linear electron accelerators. A computer is used to solve the generalized equations resulting from the nonlinear analysis of the oscillator by the Lagrange method in a one-dimensional system; Fourier analysis is used to calculate the space-charge field.

The calculations reveal the following general features:

1. In a structure with a constant phase velocity the modulation depth of the beam increases with increasing velocity detuning, but the self-excitation conditions are satisfied for a long structure.

2. The formation of two or more bunches is not observed, implying that such devices can be used for bunching in accelerators. A possible explanation for this behavior is that the bunching occurs in a field which decays to zero, in contrast with the situation in traveling-wave tubes or waveguide bunchers, in which bunches are isolated at high signal levels.

3. An increase in the amplitude of the output signal A(0), in the beam current I_0, and in the characteristic impedence Z_0, correspond to a contraction of the phase spectrum, as does a decrease in the injection voltage V_0.

4. The self-excitation conditions are satisfied for a structure length of $N_S = Z/\lambda_S = 6$-10 (λ_S is the wavelength); at the output about 80% of the particles are bunched into a phase interval shorter than 60°, and the spectral width at half-height does not exceed 20°.

5. A general property is the existence of tails in the accelerating field region in the phase spectra and, at low energies, in the energy spectra. As the structure is lengthened the phase spectra contract, while the energy spectra expand.

As an example, Fig. 1 shows the phase spectra of the particles at the exit from the structure (where the field amplitude vanishes) for two phase-velocity cases for the case of uniform injection; the corresponding energy spectra are shown in Fig. 2. Here b' is the beam radius, f_S is the oscillation frequency, $C = (Z_0I_0/4V_0)^{1/3}$ is the coupling parameter, $y = 2\pi CN_S$ is the normalized length, b =

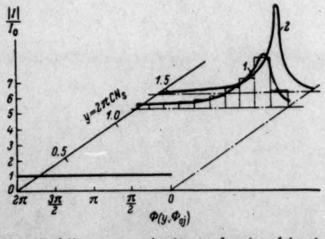

Fig. 1. Normalized linear current density as a function of the electron phase for equilibrium injection. $I_0 = 0.5$ A, $V_0 = 120$ kV, $Z_0 = 40\ \Omega$, b' = 5 mm, $f_s = 3000$ MHz, A(0) = 0.2. 1) b = 0.5, y = 1.2 (the approximating histogram is shown); 2) b = 1.5, y = 1.4.

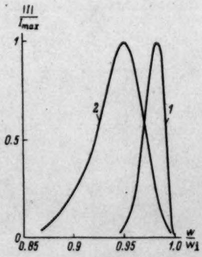

Fig. 2. Energy spectra corresponding to the cases shown in Fig. 1. W_I is the injection energy.

$(u_0-v_0)/Cv_0$ is the velocity-detuning parameter, $A(y) = CV(y)/Z_0I_0$ is the normalized voltage amplitude, $V(y)$ is the voltage across the structure, u_0 is the injection velocity, v_0 is the phase velocity of the unperturbed (cold) wave, $\Phi(y, \Phi_{0j})$ is the phase position of a particular group of charges with respect to the hot wave, and Φ_{0j} is the phase position at the instant of injection.

As a typical example we assume a system with I_0 = 1 A, W_i = 200 keV, b' = 6 mm, f_s = 3000 MHz, Z_0 = 40 Ω (a typical value for structures of the limited-waveguide type), and b = 0.1. We assume that the self-excitation conditions are satisifed when the structure is about 60 cm long; the generated power is almost 10% of the beam power, i.e., 20 kW, and the particles are bunched into a phase interval of 60°.

These results indicate that systems of this kind satisfy the requirements imposed by the prevailing parameters of radio-frequency power supplies (a long pulse and a frequency instability)[4] and by the tolerances involved in the construction of the waveguides[5] and can be used to bunch particles in linear accelerators.

The phase focusing can be improved through the use of well-known methods for increasing the efficiency of TWT devices; in particular, structures with a varying phase velocity can be used. We assume that such a system can be used to achieve a phase bunching no worse than that achieved in most of the existing bunchers, primarily, prebunchers; the system would have similar structural parameters, but would have the important advantage of not requiring a separate power supply.

Furthermore, the beam signal generated in the buncher can be used as a master signal in the accelerator sections.

---

[1] O. A. Val'dner, A. D. Vlasov, and A. V. Shal'nov, Linear Accelerators (in Russian), Atomizdat, Moscow (1969).

[2] S. N. Bychkov, N. I. Burenin, and R. T. Safarov, Frequency Stabilization of Microwave Oscillators (in Russian), Izd. Sov. Radio, Moscow (1962).

[3] J. E. Rowe, Nonlinear Electron-Wave Interaction Phenomena, Academic Press, New York (1965).

[4] G. P. Aver'yanov, A. V. Nesterovich, and A. V. Shal'nov, Proceedings of the Second All-Union Conference on Particle Accelerators [in Russian], Vol. 2, Izd. Nauka, Moscow (1972), p. 65.

[5] G. P. Aver'yanov, A. V. Nesterovich, and A. V. Shal'nov, Zh. Tekh. Fiz., 41, 1231 (1971) [Sov. Phys.-Tech. Phys., 16, 970 (1971)].

Self-acceleration of an intense electron beam

I. A. Grishaev, A. N. Dedik, V. V. Zakutin, I. I. Magda,
Yu. V. Tkach, and A. M. Shenderovich

(Submitted June 18, 1973)
Zh. Tekh. Fiz., 44, 1743-1748 (August 1974)

The present work describes an experiment on the self-acceleration of an electron beam in a shock-excited resonator. The experiment is performed at beam energies between 500 and 800 keV and beam current between 5 and 15 kA. The increase of 200-250 keV in the beam energy agrees with the calculations. High-frequency modulation of the current in the resonator walls is observed at high currents.

INTRODUCTION

Self-acceleration with the aid of a resonator is one of the most promising methods of accelerating an intense electron beam.[1-5] The method is based upon shock excitation of a resonator by the beam and the acceleration of the beam in the strong electric fields developed by the shock excitation. Fields excited by the leading edge[1] or trailing edge[2-5] of the beam pulse through the resonator can be used for this purpose.

Earlier papers have reported on theoretical investigations of the self-acceleration of a beam,[1-5] measurements on resonators,[4] and measurements of the accelerating fields which had been excited by a beam of low energy and low intensity.[5] The present work is a description of an experiment on the self-acceleration of an intense electron beam with the aid of a resonator.

1. ACCELERATING RESONATOR

The accelerating system is a resonator (Fig. 1) consisting of a coaxial line with the accelerating gap as a load. A resonator of this type is characterized by the advantage that parameters such as the length of the accelerating gap, the characteristic impedance ρ, and the resonance frequency can be varied independently. In particular, a relatively high characteristic impedance can be obtained with small accelerating gaps. The design calculation for this resonator is based on an equivalent circuit approach and summation of voltage and current waves incident and reflected, in sequence, from the short-circuited end of the coaxial line.[4] The first wave, which is excited by the beam, can be determined from the condition U(t) = ρJ(t), where ρ denotes the characteristic impedance of the resonator and J(t), the beam current.

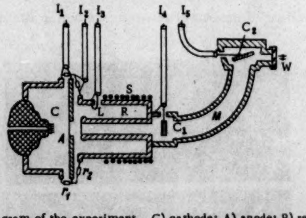

Fig. 1. Diagram of the experiment. C) cathode; A) anode; R) resonator; C_1, C_2) Faraday cylinders; M) magnetic analyzer; W) window through which the light leaves; L) loop for measurement of the field in the resonator; S) solenoid; r_1, r_2) 1/16 Ω resistors for the measurement of the beam current; I_1) current pulse of the gun; I_2) current pulse of the beam in the resonator; I_3) dH/dt pulse in the resonator; I_4) current pulse of the beam from C_1; I_5) current pulse of the beam from C_2.

When the influence of the accelerating gap upon the wave propagation is negligible, the excitation of the coaxial resonator by the beam can be determined by a field approach. This calculation makes it possible to verify the validity of the equivalent-circuit method.

Let us consider a coaxial line which is short-circuited at both ends (Fig. 2). The exciting beam passes through the cross section z = 1/2 and the current density of the beam is

$$j_z = j_\varphi = 0;$$
$$j_r = \frac{\delta\left(z - \frac{l}{2}\right)}{2\pi r} J(r - vt), \qquad (1)$$

where v denotes the beam velocity.

We restrict our considerations to the excitation of TEM waves because TE waves are not excited by a current of the type described by Eq. (1) and because the influence of TM waves is small in cases of practical interest. Let us determine the vector potential A of the excited field in the form of an expansion in eigenmodes:

$$A \equiv A_r(r, z, t) = \frac{1}{r} \sum_{m=0}^{\infty} q_m(t) \sin \frac{\pi m}{l} z. \qquad (2)$$

Substituting Eq. (2) into the wave equation, we obtain

$$\ddot{q}_m + \omega_m^2 q_m = \frac{4c \sin \frac{\pi m}{2}}{l \ln \frac{R}{r_0}} \int_{r_0}^{R} \frac{J(r - vt)}{r} dr, \qquad (3)$$

where $\omega_m = \pi mc/l$.

Solving Eq. (3) and substituting into Eq. (2), we obtain

$$A = \frac{4}{\pi r \ln \frac{R}{r_0}} \int_0^t dt' \int_{r_0}^{R} \frac{J(r - vt')}{r} dr \sum_{m=0}^{\infty} \frac{\sin \frac{\pi m}{2}}{m} \sin \frac{\omega_m}{c} z \sin \omega_m (t - t'). \qquad (4)$$

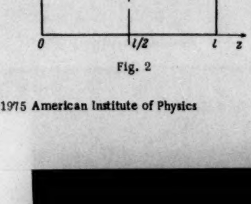

Fig. 2

We are interested in the field at the point $z = l/2$, through which the beam passes. For $t < l/c$, i.e., before the first reflected wave appears, the sum of Eq. (4) is equal to $\pi/4$ or to $-\pi/4$ for various t' values, which, in physical terms, indicates the appearance of a reflected wave. The dt' interval is split into a larger number of terms of alternating signs at greater t values, which in physical terms corresponds to the effect of multiply reflected waves.

We restrict our considerations to the first incident wave ($t < l/c$). According to Eq. (4) the electric field of the first incident wave is (we disregard the influence of space charge)

$$E = -\frac{1}{c}\frac{\partial A}{\partial t} = -\frac{1}{cr \ln \frac{R}{r_0}} \int_{r_0}^{R} \frac{J(r - vt)}{r} dr. \qquad (5)$$

Let us consider a linearly increasing current:

$$J = J_0 \frac{vt + r_0 - r}{t_e v}. \qquad (6)$$

Thus, for $t > (R-r)v$ we have

$$E = -\frac{J_0}{rct_e}\left[t + \frac{r_0}{v} - \frac{R - r_0}{v \ln \frac{R}{r_0}}\right]. \qquad (7)$$

Since it is usually true that $t_e \gg r_0/v$ and $t_e \gg (R-r_0)/v \cdot \ln(R/r_0)$, times $t \gg r_0/v$ and $t \gg (R-r_0)/v \ln(R/r_0)$ are of real interest. The second and third terms in Eq. (7) can be ignored for these times; hence, Eq. (7) coincides with the results of the equivalent-circuit calculation.

According to Eq. (7), the maximum of the retarding voltage is

$$U_{\max} = -\rho J_0 \frac{\Delta t}{t_e}, \qquad (8)$$

where $\Delta t = l/c$.

A calculation similar to the calculation performed here shows that if $t_e/\Delta t$ is an integer, the accelerating voltage has the above value during the flat section of the pulse. When the front does not increase according to a linear law or when $t_e/\Delta t$ is not an integer, the calculations show that U differs from that of Eq. (8), but the difference is not substantial.

When the length of the leading edge of the current pulse is much greater than t_{tr}, the length of the trailing edge, the accelerating voltage is given by Eq. (8) during the trailing edge, but t_e must be replaced by t_{tr}. When t_{tr} is comparable to t_e (and also if the trailing edge is nonlinear), U can differ slightly from U in Eq. (8) as a consequence of the waves which were excited in the resonator by the leading edge.

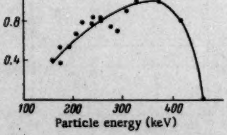

Fig. 3. Spectrum of the accelerator–injector.

Thus, Eq. (8) can be used to estimate the accelerating voltage in both cases.

In the experiments we use a resonator with $\rho = 100\ \Omega$ and $\Delta t = 3 \cdot 10^{-9}$ sec. Calculations with Eq. (8) have shown that the accelerating voltage is $2 \cdot 10^5$ V for $I_0 = 10^4$ A and $t_e = 15 \cdot 10^{-9}$ sec (or $t_{tr} = 15 \cdot 10^{-9}$ sec).

2. METHOD OF THE MEASUREMENTS

Figure 1 shows the experiment. After passing through the grid anode (A), the beam from an injector enters the accelerating gap, excites the resonator, and is accelerated, entering the magnetic analyzer M, in which the beam energy is measured with the aid of a Faraday cylinder C_2.

A direct acceleration, high-current linear accelerator is used as the injector.[6] Measurements are made at accelerator-beam energies between 500 and 800 keV and beam currents I_0 of 5-15 kA in the resonator. Figure 3 shows the spectrum measured in one mode of operation of the injector; the spectrum is obtained from the voltage pulses derived from Faraday cylinder C_2.

The pulses of the beam current in the gun and of the beam current in the resonator are measured with 1/16 Ω resistors r_1, r_2 (Fig. 1) in the form of loops that go around the flanges on which resistors, 1 Ω each, are uniformly distributed on a circle. The design of these loops allows undistorted measurements of pulse fronts of about 1 nsec.

It follows from theoretical considerations that the current pulse in resistor r_2 has both the same amplitude and the same form as the current pulse of the beam. As a matter of fact, by summing the series in Eq. (4) and by differentiating with respect to z, we find that the sum of the oppositely directed currents over the walls of the tube is at the point $z = 0$ (Fig. 2) (for any t and not only for $t < l/c$).

$$J_{\text{wall}} = \frac{1}{\ln \frac{R}{r_0}} \int_{r_0}^{R} J(r - vt) \frac{dr}{r}.$$

In cases of practical interest, in which the beam cur-

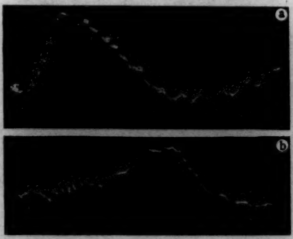

Fig. 4. Beam current pulses in the resonator. A sinusoidal voltage with a frequency of 100 MHz is used for the time scale.

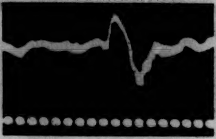

Fig. 5. Voltage pulse derived from the loop (L) in the resonator. Time marks every 20 nsec.

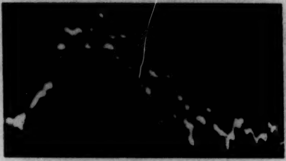

Fig. 6. Current pulse in resistor r_2; the current pulse is modulated by a high frequency.

rent changes only slightly during the time of flight from r_0 to R (see Sec. 1), we find from Eq. (9) that $I_{wall} \approx I$.

Figure 4 shows typical oscillograms of the current pulse of the beam in the resonator.

The beam–current pulses beyond the resonator and beyond the magnet are measured with the aid of cylinders C_1 and C_2, which provide nansecond time resolution. The ends of cables I_4 and I_5 have no load resistances so that the total charge absorbed by the cylinders can be measured. Moreover, a SnS scintillation layer is applied to cylinder C_2 so that visual observation of the electron beam is possible.

3. EXPERIMENTAL RESULTS

Three series of measurements were made to observe the accelerated particles. In the first two of these series, the resonator is initially shorted out and the maximum beam energy is determined by varying the field in the magnet (M); the resonator is then shorted out again and the maximum beam energy is determined again. The electrons are detected on the basis of the luminescence radiation emitted from the scintillating layer applied to C_2. In the first series, in which the anode–cathode gap of the electron gun has a width of 6 mm, an increase in the maximum beam energy from 750 keV to 1 MeV is observed, i.e., the energy increase amounts to 250 keV. In the second series, in which the cathode–anode gap has a width of 4 mm and the initial energy amounts to 550 keV, an energy increase amounting to 200 keV is observed. The accelerating gap of the resonator is 12 mm in these measurements, i.e., the strength of the accelerating field is about 200 kV/cm.

The values which are obtained for the energy increase agree with the theoretical values at this amplitude (10-15 kA) and the form (Fig. 4) of the pulse of the beam current at which the measurements are made [see the above estimate with Eq. (8)].

In the third series, in which the total charge absorbed by cylinder C_2 is measured, a greater energy increase amounting to 500-1000 keV is observed. However, these results are not reliable in view of the strong induction, which resulted in a charging of C_2 even without a beam. The form of the pulse of the beam current is not fixed in this series.

Excitation of the resonator by the beam is observed during the measurements of the first and second series (these observations are made with the loop L of Fig. 1). Both amplitude and shape of the excited magnetic field pulse (Fig. 5) coincide with the calculated values. Moreover, a breakdown of the resonator is observed after passage of the beam, which means that the electric field excited by the beam is very strong.

A high-frequency modulation of the current pulse in the walls of the resonator is detected in the experiments and recorded with the r_2 resistors (Fig. 6). The modulation frequency is close to the double eigenfrequency of the resonator, being about 300 MHz. Modulation occurs at a current in excess of 6 kA and the amplitude of the modulation increases with increasing current.

As has been mentioned above, in the specified-current approximation the shape of the current pulse in r_2 coincides with the shape of the current pulse of the beam. Accordingly, the modulation indicates that feedback in the beam–resonator system exists. The feedback may be related to the development of a longitudinal instability discussed in ref. 7.

CONCLUSIONS

We have established that the self-acceleration of an intense electron beam in the kiloampere range is possible by a shock excitation of a resonator. The resulting increase of 200-250 keV in the beam energy agrees with the theoretical values. Both the excitation of the resonator and the acceleration are observed in the case of a relatively short leading edge and a long trailing edge of the current pulse of the beam (Fig. 4a), as well as in the case of a long leading edge and a relatively short trailing edge of the current pulse (Fig. 4b). Thus, two acceleration mechanisms are observed: in the first case, the self-acceleration of Eq. (1) and, in the second case, the acceleration developing upon interruption of the beam.[2-5] The two mechanisms are simultaneously effective in certain cases. (A short communication on the main results of this experiment has been published in ref. 8.)

---

[1] L. N. Kazanskii, A. V. Kisletsov, and A. N. Lebedev, Atom. Energ., 30, 27 (1971).

[2] G. A. Askar'yan, Atom. Energ., 6, 658 (1959).

[3] Yu. I. Bashmakov, K. A. Belovintsev, E. G. Bessonov, Ya. A. Vazdik, and P. A. Cherenkov, Kr. Soobshch. po Fiz., Sb. FIAN SSSR, No. 5, 10 (1971).

[4] I. A. Grishaev, A. N. Dedik, V. V. Zakutin, and A. M. Shenderovich, Math. Symposium on Collective Methods of Acceleration [in Russian] (Dubna, September 1972), JINR, Dubna (1972), p. 133.

[5] I. A. Grishaev and A. M. Shenderovich, Zh. Tekh. Fiz., 42, 2409 (1972) [Sov. Phys.–Tech. Phys., 17, 1871 (1973)].

[6] Yu. V. Tkach, Ya. Yu. Fainberg, I. I. Magda, V. D. Shapiro, V. I. Shevchenko, A. I. Zykov, E. M. Lemberg, I. N. Mondrus, and N. P. Gadetskii, ZhETF Pis. Red., 16, 368 (1972) [JETP Lett., 16, 259 (1972)].

[7] V. I. Kurilko and V. A. Shendrik, Math. Symposium on Collective Methods of Acceleration [in Russian] (Dubna, September 1972), JINR, Dubna (1972), p. 122.

[8] I. A. Grishaev, A. N. Dedik, V. V. Zakutin, I. I. Magda, Yu. V. Tkach, and A. M. Shenderovich, in: Problems of Atomic Science and Technology [in Russian], High-Energy and Atomic Nucleus Physics Series, No. 4 (6), 34, Khar'kov (1973).

General

Secondary-electron energy in a resonance discharge in a three-electrode system

Yu. A. Kulikov, V. V. Ogienko, and Yu. M. Trifonov

(Submitted September 24, 1973; resubmitted January 16, 1974)
Zh. Tekh. Fiz., 44, 1749-1752 (August 1974)

The energy with which the secondary emitters are bombarded by electrons from a secondary-electron-resonance discharge has been studied experimentally in the microwave range in the primary and secondary discharge zones. The discharge is excited in a three-electrode system in which the microwave voltage between one of the emitters and the anode is much lower than the anode potential, which is positive with respect to the emitters. The envelope of the energy spectrum of the electrons bombarding the emitters has a clearly defined peak corresponding to resonance electrons. A large fraction of the electrons from the emitters have energies approximately equal to the resonance value.

The excitation range for secondary-electron-resonance discharges in three-electrode systems has been studied theoretically and experimentally[1,2] for the case in which the microwave voltage applied between one of the emitters and the anode is much lower than the anode potential, which is positive with respect to the emitters. It has been shown that such a discharge in a three-electrode system differs in several fundamental ways from a similar discharge in a high-frequency gap. For example, in a three-electrode system with a constant anode voltage considerably higher than the microwave amplitude the phase condition for excitation is a weak function of the microwave voltage, being governed primarily by the constant anode voltage, the microwave frequency, and the interelectrode distances. The range of favorable starting phases, from which electrons are pulled toward the phase of a resonant electron, is much broader and varies over the volume.

In a three-electrode system, as in a high-frequency gap, the mechanism responsible for the excitation and the maintenance of the secondary-electron-resonance discharge is related to the possible formation of an electron "packet" centered around a resonant electron. Below we report on an experimental study of the energy spectrum of electrons in the packets formed in a secondary-electron-resonance discharge.

The energy spectrum is studied in the microwave range with the apparatus described in ref. 1, supplemented with a two-electrode electron-velocity analyzer. Figure 1a shows the electrodes of the apparatus and the velocity analyzer. The apparatus includes secondary emitters 1 and 2, 10 mm in diameter, with focusing electrodes 7, used to confine oscillating electrons in the interaction region. Anode 3, a quarter-wave cup, is at the end of an open coaxial line; it has a drift tube 10 mm in diameter and 8 mm long. Emitter 1 is at the end of the central conductor of the coaxial line along which the microwave power is supplied to the interaction region. The emitters are 28 mm apart. At the centers of emitters 1 and 2 there are circular apertures 0.4 mm in diameter. Behind the emitters are collectors 4 and 5, Faraday cups with entrance apertures 1.5 mm in diameter. The leads to the analyzer, on the microwave-line guide, lie within the central conductor of the coaxial line. The operating principles of the analyzers are described in refs. 3 and 4. The analyzers are calibrated by recording the retardation curves for an electron flux with a known energy distribution.[3] The secondary emitters 1 and 2 are foils of a Pt−Ba alloy.[5] Electron collectors 4 and 5 contain heaters 6, used to activate the emitters; these also provide the heating needed to produce the thermionic current required to calibrate the analyzers. After calibration we are able to study the electron energy spectrum in the secondary-electron-resonance discharge without any problem. Figure 1b shows the calibration curves. The scatter in the calibration curves in the region up to $U_r = -50$ V is due to secondary emission from the edges of the aperture. In our case this region is not important, so no special measures are used to eliminate the error in this region. The experiments are carried out under pulsed conditions with cold emitters; the chamber pressure does not exceed 10^{-6} torr. The microwave pulses are 30 μsec long. The klystron operates at 850 MHz. The pulse repetition frequency is 50 Hz. The microwave voltage between emitter 1 and anode 3 is determined as in ref. 1, but the power absorption in the discharge is taken into account.

Figure 2a shows the currents of emitters 1 and 2 at $P_{ref} = 1.8$ kW, and the change in the reflected microwave power within the primary and secondary discharge zones.

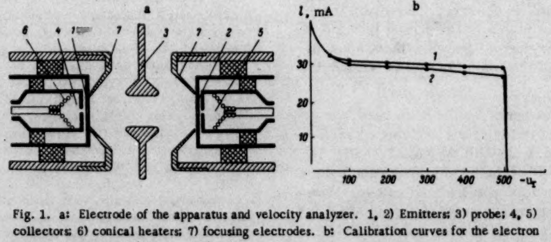

Fig. 1. a: Electrode of the apparatus and velocity analyzer. 1, 2) Emitters; 3) probe; 4, 5) collectors; 6) conical heaters; 7) focusing electrodes. b: Calibration curves for the electron velocity analyzers. 1) I_{an-em_1}; 2) I_{an-em_2}.

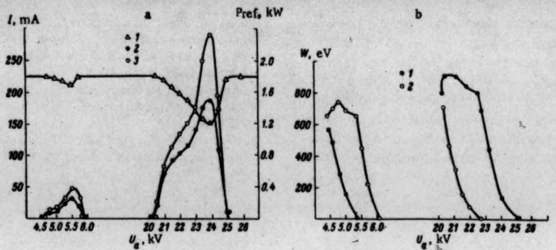

Fig. 2. a: Emitter currents and reflected power in the primary and secondary discharge zones. 1) P_{ref}; 2) I_{em2}; 3) I_{em1}. b: Energies at which the emitters are bombarded by resonant electrons in the primary and secondary discharge zones. 1) W_{em1}; 2) W_{em2}.

The microwave voltage between emitter 1 and the anode varies from 900 to 640 V within the primary discharge zone as a result of power absorption by the discharge, and it varies from 900 to 800 V in the secondary discharge zone. Retardation curves are taken for three values of the anode voltage in each zone. Graphical differentiation of the retardation curves yields the curves in Fig. 3, which show the electron energy spectra.

It follows from the results in Fig. 3 that the electron energy distribution in a secondary-electron-resonance discharge in a three-electrode system has a clearly defined peak. In the primary discharge zone for the electrons bombarding emitter 1 the peak of the energy distribution occurs at a position nearly independent of the anode voltage; for electrons bombarding emitter 2 it shifts toward lower energies between the beginning and end of the zone (Fig. 3a). In the secondary discharge zone (Fig. 3b) we find the opposite pattern: The position of the energy-distribution peak shifts toward lower energies for the electrons incident on emitter 1 and remains relatively constant in the bombardment of emitter 2. We also see that the scatter in electron velocities increases with increasing anode voltage.

In discussing the experimental results we use the prediction of the elementary theory of ref. 1 regarding the energy with which an emitter is bombarded by a resonant electron as a function of the anode voltage. Figure 2b shows this functional dependence, obtained for emitters 28 mm apart, F = 850 MHz, and a microwave voltage of 1 kV between emitter 1 and the anode. Here, W_1 is the energy with which emitter 1 is bombarded and W_2 is the energy with which emitter 2 is bombarded. The energy of a resonant electron incident on emitter 2 falls off rapidly from the beginning of the primary discharge zone to its end, vanishing at U_a = 22.7 kV. The energy with which emitter 1 is bombarded by a resonant electron is roughly constant up to U_a = 22.7 kV; then it falls off to zero at the end of the zone. Here, U_a = 20.4 to 22.7 kV is the range of the two-surface discharge, and U_a = 22.7 to 25.2 kV is the range of the single-surface discharge from the side of emitter 1. For the secondary zone the energy of the resonant-electron bombardment of the second emitter displays a behavior opposite that for the first emitter. Comparison of the results in Figs. 3 and 2b shows that the displacement of the energy-distribution peaks for electrons incident on emitters 1 and 2 corresponds to the functional dependence on the anode voltage of the energy with which the emitters are bombarded by resonant electrons in both the primary and secondary zones. Similar results are obtained at other microwave power levels. On the basis of these results we conclude that the peak of the energy distribution is formed around the resonance value, confirming arguments regarding the resonant nature of the discharge in a three-electrode system. In our apparatus we do not observe a transition from a two-surface

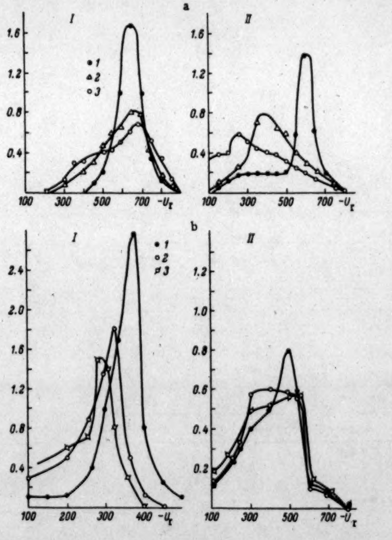

Fig. 3. Envelopes of the energy spectra of the electrons bombarding the emitters, obtained through graphical differentiation of the retardation curves. a: In the primary discharge zone. I) For I_{an-em1}; II) for I_{an-em2}. U, kV: 1) 21.5; 2) 23.5; 3) 24.5. b: In the secondary discharge zone. 1) For I_{an-em1}; II) for I_{an-em2}. U, kV: 1) 4.8; 2) 5.4; 3) 5.7.

discharge to a single-surface discharge, probably because the transit angles are not the same for electrons starting from the center and the periphery of the emitters, because the potential dips in the anode drift tube. In this connection we do not rule out the possibility that two-surface and single-surface discharges exist simultaneously at the end of the zones; this could explain the increase in the electron velocity scatter toward the end of the zone.

---

[1] Yu. M. Trifonov, Yu. A. Kulikov, G. V. Okhmatovskii, and A. S. Malinovskii, Radiotekh. Elektron., 1, 16, 166 (1971).

[2] R. Kh. Biboletov, B. V. Eliseev, Yu. A. Kulikov, and Yu. M. Trifonov, Radiotekh. Elektron., 9, 16, 1968 (1971).

[3] K. Krebs and H. Meerbach, Ann. Phys., 6, B. 18 (1956).

[4] D. A. Ganichev, V. A. Stanskii, and B. V. Khrisanfov, Zh. Tekh. Fiz., 38, 10 (1968).

[5] B. Ch. Dyubua, L. A. Ermolaev, E. P. Esaulov, I. P. Starodubov, and L. P. Yakimenko, Radiotekh. Elektron., 12, 8, 1523 (1967).

Microcells in cold cathodes

N. P. Kozlov, A. A. Lyapin, and V. I. Khvesyuk

N. É. Bauman Moscow Higher Technical School

(Submitted April 26, 1973)
Zh. Tekh. Fiz., 44, 1753-1757 (August 1974)

An approximate method for analysis of a cold cathode is proposed; this method can be used to determine the basic parameters of the cathode region. Results calculated for a mercury cathode are reported. Analysis of the original system of equations shows that the allowed cell currents lie in a narrow range which is a function of the thermal and emission properties of the cathode material and of the cross section for inelastic electron–atom interactions.

We propose here an approximation method for analyzing a cold cathode which can be used to determine the basic parameters of the cathode region: the current density j, the electronic fraction of a current s, the temperature of the cathode surface T, the density of neutrals n_g, and the electric field E as a function of the characteristics of the material (the heat of vaporization, the thermal conductivity, the cross section for excitation to a metastable level, the work function, etc.), the current in the microscopic cell I, and the cathode potential drop V_C. A similar method could be based on a common analysis of the processes in the cathode region and in the cathode. The system of equations describing these processes is given in ref. 1.

The solution of the equations describing the processes in the cathode region yields equations relating the cathode potential drop and the electric field at the cathode surface to the dimensions of the cathode zones:[2]

$$V_c - V_m = \frac{1}{2} A a^2, \tag{1}$$

$$E = \frac{1}{2} A a, \tag{2}$$

$$A^3 = -\frac{2(1+s) M (n_g \sigma_m 4\pi j)^2}{e \ln\left(3 - \frac{2}{s}\right)} \left[3 - \frac{2}{s} - s\left(3 - \frac{2}{s}\right)^{3/2}\right],$$

$$a = -\frac{1}{2 n_g \sigma_m} \lg\left(3 - \frac{2}{s}\right),$$

where V_m is the potential for the excitation of a cathode atom to the metastable level, M is the mass of this atom, and σ_m is the cross section for the excitation to the metastable level.

Working from the results of ref. 2, we take account only of the surface heat source. We assume that the heat flux q is supplied over the surface of a hemisphere of radius b. Then, in the steady-state approximation the surface temperature for a semiinfinite cathode is

$$T = \frac{b}{\lambda} q, \tag{3}$$

where λ is the thermal conductivity and

$$b = \left(\frac{I}{\pi j}\right)^{1/2}. \tag{4}$$

The heat flux q is determined from the energy-balance equation at the cathode:[3]

$$q = (1-s)(V_i + V_c - \varphi) j + W_{st}. \tag{5}$$

It is legitimate to use the steady-state approximation, since the experimental lifetimes of the microspots[4] τ are much longer than the characteristic times for the establishment of a steady-state temperature distribution, given by[5]

$$\tau^* = \frac{cb^2}{\lambda},$$

where c is the specific heat.

Evaporation is calculated on the basis of the Langmuir equation, which has been shown[6,7] to hold in the case of high vapor concentrations above the surface:

$$G = 0.0583\beta \sqrt{\frac{A}{T}} \exp\left(-\frac{\Lambda}{T}\right), \tag{6}$$

where β is a constant, A is the molecular weight of the cathode atoms, and Λ is the reduced heat of the vaporization. The emission equation is the Fowler–Nordheim equation:[8]

$$j_e = 1.395 \cdot 10^6 \frac{E^2}{\varphi} \exp\left[-\frac{1.19 \cdot 10^9 \varphi^{3/2}}{E} \theta(y)\right], \tag{7}$$

where θ(y) is the Nordheim function and

$$y = \frac{2.09 \cdot 10^{-5} E^{1/2}}{\varphi}. \tag{8}$$

In the calculation we use equations relating the cathode erosion G and the ion-current density j_i to the density of neutrals:

$$j_i = \alpha e n_g v_i; \tag{9}$$

$$G = M n_g v_g, \tag{10}$$

where α is the degree of ionization in the cathode region,

$$v_i = \left(\frac{eV_c}{2M}\right)^{1/2}$$

is the ion velocity, and

$$v_g = \left(\frac{kT}{2\pi M}\right)^{1/2}$$

is the velocity of the neutrals, assumed to be equal to the thermal velocity.

To determine the electric field we use the Mackeown equation[9] instead of Eq. (2),

$$E^2 = 16\pi \left(\frac{m_e}{2e}\right)^{1/2} V_c^{1/2} \frac{j}{1 - \frac{j_i}{j_e}} \left[\left(\frac{M}{m_e}\right)^{1/2} \frac{j_i}{j_e} - 1\right], \tag{11}$$

since these equations give approximately the same values of E, and the use of Eq. (11) simplifies the calculations.

This system of equations is highly nonlinear and cannot be solved analytically in general form. We used the circumstance[1] $f = 1 - s \leq 0.1$ to simplify Eqs. (1) and (11).

To analyze this system of equations we substitute (10) into (6), finding

$$n_g = \frac{0.1463\sqrt{A}}{\sqrt{kMT}} \exp\left(-\frac{\Lambda}{T}\right), \qquad (12)$$

where k is the Boltzmann constant.

Substituting Eqs. (5) and (4) into (3), we find

$$n_g = \frac{7.25 \cdot 10^{8} \lambda^{4/3} M^{1/3}}{\sigma_m^{2/3} \alpha^{1/3} V_c^{1/6} I^{2/3} (V_i + V_e - \varphi)^{4/3} (V_e - V_m)^{1/2}} T^{4/3}. \qquad (13)$$

Equations (12) and (13) are shown graphically in Fig. 1. We see that there are two possible solutions to the problem; in a previous paper[10] we only found solution I. This solution is stable, but the characteristic density and temperature are too high [$n_g \sim 10^{22}$ cm^{-3}; $T \sim (3\text{–}6) \cdot 10^3$ °K]. Solution II is unstable. It has been shown[4,11] that an internal instability is associated with processes at a cold cathode; thus, solution II may, in fact, reflect the actual situation.

We have carried out calculations for a mercury cathode, assuming $V_c = 10$ V, $I = 0.08$ A (ref. 4), and $\varphi_{eff} = 2$ eV. We choose the condition $\varphi_{eff} < \varphi$, which takes account of the effect of the local fields (solution II): $j = 1.55 \cdot 10^6$ A/cm^2, $n_g = 4.2 \cdot 10^{20}$ cm^{-3}, $E = 1.55 \cdot 10^7$ V/cm, $f = 0.11$, $\alpha = 1.6 \cdot 10^{-2}$, and $T = 1.3 \cdot 10^3$ °K.

We see from Fig. 1 that a solution does not exist for certain values of the initial parameters, since the corresponding curves do not have intersections. The condition for the existence of a solution is found by equating Eqs. (12) and (13) and their derivatives with respect to the temperature; it is

$$\alpha I^2 = \frac{1.06 \cdot 10^{-34} \lambda^4 M \Lambda^7}{\beta^3 \sigma_m^2 V_c^{1/2} (V_i + V_e - \varphi)^4 (V_e - V_m)^{3/2}}. \qquad (14)$$

The free parameters are V_c and I; however, since V_c is known quite well from experiment,[4,12] we turn to a determination of the allowable range of cell currents I. We see from (13) that there is a certain minimum current I_{min} below which no solution exists for Eqs. (12) and (13). An equation for I_{min} is obtained from the general solution of the system of equations, taking condition (14) into account:

$$\lg A_2 - \frac{3}{2}\lg A_1 + \lg I_{min} + \frac{1}{2}\lg n_{ge} = \frac{2.58 \cdot 10^{8} \varphi^{3/2} I_{min}}{B_1 A_1^{3/4} n_{ge}^{1/2}} \theta(y),$$

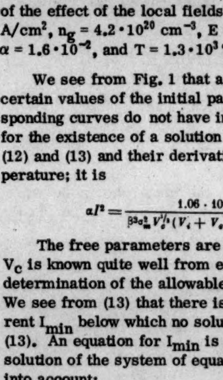

Fig. 1. Typical shapes of the calculated curves. 1) Eq. (12); 2) Eq. (13).

where n_{ge} is determined from

$$\frac{7}{4}\lg n_{ge} + \frac{3}{4}\lg A_1 = -\lg A + \frac{3}{4}\lg B - \frac{0.435\Lambda B^{3/4}}{n_{ge}^{3/4} A_1^{3/4}},$$

$$\lg A = -18.346 - \lg\beta,$$

$$A_1 = \frac{1.44 \cdot 10^{-18} \lambda^{4/3} M^{1/3} \Lambda^{7/3}}{\beta \sigma_m^{2/3} V_c^{1/6} (V_i + V_e - \varphi)^{4/3} (V_e - V_m)^{1/2}},$$

$$\lg A_2 = \lg B_2 - 9.778,$$

$$B = \frac{2.2 \lambda^{4/3} M^{1/3}}{\sigma_m^{2/3} V_c^{1/6} (V_i + V_e - \varphi)^{4/3} (V_e - V_m)^{1/2}},$$

$$B_1 = 3.31\sqrt{V_c},$$

$$\lg B_2 = 16.693 + \frac{1}{4}\lg V_c - \lg\varphi + \frac{1}{2}\lg M + \lg\sigma_m + \frac{3}{4}\lg(V_e - V_m),$$

θ(y) is the Nordheim function, and

$$y = \frac{9.35 \cdot 10^{-3} B_1^{1/2} A_1^{3/4} n_{ge}^{1/4}}{I_{min}^{1/2} \varphi}.$$

If we assume further that (12) does not hold at high vapor concentrations above the surface and that the equation corresponding to (12) is such that a solution of Eqs. (12) and (13) exists for any T, there is still a lower boundary on the cell current, determined from the condition

$$n_g < n_{solid}.$$

The upper limit on the cell current is determined from the obvious condition $\alpha \leq 1$:

$$\frac{7}{4}\lg n_{gr} = -\lg A_3 + \frac{3}{4}\lg B - \frac{1}{2}\lg I_{max} - \frac{3.37 \cdot 10^4 \Lambda B^{3/4}}{n_{gr}^{3/4} I_{max}^{1/2}},$$

where h_{gr} is found from

$$\lg B_2 + \frac{1}{2}\lg n_{gr} = \frac{1.55 \cdot 10^{13} \varphi^{3/2}}{B_1 n_{gr}^{1/2}} \theta(y),$$

$$\lg A_3 = \lg A - 4.889;$$

$$y = \frac{1.21 \cdot 10^{-7} B_1^{1/2} n_{gr}^{1/2}}{\varphi}.$$

For a mercury cathode and under the conditions given above, we find the following limits on the cell current: $I_{min} = 0.043$ A and $I_{max} = 0.42$ A.

On the basis of this discussion we can draw the following conclusions:

1. The calculated results agree with the data of several experimental papers with regard to current density,[13] relative ion current,[14,15] and density of neutrals.[16]

2. The range of currents I over which a solution exists is narrow and is a function of the thermal and emission characteristics of the cathode material. We note that the experimental cell currents of refs. 4, 17 lie within the range found here.

3. As the thermal conductivity λ increases, the current range shifts toward larger values, also in agreement with experimental data.[4]

4. A reduction of the heat of vaporization Λ shifts the current range toward lower values.

5. If a film cathode is used (or, correspondingly, if

the thermal conductivity λ is reduced), the I range is shifted toward lower values.[4]

6. As the cross section for excitation to a metastable level σ_m is increased the current range shifts toward lower values.

---

[1] N. P. Kozlov and V. I. Khvesyuk, Zh. Tekh. Fiz., 41, 2135 (1971) [Sov. Phys.–Tech. Phys., 16, 1691 (1972)].

[2] N. P. Kozlov and V. I. Khvesyuk, Zh. Tekh. Fiz., 41, 2142 (1971) [Sov. Phys.–Tech. Phys., 16, 1697 (1972)].

[3] V. L. Granovskii, Electric Currents in Gases [in Russian], Izd. Nauka, Moscow (1971).

[4] I. G. Kesaev, Cathode Processes in an Electric Arc [in Russian], Izd. Nauka, Moscow (1968).

[5] R. Holm, J. Appl. Phys., 19, 361 (1948).

[6] S. I. Anisimov, Ya. I. Imas, G. S. Romanov, and Yu. V. Khodyko, Effect of Intense Radiation of Metals [in Russian], Izd. Nauka, Moscow (1970).

[7] S. I. Anisimov and A. Kh. Rakhmatulina, Zh. Eksp. Teor. Fiz., 64, 869 (1973).

[8] M. I. Elinson and G. F. Vasil'ev, Field Emission [in Russian], GIFML, Moscow (1958).

[9] S. S. Mackeown, Phys. Rev., 34, 611 (1929).

[10] N. P. Kozlov, A. A. Lyapin, and V. I. Khvesyuk, Abstracts of Reports, Fifth All-Union Conference on Cool-Plasma Sources, Novosibirsk, 1972.

[11] I. G. Kesaev, Cathode Processes in a Mercury Arc and Questions of Its Stability [in Russian], Énergoizdat, Moscow (1961).

[12] V. E. Grakov, Zh. Tekh. Fiz., 37, 396 (1967) [Sov. Phys.–Tech. Phys., 12, 286 (1967)].

[13] K. D. Froome, Proc. Phys. Soc. (London), 62, 805 (1949).

[14] T. Z. Wasserrab, Phys., 130, 511 (1951).

[15] W. Weizel, Phys., 131, 170 (1952).

[16] H. Hull, J. Appl. Phys., 35, 490 (1964).

[17] S. S. Mackeown, F. W. Bowden, and I. D. Cobine, El. End., 53, 1081 (1934).

Evaporation rates of the system ZrC + x% W for the temperature range 2300-3000°K

N. M. Karnaukhova, V. A. Luknitskii, and I. A. Maslov

A. F. Ioffe Physicotechnical Institute,
Academy of Sciences of the USSR, Leningrad

(Submitted March 19, 1973)
Zh. Tekh. Fiz., 44, 1758-1764 (August 1974)

The evaporation rate of solids in vacuum is measured by letting the test substance condense onto a water-cooled metal collector whose removable part is an aluminum foil. The collector and the condensate are irradiated by neutrons in a nuclear reactor; after the irradiation the condensate is removed in a mixture of nitric and hydrofluoric acids. Evaporation rates are measured for ZrC, W, and ZrC + x% W (x ≃ 10 and 30%). The amounts of zirconium (according to ^{95}Zr) and tungsten (according to ^{187}W) are determined from direct γ spectrometry of the solution. For the compounds ZrC + x% W a radiochemical procedure is proposed for separation; the procedure involves extraction with α-benzoinoxime in chloroform. The evaporation experiment is carried out in a metal apparatus at 10^{-7}-10^{-8} torr, with the mass composition of the residual gases being monitored. The emissivities of the evaporating substances are measured under the vacuum conditions.

INTRODUCTION

Measurements of the evaporation rates of refractory materials based on zirconium carbide are of considerable practical interest because of the proven and potential technological applications of these materials – in thermionic convecters, protective coatings, etc. One such promising material is the compound ZrC + x% W, in which tungsten is used to reduce the evaporation rate of the carbide.

If pure tungsten is used in a study of the evaporation rate of such materials in vacuum as a function of the tungsten content, as in our case, in which this content is varied from 0% to 100% (by weight), special precautions are necessary.

First, any trace of moisture leads to a gas-transport reaction in which tungsten is transported from relatively hot regions to relatively cool regions.[1] Accordingly, experiments of this type must be carried out in a high vacuum and the mass composition of the residual gas must be monitored for water, oxygen, and organic matter.

Second, accurate measurement of the temperature of a particular sample requires knowledge of its emissivity, which is a function of the composition of the material and, probably, the residual gas composition. It follows that the emissivity must be measured under experimental conditions designed to eliminate the need for indirect conversions, which lead to errors.

Both these requirements are met by the apparatus designed for these experiments. Furthermore, since the range of relatively low temperatures which we study (of practical importance in connection with thermionic conversion) is characterized by comparatively low evaporation rates and very small amounts of condensate, the apparatus is designed with provision for the collection of the condensate on the collector and for subsequent neutron-activation analysis of the zirconium and tungsten contents.1)

We have not been able to determine the amount of evaporated material by direct γ spectroscopy because of the significant interference of ^{24}Na formed from the collector material (Al) during the reactor irradiation in the reaction $^{27}\mathrm{Al}(n, \alpha)\,^{24}\mathrm{Na}$. The sodium passes into solution during the scouring of the condensate. Furthermore, the resolution of the NaI(Tl) detector is inadequate for distinguishing the necessary γ lines: those of ^{187}W (480 and 686 keV), ^{95}Zr (750 keV), and ^{97}Zr (666 and 750 keV). We therefore use a radiochemical method for separating the radioactive Zr and W isotopes.

EXPERIMENTAL APPARATUS AND PROCEDURE

The experimental apparatus is designed for operation in a vacuum of 10^{-7}-10^{-8} torr (most of the measurements are carried out at a residual gas pressure $< 10^{-7}$ torr); at these pressures ($P_{O_2} \leq 10^{-8}$ torr) there are no oxides in the vapor phase during the evaporation of tungsten, and only atomic tungsten particles are observed.[3] The metal apparatus is made of stainless steel with six removable flanges with copper seals. The system of traps and valves provides complete isolation of the working chamber from oil vapor after the general degassing by heating, which is carried out for 7-8 h at 330°C. The vacuum is monitored by LT-2, LM-2, and IM-12 gauges and an RMO-4S omegatron gauge. The temperature is measured through a glass window, which is covered in the intervals between temperature measurements by an internal shutter or by the collector itself.

Rods of the material being tested (1.5-1.7 mm in diameter and 40 mm long) are mounted on water-cooled copper leads with tungsten tips, through which heating is car-

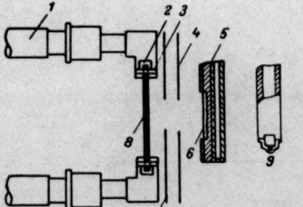

Fig. 1. The evaporation apparatus. 1) Cooled heater-current leads; 2) tungsten tips; 3) tantalum clamp; 4) tantalum shield; 5) cooled copper collector disk; 6) aluminum collector; 7) additional W shield; 8) test rod; 9) device for attaching the test rod to the current lead (view along the rod axis).

ried out by current at the line frequency. Two shields (tungsten and tantalum) with irises are used to cut out the flux of evaporated material from the central part of the rod, which exhibits a temperature drop of less than 20°.

Figure 1 shows the evaporation apparatus.[2] The collector is aluminum tape (99.999% pure), 80 mm long, 30 mm wide, and 0.09 mm thick, pressed against a copper half-cylinder cooled by running water.

A special mechanism makes it possible to carry out the evaporation four times on different parts of the tape (an individual spot of condensate has dimensions of 8 × 16 mm), and the collector can be moved aside for the time required to bring the apparatus to working conditions and for the time required to measure the temperature.

The rod temperature is measured at intervals of 10-20 min and held constant within ± 20° during an experiment.

At the end of an evaporation cycle (consisting of four exposures for a single temperature), the aluminum tape with the deposit of evaporated material is sent to a VVR-M reactor for neutron irradiation and for subsequent activation analysis.

The evaporation rate is calculated as in ref. 2.

Before the irradiation the collector tape is rolled up into thin aluminum foil (0.02 mm thick) and placed in a container unit. Up to 16 collectors are irradiated simultaneously in a single container unit. Reference samples packed in quartz ampoules are irradiated along with the collectors. For the case of Zr these reference samples consist of $5 \cdot 10^{-3}$g of zirconyl chloride ($ZrOCl_2 8H_2O$), and in the case of tungsten they consist of $2 \cdot 10^{-6}$g of tungstic acid (H_2WO_4).

After irradiation in a vertical reactor channel [flux $(3\text{-}5) \cdot 10^{13}$ neutrons/($cm^2 \cdot sec$) for 24 to 100 h], the radioactive zirconium and tungsten isotopes are separated radiochemically. The condensate is scoured in a Teflon cup in 2-3 ml of a mixture consisting of 2 parts of HNO_3 (1:1) and 1 part of concentrated HF. First, 0.2 ml of the tungsten-carrier solution (H_2WO_4, 10^{-5} g) is added to the mixture. The collector is cut into the four parts corresponding to the four evaporation exposures, and each part is etched[2)] separately for 1 min. An experimental check shows that the condensate is removed essentially completely by a single etching. The thickness of the film removed in a single etching is about $5 \pm 0.005\mu$ and the same with triple etching.

The Zr and W are separated by an extraction method with α-benzoinoxime in chloroform. The separation procedure used for the case of pure zirconium carbide is described in ref. 4. To the solution of the condensate we add 17 ml of water and 1 ml of concentrated HCl; then the tungsten is extracted twice with 15 ml of a 0.15% solution of α-benzoinoxime in chloroform. The chemical yield[3)] of tungsten in the organic phase is 98%. The zirconium activity is measured in the aqueous phase.

For a quantitative determination of the zirconium content we measure its activity on the basis of the isotopes $^{95}Zr + ^{95}Nb$ (the γ lines at 750 and 770 keV); in the case of tungsten we use the isotope ^{187}W (the γ lines at 480 and 686 keV). The γ activity is measured by a spectrometer consisting of a scintillation unit with a NaI(Tl) crystal (63 × 63 mm in size, having a 9% resolution at the 662-keV line) and an AI-256 multichannel pulse-height analyzer. The count rate − the area of the γ spectral peak − ranges from 2 to 1000 sec^{-1} for the various samples.

Analysis of eight samples (including the cooling of the irradiated samples, the radiochemical separation, and the activity measurements) requires about three days. The samples of the compositions studied are prepared by the powder-metallurgy method from zirconium carbide and "especially pure" tungsten.[4)]

EMISSIVITY MEASUREMENTS

To determine the emissivity we select rods of those lots for which evaporation experiments have been carried out (except for the case of pure tungsten, for which we use the tabulated values[6]) and we construct a "blackbody" of each compound. For this purpose we use an electric-spark method to machine a depression 0.15 mm in diameter and 1 mm deep in the central part of a rod. The actual temperature is measured by training an LMP-066 optical micropyrometer onto the bottom of the depression and the brightness temperature is measured by training it onto the rod surface. All the measurements are carried out in the same apparatus, in the same high vacuum as in the evaporation experiments. An estimate of the error in the measurements of the actual temperature due to the imperfections in the blackbody model[7] shows this error to be less than 1%. The calculations are carried out on the basis of the standard equation.[8] The results are shown in Fig. 2.

We see from these figures that there is a tendency for ε_λ to decrease with increasing temperature for all the materials studied, in agreement with the data for tungsten[6] and zirconium carbide.[8] Then, as the tungsten content is increased, the values of ε_λ for these compositions decrease, approaching the values characteristic of tungsten.[5)] The brightness temperature in these measurements is detected by an OPIR-17 optical pyrometer, and the accuracy of its indications is monitored by means of an LMP-066 micropyrometer. The values of $\varepsilon_\lambda(ZrC)$ and

TABLE 1

Composition	wt.%				
	c_{tot}	c_{free}	Zr	W	N_2
ZrC	10.83	0.09	88.7	—	0.12
ZrC+10% W	9.72	Нет	78.0	11.0	0.58
ZrC+30% W	7.78	Нет	58.0	34.0	0.45

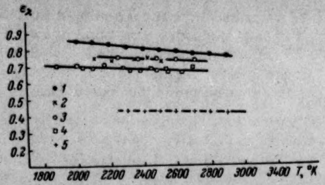

Fig. 2. Emissivity as a function of the temperature for zirconium carbide, zirconium carbide with tungsten, and tungsten. 1) ZrC (ref. 8); 2) ZrC, this work; 3) ZrC + 10% W, this work; 4) ZrC + 30% W, this work; 5) W (ref. 6).

ε_λ(ZrC + 10% W) are essentially the same. There is some discrepancy between our results and those of ref. 8, probably because of differences in the materials and in the vacuum conditions.

MASS COMPOSITION OF THE RESIDUAL GASES

The residual gases must strongly influence the evaporation of hot metal carbides as a result of the interaction with the surfaces of these carbides.[10]

In the unheated evacuated apparatus, with an oil vapor pump, the pressure in the system is governed primarily by gases containing oxygen (H_2O, CO, CO_2) and by hydrocarbons (C_xH_y); the water content can reach 90% of the total pressure.[11] In working out the heating conditions for our apparatus we study the mass composition of the residual gases under all operating conditions. The partial pressures of the residual gases are measured by an IPDO-1 apparatus with an RMO-4S omegatron gauge. Figure 3a shows a typical residual-gas spectrum, for the heating of ZrC + 10% W. An important change in the mass composition is observed near the beginning of an exposure.

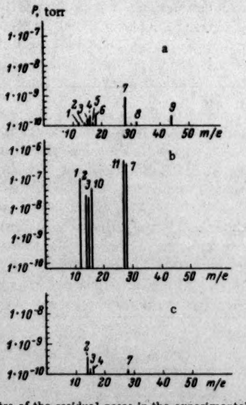

Fig. 3. Mass spectra of the residual gases in the experimental apparatus (ZrC + 10% W). a: Apparatus heated under the oven. $P_{res} = 6 \cdot 10^{-8}$ torr, T = 293°K, ZrC + 10% W. b: Sample heated to 2480°K. $P_{res} = 18 \cdot 10^{-5}$ torr. c: Vacuum conditions at the time of the measurements for exposures. $P_{res} = 4 \cdot 10^{-8}$ torr, T = 2480°K. 1) C^+; 2) N^+, CH_2^+; 3) CH_3^+; 4) O^+, CH_4^+; 5) OH^+; 6) H_2O^+; 7) N_2^+, CO^+; 8) O_2^+; 9) CO_2^+; 10) CH_4, 11) $C_2H_3^+$.

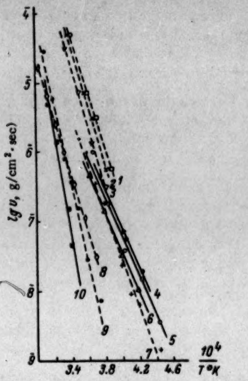

Fig. 4. Evaporation rates of ZrC, W, and samples made from them. 1) ZrC (ref. 9); 2) ZrC + 10% (ref. 9); 3) ZrC + 30% W (ref. 9); 4) ZrC (this work); 5) ZrC + 10% W (this work); 6) ZrC + 30% W (this work); 7) ZrC (ref. 10); 8) W (ref. 6); 9) W (ref. 12); 10) W (this work).

For example, masses at 17, 18, 32, and 44 (OH^+, H_2O^+, O_2^+, CO_2^+) are not observed; the peaks with masses of 14, 15, 16, and 28 (N^+, CH_2^+, CH_3^+, O^+, CH_4^+, N_2^+, CO^+) remain considerably lower than those according to the corresponding data of ref. 10. We see that our experiments have been carried out under qualitatively better vacuum conditions, with a higher total vacuum.

EXPERIMENTAL RESULTS AND DISCUSSION

The experimental results are shown in Table 2 and Fig. 4; the figure also shows data of other investigators.

Analysis of these results reveals that zirconium carbide evaporates fastest. The composition with 30% tungsten displays an evaporation rate about half as large over the temperature range studied. The lowest evaporation rate is of course that of tungsten.

Our values for the evaporation rates of ZrC, ZrC + 10% W, and ZrC + 30% W are considerably lower than the values of ref. 9; this result is to be expected since our measurements are carried out in a considerably higher vacuum. The results of ref. 10, found under relatively better vacuum conditions, show better agreement with the present results.

The discrepancy between the line slopes, which give the heats of vaporization, can also be attributed to differences in the vacuum conditions (the pressure and the mass composition of the residual gases), and perhaps to differences in the chemical compositions of the materials studied. It is interesting to note the clearly defined tendency for the residual gas pressure to affect the slopes of the lines for pure tungsten and the slopes of the lines for the compositions including zirconium carbide in opposite manners.

In the former case, as the pressure is reduced [10^{-5} torr (ref. 6), $8 \cdot 10^{-7}$ torr (ref. 12), and $1.4 \cdot 10^{-7}$ torr (the

TABLE 2. Evaporation Rates of ZrC, W, and ZrC + x% W with an Exposed Surface in Vacuum

Composition	T, °K	Delay, t, sec	Evaporation rate, v, g/cm²· sec)	Composition	T, °K	Delay, t, sec	Evaporation rate, v, g/(cm² · sec
ZrC	2365	9000	$2.1\cdot10^{-8}$	ZrC+30% W	2390	18000	$9.5\cdot10^{-9}$
	2365	9000	$1.9\cdot10^{-8}$		2390	18000	$7.9\cdot10^{-9}$
	2365	14400	$1.6\cdot10^{-8}$		2390	18000	$9.0\cdot10^{-9}$
	2365	14400	$1.6\cdot10^{-8}$		2390	21600	$7.3\cdot10^{-9}$
	2365	17100	$2.3\cdot10^{-8}$		2390	21600	$11.0\cdot10^{-9}$
	2365	18000	$1.8\cdot10^{-8}$		2510	6000	$3.8\cdot10^{-8}$
	2365	18000	$1.8\cdot10^{-8}$		2510	6000	$2.8\cdot10^{-8}$
	2480	7200	$7.2\cdot10^{-8}$		2510	7200	$2.9\cdot10^{-8}$
	2480	7200	$8.1\cdot10^{-8}$		2510	7200	$2.7\cdot10^{-8}$
	2480	7200	$6.6\cdot10^{-8}$		2510	6000	$4.1\cdot10^{-8}$
	2480	7200	$5.4\cdot10^{-8}$		2510	7200	$2.3\cdot10^{-8}$
	2460	6000	$6.5\cdot10^{-8}$		2510	6000	$3.8\cdot10^{-8}$
	2460	6000	$6.0\cdot10^{-8}$		2630	2400	$1.4\cdot10^{-7}$
	2460	7200	$5.0\cdot10^{-8}$		2630	3600	$1.5\cdot10^{-7}$
	2460	7200	$5.4\cdot10^{-8}$		2630	3600	$1.2\cdot10^{-7}$
	2598	2400	$6.3\cdot10^{-7}$		2750	900	$4.3\cdot10^{-7}$
	2598	3000	$4.3\cdot10^{-7}$		2750	600	$4.4\cdot10^{-7}$
	2598	3000	$5.7\cdot10^{-7}$		2750	600	$4.5\cdot10^{-7}$
ZrC+10% W	2250	54000	$4.1\cdot10^{-9}$		2750	1200	$4.6\cdot10^{-7}$
	2250	27600	$3.7\cdot10^{-9}$		2750	600	$4.9\cdot10^{-7}$
	2367	10800	$2.0\cdot10^{-8}$	W	2930	1800	$4.6\cdot10^{-8}$
	2367	10800	$2.1\cdot10^{-8}$		2930	3060	$4.6\cdot10^{-8}$
	2367	14400	$1.1\cdot10^{-8}$		2930	600	$5.8\cdot10^{-8}$
	2367	10800	$1.8\cdot10^{-8}$		2930	1200	$3.7\cdot10^{-8}$
	2367	14400	$1.2\cdot10^{-8}$		2960	2700	$1.5\cdot10^{-7}$
	2367	10800	$0.7\cdot10^{-8}$		2960	1800	$1.6\cdot10^{-7}$
	2480	7200	$4.1\cdot10^{-7}$		2960	1800	$1.5\cdot10^{-7}$
	2480	7200	$4.1\cdot10^{-7}$		2960	1800	$1.4\cdot10^{-7}$
	2480	7200	$3.1\cdot10^{-7}$		3080	1200	$1.4\cdot10^{-6}$
	2480	5400	$3.3\cdot10^{-7}$		3080	720	$1.7\cdot10^{-6}$
ZrC+10% W	2547	3600	$2.0\cdot10^{-7}$		3080	120	$1.5\cdot10^{-6}$
	2547	3600	$1.4\cdot10^{-7}$		3195	300	$4.6\cdot10^{-6}$
	2547	3600	$1.9\cdot10^{-7}$		3195	420	$4.9\cdot10^{-6}$
	2547	3600	$2.0\cdot10^{-7}$		3195	300	$4.8\cdot10^{-6}$
	2547	3600	$1.5\cdot10^{-7}$				
	2720	600	$0.9\cdot10^{-6}$				
	2720	600	$1.3\cdot10^{-6}$				
	2720	600	$1.0\cdot10^{-6}$				

present experiments)], the line slope increases. In the latter case [$(1\text{–}2)\cdot10^{-5}$ torr (ref. 9), $4\cdot10^{-7}$ torr (ref. 10), and 10^{-7}–10^{-8} torr (the present experiments)], we find the opposite tendency. While in the case of tungsten this tendency could be interpreted as a change in the evaporation mechanism, from oxide evaporation to evaporation of the pure metal, with a corresponding increase in the heat of vaporization, in the case of the materials based on zirconium carbide the data available allow us only to note a significant change in the evaporation process as the vacuum in the evaporation apparatus is improved.

---

[1] A similar procedure for ZrC evaporation in a vacuum of 10^5–10^6 torr has been described previously.[2]

[2] Before the deposition, the collector surface is treated with similar threefold etching.

[3] The authors thank G. I. Karazhanova, who was very helpful in solving the chemical questions.

[4] The samples have been synthesized at the State Institute of Applied Chemistry and graciously furnished by R. G. Avarbé and T. A. Nikol'skaya, whom the authors thank. The synthesis procedure is described in ref. 5. The chemical composition of the original samples is shown in Table 1. The sample porosities were 16% for ZrC, 7% for ZrC + 10% W, and 5% for ZrC + 30% W.

[5] In light of these results we note that the literature reveals significantly different results[9] for "poor vacuum conditions" for the analogous materials: $\varepsilon_\lambda = 0.51$ for ZrC + 10% W and $\varepsilon_\lambda = 0.53$ for ZrC + 30% W.

---

[1] H. Schaefer, Chemical Transport Reactions, Academic, New York (1964).

[2] N. M. Karnaukhova, G. I. Karkzhanova, V. A. Luknitskii, I. A. Maslov, and Z. P. Terent'eva, in: Methods and Applications of Neutron Activation Analysis [in Russian], Izd. Zinatne, Riga (1969), p. 167; I. A. Maslov, V. A. Luknitski (Lucknitskii), N. M. Karnaukhova (Karnauchova), and G. I. Karnaganova, Nucl. Appl. Technol., 7, 389 (Oct. 1969).

[3] A. Ya. Tontegode, Candidate's Dissertation [in Russian], FTI Akad. Nauk SSSR, Leningrad (1965).

[4] Ping Y. Peng and E. V. Sandell, Anal. Chim. Acta, 29, 325 (1963).

[5] I. N. Dranitsyna, Yu. N. Vil'k, R. G. Avarbé, Yu. A. Omel'chenko, and T. P. Ryzhkova, Zh. Prikl. Khim., 41, 492 (1968).

[6] W. Espe, Materials for Vacuum Technology, Pergamon (1965).

[7] V. B. Fedorov and V. S. Egorov, Teplofiz. Vys. Temp, No. 6, 498 (1968) [High Temp.]

[8] V. A. Petrov, V. Ya. Chekhovskii, A. E. Sheindlin, V. A. Nikolaeva, and L. P. Fomina, Teplofiz. Vys. Temp., No. 5, 995 (1967).

[9] T. A. Nikol'skara and Yu. N. Vil'k, Zh. Tekh. Fiz., 42, 429 (1972) [Sov. Phys.—Tech. Phys., 17, 341 (1972)].

[10] V. K. Vlasov, Candidate's Dissertation [in Russian], MGU (1970).

[11] K. V. Cherepin, Fundamentals of Cleaning, Outgassing, and Pumping in Vacuum Technology [in Russian], Izd. Sov. Radio, Moscow (1967), p. 167.

[12] I. V. Golubtsov, A. N. Nesmeyanov, Vestn. MGU, Ser. II, Khimiya, No. 5, 31 (1965).

Mass-spectrometer study of the ion composition of a glow discharge

N. P. Egorov and V. N. Komarov

L. Ya. Karpov Scientific-Research Physicochemical Institute, Moscow

(Submitted April 9, 1973)
Zh. Tekh. Fiz., 44, 1765-1769 (August 1974)

The composition of the beams and the ion composition have been studied in the negative glow of glow discharges in nitrogen, mixtures of nitrogen with helium and argon, air, and carbon dioxide. The discharges are studied over the pressure range 0.1-0.8 torr and at current densities ~ 10^{-4} A/cm². The experimental apparatus and procedure are described. A KM-1 quadrupole mass spectrometer is used as mass analyzer. A system of grids is used to study the energy distribution of the ions emitted from the discharge tube. The ions are extracted from the negative glow through an aperture in the anode. The extraction mechanism is discussed.

We report here on a study of the ion composition in the cathode region of a glow discharge. A mass-spectrometer method has been developed for this purpose. The literature reveals several cases[1-13] in which the positive-ion composition in a dc discharge has been studied by mass-spectrometer methods. The work can be divided into two groups: 1) studies of channeled beams;[7-10] 2) study of the positive column, the negative glow, and the Faraday dark space.[1-6,11,12] In a study of channeled beams the ions are extracted through an aperture in the cathode; in studies of the intermediate parts of a discharge the extraction is carried out through an aperture in the side wall of the discharge tube. In the present experiments, in contrast, an analysis of the channeled beams is combined with an analysis of the positive ions in the negative glow. In this procedure the positive ions are extracted through an aperture in the anode, which is in the negative glow (in this case, there is no anode region, positive column, or Faraday dark space). The extraction is assumed to occur as the result of a negative potential drop. The energy spread of the ions emitted from the aperture in the anode is 2-5 eV.

Ions approaching the cathode of a glow discharge have a broad energy distribution (up to several hundred volts). Accordingly, in the study of channeled beams we use a quadrupole mass spectrometer (the KM-1; ref. 14), which has the important advantage of a resolution which is not a function (within a certain range) of ion energy. It is possible to collect efficiently ions with a large energy spread. Other characteristics[15] of the quadrupole mass spectrometer indicate that this type of spectrometer is highly suitable for plasma studies.

Figure 1 shows the experimental apparatus. The ions are extracted through an aperture 0.1 mm in diameter in electrode 3, which can serve as either the anode or the cathode of discharge tube 1. The other electrode, 2, can be moved by means of a magnet. Both electrodes are made of stainless steel and have diameters of 2.2 cm, approximately equal to that of the discharge tube. The discharge tube is made from molybdenum glass. Conical electrode 4 performs accelerating and focusing functions. Grid system 5 is used to record the ion distribution with respect to kinetic energy. Ionization box 6 is used to analyze the neutral component in the discharge. In front of the quadrupole rods 10 are the extracting and focusing irises of the KM-1 quadrupole mass spectrometer. After mass analysis the ion beam strikes secondary electron multiplier 11.

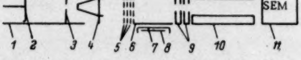

Fig. 1. The experimental apparatus. 1) Discharge tube; 2) movable electrode; 3) electrode with aperture; 4) accelerating and focusing electrode; 5) grids for recording the ion energy distribution; 6) ionization box; 7) heater filament; 8) reflector; 9) extracting and focusing irises of the KM-1; 10) quadrupole rods; 11) secondary electron multiplier.

The analyzer is evacuated by an ÉRA-100 vacuum pump. When the pressure in the discharge cell is in the range 0.2-0.8 torr the corresponding pressure in the analyzer is $5\cdot10^{-6}$-$2\cdot10^{-5}$ torr. The gases and mixtures to be tested are admitted into a chamber having a volume of ~15 liters connected to the discharge. The large volume makes it possible to operate continuously without any appreciable pressure change in the discharge tube due to the escape of gas through the extraction aperture. The pressure in the discharge tube is assumed to be equal to the pressure in the chamber and is measured with an LT-2 thermocouple gauge.

We use technical grade nitrogen, spectrally pure helium and argon, and carbon dioxide.

EXPERIMENTAL RESULTS AND DISCUSSION

Most of the ions in the channeled beams from the discharge in nitrogen are N_2^+ and N^+ ions. There is also a contribution to the ion current with m/e = 14 from N_2^{++} ions, as can be inferred from the existence of ions with kinetic energies higher than the voltage across the discharge tube. We also observe N^{++} and N_3^+ ions and impurity Ar^+ ions. The N_3^+ current is about 1% of the total ion current.

A change in the anode–cathode separation does not affect the composition of the channeled beams until the anode approaches the boundary of the cathode dark space and the negative glow. This observation implies that ions

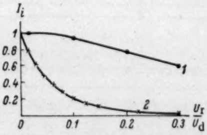

Fig. 2. Reduced ion current J_i in the channeled beam as a function of the retardation potential U_r. The discharge is in nitrogen at a pressure of p = 0.3 torr, and the current density is j = $2\cdot10^{-4}$ A/cm². Here U_d is the voltage across the discharge tube. 1) N^+; 2) N_2^+.

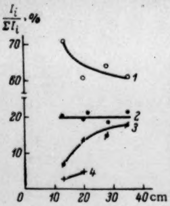

Fig. 3. Relative ion current in the negative glow as a function of the distance between the cathode and the anode. Discharge in nitrogen, p = 0.3 torr, j = $2 \cdot 10^{-4}$ A/cm². The ions are extracted through an aperture in the anode. 1) N_2^+; 2) N^+; 3) N_4^+; 4) N_3^+.

produced in the cathode dark space or in the first part of the negative glow move toward the cathode. Figure 2 shows the ion current as a function of the retardation potential. The distribution of N_2^+ ions with respect to kinetic energy agrees qualitatively with the distribution obtained on the basis of a model in which resonant charge exchange is treated as the decisive factor governing this distribution:[7]

$$\frac{V_c}{N_0}\frac{dN}{dV}=\frac{L}{2l}e^{-\frac{L}{2l}\frac{V_x}{V_c}}, \tag{1}$$

where l is the characteristic length for resonant charge exchange, N_0 is the number of ions coming from the negative glow, L is the length of the cathode dark space, V_c is the cathode potential drop, and V_x is the potential corresponding to the ion energy.

As expected, the width of the distribution is inversely proportional to the pressure ($l \sim 1/p$).

A mechanism which affects the particle energy distribution like resonant charge exchange is gas ionization in the cathode dark space by electrons; furthermore, there is the possible dissociation

$$N_2^+ + N_2 \rightarrow N^+ + N + N_2. \tag{2}$$

The distribution for N^+ ions is broader than that for N_2^+ ions; there are no ions of zero kinetic energy.

The increase in the contribution of the N_2^+ ions to the total ion current from 80% to 90% as the pressure is raised from 0.2 to 0.7 torr may be due to a reduced contribution of process (2) to the observed ion currents. It would be interesting to compare the ion composition in the negative glow with that of the channeled beams. We see from Fig. 3 that in the negative glow there are a large number of N_4^+ ions; the relative number of these ions in the total ion current increases with distance from the boundary of the cathode potential drop into the negative glow. The fact that the weakly bound N_4^+ ion is not observed in the channeled beams is evidently due to its dissociation in collisions with gas molecules in the region in which the electric field is strong.

We have studied the ion composition in discharges in mixtures of nitrogen with argon and helium. We find that in the case of the nitrogen–argon mixture the ratio of the current of Ar^+ ions to the sum of the N_2^+ and N^+ currents in the negative glow agrees well with the ratio calculated from the relative abundances of the two components and the cross sections for ionization by the electron beam. It should also be noted that we have detected ArN_2^+ and ArN^+ ions in the negative glow; the relative concentration of the ArN_2^+ ion increases with distance from the cathode, in agreement with the assumption that this ion is formed in a reaction involving an excited argon atom:[16]

$$Ar^* + N_2 \rightarrow ArN_2^+ + e. \tag{3}$$

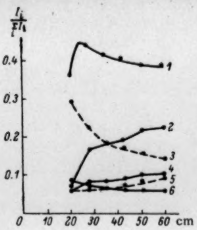

Fig. 4. Relative ion current from the negative glow as a function of the cathode–anode separation. Discharge in carbon dioxide, p = 0.1 torr, j = $2 \cdot 10^{-4}$ A/cm². 1) O_2^+; 2) $H_2CO_2^+$; 3) CO_2^+; 4) H_2CO^+; 5) H_3O^+; 6) CO^+. The HCO^+ currents (~ 0.07 of the total ion current) are not shown, nor are the small currents corresponding to O^+ and C^+ ions.

In the helium–nitrogen mixture the behavior of the ion currents is very different from that in the case just discussed. Near the cathode the ion current is governed primarily by N_2^+ and N^+ ions, even at concentrations on the order of 1%. It is difficult to explain this result under the assumption that the ions are formed only as a result of electron impact. In the negative glow a current of helium ions is detected only near the boundary of the negative glow, and its relative contribution to the total current is an order of magnitude lower than that near the cathode. The ratio of ion currents in the He discharge can be attributed to the contribution of Penning ionization,

$$He^* + N_2 \rightarrow He + N_2^+ + e,$$

or the reaction[17]

$$He^+ + N_2 \begin{cases} \nearrow He + N_2^+, \\ \searrow He + N^+ + N. \end{cases}$$

The positive ions in the carbon dioxide are analyzed at pressures in the range p = 0.1-0.8 torr and at currents in the range 0.08-6 mA. Most of the ions in the channeled beams are CO_2^+, O_2^+, CO^+ and C^+ ions; there are also O^+ (~ 6%) and H_2O^+ (~ 1%) ions. As the discharge current is

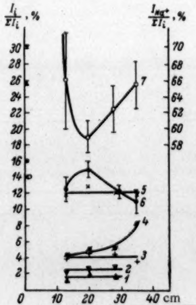

Fig. 5. Relative ion current as a function of the distance to the cathode. Discharge in air, p = 0.3 torr, j = $2 \cdot 10^{-4}$ A/cm². The values for zero distance to the cathode are the ion contributions to the channeled beams. 1) O^+; 2) N^+; 3) N_2O^+; 4) H_3O^+; 5) O_2^+; 6) N_2^+; 7) NO^+.

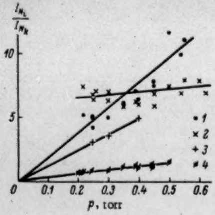

Fig. 6. Ratios of ion currents as functions of the pressure in the discharge tube. Discharge in air, $j = 2 \cdot 10^{-4}$ A/cm². 1) $I_{NO^+}/I_{N_2^+}$; 2) $I_{NO^+}/I_{O_2^+}$; 3) I_{NO^+}/I_{N^+}; 4) $I_{O_2^+}/I_{N_2^+}$.

raised from 0.08 to 2 mA ($p = 0.25$ torr), the relative CO_2^+ contribution falls off from 50% of the total ion current to 20%, while the contributions of O_2^+ and CO^+ increase from 17% to 24% and from 6% to 40%, respectively. Of primary interest in the negative-glow region (Fig. 4) is the intense peak with $m/e = 46$ ($H_2CO_2^+$); this peak is not observed in the neutral composition. In addition to $H_2CO_2^+$ we detected other ions containing hydrogen: H_3O^+, H_2CO^+, HCO^+, and HCO_2^+. We note that, as in ref. 12, at a sufficiently high current density the O_2^+ ions are predominant.

Figure 5 shows the results obtained for discharges in air. Most of the ions in the negative glow are NO^+, N_2^+, O_2^+, H_2O^+, H_3O^+, N^+, O^+, N_2O^+, and Ar^+ ions. As the pressure is raised from 0.3 to 0.6 torr the relative NO^+ current increases from 60% to 80% of the total ion current. The large ratio of the O_2^+ current to the N_2^+ (~ 1, although the mixture contains only ~ 20% oxygen) can be attributed to the formation of O_2^+ in charge exchange $N_2^+ + O_2 \rightarrow N_2 + O_2^+$ or to the consumption of N_2^+ ions in the ion–molecular reaction

$$N_2^+ + O_2 \rightarrow NO^+ + NO.$$

A further contribution to the formation of NO^+ ions probably comes from the reaction

$$N^+ + O_2 \rightarrow NO^+ + O.$$

These mechanisms are consistent with the functional dependences of the relative ion currents on the pressure shown in Fig. 6. In contrast with the case in the negative glow, the intensities of the NO^+, O_2^+, and N_2^+ currents in the channeled beams are about the same (~ 15%), and the N^+ and O^+ intensities increase sharply (~ 30%), probably because of the dissociation of the molecular ions in the high-energy part of the cathode fall.

---

[1] P. F. Knewstubb and A. W. Tickner, J. Chem. Phys., 36, 674 (1961).

[2] P. F. Knewstubb and A. W. Tickner, J. Chem. Phys., 36, 684 (1961).

[3] P. F. Knewstubb and A. W. Tickner, J. Chem. Phys., 37, 2941 (1962).

[4] M. Pahl, Z. Naturforsch., 14a, 239 (1959).

[5] J. P. Gaur and L. M. Chanin, J. Appl., Phys., 40, 256 (1969).

[6] J. P. Gaur and L. M. Chanin, Phys. Rev., 182, 167 (1969).

[7] W. D. Davis and T. A. Vanderslice, Phys. Rev., 131, 219 (1963).

[8] A. V. Bondarenko and E. M. Buryak, First All-Union Conference on Mass Spectrometry. Abstracts, Annotated Reports, and Discussions [in Russian], Leningrad (1969), p. 118.

[9] A. V. Bondarenko, Chemistry and Physics of Cool Plasmas [in Russian], Izd. Moscow Univ. (1971), p. 118.

[10] M. M. Shanin, J. Chem. Phys., 43, 1798 (1965).

[11] J. Freudenthal, J. Appl. Phys., 41, (6), 2447 (1970).

[12] P. H. Dawson and A. W. Tickner, Proceedings of the Sixth International Conference on Ionization Phenomena in Gases, Paris (1963), p. 79.

[13] H. Held, J. L. Gilkinson, and L. M. Chanin, J. Appl. Phys., 40, (11) 4395 (1969).

[14] G. L. Slobodenyuk, A. I. Titov, V. S. Voronin, and V. I. Ivashkin, Zavod. Lab., No. 6, 745 (1970).

[15] M. Mosharrafa and H. J. Oskam, Physica, 32, 1759 (1966).

[16] W. Kaul and R. Fucks, Z. Naturforsch., 15a, 326 (1960).

[17] D. B. Dunkin, F. C. Fehsenfeld, A. L. Schmeltekopf, and E. E. Ferguson, J. Chem. Phys., 49, 1365 (1968).

Energy losses of slow electrons reflected from molybdenum and tungsten single crystals

O. M. Artamonov, B. B. Bolotov, and M. V. Kremkov

A. A. Zhdanov State University, Leningrad

(Submitted August 30, 1973; resubmitted January 3, 1974)
Zh. Tekh. Fiz., 44, 1770-1773 (August 1974)

The energy spectra of scattered electrons and secondary electrons are obtained for various states of the surfaces of the (100) face of Mo and the (110) face of W. A change in the position of the maxima of the energy losses is observed when the single-crystal surfaces are outgassed. Keeping the samples in N_2 or H_2 or in an atmosphere of residual gases increases the intensity of both the elastic and inelastic maxima and, at the same time, raises the work function of the surface.

The energy losses of slow electrons reflected from a surface are of interest for studying the interaction of electrons with a solid and for investigating the energy conditions at the surface of a crystal. Groups of electrons losing an energy of 1.5 or 4.3 eV upon excitation of the energy transitions to subsurface bands are reported in refs. 1 and 2 for the (100) face of W. Similar energy losses at 3.0 and 5.4 eV are observed in ref. 3 in the case of the (110) face of W. Maxima which are associated with the excitation of oscillations of gas molecules adsorbed on the surface,[1] or with the excitation of electron transitions from the levels of adsorbed O_2, CO, and H_2O molecules,[2] or with the excitation of plasma oscillations of the valence electrons of tungsten[4] are identified in the spectra of the energy losses. In investigations of the energy losses of the (100) Mo face, only maxima resulting from the excitation of plasma oscillations[5,6] were detected, although it is shown in ref. 7 that the energy losses are independent of the type of the adsorbed gases.

The goal of the present work is to use the (100) Mo and the (110) W faces of single crystals as examples to show how the energy losses of slow electrons with energies $E_p = 5$-200 eV depend upon the state of the surface.

Molybdenum and tungsten have a volume-centered cubic lattice with similar lattice constants. The energy characteristics of these elements are similar. In particular, the form of the Fermi surface and density of the electron states in the conductivity bands are similar.[8] Consequently, characteristic details in the spectrum of the energy losses of slow electrons (e.g., the maxima resulting from the excitation of plasma oscillations) appear at close values of the energy losses.[4,6,9]

The spectra of the energy losses are recorded with an electrostatic 180° analyzer having a system of retarding three-electrode lenses and an analyzer resolution[10] of 0.15 eV. Both the scattered electrons and secondary electrons are recorded in the direction of the (00) diffraction maximum at an angle of 20° relative to the normal to the surface. The spectra of the energy losses are studied on an outgassed surface of the single crystals, or on surfaces with adsorbed N_2 or H_2 molecules or with adsorbed residual gases. The spectra of the energy losses are also measured in the thermally stimulated desorption in vacuum between $2 \cdot 10^{-6}$ and $6 \cdot 10^{-10}$ torr. The composition of the residual gases is checked with the aid of an IPDO-1 instrument. The spectra reveal CO_2 (18%), CO (40%), H_2O (12%), and H_2 (18%). When the target is cleaned by high-temperature flashes, the CO_2, CO, and H_2 concentrations increase. The state of the surface is monitored by observing changes in the sample work function, which is measured with an accuracy of 0.05-1.1 eV, and by observing changes in the intensity of the maxima of elastically reflected and slow secondary electrons. The relative change in the work function is recorded from the shift of the curves representing the delay of the primary electron current at the target and from changes of the energy interval encompassing the full spectrum of both scattered and secondary electrons relative to the peak of the elastically reflected electrons. The surface which is used on the single crystals is mechanically polished and treated with an electropolishing etching agent. The accuracy with which a crystal face appears on the surface is checked with Laue diagrams, being about 1.5°. Repeated, extended heating to 2000°K by radiation or electron bombardment of the rear surface of the target is used for surface cleaning. The final cleaning step consists of several short high-temperature heating cycles to which the sample is subjected in a vacuum of $1 \cdot 10^{-9}$ torr. The thermal treatment of the target leads to the removal of adsorbed molecules and chemical compounds from the surface but does not render a surface fully cleaned from carbon.[6,11]

The spectra of the slow electrons reflected from the surface are displayed in Figure 1. At energies $E_p = 18$-22 and 70-80 eV, maxima of energy losses with an intensity ratio of genuine secondary electrons to background depending upon E_p appear near the peak of the elastically reflected electrons. The energy losses ΔE_i of the surfaces of the (100) Mo and (110) W faces, which have or have not been outgassed, are listed in Table 1.

The loss value of 9.5 eV in the case of molybdenum corresponds to the approximate excitation energy of a surface plasmon. The excitation energy amounts to 10-11 eV, according to the results of optical measurements[12] of the dielectric constant ε. In the case of outgassed

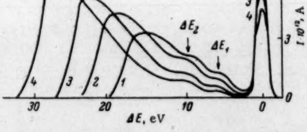

Fig. 1. Spectra of the energy losses of slow electrons reflected from the surface of the (110) faces of W at various energies of the primary electrons. E_p (eV): 1) 18; 2) 22; 3) 27; 4) 33.

TABLE 1

State of the sample's surface	Energy loss (eV)				
	(100) Mo		(110) W		
	ΔE_1	ΔE_3	ΔE_1	ΔE_2	ΔE_3
Surface not outgassed	6.5±0.5	25.5±1.5	6.5±0.5	10.5±0.5	24.0±1.0
Surface outgassed	9.5±0.5	22.0±1.0	5.5±0.5	11.0±0.5	22.5±1.5

tungsten, the loss figure of 11 eV is close to the excitation energy of a surface plasmon; the excitation energy is in approximate agreement with the energy value of 10 eV obtained in ε measurements.[13]

When a molybdenum target is kept for an extended period of time in an atmosphere of residual gases under a pressure of $1 \cdot 10^{-6}$ torr, the ΔE_1 peak is shifted to 6.5 eV and becomes stronger; on the other hand, absorption of N_2 and H_2 under similar pressures only increases the intensity of the maximum, which agrees with the results of ref. 6. A shift of the peak of the surface plasmons toward lower energies in the presence of a layer of adsorbed molecules of residual gases on the surface can be explained by an increase in the ε value of the layer at the metal–vacuum interface[4] or by possible additional energy losses, which are associated with the excitation of electrons from the level of CO and H_2O molecules adsorbed on the surface;[2] these electrons distort the plasmon peak.

Thermal desorption of adsorbed molecules of residual gases shifts the maximum of the surface plasmon toward increased energy losses. The work function $l\Delta\varphi$ of the surface decreases by the value $l\Delta\varphi = -0.3$ eV and passes through the minimum $l\Delta\varphi = -0.6$ eV at a sample temperature of 700°K. The majority of the adsorbed molecules are desorbed at temperatures of 600–800°K when the maximum change of $l\Delta\varphi$ is observed and when the peaks of the elastically and inelastically scattered electrons reach the intensity maxima. CO molecules are the main component of the gas molecules desorbed from the surface. When CO is adsorbed on the (100) Mo face, an increase by 0.35–0.6 eV is observed in the work function of refs. 11 and 15. This observation agrees with the results of our experiments. The desorption of the molecules of the residual gases from the surface of the (100) face of W reduces the work function by 0.5–0.6 eV, whereas adsorption of N_2 on the (110) face of W increases the work function by 0.3 eV and by 0.5 eV in the case of the (100) face of Mo of our experiments. These figures are consistent with the results of other authors.[11,16] When the outgassed target is kept in an N_2 atmosphere or in an atmosphere of residual gases under pressures of $1 \cdot 10^{-6}$ torr, a relatively stronger increase in the intensity of the elastic peak and the peaks of the energy losses is obtained in (100) Mo than in (110) W. The observed shift of the maxima of the energy losses is more pronounced in molybdenum when the target has been outgassed.

The very intensive, broad peak around about 23 eV can be explained[4,6,9] by the excitation of plasma oscillations of hexavalent electrons in the peak of Mo and W. This interpretation of the maximum is confirmed by the change in the intensity of the peak relative to the peak of surface plasmons. At energies E_p up to 100 eV the surface plasma peak has the highest intensity in the spectrum, whereas at higher E_p values the volume peak dominates. The absorption of the molecules of the residual gases on the surface of an outgassed target leads to a shift of the peak of the bulk plasmon toward higher energies, with the shift amounting to 1–2 eV. In the case of polycrystalline tungsten, a similar change is observed in the spectrum by the authors of ref. 17. An additional inelastic scattering of the electrons during their passage through the layer of adsorbed molecules is the most likely explanation.

In the case of the outgassed W surface, a 5.5 eV peak is observed in the spectrum of the energy losses within the range E_p = 18–40 eV. Similar behavior at 5.4 eV is observed in ref. 3 in the case of the (110) face of W. The authors of ref. 3 associate the peak with the excitation of electron transitions in the near-surface conduction band of tungsten.

Our investigations of the spectra of energy losses of slow electrons reflected from the surface of the (100) Mo and (110) W faces show that the state of the surface of a crystal has a strong influence upon the interaction of electrons with solids.

---

[1] F. M. Propst and T. C. Piper, J. Vac. Sci. Tech., 4, 53 (1967).
[2] D. Edwards, Jr., and F. M. Propst, J. Chem. Phys., 55, 5175 (1971).
[3] N. R. Avery, Surf. Sci., 32, 477 (1972).
[4] V. V. Korablev, Fiz. Tverd. Tela, 12, 1638 (1970) [Sov. Phys.–Solid State, 12, 1298 (1970)].
[5] U. A. Arifov, A. A. Aliev, and R. M. Tangribergenov, in: Atomic Collisions on the Surface of Solids [in Russian], Chapter 5, Izd. Fan, Tashkent (1972).
[6] G. J. Dooley and T. W. Haas, J. Chem. Phys., 52, 993 (1970).
[7] J. Lecante and D. A. Degras, J. Phys., 31, C1-63 (1970).
[8] J. Petroff and C. R. Viswanathan, Phys. Rev. B, 4, 799 (1971).
[9] D. Pines, Usp. Fiz. Nauk, 62, 399 (1957).
[10] O. M. Artamonov, B. B. Bolotov, V. D. Gelever, and M. V. Kremkov, Prib. Tekh. Eksp., 6, 30 (1973).
[11] K. Hayek, H. E. Farnsworth, and R. L. Park, Surf. Sci., 10, 429 (1968).
[12] M. M. Kirillova, G. A. Bolotin, and V. M. Maevskii, Fiz. Met. Metalloved., 24, 95 (1967).
[13] D. W. Juenker, J. Opt. Soc. Am., 58, 164 (1968).
[14] E. A. Stern and R. A. Ferrell, Phys. Rev., 120, 130 (1960).
[15] L. D. Matthews, Surf. Sci., 24, 248 (1971).
[16] B. J. Hobkins and S. Usami, in: The Structure and Chemistry of Solid Surfaces (ed. by G. A. Somorjai), 67-1 (1969).
[17] C. J. Powell, J. L. Robins, and J. B. Swan, Phys. Rev., 110, 657 (1958).

Diffusion and solubility of helium in potassium chloride

A. Ya. Kupryazhkin, P. V. Volobuev, and P. E. Suetin

S. M. Kirov Ural Polytechnical Institute, Sverdlovsk

(Submitted June 26, 1973; resubmitted January 7, 1974)
Zh. Tekh. Fiz., 44, 1774-1778 (August 1974)

The diffusion coefficients and solubilities of helium in potassium chloride crystals have been measured. An experimental apparatus for measuring the diffusion properties of inert gases in ionic crystals is described. Over the temperature range 160-300°C the diffusion coefficient is described by the Arrhenius equation

$$D=3.9\cdot10^{-5}\exp\left\{-\frac{10.6}{RT}\right\}\ \mathrm{cm^2/sec}$$

The solubility is also an exponential function of the temperature in this range:

$$S=2.4\cdot10^{14}\exp\left\{\frac{3.8}{RT}\right\}\ \mathrm{cm^{-3}}$$

All the measurements are carried out at a saturation pressure of 800 torr. The results are compared with experimental data on helium diffusion in sodium chloride. It is concluded that a vacancy mechanism is responsible for the dissolution in these systems.

The more stringent requirements being imposed on the gas permeability of various crystalline materials require a detailed understanding of the microscopic processes involved in the diffusion of gases in solids and of the macroscopic consequences of these processes under various conditions. In particular, it would be difficult to describe the evolution of inert gases from fuel elements in nuclear reactors without an accurate understanding of the diffusion mechanisms and the parameters of the interaction between gas molecules and solids. To acquire this knowledge it is necessary to study the given processes in detail in simple systems by independent methods. One such simple system is that of an inert gas and an alkali halide crystal.

We have been carrying out an experimental study of helium diffusion in potassium chloride by a method involving desorption from previously saturated crystals.[1] This method, in contrast with that in which the inert gas is produced in the crystal through neutron bombardment, does not damage the lattice, so it is preferable. However, since only a few systems have been studied, since the sensitivity is low, and since the background in the chamber in which the sample is saturated is high, we have now improved the apparatus and carried out additional measurements.

Figure 1 shows the experimental apparatus. The sensitive element is differential capacitive gauge[2] 5, whose membranes form the capacitance in high-frequency oscillator 19, which uses a single transistor. The indicating device is a ChZ-11 digital frequency meter. The sensitivity of the measurement circuit is $1.7\cdot10^{-6}$ torr/Hz. The stability with bypass valve 6 open is ±1 Hz over a 10-min period. For increased thermal stability of the measurement circuit the oscillator is mounted directly on the gauge and placed with it in a quiet oil bath 7. During the measurements the reference cavity of the gauge is evacuated continuously by forepump 11 and diffusion pump 10. The pressure in the system is monitored by the ionization tube 20 of vacuum gauge 16 and by oil 8 and mercury 9 gauges.

The apparatus has two chambers 3; one holds the sample, while the other is used to monitor outgassing from the walls. The chambers are made primarily from aluminum, because it is relatively impermeable to gases. Since aluminum conducts heat well, the sample can be heated uniformly. The chamber is connected to the system by means of a conical stainless steel gasket. This connection remains vacuum-tight over the entire operating-temperature range. Both chambers are placed in oven 2, whose temperature is regulated within ±0.1°C by temperature-regulation and -sensing system 17, which receives signals from thermocouple 18, mounted on the oven housing. The temperature is measured by three thermocouples 1 at various points along the length of the chambers. In the measurements the temperature gradient is less than 1°C. Gas is injected from bottle 10 through nitrogen trap 13; the injection is monitored by the spring gauge 12 and mercury gauge 9.

In the experiments we use "pure" KCl crystals sifted through a screen with a mesh size of 0.0125–0.0160 cm. The total volume of the salt is V = 13.6 cm³. Before an experiment the chamber and sample are outgassed continuously for 15 days at the maximum temperature. Then the sample is saturated with the gas to be studied. At time t = 0 the gas is evacuated, and the chamber is connected to the measurement system. Pressure changes in the system change the frequency of oscillator 19, and these latter changes are detected by frequency meter 15. The rate of change of the frequency, which corresponds to the rate of change of the pressure in the chamber, is recorded

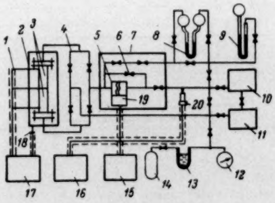

Fig. 1. The experimental apparatus.

over 1 min intervals. Through the use of valves 4, which do not change the volume of the system, the two chambers can be connected separately to the vacuum and measurement units. The outgassing of the empty chamber can thus be monitored at any time. Figure 2 shows typical curves recorded by the measurement system.

We see that the effect of helium dissolution in the chamber walls is small, and after a certain time we find $\Delta f/\Delta t = \text{const}$ for the empty chamber. The value of this constant is an order of magnitude lower than that for a fused quartz chamber.[1] Since the desorption data are generally processed 50 min after the beginning of the measurements, the empty chamber is used solely to monitor the outgassing upon a change in the thermal conditions.

An equilibrium is established between the adsorbed gas atoms and the gaseous phase in the system within $1 \cdot 10^{-12}$ sec (ref. 3). Gas accumulates in the surface layer of the crystal by physical mechanisms; no chemical reactions occur. It is found experimentally that the system obeys ideal laws. The outgassing pressure and the saturation pressure differ by four orders of magnitude. Accordingly, after a certain period of time the outgassing can be described by the first term of the general solution of Fick's second law,[1] obtained under the assumption of an instantaneous desorption reaction at the crystal–vacuum interface,[1] an assumption which is widely used in studies of the diffusion of gases in solids. The behavior of the pressure in the system as a function of the time is given by

$$\frac{dP}{dt}=\frac{1536DSN\bar{a}kT_2}{\pi^4V_2\left[1+\frac{V_1}{V_2}\left(\frac{T_2}{T_1}\right)^{1-\gamma}\right]}\exp\left\{-\frac{3\alpha}{\bar{a}^2}Dt\right\}, \tag{1}$$

where a is the average crystal dimension, P is the pressure, t is the time, k is the Boltzmann constant, S is the solubility, N is the number of salt crystals, V_1 and T_1 are the volume and temperature of the cold part of the measurement system, V_2 and T_2 are the same for the hot part, $\alpha = 8.4$ is the approximation constant, and γ is the thermomolecular pressure-difference constant, calculated for each specific temperature and for each specific pressure range for a connecting-tube diameter of 0.5 cm (see ref. 5).

To check the reproducibility of the results, we have repeated the measurements after one month. Between series of measurements the working chamber is opened to the atmosphere. Figures 3 and 4 show the experimental results for the diffusion coefficient and the solubility; the results of both series of measurements are shown in Fig. 3 to illustrate the reproducibility. We see that the scatter of the points does not exceed the experimental error. The functional dependences of the diffusion coefficient and the solubility of helium in KCl on the temperature at a saturation pressure of 800 torr are

$$\left.\begin{aligned} D&=3.9\cdot10^{-5}\exp\left\{-\frac{10.6}{RT}\right\}\ \text{cm}^2/\text{sec}\\ S&=2.4\cdot10^{14}\exp\left\{\frac{3.8}{RT}\right\}\ \text{cm}^{-3}\,, \end{aligned}\right\} \tag{2}$$

The mean-square relative deviation of the experimental results from Eq. (2) for the diffusion coefficient is 10%, and that for the solubility is 8%.

Unfortunately, we have found no other data in the literature with which to compare our results, so that we can compare our results only with data on helium diffusion in NaCl (ref. 1). It is evident that the diffusion coefficients are described by the same equations in the two cases, while the activation energy of the solubility has different signs in the two cases. A negative value of this activation energy could be attributed to the influence on the overall effect of surface adsorption and dissolution at dislocations and in vacancies of the crystal. However, experiments on the adsorption of inert gases on alkali halide crystals[6] reveal a low adsorption energy even for argon; second, the sign of the energy must be the same, regardless of the sample; and third, the procedure used to process the data completely eliminates this effect, since the lifetime of helium on the surface amounts to a fraction of a second. In the case of dissolution at dislocations, a helium molecule would very probably diffuse along dislocations; since the corresponding diffusion coefficients[7] are one or two orders of magnitude higher than the values which we found,

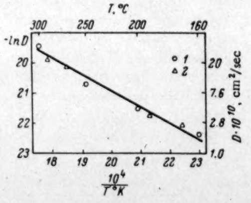

Fig. 3. Diffusion coefficient of helium in KCl as a function of the temperature. 1) First series of measurements; 2) second series.

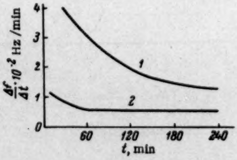

Fig. 2. Experimental rate of change of the frequency of oscillator 19 as a function of the time (T = 163°C). 1) Chamber with salt; 2) chamber without salt.

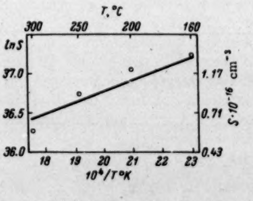

Fig. 4. Solubility of helium in KCl as a function of the temperature.

this mechanism should be more apparent early in the experiment and should also be eliminated in the procedure used to analyze the data.

On the basis of the vacancy mechanism for dissolution we can explain both the negative value of the dissolution energy and the difference between the signs for two crystals. Experimental study of the electrical conductivity[8] has shown that at low temperatures the vacancies are predominantly cation vacancies, resulting from the presence of divalent impurities in the crystals. The concentration of these vacancies is not a function of the temperature. In these systems the energy for the interaction of the inert gas with the ions of the alkali halide crystal can be interpreted by means of a binary-interaction potential, usually the Lennard-Jones 6−12 potential:[9]

$$U(r)=4\varepsilon\left\{\left(\frac{\sigma}{r}\right)^{12}-\left(\frac{\sigma}{r}\right)^{6}\right\}, \tag{3}$$

where σ is the value of r at which U(r) = 0, and ε is the depth of the potential well.

The sign of the energy depends on the distance between the interacting particles. In the case of helium at a cation vacancy we can, in a first approximation, consider only the nearest neighbors, neglecting relaxation of the lattice ions around the vacancy. Then an evaluation of the interaction of helium with the crystal in the case of either lattice reduces to an evaluation of the interaction of helium with chloride ions in the unperturbed lattice. The functional dependence of this energy for a mole of the gas on the distance between the particles should have the same form as the interaction potential, and the energies corresponding to the interaction of helium with the nearest-neighbor ions, corresponding to definite distances, must lie on this curve. In the first case the distance is r_1 = 2.81 Å, and in the second it is r_2 = 3.14 Å; the energies are U_1 = 3.2 kcal/mole and U_2 = 3.8 kcal/mole. Since $\Delta r = r_2 - r_1$ is small in comparison with the width of the potential well, it is reasonable to assume that both points lie on a single branch of the potential curve. Using a linear interpolation between the points, we find

$$\sigma_{He-Cl}=\frac{1}{2}(\sigma_{He-He}+\sigma_{Cl-Cl}), \tag{4}$$

and knowing the ionic radius of chlorine we can evaluate σ_{He-He}. Taking this radius from ref. 10, we find σ_{He-Cl} = 3.0 Å and σ_{He-He} = 2.4 Å. The latter value agrees reasonably with the value obtained from measurements of the viscosity of helium:[9] σ_{He-He} = 2.576 Å. We note that taking account of the relaxation of chloride ions around the helium does not increase the discrepancy between these results by more than 15%.

Even in view of the roughness of the assumptions used, these arguments imply a vacancy mechanism for the dissolution of helium in these systems. In turn, the method used to demonstrate the dissolution mechanism allows us to use data on the solubility of gases in crystals differing by only one ion species to evaluate the parameters of the interaction potentials of the systems.

---

[1] N. N. Alekseenko, P. V. Volobuev, and P. E. Suetin, Fiz. Tverd. Tela, 14, 2398 (1972) [Sov. Phys.—Solid State, 14, 2073 (1973)].

[2] P. E. Suetin and P. V. Volobuev, Zavod. Lab., 30, 374 (1964).

[3] J. H. De Boer, Dynamical Character of Adsorption, Oxford Univ. Press (1953).

[4] L. L. Kunin, A. M. Golovin, Yu. N. Surovoi, and V. M. Khokhrin, Problems of the Outgassing of Metals [in Russian], Izd. Nauka, Moscow (1972).

[5] V. G. Chernyak, B. T. Porodnov, and P. E. Suetin, Inzh.-Fiz. Zh., 24, 227 (1973).

[6] B. G. Aristov, A. V. Kiselev, V. M. Luk'yanovich, V. I. Trofimov, and S. Shpigel', Zh. Fiz. Khim., 42, 984 (1968).

[7] Ya. E. Geguzin and E. R. Dobrovinskaya, Fiz. Tverd. Tela, 7, 2058 (1965) [Sov. Phys.—Solid State, 7, 1660 (1966)].

[8] A. M. Murin and B. G. Lur'e, Diffusion of Tracer Atoms in and Conductivity of Ionic Crystals [in Russian], LGU (1967).

[9] J. O. Hirschfelder, C. F. Curtis, and R. B. Bird, Molecular Theory of Gases and Liquids, Wiley, New York (1954).

[10] L. Pauling, Nature of the Chemical Bond, Third Edition, Cornell Univ. Press, Ithaca (1960).

Pulsed ion beams from a high-current plasma diode

B. A. Tskhadaya, A. A. Plyutto, and K. V. Suladze

(Submitted October 13, 1973)
Zh. Tekh. Fiz., 44, 1779-1780 (August 1974)

In a study of pulsed ion beams in a high-current plasma diode it has been found that an ion beam of $6\cdot10^2$ A is produced when a critical diode current is reached and a discontinuity appears in the plasma. The ion beam has a large energy spread, but the average energy is approximately equal to the initial voltage, $U_0 = 30$-50 kV. The linear functional dependence of the ion-beam current on the critical diode current implies that ion beams with currents of $2\cdot10^4$ A can be achieved at diode currents of 10^6 A.

The present interest in the production of high-current ion beams results from their possible use in thermonuclear research and in producing intense neutron radiation.[1] Ion beams are usually produced by extraction from a plasma surface.[2] New techniques for producing charged-particle beams have led to the concept of preliminary filling of a diode with plasma.[3-6] Ion beams with currents up to 20 A have been produced in diodes in the collapse of the anode plasma when the plasma source is located at the cathode.[7] Pulsed neutral ion beams with considerably higher currents and current densities can be produced if the diode and the drift region are first filled with a plasma from a source located at the anode. The experiments have been carried out in an apparatus similar to that described in refs. 5 and 6.

When an external electric field is applied to a plasma-filled diode (in which the plasma density at the cathode is 10^{13}-10^{14} cm^{-3}), the electron current reaches its critical value in a time $t = 10^{-7}$ sec and is then cut off (Fig. 1a); at this point the voltage across the gap increases sharply[4] to $(1.5$-$2)U_0$ ($U_0 = 30$-50 kV) (Fig. 1b). At this point a discontinuity appears in the plasma,[4,7,8] and an ion beam is produced; it moves in the neutralized state in the drift region. A transverse magnetic field $(2$-$3)\cdot10^2$ Oe is applied to the beam to separate the plasma electrons from the ions near the collector ($l = 50$ mm), which measures the ion current. The ion current appears when the current is cut off (Fig. 1c). The ion current increases linearly with critical electron current. At $I_{cr} = 3\cdot10^4$ A a proton beam of $6\cdot10^2$ A, with an average length of $(3$-$4)\cdot10^{-7}$ sec and a current density of 10^2 A/cm^2, has been achieved (in this case the distance to the collector is 8-10 cm). Oscilloscope and calorimetric measurements of the average ion-beam current yield consistent results. When the collector is moved to 30-40 cm the ion-current signal is delayed by the transit time with respect to the voltage signal.

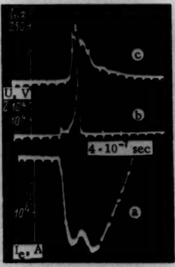

Fig. 1. Oscillograms: a) total diode current; b) voltage across the diode; c) ion current to the collector.

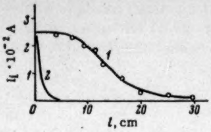

Fig. 2. Profile of the current density along the beam. 1) Experimental; 2) calculated for the case in which the beam is not neutralized.

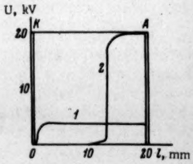

Fig. 3. Potential distribution in the diode. 1) In the initial stage of the increase in the total current; 2) in the stage in which the total current is cut off.

Study of the divergence of the ion beam shows that the collector current varies slightly over the distance 8-10 cm but then falls off (Fig. 2). The divergence angle is below 6° at distances up to 10 cm.

A Thomson mass analyzer is used to study the composition and energy distribution of the particles. The beam is found to be predominantly protons, but charged carbon ions C^{+1}, C^{+2}, C^{+3}, C^{+4} are also observed. The ions have a large energy spread, but the average beam energy is approximately equal to the initial voltage on the capacitor bank, U_0. The maximum proton energy is $\sim(1.5$-$2)U_0$, apparently because of the overvoltage which results from the cutoff of the electron current.

Fast electrons, with energies of 10^3-10^4 eV (at $U_0 = 30$ kV), move in the same direction as the ion beam; the reason is not clear. The energy acquired by these electrons does not significantly affect the calorimetric measurements of the ion current.

On the basis of these experimental results we propose that high-current pulsed ions beams can be produced in the discontinuity in a plasma. This method differs fundamentally from the method in which beams are produced from a plasma boundary, in which case the potential drop occurs between the cathode and the plasma. A state with a cathode potential drop is observed (when the gap is filled with plasma) in the initial stage of the current rise, when the space-charge shell is near the cathode and the voltage drop is $0.2U_0$ (curve 1 in Fig. 3). The appearance of electron-emission centers at the cathode changes this state considerably. The plasma from the emission centers destroys the ion space-charge sheath, and the conductivity near the cathode increases. When the electron current reaches its critical value, a discontinuity occurs in the plasma;[4,7,8] most of the potential drop occurs in this region (curve 2 in Fig. 3). An electron beam,[4] which evaporates the working medium of the source and which generates a dense plasma, is also produced in the discontinuity. As a result, the ion current is an order of magnitude larger than that in ref. 7.

Because of the space-charge neutralization and focusing by the magnetic field of the electron current, the ion beam accelerated in the discontinuity has a high current density and can propagate over a considerable distance in the drift region. The linear functional dependence of the ion-beam current on the critical electron current implies that ion beam currents of $2 \cdot 10^4$ A can be achieved at diode currents of 10^6 A.

The basic advantage of this method of producing an intense ion beam (electrostatic acceleration of ions in the discontinuity) as compared with the electrodynamic method is that the ion energy can be adjusted by changing U_0. It is possible to increase the ion energy to 10^5–10^6 eV.

In conclusion the authors thank I. F. Kvartskhava, V. N. Ryzhkov, and L. P. Skripal' for valuable comments.

---

[1] R. L. Hirsch, J. Appl. Phys., 38, 4522 (1967).

[2] M. D. Gabovich, Physics and Technology of Plasma Ion Sources [in Russian], Atomizdat, Moscow (1972).

[3] A. A. Plyutto et al., ZhETF Pis. Red., 6, 540 (1967) [JETP Lett., 6, 61 (1967)].

[4] K. V. Suladze, B. A. Tskhadaya, and A. A. Plyutto, ZhETF Pis. Red., 10, 282 (1969) [JETP Lett., 10, 180 (1969)].

[5] A. A. Plyutto, K. V. Suladze, and V. N. Ryzhkov, Proceedings of the Seventh Intern. Conf. on High-Energy Particle Accelerators [in Russian], Vol. 2, Erevan (1969), p. 505.

[6] A. A. Plyutto, K. V. Suladze, S. M. Temchin, and E. D. Koron, At. Energ., 27, 418 (1969).

[7] K. V. Suladze, ZhETF Pis. Red., 15, 648 (1972) [JETP Lett., 15, 459 (1972)].

[8] A. A. Plyutto, K. V. Suladze, E. D. Korop, and V. N. Ryzhkov (Rushkov), Fifth Intern. Symp. on Discharges and Electrical Insulation in Vacuum, Poznan, Poland, 1972.

Parallel-plate capacitor as a charged-particle spectrometer

Yu. D. Kornyushkin

Leningrad Institute of Precision Mechanics and Optics

(Submitted February 1, 1973; resubmitted February 6, 1974)
Zh. Tekh. Fiz., 44, 1781-1784 (August 1974)

We discuss the possibility of using the uniform electrostatic field of a parallel-plate capacitor for the energy and angle analysis of charged-particle beams in the most general case in which the source of charged particles is in the interelectrode space. We show that there are operating conditions favorable for the energy and angle analysis of a beam of charged particles. We obtain equations and curves for the dispersion in energy and angle. We show the possibility of using the electric method to analyze the angle of emission distribution of charged particles.

Among electrostatic spectrometers the simplest seems to be one employing a parallel-plate capacitor to deflect a stream of charged particles to one plate.[1] Such a device was first discussed in some detail in refs. 2 and 3. In particular, the optimum condition for energy analysis based on the use of first-order focusing was formulated. The analysis of the properties of an electrostatic spectrometer with plane-parallel plates was continued in refs. 4 and 5, and the operating conditions for second-order focusing were found. Subsequently the electron-optical properties of such a spectrometer were investigated in ref. 6 for relativistic particles. Nevertheless the analysis of the electron-optical properties of such a spectrometer performed in refs. 1-6 is still incomplete and the possibility of obtaining the angle distribution of charged particles has not been completely evaluated. In the present paper we investigate the properties of a parallel-plate capacitor used to find the angle distribution of charged particles.

ANALYSIS OF THE OPERATION OF THE CHARGED-PARTICLE SPECTROMETER

The spectrometer consists of parallel plates with a potential difference between them. In the general case a source of charged particles is located in the space between the plates; therefore for a given potential difference between the plates and a given energy $\mathcal{E}_0$ of the charged particles only those particles which leave the source at the angle of emission α (Fig. 1) pass through the point of the exit slit a distance x_0 from the source. None of the other charged particles with different angles of emission pass through the indicated point of the exit slit. It is assumed that the effect of the inhomogeneity of the electrostatic field at the edges of the plates on the charged particle trajectories is eliminated in one way or another. In general the charged particles can move in both decelerating and accelerating fields.

We use the following sign convention for measuring the angles of emission relative to the horizontal line passing through the source; $\alpha > 0$ for angles measured counterclockwise and $\alpha < 0$ for angles measured clockwise (Fig. 1).

We assume that the motion of the charged particles is at all times in the xoy plane and that the space charge density in the interelectrode space is negligibly small. Then the distance between the source of charged particles and the exit slit in the x direction can be found in relative units from the expression

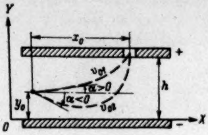

Fig. 1. Schematic diagram of spectrometer.

$$X_0 = 2E_0 \cos\alpha \left[\sqrt{\sin^2\alpha + \frac{1}{a}} - \sin\alpha\right], \tag{1}$$

where

$$X_0 = \frac{x_0}{h}, \quad E_0 = \frac{U_p}{U} > 0, \quad a = \frac{E_0}{1 - Y_0},$$
$$Y_0 = \frac{y_0}{h}, \tag{2}$$

x_0 is the distance from the particle source to the slit in the x direction, y_0 is the distance from the particle source to the lower plate in the y direction, h is the distance between the plates, α is the angle of emission of the particles from the source, U is the potential difference between the plates, and qU_p is the kinetic energy of the particles leaving the source, where U_p is the potential difference and q is the particle charge.

If the beam is monoenergetic Eq. (1) shows that $X_0 = X_0(\alpha)$ can lead to the same value of X_0. Then the conditions $E_0 = \text{const}$, $X_0 = \text{const}$ will correspond to a family of trajectories lying to the left of the limiting trajectory bounding this family on the right and satisfying the condition $X_0 = X_{0\max}$. Therefore charged particles can reach the largest value $X = X_{0\max}$ only for certain angles α_0, which can be found from the extremum condition $(dX_0/d\alpha)_{E=\text{const}} = 0$.

By investigating Eq. (1) at the extremum we find the limiting angle

$$\sin\alpha_0 = \frac{-1}{\sqrt{2 + \frac{1}{a}}}. \tag{3}$$

It is also clear from Eq. (1) that $E = E_0(\alpha)$ is a multivalued function of the angle of emission α ($X_0 = \text{const}$). This means that to one value of E_0 there can correspond various values of α and therefore various trajectories. As in the preceding case, among the possible values of energies and angles there are limits which correspond to a given value of $X_0 = \text{const}$. By using the extremum condition $(dE/d\alpha)_{X_0=\text{const}} = 0$ it can be shown that the limiting angle of emission α_0 is also determined from Eq. (3). In combining the two limiting cases $X_{0\max}$ and $E_{0\max}$ Eq. (3) corresponds to the condition for focusing charged particles in the plane of the exit slit.

It follows from Eq. (1) and Fig. (1) that for any value of $\alpha > 0$ it is possible to choose a value of E_0 such that the charged particles pass through the exit slit; motion of the charged particles is possible for any angles of emission in the range $0 \le \alpha \le \pi/2$. Particles with negative angles of emission move initially in a decelerating field and can reach the plane of the exit slit only for certain angles $\alpha < 0$, since in moving in the decelerating field the charged particles must not strike the lower plate. Then the condition corresponding to the particles not reaching the lower plate can be written as the inequality

$$\sin^2 \alpha_1 \leqslant \frac{Y_0}{a(1-Y_0)}, \tag{4}$$

where for $\alpha_1 < 0$ we have $\sin^2\alpha_0 < \sin^2\alpha_1$, i.e., $E_0 > Y_0 - 1/2$.

Various specific operating conditions can be investigated by an analytic study of Eq. (1).

ANGLE ANALYSIS

The analyzing properties of the spectrometer are determined by the value of the dispersion and the quality of the focusing. Direct differentiation of Eq. (1) gives the following expressions for the energy and angle dispersion:

$$D_E = \frac{\cos\alpha}{a\sqrt{\sin^2\alpha + \frac{1}{a}}}\left[1 + 2a\sin\alpha\left(\sin\alpha - \sqrt{\sin^2\alpha + \frac{1}{a}}\right)\right], \tag{5}$$

$$D_\alpha = \frac{2a(1-Y_0)}{\sqrt{\sin^2\alpha + \frac{1}{a}}}\left[\left(\sin\alpha - \sqrt{\sin^2\alpha + \frac{1}{a}}\right)\cos 2\alpha - \frac{\sin\alpha}{a}\right]. \tag{6}$$

Figure 2 shows curves of Eqs. (5) and (6) for D_E and D_α. It is clear from the curves that in principle two limiting sets of operating conditions are possible, one for angle analysis and one for energy analysis. In the first case the spectrometer is adjusted so that it is insensitive to a change in the energy of the charged particles but very sensitive to a change in the angle of emission α ($D_E \ll D_\alpha$); in the second case the spectrometer must be insensitive to a change in the angle of emission and very sensitive to a change in the energy of the particles ($D_E \gg D_\alpha$).

If the beam is stopped down sufficiently and the operating conditions correspond to a small value of D_α, the absolute resolving power can be found from the expression

$$\Delta U_p = \frac{\Delta x_{\text{out}}}{h}\frac{U}{D_E}. \tag{7}$$

Here it is assumed that $\Delta x_{\text{out}} \gg \Delta x_{\text{in}}$, where Δx_{out} and Δx_{in} are the widths of the exit and entrance slits.

An analysis of the family of curves of D_α shown in Fig. 2 and Eq. (6) shows that the largest angle dispersion occurs at $Y_0 = 0$. In the angle analysis process the energy dispersion D_E must be a minimum in order that the instrument be insensitive to the energy analysis of the charged particles.

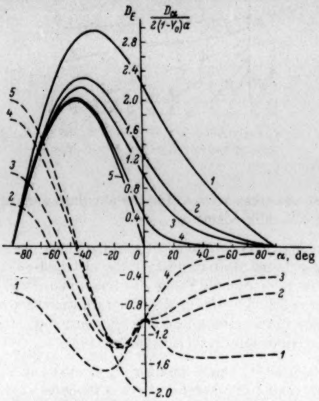

Fig. 2. Curves of energy (solid curves) and angle (open curves) dispersion. a: 1) 0.2; 2) 0.6; 3) 1.0; 4) 5.0; 5) ∞.

The family of curves of D_E in Fig. 2 shows that over a broad range of emission angles α minimum values of D_E exist only for $\alpha > 0$. Consequently the optimum conditions for angle analysis require an accelerating field. Thus it is clear from Fig. 2 that for $a \ge 5$ and $\alpha \ge +25°$ the angle dispersion ($Y_0 = 0$) lies in the range $0.8 \le D_\alpha < 3.4$. Then for $\alpha = 50°$ and $h = 40$ mm $D_\alpha = 60$ mm/rad $= 1.05$ mm/deg, i.e., under these conditions the system is sufficiently sensitive for the angle analysis of a beam of charged particles.

It is frequently necessary to investigate the angle distribution in space of a beam of charged particles in which the energy varies continuously from 0 to qU_p. This case is commonly encountered in the analysis of the interaction of primary charged particles with matter and the study of various characteristics of beams of secondary charged particles. Here it is important that in the range of angles of emission from α to $\alpha + \Delta\alpha$ particles with the largest possible range of energies pass through the exit slit of the spectrometer. The fraction of the spectrum corresponding to the energies of the charged particles which pass through the exit slit is determined from the expression

$$N = \frac{\Delta x_{\text{out}}}{h}\frac{1}{E_0 D_E}, \tag{8}$$

where $N = \Delta U_p/U_p$.

The absolute angle resolving power is given by

$$\Delta\alpha = \frac{\Delta x_{\text{out}}}{h}\frac{1}{D_\alpha}. \tag{9}$$

It follows from Fig. 2 that for $a = 5$ and $\alpha > 35°$, $D_E \le 0.02$. In angle analysis it is expedient to have $Y_0 = 0$, so that $a = E_0 = 5$. For $h = 40$ mm and $\Delta x_{\text{out}} = 4$ mm we find $N = 1$ from Eq. (8). Thus all charged particles in the energy range from 0 to qU_p pass through an exit slit 4 mm wide for $35° < \alpha < 90°$. The substitution of these values

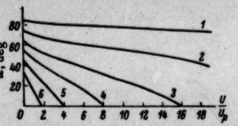

Fig. 3. Angle of emission α as a function of X_0 and E_0. X_0: 1) 0.1; 2) 0.28; 3) 0.5; 4) 0.7; 5) 1.0; 6) 1.5. $Y_0 = 0$.

into Eq. (9) gives $\Delta\alpha = 6'$ for the absolute angle resolving power, which is adequate.

By appropriate choice of spectrometer operating conditions it is possible to analyze the charged-particle distribution in a selected range of emission angles, i.e., to make a detailed analysis of the angle distribution of charged particles for a given initial energy. In many cases this is of considerable experimental interest.

Equation (1) shows that for X_0 = const and Y_0 = const various angles of emission α correspond to various values of E_0. But E_0 can vary not only due to a change in U_p but also because of a change in U – the deflecting potential difference between the spectrometer plates. Hence an angle analysis can be performed by the electric method, in which the continuous variation of U will correspond to a continuous change in the angle of emission α corresponding to the passage of the beam of charged particles through the exit slit.

In the angle analysis it is convenient to have a linear relation between the deflecting voltage and the angle of emission; thus it is expedient to determine the region in which such a relation holds. If the relation $\alpha = \alpha(U)$ is nonlinear it is expedient to approximate the nonlinear relation by some simple function so that the potential difference U can be varied according to that law in the given range of values.

Figure 3 shows curves of $\alpha = \alpha(1/E_0)$, from which the necessary operating conditions for angle analysis can be selected. If the experimental conditions permit U_p = const, $\alpha = \alpha(U)$. The curves of Fig. 3 show that there is an appreciable range within which we can write

$$\alpha = \alpha_i - b_i \frac{U}{U_p}, \tag{10}$$

where α_i and b_i are constants depending on the choice of operating conditions.

Suppose there is a flux of monoenergetic charged particles (U_p = const) in space. By using (10) the angle analysis can be performed rather simply by the electric method. But Eq. (2) shows that a change in U produces a change in E_0 (U_p = const); therefore, according to (5) and (6) the angle and energy dispersions will change. For a monoenergetic beam the change in energy dispersion can be neglected, but the uncontrollable change in angle dispersion can distort significantly the true picture of the angle distribution. Therefore the signal must be corrected to take account of this change. An initial operating point (Fig. 3) should be selected so that measurements can be performed with sufficient sensitivity to the angle of emission over the broadest range of angles α, e.g., $0.5 \le X_0 \le 1.5$.

If the beam of charged particles under study is not monoenergetic the requirements for choosing the operating point are more rigid, since the spectrometer must operate under conditions such that D_E is always small. This condition is satisfied by $a > 1$ and $\alpha > 30°$, and as can be seen from Fig. 3, the possible range of the anglee analysis is appreciably decreased. Thus for $0.7 \le X_0 \le 1.0$ the range of angles of emission relevant to the investigation is of the order of 10°. Therefore in the analysis of the angle distribution over a wide range of angles it is expedient to use a combination of the methods of investigation by mechanically rotating the specimen 10° and then making an angular analysis over a 10° range by the electric method.

---

[1] I. G. Kozlov, Energy Analysis Methods for Electron Beams [in Russian], Atomizdat, Moscow (1971).

[2] G. D. Yarnol and H. C. Bolton, J. Sci. Instrum., 26, 38 (1949).

[3] G. A. Harrower, Rev. Sci. Instrum., 26, 850 (1955).

[4] V. F. Litvin, Prib. Tekh. Eksp., No. 3, 32 (1958).

[5] T. S. Green and G. A. Proca, Rev. Sci. Instrum., 41, 1409 (1970); G. A. Proca and T. S. Green, Rev. Sci. Instrum., 41, 1778 (1970).

[6] M. Bitter and G. Proca, Rev. Sci. Instrum., 43, 1125 (1972).

Energy exchange between electrons and molecular vibrational states in resonance collisions

A. Kh. Mnatsakanyan and G. V. Naidis

Institute of High Temperatures
Academy of Sciences of the USSR, Moscow

(Submitted January 2, 1974)
Zh. Tekh. Fiz., 44, 1785-1787 (August 1974)

An expression is obtained for the energy exchange between electrons and the molecular vibrational states in resonance collisions when the width of the resonance is much smaller than the vibrational frequency. A comparison is made with conventional expressions for the energy exchange rate in N_2.

In many molecules the excitation of vibrational levels by electron impact is of a resonance character due to the formation, as an intermediate state of the reaction, of an unstable negative ion. The theory of the resonance interaction of electrons with molecules is developed in refs. 1-3; the results of numerical calculations of the cross sections are in good agreement with experiment.[4] In many cases, however, interest centers not so much on the cross constants of the transitions between individual levels, as on the total rate of exchange of energy between the molecular vibrational states and the electrons. In the calculation of an averaged characteristic of the process (averaged with the electrons distributed over energies and the molecules over the vibrational levels) it is possible to utilize less exact values of the cross sections and thereby obtain an analytically simple approximate expression for the energy exchange rate.

1. The rate of exchange of energy between electrons and molecular vibrational states for a Maxwellian electron energy distribution and a Boltzmann distribution over vibrational levels with temperatures T_e and T_v respectively, is given by

$$\omega' N_e \sum_{m,n} (m-n) N_n P_{nm}$$
$$= \omega' N_e N (1-q) \sum_{m,n} (m-n) q^n P_{nm} = \omega' N_e N K (T_e, T_v). \tag{1}$$

Here, $N_n = N(1-q)q^n$ is the population of molecules in the n-th vibrational level,

$$N = \sum_n N_n, \quad q = e^{-\omega'/T_v}, \quad P_{nm} = A \int_0^\infty \varepsilon \sigma_{nm}(\varepsilon) e^{-\varepsilon/T_e} d\varepsilon,$$

is the rate constant of the transition n → m induced by electron impact, $A = \sqrt{8/\pi m_e T_e^3}$, σ_{nm} is the corresponding cross section for the transition, ε and m_e are the energy and mass of the electron, ω is the molecular vibrational frequency and N_e is the electron density.

In the simplest version of the theory, in which the width of the resonance vibrational levels of the ion is regarded as independent of the number of the level, σ_{nm} the cross section for a transition from the n-th vibrational state to the m-th near resonance has the form[2]

$$\sigma_{nm}(\varepsilon) = \frac{\sigma_0}{\varepsilon} \left| \sum_\lambda \frac{\langle n|\lambda\rangle \langle \lambda|m\rangle}{\varepsilon - \varepsilon_0 + n\omega' - \lambda\omega'' + i\frac{\Gamma}{2}} \right|^2, \tag{2}$$

where ε_0 is the energy difference between the ground states of the ion and the molecule, $\langle n|\lambda\rangle$ is the overlap integral for the wave functions of the corresponding vibrational states of the molecule and the ion, ω'' is the ion vibrational frequency, Γ is the width of the resonance, and σ_0 is a normalizing constant, the choice of which is discussed below.

We consider the cases $\omega \ll \varepsilon_0$ (resonance region located far beyond threshold) and $\Gamma/2 \ll \omega$ (a sharp resonance). It is precisely these conditions that are realized for the molecules N_2 and CO. The discussion is restricted to the calculation of the rate constant for energy exchange at high electron temperatures $T_e \gg \omega$. The main contribution to the rate constant then comes from a region close to the resonance region and (2) is valid over the entire energy region. We take $\langle n|\lambda\rangle$ to be the overlap integral of the wave functions for harmonic oscillators with different equilibrium internuclear distances, r_e' and r_e'', and the same frequency $\omega = (\omega' + \omega'')/2$ (following ref. 5, where the absorption cross section of the molecules is averaged over the vibrational distribution).

2. The quantity K can be expressed in terms of an auxiliary function $R(a, b) = \sum_{n,m} a^n b^m P_{nm}$ in the following manner:

$$K = (1-q) \left\{ \frac{dR(q, r)}{dr} \bigg|_{r=1} - q \frac{dR(q, 1)}{dq} \right\}. \tag{3}$$

Expressing the denominators in (2) in the form of integrals of exponentials, setting $\omega' = \omega'' = \omega$, and integrating with respect to ε, we obtain

$$R(a, b) = \sigma_0 A \iint_0^\infty dt\,ds \frac{\exp\left[i\varepsilon_0(s-t) - \frac{\Gamma}{2}(s+t)\right]}{\frac{1}{T_e} + i(s-t)}$$
$$\times S(a e^{-i\omega(s-t)}, b, e^{-i\omega t}, e^{i\omega s}), \tag{4}$$

where

$$S(a, b, c, d) = \sum_{n,m,\lambda,\mu} a^n b^m c^\lambda d^\mu \langle n|\lambda\rangle \langle \lambda|m\rangle \langle m|\mu\rangle \langle \mu|n\rangle.$$

Utilizing the calculational technique described in detail in a previous paper,[5] we write generating function S in the explicit form

$$S(a, b, c, d) = \frac{1}{1-abcd} \exp\left\{ -\Lambda \frac{2 - (a+b)(1+cd) - (c+d)(1+ab) + (a+b)(c+d) - 2abcd}{1-abcd} \right\}. \tag{5}$$

where $\Lambda = \mu\omega/2\hbar\,(r_e^{I} - r_e^{II})^2$ and μ is the reduced mass of the molecule. We note that $S(a, b, c, 1) = \sum\limits_{n,\lambda} (ab)^n c^\lambda \cdot |\langle n|\lambda\rangle|^2 = S_3(ab, c)$, where S_3 is the generating function calculated in ref. 5. It is worth mentioning that Eq. (5) can be of use in a number of other applications.

Inserting (5) and (4) into (3), introducing the variable $u = t - s$, and integrating with respect to s, we obtain

$$K = \frac{\sigma_0 A}{1-q}\frac{\Lambda\omega}{\Gamma(\omega^2+\Gamma^2)} J,$$

$$J = \int\limits_{-\infty}^{\infty} du \frac{(e^{-i\omega u} - q)\,[\omega(1+e^{i\omega u}) + i\Gamma\delta(u)(1-e^{i\omega u})]}{\frac{1}{T_e} - iu}$$

$$\times \exp\left[-\frac{\Gamma}{2}|u| - i\varepsilon_0 u + \Lambda\frac{(e^{-i\omega u}-q)(1-e^{i\omega u})}{1-q}\right], \quad \delta(u) = \frac{u}{|u|}. \quad (6)$$

3. In order to estimate the latter integral, which, in the long run, determines K, we apply the conditions $\Gamma/2 \ll \omega \ll \varepsilon_0$, $\omega \ll T_e$, $\Lambda \sim 1$. Furthermore, we require that $T_v \lessdot T_e$, $T_v \lessdot (\varepsilon_0 + \Lambda\omega)^2/8\omega\Lambda$ ($T_e \lessdot 1.5$ eV for N_2). Then

$$K = \frac{2\Lambda\sigma_0 A\pi}{\Gamma}\frac{(1+p)(p-q)}{p(1-q)}\exp\left(-\frac{\varepsilon_0 + \Lambda\omega\frac{p-q}{p(1-q)}}{T_e}\right), \quad p = e^{-\omega/T_e}. \quad (7)$$

If we neglect the dependence of the exponent of the exponential on q (this dependence is weak for $\Delta\omega \ll T_e$), then K can be expressed in terms of the vibrational energy $\varepsilon_v = q/(1-q)$ in the following manner:[1)]

$$K(T_e, T_v) = K(T_e, 0)\left[1 - \frac{\varepsilon_v}{\varepsilon_e}\right], \quad \varepsilon_e = \frac{p}{1-p}. \quad (8)$$

The normalizing constant σ_0 appears in (2) and (7). When Γ is independent of the number of the level theory[2] gives $\sigma_0 = \pi\hbar^2\Gamma^2/2m_e$. On the other hand the energy exchange rate in N_2 can be normalized using the known[7] value of the total cross section for vibrational excitation by electron impact at its maximum: $\sum\limits_m \sigma_{0m}(2.2\text{ eV}) = 5.5 \cdot 10^{-16}\text{ cm}^2$. The value $\varepsilon_M = 2.2$ eV corresponds to a resonance with $\lambda = 1$ ($\varepsilon_M = \varepsilon_0 + \omega$). Remembering that $\Gamma/2 \ll \omega$, we obtain

$$\sum_m \sigma_{0m}(\varepsilon_M) = \frac{4\sigma_0}{\varepsilon_M\Gamma^2}|\langle 0|1\rangle|^2(1 - |\langle 0|1\rangle|^2). \quad (9)$$

Using the value of $\langle 0|1\rangle$ for harmonic oscillators with equal frequencies, we obtain σ_0/Γ^2, which differs from $\pi\hbar^2/2m_e$ by only 5%. This agreement may be accidental and if the absolute values of the cross sections are available it is better to use them in the normalization.

The cross sections obtained by Chen[2] are averaged in ref. 8 for a Maxwellian electron distribution, and it is shown that for modest n and k the quantity $P_{n+k,\,n}$ is weakly dependent on n and k. The following relation is then derived in ref. 9:

$$\left.\begin{aligned} K(T_e, T_v) &= P_{10}\varepsilon_e(1+\varepsilon_e)\,r_m(p)\left\{1 - \frac{\varepsilon_v(1+\varepsilon_v)\,r_m(q)}{\varepsilon_e(1+\varepsilon_e)\,r_m(p)}\right\}, \\ r_m(x) &= 1 - (m+1)x^m + mx^{m+1}. \end{aligned}\right\} \quad (10)$$

Here, m is the maximum number of transferred photons.

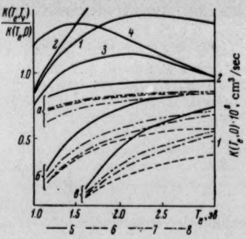

Fig. 1. Rate of energy exchange between molecules and vibrations of electrons $K(T_e, 0)$: 1) Eq. (10), m = 8; 2) Eq. (10), m = 8, approximation of ref. 8 used for P_{10}; 3) Nighan's results;[11] 4) Eq. (7). Ratio $K(T_e, T_v)/K(T_e, 0)$ for various values of vibrational temperature T_v(eV): a) 0.5; b) 1.0; c) 1.5; curves 5) Eq. (10), m = ∞; curves 6) Eq. (10), m = 8; curves 7) Eq. (7); curves 8) Eq. (8).

In ref. 10 use is made of an expression for K obtained on the assumption that only the lowest group of levels, with number up to a certain m, participate in vibrational exchange.

Equations (7), (8), and (10) with m = 8 and ∞ are used to calculate the ratio $K(T_e, T_v)/K(T_e, 0)$ as a function of T_e for various values of T_v. The results of the calculations are presented in Fig. 1. We note that expression (7) obtained in the present paper gives a value for this ratio that lies between the values given by (10) for m = 8 and m = ∞. The figure also gives the absolute values of $K(T_e, 0)$ obtained from (7) and (10) for m = 8 and also from ref. 11, where the cross section is averaged with an electron distribution satisfying Boltzmann's equation. The following values are used for the parameters (7): $\Lambda = 1.65$, $\omega = 0.26$ eV, $\Gamma = 0.15$ eV, $\varepsilon = 1.95$ eV.

We note that (10) and, to a greater extent, the equations of ref. 10 are nonlinear in ε_v, which can give rise to difficulties in the application of these results. Thus, in ref. 10 a study is made of the distribution of N_2 molecules in a discharge. The equation for the vibrational energy, allowing for pumping by electron impact and for the diffusion of vibrationally excited molecules to the walls of the discharge tube, is solved approximately. The use of (8) enables the problem to be solved exactly.

A direct comparison of the results for $T_e \lessdot 1.5$ eV with experimental data is not possible at the present time in view of the lack of experimental data. Preliminary calculations[8,9] for $T_e \lessdot 1$ eV are in satisfactory agreement with experiment (see the discussion in the review article by Mnatsakanyan[12]).

[1)] We note that K depends on T_v in this same manner in the opposite limiting case $\Gamma \gg \omega$, which is realized[6] for the molecules H_2 and CO_2.

[1] A. Herzenberg and F. Mandl, Proc. Roy. Soc., A270, 48 (1962).
[2] J. C. Y. Chen, J. Chem. Phys., 40, 3507, 3513 (1964).
[3] D. B. Birtwistle and A. Herzenberg, J. Phys., B4, 53 (1971).
[4] G. J. Schulz, Phys. Rev., 125, 229 (1962); 135A, 988 (1964).
[5] A. Kh. Mnatsakanyan, Opt. Spektrosk., 30, 1015 (1971).
[6] A. A. Likal'ter and A. Kh. Mnatsakanyan, Teplofiz. Vys. Temp., 11, 202 (1973).

[7] A. G. Engelhardt, A. V. Phelps, and C. G. Risk, Phys. Rev., 135A, 1566 (1964).

[8] L. M. Biberman and A. Kh. Mnatsakanyan, Report No. SM74/215 [in Russian], Intern. Symp. on MHD Energy Conversion, Salzburg, 1966.

[9] M. B. Zheleznyak, A. Kh. Mnatsakanyan, and I. T. Yakubov, Izv. AN SSSR, Mekhan. Gaza, No. 4, 161 (1970).

[10] A. Kh. Mnatsakanyan and G. V. Naidis, Teplofiz. Vys. Temp., 11, 932 (1973).

[11] W. L. Nighan, Phys. Rev., A2, 1989 (1970).

[12] A. Kh. Mnatsakanyan, Teplofiz. Vys. Temp., 12 (1974).

Plasma decay instability in crossed fields

V. I. Farenik, V. V. Vlasov, A. M. Rozhkov, and A. A. Kozharin
A. M. Gor'kii Khar'kov State University

(Submitted June 28, 1973)
Zh. Tekh. Fiz., 44, 1788-1789 (August 1974)

An experimental study is made of the nonlinear interaction of characteristic plasma oscillations which obey the decay conditions over a wide range of external fields.

The relative motion between the components of a plasma located in crossed electric and magnetic fields can result in the appearance of various instabilities.[1,2] In the present work an experimental study is made of the excitation and nonlinear interaction of high-frequency ($\omega \gg \omega_{Hi}$, ω_{Hi} is the ion gyrofrequency) longitudinal oscillations in a plasma in external crossed fields, a radial electric field E_r, and an axial magnetic field H.

Oscillations are found to be excited in the plasma with a frequency close to the drift frequency:

$$\omega_0 = k_\varphi V_\varphi, \tag{1}$$

where $k_\varphi = m/r$ is the azimuthal wave number and $V_\varphi = -cE_r/H$ is the electron drift velocity ($E_r < 0$). These oscillations decay into two modes, which satisfy selection rules

$$\omega_0 = \omega_2 - \omega_1, \quad m_0 = m_2 - m_1, \tag{2}$$

where the frequency ω_1 is close to the ion plasma frequency. Plasma heating is observed under conditions of a well-developed nonlinear interaction.

The experiments are performed in the gas discharge with a cold cylindrical diode in an axial magnetic field at a pressure (air) of $(0.25\text{-}5) \cdot 10^{-5}$ mm Hg. The potential difference between the electrodes of the diode $U = \varphi_1 - \varphi_2$ ($\varphi_1 > \varphi_2 = 0$, φ_1, φ_2 are respectively the potentials of the outer and inner electrodes) is varied in the range 0-3 kV. The magnetic field is varied in the range H = 0-3 kOe. The discharge current is varied from 0.5 to 5 mA. The parameters of the plasma and their spatial distribution are determined using movable Langmuir and heated probes. The characteristics of the oscillations of the plasma are determined by means of floating probes.

For values of H and U satisfying the relationship[3]

$$H \geqslant H_{cr} \approx \frac{2c\sqrt{2m_e U}}{r_1\sqrt{e}}.$$

there is formed in the diode at the given pressure a gas-discharge plasma of density $n = 10^8\text{-}10^9$ cm^{-3} ($n_e > n_i$, $n_{e,i}$ are the densities of the components of the plasma) with a temperature $T_e = 20\text{-}100$ eV $> T_i \approx 0.1\ T_e$. The inhomogeneity of the plasma along the radius r is not large:

$$\frac{1}{n}\frac{dn}{dr} \sim \frac{1}{T_e}\frac{dT_e}{dr} \leqslant 1\ \text{cm}^{-1}.$$

The radial electric field in the plasma E_r increases monotonically with radius. The experimentally measured dependence of E_r on U and r can be expressed as $E_r = Ur/A$ V/cm, where $A = 2r_1$ (r_1 is the radius of the outer electrode).

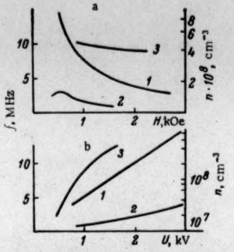

Fig. 1. Experimental plots of oscillation frequencies f_0 (1) and f_1 (2) and plasma density n (3) versus magnetic field intensity H (a) and potential difference across electrodes U (b).

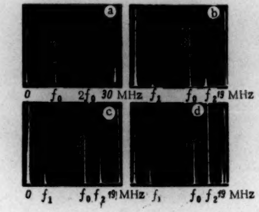

Fig. 2. Spectrograms of observed oscillations for various discharge conditions.

Oscillations are observed in the floating potential and in the discharge current under almost all operating conditions of the discharge. A study of how these oscillations depend on the external parameters of the plasma shows that for $1.1H_{cr} \leqslant H \leqslant 1.2H_{cr}$ only oscillations with a frequency f_0 = 5-15 MHz are excited, accompanied by the appearance of oscillations with frequencies $f_n = nf_0$ (n = 2, 3, 4...). The frequency f_0 is proportional to U/H and is independent of pressure and discharge current. Plots of f_0 versus H and U shown in Fig. 1 agree with (1), while the frequency of the observed oscillations is $\omega_0/2\pi$ with $m = m_0 = 2$. The amplitude of these oscillations increases with increasing magnetic field, up to $H \leqslant 1.2H_{cr}$, and the amplitudes of the higher harmonics nf_0 can be comparable to or greater than the amplitude of the oscillations at the fundamental frequency.

When the amplitude of the drift oscillations reaches the maximum value, frequencies $f_1 \ll f_0$ and $f_2 > f_0$ (Fig. 2b) appear in the spectrum of the plasma oscillations, and under certain discharge conditions the harmonics of these frequencies appear as well. Decay condition (2) holds for these frequencies.[4] As the amplitudes of the oscillations

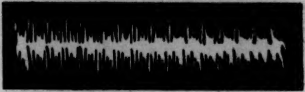

Fig. 3. Oscillogram of plasma oscillations for well-developed three-wave interaction. Sweep length is 10 μsec.

at f_1 and f_2 increase, the amplitude of the oscillations at frequency f_0 decreases. Plots of f_1 versus H and U are shown in Fig. 1. Unlike f_0, the frequency f_1 varies with pressure and discharge current. Simultaneous measurements of f_1 and the density n as a function of the external parameters show that $f_1 \sim \sqrt{n}$. For $n = 4 \cdot 10^8$ cm^{-3} the value of $\omega_{pi}/2\pi \approx 1$ MHz, which is in good agreement with the experimentally observed frequency. The oscillations with frequency f_1 can thus be identified with ion plasma oscillations. As can be seen from Fig. 3, these oscillations are also observed as low-frequency beats between two high-frequency signals at close frequencies.

For all modes of oscillation we measured the phase shift between the signals from probes movable in azimuth. The azimuthal mode numbers satisfy relationship (2): $m = 2$, $m_1 = -1$, $m_2 = 1$. No phase shift is detected along the axis of the system, i.e., the oscillations propagate in a direction perpendicular to the magnetic field.

We note that the harmonics of the oscillations with fundamental frequencies f_0, f_1, f_2 also satisfy the decay condition

$$f_{mn} = nf_0 + mf_1, \quad f_2 \equiv f_{11},$$

the amplitude being the greatest for oscillations with m = n (m and n are the harmonic numbers). In the harmonic spectrum of oscillations of frequency f_{mn}, the amplitude for a well-developed nonlinear interaction is greatest for oscillations with frequency f_{33}.

Under conditions of a well-developed three-wave interaction the elctron temperature reaches a value $T_e \approx 100$ eV, i.e., 5-10 times greater than the value $T_e \approx 10$-20 eV under conditions when oscillations are absent.

We are indebted to K. N. Stepanov for suggesting the problem and for valuable remarks. Thanks are also due to A. G. Pokroev, M. V. Sosipatrov, and M. G. Krivonos for their assistance in setting up the experiments.

---

[1] A. M. Rozhkov, K. N. Stepanov, V. A. Suprunenko, V. I. Farenik, and V. V. Vlasov, Plasma Phys., 12, 519 (1970).

[2] V. V. Dolgopolov, V. L. Sizonenko, and K. N. Stepanov, UZhF, 18, 621 (1973).

[3] É. M. Reikhrudel' and É. P. Sheretov, Radiotekh. Elektron., 9, 729 (1964).

[4] B. B. Kadomtsev, Reviews of Plasma Physics, Vol. 4, Consultants Bureau, New York (1966).

Titanium adsorption on tungsten

Yu. K. Ustinov and S. V. Fedichev
A. F. Ioffe Physicotechnical Institute,
Academy of Sciences of the USSR, Leningrad
(Submitted January 22, 1974)
Zh. Tekh. Fiz., 44, 1790-1792 (August 1974)

Titanium adsorption on tungsten has been studied by the flash method in a pulsed time-of-flight mass spectrometer. Titanium is found to desorb from two states bound to the tungsten. The first state, an adsorption state, has the following characteristics: $E = 80$ kcal/mole and $C = 10^{13}$ $\sec^{-1}$. The second state is of a diffusive nature, characterized by $E = 25$ kcal/mole and $C = 3 \cdot 10^{3}$ $\sec^{-1}$.

The getter properties of sputtered titanium films are widely used in high-vacuum technology. Titanium is also known to catalyze the formation of methane from molecules containing hydrogen and carbon. To study the simplest reaction, in which methane is formed from hydrogen and carbon dioxide on a titanium catalyst $H_2 + CO \rightarrow CH_4$ we use the thermal-flash method in a pulsed time-of-flight mass spectrometer.[1]

We use titanium films sputtered in high vacuum onto a tungsten substrate, which is neutral with respect to methane synthesis, for better purification of the titanium sorbed gases and for more complete titanium detection during the experiments.

Preliminary experiments on the adsorption of titanium on tungsten are given below.

The substrate is a tungsten ribbon 40 × 0.5 × 0.05 mm; after the appropriate heat treatment, its surface is dominated by the ⟨100⟩ face. The ribbon is heated by electric current. The titanium evaporators are tantalum strips 40 × 0.7 × 0.1 mm in size, to one or both sides of which titanium strips are spot-welded. Figure 1 shows the arrangement of the substrate and evaporators. Fluxes of titanium atoms from the sides of evaporator 3 and the flux desorbed from the substrate can enter the ion source of the pulsed time-of-flight mass spectrometer. Deposition of titanium from evaporator 1 onto the side of the substrate opposite the ion source shows that titanium atoms do not migrate to the opposite side of the substrate (facing the ion source) during the subsequent thermal desorption.

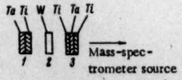

Fig. 1. Arrangement of adsorbent and titanium sputterers with respect to the source of the pulsed time-of-flight mass spectrometer.

The residual pressure in the spectrometer during the experiments is $5 \cdot 10^{-9}$ torr; the residual gases are primarily H_2 and CO, with partial pressures in the ratio 3 : 1. During titanium deposition an appreciable amount of methane appears in the mass spectrum of the residual gases.

The measurement procedure is as follows: The substrate is cleaned by heating to T = 2300°K and then cooled to room temperature. Then a titanium film is deposited on its surface for a certain time t_a, the evaporator is turned off, and the flash occurs. In certain experiments the substrate is cooled to 130°K or heated to 850°K during titanium adsorption. Figure 2 shows the current of Ti^+ ions as a function of the time, i(t), after the beginning of the flash for various titanium-adsorption times. During the flash we observe only the atomic ions Ti^+ and Ti^{++}. The same figure shows the increase in the substrate temperature during the flash, T(t). This functional dependence is determined by the method described in ref. 1.

We note the following features of the i(t) curves: 1) The titanium desorption begins at the same substrate temperature, regardless of the adsorption time t_a. 2) The peaks of the desorption curves, i_{max}, shift toward higher temperatures with increasing t_a. 3) As t_a increases the descending branches of the i(t) curves shift appreciably toward larger values of T, in the manner characteristic of diffusive desorption.

The ion current detected in the mass spectrometer during the flash is proportional to the flux of desorbed titanium atoms, i.e., $i(t) = 1/B\nu(t)$. The proportionality coefficient B is a function of the probability for the ionization of atoms in the ion source, the transmission of the mass spectrometer, and the ion–electron emission yield at the first dynode of the secondary-electron multiplier. The value of B is also a function of the substrate temperature T (it is proportional to $\sqrt{T}$ in the case of a Maxwell energy distribution for the particles), but over a narrow range of T this functional dependence is slight, so

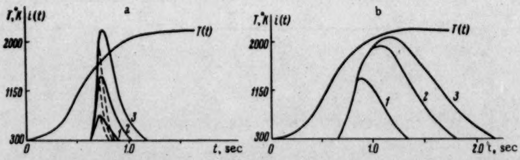

Fig. 2. Curves showing the desorption of titanium from a tungsten surface for various exposure times. a: t_a, min: 1) 0.5; 2) 1.0; 3) 2.0. b: t_a, min: 1) 5.0; 2) 10.0; 3) 20.0.

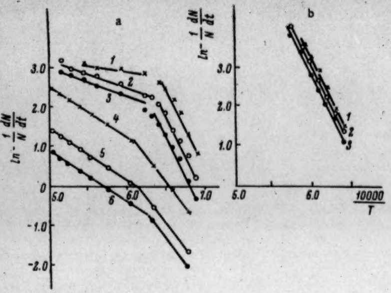

Fig. 3. Arrhenius curves. a: Arrhenius curves for titanium desorption. t_a, min: 1) 0.5; 2) 1.0; 3) 2.0; 4) 5.0; 6) 10.0; 6) 20.0. b: Arrhenius curves for titanium desorption from the first state. t_a, min: 1) 0.5; 2) 1.0; 3) 2.0.

we ignore it. To determine the value of B we use the flux of titanium atoms from evaporator 3 (Fig. 1), calculated from the known values of the titanium vapor pressure.[2]

Under the assumption that the atoms are desorbed according to first-order desorption kinetics, we can write the desorbed flux at any time t after the beginning of the flash as

$$\nu(t) = Bi(t) = -\frac{dN}{dt} = CN\exp\left(-\frac{E}{RT}\right), \qquad (1)$$

where N is the concentration of adsorbed atoms on the surface and E is the desorption activation energy. With E independent of N, we find from (1)

$$N(t) = N_a - B\int_0^t i\,dt = B\int_t^\infty i\,dt, \qquad (2)$$

where N_a is the concentration of adsorbed atoms before the flash at t = 0. For any time t the value of N(t) is proportional to the area under the desorption curve to the right of the i(t) ordinate (Fig. 2). The value of N_a is proportional to the entire area bounded by the desorption curve. The values of N_a, N(t), and dN/dt are found from the experimental i(t) functional dependences.

Comparing for each t the corresponding values of dN/dt and N(t), and using (1), we construct the functional dependences $\ln[(-1/N)(dN/dt)] = \Phi(1/T)$ with E = const; these curves are line segments whose slopes give E and whose ordinate intercepts give the constant ln C. Functional dependences of this type, calculated from the data in Fig. 2, are shown in Fig. 3a. These are approximated by two line segments with different slopes. The two different types of functional dependence imply that there are two different groups of sorbed titanium atoms.

Numerical estimates show that curve 1 in Fig. 2a corresponds to the desorption of a monolayer adsorbed before the titanium flash; correspondingly, curves 2 and 3 are associated with initial coverages greater than a monolayer. During the flash the titanium desorption occurs at T > 1500°K. We propose that as the temperature is raised (before desorption begins) a large fraction of the titanium atoms dissolve in the tungsten lattice. When desorption begins the concentration of adsorbed titanium atoms remaining on the surface is smaller than that corresponding to a monolayer $N < N_0$. Initially, it is these atoms remaining on the surface which are desorbed; their desorption governs the shape of the initial parts of the i(t) flash curves in Fig. 2a and the low-temperature parts of the curves in Fig. 3a. When the concentration of adsorbed atoms has fallen off as a result of the desorption we observe a diffusive flux of atoms from the tungsten lattice to the surface. This assumption is consistent with the fact that a Ti–W solid solution exists in the range[3] 800–1200°K. This second and slower process stretches out the i(t) desorption curves and corresponds to the high-temperature regions in Fig. 3a. During the flash, both processes of course occur at the same time, at different rates, and it is necessary to distinguish between them in order to determine the corresponding kinetic characteristics.

In first-order desorption kinetics, the peak on the desorption curve, i_{max} at T_{max}, is independent of the initial concentration of adsorbed atoms before the flash; under the assumption that the contribution of bulk diffusion is minimal during the desorption of a monolayer (curve 1 in Fig. 2a), we add the symmetric decaying parts (the dashed branches in Fig. 2a) to the desorption curves (rising front) at point T_{max}. In this manner we extract from the i(t) curves the part in which the flash is due primarily to the desorption of adsorbed atoms. After plotting $\ln[(-1/N)(dN/dt)] = \Phi(1/T)$ for these parts from the i(t) curves, we obtain the curves in Fig. 3b, whose slopes are independent of the initial concentration of titanium atoms in the film. The values E = 80 ± 5 kcal/mole and $C = 10^{13}$ sec^{-1} found from these curves are the kinetic characteristics of the thermal desorption of adsorbed titanium atoms from the tungsten ⟨100⟩ face. We recall that the heat of sublimation of titanium is E = 112 kcal/mole (ref. 2).

To test the validity of our method for determining T_{max} we calculate the leading parts of the desorption curves in Fig. 2a by a different method – that proposed by Redhead.[4] We find E = 75 ± 3 kcal/mole, in agreement with the value E = 80 ± 5 kcal/mole found from Fig. 3b.

At large initial concentrations of titanium atoms (corresponding to several monolayers), the slopes of the high-temperature parts of the curves in Fig. 3a apparently correspond to the desorption of dissolved titanium. The kinetic characteristics for the thermal desorption of dissolved titanium, found from the curves in Fig. 3a, turn out to be E = 25 ± 3 kcal/mole and $C = 3 \cdot 10^3$ sec^{-1}.

The parameters characteristic of titanium desorption from tungsten are necessary for studying the production of methane on titanium films deposited on tungsten.

---

[1] V. N. Ageev, N. I. Ionov, and Yu. K. Ustinov, Zh. Tekh. Fiz., 34, 2056 (1964) [Sov. Phys.-Tech. Phys., 9, 1581 (1965)].

[2] A. N. Nesmeyanov, Vapor Pressures of the Chemical Elements [in Russian], Izd. Akad. Nauk SSSR, Moscow (1961).

[3] A. D. McQuillan and M. K. McQuillan, Titanium, Academic Press, New York (1956).

[4] P. Redhead, Vacuum, 12, No. 4 (1962).

Effect of the radiation density on ion drift velocity in a cadmium–helium laser

G. N. Tolmachev, E. L. Latush, and V. S. Mikhalevskii

Scientific-Research Institute of Physics, Rostov-on-Don

(Submitted October 22, 1973)
Zh. Tekh. Fiz., 44, 1792-1794 (August 1974)

The effect of the radiation density in the cavity of a Cd–He laser on the drift velocity of cadmium ions in the $D_{5/2}$* state is determined. This state is the upper level for the 4416 Å laser transition.

1. The experiments reported here are carried out with an annular cataphoretic cadmium–helium laser with a cavity circumference of 3 m. The cavity is formed by two spherical mirrors (radii of curvature 2 m) and a plane mirror. The discharge tube, 1.8 mm in diameter with an active region 45 cm long, is placed between the spherical mirrors. Two rotatable plane-parallel plates are placed in the laser cavity to introduce a calibrated loss. A mirror system guides the rays moving in opposite directions onto a Fabry–Perot scanning interferometer. The drift velocities of the cadmium ions are measured by the method described in ref. 1, under the discharge conditions optimum for lasing: a helium pressure of 5 torr and a discharge current of 80 mA.

2. The measurements show that the drift velocity of the $D_{5/2}$* Cd II ions is a nonlinear function of the cadmium vapor pressure in the discharge; the functional dependence displays a clear minimum at pressures corresponding to the maximum radiation power.

It is reasonable to suggest that this functional dependence of the drift velocity on the cadmium vapor pressure is related to the power level in the cavity. This assumption is supported by the experimental functional dependence of the cadmium-ion drift velocity on the radiation power at the (constant) vapor pressures and other discharge parameters which are optimum for lasing (Fig. 1). The radiation power is varied by introducing loss in the cavity. It follows from the data in Fig. 1 that an increase in the radiation power in the cavity leads to a significant reduction of the drift velocity.

3. These results can be understood by noting that in the cadmium–helium laser the lifetime of the upper level is long ($\tau \approx 0.6$ μsec) (ref. 2), and this level is populated, according to current ideas, by Penning collisions from the ground state of the atom.[3,4] Since the drift velocity of the atoms is much lower than the ion drift velocity (even zero), a cadmium atom arrives in the upper ionic state with essentially zero average velocity; then it is accelerated in the axial electric field. Since the lifetime of the $D_{5/2}$* ion is long, the average velocity it acquires can be large. However, if the ion moves in the laser field, its lifetime is reduced because of the stimulated emission,[4] so that the velocity which it can reach is reduced.

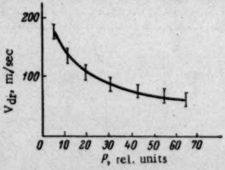

Fig. 1. Cadmium-ion drift velocity as a function of the radiation power in the cavity.

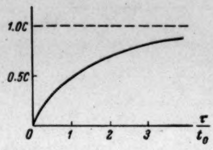

Fig. 2. Position of the maximum of the distribution function, in units of the thermal velocity (C), as a function of the ratio of the lifetime τ to the time required for the establishment of a steady-state ion drift velocity t_0.

4. To show the effect of the laser-radiation field in the cavity on the drift velocity we calculate the ion velocity distribution as a function of the ion lifetime, taking collisions into account. The momentum p of an ion satisfies

$$\frac{dp}{dt} = eE - \delta\langle VQ\rangle N_{He}p. \tag{1}$$

Here, $\delta = M_{He}/M_{Cd}$ is the part of the momentum given up in a collision of a Cd^+ ion with a He atom, Q is the momentum-transfer cross section, V is the relative velocity of the Cd^+ ion and the He atom, N_{He} is the density of helium atoms, and E is the field. The solution of the equation for the directed velocity V_z is

$$V_z = V_{z0} + \frac{eEt_0}{M_{Cd}}\left(1 - e^{-t/t_0}\right), \tag{2}$$

where

$$t_0 = \frac{1}{\delta\langle QV\rangle N_{He}} \tag{3}$$

is the characteristic time for the establishment of a directed ion velocity, and V_{z0} is the initial ion velocity.

The probability for the emission of a photon by an ion in time interval dt a time t after excitation is[5]

$$dW = e^{-t/\tau}\frac{dt}{\tau}, \tag{4}$$

where τ is the ion lifetime.

Solving Eqs. (2) and (4) simultaneously, we find the probability that the directed velocity of the ions will reach the value V_z:

$$dW = \left(1 - \frac{V_z - V_{z0}}{\frac{eEt_0}{M_{Cd}}}\right)^{\frac{t_0}{\tau}-1} \frac{dV_{z0}}{\frac{eE\tau}{M_{Cd}}}. \tag{5}$$

Then the z-velocity distribution function of the emitting ions is

$$F(V_z) = \text{const} \int\limits_{V_z - \frac{eE}{M_{\text{Cd}}} t_0}^{V_z} \left(1 - \frac{V_z - V_{z0}}{\frac{eEt_0}{M_{\text{Cd}}}}\right)^{\frac{t_0}{\tau} - 1} e^{-\frac{V_{z_0}^2}{2kT} M_{\text{Cd}}} \, dV_{z0}. \quad (6)$$

Because of the radiation field there is a change in the lifetime τ; the integral in (6) must be evaluated with this lifetime as a parameter. The distance from the velocity zero to the distribution peak gives the Doppler shift, which is measurable in practice, and the cadmium-ion drift velocity. Figure 2 shows the positions of the ion distribution peaks in units of the most probable thermal velocity $\sqrt{2kT/M_{\text{Cd}}}$, calculated under the assumption that the maximum attainable directed velocity is of the order of the thermal velocity (i.e., under the assumption $t_0eE/M_{\text{Cd}} = \sqrt{2kT/M_{\text{Cd}}} = C$). We see that the distribution peak shifts toward a zero average velocity as the lifetime decreases. This theoretical functional dependence is in qualitative agreement with the experimental data.

Figure 2 also shows that the drift velocity displays a functional dependence on the radiation power in the case in which the ion lifetime is comparable to the time required for the establishment of a steady-state drift velocity. Our estimates show that this condition is satisfied in the Cd−He laser.

This phenomenon is not observed in the argon laser, in which large ion drift velocities are observed,[6] because of the brief lifetime of the excited ion levels and because these levels are populated from the ground state of the ion, rather than the atom.

Accordingly, the drift velocity of the $D^*_{5/2}$ cadmium ions decreases with increasing laser power ($\lambda = 4416$ Å) because the lifetime of these ions is reduced by the stimulated emission; accordingly, the unperturbed ion drift velocities should be measured at low radiation-power levels in such lasers.

This effect can cause a contraction of the emission spectrum of this type of laser, and must be taken into account in analyzing the mode structure. This effect is further evidence that the $D^*_{3/2,\,5/2}$ Cd II levels are populated from the ground state of the atom under optimum conditions. This conclusion agrees with the mechanism of Penning collisions with metastable helium atoms.

It is hoped that future study of this phenomenon can be used to examine the lifetimes and the dynamics of drift velocities under typical discharge conditions.

---

[1] L. D. Mash, B. M. Rabkin, and B. V. Rybakov, ZhETF Pis. Red., 13, 240 (1971) [JETP Lett., 13, 169 (1971)].

[2] D. T. Hodges, Appl. Phys. Lett., 17, 11 (1970).

[3] W. T. Silfvast, Appl. Phys. Lett., 15, 23 (1969).

[4] I. G. Ivanov, E. L. Latush, V. F. Papakin, and M. F. Sém, Izv. VUZ Fiz., No. 8, 87 (1972).

[5] V. M. Zakharova and Yu. M. Kagan, in: Spectroscopy of a Gas-Discharge Plasma [in Russian], Izd. Nauka, Leningrad (1970), p. 291.

[6] W. W. Rigrod and T. J. Bridges, IEEE, QE-1, 298 (1965).

Dielectric strength of a vacuum gap with electrodes irradiated with He$^+$ and H$^+$ ions

A. P. Solodovnikov and Yu. M. Khirnyi

(Submitted June 25, 1973; resubmitted December 12, 1973)
Zh. Tekh. Fiz., 44, 1795-1796 (August 1974)

The dielectric strength of the vacuum gap between electrodes of metals differing in crystal structure and containing implanted He$^+$ atoms has been studied. The mechanism by which the atoms implanted in the electrodes affect the dielectric strength of the evacuated gap is discussed.

Measurements of the dielectric strength of a vacuum gap with stainless steel electrodes irradiated beforehand with inert-gas and nitrogen ions are reported in refs. 1 and 2. The dielectric strength is determined in ref. 1, where a working hypothesis is also offered for the mechanism for the enhanced dielectric strength of such gaps. Implanted He atoms evidently produce a dense layer of relatively tightly bound atoms at the electrode surface; these atoms stabilize sorption and diffusion processes at the electrodes, inhibiting ionization and bulk processes responsible for the predischarge current. The microscopic surface geometry of the electrodes is assumed to remain essentially constant. Evidence in favor of this assumption is the fact that the greatest increase in the dielectric strength occurs when the electrodes are bombarded with helium atoms rather than heavier ions, which would cause more damage to the metal surface during the bombardment.

We report here a study of the changes in the dielectric strength following helium bombardment of Mg, Al, Ti, Cu, Nb, and Mo electrodes, which have three types of crystal structure and which differ markedly in sputtering coefficient. The dielectric strengths of the gaps are shown in Table 1.

TABLE 1

	Electrodes						
	Mg	Al	Ti	Cu	Nb	Mo	stainless steel
Dielectric strength,	230	240	400	260	310	300	300

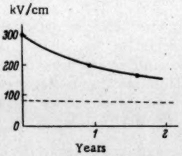

Fig. 1

In all cases at voltages above 200 kV the values of the dielectric strength are corrected to d = 10 mm. The electrodes are bombarded by ions at $E_i = 20$ keV; the total bombardment charge is $Q = 2 \cdot 10^{16}$ ions/cm^2, the optimum value for stainless steel electrodes bombarded by helium.

The dielectric strength is apparently not explicitly related to the type of crystal lattice, because in electrodes made of metal with the same hexagonal lattice – Mg and Ti – the values of the dielectric strength are 230 and 400 kV/cm, respectively.

Nor is the sputtering coefficient (which determines the degree of microscopic working of the electrode surface during the bombardment) the basic reason for the increase in the dielectric strength, since the maximum strength, 400 kV/cm, is obtained for Ti, whose sputtering coefficient is small; for Al, which also has a small sputtering coefficient, the strength is only 240 kV/cm. These experiments of course in no way rule out an effect of the microscopic surface geometry on the predischarge current. Using ions of the same species to bombard the electrodes, and varying the energy, intensity, and bombardment angle, i.e., by changing from ion bombardment to ion etching, one can produce a microscopic geometry such that the dielectric strength of the gap falls below the value characteristic of the unirradiated electrodes; this circumstance is also noted in ref. 3, although that work focused on the electric strength.

With stainless steel electrodes bombarded by He ions the dielectric strength decreases after the electrodes are held for a prolonged period of time under ordinary atmospheric conditions (Fig. 1). This decrease can be explained on the basis of the hypothesized decrease in the density of the layer of implanted He atoms due to diffusion. Hydrogen is known to diffuse more rapidly than inert gases in metals, so we have measured the dielectric strength as a function of the storage time of Ti electrodes bombarded by hydrogen ions in order to determine the role of the change in the density of implanted atoms on the magnitude of the dielectric strength. The extremely small change in the dielectric strength between such electrodes over five months apparently implies that the diffusion of hydrogen ions implanted into a metal by bombardment is not identical to the diffusion of hydrogen dissolved from the gas phase.

---

[1] Yu. M. Khirnyi and A. P. Solodovnikov, Prib. Tekh. Eksp., No. 2, 144 (1972).

[2] A. P. Solodovnikov and Yu. M. Khirnyi, Zh. Tekh. Fiz., 43, 861 (1973) [Sov. Phys.-Tech. Phys., 18, 543 (1973)].

[3] A. S. Pokrovskaya-Soboleva, V. V. Kraft, T. S. Borisova, and L. K. Mazurova, Zh. Tekh. Fiz., 42, 1318 (1972) [Sov. Phys.-Tech. Phys., 17, 1047 (1972)].

Hydrodynamic stability of the Uragan stellarator

V. M. Zalkind, Yu. K. Kuznetsov, V. K. Pashnev, and V. M. Tonkopryad

(Submitted January 28, 1974)
Zh. Tekh. Fiz., 44, 1796-1799 (August 1974)

The hydrodynamic stability of the $l = 3$ Uragan stellarator has been studied by measuring magnetic-field perturbations outside the plasma. A hydrodynamic instability has been studied. The perturbations have the spatial structure m = 1, n = 1. The possible connection between the hydrodynamic perturbations and the macroscopic plasma instability observed for increasing current is discussed.

Investigations of the current-carrying plasma in the $l = 3$ Uragan racetrack stellarator with large shear show[1] that increasing the current to a particular critical value causes an abrupt transition into an unstable regime. This regime is characterized by substantial fluctuations in loop voltage, plasma density, and other parameters, and increased losses of particles and energy from the plasma; therefore, further attempts to increase the energy containment by increasing the introduced power have little effect.

In the present work we investigate the hydrodynamic instability of a current-carrying pinch as one of the most probable causes of the observed effect.

EXPERIMENTAL MEASUREMENT

The main investigations on the Uragan stellarator are carried out in the optimum regime for obtaining the maximum plasma parameters. In this regime the mean radius of the outer unperturbed surface $r_0 = 6.8$ cm (radius of chamber $r_c = 10$ cm) and the rotational transform of the magnetic lines of force, forming this surface, for a single circuit (L = 1035 cm) is $i_0^b = 1.5\pi$. The direction of the ohmic heating current is such as to increase the rotational transform. The pressure of the working gas (helium) is $P = 10^{-4}$ mm Hg. The experiments are carried out with a magnetic field $H_0 \leq 7.2$ kOe.

The critical current is determined mainly by the magnetic field: $J_{cr}(\text{kA}) = 0.4\text{–}0.7\ H_0\ (\text{kOe})$. The coefficient of proportionality varies within the limits 0.4-0.7, depending on the current rise time in the initial phase of the discharge. We obtain the following maximum plasma parameters in the optimum regime: $\bar{n}_e = 8 \cdot 10^{12}\ \text{cm}^{-3}$, $\bar{T}_e = 300$ eV, $\bar{T}_i = 30$ eV.

The hydrodynamic plasma perturbations are studied by measuring magnetic-field perturbations outside the plasma using magnetic probes. Perturbations with m = 1 and n = 0.1, which are most probable under our conditions, can also be measured directly by distributed windings, inductively coupled to the given modes. The probes and windings are located outside the chamber and the helical winding at a distance of 14 cm from the axis. There is also a probe inside the chamber which can be moved in the radial direction. This probe and probes intended for studying the azimuthal structure of the perturbations are located along the straight section of the stellarator, where the shape of the cross section of the plasma is nearly circular because of the presence of the circularizer. In the measurements we process signals with lifetime 0.5-1.0 msec; these satisfy the condition that the process be stationary. The frequency spectrum and spatial structure of the oscillations are determined by correlation measurements.

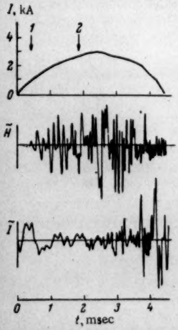

Fig. 1. Oscillograms of the current, oscillations of magnetic field $\tilde{H}$, and oscillations of current $\tilde{J}$. $H_0 = 4.8$ kOe.

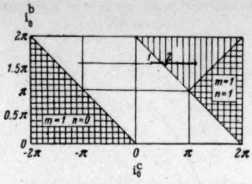

Fig. 2. Diagram of stability of current-carrying plasma in a stellarator with respect to perturbations with m = 1.

MEASUREMENT RESULTS AND THEIR DISCUSSION

Oscillograms that illustrate the hydrodynamic instability are presented in Fig. 1. The figure also shows magnetic-field oscillations (measured by the winding) corresponding to m = 1, n = 1, and the first mode of the helical instability; we also show oscillations of the total current (from the signal output of the Rogowski loop, proportional to J,) using a high-frequency filter. The arrows 1 and 2 indicate the transition to the unstable regime.

On the basis of the theory of hydrodynamic stability of a current-carrying plasma in a stellarator[2] we conclude that the difference between a stellarator and a tokamak in the present context is the additional rotational transform due to the helical windings. Therefore we propose that the theoretical results on the helical instability in a tokamak obtained by Shafranov[3] and other authors apply for a stellarator, if the additional rotational transform is taken into account. The chief parameter determining the stability of a current-carrying plasma is the rotational transform at the surface i_0. To calculate i_0 we use the simple summation of i_0^b and the rotational

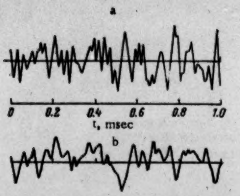

Fig. 3. Characteristic realizations of magnetic-field oscillations: a) inside; b) outside the chamber.

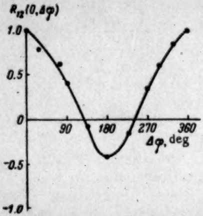

Fig. 4. Azimuthal cross-correlation function of magnetic-field oscillation $R(0, \Delta\varphi) = \langle\tilde{H}_1\tilde{H}_2\rangle/\sqrt{\langle\tilde{H}_1^2\rangle\langle H_2^2\rangle}$.

transform generated by the current $i_0^c = H_\varphi(r_0)L/H_z r_0$. Actually the mean radius of the configuration depends on the magnitude and direction of the current, and i_0 is determined by i_0^b and i_0^c in a more complicated way. However, as is shown by appropriate calculations, under the conditions of our experiments the error in the determination of i_0 due to these effects is less than 10%.

To compare the experimental data on the instability with the theoretical predictions we present a theoretical diagram of the stability of a current-carrying plasma in a stellarator taken from ref. 2 (Fig. 2). Since $i_0^b = 1.5\pi$ in our case, perturbations with $m \geq 2$, which play an important role in Tokamak experiments,[4] should not be excited and the most dangerous mode is the $m = 1$ mode; the region corresponding to this mode is cross-hatched on the diagram (Fig. 2). In the region with cross-hatching ($i_0^c > i_0^b$) an instability is expected for arbitrary values of the distribution over the cross section and the finite plasma conductivity broadens the instability region; the universal condition for suppression of the mode $m = 1$ has the form[3] $i_0 < 2\pi$.

The horizontal line in Fig. 2 shows the range of variation of i_0^c in the experiment, and the values of i_0^c for which oscillations with $m = 1$ arise and a transition to an unstable regime occurs are noted.

In qualitative agreement with the theory, a change in direction of current ($i_0^c < 0$) leads to the suppression of the $n = 1$ mode and the appearance of perturbations with $n = 0$. However, in contrast with the theoretical criterion, the $n = 0$ mode is excited for comparatively small currents ($i_0^c < 0.5\pi$), for which the condition $i_0 = 0$ is not satisfied at the boundary but somewhere within the plasma.

The excitation of the $m = 1$ mode in the fundamental regime is also verified by probe measurements. Characteristic magnetic-field oscillations used for the correlation analysis are presented in Fig. 3. Evidently the oscillations are rather irregular. The conducting chamber distorts the information on the frequency spectrum of the perturbations when the probes are outside the chamber. The measurements with the probe inside the chamber show that the frequency spectrum occupies the range f = 2-20 kHz with maximum power density at f = 8-12 kHz. The growth rates of perturbations corresponding to these frequencies are 5-10 times smaller than the theoretical estimate.[3]

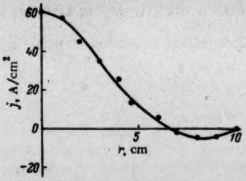

Fig. 5. Current-density distribution along radius, measured by a magnetic probe in an unstable regime.

The example of an azimuthal cross-correlation function is shown in Fig. 4; it indicates that an $m = 1$ mode is excited. The experimental data also indicate the presence of higher harmonics in the azimuthal structure. The total power of oscillations with $m = 0.1$, measured by the windings and the Rogowski loop, is usually less than the power of the oscillations received by the magnetic probe. The radial dependences of the mean amplitude obtained using the movable probe are indicated by this. For the $m = 1$ mode the magnetic perturbation field should decrease according to a quadratic law: $\tilde{H}(r) = \tilde{H}_0(r_0/r)^{m+1}$; in most regimes we observe a stronger dependence. The presence of higher harmonics can be due to strong nonlinear distortions of the $m = 1$ structure although the theory does not exclude the possibility of excitation of different branches of short-wave instabilities.[2] It is impossible to investigate the spatial structure more thoroughly in our experiments because the probes are located at a considerable distance from the plasma surface and experience a strong shielding effect due to the conducting chamber. Thus, the magnetic field of the short-wave perturbations is weakened considerably and the accuracy of the correlation analysis is poor.

If we assume that the current density is perturbed by surfaces localized at a radius $r \approx r_0$, then the value of the perturbed currents J_{pert} calculated from the measured values of $\tilde{H}$ reaches $J_{\text{pert}} \approx 0.05$ J. Oscillations of the total current J usually exhibit a considerably lower level.

The experimental data do not allow us to verify that the observed hydrodynamic perturbations are the cause of the macroscopic instability. The perturbations are not large enough for them to be considered as the direct mechanism for the increased loss of plasma. The sharp transition of the discharge to an unstable regime is not accompanied by any special features in the magnetic-probe signals. It is possible that the helical instability is the initial phase and causes some complicated instability. In particular, it is entirely probable that the transition to the unstable regime in our case is similar to the disruptive instability in tokamaks.[3] The following result favors this interpretation. An important feature of the disruptive instability is the contraction of the current channel, which precedes it. In these experiments we observe a rapid increase in the major radius,[1] which can also be explained by a contraction of the current channel.

In conclusion we note interesting results obtained by measurements of the function $H_{\varphi}(r)$ with a movable probe. The corresponding current-density profiles, constructed assuming axial symmetry, have negative values near the pinch boundary (Fig. 5). According to these measurements, a reverse current is excited in the unstable regime and can be a considerable fraction of the total current. Since the use of probes for measuring the current density introduces uncertainties, we also check all the other measurable parameters of the discharge. There is no noticeable effect, even when the probe is inserted at the radius r = 5 cm. This gives us a basis for assuming that the data on the excitation of negative currents are reliable. The possibility of the appearance of such a current is indicated, in particular, by the nonlinear theory of the helical instability given by Kadomtsev and Pogutse.[5] This effect can also be explained by the formation of a longitudinal electric field owing to the anomalously rapid expansion of the plasma pinch across the azimuthal component of the helical field and current field.

The authors thank V. A. Suprunenko for helpful remarks.

---

[1] A. G. Dikii (Diky), Yu. (Ju). K. Kuznetsov, O. S. Pavlichenko, Yu. (Ju.) I. Samoilenko, V. A. Suprunenko, and V. M. Tomkoryad (Tonkorjad), Proc. Third Intern. Symp. on Toroidal Plasma Confinement, Paper D-12, Garching, March 26-30 (1973).

[2] R. M. Sinclair, S. Yoshikawa, W. L. Harries, K. M. Young, K. E. Weimer, and J. L. Johnson, Phys. Fluids, 8, 118 (1965).

[3] V. D. Shafranov, Zh. Tekh. Fiz., 40, 241 (1970) [Sov. Phys.—Tech. Phys., 15, 175 (1970)].

[4] S. V. Mirnov and I. B. Semenov, Zh. Eksp. Teor. Fiz., 60, 2105 (1971) [Sov. Phys.—JETP, 33, 1134 (1971)].

[5] B. B. Kadomtsev and O. P. Pogutse, Zh. Eksp. Teor. Fiz., 65, 575 (1973).

Equations and boundary conditions for a three-dimensional quasistationary field

V. I. Yurchenko

Institute of Nuclear Physics, Siberian Branch,
Academy of Sciences of the USSR

(Submitted November 22, 1973)
Zh. Tekh. Fiz., 44, 1799-1802 (August 1974)

The problem of determining a quasistationary three-dimensional field is formulated. The source is described in the equations by means of an auxiliary vector $\mathbf{E}^a$ on which are imposed certain simple limitations. It is shown that the magnetic field is then uniquely defined by the magnitude of the emf of the source and does not depend on the form of $\mathbf{E}^a$. Sets of equations and boundary conditions for the electromagnetic potentials **A** and φ and the electromagnetic fields are given. The electric field vector is represented as a sum of a solenoidal vector $\mathbf{E}^r$ and a gradient vector $\mathbf{E}^g$. It is possible to eliminate either the vector $\mathbf{E}^r$ or **B** from the equations, and to set down two different sets of equations. The latter are not as tractable as the equations for **A** and φ. It is noted that violation of charge conservation is permissible in the quasistationary approximation. As a result, unless special conditions are invoked the equations of the quasistationary field do not have a unique solution.

In the analysis of a magnetic field allowing for the skin effect there are many applications in which one requires a matched solution in a mixed conductor–vacuum region or in which the current in a circuit has to be matched to the characteristics of the voltage source. The complexity of such problems is such that exact solutions can be obtained only in certain cases which reduce, in the long run, to the one-dimensional case.[1,2] In two-dimensional problems, if the accuracy of estimates is insufficient, one is obliged to seek a solution by numerical methods. Some contemporary examples of such calculations are found in refs. 3-8.

The transition to three measurements requires special consideration. This is due both to the increase in the number of measurements and also to the need to introduce into the field equations certain quantities characterizing the voltage source. In the strict formulation, the field must be uniquely determined by these quantities. This requires that the formulation of the problem be given special consideration, and it is with this problem that the present paper is concerned. For simplicity the relative dielectric and magnetic permitivities of the medium are set equal to unity, $\varepsilon = \mu = 1$, while the conductivity σ is taken to be a function which has a constant value in the domain of a conductor and which equals zero in vacuum.

1. The source is most easily introduced into the equations by means of the generalized Ohm's law

$$\mathbf{j} = \sigma(\mathbf{E} + \mathbf{E}^a), \tag{1}$$

the vector $\mathbf{E}^a$ in the conductor being regarded as a given function of the coordinates and time (see Fig. 1). The initial set of equations, obtained by combining (1) with Maxwells equations, is written in the form (the displacement current is neglected)

$$\operatorname{curl} \mathbf{B} = \mu_0 \mathbf{j}, \tag{2}$$

$$\operatorname{div} \mathbf{B} = 0, \tag{3}$$

$$\operatorname{curl} \mathbf{E}^r = -\frac{\partial \mathbf{B}}{\partial t}, \tag{4}$$

$$\operatorname{div} \mathbf{E}^r = 0, \tag{5}$$

$$\operatorname{curl} \mathbf{E}^g = 0 \tag{6}$$

$$\operatorname{div} \mathbf{E}^g = \frac{\rho}{\varepsilon_0}, \tag{7}$$

$$j = \sigma(\mathbf{E}^r + \mathbf{E}^g + \mathbf{E}^a). \tag{8}$$

Here we have represented the vector electric field **E** as the sum of a solenoidal vector $\mathbf{E}^r$ and a gradient vector $\mathbf{E}^g$, i.e., we have split it up into two simpler vectors that are different in mathematical (and physical) respects. This sort of decomposition is utilized in the determination of vector fields[9] and simplifies the formulation of the problem. From (2) div $\mathbf{j} = 0$ everywhere, and consequently $\mathbf{j}_\perp = 0$ (otherwise div **j** becomes infinite on the surface of the conductor). This is the only boundary condition needed to solve the problem, and it follows directly from the equations. In Eqs. (2)-(8) the vector $\mathbf{E}^a$ is prescribed; the quantities **B**, $\mathbf{E}^r$, $\mathbf{E}^g$, **j**, ρ are to be determined.

2. We now write equations for **A** and φ. We take div **A** = 0. The vector potential then only describes solenoidal fields:1) $\mathbf{B} = \operatorname{curl} \mathbf{A}$, $\mathbf{E}^r = -\partial \mathbf{A}/\partial t$, $\mathbf{E}^r = -\nabla\varphi$, and from (2)-(8)

$$\Delta \mathbf{A} = -\mu_0 \mathbf{j},$$

$$\Delta\varphi = -\frac{\rho}{\varepsilon_0},$$

$$\mathbf{j} = \sigma\left(-\frac{\partial \mathbf{A}}{\partial t} + \mathbf{E}^g + \mathbf{E}^a\right).$$

By eliminating ρ and **j** from these equations (to eliminate ρ it is necessary to use div $\mathbf{j} = 0$, div $\mathbf{A} = 0$) we obtain the equations

$$\gamma \frac{\partial \mathbf{A}}{\partial t} = \Delta \mathbf{A} + \gamma(\mathbf{E}^g + \mathbf{E}^a), \tag{9}$$

$$\Delta\varphi = \operatorname{div} \mathbf{E}^a, \tag{10}$$

where $\gamma = \sigma\mu_0$, with the boundary condition

$$E^g_{\perp i} = -E^a_{\perp i} + \frac{\partial A_{\perp i}}{\partial t} \quad (j_\perp = 0). \tag{11}$$

Here and below the index i indicates that a quantity is taken at the interior side of the conductor surface and e that it is taken at the exterior side, $\perp$ indicates the projection of the vector on the interior normal **n**.

Equation (10) holds only within the conductor: It does not allow for surface charges ρ_S or for charges in vacuum. However, the value of $\mathbf{E}^g$ in vacuum has no effect on **A** and does not enter into boundary condition (11). It is therefore sufficient to know it only in the conductors. For this we have the problem (10)-(11). The distribution of $\mathbf{E}^g$ in vacuum can be found by solving the external boundary problem for $\Delta\varphi = -\rho/\varepsilon_0$ with the boundary value of the potential obtained from (10)-(11).

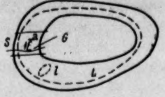

Fig. 1

It is important to note that the potential in (10)-(11) is determined to within an arbitrary constant and that this is a consequence of the approximation under consideration. Because of the absence of displacement current in (2)-(8) it is possible for charge conservation to be violated. To $\mathbf{E}^g$ one can add the electric field of charges arbitrarily dependent on time, and to ρ one can add their density, provided the charges are distributed in vacuum and on the surfaces of the conductors in such a manner that the boundaries of the conductors coincide with equipotentials of their electric field. This does not affect the remaining quantities. If the charges are assumed to be independent of time then this can also be done in the general case in which the displacement current is incorporated in the equations. Here, however, the lack of uniqueness is removed by prescribing the initial value of $\mathbf{E}^g$ in vacuum. This is not possible in the quasistationary approximation. In this case it is necessary to fix the value of ρ outside the conductors (below we assume that $\rho = 0$ there) when the lack of uniqueness in a problem like (10)-(11) can be removed by prescribing either the total charge on the conductor[10] or the value of the potential at any point of the conductor.

We note that Eq. (9) for $\mathbf{A}$ is formally like an inhomogeneous equation for thermal conductivity in which the coefficient γ depends on the coordinates. By writing it in the conductors in the form $\mathbf{E}^g + \mathbf{E}^a = -1/\gamma\ \Delta\mathbf{A} - \mathbf{E}^r$ we see that $(-1/\gamma)\Delta\mathbf{A}$ corresponds to the ohmic voltage drop per unit length, $\mathbf{E}^r$ corresponds to the induced emf per unit length, and $\mathbf{E}^g + \mathbf{E}^a$ corresponds to the total voltage drop per unit length. In the language of electrical engineering Eq. (9) can be regarded as the voltage law in a circuit consisting of a source and a resistor and inductor in series. It is necessary to prescribe the initial value $\mathbf{A}(\mathbf{r}, 0) = \mathbf{f}(\mathbf{r})$ for $\mathbf{A}$ in (9) subject to the condition $\operatorname{div}\mathbf{f} = 0$.

3. Let us manipulate (2)-(8), eliminating certain of the dependent quantities. As above, we can eliminate ρ and $\mathbf{j}$. Then, from (4)-(5), we obtain

$$\mathbf{E}^r = -\operatorname{curl}\iiint\limits_V \frac{\partial\mathbf{B}(\mathbf{r}', t)}{\partial t}\frac{d^3r'}{4\pi|\mathbf{r}-\mathbf{r}'|},$$

where the integration is extended over all space; we thus eliminate $\mathbf{E}^r$ from the remaining equations. Taking the curl of (2) and utilizing (3), we obtain an equation for $\mathbf{B}$

$$\gamma\frac{\partial\mathbf{B}}{\partial t} = \Delta\mathbf{B} + \gamma\operatorname{curl}\mathbf{E}^a + \mathbf{q}, \tag{12}$$

where $\mathbf{q}$ is the surface source due to the jump of σ at the boundary of the conductor. The surface density is

$$\gamma_i\left[\mathbf{n}\times\left(-\operatorname{curl}_i\iiint\limits_V \frac{\partial\mathbf{B}(\mathbf{r}', t)}{\partial t}\frac{d^3r'}{4\pi|\mathbf{r}-\mathbf{r}'|} + \mathbf{E}_i^g + \mathbf{E}_i^a\right)\right].$$

We write (12) inside and outside the conductor; then, in addition to taking

$$E^g_{\perp i} = \operatorname{curl}_{\perp i}\iiint\limits_V \frac{\partial\mathbf{B}(\mathbf{r}', t)}{\partial t}\frac{d^3r'}{4\pi|\mathbf{r}-\mathbf{r}'|} - E^a_{\perp i} \tag{13}$$

($j_\perp = 0$) it is necessary to prescribe the condition of continuity

$$\mathbf{B}_i = \mathbf{B}_e \tag{14}$$

and the condition on the jump of $\partial\mathbf{B}/\partial n$ allowing for $\mathbf{q}$. As in the case of the normal derivative of the potential of a simple layer in passing through a surface containing charges, we obtain

$$\left.\frac{\partial\mathbf{B}}{\partial n}\right|_e - \left.\frac{\partial\mathbf{B}}{\partial n}\right|_i = \gamma_i\left[\mathbf{n}\times\left(-\operatorname{curl}_i\iiint\limits_V \frac{\partial\mathbf{B}(\mathbf{r}', t)}{\partial t}\frac{d^3r'}{4\pi|\mathbf{r}-\mathbf{r}'|} + \mathbf{E}_i^g + \mathbf{E}_i^a\right)\right] \tag{15}$$

Thus (2)-(8) can be replaced by:

$$\left.\begin{array}{l}\left.\begin{array}{c}\gamma\dfrac{\partial\mathbf{B}}{\partial t} = \Delta\mathbf{B} + \gamma\operatorname{curl}\mathbf{E}^a\\ \Delta\varphi = \operatorname{div}\mathbf{E}^a\end{array}\right\}\text{in the conductor}\\ \quad\Delta\mathbf{B} = 0 \quad \text{in vacuo}\end{array}\right\} \tag{16}$$

with boundary conditions (13)-(15). Similarly, by eliminating $\mathbf{B}$ from (2)-(8) we obtain the following set of equations for $\mathbf{E}^g$ and $\mathbf{E}^r$:

$$\left.\begin{array}{c}\gamma\dfrac{\partial\mathbf{E}^r}{\partial t} = \Delta\mathbf{E}^r - \gamma\dfrac{\partial}{\partial t}(\mathbf{E}^g + \mathbf{E}^a),\\ \Delta\varphi = \operatorname{div}\mathbf{E}^a,\\ E^g_{\perp i} = -(E^a_{\perp i} + E^r_{\perp i}),\end{array}\right\} \tag{17}$$

which is simpler than (13)-(16).

We make two remarks. The representation $\mathbf{E} = \mathbf{E}^r + \mathbf{E}^g$ enables us to obtain equations and boundary conditions that do not contain ρ_S. If this representation is not used and if one prescribes $\Delta\mathbf{E} = 0$ in vacuum, $\gamma(\partial\mathbf{E}/\partial t) = \Delta\mathbf{E}\,(\mathbf{E}^a = 0)$ in the conductor, and $E_{\parallel i} = E_{\parallel e}$ and $E_{\perp i} - E_{\perp e} = \rho/\varepsilon_0$ on the boundary, then an incomplete set is obtained since ρ_S, like $\mathbf{E}$, is unknown; in this scheme the second boundary condition is nothing more than a renaming of the variables. The formulation of the problem for the vector $\mathbf{E}$ that does not involve splitting the latter into a solenoidal and a gradient part thus seems to us to be difficult.

It is easy to eliminate $\mathbf{E}^r$ or $\mathbf{B}$ from (2)-(8), but not $\mathbf{E}^g$. If the surface charges are taken into account in the right side of $\Delta\varphi = \operatorname{div}\mathbf{E}^a$, the solution is written in free space, and after this $\mathbf{E}^g = -\nabla\varphi$ is substituted into the equations and boundary conditions, we eliminate $\mathbf{E}^g$, but in place of $\mathbf{E}^g$ in the equations there appears another unknown quantity, ρ_S.

We note that the set of equations given in the present section, (13)-(16) and (17), are less convenient for obtaining solutions than (9)-(11) as they contain equations of higher order either in the space variables or in time.

4. In Maxwell's equations the arbitrarily prescribed vector $\mathbf{E}^a$ is an external quantity. Restrictions corresponding to the conditions of the problem must be imposed upon it.

The circulation of $\mathbf{E}^a$ around any contour of type L (see Fig. 1) must always have the same value, equal to the emf of the voltage generator. This requires that the circulation around any contour of type l must equal zero. Whence follows the first restriction, curl $\mathbf{E}^a = 0$. (The condition $\mathbf{E}^a = 0$ does not imply that $\mathbf{E}^a$ is a gradient vector. For this the circulation of $\mathbf{E}^a$ around contour L must equal zero[11].) For a given emf, the vector $\mathbf{E}^a$ with this restriction can be specified in an infinite number of ways, although the vector **A** does not depend on the form of $\mathbf{E}^a$. Let us consider the stationary case in which $\partial\mathbf{A} \cdot (\partial t)^{-1} = 0$ in (9)-(11). Suppose for different $\mathbf{E}_1^a$, $\mathbf{E}_2^a$ corresponding to the same value of the emf we find respectively $\mathbf{E}_1^g$, $\mathbf{E}_2^g$ and $\mathbf{j}_1 = \sigma(\mathbf{E}_1^g + \mathbf{E}_1^a)$, $\mathbf{j}_2 = \sigma(\mathbf{E}_2^g + \mathbf{E}_2^a)$. Evidently, the circulation of $\mathbf{j}_2 - \mathbf{j}_1$ around any contour in the conductor is equal to zero; accordingly $\mathbf{j}_2 - \mathbf{j}_1 = \Delta\psi$. For ψ we obtain $\nabla\psi = 0$, $d\psi/dn|_1 = 0$. The solution of this problem is an arbitrary constant, so that $\mathbf{j}_1 = \mathbf{j}_2$. Having made the substitution $\mathbf{E}^a - \Delta\varphi_0 \to \mathbf{E}^a$, $\varphi - \varphi_0 \to \varphi$ is the potential determined from (10)-(11) for $\partial\mathbf{A}/\partial t = 0$ in (9)-(11) we obtain equations for **A** that are independent of the initial form of $\mathbf{E}^a$. Thus, to determine $\mathbf{j}$, $\mathbf{E}^r$, **B** (the quantities most frequently encountered in practical applications), any convenient form of $\mathbf{E}^a$ may be chosen, not necessarily localized in the region of the generator G. The latter feature is significant for the determination of φ.

Assume that Eqs. (9)-(11) are solved for a prescribed $\mathbf{E}^a$. Assume that the conductor is bounded by a surface S (see Fig. 1) such that the region occupied by the conductor is singly connected (any contour in this region is a contour of type l); let us redefine the potential by $\varphi = C(t) - \int_{\mathbf{r}_0}^{\mathbf{r}} (\mathbf{E}^g + \mathbf{E}^a) \cdot d\mathbf{r}$ where $\mathbf{r}_0$ is a point taken on either side of S and C(t) is an arbitrary function of time (the ambiguity of the potential is discussed in Sec. 2 above). Let the integration be taken within the conductor without intersecting S. With this definition of the potential the region of the generator reduces to an infinitesimally thin layer on the surface S, and the value of the potential is independent of the form of the vector $\mathbf{E}^a$ chosen for the calculations.

I thank B. V. Chirikov for useful discussion.

[1)] This is also valid for $\partial/\partial t$ div $\mathbf{A} = 0$. For any other gauge the vector potential also describes a part of the gradient field.

---

[1] G. Caden, Electromagnetic Screens [Russian translation], Gosenergoizdat, Moscow–Leningrad (1957).

[2] V. I. Yurchenko, Zh. Tekh. Fiz., 43, 1866 (1973) [Sov. Phys.–Tech. Phys., 18, 1180 (1974)].

[3] O. V. Tozoni, Computer Calculation of Electromagnetic Fields [in Russian], Izd. Tekhnika, Kiev (1967).

[4] É. V. Kolesnikov and D. D. Savvin, Izv. VUZ Elektromekhanika, No. 8, 827 (1968).

[5] É. V. Kolesnikov, Izv. VUZ, Elektromekhanika, No. 12, 1294 (1970).

[6] É. V. Kolesnikov, Izv. VUZ. Elektromekhanika, No. 1, 3 (1971).

[7] N. I. Doinkov, Zh. Tekh. Fiz., 43, 897 (1973) [Sov. Phys.–Tech. Phys., 18, 571 (1973)].

[8] V. I. Yurchenko, Preprint Institute of Nuclear Physics, Siberian Branch, Academy of Sciences of the USSR [In Russian], 94-73 (1973).

[9] A. N. Tikhonov and A. A. Samarskii, The Equations of Mathematical Physics [in Russian], Izd. Nauka, Moscow (1966).

[10] G. A. Grinberg, Selected Topics in the Mathematical Theory of Electrical and Magnetic Phenomena [in Russian], Izd, AN SSSR, Moscow–Leningrad (1948).

[11] Ya. B. Zel'dovich and A. D. Myshkis, The Elements of Applied Mathematics [in Russian], Izd. Nauka, Moscow (1965).

Steady-state operation of a surface-ionization thermionic converter

N. V. Volkov, Yu. K. Gus'kov, Yu. I. Kostikov, and V. P. Pashchenko

(Submitted August 7, 1973; resubmitted January 2, 1974)
Zh. Tekh. Fiz., 44, 1802-1804 (August 1974)

The transient waveform obtained by switching a thermionic converter from open-circuit to short-circuit conditions is studied. The analysis centers on processes with characteristic time much greater than the diffusion time. It is shown that these slow processes are a feature of underneutralized operation, and are absent in overneutralized regimes. The cathode temperature is varied in the range 1000-1500°K and the cesium vapor pressure in the range 10^{-3} 0.3 torr.

It has been noted in a previous paper[1] that two time constants are associated with the establishment of steady-state conditions in a converter subsequent to a stepwise switching operation. The shorter, τ_1, is determined by the diffusion time. The character of the processes responsible for the longer time constant, τ_2, was tentatively ascribed to the effect of "well filling" by thermally emitted ions.

In the present paper we present the results of transient-recovery measurements for times much greater than the diffusion time. An experiment has shown that edge effects have a strong influence on the time dependence of the current; accordingly the device is placed in an axial magnetic field of 400 Oe. The electrodes of the device, with an area 1 cm^2, are made from molybdenum. The cathode is indirectly heated. Temperatures are measured by thermocouples. The cesium vapor pressure in the device varies from 10^{-3}–3.10^{-1} torr; the variation of the cathode temperature lies in the range 1000–1500°K.

Figure 1 shows typical transient current and voltage waveforms obtained when the converter is switched (in a time of order 0.2 μsec) from open-circuit to short-circuit conditions. In the time interval (0, τ_1) the recovery is determined by the diffusion time and τ_1 coincides with the ambipolar diffusion time.[1] It is also evident from Fig. 1 that in the absence of an axial magnetic field the current variation in the interval $\tau > \tau_1$ is very weak; when an axial field is applied and edge effects thereby eliminated, the current can vary by a factor of 1.5–2. The time required to establish the voltage does not exceed the switching time (0.2 μsec). The quantity τ_2 is determined from the experimental curves as the time required for the current to reach 95% of its steady-state value, as the precise time at which the latter value is achieved cannot be determined accurately.

Slow variations of current (in a time $\tau > \tau_1$) are observed only in the underneutralized regime (defiency of ions); when short-circuiting occurs an ion trap is formed in the interelectrode gap (which can freely pass to the anode when the diode is open-circuited). Figure 2 shows the volt–ampere characteristic and the current recovery times for switching of the converter from open circuit to a given point on the volt–ampere characteristic. As the amplitude of the voltage pulse increases the recovery time first increases; then, reaching a maximum value in the current saturation region it decreases. The quantity τ_2 falls sharply when an arc discharge is established.

The calculated time to reach steady-state conditions is shown in Fig. 2. In the current saturation region this time is defined as the time required to establish an equilibrium density for the Saha–Langmuir current:

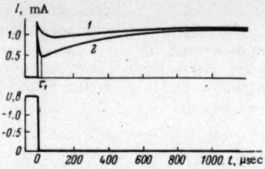

Fig. 1. Oscillograms of current and voltage transient behavior. Pressure p = 0.12 torr, T = 1200 °K. Axial magnetic field H (Oe): 1) 0; 2) 400.

$$\tau_2 = \frac{n_0}{I_c} L,$$

where n_0 is the equilibrium density of the plasma, J_C is the Saha–Langmuir current, L = L – Δ is the effective interelectrode gap, L_0 = 0.2 cm is the geometric gap, and Δ is the reduction of the region occupied by the plasma due to penetration of the electric field when a positive potential is applied to the converter anode; Δ is determined through the equations of refs. 2 and 3. In the above expression the product n_0L determines the total number of cesium ions in the interelectrode gap for an electrode area of 1 cm^2. In the calculation of J_C we use the data of Aamodt et al.[4] on the work function of molybdenum in cesium vapor.

As can be seen from Fig. 2, the experimental and calculated times agree in the current saturation region. On the tail of the volt–ampere characteristic the plasma density is below equilibrium,[5] and the time required to establish the steady state is correspondingly small. At the point on the volt–ampere characteristic at which the near-anode potential jump is approximately zero, the well-filling time is 250 μsec and exceeds the calculated time (200 μsec) for L = L_0. This probably occurs because the

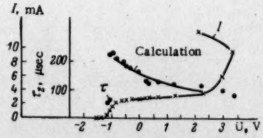

Fig. 2. Dependence of transient duration on anode voltage. p = $2.2 \cdot 10^{-2}$ torr; T = 1250°K; H = 400 Oe.

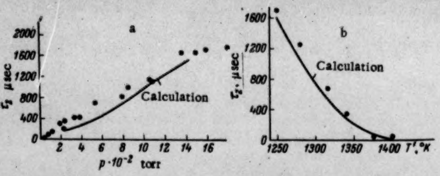

Fig. 3. Dependence of τ_2 on cesium vapor pressure (a): T = 1250°K, U = 0, H = 400 Oe; and on cathode temperature (b): p = 0.16 torr, U = 0, H = 400 Oe.

confinement of the ions in the interelectrode gap is not efficient at small positive potential jumps. The quantity τ_2 begins to fall strongly for U > 3 V on account of ions generated in the near-anode region. In this case a glow can be visually observed in the anode region and the current increases sharply.

Figure 3 shows the experimental and calculated variation of the duration of the transient with cesium vapor pressure (Fig. 3a) and cathode temperature (Fig. 3b). Evidently τ_2 decreases with increasing cathode temperature and increases with increasing cesium vapor pressure because of the increase in the cathode work function and the associated increase in the ion flux from the emitter.

The experimental and calculated curves are in good agreement; accordingly the time τ_2 can be used to estimate the cathode work function in the underneutralized regime.

In conclusion we thank R. Ya. Kucherov for useful discussion.

---

[1] N. V. Volkov, Yu. K. Gus'kov, and V. P. Pashchenko, in: Topics in the Physics of Low-Temperature Plasmas [in Russian], Izd. Nauka i Tekhnika, Minsk (1970), p. 532.

[2] R. Ya. Kucherov and L. É. Rikenglaz, Zh. Tekh. Fiz., 32, 1275 (1962) Sov. Phys.–Tech. Phys., 7, 941 (1962)].

[3] I. G. Gverdtsiteli, V. Ya. Karakhanov, R. Ya. Kucherov, Z. A. Oganezov, and V. K. Tskhakaya, in: Reports presented by Soviet Scientists at Second Intern. Conf. on Thermionic Conversion of Energy [in Russian], Izd. VNIIT, Moscow (1969), p. 95.

[4] R. L. Aamodt, L. I. Brown, and B. D. Nichols, J. Appl. Phys., 33, 2080 (1962).

[5] V. P. Karmazin, I. I. Kasikov, and I. P. Stakhanov, Izv. AN SSSR, Ser. Fiz., 28, 1541 (1964).

Transient thermionic-field emission from a point cathode

E. A. Litvinov and A. F. Shubin

Institute of Atmosphere Optics, Tomsk

(Submitted June 8, 1973; resubmitted January 30, 1974)
Zh. Tekh. Fiz., 44, 1804-1806 (August 1974)

The variation of the electron and phonon temperatures of the cathode material under condition of intense thermionic-field emission is investigated. A numerical calculation shows that the electron temperature can exceed the lattice temperature. This feature introduces certain changes in the time criteria for the onset of vacuum breakdown and opens the possibility of obtaining short-duration pulses of emission current with density 10^{10}-10^{11} A/cm^2.

It has been shown by Kartsev et al.[1] that the prebreakdown emission current density j and the delay t_d in vacuum breakdown (with respect to the application of the voltage pulse) are related by $j^2 t_d \simeq 4.5 \cdot 10^9$ A^2·sec/cm^4 (for tungsten). Calculations performed in a previous paper[2] for a cylindrical point emitting under thermionic-field conditions show that the field-emission current density j_0 and t_d are related by $j_0^2 t_d \simeq 2.2\,\rho C/\varkappa_0$, where ρ is the density of the cathode material and C is its specific heat, $\varkappa_0$ is the temperature coefficient of the resistivity, i.e., $\varkappa = \varkappa_0 T$ (T is temperature in degrees K). Numerical estimates of t_d via the equation of ref. 2 are in good agreement with the experimental results of ref. 1.

In the present paper a more detailed analysis is given of the processes at the cathode accompanying intense thermionic-field emission. A more realistic emitter geometry is used: an emitter in the form of a truncated cone with emitting tip radius r_{em}, base radius r_0, and apex angle 2θ. When a high-density emission current is drawn the temperature of the electrons in the metal T_e increases by Joule heating and the Nottingham effect.[3] The latter is due to the fact that the mean energy carried by conduction electrons to the emitting metal–vacuum boundary differs from the mean energy that is removed by the emitted electrons. The lattice temperature of the cathode metal, T_{ph}, increases as a result of electron–phonon interaction.

The following two-temperature model can be used to describe the situation:

$$\left.\begin{aligned}
&C_e\frac{\partial T_e}{\partial t}=\lambda_e\left(\frac{\partial^2 T_e}{\partial r^2}+\frac{2}{r}\frac{\partial T_e}{\partial r}\right)\\
&\quad+\frac{jC_e}{en_e}\left(\frac{r_{em}}{r}\right)^2\frac{\partial T_e}{\partial r}+j^2\left(\frac{r_{em}}{r}\right)^4\varkappa_0 T_{ph}-\dot{\varepsilon},\\
&C_{ph}\frac{\partial T_{ph}}{\partial t}=\dot{\varepsilon};\quad T_e=T_{ph}\big|_{t=0}=T_0;\quad T_e=T_{ph}\big|_{r=r_0}=T_0;\\
&\lambda_e\frac{\partial T_e}{\partial r}\bigg|_{r=r_{em}}=-\frac{2kT_u j}{e}\left[\frac{\pi^2 kT_e^2}{4\mu T_u}+\frac{\pi T_e}{2T_u}\operatorname{ctg}\frac{\pi T_e}{2T_u}\right],\\
&j=\frac{j_0\dfrac{\pi T_e}{2T_u}}{\sin\dfrac{\pi T_e}{2T_u}};\quad T_u\,[^\circ\mathrm{K}]=\frac{5.67\cdot 10^{-5}E}{\sqrt{\varphi}},
\end{aligned}\right\}\qquad(1)$$

$$r_0=\frac{r_{em}}{\sin\theta};\quad r_{em}=\frac{r_{em}}{\sin\theta}.$$

Here, $C_{ph} = \rho C$ is the phonon specific heat, C_e is the electronic specific heat, λ_e is the electronic thermal conductivity, n_e is the density of conduction electrons, e is the electron charge, μ is the Fermi level, φ (eV) is the work function, E (V/cm) is the electric field at the cathode, and k is Boltzmann's constant. The emission characteristics of the cathode are written for strong electric fields and relatively low temperatures ($\pi T_e/2T_u \le 2$) (see ref. 5).

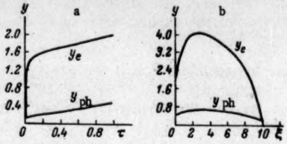

Fig. 1. Dimensionless temperature $y = \pi T_e/2T_u$ versus: a) a time $\tau = (j_0^2\varkappa_0/c\,C_{ph})t$ (for $\xi = 0$) and b) distance from emitter tip $\xi = (j_0^2\varkappa_0/\lambda_e)^{1/2}(r - r_{em})$ (for $\tau = 1$). $E = 1.2\cdot 10^8$ V/cm, $j_0 = 1.25\cdot 10^9$ A/cm^2, $r - r_{em} = 4\cdot 10^{-6}\,\xi$ cm, $t = 1.3\cdot 10^{-11}\,\tau$ sec, $T = 2\cdot 10^3\,y$ °K.

The quantity $\dot{\varepsilon}$ characterizes the rate of transfer of energy from the electronic subsystem to the lattice. This process has been examined in detail[4] and the following equation obtains:

$$\dot{\varepsilon}=AT_D\left[\left(\frac{T_e}{T_D}\right)^5\int_0^{T_D/T_e}\frac{x^4dx}{e^x-1}-\left(\frac{T_{ph}}{T_D}\right)^5\int_0^{T_D/T_{ph}}\frac{x^4dx}{e^x-1}\right],\qquad(2)$$

where T_D is the Debye temperature. Estimates in ref. 6 indicate that the coefficient $A \simeq 2\cdot 10^{11}$ J/cm^3·sec·deg.

The problem has been solved numerically for the case of tungsten ($C_{ph} = 2.73$ J/cm^3·sec·deg, $\lambda_e = 1.68$ J/cm·sec·deg, $\mu = 1.12\cdot 10^{-18}$ J, $\varkappa_0 = 3\cdot 10^{-8}$ Ω·cm/deg, $\varphi = 4.52$ eV, $n_e = 10^{23}$ cm^{-3}, $T_0 = 300$°K, $T_D = 350$°K, $r_{em} = 3\cdot 10^{-5}$ cm, $\theta = 5°$). The results of the calculations are presented in Figs. 1 and 2.

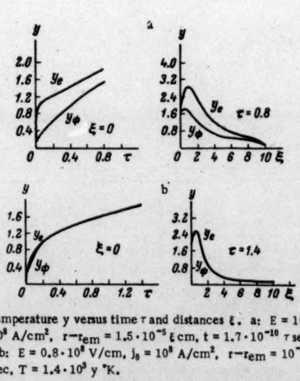

ig. 2. Temperature y versus time τ and distances ξ. a: $E = 10^8$ V/cm, $j_0 = 6.8\cdot 10^8$ A/cm^2, $r - r_{em} = 1.5\cdot 10^{-5}\,\xi$ cm, $t = 1.7\cdot 10^{-10}\,\tau$ sec, $T = 1.7\cdot 10^3\,y$ °K. b: $E = 0.8\cdot 10^8$ V/cm, $j_0 = 10^8$ A/cm^2, $r - r_{em} = 10^{-4}\,\xi$ cm, $t = 8\cdot 10^{-9}\,\tau$ sec, $T = 1.4\cdot 10^3\,y$ °K.

It follows from the curves that the basic features established in ref. 2 apply for cathode fields $E \leq 0.8 \cdot 10^8$ V/cm. At fields $E \geq 10^8$ V/cm new and interesting effects appear. The electron temperature T_e can exceed the lattice temperature T_{ph}. The value of t_d is not determined by the current density j_0 but more by the rate of transfer of energy from the electrons to the lattice. For example, Fig. 1 shows that in fields $E = 1.2 \cdot 10^8$ V/cm the electron temperature rises in a characteristic time of 10^{-12} sec on account of the Nottingham effect. The lattice temperature T_{ph} approaches the melting point of the cathode material ($T_{ph} \simeq 1500$°K, $T_{melt} = 3600$°K) in a characteristic time of $1.3 \cdot 10^{-11}$ sec. It follows from ref. 7 that the minimum value of the experimental t_d is close to this value, $1.3 \cdot 10^{-11}$ sec.

We note in conclusion that it is probably possible to obtain short-duration [$\tau \simeq 4C_{ph}/A \simeq (10^{-11}-10^{-10})$ sec] pulses of emission current with density $j \simeq (10^{10}-10^{12})$ A/cm^2. A value $j = 10^{12}$ A/cm^2 means that the current removes all conduction electrons ($j = en_e v_F = 10^{-19} \cdot 10^{23} \cdot 10^8 = 10^{12}$ A/cm^2).

---

[1] G. K. Kartsev, G. A. Mesyats, D. I. Proskurovskii, V. P. Rotshtein, and G. N. Fursei, Dokl. Akad. Nauk SSSR, 192, 309 (1970).

[2] E. A. Litvinov, G. A. Mesyats, and A. F. Shubin, Izv. VUZ. Fiz., 4, 147 (1971).

[3] W. B. Nottingham, Phys. Rev., 59, 906 (1941).

[4] V. P. Shabanskii, Zh. Eksp. Teor. Fiz., 27, 142, 147 (1954); V. L. Ginzburg and V. P. Shabanskii, Dokl. Akad. Nauk SSSR, 100, 445 (1955); M. I. Kaganov, M. I. Lifshits, and L. V. Tanatarov, Zh. Eksp. Teor. Fiz., 31, 232 (1956) [Sov. Phys.–JETP, 4, 173 (1957)].

[5] E. L. Murphy and R. H. Good, Phys. Rev., 102, No. 6, 1464 (1956).

[6] S. I. Anisimov, Ya. A. Imas, G. S. Romanov, and Yu. V. Khodyko, The Effect of High-Intensity Radiation on Metals [in Russian], Izd. Nauka, Moscow (1970).

[7] B. Lüttner, W. Rohrbeck, and H. Wolff, Beitrag Plasmaphys., 10, 383 (1970).

Recent developments in surface ionization (review)*

É. Ya. Zandberg

A. F. Ioffe Physicotechnical Institute,
Academy of Sciences of the USSR, Leningrad

(Submitted February 1, 1974)
Zh. Tekh. Fiz., 44, 1809-1828 (September 1974)

Recent work on surface ionization, carried out primarily over the period 1970-1973, is reviewed. General questions related to surface ionization, the surface ionization of organic compounds in weak electric fields, and applications of surface ionization in electronics and physical-chemistry research are discussed.

I. CERTAIN GENERAL QUESTIONS OF SURFACE IONIZATION

Since surface ionization was discovered 50 years ago by Langmuir and Kingdon,[1] we have acquired a clear overall picture of this phenomenon, although a detailed quantum-mechanical theory has not yet been worked out. Equations for the ion currents for the ionization of atomic and molecular fluxes involving the production of positive and negative ions at homogeneous and polycrystalline emitters have been derived and, in general, experimentally verified with weak and strong electric fields at the emitter surface. These questions are treated in ref. 2. Over the time period reviewed here, some of these questions have been refined and developed further. In this review we discuss only those aspects of the recent work which are most interesting.

1. Ion Emission by Film Systems Involving a First-Order Phase Transition in a Chemisorbed Film

Until recently there had been essentially no investigations of the surface ionization of particles on emitters consisting of synthesized film systems. The search for efficient thermionic emitters has spurred interest in film systems, and research in this field by various methods is increasing in intensity.

Film emitters can be efficient emitters of positive ions as well as of thermionic electrons. Furthermore, even the earliest studies of ionization with the film system Ir (III) − C showed that the surface ionization of elements which are not readily ionized is, when combined with thermionic emission, a very useful tool for studying several properties of film systems, since first-order phase transitions in the films can be easily detected.[3]

The study of ion emission in film systems undergoing first-order phase transitions is a new field in emission electronics and an important one, since features observed in ion emission are also manifested in the electron emission of such systems.

We now know that first-order phase transitions occur in many two-dimensional films over the temperature range which can be studied experimentally. For example, such transitions occur in a system consisting of a platinum-group metal and carbon;[3-4] in sodium films on the tungsten (100) face;[5] in barium films on many metal substrates;[6] in zirconium, hafnium,[7-11] and platinum[12] films on refractory metals; and, apparently, in gold and copper films on graphite[13] and in other film systems. First-order phase transitions, including transitions of the condensation type, can occur even in two-dimensional films of electropositive atoms, despite the large effective charge of the adsorbed atoms and the repulsive nature of the interaction between them. This possibility has been pointed out in theoretical papers[14,15] on the properties of adsorbed films of alkali metals on refractory-metal substrates. The phase transitions in these systems arise in contraction of the film, which reduces the effective charge of the adsorbed atoms.

Systems with homogeneous metal substrates become inhomogeneous with respect to emission as a result of first-order phase transitions, in particular, transitions of the condensation type. Accordingly, phase transitions can be detected if the experimental method is sensitive to inhomogeneity in emission, and we can expect that as such methods are developed a large number of systems in which phase transitions occur in a film will be discovered. Among such methods are field microscopy, low-energy electron diffraction, and a method combining thermionic emission and surface ionization of elements which are not readily ionized.[2,3] The latter method is particularly good for film systems which are studied at high temperatures; with this method the work function of each phase of the film coating can be found directly at these temperatures and the critical coverage ĉan be determined.

Figure 1 (from ref. 3) shows the behavior of the thermionic-emission current and the current of positive In^+ ions during a change in the average carbon coverage of the (111) Ir face. Figure 2 (also from ref. 3) shows the behavior of the work function of the Ir (111) − C film system. We see that the emitter initially remains homogeneous and its work function increases with increasing coverage; then a phase transition occurs, causing the system to become inhomogeneous with respect to emission. The emission becomes homogeneous again at a coverage $\Theta = 1$. We see from Fig. 2 that the work function of the (111) Ir face is ~ 5.8 V, that of the adsorbed gaseous carbon phase on this face is ~ 6 V, and that of the condensed carbon phase is ~ 4.8 V.

A general approach to the description of the emission of systems in which a first-order phase transition of the

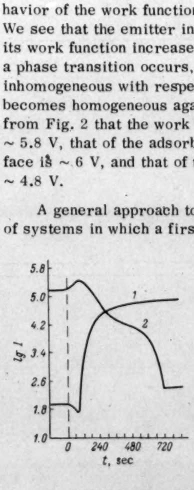

Fig. 1. Thermionic current (1) and current of In^+ ions (2) in carbon deposition on the (111) Ir face; the atomic flux is constant in time. The iridium temperature is T= 1685°K.

condensation type occurs has now been worked out. The occurrence of a transition at a given temperature in a given system (if possible) requires that the surface coverage Θ reach a certain (critical) value Θ_{cr}. At $\Theta < \Theta_{cr}$ the film consists of simply a two-dimensional adsorbed gaseous phase and is homogeneous if the substrate is homogeneous. A subsequent increase in the number of particles in the film leads to the condensation of the excess particles in islands, and the system becomes a two-phase system with a coverage Θ_{cr} in the adsorbed gaseous phase and $\Theta \approx 1$ in the adsorbed condensed phase. A further increase in the number of particles in the film leads to an increase in the area of the condensed phase through a contraction of the area of the gaseous phase; the system again becomes a single-phase system at a monolayer coverage, at which only the condensed phase remains. The example of the Ir (111)−C system shows that the gaseous and condensed phases can differ significantly in characteristics other than the work function: the heat of vaporization, the sticking probability, the particle-reflection coefficient, the catalytic activity, etc.[3,16,17]

The emission properties of these systems, which become inhomogeneous as a result of phase transitions, differ significantly from those of inhomogeneous polycrystalline emitters, for which the behavior has been studied thoroughly. It is shown in refs. 3, 17–19 that, for film systems in which a first-order phase transition of the condensation type occurs in a film, the emission features are governed by the following properties of these systems:

1. The areas occupied by the phases are functions of the average coverage at a constant temperature or of the temperature at a constant average coverage. This latter functional dependence results from the temperature dependence of the critical coverage Θ_{cr}, at which the phase transition occurs.

2. Changes in the substrate temperature can affect the work function of the gaseous phase but have little effect on the work function of the condensed phase.

3. The redistribution of phase areas which occurs upon changes in the degree of coverage or the temperature leads to a change in the effect on the emission of the contact fields of the spots at a constant external electric field. When the average coverage is higher than the critical coverage, but only slightly so, it is essentially impossible to produce an external field sufficient to balance the contact spot fields above regions of condensed phase, and as $\bar{\Theta}$ approaches $\Theta = 1$ it is essentially impossible to produce fields sufficient to balance the contact spot fields above the remaining areas of a two-dimensional gaseous phase.

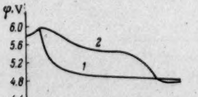

Fig. 2. Work function calculated from the total thermionic current (1) and from the total current of In^+ ions (2) in the Ir (111)−C system during carbon deposition on the (111) Ir face. T = 1685°K. The changes in φ correspond to the changes in the currents in Fig. 1.

A method has been worked out[17] for finding a quantitative description of the thermionic emission of electrons and ions by film emitters in which there is a two-dimensional condensation of particles in a film. This method takes into account the continuously changing degree of compensation of the contact spot fields with increasing amounts of adsorbate, and it permits the relative areas occupied by each coverage phase on the emitter surface to be determined from the electron and ion currents at all coverages $\bar{\Theta} > \Theta_{cr}$.

It has been pointed out that because of these features of film systems characterized by first-order phase transitions the methods for determining various physicochemical characteristics on the basis of temperature changes cannot be used. Among these methods are the widely used nonisothermal methods for determining the heat of vaporization and the heat of desorption for atoms and ions, methods in which the work function is determined from the temperature dependences of the ion and electron currents, etc.[18,19] It has been shown that the large temperature coefficient of the work function in such a system is not a consequence of the functional dependence of the Fermi level on the temperature; instead it is due to a redistribution of the areas of the phases due to a change in the temperature. It has also been pointed out that there may be errors in the functional dependence of the work function on the concentration, $\varphi(\Theta)$ obtained at a constant temperature by the contact-potential difference methods worked out for obtaining the functional dependence $\varphi(\Theta)$ for homogeneous systems. This question is studied in ref. 20, where a study is made of the displacement of the retardation curves for the positive ions produced by surface ionization and for thermionic electrons corresponding to changes in the average coverage in a film system with two-dimensional condensation. Analytic equations are derived for the retardation curves for the cases of balanced and unbalanced contact spot fields (the electrodes are assumed to be in a planar arrangement, the spots are assumed to be sharply defined, and the "normal energy" approximation is used). It follows from this analysis[20] that under the conditions corresponding to two-dimensional adsorbate condensation the method based on the displacement of the retardation curves upon changes in the average coverage does not unambiguously give the changes in work function. This situation is illustrated by Fig. 3 (from ref. 20).

Finally, we emphasize that the question of phase transition in films at the pertinent operating temperatures of

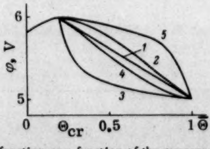

Fig. 3. The work function as a function of the average coverage, $\varphi(\bar{\Theta})$, of the (111) Ir face by carbon. 1) The function $\bar{\varphi} = f(\bar{\Theta})$ determined by the vibrating-capacitor method; 2–5) the same, obtained from the displacement of the linear regions of the retardation curves for thermionic electrons and ions of readily ionizable elements [2) from the displacement of the retardation curves for thermionic electrons in an unbalanced spot field; 3) in a balanced spot field; 4) from the displacement of the ion retardation curves in an unbalanced spot field; 5) in a balanced spot field].

film emitters should be studied further; it is necessary to determine the work function and heat of vaporization of particles from the film as functions of the concentration and to determine other characteristics of these systems and of their interactions with foreign particles adsorbed on them, by the methods developed for homogeneous systems. The possibility of phase transitions in films has frequently been neglected.

2. Ion Emission from Inhomogeneous Emitters When the Contact Spot Field Is Not Balanced

This case occurs in thermionic converters and film systems with phase transitions at average coverages for which the emitting spots are very small. It was assumed previously that the ions from spots with a work function larger than the average value move in the retarding field of the spots and must overcome an additional potential barrier,[2] but reflection of the desorbed ions from a barrier was neglected. As a result, the particle flux of homogeneous density directed toward the emitters converted into an inhomogeneous flux within the effective range of the contact fields (Fig. 4). Taking account of this feature in ref. 21 leads to a change in the expression for the ion current taken from an exposed surface in the ionization of a flux of neutral particles of a specified density ν_0 far from the emitter. This equation is now written

$$I = \nu_0 S_0 A e \left[\sum_k \frac{s_k}{A + \exp \frac{e}{kT}(V - \varphi_k)} + \sum_i \frac{s_i}{A + \exp \frac{e}{kT}(V - \varphi)} \right], \quad (1)$$

where S_0 is the total area of the emitting surface, A is the ratio of the statistical sum for the ion states to that for the states of the neutral, ionizable particles, s_k and s_i are the relative areas of spots having work functions $\varphi_k < \bar{\varphi}$; (the average over the surface $\varphi_i > \bar{\varphi}$, V is the ionization potential of the particles being ionized, and e, k, and T have their usual meanings. The first term in brackets gives the current from spots with $\varphi_k < \bar{\varphi}$, while the second gives that from spots with $\varphi_i > \bar{\varphi}$. As in ref. 2, the equation for the current is derived under the assumption that the spots have sharp boundaries, in the normal-energy approximation; the spot dimensions are assumed to be small in comparison with the dimension of the total emitting surface area and in comparison with the distance between the emitter and collector; migration and the space-charge field are neglected.

Equation (1) shows that during the ionization of readily ionizable elements [for which the condition $e(\varphi_{\min} - V) \gg kT$ is satisfied], i.e., under the condition $V \ll \bar{\varphi}$, there is complete ionization of the incident particle flux, since $I = e\nu_0 S_0$. The current cannot be a function of the external electric field, so that there can be neither a normal nor anomalous Schottky effect. Accordingly, the effect of the external field on the surface-ionization current of readily ionizable elements differs markedly from the effect on the thermionic-emission current: In the ionization of Cs atoms ($V \simeq 3.9$ V) on the two-phase surface of the film system Ir(111)–C with $\varphi \sim 6$ V for the gaseous phase of carbon and ~ 4.8 V for the condensed phase, an anomalous electronic Schottky effect is observed, but the anomalous ion Schottky effect is not observed at any coverage.

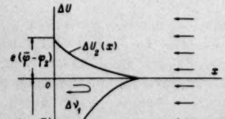

Fig. 4. Changes in the ion potential energy ΔU above spots having φ_1 and φ_2 ($\varphi_1 > \varphi_2$). Some of the ions produced at spots having φ_1 are reflected from the spot field barrier.

3. Surface Ionization of Molecules

In surface ionization of molecules it is not only the molecules which can undergo ionization, but also the products of all reactions which the molecules and the particles which they form undergo in the adsorbed film on the emitter. In fact, it is usually the products of reactions (primarily, dissociation reactions) which are ionized, since their ionization potentials are generally lower than those of the corresponding molecules.

Calculation of the ion currents of various chemical compositions requires a determination of the concentration of the particles of each species formed on the emitter. This problem is simpler to deal with if a state near chemical equilibrium is established in the adsorbed film; then the equilibrium constants for the reactions can be used to determine the numbers of particles of the various species.[22] This case apparently arises over a broad temperature range in the ionization of alkali halide molecules on metals.[23] A special experimental study is required in each particular case in order to determine the chemical equilibrium in the adsorbed particle film. It has been recently demonstrated that an equilibrium cannot occur in an adsorbed film in the case of adsorption of the vapor of metallic bismuth, which has a complex composition, on the (100) face of tungsten.[24]

A more general approach to the problem would be to analyze the conditions for a steady state, giving the conservation law for the particles of each chemical species; the case of the chemical equilibrium of particles in an adsorbed film is a particular case. This approach, proposed in ref. 25, has been used in the surface ionization of MX molecules of alkali halide salts.[25,26]

A chemical equilibrium between the particles in an adsorbed film is possible when $(\nu_0 - \nu_{MX})/\nu_d \ll 1$, where ν_0 is the molecular flux to the emitter, ν_{MX} is the inverse flux of molecules evaporated from the emitter, and ν_d is the effective particle flux to the surface (taking dissociation into account). Lacking information on the heats of vaporization of molecules from emitters of various materials and lacking information on the dissociation energies of molecules on various materials, we cannot predict in which metal–molecule systems and at what temperatures

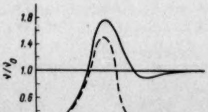

Fig. 5. Dissociation rate (solid curve) and association rate (dashed curve) as functions of the temperature for the ionization of LiCl molecules on Re.

this chemical-equilibrium condition can be satisfied. For a given system a chemical equilibrium can be approached very closely in an adsorbed film at a low temperature, at which the rate of particle desorption from the surface is low; at a high temperature, because of the rapid disruption of reaction products, the predominant reaction is molecular dissociation, whose rate is comparable to the rate at which particles reach the surface, so that the chemical equilibrium is disrupted. This situation is illustrated in Fig. 5 (from ref. 26), which shows the calculated rates for the forward and reverse reactions $MX \rightleftharpoons M + X$ for ionization of LiCl on Re in the case in which the rate constants for particle desorption are higher than the rate constants for particle dissociation on the emitter surface.

Coverage of metals by foreign particles can affect the ratio of dissociation and evaporation rates. If the work function does not change, or if it changes in a controllable manner, the ion current gives information about the changes in the degree of molecular dissociation in the adsorbed film. It follows that surface ionization can be used to study the effects of various adsorbates on the course of heterogeneous catalytic reactions which involve a dissociation step. This method has been used to determine the mechanism for the poisoning effect of carbon on molecular-dissociation reactions on metals of the platinum group.[16]

4. Transient Behavior of the Ion Current After a Change in Emitter Temperature

The functional dependences of the currents on the temperature yield several important characteristics, e.g., the work function, the ionization potential, the electron affinity, and the heat of vaporization of ions. Accordingly, it is important to record these functional dependences in undistorted form. However, the literature reveals that in certain cases the establishment of a steady-state current after a change in the emitter temperatures takes a long time – a time much longer than that required for the establishment of a steady-state emitter temperature. The time required to establish a steady-state current is particularly long if the temperatures involved are low.[2] The reasons for the transient behavior of the currents have not been studied; the experimentalist usually records the transient currents corresponding to an arbitrarily chosen delay time.

The temporal behavior of the currents has been studied recently in an ionization experiment in which the particle flux to the emitter is held constant in time.[27,28] It is shown that a neglect of the temporal changes leads, in certain cases, to serious distortions of the functional dependences on the temperature, e.g., false thresholds can appear, as are observed in the ionization of barium atoms on the (111) Ir face (Fig. 6, from ref. 28).

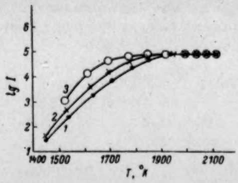

Fig. 6. Current of Ba⁺ ions as a function of the temperature for the ionization of Ba atoms on the (111) Ir face. The delay times for the current measurements are: 1) 30, 2) 240, 3) 600 sec.

Transient currents occur after a change in the emitter temperature T because when T is changed rapidly from T_1 to T_2 the equilibrium coverage N_1 of the emitter by ionizable particles at T_1 becomes a nonequilibrium coverage at T_2 and approaches the equilibrium coverage N_2 at the new temperature only after a finite time. Using the familiar equation

$$\frac{dN}{dt} + W(T_2)N = \nu_0,$$

where $W(T_2)$ is the probability for particle evaporation in the form of ions and neutrals from the emitter surface at temperature T_2, and ν_0 is the flux of particles incident on the emitter, and assuming that the heats of vaporization of the ions, l_+, and the neutrals, l_0, are independent of the degree of coverage over the possible range of this coverage, we find

$$t^* = \frac{\ln\left[\frac{1}{1-\gamma}\left(1 - \frac{W(T_2)}{W(T_1)}\right)\right]}{W(T_2)}, \tag{2}$$

where t^* is the time required to obtain at T_2 a coverage $N = \gamma N_2$ $(\gamma \leq 1)$; $W(T) = C \exp(-l_+/kT) + D \exp(-l_0/kT)$.

It follows from Eq. (2) that in the ionization of specified particles and with a selected value of γ the time t^* is a strong function of T_2 and the difference $T_1 - T_2$: The larger the heats of desorption of the atoms and ions (l_0 and l_+), the longer the time required to establish a steady-state current. To illustrate this point, in Fig. 7 we show the $t^*(l_+)$ functional dependences calculated from Eq. (2) in ref. 28 for the ionization of readily ionizable particles for the case $\gamma = 0.9$, $T_1 - T_2 = 100°$, and various temperatures. We see that at large l_+ and low T the attainment of a coverage with $\gamma = 0.9$ requires long delay times (the dashed line in Fig. 7 corresponds to 100 sec). The larger l_+, the higher the temperatures at which significantly time-dependent currents are observed. It is for this reason that time-dependent currents are only observed at low threshold temperatures in the ionization of alkali metal atoms ($l_+ \approx 2$ eV), while such currents are observed in the ionization of Ba on the (111) Ir face also at extremely high temperatures ($l_+ \simeq 5$ eV).

It follows from Eq. (2) and from the equation for W(T) that the desorbed fluxes of neutral particles should also be functions of the time, especially if the corresponding heats of desorption are large. This circumstance must be kept in mind in determining the heats of desorption of neutral particles by any nonisothermal method.

5. Aspects of Ionization in Strong Electric Fields

Opinion is divided on the mechanism for ionization in strong electric fields produced at the surface of a point emitter in field-ion microscopes and field-ion sources. In the literature from outside the Soviet Union the ionization of atoms having high ionization potentials is frequently attributed to field ionization, regardless of whether the atoms involved pass through an adsorption step. The ionization of atoms of the point material (field evaporation) and of adsorbed atoms (field desorption), on the other hand, are treated as the evaporation of ions under conditions such that the field lowers the potential barrier at the surface.[29,30]

An approach like that used for surface ionization in strong electric fields[2,31-33] has been proposed for dealing with all ionization phenomena in strong fields in which the particles being ionized pass through a step in which they are on the emitter. This approach has led to explanations for many of the features observed experimentally for each of these processes, and a study has been made of the energy distribution of the ions produced by surface ionization in strong electric fields.[2,33] (An error has been made here in taking into account the effect of the surface potential at the collector on the ions; it is corrected in ref. 34.)

The motion of ions from an emitter to a collector through an accelerating grid is studied in ref. 34 for external electric fields weaker than those required to balance the surface field; stronger fields are also studied. The ions are assumed to have an initial Maxwellian velocity distribution (characteristic of surface ionization), and the emitter and collector are assumed to be homogeneous with respect to work function (in this case the ion retardation curves consist of two linear regions; Fig. 8). The following equation has been derived for the potential U_0 at which these linear regions intersect:

$$eU_0 = e(V - \varphi') + kT \ln \frac{\alpha}{A}, \tag{3}$$

where V is the ionization potential of the atoms being ionized, φ' is the work function of the ion collector, A is the ratio of the statistical sums for the states of the ions and atoms, and α is the degree of ionization of particles at the emitter in the applied field.

Retardation curves for the ions produced at the emitters in strong electric fields can be determined experimentally only if the currents are large, i.e., if the degree of ionization is not too small. By appropriately choosing the field, the condition $\alpha \approx A$ can be arranged. Under this condition, when elements have different values of V are undergoing ionization, the retardation curves should be displaced (Fig. 8) according to

$$e(U_{01} - U_{02}) \approx e(V_1 - V_2). \tag{4}$$

If the ionization potential is not known for one of the particles, it can be found with respect to that of a reference particle from the displacement of the retardation curves. In the case of complex particles, e.g., molecules and radicals of organic compounds, the ratios of statistical sums are approximately equal to unity. If the ionization of two substances occurs at approximately equal pressures of these substances and leads to approximately equal currents at various field intensities, we would have $\alpha_1 \approx \alpha_2$; here the absolute values of the difference $kT(\ln \alpha_1/A_1 - \ln \alpha_2/A_2)$ are small, and we can assume that Eq. (4) holds. For organic compounds, for which the ionization potentials are not known for many molecules and, especially radicals, a determination of the ionization potentials on the basis of the displacement of the retardation curves could be very useful.

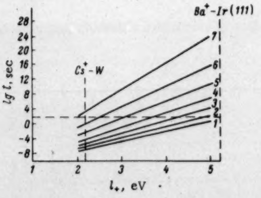

Fig. 7. Delay time required to obtain $\theta = 0.9$ of the equilibrium value as a function of the heat of vaporization of ions in the ionization of readily ionizable elements. The changes in T (°K) are as follows: 1) 2000 → 1900; 3) 1600 → 1500; 5) 1200 → 1100; 7) 800 → 700.

The retardation-potential method has recently been used independently to measure the energy distributions of polyatomic ions produced in the ionization of organic compounds of various classes in strong electric fields produced at the surfaces of sharp points.[35] Here the concept of surface ionization is not used in analyzing the experimental results, and the displacement of the energy distributions as a function of the ionization potentials of the ionizing particles is explained on the basis of the energy balance for the ions produced in the strong field, at a critical distance from the surface. The equation obtained in this manner for the displacement of the initial ion currents in the ionization of particles with different values of V is essentially the same as Eq. (4), differing only in small correction terms, which are not used in analyzing the experimental results. As measurements of the ionization potentials for many compounds with known values of V have shown, the error in the determination of the ionization potential does not exceed 0.1 V; the previously unknown values of V for several compounds of various classes have been determined within this error.

The results of the experiments which have been reported are consistent with the concept that ionization in a strong field is a surface-ionization process. The curves of the molecular ion distributions should be parallel, and if the small correction terms in the equations for determining V from the displacement of the ion energy distributions are neglected, it does not matter how V is determined – from the intersection of the linear parts of the charging curve or from the intercept at the retarding-potential axis.

Several schemes for energy analyzers in mass spectrometers involving particle ionization in a strong field are analyzed in ref. 36, where it is shown that the ion energy distributions are distorted least if the energy analyzer is placed directly behind the ion source, rather than near the ion collector.

II. SURFACE IONIZATION OF ORGANIC COMPOUNDS IN WEAK ELECTRIC FIELDS

1. Positive Ions

In recent experimental work on the surface ionization of organic compounds leading to the formation of positive ions an attempt has been made to determine the behavior of the ionization of complex particles, to search for compounds capable of being ionized efficiently, and to make practical use of the ionization of compounds of this type.

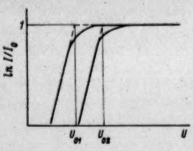

Fig. 8. Displacement of the ion retardation curves for ionization in a strong electric field of particles having ionization potentials V_1 and V_2.

Studies have been made of the composition of the ions produced, the ionization coefficients of particles of various chemical composition, the absolute current densities, the functional dependences of the currents on the temperature, reactions at the emitter surfaces, and monomolecular decay of the ions during their free motion. Surface-ionization methods have been used to determine or estimate the ionization potentials of many radicals.[37]

It has been found that certain compounds are ionized particularly efficiently: compounds of nitrogen, including alkyl-substituted amines[38] and hydrazines,[39] and many cyclic compounds, including alkaloids[40] (the amines are compounds of the type 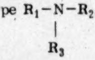 $R_1-\underset{\underset{R_3}{|}}{N}-R_2$, e.g., 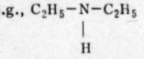 $C_2H_5-\underset{\underset{H}{|}}{N}-C_2H_5$

while the hydrazines are of the type 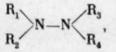 , e.g., 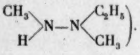).

On the basis of evidence acquired recently we can draw several conclusions.[40] It has been shown that the mass spectra for the surface ionization of compounds of nitrogen contain fewer lines than those corresponding to ionization by electrons, consisting of a set of characteristic lines corresponding to the following species: M^+ (molecular ions); $(M + H)^+$, associative ions (with an attached hydrogen atom); $(M - R_i)^+$, ionized products of the dissociation on the emitter of molecules from which radicals R_i are detached; and $(M - nH)^+$ ions, where n is an odd number.

In an explanation of the mass spectra of the compounds of nitrogen the ion charge can be assumed to be localized at the nitrogen atom; the nitrogen ion is tetravalent because of orbital hybridization; the ions which are formed are primarily those in which the valence bonds of the nitrogen ion are saturated. The bond saturation also determines the course of the particle dissociation at the emitter, and the chemical composition of the product ions can be explained on this basis. The relatively few lines in the mass spectra result from the selectivity of the surface-ionization process, itself a result of the strong functional dependence of the degree of ionization on the ionization potentials of the particles being ionized. Rules are given in ref. 40 for the formation of ions in the surface ionization of organic compounds containing nitrogen; these rules can be used to predict the ion composition in the mass spectra of the surface ionization of these substances. This capability is of practical value in solving several analytic problems.

A study has been made of the surface ionization of the new classes of heteroorganic compounds containing phosphorus and arsenic heteroatoms.[41] It has been shown that the alkyl-substituted phosphines 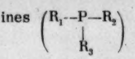 $\left(R_1-\underset{\underset{R_3}{|}}{P}-R_2\right)$ and arsines 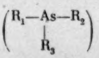 $\left(R_1-\underset{\underset{R_3}{|}}{As}-R_2\right)$ ionize, forming ions of the same type as the amines, but at a vastly lower efficiency, and it has been shown that the intensity distribution among the lines in the mass spectra of these compounds is different than that in the case of the amines. These ionization features are attributed to differences in the orbitals of unshared pairs of nitrogen, phosphorus, and arsenic heteroatoms in the molecules and to the circumstance that phosphorus and arsenic have incomplete d orbitals at relatively low energies, so that they are capable of inversely accepting electrons.

There has been further study of monomolecular decay of ions of complex composition produced in surface ionization as they move freely after desorption from the emitter. The decay results from a statistical redistribution in the freely moving ions of the vibrational energy accumulated over the time they spend at the emitter; it leads to the formation of simpler charged particles and neutral fragments. In contrast with decays of impact ionization by electrons or photons, the decay schemes for polyatomic ions in the case of surface ionization can be mapped out well. It has been shown for the amines that the course of the monomolecular decay of the ions is the same in surface ionization as in impact ionization.[42] Accordingly, a study of the decay of ions formed in surface ionization can facilitate identification of the multistage decay which occurs within ion sources in which ionization is achieved with electrons. Serious experimental difficulties are involved in determining the path of ion decay in ionization chambers. The decay path must be known in order to derive a theory for the impact-ionization mass spectra of polyatomic molecules.

The circumstance that the vibrational-excitation states in equilibrium surface-ionization processes are the same as in nonequilibrium impact-ionization processes implies that the ion decay path is governed by the properties of the ion and is relatively independent of the ionization mechanism. This circumstance was also noted in a comparison of field and impact ionization.

The monomolecular decay of freely moving ions of complex composition obtained by surface ionization can be described by means of the statistical theory of mass spectra.[43-45] Since the ions have a Boltzmann distribution of

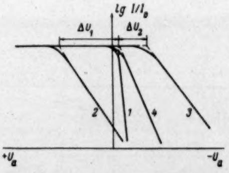

Fig. 9. Retardation curves for the negative ions produced in various processes. 1) Surface ionization; 2) dissociative resonant capture of electrons; 3) conversion of positive ions to negative ions on the emitter; 4) secondary ion–ion emission from the emitter and resonant capture of electrons having a very low energy.

TABLE 1

Substance	Emitters	Primary ions	Secondary ions
Carbon tetrachloride, CCl_4	W	Cl^-	CCl^-, CCl_2^-, C_2^-, CH^-, C_2H^-, etc.
	C	Cl^-	C_n^-, C_nCl^-, C_nH^-, Cl_2^-
Benzene, C_6H_6	W	—	C_2^-, C_2H^-
	C	—	C^-, C_2^-, C_3^- etc.
Acetone, $CO(CH_3)_2$	W	—	C_2^-, C_2H^-
	LaB_6	—	CN^-, C_2^-, C_2H^- background
Silicon tetrachloride, $SiCl_4$	Ta	Cl^-, $SiCl_3^-$, Si^-	$SiCl^-$, Cl_2^-, $SiCl_2^-$
Aniline, $C_6H_5NH_2$	W	CN^-	C_2^-, C_2H^-
	C	CN^-	C_n^-, $C_{(n-1)}N^-$
Bromoform, $HCBr_3$	W	Br^-	C_2^-, C_2H^-, Br_2^-
Chlorobenzene, C_6H_5Cl	W	Cl^-	C_2^-, C_2H^-, Cl_2^-
Pyrrole, C_6NH_5	Ta	CN^-	C_2^-
Thiophene, C_4SH_4	Ta	S^-	C_2^-, C_2H^-
Diethylamine, $C_4H_{11}N$	W	CN^-	C_2^-

initial energies in this case, there is more justification for using the statistical theory to describe the decay than in the case in which the ions are produced as a result of impact ionization. A method for determining the activation energy for the ion decay from the experimental functional dependences of the decay rate on the temperature is proposed in ref. 43 for the simple case of monomolecular decay not involving a change in the particle structure, and a method is proposed in ref. 45 for decay which does involve a change in the ion structure.

2. Negative Ions

According to data in the literature, many organic compounds form molecular and radical negative ions of complex composition through surface ionization. The magnetron surface ionization method has even been used to determine the electron affinities of many molecules and radicals.[46] It turns out that these determinations are erroneous[47] and that negative ions of complex composition generally are not produced in surface ionization. This circumstance can be explained on the basis of the inadequate thermal excitation of electronic states at small values of the electron affinity and on the basis of effective dissociation of the compounds on emitters at the high temperatures required for ionization in the case.

Negative ions are produced in thermionic emission sources in secondary processes not related to surface ionization. These secondary processes begin with the accompanying thermionic emission of electrons by the emitter: in resonant capture of thermionic electrons by free molecules, through conversion at the emitters of the positive ions produced in ionization by electrons, and in secondary emission under the influence of these positive ions.[47] Table 1, from ref. 47, illustrates the situation for several compounds. An explanation of the "origin" of negative ions in surface-ionization experiments requires a special study of the functional dependences of the ion currents and, especially, of the ion energy distributions on the temperature. Figure 9, also from ref. 47, shows the retardation curves for the ions produced in the various processes; we see that the curves corresponding to the different processes are quite different.

Although they do not form ions in surface ionization, many complex organic compounds yield rich mass spectra of negative ions in the bombardment of adsorbed films by positive ions. Apparently, something like a gas-discharge plasma is produced near the impact point in the adsorbed film, since the ion composition of the mass spectra are similar to those of gas-discharge spectra, and the ion energy distributions are not homogeneous and are governed by the complexity of the chemical composition.[48]

Figure 10 shows a negative-ion source, in which the efficiency of the surface ionization of the vapor of a compound can be compared with the efficiencies of ion bombardment and ionization by electrons.[49] The positive ions used for the bombardment are produced in the source through ionization of the vapor of the working material by electrons when the auxiliary cathode is activated. Like an ion-bombardment source, it operates stably over time due to continuous regeneration of the vapor film at the target, held at room temperature, and its service life is governed by the useful lifetime of only a single element – the thermionic cathode. Comparison of the three types of ionization under comparable conditions reveals that the mass spectra of the surface ionization of organic compounds are extremely poor in comparison with those of other types of ionization and that the line intensity in the ion-bombardment case is greater than in the case in which the negative ions are produced through ionization of vapor by electrons.

Finally, we should point out that secondary processes leading to the formation of negative ions also occur in the ionization of atomic fluxes; these processes introduce errors into the determination of the atomic affinities by sur-

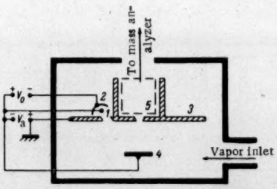

Fig. 10. Ion source designed for comparing the efficiencies at which negative ions are produced in various processes. 1, 2) Thermionic electron source for producing positive ions near electrodes 3 and 4 (4 is a thermionic emitter for producing ions through surface ionization and target for secondary ion emission); 5) Nier source for producing negative ions in resonant electron capture.

face-ionization methods, particularly when the affinities are low. This question is examined in detail in ref. 50.

III. APPLICATIONS OF SURFACE IONIZATION

The traditional applications of surface ionization have been in the production of charged particles, the detection of neutral particles, and in various physicochemical studies.[2] Over the time period with which we are concerned here, each of these fields has expanded significantly.

1. Ion Production

Surface ionization is used to produce atomic ions in order to form plasma, to provide a jet thrust in low-thrust engines, to neutralize electronic space charge (e.g., in thermionic converters), for alloying materials, for isotopic and chemical analysis, to study the elementary interactions between particles and between particles and solid surfaces, and for many other purposes. The variety of applications has lead to a wide variety of ion sources. Recently developed positive-ion sources are distinguished by the use of refractory metals with high work functions (rhenium and iridium) as the emitter material. The (111) Ir face has the highest work function known for a metal, $\varphi \approx 5.8$ V, so that emitters having a (111) working surface are the most efficient emitters for producing positive ions, especially of elements which are not easily ionized. When iridium emitters are used, however, it must be kept in mind that the adsorption of carbon to a surface coverage $\Theta > \Theta_{cr}$ significantly reduces the work function so that such emitters should be used only in evacuated devices not containing traces of hydrocarbon vapor.[51] A source having an iridium emitter has been described for producing ions on elements having ionization potentials Al^+, Ga^+, In^+, Tl^+, and Ba^+ ions at a current density of $j \approx 10 \mu A \cdot cm^{-2}$ (ref. 52). A source of Ba^+ ions having the same current density and using a rhenium emitter has also been reported.[53]

It is now possible to produce Na^+ and Li^+ ions at current densities of up to tens[54] and even hundreds[55] of microamperes per square centimeter.

The most efficient use of material is also achieved in sources of the capillary type, in which the substance to be ionized is passed through narrow channels in the emitter.[56-58] The best examples of this design are sources in which the material to be ionized reaches the emitter surface by diffusion through pores in the emitter.[2,59] Ionization on porous emitters is used in low-thrust ion rockets used to correct the trajectories of space vehicles outside the earth's atmosphere.[2] An effort is still being made to improve the efficiency of ion sources used in low-thrust ion rockets (see, e.g., ref. 60).

Surface ionization in weak and strong electric fields is used to produce polyatomic ions of organic compounds. In the case of weak fields, selective ion sources are used for certain compounds having comparatively low ionization potentials. In the ionization of certain compounds on the oxides of transition metals an ion current density can be reached which is comparable to the current density of the ions of alkali metals in the case of their ionization on tungsten wires.[61] Sources having a strong electric field — "field sources" — are very versatile and are widely used in the mass spectrometry of organic compounds in analytic chemistry. In these sources the emitters are needles, fine wires, knife edges, or arrays of needles of various metals. The applications of field mass spectrometry in analytic chemistry have been discussed most thoroughly in ref. 62.

2. Detection of Neutral Particles

Surface ionization is used to detect atomic fluxes in vacuum in a variety of applications: in determining the thickness of a deposited alkali-metal film, in the development of ion sources for low-thrust rockets for space vehicles having a minimal emission of neutral particles, in the detection atomic and molecular fluxes, in studies of chemical reactions in molecular beams, etc.

The production and use of ultrapure materials requires detection of traces of various elements in the air. There has been a report of the analysis of microimpurities of elements with ionization potentials up to 8 V (there are 56 such elements) in air by means of a mass spectrometer with a surface-ionization ion source, in which the emitter is a rhenium tape.[63]

Important practical problems are the detection of microimpurities in chromatographic analysis of substances and the detection of traces of certain organic compounds in the atmosphere during the production and storage of these substances.

Evacuated surface-ionization detectors can detect fluxes of molecules of many amines and hydrazines at partial pressures of 10^{-13}–10^{-14} torr (ref. 61). The theoretical threshold sensitivity for the detection of these compounds with these detectors is several orders of magnitude better than that of the most sensitive selective detectors.

Further improvements in the sensitivity of detectors intended for detecting traces of compounds in the atmosphere and efforts to simplify the operation of these detectors require that the detector operate, not in vacuum, but directly at atmospheric pressure. Emitters of oxidized tungsten are not suitable for such purposes, so a search has been carried out for materials capable of efficient ionization of organic compounds and suitable for use at atmospheric pressure.[64] The best material found so far is oxidized molybdenum, even though its emission properties gradually become degraded (the emitter becomes "poisoned"). The degradation occurs because the products resulting from the decomposition on the emitter of organic compounds are reduced and a carbon coating is therefore formed. The poisoning of oxidized molybdenum occurs more slowly in air than in vacuum. The poisoning

TABLE 2

Element	s, V	
	SI	PD
Si	1.24±0.02 [67,50]	
Ge	1.14±0.08 [67,50]	
Sn	1.16±0.06 [66,50]	
Pb	1.05±0.08 [66,50]	
Sb	0.90±0.07 [65,50]	
Bi	1.16±0.06 [65,50]	
Cu	1.18±0.06 [66,50]	1.226 ±0.010 [68]
Ag	1.38±0.10 [50]	1.303 ±0.010 [68]
Au	2.34±0.10 [50]	2.3086±0.0007 [69]

can be either reversible or irreversible, depending on the total number of particles supplied to the emitter surface in the detection of compounds having a specified chemical composition. Where the poisoning is reversible, a brief heating of the emitter to a temperature above the working temperature restores the emitter properties; oxygen diffuses from the interior of the oxide to the emitter surface and converts carbon into carbon dioxide, which evaporates from the surface, leaving the surface film oxidized to the original degree.

3. Surface Ionization as a Tool of Physicochemical Research

a) Determination of ionization potentials. We have already mentioned the use of surface ionization in weak and strong electric fields for estimates and precise determinations of the ionization potentials of molecules and radicals of organic compounds. The first experiments on the determination of the ionization potentials for molecules of complex organic compounds through a comparison of the distributions of ions formed on emitters in strong electric fields demonstrated the usefulness of this method. This method, based on a displacement of the energy distributions during surface ionization in strong fields, will probably find a wide variety of future applications. It has already been used for compounds of various classes. Another virtue of this method is that it does not require a complicated procedure, and the results obtained with it are extremely simple to interpret.

b) Determination of the electron affinities of atoms. Determination of the electron affinities of atoms through surface ionization has been extended to atoms with relatively low affinities.[50,65–67] This method has been used as both an absolute method[2] and as a comparison method,[65] in which the reference element is silver. Table 2 illustrates the results. Shown for comparison here are the affinities determined very recently for copper, silver, and gold by photodissociation methods employing laser light sources.[68,69] These methods are highly accurate. We see that the differences in the values of the affinities are of the order of a hundredth of a volt. Although surface-ionization methods are not as accurate as optical methods for determining affinities, their relative simplicity makes them convenient for primarily experimental estimates. They are used where the affinity is $S \geq 1$ V.

c) Studies of particle desorption from solid surfaces. In recent work, desorption characteristics have been determined for various particle–solid combinations by surface-ionization methods or in experiments in which surface ionization is used to detect the desorbed particles.

TABLE 3

Adsorbate	Substrate	Ref.
Cs, K, Na, Li	Mo	[70]
Cs	W (110), (100)	[71]
Cs, K, Na, Li	Si (111)	[72]
F, Cl, Br	Mo	[73]
U	W	[74]
Th, Nb	W	[75]
U	Re	[76]
Ba	Ir (111)	[28]
K, Na, Li	W + O_2	[77]
Ca, Sr, Ba	W + O_2	[78]
CsI	W	[79]

Most of the determinations have been carried out by the modulated-flux method.[28,70–79] Table 3 shows the absorbate–substrate systems which have been studied. We see that the method has been used to study the adsorption of atoms of many metals on the various faces of metal and semiconducting single crystals as well as on metal surfaces covered by films of different particles. It is the first method which has been used to study the desorption characteristics of molecules. The possibilities of this method have by no means been exhausted; in fact they are being realized at an increasing rate.

In a few experiments the desorption kinetics of atoms and ions of alkali metals has been studied by the flash method with the temperature changing as a linear function of the time.[80,81]

A new method which has been proposed for determining desorption characteristics is the constant-coverage method[27] or the "temperature-modulation method." In this method, with a constant particle flux to the emitter, the emitter temperature is changed from T_1 to T_2 so rapidly that the equilibrium surface coverage at T_1 does not manage to change as fast as the temperature. The coverage gradually changes, approaching the equilibrium coverage at T_2, as is observed in the subsequent time dependence of the flux of desorbed particles. If the particle flux ν_1 desorbed at T_1 (these particles are atoms or positive or negative ions) is given by $\nu_1 = N_1 C \exp(-l/kT_1)$, then the flux initially desorbed after an abrupt change from T_1 to T_2 is, by virtue of the conservation of the original surface coverage N_1, $\nu_2 = N_1 C \exp(-l/kT_2)$. It follows from the equations for ν_1 and ν_2 that

$$l = \frac{\ln \frac{\nu_1}{\nu_2}}{\left(\frac{1}{kT_2} - \frac{1}{kT_1}\right)}. \tag{5}$$

In a determination of the heat of vaporization for positive or negative ions the ratio of particle fluxes is replaced by the ratio of the corresponding currents. Tontegode and Yusifov[27] have analyzed the range of applicability of this method (assuming conservation of the coverage at the initial instant following the temperature change) and have shown how to use the method to determine the average time spent by particles on the emitter surface. The isothermal heats of vaporization and average "lifetimes" have been determined experimentally for the adsorption systems Ir (111)–In (ref. 27) and Ir (111)–Ba (ref. 28). This method has the advantages of versatility (it can be used with particles having any charge) and simplicity in the procedure for experimentally determining the desorption characteristics.

Ionov et al.[82] analyzed the method further, showing how it could be used if the initial coverage manages to change during the temperature change. The kinetic characteristics have been determined for the desorption of atoms and ions for 13 lanthanides from tungsten surfaces.[82,83] The heats of vaporization for the lanthaide atoms display a periodic dependence on the atomic number;[83] a study of the reasons for this periodicity would be interesting.

A method based on an analysis of the threshold regions in the functional dependences of the currents on the temperature for various flux densities of the particles being ionized was extended to the determination of the heats of desorption for negative ions.[84] It should be noted that the methods for determining desorption characteristics on the basis of surface ionization are finding increasing use.

d) Study of the emission homogeneity of thermionic emitters. In studies of the emission properties of various faces of single crystals, in studies of the processes occurring on such surfaces, and in many other cases it is important to know the inhomogeneity of the surface with respect to emission. This information is difficult to obtain by thermionic-emission methods alone, especially when the emitter has a high work function. In this latter case a contamination of the surface by foreign particles tends to reduce the value of φ. Under these circumstances, it is being found increasingly useful to combine the surface ionization of elements not readily ionized with a thermionic-emission method to determine the emission inhomogeneity: The emitter is judged homogeneous if the values of φ found by the two emission methods are the same. The reader is referred to refs. 3 and 85-89 for recent examples of the use of surface ionization. This double method is particularly useful in studying the properties of film systems: As mentioned previously, this method easily detects first-order phase transitions in films if these transitions occur at emission temperatures; it reveals the critical coverages and their functional dependence on the substrate temperature, and it reveals the work functions of different phases and the areas which they occupy. This method has been used to study phase transitions in systems formed by carbon on metals of the platinum group.[3,4] Its use to study film systems is just beginning.

e) Study of certain problems of catalysis. We already pointed out that study of the dissociation of molecules on the surface of an emitter covered by foreign particles is one problem in catalysis.

The surface ionization of alkali halide molecules has been used successfully to determine the mechanism for carbon poisoning of platinum-group metals in heterogeneous dissociation reactions. Alkali halide molecules have been selected for study because of the convenience of detecting the alkali metal atoms formed on the emitter surface in the dissociation reactions, through surface ionization. The efficiency with which the molecules dissociate on graphite and on the various carbon phases jointly present on a platinum-group metal after a first-order phase transition in a carbon film has been determined. It has been found that the efficiency of the dissociation on monolithic graphite is lower by a factor of 10 than that of dissociation on metals, that the phase of a two-dimensional adsorbed carbon gas has essentially no effect on the dissociation, and that a condensed carbon phase reduces the dissociation by a factor of 10^3-10^4, depending on the temperature of the substrate metal. The results are illustrated in Figs. 11-13 (from refs. 16, 90). Since the states of the carbon atoms on the surface differ in the degree of saturation of the valence bonds in these cases, it is concluded from the results that the effects of poisons in heterogeneous dissociation reactions on metal catalysis are governed by the type of structure formed on the surface as well as by the chemical composition of the poisons: Only those adsorbates which form structures having a high degree of valence saturation become poisons.[16]

f) Study of carbon diffusion in metals. An interesting application of surface ionization of alkali halide molecules has been in the study of carbon diffusion across the boundary between metal crystals not forming bulk carbides.[91] There have been few experimental studies of particle diffusion across metal boundaries because sensitive methods have not been available for detecting particles on the surface and in the surface layer. The diffusion of carbon is particularly interesting, since carbon is one of the principal impurities in metals. The sensitive detection of carbon on the surfaces of these metals is made possible by a change in the efficiency of the surface ionization of alkali halide molecules on two-dimensional carbon films having the graphite structure.[16] The use of this method for detecting carbon on surfaces has revealed the general features of the "diffusive penetration" of atoms across a metal—gas interface. These features were explained in ref. 92.

g) Temperature measurements by means of retardation curves for the positive ions produced in surface ionization. According to the theory for the retardation curves of ions produced in surface ionization, the slope of the linear region in the range of potentials retarding ions is related to the emitter temperature by $d\ln I/dU = -e/kT$, for ionization on both

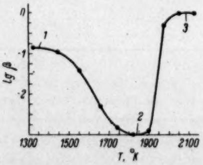

Fig. 11. Changes in the ionization coefficient for CsCl molecules as a dense carbon film deposited beforehand from a carbon filament is evaporated from iridium. 1) Graphite film on iridium; 2) monolayer coverage; 3) Ir surface cleansed of carbon.

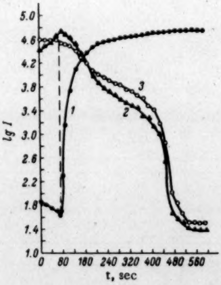

Fig. 12. Changes in the currents during carbon deposition on the (111) Ir face. T = 1685°K. 1) Thermionic electrons; 2) In^+ ions; 3) Cs^+ ions formed during the ionization of CsCl molecules. We see that this current begins to change only after the phase transition occurs in the carbon film.

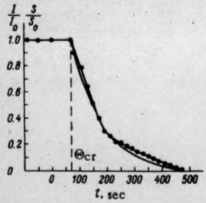

Fig. 13. Changes in the relative areas of the condensed carbon phase on the (111) Ir face during a change in the carbon coverage as a function of the deposition time, calculated from the data in Fig. 12; relative current of Cs^+ ions during ionization of CsCl molecules on this emitter.

homogeneous and inhomogeneous emitters. The ion retardation curves can thus be used to determine emitter temperatures.[2]

The integrated values of the emissivity, ε, and the monochromatic values, ε_λ, are known for many metals and semiconductors, so that there is no particular difficulty in determining their temperatures, but the emissivities for most binary and more complicated systems and the functional dependences of these emissivities on the composition are not known.

Tontegode and Yusifov[93] found that, as carbon diffuses from the surface into the interior of rhodium, bulk phase transitions occur in a surface layer at certain temperatures and lead to a spatial redistribution of the carbon atoms and to the precipitation or dissolution in this layer of microscopic carbon grains. The process is accompanied by changes in ε_λ and ε. Determining T from the retardation curves for Cs^+ ions, Tontegode and Yusifov followed the changes in ε_λ accompanying the phase transition and showed that large changes in ε_λ correspond to relatively low concentrations of carbon dissolved in the surface layer and to a small amount of carbon in the microscopic grains which form. It follows from these experiments that the retardation-curve method can be used successfully to determine the actual temperature of binary and more complicated systems in an effort to determine the spectral characteristics of their emission.

CONCLUSION

The recent papers show that all the traditional fields in surface-ionization research have continued to develop. New results have been obtained in studies of the surface ionization of simple and complicated molecules. The research has led to the development of new applications of the phenomenon of surface ionization.

Modern vacuum techniques, techniques for obtaining perfect single crystals and pure materials, and, especially, the development of new methods for studying the state of surface layers in solids (see, e.g., ref. 94) lay the groundwork for several new studies of fundamental importance. One such study is the determination of the absolute ionization coefficients of atoms, a study which is particularly interesting in the cases of the ionization of atoms having complicated electronic shells and of the ionization of atoms on semiconducting crystals in weak and strong electric fields. The results of this research cannot be predicted; fine details of the phenomena may be revealed, and information may be obtained on the reflection coefficients of particles at the potential barrier near a surface and on the shape of this barrier.

Further study of the surface ionization of molecules of various compositions in weak and strong electric fields would be interesting. We can expect that such research will broaden our understanding of the ionization and adsorption of complex particles and will yield much information about many physicochemical properties of molecules and radicals, about their state in adsorbed films, and about the catalytic properties of various solids with respect to many heterogeneous reactions.

Finally, there is interest in a further development of research in the field of the surface ionization of atoms and molecules on film systems – new emitters for surface ionization. On the basis of the first results in this field we can assume that this research will lead to an understanding of the features of ionization on such emitters and that experiments of this type, combined with other methods for studying surfaces, will yield information on the adsorption of simple and complex particles on film systems. We will also gain more information on the properties of film systems, especially on first-order phase transitions in films.

---

*Based on a report delivered at the 15th All-Union Conference on Emission Electronics, Kiev, December 10-14, 1973.

---

[1] K. H. Kingdon and I. Langmuir, Phys. Rev., 21, 380 (1923).
[2] É. Ya. Zandberg and N. I. Ionov, Surface Ionization [in Russian], Izd. Nauka, Moscow (1969).
[3] É. Ya. Zandberg, A. Ya. Tontegode, and F. K. Yusifov, Zh. Tekh. Fiz., 41, 2420 (1971) [Sov. Phys. – Tech. Phys., 16, 1920 (1972)].
[4] A. Ya. Tontegode and F. K. Yusifov, Zh. Tekh. Fiz., 43, 1049 (1973) [Sov. Phys. – Tech. Phys., 18, 661 (1973)].
[5] V. K. Medvedev, A. G. Naumovets, and A. G. Fedorus, Fiz. Tverd. Tela, 12, 375 (1970) [Sov. Phys. – Solid State, 12, 301 (1970)].
[6] Yu. S. Vedula and A. G. Naumovets, Ukr. Fiz. Zh., 18, 1000 (1973).
[7] V. N. Shrednik, Fiz. Tverd. Tela, 1, 1134 (1959) [Sov. Phys. – Solid State, 1, 1037 (1960)].
[8] V. N. Shrednik, Fiz. Tverd. Tela, 3, 1750 (1961) [Sov. Phys. – Solid State, 3, 1268 (1961)].
[9] V. N. Shrednik and G. A. Odishariya, Izv. Akad. Nauk SSSR, Ser. Fiz., 33, 536 (1969).
[10] G. A. Odishariya and V. N. Shrednik, Dokl. Akad. Nauk SSSR, 182, 542 (1968) [Sov. Phys. – Dokl., 13, 929 (1969)].
[11] V. N. Shrednik and G. A. Odishariya, Fiz. Tverd. Tela, 11, 1844 (1969) [Sov. Phys. – Solid State, 11, 1487 (1970)].
[12] D. W. Basset, Surf. Sci., 23, 140 (1970).
[13] J. R. Arthur and A. Y. Cho, Surf. Sci., 36, 641 (1973).
[14] L. A. Bol'shov, Fiz. Tverd. Tela, 13, 1679 (1971) [Sov. Phys. – Solid State, 13, 1404 (1971)].
[15] L. A. Bol'shov and A. P. Napartovich, Zh. Eksp. Teor. Fiz., 64, 1404 (1973).
[16] É. Ya. Zandberg, A. Ya. Tontegode, and F. K. Yusifov, Zh. Tekh. Fiz., 42, 171 (1972) [Sov. Phys. – Tech. Phys., 17, 134 (1972)].
[17] N. D. Potekhina and A. Ya. Tontegode, Zh. Tekh. Fiz., 42, 162 (1972) [Sov. Phys. – Tech. Phys., 17, 127 (1972)].
[18] É. Ya. Zandberg and A. Ya. Tontegode, Fiz. Tverd. Tela, 14, 2144 (1972) [Sov. Phys. – Solid State, 14, 1850 (1973)].
[19] É. Ya. Zandberg and A. Ya. Tontegode, Abstracts of Reports, Second Seminar on Problems of Work Function and Adsorption, Ryazan (1971), p. 15.
[20] N. I. Ionov, Zh. Tekh. Fiz., 43, 159 (1973) [Sov. Phys. – Tech. Phys., 18, 102 (1973)].
[21] É. Ya. Zandberg, N. D. Potekhina, and A. Ya. Tontegode, Zh. Tekh. Fiz., 42, 2560 (1972) [Sov. Phys. – Tech. Phys., 17, 1989 (1973)].
[22] G. M. Pyatigorskii, Zh. Tekh. Fiz., 35, 1127 (1965) [Sov. Phys. – Tech. Phys., 10, 867 (1965)].
[23] G. M. Pyatigorskii, Zh. Tekh. Fiz., 41, 1723 (1971) [Sov. Phys. – Tech.

Phys., 16, 1358 (1972)].

[24] M. A. Mittsev, Zh. Tekh. Fiz., 44, 1292 (1974) [Sov. Phys. – Tech. Phys., 19, 811 (1974)].

[25] N. D. Potekhina, Zh. Tekh. Fiz., 35, 1658 (1965) [Sov. Phys. – Tech. Phys., 10, 1280 (1966)].

[26] N. D. Potekhina, Zh. Tekh. Fiz., 40, 620 (1970) [Sov. Phys. – Tech. Phys., 15, 479 (1970)].

[27] A. Ya. Tontegode and F. K. Yusifov, Zh. Tekh. Fiz., 41, 1717 (1971) [Sov. Phys. – Tech. Phys., 16, 1353 (1972)].

[28] É. Ya. Zandberg, E. V. Rut'kov, and A. Ya. Tontegode, Zh. Tekh. Fiz., 44, 419 (1974) [Sov. Phys. – Tech. Phys., 19, 261 (1974)].

[29] J. J. Hren and S. Ranganathan (editors), Field-Ion Microscopy, Plenum, New York (1968).

[30] E. W. Müller and T. T. Tsong, Field-Ion Microscopy, American Elsevier, New York (1969).

[31] L. N. Dobretsov, Zh. Tekh. Fiz., 23, 417 (1953).

[32] N. I. Ionov, Zh. Tekh. Fiz., 39, 716 (1969) [Sov. Phys. – Tech. Phys., 14, 538 (1969)].

[33] N. I. Ionov, Zh. Tekh. Fiz., 39, 721 (1969) [Sov. Phys. – Tech. Phys., 14, 542 (1969)].

[34] N. I. Ionov, Zh. Tekh. Fiz., 44, 225 (1974) [Sov. Phys. – Tech. Phys., 19, 146 (1974)].

[35] I. V. Gol'denfel'd, I. Z. Korostyshevekii, B. G. Miskanchuk, and V. A. Pokrovskii, Dokl. Akad. Nauk SSSR, 213, 626 (1973).

[36] I. Z. Korostyshevskii and B. G. Miskanchuk, Prib. Tekh. Eksp., No. 4, 193 (1973).

[37] É. Ya. Zandberg, Proceedings of the First All-Union Conference on Mass Spectrometry (October 20-24, 1969, Leningrad) [in Russian], Izd. Nauka, Leningrad (1972), p. 180.

[38] É. Ya. Zandberg, U. Kh. Rasulev, and M. R. Sharapudinov, Zh. Eksp. Teor. Khim., 7, 363 (1971).

[39] U. Kh. Rasulev, Zh. Organ. Khim., 9, 1573 (1973).

[40] É. Ya. Zandberg and U. Kh. Rasudev, Zh. Teor. Eksp. Khim., 8, 658 (1972).

[41] U. Kh. Rasulev, É. Ya. Zandberg, and G. M. Bogolyubov, Zh. Obshch. Khim., No. 10, 44 (1974).

[42] É. Ya. Zandberg, U. Kh. Rasulev, and Sh. M. Khalikov, Zh. Organ. Khim., 10, 1137 (1974).

[43] N. D. Potekhina, Zh. Teor. Eksp. Khim., 6, 339 (1970).

[44] N. D. Potekhina, Proceedings of the First All-Union Conference on Mass Spectrometry, (October 20-24, 1969, Leningrad) [in Russian], Izd. Nauka, Leningrad (1972), p. 224.

[45] N. D. Potekhina, Zh. Teor. Eksp. Khim., 9, 606 (1973).

[46] F. M. Page and G. G. Goode, Negative Ions and the Magnetron, Wiley–Interscience, New York (1969).

[47] É. Ya. Zandberg and V. I. Paleev, Zh. Tekh. Fiz., 42, 844 (1972) [Sov. Phys. – Tech. Phys., 17, 665 (1972)].

[48] V. I. Paleev and É. Ya. Zandberg, Khim. Vys. Energ. (1974).

[49] V. I. Paleev and É. Ya. Zandberg, Prib. Tekh. Eksp., No. 2, 163 (1974).

[50] É. Ya. Zandberg, A. G. Kamenev, and V. M. Paleev, Zh. Tekh. Fiz., 44, 517 (1974).

[51] É. Ya. Zandberg and A. Ya. Tontegode, Fiz. Tverd. Tela, 12, 1124 (1970) [Sov. Phys. – Solid State, 12, 878 (1970)].

[52] D. M. Jamba, Rev. Sci. Instr., 40, 1072 (1969).

[53] R. K. Feeney, F. M. Bacon, M. T. Elford, and J. W. Hooper, Rev. Sci. Instr., 43, 540 (1972).

[54] F. Bernhard and H. Kerkow, Exp. Tech. Phys., 21, 317 (1973).

[55] H. D. Daley and J. Perel, Rev. Sci. Instr., 42, 1324 (1971).

[56] L. N. Gall', R. N. Gall', V. A. Lednev, and L. K. Veselova, Zh. Tekh. Fiz., 40, 1534 (1970) [Sov. Phys. – Tech. Phys., 15, 1185 (1971)].

[57] M. Remy and R. Haug, Rev. Sci. Instr., 41, 650 (1970).

[58] A. S. Avakov, S. F. Belykh, V. V. Evstifeev, and R. N. Evtukhov, Prib. Tekh. Eksp., No. 4, 33 (1974).

[59] N. I. Ionov, "Surface ionization and its applications," in: Progress in Surface Science, Vol. 1, Pergamon Press, New York (1972), p. 3.

[60] G. E. Le and L. Jean, J. Spacecraft and Rockets, 10, No. 2, 113 (1973).

[61] É. Ya. Zandberg and U. Kh. Rasulev, Zh. Anal. Khim., 27, 2459 (1972).

[62] H. D. Beckey, Field Ionization Mass-Spectrometry, Pergamon Press, New York (1971).

[63] W. D. Davis, J. Vac. Sci. and Technol., 10, 278 (1973).

[64] É. Ya. Zandberg, U. Kh. Rasulev, and Sh. M. Khalikov, Abstracts of Reports, 15th All-Union Conference on Emission Electronics, December 10-14, 1973, Kiev, p. 62.

[65] É. Ya. Zandberg and V. I. Paleev, Dokl. Akad. Nauk SSSR, 190, 562 (1970) [Sov. Phys. – Dokl., 15, 52 (1970)].

[66] É. Ya. Zandberg, A. G. Kamenev, and V. I. Paleev, Zh. Tekh. Fiz., 41, 1057 (1971) [Sov. Phys. – Tech. Phys., 16, 832 (1971)].

[67] É. Ya. Zandberg, A. G. Kamenev, and V. I. Paleev, Zh. Tekh. Fiz., 41, 1983 (1971) [Sov. Phys. – Tech. Phys., 16, 1567 (1972)].

[68] H. Hofop, R. A. Bennet, and W. C. Lineberger, J. Chem. Phys., 58, 2373 (1973).

[69] H. Hofop and W. C. Lineberger, J. Chem. Phys., 58, 2379 (1973).

[70] M. D. Scheer, R. Klein, and J. D. McKinley, J. Chem. Phys., 55, 3577 (1971).

[71] T. J. Lee and R. E. Stickney, Surf. Sci., 32, 100 (1972).

[72] É. F. Chaikovskii and L. I. Kaisheva, Zh. Tekh. Fiz., 42, 1315 (1972) [Sov. Phys. – Tech. Phys., 17, 1043 (1972)].

[73] M. D. Scheer, R. Klein, and J. D. McKinley, Surf. Sci., 30, 251 (1972).

[74] D. H. Smith, J. Chem. Phys., 53, 299 (1971).

[75] D. H. Smith, A. E. Kameron, and J. A. Dean, J. Chem. Phys., 54, 170 (1971).

[76] D. H. Smith, J. Chem. Phys., 55, 4152 (1971).

[77] H. D. Daley, A. Y. Yahíku, and J. Perel, J. Chem. Phys., 52, 3577 (1970).

[78] R. Müller and H. W. Wassmuth, Surf. Sci., 34, 249 (1973).

[79] B. Ya. Kolesnikov, A. M. Kolchin, and G. M. Panchenkov, Zh. Tekh. Fiz., 40, 868 (1970) [Sov. Phys. – Tech. Phys., 15, 673 (1970)].

[80] E. K. Stefanakos and A. A. Fald, Surf. Sci., 28, 221 (1971).

[81] R. V. Hill, E. K. Stefanakos, and R. F. Tinder, J. Appl. Phys., 43, 1976 (1972).

[82] N. I. Ionov, Ts. S. Marinova, and B. V. Yakshinskii, Fiz. Tverd. Tela, 14, 3181 (1972) [Sov. Phys. – Solid State, 14, 2717 (1973)].

[83] B. K. Medvedev, N. I. Ionov, and Yu. I. Belyakov, Fiz. Tverd. Tela, 15, 2620 (1973) [Sov. Phys. – Solid State, 15, 1743 (1974)].

[84] É. F. Chaikovskii, L. G. Mel'nik, and G. M. Pyatigorskii, Single Crystals and Technology (Khar'kov) [in Russian], No. 1 (1970).

[85] R. Müller, W. Walcher, and H. W. Wassmuth, Z. Naturforsch., 27a, 794 (1972).

[86] L. I. Kaisheva, Fiz. Tverd. Tela., 14, 2438 (1972) [Sov. Phys. – Solid State, 14, 2108 (1973)].

[87] N. G. Imangulova and E. P. Sytaya, Izv. Akad. Nauk UzSSR, Ser. Fiz. Mat., No. 2, 45 (1973).

[88] K. Zh. Zhanabergenov, N. G. Imangulova, and E. P. Sytaya, in: Structure and Properties of Refractory-Metal Single Crystals, ed. by E. M. Savitskii [in Russian], Izd. Nauka, Moscow (1973), p. 207.

[89] K. Zh. Zhanabergenov and E. P. Sytaya, Izv. Vuz. Fiz., No. 6 (1970).

[90] A. Ya. Tontegode and É. Ya. Zandberg, Zh. Tekh. Fiz., 40, 626 (1970) [Sov. Phys. – Tech. Phys., 15, 483 (1970)].

[91] A. Ya. Tontegode and F. K. Yusifov, Zh. Tekh. Fiz., 43, 1049 (1973) [Sov. Phys. – Tech. Phys., 18, 661 (1973)].

[92] A. Ya. Tontegode, Zh. Tekh. Fiz., 43, 1042 (1973) [Sov. Phys. – Tech. Phys., 18, 657 (1973)].

[93] A. Ya. Tontegode and F. K. Yusifov, Zh. Tekh. Fiz., 43, 1105 (1973) [Sov. Phys. – Tech. Phys., 18, 708 (1973)].

[94] C. B. Duke and R. L. Park, Physics Today 25(8), 23 (1972).

Plasma

Transverse-current plasma instability

D. G. Lominadze and V. L. Sizonenko

(Submitted November 22, 1973)
Zh. Tekh. Fiz., 44, 1829-1838 (September 1974)

The stability of a low-β plasma with a current perpendicular to the magnetic field is analyzed. Ion-acoustic waves that propagate across the magnetic field have a high excitation threshold and are not excited if the magnetic field is large when the directed velocity u is lower than the electron thermal velocity v_{Te}. Electron cyclotron waves for $u \sim v_{Te}$ and the Buneman instability $u \gg v_{Te}$ are analyzed.

INTRODUCTION

Instabilities and turbulence in a plasma with an electric current perpendicular to the magnetic field play an important role in many plasma experiments (in θ pinches, in the propagation of large-amplitude waves in a plasma, in plasma formations interacting with magnetic field, in plasma guns, etc.) and in plasmas of astrophysical interest. Many theoretical and experimental papers have appeared on these topics in recent years (see refs. 1, 2 and the cited literature).

In this paper we are concerned with instabilities of this type for the case of a low-β plasma in which the waves propagate across the magnetic field. We find that ion-acoustic waves have a high excitation threshold in this case and that they are not excited in a strong magnetic field provided that the relative velocity of the electrons and ions **u** is lower than the electron thermal velocity v_{Te}. We analyze the excitation of electron cyclotron waves when $u \sim v_{Te}$ and the Buneman instability when $u \gg v_{Te}$. In addition to the hydrodynamic Buneman instability there are kinetic instabilities with the same growth rate as the hydrodynamic instability.

1. DISPERSION RELATION

In this section we derive the dispersion relation for a plasma with a transverse current for extraordinary electromagnetic waves that propagate across the magnetic field. Taking account of the small inhomogeneities in the temperature, density, and equilibrium magnetic field, and adopting the local approximation, we write this relation as[3]

$$\varepsilon_{00}\left(\varepsilon_{22}-\frac{k^2c^2}{\omega^2}\right)+\varepsilon_{02}^2=0. \qquad (1.1)$$

In this case, in which the growth rate is much larger than the ion gyrofrequency and the wavelength is much smaller than the ion Larmor radius, we can assume the ions to be unmagnetized. Then the ions contribute to the longitudinal dielectric constant only

$$\varepsilon_{00}=\varepsilon_{00}^{(i)}+\varepsilon_{00}^{(e)}+1, \qquad (1.2)$$

where

$$\varepsilon_{00}^{(i)}=\frac{\omega_{pi}^2}{k^2v_{Ti}^2}\left[1+i\sqrt{\pi}z_iW(z_i)\right],$$

and

$$\omega_{pi}=\left(\frac{4\pi n_0e^2}{m_i}\right)^{1/2}, \quad v_{Ti}=\left(\frac{T_i}{m_i}\right)^{1/2},$$

$$W(z)=e^{-z^2}\left(1+\frac{2i}{\sqrt{\pi}}\int_0^z e^{t^2}dt\right), \quad z_i=\frac{\omega-\mathbf{ku}}{\sqrt{2}kv_{Ti}}.$$

The other components of the tensor ε_{ij} are given by Mikhailovskii:[3]

$$\left.\begin{aligned}\varepsilon_{00}^{(e)}&=\frac{\omega_{pe}^2}{k^2v_{Te}^2}\left[1-\frac{\omega}{n_0}\hat{l}\sum_{n=-\infty}^{\infty}\int d\mathbf{v}f_eJ_n^2(a)\zeta_n\right],\\ \varepsilon_{22}&=1-\frac{\omega_{pe}^2}{n_0\omega v_{Te}^2}\hat{l}\sum_{n=-\infty}^{\infty}\int d\mathbf{v}v_\perp^2f_e[J_n'(a)]^2\zeta_n,\\ \varepsilon_{02}&=-i\frac{\omega_{pe}^2}{n_0kv_{Te}^2}\hat{l}\sum_{n=-\infty}^{\infty}\int d\mathbf{v}v_\perp f_eJ_n(a)J_n'(a)\zeta_n,\end{aligned}\right\} \qquad (1.3)$$

where

$$\hat{l}=1+\frac{k_xv_{Te}^2}{\omega\omega_{He}}\left(\frac{\partial n_0}{\partial y}\frac{\partial}{\partial n_0}+\frac{\partial T_e}{\partial y}\frac{\partial}{\partial T_e}\right),$$

$$a=\frac{kv_\perp}{\omega_{He}}, \quad \zeta_n=\left(\omega-n\omega_{He}+\frac{k_x\varkappa_Hv_\perp^2}{2\omega_{He}}\right)^{-1}, \quad \varkappa_H=\frac{1}{H_0}\frac{\partial H_0}{\partial y},$$

$$\omega_{pe}^2=\left(\frac{4\pi n_0e^2}{m_e}\right), \quad \omega_{He}=\frac{eH_0}{m_ec}, \quad v_{Te}=\left(\frac{T_e}{m_e}\right)^{1/2}.$$

Here ω and **k** are the frequency and wave vector, n_0 is the plasma density, J_n is the Bessel function, and **u** is the directed velocity along the x axis. In the absence of a current the equilibrium distribution functions of the plasma ions and electrons are assumed to be Maxwellian distributions, and the density, temperature, and magnetic field are assumed to be slowly varying functions of the y coordinate. The magnetic field is parallel to the axis.

Writing (1.3) in terms of single integrals, we find sums of the type

$$Q_1\equiv\sum_{n=-\infty}^{\infty}\int d\mathbf{v}f_eJ_n^2(a)\zeta_n.$$

Using

$$\frac{1}{\omega-n\omega_{He}+bv_\perp^2}\equiv-i\int_0^\infty d\xi\exp\left[i\xi(\omega-n\omega_{He}+bv_\perp^2)\right], \qquad (1.4)$$

where $b\equiv k_x\varkappa_H/2\omega_{He}$, and where convergence of the integral as $\xi\to\infty$ is ensured by Im $\omega > 0$, we find

$$Q_1=-i\sum_{n=-\infty}^{\infty}\int_0^\infty d\xi e^{i(\omega-n\omega_{He})\xi}\frac{n_0}{v_{Te}^2}\int_0^\infty dv_\perp v_\perp J_n^2(a)e^{-\frac{v_\perp^2}{2v_{Te}^2}+ib\xi v_{Te}^2}$$

$$=-in_0\sum_{n=-\infty}^{\infty}\int_0^\infty d\xi e^{i(\omega-n\omega_{He})\xi}Ae^{-\mu A}I_n(\mu A),$$

where $A\equiv(1-2ib\xi v_{Te}^2)^{-1}$, $\mu\equiv(kv_{Te}/\omega_{He})^2$, and I_n is the modified Bessel function. Then, using

$$\sum_{n=-\infty}^{\infty}e^{-in\omega_{He}\xi}I_n(z)=e^{z\cos(\omega_{He}\xi)},$$

we write Q_1 as

$$Q_1 = -\frac{in_0}{|\omega_{He}|}\int\limits_0^\infty d\varphi e^{i\frac{\omega}{|\omega_{He}|}\varphi + \frac{\mu(\cos\varphi - 1)}{(1-i\rho\varphi)}} \frac{1}{1-i\rho\varphi}, \qquad (1.5)$$

where $\rho = k_x \varkappa_H v_{Te}^2 / |\omega_{He}| \omega_{He}$. We now introduce the function

$$R(p) = \int\limits_0^\infty d\varphi e^{i\frac{\omega}{|\omega_{He}|}\varphi - \frac{\mu(1-\cos\varphi)}{1-i\rho\varphi}} \frac{1}{p - i\rho\varphi} \qquad (1.6)$$

and its derivatives at p = 1:

$$R_n = \frac{d^n R(p)}{dp^n}\bigg|_{p=1} \quad (n = 0,\ 1,\ 2,\ \ldots). \qquad (1.7)$$

We then find

$$Q_1 = -\frac{in_0}{|\omega_{He}|} R_0. \qquad (1.8)$$

Using (1.4) in

$$Q_2 \equiv \sum_{n=-\infty}^{\infty} \int d\mathbf{v} v_\perp^2 f_e [J_n'(a)]^2 \zeta_n$$

and integrating over $v_\perp$ as above, we find

$$Q_2 = \frac{in_0|\omega_{He}|}{k^2}\left\{ i\frac{\omega}{|\omega_{He}|} - \left(\frac{\omega}{\omega_{He}}\right)^2 R_0 + 2i\mu^2\frac{dR_1}{d\mu} + \rho\left[i(1-2\mu) + 2\frac{\omega}{|\omega_{He}|}R_1 + \frac{\omega}{|\omega_{He}|}\mu R_2\right] - \rho^2\left[R_2 + \frac{2}{3}\mu R_3 + \frac{1}{24}\mu^2 R_4\right]\right\}. \qquad (1.9)$$

Similarly, for

$$Q_3 \equiv \sum_{n=-\infty}^{\infty} \int d\mathbf{v} v_\perp f_e J_n(a) J_n'(a) \zeta_n$$

we find

$$Q_3 = \frac{in_0}{k}\mu\frac{dR_0}{d\mu}. \qquad (1.10)$$

Now substituting (1.8)-(1.10) into the components of the tensor ε_{ij}, and neglecting unity in comparison with k^2c^2/ω^2, we rewrite dispersion relation (1.1) as

$$\left[1 + k^2\lambda_D^2 + \frac{T_e}{T_i}(1 + i\sqrt{\pi}z_i W(z_i)) + i\frac{\omega}{n_0|\omega_{He}|}\hat{l}n_0R_0\right] \times \left[\frac{|\omega_{He}|}{\omega}\frac{1}{n_0}\hat{l}n_0 S + \frac{\omega_{He}^2}{\omega^2}\frac{\mu^2}{\beta_e}\right] = \left(\frac{1}{n_0}\hat{l}n_0\mu\frac{dR_0}{d\mu}\right)^2, \qquad (1.11)$$

where

$$S \equiv -2\mu^2\frac{dR_1}{d\mu} - \frac{\omega}{|\omega_{He}|} - i\left(\frac{\omega}{\omega_{He}}\right)^2 R_0 + \rho\left(2\mu - 1 + 2i\frac{\omega}{|\omega_{He}|}R_1 + i\frac{\omega}{|\omega_{He}|}R_2\mu\right) - i\rho^2\left(R_2 + \frac{2}{3}\mu R_3 + \frac{1}{24}\mu^2 R_4\right),$$

where $\lambda_D = (v_{Te}/\omega_{pe})$ and $\beta_e = 4\pi n_0 T_e/H_0^2$.

Using

$$\varkappa_n = \frac{4\pi e n_0 u}{cH_0}, \qquad (1.12)$$

which follows from the Maxwell equation curl H = 4π/cj, we see that in a plasma with a low electron pressure ($\mu^2/\beta_e \gg 1$) the principal contribution to Eq. (1.11) comes from the terms due to the electrostatic part of the electric field of the waves. In this case Eq. (1.12) becomes $\varepsilon_{00} = 0$ or

$$1 + k^2\lambda_D^2 + \frac{T_e}{T_i}(1 + i\sqrt{\pi}z_i W(z_i)) + i\frac{\omega}{n_0|\omega_{He}|}\hat{l}n_0R_0 = 0. \qquad (1.13)$$

This equation is analyzed in refs. 5 and 6 in a study of the excitation of electron cyclotron waves.

In the case of a high directed velocity ($u \sim v_{Te}$) and finite electron pressure ($\beta_e \sim 1$), Eq. (1.13) cannot be used to describe the excitation of these waves; instead we must use Eq. (1.11), in which the nonelectrostatic terms play an important role.

2. ION-ACOUSTIC INSTABILITIES IN A LOW-β PLASMA

In a low-β plasma ($\beta_e \ll 1$) with cold ions and hot electrons ($T_e \gg T_i$), electron cyclotron and ion-acoustic waves are known to be excited when $u \ll v_{Te}$. Although such instabilities have received considerable attention,[1,2,7] the effect of magnetization of the electrons on the growth of ion-acoustic waves propagating across the magnetic field has not been fully resolved. We show below that the ion-acoustic instability occurs when $u < v_{Te}$ only at sufficiently high directed velocities, $u > u_{cr} \sim v_{Te}\omega_{He}/\omega_{pi}$. Accordingly, in a plasma in a strong magnetic field, in which $\omega_{He} > \omega_{pi}$ at $u < v_{Te}$, the ion-acoustic instability does not occur. The characteristic wavelength of the ion-acoustic waves is known to be of the order of λ_D ($k\lambda_D \sim 1$); hence, when $\omega_{pe} \gg \omega_{He}$ we have $kv_{Te} \sim \omega_{pe} \gg \omega_{He}$. Since the growth rate of the ion-acoustic instability γ is of order $\gamma \sim \omega_{pi}(u/v_{Te})$ (ref. 1), the condition $\gamma \gg \omega_{He}$ may not hold, so that the effect of a magnetic field on the instability should be taken into account. If the wave vector has a nonvanishing component along the magnetic field ($k_z \neq 0$), the function R_0 (for $\beta_e \sim \rho \to 0$), would be

$$R_0 = \int\limits_0^\infty d\varphi e^{i\frac{\omega}{|\omega_{He}|}\varphi - \frac{k_\perp^2 v_{Te}^2}{\omega_{He}^2}(1-\cos\varphi) - \frac{k_z^2 v_{Te}^2}{2\omega_{He}^2}\varphi^2}. \qquad (2.1)$$

In this case, with $k_z \gtrsim \omega_{He}/v_{Te}$, the integral converges as $\varphi \to \infty$ because of the terms containing k_z. Furthermore, in the integration over φ by the method of steepest descent (since $k^2v_{Te}^2/\omega_{He}^2 \gg 1$), account need be taken of only the contribution of the region $\varphi \lesssim \omega_{He}/k_\perp v_{Te} \ll 1$, since the integrals near other points $\varphi \simeq 2n\pi$ are exponentially small. In this case we have

$$R_0 \doteq \sqrt{\frac{\pi}{2}}\frac{|\omega_{He}|}{k_\perp v_{Te}} W(z_e), \quad z_e = \frac{\omega}{\sqrt{2}kv_{Te}}$$

and the electrons are unmagnetized. Accordingly, the magnetic field only affects waves with $k_z \ll \omega_{He}/v_{Te}$. Then, neglecting terms containing k_z, we can convert the function R(p) (for $\beta_e \sim \rho \to 0$) to the form[8]

$$R(p) = \left(\frac{\pi}{2}\right)^{1/2}\frac{1}{p}\frac{|\omega_{He}|}{k_\perp v_{Te}}\left[\frac{\xi+1}{\xi-1}e^{-z_e^2} + \frac{2i}{\sqrt{\pi}}e^{-z_e^2}\int\limits_0^{z_e} e^{t^2}dt\right], \qquad (2.2)$$

where $\xi = \exp(-2\pi i\omega/|\omega_{He}|)$.

Below we call those waves for which ω is not approximately equal to $n\omega_{He}$ "ion-acoustic," and we call those for which we have $\omega \approx n\omega_{He}$ "electron cyclotron." Assuming $\mathrm{Re}\,\omega \sim \omega_{pi} > |\omega_{He}|$ and using the condition $z_e \sim u/v_{Te} \ll 1$ for ion sound, we find

$$R(p) = \frac{1}{p}\sqrt{\frac{\pi}{2}}\frac{|\omega_{He}|}{kv_{Te}}\frac{\eta^2 - 1 + 2i\eta\sin\psi}{\eta^2 + 1 - 2\eta\cos\psi}, \qquad (2.3)$$

where

$$\eta \equiv \exp\left(2\pi\frac{\gamma}{|\omega_{He}|}\right), \quad \psi \equiv 2\pi\frac{\mathrm{Re}\,\omega}{|\omega_{He}|} \geqslant 2\pi.$$

Now substituting (2.3) into (1.13) and neglecting (for simplicity) the inhomogeneity of the density and temperature, we find the following dispersion relation for the ion-acoustic waves:

$$1-\frac{\omega_{pi}^2}{(\omega-\mathbf{ku})^2}+\frac{\omega_{pe}^2}{k^2v_{Te}^2}\left(1+i\sqrt{\pi}z_e\frac{\eta^2-1}{\eta^2+1-2\eta\cos\psi}\right)=0. \quad (2.4)$$

From (2.4) we find the wave frequency,

$$\operatorname{Re}\omega=\mathbf{ku}+\omega_s,\quad \omega_s=\frac{kv_s}{\sqrt{1+k^2\lambda_D^2}},$$

and an equation for the growth rate,

$$F(b)\equiv b\frac{e^{2b}+1-2e^b\cos\psi}{e^{2b}-1}=-\sqrt{\frac{\pi^3}{2}\frac{m_e}{m_i}}\frac{(\mathbf{ku}+\omega_s)}{|\omega_{He}|(1+k^2\lambda_D^2)^{3/2}}, \quad (2.5)$$

where $b \equiv 2\pi(\gamma/|\omega_{He}|)$.

The function F(b) is given in the asymptotic limit $|b| \gg 1$ by $F(b) \approx |b|$; it reaches a minimum at $b = 0$, and near the origin it is given approximately by

$$F(b)\approx 1-\cos\psi+\frac{b^2}{3}\left(1+\frac{\cos\psi}{2}\right).$$

Accordingly, when

$$-\sqrt{\frac{\pi^3}{2}\frac{m_e}{m_i}}\frac{(\mathbf{ku}+\omega_s)}{|\omega_{He}|(1+k^2\lambda_D^2)^{3/2}}\gg 1$$

the growth rate becomes the same as in an unmagnetized plasma, and when

$$-\sqrt{\frac{\pi^3}{2}\frac{m_e}{m_i}}\frac{(\mathbf{ku}+\omega_s)}{|\omega_{He}|(1+k^2\lambda_D^2)^{3/2}}\leqslant 1-\cos\psi \quad (2.6)$$

the unstable solutions vanish.

Accordingly, when $k_z \ll |\omega_{He}|/v_{Te}$ the ion-acoustic instability exists only when $u > u_{cr}$. The threshold current velocity u_{cr} can be evaluated for the case $u_{cr} \gg v_s$ in the following manner: Setting $\mathbf{ku} = -ku$ and requiring that the equation in (2.6) hold,

$$\sqrt{\frac{\pi^3}{3}\frac{m_e}{m_i}}\frac{u}{v_{Te}}\frac{\omega_{pe}}{|\omega_{He}|}\frac{k\lambda_D}{(1+k^2\lambda_D^2)^{3/2}}=1-\cos\psi, \quad (2.7)$$

using $1-\cos\psi \sim 1$, and choosing the maximum value of the quantity $k\lambda_D(1+k^2\lambda_D^2)^{-3/2}=2/3\sqrt{3}$, we find that u_{cr} is of order

$$u_{cr}\simeq v_{Te}\frac{|\omega_{He}|}{\omega_{pi}}<v_{Te}. \quad (2.8)$$

In a stronger magnetic field, with $\omega_{pi} \ll |\omega_{He}|$, we have $2\pi\omega/|\omega_{He}| \ll 1$ and $R(p) \simeq i\omega_{He}^2/\sqrt{2\pi}pkv_{Te}\omega$, so that Eq. (1.13) becomes

$$1-\frac{\omega_{pi}^2}{(\omega-\mathbf{ku})^2}+\frac{\omega_{pe}^2}{k^2v_{Te}^2}\left\{1-\frac{|\omega_{He}|}{\sqrt{2\pi}kv_{Te}}\right\}=0,$$

and there is no instability.

Accordingly, in a plasma with $\omega_{pi} < |\omega_{He}|$ the ion-acoustic waves are stable, and only electron cyclotron waves can be excited.

3. EXCITATION OF ELECTRON CYCLOTRON WAVES IN THE CASE $\mathbf{u} \sim v_{Te}$ AND $\beta_e \ll 1$

We turn now to the excitation of electron cyclotron waves in a low-β plasma in which the current velocity is the order of the electron thermal velocity. Using the condition $\omega \sim ku \sim \omega_{He}$ we find that the wavelength of these waves is of the order of the electron Larmor radius $k\rho_e \sim 1$. Over the wavelength range $k \sim (\omega_{He}/v_{Te})$ the natural frequencies of the waves in this case are not close to $n\omega_{He}$ (where n is an integer) (see e.g., ref. 9). In a plasma without a current the ion terms are unimportant because of the inequalities

$$z_i\sim\frac{\omega_{He}}{kv_{Ti}}\sim\frac{v_{Te}}{v_{Ti}}\gg 1,\quad \frac{\omega_{pi}^2}{\omega^2}\sim\frac{\omega_{pi}^2}{\omega_{He}^2}\ll\frac{\omega_{pe}^2}{k^2v_{Te}^2}.$$

When there is a current the ion terms are important when the natural frequency of the electron cyclotron waves, $\omega = \omega(k)$, intersects the beam branch $\omega = \mathbf{ku}$. Since the ion terms appear only in ε_{00}, dispersion relation (1.1) should be written

$$\frac{\omega_{pi}^2}{k^2v_{Ti}^2}[1+i\sqrt{\pi}z_iW(z_i)]=\frac{\varepsilon_{02}^2}{\left(\frac{kc}{\omega}\right)^2-\varepsilon_{22}}-\varepsilon_{00}^{(e)}-1. \quad (3.1)$$

Equating to zero the right-hand side of Eq. (3.1), and neglecting terms containing $\varkappa_n$, $\varkappa_T$, and $\varkappa_H$, we find the dispersion relation studied previously (see ref. 9 and the literature cited there). Neglecting the nonelectrostatic terms, other workers have studied Eq. (3.1) in detail for the case $u \ll v_{Te}$ (see, e.g., ref. 7 and the literature cited there). The growth rate is found in ref. 10 for the case $u \sim v_{Te}$ in certain limiting approximations.

Now assuming that the wave frequency is approximately equal to $\omega(k)$ when the ion terms are taken into account, and expanding the right-hand side of (3.1) in the small parameter $\omega-\omega(k)$, we can replace (3.1) by the dispersion relation

$$D(\omega-\omega(k))+\frac{\omega_{pi}^2}{k^2v_{Ti}^2}[1+i\sqrt{\pi}z_iW(z_i)]=0, \quad (3.2)$$

where

$$D\equiv\frac{\partial}{\partial\omega}\left\{1+\varepsilon_{00}^{(e)}-\frac{\varepsilon_{02}^2}{(kc/\omega)^2-\varepsilon_{22}}\right\}\Big|_{\omega=\omega(k)}.$$

It follows from Eq. (1.11) that with $\beta_e \ll 1$, $\mu \sim 1$, and $\omega \sim \omega_{He}$ the nonelectrostatic terms are smaller than the electrostatic terms by a factor of $1/\beta_e$. Also noting that $k_\perp v_{Te}^2\varkappa_{n, T}/\omega\omega_{He} \sim \varkappa_{n, T}v_{Te}/\omega_{He} \ll 1$ and $k_\perp v_{Te}^2\varkappa_H \cdot (\omega\omega_{He})^{-1} \sim \beta_e \ll 1$, we find that we can in fact neglect in the ε_{ij} components those terms having $\varkappa_n$, $\varkappa_T$, and $\varkappa_H$, and we can set $\hat{I} = 1$. It is not difficult to see that in this case

$$D\approx\frac{\omega_{pe}^2}{k^2v_{Te}^2|\omega_{He}|}D_0,$$

where

$$D_0\equiv i\left\{\frac{\partial}{\partial\omega}\omega R_0(\omega)\right\}_{\omega=\omega(k)}\sim 1.$$

Equation (3.2) can now be rewritten as

$$z_i-z_0+\eta[1+i\sqrt{\pi}z_iW(z_i)]=0, \quad (3.3)$$

where

$$z_0\equiv\frac{\omega(k)-\mathbf{ku}}{\sqrt{2}kv_{Ti}},\quad \eta\equiv\frac{T_e}{T_i}\frac{|\omega_{He}|}{\sqrt{2}kv_{Ti}D_0}.$$

With $z_0 = 0$, Eq. (3.3) is the same as the equation given in ref. 11. With $\eta = 1$ and $z_0 = 0$ we have $z_i = -0.46 + i0.36$; with $|\eta| \leq 1$ and $|z_0| \leq 1$ Eq. (3.3) has an unstable solution with $\operatorname{Re} z_i \sim \operatorname{Im} z_i \sim 1$.

In the case $T_e/T_i \lesssim (m_e/m_i)^{1/3}$, $|z_0| \lesssim 1$, the electron cyclotron waves thus interact resonantly with the ions and the growth rate is given in order of magnitude by

$$\gamma \sim \left(\frac{T_i}{T_e}\omega_{He}\omega_{Hi}\right)^{1/2}. \tag{3.4}$$

We note that in a plasma having $T_i \gg T_e$ growth rate (3.4) can be much larger than $(\omega_{He}\,\omega_{Hi})^{1/2}$, so that these instabilities can play an important role in energy dissipation at the front of a collisionless shock wave.

In the case $(T_e/T_i) \gg (m_e/m_i)^{1/3}$ we find $|\eta| \gg 1$, so that Eq. (3.3) is satisfied only for $|z_i| \gg 1$. Then at $z_0 = 0$ we find the cubic equation $z_i^3 = (\eta/2)$, from which we can easily find the growth rate for the waves:

$$\gamma = \left(\frac{3}{2}\right)^{1/2}\left(\frac{\eta}{2}\right)^{1/3} kv_{Ti} \sim |D_0|^{-1/3}\left(\frac{m_e}{m_i}\right)^{1/3}|\omega_{He}|. \tag{3.5}$$

If the growth rates in (3.4) and (3.5) are smaller than the corresponding growth rates for electron cyclotron waves found in the case $u \ll v_{Te}$ (ref. 7), then with a large current velocity, $v \sim v_{Te}$, it is primarily waves whose wave vector $\mathbf{k}$ is nearly perpendicular to current velocity $\mathbf{u}$ which should be excited. Setting $\mathbf{ku} = k_x u = ku_{\text{eff}}$ ($u_{\text{eff}} \ll u_{Te}$), we can make u_{eff} quite small and convert to the case of the excitation of electron cyclotron waves, which have the largest growth rate.

If, on the other hand, the growth rates in (3.4) and (3.5) are larger than the corresponding growth rates for electron cyclotron waves, it would be primarily waves propagating along the current which are excited, at a wavelength on the order of the electron Larmor radius. We note that the excitation of electron cyclotron waves by an ion beam moving across a magnetic field in a plasma has been detected experimentally.[12]

4. BUNEMAN INSTABILITY IN A LOW-β PLASMA

We turn now to the excitation of waves in the case $u \gg v_{Te}$ and $\beta \ll 1$. The instability of the Buneman type was analyzed in refs. 13-16, where account is taken of the inhomogeneity of the plasma density in the presence of a longitudinal current, as in this section; for the case of magnetized electrons ($\omega \ll \omega_{He}$, $kv_{Te} \ll \omega_{He}$) with a transverse current it is analyzed in ref. 17 (see also ref. 18). The Buneman instability occurs when $|\mathbf{ku}| \lesssim \omega_{pe}$; in order-of-magnitude terms

$$\rho = \beta_e \ll 1,\ \mu \sim \frac{v_{Te}^2}{\omega_{He}^2}\frac{\omega_{pe}^2}{u^2}\left(\frac{k_\perp}{k_x}\right)^2,$$

$$\frac{k_x v_{Te}^2 \varkappa_{n,T}}{\omega|\omega_{He}|} \sim \frac{v_{Te}}{u}\frac{\varkappa_{n,T}v_{Te}}{|\omega_{He}|} \ll 1,\quad \hat{l} \approx 1.$$

Now assuming μ^2/β to be large enough to satisfy Eq. (1.13) for electrostatic waves, and writing R(p) as in (2.2) (for the case $\mu \gg 1$, $\beta_e \ll 1$), we find the following dispersion relation for the unstable waves:

$$1 + k^2\lambda_D^2 + \frac{T_e}{T_i}[1 + i\sqrt{\pi}\,z_iW(z_i)] + i\frac{\sqrt{\pi}}{n_0}\hat{l}n_0 z_e \times \left[\frac{\xi+1}{\xi-1}e^{-z_e^2} + \frac{2i}{\sqrt{\pi}}e^{-z_e^2}\int_0^{z_e} e^{t^2}dt\right] = 0. \tag{4.1}$$

For waves with $|z_e| \gg 1$ we then find

$$k^2\lambda_D^2 + \frac{T_e}{T_i}[1 + i\sqrt{\pi}z_iW(z_i)] - \frac{1}{n_0}\hat{l}n_0\left[\frac{1}{2z_e^2} - i\sqrt{\pi}\frac{\xi+1}{\xi-1}z_e e^{-z_e^2}\right] - \frac{k_x v_{Te}^2\varkappa_n}{\omega\omega_{He}} = 0. \tag{4.2}$$

If $\omega \neq n\omega_{He}$ and $|\mathbf{ku}| \neq \omega_{pe}$, we can neglect the terms preceded by minus signs in (4.2) and set $\hat{l} = 1$; we then find

$$1 - \frac{\omega_{pe}^2}{\omega^2} + \frac{\omega_{pi}^2}{k^2v_{Ti}^2}[1 + i\sqrt{\pi}z_iW(z_i)] - \frac{k_x\varkappa_n\omega_{pe}^2}{k^2\omega\omega_{He}} = 0. \tag{4.3}$$

When the last term in Eq. (4.3) is dropped, this equation becomes the familiar dispersion relation for the Buneman instability.[1]

We now set $\omega \approx k_x u$ in (4.3) and assume $|z_i| \gg 1$, finding

$$1 - \frac{\varkappa_n\omega_{pe}^2}{k^2\omega_{He}u} - \frac{\omega_{pe}^2}{\omega^2} - \frac{\omega_{pi}^2}{(\omega - k_xu)^2} = 0. \tag{4.4}$$

When $k_xu \neq \omega_{pe}$ Eq. (4.4) has the solution

$$\omega = k_xu \pm \frac{i\omega_{pi}}{\left(\frac{\omega_{pe}^2}{k_x^2u^2} + \frac{\varkappa_n\omega_{pe}^2}{k^2\omega_{He}u} - 1\right)^{1/2}}. \tag{4.5}$$

It follows that with $|\varkappa_n u/\omega_{He}|(k_x/k)^2 \gtrsim 1$ the contribution from the density inhomogeneity is important. Under the resonance condition $\omega_{pe}^2/k_x^2u^2 = 1 - \varkappa_n\omega_{pe}^2/k^2\omega_{He}u$ the growth rate increases and is given by

$$\gamma = \frac{\sqrt{3}}{2^{4/3}}\omega_{pe}\left(\frac{m_e}{m_i}\right)^{1/3}\left(1 + \frac{k_x^2}{k^2}\frac{\varkappa_nu}{\omega_{He}}\right)^{1/3}\left(1 + \frac{\varkappa_nu}{2\omega_{He}}\frac{k_x^2}{k^2}\right)^{-1/3}. \tag{4.6}$$

Hydrodynamic equations (4.4)-(4.6) can be used in the case $\gamma \gg kv_{Ti}$, i.e., in the case

$$\left(1 + \frac{k_x^2}{k^2}\frac{\varkappa_nu}{\omega_{He}}\right)^{2/3}\frac{T_i}{T_e} \ll \left(\frac{k_x}{k}\right)^2\left(\frac{u}{v_{Te}}\right)^2\left(\frac{m_i}{m_e}\right)^{1/3}.$$

If this inequality does not hold, we must take the thermal motion of the ions into account in determining the growth rate. In this case Eq. (4.3) reduces to an equation like (3.3), in which

$$\left.\begin{aligned} \eta &= \frac{m_e}{m_i}\left(\frac{k_xu}{\sqrt{2}\,kv_{Ti}}\right)^3\left(1 + \frac{k_x^2}{2k^2}\frac{\varkappa_nu}{\omega_{He}}\right)^{-1}, \\ z_0 &= \frac{k_xu}{2\sqrt{2}\,kv_{Ti}}\left(1 + \frac{k_x^2}{k^2}\frac{\varkappa_nu}{\omega_{He}} - \frac{k_x^2u^2}{\omega_{pe}^2}\right)\left(1 + \frac{k_x^2}{2k^2}\frac{\varkappa_nu}{\omega_{He}}\right)^{-1}. \end{aligned}\right\} \tag{4.7}$$

With $\eta \sim 1$ and $|z_0| \lesssim 1$ we find from (3.3) that the growth rate is given in order of magnitude by (4.6).

Thermal motion of the electrons can be neglected ($|z_e| \gg 1$) for solutions (4.4)-(4.6) in all cases except that in which the waves are propagating nearly perpendicular to the beam ($k_k \ll k$). In this case, instead of (2.4) we find from (4.1) the following equation, which holds for cold ions:

$$1 + k^2\lambda_D^2 - \frac{k^2v_e^2}{(\omega - k_xu)^2} - \sqrt{\pi}z_e e^{-z_e^2}\operatorname{ctg}\pi\frac{\omega}{|\omega_{He}|} - 2z_e e^{-z_e^2}\int_0^{z_e} e^{t^2}dt = 0. \tag{4.8}$$

Setting $\omega = k_xu + i\gamma$ ($\gamma \ll k_xu$) we find

$$\gamma = kv_e|f(z_e)|^{-1/2}, \tag{4.9}$$

where

$$f(z_e) = \left[\sqrt{\pi}z_e e^{-z_e^2}\operatorname{ctg}\pi\frac{k_xu}{|\omega_{He}|} + 2z_e e^{-z_e^2}\int_0^{z_e} e^{t^2}dt - 1 - k^2\lambda_D^2\right], \tag{4.10}$$

and $z_e = k_x u/\sqrt{2}kv_{Te}$. If $k_x/k \sim v_{Te}/u \ll 1$, then $z_e \sim 1$ and $\gamma \sim kv_s$. With $z_e \gg 1$ we find from (4.9) an equation for Im ω, which follows from (4.5) if terms $\sim \varkappa_n$ are neglected there.

At resonance, with $f(z_e = 0)$, (4.9) is replaced by the following growth rate:

$$\gamma = \frac{\sqrt{6}}{2^{4/3}}\left(\frac{m_e}{m_i\,|f'(z_e)|}\right)^{1/3} kv_{Te}. \tag{4.11}$$

If $k\lambda_D \sim 1$ and $z_e \sim 1$, then it follows from (4.11) that $\gamma \sim \omega_{pe}(m_e/m_i)^{1/3}$. We note that the growth rate is even larger at a double resonance with $f(z_e) = 0$ and $f'(z_e) = 0$. In this case, setting $\omega = k_x u + \Delta\omega$, we find

$$(\Delta\omega)^4 = \frac{4k^4 v_s^2 v_{Te}^2}{f''(z_0)}. \tag{4.12}$$

Hence the growth rate for $k\lambda_D \sim 1$ is

$$\gamma \sim \omega_{pe}(m_e/m_i)^{1/4}. \tag{4.13}$$

At the intersection of the "beam" frequency $\omega = k_x u$ with the gyrofrequencies ($k_x u \approx n|\omega_{He}|$) the growth rate for this instability is lower than in (4.11)-(4.13).

In conclusion the authors thank K. N. Stepanov for useful discussion.

---

[1] A. B. Mikhailovskii, Theory of Plasma Instabilities, Vol. 1, Consultants Bureau, New York (1973).

[2] L. I. Grigor'eva, A. V. Longinov, A. I. Pyatak, V. L. Sizonenko, B. I. Smerdov, K. N. Stepanov, and V. V. Chechkin, Plasma Physics and Controlled Nuclear Fusion Research Conference, Madison, Wisconsin, June 17-23, 1971, Vol. 3, IAEA, Vienna (1971), p. 573.

[3] A. B. Mikhailovskii, in: Reviews of Plasma Physics, Vol. 3, Consultants Bureau, New York (1967).

[4] L. I. Pyatak, V. L. Sizonenko, and K. N. Stepanov, Zh. Tekh. Fiz., 43, 475 (1973) [Sov. Phys. – Tech. Phys., 18, 304 (1973)].

[5] S. P. Gary, J. Pl. Phys., 4, 753 (1970); 7, 417 (1972).

[6] J. J. Sanderson and E. R. Priest, Pl. Phys., 14, 959 (1972).

[7] D. G. Lominadze, Zh. Eksp. Teor. Fiz., 63, 1300 (1972) [Sov. Phys. – JETP, 36, 686 (1973)].

[8] V. L. Sizonenko and K. N. Stepanov, Ukr. Fiz. Zh., 16, 438 (1971).

[9] T. D. Kaladze, D. G. Lominadze, and K. N. Stepanov, Zh. Tekh. Fiz., 42, 243 (1972) [Sov. Phys. – Tech. Phys., 17, 196 (1972)].

[10] G. I. Machabeli, Zh. Tekh. Fiz., 43, 938 (1973) [Sov. Phys. – Tech. Phys., 18, 595 (1973)].

[11] V. L. Sizonenko and K. N. Stepanov, Radiofizika, 15, 144 (1972).

[12] B. H. Ripin and R. L. Stenzel, Phys. Rev. Lett., 30, 45 (1973).

[13] V. V. Arsenin, Dokl. Akad. Nauk SSSR, 156, 766 (1964) [Sov. Phys. – Dokl., 9, 456 (1964)].

[14] A. B. Mikhailovskii, Zh. Tekh. Fiz., 35, 1945 (1965) [Sov. Phys. – Tech. Phys., 10, 1498 (1966)].

[15] V. V. Vladimirov, Dokl. Akad. Nauk SSSR, 162, 785 (1965) [Sov. Phys. – Dokl., 10, 519 (1965)].

[16] E. E. Lovetskii and A. A. Rukhadze, Nuclear Fusion, 6, 9 (1966).

[17] A. B. Mikhailovskii and V. S. Tsypin, ZhETF Pis. Red., 3, 247 (1966) [JETP Lett., 3, 158 (1966)].

[18] A. B. Mikhailovskii, Theory of Plasma Instabilities, Vol. 2, Consultants Bureau, New York (1973).

Plasma instability due to an anisotropic electron distribution

D. G. Lominadze and V. L. Sizonenko

(Submitted November 22, 1973)
Zh. Tekh. Fiz., 44, 1839-1845 (September 1974)

The stability of a uniform plasma with a nonmonotonic electron velocity distribution in a plane perpendicular to the magnetic field is studied with a transverse current. It is shown that ion plasma instabilities due to a loss cone in the electron distribution in the presence of a transverse current occur even when the loss cone is almost filled. In turn, the appearance of the loss cone leads to an increase in the growth rate for electron cyclotron oscillations; these are unstable because of the transverse current.

The nonmonotonic form of the electron velocity distribution and the presence of relative electron and ion motion perpendicular to the magnetic field are the reasons for the numerous anisotropic and beam-type instabilities in a plasma.[1] In particular, a current can drive electrostatic electron cyclotron instabilities; the radiation due to these has recently received considerable attention.[2-28] In practical situations electrons often have a nonmonotonic velocity distribution in the plane perpendicular to the magnetic field (for example, due to the particles drifting out of adiabatic traps).

1. In this paper we investigate the effect of a nonmonotonic particle velocity distribution on the development of an instability at the electron cyclotron frequency in the presence of a transverse current; it is shown that the growth rate of these instabilities in the presence of a loss cone increases considerably. In addition, in a weak magnetic field the presence of a loss cone leads to the appearance of a distinctive conical instability in the ion plasma oscillation, which also develops when there is no transverse current (in the presence of a transverse current the electron cone instability can also develop in the case when the loss cone is almost filled).

2. We assume that the frequency ω and the growth rate are much greater than the ion cyclotron frequency, and that the wavelength is much smaller than the ion Larmor radius so that the ions can be assumed to be unmagnetized. If the ions are cold ($\gamma \gg kv_{Ti}$, $v_{Ti} = \sqrt{2T_i/m_i}$) the dispersion equation transverse to the magnetic field is[1]

$$1-\frac{\omega_{pi}^2}{(\omega-\mathbf{ku})^2}+2\pi F(0)\frac{\omega_{pe}^2}{k^2}$$

$$+\frac{\omega_{pe}^2}{k^2}\sum_{n=-\infty}^{\infty}\frac{\omega}{\omega-n\omega_{He}}2\pi\int_0^\infty dv_\perp J_n^2\left(\frac{kv_\perp}{\omega_{He}}\right)\frac{\partial F(v_\perp)}{\partial v_\perp}=0, \tag{1}$$

where $F(v_\perp)=\int_{-\infty}^{\infty} dv_\parallel f(v_\perp, v_\parallel)$; $\omega_{p\alpha}=(4\pi n_0e^2/m_\alpha)^{1/2}$; $f(v_\parallel, v_\perp)$ is the equilibrium electron velocity distribution function, normalized to unity, J_n is the Bessel function, and $\mathbf{u}$ is the directed velocity.

We assume that the electron distribution function has the form[1]

$$F(v_\perp)=\frac{1}{\pi v_0^2}\left[q+(1-q)\frac{1}{j!}\left(\frac{v_\perp}{v_0}\right)^{2j}\right]e^{-\left(\frac{v_\perp}{v_0}\right)^2}\quad (j=1,\ 2,\ 3,\ \ldots). \tag{2}$$

The distribution function (2) when $q = 1$ is a Maxwellian velocity distribution, in which v_0 means the thermal velocity; when $q = 0$ the function $F(v_\perp)$ describes the characteristic electron distribution when there is a loss cone. Hence, by changing q from zero to unity we can investigate the change in the nature of the instability as the loss cone becomes filled.

For the distribution function given by Eq. (2), Eq. (1) takes the form

$$1-\frac{\omega_{pi}^2}{(\omega-\mathbf{ku})^2}+2\frac{\omega_{pe}^2}{k^2v_0^2}\left[q-\sum_{n=-\infty}^{\infty}\frac{\omega}{\omega-n\omega_{He}}Q_n(q)\right]=0, \tag{3}$$

where

$$Q_n(q)=\hat{S}(q)\exp\left(-\frac{\mu}{\rho}\right)\frac{1}{\rho}I_n\left(\frac{\mu}{\rho}\right)\Big|_{\rho=1}, \tag{4}$$

$$\hat{S}(q)=\left[q+(-1)^j\frac{(1-q)}{j!}\frac{\partial^j}{\partial\rho_j}+(-1)^j\frac{(1-q)}{(j-1)!}\frac{\partial^{(j-1)}}{\partial\rho_{j-1}}\right],$$

$$\mu=\frac{1}{2}\left(\frac{k^2v_0^2}{\omega_{He}^2}\right). \tag{5}$$

Below we will investigate shortwave oscillations with wavelength which is considerably smaller than the electron Larmor radius. Using the asymptotic expression[29] for the sum

$$i\sum\frac{\omega_{He}e^{-x}J_n(x)}{\omega-n\omega_{He}}=\int_0^\infty d\varphi e^{x(\cos\varphi-1)+\frac{\omega}{\omega_{He}}\varphi}$$

$$=\sqrt{\frac{\pi}{2}x}\,e^{-z^2}\left(1+\frac{2i}{\sqrt{\pi}}\int_0^z e^{t^2}dt\right)+\sqrt{\frac{2\pi}{x}}\,e^{-z^2}\frac{1}{e^{-\xi}-1},$$

where $z = (\omega/\omega_{He})\sqrt{1/2x}$, $\xi = 2\pi i\omega/\omega_{He}$ holds for $x \gg 1$, we can reduce Eq. (3) to the following form:

$$1-\frac{\omega_{pi}^2}{(\omega-\mathbf{ku})^2}$$

$$+2\frac{\omega_{pe}^2}{k^2v_0^2}\left\{q+i\sqrt{\pi}\,z_0\hat{S}(q)\frac{e^{-z_0^2}}{\sqrt{\rho}}\rho\left[\frac{2i}{\sqrt{\pi}}\int_0^{z_0\sqrt{\rho}}e^{t^2}dt+\frac{e^{-\xi}+1}{e^{-\xi}-1}\right]\right\}_{\rho=1}=0, \tag{6}$$

where $z_0 = \omega/kv_0$.

We confine ourselves to the case $z_0 \ll 1$, in which case Eq. (6) becomes

$$1-\frac{\omega_{pi}^2}{(\omega-\mathbf{ku})^2}+2\frac{\omega_{pe}^2}{k^2v_0^2}\left[q+i\sqrt{\pi}z_0S_j\frac{e^{-\xi}+1}{e^{-\xi}-1}\right]=0; \tag{7}$$

here $S_j = -A_j\,(1-q/q_j)$, $q_j = A_j/(1+A_j)$, $A_j = (2j-3)!!/2^jj!$ $(j \geq 2)$, $A_1 = 1/2$, $q_1 = 1/3$.

3. We first investigate all the instabilities in the plasma with no current ($\mathbf{u} = 0$). We assume that the condition $2\pi\gamma/\omega_{He} \gg 1$ is satisfied for unstable modes so that $|e^{-\xi}| \gg 1$. In this case the effect of the magnetic field on the electrons can be neglected, and Eq. (7) takes the form

$$1-\frac{\omega_{pi}^2}{\omega^2}+2\frac{\omega_{pe}^2}{k^2v_0^2}\left[q+i\sqrt{\pi}\frac{\omega}{kv_0}S_j\right]=0. \tag{8}$$

Introducing the dimensionless variables

$$y \equiv \frac{\omega}{\omega_{pi}}, \quad a \equiv 1 + 2q\frac{\omega_{pe}^2}{k^2 v_0^2}, \quad b \equiv 2\sqrt{\pi}\frac{\omega_{pe}^2 \omega_{pi}}{k^3 v_0^3} S_j,$$

we can write Eq. (8) in the form

$$iby^3 + ay^2 - 1 = 0. \tag{9}$$

In the region of fairly small wavelengths where $2q\omega_{pe}^2/k^2v_0^2 \ll 1$ and $a \approx 1$, Eq. (9) has the following solutions:

$$y_{1,2} = \pm 1 - i\frac{b}{2}, \; y_3 = i\frac{1}{b} \; (b \ll 1), \tag{10}$$

$$y_{1,2} = -\frac{(i \pm \sqrt{3})}{2b^{1/3}}, \; y_3 = i\frac{1}{b^{1/3}} \; (b \gg 1). \tag{11}$$

If $q < q_j$, $S_j < 0$ $(b < 0)$, the solution $y_{1,2}$ is unstable and the growth rate is

$$\gamma = \omega_{pi}(|b|/2) \; (|b| \ll 1), \tag{12}$$

$$\gamma = \omega_{pi}\left(\frac{1}{2|b|^{1/3}}\right) \; (|b| \gg 1). \tag{13}$$

It follows that the growth rate reaches a maximum value when $|b| \sim 1$; this value is of order

$$\gamma \sim \omega_{pi} \quad \left(k \approx \frac{\omega_{pe}}{v_0}\left(\frac{m_e}{m_i}\right)^{1/6}(2\sqrt{\pi}|S_j|)^{1/3}\right). \tag{14}$$

The condition $2q\omega_{pe}^2/k^2v_0^2 \ll 1$ for the solution (14) is satisfied when $q \ll (m_e/m_i)^{1/3}(2\sqrt{\pi}|S_j|)^{2/3}$. The solution y_3 when $q < q_j$ is a damped solution, and when $q > q_j$ is a growing solution, but is inapplicable since it does not satisfy the condition $z_0 \ll 1$.

It is easy to show that Eq. (9) also has unstable solutions when $q \gtrsim (m_e/m_i)^{1/3}(2\sqrt{\pi}|S_j|)^{2/3}$ (but $q < q_j$). Assuming, for example, that $a \gg 1$, we obtain the following unstable solution of Eq. (9) for $|b| \ll 2a^{3/2}$:

$$y_{1,2} = \pm\frac{1}{a^{1/2}} - i\frac{b}{2a^2}. \tag{15}$$

The growth rate is

$$\gamma = -\omega_{pi}\frac{|b|}{2a^2} = -\frac{\sqrt{\pi}}{4}S_j\frac{\omega_{pi}^2}{\omega_{pe}^2}\frac{kv_0}{q^2}. \tag{16}$$

Expression (16) increases with k, and the growth rate reaches a maximum value given by Eq. (14) when $a \sim 1$.

This instability is due to the nonmonotonic behavior[30] of the electron distribution function $F(v_\perp)$ and can be called by analogy with the instability described,[1] which is due to the nonmonotonic behavior of the ion distribution function, the electron loss-cone instability. The above consideration shows that this instability occurs everywhere in the region $q < q_j$, and in this case for $0 < q \lesssim (m_e/m_i)^{1/3} \cdot (2\sqrt{\pi}|S_j|)^{2/3}$ the growth rate is of the order of the ion plasma frequency, and decreases monotonically to zero in the region $(m_e/m_i)^{1/3}(2\sqrt{\pi}|S_j|)^{2/3} \lesssim q \lesssim q_j$.

If the filling of the loss cone is fairly large $(q > q_j)$, the quantity S_j changes sign, and the increase in the oscillations changes to attenuation, so that in this region there is no electron cone instability.

4. For the growth rate (14) the condition that the electrons should be unmagnetized $2\pi\gamma/\omega_{He} \sim 2\pi\omega_{pi}/\omega_{He} \gg 1$ is only satisfied when the magnetic field is fairly weak. We now investigate the electron loss-cone instability with no current; the plasma is strong in a magnetic field $2\pi\gamma/\omega_{He} \ll 1$, and we assume that this instability does not develop even when $q = 0$.

For convenience we introduce the phase ψ according to the relation $\psi = 2\pi \operatorname{Re} \omega/\omega_{He}$; then for ψ not close to $2n\pi(|1 - \cos\psi| \gg 2\pi\gamma/\omega_{He})$, Eq. (7) takes the form

$$\left(\frac{\omega}{\omega_{pi}}\right)^2 - 1 - 2\sqrt{\pi}\left(\frac{\omega_{pe}}{kv_0}\right)^3 S_j\left(\frac{m_e}{m_i}\right)^{1/2}\left(\frac{\omega}{\omega_{pi}}\right)^2\frac{\sin\psi}{1-\cos\psi} = 0 \quad (\gamma \ll \operatorname{Re}\omega). \tag{17}$$

Assuming that $\omega_{He}^2/4\pi^2 \gg \omega_{pi}^2$ when $\psi \sim 1$ Eq. (17) reduces to the form

$$\frac{\psi}{2}\operatorname{ctg}\frac{\psi}{2} = \frac{\sqrt{\pi}}{2S_j}\left(\frac{m_i}{m_e}\right)^{1/2}\frac{\omega_{pi}}{\omega_{He}}\left(\frac{kv_0}{\omega_{pe}}\right)^3. \tag{18}$$

It is easy to show graphically that this equation has a purely real solution.

For $\psi \approx 2n\pi$ $(\omega \approx n\omega_{He})$, we obtain from Eq. (7)

$$1 - \frac{\omega_{pi}^2}{\omega^2} - \frac{2}{\sqrt{\pi}}\frac{\omega_{pe}^2 n\omega_{He}^2 S_j}{k^3v_0^3(\omega - n\omega_{He})} = 0. \tag{19}$$

Assuming that $(\omega_{pi}/\omega)^2 \approx (\omega_{pi}/n\omega_{He})^2 \ll 1$, we find

$$\omega \approx n\omega_{He} + \frac{2}{\sqrt{\pi}}\frac{n\omega_{He}^2\omega_{pe}^2}{k^3v_0^3}S_j. \tag{20}$$

It is easy to show that there is also no instability in the frequency range $\omega \ll \omega_{He}$.

Hence, for fairly high magnetic fields $2\pi\omega_{pi}/\omega_{He} \ll 1$ there is no electron loss-cone instability with zero current. Consequently, the instabilities considered above would only be expected when the following inequality is satisfied:

$$2\pi\frac{\omega_{pi}}{\omega_{He}} \geqslant 1. \tag{21}$$

5. When a transverse current is present it is necessary to use Eq. (7) to describe the loss-cone instability; this equation reduces to the form (9) in the case of magnetized electrons $(2\pi\gamma/\omega_{He} \gg 1)$. In this case, the coefficient b in Eq. (9) remains as before, whereas the coefficient a must be changed to the following:

$$a = 1 + 2q\frac{\omega_{pe}^2}{k^2v_0^2} + 2i\sqrt{\pi}\frac{u}{v_0}\frac{\omega_{pe}^2}{k^2v_0^2}S_j.$$

Investigation of the solutions of Eq. (9) in this case shows that when $q \lesssim q^* \equiv (m_e/m_i)^{1/3}(2\sqrt{\pi}|S_j|)^{2/3}(1 + u/u_0)$ the maximum growth rate, as before, is determined by the estimate (14), while the wave vector k in the presence of a current is changed, being of order

$$k \sim \frac{\omega_{pe}}{v_0}(2\sqrt{\pi}|S_j|)^{1/3}\left(\frac{m_e}{m_i}\right)^{1/6}\sqrt{1 + \frac{u}{u_0}}, \tag{22}$$

where

$$u_0 \equiv \frac{v_0}{(2\sqrt{\pi}|S_j|)^{1/3}}\left(\frac{m_e}{m_i}\right)^{1/2}.$$

When q increases in the region $q > (m_e/m_i)^{1/3} \cdot (2\sqrt{\pi}|S_j|)^{1/3}$ the growth rate decreases, and remains positive even when $q > q_j$.

It is easy to show that when $q > q_j$ and $u \gg v_0(m_e/m_i)^{1/2}$.

$q^{-1/2}$, growth rate γ has the form

$$\gamma=\left(\frac{\pi}{2}\frac{m_e}{m_i}\right)^{1/2}ku\,|S_j|\left(2q+\frac{k^2v_0^2}{\omega_{pe}^2}\right)^{-3/2}. \tag{23}$$

When q = 1 Eq. (23) is identical with the well-known expression for the growth rate of ion-acoustic oscillations in the limiting case when $u \gg v_s = (T_e/m_i)^{1/2}$. As can be easily shown, the growth rate (23) reaches a maximum when $k = (\omega_{pe}/v_0)q^{1/2}$, given by

$$\gamma_{\max}=\frac{1}{3}\omega_{pi}\left(\frac{\pi}{6}\right)^{1/2}\frac{|S_j|}{q}\frac{u}{v_0}. \tag{24}$$

Hence, the growth rate in a plasma with a current decreases monotonically as q increases; when q = 1 it is identical with the well-known expression for the growth rate of ion-acoustic oscillations.

The behavior of the growth rate as a function of q is shown schematically in Fig. 1. As the figure shows, in the region $0 < q \leqslant q^*$ there is a loss-cone instability ($\gamma \sim \omega \sim \omega_{pi}$), and its growth rate decreases monotonically as q increases. When there is no current, the instability ceases when $q = q_j$; when there is a current present it also exists in the region $q > q_j$, and when q = 1 it changes into the usual ion-acoustic instability.

6. We will now consider the effect of the loss cone on the excitation of electron cyclotron waves (the Bernstein mode) in a plasma with a transverse current, assuming that $(2\pi\gamma/\omega_{He}) \ll 1$. Taking the condition $|\omega - n\omega_{He}| \ll \omega_{He}$ into account, Eq. (7) can be simplified and reduced to the form

$$ay^3+(Aa-B)y^2-y-A=0, \tag{25}$$

where

$$a=1+2q\frac{\omega_{pe}^2}{k^2v_0^2},\quad A=\frac{ku-n\omega_{He}}{\omega_{pi}},$$
$$B=\frac{2n\omega_{pe}^2\omega_{He}^2}{\sqrt{\pi}\,\omega_{pi}k^3v_0^3}S_j,\quad y=\frac{\omega-\mathbf{ku}}{\omega_{pi}}.$$

We will investigate the solution of dispersion equation (25) in a number of special cases.

If $Aa = B$ and $|y| \ll A$, Eq. (25) takes the form $y^3a = A$, and its solution gives the following growth rate:

$$\gamma=\sqrt{3}\left(\frac{1}{16\sqrt{\pi}}\frac{m_e}{m_i}\frac{v_0}{u}\right)^{1/3}\left(\frac{n^2|S_j|}{(q+k^2\lambda_{De}^2)^2}\right)^{1/3}\omega_{He},\quad \lambda_{De}=(v_{Te}/\sqrt{2}\omega_{pe}). \tag{26}$$

The condition $|y| \ll A$ is satisfied in this case if

$$\left(\frac{u}{v_0}\right)^2 \gg n\left(\frac{\pi}{2}\right)^{1/2}\frac{(q+k^2\lambda_{De}^2)^{1/2}}{S_j}\left(\frac{m_e}{m_i}\right)^{1/2}. \tag{27}$$

When q = 1 the growth rate (26) is identical with the growth rate of electron cyclotron frequencies in the region where the cyclotron and bunch branches of the oscillations intersect.[2,28] In this case the condition $aA = B$ represents exactly the condition for the branches of the oscillations to intersect.

We will now consider the case when $aA^2 = 1$. Assuming $y = -A + \Delta y$, where $|\Delta y| \ll A$, we obtain from Eq. (25) the equation

$$\Delta y = \pm i\,(B/2a^{3/2})^{1/2}. \tag{28}$$

From expression (28) we obtain the growth rate

$$\gamma=\left(\frac{1}{8\pi}\frac{m_e}{m_i}\right)^{1/4}\frac{n^{1/2}\omega_{He}|S_j|^{1/2}}{(q+k^2\lambda_{De}^2)^{3/4}}. \tag{29}$$

The condition $|\Delta y| \ll A$ is satisfied if

$$\left(\frac{u}{v_0}\right)^2 \ll n\left(\frac{\pi}{2}\right)^{1/2}\left(\frac{m_e}{m_i}\right)^{1/2}\frac{(q+k^2\lambda_{De}^2)^{1/2}}{S_j}. \tag{30}$$

When q = 1, the growth rate given by Eq. (29) is identical with the well-known expression (see, for example, refs. 2, 3, 7–9, 17–20, 28) for the growth rate of ion-acoustic oscillations, when their frequency is close to $n\omega_{He}$. The equation $aA^2 = 1$ also represents the condition for the frequency of ion sound and the electron cyclotron harmonic to intersect.

Note that condition (30), which is the criterion for the solution (29) to be applicable, is an inequality which is the opposite of the inequality (27). Hence, the solutions (26) and (29) can be regarded as solutions of Eq. (25), obtained in two opposite limiting cases, which can be obtained by changing the parameter q for a fixed value of $k = n\omega_{He}/u$.

The characteristic relationship $\gamma = \gamma(q)$ obtained on the basis of the solutions (26) and (29), is shown schematically in Fig. 2. When q = 0 the growth rate is

$$\gamma=\sqrt{3}\left(\frac{1}{4\sqrt{\pi}}\frac{m_e}{m_i}\frac{\omega_{pe}}{n^2\omega_{He}}S_j\right)^{1/3}\omega_{pe}\frac{u}{v_0},\quad \text{if}\quad \frac{u}{v_0}>\left\{\frac{n^2}{2}\sqrt{\pi\frac{m_e}{m_i}}\frac{\omega_{He}}{\omega_{pe}S_j}\right\}^{1/3}, \tag{31}$$

$$\gamma=\left(\frac{1}{8\pi}\frac{m_e}{m_i}\right)^{1/4}\left(\frac{u}{v_0}\right)^3\frac{\omega_{pe}^3}{\omega_{He}^2}\frac{2^{3/2}S_j^{1/2}}{n^3},\quad \text{if}\quad \frac{u}{v_0}<\left\{\frac{n^2}{2}\sqrt{\pi\frac{m_e}{m_i}}\frac{\omega_{He}}{\omega_{pe}}\frac{1}{S_j}\right\}^{1/3}. \tag{32}$$

When $q = q_j$, as follows from Eq. (29), the growth rate becomes zero. When $q = q_m$ the growth rate reaches a maximum, and is given by the following expression if inequality (27) holds:

$$\gamma=\gamma_m=\sqrt{3}\left(\frac{1}{16\sqrt{\pi}}\frac{m_e}{m_i}\frac{v_0}{u}\right)^{1/3}\left[\frac{n^2(1+A_j)}{4(q_j+k^2\lambda_{De}^2)}\right]^{1/3}\omega_{He},\quad q_m=2q_j+k^2\lambda_{De}^2. \tag{33}$$

When the inequality opposite to (27) holds, the maximum growth rate is

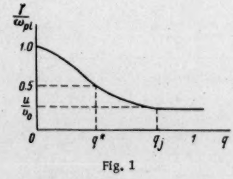

Fig. 1

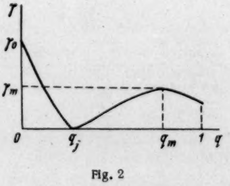

Fig. 2

$$\gamma_m=\left(\frac{1}{8\pi}\frac{m_e}{m_i}\right)^{1/3}\left[\frac{2n(1+A_j)}{3\sqrt{3}\,(q_j+k^2\lambda_{De}^2)^{1/2}}\right]^{1/2}\omega_{He}, \qquad (34)$$

where $q_m = 3q_j + 2k^2\lambda_{De}^2$.

It should be noted that the point $q = q_m$ can be both to the left and to the right of the point $q = 1$. The case when $k^2\lambda_{De}^2 \ll 1$ is particularly interesting. In this case the point q_m is to the left of the point $q=1$, and $\gamma \gg \gamma_m$. Hence, when $k^2\lambda_{De}^2 \ll 1$ the growth rate of electron cyclotron oscillations when there is a conical distribution is much greater than the growth rate obtained in the case of a Maxwellian distribution.

We wish to thank K. N. Stepanov for discussion.

---

[1] A. B. Mikhailovskii, Theory of Plasma Instabilities, Vol. 1, Consultants Bureau, New York (1973)

[2] V. I. Kurilko and V. I. Miroshnichenko, in: Plasma Physics and Problems of Controlled Thermonuclear Reactions [in Russian], No. 3, AN UkrSSR, Kiev (1963), p. 161.

[3] C. N. Lashmore-Davies, J. Phys., A3, 40 (1970).

[4] C. N. Lashmore-Davies, Phys. Fluids, 14, 1451 (1971).

[5] C. N. Lashmore-Davies and T. J. Martin, Nucl. Fusion, 13, 193 (1973).

[6] S. P. Gary and J. J. Sanderson, J. Pl. Phys., 4, 739 (1970); 4, 753 (1970).

[7] S. P. Gary, J. Pl. Phys., 6, 561 (1971).

[8] S. P. Gary, J. Pl. Phys., 7, 417 (1972).

[9] S. P. Gary, J. Pl. Phys., 15, 399 (1973).

[10] S. P. Gary and B. Biskomp, J. Phys., A4, 27 (1971).

[11] H. V. Wong, Phys. Fl., 13, 757 (1970).

[12] D. W. Forslund, R. L. Morse, and C. W. Nielson, Phys. Rev. Lett., 25, 1266 (1970).

[13] D. W. Forslund, R. L. Morse, and C. W. Nielson, Proc. Fourth Intern. Conf. Plasma Phys. and Nucl. Fus. Res. Vienna, IAEA, II (1971), p. 277.

[14] D. W. Forslund, R. L. Morse, and C. W. Nielson, Phys. Rev. Lett., 27, 1424 (1972).

[15] D. W. Forslund, R. L. Morse, C. W. Nielson, and J. Fu, Phys. Fl., 15, 1303 (1972).

[16] D. W. Forslund, R. L. Morse, and C. W. Nielson, Phys. Fl., 15, 2363 (1972).

[17] M. Lampe, J. B. Mc'Bride, J. M. Orens, and R. Sudan, Phys. Lett., 35A, 131 (1971).

[18] M. Lampe, W. Manheimer, J. B. Mc'Bride, J. Orens, R. Shanny, and R. Sudan, Phys. Rev. Lett., 26, 1221 (1972).

[19] M. Lampe, W. Manheimer, J. B. Mc'Bride, J. Orens, K. Papadopoulos, R. Shanny, and R. Sudan, Phys. Fl., 15, 662 (1972).

[20] M. Lampe, W. Manheimer, J. B. Mc'Bride, and J. Orens, Phys. Fl., 15, 2356 (1972).

[21] J. Sanderson and E. Priest, J. Phys., A4, L65 (1971).

[22] J. Sanderson and E. Priest, Pl. Phys., 14, 951 (1972).

[23] D. Biskamp and R. Chodura, Fifth European Conf. on Contr. Fus. and Plasma Phys., Grenoble, 21-25 August 1972, Invited Papers, p. 43.

[24] A. Rogister, Phys. Rev. Lett., 30, 86 (1973).

[25] A. Rogister, Phys. Fl., 16, 282 (1973).

[26] C. Wu and R. Fredericks, J. Geoph. Res., 77, 5585 (1972).

[27] A. A. Galeev, D. G. Lominadze, A. D. Pataraya, R. Z. Sageev, and K. N. Stepanov, ZhETF Pis. Red., 15, 417 (1972) [JETP Lett., 15, 294 (1972)].

[28] D. G. Lominadze, Zh. Eksp. Teor. Fiz., 63, 1300 (1972) [Sov. Phys. – JETP, 36, 686 (1973)].

[29] V. L. Sizonenko and K. N. Stepanov, Ukr. Fiz. Zh., 16, 438 (1971).

[30] L. V. Korablev, ZhETF Pis. Red., 5, 137 (1967) [JETP Lett., 5, 111 (1967)].

Stochastic acceleration of electrons in nanosecond discharges

L. P. Babich

(Submitted June 19, 1973; resubmitted October 15, 1973)
Zh. Tekh. Fiz., 44, 1846-1851 (September 1974)

Stochastic acceleration is possible for some electrons in field-emission beams in the cathode plasma of nanosecond discharges in air at atmospheric pressure. Equations are derived which relate the energy of the stochastically accelerated electrons to the density and energy of the beam, the density and temperature of the plasma electrons, and the beam dimensions.

In refs. 1 and 2 it is reported that in nanosecond vacuum and gas discharges with average fields $E_0 \sim 10^5\ \mathrm{V\cdot cm^{-1}}$ electrons are detected with ε greater than the applied voltage U_0. It is known at the present time that fast electrons and ions are observed frequently in nature and in laboratory experiments involving discharges and plasmas over a wide range of conditions (see, for example, refs. 3-12); as a rule, the acceleration effects are correlated with intense oscillations in the plasma[13,14] (stochastic acceleration). In a nanosecond discharge a field-emission beam–plasma system is produced in the region of micrononuniformities on the surface of the cathode; this plasma can be unstable with respect to the generation of plasma oscillations.[15] Hence, there is a probable stochastic mechanism for the acceleration of that part of the electrons of the field-emission beams, for which the derivative of the distribution function $\partial f_a/\partial \mathbf{v} < 0$.

To obtain appropriate estimates it is necessary to know the plasma density n_0, the degree of ionization $i = n_0/N$, the electron temperature T_e, and the density n_1 and the energy of the electrons ε_1 in the beams. Under the conditions described in refs. 1 and 2 these characteristics are unknown. However, the quantities n_0, n_1, and ε_1 in nanosecond discharges in air at atmospheric pressure can be estimated using certain indirect data. On photographs of the external form of nanosecond discharges in air at atmospheric pressure, given in ref. 2 under conditions for which electrons with $\varepsilon > eU_0$ are generated, one can see plasmoids in the region of the cathode; these have dimensions $h_0 \sim 0.1$ cm, and are formed near microprojections which initiate the discharge. Weak diffuse fluorescence which propagates to the anode is also observed. In ref. 16, in diffuse channels (the channel diameter approximately 0.2 cm and the length approximately 0.6 cm) of nanosecond discharges in air at atmospheric pressure values of $i \sim 10^{-2}$ are recorded, and the possibility of a local excess of i above the value obtained is noted. In ref. 2 the slope of the leading edge of the voltage pulse dU/dt and its amplitude exceed the values of these characteristics in ref. 16 and the voltage pulse length is very much shorter than in ref. 16; thus, the energy of the emission beam in ref. 2 is used to generate a plasma and to heat it more effectively than in ref. 16. This is confirmed by the external form of the discharges.[2] It can be assumed that in ref. 2 (at least in the denser parts of the plasma in the region of the microprojections,) values of $i \sim 1$ ($n_0 \sim 10^{20}\ \mathrm{cm^{-3}}$) are reached exactly as in the cathode bursts of nanosecond vacuum discharges.[17]

We estimate the characteristics of the beam n_1 and ε_1 starting from the fact that in nanosecond gas discharges at high overvoltages explosion of microprojections on the cathode surface is possible.[18] A relation is proposed in ref. 19 between the density of the emission current j_e, which ensures explosion of a tungsten point, and the delay time of the explosion

$$j_e^2 t_d \simeq 4\cdot 10^9\ \mathrm{A^2\cdot cm^{-1}\cdot sec}.$$

Assuming $t_d \sim 10^{-9}$ sec, we obtain $j_e \simeq 2\cdot 10^9\ \mathrm{A\cdot cm^{-2}}$, for which the field intensity in the region of the micropoint[20] should be $E \simeq 10^8\ \mathrm{V\cdot cm^{-1}}$. A field with this intensity can be obtained by amplification of the external field at the microprojections and by amplification due to the space-charge field.[21]

The cathode potential drop, which occurs as a result of polarization in the external field E_0 of a plasma layer of thickness h_0, is $\Delta\varphi \simeq (1/2)E_0h_0 \simeq 5$ kV. If we assume that the plasma is uniform[16] and $i = 10^{-2}$, the field in the region of the cathode drop[21] $E_k = (1/2)\,(eiNE_0h_0/6)^{1/2} \simeq 4\cdot 10^6\ \mathrm{V\cdot cm^{-1}}$. Projections which amplify this field by a factor of 25 must explode. The observed gains of the external field in the region of the microprojections lie[18] in the range 10–300.

In fields of approximately $10^6\ \mathrm{V\cdot cm^{-1}}$ the energy losses of the electrons are small,[22] and $\varepsilon_1 \simeq e\Delta\varphi = 5$ keV, $n_1 \simeq j_e/ev_1 = 10^{18}\ \mathrm{cm^{-3}}$.

The energy spread of the electrons emitted from a single point of the surface of a microprojection[20] $\Delta\varepsilon \ll \varepsilon_1$. It can be shown that for a semiellipsoidal isolated projection[23] the spread of the electron velocity component along the external field

$$\frac{\Delta v_z}{v_z} = \frac{\sin^2\theta}{(\cos\theta)^2} \simeq \frac{4\theta\sin^2\theta}{2\theta + \sin 2\theta}, \tag{1}$$

where θ is the angle of divergence of the electron beam. Assuming[23] $\theta = 20°$, we obtain $\Delta v_z/v_z \simeq 0.12 < (n_1/n_0)^{1/3} \simeq 0.22$. In fact, the angular divergence of the beam is somewhat smaller because of the focusing effect of the fields of a plane cathode and the neighboring microprojections. Hence, initially the instability of the beam in the densest part of the plasma is hydrodynamic with a growth rate[5]

$$\gamma_h = \sqrt{3}\left(\frac{n_1}{16 n_0}\right)^{1/3}\omega_{p0} \simeq 10^{14}\ \mathrm{sec^{-1}}, \tag{2}$$

where $\omega_{p0} = \sqrt{4\pi n_0 e^2/m_e}$ is the plasma frequency.

The hydrodynamic instability along the path $\sim v_1\gamma_h^{-1} \simeq 4\cdot 10^{-5}$ cm increases the velocity spread up to $(n_1/n_0)^{1/3}$, and further relaxation of the beam is determined by the quasilinear stage. The characteristic relaxation time[24] to $v_{\min}$ is

$$t_q = \left(\frac{v_1}{v_{\min}} - 1 + \ln\frac{v_{\min}}{v_1}\right)\frac{\Lambda}{\pi}\,\frac{n_0}{n_1}\,\omega_{p0}^{-1}, \tag{3}$$

where Λ is the Coulomb logarithm

$$v^{\min} = v_{Te}\left[2\ln\left(\frac{n_0 v_1}{n_1 v_{Te}}\right)\right]^{1/2},$$

and $v_{Te} = (T_e/m_e)^{1/2}$ is the thermal velocity of the plasma electrons.

The energy density of the plasma oscillations excited in the beam instability is[13,14]

$$\dot{W} = \left[2 - \frac{v_{\min}}{v_1} - \left(\frac{v_{\min}}{v_1}\right)^2\right]\frac{n_1\varepsilon_1}{3} \simeq \frac{2}{3}n_1\varepsilon_1, \tag{4}$$

and the spectral density is[14,25]

$$W_k = \frac{n_1 m_e \omega_{p0}^3}{v_1 k^4}. \tag{5}$$

In order to ensure the resonance condition of the accelerated particles with a large number of oscillations it is necessary to take account of the spectral transfer of turbulent energy from the generation region $k \geq \omega_{p0}/v_1$ to the acceleration region $k \leq \omega_{p0}/v_1$.

In the cathode plasma of nanosecond gas discharges one might expect a considerable difference between the electron temperature T_e and the ion temperature T_i. In a strongly nonisothermal plasma ($T_e \gg T_i$) the following interactions are available to increase the length of the plasma waves: decay of the plasma wave into an ion-acoustic wave and a plasma wave with a longer wavelength:[13,14]

$$l \rightarrow S + l' \tag{6}$$

and scattering of the plasma waves by thermal ions

$$l + i \rightarrow l' + i' \tag{7}$$

and by plasma electrons

$$l + e \rightarrow l' + e. \tag{8}$$

We neglect slow ion-acoustic oscillations in the transfer processes because of the extremely small lifetime of the plasma investigated in ref. 2.

The efficiency of the stochastic acceleration of particles in a turbulent plasma is determined by the spectral distribution of the turbulent pulses which build up in the transfer process. In a hot isothermal plasma in which nonlinear scattering of plasmons by ions is the main process by which turbulent energy is saturated at high phase velocities v_p, the spectrum which is established is not suitable for particle acceleration.[13] However, in a nonisothermal plasma with heavy ions the range of values of v_p for which the spectrum of plasma turbulence is determined by electron scattering is broadened.

The plasma rapidly becomes isotropic when spectral transfer of the oscillations takes place.[14,25] Hence, the turbulence is assumed to be isotropic below.

The change in the spectral energy density W_k of isotropic turbulent pulses due to scattering on electrons and damping in binary electron collisions is

$$\frac{\partial W_k}{\partial t} = (\gamma_e^l - 2\nu_e)W_k, \tag{9}$$

where the rate of scattering of plasmons[14] by electrons γ_e^l is

$$\gamma_e^l = \frac{6v_{Te}\sqrt{2\pi}}{4m_e n_0 \omega_{p0}^2}\left\{\int_k^\infty dk_1 W_{k_1}\frac{k^2}{k_1^3}(k_1^2 - k^2)\right.$$
$$\left.\times\left(\frac{1}{3}k_1^2 + \frac{4}{7}k^2\right) - \int_0^k dk_1 W_{k_1}\frac{k_1^2}{k^3}(k^2 - k_1^2)\left(\frac{1}{3}k^2 + \frac{4}{7}k_1^2\right)\right\}. \tag{10}$$

Assuming $W_k = T(t)K_k(k)$, Eq. (9) reduces to the following equations:

$$\dot{T} + 2\nu_e T = \mathrm{const}\, T^2, \tag{11}$$

$$\int_k^\infty K_{k_1}dk_1\frac{k^2}{k_1^3}(k_1^2 - k^2)\left(\frac{1}{3}k_1^2 + \frac{4}{7}k^2\right) - \int_0^k K_{k_1}dk_1\frac{k_1^2}{k^3}(k^2 - k_1^2)$$
$$\times\left(\frac{1}{3}k^2 + \frac{4}{7}k_1^2\right) = \mathrm{const}. \tag{12}$$

The solution of Eq. (12) which satisfies the condition that the transfer of energy along the spectrum is local, has[14] the form $K_k \sim k^{-5/2}$, in which case const $= 0$. Then $T \sim \exp(-2\nu_e t)$, and

$$W_k = Ak^{-5/2}\exp(-2\nu_e t). \tag{13}$$

The constant A is found by matching Eq. (13) with Eq. (5) at $t = 0$ at the point $k = \omega_{p0}/v_1$. Finally we obtain

$$W_k = \frac{n_1 m_e v_1^3}{\omega_{p0}}\left(\frac{\omega_{p0}}{v_1 k}\right)^{5/2}\exp(-2\nu_e t). \tag{14}$$

We find the mean energy acquired by electrons of the beam accelerated stochastically by turbulent pulses of this spectrum in a plasma layer of thickness h. In the nonrelativistic approximation the rate of acceleration is determined solely by the spectrum[14,25]

$$\dot{\varepsilon} = \frac{\pi}{2}\frac{\omega_{p0}^2 m_e}{n_0\sqrt{2m_e\varepsilon}}W_k\bigg|_{k=\omega_{p0}\sqrt{\frac{m_e}{2\varepsilon}}}. \tag{15}$$

The solution of Eq. (15) with W_k defined by Eq. (14), and with the initial condition $\varepsilon(t = 0) = \varepsilon_1 \ll \varepsilon$ has the following form:

$$\varepsilon = \varepsilon_\infty(1 - e^{-2\nu_e t})^4, \tag{16}$$

where

$$\varepsilon_\infty = \left[3\left(\frac{\pi}{2}\right)^2\sqrt{2\pi}\frac{n_1 d_{p0}^3}{\Lambda}\right]^4\varepsilon_1, \tag{17}$$

$d_{p0} = v_{Te}/\omega_{p0}$ is the Debye radius of the plasma. Assuming that $h = \int_0^{t(\varepsilon)} v(t')dt'$, where $t(\varepsilon)$ is determined from Eq. (16), we find the relation between the mean energy of the accelerated electrons ε and the dimensions of the plasma h:

$$h = -\frac{1}{2\nu_e}\sqrt{\frac{2\varepsilon_\infty}{m_e}}\left\{\ln\left[1 - \left(\frac{\varepsilon}{\varepsilon_\infty}\right)^{1/4}\right] + \left(\frac{\varepsilon}{\varepsilon_\infty}\right)^{1/4} + \frac{1}{2}\left(\frac{\varepsilon}{\varepsilon_\infty}\right)^{1/2}\right\}. \tag{18}$$

We do not know the electron temperature in the plasma in ref. 2. Hence, taking as the base of the acceleration h the dimension of the densest part of the plasma, which in ref. 2 is approximately 10^{-2} cm, we find from Eq. (18) that for stochastic acceleration of the electrons in a completely ionized plasma with $n_0 \sim 10^{20}$ cm^{-3} up to an energy[2] $\varepsilon \simeq 300$ keV we require $T_e \sim 200$ eV.

In such a plasma the quasilinear relaxation time $t_q \simeq 10^{-13}$ sec. Since the Landau damping $\gamma_L(v^{\min}) \simeq 5 \cdot 10^{12}$ sec^{-1}, and the frequency of binary electron collisions $\nu_e \simeq 0.7 \cdot 10^{12}$ sec^{-1}, relaxation of the beam takes place completely without dissipative processes. The characteristic scale of the plasma nonuniformities, capable of stabilizing the instability,[25] is

$$L \leqslant v_g t_q \simeq 3 \frac{v_{T_e}^2}{v_p} t_q \simeq (2 \div 5) \cdot 10^{-5} \text{ cm}.$$

where v_g is the group velocity of the plasma waves. It can be assumed that the characteristic scale of the nonuniformities of the densest part of the plasma in ref. 2 is not smaller than the dimensions of the microprojections [$\sim 10^{-4}$ cm (ref. 26)], and that there is no stabilization of the instability by the nonuniformities.

Comparing the characteristic rate of scattering of plasma oscillations by electrons for $v_p/v_{Te} \ll (3m_i/m_e)^{1/3}$

$$\gamma_e = 3\sqrt{\frac{\pi}{2}}\, \omega_{p0} \frac{W}{n_0 T_e} \left(\frac{v_{T_e}}{v_p}\right)^3 \simeq 2.8 \cdot 10^{12} \text{ sec}^{-1}$$

with the rate of differential transfer to ions[14] ($v_p/v_{Te} \ll 3v_{Te}/v_{Ti}$)

$$\gamma_i = \frac{\pi}{27} \omega_{p0} \frac{W}{n_0 T_e} \left(\frac{v_p}{v_{T_e}}\right)^2 \left(1 + \frac{T_e}{T_i}\right)^{-2},$$

we obtain the region v_p where scattering by electrons predominates over scattering by ions:

$$\left(\frac{v_p}{v_{T_e}}\right)^5 \ll \frac{9 \cdot 2^{1/2}}{\pi^{5/2}} \frac{m_i}{m_e} \left(1 + \frac{T_e}{T_i}\right)^2. \tag{19}$$

In our case the time taken to transfer energy from electrons to ions considerably exceeds the lifetime of the plasma ($t_{ei} \sim 10^{-7}$ sec) and T_i is not greater than the mean electron energy in single avalanches, which for $E \sim 10^5$ V · cm^{-1} and p = 760 torr in air and Eq. (19) is satisfied over the whole region of acceleration. The anisotropic nature of the overshoot of the fast electrons observed in ref. 2 can obviously be explained by the fact that the oscillations are not completely isotropic.

The phenomenon of stochastic acceleration of electrons is connected with the excitation in the plasma of high-frequency slow waves with phase velocities smaller than the velocity of light. Besides oscillations of the electrostatic type with frequencies of the order of ω_{p0}, these include electromagnetic waves with frequencies below[27,28] the electron cyclotron frequency ω_{He} (whistlers). We assume that all the stored charge in the experiments described in ref. 2 passes through a plasma bunch. Then

$$\omega_{He} = \mu_0 \frac{e}{m_e} H \simeq \mu_0 \frac{e}{m_e} \frac{CU_0}{2\pi t r}.$$

Assuming[2] $C \simeq 4 \cdot 10^{-11}$ F, $U_0 \simeq 10$ V, and $r \simeq 10^{-4}$ cm (the characteristic dimensions of the emitting point), we obtain $\omega_{He} \sim 10^{12}$ sec$^{-1} \sim \nu_e$. Consequently, the whistlers are strongly attenuated and stochastic acceleration of the electrons[2] can only be connected with the Langmuir turbulence.

Hence, the above estimates indicate that the nature of the fast electrons generated in nanosecond gas discharges may be related to stochastic acceleration of part of the electrons of the field-emission beams by turbulence excited by beams in the cathode plasma. To get better estimates it is necessary to determine experimentally the plasma electron temperature, for example, by investigating its radiation in the first nanoseconds of the discharge.

---

[1] N. G. Pavlovskaya and T. V. Kudryavtseva, Prib. Tekh. Eksp., No. 2, 198 (1972).

[2] L. P. Babich, L. V. Tarasova, and T. V. Loiko, Proc. Symposium on Emission Plasma High-Current Electronics, Tomsk (1973).

[3] S. Yu. Luk'yanov and I. M. Podgornyi, At. Energ., 3, 97 (1956).

[4] A. A. Plyutto, I. F. Kvartskhava, and K. N. Kervalidze, At. Energ., 3, 153 (1957).

[5] I. F. Kharchenko, Ya. B. Fainberg, R. M. Nikolaev, E. A. Kornilov, E. I. Lutsenko, and N. S. Pedenko, Nucl. Fusion III (1962).

[6] L. Alexeff, R. Neidigh, W. Peed, and E. Shipley, Phys. Rev. Lett., 10, 273 (1963).

[7] V. L. Ginzburg and S. I. Syrovatskii, Cosmic Rays [in Russian], Nauka, Moscow (1963).

[8] S. K. Handel, Brit. J. Appl. Phys., 14, 181 (1963).

[9] L. N. Khudyakova, E. K. Gutnikova, and L. V. Tarasova, Zh. Tekh. Fiz., 34, 2044 (1964) [Sov. Phys. – Tech. Phys., 9, 1572 (1965)].

[10] R. V. Neidigh, L. Alexeff, G. E. Guert, W. D. Ioner, D. C. Montgomery, D. I. Rose, and W. L. Stirling, Conf. Proc. Novosibirsk (1968), II, p. 6393, Vienna (1969).

[11] A. N. Karkhov, Zh. Eksp. Teor. Fiz., 59, 356 (1970) [Sov. Phys. – JETP, 32, 192 (1971)].

[12] I. R. Conrad, I. E. Walsh, C. I. Diaz, and K. B. Freese, Phys. Rev. Lett., 30, 827 (1973).

[13] V. N. Tsytovich, Nonlinear Effects in Plasma, Plenum, New York (1970).

[14] V. N. Tsytovich, Theory of Turbulent Plasma, Consultants Bureau, New York (1973).

[15] A. B. Mikhailovskii, Theory of Plasma Instabilities, Vol. 1, Consultants Bureau, New York (1973).

[16] Yu. I. Bychkov, Yu. D. Korolev, and P. A. Gavrilyuk, Zh. Tekh. Fiz., 42, 1674 (1972) [Sov. Phys. – Tech. Phys., 17, 1337 (1973)].

[17] R. B. Baksht, A. P. Kudinov, and E. A. Litvinov, Zh. Tekh. Fiz., 43, 146 (1973) [Sov. Phys. – Tech. Phys., 18, 94 (1973)].

[18] G. A. Mesyats, Yu. I. Bychkov, and V. V. Kremnev, Usp. Fiz. Nauk, 107, 201 (1972) [Sov. Phys. – Usp., 15, 282 (1972)].

[19] E. A. Litvinov, G. A. Mesyats, and A. F. Shubin, Izv. VUZ. Fizika, 4, 147 (1970).

[20] M. I. Elinson and G. F. Vasil'ev, Field Emission [in Russian], Fizmatgiz, Moscow (1958).

[21] V. S. Bosamykin and A. I. Pavlovskii, Zh. Tekh. Fiz., 41, 2002 (1971) [Sov. Phys. – Tech. Phys., 16, 1584 (1972)].

[22] L. R. Peterson and A. E. S. Green, I. Phys. B. (At. Mol. Phys.), 1, No. 6, 1131 (1968).

[23] I. I. Slivkov, Insulation and Discharge in a Vacuum [in Russian], Atomizdat, Moscow (1972).

[24] M. A. Leontovich (ed.), Reviews of Plasma Physics, Vol. 6, Atomizdat, Moscow (1972).

[25] S. A. Kaplan and V. N. Tsytovich, Plasma Astrophysics [in Russian], Nauka, Moscow (1972).

[26] G. A. Bogdanovskii, Fiz. Tverd. Tela, 1, 1281 (1959) [Sov. Phys. – Solid State, 1, 1171 (1960)].

[27] D. Meek and D. Craggs, Electrical Breakdown in Gases [Russian translation], IL, Moscow (1960).

[28] M. A. Leontovich (ed.), Reviews of Plasma Physics, Vol. 3, Consultants Bureau, New York (1967).

Nonlinear interaction between a monochromatic ion-acoustic wave and a plasma

V. P. Indykul

(Submitted July 4, 1973; resubmitted October 31, 1973)
Zh. Tekh. Fiz., 44, 1852-1856 (September 1974)

The nonlinear interaction between a monochromatic, finite-amplitude ion-acoustic wave and a collisionless nonisothermic plasma is considered. The nonlinear damping and frequency shift are obtained. The nonlinear damping of the ion-acoustic wave is due primarily to the ions, whose interaction with the wave is much stronger because the resonant-ion period is longer than the electron period. The nonlinear frequency shift of the ion-acoustic wave due to the interaction with the resonant plasma particles is determined primarily by the electrons.

1. The resonant interaction of waves with particles in a Maxwellian plasma underlies the collisionless damping – Landau damping. The interaction with the wave causes the distribution function in the resonant velocity region to become so distorted that energy exchange between the particles and the wave stops.

The equations of the quasilinear theory[1,2] can be used to study the damping of broad wave packets in a plasma. In this case the change in the distribution function associated with a particular harmonic is small, and the cumulative effect of all of the harmonics leads to diffusion of the resonant particles in velocity space. This diffusion is described by Fokker–Planck equations for the distribution functions.

The damping of a monochromatic wave of finite amplitude in a plasma is completely different. In this case the interaction between the resonant particles and the wave is completely nonlinear and leads to trapping of the resonant particles by the wave. An analytic solution for the problem of nonlinear Landau damping can be obtained when

$$\gamma^L \tau_0 \ll 1,$$

where γ^L is the linear damping and $\tau_0 = (keE_0/m)^{-1/2}$ is the characteristic oscillation period of particles trapped by the wave (k and E_0 are the wave number and amplitude of the monochromatic wave). The motion of the resonant particles is first considered in the field of a wave of constant amplitude; then the effect of the particles on the wave is taken into account. The earliest analyses of the damping of a monochromatic plasma wave are given in refs. 3-5.

An essential feature of the nonlinear interaction of monochromatic waves with a plasma is the presence of a large group of thermal (nonresonant) particles which determine the dispersion of the wave and whose motion in the field of the wave is linear. The interaction of a wave with a plasma is therefore usually studied under the assumption that the shape of the wave remains constant. It has been shown,[6] however, that the nonlinear interaction of the resonant particles with the wave causes a small nonlinear phase shift; this in turn causes a small nonlinear shift of the frequency of the plasma oscillations as compared to the frequency ω_L determined by the linear dispersion equation.

In the present work we consider the nonlinear interaction between a nonisothermal ($T_e \gg T_i$) plasma and a monochromatic ion-acoustic wave of finite amplitude whose electric field is

$$E(t,\ z) = E_0(t) \sin (kz - v_p t + \alpha). \tag{1}$$

Here, $v_p \simeq c_s = \sqrt{T_e/m_i}$ is the phase velocity of the wave, and α is the small nonlinear phase shift.

The nonlinear properties of an ion-acoustic wave are conveniently studied with the Poisson equation

$$\varepsilon(\omega_L + \Delta\hat{\omega}) \operatorname{div} \mathbf{E} + \text{c.c.} = 8\pi\rho, \tag{2}$$

which must be satisfied by the field given by Eq. (1). Here, ρ is the particle charge density,

$$\varepsilon(\omega_L) = 1 - \frac{\omega_{0i}^2}{\omega_L^2} + \frac{1}{k^2\lambda_{De}^2} = 0$$

is the linear dispersion equation for the longwave ion-acoustic mode, and $\Delta\hat{\omega}$ is a complex frequency shift operator, whose action on the field is defined by the equation

$$\Delta\hat{\omega} E = i \frac{\partial E}{\partial t}. \tag{3}$$

Utilizing the fact that $|\Delta\hat{\omega}|$ is small compared with ω_L, we can expand $\varepsilon(\omega_L + \Delta\hat{\omega})$ in powers of $\Delta\hat{\omega}/\omega_L$ (the zeroth-order term vanishes by virtue of the linear dispersion equation). Using this expansion and Eq. (3), and substituting (1) into (2), we obtain the result (in the wave reference frame)

$$\hat{\delta\omega} - i\gamma = \frac{8\pi e}{kE_0}\left(\frac{d\varepsilon}{d\omega_L}\right)^{-1} \int_{-\infty}^{\infty} dv_0 \int_{-\lambda/2}^{\lambda/2} \frac{dz_0}{\lambda} \{[f_{0i}(v_0 + v_p) - f_i^L(v_0 + v_p)] - [f_{0e}(v_0 + v_p) - f_e^L(v_0 + v_p)]\} e^{-ikz - i\alpha}, \tag{4}$$

where γ and $\delta\omega$ are the nonlinear damping and frequency shift of the ion-acoustic wave, and

$$f_{i,e}^L(v_0 + v_p) = \mp \frac{eE_0}{km_{i,e}} \frac{1}{v_0} \frac{\partial f_{0i,e}}{\partial v_0} \cos(kz + \alpha).$$

We assume that the following condition holds:

$$\frac{m_e}{m_i} \ll \frac{eE_0}{kT_e} \ll \left(\frac{T_i}{T_e}\right)^2. \tag{5}$$

The motions of the main nonresonant ions and electrons, which move with the thermal velocities, can be regarded as linear for these amplitudes. The nonlinear effects are due to the resonant particles, whose interaction with the wave is strong. The contribution of the linear approximation has therefore been subtracted from the right-hand side of Eq. (4).

By making use of the fact that the nonlinear damping and frequency shift are small compared with ω_L, we can make the approximation that $\alpha = 0$ in the right-hand side of Eq. (4). By separating the imaginary and real parts in Eq. (4), we obtain the following expressions for the nonlinear damping and frequency shift of the ion-acoustic wave:

$$\gamma=-\frac{8\pi e}{kE_0}\left(\frac{d\varepsilon}{d\omega_L}\right)^{-1}\int\limits_{-\infty}^{\infty}dv_0\int\limits_{-\lambda/2}^{\lambda/2}\frac{dz_0}{\lambda}\left[f_{0i}(v_0+v_p)-f_{0e}(v_0+v_p)\right]\sin kz, \tag{6}$$

$$\delta\omega=\frac{8\pi e}{kE_0}\left(\frac{d\varepsilon}{d\omega_L}\right)^{-1}\int\limits_{-\infty}^{\infty}dv_0\int\limits_{-\lambda/2}^{\lambda/2}\frac{dz_0}{\lambda}\{[f_{0i}(v_0+v_p)-f_i^L(v_0+v_p)]$$
$$-[f_{0e}(v_0+v_p)-f_e^L(v_0+v_p)]\}\cos kz. \tag{7}$$

If the particle velocity distribution is Maxwellian, making use of (5) we find

$$\left.\begin{aligned}f_{0i}(v_0+v_p)&\simeq\frac{n}{\sqrt{2\pi}\,v_{Ti}}e^{-v_p^2/2v_{Ti}^2}\left(1-\frac{v_0v_p}{v_{Ti}^2}-\frac{1}{2}\frac{v_0^2}{v_{Ti}^2}\right),\\ f_{0e}(v_0+v_p)&\simeq\frac{n}{\sqrt{2\pi}\,v_{Te}}\left(1-\frac{v_0v_p}{v_{Te}^2}-\frac{1}{2}\frac{v_0^2}{v_{Te}^2}\right).\end{aligned}\right\} \tag{8}$$

It is easy to show that the terms in Eq. (8) which are linear in v_0 contribute only to the damping; the quadratic terms contribute only to the nonlinear frequency shift. It then follows from Eqs. (6), (7), and (8) that

$$\gamma=\frac{8\pi}{\sqrt{2\pi}}\frac{en}{kE_0}\left(\frac{d\varepsilon}{d\omega_L}\right)^{-1}\int\limits_{-\infty}^{\infty}dv_0\int\limits_{-\lambda/2}^{\lambda/2}\frac{dz_0}{\lambda}\left[\frac{v_pv_0}{v_{Ti}^3}\sin kz'+\frac{v_pv_0}{v_{Te}^3}\sin kz\right], \tag{9}$$

where $kz' = kz-\pi$ and

$$\delta\omega=-\frac{8\pi}{\sqrt{2\pi}}\frac{en}{kE_0}\left(\frac{d\varepsilon}{d\omega_L}\right)^{-1}\int\limits_{-\infty}^{\infty}dv_0\int\limits_{-\lambda/2}^{\lambda/2}\frac{dz_0}{\lambda}\left\{\frac{1}{v_{Ti}^3}\left(\frac{v_0^2}{2}+v_i^2\cos kz'\right)\cos kz'\right.$$
$$\left.+\frac{1}{v_{Te}^3}\left(\frac{v_0^2}{2}+v_e^2\cos kz\right)\cos kz\right\}, \tag{10}$$

where $v_{i,e}^2 = eE_0/km_{i,e}$.

2. We first study the nonlinear damping of the ion-acoustic wave due to resonant ions. In order to solve the equations of motion for the ions, i.e., to find the dependence of $\sin kz'$ and $\cos kz'$ on z_0 and v_0, we divide the ions into two groups: those which are trapped and oscillate in the potential well, and those which are in transit. Integration of the equations of motion gives

$$F(\xi,\varkappa)=F(\xi_0,\varkappa)\pm\frac{t}{\varkappa\tau_{0i}},\quad \varkappa^2\equiv\frac{2eE_0}{kW+eE_0}<1 \tag{11}$$

for the transit ions, and

$$F\left(\zeta,\frac{1}{\varkappa}\right)=F\left(\zeta_0,\frac{1}{\varkappa}\right)\pm\frac{t}{\tau_{0i}},\quad \varkappa>1 \tag{12}$$

for the trapped ions. Here, W is the energy of the particles in the wave field (1), $\tau_{0i} = (ekE_0)/m_i)^{-1/2}$ is the period of oscillation of the particles in the potential well, $\xi = kz'/2$, F(x) is an elliptic integral of the first kind, and the quantities ξ and ζ are related by the equation $\varkappa \sin\xi = \sin\zeta$.

The upper sign in Eqs. (11) and (12) corresponds to ions with $v_0 > 0$, while the lower sign corresponds to ions with $v_0 < 0$. From Eqs. (11) and (12), it follows that

$$\left.\begin{aligned}\sin kz'&=2\,\mathrm{sn}\left(F\pm\frac{t}{\varkappa\tau_{0i}}\right)\mathrm{cn}\left(F\pm\frac{t}{\varkappa\tau_{0i}}\right),\quad \varkappa<1,\\ \sin kz'&=\frac{2}{\varkappa}\,\mathrm{sn}\left(F\pm\frac{t}{\tau_{0i}}\right)\mathrm{dn}\left(F\pm\frac{t}{\tau_{0i}}\right),\quad \varkappa>1,\end{aligned}\right\} \tag{13}$$

where snu, cnu, and dnu denote the elliptic sine and cosine and the Jacobi delta.

If we substitute Eqs. (13) into Eq. (9), integrate over $\varkappa$ and $F(\xi_0, \varkappa)$ for the particles in transit ($\varkappa < 1$) and over $1/\varkappa$ and $F(\zeta_0, 1/\varkappa)$ for the trapped particles ($\varkappa > 1$), and use the Fourier expansion of the elliptic functions,[7] the nonlinear damping due to the ions is found to be

$$\gamma_i=\gamma_i^L 128\pi\sum_{n=1}^{\infty}\int\limits_0^1 d\varkappa$$
$$\times\left\{\frac{nq^{2n}}{\varkappa^5K^2(1+q^{2n})^2}\sin\frac{n\pi t}{\varkappa K\tau_{0i}}+\frac{\varkappa\left(n-\frac{1}{2}\right)q^{2n-1}}{K^2(1+q^{2n-1})^2}\sin\frac{\left(n-\frac{1}{2}\right)\pi t}{K\tau_{0i}}\right\}, \tag{14}$$

where γ_i^L is the ion linear Landau damping, K is the total elliptic integral of the first kind, and $q = \exp\{-\pi K(\sqrt{1-\varkappa^2})\cdot[K(\varkappa)]^{-1}\}$.

It follows from Eq. (14) that for $t \ll \tau_{0i}$ the damping is identical with the linear damping; for $t \sim \tau_{0i}$ it oscillates about zero, causing oscillations of the wave amplitude. Since the period of the oscillations of the resonant particles which cause this temporal behavior of the wave is a function of their energy, a "phase mixing" of these particles occurs which results in damping of the oscillations after a long time $t \gg \tau_{0i}$. A stationary value of the field amplitude is thus established which is given by the equation

$$E(\infty)=E(0)\exp(-\Gamma),$$

where

$$\Gamma=\Gamma_i+\Gamma_e\equiv\int\limits_0^{\infty}\gamma_i(t)\,dt+\int\limits_0^{\infty}\gamma_e(t)\,dt.$$

The quantity $\Gamma_{i,e}$ is calculated by a method which has been previously discussed,[5] with the result that

$$\Gamma_{i,e}=\gamma_{i,e}^L\tau_{0i,e}\frac{64}{\pi}\int\limits_0^1 d\varkappa\left\{\frac{1}{\varkappa^4}\left[\frac{E}{\pi}-\frac{\pi}{4K}\right]+\frac{\varkappa}{\pi}[E-(1-\varkappa^2)K]\right\}, \tag{15}$$

where $E \equiv E(\varkappa)$ denotes the total elliptic integral of the second kind.

For realistic plasma parameters

$$\frac{\Gamma_i}{\Gamma_e}=\frac{m_i}{m_e}\left(\frac{T_e}{T_i}\right)^{3/2}\exp\left[-\frac{T_e}{2T_i}\right]\gg 1, \tag{16}$$

i.e., the ion contribution to the nonlinear damping of an ion-acoustic wave is much larger than the electron contribution. This fact can be explained as follows: Since τ_{0e} the period of the electron oscillations in the wave field is much smaller than the ion period τ_{0i}, the electron damping disappears after a time $\tau_{0e} \ll t \lessdot \tau_{0i}$; however, the ions continue to interact with the wave and determine the further evolution of the amplitude.

3. Let us now consider the nonlinear frequency shift caused by the interaction of the ion-acoustic wave with the resonant plasma particles. We first consider the effect of the electrons. From the electron equations of motion we have the following integral of the motion:

$$\frac{m_ev^2}{2}-m_ev_e^2\cos kz=W=\mathrm{const},$$

which is to be interpreted as the total energy of the electrons in the field (1) of the ion-acoustic wave. By taking this into account, it is easy to transform Eq. (10) to the form

$$\delta\omega_e = \frac{8}{\pi\sqrt{2\pi}}\frac{\omega_{0e}^2}{k^2 v_{Te}^2}\left(\frac{d\varepsilon}{d\omega_L}\right)^{-1}\left\{\int_0^1 \frac{d\varkappa}{\varkappa^2}\int_{-K}^{K} dF\,\mathrm{sn}^2 F\left[1 - 2\,\mathrm{sn}^2\left(F + \frac{t}{\varkappa T_{0e}}\right)\right]\right.$$
$$\left. + \int_0^1 \varkappa^3 d\varkappa \int_{-K}^{K} dF\,\mathrm{sn}^2 F\left[1 - 2\varkappa^2\,\mathrm{sn}^2\left(F + \frac{t}{\tau_{0e}}\right)\right]\right\}. \qquad (17)$$

If we now use the expansion[8]

$$\mathrm{sn}^2 u = \frac{K - E}{\varkappa^2 K} - \frac{2\pi^2}{\varkappa^2 K^2}\sum_{n=1}^{\infty}\frac{nq^n}{1 - q^{2n}}\cos\frac{n\pi u}{K}$$

we then obtain from Eq. (10)

$$\delta\omega_e = \frac{16}{\pi\sqrt{2\pi}}\frac{\omega_{0e}^2}{k^2 v_{Te}^2}\frac{v_e}{v_{Te}}\left(\frac{d\varepsilon}{d\omega_L}\right)^{-1}\int_0^1 \frac{d\varkappa}{\varkappa^6 K}\left\{(K - E)\left[\varkappa^2 K + 2(E - K)\right]\right.$$
$$\left. - \frac{4\pi^4}{K^2}\sum_{n=1}^{\infty}\frac{n^2 q^{2n}}{(1 - q^{2n})^2}\cos\frac{n\pi t}{\varkappa K \tau_{0e}}\right\}$$
$$+ \frac{16}{\pi\sqrt{2\pi}}\frac{\omega_{0e}^2}{k^2 v_{Te}^2}\frac{v_e}{v_{Te}}\left(\frac{d\varepsilon}{d\omega_L}\right)^{-1}\int_0^1 \frac{\varkappa\, d\varkappa}{K}\left\{(K - E)(2E - K)\right.$$
$$\left. - \frac{4\pi^4}{K^2}\sum_{n=1}^{\infty}\frac{n^2 q^{2n}}{(1 - q^{2n})^2}\cos\frac{n\pi t}{K\tau_{0e}}\right\}. \qquad (18)$$

Here, the first term represents the contribution of the transiting particles and the second term represents the contribution of the trapped particles.

After a long interval of time $t \gg \tau_{0e}$, the nonlinear frequency shift becomes constant, being equal to

$$\delta\omega_e(\infty) = \frac{8}{\pi\sqrt{2\pi}}\,\omega\sqrt{\frac{eE_0}{kT_e}}\int_0^1 \frac{d\varkappa}{K}\left\{\frac{K - E}{\varkappa^6}\left[\varkappa^2 K\right.\right.$$
$$\left.\left. + 2(E - K)\right] + \varkappa(K - E)(2E - K)\right\}. \qquad (19)$$

It is easy to obtain expressions for the ions which are similar to Eqs. (18) and (19), and to show that

$$\frac{\delta\omega_e(\infty)}{\delta\omega_i(\infty)} = \left(\frac{T_i}{T_e}\right)^{1/2}\exp\left[\frac{T_e}{2T_i}\right] \gg 1. \qquad (20)$$

This means that the electronic contribution to the nonlinear change of the dispersion of an ion-acoustic wave is much larger than the ion contribution.

In conclusion, we thank V. D. Shapiro and V. I. Shevchenko for guidance.

---

[1] A. A. Vedenov, E. P. Velikhov, and R. Z. Sagdeev, Nuclear Fusion [in Russian], 1962 Supplement, Part 2, p. 465.
[2] W. E. Drummond and D. Pines, Nuclear Fusion, 1962 Supplement, Part 3, p. 1049.
[3] R. K. Mazitov, Prikl. Mekh. Tekh. Fiz., 1, 27 (1965).
[4] L. M. Al'tshul' and V. I. Karpman, Zh. Eksp. Teor. Fiz., 49, 515 (1965) [Sov. Phys.–JETP, 22, 361 (1966)].
[5] T. M. O'Neil, Phys. Fluids, 8, 2255 (1965).
[6] G. J. Morales and T. M. O'Neil, Phys. Rev. Lett., 28, 417 (1972).
[7] I. S. Gradshtein and I. N. Ryzhik, Tables of Integrals, Sums, Series, and Products, Academic Press, New York (1965).
[8] E. Whittaker and G. Watson, Modern Analysis, 4th ed., Cambridge Univ. Press, New York (1927).

High-frequency instabilities in an inhomogeneous, anisotropic finite-β plasma

V. D. Egorenkov and A. I. Pyatak

(Submitted July 30, 1973; resubmitted October 16, 1973)
Zh. Tekh. Fiz., 44, 1857-1861 (September 1974)

The electromagnetic instabilities in an inhomogeneous hot-electron ($T_e \gg T_i$) finite-β plasma with an anisotropic velocity distribution function are investigated. At frequencies $\omega_{Bi} \ll \omega \ll \omega_{Be}$ and wavelengths $v_{Te}/\omega_{Be} \ll \lambda_\perp \ll v_{Ti}/\omega_{Bi}$ firehose and mirror instabilities can develop in an anisotropic inhomogeneous plasma. In particular, the instabilities are related to the ion-acoustic mode and the whistler mode of a homogeneous plasma. The inhomogeneity in the plasma density and the external magnetic field has a strong effect on modes whose wavelength in the direction of the magnetic field $\lambda_\parallel$ is large compared to the inhomogeneity scale length for the equilibrium plasma parameters.

1. It is well-known[1-5] that in a homogeneous magnetoactive finite-β plasma anisotropies in the electron and ion pressures can produce firehose and mirror instabilities at frequencies $\omega \ll \omega_{Bi}$. It is shown in ref. 6 that these instabilities also develop in the frequency range $\omega_{Bi} \ll \omega \ll \omega_{Be}$. In a plasma with hot electrons and cold ions the long-wave modes ($kc \lesssim \omega_{pe}$), which correspond to ion-acoustic modes and whistler modes in an isotropic plasma, are unstable.

The papers cited above do not consider the inhomogeneity of the equilibrium plasma parameters (density, external magnetic field, etc.). It is clear, however, that the Larmor ($\nabla n_0 \neq 0$) and magnetic ($\nabla B \neq 0$) particle drifts can affect the dispersion properties of waves that propagate across the magnetic field. It will be shown in the present paper that this effect can be neglected if the wavelength along the magnetic field is smaller than the characteristic dimension of the inhomogeneity of the plasma parameters across the magnetic field.

In the present paper the stability of a finite-β plasma [$\beta = 4\pi n_0(T_e + T_i)/B_0^2 \sim 1$] with hot electrons and cold ions ($T_e \gg T_i$) is investigated in the frequency region $\omega_{Bi} \ll \omega$, $\gamma \ll \omega_{Be}$ for the case in which the wavelength along the magnetic field is of the same order as the characteristic scale size of the inhomogeneity. The inhomogeneity is to be assumed weak, i.e., the electron Larmor radius is assumed to be appreciably smaller than the characteristic dimension of the inhomogeneity. It is shown that the inhomogeneity has a strong effect on the dispersion properties; with a strong inhomogeneity the conditions for instability in a homogeneous plasma obtained in ref. 6 are modified.

2. We consider electromagnetic modes in a nonisothermal plasma with an anisotropic electron velocity distribution and cold ions. Let the external magnetic field be in the direction of the z axis, and let its magnitude vary slowly along the y axis. This variation will be considered small over distances of the order of the electron Larmor radius ($\varkappa_B v_e/\omega_{Be} \ll 1$, where $\varkappa_B = \partial \ln B_0/\partial y$ and v_e is the characteristic electron thermal velocity). Since we are interested in a finite-β plasma ($\beta \sim 1$) the condition for weak inhomogeneity of the magnetic field leads to a condition on weak inhomogeneity of the kinetic pressure. However, we assume a uniform plasma temperature and only consider the density inhomogeneity ($\varkappa_n v_e/\omega_{Be} \ll 1$, where $\varkappa_n = \partial \ln n/\partial y$). In describing the plasma we start with the kinetic equation for the electrons in the drift approximation and the hydrodynamic equations without a magnetic field for the ions together with Maxwell's equations.

We consider phase velocities that are appreciably smaller than the electron thermal velocity along the magnetic field and with wavelengths across the magnetic field that exceed the electron Larmor radius. We also assume $\varkappa \sim k_z \ll k$. Instead of using the vectors **E** and **H** of the electromagnetic field we introduce the scalar ψ and vector **A** potentials. Then the dispersion equation in the local approximation (see ref. 7) is

$$\varepsilon_{00}\frac{k^4c^4}{\omega^4} + [\varepsilon_{03}^2 - \varepsilon_{00}(\varepsilon_{33} + \varepsilon_{22}) - \varepsilon_{02}^2]\frac{k^2c^2}{\omega^2} + \varepsilon_{00}\varepsilon_{23}^2 + \varepsilon_{33}\varepsilon_{02}^2 + 2\varepsilon_{02}\varepsilon_{03}\varepsilon_{23} + \varepsilon_{22}(\varepsilon_{00}\varepsilon_{33} - \varepsilon_{03}^2) = 0, \tag{1}$$

$$\left.\begin{aligned}
\varepsilon_{00} &= \frac{\omega_{pi}^2}{k^2u_s^2} - \frac{\omega_{pi}^2}{\omega^2},\\
\varepsilon_{02} &= -i\frac{\omega_{pi}^2}{\omega\omega_{Bi}}\delta,\\
\varepsilon_{03} &= \frac{\omega_{pi}^2}{kk_zu_s^2} + \frac{\omega_{pi}^2}{\omega\omega_{Bi}}\frac{k_x\varkappa_B}{kk_z}\delta - \frac{\omega_{pi}^2}{\omega\omega_{Bi}}\frac{k_x\varkappa_n}{kk_z},\\
\varepsilon_{22} &= -\frac{\omega_{pi}^2}{\omega^2}\frac{k^2v_{2e}^2}{\omega_{Bi}^2},\\
\varepsilon_{23} &= i\frac{\omega_{pi}^2}{\omega\omega_{Bi}}\frac{k}{k_z}\lambda - i\frac{\omega_{pi}^2}{\omega^2}\frac{k}{k_z}\frac{k_x\varkappa_B(v_A^2 + v_{2e}^2)}{\omega_{Bi}^2},\\
\varepsilon_{33} &= \frac{\omega_{pi}^2}{k_z^2u_s^2} - \frac{\omega_{pi}^2}{\omega^2}\frac{k^2v_{1e}^2}{\omega_{Bi}^2} + \frac{\omega_{pi}^2}{\omega\omega_{Bi}}\frac{k_x\varkappa_B}{k_z^2}(\delta + \lambda)\\
&\quad - \frac{\omega_{pi}^2}{\omega\omega_{Bi}}\frac{k_x\varkappa_n}{k_z^2} - \frac{\omega_{pi}^2}{\omega^2}\frac{k_x^2\varkappa_B^2(v_A^2 + v_{2e}^2)}{k_z^2\omega_{Bi}^2},
\end{aligned}\right\} \tag{2}$$

where

$$\frac{1}{u_s^2} = -\frac{m_i}{m_e}\frac{1}{n_0}\int d\varepsilon_\perp dv_z\frac{\partial F}{\partial\varepsilon_z},\quad n_0 = \int d\varepsilon_\perp dv_z F,$$

$$\delta = \frac{1}{n_0}\int \varepsilon_\perp d\varepsilon_\perp dv_z\left(\frac{\partial F}{\partial\varepsilon_z} - \frac{\partial F}{\partial\varepsilon_\perp}\right),$$

$$\lambda = \frac{1}{n_0}\int \varepsilon_\perp d\varepsilon_\perp dv_z\frac{\partial F}{\partial\varepsilon_z},$$

$$v_{1,e}^2 = -\frac{m_e}{m_i}\frac{1}{n_0}\int \varepsilon_\perp d\varepsilon_\perp v_z^2 dv_z\left(\frac{\partial F}{\partial\varepsilon_z} - \frac{\partial F}{\partial\varepsilon_\perp}\right),$$

$$v_{2,e}^2 = \frac{m_e}{m_i}\frac{1}{n_0}\int \varepsilon_\perp^2 d\varepsilon_\perp dv_z\left(\frac{\partial F}{\partial\varepsilon_z} - \frac{\partial F}{\partial\varepsilon_\perp}\right),\quad v_A^2 = c^2\frac{\omega_{Bi}^2}{\omega_{pi}^2},$$

$$\varepsilon_\perp = \frac{v_\perp^2}{2},\quad \varepsilon_z = \frac{v_z^2}{2},\quad \omega_{pi}^2 = \frac{4\pi e^2n_0}{m_i},\quad \omega_{Bi} = \frac{|e|B_0}{m_ic},$$

and $F = F(v_\perp, v_z)$ is the electron velocity distribution function.

Solving Eq. (1) for the frequency ω we obtain the following expression for the normal modes of an inhomogeneous anisotropic finite-β plasma:

$$\omega^4 + m\omega^3 + p\omega^2 + n\omega + q = 0, \tag{3}$$

where

$$\left.\begin{aligned} m &= \sigma\frac{k_z k}{\omega_{Bi}\varkappa_n}\{(v_A^2+v_{2s}^2)(\varkappa_B+\varkappa_n)+u_s^2[\varkappa_B\delta^2+\varkappa_n\delta(\lambda-1)]\},\\ p &= -\frac{k_z^2k^2}{\omega_{Bi}^2}(v_A^2+v_{1s}^2)(v_A^2+v_{2s}^2+u_s^2\delta^2)\\ &\quad -k^2(v_A^2+v_{2s}^2+u_s^2\lambda^2)-\sigma^2\frac{k_z^2k^2}{\omega_{Bi}^2}u_s^2(v_A^2+v_{2s}^2),\\ n &= -\sigma\frac{k_z k}{\omega_{Bi}\varkappa_n}k^2u_s^2(v_A^2+v_{2s}^2)(\varkappa_B-\varkappa_n),\\ q &= k_z^2u_s^2\frac{k^4}{\omega_{Bi}^2}(v_A^2+v_{1s}^2)(v_A^2+v_{2s}^2),\quad \sigma\equiv\frac{k_x\varkappa_n}{k_z k}. \end{aligned}\right\}\quad(4)$$

The case of a homogeneous plasma corresponds to $\sigma = 0$. Here we obtain an equation that was investigated previously in ref. 6.

3. We now consider an inhomogeneous anisotropic plasma. We first consider short wavelengths ($k_z v_s/\omega_{Bi} \gg 1$). Equation (3) has the solutions

$$\omega^2 = k^2u_s^2\frac{(v_A^2+v_{1s}^2)(v_A^2+v_{2s}^2)}{(v_A^2+v_{1s}^2)(v_A^2+v_{2s}^2+u_s^2\delta^2)+\sigma^2u_s^2(v_A^2+v_{2s}^2)},\quad(5)$$

$$\begin{aligned}&\omega^2+\sigma\frac{k_z k}{\omega_{Bi}\varkappa_n}\{(v_A^2+v_{2s}^2)(\varkappa_B+\varkappa_n)+u_s^2[\varkappa_B\delta^2+\varkappa_n\delta(\lambda-1)]\}\,\omega\\ &-\sigma^2\frac{k_z^2k^2}{\omega_{Bi}^2}u_s^2(v_A^2+v_{2s}^2)-\frac{k_z^2k^2}{\omega_{Bi}^2}(v_A^2+v_{1s}^2)(v_A^2+v_{2s}^2+u_s^2\delta^2)=0.\quad(6)\end{aligned}$$

When the wavelength along the magnetic field is appreciably smaller than the characteristic dimensions of the inhomogeneities ($k_z \gg \varkappa_n$) the instability condition for the frequency, Eq. (5) becomes

$$-u_s^2\delta^2 < v_A^2+v_{2s}^2 < 0,\quad(7)$$

and the instability condition for (6) becomes

$$\left.\begin{aligned}&v_A^2+v_{1s}^2<0\\ \text{or}\quad&\\ &v_A^2+v_{2s}^2+u_s^2\delta^2<0.\end{aligned}\right\}\quad(8)$$

The homogeneous-plasma approximation is valid for these modes. However, when the wavelength along the magnetic field is much larger than the scale of the magnetic field inhomogeneity the instability condition for (5) becomes

$$v_A^2+v_{1s}^2<0,\quad(9)$$

and the instability condition for (6) becomes

$$\frac{1}{\varkappa_n^2}\{(v_A^2+v_{2s}^2)(\varkappa_B+\varkappa_n)+u_s^2[\varkappa_B\delta^2+\varkappa_n\delta(\lambda-1)]\}^2+4u_s^2(v_A^2+v_{2s}^2)<0.\quad(10)$$

To make conditions (9) and (10) more explicit we substitute a model electron velocity distribution function

$$F\sim\exp\left\{-\frac{mv_\perp^2}{2T_\perp}-\frac{mv_z^2}{2T_\parallel}\right\}$$

and introduce the following notation:

$$\beta_\perp=\frac{T_\perp}{m_iv_A^2},\quad \beta_\parallel=\frac{T_\parallel}{m_iv_A^2}.$$

Then, (9) takes the following form:

$$\beta_\parallel>1+\beta_\perp.\quad(11)$$

This is the usual condition for the firehose instability, which, in the given case, develops in an inhomogeneous plasma.

For explicitness in the case of an almost-isotropic plasma ($T_\perp \approx T_\parallel$) we write (10) near the limit of the necessary condition for instability as

$$1+\frac{v_{1s}^2}{v_A^2}=-\nu\quad(1\gg\nu>0).$$

Condition (10) is written in the following simple form:

$$\frac{1}{4}<\beta_\perp\nu<\frac{9}{4}.\quad(12)$$

We now consider long wavelengths ($k_z v_s/\omega_{Bi} \ll 1$). Equation (3) has the solutions

$$\omega^2=k^2(v_A^2+v_{2s}^2+u_s^2\lambda^2),\quad(13)$$

$$\begin{aligned}&-k^2(v_A^2+v_{2s}^2+u_s^2\lambda^2)\,\omega^2-\sigma\frac{k_z k}{\omega_{Bi}\varkappa_n}k^2u_s^2(v_A^2+v_{2s}^2)(\varkappa_B-\varkappa_n)\,\omega\\ &+k_z^2u_s^2\frac{k^4}{\omega_{Bi}^2}(v_A^2+v_{1s}^2)(v_A^2+v_{2s}^2)=0.\quad(14)\end{aligned}$$

Solution (13) does not depend on the inhomogeneity dimension. It has exactly the same form as the solution for a fast magnetosound mode obtained in ref. 6 for a homogeneous plasma and the same instability region. With regard to solution (14), the homogeneous-plasma approximation is valid for wavelengths along the magnetic field that are appreciably smaller than the dimension of the magnetic field inhomogeneity, and the instability^6 condition is

$$v_A^2+v_{1s}^2<0\quad(15)$$

or

$$-u_s^2\lambda^2<v_A^2+v_{2s}^2<0,\quad(16)$$

whereas for wavelengths along the magnetic field that appreciably exceed the dimension of magnetic field inhomogeneities, the modes for (14) are aperiodically stable ($\omega^2 > 0$).

Finally, we consider very long wavelengths ($k_z \ll \varkappa_n$) or fairly strong inhomogeneities, making no assumptions as to the magnitude of $k_z v_s/\omega_{Bi}$. In this case Eq. (3) splits into two equations, one of which is identical to the limiting equation (6) for $k_z \ll \varkappa_n$. This case has already been analyzed and the instability condition is expressed by (10). The second equation reads

$$\begin{aligned}&\Big[-\sigma^2\frac{k_z^2k^2}{\omega_{Bi}^2}u_s^2\omega^2-\sigma\frac{k_z k}{\omega_{Bi}\varkappa_n}k^2u_s^2(\varkappa_B-\varkappa_n)\,\omega\\ &+k_z^2u_s^2\frac{k^4}{\omega_{Bi}^2}(v_A^2+v_{1s}^2)\Big](v_A^2+v_{2s}^2)=0.\quad(17)\end{aligned}$$

In the limiting case $k_z v_s/\omega_{Bi} \gg 1$ this equation leads to aperiodically unstable oscillations, whose instability condition is determined by (9). In the opposite limiting case $k_z v_s/\omega_{Bi} \ll 1$ both solutions of (17) are aperiodically stable.

4. Thus it has been shown that it is important to take account of density and magnetic-field inhomogeneities for wavelengths along the magnetic field of the order of the inhomogeneity scale. For a plasma with $T_\perp < T_\parallel$ and $\omega_{Bi}/v_s \ll k_z \ll \varkappa_n$ the instability (5) is similar to the acoustic branch, and condition (9) coincides with the condition for generation of a firehose instability in a homogeneous plasma. For a plasma with $T_\perp > T_\parallel$ and $\omega_{Bi}/v_s \ll k_z \ll \varkappa_n$ the instability (6) develops from the whistler mode while condition (12) is somewhat more rigorous than the condition for the mirror instability in a homogeneous plas-

ma. A mirror instability develops in an inhomogeneous high-pressure plasma ($\beta \gg 1$) only for a low anisotropic temperature ($T_{\perp} \approx T_{\parallel}$) [see condition (12)]. If $k_z \ll \varkappa_n, \omega_{Bi}/v_s$, when $\varkappa_n v_s/\omega_{Bi} \gg 1$ the instability develops for (13), which coincides with the corresponding mode in a homogeneous plasma. When $\varkappa_n v_s/\omega_{Bi} \ll 1$ there is no instability.

In conclusion the authors thank K. N. Stepanov for guidance.

---

[1] L. I. Rudakov and R. Z. Sagdeev, in: Plasma Physics and Controlled Thermonuclear Reactions [in Russian], Vol. 3, Izd. AN SSSR, Moscow (1958), p. 268.

[2] S. Chandrasekhar, A. N. Kaufman, and K. M. Watson, Proc. R. Soc. A, 245, 435 (1958).

[3] A. B. Kitsenko and K. N. Stepanov, Zh. Eksp. Teor. Fiz., 38, 1840 (1960) [Sov. Phys. – JETP, 11, 1323 (1960)].

[4] V. F. Aleksin and V. I. Yashin, Zh. Eksp. Teor. Fiz., 40, 1115 (1961) [Sov. Phys. – JETP, 13, 787 (1961)].

[5] A. B. Mikhailovskii, in: Reviews of Plasma Physics [in Russian], Vol. 6, Atomizdat, Moscow (1972), p. 70.

[6] V. D. Egorenkov and K. N. Stepanov, Ukr. Fiz. Zh., 15, 324 (1970).

[7] A. B. Mikhailov, in: Reviews of Plasma Physics, Vol. 3, Consultants Bureau, New York (1967).

Modulation of microwaves by density fluctuations in a plasma

L. A. Dushin, A. V. Serikov, A. I. Skibenko, E. V. Krivorukov, and I. P. Fomin

(Submitted October 22, 1973)
Zh. Tekh. Fiz., 44, 1862-1870 (September 1974)

To determine the parameters of a fluctuating plasma from modulation of electromagnetic waves, we have investigated the frequency spectrum and the plasma particle density by spectral analysis of fluctuations in the level of a microwave signal transmitted through the plasma. Analytical relations are obtained for the partial and integrated modulation coefficients for the regular and random components of density and on the effective collisions frequency averaged over the path. The experimental arrangement allows investigation of the temporal variation of the spectrum and the level of the high-frequency signal transmitted through the plasma in the frequency range 0.05-5 MHz, by recording short samples at different time intervals of the pulse. Spectral analysis of fluctuations in the microwave signal level (λ = 8 mm) gives the spectrum and the level of plasma density oscillations whose mean value falls in the range 5.10^{11} to 10^{13} cm^{-5}. The range of characteristic frequencies of the density oscillations is 0.05 to 1 MHz. The level of relative density fluctuations in a 40 kHz band near the characteristic maxima of the oscillations is 2 to $7 \cdot 10^{-3}$. The high-frequency spectra are compared with the signal from a zero-bias double probe.

Probes[1] are frequently used to determine the intensity and spectral composition of fluctuations in a turbulent plasma. However, noncontact methods of measurement are to be preferred. Therefore, there is interest in investigating modulation of microwaves passing through a plasma with fluctuating parameters, both from the viewpoint of propagation of the electromagnetic oscillation, and from the viewpoint of noncontact diagnostics. However, the possibility of using modulation of a propagating wave for diagnostics of a dense plasma has only been investigated in the approximation in which the oscillation of the plasma parameters is monochromatic.[2,3] The spectrum of scattered radiation at large angles has been studied for diagnostic purposes.[4,5] An experimental investigation of modulation of microwave signals inside a tube has been performed by us (see ref. 6). The present paper is a continuation of ref. 6 with the objective of developing a method of determining the spectral distribution of the fluctuations of the plasma parameters from the fluctuation in the level of a microwave signal passing through the plasma.

1. DERIVATION OF THE BASIC RELATIONS

If the density N and the effective collision frequency ν in a plasma are random functions of time we can write[7]

$$N(t) = N_0(t) + \int\limits_{\Omega'_m}^{\Omega''_m} N(\Omega_m)\, e^{i(\Omega_m t + \varphi_{0m})} d\Omega, \tag{1}$$

$$\nu(t) = \nu_0(t) + \int\limits_{\Omega'_n}^{\Omega''_n} \nu(\Omega_n)\, e^{i(\Omega_n t + \varphi_{0n})} d\Omega, \tag{2}$$

where $N(\Omega_m)$ and $\nu(\Omega_n)$ are the spectral densities of the random functions $\overset{\circ}{N}(t)$ and $\overset{\circ}{\nu}(t)$; $N_0(t)$ and $\nu_0(t)$ are slow functions of time as compared with $\exp[i(\Omega_m(t) + \varphi_{0m})]$ and $\exp[i(\Omega_n t + \varphi_{0n})]$, respectively; φ_{0m}, φ_{0n} are the initial phases.

In the linear approximation the plasma must have components of the high-frequency complex conductivity σ_ω and $\sigma_{\omega \pm \Omega_{m,n}}$, corresponding to the probe frequency ω and the sideband components $\omega \pm \Omega_{m,n}$. Under the assumption that $\Omega_m \ll \omega$, $\Omega_n \ll \omega$, and

$$\left| \int\limits_{\Omega'_m}^{\Omega''_m} \frac{N(\Omega_m)}{N_0} e^{i(\Omega_m t + \varphi_{0m})} d\Omega \right| \ll 1, \quad \left| \int\limits_{\Omega'_n}^{\Omega''_n} \frac{\nu(\Omega_n)}{i\omega + \nu_0} e^{i(\Omega_n t + \varphi_{0n})} d\Omega \right| \ll 1,$$

neglecting second-order quantities we can write the conductivity components in the form

$$\sigma_\omega = \sigma_0 \left[1 + \int\limits_{\Omega'_m}^{\Omega''_m} \frac{N(\Omega_m)}{N_0} e^{i(\Omega_m t + \varphi_{0m})} d\Omega - \int\limits_{\Omega'_n}^{\Omega''_n} \frac{\nu(\Omega_n)}{i\omega + \nu_0} e^{i(\Omega_n t + \varphi_{0n})} d\Omega \right], \tag{3a}$$

$$\sigma_{\omega \pm \Omega_{m,n}} = \sigma_\omega \left[1 \mp \frac{i\Omega_{m,n}}{i\omega + \nu} \right], \tag{3b}$$

where $\sigma_0 = e^2 N_0 / m(i\omega + \nu_0)$ is the conductivity of the unperturbed plasma at frequency ω. A plane electromagnetic wave propagating through the plasma will have components of electric field

$$\left. \begin{array}{c} E_0 \exp\{i(\omega t + \varphi_0)\};\ E_m(\omega) \exp\{i[(\omega \pm \Omega_m) t + \varphi_0 \pm \varphi_{0m}]\} d\omega, \\ E_n(\omega) \exp\{i[(\omega \pm \Omega_n) t + \varphi_0 \pm \varphi_{0n}]\} d\omega, \end{array} \right\} \tag{4}$$

where $E_m(\omega)$ and $E_n(\omega)$ are the spectral densities of the components of the electric field, and φ_0 is the initial phase of the plane monochromatic wave incident on the plasma.

The analytical dependence of the fluctuations of the electromagnetic wave passing through the plasma on the parameters of the turbulent plasma can be obtained by solving the wave equation

$$\frac{\partial^2 E}{\partial x^2} - \frac{1}{c^2} \frac{\partial^2 E}{\partial t^2} = \frac{4\pi}{c^2} \frac{\partial J}{\partial t} \tag{5}$$

taking account of the fact that the wave propagates in the positive 0x direction, and that $\partial/\partial y = \partial/\partial z = 0$. Substituting the conductivity values from Eqs. (3a) and (3b) and values of the electric field components from Eq. (4) into Eq. (5), we obtain linear second-order differential equations for the field components:

$$\frac{\partial^2 \varepsilon_0}{\partial x^2} + b_0^2 \varepsilon_0 = 0, \tag{6a}$$

$$\frac{\partial^2 \varepsilon_{1,2m,n}(\omega)}{\partial x^2} + b_{1,2m,n}^2 \varepsilon_{1,2m,n}(\omega) = d_{1,2m,n} \varepsilon_0, \tag{6b}$$

where

$$b_0^2 = \left(1 - \frac{4\pi i \sigma_0}{\omega}\right) k^2; \quad k = \frac{\omega}{c},$$

$$b^2_{1,2m,n}=\left[\frac{(\omega\pm\Omega_{m,n})^2}{\omega^2}-\frac{4\pi i\,(\omega\pm\Omega_{m,n})}{\omega^2}\sigma_{\omega\pm\Omega_{m,n}}\right]k^2,$$

$$d_{1m,n}=\frac{2\pi i\,(\omega+\Omega_{m,n})}{\omega^2}a_{m,n}k^2;\quad d_{2m,n}=\frac{2\pi i\,(\omega-\Omega_{m,n})}{\omega^2}\tilde{a}_{m,n}k^2,$$

$$a_m=\frac{N(\Omega_m)}{N_0}\sigma_0;\quad \tilde{a}_m=\frac{N(\Omega_m)}{N_0}\sigma_0\exp[i2(\Omega_m t+\varphi_{0m})],$$

$$a_n=\frac{\nu(\Omega_n)}{i\omega+\nu_0}\sigma_0;\quad \tilde{a}_n=\frac{\nu(\Omega_n)}{i\omega+\nu_0}\sigma_0\exp[i2(\Omega_n t+\varphi_{0n})],$$

$$\varepsilon_0=\frac{E_0}{E_{00}};\quad \varepsilon_{1,2m,n}(\omega)=\frac{E_{1,2m,n}(\omega)}{E_{00}},$$

ω is the frequency of the probe wave; c is the speed of light in vacuum; E_{00} is the electric field wave incident on the plasma.

The solution of Eq. (5) with $m \neq 0$, $n = 0$ or $m = 0$, $n \neq 0$ and the initial conditions

$$\varepsilon_{1,2m,n}(\omega)|_{x=0}=0,\quad \left.\frac{\partial\varepsilon_{1,2m,n}(\omega)}{\partial x}\right|_{x=0}=0$$

has the form

$$\varepsilon_0=D_0e^{ib_0x}, \tag{7a}$$

$$\varepsilon_{1,2m,n}(\omega)=\frac{d_{1,2m,n}D_0}{b_0^2-b_{1,2m,n}^2}[e^{ib_{1,2m,n}x}-e^{ib_0x}]. \tag{7b}$$

Taking account of Eqs. (1), (2), (7a), and (7b) we write the normalized field in the plasma in the form

$$\varepsilon(t)=\varepsilon_0e^{i(\omega t+\varphi_0)}+\int\limits_{\omega'_{1m}}^{\omega''_{1m}}\varepsilon_{1m}(\omega)\,e^{i(\omega_{1m}t+\varphi_{1m})}d\omega+\int\limits_{\omega''_{2m}}^{\omega'_{2m}}\varepsilon_{2m}(\omega)\,e^{i(\omega_{2m}t+\varphi_{2m})}d\omega$$
$$+\int\limits_{\omega'_{1n}}^{\omega''_{1n}}\varepsilon_{1n}(\omega)\,e^{i(\omega_{1n}t+\varphi_{1n})}d\omega+\int\limits_{\omega''_{2n}}^{\omega'_{2n}}\varepsilon_{2n}(\omega)\,e^{i(\omega_{2n}t+\varphi_{2n})}d\omega$$
$$=\varepsilon_0[1+\dot{M}(t)]\,e^{i(\omega t+\varphi_0)}, \tag{8}$$

where

$$\omega_{1n,m}=\omega+\Omega_{m,n};\ \omega_{2m,n}=\omega-\Omega_{m,n};$$

$$\varphi_{1m,n}=\varphi_0+\varphi_{0m,n};\ \varphi_{2m,n}=\varphi_0-\varphi_{0m,n}.$$

The instantaneous value of the complex modulation amplitude of the electromagnetic wave passing through the plasma is a random quantity

$$\dot{M}(t)=\int\limits_{\Omega'_m}^{\Omega''_m}\dot{M}(\Omega_m)\,e^{i(\Omega_m t+\varphi_{0m})}d\Omega+\int\limits_{\Omega'_n}^{\Omega''_n}\dot{M}(\Omega_n)\,e^{i(\Omega_n t+\varphi_{0n})}d\Omega. \tag{9}$$

The spectral distribution of the modulation coefficients can be represented by the expressions

$$\dot{M}(\Omega_m)=\left\{\frac{(\omega+\Omega_m)}{b_0^2-b_{1m}^2}[e^{i(b_{1m}-b_0)x}-1]\right.$$
$$\left.+\frac{(\omega-\Omega_m)}{b_0^2-b_{2m}^2}[e^{i(b_{2m}-b_0)x}-1]\right\}\frac{2\pi i\sigma_0}{\omega^2}k^2\frac{N(\Omega_m)}{N_0}, \tag{10}$$

$$\dot{M}(\Omega_n)=\left\{\frac{(\omega+\Omega_n)}{b_0^2-b_{1n}^2}[e^{i(b_{1n}-b_0)x}-1]\right.$$
$$\left.+\frac{(\omega-\Omega_n)}{b_0^2-b_{2n}^2}[e^{i(b_{2n}-b_0)x}-1]\right\}\frac{2\pi i\sigma_0}{\omega^2}k^2\frac{\nu(\Omega_n)}{i\omega+\nu_0}. \tag{11}$$

If we neglect the collision frequency and assume that the plasma oscillations are of low frequency, and that their level is low, i.e., $\nu \ll \omega$, $\Omega_m \ll \omega$, $|i(b_m-b_0)x| \ll 1$, then, taking into account Eqs. (3a), (3b), (5a), (5b), (9), and (10), the modulus of the spectral distribution of the modulation coefficient can be represented by the expression

$$|\dot{M}(\Omega_m)|=\frac{1}{2}\frac{\omega}{c}x\left(1-\frac{N_0}{N_{cr}}\right)^{-1/2}\frac{N_0}{N_{cr}}\frac{N(\Omega_m)}{N_0}. \tag{12}$$

The modulus of the modulation coefficient is then equal to

$$M=\frac{1}{2}\frac{\omega}{c}x\frac{N_0}{N_{cr}}\left(1-\frac{N_0}{N_{cr}}\right)^{-1/2}\left\{\left[\int\limits_{\Omega'_m}^{\Omega''_m}\frac{N(\Omega_m)}{N_0}\sin(\Omega_m t+\varphi_{0m})\,d\Omega\right]^2\right.$$
$$\left.+\left[\int\limits_{\Omega'_m}^{\Omega''_m}\frac{N(\Omega_m)}{N_0}\cos(\Omega_m t+\varphi_{0m})\,d\Omega\right]^2\right\}^{1/2}. \tag{13}$$

Replacing the random functions by their variances we write the expression for the mean-square value of the modulation amplitude in the form

$$\overline{M}=\frac{1}{2}\frac{\omega}{c}x\frac{N_0}{N_{cr}}\left(1-\frac{N_0}{N_{cr}}\right)^{-1/2}\frac{\sqrt{\overline{N}^2}}{N_0}, \tag{14}$$

where $\overline{N}^2$ is the variance of the density fluctuation. Thus, by measuring the spectral distribution of the fluctuations in the level of a microwave signal, we can determine the spectrum of density fluctuations; from the variance of the signal level fluctuations we can determine the mean-square deviation of density from its mean value.

2. MEASUREMENT TECHNIQUE AND RESULTS

An experimental investigation of the modulation of an electromagnetic wave caused by a spectrum of plasma oscillations has been carried out on the high-power cold cathode reflex discharge facility described in ref. 6. The discharge takes place in hydrogen at 10^{-2} torr in a mag-

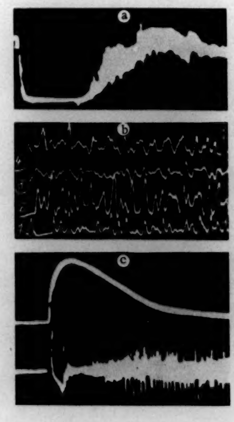

Fig. 1. a) Microwave signal passed through the plasma, with sweep length 2 μsec; b) microwave signals delayed by 1.2, 1.4, 1.6, and 1.8 μsec relative to the start of the discharge (curves 1-4, respectively), length 50 μsec; c) discharge current and signal from the zero-bias twin electrical probe (sweep is 2 μsec).

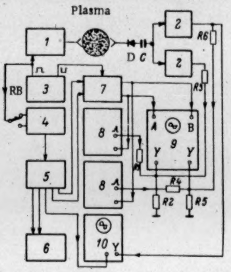

Fig. 2. Schematic diagram of the measurement system. 1) Microwave generator; 2) amplifier; 3) G5-15 generator; 4) individual record trigger; 5) triggering unit; 6) electrical circuit; 7) matched electronic gates; 8) sawtooth voltage generator; 9) S1-33 oscilloscope; 10) S1-16 oscilloscope.

netic field. The plasma is probed by means of electromagnetic waves at λ = 8 mm, with $E \parallel H_{ext}$. Horns mounted in matched diagnostic ports are used to form beams of the order of the antenna aperture.

It has been noted earlier[6] that for certain conditions in a discharge of this type there are intense low-frequency oscillations of the plasma, whose spectrum varies during the discharge. In order to study the temporal variation of the spectrum of the oscillations the spectral composition is investigated for samples of a given length ($\Delta t = 50$ μsec), these being chosen by introducing a different delay relative to the start of the discharge (Fig. 1).

To carry out these measurements a system (Fig. 2) has been developed to allow recording of both the random fluctuations of the microwave signal level, and also the mean value. To determine the level of the signal a continuous sequence of pulses is fed from a reference oscillator 3 to the reflector of the klystron oscillator 1, the pulse length being t_p, and the repetition period T_p. The mean level of the signal passing through the plasma is determined from the cutoff (Fig. 1b). To record the short samples of the progress of the process, multiple recordings are taken on two channels of oscilloscope 9, with independent sweeps. To do this a signal is fed from oscillator 3 to the matched "electronic gates" 7 (Fig. 3) and through the record button RB to the separate record trigger 4. The first pulse to pass through after the contact RB closes flips the trigger 4. A positive pulse appears at the trigger output which arrives at the input to the multichannel generator of synchropulses with a controlled delay. At a given time relative to the start of the discharge the first channel of the electronic gate 7 is recorded by unit 5, and at its output a sequence of pulses appears which gives a multiple sweep of the first channel beam on the oscilloscope 9. Similarly, the second channel of unit 7 gives a multiple recording of the sweep of the second beam of oscilloscope 9 at later times than for the first channel. Vertical displacement of the beams during the multiple recording on oscilloscope 9 is achieved by sawtooth voltage pulses of length $t_{sp} \geq (n-1)T_n$, which come from generator 8 synchronously with the oscilloscope recording. The resistor networks, R1, R2, R3, and R4, R5, R6 allow decoupling of the output of the amplifiers 2 and the generators 8. Oscilloscope 10 is used to record variation in the level of the microwave that is passed through the plasma during the entire process (Fig. 1a).

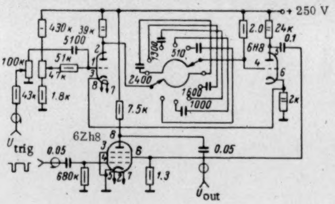

Fig. 3. Circuit diagram of the electronic gates.

A similar arrangement is also used to record the signals from the zero-bias electrical double probe. The coupling element between the probe and amplifiers 2 is a wideband symmetric transformer with a 3 dB band from 0.01 to 10 MHz. An oscillogram of the probe signal is shown in Fig. 1c.

The level of the signal that is passed through the plasma can be represented by the function

$$A(t) = A_0(t) + \tilde{A}(t), \tag{15}$$

where $A_0(t)$ is a slowly varying function of time; $\tilde{A}(t)$ is a centered random function, describing random fluctuations of the level.

The recorded signal oscillograms (Fig. 1b) are processed and a continuous sample is transformed into a random sequence. Digitalization and measurement of the samples is semiautomatic. The initial sequence of points thus obtained, measured in an arbitrary manner along the time axis, is transformed following interpolation into an equidistant sequence of the desired size.

Following transformation of the random function into a stationary centered sequence, the mathematic expectation, the variance, and the autocorrelation function can be represented, respectively, in the form[9]

$$A_0^* = \frac{1}{n} \sum_{j=1}^{n} A_j^{1/\gamma}, \tag{16}$$

$$\bar{A}_d^{*2} = \frac{1}{n} \sum_{j=1}^{n} [A_j^{1/\gamma} - A_0^*]^2, \tag{17}$$

$$R_A = \frac{1}{n} \sum_{j=1}^{n-k} A_j^{1/\gamma} A_{j+k}^{1/\gamma} \tag{18}$$

(k = 0, 1, 2, ... is the number of intervals of the digitalization, A_j is the deviation of the j-th point from the zero level; and γ is the exponent determining the volt–ampere characteristic of the sensor). The spectral density of the level fluctuations in the interval $0 \leq f \leq 1/2\Delta$ is[8]

$$\bar{A}^{*2}(f) = 2\Delta \sum_{k=0}^{p-1} R_A e^{-i2\pi k\Delta f}$$

($f = \Omega/2\pi$; Δ is the digitalization interval).

Thus, the mean-square value of the modulation coefficient and its spectral distribution in the interval Δt has the form

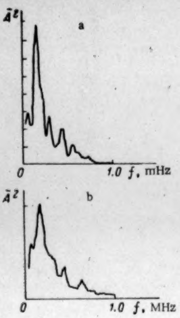

Fig. 4. Spectral distributions of oscillations of a microwave signal transmitted through a plasma (a), and of a probe signal (b), for a time t = 1.6 μsec relative to the start of the discharge.

$$\bar{M}=\frac{(\bar{A}_{\sim}^{*2})^{1/2}}{A_0^*}, \tag{19}$$

$$M^2(f)=\frac{\bar{A}^{*2}(f)}{A_0^{*2}}. \tag{20}$$

By recording and processing oscillograms of the fluctuations in the signal level (Fig. 1b) in the above manner, using a type M-220 computer, we have been able to determine the spectral distribution at different times (Fig. 4a) and the mean value of the transmitted signal. Thus we find the spectral distribution of the modulation coefficient and its integrated value, both in a narrow frequency range near the characteristic frequency, and also in the wide range of frequencies investigated (Fig. 5). From these relationships and the time variation of the mean density (Fig. 6) we have calculated the time (Fig. 7) and frequency (Fig. 8) dependences of the relative density fluctuations $\bar{N}(t)/N_0$ and $\bar{N}(f)/N_0$.

Comparison of Figs. 6 and 7 shows that, as the density N_0 decreases, the level of $\bar{N}(t)/N_0$ first increases, reaches a maximum, and then decreases. The value of $\bar{N}(f)/N_0$ decreases as the frequency f increases, and the position of the maximum is displaced towards lower densities (at later time). The cause of the observed fluctuations in the signal level, besides low-frequency large-scale density oscillations, may also be other factors; fluctuations in the frequency of collisions, regular refraction, scattering of the wave at large angles, followed by reflection and combination with the transmitted wave.

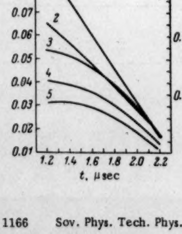

Fig. 5. Time dependence of the integral (1) and partial modulation coefficients in a 40 kHz band near the characteristic plasma oscillation frequencies: 2) 200; 3) 300; 4) 400; 5) 500 kHz.

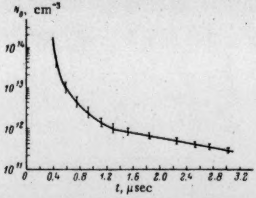

Fig. 6. Time dependence of the mean plasma density across the probe section. p = 10^{-2} torr, H = 320 kA/m, U_{el} = 3.6 kV.

It can be shown from Eqs. (10) and (11) that the ratio of the modulation coefficients due to fluctuations in the frequency of collisions and of the density is

$$\frac{M_\nu}{M_N}=\frac{\nu_0}{\omega}\frac{\tilde{\nu}}{\nu_0}\left(\frac{\bar{N}}{N_0}\right)^{-1}. \tag{21}$$

In our case ($\nu \leqslant 0.04\ \omega$) for the same level of fluctuations of the two parameters, $M_\nu \leq 0.04\ M_N$. Calculation of the refraction shows that the increase in dispersion of the ray tube due to this factor is less than 1° for $N \leq 0.1\ N_{cr}$.

It is known that the integrated scattering coefficient is[11]

$$\Gamma=\frac{\pi^3 d}{\lambda^2}\left(\frac{\bar{N}}{N_{cr}}\right)^2\left[1-\exp\left\{-\left(\frac{2\pi d}{\lambda}\right)^2\right\}\right], \tag{22}$$

where d is the scale of the nonuniformity. Assuming d ≈ 1 cm, and $\bar{N}/N_{cr} \approx 0.5$, and that the fraction of the scattered flux reaching the receiving antenna is proportional to the ratio of the area of the antenna aperture (0.8 Δb^2) to the area of the part of the chamber reflecting the scattered radiation, equal to $2\pi R\Delta b$ (Δb is the width of the antenna aperture), we obtain a modulation coefficient of 0.06.

Taking into account that, for the plasma parameters chosen and for a single transmission, the radiation is attenuated roughly by a factor of 2, the effect of large-scale scattering will be less than the modulation level in the ray tube by a factor of roughly 3 to 4.

Simultaneously with measurement of the spectrum of signal level fluctuations, a study is made of the spectrum of current fluctuations in the zero-bias electrical double

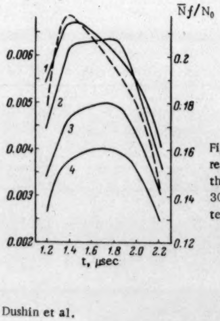

Fig. 7. Temporal dependence of the relative fluctuations of density near the characteristic frequency 1) 200; 2) 300; 3) 400; 4) 500 kHz, and their integrated value (dashed line).

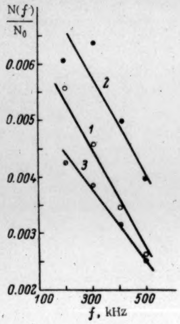

Fig. 8. Frequency dependence of the relative fluctuations of plasma particle density at different times relative to the start of discharge. 1) t = 1.2, 2) 1.8; 3) 2.2 μsec.

probe, which is mounted in the same section at a distance of (1/3)R from the discharge axis (Fig. 4). A comparison of the fluctuations in the level and in the probe signals shows that their spectra coincide. Therefore, we can consider that the fluctuations in signal level are due to fluctuations of parameters in the plasma volume, and do not result from interference by multiple reflection in the chamber. The two sensors do not record oscillations when the discharge current duration is small. The nature of the time variations in the probe signal fluctuations is qualitatively similar to the fluctuation in the signal level.

Thus, large-scale low-frequency oscillations predominate in the discharge; their intensity decreases linearly as frequency increases.

An analysis of the time dependence of the fluctuations in signal level and of the probe signal (Fig. 1, a and c) shows that the fluctuations are generated at the density growth stage and are attenuated when the discharge current and the density have their maximum values. At the density decrease stage the amplitude of the oscillations increases to a maximum and again decreases. When the oscillations are attenuated the plasma decays more slowly.

Preliminary investigations of the dependence of the fluctuation spectrum on the level of the external magnetic field, and estimates of the temperature gradients and the density support the view that the observed plasma oscillations can be interpreted as drift oscillations of a nonuniform plasma with an isotropic particle distribution function in the presence of an external magnetic field; these oscillations exist in a nonisothermal plasma[10] with $T_e \gg T_i$. Since the drift oscillations are generated at density gradients, the size of a nonuniformity must be less than the radius of the plasma (R = 100 mm), and the least size of nonuniformity for which radiation does not emerge from the ray tube is of the order[6] of 24 mm.

Thus, spectral analysis of fluctuations of the level of microwaves used to probe a plasma has generated the spectral distribution and the value of large-scale low-frequency density fluctuations in the vicinity of the characteristic frequencies of plasma oscillations, as well as the integral value of plasma oscillations over the entire frequency range.

The experimental technique used has allowed investigation of the time variation of the spectrum of plasma oscillations in a single discharge.

In conclusion the authors thank A. Ya. Omel'chenko and B. I. Smerdov for useful comments.

---

[1] M. P. Vasil'ev, O. S. Pavlichenko, and F. F. Tereshchenko, in: Plasma Physics and Problems of Controlled Thermonuclear Fusion, No. 4, 195, [in Russian], Izd. Naukova Dumka, Kiev (1973).

[2] M. S. Sodak and C. J. Palumbo, Canad. J. Phys., 42, No. 8, 1335 (1964).

[3] C. J. K. Virmani, Plasma Phys., 14, No. 11, 1047 (1972).

[4] M. M. Larionov and V. V. Rozhdestvenskii, Zh. Tekh. Fiz., 38, 279 (1968) [Sov. Phys. – Tech. Phys., 13, 202 (1968)].

[5] M. M. Larionov, V. A. Rodichkin, V. V. Rozhdestvenskii, and A. M. Timonin, Plasma Phys. and Controlled Nucl Fus. Res., I, CN-24/B = 5, 225 (1969).

[6] L. A. Dushin, A. I. Skibenko, and I. P. Fomin, Zh. Tekh. Fiz., 43, 317 (1973) [Sov. Phys. – Tech. Phys., 18, 207 (1973)].

[7] V. S. Pugachev, Theory of Random Functions and Its Application to Problems of Automatic Control [in Russian], Fizmatgiz, Moscow (1962).

[8] G. Jenkins and D. Beattie, Spectral Analysis and Its Application, Pt. I, [Russian translation], Izd. Mir, Moscow (1971).

[9] J. Bendat and A. Pearsol, Measurement and Analysis of Random Processes [in Russian], Izd. Mir, Moscow (1971).

[10] V. L. Ginzburg and A. A. Rukhadze, Waves in a Magnetoactive Plasma [in Russian], Izd. Nauka, Moscow (1970).

[11] V. E. Golant, Microwave Plasma Properties [in Russian], Izd. Nauka, Moscow (1968).

Measurement of plasma density distribution with a rectangular microwave cavity

I. N. Moskalev

(Submitted September 25, 1973)
Zh. Tekh. Fiz., 44, 1871-1876 (September 1974)

The feasbility of using multimode microwave cavities with a rectangular cross section to measure an arbitrary plasma density distribution n (r, φ) is investigated. It is shown that the loss of information associated with the odd harmonics of the Fourier expansion of the function n (r, φ) makes it impossible to measure an arbitrary distribution.

The feasibility of measuring the spatial density distribution n(r, φ, z) of a plasma by the cavity method is well known in the literature.[1–4] When a plasma is introduced into a cavity the cavity eigenfrequencies are shifted; the amount of the shift is known to be proportional to the average density of the plasma in the region occupied by the electric field. The distribution and absolute value of the plasma density can be found by determining the frequency shifts of the cavity in several modes with different electric field configurations. In most of the papers devoted to this problem for simplicity the density distribution is assumed to be axisymmetric and independent of the longitudinal coordinate. In many practical situations, however, these assumptions are not justified. For example, the plasma in a stellerator or tokamak is not axisymmetric; the plasma distribution in devices with magnetic mirrors has a strong dependence on z, etc. The density distribution with respect to z can almost always be determined by means of a cavity with small longitudinal dimensions (such as a Fabry–Perot cavity or an open beer-barrel cavity) such that the density gradient is negligible. It is not yet clear how the dependence on r and φ can be determined or whether it is even possible to do so. An analysis has shown[5] that axisymmetric cavities do not respond to the odd harmonics of the Fourier expansion of the function n(r, φ) with respect to φ. This means that such cavities cannot be used, in principle, to determine an arbitrary distribution n(r, φ), regardless of what modes or how many of them are used for the measurements.

The insensitivity of axisymmetric cavities to odd harmonics of an azimuthal perturbation (in particular, to a slight displacement of the plasma column) is a consequence of the specific form of the azimuthal dependence of the electric fields. The latter, in turn, are determined by the cavity eigenfunctions, i.e., primarily by the cavity configuration. It is reasonable to ask, therefore, whether the indicated insensitivity of such cavities to odd harmonics is not a result of their axial symmetry. If this is true, it should be possible to obtain an arbitrary distribution n(r, φ) by means of cavities with a different configuration. Since rectangular cavities are the simplest and therefore the most widely used next to the axisymmetric type, they deserve the greatest attention.

In this paper we consider the possibility of using rectangular cavities (it is immaterial whether they are open or closed) to determine an arbitrary plasma density distribution n(r, φ).

Without sacrificing generality we consider the TM_{mnq} modes of a rectangular cavity with longitudinal index q = 1 (Fig. 1). The principal field component E_z in a rectangular coordinate system associated with one of the cavity angles has the form

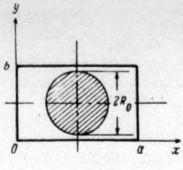

Fig. 1

$$E_z = E_0 \sin\left(\frac{\pi m}{a}x\right)\sin\left(\frac{\pi n}{b}y\right)f(z), \tag{1}$$

where $f(z)$ is the longitudinal field distribution function, which is unimportant for our problem.

Let a plasma cylinder of radius R_0 with an arbitrary density distribution with respect to the coordinates n(x, y, z) be located at the center of the cavity, i.e., at the point $\{a/2, b/2\}$.

The resonance shift of a cavity operating in the TM_{mn} mode when a plasma is introduced is given by the expression (see, e.g., ref. 4)

$$\left(\frac{\Delta\omega}{\omega}\right)_{mn} = \frac{1}{2n_{cr}}\frac{\int\limits_V E_{mn}^2(V)\,n(V)\,dV}{\int\limits_V E_{mn}^2(V)\,dV}. \tag{2}$$

Here n_{cr} is the critical density, and V is the volume of the cavity. Since we are assuming that the relative variation of the density over the length of the cavity is small and the principal field component is E_z, we can write the expression (2) for the shift in the form

$$\left(\frac{\Delta\omega}{\omega}\right)_{mn} = \frac{1}{2n_{cr}}\frac{\int\limits_S E_z^2(x, y)\,n(x, y)\,dS}{\int\limits_S E_z^2(x, y)\,dS}, \tag{3}$$

where S is the cross section of the cavity.

We introduce a cylindrical coordinate systm r, φ, z* whose center coincides with the center of the cavity, where the z* axis is parallel to the original z axis and the direction φ = 0 corresponds to the positive direction of the x axis. Expressing the variables x, y, and z in terms of r, φ, and z* = Z, substituting the resulting expression for the electric field into (3), and carrying out suitable transformations, we obtain

$$\int\limits_0^{2\pi}\int\limits_0^{R_0} E_0^2 \sin^2\left[\frac{\pi m}{a}\left(r\cos\varphi - \frac{a}{2}\right)\right]\sin^2\left[\frac{\pi n}{b}\left(r\sin\varphi - \frac{b}{2}\right)\right] n(r, \varphi)\,r\,dr\,d\varphi = B_{mn}\left(\frac{\Delta\omega}{\omega}\right)_{mn}. \tag{4}$$

Here, the constant B_{mn} includes all other quantities irrelevant to our problem.

We separate the variables in the integrand of (4). We note, accordingly, that by rewriting

$$\sin^2\left[\frac{\pi m}{a}\left(r\cos\varphi-\frac{a}{2}\right)\right] \text{ as } \frac{1}{2}\left[1-(-1)^m\cos\left(\frac{2\pi m}{a}r\cos\varphi\right)\right]$$

we can write the electric field in (4) in the form

$$\begin{aligned}E_z^2(r,\varphi)&=\frac{1}{4}\left[1-(-1)^m\cos\frac{2\pi m}{a}(r\cos\varphi)\right]\left[1-(-1)^n\cos\frac{2\pi n}{b}(r\sin\varphi)\right]\\&=\frac{1}{4}\left[1-(-1)^m\cos\left(\frac{2\pi m}{a}r\cos\varphi\right)-(-1)^n\cos\left(\frac{2\pi n}{b}r\sin\varphi\right)\right.\\&\quad\left.+(-1)^{m+n}\cos\left(\frac{2\pi n}{a}r\cos\varphi\right)\cos\left(\frac{2\pi n}{b}r\sin\varphi\right)\right].\end{aligned}\tag{5}$$

(We drop E_0^2 from now on as an inessential constant.)

We rewrite the last term in (6):

$$\begin{aligned}&(-1)^{m+n}\frac{1}{2}\left\{\cos\left[2\pi r\left(\frac{m}{a}\cos\varphi-\frac{n}{b}\sin\varphi\right)\right]\right.\\&\quad\left.+\cos\left[2\pi r\left(\frac{m}{a}\cos\varphi+\frac{n}{b}\sin\varphi\right)\right]\right\}\\&=(-1)^{m+n}\frac{1}{2}\left\{\cos\left[2\pi r\sqrt{\left(\frac{m}{a}\right)^2+\left(\frac{n}{b}\right)^2}\sin(\varphi+\varphi_0)\right]\right.\\&\quad\left.+\cos\left[2\pi r\sqrt{\left(\frac{m}{a}\right)^2+\left(\frac{n}{b}\right)^2}\sin(\varphi_0-\varphi)\right]\right\}\\&=(-1)^{m+n}\frac{1}{2}\{\cos[M(r)\sin(\varphi+\varphi_0)]+\cos[M(r)\sin(\varphi_0-\varphi)]\},\end{aligned}$$

where

$$M(r)=\cos\left[2\pi r\sqrt{\left(\frac{m}{a}\right)^2+\left(\frac{n}{b}\right)^2}\right],$$

$$\varphi_0=\operatorname{arc\,tg}\frac{mb}{na}.$$

Introducing the notation

$$\frac{2\pi m}{a}r=U(r) \text{ and } \frac{2\pi n}{b}r=W(r),$$

we write (5) in the form

$$\begin{aligned}E_z^2=E_{mn}^2=\frac{1}{4}&\left\{1-(-1)^m\cos[U(r)\cos\varphi]-(-1)^n\cos[W(r)\sin\varphi]\right.\\&+(-1)^{m+n}\frac{1}{2}\cos[M(r)\sin(\varphi+\varphi_0)]\\&\left.+(-1)^{m+n}\frac{1}{2}\cos[M(r)\sin(\varphi_0-\varphi)]\right\}.\end{aligned}\tag{6}$$

Using the relations

$$\cos(U\sin\varphi)=J_0(U)+2\sum_{p=1}^{\infty}J_{2p}(U)\cos 2p\varphi$$

and

$$\cos(U\cos\varphi)=J_0(U)+2\sum_{p=1}^{\infty}(-1)^pJ_{2p}(U)\cos 2p\varphi,$$

in which $J_p(U)$ is the Bessel function of order p, we find

$$\begin{aligned}E_{mn}^2=\frac{1}{4}&\left\{1-(-1)^m\left[J_0(U)+2\sum_{p=1}^{\infty}J_{2p}(U)\cos 2p\varphi\right]\right.\\&-(-1)^n\left[J_0(W)+2\sum_{p=1}^{\infty}(-1)J_{2p}(W)\cos 2p\varphi\right]+\frac{1}{2}(-1)^{m+n}\\&\times\left[J_0(M)+2\sum_{p=1}^{\infty}(-1)^pJ_{2p}(M)\cos 2p(\varphi+\varphi_0)\right]-\frac{1}{2}(-1)^{m+1}\\&\left.\times\left[J_0(M)+2\sum_{p=1}^{\infty}(-1)^pJ_{2p}(M)\cos 2p(\varphi-\varphi_0)\right]\right\}.\end{aligned}\tag{7}$$

Consequently, E_m^2 can be represented as a linear combination of functions depending only on one variable, r or φ.

We expand the function $n(r, \varphi)$ in a Fourier series in the interval $[0, 2\pi]$:

$$n(r,\varphi)=\frac{a_0}{2}+\sum_{k=1}^{\infty}(a_k\cos k\varphi+b_k\sin k\varphi),\tag{8}$$

where a_k and b_k are the coefficients of the expansion.

We now substitute Eqs. (7) and (8) into (4) and integrate with respect to φ from 0 to 2π. Using relations of the type

$$\int_0^{2\pi}\cos 2p\varphi\cos k\varphi d\varphi\begin{cases}0 & \text{for } k\neq 2p\\ \pi & \text{for } k=2p\end{cases} \text{ and } \int_0^{2\pi}\cos 2p\varphi\times$$

$$\times\sin k\varphi d\varphi \text{ for any integers p and k,}$$

we infer that

$$\left.\begin{aligned}&\left(\frac{\Delta\omega}{\omega}\right)_{mn}=\pi\int_0^{R_0}\left(a_0A+2\sum_{p=1}^{\infty}a_{2p}C_{2p}\right)rdr,\\&\text{where}\\&A=1-(-1)^mI_0(U)-(-1)^nI_0(W)+(-1)^{m+n}I_{2p}(M)\cos 2p\varphi_0,\\&C_{2p}=-(-1)^{m+p}I_{2p}(U)-(-1)^nI_{2p}(W)\\&\qquad+(-1)^{m+n}I_{2p}(M)\cos 2p\varphi_0.\end{aligned}\right\}\tag{9}$$

The dependence of the right-hand side on the indices m and n is contained here in the functions U(r, m), W(r, n), and M(r, m, n).

As is evident from (9), the expression for the frequency shift does not include odd harmonics of the expansion (8); consequently, the "rectangular" cavity, like the "axisymmetric" type, does not respond to these density perturbations, and this information is therefore lost in cavity measurements.

It is interesting to note that not only are the odd harmonics of the expansion (8) missing from expression (9); all terms of the form $b_k\sin k\varphi$ are also missing; this fact seems strange because it implies, at first glance, that the x axis ($\varphi = 0$) is special by comparison with the y axis ($\varphi = \pi/2$). This cannot be the case since the electric fields are symmetric with respect to the coordinate axes.

To understand the reason for the foregoing result, i.e., to ascertain its physical meaning, we refer to Fig. 2, which shows various deformations of a plasma. We assume for simplicity that the plasma cylinder is homogeneous in its cross section and that the coefficients a_k and b_k are much smaller than a_0. The electric field E_{mn} is perpendicular to the plane of the figure (TM_{mn} modes), and the density of the contours (solid lines) is proportional to the field. Small values of m and n are used (m = 2, n = 1). The variation $\delta(\Delta\omega/\omega)_{mn}$ of the frequency shift due to perturbations of the plasma is proportional in the figure to the variation of the field flux across the plasma cross section after superposition of their perturbations.

We consider the simplest perturbations of the plasma density, $n = a_0 + a_1\cos\varphi$ and $n = n_0 + b_1\sin\varphi$, which represent, to a first approximation, displacements of the plasma

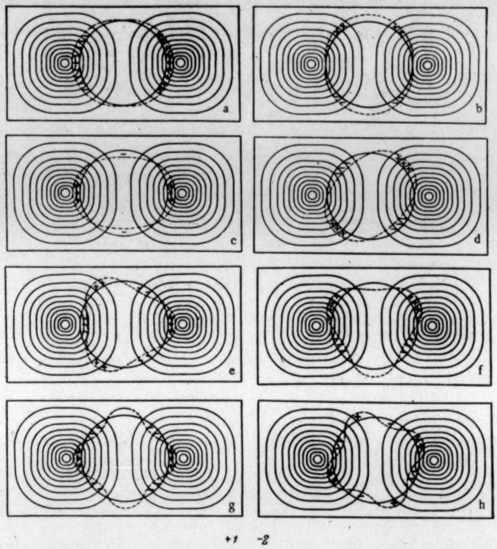

Fig. 2. Response of a cavity to various perturbations of a plasma filament. a) $n = a_0 + a_1 \cos\varphi$, $\delta(\Delta\omega) = 0$; b) $n = a_0 + b_1 \sin\varphi$, $\delta(\Delta\omega) = 0$; c) $n = a_0 + a_2 \cos 2\varphi$, $\delta(\Delta\omega) \neq 0$; d) $n = a_0 + b_2 \sin 2\varphi$, $\delta(\Delta\omega) = 0$; e) $n = a_0 + a_3 \cos 3\varphi$, $\delta(\Delta\omega) = 0$; f) $n = a_0 + b_3 \sin 2\varphi$, $\delta(\Delta\omega) = 0$; g) $n = a_0 + a_4 \cos 4\varphi$, $\delta(\Delta\omega) \neq 0$; h) $n = a_0 = b_4 \sin 4\varphi$, $\delta(\Delta\omega) = 0$. An increase in the frequency shift due to deformation of the filament is indicated by a plus sign, a decrease by a minus sign [the number of signs is proportional to the contribution to $\delta(\Delta\omega)$].

column along the x and y axes, respectively (Figs. 2a and 2b). As the figure shows, with these displacements the positive increment of the frequency shift due to entry of the plasma into the electric field domain 1 is offset by the negative increment of the shift due to its departure from the other domain 2, so that the resultant effect, i.e., the total variation $\delta(\Delta\omega)$ is equal to zero. The cavity is therefore insensitive to plasma density variation of the type $a_1 \cos\varphi$ or $b_1 \sin\varphi$.

Next we consider the perturbations $a_2 \cos\varphi$ and $b_2 \cdot \sin\varphi$ illustrated in Figs. 2c and 2d; they transform the axisymmetric plasma cylinder into an elliptical cylinder. In the case of a cosine perturbation the positive increment of $\Delta\omega$ induced by the flux across domain 1 is greater than the negative increment due to the departure of the plasma from domain 2, so that the net effect is no longer zero. A sine perturbation in this case, on the other hand, again does not change the value of $\Delta\omega$, because the positive variation $\delta(\Delta\omega)$, due to domain 1 is exactly equal to the opposite variation induced by domain 2. Accordingly, expression (9) includes the term $a_2 \sin 2\varphi$ of the expansion and not the term $b_2 \sin 2\varphi$.

A further examination of the figures (2f, 2g, and 2h) shows that the cavity has a nonzero response only for the density perturbation $a_4 \cos 4\varphi$ and, as is immediately apparent, for all perturbations symmetric with respect to both the x and the y axis simultaneously.

Therefore, contrary to first appearances based on expression (9), the cavity is actually not selective with respect to one of the directions (x or y).

The fact that the two largest and most thoroughly investigated classes of cavities, axisymmetric and rectangular, do not respond to odd harmonics of the density perturbation still does not imply that cavities should be dismissed for density distribution measurements. Under certain assumptions with respect to the form of the function $n(r, \varphi)$ [for example, if the shape of the cross section of the surfaces on which the density has the same value ("equidensity lines") is known] such multimode measurements will yield complete information about the required distribution.[5]

I wish to thank A. M. Stefanovskii and E. I. Dobrokhotov for a discussion.

---

[1] S. Braun, Radiotekh. Elektron., 4, 1244 (1959).

[2] G. Janzen, Z. Naturforsch., 24a, 1496 (1969).

[3] S. K. Sen and S. Mukhopadhyay, Internat. J. Electronics, 30, 491 (1971).

[4] V. E. Golant, Microwave Techniques of Plasma Research [in Russian], Izd. Nauka, Moscow (1968).

[5] I. N. Moskalev, and A. M. Stefanovskii, Zh. Tekh. Fiz., 42, 1224 (1972) [Sov. Phys. – Tech. Phys., 17, 974 (1972)].

Diffusion of quasistationary helical magnetic fields into the interior of cylindrical chambers. II.

V. F. Aleksin and S. S. Romanov

(Submitted May 16, 1973; resubmitted October 20, 1973)
Zh. Tekh. Fiz., 44, 1877-1882 (September 1974)

The penetration times for quasistationary magnetic fields in a conducting cylindrical shell and in a solid conducting cylinder are computed. In both cases, the penetration time of the field is determined by the conducting properties of the material and the spatial periods of the currents that excite the field.

The investigation of the diffusion of quasistationary magnetic fields into regions bounded by conductors is of interest in many problems. The increasing interest in such studies stems from the need for effective magnetic configurations for plasma confinement. The most widespread and promising of these are magnetic systems which utilize uniform and spatially periodic fields of quasistationary currents that flow inside or outside of a conducting chamber.

In the first part of this work[1] we have investigated diffusion of uniform fields. In the second part we consider the diffusion of helical magnetic fields into the interior of hollow and solid conducting cylinders.

1. DIFFUSION OF HELICAL MAGNETIC FIELDS INTO THE INTERIOR OF CONDUCTING CYLINDERS

Consider a magnetic field created by spatially periodic quasistationary currents that flow along the outer surface of a hollow conducting cylinder of radius a. In a cylindrical coordinate system (r, φ, z) with z axis directed along the cylinder axis, with periodically distributed currents with period $2\pi/l$ relative to φ and L relative to z, the components of the magnetic field can be represented by a double Fourier series in φ and z. We limit ourselves to the case of helical symmetry, in which the current components are periodic functions of the period 2π relative to the combination $\theta = l\varphi - hz$, where $h = 2\pi/L$.

Despite these constraints, the case under consideration remains fairly general, and from it for $l = 0$ we obtain the case of a "corrugated" magnetic field and for $h = 0$ the case of a field of periodically distributed longitudinal currents.

We represent the components of the helical currents by a Fourier series in complex form:

$$\left.\begin{aligned} j_z(\theta, t) &= \sum_{n=-\infty}^{n=+\infty} j_{nz}(t)\, e^{in\theta}, \\ j_\varphi(\theta, t) &= \sum_{n=-\infty}^{n=+\infty} j_{n\varphi}(t)\, e^{in\theta}. \end{aligned}\right\} \tag{1.1}$$

The condition that the current density be continuous (div j = 0) implies that

$$j_{n\varphi}(t) = \frac{ha}{l} j_{nz}(t) \equiv j_n(t), \tag{1.2}$$

i.e., the helical currents can be specified by one component. The ratio ha/l represents the tangent of the angle between the direction of the current and the generator of the cylinder ($\tan \vartheta = ha/l$).

The components of the magnetic field with helical symmetry can also be represented by a Fourier series:

$$\left.\begin{aligned} H_r(r, \theta, t) &= \sum_n f_n(r, t)\, e^{in\theta}, \\ H_\varphi(r, \theta, t) &= \sum_n g_n(r, t)\, e^{in\theta}, \\ H_z(r, \theta, t) &= \sum_n q_n(r, t)\, e^{in\theta}. \end{aligned}\right\} \tag{1.3}$$

To be specific we consider the case of positive n ($n > 0$). Because the components of the magnetic field are real, the Fourier coefficients with negative n must be the complex conjugates of the corresponding coefficient with positive n. The case $n = 0$ has been considered earlier.[1]

The Laplace transformations with respect to time for the Fourier coefficients of the magnetic field components $\bar{f}_n(r)$, $\bar{g}_n(r)$, $\bar{q}_n(r)$ can be found from the solution of Maxwell's equations ((1.5)-(1.7) in ref. 1).

The solutions for Maxwell's equations for the Fourier coefficients inside a cylindrical shell that are finite on the cylinder axis and outside the cylinder that are finite at infinity can be written in the form

$$\left.\begin{aligned} \bar{f}_n^{(i)}(r) &= iC_n^{(i)} I'_{nl}(nhr), \\ \bar{q}_n^{(i)}(r) &= -\frac{hr}{l} \bar{g}_n^{(i)}(r) = C_n^{(i)} I_{nl}(nhr), \\ \bar{f}_n^{(e)}(r) &= iC_n^{(e)} K'_{nl}(nhr), \\ \bar{q}_n^{(e)}(r) &= -\frac{hr}{l} \bar{g}_n^{(e)} = C_n^{(e)} K_{nl}(nhr). \end{aligned}\right\} \tag{1.4}$$

Here, the prime denotes derivatives with respect to the argument.

Inside the cylinder walls, the Fourier coefficients are related by the expressions

$$\left.\begin{aligned} \bar{f}_n(r) + i\bar{g}_n(r) &= A_{1n} I_{nl+1}(\varkappa_n r) + B_{1n} K_{nl+1}(\varkappa_n r), \\ \bar{f}_n(r) - i\bar{g}_n(r) &= A_{2n} I_{nl-1}(\varkappa_n r) + B_{2n} K_{nl-1}(\varkappa_n r), \\ \bar{q}_n(r) &= \frac{i\varkappa_n}{2nh}[-(A_{1n} + A_{2n}) I_{nl}(\varkappa_n r) + (B_{1n} + B_{2n}) K_{nl}(\varkappa_n r)], \end{aligned}\right\} \tag{1.5}$$

where $\varkappa_n^2 = q^2 + n^2h^2$, $q^2 = p/\chi^2$, $\chi^2 = c^2/4\pi\sigma$. As before,[1] we assume that $\mu = 1$.

The constants $C_n^{(i)}$, $C_n^{(e)}$, A_{1n}, A_{2n}, B_{1n}, and B_{2n} depend on n, l, h, and $\varkappa_n$, and can be found from the continuity conditions for the magnetic field components on the inner side of the cylindrical shell ($r = b = a - \Delta$):

$$\bar{f}_n^{(i)}(b) = \bar{f}_n(b), \quad \bar{g}_n^{(i)}(b) = \bar{g}_n(b), \quad \bar{q}_n^{(i)}(b) = \bar{q}_n(b) \tag{1.6}$$

and the boundary conditions on the interior side of the cylinder, which allow for the discontinuity in the tangential components of the magnetic field as a result of the surface current:

$$\left.\begin{array}{c}\bar f_n^{(e)}(a)=\bar f_n(a),\quad \bar g_n^{(e)}(a)=\bar g_n(a)+\frac{4\pi l}{cha}\bar j_n,\\ \bar q_n^{(e)}(a)=\bar q_n(a)-\frac{4\pi}{c}\bar j_n,\end{array}\right\}\qquad(1.7)$$

where $\bar{j}_n$ is the Laplace transformation of the Fourier coefficient of the current $j_n(t)$.

We omit the calculations and give expressions for the coefficients $C_n^{(i)}$, $C_n^{(e)}$ and the determinant $D_n(p)$. To abbreviate the notation we introduce functions which represent combinations of cylindrical functions:

$$\left.\begin{array}{l}M_{n,m}\equiv M_{n,m}(a,\ b)=I_n(\varkappa_n a)K_m(\varkappa_n b)-I_m(\varkappa_n b)K_n(\varkappa_n a),\\ N_{n,m}\equiv N_{n,m}(a,\ b)=I_n(\varkappa_n a)K_m(\varkappa_n b)+I_m(\varkappa_n b)K_n(\varkappa_n a).\end{array}\right\}(1.8)$$

Then these coefficients can be written in the form

$$\left.\begin{array}{l}C_n^{(i)}=-\frac{4\pi}{c}\bar j_n nhaG_n^{(i)}(p)D_n^{-1}(p)K'_{nl}(nha),\\ C_n^{(e)}=-\frac{4\pi}{c}\bar j_n nhaG_n^{(e)}(p)D_n^{-1}(p)I'_{nl}(nha),\end{array}\right\}\qquad(1.9)$$

where

$$G_n^{(i)}(p)=\frac{1}{2n^2h^2ab}\left(M_{nl-1,\,nl-1}+M_{nl+1,\,nl+1}+\frac{2l^2}{h^2ab}M_{nl,\,nl}\right),\qquad(1.10)$$

$$G_n^{(e)}(p)=\frac{I'_{nl}(nhb)}{nhaI'_{nl}(nha)}\Big\{\Big[M_{nl-1,\,nl-1}M_{nl+1,\,nl+1}$$
$$+\frac{\varkappa_n^2}{4n^2h^2}(M_{nl+1,\,nl+1}-M_{nl-1,\,nl-1})^2$$
$$-\frac{\varkappa_n l^3}{2nh^4a^2b}(N_{nl,\,nl+1}-N_{nl,\,nl-1})^2\Big]\frac{I_{nl}(nhb)}{I'_{nl}(nhb)}+\frac{\varkappa_n}{2nh}\Big[N_{nl+1,\,nl}M_{nl-1,\,nl-1}$$
$$+N_{nl-1,\,nl}M_{nl+1,\,nl+1}+\frac{l^2}{h^2a^2}M_{nl,\,nl}(N_{nl,\,nl+1}+N_{nl,\,nl-1})\Big]\Big\}.\qquad(1.11)$$

The determinant is

$$D_n(p)=M_{nl-1,\,nl-1}M_{nl+1,\,nl+1}I_{nl}(nhb)K_{nl}(nha)+\frac{\varkappa_n}{2nh}[N_{nl,\,nl+1}I_{nl}(nhb)$$
$$\times K_{nl+1}(nha)+N_{nl+1,\,nl}I_{nl+1}(nhb)K_{nl}(nha)]M_{nl-1,\,nl-1}+\frac{\varkappa_n}{2nh}M_{nl+1,\,nl+1}$$
$$\times[N_{nl,\,nl-1}I_{nl}(nhb)K_{nl-1}(nha)+N_{nl-1,\,nl}I_{nl-1}(nhb)K_{nl}(nha)]+$$
$$+\frac{\varkappa_n^2}{4n^2h^2}M_{nl,\,nl}[M_{nl+1,\,nl-1}I_{nl+1}(nhb)K_{nl-1}(nha)+M_{nl-1,\,nl+1}I_{nl-1}(nhb)$$
$$\times K_{nl+1}(nha)+M_{nl-1,\,nl-1}I_{nl+1}(nhb)K_{nl+1}(nha)+M_{nl+1,\,nl+1}$$
$$\times I_{nl-1}(nhb)K_{nl-1}(nha)].\qquad(1.12)$$

For $a = b$ or $\sigma = 0$ ($\varkappa_n = nh$) the products $G_n^{(i)}(p)D_n^{-1}(p)$ and $G_n^{(e)}(p)D_n^{-1}(p)$ become unity and the values of the coefficients $C_n^{(i)}$ and $C_n^{(e)}$, as expected, are equal to their values when there is no conducting medium.

Let us first investigate the transient process. The roots of the determinant (1.12) in the general case of arbitrary a_n and Δ can be determined by numerical methods.

For thin walls, where the condition $nh\Delta \ll 1$ holds, the minimum root of the determinant that satisfies the condition $\varkappa_n\Delta \ll 1$ can be found by series expansion of the determinant in powers of $nh\Delta$ and $\varkappa_n\Delta$.

Using the series expansion of Bessel function we obtain the following expression for the determinant:

$$D_n(p)=\frac{\Delta}{n^2h^2a^3}\left[1+\frac{l^2}{h^2a^2}-\frac{pa\Delta}{\chi^2}I'_{nl}(nha)K'_{nl}(nha)\right].\qquad(1.13)$$

The unique root of the determinant in this approximation is

$$p=\frac{\chi^2}{a\Delta}\left(1+\frac{l^2}{h^2a^2}\right)\frac{1}{I'_{nl}(nha)K'_{nl}(nha)}.\qquad(1.14)$$

The applicability condition for the expansion in powers of $\varkappa_n\Delta \ll 1$ yields a constraint on the ratio Δ/a of the form

$$\frac{\Delta}{a}\ll\frac{h^2a^2}{l^2+h^2a^2}I'_{nl}(nha)\,|K'_{nl}(nha)|.\qquad(1.15)$$

When this condition is not observed other roots of the equation $D_n(p) = 0$ appear, but the minimum root, which essentially determines the diffusion time of the field, remains (1.14), as before. Equation (1.14) is valid for arbitrary nha. If $nha \ll 1$, we have

$$p=-\frac{2\chi^2}{a\Delta}nl=-\frac{2\chi^2}{a\Delta}nha\operatorname{ctg}\vartheta\qquad(1.16)$$

for nonzero l values, and

$$p=-\frac{2\chi^2}{a\Delta}\qquad(1.17)$$

for $l = 0$.

For large nha values and arbitrary angles ϑ, with $nh\Delta \ll 1$, the minimum root of the determinant is

$$p=-\frac{2\chi^2}{a\Delta}nl\sqrt{1+\frac{l^2}{h^2a^2}}.\qquad(1.18)$$

Expression (1.18) implies that the minimum root increases with the harmonic number and hence the duration of the transient decreases.

Let us consider the steady-state process for a current that varies harmonically:

$$j_n(t)=j_{n0}\sin\omega t\qquad(1.19)$$

with frequency ω and amplitude j_{n0}.

The Fourier components $\tilde f_n(r,\ t)$, $\tilde g_n(r,t)$, and $\tilde q_n(r,\ t)$ that describe the steady-state process can be written in the following form in accordance with (1.19):

$$\left.\begin{array}{r}\tilde f_n^{(i)}(r,\ t)\\ \tilde q_n^{(i)}(r,\ t)=-\frac{hr}{l}\tilde g_n^{(i)}(r,\ t)\end{array}\right\}$$
$$=-\frac{4\pi}{c}j_{n0}nhaF_n^{(i)}\sin(\omega t-\Phi_n^{(i)})K'_{nl}(nha)\begin{array}{l}iI'_{nl}(nha),\\ I_{nl}(nha),\end{array}\qquad(1.20)$$

$$\left.\begin{array}{r}\tilde f_n^{(e)}(r,\ t),\\ \tilde q_n^{(e)}(r,\ t)=-\frac{hr}{l}\tilde g_n^{(e)}(r,\ t)\end{array}\right\}$$
$$=-\frac{4\pi}{c}j_{n0}nhaF_n^{(e)}\sin(\omega t-\Phi_n^{(e)})I'_{nl}(nha)\begin{array}{l}iK'_{nl}(nha),\\ K_{nl}(nha),\end{array}\qquad(1.21)$$

where the quantities $F_n^{(i)}$, $F_n^{(e)}$, $\Phi_n^{(i)}$, $\Phi_n^{(e)}$ that characterize the changes in the amplitudes and the phase shifts of the field introduced by the conducting medium are determined by the expressions

$$F_n^{(i)}=|G_n^{(i)}(i\omega)|\,|D_n^{-1}(i\omega)|^{-1},\quad \Phi_n^{(i)}=\arg[D_n(i\omega)G_n^{(i)-1}(i\omega)],\qquad(1.22)$$

$$F_n^{(e)}=|G_n^{(e)}(i\omega)|\,|D_n(i\omega)|^{-1},\quad \Phi_n^{(e)}=\arg[D_n(i\omega)G_n^{(e)-1}(i\omega)].\qquad(1.23)$$

Expressions (1.20) and (1.21) for the Fourier coefficients of the magnetic field become much simpler for thin walls; when $nh\Delta \ll 1$ the ratio of the wall thickness to the skin depth δ is much less than unity.

Using expression (1.13) for the determinant and the expansion of the functions $G_n^{(i)}$ and $G_n^{(e)}$ from the general equation (1.19), we find

$$\left.\begin{array}{c} f_n^{(i)}(r,t), \\ q_n^{(i)}(r,t) = -\frac{hr}{l} g_n^{(i)}(r,t) \end{array}\right\} = -\frac{4\pi}{c} j_{n0} nha \Psi_n(\omega, t) K'_{nl}(nha) \begin{array}{c} iI'_{nl}(nhr) \\ I_{nl}(nhr), \end{array} \tag{1.24}$$

$$\left.\begin{array}{c} f_n^{(e)}(r,t), \\ q_n^{(e)}(r,t) = -\frac{hr}{l} g_n^{(e)}(r,t) \end{array}\right\} = -\frac{4\pi}{c} j_{n0} nha \Psi_n(\omega, t) I'_{nl}(nha) \begin{array}{c} iK'_{nl}(nhr) \\ K_{nl}(nhr), \end{array} \tag{1.25}$$

where

$$\Psi_n(\omega, t) = [\sin(\omega t - \Phi_n) + e^{-t/\tau_n} \sin \Phi_n] \cos \Phi_n, \tag{1.26}$$

and the phase is determined from the equation

$$\operatorname{tg} \Phi_n = \omega\tau_n = -\frac{2a\Delta}{\delta^2} \frac{h^2a^2}{l^2 + h^2a^2} I'_{nl}(nha) K'_{nl}(nha). \tag{1.27}$$

It turns out that $\Psi_n(\omega, t)$ is a universal function that describes the penetration of spatially periodic fields into a cavity for which the thickness of the conducting walls is much less than the skin depth and spatial period of the field. This conclusion will evidently hold for any cavity. As a result, to determine the magnetic field as a function of time when there is a conducting chamber, it suffices to know the solutions for the field components in a vacuum (without conducting walls) and to replace $\sin \omega t$ by the function $\Psi_n(\omega, t)$ in them. This function is determined by the duration of the transient τ_n, which depends on the geometry of the cavity and the current distribution.

In the other limiting case, in which $\Delta/\delta = \xi \gg 1$ and $n^2h^2\delta^2 \ll 1$, the functions (1.22) and (1.23) are given by

$$F_n^{(i)} = -\sqrt{2} e^{-\zeta} \frac{\delta}{\sqrt{ab}} \left(1 + \frac{l^2}{h^2a^2}\right) \frac{1}{I'_{nl}(nha) K'_{nl}(nha)}, \quad \Phi_n^{(i)} = \zeta + \frac{\pi}{4}, \tag{1.28}$$

$$F_n^{(e)} = -\sqrt{2} \frac{\delta}{a} \left(1 + \frac{l^2}{h^2a^2}\right) \frac{1}{I'_{nl}(nha) K'_{nl}(nha)}, \quad \Phi_n^{(e)} = \frac{\pi}{4}. \tag{1.29}$$

The field amplitude in the chamber is exponentially small in this case, while the phase is arbitrary.

2. PENETRATION OF A HELICAL FIELD INTO A SOLID CONDUCTING CYLINDER

Let us consider the diffusion of a helical field into a solid conducting cylinder.

The Fourier coefficients for the Laplace transformations of the field components are described by expressions (1.4) and (1.5), as before, in which we must set the coefficients $C_n^{(i)}$, B_{in}, and B_{2n} equal to zero. The nonzero coefficients are

$$\left.\begin{aligned} C_n^{(e)} &= -\frac{4\pi}{c} J_n nha G_n(p) D_n^{-1}(p) I'_{nl}(nha), \\ A_{1n,2n} &= -\frac{4\pi i}{c} J_n D_n^{-1}(p) \left[I'_{nl\mp1}(\varkappa_n a) \mp \frac{\varkappa_n l}{nh^2a} I_{nl}(\varkappa_n a) \right] K'_{nl}(nha), \end{aligned}\right\} \tag{2.1}$$

where

$$\left.\begin{aligned} G_n(p) &= \frac{1}{nhaI'_{nl}(nha)} \left[I'^2_{nl}(\varkappa_n a) + \frac{l^2q^2}{\varkappa_n^2 h^2a^2} I^2_{nl}(\varkappa_n a) \right], \\ D_n(p) &= \left[I'^2_{nl}(\varkappa_n a) + \frac{q^2l^2}{\varkappa_n^2 h^2a^2} I^2_{nl}(\varkappa_n a) \right] K_{nl}(nha) \\ &\quad - \frac{\varkappa_n}{nh} I_{nl}(\varkappa_n a) I'_{nl}(\varkappa_n a) K'_{nl}(nha). \end{aligned}\right\} \tag{2.2}$$

Let us investigate the roots of the determinant in the limiting cases. If $q^2 \ll n^2h^2$, the determinant can be written in the form

$$D_n(p) = D_0 + \frac{q^2}{n^2h^2} D_1, \tag{2.3}$$

where

$$\left.\begin{aligned} D_0 &= \frac{I'_{nl}(nha)}{nha}, \\ D_1 &= \left(1 + \frac{l^2}{h^2a^2}\right) I_{nl}(nha) + \left[\frac{l^2}{h^2a^2} I^2_{nl}(nha) - I'^2_{nl}(nha)\right] K_{nl}(nha) \\ &\quad + \frac{nha}{2} \left[\left(1 + \frac{l^2}{h^2a^2}\right) I^2_{nl}(nha) - I'^2_{nl}(nha)\right] K'_{nl}(nha). \end{aligned}\right\} \tag{2.4}$$

The minimum root of the determinant is

$$p = -\chi^2 n^2 h^2 \frac{D_0}{D_1}. \tag{2.5}$$

The condition $q^2 \ll n^2h^2$ holds for any nha if $n^2l^2 \gg 1$. If $nha \ll 1$, the penetration time is

$$\tau_n = -\frac{1}{p} = \frac{\pi\sigma l}{c^2nh^2}. \tag{2.6}$$

It is independent of the dimensions of the conducting cylinder and determined by the spatial periods of the distribution of the currents that create the field.

For a steady-state process we can write the Fourier components in the form

$$\left.\begin{array}{c} \tilde f_n^{(e)}(r,t), \\ \tilde q_n^{(e)}(r,t) = -\frac{hr}{l} \tilde g_n^{(e)}(r,t) \end{array}\right\} = -\frac{4\pi}{c} j_{n0} nha F_n^{(e)} I'_{nl}(nha) \sin(\omega t - \Phi_n^{(e)}) \begin{array}{c} iK'_{nl}(nhr) \\ K_{nl}(nhr), \end{array} \tag{2.7}$$

$$\left.\begin{aligned} \tilde f_n(r,t) &= -\frac{4\pi i}{c} j_{n0} nha I'_{nl}(nhr) K'_{nl}(nha) \sin[\omega t - \Phi_r(r)], \\ \tilde g_n(r,t) &= \frac{4\pi}{c} j_{n0} \frac{nla}{r} I_{nl}(nhr) K'_{nl}(nha) \sin[\omega t - \Phi_\varphi(r)], \\ \tilde q_n(r,t) &= -\frac{4\pi}{c} j_{n0} nha I_{nl}(nhr) K_{nl}(nha) \sin[\omega t - \Phi_z(r)], \end{aligned}\right\} \tag{2.8}$$

$$\operatorname{tg} \Phi_\alpha(r) = \frac{\omega^2}{\chi^2 n^2 h^2} \left(\frac{D_1}{D_0} - f_\alpha\right), \tag{2.9}$$

α taking the values r, φ, z, where

$$\left.\begin{aligned} f_r &= -1 + \frac{nha}{2}\left(1 + \frac{l^2}{h^2a^2}\right) \frac{I_{nl}(nha)}{I'_{nl}(nha)} \\ &\quad + \left[\frac{l^2 I_{nl}(nha)}{h^2arI'_{nl}(nha)} + \frac{nhr}{2}\left(1 + \frac{l^2}{h^2r^2}\right)\right] \frac{I_{nl}(nhr)}{I'_{nl}(nhr)}, \\ f_\varphi &= -1 + \frac{nha}{2}\left(1 + \frac{l^2}{h^2a^2}\right) \frac{I_{nl}(nha)}{I'_{nl}(nha)} \\ &\quad + \left[\frac{I_{nl}(nha)}{I'_{nl}(nha)} + \frac{nhr}{2}\right] \frac{I'_{nl}(nhr)}{I_{nl}(nhr)}, \\ f_z &= \frac{nha}{2}\left[\left(1 + \frac{l^2}{h^2a^2}\right) \frac{I_{nl}(nha)}{I'_{nl}(nha)} + \frac{rI'_{nl}(nhr)}{aI_{nl}(nhr)}\right]. \end{aligned}\right\} \tag{2.10}$$

On the axis, the phase shift of each component is nonzero.

Using the summation equations, we can obtain expressions for the phase shifts in the case of stellarator and torsatron windings.

---

[1] V. F. Aleksin and S. S. Romanov, Zh. Tekh. Fiz., 43, 1153 (1973) [Sov. Phys. – Tech. Phys., 18, 734 (1973)].

[2] A. I. Morozov and L. S. Solov'ev, Reviews of Plasma Physics, Vol. 2, Consultants Bureau, New York (1966).

Quantum electronics

Solid-state laser with externally forced Q switching

N. M. Galaktionova, A. A. Mak, and A. P. Khyuppenen

(Submitted September 6, 1973)
Zh. Tekh. Fiz., 44, 1883-1889 (September 1974)

An experimental investigation of the modulation of the radiation of a stabilized YAG : Nd^{3+} laser is reported; the resonator loss is modulated over a wide range of frequencies and modulation indices. By varying the loss modulation of a single-mode laser all the usual operating conditions of solid state lasers can be obtained. The modulation indices are measured. The results are in good agreement with the solutions of the linearized kinetic equation over a wide range of modulation. The mechanisms by which the resonator loss is modulated is discussed.

1. Despite the large number of published papers in the field, at the present time many modes of operation of solid state lasers have not received a satisfactory explanation. Various mechanisms have been used to interpret the different modes of operation. Spike generation[1–3] is explained by fluctuations in the loss and pumping inside the active medium. These fluctuations[4] are due to instabilities in the shape of the resonator and its optical length. Regular pulse operation, which, as a rule, is obtained when a large number of transverse modes are generated in spherical resonators,[5–7] is due to the interaction of transverse modes which are very close in frequency,[8] or saturation absorption.[5,7] The mechanism by which periodic packets of spikes are emitted is still unclear.[9] Hence, all the explanations of the kinetic modes of operation reduce to some form of modulation (random or periodic) of the loss or gain of the active medium. Experimental investigations of the emission kinetics have been carried out; but without good stabilization of the laser parameters one cannot determine the origin of this modulation.[6,10,11]

In the present paper we show experimentally that both under single-mode and multimode conditions all the well-known dynamic modes of operation can be obtained by harmonic modulation of the resonator loss; simulation of these modes of operation can be achieved by changing the frequency and the depth of modulation in Q-switching.

2. In the experiments we use a stabilized cw YAG: Nd^{3+} laser; the resonator construction and the measures taken to ensure stability are described in ref. 12. The optical arrangement of the laser and the experimental apparatus are shown in Fig. 1. The laser is pumped with high-pressure krypton arc lamps in circular cylindrical exciters with a diffuse scattering coating. We use active elements 3 mm in diameter and 50 mm in length. The thermal birefringence of the active elements is compensated with a 90° rotator. All the elements inside the resonators are clear and inclined to the axis of the resonator. The Q switch consisted of a Glan prism and a Pockels call which contains lithium niobate. The optic axis of the crystal is perpendicular to the cut. The x and y crystallographic axes make an angle of 45° with the plane of the electric vector transmitted by the polarizer. The electric field in the cell is parallel to the plane of the extraordinary ray. The dependence of the loss on the voltage and the frequency characteristic of the modulator are checked by modulating the constant flux when the modulator is removed from the resonator. The loss is calibrated by internal-resonator modulation at low frequencies, the modulation in which is independent of frequency. We thus measure the modulation factor of the radiation m_p for a given value of the modulator voltage, and the modulation factor of the loss m_γ is found from the equation[12]

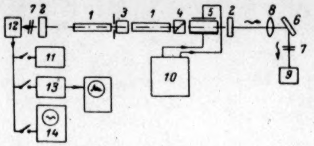

Fig. 1. Experimental arrangement. 1) Active elements; 2) resonator mirrors [τ_1 = 0.05%, τ_2 = 3%]; 3) polarization rotator; 4) Glan prism; 5) Pockels cell; 6) rotatable mirror; 7) neutral filters; 8) focusing lens; 9) image-converter tube; 10) sonic generator; 11) DC voltmeter, 12) photodiode; 13) measuring amplifier; 14) spectrum analyzer; 15) oscilloscope.

$$m_p = m_\gamma \frac{n}{n-1}, \tag{1}$$

where n is the excess of the pumping above the threshold. The amplitude of the loss rate introduced into the resonator in modulation is defined as $\Delta\gamma = m_\gamma\gamma$; where γ is the

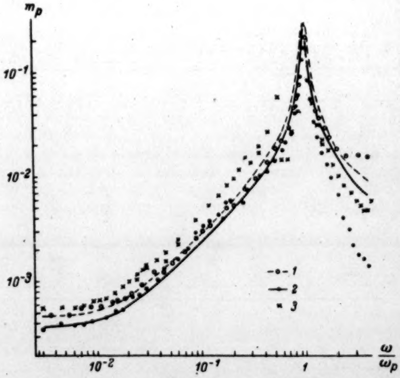

Fig. 2. Frequency characteristics of the emission modulation. 1) Theoretical and experimental values when an axial transverse mode is generated, $m_\gamma = 6.6 \cdot 10^{-5}$, $n = 1.15$, $\omega_p = 3.6 \cdot 10^5$ sec^{-1}; 2) the same quantities and spectral composition of the emission, $m_\gamma = 8.1 \cdot 10^{-5}$, $n = 1.3$, $\omega_p = 4.3 \cdot 10^5$ sec^{-1}; 3) experimental values when several transverse modes are generated, $m_\gamma = 1.5 \cdot 10^{-4}$, $n = 1.5$, $\omega_p = 4.2 \cdot 10^5$ sec^{-1}.

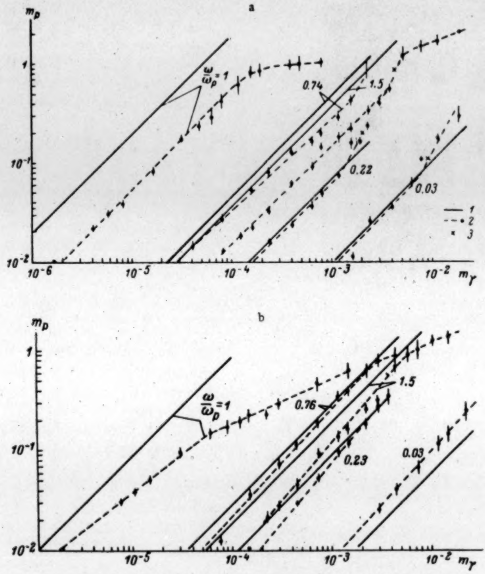

Fig 3. Amplitude characteristics of the emission modulation. 1) Theoretical values; 2) experimental values; 3) values for which random radiation pulses begin. a) $m_\gamma = 6.6 \cdot 10^{-5}$, $n = 1.15$, $\omega_p = 3.6 \cdot 10^5$ sec^{-1} when generating the fundamental transverse mode; b) $m_\gamma = 1.5 \cdot 10^{-4}$, $n = 1.5$, $\omega_p = 4.2 \cdot 10^5$ sec^{-1} when generating several transverse modes.

loss rate of the resonator, which is found by measuring the frequency of relaxation oscillations ω_p, and is given by[12]

$$\gamma = \frac{\omega_p^2 \tau}{n-1}, \qquad (2)$$

where τ is the lifetime of the upper excited level of the working transitions, $\tau = 2 \cdot 10^{-4}$ sec.

The modulation of the emission is measured by a dc voltmeter (the constant component) and an amplifier (the variable component of the photodiode signal). The frequency spectrum of the modulation is monitored by ASChKh-1 and SCh-8 analyzers. The emission output is photographed from the screen of an oscilloscope. The transverse modes are monitored on an image-converter tube, onto the cathode of which we project the far field radiation by means of a lens. The spectrum of the longitudinal modes consists of two to three groups with three to four modes in each group. The overall width of the spectrum is less than 0.2 Å. The laser noise in the measuring apparatus enables us to measure the modulation factor of the radiation in the frequency range from 20 Hz to 300 KHz up to a value of $3 \cdot 10^{-3}$. Measurement of the harmonic oscillations, previously calibrated by the spectrum analyzer, increases the range of sensitivity to 10^{-4}.

3. The frequency and amplitude characteristics are measured in the following sequence. A stop 1.5 mm in diameter is placed in the resonator, the modulator is calibrated, and readings are taken of the modulation characteristic under single-mode conditions. The stop is then removed, and without changing the pumping or adjusting the mirrors, we investigate multimode operation at the same frequencies and modulator voltage. In measuring the amplitude characteristics for different depths of loss modulation we photograph the emission signal. The results of the measurements of single-mode radiation modulation are compared with the results of calculations carried out using the equation[12]

$$m_p = \Delta\gamma \left[\frac{\omega^2 + 4\beta^2}{(\omega^2 - \omega_p^2)^2 + 4\beta^2\omega^2} \right]^{1/2}, \qquad (3)$$

where ω is the angular modulation frequency, and $\beta = n/2\tau$ is the attenuation constant.

Figures 2 and 3 show the results of measurements of the emission modulation. The measurements show that when an axial transverse mode is generated the modulation is less than the theoretical value. This tendency is pronounced for $\omega \geq \omega_p$. Under multimode conditions the amplitude and frequency characteristics of the overall emission with the exception of the region around $\omega = \omega_p$, are close to single-mode operation.

Figure 4 shows the emission in single-mode lasing for different frequencies and modulation depths. Harmonic modulation of the loss up to a certain value of the modulation depth independent of the ratio ω/ω_p, gives rise to harmonic modulation of the emission, the value of which

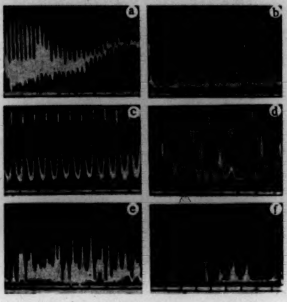

Fig. 4. Oscillograms of the radiation for different values of the loss modulation parameters. a) $\omega/\omega_p = 3\cdot10^{-2}$, $m_\gamma = 1.1\cdot10^{-2}$, i_p = 50 μsec/div; b) 0.37, $0.7\cdot10^{-2}$ 20 μsec/div; c) 1, $5.3\cdot10^{-4}$, 20 μsec/div; d) 0.12, $0.1\cdot10^{-2}$, 15 μsec/div; e) 0.49, $5.3\cdot10^{-3}$, 20 μsec/div; f) 2.6, $2.7\cdot10^{-2}$, 20 μsec/div.

is proportional to the loss modulation factor. The limiting value $m_\gamma^{\lim}$, up to which the emission follows the loss modulation is a minimum for $\omega = \omega_p$, and is $\sim 0.6\cdot10^{-4}$, and increases as the difference $(\omega - \omega_p)$ increases. Thus, for $\omega/\omega_p = 0.03$, $m_\gamma^{\lim} \sim 10^{-2}$. The modulation factor for the limiting values of $m_\gamma^{\lim}$ at all frequencies lies in the range 0.1-0.3. A further increase in the modulation depth of the loss gives rise to another mode of operation, the form of which depends on the ratio ω/ω_p. The damped-pulse mode of operation is obtained at low modulating frequencies $\omega/\omega_p = 0.02$-0.06 (Fig. 4a). Equidistant packets of regular pulses occur for $\omega/\omega_p = (0.1$-$0.4)$. The repetition period of the packets is equal to or a multiple of the modulation period, while the pulses in a packet follow one another at the frequency of the relaxation oscillations. This mode of operation is unstable, and with fixed modulation parameters we observed from one to three or four pulses in each packet (Fig. 4b, d). At frequencies close to the relaxation frequency regular pulses are observed (Fig. 4c). Spikes which are random in amplitude and repetition frequency are observed (Fig. 4e), at higher loss modulation factors; the values are smaller the closer the modulation frequency is to the relaxation frequency. This value is smaller than 10^{-2} for all the modulation frequencies, and is 10^{-4} for $\omega = \omega_p$. At frequencies greater than ω_p the spikes follow each other at intervals which are a multiple of the modulation period τ_M. For example, in Fig. 4f the time between the first two pulses is $8\tau_M$, between the four following pulses is $3\tau_M$, and between the two following pulses is $7\tau_M$. A similar sequence is also observed for multimode operation.

4. Stable lasing in the absence of loss modulation, and the possibility of simulating the kinetics of harmonic loss modulation leads to the assumption that such modulation of the laser parameters is always present. One of the probable reasons for this in pulsed lasers is natural longitudinal and transverse mechanical oscillations excited in the active element by thermal shock. In this case, if the active element is a weak selector for long waves λ_0, determined by the length of the resonator, the losses in such a resonator depend on the transmission of the selector. Modulation of the transmission of such a selector when the optical length of the element is changed with frequency Ω, can be represented in the form

$$\left.\begin{aligned}\tau &= 1-\frac{F}{2}\left[1-J_0(\beta)+2\sum_{k=1}^{\infty}J_{2k}(\beta)\cos 2k\Omega t\right],\\ \beta &= \frac{4\pi}{\lambda_0}h,\quad F=\frac{4R}{(1-R)^2},\quad \Delta\omega = 2(1+\beta)\Omega,\end{aligned}\right\} \tag{4}$$

where R is the reflectance of the ends of the element, $\Delta\omega$ is the width of the modulation frequency spectrum, h and Ω are the amplitude and frequency of the natural longitudinal oscillations of the active element respectively, and J_k are the Bessel functions of the first kind and k-th order.

Numerical calculation shows that for $h \sim \lambda_0/2$ the frequency of the relaxation oscillations lies in the modulation frequency bands. When the ends of the element are cut at the Brewster angle, Q switching gives rise to natural transverse modes of oscillation, which are excited in the element when there is pulsed heating which is nonuniform over the cross section. As our experiments have shown,[12] even for a spherical resonator, an amplitude of the angular oscillations of the ends of approximately 1" leads to spike generation. It can be shown that in the case of transverse oscillations the frequency of relaxation oscillations lies in the modulation frequency band.

Hence, we can conclude that modulation of the radiation of single-mode solid state lasers is induced, and is determined by the modulation of the loss and the pumping. The variety of kinetic modes of operation is determined by the nature of the transients in solid state lasers, and by nonlinear interaction between the modulated electromagnetic field and the active medium.

The authors thank V. B. Volkonskii for the modulator and for consultation.

---

[1] N. M. Galaktionova, V. F. Egorova, and B. M. Sedov, Proc. of the Conference on Quantum Electronics, Erevan (1967).

[2] N. M. Galaktionova, V. F. Egorova, and A. A. Mak, Opt. Spektrosk., 25, 305 (1968).

[3] B. N. Lifshits, Dokl. Akad. Nauk SSSR, 194, 1298 (1970) [Sov. Phys. – Dokl., 15, 949 (1971)].

[4] G. N. Vinokurov, N. M. Galaktionova, V. F. Egorova, A. A. Mak, B. M. Sedov, and Yu. I. Khanin, Zh. Eksp. Teor. Fiz., 60, 489 (1971) [Sov. Phys.– JETP, 33, 262 (1972)].

[5] H. Laig-Hörstebrock and H. Weber, Z. Angew. Phys., 23, 1 (1967).

[6] Yu. E. Pol'skii and A. A. Yakutenkov, Zh. Eksp. Teor. Fiz., 64, 438 (1973) [Sov. Phys. – JETP, 37, 223 (1973)].

[7] A. M. Bonch-Bruevich, S. E. Potapov, and Ya. I. Khanin, Opt. Spektrosk., 28, 203 (1970).

[8] N. G. Basov, V. N. Morozov, and A. N. Oraevskii, Zh. Eksp. Teor. Fiz., 49, 895 (1965) [Sov. Phys. – JETP, 22, 622 (1966)].

[9] M. I. Dzhibladze, T. M. Murina, and A. M. Prokhorov, Opt. Spektrosk., 27, 464 (1969).

[10] E. Bayer, K. H. Hellwege, and G. Schaack, Z. Naturforsch., 20a, 1181 (1965).

[11] H. G. Danielmeyer, J. Appl. Phys., 41, 4014 (1970).

[12] N. M. Galaktionova, A. A. Mak, and A. P. Khyuppenen, Zh. Tekh. Fiz., 44, 770 (1974) [Sov. Phys. – Tech. Phys., 19, 486 (1974)].

Aberrations in systems with plane and spherical detection apertures

V. V. Izokh, A. V. Sergeev, and I. Yu. Shmidov

V. I. Lenin Belorussian State University, Minsk

(Submitted July 4, 1973; resubmitted January 19, 1974)
Zh. Tekh. Fiz., 44, 1889-1895 (September 1974)

A computer comparison has been made of the ray aberrations in the images obtained from systems with plane and spherical detection apertures. The aberrations in the image of object points lying near the origin of coordinates of the object plane for a spherical aperture are smaller than the aberrations of a plane aperture for a given angular aperture. As the distance from the center of the object increases the aberrations in a spherical detecting aperture exceed those for a plane aperture. Furthermore, an increase in the angular aperture of the detection apertures of the imaging system leads to an increase in the size of the regions in the object plane for which the aberrations for a spherical receiving aperture do not exceed those for a plane aperture.

Digital holography is currently the subject of considerable interest. It is difficult to overestimate the usefulness of computers in constructing images in acoustic and microwave holography. There is a possibility of using an amplitude detector to measure the diffraction field of an object without a reference wave and to reconstruct the object from this field by means of a computer. This possibility has been studied theoretically[1,2] and demonstrated experimentally.[3] In this note we carry out a comparative evaluation of the aberrations in the images constructed from a measurement of the diffraction field of an object at points in the plane of the detection aperture at a distance z = d from the object and at points in a spherical aperture of radius $\rho = a$ (Fig. 1).

We turn first to the aberrations of an image constructed from the field values measured at points in a plane detection aperture.

According to the theory of inverse diffraction,[4] the field distribution in the plane of the reconstructed image is related to the field distribution in the object plane, $U_1(x_1, y_1, 0)$, by

$$U_3(x_3, y_3, z_3) = -\frac{1}{4\pi^2}\iiiint\limits_{-\infty}^{\infty} U_1(x_1, y_1, 0)\left[\frac{\partial}{\partial z_1}\frac{\exp jk_1 r_{1p}}{r_{1p}}\right]_{z_1=0} \times\left[\frac{\partial}{\partial z_2}\frac{\exp - jk_2 r_{2p}}{r_{2p}}\right]_{z_2=d}\operatorname{rect}\left(\frac{x_{2p}}{D_{xp}}\right)\operatorname{rect}\left(\frac{y_{2p}}{D_{yp}}\right)dx_1 dy_1 dx_{2p} dy_{2p}, \quad (1)$$

where

$$r_{1p} = [(x_{2p} - x_1)^2 + (y_{2p} - y_1)^2 + d^2]^{1/2}, \quad (2)$$

$$r_{2p} = [(x_3 - x_{2p})^2 + (y_3 - y_{2p})^2 + (z_3 - d)^2]^{1/2}, \quad (3)$$

D_{xp} and D_{yp} are the dimensions of the plane detection aperture, subscript "p" corresponds to the field in the plane, $k_1 = 2\pi/\lambda_1$, λ_1 is the wavelength of the illuminating wave, $k_2 = 2\pi/\lambda_2$, λ_2 is the wavelength of the reconstruction wave, and

$$\operatorname{rect}(x) = \begin{cases} 1 & \text{for } |x| \leqslant \frac{1}{2}, \\ 0 & \text{otherwise.} \end{cases} \quad (4)$$

According to the theory for the formation of images by linear systems,[5] Eq. (1) implies that

$$H_p = \iint\limits_{-\infty}^{\infty}\left[\frac{\partial}{\partial z_1}\frac{\exp jk_1 r_{1p}}{r_{1p}}\right]_{z_1=0}\left[\frac{\partial}{\partial z_2}\frac{\exp - jk_2 r_{2p}}{r_{2p}}\right]_{z_2=d} \times \operatorname{rect}\left(\frac{x_{2p}}{D_{xp}}\right)\operatorname{rect}\left(\frac{y_{2p}}{D_{yp}}\right)dx_{2p} dy_{2p} \quad (5)$$

is the pulsed response of the system. Carrying out the corresponding calculations in the integrand in (5), we find

$$H_p = \iint\limits_{-\infty}^{\infty} A_p(x_{2p}, y_{2p}) \exp j\varphi_p(x_{2p}, y_{2p})\, dx_{2p} dy_{2p}, \quad (6)$$

where

$$A_p(x_{2p}, y_{2p}) \simeq \frac{k_1 k_2}{d\,|z_3 - d|}\operatorname{rect}\left(\frac{x_{2p}}{D_{xp}}\right)\operatorname{rect}\left(\frac{y_{2p}}{D_{yp}}\right), \quad (7)$$

$$\varphi_p(x_{2p}, y_{2p}) \simeq k_1 r_{1p} - k_2 r_{2p} - \pi \quad (8)$$

with

$$k_1 r_{1p} \gg 1, \quad k_2 r_{2p} \gg 1. \quad (9)$$

According to ref. 5, the image aberrations are governed by the phase component of the pulsed response of the system, (8). The structure of (8) allows us to use the method proposed in ref. 6 for calculating the third-order aberrations; using this method, we find that the aberrations of an image formed by a system with a plane detection aperture are described by

$$\Delta_p = \frac{1}{8}\left(\frac{k_2}{|z_3 - d|^3} - \frac{k_1}{d^3}\right)\beta_p^4 + \left(\frac{k_1}{d^3} - \frac{k_2 M_p}{|z_3 - d|^3}\right)\beta_p^2\alpha_p^2 + \frac{1}{2}\left(\frac{k_2 M_p^2}{|z_3 - d|^3} - \frac{k_1}{d^3}\right)\alpha_p^4 + \frac{1}{4}\left(\frac{k_2 M_p^2}{|z_3 - d|^3} - \frac{k_1}{d^3}\right)\beta_p^2\gamma^2 + \frac{1}{2}\left(\frac{k_1}{d^3} - \frac{k_2 M_p^3}{|z_3 - d|^3}\right)\gamma^2\alpha_p^2, \quad (10)$$

where

$$\beta_p^2 = x_{2p}^2 + y_{2p}^2, \quad \alpha_p^2 = x_1 x_{2p} + y_1 y_{2p}, \quad \gamma^2 = x_1^2 + y_1^2, \quad (11)$$

$$M_p = \frac{|z_3 - d|}{d}\frac{k_1}{k_2}. \quad (12)$$

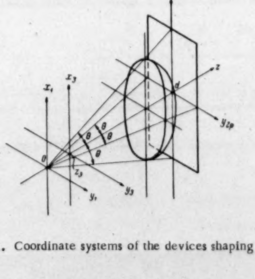

Fig. 1. Coordinate systems of the devices shaping the image.

The first term in (10) corresponds to spherical aberration, the second to coma, the third to astigmatism, the fourth to field curvature, and the fifth to distortion.[7]

Let us find the conditions under which these aberrations vanish. There is no spherical aberration if

$$\frac{k_2}{|z_3-d|^3}-\frac{k_1}{d^3}=0 \quad \text{or} \quad \frac{|z_3-d|^3\lambda_2}{d^3\lambda_1}=1. \tag{13}$$

Coma vanishes if

$$\frac{k_1}{d^3}-\frac{k_2M_p}{|z_3-d|^3}=0 \quad \text{or} \quad \frac{|z_3-d|^3\lambda_2}{d^3\lambda_1}=M_p. \tag{14}$$

Using (12) we find

$$|z_3-d|=d. \tag{15}$$

There is no astigmatism or field curvature if

$$\frac{k_2M_p^2}{|z_3-d|^3}-\frac{k_1}{d^3}=0 \quad \text{or} \quad \frac{\lambda_2}{\lambda_1}=\frac{|z_3-d|}{d}. \tag{16}$$

Distortion vanishes if

$$\frac{k_1}{d^3}-\frac{k_2M_p^3}{|z_3-d|^3}=0 \quad \text{or} \quad \lambda_1=\lambda_2. \tag{17}$$

We see from (13)-(17) that if the magnification satisfies $M_p \neq 1$, it is impossible to simultaneously suppress all aberrations.

We turn now to the aberrations of an image reconstructed from measurements of the field at points in a spherical detection aperture of radius $\rho = d$. The pulsed response of the system in this case is

$$H_s=\int_0^{\rho}\int_0^{2\pi}\left[\frac{\partial}{\partial z}\frac{\exp jk_1r_{1s}}{r_{1s}}\right]_{z_1=0}\left[\frac{\partial}{\partial \rho}\frac{\exp -jk_2r_{2s}}{r_{2s}}\right]_{\rho=d} r\,dr\,d\varphi, \tag{18}$$

where

$$r_{1s}=[(x_{2s}-x_1)^2+(y_{2s}-y_1)^2+z_{2s}^2]^{1/2}, \tag{19}$$

$$r_{2s}=[(x_3-x_{2s})^2+(y_3-y_{2s})^2+(z_3-z_{2s})^2]^{1/2}, \tag{20}$$

$$x_{2s}=r\cos\varphi,\ \ y_{2s}=r\sin\varphi,\quad z_{2s}=(d^2-r^2)^{1/2},\ \ r=d\sin\theta. \tag{21}$$

Here, the subscript "s" corresponds to the field at points of the spherical detection aperture. In general, it is extremely complicated to evaluate Eq. (18), so we will simplify it, using power-series expansions of r_{1s} and r_{2s}:

$$r_{1s}=[d^2+\gamma^2-2(x_1x_{2s}+y_1y_{2s})]^{1/2}\simeq d+\frac{\gamma^2}{2d}-\frac{x_1x_{2s}+y_1y_{2s}}{d}$$
$$-\frac{1}{8d^3}[\gamma^4-4\gamma^2(x_1x_{2s}+y_1y_{2s})+4(x_1x_{2s}+y_1y_{2s})^2]+\dots \tag{22}$$

under the condition

$$\gamma^2-2(x_1x_{2s}+y_1y_{2s})<d^2, \tag{23}$$

and

$$r_{2s}=[d^2+\rho_s^2-2(x_3x_{2s}+y_3y_{2s}+z_3z_{2s})]^{1/2}$$
$$\simeq d+\frac{\rho_s^2}{2d}-\frac{x_3x_{2s}+y_3y_{2s}+z_3z_{2s}}{d} \tag{24}$$
$$-\frac{1}{8d^3}[\rho_s^4-4\rho_s^2(x_3x_{2s}+y_3y_{2s}+z_3z_{2s})$$
$$+4(x_3x_{2s}+y_3y_{2s}+z_3z_{2s})^2]+\dots \tag{24}$$

under the condition

$$\rho_s^2-2(x_3x_{2s}+y_3y_{2s}+z_3z_{2s})<d^2, \tag{25}$$

where

$$d^2=x_{2s}^2+y_{2s}^2+z_{2s}^2, \tag{26}$$

$$\rho_s^2=x_3^2+y_3^2+z_3^2. \tag{27}$$

We also use the conditions

$$k_1r_{1s}\gg 1,\ \ k_2r_{2s}\gg 1. \tag{28}$$

Retaining, in (18), the second-degree expansion terms in (22) and (24), and using (28), we find that the field distribution of a point image shaped by our system in the paraxial approximation, specified by the condition[8]

$$0\leqslant r\leqslant r_s\ll d, \tag{29}$$

is

$$H_s=\int_0^{r_s}\int_0^{2\pi}B_s\exp j\left[k_1\left(d+\frac{\gamma^2}{2d}\right)-k_2\left(d+\frac{\rho_s^2}{2d}+z_3\right)\right.$$
$$\left.-\frac{rD}{d}\cos(\varphi-\delta)\right]r\,dr\,d\varphi, \tag{30}$$

where

$$B_s=\frac{d-z_3}{d^2}\left[\left(\frac{k_1+k_2}{d}\right)^2+\left(k_1k_2-\frac{1}{d^2}\right)^2\right]^{1/2}, \tag{31}$$

$$D=[(k_1x_1-k_2x_3)^2+(k_1y_1-k_2y_3)^2]^{1/2}, \tag{32}$$

$$\delta=\operatorname{arc\,tg}\frac{k_1y_1-k_2y_3}{k_1x_1-k_2x_3}. \tag{33}$$

We see from (30) that the ideal image of a point occurs, in the paraxial approximation, under the condition

$$k_1\gamma^2-k_2\rho_s^2=0 \tag{34}$$

and is equal to

$$H_{si}=B_s\frac{r_sJ_1\left(r_s\frac{D}{d}\right)}{\frac{D}{d}}, \tag{35}$$

where $J_1(x)$ is the Bessel function of the first kind of index unity.

To find the transverse magnification of the image formed by our system, M_s, we exploit its circular symmetry, finding from (34)

$$M_s=\left(\frac{\lambda_2}{\lambda_1}-\frac{z_3}{\gamma^3}\right)^{1/2}. \tag{36}$$

We turn now to the aberrations of an image reconstructed from the field values at points of a spherical detection aperture. As in the case of a plane aperture, we must analyze the quantity

$$\Delta_s=k_1r_{1s}-k_2r_{2s}. \tag{37}$$

Substituting (22) and (24) into (37), and carrying out the corresponding calculations, we find

$$\Delta_s=\frac{1}{8d^3}(k_2M_s^4-k_1)\gamma^4+\frac{1}{2d^3}(k_1-k_2M_s^3)\gamma^2\alpha_s^2$$
$$+\frac{1}{2d^3}(k_2M_s^2-k_1)\alpha_s^4+\frac{k_2}{8d^3}$$
$$\times[z_3^3-4z_{2s}z_3+4z_{2s}^2z_3+2M_s^2(z_3-2z_{2s})\gamma^2$$
$$+2M_s(z_{2s}-2z_3)\alpha_s^2]\,z_3, \tag{38}$$

where

$$\alpha_s^2=x_1x_{2s}+y_1y_{2s}. \tag{39}$$

According to ref. 7, the first term in (38) does not cause image aberrations, the second gives the distortion, the third gives the astigmatism, and the fourth gives the defocusing, which occurs because the image plane does not coincide with the object plane.

Let us find the conditions under which these aberrations vanish. The distortion vanishes if

$$M_s^3=\frac{\lambda_2}{\lambda_1}. \tag{40}$$

The astigmatism vanishes if

$$M_s^2=\frac{\lambda_2}{\lambda_1}. \tag{41}$$

The defocusing vanishes if the image and object planes coincide, i.e., if $z_3 = 0$.

Accordingly, all the aberrations can be suppressed simultaneously only under the conditions $z_3 = 0$ and $\lambda_1 = \lambda_2$, i.e., with $M_s = 1$.

Comparing the aberrations of the images reconstructed from field values at points of a plane receiving aperture with those of a spherical aperture we see that the astigmatism and distortion are common to both images.

Equations (10) and (38) cannot be used directly for a quantitative comparison of the image aberrations in the two cases, so we compare the ray aberrations associated with Δ_p and Δ_s according to ref. 7.

For the components of the ray aberrations in the case of a plane detection aperture we have

$$\begin{aligned}\delta x_p=|z_{3_p}-d|\frac{\partial\Delta_p}{\partial x_{2p}}&=|z_{3_p}-d|\Big[\frac{1}{2}\Big(\frac{k_2}{|z_{3_p}-d|^3}-\frac{k_1}{d^3}\Big)\beta_p^2x_{2p}\\&+\frac{1}{2}\Big(\frac{k_1}{d^3}-\frac{k_2M_p}{|z_{3_p}-d|^3}\Big)(\beta_p^2x_1+2\alpha_p^2x_{2p})+\Big(\frac{k_2M_p^2}{|z_{3_p}-d|^3}-\frac{k_1}{d^3}\Big)\alpha_p^2x_1\\&+\frac{1}{2}\Big(\frac{k_2M_p^2}{|z_{3_p}-d|^3}-\frac{k_1}{d^3}\Big)\gamma^2x_{2p}+\frac{1}{2}\Big(\frac{k_1}{d^3}-\frac{k_2M_p^3}{|z_{3_p}-d|^3}\Big)\gamma^2x_1\Big],\end{aligned} \tag{42}$$

$$\begin{aligned}\delta y_p=|z_{3_p}-d|\frac{\partial\Delta p}{\partial y_{2p}}&=|z_{3_p}-d|\Big[\frac{1}{2}\Big(\frac{k_2}{|z_{3_p}-d|^3}-\frac{k_1}{d^3}\Big)\beta_p^2y_{2p}\\&+\frac{1}{2}\Big(\frac{k_1}{d^3}-\frac{k_2M_p}{|z_{3_p}-d|^3}\Big)(\beta_p^2y_1+2\alpha_p^2y_{2p})+\Big(\frac{k_2M_p^2}{|z_{3_p}-d|^3}-\frac{k_1}{d^3}\Big)\alpha_p^2y_1\\&+\frac{1}{2}\Big(\frac{k_2M_p^2}{|z_{3_p}-d|^3}-\frac{k_1}{d^3}\Big)\gamma^2y_{2p}+\frac{1}{2}\Big(\frac{k_1}{d^3}-\frac{k_2M_p^3}{|z_{3_p}-d|^3}\Big)\gamma^2y_1\Big],\end{aligned} \tag{43}$$

and in the case of a spherical aperture we have

$$\begin{aligned}\delta x_s=|z_{3s}-d|\frac{\partial\Delta_s}{\partial x_{2s}}&=|z_{3s}-d|\Big[\frac{1}{2d^3}(k_1-k_2M_s^3)\gamma^2x_1\\&+\frac{1}{d^3}(k_2M_s^2-k_1)\alpha_s^2x_1+\frac{k_2M_s}{4d^3}(d\cos\theta-2z_{3s})x_1z_{3s}\Big],\end{aligned} \tag{44}$$

$$\begin{aligned}\delta y_s=|z_{3s}-d|\frac{\partial\Delta_s}{\partial y_{2s}}&=|z_{3s}-d|\Big[\frac{1}{2d^3}(k_1-k_2M_s^3)\gamma_2y_1\\&+\frac{1}{d^3}(k_2M_s^2-k_1)\alpha_s^2y_1+\frac{k_2M_s}{4d^3}(d\cos\theta-2z_{3s})y_1z_{3s}\Big],\end{aligned} \tag{45}$$

where

$$z_{3_p}=d\Big(1-M_p\frac{\lambda_1}{\lambda_2}\Big), \tag{46}$$

$$z_{3s}=\gamma\Big(\frac{\lambda_2}{\lambda_1}-M_s^2\Big)^{1/2}, \tag{47}$$

and θ is the angular aperture of the detection apertures of the imaging systems.

We see from Eqs. (42)-(45) that δy_p and δy_s contain no information about the behavior of the ray aberrations

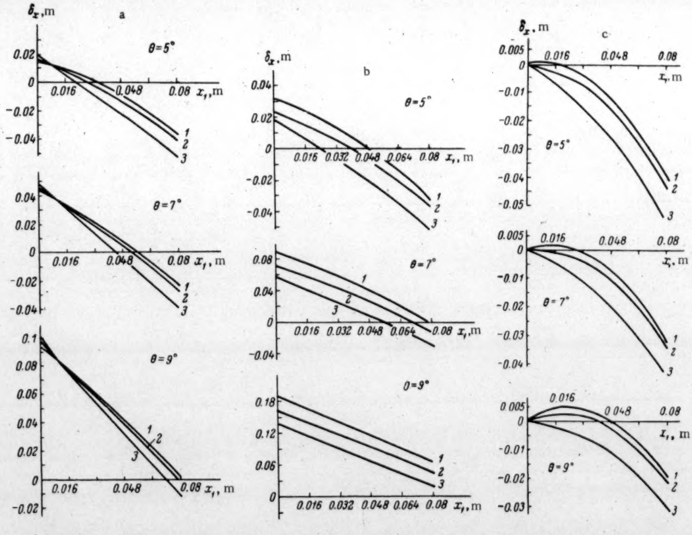

Fig. 2. Difference between the magnitudes of the image aberrations in the cases of plane and spherical apertures as a function of the position of the object points. a) x_{2_p} = d tan θ, y_{2_p} = 0, x_{2s} = d sin θ, y_{2s} = 0; b) x_{2_p} = d tan θ, y_{2_p} = d tan θ; x_{2s} = d sin θ/√2, y_{2s} = d sin θ/√2; c) x_{2_p} = 0, y_{2_p} = d tan θ, x_{2s} = 0, y_{2s} = d sin θ. The coordinates of the object points along the y_1 axis are: 1) 0; 2) 0.04; 3) 0.08 m.

not contained in δx_p and δx_s, so that it is sufficient to compare these latter two quantities.

We have used a Minsk-22 computer to calculate from Eqs. (42) and (44) the values of the difference

$$\delta x = |\delta x_p| - |\delta x_s| \tag{48}$$

for $M_p = M_s = 0.8$, $\lambda_1 = \lambda_2 = 0.1$ m, and $d = 1$ m as a function of x_1, y_1, and θ. Figure 2 shows the results calculated for three different points in the detection aperture.

We see that in the case of a spherical detection aperture the aberrations in the images of object points lying near the origin of coordinates in the object plane do not exceed the aberrations corresponding to a plane aperture for a given angular aperture. As the distance from the center of the object increases, the aberrations in the spherical detection aperture begin to exceed those corresponding to a plane aperture. Furthermore, as the angular aperture of the detection apertures of the imaging systems increases there is an enlargement of the regions in the object plane for which the aberrations in a spherical aperture are no larger than those in a plane aperture.

The authors thank V. G. Tyukul'min and B. D. Maleev for assistance in the calculations.

---

[1] E. Lalor, J. Math. Phys., 9, 2001 (1968).
[2] J. R. Shewell and E. Wolf, J. Opt. Soc. Amer., 58, 1596 (1968).
[3] M. M. Sindhi, J. Acoust. Soc. Amer., 46, 1158 (1969).
[4] T. Jannson and B. Karczewski, Optics Commun., 2, 201 (1970).
[5] J. W. Goodman, Introduction to Fourier Optics, McGraw-Hill, New York (1968).
[6] J. A. Armstrong, IBM J., 9, 171 (1965).
[7] M. Born and E. Wolf, Principles of Optics, Pergamon, New York (1959).
[8] E. L. O'Neill, Introduction to Statistical Optics, Addison-Wesley, Reading, Mass. (1963).

Correlation analysis of fine-structure images

A. A. Kolesnikov and N. V. Lapteva
A. F. Ioffe Physicotechnical Institute,
Academy of Sciences of the USSR, Leningrad

(Submitted August 3, 1973; resubmitted March 1, 1974)
Zh. Tekh. Fiz., 44, 1896-1902 (September 1974)

The solution of several technical problems, such as study of certain physical processes, ultimately reduces to an analysis of fine-structure images, i.e., images consisting of elements whose dimensions are much smaller than that of the image itself (the analysis field). The final goals of the analysis are different in different cases, but they can usually be reached if the integral distribution of these elements with respect to their dimensions is found. Among such problems are the analysis of thin sections in metallography, the study of noise in photographic materials, the study of the composition of powders, the study of the populations of microorganisms, etc.

Direct methods of statistical analysis involving a systematic measurement of a large number of elements are extremely cumbersome and laborious. Indirect measurement methods frequently permit a simpler solution. For example, in certain cases in which it is possible to exploit a priori information about the elements of the image the problem can be solved by analyzing the autocorrelation function of the image, which can be measured quite simply. The correlation-analysis method opens up certain possibilities regarding automatic measurements and thus automatic control of technological or physical processes.

NOTATION AND STATEMENT OF THE PROBLEM

Assume that we are to analyze some region Ω of area S containing N elements of arbitrary shape (Fig. 1). For generality, we assume that the elements can overlap in some arbitrary manner. We will use the following notation: x, y are the values of the coordinates X and Y with respect to the origin; x_i, y_i are the coordinates of the conventional center of element i; R is the radius vector running from the origin to point x, y; R_i is the radius vector of the conventional center of element i; R_{0i} is the radius vector of a point with respect to the i-th center; $\tau(X, Y)$ is the transparency at point X, Y from the i-th element; t(X, Y) is the transparency at point X, Y of the analysis region; P(r) and W(r) = dP(r)/dr are the integral and differential distributions of the length of the vector running from the center of an element to its boundary at angle φ; $P_\tau\{t_i, x_i\ y_i\}$ is the distribution with respect to transparency; and $W_{2N}(x_1, x_2 \ldots x_N; y_1, y_2 \ldots y_N)$ is the 2N-dimensional density distribution of the coordinates of the centers of the elements. In its most general form the problem is one of determining $P(r, \varphi) = \text{Bep}\{R < r\}$ from the measured two-dimensional autocorrelation function $B_t(X, Y, \Delta X, \Delta Y)$.

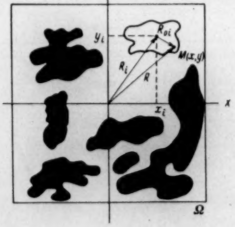

Fig. 1

SOLUTION OF THE PROBLEM

The solution of the problem can be divided arbitrarily into two steps. The first step is that of calculating the autocorrelation function for the given model of the object. We note that the choice of a model significantly affects both the calculation difficulties and the generality of the results. The best model for a particular application depends on the a priori information available about the object. As more a priori information is used, the algorithm for the analysis can be simplified, as can the apparatus itself.

The second step in the solution is that of determining the unknown distribution law from the autocorrelation function, which we assume known (measured). As is shown below, in this step also it is extremely important to have a priori information about the object being analyzed, since the problem generally does not have an unambiguous solution.

In the first step of the solution we use the method described in ref. 1. We define the transparency at any point of the analysis region as the product of the transparencies of each of the elements covering this point:

$$t(X,\ Y)=\prod_{i=1}^{N}\tau_i[X-x_i,\ Y-y_i]=\prod_{i=1}^{N}\tau(R_{0i}). \tag{1}$$

The autocorrelation function for the transparency of the object can be found by averaging the product:

$$B(X,\ Y,\ \Delta X,\ \Delta Y)=\underset{\tau_i}{E}\ \underset{x_iy_i}{E}\ t(X,\ Y)t^*(X-\Delta X,\ Y,\ \Delta Y), \tag{2}$$

where $\underset{\tau_i}{E}$ denotes an averaging over the transparencies of all spots, and $\underset{x_iy_i}{E}$ denotes an averaging over the distribution of the centers of the elements in the analysis region. In integral form, Eq. (2) is

$$\begin{aligned}B(X,\ Y,\ \Delta X,\ \Delta Y)=\iint_0^\infty\Big\{\iint_\Omega\cdots\int\prod_{i=1}^{N}\tau_i(X-x_i,\ Y-y_i)\\ \times\prod_{i=1}^{N}\tau_i^*(X-\Delta X-x_i,\ Y-\Delta Y-y_i)\\ \times W_{2N}(x_1,\ x_2,\ \ldots x_N;\ y_1,\ y_2\ldots y_N)\\ \times dx_1dx_2\ldots dy_N\Big\}W_\tau(X,\ Y,\ \Delta X,\ \Delta Y)\,d\tau d\tau^*.\end{aligned} \tag{3}$$

For a uniform and independent determination of the centers of the elements in the analysis region we can use

$$W_{2N}=\prod_{i=1}^{N} W_i(x_i)\prod_{i=1}^{N} W_i(y_i);\; W(x_i)W(y_i)=\begin{cases}\frac{1}{S} & \begin{smallmatrix}x_i\\ y_i\end{smallmatrix} \in \Omega\\ 0, & \begin{smallmatrix}x_i\\ y_i\end{smallmatrix} \bar{\in} \Omega,\end{cases} \qquad (4)$$

where S is the analysis area.

We assume that the elements are absolutely opaque, i.e., that

$$W_\tau(X,\ Y)=\begin{cases}\delta(0), & \text{if the point belongs to the element,}\\ \delta(1), & \text{if the point does not belong to the element.}\end{cases}$$

Then we can use (4) to significantly simplify (3):

$$B(X,\ Y,\ \Delta X,\ \Delta Y)=\rho^N, \qquad (5)$$

where

$$\rho=\frac{1}{S}\iint\limits_{\Omega}\tau(X-x_0,\ Y-y_0)\,\tau^*(X-\Delta X-x_0,\ Y-\Delta Y-y_0)\,dx_0dy_0 \qquad (6)$$

is the desired function, which is determined solely by the statistical properties of the elements. If, in addition, the number of elements and the analysis region are large, we can write (5) in exponential form:

$$B(X,\ Y,\ \Delta X,\ \Delta Y)=\exp\{-N[1-\rho(X,\ Y,\ \Delta X,\ \Delta Y)]\}. \qquad (7)$$

Under these assumptions the integrand in (6) can take on only two values: 0 or 1. We can therefore calculate ρ as the probability of an event in which elements whose centers are at point (X, Y) do not simultaneously overlap points $(X-\Delta X,\ Y-\Delta Y)$ and $(X-\Delta X-x_0,\ Y-\Delta Y-y_0)$.

Equation (6) can be written in polar coordinates:

$$\rho(r,\ \Delta R)=\frac{1}{S}\iint\limits_{\Omega}P(r-r_0)\,P(r-r_0-\Delta R)\,r_0dr_0d\varphi. \qquad (8)$$

The second step thus reduces to solving an integral equation of the type

$$\ln B(r,\ \varphi,\ \Delta R)=-\frac{N}{S}\left[S-\iint\limits_{\Omega}P(r-r_0)\,P(r-r_0-\Delta R)\,r_0dr_0d\varphi\right] \qquad (9)$$

for P(r).

In general this problem has an infinite set of solutions. Below we show that when we have a priori information about the objects being analyzed we can find a unique solution.

Example 1. We make the a priori assumptions that all the elements of the image are circular, that their centers are distributed uniformly over the analysis region, that the statistics of the elements are identical, and that the number of elements is large, so that we can assume the distribution law to be invariant with respect to direction, i.e., $P(r,\varphi)=P(r)$.

We choose the origin of coordinates as shown in Fig. 2, and we assume for simplicity that the analysis region is infinitely large. The probability that the center of a spot falls in an area $dS = r\,dr\,d\varphi$, does not cover the point $(x+\Delta R/2,\ 0)$, and, since the elements are circular, does not cover the point $(x-\Delta R/2,\ 0)$ is

$$d\rho=1\cdot P(r)\frac{r\,dr\,d\varphi}{S}.$$

Integrating in the right-hand half-plane, and multiplying by two, we find

$$\rho(r,\ \Delta R)=\frac{2}{S}\left\{\int\limits_0^{\Delta R/2}\int\limits_0^{2\pi}P(r)\,r\,dr\,d\varphi+2\int\limits_{\Delta R/2}^{\infty}\int\limits_{\arccos\Delta R/2r}^{\pi}P(r)\,r\,dr\,d\varphi\right\}$$

$$=\frac{4\pi}{S}\left\{\int\limits_0^{\infty}P(r)\,r\,dr-\frac{1}{\pi}\int\limits_{\Delta R/2}^{\infty}P(r)\,r\arccos\frac{\Delta R}{2r}\,dr\right\}.$$

Then the autocorrelation function is

$$\ln B(\Delta R)=-\frac{N}{S}\times\left\{S-4\pi\left[-\int\limits_0^{\infty}P(r)\,r\,dr-\frac{1}{\pi}\int\limits_{\Delta R/2}^{\infty}P(r)\,r\arccos\frac{\Delta R}{2r}\,dr\right]\right\}. \qquad (10)$$

A similar result is obtained in ref. 2. We can show that (10) can be solved for P(r). For this purpose we differentiate (10) with respect to ΔR, make the variable replacement $y = 1/r^2$, and introduce the following notation:

$$\Phi(y)=P\left(\frac{1}{\sqrt{y}}\right)y^{-3/2};\; h=\left(\frac{2}{\Delta R}\right)^2;$$

$$F(\Delta R)=\frac{\Delta R S}{2NB(\Delta R)}\frac{dB(\Delta R)}{d(\Delta R)}.$$

We then find the integral equation

$$F(\Delta R)=\int\limits_0^{h}\frac{\Phi(y)}{\sqrt{h-y}}\,dy,$$

which is called the Abel equation. After some straightforward manipulations, we find

$$\Phi(y)=\frac{S}{N}\left\{\int\limits_0^{y}\frac{B'(\Delta R)}{B(\Delta R)}\frac{d(\Delta R)}{\sqrt{y-\Delta R}}+\int\limits_0^{y}\Delta R\,\frac{B''(\Delta R)}{B(\Delta R)}\frac{d\,\Delta(R)}{\sqrt{y-\Delta R}}-\int\limits_0^{y}\Delta R\left[\frac{B'(\Delta R)}{B(\Delta R)}\right]^2\frac{d(\Delta R)}{\sqrt{y-\Delta R}}\right\}. \qquad (11)$$

This result can be used to calculate P(r) from the measured B(ΔR). The algorithm for processing the measured results is uncomplicated and easily programmable.

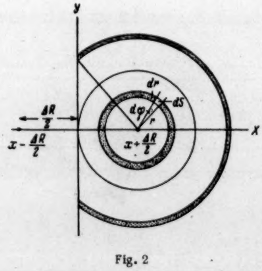

Fig. 2

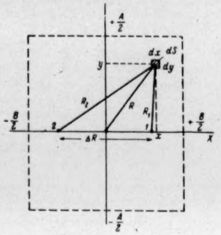

Fig. 3

Example 2. We now assume that the elements of the image are of an arbitrary shape but that the integral distribution of the lengths of the radius vectors P(r) can be approximated by a Rayleigh distribution:

$$P(r)=1-\exp\left(-\frac{r^2}{2\sigma^2}\right).$$

Figure 3 shows the analysis region, which is bounded by certain rectangles, within which there is a set of elements of arbitrary shape. Our previous assumptions remain valid. We will calculate $\rho(\Delta R)$ in accordance with (8). Using

$$P(r_1)=1-\exp\left[-\frac{y^2+(x-\Delta R)^2}{2\sigma^2}\right],$$

we find

$$P(r_2)=1-\exp\left[-\frac{y^2+(x+\Delta R)^2}{2\sigma^2}\right].$$

Then

$$\rho(\Delta R)=1-\frac{4\pi\sigma^2}{AB}\Phi\left(\frac{A}{2\sigma\sqrt{2}}\right)\Phi\left(\frac{B}{2\sigma\sqrt{2}}\right)+\frac{\sqrt{2\pi}}{A\sigma}\Delta R^2e^{-\frac{B^2}{8\sigma^2}}\Phi\left(\frac{A}{2\sigma\sqrt{2}}\right)$$
$$+\frac{\pi\sigma^2}{AB}e^{-\frac{\Delta R^2}{\sigma^2}}\Phi\left(\frac{A}{2\sigma}\right)\Phi\left(\frac{B}{2\sigma}\right), \qquad (12)$$

where

$$\Phi(x)=\frac{2}{\sqrt{\pi}}\int_0^x e^{-t^2}dt$$

is the Laplace function.

Substituting this equation into (7) and normalizing, we find

$$B_N=\frac{\exp\left\{-N\frac{2\pi\sigma^2}{AB}\left[4-e^{-\frac{\Delta R^2}{\sigma^2}}\right]\right\}-\exp\left(-N\frac{8\pi\sigma^2}{AB}\right)}{\exp\left\{-N\frac{6\pi\sigma^2}{AB}\right\}\left[\exp\left(N\frac{2\pi\sigma^2}{AB}\right)-1\right]}. \qquad (13)$$

This equation can be solved for σ, although the calculation is lengthy. However, if the dimensions of the analysis region are large, so that

$$\Phi\left(\frac{A}{2\sigma\sqrt{2}}\right)=\Phi\left(\frac{B}{2\sigma\sqrt{2}}\right)\simeq 1,$$

and if the exponential function in (13) can be approximated by the first two terms of its series expansion,

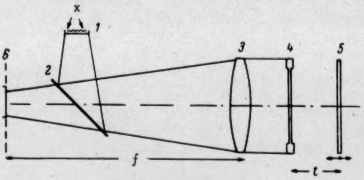

Fig. 4

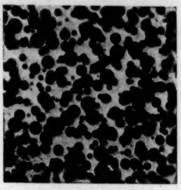

Fig. 5

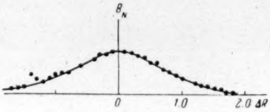

Fig. 6

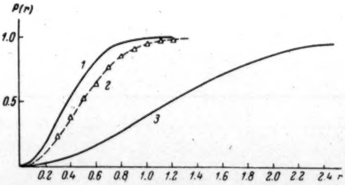

Fig. 7

$$\exp\left(N\frac{2\pi\sigma^2}{AB}\right)=1+N\frac{2\pi\sigma^2}{AB},$$

then the solution simplifies considerably, becoming

$$B_N=\frac{B(\Delta R)}{B(0)}\simeq e^{-\frac{\Delta R^2}{\sigma^2}}. \qquad (14)$$

Obviously, σ can be calculated from the measured B(ΔR).

EXPERIMENTAL RESULTS

In our experiments we use the optical-correlator arrangement shown in Fig. 4. The correlator consists of a light source 1, mirrors 2 and 5, lens 3, and object 4 (a transparency). The two-dimensional autocorrelation function is formed in the focal plane 6 of lens 3. The position of mirror 5 with respect to the transparency determines the maximum displacement with respect to each coordinate, due to the ratio $M = f/2t$, where f is the focal length of the lens and t is the distance along the optical axis between transparency 4 and mirror 5.

We studied a transparency (Fig. 5) consisting of $N = 500$ circles, whose centers were distributed uniformly over the analysis field. This uniformity was achieved by choosing the coordinates of each point from tables of random numbers;[4] an arbitrary overlap of the circles was permitted. The distribution of the radii of these circles obeys a Rayleigh law with $\sigma = 0.32$. Figure 6 shows the result of photometry of the autocorrelation function. Calculations from (14) yield $\sigma = 0.41$, quite close to the original value. Figure 7 shows curves of the function $P(r) = 1 - \exp(-r^2/2\sigma^2)$ plotted for $\sigma = 0.32$, 0.41, and 1.0 (curves 1-3, respectively). We see that the experimental curve for $\sigma = 0.41$ differs only slightly from that for $\sigma = 0.32$; the primary reason for the discrepancy is that the distribution of radii on the transparency obeys a discrete law, rather than the purely Rayleigh law, for which Eq. (14) holds.

CONCLUSIONS

1. We have shown that when certain a priori information is available about the elements of the image being studied the size distribution of elements can be determined from the measured autocorrelation function.

2. Simple equations have been derived for certain common cases: circular objects or objects of arbitrary shape for which the lengths of the radius vectors obey a Rayleigh law.

3. This calculation procedure can be used for objects of other shapes: rectangles, ellipses, etc., with arbitrary distribution laws.

4. The relatively simple algorithms for processing the measured results can be used for automatic analysis of fine-structure images.

---

[1] S. A. Benton and R. F. Kronamer, J. Opt. Soc. Amer., 61, No. 4, 524 (1971).

[2] E. L. O'Neill, Introduction to Statistical Optics, Addision-Wesley, Reading, Mass. (1963).

[3] S. G. Mikhlin, Lectures on Linear Integral Equations [in Russian], Fizmatgiz (1959).

[4] Tables for Mathematical Statistics [in Russian], Vychislitel'nyi Tsentr Akad. Nauk SSSR, Moscow (1968).

Coherent instability of a beam in a vacuum chamber with an irregular boundary

E. S. Masunov

(Submitted January 15, 1973; resubmitted October 23, 1973)
Zh. Tekh. Fiz., 44, 1903-1908 (September 1974)

The longitudinal stability of charged-particle beams in accelerators and storage rings is analyzed. A general dispersion relation is derived for the case in which the vacuum chamber has an arbitrary irregularity which violates the azimuthal symmetry of the system. The growth rates are calculated taking account of the interaction of harmonics of the space-charge density waves. The motion of a single beam and of the simultaneous motion of two beams are analyzed separately.

The longitudinal instability of beams in charged-particle accelerators and storage rings is usually analyzed under the assumption that the transverse dimensions of the chamber and other external elements surrounding the beam are independent of the azimuthal angle θ (refs. 1-4). On the other hand, it is well known that the azimuthal symmetry is always violated in a real system. In large accelerators and storage rings the toroidal chamber will consist of separate regions with different transverse cross sections. The azimuthal symmetry can also be violated when there are any other irregularities in the shape of the chamber boundary, when deflecting plates are placed at certain points in the ring, when azimuthal cuts are provided in a waveguide for focusing a toroidal bunch,[5] etc.

In ref. 6 an attempt is made to take account of boundary irregularities, and the impedance of a chamber containing a beam is calculated for a particular case. It should be noted that it is assumed in this calculation[6] that the different harmonics of the space-charge density waves are independent; but this assumption is strictly valid only for regular systems, and it does not permit an analysis of effects due to an irregularity.

Our purpose here is to analyze the stability of the motion of one or several circulating beams in an arbitrary irregular chamber, taking harmonic interactions into account. The analogous problem for the case of a linear geometry is studied in ref. 7.

1. For simplicity we first consider a single freely circulating beam. The kinetic equation describing the longitudinal motion of the particles in the beam is

$$\frac{\partial f}{\partial t}+\Omega(W)\frac{\partial f}{\partial\theta}+2\pi eR\frac{df_0}{dW}\langle E_\theta\rangle=0, \tag{1}$$

where θ is the azimuth and W is the canonically conjugate momentum. Here, the angle brackets denote averaging of the longitudinal field over the transverse coordinates of the particles in the bunch. This averaging is valid if the frequency of the transverse oscillations differs markedly from that of the longitudinal oscillations in the beam. Since our basic purpose below is to analyze the longitudinal motion of the beam, independently of the transverse motion, we assume that this latter condition is always satisfied.

We assume that the chamber has N-fold symmetry in the azimuthal direction, i.e., it consists of N identical inhomogeneous parts. Then we seek the current density of the circulating beam in the form

$$j(\mathbf{r}^{\perp},\theta)=\lambda(\mathbf{r}^{\perp})\sum_{\hat m}j(\hat m)e^{i\hat m\theta-i\omega t}. \tag{2}$$

Here $\hat m = k+Nl$ are integers; $|k| \leq N/2$ for even N or $|k| \leq N-1/2$ for odd N; and $l = 0, \pm 1\ldots$. The field produced by the beam in the chamber can also be written in form (2). In an analysis of stability it is customary to analyze the total coupling impedance Z instead of $\langle E(\hat m)\rangle$. For the case of an irregular boundary the impedance should be defined by

$$2\pi R\langle E(\hat m)\rangle=\sum_{\hat n}Z_{\hat m,\hat n}j(\hat n). \tag{3}$$

Each diagonal element of the matrix Z is the average over the azimuth of the impedance corresponding to the given harmonic of the orbiting frequency. The off-diagonal elements $Z_{\hat m\hat n}$ are nonvanishing for irregular systems and can be calculated as described in the Appendix. It follows from the general form of $Z_{\hat m\hat n}$(A7) that the matrix Z is anti-Hermitian if we neglect damping at the walls.

Substituting (3) into the kinetic equation (1), we find a general dispersion relation for determining the growth rates for longitudinal instability of the beam:

$$\det\|I_{\hat n}\delta_{\hat m,\hat n}-ie^2\omega Z_{\hat m,\hat n}\|=0, \tag{4}$$

where

$$I_{\hat n}^{-1}=\frac{1}{\hat n}\int\frac{\frac{df_0}{dW}}{\hat n\Omega-\omega}dW. \tag{4a}$$

In addition to the ordinary radiative instability and the negative-mass instability, Eq. (4) can be used to analyze a specific instability (specific to irregular systems) due to the parametric interaction of space-charge density waves. Let us consider the solution of Eq. (4) for frequencies near $\omega_{\hat m,\hat n} = [2\hat m\hat n/(\hat m+\hat n)]\Omega_0$ (Ω_0 is the averaging orbiting frequency of the particles). We assume that $\omega_{\hat m,\hat n}$ differs significantly from the resonant frequencies of the chamber corresponding to the $\hat m$ and $\hat n$ harmonics and that the negative-mass instability also does not occur (for a monoenergetic beam this latter condition is satisfied if $\eta\,\mathrm{Im}\,Z_{\hat m,\hat n}/\hat m$ and $\eta\,\mathrm{Im}\,Z_{\hat n\hat n}/\hat n$, where $\eta = 1/\gamma^2 - 1/\gamma_{\mathrm{crit}}^2$, are negative). Then it can be shown that if the beam properties satisfy

$$4\left(\frac{\hat m-\hat n}{\hat m+\hat n}\right)^2\approx F_1+F_2^2, \tag{5}$$

where

$$F_1=i\frac{\alpha c}{2\pi\beta}\frac{Z_{\hat m,\hat n}}{\hat n},\quad F_2=i\frac{\alpha c}{2\pi\beta}\frac{d}{d\omega}\left[\omega\frac{Z_{\hat n\hat n}}{\hat n}\right]_{n\Omega_0},\quad \alpha=\frac{r_0N_e\eta}{2\pi R\gamma}, \tag{5a}$$

Eq. (4) has complex solutions. In the case in which Eq. (5) holds exactly, the growth rate μ is a maximum:

$$\mu = \pm i \frac{\omega_{\hat m,\hat n}}{\hat m - \hat n} \frac{c}{2\pi\beta} |\alpha Z_{\hat m,\hat n}|. \tag{6}$$

For a specified difference $\hat{m} - \hat{n} > 0$ the width of the resonance band is found from the condition

$$-\frac{\omega_{\hat m,\hat n}}{\Omega_0} \frac{c}{\pi\beta} \frac{|\alpha Z_{\hat m,\hat n}|}{\hat m^2 - \hat n^2} < \frac{\hat m + \hat n}{2(\hat m - \hat n)} \sqrt{F_1 + F_2^2}$$

$$-1 - \frac{F_2}{2} < \frac{\omega_{\hat m,\hat n}}{\Omega_0} \frac{c}{\pi\beta} \frac{|\alpha Z_{\hat m \hat n}|}{\hat m^2 - \hat n^2}, \tag{7}$$

from which we can determine the total number of interacting harmonics if we know $Z_{\hat m \hat n}$.

It follows from condition (5) that for beams with a large space-charge density (e.g., in the toroidal electron bunches used in ring systems,[5] with $N_e \sim 10^{13}$-10^{14}, $R \sim 5$ cm) the parametric interaction of the density waves becomes important even at low harmonics $\hat{m}$ and $\hat{n}$. As the violation of the azimuthal symmetry of the system surrounding the beam becomes more pronounced, the value of $|Z_{\hat m \hat n}|$ increases, and so does the growth rate.

When η Im $Z_{\hat n \hat n}/\hat n > 0$ the negative-mass instability is not dangerous if the relative spread in orbiting frequencies, Δ, satisfies

$$\Delta^2 > |F_1|. \tag{8}$$

Nevertheless, even in this case the effect considered above leads to a beam instability with a growth rate (6), although it is true that the resonance conditions themselves are slightly different; (5) and (7) should be replaced by analogous equations with F_1 replaced by $F_1 + \Delta^2$.

The result obtained above has a simple physical meaning: In a regular waveguide, as in free space, the harmonics of the fast and slow space-charge waves propagate independently at any beam density. An irregular boundary can lead to a coupling of the m-th harmonic of the fast wave and the n-th harmonic of the slow wave. Since the coupling between the slow and fast waves is active, the energy is continuously pumped from the slow wave to the fast wave. The slow wave carries a negative kinetic power, while the fast wave carries a positive kinetic power. Accordingly, the amplitudes of both waves grow, leading to the beam instability.

2. We now consider a slightly different case, in which two beams circulate simultaneously in an irregular chamber, instead of the single beam discussed above. We are interested in the longitudinal stability of such a two-beam system; we assume that the conditions for transverse stability are satisfied.

The dispersion relation (4) is replaced by

$$\det \| \delta_{\hat m,\hat n} - ie^2 \omega Z_{\hat m,\hat n} \{ I_{1,\hat n}^{-1} + I_{2,\hat n}^{-1} \} \| = 0, \tag{9}$$

where

$$I_{i,\hat n}^{-1} = \frac{1}{\hat n} \int \frac{\frac{df_{i0}}{dW}}{\hat n \Omega_i - \omega} dW, \tag{9a}$$

and Ω_i is the angular velocity of the first ($i = 1$) or second ($i = 2$) beam. If the particles are revolving in different directions, the Ω_i have opposite signs.

If the external system is azimuthally symmetric, Eq. (9) has complex solutions when the number of particles in orbit is $N_{1,2} \geqslant \gamma^3 R/r_0$. This case corresponds to the ordinary two-stream instability of the Buneman type;[2] the particle density per unit length does not reach this threshold in any existing accelerator.

Of much more interest is the beam interaction in the case $Z_{\hat m \hat n} \neq 0$. We see from (9) that under the condition

$$\hat m \Omega_1 + \hat n \Omega_2 = 0 \tag{10}$$

there is an intense interaction between the particles of the different beams, leading to an instability even when the space charge is small.

We first assume that $\eta_1 \operatorname{Im} Z_{\hat m, \hat m}/\hat m$ and $\eta_2 \operatorname{Im} Z_{\hat n \hat n}/\hat n$ are negative, corresponding to the case in which each of the beams is individually stable. Taking account of the resonant interaction between bunches we can show that (9) has complex solutions if

$$-Z_{\hat m,\hat m} Z_{\hat n,\hat n} < |Z_{\hat m,\hat n}|^2. \tag{11}$$

This latter condition is independent of $N_{1,2}$, and in the case of a toroidal chamber, with $Z_{\hat m,\hat n}$ given by Eq. (A7), this condition can be rewritten as

$$\frac{G^{(0)}}{\gamma_1 \gamma_2} < (1 \pm \beta_1 \beta_2) |G^{(\hat m - \hat n)}|. \tag{12}$$

The upper sign corresponds to the case of beams moving in opposite directions, and the lower sign corresponds to the case of the same direction.

If the quantities $\eta_1 \operatorname{Im} Z_{\hat m \hat m}/\hat m$ and $\eta_2 \operatorname{Im} Z_{\hat n \hat n}/\hat n$ have different signs (e.g., if $\eta_1 \operatorname{Im} Z_{\hat m \hat m}/\hat m > 0$ and $\eta_2 \operatorname{Im} Z_{\hat n \hat n}/\hat n < 0$), an instability of the first beam would lead to an instability of the second. An exceptional case is that in which

$$\alpha_2 \frac{\hat n^2}{\gamma_2^2} > -\alpha_1 \frac{\hat m^2}{\gamma_1^2}. \tag{13}$$

Now the second beam can stabilize the first beam, under the condition

$$\frac{G^{(0)}}{\gamma_1 \gamma_2} (1 \pm \beta_1 \beta_2) |G^{\hat m - \hat n} < \frac{G^{(0)}}{2 \hat m \hat n} \frac{1}{\sqrt{|\alpha_1 \alpha_2|}} \left[\alpha_2 \frac{\hat n^2}{\gamma_2^2} - \alpha_1 \frac{\hat m^2}{\gamma_1^2} \right]. \tag{14}$$

Finally, with $\eta_1 \operatorname{Im} Z_{\hat m \hat m}/\hat m > 0$ and $\eta_2 \operatorname{Im} Z_{\hat n \hat n}/\hat n > 0$, there is always an instability. Each of the beams can be stabilized separately if the relative spread in orbiting frequency $\Delta_{1,2}$ satisfies condition (8). But even in this case a resonant interaction can lead to an instability of the two-beam system, under the condition

$$\left(G^{(0)} + \frac{\Delta_1^2 \beta_1^2 \gamma_1^2}{\alpha_1} \right) \left(G^{(0)} + \frac{\Delta_2^2 \beta_2^2 \gamma_2^2}{\alpha_2} \right) < \gamma_1^2 \gamma_2^2 (1 \pm \beta_1 \beta_2)^2 |G^{(\hat m - \hat n)}|. \tag{15}$$

In particular, when particles with the same rest mass collide, we find from (15)

$$\frac{\Delta^2 \beta^2 \gamma^2}{|\alpha| G^{(0)}} - 1 < \gamma^2 (1 + \beta^2) \left| \frac{G^{(2\hat n)}}{G^{(0)}} \right|. \tag{16}$$

The longitudinal two-stream instability in a chamber having an irregular boundary is of the same nature as the instability in the case of a single beam; a parametric interaction between the fast space-charge wave of one beam and the slow wave of the second beam can occur, as was shown above, even when the particle density in the bunches is low. At large γ this instability can be dangerous for all low-frequency harmonics, e.g., in the case of a vacuum chamber in which there is an abrupt change in the cross section, $G^{(2n)}$ falls off no more rapidly than $1/\hat{n}$, and the quantity on the right-hand side of inequality (16) can be larger than or comparable to unity for all $\hat{n} < \gamma^2$.

It should be noted that at very large $\hat{n}$, corresponding to microwave frequencies, equations like (5) and (16) become invalid, since the analysis of the parametric interaction of space-charge density waves must now incorporate the approximate equality of ω and the resonant frequencies of the irregular parts of the chamber. This problem is solved in ref. 7 for linear geometry; it is shown that the approximate equality of ω and the resonant frequencies can both increase the growth rate or suppress the instability altogether. Analysis of these effects for cyclic systems having one or two beams is of independent interest and requires a separate analysis.

APPENDIX

To determine the field excited by the beam in any cross section of the chamber with a longitudinal coordinate θ, it is better to use the method of transverse cross sections.[8] The longitudinal component of the field E is sought in this case in the form

$$E_\theta = -i\sum_{\hat{m}}\left\{\sum_s A_{\hat{m},s}\nu_s^2\Phi_s + \frac{4\pi}{\omega}\lambda(\mathbf{r}^\perp)\, j(\hat{m})\right\} e^{i\hat{m}\theta - i\omega t}, \tag{A.1}$$

where $\Phi_s(\mathbf{r}^\perp, \theta)$ is the eigenfunction for the boundary-value problem

$$\nabla_\perp^2\Phi_s + \nu_s^2\Phi_s = 0 \tag{A.2}$$

with the boundary condition $\Phi_s = 0$ on the contour bounding the cross section $S_\perp$ perpendicular to the beam. In Eqs. (A.1) and (A.2), ν_s is the eigenvalue corresponding to the eigenfunction Φ_s. The unknown quantities $A_{\hat{m},s}$ can be found as in ref. 8. In the case in which the orbital radius is much larger than the transverse dimensions of the chamber, and the transverse beam current can be neglected, the $A_{\hat{m},s}$ are the solutions of

$$\sum_{\hat{m},s_1}\left\{M^{\hat{n},\hat{m}}_{s,s_1} + i\frac{\omega}{c}\zeta D^{\hat{n},\hat{m}}_{s,s_1}\right\} A_{\hat{m},s_1} = \frac{4\pi}{\omega}\sum_{\hat{m}}[\nu_s^2\langle\Phi_s\rangle]^{(\hat{n}-\hat{m})}\, j(\hat{m}). \tag{A.3}$$

Here the matrix M is Hermitian, and all its elements can be written in terms of the functions Φ_s and their derivatives:

$$M^{\hat{n},\hat{m}}_{s,s_1} = \left(\frac{\omega^2}{c^2} - \frac{\hat{n}^2}{R^2}\right)\delta_{s,s_1}\delta_{\hat{n},\hat{m}} - [\nu_s^2]^{(\hat{n}-\hat{m})}\delta_{s,s_1} + \frac{i}{R}\left(\hat{n}Q^{\hat{n},\hat{m}}_{s,s_1} - \hat{m}Q^{\hat{n},\hat{m}}_{s,s_1}\right) - \Lambda^{\hat{n},\hat{m}}_{s,s_1},$$

$$Q^{\hat{n},\hat{m}}_{s,s_1} = \frac{1}{2\pi R}\oint d\theta\int dS_\perp\left(\nabla_\perp\Phi_s,\ \nabla_\perp\frac{\partial\Phi_{s1}}{\partial\theta}\right)e^{i(\hat{m}-\hat{n})\theta},$$

$$\Lambda^{\hat{n},\hat{m}}_{s,s_1} = \frac{1}{2\pi R^2}\oint d\theta\int dS_\perp\left(\nabla_\perp\frac{\partial\Phi_s}{\partial\theta},\ \nabla_\perp\frac{\partial\Phi_{s1}}{\partial\theta}\right)e^{i(\hat{m}-\hat{n})\theta},$$

$$[\nu_s^2]^{(\hat{n}-\hat{m})} = \frac{1}{2\pi}\oint d\theta\,\nu_s^2(\theta)\, e^{i(\hat{m}-\hat{n})\theta}. \tag{A.4}$$

The matrix $D^{\hat{n},\hat{m}}_{s,s_1}$ gives the damping at the walls, whose surface impedance is ζ. The elements of matrix D themselves can be expressed in terms of the functions Φ_s:

$$D^{\hat{n},\hat{m}}_{s,s_1} = \frac{1}{2\pi}\oint d\theta\int dS_\perp\frac{\partial\Phi_s}{\partial\tau}\frac{\partial\Phi_{s1}}{\partial\tau}e^{i(\hat{m}-\hat{n})\theta}, \tag{A.5}$$

where τ is the unit vector normal to the contour bounding cross section $S_\perp$.

From the solutions found for Eq. (A.3) we can calculate the field in (A.1) and the elements of matrix $Z_{\hat{m},\hat{n}}$. Without going into the details of the method used to seek the solutions of $A_{\hat{m},s}$ for an arbitrary frequency ω, we write $Z_{\hat{m},\hat{n}}$ in the long-wavelength approximation:

$$Z_{\hat{m},\hat{n}} = i\frac{8\pi^2 R}{\omega}\sum_{\substack{s,s_1\\ \hat{m}_1,\hat{n}_1}}\langle\Phi_s\rangle^{(\hat{m}-\hat{m}_1)}\langle\Phi_{s1}\rangle^{(\hat{n}_1-\hat{n})}\left\{\left(\frac{\omega^2}{c^2} - \frac{\hat{n}_1^2}{R^2}\right)\delta_{s,s_1}\delta_{\hat{n}_1\hat{m}_1} + \frac{i}{R}\left(\hat{m}_1 Q^{\hat{m}_1,\hat{n}_1}_{ss_1} - \hat{n}_1 Q^{\hat{m}_1,\hat{n}_1}_{s_1 s}\right) - \Lambda^{\hat{m}_1\hat{n}_1}_{ss_1} + i\frac{\omega}{c}\zeta D^{\hat{m},\hat{n}_1}_{ss_1}\right\}. \tag{A.6}$$

This equation simplifies if the particular shape of the cross section is specified. Let us assume, e.g., that the waveguide has a circular cross section. Then by writing the functions Φ_s as in (2) in ref. 8, and expressing the matrices Q and Λ in terms of the roots of the Bessel function, again as in ref. 8 [see Eq. (4a)], we find, after summing over s, s_1, $\hat{m}_1$, and $\hat{n}_1$, that Eq. (A.6) becomes

$$Z_{\hat{m},\hat{n}} = i\frac{2\pi R}{\omega}\left(\frac{\omega^2}{c^2} - \frac{\hat{m}\hat{n}}{R^2}\right)G^{(\hat{m}-\hat{n})} + 2i\frac{\omega}{c}\zeta\oint d\theta\sqrt{\frac{1}{b^2} + \left(\frac{db}{Rd\theta}\right)^2}\, e^{i(\hat{n}-\hat{m})\theta}. \tag{A.7}$$

Here

$$G^{(\hat{m}-\hat{n})} = \frac{1}{2\pi}\oint\left(\frac{1}{2} + 2\ln\frac{b(\theta)}{a}\right)e^{i(n-m)}d\theta, \tag{A.8}$$

$b(\theta)$ is the variable radius of the cross section, and a is the beam radius.

If we set $\hat{m} = \hat{n}$ in (A.8) and assume that $b(\theta)$ is a piecewise-constant function, we find the equation of ref. 6 for $G^{(0)}$.

---

[1] A. A. Kolomenskii and A. N. Lebedev, At. Energ., 7, 549 (1959).
[2] C. Nielsen, A. Sessler, and K. Symon, Proceedings of the International Conference on High-Energy Accelerators and Instrumentation, Geneva, 1959, p. 239.
[3] A. A. Kolomenskii, At. Energ., 17, 57 (1964).
[4] A. G. Bonch-Osmolovskii and É. A. Perel'shtein, Preprints R9-4424 and R9-4425, Joint Institute for Nuclear Research, Dubna, 1969.
[5] G. V. Dolbilov, I. N. Ivanov, É. A. Perel'shtein, V. P. Sarantsev, and V. F. Shevtsov, Proceedings of the Seventh Intern. Conference on High-Energy Particle Accelerators [in Russian], Vol. 2, Erevan (1970), p. 535.
[6] E. Keil and B. Zotter, CERN-ISR-TH/70-30, 33.
[7] É. S. Masunov, Izv. VUZ. Radiofiz., 14, 1611 (1971).
[8] É. S. Masunov, in: Accelerators [in Russian], No. 12, Atomizdat, Moscow (1970), p. 44.

Magnetic-field transport of a high-current electron beam

A. V. Agafonov, V. S. Voronin, A. N. Lebedev, and K. N. Pazin

P. N. Lebedev Physics Institute,
Academy of Sciences of the USSR, Moscow
(Submitted October 11, 1973)
Zh. Tekh. Fiz., 44, 1909-1916 (September 1974)

The steady state of a high-current relativistic electron beam in a homogeneous external magnetic field is analyzed; diamagnetism and space charge are taken into account. The relations between the current and the minimum external field required for beam transport are derived. Currents considerably above the Alfvén limit can only be transported by hollow beams.

INTRODUCTION

The recent interest in high-current electron beams with 10^4-10^6 A and particle energies of 10^5-10^7 eV stems from the strong self-fields and the large amount of stored energy, which can be used effectively in a variety of applications.[1-5] A problem which arises in this connection is that of developing efficient methods for shaping and transporting these beams.

The transport methods used in practice generally involve gas focusing at pressures of the order of 10^{-2}-1 torr, but in certain applications the presence of gas in the chamber is either undesirable or ruled out altogether. Accordingly, there is interest in the possibility of beam transport in vacuum by a longitudinal magnetic field, which, in practice, must be comparable to the self-field of the beam.

Our purpose here is to determine the external magnetic field required for the flow of a specified total current and a specified total particle energy, taking the beam diamagnetism and space charge into account. Even in this formulation the problem is not unambiguous since the result must depend on the particle distribution in phase space, which is governed by conditions prevailing at the cathode. The most graphic model, which is the one usually adopted in the theory of low-current beams[6] and which is generalized below to the case of high-current electron beams, is the "laminar-flow model," described by the self-consistent hydrodynamic equations at zero temperature.[7] In cases of practical interest, however, the motion of the particles in a high-current electron beam differs markedly from laminar flow, and the kinetic approach must be adopted. We believe that the use of the hydrodynamic equations for a beam with a local Maxwellian temperature[8] is difficult to justify under conditions such that particle collisions can essentially be neglected.

We adopt a system of units in which e = m = c = 1; the unit of current is then 17 kA, the unit of energy is 0.511 MeV, the unit of magnetic stiffness is 1.7 kG · cm, and the unit of power is 8.7 GW.

1. HYDRODYNAMIC BEAM

We consider nonintersecting particle trajectories in the beam, which is assumed to be steady-state, axisymmetric, and homogeneous in the propagation direction (the z axis). The system of equations describing this state is

$$(\boldsymbol{\beta}\nabla)\boldsymbol{\beta}\gamma = \mathbf{E} + [\boldsymbol{\beta}\mathbf{B}]; \operatorname{curl}\mathbf{B} = 4\pi\rho\boldsymbol{\beta}; \ \operatorname{div}\mathbf{E} = 4\pi\rho, \tag{1}$$

where **E** and **B** are the electric and total magnetic fields, β and γ are the particle velocity and energy, and ρ is the charge density. All quantities are functions of the radius r alone in the polar coordinate system; we have $\beta_r \equiv 0$, so that the continuity equation is satisfied automatically. We can then write

$$\left.\begin{array}{c} \dfrac{\gamma\beta_\theta^2}{r} + E_r + \beta_\theta B_z - \beta_z B_\theta = 0, \\ B_z' = -4\pi\rho\beta_\theta; \ (rB_\theta)' = 4\pi\rho r\beta_z; \ (rE_r)' = 4\pi\rho r \end{array}\right\} \tag{2}$$

with the boundary conditions $B_z(r_e) = B_e$, $B_{\theta i} = 0$, $E_{ri} = 0$. Below, the subscripts "i" and "e" denote quantities at the inner and outer surfaces of the (generally hollow) beam; B_e represents the external magnetic field.

The hydrodynamic system thus only yields four equations for six quantities: ρ, β_z, β_θ, E_r, B_θ, and B_z. We can express two of these quantities as functions of the radius, reflecting the ambiguity mentioned above. As one auxiliary condition we take the total energy of the particles over a cross section to be constant; this case corresponds to the injection of a monoenergetic beam. We write the corresponding condition as

$$\gamma' = E_r. \tag{3}$$

We are now left with only a single relation between hydrodynamic quantities; the various forms of this relation lead to various models for the beam.[1)] In choosing this relation we must take account of the physical restrictions: The density and longitudinal velocity must be nonnegative.

As a typical model, for which we can find an analytic solution, we consider a monochromatic beam, i.e., one in which the longitudinal velocity is uniform over the cross section. Using the notation

$$\gamma_\parallel = (1-\beta_z^2)^{-1/2}; \ \gamma_\perp = \frac{\gamma}{\gamma_\parallel} \tag{4}$$

and eliminating the fields and densities from (2), we find an equation for $\gamma_\perp$:

$$[\gamma_\perp' r(\gamma_\perp^2-1)^{-1/2}]' = \frac{\gamma_\perp(\gamma_\perp^2-1)^{3/2}}{r}, \tag{5}$$

The solution of this equation can be expressed in terms of elliptic Jacobi functions and depends on the single parameter C, which takes on any value between $-\infty$ and γ_e^2:

$$\gamma_\perp(r) = \begin{cases} \sqrt{C}\, cn\left(i\sqrt{C-1}\ln\dfrac{r}{r_i}; \sqrt{\dfrac{C}{(C-1)}}\right) \text{ for } C > 1, \\ cn\left(i\sqrt{1-C}\ln\dfrac{r}{r_i}; (1-C)^{-1/2}\right) \text{ for } C < 1. \end{cases} \tag{6}$$

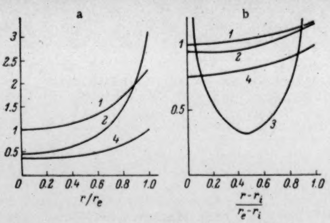

Fig. 1. Distribution of the principal electrodynamic quantities over the beam cross section. a) Continuous hydrodynamic beam, $\gamma_e = 3$, $I = I_{max} = 1.8$ (30.7 kA), $r_eB_e = 6.93$ (11.8 kG·cm); b) hollow kinetic and hydrodynamic beams, $\gamma_e = 3$, $I = 17.7$ (300 kA), $r_eB_e = 27$ (45.5 kG·cm). 1) Transverse energy $\gamma_\perp$; 2) charge density ρ for a hydrodynamic beam; 3) ρ for a kinetic beam; 4) longitudinal magnetic field B_z.

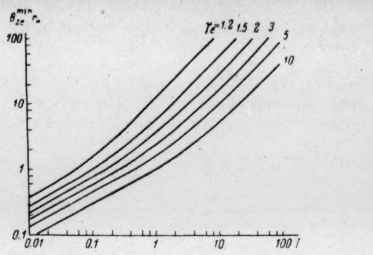

Fig. 2. Minimum external magnetic field B_e as a function of the total beam current I for the hollow hydrodynamic model and for various total energies γ_e (the curves are labelled).

We write the principal physical quantities in terms of $\gamma_\perp(r)$ as follows:

$$\left.\begin{aligned} E_r &= \frac{\gamma_\parallel}{r}[(\gamma_\perp^2-1)(\gamma_\perp^2-C)]^{1/2};\\ rB_z &= (\gamma_\perp^2-1)^{1/2}+\gamma_\perp(\gamma_\perp^2-C)^{1/2},\\ 4\pi\rho &= \frac{\gamma_\parallel\gamma_\perp}{r^2}[2\gamma_\perp^2-1-C]. \end{aligned}\right\} \tag{7}$$

The total beam current I and the external field are related by the parametric relations

$$I = \frac{1}{2}\beta_z\gamma_\parallel[(\gamma_{\perp e}^2-1)(\gamma_{\perp e}^2-C)]^{1/2};$$

$$r_eB_e = (\gamma_{\perp e}^2-1)^{1/2}+\gamma_{\perp e}(\gamma_{\perp e}^2-C)^{1/2}. \tag{8}$$

From (6) we can determine, in terms of the same parameters C and $\gamma_{\perp e}$, the hollowness coefficient of the current, $\mu = r_i/r_e$. We note that with $C > 1$ the quantity $\gamma_{\perp i}^2$ is equal to C; with $C < 1$ we have $\gamma_{\perp i} = 1$, corresponding to purely longitudinal particle motion at the linear beam surface. Figure 1 shows a typical distribution of the hydrodynamic quantities over the beam cross section.

Specification of the total particle energy γ_e determines $\gamma_{\perp e} = \gamma_e/\gamma_\parallel$, so that the $r_eB_e(I)$ curves for γ_e = const must be a single-parameter family. Interestingly, if we choose the hollowness coefficient of the current as this parameter, we find that these curves are double-valued, implying the existence of a limiting current. Increasing the current for a given hollowness coefficient increases the sag in the potential and the transverse-motion energy. If this energy becomes comparable to the total energy we find that the longitudinal velocity and thus, the current, begin to decrease, although the magnetic stiffness and charge density in the beam continue to increase. In a beam with a low hollowness coefficient the limiting transportable current is of the order of the Alfvén current, although the physical origin of this limitation is the transverse sag of the potential, rather than the self-magnetic field.

Transport of currents considerably higher than the Alfvén limit $I_A = \sqrt{\gamma_e^2 - 1}$ in a magnetic field is possible, according to (8), only at large negative values of C, since both $\gamma_\parallel$ and $\gamma_{\perp e}$ are always smaller than γ_e. On the one hand, this restriction implies $\gamma_{\perp i} = 1$, i.e., that the particles have only a longitudinal velocity at the inner surface of the hollow beam. On the other hand, the asymptotic form of (6) for $C \to -\infty$ yields

$$\mu = 1 - \frac{\operatorname{arch}\gamma_{\perp e}}{|C|^{1/2}}, \tag{9}$$

from which we see that the beam must have a strongly defined hollow structure. In principle, the transported current can be arbitrarily large if the hollow nature is sufficiently pronounced and if the magnetic stiffness is sufficiently high.

Of more interest in practice is the optimum beam, corresponding to the lowest magnetic stiffness for a given current, i.e., corresponding to the optimum choice of a hollowness coefficient. Possibilities of this optimization are illustrated in Fig. 2, which shows the envelopes of the family discussed above for various total energies. At small currents $r_eB_e^{min} \sim I^{1/2}$; at large currents $r_eB_e^{min} \sim I$, and the complete behavior of the curves is described, with an accuracy sufficient in practice, by the approximation

$$r_eB_e^{min} \approx \frac{2}{\gamma_e}\sqrt{\gamma_e^2-1}\left[\frac{I}{I_0}+\frac{I^2}{I_0^2}\right]^{1/2};\ I_0 = \frac{(\gamma_e^2-1)^{3/2}}{2\gamma_e^2}. \tag{10}$$

The optimum hollowness coefficient increases with increasing current.

This model of a monochromatic beam is not, of course, clearly defined. However, a study of other models (e.g., that with ρ = const) by numerical methods yields qualitatively the same results. Furthermore, in the high-current limit, for which the hollowness coefficient approaches unity and the details of the "internal" beam structure become unimportant, the asymptotic behavior turns out to be the same for the various models.

2. KINETIC DESCRIPTION OF THE BEAM

As mentioned above, real high-current beams generally have a relativistic "temperature," i.e., there is a difference between the energy of the microscopic motion and the energy corresponding to the average macroscopic velocity. Let us examine how seriously this effect influences the transport properties of the magnetic field and the beam diamagnetism.

When the system is homogeneous with respect to θ and z and steady-state in time, the kinetic equation without a collision term is satisfied identically by an arbitrary nonnegative function $f(H, P_\theta, P_z)$ of three integrals of motion: the Hamiltonian, the generalized angular momentum, and the generalized longitudinal momentum, which are related to the particle momentum **p** and the electromagnetic potentials Φ, A_θ, and A_z by

$$H = [1 + p_r^2 + p_\theta^2 + p_z^2]^{1/2} + \Phi;\quad P_\theta = r(p_\theta + A_\theta);\quad P_z = p_z + A_z. \tag{11}$$

The charge and current densities are then

$$\rho = \int f d\mathbf{p} = -\frac{\partial U}{\partial \Phi};\quad j_\theta = \int f \frac{p_\theta}{H - \Phi} d\mathbf{p} = \frac{\partial U}{\partial A_\theta};$$

$$j_z = \int f \frac{p_z}{H - \Phi} d\mathbf{p} = \frac{\partial U}{\partial A_z}, \tag{12}$$

where

$$U(\Phi, A_\theta, A_z, r) = \frac{2}{r} \int f p_r^2 dH dP_\theta dP_z, \tag{13}$$

and the integration is carried out over the region in phase space in which $p_x^2 \geq 0$.

By virtue of the symmetry of Eqs. (12), self-consistent equations for the potentials Φ, A_θ, and A_z can be written in the form

$$\begin{pmatrix} \frac{1}{r}\frac{d}{dr} r \frac{d}{dr} & 0 & 0 \\ 0 & \frac{d}{dr}\frac{1}{r}\frac{d}{dr} r & 0 \\ 0 & 0 & \frac{1}{r}\frac{d}{dr} r \frac{d}{dr} \end{pmatrix} \mathbf{R} = 4\pi \nabla_{\mathbf{R}} U(\mathbf{R}, r), \tag{14}$$

where **R** is the three-dimensional vector with components $\{-\Phi, -iA_\theta, -iA_z\}$.

For comparison with the laminar flow discussed above we again consider monoenergetic and monochromatic beams. We also assume that all particles have the same generalized angular momentum. On the one hand, this condition corresponds to the actual conditions that prevail for injection from a ring cathode in a longitudinal magnetic field; on the other, it ensures that each particle moves from the outer beam radius to the inner beam radius. For our purposes, this situation is the limiting case opposite that of the laminar flow discussed in Sec. 1.

The distribution functions corresponding to this model are

$$f = f_0 \delta(H) \delta(P_\theta) \delta(P_z) \tag{15}$$

and

$$U(\mathbf{R}, r) = \frac{2f_0}{r}(R^2 - 1)^{1/2}. \tag{16}$$

The addition of arbitrary constants to the arguments of the δ functions is equivalent to the addition of constants to the potentials and thus does not alter the physical state. In this case, over the entire volume occupied by the beam, $\Phi \equiv -\gamma$, $A_\theta \equiv -p_\theta$, and $A_z \equiv -p_z$. The boundary conditions for Eqs. (14) are conveniently specified at the inner beam surface:

$$\mathbf{R}_i = \{\sqrt{1 + p_{\theta i}^2 + p_{zi}^2};\ ip_{\theta i};\ ip_{zi}\};\quad \mathbf{R}_i' = \left\{0;\ -iB_{zi} - \frac{ip_{\theta i}}{r_i};\ 0\right\}. \tag{17}$$

We can now show that distribution function (15) actually corresponds to a monochromatic beam. Multiplying the first component of (14) by A_z, multiplying the third by Φ, and taking the difference we find, taking account of the boundary conditions, the first integral

$$p_z = \text{const}\,\gamma,$$

from which we see that the longitudinal velocity is constant over the cross section and that Eq. (14) is in fact two-dimensional.

The solution of Eq. (14) allows us to write the following equations in terms of the properties at the inner boundary:

$$\gamma_e = -\Phi_e;\quad r_e B_e = \frac{d}{dr} r A_\theta \Big|_e;\quad I = -\frac{r_e}{2} \beta_z \frac{d\Phi}{dr}\Big|_e;\quad p_{\theta e} = -A_{\theta e}. \tag{18}$$

We can also write an equation for the dimensionless outer beam radius $f_0 r_e$, determined from the condition $R_e^2 = 1$ (we note that the normalization constant f_0 only determines the absolute dimension of the beam and does not appear in the final results). Used along with a kinematic equation at the outer boundary, $p_{\theta e}^2 = \gamma_e^2/\gamma_\parallel^2 - 1$, this equation allows us to write the magnetic stiffness $r_e B_e$ and the current in terms of the three quantities γ_e, B_z, and $\mu = r_i/r_e$, as in Sec. 1.

In the limiting case of a low beam density, to a first approximation we then have

$$B_e r_e \approx -\frac{2p_e}{1 \mp \mu};\quad I \approx \frac{1}{2} \beta_z \frac{(\gamma_e - \gamma_i)}{\ln \frac{2}{1 + \mu}}, \tag{19}$$

where the upper sign corresponds to $p_i \approx -p_e$ and the lower to $p_i \approx p_e$, corresponding to two different projections on the beam cross section (Figs. 3a and 3b). The first of these states, which is somewhat analogous to that of the hydrodynamic case with $c < 1$, permits a greater range of possibilities in high-current transport, while the second has marked diamagnetic properties. By varying the hollowness coefficient we can easily find the envelope of this family, i.e., the minimum field required for propagation of a given (small) current:

$$\gamma_i = \gamma_\parallel;\quad r_e B_e^{\min} \approx 4\sqrt{\ln 2}\, I^{1/2} (\gamma_e^2 - 1)^{-1/4}. \tag{20}$$

Condition (20) differs from the corresponding limiting case in (10) only in that the coefficient $4\sqrt{\ln 2} \approx 3.33$ appears instead of $2\sqrt{2} \approx 2.83$.

As in the hydrodynamic case the current is limited by the transverse sag of the electrostatic potential; hence it is reasonable to expect that a high current can only propagate in a hollow beam; then neglecting 1/r in com-

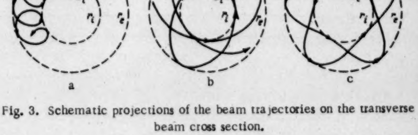

Fig. 3. Schematic projections of the beam trajectories on the transverse beam cross section.

parison with d/dr, we find the plane approximation, in which Eq. (14) becomes

$$\mathbf{R}''=\frac{8\pi I_0}{r_i}\nabla_R\sqrt{R^2-1} \tag{21}$$

and agrees formally with the equation describing the nonrelativistic motion of a material point in a centrally symmetric field. Without going into the details of the solution (see ref. 10), we write the distribution of the principal electrodynamic quantities over the cross section:

$$\left.\begin{aligned}\gamma_\perp\equiv-\frac{\Phi}{\gamma_\parallel}=R\cosh(\varepsilon-\psi);\ p_\theta\equiv-A_\theta=R\sinh(\varepsilon-\psi),\\ p_z\equiv-A_z=\beta_z\gamma_\perp\gamma_\parallel,\end{aligned}\right\} \tag{22}$$

where sinh ε = $p_{\theta i}$ and where the functions R(r) and ψ(r) are written implicitly in quadratures [the r(R) functional dependence is double valued]:

$$\left.\begin{aligned}r-r_i=\int_1^R\frac{RdR}{Q(R)};\quad \psi(r)=B_{zi}\int_1^{R(r)}\frac{dR}{RQ(R)},\\ Q=\left[\frac{8\pi I_0}{r_i}R^2\sqrt{R^2-1}-B_{zi}^2(R^2-1)\right]^{1/2}.\end{aligned}\right| \tag{23}$$

From simple physical considerations and (22) it again follows that the maximum transportable current corresponds to ε = 0, i.e., to the case in which there is no orbiting motion at the inner boundary of the beam. The density distribution for this case is also shown in Fig. 1. Despite the pronounced difference between this density distribution and that of the hydrodynamic case we note that the potential and magnetic field behave in essentially the same manner within the beam.

Corresponding to the optimum beam, i.e., to the minimum magnetic field for a specified current, there is also a definite longitudinal velocity,

$$\beta_z^{\text{opt}}=\sqrt{\frac{(\gamma_e^2-1)}{(\gamma_e^2+1)}}, \tag{24}$$

for which we have the following relation between the field and the current:

$$r_eB_e^{\min}=\frac{4\gamma_e}{\gamma_e^2-1}I,\quad I\gg\gamma_e, \tag{25}$$

which agrees exactly with hydrodynamic equation (10) over its entire range of applicability. Accordingly, the "temperature" effect turns out to be important in the transport of optimum beams only at low currents.

3. DIAMAGNETISM OF A HIGH-CURRENT ELECTRON BEAM

We see from the discussion above that in any finite magnetic field a charged beam rotates, i.e., produces diamagnetic currents which displace the magnetic field from the beam volume. This effect becomes particularly important for total currents on the order of I_A, for which the orbital velocity is relativistic.

In general, beam states providing the maximum transportable current yield a relatively low diamagnetism, for the particles in them must have a minimum transverse energy, due primarily to the sag of the electrostatic potential. In the hydrodynamic case the maximum diamagnetism comes from states for which C → 1 [see (7) and (8)] and

$$\frac{B_{ze}}{B_{zi}}\to\frac{(\gamma_{\perp e}+1)^2}{4}; \tag{26}$$

the ratio of the internal radius to the external radius tends toward zero, or the beam becomes continuous. We note that the diamagnetism increases with increasing total particle energy and with decreasing longitudinal energy ($\gamma_{\perp e}\to\gamma_e$). In all cases, however, the internal field has the same sign as the external field; otherwise a hydrodynamic equilibrium would not be possible.

In general, the kinetic beam model yields analogous results. For a highly hollow beam the diamagnetism corresponding to the transport of high currents is relatively low; from Eqs. (22) and (23) we find

$$\frac{B_{ze}}{B_{zi}}=\cosh(\psi_e-2\varepsilon)=\gamma_{\perp e}\gamma_{\perp i}+\sqrt{(\gamma_{\perp e}^2-1)(\gamma_{\perp i}^2-1)}, \tag{27}$$

and in the optimum beam ($\gamma_{\perp i}=1$) this ratio decreases even further, to $\gamma_{\perp e}$. We note that in this approximation only trajectories of the type shown in Fig. 2a are described, for which the inner part of the beam rotates in the direction opposite the rotation of the outer part. Obviously, motion like that in Fig. 3b, which is possible in the case of a small hollowness coefficient, provides a large azimuthal current and, correspondingly, a large diamagnetism. Numerical solution of Eq. (14) confirms this conclusion; as the diamagnetism increases, the hollowness coefficient decreases. We note that trajectories of the type in Fig. 3b correspond to negative values of the generalized angular momentum; this case is possible, e.g., when a cathode moves in a magnetic field directed opposite to the guiding field.

Also of interest is the hypothetical situation in which the internal field is directed opposite the external field. Such an equilibrium state, or "E layer," is known to actually be possible in the case of neutralized beams[11] and has been achieved in practice.[12] For charged beams this state should correspond to the trajectories shown in Fig. 3c, which do not qualitatively contradict the conditions for a force equilibrium. However, in the numerical study of the equations for values of r_eB_e and γ_e which are achievable in practice, no such states were found.

The authors thank A. A. Kolomenskii for his interest and É. N. Chaikovskaya for the extensive numerical calculations.

[1)] The second condition in ref. 9, although not contradictory, does not follow, as the author asserts, from any physical consideration; it is an artificial restriction.

---

[1] L. N. Kazanskii, A. V. Kisletsov, and A. N. Lebedev, At. Energ., 30, 27 (1971).
[2] A. A. Kolomenskii and I. I. Logachev, Proceedings of the Eighth International Conference on Accelerators, CERN, Geneva (1971), p. 587.
[3] I. M. Vitkovitsky, L. S. Levine, D. Mosher, and S. J. Stephanakis, Appl. Phys. Lett., 23, No. 1, 9 (1973).
[4] J. A. Nation and W. L. Gardner, Nucl. Fusion, 2, 55 (1972).
[5] M. Friedman and M. Herndon, Phys. Rev. Lett., 29, No. 1, 55 (1972).
[6] P. T. Kirstein et al., Space-Charge Flow, McGraw-Hill, New York (1967).
[7] M. Andrews, J. Bzura, H. H. Fleishmann, and N. Rostoker, Phys. Fluids, 13, No. 5, 1322 (1970).

[8] J. L. Synge, The Relativistic Gas, Interscience, New York (1957).
[9] A. J. Toepfer, Phys. Rev., A3, No. 4, 1444 (1971).
[10] V. S. Voronin and A. N. Lebedev, Zh. Tekh. Fiz., 43, 2591 (1973) [Sov. Phys. – Tech. Phys., 18, 1627 (1974)].
[11] L. Tonks, Phys. Rev., 114, No. 3, 637 (1959); Phys. Rev., 118, No. 4, 390 (1960).
[12] M. L. Andrews, H. Davitian, H. H. Fleishmann, B. Kusse, R. E. Kribel, and J. A. Nation, Phys. Rev. Lett., 27, No. 21, 1428 (1971).

Electron energy spectrum in a high-current vacuum diode

S. P. Bugaev, V. I. Koshelev, and M. N. Timofeev

Institute of Atmospheric Optics, Siberian Branch,
Academy of Sciences of the USSR, Tomsk

(Submitted August 3, 1973)
Zh. Tekh. Fiz., 44, 1917-1921 (September 1974)

In an experimental study of the electron energy spectrum in a high-current vacuum diode it is found that the energy spectra for single-point and multipoint cathodes are similar in shape. When current flows stably from the surface of the cathode-burst plasma the spectrum is smooth; when the current is unstable, the spectrum displays lines. The measured spectrum agrees satisfactorily with that constructed from current and voltage oscillograms recorded simultaneously. The maximum energy of the beam electrons is studied as a function of the cathode–anode gap and the length of the voltage pulse. Anomalous electrons, with energies above the applied voltage, are detected. It is concluded from the experimental results that the limiting energy of these anomalous electrons is not a function of the length of the voltage pulse (10^{-8}-10^{-7} sec) or the gap size (d = 4-32 mm) but is a function of the maximum energy of the beam electrons (E_{max} = 150-300 kV). For a multipoint cathode this limiting energy is $E_{lim} \approx 3E_{max}$; for a single-point cathode it is $E_{lim} \approx 2E_{max}$. The experimental data do not furnish an adequate basis for discussing in detail the mechanism by which electrons are accelerated to energies exceeding the applied voltage.

Study of the shaping of electron beams in plasma-cathode diodes has revealed stable and unstable current-flow regimes.[1,2] In the unstable case electrons are detected at energies above the applied voltage,[3] and ions are found to be accelerated in electron beams.[4] Refinements in the techniques for shaping intense electron beams[5,6] led to the use of cathodes with explosive electron emission.[7] Study of this phenomenon revealed high-energy electrons[8] and ions of the cathode-burst plasma accelerated toward the anode[9] and cathode.[10]

Below we report a study of the electron energy spectrum during stable and unstable current flow from the surface of a cathode-burst plasma. We present data on the properties of the high-energy electrons as a function of the diode geometry and the length of the high-voltage pulse.

EXPERIMENTAL APPARATUS AND PROCEDURE

Figure 1 shows the experimental apparatus. A negative voltage pulse is shaped by a lumped-capacitance (C_{pu} = 400 pF) GIN-300 generator (1). The pulse height is 300 kV and its rise time is τ_{fr} = 5 nsec. The pulse length is varied over the range 10^{-8}-10^{-7} sec by a cutoff switch in vacuum chamber 2. The vacuum, produced by an oil-vapor pump, is $5 \cdot 10^{-5}$ torr.

The cathode in the experiments consists of a single point (Cu, Mo) or a multipoint copper cathode with a packing density of 10^2 cm^{-2}. The interelectrode gap is 4-32 mm. The anode is a high-transmission molybdenum grid.

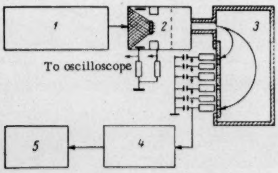

Fig. 1. Block diagram of the experimental apparatus.

A simultaneous oscilloscope display is made of the current pulse (taken from a Rogowski loop) and the voltage pulse (from a capacitative divider), and the energy spectrum is measured by semicircular-focusing spectrometer[11] 3. The recording circuit of the spectrometer uses 20 aluminum sheets with memory elements using FT-1 capacitors. A readout device sends a signal to amplifying electrometer 4 (input resistance of 1000 Ω); the signal is recorded by a KSP-4 electronic potentiometer 5.

A graphical method is used to construct the electron energy spectrum for various gaps from the simultaneously recorded current and voltage oscillograms. For this purpose the amplitude of the voltage pulse, $U_d(t)$, is partitioned into a certain number of intervals in steps of ΔU. The average current for the given time interval, i(t), is then determined. Then the data are analyzed on the basis of the equation

$$\frac{dN}{dU_d} = \frac{i(t)}{e}\left(\frac{dU_d}{dt}\right)^{-1}, \tag{1}$$

where e is the electron charge and N is the number of electrons. A similar problem is solved in ref. 12.

EXPERIMENTAL RESULTS

The energy spectra corresponding to the single-point cathode and the multipoint cathode are similar, so we will discuss only the spectra for the multipoint cathode.

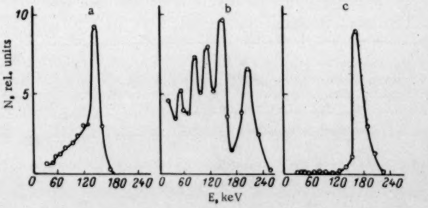

Fig. 2. Energy spectra. a) d = 4 mm, τ_p = 100 nsec; b) 20 mm, 100 nsec; c) 20 mm, 12 nsec.

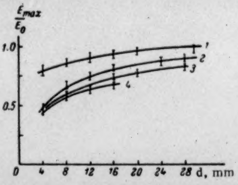

Fig. 3. Maximum electron energy in the beam as a function of the anode–cathode gap. 1) Single point, τ_p = 10 to 100 nsec; 2) multipoint cathode, τ_p = 100 nsec; 3) multipoint cathode, τ_p = 12 nsec; 4) multipoint cathode, τ_p = 10 nsec.

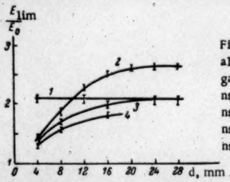

Fig. 4. Limiting energy of the anomalous electrons as a function of the gap. 1) Single point, τ_p = 10 to 100 nsec; 2) multipoint cathode, τ_p = 100 nsec; 3) multipoint cathode, τ_p = 12 nsec; 4) multipoint cathode, τ_p = 10 nsec.

Figure 2 shows the energy spectra for various gaps and pulse lengths. As the gap is increased in size, the spectrum changes markedly, going from a single-peak spectrum into a line spectrum. A high-voltage pulse with a length of $\sim 1 \cdot 10^{-8}$ sec is used to obtain an electron beam with a narrow energy spectrum (half-width 10-15%).

Figure 3 shows the maximum energy of the electrons in the beam found for single-point and multipoint cathodes as a function of the cathode–anode gap and the length of the voltage pulse. The energies are given in relative units; E_0 is the electron energy at the maximum voltage across the diode (300 kV). The maximum electron energy for the single-point cathode is slightly larger and is independent of the voltage-pulse length.

Study of the energy characteristics of the electron beam shows electrons at energies above the applied voltage (anomalous electrons); they make up 0.1-1% of the total charge which flows. The limiting energy of the anomalous electrons, detected by the spectrometer, is independent of the gap and the length of the voltage pulse (within the experimental errors) for the case of a single-point cathode; for a multipoint cathode it is higher, and its functional dependence on the gap typically displays saturation (Fig. 4). To confirm that these are actually high-energy electrons, rather than the results of the incidence of reflected electrons on the sheets, we place irises in the vacuum chamber of the spectrometer, which block the low-energy part of the spectrum. We find no change in the shape of the high-energy tail of the distribution.

Using the simultaneous recordings of the current and voltage as described above, we construct the spectrum. Figure 5 shows the constructed and measured spectra for a gap of 12 mm. We see that the agreement is satisfactory.

DISCUSSION OF RESULTS

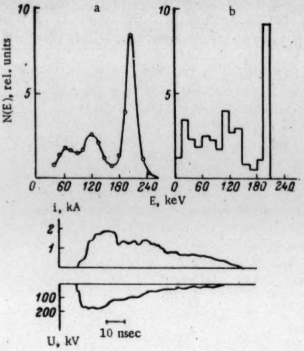

Fig. 5. Energy spectra. a) Measured (d = 12 mm, τ_p = 100 nsec); b) spectrum constructed from the current and voltage oscillograms (d = 12 mm, τ_p = 100 nsec).

The energy characteristics of the electron beam are functions of the nature of the high-voltage pulse generator, the parameters of the discharge circuit, and the physical processes involved in the current flow from the surface of the cathode-burst plasma.[13,14] In numerical calculations we determine the shape of the energy spectrum of an electron beam shaped by a lumped-capacitor generator; the equivalent circuit is shown in Fig. 6. The switching is assumed ideal. The calculation is carried out for a plane diode with a constant perveance p; this is a legitimate assumption in the case of large gaps, for which we can neglect the penetration of the cathode plasma into the gap. The spectrum is analyzed on the basis of the system of equations

$$\left.\begin{aligned} \int_0^{t_p} \frac{i(t)}{C}\,dt + L\frac{di(t)}{dt} - U_d(t) = 0, \\ i(t) = pU_d^{3/2}(t), \\ \frac{dN}{dU_d} = \frac{i(t)}{e}\left(\frac{dU_d}{dt}\right)^{-1}, \end{aligned}\right\} \qquad (2)$$

where L and C are the inductance and capacitance, respectively, of the generator. Solution of this system of equations is trivial for the discharge of the capacitance; the energy spectrum is "table-shaped" (1 in Fig. 6). The inductance is taken into account in a calculation of the spectrum on an M-220 computer (2 in Fig. 6); the result agrees satisfactorily with the experimental results.

However, it is found experimentally that the shape of the energy spectrum depends on the current-flow conditions; in the case of stable current flow, the spectrum is smooth (Fig. 2a), but as the gap is lengthened (d > 10 mm), a modulation appears in the electron current. There are

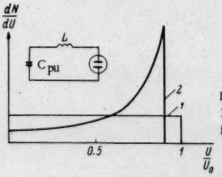

Fig. 6. Theoretical spectral shape. 1) Inductance of generator not taken into account; 2) taken into account.

spikes exceeding the amplitude of the basic signal by a factor of 1.5-2, implying an unstable current flow. Here the spectrum has lines (Figs. 5 and 2b). The spectral oscillations are observed at low energies. At a voltage pulse length of 12 nsec an electron beam with a smooth spectrum is shaped (Fig. 2c), so we conclude that the time over which the unstable current flow sets in is longer than $1 \cdot 10^{-8}$ sec.

It follows from the experimental results on the electron-beam energy spectrum (4 in Fig. 3) that the limiting energy of the anomalous electrons is not a function of the voltage pulse length or the gap size, but is a function of the maximum energy of the beam electrons. Over the range $E_{\max}$ = 150-300 keV (Fig. 3), the energy $E_{\lim}$ is essentially a linear function of $E_{\max}$, described by $E_{\lim} \approx 3E_{\max}$ for the multipoint cathode and $E_{\lim} \approx 2E_{\max}$ for the single-point cathode. No functional dependence of the limiting electron energy on the cathode material is found. The independence of the limiting energy from the gap size implies that the current-flow conditions do not affect the acceleration, and the independence of this energy from the length of the voltage pulse implies short characteristic acceleration times. The appearance of electrons at an anomalously high energy can result from an overvoltage across the accelerating gap. Another possible mechanism is stochastic acceleration of electrons in the cathode-burst plasma by the plasma turbulence,[15] which occurs as a result of the electron-drift instability.[16,17] It should be noted that the operating conditions are different for the single-point and multipoint cathodes: In the case of the multipoint cathode the current from a single point is two or three orders of magnitude lower than that in the case of a single-point cathode. There is also an important difference in the topology of the electric field at the cathodes. These factors apparently influence the acceleration efficiency. These experimental results do not furnish an adequate basis for a detailed discussion of the mechanism accelerating electrons to energies exceeding the applied voltage.

In studying the procedure for constructing the spectrum from the current and voltage oscillograms we construct spectra for two current-flow regimes. In the case of large gaps (d = 20 mm), in which case the modulation of the electron current is pronounced, a large number of partitions is required if the current over a single interval is to be essentially constant. This circumstance gravely complicates construction of the spectrum. This method seems to be workable if the modulation of the electron current and of the voltage is weak. The method can distinguish energy peaks in the spectrum separated by ~60 keV (Fig. 5).

The authors thank V. V. Kremnev for useful discussion.

---

[1] P. E. Belensov, A. T. Kapin, A. A. Plyutto, and V. N. Ryzhikov, Zh. Tekh. Fiz., 34, 2120 (1964) [Sov. Phys.-Tech. Phys., 9, 1633 (1965)].

[2] K. V. Suladze and A. A. Plyutto, Zh. Tekh. Fiz., 37, 72 (1967) [Sov. Phys.-Tech. Phys., 12, 48 (1967)].

[3] A. A. Plyutto, V. N. Ryzhkov, P. E. Belensov, and A. G. Kapin, Report No. 2409 (A), Siberian Physicotechnical Institute, (1967).

[4] A. A. Plyutto, P. E. Belensov, E. D. Korop, G. P. Mkheidze, V. N. Ryzhkov, K. V. Suladze, and S. M. Temchin, ZhETF Pis. Red., 6, 540 (1967) [JETP Lett., 6, 61 (1967)].

[5] W. T. Link, Trans. Nucl. Sci., NS-14, 777 (1967).

[6] T. H. Martin, IEEE Trans., NS-16, 59 (1969).

[7] S. P. Bugaev, A. M. Iskol'dskii, G. A. Mesyats, and D. I. Proskurovskii, Zh. Tekh. Fiz., 37, 2206 (1967) [Sov. Phys.-Tech. Phys., 12, 1625 (1968)].

[8] N. G. Pavlovskaya and T. V. Kudryavtseva, Prib. Tekh. Eksp., 2, 198 (1972).

[9] E. D. Korop and A. A. Plyutto, Zh. Tekh. Fiz., 40, 2534 (1970) [Sov. Phys.-Tech. Phys., 15, 1986 (1971)].

[10] E. D. Korop and A. A. Plyutto, Izv. VUZ. Fiz., 4, 131 (1973).

[11] A. P. Gerasimov, E. G. Dubinov, and B. G. Kudasov, Prib. Tekh. Eksp., 3, 31 (1971).

[12] S. E. Graybill, Atomnaya Tekhnika za Rubezhom, 3, 29 (1973).

[13] S. E. Graybill and S. V. Nablo, Appl. Phys. Lett., 8, 18 (1966).

[14] C. Andelfinger, W. Dommaschk, and W. Ott, Proceedings of the Fifth International Symposium (Poznan, 1972), p. 383.

[15] V. N. Tsytovich, Theory of Turbulent Plasma, Consultants Bureau, New York (1973).

[16] O. Buneman, Phys. Rev., 115, 503 (1959).

[17] H. M. Epstein, W. T. Gallagher, P. J. Mollozzi, and T. E. Strotton, Phys. Rev., A, 2, 146 (1970).

Multiphase, uniform, secondary-emission microwave discharge at a solid surface

G. S. Luk'yanchikov

P. N. Lebedev Physics Institute,
Academy of Sciences of the USSR, Moscow

(Submitted June 4, 1973; resubmitted February 19, 1974)
Zh. Tekh. Fiz., 44, 1922-1928 (September 1974)

The electron velocity distribution function, the threshold for the onset of the secondary-emission discharge, and the growth rate are determined for the case in which the high-frequency electric field is perpendicular to the surface. The results are applied to a microwave system with a large distance between the walls and to a single-ended discharge with a weak restoring force.

INTRODUCTION

In many theoretical papers on secondary-emission rf discharges at surfaces perpendicular to the high-frequency electric field (e.g., refs. 1-4), it is assumed that only electrons emitted in a narrow phase range (single phase) $\Delta\varphi_1 \ll \pi/2$, in resonance with the field, participate in the discharge.

It is thus assumed that most of the electrons participating in the discharge are monoenergetic. A condition for the occurrence of the discharge is that the field reach a level such that the secondary-emission yield is $\sigma > 1$ for electrons in resonance with the field. The spread of the initial electron velocities and the functional dependence on the collision energy W_c are neglected (only a single point in the functional dependence of σ on the energy is used − that energy W_1 at which the yield is $\sigma = 1$).

This approach is justified if the transit time of an electron between the two walls (a double-ended discharge) or the time interval between emission and collision with the same surface (a single-ended discharge) is so short that the spread in the initial electron velocities does not lead to a large spread in the field phases corresponding to the collision with the wall. A typical situation in which this resonant treatment is legitimate is that of a discharge in the narrow "capacitance" gap of a cavity resonator. However, in an apparatus in which a high level of microwave power is used and in which the walls are far apart (e.g., rf heating in thermonuclear devices, cavity resonators, waveguides, etc.), the approximation based on monoenergetic, in-phase electrons is not valid; even the thermal spread of initial velocities[1)] leads, over the long transit time, to an important spread in field phases at collision or at secondary emission.

In the discharge a distribution of electrons with respect to emission phase is established, and since electrons from a broad energy interval[2)] participate in the discharge, it is necessary to take account of the functional dependence of σ on energy over the entire range of energies which an electron can acquire in the microwave field. It is necessary to determine this distribution function in order to study the secondary-emission discharge.

Miller et al.[7] have determined the distribution functions for certain particular cases through numerical experiments, and Stanskii et al.[8] found the conditions for onset of a discharge for an arbitrary electron distribution function.

STATEMENT OF THE PROBLEM

We are concerned here with the initial stage of the discharge, in which we can neglect space-charge effects; we are to find the electron distribution with respect to emission phase and determine the threshold field for a discharge between two infinite plates in an alternating electric field perpendicular to the surface and exerting a force $F\sin\omega t$ on an electron. We make the following assumptions.

1. The time between electron emission, t_1, and collision with the second wall is so long that electrons emitted at any phase $\varphi_1 + 2\pi k$ (k is an integer, and $\varphi_1 = \omega t_1$) can be assumed to be distributed uniformly in the region in front of the surface with which they will collide. It is not difficult to show that condition for a uniform distribution of in-phase electrons is

$$\frac{t_f}{T} \gg \frac{v_m}{\Delta v}. \tag{1}$$

Here $T = 2\pi/\omega$, Δv is the half-width of the distribution with respect to initial velocities of the in-phase electrons (at $T_e = 2$-4 eV, we have $\Delta v \sim 10^6$ m/sec), $v_m = F/m\omega$, m is the electron mass, and t_f is the time the electron spends in the field between the walls. This condition holds, e.g., in a standard centimeter-range waveguide at a microwave power of 100-1000 kW for the case of a double-ended discharge between walls or a single-ended discharge on any structural element, in the presence of a force which turns emitted electrons back toward the surface (e.g., electrostatic forces). It is easy to show that if the transit time of the electron in the restoring field satisfies (1) a single-ended discharge is analogous to a double-ended discharge.

2. We assume that the functional dependence of σ on the collision energy is

$$\sigma = \frac{W_c}{W_1}, \tag{2}$$

which is a good approximation of the secondary-emission characteristics for most materials in the initial stage.

3. In analyzing the electron dynamics in front of the discharge surface we neglect the initial velocity[3)] and assume that the electron motion is governed completely by the microwave field. This assumption is valid since most of the electrons must have an energy[4)] $W_c \sim W_1 \gg 2$-4 eV.

EQUATIONS OF MOTION

Integrating $\ddot{x} = (F/m)\sin\omega t$ (the x axis is perpendicular to the emitting surface and parallel to F), and using assumption 3, we find equations for the electron velocity to the wall and for the dimensionless coordinate of an arbitrary electron, $\xi = xm\omega^2/F$:

$$\dot{x} = \frac{F}{m\omega}(-\cos\varphi + \cos\varphi_1), \tag{3}$$

$$\xi = -\sin\varphi + \varphi\cos\varphi_1 + c. \tag{4}$$

Here, $\varphi = \omega t$. Since the in-phase electrons are distributed uniformly, c can take on any value.

PHASE RANGE FOR THE PRIMARY AND SECONDARY CURRENTS

First we note that only electrons created at the wall in the phase range $\varphi_1 = (0-\pi/2) + 2\pi k$ can leave the wall and participate in the discharge, since they have a velocity component $(F/m\omega)\cos\varphi_1$ directed away from the wall.

We seek the phase range over which electrons can strike an obstacle in their path. Figure 1c shows the electron coordinate as a function of the field phase according to Eq. (4). As an example, we consider an electron with a dc velocity component corresponding to the creation phase $\pi/3$. We see from Fig. 1c that, between phase a_2, at which the electron velocity vanishes (Fig. 1b), and phase a_1, no electron having this dc velocity can reach an object in the x direction. Over the range a_1-a_2, on the other hand, the number of particles reaching the opposite surface is proportional to electron velocity (3) (Fig. 1b). It is easy to see that $a_2 = 2\pi k - \varphi_1$ (where k is any integer). We find point a_1 from (4), assuming that the coordinate of an electron at phase a_2 is equal to that of an electron at phase a_1: $\xi(a_1) - \xi(a_2) = 0$. As a result, we find an equation for the point a_1:

$$\sin a_1 = a_1\cos\varphi_1 + \varphi_1\cos\varphi_1 - \sin\varphi_1. \tag{5}$$

Through numerical solution of Eq. (5) we find that electrons created in the phase range $(0-1.35) + 2\pi k$ lead to $a_1 \leq \pi + 2\pi k$. Obviously, for these particles $a_2 > 3\pi/2 + 2\pi k$ (Fig. 1b).

This result means that an object lying in the path of the electrons is struck by electrons with dc velocity components corresponding to creation phases between 0 and 1.35 in such a manner that the electrons have a cosine distribution between phases $\pi + 2\pi k$ and $3\pi/2 + 2\pi k$ (Fig. 1b). The phase range $(\pi - 3\pi/2) + 2\pi k$ is precisely that over which secondary electrons created at the opposite surface can escape from this surface toward the original wall, since they have dc velocity components directed away from the surface.

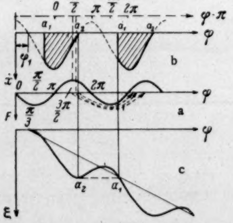

Fig. 1. a) Force exerted on an electron; b) cosine function corresponding to the velocity of electrons emitted at phase $\varphi_1 = 1.05$ (the cross-hatching shows the flow density of in-phase electrons at various field phases; c) dimensionless electron coordinate as a function of the field phase.

DISTRIBUTION FUNCTIONS OF THE PRIMARY AND SECONDARY CURRENTS

Since particles with the same translational velocity are distributed uniformly over the direction of motion with the density n_1, the current i_1 that they produce to a unit area of the wall is given as a function of the field phase by

$$i_1 = \frac{F}{m\omega}(-\cos\varphi + \cos\varphi_1)\,n_1,$$

if $0 < \varphi_1 - 2\pi k < 1.35$. Multiplying and dividing by $\cos\varphi_1$, we find

$$i_1 = \frac{(-\cos\varphi + \cos\varphi_1)}{\cos\varphi_1} I_1, \tag{6}$$

where $I_1 = (Fn_1/m\omega)\cos\varphi_1$ is the time average of the current to a unit surface area of particles with the translational velocity corresponding to creation phase φ_1.

Since we treat the surface on which the electrons are incident as an emitting surface, it is more convenient to shift the reference point for the phase φ by π, so that the active phase range, i.e., that over which electrons can escape the surface, gives from 0 to $\pi/2$, rather than from π to $3\pi/2$ (the dashed axis at the top of Fig. 1). Now Eq. (6) becomes

$$i_1 = \frac{\cos\varphi + \cos\varphi_1}{\cos\varphi_1} I_1. \tag{7}$$

Equation (7) gives the distribution of the current of primary particles with respect to arrival phase φ. We find the distribution of the secondary current i with respect to emission phase by multiplying (7) by σ, in accordance with (2) and (3):

$$i(\varphi) = \frac{W}{W_1}\frac{(\cos\varphi + \cos\varphi_1)^3}{\cos\varphi_1} I_1. \tag{8}$$

where $W = F^2/2m\omega^2$. We see that I_1, any current of primary particles emitted at phase φ_1, produces a current of secondary particles distributed with respect to creation phase φ according to

$$\cos^3\varphi + a\cos^2\varphi + b\cos\varphi + c, \tag{9}$$

where $0 \leq a \leq 3$, $0 \leq b \leq 3$, and $0 \leq c \leq 1$. These coefficients are functions of the emission phase of the primary electron current, φ_1.

Up to this point we have used $_1$ as the creation phase of the primary electrons at one surface and φ as the arrival phase of the primary electrons and the creation of the secondary electrons at the other surface.

It is not difficult to show that the total secondary current, which consists of the sum of the secondary currents i due to the primary electron I_1 with various creation phases φ_1, is also distributed with respect to creation phase according to (9): $D_1(\cos^3\varphi_1 + A_1\cos^2\varphi_1 + B_1\cos\varphi + C_1)$, where D_1 is a coefficient with units of particles per square centimeter per second; A_1, B_1, and C_1 can take on any values in the range specified above for *a*, b, and c.

We now find the numerical values of A_1, B_1, and C_1.

OPERATOR PRODUCING THE SECONDARY DISTRIBUTION FOR A SPECIFIED PRIMARY DISTRIBUTION

We replace I_1 in (8) by $(D_1/2\pi)(\cos^3\varphi_1 + A_1\cos^2\varphi_1 + B_1\cos\varphi_1 + C_1)\Delta\varphi_1$, which is the average current of electrons emitted in the narrow phase range $\Delta\varphi_1 \ll \pi/2$.

Integrating the resulting equation over φ_1 from 0 to 1.35, after converting from $\Delta\varphi$ to $d\varphi$, we find the distribution of secondary electrons with respect to creation phase $D(\cos^3\varphi + A\cos^2\varphi + B\cos\varphi + C)$:

$$\frac{W}{2\pi W_1}\int_0^{1.35}\frac{(\cos\varphi+\cos\varphi_1)^3}{\cos\varphi_1}D_1(\cos^3\varphi_1+A_1\cos^2\varphi_1+B_1\cos\varphi_1+C_1)\,d\varphi_1 = D(\cos^3\varphi+A\cos^2\varphi+B\cos\varphi+C). \tag{10}$$

We simplify the notation by defining

$$\frac{2\pi DW_1}{D_1W}=H. \tag{11}$$

Expanding the quantity in parentheses in the integrand, and assuming the coefficients of a given power of φ on the left-hand and right-hand sides of the equation to be equal, we find, after integration,

$$\left.\begin{aligned} A_1\cdot 0.976+B_1\cdot 1.36+C_1\cdot 2.5+0.785&=H,\\ A_1\cdot 2.36+B_1\cdot 2.93+C_1\cdot 4.07+2&=HA,\\ A_1\cdot 2+B_1\cdot 2.36+C_1\cdot 2.93+1.76&=HB,\\ A_1\cdot 0.588+B_1\cdot 0.666+C_1\cdot 0.785+0.534&=HC.\end{aligned}\right\} \tag{12}$$

Equation (12) gives the relationships among the parameters of the primary current (D_1, A_1, B_1, C_1) and the secondary current (D, A, B, C).

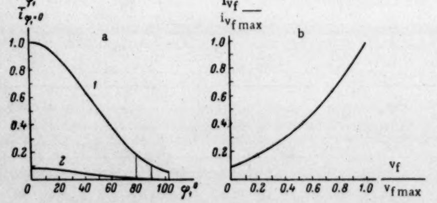

Fig. 2. a) Relative current density of the particles which is established during the discharge as a function of the creation phase φ_1; b) relative current density as a function of the relative translational velocity $v_f = (F/m\omega)\cos\varphi_1$ ($v_{f\,max} = F/m\omega$).

STEADY-STATE DISTRIBUTION FUNCTION AND THE THRESHOLD FIELD

We seek that distribution function which is not changed as a result of the interaction of the current with the wall, i.e., that for which $A_1 = A$, $B_1 = B$, and $C_1 = C$. For this purpose we solve system (12) under the assumptions $A_1 = A$, $B_1 = B$, $C_1 = C$.

A computer solution of Eq. (12) yields the unique solution $A_0 = 2.18$, $B_0 = 1.78$, $C_0 = 0.51$, $H_0 = 6.66$.

Accordingly, the basic current is distributed with respect to creation phase φ_1 according to

$$i_1(\varphi_1) = D_1(\cos^3\varphi_1 + 2.18\cos^2\varphi_1 + 1.78\cos\varphi_1 + 0.51). \tag{13}$$

This equation gives the current distribution with respect to the relative translational velocity (Fig. 1), since $\cos\varphi_1 = v_f m\omega/F$, where v_f is the translational velocity [see (3)].

We can now easily find the condition for which the discharge is self-sustaining. At the threshold power $D/D_1 = 1$; from (11) we find $W/W_1 = 2\pi/6.66$. Accordingly, the threshold field required for the discharge is found from the simple equation

$$W = 0.94W_1. \tag{14}$$

STABILITY OF THE DISTRIBUTION FUNCTION. GROWTH RATE OF THE DISCHARGE

Function (13) is the solution of our original problem only if it is stable. Let us analyze the stability of distribution function (13) with respect to small deviations of A, B, and C from the values $A_0 = 2.18$, $B_0 = 1.78$, $C_0 = 0.51$.

In (12) we replace A_1, B_1, C_1 by $A_0 + A_n$, $B_0 + B_n$, $C_0 + C_n$, respectively, where A_n, B_n, C_n are much smaller than A_0, B_0, C_0, respectively. We find the deviations ΔA_{n+1}, ΔB_{n+1}, ΔC_{n+1} from A_0, B_0, C_0, which are acquired by the secondary distribution function after the interaction of the primary distribution function with the wall. Neglecting terms of second order with respect to ΔA_n, ΔB_n, ΔC_n, we find

$$\left.\begin{aligned} \Delta A_{n+1}&=\Delta A_n\frac{(k_{aa}-A_0k_{ha})}{H_0}+\Delta B_n\frac{(k_{ab}-A_0k_{hb})}{H_0}+\Delta C_n\frac{(k_{ac}-A_0k_{hc})}{H_0},\\ \Delta B_{n+1}&=\Delta A_n\frac{(k_{ba}-B_0k_{ha})}{H_0}+\Delta B_n\frac{(k_{bb}-B_0k_{hb})}{H_0}+\Delta C_n\frac{(k_{bc}-B_0k_{hc})}{H_0},\\ \Delta C_{n+1}&=\Delta A_n\frac{(k_{ca}-C_0k_{ha})}{H_0}+\Delta B_n\frac{(k_{cb}-C_0k_{hb})}{H_0}+\Delta C_n\frac{(k_{cc}-C_0k_{hc})}{H_0}.\end{aligned}\right\} \tag{15}$$

Here k_{aa}, k_{ab}, k_{ac}, ... are the coefficients in system (12), and $H_0 = 6.66$. Substituting in the numerical values we find

$$\left.\begin{aligned} \Delta A_{n+1}&=3.6\cdot 10^{-2}\Delta A_n \quad -4.5\cdot 10^{-3}\Delta B_n \quad -0.21\Delta C_n,\\ \Delta B_{n+1}&=3.9\cdot 10^{-2}\Delta A_n \quad -9\cdot 10^{-3}\Delta B_n \quad -0.23\Delta C_n,\\ \Delta C_{n+1}&=1.3\cdot 10^{-2}\Delta A_n \quad -5.1\cdot 10^{-3}\Delta B_n \quad -7.3\cdot 10^{-2}\Delta C_n.\end{aligned}\right\} \tag{16}$$

If each deviation ΔA_{n+1}, ΔB_{n+1}, ΔC_{n+1} is smaller in absolute value than the preceding deviation ΔA_n, ΔB_n, ΔC_n, respectively, the function is stable. It is easy to see that for (16) we have

$$|\Delta A_{n+1}|<|\Delta A_n|;\ |\Delta B_{n+1}|<|\Delta B_n|;\ |\Delta C_{n+1}|<|\Delta C_n|. \qquad (17)$$

Consequently, function (13) is stable with respect to small perturbations in A, B, and C.

To evaluate the growth rate of the discharge we denote by τ the time over which most of the electrons manage to move from one surface to the other. From (11) for the case $H = H_0$ we find $D/D_1 = (W/W_1)\,1.06$. Then we easily find the time evolution of the discharge:

$$D_1 = D_0 e^{\frac{(1.06W/W_1-1)}{\tau}t}, \qquad (18)$$

where D_0 is the amplitude of function (13) at time $t = 0$.

CONCLUSION

There exists a single stable distribution (13) which can remain constant over time; we have found the threshold field for the occurrence of a discharge for this distribution. A question which remains is that of whether there can exist a group of unstable distribution functions, whose coefficients A, B, C are not equal to A_0, B_0, C_0, which vary with the time and which have a threshold field lower than (14). Such functions apparently do not exist, for otherwise we would observe a change in the form of function (13) at the threshold field [since we can always distinguish in the current a small group of particles having function (13) and which are distributed arbitrarily with respect to creation phase.] Since this change is in fact not observed, the very existence of a stable function implies that there are no unstable functions having a threshold lower than that in (14).

Equation (10) has been integrated over the range 0-1.35, while the active range of field phases is 0-1.57 + 2πk. The explanation is that, if $1.35 < \varphi_1 - 2\pi k < 1.57$, then $a_1 > 0$ (the dashed axis in Fig. 1b); particles with these emission phases do not lead to cosine distribution (7) over the entire active range $0 < \varphi - 2\pi k < 1.57$. In addition to this phase range, which we have not considered, there is the range $1.57 < \varphi_1 - 2\pi k < 1.78$ (the vertical dashed lines in Figs. 1a and 1b), which, although passive, contributes to the discharge, since secondary electrons from this range reach the active range $0 < \varphi - 2\pi k < 1.57$ after times shorter than T (the dashed curves in Fig. 1a). Analysis of the role of these small ranges under the assumption that most of the electrons obey function (13) leads to a refinement of threshold field (14):

$$W \approx 0.92W_1. \qquad (19)$$

Figure 2a (curve 2) (for which the scale is five times larger) shows the additional correction function, which takes the role of these small ranges into account in a first approximation. Curve 1 is the basic distribution.

Since the maximum possible value is $W_c = 4W$, we see from (19) that this entire analysis holds for materials for which the linearity of σ continues to $\sigma \geq 3.68$. If the functional dependence of σ on W_c becomes a horizontal line at values $\sigma < 3.68$, a field stronger than that according to (19) would be required for a secondary-emission discharge.

A uniform multiphase discharge can occur in many microwave devices for which (1) holds. In particular, an understanding of the behavior of secondary-emission discharges yields a correct interpretation of many experiments on microwave-plasma interactions carried out in systems in which the walls are far apart.[9-11]

In conclusion the author thanks I. E. Andreev, A. I. Kossyi, and V. A. Silin for help and valuable comments, and G. M. Batanov and M. M. Savchenko for useful discussion.

---

1) The initial velocities of secondary electrons are known to have an approximately Maxwellian distribution with $T_e \sim$ 2-4 eV, which is a weak function of the energy of the primary electrons.[5]

2) Gorovets and Rybak[6] were the first to point out the possible existence of secondary-emission discharges with electrons emitted in a broad phase range.

3) However, a spread in these initial velocities leads to a spatial equilibration of the density of in-phase electrons along the x direction.

4) We are not able to incorporate the role of reflected electrons, which usually constitute 10-20% of the total number of secondary electrons.[5] We can assume that they do not play a very important role in the discharge: Although they are characterized by a large value of σ, because of their high velocity, it is shown in the analysis below that fast particles have a good chance of reaching the wall during the unfavorable phase of the field and do not produce another generation of electrons. However, this question requires special study.

---

[1] A. I. Hatch and H. B. Williams, J. Appl. Phys., 25, 417 (1954).
[2] A. I. Hatch and H. B. Williams, Phys. Rev., 112, 681 (1958).
[3] S. C. Brown, Basic Data of Plasma Physics, MIT Press, Cambridge, Mass. (1959).
[4] V. I. Petrunin, in: Electrophysical Apparatus [in Russian], No. 1, Atomizdat, Moscow (1963), p. 97.
[5] I. M. Bronshtein and B. S. Fraiman, Secondary Electron Emission [in Russian], Izd. Nauka, Moscow (1969).
[6] V. S. Gorovets and S. A. Rybak, Zh. Tekh. Fiz., 37, 387 (1967) [Sov. Phys.-Tech. Phys., 12, 279 (1967)].
[7] A. Miller, H. Williams, and O. Theimer, J. Appl. Phys., 34, 1674 (1963).
[8] V. A. Stanskii, D. A. Ganichev, and S. A. Fridrikhov, Zh. Tekh. Fiz., 43, 1750 (1973) [Sov. Phys.-Tech. Phys., 18, 1103 (1974)].
[9] I. R. Gekker and O. V. Sizukhin, ZhETF Pis. Red., 9, 408 (1969) [JETP Lett., 9, 243 (1969)].
[10] K. F. Sergeichev and V. E. Trofimov, ZhETF Pis. Red., 13, 236 (1971) [JETP Lett., 13, 166 (1971)].
[11] G. M. Batanov and K. A. Sarksyan, Trudy FIAN, 73, 104 (1973).

Discharge in a cylindrical diode with surface ionization

V. P. Osoka and A. V. Potarov

(Submitted April 18, 1973; resubmitted November 30, 1973)
Zh. Tekh. Fiz., 44, 1929-1937 (September 1974)

A low-pressure discharge in a cylindrical diode is analyzed for the case in which surface ionization plays a role in addition to volume ionization. Results are calculated for a series of discharges which differ in gap length. Surface ionization at the anode can affect the electron density distribution over the length of the discharge. A cutoff of the steady-state discharge which is observed in long gaps is explained.

INTRODUCTION

An electrical discharge in a cylindrical diode is analyzed theoretically in refs. 1 and 2 on the basis of the transport equations for a nonisothermal, partially ionized gas using the Grad 13-moment method. Surface ionization is assumed to be unimportant. However, under certain conditions surface ionization can affect the characteristics of the plasma sheath, particularly at the anode.[3,4] Just how strongly surface ionization affects the parameter distribution in the discharge as a whole has not been clarified. Since alkali metals are widely used in practice, either as an ionizing impurity or as the basic plasma material, we feel it is worthwhile to study numerically discharges with surface ionization taken into account. We base our analysis on the magnetogasdynamic equations of the Grad 13-moment approximation.[5-7] We consider a discharge in a cylindrical diode with an azimuthal magnetic field, like that in coaxial sources and plasma accelerators. One of the cases for which calculations are carried out corresponds to refs. 1 and 2 in terms of geometric dimensions. We analyze separately the establishment of limits for the existence of a discharge and determine why a steady-state discharge cannot be maintained in short gaps or long gaps.

The system of equations used here differs from that of ref. 1 in that the electron-production rate is written in a different manner; several secondary terms, proportional to the degree of ionization, are taken into account. The limits of the applicability of this system of equations are examined in ref. 1. The boundary conditions are written more precisely, in accordance with ref. 3. The boundary conditions take account of surface ionization at the cathode and at the anode.

The solution obtained here can be interpreted as dealing with a plasma moving along the axis of a cylindrical gap, with the restrictions specified in ref. 1.

SYSTEM OF EQUATIONS

After conversion to a form convenient for our calculations, we write the system of differential equations for the problem of a cylindrical discharge in an azimuthal field in the following manner:

$$J_{ir} = -D_{ia}\left(1+\frac{T_e}{T}\right)\frac{dn_e}{dr} - D_{ia}\frac{n_e}{T}\left\{\frac{dT}{dr}+\frac{dT_e}{dr}+\frac{\alpha_{Ta}}{\lambda_e}\left[q_{er}+\left(\frac{5}{2}kT_e+e\mathcal{E}\right)\frac{j_r}{e}\right] - \frac{\alpha}{kn_e}\frac{dp}{dr}-\frac{\chi_e}{\lambda_e\nu_0}\left[j_r\tau_{ea}^{-1}-(1-\alpha)\omega j_z\right]\right\}, \tag{1}$$

$$q_{er} = -\frac{\lambda_e}{1+(\gamma\omega\tau_0)^2}\frac{dT_e}{dr}-\left(\frac{5}{2}kT_e+e\mathcal{E}\right)\frac{j_r}{e}+\frac{\chi_e}{1+(\gamma\omega\tau_0)^2}(j_r+\gamma\omega\tau_0 j_z), \tag{2}$$

$$q_{ir}+q_{ar} = -\lambda_T\frac{dT}{dr}, \tag{3}$$

$$\frac{1}{r}\frac{d}{dr}\left[r\left(J_{ir}-\varepsilon\alpha\frac{j_r}{e}\right)\right] = K_1 n_a n_e - \Gamma_2 \equiv \Gamma, \tag{4'}$$

if $\Gamma \geq 0$. If, on the other hand, $\Gamma < 0$, we have

$$\frac{1}{r}\frac{d}{dr}\left[r\left(J_{ir}-\varepsilon\alpha\frac{j_r}{e}\right)\right] = \Gamma_1 - \frac{Sn_e^3}{T_e^{3/2}}, \tag{4''}$$

$$\frac{1}{r}\frac{d}{dr}(rq_{er}) = j_r E'_r - 3k\varkappa n_e\tau_0^{-1}(T_e-T), \tag{5}$$

$$\frac{1}{r}\frac{d}{dr}[r(q_{ir}+q_{ar})] = 3k\varkappa n_e\tau_0^{-1}(T_e-T), \tag{6}$$

$$\frac{dp}{dr} = -\frac{1}{c}j_z B, \tag{7}$$

$$\frac{dJ}{dr} = 2\pi r j_z, \tag{8}$$

$$\frac{1}{r}\frac{d}{dr}(rj_r) = 0, \tag{9}$$

$$\frac{d\varphi}{dr} = -E'_r. \tag{10}$$

We supplement this system with the equations

$$E'_r = \frac{j_r[A^2+(G\omega\tau_0)^2]}{A\sigma} - \frac{k}{e}\left\{\frac{T_e}{n_e}\frac{dn_e}{dr}+\left[1-\alpha_T\frac{1-\frac{\gamma(\omega\tau_0)^2G}{A}}{1+(\gamma\omega\tau_0)^2}\right]\frac{dT_e}{dr} + \frac{\varkappa(\omega\tau_0)^2G}{A}\left[\frac{\alpha}{kn_e}\frac{dp}{dr}-\frac{dT}{dr}-\frac{dT_e}{dr}-\frac{T+T_e}{n_e}\frac{dn_e}{dr}\right]\right\}, \tag{11}$$

$$j_z = -\frac{\omega\tau_0}{1-\Delta+\varkappa(1-\alpha)(\omega\tau_0)^2}\left\{j_r+\frac{\alpha_T^2}{\frac{5}{2}\chi_e}\left[q_{er}+\left(\frac{5}{2}kT_e+e\mathcal{E}\right)\frac{j_r}{e}\right]\right\}, \tag{12}$$

$$p = n_e kT_e + (n_a+n_e)kT, \tag{13}$$

$$\alpha = \frac{n_e}{n_e+n_a}, \tag{14}$$

$$B = \frac{2J}{cr} \tag{15}$$

and equations for the kinetic coefficients,

$$\frac{1}{\tau_{ai}} = \frac{16}{3}n_e\left(\frac{kT}{\pi m}\right)^{1/2}Q_{ai},\quad \frac{1}{\tau_{aa}} = \frac{16}{3}n_a\left(\frac{kT}{\pi m}\right)^{1/2}Q_{aa},$$

$$\frac{1}{\tau_{ea}} = \frac{16}{3}n_a\left(\frac{kT_e}{2\pi m_e}\right)^{1/2}Q_{ea},\quad \frac{1}{\tau_{ia}} = \frac{n_a}{n_e}\frac{1}{\tau_{ai}},$$

$$\Lambda_{ei} = \frac{3kT_e}{2e^3}\left[\frac{kT_eT}{\pi n_e(T+T_e)}\right]^{1/2},\quad \Lambda_{ii} = \frac{T}{T_e}\Lambda_{ei},$$

$$\frac{1}{\tau_{ei}} = \frac{16}{3}n_e\left(\frac{2\pi kT_e}{m_e}\right)^{1/2}\left[\frac{e^2}{2kT_e}\right]^2\ln\Lambda_{ei},\quad \frac{1}{\tau_{ee}} = \frac{\sqrt{2}}{\tau_{ei}},$$

$$\frac{1}{\tau_{ii}}=\frac{16}{3}n_e\left(\frac{4\pi kT}{m}\right)^{1/2}\left[\frac{e^2}{2kT}\right]^2\ln\Lambda_{ii},$$

$$\tau_0^{-1}=\tau_{ei}^{-1}+\tau_{ea}^{-1},$$

$$\tau_e^{*-1}=0.4\tau_{ee}^{-1}+1.3\tau_0^{-1},$$

$$\tau_i^{*-1}=0.4\tau_{ii}^{-1}+0.7375\tau_{ia}^{-1},$$

$$\tau_a^{*-1}=0.4\tau_{aa}^{-1}+0.7375\tau_{ai}^{-1},$$

$$b_{ia}=-0.3375\tau_i^*\tau_{ai}^{-1},$$

$$b_{ai}=--0.3375\tau_a^*\tau_{ia}^{-1},$$

$$\delta=1-b_{ia}b_{ai},$$

$$\omega=\frac{eB}{m_ec},\quad \varepsilon=\frac{m_e}{m},$$

$$\lambda_e=\frac{5}{2}\frac{k^2n_eT_e}{m_e}\tau_e^*,$$

$$\lambda_i=\frac{5}{2}\frac{k^2n_eT}{m}\tau_i^*,$$

$$\lambda_a=\frac{5}{2}\frac{k^2n_aT}{m}\tau_a^*,$$

$$\nu_0=-0.6\tau_{ei}^{-1}+0.2\tau_{ea}^{-1},$$

$$\lambda_T=\lambda_a+\lambda_i\frac{(1-b_{ai})^2}{\delta\left[1+(\varepsilon\omega\tau_i^*\delta^{-1})^2\right]},$$

$$\chi_e=\alpha_T\frac{kT_e}{e},$$

$$\alpha_T=\frac{5}{2}\tau_e^*\nu_0,$$

$$\gamma=\tau_e^*\tau_0^{-1},$$

$$\alpha_{Ta}=\frac{1}{2}\tau_e^*\tau_{ea}^{-1},$$

$$\Delta=\alpha_T\nu_0\tau_0,$$

$$\varkappa=2\varepsilon\tau_0^{-1}\tau_{ai}\alpha,$$

$$\sigma=\frac{n_ee^2}{m_e}\tau_0,$$

$$D_{ia}=\frac{2\tau_{ai}\alpha kT}{m},$$

$$A=1-\frac{\Delta}{1+(\gamma\omega\tau_0)^2}+\varkappa(1-\alpha)(\omega\tau_0)^2,$$

$$G=1+\frac{\gamma\Delta}{(1+\gamma\omega\tau_0)^2},$$

$$S=\frac{4\pi\sqrt{2\pi}\,e^{10}\ln\sqrt{2}}{9m_e^{1/2}k^{9/2}}. \tag{16}$$

Here, r, θ, z are cylindrical coordinates; the z axis runs parallel to the magnetizing current J. Also, m_e, m, T_e, T are the masses and temperatures of the electrons and heavy particles, respectively; n_e, n_a are the densities of electrons and atoms; q_{ir}, q_{ar}, q_{er} are the radial components of the specific energy fluxes of ions, neutrals, and electrons, respectively; J_{ir} is the radial specific diffusive flux of ions; j_r, j_z are the radial and longitudinal components of the current density; p is the pressure; E_r' is the radial component of the electric field in the coordinate system fixed in the plasma; B is the magnetic induction, which is directed azimuthally; α is the degree of ionization; Q_{aa}, Q_{ea} are the diffusion cross sections; K_1 is the ionization-rate coefficient; $\mathcal{E}$ is the ionization potential; k is the Boltzmann constant; e is the electron charge; and c is the speed of light in vacuum.

Equation (1) describes the diffusive ion flux,$^{1)}$ Eqs. (2) and (3) describe the energy fluxes, Eqs. (5) and (6) describe conservation of the electron and heavy-particle energy, Eq. (8) is the definition of the magnetization energy, Eq. (9) is the current-conservation equation, Eq. (10) is the definition of the potential φ, and Eq. (7) is a particular case of the equation of motion, written under the assumption that there is no radial projection of the mean mass velocity. When this equation is satisfied the total flux of atoms and ions toward the walls vanishes. Equation (4) is the ion-balance equation. The term Γ, which describes the rate of charged-particle formation, assumes different forms, depending on whether ionization predominates over recombination. If so, ionization is incorporated through the ionization-rate coefficient[1] K_1, and the recombination term Γ_2 is chosen in accordance with the principle of detailed balance through the use of the statistical equation from ref. 8. If, on the other hand, recombination predominates over ionization, the equation for the recombination rate from ref. 9 is used, and the ionization term Γ_1 is written taking account of the statistical relation.

BOUNDARY CONDITIONS

The boundary conditions at the cathode, $r = r_k$, are the conditions which hold at the outer boundary of the corresponding sheath:

$$J_{ir}-\varepsilon\alpha\frac{j_r}{e}=-\frac{1}{4}(\xi_i^-)^*n_ev_i, \tag{17}$$

$$q_{er}=\frac{j_{\text{E}}^{(k)}}{e}(2kT+e\varphi_k+e\mathcal{E})-\frac{1}{4}\xi_e^-n_ev_e$$
$$(2kT_e+e\varphi_k+e\mathcal{E})\exp\left(-\frac{e\varphi_k}{kT_e}\right), \tag{18}$$

$$T=T_k, \tag{19}$$

$$p=p_k, \tag{20}$$

$$J=J_k, \tag{21}$$

$$j_r=j_k, \tag{22}$$

$$\varphi=0. \tag{23}$$

These are supplemented by the equations for the cathode potential barrier $\varphi_k > 0$:

$$\left.\begin{aligned}&e\varphi_k=kT_e\ln\left[\frac{(1+\mathscr{K})(1-R_e)}{2\mathscr{K}}\right],\\&\mathscr{K}=\frac{en_ev_i\left(1-\frac{\beta}{\alpha}\right)+2(j_r+j_{\text{E}}^{(k)})}{en_ev_e-2j_{\text{E}}^{(k)}},\quad \beta=\frac{\exp\left(-\frac{e\varphi_k}{kT_k}\right)}{\frac{1}{\beta_k}-1+\exp\left(-\frac{e\varphi_k}{kT_k}\right)}.\end{aligned}\right\} \tag{24}$$

Here

$$v_i=\sqrt{\frac{8kT}{\pi m}},\quad v_e=\sqrt{\frac{8kT_e}{\pi m_e}},\quad \beta_k=\frac{\alpha_k}{1+\alpha_k},\quad (\xi_i^-)^*=2\left(1-\frac{\beta}{\alpha}\right),$$

$$\alpha_k=A^*\exp\left(\frac{e\varphi_k^*-e\mathcal{E}}{kT_k}\right),\quad \xi_e^-=\frac{2-j_{\text{E}}^{(k)}\left(\frac{1}{4}en_ev_e\right)^{-1}}{2-(1-R_e)\exp\left(-\frac{e\varphi_k}{kT_e}\right)},$$

$j_{\text{E}}^{(k)}$ is the thermionic-emission current density, $e\varphi_k^*$ is the effective work function for surface ionization, A^* is the coefficient in the equation for the degree of positive surface ionization, R_e is the elastic-reflection coefficient for electrons, and v_i and v_e are the mean thermal velocities of ions and electrons.

The boundary conditions at the anode, $r = r_a$, are

$$J_{ir}-\varepsilon\alpha\frac{j_r}{e}=\frac{1}{4}(\xi_i^-)^*n_ev_i, \tag{25}$$

$$q_{er}=-\frac{j_{\text{E}}^{(a)}}{e}(2kT+e\varphi_a+e\mathcal{E})+$$

$$+\frac{1}{4}\xi_e^- n_e v_e (2kT_e + e\varphi_a + e\mathcal{E}) \exp\left(-\frac{e\varphi_a}{kT_e}\right), \qquad (26)$$

$$T = T_a. \qquad (27)$$

To determine the anode potential barrier $\varphi_a > 0$ (the plasma potential near the anode is higher than the electrode potential) we have the system of equations

$$\left.\begin{aligned} e\varphi_a &= kT_e \ln\left[\frac{(1+\mathscr{K})(1-R_e)}{2\mathscr{K}}\right], \\ \mathscr{K} &= \frac{en_e v_i\left(1-\frac{\beta}{\alpha}\right)+2\left(-j_r+j_E^{(a)}\right)}{en_e v_e - 2j_E^{(a)}}, \quad \beta = \frac{\exp\left(-\frac{e\varphi_a}{kT_a}\right)}{\frac{1}{\beta_a}-1+\exp\left(-\frac{e\varphi_a}{kT_a}\right)} \end{aligned}\right\} \qquad (28)$$

where

$$\beta_a = \frac{\alpha_a}{1+\alpha_a},$$

$$\alpha_a = A^* \exp\left(\frac{e\varphi_a^* - e\mathcal{E}}{kT_a}\right),$$

$$\xi_e^- = \frac{2 - j_E^{(a)}\left(\frac{1}{4}en_e v_e\right)^{-1}}{2-(1-R_e)\exp\left(-\frac{e\varphi_a}{kT_e}\right)},$$

$$(\xi_i^-)^* = 2\left(1-\frac{\beta}{\alpha}\right),$$

$j_E^{(a)}$ is the thermionic-emission current density, and $e\varphi_a^*$ is the effective work function for surface ionization.

In Eqs. (17) and (25) the term $\varepsilon\alpha(j_r/e)$ gives a correction to the motion of the center of mass of an element of the plasma with respect to the electrode.

CALCULATION PROCEDURE

System (1)-(10) with boundary conditions (17)-(23) is integrated numerically from the cathode to the anode by the Runge–Kutta method. This integration requires a knowledge of auxiliary parameters at the initial boundary: n_e, T_e, and $q_{ir} + q_{ar}$. In general, the integration yields parameters at the final boundary which differ from the boundary conditions there, conditions (25)-(27). The discrepancies are used in Newton's method to refine the values of these auxiliary parameters at the initial boundary; then the calculation is repeated. The calculation is iterated until the desired agreement is achieved between the values of the parameters at the final boundary. The initial approximation at the initial boundary is found by a random-search method.

NUMERICAL CALCULATIONS

We report here the results calculated for a series of cylindrical diodes2) with anode radius $r_a = 2.5$ cm and cathode radius $r_k = 1.85$-2.4 cm. A lithium plasma is assumed; the kinetic and gas-kinetic characteristics are taken from ref. 1. The cathode and anode temperatures are assumed to be $T_k = T_a = 2700$°K, the current density of the discharge at the cathode is assumed to be $|j_k| = 2.5$ A/cm^2, the plasma pressure at the cathode is assumed to be $p_k = 85$ μbar, and the azimuthal magnetic field is assumed to be $B_k = 50$ G. The thermionic-emission current density is assumed to be $j_E^{(k)} = 2$ A/cm^2. We also use $R_e = 0.15$ and $A^* = 0.5$.

The results of the numerical solution are shown in Figs. 1-4. Figure 1 shows the characteristic plasma parameters as a function of the cathode radius. Here

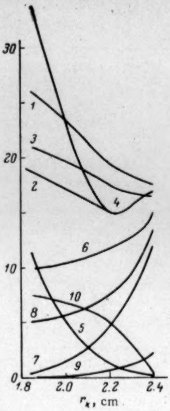

Fig. 1. Characteristic plasma parameters as a function of the cathode radius at a fixed anode radius ($r_a = 2.5$ cm). 1) $(n_e)_{\max} \cdot 10^{-12}$, cm^{-3}; $(n_e)_{\min} \cdot 10^{-12}$ cm^{-3}; 3) $(n_e)_k \cdot 10^{-12}$ cm^{-3}; 4) $(n_e)_a \cdot 10^{-12}$ cm^{-3}; 5) $(T - T_W)_{\max} \cdot 10^{-1}$ °K; 6) $(T_e)_k \cdot 10^{-3}$ °K; 7) $(T_e)_a \cdot 10^{-3}$ °K; 8) φ_k, V; 9) φ_a V; 10) $\Delta\varphi \cdot 10$ V.

$(\Delta T)_{\max} = T_{\max} - T_k$, and $\Delta\varphi$ is the potential difference between the given spatial point and the outer boundaries of the sheaths at the anode and cathode. Figure 2 shows the profiles of the plasma parameters for $r_k = 2$ cm, under which conditions we find $\varphi_k = 5.574$ V and $\varphi_a = 0.186$ V. Here $\delta = (r - r_k)/(r_a - r_k)$, $q_{rr} = q_{ar} + q_{ir}$, and φ is the potential difference between the given spatial point and the outer boundary of the cathode sheath. Figure 2 shows profiles of gas-kinetic quantities characteristic of viscous effects: the times5 τ_e, τ_i, and τ_a; the mean free paths3) $l_e = v_e\tau_e$, $l_i = v_i\tau_i$, $l_a = v_i\tau_a$; and the quantity $\omega\tau_0$ for the case $r_k = 2$ cm.

Figure 4 shows the change in the profile of the degree of ionization α due to a lengthening of the interelectrode gap. The points are the calculated degrees of ionization at the outer boundaries of the cathode and anode sheaths.

The extreme values adopted for the length of the interelectrode gap are at the boundaries for the existence of a solution. Numerical determination of the exact boundaries requires a great deal of computer time.

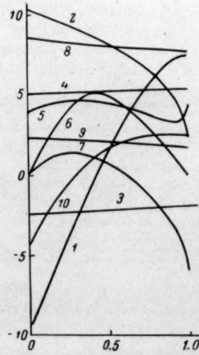

Fig. 2. Profiles of the plasma parameters in the interelectrode region. 1) $q_{Tr} \cdot 10^2$, W/cm^2; 2) $T_e \cdot 10^{-3}$ °K; 3) j_r, A/cm^2; 4) $I \cdot 10^{-2}$, A; 5) $n_e \cdot 10^{-13}$, cm^{-3}; 6) $(T - T_W) \cdot 10^{-1}$ °K; 7) $\varphi \cdot 10$, V; 8) $p \cdot 10^{-1}$ μbar; 9) $q_{er} \cdot 10^{-1}$ W/cm^2; 10) $j_{ir} \cdot 10$, A/cm^2.

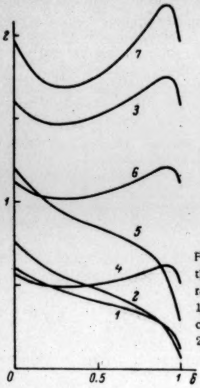

Fig. 3. Profiles of the characteristic times, mean free paths, and Hall parameters in the interelectrode region. 1) $\omega\tau_0 \cdot 0.5$; 2) $l_e \cdot 10$, cm; 3) $l_i \cdot 10^2$ cm; 4) l_a, cm; 5) $\tau_e \cdot 10^9$ sec; 6) $\tau_i \cdot 2 \cdot 10^7$, sec; 7) $\tau_a \cdot 10^6$ sec.

ANALYSIS OF THE DATA

An inspection of Fig. 3 reveals that the characteristic times and mean free paths for the various plasma components differ markedly. The atoms have the longest mean free path. The characteristic mean free paths for diffusion effects, l_a^*, lie in the range[5] $0.33\, l_a < l_a^* < 0.53\, l_a$. In the case of narrow gaps the Knudsen numbers for neutrals, $\mathrm{Kn}_a = l_a^*/(r_a - r_k)$, are larger than unity, so that these results on the characteristics of the heavy component should be considered formal but instructive in these discharge cases, e.g., they are useful for estimating the order of magnitude of the change in the discharge energy.

This circumstance has essentially no effect on the accuracy of the values found for the plasma properties associated with the electron component: The maximum deviation of the heavy-particle temperature from the wall temperature according to these calculations is about 4%, and we can assume that the state of the atoms, which is incorporated in the calculation of the properties of the electronic gas, is described within an error much smaller than this.

The quantities τ_a, l_e, and $\omega\tau_0$ are highly inhomogeneous over the gap. The calculations show that this inhomogeneity arises and becomes more pronounced as the gap is lengthened. From Fig. 2 we see that the potential φ near the cathode generally rises somewhat and then decreases over the greater part of the gap, acquiring a value at the anode lower than that at the cathode. The electron temperature falls off from the cathode toward the anode, and the decrease becomes more pronounced as the gap is lengthened; the temperature near the anode can be lower than the heavy-particle temperature and the anode temperature. The profile of the electron density in the case of long gaps is qualitatively different for that in the case of short gaps: In long gaps the density increases in the immediate vicinity of the anode surface, and a minimum is formed in the $n_e(r)$ profile near the electrode. Figure 1 shows that lengthening of the gap is accompanied by a significant decrease in the anode potential drop φ_a. Accordingly, the observed local increase in the electron density at the anode results from the establishment of conditions favoring emission from the plasma sheath of ions produced by surface ionization.

Figure 4 shows that the degree of ionization in the gap in the case of surface ionization changes significantly as the gap is lengthened. The convex $\alpha(r)$ profile for short gaps is replaced by a more complex profile, having a concave region on the anode side. The degree of ionization at the cathode and that at the anode reach minima at certain intermediate gap lengths. The maximum value of n_e in the plasma displays the same behavior. The maximum degree of ionization in the plasma increases with the gap length, but a reduction of the cathode radius for a given distance from the anode (r_a = const) causes a reduction of the density n_e.

According to Fig. 1, lengthening of a gap leads to an increase in the densities $(n_e)_{\max}$ and $(n_e)_k$, an increase in the potential difference between the outer boundaries of the sheath at the anode and cathode, $\Delta\varphi$, and a reduction of the temperatures $(T_e)_k$ and $(T_e)_a$ and of the potential drops near the electrodes in the sheath, φ_k and φ_a. The electron density near the anode, $(n_e)_a$, and the minimum density in the plasma, $(n_e)_{\min}$, reach their lowest values at a certain intermediate gap length. In the case of short gaps the minimum electron density is observed near the anode, in long gaps it is observed in the plasma. In long gaps the absolute maximum of the electron density occurs near the anode. This absolute maximum near the anode does not yet lead, in the cases for which calculations were carried out, to an absolute maximum of the degree of ionization in the same part of the discharge, since the reduction of the electron temperature near the anode is accompanied at p_k = const by an increase in n_a.

Inspection of these results shows why no solutions exist for a steady-state discharge in the case of short or long gaps.[4)] With a short gap, a discharge cannot occur at a current $|j_k| > j_E^{(k)}$ at any value of T_e and φ_k because the production of ions in the plasma is inadequate; the current of these ions is required to make up the difference $(|j_k| - j_E^{(k)})$. The limit on the existence of solutions at long gaps is determined by the limit $(T_e)_a \to 0$. As shown above, lengthening of the gap is accompanied by an increase in the electron density at the outer boundary of the cathode sheath, due to an increase in the total number of charged particles produced in the plasma. According to the boundary conditions adopted here, an increase in the electron density at the cathode results in a reduction of the cathode potential drop φ_k. Thus the electron energy

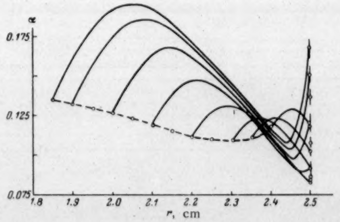

Fig. 4. Profiles of the degree of ionization as a function of the width of the interelectrode gap for a fixed anode radius (r_a = 2.5 cm).

and temperature in the plasma near the cathode fall off. As the gap is lengthened, the energy expended by the electron gas in plasma ionization is increased. The initial electron energy in the plasma near the cathode and the energy acquired from the electric field in the case of long gaps is inadequate to maintain a positive absolute temperature for the electrons over the entire gap.

---

1) This corresponds to ion motion with respect to the center of mass of the plasma under conditions such that the ion flux is equal in magnitude but opposite in direction to the diffusive flux of atoms.

2) The computer program, worked out for use over broad ranges of discharge parameters, is applied here to the case in which certain terms in the equations can be neglected. However, a calculation on the basis of the complete program yields important information required for choosing the zeroth approximations in more complicated cases and for developing approximate-calculation methods. The parameters for the calculation are chosen so that the results of refs. 1 and 2 can be used in the numerical solution.

3) The characteristic mean free paths shown in this figure give an idea of the differences and inhomogeneities over the cross section of the corresponding Knudsen numbers.

4) In the case of short gaps or long gaps the discharge can apparently exist only in a different form, an oscillatory form, consisting of contracted arcs, as the electrode material, as the vapor of the electrode material undergoes combustion.

---

[1] A. V. Potapov and A. S. Margevich, Zh. Tekh. Fiz., 41, 2126 (1971) [Sov. Phys.-Tech. Phys., 16, 1684 (1972)].

[2] A. S. Margevich and A. V. Potapov, Zh. Prikl. Mekh. Tekh. Fiz., No. 6, 17 (1971).

[3] A. V. Potapov and G. V. Babkin, Teplofiz. Vys. Temp., No. 4, 137 (1970).

[4] G. V. Babkin and A. V. Potapov, Zh. Prikl. Mekh. Tekh. Fiz., No. 4, 137 (1970).

[5] V. M. Zhdanov, Prikl. Matem. Mekhan., 26, 280 (1962).

[6] M. Ya. Alievskii and V. M. Zhdanov, Zh. Prikl. Mekh. Tekh. Fiz., No. 5, 11 (1963).

[7] M. Ya. Alievskii, V. M. Zhdanov, and V. A. Polyanskii, Zh. Prikl. Mekh. Tekh. Fiz., No. 3, 32 (1964).

[8] A. V. Potapov, Teplofiz. Vys. Temp., 4, 55 (1966).

[9] A. V. Gurevich and L. P. Pitaevskii, Zh. Eksp. Teor. Fiz., 46, 1281 (1964) [Sov. Phys.-JETP, 19, 870 (1964)].

Kinetic energy of ions produced by surface ionization.
I. Distribution over the velocity components

L. V. Sumin
Scientific-Research Institute of Minerals, Moscow
(Submitted October 29, 1973; resubmitted January 22, 1974)
Zh. Tekh. Fiz., 44, 1938-1945 (September 1974)

The experimental ion distribution over velocity components is obtained taking account of the angular distribution of particles from the surface. The experimental ion distribution corresponds to the calculated distribution. Surface ionization of silver on oxidized tungsten is used to show the dependence of the ion current on the ionizer temperature according to the Saha–Langmuir equation. Ionizer surface temperature in the range 1365–1100°K obtained from the experimental distribution curves and those measured by an optical pyrometer agree to within ±10°.

The energy and angle distributions of particles from a surface is of considerable interest and can be one of the most productive methods for studying the state of desorbed particles, the properties of a surface, and the interaction between particles and a surface.

The measurement of the kinetic energies of the positively charged component of a beam of desorbed particles is less complicated technically and can answer many of the questions involving surface ionization. The study of the distribution of initial ion energies in surface ionization of molecular beams can help to explain many characteristics of the state of thermal equilibrium and dissociative ionization on a surface.

In these experiments the distribution of initial energies of positively charged ions is measured for ionization on hot tungsten and rhenium surfaces. In this part the equation for the shape of the experimentally observed particle distribution over velocity components is derived and the ion source and the results of control measurements of the ionizer surface temperature are described. Measurements of the initial energies of ions produced in surface ionization of atoms and simple inorganic molecules are given in Part II.

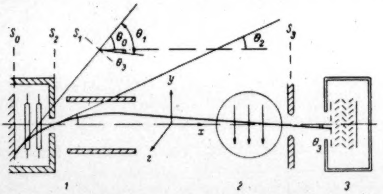

Fig. 1. Simplified diagram of ion motion in a mass spectrometer. 1) Ion source; 2) mass analyzer; 3) electron multiplier.

TEMPERATURE DEPENDENCE OF THE EXPERIMENTAL DISTRIBUTION CURVE

The kinetic energies of ions produced on an ionizer surface have been investigated on an MI 13-09 mass spectrometer with a special ion source, using the so-called deflection method.[1] When analyzing initial energies, the deflection method is used to investigate ion motion in the direction coinciding with the force lines of the magnetic field of the mass analyzer and corresponding to the motion "along the slit" of a Nier, or similar type, source with an ion-optical slit system (the y direction, Figs. 1 and 2). In principle, this method gives the energy of ions in the direction studied to within $1 \cdot 10^{-3}$ eV. The basis of the deflection method is that only those particles whose velocity in the y direction is compensated by the voltage of the deflecting capacitor are incident on the ion collector of the mass spectrometer. Since the initial (here, thermal) ion velocity V_y in this direction cannot be distorted, or distorted only negligibly, the dependence of the current taken from the ion collector on the deflecting voltage contains information on the ion distribution over the velocity component V_y. To analyze this distribution it is necessary to obtain an expression for the ion current density through the plane of the collector.

Only singly charged positive ions are considered.

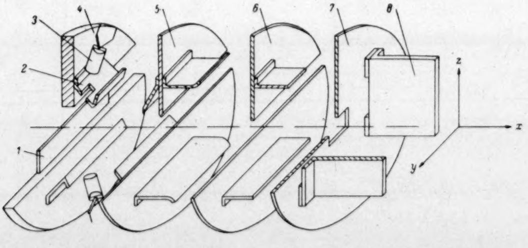

Fig. 2. Schematic diagram of the ion source. 1) Ionizer; 2) evaporator shield; 3) evaporator; 4) thermocouple; 5, 6, 7) extracting, accelerating, and collimating electrodes, respectively; 8) deflecting capacitor.

When atomic or molecular ions are produced the velocity distribution coincides with the Maxwell–Boltzmann distribution of the neutrals; the number of particles per phase volume element is

$$dn = C\exp\left[-\frac{mc^2}{2kT}\right]c^2 dc\, d\Omega\, d\tau$$

$$= C'\exp\left[-\frac{m(V_x^2+V_y^2+V_z^2)}{2kT}\right]dV_x dV_y dV_z d\tau, \tag{1}$$

where C is a constant, $c = \sqrt{V_x^2 + V_y^2 + V_z^2}$ is the ion thermal velocity, $d\Omega = \sin\theta d\varphi d\theta$ is the solid angle element, $d\tau_g = dxdydz$ for particles in the gaseous phase, (ionization by electrons and photons), and $d\tau_s = dydz$ for particles departing from the surface (the ionization surface in particular). In both cases the element $d\tau$ refers to the ionization region. Momentum transfer during ionization due to electron impact[2] is not taken into account here. The value of T is either the temperature of the ionizer surface or the temperature of the walls of the ionization chamber. From the time the ions are produced until they are deflected after acceleration to an energy ev, the ion velocity vector varies in magnitude from $V_0 = c$ to $V = \sqrt{c^2 + 2ev/m}$ and its direction in the laboratory coordinate system varies through an angle $\theta_1 = \theta_0 + \theta_3$ (Fig. 1), where θ_0 is the angle between the direction $\bar{c}$ and the normal to the plane of the ionization S_0; θ_3 is angle of incidence of the ions on the collector (the plane S_3). The particle flux density from the surface S_0 at the solid angle element $d\Omega$ equals the flux through the area dS_1, the normal to which is formed by the angle θ_0 with the normal to dS_0

$$d\nu_1 = C_1 V_0 \exp\left[-\frac{mc^2}{2kT}\right]c^2 dc\, d\Omega\, dS_1. \tag{2}$$

The flux of accelerated ions exiting from the slit of the source in the plane S_2 is

$$d\nu_2 = C_2 V\cos\theta_0 \exp\left[-\frac{mc^2}{2kT}\right]c^2 dc\, d\Omega\, dS_2$$

$$= C_2 V\cos\theta_0\cos\theta_2 \exp\left[-\frac{mc^2}{2kT}\right]c^2 dc\, d\Omega\, dS_0, \tag{3}$$

where $\cos\theta_2 = \sqrt{V_x^2 + 2ev/m}/\sqrt{c^2 + 2ev/m}$, and the normalization constant C_2 must include the decrease in ion density due to acceleration (the condition for a constant number of particles). When ev = 0, $\theta_2 = \theta_0$, and c = const, Eq. (3) becomes the well-known expression[3,4] for a radiative flux.

Considering the plane of the collector S_3, we obtain

$$d\nu_3 = C_3 V\cos\theta_0\cos\theta_2\cos\theta_3 \exp\left[-\frac{mc^2}{2kT}\right]c^2 dc\, d\Omega\, dS_0$$

$$= C_3 V_x\cos\theta_0\cos\theta_3 \exp\left[-\frac{mc^2}{2kT}\right]c^2 dc\, d\Omega\, dS_0. \tag{4}$$

Usually in mass analysis the ions are accelerated to energies of several kiloelectron volts (here, ev = 3 keV), and the thermal energy of the particles, taken over one degree of freedom in the case of surface ionization, is ≤ 0.1 eV $\ll$ ev. It can be assumed that $\theta_3 \simeq 1$, $\cos\theta_2 \simeq 1$, and $V_x \simeq \sqrt{2ev/m} \simeq$ const to within $2\cdot 10^{-5}$. This situation has theoretical significance and leads to the absence of a dependence of the limits of integration with respect to $d\tau$ on the initial velocity projection. Integration cannot be taken directly over $d\tau$ and dV_y since the ratio of the area of effective ionization to the square of the distance between the ionizer and the collector (with a correction for acceleration) is ~0.005. The small working area is determined in one measurement by the width of the ionizer or of the slit of the source (0.2–0.4 mm), and in the other by the length of the collimating slit, reduced to 0.6 mm, and the slit of the ion collector. Thus, one can assume with fair accuracy that the detection currents are proportional to the flux from the volume element or from the area element. The error introduced by this approximation is several times smaller than the instrumental distortions (see below), and henceforth when treating the experimental data it will be included with them.

Thus, the current across the collector is

$$dI_n \simeq C_4 \exp\left[-\frac{mc^2}{2kT}\right]c^2\cos\theta_0 dc\, d\Omega$$

$$= C_4' \exp\left[-\frac{m(V_x^2+V_y^2+V_z^2)}{2kT}\right]\frac{V_x}{\sqrt{V_x^2+V_y^2+V_z^2}}dV_x dV_y dV_z. \tag{5}$$

In the analysis of initial velocities using the deflection method the ions incident on the collector have a velocity in the Y direction from V_y to $V_y + dV_y$, an arbitrary initial velocity in the X direction, and, in the limits from $-V_{z0}$ to V_{z0}, which are determined by discrimination at the slits, in the z direction. Thus, the ion flux density from the surface incident on the collector is

$$\frac{dI_n}{dV_y} = C_5 \int\limits_{-V_{z0}}^{V_{z0}} dV_z \int\limits_0^{\infty} \exp\left[-\frac{m(V_x^2+V_y^2+V_z^2)}{2kT}\right]\frac{V_x dV_x}{\sqrt{V_x^2+V_y^2+V_z^2}}. \tag{6}$$

The measured voltage U across the deflecting capacitor is related to the projection of velocity V_y by

$$U = \varkappa V_y\sqrt{\frac{m}{2}} = \varkappa\sqrt{E_y},$$

where $\varkappa$ is the instrumental constant. For convenience considering energies $E_x = mV_x^2/2$ and $E_z = mV_z^2/2$, we obtain

$$\frac{dI_n}{dU} = C_6\frac{dI_n}{dV_y} = C_6' \int\limits_{-\sqrt{E_{z0}}}^{\sqrt{E_{z0}}} d(\sqrt{E_z}) \int\limits_0^{\infty} \exp\left[-\frac{E_x + E_z + \varkappa^2 U^2}{kT}\right]$$

$$\times\sqrt{\frac{E_x}{E_x + E_z + \varkappa^2 U^2}}\, d(\sqrt{E_x}). \tag{7}$$

For ions produced in the gaseous phase we obtain the well-known result confirmed by experiment:[5]

$$\frac{dI_{r.}}{dU} = C''\exp\left[-\frac{\varkappa^2 U^2}{kT}\right].$$

ERRORS

Since the absolute value of the ion thermal energies is small and only fairly precise measurements are of practical interest, the instrumental errors should be calculated to within ±0.001 eV. With regard to the inhomogeneity of the surface of the metal ribbons used as ionizers the distribution of initial ion energies can be distorted both by the contact field of spots and by the strong electric field applied to compensate for it. In practice, the smallest errors of the true distribution are attained for a certain compromise value of the electric field voltage, which in the experiments is $F \simeq 2\cdot 10^3$ V/cm. Experiment shows that the measured energy kT* has a time-constant instrumen-

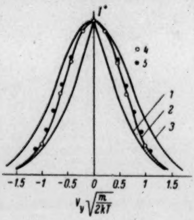

Fig. 3. Distribution of ions over V_y for a fixed temperature in the interval 1700-2100°K. 1) Calculated curve corresponding to the absence of errors and strong discrimination with respect to V_z; 2) experimental distribution of $^{107}Ag^+$, $^{208}pb^+$, $^{39}K^+$, and $^{23}Na^+$ ions (surface ionization beams); 3) calculated distribution curve for ions from the gaseous phase; 4) points calculated from Eq. (8); 5) experimental points of the distribution of $^{184}W^+$, $^{187}Re^+$, $^{39}K^+$, and $^{23}Na^+$ thermions.

tal correction $\mathcal{E} = 0.021$ eV, which also includes the effect of the finite dimensions of the ionization region and the collector. For a change in the optimum field voltage of 25% the value of $\mathcal{E}$ had a two-fold increase. Examination of the possible cases indicates that the instrumental effect appears in the form of an error of the initial angular distribution of ions due to an artificial increase in E_y. Taking this error mechanism into account, we obtain an expression relating the recorded curve to the Maxwellian distribution of ions:

$$\frac{dI_n}{dU} = \text{const} \int\limits_{-\sqrt{E_{z0}}}^{\sqrt{E_{z0}}} d(\sqrt{E_z}) \int\limits_0^{\infty} \exp\left[-\frac{E_x + E_z + \varkappa^2 U^2}{kT}\right] \times \sqrt{\frac{E_x}{E_x + E_z + \varkappa^2 U^2 + \mathcal{E}}}\, d(\sqrt{E_x}). \quad (8)$$

The absolute value of the error can be obtained directly from the experimental curves if the ionizer temperature is known to within 100-200°K and if it is assumed that the kinetic energy of the ion corresponds to the temperature of the ionizer surface.[6]

Equation (8) is used to determine $\mathcal{E}$. When $\varkappa^2U^2 = \mathcal{E}$, the half-width of the distribution at a height determined by (8) should be $\sqrt{\mathcal{E}}$. The equation can be solved by numerical methods.

The thermal energy kT can be determined from the half-width of the experimental curve at a height determined by (8) under the condition $\varkappa^2U^2 = kT$. For this purpose we can use the half-width of the line at a height 0.157 I_0, which for $\mathcal{E} \to 0$ and $V_{z0} \to 0$ should be kT (curve 1 in Fig. 3), and we can use the equality $kT \simeq kT^* - \mathcal{E} - E_{z0}$ which is satisfied with fair accuracy for $\mathcal{E} \leq 0.04$ eV.

EXPERIMENTAL PART

The measurements are carried out with an ion source with slits which produce a field with axial symmetry (Fig. 2). This kind of ion-optical system allows the ion thermal velocities to be measured in the direction of the axis of symmetry and is independent to a considerable degree of the contamination of the electrodes. The distribution function is recorded by an ÉPP-09 automatic potentiometer with continuous scanning of the deflecting voltage. The ion currents are enhanced by a secondary electron multiplier.

Taking account of the geometry of the MI 13-09 instrument, the dimensions of the deflecting plates, and the distance between them and the stray field, the constant $\varkappa$ for an accelerating voltage of 3 kV is 0.0986 $eV^{1/2}$ per 1 V of deflecting voltage. The change in scale on the abscissa for an accelerating voltage of 1.5 kV corresponds completely to this variation, which indicates that distortions of the ion velocity are absent in the region from the extracting electrode to the collector (the field voltage at the ionizer surface does not change in these experiments).

A necessary reduction in the length of the source and collector slits produces a perceptible loss of current strength. For this reason, atomic beams of fairly high intensity are used to obtain experimental curves with fairly small fluctuations in the ion current. In particular, in the case of tungsten ionization the beam density of atomic silver is ~ 10^{14} and for ionization in oxidized tungsten and rhenium it is 10^{13} $cm^{-2} \cdot sec^{-1}$.

To inhibit electron emission from the ionizer, potential of + 100 V is applied to it with respect to the evaporator screen.

A uniform surface temperature of the working area[7] should provide an equally probable ionization of beams with an arbitrary projection of velocity – from zero to the maximum that can be recorded. The uniformity of the ionizer temperature and the beams incident on it is checked experimentally by recording the distribution function for tungsten and rhenium (the ionizer material) thermions, potassium (the impurity atoms) thermions, and ions incident on the ionizer from silver and lead beams. There is a very different dependence of the yield of these ions on the ionizer temperature; therefore, any change in the temperature along the length of the working area of the ionizer (or for the incident beams and their inhomogeneity) leads to a different shape of the experimental distribution curves.

The ionizer is a wire 0.2 mm in diameter or a ribbon 0.02 × 0.5 mm with the same length 16 mm. The current conductors are plane molybdenum springs with a cross section 0.1 × 5 mm and a length of 15 mm. The evaporators are heated open nickel cylinders 1.5 mm in diameter and 1.5-2 mm long. The distribution recorded for a series of ions in an experiment with tungsten wire ionizer 0.15 mm in diameter and 32 mm long coincides with the other measurements. After a period in which the ion source is not in use, the distribution curves are reproduced in all the experiments to within ±0.5% during the entire time of the experiments, regardless of changes in the ionizers and replacement of ribbons by wires, and vice versa.

For a Langmuir treatment[8] of each new ionizer and for oxidation of tungsten according to the method of ref. 9, the temperature of the wires and ribbons is established from the distribution of potassium ions. When oxygen is admitted, the filament voltage of the ionizer is increased until the resistance of the oxidized wire or ribbon is equal to the resistance in vacuum for a given temperature.

A 50-100° change in the ionizer temperature in the 2000°K region changes the evaporator temperature by several degrees. A constant evaporator temperature is maintained to within ±1° by regulating the filament current and monitoring the emf of the thermocouple of the PP-51 potentiometer.

The experiments are carried out at a pressure of $p = 5 \cdot 10^{-8}$–$1 \cdot 10^{-7}$ torr, which is measured with an ion pump.

CONTROL MEASUREMENTS

A comprehensive method is used to check the validity of Eq. (8) and its constants. First, the temperature of the working surface of the ionizer is determined by an optical pyrometer independently of the other measurements. Second, the use of an ionizing surface with a known work function φ^* and a beam of hard-to-ionize atoms with a known ionization potential J is used to check the correspondence between the temperature dependence of the ion current and the Saha–Langmuir equation:

$$I = C \exp\left[\frac{e(\varphi^* + \sqrt{eF} - J)}{kT}\right], \tag{9}$$

in which the values of kT obtained from the experimental distribution curves should appear.

Since the measurement of the ionizer temperature by an optical pyrometer simultaneously with the measurement of the ion currents and the recording of the distribution function would require a considerable alteration of the chamber or ion source of the mass spectrometer, these two measurement processes are performed separately. In these experiments the ionizer is an oxidized tungsten wire. The resistance of this ionizer is constant during the measurements; therefore, it is possible to first obtain the dependence of the surface temperature, measured from the ion distribution over the velocity projection, on the filament current, and then to obtain the same dependence using an optical pyrometer and to compare the data. The pyrometric measurements are carried out in a separate system in a vacuum of $1 \cdot 10^{-5}$ torr. During the optical measurements the temperature of the wire is increased from 1200 to 1600°K in order to obtain the dependence of its radiant emittance on the filament current before and after evaporation of the oxides. In the temperature interval under investigation this dependence is represented by two parallel segments of a straight line shifted according to the measured value of the temperature by 10±5° at a temperature of 1488°K, where evaporation of the tungsten oxides evidently terminates, and it corresponds to the best emissivity of an oxidized surface compared to a purely metallic surface. This correction was taken into account when correcting the pyrometer readings.[10] The values of the temperature determined using a Ribaud optical pyrometer are shown in Fig. 4 at points corresponding to the same value of the filament current of the ionizer in measurements using both methods.

RESULTS AND DISCUSSION

As indicated by control measurements of the temperature of the ionizer surface using the optical method, the true temperature and the values obtained from the distribution of silver ions over the velocity projection coincide to within ±10° (Fig. 4). The value of $J - \varphi^*$ obtained for the pair silver–oxidized tungsten, 0.91±0.10 eV, also agrees well with the literature value[6] of 0.81 eV.

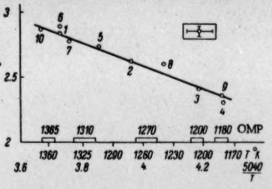

Fig. 4. Dependence of Ag$^+$ ion current on the temperature of the surface ionizer (oxidized tungsten). The values obtained using an optical pyrometer are shown in the upper row above the abscissa. The temperature values in the lower row are obtained from the ion distribution over the velocity projection. On the upper right, the limits of experimental error are shown and they are the same on the average for all the points.

The results confirm Eq. (8). The equality of the measured values of $J - \varphi^*$ and the published values corresponds to thermal equilibrium on the surface. We have used this method of analysis to investigate equilibrium in the case of silver and lead ions produced on different surfaces at temperatures up to 2600°K (see Part II). Under equilibrium the recorded distribution should be the same for all ions. Actually, in all such cases, some of which are shown in Fig. 3 for illustration, agreement between the distribution curves is observed within the experimental error ±0.001 eV. In these experiments beams of different atoms are ionized along with silver, which serves as a standard of comparison. Points calculated from Eq. (8) are plotted on this graph and they coincide with the experimental curve. It can be seen from Fig. 3 that the distribution over V_y obtained for thermionic ions of the ionizer material and the potassium and sodium impurities in them is somewhat broadened. The absolute value of the broadening is different for each ribbon and varies from 2 to 15%. However, the distribution of ions obtained during surface ionization of beams is stable over time and independent of the material and geometry of the ionizer; this has been checked by numerous determinations of the value of $J - \varphi^*$.

The presence of errors together with the poor discrimination with respect to the velocity V_z ($E_{z_0} = 0.017$ eV) means that the recorded function has a form very similar to that of $\sim \exp[-\varkappa^2 U^2/kT^*]$ where an incorrect interpretation of the experimental data can cause the temperature T^* to differ appreciably from the true temperature. For this reason, an experimental check of the method should be based not only on a comparison of the shape of the ion distribution curve, but also on the agreement between it and the temperature of the ionizing surface.

The distribution over the velocity projection of ions produced during surface ionization was first studied in ref. 11. The curves obtained have a form $I = I_0 \exp[-\alpha^2 U^2]$ and are evidently an integral distribution over two or several variables in velocity and coordinate space or an indication that distortions of type (8) are present.

In principle, analysis of the kinetic energies of ions can be a fairly precise method for measuring any surface temperature, including the range where optical pyrometry is not applicable. In particular, this method is promising for measurements where the emission properties of the surface are unknown or vary, for example, due to the interaction with the incident particle flux. The same applies to the determination of the work function of heated surfaces.

In combination with an independent method for measuring the temperature, the distribution of ions over the velocity projection allows us to obtain data on the spatial distribution of particles from the surface. With ionization of molecules, comparison of the distributions of molecular and atomic fragment ions with the temperature of the ionizing surface can give information on details of thermal equilibrium in a gas–surface system.

In conclusion, the author thanks M. V. Gur'ev, Yu. N. Lyubitov, and V. S. Senashenko for discussion.

The temperature measurements using an optical pyrometer were carried out by the author at the High-Temperature Institute of the Academy of Sciences of the USSR in the L. N. Gorokhov laboratory; the author thanks Yu. S. Khodeev for his help.

---

[1] C. Berry, Phys. Rev., 78, 597 (1950).
[2] L. V. Sumin and V. M. Gur'ev, Zh. Eksp. Teor. Fiz., 62, 2026 (1972) [Sov. Phys. – JETP, 35, 1057 (1972)].
[3] Yu. N. Lyubitov, Calculation of the Interaction between Molecular Beams and the Vessels Surrounding Them [in Russian], Nauka, Moscow (1964).
[4] J. V. Walsh, Proc. R. Soc. Lond., 32, 59 (1919).
[5] V. L. Tal'roze and E. L. Frankevich, Zh. Tekh. Fiz., 26, 497 (1956) [Sov. Phys. – Tech. Phys., 1, 479 (1956)].
[6] É. Ya. Zandberg and N. I. Ionov, Surface Ionization [in Russian], Nauka, Moscow (1969).
[7] V. Ya. Frenkel' and M. A. Shepsenvol, Zh. Tekh. Fiz., 28, 1477 (1958) [Sov. Phys. – Tech. Phys., 3, 1368 (1959)].
[8] H. A. Jones and I. Langmuir, Gen. Electr. Rev., 30, 310 (1927).
[9] É. Ya. Zandberg and U. Kh. Rasulev, Zh. Tekh. Fiz., 38, 1793 (1968) [Sov. Phys. – Tech. Phys., 13, 1446 (1969)].
[10] G. Ribaud, Optical Pyrometry, Paris (1931).
[11] N. I. Ionov and V. I. Karataev, Zh. Tekh. Fiz., 32, 626 (1962) [Sov. Phys. – Tech. Phys., 7, 454 (1962)].

Dielectric strength of spark gaps following strong current pulses

E. P. Bel'kov

M. I. Kalinin Polytechnical Institute, Leningrad

(Submitted August 2, 1972; resubmitted January 22, 1974)
Zh. Tekh. Fiz., 44, 1946-1951 (September 1974)

The dielectric strength of various gases is determined when the spark channel undergoes natural cooling.

The restoration of the dielectric strength following a spark discharge (or an arc discharge) is closely associated with the cooling of both the gas in the gap and the electrodes. Restoration of the dielectric strength begins when the temperature of the gas in the gap falls to 3000–4500°K. Below ~ 2000–2500°K the breakdown voltage of the gap depends on the density of the gas. The breakdown voltage obeys a generalized Paschen law and the deviations from the Paschen law[1,2] do not exceed ~ 15–20%.

A theoretical analysis of the cooling of the gas in the discharge gap is given in refs. 2-7 for the time following spark or arc discharges. It is proposed in refs. 2-4 that cooling in the cylindrical column of hot gas which remains after a discharge results from heat conduction due to thermal currents from the hot gas to the cold electrodes. Another hypothesis is developed in refs. 5-7, where it is assumed that the heat is removed from the channel in the radial direction toward the surrounding cold gas. Heat is transferred by molecular heat conduction and the influx of a mass of cold gas into the channel. As has been shown by the author in ref. 8, turbulent heat conduction is also of importance in addition to the above factors. Turbulent motion of the gas develops during the cooling of the channel. This detail of the gas cooling has not been considered in the earlier work. The present work therefore deals, in further detail, with the cooling of a gas and the restoration of the dielectric strength after a spark discharge. Another problem is that of determining the basic relationships of these processes in various gases and for various gap lengths.

The cooling of a gas has been qualitatively studied with a shadow setup similar to that described in ref. 9.

Restoration of the dielectric strength has been investigated in air, elegaz, hydrogen, argon ($p = 1$ atm), and in compressed air ($p = 2.5$ atm) after the passage of current pulses whose parameters are listed in Table 1.

The electrodes of the tested gaps are hemispherical and 30 mm in diameter; St-3 steel and copper are used. In the tests in air the spark gaps are inserted into a chamber with a volume of ~ 0.25 m^3 and weak exhaust ventilation (0.05 m^3/min); in the tests involving other gases the spark gap is placed in a hermetically sealed chamber with a volume of ~ 1 dm^3. In all cases the gap tested received a bias illumination from a mercury lamp located at a distance of 10 cm from the electrodes. The bias illumination passes through a quartz window in the tests made with the hermetically sealed chamber.

The restoration of the dielectric strength is investigated at a repetition rate of 1 Hz for the current pulses. The probing voltage pulses have a form of 1.5/500 μsec. For a given exposure time the curves representing the probability of breakdown of the gap as a function of the probing voltage are recorded at the end of the current pulse, with the probability of breakdown varying between 3 and 97%. The results are used to plot the curves representing the restoration of the dielectric strength of the spark gaps for the breakdown probability 50% and to calculate the mean-square spread σ of the breakdown voltages.

After a spark discharge the gaps have zero dielectric strength for 200–300 μsec (Figs. 1–3). The length of this time interval depends weakly upon the magnitude of the current pulse, the type of the gas, the distance between the electrodes (for $S > 2$ mm), and the electrode material. The gas temperature in the gap exceeds ~ 5000–6000°K in this time period; hence, the electrical conductivity of the gas is high. After a spark discharge involving a quantity of electricity $Q < 0.1$ C (I_3, I_4), the dielectric strength is restored to $(0.85–0.9)U_0$ according to an exponential law. The time required for restoring the dielectric strength $0.9\,U_0$ is 3-5 msec in hydrogen, 4-7 msec in air and argon, and 10-12 msec in elegaz and compressed air (Fig. 1). This time is independent of the material used for the electrodes and increases slightly when the length of the gap is increased.

After a powerful spark discharge involving a quantity of electricity $Q > 0.25$ C (I_1, I_2), the dielectric strength is initially restored at the same rate as after current pulses of a spark discharge with $Q < 0.1$ C (Fig. 1). Then the restoration of the dielectric strength is retarded. Accordingly, the curves representing the restoration of the dielectric strength, which are plotted on a semilog scale, have two sections of greatly different curvature. The first curved section is characterized by a restoration rate which is independent of the material of the electrodes and which

TABLE 1

	First current peak I_m, kA	Frequency of the oscillations f, kHz	Damping of the oscillations, Δ	Pulse length t_p, μsec	Quantity of electricity Q, C	Remarks
I_1	90	250	1.33	40	1	powerful spark discharge; Q > 0.25 C
I_2	60	200	2.7	15	0.25	
I_3	20	600	1.67	10	0.05	spark discharge, Q < 0.1 C
I_4	4	1600	2.3	3	0.003	
I_5	0.65	18.2	1.08	1500	0.3	arc current

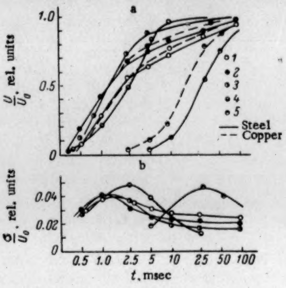

Fig. 1. Restoration of the dielectric strength of a 10 mm spark gap in air (U_0 = 30 kV) after current pulses. a) 50% breakdown voltage of the gap; b) mean-square deviations σ of the breakdown voltage from the 50% value for the curves of Fig. 1a. I_m (kA): 1) 90; 2) 60; 3) 20; 4) 4; 5) 0.65; t_p (μsec): 1) 40; 2) 15; 3) 10; 4) 3; and 5) 1500.

changes only slightly when the parameters of the current pulses are varied. In the flat section of the curves, the restoration rate of the dielectric strength depends, though only weakly upon the thermal conductivity of the electrode material. When the amplitude and the length of the current pulses increase these sections of the curves are shifted downward.

After an arc discharge the dielectric strength is restored more slowly than after a spark discharge. Except for elegaz, the gaps have (2.5-5 msec after the end of a discharge) low dielectric strength in all gases on the level of 300-500 V (Fig. 2). The dielectric strength of elegaz is restored much earlier than in the other gases, 100-200 μsec after the end of the pulse. The dielectric strength is most rapidly restored to its full extent in elegaz and hydrogen. The time required for complete restoration of the dielectric strength depends upon the heat conductivity of the electrode material and the spacing of the electrodes (Figs. 1 and 3).

The laws governing the restoration of the dielectric strength after spark and arc discharges can be explained by gas cooling in the gap. As can be inferred from the shadow photographs (Fig. 4), the gas volume which is heated by the discharge continues to expand after the current pulse. This is not a consequence of the adiabatic expansion of the gas, because the pressure in the channel is approximately equal to the atmospheric pressure at the end of the current pulse for both a spark discharge, or an arc discharge. The expansion of the volume of the hot gas during its cooling under constant pressure indicates that the energy of the hot gas gradually propagates to the adjacent layers of the cold gas, heating the latter. The mass of the hot gas increases and its volume increases. The boundary of the hot gas with the cold undisturbed gas remains sharp for a long time because the relation between the heat conductivity of a gas (air) and the temperature is nonlinear. This means that a high temperature (density) gradient exists at the boundary.

Intense turbulent motion is observed inside the hot gas volume. The processes leading to the development of this motion can be envisaged as follows. After the current pulse, the discharge channel is cooled by heat conduction, and, to some extent, by radiation. Since the density of a gas decreases during cooling, gas moves from the periphery to the center inside the channel. The motion develops under the influence of the external pressure forces. Gas particles which are far from the center of the channel acquire a particularly high radial velocity. The velocity of the radial motion of the gas decreases toward the center of the channel and vanishes at the center proper. Therefore, the gas particles which are accelerated far from the center of the channel must necessarily reduce their radial velocity component in proportion to the approach to the center. Moving by inertia, these gas particles form eddy currents. Thus, turbulent motion develops in the cooling discharge channel.

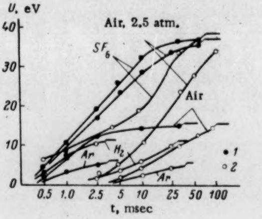

Fig. 2. Restoration of the dielectric strength of a 5 mm spark gap in various gases after current pulses. 1) I_m (kA): 1) 20; 2) 0.65; t_p(μsec): 1) 10; 2) 1500. Steel was the material of the electrodes.

Heat is transferred in the turbulent motion. The equation of energy transfer for a cylindrical model of the channel (the removal of heat onto the electrodes is ignored[8]) can be written in the following form when the turbulent transfer is taken into account:[10]

$$\rho\frac{\partial\bar{\varepsilon}}{\partial t}=\frac{1}{r}\frac{\partial}{\partial r}\left[r\frac{\lambda}{C_p}(1+\mathrm{Pe})\frac{\partial\bar{\varepsilon}}{\partial r}\right]-\frac{\partial\bar{\varepsilon}}{\partial r}\frac{1}{r}\int_0^r r\frac{\partial\rho}{\partial\bar{\varepsilon}}\frac{\partial\bar{\varepsilon}}{\partial t}dr, \tag{1}$$

where $\bar{\varepsilon}$ denotes the enthalpy of the gas; a bar on top of a symbol denotes an average over time; ρ, λ, and C_p denote the density, the heat conductivity, and the specific heat of the gas, respectively, i.e., quantities which depend upon $\bar{\varepsilon}$; Pe denotes the average Peclet criterion for the entire volume of the hot gas (independent of the coordinates).

The Peclet criterion is defined as

$$\mathrm{Pe}=\frac{\rho_{\mathrm{av}}Lv'_{\mathrm{av}}}{\left(\frac{\lambda}{C_p}\right)_{\mathrm{av}}}.$$

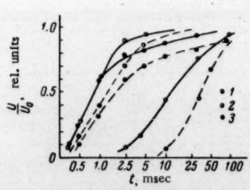

Fig. 3. Restoration of the dielectric strength of air gaps S = 2 mm (U_0 = 7.8 kV) and S = 15 mm (U_0 = 43 kV) after current pulses. I_m (kA): 1) 60; 2) 20; 3) 0.65; t_p (μsec): 1) 15; 2) 10; 3) 1500. The electrodes are steel. S = 2 mm is indicated by the solid lines; S = 15 mm is indicated by the dashed lines.

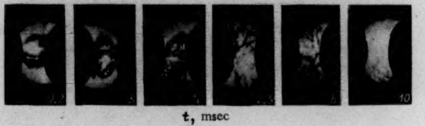

Fig. 4. Shadow photographs of the gas heated by a discharge channel through which a current pulse with $I_m = 20$ kA and $t_p = 10$ μsec passes. The photographs were taken at various times t after the termination of the discharge current.

where ρ_{av} denotes the average density of the gas in the volume; L denotes the scale of turbulence; $(\lambda/C_p)_{av}$ denotes a function of the average enthalpy of the gas in the volume; ε_{av}; and v'_{av} denotes the average velocity of the pulsating motion of the gas. This average velocity is given by the energy of the turbulent motion of the gas in the volume:

$$v'_{av} = \sqrt{\frac{2W_t}{M}},$$

where M denotes the mass of the gas in the volume. The energy of the turbulent motion of a gas can be obtained by integrating the product of the decelerating force exerted upon the gas times path over both time and the volume bounded by the radius r_m (Fig. 6):

$$W_t = \int_0^t \int_0^{r_m} 2\pi r\rho v_r^2 \frac{\partial v_r}{\partial t}\, dr\, dt. \tag{2}$$

While turbulent energy is generated in the gas volume, this energy is also spent by friction. We use an equation of ref. 11 to calculate the dissipation of the turbulent energy:

$$\frac{dv'}{dt} = -10\mu \left(\frac{v'}{L}\right)^2,$$

where μ denotes the coefficient of kinematic viscosity.

The boundary conditions of the problem are as follows:

$$\left.\begin{array}{l} r > r_0,\ \varepsilon(r,\ t) = \varepsilon_0, \\ r < r_0,\ \varepsilon(r,\ t) = \varepsilon_1(r,\ t) + \varepsilon_0, \end{array}\right\} \tag{3}$$

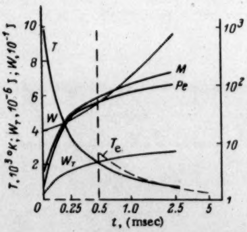

Fig. 5. Results of a calculation of the gas cooling after a current pulse with $I_m = 4$ kA and $t_p = 3$ μsec. T denotes the temperature on the axis of the cooling channel; M denotes the mass, W, the thermal energy, and W_t, the energy of turbulent motion of the gas calculated per centimeter channel length; Pe denotes the Peclet criterion; and T_e denotes the temperature deduced from the experimental results.

for

$$t = 0,\ \varepsilon(r,\ 0) = \varepsilon_{01}\left(1 - \frac{r}{r_0}\right)^{1/m} + \varepsilon_0$$

$$W_t = W_{t0}.$$

A cylindrical model of the cooling of a channel is developed in refs. 5-7, where turbulent transfer is disregarded [Pe = 0 in Eq. (1)]. The solution of Eq. (1) then produces a very slow cooling of the channel, particularly at temperatures below ~ 4500°K where the heat conductivity of air decreases sharply. Equation (1) is solved numerically when we include the turbulent transfer in the present work. The results of the calculation of the gas cooling are shown in Figs. 5 and 6 for a spark channel with a radius of 0.4 cm at the end of the current pulse (which corresponds to a current pulse with $J_m = 4$ kA and $t_p = 3$ μsec). It is assumed that removal of heat by radiation is the dominant process when the channel cools to ~ 10,000°K. In this case, an energy of turbulent motion

$$W_{t0} = \frac{\pi}{64} \frac{(\Delta\rho)^3}{(\rho_{av}\Delta t)^2} r_0^4,$$

accumulates in the channel, where Δt denotes the time within which, the gas cools to 10,000°K; $\Delta\rho$ denotes the density change corresponding to this cooling.

It follows from calculations that turbulent heat transfer Pe > 2 is of great importance in the cooling of the channel as early as 10-20 μsec after the end of the discharge, with the importance of turbulent heat transfer increasing continuously (Pe reaches the value 10^2 in the calculation). This behavior results from the fact that W_t the energy of the turbulent gas motion in the volume increases with time. A particularly fast increase in turbulent energy occurs at the beginning of the cooling process 200-250 msec after the end of the current pulse. The gas cools rapidly in this time interval and the velocity of directed radial gas motion in the volume reaches high values (Fig. 6). The gas is accelerated far from the center of the channel. The kinetic energy of the gas is converted into energy of turbulent motion when the gas approaches the center of the channel. About 2/3 of the turbulent energy of the gas in the volume is accumulated when the gas has cooled to 5000-6000°K. The turbulent energy greatly increases the turbulent heat conductivity of the gas and, hence, the gas volume continues to cool rapidly despite the fact that molecular heat conduction of the gas is low at low temperatures.

Calculations have shown that the rate of gas cooling is essentially independent of the channel radius after a spark

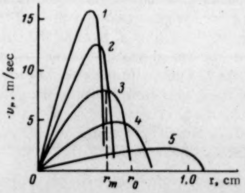

Fig. 6. Velocity of radial gas motion in the cooling of the channel. $I_m = 4$ kA, $t_p = 3$ μsec, $r_m = r_m(t)$ and $r_0 = r_0(t)$. Time (msec) after the end of the discharge: 1) 0.05; 2) 0.1; 3) 0.2; 4) 0.5; and 5) 1.0.

discharge. This is explained by the fact that at a certain initial rate of gas cooling by radiation the energy of turbulent motion developing in the volume is proportional to r_0^4, whereas the coefficient of turbulent transfer is $A_q \sim r_0^2$. Since the thermal energy of the gas in the channel is also proportional to r_0^2, the constant of the cooling time of the gas, $\tau \sim r_0^2/A_q$, is independent of the channal radius. This detail accounts for the fact that the rate at which the dielectric strength is restored after a spark discharge is almost independent of both magnitude and duration of the current pulses even when the parameters are varied over very wide limits.

After an arc discharge the gas begins to cool from a temperature of 7000-8000°K. There is no fast initial cooling of the gas. Turbulent energy accumulates slowly in the gas volume and, accordingly, the gas also cools slowly.

The observed experimental relationships in the restoration of the dielectric strength after both spark and arc discharges can be explained by gas cooling in the spark gap. Shortly after the end of the current pulse, turbulent gas motion develops in the cooling channel and the turbulent motion stimulates the entire subsequent gas cooling in the gap.

The author thanks P. I. Shkuropat for valuable comments.

---

[1] D. E. Poole, A. B. Parker, and R. J. Churchill, J. Electr. Contr., 15, 131 (1963).

[2] A. B. Parker and D. E. Poole, Brit. J. Appl. Phys., 15, 1011 (1964).

[3] F. L. Curzon and M. S. Gautom, Brit. J. Appl. Phys., 8, 79 (1967).

[4] H. Edels and J. C. Holme, Brit. J. Appl. Phys., 17, 1595 (1966).

[5] D. Whittaker, Fourth Intern. Conf. on Ionization Phenomena in Gases, Amsterdam (1960), p. 381.

[6] R. L. Phillips, Z. Physik, 211, 113 (1968).

[7] G. R. Jones and G. Freeman, Z. Physik, 229, 177 (1969).

[8] E. P. Bel'kov, Zh. Tekh. Fiz., 41, 1678 (1971) [Sov. Phys. – Tech. Phys., 16, 1321 (1972)].

[9] M. P. Vanyukov, V. I. Isaenko, and L. D. Khazov, Zh. Tekh. Fiz., 25, 1248 (1955).

[10] L. G. Loitsyanskii, Mechanics of Liquids and Gases [in Russian], Nauka, Moscow (1970).

[11] Bay-Shi-Yee, Turbulent Flow of Liquids and Gases [Russian translation], IL, Moscow (1962).

Electrical conductivity of a pseudoliquefied layer in an electric field

V. V. Gal', V. I. Konov, and K. A. Nikitin

Institute of High Temperatures, Academy of Sciences of the USSR, Moscow

(Submitted October 8, 1973)
Zh. Tekh. Fiz., 44, 1952-1954 (September 1974)

The electrical conductivity of pseudoliquefied layers of graphite, niobium, and zirconium oxycarbonitride is investigated in a weak electric field, i.e., below 1 V/cm. It is shown that an electric current can flow through pseudoliquefied zirconium oxycarbonitride and niobium layers only above a threshold voltage, the breakdown voltage. The dependence of the breakdown voltage on the experimental parameters is investigated. The results are evaluated in connection with contact conductivity and the breakdown of thin dielectric oxide layers on particle surfaces.

Heating a pseudoliquefied layer of particles through which an electric current flows is one of the promising methods of generating high temperatures. Carbon-containing materials which are electrical conductors are usually employed as pseudoliquefied layers.[1-6] However, this technique of heating pseudoliquefied layers has not been thoroughly investigated, particularly in regard to materials which do not contain carbon. When a current passes through a pseudoliquefied layer, its structure obviously differs from that of a layer through which no current flows.

It is important to investigate the electrical conductivity of pseudoliquefied layers of various materials (graphite, oxycarbonitride of zirconium, niobium), when an electric field which does not change the layer structure is applied.

Suspended layers are produced in a cylindrical reaction vessel 40 mm in diameter (one electrode); a central electrode is inserted into the reaction vessel in a coaxial position. Gas is admitted to the pseudoliquefied layers through a diffusor situated in the lower section of the reaction vessel. A voltage from a dc source is applied to the electrodes and the voltage–current characteristics of the pseudoliquefied layers are recorded. Figure 1 shows a typical voltage–current characteristic. The measurements are used to determine the smallest potential difference U_{appl} for a stable, fixed current in the layer. The sensitivity of the voltage measurements is $5 \cdot 10^{-5}$ V.

The quantity U_{appl} has the meaning of the breakdown voltage of the pseudoliquefied layer. This quantity depends upon several factors. The most important of these factors are the electrophysical properties of the solid and the gaseous phases, and the structure of the suspended layer. With $U_{appl} = 0$ a number of contacts sufficient to produce an electrical conductivity exists in the pseudoliquefied layer, and these extend from one electrode to the other. When $U_{appl} > 0$ (more precisely, when U_{appl} is greater than the sensitivity threshold of the voltage measurements), no contacts with purely resistive conductivity are present in the pseudoliquefied layers. The quantity U_{appl} is therefore an indicator of the contact circuits of the conductivity of pseudoliquefied layers and is characteristic of the layer structure. The homogeneity of a pseudoliquefied layer through which an electric current flows increases with decreasing U_{appl}.

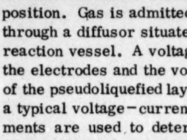

Fig. 1. Voltage–current characteristic of a pseudoliquefied layer of zirconium oxycarbonitride (at an Ar consumption of 12 liter/min).

We investigate the dependence of U_{appl} upon the solid phase and the consumption of liquefied gas. The basic results of the U_{appl} measurements are given in Table 1 (the distance between the electrodes is kept constant at 16 mm).

In a pseudoliquefied graphite layer, $U_{appl} = 0$ when the parameters of the experiment are varied over wide limits. This means that a large number of contact loops exist in the layer.

In niobium and zirconium oxycarbonitride, U_{appl} is nonvanishing even for fixed layers. This result can be explained by the fact that the contact points of the particles are nonconductive.

The possible reasons for the increase in U_{appl} with increasing layer porosity are: The formation of longer loops of contact conductivity is characteristic of increasing porosity (this results in an increase in the number of nonconductive contacts); furthermore, when the porosity increases the number of conductive loops with gas-filled inclusions also increases.

We note that the specific resistivity of pseudoliquefied layers is greater by several orders of magnitude than that of the compact material (six to seven orders of magnitude in graphite). The increased specific resistivities of pseudoliquefied layers apparently originate from the small contact areas of the particles and the high resistance of the contacts. The higher value of U_{appl} at higher porosity is due to a reduction of the number of conductivity in loops per unit of layer cross section.

The dependence of U_{appl} upon the electrode spacing has been investigated (see Table 2). In niobium, whose particles, when in contact with air, are covered by a thin film of lower oxides, U_{appl} increases in proportion to the increase in the length of the contact circuits (i.e., with the increasing effective thickness of the dielectric). U_{appl} of graphite is always equal to zero. The specific resistivity of the pseudoliquefied layer is essentially independent of the electrode spacing.

A significant dependence of the specific resistivity of the pseudoliquefied layers upon the current density should be noted (fraction 315-500 μ; see Table 3).

It is interesting to compare the electrical conductivity of pseudoliquefied layers with electrical phenomena

TABLE 1. Basic Results of the Experiments

Material	Fraction (μ)	Electrode materials	Gas	Flow of liquefied gas (liter/mm)	Porosity of pseudoliquefied layer	U_{appl}, (mV)	$\rho(\Omega \cdot cm)$
Graphite	315—500	Graphite—graphite	—	Fixed layer	0.62	0	$2 \cdot 10^{-4}$
	315—500	Same	N_2	12	Not determined	0	Not determined
	315—500		Ar	9		0	
	315—500	Steel—niobium	—	Fixed Layer	0.62	0	$2 \cdot 10^{4}$
	315—500	Same	—	15	0.79	0	10^{5}
	315—500		—	30	0.89	0	$4 \cdot 10^{5}$
Zirconium oxycarbonitride	500—1000	Graphite—graphite	—	Fixed layer	0.81	0.2—0.4	$2 \cdot 10^{4}$
	500—1000	Same	Ar	12	0.84	1—2	10^{5}
	500—1000	"		16	0.86	9—14	$5 \cdot 10^{5}$
	500—1000	"		20	0.90	25—30	$2 \cdot 10^{6}$
	500—1000	"	N_2	35	Not determined	56—60	Not determined
Niobium	400—500	Steel—niobium	—	Fixed layer	0.70	150—210	$2 \cdot 10^{4}$
	400—500	Same	Ar	15	0.75	210—300	$2 \cdot 10^{7}$
	400—500	"		30	0.83	480—750	$6 \cdot 10^{7}$
	50—100	"		7.3	0.75	300—440	$5 \cdot 10^{7}$
	50—100	"		15	0.87	390—450	$7 \cdot 10^{7}$
	50—100	"		20	0.91	370—430	$8 \cdot 10^{7}$
	50—100	"		30	0.96	400—500	$2 \cdot 10^{8}$
	56—71	"	N_2	35	Not determined	500—600	Not determined

TABLE 2. Electrical Conductivity of Fixed Layers of Granular Materials

Material	Fraction (μ)	Distance between electrodes	Porosity of pseudoliquefied layer	U_{appl} (mV)	$\rho(\Omega \cdot cm)$ of pseudoliquefied layers
Niobium	400—500	7.5	0.70	6—10	$1.5 \cdot 10^{7}$
	400—500	12	0.70	20—30	$2 \cdot 10^{7}$
	400—500	16	0.70	50—150	$1.2 \cdot 10^{7}$
Graphite	100—315	10	0.75	0	110
	100—315	25	0.75	0	104
	100—315	45	0.75	0	94
	100—315	60	0.75	0	92

Note: Material of the electrodes: Graphite—graphite; fixed layer.

TABLE 3. Specific Resistivity of Graphite Powder

Current density (A/cm^2)	$\rho_{ps.l}(\Omega \cdot cm)$
10^{-7}	10^{4}
10^{-3}	10^{2}
10^{-1}	10

in suspensions of electrically conductive powders. The electric breakdown of suspensions of Al and soot in dielectric liquid is studied in refs. 6 and 7. It is shown that the electric breakdown in suspensions with concentrations of about 1% of the conductive particles results in a structuring of the suspensions at fields of 10^3-10^4 V/cm The effects of aggregation and the interactions of the conducting chains with the electrodes are considered.

The similarity in the behavior of suspensions and pseudoliquefied layers in an electric field is noteworthy. The similarity resides in the fact that electric breakdown occurs in pseudoliquefied layers, as in suspensions with the breakdown voltage increasing in direct proportion to the distance between the electrodes. However, in addition to the similarities between pseudoliquefied layers and suspensions, there is an important difference: In pseudoliquefied layers the average field is about four orders of magnitude lower and the concentration of the particles is one order of magnitude greater than that in suspensions. The circuits for contact conductivity formed in suspensions are stable during the entire time in which an electric field is applied because the circuits are maintained by the forces generated by the electric field. In pseudoliquefied layers, the circuits of the contact conductivity, which are formed by the much weaker applied field, exist for a short time, which depends upon the porosity fluctuations in the layer, and disintegrate. New circuits are formed at the same time, i.e., a stationary equilibrium exists between the number of circuits being created and destroyed. A description of electrical phenomena in pseudoliquefied layers in an electric field which changes the layer structure will be communicated in subsequent publications.

---

[1] W. M. Goldberger and I. E. Hanway, Chem. Eng. Progress, 61, No. 2 (1965).

[2] H. S. Johnson, Canad. J. Chem. Eng., 39, No. 3 (1961).

[3] W. M. Goldberger and H. W. Nack, Batelle Tech. Rev., 13, No. 11 (1964).

[4] E. Wicke, Chem. Eng. Sci., 6, 160 (1957).

[5] G. B. Read, Int. Sci. Technol., No. 6, 42 (1962).

[6] L. G. Gidin, Ya. I. Frenkel', and O. A. Shpanskaya, Zh. Tekh. Fiz., 20, 937 (1950).

[7] L. G. Gidin, A. E. Vol'pyan, I. F. Galkin, and V. E. Gul', Physicochemical Mechanics of Disperse Structures; Collection of Articles [in Russian], Nauka, Moscow (1966).

Multiple scattering of a focused beam of monoenergetic electrons

G. N. Vyalov

(Submitted October 12, 1973; resubmitted January 10, 1974)
Zh. Tekh. Fiz., 44, 1955-1960 (September 1974)

The mean-square dimensions of an axisymmetric focused beam of monoenergetic electrons subject to multiple scattering are determined. The mean-square dimensions in a longitudinal magnetic field are calculated for arbitrary total scattering angles. The scattering of a magnetically self-focused charge-neutralized beam is also calculated. An approximate expression valid for small total scattering angles is obtained for the mean-square dimensions. The beam current is estimated by assuming that the beam propagates without significant change in the transverse dimension. The calculation is performed by determining the trajectory of a single electron, taking account of random forces, and then averaging over the trajectories.

1. In a number of applications of an electron beam related to its propagation in a gaseous medium it is important to take account of the effect of electron scattering on the properties of the beam.[1)] In particular, the scattering leads to an increase in the transverse dimensions of the beam, and to a reduction in its specific power. Extreme broadening of the beam at distances less than the slowing-down length can be inhibited by external focusing, for example, by a longitudinal magnetic field. For small total angles of deflection of the electrons from their initial direction the mean-square dimensions of the beam can be estimated, for example, by the method used by Vyalov and Fiks.[1] We show below that the similar problem of finding the shape of a scattered beam in a uniform longitudinal magnetic field can be solved without restricting the size of the total scattering angles. An approximate equation is derived for the transverse dimensions of a self-focused weakly divergent electron beam.

2. In order to simplify the problem we assume that the energy lost by electrons in slowing down in the medium is negligibly small. This means that the propagation distance of the beam in the medium is less than the slowing-down length.

It can be shown that to an accuracy sufficient for the calculation of the mean-square dimensions of the beam the change in direction of the momentum **p** of a single electron with a given energy in a scattering medium without a magnetic field is

$$\frac{d\mathbf{p}}{dt}=\frac{1}{\tau}(-A\mathbf{p}+Bp\mathbf{n}),\quad p=|\mathbf{p}|,\tag{1}$$

where τ is the average time between collisions, **n** is a random unit vector quasiorthogonal to **p**, i.e., orthogonal to **p** to order A/B; $B\approx\bar{\theta}$ is the average angle of deflection of the momentum in a single collision, $A\approx\bar{\theta}^2/2\approx\overline{\theta^2}/2$. We assume multiple Coulomb scattering, with small average and mean-square scattering angles in a simple interaction. The quantity $\theta_i=\theta(t_i)$, where i is the number of the scatter, varies randomly from collision to collision. Assuming that the collisions are sufficiently frequent we use the quasicontinuous collision approximation to replace the functions $\theta(t_i)$ and $\theta^2(t_i)$ by their average values determined by the Rutherford equation for small-angle scattering. The characteristics of the beam can be calculated up to the second moments by supplementing the above assumptions with the following rules for averaging over the directions of the random vector **n**(t):

$$\left.\begin{aligned}&\langle\mathbf{n}(t)\rangle\simeq 0,\\&\langle n_i(t)\,n_k(t')\rangle\simeq\frac{1}{2}\left[\delta_{ik}-\langle\pi_i(t)\,\pi_k(t)\rangle\right]\delta(t-t'),\end{aligned}\right\}\tag{2}$$

where $\boldsymbol{\pi}=\mathbf{p}/p$, with the usual notation for the unit tensor δ_{ik} and the Dirac delta function $\delta(t-t')$.

If it is assumed that initially all the electrons have the same direction described by the unit vector $\boldsymbol{\pi}_0$, then by averaging Eq. (1) and solving the averaged equation we obtain the change of the average longitudinal momentum in the beam

$$\langle\pi_{\parallel}\rangle=\langle\boldsymbol{\pi}\boldsymbol{\pi}_0\rangle=e^{-At/\tau}=e^{-t/\tau_s},\tag{3}$$

where

$$\tau_s=\left(\frac{\tau}{A}\right)=\frac{2\tau}{\overline{\theta^2}},\tag{4}$$

which agrees with Eq. (14.9) of ref. 2 obtained using the Boltzmann equation. It follows that the average longitudinal displacement of monoenergetic electrons in a scattering medium is limited by the value of $v\tau_s$, where v is the velocity of the electrons.

Similarly, using the formal solution of Eq. (1) in the form

$$\mathbf{p}=\mathbf{p}_0e^{-\frac{At}{\tau}}+\frac{Bp}{\tau}\int\limits_0^t e^{-\frac{A(t-t')}{\tau}}\mathbf{n}(t')\,dt',\tag{5}$$

we obtain an integral equation for the mean-square longitudinal momentum $T=\langle\pi_{\parallel}^2\rangle$:

$$T=e^{-\frac{2At}{\tau}}+\frac{B^2}{2\tau}\int\limits_0^t e^{-\frac{2A}{\tau}(t-t')}(1-T')\,dt'\tag{6}$$

where T' denotes the value of T at time t'. The integral equation (6) is equivalent to the differential equation

$$\frac{dT}{dt}\equiv\dot{T}=\frac{B^2}{2\tau}-\frac{T}{\tau}\left(\frac{B^2}{2}+2A\right)\rightarrow\frac{B^2}{2\tau}-\frac{3B^2}{2\tau}T\ \text{for}\ A=\frac{B^2}{2},\tag{7}$$

which has the solution

$$T=\frac{B^2+4Ae^{-\frac{t}{\tau}\left(\frac{B^2}{2}+2A\right)}}{B^2+4A}\rightarrow\frac{1}{3}\left(1+e^{-\frac{3B^2t}{\tau}}\right)\ \text{for}\ A=\frac{B^2}{2},\tag{8}$$

agreeing with Eq. (14.9) of ref. 2 for $A=B^2/2=\overline{\theta^2}/2$, written for the average of the square of the transverse momentum $\langle\pi_{\perp}^2\rangle=1-T$, obtained by using the Boltzmann equation.

The mean-square dimensions of the beam can be calculated by using Eqs. (5) and (8). We note also that according to Eq. (5) the mean-square momentum of an electron in the beam is conserved $\langle \overline{p}^2 \rangle = p_0^2$, in accord with the assumption that slowing down can be neglected.

3. The equations of motion of an electron in a scattering medium in the presence of a magnetic field H can be written in the form

$$\frac{d\mathbf{p}}{dt}=\frac{1}{\tau}(-A\mathbf{p}+Bp\mathbf{n})-\frac{e}{\gamma mc}[\mathbf{pH}], \tag{9}$$

where $\mathbf{p} = \gamma m\mathbf{v}$ is the momentum of the electron, γ is the relativistic factor, $-e$ is the charge of the electron, and c is the velocity of light.

For the motion of a beam in a uniform longitudinal magnetic field along the z axis p_x, p_y and n_x, n_y are replaced by the complex quantities

$$\Pi=p_x+ip_y;\quad n=n_x+in_y. \tag{10}$$

The vector equation (9) is equivalent to the system

$$\left.\begin{aligned}\dot{\Pi}&=-\left(\frac{A}{\tau}-i\omega\right)+\frac{pB}{\tau}n,\\ \dot{p}_z&=-\frac{A}{\tau}p_z+\frac{pB}{\tau}n_z.\end{aligned}\right\}. \tag{11}$$

The formal solution of system (11) with the initial conditions

$$\Pi(0)=\Pi_0;\quad p_z(0)=p_{z0}$$

is

$$\left.\begin{aligned}\Pi&=\Pi_0e^{-t\left(\frac{A}{\tau}-i\omega\right)}+\frac{pB}{\tau}\int_0^t e^{\left(\frac{A}{\tau}-i\omega\right)(t'-t)}n(t')\,dt',\\ p_z&=p_{z0}e^{-\frac{At}{\tau}}+\frac{pB}{\tau}\int_0^t e^{\frac{A}{\tau}(t'-t)}n_z(t')\,dt'.\end{aligned}\right| \tag{12}$$

The complex transverse displacement w = x + iy and the longitudinal displacement z are

$$\left.\begin{aligned}w&=w_0+\frac{\Pi_0}{\gamma m\left(\frac{A}{\tau}-i\omega\right)}\left[1-e^{-t\left(\frac{A}{\tau}-i\omega\right)}\right]\\ &+\frac{vB}{\tau}\int_0^t\frac{dt'n(t')}{\frac{A}{\tau}-i\omega}\left[1-e^{\left(\frac{A}{\tau}-i\omega\right)(t'-t)}\right],\\ z&=z_0+\frac{p_{z0}\tau}{\gamma mA}\left(1-e^{-\frac{At}{\tau}}\right)+\frac{vB}{A}\int_0^t dt'n_z(t')\left[1-e^{\frac{A}{\tau}(t'-t)}\right].\end{aligned}\right\} \tag{13}$$

We note that the equation for the longitudinal momentum does not contain the field H. Therefore the mean-square longitudinal momentum is determined by Eq. (8).

The mean-square dispersions of the displacement due to multiple scattering are

$$\left.\begin{aligned}\langle\Delta w\Delta w^*\rangle&=\frac{v^2B^2}{A^2+\omega^2\tau^2}\int_0^t\int_0^t dt'dt''\langle n(t')n^*(t'')\rangle\\ &\times\left[1-e^{\left(\frac{A}{\tau}-i\omega\right)(t'-t)}\right]\left[1-e^{\left(\frac{A}{\tau}+i\omega\right)(t-t'')}\right],\\ \langle\Delta z^2\rangle&=\frac{v^2B^2}{A^2}\int_0^t\int_0^t dt'dt''\langle n_z(t')n_z(t'')\rangle\\ &\times\left[1-e^{\frac{A}{\tau}(t'-t)}\right]\left[1-e^{\frac{A}{\tau}(t''-t)}\right],\end{aligned}\right\} \tag{14}$$

where the asterisk denotes the complex conjugate.

According to rules (2) for averaging we have

$$\left.\begin{aligned}\langle n(t')n^*(t'')\rangle&=\frac{1}{2}\delta(t'-t'')[1+T(t')],\\ \langle n_z(t')n_z(t'')\rangle&=\frac{1}{2}\delta(t'-t'')[1-T(t')].\end{aligned}\right\} \tag{15}$$

By taking account of (8) we obtain for T(t):

$$\left.\begin{aligned}\langle\Delta w\Delta w^*\rangle&=\frac{v^2B^2\tau}{3(A^2+\omega^2\tau^2)}\int_0^t dt'\left(2+e^{-\frac{3At'}{\tau}}\right)\\ &\left[1-2e^{\frac{A(t'-t)}{\tau}}\cos\omega(t'-t)+e^{\frac{2A(t'-t)}{\tau}}\right],\\ \langle\Delta z^2\rangle&=\frac{v^2B^2\tau}{3A^2}\int_0^t dt'\left(1-e^{-\frac{3At'}{\tau}}\right)\left[1-2e^{\frac{A(t'-t)}{\tau}}+e^{\frac{2A(t'-t)}{\tau}}\right].\end{aligned}\right\} \tag{16}$$

Integrating gives the form

$$\left.\begin{aligned}\langle\Delta w\Delta w^*\rangle&=\frac{v^2B^2\tau}{3(A^2+\omega^2\tau^2)}\left\{2\left[t-\frac{2\tau^2}{A^2+\omega^2\tau^2}\left(e^{-\frac{At}{\tau}}\left(\omega\sin\omega t\right.\right.\right.\right.\\ &\left.\left.\left.-\frac{A}{\tau}\cos\omega t\right)+\frac{A}{\tau}\right)+\frac{\tau}{2A}\left(1-e^{-\frac{2At}{\tau}}\right)\right]\\ &+e^{-\frac{3At}{\tau}}\left[\frac{\tau}{A}\left(\frac{1}{3}e^{\frac{3At}{\tau}}+e^{\frac{At}{\tau}}-\frac{4}{3}\right)\right.\\ &\left.\left.-\frac{4A\tau}{4A^2+\omega^2\tau^2}\left(e^{\frac{2At}{\tau}}\left(\cos\omega t+\frac{\omega\tau}{2A}\sin\omega t\right)-1\right)\right]\right\},\\ \langle\Delta z^2\rangle&=\frac{v^2B^2\tau}{3A^2}\left[t+\frac{\tau}{A}\left(-\frac{11}{6}+3e^{-\frac{At}{\tau}}-\frac{3}{2}e^{-\frac{2At}{\tau}}+\frac{1}{3}e^{-\frac{3At}{\tau}}\right)\right].\end{aligned}\right\} \tag{17}$$

Strong magnetic fields, for which

$$\omega\tau\gg 2A=\theta^2\quad\text{or}\quad H\gg\frac{m\gamma c}{e\tau}\theta^2=\frac{1700\beta\gamma}{Z_p}\,[\text{Oe}], \tag{18}$$

are of particular interest.

In this case we have

$$\begin{aligned}\langle\Delta w\Delta w^*\rangle&\simeq\frac{v^2B^2}{3\omega^2\tau}\left\{2\left[t-\frac{2}{\omega}\sin\omega te^{-\frac{At}{\tau}}+\frac{\tau}{2A}\left(1-e^{-\frac{2At}{\tau}}\right)\right]\right.\\ &\left.+e^{-\frac{3At}{\tau}}\left[\frac{\tau}{A}\left(\frac{1}{3}e^{\frac{3At}{\tau}}+e^{\frac{At}{\tau}}-\frac{4}{3}\right)-\frac{2}{\omega}e^{\frac{2At}{\tau}}\sin\omega t\right]\right\}.\end{aligned}$$

In the limiting case of small times, $3At/\tau \ll 1$, or $z \ll 2z_p/3$, where $z_p = v\tau/\theta^2$ is the scattering length, we obtain the simple expressions

$$\left.\begin{aligned}\langle\Delta w\Delta w^*\rangle&\simeq\frac{2v^2B^2}{\omega^2\tau}\left(t-\frac{1}{\omega}\sin\omega t\right)=\frac{2\rho^2}{z_p}\left(z-\rho\sin\frac{z}{\rho}\right)\simeq\frac{2\rho^2z}{z_p},\\ \langle\Delta z^2\rangle&\simeq\frac{v^2B^2At^4}{12\tau^2}=\frac{z^4}{24z_p^2};\quad\rho=\frac{v}{\omega}.\end{aligned}\right\} \tag{19}$$

Thus in a strong magnetic field the transverse diffusion of the beam electrons is established rather rapidly. The square of the transverse dimensions increases linearly with the time. In the absence of a magnetic field the beam spreads much more rapidly, the square of the dimensions increasing as the cube of the time.

The longitudinal diffusion of the beam can be established only after a time $t \gg \tau/A = 2\tau/\theta^2$. For small times the law for the change of the longitudinal dispersion ($\Delta Z^2 \sim t^4$) differs markedly from the diffusion law.

4. The equations of motion of an electron in a scattering medium in the form (9) can, in principle, also be applied for a magnetic field of arbitrary configuration, or for other force fields. It is also possible to take account of slowing down, for example by ionization, by introducing an appropriate retarding force on the right-hand side of (9). The equations obtained in this way are generally quite complicated and can only be solved numerically.

Because of the complexity of the problem of the motion of a high-current electron beam in a scattering medium (self-focused by its self-magnetic field) it is difficult to obtain the change of the mean-square dimensions of the beam for any time from the instant of emission of the electron. Simplification of the problem of motion of a beam in an axisymmetric transverse magnetic field which increases linearly with the radius by assuming that the deflection from the initial direction is small and the longitudinal momentum is constant gives an answer identical with that of ref. 3 obtained by the Boltzmann equation (cf. also ref. 4). In the approximation of constant longitudinal momentum p_z it is relatively simple to take account also of the decrease in the transverse momentum related to the factor A of Eq. (9). If necessary the correction to the change in p_z can be calculated by perturbation theory.

In a similar way, the average of the square of the radius a^2 of a self-focused electron beam for relatively small total scattering angles can be estimated by assuming that the transverse dimensions change slowly and that the self-magnetic field inside a charge-neutralized beam can be written in the form

$$H = \frac{2Jr}{ca^2}. \qquad (20)$$

In this case the mean-square dimensions of the beam can be estimated by the equation

$$a^2 \simeq a_0^2\left(\cos\frac{\varkappa z}{a} + \frac{a}{\varkappa f}\sin\frac{\varkappa z}{a}\right)^2 + \frac{a^2\Gamma^2}{\varkappa^2}\sin^2\left(\frac{\varkappa z}{a}\right) + \frac{a^2}{2\varkappa^2 z_p}\left(z - \frac{a}{2\varkappa}\sin\frac{2\varkappa z}{a}\right), \qquad (21)$$

which is valid when

$$\frac{d\ln a}{d\ln z} \ll 1, \qquad (22)$$

where a_0 and Γ are respectively the initial mean-square dimensions of the beam and the angular spread; $\varkappa^2 = 2I/I_0\beta\gamma$; $I_0 = mc^3/e$ is a universal current, equal to 17,000 A; f is the focal length, i.e., the distance at which a beam with a zero current and $\Gamma = 0$ would converge to a point if there were no scattering. For a sufficiently large current and $\Gamma^2 \approx (\varkappa^2/a^2)a_0^2 \approx \varkappa^2$ the beam dimensions can be estimated by the simple relation

$$a^2 \approx \frac{a_0^2}{\dfrac{z}{1-(2\varkappa^2 z_p)}}. \qquad (23)$$

The expression is satisfied approximately when its value is close to unity. By requiring that this condition be satisfied at least at distances $Z \leqslant (1/2)\, z_p$ we obtain a restriction on the current ensuring the propagation of a self-focused beam the indicated distance, $\varkappa^2 > 1/4$ or $I > (1/8)\, I_0\beta\gamma$. In general it is necessary that

$$J > \frac{1}{4} J_0\beta\gamma\frac{z}{z_p}. \qquad (24)$$

This estimate assumes also that in a distance z an electron performs a large number of transverse oscillations in the self-field of the beam, i.e., $2\varkappa z/a \gg 1$.

[1)] The role of scattering in the propagation of a relativistic electron beam in a dense gas is discussed, for example, in an experimental paper by Miller and Gerardo.[5]

---

[1] G. N. Vyalov and M. M. Fiks, Usp. Fiz. Nauk, 89, 437 (1966) [Sov. Phys.—Usp., 9, 525 (1967)].

[2] B. A. Trubnikov, in: Reviews of Plasma Physics, Vol. 1, Consultants Bureau, New York (1965).

[3] R. L. Kimmel' and O. N. Salimov, Zh. Tekh. Fiz., 41, 2628 (1971) [Sov. Phys.—Tech. Phys., 16, 2089 (1972)].

[4] V. P. Kartashev, V. I. Kotov, and R. A. Rzaev, Zh. Tekh. Fiz., 43, 641 (1973) [Sov. Phys.—Tech. Phys., 18, 402 (1973)].

[5] P. A. Miller and J. B. Gerardo, J. Appl. Phys., 43, 3008 (1972).

Double focusing in a system of 1/r electric and magnetic fields

V. V. Zashkvara and V. N. Demin

Institute of Nuclear Physics,
Academy of Sciences of the Kazakh SSR, Alma-Ata

(Submitted October 11, 1973; resubmitted March 18, 1974)
Zh. Tekh. Fiz., 44, 1961-1963 (September 1974)

We discuss an ion-optical mass spectrometer in which spatial focusing and energy focusing of a beam of charged particles are accomplished simultaneously (double focusing). The spectrometer consists of two analyzing elements in tandem: a cylindrical electrostatic mirror and a magnetic analyzer with a 1/r field.

Electrostatic energy analyzers of the cylindrical mirror type[1-4] have been widely used in the spectroscopy of charged-particle beams because of their good ion-optical characteristics and simple construction. It is tempting to consider the possibility of using a cylindrical mirror in combination with a magnetic field in a double-focusing mass spectrometer to increase the transmission. A magnetic field varying as 1/r, where r is the distance from the axis of symmetry, corresponds most closely to a cylindrical mirror in the character of its spatial focusing of a beam. This field has been known for a long time in the spectroscopy of charged-particle beams and is the basis for high-transmission beta spectrometers.[5-8] A magnetic field varying as 1/r surrounds a straight wire carrying a current or, according to ref. 5, can be obtained between two inclined pole faces of a magnet as shown in Fig. 1. In a cylindrical coordinate system the field components are: $H_r = 0$, $H_\theta = h/r$, $H_z = 0$, where h is a constant characterizing the field intensity. Far from the edges of the magnet the lines of force are concentric circles and the equipotential lines are radii. There is a close analogy between the ion-optical properties of a cylindrical electrostatic field and a 1/r magnetic field. We assume that a point source at point 0 on the axis of symmetry of the magnetic field (Fig. 1) emits particles of mass m, charge q, and velocity v which enter the magnetic analyzer in a beam with an angular divergence of $2\Delta\alpha$ in an axial plane, and $2\theta_0$ in a plane perpendicular to the axis of symmetry. The boundaries of the pole faces of the magnet are rectilinear, and we assume that the axis of the beam is perpendicular to the boundary of the analyzer. The spatial focusing of a beam in a 1/r magnetic field with rectilinear boundaries (Fig. 1) and in a cylindrical electrostatic mirror are very similar. Neglecting edge effects it can be shown that the 1/r magnetic field, like the electrostatic field of a cylindrical mirror, focuses a beam of charged particles on the axis of symmetry z to second order in $\Delta\alpha$ and exactly with respect to the azimuthal angle θ. If the 1/r magnetic field is sharply defined at the edges of the pole faces and the boundary where the beam enters and leaves the field is a cylindrical surface of radius r_m passing through the edges of the poles (Fig. 1), then the resolution of the focal length L in terms of the small perturbations $\Delta\alpha$ and $\delta p = \Delta(mv)/mv$ the relative momentum spread in the beam of charged particles, is

$$L = r_m \{l_0 + B_1\Delta\alpha + B_2\delta p + B_{11}(\Delta\alpha)^2 + B_{12}\Delta\alpha\delta p + B_{22}(\delta p)^2 + B_{111}(\Delta\alpha)^3 + \ldots,\} \quad (1)$$

under conditions of angular focusing with respect to $\Delta\alpha$

$$l_0 = 2.71,\quad B_1 = 0,\quad B_2 = 4.31,\quad B_{11} = 0,\quad B_{12} = 5.22,\quad B_{22} = 4.30,\quad B_{111} = -1.0, \quad (2)$$

where B_2 is the linear momentum dispersion in the direction of the z axis. The numerical values of B_{111}, B_{12}, and B_{22} characterize the relative aberrations of the third order in $\Delta\alpha$ and the second order in $\Delta\alpha$ and δp in the direction of the dispersion. It should also be added that the condition for second-order angular focusing occurs at $mv/qh = 0.74$ and $r_{max} = 2.10\ r_m$ (Fig. 1). These are the optical characteristics of a magnetic analyzer if we neglect fringing fields. Actually the fringing field is the cause of the extra aberrational spread of the image in the direction of the dispersion, an effect which increases with the azimuthal divergence of the beam $2\theta_0$. Henceforth we assume that θ_0 is chosen to achieve a compromise between the aberrations due to the effect of fringing and the loss of transmission produced by the decrease in those aberrations, so that in the first approximation the expansion coefficients (1) and (2) shown above give a good description of the ion-optical properties of the magnetic analyzer. Unfortunately the value of θ_0 corresponding to these conditions cannot be estimated without knowing the actual trajectories.

We now consider a double-focusing mass spectrometer. Figure 2 shows the ion-optical scheme of such

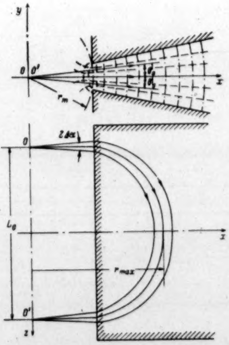

Fig. 1. Analyzer with a magnetic field varying as 1/r.

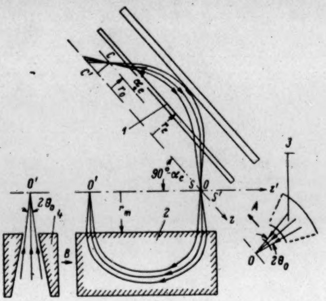

Fig. 2. Ion-optical scheme of a double-focusing mass spectrometer. 1) Electrostatic analyzer of the cylindrical mirror type; 2) magnetic analyzer with a 1/r field; 3) view of electrostatic analyzer along arrow A; 4) view of magnetic analyzer along arrow B.

an instrument consisting of a cylindrical electrostatic mirror 1 and a matching magnetic analyzer 2 with a 1/r field. We assume that the cylindrical mirror is adjusted for second-order focusing by one of the schemes of the annulus-axis type.[9] CC' is an annular slit of radius r_0 serving as the ion-optical source. The entrance angle α_e satisfies the condition of second-order angular focusing in the cylindrical mirror and, according to ref. 9, can take on values from 42°18', when the ion-optical source is a point and $r_0/r_e = 0$, to 38°50', when the ion-optical source is a narrow annular slit on the surface of the mirror z and the axis of symmetry of the magnetic field z' in the plane of Fig. 2 and the angle between them is $90° - \alpha_e$. Angular focusing is achieved in the system of fields by the coincidence of the foci of the component elements at point 0. The narrow slit SS' is located on the axis of symmetry of the cylindrical mirror; its extension along the z axis determines the energy range of ions in the beam entering the magnetic field, and the slit width determines the separation of the nonaxial trajectories leaving the source.[4] Energy focusing in this scheme is achieved if the characteristic dimensions of the analyzer r_e and r_m satisfy a relation which follows from the requirement that the linear energy dispersions of the cylindrical mirror and the magnetic analyzer be equal:

$$\frac{r_m}{r_e} = 2\frac{A_2}{B_2}\sin\alpha_e. \tag{3}$$

Data on the linear dispersion coefficient A_2 and the other parameters characterizing the ion-optical properties of a cylindrical mirror are given in ref. 9.

The proposed mass spectrometer should be useful in measuring mass spectra of low-intensity ion beams when the mass resolution requirements are not so rigid and an increase in transmission is necessary, for example in ion microanalyzers.

---

[1] V. V. Zashkvara, M. I. Korsunskii, and O. S. Kosmachev, Zh. Tekh. Fiz., 36, 132 (1966) [Sov. Phys.–Tech. Phys., 11, 96 (1966)].

[2] V. V. Zashkvara and V. S. Red'kin, Zh. Tekh. Fiz., 39, 1452 (1969) [Sov. Phys.–Tech., 14, 1089 (1970)].

[3] V. V. Zashkvara, M. I. Korsunskii, V. S. Red'kin, and V. E. Masyagin, Prib. Tekh. Eksp., 2, 39 (1970).

[4] V. V. Zashkvara, M. I. Korsunskii, V. S. Red'kin, and V. P. Lavrov, Prib. Tekh. Eksp., 5, 44 (1970).

[5] H. O. Richardson, Proc. Phys. Soc., 59, 791 (1947).

[6] O. Kofoed-Hansen, J. Lindhard, and O. B. Nielsen, Mat. Fys. Medd. Dan. Vid. Selsk, 25, No. 16 (1950).

[7] O. B. Nielsen and O. Kofoed-Hansen, Mat. Fys. Medd. Dan. Vid. Selsk, 19, No. 6 (1955).

[8] S. J. Kato, Phys. Soc. Japan, 13, 544 (1958).

[9] V. V. Zashkvara, Zh. Tekh. Fiz., 41, 829 (1971) [Sov. Phys.–Tech. Phys., 16, 651 (1971)].

Numerical experiments on electron bombardment in crossed fields

P. V. Romanov and A. S. Roshal'

Moscow Physical Engineering Institute

(Submitted October 5, 1973)
Zh. Tekh. Fiz., 44, 1964-1968 (September 1974)

The statistical characteristics of electron bombardment in magnetrons are obtained by numerical experiments using the giant particle method. Cylindrical and planar electrodes are considered. The effects of the anode potential and of an rf voltage on the distributions of thermal losses, energy, velocity, and electron incidence angle are considered. Nonequilibrium distributions of mean electron energies of incidence at the cathode are enhanced with increasing dc and rf potentials. The distribution of incident electron energies lies in the low-energy region (100-200 eV). The electron distribution over an incidence angle is also a nonequilibrium distribution and has a noticeable maximum in the negative angle region, indicating the cycloidal nature of the electron motion in the immediate neighborhood of the cathode. The nonequilibrium nature of the thermal loss distribution is much stronger at the anode than the cathode. The results lead to better development on design requirements for cathodes and anodes, cathode emission characteristics, and cooling for given performance characteristics.

1. STATEMENT OF THE PROBLEM

The cathode and anode of a magnetron undergo intense electron bombardment which affects the lifetime and performance.[1-4] A study of electron bombardment in magnetron devices is necessary to understand physical phenomena in the electron cloud and to improve construction and operation characteristics. Experimental studies of electron bombardment are difficult.[1,2] It is therefore fruitful to use numerical methods, **i.e., computer simulation** of magnetron devices with an appropriate statistical formulation of stochastic processes such as electron collisions with electrodes.

Electron bombardment in an amplitron has been evaluated[4] in the adiabatic approximation. In this paper we characterize electron bombardment in magnetrons statistically, performing numerical experiments by means of the giant particle method.[5,6] Processes are simulated in 3 cm magnetrons region with secondary-emission cathodes. The region corresponding to one pair of magnetron resonators is considered.

Let P be one of the parameters characterizing electron bombardment, and let $0 \le x \le 96$ be the dimensionless coordinate along the electrode surface (cathode or anode). The origin of coordinates is chosen so that the maximum rf anode potential is located at $x = 24$. In the simulation the expectation values are found:

$$P(x) \equiv M[P[x]] = \int_{-\infty}^{\infty} P \frac{w(P,\ x)}{w_P(x)}\, dP, \tag{1}$$

where the one-dimensional distribution function

$$w_P(x) = \int_{-\infty}^{\infty} w(P,\ x)\, dP$$

and the distribution function

$$w(P) = \int_0^{96} w(P,\ x)\, dx. \tag{2}$$

The quantity P(x) characterizes the distribution of the parameter P along the electrode, and w(P) the spread in P for the electrode as a whole. In addition, the average parameter value

$$\bar{P} = \int_{-\infty}^{\infty} \int_0^{96} P w(P,\ x)\, dP dx \tag{3}$$

is calculated for the electrode as a whole.

As parameters we take the current density j, thermal losses P_l, the incident electron kinetic energy E_p, the incidence angle θ_p measured from the normal to the electrode surface, the velocity components, their squares, and the electron temperature T_e, i.e., the velocity spread of the incident electrons.[6] Calculations by Eqs. (1)-(3) are performed by averaging simulation results of stationary magnetron results over 8-15 cyclotron periods. The average number of particles in the region selected is 1800-2300. The sample volume, i.e., the number of particles arriving at the electrode in the average time, is 3500-7500 for the cathode and 300-1700 for the anode.

The results of the numerical experiment are given in Figs. 1-7. The curves 1-3 are calculated for cylindrical electrode configurations, and curves 4-6 for planar electrodes. The constant anode potential U_a and the peak rf voltage at the anode U_{st} for curves 1-6 are, respectively (in kV): 1) 15.0, 4.71; 2) 15.0, 0.67; 3) 14.0, 4.71; 4) 25.3, 6.90; 5) 15.9, 6.90; 6) 15.9, 8.68. Curve 2 is calculated for the case when the anode current and the generated power are small, and the other curves for external generation.

2. CATHODE BOMBARDMENT

The nonequilibrium distribution of incident energy $E_p(x)$ at the cathode increases with both the dc U_a and rf

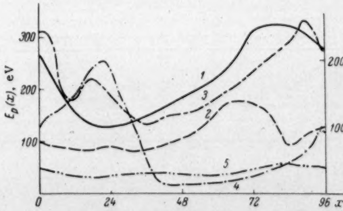

Fig. 1. Energy distribution of incident electrons $E_p(x)$. For curves 1-3 the ordinate axis is on the left, and for 4, 5 on the right.

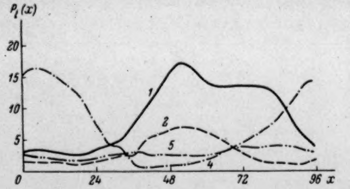

Fig. 2. Distribution of thermal losses $P_l(x)$ (in dimensionless units).

U_{st} potentials (Fig. 1). As seen from Fig. 1, the maximum position of $E_p(x)$ depends on the electrode geometry and on the operational region. The distribution of thermal losses $P_l(x)$ along the cathode (Fig. 2) is also nonequilibrium. The nonequilibrium distribution $P_l(x)$ is enhanced with increasing anode potential U_a and rf potential amplitude U_{st}. The total thermal loss at the cathode in oscillation is 5-8% of the input power, which is in good agreement with experimental data.

Strong space charge close to the cathode reduces the potential significantly. Figure 3 shows the total potential $U_1(x)$ at the first grid close to the cathode (at a distance 0.02 mm from it), which is used in solving the Poisson equation numerically. In the absence of a space charge the total potential in this region is about 300 V. The location of the potential minimum coincides with the maximum position of the current density j of the returning electrons (not shown in the figure).

The electron distribution over incidence angle $w(\theta_p)$ has a noticeable maximum (mode) $\tilde{\theta}_p$ in the negative angle region: $\tilde{\theta}_p \simeq -(0.3\text{-}0.4)\pi$, which indicates the cycloidal nature of electron motion in the immediate neighborhood of the cathode (Fig. 4). The rise of the curves close to $\theta_p \simeq \pi/2$ is due to the same emitted electrons which enter the retarding field and returns to the cathode. For these values the cycloid is restricted to a point and the incidence angle is $\pi/2$. With increasing rf field amplitude the mode position $\tilde{\theta}_p$ is somewhat displaced to the positive side (curves 1 and 2). The average incidence angle $\bar{\theta}_p = -(0.16\text{-}0.23)\pi$, the halfwidth of the curve $\omega(\theta p)$ around the mode $\bar{\theta}_p$, is about $\pi/4$.

The mode $\tilde{E}_p$ of the distribution $w(E_p)$ of incident electron energy is also strongly expressed and located in the low energy region: $\tilde{E}_p \simeq 100\text{-}200$ eV (Fig. 5), with E_p increasing with the constant potential U_a. This indicates that in the region of space-charge limiting a significant number of electrons return to the cathode. The energy of these electrons is of the order of their initial energy, i.e., it is low. For the secondary emission used the most probable initial energy is about 3.5 eV. With increasing constant potential U_a the field is enhanced in the interaction space and the space-charge limiting is reduced, i.e., a small part of the emitted electrons returns to the cathode and E_p increases. The average incidence energy is $\tilde{E}_p \cong 100\text{-}200$ eV, and the halfwidth of the curve $w(E_p)$ is 500-600 eV. The calculated incidence energies are in good agreement with the results of refs. 1 and 4.

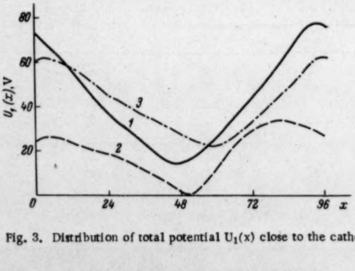

Fig. 3. Distribution of total potential $U_1(x)$ close to the cathode.

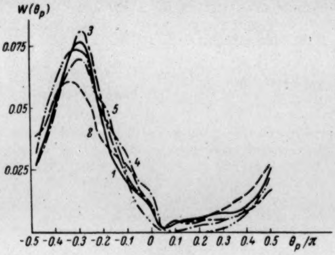

Fig. 4. Electron distribution in the incidence angle θ_p.

For the platinum emitter used the secondary emission coefficient $\sigma(E_p)$ becomes larger than unity at $E_p > E_{p1} \simeq 70$ eV and reaches a maximum $\sigma_m = 1.8$ at $E_p = E_{pm}$ 850 eV. The secondary emission coefficient $\sigma(\tilde{E}_p)$ at $\tilde{E}_p = 100\text{-}200$ eV is located at the rising branch of the curve $\sigma(E_p)$ close to $\sigma(E_{p1}) = 1$. In the regions calculated the average value is $\bar{\sigma} \simeq 1.00\text{-}1.35$. The behavior of the curve $\sigma(E_p)$ in the region $E_{p1} \leq E_p \leq E_{pm}$ requires most careful experimental investigation, as it determines the complete space charge in the interaction region and is related to the device characteristics.

The electron temperature of the current that bombards the cathode is $(0.6\text{-}1.5) \cdot 10^6$ deg K.

3. ANODE BOMBARDMENT

In the region considered the anode current I_a is less than the current I_c of electrons returning to the cathode. This is seen from the quantity $\bar{\sigma}$; for secondary emission cathodes we have $\bar{\sigma} \simeq 1 + I_a/I_c$ by the conservation of the average charge. The energy and incidence angle of the electrons hitting the anode are determined by the cycloidal

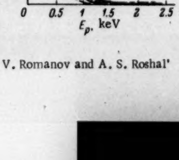

Fig. 5. Electron distribution in the incidence energy E_p.

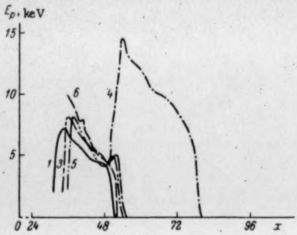

Fig. 6. Distribution of electron incidence energy $E_p(x)$.

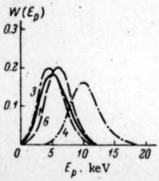

Fig. 7. Electron distribution in the incidence energy E_p.

motion in the immediate neighborhood of the anode and therefore depend strongly on the constant and rf voltages. Thus, for example, for the regions 4-6 (Fig. 4) the most probable incidence angle $\tilde{\theta}_p$ is, respectively, 0.1 π, 0.14 π, and π/4, and the halfwidth of the density distribution of $w(\theta_p) \simeq 0.08\pi$, 0.12π, and 0.20π. In the anode region (in the "spoke") the electrons regroup, with the degree of regrouping also dependent on the rf potential amplitude.

The nonequilibrium **energy distribution $E_p(x)$ enhanced** with increasing constant anode potential U_a **and with the rf** potential amplitude U_{st} (Fig. 6). The nonequilibrium nature of the distribution of thermal losses $P_l(x)$ along the anode is considerably stronger than at the cathode due to the small area the electrons hit with a large velocity spread. The total power of anode **thermal losses is 35% of** the input power, exceeding cathode losses by a factor of 4-7. The most probable electron incidence energy at the anode is $\tilde{E}_p \simeq \bar{E}_p \simeq 5$-11 keV (Fig. 7), which is 30-40% of the potential energy eU_a. The halfwidth of the distribution $w(E_p)$ is about 4.5-6 keV.

The electron temperature of the current hitting the anode is $(2-4)\cdot 10^6$ deg K.

The results of the numerical experiment provide important information on the distribution of thermal losses, energy, velocity and angle of electron incidence along the cathode and anode, and also on their dependence on the electrode geometry and on the operational region. Since the difficulties in carrying out similar physical experiments are obvious, numerical simulation is a very useful method of reproducing "ideal," i.e., unperturbed, physical observation. The data are useful in evaluating electrode design, cathode emission characteristics, and cooling requirements.

---

[1] V. K. Rosnovskii, Elektron. Tekh., Ser. Elektronika SVCH, No. 3, 163 (1969).

[2] J. R. M. Vaughan, IEEE Trans., ED-15, No. 11, 883 (1968).

[3] G. G. Sominskii, Zh. Tekh. Fiz., 35, 162 (1965) [Sov. Phys. - Tech. Phys., 10, 129 (1965)].

[4] G. Dombrowski and T. Ruden, Large signal calculation of amplitron performance, "Microwaves," Proc. of the Fourth Intern. Congress on Microwave Tubes, Scheweningen, Holland, 1962; Centrex, Eindhoven (1963).

[5] P. V. Romanov, A. S. Roshal', and V. N. Galimulin, Izv. Vuz. Radiofizika, 13, 1096 (1970).

[6] A. S. Roshal' and P. V. Romanov, Zh. Tekh. Fiz., 42, 2501 (1972) [Sov. Phys. - Tekh. Phys., 17, 1948 (1973)].

Effect of a high-current relativistic electron beam on a metal

**B. I. Dmitrenko, L. V. Leskov, G. P. Maksimov, S. L. Nedoseev,
V. V. Savichev, V. P. Smirnov, and A. M. Spektor**

(Submitted September 14, 1973; resubmitted January 2, 1974)
Zh. Tekh. Fiz., 44, 1969-1972 (September 1974)

Samples of stainless steel and M-1 copper are irradiated with 55 nsec pulses of 0.8 MeV electrons. The beam current is $\leqslant 25$ kA. For current densities appreciably larger than 1 kA/cm^2 a shock wave is produced in the sample, and splitting is observed on the rear surface. For current densities ~ 1 kA/cm^2 microcavities $\sim 10^{-4}$ cm across are observed in the samples. In the copper samples these are in the form of elongated chains or filaments. The distance between filaments is $\sim 10^{-2}$ cm. Possible causes of the observed phenomena are discussed.

High-current beams of relativistic electrons with a total energy $\leqslant 10^5$ J and intensities up to 10^9–10^{11} W/cm^2 incident on a solid surface for times $< 10^{-7}$ sec should produce pronounced structural changes. The effects of pure radiation damage to the crystal lattice by the beam electrons described in refs. 1 and 2 appear to be significantly masked by the consequences of strong heating and the production of high pressures in the material.[3] The pressure in the irradiated material after termination of energy transfer from the beam to the crystal lattice is determined by the heating and the elastic properties of the material and by the depth and uniformity of the penetration of the electrons. For a high enough pressure shock waves can develop in the sample, as observed by Zelenskii et al.,[4] in addition to elastic waves.

It has been shown in a number of papers[5–8] that the pressure and the directly related depth of penetration of the beam electrons, determined by the form and amplitude of the compression wave, are in satisfactory agreement with the values calculated by the single-particle theory of the interaction of electrons with matter. Honnold et al.[9] have obtained the unexpected result that a torsional wave is produced by the uniform irradiation of a sample. Apparently the torsion of the sample is related to the nonuniform penetration of the beam due to collective effects. The possibility of collective processes at large current density is confirmed by the observation of the self-focusing of a beam in a dielectric and the anomalous damage to ionic crystals.[10,11] One method of studying the way a beam penetrates matter is to investigate the uniformity and depth of structural changes in the material irradiated by the beam. In the work described below we present the first results of such studies of samples of stainless steel and copper.

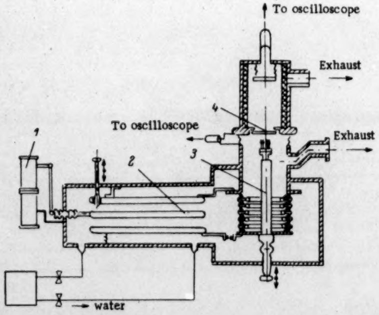

Fig. 1. 1) Voltage pulse generator; 2) shaping line; 3) cathode holder; 4) anode.

The experiments were performed at the Neptune accelerator,[12] shown schematically in Fig. 1. The double shaping line of the accelerator is charged from the voltage pulse generator for 0.5 μsec to $V_0 \approx 0.8$ Mv. During charging a prepulse of $0.15\ V_0$ appears at the cathode of the accelerator. In a number of experiments the size of the prepulse has been substantially reduced by using a special sparkgap.[12] The main voltage pulse with height $\leqslant 0.8$ MV and length 55 nsec is applied to a disk plasma cathode 4 cm in diameter. A plasma sheath is produced at the cathode by a discharge over the surface of epoxy resin filling holes 1.2 mm in diameter and 2 mm deep in the metal disk. Up to 200 holes are drilled in the cathode surface. In the matching mode the beam current is 25 kA. The distribution of current density at the exit foil, averaged over the time of a pulse and over an area of ~ 4 mm^2, is determined by the luminescence of scintillators and the blackening of glass. Under typical conditions it is nearly uniform over a circle 5 cm in diameter. As the pressure of the neutral gas in the accelerator gap is increased to $\sim 3 \cdot 10^{-4}$ torr pronounced inhomogeneities ≤ 5 mm in diameter appear in the current density. These are recorded by the luminescence of a scintillator and are typically ≤ 5 mm in diameter. The inhomogeneities are explained by the appearance of a plasma in the accelerator gap as a result of the prepulse. In this case, as is shown in ref. 13, the beam current density is increased appreciably.

This feature permits the irradiation of samples by beams which are either uniform or nonuniform over the cross section. A disk-shaped sample 1.2 mm thick and 120 mm in diameter is used as the anode of the accelerator. In a number of cases the sample is placed behind a titanium foil 50 μ thick to eliminate the possibility of the residual gas discharge in the accelerator gap acting on the surface of the target. The targets are made of 1Kh18N9T stainless steel and M-1 copper. The surface and volume of the samples are examined before and after irradiation using metallographic and profilometric analyses and a scanning electron microscope having a spatial resolution no better than $2 \cdot 10^{-5}$ cm.

A nonuniform beam causes significant metal failure including splitting on the rear surface of the disk. Figure 2 shows a microsection through one such region of failure on a stainless steel disk. A layer of metal 200 μ thick is peeled off the rear surface. Part of the layer, about 3 mm^2 in area, is completely separated from the base material, as is confirmed by the character of the

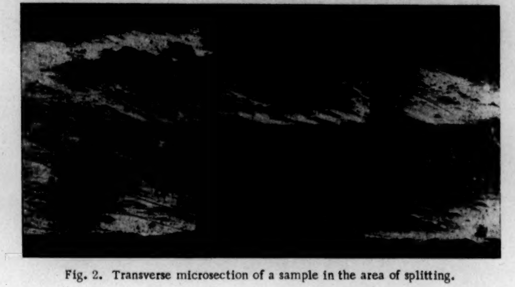

Fig. 2. Transverse microsection of a sample in the area of splitting.

surface where the splitting occurs. Close to the splitting region there are many cavities typically ~ 40 μ in size stretched out parallel to the plane of cleavage. Similar failures are recorded on the copper samples. After a hundred irradiations by a beam having a uniform current density a transverse section of a stainless steel target shows microcavities $1\text{-}2\cdot10^{-4}$ cm long and $3\cdot10^{-5}$ cm wide. The microcavities are distributed at random over the section. This effect is studied in more detail on the copper disk. Figure 3 shows a transverse section of a copper sample after five irradiations. The microcavities form filaments drawn out along the direction of propagation of the beam with typical widths of 10^{-4} cm. The average angle between a filament and the axis of the beam is a few degrees, and this prevents the observation of longer filaments. The filaments are uniformly distributed both over the cross section of the beam and over its depth, and are separated from one another by distances of a few tens to a few hundreds of microns. A rough estimate on one exposure indicates ~ 10^5 filaments in the target.

The splitting observed in these experiments is explained by the production of shock waves in the metal as a result of heating by the electron beam.[4] The appearance of the filaments is harder to understand. We note that microcavities are observed up to a depth four times the mean free path of 0.8 MeV electrons. Evidently the formation of microcavities cannot be explained by the characteristics of the metal structure.

It is possible that the formation of filaments is related to the small-scale inhomogeneities of the beam current density in the accelerator gap, or to the separation of the beam into individual filaments in the sample under study.

Fig. 3. Microcavities in a copper sample. Typical width of a cavity is ~ 10^{-4} cm.

In conclusion the authors thank E. K. Zavoiskii and L. I. Rudakov for helpful discussions, and E. S. Trekhov and E. D. Titov for help in studying the samples.

---

[1] R. Bullough and A. B. Lidiard, Comm. Sol. State Phys., Part B, 4, 69 (1962).

[2] A. Seeger, Comm. Sol. State. Phys., Part B, 4, 79 (1972).

[3] O. V. Bogdankevich and A. A. Rukhadze, ZhETF Pis. Red., 13, 517 (1971) [JETP Lett., 13, 369 (1971)].

[4] K. F. Zelenskii, O. P. Pecherskii, and V. A. Tsukerman, Zh. Tekh. Fiz., 38, 1581 (1968) [Sov. Phys.—Tech. Phys., 13, 1284 (1969)].

[5] D. R. Schallhorn and L. D. Buxton, IEEE Trans. Nucl. Sci., NS-16, 242 (1969).

[6] R. A. Graham and R. E. Hutchison, Appl. Phys. Lett., 11, 69 (1967).

[7] R. B. Oswald, D. R. Shcallhorn, and H. A. Eisen, IEEE Trans. Nucl. Sci., NS-15, 187 (1968).

[8] F. C. Perry, Appl. Phys. Lett., 17, 478 (1970).

[9] V. R. Honnold, C. C. Berggren, and W. M. Peffley, IEEE Trans. Nucl. Sci., NS-16, 255 (1969).

[10] R. Little, T. Ottesen, and E. K. Childers, IEEE Trans. Nucl. Sci., NS-16, 250 (1969).

[11] A. I. Vaisburd and I. N. Balychev, ZhETF Pis. Red., 15, 537 (1972) [JETP Lett., 15, 380 (1972)].

[12] S. S. Kingsep, G. P. Maksimov, Yu. L. Sidorov, V. P. Smirnov, and A. M. Spektor, Prib. Tekh. Eksp., 2, 26 (1973).

[13] S. L. Nedoseev, V. P. Smirnov, A. M. Spektor, and D. G. Fil'kin, Zh. Tekh. Fiz., 42, 2520 (1972) [Sov. Phys.—Tech. Phys., 17, 1961 (1973)].

Explosion driven magnetic generator with a matched inductive load

L. S. Gerasimov

(Submitted July 10, 1973; resubmitted January 9, 1974)
Zh. Tekh. Fiz., 44, 1973-1980 (September 1974)

The conditions for maximum energy transfer and peak power from an explosion-driven magnetic generator (EMG) acting on an inductive load are considered for three circuits: transformerless, with transformer outside the explosion chamber, and transformer inside the explosion chamber. Optimum regimes are described. The parameter ranges are determined for which one of the circuits is preferable to the other two.

Explosion-driven magnetic generators (EMG) are gaining wider application in experimental physics as a means of obtaining powerful current pulses. It is well-known[1] that such pulses can also be obtained from condenser banks; however, the specific energy obtained from an EMG is greater by more than an order of magnitude. Clearly, a laboratory device for the conversion of the energy of an explosion into electromagnetic energy (explosion chamber and necessary equipment) is only justified when the energy supplied to the load is considerably greater than that which can be stored in a condenser bank. Often (for example, in plasma experiments), the more important property is not the energy, but the power of the electromagnetic pulse.[2] In any case, the EMG or condenser bank must be matched to the load to ensure optimum results.

TRANSFORMERLESS CIRCUITS

In order to simplify the analysis, we neglect the resistance of the condenser bank, generator, and connectors. We then obtain the electric circuit shown in Fig. 1a. We denote the working inductance of the generator by

$$L(t)=L_0 \text{ for } t=0,$$
$$L(t)=0 \text{ for } t=T$$

where T is the cycle length, the inductance of the connection between generator and load (output from the chamber) by L_{out}, the bank inductance by L_c, and the stored energy by E_0. If the magnetic field is trapped (dotted line in Fig. 1a) when the current is a maximum (zero bank voltage), then

$$E_0=\frac{1}{2}(L_0+L_b+L_{out}+L_L)\,i_0^2,$$

where $i_0 = i(0)$ is the feed current to the generator and the energy delivered to the load is

$$E_{\text{н.}}=E_0\left(\frac{L_0+L_{out}+L_L}{L_{out}+L_L}\right)^2\frac{L_L}{L_0+L_b+L_{out}+L_L}.$$

a) Condition for maximum energy transfer. We can estimate the efficiency of the system as

$$\frac{E_L}{E_0}=\frac{\left(1+\frac{1}{l_{out}+l_L}\right)^2}{1+\frac{1+l_b+l_{out}}{l_L}}, \tag{1}$$

where, for convenience, the dimensionless inductances

$$l_b=\frac{L_b}{L_0},\ l_{out}=\frac{L_{out}}{L_0},\ l_L=\frac{L_L}{L_0}.$$

are used.

In order to have $E_L/E_0 \geq 1.5$ it is necessary that

$$l_b \ll 1,\ l_{out} \ll 1,\ l_L \leqslant 1.$$

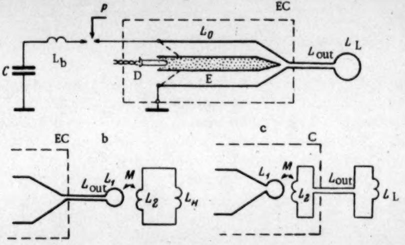

Fig. 1. Electric circuits for an explosion-driven magnetic generator with an inductive load. a) Transformerless; b) with transformer outside explosion chamber; c) with transformer inside explosion chamber; C) condenser bank; L_b) inductance of connector between bank and generator; P) spark gap switch; EC) explosion chamber; E) explosive; D) detonator; L_{out}) output inductance of EC; L_L) load inductance; L_1) inductance of transformer primary; L_2) inductance of secondary; M) mutual inductance of windings.

For example, for $l_b = l_{out} = l_L = 0.2$, $E_L/E_0 \simeq 1.5$, and for $l_b = l_{out} = l_L = 0.1$, $E_L/E_0 \simeq 2.8$. If L_L is greater than L_b and L_{out} by an order of magnitude or more, then

$$\frac{E_L}{E_0}\cong 1+\frac{1}{l_L},$$

i.e., the efficiency of energy transfer is limited by the value of l_L. Evidently, the output from the explosion chamber should be such that its inductance is two to three times less than the load inductance (further reduction has little effect). Thus, for $l_b = l_L = 0.1$ and $l_{out} = 0.05$, $E_L/E_0 = 4.7$ (as opposed to 2.8 in the second example). It is desirable to have a value $l_b = 0.2$-0.1 for the bank inductance (further reduction also has no effect). If L_L is reduced with fixed L_b and L_{out} then E_L/E_0 will begin to grow at first and then fall. The optimum value of L_{out} depends on L_b and L_{out} in a complicated manner; however, in the most interesting practical case, $l_b \ll 1$ and $l_{out} \ll 1$, we may assume that $(l_L)_{opt} = l_{out}$ to a sufficient degree of accuracy. In this case the efficiency is a maximum, given by

$$\frac{E_L}{E_0}=\frac{\left(1+\frac{1}{2l}\right)^2}{2+\frac{1}{l_{out}}},$$

which is shown in Fig. 2 (curve 1). Thus, the limiting

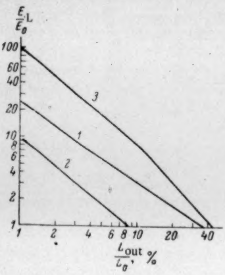

Fig. 2. Generator efficiency E_L/E_0 as a function of L_{out}/L_0. 1) Transformerless circuit under optimum conditions ($L_b/L_0 \ll 1$, $L_{out}/L_0 \ll 1$, $L_L/L_0 = L_{out}/L_0$); 2) apparatus with optimized transformer outside the explosion chamber with $k = 0.9$ and $L_b/L_0 = 0$; 3) apparatus with transformer inside the explosion chamber with $k = 0.9$, $L_b/L_0 = 0$, $L_1/L_{out} = 1$, $L_L/L_0 = 1$.

values of E_L/E_0 can be attained for $l_{out} \ll 1$ and $l_L \ll 1$.

b) Condition for maximum generated power. The energy delivered to the load up to time t is

$$E_L(t) = E_0\left[\frac{L_0 + L_{out} + L_L}{L(t) + L_{out} + L_L}\right]^2 \frac{L_L}{L_0 + L_b + L_{out} + L_L}.$$

Assuming a linear variation of the inductance of the generator, we find that the power $P = dE_L/dt$ is a maximum at the end of the cycle (for $t = T$), being equal to

$$P = \frac{2E_0(L_0 + L_{out} + L_L)^2 L_0 L_L}{(L_0 + L_b + L_{out} + L_L)(L_{out} + L_L)^3 T}.$$

We estimate the efficiency of a system with an EMG by the ratio of P to the limiting power which is delivered to an optimum load when it is directly connected to the condenser bank. In this case the power is

$$P_1 = L_L i \frac{di}{dt},$$

where

$$i = i_m \sin\omega_0 t,\quad i_m^2 = \frac{2E_0}{L_b + L_L},\quad \omega_0^2 = \frac{1}{(L_b + L_L)C}.$$

Expressing ω_0 as a function of the energy[1] and charging voltage, u_0, we have

$$\omega_0 = \frac{u_0}{\sqrt{2(L_b + L_L)E_0}},$$

and the peak power amplitude is

$$P_{1m} = \frac{u_0\sqrt{E_0}L_L}{\sqrt{2}(L_b + L_L)^{3/2}}.$$

Taking the optimum value $(L_L)_{opt.} = 2L_0$, we obtain the limiting power of the bank,

$$P_b = 0.272u_0\sqrt{\frac{E_0}{L_b}}$$

and the power efficiency of the EMG is

$$\frac{P}{P_b} = 7.36\frac{\sqrt{L_0E_0}}{u_0T}\frac{\left(1 + \frac{1}{l_{out} + l_L}\right)^2\sqrt{l_b}}{\left(1 + \frac{1 + l_b + l_{out}}{l_L}\right)(l_{out} + l_L)}. \qquad (2)$$

It is clear that P/P_b depends on two factors: One is determined by the basic parameters of the bank (u_0, E_0) and the generator (L_0, T) and the other by the parasitic parameters and the load inductance. For condenser banks with $E_0 = 10^4$–10^6 J and $u_0 = 5\cdot10^3$–$5\cdot10^4$ V and generators with $L_0 = 10^{-4}$–$5\cdot10^{-7}$ H and $T = 2\cdot10^{-5}$–10^{-4} sec, the first factor lies between 0.1 and 736. In order that the second factor be greater than unity it is necessary [as for Eq. (1)] that the conditions

$$l_b \ll 1,\ l_{out} \ll 1,\ l_L \leqslant 1$$

hold.

Thus, as an example, for $l_b = l_{out} = l_L = 0.2$ we obtain 1.7 and for $l_b = l_{out} = l_L = 0.1$ we obtain 4.4. For fixed l_b and l_{out}, as l_L increases this factor at first rises, but later falls. The optimum value of l_L for $l_b \ll 1$ and $l_{out} \ll 1$ is equal to $(l_L)_{opt} \simeq l_{out}/2$ and corresponds to a maximum of the factor equal to

$$\frac{4}{27}\frac{\sqrt{l_b}}{l_{out}^2}.$$

The limiting power, like the limiting energy, is obtained with $l_{out} \ll 1$ and $l_L \ll 1$. Both these conditions are troublesome as the first is difficult to ensure in practice and the second means that the dimensions of the generator must be significantly larger than those of the load coil.

In several cases it is possible to avoid these limitations by connecting the load through a pulse transformer. Then two approaches can be used: placing the transformer outside (Fig. 1b) and inside (Fig. 1c) the explosion chamber. With the first variant it is possible to relax the limitations on the value of the load inductance since L_{out} does not change. In the second case, the generator coil in which the magnetic flux is displaced serves as the first winding of a transformer; thus, the inductance of the connectors to the primary can be reduced to zero. The output of the chamber is through the secondary winding. The effect of L_b on the efficiency of the system is greatly reduced. In this variant high efficiencies, E_L/E_0 and P/P_b, can be obtained with reduced demands on L_{out} and L_L. However, the transformer will be destroyed in each experiment.

ARRANGEMENT WITH A TRANSFORMER OUTSIDE THE EXPLOSION CHAMBER

We now consider the first variant (Fig. 1b). Using the known solution[1] for this circuit it is easy to show that for flux trapping at the current maximum we have

$$i_L = \frac{k\sqrt{L_1L_2}}{L_2 + L_L}\frac{L_0 + L_{out} + L_1\left(1 - k^2\frac{L_2}{L_2 + L_L}\right)}{L(t) + L_{out} + L_1\left(1 - k^2\frac{L_2}{L_2 + L_L}\right)} \times\sqrt{\frac{2E_0}{L_0 + L_b + L_{out} + L_1\left(1 + 3k^2\frac{L_2}{L_2 + L_L}\right)}}, \qquad (3)$$

where $k \leq 1$ is the coupling coefficient of the transformer winding.

a) Condition for maximum energy. In Eq. (3) we set L(t) = 0, and write it as a product of three factors:

$$i_{\mathrm{L}} = k\sqrt{\frac{2E_0}{L_{\mathrm{L}}}}\,\frac{\sqrt{\frac{L_1}{L_{\mathrm{out}}}\frac{L_2}{L_{\mathrm{L}}}}}{\left(1+\frac{L_1}{L_{\mathrm{out}}}\right)\left(1+\frac{L_2}{L_{\mathrm{L}}}\right)-k^2\frac{L_1}{L_{\mathrm{out}}}\frac{L_2}{L_{\mathrm{L}}}}$$

$$\times\frac{1+\frac{L_0}{L_{\mathrm{out}}}+\frac{L_1}{L_{\mathrm{out}}}\left(1-k^2\frac{\frac{L_2}{L_{\mathrm{L}}}}{1+\frac{L_2}{L_{\mathrm{L}}}}\right)}{\sqrt{1+\frac{L_0}{L_{\mathrm{out}}}+\frac{L_{\mathrm{b}}}{L_{\mathrm{out}}}+\frac{L_1}{L_{\mathrm{out}}}\left(1+3k^2\frac{\frac{L_2}{L_{\mathrm{L}}}}{1+\frac{L_2}{L_{\mathrm{L}}}}\right)}}.$$

The first of these factors is independent of L_1 and L_2; the third depends on them weakly. Actually, for efficient operation it is necessary that $L_0/L_{\mathrm{out}} \geq 10$; thus, for variation of L_1/L_{out} and L_2/L_{L} in the range 1 to 3 (which corresponds to the maximum energy in the load, as will be shown below) the third factor changes insignificantly. Therefore, we treat the L_1 and L_2 dependence of the second factor only:

$$f(L_1, L_2) = \frac{\sqrt{\frac{L_1}{L_{\mathrm{out}}}\frac{L_2}{L_{\mathrm{L}}}}}{\left(1+\frac{L_1}{L_{\mathrm{out}}}\right)\left(1+\frac{L_2}{L_{\mathrm{L}}}\right)-k^2\frac{L_1}{L_{\mathrm{out}}}\frac{L_2}{L_{\mathrm{L}}}},$$

For arbitrary fixed L_2 = const the optimum values are

$$\left(\frac{L_1}{L_{\mathrm{out}}}\right)_{\mathrm{opt}} = \frac{1}{1-k^2\frac{\frac{L_2}{L_{\mathrm{L}}}}{1+\frac{L_2}{L_{\mathrm{L}}}}}, \tag{4}$$

and the corresponding maximum is equal to

$$f_1 = \frac{1}{2\left(1+\frac{L_2}{L_{\mathrm{L}}}\right)}\sqrt{\frac{L_2/L_{\mathrm{L}}}{1-k^2\frac{L_2/L_{\mathrm{L}}}{1+L_2/L_{\mathrm{L}}}}}. \tag{5}$$

For arbitrary L_1 = const the optimum for L_2 is given by

$$\left(\frac{L_2}{L_{\mathrm{L}}}\right)_{\mathrm{opt}} = \frac{1}{1-k^2\frac{L_1/L_{\mathrm{out}}}{1+L_1/L_{\mathrm{b}}}} \tag{6}$$

and the corresponding maximum is

$$f_2 = \frac{1}{2\left(1+\frac{L_1}{L_{\mathrm{out}}}\right)}\sqrt{\frac{L_1/L_{\mathrm{out}}}{1-k^2\frac{L_1/L_{\mathrm{out}}}{1+L_1/L_{\mathrm{out}}}}}. \tag{7}$$

Equations (4) and (5) are the same functions of L_2/L_{L} as (5) and (6) are of L_1/L_{out}. These functions are shown in Fig. 3. It is clear that this function has a mildly sloping maximum: When the winding inductance changes from 0.5 to 5 times its optimum, i_{L} is reduced from its maximum by less than 25%. The global maximum, f_{max}, corresponding to simultaneous optimization for both windings, is reached when

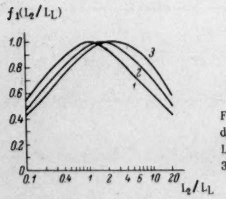

Fig. 3. The function $f_1(L_2/L_L)$, which defines the load current for optimum L_1 and arbitrary L_2. k: 1) 0.4; 2) 0.8; 3) 0.9.

$$\frac{L_1}{L_{\mathrm{out}}} = \frac{L_2}{L_{\mathrm{L}}} = \frac{1}{\sqrt{1-k^2}}.$$

being

$$f_{\mathrm{max}} = \frac{1}{2}\,\frac{1}{1+\sqrt{1-k^2}}.$$

For k = 0.95, $L_1/L_{\mathrm{out}} = L_2/L_{\mathrm{L}} = 3.16$, while for k = 0.4, $L_1/L_{\mathrm{out}} = L_2/L_{\mathrm{L}} = 1.1$. Thus, it is almost always true that $1 < L_1/L_{\mathrm{out}} < 3$. In view of the last two expressions we find

$$\left(\frac{E_{\mathrm{L}}}{E_0}\right)_{\mathrm{max}} = \frac{1}{4}\left(\frac{k}{1+\sqrt{1-k^2}}\right)^2\frac{\left(2+\frac{1}{l_{\mathrm{out}}}\right)^2}{\frac{1}{l_{\mathrm{out}}}+\frac{l_{\mathrm{b}}}{l_{\mathrm{out}}}+\frac{4}{\sqrt{1-k^2}}-2}. \tag{8}$$

From this it is clear that use of a transformer actually removes the limitation on l_{L}. The efficiency of the system does not depend on the load if both transformers are optimized. In this case, however, the efficiency depends strongly on the coupling coefficient. A high efficiency of energy transfer to the load is possible only for very small values of l_{out} (for k = 0.9 and $l_{\mathrm{b}} = 0$, $E_{\mathrm{L}}/E_0 \geq 1$ if $l_{\mathrm{out}} \leq 8\%$). The dependence of $(E_{\mathrm{L}}/E_0)_{\mathrm{max}}$ on l_{out} for k = 0.9 and $l_{\mathrm{b}} = 0$ is shown in Fig. 2 (curve 2). A comparison of this variant with the transformerless circuit can be carried out as follows. We equate the right-hand sides of Eqs. (1) and (8) and determine l_{L} from this equation. For $(E_{\mathrm{L}}/E_0)_{\mathrm{max}} > 1$, two values of l_{L} (see Table 1) correspond to each value of l_{out}. If l_{L} lies between these two values, then for the corresponding value of l_{out} the transformerless circuit has the greater efficiency. For l_{L} outside this region the opposite holds. Thus, the table indicates the region of l_{out} and l_{L} over which the use of a circuit with a transformer in the first variant is reasonable.

The ratio of the number of turns (W_1, W_2) in the windings of an optimized transformer is found from the ratio $L_2/L_1 = L_{\mathrm{L}}/L_{\mathrm{out}}$. For $k \simeq 1$, we have

$$\frac{W_2}{W_1} \simeq \sqrt{\frac{L_2}{L_1}} = \frac{L_{\mathrm{L}}}{L_{\mathrm{out}}}$$

b) Condition for maximum power. Using a linear dependence of generator inductance on time we find from Eq. (3) that the power $P = L_{\mathrm{L}} i_{\mathrm{L}} di_{\mathrm{L}}/dt$ is maximum for t = T and L(t) = 0. Dividing this quantity by P_{b}, we have

$$\frac{P}{P_{\mathrm{b}}} = 7.36\,\frac{\sqrt{L_0 E_0}}{u_0 T}k^2\sqrt{\frac{L_{\mathrm{b}}}{L_0}}\,\frac{L_0}{L_{\mathrm{out}}}\,\frac{\frac{L_1}{L_{\mathrm{out}}}\frac{L_2}{L_{\mathrm{L}}}\left(1+\frac{L_2}{L_{\mathrm{L}}}\right)}{\left[\left(1+\frac{L_1}{L_{\mathrm{out}}}\right)\left(1+\frac{L_2}{L_{\mathrm{L}}}\right)-k^2\frac{L_1}{L_{\mathrm{out}}}\frac{L_2}{L_{\mathrm{L}}}\right]^3}$$

$$\times\frac{\left[1+\frac{L_0}{L_{\mathrm{out}}}+\frac{L_1}{L_{\mathrm{out}}}\left(1-k^2\frac{L_2/L_{\mathrm{L}}}{1+L_2/L_{\mathrm{L}}}\right)\right]^2}{1+\frac{L_0}{L_{\mathrm{out}}}+\frac{L_{\mathrm{b}}}{L_{\mathrm{out}}}+\frac{L_1}{L_{\mathrm{out}}}\left(1+3k^2\frac{L_2/L_{\mathrm{L}}}{1+L_2/L_{\mathrm{L}}}\right)}.$$

TABLE 1. Values of l_L for Equal Efficiencies, E_L/E_0, of Transformer and Transformerless EMG Circuits (for k = 0.9 and l_b = 0 in both circuits).

	l_{out}							
	0.01	0.02	0.03	0.04	0.05	0.06	0.07	0.08
l_L 1	0.096	0.220	0.405	0.680	1.11	1.97	4.20	15.1
l_L 2	0.0012	0.0023	0.0033	0.0043	0.0050	0.0059	0.0069	0.0075
E_{out}/E_0	9.70	4.75	3.06	2.26	1.78	1.45	1.23	1.06

Only the second term depends significantly on the parameters L_1 and L_2. Optimizing this term simultaneously for both transformer windings we find

$$\left(\frac{L_1}{L_{out}}\right)_{opt}=\frac{1}{2\sqrt{1-k^2}},\quad \left(\frac{L_2}{L_L}\right)_{opt}=\frac{1}{\sqrt{1-k^2}},$$

for which

$$k^2\sqrt{\frac{L_b}{L_0}\frac{L_0}{L_{out}}}\frac{\frac{L_1}{L_{out}}\frac{L_2}{L_L}\left(1+\frac{L_2}{L_L}\right)}{\left[\left(1+\frac{L_1}{L_{out}}\right)\left(1+\frac{L_2}{L_L}\right)-k^2\frac{L_1}{L_{out}}\frac{L_2}{L_L}\right]^3}=\frac{4}{27}\frac{\sqrt{l_b}}{l_{out}}\left(\frac{k}{1+\sqrt{1-k^2}}\right)^2.$$

We note that the optimum values of the inductance of the secondary winding obtained from the conditions for maximum energy and maximum power agree and that for the primary winding they differ only by a factor of 2. It then follows that by choosing some average value for L_1/L_{out} it is possible to ensure both conditions in practice, since the maxima of the power and energy curves are weakly defined.

ARRANGEMENT WITH A TRANSFORMER INSIDE THE EXPLOSION CHAMBER

We define the load current using Eq. (3), setting L(t) = 0 and L_{out} = 0, and replacing $(L_L + L_{out})$ by L_L to obtain

$$i_L=k\sqrt{\frac{2E_0}{L_L}}\frac{\sqrt{\frac{L_{out}}{L_1}\frac{L_2}{L_L}}}{1+(1-k^2)\frac{L_2}{L_L}+\frac{L_{out}}{L_L}}\frac{\frac{L_0}{L_{out}}+\frac{L_1}{L_{out}}\left(1-k^2\frac{L_2/L_L}{1+L_2/L_L+L_{out}/L_L}\right)}{\sqrt{\frac{L_0}{L_{out}}+\frac{L_b}{L_{out}}\frac{L_1}{L_{out}}\left(1+3k^2\frac{L_2/L_L}{1+L_2/L_L+L_{out}/L_L}\right)}}.$$

As before, we only take account of the dependence of the second factor on L_1/L_{out} and L_2/L_L; we note that i_L increases without bound as L_1/L_{out} decreases. Thus, in using a pulse transformer in a self-destructive assembly it is necessary to obtain the lowest possible values of L_1 provided this does not lead to a reduction in the coupling coefficient. The maximum efficiency of energy transfer obtains when

$$\left(\frac{L_2}{L_L}\right)_{opt}=\frac{1+\frac{L_{out}}{L_L}}{1-k^2} \tag{9}$$

and is equal to

$$\left(\frac{E_L}{E_0}\right)_{max}=\frac{1}{4}\frac{k^2}{1-k^2}\frac{\left[\frac{L_0}{L_{out}}+\frac{L_1}{L_{out}}\left(1-\frac{k^2}{2-k^2}\right)\right]^2}{\frac{L_1}{L_{out}}\left(1+\frac{L_{out}/L_0}{L_L/L_0}\right)\left[\frac{L_0}{L_{out}}+\frac{L_b}{L_{out}}+\frac{L_1}{L_{out}}\left(1+\frac{3k^2}{2-k^2}\right)\right]}.$$

The first variant depends on k, L_{out}/L_0, L_b/L_0 and on L_1/L_{out} and L_L/L_0. We take k = 0.9, L_b/L_0 = 0, L_1/L_{out} = 1, and L_L/L_0 = 1. Then

$$\left(\frac{E_L}{E_0}\right)_{max}=1.06\frac{\left(\frac{L_0}{L}+0.32\right)^2}{\left(1+\frac{L_{out}}{L_0}\right)\left(\frac{L_0}{L_{out}}+3.04\right)}.$$

This relation is shown in Fig. 2 (curve 3). It is clear that this circuit has an energy-transfer efficiency which exceeds that of the variant with a transformer outside the chamber by an order of magnitude and that of the transformerless variant by two to five times.

The power efficiency of this system,

$$\frac{P}{P_b}=7.36\frac{\sqrt{L_0E_0}}{u_0T}k^2\sqrt{\frac{L_b}{L_0}\frac{L_0}{L_{out}}}\frac{\frac{L_2}{L_L}\left(1+\frac{L_{out}}{L_L}+\frac{L_2}{L_L}\right)}{\left(\frac{L_1}{L_{out}}\right)^2\left[1+\frac{L_{out}}{L_L}+(1-k^2)\frac{L_2}{L_L}\right]^3}$$

$$\times\frac{\left[\frac{L_0}{L_{out}}+\frac{L_1}{L_{out}}\left(1-k^2\frac{L_2/L_L}{1+L_{out}/L_L+L_2/L_L}\right)\right]^2}{\frac{L_0}{L_{out}}+\frac{L_b}{L_{out}}+\frac{L_1}{L_{out}}\left(1+3k^2\frac{L_2/L_L}{1+L_{out}/L_L+L_2/L_L}\right)}$$

increases without bound as L_1/L_{out} decreases (as does the energy efficiency). The optimum value for L_2/L_L,

$$\left(\frac{L_2}{L_L}\right)_{opt}=\frac{1+\frac{L_{out}}{L_L}}{1-k^2}k^2\left(1+\sqrt{1+\frac{1-k^2}{k^4}}\right)$$

differs somewhat from the corresponding condition, Eq. (9), for the maximum energy. For k = 0.7-0.9 this difference is not more than 1.75 times bigger. Thus even in this case, it is possible to choose a regime which is simultaneously near the optimum for both power and energy.

CONCLUSIONS

1. The energy transferred to an inductive load from an explosion-driven magnetic generator without a transformer can exceed the energy of the condenser bank by several times only when the inductance of the bank, the chamber output connection, and the load are considerably less than that of the generator. Thus for transfer of three times the energy to the load it is necessary that these inductances not exceed 10% of the generator inductance.

2. An arrangement with a transformer outside the explosion chamber will transfer more energy (compared to a transformerless circuit) to a load only when the out-

put inductance does not exceed 8% of the generator inductance and the load inductance lies outside a given range (see Table 1). The coupling coefficient of the windings must be near unity and the inductances of the windings must not differ from the optimum by more than two times.

3. An arrangement with a transformer inside the explosion chamber has an energy transfer efficiency which exceeds that of the arrangement with a transformer outside the chamber by an order of magnitude and exceeds that of an optimum transformerless circuit by two to five times. In this case the transformer primary must have as low an inductance as possible and there is an optimum inductance for the secondary.

4. The power efficiency of an EMG is defined in terms of the basic parameters of the bank (E_0, u_0) and generator (L_0, T) and also by the parasitic circuit parameters.

5. The conditions for optimization of the circuit with respect to power and energy differ for the three cases by more than a factor of 2. The power efficiency depends significantly more on L_b than does the energy efficiency.

The author is grateful to A. E. Voitenko and E. P. Matochkin for useful comments.

---

[1] H. Knoepfel, Pulse High Magnetic Fields, Amsterdam – London (1970).

[2] L. A. Artsimovich, Controlled Thermonuclear Reactions [in Russian], Moscow, Fizmatgiz (1961).

Impurities and crystal dimensions in zone refining

V. G. Glebovskii and B. M. Shipilevskii

(Submitted September 18, 1973; resubmitted January 21, 1974)
Zh. Tekh. Fiz., 44, 1981-1989 (September 1974)

Equations describing the radius of a growing crystal and the impurity concentration in the liquid zone are derived and solved for the first pass in zone refining. The results are used to determine the characteristic distributions of relatively volatile and nonvolatile impurities in the crystal. The limiting radius is found for crystals of several elements over a broad range of crystallization rates. Experimental data which support the calculated results are reported.

Vacuum refining is one of the most promising methods for growing especially pure metal single crystals. A fundamental feature of this method is that the recrystallization is accompanied by rapid evaporation of impurities and the host material from the surface of the liquid zone as well as by a redistribution of the components at the crystal–liquid interface. This evaporation introduces a serious difficulty in the calculations, but if we assume the vapor pressure of the host to be negligible we can solve the problem rigorously for an arbitrary number of zone passes.[1] This simplification is justified at high crystallization rates; at low and intermediate rates ($1\text{-}10^{-1}$ mm · min^{-1}) there is an appreciable depletion of the amount of molten host component so that the radius of the growing crystal is smaller than that of the original sample. In this work we evaluate the influence of these factors on the impurity distribution after a single pass. This problem has been treated in ref. 2, but there the linear approximation is used for the functional dependence of the radius of the growing crystal on the distance, and this approximation is too crude. Also, the steady-state impurity concentration is calculated on the basis of the unjustified assertion that the dimensions of the growing crystal and the concentrations of each impurity in the melt reach steady-state values simultaneously. The changes in the impurity concentration in the zone due to changes in both the amount of impurity and the amount of host material are neglected altogether.[2]

To obtain kinetic equations for the mass balance of the crystal–liquid system in vacuum we start from an obvious equation for the total differential of the concentration of impurity i in the zone:

$$dC_i = \sum_k \frac{\partial C_i}{\partial N_k} dN_k, \tag{1}$$

where C_i is the concentration of impurity i in the liquid zone (atomic fraction), and N_k is the number of gram-atoms (or moles) of each component in the liquid zone.

Then, assuming, $\sum\limits_{k\neq 0} N_k \ll N_0$, we can write1)

$$\frac{\partial C_i}{\partial N_i} = \frac{1}{N_0}; \quad \left(\frac{\partial C_i}{\partial N_k}\right)_{k\neq i,\,0} \simeq 0; \quad \frac{\partial C_i}{\partial N_0} = -\frac{C_i}{N_0}$$

or, after substituting the derivatives into (1),

$$dC_i = \frac{dN_i - C_i dN_0}{N_0}. \tag{2}$$

We assume that the following are valid under the condition prevailing in vacuum refining: 1) The solutions of the impurities in the host component obey Henry's law (γ_i = const); 2) evaporation occurs only from the lateral surface of the liquid zone; 3) convective diffusion of impurity atoms from the interior of the zone to its surface does not limit evaporation; 4) the evaporation regime is approximately molecular, and the evaporation rate is given by the Knudsen–Langmuir equation: $dN_0/dt = -\alpha_0 S/\tau_0$ (moles/sec) for the host component and $dN_i/dT = (-\alpha_i S/\tau_i) \cdot \gamma_i C_i$ (moles/sec) for an impurity. Here, $\tau = (17.16/P^0) \cdot \sqrt{\mu T/\nu}$ [moles/(cm^2 · sec)] is the molar evaporation time for the substance in its pure state, tabulated in ref. 1 for the metallic elements; t is the evaporation time (seconds); α is the accommodation coefficient; S is the evaporation surface area (square centimeters); P^0 is the saturation vapor pressure of the substance in its pure state at the Kelvin temperature (torr); μ is the atomic weight of the evaporating substance in the condensed phase; ν is the number of atoms in the vapor molecule; and γ is the activity coefficient of the impurity; 5) the liquid–crystal interface is planar.

We write the linear dimensions of the zone, l, and the average temperature at its surface ($\tilde{T}$°K), to which the molar evaporation time of the substance, τ, is referred, in the form $l = l_0 + \varkappa(\nu - r_0)$ and $\tilde{T} = \tilde{T}_0 + p(r - r_0)$, where $\varkappa$ and p are certain numerical factors, l_0 and T_0 are the original length and average surface temperature of the zone, and r_0 and r are the initial and instantaneous radii of the zone at the crystallization front. We assume the crystallization $\varkappa(r - r_0) \ll l_0$ and $p(r - r_0) \ll \tilde{T}_0$, i.e., we assume that changes in the linear dimension and average surface temperature of the zone are negligible.

Under these assumptions we can describe the change in the impurity content in the zone in time $dt = dx/f$ by

$$dN_i = \sum_{k=1}^{3} dN_i^{(k)}, \tag{3}$$

where

$$dN_i^{(1)} = -\frac{\alpha_i \gamma_i C_i S}{\tau_i f} dx, \quad dN_i^{(2)} = -\frac{\pi r^2 \rho_0 k_i C_i}{\mu_0} dx, \quad dN_i^{(3)} = \frac{\pi r_0^2 \rho_0 C_i^0}{\mu_0} dx$$

are the amount of evaporating impurity, the amount of impurity which has left the zone containing the solidified part of the crystal, and the amount of impurity supplied from the other end of the zone, respectively.

Here we have adopted the following notation: ρ_0 is the density of the host component (grams per cubic centimeter) (we assume the densities in the liquid and solid phases to be equal), f is the zone velocity (centimeters per second), k_i is the effective coefficient for the Burton–Prim–Slichter distribution of the impurity, and C_i^0 is the impurity concentration in the initial sample.

Similarly, for the host component:

$$dN_0 = \sum_{k=1}^{3} dN_0^{(k)}, \tag{4}$$

where

$$dN_0^{(1)} = -\frac{\alpha_0 S}{\tau_0 f}\,dx,\quad dN_0^{(2)} = -\frac{\pi r^2 \rho_0}{\mu_0}\,dx,\quad dN_0^{(3)} = \frac{\pi r_0^2 \rho_0}{\mu_0}\,dx.$$

For our purposes it is convenient to write the area of the lateral surface and the volume of the liquid zone as

$$S = 2\pi r l \theta,\quad \Omega = \pi r^2 l \omega. \tag{5}$$

The functions θ and ω in Eqs. (5) take account of the deviations of S and Ω for the zone from the area of the lateral surface and the volume of a regular cylinder of length l and radius r.

Substituting Eqs. (3) and (4) into (2), and using

$$N_0 = \frac{\Omega \rho_0}{\mu_0} = \frac{\pi r^2 l \rho_0}{\mu_0}\,\omega,$$

we find the desired differential equation for C_i:

$$\omega \frac{dC_i}{d\xi} = \left[1 + \frac{(g_0 - g_i)\,\theta}{\eta} - \left(k_i + \frac{1}{\eta^2}\right)\right] C_i + \frac{C_i^0}{\eta^2}, \tag{6}$$

where g_0 is the reduced evaporation coefficient of the host component, equal to $2\mu_0\alpha_0 l/f\tau_0\rho_0 r_0$; g_i is the reduced evaporation coefficient of the impurity, equal to $(2\mu_0\alpha_i l/f\tau_i\rho_0 r_0)\cdot\gamma_i$; ξ is the dimensionless instantaneous coordinate of the crystal in units of the zone length, equal to x/l; and η is the dimensionless zone radius at the crystallization front in units of the original radius, equal to r/r_0.

A relationship among the functions η, ω, and θ is established by differential equation (4); using the substitution $dn_0 = (\pi l \rho_0/\mu_0)d[r^2\omega]$, we write this relationship explicitly as

$$\frac{d\,[\eta\omega]}{d\xi} + \omega \frac{d\eta}{d\xi} = \frac{1}{\eta} - \eta - g_0\theta. \tag{7}$$

Below we distinguish between quasisteady-state recrystallization, in which the impurity concentration and crystal dimensions become essentially constant as the zone moves, and nonsteady-state recrystallization, in which these quantities change more or less rapidly as they approach their constant values.

Quasisteady-state refining. In this case, in which the derivatives $(C_i)'_\xi$, $(C_i)''_\xi$, $(\eta)'_\xi$, $(\omega)'_\xi$, and $(\theta)'_\xi$ tend to zero, and the zone parameters (ω, θ), the radius of the growing crystal, and the impurity concentration in the melt tend toward the limiting values ω_*, θ_*, η_*, and C_i^*, we can reduce system of differential equations (6), (7) to the algebraic system

$$\left\{\omega \frac{dC_i}{d\xi}\right\}^* = \left[1 + \frac{(g_0 - g_i)\,\theta_*}{\eta_*} - \left(k_i + \frac{1}{\eta_*^2}\right)\right] C_i^* + \frac{C_i^0}{\eta_*^2} = 0, \tag{8}$$

$$\left\{\frac{d\,[\eta\omega]}{d\xi} + \omega \frac{d\eta}{d\xi}\right\}^* = \frac{1}{\eta_*} - \eta_* \cdot \quad \xi_0\theta_* = 0, \tag{9}$$

from which we find

$$C_i^* = \frac{C_i^0}{1 + (k_i - 1)\,\eta_*^2 + (g_i - g_0)\,\theta_*\eta_*}, \tag{10}$$

$$g_0\theta_* = \frac{1 - \eta_*^2}{\eta_*}. \tag{11}$$

Strictly, speaking, the limits ω_*, θ_*, η_*, and C_i^* are reached only at infinity ($\xi \to \infty$). In practice, it is useful to assume that the quasisteady-state changes in the zone dimensions begin at the characteristic distance ξ_s, and that the quasisteady-state change in the value of C_i in the melt begins at the characteristic distance ξ_i^*; at these characteristic distances, we have the inequalities

$$|\eta - \eta_*| \leqslant 0.01,\quad \xi \geqslant \xi_s, \tag{12}$$

$$\left|\frac{C_i - C_i^*}{C_i^*}\right| \leqslant 0.1,\quad \xi \geqslant \xi_i^*. \tag{13}$$

Equation (10) holds if both inequalities (12) and (13) are satisfied. For convenience we write

$$\beta_i^* = \frac{C_i^* k_i}{C_i^0} = \frac{C_i^*\ (SO)}{C_i^0}.$$

After some manipulation, we find from (10) and (11)

$$\beta_i^* = [1 + g_0\theta_*\eta_*(\lambda_i - 1)]^{-1} \quad \text{or} \quad \beta_i^* = [\eta_*^2 + \lambda_i(1 - \eta_*^2)]^{-1}, \tag{14}$$

where $\lambda_i = g_i/g_0 k = \tau_0\gamma_i\alpha_i/\tau_i k_i \alpha_0$ is the directionality criterion for the process, which incorporates the basic parameters of the vacuum zone recrystallization. If $\lambda_i > 1$, then $\beta_i^* < 1$, and the evaporation facilitates the removal of impurity; if $\lambda_i = 1$, then $\beta_i^* = 1$, and the evaporation does not affect the limiting impurity distribution; finally, if $\lambda_i < 1$, then $\beta_i^* > 1$, and the evaporation favors the accumulation of impurity. Accordingly, whether the crystal is depleted of or enriched in the impurity can be largely determined from the magnitude of the zone effect, and not only on the basis of the ratio of vapor pressures of the host and impurity, as was assumed in refs. 2 and 3. In fact, even in the case $g_0 > g_i$ with $k_i \ll 1$, according to Eq. (14), a significant removal of impurity can be achieved, and vice versa. In the case $\lambda_i \ll 1$, in which the impurity is relatively nonvolatile, Eq. (14) takes the extremely simple form

$$\beta_i^* = (\eta_*)^{-2},\quad \lambda_i \ll 1. \tag{15}$$

It follows from (15) that the limiting concentration of any relatively nonvolatile, impurity is governed solely by the conditions prevailing in the refining of the host.

Let us compare the changes in the limiting radius η_* for certain crystals as the crystallization rate is varied over a range of two orders of magnitude. For this purpose we rewrite (11) as

$$\eta_* = \sqrt{1 + s^2} - s, \tag{11'}$$

where

$$s = \frac{\alpha_0 \mu_0 l \theta_*}{f \tau_0 r_0 \rho_0}.$$

Figure 1 shows plots of the function $\eta_* = \eta_*(f)$ calculated from Eq. (11') for several metals and silicon. The

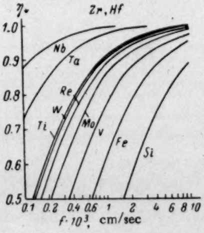

Fig. 1. Limiting crystal radius as a function of the crystallization rate for various elements. Here the zone parameters are $\widetilde{\Delta}T$ = 100°C, θ_* = 1, l/r = 2.

calculations apply for the most common zone parameters: $l/v_0 = 2$ and $\widetilde{\Delta T} = \widetilde{T} - T_{me} = 100°C$. The values of $\tau_0(\widetilde{T})$ are taken from the tables of $\log \tau = \varphi(1/T)$ in ref. 1. We also use the approximation $\rho_0(\widetilde{T}) \simeq 0.9\, \rho_0$ (273°K) and assume $\theta_* = 1$ (the calculations are continued until the values $\eta_* = 0.5$ are reached, since the zone becomes unstable[2] at $\eta_* \leqslant 0.5$). We see that the refining at rates $f < 10^{-2}$ cm/sec for many metals (Fe, V, Mo, Re, Ti, W) is accompanied by an appreciable change in the crystal radius in comparison with its initial value; the change is particularly marked at rates in the range $f \leqslant 10^{-3}$ cm/sec. In practice, the rates most frequently used are $f < 10^{-2}$ cm/sec, so that the limiting impurity concentration for these elements should be determined on the basis of (10). At higher rates, i.e., at $f > 10^{-2}$ cm/sec, the change from the initial radius is small, and the calculation method proposed in ref. 1 is completely justified. We note that at any concrete values of the zone parameters l/r_0, $\widetilde{\Delta T}$, and θ_* the limiting radius η_* can be easily determined by means of Fig. 1, through a direct replacement of f by the reduced rate $f_{li} = f\Delta_{li}$, where

$$\Delta_{li} = \frac{2r_0\tau_0(\widetilde{\Delta T})}{l\tau_0(100°\,C)\theta_*}. \qquad (16)$$

The changes in the crystal radius in vacuum refining have been studied for molybdenum and vanadium in a vacuum of 10^{-6} torr. The initial samples, 10 mm in diameter, are refined at a rate of about 10 mm/min to eliminate metal spray; then a single pass of the zone is carried out for each sample at rates of 0.2, 0.4, 0.6, 1.2, and 3.0 mm/min. The average heating of the zone surface, $\widetilde{\Delta T}_{Mo} = 110 \pm 20°C$ for molybdenum and $\widetilde{\Delta T}_V = 50 \pm 10°C$ for vanadium, is determined with an optical pyrometer and a special optical system. The zone length and the radius ratio r_*/r_0 in the steady-state region are determined by measuring the parameters of the liquid zone from a photograph. It is found that the zone length is essentially independent of the rate, amounting to $l_{Mo} = 1.7r_0$ for molybdenum and $l_V = 1.8r_0$ for vanadium. Figure 2 shows a photograph of the liquid zone of vanadium in the final stage of the formation of the quasisteady-state radius for a crystallization rate of 0.4 mm/min. Table 1 shows the measured limiting radius $\eta_* = r_*/r_0$ for the various crystallization rates studied.

Using the results, we check (11) for the refining of vanadium and molybdenum. According to this equation, the functional dependence $\eta_* = \eta_*(f)$ should become linear when plotted as $\eta_*/(1-\eta_*^2)$ vs f, since the parameters θ_* and τ_0 are weak functions of the crystallization rate. We see from Fig. 3 that the experimental points agree with the straight lines calculated from (10) with the zone parameters $l/r_0 = 1.7$, $\widetilde{\Delta T}_{Mo} = 120°C$ for molybdenum and $l/v_0 = 1.8$, $\widetilde{\Delta T} = 40°C$ for vanadium; the values of $\widetilde{\Delta T}$ agree with the experimental values within the corresponding errors. Accordingly, Eq. (11) holds satisfactorily over a broad range of crystallization rates.

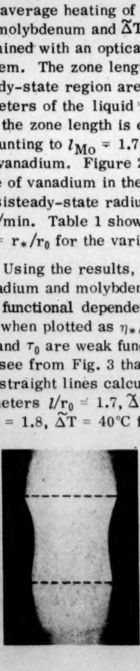

Fig. 2. Photograph of the liquid zone of vanadium when the quasisteady-state radius is established at a crystallization rate of 0.4 mm/min. The upper line is the melting front, and the lower dashed line is the crystallization front.

TABLE 1

	f, mm/min				
	3	12	0.6	0.4	0.2
η_*^{Mo}	0.97	0.93	0.87	0.82	0.66
η_*^{V}	0.98	0.95	0.9	0.86	0.73

The applicability of Eq. (14) can be demonstrated on the basis of data[4] on the zirconium distribution after a single-pass refining of molybdenum. The zone refining and growth of the molybdenum, 10 mm in diameter, are carried out at rates of 0.3 and 1.0 mm/min, with the sample rotating at 60 rpm, in a vacuum 10^{-5} torr. According to precision analysis of samples from the steady-state part of the crystal, the values of β^*_{Zr} are 0.61 and 0.44 for rates of 1.0 and 0.3 mm/min, respectively. The coefficients of the zirconium distribution in molybdenum, K_{Zr}, calculated by the method of ref. 1 for these rates are 0.31 and 0.52 at rates of 1.0 and 0.3 mm/min, respectively, i.e., the ratio of these coefficients is $k^{(0.3)}_{Zr}/k^{(1)}_{Zr} \simeq 1.7$. On the other hand, it is known[5] that as the crystallization rate is reduced the processes occurring at the crystal–liquid interface approach equilibrium, so that k_{Zr} should decrease. On the basis of the high temperatures and intense mixing in the zone, we assume that $k^{(0.3)}_{Zr}/k^{(1)}_{Zr} \simeq 1$ is near equilibrium even at a rate of 1 mm/min, so that we expect $k^{(0.3)}_{Zr} \cdot (k^{(1)}_{Zr})^{-1} \simeq 1$. Calculations based on Eq. (14) taking account of the evaporation of the molybdenum host lead to a ratio $k^{(0.3)}_{Zr}/k^{(1)}_{Zr}$ close to the expected value: According to the experimental conditions, we have $\Delta_{li} \simeq 2$, so that for molybdenum (Fig. 4)

$$\eta_*^{(0.3)} = 0.87, \quad \eta_*^{(1)} = 0.95.$$

It has been pointed out previously[4] that the weight loss of molybdenum after a single pass at 1.0 mm/min is about 10%. This value agrees with the value found above. If we rewrite Eq. (14) as

$$\lambda_{Zr} = \frac{\frac{1}{\beta^*_{Zr}} - \eta_*^2}{1 - \eta_*^2}$$

and substitute the corresponding values of β^*_{Zr} and η_* into the result, we find $\lambda^{(0.3)}_{Zr} \simeq 6.4$ and $\lambda^{(1)}_{Zr} \simeq 7.4$, so that the

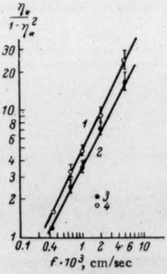

Fig. 3. Limiting radius of molybdenum and vanadium crystals as a function of the crystallization rate. Lines) calculated; points) experimental. $\widetilde{\Delta T}$, °C: 1) 40, 2) 120; 3) Mo, 4) V.

ratio of distribution coefficients is

$$\frac{k_{\mathrm{Zr}}^{(0.3)}}{k_{\mathrm{Zr}}^{(1)}} = \frac{\lambda_{\mathrm{Zr}}^{(1)}}{\lambda_{\mathrm{Zr}}^{(0.3)}} \simeq 1.15.$$

Transient regime. To evaluate the periods of the transient behavior, ξ_s and ξ_i^*, we note that in the region $\xi \geq \xi_s$ differential equation (6) becomes

$$\omega_* \frac{dC_i}{d\xi} = \left[1 + \frac{(g_0 - g_i)\theta_*}{\eta_*} - \left(k_i + \frac{1}{\eta_*^2}\right)\right] C_i + \frac{C_i^0}{\eta_*^2}. \tag{17}$$

Integrating (17), using the initial condition $C_i|_{\xi=\xi_s} = C_i^s$, we find

$$C_i - C_i^* = (C_i^s - C_i^*) \exp\left\{-\frac{k_i(\xi - \xi_s)}{\beta_i^* \eta_*^2 \omega_*}\right\},$$

from which we then find, using (13),

$$\xi_i^* - \xi_s = \frac{2.3\beta_i^* \eta_*^2 \omega_*}{k_i}\left\{1 + \lg\left|\frac{\Delta C_i^s}{C_i^*}\right|\right\}, \tag{18}$$

where $\Delta C_i^s = C_i^s - C_i^*$.

Then using the obvious inequality

$$\left|\frac{\Delta C_i^s}{C_i^*}\right| \leqslant \left|\frac{k_i - \beta_i^*}{\beta_i^*}\right|$$

we find the rough estimate

$$\frac{\xi_i^* - \xi_s}{\omega_*} \leqslant 2.3(k_i + g_i)^{-1}. \tag{19}$$

To evaluate ξ_s, we set $\omega \equiv \omega_*$ and $\theta \equiv \theta_*$ in Eq. (7) as a first approximation. Then introducing the variable $\zeta = \eta - \eta_*$ and integrating (7) with the initial condition $\zeta_0 = \zeta|_{\xi=0} = 1 - \eta_*$, we find

$$\xi = \frac{2\omega_*}{1 + \eta_*^2}\left\{\ln\left(\frac{\zeta_0 + \varepsilon}{\zeta + \varepsilon}\right) + \eta_*^2 \ln\frac{\zeta_0}{\zeta}\right\}, \tag{20}$$

where $\varepsilon = (1 + \eta_*^2)/\eta_*$.

Using (12), we easily find from (20) an equation for ξ_s:

$$\xi_s \simeq \frac{2\omega_*}{1 + \eta_*^2}\left\{\ln\left(\frac{1 + \eta_*}{1 + \eta_*^2}\right) + \eta_*^2\left(\frac{1 - \eta_*}{0.01}\right)\right\}. \tag{21}$$

Figure 4 shows a plot of the function $\xi_s/\omega_* = f(\eta_*)$. Usually, we would have $\omega_* \lessdot 1$, so that, as we see from Fig. 4, we would have $\xi_s \lessdot 2.5$, in agreement with the experimental data available.

Accordingly, when $k_i + g_i \gtrdot 1$ we have $\xi_i^* \lessdot 5$, i.e., the impurity concentration along the crystal is essentially steady-state, given by (14), since the total length of the crystal is usually equal to some 30-100 zone lengths. Under the condition $k_i + g_i < 1$ the region in which the concentration is not in a steady state can span a large part of the crystal. In this case Eq. (6) can be integrated. As before, we assume $\omega \equiv \omega_*$ and $\theta \equiv \theta_*$ in a first approximation. Then eliminating ξ from (6) by means of (7), we find

$$\frac{dC_i}{d\eta} + z(\eta)\{(1 - k_i)\eta^2 + g_0\theta_*\eta(1 - \lambda_i k_i) - 1\} C_i + z(\eta) C_i^0 = 0,$$
$$z(\eta) = \frac{2}{\eta(\eta^2 + g_0\theta_*\eta - 1)}. \tag{23}$$

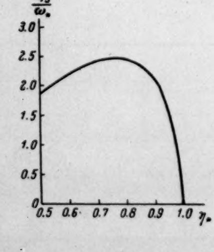

Fig. 4. Distance over which a quasi-steady-state crystal radius is established as a function of the limiting value of this radius.

Using ζ to replace η in (23) [see (20)], and integrating, using the initial condition $C_i|_{\zeta=\zeta_0} = C_i^0$, we find[3)]

$$\frac{C_i(\mathrm{SO})}{C_i^0} = \frac{[k_i - \beta_i^*\eta_*^2\Gamma(\zeta_0)]}{(\zeta + \eta_*)^2}\left(\frac{\zeta}{\zeta_0}\right)^{\nu_1}\frac{\varepsilon + \nu_2\zeta}{\varepsilon + \nu_2\zeta_0} + \frac{\beta_i^*\eta_*^2\Gamma(\zeta)}{(\zeta + \eta_*)^2}, \tag{24}$$

where

$$\Gamma(\zeta) = \left(1 + \frac{\nu_2\zeta}{\varepsilon}\right)(1 + \sigma\zeta + \delta\zeta^2), \quad \sigma = \frac{\nu_1}{\nu_1 - 1}\left(\frac{1}{\eta_*} - \frac{\nu_2 + 1}{\varepsilon}\right),$$
$$\delta = \frac{\nu_1}{1 + \eta_*^2}\left(\frac{\nu_2 + 1}{2 - \nu_1}\right), \quad \nu_1 = \frac{2k_i}{(1 + \eta_*^2)\beta_i^*}, \quad \nu_2 = \frac{2k_i}{1 + \eta_*^2}\left(\frac{\beta_i^* - 1}{\beta_i^*} + \eta_*^2\right).$$

Using system (20), (24) we can find the impurity distribution in the crystal for the case in which the transient period ξ_i^* becomes large. To illustrate this point, we show in Fig. 5 some results calculated for the distribution of a relatively nonvolatile impurity ($\lambda_i \ll 1$) along a crystal for $\eta^* = 0.7$, $\beta^* \equiv 2$, and $\omega_* = 0.9$. We see that the concentration of such an impurity tends monotonically toward a steady-state value over this range of distribution coefficients k_i. A shift of the quantity $k_i + g_i$ toward higher values leads to the appearance of an extremum at some point $\xi_i^M < \xi_s$ on the plot of the impurity concentration against the crystal coordinate. This extremum occurs because the impurity concentration in the zone changes faster than the radius of the solidified crystal can change. This conclusion follows directly from (2), according to which there are two ways in which the first derivative of the impurity concentration with respect to coordinate ξ can vanish: a) $(C_i)'_\xi \to 0$ as $\xi \to \infty$, in which case the derivatives $(N_i)'_\xi$, $(N_0)'_\xi$, and $(C_i)''_\xi$ tend toward zero; b) $(C_i)'_\xi = 0$ at the point $\xi = \xi_i^M$, at which we have $(N_i)'_\xi = C_i(N_0)'_\xi$, but at which the derivatives $(N_0)'_\xi$ and $(C_i)''_\xi$ are nonvanishing.

The situation is illustrated in Fig. 6, which shows the impurity concentration as a function of the crystal coordinate according to Eqs. (20) and (24) with the values $\eta_* = 0.5$, $\beta^* \equiv 0.8$, and $\omega_* = 0.9$. [in this case $\nu_2 = 0$, so series (25) contains only a single term, and Eq. (24) holds for any k and g.] It is evident that when $k/\beta^* < 1$ the im-

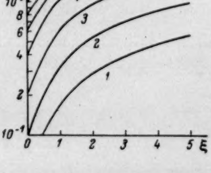

Fig. 5. Distribution of relatively nonvolatile impurities having distribution coefficients in the range 0.05-1 along a semiinfinite crystal. $\eta_* = 0.7$, $\beta^* \equiv 2$, $\omega_* = 0.9$. k: 1) 0.05; 2) 0.1; 3) 0.2; 4) 0.4; 5) 0.6; 6) 0.8; 7) 1.

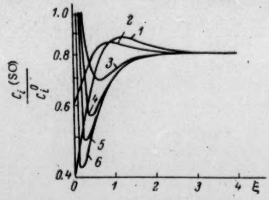

Fig. 6. Distribution of impurities having distribution coefficients in the range 0.4-10 along a semiinfinite crystal. $\eta_* = 0.5$, $\beta_* \equiv 0.8$, $\omega_* = 0.9$. k: 1) 0.4; 2) 0.6; 3) 1.5; 4) 3; 5) 5; 6) 10.

purity concentration passes through a **maximum; with** $k/\beta^* > 1$ it **through a minimum.**

A phenomenon of this type is apparently observed experimentally in ref. 4 in a study of the distribution of a Zr impurity in Mo after a single pass of the zone at rates of 0.3 and 1.0 mm/min. For both rates $(k/\beta^*)_{Zr} < 1$, and the zirconium concentration in the first part of the crystal ($\xi \sim 0.5$-1.0) is higher than the steady-state value.

In conclusion we note that, first, although we **originally assumed the length** of the zone and the average temperature of the zone surface to remain relatively constant over the course of the recrystallization, this assumption of course does not restrict the applicability of Eqs. (14) and (11). All the quantities which appear in these equations refer to the quasisteady-state region and can be easily measured, regardless of their history. Furthermore, Eq. (14) can be used for estimates simply by measuring the average heating in the zone and the limiting crystal radius for known values of k and γ; in this regard, Eq. (14) is particularly convenient.

Second, in large-diameter crystals ($d \geqslant 20$-25 mm) the elimination of relatively volatile impurities apparently becomes limited by the convective supply of atoms from the interior of the zone to its surface; this circumstance could be responsible for the discrepancy between the calculated and experimental data.

Finally, we mention the effect of the period in which the initial zone is formed, t_f, during which the concentration of relatively volatile impurities in the zone can decrease perceptibly. This circumstance can be taken into account by substituting the initial condition $C_i|_{\zeta=\zeta_0} = C_i(t_f) \simeq C_i^0 \exp[(g_0 - g_i)t_f]$ into (23) (see, e.g., ref. 3).

[1)] Here the subscript "0" denotes the host component.

[2)] The accommodation coefficient α_0 is approximately equal to unity for metallic elements.

[3)] In integrating (23) we use a series expansion of the coefficient $(\zeta+\varepsilon)^{\nu_2}$ in powers of

$$(\zeta+\varepsilon)^{\nu_2} = \varepsilon^{\nu_2}\left[1 + \frac{\nu_2\zeta}{\varepsilon} + \frac{\nu_2(\nu_2-1)}{2!}\left(\frac{\zeta}{\varepsilon}\right)^2 + \dots\right]. \qquad (25)$$

The condition $k_i + g_i < 1$ leads to a rapid convergence of this series, so that it is sufficient to retain only the first two terms. We note that in the case $\nu_1 = 1$ or 2, in which case σ and δ are not meaningful, Eq. (23) can be integrated directly.

[1] Sh. I. Peizulaev, Izv. Akad. Nauk SSSR, Neorgan. Mat., 3, 1523 (1967).
[2] M. V. Pikunov, Izv. Akad. Nauk SSSR, Metally, 5, 160 (1967).
[3] G. E. Chuprikov, in: Single Crystals of Refractory and Rare Earth Metals [in Russian], Izd. Nauka, Moscow (1971), p. 32.
[4] Sh. I. Peizulaev, V. N. Bykov, S. S. Budagovskii, M. I. Zakharova, V. N. Zolotukhin, and L. K. Popova, in: Physicochemical Principles of Crystallization Processes in Extreme Purification of Metals, Izd. Nauka, Moscow (1970), p. 62.
[5] J. A. Burton, R. C. Prim, and W. P. Slichter, J. Chem. Phys., 21, 1987 (1953).

Hydrogen-ion mobility in a high-pressure unipolar corona

A. G. Lyapin

G. M. Krzhizhanovskii Scientific Research Institute, Moscow

(Submitted April 2, 1973)
Zh. Tekh. Fiz., 44, 1990-1995 (September 1974)

A simplified method is proposed to determine the mobility of hydrogen ions, averaged over the interelectrode gap, over a wide pressure range in highly nonuniform fields. The experimental data show that at high pressure the mobility has a complicated dependence on p. Up to a critical pressure ($p \simeq 8$ atm) the mobility of negative ions changes by more than two orders of magnitude; the positive-ion mobility is approximately inversely proportional to the pressure. For hydrogen pressures greater than the critical value the mobilities of positive and negative ions are about the same and essentially independent of p. The drift velocity of the ions in a corona field is compared with data in the literature. The agreement with the available data confirms the assumptions made here.

In recent years there has been a rapid increase in technological applications of electric fields produced in the interelectrode gap of high voltage sources in the range 80 kV to 1.2 MV. In such sources both hydrogen and anisotropic mixtures of fluorochlorohydrocarbons with H_2 or N_2 are used as basic insulator materials.

The dielectric strength of these materials and the conditions for electrical discharges are determined chiefly by the volume charge distribution in the interelectrode gap. In refs. 1-3 it is shown that the latter is determined by the ion mobility.

We consider here the results of an experimental determination of the averaged (over the gap) ion mobility of clean, dry hydrogen in the field of a unipolar corona in a cylindrical electrode geometry with $30 \leq R/r_0 \leq 600$ at high pressures ($0.5 \leq p \leq 25$ atm).

An advantage of this electrode geometry is the fact that in the outer zone of the corona in the field of a cylindrical condenser the electric field is given by

$$E_x = \sqrt{\frac{I}{2\pi\varepsilon_0 l_k K}\left[1-\left(\frac{r_0}{r_x}\right)^2\right]+\left(E_0\frac{r_0}{r_x}\right)^2}, \tag{1}$$

where I is the corona current, r_0 and r_x are the radii of the corona electrode and of the zone in which the field gradient is evaluated, l_k is the length of the corona electrode, E_0 is the electric field at the surface of the corona electrode corresponding to the voltage, U_0, at which corona is initiated, and K is the ion mobility.

For a developed corona $I > 20$ mA/m, as is shown in ref. 4, and Eq. (1) takes the form

$$E_x = \left(\frac{I}{2\pi\varepsilon_0 K l_k}\right)^{1/2}. \tag{2}$$

For an outer corona zone with $r_x \geq 10\, r_0$ and a developed corona ($m = U/U_0 > 3$, where U is the voltage across the gap) the electric field is independent of the coordinate r_x and remains (beginning with some $r_x > r_{x_{cr}}$) constant.[5] Thus, for $r > r_{x_{cr}}$, we assume

$$K = \frac{I}{2\pi\varepsilon_0 l_k E_{x\,cr}^2} = aIE_{x\,cr}^{-2}. \tag{3}$$

If we take the volt–ampere characteristics $I = f(U)$ for a given corona electrode with two different outer cylinder dimensions R for each given value of corona current we have

$$E_x = \frac{U_2 - U_1}{R_2 - R_1} = \frac{\Delta U}{\Delta R}, \tag{4}$$

where R_1 and R_2 are the dimensions of the outer cylinders; ΔU is the difference in voltage across the gap for a fixed value of corona current (I/l_k = const) when the boundary of the outer zone is changed from R_1 to R_2.

In other words, the gradient of the electric field, E_x, depends on the voltage difference applied to two cylindrical condensers, R_1/r_0 and R_2/r_0, with the same corona current. Thus,

$$K_{av} = \frac{I_i \Delta R^2}{2\pi\varepsilon_0 l_k \Delta U_i^2} = GI_i\Delta U_i^{-2} \tag{5}$$

or

$$\bar{V} = KE = G'I_i\Delta U_i. \tag{6}$$

For a given current (corona current per unit length of corona electrode) the coefficients G and G' are determined only by the electrode dimensions.

The mobility of hydrogen (a basic insulator gas in high-voltage electrophysical apparatus) is determined from experimental volt–ampere characteristics with positively and negatively polarized inner electrodes of a cylindrical condenser. The R/r_0 geometry is varied by using three outer cylinders: R_i = 2.0, 3.0, and 5.0 cm. The inner working surface of the shielding elements of the noncorona electrode corresponded, for given R, to a Rogowski profile with $\psi = \pi/2$. Stainless steel wires $0.01 \leq r_0 \leq 0.175$ cm in diameter serve as corona electrodes.

Over the entire range of R/r_0 and p studied here the volt–ampere characteristics are obtained in the usual way (point-by-point) and with an x–y chart recorder (N359/P).

From the analyzed volt–ampere characteristics for R/r_0 it follows that the current for a negative unipolar corona is significantly higher than the analogous quantity for positive polarization for a given U, regardless.

Typical volt–ampere characteristics for positive (solid curves) and negative (dotted) polarity and for a number of pressures for r_0 = 0.025 cm are shown in Fig. 1.

The function $I = f(U)$ allows us (with an accuracy $\sigma_m \simeq 1\%$ at a certainty level $\Delta\sigma_m = 0.94$) to plot intermediate curves $\Delta U_i = \varphi(p)$ at r_0 = const for $2 \leq I_i \leq 200$ μA/m. For a positive unipolar corona this dependence has an exponential form, whose growth rate depends, for

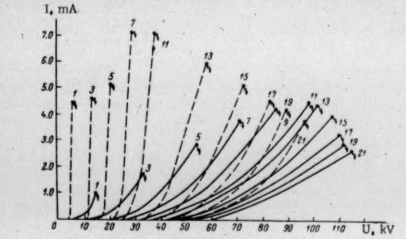

Fig. 1. Typical volt–ampere characteristics for unipolar corona in hydrogen. $R/r_0 = 100$, $R_1 = 3.0$ cm. The numbers on the curves denote pressure; the downward arrows, breakdown.

a given r_0, on the overvoltage relative to the corona threshold. That is, it is determined by the intensity with which the corona "burns." In the case of negative corona this dependence has two distinct zones: a) For $0.5 \leq p \leq 5$ atm ΔU_i is essentially proportional to the square root of the pressure; and b) for $8 \leq p \leq 15$ atm, $\Delta U_i = \varphi(p)$ is nearly exponential.

The intermediate curves $\Delta U_i = \varphi(p)$ for all R/r_0, $s = R - r_0$, p, and corona electrode polarities which were studied enable us to plot the basic dependence $\bar{K}_{av} = f(p)$, as shown in Fig. 2. Here, $\bar{K}_{av}$ means the value of K averaged over an entire series of runs (arithmetic mean). In order to simplify the analysis the average mobility of hydrogen ions is also shown as a function of lifetime [$K_{av} = \varphi(t)$] and as a function of the electric field gradient [$K_{av} = \psi(E/p)$].

The function $\bar{K}_{av} = f(p)$ for ions of both sign is qualitatively the same for the pressures and electrode distances considered here (this does not contradict the conclusions of ref. 6). Quantitatively, however, there is a substantial difference between the curves $\bar{K}^-_{av} = f(p)$ and $\bar{K}^+_{av} = f(p)$.

For positive ions over the entire range of pressure studied here $\bar{K}^+_{av}$ falls by five or six times as p increases; for negative polarity the drop is almost two orders of magnitude. Then a sharp drop in K_{av} for positive and negative ions occurs over a range up to the critical pressure for hydrogen, which at normal temperature (according to ref. 7) reaches 7 atm. Over the remaining portion of this pressure range ($8 \leq p \leq 25$ atm) the ion mobility changes insignificantly (up to 20%). In the range $0.5 \leq p \leq 7$ atm the mobility of the negative ions falls by more than 50 times.

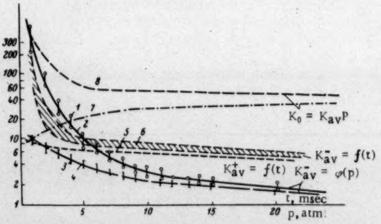

Fig. 2. Change in mobility, averaged over the interelectrode gap, of negative and positive ions with H_2 pressure or ion lifetime. 1) Spread in $\bar{K}_{av} = \varphi(p)$; 2) generalized dependence $K^- = \psi(p)$ (over the whole series of experiments); 3) spread in $K^+_{av} = \varphi(p)$; 4) generalized dependence $K^+_{av} = \varphi(p)$; 5) dependence $K^+_{av} = f(t)$; 6) spread in $K^-_{av} = f(t)$; 7, 8) K^+_0 and K^-_0, respectively, for the pressure range studied.

For p > 7-8 atm the mobility of both positive and negative ions is pressure-independent and it is assumed that $\bar{K}^-_{av} = \bar{K}^+_{av}$ in this range.

In the case of a negative unipolar corona for p < 5 atm the mobility of the ions exceeds 100 cm²/V · sec. This experimental result indicates that if clean, dry hydrogen is compressed slightly the principal charge carriers in a negative corona may be the electrons. This conclusion agrees with the data of refs. 8 and 9.

The equal positive- and negative-ion mobilities at high pressures (p > 12 atm), for which K_{av} reaches similar values to those representative of normal ions at atmospheric pressure, indicates that in this pressure range the mobility of the charge carriers is affected by the presence of chemical impurities and additives in the hydrogen. The chief impurities are water vapor (< 0.0012%) and compounds of the KOH groups (< 0.001%). The sublimation technique (freezing during pumping) used in these experiments to dry the hydrogen does not remove these additives.

Another important result is indicated by the present data. For positive hydrogen ion lifetimes, $1 \leq t \leq 30$ msec, the relation between K and t can be written in the form

$$K^+(t) = 5.9 + 2.13\exp(-0.38pt). \qquad (7)$$

We note that the ion lifetimes are calculated by the method of ref. 4 for given overvoltage m, that is,

$$t = \frac{E_0}{KI_i}\left\{\sqrt{G\frac{I_i}{\Delta U_i^2}} - 1\right\}. \qquad (8)$$

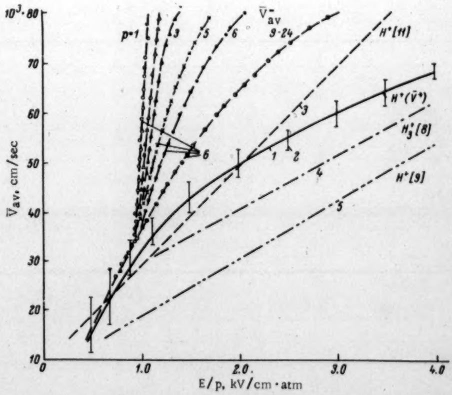

Fig. 3. Ion drift speed as a function of E/p. $R/r_0 = 60$-240, $R_1 = 3.0$ cm, $R_2 = 6.0$ cm. 1) Averaged dependence $\bar{V}^+ = f(E/p)$; 2) spread in $\bar{V}^+$; 3) $\bar{V}^+ = f \cdot (E/p)$ according to ref. 11; 4) same, from ref. 8; 5) same, from ref. 9; 6) $\bar{V}^- = f(E/p)$.

It has not been possible to obtain a unique dependence $K_{av}^{-} = \psi(t)$, whose analytic form approximates a relationship like Eq. (7), for negative ions. This difficulty can be explained only by the effect of the electron component in the corona current on the character of $K_{av}^{-} = \psi(t)$.

Attempts to isolate the ion component (using grids) in the plot of unipolar current at negative polarity have been unsuccessful.

This difficulty, in our opinion, is most fully illustrated by a curve of the ion drift speed as a function of the electric field divided by the pressure, which is plotted in Fig. 3. This curve shows that the drift speed of the hydrogen ions over the entire range of E/p and p studied here has a complicated structure due to changes in the form of the corona discharge.

For a negative unipolar corona with $0.3 \leq E/p \leq 1$ kV · (cm · atm)$^{-1}$, the drift speed is proportional to E/p and can be approximated by the analytic expression

$$\bar{V}^{+} = 1.5\left(\frac{E}{p} - 1.5\right) \cdot 10^{4}, \text{ cm/sec.} \qquad (9)$$

This expression agrees with the data of ref. 9. For high values of E/p (E/p > 1.0 kV/cm-atm) the drift speed increases much more slowly than E/p, that is, saturation is reached in the curve $\bar{V}^{-} = \varphi(E/p)$.

On the other hand, for a positive corona the drift speed is approximated by the analytic expression

$$\bar{V}^{-} = 5.6\left(\frac{E}{p} - 0.3\right) \cdot 10^{4}, \text{cm/sec.} \qquad (10)$$

only for $E/p \geq 1.5$ kV/cm · atm.

For lower values of E/p the positive ion drift speed depends on the absolute pressure, p.

All these data agree with ref. 10.

The ion mobility values obtained from volt—ampere characteristics yield another important result: The constancy of Kp, usually assumed in estimates of the dielectric strength of corona gaps, holds only at high pressures (i.e., for $K_{av}^{+} = K_{av}^{-}$). For the range of pressures of interest in the construction of apparatus ($3 \leq p \leq 16$ atm) the product of ion mobility and pressure depends on the polarity of the corona electrode and the relationship is complicated.

Optical observations of the character of the corona for given electrode geometries as the pressure is varied show not only that the latter depend on the polarity of the corona electrode but also on the form of the corona. For p > 7 atm a streamer corona in the form of separate filaments, several of which cross the entire discharge gap, is observed independent of polarity.

The data on hydrogen ion mobility obtained using the techniques described here are in good agreement with data obtained by the classical methods of determining K. Thus, it is possible to determine the mobility of the ions in analyzing the electrical characteristics of compressed gases by taking volt—ampere characteristics in the pressure range of practical interest.

---

[1] Collection: Foreign Electrotechnical Industry [in Russian], TS-12 (OI-518), Central Scientific and Technical Research Institute of the Electrical Industry (TsINTI Elektroprom.), Moscow (1963) p. 69.

[2] B. Rossi and G. Staub, Ionization Chambers and Counters [Russian translation] (1951).

[3] V. I. Levitov, AC Corona [in Russian], Moscow, Énergiya (1967), p. 74.

[4] V. I. Popkov, Dokl. Akad. Nauk SSSR, 58, 1043 (1947).

[5] V. D. Kravchenko and V. I. Levitov, Elektroenergetika, No. 6, 17 (1962).

[6] L. Frommhold, Zs. Phys., 156, 259 (1959).

[7] M. Knoll, Gasenthadungstabellen. Handbuch der Physik, 15, 173, Springer, Berlin (1967).

[8] A. N. Prasad, Brit. J. Appl. Phys. 18, 185 (1967).

[9] J. Jowke, Zs. Angew. Phys., 107, 113 (1968); D. Bates, Atomic and Molecular Processes, Academic, New York (1962).

[10] H. Hessenauer, Zs. Phys., 204, 142 (1967).

[11] M. Saporoschenko, Phys. Rev., 139A, 349 (1965).

Absolute-photometry determination of the rate constant of the gas-phase reaction of the radical compound C_3F_7 and $I(^2P_{3/2})$

G. A. Skorobogatov, V. S. Komarov, and V. G. Seleznev
A. A. Zhdanov Leningrad State University

(Submitted September 24, 1973)
Zh. Tekh. Fiz., 44, 1996-2001 (September 1974)

A method described elsewhere has been used to measure the differential quantum yield of the stimulated emission of a C_3F_7I laser at peak output: (140 ± 20)% and (148 ± 12)% for initial perfluorinated propyl iodide pressures of 22.3 and 74.2 torr, respectively. Calculations based on these quantum yields yield a rate constant of $k_{11}(360°K) = (1.5 \pm 0.5) \cdot 10^{-10}$ cm³/(molecule · sec) for the gas-phase reaction $C_3F_7 + I(^2P_{3/2}) \rightarrow C_3F_7I$.

INTRODUCTION

Photolysis of the perfluorinated alkyl iodides has been studied intensively in recent years because of the discovery of photodissociative iodine lasers.[1,2] In the early work[1,3-5] it was assumed that the radical R formed in the photolysis

$$RI + h\nu_1 \rightarrow R + I(^2P_{1/2}) \qquad (1)$$

recombines rapidly,

$$2R \xrightarrow{k_2} R_2 \qquad (2)$$

and has no effect on the behavior of the $I(^2P_{1/2})$ atoms. The $I(^2P_{1/2})$ atoms, on the other hand, are assumed to lose their electronic excitation in some undetermined way:

$$I(^2P_{1/2}) \rightarrow I(^2P_{3/2}) + h\nu_3, \qquad (3)$$

$$I(^2P_{1/2}) + h\nu_3 \rightarrow I(^2P_{3/2}) + 2h\nu_3, \qquad (4)$$

$$I(^2P_{1/2}) + M \rightarrow I(^2P_{3/2}) + M \quad (M \equiv RI,\ I_2)\ . \qquad (5)$$

Then they are assumed to recombine to molecular iodine:

$$2I(^2P_{3/2}) + M \rightarrow I_2 + M \quad (M \equiv RI,\ I_2). \qquad (6)$$

However, these assumptions do not explain all features of the photolysis of the perfluorinated alkyl iodides (with or without the laser effect), so it has been suggested that an important role is played in these processes by either pyrolysis of the irradiated material,[2,6]

$$RI \rightarrow R + I(^2P_{3/2}), \qquad (7)$$

or reactions involving excited photolysis products,[7-10]

$$I(^2P_{1/2}) + RI \rightarrow I_2 + R, \qquad (8)$$

$$\tilde{R} + RI \rightarrow R_2 + I(^2P_{1/2}), \qquad (9)$$

where $\tilde{R}$ is the vibrationally excited R radical. However, direct measurements[11] show that the rate constants for reactions (8) and (9) do not exceed 10^{-16}-10^{-17} cm³ · (molecule · sec)$^{-1}$. A theoretical analysis shows[12,13] that with these low values of k_8 and k_9 it would not be possible to explain fundamental features of the photolysis of the perfluorinated alkyl iodies such as the laser effect; the situation is not saved by taking process (7) into account.[14]

1. KINETIC MODEL

In accordance with the discussion in the introduction we assume that only processes (1), (3), (4), and (11) occur in the working volume of a C_3F_7I laser before peak output is reached, at t_{max}. We describe the time evolution of the concentrations [RI], $[I(^2P_{1/2})]$, $[I(^2P_{3/2})]$, and $[C_3F_7]$, and the intensity of the stimulated transitions G(t) in the approximation of Part I of ref. 18. Then for a pumping pulse

$$\varphi(t) = \varphi\Theta(t), \qquad (12)$$

where Θ(t) is the Heaviside function, and for zero critical inversion (P = 0), we find that Eqs. (20)-(28) of ref. 18 become

$$\Gamma(\tau) = y + \frac{1}{2}Kvz, \qquad (13)$$

$$\frac{dy}{d\tau} = -\frac{dz}{d\tau} = -y + Kvz \quad [y(0) = 1;\ z(0) = 0], \qquad (14)$$

$$\frac{du}{d\tau} = y - \frac{2}{3}\Gamma(\tau) = \frac{1}{3}y - \frac{1}{3}Kvz \quad [u(0) = 0], \qquad (15)$$

$$\frac{dv}{d\tau} = \frac{2}{3}\Gamma(\tau) - Kvz = \frac{2}{3}y - \frac{2}{3}Kvz \quad (v(0) = 0), \qquad (16)$$

where

$$\left.\begin{array}{c} K = \dfrac{nk_{11}}{\sigma(RI)\varphi}, \quad \Gamma(\tau) \equiv \dfrac{3G(t)}{2\sigma(RI)\varphi n}, \\ y \equiv \dfrac{1}{n}[C_3F_7I], \quad z \equiv \dfrac{1}{n}[C_3F_7], \\ u \equiv \dfrac{1}{n}[I(^2P_{1/2})], \quad v \equiv \dfrac{1}{n}[I(^2P_{3/2})], \\ \tau \equiv \sigma(RI)\varphi t, \quad n = [RI]_{t=0} \end{array}\right\} \qquad (17)$$

and σ(RI) is the cross section for photon absorption by the RI molecule averaged over the band.

The system of four equations in (14)-(16) has three independent integrals

$$u - \frac{1}{2}v = 0, \quad z = 1 - y, \quad v = \frac{2}{3}(1 - y), \qquad (18)$$

so that the solution of system (14)-(16) reduces to the solution of one equation. For example, using the last two integrals in (18) we find from (14)

$$\frac{dy}{d\tau} = \frac{2}{3}K\left[y^2 - 2\left(1 + \frac{3}{4K}\right)y + 1\right], \quad [y(0) = 1]. \qquad (19)$$

No significant process was made toward an understanding of the mechanism for the photolysis of the perfluorinated alkly iodides until Pimentel's group reported[15] experimental results indicating a decisive role in these processes of fast reactions involving the R radical:

$$\mathrm{I}(^2P_{1/2}) + R \xrightarrow{k_{10}} \mathrm{I}(^2P_{3/2}) + R, \qquad (10)$$

$$\mathrm{I}(^2P_{3/2}) + R \xrightarrow{k_{11}} R\mathrm{I}, \qquad (11)$$

for which the rate constants are comparable to k_2. For the case in which R is CF_3, e.g., the value of k_{10} increases with increasing temperature and at 300-500°C is 100 times the value of k_5 for the case $M \equiv I_2$ (ref. 16). As a result, process (10) turns out to be responsible for the quenching of the generation of a CF_3I laser at a pumping flux density of $> 10^{22}$ photons/(cm^2 • sec) in the CF_3I absorption band.[17]

In contrast, in the photolysis of perfluorinated propyl iodide, reactions (2) and (10) should play a less important role, and reaction (11) should play a more important role than in the photolysis of trifluoromethyl iodide since, according to refs. 2 and 6, the energy yield of the stimulated emission from a unit volume of the active medium of a C_3F_7I laser is twice that for a CF_3I laser.

We have evaluated the absolute value of k_{11} for the case $R \equiv C_3F_7$ by measuring the differential quantum yield of the stimulated emission of a C_3F_7I laser at peak output.

If we assume k_{11} to be independent of the temperature and thus of the time, we can write the solution of the Cauchy problem for Eq. (19) as

$$y(\tau) = 1 + \frac{3}{4K} - \frac{3}{4K} A \frac{A \operatorname{sh}\frac{1}{2}\tau A + \operatorname{ch}\frac{1}{2}\tau A}{\operatorname{sh}\frac{1}{2}\tau A + A \operatorname{ch}\frac{1}{2}\tau A} \quad \left(A = \sqrt{\frac{8}{3}K + 1}\right). \qquad (20)$$

The problem is solved completely, since from (20) and (18) we find the functional dependences of the other concentrations (u, v, z) on the time, and by substituting (18) into (13) we find the differential quantum yield of the stimulated transitions:

$$\Gamma(\tau) = y(\tau) + \frac{1}{3} K (1 - y(\tau))^2. \qquad (21)$$

From (20) and (21) we find the asymptotic values of the functions y and Γ in the case $\tau \to \infty$:

$$y(\infty) = 1 + \frac{3}{4K}\left(1 - \sqrt{\frac{8}{3}K + 1}\right), \qquad (22)$$

$$\Gamma(\infty) = 1\frac{1}{2} + \frac{3}{4K}\left(1 - \frac{3}{2}\sqrt{\frac{8}{3}K + 1}\right) \quad (K > 0), \qquad (23)$$

$$\Gamma(\infty) \simeq 1.5\left(1 - \sqrt{\frac{3}{2K}}\right) \quad (K \gg 1). \qquad (24)$$

In a real RI laser, because of the temperature increase in the working volume and because of processes (2), (5)-(7), and (10), the value of Γ sooner or later falls below the limiting value (23) before it vanishes. Accordingly, in a real RI laser Eqs. (22)-(24) hold only in the range $\tau_{\mathrm{asymp}} \leq \tau \leq \tau_{\max}$, where $\tau_{\max}$ is the time at which the output reaches its peak and where $A\tau_{\mathrm{asymp}} \gg 1$. We assume

$$\tau_{\mathrm{asymp}} = 4A^{-1}. \qquad (25)$$

If we have

$$\tau_{\mathrm{asymp}} < \tau_{\max} \qquad (26)$$

in a real laser, then there is a range of times $\tau_{\mathrm{asymp}} < \tau < \tau_{\max}$ in which the measured quantum yield $\Gamma(\tau_{\max})$ obeys (23) or (24). If, on the other hand, inequality (26) does not hold, then Eqs. (22)-(24) are not applicable for the given RI laser, and $\Gamma(\tau_{\max})$ is smaller than the limiting value in (23).

2. EXPERIMENTAL PROCEDURE AND APPARATUS

The quartz laser cell (inside diameter 5.4 mm, length 250 mm, and working volume 5.7 cm^3), with end windows making an angle of 90° with the axis of the cell, is surrounded by four IFP-5000 lamps wrapped in aluminum foil. The IFP-5000 lamps are placed inside a copper tube (100 mm in diameter and 350 mm long) so that the discharge current passes through the lamps and the copper tube to ground through a low-inductance circuit. The pumping pulses are produced by supplying the lamps a voltage of up to 30 kV through a coaxial air spark switch from two KMK-40-4 capacitors (C_{tot} = 7.6 μF, L = 15 nH). For a discharge energy of 500 J the length of the voltage pulse in the UV region is 10 μsec at half-height, and that at an energy of 3600 J is 20 μsec.

The cavity is formed by an opaque mirror and one with a dielectric coating which reflects 10% of the radiation at 1300 nm. The radius of curvature of the mirrors is 1 m, and the mirrors are 750 mm apart. Part of the stimulated emission (12-20%) is reflected by a quartz plate; after attenuation by a factor of ~100, it reaches a light guide to the pickup (a type FD9É111B photodiode) of an S1-29 storage oscilloscope. The other 80-88% of the radiation reaches the entrance of an IKT-1M calorimeter. When a cell having Brewster-angle windows is used the stimulated-emission energy per cm^3 of the working volume is not significantly increased.

The trifluoromethyl iodide (99.8% pure) is purified until the impurity peaks on the chromatograms disappear completely, by means of 8-10 vacuum distillations. The perfluorinated propyl iodide is purified in a similar manner, and the product used in the experiments contains 2-3 mole % of inert impurities of the type C_6F_{14}.

3. ABSOLUTE PHOTOMETRY

Table 1 shows, for each initial pressure n = $[RI]_0$, the pumping energy E_{pump}; the measured stimulated-emission energy per cm^3 of the working volume, E_{gen}; the time at which the generation reaches its maximum, $t_{\max}$; and the time at which generation is cut off, t_{cut}. This table also shows values of the integrated quantum yield of the stimulated emission, calculated from

$$\Gamma_{\Sigma}(\%) = \frac{(\quad 0.988 \cdot 10^{19} E_{\mathrm{gen}}(\mathrm{J/cm^3})}{n\,(\mathrm{molecules/cm^3})} \cdot 100 \qquad (27)$$

as a percentage of the maximum possible value $2/3[RI]_0$:

$$\Gamma_{\Sigma} = \frac{3}{2n} \int_0^{t_{\mathrm{cut}}} G(t)\,dt = \int_0^{\tau_{\mathrm{cut}}} \Gamma(\tau)\,d\tau. \qquad (28)$$

Then, using the measured values of E_{gen} and the shapes of the pulses (Fig. 1), we calculate the maximum

TABLE 1. Rate Constants for the Combination of the C_3F_7 Radical and the $I(^2P_{3/2})$ Atom Calculated from the Experimental Data

$[RI]_0 \equiv n$		E_{pump}, J	R	E_{gen}, mJ · cm^{-3}	t_{max}, μsec	t_{cut}, μsec	r_Σ, %	G_{max}, photons · $(cm^3 \cdot sec)^{-1}$	φ^{RI}_{max}, photons · $(cm^2 \cdot sec)^{-1}$	$\varphi^{C_3F_7I}_{max} / \varphi^{CF_3I}_{max}$	$(\varphi^{C_3F_7I}_{max} / \varphi^{CF_3I}_{max})_{av}$	$k_{11}^{C_3F_7}$, $cm^3/(mol. \cdot sec)$	τ_{asymp}	τ_{max}
torr	mole/cm^3													
22.3	$7.34 \cdot 10^{17}$	3420	CF_3	4.6	0.5	5.0	6.2	$2.03 \cdot 10^{22}$	$1.04 \cdot 10^{23}$	—	—	—	—	0.020
			C_3F_7	18.1	0.6	10.5	24.3	$3.41 \cdot 10^{22}$	$1.66 \cdot 10^{23}$	1.12	1.40±0.20	$3 \cdot 10^{-11}$	0.133	0.031
			C_3F_7	15.8	0.5	9.0	21.3	$4.40 \cdot 10^{22}$	$1.50 \cdot 10^{23}$	1.44				
			C_3F_7	16.7	0.6	7.0	22.5	$5.04 \cdot 10^{22}$	$1.72 \cdot 10^{23}$	1.65				
74.2	$2.44 \cdot 10^{18}$	2570	CF_3	15.3	0.6	5.0	6.2	$5.76 \cdot 10^{22}$	$8.88 \cdot 10^{22}$	—	—	—	—	0.018
			C_3F_7	48.2	0.5	9.0	19.5	$1.21 \cdot 10^{23}$	$1.24 \cdot 10^{23}$	1.40	1.48±0.12	$1.8 \cdot 10^{-10}$	0.026	0.027
			C_3F_7	48.0	0.6	11.0	19.4	$1.20 \cdot 10^{23}$	$1.22 \cdot 10^{23}$	1.38				
			C_3F_7	48.3	0.5	9.5	19.6	$1.45 \cdot 10^{23}$	$1.49 \cdot 10^{23}$	1.67				

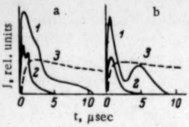

Fig. 1. Intensities J of the pumping pulses and the generation of CF_3I and C_3F_7I lasers. a) E_{pump} = 3420 J, [RI] = 22.3 torr; b) E_{pump} = 2570 J, [RI] = 74.2 torr. 1) C_3F_7I; 2) CF_3I; 3) pumping.

power per unit working volume of the stimulated emission, E_{max} (joules per cubic centimeter per second). These values are shown, in units of photons per cubic centimeter per second (G_{max}), in the ninth column of Table 1. The 10th column shows the apparent pumping radiation flux in the RI absorption band at the time of peak output, t_{peak}, calculated from

$$\varphi^{RI}_{max}[\text{photons}/(\text{cm}^2 \cdot \text{sec}) = \frac{1.5G_{max}[\text{photons}/(\text{cm}^3 \cdot \text{sec})]}{n\sigma(RI)}. \quad (29)$$

We assumed $\sigma(CF_3I) = 4 \cdot 10^{-19}$ and[3,19] $\sigma(C_3F_7I) = 6 \cdot 10^{-19}$ cm^2/molecule.

We also assert that the apparent flux $\varphi^{CF_3I}_{max}$ is equal to the actual pumping flux on the basis of four arguments used to derive fundamental equation (2) of ref. 20 [Eq. (29) with $R \equiv CF_3$ was derived from this equation]. Column 11 in Table 1 shows the ratios $\varphi^{C_3F_7I}_{max} / \varphi^{CF_3I}_{max}$ calculated from data in the 10th column, while column 12 shows the average values of these ratios, $(\varphi^{C_3F_7I}_{max} / \varphi^{CF_3I}_{max})_{av}$. Since the values of t_{max} are the same for CF_3I and C_3F_7I lasers, we can conclude from the assertion above that

$$\Gamma^{C_3F_7I}(t_{peak}) = (\varphi^{C_3F_7I}_{max} / \varphi^{CF_3I}_{max})_{av} \quad (30)$$

Furthermore, if (26) holds we can assume that the value of $\Gamma(\infty)$ for the model in Sec. 1 is equal to the experimental value $\Gamma^{C_3F_7I}(t_{max})$; then we find from (17), (24), and (30) that

$$k_{11} = \frac{3}{2}\sigma(CF_3I)\,\varphi^{CF_3I}_{max}\left\{[CF_3I]_0\left[1 - \frac{2}{3}(\varphi^{C_3F_7I}_{max} / \varphi^{CF_3I}_{max})_{av}\right]^2\right\}^{-1}. \quad (31)$$

The values of $k_{11}^{C_3F_7}$ calculated from (31) are shown in column 13 of the table. To check the legitimacy of the model in Sec. 1, we calculate τ_{asymp} and τ_{max} from Eqs. (25) and (17) (columns 14 and 15, respectively). We see from the data that Eq. (26) holds for n = 74.2 torr but does not hold for n = 22.3 torr. The value $k_{11} = 1.8 \cdot 10^{-10}$ is more reliable. Quantitative estimates show that $k_{11} \geq 10^{-10}$ for $\Gamma^{C_3F_7I}(t)$ to reach a value of 1.4 by t_{max} when n = 22.3 torr.

The relative amount of the CF_3I working medium at peak output is, in a first approximation, equal to $g(t_{max}) = \exp(-\tau_{max})$. From this equation and the data in column 15 of the table we see that the assumption[20] $[CF_3I] \simeq [CF_3I]_0$ used in deriving Eq. (29) holds within 1-2%.

We are left with the problem of evaluating the temperature of the photolyzed perfluorinated propyl iodide at time t_{max}. The absorption of one pumping photon leads to an increase of 3.6 eV in the energy of the working gas. We adopt 34 cal/(deg · mole) as the specific heat C_3F_7I. Then in the approximation of Sec. 2 of ref. 18, we find, using Eq. (45) of ref. 18, that we would have $T(t_{peak})$ = 368°K in an experiment with n = 22.3 torr and $T(t_{peak})$ = 358°K in an experiment with n = 74.2 torr. Our experimental results thus yield the value $k_{11}^{C_3F_7}(360°K) = (1.5 \pm 0.5) \cdot 10^{-10}$ cm^3/(molecule · sec).

Publisher's note: The numbering system used for the equations corresponds to the Russian original.

[1] J. V. V. Kasper and G. C. Pimentel, Appl. Phys. Lett., 5, 231 (1964).
[2] J. V. V. Kasper, J. H. Parker, and G. C. Pimentel, J. Chem. Phys., 43, 1827 (1965).
[3] A. J. De Maria and C. J. Ultee, Appl. Phys. Lett., 9, 67 (1966).
[4] M. A. Pollack, Appl. Phys. Lett., 8, 36 (1966).
[5] V. Yu. Zalesskii and A. A. Venediktov, Zh. Eksp. Teor. Fiz., 55, 2088 (1968) [Sov. Phys.-JETP, 28, 1104 (1969)].
[6] V. Yu. Zalesskii and E. I. Moskalev, Zh. Eksp. Teor. Fiz., 57, 1884 (1969) [Sov. Phys.-JETP, 30, 1019 (1970)].
[7] N. G. Basov, L. K. Gavrilina, Yu. S. Leonov, and V. A. Sautkin, ZhETF Pis. Red., 8, 178 (1968) [JETP Lett., 8, 106 (1968)].
[8] T. L. Andreeva, V. I. Malyshev, A. I. Maslov, I. I. Sobel'man and V. N. Sorokin, ZhETF Pis. Red., 10, 423 (1969) [JETP Lett., 10, 271 (1969)].
[9] P. Gensel, K. Hohla, and K. L. Kompa, Appl. Phys. Lett., 18, 48 (1971).
[10] D. E. O'Brien and J. R. Bowen, J. Appl. Phys., 40, 4767 (1969).
[11] V. Yu. Zalesskii and T. I. Krupenikova, Opt. Spektrosk., 30, 813 (1971).
[12] G. A. Skorobogatov and V. E. Khomenko, Vestnik LGU, No. 16, 109 (1972).
[13] G. A. Skorobogatov, Vestnik LGU, No. 22, 84 (1972).
[14] G. A. Skorobogatov and V. E. Khomenko, Vestnik LGU, No. 10, 170 (1970).
[15] T. Ogawa, G. A. Carlson, and G. C. Pimentel, J. Phys. Chem., 74, 2090 (1970).
[16] J. J. Deakin and D. Husain, J. Chem. Soc. (Far. Trans), 68 II, 1603 (1972).
[17] G. A. Skorobogatov, V. M. Tret'yak, and V. S. Komarov, Zh. Tekh. Fiz., 44, 784 (1974) [Sov. Phys.-Tech. Phys., 19, 558 (1974)].
[18] G. A. Skorobogatov, Vestnik LGU, No. 4, 144 (1970).
[19] K. Hohla and K. L. Kompa, Z. Naturforsch., 27a, 938 (1972).
[20] V. S. Komarov, V. G. Seleznev, and G. A. Skorobogatov, Zh. Tekh. Fiz., 44, 875 (1974) [Sov. Phys.-Tech. Phys., 19, 495 (1974)].

Optical methods for studying amplification of elastic surface waves in a stratified system

I. B. Yakovkin, V. V. Petrov, and S. V. Bogdanov

Institute of Semiconductor Physics, Siberian Branch, Academy of Sciences of the USSR, Novosibirsk

(Submitted July 3, 1973)
Zh. Tekh. Fiz., 44, 2002-2007 (September 1974)

The amplification (damping) of elastic surface waves (ESW) in a layer-type amplifier is studied using the scattering of light on ESW. The distribution of the acoustic field is determined both in the amplifying and damping regimes for various levels of acoustical input power. The resulting curves indicate a nonlinearity in density at large ESW amplitudes. A method is shown for determining the magnitude of the "mechanical" damping caused by scattering of ESW and their transformation into other types of waves.

Elastic surface waves (ESW) can be amplified in piezoelectric crystals using the drift of free charge carriers.[1] From a physical viewpoint the most interesting ESW amplifying system is a piezoelectric substrate, in which an ESW is excited, to which is clamped a layer of semiconductor in which the electrons (holes) drift due to a driving electric field, E_T. With such a system it is possible to investigate the interaction of the charge carriers with the ESW and to determine several electrophysical parameters of the semiconductor. The usual method of studying such systems,[2] which involves measuring the signal at a receiver transducer as a function of a variable parameter, only yields an integral value of those quantities which characterize the interaction of the surface wave with the moving carriers. In order to obtain the local characteristics of the interaction we can find the spatial distribution of the acoustic field of ESW in the amplifier by means of scattering of light[3] from the ESW. In particular, by this method it is possible to determine the local amplification coefficient, to determine the coordinates of points where the deviation from linearity becomes noticeable, to explain the effect of various mechanisms for ESW scattering, etc.

We shall discuss the construction of the amplifier, the experimental arrangement, the measured quantities, and the errors involved. The amplifier, which consists of an acoustic line ($LiNbO_3$, Y–Z shear plane) on which ESW are excited by means of opposed rod transducers (f_0 = 85 MHz; aperture 0.18 cm; 16 electrode pairs), is shown in Fig. 1. Charge carrier drift arises in a layer of n-type silicon (resistivity, ρ = 0.6 cm; mobility, μ = 1200 $cm^2/V \cdot sec$; equilibrium concentration in conduction zone, $n_0 = 9 \cdot 10^{15}$ cm^{-3}) epitaxially grown on a p-type silicon substrate. Light from a He–Ne laser (λ = 6328 Å; polarized along the X axis of the crystal; beam diameter 0.2 cm) passes through a lens (L_1 and L_2) and diaphragm (D) system and falls on the backing near normal incidence. Propagating into the crystal and interacting with an ESW, the light beam is split into a basic beam of intensity I_0 and a scattered beam of intensity I_1. It should be noted that the intensity of the scattered light is determined by two factors. These are the phase shift of light rays when they are reflected from periodic curved surfaces and the phase shift due to changes in the refractive index of the layer near the surface[3] due to ESW. Restricting ourselves to small arguments of the Bessel function, it is easy to obtain a simple relation between the experimentally measured ratio I_1/I_0 and the amplitude, u_0, of a surface wave for a given interaction geometry and incident polarization:

$$\frac{I_1}{I_0} = J_1^2\left[\frac{4\pi}{\lambda}\left(u_0 + \int_0^\infty \Delta n dy\right)\right] = J_1^2\left[\frac{4\pi u_0}{\lambda}(1 + 0.1\pi n_0^3)\right], \qquad (1)$$

where J_1 is the first-order Bessel function of the first kind, λ is the wavelength of the light, Δn is the change in refractive index due to the photoelastic effect, and n_0 is the refractive index of lithium niobate.

The amplitude of the ESW calculated from this equation agrees with the amplitude found by the independent technique (diffraction of light reflected from a metallized surface for constant ESW power). The measurement error of 10% in u_0 is determined by the photomultiplier and the instability of the laser.

We note here several additional distinctive features which arise in the measurements.

1. The light is scattered by a spatially damped (growing) elastic wave. This causes the scattered light inten-

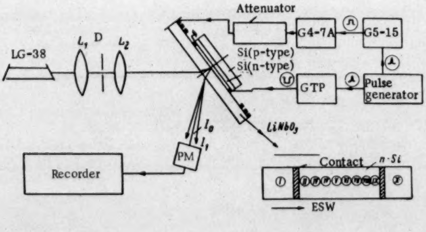

Fig. 1. Diagram of experimental apparatus.

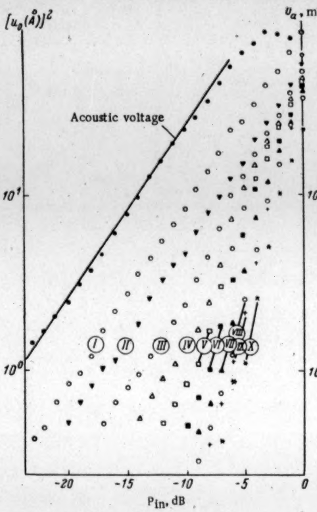

Fig. 2. Dependence of u_0^2 and the acoustic voltage, v_a, on P_{in} at various points in the amplifier for $E_T = 0$.

sity to depend not only on the amplitude of the ESW but also on the damping (amplification) coefficient, which is shown in Eq. (1) by an additional factor,[4] $\exp[(\alpha^2)/2\pi p^2]$, where α is the damping coefficient and p is the Gaussian parameter of the beam intensity distribution $[I \sim \exp\cdot(-\pi p^2 x^2)]$. This factor is of order unity in our experiments; thus, it is ignored in calculating u_0.

2. The electrophysical properties of the silicon layer change due to the light; hence, the amplification conditions change at this point. If the layer is homogeneous the mapping of the distribution of the acoustic field in the ESW amplifier obtained by means of the laser beam will be close to the true distribution. This is confirmed by a special experiment, in which the entire sample is illuminated by the same kind of laser. The form of the distribution is the same for both cases (with illumination and without) within the error limits of the experiment.

3. Measurement of the acoustic field distribution at very small ESW energies is not possible due to noise limits caused by loading of the photomultiplier by light incident on its cathode, which is scattered by inhomogeneities in the substrate.

4. In order to eliminate error in measuring the scattered light caused by shear waves,[5] the latter are eliminated by means of special absorbers of polystyrene tape dissolved in toluene attached to the ends of the acoustic line.

5. The electronic damping (amplification) and mechanical damping of the ESW are measured simultaneously by the optical method as well as by acoustoelectric measurements. The mechanical damping arises due to scattering of ESW, i.e., their transformation into other types of waves at the places of mechanical contact between the semiconductor layer and the substrate.

The goal of this experiment is to study the distribution of the acoustic field in the ESW amplifier in detail both for damping and amplifying regimes with various acoustical input power levels, to measure the amplification (damping) coefficient at each point of the amplifier, and to determine the spatial origin of nonlinear processes in the amplifier.

The relative intensity of scattered light is measured for reflection from the points I to X (Fig. 1, lower right) as a function of the acoustic power emitted by the transducer. The distance between neighboring points is 0.2 cm. This dependence is shown in Figs. 2 and 3 for damping and amplification, respectively. The 0 dB level (on the abscissa) corresponds to an acoustic power of 16 mW. It is possible to raise the maximum amplification (damping) coefficient by means of additional illumination. With the illumination chosen here the maximum amplification is observed for $E_T = 820$ V/cm. Damping is measured for the same illumination at $E_T = 0$. From the data of Figs. 2 and 3 it is possible to determine the acoustic field distribution along the amplifier for various values of input acoustical power, P_{in}. The resulting distributions are shown in Fig. 4. The damping (amplification) coefficient at every point of the amplifier for several values of P_{in} is shown in Fig. 5.

DISCUSSION OF RESULTS

In following the curves of Figs. 2 and 3 we distinguish three amplification (damping) regimes depending on the input acoustical power: a) for $P_{in} = -20$ dB and less the damping (amplification) coefficient is large and is independent of the input acoustic power (linear regime); b) for P_{in} between −15 and −7 dB the damping (amplification) coefficient decreases as the input power increases; and c) for P_{in} greater than −2 dB the electron damping (amplification) goes to zero. Only "mechanical" damping remains and its magnitude remains constant for larger P_{in}.

Apparently, the nonlinear behavior of the ESW amplitude in damping and amplification is due to a concentration effect. For $u_0 = 2.6$ Å the deviation from linearity reaches 10%.

The dependence of the acoustic voltage on P_{in} also indicates a concentration nonlinearity in ESW damping, since the deviation from linearity is observed for the same values of P_{in} both for the damping and amplification curves. It should be noted that the acoustic voltage is produced not only by the fundamental of the wave emitted in the wave transformation but also by its higher harmonics, which arise because of the nonlinearity of the system. Thus, although the coefficient of electronic damping (amplification) at the first harmonic for $P_{in} = -2$ dB is zero, the total acoustic voltage does not go to zero (cf. Fig. 2).

In order to verify this assumption of a concentration nonlinearity we calculate the nonequilibrium electron concentration due to the piezoelectric field of the ESW and compare it with the equilibrium concentration in the conduction zone. The mechanical stress is given by

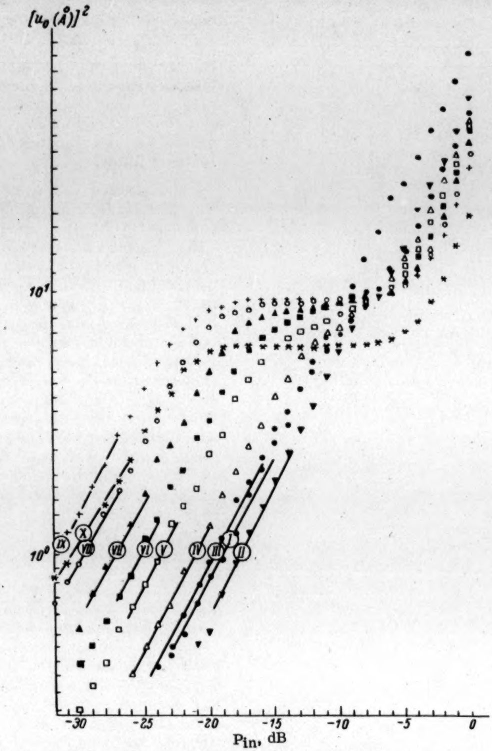

Fig. 3. Dependence of u_0^2 on P_{in} at various points in the amplifier for E_T = 820 V/cm.

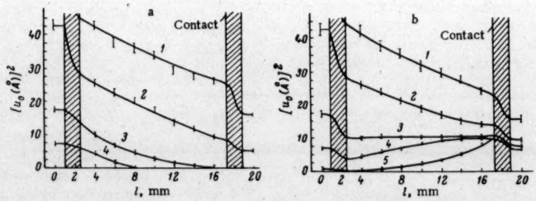

Fig. 4. Distribution of u_0^2 along the amplifier for various P_{in} with: a) E_T = 0; b) E_T = 820 V/cm. 1) −1 dB; 2) −3 dB; 3) −7 dB; 4) −11 dB; 5) −20 dB.

$$\sigma_{kl}=C_{ijkl}\zeta_{ij}-\frac{1}{4\pi}h_{nkl}D_n \qquad (2)$$

which goes to zero at a free boundary, while

$$\operatorname{div}\bar{D}=4\pi e\tilde{n}, \qquad (3)$$

where ζ_{ij} are the elastic deformations, c_{ijkl} is the matrix of elastic coefficients, h_{nkl} is the matrix of piezoelectric

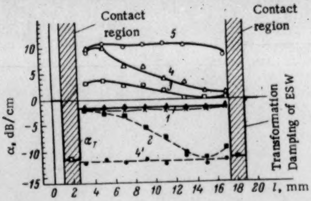

Fig. 5. Amplification (damping) coefficient in different parts of the amplifier for various values of P_{in}. 1) 0 dB; 2) −5 dB; 3) −10 dB; 4, 4')− 15; 5) −25 dB. E_T: 1, 3-5) 820 V/cm; 4) 0.

constants, $\bar{D}$ is the electric induction vector, e is the electronic charge, and $\tilde{n}$ is the nonequilibrium electron concentration.

Simulateneous solution of these equations for the semiconductor and the piezoelectric yields a relation between U_0 and $\tilde{n}$:

$$\tilde{n}=\frac{k^2u_0}{eh_{31}}\left[c_{13}+c_{11}-2\frac{h_{22}}{h_{15}}c_{44}+\left(2-\frac{h_{22}}{h_{15}}\right)c_{14}\right], \qquad (4)$$

where k is the wave vector of the ESW. Substituting the known values of constants and putting u_0 = 2.6 Å in Eq. (4) we obtain

$$\tilde{n}=9.5\cdot 10^{15}\,\mathrm{cm}^{-3}, \text{i.e., } \tilde{n}\simeq n_0.$$

These estimates confirm that when the amplitude of the displacement reaches 2.6 Å a concentration nonlinearity begins. As is known, under these conditions the second harmonic of the fundamental signal appears. We have made an attempt to measure it directly. For this, the intensity of light scattered at twice the scattering angle for the fundamental is measured (according to our estimates, second-order scattering from the ESW at the fundamental frequency is two orders of magnitude less than first-order scattering at the second harmonic of the ESW. It seems that in the nonlinear regime the second harmonic still only grows insignificantly, while the fundamental is no longer amplified. In fact, the measured amplitude of the second harmonic at the point X is three times larger than at point I.

Following the curves of Fig. 3 it is possible to calculate a dynamic amplification zone, which, when the silicon layer is strongly pressed to the acoustic line, is bounded above for an acoustic input power of 160 μW. For a weaker compression the dynamic zone widens considerably due to the nonuniform gap.

For P_{in} > 2 dB the mechanical damping is independent of the input signal magnitude and we conclude that the Hooke nonlinearity does not appears. Thus, if it is necessary to determine exactly the magnitude of the mechanical (transformation) damping, it is sufficient to take the acoustic field distribution in a known nonlinear regime. Hence, from Fig. 5 it is clear that for P_{in} = 0 dB the damping at each of the aluminum contacts of width 0.13 cm is of order 1.75 dB, while transformation damping at the silicon−lithium niobate interface of length 1.45 cm leads to mechanical losses of 2 dB.

The authors thank M. D. Levin for useful discussion.

---

[1] Yu. V. Gulyaev and V. I. Pustovoit, Zh. Eksp. Teor. Fiz, 20, 1508(1965).

[2] J. H. Collins, K. M. Lakin, C. F. Quate, and H. J. Shaw, Appl. Phys., Lett., 13, 314 (1968).

[3] S. V. Bogdanov, A. V. Kovalev, D. V. Petrov, and I. B. Yakovkin, Zh. Tekh. Fiz., 41, 1511(1971)[Sov. Phys.−Tech. Phys., 16, 1186 (1972)].

[4] R. J. Hallermeier and W. G. Mayer, IEEE Trans., SU-18, 176 (1971).

[5] D. V. Petrov and I. B. Yakovkin, Zh. Tekh. Fiz., 42, 2556 (1972) [Sov. Phys.−Tech. Phys., 17, 1986 (1973)].

Magnetohydrodynamic stability of a neutral current layer in a plasma

S. V. Bulanov

P. N. Lebedev Physics Institute,
Academy of Sciences of the USSR, Moscow

(Submitted February 26, 1974)
Zh. Tekh. Fiz., 44, 2008-2010 (September 1974)

The stability of a bounded plane layer of a current-carrying plasma has been investigated. The low-conductivity limit is considered, taking account of the compressibility of the medium and the thermal conductivity. The layer is found to be unstable in the long-wave limit. The characteristic decay rate is of the order of the isothermal acoustic velocity.

The investigation of the stability of a neutral current layer is of interest both for astrophysical applications,[1,2] and also for a laboratory plasma.[3] It is known that a plane current layer is stable in the infinite-conductivity limit. Taking account of the finite electrical conductivity leads to various instabilities.[4] The most interesting of these instabilities for astrophysical applications is the tearing-mode type. As a result of this instability the current layer splits into plasmoids, stretched along the current direction, and it is possible to have electric fields (in the limit of the order of the magnetic-field intensity outside the layer) and effective acceleration of charged particles. The tearing instability has been considered in many papers, both in the magnetohydrodynamic (MHD) approximation,[4] and also within the framework of the Vlasov equation.[5,6]

Below we will consider the stability of a current layer in the MHD approximation in the low-conductivity limit. This corresponds to the approximation S → 0, where $S = \sqrt{4\pi}\sigma h^2 L^2/\rho^{1/2} c^2$. Here σ is the electrical conductivity, h is the magnetic-field gradient inside the layer, L is the half-thickness of the layer, and ρ is the density. The tearing instability has been considered in this limit in the MHD approximation in an incompressible homogeneous fluid in ref. 4. However, in the low-conductivity limit in the problem being considered, it is imposible to disregard the compressibility of the medium.1) Moreover, the limit $\sigma \to 0$ indicates that the Joule dissipation of the magnetic field is large; therefore, in this case it is necessary to consider heat-transfer processes

1. We consider a plane layer of plasma of thickness 2L, located in the yz plane. The plasma is confined by the magnetic field produced by the current flowing in it. The current is directed along the oz axis. The magnetic field has only a y component H_y, equal to hx inside the layer ($|x| < L$) and hL outside the layer ($|x| > L$). The density distribution that corresponds to the equality of the magnetic and gas pressures at constant temperature (T_0 = const) is $\rho_0(x) = \rho(0)(1 - x^2/L^2)$. There is no plasma outside the layer. We neglect the viscosity. In this case the system of MHD equations can be written in the form

$$\frac{\partial \mathbf{v}}{\partial t} + (\mathbf{v}\nabla)\mathbf{v} = -\frac{1}{\rho}\nabla p + \frac{1}{4\pi\rho}[\mathrm{curl}\,\mathbf{H}, \mathbf{H}], \tag{1}$$

$$\frac{\partial \rho}{\partial t} + \mathrm{div}\,(\rho\mathbf{v}) = 0, \tag{2}$$

$$\frac{\partial \mathbf{H}}{\partial t} = \mathrm{curl}[\mathbf{v}, \mathbf{H}] - \frac{c^2}{4\pi}\mathrm{curl}\frac{1}{\sigma}\mathrm{curl}\mathbf{H}, \tag{3}$$

$$\mathrm{div}\,\mathbf{H} = 0, \tag{4}$$

$$\rho T\left(\frac{\partial s}{\partial t} + \mathbf{v}\nabla s\right) = \mathrm{div}\,(\chi\nabla T) + \frac{c^2}{(4\pi)^2\sigma}(\mathrm{curl}\mathbf{H})^2. \tag{5}$$

A high-temperature plasma can be assumed to be an ideal gas; the pressure is then

$$p = \frac{(1+z)\varkappa}{M}\rho T = \rho v_T^2, \tag{6}$$

where z is the effective ion charge, M is the ion mass, and $v_T^2 = (1 + z)\varkappa T/M$ is the square of the isothermal acoustic velocity. The entropy per unit mass is

$$s = \frac{(1+z)\varkappa}{M}\ln\frac{T^{3/2}}{\rho}. \tag{7}$$

We neglect the weak density dependence of the coefficients of electrical and thermal conductivity. We assume that $\sigma(T_0) \sim T_0^{3/2}$ is constant inside the layer and is zero outside it. The thermal conductivity $\chi(T_0) \sim T_0^{5/2}$ is assumed to be everywhere constant.

2. We now investigate the stability of a neutral current layer with respect to small perturbations. We represent the perturbed quantities in the form $f_1(x, y, t) = f_1(x)\exp(-i\omega t + iky)$. We consider the perturbations to be homogeneous in z. Linearizing the system of equations (1)-(5) taking account of T_0 = const, we obtain

$$(\rho_0 v_{1x})'' - q_T^2\rho_0 v_{1x} = -i\omega\left(\frac{\rho_0 T_1}{T_0}\right)' - \frac{hxq_T^2}{4\pi\omega k}(H_{1x}'' - k^2 H_{1x}) + \frac{\omega h}{4\pi k v_T^2}H_{1x}' + \frac{kh}{4\pi\omega}H_{1x}(\delta(x+L) - \delta(x-L)), \tag{8}$$

$$H_{1x}'' - \left(k^2 - i\frac{4\pi\sigma_0\omega}{c^2}\right)H_{1x} = -i\frac{4\pi\sigma_0 hxk}{c^2}v_{1x} - i\frac{3}{2}\frac{kh}{T_0}T_1 + v_{1x}\frac{kh}{\omega}(\delta(x+L) - \delta(x-L)), \tag{9}$$

$$\begin{aligned} T_1'' - \left[k^2 + \frac{3c^2h^2}{2(4\pi)^2\sigma_0\chi_0 T_0} - i\omega\frac{v_T^2\rho_0\left(\frac{3}{2}q_T^2 + k^2\right)}{T_0\chi_0 q_T^2}\right]T_1 &= -i\frac{2c^2h}{(4\pi)^2\sigma_0\chi_0 k}(H_{1x}'' - k^2H_{1x}) - \frac{\omega kh}{4\pi q_T^2\chi_0}H_{1x} \\ &+ i\frac{c^2h^2}{(4\pi)^2\omega\chi_0\sigma_0}v_{1x}[\delta(x+L) - \delta(x-L)] \\ &- \frac{\omega^2}{q_T^2\chi_0}(\rho_0 v_{1x})' - \frac{v_T^2}{\chi_0}\rho_0' v_{1x}. \end{aligned} \tag{10}$$

In the low-conductivity limit (S → 0) we obtain

$$(\rho_0 v_{1x})'' - q_T^2 \rho_0 v_{1x} = -i\omega\left(\frac{\rho_0}{T_0} T_1\right)' + \frac{\omega h}{4\pi k v_T^2} H'_{1x}$$

$$+ i\frac{3}{2}\frac{h^2 x q_T^2}{4\pi\omega T_0} T_1 - \left(\frac{h^2 x q_T^2}{4\pi\omega^2} v_{1x} - \frac{kh}{4\pi\omega} H_{1x}\right)(\delta(x+L) - \delta(x-L)), \quad (11)$$

$$H''_{1x} - k^2 H_{1x} = -i\frac{3}{2}\frac{kh}{T_0} T_1 + \frac{kh}{\omega} v_{1x}(\delta(x+L) - \delta(x-L)), \quad (12)$$

$$T''_1 - Q^2 T_1 = -i\frac{c^2 h^2}{(4\pi)^2 \omega\sigma_0\chi_0} v_{1x}(\delta(x+L) - \delta(x-L)). \quad (13)$$

Here $q_T^2 = k^2 - \omega^2/v_T^2$, $Q^2 = k^2 - 3c^2h^2/(4\pi)^2 2\sigma_0\chi_0 T_0$. The boundary conditions are represented in the form of sources on the right sides of the equations. Below we consider perturbations, corresponding to tearing, that are mirror symmetric with respect to the plane x = 0, i.e., $v_{1x}(x) = -v_{1x}(-x)$, $H_{1x}(x) = H_{1x}(-x)$, $T_1(x) = T_1(-x)$. Then the solution of the system (11)-(13) will be

$$T_1(x) = -i\frac{c^2h^2 e^{-QL} v(L)}{(4\pi)^2 \sigma_0\chi_0 Q\omega} \operatorname{ch} Qx, \quad (14)$$

$$H_{1x}(x) = \left(\frac{3c^2h^2e^{-QL}}{4(4\pi)^2\sigma_0\chi_0 Q T_0}\int_{-L}^{L} e^{-k|x-x'|}\operatorname{ch}(Qx')\,dx' + e^{-kL}\operatorname{ch}(kx)\right)\frac{h}{\omega} v(L), \quad (15)$$

$$\rho_0 v_{1x}(x) = \Biggl\{\frac{-c^2e^{-QL}}{8\pi\sigma_0\chi_0 Q T_0}\int_{-L}^{L} e^{-q_T|x-x'|}\operatorname{sign}(x-x')\,\rho_0(x')\operatorname{ch} Qx'\,dx'$$

$$-\frac{3c^2h^2e^{-QL}q_T}{(4\pi)^2 4\omega^2\sigma_0\chi_0 Q T_0}\int_{-L}^{L} e^{-q_T|x-x'|}x'\operatorname{ch} Qx'\,dx'$$

$$-\frac{q_T L e^{-q_T L}}{\omega^2}\operatorname{sh} q_T x + \frac{k e^{-q_T L}}{\omega^2 q_T}\operatorname{sh} q_T x$$

$$\times\left[\frac{3c^2h^2e^{-(Q+k)L}}{4(4\pi)^2\sigma_0\chi_0 Q T_0}\left(\frac{\operatorname{sh}(k+Q)L}{(k+Q)L} + \frac{\operatorname{sh}(k-Q)L}{(k-Q)L}\right) + e^{-kL}\operatorname{ch} kL\right]$$

$$+\frac{1}{2v_T^2 q_T}\Biggl[\frac{3c^2h^2e^{-QL}}{4(4\pi)^2\sigma_0\chi_0 Q T_0}$$

$$\times\int_{-L}^{L}\int_{-L}^{L} e^{-q_T|x-x'|-k|x'-x''|}\operatorname{sign}(x'-x'')\operatorname{ch} Qx''\,dx'\,dx''$$

$$-e^{-kL}\int_{-L}^{L} e^{-q_T|x-x'|}\operatorname{sh} kx'\,dx'\Biggr\}\frac{h^2}{4\pi} v(L). \quad (16)$$

Here v (L) is the value of v_{1x} on the boundary x = +L. Taking into account that $\rho_0 v_{1x}(x = \pm L) = 0$ (the material flow through the boundary equals zero), we obtain from (16), setting x = L, a dispersion equation relating ω and k.

We consider perturbations with wavelength much greater than the layer thickness. In other words, we assume the inequalities $kL \ll 1$ and $q_T L \ll 1$ to be satisfied. In this limit we obtain the instability growth rate from (16):

$$\gamma = \frac{\sqrt{kL}}{\tau_T}$$

$$\times\left\{\frac{1 + \left(1 - \frac{k^2}{Q^2}\right)e^{-QL}\operatorname{sh} QL}{\dfrac{1 + \left(1 - \frac{k^2}{Q^2}\right)e^{-QL}\operatorname{sh} QL\left[Q^2L^2 + (1 - QL\operatorname{cth} QL)\left(3 + \frac{4}{3}\frac{\tau_A^2}{\tau_T^2}\right)\right]}{Q^2L^2}}\right\}^{1/2}. \quad (17)$$

Here,

$$\tau_T = \frac{L}{v_T}, \quad \tau_A = \frac{L}{v_A} \equiv \frac{\sqrt{4\pi\rho(0)}}{h}. \quad (18)$$

In the limit $Q^2 \to k^2$, which corresponds to $\chi_0 \to \infty$ (high thermal conductivity), we obtain $\gamma = \sqrt{kL}/\tau_T$. Low thermal conductivity ($\chi_0 \to 0$) corresponds to $L^2Q^2 \to \infty$. In this case also $\gamma = \sqrt{kL}/\tau_T$. We can show[7] that for short-wave perturbations ($kL \gg 1$) the layer is stable.

Thus, we see that in the MHD approximation in the low-conductivity limit a neutral current layer is unstable. The characteristic instability growth rate is of order τ_T and depends weakly on thermal conductivity.

In conclusion we thank A. A. Rukhadze and S. I. Syrovatskii for their interest.

---

[1] This fact was brought to our attention by A. A. Rukhadze.

---

[1] B. Coppi, G. Laval, and R. Pellat, Phys. Rev. Lett., 16, 1207 (1966).
[2] S. I. Syrovatskii, in: Solar Flares and Space Research, ed. by C. de Jager and Z. Svestka, North-Holland, Amsterdam (1969), p. 346.
[3] A. A. Rukhadze and S. A. Triger, PIAS Preprint, No. 168 (1968); PIAS Preprint, No. 26 (1969); Prikl. Mekh. Tekh. Fiz., No. 3, 11 (1968).
[4] H. P. Furth, J. Killeen, and M. N. Rosenbluth, Phys. Fluids, 6, 459 (1963).
[5] G. Laval, R. Pellat, and M. Vuillemin, Proc. of a Conf. on Plasma Physics and Controlled Nuclear Fusion Research, Vol. 2, Culham, 1965, IAEA, Vienna (1966), p. 259.
[6] D. Biskamp, R. Z. Sagdeev, and K. Schindler, Cosmic Electrodynamics, 1, 297 (1970).
[7] H. P. Furth, in: "The stability of plane plasmas," Proceedings of the ESRIN Study Group, Frascati (Rome), Italy, December 4-8, 1967, ESRO-SP-36, July (1968), p. 21.

Radiation of electromagnetic waves by a modulated electron beam

S. G. Pankratov

(Submitted December 24, 1973)
Zh. Tekh. Fiz., 44, 2011-2014 (September 1974)

We calculate the intensity of coherent electromagnetic radiation from a velocity-modulated beam of charged particles. The radiation field is calculated by using the velocity distribution function for the beam particles found in the first approximation in the small parameter eI/mv_0^3, where I is the beam current. We show that the spectral distribution of the radiation intensity has sharp maxima at the modulation frequency and its harmonics. The results are valid in the region in which spreading of the beam affects the radiation.

1. In the study of electron beams particular attention is focused on the interaction of beams with a plasma.[1-4] The radiation of electromagnetic waves by an electron beam itself has not been adequately investigated. Experiment shows that the electromagnetic radiation from a modulated electron beam is intense enough[5] to permit the use of a beam as a radiator. The spectral distribution of the radiation intensity has sharp maxima at the modulation frequency and its harmonics.[5-7] The use of such a radiator can be justified, for example, if it is necessary to transmit information through a dense plasma layer. Electromagnetic waves are appreciably attenuated in passing through a plasma layer of thickness l larger than $c/\omega\sqrt{\varepsilon}$. If the density of the beam remains higher than that of the plasma in the region near the injector, where the spreading of the beam can be neglected, the plasma has a negligible effect on the motion of the beam. The characteristic spreading length of a beam is of the order $amv_0^3/2eI$, where a is the initial radius of the beam, v_0 is the initial velocity of the electrons, and I is the beam current. Thus, for $l \ll amv_0^3/2eI$ electromagnetic power is transmitted beyond the limits of the plasma layer.

2. The electric and magnetic fields produced by the beam are given by

$$\left.\begin{aligned}\Delta\mathbf{E}-\frac{1}{c^2}\frac{\partial^2\mathbf{E}}{\partial t^2}&=4\pi e\int d^3v\left(\nabla f+\frac{\mathbf{v}}{c^2}\frac{\partial f}{\partial t}\right),\\ \Delta\mathbf{H}-\frac{1}{c^2}\frac{\partial^2\mathbf{H}}{\partial t^2}&=\frac{4\pi e}{c}\int d^3v\,[\mathbf{v}\nabla]\,f,\end{aligned}\right\} \tag{1}$$

where $f(\mathbf{r}, \mathbf{v}, t)$ is the distribution function for the beam electrons. This function satisfies the collisionless Boltzmann equation which, in turn, contains E and H

$$\frac{\partial f}{\partial t}+\mathbf{v}\frac{\partial f}{\partial \mathbf{r}}+\frac{e}{m}\left\{\mathbf{E}+\frac{1}{c}[\mathbf{vH}]\right\}\frac{\partial f}{\partial \mathbf{v}}=0. \tag{2}$$

Using Fourier components we can write the solution of Eq. (1) at large distances, $R \gg kL^2$, $kR \gg 1$, where $k = \omega/c$ and $L \lessdot amv_0^3/2eI$ is the effective length of the beam, in the form[8]

$$\mathbf{H}_\omega \approx \frac{ie^{ikR}}{cR}[\mathbf{kj}(\mathbf{k},\omega)];\quad \mathbf{E}_\omega=[\mathbf{H}_\omega\mathbf{n}];\quad \mathbf{n}=\frac{\mathbf{R}}{R}, \tag{3}$$

where we have used the notation

$$\mathbf{j}(\mathbf{k},\omega)=e\int d^3r\int_{-\infty}^{\infty}dt\,e^{i\omega t-i\mathbf{kr}}\int d^3v\,\mathbf{v}f(\mathbf{r},\mathbf{v},t);\quad \mathbf{k}=\frac{\omega}{c}\mathbf{n}. \tag{4}$$

The distribution function $f(\mathbf{r}, \mathbf{v}, t)$ can be found by using the fact that the velocity of the electrons is small in comparison with the velocity of light. The terms on the right-hand sides of Eq. (1) containing v/c are omitted and the effect of the magnetic field on the motion of the particles is neglected. If the effective beam dimensions are small in comparison with the wavelength, the self-consistent field is reduced to the Coulomb repulsion of the charges

$$\mathbf{E}(\mathbf{r},t)=-e\int d^3v\,d^3r'\frac{\partial}{\partial \mathbf{r}}\frac{f(\mathbf{r}',\mathbf{v},t)}{|\mathbf{r}-\mathbf{r}'|}. \tag{5}$$

The system of equations (1) and (2) must be supplemented by the boundary condition which determines the way the beam is modulated. As an example we consider velocity modulation. By taking the x axis along the initial velocity of the beam we can write

$$f(\mathbf{r},\mathbf{v},t)|_{x=0}=\Theta(a-r_\perp)\,n_0\varphi(\mathbf{v}_\perp,\ v_x-v_0-\Delta v\cos\Omega t), \tag{6}$$

where $\varphi(\mathbf{v})$ is the initial electron velocity distribution function, normalized to unity, and Ω is the modulation frequency

$$\Theta(a-r_\perp)=\begin{cases}0, & r_\perp>a,\\ 1, & r_\perp\leqslant a.\end{cases} \tag{7}$$

We solve Eq. (2) by successive approximations, using the fact that the interaction energy of the electrons is small in comparison with the kinetic energy

$$\frac{U_{\text{eff}}}{\dfrac{mv_0^2}{2}}\sim\frac{2\pi a^2n_0e^2}{mv_0^2}=\frac{2eI}{mv_0^3}\ll 1. \tag{8}$$

In the zeroth approximation in the interaction parameter the distribution function has the form

$$f^{(0)}=\Theta(a-r_\perp)\,n_0\varphi\left[v_\perp,\ v_x-v_0-\Delta v\cos\Omega\left(t-\frac{x}{v_x}\right)\right], \tag{9}$$

while the perturbation of the distribution function, including the interaction of the beam electrons, is

$$\frac{\partial f^{(1)}}{\partial t}+\mathbf{v}\frac{\partial f^{(1)}}{\partial \mathbf{r}}-\frac{e^2}{m}\left(\int d^3v'd^3r'\frac{\partial}{\partial \mathbf{r}}\frac{f^{(0)}(\mathbf{r}',\mathbf{v}',t)}{|\mathbf{r}-\mathbf{r}'|}\right)\frac{\partial f^{(1)}}{\partial \mathbf{v}}=0. \tag{10}$$

In this equation the electric field which acts on the beam particles can be written in the form

$$\mathbf{E}^0(\mathbf{r},t)=-e\frac{\partial}{\partial \mathbf{r}}\int d^3r'd^3v\frac{f^{(0)}(\mathbf{r}',\mathbf{v},t)}{|\mathbf{r}-\mathbf{r}'|}=$$

$$=-4\pi en_0a\frac{\partial}{\partial \mathbf{r}}\sum_{\nu=-\infty}^{\infty}i^\nu e^{i\nu\Omega t}\int_{-\infty}^{\infty}\frac{ds}{2\pi}g\left(\frac{s}{\Delta v}\right)J_\nu(s)\int_{-\infty}^{\infty}d\xi\,e^{-is\xi-\frac{i\nu\Omega x}{v_0+\xi\Delta v}}\times$$

$$\times \int_0^\infty \frac{dl_\perp J_0(l_\perp r_\perp) J_1(l_\perp a)}{l_\perp^2 + \left(\frac{\nu\Omega}{v_0 + \xi\Delta v}\right)^2}, \tag{11}$$

where

$$g(x) = \int_{-\infty}^{\infty} du e^{iux} \int d^2 v_\perp \varphi(\mathbf{v}_\perp, u) \tag{12}$$

is the Fourier transform of the initial longitudinal velocity distribution function, $\xi \equiv (v_\parallel - v_0)/\Delta v$, and $J_\nu(s)$ is the Bessel function.

The effective values of ξ which contribute to the integral in (11) are of the order of unity; therefore the term $\xi\Delta v$ in the denominator can be neglected in comparison with v_0. The quantity $\xi\Delta v$ in the exponent cannot be neglected. It is evident that in this case the time dependence of the field vanishes. However, using the fact that $\Delta v/v_0 \ll 1$ the exponent can be expanded in powers of $\Delta v/v_0$. If the effective values of ν in the sum are such that

$$\frac{\nu\Omega L}{v_0}\left(\frac{\Delta v}{v_0}\right)^2 \ll 1, \tag{13}$$

only the first two terms in the expansion in the exponent need be retained. Condition (13) is not too stringent since those harmonics whose wavelengths are comparable with the length of the beam, i.e., $\nu \sim c/\Omega L$, make a significant contribution to the radiation. Thus when the condition

$$\left(\frac{\Delta v}{v_0}\right)^2 \ll \frac{v_0}{c} \tag{14}$$

is satisfied, after performing the integration in (11) we have

$$\mathbf{E}^0 = 4\pi e n_0 a^2 \frac{\partial}{\partial \mathbf{r}} \sum_{\nu \neq 0} i^\nu e^{i\nu\Omega\left(t - \frac{x}{v_0}\right)} \frac{I_0\left(\frac{\nu\Omega r_\perp}{v_0}\right) K_1\left(\frac{\nu\Omega a}{v_0}\right)}{\frac{\nu\Omega a}{v_0}} \times g\left(\frac{\nu\Omega x}{v_0^2}\right) J_\nu\left(\frac{\nu\Omega x}{v_0}\frac{\Delta v}{v_0}\right), \tag{15}$$

where $I_0(x)$ is the Bessel function and $K_1(x)$ is the Macdonald function. $\mathbf{E}^0(\mathbf{r}, t)$ is the variable part of the electric field produced by the modulated beam when spreading can be neglected. In the region in which the spreading of the beam is small the Coulomb repulsion of the electrons changes the velocities of the particles by an amount which is small in comparison with the initial velocity

$$|\mathbf{v} - \mathbf{v}_0| \ll v_0. \tag{16}$$

When condition (16) is satisfied $\mathbf{v}$ can be replaced by $\mathbf{v}_0$ in Eq. (10). Then the solution of Eq. (10) can be written in the form

$$f^{(1)} = n_0 \Theta(a - r_\perp) \varphi\left\{\mathbf{v}_\perp - \frac{e}{mv_0}\int_0^x dx' \mathbf{E}_\perp^{(0)}\left(t - \frac{x - x'}{v_0}\right);\right.$$

$$\left. v_\parallel = v_0 - \Delta v \cos\Omega\left(t - \frac{x}{v_0}\right) - \frac{e}{mv_0}\int_0^x dx' \mathbf{E}_\parallel^0\left(\mathbf{r}_\perp, x', t - \frac{x - x'}{v_0}\right)\right\}. \tag{17}$$

Using (15) it is easy to see that the inequality (16) is equivalent to

$$L \ll a \frac{mv_0^2}{2eI}. \tag{18}$$

3. In calculating the radiation it is convenient to rewrite (3) in the form

$$\mathbf{E}_\omega = -\frac{ik}{cR} e^{ikR} \boldsymbol{\theta} [j_\parallel(\omega, \mathbf{k}) \cos\theta - j_\perp(\omega, \mathbf{k}) \sin\theta]$$

$$= \frac{k}{cR} e^{ikR} \int_{-\infty}^{\infty} dt e^{i\omega t} \int d^3 r e^{-i\mathbf{kr}} \left[\mathbf{n}\left[\mathbf{n}\frac{\partial}{\partial \mathbf{q}}\right]\right] f^{(1)}(\mathbf{r}, \mathbf{q} = 0, t), \tag{19}$$

where $\boldsymbol{\theta}$ is a unit vector in a spherical coordinate system with its polar axis along the x axis; the vector $\mathbf{j}(\omega, \mathbf{k})$ is given by (4), and $f(\mathbf{r}, \mathbf{q}, t) = \int d^3 v e^{-i\mathbf{qv}} f(\mathbf{r}, \mathbf{v}, t)$.

Using (15) and assuming that the radius of the beam is small in comparison with the wavelength of the radiation we obtain the following expression for the field at large distances:

$$\mathbf{E}_\omega = -\frac{ike^{ikR}}{cR} \boldsymbol{\theta} 8\pi I \sin\theta \frac{2eI}{mv_0^3} \sum_{\nu \neq 0} i^\nu D_\nu(\cos\theta) \frac{K_1\left(\frac{\nu\Omega a}{v_0}\right) I_1\left(\frac{\nu\Omega a}{v_0}\right)}{\left(\frac{\nu\Omega a}{v_0}\right)^2}, \tag{20}$$

where

$$D_\nu(\cos\theta) \equiv \int_0^\infty dx e^{-i\left(k\cos\theta + \frac{\nu\Omega}{v_0}\right)x} g\left(\frac{\nu\Omega x}{v_0^2}\right) J_\nu\left(\frac{\nu\Omega x}{v_0}\frac{\Delta v}{v_0}\right). \tag{21}$$

The upper limit of the integral in (21) is taken as infinity. This is admissible if

$$\frac{\Omega L}{v_0} \sim \frac{\Omega a}{v_0}\frac{mv_0^3}{2eI} \gg 1, \tag{22}$$

i.e., the beam is long enough to contain several bunches.

Assuming that the initial velocity distribution is Maxwellian with a longitudinal temperature T, from (12) we obtain

$$g\left(\frac{\nu\Omega x}{v_0^2}\right) = \exp\left\{-\frac{T}{2mv_0^2}\left(\frac{\nu\Omega x}{v_0}\right)^2\right\}. \tag{23}$$

We note that the condition $T \ll mv_0^2$ does not ensure that the beam is cold since the initial narrow distribution function spreads as the distance from the point of injection increases. This spreading is greater for higher modulation frequencies and for higher harmonics. The decrease in the intensity of coherent radiation due to thermal velocities can be neglected if the temperature and the effective beam length satisfy the inequality

$$\frac{T}{mv_0^2}\left(\frac{\Omega L}{v_0}\right)^2 \ll 1, \tag{24}$$

which can be rewritten in the form

$$T \ll e^2 n_0 a^2 \frac{e^2 n_0}{m\left(\frac{\Omega}{2\pi}\right)^2}. \tag{25}$$

If conditions (24) and (25) are satisfied the longitudinal velocity distribution function can be considered a delta function over the region in which spread of the beam is small. In this case $g(\nu \Omega x/v_0^2) = 1$. Using the value of integral (21) given in ref. 9 we obtain

$$D_\nu(\cos\theta) = \frac{e^{-\frac{i\pi}{2}(\nu+1)}\left(\frac{\nu\Omega}{v_0}\right)^\nu\left(\frac{\Delta v}{v_0}\right)^\nu}{\sqrt{\left(\frac{\nu\Omega}{v_0}+k\cos\theta\right)^2-\left(\frac{\nu\Omega}{v_0}\right)^2\left(\frac{\Delta v}{v_0}\right)^2}\left(\frac{\nu\Omega}{v_0}+k\cos\theta+\sqrt{\left(\frac{\nu\Omega}{v_0}+k\cos\theta\right)^2-\left(\frac{\nu\Omega}{v_0}\frac{\Delta v}{v_0}\right)^2}\right)^\nu}. \tag{26}$$

Substituting (26) into (20) and retaining only the first nonvanishing term in the expansion in v_0/c (quadrupole) we obtain the radiation field

$$\mathbf{E}_\omega \approx -\frac{ke^{ikR}}{cR}\,64\pi I\sin 2\theta\,\frac{2eI}{mv_0^3}\,\frac{ka^2}{\left(\frac{\Omega a}{v_0}\right)^4}\sum_{\nu=1}^{\infty}\frac{\nu+1}{\nu^4}\,\frac{\left(\frac{\Delta v}{v_0}\right)^\nu}{2^\nu} \times K_1\left(\frac{\nu\Omega a}{v_0}\right)I_1\left(\frac{\nu\Omega a}{v_0}\right)\delta(\omega-\nu\Omega). \tag{27}$$

Since the field decreases rapidly as the harmonic number increases, we can limit ourselves to the term with $\nu = 1$. In the limiting case of a narrow beam, $a \ll v_0/\Omega$, the energy radiated by the beam per unit time is

$$\frac{d\varepsilon(\mathbf{n},\omega)}{d\Omega d\omega} = \frac{c}{4\pi^2}|\mathbf{E}_\omega|^2 \approx \frac{I^2\sin^2 2\theta}{c}\,\frac{(ka)^4}{\left(\frac{\Omega a}{v_0}\right)^8}\left(\frac{\Delta v}{v_0}\right)^2\left(\frac{2eI}{mv_0^3}\right)^2\delta(\omega-\Omega).$$

We note that for high modulation frequencies (22) the radiation intensity decreases as the frequency increases.

---

[1] A. I. Akhiezer and Ya. B. Fainberg, Zh. Eksp. Teor. Fiz., 21, 1962 (1951).

[2] D. Bohm and E. P. Gross, Phys. Rev., 75, 1864 (1949).

[3] A. B. Mikhailovskii, Theory of Plasma Instabilities, Vol. 1, Consultants Bureau, New York (1973).

[4] R. J. Briggs, Electron-Stream Interaction with Plasmas, MIT Press, Cambridge (1964).

[5] E. G. Katyshev, V. S. Panasyuk, S. G. Pankratov, V. F. Romanovskii, Yu. K. Samoshenkov, A. A. Sokolov, Ya. M. Spektor, and B. M. Stepanov, Zh. Tekh. Fiz., 42, 2446 (1972) [Sov. Phys.–Tech. Phys., 17, 1905 (1973)].

[6] S. G. Pankratov, Yu. K. Samoshenkov, and A. A. Sokolov, Zh. Tekh. Fiz., 42, 1320 (1972) [Sov. Phys.–Tech. Phys., 17, 1050 (1972)].

[7] N. P. Kalashnikov, S. G. Pankratov, V. S. Remizovich, and M. I. Ryazanov, Radiotekh. Elektron., 18, 1095 (1973).

[8] L. D. Landau and E. M. Lifshitz, The Classical Theory of Fields, Addision-Wesley, Reading (1962).

[9] G. N. Watson, Treatise on the Theory of Bessel Functions, Cambridge, New York (1944).

Skin effect in a constant magnetic field

Z. K. Yankauskas, V. I. Chesonis, and V. G. Skripnik

(Submitted October 10, 1973)
Zh. Tekh. Fiz., 44, 2015-2017 (September 1974)

The skin effect is studied in a conducting plate in alternating and constant magnetic fields. The effective magnetic permeability is determined in the alternating magnetic field.

We consider an infinite conducting plate bounded by the planes $z = \pm a$. A conductor is wound around the plate perpendicularly to the x axis. An alternating current of frequency ω flows through the conductor producing an alternating magnetic field (Fig. 1).

$$\mathscr{H} = H\cos\omega t, \quad |z| = a. \tag{1}$$

In the classical skin effect the field $\mathscr{H}_x$ penetrates the conducting plate[1] only to the skin depth δ. For $a \gg \delta$ the alternating magnetic field inside the plate is essentially zero.

If the plate is in a sufficiently strong constant magnetic field along the z axis, helical waves (helicons) are excited in the plate,[2] and the alternating magnetic field $\mathscr{H}_x$ penetrates well beyond the skin depth. The distribution of helical waves at microwave frequencies in a waveguide is calculated in ref. 3. We consider the skin effect for a range of low and high frequencies (up to ~ 100 MHz) in the presence of helicons.

If there is no constant magnetic field the alternating magnetic field $\mathscr{H}_x$ given by Eq. (1) excites eddy currents in the plate in planes perpendicular to the x axis. When there is a constant magnetic field $H_z = H_0$ in the plate Hall currents are produced in planes perpendicular to the y axis.[4]

Since we are considering an infinite plate, i.e., one whose transverse dimensions are much greater than its thickness, we can limit ourselves to the transverse current components j_x and j_y (plane wave approximation). Assuming for simplicity that the conductivity of the plate is due to electrons with an isotropic mass, we write the equations for the current components j_x and j_y:

$$\left.\begin{aligned}\frac{d}{dt}j_x + \tau^{-1}j_x - \frac{eH_0}{mc}j_y = \frac{Ne^2}{m}E_x,\\ \frac{d}{dt}j_y + \tau^{-1}j_y + \frac{eH_0}{mc}j_x = \frac{Ne^2}{m}E_y,\end{aligned}\right\} \tag{2}$$

where e, m, N, and τ are respectively the electron charge, effective mass, density, and mean free time; E_x and E_y are the components of the alternating electric field, and H_0 is the constant magnetic field along the z axis. The effect of the alternating magnetic field is neglected in comparison with H_0.

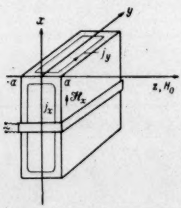

Fig. 1

Equation (2) must be considered together with Maxwell's equations

$$\left.\begin{aligned}\operatorname{curl}\mathscr{E} = -\frac{1}{c}\frac{\partial\mathscr{H}}{\partial t},\\ \operatorname{curl}\mathscr{H} = \frac{1}{c}\frac{\partial\mathscr{E}}{\partial t} + \frac{4\pi}{c}J.\end{aligned}\right\} \tag{3}$$

We seek the solution of the system of equations (2) and (3) in the form

$$\mathscr{E} = \operatorname{Re}\bar{E}\exp(-i\omega t), \quad \mathscr{H} = \operatorname{Re}\bar{H}\exp(-i\omega t), \quad J = \operatorname{Re}\bar{J}\exp(-i\omega t), \tag{4}$$

where the complex amplitudes $\bar{E}$, $\bar{H}$, and $\bar{J}$ depend only on the z coordinate and have only x and y components.

Since the frequency ω of the alternating magnetic field is appreciably smaller than the reciprocal of the mean free time $\tau^{-1} = 10^{11}$-10^{13} Hz, the time derivatives in Eq. (2) can be neglected. Expressing $\bar{E}$ and $\bar{J}$ in terms of $\bar{H}$ and neglecting the displacement currents in comparison with conduction currents, we obtain a system of equations for the complex amplitudes H_x and H_y from (2)-(4):

$$\left.\begin{aligned}c^2\frac{\partial^2}{\partial z^2}H_x + i\omega\sigma_{11}H_x + i\omega\sigma_{12}H_y = 0,\\ c^2\frac{\partial^2}{\partial z^2}H_y + i\omega\sigma_{22}H_y - i\omega\sigma_{12}H_x = 0,\end{aligned}\right\} \tag{5}$$

where the components of the conductivity tensor σ are

$$\sigma_{11} = \sigma_{22} = \sigma_0\frac{1}{1+\left(\frac{eH\tau}{mc}\right)^2}, \quad \sigma_{12} = \sigma_0\frac{\frac{eH\tau}{mc}}{1+\left(\frac{eH\tau}{mc}\right)^2}, \quad \sigma_0 = \frac{Ne^2\tau}{m}. \tag{6}$$

It follows from (1) that we must solve the system of equations for the boundary conditions

$$\left.\begin{aligned}H_x = H, \quad H_y = 0 \quad \text{for} \quad z = \pm a,\\ \frac{\partial H_x}{\partial z} = \frac{\partial H_y}{\partial z} = 0 \quad \text{for} \quad z = 0.\end{aligned}\right\} \tag{7}$$

The solutions satisfying these conditions are

$$H_x = \frac{1}{2}H\left(\frac{\cos k_- z}{\cos k_- a} + \frac{\cos k_+ z}{\cos k_+ a}\right), \tag{8a}$$

$$H_y = \frac{1}{2}iH\left(\frac{\cos k_+ z}{\cos k_+ a} - \frac{\cos k_- z}{\cos k_- a}\right), \tag{8b}$$

where $k_\pm$ are determined from the characteristic equation

$$c^2k_\pm^2 = \frac{\omega_p^2\omega}{\pm\omega_H + i\tau^{-1}}, \quad \omega_p^2 = \frac{4\pi Ne^2}{m}, \quad \omega_H = \frac{eH}{mc}. \tag{9}$$

The terms in (8) with the argument $k_- z$ are due to helicons. The magnetic fluxes per unit transverse length are

$$\Phi_x = \int_{-a}^{a} H_x dz = H\left(\frac{\operatorname{tg}k_- a}{k_-} + \frac{\operatorname{tg}k_+ a}{k_+}\right), \tag{10a}$$

$$\Phi_y = \int_{-a}^{a} H_y dz = iH\left(\frac{\operatorname{tg} k_+ a}{k_+} - \frac{\operatorname{tg} k_- a}{k_-}\right). \qquad (10b)$$

Equations (8) and (9) determine the complex field amplitudes and the flux as functions of the constant magnetic field H_0, the frequency ω, and the thickness of the plate a. As a consequence of the Hall currents an alternating magnetic field appears in the plate perpendicular to the exciting field.

From Eq. (10a) we find the effective magnetic permeability of the plate:

$$\mu_{\text{eff}} = \frac{\Phi_x}{2aH} = \frac{\operatorname{tg} k_- a}{2k_- a} + \frac{\operatorname{tg} k_+ a}{2k_+ a}. \qquad (11)$$

When $\omega_H \tau \gg 1$, from (9)

$$k_- = \sqrt{\frac{\omega_p^2 \cdot \omega}{\omega_H c^2}}\left(1 + \frac{i}{\omega_H \tau}\right), \qquad (12)$$

μ_{eff} is maximum at resonance

$$(\operatorname{Re} k_-)a = \frac{n\pi}{2}, \quad n = 1, 3, 5, \ldots \qquad (13)$$

and is equal to

$$\max \mu_{\text{eff}} \cong \frac{2i\omega_H \tau}{n^2\pi^2}, \quad n = 1, 3, 5, \ldots \qquad (14)$$

Thus at resonance the impedance Z of the induction coil with a conducting core is purely resistive

$$Z = -i\omega L_0 \mu_{\text{eff}} = \frac{2\omega_H \tau}{n^2\pi^2}\omega L_0 \qquad (15)$$

with absolute magnitude appreciably ($2\omega_H \tau/n^2\pi^2$ times) larger than the inductive reactance ωL_0 of the coil without a core, where L_0 is the inductance of the coil without a core. The intensity of the resonance peak decreases with an increase in the resonance number n = 1, 3, ...

The most suitable core material is InSb for which $\omega_H \tau = 1$ at room temperature in a magnetic field of ~ 1000 Oe.

---

[1] V. A. Govorkov, Electric and Magnetic Fields [in Russian], Energiya, Moscow (1968).

[2] É. A. Kaner and V. G. Skobov, Usp. Fiz. Nauk, 89, 367 (1966) [Sov. Phys.-Usp., 9, 480 (1967)].

[3] F. G. Bass, A. Ya. Blank, and M. L. Kaganov, Zh. Eksp. Teor. Fiz., 45, 1081 (1963) [Sov. Phys.-JETP, 18, 747 (1964)].

[4] Z. K. Yankauskas, Fiz. Tverd. Tela, 11, 2642 (1969) [Sov. Phys.-Solid State, 11, 2131 (1970)].

Graphical methods for constructing trajectories of small particles in electrostatic fields

N. I. Shtepa

(Submitted October 10, 1973)
Zh. Tekh. Fiz., 44, 2017-2020 (September 1974)

Graphical methods are described for the velocity increments and radii of curvature for trajectories of small (10^{-1}-10^{-4} cm) statically charged particles in strong electrostatic fields. An example is presented.

The focusing of small (10^{-1}-10^{-4} cm) statically charged particles by strong electrostatic fields is discussed in refs. 1-4. The analysis of the focusing is based on the general form of the differential equations describing the motion of particles in the fields under study. Focusing results from the linearity of the second-order differential equations in the paraxial approximation. Analytic expressions for the focusing parameters can be obtained in general form only for the fields of so-called thin lenses.

In order to find the focusing parameters of the practically important electrostatic fields of thick lenses and to explain their special features it is necessary to know how to find particle trajectories in each particular problem.

Finding the trajectories with sufficient accuracy is generally quite difficult and requires the use of a computer.

Relatively simple graphical methods similar to the methods of electron optics[5-7] can be used to find approximate trajectories. However, in contrast with electron-optical problems the calculational equations are somewhat complicated in the cases under consideration because of the effect of dissipative forces on the motion of particles in viscous media.

We describe below graphical methods for the velocity increments and radii of curvature for the construction of trajectories of small statically charged particles in strong electrostatic fields. As in refs. 1-4, it is assumed that the particles are homogeneous, isotropic, spherical, and small enough so that the variation in the guide field is negligible, but large enough so that fluctuation phenomena can be neglected. In steady flow in a viscous medium the particle velocities are limited by Stokes' law.

VELOCITY INCREMENTS METHOD

Under the limitations assumed the differential equation of motion of a particle in an electrostatic field can be written in the form[1]

$$m\frac{d\mathbf{v}}{dt}=\mathbf{F}_q+\mathbf{F}_p+\mathbf{F}_b+\mathbf{F}_a+\mathbf{F}_c, \tag{1}$$

where $\mathbf{v}$ is the velocity of the particle

$$m=\frac{4}{3}\pi R^3\rho_1 \tag{2}$$

is the mass of the particle, R is its radius, ρ_1 is its density,

$$\mathbf{F}_q=q\mathbf{E} \tag{3}$$

is the force due to the free charge q of the particle, $\mathbf{E}$ is the intensity of the electrostatic field,[1)]

$$\mathbf{F}_p=R^3\frac{(\varepsilon-1)}{(\varepsilon+2)}(\mathbf{E}\nabla)\mathbf{E} \tag{4}$$

is the force due to the polarization of the particle, ε_1 and ε_2 are respectively the permittivities of the particle and the medium, $\varepsilon = \varepsilon_1/\varepsilon_2$,

$$\mathbf{F}_b=\frac{4}{3}\pi R^3\rho_1\mathbf{g} \tag{5}$$

is the weight, $\mathbf{g}$ is the acceleration due to gravity,

$$\mathbf{F}_a=-\frac{4}{3}\pi R^3\rho_2\mathbf{g} \tag{6}$$

is the buoyant force, ρ_2 is the density of the medium,

$$\mathbf{F}_c=-6\pi\mu R(\mathbf{v}-\mathbf{u}) \tag{7}$$

is the viscous force, μ is the coefficient of viscosity, and $\mathbf{u}$ is the velocity of the medium.

We represent the displacement Δs of a particle along its trajectory in terms of Δx, Δy, and Δz. For a sufficiently small displacement Δs the velocity increments can be written to second order as follows:

$$\Delta v_x=\frac{\Delta x}{v_x}\left[\eta E_x+aE\frac{\partial E}{\partial x}+kg_x-\lambda(v_x-u_x)\right], \tag{8}$$

$$\Delta v_y=\frac{\Delta y}{v_y}\left[\eta E_y+aE\frac{\partial E}{\partial y}+kg_y-\lambda(v_y-u_y)\right], \tag{9}$$

$$\Delta v_z=\frac{\Delta z}{v_z}\left[\eta E_z+aE\frac{\partial E}{\partial z}+kg_z-\lambda(v_z-u_z)\right], \tag{10}$$

where

$$\eta=\frac{3q}{4\pi R^3\rho_1},\quad a=\frac{3(\varepsilon-1)}{4\pi(\varepsilon+2)\rho_1},\quad k=1-\frac{\rho_2}{\rho_1},\quad \lambda=\frac{9\mu}{2R^2\rho_1}. \tag{11}$$

Equations (8)-(10) are the basic calculational equations of the velocity increments method.

In this method the trajectory is constructed step by step in two projections, for example on the xoy and xoz planes, in the following way (Fig. 1). Starting from the projections A_{u_0} and A_{w_0} of the initial point A_0 on the coordinate planes, the components v_{u_0} and v_{w_0} of the initial velocity are constructed. Replacing the true motion of a point along a small segment by its motion along a tangent, v_{u_0} and v_{w_0} are used to find the projections A_{u_1} and A_{w_1} of the next point A_1 of the trajectory corresponding to a small increment Δx_0. Equations (8)-(10) are used to calculate the increments in the velocity components Δv_{x_0}, Δv_{y_0}, Δv_{z_0} corresponding[2)] to the step of the construction, and the velocity components v_{u_1}, and v_{w_1} at point A_1 are found from $v_{x_1} = v_{x_0} + \Delta v_{x_0}$, $v_{y_1} = v_{y_0} + \Delta v_{y_0}$, $v_{z_1} = v_{z_0} + \Delta v_{z_0}$. A similar construction is then performed for the next portion, and this process is continued until the whole trajectory is constructed.

The accuracy of the method is improved if the displacement along the tangent is replaced by the displacement along the bisector of the angle between the tangents at the initial and end points of the interval. The final position of each point is recalculated after the main construction, which increases the volume of the work somewhat.

RADII OF CURVATURE METHOD

In this method a trajectory is constructed from a succession of arcs of osculating circles of projections on the coordinate planes xoy and xoz.

The radii of curvature of the projections of the trajectory are

$$R_u = \frac{(v_x^2 + v_y^2)^{3/2}}{v_y \frac{dv_x}{dt} - v_x \frac{dv_y}{dt}}, \tag{12}$$

$$R_w = \frac{(v_x^2 + v_z^2)^{3/2}}{v_z \frac{dv_x}{dt} - v_x \frac{dv_z}{dt}} \tag{13}$$

which, by taking account of (1), can be rewritten in the form

$$R_u = \frac{(v_x^2 + v_y^2)^{3/2}}{\eta\,(v_y E_x - v_x E_y) + aE\left(v_y \frac{\partial E}{\partial x} - v_x \frac{\partial E}{\partial y}\right) + k\,(v_y g_x - v_x g_y) + \lambda\,(u_x v_y - u_y v_x)}, \tag{14}$$

$$R_w = \frac{(v_x^2 + v_z^2)^{3/2}}{\eta\,(v_z E_x - v_x E_z) + aE\left(v_z \frac{\partial E}{\partial x} - v_x \frac{\partial E}{\partial z}\right) + k\,(v_z g_x - v_x g_z) + \lambda\,(u_x v_z - u_z v_x)}. \tag{15}$$

The construction of a trajectory on the coordinate planes xoy and xoz is started from the projections A_{u_0} and A_{w_0} of the initial point A_0 (Fig. 2). At this point Eqs. (14) and (15) are used to calculate the radii of curvature R_{u_0} and R_{w_0}. Using the values found for the radii the centers of curvature O_{u_0} and O_{w_0} are located along the perpendiculars to the velocity components v_{u_0} and v_{w_0} at the initial point, and the arcs $A_{u_0}A_{u_1}$ and $A_{w_0}A_{w_1}$ corresponding to the small increment Δx_0 are constructed. The end points of the arcs, A_{u_1} and A_{w_1}, determine the succeeding point of the trajectory A_1. The next part of the trajectory is then constructed from this point, etc.

The velocity components v_x, v_y, v_z needed to calculate the subsequent radii of curvature in the construction process are found by calculating their increments Δv_x, Δv_y, Δv_z from Eqs. (8)-(10).

As an example Table 1 lists the results of constructing the trajectory of an ice particle of radius $R = 0.5 \cdot 10^{-2}$ cm moving in the electrostatic field of a cylindrical capacitor with a vertical axis. The air between the capacitor plates is at rest (u = 0); the intensity of the electric field is E = A/r, the charge of the particle and its initial velocity are chosen so that

$$\eta = \lambda\sqrt{a},\quad \dot{r}_0 = \frac{A\sqrt{a}}{r_0},\quad \dot{z}_0 = \frac{kg}{\lambda},\quad \dot{\vartheta}_0 = 0$$

(r, z, ϑ are cylindrical coordinates with the z axis along the axis **g** of the cylinder). The differential equation of the trajectory can be integrated exactly:

$$z = \frac{kg}{2\lambda A\sqrt{a}}(r^2 - r_0^2),\quad \vartheta = \text{const}$$

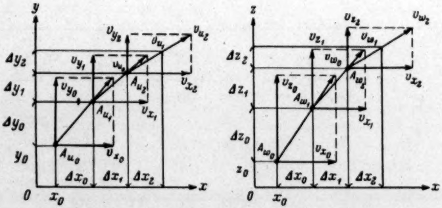
y
v_{y_2}
v_{u_2}
v_{u_1}
Δy_2
v_{y_1}
v_{u_0}
Δy_1
v_{y_0}
A_{u_2}
v_{x_2}
A_{u_1}
v_{x_1}
Δy_0
y_0
A_{u_0}
v_{x_0}
Δx_0
Δx_1
Δx_2
x
0
x_0
z
v_{z_2}
v_{w_2}
v_{z_1}
v_{w_1}
Δz_2
v_{w_0}
Δz_1
v_{z_0}
A_{w_2}
v_{x_2}
A_{w_1}
v_{x_1}
Δz_0
A_{w_0}
v_{x_0}
z_0
Δx_0
Δx_1
Δx_2
x
0
x_0

Fig. 1

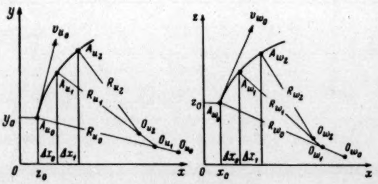
y
v_{u_0}
A_{u_2}
A_{u_1}
R_{u_2}
R_{u_1}
y_0
A_{u_0}
R_{u_0}
O_{u_2}
O_{u_1}
O_{w_0}
Δx_0
Δx_1
0
x_0
x
z
v_{w_0}
A_{w_2}
A_{w_1}
R_{w_2}
z_0
A_{w_0}
R_{w_1}
R_{w_0}
O_{w_2}
O_{w_1}
O_{w_0}
Δx_0
Δx_1
0
x_0
x

Fig. 2

TABLE 1

	z, cm										
r, cm	0	1	2	3	4	5	6	7	8	9	10
Exact value	1	1.60	2.02	2.37	2.68	2.95	3.20	3.44	3.65	3.86	4.06
Velocity increments	1	1.55	1.94	2.25	2.55	2.85	3.10	3.33	3.55	3.66	3.86
Radii of curvature	1	1.77	1.99	2.35	2.62	2.87	3.12	3.37	3.58	3.78	3.97

assuming $z_0 = 0$. The construction is performed for the following values: $A = 2 \cdot 10^3$ V, $\varepsilon_1 = 2.8$, $\varepsilon_2 = 1$, $\rho = 0.9$ g/cm^3, $g = 981$ cm/sec^2, $k = 1$, $\mu = 1.8 \cdot 10^{-4}$ g/cm$\cdot$sec, and $r_0 = 1$ cm. The trajectory is constructed from $z_0 = 0$ to $z = 10$ cm in steps $\Delta z_i = 1$ cm.

Table 1 shows that the approximate trajectories found by graphical methods are close to the exact values.

In conclusion we note that the main virtue of the methods described is their relative simplicity and universality. They can be used when the guide fields are described either analytically or numerically. The latter is important since in practice the electrostatic fields of complex configurations (calculated or simulated) are ordinarily given in the form of numerical values of the potential. An important shortcoming of the methods is the lack of reliable methods of estimating accuracy. In practice the accuracy can be judged by the difference between trajectories constructed by different methods or for various partitions into segments.

---

1) The factor ε_2 appears by mistake in the expression for $\vec{F}_p$ in refs. 1-4.

2) For a potential distribution $\varphi(x, y, z)$ given analytically or numerically the values of E, E_x, $\partial E/\partial x, \ldots$ at the point of construction are found exactly or approximately from $\mathbf{E} = -\operatorname{grad} \varphi$.

[1] N. I. Shtepa, Zh. Tekh. Fiz., 36, 470 (1966) [Sov. Phys.–Tech. Phys., 11, 347 (1966)].

[2] N. I. Shtepa, Zh. Tekh. Fiz., 38, 1060 (1968) [Sov. Phys.–Tech. Phys., 13, 803 (1968)].

[3] N. I. Shtepa, Zh. Tekh. Fiz., 40, 1976 (1970) [Sov. Phys.–Tech. Phys., 15, 1540 (1971)].

[4] N. I. Shtepa, Ukr. Fiz. Zh., 12, 1973 (1967).

[5] V. Kel'man and S. Yavor, Electron Optics [in Russian], Izd. AN SSSR, Moscow–Leningrad (1959).

[6] N. S. Zinchenko, A Course of Lectures on Electron Optics [in Russian], Khar'kov State University (1961).

[7] N. I. Shtepa, Zh. Tekh. Fiz., 28, 2587 (1958) [Sov. Phys.–Tech. Phys., 3, 2370 (1959)].

Cumulative destruction of transparent dielectrics in repeated laser irradiation

L. D. Khazov, I. A. Fersman, and V. Yu. Bortniker

(Submitted June 4, 1973)
Zh. Tekh. Fiz., 44, 2020-2022 (September 1974)

We obtain a relation between the number of laser shots needed to destroy a K-8 glass surface and the energy density in the laser beam. We find that the scattering of light at the glass surface increases with the number of laser shots. This means that microdefects accumulate during repeated irradiation.

The relation between the number of laser shots needed to destroy a sample and the energy density in the laser beam (lifetime curves) has been obtained by several researchers for various materials such as nonlinear $LiNbO_3$ and $Ba_2NaNb_5O_{15}$ crystals,[1] polymers,[2] and reflecting dielectric coatings.[3]

Two explanations of the reduced destructive energy density of a laser beam have been described in the literature. Bass[4] has proposed a statistical form of destruction, i.e., he assumes that the probability of destruction depends linearly upon the intensity of the laser light.

In another explanation[1-3] for the reduced threshold, an accumulation of irreversible, residual changes in the properties of the material and an increase in the number of defects, which results in aging of the material, are assumed.

We have investigated the destruction resulting from multiple irradiations of K-8 glass which has its surface polished according to usual standards. In order to explain the reduced transparency of the surface after repeated irradiation, we record the scattering of the laser light at the surface in addition to investigations of the lifetime. Figure 1 shows the optical arrangement of the apparatus. The radiation emitted by the single-pulse ruby laser 1, which is operated in a single, transverse mode, is focused by a lens 4 with great focal length (f = 235 mm) upon sample 5.

A K-8 glass sample ϕ 30 × 4 mm is placed in a movable mounting and forms the window of the blackened housing 10. It is assumed that if microdefects are generated, scattering must occur at the defects. The forward scattering is recorded, because the scattering is a maximum in the forward direction. In order to record the scattering at small angles inside the housing a concave mirror 8 with a center opening for the basic laser beam is mounted inside the housing. The laser beam is attenuated behind the mirror with the aid of a filter 9. The scattered light, which is reflected by the mirror, is directed with a total internal reflection prism 13 onto an FÉU-14 photomultiplier 11. In order to attenuate spurious signals which reduce the sensitivity of the apparatus, all components surrounding the beam are blackened and the basic laser beam is transmitted in a blackened tube. A neutral KS-19 filter 12 is placed in front of the photomultiplier to prevent light from incandescent lamps from being recorded. In order to preclude bias illumination by the luminescence flux, an iris 3 mm in diameter is placed in front of the lens. The residual scattering signal (without sample) is reduced to half the magnitude of the scattering signal in undamaged glass by these measures. The moment at which the surface is destroyed is indicated by the formation of a plasma whose bright flash generates a strong signal in an oscilloscope.

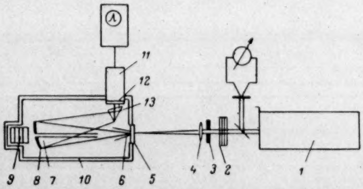

Fig. 1. Optical scheme of the recording apparatus. 1) Single-pulse single-mode ruby laser; 2) set of calibrating neutral filters; 3) diaphragm; 4) collector lens; 5) sample; 6) blackened cone; 7) tube; 8) concave mirror with center opening; 9) cassette with a set of neutral filters; 10) housing; 11) FÉU-14 photomultiplier; 12) NS-9 and KS-19 filters; 13) prism.

In order to obtain the lifetime characteristics a series of statistical tests is made. The destruction threshold obtained with the first shot is defined as the energy density at which destruction occurs with a probability of about 50%. This limit is termed "resistance of light." Since the resistance to light is inhomogeneous, the transition region near the threshold is very large (Figure 2a).

The following method is used to obtain the threshold of destruction of the surface after a series of shots. For a given adjustable energy of the shot, the irradiation shots are repeated until a large signal generated by a spark appears on the oscilloscope. After this series, the average energy of a shot and the energy spread in a series are calculated. The high inhomogeneity of the resistance to

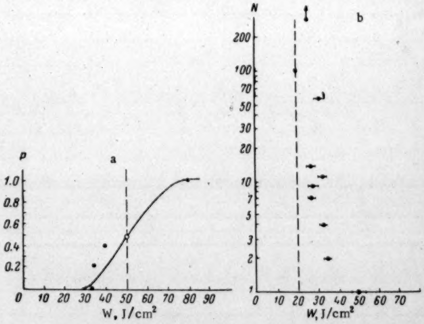

Fig. 2. a) Dependence of the probability of destruction with the first shot upon the energy density of the radiation. The diameter of the irradiated section is 126 μ. b) Dependence of the number of shots needed for destruction on the energy density in the beam. The horizontal arrows denote the spread of the radiation energy in a series. The vertical arrows indicate that after a particular number of flashes, destruction does not occur at the given energy density.

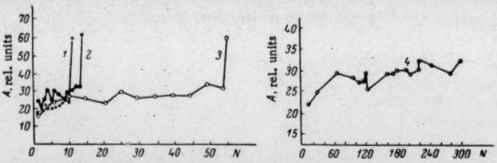

Fig. 3. Dependence of the magnitude of the scattering signal upon the number of irradiation pulses. Curves 1 and 2 are recorded with W ≈ 38 J/cm^2, curve 3, with W ≈ 33 J/cm^2, and curve 4, with W ≈ 29 J/cm^2.

light implies that for similar values of the average energy of a shot, there appear points which are destroyed after seven shots, as well as points which are not destroyed even after 300 shots (Fig. 2b). At an energy density of 29 J/cm^2 in the beam, no sample destruction takes place at seven points of a sample even after 100 irradiation pulses.

There probably exists an energy below which no destruction occurs even for $N \to \infty$ (dashed line in Fig. 2b). This energy density is termed the stability limit of a particular sample. Several thousand shots must be applied for a correct determination of the stability limit. This is not possible for technical reasons.

The dimensional effect of ref. 5 must be recalled when the quantitative data of Fig. 2 are used.

The scattering signal increases in proportion to the increasing number of radiation shots which do not yet cause destruction (Fig. 3). The slight increase in the scattering signal in the subthreshold region is followed by a sharp discontinuity of the signal, with the discontinuity resulting from the spark of a surface discharge. Values of the scattering signal obtained at constant radiation energy are used to construct the curves.

The increase in the scattering signal indicates the generation of microdefects in the surface layer of the sample in multiple shots. The microdefects accumulate from shot to shot and result in aging of the sample and reduced sample transparency.

---

[1] M. Bass, Papers of the Symposium "Damage to Materials by Laser Radiation" Organized by the American Society for Testing and Materials in the National Bureau of Standards, June 24-25, 1970, Boulder, Colorado.

[2] M. V. Agranat, I. K. Krasyuk, N. P. Novikov, V. P. Perminov, Yu. P. Yudin, and P. A. Yampol'skii, Zh. Eksp. Teor. Fiz., 60, 1748 (1971) [Sov. Phys.—JETP, 33, 944 (1971)]; V. A. Likhachev, S. M. Ryvkin, V. M. Salmanov, and N. D. Yaroshetskii, Fiz. Tverd. Tela, 8, 3432 (1966) [Sov. Phys.—Solid State, 8, 2754 (1967)].

[3] A. Ya. Kuznetsov, I. S. Varnashova, A. A. Poplavskii, and G. P. Tikhomirov, OMP, No. 3, 39 (1972).

[4] A. J. Glass and A. H. Guenther, Appl. Opt., 11, No. 4, 832 (1972).

[5] L. A. Nesterov, A. A. Poplavskii, I. A. Fersman, and L. D. Khazov, Zh. Tekh. Fiz., 40, 651 (1970) [Sov. Phys.—Tech. Phys., 15, 505 (1970)].

Ion energy spectra and collective effects in a Penning ion source

V. I. Farenik, V. V. Vlasov, A. M. Rozhkov, and A. A. Kozharin

A. M. Gor'kii Khar'kov State University

(Submitted July 17, 1973; resubmitted February 12, 1974)
Zh. Tekh. Fiz., 44, 2023-2025 (September 1974)

It has been shown experimentally that the energy spectrum of an ion beam extracted along the magnetic field from a Penning source is governed by any instability which occurs in the source plasma. In the case of the ion-cyclotron instability the spectral half-width is much larger than in the case of low-frequency ($\omega_{LF} < \omega_{Hi}$) drift waves. The regimes corresponding to ion-cyclotron and drift instabilities are determined.

In many applications of ion beams from plasma sources the ions must have a small energy spread. Various methods are known for reducing this spread:[1] in general, reducing the maximum beam energy, using various types of extracting probes, choosing appropriate materials for the source electrodes, etc. It has also been pointed out[1] that oscillatory processes involving a collective interaction between the electron and ion beams with the plasma affect the conditions under which the ion beam is produced and affect the characteristics of this beam. However, these questions have not been studied adequately; in particular, an unambiguous relationship has not been established between the width of the ion energy spectrum and the characteristic waves in a Penning source.

We report here an experimental study of the energy spectra of ion beams extracted along the magnetic field from a Penning source in the case in which ion-cyclotron waves and low-frequency drift waves exist in the plasma, at frequencies ω_{Hi} and $\omega_{LF} < \omega_{Hi}$.

The experimental apparatus and the configurations of the magnetic and electric fields are described in ref. 2. The magnetic field is varied over the range H = 0-1.5 kOe, the anode voltage over the range V_a = 1-2 kV and the working-gas (air) pressure over the range P = $(0.5-2)\cdot 10^{-4}$ torr. The ion energy spectra are determined by a special electrostatic analyzer which can be used to measure the ion energy over the radial cross section of the beam. The plasma waves are detected by a system of single probes at the floating potential and a standard radio receiver.

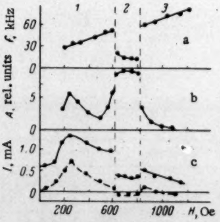

Fig. 1. Functional dependences of the magnetic field H of various quantities. a) Plasma-wave frequency f; b) plasma-wave amplitude A; c) anode current I_a (solid curve) and current to reflecting electrodes (dashed curve). It should be kept in mind that the anode current and the current to the reflecting electrodes have different polarities. Ion-cyclotron waves (regions 1 and 3) and low-frequency drift waves (region 2) occur in the discharge. V_a = 1.2 kV, P = $6\cdot 10^{-5}$ torr.

A resonant cyclotron instability, accompanied by the excitation of waves at the ion gyrofrequency (region 1 in Fig. 1) occurs in the discharge when the crossed radial electric field E_r and longitudinal magnetic field H satisfy

$$H = H_{cr} \approx \sqrt{\frac{2m_i c^2 E_r}{e_i r}} \tag{1}$$

where m_i is the mass of atomic nitrogen, c is the speed of light, e_i is the ion charge, r is the plasma radius $E_r = 0.3\cdot 10^{-2}\, V_a/\delta$, and δ is the distance between the anode and the reflecting electrode. This instability leads to an effective heating of the ion plasma component,[3] so that the ion velocity distribution becomes an equilibrium distribution (Fig. 2, curve 1). In this case the spectral half-width is a maximum at $H = H_{cr}$. At $H > H_{cr}$, a saturation region (or plateau) appears in the ion distribution, due to nonlinear effects which tend to increase the average ion energy.

At $H \approx 3\, H_{cr}$ the amplitude of the cyclotron waves falls abruptly (region 2 in Fig. 1), and large-amplitude, low-frequency waves ($f_{LF} < \omega_{Hi}/2\pi$) appear. We identify them as drift waves:[4]

$$f_{LF} \sim \frac{E_r}{H}, \quad \cos\theta = \frac{k_\parallel}{k_\perp} \ll 1,$$

where θ is the angle between the magnetic field and the wave-propagation direction, $k_\parallel$ and $k_\perp$ are the components of the wave number, and the wave propagates in the direction of the ion Larmor drift. The value of the frequency

$$f_{LF} \approx \frac{m f_{Hi}}{2\pi}\frac{\rho_i^2}{r} \approx 0.3 f_{Hi},$$

where m is the index of the azimuthal mode and ρ_i is the ion Larmor radius, agrees well with the results of ref. 4.

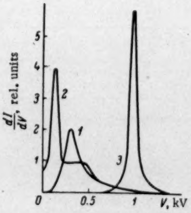

Fig. 2. Energy spectra of the ion beams. 1,2) Cyclotron instability; 3) low-frequency drift waves. V_a = 1.2 kV; P = $6\cdot 10^{-5}$ torr; dI/dV is the derivative of the function I = f(V); I is the collector current in the electrostatic analyzer, V is the retarding potential.

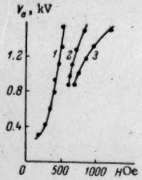

Fig. 3. Experimental dependence on the magnetic field H for the anode voltage V_a corresponding to the excitation of cyclotron (1,3) and low-frequency (2) waves in the plasma.

Under these conditions the emission of particles, particularly electrons, from the plasma is significantly lower. Figure 1c shows the abrupt decreases in the anode current and the current to the reflecting electrode. These decreases are accompanied by pronounced changes in the energy spectrum of the ion beam (Fig. 2), where the half-width falls below $0.1V_a$. It is particularly important to note that the maximum beam energy is comparable to the potential drop across the electrodes and can be changed easily by changing this potential drop. Furthermore, while in the cyclotron-instability region the beam energy and intensity are smoothly varying functions of the radius (the functional dependences are "bell-shaped"), they are concentrated near the center of the discharge in the region of low-frequency drift waves.

With a further increase in the magnetic field, at $H > (4\text{-}4.5)H_{cr}$ the ion cyclotron instability sets in (region 3 in Fig. 1), and the energy spectrum of the ion beam becomes thermal. The entire process behaves as if the anode voltage were changed at H = const. Figure 3 shows the functional dependences $V_a = f(H)$, which give the thresholds for the onset of the cyclotron (curves 1 and 3) and drift-wave (curve 2) instabilities. For values of H and V_a lying between curves 2 and 3 the ions display a minimal energy spread.

We cannot go into detail here on the nature of the excitation of the drift and cyclotron (region 3 in Fig. 1c) waves, which result from the relative azimuthal motion of the plasma components in a cylindrically symmetric system (see, e.g., ref. 5), but we note that one reason for the abrupt change in the plasma-wave frequency f as a function of **H** (Fig. 1) can be a nonlinear interaction between the strong high-frequency waves in this discharge with the low-frequency ions waves (a parametric interaction) (refs. 6, 7). The possibilities for reducing the width of the ion-beam energy spectrum are apparently not exhausted by a study of the low-frequency spectrum of collective instabilities ($\omega \nless \omega_{Hi}$), but we can conclude that an important first step in producing an ion beam having a small energy spread is to suppress the ion cyclotron instability, which leads to an effective heating of the ion component.

The authors thank K. I. Stepanov and V. A. Suprunenko for useful discussions.

---

[1] M. D. Gabovich, Physics and Technology of Plasma Ion Sources [in Russian], Atomizdat, Moscow (1972).

[2] A. M. Rozhkov, K. N. Stepanov, V. A. Suprunenko, V. I. Farenik, and V. V. Vlasov, Ukr. Fiz., Zh., 14, 1856 (1969).

[3] A. M. Rozhkov, K. N. Stepanov, V. A. Suprunenko, V. I. Farenik, and V. V. Vlasov Author's Certificate No. 352610; Byull. Izobret., No. 4, 164 (1973).

[4] A. B. Mikhailovskii, Nuclear Fusion, 5, 125 (1965).

[5] Yu. A. Kirochkin, V. L. Sizonenko, and K. N. Stepanov, Ukr. Fiz. Zh., 18, 621 (1973).

[6] V. F. Tarasenko, A. B. Kitsenko, V. I. Panchenko, and K. N. Stepanov, Zh. Tekh. Fiz., 42, 1996 (1972) [Sov. Phys.-Tech. Phys., 17, 1599 (1973)].

[7] V. I. Farenik, V. V. Vlasov, and A. M. Rozhkov, ZhETF Pis. Red., 18, 409 (1973) [JETP Lett., 18, 240 (1973)].

Turbulent plasma heating and the Buneman instability

V. L. Sizonenko
Physicotechnical Institute,
Academy of Sciences of the Ukrainian SSR, Khar'kov

(Submitted February 25, 1974)
Zh. Tekh. Fiz., 44, 2025-2027 (September 1974)

The nonlinear stage of the kinetic Buneman instability is analyzed. The scattering of resonant electrons by fluctuations of the electric field leads to an anomalously rapid increase in the electron thermal velocity to the velocity characteristic of the current.

Kinetic wave branches as well as hydrodynamic Buneman instabilities[2-4] are excited efficiently in an unmagnetized plasma.[1] Below we analyze the nonlinear stage of these kinetic instabilities, finding that the primary nonlinear effect is a rapid electron heating.

We start from the following relations[1] for the kinetic instability in a plasma with $T_e \gg T_i$:

$$\gamma \equiv \operatorname{Im}\omega \sim \operatorname{Re}\omega \sim \omega_{pi},\ k \sim r_D^{-1},\ \cos\vartheta \sim \frac{v_{Te}}{u} \ll 1, \tag{1}$$

where **k** is the wave vector, ω is the complex frequency, **u** is the ordered velocity corresponding to the current, $r_D = (v_{Te}/\omega_{pe})$, $v_{T\alpha} = (T_\alpha/m_\alpha)^{1/2}$, $\omega_{p\alpha} = (4\pi e^2 n_0/m_\alpha)^{1/2}$, $\alpha = (e, i)$, and ϑ is the angle between **k** and **u**.

To describe the nonlinear stage of the instability we use the weak coupling kinetic model of Kadomtsev,[5] according to which

$$\varepsilon(\mathbf{k}, \omega) \equiv 1 - \frac{\omega_{pi}^2}{\omega^2} + \frac{4\pi e}{k^2}\int dv\,(\mathbf{k}\mathbf{g}_{\mathbf{k}\omega}) f_0 + \Delta\varepsilon(\mathbf{k}, \omega), \tag{2}$$

$$\eta_{\mathbf{k}\omega} P_{\mathbf{k}\omega} = \frac{\partial}{\partial v_i} A_{ij} \frac{\partial P_{\mathbf{k}\omega}}{\partial v_j},\ A_{ij} = \left(\frac{e}{m_e}\right)^2 \int d\mathbf{k}'d\omega' \frac{k_i' k_j' I_{\mathbf{k}'\omega'}}{\omega'' - \mathbf{k}''\mathbf{v} + \eta_{\mathbf{k}''\omega''}}, \tag{3}$$

$$P_{\mathbf{k}\omega} = I_{\mathbf{k}\omega}(\mathbf{k}\mathbf{g}_{\mathbf{k}\omega}) f_0 + \Delta P_{\mathbf{k}\omega},\ \mathbf{g}_{\mathbf{k}\omega} \equiv \frac{e}{m_e} \frac{1}{\omega - \mathbf{k}\mathbf{v} + \eta_{\mathbf{k}\omega}} \frac{\partial}{\partial \mathbf{v}}, \tag{4}$$

where $\mathbf{k}'' = \mathbf{k} - \mathbf{k}'$, $\omega'' = \omega - \omega'$, $I_{\mathbf{k}\omega} = \langle|\varphi_{\mathbf{k}\omega}|^2\rangle$, $P_{\mathbf{k}\omega} = \langle\varphi^*_{\mathbf{k}\omega} f_{\mathbf{k}\omega}\rangle$, and $\varphi_{\mathbf{k}\omega}$ and $f_{\mathbf{k}\omega}$ are the Fourier components of the potential φ and the electron distribution function. The background electron distribution f_0 satisfies

$$\frac{\partial f_0}{\partial t} = \frac{e}{m_e} E_0 \frac{\partial f_0}{\partial v_z} - \frac{e}{m_e} \frac{\partial}{\mathbf{v}\varrho} \int d\mathbf{k}\, d\omega\, \mathbf{k} \operatorname{Im} P_{\mathbf{k}\omega}, \tag{5}$$

where $\mathbf{E}_0$ is the external electric field. The nonlinear terms for ions are neglected [for monoenergetic ions, $(\gamma/kv_{Ti}) \sim (T_e/T_i)^{1/2} \gg 1$, this simplification is valid if $W \equiv (1/8\pi)(\nabla\varphi)^2 \ll n_0 T_e$]. The terms $\Delta\varepsilon(\mathbf{k}, \omega)$ and $\Delta P_{\mathbf{k}\omega}$ describe the nonlinear wave interaction.

The quantity $\eta_{\mathbf{k}\omega}$ gives the resonance broadening and is a complicated function of the variable $\zeta \equiv \mathbf{kv}/kv$. Under the assumption that the nonlinear wave interaction is weak $[|\Delta\varepsilon(\mathbf{k}, \omega)| \ll 1,\ |\Delta P_{\mathbf{k}\omega}| \ll |P_{\mathbf{k}\omega}|]$, taking account of the strong functional dependence on ζ of the quantities $P_{\mathbf{k}\omega}$ and $\eta_{\mathbf{k}\omega}$ in the resonance region, $|\omega - \mathbf{kv}| \lesssim |\eta_{\mathbf{k}\omega}|$, $|\zeta| \lesssim |\eta_{\mathbf{k}\omega}/kv| \ll 1$, we find from (3)

$$\eta_{\mathbf{k}\omega} P_{\mathbf{k}\omega} = A \frac{\partial^2 P_{\mathbf{k}\omega}}{\partial\zeta^2},\ A = \left(\frac{e}{m_e}\right)^2 \frac{1}{k^2 v^2} \int d\mathbf{k}'d\omega' \frac{(\mathbf{k}\mathbf{k}')^2 I_{\mathbf{k}'\omega'}}{\omega'' - \mathbf{k}''v + \eta_{\mathbf{k}''\omega''}} \approx \text{const.} \tag{6}$$

Eliminating $\eta_{\mathbf{k}\omega}$ from (4) and (6), we find an equation for $P_{\mathbf{k}\omega}$:

$$\frac{\partial^2 P_{\mathbf{k}\omega}}{\partial\zeta^2} - \left(\zeta - \frac{\omega}{kv}\right)\frac{kv}{A} P_{\mathbf{k}\omega} = \frac{e}{m_e} \frac{I_{\mathbf{k}\omega}}{A}\left(\mathbf{k}\frac{\partial f_0}{\partial \mathbf{v}}\right). \tag{7}$$

It follows from (7) that the width of the resonance region is of order $\Delta\zeta \sim |A/kv|^{1/3} \sim (W/n_0T_e)^{1/3}$. It is not difficult to show on the basis of the structure of Eq. (7) that

$$J \equiv \int_{-\infty}^{\infty} d\zeta \operatorname{Im} P_{\mathbf{k}\omega} = -\frac{\pi}{kv}\frac{e}{m_e} I_{\mathbf{k}\omega}\left(\mathbf{k}\frac{\partial f_0}{\partial \mathbf{v}}\right)\Big|_{\omega = \mathbf{kv}}, \tag{8}$$

i.e., with $W \ll n_0T_e$, the resonance broadening is negligible for the integral J, which describes the resonant interaction of the waves with the particles. We can find the quantities $\Delta\varepsilon(\mathbf{k}, \omega)$ and $\Delta P_{\mathbf{k}\omega}$ (in order of magnitude) by simplifying the problem, assuming that $\eta_{\mathbf{k}\omega}$ is independent of **v** and is a slowly varying function of **k**. Then $\eta_{\mathbf{k}\omega}$ plays the role of a complex increment in the frequency ω, and a calculation of the nonlinear wave interaction would be the same as that for the case of the ion-acoustic instability.[6] Replacing ω by $\omega + \eta_{\mathbf{k}\omega}$ in the equations of ref. 6, we can easily show that the following holds for the case of Buneman instabilities:[1]

$$\operatorname{Im}\Delta\varepsilon(\mathbf{k}, \omega) \sim \operatorname{Re}\Delta\varepsilon(\mathbf{k}, \omega) \sim \frac{W}{n_0T_e}\left[\frac{m_e}{m_i} + \left|\frac{\eta_{\mathbf{k}\omega}}{\omega_{pe}}\right|^2\right]^{-1} \sim \frac{W}{n_0T_e}\left[\frac{m_e}{m_i} + \left(\frac{W}{n_0T_e}\right)^{2/3}\right]^{-1}. \tag{9}$$

Accordingly, in the case $1 \gg (W/n_0T_e) > (m_e/m_i)^{3/2}$ the nonlinear increment $\Delta\varepsilon(\mathbf{k}, \omega)$, like $\Delta P_{\mathbf{k}\omega}$, is smaller by a factor of $(n_0T_e/W)^{1/3}$ than the linear terms[1)] $\varepsilon(\mathbf{k}, \omega)$. Also using (8) we conclude that with $W \ll n_0T_e$ for these instabilities, the scattering of electrons by the oscillations leads primarily to an increase in the transverse electron temperature $(k_\parallel/k_\perp) \sim (v_{Te}/u) \ll 1$ and is described by the diffusion equation

$$\frac{\partial f_0}{\partial t} = \frac{1}{v_\perp}\frac{\partial}{\partial v_\perp} v_\perp D_\perp \frac{\partial f_0}{\partial v_\perp},\ D_\perp \equiv \left(\frac{e}{m_e}\right)^2 \frac{1}{v_\perp^2} \int d\mathbf{k}\, d\omega \frac{(\mathbf{ku})^2 I_{\mathbf{k}\omega}}{\sqrt{k_\perp^2 v_\perp^2 - (\mathbf{ku})^2}}. \tag{10}$$

Using estimate (1), we find from (10) that $n_0(\partial T_{\perp e}/\partial t) \sim \omega_{pe} W$; we then find $n_0 T_{\perp e} \sim W(m_i/m_e)^{1/2}$.

As the electrons are heated, waves with increasingly large values of $|\cos\vartheta| \sim v_{Te}/u$ become "kinetic," so that the electron spread with respect to longitudinal energy is also accelerated; then at a noise level

$$W \sim n_0 T_e (m_e/m_i)^{1/2}, \tag{11}$$

we would obviously have $T_{\perp e} \sim T_{\parallel e}$ and $u \sim v_{Te}$. More information about the growth of the instability can be obtained by solving the equations of the quasilinear theory under the condition $u \lesssim v_{Te}$. Obviously, an anomalous plasma resistance can also appear with $u \lesssim v_{Te}$, in which case the quasilinear effects lead to $\gamma \lesssim kv_{Ti}$, and the instability is stabilized completely by nonlinear scattering of the waves by ions. This conclusion is consistent with the experimental data of refs. 9 and 10, for which the condition $u \lesssim v_{Te}$ is satisfied even when the plasma conductivity reaches the second plateau. It is also possible that the instability leads to a regime in which there is no anomalous plasma resistivity.[11]

On the basis of this analysis we can assume that hydrodynamic instabilities do not significantly affect a plasma carrying a current, since such an effect would require too high a noise level, $W \sim n_0 m_e u^2$ (ref. 12).

The author thanks K. N. Stepanov for discussion.

---

1)An analogous conclusion is reached in ref. 7 for the ion-acoustic instability.

[1] V. L. Sizonenko and K. N. Stepanov, Zh. Tekh. Fiz., 42, 484 (1972) [Sov. Phys.-Tech. Phys., 17, 385 (1972)].

[2] J. R. Pierce, J. Appl. Phys., 19, 231 (1948).

[3] G. I. Budker, At. Energ., 5, 9 (1956).

[4] O. Buneman, Phys. Rev. Lett., 1, 104 (1958).

[5] B. B. Kadomtsev, Reviews of Plasma Physics, Vol. 4, Consultants Bureau, New York (1966).

[6] V. L. Sizonenko and K. N. Stepanov, ZhETF Pis. Red., 9, 468 (1969) [JETP Lett., 9, 282 (1969)].

[7] L. I. Rudakov and V. N. Tsytovich, Plasma Phys., 13, 213 (1971).

[8] A. A. Vedenov, E. P. Velikhov, and R. Z. Sagdeev, Usp. Fiz. Nauk, 73, 701 (1961) [Sov. Phys.-Usp., 4, 332 (1961)].

[9] S. M. Hamberger and M. Friedman, Phys. Rev. Lett., 21, 674 (1968).

[10] S. M. Hamberger, J. Jancarik, J. H. Adam, and J. E. Sharp, "Turbulent Heating In a Toroidal Stellarator," International Conference on Plasma Confinement in Closed Systems, Dubna, USSR, September 29-October 3, 1969, Abstracts of Reports [Russian translation], Moscow (1969), p. 44.

[11] G. E. Vekshtein, D. D. Ryutov, and R. Z. Sagdeev, Zh. Eksp. Teor. Fiz., 60, 2142 (1971) [Sov. Phys.-JETP, 33, 1152 (1971)].

[12] V. L. Sizonenko and K. N. Stepanov, Plasma Phys., 13, 1033 (1971).

Gas polymerization wave excited by monochromatic light

A. I. Plis and V. A. Shcheglov

Moscow Energetics Institute

(Submitted February 19, 1974)
Zh. Tekh. Fiz., 44, 2027-2030 (September 1974)

The profiles of the intensity and reactant densities are obtained in an analysis of photochemical polymerization waves in a gaseous medium. An equation for the wave velocity is derived for the general case. This velocity is found for the particular case in which the elementary steps of the polymerization chain reaction have equal rate constants. The molecular weight of the mixture is calculated.

The propagation of photodissociation waves in gaseous media is analyzed in refs. 1-3, and the photochemical waves propagating in gaseous mixtures with chain and branched-chain conversion mechanisms are analyzed in refs. 4-6. It has been shown[4-6] that secondary (with respect to the photolysis) chemical reactions involving the annihilation of the photodissociating reactant lead to an increase in the velocity of the "intensification" wave. This is an extremely important circumstance from the physical standpoint, since it yields information about the dynamics of the processes involved in photochemical conversions in a gaseous medium.

We are concerned here with photochemical polymerization waves in a gaseous medium. Polymerization waves initiated by quasimonochromatic light are of interest primarily from the practical standpoint; a point of physical interest is the unusual kinetics of the polymerization process (see, e.g. ref. 7).

The initial reactant is a monomer molecule A = B having a double bond. When light having a certain photon energy $h\nu_0$ acts on the monomer, one of the bonds is ruptured, and the active radical −A−B− is formed. The reaction of this radical with the initial monomer leads to the formation of the dimer radical −A−B−A−B−, which in turn, by interacting with the A = B monomer, forms a trimer; etc. Corresponding to this chain mechanism is the scheme

$$\left.\begin{array}{l} (AB)_1 + h\nu_0 \xrightarrow{\sigma} (AB^*)_1, \\ (AB^*)_1 + (AB)_1 \xrightarrow{k_1} (AB)_2, \\ (AB)_2 + (AB)_1 \xrightarrow{k_2} (AB)_3, \\ (AB)_3 + (AB)_1 \xrightarrow{k_3} (AB)_4, \\ \cdots\cdots\cdots\cdots \end{array}\right\} \quad (1)$$

According to (1) the photochemical polymerization wave is described by a system of equations consisting of the one-dimensional radiation-transport equation and the kinetic equations

$$\left.\begin{array}{c} \left(\frac{1}{c}\frac{\partial}{\partial t}+\frac{\partial}{\partial x}\right)I=-\sigma IN_1;\ \frac{\partial N_1}{\partial t}=-\sigma IN_1-k_1N_1^*N_1-\left(\sum_{i=2}^{\infty}k_iN_i\right)N_1, \\ \frac{\partial N_1^*}{\partial t}=\sigma IN_1-k_1N_1^*N_1;\ \frac{\partial N_2}{\partial t}=k_1N_1^*N_1-k_2N_2N_1, \\ \frac{\partial N_i}{\partial t}=k_{i-1}N_{i-1}N_1-k_iN_iN_1,\ i\geqslant 3, \end{array}\right\} \quad (2)$$

where I (photons per square centimeter per second) is the radiation flux density; σ is the photoinitiation cross section; k_i are the rate constants for the corresponding reactions; and the densities of reactants $(AB)_1$, $(AB^*)_1$, $(AB)_2$, etc., are denoted by N_1, N_1^*, N_2, etc. System (2) is to be supplemented with the initial and boundary conditions

$$\left.\begin{array}{c} t=0,\ N_1=N_0,\ N_1^*=N_2=\ldots=0,\ I=0\ (0<x<\infty), \\ x=0,\ I=I_0\ (0<t<\infty). \end{array}\right\} \quad (3)$$

We seek a solution of system (2) in the form of a stationary wave whose velocity D is to be determined. For such a wave the particle densities and radiation flux densities are functions of the argument $x' = x - Dt$ only, so we can write system (2) as

$$\left.\begin{array}{c} \frac{D^{-1}dI}{d\tau}=-\sigma IN_1;\ \frac{dN_1}{d\tau}=\sigma IN_1+k_1N_1^*N_1+\left(\sum_{i=2}^{\infty}k_iN_i\right)N_1, \\ \frac{dN_1^*}{d\tau}=-\sigma IN_1+k_1N_1^*N_1;\ \frac{dN_2}{d\tau}=-kN_1^*N_1+k_2N_2N_1, \\ \frac{dN_i}{d\tau}=-k_{i-1}\overset{\bullet}{N}_{i-1}N_1+k_iN_iN_1,\ i\geqslant 3, \end{array}\right\} \quad (4)$$

where $\tau = x'/D = (x-Dt)/D$ and where we have assumed $D/c \ll 1$ in a first approximation. System (4) describes a stationary polymerization wave propagating in the positive x direction. It is not difficult to see that system (4) has the integral

$$N_1^* + \sum_{i=2}^{\infty} N_i = \frac{I}{D}, \quad (5)$$

which expresses "photon-particle" conservation. From (4) we also find the obvious relation (conservation of elements)

$$N_0 = N_1 + N_1^* + \sum_{i=2}^{\infty} iN_i.$$

Using (3) and (4) we can find a relation between the densities of the reactants and the radiation flux density:

$$N_1^* = \frac{I}{D}\frac{1}{(1+a_1)},$$

$$N_i = \frac{I}{D}\frac{a_1a_2\ldots a_{i-1}}{(1+a_1)(1+a_2)\ldots(1+a_i)}, \quad (6)$$

where $a_i = k_i/\sigma D$. Using (6) and the first two equations in (4) we find a relation between the density of the initial monomer and the intensity:

$$N_1 + A\frac{I}{D} = C, \quad (7)$$

$$A = 1 + \frac{a_1}{1+a_1} + \frac{a_1a_2}{(1+a_1)(1+a_2))} + \ldots$$

$$+ \frac{a_1a_2\ldots a_{i-1}}{(1+a_1)(1+a_2)\ldots(1+a_i)} + \ldots. \quad (8)$$

Using $N_1 = 0$ and $I = I_0$ at $\tau = -\infty$, and then using N_1 =

N_0 and I = 0, we find

$$C = N_0 = \frac{I_0}{D} A. \tag{9}$$

Equation (9) gives the velocity of the photochemical wave. From (7) and (9) we can determine the intensity profile:

$$\frac{I}{I_0} = [1 + e^{\sigma I_0 A\tau}]^{-1}. \tag{10}$$

The profiles of the densities of the corresponding reactants are determined from (6) and (7). Equations (6)-(10) thus completely define the solution of the problem. For the profile of the total particle density we easily find

$$N = \frac{I_0}{D_0} + I\left(\frac{1}{D} - \frac{1}{D_0}\right). \tag{11}$$

Finally, we can show that the profile of the molecular weight of the reactant system, M, is

$$\frac{M}{M_0} = \frac{1}{N}\left\{\frac{1}{D_0}(I_0 - I) + \frac{I}{D}\left[\frac{1}{(1+a_1)} + \frac{2a_1}{(1+a_1)(1+a_2)} + \ldots + \frac{i a_1 a_2 \ldots a_{i-1}}{(1+a_1)(1+a_2)\ldots(1+a_i)}\right]\right\}, \tag{12}$$

where M_0 is the molecular weight of the original monomer.

In the case of equal rate constants for the elementary steps of the polymerization reaction [$k_i \equiv k$ (i = 1, 2, ...)] the analysis simplifies; in particular, Eq. (8) becomes

$$A = 1 + a = 1 + \frac{k}{\delta D},$$

so that the wave velocity is given by

$$y^2 - y - \xi = 0, \tag{13}$$

where $y = D/D_0$ and $\xi = kN_0/\sigma I_0$. From (13) we find

$$y = \frac{1}{2} + \left[\frac{1}{4} + \xi\right]^{1/2}.$$

The densities of the reactants and the radiation intensity in this case are related by

$$N_1 = N_0 - \frac{I}{D}(1 + a),$$

$$N_1^* = \frac{I}{D}\frac{1}{(1 + a)},$$

$$N_i = \frac{I}{D}\frac{a^{i-1}}{(1 + a)^i} (i \geqslant 2); \quad a = \frac{\xi}{y}.$$

The molecular weight of the mixture is given by

$$\frac{M}{M_0} = \left[1 + \frac{I}{I_0}\left(\frac{D_0}{D} - 1\right)\right]^{-1}.$$

The maximum molecular weight is obviously reached at the wave front:

$$\frac{M_{\max}}{M} = \frac{D}{D_0}.$$

As an example, we consider the case of equal rate constants for the elementary steps, with $K \sim 10^{-13}$ cm^3 · (particle · sec)$^{-1}$, $N_0 \sim 10^{18}$ particles/cm^3, $\sigma \sim 10^{-18}$ cm^2, and $I_0 \sim 10^{21}$ photons/(cm^2 · sec); we find the velocity of the photochemical polymerization wave to be $D \sim 10^4$ cm/sec, the width of the wave profile to be $\Delta x \sim 1$ cm, and the maximum molecular weight of the reactant mixture to be $M \sim 10M_0$.

We note in conclusion that we have focused primarily on questions of the propagation of photochemical polymerization waves in a gaseous medium here. We have not taken up several processes – the bond-rupture reaction, thermal effects, etc. – so that the generality of our analysis is limited. A more complete analysis, incorporating these processes, is planned for a future paper.

---

[1] V. E. Khartsiev, Zh. Eksp. Teor. Fiz., 54, 867 (1968) [Sov. Phys.–JETP, 27, 464 (1968)]; 53, 3 (1967).

[2] B. L. Borovich, V. S. Zuev, and O. N. Krokhin, Zh. Eksp. Teor. Fiz., 64, 1184 (1973) [Sov. Phys.–JETP, 37, 602 (1973)].

[3] B. L. Borovich, V. Ya. Karpov, N. I. Kozlov, Yu. Yu. Stoilov, and A. A. Filyukov, Zh. Eksp. Teor. Fiz., 64, 1211 (1973) [Sov. Phys.–JETP, 37, 616 (1973)].

[4] A. N. Oraevskii and V. A. Shcheglov, Zh. Eksp. Teor. Fiz., 59, 845 (1970) [Sov. Phys.–JETP, 32, 462 (1971)]; Kratk. Soobshch. Fiz. (FIAN), No. 5 (1970).

[5] A. N. Oraevskii, V. P. Pimenov, and V. A. Shcheglov, Zh. Eksp. Teor. Fiz., 62, 89 (1972) [Sov. Phys.–JETP, 35, 48 (1972)]; Kratk. Soobshch. Fiz. (FIAN), No. 9 (1971).

[6] A. N. Oraevskii, V. P. Pimenov, and V. A. Shcheglov, Preprint No. 162, P. N. Lebedev Physics Institute, (1973).

[7] A. A. Strepikhiev and V. A. Derevitskaya, Principles of the Chemistry of High-Molecular Compounds [in Russian], Goskhimizdat, Moscow (1961).

Luminosity of a cylindrical spectrometer with a small off-axis source

V. V. Zashkvara
Institute of Nuclear Physics,
Academy of Sciences of the Kazakh SSR, Alma-Ata

(Submitted July 9, 1973)
Zh. Tekh. Fiz., 44, 2030-2032 (September 1974)

Our purpose here is to calculate the luminosity of a cylindrical-mirror analyzer[1] as a function of radial position of a small source. This functional dependence is of practical interest in connection with the development of a scanning microprobe analyzer for studying the distribution of chemical elements over solid surfaces on the basis of the characteristic Auger-electron spectra. Figure 1 shows the Auger microanalyzer. Here 1 and 2 are the inner and outer electrodes of a cylindrical-mirror analyzer. The surface of the specimen, 3, is in the plane perpendicular to the symmetry axis of the mirror electrodes and intersecting the axis at point 0. This point corresponds to the position of a point source in an ion-optics system for second-order angular focusing of a beam of electrons to be analyzed. The central ray of this beam makes an angle of 42°18' with the z axis.[1] Auger electrons are excited in the atoms of the surface layer of the specimen under the influence of a beam of primary electrons brought to a sharp focus near point 0. This beam is shaped by electron gun 4. Then the Auger electrons enter the analyzer. Here 5 are annular slits at the surface of inner cylindrical electrode 1, covered by high-transmission metal grids. Receiving iris 6 has a circular aperture 7 of small radius $\Delta r_r = r_1\rho_r$ (r_1 is the radius of the inner cylindrical electrode, 1). This aperture is centered on the z axis, at a second-order focal point. Beyond the iris is some detector, which we will not discuss here. We assume that the dimension of the microprobe on the surface of the specimen is much smaller than Δr_r. In the course of a measurement, the microprobe scans the specimen surface within a certain area 8 (dashed circle) having dimensions comparable to Δr_r. To design a detection system for the microanalyzer we must determine how the signal level at the peak varies as the microprobe is moved radially away from point 0. We can find this information by calculating the luminosity of a cylindrical mirror of this type having an off-axis source of monoenergetic charged particles under conditions such that the analyzer operates in the regime of second-order angular focusing. We assume that the particle emission by the source surface obeys Lambert's law; then the luminosity of the analyzer is given by the double integral

$$L = \int dS d\Omega \cos i \tag{1}$$

over the area of the source and over the solid angle subtended by the beam to be analyzed. This integral is calculated for all the trajectories issuing from the source and intersecting the plane of the entrance aperture of the receiving iris. In Eq. (1) i is the angle between the normal to area ds and the given direction. Figure 2 shows a projection on the plane perpendicular to the symmetry axis of the analyzer of certain elements shown in Fig. 1, for assistance in understanding the calculations. The entrance aperture of the receiving iris describes a circle of radius $\Delta r_r = r_1\rho_r$. The circle of radius r_1 corresponds to the inner cylindrical electrode. Line 1 is the projection of an arbitrary ray coming from the region of the off-axis source, which has small dimensions and an area S. The deviation of this ray from the axis is characterized by the angle ψ. The dashed lines in Fig. 2 nominally bound the range of angles ψ including all trajectories emerging from source S and ending at the entrance aperture of the receiving iris.

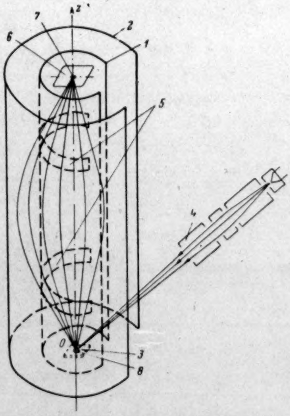

Fig. 1. The Auger microanalyzer. 1, 2) Inner and outer electrodes of the cylindrical analyzer; 3) specimen; 4) electron gun; 5) annular slits; 6) receiving iris; 7) entrance aperture of receiving iris; 8) region on the specimen surface over which the microprobe is scanned..

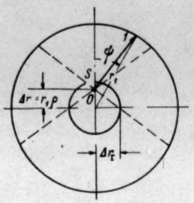

Fig. 2.

Under these conditions Eq. (1) can be rewritten as

$$L = 4S \iint\limits_{\alpha_0-\Delta\alpha}^{\alpha_0+\Delta\alpha} \cos\alpha \sin\alpha \, d\alpha d\psi \simeq 4S \cos\alpha_0 \sin\alpha_0 \int\limits_{\alpha_0-\Delta\alpha}^{\alpha_0+\Delta\alpha} \psi(\rho, \alpha - \alpha_0)\, d\alpha, \tag{2}$$

where $\alpha_0 = 42°18'$ is the angle between the z axis and the central ray in the beam to be analyzed, $\Delta\alpha$ is the divergence half-angle of the beam in the axial plane, and ρ is the relative displacement of source S from the z axis. In Eq. (2) the cos α and sin α are taken through the integral sign, since they are slowly varying functions over the integration range. A necessary condition for the evaluation of integral (2) is the condition governing the passage of the trajectories through the aperture of the receiving limiter of the cylindrical analyzer. This condition, derived in ref. 2, takes the following form for the case of second-order angular focusing:

$$\rho \sin\psi \leqslant \sqrt{\rho_r^2 - \mathrm{tg}^2\,\alpha_0 A_{III}^2 (\alpha - \alpha_0)^6}, \tag{3}$$

where A_{III} is the coefficient of cubic angular aberration.[1] Using the substitution $x = |\alpha - \alpha_0|$ in (2) we find

$$L = 8 \sin\alpha_0 \cos\alpha_0 S \int_0^{\Delta\alpha} \psi(\rho,\ x)\, dx, \tag{4}$$

where, in accordance with condition (3),

$$\psi = \begin{cases} \dfrac{\pi}{2}, & \text{if} \quad \rho \leqslant \sqrt{\rho_r^2 - \mathrm{tg}^2\alpha_0 A_{III}^2 x^6}, \\ \arcsin \dfrac{\sqrt{\rho_r^2 - \mathrm{tg}^2\alpha_0 A_{III}^2 x^6}}{\rho}, & \text{if} \quad \rho > \sqrt{\rho_r^2 - \mathrm{tg}^2\alpha_0 A_{III}^2 x^6}. \end{cases} \tag{5}$$

Let us consider several possible positions for the off-axis source.

1. $\rho = 0$. The source is on the symmetry axis. It follows from (4) and (5) that $\psi = \pi/2$ and

$$L_0 = 4\pi \sin\alpha_0 \cos\alpha_0 S\Delta\alpha. \tag{6}$$

In this case the luminosity is a maximum.

2. $\rho < \rho_r$. From (4) and (5) we find

$$\int_0^{\Delta\alpha} \psi(\rho,\ x)\, dx = \frac{\pi}{2} x_e + \int_{x_e}^{\Delta\alpha} \arcsin \frac{\sqrt{\rho_r^2 - \mathrm{tg}^2\alpha_0 A_{III}^2 x^6}}{\rho}\, dx, \tag{7}$$

where

$$x_e = \left[\frac{\rho_r}{|A_{III}|\,\mathrm{tg}\,\alpha_0}\right]^{1/3} \left[1 - \left(\frac{\rho}{\rho_r}\right)^2\right]^{1/6}.$$

The quantity

$$\left[\frac{\rho_r}{|A_{III}|\,\mathrm{tg}\,\alpha_0}\right]^{1/3} = \Delta\alpha_{li}$$

is the limiting divergence half-angle of the beam. As is shown in ref. 2, the luminosity of a cylindrical analyzer increases nearly linearly with increasing beam divergence over the range $\Delta\alpha \le \Delta\alpha_{li}$; then, at $\Delta\alpha > \Delta\alpha_{li}$, it becomes constant, and the instrumental line shape becomes blurred at the base. Under these conditions, therefore, $\Delta\alpha_{li}$ is the optimum value of the divergence half-angle for the beam to be analyzed in the axial plane. We assume $\Delta\alpha = \Delta\alpha_{li}$; then by using the substitution $z = x/\Delta\alpha_{li}$ in (7) we find

$$L = 8 \sin\alpha_0 \cos\alpha_0 S\Delta\alpha_{li} \left\{ \frac{\pi}{2}\left[1 - \left(\frac{\rho}{\rho_r}\right)^2\right]^{1/6} + \int_{\left[1-\left(\frac{\rho}{\rho_r}\right)^2\right]^{1/6}}^{1} \arcsin\left[\frac{\rho_r}{\rho}\sqrt{1 - z^6}\right] dz. \right. \tag{8}$$

3. In the case $\rho = \rho_r$ we find from (8)

$$L = 8 \sin\alpha_0 \cos\alpha_0 S\Delta\alpha_{li} \int_0^1 \arccos(z^3)\, dz. \tag{9}$$

4. $\rho > \rho_r$. In this case we find from (4) and (5)

$$L = 8 \sin\alpha_0 \cos\alpha_0 S\Delta\alpha_{li} \int_0^1 \arcsin\left[\frac{\rho}{\rho_r}\sqrt{1 - z^6}\right] dz. \tag{10}$$

Using Eqs. (6) and (8)-(10) we calculate the relative luminosity $l = L/L_0$ as a function of ρ/ρ_r over the range 0-4 (Fig. 3). We see that with $\rho \ge \rho_r$ the luminosity of the analyzer falls off considerably. If the region in which the microprobe is scanned over the specimen surface is bounded by a circle $\rho \le 0.8\rho_r$, then the changes in the luminosity and thus in the intensity of the detected signal due to the displacement of the microprobe from the symmetry axis do not exceed 5% of the maximum luminosity, corresponding to the placement of the microprobe on the symmetry axis.

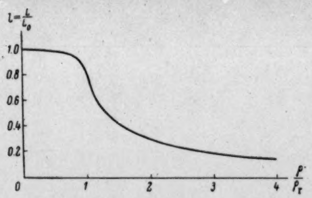

Fig. 3. Relative luminosity of the cylindrical mirror, $l = L/L_0$, as a function of the relative radial displacement of the source from the symmetry axis, ρ/ρ_r.

---

[1] V. V. Zashkvara, M. I. Korsunskii, and O. S. Kosmachev, Zh. Tekh. Fiz., 36, 132 (1966) [Sov. Phys.-Tech. Phys., 11, 96 (1966)].

[2] V. V. Zashkvara, V. F. Tarasov, and S. S. Kiseleva, Zh. Tekh. Fiz., 43, 1833 (1973) [Sov. Phys.-Tech. Phys., 18, 1161 (1974)].

BLANK
PAGE

Theoretical and mathematical physics

Heat transport problems with time-varying boundary conditions or moving boundaries (Stefan problem)

G. A. Grinberg

A. F. Ioffe Physicotechnical Institute, Academy of Sciences of the USSR, Leningrad

(Submitted April 24, 1974)
Zh. Tekh. Fiz., 44, 2033-2042 (October 1974)

We propose a certain general method for investigating problems described by equations like $\Delta u + Q(x, y, z, \tau) = \partial u/\partial\tau$, where $Q(x, y, z, \tau)$ is a given function. The method is based on a set of special functions φ_m ($m = 0, 1, 2, \ldots, \infty$) which depend only on the coordinates and not on the time; these make it possible to reduce the problem to an infinite system of simple differential-difference equations. Using this system we can obtain a relation between the time-varying boundary condition and the outer surface of the medium being considered [Eq. (17)]; in addition, using the Laplace transform and generating function $\varphi(\lambda) = \sum_{m=1}^{\infty} \lambda^m \varphi_m$ we can form integral equations, one of which serves for determining the unknown functions on the moving boundary if the motion of the boundary is given [Eq. (29)], or, in the case of problems of the Stefan type,[1] for determining the unknown boundary motion [Eq. (30)]. When the solution of the appropriate equation (29) or (30) is known (or is assumed to be known – the inverse problem), to find the function u, we must use Eq. (28). The general theory is illustrated with a number of examples. In particular, when the shape of the boundary is known a priori in the Stefan problem and only the law of its displacement in time is unknown (when the solution depends on only one Cartesian coordinate or has cylindrical or spherical symmetry), a connection is developed between the second stage of the solution of the problem indicated above and the expansion of the unknown solution in "instantaneous" eigenfunctions of the problem. The proposed method allows a direct extension to equations of the form $\Delta u = a\partial^2 u/\partial\tau^2 = b\,\partial u/\partial\tau + cu + Q(x, y, z, \tau)$, where a, b, and c are constants.

1. We proceed to the problem. Let a medium fill some simply connected or multiply connected time-varying volume $V = V(\tau)$ which is bounded by the surface $f = f_1 + f_2 + f_3 + f_\tau$; the segments f_1, f_2, and f_3 are fixed, and on these we are given boundary conditions of the first, second, or third kind, respectively, i.e.,

$$\left.\begin{aligned} u|_{f_1} &= F_1(M, \tau),\\ \left.\frac{\partial u}{\partial n}\right|_{f_2} &= F_2(M, \tau),\\ \left.\left(\frac{\partial u}{\partial n} + \gamma u\right)\right|_{f_3} &= F_3(M, \tau), \end{aligned}\right\} \tag{1}$$

where M is a point on the corresponding part of the surface, $\partial u/\partial n$ is the derivative of u normal to the surface, and $F_k(M, \tau)$ ($k = 1, 2, 3$) are specified functions of M and τ. The segment f_τ is displaced in a specified way, and on it we are given boundary conditions of first, second, or third kind. In another formulation the Stefan conditions are satisfied on this segment, i.e.,

$$u|_{f_\tau} = 0; \quad \left.\frac{\partial u}{\partial n}\right|_{f_\tau} = -\alpha v_n, \tag{2}$$

where α is a known constant, v_n is the component of the velocity normal to the surface of f_τ; this component is unknown and is to be determined.

Inside the volume the function u everywhere satisfies the equation

$$\Delta u + Q = \frac{\partial u}{\partial \tau}, \quad Q = Q(x, y, z, \tau) \tag{3}$$

and the initial condition

$$u|_{\tau=0} = u^0(x, y, z), \tag{4}$$

which is satisfied inside the initial volume $V|_{\tau=0} = V_0$.

We construct a sequence of functions $\varphi_m = \varphi_m(x, y, z)$, independent of τ, such that $\Delta\varphi_0 = 0$ and

$$\Delta\varphi_{m+1} = \varphi_m, \quad m \geqslant 0, \tag{5}$$

where we take[2]

$$\varphi_m|_{f_1} = 0; \quad \left.\frac{\partial \varphi_m}{\partial n}\right|_{f_2} = 0; \quad \left.\left(\frac{\partial \varphi_m}{\partial n} + \gamma\varphi_m\right)\right|_{f_3} = 0, \quad m \geqslant 0. \tag{6}$$

We introduce the notation (here $m \geq 0$ everywhere)

$$u_m = u_m(\tau) = \int_V u\varphi_m dV, \tag{7}$$

$$Q_m = Q_m(\tau) = \int_V Q\varphi_m dV, \tag{8}$$

$$a_m = a_m(\tau) = \int_{f_\tau} \left[\left(\frac{\partial u}{\partial n} + v_n u\right)\varphi_m - u\frac{\partial \varphi_m}{\partial n}\right] df_\tau, \tag{9}$$

$$b_m = b_m(\tau) = -\int_{f_1} F_1 \frac{\partial \varphi_m}{\partial n} df_1 + \int_{f_2} F_2\varphi_m df_2 + \int_{f_3} F_3\varphi_m df_3. \tag{10}$$

For the Stefan problem we have

$$a_m = -\alpha \int_{f_\tau} v_n\varphi_m df_\tau, \tag{9'}$$

when f_τ moves in a specified way and on f_τ we are given values of u; in this case Eq. (9) contains a single unknown term $\int_{f_\tau} (\partial u/\partial n)\varphi_m df_\tau$, for boundary conditions of the second kind

$$-\int_{f_\tau} u\left(v_n\varphi_m - \frac{\partial \varphi_m}{\partial n}\right) df_\tau,$$

For boundary conditions of the third kind we can replace one of the quantities u or ∂u/∂n by the other so that both are expressed in terms of one unknown quantity.

Denoting the total time derivative by d/dτ, we obtain

$$\int_V (\varphi_{m+1}\Delta u - u\Delta\varphi_{m+1})\,dV + u_m + Q_{m+1} = \int_V \varphi_{m+1}\frac{\partial u}{\partial \tau}\,dV$$

$$= u_m + Q_{m+1} + \int_f \left(\varphi_{m+1}\frac{\partial u}{\partial n} - u\frac{\partial \varphi_{m+1}}{\partial n}\right)df = \frac{du_{m+1}}{d\tau} - \int_{f_\tau} \varphi_{m+1}v_n u\,df_\tau,$$

i.e.,

$$\frac{du_{m+1}}{d\tau} = u_m + a_{m+1} + b_{m+1} + Q_{m+1},\ m \geqslant 0, \tag{11}$$

$$\frac{du_0}{d\tau} = a_0 + b_0 + Q_0. \tag{12}$$

For brevity we write

$$a_m + b_m + Q_m = -c_m, \tag{13}$$

and rewrite Eqs. (11) and (12) in the form

$$u_m = u'_{m+1} + c_{m+1},\quad m \geqslant 0, \tag{11'}$$

$$0 = c_0 + u'_0, \tag{12'}$$

whence, by differentiating n times with respect to τ we obtain the relation

$$u_m^{(n)} = u_{m+1}^{(n+1)} + c_{m+1}^{(n)},\ m \geqslant 0. \tag{14}$$

Equations (12)-(14) give

$$0 = c_0 + u'_0 = c_0 + c'_1 + u''_1 = \ldots = \sum_{k=0}^{k=m} c_k^{(k)} + u_m^{(m+1)}. \tag{15}$$

If the selected system of functions φ_m is such that $\lim\limits_{m=\infty} u_m{}^{(m+1)} = 0$, then (15) can be written as

$$\sum_{k=0}^{\infty} c_k^{(k)} = 0 = \sum_{k=0}^{\infty} a_k^{(k)} + \sum_{k=0}^{\infty} (b_k^{(k)} + Q_k^{(k)}),$$

i.e.,

$$\sum_{k=0}^{\infty} \frac{d^k}{d\tau^k}\int_{f_\tau}\left[\left(\frac{\partial u}{\partial n} + v_n u\right)\varphi_k - u\frac{\partial \varphi_k}{\partial n}\right]df_\tau = -\sum_{k=0}^{\infty}(b_k^{(k)} + Q_k^{(k)}), \tag{16}$$

whence, in particular, for the Stefan problem we obtain

$$\alpha\sum_{k=0}^{\infty}\frac{d^k}{d\tau^k}\int_{f_\tau} v_n\varphi_k\,df_\tau = \sum_{k=0}^{\infty}(b_k^{(k)} + Q_k^{(k)}), \tag{17}$$

relations in which the distribution of the function u over the volume V does not enter, the right side is the known function τ, and the left side contains the value of u or ∂u/∂n, unknown on the surface f_τ, and for the case of the Stefan problem – the quantity (9').

On the other hand, using the Laplace transform in (11) and (12) and introducing the notation

$$\bar{\psi} \equiv \bar{\psi}(p) = \int_0^\infty e^{-p\tau}\psi(\tau)\,d\tau$$

[ψ(τ) is some function of τ], we obtain

$$\bar{u}_m = p\bar{u}_{m+1} - u_{m+1}(0) + \bar{c}_{m+1} = r_{m+1} + p\bar{u}_{m+1},\quad m \geqslant 0, \tag{18}$$

$$0 = p\bar{u}_0 - u_0(0) + \bar{c}_0 = r_0 + p\bar{u}_0, \tag{19}$$

where

$$r_m = -[\bar{a}_m + \bar{b}_m + \bar{Q}_m + u_m(0)],\quad m \geqslant 0, \tag{20}$$

where $\bar{b}_m$, $\bar{Q}_m$, and $u_m(0)$ are known quantities.[3]

From (18) and (20) we have

$$0 = r_0 + p\bar{u}_0 = r_0 + pr_1 + p^3\bar{u}_1 = \ldots = \sum_{s=0}^{s=n} p^s r_s + p^{n+1}\bar{u}_n, \tag{21}$$

from which it also follows that if $\lim\limits_{n\to\infty} p^{n+1}\bar{u}_n \mid 0$, then

$$\sum_{s=0}^{\infty} p^s r_s = 0. \tag{21'}$$

Below, we assume that this limit actually is equal to zero for the selected φ_m. This assumption must be verified later when the solution obtained in this approximation has been found.

Equation (21) can be rewritten as

$$\bar{u}_n = -\sum_{s=0}^{s=n}\frac{r_s}{p^{n+1-s}}.\quad n \geqslant 0. \tag{21''}$$

Introducing the generation function[4]

$$\varphi(x,\ y,\ z,\ \lambda) \equiv \varphi(\lambda) = \sum_{n=0}^{\infty}\lambda^n\varphi_n, \tag{22}$$

and the functions

$$\bar{M}(\lambda,\ p) = \sum_{n=0}^{\infty}\lambda^n\bar{u}_n, \tag{23}$$

$$N(\lambda,\ p) = \sum_{s=0}^{\infty}\lambda^s r_s = -\sum_{s=0}^{\infty}\lambda^s(\bar{a}_s + \bar{b}_s + \bar{Q}_s) - \sum_{s=0}^{\infty}\lambda^s u_s(0)$$

$$\equiv -\bar{w}(\lambda,\ p) - M(\lambda,\ 0), \tag{24}$$

which can be considered as Laplacians, transformed from the functions

$$M(\lambda,\ \tau) = \int_V u\varphi(\lambda)\,dV \tag{25}$$

and

$$w(\lambda,\ \tau) = \int_{f_\tau}\left[\left(\frac{\partial u}{\partial n} + v_n u\right)\varphi(\lambda) - u\frac{\partial\varphi(\lambda)}{\partial n}\right]df_\tau$$

$$-\int_{f_1} F_1\frac{\partial\varphi(\lambda)}{\partial n}df_1 + \int_{f_2} F_2\varphi(\lambda)\,df_2 + \int_{f_3} F_3\varphi(\lambda)\,df_3 + \int_V Q\varphi(\lambda)\,dV \tag{26}$$

respectively, it is easy to verify that[5]

$$\bar{M}(\lambda,\ p) = -\frac{N(\lambda,\ p)}{p-\lambda} = \frac{\bar{w}(\lambda,\ p)}{p-\lambda} + M(\lambda,\ 0)\frac{1}{p-\lambda}. \tag{27}$$

Converting from the transformed functions to the inverse transforms, taking account of (20) and using Duhamel's theorem, we obtain the equation

$$M(\lambda, \tau)=\int_V u\varphi(\lambda)\,dV=e^{\lambda\tau}\left[\int_0^\tau e^{-\lambda\eta}w(\lambda, \eta)\,d\eta+\int_{V_0} u^0\varphi(\lambda)\,dV_0\right]. \quad (28)$$

It can be obtained more simply, as will be shown below, by the method in Sec. 2. When (24) and (26) are used Eq. (21') becomes

$$\int_0^\infty e^{-p\tau}d\tau\int_{f_\tau}\left[\left(\frac{\partial u}{\partial n}+v_n u\right)\varphi(p)-u\frac{\partial\varphi(p)}{\partial n}\right]df_\tau=\int_0^\infty e^{-p\tau}d\tau\left\{\int_{f_1}F_1\frac{\partial\varphi(p)}{\partial n}df_1\right.$$

$$\left.-\int_{f_2}F_2\varphi(p)\,df_2-\int_{f_3}F_3\varphi(p)\,df_3-\int_V Q\varphi(p)\,dV\right\}-\int_{V_0}u^0\varphi(p)\,dV_0. \quad (29)$$

Here, the right side is known, so that when the motion of the boundary of f_T is given, this relation is an integral equation for finding whichever of the quantities u or ∂u/∂n is unknown. In the Stefan problem, Eq. (29) takes the form

$$\alpha\int_0^\infty e^{-p\tau}d\tau\int_{f_\tau}v_n\varphi(p)\,df_\tau=\int_0^\infty e^{-p\tau}d\tau\left\{-\int_{f_1}F_1\frac{\partial\varphi(p)}{\partial n}df_1\right.$$

$$\left.+\int_{f_2}F_2\varphi(p)\,df_2+\int_{f_3}F_3\varphi(p)\,df_3+\int_V Q\varphi(p)\,dV\right\}+\int_{V_0}u^0\varphi(p)dV_0, \quad (30)$$

and equations of this kind can be used to find the motion of the phase boundary f_T. This generally requires construction and use of an infinite set of functions φ(p) which form a complete (in a specific sense) set. The solution of the inverse problem is simpler when the motion of the phase boundary is known and it is required to determine the distribution of the external surface and volume sources that are responsible for such motion. Below, we give examples.

2. Returning now to the function $\varphi(\lambda)$, using Eq. (22) and the condition $\Delta\varphi_0 = 0$, we verify directly that it satisfies the equation

$$\Delta\varphi(\lambda)=\lambda\varphi(\lambda), \quad (31)$$

and since all the functions φ_m satisfy the boundary conditions (6) on f_1, f_2, and f_3 of the boundary surface, the same boundary conditions must also be satisfied by the function φ, i.e.,

$$\varphi|_{f_1}=0, \quad (32)$$

$$\frac{\partial\varphi}{\partial n}\Big|_{f_2}=0, \quad (33)$$

$$\left(\frac{\partial\varphi}{\partial n}+\gamma\varphi\right)\Big|_{f_3}=0. \quad (34)$$

This gives a direct method for constructing the functions $\varphi(\lambda)$, which can be any holomorphic solutions of (31) at the point $\lambda = 0$ which satisfy[6] the boundary conditions (32)-(34). At the same time, since the function $\varphi(\lambda)$ is a generating function for the functions φ_m, the latter can be obtained from the former by a simple expansion[7] in powers of λ.

Note that Eqs. (28) and (29) can be obtained directly from Eqs. (3) and (31). Actually,

$$\int_V[\varphi(\lambda)\,\Delta u-u\Delta\varphi(\lambda)]\,dV+\int_V Q\varphi(\lambda)\,dV+\int_{f_\tau}\varphi u v_n df_\tau=-\int_{f_1}F_1\frac{\partial\varphi(\lambda)}{\partial n}df_1$$

$$+\int_{f_2}F_2\varphi(\lambda)\,df_2+\int_{f_3}F_3\varphi(\lambda)df_3+\int_{f_\tau}\left[\left(\frac{\partial u}{\partial n}+v_n u\right)\varphi(\lambda)-u\frac{\partial\varphi(\lambda)}{\partial n}\right]df_\tau$$

$$+\int_V Q\varphi(\lambda)\,dV=\frac{dM(\lambda, \tau)}{d\tau}-\lambda M(\lambda, \tau);$$

integrating this equation for the initial condition $M(\lambda, 0) = \int_{V_0} u^0\varphi(\lambda)dV_0$, we obtain (28). Assuming that $\mathrm{Re}(\lambda) > 0$, multiplying (28) by $e^{-\lambda\tau}$ and taking the limit $\tau = \infty$, we obtain Eq. (29).

3. In the integrals over τ on the right side of Eq. (28) we take λ to be a constant. However, after the calculation is performed it is possible to determine $\lambda(\tau)$ the time dependence of λ. This follows since both the left and right sides of this equation contain analytic functions of λ and these must be identical.

4. In order to illustrate the general theory we first consider the simplest case of a Stefan problem, in which the solution depends only on a single Cartesian coordinate x or only on the radius r in cylindrical or spherical coordinate systems.

a) Process depends only on x. We denote the coordinate of the moving boundary by $\xi(\tau)$, so that $v_n = \dot{\xi}$; we note that in the present case the volume V means a cylinder of height ξ with cross section f_T equal to unity, i.e., $\int_V \psi dV = \int_0^\xi \psi dx$ and $\int_{f_\tau} \psi df_T = \psi$, where ψ is any function of x and τ. Moreover, on the moving boundary $\partial/\partial n = \partial/\partial x$, and on f_1, i.e., for $x = 0$, $\partial/\partial n = -\partial/\partial x$. Since the function $\varphi(\lambda)$ must satisfy the equation $d^2\varphi/dx^2 = \lambda\varphi$ and any one of the three boundary conditions (32)-(34) and be a holomorphic function of λ at the value $\lambda = 0$, then the corresponding three functions are

$$\varphi^{(1)}(\lambda)=\frac{\operatorname{sh}\sqrt{\lambda}x}{\sqrt{\lambda}}=\sum_{m=0}^\infty\lambda^m\frac{x^{2m+1}}{(2m+1)!},\quad\varphi_m^{(1)}=\frac{x^{2m+1}}{(2m+1)!}, \quad (35)$$

$$\varphi^{(2)}(\lambda)=\operatorname{ch}\sqrt{\lambda}x=\sum_{m=0}^\infty\lambda^m\frac{(x^{2m})!}{(2m)!};\quad\varphi_m^{(2)}=\frac{x^{2m}}{(2m)!}, \quad (36)$$

$$\varphi^{(3)}(\lambda)=\gamma\varphi^{(1)}-\varphi^{(2)}. \quad (37)$$

Note that for m ≥ 1 and k = 1, 2, 3 the following expression is obtained:

$$\varphi_m^{(k)}\big|_{x=0}=\frac{d\varphi_m^{(k)}}{dx}\Big|_{x=0}=0,$$

by virtue of which $b_m = 0$ for m ≥ 1 [cf. (10)].

For the case of boundary conditions of the first kind, Eq. (17) gives

$$\alpha\sum_{k=0}^\infty\frac{d^k}{d\tau^k}\left[\frac{\xi^{2k+1}}{(2k+1)!}\dot{\xi}\right]=\sum_{n=1}^\infty\frac{1}{(2n)!}\frac{d^n}{d\tau^n}(\xi^{2n})$$

$$=F_1(\tau)+\sum_{k=0}^{\infty}\frac{1}{(2k+1)!}\frac{d^k}{d\tau^k}\int_0^{\xi}Q(x,\tau)x^{2k+1}dx, \qquad (38)$$

where $F_1(\tau) = u|_{x=0}$, and similar equations for the cases of boundary conditions of the second and third kind. These equations coincide for $Q(x, \tau) = 0$ with the corresponding equations in refs. 1-3, where they were obtained by different methods, and extend the equations to the case[8] of a medium containing volume sources with density $Q(x, \tau)$.

Substituting the function $\varphi^{(1)}(\lambda)$ into (30), we obtain the equation

$$\alpha\int_0^{\infty}e^{-p\tau}\frac{\operatorname{sh}\sqrt{p}\,\xi(\tau)}{\sqrt{p}}\xi(\tau)\,d\tau=-\frac{\alpha\operatorname{ch}[\sqrt{p}\,\xi(0)]}{p}+\alpha\int_0^{\infty}e^{-p\tau}\operatorname{ch}[\sqrt{p}\,\xi(\tau)]\,d\tau$$
$$=F_1(p)+\frac{1}{\sqrt{p}}\left[\int_0^{\xi(\tau)}Q(x,\tau)\operatorname{sh}\sqrt{p}x\,dx+\int_0^{\xi(0)}u^0\operatorname{sh}\sqrt{p}x\,dx\right], \qquad (39)$$

whereas substitution into (28) gives

$$\int_0^{\xi(\tau)}u\frac{\operatorname{sh}\sqrt{\lambda}x}{\sqrt{\lambda}}dx=\int_0^{\tau}e^{\lambda(\tau-\eta)}\left[F_1(\eta)+\int_0^{\xi(\eta)}Q(x,\eta)\frac{\operatorname{sh}\sqrt{\lambda}x}{\sqrt{\lambda}}dx\right.$$
$$\left.-\alpha\frac{\operatorname{sh}\sqrt{\lambda}\,\xi(\eta)}{\sqrt{\lambda}}\xi'(\eta)\right]d\eta+e^{\lambda\tau}\int_0^{\xi(0)}u^0\frac{\operatorname{sh}\sqrt{\lambda}x}{\sqrt{\lambda}}dx. \qquad (40)$$

Similarly we obtain corresponding equations for the case of boundary conditions of the second and third kind.

When $Q(x, \tau) = 0$ Eq. (39) coincides with Eq. (2.5) in ref. 4 for $\xi(0) = 0$, and with Eq. (4.8) in ref. 6 for $\xi(0) \neq 0$, and (40) – with (4.7) in ref. 6, in which both these equations and also similar equations for problems with cylindrical and spherical symmetry are obtained with the help of special integral transformations, which are only useful in "one-dimensional" problems. In ref. 6 it is noted that integral relations of form (39) and similar relations for problems with cylindrical and spherical symmetry can be used to find the motion of the phase boundary.

An important result in Eq. (40) has not been indicated in these papers: When the boundary motion is known it is then possible to get the complete solution of the problem, i.e., the function u at any τ for any point in the medium. We now show this using Eq. (40).

Assuming that $\sqrt{\lambda} = ik\pi/\xi(\tau)$, where k is any integer, $k \geq 0$ (this is admissible, as was indicated in Sec. 3), we obtain

$$\int_0^{\xi(\tau)}u\sin\frac{\pi kx}{\xi(\tau)}dx\equiv u_k^{(1)}(\tau)=e^{-\frac{\pi^2k^2}{\xi^2(\tau)}\tau}\int_0^{\xi(0)}u_0(x)\sin\frac{\pi kx}{\xi(\tau)}dx$$
$$+\int_0^{\tau}e^{-\frac{\pi^2k^2(\tau-\eta)}{\xi^2(\tau)}}\left[\frac{\pi k}{\xi(\tau)}F_1(\eta)-\alpha\xi'(\eta)\sin\frac{\pi k\xi(\eta)}{\xi(\tau)}\right.$$
$$\left.+\int_0^{\xi(\eta)}Q(x,\eta)\sin\frac{\pi kx}{\xi(\tau)}dx\right]d\eta. \qquad (41)$$

The integrals on the left, however, are nothing more than the coefficients of the expansion of the function $u(x, \tau)$, determined at time τ in the interval $[0, \xi(\tau)]$ according to the system of "instantaneous" eigenfunctions (see ref. 7) $v_k^{(1)}(x, \tau) = \sin\pi kx/\xi(\tau)$, $k \geq 1$, corresponding to the boundary conditions of the first kind for $x = 0$ and for $x = \xi(\tau)$, where

$$u(x,\tau)=\frac{2}{\xi(\tau)}\sum_{k=1}^{\infty}u_k^{(1)}(\tau)\sin\frac{\pi kx}{\xi(\tau)},\quad 0<x<\xi(\tau). \qquad (42)$$

Therefore, if $\xi(\tau)$ is known, Eqs. (41) and (42) give the final solution of the initial problem.[9] Thus, e.g., if $\xi = 2\beta\sqrt{\tau}$, where $\beta = \text{const}$, such that $\xi(0) = 0$, and if $Q(x, \tau) = 0$, then (38) gives

$$F_1(\tau)=\alpha\sum_{n=1}^{\infty}\frac{n!}{(2n)!}(2\beta)^{2n}=\alpha\left[\int_0^{\infty}e^{-t}\operatorname{ch}2\beta\sqrt{t}\,dt-1\right]$$
$$=\alpha\sqrt{\pi}\beta e^{\beta^2}\Phi(\beta)\equiv U^0, \qquad (43)$$

where $\Phi(\beta) = (2/\sqrt{\pi})\int_0^{\beta}e^{-y^2}dy$, and (41), after simple transformations, takes the form

$$u_k^{(1)}(\tau)=\frac{2\beta\sqrt{\tau}}{\pi k}\left\{U^0\left(1-e^{-\frac{\pi^2k^2}{4\beta^2}}\right)-2\alpha\beta e^{-\frac{\pi^2k^2}{4\beta^2}}\int_0^{k\pi/2\beta}e^{y^2}\sin 2\beta y\,dy\right\}. \qquad (44)$$

Using the equation

$$\int_0^{b}e^{y^2}\sin 2\beta y\,dy=e^{\beta^2}\left[e^{b^2}\int_0^{\beta}e^{-x^2}\cos 2bx\,dx-\int_0^{\beta}e^{-x^2}dx\right], \qquad (45)$$

where b is an arbitrary constant, and using Eq. (43) it is easy to verify, by a direct calculation, that the quantities (44) coincide with the expansion coefficient in the series of the considered type of function

$$u(x,\tau)=U^0\left[1-\frac{\Phi\left(\frac{x}{2\sqrt{\tau}}\right)}{\Phi(\beta)}\right], \qquad (46)$$

which, as is known, is in fact a solution of the formulated problem.

We consider the solution of the problem for boundary conditions of the first kind. For boundary conditions of the second and third kind the calculations are similar, and we shall not discuss them. For example, note that for conditions of the second kind we find from Eq. (28) the quantities

$$u_k^{(2)}(\tau)=\int_0^{\xi(\tau)}u(x,\tau)\cos\frac{\pi kx}{\xi(\tau)}dx,$$

the expansion coefficients of the solution in a series of the form

$$u(x,\tau)=\frac{u_0^{(2)}(\tau)}{\xi(\tau)}+\frac{2}{\xi(\tau)}\sum_{k=1}^{\infty}u_k^{(2)}(\tau)v_k^{(2)}(x,\tau) \qquad (47)$$

according to the instantaneous functions $v_k^{(2)}(x, \tau) = \cos\pi kx/\xi(\tau)$, which satisfy boundary conditions of the second kind for x = 0 and x = $\xi(\tau)$ for conditions of the third kind.

b) Process depends only on cylindrical coordinate r. Then

$$\Delta\varphi=\frac{1}{r}\frac{d}{dr}\left(r\frac{d\varphi}{dr}\right)=\lambda\varphi,$$

and the solution, holomorphic at $\lambda = 0$, becoming zero at $r = a$, will be

$$\varphi^{(1)}(r,\ \lambda)=K_0(\sqrt{\lambda}\,a)\,I_0(\sqrt{\lambda}\,r)-I_0(\sqrt{\lambda}\,a)\,K_0(\sqrt{\lambda}\,r), \tag{48}$$

whereas for conditions of the second kind[10)]

$$\varphi^{(2)}(\lambda,\ r)=\frac{K_1(\sqrt{\lambda}\,a)\,I_0(\sqrt{\lambda}\,r)+I_1(\sqrt{\lambda}\,a)\,K_0(\sqrt{\lambda}\,r)}{\sqrt{\lambda}}. \tag{49}$$

Assuming the radius of the moving boundary to be equal to $\rho(\tau)$ as in the plane problems, we obtain a system of relations for determining $\rho(\tau)$ and for finding the function $u(r, \tau)$ based on known $\rho(\tau)$, initial state, and distribution of sources $Q(r, \tau)$. At the same time, Eq. (28) again gives, with substitution in it of the appropriate values of λ, the coefficients of the expansion $u(r, \tau)$ based on the corresponding system of instantaneous eigenfunctions. For boundary conditions of the first kind these eigenvalues $\lambda = \lambda(\tau)$ should be determined from the condition: $\varphi^{(1)}[\rho(\tau), \lambda(\tau)] = 0$, and for conditions of the second kind from the equation

$$\left.\frac{\partial\varphi^{(2)}(r,\ \lambda)}{\partial r}\right|_{r=\rho(\tau)}=0.$$

c) We now consider the Stefan problem for the half-space $z > 0$, on the boundary of which, i.e., for $z = 0$, we are given the values of $u|_{z=0} = F_1(x, y)$ or $\partial u/\partial z|_{z=0} = F_2(x, y)$ (three-dimensional problems).

In the first case we take $\varphi^{(1)}$ to be the function

$$\varphi^{(1)}=\frac{\operatorname{sh}\sqrt{\lambda+k^2+l^2}\,z}{\sqrt{\lambda+k^2+l^2}}\,e^{i(kx+ly)}, \tag{50}$$

where k and l are arbitrary real numbers. It satisfies Eq. (31) and is an entire function of λ. Since

$$\varphi^{(1)}|_{z=0}=0,\text{ and }\left.\frac{\partial\varphi^{(1)}}{\partial z}\right|_{z=0}=e^{i(kx+ly)}=\left.\frac{\partial\varphi_0^{(1)}}{\partial z}\right|_{z=0},$$

for all values of λ, we have the relations

$$\varphi_m^{(1)}|_{z=0}=0,\ m\geqslant 0\text{ and }\left.\frac{\partial\varphi_m^{(1)}}{\partial z}\right|_{z=0}=0,\ m\geqslant 1,$$

such that for $m \geq 1$, $b_m = 0$ [cf. (10)].

In the second case we set

$$\varphi^{(2)}=\operatorname{ch}(\sqrt{\lambda+k^2+l^2}\,z)\,e^{i(kx+ly)}, \tag{51}$$

where

$$\varphi_m^{(2)}|_{z=0}=0,\ m\geqslant 1;\ \left.\frac{\partial\varphi_m^{(2)}}{\partial z}\right|_{z=0}=0,\ m\geqslant 0.$$

Equation (10) shows that in both cases only the quantity b_0 is nonzero, whereas for $m \geq 1$, $b_m = 0$.

We assume that we know some possible law of displacement of the boundary f_τ and we pose the question of the nature of those external conditions on the plane $z = 0$ that cause such a motion, assuming that $Q(x, y, z, \tau) = 0$. Since we know the law of motion of the surface f_τ, we also know at each moment the normal component v_n of the velocity of displacement of all its elements; then we know the function of time and all the integrals of the form $\int_{f_\tau} v_n\varphi_k^{(s)}df_\tau$, s = 1, 2, appearing on the left side of Eq. (17). From this we therefore also find the sum appearing on its right side, which, according to what has been said above, reduces to the single term b_0, which in the case of the first boundary-value problem is

$$b_0\equiv b_0^{(1)}(k,\ l)=\int\limits_{x=-\infty}^{\infty}\int\limits_{y=-\infty}^{\infty}F_1(x,\ y)\,e^{i(kx+ly)}\,dxdy, \tag{52}$$

and for a condition of the second kind

$$b_0\equiv b_0^{(2)}(k,\ l)=\int\limits_{-\infty}^{\infty}\int\limits_{-\infty}^{\infty}F_2(x,\ y)\,e^{i(kx+ly)}\,dxdy. \tag{53}$$

Transformation of these equations using the Fourier integral gives

$$F_1(x,\ y)=\frac{1}{4\pi^2}\int\limits_{-\infty}^{\infty}\int\limits_{-\infty}^{\infty}b_0^{(1)}(k,\ l)\,e^{-i(xk+yl)}\,dkdl, \tag{54}$$

$$F_2(x,\ y)=\frac{1}{4\pi^2}\int\limits_{-\infty}^{\infty}\int\limits_{-\infty}^{\infty}b_0^{(2)}(k,\ l)\,e^{-i(xk+yl)}\,dkdl, \tag{55}$$

and this is also the complete solution of the formulated problem.

d) As a last example we consider one more problem with the boundary moving in a given way, where we assume that everything depends only on x, and on the moving boundary $\xi(\tau)$ we are given one of the values: $u|_{x=\xi} = \psi_1(\tau)$ or $\partial u/\partial x|_{x=\xi} = \psi_2(\tau)$, for x = 0 – the value $u|_{x=0} = F_1(\tau)$, and $u|_{\tau=0} = u^0(x)$. Equations (29) and (35) then give, for example, in the first of the indicated cases, if we set $\partial u/\partial n|_{x=\xi} = q(\tau)$

$$\begin{aligned}\int\limits_0^{\infty}e^{-p\tau}q(\tau)\operatorname{sh}[\sqrt{p}\,\xi(\tau)]\,d\tau&=-\sqrt{p}\,F_1(p)-\int\limits_0^{\xi(0)}u^0(x)\operatorname{sh}\sqrt{p}\,x\,dx\\&+\int\limits_0^{\infty}e^{-p\tau}\Big\{\psi_1(\tau)[\sqrt{p}\operatorname{ch}\sqrt{p}\,\xi(\tau)-\dot{\xi}(\tau)\operatorname{sh}\sqrt{p}\,\xi(\tau)]\\&-\int\limits_0^{\xi(\tau)}Q(x,\ \tau)\operatorname{sh}\sqrt{p}\,x\,dx\Big\}\,d\tau,\end{aligned} \tag{56}$$

and this equation, the right side of which is known, should also serve for finding the function $q(\tau)$. After $q(\tau)$ has been found, the right side of Eq. (28) becomes known [cf. (26)], and since its left side in the given case equals $\int_0^{\xi(\tau)} u(\operatorname{sh}\sqrt{\lambda}x/\sqrt{\lambda})dx$, the equation obtained agrees in type with Eq. (40) and can be solved immediately by the method given in Sec. 3.

The case when on the moving boundary we are given the value $\partial u/\partial x|_{x=\xi} = \psi_2(\tau)$ or when $x = 0$ we are given the values $\partial u/\partial x|_{x=0} = -F_2(\tau)$ or $(\partial u/\partial x - \gamma u)|_{x=0} = -F_3(\tau)$ can be considered in a completely similar way.

---

[1] By a Stefan problem we shall here mean the particular case in which one of two adjoining phases is at the temperature of the phase transition and the phase boundary is displaced laterally. The boundary conditions on the boundary surface will have the form (2) (the transition temperature is assumed to be zero).

[2] We note that in the selection of such a system of functions we have some arbitrariness because on the part f_τ of the surface bounded by V no conditions are placed on the functions. We assume that these functions have all the properties that are necessary for the validity of the further calculations.

[3] The quantity $u_m(0)$ is the value of the integral (7) for $\tau = 0$, i.e., at the initial time.

[4] Here and below, we everywhere assume that all the series introduced in the course of the calculations converge uniformly in the ranges of the variables being considered so that we can interchange the order of summation and integration.

[5] Comparing the coefficients for identical powers of λ from the right and from the left.

[6] As indicated above, the conditions for the function $\varphi(\lambda)$ are not unique.

[7] It is sometimes advantageous to obtain these directly from the system (5), (6).

[8] In ref. 5, similar relations are also obtained for a continuous cylinder and sphere, on the external surface of which the Stefan conditions are satisfied.

[9] We recall that the function $F_1(\tau)$ that appears in (41) is also known, because it is obtained with known $\xi(\tau)$ from Eq. (38).

[10] It is easy to verify that, although the functions $K_0(\sqrt{\lambda}r)$ and $K_1(\sqrt{\lambda}r)$ contain ln λ, it drops out of the combinations (48) and (49).

---

[1] B. Ya. Lyubov, Dokl. Akad. Nauk SSSR, 98, 847 (1949).

[2] V. T. Borisov, B. Ya. Lyubov, and D. E. Temkin, Dokl. Akad. Nauk SSSR, 104, 223 (1955).

[3] O. M. Chekmareva, Zh. Tekh. Fiz., 40, 2032 (1970) [Sov. Phys. – Tech. Phys., 15, 1584 (1971)].

[4] G. A. Grinberg and O. M. Chekmareva, Zh. Tekh. Fiz., 40, 2025 (1970) [Sov. Phys. – Tech. Phys., 15, 1579 (1971)].

[5] O. M. Chekmareva, Zh. Tekh. Fiz., 41, 1071 (1971) [Sov. Phys. – Tech. Phys., 16, 846 (1971)].

[6] O. M. Chekmareva, Zh. Tekh. Fiz., 41, 1115 (1971) [Sov. Phys. – Tech. Phys., 16, 882 (1971)].

[7] G. A. Grinberg, Prikl. Matem. Mekhan., 31, No, 2, 193 (1967).

Stefan problem with motion of the phase-transition surface described by $y(\tau) = \sqrt{A\tau^2 + B\tau + h^2}$

O. M. Chekmareva

A. F. Ioffe Physicotechnical Institute, Academy of Sciences of the USSR, Leningrad

(Submitted November 30, 1973)
Zh. Tekh. Fiz., 44, 2043-2050 (October 1974)

The generalized Cauchy series for the heat-conduction equation is used to find new exact solutions for the one-dimensional Stefan problem in a plane region and in a region with spherical symmetry; the phase boundary moves according to $y(\tau) = \sqrt{A\tau^2 + B\tau + h^2}$, where A, B, and h are known constants. The solution for the corresponding problem is given when the boundary moves according to $y(\tau) = \sqrt{A\tau^2 + B\tau}$ for a region bounded by a cylindrical phase-transition surface with an interior heat source located along the axis.

1. In this work, using the generalized Cauchy series we obtain exact solutions of certain single-phase Stefan problems.

We consider the following problem. Let the region $0 < x < h$ be initially filled with a substance in which there is some initial temperature distribution $\varphi(x)$ such that $\varphi(h) = 0$; in the region $x > h$ this substance is at its melting point, which we take equal to zero. As a result of heating or cooling of the medium from the surface $x = 0$ to the plane $x = h$, at time $\tau = 0$ a phase transition arises; this propagates continuously to the right.

We obtain the following system of equations for the problem:

$$\frac{\partial^2 u}{\partial x^2} = \frac{\partial u}{\partial \tau}, \quad 0 < x < y(\tau), \ \tau > 0, \tag{1.1}$$

$$u(x, 0) = \varphi(x), \quad 0 < x < h = y(0), \quad \varphi(h) = 0, \tag{1.2}$$

$$u[y(\tau), \tau] = 0, \tag{1.3}$$

$$\alpha \left.\frac{\partial u}{\partial x}\right|_{x=y(\tau)} = \frac{dy}{d\tau}. \tag{1.4}$$

Beginning at the time $\tau = 0$ on the surface $x = 0$ we are given one of the three boundary conditions

$$u(0, \tau) = f_1(\tau), \tag{1.5a}$$

$$\left.\frac{\partial u}{\partial x}\right|_{x=0} = f_2(\tau), \tag{1.5b}$$

$$\left.\frac{\partial u}{\partial x}\right|_{x=0} = \chi[u(0, \tau) - f_3(\tau)], \tag{1.5c}$$

where $y(\tau)$ is the coordinate of the moving surface, α is a constant, which can be greater than or less than zero, χ is a known coefficient, and τ is the dimensionless time.

Replacing x by ξ in Eq. (1.1) we multiply it by $\xi - x$ and integrate over ξ from x to $y(\tau)$. Then, as a result of successive integration by parts (as in ref. 1), we obtain

$$u(x, \tau) = -\sum_{n=0}^{\infty} \frac{\partial^n}{\partial \tau^n} \left\{ \frac{[y(\tau) - x]^{2n+1}}{(2n+1)!} \left[\dot{y}(\tau) u(y(\tau), \tau) + \left.\frac{\partial u}{\partial x}\right|_{x=y(\tau)} \right] \right\} + \sum_{n=0}^{\infty} \frac{\partial^n}{\partial \tau^n} \left\{ \frac{[y(\tau) - x]^{2n}}{(2n)!} u(y(\tau), \tau) \right\}, \quad x < 0 < y(\tau). \tag{1.6}$$

Equation (1.6) is a generalized Cauchy series for the heat-conduction equations, when the Cauchy conditions are given along some analytic arc $x = y(\tau)$.

Using conditions (1.3) and (1.4) we obtain

$$u(x, \tau) = -\frac{1}{\alpha} \sum_{n=1}^{\infty} \frac{1}{(2n)!} \frac{\partial^n}{\partial \tau^n} [y(\tau) - x]^{2n}, \quad 0 < x < y(\tau). \tag{1.7}$$

Using the boundary conditions (1.5) we obtain the relations

$$f_1(\tau) = -\frac{1}{\alpha} \sum_{n=1}^{\infty} \frac{1}{(2n)!} \frac{d^n}{d\tau^n} y^{2n}(\tau), \tag{1.8a}$$

$$f_2(\tau) = \frac{1}{2} \sum_{n=1}^{\infty} \frac{1}{(2n-1)!} \frac{d^n}{d\tau^n} [y(\tau)]^{2n-1}, \tag{1.8b}$$

$$-\alpha f_3(\tau) = \sum_{n=1}^{\infty} \frac{d^n}{d\tau^n} \left[\frac{y^{2n}(\tau)}{(2n)!} + \frac{1}{\chi} \frac{y^{2n-1}(\tau)}{(2n-1)!} \right]. \tag{1.8c}$$

To these equations we must add an initial condition, which follows from (1.2) and (1.7):

$$\varphi(x) = -\frac{1}{\alpha} \sum_{n=1}^{\infty} \frac{1}{(2n)!} \left\{ \frac{\partial^n}{\partial x^n} [y(\tau) - x]^{2n} \right\}_{\tau=0}, \quad 0 < x < h. \tag{1.9}$$

Equations (1.7) and (1.9) can be written in a more convenient form. Since the solution of Eq. (1), $u(x, \tau)$, and its derivative $\partial u/\partial x$ on the surface $x = 0$ become, respectively, the functions $f_1(\tau)$ and $f_2(\tau)$, we can use the well-known (see ref. 2) expansion of the integral of the heat-conduction equation (1.1) in a series in powers of x:

$$u(x, \tau) = \sum_{n=0}^{\infty} \frac{x^{2n}}{(2n)!} \frac{d^n}{d\tau^n} f_1(\tau) + \sum_{n=0}^{\infty} \frac{x^{2n+1}}{(2n+1)!} \frac{d^n}{d\tau^n} f_2(\tau); \tag{1.10}$$

hence

$$\varphi(x) = \sum_{n=0}^{\infty} \frac{x^{2n}}{(2n)!} \left[\frac{d^n}{d\tau^n} f_1(\tau) \right]_{\tau=0} + \sum_{n=0}^{\infty} \frac{x^{2n+1}}{(2n+1)!} \left[\frac{d^n}{d\tau^n} f_2(\tau) \right]_{\tau=0}. \tag{1.11}$$

Equations (1.7)-(1.9) can be considered as the solution of an inverse Stefan problem in the following sense: If a law of motion of the boundary $y(\tau)$ is given, then the function $u(x, \tau)$, defined by (1.7), is a solution of the heat-conduction equation (1.1) which satisfies conditions (1.3) and (1.4) on the boundary $x = y(\tau)$. Then Eqs. (1.5) and (1.9) give the boundary values $f_i(\tau)$ and the initial distribution

$\varphi(x)$, corresponding to a given law of motion of the phase-boundary surface.

2. We assume that the phase-transition surface moves according to

$$y(\tau)=\sqrt{A\tau^2+B\tau+h^2}, \qquad (2.1)$$

where A and B are known coefficients.

We investigate thermal regimes for which such motions are possible. We determine the conditions on the boundary x = 0 corresponding to the given motion of the front of the phase boundary. We first find the temperature on the surface x = 0. We substitute (2.1) into Eq. (1.8a):

$$f_1(\tau)=-\frac{1}{a}\sum_{n=1}^{\infty}\frac{1}{(2n)!}\frac{d^n}{d\tau^n}(A\tau^2+B\tau+h^2)^n. \qquad (2.2)$$

We rewrite y(τ) in the form

$$y^2(\tau)=A\tau^2+B\tau+h^2=\left(\sqrt{A}\,\tau+\frac{B}{2\sqrt{A}}\right)^2-\frac{B^2}{4A}+h^2=\beta^2(z^2-1). \qquad (2.3)$$

where

$$\beta^2=\frac{B^2}{4A}-h^2,\quad z^2=\frac{1}{\beta^2}\left(\sqrt{A}\,\tau+\frac{B}{2\sqrt{A}}\right)^2; \qquad (2.4)$$

then

$$f_1(\tau)=-\frac{1}{a}\sum_{n=1}^{\infty}\frac{\beta^{2n}}{(2n)!}\frac{d^n}{d\tau^n}\left[\frac{\left(\sqrt{A}\,\tau+\frac{B}{2\sqrt{A}}\right)^2}{\beta^2}-1\right]^n$$
$$=-\frac{1}{a}\sum_{n=1}^{\infty}\frac{A^{n/2}\beta^n}{(2n)!}\frac{d^n}{dz^n}(z^2-1)^n. \qquad (2.5)$$

The right side of (2.5) is a series in Legendre polynomials, which, for all real or complex z, are defined by the Rodrigues equation[3]

$$P_n(z)=\frac{1}{2^n n!}\frac{d^n}{dz^n}(z^2-1)^n.$$

Hence

$$f_1(\tau)=-\frac{1}{a}\sum_{n=1}^{\infty}\frac{A^{n/2}\beta^n}{(2n-1)!!}P_n\left(\frac{\tau\sqrt{A}+\frac{B}{2\sqrt{A}}}{\beta}\right). \qquad (2.6)$$

Using Eq. (A.1) of the Appendix, we obtain

$$f_1(\tau)=-\frac{1}{a}\int_0^1\frac{1}{\sqrt{1-\zeta}}\frac{d}{d\zeta}e^{\frac{\sqrt{A}\beta}{2}z\zeta}I_0\left(\frac{\beta\sqrt{A}}{2}\zeta\sqrt{z^2-1}\right)d\zeta$$
$$=-\frac{1}{a}\int_0^1 e^{\frac{\sqrt{A}\beta z}{1}\zeta}\left[\frac{\sqrt{A}\beta}{2}zI_0\left(\frac{\sqrt{A}\beta}{2}\zeta\sqrt{z^2-1}\right)\right.$$
$$\left.+\frac{\beta\sqrt{A}}{2}\sqrt{z^2-1}\,I_1\left(\frac{\sqrt{A}\beta}{2}\zeta\sqrt{z^2-1}\right)\right]\frac{d\zeta}{\sqrt{1-\zeta}}\ ; \qquad (2.7)$$

taking account of (2.3) and (2.4), we obtain the final expression for $f_1(\tau)$:

$$f_1(\tau)=-\frac{1}{2a}\int_0^1 e^{\frac{y(\tau)\dot{y}(\tau)}{2}\zeta}\left\{y(\tau)\dot{y}(\tau)I_0\left[\frac{\sqrt{A}}{2}y(\tau)\zeta\right]\right.$$
$$\left.+\sqrt{A}y(\tau)I_1\left[\frac{\sqrt{A}}{2}y(\tau)\zeta\right]\right\}\frac{d\zeta}{\sqrt{1-\zeta}}. \qquad (2.8)$$

We now calculate the value of the heat flux on the surface x = 0. After substituting (2.1) into Eq. (1.8b) we obtain

$$f_2(\tau)=\frac{1}{a}\sum_{n=1}^{\infty}\frac{A^{n/2}\beta^{n-1}}{(2n-1)!}\frac{d^n}{dz^n}(z^2-1)^{n-1/2}. \qquad (2.9)$$

By definition, for every real and complex z we have

$$\frac{\sqrt{z^2-1}}{(2n-1)!!}\frac{d^n}{dz^n}(z^2-1)^{n-1/2}=T_n(z),\ |z|\geqslant 1,$$

where the $T_n(z)$ are Tschebyshev polynomials of the first kind; then

$$f_2(\tau)=\frac{1}{a\sqrt{z^2-1}}\sum_{n=1}^{\infty}\frac{A^{n/2}\beta^{n-1}}{2^{n-1}(n-1)!}T_n(z)=\frac{\sqrt{A}}{a\sqrt{z^2-1}}\sum_{n=0}^{\infty}\frac{A^{n/2}\beta^n}{2^n n!}T_{n+1}(z). \qquad (2.10)$$

Since

$$T_n(z)=\operatorname{ch}(n\operatorname{arch}z)=\frac{1}{2}[(z+\sqrt{z^2-1})^n$$
$$+(z-\sqrt{z^2-1})^n],\ |z|\geqslant 1, \qquad (2.11)$$

then Eq. (2.10) can be summed:

$$f_2(\tau)=\frac{\sqrt{A}}{2a\sqrt{z^2-1}}\sum_{n=0}^{\infty}\frac{A^{n/2}\beta^n}{2^n n!}[(z+\sqrt{z^2-1})^{n+1}+(z-\sqrt{z^2-1})^{n+1}]$$
$$=\frac{\sqrt{A}}{a\sqrt{z^2-1}}e^{\frac{\sqrt{A}\beta}{2}z}\left[z\operatorname{ch}\frac{\beta\sqrt{A}}{2}\sqrt{z^2-1}+\sqrt{z^2-1}\operatorname{sh}\frac{\sqrt{A}}{2}\beta\sqrt{z^2-1}\right].$$

Thus,

$$f_2(\tau)=\frac{1}{a}e^{\frac{y(\tau)\dot{y}(\tau)}{2}}\left\{\dot{y}(\tau)\operatorname{ch}\left[\frac{\sqrt{A}}{2}y(\tau)\right]+\sqrt{A}\operatorname{sh}\left[\frac{\sqrt{A}}{2}y(\tau)\right]\right\}. \qquad (2.12)$$

If the phase-transition surface moves according to $y(\tau)=\sqrt{B\tau+h^2}$ from Eqs. (2.8) and (2.12) we have

$$f_1(\tau)=-\frac{\sqrt{\pi B}}{2a}e^{B/4}\Phi\left(\frac{\sqrt{B}}{2}\right), \qquad (2.13)$$

$$f_2(\tau)=\frac{Be^{B/4}}{2a\sqrt{B\tau+h^2}}, \qquad (2.14)$$

and from (1.10) and (1.11)

$$u(x,\tau)=-\frac{\sqrt{\pi B}}{2a}e^{B/4}\left[\Phi\left(\frac{\sqrt{B}}{2}\right)-\Phi\left(\frac{x}{2}\sqrt{\frac{B}{B\tau+h^2}}\right)\right],\ 0<x<y(\tau), \qquad (2.15)$$

$$\varphi(x)=-\frac{\sqrt{\pi B}}{2a}e^{B/4}\left[\Phi\left(\frac{\sqrt{B}}{2}\right)-\Phi\left(\frac{\sqrt{B}}{2}\frac{x}{h}\right)\right],\ 0<x<h, \qquad (2.16)$$

where

$$\Phi(z)=\frac{2}{\sqrt{\pi}}\int_0^z e^{-\zeta^2}d\zeta.$$

If the velocity of the boundary is such that the quantity B/12 can be neglected in comparison with unity, then the initial temperature distribution, corresponding to motion of the boundary according to $y(\tau) = \sqrt{B\tau + h^2}$, is essentially linear:

$$\varphi(x)\simeq\frac{B}{2\alpha}\left(1-\frac{x}{h}\right). \qquad (2.17)$$

3. Using the same method we can investigate a similar problem for a spherically symmetric layer. The equations of the problem have the form

$$\frac{1}{r^2}\frac{\partial}{\partial r}r^2\frac{\partial u(r,\tau)}{\partial r}=\frac{\partial u}{\partial\tau},\quad a<r<R(\tau), \qquad (3.1)$$

$$u[R(\tau),\tau]=0,\quad R(0)=b\geqslant a, \qquad (3.2)$$

$$\alpha\frac{\partial u}{\partial r}\Big|_{r=R(\tau)},\quad \dot{R}(\tau), \qquad (3.3)$$

$$u(r,0)=\varphi(r),\quad 0<r<R(0)=b. \qquad (3.4)$$

On the interior fixed boundary we are given one of the two conditions

$$u(a,\tau)=f_1(\tau), \qquad (3.5a)$$

$$\frac{\partial u}{\partial r}\Big|_{r=a}=f_2(\tau). \qquad (3.5b)$$

Assuming, as usual, that

$$v(r,\tau)=ru(r,\tau),\quad x=r-a, \qquad (3.6)$$

we obtain the following system of equations for the function $v(x, \tau)$:

$$\frac{\partial^2 v}{\partial x^2}=\frac{\partial v}{\partial\tau},\quad 0<x<y(\tau)=R(\tau)-a, \qquad (3.7)$$

$$v[y(\tau),\tau]=0, \qquad (3.8)$$

$$\alpha\frac{\partial v}{\partial x}\Big|_{x=y(\tau)}=[y(\tau)+a]\dot{y}(\tau), \qquad (3.9)$$

$$v(x,0)=\varphi(x)(x+a),\quad 0<x<h=b-a, \qquad (3.10)$$

$$v(0,\tau)=af_1(\tau), \qquad (3.11a)$$

$$\left(\frac{\partial v}{\partial x}-\frac{v}{a}\right)_{x=0}=af_2(\tau). \qquad (3.11b)$$

If we now use Eqs. (1.6), (1.8a), (1.8b), and (1.11), we obtain

$$v(x,\tau)=-\frac{1}{\alpha}\sum_{n=0}^{\infty}\frac{1}{(2n+1)!}\frac{\partial^n}{\partial\tau^n}\{[y(\tau)-x]^{2n+1}[y(\tau)+a]\dot{y}(\tau)\}, \quad 3.12)$$

$$af_1(\tau)=-\frac{1}{\alpha}\sum_{n=0}^{\infty}\frac{1}{(2n+1)!}\frac{d^n}{d\tau^n}\{y^{2n+1}(\tau)[y(\tau)+a]\dot{y}(\tau)\}, \qquad (3.13)$$

$$af_2(\tau)=-f_1(\tau)+\frac{1}{\alpha}\sum_{n=0}^{\infty}\frac{1}{(2n)!}\frac{d^n}{d\tau^n}\{[y(\tau)]^{2n}[y(\tau)+a]\dot{y}(\tau)\}, \qquad (3.14)$$

$$\varphi(x)(x+a)=a\sum_{n=0}^{\infty}\frac{x^{2n}}{(2n)!}\left[\frac{d^n}{d\tau^n}f_1(\tau)\right]_{\tau=0}$$
$$+\sum_{n=0}^{\infty}\frac{x^{2n+1}}{(2n+1)!}\left\{\frac{d^n}{d\tau^n}[af_2(\tau)+f_1(\tau)]\right\}_{\tau=0}. \qquad (3.15)$$

We present here (omitting the calculations) values of the temperature and heat flux on the surface r = a, if the phase-boundary surface moves according to

$$y(\tau)=R(\tau)-a=\sqrt{A\tau^2+B\tau+(b-a)^2}=\sqrt{A\tau^2+B\tau+h^2}, \qquad (3.16)$$

$$af_1(\tau)=-\frac{2}{\alpha}e^{\frac{1}{2}\left(A\tau+\frac{B}{2}\right)}\left\{\frac{1}{\sqrt{A}}\left(A\tau+\frac{B}{2}-2\right)\operatorname{sh}\left[\frac{\sqrt{A}}{2}y(\tau)\right]\right.$$
$$\left.+y(\tau)\operatorname{ch}\left[\frac{\sqrt{A}}{2}y(\tau)\right]\right\}-\frac{a}{\alpha}\int_0^1\frac{1}{\sqrt{1-\zeta}}\frac{d}{d\zeta}e^{\frac{1}{2}y(\tau)\dot{y}(\tau)\zeta}I_0\left[\frac{\sqrt{A}}{2}\zeta y(\tau)\right]d\zeta, \qquad (3.17)$$

$$af_2(\tau)=-f_1(\tau)+\frac{S}{\alpha}, \qquad (3.18)$$

$$S=\frac{a\sqrt{A}}{\sqrt{z^2-1}}e^{\frac{\beta\sqrt{A}}{2}z}\left[z\operatorname{ch}\left(\frac{\beta\sqrt{A}}{2}\sqrt{z^2-1}\right)+\sqrt{z^2-1}\operatorname{sh}\left(\frac{\beta\sqrt{A}}{2}\sqrt{z^2-1}\right)\right]$$
$$+\beta\sqrt{A}z+\frac{\beta^2Az^2}{2}\int_0^1 e^{\frac{\beta\sqrt{A}}{2}\zeta z}I_0\left(\frac{\beta\sqrt{A}}{2}\zeta\sqrt{z^2-1}\right)\frac{d\zeta}{\sqrt{1-\zeta}}$$
$$+\beta^2A\sqrt{z^2-1}\int_0^1 e^{\frac{\beta\sqrt{A}}{2}z\zeta}\left(z-\frac{1}{\beta\sqrt{A}\zeta}\right)I_1\left(\frac{\beta\sqrt{A}}{2}\zeta\sqrt{z^2-1}\right)\frac{d\zeta}{\sqrt{1-\zeta}}$$
$$+\beta^2A\frac{z^2-1}{2}\int_0^1 e^{\frac{\beta\sqrt{A}}{2}z\zeta}I_0\left(\frac{\beta\sqrt{A}}{2}\zeta\sqrt{z^2-1}\right)\frac{d\zeta}{\sqrt{1-\zeta}}, \qquad (3.19)$$

where

$$\beta\sqrt{z^2-1}=y(\tau),\quad \frac{\beta\sqrt{A}}{2}z=\frac{1}{2}\left(A\tau+\frac{B}{2}\right)$$
$$=\frac{1}{2}y(\tau)\dot{y}(\tau),\quad \beta^2=\frac{B^2}{4A}-h^2.$$

If A = 0, i.e., $y(\tau) = R(\tau) - a = \sqrt{B\tau + h^2}$, then

$$af_1(\tau)=-\frac{B}{2\alpha}e^{B/4}\sqrt{B\tau+h^2}-\frac{a\sqrt{\pi B}}{2\alpha}e^{B/4}\Phi\left(\frac{\sqrt{B}}{2}\right), \qquad (3.20)$$

$$af_2(\tau)=\frac{B}{2\alpha}e^{B/4}\left[\frac{1}{a}\sqrt{B\tau+h^2}+\frac{a}{\sqrt{B\tau+h^2}}+\frac{\sqrt{\pi}}{\sqrt{B}}\Phi\left(\frac{\sqrt{B}}{2}\right)\right.$$
$$\left.+\frac{\sqrt{\pi B}}{2}\Phi\left(\frac{\sqrt{B}}{2}\right)\right]+\frac{B}{2\alpha}, \qquad (3.21)$$

$$\varphi(x)(x+a)=-a\frac{\sqrt{\pi B}}{2\alpha}e^{B/4}\left[\Phi\left(\frac{\sqrt{B}}{2}\right)+\Phi\left(\frac{x}{h}\frac{\sqrt{B}}{2}\right)\right]$$
$$+\frac{Bx}{2\alpha}\left[1+\frac{\sqrt{\pi B}}{2}e^{\frac{B}{4}}\Phi\left(\frac{\sqrt{B}}{2}\right)\right]-\frac{Bh}{2\alpha}e^{\frac{B}{4}\left(1-\frac{x^2}{h^2}\right)}\left[1+\frac{x}{h}\frac{\sqrt{\pi B}}{2}e^{\frac{B}{4}\frac{x^2}{h^2}}\Phi\left(\frac{x}{h}\frac{\sqrt{B}}{2}\right)\right]. \qquad (3.22)$$

If B/12 ≪ 1, then

$$\varphi(r) \simeq -\frac{B}{2a}\frac{b}{b-a}\frac{b-r}{r}, \quad a<r<b. \tag{3.23}$$

4. In conclusion we present a solution of an axisymmetric problem with an interior heat source located on the axis.

The general equations for such a problem are as follows:

$$\frac{1}{r}\frac{\partial u}{\partial r} r \frac{\partial u}{\partial r} = \frac{\partial u}{\partial \tau}, \quad 0<r<R(\tau), \tag{4.1}$$

$$u[R(\tau), \tau] = 0, \tag{4.2}$$

$$a \frac{\partial u}{\partial r}\Big|_{r=R(\tau)} = \frac{dR(\tau)}{d\tau}, \quad R(0)=0, \tag{4.3}$$

$$\lim_{r\to 0} 2\pi r \frac{\partial u}{\partial r} = f_2(\tau). \tag{4.4}$$

Proceeding in the same way as in ref. 4, we multiply (4.1) by $2\pi r$ and integrate over r from 0 to $R(\tau)$. We obtain

$$f_2(\tau) = \frac{2\pi}{a}\sum_{n=0}^{\infty}\frac{1}{[(2n)!!]^2\, 2(n+1)}\frac{d^{n+1}}{d\tau^{n+1}} R^{2n+2}(\tau). \tag{4.5}$$

If the boundary moves according to

$$R(\tau) = \sqrt{Ar^2 + B\tau}, \tag{4.6}$$

after substituting (4.6) into (4.5) and making transformations similar to those in the preceding sections, we find that the power of the source corresponding to such motion should be as follows:

$$\left.\begin{aligned} f_2(\tau) = \frac{4\pi}{a} e^{\frac{R(\tau)\dot{R}(\tau)}{2}} \Big\{ & \frac{R(\tau)\dot{R}(\tau)}{2} I_0\Big[\frac{\sqrt{A}}{2}R(\tau)\Big] \\ & + \frac{\sqrt{A}}{2}R(\tau) I_1\Big[\frac{\sqrt{A}}{2}R(\tau)\Big]\Big\}, \\ R(\tau) = \sqrt{A\tau^2 + B\tau}. & \end{aligned}\right\} \tag{4.7}$$

When A = 0, i.e., $R(\tau) = \sqrt{B\tau}$, we obtain the solution for the case of a source of constant power:

$$\lim_{r\to 0} 2\pi r \frac{\partial u}{\partial r} = Q = \frac{4\pi}{a}\frac{B}{4} e^{B/4}, \tag{4.8}$$

which agrees with the known case.[5]

APPENDIX

We consider the series

$$\sum_{n=1}^{\infty}\frac{\gamma^{n-\frac{1}{2}}}{(2n-1)!!}P_n(z) = F(\gamma, z).$$

We apply a Laplace transformation with respect to γ. We then obtain

$$\int_0^{\infty} e^{-p\gamma}F(\gamma, z)\,d\gamma = \int_0^{\infty} e^{-p\gamma}\Bigg[\sum_{n=1}^{\infty}\frac{\gamma^{n-\frac{1}{2}}}{(2n-1)!!}P_n(z)\Bigg]d\gamma$$

$$= \sum_{n=1}^{\infty}\frac{P_n(z)}{(2n-1)!!}\frac{(2n-1)!!}{2^n p^n}\int_0^{\infty}\frac{e^{-p\gamma}d\gamma}{\sqrt{\gamma}} = \sqrt{\pi}\sum_{n=1}^{\infty}\frac{P_n(z)}{2^n p^{n+\frac{1}{2}}},$$

i.e., the function $\overline{F}(p, z)$ is correct at an infinitely distant point, and has in its neighborhood a Laurent expansion

$$F(p, z) = \sqrt{\frac{\pi}{p}}\sum_{n=1}^{\infty}\frac{P_n(z)}{2^n p^n}.$$

Using the first expansion theorem and the multiplication theorem we obtain

$$F(\gamma, z) = \int_0^{\gamma}\sum_{n=1}^{\infty}\frac{P_n(z)\,\eta^{n-1}}{2^n(n-1)!}\frac{d\eta}{\sqrt{\gamma-\eta}} = \int_0^{\gamma}\frac{1}{\sqrt{\gamma-\eta}}\frac{\partial}{\partial\eta}\sum_{n=1}^{\infty}\frac{P_n(z)}{2^n n!}\eta^n d\eta$$

$$= \int_0^{\gamma}\frac{1}{\sqrt{\gamma-\eta}}\frac{\partial}{\partial\eta}\sum_{n=0}^{\infty}\frac{P_n(z)\,\eta^n}{2^n n!}\,d\eta.$$

In view of the generating function for Legendre polynomials[3]

$$\sum_{n=0}^{\infty}\frac{P_n(z)\,\eta^n}{n!} = e^{\eta z} I_0(\eta\sqrt{z^2-1}), \quad |z| \geqslant 1,$$

we obtain

$$F(\gamma, z) = \sum_{n=1}^{\infty}\frac{\gamma^{n-\frac{1}{2}}}{(2n-1)!!}P_n(z) = \int_0^{\gamma}\frac{1}{\sqrt{\gamma-\eta}}\frac{d}{d\eta}\Big\{e^{\frac{z\eta}{2}} I_0\Big[\frac{\eta}{2}\sqrt{z^2-1}\Big]\Big\}d\eta$$

$$= \frac{1}{\sqrt{\gamma}}\int_0^{1}\frac{1}{\sqrt{1-\zeta}}\frac{d}{d\zeta}e^{\frac{\gamma z}{2}\zeta} I_0\Big[\frac{\gamma}{2}\zeta\sqrt{z^2-1}\Big]d\zeta. \tag{A.1}$$

---

[1] O. M. Chekmareva, Zh. Tekh. Fiz., 40, 2032 (1970) [Sov. Phys. – Tech. Phys., 15, 1584 (1971)].

[2] E. Goursat, A Course in Mathematical Analysis, Dover (1959), Vol. 3, Part 1.

[3] A. Erdélyi (ed.), Higher Transcendental Functions, Vol. 2, McGraw-Hill (1953), Chap. 10, p. 179.

[4] O. M. Chekmareva, Zh. Tekh. Fiz., 41, 1071 (1971) [Sov. Phys. – Tech. Phys., 16, 846 (1971)].

[5] H. S. Carslaw and J. C. Jaeger, Conduction of Heat in Solids, 2nd ed., Oxford Univ. Press (1959), Chap. 11.

[6] M. N. Lavrent'ev and B. V. Shabat, Methods in the Theory of Functions of a Complex Variable [in Russian], Izd. AN SSSR, Moscow (1958).

Magnetic topography of toroidal systems

M. N. Skoblik, V. E. Ziser, A. V. Georgievskii, and V. G. Peletminskaya

(Submitted September 21, 1973)
Zh. Tekh. Fiz., 44, 2051-2057 (October 1974)

Magnetic fields of toroidal systems are calculated, taking account of the finite size of the elements producing the field. The rule for locating the helical windings on the surface of the torus is discussed in general form, yielding the choice of the optimum pitch for a given device. An algorithm is developed and a computer program is given for calculating the field at any point in space from a single helix or a set of n-helical windings. Results for specific thermonuclear devices are presented.

INTRODUCTION

The mathematical simulation of all kinds of systems and processes has long ago justified itself and is more and more widely used in various fields of science and technology, including the construction of various magnetic systems.

In order to investigate the magnetic field of a device, to calculate the ponderomotive forces, which control the capacity rating of the structure, to analyze the effectiveness of the use of superconducting materials, etc., it is first necessary to determine the magnetic field inside and outside the current elements.

The field can be determined experimentally only after the system has been constructed, and an accurate measurement of the field is difficult close to a conductor wound on a torus, and almost impossible inside the conductor. By mathematical simulation one can choose the optimum values of the geometrical and other parameters and perform a detailed calculation of the system before construction.

The creation of a mathematical model which reflects physical reality makes it possible to investigate magnetic systems and to determine the dependence of the physical parameters of the systems on geometry, etc. The development of a calculational procedure greatly increases the possibilities of optimizing the system parameters with minimum effort.

Magnetic fields of helical coils wound on a torus are analyzed in refs. 1-3, but under the assumption that the wire is infinitesimally thin. Alexander and Downing[4] take account of the finite size of the conductor, but for circular cylindrical coils.

We discuss the simulation of magnetic systems whose elements are helical coils wound on a torus, taking account of the finite size of the elements producing the field.

1. DESCRIPTION OF THE MODEL

In actual physical devices an element producing the field is finite in width and thickness. If the field point, i.e., the point at which the field is calculated, is sufficiently far from the current element its dimensions can be neglected and the field can be assumed to be produced by an infinitesimally thin conductor. As the field point approaches the conductor its width begins to matter first. To take account of the width the conductor is replaced by an infinitesimally thin sheet with width equal to the actual width of the conductor. If the field point is very close to the element or inside it the thickness of the element must be taken into account by replacing the conductor by a stack of k very thin uniformly spaced sheets (Fig. 1).

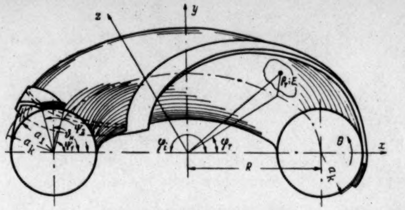

Fig. 1. System of coordinates.

Expansion of the field in spatial harmonics is inappropriate in calculating the magnetic field at a point inside a conductor or very near it, so the exact Biot–Savart law must be used. The field of an infinitesimally thin conductor is

$$\mathbf{H}=\frac{I}{c}\int\limits_{l}\frac{[d\mathbf{l}\mathbf{r}]}{r^3}, \tag{1.1}$$

where **dl** is an element of the conductor producing the field, **r** is the radius vector from the element to the field point, and I is the current in the conductor.

As already noted, however, the intensity can be calculated by assuming that the current element is infinitesimally thin only when the field point is sufficiently far from the element. If the point is close to the current element or inside it the finite dimensions of the element must be taken into account to obtain the intensity with sufficient accuracy. Its width is $\psi_2 - \psi_1$ and its thickness is $a_2 - a_1$ (Fig. 1), where ψ_i is the polar angle in a cross section at a fixed φ.

By integrating Eq. (1.1) over ψ from ψ_1 to ψ_2 we obtain the field of an infinitesimally thin sheet. By considering a stack of k very thin uniformly spaced sheets, each of width $\psi_{2k} - \psi_{1k}$, and summing over k, we find the magnetic field due to a conductor of finite cross section:

$$\mathbf{H}=\sum_{k}\frac{I_k}{c\,(\psi_{2k}-\psi_{1k})}\int\limits_{\psi_{1k}}^{\psi_{2k}}\int\frac{[d\mathbf{l}_k\mathbf{r}_k]}{r_k^3}\,d\psi, \tag{1.2}$$

where a_k is the radial distance to the k-th sheet. The current in the k-th sheet is

$$I_k=\frac{Ia_k}{\sum\limits_k a_k}. \tag{1.3}$$

Let us consider the magnetic field of a helical coil wound on a torus of minor radius a and major radius R (Fig. 1). The final expressions for the quantities entering the integrand depend on the choice of coordinate system, on the rule for winding the coil, and on the method of specifying the coordinates of the field point (x_T, y_T, z_T).

The field components in the XYZ Cartesian coordinate system are

$$\left.\begin{aligned} H_x &= \sum_k \frac{I_k}{c(\psi_{2k}-\psi_{1k})} \int\limits_{\psi_{1k}}^{\psi_{2k}} \int\limits_{l_k} \frac{1}{r^3}[dl_{yk}(z_T-z_k)-dl_{zk}(y_T-y_k)]\,d\psi_k, \\ H_y &= \sum_k \frac{I_k}{c(\psi_{2k}-\psi_{1k})} \int\limits_{\psi_{1k}}^{\psi_{2k}} \int\limits_{l_k} \frac{1}{r^3}[dl_{zk}(x_T-x_k)-dl_{xk}(z_T-z_k)]\,d\psi_k, \\ H_z &= \sum_k \frac{I_k}{c(\psi_{2k}-\psi_{1k})} \int\limits_{\psi_{1k}}^{\psi_{2k}} \int\limits_{l_k} \frac{1}{r^3}[dl_{xk}(y_T-y_k)-dl_{yk}(x_T-x_k)]\,d\psi_k, \end{aligned}\right\} \tag{1.4}$$

where $r^3 = [(x_T - x_k)^2 + (y_T - y_k)^2 + (z_T - z_k)^3]^{3/2}$; x_k, y_k, z_k are the running coordinates of the current element; x_T, y_T, z_T are the coordinates of the field point.

Let us consider the general expression for the location of the helical windings in parametric form,[5]

$$m\varphi = \pm(\theta - \alpha\sin\theta - \beta\sin 2\theta), \tag{1.5}$$

where φ is the azimuthal angle in the plane containing the major radii of the torus, θ is the polar angle in a cross section of the torus at constant φ, m is the number of the periods of the field, and α and β are variable parameters:

$$\alpha = \varkappa\alpha_0;\quad \beta = \varkappa\beta_0,$$

$$\alpha_0 = \frac{a}{R}\left(\ln\frac{8R}{a} - \frac{1}{2}\right);\quad \beta = \frac{a^2}{8R^2}\left(\frac{17}{4} - 4\ln\frac{8R}{a}\right).$$

By varying α and β the optimum relation for locating the helical windings for a specific arrangement can be found. The ± signs distinguish right- and left-hand windings. Below we assume right-hand windings, which does not affect the generality of the discussion.

Then in the XYZ system the running coordinates of the conductor producing the field, and the quantities dl, dl_y, dl_z entering the integrand, divided by the radius, are

$$\left.\begin{aligned} x &= (R_1 + \cos\theta)\sin\varphi, \\ y &= \sin\theta, \\ z &= (R_1 + \cos\theta)\cos\varphi, \\ dl_x &= [(R_1 + \cos\theta)\cos\varphi f - \sin\theta\sin\varphi]\,d\theta, \\ dl_y &= \cos\theta\, d\theta, \\ dl_z &= -[(R_1 + \cos\theta)\sin\varphi f + \sin\theta\cos\varphi]\,d\theta, \end{aligned}\right\} \tag{1.6}$$

where $R_1 = R/a$; $f = (1/m)(-\theta + \alpha\cos\theta + 2\beta\cos 2\theta)$.

The field point is specified in polar coordinates ρ_T, ξ in a cross section at a given value of φ. In the XYZ system the coordinates of the field point are

$$\left.\begin{aligned} x_T &= \frac{1}{a}[A\cos(\varphi_i + \theta_i) + B\sin(\varphi_i + \theta_i)], \\ y_T &= \frac{1}{a}\rho_T \sin\xi, \\ z_T &= \frac{1}{a}[A\sin(\varphi_i + \theta_i) - B\cos(\varphi_i + \theta_i)], \end{aligned}\right\} \tag{1.7}$$

where

$$\left.\begin{aligned} A &= (R + \rho_T\cos\xi)\cos\varphi_T - a_i - R\cos\varphi_i, \\ B &= (R + \rho_T\cos\xi)\sin\varphi_T - R\sin\varphi_i, \end{aligned}\right\} \tag{1.8}$$

φ_T is the value of φ in the cross section which contains the field point; a_i, φ_i, and θ_i locate the coordinate system fixed at the origin of the current element relative to the XYZ system.

Using the fact that in calculating the field of finite-sized conductors the running coordinate is $\theta_n = \theta - \psi$, the final expressions for the field components in electromagnetic units from n-helical conductors are

$$H_x = \sum_k \frac{0.1}{(\psi_{2k}-\psi_{1k})} \int\limits_{\psi_{1k}}^{\psi_{2k}} \Bigg\{ \sum \frac{I_k}{a_k} \int\limits_{\theta_{1n}}^{\theta_{2n}} \frac{1}{r^3} \Big\{ \cos\theta_n \Big[\frac{1}{a}\{A\sin(\varphi_i + \theta_i)$$
$$- B\cos(\varphi_i + \theta_i)\} - (R_1 + \cos\theta_n)\cos\varphi\Big] + [(R_1 + \cos\theta_n)\cos\varphi m^{-1}$$
$$\times(-1 + \alpha\cos\theta_n + 2\beta\cos 2\theta_n)$$
$$+ \sin\theta_n\sin\varphi]\left(\frac{\rho_T}{a}\sin\xi - \cos\theta_n\right)\Big\}\, d\theta_n \Bigg\}\, d\psi_k,$$

$$H_y = \sum_k \frac{0.1}{\psi_{2k}-\psi_{1k}} \int\limits_{\psi_{1k}}^{\psi_{2k}} \Bigg\{ \sum_n \frac{I_k}{a_k} \int\limits_{\theta_{1n}}^{\theta_{2n}} \frac{1}{r^3} \Big\{ [(R_1 + \cos\theta_n)\sin\varphi(1 - \alpha\cos\theta_n$$
$$- 2\beta\cos\theta_n) - \sin\theta_n\cos\varphi]\Big[\frac{1}{a}[A\cos(\varphi_i + \theta_i) - B\sin(\varphi_i + \theta_i)]$$
$$- (R_1 + \cos\theta_n)\sin\varphi\Big] - [(R_1 + \cos\theta_n)$$
$$\cos\varphi(-1 + \alpha\cos\theta_n + \beta\cos 2\theta_n)m^{-1}$$
$$- \sin\theta_n\sin\varphi]\Big[\frac{1}{a}[A\sin(\varphi_i + \theta_i) - B\cos(\varphi_i + \theta_i)]$$
$$- (R_1 + \cos\theta_n)\cos\varphi\Big]\Big\}\, d\theta_n \Bigg\}\, d\psi_k,$$

$$H_z = \sum_k \frac{0.1}{\psi_{2k}-\psi_{1k}} \int\limits_{\psi_{1k}}^{\psi_{2k}} \Bigg\{ \sum_k \frac{I_k}{a_k} \int\limits_{\theta_{1n}}^{\theta_{2n}} \frac{1}{r^3} [(R_1 + \cos\theta_n)\cos\varphi(-1 + \alpha\cos\theta_n$$
$$+ \beta\cos 2\theta_n)m^{-1} - \sin\theta_n\sin\varphi]\left(\frac{\rho_T}{a}\sin\xi - \sin\theta_n\right)$$
$$- \cos\theta_n\Big[\frac{1}{a}[A\cos(\varphi_i + \theta_i)$$
$$+ B\sin(\varphi_i + \theta_i)] - (R_1 + \cos\theta_n)\sin\varphi\Big]\Big\}\, d\theta_n \Bigg\}\, d\psi_k,$$

where

$$r^3 = \Big\{\Big[\frac{1}{a}[A\cos(\varphi_i + \theta_i) + B\sin(\varphi_i + \theta_i)] - (R_1 + \cos\theta_n)\sin\varphi\Big]^2$$
$$+ \left(\frac{\rho_T}{a}\sin\xi - \sin\theta_n\right)^2 + \Big[\frac{1}{a}[A\sin(\varphi_i + \theta_i) - B\cos(\varphi_i + \theta_i)]$$
$$- (R_1 + \cos\theta_n)\cos\varphi\Big]^2\Big\}^{3/2}; \tag{1.9}$$

the summation over n is a summation over the number of conductors.

In stellarators the windings for producing a magnetic field with a rotational transform consist of several helical conductors uniformly spaced in φ. The resulting field of such windings can be obtained by summing the fields of the separate conductors, each of which has its own value of the angle φ where the helical winding begins. The transition from conductor to conductor is accomplished by the substitution

$$\varphi_i=\vartheta_0+\frac{2\pi}{mn}(i-1);\quad i=1,\ 2,\ \ldots,\ n, \tag{1.10}$$

where ϑ_0 is the initial angle of the first conductor, and n is the number of identical helical conductors spaced in φ. In this case expressions are obtained for the field components for helical windings of torsatrons,[4] i.e., when equal currents flow in the same direction in adjacent conductors.

For stellarators, i.e., when there are 2n-helical conductors with the current flowing in opposite directions in adjacent conductors, the summation is performed with the factor $(-1)^k (k = 1, 2, \ldots, 2n)$ and in addition n is replaced by 2n in Eq. (1.10). θ_{1n} and θ_{2n} are found in terms of φ by an iterative method.[6] As a first approximation $\theta_{1n} = 2\pi m(i-1)$. In special cases integrations over θ are replaced by integration1) over φ:

$$\theta=\vartheta_0+\frac{2\pi}{n}(i-1)-\psi,\quad i=1,\ 2,\ \ldots,\ n \text{ for a torsatron,}$$

$$\theta=\vartheta_0+\frac{2\pi}{2n}(i-1)-\psi,\quad i=1,\ 2,\ \ldots,\ 2n \text{ for a stellarator.}$$

2. DESCRIPTION OF THE PROGRAM AND THE CALCULATIONAL PROCEDURE

For arbitrary values of the parameters of the torus and the current element and an arbitrary field point Eq. (1.9) is suitable for computer calculations. Only one restriction is imposed on the location of the field point: It must not coincide with a point current element or lie on a thin plate element. No restrictions are imposed on the parameters of the torus and the current element.

The calculation is programmed for an M-220 computer. In one manipulation the field intensity can be computed at $N \le 100$ points from several ($k \le 25$) n-helical windings. The integration is performed by Simpson's rule.[6] All three integrals are computed simultaneously, and in order to save machine time the trigonometric functions in the integrand are computed by the formulas for the sums of angles. The limits of integration θ_{1n} and θ_{2n} are found by an iteration method[6] using Eq. (1.5) for $\varphi = \varphi$ initial and $\varphi = \varphi_{\text{final}}$.

The number of steps in the internal integral per field period for satisfactory accuracy is determined in the process of checking out the program by comparing the results for h and h/2, where h is the integration step. If the field point is outside the element it is sufficient for the internal integral to take $(\theta_{2n} - \theta_{1n})/\text{nmh} = 100$; if the point is inside the element $(\theta_{2n} - \theta_{1n})/\text{nmh} \ge 200$.

As previously noted, a current element can be considered a point (having no transverse dimensions) when the field point is far enough away from the conductors. It has been established in the calculational process that if an element of thickness $a_2 - a_1$ is replaced by a point conductor at the radius $a = (a_2 - a_1)/2$ the field components are determined with 1% accuracy for $\rho_T \ge 1.2a_2$ or $\rho_T \le 0.55a_1$.

To achieve 1% accuracy for $0.55a_1 < \rho_T < 0.8a_1$ and $1.05a_2 < \rho < 1.2a_2$ the element must be replaced by an infinitesimally thin sheet having the actual width of the conductor $\psi_2 - \psi_1$ and located at the same place as the point conductor, i.e., $a = (a_2 - a_1)/2$.

In all other cases 1% accuracy is achieved by replacing the element by a set of k sheets uniformly spaced from a_1 to a_2. The current in the sheets is given by Eq. (1.3). It is sufficient to take the number of sheets k = 12 since there is no significant change in the field components for

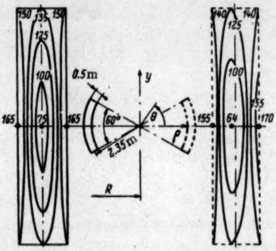

Fig. 2. Distribution of magnetic field intensity inside a current element. $\alpha = \beta = 0$, $a = 2.35$, R = 12, m = 5.33, n = 3, $a_2 - a_1 = 0.5$ m, $\psi_2 - \psi_1 = 60°$, $H_0 = 90$ kOe.

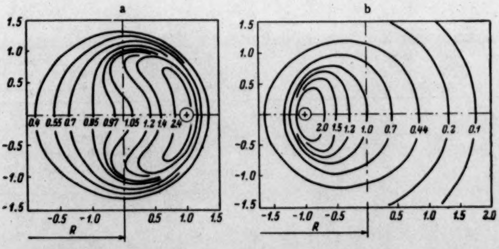

Fig. 3. Distribution of magnetic field intensity in the active volume of a torsatron. a) φ = period of the field; b) φ = 1/2 period of the field. $a = 7.25$ cm, R = 13.5 cm, n = 1, $\alpha = 0.875\alpha_0$, $\beta = 0.875\beta_0$, m = 13.

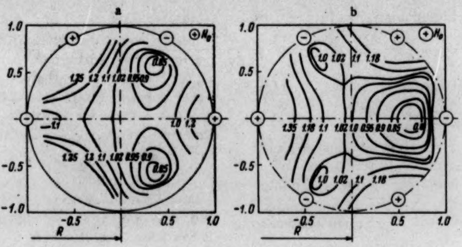

Fig. 4. Distribution of magnetic field intensity in the active volume of a stellarator. a) φ = period of the field; b) φ = 1/2 period of the field. a = 10 cm, R = 35.6 cm, n = 3, m = 2.666, $\alpha = \beta = 0$.

a further increase in k.

Using the program developed here calculations have been reformed to select the magnetic systems of such thermonuclear devices as Saturn-1 (ref. 3), Vint-20 (ref. 7), and others. A study of the structure of the magnetic fields of these devices shows that in principle a stellarator can be used to construct a thermonuclear reactor.[8] As an illustration of the use of the algorithm and the program the results of some of the calculations are presented below.

Figure 2 shows the lines $H = \sqrt{H_x^2 + H_y^2 + H_z^2}$ = const inside a current element for the magnetic system of a torsatron. The calculation is performed according to the procedure described above. The element is replaced by very thin sheets of radius $a_k = a_1 \pm (a_2 - a_1)/12$ with the current given by Eq. (1.3).

In the investigation of the magnetic system of a stellarator reactor[8] the calculation of the magnetic field inside an element and the construction of the lines H = const permit a determination of the ponderomotive forces acting on the windings and give a basis for the choice of material for the winding.

Figures 3 and 4 show the lines H = const in the active volume of the single-helix torsatron Vint-20 and the l = 3 stellarator Saturn-1. The principal characteristics of the magnetic field (absolute value of the field intensity in the active volume, ratio of maximum to minimum intensity, etc.) are calculated from these data.

The algorithm and program described can be used as a component in calculating the topography of the magnetic lines of force of closed toroidal systems. The algorithm and calculational program for the topography of the magnetic lines of force will be described later.

The machine time for the calculation depends on the parameters of the device being calculated, but is acceptable in all the cases examined here.

---

1) If $\alpha = \beta = 0$ Eq. (1.5) is easily solved for θ, and the integration over θ can be replaced by an integration over φ.

[1] A. Gibson, Phys. Fluids, 10, 1553 (1967).
[2] V. S. Voitsenya, A. V. Georgievskii, V. E. Ziser, D. F. Pogozhev, S. I. Solodovchenko, V. A. Suprunenko, and V. T. Tolok, Atom. Energ., 31, 536 (1971).
[3] C. Gourdon and M. Vuillemin, EUR-CEA-391 (1966).
[4] N. B. Alexander and A. C. Downing, Phys. and Math., ORNL - 2828.
[5] P. Herbert, EUR-CEA-F1-533 (1970).
[6] Programmer's Handbook [in Russian], Sudpromgiz, Leningrad (1963).
[7] A. V. Georgievskii, V. A. Suprunenko, and E. A. Sukhomlin, Atom. Energ., 34, 415 (1973).
[8] A. V. Georgievskii (Georgievsky), V. E. Ziser (Zisser), Yu. A. Litvinenko, M. N. Skoblik, V. A. Suprunenko, and V. T. Tolok, Proc. Intern. Working Session on Fusion Reactor Technology, 352, Oak Ridge (1971).

Rectangular conducting wedge in a moving electromagnetic field

I. D. Maergoiz and L. P. Nizhnik

(Submitted October 8, 1973; resubmitted February 26, 1974)
Zh. Tekh. Fiz., 44, 2058-2068 (October 1974)

The problem of determining the eddy current distribution over the surface of a rectangular conducting wedge in the field of a moving current sheet is discussed. Analytic solutions are found when the surface of the wedge is perfectly conducting and for the Leontovich impedance boundary condition. Eddy current distribution patterns are constructed. A solution is also presented for another method of exciting the external field.

INTRODUCTION

In a number of technical problems, for example the design of electrical machines with solid rotors, the magnetic field and eddy current distributions in the end zones of solid conducting cylinders are of interest. The solution of this problem with a detailed account of the geometry of the conducting body and the extent of the penetration of the electromagnetic field into its interior presents considerable mathematical difficulties. The purpose of the present paper is to show that these difficulties can be overcome under the following simplifying assumptions: 1) The solid conducting cylinder is replaced by an infinite rectangular wedge; 2) the skin effect is well defined. By assuming the sharp manifestation of the skin effect approximate boundary conditions can be assumed on the surface of the conducting body, and the calculation of the field can be reduced to the solution of the exterior boundary-value problem. If the conducting body is nonmagnetic ($\mu = \mu_0$) it is expedient to take the perfect conductivity boundary condition; for a ferromagnetic ($\mu \gg \mu_0$) conducting body the Leontovich impedance boundary conditions are used. We note that the use of approximate boundary conditions is not rigorously justified in the immediate vicinity of the edge of the dihedral corner. One expects, however, that the calculated results will be in error only in the vicinity of the edge and that the general character of the field and eddy current distributions will not be changed. The use of approximate boundary conditions to calculate the field in corner regions is transitional;[1-3] it significantly simplifies the calculation and leads to analytic solutions.

STATEMENT OF THE PROBLEM

Let us consider the problem of calculating the electromagnetic field produced by a current sheet which is infinite in the x direction and moves in the z direction above a dihedral conducting corner (Fig. 1). We write the magnetic field in vacuum as the sum of two terms:

$$\dot{\mathbf{H}} = \dot{\mathbf{H}}^J + \dot{\mathbf{H}}^0,$$

where $\dot{\mathbf{H}}^J$ is the magnetic field produced by the current sheet of density $\dot{\mathbf{J}} = \mathbf{k}_x j e^{j\alpha z}$ moving in a region of uniform permeability μ_0; $\dot{\mathbf{H}}^0$ is the field produced by the eddy currents and the magnetization of the medium of the dihedral corner. The following equations hold for $\dot{\mathbf{H}}^J$:

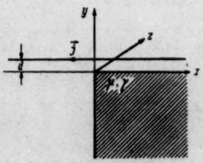

Fig. 1

$$\left.\begin{aligned} \dot{H}^J_y &= -j\frac{J e^{-\alpha d}}{2} e^{\alpha y} e^{j\alpha z}, \\ \dot{H}^J_x &= \frac{J e^{-\alpha d}}{2} e^{\alpha y} e^{j\alpha z}, \end{aligned}\right\} \tag{1}$$

if y < d, and

$$\left.\begin{aligned} \dot{H}^J_y &= -j\frac{J e^{\alpha d}}{2} e^{-\alpha y} e^{j\alpha z}, \\ \dot{H}^J_x &= -\frac{J e^{\alpha d}}{2} e^{-\alpha y} e^{j\alpha z}, \end{aligned}\right\} \tag{2}$$

if y > d.

The principal difficulty is the calculation of the secondary field $\dot{\mathbf{H}}^0$. In the quasistationary approximation the field $\dot{\mathbf{H}}^0$ has a zero curl; hence, a scalar potential can be introduced in the region outside the corner

$$\begin{gathered} \dot{\mathbf{H}}^0 = -\operatorname{grad} \dot{\varphi}, \\ \dot{\varphi}(x, y, z) = \dot{\Phi}(x, y) e^{j\alpha z}, \end{gathered} \tag{3}$$

where $\dot{\Phi}(x, y)$ satisfies the equation

$$\frac{\partial^2 \Phi}{\partial x^2} + \frac{\partial^2 \Phi}{\partial y^2} - \alpha^2 \Phi = 0. \tag{4}$$

If the medium inside the dihedral corner is assumed to be perfectly conducting

$$(\mathbf{n}, \dot{\mathbf{H}}) = 0. \tag{5}$$

Using (1)-(3) and (5) we obtain the boundary conditions for $\dot{\Phi}(x, y)$

$$\frac{\partial \Phi}{\partial y}(x, 0) = \dot{A}; \; x > 0; \; \dot{A} = -j\frac{J e^{-\alpha d}}{2}, \tag{6}$$

$$\frac{\partial \Phi}{\partial x}(0, y) = 0; \; y < 0. \tag{7}$$

Thus the calculation of the field is reduced to solving the Neumann boundary-value problem (4), (6), (7).

For a ferromagnetic conducting medium ($\mu \gg \mu_0$) the magnetic field lines are drawn in; therefore even for a sharply defined skin effect there will be a strong deviation from boundary condition (5). In this situation we use the Leontovich boundary condition

$$[\mathbf{n}, \dot{\mathbf{E}}] = (1 + j)\sqrt{\frac{\omega\mu}{2\gamma}}[\mathbf{n}, [\mathbf{n}, \dot{\mathbf{H}}]]. \tag{8}$$

Let us reformulate this boundary condition as a boundary condition for $\dot{\Phi}(x, y)$.

We consider, for example, the side $y = 0, x > 0$. Here (8) takes the form

$$\dot{E}_z = (1+j)\sqrt{\frac{\omega\mu}{2\gamma}}\,\dot{H}_x;\ \dot{E}_x = -(1+j)\sqrt{\frac{\omega\mu}{2\gamma}}\,\dot{H}_z. \tag{9}$$

Using Maxwell's equations we obtain from (9)

$$\mathrm{curl}_y\,\dot{\mathrm{E}} = \frac{\partial \dot{E}_x}{\partial z} - \frac{\partial \dot{E}_z}{\partial x} = -j\omega\mu_0 \dot{H}_y$$

$$= (1+j)\sqrt{\frac{\omega\mu}{2\gamma}}\left(\frac{\partial \dot{H}_z}{\partial z} + \frac{\partial \dot{H}_x}{\partial x}\right) = -(1+j)\sqrt{\frac{\omega\mu}{2\gamma}}\frac{\partial \dot{H}_y}{\partial y},$$

from which

$$\frac{\partial \dot{H}_y}{\partial y} - (1+j)\sqrt{\frac{\omega\gamma\mu_0^2}{2\mu}}\,\dot{H}_y = 0. \tag{10}$$

Using (1)-(3) we find from (10)

$$\frac{\partial^2 \Phi}{\partial y^2} - \dot{\beta}\frac{\partial \Phi}{\partial y} = \dot{A} \text{ for } y = 0,\ x > 0. \tag{11}$$

Here,

$$\dot{\beta} = (1+j)\sqrt{\frac{\omega\gamma\mu_0^2}{2\mu}};\ \ \dot{A} = -j\frac{f e^{-\alpha d}(\alpha - \dot{\beta})}{2}. \tag{12}$$

In complete analogy with the above

$$\frac{\partial^2 \Phi}{\partial x^2} + \dot{\beta}\frac{\partial \Phi}{\partial x} = 0 \text{ for } x = 0,\ y < 0. \tag{13}$$

Thus when impedance boundary conditions are used the calculation of the field is reduced to solving the boundary-value problem (4), (11), (13).

SOLUTION OF THE PROBLEM FOR A PERFECTLY CONDUCTING MEDIUM

Since the right-hand sides of boundary conditions (6) and (7) are constants we can use the following simple method of solution. We introduce the new function

$$\Psi(x, y) = \frac{\partial^2 \Phi}{\partial x \partial y}, \tag{14}$$

and from (4), (6) and (7) we obtain the following homogeneous boundary-value problem:

$$\frac{\partial^2 \Psi}{\partial x^2} + \frac{\partial^2 \Psi}{\partial y^2} - \alpha^2 \Psi = 0, \tag{15}$$

$$\Psi(x, 0) = 0,\ x > 0, \tag{16}$$

$$\Psi(0, y) = 0,\ y < 0. \tag{17}$$

We note that a similar scheme for solving boundary-value problems for a rectangular wedge, based on the introduction of auxiliary functions,$^{1)}$ was developed earlier.[4]

The solution of the boundary-value problem (15)-(17) is easily obtained by separating variables in polar coordinates

$$\Psi(x, y) = \sum_{i=1}^{\infty} \dot{B}_{2i/3} K_{2i/3}(\alpha r) \sin\frac{2i}{3}\theta. \tag{18}$$

Here, the $K_{2i/3}$ are Macdonald functions and the $\dot{B}_{2i/3}$ are arbitrary constants. It is physically obvious that the field $\dot{H}^0$ can have only integrable singularities in the neighborhood of the edge of the dihedral corner. Therefore only two terms need be retained in (18), i.e.

$$\Psi(x, y) = \dot{B}_{2/3} K_{2/3}(\alpha r) \sin\frac{2}{3}\theta + \dot{B}_{4/3} K_{4/3}(\alpha r) \sin\frac{4}{3}\theta. \tag{19}$$

From (19) and (14) we find

$$\frac{\partial \Phi}{\partial x}(x, y) = -\dot{B}_{2/3}\int_y^{\infty} K_{2/3}(\alpha r) \sin\frac{2}{3}\theta dy_1 - \dot{B}_{4/3}\int_y^{\infty} K_{4/3}(\alpha r)\sin\frac{4}{3}\theta dy_1, \tag{20}$$

$$\frac{\partial \Phi}{\partial y}(x, y) = \dot{B}_{2/3}\int_{-\infty}^{x} K_{2/3}(\alpha r) \sin\frac{2}{3}\theta dx_1 + \dot{B}_{4/3}\int_{-\infty}^{x} K_{4/3}(\alpha r)\sin\frac{4}{3}\theta dx_1. \tag{21}$$

The constants $\dot{B}_{2/3}$ and $\dot{B}_{4/3}$ are determined from boundary conditions (6) and (7). In order to satisfy these boundary conditions it is necessary to let $x \to 0 (y < 0)$ and $y \to 0 (x > 0)$ in (20) and (21). However, going to the limit directly in (20) and (21) leads to divergent integrals. To overcome this difficulty we use the easily proved relation

$$K_{4/3}(\alpha r)\sin\frac{4}{3}\theta = -\frac{2}{\alpha}\frac{\partial}{\partial y}\left(K_{1/3}(\alpha r)\cos\frac{1}{3}\theta\right) - K_{2/3}(\alpha r)\sin\frac{2}{3}\theta \tag{22}$$

and transform (20) to the form

$$\frac{\partial \Phi}{\partial x}(x, y) = (\dot{B}_{4/3} - \dot{B}_{2/3})\int_y^{\infty} K_{2/3}(\alpha r)\sin\frac{2}{3}\theta dy_1 - \frac{2}{\alpha}\dot{B}_{4/3}K_{1/3}(\alpha r)\cos\frac{1}{3}\theta. \tag{23}$$

Taking account of (7) we find from (23)

$$\lim_{\substack{x \to 0 \\ y < 0}} \frac{\partial \Phi}{\partial x}(x, y) = (\dot{B}_{4/3} - \dot{B}_{2/3})\frac{\sqrt{3}}{2}\int_0^{\infty} K_{2/3}(\alpha y)\, dy = 0,$$

hence

$$\dot{B}_{4/3} = \dot{B}_{2/3}. \tag{24}$$

Similarly we transform (21) to the form

$$\frac{\partial \Phi}{\partial y}(x, y) = (\dot{B}_{2/3} + \dot{B}_{4/3})\int_{-\infty}^{x} K_{2/3}(\alpha r)\sin\frac{2}{3}\theta dx_1 - \frac{2}{\alpha}\dot{B}_{4/3}K_{1/3}(\alpha r)\sin\frac{1}{3}\theta, \tag{25}$$

from which, according to (6),

$$\lim_{\substack{y \to 0 \\ x > 0}} \frac{\partial \Phi}{\partial y}(x, y) = (\dot{B}_{2/3} + \dot{B}_{4/3})\frac{\sqrt{3}}{2}\int_{-\infty}^{0} K_{2/3}(\alpha x)\, dx = \dot{A}.$$

Using (24) and the fact that[5]

$$\int_{-\infty}^{0} K_{2/3}(\alpha x)\, dx = \int_0^{\infty} K_{2/3}(\alpha x)\, dx = \frac{\pi}{\alpha}, \tag{26}$$

we obtain

$$\dot{B}_{1/3}=\dot{B}_{2/3}=\frac{\alpha\dot{A}}{\pi\sqrt{3}}=-j\frac{\alpha\dot{J}e^{-\alpha d}}{2\pi\sqrt{3}}. \qquad (27)$$

From (27), (23), (25), and (3) we find

$$\dot{H}_x^0=-\frac{\partial\Phi}{\partial x}e^{j\omega t}=-j\frac{\dot{J}e^{-\alpha d}}{\pi\sqrt{3}}K_{1/3}(\alpha r)\cos\frac{1}{3}\theta e^{j\omega t}, \qquad (28)$$

$$\dot{H}_y^0=-\frac{\partial\Phi}{\partial y}e^{j\omega t}$$

$$=\left(\frac{j\alpha\dot{J}e^{-\alpha d}}{\pi\sqrt{3}}\int\limits_{-\infty}^{x}K_{2/3}(\alpha r)\sin\frac{2}{3}\theta dx_1-j\frac{\dot{J}e^{-\alpha d}}{\pi\sqrt{3}}K_{1/3}(\alpha r)\sin\frac{1}{3}\theta\right)e^{j\omega t}, \qquad (29)$$

$$\dot{H}_z^0=-j\alpha\Phi e^{j\omega t}=\frac{\alpha\dot{J}e^{-\alpha d}}{\pi\sqrt{3}}\int\limits_{-\infty}^{x}K_{1/3}(\alpha r)\cos\frac{1}{3}\theta dx_1 e^{j\omega t}. \qquad (30)$$

SOLUTION OF THE PROBLEM FOR IMPEDANCE BOUNDARY CONDITIONS

Since the right-hand sides of boundary conditions (11) and (13) are constants a method similar to that of the previous section can be used to solve the boundary-value problem (4), (11), (13). We introduce the auxiliary function

$$\Psi(x,\ y)=\left(\frac{\partial}{\partial x}+\dot{\beta}\right)\left(\frac{\partial}{\partial y}-\dot{\beta}\right)\Phi(x,\ y)$$

$$=\frac{\partial}{\partial x}\left(\frac{\partial\Phi}{dy}-\beta\Phi\right)+\dot{\beta}\left(\frac{\partial\Phi}{\partial y}-\beta\Phi\right)=\frac{\partial}{\partial y}\left(\frac{\partial\Phi}{\partial x}+\beta\Phi\right)-\dot{\beta}\left(\frac{\partial\Phi}{\partial x}+\beta\Phi\right). \qquad (31)$$

From (31), (4), (11), and (13) we find that $\dot{\Psi}(x, y)$ is a solution of the following boundary-value problem:

$$\frac{\partial^2\Psi}{\partial x^2}+\frac{\partial^2\Psi}{\partial y}-\alpha^2\Psi=0, \qquad (32)$$

$$\frac{\partial\Psi}{\partial y}(x,\ 0)=\dot{\beta}\dot{A},\ x>0, \qquad (33)$$

$$\frac{\partial\Psi}{\partial x}(0,\ y)=0,\ y<0; \qquad (34)$$

here $\dot{\beta}$ and A are given by (12).

The boundary-value problem (32), (33), (34) is similar to the boundary-value problem (4), (6), (7) whose solution is discussed in the preceding section. Therefore if we do not require that the solution of problem (32)-(34) be bounded, its general form is

$$\Psi(x,\ y)=\Psi_0(x,\ y)+\sum_{i=0}^{\infty}\dot{B}_{2i/3}K_{2i/3}(\alpha r)\cos\frac{2i}{3}\theta, \qquad (35)$$

$$\Psi_0(x,\ y)=\dot{B}_{1/3}\int\limits_{-\infty}^{x}K_{1/3}(\alpha r)\cos\frac{1}{3}\theta dx_1, \qquad (36)$$

$$\dot{B}_{1/3}=-\frac{2}{\pi\sqrt{3}}\dot{\beta}\dot{A}=\frac{j\dot{J}e^{-\alpha d}\dot{\beta}(\alpha-\dot{\beta})}{\pi\sqrt{3}}. \qquad (37)$$

We find from (31)

$$\frac{\partial^2\Phi}{\partial y^2}-\dot{\beta}\frac{\partial\Phi}{\partial y}=\int\limits_{-\infty}^{x}e^{-\dot{\beta}(x-x_1)}\frac{\partial\Psi}{\partial y}(x_1,\ y)dx_1, \qquad (38)$$

$$\frac{\partial^2\Phi}{\partial x^2}+\dot{\beta}\frac{\partial\Phi}{\partial x}=-\int\limits_{y}^{\infty}e^{\dot{\beta}(y-y_1)}\frac{\partial\Psi}{\partial x}(x,\ y_1)dy_1. \qquad (39)$$

. . It can be shown from (38) and (39) that $\partial^2\dot{\Phi}/\partial y^2-\beta\partial\Phi/\partial y=0$ and $\partial^2\dot{\Phi}/\partial x^2+\dot{\beta}\partial\dot{\Phi}/\partial x$ will be bounded in the neighborhood of the edge of the dihedral corner; consequently boundary conditions (11) and (13) can be satisfied only if $\dot{\Psi}(x, y)$ increases no faster than $1/r$ in the neighborhood of the edge. Hence it follows that in the infinite sum in (35) only the first two terms need be retained, i.e.,

$$\Psi(x,\ y)=\Psi_0(x,\ y)+\dot{B}_0K_0(\alpha r)+\dot{B}_{2/3}K_{2/3}(\alpha r)\cos\frac{2}{3}\theta. \qquad (40)$$

Since $\dot{\Psi}_0(x, y)$ satisfies boundary conditions (33) and (34),

$$\lim_{\substack{y\to0\\x>0}}\int\limits_{-\infty}^{x}e^{-\dot{\beta}(x-x_1)}\frac{\partial\Psi_0}{\partial y}(x_1,\ y)dx_1=\dot{\beta}\dot{A}\int\limits_{0}^{x}e^{-\dot{\beta}(x-x_1)}dx_1$$

$$+\lim_{\substack{y\to0\\x>0}}\int\limits_{-\infty}^{0}e^{-\dot{\beta}(x-x_1)}\frac{\partial\Psi_0}{\partial y}(x_1,\ y)dx_1$$

$$=\dot{A}(1-e^{-\dot{\beta}x})+\lim_{\substack{y\to0\\x>0}}\int\limits_{-\infty}^{0}e^{-\dot{\beta}(x-x_1)}\frac{\partial\Psi_0}{\partial y}(x_1,\ y)dx_1. \qquad (41)$$

Since $\dot{\Psi}_0(x, y)$ is a bounded solution of the boundary-value problem (32)-(34), according to the results of the preceding section (cf. 29)

$$\frac{\partial\Psi_0}{\partial y}(x_1,\ y)=-\alpha\dot{B}_{1/3}\int\limits_{-\infty}^{x_1}K_{2/3}(\alpha r)\sin\frac{2}{3}\theta dx_2+\dot{B}_{1/3}K_{1/3}(\alpha r)\sin\frac{1}{3}\theta.$$

Substituting the last expression into (41), integrating by parts, and making some simple transformations we find

$$\lim_{\substack{y\to0\\x>0}}\int\limits_{-\infty}^{x}e^{-\dot{\beta}(x-x_1)}\frac{\partial\Psi_0}{\partial y}(x_1,\ y)dx_1=\dot{A}(1-e^{-\dot{\beta}x})$$

$$+\dot{B}_{1/3}\frac{\sqrt{3}}{2}\left[\frac{\alpha}{\dot{\beta}}\left(-\int\limits_{0}^{\infty}K_{2/3}(\alpha x)dx+\int\limits_{0}^{\infty}e^{-\dot{\beta}x}K_{2/3}(\alpha x)dx\right)\right.$$

$$\left.+\int\limits_{0}^{\infty}e^{-\dot{\beta}x}K_{1/3}(\alpha x)dx\right]e^{-\dot{\beta}x}. \qquad (42)$$

It is easy to see that

$$\lim_{y\to+0}\frac{\partial K_0(\alpha r)}{\partial y}=-\pi\delta(x),\quad \lim_{x\to-\infty}\frac{\partial K_0(\alpha r)}{\partial x}=\pi\delta(y), \qquad (43)$$

where δ is the Dirac delta function. Therefore

$$\lim_{\substack{y\to+\infty\\x>0}}\dot{B}_0\int\limits_{-\infty}^{x}e^{-\dot{\beta}(x-x_1)}\frac{\partial K_0(\alpha r)}{\partial y}dx_1=-\pi\dot{B}_0e^{-\dot{\beta}x}. \qquad (44)$$

Using the easily proved relation

$$\frac{\partial}{\partial y}\left(K_{2/3}(\alpha r)\cos\frac{2}{3}\theta\right)=\frac{\partial}{\partial x}\left(K_{2/3}(\alpha r)\sin\frac{2}{3}\theta\right)-\alpha K_{1/3}(\alpha r)\sin\frac{1}{3}\theta \quad (45)$$

and integrating by parts we find, after some simple transformations,

$$\lim_{\substack{y\to 0\\ x>0}}\dot{B}_{2/3}\int_{-\infty}^{x}e^{-\dot{\beta}(x-x_1)}\frac{\partial}{\partial y}\left(K_{2/3}(\alpha r)\cos\frac{2}{3}\theta\right)dx_1$$

$$=-\dot{B}_{2/3}\frac{\sqrt{3}}{2}\left(\dot{\beta}\int_0^\infty e^{-\dot{\beta}x}K_{2/3}(\alpha x)\,dx+\alpha\int_0^\infty e^{-\dot{\beta}x}K_{1/3}(\alpha x)\,dx\right)e^{-\dot{\beta}x}. \quad (46)$$

It follows from (38), (40), (42), (44), and (46) that boundary condition (11) will be satisfied if the constants $\dot{B}_0$ and $\dot{B}_{2/3}$ satisfy the equation

$$-\dot{A}+\dot{B}_{1/3}\frac{\sqrt{3}}{2}\left[\frac{\alpha}{\dot{\beta}}\left(-\int_0^\infty K_{2/3}(\alpha x)\,dx\right.\right.$$

$$\left.\left.+\int_0^\infty e^{\dot{\beta}-x}K_{2/3}(\alpha x)\,dx\right)+\int_0^\infty e^{-\dot{\beta}x}K_{1/3}(\alpha x)\,dx\right]$$

$$-\pi\dot{B}_0-\dot{B}_{2/3}\frac{\sqrt{3}}{2}\left(\dot{\beta}\int_0^\infty e^{-\dot{\beta}x}K_{2/3}(\alpha x)\,dx+\alpha\int_0^\infty e^{-\dot{\beta}x}K_{1/3}(\alpha x)\,dx\right)=0. \quad (47)$$

Using (43) and the relation

$$\frac{\partial}{\partial x}\left(K_{2/3}(\alpha r)\cos\frac{2}{3}\theta\right)=-\frac{\partial}{\partial y}\left(K_{2/3}(\alpha r)\sin\frac{2}{3}\theta\right)-\alpha K_{1/3}(\alpha r)\cos\frac{1}{3}\theta,$$

we find similarly from (39) and (40) that boundary condition (13) is satisfied if the constants $\dot{B}_0$ and $\dot{B}_{2/3}$ satisfy the equation

$$\dot{B}_{1/3}\frac{\sqrt{3}}{2}\int_0^\infty e^{-\dot{\beta}y}K_{1/3}(\alpha y)\,dy+\pi\dot{B}_0$$

$$-\dot{B}_{2/3}\frac{\sqrt{3}}{2}\left(\dot{\beta}\int_0^\infty e^{-\dot{\beta}y}K_{2/3}(\alpha y)\,dy+\alpha\int_0^\infty e^{-\dot{\beta}y}K_{1/3}(\alpha y)\,dy\right)=0. \quad (48)$$

Using (26) and (27) we obtain from (47) and (48)

$$\dot{B}_{2/3}=\frac{\dot{B}_{1/3}}{\dot{\beta}}\frac{\frac{1}{2\dot{\beta}}\int_0^\infty e^{-\frac{\dot{\beta}}{\alpha}x}K_{2/3}(x)\,dx+\int_0^\infty e^{-\frac{\dot{\beta}}{\alpha}x}K_{1/3}(x)\,dx}{\int_0^\infty e^{-\frac{\dot{\beta}}{\alpha}x}K_{2/3}(x)\,dx+\frac{\alpha}{\dot{\beta}}\int_0^\infty e^{-\frac{\dot{\beta}}{\alpha}x}K_{1/3}(x)\,xd}, \quad (49)$$

$$\dot{B}_0=\frac{\sqrt{3}\dot{B}_{1/3}}{4\pi\dot{\beta}}\int_0^\infty e^{-\frac{\dot{\beta}}{\alpha}x}K_{2/3}(x)\,dx. \quad (50)$$

The integrals in (49) and (50) are tabulated,[5] and therefore (49) and (50) can be simplified to

$$\dot{B}_{2/3}=\frac{\dot{B}_{1/3}\left(\frac{\dot{\varkappa}}{2}\operatorname{sh}\frac{2}{3}u+\operatorname{sh}\frac{1}{3}u\right)}{\dot{\beta}\left(\operatorname{sh}\frac{2}{3}u+\dot{\varkappa}\operatorname{sh}\frac{1}{3}u\right)};\quad \dot{B}_0=\frac{\dot{B}_{1/3}\operatorname{sh}\frac{2}{3}u}{\dot{\beta}\operatorname{sh}u}, \quad (51)$$

where

$$\dot{\varkappa}=\frac{\dot{\beta}}{\alpha}\operatorname{ch}u. \quad (52)$$

It follows from (40), (31), and (36) that

$$\Phi(x,\ y)=\frac{\dot{B}_{1/3}}{\dot{\beta}}\int_{-\infty}^{x}\int_{y}^{\infty}e^{\dot{\beta}(y-y_1)}K_{1/3}(\alpha r)\cos\frac{1}{3}\theta\,dx_1dy_1$$

$$+\int_{-\infty}^{x}\int_{y}^{\infty}e^{-\dot{\beta}[(x-x_1)-(y-y_1)]}\left\{\frac{\dot{B}_{1/3}}{\dot{\beta}}K_{1/3}(\alpha r)\cos\frac{1}{3}\theta-\dot{B}_0K_0(\alpha r)\right.$$

$$\left.-\dot{B}_{2/3}K_{2/3}(\alpha r)\cos\frac{2}{3}\theta\right\}dx_1dy_1. \quad (53)$$

Equations (53), (52), (51) and (37) give a complete solution of the boundary-value problem (4), (11), (12), (13).

RESULTS AND DISCUSSION

In the problem under discussion the greatest interest is in the distribution of the tangential components of the magnetic intensity and the eddy currents over the surface of the conducting wedge. The magnetic field is simply expressed in terms of $\dot{\Phi}(x, y)$ by using Eqs. (1)-(3). We show that the eddy current pattern can be constructed from the values of $\dot{\Phi}(x, y)$ on the surface of the dihedral corner.

Let Q be an arbitrary point, and $L_{Q,\infty}$ some open contour on the surface of the wedge, one end of which coincides with Q; the other extends to infinity in the y direction along the boundary x = 0. We introduce the stream function

$$\Psi(Q,\ t)=\int_{L_{Q,\infty}}\delta_\nu(Q,\ t)\,dl_Q=\gamma\operatorname{Re}\int_{L_{Q,\infty}}([\mathbf{n},\ \dot{\mathbf{E}}(Q)],\ d\mathbf{l}_Q), \quad (54)$$

where $\delta(Q, t)$ is the component of the current density on the surface of the dihedral corner normal to $L_{Q,\infty}$, and the integration is extended from infinity to the point Q. It follows from (54) that at any time t the level lines of the stream function coincide with the eddy current lines.

Using the impedance boundary condition (8), Eq. (54) can be put in the form

$$\Psi(Q,\ t)=\operatorname{Re}(1+j)\sqrt{\frac{\omega\mu\gamma}{2}}\int_{L_{Q,\infty}}\mathbf{H}(Q)\,d\mathbf{l}_Q$$

$$=\operatorname{Re}(1+j)\sqrt{\frac{\omega\mu\gamma}{2}}\,(\dot{\varphi}(Q)+\dot{\varphi}^J(Q))$$

$$=\sqrt{\omega\mu\gamma}\,(\dot{\varphi}(Q)+\dot{\varphi}^J(Q))\cos\left[\omega t+\frac{\pi}{4}+\arg(\dot{\varphi}(Q)+\dot{\varphi}^J(Q))\right]. \quad (55)$$

In the last expression $\dot{\varphi}^J(Q)$ is the potential of the field $\dot{H}^J$, which is equal to $[(jJe^{-\alpha d}e^{\alpha y})/2A]e^{j\alpha z}$ for $y < d$. In a similar way it can be shown that for a perfectly conducting medium

$$\Psi(Q,\ t)=\varphi(Q,\ t)+\varphi^J(Q,\ t), \quad (56)$$

where

$$\Psi(Q,\ t)=\int_{L_{Q,\infty}}i_\nu(Q,\ t)\,dl_Q, \quad (57)$$

where $\mathbf{i}(Q, t)$ is the surface current density vector. It follows from (55) and (56) that it is easy to construct the streamlines if $\dot{\Phi}(x, y)$ has been computed on the surface of the dihedral corner. To calculate $\dot{\Phi}(x, y)$ it is expedient to go over to dimensionless coordinates and to write the expression for $\dot{\Phi}(x, y)$ in dimensionless form.

Introducing the coordinates $X = \alpha x$, $Y = \alpha y$, and the notation $R = \alpha r$, we transform (37), (51), and (53)

$$\Phi(X, Y) = -\dot{C}_{1/3} \int_{-\infty}^{X} \int_{Y}^{\infty} e^{\dot{\varkappa}(Y-Y_1)} K_{1/3}(R) \cos\frac{1}{3}\theta \, dX_1 dY_1$$

$$+ \int_{-\infty}^{X} \int_{Y}^{\infty} e^{-\dot{\varkappa}[(X-X_1)-(Y-Y_1)]} \left\{ \dot{C}_{1/3} K_{1/3}(R) \cos\frac{1}{3}\theta \right.$$

$$\left. - \dot{C}_0 K_0(R) - \dot{C}_{2/3} K_{2/3}(R) \cos\frac{2}{3}\theta \right\} dX_1 dY_1, \quad (58)$$

$$\dot{C}_{1/3} = -\frac{2(1-\dot{\varkappa})}{\sqrt{3}\pi} \dot{M}; \quad \dot{C}_0 = \dot{C}_{1/3} \frac{\operatorname{sh}\frac{2}{3}u}{2\operatorname{sh}u}, \quad (59)$$

$$\dot{C}_{2/3} = \dot{C}_{1/3} \frac{\frac{\dot{\varkappa}}{2}\operatorname{sh}\frac{2}{3}u + \operatorname{sh}\frac{1}{3}u}{\operatorname{sh}\frac{2}{3}u + \dot{\varkappa}\operatorname{sh}\frac{1}{3}u}; \quad \dot{M} = -\frac{j\dot{J}e^{-\alpha d}}{2\alpha}, \quad (60)$$

$$\dot{\varkappa} = \frac{\dot{\beta}}{\alpha} = (1+j)\sqrt{\frac{\omega\mu_0^2\gamma}{2\mu\alpha^2}} = \operatorname{ch}u. \quad (61)$$

In accord with Eqs. (58)-(61) a program was written in FORTRAN for a BÉSM-6 computer to calculate the distribution of $\dot{\Phi}(x, y)$ on the surface of the dihedral angle.

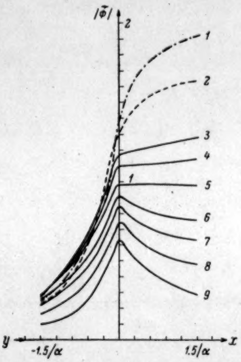

Fig. 2

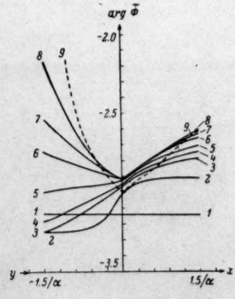

Fig. 3

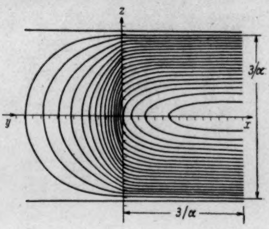

Fig. 4

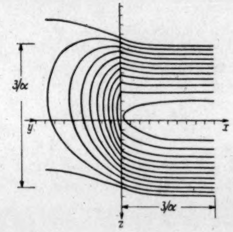

Fig. 5

This program was used to calculate the normalized total distribution $\dot{\tilde{\Phi}} = \dot{\Phi}/M - 1$, that is, taking account of the field of the current sheet. The results were checked by comparing the calculated values of $\dot{\tilde{\Phi}}$ for Y = 0 and large X with $\dot{\tilde{\Phi}}(\infty, 0) = -2\dot{\varkappa}(1 + \dot{\varkappa})$. The distribution of $\dot{\tilde{\Phi}}(X, Y)$ for a perfect conductor is given by

$$\dot{\Phi}(X, Y) = \frac{\Phi(X, Y)}{\dot{M}} - 1 = -\frac{2}{\pi\sqrt{3}} \int_{-\infty}^{x} K_{1/3}(R) \cos\frac{1}{3}\theta \, dX_1 - 1. \quad (62)$$

The results of the calculations are shown in Figs. 2 and 3. Here, curve 1 is for a perfectly conducting wedge; curves 2-9 are calculated by Eqs. (58)-(61) and correspond to the following values of $\dot{\varkappa}$: $\dot{\varkappa}_2 = 2 + 2j$, $\dot{\varkappa}_3 = 1 + j$, $\dot{\varkappa}_4 = 0.8 - 0.8j$, $\dot{\varkappa}_5 = 0.6 + 0.6j$, $\dot{\varkappa}_6 = 0.4 + 0.4j$, $\dot{\varkappa}_7 = 0.3 + 0.3j$, $\dot{\varkappa}_8 = 0.2 + 0.2j$, $\dot{\varkappa}_9 = 0.1 + 0.1j$. On the basis of these results and the procedure described above, diagrams of the streamlines have been constructed for perfect conductivity $\dot{\varkappa} = \infty$ (Fig. 4), $\dot{\varkappa} = 1 + j$ (Fig. 5) and $\dot{\varkappa} = 0.3 + 0.3j$ (Fig. 6). In Fig. 4 the increment of the stream function in going from one line of force to another is $\Delta\psi = 0.1|\dot{M}|$, in Fig. 5 $\Delta\psi = 0.12\sqrt{\omega\mu\gamma}|\dot{M}|$, and in Fig. 6 $\Delta\psi = 0.085\sqrt{\omega\mu\gamma}|\dot{M}|$. In contrast with perfect conductivity, in which the phase of the stream function is the same at all points, with the impedance boundary conditions the phase of the stream function varies from point to point, which leads to asymmetry of the streamlines. In this case in the neighborhood of the edge of the dihedral corner there is always a phase lag of the stream function relative to its values at distant points along the X axis (Fig. 3). For small absolute values of $\dot{\varkappa}$ local closed streamlines are observed in the neighborhood of the edge of the dihedral corner (Fig. 6). This can be explained by the fact that small absolute values of $\dot{\varkappa}$ correspond to large values

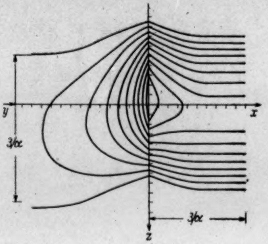

Fig. 6

of μ. For large μ magnetic lines of force are strongly drawn in near the edge of the dihedral corner, and this leads to the production of closed streamlines in this location. Generally the skin effect in a ferromagnetic conducting body involves two opposite tendencies: The drawing of magnetic lines of force into the body because of the large magnetic permeability, and the expulsion of lines of force by the eddy currents produced in the body. For various values of the parameters of a conducting ferromagnet one or the other phenomenon can predominate, and the streamline pattern changes sharply as shown in Figs. 4, 5, and 6. We note that the streamline patterns for other values of $\dot{\varkappa}$ can be constructed by using Figs. 2 and 3.

SOLUTION OF THE PROBLEM FOR ANOTHER METHOD OF EXCITING THE EXTERNAL FIELD

More complicated problems can be solved by using the results of the preceding sections. Let us consider a conducting wedge in the magnetic field of a line current $\dot{I}$ parallel to the x axis. Expanding the current axis into a continuous superposition of current sheets moving in the z direction with values of the parameter α varying from $-\infty$ to $+\infty$, using for each value of α the solution found in the preceding sections, and integrating over α gives the solution of the original problem. For a perfectly conducting medium the integrals which arise can be evaluated exactly[5] and the final result is

$$\dot{\varphi}(x,\ y,\ z)=-\frac{\dot{I}}{3\pi}\int\limits_{-\infty}^{x}\frac{1}{r}\left(\frac{\operatorname{sh}\frac{1}{3}u}{\operatorname{sh}u}+\frac{\operatorname{sh}\frac{1}{3}v}{\operatorname{sh}v}\right)\cos\frac{1}{3}\theta\,dx_1. \quad (63)$$

Here, $\dot{\varphi}$ is the potential of the secondary magnetic field, $\operatorname{ch}u = (d - jz)/r$, $\operatorname{ch}v = (d + jz)/r$, $r = \sqrt{x^2 + y^2}$, $\theta = \arctan y/x$, d is the ordinate of the current axis, and its z coordinate is taken as zero.

More complicated expressions arise for impedance boundary conditions. Here numerical results can be obtained by using the program described in the last section or the data shown in Figs. 2 and 3.

By using the superposition principle solutions can be obtained for several parallel current axes.

CONCLUSION

In treating boundary effects in solid rotors the "angular" character of a region is generally not taken into account. As a rule the end zone is rectified and considered as an extension of the active zone.[6-7] In this connection the authors hope their work can be used for a more accurate study of boundary effects.

Our method of solution is special and uses specific boundary conditions. Nevertheless there are many problems which are amenable to this method of solution.

---

1)The reviewer kindly called this to the authors' attention.

[1] G. D. Malyuzhinets, Dokl. Akad. Nauk SSSR, 121, 436 (1958) [Sov. Phys. – Dokl., 3, 752 (1958)].

[2] N. N. Lebedev and I. P. Skal'skaya, Zh. Tekh. Fiz., 32, 1174 (1962) [Sov. Phys. – Tech. Phys., 7, 867 (1963)].

[3] V. A. Borovikov, Diffraction by Polygons and Polyhedra [in Russian], Nauka, Moscow (1968).

[4] S. N. Karp and F. C. Karal, Commun. on Pure and Appl. Mathem., 12, 435 (1959).

[5] I. M. Ryzhik and I. S. Gradshtein, Tables of Integrals, Sums, Series, and Products [in Russian], GITTL, Moscow–Leningrad (1951).

[6] V. M. Kutsevalov, Problems in the Theory and Design of Asynchronous Machines with Solid Rotors [in Russian], Energiya, Moscow (1966).

[7] A. J. Wood and C. Concordia, Trans. AIEE, 78, February (1960).

Diffusion regime for electrostatic probes as singular-perturbation problem

I. B. Chekmarev
A. F. Ioffe Physicotechnical Institute, Academy of Sciences of the USSR, Leningrad

(Submitted November 30, 1973)
Zh. Tekh. Fiz., 44, 2069-2074 (October 1974)

Singular perturbation theory is used to analyze a flat electrostatic probe in a weakly ionized collisional plasma in a uniform external magnetic field parallel to the surface of the probe. The voltage—current characteristic is obtained in analytic form in the zeroth approximation. Higher approximations are discussed.

The study of the structure of the transition region between an unperturbed plasma and the walls confining it, which started with the well-known work of Langmuir, remains one of the most important topics in gas discharge.

In extensive studies of the properties of a weakly ionized gas during the last decade considerable attention has been focused on the development of the diffusion theory for the boundary layer close to the walls, particularly when the mean free path of the charged particles is small in comparison with the thickness of the sheath, which in turn is small in comparison with the macroscopic linear dimensions in the problem.[1-8]

In the present work it is shown that the collisional Debye sheath can be treated as a problem in singular perturbation theory. The use of singular-perturbation theory is illustrated by the example of a flat probe in a transverse magnetic field.

For weak ionization and constant temperatures of the components the behavior of the electrons and ions is described by the following system of equations (α = e, i):

$$\left.\begin{aligned} &\nabla\Gamma_\alpha = \nu_I n_e - \beta_R n_e^2 n_i,\\ &\nabla p_\alpha + e_\alpha n_\alpha \nabla\varphi - e_\alpha \Gamma_\alpha \times \mathbf{B} = -\frac{m_\alpha}{\tau_\alpha}\Gamma_\alpha,\\ &\Delta\varphi = \frac{e}{\varepsilon_0}(n_e - n_i).\end{aligned}\right\} \tag{1}$$

We introduce the dimensionless quantities

$$\mathbf{R} = \frac{\mathbf{r}}{L},\ g_\alpha = \frac{n_\alpha}{n_0},\ \mathbf{G}_\alpha = \frac{\Gamma_\alpha}{\Gamma_0},\ \Phi = \frac{\varphi}{\varphi_0},\ \mathbf{b} = \frac{\mathbf{B}}{B},$$

where

$$L = \sqrt{\frac{D}{\nu_I}},\ \Gamma_0 = \frac{Dn_0}{L},\ D = \frac{k(T_e + T_i)\tau_i}{m_i},$$
$$\varphi_0 = \frac{kT_e}{e},\ \mu_\alpha = \frac{e\tau_\alpha}{m_\alpha},\ \nu_I n_0 - \beta_R n_0^3 = 0.$$

Then system (1) becomes

$$\left.\begin{aligned} &\nabla\mathbf{G}_\alpha = g_e - g_e^2 g_i,\\ &\nabla g_e - g_e\nabla\Phi + \frac{T_e + T_i}{T_e}\omega_i\tau_i\mathbf{G}_e \times \mathbf{b} = -\frac{T_e + T_i}{T_e}\frac{\mu_i}{\mu_e}\mathbf{G}_e,\\ &\frac{T_i}{T_e}\nabla g_i + g_i\nabla\Phi - \frac{T_e + T_i}{T_e}\omega_i\tau_i\mathbf{G}_i \times \mathbf{b} = -\frac{T_e + T_i}{T_e}\mathbf{G}_i,\\ &\varepsilon\Delta\Phi = g_e - g_i.\end{aligned}\right\} \tag{2}$$

Since $\lambda_\alpha \ll \lambda_D \ll L$ ($\lambda_D^2 = \varepsilon_0 kT_e/e^2 n_0$) and $\varepsilon = (\lambda_D/L)^2 \ll 1$, the coefficient of the highest derivative in the last equation is a small parameter, making this a problem in singular perturbation theory.[9-11]

We take the x and z axes of a right-handed coordinate system in the surface of the flat probe with the y axis directed into the region occupied by the plasma and the x axis in the direction of the uniform external magnetic field **B**.

Then system (2) is reduced to the equations

$$\left.\begin{aligned} &\frac{dG_e}{dy} = g_e - g_e^2 g_i,\ \frac{dG_i}{dy} = g_e - g_e^2 g_i,\\ &\frac{dg_e}{dy} - g_e\frac{d\Phi}{dy} + \frac{T_e + T_i}{T_e}\frac{\mu_i}{\mu_e}\left(1 + \frac{\mu_e}{\mu_i}\beta\right)G_e = 0,\\ &\frac{T_i}{T_e}\frac{dg_i}{dy} + g_i\frac{d\Phi}{dy} + \frac{T_e + T_i}{T_e}\left(1 + \frac{\mu_i}{\mu_e}\beta\right)G_i = 0,\\ &\varepsilon\frac{d^2\Phi}{dy^2} = g_e - g_i,\end{aligned}\right\} \tag{3}$$

where $\beta = \omega_e\tau_e\omega_i\tau_i$.

We assume that the conducting surface of the probe is also a perfect absorber. Then the total fluxes of reflected particles vanish. We then have the following dimensionless boundary conditions at the wall:

$$y = 0,\ g_e = -\frac{c_i}{c_e}hG_e,\ g_i = -hG_i,\ \Phi = 0, \tag{4}$$

where

$$c_\alpha = \sqrt{\frac{8kT_\alpha}{\pi m_\alpha}},\ h = \frac{\pi}{4}\frac{T_e + T_i}{T_i}\left(\frac{\lambda_i}{L}\right).$$

We also have

$$y \to \infty,\ g_e \to 1,\ g_i \to 1. \tag{5}$$

As a last condition we specify the current

$$j = G_i - G_e. \tag{6}$$

Following the method of singular-perturbation theory we seek the "outer" solution of system (3) in the form (u = g_e, g_i, G_e, G_i, Φ)

$$u = u_0(y) + \sqrt{\varepsilon}\,u_1(y) + \varepsilon u_2(y) + \dots. \tag{7}$$

In the original system (3) we transform to a new independent variable $\eta = y/\sqrt{\varepsilon}$ and seek the "inner" solution of the system in the form ($\tilde{u}$ = $\tilde{g}_e$, $\tilde{g}_i$, $\tilde{G}_e$, $\tilde{G}_i$, Φ)

$$\tilde{u} = \tilde{u}_0(\eta) + \sqrt{\varepsilon}\,\tilde{u}_1(\eta) + \varepsilon\tilde{u}_2(y) + \dots. \tag{8}$$

Omitting the obvious intermediate steps we obtain the following equations in the zeroth approximation:

for the outer solution

$$\left.\begin{aligned} &g_{e0} = g_{i0} = g,\\ &\frac{dG_{e0}}{dy} = g - g^3,\ \frac{dG_{i0}}{dy} = g - g^3,\\ &\frac{dg}{dy} - g\frac{d\Phi_0}{dy} + \frac{T_e + T_i}{T_e}\frac{\mu_i}{\mu_e}\left(1 + \frac{\mu_e}{\mu_i}\beta\right)G_{e0} = 0,\\ &\frac{T_i}{T_e}\frac{dg}{dy} + g\frac{d\Phi_0}{dy} + \frac{T_e + T_i}{T_e}\left(1 + \frac{\mu_i}{\mu_e}\beta\right)G_{i0} = 0\end{aligned}\right\} \tag{9}$$

with the boundary conditions

$$y \to \infty,\ g \to 1,\ j = G_{i0} - G_{e0}, \tag{10}$$

for the inner solution (the case $\sqrt{\varepsilon}\,\beta \sim 1$ is not considered)

$$\left.\begin{gathered}\frac{d\bar G_{e0}}{d\eta} = 0,\ \frac{d\bar G_{i0}}{d\eta} = 0,\\ \frac{d\bar g_{e0}}{dy} - \bar g_{e0}\frac{d\Phi_0}{dy} = 0,\ \frac{T_i}{T_e}\frac{d\bar g_{i0}}{d\eta} + \bar g_{i0}\frac{d\Phi_0}{d\eta} = 0,\\ \frac{d^2\Phi_0}{d\eta^2} = \bar g_{e0} - \bar g_{i0}\end{gathered}\right\} \tag{11}$$

with the boundary conditions

$$\eta = 0,\ \bar g_{e0} = -\frac{c_i}{c_e} h\bar G_{e0},\ \bar g_{i0} = -h\bar G_{i0},\ \Phi_0 = 0. \tag{12}$$

The asymptotic matching of the outer and inner solutions provides the missing five conditions for the solution of systems (9) and (11). By transforming from the variables y and η to the intermediate variable $\tau = y/\delta(\varepsilon) = [\sqrt{\varepsilon}/\delta(\varepsilon)]\eta$, where $\sqrt{\varepsilon}/\delta(\varepsilon)|_{\varepsilon\to 0} \to 0$, in the region of overlap of the outer and inner solutions we obtain the matching condition in the zeroth approximation for the electron density:

$$\begin{aligned}\lim_{\substack{\varepsilon\to 0\\ \tau\ \text{fixed}}} [g_e - \bar g_e] = \lim_{\substack{\varepsilon\to 0\\ \text{fixed}}} \Big\{ & g[\delta(\varepsilon)\tau] + \sqrt{\varepsilon}\, g_{e1}[\delta(\varepsilon)\tau] + \ldots\\ & - \bar g_{e0}\left[\frac{\delta(\varepsilon)}{\sqrt{\varepsilon}}\tau\right] - \sqrt{\varepsilon}\,\bar g_{e1}\left[\frac{\delta(\varepsilon)}{\sqrt{\varepsilon}}\tau\right] + \ldots\Big\} = 0\end{aligned}$$

and similar relations for g_i, G_e, G_i, and Φ. Hence we find that as $y \to 0$, $\eta \to \infty$

$$\left.\begin{gathered}\bar g_{e0} \to g(0),\ \bar g_{i0} \to g(0),\ \bar G_{e0} \to G_{e0}(0),\\ \bar G_{i0} \to G_{i0}(0),\ \Phi_0 \to \Phi_0(0).\end{gathered}\right\} \tag{13}$$

We consider system (9). It follows from the first two equations that

$$G_{i0} - G_{e0} = \text{const} = j. \tag{14}$$

Combining the last two equations and eliminating G_{e0} and G_{i0} by differentiating we obtain

$$\frac{d^2 g}{dy^2} + (1+\beta)(g - g^3) = 0. \tag{15}$$

Using (14) we eliminate G_{e0} and G_{i0} in turn and express the fluxes in terms of j and g

$$\left.\begin{aligned}G_{e0} &= -\frac{1}{1+\beta}\left[\frac{dg}{dy} + \left(1 + \frac{\mu_i}{\mu_e}\beta\right) j\right],\\ G_{i0} &= -\frac{1}{1+\beta}\left[\frac{dg}{dy} - \frac{\mu_i}{\mu_e}\left(1 + \frac{\mu_e}{\mu_i}\beta\right) j\right].\end{aligned}\right\} \tag{16}$$

The solution of Eq. (15) can be written in the form

$$g = \operatorname{th}\left[\operatorname{arth} g(0) + \sqrt{\frac{1+\beta}{2}}\, y\right],\ \frac{dg}{dy} = \sqrt{\frac{1+\beta}{2}}\,(1 - g^2), \tag{17}$$

where g(0) is the as yet unknown value of g at y = 0.

We turn now to the inner system (11). Using the matching conditions we find

$$\left.\begin{aligned}\bar G_{e0} &= -\frac{1}{1+\beta}\left[\sqrt{\frac{1+\beta}{2}}\,(1 - g^2(0)) + \left(1 + \frac{\mu_i}{\mu_e}\beta\right) j\right] = \text{const},\\ \bar G_{i0} &= -\frac{1}{1+\beta}\left[\sqrt{\frac{1+\beta}{2}}\,(1 - g^2(0)) - \frac{\mu_i}{\mu_e}\left(1 + \frac{\mu_e}{\mu_i}\beta\right) j\right] = \text{const}.\end{aligned}\right\} \tag{18}$$

Integration of the middle two of Eqs. (11) with boundary conditions (12) gives

$$\bar g_{e0} = -\frac{c_i}{c_e} h\bar G_{e0}\exp(\Phi_0),\ \bar g_{i0} = -h\bar G_{i0}\exp\left(-\frac{T_e}{T_i}\Phi_0\right). \tag{19}$$

By applying the matching conditions to (19) we obtain relations for determining g(0) and $\Phi_0(0)$

$$\begin{aligned}g(0) = {} & \frac{h}{1+\beta}\left\{\frac{c_i}{c_e}\left[\sqrt{\frac{1+\beta}{2}}\,(1 - g^2(0)) + \left(1 + \frac{\mu_i}{\mu_e}\beta\right) j\right]\right\}^{\frac{T_e}{T_e+T_i}}\\ & \times\left[\sqrt{\frac{1+\beta}{2}}\,(1 - g^2(0)) - \frac{\mu_i}{\mu_e}\left(1 + \frac{\mu_e}{\mu_i}\beta\right) j\right]^{\frac{T_i}{T_e+T_i}},\end{aligned} \tag{20}$$

$$\Phi_0(0) = \frac{T_i}{T_e + T_i}\ln\left[\frac{c_e}{c_i}\,\frac{\sqrt{\frac{1+\beta}{2}}\,(1 - g^2(0)) - \frac{\mu_i}{\mu_e}\left(1 + \frac{\mu_e}{\mu_i}\beta\right) j}{\sqrt{\frac{1+\beta}{2}}\,(1 - g^2(0)) + \left(1 + \frac{\mu_i}{\mu_e}\beta\right) j}\right], \tag{21}$$

where the second equation is the voltage–current characteristic of the sheath.

We write the equations and boundary conditions of the first approximation. For the outer solution we obtain

$$\left.\begin{gathered}g_{e1} = g_{i1} = g_1,\ G_{e1} = G_{i1} = G_1,\\ \frac{dG_1}{dy} = (1 - 3g^2)\, g_1,\\ \frac{dg_1}{dy} - g_1\frac{d\Phi_0}{dy} - g\frac{d\Phi_1}{dy} + \frac{T_e + T_i}{T_e}\frac{\mu_i}{\mu_e}\left(1 + \frac{\mu_e}{\mu_i}\beta\right) G_1 = 0,\\ \frac{T_i}{T_e}\frac{dg_1}{dy} + g_1\frac{d\Phi_0}{dy} + g\frac{d\Phi_1}{dy} + \frac{T_e + T_i}{T_e}\left(1 + \frac{\mu_i}{\mu_e}\beta\right) G_1 = 0,\end{gathered}\right\} \tag{22}$$

with the boundary conditions

$$y \to \infty,\ g_1 \to 0.$$

We find for the inner solution

$$\left.\begin{gathered}\bar G_{e1} = \bar G_{i1} = \bar G_1,\\ \frac{d\bar G_1}{d\eta} = \bar g_{e0} - \bar g_{e0}^2\bar g_{i0},\\ \frac{d\bar g_{e1}}{d\eta} - \bar g_{e1}\frac{d\Phi_0}{d\eta} - \bar g_{e0}\frac{d\Phi_1}{d\eta} + \frac{T_e + T_i}{T_e}\frac{\mu_i}{\mu_e}\left(1 + \frac{\mu_e}{\mu_i}\beta\right)\bar G_{e0} = 0,\\ \frac{T_i}{T_e}\frac{d\bar g_{i1}}{d\eta} + \bar g_{i1}\frac{d\Phi_0}{d\eta} + \bar g_{i0}\frac{d\Phi_1}{d\eta} + \frac{T_e + T_i}{T_e}\left(1 + \frac{\mu_i}{\mu_e}\beta\right)\bar G_{i0} = 0,\\ \frac{d^2\Phi_1}{d\eta^2} = \bar g_{e1} - \bar g_{i1}\end{gathered}\right\} \tag{23}$$

with the boundary conditions

$$\eta = 0,\ \bar g_{e1} = -\frac{c_i}{c_e} h\bar G_1,\ \bar g_{i1} = -h\bar G_1,\ \Phi_1 = 0.$$

By definition of an asymptotic expansion the matching condition for the first approximation has the form

$$\begin{aligned}&\lim_{\substack{\varepsilon\to 0\\ \tau\ \text{fixed}}}\frac{1}{\delta(\varepsilon)}\left[g(\delta\tau) + \sqrt{\varepsilon}\, g_1(\delta\tau) + \ldots - \bar g_{e0}(\eta) - \sqrt{\varepsilon}\,\bar g_{e1}(\eta) + \ldots\right]\\ &= \lim_{\substack{\varepsilon\to 0\\ \tau\ \text{fixed}}}\frac{1}{\delta(\varepsilon)}\Big[g(0) + \delta\tau g'(0) + \ldots + \frac{\delta\tau}{\eta} g_1(\delta\tau) + \ldots\\ &\qquad - \bar g_{e0}(\eta) - \frac{\delta\tau}{\eta}\bar g_{e1}(\eta) + \ldots\Big] = 0,\end{aligned}$$

from which it follows that as $\eta \to \infty$

$$g'(0)\,\eta + g_1(0) - \bar g_{e1}(\eta) \to 0,$$

We obtain similar relations for the remaining unknowns as $\eta \to \infty$

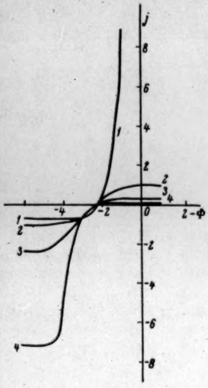

Fig. 1. $T_e = T_i$, $c_e/c_i = 10^2$, $\mu_e/\mu_i = 10^3$; 1) $\beta = 0$; 2) 1; 3) 10; 4) 100.

$$g'(0)\eta + g_1(0) - \tilde{g}_{e1}(\eta) \to 0,$$
$$G'_{e0}(0)\eta + G_1(0) - \tilde{G}_1(\eta) \to 0,$$
$$\Phi'_0(0)\eta + \Phi_1(0) - \tilde{\Phi}_1(\eta) \to 0.$$

The sequence of solving the equations of the outer and inner expansions is the same as in the zeroth approximation.

We note that in the case under consideration $\sqrt{\varepsilon\beta} \ll 1$ the effect of the fluxes on the distribution of charged particles in the Debye sheath appears only in the first approximation. In the quasineutral layer the electron and the ion densities are equal in both the zeroth and first approximations. A difference appears only in the second approximation.

In conclusion we return to Eqs. (20) and (21). Since $g(0) \ll 1$ we have as a good approximation

$$g(0) = \frac{h}{1+\beta}\left\{\frac{c_i}{c_e}\left[\sqrt{\frac{1+\beta}{2}} + \left(1 + \frac{\mu_i}{\mu_e}\beta\right)j\right]^{\frac{T_e}{T_e+T_i}}\right.$$
$$\times\left[\sqrt{\frac{1+\beta}{2}} - \frac{\mu_i}{\mu_e}\left(1 + \frac{\mu_e}{\mu_i}\beta\right)j\right]^{\frac{T_i}{T_e+T_i}}, \qquad (24)$$

$$\Phi_0(0) = \frac{T_i}{T_e+T_i}\ln\left[\frac{c_e}{c_i}\,\frac{\sqrt{\frac{1+\beta}{2}} - \frac{\mu_i}{\mu_e}\left(1+\frac{\mu_e}{\mu_i}\beta\right)j}{\sqrt{\frac{1+\beta}{2}} + \left(1+\frac{\mu_i}{\mu_e}\beta\right)j}\right]. \qquad (25)$$

The value of the floating potential

$$\Phi_f = \Phi_0(0)\big|_{j=0} = \frac{T_e}{T_e+T_i}\ln\left(\frac{c_e}{c_i}\right) \qquad (26)$$

in the zeroth approximation does not depend on the magnetic parameter β. All the voltage–current characteristics pass through the point $j = 0$, $\Phi = \Phi_f$ (Fig. 1).

In the limiting case of an ion saturation current

$$j_i = -\frac{\sqrt{\frac{1+\beta}{2}}}{1+\frac{\mu_i}{\mu_e}\beta} \qquad (27)$$

in the sheath $\tilde{G}_{e0} = 0$, $\tilde{g}_{e0} = 0$.

In the other limiting case of an electron saturation current

$$j_e = \frac{\mu_e}{\mu_i}\,\frac{\sqrt{\frac{1+\beta}{2}}}{1+\frac{\mu_e}{\mu_i}\beta} \qquad (28)$$

in the sheath $\tilde{G}_{i0} = 0$, $\tilde{g}_{i0} = 0$.

Since the absolute value of the ratio of the saturation currents

$$\left|\frac{j_i}{j_e}\right| = \frac{\mu_i}{\mu_e}\,\frac{1+\frac{\mu_e}{\mu_i}\beta}{1+\frac{\mu_i}{\mu_e}\beta} \qquad (29)$$

depends only on the mobility of the charged particles and the magnetic parameter β, a flat electrostatic probe can be used to measure the strength of the magnetic field.

---

[1] G. A. Lyubimov and V. N. Mikhailov, MZhG, 3, 9 (1968).
[2] V. S. Yuferev, MZhG, 1, 61 (1971).
[3] V. N. Mikhailov, Zh. Prikl. Mekh. Tekh. Fiz., 4, 3 (1971).
[4] A. A. Yastrebov, Zh. Tekh. Fiz., 42, 1143 (1972) [Sov. Phys. – Tech. Phys., 17, 910 (1972)].
[5] I. M. Cohen, Phys. Fluids, 6, 1492 (1963).
[6] S. H. Lam, AIAA J., 2, 256 (1964).
[7] I. M. Cohen, Phys. Fluids, 13, 889 (1970).
[8] K. J. Touryan and P. M. Chung, AIAA J., 9, 365 (1971).
[9] M. D. Van Dyke, Perturbation Methods in Fluid Mechanics, Academic Press, New York (1964).
[10] J. D. Cole, Perturbation Methods in Applied Mathematics, Blaisdell, Waltham (1968).
[11] A. B. Vasil'eva and V. F. Butuzov, Asymptotic Expansions of Singularly Perturbed Equations [in Russian], Nauka, Moscow (1973).

Electromagnetic pulse radiated by a moving charged bunch in matter

N. A. Zvonnikov

V. I. Lenin Moscow Pedagogical Institute

(Submitted July 14, 1972; resubmitted April 18, 1974)
Zh. Tekh. Fiz., 44, 2075-2080 (October 1974)

The Cerenkov radiation from moving cylindrical and ellipsoidal charge bunches is discussed. As a result of the interference of the radiation fields produced by the various elements of the bunch the characteristic frequency of the radiation can lie outside the dispersion region. The electromagnetic field is found as a function of time and position for this case.

In the study of Cerenkov radiation from systems of electric charges the spectral characteristics of the radiation are generally investigated.[1-2] The duration of a pulse of Cerenkov radiation has been considered only for a point charge.[3] However, it is important to know the spatial and temporal structure of the radiation from a charged bunch in certain problems of microwave spectroscopy and radiation detection.

We consider Cerenkov radiation from uniformly charged cylindrical and ellipsoidal bunches moving with constant velocity in an infinite homogeneous medium. As a result of the interference of the radiation fields produced by various elements of the bunch the characteristic frequency of the radiation can lie outside the dispersion region. We obtain the temporal and spatial dependence of the electromagnetic field, taking account of the parameters of the bunches for this case.

1. Assume that a cylindrical bunch of length l and radius R moves with constant velocity v in an infinite homogeneous medium of permittivity ε. The longitudinal component E_z and the transverse component E_r of the electric field of a uniformly charged bunch with total charge q moving along the z axis of a cylindrical coordinate system are

$$E_z(z,\ r,\ t)=-\frac{2q}{\pi v}\int\limits_{-\infty}^{\infty}\frac{(\varepsilon\beta^2-1)\,\omega}{\varepsilon}e^{i\frac{\omega}{v}(z-vt)}\frac{2v}{\omega l}\sin\frac{\omega l}{2v}$$
$$\times\frac{I_1\left(-i\frac{\omega}{v}\sqrt{\varepsilon\beta^2-1}\,R\right)}{\sqrt{\varepsilon\beta^2-1}\,\omega R}K_0\left(-i\frac{\omega}{v}\sqrt{\varepsilon\beta^2-1}\,r\right)d\omega, \tag{1}$$

$$E_r(z,\ r,\ t)=\frac{2q}{\pi v}\int\limits_{-\infty}^{\infty}\frac{\sqrt{\varepsilon\beta^2-1}\,\omega}{\varepsilon}e^{i\frac{\omega}{v}(z-vt)}\frac{2v}{\omega l}\sin\frac{\omega l}{2v}$$
$$\times\frac{I_1\left(-i\frac{\omega}{v}\sqrt{\varepsilon\beta^2-1}\,R\right)}{\sqrt{\varepsilon\beta^2-1}\,\omega R}K_1\left(-i\frac{\omega}{v}\sqrt{\varepsilon\beta^2-1}\,r\right)d\omega \tag{2}$$

in the region $r \geq R$. Here, I_1 is the Bessel function of imaginary argument, K_0 is the Macdonald function, and $\beta = v/c$, where c is the velocity of light.

Equations (1) and (2) contain characteristic interference terms depending on the length and radius of the bunch

$$\frac{2v}{\omega l}\sin\frac{\omega l}{2v}\ \text{and}\ \frac{I_1\left(-i\frac{\omega v}{v}\sqrt{\varepsilon\beta^2-1}\,\beta\right)}{\sqrt{\varepsilon\beta^2-1}\,\omega R}.$$

For fixed l and R high frequencies make a negligible contribution to the electromagnetic field; it should then be expected that the dispersion of the permittivity can be neglected in certain real dielectrics. It is easy to estimate the order of magnitude of the duration of the perturbation Δt at points with coordinates z and r by noting that the range of frequencies $1/\Delta t$ in which the main part of the radiation is concentrated, and for which Eqs. (1) and (2) are markedly different from zero, is determined by the inequality $\omega < \min\{2v/l,\ v\sqrt{\varepsilon\beta^2-1}R\}$, so that

$$\Delta t\sim\frac{1}{\min\left\{\frac{2v}{l},\ \frac{v}{\sqrt{\varepsilon\beta^2-1}\,R}\right\}}. \tag{3}$$

Calculations performed below for a nondispersive medium show that the duration of the oscillation of the electromagnetic field in each half-wave is determined by the smallest characteristic size of the variation of charge density. The value agrees with estimate (3) in order of magnitude.

We first calculate the longitudinal component of the electric field. Using the relation

$$\sin\frac{\omega l}{2v}=\frac{e^{i\frac{\omega l}{2v}}-e^{-i\frac{\omega l}{2v}}}{2i},$$

we write Eq. (1) in the form

$$E_z=E_z(t)-E_z\left(t-\frac{l}{R\sqrt{\varepsilon\beta^2-1}}\right), \tag{4}$$

where

$$t\equiv t-\frac{z}{R\sqrt{\varepsilon\beta^2-1}}+\frac{l}{2R\sqrt{\varepsilon\beta^2-1}}+1$$

is the time counted from the arrival of the wave at point $r = R$ in units of $R\sqrt{\varepsilon\beta^2-1}/v$,

$$E_z(t)=-\frac{4q\sqrt{\varepsilon\beta^2-1}}{Rl}\frac{1}{2\pi i}\int\limits_{-i\infty}^{i\infty}e^{pt}K_0(kp)\frac{e^{-p}I_1(p)}{p}dp,\ k=\frac{r}{R}.$$

Substituting into the convolution integral from the tables[4] the inverse transforms of the functions in the last integral we have

$$E_z(t)=-\frac{4q\sqrt{\varepsilon\beta^2-1}}{Rl\varepsilon\pi}\begin{cases}\displaystyle\int\limits_0^{t-k}\frac{\sqrt{\tau(2-\tau)}}{\sqrt{(t-\tau)^2-k^2}}d\tau, & 0<t-k<2,\\ \displaystyle\int\limits_0^{2}\frac{\sqrt{\tau(2-\tau)}}{\sqrt{(t-\tau)^2-k^2}}d\tau, & t-k\geqslant 2.\end{cases} \tag{5}$$

The second part of the longitudinal field differs from $E_z(t)$ only by a time displacement $l/R\sqrt{\varepsilon\beta^2-1}$.

The transverse component of the electric field is found in the same way as the longitudinal component E_z:

$$E_r = E_r(t) - E_r\left(t - \frac{l}{R\sqrt{\varepsilon\beta^2-1}}\right), \tag{6}$$

$$E_r(t) = \frac{4q}{rl\varepsilon\pi}\begin{cases} \displaystyle\int_0^{t-k} \frac{(t-\tau)\sqrt{\tau(2-\tau)}}{\sqrt{(t-\tau)^2-k^2}}\,dt, & 0 < t-k < 2, \\ \displaystyle\int_0^{2} \frac{(t-\tau)\sqrt{\tau(2-\tau)}}{\sqrt{(t-\tau)^2-k^2}}\,d\tau, & t-k \geqslant 2. \end{cases} \tag{7}$$

To investigate the expressions obtained we evaluate integrals (5) and (7) approximately. For $0 < t-k < 2$, to $\approx 1/2(k+1)$

$$E_z(t) \simeq -\frac{4q\sqrt{\varepsilon\beta^2-1}}{Rl\varepsilon\pi\sqrt{u+2k}}f(u), \tag{8}$$

$$E_r(t) \simeq \frac{4q}{Rl\varepsilon\pi}\left(\frac{\sqrt{u+2k}}{k} - \frac{1}{\sqrt{u+2k}}\right)f(u) \tag{9}$$

and for $t \gg k + 2$

$$E_z(t) \simeq -\frac{2q\sqrt{\varepsilon\beta^2-1}}{Rl\varepsilon\sqrt{u(u+2k)}}, \tag{10}$$

$$E_r(t) \simeq \frac{2q(u+k)}{Rl\varepsilon\sqrt{u(u+2k)}\,k}. \tag{11}$$

Here, $u = t - k$, $F(\pi/2, \sqrt{u/2})$ and $E(\pi/2, \sqrt{u/2})$ are elliptic functions of the first and second kind

$$f(u) = \frac{2\sqrt{2}}{3}\left[(2-u)F\left(\frac{\pi}{2}, \sqrt{\frac{u}{2}}\right) + 2(u-1)E\left(\frac{\pi}{2}, \sqrt{\frac{u}{2}}\right)\right] + \frac{4}{3}(2-u)\sqrt{\frac{u}{2}}.$$

It follows from Eqs. (4), (6), (8)-(11) that at each point in space the field components E_z and E_r are positive and negative respectively from the beginning to the time $t \sim l/R\sqrt{\varepsilon\beta^2-1}$; after that time they change sign. The field decreases as $1/\sqrt{r}$ where r is the distance from the axis. Using these expressions the quantities E_z and E_r are calculated for $k = r/R = 2$, and curves are plotted for $l/R\sqrt{\varepsilon\beta^2-1} = 3$ (Fig. 1).

We also present equations for the components of the radiation field of a uniformly moving line charge of length l. Letting $R \to 0$ in (5) and (7) ($k \to \infty$, $t \to \infty$) and using the value of the integral $\int_0^2 \sqrt{\tau(2-\tau)}\cdot d\tau = \pi/2$ we obtain

$$E_{z|R\to0} = -\frac{2q\sqrt{\varepsilon\beta^2-1}}{rl\varepsilon}\left[\frac{1}{\sqrt{t^2-1}}\eta(t-1) - \frac{1}{\sqrt{\left(t-\frac{l}{r\sqrt{\varepsilon\beta^2-1}}\right)^2-1}}\eta\left(t-\frac{l}{r\sqrt{\varepsilon\beta^2-1}}-1\right)\right], \tag{12}$$

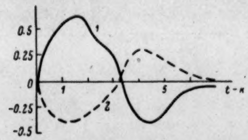

Fig. 1. Time dependence of components of the electromagnetic field of a cylindrical charge bunch. Time is in units of $R\sqrt{\varepsilon\beta^2-1}/v$. 1) E_r/E_r^0; 2) E_z/E_z^0. $E_r^0 = 4q/Rl\varepsilon$, $E_z^0 = \sqrt{\varepsilon\beta^2-1}E_r^0$, $H_\varphi = -\varepsilon\beta E_r$.

$$E_{r|R\to0} = \frac{2q}{rl\varepsilon}\left[\frac{t}{\sqrt{t^2-1}}\eta(t-1) - \frac{\left(t-\frac{l}{r\sqrt{\varepsilon\beta^2-1}}\right)}{\sqrt{\left(t-\frac{l}{r\sqrt{\varepsilon\beta^2-1}}\right)^2-1}}\eta\left(t-\frac{l}{r\sqrt{\varepsilon\beta^2-1}}-1\right)\right], \tag{13}$$

where

$$t \equiv t - \frac{z}{r\sqrt{\varepsilon\beta^2-1}} + \frac{l}{2r\sqrt{\varepsilon\beta^2-1}}$$

is the time in units of $r\sqrt{\varepsilon\beta^2-1}/v$, and $\eta(t)$ is the unit step function.

At the instants waves arrive from the front and rear ends of the line charge the field becomes infinite with opposite signs. The change in sign of the field occurs in a time l/v.

When both the radius and the length of the cluster are small the well-known equations of Tamm and Frank[3] for the Cerenkov radiation from a point charge are obtained from Eqs. (12) and (13) as $l \to 0$.

2. Following ref. 1 let us consider the electromagnetic field of a moving ellipsoidal bunch whose charge density in cylindrical coordinates is

$$\rho(r, z) = \begin{cases} \frac{3q}{4\pi ab^2}; & |z-vt| < a,\ r < b\sqrt{1-\frac{z^2}{a^2}}, \\ 0 - \text{in all other cases}. \end{cases} \tag{14}$$

In view of the axial symmetry of the problem the Fourier transform $\rho(k, \omega)$ of the distribution $\rho(r, z)$ is given by

$$\rho(k, \omega) = 2\pi\int_{-\infty}^{\infty}\int_0^{\infty}\rho(r, z)e^{-r\frac{\omega}{v}}rJ_0(rk)\,dz\,dr,$$

for the charge distribution (14) we have

$$\rho(k, \omega) = 3q\left[\frac{\sin\sqrt{b^2k^2+\frac{\omega^2}{v^2}a^2}}{\left(k^2b^2+\frac{\omega^2}{v^2}a^2\right)^{3/2}} - \frac{\cos\sqrt{k^2b^2+\frac{\omega^2}{v^2}a^2}}{\left(k^2b^2+\frac{\omega^2}{v^2}a^2\right)}\right]. \tag{15}$$

We note that if a parameter ξ is introduced into the sine term in (15) the expression for $\rho(k, \omega)$ can be written as the difference of two terms, the second of which is the derivative of the first with respect to ξ:

$$\left.\begin{aligned}\rho(k,\ \omega)&=\left[\rho^*(\xi)-\frac{\partial\rho^*(\xi)}{\partial\xi}\right]_{\xi=1},\\ \rho^*(k,\ \omega,\ \xi)&=\frac{3q\sin\xi\sqrt{k^2b^2+\frac{\omega^2}{v^2}a^2}}{\left(k^2b^2+\frac{\omega^2}{v^2}a^2\right)^{3/2}}.\end{aligned}\right\}\tag{16}$$

With the Fourier transform $\rho(k, \omega)$ in the form (16) the method of ref. 1 for calculating the field of a cylindrical bunch can be used to obtain the following expressions for the longitudinal component of the electromagnetic field E_z and the transverse component E_r in the region $r \geq b$:

$$E_z=\left[E_z^*(\xi)-\frac{\partial E_z^*(\xi)}{\partial\xi}\right]_{\xi=1},\tag{17}$$

$$E_z^*=\frac{3qvi}{\pi}\int\limits_{-\infty}^{\infty}\frac{(\varepsilon\beta^2-1)}{\varepsilon}\frac{\sin\left(\xi\frac{\omega}{v}\sqrt{(\varepsilon\beta^2-1)\,b^2+a^2}\right)}{\omega^2\left[(\varepsilon\beta^2-1)\,b^2+a^2\right]^{3/2}}$$

$$\times e^{i\frac{\omega}{v}(z-vt)}K_0\left(-i\frac{\omega}{v}\sqrt{\varepsilon\beta^2-1}\,r\right)d\omega,\tag{18}$$

$$E_r=\left[E_r^*(\xi)-\frac{\partial E_r^*(\xi)}{\partial\xi}\right]_{\xi=1},\tag{19}$$

$$E_r^*=-\frac{3qvi}{\pi}\int\limits_{-\infty}^{\infty}\frac{(\varepsilon\beta^2-1)^{1/2}}{\varepsilon}\frac{\sin\left(\xi\frac{\omega}{v}\sqrt{(\varepsilon\beta^2-1)\,b^2+a^2}\right)}{\omega^2\left[(\varepsilon\beta^2-1)\,b^2+a^2\right]^{3/2}}$$

$$\times e^{i\frac{\omega}{v}(z-vt)}K_1\left(-i\frac{\omega}{v}\sqrt{\varepsilon\beta^2-1}\,r\right)d\omega.\tag{20}$$

As in the preceding case, the components of the electric field contain interference terms which limit the high-frequency contribution. The order of magnitude of the duration of the perturbation Δt can be estimated by comparing it with $1/\Delta\omega$, where $\Delta\omega$ is the frequency spread:

$$\Delta t\sim\frac{v}{\sqrt{(\varepsilon\beta^2-1)\,b^2+a^2}}.\tag{21}$$

To evaluate (18) we write it in the form

$$E_z^*=E_z^*(t+\xi c)-E_z^*(t-\xi c),$$

where $t = t - z/b\sqrt{\varepsilon\beta^2-1}$ is the time from the instant the wave arrives at the point $r = b$ in units of $b\sqrt{\varepsilon\beta^2-1}/v$,

$$E_z^*(t)=\frac{3q(\varepsilon\beta^2-1)^{3/2}}{\varepsilon\left[(\varepsilon\beta^2-1)\,b^2+a^2\right]^{3/2}}\frac{1}{2\pi i}\int\limits_{-i\infty}^{i\infty}e^{pt}\frac{K_0(kp)}{p^3}dp,$$

$$c=\frac{\sqrt{(\varepsilon\beta^2-1)\,b^2+a^2}}{\sqrt{\varepsilon\beta^2-1}\,b},\ k=\frac{r}{b}.$$

Evaluating the last integral[4] and substituting the value of $E_z^*(t)$ into (17) we obtain

$$E_z=\frac{3q(\varepsilon\beta^2-1)^{3/2}b}{\varepsilon\left[(\varepsilon\beta^2-1)\,b^2+a^2\right]^{3/2}}\left\{\left[t\ln\left(\frac{t+c-\sqrt{(t+c)^2-k^2}}{k}\right)\right.\right.$$

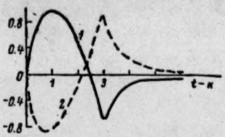

Fig. 2. Time dependence of the components of the electromagnetic field of an ellipsoidal bunch. $\sqrt{(\varepsilon b^2-1)b^2+a^2}/\sqrt{\varepsilon b^2-1}b = 3/2$, $k = r/b = 2$. Time units of $b\sqrt{\varepsilon b^2-1}/v$. 1) E_r/E_r^0; 2) E_z/E_z^0. $E_r^0 = 3q(\varepsilon b^2-1)b/\varepsilon[(\varepsilon\beta^2-1)b^2+a^2]^{3/2}$, $E_z^0 = \sqrt{\varepsilon b^2-1}E_r^0$, $H_\varphi = -\varepsilon\beta Er$.

$$\left.-\sqrt{(t+c)^2-k^2}\right]\eta(t+c-k)$$

$$\left.-\left[t\ln\left(\frac{t-c-\sqrt{(t-c)^2-k^2}}{k}\right)-\sqrt{(t+c)^2-k^2}\right]\eta(t-c-k)\right\}.\tag{22}$$

The component E_r is evaluated in a similar way:

$$E_r=\frac{3q(\varepsilon\beta^2-1)\,b}{\varepsilon\left[(\varepsilon\beta^2-1)\,b^2+a^2\right]^{3/2}}\left\{\left[\frac{k}{2}\ln\left(\frac{t+c-\sqrt{(t+c)^2-k^2}}{k}\right)\right.\right.$$

$$\left.-\frac{(t-c)\sqrt{(t+c)^2-k^2}}{2k}\right]\eta(t+c-k)$$

$$\left.-\left[\frac{k}{2}\ln\left(\frac{t-c-\sqrt{(t-c)^2-k^2}}{k}\right)-\frac{(t+c)\sqrt{(t-c)^2-k^2}}{2k}\right]\eta(t-c-k)\right\}.\tag{23}$$

Thus the electromagnetic field of an ellipsoidal bunch is expressed in terms of elementary functions and differs somewhat from the field of a cylindrical bunch (Fig. 2). The duration of the oscillation in each half-wave is of the same order of magnitude as estimate (21). It is easy to see from (22) and (23) that as $b \to 0$ the form of the radiation field function for an infinitesimally thin moving bunch (a line charge of length $2a$) is not changed, and as a consequence the field is everywhere finite in contrast with (12) and (13). This is a result of the fact that the density of the line charge obtained from an ellipsoidal bunch is not uniform.

In conclusion it should be noted that although the present analysis applies to nondispersive media it gives the correct result for media in which the dispersion region begins with wavelengths shorter than the scale of the characteristic variation of the charge density function in the bunch. The expressions for the fields of bunches depend on parameters (the linear dimensions of the bunches) which are not revealed by spectral analysis. We note that a similar method can be used to find the electromagnetic field inside a bunch. This permits a qualitative treatment of the important problem of the stability of a system of charged particles.

The author thanks K. A. Barsukov for posing the problem and for discussion.

---

[1] B. M. Bolotovskii, Trudy FIAN, 22, Nauka, Moscow (1964).

[2] Millimeter and Submillimeter Waves [in Russian], IL, Moscow (1959).

[3] I. E. Tamm, J. Phys. (USSR), 1, 439 (1939).

[4] V. A. Ditkin and A. P. Prudnikov, Handbook of Operational Calculus [in Russian], Vysshaya Shkola, Moscow (1965).

State of a gas moving near a solid surface

S. P. Bakanov and B. M. Markeev

Institute of the Problems of Mechanics, Academy of Sciences of the USSR, Moscow

(Submitted November 21, 1973)
Zh. Tekh. Fiz., 44, 2081-2084 (October 1974)

The range of applicability of the method of half-range expansions to describe the state of a gas close to a phase interface is discussed. It is shown that by starting from physical premises the accuracy of the method can be estimated without having to resort to the very cumbersome evaluation of the succeeding terms. The velocity of slip is calculated for an arbitrary law of interaction of the gas molecules with the interface.

For a gas moving along a solid surface the distribution of velocities in the Knudsen layer differs significantly from that in the main volume of the gas. Maxwell[1] first called attention to this fact. The first attempt to find the distribution function of gas molecules in the Knudsen layer appeared in papers by Gross et al.,[2-3] treating the Couette flow of a monatomic gas between two plates. It was noted in ref. 4, however, that the results in ref. 3 contain errors of fundamental significance. In particular, the solution given in ref. 3 does not satisfy the most important physical requirement that at a point between two widely separated plates, sufficiently far from each of them, the distribution functions for the velocities of molecules moving in opposite directions must be the same. In those papers[2,3] the distribution functions for falling and rising fluxes are different even halfway between plates any distance apart.

It is shown below that this physically meaningless result[3] can be eliminated by taking account of the accuracy of the calculation of the moments of the collision integral.

It should be noted that the above difficulty has not gone unnoticed. Several papers[5,6] have treated the contradiction by matching the solution obtained for the Knudsen layer with the Chapman–Enskog solution. In an interesting paper by Cercignani it is pointed out correctly that if the distribution function is expanded in terms of a finite number of polynomials the expansion coefficients depend on velocity. Therefore, the author notes that the violation of the physical principle corresponding to the Chapman–Enskog solution is not the result of mistakes in evaluating the integrals, but arises from the nature of the approximation, which assumes that the expansion coefficients mentioned above are velocity independent. Yielding to the correct physical intuition, Cercignani had to note that his statement of the problem was not very helpful and that it is similar to attempts to obtain an exact solution of the linearized Boltzmann equation. At the same time the method of polynomial expansions, though approximate, enables one to solve the problem completely, of course not avoiding an estimate of the accuracy of the method.

In view of the above it is appropriate to return to the problem.

Let us consider the problem of Couette flow of a gas between two infinite parallel plates, using the method developed by Gross et al.[2-3]

Let the distance between the plates be 2L, and suppose they are both maintained at temperature T. The upper plate moves in the z direction with a velocity $u_0'/2$, and the lower plate with the velocity $-u_0'/2$. The x axis is perpendicular to the plates.

The distribution function for gas molecules $f(\mathrm{r}, \mathrm{v})$ depends on a single spatial coordinate. We assume that a stationary state exists so that $f(\mathrm{r}, \mathrm{v})$ does not depend on time. We also assume that the relative velocity of the plates u_0' is small in comparison with the mean thermal velocity of the gas molecules.

The distribution function for gas molecules satisfies the Boltzmann equation. We seek it in the form

$$f = f_0[1 + \varphi(x, c)], \tag{1}$$

where $c = (m/2kT)^{1/2}v$ and v is the velocity of a molecule. The remaining notation is standard.

We find the function $\varphi(c, x)$ from the equation

$$c_x \frac{\partial\varphi}{\partial x} = J(\varphi), \tag{2}$$

where $J(\varphi)$ is the collision integral.

We introduce two distribution functions, $f^+(v, x)$ for molecules with $v_X > 0$ and $f^-(v, x)$ for molecules with $v_X < 0$, and assume that $f^+(v_X, x) = 0$ for $v_X < 0$ and $f^-(v_X, x) = 0$ for $v_X > 0$. We take the usual boundary conditions: A fraction ε of the molecules are reflected diffusely, and a fraction 1 − ε specularly. Since $u_0'/v_Z \ll 1$, we have

$$\left.\begin{aligned}\varphi^+(c, -L) &= \varepsilon u_0 c_z + (1-\varepsilon)\varphi^-(-c_x, c_y, c_z, -L) \text{ for } c_x > 0,\\ \varphi^-(c, L) &= -\varepsilon u_0 c_z + (1-\varepsilon)\varphi^+(-c_x, c_y, c_z, L) \text{ for } c_x < 0,\end{aligned}\right\} \tag{3}$$

where

$$u_0 = u_0'\left(\frac{m}{2kT}\right)^{1/2}.$$

We seek a solution of Eq. (2) in the form

$$\varphi^\pm(c, x) = a_0^\pm(x)c_z + a_1^\pm(x)c_x c_z. \tag{4}$$

Boundary condition (3) will be satisfied by setting

$$\left.\begin{aligned}a_0^\pm(\mp L) &= \pm\varepsilon u_0 + (1-\varepsilon)\alpha_0^\mp(\mp L),\\ a_1^\pm(\mp L) &= -(1-\varepsilon)a_1^\mp(\mp L).\end{aligned}\right\} \tag{3'}$$

Introducing the auxiliary function

$$\operatorname{sign} c_x = \begin{cases} 1 \text{ for } c_x > 0,\\ -1 \text{ for } c_x < 0,\end{cases}$$

we have

$$\varphi(c, x) = \varphi^+\frac{1+\operatorname{sign} c_x}{2} + \varphi^-\frac{1-\operatorname{sign} c_x}{2}. \tag{5}$$

Substituting (5) into (2), multiplying successively by

$c_z(1 \pm \text{sign } c_x)e^{-c^2}dc$ and $c_x c_z(1 \pm \text{sign } c_x)e^{-c^2}dc$, and integrating with respect to c from $-\infty$ to ∞ we obtain a system of differential equations for $a_0^{\pm}(x)$ and $a_1^{\pm}(x)$:

$$\left.\begin{aligned} \frac{d}{dx} a_0^{\pm} &= (a_0^{+} - a_0^{-}) A_1 + (a_1^{+} + a_1^{-}) A_2 \mp (a_1^{+} - a_1^{-}) A_3, \\ \frac{d}{dx} a_1^{\pm} &= \pm (a_0^{+} - a_0^{-}) B_1 \pm (a_1^{+} + a_1^{-}) B_2 + (a_1^{+} - a_1^{-}) B_3, \end{aligned}\right\} \quad (6)$$

where A_i and B_i are functions of the pressure of the gas depending on the law of interaction between its molecules.[4]

The standard procedure for solving a system of ordinary differential equations with boundary conditions (3) gives

$$\left.\begin{aligned} a_0^{\pm} &= \frac{u}{F}\left\{\mp \frac{B_2}{B_1} - 2\left[\frac{B_2}{B_1} A_1 - A_2\right] x \pm \frac{2-\varepsilon}{N}\left[A e^{\pm \alpha x} - B e^{\mp \alpha x}\right]\right\}, \\ a_1^{\pm} &= \frac{u}{F}\left\{1 + \frac{2-\varepsilon}{N}\left[D e^{\pm \alpha x} - C e^{\mp \alpha x}\right]\right\}, \end{aligned}\right\} \quad (7)$$

where

$$\left.\begin{aligned} A &= \alpha\sqrt{\pi} - 4B_1\left(1 - \frac{\sqrt{\pi}}{2}\frac{B_2}{B_1}\right), \\ B &= -\alpha\sqrt{\pi} - 4B_1\left(1 - \frac{\sqrt{\pi}}{2}\frac{B_2}{B_1}\right), \\ C &= 2\left[\alpha + 2B_1\left(\frac{\sqrt{\pi}}{2} - \frac{B_2}{B_1}\right)\right], \\ D &= 2\left[-\alpha + 2B_1\left(\frac{\sqrt{\pi}}{2} - \frac{B_2}{B_1}\right)\right], \\ \alpha^2 &= -4B_1B_2\left(\frac{\sqrt{\pi}}{2} - \frac{B_2}{B_1}\right), \\ F &= -2A_2L + \frac{2-\varepsilon}{\varepsilon}\frac{M}{N}, \\ M &= [A - B(1-\varepsilon)]e^{-\alpha L} - [B - A(1-\varepsilon)]e^{\alpha L}, \\ N &= [C(1-\varepsilon) - D]e^{-\alpha L} - [D(1-\varepsilon) - C]e^{\alpha L}. \end{aligned}\right\} \quad (8)$$

It is clear from (7) and (8) that the distribution function for the molecules is discontinuous at the point $c_x = 0$. Physically the presence of a discontinuity is justified for large Knudsen numbers, but is completely inadmissible for $\lambda/L \ll 1$, i.e., distances from the plates appreciably larger than the mean free path of the molecules. Calculations show that the magnitude of the discontinuity depends on the law of interaction between the molecules. Actually we have

$$\frac{f^{+}(x, c_x = 0) - f^{-}(x, c_x = 0)}{f^{+}(x, c_x = 0) + f^{-}(x, c_x = 0)} \simeq \frac{B_2}{B_1}.$$

For the hard sphere model $B_2/B_1 = 0.013$; for Maxwell's law[8] $B_2/B_1 = 0$. In this way the physically reasonable result used in the approximation of the distribution function (4) is realized with a certain accuracy depending on the model of the molecular interaction assumed. The statement[4] that $B_2 = 0$ must be understood in this sense.

Thus the accuracy of expansion (4) can be estimated without having to perform the very cumbersome calculation of the succeeding terms. On the other hand without performing this estimate a more accurate evaluation of the integrals is not justified.[9]

It is easy to compute the flow rate of the gas in the space between the plates:

$$q_s(x) = \frac{u_0'}{2}\frac{\varepsilon}{M}\,\frac{2A_2\dfrac{N}{2-\varepsilon}x + \left(A + B + \dfrac{C+D}{\sqrt{\pi}}\right)\operatorname{sh}\alpha x}{1 - 2A_2L\dfrac{\varepsilon}{2-\varepsilon}\dfrac{N}{M}}. \quad (9)$$

The true q_s and the "apparent" q_s^* velocities of slip are given by the relations

$$q_s(L) = -\frac{u_0'}{2} - q_s(L),$$

$$q_s^*(L) = -\frac{u_0'}{2} - L\left(\frac{\partial q}{\partial x}\right)\Big|_{x=0}.$$

Hence

$$\left.\begin{aligned} q_s(L) &= -\frac{u_0'}{2}\,\frac{1 + \dfrac{\varepsilon}{M}\left(A + B + \dfrac{C+D}{\sqrt{\pi}}\right)\operatorname{sh}\alpha L}{1 - 2A_2L\dfrac{\varepsilon}{2-\varepsilon}\dfrac{N}{M}}, \\ q_s^*(L) &= -\frac{u_0'}{2}\,\frac{1 + \dfrac{\varepsilon}{M}\left(A + B + \dfrac{C+D}{\sqrt{\pi}}\right)\alpha L}{1 - 2A_2L\dfrac{\varepsilon}{2-\varepsilon}\dfrac{N}{M}}. \end{aligned}\right. \quad (10)$$

For specular reflection ($\varepsilon = 0$) the gas is stationary and slips along the surface of a plate with the velocity of the plate itself. The velocity gradient of the gas $\partial q/\partial x$ is of course zero. It should be noted that it is difficult to interpret the results of refs. 10 and 11 in this respect.

In conclusion the authors thank V. V. Struminskii and A. A. Rukhadze for helpful discussion.

---

[1] J. C. Maxwell, Phil. Trans. Roy. Soc., 170, 231 (1879).

[2] E. P. Gross, E. A. Jackson, and S. Ziering, Ann. Phys., 1, 141 (1957).

[3] E. P. Gross and Z. Ziering, Phys. Fluids, 1, 215 (1958).

[4] S. P. Bakanov and B. V. Deryagin, Dokl. Akad. Nauk, SSSR, 139, 71 (1961) [Sov. Phys.–Dokl., 6, 588 (1962)].

[5] S. L. Gorelov and M. N. Kogan, Izv. AN SSSR, MZhG, No. 6 (1968).

[6] M. M. Kuznetsov, Prikl. Mekh. Tekh. Fiz., No. 4 (1971).

[7] C. Cercignani, Nuovo Cimento, 27, 1240 (1963).

[8] S. Ziering, AIAA, 1, No. 3 (1963).

[9] P. E. Suétin and B. T. Porodnov, Zh. Tekh. Fiz., 37, 171 (1967) [Sov. Phys. – Tech. Phys., 12, 120 (1967)].

[10] I. N. Ivchenko and Yu. I. Yalamov, Izv. AN SSSR, MZhG, No. 6 (1968).

[11] B. T. Porodnov and P. E. Suétin, Zh. Tekh. Fiz., 39, 748 (1969) [Sov. Phys. – Tech. Phys., 14, 563 (1969)].

Plasma

Drift instability in a weakly ionized plasma

S. V. Putvinskii and A. V. Timofeev

(Submitted November 19, 1973)
Zh. Tekh. Fiz., 44, 2085-2094 (October 1974)

It is shown that low-frequency ($\omega \ll \nu_i$) drift waves can be excited spontaneously in a current-free discharge when the ions are not fully magnetized ($\omega_i/\nu_i \sim 1$, $\rho_i/a \sim 1/2$-$1/3$). Here, ω_i is the ion cyclotron frequency, ν_i is the ion–neutral collision frequency, ρ_i is the ion Larmor radius and a is the characteristic scale length for changes in the plasma density. A comparison of theoretical and experimental results indicates that this instability has been observed.[1,2] In strong magnetic fields ($\omega_i/\nu_i \gg 1$, $\rho_i/a \ll 1$) the residual effect of incomplete ion magnetization has a stabilizing influence on the drift instability.

INTRODUCTION

A high-frequency gas discharge in a magnetic field exhibits an instability at a frequency which changes in a nonmonotonic fashion with the magnetic field and forms a characteristic sawtooth shape.[1,2] The absolute value of the frequency can be small compared to the ion–neutral collision frequency so that the instability is not a drift-dissipative instability.[3] However, the mechanism considered in ref. 4 can cause low-frequency instabilities. This is the case if the plasma is charged negatively with respect to the walls and the resultant radial electric field is strong. The authors of refs. 1 and 2 have used the results of the theory developed in ref. 4 to explain the increase of frequency with magnetic field. However, the decreasing branch can be excited even with a positive plasma charge.

The experimental conditions in refs. 1 and 2 are such that the mechanism related to violation of neutrality[5] is not effective because of the high charged-particle density.

The theoretical model of the phenomenon proposed here is based on certain properties of the unstable plasma state. The most important of these in refs. 1 and 2 is the fact that the ion component of the weakly ionized plasma is not fully magnetized; in the unstable state the ion cyclotron frequency ω_i is close to the ion–neutral collision frequency ν_i, and the ion Larmor radius ρ_i is a considerable fraction (of the order of 1/2-1/3) of the tube radius a. Under these conditions the ion drift velocity in crossed fields (the electric field of the wave and the constant magnetic field) is significantly different from the electron drift velocity. According to ref. 6, a difference on the drift speeds can lead to low-frequency drift in stabilities in a nonuniform plasma.

An analysis of the behavior of a plasma with a large ion Larmor radius presents considerable mathematical difficulties. In order to simplify the calculations we make use of an expansion in the parameter ρ_i/a, taking the Larmor radius to be small. For $\rho_i/a \sim 1/2$-$1/3$ the results are not highly accurate and are only illustrative. We therefore put most emphasis on the interpretation of the qualitative effects observed in the experiments of the variation in frequency with the magnetic field, the variation of the critical field with density, etc.

The ion component is described by the kinetic equation with the Batnager–Gross–Crook collision integral. It is well known that this collision integral works for a weakly ionized plasma where the denominating collisions are those with neutrals. The use of the kinetic approach is due to the necessity of allowing for the finite Larmor radius. If the plasma is fully ionized the effect of the finite Larmor radius is taken into account in the hydrodynamic treatment by means of the viscosity. However, the normal hydrodynamic treatment is not applicable to a weakly ionized plasma.[7] In the derivation of the hydrodynamic equations it is assumed that collisions do not change the total momentum and energy; however, in collisions with neutrals, neither the momentum nor the energy of the charged particles is observed. The formal use of the hydrodynamic treatment in the present case leads to erroneous results. (Corrections for the effects of finite Larmor radius are ambiguous in sign.)

1. BASIC EQUATIONS.
INITIAL STATE

We describe the ion component of a weakly ionized plasma by the kinetic equation

$$\frac{\partial f}{\partial t}+(\mathbf{v}\nabla)f+\frac{e}{m_i}\left(\mathbf{E}+\frac{1}{c}[\mathbf{v}\mathbf{H}]\right)\frac{\partial}{\partial \mathbf{v}}f=\mathrm{St}(f). \qquad (1)$$

Here, the collision term is taken in a form which allows for the conservation of the number of ions in collisions with neutrals:

$$\mathrm{St}(f)=-\nu_i(f-f_{00})+\nu_i\frac{f_{00}}{n_0}\int(f-f_{00})\,d\mathbf{v}, \qquad (2)$$

where ν_i is the ion–neutral collision frequency,

$$f_{00}=\left(\frac{m_i}{2\pi T_i}\right)^{3/2}n_0(r)\,e^{-\frac{m_i v^2}{2T_i}},$$

T_i is the temperature of the neutral gas. It is assumed that the collisions bring the ions into thermal equilibrium with the neutrals.

Discharge tubes are axially symmetric and in the absence of instabilities the density gradient and the electric field are radial. In order to simplify the problem we introduce an equivalent system with plane symmetry in which OX represents the radial direction and OZ the azimuthal direction. The OZ axis coincides with the magnetic field. Solving (1) under the conditions

$$\left|\rho_i\frac{1}{n_0}n_0'\right|\ll 1,\quad \left|\frac{c}{H}\left(\frac{T_i}{m_i}\right)^{-1/2}\varphi_0'\right|\ll 1,$$

we find

$$f_0=f_{00}\left\{1+\left(\frac{n_0'}{n_0}+\frac{e\varphi_0'}{T_i}\right)(\omega_i v_y-\nu_i v_x)\frac{1}{\omega_i^2+\nu_i^2}+\right.$$

$$+\left(\frac{n_0'}{n_0}\frac{e\varphi_0'}{T_i}+\frac{1}{2}\frac{n_0''}{n_0}+\frac{1}{2}\frac{e\varphi_0''}{T_i}+\frac{1}{2}\left(\frac{e\varphi_0'}{T_i}\right)^2\right)\frac{v_x^2+v_y^2}{\omega_i^2+\nu_i^2}$$
$$-\left(\frac{n_0'}{n_0}\frac{e\varphi_0'}{T_i}+\frac{m_i}{T_i}\left(\frac{e\varphi_0'}{m_i}\right)^2\right)\frac{1}{\omega_i^2+\nu_i^2}\Bigg\}. \tag{3}$$

In the expansion (3) we take only those second-order terms which affect the density.[1] The velocity is defined by the first term of the expansion

$$V_{0ix}=-b_{i\perp}\varphi_0'-D_{i\perp}\frac{n_0'}{n_0}, \tag{4}$$

$$V_{0iy}=b_{i\perp}\varphi_0'-D_{i\perp}\frac{n_0'}{n_0}. \tag{5}$$

Here $b_i = e/m_i\nu_i$ is the mobility of the ions, $D_i = T_i/m_i\nu_i$ is the diffusion coefficient, $b_{i\perp} = b_i(\nu_i^2/\omega_i^2 + \nu_i^2)$; $b_{i\perp} = (\omega_i/\nu_i)b_i$; $D_{i\perp} = D_i(\nu_i^2/\omega_i^2 + \nu_i^2)$; $D_{i\perp} = D_{i\perp}\omega_i/\nu_i$.

It is usually assumed that even with collisions the unperturbed state of the plasma can be described by a function of the integrals of motion v^2, $x + v_y/\omega_i$. In the present case this approach leads to an incorrect expression for the ion velocity.

Since the Larmor radius of the electrons is small, their motion can be described by means of the continuity equation

$$\frac{\partial n}{\partial t}+\operatorname{div}(n\mathbf{V}_e)=0 \tag{6}$$

and the momentum balance equation

$$0=-T_e\nabla n+en\nabla\varphi-\frac{en}{c}[\mathbf{V}H]-m_e n\mathbf{V}_e\nu_e. \tag{7}$$

It is assumed here that the neutrality condition $n_e = n_i = n$ is satisfied and that the temperature (average energy) of the electrons is not changed in the instabilities. By means of (7) we can find an expression for the components of the initial electron velocity and these will differ from (4) and (5) only in the sign in front of the mobility and in the subscript used (i → e).

In dielectric discharge tubes the rate of electron and ion motion to the walls of the tubes must be equal. This condition then defines the ambipolar electric field

$$E_0=\frac{D_{i\perp}-D_{e\perp}}{b_{i\perp}+b_{e\perp}}\frac{n_0'}{n_0}. \tag{8}$$

2. LOW-FREQUENCY DRIFT OSCILLATIONS

The study of drift oscillations usually makes use of the so-called local quasiclassical approximation; we treat small perturbations in the electric field, the ion distribution function, and the density in the form of plane waves traveling in the plane perpendicular to OX, $e^{-i\omega t+ik_z z+ik_y v}$, $k_y \gg \varkappa$, $\varkappa = n'_0/n_0 \sim a^{-1}$.

We consider modes with $k_y \gg k_z$, $\omega \ll \nu_i$. We consider the electrons as magnetized $\omega_e \gg \nu_e$, and the initial electric field as weak $|\varkappa u/\omega_i| \ll 1$. Here $u = (c/H)(d\varphi_0 \cdot dx)^{-1}$, and the conditions $\varkappa\rho_i \ll 1$, $|\varkappa u/\omega_i| \ll 1$ allow us to retain only the first two terms in the expression f_0. Considering the motion of the electrons and ions in the wave field, we get the following relationships between the perturbations in density and potential (remembering that the plasma is neutral):

$$\left.\begin{aligned}&\left(-i\omega+ik_y u+D_e\left(k_y^2\frac{\nu_e^2}{\omega_e^2}+k_z^2\right)\right)\frac{n_1}{n_0}+\\&+\left(-k_y^2\frac{\nu_e}{\omega_e}-k_z^2\frac{\omega_e}{\nu_e}-ik_y\varkappa\right)\frac{c\varphi_1}{H}=0,\\&\left(-i\omega+ik_y u\frac{\omega_i^2}{\omega_i^2+\nu_i^2}(1+\delta)+D_i k_y^2(1-\beta)\frac{\nu_i^2}{\omega_i^2+\nu_i^2}\right)\frac{n_1}{n_0}\\&+\left(k_y^2\frac{\nu_i\omega_i}{\omega_i^2+\nu_i^2}(1-\beta)-ik_y\varkappa\frac{\omega_i^2}{\omega_i^2+\nu_i^2}(1-\alpha)\right)\frac{c\varphi_1}{H}=0,\end{aligned}\right\} \tag{9}$$

and α, β, and δ are corrections related to the finite ion Larmor radius

$$\left.\begin{aligned}\alpha&=1-\frac{\eta_0(z_i)+2\sum\limits_{n=1}^{\infty}\frac{\eta_n(z_i)\nu_i^2}{\nu_i^2+n^2\omega_i^2}}{1-4\sum\limits_{n=1}^{\infty}\frac{\eta_n(z_i)n^2\omega_i^2\nu_i^2}{(\nu_i^2+n^2\omega_i^2)^2}},\\\beta&=1-\frac{1}{z_i}\frac{1-\eta_0(z_i)-2\sum\limits_{n=1}^{\infty}\frac{\eta_n(z_i)\nu_i^2}{\nu_i^2+n^2\omega_i^2}}{1-4\sum\limits_{n=1}^{\infty}\frac{\eta_n(z_i)n^2\omega_i^2\nu_i^2}{(\nu_i^2+n^2\omega_i^2)^2}},\\\delta&=-1+\frac{1+\frac{\nu_i^2}{\omega_i^2}\left(1-\frac{2}{z_i}\sum\limits_{n=1}^{\infty}\frac{\eta_n(z_i)n^2(\nu_i^2+\omega_i^2)}{\nu_i^2+n^2\omega_i^2}\right)}{1-4\sum\limits_{n=1}^{\infty}\frac{\eta_n(z_i)n^2\omega_i^2\nu_i^2}{(\nu_i^2+n^2\omega_i^2)^2}}.\end{aligned}\right\} \tag{10}$$

The following notation has been used in (10): $z_i = k_y^2\rho_i^2$; $\rho_i = \omega_i^{-1}(T_i/m_i)^{1/2}$ is the ion Larmor radius, $I_n(z_i)$ is the Bessel function of imaginary argument, $\eta_n(z_i) = I_n(z_i)e^{-z_i}$. We get the dispersion equation by equating the determinant of (9) to zero. From the dispersion equation we then find the frequency at the instability boundary (Im ω = 0)

$$\omega=\frac{\omega_i^2}{\nu_i^2+\omega_i^2}\left\{k_y u\left(1+\delta+(1-\beta)\left(\frac{k_y}{k_0}\right)^2\frac{\nu_i\nu_e}{\omega_i\omega_e}\right)\right.$$
$$\times\left(1+(1-\beta)\left(\frac{k_y}{k_0}\right)^2\frac{\omega_i\nu_i\nu_e}{\omega_e(\nu_i^2+\omega_i^2)}\right)^{-1}-D_e k_y\varkappa\frac{\nu_e}{\omega_e}$$
$$\left.\times\left(1-\alpha-(1-\beta)\frac{T_i}{T_e}\left(\frac{k_y}{k_0}\right)^2\frac{\nu_i\nu_e}{\omega_i\omega_e}\right)\left(1+(1-\beta)\left(\frac{k_y}{k_0}\right)^2\frac{\omega_i\nu_i\nu_e}{\omega_e(\nu_i^2+\omega_i^2)}\right)^{-1}\right\} \tag{11}$$

and the condition for onset:

$$D_e k_0^2\left(1+\frac{T_i}{T_e}\right)\leqslant-\omega\frac{\varkappa}{k_y}\left(1+\alpha\frac{\omega_i^2}{\nu_i^2}\right)\frac{\nu_i}{\omega_i}(1-\beta)^{-1}$$
$$+\varkappa u\frac{\omega_i}{\nu_i}(\alpha+\delta)(1-\beta)^{-1}. \tag{12}$$

In (11) and (12), $k_0^2 = k_z^2 + k_y^2(\nu_e/\omega_e)^2$.

It is shown in ref. 3 that the drift frequency in a weakly ionized plasma must be greater than the collision frequency of ions with neutrals: $\omega > \nu_i$. It follows from (11) however, that if the plasma is positively charged relative

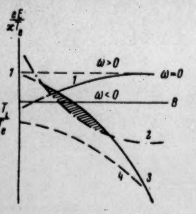

Fig. 1. 1) Electric field for which $\omega = 0$; the frequency (phase velocity) is positive above this curve; 2) characteristic experimental variation of electric with magnetic field; 3) critical electric field; the oscillations are unstable when $E < E_{cr}$; 4) critical field obtained in ref. 4.

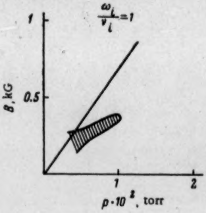

Fig. 3. Calculated stability boundaries for the decreasing frequency branch of the low-frequency mode. $k_{\parallel}$ corresponds to a solenoid with L = 60 cm.

to the walls $\varkappa u > 0$, the frequency of the oscillations can in fact go to zero. The instability condition (12) is then satisfied if the corrections for the effect of a finite Larmor radius (α, δ) in the second term on the right of (12) are large enough. We note that the instability mechanism considered in ref. 4 acts for an electric field of the opposite sign ($\varkappa u < 0$), in which case the first term on the right of (12) is the dominant one.

These ideas are illustrated in Fig. 1. The region of instability is that below the curve 3. As the magnetic field increases (Larmor radius decreases), this curve goes over to 4, which gives the critical field for the instability considered in ref. 4. A typical variation of the electric field with the magnetic field for the conditions of the experiments discussed here is shown by curve 2. The instability region lies between 2 and 3 (shaded area). The frequency (phase velocity) goes to zero on curve 1. Above 1 is the region in which the oscillations have a positive phase velocity, i.e., go over to the electron side (falling branch).

3. NUMERICAL RESULTS.
COMPARISON WITH EXPERIMENT

Expressions are obtained from (9) and (10) for the frequency ω and the growth rate γ. Since these expressions are rather cumbersome, numercial calculations are used to find the dependence of the frequency on the magnetic field. In order to compare the results with experiment the values of the parameters in the dispersion equations are taken to be those in ref. 2 for which the most extensive data are available. We use the experimental values of the stationary electric field. We note that this field exceeds the ambipolar field of (8) by about an order of magnitude. The ions can thus acquire a considerable amount of energy between collisions with neutrals – significantly higher in fact than the thermal energy of the neutrals. The effective ion temperature is calculated from the equation

$$T_{i\,\mathrm{eff}} = T_0 + \frac{eE_0}{l_i^{-1} + \rho_i^{-1}}.$$

Here, T_0 is the neutral temperature, l_i and ρ_i are the mean free path and Larmor radius of the ions. The electron temperature in ref. 2 is 2 eV. The value of $\varkappa \approx -2$ cm^{-1} is determined from the experimental distribution of the initial density n_0. Since we have solved the plane problem rather than the cylindrical of wave number $k_y = |\varkappa|$. The second mode corresponds to $k_y = 2|\varkappa|$, etc.

The waves observed in the experiment represent the fundamental mode in the longitudinal direction, i.e., a single half-wavelength along the axis of the tube. The length of the discharge tube exceeds that of the solenoids so that the length of the plasma along the magnetic field is equal to the length of the solenoid. Thus, the longitudinal wave numbers are 0.156, 0.104 and 0.052 cm^{-1} for solenoid lengths of 20, 40 and 60 cm, respectively.

Figure 2 shows how the frequencies varies with the magnetic field for various pressures and Fig. 3 shows the variation of the instability region with pressure and magnetic field for the decreasing branch of the oscillations. The experimental results are shown[2] in Figs. 4 and 5. For comparison of theory and experiment we have in Figs. 3 and 5 separated out the oscillations on the branch where the frequency decreases with magnetic field. There are two reasons for doing this: First, these modes exist over a narrow range of the parameters and second, it is in these modes that the effects of incomplete ion magnetization, and in particular of finite Larmor radius, are most clearly seen. The oscillations with increasing frequency can build up in a negative electric field of sufficient strength even when the ion Larmor radius is equal to zero.[4] (In Fig. 1, curves 3 and 4 approach each other as $|E|$ increases.) The frequency variation of the unstable modes derived from the theory has the same form as that

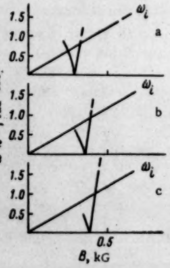

Fig. 2. Theoretical variation of the frequency of unstable oscillations with the magnetic field, calculated for an argon plasma. $k_{\parallel}$ corresponds to a solenoid with L = 60 cm; a) $p = 5 \cdot 10^{-3}$; b) $8 \cdot 10^{-3}$; c) $1 \cdot 10^{-2}$ torr.

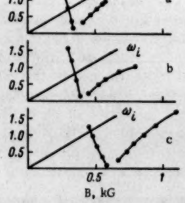

Fig. 4. Experimental variation of the frequency in an argon plasma with magnetic field for L = 60 cm. a) $p = 8 \cdot 10^{-3}$; b) 1.10^{-2}; c) $1.5 \cdot 10^{-2}$ torr.

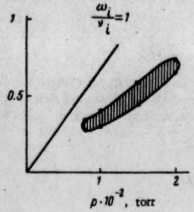

Fig. 5. Experimental boundary for the existence of the decreasing branch of the low-frequency oscillations in an argon plasma in a solenoid with L = 60 cm.

observed in the experiment. However, the whole picture is shifted to lower magnetic field values. This discrepancy is obviously due to the simplified nature of the model. Although the absolute values of the magnetic field and pressure in the instability region differ from the experimental values, there is good agreement in the dimensionless parameter ω_i/ν_i. The fact that this parameter is close to unity is understandable because in this case the ions are sufficiently magnetized as is necessary for the existence of drift instabilities and at the same time the difference in the drift velocities for crossed fields is a maximum. We recall that this quantity plays an important role in the instability.[6]

If we consider the condition $\omega_i/\nu_i \approx 1$ as necessary for the instability, then we have an explanation for the fact that the instability region is bounded on the low-pressure side. In fact, as the pressure decreases, the magnetic field in the instability region must also fall. The instability is quenched when the ion Larmor radius becomes comparable to the radius of the tube. Estimates of the lower limit in pressure made in this way agree with the experimental data.

Electron diffusion along the magnetic field plays a double role. On the one hand, it is necessary for excitation to occur.[6] On the other, it has a stabilizing effect at small longitudinal wavelengths. It is for this second reason, apparently, that the instability is not observed for the smallest solenoid length of 20 cm.

The instabilities have been observed only in the heavy gases Ar, Kr, and Xe and not He and Ne. We take this as direct proof of the important effect of the finite Larmor radius in the instability mechanism.

4. EFFECTS OF THE FINITE ION LARMOR RADIUS ON DRIFT WAVES IN A WEAKLY IONIZED MAGNETIZED PLASMA

In the majority of papers on the instabilities in a weakly ionized plasma, the ions are assumed to be cold. A smaller ion temperature ($T_i \ll T_e$) is characteristic of hf discharges and positive columns. For a discharge plasma, however, the afterglow is isothermal ($T_i \approx T_e$). In this case, as has been noted in ref. 6, the effects of the finite Larmor radius have a considerable influence on the drift waves in strong magnetic fields $\omega_i/\nu_i \gg 1$. When $\omega_i/\nu_i \gg 1$, drift waves can build up under the action of the drift-dissipative mechanism.[3,6] The unstable oscillations are then the "high-frequency" ones with $\omega \gg \nu_i$, and so in what follows we have taken the ion inertia into account.

When $\omega_i/\nu_i \gg 1$, the electrons and ions drift under the action of the stationary radial electric field with almost the same velocities $[|V_{0ey} - V_{0iy}| \approx |(cE_0/H)\,\nu_i^2/\omega_i^2| \ll |cE_0/H|]$. This motion only produces a Doppler frequency shift in the laboratory system. The small difference in the drift velocities causes an azimuthal current which in general can affect the plasma stability.[4] However, if the electric field is ambipolar, its effect is too weak and we can neglect it.

Thus from (A.1) and (2) we have

$$(-i\omega + D_e k_0^2)\frac{n_1}{n_0} + \left(-k_0^2\frac{\omega_e}{\nu_e} - ik_y\varkappa\right)\frac{c\varphi_1}{H} = 0, \tag{13}$$

$$\left(-i\omega + D_i k_y^2 \frac{\nu_i^2}{\omega_i^2}\frac{1-\eta_0(z_i)}{z_i}\right)\frac{n_1}{n_0}$$
$$+\left(k_y^2\frac{\nu_i}{\omega_i}\left(1-\frac{i\omega}{\nu_i}\right)\frac{1-\eta_0(z_i)}{z_i} - ik_y\varkappa\eta_0(z_i)\right)\frac{c\varphi_1}{H} = 0. \tag{14}$$

Here $k_0^2 = k_z^2 + k_y^2\nu_e^2/\omega_e^2$, $\eta_0(z_i) = e^{-z_i}I_0(z_i)$. Equations (13) and (14) give the frequency and the instability boundary ($\mathrm{Im}\,\omega = 0$)

$$\omega = -D_e k_y \varkappa \frac{\nu_e}{\omega_e}\left(\eta_0 - t\left(\frac{k_y}{k_0}\right)^2 \frac{1-\eta_0(z_i)}{z_i}\frac{\nu_i\nu_e}{\omega_i\omega_e}\right)$$
$$\times\left(1 + \left(\frac{k_y}{k_0}\right)^2 \frac{1-\eta_0(z_i)}{z_i}\frac{\nu_i\nu_e}{\omega_i\omega_e} + D_e k_y^2 \frac{1-\eta_0(z_i)}{z_i}\frac{\nu_e}{\omega_i\omega_e}\right)^{-1}, \tag{15}$$

$$D_e k_0^2(1+t) \leqslant \frac{\omega^2}{\nu_i} - \omega\frac{\varkappa}{k_y}z_i\frac{\omega_i}{\nu_i}. \tag{16}$$

Substitution of (15) into (16) gives

$$q \leqslant \xi^2 \frac{\eta_0(z_i) - t\,\dfrac{1-\eta_0(z_i)}{z_i}\,q^{-1}}{\left(1 + \dfrac{1-\eta_0(z_i)}{z_i}\,q^{-1} + \dfrac{1-\eta_0(z_i)}{t}\right)^2}, \tag{17}$$

where

$$q = \left(\frac{k_0}{k_y}\right)^2\frac{\omega_i\omega_e}{\nu_i\nu_e}, \quad \xi^2 = \frac{T_e\varkappa^2}{m_i\nu_i^2}, \quad t = \frac{T_i}{T_e}.$$

The inequality (17) can be written

$$\xi^2 \geqslant \frac{[qz_i(1+t-\eta_0(z_i)) + (1-\eta_0(z_i))\,t]^2}{z_i t^2[z_i\eta_0(z_i)\,q - (1-\eta_0(z_i))\,t]}. \tag{18}$$

An analysis of this inequality has shown that as ξ increases (i.e., as the pressure of the neutral gas decreases), the first modes to become unstable are those which are extended along the magnetic field with $k_z^2 \approx k_y^2(1+2t)(\nu_i\nu_e/\omega_i\omega_e)$. The critical value of ξ is $\xi^* = 2(1+T_i/T_e)^{1/2}$. When T = 0, this result coincides with that in ref. 3. Thus with increase in the ion temperature, the drift instability requires a higher gradient in the plasma density or a smaller neutral gas pressure. The stabilizing effect is apparently due to ion diffusion.

The authors are grateful to B. B. Kadomtsev and B. N. Shvilkin for useful discussions.

APPENDIX

DERIVATION OF THE DISPERSION EQUATION

The kinetic equation for a perturbation in the ion distribution function

$$\frac{\partial f_1}{\partial t}+\frac{e}{m_i}\mathbf{E}_0\frac{\partial f_1}{\partial \mathbf{v}}+\frac{e}{m_i c}[\mathbf{vH}]\frac{\partial f_1}{\partial \mathbf{v}}-\frac{e}{m_i}\nabla\varphi\frac{\partial f_0}{\partial \mathbf{v}}=-\nu_i\left(f_1-n_1 f_{00}(v)\right) \quad (\mathrm{A.1})$$

is obtained by linearizing (1). In (A.1), f_1 is the perturbed distribution function, f_0 is the initial distribution function, φ_1 and n_1 are the potential and ion-density perturbations. The initial electric field is taken to be constant E_0 = const; in the solution of (A.1) it is convenient to go over to a coordinate system in which the initial electric vanishes:

$$v'_y=v_y-u, \qquad v'_x=v_x,$$

v'_x and v'_y are the ion velocity in the new coordinate system and $u_y = -cE_0/H$ in the drift velocity in the crossed fields. Equation (A.1) becomes

$$\frac{\partial f_1}{\partial t}+\frac{e}{m_i c}[\mathbf{v}'\mathbf{H}]\frac{\partial f_1}{\partial \mathbf{v}'}-\frac{e}{m_i}\nabla\varphi_1\frac{\partial f_0}{\partial \mathbf{v}'}=-\nu_i\left(f_1-n_1 f_{00}(\mathbf{v}'+\mathbf{u})\right). \quad (\mathrm{A.2})$$

This equation has been solved by integration along the characteristic

$$v'_x=v_\perp\sin(\omega_i t+\alpha), \qquad v'_y=v_\perp\cos(\omega_i t+\alpha),$$

$$x'=x_0-\frac{v_\perp}{\omega_i}\cos(\omega_i t+\alpha)+\frac{v_\perp}{\omega_i}\cos\alpha,$$

$$y'=y_0+\frac{v_\perp}{\omega_i}\sin(\omega_i t+\alpha)-\frac{v_\perp}{\omega_i}\sin\alpha$$

We now drop the primes with v_x, v_y, x, and y.

The perturbation in the ion distribution function is

$$\frac{df_1}{dt}=\frac{e}{m_i}\nabla\varphi_1\frac{\partial f_0}{\partial \mathbf{v}}-\nu_i f_1+\nu_i n_1 f_{00}(\mathbf{v}+\mathbf{u}). \quad (\mathrm{A.3})$$

The potential and density perturbations $[\varphi_1(\mathbf{r}, t)]$ and $[n_1(\mathbf{r}, t)]$ are taken in the form $e^{-i\omega t+ik_y y+ik_z z}$. By integrating (A.3) we get the following expression for $f_1(\mathbf{r}, t)$:

$$f_1(\mathbf{r},t)=i\nu_i n_1 f_{00}e^{-\frac{m_i u^2}{2T_i}}\sum_{n=-\infty}^{\infty}\frac{J_n\left(\xi(1-\beta_i^2)^{1/2}\right)}{\omega+i\nu_i-k_z v_z-n\omega_i}e^{-i\xi\sin\alpha+in(\alpha+\psi)}$$
$$-\frac{e\varphi_1}{T_i}f_{00}\Big\{n_0\Big(1+\varkappa\Big(x+\frac{v_y}{\omega_i}\Big)\Big)-n_0\Big[\Big(1+\varkappa\Big(x+\frac{v_y}{\omega_i}\Big)\Big)(\omega+i\nu_i)$$
$$-\frac{T_i}{m_i}\frac{k_y\varkappa\omega_i}{(\nu_i^2+\omega_i^2)}\Big(1-\frac{\nu_i^2 m_i u}{\omega_i\varkappa T_i}\Big)\Big]$$
$$\times\sum_{n=-\infty}^{\infty}\frac{J_n(\xi)e^{-i\xi\sin\alpha+in\alpha}}{\omega+i\nu_i-k_z v_z-n\omega_i}-\frac{i\nu_i}{\omega_i}\frac{n_0\varkappa}{\nu_i^2+\omega_i^2}\Big(1+\frac{m_i u\omega_i}{T_i\varkappa}\Big)$$
$$\times v_\perp\Big[\omega_i\omega\sum_{n=-\infty}^{\infty}J'_n(\xi)\frac{e^{-i\xi\sin\alpha+in\alpha}}{\omega+i\nu_i-k_z v_z-n\omega_i}-(\omega_i^2-i\nu_i(\omega+i\nu_i))$$
$$\times\sum_{n=-\infty}^{\infty}\frac{nJ_n(\xi)}{\xi}\frac{e^{-i\xi\sin\alpha+in\alpha}}{\omega+i\nu_i-k_z v_z-n\omega_i}\Big]\Big\}. \quad (\mathrm{A.4})$$

Here $v_\perp^2 = v_x^2 + v_y^2$, $\xi = kv_\perp/\omega_i$, $\beta_i = m_i u\omega_i/kT_i$, $\sin\psi = \beta_i/\sqrt{\beta_i^2-1}$. Integrating (A.4) over velocity, we get

$$\frac{n_1}{n_0}\Big(1-\frac{i\nu_i\sqrt{\pi}}{k_z v_T}\sum_{n=-\infty}^{\infty}I_n\big(z_i\sqrt{1-\beta_i^2}\big)e^{-z_i}W(p_n)\Big(\frac{1-\beta_i}{1+\beta_i}\Big)^{n/2}\Big)$$
$$=-\frac{e\varphi_1}{T_i}\Bigg\{1+i\sqrt{\pi}\,\frac{\omega+i\nu_i-\frac{T_i k_y\varkappa}{m_i\omega_i}\frac{\omega_i^2}{\nu_i^2+\omega_i^2}\Big(1-\frac{\nu_i^2 m_i u}{\omega_i\varkappa T_i}\Big)}{k_z v_T}$$
$$\times\sum_{n=-\infty}^{\infty}I_n(z_i)e^{-z_i}W(p_n)$$
$$+\frac{i\sqrt{\pi}}{k_z v_T}\frac{\omega_i\omega}{\omega_i^2+\nu_i^2}\Big(1+\frac{m_i u\omega_i}{T_i\varkappa}\Big)\frac{\varkappa}{k_y}\Bigg[\omega_i\Bigg(1+\frac{\nu_i^2}{\omega_i^2}\Big(1+\frac{i\nu_i}{\omega_i}\Big)\frac{k_y u}{1+\frac{m_i u\omega_i}{T_i\varkappa}}\Bigg)$$
$$\times\sum_{n=-\infty}^{\infty}nI_n(z_i)e^{-z_i}W(p_n)+i\nu_i\Big(1-\frac{k_y u}{\omega}\frac{T_i\varkappa}{T_i\varkappa+m_i u\omega_i}\Big)$$
$$\times\sum_{n=-\infty}^{\infty}z_i e^{-z_i}\left(I'_n(z_i)-I_n(z_i)\right)W(p_n)\Bigg]\Bigg\}. \quad (\mathrm{A.5})$$

The following notation has been used in (A.5): $W(p_n)$ is the probability integral of the complex argument $p_n = (\omega + i\nu - n\omega_i)/k_z v_T$; $I_n(z_i)$ is the Bessel function of the imaginary argument $z_i = k_y^2\rho_i^2$; $v_T = \sqrt{T_i/m_i}$. When $\omega \ll \nu_i$, $\beta_i \ll 1$, $|(\omega+i\nu_i-n\omega_i)/k_z v_T| \gg 1$, (A.5) can be rewritten as

$$\frac{n_1}{n_0}\Big\{\omega(1-S_2)-k_y u(1+S_3)\frac{\omega_i^2}{\omega_i^2+\nu_i^2}+i\nu_i(1-\eta_0(z_i)-S_1)\Big\}$$
$$=-\Big\{i\nu_i(1-\eta_0(z_i)-S_1)+\frac{T_i}{m_i}\frac{k_y\varkappa}{\omega_i}\frac{\omega_i^2}{\omega_i^2+\nu_i^2}(\eta_0+S_1)\Big\}\frac{e\varphi_1}{T_i}. \quad (\mathrm{A.6})$$

Here

$$\eta_n(z_i)=I_n(z_i)e^{-z_i},$$

$$S_1=2\sum_{n=1}^{\infty}\eta_n(z_i)\frac{\nu_i^2}{\nu_i^2+n^2\omega_i^2},$$

$$S_2=4\sum_{n=1}^{\infty}n^2\eta_n(z_i)\frac{\omega_i^2\nu_i^2}{(\nu_i^2+n^2\omega_i^2)^2},$$

$$S_3=S_2+\frac{\nu_i^2}{\omega_i^2}\Big(1-\frac{2}{z_i}\sum_{n=1}^{\infty}n^2\eta_n(z_i)\frac{\nu_i^2+\omega_i^2}{\nu_i^2+n^2\omega_i^2}\Big).$$

Equation (A.6) is written in the laboratory system of coordinates ($\omega \to \omega' - ku$). For magnetized ions $\omega_i/\nu_i \gg 1$ with $\omega \gtrless \nu_i$, and from (A.5)

$$\Big(-i(\omega-k_y u)+D_i k_y^2\frac{\nu_i^2}{\omega_i^2}\frac{1-\eta_0(z_i)}{z_i}\Big)\frac{n_1}{n_0}$$
$$+\Big(k_y^2\frac{\nu_i^2}{\omega_i^2}\frac{1-\eta_0(z_i)}{z_i}\Big(1-i\frac{\omega-k_y u}{\nu_i}\Big)-ik_y\varkappa\eta_0(z_i)\Big)\frac{c\varphi_1}{H}=0.$$

---

1) The expression for f_0 satisfies the normalization condition. This can be seen by allowing for the connection between the density and potential profiles as found from the continuity equation.

[1] B. N. Shvilkin and S. A. Postnikov, 10th Intern. Conf. on Phenomena in Ionized Gases, London (1971), p. 276.

[2] B. N. Shvilkin, Dokl. Akad. Nauk SSSR, 199, 1286 (1971) [Sov. Phys. – Dokl., 16, 661 (1972)].

[3] A. B. Timofeev, Dokl. Akad. Nauk SSSR, 152, 84 (1963) [Sov. Phys. – Dokl., 8, 890 (1964)].

[4] A. Simon, Phys. Fluids, 6, 382 (1963).

[5] A. P. Zhilinskii, Zh. Tekh. Fiz., 42, 925 (1972) [Sov. Phys. – Tech. Phys., 17, 734 (1972)].

[6] A. V. Timofeev, Zh. Tekh. Fiz., 33, 909 (1963) [Sov. Phys. – Tech. Phys., 8, 682 (1964)].

[7] A. V. Timofeev, Zh. Tekh. Fiz., 40, 192 (1970) [Sov. Phys. – Tech. Phys., 15, 140 (1970)].

Nonlinear statistical theory for condensation of Langmuirplasmons. III. Energy flux for plasma turbulence

F. Kh. Khakimov and V. N. Tsytovich
V. I. Lenin Tadzhik State University, Dushanbe

(Submitted November 11, 1973)
Zh. Tekh. Fiz., 44, 2095-2100 (October 1974)

Analysis of the nonlinear stage of the modulation instability shows that the establishment of a steady-state spectrum and a level of modulation waves is accompanied by a change in the direction of spectral pumping; plasmons are transferred from the "condensate" into the Landau-absorption region.

INTRODUCTION

We have previously[1] developed a nonlinear theory for the modulation instability,[2,3] which is driven at a certain level of plasma turbulence and leads to a stochastic heating of the plasma particles. Our purpose here is to analyze the overall energy balance of the plasma under conditions such that the plasma turbulence drives the modulation instability.

The general scheme of the energy fluxes can be described as follows: First, as a result of the conversion of turbulent energy, a "condensate of Langmuir plasmons" arises. This condensate is unstable and drives low-frequency modulation waves at $v_p/v_{Te} \gg 3\sqrt{m_i/m_e}$ with $W/nT > m_e/m_i$. Energy is transferred to low-frequency waves. It is shown below that this energy flux results from a resonance of the plasmons and the (low-frequency) modulation waves when $\omega_1 \approx k_1 v_{\parallel i}$ in the case of a nonlinear balance in which the excitation of waves is balanced by a nonlinear outflow. As a result, low-frequency waves with $\omega/k \ll v_{Te}$ are excited.

The energy subsequently moves through the low-frequency wave spectrum toward increasing phase velocities, up to v_{Te}. At a turbulent-energy level $W/nT > \sqrt[5]{(m_e/m_i)^2}$, the sign of the nonlinear Landau damping changes, i.e., low-frequency waves increase in frequency as a result of the nonlinear resonant interactions with particles. The result is an increase in the phase velocities. Decay processes operate in the same direction.

Finally, there is the energy transfer between low-frequency modulation waves with sufficiently large phase velocities and plasma particles.

We now consider this energy-flux scheme.

1. ENERGY FLUX FROM HIGH FREQUENCIES TO LOW FREQUENCIES

We determine the time rate of change of the total high-frequency energy:

$$\frac{dW^T}{dt}=\int \gamma^T_{k_1,\omega_1} W^T_{k_1,\omega_1} dk_1 d\omega_1, \tag{1}$$

where

$$\gamma^T_{k_1,\omega_1}=-\mathrm{Im}\,\frac{\varepsilon^T_{k_1},\ \omega_1^T}{\frac{\partial}{\partial\omega_1}\mathrm{Re}\,\varepsilon^T_{k_1,\omega_1}}. \tag{2}$$

To find $\gamma^T_{k_1,\omega_1}$ we use the dielectric constant of the high-frequency waves in the presence of modulation waves, found in ref. 1:

$$\varepsilon^T_{k_1,\omega_1}=\frac{\frac{\omega_{pe}^3}{n_0^3 m_e}}{1+\frac{n_0 m_e}{T_e+T_i}d_2}\int \frac{|c_{k,\omega}|^2}{|1+\beta_{k,\omega}|^2}\,\frac{w_{k,\omega}dk d\omega}{\tilde{\varepsilon}(k-k_1,\ \omega-\omega_1)}. \tag{3}$$

We see that the imaginary part of $\varepsilon^T_{k_1,\omega_1}$ is coupled only to the imaginary part of $1/\tilde{\varepsilon}(k-k_1,\omega-\omega_1)$. If we assume the imaginary part of $\varepsilon_{k_1,\omega_1}$ to be small, we can write[1]

$$\mathrm{Im}\,\frac{1}{\tilde{\varepsilon}_{k_1,\omega_1}}\approx-\pi\delta[\tilde{\varepsilon}(k-k_1,\ \omega-\omega_1)].$$

Accordingly, the damping can result from a wave resonance of the plasmons and modulation waves; we can describe this resonance approximately by $\omega_1 \approx k_1 v_{\parallel i}$. It is this resonance which is responsible for the energy flux from high frequencies to low frequencies:

$$\frac{dW^T}{dt}=-\frac{\pi}{2}\,\frac{\frac{\omega_{pe}^3}{n_0^3 m_e}}{1+\frac{n_0 m_e}{T_e+T_i}d_2}\int \frac{|c_{k,\omega}|^2}{|1+\beta_{k,\omega}|^2}W^T_{k_1,\omega_1} \times w^R_{k,\omega}\delta(\tilde{\varepsilon}(|k-k_1|,\ |\omega-\omega_1|))\,dk dk_1 d\omega d\omega_1. \tag{4}$$

We note that in the region of acoustic waves, $\omega \ll \omega_1$, the high-frequency waves are absorbed; if we neglect the nonlinear corrections $\beta_{k,\omega}$ and d_2, we find that this absorption is the same as in ref. 4.

We now treat the true rate of change of the low-frequency energy:

$$\frac{dw^R}{dt}=\int \gamma^R_{k,\omega} w^R_{k,\omega} dk d\omega. \tag{5}$$

Using the dielectric constant of the plasma taking account of the effect of high-frequency plasma waves found in ref. 5,

$$\varepsilon^R_{k,\omega}\simeq\left(\frac{e}{m_e}\right)\frac{\frac{\omega_{pe}^4}{n_0^2}}{1+\frac{n_0 m_e}{T_e+T_i}d_2}\int \frac{|c_{k,\omega}|^2}{|1+\beta_{k,\omega}|^2}\,\frac{J^T_{k_1,\omega_1}dk_1 d\omega_1}{\tilde{\varepsilon}(k_1-k,\ \omega_1-\omega)\,\omega_1^4} \tag{6}$$

taking the imaginary part of (6), and substituting into (5), we find

$$\frac{dw^R}{dt}=\frac{\pi}{2}\,\frac{\frac{\omega_{pe}^3}{n_0^3 m_e}}{1+\frac{n_0 m_2}{T_e+T_i}d_2}\int \frac{|c_{k,\omega}|^2}{|1+\beta_{k,\omega}|^2}W^T_{k_1,\omega_1}w^R_{k,\omega} \times \delta(\tilde{\varepsilon}(|k_1-k|,\ |\omega_1-\omega|))\,dk dk_1 d\omega d\omega_1. \tag{7}$$

We see that Eqs. (7) and (4) are identical. Thus

$$\frac{d}{dt}(W^T+w^R)=0. \tag{8}$$

2. TRANSFER OF PLASMA ENERGY THROUGH THE LOW-FREQUENCY SPECTRUM

To study the energy transfer through the low-frequency spectrum we must first carry out several auxiliary calculations, i.e., we must determine the nonlinear dielectric constant of the plasma in the presence of the modulation instability. Using

$$E^R_{k,\omega}=\frac{4\pi ie}{k}\int f^{Re}_{k,\omega}dkd\omega, \tag{9}$$

multiplying by $E^R_{k',\omega'}$ and averaging over the low frequencies, we find the following equation for the correlation function of the low-frequency waves:[1]

$$w^R_{k,\omega}=i\frac{e}{k}\int\langle E^R_{k',\omega'}f^R_{k,\omega}\rangle_L\,dk'd\omega'dv. \tag{10}$$

The distribution function of the "quasiparticles" (dressed particles) in the plasma $f^R_{k,\omega}$ can be expanded in a series in the field E^R:

$$f^R_{k,\omega}\simeq f^{R(1)}_{k,\omega}+f^{R(2)}_{k,\omega}+f^{R(3)}_{k,\omega}+\ldots, \tag{11}$$

where $f^{R(1)}_{k,\omega}$ describes the linear properties of the plasma, and $f^{R(2)}_{k,\omega}$ and $f^{R(3)}_{k,\omega}$ describe the nonlinear properties. Using[6]

$$f^{R(1)}_{k,\omega}=i\frac{e}{m_e}\frac{E^R_{k,\omega}}{1+\beta_{k,\omega}}\left(\frac{1}{\omega-kv}\frac{\partial\Phi}{\partial v}+\frac{\beta_{k,\omega}}{k}\frac{\partial^2\Phi}{\partial v^2}\right) \tag{12}$$

and substituting into (10), we find an equation for the linear dielectric constant of the plasma which incorporates the renormalization under the influence of the high-frequency plasma fluctuations ($\beta_{k,\omega}$):

$$\varepsilon^{Re}_{k,\omega}\approx\frac{\frac{\omega^2_{pe}}{k^2v^2_{Te}}}{1+\beta_{k,\omega}}. \tag{13}$$

To find the nonlinear dielectric constant we use[1]

$$\begin{aligned}f^{R(2)}_{k,\omega}={}&i\frac{e}{m_e}\frac{1}{\omega-kv}\frac{\partial}{\partial v}\int\left(E^R_{k_1,\omega_1}f^{R(1)}_{k_2,\omega_2}-\langle E^R_{k_1,\omega_1}f^{R(1)}_{k_2,\omega_2}\rangle_L\right)\\&\times\delta(k-k_1-k_2)\,\delta(\omega-\omega_1-\omega_2)\,dk_1dk_2d\omega_1d\omega_2\\&+i\frac{e}{m_e}\frac{a}{1+\beta_{k,\omega}}\frac{1}{\omega-kv}\frac{\partial}{\partial v}(\omega-kv)\frac{\partial\Phi}{\partial v}\int\frac{dv}{\omega-kv}\frac{\partial}{\partial v}\\&\times\left(E^R_{k_1,\omega_1}f^{R(1)}_{k_2,\omega_2}-\langle E^R_{k_1,\omega_1}f^{R(1)}_{k_2,\omega_2}\rangle_L\right)\delta(k-k_1-k_2)\\&\times\delta(\omega-\omega_1-\omega_2)\,dk_1dk_2d\omega_1d\omega_2,\end{aligned} \tag{14}$$

$$\begin{aligned}f^{R(3)}_{k,\omega}={}&i\frac{e}{m_e}\frac{1}{\omega-kv}\frac{\partial}{\partial v}\int\left(E^R_{k_1,\omega_1}f^{R(2)}_{k_2,\omega_2}-\langle E^R_{k_1,\omega_1}f^{R(2)}_{k_2,\omega_2}\rangle_L\right)\\&\times\delta(k-k_1-k_2)\,\delta(\omega-\omega_1-\omega_2)\,dk_1dk_2d\omega_1d\omega_2-\left(\frac{e}{m_e}\right)^2\frac{1}{\omega-kv}\frac{\partial}{\partial v}\\&\times\int\frac{\omega-kv}{(\omega_1-k_1v)(\omega_2-k_2v)}\left(\langle E^{T(0)}_{k_1,\omega_1}E^{T(3)}_{k-k_1,\omega-\omega_1}+E^{T(1)}_{k_1,\omega_1}E^{T(2)}_{k-k_1,\omega-\omega_1}\rangle_L\right)\\&\times\frac{\partial\Phi}{\partial v}\delta(k-k_1-k_2)\,\delta(\omega-\omega_1-\omega_2)\,dk_1dk_2d\omega_1d\omega_2.\end{aligned} \tag{15}$$

Solving the integral equation for the correlation function $\langle E^{T(0)}_{k_1,\omega_1}E^{T(3)}_{k-k_1,\omega-\omega_1}\rangle_H$, which is of the same order as $\langle E^{T(1)}_{k_1,\omega_1}E^T_{k-k_1,\omega-\omega_1}\rangle_H$, i.e.,

$$\begin{aligned}&\varepsilon(k-k_1,\ \omega-\omega_1)\langle E^{T(0)}_{k_1,\omega_1}E^{T(3)}_{k-k_1,\omega-\omega_1}\rangle_H-\left(\frac{e}{m_e}\right)^2J_{k_1,\omega_1}\\&\times\int dk'_2d\omega'_2\langle E^{T(0)}_{k'_2,\omega'_2}E^{T(3)}_{k-k'_2,\omega-\omega'_2}\rangle_H\left[\Sigma_{k-k_1,\omega-\omega_1;\,k'_1,\omega'_1;\,-k_1,-\omega_1;\,k-k'_2,\omega-\omega'_2}\right.\\&\left.+\Sigma_{k-k_1,\omega-\omega_1;\,k-k'_2,\omega-\omega'_2;\,-k_1,-\omega_1;\,k'_1,\omega'_1}\right]\\&-\left(\frac{e}{m_e}\right)^2\int\langle E^{T(0)}_{k_2,\omega_2}E^{T(1)}_{k'-k_2,\omega'-\omega_2}\rangle_H\left(\langle E^{T(0)}_{k'_2,\omega'_2}E^{T(2)}_{k''-k'_1,\omega''-\omega'_1}\rangle_H\right.\\&\left.+\langle E^{T(1)}_{k'_2,\omega'_2}E^{T(1)}_{k''-k'_1,\omega''-\omega'_1}\rangle_H\right)\left[\Sigma_{k-k_1,\omega-\omega_1;\,k'_1,\omega'_1;\,k''-k'_1,\omega''-\omega'_1;\,k'-k_1,\omega'-\omega_1}\right.\\&\left.+\Sigma_{k-k_1,\omega-\omega_1;\,k''-k'_1,\omega''-\omega'_1;\,k'_1,\omega'_1;\,k'-k_1,\omega'-\omega_1}\right]\\&\times\delta(k-k'-k'')\,\delta(\omega-\omega'-\omega'')\,dk'dk''d\omega'd\omega''=G,\end{aligned} \tag{16}$$

where

$$\begin{aligned}G={}&-\frac{\omega^2_{pe}}{n_0}\int\frac{J_{k_1,\omega_1}dk_1d\omega_1}{(k-k_1)[\omega-\omega_1-(k-k_1)v]}\frac{\partial f^{R(3)}_{k,\omega}}{\partial v}\\&-\frac{\omega^2_{pe}}{n_0}\int\frac{dv}{(k-k_1)[\omega-\omega_1-(k-k_1)v]}\\&\times\left(\frac{\partial f^{R(1)}_{k'',\omega''}}{\partial v}+i\frac{e}{m_e}E^R_{k'',\omega''}\frac{\partial}{\partial v}\frac{1}{\omega'-\omega_1-(k'-k_1)v}\frac{\partial\Phi}{\partial v}\right)\langle E^{T(0)}_{k_1,\omega_1}E^{T(2)}_{k'-k_1,\omega'-\omega_1}\rangle_H\\&\times\delta(k-k'-k'')\,\delta(\omega-\omega'-\omega'')\,dk'dk''d\omega'd\omega''\\&-\frac{\omega^2_{pe}}{n_0}\int\frac{dv}{(k-k_1)[\omega-\omega_1-(k-k_1)v]}\frac{\partial f^{R(2)}_{k'_2,\omega'_2}}{\partial v}\langle E^{T(0)}_{k_1,\omega_1}E^{T(1)}_{k'_1,\omega'_1}\rangle_H\\&\times\delta(k_2-k'_1-k'_2)\,\delta(\omega_2-\omega'_1-\omega'_2)\,dk'_1dk'_2d\omega'_1d\omega'_2,\end{aligned} \tag{17}$$

we find the following equation for $f^{R(3)}_{k,\omega}$:

$$\begin{aligned}f^{R(3)}_{k,\omega}={}&i\frac{e}{m_e}\frac{1}{\omega-kv}\frac{\partial}{\partial v}\int\left(E^R_{k_1,\omega_1}f^{R(2)}_{k_2,\omega_2}-\langle E^R_{k_1,\omega_1}f^{R(2)}_{k_2,\omega_2}\rangle_L\right)\\&\times\delta(k-k_1-k_2)\,\delta(\omega-\omega_1-\omega_2)\,dk_1dk_2d\omega_1d\omega_2+i\frac{e}{m_e}\frac{a}{1+\beta_{k,\omega}}\\&\times\frac{1}{\omega-kv}\frac{\partial}{\partial v}(\omega-kv)\frac{\partial\Phi}{\partial v}\int\frac{dv}{\omega-kv}\frac{\partial}{\partial v}\left(E^R_{k_1,\omega_1}f^{R(2)}_{k_2,\omega_2}\right.\\&\left.-\langle E^R_{k_1,\omega_1}f^{R(2)}_{k_2,\omega_2}\rangle_L\right)\delta(k-k_1-k_2)\,\delta(\omega-\omega_1-\omega_2)\,dk_1dk_2d\omega_1d\omega_2.\end{aligned} \tag{18}$$

Substituting (18) and (14) into (10) and carrying out some straightforward calculations, we find

$$\begin{aligned}\varepsilon^{RN}_{k,\omega}\approx{}&-\left(\frac{e}{m_e}\right)^2\frac{1}{|1+\beta_{k,\omega}|^2}\frac{1}{1+\beta_{k-k_1,\omega-\omega_1}}\\&\times\int\Sigma_{k,\omega;\,k_1,\omega_1;\,k,\omega;\,-k_1,-\omega_1}w^R_{k_1,\omega_1}dk_1d\omega_1\\&-\left(\frac{e}{m_e}\right)^2\frac{\frac{\beta_{k,\omega}}{k}}{|1+\beta_{k,\omega}|^2}\frac{1}{1+\beta_{k-k_1,\omega-\omega_1}}\frac{\omega^2_{pe}}{n_0}\\&\times\int\frac{dv}{(\omega-kv)^2}\left[\frac{2k}{\omega-kv}+\frac{k-k_1}{\omega-\omega_1-(k-k_1)v}\right]\\&\times\frac{1}{\omega-\omega_1-(k-k_1)v}\frac{\partial^2\Phi}{\partial v^2}w^R_{k_1,\omega_1}dk_1d\omega_1.\end{aligned} \tag{19}$$

Equation (19) which gives the electric constant of the plasma, takes account of the nonlinear interaction of low-frequency waves. Equation (19) can be used to calculate the nonlinear growth rate:

$$\gamma^{RN}_{k,\omega}=-\frac{\operatorname{Im}\varepsilon^{RN}_{k,\omega}}{\frac{\partial}{\partial\omega}\operatorname{Re}\varepsilon^{RN}_{k,\omega}}. \tag{20}$$

Neglecting the influence of the modulation waves, i.e., setting $\beta_{k,\omega}=0$, we find the following equation for the induced scattering by ions, $\omega-\omega_1<|k-k_1|v_{Ti}$ (ref. 6):

$$\gamma_1^{RN} \simeq \frac{1}{30}\left(\frac{\omega_{pe}}{kv_{Te}}\right)^2 \frac{w}{n_0 T}\frac{m_e}{m_i}, \tag{21}$$

which gives the energy transfer toward low frequencies.

Taking account of the nonlinear corrections $\beta_{k,\omega}$ for this case, we find that the term which arises from the second term in (19) is the predominant term, i.e., the predominant term is

$$\operatorname{Im} \varepsilon_{k,\omega}^{RN} \approx -\left(\frac{e}{m_e}\right)^2 \frac{\frac{\operatorname{Re} \beta_{k,\omega}}{k}}{|1+\beta_{k,\omega}|^2} \frac{\operatorname{Im} \beta^*_{k-k_1,\,\omega-\omega_1}}{|1+\beta_{k-k_1,\,\omega-\omega_1}|^2} \operatorname{Re} J_1, \tag{22}$$

where

$$J_1 = \frac{\omega_{pe}^2}{n_0} \int \frac{dv}{(\omega - kv)^2}\left[\frac{2k}{\omega - kv} + \frac{k - k_1}{\omega - \omega_1 - (k - k_1)v}\right]$$
$$\times \frac{1}{\omega - \omega_1 - (k - k_1)v} \frac{\partial^2 \Phi}{\partial v^2} w^R_{k_1,\omega_1} dk_1 d\omega_1. \tag{23}$$

Using (22) and (23) we can find the growth rate governing the energy transfer toward high frequencies:

$$\gamma_2^{RN} \approx -8\sqrt{\frac{\pi}{2}}\left(\frac{\omega_{pe}}{kv_{Te}}\right)^5 \frac{w}{nT}\frac{\xi^3}{|1+\xi|^4}, \tag{24}$$

where

$$\xi = \frac{n_0}{v_{Te}^2}\alpha = \frac{\frac{n_0 m_e}{T_e} d_1}{1 + \frac{n_0 m_e}{T_e + T_i} d_2} \approx \frac{1}{1 + \frac{\omega^2}{k^2 v_\sim^2}},$$

and $v_\sim^2 = 3W/4n_0 m_e$.

When we take $\beta_{k,\omega}$ into account in (21) we find a factor $1/|1 + \xi|^3$. Comparing Eqs. (21) and (24) we see that the transfer of plasma energy undergoes a change when the plasma turbulence reaches a level

$$\left(\frac{\omega_{pe}}{kv_{Te}}\right)^3 \frac{\xi^2}{|1+\xi|} > \frac{m_e}{m_i}. \tag{25}$$

Introducing $\lambda = \omega/kv_{Te}$ and $\lambda_0^2 = 3W/4n_0T$, we can rewrite inequality (15) as

$$\frac{\lambda^3}{\left(1 + \frac{\lambda^2}{\lambda_0^2}\right)\left(2 + \frac{\lambda^2}{\lambda_0^2}\right)} > \frac{m_e}{m_i}. \tag{26}$$

In the case $\lambda \gg \lambda_0$

$$\frac{W}{nT} > \left(\frac{m_e}{m_i}\right)^{2/5}. \tag{27}$$

The decay processes taken into account in ref. 4 also lead to transfer toward high frequencies.

3. ENERGY BALANCE OF THE LOW-FREQUENCY PARTICLE OSCILLATIONS

To determine the change in the total particle energy per unit time we use a quasilinear equation describing the motion of particles in the presence of the modulation instability:[1]

$$\frac{\partial \Phi}{\partial t} + v\frac{\partial \Phi}{\partial z} = I_1, \tag{28}$$

where

$$I_1 = i\frac{4\pi e^2}{m_e^2}\frac{\partial}{\partial v}\int \frac{w^R_{k,\omega}}{1+\beta_{k,\omega}} \frac{dk d\omega}{\omega - kv}\frac{\partial \Phi}{\partial v}. \tag{29}$$

Multiplying Eq. (28) by $mv^2/2$ and integrating over v, we find

$$\frac{dE}{dt} = \int I_1 \frac{mv^2}{2} dv = -i\frac{4\pi e^2}{m_e}\int \frac{\omega}{k}\frac{w^R_{k,\omega}}{1+\beta_{k,\omega}}$$
$$\times \frac{1}{\omega - k\omega}\frac{\partial \Phi}{\partial v} dv dk d\omega = -i\frac{4\pi e^2}{m_e}\frac{\omega}{k}\frac{c_{k,\omega}}{1+\beta_{k,\omega}} w^R_{k,\omega} dk d\omega, \tag{30}$$

where

$$\beta_{k,\omega} = \alpha k c_{k,\omega};\ c_{k,\omega} = \int \frac{1}{\omega - kv}\frac{\partial \Phi}{\partial v} dv.$$

Since the left-hand side of Eq. (30) is real, we find

$$\operatorname{Im}\frac{c_{k,\omega}}{1+\beta_{k,\omega}} = \operatorname{Im}\frac{c_{k,\omega}(1+\beta^*_{k,\omega})}{|1+\beta_{k,\omega}|^2} = \operatorname{Im}\frac{c_{k,\omega} - \alpha k|c_{k,\omega}|^2}{|1+\beta_{k,\omega}|^2}. \tag{31}$$

The second term vanishes since it is of odd parity. We can thus write

$$\frac{dE}{dt} = \frac{4\pi e^2}{m_e}\int \frac{\omega}{k}\frac{\operatorname{Im} c_{k,\omega}}{|1+\beta_{k,\omega}|^2} w^R_{k,\omega} dk d\omega. \tag{32}$$

On the other hand, the change in the energy of the low-frequency oscillations per unit time is

$$\frac{dw^R}{dt} = \int \gamma^R_{k,\omega} w^R_{k,\omega} dk d\omega. \tag{33}$$

Using

$$\gamma^R_{k,\omega} = \frac{-\operatorname{Im}\varepsilon^R_{k,\omega}}{\frac{\partial}{\partial \omega}\operatorname{Re}\varepsilon^R_{k,\omega}} \approx -\frac{4\pi e^2}{m_e}\frac{\omega}{k}\frac{\operatorname{Im} c_{k,\omega}}{|1+\beta_{k,\omega}|^2} \tag{34}$$

for the damping by electrons, we find

$$\frac{dw^R}{dt} = -\frac{4\pi e^2}{m_e}\int \frac{\omega}{k}\frac{\operatorname{Im} c_{k,\omega}}{|1+\beta_{k,\omega}|^2} w^R_{k,\omega} dk d\omega, \tag{35}$$

which, in particular, is the same as (32).

We thus find that the energy exchange occurs only between low-frequency oscillations and particles:

$$\frac{d}{dt}(E + w^R) = 0. \tag{36}$$

---

[1] In principle, there could also be cases in which this imaginary part is not small.

---

[1] F. Kh. Khakimov and V. N. Tsytovich, Zh. Eksp. Teor. Fiz., 64, 1261 (1973) [Sov. Phys. – JETP, 37, 641 (1973)].

[2] A. A. Vedenov and L. I. Rudakov, Dokl. Akad. Nauk SSSR, 159, 767 (1964) [Sov. Phys. – Dokl., 9, 1073 (1965)].

[3] A. Gailitis, Izv. Akad. Nauk LatvSSR, Ser. Fiz.-Tekh. Nauk, 4, 13 (1965).

[4] V. N. Tsytovich, Nonlinear Effects in Plasma, Plenum, New York (1970).

[5] F. Kh. Khakimov and V. N. Tsytovich, Zh. Tekh. Fiz., 43, 2481 (1973) [Sov. Phys. – Tech. Phys., 18, 1563 (1974)].

[6] V. N. Tsytovich, Theory of Turbulent Plasma, Consultants Bureau, New York (1973).

Energy of charged particles accelerated by electromagnetic waves in a plasma with a spatially decreasing density

V. Ya. Davydovskii and A. S. Ukolov

Taganrog Radiotechnical Institute

(Submitted October 26, 1973; resubmitted February 6, 1974)
Zh. Tekh. Fiz., 44, 2101-2108 (October 1974)

The energies of charged particles trapped by an electromagnetic wave propagating in a plasma are found when the electron density decreases exponentially in the direction of propagation. It is shown that an adiabatic treatment, in which the wave velocity is a slowly varying function, is valid for the entire acceleration process. Two mechanisms are considered for the loss of particles from the trapped state: the reduction in the amplitude of the wave and collisions. In the latter case the shape of the energy spectrum coincides with the spectrum observed for cosmic rays. The existence of a lower limit of the spectrum is indicated.

The motion of charged particles trapped by plane electromagnetic waves is considered in refs. 1 and 2 in the adiabatic approximation, in which the variation in wave parameters over a period can be neglected. The acceleration of particles by waves with an increasing propagation velocity is proposed in ref. 3 as a mechanism for the acceleration of cosmic particles. This mechanism can even operate in the solar atmosphere. Long-range Coulomb collisions do not untrap particles (the numerical estimates for the sun are given in ref. 4), and the mean free path of the particles, calculated on the basis of an impact parameter of the order of the classical electron radius e^2/mc^2, is much larger than the solar radius $R_\odot$, even for electron densities corresponding to the lower layers of the corona.

In the present work we investigate a possible shape for the energy spectrum of particles accelerated by the mechanism under discussion. It is assumed below that the medium is a plasma with an electron density that varies as

$$N(z)=N_0 e^{-\alpha z}.$$

Such a medium is fairly typical of cosmic conditions. For the sun, depending on height, the parameter $1/\alpha$ varies from 0.01-0.5 $R_\odot$.

The electromagnetic wave is described by the vector potential

$$\left.\begin{array}{l} A_x=\lambda\cos\omega\theta,\ A_y=-\lambda\sin\omega\theta,\ A_z=0,\\ \lambda=\dfrac{eE}{mc\omega},\ \omega=\text{const},\ \theta=t-\displaystyle\int_0^z n(z)\,dz, \end{array}\right\} \qquad (1)$$

where E is the electric field of the wave, and n(z) is a function which plays the role of the refractive index, being related to the group velocity by the expressions

$$n(z)=\frac{1}{v(z)}=\left[1-\frac{4\pi e^2}{m\omega^2}N(z)\right]^{-1/2}=\left[1-\frac{\omega_0^2}{\omega^2}e^{-\alpha z}\right]^{-1/2}, \qquad (2)$$

where ω_0 is the plasma frequency at the point z = 0. All velocities are expressed in units of c and distances in units of light seconds.

In the numerical estimates we set $E = 10^{-4}$ V/cm, which is twice the values observed for radio emission from the quiet sun calculated back to the source. Amplitudes have been observed in radio bursts that are four to five orders of magnitude higher than the value assumed here. The wave frequency ω is taken to be $2\cdot10^9$ sec^{-1}, which corresponds to the meter range. Also, $\lambda\simeq5\cdot10^{-9}$ for electrons, and $\lambda\simeq2.5\cdot10^{-12}$ for protons.

It is pointed out in ref. 5 that it is not necessary to choose the wave in the form of (1); it is only necessary that the field of the wave confine the particle.

The adiabatic treatment of the particle motion is valid if

$$\left|\frac{dn}{dz}\right|\ll\frac{n}{Z}, \qquad (3)$$

where Z is the distance the particle is displaced during a period.[1,2] It is easy to verify that condition (3) is satisfied in the solar corona for waves in the meter range.

The parameter τ is related to the amplitude of phase oscillations of the particle $\Delta\theta_{\max}$ by the relation[1,2]

$$\tau=\sin^2\frac{1}{2}\omega\Delta\theta_{\max}. \qquad (4)$$

With $\tau = 0$ there are no phase oscillations; when $\tau > 1$ the particles are not confined by the wave.

For wave propagation along the z axis the average energy of the trapped particles increases as

$$\beta=n\left[\frac{4C\lambda\tau+1+(C-\lambda)^2}{n^2-1}\right]^{1/2}=\frac{\omega}{\omega_0}\sqrt{4C\lambda\tau+1+(C-\lambda)^2}\,e^{\frac{\alpha z}{2}}. \qquad (5)$$

The particle energy β is divided by the rest energy mc^2. We will assume that the energy spectrum of particles accelerated by the described mechanism is determined by the following consideration: The final energy of the particle is related by Eq. (5) to the value of n(z) at the point at which the particle becomes untrapped. For simplicity we assume everywhere that the constant C is the same for all the particles. In the estimates we set C = 1.

The desired energy spectrum is determined by mechanisms that break down the confinement of the particle by the wave. We will show, first, that the violation of adiabaticity cannot be such a mechanism. Using (2) and (4), and setting $\tau = 0$ we write instead of (3)

$$\sqrt{\frac{1+(C-\lambda)^2}{C\lambda}}\ll\frac{\omega}{4\alpha}, \qquad (6)$$

which is satisfied for the assumed values. If condition (6) is not satisfied, an adiabatic treatment is impossible for any values of τ. Otherwise, there exists a $\tau_{\max}$ determined by

$$K(\tau_{\max})\sqrt{\tau_{\max}+\frac{1+(C-\lambda)^2}{4C\lambda}}=\frac{\omega}{4\alpha}$$

such that when $\tau \ll \tau_{\max}$, there exists an adiabatic invariant[1,2]

$$\tau B(\tau)\sqrt{\frac{\lambda}{n^2-1}}=I=\text{const.} \tag{7}$$

In our case it is practical to set $\tau_{\max} = 1$.

It follows from (7) that for a decrease in n the parameter τ only decreases if $\lambda(z)$ does not decrease faster than n^2-1. In this case condition (6) is only enhanced, which means that it is impossible for the particles to escape from the trapped state as a result of a violation of adiabaticity. We note also that on the basis of the above discussion the parameter τ decreases for trapped particles as the acceleration increases.

The particles escape from the trapped state due to a decrease in the wave amplitude, collisions with the particles of the medium, and a change in wave mode due to dispersion. Assuming that the particles attain high energies for values of n close to unity, when the electron density is small and dispersion is negligible, we restrict the investigation to the first two mechanisms. For this reason we neglect damping of the wave due to interaction with the medium, assuming that the decrease in wave amplitude results from energy transfer between the wave and the particles. The latter effect is considered in ref. 5 under the assumption that the particles have the same initial parameters and therefore that they are untrapped simultaneously. If this assumption is not made then the accelerated particles have an energy distribution.

We assume that condition (3) is satisfied, so that there is an adiabatic invariant (7). Then at the point of untrapping, for which $\tau = 1$, we have

$$\sqrt{\frac{E}{n^2-1}}=A_1\tau_0 B(\tau_0). \tag{8}$$

Here, $A_1=\sqrt{E_0/(n_0^2-1)}$ and the subscript 0 denotes quantities at some initial reference point.

Assume that the wave imparts energy only to trapped particles whose flux j decreases. Then we have

$$d(S+j\beta)=\beta dj, \tag{9}$$

where S(n, E) is the wave energy flux density.

We introduce the function $f(\tau_0)$, which characterizes the initial distribution of particles over the parameter τ_0: $dj_0 = f(\tau_0)d\tau_0$. In the interval corresponding to a change in the refractive index by dn, particles with values of τ_0 within the interval $d\tau_0$ escape from the trapped state. The number of such particles in the flux j is $f(\tau_0)d\tau_0$. Thus,

$$dj=f(\tau_0)\,d\tau_0. \tag{10}$$

Assuming that the particle energy at untrapping time is related to n by (5), where we set $\tau = 1$,

$$\beta=n\left[\frac{1+(C+\lambda)^2}{n^2-1}\right]^{1/2}=\frac{\omega}{\omega_0}\sqrt{1+(C+\lambda)^2}\,e^{\alpha z/2}, \tag{11}$$

we can, theoretically, use Eqs. (8)-(10) to find the energy spectrum of the accelerated particles. We solve this problem under the following assumptions, which are fairly realistic:

1. We assume $n \gg 1$ since particle acceleration becomes important for values of n close to unity. On the basis of (2), this assumption is equivalent to $\exp(\alpha z) \gg (\omega_0/\omega)^2$.

2. The form of the wave energy flux density is $S = A_2E^2n^{-1}$, $A_2 = 1.2\cdot10^{12}$ sec/g-cm. Throughout, the estimates are satisfactory with regard to protons. Under these assumptions, equality (9) becomes

$$2A_2\frac{E}{n}\,dE+j\,d\beta=0. \tag{12}$$

Here, the change in wave amplitude related to the increase in wave velocity is neglected; only the change due to the increase in particle energy is considered. Obviously, this procedure is valid when $n \to 1$. Substituting into (12) the value of j obtained from (10), $j=\int_0^{\tau_0} f(x)dx$, expressing τ_0 in terms of E and n through (8), where $B(\tau_0) = 1$ [actually, B(x) varies from $\pi/4$ to 1 when x varies from 0 to 1], and finding $d\beta$ from (11), we obtain a differential equation for E(n):

$$2A_2EdE-\sqrt{1+(C+\lambda)^2}\,\frac{dn}{(n^2-1)^{3/2}}\int\limits_0^{\frac{1}{A_1}\sqrt{\frac{E}{n^2-1}}} f(x)\,dx. \tag{13}$$

It is evident from this equation that the shape of the spectrum depends essentially on the shape of $f(\tau_0)$, which is determined by a number of factors that are hard to evaluate: the trapping mechanism, the behavior of the flux and the wave up to the point chosen as the initial point, etc. Therefore, certain assumptions will be made with regard to the shape of $f(\tau_0)$.

The trapped particle represents an oscillator[1] with a maximum energy

$$\beta_{\max}=\beta+\sqrt{\frac{C\lambda\tau}{n^2-1}}$$

that obviously coincides with the total energy. Assuming that at the initial time the oscillators are governed by Boltzmann statistics, we write

$$dj_0=2A_3e^{-\gamma\sqrt{\tau_0}}d(\sqrt{\tau_0}),\ A_3=\text{const},\ f(\tau_0)=A_3\frac{e^{-\gamma\sqrt{\tau_0}}}{\sqrt{\tau_0}}, \tag{14}$$

after which E(n), given by (13), takes the form

$$A_2 d(E^2)+\frac{A_3}{\gamma}\sqrt{1+(C+\lambda)^2}$$

$$\times\left\{\exp\left[-\frac{\gamma E^{1/4}}{A_1^{1/4}(n^2-1)^{1/4}}\right]-1\right\}\frac{d(n^2)}{(n^2-1)^{3/2}}=0. \qquad (15)$$

We take $A_3 = 10^4$ sec^{-1}, which corresponds to fluxes observed near the earth, which are of order 1 cm^{-2}. sec^{-1}. To integrate (15) we assume $\sqrt{1+(C+\lambda)^2}$ = const since usually $\lambda \ll 1$.

In (15) we take

$$\tau_1 \ll \frac{1}{\gamma^2}, \qquad (16)$$

which is valid not only for small τ_0 for any temperature of excitation of phase oscillations $1/\gamma$, but also for $\gamma \ll 1$ for any values of τ_0. Integrating (15) and using (16), we find E(n) for n ~ 1:

$$E=\left\{E_0^{7/4}+\frac{7A_3}{6A_2}\sqrt{\frac{1+(C+\lambda)}{A_1}}\,[(n_0^2-1)^{-3/4}-(n^2-1)^{-3/4}]\right\}^{4/7}. \quad (17)$$

It is evident that for n → 1 a value of n is reached such that the wave amplitude vanishes and confinement becomes impossible. Introducing the notation

$$a=E_0^{7/4}+(n_0^2-1)^{-3/4}\frac{7A_3}{6A_2}\sqrt{\frac{1+(C+\lambda)^2}{A_1}}$$

and expressing n in terms of β with the aid of (11), where it is assumed that $n \approx 1$, we rewrite (17) in the form

$$E=\left\{a-\frac{7A_3}{6A_2\sqrt{A_1}}\frac{\beta^{3/4}}{[1+(C+\lambda)^2]^{1/4}}\right\}^{4/7}.$$

It follows that there exists a limiting energy β_{lim} for which the wave vanishes:

$$\beta_{\text{lim}}=\left\{\frac{6A_2\sqrt{A_1}\,a\,[1+(C+\lambda)^2]^{1/4}}{7A_3}\right\}^{4/3}.$$

The larger β_{lim} the larger E_0, the later the particles are captured (the smaller $n_0^2 - 1$), and the smaller the initial particle flux (the smaller A_3).

Assuming $n_0^2 - 1 = 1$, we obtain $\beta_{\text{lim}} \simeq 1.3$; this corresponds to 300 MeV protons, which is comparable to the energy of protons of solar origin.

It is also easy to establish the lower limit of the spectrum; this is determined by the vanishing of the derivative of the expression $[E(n^2-1)^{-1}]^{-1/2}$; at this point the increase due to the reduction in $n^2 - 1$ is offset by the reduction due to the decreasing wave amplitude E caused by the fact that the energy of the wave is absorbed by the accelerated particles. At this point the reduction in τ [as can be seen from (7)] becomes an increase and when τ = 1 the particles escape from the trap. Therefore, the lower boundary of the particle energies in the spectrum is β_{low}, which is determined by $\beta_{\text{low}} = (0.7)^{2/3}\beta_{\text{lim}} \simeq 0.7884 \cdot \beta_{\text{lim}}$, which follows from

$$\frac{d}{d\beta}\left(\frac{E}{n^2-1}\right)=0.$$

Assuming (14) in the limiting case (16) the differential energy spectrum of the accelerated particles $F(\beta)$ with $\beta \leqslant \beta_{\text{lim}}$ is

$$F(\beta)=\text{const}\,\beta\left[1-\left(\frac{\beta}{\beta_{\text{lim}}}\right)^{3/4}\right]^{-4/7}. \qquad (18)$$

In the opposite limiting case to (16),

$$\gamma^2 \gg \frac{1}{\tau_0}, \qquad (19)$$

the wave amplitude is

$$E=\left\{E_0^2+\frac{2A_3}{A_2\gamma}\sqrt{1+(C+\lambda)^2}\,[(n_0^2-1)^{-1/2}-(n^2-1)^{-1/2}]\right\}^{1/2}.$$

In this case the limiting energy at which the field vanishes is

$$\beta_{\text{lim}}=\frac{A_2\gamma b}{2A_3},$$

where

$$b=E_0^2+\frac{2A_3}{A_2\gamma}\sqrt{\frac{1+(C+\lambda)^2}{n_0^2-1}}.$$

When $\gamma \simeq 10$ we obtain $\beta_{\text{lim}} \simeq 1.4$. The lower boundary of the spectrum is $\beta_{\text{low}} = 0.8\beta_{\text{lim}}$. Obviously, the limiting case (19) is realized at low excitation temperatures, in which case γ is large; this holds when there are no particles with small τ_0 in the initial distribution over τ_0. Assuming that the spectrum only contains particles with $\tau_0 \simeq 1$ we find the following differential spectrum for $\beta \sim \beta_{\text{lim}}$:

$$F(\beta)=\text{const}\,\beta^{1/2}\left(1-\frac{\beta}{\beta_{\text{lim}}}\right)^{-1/2}. \qquad (20)$$

Equations (18) and (20) do not coincide with the spectrum observed for cosmic radiation. We now find the form of $f(\tau_0)$ for which the energy spectrum of the accelerated particles is like the observed power spectrum:

$$j=A_4\beta^{-x},\ A_4=\text{const}. \qquad (21)$$

Taking n ~ 1 in (12), we find

$$E=E_0\left[1-\left(\frac{\beta}{\beta_{\text{lim}}}\right)^{1-x}\right]^{1/2}\left[1-\left(\frac{\beta_0}{\beta_{\text{lim}}}\right)^{1-x}\right]^{-1/2}, \qquad (22)$$

$$\beta_{\text{lim}}^{1-x}=\frac{E_0^2A_3(1-\gamma)}{A_4}+\beta_0^{1-x}. \qquad (23)$$

Thus, if the particles are accelerated by the mechanism under consideration, their energy spectrum is not expressed by (21) but has the form

$$j(\beta)=\begin{cases} A_4\beta^{-x} & \text{for } \beta\leqslant\beta_{\text{lim}} \\ A_4\beta^{-x} & \text{for } \beta>\beta_{\text{lim}}. \end{cases}$$

For (21), the lower boundary is

$$\beta_{\text{low}}^{1-x}=\beta_{\text{lim}}^{1-x}\frac{4}{5-x}.$$

The form of $f(\tau_0)$ is determined by (8), (10), and (11). Setting x = 3 and $B(\tau_0) = 1$ we obtain

$$f(\tau_0)=\frac{6A_3}{\beta^3_{\text{lim}}}\frac{1+(C+\lambda)^2}{n_0^2-1}(\beta^2_{\text{lim}}-\beta_0^2)\tau_0^3. \tag{24}$$

Here, $\beta_{\text{low}} = \beta_{\text{lim}}/\sqrt{2}$. Equation (24) is valid when

$$2\frac{1+(C+\lambda)^2}{n_0^2-1}(\beta^2_{\text{lim}}-\beta_0^2)^{1/2}\tau_0^2\ll\beta^3_{\text{lim}},$$

i.e., for small τ_0 and, thus, high energies.

Equations (22) and (23) become

$$E=E_0\frac{\beta_0}{\beta}\sqrt{\frac{\beta^2_{\text{lim}}-\beta^2}{\beta^2_{\text{lim}}-\beta_0^2}},\quad \beta^2_{\text{lim}}=\frac{A_4\beta_0^2}{A_4-2S_0}. \tag{25}$$

If the initial amplitude is large and the initial flux of trapped particles is small, $2S_0 > A_4$ the latter expression is meaningless, and thus total absorption of the wave is impossible and there is a limiting value of the amplitude:

$$E_{\text{lim}}=E_0\left(1-\frac{\beta^2_{\text{lim}}}{\beta_0^2}\right)^{-1/2}=E_0\sqrt{1-\frac{A_4}{2S_0}}.$$

In this case the entire spectrum is described by (21). Collisions can also cause untrapping of particles. The relation describing the decrease in particle density due to collisions can be written

$$dj=-g(z)\,j\,dz, \tag{26}$$

where g(z) is a function which acts as the reciprocal mean free path. As a first approximation we take

$$g(z)=g_0=\text{const}, \tag{27}$$

and find from (11)

$$j=j_0\left(\frac{\omega\sqrt{1+(C+\lambda)^2}}{\omega_0}\right)^{\frac{\alpha}{2g_0}}\beta^{-\frac{2g_0}{\alpha}},$$

i.e., a power spectrum with exponent $2g_0/\alpha$; in the differential energy spectrum the exponent is $i = 2g_0/\alpha + 1$.

Acceleration of charged particles in waves with an increasing propagation velocity is obviously effective when the mean free path of the trapped particles $1/g_0$ is comparable to or larger than the distance of the characteristic change in energy $1/\alpha$. When $1/2 < g_0/\alpha < 2$ agreement is obtained with the spectrum observed for cosmic radiation of galactic or solar origin, for which i = 2–5.

When particles escape from the trap due to collisions the function g(z) theoretically cannot be considered constant since a decrease in the density of the medium is necessary for particle acceleration, and the function g(z) must decrease along with the decrease in density. Therefore, we set $g(z) = g_0 \exp(-qz)$, and q can coincide with α, which characterizes the decrease in medium density. Then, from (26), we have

$$j=j_0\exp\left[\frac{g_0}{q}(e^{-qz}-1)\right]. \tag{28}$$

From (11), it is easy to find the spectrum

$$j=j_0e^{g_0/q}\exp\left\{\frac{g_0}{q}\left(\frac{\omega_0{}^3}{\omega\sqrt{1+(C+\lambda)^2}}\right)^{-2q/\alpha}\right\}. \tag{29}$$

We now consider the form of the energy spectrum of accelerated particles for different assumptions. The spectrum concides with the experimentally observed spectrum only for (26) and (27). However, we feel that the most realistic picture of the acceleration of charged particles is given by a combination of the two mechanisms under consideration. At first, when the wave has not yet imparted its energy to the trapped particles, it is fairly powerful and confines the particles well. This feature is indicated by the fact that the parameter τ decreases according to (7) with decreasing n in spite of the decrease in the wave amplitude. For a value of n corresponding to a particle energy equal to the lower limit of the spectrum β_{low}, the parameter τ begins to increase. When $\tau \simeq 1$ particles can escape from the trapped state by collisions. Therefore the collision mechanism comes into play only at a certain value of the z coordinate. In this case there is a more or less sharp lower boundary of the spectrum. The parameters g_0 and q depend not only on the kind of collision and the density of the medium, but also on the portion of the trapped particles for which τ has reached values close to unity.

In any case, it can be seen from (29) that a necessary condition for a substantial decrease in the initial particle flux is $g_0 \gg q$, which means that the average mean free path of the trapped particles should vary slowly. In (28) we take

$$z\gg\frac{1}{q}\ln\frac{g_0}{q}, \tag{30}$$

and expand the exponential

$$j=j_0e^{-g_0/q}\left(1+\frac{g_0}{q}e^{-qz}\right).$$

If the coordinates for particle untrapping satisfy the condition $z \gg 2/\alpha$ as well as (30), the trapped particles are effectively accelerated by the mechanism in question. For the hard part of the spectrum, for which (30) is valid, a power differential spectrum is obtained with an exponent $i = 2q/\alpha + 1$. This exponent coincides with that observed for $q \sim \alpha$ and is fairly realistic since it means that substantial variation of the mean free path of the trapped particles and the electron density of the medium occurs at comparable distances.

The maximum energies that can be attained by protons in the sun are easy to estimate from the following considerations. The particle energy is related to n by (5), which for $n \sim 1$ can be written as $\beta = \text{const}(n^2-1)^{-1/2}$. Using (2), we obtain $\beta/\beta_0 = (N/N_0)^{1/2}$. Setting $\beta_0 \simeq 1$ and $N_0 \simeq 10^9$ cm^{-3} (the lower corona layers), for the upper corona, where $N \simeq 10^5$ cm^{-3}, we have $\beta \simeq 10^2$ and this corresponds to energies of $\sim 10^{11}$ eV. Energies of the same order of magnitude have been observed for the most energetic protons from the sun (for example, see ref. 6).

If the flux of trapped particles encounters a magnetic inhomogeneity they are untrapped. The synchrotron radiation of these particles can generate radio bursts.

In conclusion, we summarize results that are of interest for astrophysical problems.

1. Violation of the adiabatic condition is not an important mechanism for particle untrapping.

2. If a fairly large portion of the particles in the initial flux have low phase oscillation amplitudes, when $\tau_0 \ll 1$ the wave is strongly absorbed. If there are many trapped particles, the acceleration is negligible. Thus, high-energy trapped particles accelerated by the wave can appear unaccompanied by electromagnetic radiation.

3. The mechanism explains the existence of a lower boundary in the spectrum.

4. Fairly realistic assumptions are used to obtain a form of the spectrum that coincides with the spectrum observed for cosmic particles of galactic or solar origin.

5. Numerical estimates indicate that even under solar conditions with amplitudes corresponding to radio emission from the quiet sun the mechanism in question can generate particles over a very broad energy range. Energies corresponding to the hardest protons of solar origin are attained through acceleration by waves generated by powerful chromospheric flares.

---

[1] V. Ya. Davydovskii and E. M. Yakushev, Zh. Eksp. Teor. Fiz., 52, 1068 (1967) [Sov. Phys.–JETP, 25, 709 (1967)].

[2] V. Ya. Davydovskii and E. M. Yakushev, Zh. Tekh. Fiz., 41, 2259 (1971) [Sov. Phys.–Tech. Phys., 16, 1796 (1972)].

[3] V. Ya. Davydovskii and E. M. Yakushev, Izv. Akad. Nauk SSSR, Ser. Fiz., 32, 1796 (1968).

[4] V. Ya. Davydovskii and A. S. Ukolov, Izv. SKNTs VSH, Ser. Estestv. Nauk, No. 2 (1974).

[5] V. Ya. Davydovskii and E. M. Yakushev, Zh. Tekh. Fiz., 39, 2236 (1969) [Sov. Phys.–Tech. Phys., 14, 1687 (1970)].

[6] S. M. Schindler and P. D. Kearney, Nature, 237, 503 (1972).

Nonmonotonic potential distribution in the electrode region

A. I. Loshkarev

(Submitted October 25, 1973)
Zh. Tekh. Fiz., 44, 2109-2115 (October 1974)

Low-voltage arcs with a nonmonotonic potential distribution in the electrode sheath are examined. The inclusion of electron and ion scattering is important because it provides correct matching to the neutral plasma. Simple analytic expressions are obtained for the potential drop near the cathode; these agree with the experimental data. The space charge at the minimum potential is fairly small, making it possible to match the solution to the neutral plasma at the minimum. This matching is equivalent to the existence of a solution with fixed striations, which have been observed experimentally in cesium discharges. Moving striations are also discussed.

The nonmonotonic potential distribution in the electrode sheath has attracted the attention of many investigators. As a rule, the solution is obtained from the Vlasov (collisionless) equation or from the beam approximation. Difficulties arise with regard to correct matching of the kinetic equation to the diffusion equation at the boundary of a dense neutral plasma. In certain cases formal satisfaction of the boundary conditions, i.e., zero first derivative of the potential at the minimum near the electrode and at the boundary of the diffusion region, means that the square of the derivative of the potential, obtained as the first integral of the Poisson equation, must be negative over most or all of the region in which the potential varies in the electrode sheath. A detailed review of the literature involving this problem is contained in ref. 1. That paper also emphasizes the difficulties involved in matching and the resulting error in the sign of the second derivative of the potential at the minimum. Consideration of charged-particle scattering allows us to obtain a correct solution which can be matched to the diffusion equation.

We will use transport equations in hydrodynamic form. The accuracy of these equations is no worse than that of the kinetic equations if the frictional forces, viscous terms, etc. are determined appropriately.

The conservation of momentum for electrons and ions can be written

$$\frac{dn_e}{dx}+n_e\left(\frac{d\ln T_e}{dx}-\frac{e}{T_e}\frac{d\varphi}{dx}\right)=\frac{1}{T_e}\left(R_e-\frac{d\tau_{exx}}{dx}-m_e\Gamma_e\frac{du_e}{dx}\right)\equiv\frac{R_e^*}{T_e}, \tag{1}$$

$$\frac{dn_i}{dx}+n_i\left(\frac{d\ln T_i}{dx}+\frac{e}{T_i}\frac{d\varphi}{dx}\right)=\frac{1}{T_i}\left(R_i-\frac{d\tau_{ixx}}{dx}-m_i\Gamma_i\frac{du_i}{dx}\right)\equiv\frac{R_i^*}{T_i}, \tag{2}$$

where $m_{e,i}$ is the electron (ion) mass, $n_{e,i}$ is the electron (ion) density, $T_{e,i}$ is the electron (ion) temperature, φ is the electric potential, $R_{e,i}$ is the electron (ion) frictional force produced by interactions with the other plasma particles, $\tau_{e,ixx}$ is the viscous stress component, $\Gamma_{e,i} \equiv n_{e,i}u_{c,i}$ is the electron (ion) flux expressed in terms of the density and the average drift velocity $u_{e,i}$. The quantities are expressed in terms of moments of the distribution function and the collision integrals.[2]

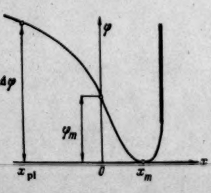

Fig. 1. Potential distribution in the electrode sheath.

In Eqs. (1) and (2), generalized frictional forces $R_{e,i}^*$ are introduced which include viscous and inertial terms. The formal solutions of the equations are:

$$n_e=\frac{T_{e0}}{T_e}\exp\left(\int_0^x\frac{e}{T_e}\frac{d\varphi}{dx'}\,dx'\right)\left[n_{e0}+\int_0^x\frac{R_e^*}{T_{e0}}\exp\left(-\int_0^{x'}\frac{e}{T_e}\frac{d\varphi}{dx''}dx''\right)dx'\right],$$

$$n_i=\frac{T_{i0}}{T_i}\exp\left(-\int_0^x\frac{e}{T_i}\frac{d\varphi}{dx'}\,dx'\right)\left[n_{i0}+\int_0^x\frac{R_i^*}{T_{i0}}\exp\left(\int_0^{x'}\frac{e}{T_i}\frac{d\varphi}{dx''}\,dx''\right)dx'\right].$$

These relations show that the inclusion of the comparatively weak temperature variation across the electrode sheath should not lead to qualitative (or significant quantitative) changes in the solutions. For simplicity therefore, we assume below that the electron and ion temperatures in the sheath are constant.

It is convenient to choose the origin at the point of inflection of the potential curve (Fig. 1), where $n_e = n_i = n_0$; the potential calculated from the minimum is φ_m. Introducing the notation

$$\eta=\frac{e(\varphi_m-\varphi)}{T_i};\ \xi=\frac{x}{r_i};\ r_i=\sqrt{\frac{T_i}{4\pi e^2n_0}},$$

we write the Poisson equation

$$\frac{d^2\varphi}{dx^2}=4\pi e\,(n_e-n_i)$$

in dimensionless form:

$$\frac{d^2\eta}{d\xi^2}+\left\{\frac{1}{\eta}\left[e^{-\frac{\eta}{\theta}}\left(1+\int_0^\xi a_e^*e^{\frac{\eta}{\theta}}d\xi'\right)-e^{\eta}\left(1+\int_0^\xi a_i^*e^{-\eta}d\xi'\right)\right]\right\}\eta=0, \tag{3}$$

where $a_{e,i}^* = R_{e,i}^*r_i/T_{e,i}n_0$; $\theta = T_e/T_i$.

Using the continuity equation in the form

$$\frac{d\Gamma_{e,i}}{dx}=\frac{d\,(n_{e,i}u_{e,i})}{dx}=0,$$

i.e., assuming that volume production and recombination can be neglected in the sheath, we obtain the following relations for the dimensionless generalized frictional forces:

$$a_e^*\left(1-\frac{m_e\Gamma_e^2}{T_en_e^2}\right)=\frac{\left(R_e-\frac{d\tau_{exx}}{dx}\right)r_i}{T_en_0}-\frac{m_e\Gamma_e^2}{T_en_e^2}\frac{n_e}{n_0}\frac{1}{\theta}\frac{d\eta}{d\xi}, \tag{4}$$

$$a_i^*\left(1-\frac{m_i\Gamma_i^2}{T_i n_i^2}\right)=\frac{\left(R_i-\frac{d\tau_{ixx}}{dx}\right)r_i}{T_i n_0}+\frac{m_i\Gamma_i^2}{T_i n_i^2}\frac{n_i}{n_0}\frac{d\eta}{d\xi}. \qquad (5)$$

The electron and ion fluxes at the boundary of the quasineutral plasma, expressed in terms of random fluxes, are

$$\Gamma_e=\frac{b_e}{4}n_{\mathrm{pl}}v_{eT};\ \Gamma_i=\frac{b_i}{4}n_{\mathrm{pl}}v_{iT}. \qquad (6)$$

Here, $b_{e,i}$ must be negative if the corresponding flux is directed away from the electrode. Note that in these relations n_{pl} does not coincide with n_{el}, which is the analytic continuation (extrapolation) of the solution of the neutral diffusion equations to the electrode surface.

Using (6), we obtain

$$\frac{m_i\Gamma_i^2}{T_i n_{\mathrm{pl}}^2}=\frac{b_i^2}{2\pi};\ \frac{m_e\Gamma_e^2}{T_e n_{\mathrm{pl}}^2}=\frac{b_e^2}{2\pi}\approx\frac{1}{2\pi}\left[\frac{\Gamma_e}{\Gamma_{\mathrm{et}}-\Gamma_e}\exp\left(-\frac{e\Delta\varphi}{T_e}\right)\right]^2,$$

where Γ_{et} is the portion of the electron flux emitted by the cathode that passes through the potential barrier into the plasma.

In order that the ion density drop off from the boundary of the neutral plasma to the regions of strong fields, where the field term in the right side of (5) is decisive, it is necessary that at least the following condition be satisfied:

$$b_i^2>2\pi.$$

It follows from (1) and (2) that at the boundary of the neutral plasma ($n_e = n_i = n_{\mathrm{pl}}$)

$$\left.\frac{d\eta}{d\xi}\right|_{\xi=\xi_{\mathrm{pl}}}=(a_e^*-a_i^*)_{\mathrm{pl}}\frac{n_0}{n_{\mathrm{pl}}}\left(1+\frac{1}{\theta}\right)^{-1}. \qquad (7)$$

We transform (7), taking (4) and (5) into account:

$$\left[\frac{2\pi}{2\pi-b_e^2}\left(R_e-\frac{d\tau_{exx}}{dx}\right)\frac{1}{T_e}-\frac{2\pi}{2\pi-b_i^2}\left(R_i-\frac{d\tau_{ixx}}{dx}\right)\frac{1}{T_i}\right]\frac{r_i}{n_{\mathrm{pl}}}\left.\frac{d\xi}{d\eta}\right|_{\xi=\xi_{\mathrm{pl}}}$$
$$=1+\frac{1}{\theta}+\frac{b_e^2}{2\pi-b_e^2}+\frac{b_i^2}{2\pi-b_i^2}. \qquad (8)$$

Since Coulomb scattering can be neglected at the boundary, with the introduction of effective frequencies for electron and ion collisions with atoms $\tau_{e,ia}^{-1} = v_{e,iT}/\lambda_{e,i}$

$$R_e\approx-\frac{\Gamma_e m_e}{\tau_{ea}}\ll|R_i|\approx\left|-\frac{\Gamma_i m_i}{\tau_{ia}}\right|,$$

and $b_e^2 \ll 1$, for the derivative of the dimensionless potential at the boundary to be positive $d\eta/d\xi|_{\mathrm{pl}} > 0$ it is necessary that

$$1+\frac{1}{\theta}+\frac{b_i^2}{2\pi-b_i^2}<0.$$

This condition determines the upper limit of b_i, which is thus restricted by the relations

$$(1+\theta)2\pi>b_i^2>2\pi.$$

It is interesting to note that in the limiting case $\theta \ll 1$, $b_i^2 = 2\pi$. This result agrees with the result obtained in ref. 3 for a kinetic treatment of the neutral electrode sheath for $\theta \ll 1$.

Under the above-mentioned conditions with $n_{e,i} \leq n_0 \ll n_{\mathrm{pl}}$

$$\left.\begin{aligned}a_e^*&\approx\frac{r_i}{T_e n_0}\left(R_e-\frac{d\tau_{exx}}{dx}\right)-\frac{m_e\Gamma_e^2}{T_e n_{\mathrm{pl}}^2}\frac{n_{\mathrm{pl}}^2}{n_e^2}\frac{n_e}{n_0}\frac{1}{\theta}\frac{d\eta}{d\xi},\\ a_i^*&\approx-\frac{r_i}{T_i n_0}\left(R_i-\frac{d\tau_{ixx}}{dx}\right)\left(\frac{m_i\Gamma_i^2}{T_i n_{\mathrm{pl}}^2}\frac{n_{\mathrm{pl}}^2}{n_i^2}\right)^{-1}-\frac{n_i}{n_0}\frac{d\eta}{d\xi},\end{aligned}\right\} \qquad (9)$$

since

$$\frac{m_e\Gamma_e^2}{T_e n_{\mathrm{pl}}^2}\frac{n_{\mathrm{pl}}^2}{n_e^2}\ll 1;\ \frac{m_i\Gamma_i^2}{T_i n_{\mathrm{pl}}^2}\frac{n_{\mathrm{pl}}^2}{n_i^2}\gg 1. \qquad (10)$$

We denote the term in curly brackets in (3) by $C^2(\xi)$ which is permissible for the postulated potential distribution. A formal approximate solution of (3) with boundary condition

$$\eta=0 \text{ for } \xi=0$$

can be found by the WKB method[4] and written in the form

$$\eta=\frac{A}{\sqrt{C(\xi)}}\sin\int_0^{\xi}C(\xi')\,d\xi', \qquad (11)$$

where $A = \eta_m C_m^{1/2}\left[\sin\int_0^{\xi_m}C(\xi')d\xi'\right]^{-1}$ (the subscript indicates that the term is taken at the corresponding point).

Note that the solution in the form of (11) is exact if $C^2(\xi) = (D\xi + B)^{-4}$, where D and B are arbitrary constants, i.e., this solution is also applicable for rapidly varying $C^2(\xi)$ in the range in question. To satisfy the second boundary condition

$$\frac{d\eta}{d\xi}=0 \text{ for } \xi=\xi_m$$

it is necessary that

$$-\frac{1}{2C_m^2}\left.\frac{dC}{d\xi}\right|_m\sin\int_0^{\xi_m}C(\xi')\,d\xi'+\cos\int_0^{\xi_m}C(\xi')\,d\xi'=0. \qquad (12)$$

It is easy to see that when (9) is used

$$C_0^2=(a_e^*-a_i^*)_0\left.\frac{d\xi}{d\eta}\right|_0-\left(1+\frac{1}{\theta}\right)$$
$$\approx\left[\frac{r_i}{T_e n_0}\left(R_e-\frac{d\tau_{exx}}{dx}\right)+\frac{r_i}{T_i n_0}\left(R_i-\frac{d\tau_{ixx}}{dx}\right)\left(\frac{m_i\Gamma_i^2}{T_i n_0^2}\right)^{-1}\right]_0\left.\frac{d\xi}{d\eta}\right|_0-\frac{1}{\theta}.$$

If viscous terms are neglected and it is assumed that $R_i < 0$, to obtain a nonmonotonic potential distribution it is necessary that $R_e > 0$, i.e., the total electron flux must move from the electrode into the plasma and must be fairly large.

Substituting the derivative calculated from (11) into the expression for C_0^2, we obtain

$$\frac{\eta_m C_m^{1/2}}{\sin\int_0^{\xi_m}C(\xi')\,d\xi'}\left(C_0^{3/2}+\frac{1}{\theta}C_0^{1/2}\right)\approx a_e+a_i\left(\frac{m_i\Gamma_i^2}{T_i n_0^2}\right)^{-1}, \qquad (13)$$

where

$$a_e = \frac{R_e r_i}{T_e n_0} \approx \frac{2}{\pi} \frac{\exp\left[-\frac{1}{\theta}\left(\eta_m + \frac{\eta_{\text{pl}}}{2}\right)\right]}{\frac{\Gamma_{\text{et}}}{\Gamma} - 1} \frac{11}{\theta^{1/2}} \frac{r_e}{\lambda_e} \ll 1; \quad r_e = \sqrt{\frac{T_e}{4\pi e^2 n_{\text{pl}}}},$$

$$a_i = \frac{R_i r_i}{T_i n_0} \approx -\frac{2}{\pi} \frac{b_i}{\theta^{1/2}} \exp\left(-\frac{3}{2}\frac{\eta_{\text{pl}}}{\theta}\right)\frac{r_e}{\lambda_i}; \quad \frac{n_0}{n_{\text{pl}}} \approx \exp\left(\frac{\eta_{\text{pl}}}{\theta}\right).$$

It will be shown later that $\eta_{\text{pl}} \approx -3$ and the second term on the right side of (13) is considerably smaller than the first.

When the basic variation in the potential is concentrated in a region of the order of the Debye radius (ξ_m is the order of unity), it is necessary that C_0 also be of the order of unity. [For $C^2(\xi)$ = const it follows from (12) that $C\xi_m = \pi/2$.] Then, (13) should be satisfied for $C_m^{1/2} \sim a_e$, i.e., for small space charge at the minimum potential. To restrict the first term in (12) it is necessary that

$$\left.\frac{dC}{d\xi}\right|_m \sim a_e^4.$$

Differentiation of $C^2(\xi)$ leads to

$$2C\frac{dC}{d\xi} = \left\{C^2 - \frac{1}{\eta}\left[C^2 + \left(1 + \frac{1}{\theta}\right)\frac{n_e}{n_0}\right]\right\}\frac{d\eta}{d\xi} + \frac{1}{\eta}(a_e^* - a_i^*), \tag{14}$$

and to within terms $\sim a_e^6$

$$(a_e^* - a_i^*)_m = 0. \tag{15}$$

Relation (15) again indicates that for a potential minimum to exist in the sheath the electron and ion fluxes must move in opposite directions.

If viscous terms are neglected, using (9) we have

$$\frac{|\Gamma_e|}{\Gamma_i}\left(\frac{m_e}{m_i}\right)^{1/2} = \theta^{-1/2}\frac{\sigma_{ia}}{\sigma_{ea}}\frac{\sqrt{2}\pi}{b_i^2}\frac{n_{im}^2}{n_{\text{pl}}^2} \ll 1. \tag{16}$$

The value of n_{im} can be determined when the dimensionless space charge at the minimum is

$$\frac{(n_e - n_i)_m}{n_0} = C_m^2 \eta_m \sim a_e^4.$$

The electron density at the minimum n_{em}, with the distribution function approximated by the sum of two semi-Maxwellian functions and with the usual expression for the electron flux

$$|\Gamma_e| = \Gamma_{\text{et}} - \frac{1}{4} n_{\text{pl}} v_{eT} \exp\left(-\frac{e\Delta\varphi}{T_e}\right) = \Gamma \tag{17}$$

is represented in the form

$$n_{em} = \frac{1}{2} n_{\text{pl}}\left(1 + \theta^{1/2}\frac{\frac{\Gamma_{\text{et}}}{\Gamma}}{\frac{\Gamma_{\text{et}}}{\Gamma} - 1}\right)\exp\left(-\frac{e\Delta\varphi}{T_e}\right).$$

The following equality is valid to within terms $\sim a_e^4$:

$$\frac{n_{im}}{n_0} \approx \frac{n_{em}}{n_0} \sim \exp\left(-\frac{\eta_m}{\theta}\right) \gg a_e^4,$$

and (15) can be rewritten

$$2\left(\frac{\sigma_{ea}}{\sigma_{ia}}\frac{b_i}{\sqrt{2}\pi}\right)^{1/2}\exp\left(\frac{e\Delta\varphi}{2T_e}\right) = \frac{1 + \theta^{1/2}}{\theta^{1/2}}\sqrt{\frac{\Gamma_{\text{et}}}{\Gamma} - 1} + \frac{1}{\sqrt{\frac{\Gamma_{\text{et}}}{\Gamma} - 1}}. \tag{18}$$

The error introduced by the assumptions does not exceed the error of the ratio σ_{ia}/σ_{ea} and is therefore negligible.

The right side of (18) has a lower limit and the minimum value of the electrode jump in the presence of the virtual cathode is

$$\frac{e\Delta\varphi_{\min}}{T_e} = \ln\left(\frac{1 + \theta^{1/2}}{\theta^{1/2}}\frac{\sqrt{2}\pi}{b_i}\frac{\sigma_{ia}}{\sigma_{ea}}\right), \tag{19}$$

which is realized for

$$\left(\frac{\Gamma_{\text{et}}}{\Gamma}\right)_{\Delta\varphi_{\min}} = 1 + \frac{\theta^{1/2}}{1 + \theta^{1/2}}.$$

A unique determination of $\Delta\varphi$ requires the use of the energy balance equation for the electron gas. If the electron distribution function at the boundary of the neutral plasma is approximated by the sum of two semi-Maxwellian functions with temperature T_e, then the energy balance equation[5] takes the simple form

$$\frac{e\Delta\varphi}{2T_e} = \frac{\Gamma_{\text{et}}}{\Gamma}\left(1 - \frac{1}{\theta}\right). \tag{20}$$

A joint solution of (19) and (20) allows us to determine $e\Delta\varphi/T_e$ and $(\Gamma_{\text{et}}/\Gamma)_{\Delta\varphi}$ which in this approximation depend only on θ and $b_i\sigma_{ea}/\sigma_{ia}$.

The dependence of $e\Delta\varphi/T_e$, $e\Delta\varphi_{\min}/T_e$, $(\Gamma_{\text{et}}/\Gamma)_{\Delta\varphi}$ and $(\Gamma_{\text{et}}/\Gamma)_{\Delta\varphi_{\min}}$ on θ is shown in Figs. 2 and 3. Comparison of the theoretical values of $\Delta\varphi$ with the appropriate experimental results[6] indicates good agreement between theory and experiment.

We consider the magnitude of the basic parameters at the boundary of the neutral plasma. It follows from (7) and (14) that at the boundary

$$\frac{\eta_{\text{pl}} - 1}{\eta_{\text{pl}}}\left.\frac{d\eta}{d\xi}\right|_{\text{pl}} = \frac{2}{C_{\text{pl}}}\left.\frac{dC}{d\xi}\right|_{\text{pl}}.$$

The differential expression (11) gives

$$\frac{1}{A}\frac{d\eta}{d\xi} = -\frac{1}{2C^{3/2}}\frac{dC}{d\xi}\sin\int_0^\xi C(\xi')\,d\xi' + C^{1/2}\cos\int_0^\xi C(\xi')\,d\xi'.$$

Excluding $dC/d\xi$ we obtain

$$\eta_{ux} = -3 + 4\eta_m C_m^{1/2} C_{\text{pl}}^{1/2}\,\mathrm{ctg}\left[\int_0^{\xi_{\text{pl}}} C(\xi')\,d\xi'\right]\left.\frac{d\xi}{d\eta}\right|_{\text{pl}}. \tag{21}$$

However, it follows from (8) that

$$\left.\frac{d\xi}{d\eta}\right|_{\text{pl}} = \frac{\theta^{1/2}}{4b_i}\left[\left(1 + \frac{1}{\theta}\right)(2\pi - b_i^2) + b_i^2\right]\exp\left(\frac{\eta_{\text{pl}}}{2\theta}\right)\frac{\lambda_i}{r_e}.$$

Since

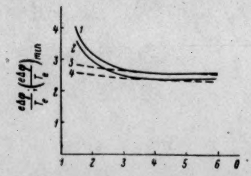

Fig. 2. $e\Delta\varphi/T_e$ (solid lines) and $(e\Delta\varphi/T_e)_{min}$ (dashed) as functions of θ. 1,3) $\alpha \equiv [(\sigma_{ea}/\sigma_{ia})b_i/\sqrt{2\pi}]^{1/2} = 0.325$; 2,4) 0.364.

$$A = \eta_m \frac{C_m^{1/2}}{\sin\int_0^{\xi_m} C(\xi')\,d\xi'} = \eta_{pl} \frac{C_{pl}^{1/2}}{\sin\int_0^{\xi_{pl}} C(\xi')\,d\xi'},$$

relation (13) gives $C_{pl}^{1/2} \sim a_e$, i.e., a small value for the space charge, as expected. Thus, the second term on the right side of (21) is of order a_e^2 and can be neglected. An interesting result is that the potential drop from the point of inflection to the boundary of the neutral plasma is almost constant and equal to $3T_i/e$.

If the results of ref. 3 are used, the relationship between n_{pl} and n_{el} at a nonemitting electrode is given by the following expression which is obtained by assuming $\theta \ll 1$:

$$n_{el} = \frac{\sqrt{2}}{1+\theta}\left(1.016 + \frac{\theta}{\sqrt{2}}\right) n_{pl}; \quad b_i = \sqrt{2\pi} \approx 2.5.$$

To obtain correct results for $\theta \approx 1$ we have recommended[11] that T_i be replaced by T_e, which corresponds to $\theta = 1$ in the expression obtained above. Then $n_{el} \approx 1.22 n_{pl}$ and $b_{i\,el} \approx 2$, i.e., we obtain the usual relation for the particle flux to the nonemitting wall, which is twice the random flux.

We now give certain results. An electrode sheath with a nonmonotonic potential distribution can occur only at an emitting electrode operating in the cathode mode with small ion emission. An electrode sheath with a nonmonotonic potential distribution cannot be produced in the working quadrant even with a hot anode with a uniform work function over its surface, although such a distribution can appear if the reverse currents are eliminated. The latter feature is confirmed by the experimental voltage–current characteristic curves given in Fig. 45 of ref. 7, which have an intermediate plateau in the reverse-current branch; this is due to the nonmonotonic potential distribution at the hot anode working in the cathode mode.[8] An important role can be played by the "spottiness" of the electrode in which a monotonic potential jump is "attached" to the spots with an increased work function, and the virtual electrodes are aligned over the spots with a reduced work function. Since the space charge is close to zero at the potential minimum, the solution is well matched to the neutral plasma at the minimum. This corresponds to the striations in a cesium discharge that are observed experimentally in ref. 9. A mode with a sharp variation in the potential within the limits of the Debye radius can be interpreted as a shock wave produced by the interaction between oppositely traveling electron and ion fluxes in a scattering medium.

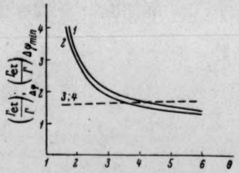

Fig. 3. $(\Gamma_{et}/\Gamma)_{\Delta\varphi}$ ($1 - \alpha = 0.325$, $2 - 0.364$) and $(\Gamma_{et}/\Gamma)_{\Delta\varphi\min}$ (3, 4) as functions of θ.

The simplest energy balance equation for the electron gas (20) is an approximation. Near the cathode of an arc discharge or at the head of a striation, thermal conductivity processes[10] that should reduce the value of Γ_{et}/Γ to obtain the given θ can be important. Thus, calculation of the detailed potential distribution and the density and temperature distributions requires that the appropriate closed system of diffusion equations be solved using the expression obtained for the potential drop in the Debye sheath as the boundary condition. However, if we only calculate the total potential drop across the gap or across a striation up to the head of the next striation, then correct results can be obtained by writing the voltage and energy balance equations for the interval as a whole under the assumption of constant T_e over the entire interval (see refs. 5 and 11). In analyzing the striations in the positive column of a long discharge tube, the two-dimensional problem should be solved with the escape of ions and hot electrons to the wall of the discharge tube taken into account. Moving striations can be obtained if the solution is found in a coordinate system coupled to the striation. Also, in the equations of conservation of momentum it is necessary to change the expression for $R_{e,i}$ in the appropriate manner since the neutral gas cannot be considered at rest in this coordinate system.

---

[1] P. P. Shcherbinin, Zh. Tekh. Fiz., 42, 2490 (1972) [Sov. Phys. – Tech. Phys., 17, 1941 (1972)].

[2] S. I. Braginskii, in: Reviews of Plasma Physics, Vol. 1, Consultants Bureau, New York (1965).

[3] I. P. Stakhanov and P. P. Shcherbinin, Prikl. Mekh. Tekh. Fiz., No. 3, 47 (1969); No. 2, 4 (1970).

[4] N. Froman and P. O. Froman, The WKB Approximation, North-Holland, Amsterdam (1965).

[5] I. P. Stakhanov and I. I. Kasikov, Zh. Tekh. Fiz., 39, 1496 (1969) [Sov. Phys. – Tech. Phys., 14, 1122 (1970)].

[6] F. G. Baksht, G. A. Dyuzhev (Djuzhev), V. B. Kaplan, I. L. Korobova, A. M. Martsinovskii (Martzinovskiy), B. Ya. Moizhes, G. A. Shanasarova (Shahnasarova), and V. G. Yur'ev (Yuriev), in: Proceedings of the International Conference on Thermoelectrical Power Generation, Genoa, Italy, 1968.

[7] I. P. Stakhanov, A. S. Stepanov, V. P. Pashchenko, and Yu. K. Gus'kov, in: Physical Principles of Thermionic Converters [in Russian], Atomizdat, Moscow (1973).

[8] R. Ya. Kucherov and L. É. Rikenglaz, Zh. Tekh. Fiz., 32, 1275 (1962) [Sov. Phys. – Tech. Phys., 7, 941 (1963)].

[9] A. I. Kiryushchenko and M. A. Lebedev, Zh. Tekh. Fiz., 42, 1657 (1972) [Sov. Phys. – Tech. Phys., 17, 1322 (1973)].

[10] A. V. Nedospasov, Usp. Fiz. Nauk, 94, 439 (1968) [Sov. Phys. – Usp., 11, 174 (1968)].

[11] A. I. Loshkarev, Zh. Tekh. Fiz., 42, 2127 (1972) [Sov. Phys. – Tech. Phys., 17, 1684 (1973)].

Nonlinear effects for the "kink" instability in an electron-ion ring

G. P. Berman

Novosibirsk University

(Submitted July 11, 1973; resubmitted December 18, 1973)
Zh. Tekh. Fiz., 44, 2116-2125 (October 1974)

The influence of a nonlinear polarization force on damping of the "kink" instability in an electron–ion ring is investigated. An explicit expression is found for the polarization force produced by relative displacement of the beam centers of gravity. Conditions are found for which there is no nonlinear stabilization at low amplitudes. Nonlinear saturation amplitudes are estimated for different instability regions.

In an electron–ion ring an instability can be produced by relative transverse displacement of the center of gravity of the electrons with respect to the ions without changing the shape of the transverse cross section of the beams ("kink" instability).[1,2] This problem is considered in detail in ref. 2 in the linear approximation. In particular, it is shown that an instability always exists for a continuous wave-number spectrum. For a discrete spectrum $k_n = n/R$ (R is the radius of the ring, and $n = \pm 1, \pm 2, \ldots$), it follows from the results of ref. 2 that an instability is possible only for certain wave numbers k_n (in Fig. 1, the boundaries of the instability region are denoted by k_- for the lower boundary and by k_+ for the upper boundary).

However, the exponential increase in the amplitude $a(t)$ predicted by linear theory is valid only for the initial stage of the instability, when the oscillation amplitudes are small. Therefore, a nonlinear treatment is necessary to estimate the maximum amplitude.

The transverse instability is considered in ref. 3 in the approximation of a small nonlinear polarization force for a single unstable mode with $n \geq 1$. The beam parameters are chosen near the upper boundary of the instability region. In ref. 3 a solution is obtained in the form of a nonlinear stationary wave in the absence of external focusing [$\lambda = 0$, see (1.5)]. The oscillation saturation amplitude is found in the presence of an external focusing field and is small compared to the characteristic beam dimensions.

However, the approximation for a small nonlinearity is valid only near the boundary of the instability region, where the maximum oscillation amplitudes, which are proportional to γ (the growth rate), are small. Furthermore, as will be shown later, there are conditions for which nonlinear stabilization is impossible, even for small γ. This situation occurs for wave numbers near the lower boundary of the instability region ($k \geqslant k_-$), where the weakly nonlinear polarization force leads to an increase in the growth rate of the displacement between the electrons and ions. This result comes from the approximate treatment of the problem: Physically, it is clear that the interaction between beams is attenuated as $y - x$ increases (x and y are the electron and ion displacements, respectively). As a result the instability should be damped, although possibly not for small amplitudes of the electron and ion displacements. Therefore, further investigation of the instability requires that the explicit form of the interaction force produced by transverse displacements of the beam be known. Furthermore, it is necessary to investigate the instability without the assumption of a small nonlinearity. The explicit form of the interaction force is also necessary for estimates of the maximum oscillation amplitudes near the boundary of the instability region.

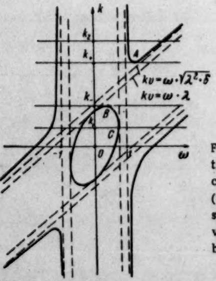

Fig. 1. Form of the dispersion relation $k = k(\omega)$ given by Eq. (1.8). The coordinates of point C are: $\bar{\omega} = \bar{k}v = (1 + \delta/\Lambda^2)^{-1/2}$. The boundaries of the stability region are: $A(k_+)$, $B(k_-)$. The vectors k_1 and k_2 are in the linear stability region.

In the present paper, the transverse instability of an electron–ion ring is considered in a rigid-beam model with a Gaussian distribution of the particle density over the cross section. An explicit expression is found for the interaction force between the beams $F(y - x)$. An expression is obtained for the complex amplitude $\Phi(\xi, \tau)$ for a single mode (ξ and τ characterize the slow variation of the amplitude with z and t, respectively); the time development is also investigated (see Sec. 2). Physically, the situation is the following: The electron beam makes many turns during the change in oscillation amplitude; therefore, the spatial evolution of the oscillation amplitude is not considered in the present paper. The effect of nonlinearity on damping of instabilities corresponding to different areas of the instability region is investigated. Near the lower boundary of the instability region ($k \geqslant k_-$) conditions are found for the absence of stabilization due to nonlinearity at small amplitudes. Near the upper boundary of the instability region ($k \leq k_+$) estimates are obtained for the maximum amplitudes and the saturation amplitudes of oscillation due to nonlinearity.

1. FUNDAMENTAL EQUATIONS

We consider two interpenetrating beams: an electron beam and an ion beam; the particle density over the transverse cross sections is a Gaussian:

$$n_{e,i}(r_\perp) = n_{e,i}^{(0)} \exp\left(-\frac{r_\perp^2}{a^2}\right), \tag{1.1}$$

where a characterizes the beam radius. The beams can be displaced with respect to each other in the vertical direction (the X axis). The polarization force resulting from the relative displacement, calculated for one particle, is

$$F_{e,i}(\Delta_1, \Delta_2) = -\frac{\frac{\partial U(\Delta_1, \Delta_2)}{\partial \Delta_1 (\partial \Delta_2)}}{N_{e,i}}, \tag{1.2}$$

where Δ_1 and Δ_2 are the electron and ion displacements, respectively; $U(\Delta_1, \Delta_2)$ is the beam interaction energy

$$U(\Delta_1, \Delta_2) = \int \frac{dv_1 dv_2 n_e(x_1 - \Delta_1, y_1, z_1)\, n_i(x_2 - \Delta_2, y_2, z_2)}{|\mathbf{r}_1 - \mathbf{r}_2|}, \tag{1.3}$$

$$N_{e,i} = \int n_{e,i} dv_{e,i}.$$

The calculation of $F_{e,i}$ is fairly laborious and will not be given here. We note only that it is convenient to differentiate the expression for $U(\Delta_1, \Delta_2)$ in (1.3) with respect to $\Delta_1(\Delta_2)$ and then to integrate. We give the final result of the calculations

$$\left.\begin{aligned} F_{e,i}(\Delta) &= \pm \frac{2\pi e^2 n_{i,e}^{(0)} a^2}{\Delta}\left(1 - e^{-\Delta^2/2a^2}\right), \\ \Delta &= \Delta_2 - \Delta_1. \end{aligned}\right\} \tag{1.4}$$

In addition to the polarization force (1.4), there are external focusing forces which act on the electrons; these are proportional$^{1-3}$ to Δ_1: $f_{ex} = -\gamma m_e \lambda^2 \Delta_1$ where $\gamma = (1 - v^2/c^2)^{-1/2}$ c is the velocity of light, v is the velocity of the electron beam along the Z axis, m_e is the electron rest mass, and λ is the electron oscillation frequency in the external focusing field. Taking account of the polarization and focusing forces acting on the particle, we write the Lagrangian equation for the displacements Δ_1 and Δ_2

$$\left.\begin{aligned} m_e\gamma\ddot{\Delta}_1 + m_e\gamma\lambda^2\Delta_1 &= F_e(\Delta_2 - \Delta_1), \\ m_i\ddot{\Delta}_2 &= F_i(\Delta_2 - \Delta_1), \end{aligned}\right\} \tag{1.5}$$

where m_i is the ion rest mass. The dots in (1.5) denote the total derivative with respect to time: $d/dt = \partial/\partial t + v\partial/\partial z$. As noted above, the system (1.5) is used in refs. 1 and 2 to investigate stability in an approximation linear in $\Delta_{1,2}$ for perturbations of the form $\Delta_{1,2} \sim \exp i(kz - \omega t)$. Here, we consider the nonlinear stage of such perturbations.

We only consider a weak nonlinearity: $\Delta_{1,2}/a \ll 1$. Substituting (1.4) into (1.5) and expanding $F_{e,i}(\Delta)$ in a series in the parameter Δ/a (we only keep the first two terms of the expansion), we obtain a system of equations for the dimensionless displacements $x = \Delta_1/a$, $y = \Delta_2/a$:

$$\left.\begin{aligned} \ddot{x} + \lambda^2 x &= \delta\omega_0^2 (y - x)\left[1 - \frac{1}{4}(y - x)^2\right], \\ \ddot{y} &= -\omega_0^2 (y - x)\left[1 - \frac{1}{4}(y - x)^2\right], \end{aligned}\right\} \tag{1.6}$$

where $\omega_0 = (\pi e^2 n_e^{(0)}/m_i)^{1/2}$ is the ion oscillation frequency in the electron field (below we take $\omega_0 = 1$); $\delta = n_i^{(0)} m_i \cdot (\gamma n_e^{(0)} m_e)^{-1}$.

The solution of (1.6) is sought by using the method of stretched coodinates developed in refs. 4-6. We introduce the slowly varying variables

$$\tau = \varepsilon t; \quad \xi = \varepsilon^2 z; \quad \varepsilon \ll 1$$

and seek the solution of (1.6) in the form of a series in powers of the parameter ε

$$\begin{pmatrix} x \\ y \end{pmatrix} = \sum_{j=1}^{\infty} \varepsilon^j \sum_{l=1}^{\infty} \begin{pmatrix} x_l^{(j)} & (\xi, \tau) \\ y_l^{(j)} & (\xi, \tau) \end{pmatrix} e^{il(kz - \omega t)} + \text{c.c.}, \tag{1.7}$$

Here, k and ω are the wave vector and the frequency.

To first order in E we obtain the dispersion relation of the linear theory^2

$$F(\omega) = \frac{1}{\omega^2} + \frac{\delta}{(\omega - kv)^2 - \lambda^2} = 1. \tag{1.8}$$

We also obtain the relation: $\alpha x_1^{(1)} = y_1^{(1)} \equiv \Phi(\xi, \tau)$, $\alpha \equiv 1 - \omega^2$. Below we will obtain an equation for $\Phi(\xi, \tau)$ near the boundary of the instability region, i.e., for the additional condition $\partial F(\omega)/\partial\omega = 0$. From the latter condition and (1.8), we obtain a condition that is valid at the boundary of the instability region

$$1 - \frac{kv}{\omega} = -\frac{\delta}{\alpha^2}\bigg|_{A;\,B}. \tag{1.9}$$

The relation $k = k(\omega)$ given by (1.8) is plotted in Fig. 1. The points A and B denote the boundaries of the instability region: A the upper boundary (k_+), corresponds to the electron-ion resonance; B, the lower boundary (k_-) corresponds to resonance at electron Doppler oscillation frequencies in the magnetic field. These frequencies appear because electrons oscillate with frequency λ in the external focusing field. Terms refering to points A(B) will henceforth be denoted by the subscripts "+" and "-", respectively.

To order E^2, with (1.9) taken into account, we have

$$x_1^{(2)} - \alpha y_1^{(2)} = -2i\omega\frac{\partial\Phi}{\partial\tau}. \tag{1.10}$$

We introduce the parameter μ

$$\mu = \frac{v_0 - v}{v_0}; \quad |\mu| \ll 1, \tag{1.11}$$

where v_0 is the velocity at the boundary (at point A or B). By changing the sign of μ we shift from the boundary A (or B) either to the region of linear stability or to the region of linear instability. Near the boundary of the instability region we can assume $\mu \sim \varepsilon^2$ (see Ref. 6). The relationship between μ and the shift in the wave number k: $\delta k = k - k_\pm$ will be seen from the equation for Φ. Assuming $\mu \sim E^2$ we obtain the equation for Φ to order E^3:

$$i\frac{\partial\Phi}{\partial\xi} = q\frac{\partial^2\Phi}{\partial\tau^2} - (b|\Phi|^2 + c)\Phi, \tag{1.12}$$

$$q = -\frac{\left(\frac{4\omega^2\delta}{\alpha} + \frac{\alpha^2 k v_0}{\omega}\right)}{2v_0\omega\delta},$$

$$b = -\frac{3}{4v_0\omega}(1 - \alpha)^4; \quad c = \frac{\mu}{|\mu|}k. \tag{1.13}$$

An equation similar to (1.13) is obtained in ref. 3 for the two-stream instability in a plasma.

We note that displacement from boundary A or B can occur not through a shift of the beam [see (1.11)] from the equilibrium value v_0 at the boundary ($k_\pm$ is taken at the boundary), but through a direct shift of the wave number $k = k_\pm + \delta k$ (the beam velocity is assumed to be v_0 at the boundary). Actually, it can be seen from (1.13) that the linear term in parentheses can be obtained without representing the electron beam velocity by (1.11), but by using the formal substitution

$$\Phi = \bar{\Phi}\exp\left(-i\frac{\mu}{|\mu|}k\xi\right) = \bar{\Phi}\exp\left(-i\frac{\mu}{|\mu|}k\varepsilon^2 z\right). \tag{1.14}$$

Thus, the displacement from the boundary of the stability region with respect to k is given by $\delta k \approx (\mu/|\mu|)\, E^2 k_\pm$. Depending on the sign of μ, in the linear approximation we have

$$\operatorname{sign} \mu = \begin{cases} +, \text{ instability near point A, stability near point B} \\ -, \text{ stability near point A, instability near point B.} \end{cases}$$

2. TIME EVOLUTION

We consider the effect of the nonlinearity on the time evolution near the instability boundary. The solution of (1.12) is sought in the form

$$\Phi(\xi, \tau) = A(\tau) \exp(-i\psi(\tau)). \tag{2.1}$$

Solution (2.1) is obviously a particular solution of (1.12). This solution only reflects the time evolution of the complex oscillation amplitude. As noted in the introduction, physically this means that the electron beam executes many turns during the change in oscillation amplitude. A similar solution is considered, for example, in ref. 5 for the beam–plasma instability. In the present paper, we only consider solutions like (2.1) type for Eq. (1.12).

We substitute (2.1) into (1.2), separate the real and imaginary parts, and use conservation of "momentum"

$$A^2 \frac{d\psi}{d\tau} = M = \text{const}, \tag{2.2}$$

to integrate the equation for $A(\tau)$. We obtain

$$\frac{1}{2}\left(\frac{dA}{d\tau}\right)^2 + V(A) = H = \text{const}, \tag{2.3}$$

where H is a constant of integration and

$$V(A) = -\frac{M^2}{A^2} - \frac{b}{4q} A^4 - \frac{c}{2q} A^2. \tag{2.4}$$

Thus, the time evolution can be interpreted as the motion of a "particle" of unit mass in the potential V(A), which is axially symmetric with respect to the phase ψ. Oscillations with M = 0 are of interest since the potential (2.4) gives a deep "well" at the origin for $M \neq 0$.

We consider two cases: a narrow instability region with respect to k, i.e., $\sqrt{\delta/\lambda} \ll 1$, $\lambda \gg 1$ or $\lambda \sim 1$ (see the Appendix, case $I_\pm$), and a broad instability region with respect to k, $\lambda^2/\delta^{2/3} \ll 1$ (see the Appendix, case $II_\pm$).

The terms q and b in the coefficients of (1.13) are calculated for cases I and II in the Appendix.

The solutions of (2.3) for cases I_+ and II_+ have the form:

for $V_0 \leq H \leq 0$ (trajectory 1 in Fig. 2a)

$$\left.\begin{aligned} &A(\tau) = \sqrt{1+\theta_1}\, A_0 \operatorname{dn}\left[\sqrt{\frac{1}{2}\left|\frac{c}{q}\right|}(2+\theta_1)\tau,\ \frac{2\theta_1}{1+\theta_1}\right], \\ &\theta_1 = \sqrt{1 - \left|\frac{H}{V_0}\right|};\ V_0 = -\frac{c^2}{4|qb|};\ A_0 = \sqrt{\left|\frac{c}{b}\right|}. \end{aligned}\right\} \tag{2.5}$$

for $H \geq 0$ (trajectory 2 in Fig. 2a)

$$A(\tau) = A_1 \operatorname{cn}\left[\sqrt{\frac{1}{2}\left|\frac{b}{q}\right|(A_1^2 + A_2^2)}\,\tau,\ \theta_2\right],$$

$$A_{1,2} = A_0\left[\left(1 + \frac{H}{|V_0|}\right)^{1/2} \pm 1\right]^{1/2};\quad \theta_2 = \frac{A_1}{\sqrt{A_1^2 + A_2^2}}.$$

Thus, we have stabilized the linearly unstable oscillations near the upper boundary of the instability region produced by the nonlinearity of the polarization force. The maximum value of the amplitude A is $A_{\max} = \sqrt{2|c/b|}$. In the linear theory the growth rate γ is related to E by [see (1.2)] $\gamma = E\sqrt{|c/q|}$; thus $A_{\max} = (\gamma/E)\sqrt{2|q/b|}$. Calculations give

$$A_{\max}(I_+) \approx 2\sqrt{\frac{2}{3}}\,\frac{\gamma}{E\sqrt{\varepsilon}};\quad \varepsilon = \sqrt{\frac{\delta}{\lambda}} \ll 1, \tag{2.6}$$

$$A_{\max}(II_+) \approx \frac{\gamma}{E}\,\frac{1}{\delta^{1/3}};\quad \delta \gg 1. \tag{2.7}$$

Since $(y-x)_{\max} \approx E(1-\alpha)\Phi + \text{c.c.} \approx 2E(1-\alpha)A_{\max}$ we find the expressions for $(y-x)_{\max}$

$$I_+)\quad (y-x)_{\max} \approx 4\sqrt{\frac{2}{3}}\,\frac{\gamma}{\sqrt{\varepsilon}}, \tag{2.6'}$$

$$II_+)\quad (y-x)_{\max} \approx \frac{2\gamma}{\delta^{1/3}}. \tag{2.7'}$$

In case I_+, $\gamma_{\max} = (1/2)\varepsilon$ (see ref. 2); therefore, near point A the condition $(y-x)_{\max} \ll 1$ is satisfied. Thus, near point $A(k_+)$ the nonlinearity damps the instability at small amplitudes proportional to γ. Note that substitution of the parameters for the upper boundary of the instability region in case I_+ gives saturation amplitude as found by another method in Ref. 3, which coincides with (2.6) to within a numerical factor of order unity.

We now consider the effect of nonlinearity on damping of instability near the lower boundary of the instability region (point B). In this wave-number region the nonlinearity does not damp the instability; indeed, the nonlinearity acts to destabilize. For $\mu < 0$ $(k \gtrsim k_-)$ under these conditions we have $b/q > 0$, i.e., the nonlinear term in potential (2.4) has a negative sign (Fig. 2b). It follows that damping due to the nonlinearity does not occur at small amplitudes near the lower boundary of the instability region; hence the approximation of a small nonlinearity $x, y \ll 1$, used above, is not applicable here.

We now consider the behavior inside the instability region for $k_- \lessapprox k \lessapprox k_+$. We represent ω in (1.7) in the form $\omega = \mathrm{Re}\,\omega + i\gamma$ and make use of the following situation: Far from the boundary A there is a wave-number region for which damping begins at $(y-x)_{\max} \sim \sqrt{\gamma}$. On

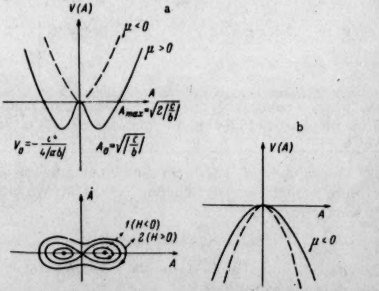

Fig. 2. a) Shape of the potential and phase trajectories for cases I_+ and II_+ (nonlinear stabilization near point A); b) shape of the potential for cases I_- and II_- (nonlinear enhancement near point B shown by dashed curve).

the other hand, near A: $(y-x)_{\max} \sim \gamma$. We take this into account by introducing the slow time evolution (as before, we assume $\gamma \ll 1$) according to the equation $\tau = E^2 t$. We obtain the dispersion relation (1.8) to within ε. To order E^2 we have

$$\left.\begin{aligned} -2i(\omega-kv)\frac{\partial x_1^{(1)}}{\partial\tau}+\frac{\delta}{\alpha}x_1^{(2)}-\delta y_1^{(2)}=-\frac{3}{2}|y_1^{(1)}|^2 y_1^{(1)} \\ \times(1-\alpha)|1-\alpha|^2 e^{2\gamma t}, \\ -2i\omega\frac{\partial y_1^{(1)}}{\partial\tau}+\alpha y_1^{(2)}-x_1^{(2)}=\frac{3}{2}|y_1^{(1)}|^2 y_1^{(1)}(1-\alpha)|1-\alpha|^2 e^{2\gamma t}, \end{aligned}\right\} \quad (2.8)$$

where $\alpha = 1-\omega^2(\operatorname{Im}\alpha \neq 0)$. We multiply the first equation in (2.8) by α/δ and combine it with the second, obtaining

$$\frac{d\Phi}{d\tau}=\frac{3i\delta|1-\alpha|^2(1-\alpha)^2 e^{\frac{2\gamma\tau}{E^2}}|\Phi|^2\Phi}{4[\alpha^2(\omega-kv)+\delta\omega]}. \quad (2.9)$$

The solution of (2.9) is sought in the form of (2.1). Separating the real and imaginary parts, we obtain the equation for $A(\tau)$:

$$\frac{dA}{d\tau}=-\frac{3\delta|1-\alpha|^2\Lambda_{im}}{4}A^3\exp\left(\frac{2\gamma\tau}{E^2}\right), \quad (2.10)$$

where

$$\Lambda=\frac{(1-\alpha)^2}{[\alpha^2(\omega-kv)+\delta\omega]};\quad \Lambda_{im}=\operatorname{Im}\Lambda.$$

Integrating (2.10) with the initial condition $A(0) = A_0$, we obtain

$$A(\tau)=A_0\left[1+E^2\frac{3\delta|1-\alpha|^2\Lambda_{im}}{2\gamma}\left(e^{\frac{2\gamma\tau}{E^2}}-1\right)\right]^{-1/2}. \quad (2.11)$$

Thus, (2.11) gives the expression for the saturation amplitude

$$A_{\text{sat}}=\frac{1}{E}\sqrt{\frac{2\gamma}{3\delta|1-\alpha|^2\Lambda_{im}}}. \quad (2.12)$$

An estimate of Λ_{im} near point A for cases I_+ and II_+ gives

$$\Lambda_{im}(I_+)=\frac{\varepsilon}{\gamma\delta};\quad \Lambda_{im}(II_+)\approx\frac{1}{\gamma\delta^{1/2}}.$$

The saturation amplitudes are

$$A_{\text{sat}}(I_+)=\frac{1}{E}\sqrt{\frac{2}{3}}\frac{\gamma}{\sqrt{\varepsilon}};\quad \varepsilon=\sqrt{\frac{\delta}{\lambda}}\ll 1, \quad (2.13)$$

$$A_{\text{sat}}(II_+)\approx\frac{1}{E}\frac{\gamma}{\delta^{1/4}};\quad \delta\gg 1. \quad (2.13')$$

Expressions (2.13) and (2.13') are the same order of magnitude as (2.6) and (2.7), respectively.

In the middle section of the instability region, for case I_+ [setting $\gamma = \gamma_{\max} = (1/2)E$]: $\Lambda_{im} \approx \gamma/\delta$ so that we find from (2.12): $A_{\text{sat}} \approx 1/E$. Similarly for $(y-x)_{\text{sat}}$ we obtain a value of the order of unity. This means that in the middle section of the instability region (case I_+, $\gamma = \gamma_{\max}$) stability does not occur at small amplitudes and the approximation of a small nonlinearity is not applicable.

Thus, the entire instability region can be divided into three parts (beginning with the upper boundary): 1) $\gamma < (y-x)_{\max} < \sqrt{\gamma}$, 2) $\sqrt{\gamma} < (y-x)_{\max} < 1$, and 3) $(y-x)_{\max} \gtrsim 1$. The wave vector corresponding to $EA_{\max} = \sqrt{\gamma}$ is found from the solution for the expression (the point $p = p_0$, see the Appendix)

$$\Lambda_{im}(p_0)=\left[\frac{3}{2}|1-\alpha(p_0)|^2\right]^{-1}. \quad (2.14)$$

For wave numbers corresponding to $p_0 < p < 1$, stabilization by the nonlinearity occurs at small amplitudes. For $-1 < p < p_0$, we obtain the amplitudes $(y-x)_{\max} \gtrsim 1$. An exact solution has not been obtained for p_0. Analysis of (2.14) indicates that p_0 is close to zero for case I. Consequently, starting from the lower boundary of the instability region (point B in Fig. 1) up to the middle section, ($\gamma = \gamma_{\max}$, $p = 0$), the instability is damped at amplitudes of the order of the beam radius. And only in fairly close proximity to the upper boundary (point A in Fig. 1) is the transverse instability damped at amplitudes $(y-x)_{\max} \ll 1$. The fact that damping by the nonlinearity does not occur at small amplitudes near the lower boundary of the instability region follows formally from the consideration that the value of Λ_{im} in (2.11) near point B is negative (for example, when I_+ $\Lambda_{im} = -\varepsilon/\gamma\delta$).

To investigate the region $p < p_0$, it is necessary to solve the problem with a polarization force (1.4) without assuming a small nonlinearity. We consider the case of a relative displacement $\Delta \gg a$ (this occurs, naturally, during a limited time interval). Then the exponent in (1.4) can be neglected, and we obtain $F(\Delta) \sim 1/\Delta$. But then the system of equations for the displacements give a stable solution. Actually,

$$\left.\begin{aligned} \ddot{x}+\lambda^2 x=\frac{2\delta}{(y-x)}, \\ \ddot{y}=-\frac{2}{(y-x)}. \end{aligned}\right\} \quad (2.15)$$

We write an approximate solution of system (2.15)

$$x \sim \exp i(kz-\Omega_k t);\quad y\approx 0,$$
$$\Omega_k = kv \pm \lambda.$$

It is clear that the expression for Ω_k is real. Thus, there exists a region of amplitudes of the order of the beam radius at which the instability ceases to develop.

Note that system (1.5) with a polarization force (1.4) has a solution when $\lambda = 0$ in the form of a nonlinear stationary wave, where all the terms are functions of one variable $\eta = kz - \omega t$. Actually, in this case we obtain for the dimensionless displacement $\bar{\Delta} = \Delta/a$

$$\frac{d^2\bar{\Delta}}{d\eta^2}=-\frac{T}{\bar{\Delta}}(1-e^{-\bar{\Delta}^2/2}), \quad (2.16)$$

where

$$T=\frac{\delta}{(\omega-kv)}+\frac{1}{\omega^2}>0.$$

Integration of (2.16) leads to the equation of motion of the nonlinear oscillator

$$\frac{1}{2}\left(\frac{d\bar{\Delta}}{d\eta}\right)^2+U(\bar{\Delta})=\bar{H}=\text{const}, \quad (2.17)$$

where $\bar{H}$ is a constant of integration, and

$$U(\bar{\Delta}) = \int_0^{\bar{\Delta}} \frac{(1 - e^{-\Delta^2/2})}{\Delta} d\Delta = U(-\bar{\Delta}). \qquad (2.18)$$

It is easy to show that in the potential (2.18) the motion is finite for any finite values of $\bar{H}$ in (2.17), i.e., the expression for $\bar{\Delta}(\eta)$ has the form of a nonlinear wave with a definite period.

CONCLUSION

We have considered the damping of a transverse instability in an electron–ion ring produced by a nonlinear polarization force. It has been shown that the nonlinear polarization force does not always damp the instability at small amplitudes. In particular, the instability is not damped at small amplitudes near the lower boundary of the instability region. The appearance of instability at the lower boundary is due to resonance at Doppler electron oscillation frequencies, and at small amplitudes the nonlinear polarization force enhances the instability growth rate. Investigation of the equations for high amplitudes indicates that damping of the instability begins in this case at amplitudes of the order of the beam radius.

We thank V. I. Kurilko and B. V. Chirikov for their interest.

APPENDIX

The parameters are calculated at points A and B

$$F(\omega) = \frac{1}{\omega^2} + \frac{\delta}{(\omega - kv)^2 - \lambda^2} = 1, \qquad (A.1)$$

$$\frac{\partial F}{\partial \omega} = 0. \qquad (A.2)$$

We introduce the notation $Y = \omega^2 - 1$. From (A.1) and (A.2) we obtain the equation for Y

$$\left(1 + \frac{\lambda^2}{\delta}\right) Y^4 + Y^3 - \delta Y - \delta = 0, \qquad (A.3)$$

and

$$\omega = \sqrt{1 + Y}; \quad \omega = kv = -\frac{\delta\sqrt{1+Y}}{Y^2}.$$

Case I $(\varepsilon = \sqrt{\delta/\lambda} \ll 1;\ \lambda \gg 1$ or $\lambda \sim 1)$

$$Y = p\varepsilon + \frac{1}{4}\varepsilon^2,$$

$$\omega = 1 + \frac{p}{2}\varepsilon,$$

$$q_\pm = \frac{2k}{(1+\lambda)\varepsilon},$$

$$kv = 1 + \lambda + \frac{p}{2}\varepsilon - \frac{\lambda}{16}\varepsilon^2,$$

$$b_\pm = -\frac{3k}{2(1+\lambda)},$$

$$\alpha = -p\varepsilon - \frac{1}{4}\varepsilon^2,$$

$$\gamma = \frac{1}{2}\varepsilon\sqrt{1 - p^2} \text{ (see ref. 2)}$$

$$p = \begin{cases} +1, \text{at point } A, \\ -1, \text{at point } B. \end{cases}$$

Case II $(\lambda^2/\delta^{2/3} \ll 1)$

$$Y_+ = \delta^{1/3}; \quad Y_- = -\left(1 + \frac{\lambda^2}{\delta}\right)^{-1},$$

$$\omega_+ = \sqrt{1 + \delta^{1/3}}; \quad \omega_- = \left(1 + \frac{\delta}{\lambda^2}\right)^{-1/2},$$

$$(kv)_+ = (1 + \delta^{1/3})^{3/2}; \quad (kv)_- = \frac{\left[1 + \delta\left(1 + \frac{\lambda^2}{\delta}\right)\right]}{\sqrt{\left(1 + \frac{\delta}{\lambda^2}\right)}},$$

$$\alpha_+ = -\delta^{1/3}; \quad \alpha_- = \left(1 + \frac{\lambda^2}{\delta}\right)^{-1}.$$

The values of $q_\pm$ and $b_\pm$ are not given for Case II because of their awkwardness.

---

[1] G. I. Budker, At. Energ., 1, 9 (1956).

[2] B. V. Chirikov, At. Energ., 19, 239 (1965).

[3] N. Yu. Kazarinov, A. B. Kuznetsov, É. A. Perel'shtein, S. B. Rubin, and V. F. Shevtsov, Nonlinear phenomena in snaking instabilities in an electron–ion ring," [in Russian], Preprint P9-6284, Dubna (1972).

[4] H. Washimi and T. Taniuti, Phys. Rev. Lett., 17, 996 (1966).

[5] T. Watanabe, J. Phys. Soc. Jap., 17, 1341 (1969).

[6] Y. Midzuno and T. Watanabe, J. Phys. Soc. Jap., 28, 738 (1970).

Instabilities in interpenetrating electron and ion beams

I. A. Soloshenko and L. P. Katsubo

Institute of Physics of the Ukrainian SSR, Kiev

(Submitted October 30, 1973; resubmitted April 10, 1974)
Zh. Tekh. Fiz., 44, 2126-2131 (October 1974)

Collective oscillations are investigated in a synthesized plasma consisting of interpenetrating electron and ion beams. Instabilities are excited as in the case in which the electron component is at rest and when its velocity v_e exceeds that of the ion component v_i. The experimentally measured frequencies, growth rates, and phase velocities are found to be in qualitative agreement with theory. An effect is detected in which trapping of electrons by the wave field limits the amplitudes of the oscillations; this mechanism accelerates the electrons when $v_e = 0$ and retards them when $v_e > v_i$.

The literature contains a number of experimental investigations of the interaction between a fast ion beam and a stationary electron background. In refs. 1 and 2 an electron plasma instability is observed in such a system, and in refs. 2-4, the linear and nonlinear stages of the interaction are investigated. In the present paper the collective interaction between ions and electrons is investigated in the case in which both components have drift velocities.

The dispersion relation in a system consisting of cold electron and ion beams is

$$\frac{\omega_e^2}{(\omega-kv_e)^2}+\frac{\omega_i^2}{(\omega-kv_i)^2}=1, \tag{1}$$

where ω_e and ω_i are the plasma frequencies; v_e and v_i are the velocities of the electron and ion beams, respectively. It follows from (1) that the system is unstable when $v_e \neq v_i$. The maximum instability growth rate obtains for $k \approx \omega_{pe}/(v_i - v_e)$ and is given by

$$\gamma \approx \frac{\sqrt{3}}{2^{4/3}}\,\omega_e^{1/3}\omega_i^{2/3}. \tag{2}$$

The frequency corresponding to the maximum growth rate is

$$\omega \approx \frac{\omega_e v_i}{v_i-v_e}-\frac{1}{2^{4/3}}\,\omega_e^{1/3}\omega_i^{2/3}. \tag{3}$$

It follows from (3) that ω depends on the relationship between the electron and ion velocities. When $v_e = 0$, $\omega \approx \omega_e$ and for increasing v_e, ω increases until $v_e = v_i$, at which point the system is stable; for $v_e > v_i$ the frequency decreases as v_e increases, and for very high electron velocities ω is roughly equal to the frequency of the Buneman instability [the second term in Eq. (3)]. Below we only consider the case

$$\frac{|v_e-v_i|}{v_i} \ll 2^{4/3}\left(\frac{\omega_e}{\omega_i}\right)^{2/3}.$$

Also,

$$\omega \approx \frac{\omega_e v_i}{v_i-v_e}, \tag{4}$$

and the phase velocity of the excited waves is close to the ion beam velocity.

As in refs. 3 and 4, the exponential growth in a system consisting of an ion beam and a stationary electron background ceases at amplitudes of the potential sufficient for trapping and entrainment of the electrons by the wave field. In a system with interpenetrating electron and ion beams the amplitudes of the potential oscillations should also be restricted by this effect; thus the maximum amplitude of the wave potential $\tilde{\varphi}$ should be

$$\tilde{\varphi} \sim \frac{m\,(v_{\text{ph}}-v_e)^2}{4e} \approx \frac{m\,(v_i-v_e)^2}{4e}. \tag{5}$$

It should be noted that the electron trapping effect should lead to the equalization of the average electron and ion velocities: For $v_e < v_i$ the electrons should be accelerated and for $v_e > v_i$ they should be retarded.

A schematic diagram of the experimental apparatus is given in Fig. 1. The helium or hydrogen ions are extracted from the duoplasmatron 1, accelerated by the field of the electrode 2, and then focused by a magnetic lens 3 into a beam 4. The maximum beam current is $I_i = 40$, maximum energy $eU_0 = 40$ keV, particle density $n_i \sim 10^7$ cm^{-3}, and the beam radius $r_0 \approx 5$ cm. The electrons enter the system from the thermoionic emitter 8 located at the chamber entrance. (The pressure in the chamber $p = 5 \cdot 10^{-6}$ mm Hg, and the contribution of electrons produced by beam ionization of the gas can be ignored). The thermionic emitter–neutralizer consists of a series of tungsten

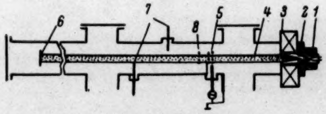

Fig. 1. Schematic diagram of the apparatus.

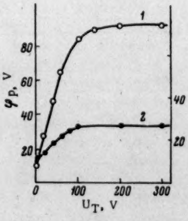

Fig. 2

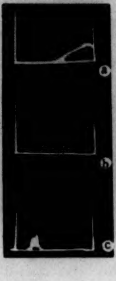

Fig. 3. Spectra of excited oscillations. a) Target potential $U_T = 0$, b) 40, c) 160 V. Ion beam current $H_2^+ I_i$ = 20 mA, and energy eU_0 = 30 keV. The marker on the left is 0 and on the right 30 MHz.

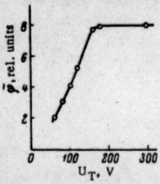

Fig. 4. Amplitude of potential oscillations as a function of the target potential. Ion beam current $H_2^+ I_i$ = 15 mA, energy eU_0 = 30 keV, and distance from the probe to the neutralizer z = 150 cm.

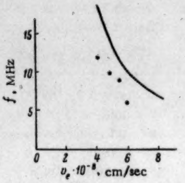

Fig. 5. Frequency of excited oscillations as a function of electron beam velocity. Ion current $H_2^+ I_i$ = 20 mA, and energy eU_0 = 30 keV.

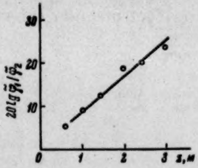

Fig. 6. Distribution of oscillation amplitude along the axis of the system. Ion current $H_2^+ I_i$ = 15 mA, energy eU_0 = 30 keV, target potential U_T = 100 V; φ_1 is the potential oscillation amplitude in the instantaneous z coordinate, φ_2 is a fixed value of the potential oscillation amplitude.

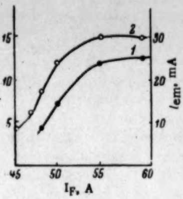

Fig. 7. Electron current from the emitter (curve 2) and potential oscillation amplitude (curve 1) as functions of the filament current. Ion current $H_2^+ I_i$ = 15 mA, energy eU_0 = 30 keV, distance to the emitter z = 150 cm.
150 cm.

needles heated to emission temperature; it is held at a potential close to the wall potential. A double-grid modulator[5] is also located at the beam entrance to the chamber and is connected to an external generator. The amplitudes of the potential oscillations are measured by insulated probes[5] 7; the signals from the probes are amplified and displayed on a spectrum analyzer. The static space potential is measured by thermionic probes located along a radius. The phase velocity of the excited waves is measured by an electronic interferometer system with a delay line.

The electron beam is formed in the sheath in which there is a potential drop between the emitter and synthesized plasma. The potential of the system can be regulated by the potential of the target 6, which is 500 cm from the neutralizer. Figure 2 gives the time-averaged space potential in the center of the beam (curve 1) and the electron current from the neutralizer (curve 2) as functions of the target potential. The beam current $H_2^+ I_i$ = 15 mA, and the energy eU_0 = 30 keV. For modest target potentials the plasma potential increases as U_T increases, and φ_P and U_T are of nearly the same order of magnitude in this region. For larger target potentials, φ_P is independent of U_T. In the latter case a sheath is formed near the target; this is the region in which the potential drop between the plasma and the target occurs. The dependence of the emitter current I_{em} on U_T behaves in similar fashion. For small U_T, according to ref. 6, $I_{em} \sim \sqrt{\bar{\varphi}}$, where $\bar{\varphi}$ is the potential difference between the emitter and the plasma averaged over the radius; with a further increase in U_T the electron current ceases to change because the space potential ceases to change.

The experiments indicate that, depending on the target potential, oscillations can be excited in the system in two spectral regions. For zero target potential, oscillations are excited at frequencies close to the electron plasma frequency (Fig. 3a); this result agrees with theory since the electrons do not have a drift velocity in this case. As the target potential increases, the oscillation amplitude drops sharply, and oscillations are not excited for U_T equal to the floating potential (Fig. 3b); this result is also consistent with theory since the average electron velocity is close to the ion velocity,[7] in this case. With a further increase in the target potential, oscillations are generated in the system at frequencies below the electron frequency (Fig. 3c). Figure 4 gives the dependence of the amplitude of these oscillations on U_T, and Fig. 5 shows the dependence of the frequency on the beam velocity, which is calculated according to $v_e = \sqrt{2e\varphi_0/m}$ where φ_0 is the static space potential in the center of the ion beam [the points are the experimental data, and the curve is calculated from Eq. (4) under the assumption that f_e = 25 MHz]. The experimental frequencies are of the same order as the calculated frequencies. Some of the difference is possibly due to the reduction in electron density at higher target potentials. The absence of oscillations at small target potentials and the increase in the amplitude with increasing U_T are evidently due to the presence of an appreciable potential drop within the ion beam. As the measurements indicate (see ref. 6), for small U_T this drop is of the same order as the potential in the beam center φ_0; therefore, the spread of electron velocities within the ion beam is of the same order as the electron drift velocity. For large U_T the radial potential drop is less than 30% of the potential φ_0 and thus the electron drift velocity exceeds the spread.

Thus, instabilities are only observed experimentally for $v_e \approx 0$ and $v_e > v_i$; the case $v_e < v_i$ has not been real-

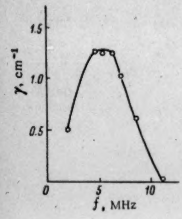

Fig. 8. Growth rate as a function of frequency. Ion current $H_2^+I_i$ = 20 mA, energy eU_0 = 30 keV, target potential U_T = 160 V.

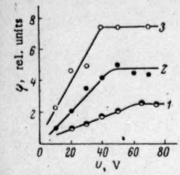

Fig. 9. Amplitude as a function of the generator voltage. 1) Target potential U_T = 0; 2) 40; 3) 80 V. Ion current $H_2^+I_i$ = 20 mA, energy eU_0 = 30 keV, distance to the neutralizer z = 150 cm, modulation frequency f = 4 MHz.

ized because of the large electron velocity spread at small target potentials.

The amplitudes of oscillations excited at large U_T increase exponentially along the beam (Fig. 6). The growth distance, which is determined from the slope of the line shown in Fig. 6, is ~100 cm; this same quantity can be estimated from Eq. (2): $l \sim v_0/\gamma \approx 25$ cm. The difference may be due to the electron velocity spread.

As expected, the instabilities are highly damped in the spectral region investigated when gas is admitted to the chamber, i.e., thermal electrons are produced due to shock ionization of the gas by the beam. Also, plasma oscillations of thermal electrons are driven by the electron current from the emitter.[2]

The instabilities are also damped when the electron current from the emitter decreases; in this case ω_e, and the instability growth rate, decreases. Figure 7 shows the emitter current (curve 1) and the oscillation amplitudes (curve 2) as functions of the filament current of the neutralizer.

To obtain the dependence of the growth rate frequency, to measure the phase velocity, and to investigate the nonlinear stage of the interaction, the ion beam is premodulated. This allows us to measure the magnitude and frequency of the initial perturbation. Figure 8 shows the measured dependence of the growth rate on the modulation frequency. The curve is resonant, and the maximum growth rate is reached at a frequency corresponding to the calculated frequency. [It follows from Eq. (4) that when f_e = 25 MHz, the maximum growth rate should correspond to f = 10 MHz].

Interferometer measurements indicate that when f = 4 MHz and U_T = 160 V the wavelength of the excited oscillations is λ = 42 cm; thus, the phase velocity is $v_{ph} = 1.68 \cdot 10^8$ cm/sec, in agreement with the calculated value for this quantity $v_{ph} \approx v_i = 1.7 \cdot 10^8$ cm/sec.

To detect the nonlinear effect of electron trapping by a wave, the oscillation amplitude is measured as a function of generator voltage. Figure 9 gives these relationships at a distance of ~200 cm from the modulator for different target potentials. In all cases the region with a linear increase in amplitude is replaced by a saturation region, and $\tilde{\varphi}$ is independent of the modulation frequency in the saturation region. It is pointed out in refs. 3 and 4 that when the electron component is at rest (U_T = 0), the maximum amplitude of the potential oscillations is $\tilde{\varphi} \approx (1/4)mv_i^2$. It follows from Eq. (4) that the maximum amplitude for the two other cases (U_T = 40 and 80 V) should increase by a factor of ~2.1 and 4.2, respectively. As can be seen from Fig. 9, the experimental ratios, 1.8 and 3, are close to the calculated ratios. The discrepancy may be due to the method of measuring the amplitude. As the target potential increases the relationship between the probe and the plasma deteriorates since the electron density, and thus the capacitance of the probe–plasma interface, decreases.

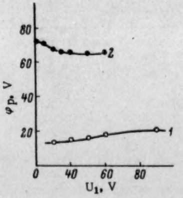

Fig. 10. Space potential in the center of the beam as a function of the generator voltage. 1) U_T = 0; 2) 160 V. Ion current $H_2^+I_i$ = 15 mA, energy eU_0 = 30 keV, f = 4 MHz.

Since the trapping of electrons changes their average velocity and average density in the region of the ion beam, a marked change in the degree of neutralization of the ion beam is to be expected with the excitation of a high-amplitude wave. Figure 10 shows the experimental dependences of the average potential in the center of the beam on the generator voltage for $v_e = 0$ (curve 1) and $v_e > v_i$ (curve 2). At a modulation amplitude sufficient for electron capture at a given point the beam potential begins to change markedly. In the first case the potential increases due to the increase in both the longitudinal and transverse electron velocity;[7] in the second case, electron capture leads to an enhanced neutralization since the average electron velocity decreases.

The present paper represents the first investigation of collective oscillations in a two-component system consisting of interpenetrating ion and electron beams. The fundamental nature of the instability has been established. An effect has been detected in which trapping of electrons restricts the amplitudes of the potential oscillations, and accelerates the electrons for $v_e = 0$ and retards them for $v_e > v_i$. The experimental results agree with theory.

In conclusion we thank M. D. Gabovich for discussion.

---

[1] W. Herrman and Th. J. Fessenden, Phys. Rev. Lett., 18, 535 (1967).

[2] M. D. Gabovich and I. A. Soloshenko, Zh. Tekh. Fiz., 41, 1627 (1971) [Sov. Phys. – Tech. Phys., 16, 1281 (1972)].

[3] M. D. Gabovich, I. A. Soloshenko, and L. S. Simonenko, Zh. Eksp. Teor. Fiz., 62, 1369 (1972) [Sov. Phys. – JETP, 35, 721 (1972)].

[4] M. D. Gabovich, I. A. Soloshenko, and L. S. Simonenko, Ukr. Fiz. Zh., 17, 1362 (1972).

[5] M. D. Gabovich, I. A. Soloshenko, and A. A. Goncharov, Zh. Tekh. Fiz., 43, 2292 (1973) [Sov. Phys. – Tech. Phys., 18, 1450 (1974)].

[6] M. D. Gabovich, I. A. Soloshenko, and A. A. Ovcharenko, Ukr. Fiz. Zh., 16, 934 (1971).

[7] M. D. Gabovich and I. A. Soloshenko, Zh. Tekh, Fiz., 43, 1656 (1973) [Sov. Phys. – Tech. Phys., 43, 1044 (1973)].

Simplified model for the initial stage of exploding wire phenomena

N. N. Stolovich, V. G. Maksimov, and N. S. Minitskaya

Institute of Heat and Mass Transfer, Academy of Sciences of the Belorussian SSR

(Submitted July 10, 1973)
Zh. Tekh. Fiz., 44, 2132-2145 (October 1974)

The initial stage of the electrical explosion of a copper wire is studied theoretically and experimentally; the wire is heated to the boiling point by a high-density current obtained by discharging a capacitor bank.

INTRODUCTION

The electrical explosion of a wire is usually understood to mean the reaction of a comparatively thin wire of given configuration and geometrical dimensions to the short-term effect of a high-density electrical current. Despite its seeming simplicity, the exploding wire phenomenon is in actuality very complex and there is no theoretical model at the present which explains it completely.

In this work we consider the initial stage of the electrical explosion of a wire (its heating to the boiling point) which is arbitrarily divided[1-3] into three phases:[1)] heating of the wire to its fusion temperature T_f, fusion, and subsequent heating of the fused wire to the boiling point T_b.

Figure 1a gives a simplified diagram of the discharge circuit which consists of the condenser C_0 charged to a voltage V_0 by the high-voltage source HVS, the spark gap P, and the exploding wire EW. Initiation of discharge is accomplished at the time $t = t_0$, for example, by applying a high-voltage pulse to one of the electrodes of the three-electrode gap P. Despite the existing nonlinearity of the initial portion of the volt–ampere characteristic for an air spark gap, it is assumed[8-10] that such a circuit containing an air gap can be replaced by an equivalent circuit with lumped parameters and that the resultant resistance of the circuit is constant (except for the resistance of the exploding wire).

The introduction of the equivalent averaged resistance R_{0k} for the spark gap and circuit conductors and the total inductance of the discharge circuit L_{0k} (excluding the inductance L_w of the exploding wire), as we have done in Fig. 1b, is obviously correct only when the time to heat the wire to its fusion temperature is greater than $0.5\pi\sqrt{L_{0k}C_0}$ since the nonlinearity of the volt–ampere characteristic of the discharge gap is insignificant from that time on.[8-12] From the work of Keilhacker[7] and Haussler,[13-14] the exploding wire is replaced by its equivalent inductance L_w and resistance R_w (Fig. 1b), the values of which vary during the flow of a discharge current along the EW.

1. HEATING EXPLODING WIRE FROM T_0 TO T_f

As shown previously,[3,15] the energy expended in radiation and heat transfer between the EW and the surrounding medium is insignificant in the initial stage of the EWP; these are neglected below. The distribution of the temperature, T, over the cross section of the EW is assumed to be uniform. It is assumed that the classical thermodynamic properties and empirical data on the temperature dependence of thermophysical characteristics of materials are also valid for the conditions obtaining in the electrical explosion of a wire.

At the high rates of energy introduction into an EW the current in the EW is initially distributed over its surface because of the skin effect and arrives at the symmetry axis of a cylindrical conductor only after a small (but finite) period of time determined by the diffusion process.[16] The relative increase R_ω/R_0 in the resistance of a cylindrical conductor because of the skin effect based on the approximation[17]

$$\frac{R_\omega}{R_0}=\begin{cases} 1+\frac{n^4}{3} & \text{for } n<1, \\ 0.997n+0.277 & \text{for } 1.5<n<10, \\ n+\frac{1}{4}+\frac{3}{64n} & \text{for } n>10, \end{cases} \tag{1}$$

depends strongly on the parameter n, the values of which for an exploding cylindrical wire can be calculated in the following manner:

$$n=\frac{r_0}{2}\left(\frac{\rho_0 T_0^*}{\pi\mu\mu_0}\right)^{-0.5}, \tag{2}$$

where r_0 is the initial radius of the EW; μ_0 is the magnetic permeability of a vacuum; μ is the relative permeability of the EW material; ρ_0 is its specific electrical resistance of an EW of radius r_0 and length l at the temperature T_0; $T_0^* = 2\pi\sqrt{(L_{0k} + L_w)C_0}$ is the period of the natural oscillations of the discharge circuit.

If we require that the inequality

$$\left|\frac{R_\omega}{R_0}-1\right|\leqslant\varepsilon, \tag{3}$$

be satisfied for $\varepsilon = 0.01$-0.1, relations are easily established, by using Eqs. (1)-(3), between the parameters of

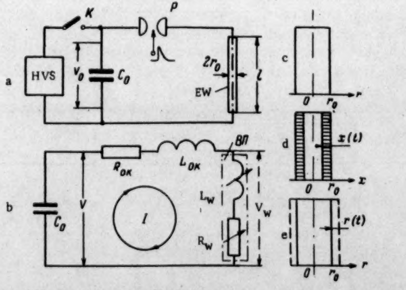

Fig. 1. a) Electrical diagram of exploding wire connected into a discharge circuit; b) equivalent circuit; c-e) choice of coordinate systems associated with the exploding wire; c) heating EW from T_0 to T_f; d) fusion; e) heating EW from T_f to T_b.

the discharge circuit and EW dimensions and materials for which the skin effect need not be considered in the initial stage of the EWP and for which the distribution of the current I can be considered uniform over the cross section of the EW. For example, the period T_0^* of the natural oscillations of the discharge circuit must not be less than $3 \cdot 10^{-5}$ sec for $\varepsilon = 0.05$ in the explosion of copper wires with diameters from 0.1 to 1 mm.

One can then write the following equations describing the transient processes in the discharge circuit and the dynamics of heating the EW from T_0 to T_f during flow of a high-density current I:

$$\frac{d}{dt}(L_{0k}+L_{w1})I+(R_{0k}+R_{w1})I-V=0, \tag{4}$$

$$\frac{dV}{dt}=-\frac{1}{c_0}I, \tag{5}$$

$$\frac{d}{dt}(mcT)=R_{w1}I^2, \tag{6}$$

where t is the time; V is the condenser voltage at time t; I is the current in the discharge circuit; c is the heat capacity of the EW material; m is the EW mass; R_{w1} and L_{w1} are the resistance and inductance of the EW in the first phase of the explosion.

The factors R_{w1}, L_{w1}, and c in Eqs. (4)-(6) are generally complex functions of time

$$c=\Phi[T(t)], \tag{7}$$

$$R_{w1}=G[T(t),\ r(t)], \tag{8}$$

$$L_{w1}=F[r(t)], \tag{9}$$

where r(t) is the radius of the thermally expanding EW at the time t.

At the present time there is no single point of view as to which heat capacity c (c_v or c_p) should be used in the numerical integration of the equation system (4)-(6).[1-7,15,18-20] Thus, Tucker[1] and Keilhacker[7] use c_p while Bennett[18,19] and Vermij[20] use c_v.

The relative increase of the EW radius r(t) with respect to its initial value r_0 during this first phase[21,22] does not exceed 5%. Therefore in Eqs. (4)-(6) with Eqs. (7)-(9) taken into account, empirical data for the specific heat capacity at constant volume c_v are used for the EW material and the variation in radius is neglected in calculations of R_{w1} and L_{w1}. The value of the density γ_0 in this phase is assumed to be constant.2)

Since it does not appear possible to establish the form of the temperature dependence $c_v(T) = \Phi(T)$ directly from the meager experimental data in the literature on measurements of the heat capacity c_v for metals, we use the approximate relation3) for c_p/c_v[23]

$$\frac{c_p(T)}{c_v(T)}=1+\frac{\alpha_v(T)\,T}{a}, \tag{10}$$

where a is the relative atomic packing density (a = 0.74 for a cubic face-centered lattice and a = 0.68 for a body-centered lattice); $\alpha_v(T)$ is the volume coefficient of expansion which to a first approximation, is equal to three times the linear coefficient of expansion α_l and increases in proportion to the first power of the increase in the temperature T.

For a copper wire, the experimental data[25,26] for α_l, converted to the corresponding values of α_v, are closely approximated by the following relation

$$\alpha_v(T)=(44.995+0.016\,T^\circ\,\mathrm{K})\,10^{-6}\ \mathrm{deg}^{-1}, \tag{11}$$

as shown by our computer calculations, with the relative error of the approximation being no more than 5% in the temperature range 293-1356°K. Computer-calculated coefficients for the relation

$$c_p(T)=a_0+a_1T+a_2T^2+a_3T^3\ \ (\mathrm{J/kg\cdot deg}), \tag{12}$$

which approximates the experimental data (on the measurement of c_p) of more than 20 authors have the following values: a_0 = 348.41, a_1 = 0.136, $a_2 = -3.35 \cdot 10^{-5}$, $a_3 = 1.19 \cdot 10^{-8}$. The relative error of this approximation is less than 3.0%.

The values of $c_v(T)$ calculated from Eq. (10) using Eqs. (11) and (12) are approximated by the linear relation

$$c_v(T)=c_v(T_0)[1+B_1(T-T_0)], \tag{13}$$

where $B_1 = 17.07 \cdot 10^{-5}\ \mathrm{deg}^{-1}$, and

$$c_v(T_0)=348.48+0.114T_0 -0.47\cdot10^{-4}T_0^2+0.117\cdot10^{-7}T_0^3\ \ (\mathrm{J/kg\cdot deg}), \tag{14}$$

with the relative error of this approximation being no more than 3-4%.

The experimental data for the specific resistance $\rho(T)$ of copper in the temperature range $T_0 - T_f$, as shown by calculation, are closely approximated by

$$\rho(T)=\rho(T_0)[1+C_1(T-T_0)], \tag{15}$$

where $C_1 = 40.151 \cdot 10^{-4}\ \mathrm{deg}^{-1}$, and

$$\rho_0=\rho(T_0)=(0.5641+30.85\cdot10^{-4}T_0+34.57\cdot10^{-7}T_0^2 +82.65\cdot10^{-11}T_0^3)\,10^{-8}\ \ (\Omega\cdot\mathrm{m}). \tag{16}$$

The EW inductance L_{0w} for this phase is calculated as[27]

$$L_{0w}=\frac{\mu_0 l}{2\pi}\ln\left(\frac{2l}{r_0}-0.75\right), \tag{17}$$

and the EW resistance R_{0w} at T_0 is calculated from

$$R_{0w}=\rho_0\frac{l}{\pi r_0^2}, \tag{18}$$

where μ_0 in Eq. (17) is the magnetic permeability of a vacuum.

Considering Eqs. (13)-(18) along with the relations

$$L_0=L_{0K}+L_{0w},\quad R_0=R_{0k}+R_{0w}, \tag{19}$$

and introducing dimensionless variables for the time τ, temperature, Θ, current in the discharge circuit, i, voltage on the condenser plates, u, and EW radius, ν, through the relations

$$\left.\begin{aligned} &u=\frac{V}{V_0},\quad \Theta=\frac{T}{T_0},\quad \tau=\frac{t}{\sqrt{L_0C_0}},\\ &i=\frac{I}{V_0}\sqrt{\frac{L_0}{C_0}},\quad \nu=\frac{r}{r_0}, \end{aligned}\right\} \tag{20}$$

the equation system (4)-(6) can be transformed to the following form:

$$\frac{dl}{d\tau}=\frac{1}{l_K+l_c}\{(u-la_0\{a_s+a_c[1+c_1(\theta-1)]\}\}, \tag{21}$$

$$\frac{du}{d\tau}=-l, \tag{22}$$

$$\frac{d\theta}{d\tau}=\frac{2\alpha_0 a_c}{q_0[1+b_1(2\Theta-1)]}[1+c_1(\Theta-1)]\,l^2, \tag{23}$$

$$\frac{d\nu}{d\tau}=0, \tag{24}$$

where $l_k, l_c, \alpha_0, a_K, a_c, q_0, c_1$, and b_1 are dimensionless parameters which are defined in terms of the parameters of Eqs. (4)-(6) in the following way:

$$\left.\begin{gathered} l_K=\frac{L_{0K}}{L_0},\quad l_c=\frac{L_{0W}}{L_0},\quad a_c=\frac{R_{0K}}{R_0},\quad a_c=\frac{R_{0W}}{R_0},\\ \alpha_0=R_0\sqrt{\frac{C_0}{L_0}},\quad q_0=\frac{2l\gamma_0\pi r_0^2c_v(T_0)\,T_0}{C_0V_0^2},\\ b_1=B_1T_0,\quad c_1=C_1T_0. \end{gathered}\right\} \tag{25}$$

The initial conditions for the solution of Eqs. (21)-(24) are given in the form

$$\text{at}\quad \tau=0\begin{cases} u=1,\ \Theta=1,\\ l=0,\ \nu=1. \end{cases} \tag{26}$$

Numerical integration of the system of (21)-(24) with the initial conditions (26) is cut off at the time τ_1, which is determined by the following condition:

$$\text{at}\quad \tau=\tau_1\ \Theta=\Theta_f=\frac{T_f}{T_0}. \tag{27}$$

The fusion process beings after the heating of the EW to the temperature Θ_f.

2. FUSION OF THE EXPLODING WIRE

It is assumed fusion of the EW occurs isothermally ($T = T_f$) and its thermal expansion is negligibly small. Fusion of the EW begins simultaneously over its entire lateral surface.[28] The solid metal−melt interface moves toward the symmetry axis of the wire during fusion (Fig. 1d), and its total resistance R_{w2} is given by

$$R_{w2}=\frac{k_f\,l\rho_0[1+C_1(T-T_0)]}{\pi(r_0-x)^2+k_f\,\pi x^2}, \tag{28}$$

where k_f is the relative increase in the resistance of the fused EW material relative to the EW resistance in the solid state at $T = T_f$; x is the coordinate of the moving solid metal−melt interface.

The equation of energy balance for the EW during fusion can be written

$$H_m\frac{dm(t)}{dt}=-R_{w2}I^2, \tag{29}$$

where H_m is the specific heat of fusion for the EW material; m(t) is the mass of the wire still in the solid state.

Since

$$m(t)=\pi x^2 l\gamma, \tag{30}$$

Eq. (29) can be rewritten in the form

$$\frac{dx}{dt}=-\frac{R_{w2}I^2}{2H_m l\gamma\pi x}, \tag{31}$$

where γ is the value of the density of the EW material assumed in the first phase.

The system of equations (4), (5), and (31) describing EW fusion and reduced to canonical form with Eqs. (25) and (28) taken into account takes the following form in terms of the dimensionless variables (20):

$$\frac{dl}{d\tau}=\frac{1}{l_k+l_c}\left\{u-\alpha_0 l\left[a_s+k_f\,a_c\frac{1+c_1(\Theta_f-1)}{(1-\xi)^2+k_f\,\xi^2}\right]\right\}, \tag{32}$$

$$\frac{du}{d\tau}=-l, \tag{33}$$

$$\frac{d\Theta}{d\tau}=0, \tag{34}$$

$$\frac{d\xi}{d\tau}=-\frac{\alpha_0 a_c k_f[1+c_1(\Theta_f-1)]}{\xi[(1-\xi)^2+k_f\,\xi^2]\,h_{\theta f}}\,l^2, \tag{35}$$

$$\frac{d\nu}{d\tau}=0, \tag{36}$$

where the following dimensionless variables and coefficients are used:

$$\xi=\frac{x}{r_0},\ h_{\theta f}=\frac{2H_m\pi r_0^2 l\gamma_0}{C_0V_0^2}. \tag{37}$$

The initial conditions for the solution of (32-(36) are determined from the results of a solution of (21)-(24) at time τ_1 and have the following form

$$\text{at}\quad \tau=\tau_1\begin{cases} u=u_{\tau_1},\ l=l_{\tau_1},\ \Theta=\Theta_f\\ \nu=1,\ \xi=1. \end{cases} \tag{38}$$

Numerical integration of (32)-(36) under the initial conditions (38) is cut off at the time τ_2 when the condition

$$\int_{\tau_1}^{\tau_2} a_0 k_f\,a_c\frac{1+c_1(\Theta_f-1)}{(1-\xi)^2+k_f\,\xi^2}\,l^2 d\tau=\frac{h_{\theta f}}{2}, \tag{39}$$

is satisfied, which corresponds to the condition

$$\xi=0\ \text{at}\ \tau=\tau_2. \tag{40}$$

3. HEATING OF THE FUSED WIRE FROM T_f TO THE BOILING POINT T_h

In considering the phase of EW heating above the fusion temperature, only its radial expansion is taken into account along with the variation of EW inductance, which is defined as[27]

$$L_W=L_{0W}+\frac{\mu_0 l}{4\pi}\ln\frac{r_0}{r(t)}, \tag{41}$$

where r(t) is the EW radius during heating from T_f to T_b (Fig. 1e).

From the condition for mass balance, one can write

$$r(t)=\frac{r_0}{\sqrt{\frac{\gamma(T)}{\gamma_0}}}, \tag{42}$$

where $\gamma(T)$ is the density of the EW material in the liquid state and in the temperature range $T_f - T_b$.

The temperature dependence of $\gamma(T)$ and $\rho(T)$ for liquid copper, as shown by our computer analysis of the experimental data of many authors, can be approximated by the following expressions:

$$\text{at} \quad T_f \leqslant T \leqslant T_b \quad \begin{cases} \gamma(T) = \gamma_l(T_f)[1 - K_\gamma(T - T_0)], & (43) \\ \rho(T) = \rho_p(T_f)[1 + C_2(T - T_0)], & (44) \end{cases}$$

where $K_\gamma = 12.81 \cdot 10^{-5}\ \text{deg}^{-1}$; $C_2 = 33.62 \cdot 10^{-5}\ \text{deg}^{-1}$; $\gamma_l(T_f)$ and $\rho_l(T_f)$ are respectively the density and specific resistance of liquid copper at T_f.

The value of $\rho_l(T_f)$ in Eq. (44) is calculated from

$$\rho_p(T_f) = \rho_0[1 + C_1(T_f - T_0)]k_f. \tag{45}$$

The relative error of approximation (43) is less than 0.6% and that of approximation (44) is less$^{4)}$ than 3%.

The temperature dependence of the heat capacity of liquid metals cannot be considered to be sufficiently investigated at the present time.[24] In a number of papers on the experimental measurement of $c_p(T)$, an increase in heat capacity with increasing temperature is noted; in others there is a reduction and in some papers the heat capacity is almost constant, and in some it varies nonmonotonically. Therefore it does not seem possible to establish the form of the temperature dependence $c_v(T)$ for metals in the liquid state, particularly for copper. In the calculations we assume a constant value for the $c_v(T)$ for copper in the temperature range $T_f - T_b$.

Using Eqs. (42) and (43) we can convert Eq. (6) for this phase of the explosion can be the following form:

$$\pi r_0^2 l \gamma_0 c_v(T_0)[1 + B_1(T_f - T_0)]\frac{dT}{dt} = k_f R_{0w}[1 + C_1(T_f - T_0)] \times [1 + C_2(T - T_0)][1 - K_\gamma(T - T_0)]I^2. \tag{46}$$

Note that Eqs. (42) and (46) indicate that

$$\frac{dr}{dt} = \frac{K_\gamma k_f R_{0w}[1 + C_1(T_f - T_0)][1 + C_2(T - T_0)]}{2\pi r_0 l c_v(T_0)[1 + B_1(T_f - T_0)]\gamma_0\sqrt{1 - K_\gamma(T - T_0)}}I^2. \tag{47}$$

Using Eqs. (46) and (47), the dimensionless variables (20) and (37), the coefficients (25) and (37), and the fact that

$$\left.\begin{aligned} \frac{L_w}{L_0} &= l_c + \frac{\Delta l_w}{2}\ln[1 - K_\gamma(T - T_0)], \\ k_\gamma &= K_\gamma T_0, \quad c_2 = C_2 T_0, \end{aligned}\right\} \tag{48}$$

where

$$\Delta l_w = \frac{\mu_0 l}{2\pi L_0}, \tag{49}$$

we can write the system of equations describing heating of the fused wire from T_f to T_b in the form

$$\frac{di}{d\tau} = \frac{1}{l_k + l_c + \frac{\Delta l_w}{2}\ln[1 - k_\gamma(\theta - 1)]} \times \Big\{u - \alpha_0 i \Big\{a_x + a_c k_f[1 + c_1(\Theta_f - 1)] \times [1 + c_2(\Theta - 1)][1 - k_\gamma(\Theta - 1)] \times \Big[1 - \Delta l_w \frac{k_\gamma}{[1 - k_\gamma(\Theta - 1)][1 + b_1(2\Theta_f - 1)]q_0} i^2\Big]\Big\}\Big\}, \tag{50}$$

$$\frac{du}{d\tau} = -i, \tag{51}$$

$$\frac{d\theta}{d\tau} = \frac{2a_0 a_c k_f[1 + c_1(\Theta_f - 1)][1 + c_2(\Theta - 1)][1 - k_\gamma(\Theta - 1)]}{q_0[1 + b_1(2\Theta_f - 1)]}i^2, \tag{52}$$

$$\frac{d\nu}{d\tau} = \frac{a_0 a_c k_f k_\gamma[1 + c_1(\Theta_f - 1)][1 + c_2(\Theta - 1)]}{q_0[1 + b_1(2\Theta_f - 1)]}i^2. \tag{53}$$

The solution of (50)-(53) under the initial conditions

$$\text{at} \quad \tau = \tau_2 \left\{\begin{matrix} u = u_{\tau_2}, & i = i_{\tau_2}, \\ \Theta = \Theta_f, & \nu = 1 \end{matrix}\right\} \tag{54}$$

should be carried out up to the time τ_3 for which the following condition

$$\text{at} \quad \tau = \tau_3 \quad \Theta = \frac{T_b}{T_0} = \Theta_b. \tag{55}$$

is satisfied.

4. RESULTS OF NUMERICAL INTEGRATION OF THE EQUATION SYSTEMS

Integration of the equation systems (21)-(24), (32)-(36), (50)-(53) under the corresponding initial conditions (26), (38), (54) is carried out numerically on a computer by the Runge–Kutta method. For this purpose the (21)-(24), (32)-(36), and (50)-(53) are formally reduced to the following system:

$$\frac{di}{d\tau} = \frac{1}{l_K + l_w}\left[u - \alpha_0 i\left(a_K + z_w + \frac{\Delta l_w}{R}k_\gamma M i^2\right)\right], \tag{56}$$

$$\frac{du}{d\tau} = -i, \tag{57}$$

$$\frac{d\theta}{d\tau} = 2B\alpha_0 M i^2, \tag{58}$$

$$\frac{d\nu}{d\tau} = +\frac{k_\gamma a_0}{\sqrt{R^3}}M i^2 - A\frac{a_0 a_c k_f P}{\nu N h_{\Theta f}}i^2, \tag{59}$$

where

$$\left.\begin{aligned} P &= 1 + c_1(n_\Theta\Theta - 1); \quad Q = 1 + c_2(n_\Theta\Theta - 1), \\ R &= 1 - k_\gamma(n_\Theta\Theta - 1), \quad z_w = a_c k_f\frac{PQR}{N}, \\ N &= [(1 + k_f)\nu^2 - 2\nu]D + 1, \quad l_w = l_c + \frac{\Delta l_w}{2}\ln R, \\ M &= \frac{z_w}{q_0[1 + b_1(2n_\Theta\Theta - 1)]}, \end{aligned}\right\} \tag{60}$$

with the following conditions being satisfied: a) in the first phase ($0 \le \tau \le \tau_1$), $A = 0$, $B = 1$, $D = 1$, $n_\Theta = 1$, and it is formally assumed $\Delta l_w = 0$, $k_\gamma = 0$, $c_2 = 0$, and $k_f = 1$; b) for the second phase ($\tau_1 \le \tau \le \tau_2$), $A = 1$, $B = 0$, $D = 1$, $n_\Theta = \Theta_f/\Theta$, and it formally assumed $\Delta l_w = 0$, $k_\gamma = 0$, and $c_2 = 0$; c) for the third phase ($\tau_1 \le \tau \le \tau_3$), $A = 0$, $B = 1$, $D = 0$, and $n_\Theta = \Theta_f/\Theta$.

Figures 2 and 3 present the results of a numerical solution of the equation system (59)-(60) under the initial conditions (26), (38), and (54) for the following values of the dimensionless coefficients (25) and (37): $l_K = 0.9828$, $l_c = 0.0172$, $a_K = 0.9155$, $a_c = 0.0845$, $\alpha_0 = 0.1304$, $q_0 = 0.001790$, and $h_{\Theta f} = 0.003735$, which correspond to the parameters of our experimental device where $C_0 = 9\,\mu F$, $L_{0k} = 3.58\,\mu H$, and $R_{0k} = 0.075\,\Omega$ for the electric explosion of a bare copper wire with a diameter $2r_0 = 0.38$ mm and a length of 50 mm at $V_0 = 25$ kV. In the calculations it is assumed $T_0 = 293°K$, $T_f = 1356°K$, $T_b = 2855°K$, $\gamma_0 = 8.93 \cdot 10^3\ kg/m^3$, $H_m = 21.39 \cdot 10^4$ J/kg, $\mu_0 = 12.57 \cdot 10^{-7}$ H/m, and $k_f = 2.5$.

5. METHOD OF MEASUREMENT AND RESULTS

A simplified block diagram of the experimental device used in our work on the electrical explosion of wires in water is shown in Fig. 4. The bank of high-voltage capacitors C1-C3 consists of three IM-50-3 capacitors with a total capacity of $9\,\mu F \pm 1\%$; the three-electrode spark gap p, the construction of which is shown in Fig. 5, is used as a switch. A study of this spark gap using a method described earlier[12] shows that the nonlinearity of the initial portion of its volt–ampere characteristic is significant only for 0.05-0.1 T_0^* at maximum discharge currents of 5-50 kA, which is somewhat different from the values given.[12] Initiation of the discharge is accomplished by a high-voltage pulse from the control panel of the SFR-2M photodetector which is fed through the split condenser 4 to electrode 15 of the gap P. Connection to the condenser bank is made with RK-50-9-11 coaxial cable.

The discharge chamber consists of two cylindrical copper electrodes submerged in a water-filled tank with the metal wire under study stretched between them. The discharge chamber is connected to the gap P by an RKG-15 cable 2.8 m long.

To measure the discharge current during electrical explosion of a wire, a noninductive coaxial current shunt is used which is similar in construction to one previously proposed[29] and which has a resistance of $(55 \pm 0.05) \cdot 10^{-4}$ Ω.

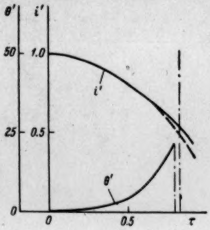

Fig. 3. Dependence of the dimensionless time rates of change for current, $i' = di/d\tau$, and for temperature, $\theta' = d\theta/d\tau$, on the dimensionless time τ.

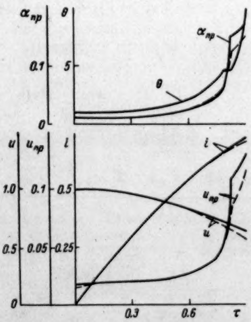

Fig. 2. The dimensionless condenser voltage u, voltage u_w across EW current i, resistance α_w, and EW temperature θ as functions of the dimensionless time τ. Here, and in Fig. 3, the solid curves are the theoretical curves and the dashed curves are experimental curves.

The voltage $V_w(t)$ on the EW is measured with a low-inductance, frequency-compensated TVO-10 resistance voltage divider (scale factor, 38.46; rise time, 10^{-7} sec at most) and is simultaneously recorded with the current I(t) on RF-3 35-mm film by photographing the screen of the cathode ray tube in the OK-17M dual-beam oscilloscope. Note that serious experimental difficulties arise in the determination of $V_w(t)$ because of the induced voltage $V_m(t)$ resulting from the presence of parasitic inductance L_m in the measuring circuit (even though the path is very short) and the high rates of change in the current flowing through it. Thus with L_m of the order of 20 mH and the current rate change of 10^7-10^{10} A/sec, the voltage $V_m(t)$ can reach several hundred volts and completely destroy the useful signal taken from the voltage divider.

The quantity $V_m(t)$ is allowed for by means of a compensation loop using a differential amplifier ahead of the oscilloscope input, as described earlier.[30] To compensate for $V_m(t)$ induced in the measuring circuit, the discharge chamber is shorted by a cylindrical copper rod in place of the exploding wire and the compensating circuit is adjusted so that the recorded time variations in voltage correspond to those which are calculated from current changes and from the resistance and inductance of the copper rod with surface effect included.

Measures are taken, similar to those described previously,[22] to reduce the nonlinearity with respect to amplitude and time in commerical models of the OK-17M oscilloscope. The amplitude nonlinearity over the working portion of the screen does not exceed 2% and the sweep non-

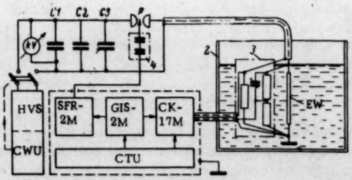

Fig. 4. Simplified Hock diagram of experimental device. HVS) high-voltage source; CWU) control and alarm unit; CTU) calibration and trigger pulse unit; GIS-2M) synchronization unit; SFR-2M) control panel of high-speed photodetector; OK-17M) double-beam oscilloscope; p) discharge gap; 1) high-voltage cable; 2) water-filled tank; 3) container for measuring equipment; EW) exploding wire.

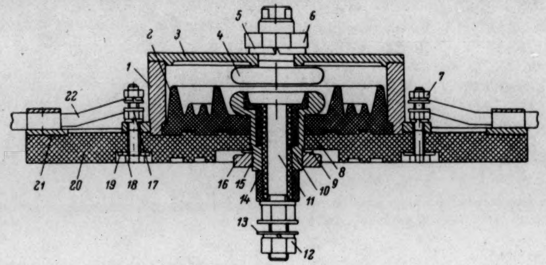

Fig. 5. Construction of spark gap. 1) Housing; 2, 8, 10, 14) insulating bushings; 3) top cover; 4, 11, 15) electrodes; 5, 9, 13, 17) washers; 6, 7, 12, 16) nuts; 18) bolt; 19) circular bus; 20) bottom cover and base; 21) cable-fastening clip; 22) high-voltage cable.

linearity is less than 0.5%. A precision calibrator using silicon stabilitrons for the production of pulses of calibrated height is used to calibrate the pulse-height and time scale factors for the oscilloscope display of $V_W(t)$ and I(t).

Because of all the measures enumerated above, we have managed to increase the accuracy of current and voltage measurements in comparison with our earlier measurements.[31] The relative error in current measurement is no more than 4%; for the voltage $V_W(t)$, it is 7-10%.

The current and voltage oscilloscope traces obtained are put in tabular form by means of an MMI-2 measuring microscope. Inclusion of the inductive component of the voltage on the EW

$$\left[L_W(t)\frac{dI(t)}{dt}+I(t)\frac{dL_W(t)}{dt}\right]$$

in calculations of the ohmic component of the voltage on the EW, and of the resistance and the energy introduced into the EW, is accomplished numerically on a computer.

The total initial circuit inductance L_{0k} and resistance R_{0k} calculated from a current trace for a short-circuited discharge chamber are the following: 3.58 μH and 0.075 Ω. The voltage V_0 on the plates of the condensers C1-C3 during charging is established with an error of no more than 1.5%.

The volume of the tank 2 (Fig. 4), which is filled with tap water, is 1.7 m^3. The water in the tank is replaced after each explosion of a wire. In the experiments, type PEL copper wire is used, the enamel insulation of which is removed with formic acid. For all bare copper-wire samples studied, the diameter and surface cleanliness are checked before installation in the discharge chamber, and the length is checked after installation.

Averaged results from five measurements of the voltage on an EW 0.19 ± 0.01 mm in radius and 50 ± 0.5 mm long, of the current in the discharge circuit and its rate of rise, and of the EW resistance, reduced to dimensionless form using (20) and (25) are shown in Figs. 2 and 3 by the dashed lines. The maximum deviation of individual measurements from the averaged curves is within the limits of accuracy of the measurements (the initial portion at τ = 0-0.1, where the maximum deviation is larger by a factor of 1.5-2, is an exception). Using the experimentally determined values for i, $di/d\tau$, and u_W, the value of the voltage on the condenser plates is calculated as

$$u=l_K\frac{di}{d\tau}+\alpha_0\alpha_K i+u_W$$

from the balance condition for the voltage in the discharge circuit.

Good agreement is observed between the calculated and experimentally measured values for α_W, i, u_W, and u, which are compared in Fig. 2, over the time period corresponding to the first phase of the EWP — heating of an EW from T_0 to T_f. As the figure indicates, theory gives a more rapid increase in the resistance of the two-phase solid metal—melt system during fusion of an EW than is observed experimentally. At time τ_2, our experimentally measured value for the ratio $\alpha_{W\tau_2}/\alpha_{W\tau_1} = k_f$ is 2-2.2 for copper, which is considerably different from the measured value of 1.83 for k_f for copper[22] in the explosion of a copper EW in air. Note that data in the literature on the measurement (or calculation) of k_f for copper by other methods is also contradictory. The value k_f = 2.5 used by us for the integration of (56)-(60) is determined by averaging independent experimental data from many authors for measurement of the specific resistance of copper in the solid and liquid states at the fusion temperature. This value is in satisfactory agreement with other data.[32,33]

As Fig. 2 indicates, the experimentally measured EW resistance α_W increases more rapidly in the time period $\tau_2 - \tau_3$ than the calculated value from the integration of equation system (56)-(60).

Better agreement with experiment than that in Fig. 2 can be obtained by assuming k_f = 2.1, as shown by calculation. Despite this, our view is that the existing considerable differences between experimentally measured and assumed values of k_f cannot be explained merely by the inaccuracy of the k_f values used in the calculations but is more likely evidence that the assumed model of isothermal fusion is very approximate (the fact that thermal expansion of the EW and the external forces opposing this expansion are not taken into account in the consideration of the first two phases of the EWP tends to reinforce this conclusion).

For this electrical explosion of a copper wire in water, we make an experimental check of the Vermij hypothesis[20] about the nonisothermal nature of the fusion process in an EWP which he observed in a study of the electrical explosion of silver wires in air. For this purpose, we compare the duration $\tau_2 - \tau_1$ of the fusion phase which is obtained by numerical solution of equation system (56)-(60) with the value calculated from the experimental curves for $u_w(\tau)$ and $i(\tau)$. The end of EW fusion (the time τ_2) is characterized by a clearly defined sharp bend in the $u_w(\tau)$ curve and therefore is comparatively simple to determine (Fig. 2). The time τ_1 is determined from the experimental curve for $\alpha_w(\tau)$ since for $T = T_f$ and $\tau = \tau_1$, the resistance of the EW is known and is

$$\alpha_{w\tau} = a_c \alpha_0 [1 + c_1 (\Theta_f - 1)].$$

In addition, the value of the energy introduced into the EW in the time $\tau_2 - \tau_1$

$$W_{J_{EW}} = \int_{\tau_1}^{\tau_2} \alpha_w i^2 d\tau,$$

is calculated.

A comparison of the indicated durations $\tau_2 - \tau_1$ shows that the experimental values of $\tau_2 - \tau_1$ are greater than the calculated values, and the experimentally determined energy $W_{J_{EW}}$ is 15-20% greater than the energy which would be expended in isothermal fusion[5] of the EW. The latter indicates that apparently the energy $W_{J_{EW}}$ will be used in part to heat the EW.

A possible reason for the nonisothermal nature of the EW fusion process may be the fact that the magnetic pressure increases as x decreases[20] ($0 \le x \le r_0$, Fig. 1d). This should lead to a dependence of the fusion temperature on the x coordinate in accordance with the Clapeyron equation even for uniform current distribution over the EW cross section and neglect of heat transfer to the surrounding medium. Then during subsequent heating of the EW, the above mentioned temperature nonuniformity over the EW cross section should lead to an "anomalous" rise in EW resistance in the time period $\tau_2 - \tau_3$, which is also observed experimentally (Fig. 2). At large current densities ($j > 10^{10}$ A/m^2), a situation is apparently possible where the boiling point can be reached on the surface of the EW even before the solid metal−melt interface reaches the EW symmetry axis (x [illegible] 0).

However, there are other points of view with respect to the reasons for the anomalous rise in EW resistance. Thus some assume[18,19] that with uniform distribution of current over the EW cross section there is observed no connection whatever between magnetic pressure and the thermodynamic processes taking place in the EW and that the anomalous rise in the resistance of a fused wire during subsequent heating results from a vaporization wave which arises even at temperatures only slightly greater than the EW fusion temperature.

Our experimental results do not allow an answer to the question of which point of view should be adopted for a description of the nonisothermal nature of the fusion and of the anomalous rise in EW resistance although the analysis performed definitely establishes the existence of a radial temperature distribution during the electrical explosion of a wire in water.

Although the proposed model for the initial stage of the EWP also does not take account of the radial distribution of temperature and is based on certain simplifying assumptions, it gives a good description of heating of the EW to its fusion temperature and gives satisfactory results for the description of the subsequent phases, for which refined models may be proposed only after additional experimental studies.

---

[1] Note that such a subdivision of the exploding wire phenomenon (EWP) into stages (or phases) is not unique or generally accepted. Thus Bennett takes as the end of the initial stage of the EWP the striking of an arc in the expanding metal vapor.[4] Manka and Hobson[5] assume the initial stage of the EWP to be one fifth of the natural oscillation period T_0^* of the discharge circuit, which corresponds approximately to the development of the EWP up to the point where fusion of the wire beings. Nash and Olsen[6] divide the explosion of a wire into three stages including in the first stage the development of the process to the point where a current break is created. Keilhacker[7] takes as the end of the first stage of the EWP the completion of fusion of the wire. Thus the duration of the initial stage of the EWP discussed here agrees with that assumed in refs. 1-3, is less than that in refs. 4 and 6, and is greater than that in refs. 5 and 7.

[2] The variation of γ does not exceed 5% during heating of a copper wire in the solid state from 293 to 1356°K.

[3] In the opinion of L. P. Filippov,[24] calculations using the equation of B. N. Oshcherin lead to better agreement with calculations based on the rigorous thermodynamic equation $c_p - c_v = \beta^{-1} v T \alpha_v^2$ than calculations using the empirical relation of Nernst and Lindemann $c_p - c_v = a c_p^2 T$, which is employed in most papers (β is the isothermal compressibility, v is atomic volume, and a is a constant.

[4] In the preceding first and second phases of the electrical explosion of a copper wire the radial expansion of the EW is neglected; hence it is necessary to substitute the value of γ_0 in place of $\gamma_l(T_f)$ in Eq. (43) in order to conserve the initial mass of the EW, which leads to an increase in the relative error of our approximation.

[5] In calculations where $k_f = 2.1$.

---

[1] T. J. Tucker, J. Appl. Phys., 32, 1894 (1961).

[2] P. Koy, Monatsberichte der deutschen Academie der Wissenschaften zu Berlin, 9, 1 (1967).

[3] R. Meininger, in: Exploding Wires, Vol. 3, ed. by W. G. Chace and H. K. Moore, Plenum, New York (1964), p. 47.

[4] F. D. Bennett, Phys. Fluids, 7, 147 (1964).

[5] A. Hobson and C. Manka, J. Appl. Phys., 37, 1897 (1966).

[6] C. P. Nash and C. W. Olsen, Phys. Fluids, 7, 209 (1964).

[7] M. Keilhacker, Z. angew, Phys., 12, No. 2, 49 (1960).

[8] R. Meininger, in: Exploding Wires, ed. by W. G. Chace and H. K. Moore, Plenum, New York (1964).

[9] W. Bertoldi, H. Kressner, and R. Winkler, Przeglad Elektrotechniczhy, 43, 300 (1967).

[10] F. D. Bennett, Phys. Fluids, 9, 471 (1966).

[11] E. H. Cullington, W. G. Chace, and R. L. Morgan, Inst. Geophys. Res., No. 5, AFORL (Sept. 1955).

[12] K. G. Moses and T. Korneff, in: Exploding Wires, Vol. 3, ed. by W. G. Chace and H. K. Moore, Plenum, New York (1964), p. 391.

[13] J. Haeusler, Elektrotechnische Z., Part A, No. 8, 171 (1969).

[14] J. Haeusler, Archiv Elektrotechnik, 53, No. 4, 197 (1970).

[15] E. Fünfer, M. Keilhacker, and G. Lehner, Z. Angew. Phys., 10, 157 (1958).

[16] R. Meininger, in: Exploding Wires, ed. by W. G. Chace and H. K. Moore, Plenum, New York (1962).

[17] B. M. Yavorskii and A. A. Detlaf, Handbook of Physics [in Russian], Izd. Nauka, Moscow (1968).

[18] F. D. Bennett, G. D. Kahl, and E. H. Wedemeyer, in: Exploding Wires, Vol. 3, ed. by W. G. Chace and H. K. Moore, Plenum, New York (1964), p. 65.

[19] F. D. Bennett and G. D. Kahl, in: Exploding Wires, Vol. 4, ed. by W. G. Chace and H. K. Moore, Plenum, New York (1968), p. 1.

[20] L. Vermij, Z. Angew. Phys., 28, 316 (1970).

[21] H. D. Edelson and T. Korneff, J. Appl. Phys., 37, 2166 (1966).

[22] M. M. Martynyuk and N. F. Ganzhela, Izv. VUZ Fiz., No. 3, 30 (1970); M. M. Martynyuk and G. E. Gerrero, Zh. Tekh. Fiz., 42, 187 (1972) [Sov. Phys. – Tech. Phys., 17, 148 (1972)].

[23] B. N. Oshcherin, Teplofiz. Vys. Temp., 2, 946 (1964).

[24] L. P. Filippov, Measurement of Thermal Properties of Solid and Liquid Metals at High Temperature [in Russian], Izd. MGU, Moscow (1967).

[25] J. A. Cahill and A. D. Kirschenbaum, J. Phys. Chem., 66, 1080 (1962).

[26] A. E. El-Mahairy and R. G. Ward, Trans. Metallur. Soc. AIME, 227, 1226 (1963).

[27] P. L. Kalantarov and L. A. Tseitlin, Calculation of Inductance [in Russian], Izd. Energiya, Leningrad (1970).

[28] J. Nasilowski, in: Exploding Wires, Vol. 3, ed. by W. G. Chace and H. K. Moore, Plenum, New York (1964), p. 295.

[29] R. Reidel and J. Blackborn, in: Exploding Wires, ed. by W. G. Chace and H. K. Moore, Plenum, New York (1964).

[30] K. G. Moses and T. Korneff, Rev. Sci. Instrum., 34, 849 (1963).

[31] N. N. Stolovich, N. S. Minitskaya, and V. G. Maksimov, in: Heat and Mass Transfer [in Russian], Vol. 2, Part 2, Minsk (1972), p. 126.

[32] A. M. Korol'kov and D. P. Shashkov, in: Studies of Metals in Liquid and Solid States [in Russian], Izd. Nauka, Moscow (1964), p. 122.

[33] D. R. Wilson, Structure of Liquid Metals and Alloys [Russian translation], Izd. Metallurgiya, Moscow (1972).

Electrical characteristics of underwater exploding wires

V. K. Sholom, E. V. Krivitskii, and V. P. Litvinenko

(Submitted August 2, 1973)
Zh. Tekh. Fiz., 44, 2146-2150 (October 1974)

Using the condition of approximate similarity for the electrical characteristics of an underwater explosion of a wire, empirical equations are obtained which make it possible to determine the inductive peak overvoltage, the minimum current value for which an arc is struck, and the maximum current in the arc stage of the discharge as functions of the parameters of the discharge circuit and the wire. The parameters of the maximum discharge are obtained, i.e., discharges corresponding to the boundary of the current break; conditions are defined for producing the maximum rate of energy deposition in the discharge gap.

The underwater electrical explosion of wires is being used increasingly in industry as a source of intense compression waves with amplitudes in the hundreds and thousands of atmospheres. In particular, the possibility of producing a discharge in comparatively small volumes, the formation of a discharge channel of preassigned shape, and the control of energy characteristics by means of the geometric dimensions and material of the wire itself, make it possible to use an underwater exploding wire (UEW) in industry for shaping various materials, for fastening tubing in the tubing sections of heat-exchange devices, for welding, etc.[1-3]

In these procedures it is very important to know (in addition to the energy relations determining the electrical characteristics of the discharge) the magnitude of the overvoltages in order to prevent breakdown of the insulation.

The qualitative picture of the variation of electrical characteristics of the discharge during explosion of a wire in various media is given rather completely by oscilloscope determination of the energy of electrical explosion of wires.[4]

However, the determination of a relation for the current variation in a circuit containing an exploding wire is complicated by the fact that the markedly nonlinear nature of the resistance of the wire during the phase transition makes it difficult to find an analytic expression.

An attempt to relate the current, voltage, and resistance of the exploding wire to each specific parameter of the discharge circuit separately[5] is not useful because the solution for the transition process in the discharge circuit is determined by a combination.

The application of similarity theory to the calculation of certain characteristics of the electrical explosion of wires[6] makes it possible, by determining the magnitude of the first maximum of the current and the time it appears, to reduce all the various factors defining the discharge at that time to two dimensionless combinations:

$$\Pi_1 = \frac{\rho_0 l}{zS}, \quad \Pi_2 = \frac{CU_0^2}{zS^2h^*}, \tag{1}$$

where ρ_0 is the initial specific resistance; l is the length of the wire; $z = \sqrt{L/C}$ is the characteristic impedance; S is the cross section of the wire; U_0 is the voltage of the charge C on the condenser bank; h^* is a constant for the wire material.

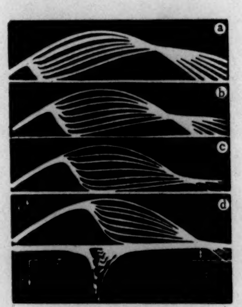

Fig. 1. Oscilloscope traces of discharge current $\bar{i}(\bar{t})$ and voltage $\bar{U}(\bar{t})$ in UEW for various Π_2 and Π_3. Π_2: a) 2.25; b) 0.442; c) 0.19; d) 0.16; $\Pi_3 = (0.0366\text{-}2)\cdot 10^{-2}$.

The fact that the shape and magnitude of the first pulse are determined by processes occurring in the wire itself rather than the nature of the surrounding medium[4] makes it possible to use the defined dimensionless combinations for a description of transition processes during UEW.

As shown below (Fig. 1), however, the two criteria alone are insufficient for the characteristics of the first pulse for a UEW in a mode with no current break.

The criterion Π_1, which defines the current variation during the time for which the wire has a metallic conductivity, has essentially no effect on the nature of the transition process. This is completely justified by the fact that the relation between the current and Π_1 is determined by a power law with an exponent $\alpha \approx 1/12$; for Π_2 = idem, the amplitude of the first pulse of the discharge current remains constant in dimensionless form. However, the trailing edge of the first pulse, which characterizes the depth of the drop, the magnitude of the peak overvoltage produced, and the condition for the onset of the current break remain undetermined.

In the determination of approximate similarity for the characteristics of UEW,[7] it appears possible to represent the system of dimensionless numerical combinations in the form of three criteria: Π_1, Π_2, and Π_3. The values of the criterion Π_2 in refs. 6 and 7 are identical except that the quantity h^* which appears in Π_2 and which is defined as a constant for the EW material with the dimensionality of "specific action," is expressed in ref. 7 in the form of the product

$$h^* \approx \rho_0 \sigma (\lambda + r), \tag{2}$$

where ρ_0 is the density of the wire material, σ is the specific conductivity, λ is the specific heat of fusion, and r is the specific heat of vaporization.

The criterion Π_3 defines the discharge process in the period after breakdown of metallic conductivity and can be determined from the expression[7-9]

$$\Pi_3 = \frac{Al^3}{U_0^2 \pi \sqrt{LC}}, \tag{3}$$

where A is a constant which characterizes state parameters and which is equal to $10^4\ V^2 \cdot sec/m^2$ for UEW.

The basic electrical characteristics are observed by oscillography of the discharge current and voltage. The inductive component of the voltage drop is compensated.[10] The scale factor of the voltage divider is selected so as to ensure recording the peak overvoltage. The parameters of the discharge circuit ($C = 9 \cdot 10^{-6}$ F, $L = 5 \cdot 10^{-6}$ H, $U_0 = 3 \cdot 10^4$ V) correspond to a range within which the conditions for approximate similarity of the UEW are satisfied.[7] The quantities Π_2 and Π_3 are varied by changing the diameter and length of the copper wire.

With Π_2 = idem, six oscilloscope traces of the exploding wire are exposed on each frame of film for various values of Π_3. The range of variation of the third criterion is bounded from above by the limiting case, in which the drop in the discharge current reaches a maximum value, and from below by the case in which there is essentially no current drop. The existence of such traces presents an opportunity to follow the nature of the transition process for all possible values of the criteria in a discharge without a current break.

Figure 1 shows traces of discharge current and voltage when the explosion occurs during the first half-cycle of the discharge current. For comparison, each frame shows the current curve in the short-circuit mode and a voltage curve in the open-circuit mode corresponding to the voltage of the charged condenser bank.

These oscilloscope traces make it clear that for certain definite values of Π_2 and Π_3 the entire energy of the condenser bank is deposited during the first current pulse (Fig. 1). The rise in the current in the first pulse coincides with the rise in the short-circuit mode and can be calculated without any particular error from the equations for R_C, L, and C of the circuit, where R_C = const is the equivalent effective resistance of the elements of the discharge circuit. The peak overvoltage increases (Fig. 2) as the time of explosion approximates the time of discharge and its value can exceed the voltage on the condenser bank by a factor of 4-5. The steepness of the current drop in the first pulse for discharges close to the "maximum" (where the current goes to zero) is practically unchanged when there are changes in Π_2. In absolute magnitude, it is approximately three times greater than U_0/L.

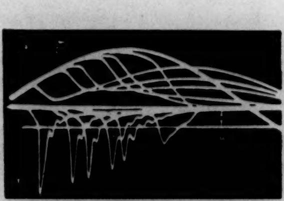

Fig. 2. Variation of peak overvoltage $\bar{U}(\bar{t})$ and of discharge current $\bar{i}(\bar{t})$ for UEW with $\Pi_2 = 2.25$-0.0515 and Π_3 = const.

From other data[4,7,11] one should expect that the transition process in the circuit during explosion of aluminum, silver, and gold wires in water would be similar to the transition process during the explosion of copper wires.

In view of the fact that the properties of the surrounding medium have little effect on the first pulse, the dependence on similarity criteria of the dimensionless current amplitude, $i_m/U_0(\sqrt{L/C})$ and the dimensionless time $\tau_m = t_m/\pi\sqrt{LC}$) for the metals in this group can be described by a power function[6] with the relation

$$\Pi_2 = \frac{1.23P}{\rho_0 \sigma (\lambda + r)} \tag{4}$$

taken into account, where

$$P = \frac{CU_0^2}{2\pi S^2},$$

and S is the cross section of the wire.

The depth of the drop, which is determined by the minimum value of the current i_{min} before the arc stage, and the amplitude of the second pulse i_{max} depend on the criteria Π_2 and Π_3:

$$\left.\begin{aligned} i_{min} &\approx 0.85 \cdot 10^3\, \Pi_2^{-1/4} (\Pi_3 - 0.025)^2, \\ i_{max} &\approx 1 - \Pi_2^{-1/3} \Pi_3^{1/4}. \end{aligned}\right\} \tag{5}$$

The magnitude of the peak inductive overvoltage produced during the explosion of a wire, which is determined by the steepness of the drop in the discharge current, can be found from the approximate expression

$$\frac{U_n}{U_0} = 20 \Pi_2^{1/4} \Pi_3^{1/3}. \tag{6}$$

Verification of Eq. (6), which is obtained from an analysis of the experimental data for the explosion of wires by a condenser bank with a capacity $C = 9 \cdot 10^{-6}$ F charged to a voltage $U_0 = 3 \cdot 10^4$ V and for a discharge circuit inductance $L = 5 \cdot 10^{-6}$ H, is carried out over the range of circuit and wire parameter variations shown in Table 1.

For a discharge without a current break, the deviation of experimental data in the indicated range, and also of other data,[2] from calculated values based on Eq. (6) does not exceed 15%.

As indicated above, the range of variation of conditions and parameters is limited to a discharge without a current break. The limiting case of such a discharge is

TABLE 1

	C, μF	U_0, kV	L, μH	d, mm	l, mm
Lower limit	1	8	1.15	0.07	28
Upper limit	99	40	10	0.9	200

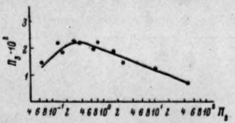

Fig. 3. Region of existence for break-free discharges bounded by the relation $\Pi_3 = f(\Pi_2)$.

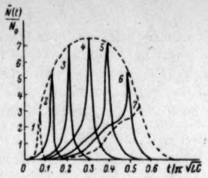

Fig. 4. Family of normalized curves for the electrical power $\tilde{N}$ in discharge modes accompanied by a current drop to zero. Π_2: 1) 9; 2) 2.56; 3) 0.68; 4) 0.228; 5) 0.154; 6) 0.104; 7) 0.065.

a discharge accompanied by a current drop to a value close to zero, with subsequent nearly instantaneous secondary breakdown (secondary initiation).

These discharges (Fig. 1), in terms of the dimensionless similarity criteria, are characterized by a region which is bounded by the curve for the dependence of the maximum value of Π_3 as a function of Π_2 (Fig. 3), above which Eq. (6) cannot be considered to be correct.

Figure 4 gives a family of normalized curves for the electrical power $N(t/\pi\sqrt{LC})/N_0$ for discharge modes accompanied by a current drop to zero in accordance with Fig. 3.

The resultant dependence of the maximum values of Π_3 has a clearly defined maximum, which corresponds to the optimum value of Π_2 from the viewpoint of rate of energy deposition.

Using the expressions for Π_2 and Π_3 as functions of the dimensional constants which characterize the parameters of the discharge circuit and of the wire, one can define conditions which provide a maximum rate of energy deposition in the discharge gap:

$$d_{\text{opt}} = 2\left(\frac{W_0}{z\rho_0\sigma(\lambda + r)}\right)^{1/6}, \tag{7}$$

$$l_{\text{opt}} = 2 \cdot 10^{-3} U_0 \sqrt[4]{LC}, \tag{8}$$

where W_0 is the stored energy. The resultant equations (7) and (8) assume deposition of the energy stored in the condenser bank during the first discharge current pulse.

Thus, the use of an approximate similarity criterion for the underwater explosion of a wire makes it possible to determine the value of the inductive peak overvoltage as a function of wire and discharge-circuit parameters and to determine the conditions corresponding to the maximum rate of energy deposition in the discharge gap.

The expressions obtained here can be used for calculating the electrical stability of special electrode systems and are basic relations determining the hydrodynamics of phenomena in devices based on UEW principles.

---

[1] Sukhara Tosiro, Kitadzima Kadzuhori, and Fukuda Sigekhisa, J. Japan Soc. Tech. Plastic., 9, 324 (1965).

[2] Hakazawa Echinori and Hara Hiroshi, Sosei To Kako, 13, 14 (1972).

[3] H. Müller, Indust. Anzeiger, 90, 73 (1968).

[4] I. F. Kvartskhava, A. A. Plyutto, A. A. Chernov, and V. V. Bondarenko, Zh. Eksp. Teor. Fiz., 30, 42 (1956) [Sov. Phys. – JETP, 3, 40 (1956)].

[5] D. Kind, J. Slage, S. Ludwig, and C. Newi, Electrotech., A92, No. 1, 46 (1971).

[6] E. I. Azarkevich, Zh. Tekh. Fiz., 43, 141 (1973) [Sov. Phys. – Tech. Phys., 18, 90 (1973)].

[7] E. V. Krivitskii and V. K. Sholom, Zh. Tekh. Fiz., 44, 1271 (1974) [Sov. Phys. – Tech. Phys., 19, 798 (1974)].

[8] Z. E. Okun', Zh. Tekh. Fiz., 39, 837 (1969) [Sov. Phys. – Tech. Phys., 14, 627 (1969)].

[9] E. V. Krivitskii and V. V. Shamko, Zh. Tekh. Fiz., 42, 83 (1972) [Sov. Phys. – Tech. Phys., 17, 62 (1972)].

[10] G. A. Ostroumov and A. A. Shteinberg, Prib. Tekh. Eksp., No. 3 (1963).

[11] W. Chace and H. K. Moore (eds.), Exploding Wires, Vol. 2, Plenum, New York (1962).

Analytic model of the cesium arc

V. P. Pashchenko, V. L. Mironovich, and I. P. Stakhanov

(Submitted November 24, 1973)
Zh. Tekh. Fiz., 44, 2151-2158 (October 1974)

An analytic expression is obtained for the voltage–current characteristic of a cesium discharge with recombination included. The main purpose is to obtain simple, limiting analytic expressions that contain the basic experimental quantities. In this regard the assumptions are more rigorous than those of ref. 1: Coulomb scattering and the electron temperature gradient are neglected. A relationship is established between individual points on the curve and the nature of the volume processes. Agreement between the experimental data and the model is shown.

1. The purpose of the present paper is to establish a relationship between the current J_e and the voltage V of a plane cesium diode with a hot cathode and a cold anode. The parameters of the plasma in the electrode gap and at the boundaries are assumed to satisfy the following relations:

$$\left.\begin{aligned} &\frac{dT_e}{dx}=0;\ \frac{dJ_e}{dx}=0;\ n_1=n_2;\ \Delta\varphi_1>0,\ \Delta\varphi_2<0,\\ &\left(D_a\frac{dn}{dx}\right)_{1,2}\gg\frac{u_i}{u_e}J_e;\quad n_0(T_e)\gg n_m\gg n_1. \end{aligned}\right\} \tag{1}$$

Here, the terms characterizing the electron and ion components are denoted by the subscripts e and i. The subscript 1 denotes quantities at the boundary near the cathode, and 2 those near the anode; the subscript 0 on the plasma density means that this term is obtained from the Saha equation with temperature T_e; n_m is the maximum plasma density in the gap. The symbols for jumps in the electrode potentials $\Delta\varphi_1$ and $\Delta\varphi_2$ are chosen under the assumption that volume ionization prevents loss of the electrons from the plasma gap. The ion production is given by

$$\frac{dJ_i}{dx}=\alpha(T_e,\ p)\,n\left(1-\frac{n^2}{n_0^2(T_e)}\right), \tag{2}$$

where the expression obtained in ref. 2 is used for the ionization coefficient α:

$$\begin{gathered} \alpha=\alpha_0\exp\left\{-\frac{E_*}{T_e}\right\},\\ \alpha_0=1.44\cdot10^{12}\,n_a v_e,\\ E_*=3.21\ \text{eV} \end{gathered} \tag{3}$$

(n_a is the density of the neutral component, and v_e is the thermal velocity of the electrons). Under these assumptions the transport equations and their boundary conditions are

$$\left.\begin{gathered} \frac{d^2n}{dx^2}=-\gamma^2\left(n-\frac{n^3}{n_0^2}\right),\\ \left(\frac{dn}{dx}\right)_{1,2}=\mp\frac{n_1}{\delta L}, \end{gathered}\right\} \tag{4}$$

where $\gamma=\sqrt{\alpha/D_a}$, $\delta=2D_a/v_iL$, and D_a is the ambipolar diffusion coefficient.

From the boundary conditions for the particle and energy fluxes, which are taken in their usual form, and with the symbols selected for the potential jumps near the electrodes, we obtain[1,3]

$$\left.\begin{gathered} \frac{eV}{T_e}-\ln\frac{J_e}{J_R-J_e}=\frac{J_e}{D_e}\int\limits_0^L\frac{dx}{n},\\ \frac{eV}{T_e}-\frac{aJ_R}{J_e}=\frac{n_1v_iE_i}{T_eJ_e}, \end{gathered}\right\} \tag{5}$$

where J_R is the emission current from the cathode; L is the electrode spacing; D_e is the electron diffusion coefficient; $a=2(1-T_1/T_e)$; v_i is the ion thermal velocity; E_i is the effective ionization potential, which is roughly equal to the cesium ionization potential 3.89 eV.

The first relation in (5) is the voltage balance for the internal potential difference. The logarithmic term is equal to the sum of the electrode jumps, and the right side gives the potential drop in the plasma. The second relation is the energy balance equation, from which it follows that Joule heating (J_eV) is expended in heating the electron component (aJ_R) and in the ionization losses represented in the right side. It should be noted that this expression is obtained in the same manner as in the model neglecting recombination[3] since the electrode potential jumps do not prevent the escape of ions from the plasma to the electrodes.

Thus, the development of an expression for the voltage–current characteristic reduces to the calculation of the integral $\int\limits_0^L dx/n$ and to the derivation of an expression for the electron temperature as a function of the density at the boundary n_1. We use Eq. (4) for this purpose. Integrating, we obtain (see ref. 4)

$$\gamma L=2\sqrt{1+k^2}\int\limits_{n_1/n_m}^{1}\frac{dt}{\sqrt{(1-t^2)(1-k^2t^2)}}, \tag{6}$$

where

$$k^2=\frac{\left(\frac{n_m}{n_0}\right)^2}{2-\left(\frac{n_m}{n_0}\right)^2},\quad n_m^2=n_0^2\left(1-\sqrt{1-\left(\frac{\sqrt{2}}{\gamma L\delta}\frac{n_1}{n_0}\right)^2}\right). \tag{7}$$

Equation (6) is used to find the electron temperature. With no recombination ($n_m \ll n_0$), we obtain $\gamma L=\pi(1-2\delta)$ from which the expression for T_e obtained in ref. 3 follows:

$$\frac{1}{T_e^0}=\frac{1}{E_*}\ln\frac{\alpha_0L^2}{\pi^2D_a}. \tag{8}$$

However, for strong recombination, $\pi\delta/\sqrt{2}\ll n_1/n_0\ll1$

$$\gamma L=\frac{n_1\sqrt{2}}{n_0\delta}\frac{1}{\sqrt{1-r_0^2}}, \tag{9}$$

where

$$r_0\approx8\exp\left\{-\frac{n_1}{n_0\delta}\right\} \tag{10}$$

makes a small correction. Neglecting r_0, we write the expression for T_e with recombination taken into account:

$$\frac{1}{T_e}=\frac{1}{T_e^0}-\frac{2}{E_i+E_*}\ln\frac{n_1}{n_{1*}}+\frac{1}{E_i+E_*}\ln\left[\left(\frac{T_e}{T_e^0}\right)^{3/2}\frac{T_1+T_e}{T_1+T_e^0}\right]. \qquad (11)$$

Here, T_1 is the cathode temperature; T_e^0 is given by (8); $n_{1*}=(\pi\delta/\sqrt{2})\cdot n_0(T_e^0)$; $n_0(T_e^0)$ is the Saha electron density corresponding to the temperature T_e^0.

In (11) the last term is small and can be neglected. Then we obtain the Saha equilibrium density for temperature T_e:

$$n_0(T_e)=n_0(T_e^0)\left(\frac{n_1}{n_{1*}}\right)^{\beta}, \quad \beta=\frac{E_i}{E_i+E_*}. \qquad (12)$$

The integral $\int\limits_0^L dx/n$ depends essentially on the small correction to the radical of Eq. (6). After several transformations it can be written $\int\limits_0^{\xi_1} d\xi/(1-\xi^2)$, where $\xi_1 = 1-[(1-k^2)/2]n_1^2/n_m^2$. Then the potential drop in the volume [i.e., the right side of the first equation in (5)] becomes

$$\frac{J_e}{D_e}\int\limits_0^L\frac{dx}{n}=\frac{J_e}{D_e}\frac{2\lambda L}{n_1}\ln\frac{2n_m}{n_1\sqrt{1-k^2}}. \qquad (13)$$

The logarithmic factor in (13) has various limiting values. In the absence of recombination [$n_m \ll n_a$, i.e., $k\approx 0$; see (7)] a valid expression is

$$\ln\frac{2n_m}{n_1\sqrt{1-k^2}}=\ln\frac{2}{\pi\delta},$$

which is the same as the expression obtained in ref. 3. If the recombination is substantial [$n_m \approx n_0$, i.e., $k\approx 1$; see (7)], then this factor increases sharply and its magnitude is determined by the small correction to the radical of Eq. (6). According to (9) and (10), we obtain

$$\ln\frac{2n_m}{n_1\sqrt{1-k^2}}=\ln\frac{2n_m}{n_1}+\frac{1}{2}\ln\frac{1}{r_0}=\ln\frac{n_m}{n_1\sqrt{2}}+\frac{n_1}{2\delta n_0}.$$

The structure of this expression indicates that all the basic changes in the potential drop related to the recombination are determined by the term $n_1/2\delta n_0$, which increases as n_1 increases. Actually, according to (12), $n_0\sim n_1^{\beta}$ and this leads to $n_1/2\delta n_0\sim n_1^{1-\beta}$. In this case $\ln n_m/n_1\sqrt{2}\leq \ln 2/\pi\delta$. Taking the above remarks into account we can approximate the logarithmic factor in (13) by

$$\ln\frac{2n_m}{n_1\sqrt{1-k^2}}=\ln\frac{2}{\pi\delta}\left(1+\frac{n_1}{2n_0\delta\ln\frac{2}{\pi\delta}}\right),$$

which has the correct limiting values for weak and strong recombination.

We introduce the dimensionless parameters

$$\left.\begin{gathered}U=\frac{eV}{T_e},\quad I=\frac{J_e}{J_R},\quad \Lambda=\ln\frac{2}{\pi\delta},\quad \varepsilon=\frac{4E_iD_a\Lambda}{T_eD_e},\\ \nu_1=\frac{n_1v_i}{J_R}\frac{E_i}{\varepsilon T_e},\quad \nu_{1*}=\frac{\pi\delta n_0(T_e^0)v_i}{\sqrt{2}J_R}=\frac{n_{1*}v_i}{J_R}\frac{E_i}{\varepsilon T_e}.\end{gathered}\right\} \qquad (14)$$

In this notation, the expression for the voltage–current characteristic becomes

$$\left.\begin{gathered}U-\frac{a}{I}=\frac{\varepsilon\nu_1}{I},\\ U-\ln\frac{I}{1-I}=\frac{I}{\nu}\left[1+\frac{\pi}{\Lambda\sqrt{8}}\left(\frac{\nu_1}{\nu_{1*}}\right)^{1-\beta}\right],\\ \frac{1}{T_e}=\frac{1}{T_e^0}-\frac{2\beta}{E_i}\ln\frac{\nu_1}{\nu_{1*}},\end{gathered}\right\} \qquad (15)$$

where, as before, $a = 2(1-T_1/T_e)$ and $\beta = E_i/(E_i+E_*)$. In a qualitative analysis we can neglect the variation of T_e with the current in the power and logarithmic functions, setting $a = 2(1-T_1/T_e^0)$ and $n_0(T_e) = n_0(T_e^0)\cdot(n_1/n_{1*})^{\beta}$ [see (12)]. Then the voltage–current characteristic can be written

$$\left(U-\ln\frac{I}{1-I}\right)\left(U-\frac{a}{I}\right)=\varepsilon+\frac{\pi\varepsilon}{\Lambda\sqrt{8}}\left(\frac{\nu_1}{\nu_{1*}}\right)^{1-\beta}, \qquad (16)$$

i.e., as a function of the parameters ε, a, ν_{1*}.

Under typical conditions $\varepsilon \leqslant 0.2$, which means that this parameter has little influence on the shape of the characteristic. The influence of the parameters a and ν_{1*} on the shape of the curve is more substantial. It follows from the structure of (16) that the voltage–current curve is in the region bounded by three intersection curves: the logarithmic asymptote $U_l = \ln I/(1-I)$, the hyperbola $U_h = a/I$, and the power curve $U_p = (\pi\varepsilon/\Lambda\sqrt{8})^{1/(1+\beta)}\cdot(I/\varepsilon\nu_{1*})^{(1-\beta)/(1+\beta)}$. The characteristic points on the curve are the inversion point (U_0, I_0) and the inflection point (U_{in}, I_{in}). A substantial role in the following discussion will be played by the point of intersection of the power-law and hyperbolic asymptotes $(U_1 I_1)$. These properties are shown in Fig. 1.

The introduction of the asymptotic curves allows us to formulate criteria for the influence of recombination. If the power asymptote goes to the left of the point of intersection of the asymptotes U_l and U_h the recombination is weak because the second term in the right side of (16) can be neglected. This term is much larger than ε (i.e., the recombination is substantial) if the point (U_1, I_1) has a much larger abscissa and a much smaller ordinate than the point of intersection of the logarithmic and hyperbolic asymptotes.

Typical families of voltage–current characteristic curves are shown in Fig. 2 for different values of a and $\varepsilon\nu_{1*}$. These curves contain the basic qualitative elements observed experimentally, i.e., they have segments of negative differential resistance, as well as inversions and inflection points that separate the segments of positive and negative curvature. For a certain relationship between the

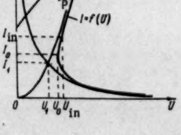

Fig. 1. The voltage–current characteristic and the asymptotic curves.

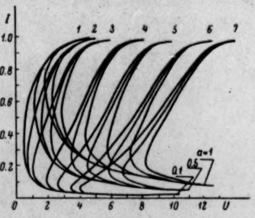

Fig. 2. Families of voltage–current characteristics with different degrees of recombination. 1) $(\varepsilon\nu_{*})^{-1} = 0$; 2) 250; 3) $2.6\cdot10^3$; 4) $3.3\cdot10^4$; 5) $1.2\cdot10^5$; 6) $3.6\cdot10^5$; 7) $6.6\cdot10^5$.

parameters a and ν_{1*}, for example $a = 0.1$ and $(\varepsilon\nu_{1*})^{-1} = 2.6\cdot10^3$ the voltage–current characteristic has a large linear segment (Fig. 2).

2. The complex, two-parameter family of curves (16) can be simplified by introducing new variables:

$$\left.\begin{aligned} &x=\frac{U}{U_1},\quad y=\frac{I}{I_1},\\ &U_1=\sqrt{\frac{\pi\varepsilon}{\Lambda\sqrt{8}}\left(\frac{a}{\varepsilon\nu_{1*}}\right)^{1-\beta}},\quad I_1=\sqrt{\frac{\Lambda\sqrt{8}}{\pi\varepsilon}a^{1+\beta}(\varepsilon\nu_{1*})^{1-\beta}}.\end{aligned}\right\}\qquad(17)$$

Then, in the coordinates x and y, Eq. (16) is written

$$(xy-1)\left[\frac{x}{y}-\frac{1}{U_1y}\ln\frac{y}{\frac{U_1}{a}-y}-\frac{\varepsilon}{U_1^2(xy-1)}-(xy-1)^{-\beta}\right]=0.\qquad(18)$$

This expression consists of two factors. Equating the first to zero, we obtain the hyperbolic asymptote, which approximates the falling branch of the voltage–current curve, i.e., that part below the inversion point (Fig. 1). Equating the second factor to zero, we obtain an approximation of the branch of the curve above the inversion point. We consider this case in more detail.

If the two terms of the second factor in (18) are negligible compared to the first two, we obtain an approximation for the characteristic in the saturation region – a logarithmic asymptote. If the relationship between the latter two terms satisfies $\varepsilon/U_1 \gg (xy-1)^{1-\beta}$ we obtain an expression for the characteristic in the absence of recombination. When $\varepsilon/U_1 \ll (xy-1)^{1-\beta}$, we have the characteristic of a process in which recombination is dominant:

$$(xy-1)\left[\frac{x}{y}-(xy-1)^{-\beta}-\frac{1}{U_1y}\ln\frac{y}{\frac{U_1}{a}-y}\right]=0.\qquad(19)$$

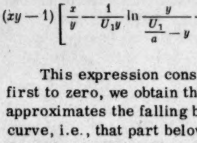

Fig. 3. Envelope (1) and families of voltage–current curves in the absence (2) and presence (3) of recombination for $a = 0.4$, $U_1 = 0.8, 2, 4, 8, 20$.

Equation (19) with parameters a and U_1 describes the family of curves with envelope

$$F(x,\ y)=x(xy-1)^{-\beta}-y=0,\qquad(20)$$

which consists of a falling branch ($y = 1/x$) and a segment with a positive derivative – a power asymptote [$y = x^{(1+\beta)(1-\beta)}$]. The inversion point $(x_0, y_0)|_{dx/dy=0}$ and the inflection point $(x_{\mathrm{in}}, y_{\mathrm{in}})|_{d^2y/dx^2=0}$ lie on the envelope. Any of the characteristic curves of a family with predominant recombination are to the right of the curve (20), lying closest to its middle section and on the falling branch. All nonrecombination characteristics in the middle section and on the falling branch are to the left of the envelope. Only in the saturation region can they enter the half-plane to the right of the envelope. Thus, the curve $F(x, y) = 0$ is a unique boundary for the recombination characteristics (Fig. 3).

We now analyze the envelope. The appropriate calculation gives the expressions

$$x_0=\beta^{-\beta/2}(1-\beta)^{\frac{\beta-1}{2}}=1.410,$$
$$y_0=\beta^{\beta/2}(1-\beta)^{-\frac{1+\beta}{2}}=1.568$$

for the coordinates of the inversion point. Calculating the inflection point, we obtain its coordinates

$$x_{\mathrm{in}}=\sqrt{\frac{2+\sqrt{1+3\beta^2}}{(1-\beta^2)\left(\frac{2+\sqrt{1+3\beta^2}}{1-\beta^2}-1\right)^{\beta}}}=1.521,$$

$$y_{\mathrm{in}}=\sqrt{\frac{2+\sqrt{1+3\beta^2}}{1-\beta^2}\left(\frac{2+\sqrt{1+3\beta^2}}{1-\beta^2}-1\right)^{\beta}}=3.174.$$

We now expand about the inversion point:

$$y=3.17+11.43(x-1.52),\qquad(21)$$

to obtain an approximate voltage–current characteristic from the inversion point to the point with coordinates $x = 2$, $y = 10$ to within 5%. The derivative $(dy/dx)|_{x_{\mathrm{in}},y_{\mathrm{in}}} = 11.43$ is the minimum value of the slope of all points of the characteristic above the inversion point.

We now consider the effect of the Richardson current on the voltage–current characteristic. On the falling branch ($y \approx a/x$) and in the saturation region [$y = U_1/a$, see (19)], the current is proportional to I_R by virtue of (17). According to these same equations and (21), in the neighborhood of the inflection point I_R has a weaker effect on the current across the converter. Here, $I \sim I_R^{(1+\beta)/2} \approx I_R^{0.77}$. Near the power asymptote ($y = x^{(1+\beta)/(1-\beta)}$) the current is independent of I_R. In this case the dimensional value of the current is

$$J=\left(\frac{\Lambda\sqrt{8}}{\pi\varepsilon}\right)^{\frac{\beta}{1-\beta}}D_e\frac{n_0(T_e^0)}{L},\qquad(22)$$

where Λ, $n_0(T_e^0)$, and ε are determined by (12) and (14). Equation (22) is satisfied when

$$\frac{JU}{a}\gg J_R\gg3\left(\frac{\Lambda\sqrt{8}}{\pi\varepsilon}\right)^{\frac{\beta}{1-\beta}}a^{\frac{1+\beta}{1-\beta}}D_e\frac{n_0(T_e^0)}{L},\qquad(23)$$

which, for experimentally reasonable values $\Lambda \approx 2$, $a \approx 0.1$ and $U \approx 10$ becomes

$$J \cdot 10^2 \gg J_R \gg 2 \cdot 10^{-2} D_e \frac{n_0(T_e^0)}{L}.$$

Consequently, (23) is self-consistent even for fairly large values of $D_e n_0(T_e^0)/I$, i.e., the parameters entering can be chosen so that the current across the converter is independent of I_R.

3. In ref. 5, the characteristic without recombination is compared to the experimental data and satisfactory agreement is noted for those experiments in which the voltage–current curves have a current saturation segment. In regard to the internal plasma parameters (n, T_e), it is found that in the middle of the electrode gap the density distribution is almost sinusoidal, and the electron temperature agrees to within 20% with the conditions for an ion discharge $\gamma L \approx \pi$. The characteristic does not agree with the experimental data in the quasisaturation region, where the Schottky effect is important.[5]

The above analysis indicates that the characteristic with recombination (19) contains all the elements usually observed for a family: a segment of negative differential resistance, a saturation region, and segments for the power and linear dependence of current on voltage (Fig. 2). This provides a basis for more detailed comparisons. As a start, we restrict the comparison to the relative values of the principal parameters: the density at the maximum and the electron temperature.

For a characteristic without recombination, T_e is independent of the current. The density at the maximum n_m is proportional to the density at the boundary. The variation with the current is expressed on the falling branch of the characteristic by

$$\frac{n_m}{n_m^*} = \left(\frac{J}{J^*}\right)^2 \tag{24}$$

and by

$$\frac{n_m}{n_m^*} = \frac{J}{J^*} \tag{25}$$

for the region near the inversion point (see ref. 5). (Throughout, n^*_m, T^*_e, and J^* are certain values of the density at the maximum, the electron temperature, and the current across the converter that are assumed for the curve of the family under analysis).

For characteristics with recombination we obtain from (15)

$$\frac{n_m}{n_m^*} = \left(\frac{J}{J^*}\right)^{\frac{2\beta}{1+\beta}}, \tag{26}$$

$$\frac{1}{T_e^*} - \frac{1}{T_e} = \frac{4\beta}{(1+\beta) E_i} \ln \frac{J}{J^*}. \tag{27}$$

Figures 4 and 5 give these functions and the experimental data published in refs. 6–8. The temperature is taken in the linear segment of the characteristic in the middle of the electrode gap. Evidently (27) correctly describes the current dependence, although the slope for this relation (Fig. 4) is lower than in experiment.

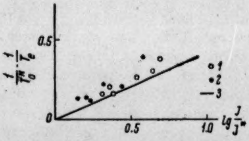

Fig. 4. Electron temperature as a function of current. 1) Data from ref. 6: p = 2-4 torr, T_1 = 1790-1900°K; 2) data from ref. 7: p = 1 torr, T_1 = 1065°K; 3) Eq. (27).

In the absence of recombination the density at the maximum has a quadratic or linear dependence on the current [see (24) and (25)]. When recombination predominates, n_m depends on the current according to a power law with an exponent $2\beta/(1+\beta) \approx 0.71$. Then, if the exponent is known for the dependence $n_m = f(J)$, one can determine whether or not the recombination affects the voltage–current characteristic. For example, the experimental data in ref. 5 do not correspond to the model given in ref. 5 but they give a much better fit with the recombination model of system (15).

For the observed families with curves having inversion points it is convenient to introduce coordinates similar to (17):

$$\left.\begin{aligned} x' &= \frac{x}{x_0} = \frac{U}{U_0} = \frac{V - \Delta\varphi_k}{V_0 - \Delta\varphi_k}, \\ y' &= \frac{y}{y_0} = \frac{I}{I_0} = \frac{J}{J_0}. \end{aligned}\right\} \tag{28}$$

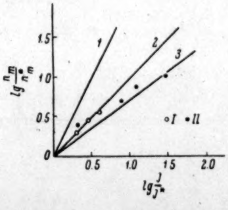

Fig. 5. Maximum density as a function of current. 1,2) Segment of the declining branch and the neighborhood of the reversal point without recombination; 3) theory with recombination included; I) data of ref. 7; II) data of ref. 8.

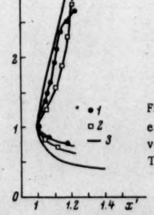

Fig. 6. Comparative behavior of the envelope (3) and the experimental voltage–current curves. p = 1.45 torr, T_1 (°K): 1) 1755; 2) 1805.

The advantage of these coordinates is that the electron temperature and Richardson current need not be known to analyze the voltage–current characteristic. Characteristics plotted in these coordinates have a common inversion point ($x' = 1$, $y' = 1$) and the relative slope in the region $y' > 1$ can be used to estimate the effect of recombination on the process. In Fig. 6, the experimental data of ref. 9 are compared with the envelope in x', y' coordinates. The experimental points for $y' > 1$ are fairly close to the envelope; for $y' < 1$ the agreement is not good. Evidently, the discrepancy between theory and experiment for regions below the inversion point is due to surface ionization, which is not taken into account in this model. This picture is even more convincing when one recalls that the ratio of the current at the inversion point to the diffusion saturation current is roughly 1.5.

In conclusion, the authors thank E. E. Sibir for compiling the experimental data.

---

[1] A. I. Loshkarev, Zh. Tekh. Fiz., 42, 2127 (1972) [Sov. Phys. – Tech. Phys., 17, 1684 (1973)].

[2] F. G. Baksht, Doctoral dissertation, Inst. Poluprovod., Akad. Nauk SSSR (1971).

[3] I. P. Stakhanov and V. A. Zherebtsov, Zh. Tekh. Fiz., 41, 1974 (1971) [Sov. Phys. – Tech. Phys., 16, 1560 (1972)].

[4] E. Jahnke, F. Emde, and F. Losch, Tables of Higher Functions, McGraw-Hill, New York (1960).

[5] V. P. Karamzin, V. P. Pashchenko, and I. P. Stakhanov, Zh. Tekh. Fiz., 42, 800 (1972) [Sov. Phys. – Tech. Phys., 17, 630 (1972)].

[6] F. G. Baksht, G. A. Dyuzhev, I. L. Korobova, V. B. Kaplan, A. M. Martsinovskii, B. Ya. Moizhes, G. A. Shakhnazarova, and V. G. Yur'ev, Zh. Tekh. Fiz., 38, 1075 (1968) [Sov. Phys. – Tech. Phys., 13, 893 (1969)].

[7] W. H. Reichelt, in: International Conference on Thermal Electrical Power Generation, London (September 1965).

[8] V. P. Pashchenko, V. A. Slobodyanyuk, N. V. Volkov, Yu. K. Gus'kov, and M. A. Lebedev, Zh. Tekh. Fiz., 40, 2167 (1970) [Sov. Phys. – Tech. Phys., 15, 1690 (1971)].

[9] V. L. Mironovich, V. P. Pashchenko, I. P. Stakhanov, and E. E. Sibir, Preprint, FEI-410, Obninsk (1973).

Thermionic emission properties of zirconium, hafnium, and titanium nitrides in cesium vapor

M. A. Eremeev, V. S. Neshpor, A. B. Novikov, E. M. Stefanovskaya, and V. P. Fedorinov

M. I. Kalinin Leningrad Polytechnical Institute

(Submitted July 2, 1973)
Zh. Tekh. Fiz., 44, 2159-2167 (October 1974)

The thermionic emission of zirconium, hafnium, and titanium nitrides in vacuum and in cesium vapor is studied when the flux density of cesium atoms varies from $4 \cdot 10^{14}$ to 10^{18} cm^{-2} · sec^{-1}. The emitters acquire new stable thermionic emission properties as a result of a long exposure in cesium vapor. The work function of these materials in the high-temperature region is reduced considerably as compared with the values obtained before exposure to cesium vapor. There are reasons to believe that cesium incorporated into the volume of the nitride exists there in a chemically combined state.

The emission properties of the nitrides of the transition metals have not been studied to any great extent. There are only a few publications[1-3] in which values of the work functions of the nitrides of Ti, Zr, V, Nb, and Ta are given; there are no experimental data for the thermionic emission parameters of hafnium nitride.

There appear to be no data on the thermionic emission properties of nitride compounds in an atmosphere of alkali metal vapor.

Because of the particular characteristics of the crystal and electronic structure of nitrides it is likely that the thermionic emission of these materials in alkali metal vapor will be uncharacteristic of the alloys and the usual intermetallic compounds. We have therefore carried out an experimental investigation of the thermionic emission parameters of zirconium, hafnium, and titanium nitrides in vacuum and in cesium vapor.

It should be noted that the thermionic emission parameters of compounds of this type can depend on the method of fabricating the specimens, their purity, their thermal dissociation during the measurement, the presence of residual gases in the system, and also on the time they are heated before the measurements are made. These features are therefore given particular attention.

EXPERIMENTAL PROCEDURE

The thermionic emission properties are investigated in sealed-off glass tubes, the construction of which is shown in Fig. 1. All the emitters are placed simultaneously in a vacuum device, which enables us to compare their emission properties under identical vacuum conditions and under identical conditions for the deposition of cesium atoms on their surfaces.

To obtain a flow of cesium atoms over the surface of the specimens the whole device is placed in a large thermostat, and the extension with a small amount of cesium metal is placed in a small thermostat. The pressure of the cesium vapor in the tube, and consequently, the intensity of the flow of cesium atoms over the surface of the emitter, is governed by the temperature of the extension. The flux density of the cesium atoms can also be determined from the surface ionization current from a tungsten filament which is placed in the tube and serves as a control emitter.

The emitters are made in the form of wires approximately 400 μ thick. In order to obtain the purest and densest emitting surfaces chemical deposition in the gas phase[4,5] is used. A tungsten alloy wire (with 20% Re) 200 μ thick is used as the core of the cathodes. This alloy, unlike tungsten, molybdenum, and tantalum cores, preserves its plasticity when the nitride emitters are deposited, which considerably facilitates further processing.

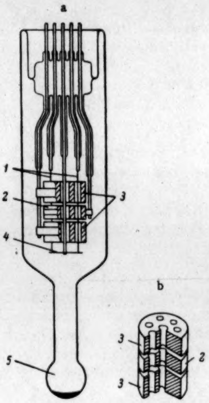

Fig. 1. Experimental device (a) and system of collectors (b). 1) Emitters; 2) measuring collector; 3) guard collectors; 4) flat tantalum spring; 5) reservoir for cesium.

The nitrides are deposited from a gas–vapor mixture containing the tetrachloride of the metal, nitrogen, hydrogen, and helium as inert diluents.

The nitride was deposited by a dissociation and exchange reaction of the gas–vapor mixture on the surface of the core in accordance with the overall equation of the reaction

$$\mathrm{MeCl_4} + 2\mathrm{H_2} + \frac{1}{2}\mathrm{N_2} = \mathrm{MeN} + 4\mathrm{HCl},$$

where Me = Ti, Zr, or Hf.

The thickness of the nitride coating is 70-100 μ. Data on the characteristics of the deposited nitride compounds are given in Table 1.

On the basis of data obtained under similar conditions[6] for more massive specimens we assume that the specimens investigated here have compositions that are approximately stoichiometric $(\mathrm{Me}_{1.0-0.97})$. This assumption is confirmed by data on the lattice periods of the nitride emitters in the initial state before their contact with cesium vapor. Analysis of x-ray powder interference patterns of the emitters shows that they contain a certain growth orientation with a predominance of the (h00) crys-

TABLE 1. Characteristics of the Nitride Emitting Layer on the Surface of a Core of W/20% Re Alloy

Emitter	Lattice period of the nitride, Å(± 0.002 Å)		Microhardness of the nitride layer, kg/mm²	
	before carrying out the experiments	after carrying out the experiments	before carrying out the experiments	after carrying out the experiments
TiN	4.213	4.245	1970±120	1890±110
ZrN	4.575	4.624	1220±106	1130±50
HfN	4.532	4.566	—	2190±250

tallographic planes in the emitter surface.

A chemical analysis of massive pyrolitic specimens of the nitrides, obtained under the same conditions, shows that they do not contain noticeable quantities of carbon and oxygen impurities (the overall content of these is less than 0.1%); the overall content of metal impurities does not exceed 0.12%. The zirconium nitrides contain up to 1.1% of hafnium impurity, while the hafnium nitrides contain up to 2.2% of zirconium impurity.

Before assembling the apparatus the surface of the emitter is polished with fine abrasive paper and subjected to electrolytic etching to obtain a smooth surface. No changes are observed in the lattice period and in the relative intensities of the x-ray lines of the specimens after this process.

The temperature of the operating part of the cathode is found by means of an LMP-066 optical micropyrometer taking account of the correction for the emission factor of the material.[7] We thus establish the relation between the temperature of the operating part and the heating current I_H for each emitter. To determine the temperature in the region below 1150°K the calibration curve $T = f(I_H)$ is extended by extrapolation into the region of lower values of I_H. During the measurements we also take account of the effect of the temperature of the large thermostat on the emitter temperature.

Unlike pure metals, the materials investigated are complex substances. Their surfaces, generally speaking, can be very nonuniform as far as work function is concerned; it is possible for the state to vary, depending on the duration and temperature of the heating which precedes the measurements, so that the thermionic emission constants can also vary. Hence, the emission properties of the compounds are first measured under vacuum conditions before they are measured in an atmosphere of alkali metal vapor.

During the measurements the pressure of the residual gases in the tube is less than 10^{-8} mm Hg. After determining the thermionic emission constants under thermionic vacuum conditions cesium is introduced into the

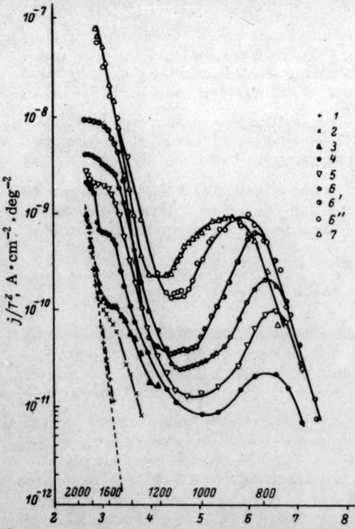

Fig. 2. Temperature dependence of thermionic emission of zirconium nitride for different flux densities of cesium atoms. The flux intensities of the cesium atoms $n \cdot 10^{17}$ (cm^{-2} · sec^{-1}) are: 1) 0.055; 2) 0.23; 3) 0.45; 4) 0.8; 5) 1.5; 6, 6', 6'') 2.5; 7) 10; the dashed curve is without cesium.

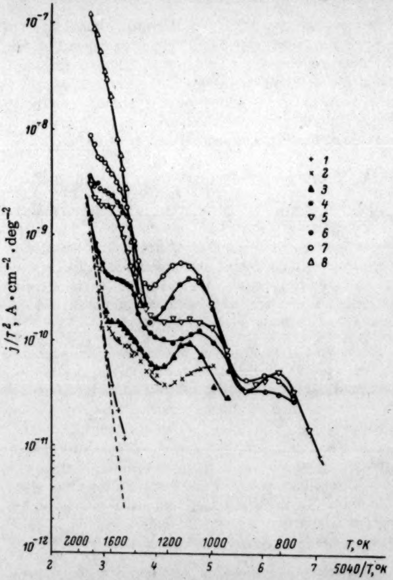

Fig. 3. Temperature dependence of the thermionic emission of hafnium nitride for different flux densities of cesium atoms. The values of the flux intensity of the cesium atom $n \cdot 10^7$ (cm^{-2} · sec^{-1}) are: 1) 0.055; 2) 0.23; 3) 0.45; 4) 0.8; 5) 1.5; 6) 2.5; 7) 4.5; the dashed curve is without cesium.

TABLE 2. Thermionic Emission Constants of the Emitters

Emitter,	Richardson's method		Total-current method		Temperature range, °K
	φ_R, eV	A_R, A/cm^2 · deg^2	φ_0, eV	α, eV/deg^{-1}	
TiN	3.75±0.05	500	3.87±0.05	$-1.1 \cdot 10^{-4}$	1350—1700
HfN	4.18±0.05	400	4.14±0.05	$-1 \cdot 10^{-4}$	1350—1800
ZrN	4.13±0.05	160	4.17±0.05	$-5.7 \cdot 10^{-5}$	1500—1860
W	4.63±0.05	160	4.40±0.05	$-3 \cdot 10^{-5}$	1900—2400

tube without disturbing the vacuum.

To obtain data on the effect of cesium atoms on the emission of nitride cathodes, for each given value of the flux of the cesium atoms we plot a family of voltage–current characteristics for different emitter temperatures. The rectilinear parts of the voltage–current characteristics are extrapolated to zero field, and in this way we determine the values of the saturation current densities at a given temperature. The values obtained for the saturation current densities enable us to represent the data on the temperature dependence of the emission current in the form of the functions $\log (j/T^2) = f(5040/T)$ (so-called S curves). From these we calculate the work function by the total-current method, and determine its temperature dependence.

All the measurements are performed for each case.

RESULTS AND DISCUSSION

The results obtained for the emission properties of the nitride cathodes in vacuum are shown in Figs. 2-5; these confirm the stability of the thermionic emission of these materials and are independent of the annealing process.

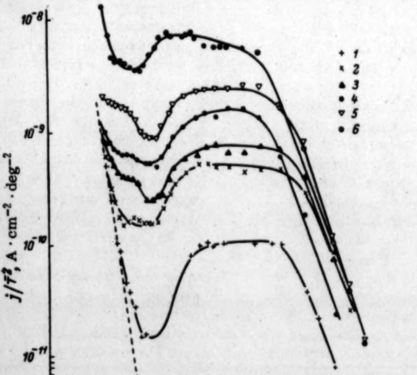

Fig. 4. Temperature dependence of the thermionic emission of titanium nitride for different flux densities of cesium atoms. The values of the flux intensities of the cesium atoms $n \cdot 10^{17}$ (cm^{-2} · sec^{-1}) are: 1) 0.055; 2) 0.23; 3) 0.45; 4) 0.8; 5) 1.5; 6) 2.5.

The values of the work function determined by Richardson's method and the total-current method are shown in Table 2. For comparison the table also gives data for a polycrystalline tungsten emitter. Figures 2-5 also show the results obtained in an atmosphere of cesium vapor.

The S curves obtained with a tungsten filament are found to be in good agreement with the data given in the literature,[8] and are not presented here. Unlike the curves for tungsten and other pure metals the S curves for zirconium, hafnium, and titanium nitrides do not exhibit a straight Richardson section corresponding to vacuum conditions. Beginning at a certain flux density of cesium atoms the curves show a kink, which becomes a "shelf" at high densities. The rectilinear parts of the curves in the high-temperature region change their slope as the flux density is increased, and shift towards lower temperatures. In the region of the maxima the curves do not have a common tangent, defining an optimum degree of coating. In addition, the S curves for the different emitters differ in the position of the extrema and the value of the current density for the same temperature and flux density.

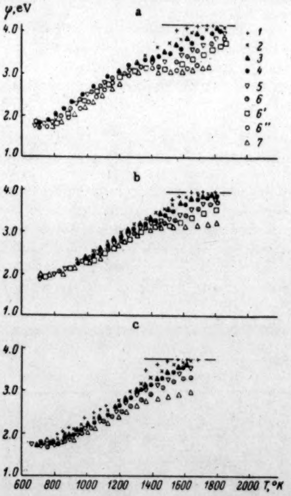

Fig. 5. Temperature dependence of the work function for different flux densities of cesium atoms. a) For zirconium nitride; b) for hafnium nitride; c) for titanium nitride. The values of the flux intensities of cesium atoms $n \cdot 10^{17}$ (cm^{-2} · sec^{-1}) are: 1) 0.055; 2) 0.23; 3) 0.45; 4) 0.8; 5) 1.5, 6, 6', 6") 2.5; 7) 10; the continuous curve is without cesium.

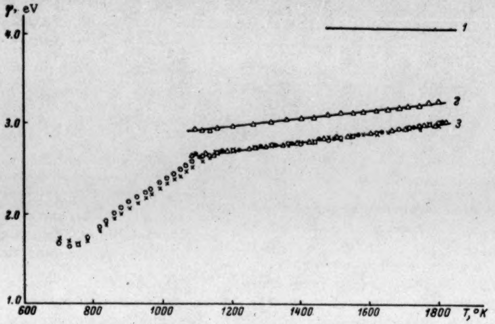

Fig. 6. Temperature dependence of the work function for zirconium nitride. 1) Without cesium; 2) in the intermediate stage of the experiment with $n = 4 \cdot 10^{14}$ $cm^{-2} \cdot sec^{-1}$; 3) at the end of the experiment with $n = 4 \cdot 10^{14}$ $cm^{-2} \cdot sec^{-1}$; 4) with $n = 4 \cdot 10^{14}$ $cm^{-2} \cdot sec^{-1}$ after emitting an ion current for three hours at T = 1860°K, and simultaneously freezing out cesium vapor with dry carbon dioxide; 5) $n = 10^{16}$; 6) $n = 10^{17}$ $cm^{-2} \cdot sec^{-1}$.

These features of the S curves of the nitride can be clearly seen from the curves of the temperature dependence of the work function shown in Fig. 5. As follows from Fig. 5, for each flux density of cesium atoms the work function increases as the emitter temperature is increased. However, the highest value of the work function for each emitter is not the same for all the curves of the family; as the flux density increases the maximum value of the work function falls.

It should be noted that the chronological sequence in which the curves are plotted is the same as the increase in flux density. Hence, the time for which the emitter remains in the atmosphere of cesium vapor increases as the flux increases.

The unusual form of the curves in Figs. 2-5 suggests that a change occurs in the material of the emitter itself while the measurements are being made. In order to check this possibility we again plot the S curves for the same flux densities of the cesium atoms. Figure 2 shows several S curves obtained for an emitter of ZrN for a flux density of $2.5 \cdot 10^{17}$ $cm^{-2} \cdot sec^{-1}$ ($T_{Cs} = 393$°K). In accordance with the sequence in which they were plotted, these curves indicate a reduction in the work function of the emitter with time.

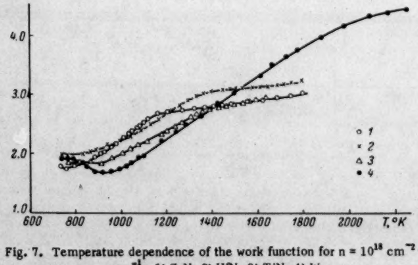

Fig. 7. Temperature dependence of the work function for $n = 10^{18}$ $cm^{-2} \cdot sec^{-1}$. 1) ZrN; 2) HfN; 3) TiN; 4) W.

The temperature dependence of the work function, obtained at different times for a flux density of the cesium atoms of $4 \cdot 10^{14}$ cm^{-2}/sec^{-1} ($T_{Cs} = 303$°K), also indicates a change in the emitter material due to exposure in an atmosphere of cesium. At the beginning of the measurements in cesium the work function of ZrN is the same as the work function obtained under vacuum conditions, and for an emitter temperature below 1500°K there is no appreciable thermionic emission current up to a vapor pressure corresponding to a flux density of cesium atoms of $2.5 \cdot 10^{16}$ $cm^{-2} \cdot sec^{-1}$; at an intermediate stage significant thermionic emission currents are observed even at a temperature of approximately 1100°K and a flux of $4 \cdot 10^{14}$ $cm^{-2} \cdot sec^{-1}$ ($T_{Cs} = 303$°K) (curve 2, Fig. 6). At the end of the measurements under these conditions curve 3 is obtained. It can be clearly seen from Fig. 6 that during the measurements the work function of zirconium nitride falls. Since the changes in the work function of the emitter are due to exposure to cesium vapor, it is natural to assume that when the electron current is emitted from it diffusion of cesium into the volume occurs. When a current of ions is emitted, diffusion to the surface must occur. Hence to answer the question of whether the change in the emitter is reversible, the specimens are annealed at a temperature T = 1860°K with the emission of a current of ions for three hours, with simultaneous freezing out of the cesium vapor with dry carbon dioxide. Curve 4, obtained with this treatment, is the same as the curve obtained previously. The agreement between these curves obviously indicates that there is no diffusion of cesium from the volume, or that the effect of this factor is negligible. In addition, the agreement between these curves indicates that the process by which the emitter changes at the end of the experiments is either completed or is close to completion. This is also confirmed by the thermionic emission data of ZrN, obtained at other vapor pressures of cesium, after the above-mentioned emitter changes had been completed. In the temperature range from 1200 to 1800°K they all lay on a single curve (Fig.

6). Hence, there can be no doubt that the change in the thermionic emission properties of zirconium nitride is due to its exposure to cesium vapor. A similar picture is also obtained for HfN and TiN, but is seen most clearly for ZrN. Thus, the final reduction in the work function for ZrN is 1 eV, for HfN it is 0.8 eV, and for TiN it is 0.7 eV.

Prolonged heating of these cathodes with the emission of an ion current and simultaneous freezing out of the cesium does not return them to their initial states, and there is no change in the thermionic emission properties obtained, which indicates the irreversible nature of the changes and their stability.

Figure 7 shows the temperature dependence of the work function for a flux density of cesium atoms of 10^{18} $cm^{-2} \cdot sec^{-1}$ ($T_{Cs} = 419°K$), for all nitrides after they had acquired stable thermionic emission properties. As follows from Fig. 7, the minimum values of the work function of zirconium and hafnium nitrides lie in the temperature range 700-750°K, i.e., almost 200°K lower than tungsten. Whereas the surface of a tungsten emitter can only be freed from cesium at a temperature of approximately 2100°K (the work function reaches values of 4.4 eV), titanium and hafnium nitrides are practically pure at a temperature of 1300°K, and zirconium nitride is practically pure even at 1100°K. The slight increase in the work function above these temperatures is most probably due to the positive temperature coefficient of the work function.

Hence, the temperature range over which a sharp change in the work function occurs due to desorption of cesium is extended by 300°K (from 800 to 1100°K) in zirconium nitride, and in tungsten this range is greater than 1000°K.

The very small temperature range over which almost complete desorption of cesium from the surface of the nitride occurs indicates the fairly low heat of evaporation of cesium from the material.

Hence, the changes which occur in the emitters during the measurements are due to their long exposure in an atmosphere of cesium vapor, and to the absence of any appreciable diffusion from the volume when the ion current is drawn off. Comparison of these factors leads to the conclusion that, obviously, sorption of cesium has a volume character, and the cesium is retained in the emitter by chemical bonding.

The changes in the emitters due to exposure to cesium vapor are also confirmed by qualitative spectral emission analysis after tests in cesium vapor, which showed that cesium is present in all the emitters in amounts greater than 1%. Specimens for analysis are made by chemical solutions of a layer of the emitter, in a mixture of fluoric and nitric acid. The solution is stopped, and the specimens are extracted from the solution as soon as the surface of the core is uncovered. Hence, the results obtained pertain only to the nitride layer.

We find no changes in the microstructure or external form of the emitters even after they have been exposed for a long time in air (for two months). This indicates that cesium impurity is present in the specimens in a chemically combined state. In favor of this idea is the increase in the lattice period of nitride emitters after they have been operating in cesium vapor, which is outside the limits of the accuracy of the measurements (Table 1), which may be due to implantation of the larger ions of cesium in the lattice of the nitride. As can be seen from Table 1, the greatest implantation of cesium occurs in an emitter of zirconium nitride.

A determination of the lattice periods of nitride emitters immediately after their removal from the apparatus and after long exposure in air does not reveal any changes.

Bearing in mind the results obtained in ref. 9 in a study of the properties of a number of carbide emitters in cesium vapor, we conclude that the implantation of cesium is probably peculiar to the majority of refractory compounds with an NaCl-type structure.

In conclusion we wish to thank V. V. Sokolov, who helped to fabricate the emitters.

---

[1] G. V. Samsonov, Nitrides [in Russian], Naukova Dumka, Kiev (1969).
[2] G. V. Samsonov, V. S. Fomenko, and T. S. Verkhoglyadova, in: The Chemistry and Physics of Nitrides [in Russian], Naukova Dumka, Kiev (1968).
[3] V. S. Fomenko, Emission Properties of Elements and Chemical Compounds, Reference Book [in Russian], Naukova Dumka, Kiev, (1970).
[4] C. Agte and K. Moers, Zs. Anorg. Allg. Chem., 198, 233 (1931).
[5] Preparation and Properties of Certain Refractory Carbides and Nitrides, GIPKh Report, Subject 147-166, 1966/1969, No. 83-69, Leningrad (1970).
[6] V. S. Neshpor, V. S. Davydov, B. G. Ermakov, and B. B. Mogilevich, Porosh. Metallurg., 2, 65 (1967).
[7] V. S. Neshpor and B. A. Fridlender, Neorg. Mater., 6, 1004 (1970); Teplofiz. Vys. Temp., No. 2, 24 (1973); Inzh. Fiz. Zh., 24, 295 (1973).
[8] I. Langmuir and K. H. Kingdon, Science, 57, 58 (1923).
[9] V. G. Bol'shov, Zh. Tekh. Fiz., 36, 331 (1966) [Sov. Phys.—Tech. Phys., 11, 239 (1966)].

Electron energy spectrum in high-energy nanosecond accelerators

V. V. Kremnev, G. A. Mesyats, and V. P. Reznikov

Atmospheric Optics Institute, Siberian Branch,
Academy of Sciences of the USSR, Tomsk

(Submitted July 13, 1973; resubmitted February 13, 1974)
Zh. Tekh. Fiz., 44, 2168-2173 (October 1974)

The effects of matching the storage line to the diode, the switching time, and circuit inductance on the electron energy spectrum of an accelerator beam are considered. The spectrum is analyzed for a linear load, a diode with a field emission cathode, a diode with a thermionic cathode (three-halves law) and a diode with explosive electron emission. Relationships are obtained for the spectrum amplitude and half-width and for the maximum electron energy in the beam. Equations are derived for estimating the effects on the energy spectrum of the electron beam of movement of the plasma front in a diode with explosive emission and of retardation in a foil at the diode output.

INTRODUCTION

Powerful nanosecond electron beams are usually obtained by discharging a storage line through a switch and vacuum diode.[1] If it is assumed that the switch is perfect, i.e., that it switches instantaneously from the nonconducting to the conducting state, that the resistance of the diode is exactly equal to the characteristic impedance of the line and that there is no inductance in the circuit, then the electrons which arrive at the anode must be strictly monoenergetic. It is not possible to achieve these conditions in real accelerators. The energy characteristics of the beam then depend on the discharge circuit, the switch, the emission mode, and processes in the diode; they also depend on the way the electron beam is extracted into the drift space. Since the switching time t_s and the time constant L/R (L is the inherent inductance of the circuit and R is the characteristic impedance of the line) are comparable with the lifetime of the nanosecond beams, the electron energy spectrum is usually very wide, several tens of per cent. The greater the electron current and the smaller the beam lifetime the wider the spectrum; this is the case because the switching time increases with the current, as does the value of L/R (owing to the reduction in R).

In this paper we analyze the effect of these factors on the spectral characteristics of the beam.

1. PRINCIPAL RELATIONSHIPS

The spectral characteristic of the beam gives the number of electrons Δn in the energy range from W to $W+\Delta W$, i.e, $\Delta n=(dn/dW)\Delta W$, where n is the total number of electrons. We assume in what follows that the beam electrons at the diode output are monochromatic and that the electron energy is defined by the potential difference applied to the diode. These conditions are satisfied when the electron thermal velocity is much smaller than the velocity at the anode and if no collective processes arise in the diode, leading to acceleration or retardation. The energy distribution function for the electrons can then be written

$$\frac{dn}{dW}=\frac{I(t)}{e}\frac{dt}{dW}, \tag{1}$$

where $W = eU(t)$, $U(t)$ is the potential across the diode at some fixed instant of time t, $I(t)$ is the electron current in the diode and e is the electron charge.

Thus, if we know the diode voltage and current, we can calculate the energy spectrum of a beam of electrons arriving at the anode of an accelerator diode.

Calculations have been carried out for the following voltage–current characteristics:

a diode with a linear characteristic

$$R_L=\frac{U(t)}{I(t)}=\text{const}, \tag{2}$$

a diode subject to the three-halves law

$$R_L=4.3\cdot 10^5\frac{d^2}{S}U(t)^{-0.5}, \tag{3}$$

and a diode with a field-emission cathode[2]

$$R_L=\frac{6.4\cdot 10^5\varphi d^2}{[U(t)\mu^2 S]}\exp\left[\frac{6.85\cdot 10^{-7}\varphi^{3/2}}{U(t)\mu}\Theta\left(\frac{1.32\cdot 10^{-7}U(t)\mu}{\varphi^2 d}\right)\right], \tag{4}$$

where Θ is the Nordheim function, which we have approximated (with an error of less than 1%) by the equation

$$\Theta(y)=1-0.5(y+y^{3/4}),$$

φ is the work function (eV), d is the length of the vacuum gap in the diode (cm), S is the emission area of the cathode (cm²), μ is the magnification of the field at a cathode whisker. The number of whiskers $n_0 \approx S/S'$, where S' is the effective emission area of a single whisker. Calculations using (4) have been performed for a tungsten cathode with an electric field $E_0 = U_0\mu/d = (9.3, 16, 22)\cdot 10^7$ V/cm. The principal relationships for the three-halves diode and the field-emission cathode diode are obtained by numerical solution. The movement of the cathode plasma in a diode with explosive emission is taken into account in Sec. 4.

2. EFFECT ON THE SPECTRUM OF MISMATCH BETWEEN STORAGE LINE AND DIODE

If $R_L > R$, $L = 0$, $t_s = 0$ (perfect switch), then with a linear load a series of voltage pulses is applied to the diode and we get a line spectrum (Fig. 1b). The final magnitude of these lines can be found by normalizing them to the amplitude of the spectral line at $R_L = R$ and $L = 0$, $t_s \to 0$, i.e., by $(dn/dW)_c$. Then for a linear load

$$\frac{\left(\frac{dn}{dW}\right)}{\left(\frac{dn}{dW}\right)_c}=2b\sum_{i=1}^{\infty}a_0^{i-1}\varphi(x-x_i), \tag{5}$$

where i is the number of the spectral line,

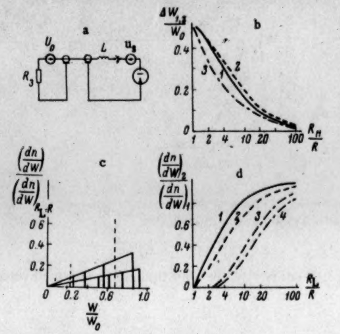

Fig. 1. a) Circuit for forming electron beam; b) typical spectral characteristics $R_L > R$ (dashed lines $R_L/R = 2$, continuous lines $R_L/R = 5$ and 10); c) Curves of $\Delta W_{1,2}/W_0$; d) curves of $(dn/dW)_2/(dn/dW)_1$. 1) Diode with linear load; 2) diode with 3/2 law; 3 and 4) field-emission diode with $E_0 = (16$ and $9.3)\cdot 10^7$ V/cm, respectively.

$$x_i = \frac{\frac{R_L}{R}}{1+\frac{R_L}{R}} a_0^{i-1}, \quad a_0 = \frac{\frac{R_L}{R}-1}{\frac{R_L}{R}+1},$$

$$b = \frac{1}{1+\frac{R_L}{R}},$$

$$\varphi(x-x_i) = \begin{cases} 0 & \text{for} \quad x \neq x_i, \\ 1 & \text{for} \quad x = x_i. \end{cases}$$

A line spectrum is also obtained for the other diode. The diode resistance during the time interval $0 < t < 2T$, where T is the electrical length of the line, is used as the criterion in these cases.

For a slight mismatch, with $R_L/R \approx 1$, the spectrum consists of a small number of lines very different in amplitude and energy level; for a severe mismatch, with $R_L/R \gg 1$, the spectrum can be characterized by the width of the envelope drawn through the 0.5 amplitude points of the line.$^{1)}$ For cases (2) and (3), the width of this envelope, referred to the maximum spectrum energy $\Delta W/W_M$, is independent of R_L/R. Thus for a linear load $\Delta W/W_M = 0.5$ and for a three-halves diode $\Delta W/W_M = 0.37$. For a diode with a field emission cathode the parameter varies weakly with R_L/R and is approximately equal to $\Delta W/W_M \approx 0.075$ and 0.1 for fields of $E_0 = (9.3$ and $16)\cdot 10^7$ V/cm, respectively. With a slight mismatch ($R_L/R \approx 1$) it is more convenient to use the relation

$$\frac{W_M - W_2}{W_0} = \frac{\Delta W_{1,2}}{W_0},$$

where W_2 is the energy of the second line in the spectrum. These relations are given for the various diodes in Fig. 1c. It is of interest to determine the ratio of the amplitudes of two neighboring lines $(dn/dW)_2/(dn/dW)_1$. This ratio is shown in Fig. 1d and for a diode with a linear load is

$$\frac{\left(\frac{dn}{dW}\right)_2}{\left(\frac{dn}{dW}\right)_1} = \frac{\frac{R_L}{R}-1}{\frac{R_L}{R}+1}.$$

It can be seen from Fig. 1d that nonlinearity of the diode characteristics brings about a decrease in the height of the following spectral line. The advantage of the field-emission cathode is indicated by the physics of the electron field-emission process, for which a small reduction in the field E at time $t \geq 2T$ causes a significant decrease in the current and, hence, in the amplitude of the second spectral line. However, if the field E_0 is increased, the field-emission electron emission from the whiskers approaches saturation and a change in E at $t \geq 2T$ has little effect on the current. The second spectral line therefore approaches the first in amplitude.

3. EFFECT OF THE SWITCHING TIME AND CIRCUIT INDUCTANCE ON THE SPECTRUM

The effect of the switching process on the electron spectrum is allowed for by assuming[1] that the voltage across the switch is given approximately by the function $U_s = U_0 e^{-at}$, where $a = 2.2/t_s$ and t_s is the switching time during which the voltage falls from $0.9\,U_0$ to $0.1\,U_0$. In the calculations we take $L = 0$, $R_s = R$ for $t \to \infty$. Only the time interval $0 < t < t_I$ is considered, where $t_I = 2T$.

The energy spectrum is characterized by the amplitude $(dn/dW)_M$, the maximum electron energy W_M and the width of the spectrum at $0.5\,(dn/dW)_M$, equal to ΔW. Figure 2, a, b, and c shows these characteristics as a function of the parameter t_I/t_s. It can be seen from Fig. 2c that ΔW depends strongly on the switching time and this is most marked for a linear load and least noticeable for a field-emission cathode diode. When $t_I/t_s > 2$, the spectral width is less than 1% of the maximum value W_M.

The effect of the inductance L on the electron spectrum is calculated for the case of an ideal switch ($t_s = 0$)

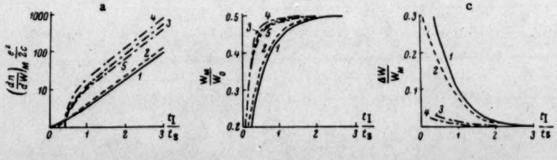

Fig. 2. Curves of $(dn/dW)e^2/2C$ (a), W_M/W_0 (b), and $\Delta W/W_M$ (c) for different diodes vs the parameter t_I/t_s. The notation for curves 1-4 is the same as in Fig. 1; 5) diode with field-emission cathode and $E_0 = 2.2\cdot 10^8$ V/cm. C is the capacity of the storage line.

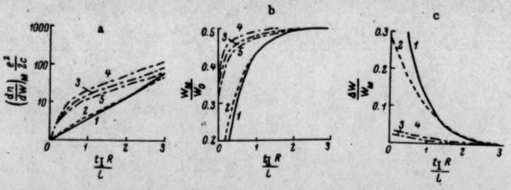

Fig. 3. Curves of $(dn/dW)_M e^2/2C$ (a), W_M/W_0 (b), and $\Delta W/W_M$ (c) for various types of diode against the parameter $t_I R/L$. The notation for curves 1-5 is the same as in Figs. 1 and 2.

in the time interval $0 < t < t_I$ with $R_L = R$. The results are shown in the curves of Fig. 3, a, b, and c. It follows from these curves that when $(R/L)t_I > 2.5$, the width of the spectrum is not more than 2% of the maximum energy. The width decreases rapidly with increasing $(R/L)t_I$ and, as in the case of a nonideal switch, the width decreases with an increase in the nonlinearity of the voltage–current curves.

4. EFFECT OF OTHER PROCESSES ON THE ELECTRON SPECTRUM

According to ref. 3, the voltage–current relationship for a diode in which the electron emission results from the explosion of whiskers on the cathode follows a 3/2 law. It must be remembered, however, that the emission boundary in such a diode moves from the cathode to the anode at a velocity $v = 2 \cdot 10^6$ cm/sec. This can be allowed for by changing from d^2 to $(d - vt)^2$ in (3). If the diode is matched to the storage line at $t = 0$, it will become mismatched at times as a result of the decrease in resistance caused by the reduction in the interelectrode gap. This leads to a broadening of the spectral lines for an ideal accelerator ($t_s = 0$, $L = 0$) when $0 < t < t_I$ and $vt/d \gg 1$:

$$\frac{\Delta W}{W_0} \approx \frac{vt}{d}. \tag{6}$$

When the line is mismatched with an explosive emission diode, the electron current pulses which arise as a result of the reflected voltage pulses cannot be calculated in the same way as for other diodes. During the interval between voltage pulses the diode becomes filled with the plasma formed by the explosion of the whiskers. This leads to a reduction in the effect of the electron space charge on the diode current and to an increase in this current.[1]

Since the electron beam is usually extracted from the diode through a metal foil at the anode, the spectrum undergoes an additional broadening. According to ref. 4, the half-width of the spectrum for a monoenergetic electron beam with energy W_0 exiting through a foil of thickness δ(cm) is given by

$$\frac{\Delta W}{W_0} \approx \frac{4\xi}{W_0}, \tag{7}$$

where $\xi = 0.154\, Z\rho\,\delta/A\beta^2$ (MeV), Z and A are the atomic number and weight of the foil element, ρ is the density of the foil (g/cm³), $\beta = v_0/c$, c is the velocity of light and v_0 is the velocity of an electron with energy W_0. Equation (7) was obtained for $\xi \gg I^*$ and $\xi \ll W_0/2$, where I^* is the average ionization energy of the atoms in the substance, $I^* \approx 13.5\, Z \cdot 10^{-6}$ MeV. The most probable energy (i.e., the energy for which the electron distribution function is a maximum) is given by

$$\frac{W_M}{W_0} = 1 - \left(\frac{\xi}{W_0}\right)\left[\ln\left(\frac{\xi}{y}\right) + 0.373\right], \tag{8}$$

where

$$\ln y = \ln\left(\frac{1-\beta^2}{2\beta^2}\,\frac{I^{*2}}{mc^2}\right) + \beta^2,$$

m is the rest mass of the electron. It follows from (7) and (8) that when $\xi W_0 < 0.01$, it is possible to neglect the effect of the foil on the electron spectrum. With an aluminum foil, for example, of thickness 20 μ and an electron beam of 1 MeV, we have $\rho = 2.7$ g/cm³, $Z = 13$, $A = 27$, $\beta \approx 1$, $\xi = 4 \cdot 10^{-4}$ MeV, $\Delta W/W_0 \approx 1.6 \cdot 10^{-3}$, $W_M/W_0 \approx 0.996$. Thus the effect of the foil is small in this case.

---

1) It should be noted that the case $R_L/R \gg 1$ is not typical of accelerators and is included here only for completeness.

---

[1] G. A. Mesyats, The Generation of Powerful Nanosecond Pulses [in Russian], Sovetskoe Radio (1974).

[2] M. I. Elinson and G. F. Vasil'ev, Field Emission [in Russian], State Publishing House for Physical and Mathematical Literature (1958).

[3] G. A. Mesyats, S. P. Bougaev, and D. I. Proskourovskii (Proskourovsky), Discharges and Electrical Insulation in Vacuum, Proc. Third Intern. Symp., Paris (1968), p. 218.

[4] L. D. Landau, Collected Works [in Russian], Vol. 1, Nauka (1965), p. 482.

Electronics

Shot noise in a thermionic cathode

A. F. Golubentsev and A. S. Shapovalov

N. G. Chernyshevskii Saratovsk State University

(Submitted October 22, 1973; resubmitted March 18, 1974)
Zh. Fiz., 44, 2174-2177 (October 1974)

One of the causes of shot noise in thermionic cathodes is investigated. The spectral density of the current fluctuations from a cathode whose emission undergoes random changes in time is calculated. The noise level of such a cathode exceeds the value given by Schottky's equation by an order of magnitude. The results can be used to calculate the spectral density of the current fluctuations for any distribution of the time intervals between the emission of successive electrons. Numerical results are given for the case in which the distribution is given by the sum of two exponentials with appropriate weighting factors.

Experimental investigations of efficient thermionic cathodes, in particular oxide cathodes, show that in a number of cases the shot noise level can exceed the value given by the Schottky equation[1-3] by a significant amount. In this paper we analyze one of the possible reasons for the anomalous shot effect.

Schottky's equation is derived on the assumption that the distribution density of the time interval τ between emission of two successive electrons is described by an exponential:[4,5]

$$f(\tau)=\lambda e^{-\lambda\tau}. \tag{1}$$

The parameter λ in this distribution represents the intensity of the electron emission process and is equal to the average number of particles emitted per unit time. Analysis of the physical–chemical processes taking place at the surface and in the bulk of the emitter shows that the "equilibrium" is not static, but dynamic in character.[6-8] Consequently, the intensity of the electron emission process λ is subject to random variations with time, and the cathode passes successively through a large number of "emission states." For this reason the distribution density of the interval τ for a practical cathode cannot always be described by the distribution (1). Hence, in this paper we calculate the spectral density of the cathode emission current fluctuations for an arbitrary distribution for the interval τ. The numerical results are presented for the case in which the distribution density of τ is described by the sum of two exponential laws with appropriate weighting factors.

The emission current observed in the plane of the emitter is represented by a random pulse process of the form

$$i(t)=\sum_{\nu=-\infty}^{\infty} e\delta(t-t_\nu),$$

where e is the electron charge, $\delta(t)$ is the delta function, and t_ν is the time an electron is emitted with index number ν. The spectral density of the current fluctuations $S_i(\omega)$ is given by[3]

$$S_i(\omega)=\lim_{T\to\infty}\frac{1}{2\pi T}M\{|i_T(\omega)|^2\}.$$

Here $i_T(\omega)=\int_{-\infty}^{+\infty} i_T(t)e^{-j\omega t}dt$ is the Fourier transform of the truncated current sample $i_T(t)$,

$$i_T(t)=\begin{cases} i(t) & \text{for } |t|\leqslant\frac{T}{2},\\ 0 & \text{for } |t|>\frac{T}{2},\end{cases}$$

and M is the mathematical expectation.

Suppose that in the time interval $(-T/2, +T/2)$ there are 2N+1 current pulses, i.e., $T\simeq(2N+1)\bar{\tau}$, where $\bar{\tau}$ is the mathematical expectation for the time interval between emission of two successive electrons. (We choose the origin of the time axis to be the time an electron is emitted with index number $\nu=0$.) Then

$$i_T(t)=\sum_{\nu=-N}^{N} e\delta(t-t_\nu),$$

$$i_T(\omega)=i_N(\omega)=\sum_{\nu=-N}^{N} ee^{-j\omega t_\nu},$$

$$S_i(\omega)=\lim_{N\to\infty}\frac{1}{2\pi(2N+1)\bar{\tau}}M\{|i_N(\omega)|^2\}.$$

Writing $|i_N(\omega)|^2$ in the form of a double sum

$$|i_N(\omega)|^2=\sum_{\nu=-N}^{N}\sum_{\mu=-N}^{N} e^2e^{-j\omega t_\nu}e^{j\omega t_\mu}$$

and carrying out simple calculations, we obtain

$$S_i(\omega)\doteq\frac{1}{2\pi\bar{\tau}}\left\{e^2+\sum_{p=1}[h_p(\omega)+h_p(-\omega)]\right\}, \tag{2}$$

where

$$h_p(\omega)=e^2M\{e^{-j\omega(t_\nu-t_\mu)}\},\quad p=\nu-\mu.$$

Since the intervals $\tau_i=t_{i+1}-t_i$ are independent and obey the same distribution we have

$$h_p(-\omega)=e^2[\varphi(\omega)]^p,\quad h_p(\omega)=e^2[\varphi^*(\omega)]^p, \tag{3}$$

where

$$\varphi(\omega)=M\{e^{j\omega\tau}\},\quad \varphi^*(\omega)=M\{e^{-j\omega\tau}\}.$$

Substituting Eq. (3) into Eq. (2), we obtain the final expression for the spectral density of the emission current fluctuations:

$$S_i(\omega)=\frac{eI_0}{2\pi}\left[1+2\,\mathrm{Re}\,\frac{\varphi(\omega)}{1-\varphi(\omega)}\right], \qquad (4)$$

where $I_0 = e/\bar{\tau}$ is the mean value of the current.

It is easy to show that for an exponential distribution of the interval τ the second term in Eq. (4) is zero, and the expression obtained is the same as Schottky's equation. In the general case this term is not zero.

For the frequencies used in electronics (including microwave frequencies) and practical currents I_0, the inequality $\omega\bar{\tau} \ll 1$ is satisfied. Expanding $M\{e^{j\omega t}\}$ in a power series and confining ourselves to terms of second order we find that for $\omega \ll 1/\bar{\tau}$ the quantity $S_i(\omega)$ is independent of frequency, being given by

$$S_i(\omega)=\frac{eI_0}{2\pi}v^2,$$

where $v = \sigma_\tau/\bar{\tau}$ is the variance of the interval, and σ_τ^2 is the dispersion of the interval.

To obtain numerical results we must make certain assumptions regarding the form of the distribution density of τ. We assume that the i-th emission state of the cathode is represented by a constant value of the intensity λ_i, the conditional distribution density of τ within a single state is described by the exponential law (1) with $\lambda = \lambda_i$, and the change of emission states is a Markov process. Then the unconditional distribution density of the interval will be given by a sum of exponentials with weighting factors which have a meaning of the probability p_i of the corresponding emission state. For simplicity we will assume that the cathode can operate under two conditions which are represented by $\lambda = \lambda_1$ and $\lambda = \lambda_2$ $(\lambda_1 > \lambda_2)$. For this mode of cathode operation the distribution density of the interval can be written

$$f(\tau)=p_1\lambda_1 e^{-\lambda_1\tau}+p_2\lambda_2 e^{-\lambda_2\tau}. \qquad (5)$$

Using Eq. (5) and assuming that $p_1 + p_2 = 1$, we find the initial times of the interval

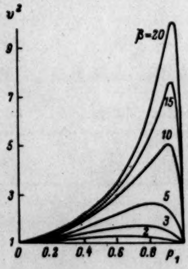

Fig. 1. The square of the variance of the interval v^2 as a function of the probability p_1 for different β.

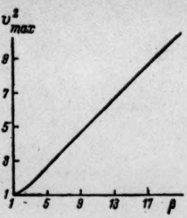

Fig. 2. The maximum value of the square of the variance of the interval $v^2_{\max}$ as a function of β.

$$\bar{\tau}=\frac{p_1}{\lambda_1}+\frac{1-p_1}{\lambda_2}, \quad \bar{\tau^2}=2\left(\frac{p_1}{\lambda_1^2}+\frac{1-p_1}{\lambda_2^2}\right)$$

and the square of the variance

$$v^2=1+2(\beta-1)^2\frac{p_1(1-p_1)}{[(1-p_1)\beta+p_1]^2}, \qquad (6)$$

where $\beta = \lambda_1/\lambda_2$ is a coefficient which represents the drop in the emissive power of the cathode when its modes of operation change.

Curves of v^2 as a function of p_1 for different β are shown in Fig. 1. For p = 0 and $p_1 = 1$ or $\beta = 1$ the functions (1) and (5) are the same and $v^2 = 1$. Consideration of the remaining cases shows that the shot noise level of a cathode with this emission mechanism can exceed several-fold the value given by the Schottky equation. The value of v^2 increases as the parameter β increases, and for $\beta = 20$ and $p_1 = 0.95$ reaches a value of 10. For each value of β a certain probability $p_1 = p_{1\max}$ exists for which the square of the variation coefficient is a maximum: $v^2 = v^2_{\max}$. These values of the parameters are given by the following expressions, which are obtained from an analysis of Eq. (6):

$$p_{1\max}=\frac{\beta}{1+\beta}, \quad v^2_{\max}=1+\frac{(1-\beta)^2}{2\beta}.$$

A curve of $v^2_{\max}$ as a function of β is given in Fig. 2. The numerical results shown in Figs. 1 and 2, and a direct analysis of (4) and (6) show that a cathode operating mechanism similar to that considered may be one of the reasons for the considerable increase in the shot noise level of emitters.

---

[1] W. Dalke and F. Dlonhy, Proc. IRE, 46, 1639 (1958).

[2] Yu. I. Nabokov and V. E. Avdeev, Izv. Akad. Nauk SSSR, Ser. Fiz., 33, 452 (1969).

[3] A. I. Popov and D. E. Kolpakov, Elektron. Tekh, Ser. 5, 35 (1971).

[4] W. B. Davenport and W. L. Root, An Introduction to the Theory of Random Signals and Noise, McGraw-Hill (1958).

[5] D. R. Cox, Renewal Theory, Wiley, New York (1962).

[6] G. Herman and S. Wagener, The Oxide Cathode [Russian translation], Gostekhizdat, Moscow–Leningrad (1949).

[7] A. N. Malakhov, Fluctuations in Self-Oscillating Systems [in Russian], Nauka, Moscow (1968).

[8] L. D. Smullin and H. A. Haus (eds.), Noise in Electron Devices, M.I.T. Press (1959).

Use of a field-emission microscope to measure the pressure of pump oil

V. Ya. Pliskovskii, M. S. Sukonnik, and V. A. Shishkin

(Submitted May 28, 1973)
Zh. Tekh. Fiz., 44, 2178-2185 (October 1974)

We describe a method for measuring the background pressure of pump oil in vacuum systems by means of a field-emission microscope. The oil molecules accumulate on a cold tungsten field-emission cathode for controlled times and undergo thermal decomposition when the cathode is heated to T = 1400°K. The emission images corresponding to the chemisorption of pyrolytic carbon on the tungsten surface are analyzed. The functional relationship between the oil vapor pressure and the time over which the surface coverage of oil is built up (required to calibrate the emission images of the pyrolytic carbon) is determined by adsorption, on the cathode, of oil evaporated from a Knudsen molecular source. As the emitter is heated the probability that the tungsten surface will capture carbon from the adsorbed oil film depends on the ratio of the flux of the oil vapor and the residual gas during the period over which the oil accumulates on the surface. This method can be used to measure oil-vapor fluxes in the range $1 \cdot 10^{9}$-$1 \cdot 10^{13}$ $cm^{-2} \cdot sec^{-1}$; the maximum measurement error is ± 50%.

INTRODUCTION

In many problems of experimental and applied physics it is necessary to have a quantitative knowledge of the backstreaming of vacuum-oil vapor into the system from the pumping system. Vacuum oils are large-molecule fluids, usually complex hydrocarbons. Since the behavior of such compounds is quite different from that of permanent gases,[1] and since serious technical difficulties arise,[2] mass-spectrometer analysis of these compounds is not very useful. Because of their high heat of adsorption, molecules of vacuum oils can accumulate on the walls of the tubing and leak into the evacuated apparatus by surface migration, while their concentration in the gas phase remains below the sensitivity of the mass spectrometer. It is thus advisable to determine the amount of oil vapor by measuring the surface concentration of the oil molecules. Most of the methods based on this principle are either technically elaborate or relatively insensitive.[3-8] Field microscopy is one of the simplest and most sensitive of such methods; the ability of a field-emission microscope to detect hydrocarbon molecules in vacuum was demonstrated long ago[9,10] and has been exploited for qualitative purposes.[11,12] It can also be used for quantitative measurements.[13] One possible procedure is to allow the oil molecules to accumulate on the surface of a cold tungsten field-emission cathode and then thermally decompose these molecules to carbon; the carbon, by becoming chemisorbed on the emitter surface, produces characteristic field-emission images with a sharp concentration gradation ("calibration emission images"). The concentration of chemisorbed carbon is proportional to the surface concentration of oil molecules which, in turn, is proportional to the flux incident on the emitter surface from the volume. With the appropriate calibration a quantitative relationship can be established between the surface concentration of carbon and the flux of oil vapor.

Below we describe the basic aspects of the method of calibration emission images, the actual procedure followed, and the results of calibrations carried out for types VM-5 and 5F4É oils under various vacuum conditions.

1. EXPERIMENTAL PROCEDURE

a) Experimental apparatus. The glass apparatus shown schematically in Fig. 1, consists of the field-emission microscope and a Knudsen molecular source, sealed to the microscope.[14] The limiter of the source is covered by a ground seal 1 by means of a magnet. In a side arm of the source, connected to the evacuation system, is an ampoule 2 containing oil which has been outgassed in vacuum. At the desired time this ampoule is broken against the wall by another magnet, and the oil spills into the source, held at a constant temperature by the vapor of a boiling coolant.

Figure 2 shows the shape of the source limiter. Its area is measured by optical projection with a magnification of 20 ×. The functional dependence of the vapor pressure on the temperature is determined beforehand with an absolute pendulum gauge[15] within ± 3% for the lots of type VM-5 vaseline oil and 5F4É polyphenyl ester chosen for the experiments.

Two versions of the apparatus, differing in the area of the source limiter, are evacuated by an oil-free apparatus with a limiting residual pressure of $1 \cdot 10^{-9}$ torr. The residual gas pressure is determined by an IM-12 gauge in the immediate vicinity of the instruments.

b) Experimental procedure. After the limiting residual pressure is reached in the apparatus the ampoule is broken, and the oil flows into the source. To achieve an equilibrium oil vapor pressure in the source ($1 \cdot 10^{-4}$-$1 \cdot 10^{-5}$ torr, varying with the type of oil), we heat the source for a long time with the vapor of a boiling

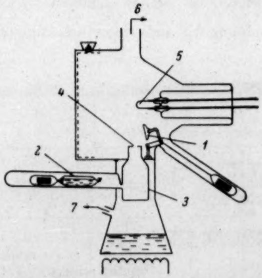

Fig. 1. Experimental apparatus. 1) Seal; 2) ampoule containing oil; 3) source; 4) limiter of source; 5) tungsten tip (the field-emission cathode); 6) pump; 7) reverse refrigerator.

coolant (water or metaxylene) with the limiter covered.

Immediately before an experiment the cleanliness of the emitter surface is checked from its emission image; if necessary, contaminants are removed by briefly heating the emitter to ~2600°K ("flashes"). After the emitter cools to room temperature the source is opened for the desired time. The adsorbed oil decomposes as the emitter is heated to ~1400°K for 20 sec; then the cathode is recooled to room temperature, a high voltage is supplied to the screen of the field-emission microscope, and the emission image is photographed.

After the emitter has been cleansed of carbon by repeated flashes and the emission image corresponding to the clean tungsten surface has been restored the entire procedure is repeated with a longer exposure. These cycles are continued until the tungsten surface becomes saturated with carbon, at which point the decomposition of more adsorbed oil does not cause any further change in the emission image.

In experiments on the effect of the residual-gas flux on the experimental results the pressure in the microscope is varied by varying the pumping rate.

c) A few necessary equations. The surface concentration of the oil on the emitter and the corresponding flux of oil vapor can be calculated with the help of Fig. 2. The flux Q of a vapor whose molecular weight is M, whose vapor pressure is p, and which is flowing through a limiter of diameter S from a source at temperature T is, under molecular-flow conditions,

$$Q = 3.51 \cdot 10^{22} \frac{pS}{\sqrt{MT}} \text{ sec}^{-1}, \tag{1}$$

where S is in square centimeters, p is in torr, and T is in Kelvin degrees.

The flux incident on a small plane area a distance r from the source is[14]

$$\nu_1 = \frac{Q}{\pi} \frac{\cos\theta \cos\varphi}{r^2}, \tag{2}$$

where θ is the angle between the normal to the small area and the flux direction, and φ is the angle between the normal to the source and the flux direction.

In calculating the surface concentration of oil on the tungsten field-emission cathode we take the following circumstances into consideration:

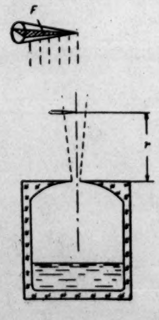

Fig. 2. Diagram used to calculate the surface concentration of oil on the emitter.

1. The literature reveals no information on the heats of adsorption q for vacuum oils on metals. However, it gives[16] q = 102 kcal/mole for ethylene on tungsten, so we can assume the heat of adsorption of an oil on a clean tungsten surface to be higher than this value. Even in the case of physical adsorption in the second layer the value of q should be no lower than the heat of vaporization, some 27-30 kcal/mole for vacuum oils.[17] The sticking probability for a substance with $M > 400$ and $q \geq 30$ kcal/mole can be set equal to unity.

2. For these values of q the lifetime of the molecules in the adsorbed state (~10^8 sec, according to the equation given by Frenkel') is much longer than the experimental time over which the oil film is deposited on the emitter (< 10^4 sec). We can thus neglect desorption of the oil.

3. At T = 300°K the rate of surface migration of adsorbed oil molecules is a few microns per second;[18] a simple geometric calculation shows that the concentration equalizes over the entire surface of the cone before the emitter is heated.

4. The emitting surface of the field-emission cathode (which is, in a first approximation, hemispherical) is several orders of magnitude smaller than a conical surface area. Accordingly, the oil concentration in this region and the oil concentration on the cone after migration is completed can be assumed to be equal.

On the basis of these arguments we can calculate the hypothetical oil concentration on the plane of an axial cros. section of the cone, N_1 (plane F in Fig. 2), and then redistribute this value over the lateral surface of the cone. The linear dimensions of plane F are much smaller than the distance r (in the actual apparatus, r is ~70 mm, while the cone of the field-emission cathode is ~1 mm long), so we can treat it as negligibly small. Since this plane makes a right angle with the axis of the limiter we have $\cos\theta = \cos\varphi = 1$; thus

$$\nu_1 = \frac{Q}{\pi r^2}, \tag{3}$$

and

$$N_1 = \nu_1 t = \frac{Q}{\pi r^2} t, \tag{4}$$

where t is the time over which the adsorption occurs.

The lateral surface of the cone is larger than surface F by a factor $\pi/\cos\alpha$, where α is the vertex half-angle of the cone. However, since the value of α for the emitters usually used in field-emission microscopes is less than 5°, we can treat the $\cos\alpha$ as unity. Then the oil concentration on the cone at the completion of migration is

$$N = \frac{N_1}{\pi} = \frac{\nu_1}{\pi} t = \nu t. \tag{5}$$

The coefficient $\nu_1/\pi = \nu$ gives the flux density uniformly distributed over the cone surface. Accordingly, the adsorption of oil molecules from the beam onto the "illuminated" side of the cone and the subsequent migration to the "shadowed" side, involving an equalization of the concentration over the entire cone surface, are equivalent to the adsorption of these molecules from a random distribution in the volume around the emitter, at a flux density at the surface smaller by a factor of π.

Finally we can write the equations for the surface concentration of the oil and the corresponding flux density:

$$N = 3.56 \cdot 10^{21} \frac{pSt}{r^2\sqrt{MT}} \text{ cm}^{-2}, \qquad (6)$$

$$\nu = \frac{N}{t} \text{ cm}^{-2} \cdot \text{sec}^{-1}. \qquad (7)$$

The experimental error involved in a determination of N from Eq. (6) is ± 10%.

2. EXPERIMENTAL RESULTS AND DISCUSSION

a) Calibration emission images. As we heat the tungsten tip to 1400°K, with various coverages of the tip by oil molecules, we find more than 10 distinct emission images. Four of the most typical images (A, B, C, and D in Fig. 3) are used as calibration images; these are formed in times in the ratios 1 : 2 : 3 : 4 (at constant ν). A distinctive feature of image A is the presence of bright lobes on two sides of the {011} faces along bands of [100], [010] and [001] zones and bright bands between {011} and {121} faces along bands of $[1\bar{1}1]$ and $[11\bar{1}]$ zones. Under the conditions corresponding to image B the lobes become broad rings around {011} faces. We also see bands of [100], [010], and [001] zones as narrow dark bands intersecting at the "poles" of {001} faces. However, the most characteristic feature of this image is the appearance of dark {334} faces. In image C the circular {334} faces are broadened and deformed into irregular hexagons, and the rings around the {011} faces join with bright formations around {121} faces. Finally, at the coverage corresponding to image D, the (001) and (010) faces are ringed with halos, within which there are dark "Maltese crosses." The {334} faces vanish, and broad bands form from the center of the {111} faces to the {011} faces. A further accumulation of pyrolytic carbon on the surface does not affect the topography of the emission image (bright spots due to carbon conglomerates appear in random positions in image D), implying the formation of a saturated film.

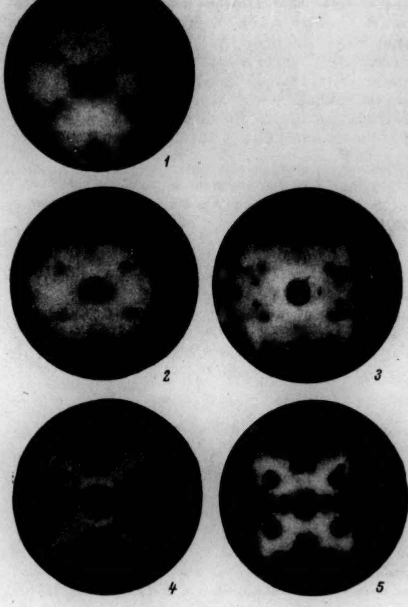

Fig. 3. "Calibration emission images." 1) Clean tungsten surface; 2) calibration image A; 3) B; 4) C; 5) D.

These emission images are obtained at cathode temperatures between 1200 and 1800°K. However, different surface concentrations of the oil correspond to the images, depending on the temperature. For example, to obtain image B at 1800°K requires roughly the same oil concentration as that required to obtain image C at 1500°K. This result, which is evidence of carbon diffusion into the surface layers of the metal, governs our choice of the oil decomposition temperature (1400°K); over the range 1200–1500°K the correlation between the surface concentration of the oil and the nature of the emission image of the carbon is not broken.

Destruction of the saturated carbon film (image D) begins at ~2300°K; at 2600°K only a few "flashes" are required to completely clean the carbon from the tungsten surface.

b) Calibration results. Calibration of the ap-

TABLE 1

Type of oil	$\nu \cdot 10^{-11}$ cm^{-2}·sec^{-1}	K	t_c, sec	$N_c \cdot 10^{-14}$, cm^{-2}	$N_c z \cdot 10^{-15}$ cm^{-2}	θ/θ_0
5F4É (z=30)	28.00	50	37	1.04	3.12	1.00
	28.00	2.7	40	1.12	3.36	0.93
VM-5 (z=35)	3.14	1.6	355	1.12	3.92	0.80
	1.60	0.3	1190	1.90	6.65	0.47
	1.60	0.03	1200	1.92	6.72	0.46
	1.60	0.02	1015	1.62	5.67	0.55
	1.60	0.005	1300	2.08	7.28	0.43
	1.05	*	1520	1.60	5.60	0.56

*Preliminary coverage of the emitter with a residual-gas monolayer.

paratus consists of a determination of the time over which the oil vapor must be adsorbed from a molecular flow of known flux density in order to produce one or several calibration emission images. At high residual gas pressures the accuracy of images A and D becomes smaller because of the adsorption of these gases on the emitter. In these cases the readings are based on images B and C, which have the best contrast. The time required for the formation of the saturated film is calculated from the proportion given above.

The time required to reach the carbon surface concentration corresponding to a given calibration image, c_c, is obviously given by

$$t_c = \frac{c_c}{\nu z \beta}, \tag{8}$$

where z is the number of carbon atoms in a molecule of the oil, and β is the probability that carbon is captured by the surface in the decomposition of the adsorbed oil. Since $\nu t_c = N_c$ we can write

$$c_c = N_c z \beta, \tag{9}$$

where N_c is the surface concentration of oil required to obtain the given calibration concentration of carbon.

If we record the same calibration concentration of carbon c_c, we see from Eq. (9) that $N_c z$ = const for any type of vacuum oil under the condition β = const. However, preliminary experiments show that this product does not remain constant but increases as the vacuum is degraded, and this result can mean only that the value of β decreases. It is not possible to determine the absolute values of the coefficient β by our method, but it is possible to follow the relative changes1) in β, setting $\beta_0 = 1$ for the adsorption of oil on a clean surface.

Table 1 shows the calibration results; for simplicity, the values of t_c and N_c are shown only for image D. The coefficient K gives the ratio of the oil flux density calculated from Eq (7) and the flux density of the residual gas, calculated from the indications of the IM-12 gauge.

Analysis of this table reveals the following:

1. The value of $N_c z$ in the case of the adsorption of type 5F4É oil directly on a clean tungsten surface (K = 50) is $(3.12 \pm 0.32) \cdot 10^{15}$ cm^{-2}. Then, according to our assumption $\beta_0 = 1$ this value can be treated as the concentration of carbon atoms in the saturated film. It is then a simple matter to calculate the values of c_c for the other calibration images.

2. The value of β falls off as the surface becomes contaminated with residual gas. Over the range 50 ≥ K ≥ 1.6 this decrease is small (~20%). Comparison of the dimensions of the oil and residual-gas molecules shows that in this range of K a large part of the "landing field" for the oil molecule is free of adsorbed gas. Nevertheless, as the emitter is heated, fragments of the oil molecules on top of adsorbed gas can desorb as radicals, carrying off part of the carbon. Over the range K = 1.6–0.3 the value of β falls another 30%. A further reduction of K, all the way to zero (the adsorption of oil on top of a residual-gas monolayer is equivalent to K = 0), does not cause any significant change in β. The different values of β obtained for this range of K reflect an experimental scatter, since the error in the indications of the calibration images in a vacuum worse than $5 \cdot 10^{-8}$ torr is ~20%.

Accordingly, we distinguish between two ranges of K, in which the average values of the coefficient β are 0.9 and 0.5, respectively:

$$\text{a)}\quad 50 \geqslant K \geqslant 1.6; \quad \nu = \frac{c_c}{t_c z \cdot 0.9}\ \text{cm}^{-2} \cdot \text{sec}^{-1} \tag{10}$$

(for this range of K the error in the determination of ν is ~± 25%);

$$\text{b)}\quad 0.3 \geqslant K \geqslant 0; \quad \nu = \frac{c_c}{t_c z \cdot 0.5}\ \text{cm}^{-2} \cdot \text{sec}^{-1} \tag{11}$$

(in this case the error in the determination of ν does not exceed ± 35%). If K cannot be evaluated, the assumption $\beta = 0.7$ should be adopted; then the error in the determination of ν is degraded to ± 50%.

To estimate the minimum value $\nu_{\min}$ detectable by this method we consider the conditions prevailing during the accumulation of oil molecules on a tungsten surface contaminated by residual gas (K < 0.3). We assume that the minimum concentration of pyrolytic carbon which can be determined from an emission image corresponds to calibration image B [$(1.56 \pm 0.16) \cdot 10^{15}$ cm^{-2}]. Then Eq. (9) shows that the surface concentration of the accumulated oil must be $1 \cdot 10^{14}$ cm^{-2}, or roughly a monolayer.[11] During the buildup of this concentration the desorption rate increases continuously, in accordance with

$$\frac{dN}{dt} = \frac{N}{\tau_0} \exp\left(-\frac{E}{RT}\right), \tag{12}$$

where $\tau_0 \simeq 10^{13}$ sec, N is the surface concentration of the oil, and E is the activation energy for the desorption. Since at equilibrium the adsorption rate is equal to the desorption rate, we can use Eq. (12) to determine the value of dN/dt at which the necessary surface concentration of oil (in this case, $1 \cdot 10^{14}$ cm^{-2}) is the equilibrium concentration. At T = 300°K and with $E \simeq q$ = 30 kcal/mole, we would have $dN/dt \simeq 1 \cdot 10^{6}$ cm$^{-2}\cdot$sec^{-1}. This value is evidently $\nu_{\min}$. At $\nu < \nu_{\min}$ the necessary oil concentration is not attained; at $\nu > \nu_{\min}$ condensation occurs immediately after the formation of a monolayer of oil.

Accordingly, Eq. (11) can be used to determine ν at T = 300°K and with $q \simeq 30$ kcal/mole only under two conditions:

1. The detected values of ν must be above $1 \cdot 10^{7}$ cm$^{-2} \cdot$ sec^{-1}; at smaller values the additional error due to oil desorption exceeds 10%.

2. The surface concentration of the accumulated oil must not exceed $\sim 1.5 \cdot 10^{14}$ cm^{-2}, since, according to Eq. (9), the tungsten surface becomes completely saturated with carbon as $N \simeq 2 \cdot 10^{14}$ cm^{-2} is approached. Accordingly, over a certain range $N > 2 \cdot 10^{14}$ cm^{-2}, regardless of the value of N, calibration image D would be obtained; with a further increase in N we would find the emission image of a nucleated carbide phase. In both cases an estimate of ν becomes problematical.

After an analogous examination of the conditions governing the applicability of Eq. (10) we conclude that N must not exceed $\sim 0.75 \cdot 10^{14}$ cm^{-2}. Under the conditions prevailing during the adsorption of the oil on the clean tungsten surface we can expect $q \gg 30$ kcal/mole and thus $\nu_{\min} \ll 10^{6}$ cm$^{-2} \cdot$ sec^{-1}.

In practice, however, it is inconvenient to determine such small values of ν, since the time required for the buildup of the required surface concentrations of oil becomes impractical ($> 10^{7}$ sec). If we restrict this time to 10^{5} sec, we can recommend this method for determining the flux density of any vacuum oil having a molecular weight of M = 400-500 and containing 30-40 carbon atoms per molecule in the range $1 \cdot 10^{9}$-$1 \cdot 10^{13}$ cm$^{-2} \cdot$ sec^{-1} (the upper limit is set by the rapid formation of a saturated carbon film). For the type VM-5 and 5F4É oils this range corresponds to $3 \cdot 10^{-6}$-$3 \cdot 10^{-2}$ mg/(cm$^{2} \cdot$ h). The oil can be accumulated on the cathode over a broad pressure range, from 10^{-2} to 10^{-11} torr, but the emission images can be observed only at a vacuum no worse than $1 \cdot 10^{-7}$ torr. For most vacuum systems the condition $K < 0.3$ holds, so it is advisable to use Eq. (11) to calculate ν.

The authors thank A. I. Ermakov and R. A Potapovich for assistance in this work, and M. L. Alashkevich and V. I. Mirimanova for furnishing data on the vapor pressures of the VM-5 and 5F4É oils.

---

1) The literature reveals no information about the mechanism for the decomposition of high-molecular hydrocarbons on hot metal surfaces, but it is shown in refs. 19 and 20 that when tungsten is heated to T > 800°K the light hydrocarbons (acetylene, ethane, ethylene, propane) adsorbed on it are completely dehydrogenated. The hydrogen desorbs into the gas phase, while the carbon skeleton of the molecules becomes tightly bound to the surface. We believe that this mechanism also holds for complex hydrocarbons.

[1] J. Blears, Proc. Roy. Soc. A, 188, 62 (1946).
[2] E. Trendelenburg, Ultrahigh Vacuum [Russian translation], Izd. Mir, Moscow (1966).
[3] M. H. Hablanian, J. Vac. Sci. Technol., 6, 265 (1969).
[4] P. Toffin, G. Legros, and R. P. Henry, Le Vide, 20, 200 (1965).
[5] R. W. Fane, W. E. J. Neal, and R. M. Rollason, Appl. Phys. Lett., 12, 265 (1968).
[6] W. K. Huber, Le Vide, 22, 260 (1967).
[7] G. Döring, G. Marx, and G. Sauerbrey, Vakuum-Technik, 15, 245 (1966).
[8] A. A. Lukashev and P. N. Chistyakov, Zh. Tekh. Fiz., 40, 236 (1970) [Sov. Phys. – Tech. Phys., 15, 171 (1970)].
[9] E. W. Müller, Ergebn. Exakt. Naturwissenschaften, 27, 290 (1953).
[10] P. Wolf, Z. Angew. Phys., 6, 34 (1954).
[11] R. A. Haefer, Vakuum-Technik, 9, 37 (1960).
[12] R. D. Gretz, J. Vac. Sci. Technol., 5, 49 (1968).
[13] V. Ya. Pliskovskii, V. A. Shishkin, and L. N. Shelikhov, Obmen Opytom v Elektronnoi Promyshlennosti, 1, No. 6, 35 (1967).
[14] L. Holland, Vacuum Deposition of Thin Films, Wiley, New York (1956).
[15] S. Dushman, Scientific Foundations of Vacuum Techniques, Wiley, New York (1962).
[16] B. M. W. Trapnell, Chemisorption, Butterworths, London (1955).
[17] A. B. Tseitlin, Vapor-Jet Vacuum Pumps [in Russian], Izd. Energiya, Moscow–Leningrad (1965).
[18] L. P. Levine and J. Landowski, J. Vac. Sci. Technol., 6, 834 (1969).
[19] R. R. Rye and R. S. Hansen, J. Chem. Phys., 50, 3585 (1969).
[20] R. S. Hansen and N. C. Gardner, J. Phys. Chem., 74, 3646 (1970).

Emission parameters of a field-emission cathode

G. N. Freiberg

Moscow Polytechnical Institute

(Submitted September 6, 1973; resubmitted February 13, 1974)
Zh. Tekh. Fiz., 44, 2186-2191 (October 1974)

It is shown theoretically that absolute determinations of the work functions, current density, and electric field at a field-emission cathode, the effective emission area, and the form factor are possible through the use of a particular parameter: the ratio of the maximum current density at the cathode to its average value over a period of the alternating electric field at the cathode. Computer calculations indicate the feasibility of such determinations. Graphical relations for finding these properties are given. A simple procedure is proposed for determining the field-emission current density at the cathode.

Current problems in the use of field-emission cathodes in vacuum-tube devices require studies of the physical processes associated with field emission. To approach this problem correctly we need to know such physical properties as the emission current density, the electric field near the cathode surface, the effective work function, the emitting surface area, and the form factor. This information is also necessary in choosing operating conditions for field-emission cathodes and for monitoring their operation.

The methods available for determining these parameters[1-3] are basically relative methods, requiring prior knowledge of one of these parameters from some other experiments. The methods by which these parameters are found through analysis of the voltage–current characteristics and the functional dependence of the field-emission current on the temperature[4,5] or of the energy distribution of the field-emission electrons[6,7] suffer from the complexity of the corresponding experiments. Furthermore, they are based on the assumption of a simplified equation for the field emission, and their results are not available during the experiment, since they require laborious calculations. Solution of the system of equations on the basis of three points on the voltage–current characteristic of the field-emission device[8] can in principle yield the values of all the parameters, if the current and voltage are measured within four or five significant figures, but a computer is required to obtain the results.

Below we propose another absolute method[9] for determining the parameters of a field-emission cathode, a method which yields results during an experiment. The time saving results from the introducing of dimensionless functions whose values can be measured during tests of the devices.

THEORY BEHIND THE METHOD

We consider the Fowler–Nordheim equation in the form

$$j=\frac{AE^{2}\exp\left[-B\varphi^{3/2}\frac{\theta(y)}{E}\right]}{\varphi v^{2}(y)^{2}},\qquad(1)$$

which is an analytic relation for the physical quantities E, j, and φ. Here, j is the field-emission current density, E is the electric field at the cathode surface, φ is the work function, $\Theta(y)$ is the tabulated Nordheim function, and $y = d\sqrt{E/\varphi}$, v(y) is defined by

$$v(y)=\Theta(y)-\frac{2}{3}y\frac{d\Theta}{dy},$$

where A, B, and D are constants.

We assume that E is specified as a function of the time:

$$E(t)=E_{m}f(\omega t),\qquad(2)$$

where E_m is the peak field, $f(\omega t)$ is an arbitrary smooth function having a period of 2π and a peak value of unity [$1 \geq |f(\omega t)| \equiv$ const; the plot of $f(\omega t)$ is rectangular], t is the time, and ω is the frequency.

We then find the current density at any time,

$$j(t)=\frac{AE_{m}^{2}f^{2}(\omega t)\exp\left\{-\frac{B\varphi^{3/2}\theta(y)}{[E_{m}f(\omega t)]}\right\}}{\varphi v^{2}(y)},\qquad(3)$$

and the maximum current density,

$$j_{m}=\frac{AE_{m}^{2}\exp\left[-\frac{B\varphi^{3/2}\theta(y_{m})}{E_{m}}\right]}{\varphi v^{2}(y_{m})},\qquad(4)$$

and the time-averaged current density,

$$j_{\text{av}}=\left[\frac{AE_{m}^{2}}{(2\pi\varphi)}\right]\int_{0}^{2\pi}\left[\frac{f^{2}(x)}{v^{2}(y)}\right]\exp\left\{-\frac{B\varphi^{3/2}\theta(y)}{[E_{m}f(x)]}\right\}dx,\qquad(5)$$

where $x = \omega t$, $y_m = D\sqrt{E_m}/\varphi$, $y = D\sqrt{E_m f(x)}/\varphi$.

We construct the new function

$$K=\frac{j_{m}}{j_{\text{av}}}.\qquad(6)$$

This function can be a function of either E_m and φ or j_m and φ [see Eqs. (4) and (5)]. We construct the family of curves $K_L(j_m, \varphi_L)$ where L = 1, 2, . . . , n (Fig. 1). In Fig. 1a we draw two straight lines through ordinates K_1

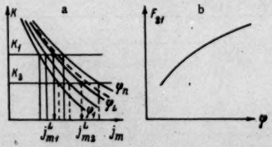

Fig. 1. a) Qualitative functional dependences of the ratio of the peak current density to the time-averaged current density on the peak current density for various work functions φ_L; b) the quantity $F_{21} = j_{m2}/j_{m1}$ as a function of φ.

and K_2 and parallel to the j_m axis. These lines intersect the family of curves $K_L(j_m, \varphi_L)$ at points with abscissas j_{m1}^L and j_{m2}^L. We also construct the function

$$F_{21} = \frac{j_{m2}^L}{j_{m1}^L} \tag{7}$$

for each work function φ_L, and plot a curve from the given points (Fig. 1b). This function, for given K_1 and K_2, is a function of the work function φ alone, i.e., $F_{21} = F_{21}(\varphi)$.

Accordingly, knowing the ratio of the peak current densities under two different sets of operating conditions of the cathode, with $j_m/j_{av} = K_1$ and $j_m/j_{av} = K_2$, we can find the work function φ for the given cathode by varying the electric field E at the cathode according to some law (2).

In practice, we deal with the total current I and the anode–cathode potential difference U. For an idealized cathode we can write

$$I = Sj, \tag{8}$$

$$E = \beta U, \tag{9}$$

where S is the area of the emitting surface and β is the form factor. By "idealized" here we mean a cathode for which φ and β are uniform along the entire surface and for which φ, β, and S are independent of the emission current density. Conditions approximating these can be achieved experimentally by recording voltage–current characteristics with probes from small regions of individual faces of single-crystal cathodes.

The quantities S and β in (8) and (9) are usually unknown, but by using (8) we can write

$$K_1 = \frac{I_{m1}}{I_{av1}}, \tag{10}$$

$$K_2 = \frac{I_{m2}}{I_{av2}}, \tag{11}$$

$$F_{21} = \frac{I_{m2}}{I_{m1}}; \tag{12}$$

i.e., dividing the peak currents I_{m2} for $K = K_2$ by I_{m1} for $K = K_1$, we find the experimental value of F_{21}, and from a plot of $F_{21}(\varphi)$ we find the unknown work function φ for the particular cathode. Then from the family of $K_L(E_m, \varphi_L)$ and $K_L(j_m, \varphi_L)$ curves constructed from the data on K_2, K_1 and φ, we find the corresponding values of E_m and j_m; knowing the corresponding values of j and U, we find from Eqs. (8) and (9) the area of the emitting surface, S, and the form factor β.

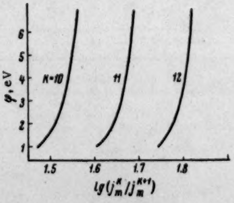

Fig. 2. Diagram used to determine the work function φ from the known value of $\log(j_m^K/j_m^{K+1})$.

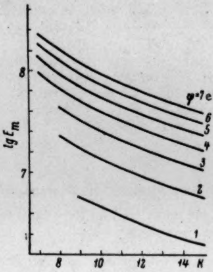

Fig. 3. Diagram used to find the field E_m from the known values of K and φ.

This solves the problem of finding the parameters of the field-emission cathode. This method is based on the Fowler–Nordheim equation alone and is absolute, so that it furnishes yet another method for testing the validity of the theory of field emission of metals for particular cathodes. We also note that this method is not rendered more complicated by the specification of some functional dependence other than that in (1), even if the functional dependence is specified implicitly.

RESULTS OF COMPUTER SOLUTIONS

We use a computer to solve the problem for the case of a sinusoidal time dependence of the electric field:

$$f(\omega t) = \sin(\omega t). \tag{13}$$

Figures 2 and 3 show the calculated results as $\varphi[\log(j_m^K/j_m^{K+1})$ and $\log E_m(K, \varphi_L)$ curves. Analysis of these curves demonstrates the feasibility of this method for determining the necessary information about the field-emission cathode.

To determine the work function φ within ± 1% it is necessary to measure the ratios of currents at their peak values, I_m, within 0.2-0.1% – which is feasible. For the other parameters the accuracy is better by a factor of 5 to 10 under the same measurement conditions.

In solving this problem we analyze the relationship between the numerical values of the width of the current pulses (we use the width at half-height, $\tau_{1/2}$; Fig. 4) and the quantity K. We find that the relative pulse width $\bar{\tau}_{1/2} = \tau_{1/2}/T$, where T is the period, is independent of the work function, being a function of K alone. Figure 5 shows the relative pulse width as a function of the ratio of the peak current to the average current over a period.

We can thus work with the relative width $\bar{\tau}_{1/2}$ instead of K, converting all the K_L curves into $\bar{\tau}_{1/2}^L$ curves; in this

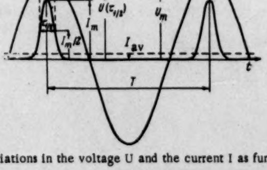

Fig. 4. Variations in the voltage U and the current I as functions of the time t.

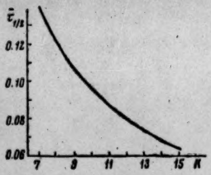

Fig. 5. Relationship between the relative width of the current pulse, $\bar{\tau}_{1/2}$, and the ratio of the peak current to the average current.

way we avoid measuring I_m, I_{av}, and their ratios and thus avoid much labor. We simply measure I_m and the relative pulse width, e.g., at half-height, by rf methods.

The computer solution of this problem reveals another important result: Over a certain range of work functions φ the emission current density can be a function of the relative width of the current pulse alone (or of the ratio $K = I_m/I_{av}$), in a first approximation. Hence we can determine the emission current density and the effective emitting area from a single value of $\bar{\tau}_{1/2}$. This capability simplifies the choice of a safe region for testing field-emission devices and studying their operation.

Figure 6 shows that for K = 10 (or $\bar{\tau}_{1/2} = 0.096$) the current density remains essentially constant as the work function is changed from 2.0 to 7.0 eV (the deviation from the average value is ≤ ± 10%).

Figure 4 also shows that to each value of $\tau_{1/2}$ there corresponds a definite relative anode voltage, since we have

$$\frac{U(\tau_{1/2})}{U_m} = \cos\left(\frac{\omega}{2}\tau_{1/2}\right). \tag{14}$$

It follows that $\bar{\tau}_{1/2}$ is a function of the relative anode voltage $\bar{U}_{1/2} = U(\bar{\tau}_{1/2})/U_m$ or, equivalently,

$$\bar{U}_{1/2} = \frac{U\left(\frac{I}{2}\right)}{U(I)}. \tag{15}$$

This result leads to the possibility of determining all the parameters at a constant voltage, i.e., at a voltage independent of the time, by using the results of the solution for the case of a sinusoidal voltage across the field-emission diode. We thus always have

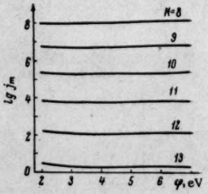

Fig. 6. The quantity $\lg j_m$ as a function of φ for various values of K.

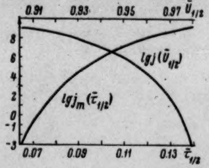

Fig. 7. Diagram used to determine the current density for known values of $\bar{\tau}_{1/2}$ or $\bar{U}_{1/2}$.

$$\tau_{1/2} = \frac{1}{\pi} \arccos \bar{U}_{1/2}. \tag{16}$$

Figure 7 shows the logarithm of the field-emission current density (error ≤ ± 10%) as a function of $\bar{\tau}_{1/2}$ and $\bar{U}_{1/2}$ for a field-emission cathode whose work function is unknown.

We thus have three methods for determing the parameters of a field-emission cathode: 1) the method based on the ratio of the peak current to the average current (the "K method"); 2) the method based on measurement of the width of the current pulse at some height (the "τ method"); 3) the method based on the ratio of the anode voltages at different currents, e.g., for currents differing by a factor of 2 (the "U method").

The U method is technically the simplest; in its essential form it requires no new instruments. In terms of the convenience and efficiency with which results are obtained, the τ method is the best.

Both methods have been tested in the laboratory in determinations of the field-emission current density; the results show that the two methods are fully consistent with each other and with the method based on the ratio of the slope of the Fowler–Nordheim line to the anode voltage.[10] We note, however, that the calculation burden associated with the method of ref. 10 is about 10 times that of our U method, for equivalent results in terms of the current density. Furthermore, because of the simplicity of the dimensionless functions we introduce here, their values can be determined during the experiment. It would be a simple matter to construct a system to automatically maintain a specified current density in the face of any changes at the cathode. Such a system could be useful, e.g., in studying the behavior of the emitting surface.

---

[1] M. I. Elinson and G. F. Vasil'ev, Field Emission [in Russian], Fizmatgiz, Moscow (1958).
[2] B. G. Smirnov and G. N. Shuppe, Zh. Tekh. Fiz., 22, 973 (1952).
[3] H. Von Vernickel, Z. Angew. Physik, 19, No. 6, 498 (1965).
[4] I. S. Andreev, Zh. Tekh. Fiz., 22, 1428 (1952).
[5] I. S. Andreev, Zh. Tekh. Fiz., 23, 849 (1953).
[6] R. D. Young and E. W. Muller, Phys. Rev., 113, 115 (1959).
[7] R. D. Young and H. E. Clark, Phys. Rev. Lett., 17, No. 7, 351 (1966).
[8] V. A. Kuznetsov, A. P. Ovchinnikov, and E. A. Tishin, Radiotekh. Elektron., No. 2, 381 (1969).
[9] G. N. Freiberg, 15th All-Union Conference on Emission Electrons, Abstracts of Reports [in Russian], Vol. 2, Kiev (1973), p. 78.
[10] A. G. J. van Oostrom, J. Phil. Res. Rept. Lett., No. 11, 102 (1966).

Composition of adsorbing and desorbing fluxes

Yu. A. Gel'man, V. I. Mikhailov, V. F. Vinogradov, and Yu. N. Lyubitov
Institute of Crystallography, Academy of Sciences of the USSR, Moscow

(Submitted May 25, 1973)
Zh. Tekh. Fiz., 44, 2192-2197 (October 1974)

Characteristics of the spatial distribution of the fluxes of sodium chloride dimers and monomers from effusion cells of various designs are reported. The conditions under which the effusion characteristics of the monomers and dimers are very different or slightly different have been determined experimentally. In particular, a study has been made of the effect of a temperature gradient in the effusion cell on the shape of the characteristics. These results make it possible to carry out experiments which show that under certain conditions the degree of dissociation of dimers incident on a tantalum target is lower than the thermodynamic equilibrium value.

These experiments are part of an effort to determine how the composition of a molecular flux incident on a target affects the composition of the flux leaving the surface. The flux leaving a tantalum target is studied in refs. 1-4 for the case of a constant incident flux of sodium chloride dimers and monomers. Different functional dependences on the target temperature are found for the flux of dimers leaving the target: There is a constant region or plateau in the dimer flux at high temperatures in refs. 1 and 2 but not in refs. 3 and 4. The difference is found to be attributable to the use of different sources for the incident flux.

We have carried out two series of experiments: 1) We have studied the fluxes from effusion chambers, like those used as the sources of the incident flux in refs. 1-4; 2) we have measured the changes in the composition and intensity of the flux leaving the surface as a function of the incident flux.

1. In the first series of experiments we study the characteristics of the spatial distribution of the monomers (NaCl) and of the dimers (Na_2Cl_2) from evaporators of various designs (Fig. 1). The evaporator in Fig. 1a, heated by radiation from a coil, is isothermal; evaporators of this kind are used in refs. 1 and 2. That in Fig. 1b is a tube of 10 μ tantalum foil, heated by a current flowing through the tube itself. In evaporators of this type there is a temperature drop ΔT between the center and edges of the evaporator which can be measured with thermocouples, as shown in Fig. 1b. The value of ΔT is varied by changing the rate at which heat is removed from the edges and by changing the pattern of the foil from which the tube is welded; it also changes as the salt is expended. An evaporator of this kind is used in refs. 3 and 4 as the source of the incident molecules.

In the present experiments an MS-1303 mass spectrometer is used, and the test evaporator is rotated around an axis passing through the effusion aperture (point 0 in Fig. 1 is the intersection of this axis with the plane of the figure). Between the evaporator and the ionization chamber of the ion source is a shield which protects the electrodes of the ion source from being sprayed with the salt. The measurable molecular beam fills an angle much smaller than 1°. Figure 2 shows effusion characteristics obtained with the evaporator of Fig. 1a. The characteristics are normalized to the maximum values of the I^{58}

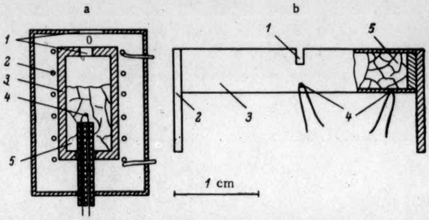

Fig. 1. Construction of the evaporators. a: 1) Effusion aperture; 2) coil; 3) stainless steel crucible; 4) thermocouple; 5) salt; 0) intersection of the rotation axis with the plane of the figure (this axis is perpendicular to this plane). b: 1) Effusion aperture; 2) current leads; 3) tantalum-foil tube; 4) thermocouples; 5) salt; 0) intersection of the rotation axis with the plane of the figure.

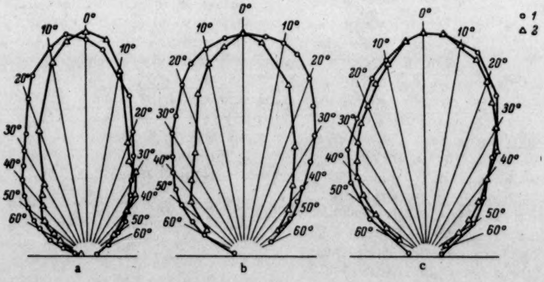

Fig. 2. Effusion characteristics of the evaporator in Fig. 1a. 1) I^{58}; 2) I^{81}; T, °C: a) 525; b) 566; c) 625.

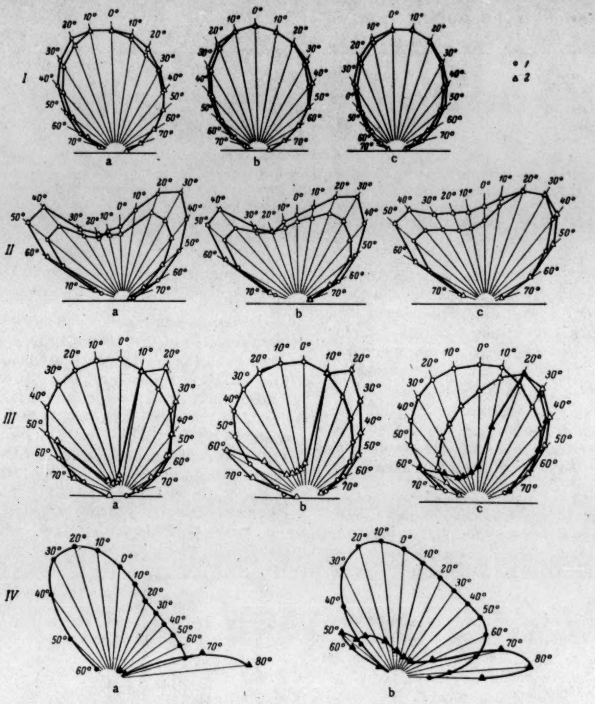

Fig. 3. Effusion characteristics of the evaporator in Fig. 1b. Here ΔT is the difference between the thermocouple readings (Fig. 1b, item 4), i.e., the evaporator temperature minus the reading of the central thermocouple. 1,2) The same as in Fig. 2. I: Evaporator full of salt, $\Delta T = 20°$ at 700°C. T, °C: a) 560; b) 630; c) 700. II: Roughly half the salt has been expended, $\Delta T = 30°$ at 700°C. T, °C: a) 560; b) 630; c) 700. III: Evaporator not full. T, °C: a) 790; b) 845; c) 890. IV: Salt at only one end of the evaporator, $\Delta T = 200°$ at 700°C. T, °C: a) 765; b) 800.

and I^{81} ion currents, which are proportional to the fluxes of the NaCl monomer (the $NaCl^+$ ion) and the Na_2Cl_2 dimer (the Na_2Cl^+ ion), respectively. The dimer contribution to the total I^{58} current (due to dissociative ionization) is neglected. With this evaporator we have $I^{58}_{max}/I^{81}_{max} = 2\text{-}3$. It is evident from Fig. 2 that at relatively low temperatures there is a greater difference between the effusion characteristics for the monomers and dimers; as the temperature is raised this difference is reduced and the characteristics become less sharp. Figure 3 shows characteristics for the second evaporator; the value of ΔT along the length of the evaporator increases from top to bottom. For the evaporator of Fig. 1b the difference between the effusion characteristics of the monomers and dimers is more pronounced than for the evaporator of Fig. 1a. There is also an increase in the difference between the characteristics with increasing ΔT in the evaporator. In contrast with the characteristics obtained with the evaporator of Fig. 1a, the shape of the characteristics obtained with the evaporator of Fig. 1b changes markedly as the charge diminishes (Fig. 3, I and II). There is also a change in the composition of the molecular flux: $I^{58}_{max}/I^{81}_{max} = 1\text{-}1.5$ for Fig. 3, I, and $I^{58}_{max}/I^{81}_{max} = 2\text{-}3$ for Fig. 3, II A change in the thermal conditions in the evaporator can also change the shape of the I^{81} characteristic (Figs. 3, III c). The open triangles show the characteristic 3 min after a change in the current through the evaporator while the solid triangles show the situation 20 min after this change. We find $I^{58}_{max}/I^{81}_{max} = 8\text{-}10$ for Fig. 3, III and $I^{58}_{max}/I^{81}_{max} = 18\text{-}25$ for Fig. 3, IV. The temperature drop ΔT is not measured for the characteristic in Fig. 3, III but on the basis of visual observation of the distribution of the brightness we conclude that this drop should lie between those corresponding to the characteristics in Fig. 3, II and Fig. 3, IV.

A difference between the partial effusion characteristics of monomers and dimers was first predicted by Voronin.[5] We have observed a substantial intensification of this effect under the influence of a temperature drop in the evaporator. The characteristics are discussed below.

The changes in the monomer and dimer fluxes with

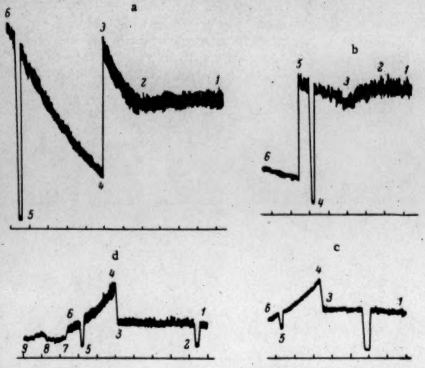

Fig. 4. Changes in the monomer (a, b) and dimer (c, d) fluxes as a function of current through the evaporator in Fig. 1b. Time elapses from right to left. a: Incident I^{58} flux. 1,2) Constant current through the evaporator; 2-6) increase in the signal with a sharp increase in the current through the evaporator; 3,4) scale is switched; 5) the incident-flux shutter is closed. b: Desired I^{58} flux; 1,2) constant current through the evaporator; 2) time at which the current decreases; 3) time at which the current increases; 3-6) gradual increase in the signal; 4) incident-flux shutter closed; 5) scale is switched. c: Incident I^{81} flux. 1-3) Constant current through the evaporator; 2) beam shutter is closed; 3) time at which the current decreases; 3-6) gradual change in signal; 5) successive increase and decrease in the current. d: Desorbed I^{81} flux. 1-3) Constant current through the evaporator; 2,5) incident-flux shutter operates; 3) current through the evaporator is decreased; 6) time at which the current increases; 8) time at which the current decreases.*

changing temperature are also different for the evaporators in Figs. 1a and 1b. That in Fig. 1a produces parallel changes in I^{58} and I^{81} as the temperature is changed, while there is a difference between the I^{58} behavior and the I^{81} behavior when the evaporator in Fig. 1b is used, with its central region free of salt (Figs. 4a and 4c). As the current through the evaporator is increased the I^{58} flux increases smoothly; as the current is reduced, the I^{58} flux decreases. As the current through the evaporator is reduced the I^{81} flux at first increases rapidly, but then decreases smoothly. A current increase causes the opposite behavior. This effect is more pronounced, the larger the temperature drop ΔT over the length of the evaporator. We can thus cause instantaneous changes in the dimer concentration in the incident flux while holding the total flux essentially constant (the monomers are predominant in the flux).

To study the effect of the composition of the incident flux on the flux leaving the target we use the evaporator in Fig. 1a, whose characteristics are shown in Fig. 3III.

2. In the second series of experiments the molecular flux is incident on a tantalum target and the composition of the flux leaving the surface is analyzed for changes in the target temperature. The experimental apparatus is the same as in refs. 1-4. The flux incident on the target spans the interval from −5° to + 5° (Figs. 2 and 3). Figure 5 shows the temperature dependences of the dimer flux (I^{81}) leaving the target. Curve a is obtained with the evaporator of Fig. 1a, while curve b is obtained with the evaporator in Fig. 1b. We see that the magnitude of the dimer flux leaving the target in the high-temperature part of the curve is much higher with the evaporator of Fig. 1a, in which case there are more dimers in the incident flux (Figs. 2 and 3, III).

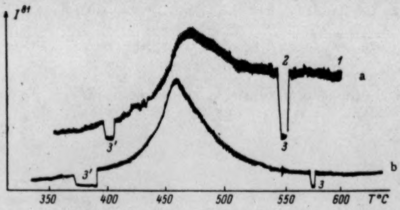

Fig. 5. Desorbed dimer flux as a function of the substrate temperature. The incident flux is from: a) the evaporator in Fig. 1a; b) that in Fig. 1b having the characteristic in Fig. 3, III. 1,2) Plateau; 3) incident-flux shutter is closed; 3') exciting-flux shutter is closed.

The data in Figs. 4, a and b, correspond to comparatively rapid changes in the temperature in the central part of the evaporator, free of salt, and comparatively slow changes in the temperature at the ends of the evaporator, which are filled with salt. We note that the temperature is always lower at the ends than at the center of these evaporators. The effect illustrated in Figs. 4, a and b, is observed in the evaporator of Fig. 1b, and in the flux leaving the target as well. Figure 4 shows the changes in I^{58} (b) and I^{81} (d) in the flux leaving the target upon a change in the current through the evaporator, with a target temperature which is constant and in the plateau region. These results imply that the dimer flux leaving the target in the plateau region is proportional to the dimer flux in the incident beam and not to the total incident flux. This result contradicts the assumption (used in ref. 5) that the desorbed fluxes are functions of the incident flux and the adsorbent temperature alone and independent of the dimer−monomer composition of the incident flux.

These experimental results (Figs. 2 and 3) can be explained by arguing that the total flux of molecules leaving the evaporator is governed primarily by the temperature of the evaporating salt. On the other hand, the composition of this flux is a function of 1) the temperature of that part of the surface which irradiates the detector, 2) whether there is a condensed phase present, and 3) the intensity and composition of the flux incident on this region (Fig. 5). Accordingly, when the detector is irradiated by the part of the evaporator filled with salt the beam has a higher dimer content than when the detector is irradiated by the hotter part of the evaporator.

These results furnish additional evidence that some of the dimers incident on a tantalum target at temperatures in the plateau region (Fig. 5) are characterized by a degree of dissociation lower than the thermodynamic equilibrium value. Further study by other experimental methods is necessary to determine the nature of the reflection of the fraction of dimers which do not participate in a dissociation reaction ($Na_2Cl_2 \rightarrow 2NaCl$) on the substrate.

The authors thank the participants of a seminar of **É. Ya. Zandberg** and **N. I. Ionov** for discussion.

Publisher's note: Point 7 in Figure 4 is not defined in the Russian original.

---

[1] Yu. A. Gel'man, A. M. Zatselyapin, Yu. N. Lyubitov, and V. I. Mikhailov, Dokl. Akad. Nauk SSSR, 195, 1813 (1970).

[2] Yu. N. Lyubitov, V. I. Mikhailov, A. M. Zatselyapin, and Yu. A. Gel'man, Zh. Fiz. Khim., 45, 1301 (1971).

[3] A. M. Zatselyapin, Candidate's Dissertation [in Russian], Moscow (1972).

[4] A. M. Zatselyapin, V. I. Mikhailov, Yu. A. Gel'man, Yu. N. Lyubitov, and A. A. Chernov, in: Crystal Growth [in Russian], Vol. 2, Izd. EGU, Erevan (1974).

[5] G. F. Voronin, Zh. Fiz. Khim., 37, 1663 (1967).

Radial distribution of density and potential in a glow discharge in CO_2 and water

A. I. Maksimov and V. F. Sokolov
Ivanov Chemicotechnological Institute

(Submitted August 7, 1973; resubmitted November 5, 1973)
Zh. Tekh. Fiz., 44, 2198-2202 (October 1974)

Expressions are obtained for the radial charge distribution when the particle currents are equal. Experimental measurements carried out in the pressure range 0.5 to 2 torr for currents of 1 mA to 5 mA show good agreement with the calculations. The experimental data are used to estimate the relative density of the negative ions $\alpha = n_-/n_e$.

The nature of the joint diffusion of electrons, positive ions, and negative ions and the charge balance with negative ions present have been considered by a number of workers.[1–5] In these papers expressions are obtained for the effective diffusion coefficients in a plasma with negative ions, and the relation between the space-charge field and the relative density of the negative ions is obtained. There are also available, certain measurements of the radial potential distribution and the radial charge density distribution in an electronegative plasma.[6]

The purpose of the present investigation is to analyze the relation between the spatial distribution of the space-charge field and the charged particle density in the column of a glow discharge in a gas capable of forming negative ions by dissociative electron trapping.

1. FUNDAMENTAL RELATIONS

The space-charge field is found from the condition that the positive and negative currents be equal:

$$\left.\begin{aligned}\Gamma_+ &= -D_+\nabla n_+ + \mu_+ n_+ E,\\ \Gamma_- &= -D_-\nabla n_- - \mu_- n_- E,\\ \Gamma_e &= -D_e\nabla n_- - \mu_e n_e E,\\ \Gamma_+ &= \Gamma_- + \Gamma_e.\end{aligned}\right\} \qquad (1)$$

Here, Γ is the current density, D is the diffusion coefficient, μ is the mobility, and n is the density. The subscripts "+", "-", and "e" refer to the positive ions, negative ions, and electrons, respectively.

From (1) we obtain the space-charge field

$$E = \frac{D_+\nabla n_+ - D_-\nabla n_- - D_e\nabla n_e}{\mu_+ n_+ + \mu_- n_- + \mu_e n_e}. \qquad (2)$$

Invoking neutrality and putting $n_-/n_e = \alpha$, we can convert Eq. (2) to the form

$$\frac{dU}{dr} = -\nabla n_+\left(D_+ - \frac{\alpha}{1+\alpha}D_- - \frac{1}{1+\alpha}D_e\right) - \nabla\alpha\left[\frac{n_+D_-}{(1+\alpha)^2} - \frac{n_+D_e}{(1+\alpha)^2}\right]. \qquad (3)$$

When $\nabla\alpha = 0$ Eq. (3) gives the ion density distribution, which has the Boltzmann form

$$n_+ = n_+^0 \exp\left(-\frac{\Delta U}{G}\right). \qquad (4)$$

Here, n_+^0 is the axial ion density, ΔU is the potential difference between the given point and the axis, and

$$G = \frac{D_+ - \frac{\alpha}{1+\alpha}D_- - \frac{1}{1+\alpha}D_e}{\mu_+ + \mu_-\frac{\alpha}{1+\alpha} + \mu_e\frac{1}{1+\alpha}}. \qquad (5)$$

When $\alpha = 0$ the quantity G is determined in practice solely by the mean electron energy, and Eq. (4) becomes the usual expression for the ambipolar diffusion condition without negative ions.[7] Note that the condition $\nabla\alpha = 0$ is equivalent to the relation (for $\alpha \gg 1$)

$$\frac{\nabla n_-}{\nabla n_e} \approx \frac{\nabla n_+}{\nabla n_e} \approx \frac{\nabla n_i}{\nabla n_e} \approx \alpha. \qquad (6)$$

This relation, which is fairly obvious qualitatively, indicates a plane radial distribution of the electron density with heavy negative ions.

An expression of the form (4) can be obtained from Eq. (3) in certain cases when $\nabla\alpha \neq 0$. When $\alpha \gg 1$, assuming that $D_e \gg D_-$, $D_e \gg D_+$, $\mu_i = \mu_- \approx \mu_+$, from Eq. (3) we have

$$\frac{dU}{dr} = -\frac{\nabla n_+\frac{D_e}{\alpha} + \nabla\alpha\frac{n_+}{\alpha^2}D_e}{n_+\left(2\mu_i + \frac{\mu_e}{\alpha}\right)} = \frac{\nabla n_+}{n_+}\frac{D_e}{2\alpha\mu_i + \mu_e} - \frac{\nabla\alpha}{\alpha}\frac{D}{2\alpha\mu_i + \mu_e}. \qquad (7)$$

Finally, if the value of α has an upper limit determined by the condition $2\alpha\mu_i + \mu_e$, or if the dependence of the sum $2\alpha\mu_i + \mu_e$ on α is small, the relation $D_e/(2\alpha\mu_i + \mu_e) = G_1$ can be assumed to be independent of radius, and Eq. (7) becomes

$$\left.\begin{aligned}\frac{n_+}{\alpha} &= \left(\frac{n_+}{\alpha}\right)_0 \exp\left(-\frac{\Delta U}{G_1}\right),\\ \ln\left(\frac{n_+}{n_+^0}\right) &= \ln\left(\frac{\alpha}{\alpha_0}\right) - \frac{\Delta U}{G_1}.\end{aligned}\right\} \qquad (8)$$

With the above assumptions this is equivalent to a Boltzmann distribution of the electron density in the space-charge field with a value G_1 which plays the role of the average electron energy.

Expression (8) only holds in the range of variation of α from 10 to 100.

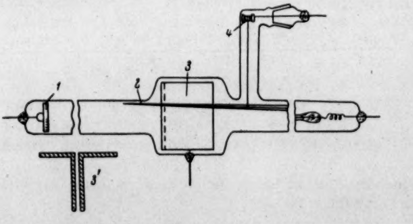

Fig. 1. Construction of the discharge tube for radial measurements. 1) cathode; 2) probe; 3) anode [3' is the view from above]; 4) moving devices.

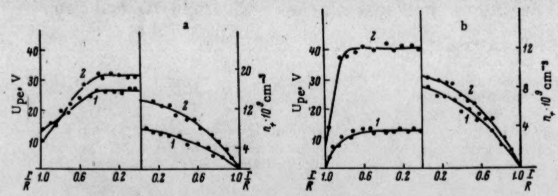

Fig. 2. Radial distribution of the positive ion density and the plasma potential. a) H_2O, p = 1.8 torr, I_p(mA): 1) 1.5; 2) 3.0, b) CO_2, p = 0.6 torr, I_p(mA): 1) 3.0; 2) 4.5.

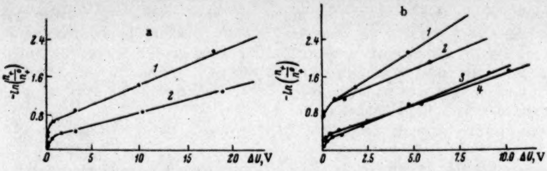

Fig. 3. Curves of $\ln(n_+/n_+^0)$ as a function of ΔU. a) H_2O, R = 1.4 cm, pR = 2.52 torr · cm, I_p(mA): 1) 1.5, 2) 3.0, b) CO_2, p(Torr), I_p(mA): 1) 0.6, 3.0; 2) 0.6, 4.5; 3) 1.2, 1.5; 4) 1.9, 1.5.

2. EXPERIMENTAL INVESTIGATIONS

We measure the radial distribution of the positive ion density and the potential in the column of a glow discharge in CO_2, and in water vapor using a single probe. The construction of the discharge tube with a probe movable in the radial direction is shown in Fig. 1. The probe is made from tungsten wire 0.065 mm in diameter and the uninsulated part is 2 mm long. The gas pressure is 0.5-2 torr, the discharge current is 1-5 mA, and the tube radius is 1.4 cm.

The radial distributions of the floating potential and space potential are found experimentally. The latter is found from the point of inflection of single-probe characteristics, plotted on a semilogarithmic scale. (The point of inflection of the curve can be measured with an accuracy better than ± 2 V).

The positive ion density is calculated from the ion branches of the probe characteristics. In calculating the radius of the collecting sheath we use the experimental values of the floating potential of the probe with respect to the plasma potential. It is also assumed that the potential of the boundary layer is determined by the mean ion energy (this holds[6] for $\alpha > 3$). The ion temperature is assumed to be equal to the temperature of the gas in the discharge; this temperature is measured using a miniature (scaled in glass) thermocouple located at the axis of the discharge.

An example of the experimentally obtained radial distribution of the positive ion density and the plasma potential in the column of the glow discharge in CO_2 and H_2O is shown in Fig. 2. The ion distribution is the usual one for diffusion decay, and the space potential exhibits a fairly flat axial part.

It follows from (8) that where $\alpha/\alpha_0 \approx$ const a linear relationship should be observed between $\ln n_+/n_+^0$ and ΔU. Plotting the experimental data in these coordinates shows that this linear relation does in fact exist (Fig. 3). From the slope of the linear part of the relation $\ln n_+/n_+^0 = f(\Delta U)$ we can estimate the values of G_1, and use it to find the radial distribution of the ratio α/α_0. The results of the calculation are shown in Fig. 4; as one moves along the radius α changes by less than a factor of 2. However, near the axis one cannot neglect $\Delta\alpha$ since the variation of α is essentially the same as the variation of n_+ for small r. This result indicates that the electron density obtained directly from Eq. (8) for the region with a flat potential distribution, is constant.

Since the presence of negative ions changes the space-charge field, it is best to compare the experimental potential distribution with that predicted by diffusion theory, which ignores the negative ions. For $\alpha = 0$, $n_+ = n_e$, and $\Delta n_+ = \Delta n_e$, it follows from Eq. (2) that

$$E \approx -\frac{\nabla n_e}{n_e}\frac{kT_e}{e} = \frac{kT_e}{e}\frac{J_1\left(\frac{2.4}{R}r\right)}{J_0\left(\frac{2.4}{R}r\right)}. \tag{9}$$

Hence, we obtain for the potential difference ΔU between the axis and the given point

$$-\frac{\Delta U e}{kT_e} = 2.4\int_0^{r/R}\frac{J_1\left(\frac{2.4}{R}r\right)}{J_0\left(\frac{2.4}{R}r\right)}\,d\left(\frac{r}{R}\right). \tag{10}$$

The curve described by Eq. (10) is shown in Fig. 5. The same figure also shows the experimental distribution of the dimensionless potential of the plasma $\Delta U/G_1$. The large difference between the theoretical and experimental curves may be due to the presence of negative ions.

Tompson[5] gives the ratio of the space-charge fields with and without negative ions in the form

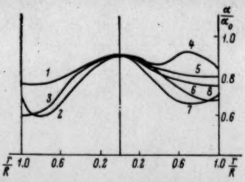

Fig. 4. Radial distribution of the relative negative ion density. CO_2, p(Torr), I_p (mA): 1) 1.9, 1.5; 2) 0.6, 3.0; 3) 0.6; 4.5, 4) 1.2, 4.5; 5) 1.2, 1.5; 6) 1.2, 3.0; H_2O: 7) 1.8, 1.5; 8) 1.8, 3.0.

$$\frac{E(\alpha)}{E(0)}=\frac{1-\frac{D_+}{D_+^{\alpha}}}{1+\alpha}\left(\frac{1+\gamma}{\gamma}\right). \qquad (11)$$

Here γ is the ratio of the mean energies of the electrons and ions, and D_+^{α} is the effective diffusion coefficient of the positive ions, which depends on α. Analysis of Eq. (11), using the expression for D_+^{α} given by Tompson, for $\gamma \gg 1$ and $\alpha \leq 100$ leads to

$$\frac{E(\alpha)}{E(0)}=\frac{1}{1+2\alpha}. \qquad (12)$$

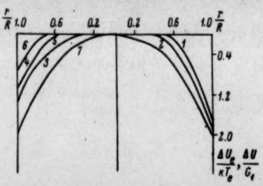

Fig. 5. Radial variation of the ratio of the space-charge field. H_2O, p(torr), I_p(mA): 1) 1.8, 1.5; 2) 1.8, 3.0; CO_2: 3) 1.2, 1.5; 4) 1.2, 3.0; 5) 0.6, 3.0; 6) 0.6, 4.5; 7) the curve given by Eq. (10).

This relation enables one to estimate the order of magnitude of α, by comparing the theoretical and experimental curves in Fig. 5. For small r, estimates give $\alpha \approx 10$.

---

[1] R. Seeliger, Ann. Phys., 6, 93 (1949).
[2] M. V. Konyukhov, Zh. Eksp. Teor. Fiz., 34, 908, 1634 (1958) [Sov. Phys.–JETP, 7, 629, 1122 (1958)].
[3] J. Wilhelm, Z. Naturwiss., 45, 19. 459 (1958).
[4] G. Albrecht and G. Ecker, Z. Naturforsch., 17a, 10, 848 (1962).
[5] J. B. Tompson, Proc. Phys. Soc. 73, 818 (1959).
[6] J. B. Tompson, Proc. R. Soc. A, 262, 503 (1961).
[7] A. von Engle, Ionized Gases Oxford Univ. Press (1965).

High-frequency modulation of atomic beams for plasma diagnostics

P. A. Demchenko, L. I. Krupnik, K. A. Leontovich, and E. S. Lyangner

(Submitted February 17, 1973; resubmitted November 21, 1973)
Zh. Tekh. Fiz., 44, 2203-2210 (October 1974)

A beam of atomic particles with an energy of $\sim 10^4$ eV modulated at a frequency $\sim 10^6$ Hz is used to probe dense plasmas (nL $\sim 10^4$-10^{15} cm^{-2}) characterized by high ultraviolet emission. A data-taking system has been developed and tested which provides measurements with high time resolution ($\tau \sim 10^{-6}$ sec) against a high-level background. The signal-to-noise ratio is 10^4. Comparison of the results of plasma density measurements (nL < 10^{15} cm^{-2}) using modulated probe beams with data obtained by other means yield good agreement. Certain conclusions regarding the potential usefulness of particle corpuscular diagnostics using modulated beams are presented.

INTRODUCTION

Wider application of active particle diagnostic techniques to the study of hot, dense plasmas is made difficult by the presence of intense fluxes of corpuscular and electromagnetic radiation from the plasma volume.

The basic problems which must be solved in order to use probe beams are those of separating the effects of interactions of probing particles with plasma particles from the background due to the intense emission from the plasma itself.[1-3]

Since monoenergetic and uniform beams of particles are used to probe plasmas, the most widely used methods of separating probe particles are based on 1) the use of electrostatic energy analyzers, 2) the use of mass-monochromators as momentum analyzers, or 3) combinations of these two methods.[4]

Detectors using energy or momentum selection have, along with their obvious advantages, a number of intrinsic shortcomings, which appear to be fundamental. In high-density plasmas scattering and energy loss play a significant role when probe-beam particles interact with the plasma.

Scattering shows up in changes in the transverse dimensions of probe beams. Energy losses and the associated smearing of the energy spectrum also lead to additional broadening of the beam in analyzing fields.

The use of neutral-particle beams for plasma diagnostics usually implies the presence of targets intended to transform neutrals into charged particles. This introduces additional scattering of probe beams. The influence of all these effects on the results of the measurements can be reduced, increasing the detector aperture; however, this is not always technically feasible. It should be noted that when particles of the same nature as those in the plasma are used for diagnostics, effective separation of probe particles from the particle emission background of the plasma is possible only when the energy of the probe beam lies outside the energy spectrum of the emitted plasma particles.

There is still another method, based on a different principle, for separating the useful signal from a high noise level. This method is based on the use of intensity modulated beams of atomic particles for plasma diagnostics. It is then possible to isolate the signal due to probe particles at the output of a detector by electronic means.

The necessity of studying rapid processes in plasmas demands high temporal resolution. This leads to a requirement for wide-band data-collecting systems for the modulated beams, such that

$$\Delta f \sim \frac{1}{\tau}, \qquad (1)$$

where τ is the required time resolution of the system and Δf is the frequency width of the recording channel.

Effective suppression of noise signals is possible if the noise signal level in the frequency band, Δf, at the chosen modulation frequency, f_M, is substantially smaller than the signal caused by changes in intensity of the probe beam. This condition can be written in the form

$$\left|\int\limits_{\Delta f} \varphi(f) e^{i2\pi f t} df\right| \ll \omega I R_{eq}, \qquad (2)$$

where $\varphi(f) = \int\limits_0^\infty \varphi(t) e^{-i2\pi f t} dt$ is the noise spectral density; $\varphi(t)$ is the signal at the load (on the beam particle detector) due to plasma particles; ΔI is the change in intensity of the equivalent probe beam current; R_{eq} is the equivalent resistance of the detector load at the modulation frequency, f_M.

It follows from Eq. (2) that to reduce noise it is necessary to reduce the passband, Δf; on the other hand, good time resolution is possible only with a wide passband [Eq. (1)].

In the majority of cases the signal at the detector output due to the plasma particles has a frequency bandwidth of several tens of hundreds of kilohertz; hence the contradictory conditions (1) and (2) can be satisfied if high-frequency modulation is used for the probe beam ($f_M > 10^6$ Hz).

Papers on the use of modulated beams for plasma diagnostics can be found in the literature. Among them is a study of a high-frequency discharge by means of beams He^0 and Ar^0 modulated[5] at 10 kHz and measurements of plasma parameters in a stellarator using beams of hydrogen atoms modulated[3] at 100 kHz.

In ref. 3 the recording channel has a bandwidth of 10 kHz, which permits a resolution time of $\tau \sim 100$ μsec. This technique of modulating the probe beam is used along with momentum analysis of the particles. The frequency response of the recording channel in ref. 5 is not stated, but it apparently does not provide a resolution time of

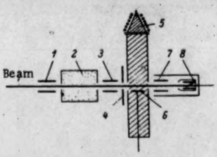

Fig. 1. Experimental arrangement

better than 10^{-3} sec and the noise is reduced basically by reducing the passband.

The present paper examines the possibility of using high-frequency ($f > 10^6$ Hz) modulation of beams of atomic particles as a diagnostic for a dense plasma.

EXPERIMENTAL ARRANGEMENT

The experiments are performed on the system shown schematically in Fig. 1.

Modulation of a monoenergetic beam of H_1^+ ions with energy $\sim 10^4$ eV is accomplished using a system, referred to below as the modulator, consisting of a plane electrostatic condenser 1, with a drift space S, and an output diaphragm 4.

The length of S is 57 cm, and the length of the condenser plates is 5 cm. The output diaphragm is 1.5 mm in diameter. A high-frequency modulated voltage from a standard sine wave generator (type GZ-41) is applied to the condenser plates. A constant bias voltage is also applied to the plates.

In order to obtain beams of neutral H_1^0 a gaseous charge exchange target 2 is located in the drift space. The protons which do not undergo charge exchange are removed from the beam by the electrostatic field of another plane condenser 3. From the modulator the beam enters a chamber into which plasma bursts are injected[6] by a conical injector 5. A metal barrier 6 can be placed in the path of the plasma flow directly adjacent to the intersection of the probe beam with the plasma.

The beam coming from the plasma is analyzed by a detection apparatus consisting of a condenser 7, which divides the complex beam according to charge, and a particle detector 8. This detector works with modulated beams of charged or uncharged particles. The construction is shown schematically in Fig. 2.

The secondary electrons from the plate 1 are collected by a cylindrical collector 2. An electric field applied between the plate and the collector ensures complete collection of the electrons by the collector. A guard cylinder 3 at negative potential with respect to the collector prevents escape of electrons from the detector volume. Shielding from external electric fields is accomplished by a copper shield 4. Insulators 5 are located between the measuring electrodes 1 and 2. The diameter of the input opening of the detector is 10 mm, which ensures an aperture of 1°. The internal capacitance of the particle detector is 27 pF, which results in an input impedance of $R_{eq} = 1.5$ kΩ at 3 MHz.

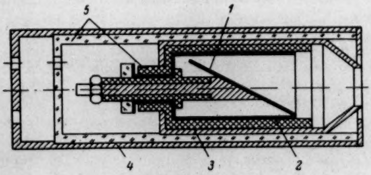

Fig. 2. Particle detector.

EXPERIMENTAL TECHNIQUES AND RESULTS

By using the above described modulator it is possible to obtain beams of charged and neutral particles modulated at frequencies of from 10^5 to $2 \cdot 10^7$ Hz, with the same modulation efficiency at all frequencies.

The choice of a detection system for modulated beams used as a plasma diagnostic is determined by the following conditions. The particle detector must have a wide dynamic range for incoming signals. It is impossible to use a system with ion-optical conversion[7] or open secondary electron multipliers as a particle detector if the signal is not preselected. The basic loading is determined by the level of plasma emission, which in most cases exceeds the signal connected with changes in intensity of the probe beams by several orders of magnitude. The basic advantages of these detectors are better time resolution, low intrinsic noise level, and high sensitivity; the last feature implies operations in a single-particle counting mode.

However, in plasma diagnostics the necessary beam intensity and, thus, sensitivity of the detectors, are determined by the allowable statistical fluctuations. The mean-square fluctuation intensity is given by

$$\frac{\overline{\Delta I^2}}{I^2}=\frac{1}{N}=\frac{e}{I\tau}.$$

where I is the beam intensity; N is the number of particles entering the detector in time τ, and e is the unit charge.

If we take the resolution time to be $\tau \sim 10^{-6}$ sec and require measurement of intensity changes in the probe beam of $\Delta I/I \approx 10^{-3}$, then the equivalent current of the beam used must be $I \geq 10^{-7}$ A.

Beams of charged and neutral particles with equivalent currents of 10^{-8}-10^{-6} A are used in these experiments. The particle detector used here has a wide dynamic range; however, it does not have sufficient gain to drive the oscilloscopes.

Preamplification is obtained by means of a bandpass amplifier developed especially for this purpose; it has a passband $2.1 < f < 3.1$ MHz, for which the gain is ~ 83 dB.

The required gain can be determined from the average intensity of the probe beam, $I \sim 10^{-7}$ A, and the output impedance of the particle detector, $R_{eq} \sim 1.5$ kΩ.

The amplifier passband, which contains the modulation frequency f_M, is chosen to be compatible with (1) and (2). To obtain the best time resolution for the given passband, $\Delta f = 1$ MHz, the modulation frequency is chosen to be $f_M = 3.1$ MHz. Since this frequency lies on the upper cutoff of the frequency characteristic, the detector circuit

Fig. 3

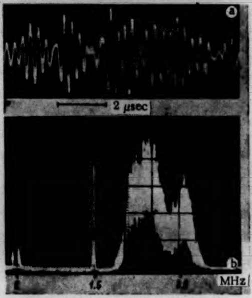

Fig. 4. a) Oscilloscope trace of the intrinsic noise voltage at the amplifier output; b) frequency spectrum of the amplifier noise.

only passes one sideband (lower) of the useful signal. The oscilloscope trace of Fig. 3 illustrates the frequency properties of the recording circuit. In this case the charged particle beam, modulated at 3.1 MHz, is deflected from the initial trajectory by a rectangular voltage pulse of 2 μsec long. The deflection voltage pulse is applied to the plates of condenser 3 (Fig. 1). A signal corresponding to weakening of the modulated beam is recorded at the detector. From the figure it follows that the circuit used provides a time resolution of $\sim 10^{-6}$ sec.

The lower limit of measured beam current is 10^{-8} A. This limit is determined by the intrinsic noise level of the amplifier. An oscilloscope trace of the intrinsic noise voltage at the output of the amplifier is shown in Fig. 4a. The maximum noise level, extrapolated to the amplifier input, is 10 μV. The frequency spectrum of the amplifier noise, taken by means of a type S4-8 spectrum analyzer, is shown in Fig. 4b. The markers on the abscissa correspond to 1.5 MHz. It follows from this figure that the spectrum of the intrinsic amplifier noise lies within its passband.

A further increase in system sensitivity will require a reduction in the intrinsic noise of the amplifier.

The modulation technique and recording system for modulated beams developed here are used to study plasma flows produced by a conical injector and to measure the densities of charged and neutral particles in the boundary layer formed when this plasma hits a metal barrier. Insertion of this barrier into the plasma flow sharply increases the level of ultraviolet emission from the plasma volume.

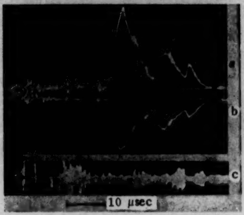

Fig. 5. Oscilloscope traces of: a) the ion saturation current in a double probe; b) the ultraviolet plasma radiation signal at the detector output; c) the signal after passing through the recording circuit.

Figure 5 shows oscilloscope traces of a) the ion saturation current in a double probe placed in the plasma, b) the signal produced at the particle detector output by ultraviolet emission from the plasma, and c) the same signal after passing through the selective circuits of a passband amplifier with a gain of $1.5 \cdot 10^4$. The maximum amplitude of the UV signal (Fig. 5b) is 0.4-0.6 V and its frequency spectrum lies within 30-200 kHz. The sensitivity of the oscilloscope is the same in Figs. 5a and b. The useful signal (due to changes in intensity of the probing beam) for a current $I = 10^{-7}$ A is less than $1.5 \cdot 10^{-4}$ V.

After passing through the bandpass amplifier the useful signal level is 2.25 V. The oscilloscope trace of Fig. 5c corresponds to conditions for which the probe beam does not enter the detector. In this figure only the intrinsic noise of the amplifier can be observed; the UV signal here is lower than the intrinsic noise level. The density of the plasma being studied in this case is $n^+L = 10^{15}$ cm^2 (n^+ is the density of charged particles per cubic centimeter and L is the path length of the probing beam in the plasma).

Thus, the selectivity of the recording circuit ensures that the intensity of modulated probe beams can be measured for a ratio

$$\frac{\text{useful signal}}{\text{noise}} \geqslant 10^{-4}.$$

at the output of the particle detector.

The density of charged and neutral particles in plasma flows are measured using the technique described above.

Oscilloscope traces of the signals due to the change in charge composition of modulated beams passing through a plasma are shown in Fig. 6. The modulation frequency f_M = 3.1 MHz.

Figure 6d shows the appearance of hydrogen atoms, H_1^0, in a proton beam due to charge exchange between probe particles and plasma neutrals. After deflection of charged particles by the field of the plane condenser, the detector only records neutrals in the probe beam. The maximum signal amplitude corresponds to transformation of about 20% of the initial H_1^+ beam intensity into H_1^0.

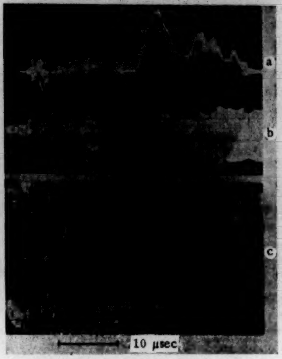

Fig. 6. Oscilloscope traces of: a) the ion saturation current in a double probe; b) the signal due to formation of H_1^0 particles in a probe beam of H_1^+; c) the signal due to attenuation of a probe beam of H_1^0.

The oscilloscope trace of Fig. 6c corresponds to attenuation of the initial intensity of an H_1^0 atom beam due to electron loss in the plasma. The relative magnitude of the attenuation can be estimated directly from the figure.

The line densities of charged (n^+L) and neutral (n^0L) particles in the plasma are determined from the change in charge composition[8,9] of probe beams H_1^0 and H_1^+. The results of measurements of these parameters obtained by means of modulated probe beams agree with the values obtained from a system without modulation.[8] Satisfactory agreement is obtained up to values of $n^+L + n^0L = 3.5 \cdot 10^{14}$ cm^{-2}.

Scattering processes begin to play an important role in thicker plasma targets. Their significance in changing the intensity of probe beams is difficult to take into account under the previous analysis and detection schemes.

With the detector used in this work it is possible to determine directly the change in beam intensity due to scattering of probe particles in the plasma at angles greater than those corresponding to the input aperture of the detector.

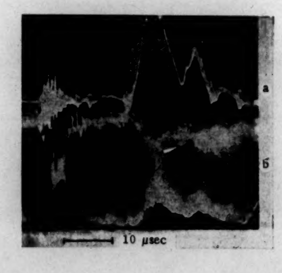

Fig. 7. Oscilloscope traces of: a) the ion saturation current in a double probe; b) the change (reduction) in intensity of a probe beam of H_1^+ due to scattering.

It is also possible to use scattering of probe particles in the plasma in order to determine the plasma density when $nL > 10^{15}$ cm^{-2}. For plasma targets with these parameters the probe particles will undergo multiple collisions in the plasma; hence, the charge composition of the passing beam does not depend on the density of the medium.

To determine the plasma density n^+L in this case it is assumed that the scattering of the proton beam in the plasma is Coulomb scattering by charged particles.

The mean square of the transverse component of momentum, $p^2_\perp$, acquired by the probe particles due to collisions is[10]

$$\overline{p_\perp^2} = \frac{16\pi e^4 \ln \lambda n^+ L}{v^2},$$

where v is the velocity of the probe particles, ln λ is the Coulomb logarithm, and e is the charge on a particle. This expression is correct if the velocity of the beam particles exceeds the speed of the particles in the plasma. The corresponding mean-square angle at which the particles initially parallel to the beam are scattered is given by

$$\theta_1^2 = \frac{\overline{p_\perp^2}}{p^2} = \frac{16\pi e^4 \ln \lambda n^+ L}{m^2 v^4} = \frac{4\pi e^4 \ln \lambda n^+ L}{E^2}, \qquad (3)$$

where $E = mv^2/2$ is the kinetic energy of the probe particles.

Since this scattering is a random process the intensity of the passing beam as a function of angle will have a normal distribution with an angular dispersion θ_1 given by

$$I(\theta) = I_0 \frac{\sqrt{2}}{\theta_1 \sqrt{\pi}} \exp\left(-\frac{\theta}{\sqrt{2}\theta_1}\right)^2.$$

Here, θ is the angle at which the particles have been scattered and I_0 is the initial beam intensity.

The equivalent beam current at the particle detector is

$$I(\varphi) = \int_0^\varphi I(\theta)\, d\theta = I_0 \Phi\left(\frac{\varphi}{\sqrt{2}\theta_1}\right),$$

where φ is the angular aperture of the receiver, and $\Phi(x) = (2/\sqrt{\pi}) \int_0^x e^{-t^2} dt$ is the probability integral. By measuring the ratio $I(\varphi)/I_0$ experimentally it is possible to calculate the angle θ_1, and thus to determine n^+L from Eq. (3).

An oscilloscope trace of the change in intensity of an H_1^+ (proton) probe beam after passing through a plasma is shown in Fig. 7b.

In this case both charged particles and neutral particles which appear in the beam are recorded simultaneously; thus, the change in total intensity of the diagnostic beam is due only to scattering of particles at angles greater than those corresponding to the input aperture of the detector. As can be seen from comparison of this oscilloscope trace with a probe signal (Fig. 7a) a correlation can be observed in this case between the intensity of the probe beam and the density of charged particles in the plasma.

The calculated line density of the plasma corresponding to the maximum amount of scattering on the oscilloscope trace of Fig. 7b is $n^+L = 3.5 \cdot 10^{15}\ \mathrm{cm}^{-2}$. Taking the finite degree of ionization of the plasma into account changes this quantity by an insignificant amount if $n^+L/n^0L \geqslant 0.5$.

The advantage of using scattering processes in active particle diagnostics of dense plasmas is that by changing the energy of the probe beam and the aperture of the particle detector it is possible to determine the particle density of the plasma over a wide range.

The development of techniques for high-frequency modulation of atomic beams and the possibility of using wide aperture detectors without initial selection of the particles opens up wide opportunities for active particle plasma diagnostics.

---

[1] V. V. Afrosimov, B. A. Ivanov, A. I. Kislyakov, and M. P. Petrov, Zh. Tekh. Fiz., 36, 89 (1966) [Sov. Phys. – Tech. Phys., 11, 63 (1966)].

[2] V. V. Afrosimov, I. P. Gladkovskii, and A. I. Kislyakov, Zh. Tekh. Fiz., 38, 1888 (1968) [Sov. Phys. – Tech. Phys., 13, 1518 (1969)].

[3] H. P. Eubank, P. Noll, and F. Tappert, Nucl. Fus., 5, 68 (1965).

[4] V. V. Afrosimov and M. P. Petrov, Zh. Tekh. Fiz., 37, 1995 (1967) [Sov. Phys. – Tech. Phys., 12, 1467 (1968)].

[5] O. V. Kozlov and V. D. Rusanov, Yad. Sint., 4, 312 (1964).

[6] Yu. S. Azovskii, I. G. Guzhovskii, and B. G. Safronov, Zh. Tekh. Fiz., 34, 841 (1964) [Sov. Phys. – Tech. Phys., 9, 641 (1964)].

[7] V. V. Afrosimov, I. P. Gladkovskii, Yu. S. Gordeev, I. F. Kalinkovich, and N. V. Fedorenko, Zh. Tekh. Fiz., 30, 1456 (1960) [Sov. Phys. – Tech. Phys., 5, 1378 (1961)].

[8] L. I. Krupnik, N. G. Shulika, and P. A. Demchenko, in: Studies on Plasma Bursts [in Russian], Kiev, Naukova Dumka (1967), p. 145.

[9] L. I. Krupnik and N. G. Shulika, in: Studies on Plasma Bursts [in Russian], Kiev, Naukova Dumka (1967), p. 159.

[10] V. D. Sivukhin, in: Reviews of Plasma Physics, Vol. 4, Consultants Bureau, New York (1966).

Doppler profile of an atomic line to the differential excitation cross section

É. S. Parilis and V. Kh. Ferleger

Electronics Institute,
Academy of Sciences of the Uzbek SSR, Tashkent

(Submitted August 6, 1973; resubmitted April 8, 1974)
Zh. Tekh. Fiz., 44, 2211-2216 (October 1974)

The spectral characteristics of Doppler line profiles for excitation and ionization by inelastic collisions are related to the differential excitation cross sections. The shape and location of the maximum and the wings of the spectrum can be used to find the differential cross section and threshold angle.

When heavy particles with velocities of 10^6-10^8 cm/sec collide, many inelastic processes are possible, including excitation and ionization of inner shells. Since the time for optical transitions (10^{-8} sec) is much greater than the collision time, while the time for radiationless transitions (10^{-13}-10^{-15} sec) is of the same order as the collision time, in many cases relaxation takes place in the system after the particles have separated.

Thus, electromagnetic radiation and characteristic electrons (for example, Auger electrons) are emitted by a rapidly moving atom whose velocity is determined by the scattering kinetics. The spectral line then shows a significant Doppler shift and broadening as do the Auger electron peaks. This feature must be taken into account in treating optical and electron spectra.[1-3]

The form of the spectral lines contains information on collision kinematics and the differential cross section for atomic excitation. If the Doppler distortion of the spectral line can be separated from the background consisting of the natural and Stark broadening, it is possible to establish a direct relationship between the line shape and the differential excitation cross section.

Using simple assumptions as to the form of the excitation function, we relate this function to line shape in this paper; a simple method is also proposed to solve the inverse problem of recovering the differential excitation cross section from the Doppler profile.

EXCITATION OF OPTICAL LINES

It is convenient to examine this case since the line shape in optical excitation is really determined by the Doppler distortion.[4]

The Doppler shift corresponding to emission at wavelength λ_0 is

$$\Delta\lambda = \lambda_0 - \lambda = \lambda_0 \frac{v(\theta)}{c} \cos\alpha. \tag{1}$$

If we ignore the changes in the kinematics due to inelastic losses, then the velocity of the scattered atom is

$$v(\theta) = v_1 \frac{\cos\theta + \sqrt{\mu^2 - \sin^2\theta}}{\mu + 1}. \tag{2}$$

Here, v_1 and θ are the velocity and scattering angle of the incident particle in the laboratory system; c is the speed of light; $\mu = m_2/m_1$ is the mass ratio of the incident, m_1, and target, m_2, atoms; and, α is the angle between the scattering direction (θ, φ) and the detector $(\theta_0, \varphi_0 = 0)$.

In the scattered atom velocity space Eq. (1) defines a surface of constant wavelength,

$$d(\lambda) = [\cos\theta + \sqrt{\mu^2 - \sin^2\theta}][\sin\theta \cos\varphi \sin\theta_0 + \cos\theta \cos\theta_0], \tag{3}$$

where

$$d(\lambda) = \frac{\Delta\lambda (1 + \mu) c}{\lambda_0 v_1}. \tag{4}$$

The intensity of emission at wavelength λ in direction θ_0 is proportional to the total number of particles whose velocity vectors form the surface described by Eq. (3) and is given by

$$J(\lambda, \theta_0) \sim \int \sigma_i(\theta) \frac{d\varphi}{d\lambda} \sin\theta d\theta, \tag{5}$$

where $\sigma_i(\theta) = (d\sigma(\theta)/d\Omega) P_i(\theta)$ is the differential cross section for excitation of the i-th spectral line, $P_i(\theta)$ is the excitation probability, and $d\sigma(\theta)/d\Omega$ is the differential cross section for scattering at angle θ. In Eq. (5) it is convenient to transform to the scattering angle, χ, in the center of mass system, where

$$\chi = \theta + \arcsin\left(\frac{\sin\theta}{\mu}\right). \tag{6}$$

Then

$$J(\lambda, \theta_0) \sim \int_{\chi_1}^{\chi_2} \frac{\sigma_i(\chi) \sin\chi d\chi}{\sqrt{\mu^2 \sin^2\chi \sin^2\theta_0 - [d(\lambda) - \mu\cos\chi\cos\theta_0 - \cos\theta_0]^2}}. \tag{7}$$

The limits of integration are

$$\left.\begin{aligned} \chi_1 &= \left|\theta_0 - \arccos\frac{d(\lambda) - \cos\theta_0}{\mu}\right|, \\ \chi_2 &= \left|2\pi n - \theta_0 - \arccos\frac{d(\lambda) - \cos\theta_0}{\mu}\right|, \end{aligned}\right\} \tag{8}$$

where

$$n = \begin{cases} 0, & \text{if} \quad \arccos\frac{d(\lambda) - \cos\theta_0}{\mu} \leqslant \pi - \theta_0, \\ 1, & \text{if} \quad \arccos\frac{d(\lambda) - \cos\theta_0}{\mu} > \pi - \theta_0. \end{cases}$$

To calculate the line profile, neglecting natural broadening, according to Eq. (7) it is necessary to know the value of $\sigma(\chi)$. If it is possible to use Firsov's formula[5] for the scattering cross section, $d\sigma(\chi)/d\Omega$, over the interval considered, then there is no general method for calculating $P_i(\chi)$. For the simplest systems, in the limit of large velocities, $P_i(\chi)$ can be obtained in the Born approximation.[6] The authors of ref. 7 calculated $P_i(\chi)$ using the molecular orbital model for a rotational $\sigma-\pi$ transition in the K shell of Ne, and in ref. 8 a function analogous to $P_i(\chi)$ is approximated by a simple dependence with a parameter whose value is chosen by comparing the theoretical curve of $J(\lambda, \theta_0)$ with experiment.

We note that several properties of the curve $J(\lambda, \theta_0)$ can be obtained by examination of Eqs. (8) without calculating the integral (7) by making some simple assumptions about the properties of $P_i(\chi)$.

1. Let $P_i(\chi)$ be defined for all angles $0 \leq \chi \leq \pi$ and increase from zero no more rapidly than $d\sigma/d\Omega$ falls off. Then:

the maximum of $J(\lambda, \theta_0)$ is reached for

$$\lambda_m = \lambda_0\left(1 - \frac{v_1}{c}\cos\theta_0\right), \tag{9}$$

the long wavelength boundary of the spectrum is

$$\lambda_l = \lambda_0\left(1 + \frac{v_1}{c}\frac{\mu - \cos\theta_0}{1+\mu}\right), \tag{10}$$

the short wavelength boundary of the spectrum is

$$\lambda_s = \lambda_0\left(1 - \frac{v_1}{c}\frac{\mu + \cos\theta_0}{1+\mu}\right), \tag{11}$$

and the full linewidth is

$$\lambda_l - \lambda_s = \lambda_0\frac{2\mu v_1}{(1+\mu)c}. \tag{12}$$

In general the distribution is asymmetric with:

a long wavelength region of width

$$\Delta\lambda_l = \lambda_l - \lambda_m = \lambda_0\frac{v_1}{c}\frac{\mu(1+\cos\theta_0)}{(1+\mu)}, \tag{13}$$

and a short wavelength region of width

$$\Delta\lambda_s = \lambda_m - \lambda_s = \lambda_0 v_1\frac{\mu(1-\cos\theta_0)}{c(1+\mu)}.$$

Only for $\theta_0 = 90°$

$$\Delta\lambda_l = \Delta\lambda_s = \lambda_0\frac{v_1\mu}{c(1+\mu)} \tag{14}$$

is the curve symmetric, in agreement with the results of refs. 4 and 8.

2. If there exists an excitation threshold in the scattering angle, that is $P_i(\chi) = 0$ for $\chi < \chi_0$, and then P grows no more rapidly than $d\sigma/d\Omega$ falls for $\chi > \chi_0$, then the position of the maximum changes compared with Eqs. (9)-(14). For $\chi_0 < \theta_0$,

$$\lambda_m = \lambda_0\left[1 - \frac{v_1}{c}\frac{\mu\cos(\theta_0 - \chi_0) + \cos\theta_0}{1+\mu}\right]$$

and for $\chi_0 > \theta_0$

$$\lambda_m = \lambda_0\left[1 - \frac{v_2}{c}\frac{\mu\cos(\theta_0 + \chi_0) + \cos\theta_0}{1+\mu}\right],$$

but the boundaries of the spectrum remain the same.

3. If $P_i(\chi) = 0$, for all $\chi > \chi_1$, then the location of the boundaries of the spectrum changes. For example, let $\chi(\lambda_e) > \chi(\lambda_s) > \chi_1$. Then the long wavelength boundary is

$$\lambda_l = \lambda_0\left[1 - \frac{v_1}{c}\frac{\mu\cos(\theta_0 + \chi_1) + \cos\theta_0}{1+\mu}\right],$$

the short wavelength boundary is

$$\lambda_s = \lambda_0\left[1 - \frac{v_1}{c}\frac{\mu\cos(\theta_0 - \chi_1) + \cos\theta_0}{1+\mu}\right],$$

and the full width is

$$\lambda_l - \lambda_s = \frac{2\lambda_0 v_1\mu\sin\theta_0\sin\chi_1}{c(1+\mu)}.$$

These relations allow us to determine χ_0 and χ_1, the threshold angles for excitation, when λ_m, λ_d, and λ_s are precisely measured spectroscopically. Furthermore, in order to be able to vary the form of $P_i(\chi)$ and to trace its effect on the Doppler distortion of a spectral line we write $P_i(\chi)$ in the form

$$P_i(\chi) = \operatorname{th} q^{-b},$$

where $q = \pi - \chi/\sqrt{\chi(2\pi - \chi)}$ is a dimensionless collision parameter for the potential of ref. 5, and b is an arbitrary parameter. The form of the function $P_i(\chi)$ for b = 0, 1, and 3 is shown in Fig. 1 (curves 1-3). Plots of $J(\lambda, \theta_0)/J_m$ for the Ar II λ_0 = 4879Å line excited by collisions with Kr, for θ_0 = 60° and E_0 = 15 keV are shown in Fig. 2. $J_m \equiv J(\lambda_m)$ is the maximum intensity. The form and half-width of the curves depend significantly on the parameter b.

Thus, the line profile is fairly sensitive to small

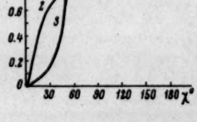

Fig. 1. The excitation probability, P(χ), as a function of scattering angle and the parameter b.

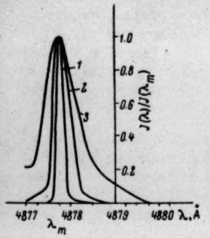

Fig. 2. Doppler profiles of the relative intensity of the Ar II λ_0 = 4879 Å line excited by collisions with Kr, for θ_0 = 60° and E_0 = 15 keV. 1) b = 0, 2) 1, 3) 3.

changes in $P_i(\chi)$, expecially at small scattering angles.

RECOVERY OF THE EXCITATION CROSS SECTION FOR OPTICAL LINES

Eq. (7) can be construed as an integral equation with respect to an unknown function $\sigma_i(\chi)$. We write $J(\lambda, \theta_0)$ in the form

$$J(\lambda, \theta_0) = \int\limits_{\chi_1(\lambda, \theta_0)}^{\chi_2(\lambda, \theta_0)} \frac{\sigma_i(\chi) \sin\chi \, d\chi}{\sqrt{(\cos\chi_1 - \cos\chi)(\cos\chi - \cos\chi_2)}}. \qquad (15)$$

Transforming to the variable $x = \cos\chi$ and writing

$$\sigma_i(\arccos\psi) = \Phi(x),$$

we obtain

$$J(\lambda, \theta_0) \equiv J(x_1, x_2) = -\int\limits_{x_1}^{x_2} \frac{\Phi(x)\, dx}{\sqrt{(x_1 - x)(x - x_2)}}, \qquad (16)$$

where $x_1 = \cos\chi_1$ and $x_2 = \cos\chi_2$. Equation (16) can be solved by setting

$$x_1(\lambda, \theta_0) = a = \mathrm{const}, \qquad (17)$$

Equation (17) gives the relationship between the observation angle, θ_0, and the measured wavelength, λ. In practice this means that for every observation angle, θ_0, the emission must be measured at the wavelength, λ, given by Eq. (17). Thus, with $a = 1$ we obtain the simple relation

$$\lambda = \lambda_0\left(1 - \frac{v_1}{c}\cos\theta_0\right). \qquad (18)$$

Evidently, for transitions associated with small energy transfers, Eq. (18) gives the location of the intensity maxima, while $J[\lambda(\theta_0), \theta_0] = I(\theta_0)$ will be the envelope of this kind of maxima obtained by continuous variation of θ_0. In the case under consideration Eq. (16) is an Abel integral equation. Using transformations analogous to those used in ref. 9 and for the boundary conditions $\sigma_i(0) = 0$, the solution may be written in the form

$$\sigma_i(\chi) = \frac{\sqrt{2}}{\pi} \frac{\sin\chi}{2} \int\limits_0^{\chi/2} \frac{\frac{dI}{d\theta_0}\, d\theta_0}{\sqrt{\cos 2\theta_0 - \cos\chi}}. \qquad (19)$$

We now consider the question of reconstructing the cross section from the entire spectrum taken at a fixed observation angle.

It is convenient to set $\theta_0 = 90°$. In this case, the result is the sum of the excitation cross sections at supplementary angles:

$$\sigma_i(\chi) + \sigma_i(\pi - \chi) = \frac{2}{\pi}\cos\chi \int\limits_{d(\lambda) = -\mu\sin\chi}^{d(\lambda) = \mu\sin\chi} \frac{\frac{dJ}{d\lambda}\, d\lambda}{\sqrt{\frac{d^2(\lambda) - \sin^2\chi}{\mu^2}}}. \qquad (20)$$

It is necessary to have an experimentally measured profile of the whole line, $J(\lambda)$, for $\theta_0 = 90°$. This method can be used to reconstruct $\sigma_i(\chi)$ for sufficiently small χ, when $\sigma_i(\pi - \chi)$ can be neglected compared with $\sigma_i(\chi)$ because of the small cross section for scattering at large angles. If the scattering cross section is known, Eqs. (19) and (20) determine $P_i(\chi)$.

Thus, two methods for reconstructing the differential cross section from the experimentally measured Doppler line profile have been proposed. The first method requires measurement of the intensities $J[\lambda(\theta_0), \theta_0]$ with continuous variation of θ_0 and that the curve $I(\theta_0)$ be obtained from them. This method is analogous to the method for measuring differential cross sections for atomic collisions. In a typical case of excitation without a threshold, $\lambda = \lambda_m$ and $I(\theta_0)$ is the envelope of the principal maxima of the spectral curves. The second method requires measurement of the entire profile $J(\lambda)$ at the fixed value $\theta_0 = 90°$ for all values of λ.

SPECTRA OF AUGER ELECTRONS AND HARD X RAYS

The emission of Auger electrons and x-ray photons in atomic collisions is connected with excitation of inner shells and is accompanied by strong scattering whose kinematics has a significant effect on the spectrum.

In calculating the discrete part of the energy spectra of electrons and the characteristic x radiation, inclusion of Doppler distortion is important.[3,10] The distinctive features of these processes as opposed to optical excitation are the significantly larger excitation thresholds with respect to scattering angle and energy[1,11] and the existence of a nonzero $P_i(\chi)$ over a rather wide range of scattering angles. This latter fact leads to an increase in the relative width of the Doppler profiles compared to the analogous profiles under optical excitation. In addition, because of the small lifetime (10^{-13}-10^{-15} sec) of the corresponding excited states, it is necessary to take the natural linewidth into account in calculating the resulting profile.

The above methods of recovering the differential excitation cross section may be applied to an isolated peak in the electron or x-ray spectrum in those cases where the Doppler distortion and broadening are predominant over other broadening mechanisms.

SPECTRA DUE TO REFLECTION OF ATOMS FROM A SOLID SURFACE

In the kinematic portion of this problem the effect of the surface reduces to a cutting off of the contribution to $J(\lambda)$ of particles whose velocity vectors are directed toward the interior of the substance. It has been noted by one of the authors[12] that atoms which have undergone multiple scattering on the surface also contribute to $J(\lambda)$. In accordance with the theory of multiple scattering spectra,[13] the energy distribution of the scattered particles shows up in $J(\lambda)$ in this case. It is also necessary to take account of the influence of the surface on changes in excitation state of the particles. Here, two groups of competing processes are the basic contributing factors. Thus, Auger relaxation with energy transfer to a target electron and resonance ionization leads to a reduction in the flux of excited particles compared to that from collisions in a gas. From the theory of atomic surface interactions the probability of conserving the excitation can be estimated from the expression

$$W=\exp\left(-\frac{A}{av_{\perp}}\right), \tag{21}$$

where $v_{\perp}$ is the component of particle velocity perpendicular to the surface; A and a are parameters whose magnitudes depend on the atom-surface pair and level being considered. On the other hand, a portion of the particles are ionized and as they move along the surface, Auger and resonance neutralization at the given level increase the flux of excited particles.

Thus, for collisions with a solid the function $P_i(\varkappa)$ (the probability for an atom to leave the surface in a given excitation state) is more complicated than the corresponding function for a gas. If the target is a monocrystal then $P_i(\chi)$ also depends on φ (the azimuthal scattering angle) since there is preferential neutralization in the directions of close packing.[14] This effect must appear in a corresponding dependence of the $J(\lambda)$ profiles on φ_0 (the azimuthal angle of rotation of the spectrometer with respect to the crystal axes).

It is obvious that the procedure discussed above for recovering the differential excitation cross section can also be applied to the case of atomic collisions with the surface of a solid. If the scattering cross section is known, the function $P_i(\chi)$ can be recovered.

---

[1] V. V. Afrosimov, Yu. S. Gordeev, M. P. Panov, and N. V. Fedorenko, Zh. Tekh. Fiz., 34, 167 (1964) [Sov. Phys.-Tech. Phys., 9, 1265 (1965)].

[2] É. S. Parilis and V. Kh. Ferleger, Abstract of Talk at Fourth All-Union Conference on Electronic and Atomic Collisions, Riga (1969).

[3] M. E. Rudd, T. Jorgensen, Jr., and D. J. Volz, Phys. Rev., 151, 28 (1966); Yu. S. Gordeev and G. N. Ogurtsov, Zh. Eksp. Teor. Fiz., 60, 2051 (1971) [Sov. Phys.-JETP, 33, 1105 (1971)].

[4] V. V. Afrosimov, Yu. S. Gordeev, V. M. Lavrov, and G. N. Ogurtsov, ZhETF Pis. Red., 14, 108 (1971) [JETP Lett., 14, 70 (1971)].

[5] O. B. Firsov, Zh. Eksp. Teor. Fiz., 34, 447 (1958) [Sov. Phys.-JETP, 7, 308 (1958)].

[6] D. R. Bates (ed.), Atomic and Molecular Processes, Academic Press (1962).

[7] J. S. Briggs and J. Macek, J. Phys. B, Atomic and Mol. Phys., 5, 579 (1972).

[8] W. F. Van der Weg and D. J. Bierman, Physica, 44, 206 (1969).

[9] L. D. Landau, Mechanics [in Russian], Moscow, Nauka (1965), p. 69.

[10] E. S. Parilis and V. Kh. Ferleger, Abstract of Talk at Fifth All-Union Conference on Electronic and Atomic Collisions, Uzhgordo (1972).

[11] B. Fastrup, G. Hermann, and K.I. Smith, Phys. Rev., A3, 1591 (1971).

[12] É. S. Parilis, Fiz. Tverd. Tela, 11, 1150 (1969).

[13] U. A. Arifov, Interaction of Atomic Particles with Solid Surfaces [in Russian], Moscow, Nauka (1968), p. 326.

[14] W. F. Van der Weg and D. I. Bierman, Physica, 44, 177 (1969).

General

Distortion of single-turn solenoids in ultrahigh magnetic fields

G. A. Shneerson

M. I. Kalinin Leningrad Polytechnic Institute

(Submitted October 1, 1973; resubmitted December 28, 1973)
Zh. Tekh Fiz., 44, 2217-2228 (October 1974)

Equations are derived and solved for the distortion of special solenoids which act to reduce the field below its calculated value. Hydrodynamic flow is assumed within the framework of spherically symmetric motion of an ideal incompressible fluid under the action of the magnetic pressure; the skin effect, the "slow" explosion of the skin layer, and a composite model are discussed. The distortion of solenoids has been investigated experimentally in fields up to 190 Wb/m². The measured values of the induction and the effective radius confirm the calculations and behave qualitatively as predicted by dimensional analysis. In particular the experimental data are compatible with the expected asymptotic dependence of the induction $B_m = \sqrt{J'}$, where J' is the initial growth rate of the current.

Three main processes determine the rate of distortion of a single-turn solenoid in an extremely high field: hydrodynamic flow, the skin effect, and the electrical explosion of the conductor.[1-9] All these processes lead to an increase in the effective inside radius of the solenoid and to a decrease in the induction below its calculated value.[3-6,9] Our calculations and experiments involve "biconical" solenoids (Fig. 1), in which the length l is proportional to the inside radius R, $l = \xi_0 R$, where $\xi_0 = 2\cot\varphi_0$. For a perfect conductor the induction at the center of such a solenoid is inversely proportional to R:

$$B(0,\ 0)=\frac{\mu_0 a_0 i}{R}, \tag{1}$$

where i is the current, a_0 is the dimensionless coefficient, equal to 0.19 for our solenoids, and $\xi_0 = 1.5$ ($\varphi_0 = 53°$). A relation of the form (1) for the induction at the center is established by measurements in a weak field produced by a 200 kHz alternating current in copper solenoids of various radii, including those deformed by the discharge. For deformations up to twice the initial radius the ratio of the length of the solenoid to the diameter of the opening varies slightly. It can thus be assumed that the flow in a biconical solenoid is nearly spherical and that the simple relation (1) for the induction can be used in the calculations and in the interpretation of the experiments. The dependence of the induction on the peak value and growth rate of the current can be traced as this dependence becomes asymptotic.

1. THE HYDRODYNAMIC MODEL AND "SLOW EXPLOSION"

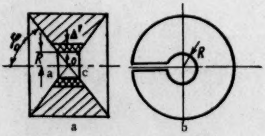

Fig. 1. Biconical solenoid.

Let us first consider hydrodynamic flow by assuming a perfect conductor, i.e., neglecting the diffusion of the field and electrical explosion. In short, solenoid effects due to compressibility and shock wave formation do not play a significant role,[7-9] and plastic flow is the principal process. This process can be likened to the motion of an ideal incompressible fluid if $B_e^2/2\mu_0 \gg \sigma_s$, where B_e is the field at the edge of the opening of the solenoid and σ_s is the dynamic yield stress.[4-10] In addition the following simplifying assumptions are made: The motion is assumed to be spherically symmetric, i.e., the displacement of the fluid through the free conical surfaces is neglected; the difference between the cylindrical surface (the part ac on Fig. 1a) and the surface of a sphere is neglected, which is admissible if $\varphi_0 \gtrsim 50°$; $B_e \approx B(0, 0)$. Under these assumptions the motion in the flow zone, where the pressure $p > \sigma_s$, becomes the same as the expansion of a sphere in an incompressible fluid.[10] Assuming that the pressure at the flow zone boundary[1)] is equal to σ_s, and neglecting elastic deformation, we obtain the following equation[10] for the magnetic pressure and the inside radius R:

$$R\,\frac{d^2R}{dt^2}+\frac{3}{2}\left(\frac{dR}{dt}\right)^2=\frac{1}{\gamma_0}\left(\frac{B_e^2}{2\mu_0}-\sigma_s\right), \tag{2}$$

where γ_0 is the density. By solving this equation together with (1) and assuming that $R = R_0$ and $dR/dt = 0$ for $B_e \leq \sqrt{2\mu_0\sigma_s}$ we find the field for a given current. This calculational model takes only very crude account of strength effects, but does reflect the threshold character of the deformation. It will be seen later that strength effects are small in an extremely high field

In the special case of a sinusoidal current of amplitude J_m and initial growth rate J' system (1) and (2) can be written in the dimensionless form

$$y\,\frac{d^2y}{dx^2}+\frac{3}{2}\left(\frac{dy}{dx}\right)^2=\frac{1}{y}\,\frac{\sin^2 k_0x}{k_0^2}-\theta_1, \tag{3}$$

$$\frac{B_e}{B_\infty}=\begin{cases}\left(\frac{2}{3}\right)^{1/4}\frac{1}{k_0}\sin k_0x & \text{for}\quad \sin k_0x\leqslant k_0\sqrt{\theta_1},\\ \left(\frac{2}{3}\right)^{1/4}\frac{1}{4k_0}\sin k_0x & \text{for}\quad \sin k_0x> k_0\sqrt{\theta_1},\end{cases} \tag{4}$$

where $x = t/t_r$, $t_r = R_0(2\gamma_0/\mu_0)^{1/4}(a_0J')^{-1/2}$; $k_0 = \omega t_r = J't_r/J_m$; $y = R/R_0$; $\theta_1 = \sigma_s(2/\mu_0\gamma_0)^{1/2}/a_0J'$; and $B_\infty = \mu_0^{3/4}(3\gamma_0)^{1/4}(a_0J')^{1/2}$. The numerical solution of Eqs. (3) and (4) shows that the maximum induction is reached before the current maximum, and that the relative change in the radius at maximum induction t_m is small. At large values of the parameter $1/k_0$ (strong fields) the maximum field is reached at the front of the sinusoid ($i = J't$). The

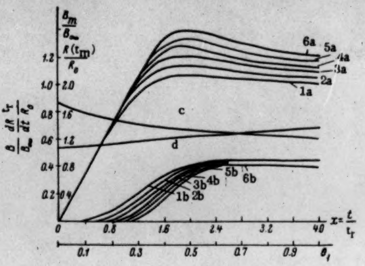

Fig. 2. Calculated time dependence of the field in a biconical solenoid for a linearly increasing current (hydrodynamic model). a) $B/B_\infty = f(x)$; b) $(dR/dt)t_r/R_0 = f(x)$; c) $R(t_m)/R_0 = f(\theta_1)$; d) $B_m/B_\infty = f(\theta_1)$. 1) $\theta_1 = 0$; 2) 0.2; 3) 0.4; 4) 0.6; 5) 0.8; 6) 1.0.

calculated curves for a linearly increasing current (Fig. 2) are close to one another if the strength parameter $\theta_1 \leqslant 0.2$–0.4. The function $B_m/B_\infty = f(x)$ has a weak maximum and then the induction approaches the limiting value

$$\lim_{x\to\infty}\frac{B_e}{B_\infty}=\left(\sqrt{1+\frac{\theta_1^2}{6}}-\frac{\theta_1}{\sqrt{6}}\right)^{-1/2}. \tag{5}$$

In the special case $\theta_1 = 0$, $B_e = B_\infty$. The solution of the equation for $\sigma_s = 0$ is also obtained in the limiting case of a source of "infinite strength" with a voltage $U_0 \approx d(\pi R^2 B_e)/dt$. In this case the induction first increases linearly ($B_e = U_0 t/\pi R_0^2$), reaches a maximum value of $B_m = 0.96(U_0/\pi R_0)^{1/2}(8\mu_0\gamma_0/9\pi)^{1/4}$ at time $t_m = 1.3R_0^{3/2}\cdot(8\mu_0\gamma_0/9\pi)^{1/4}(\pi/U_0)^{1/2}$, and then decreases: $B_e \approx [(8\mu_0\gamma_0)\cdot(9\pi t)^{-1}]^{1/3}$.

The value of the induction also depends on the skin effect and electric explosion; in short coils the most important mechanism is slow explosion – the ejection of molten metal across the faces.[7,11] To take account of the skin effect it is important to know the effective depth of penetration, the thickness of the skin layer, $\Delta' = B_e/\mu_0\delta_0$ at each time, where δ_0 is the current density at the surface of the solenoid. We have found approximation expressions[11] for Δ'. If Δ' is known the effect of the skin effect on the value of the induction at the center of a biconical solenoid can be estimated from the expression

$$B(0,\ 0)=\frac{a_0\mu_0 i}{R+\frac{\Delta'}{\pi}}=\frac{a_0\mu_0 i}{R'}, \tag{6}$$

where R' is the effective radius. Equation (6) can be obtained by assuming that the current is concentrated in the region $0 < x_1 < \Delta'/2$, with its density depending only on x_1: $\delta(x_1) = \text{const}\,[1-(2x_1/\Delta')^2]^{-1/2}$. This relation corresponds to a stationary explosion of the skin layer when the velocity of the field-conductor boundary $\Omega = dR'/dt$ is constant or slowly varying.[11] Equation (6) will be used later in the composite model of the distortion of a solenoid.

General relations giving an approximate description of a slow explosion are obtained in ref. 11. For a sinusoidal current in a biconical solenoid the slow explosion process is described by the following system of differential equations, which can be obtained from Eqs. (23)-(25) of ref. 11 by using the supplementary relation[2)] $l = \xi_0 R$ and Eq. (1):

$$P\frac{d}{dt}(B_e\Delta')=\frac{\rho_s B_e}{\mu_0(\Delta'-k_1 S)}-\frac{2B_e^2 S}{\xi_0 R\sqrt{\mu_0\gamma_0}}, \tag{7}$$

$$\frac{dS}{dt}=\frac{B_e^2\rho_0 3}{\mu_0^2 k_1\Delta'}-\frac{2SB_e}{\xi_0 R\sqrt{\mu_0\gamma_0}}, \tag{8}$$

$$B_e=\frac{1}{R}a_0\mu_0 J_m\sin\omega t, \tag{9}$$

$$\Omega=\frac{2SB_e}{\xi_0 R\sqrt{\mu_0\gamma_0}}=\frac{dR}{dt}. \tag{10}$$

The system (7)-(10) determines the field in the solenoid, the change of radius, the thickness of the skin layer, and the thickness S of the layer of molten metal ejected along the lines of force across the faces by the magnetic pressure. In Eqs. (7)-(10) ρ_s is the specific resistance of the melt, and β is the coefficient in the linearized relation for the specific resistance as a function of the volumetric energy density Q: $\rho = \rho_0(1+\beta Q)$. Specific values of the parameters P and k_1 can only be found from an exact solution of the partial differential equations describing the diffusion of the field into a medium heated by eddy currents. In the most interesting case, however, when the characteristic values vary slowly, one can take[11] P = 0.33 and k_1 = 2. Assume that the calculated peak induction $\mu_0 a_0 J_m/R_0 \gg B_s$, where $B_s = [2\mu_0(\rho_s-\rho_0)/\rho_0\beta]^{1/2}$, R_0 is the initial radius of the solenoid when the explosion begins on the linear part of the current sinusoid, and the initial conditions for the solution of system (7)-(10) can be found from a calculation of the process preceding the explosion: $t = t_s = R_0 B_s/\mu_0 a_0 J'$; $B(t_s) = B_s$; $R(t_s) = R_0$; $S(t_s) = 0$; $\Delta'(t_s) \approx (6\rho_s t_s/5\mu_0)^{1/2}$.

Equations (7)-(10) and the initial conditions can be put in dimensionless form by choosing B_s as the reference induction, $\rho_s B_s^2\mu_0^{-3}(a_0 J')^{-2}$ as the reference time, and $\rho_s B_e/\mu_0^2 a_0 J'$ as the reference length. For a sinusoidal current the behavior of the function $B_e/B_s = b = f(\tau)$ is determined by three dimensionless parameters:[3)] $\bar{r}_0 = R_0\mu_0^2 a_0 J'/\rho_s B_s$, $\eta_1 = (\mu_0\gamma_0)^{-1/2}(2B_s^2/\xi_0 a_0\mu_0 J')$, and $\eta_2 = \omega\rho_s B_s^2\mu_0^{-3}(a_0 J')^{-2}$. Numerical calculations show that when the induction is appreciably smaller than its calculated value the field at first increases linearly with a growth rate characterized by $\bar{r}_0$, and then as the current increases a quasistationary explosion regime is established with the left-hand sides of Eqs. (7) and (8) close to zero. At large values of η_1 the explosion is nearly "idealized",[11] and in this case the amplitude of the induction remains close to the threshold value B_s. For small values of η_1 the amplitude $B_m > B_s$. In the quasistationary regime the following approximate dimensionless equation can be obtained for the induction:

$$\frac{d}{d\tau}\left(\frac{\sin n_2\tau}{\eta_2 b}\right)=b\sqrt{\frac{\eta_1\eta_2(b^2-1)}{2\sin\eta_2\tau}}, \tag{11}$$

where $b = B_e/B_s$. When $b_m = B_m/B_s \gg 1\,(\eta_1\eta_2 \ll 1)$ its solution has the form

$$b\approx\left(\frac{2}{9\eta_1\eta_2}\right)^{1/3}\sin\eta_2\tau\left[\int_0^{\eta_2\tau}(\sin x)^{2/3}\,dx\right]^{-1/3}. \tag{12}$$

Hence in a slow explosion the amplitude of the induction is

$$B_m \approx \chi\mu_0\left(\frac{\gamma_0}{\mu_0}\right)^{1/12}\left(\frac{\xi_0\tau_0}{\rho_0^3}\right)^{1/6}(a_0J')^{1/2}, \tag{13}$$

where $\tau_0 = \pi/2\omega$ is the rise of time of the current, and $\chi = [(4/\pi)\sin x_m \cos^2 x_m]^{1/6} \approx 0.8$. The maximum of the induction is very flat and occurs at the time $\tau_m = \chi_m/\eta_2$, where x_m is the first nonzero root of the equation

$$3\int_0^{x_m}(\sin x)^{4/3}\,dx = \operatorname{tg} x_m \sin^{4/3} x_m.$$

The limiting regime which the system enters for a linearly increasing current ($i = J't$) is given by the following relations, which follow from Eqs. (7)-(10):

$$B_e = \mu_0\left(\frac{\gamma_0}{\mu_0}\right)^{1/12}\left(\frac{25\xi_0 t}{18\rho_0^3}\right)^{1/6}(a_0J')^{1/2}, \tag{14}$$

$$\Delta' \approx 2S = \left(\frac{\gamma_0}{\mu_0}\right)^{1/4}\left(\frac{\xi_0}{2}\rho_0\beta a_0J't\right)^{1/2}, \tag{15}$$

$$R = \left(\frac{18\rho_0^3}{25\xi_0}\right)^{1/6}\left(\frac{\mu_0}{\gamma_0}\right)^{1/12}(a_0J')^{1/2}t^{5/6}. \tag{16}$$

It is characteristic that the induction increases slowly with time ($B_e \sim t^{1/6}$) and is proportional to $\sqrt{J'}$.

2. COMPOSITE MODEL FOR THE DISTORTION OF A SOLENOID IN AN EXTREMELY HIGH MAGNETIC FIELD

Each of the models discussed above takes account of only one aspect of the distortion of a solenoid. For example, Eqs. (1) and (9) contain the geometrical inside radius R instead of the effective radius, while the slow explosion model does not take account of hydrodynamic flow outside the skin layer.

It is possible to calculate the increase in effective radius of a biconical solenoid under the combined action of the diffusion of the field, deformation, and slow explosion. This can be done by taking account of the fact that the change in inside radius is due both to the shift of the field-conductor boundary as a result of ejection, and to the hydrodynamic flow

$$\frac{dR}{dt} = \Omega + u(R). \tag{17}$$

The spherically symmetric flow velocity of an incompressible fluid at a point M(r) has the form $U_r(M) = R^2u(R)/r^2$. Substituting this value into Euler's equation

$$\gamma_0\left(\frac{\partial u_r}{\partial t} + u_r\frac{\partial u_r}{\partial r}\right) = -\frac{\partial p}{\partial r},$$

and integrating over r from R to ∞ we obtain

$$\frac{1}{\gamma_0}\left(\frac{B_e^2}{2\mu_0} - \sigma_s\right) = -\frac{1}{2}\left(\frac{dR}{dt} - \Omega\right)^2 + \int_R^\infty \frac{d}{dt}\left[R^2\left(\frac{dR}{dt} - \Omega\right)\right]\frac{dr}{r^2}$$
$$= R\frac{d^2R}{dt^2} + \frac{3}{2}\left(\frac{dR}{dt}\right)^2 - \Omega\frac{dR}{dt} - R\frac{d\Omega}{dt} - \frac{\Omega^2}{2}. \tag{18}$$

This equation must be solved together with (7), (8), (10), and the equation

$$B_e \approx B(0,\,0) = \frac{a_0\mu_0 J_m \sin\omega t}{R + \frac{\Delta'}{\pi}}, \tag{19}$$

which is used instead of (9) to take account of the skin correction in the value of the effective radius according to Eq. (6). Equations (7), (8), (10), (18), and (19) are valid when $B_e \geq B_s$; before this time $\Omega = dS/dt = 0$, and Eq. (7) has the form

$$P\frac{d}{dt}(B_e\Delta') = \frac{\rho_0 3B_e^3}{2\mu_0^2\Delta'}. \tag{20}$$

If $B_e^2/2\mu_0 < \sigma_s$ the left-hand side of Eq. (18) must be set equal to zero, and $dR/dt = \Omega$. The initial conditions for the system (7), (8), (10), (18), and (19) are: at $t = 0$, $R = R_0$, $\Delta' = 0$. For numerical calculations this system is put into dimensionless form. The reference quantities are chosen the same as in the hydrodynamic flow calculation. The details of the calculations will be published separately. Here we merely point out that the form of the relation $B/B_\infty = f(t/t_r)$ for a sinusoidal current is determined by the set of dimensionless parameters mentioned above: $k_0, \theta_1, \eta_1, \eta_2$, and ξ_0. The results of a numerical solution of the system for the specific conditions of the experiment are shown in Figs. 4-7.

3. SIMILITUDE CONDITIONS

Another approach to an estimate of the field in a coil being distorted is based on dimensional considerations. Let us assume that a sinusoidal current with an amplitude J_m and a rise time τ_0 flows through a biconical solenoid with a cylindrical opening of initial radius R_0.

The peak induction can be written as a function of the characteristic parameters4)

$$B_m = f_1(R_0,\ \xi_0,\ J_m,\ \tau_0,\ \rho_0,\ \beta,\ \gamma_0,\ \mu_0,\ \sigma_s,\ Q_s), \tag{21}$$

where $Q_s = B_s^2/2\mu_0$ is the volume energy density at the beginning of the slow explosion. Four parameters with independent dimensions can be eliminated from Eq. (21). We choose μ_0, J_m, R_0, and τ_0. With this we have

$$B_m = B_r f_2(\eta_0,\ g_1,\ g_2,\ g_3,\ g_4,\ g_5,\ g_6), \tag{22}$$

where $B_r = \mu_0 J_m/R_0$ is the reference induction,5) $g_1 = \rho_0\tau_0/\mu_0R_0^2$; $g_2 = J_m\mu_0\beta/R_0^2$; $g_3 = J_m\tau_0(\mu_0\gamma_0)^{1/2}R_0^{-2} = (1/k_0^2)\cdot(\sqrt{2}/a_0)$; $g_4 = \mu_0J_m^2/R_0^2\sigma_s = \theta_1$; $g_5 = \mu_0J_m^2/R_0^2Q_s$.

For very weak currents ($g_2 = g_3 = g_5 = 0$) we have a linear relation between B_m and J_m: $B_m = (\mu_0J_m/R_0)\varphi(\xi_0, g_1)$. The parameter g_1 takes account of the skin effect in weak fields but does not play an important role in strong fields, where there is a significant increase in the specific resistance because of heating. In such fields a characteristic quantity is the ratio of the depth of penetration Δ' to R_0 at the time t_m when the induction is maximum:12

$$\frac{\Delta'}{R_0} \approx \frac{B_m}{\mu_0R_0}\left(\frac{\rho_0 3t_m}{2}\right)^{1/2} = \frac{J_m}{R_0^2}(\rho_0\beta\tau_0)^{1/2}\left(\frac{t_m}{2\tau_0}\right)^{1/2}\frac{B_mR_0}{\mu_0J_m} = \left(\frac{t_m}{2\tau_0}\right)^{1/2}(g_1g_2)^{1/2}f_2. \tag{23}$$

Hence it follows that in a strong field the value of B_m/B_r depends on the combination $G = (g_1g_2)^{1/2} = (8\pi\eta_2)^{1/2}$.

$(a_0\xi_0\eta_1 R_0^3)$ and not on g_1 and g_2 separately. Since the amplitude of the induction varies slowly with σ_S and Q_S in strong fields one can expect f_2 to be only weakly dependent on the parameters g_1 and g_5. Consequently we have

$$\frac{B_m R_0}{\mu_0 J_m} = f_3(\xi_0,\ G,\ g_3) = f_3\left[\xi_0,\ \frac{J_m}{R_0^2}(\rho_0\vartheta\tau_0)^{1/2},\ \frac{J_m\tau_0}{R_0^2}\left(\frac{\mu_0}{\gamma_0}\right)^{1/2}\right] \tag{24}$$

or for samples of a given material and for a fixed rise time

$$\frac{B_m R_0}{\mu_0 J_m} = f_4\left(\frac{J_m}{R_0^2}\right), \tag{25}$$

since both parameters G and g_3 are proportional to J_m/R_0^2. In the experiments to be described later an attempt is made to test this conclusion.

4. DESCRIPTION OF EXPERIMENTS. COMPARISON OF THEORY AND EXPERIMENT

Preliminary results of experiments with copper and steel biconical solenoids (φ_0 = 53°; ξ_0 = 1.5) are reported in ref. 9.

Experiments have been performed on a large number of copper and steel solenoids with various initial inner radii R_0. The smallest value[6] of $R_0 = R_0^{(1)}$ = 1.7 mm. The solenoids are 20 mm in outside radius and are supported by rigid steel clamps. The insulating gap is about 1 mm wide. The field is measured with calibrated probes about 0.8 mm in radius with three to six turns. The current is measured with a Rogowski loop. Oscillograms of the induction, the current, and their derivatives are taken simultaneously. The error in the first peak of the current and the induction is 5-7%. The capacitor bank has a capacitance of 100 mF and an inductance of ~80 nH. Because of the variation in the initial voltage of the capacitor bank the current varies from 1.2 to 2.6 mA with a rise time τ_0 = 4.5 ± 0.2 μsec. The first peak induction is 190 Wb/m².

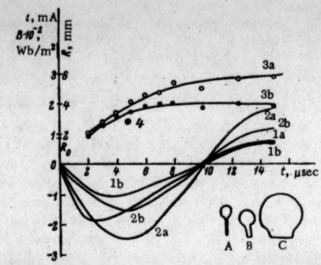

Fig. 3. Time dependence of induction, current, and effective inside radius during discharge. 1a) B(t); 2a) i(t); 3a) R'(t), copper, J_m = 2.44 mA, B_m = 184 Wb/m²; 1b, 2b, 3b) the same for steel, J_m = 1.53 mA, B_m = 113 Wb/m²; 4) value from x-ray photograph of steel; A, B, C are respectively typical x-ray photographs taken before the experiment, during the discharge, and after the experiment.

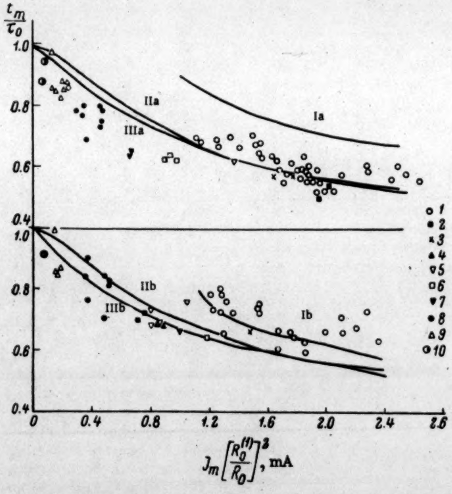

Fig. 4. Experimental points and calculated curves for the time of maximum induction as a function of the current amplitude. I) Calculated with the slow explosion model; II) calculated with the hydrodynamic model; III) calculated with the composite model. a) copper; b) steel. The points correspond to the initial radii of the samples. For copper: 1) R_0 = 1.7; 2) 1.8; 3) 1.9; 4) 2.05; 5) 2.15; 6) 2.5; 7) 3; 8) 3.4; 9) 5.1; 10) 6.8 mm; for steel: 1) 1.7; 2) 2.8; 3) 1.9; 4) 2.05; 5) 2.15; 6) 2.2; 7) 2.3; 8) 3.4; 9) 5.1; 10) 6.8 mm.

In addition to the oscilloscope measurements, in some experiments x-ray photographs are taken of the contour of the opening of the solenoid at a specified time using an exposure of $\sim 10^{-7}$ sec (Fig. 3). Examples of processed oscillograms of B(t) and i(t) are shown in Fig. 3.

It is typical that the induction maximum is reached earlier than the current maximum. This shows indirectly the increase in the effective radius at the front of the current pulse.

Figure 4 shows t_m/τ_0 as a function of $J_m(R_0^{(1)}/R_0)^2$, proportional to J_m/R_0^2. Here $R_0^{(1)} = 1.7$ mm, so that for points corresponding to this initial radius the measured rather than the calculated value of J_m is plotted along the axis of abscissas. As predicted by dimensional analysis the points for all samples lie on a common curve. For large R_0 (weak fields) the curve approaches unity. As the argument $J_m(R_0^{(1)}/R_0)^2$ increases, the ratio t_m/τ_0 decreases to 0.5-0.6 in the copper samples and to 0.6-0.7 in the steel specimens. As can be seen from Fig. 5 the

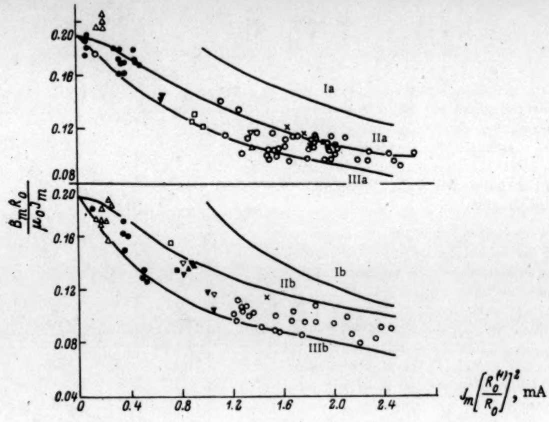

Fig. 5. Ratio of the amplitude of the induction to its calculated value. Notation is the same as in Fig. 4.

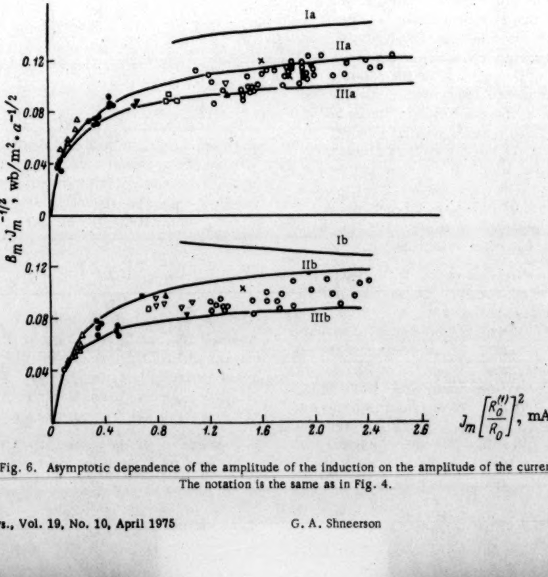

Fig. 6. Asymptotic dependence of the amplitude of the induction on the amplitude of the current. The notation is the same as in Fig. 4.

TABLE 1. Comparison of the Inside Radius R Calculated from an X-ray Photograph and the Effective Radius R'

R_0, mm	Copper			Steel		
	t_0, μsec	R, mm	R', mm	t_0, μsec	R, mm	R', mm
1.7	4.0	2.7	2.7	4.0	2.5	3.3
	4.1	2.9	3.3	4.1	2.8	3.5
	4.2	3.0	3.3	4.7	2.8	3.3
	4.2	3.5	3.0	5.1	3.4	3.8
	5.0	3.5	3.7	6.6	3.4	4.3
	7.4	4.6	5.0	7.1	3.7	4.6
	7.4	4.6	4.7			
3.4	6.5	4.3	4.3	6.9	3.7	4.5
	6.6	4.5	4.5	6.9	4.0	4.7
	7.1	4.4	4.5			

experimental points for small values of the argument lie close to the curve, clustered about the point $B_mR_0 = \mu_0J_m = 0.19$, which corresponds to the field in a perfectly conducting solenoid with a vanishingly narrow gap. As the current increases, this ratio decreases to 0.08-0.09, which corresponds to a decrease in the amplitude of the induction to less than half the calculated value.

Figure 6 shows the maximum induction as a function of the peak current in a strong field. The ratio $B_m/J_m^{-1/2}$ in strong fields does not depend on the argument $J_m \cdot (R_0^{(1)}/R_0)^2$. This agrees with the assumption in ref. 9 that the peak induction in a strong field increases as $\sqrt{J'}$ or, for a fixed rise time τ_0, as $\sqrt{J_m}$. It was shown above that this behavior of B_m in biconical solenoids follows from both the hydrodynamic model and the slow explosion model. A special consideration shows that it follows from the composite model also.

The geometrical radius R of a solenoid at a given time t_0 can be determined from the x-ray photographs (Fig. 3). The photographs show that the opening retains its shape during the first half-period of the discharge. The results of processing the x-ray photographs for a number of experiments are shown in Table 1. These results are compared with the values of the effective radius R' obtained by the processing of the oscillograms of B(t) and i(t). As in refs. 2-4, the processing technique consists in determining the instantaneous value of the effective inside radius R' from the experimental value of the ratio $g'(t) = B(t)/J(t)$, since it is known that $g' = f(R') = 0.19\ \mu_0/R'$. Examples of the curves R'(t) are shown in Fig. 3. The error in determining R'(t) is estimated as 0.2-0.3 mm for R' = 2-3 mm. The values of $R'(t_m)$, the effective radius at maximum induction, lie between 2.1 and 2.5 mm for copper solenoids with R_0 = 1.7 mm, and between 2.4 and 2.9 mm for steel solenoids.

The variation in the effective radius up to the instant of maximum induction is appreciably larger. Against the background of the spread, apparently related to the experimental errors, $R(\tau_0)/R_0$ increases monotonically with the argument $J_m(R_0^{(1)}/R_0)^2$ (Fig. 7). A comparison of the effective radius found from the oscillograms of B(t) and i(t) with the results of the x-ray measurements (Table 1) illustrates the role of the diffusion of the field into the conductor. The value of $R'(t_0)$ is always larger than the radius of the opening of the solenoid. The error in determining R_0 prevents an exact calculation of the depth of penetration and a verification of the diffusion calculation.

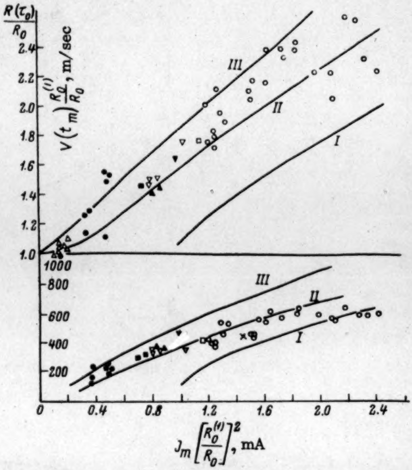

Fig. 7. Effective inside radius of a solenoid at the instant of maximum current, and the velocity at the instant of maximum induction. Copper. The notation is the same as in Fig. 4.

Because of the error in determining R' there is an appreciable error in the estimate of dR/dt, the rate of increase of the effective radius. It is simplest to determine this rate at the point of maximum induction t_m, where $dB/dt = 0$ and, consequently, $i(dg'/dt) + g'(di/dt) = 0$. Since $g' = \text{const}/R'$, the velocity at time t_m is

$$V(t_m) = \frac{dR'}{dt}(t_m) = \frac{R'(t_m)}{i(t_m)}\frac{dJ}{dt}(t_m) \approx \frac{\pi a_0\mu_0 J_m}{2B_m\tau_0}\cos\frac{\pi t_m}{2\tau_0}. \qquad (26)$$

The error in determining $V(t_m)$ is about 20%. The experimental results are shown in Fig. 7 in the form of curves of $V(t_m)R_0^{(1)}/R_0$ as functions of $J_m(R_0^{(1)}/R_0)^2$. The ratio $V(t_m)R_0^{(1)}/R_0$ is plotted: For fixed τ_0 the ratio $R_0/R_0^{(1)}$ is proportional to the reference velocity R_0/τ_0 in the system of defining parameters μ_0, J_m, R_0, and τ_0.

In our experiments the absolute value of $V(t_m)$ reaches 600-700 m/sec. The spread of experimental points in Figs. 4-7 pertaining to solenoids with various initial radii lies within the limits of experimental error. This confirms the dimensional-analysis conclusion that in strong fields the quantities $B_m R_0/\mu_0 J_m$, $R(\tau_0)/R_0$, and $V(t_m)R_0^{(1)}/R_0$ are functions of J_m^2/R_0 for a fixed rise time. Figures 4-7 show the results of numerical calculations using the hydrodynamic model (neglecting the strength term), and the slow explosion and composite models approximately satisfying the experimental conditions with $R_0 = 1.7$ mm. Under our experimental conditions the slow explosion model overestimates the amplitude of the induction and appreciably overestimates the rate of distortion. Hydrodynamic flow is the main process. Calculations with the hydrodynamic model give values of the peak induction, the radius, and the velocity close to the experimental results, although the values of B_m are somewhat overestimated. The quantitative agreement is even better than could be expected, taking account of the calculational assumptions about the nature of the flow in the distortion of a solenoid. As expected, going over to the composite model gives a smaller correction for copper solenoids than for steel, since the skin layer is thicker in steel. For both materials the composite model underestimates the induction and overestimates the velocity and the effective radius. Apparently ejection plays a somewhat smaller role than assumed in the present calculations, which do not take account of the time to establish a steady flow of heated metal in the skin layer.

The author thanks A. Kruchinin for the computer calculations.

---

1) In a field with an induction $B_e \gg \sqrt{2\mu_0\sigma_s}$ the coordinate of the flow zone boundary $R_1 \gg R$.

2) Assuming that $\Delta' \ll R$ and that the field in the skin layer is two-dimensional.

3) For example $\bar{r}_0$ can be expressed in terms of η_1, η_2, and k_0: $\bar{r}_0 = 2^{-7/4} k_0 \cdot \eta_1^{1/2}/\eta_2$. The dimensionless time $\tau = t(\alpha_0 J')^2 \mu_0^3/\rho_s B_s^2$.

4) Neglecting compressibility effects.

5) The parameter $\alpha_0 = f(\xi_0)$.

6) Of about 130 completed oscillograms 41 are for copper and 27 for steel samples having initial inside radii of 1.7 mm.

---

[1] H. P. Furth, M. A. Levine, and R. W. Waniek, Rev. Sci. Instr., 28, 799 (1957).

[2] G. A. Shneerson, Zh. Tekh. Fiz., 32, 1153 (1962) [Sov. Phys. – Tech. Phys., 7, 848 (1963)].

[3] V. P. Gordienko and G. A. Shneerson, Zh. Tekh. Fiz., 34, 376 (1964) [Sov. Phys. – Tech. Phys., 9, 296 (1964)].

[4] V. P. Gordienko and G. A. Shneerson, Zh. Tekh. Fiz., 35, 1084 (1965) [Sov. Phys. – Tech. Phys., 10, 834 (1965)].

[5] J. W. Shearer, J. Appl. Phys., 40, 4490 (1969).

[6] A. M. Andrianov, V. F. Demichev, G. A. Eliseev, and P. A. Levit, ZhETF Pis. Red., 11, 582 (1970) [JETP Lett., 11, 402 (1970)].

[7] V. S. Komel'kov (ed.), Technology of Large Pulsed Currents and Magnetic Fields [in Russian], Atomizdat, Moscow (1970).

[8] H. Knoepfel, Pulsed High Magnetic Fields, North-Holland, London (1970).

[9] G. A. Shneerson, ZhETF Pis. Red., 12, 453 (1970) [JETP Lett., 12, 315 (1970)].

[10] Ya. B. Zel'dovich and Yu. P. Raizer, The Physics of Shock Waves and High-Temperature Hydrodynamic Flows [in Russian], Nauka, Moscow (1965).

[11] G. A. Shneerson, Zh. Tekh. Fiz., 43, 419 (1973) [Sov. Phys. – Tech. Phys., 18, 268 (1973)].

[12] G. A. Shneerson, Zh. Tekh. Fiz., 37, 513 (1967) [Sov. Phys. – Tech. Phys., 12, 368 (1967)].

Dependence of the basic parameters of $Al_xGa_{1-x}As$–GaAs solar converters on temperature and optical intensity

E. B. Vinogradova, M. B. Kagan, N. S. Koroleva, T. L. Lyubashevskaya, and T. A. Nuller

(Submitted October 8, 1973)
Zh. Tekh. Fiz. 44, 2229-2234 (October 1974)

We have investigated the basic parameters of p-$Al_xGa_{1-x}As$–n-GaAs solar converters over wide ranges of temperatures and optical intensity. The low inverse saturation currents, the high constant collection coefficients over the entire spectrum, and the specific features of the electrical characteristics result in a high temperature stability of the power output and certain features over a wide range of temperatures and optical intensity.

Solar converters made of $Al_xGa_{1-x}As$-GaAs heterosystems retain their high efficiency at high temperatures. An efficiency factor of about 3% is obtained in ref. 1 and about 5% in ref. 2 at 300°C. It is noted for comparison that the best Si solar elements have an efficiency factor close to zero at T ≈ 170°C, whereas solar elements in which diffused GaAs p–n junctions are employed still have an efficiency factor[3] of about 1% at 300°C. The peculiar electrical characteristics which are described in ref. 4 may be the reason for the high temperature stability of the power delivered by the solar converters and for their efficiency. The electrical characteristics, in turn, result in a specific performance at low temperatures and at high illumination intensities; those conditions have not been considered in the literature.

The present paper reports on an investigation of the basic parameters of solar converters made of p-Al_xGa_{1-x}As–n-GaAs in the temperature range 100-200°C. In addition, the dependence of the basic parameters upon the illumination intensity in the interval (1-40)·10^3 W/m^2 is described. The results are compared with the data on homogeneous solar elements made of GaAs.

1. EXPERIMENTAL INVESTIGATIONS AND RESULTS

Figures 1 and 2 depict typical temperature dependences of the optimum power, the current delivered to an optimum load, and the short-circuit current for Al_x·Ga_{1-x}As–GaAs converters; these have been measured in the temperature range 20-200°C at a constant illumination intensity of ≈800 W/m^2. Figures 1 and 2 include, for comparison, the temperature dependence of the basic parameters which have been measured for GaAs photoelements with diffused p–n junctions under similar experimental conditions. In contrast to the latter, a decrease in the optimum power at increasing temperatures of Al_xGa_{1-x}As–GaAs converters cannot be described by a linear function with a constant negative gradient: The value $\delta = \partial P_{opt}/\partial T P_{opt}$ is much lower at temperatures up to +100°C than at higher temperatures, being 0.03-0.1 %/deg C for the various samples. The δ value for the interval 100-200°C coincides with the values which are typical for GaAs converters (≈0.25%/deg C). The Al_x·Ga_{1-x}As–GaAs converters are characterized by 1) an increase in the current $I_{sat.opt}$ at the optimum point with increasing temperature (up to 120-140°C) and 2) a positive gradient of the short-circuit current (which is much greater than in GaAs elements) $\gamma = \partial I_{sh.c.}/\partial I I_{sh.c.}$, with the gradient amounting to 0.25%/deg C in some cases. The photo-emf U_{ph} (open-circuit emf) decreases linearly at increasing temperatures and has a constant negative gradient $\delta = \partial P_{ph}/\partial T U_{ph}$ = (0.20-0.25)%/deg C (see Fig. 3).

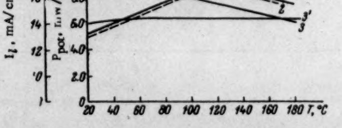

Fig. 1. Temperature dependences of the optimum power P_{opt} and the current I_l obtained with optimum load at positive temperatures. 1, 2) P = f(T) for $Al_xGa_{1-x}As$–GaAs photoconverters (experimental values); the dot–dash line indicates P = f(T) for $Al_xGa_{1-x}As$–GaAs photoconverters (computed values); 3) P = f(T) for GaAs photoconverters; 1',2') $I_l = f(T)$ $Al_xGa_{1-x}As$–GaAs photoconverters.

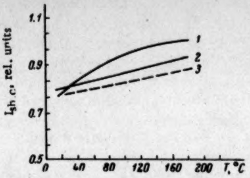

Fig. 2. Temperature dependence of the short-circuit current $I_{sh.c.}$ 1) $I_{sh.c.} = f(T)$ for $Al_xGa_{1-x}As$–GaAs photoconverters corresponding to spectral curves 1 and 1' of Fig. 4; 2) $I_{sh.c} = f(T)$ for $Al_xGa_{1-x}As$–GaAs photoconverters corresponding to spectral curves 2 and 2' of Fig. 4; 3) $I_{sh.c} = f(T)$ for GaAs photoconverters.

At low temperatures (temperatures below −100°C have been considered), the behavior of the $Al_xGa_{1-x}As$–GaAs converters is characterized by the inflection of the functions P(T) and U_{ph}(T) at a certain critical temperature which is characteristic of solar elements of Si (ref. 5) and GaAs (ref. 6), with the inflection being related to changes in the mechanism of current flow (Fig. 3). In diffused GaAs elements the sharply increased influence of surface leakage currents at $T_{cr} \approx -60$°C leads to a saturation point of the functions $I_0 = f(T)$ and $\beta = f(T)$, which, in turn, limits the increase in power at decreasing temperatures.

It is shown in ref. 4 that two exponential sections in the forward branch of the voltage–current characteristic are typical for Al_xGa_{1-x}As–GaAs converters. The experimental curves $I_0 = f(T)$ and $\beta = f(T)$ shown in Fig. 3 have a typical exponential decrease in the inverse saturation current at decreasing temperatures in the region of lowest I_0 and β. No substantial changes of the parameter β are observed.

We have investigated the temperature dependence of the spectral collection coefficient Q(λ) of $Al_xGa_{1-x}As-GaAs$ converters in order to determine the reasons for the positive temperature gradients of the photocurrent, which, when compared with GaAs elements, are abnormally large in the interval +20 to + 200°C (Fig. 4). It is observed that the form of the collection coefficient dependence on wavelength depends strongly on the initial (T = 300°K) form of the function Q(λ) at increasing temperatures. The greatest change of Q(λ) = *f*(T) and, hence, the maximum increment of the integrated photocurrent $\gamma \sim 0.25\%$/deg C are observed in converters with an initial function Q(λ) of type 1 (Fig. 4), i.e., with a sharp drop of the collection coefficient in the long-wave part of the spectrum. A wavelength dependence of type 2 (Fig. 4) corresponds to a smaller temperature gradient of the photocurrent ($\gamma \sim 0.1\%$/deg C). A shift of both long-wave and short-wave edges of the function Q(λ) is observed in all cases in accordance with the temperature dependences of the widths of the forbidden-energy gaps in GaAs and $Al_xGa_{1-x}As$.

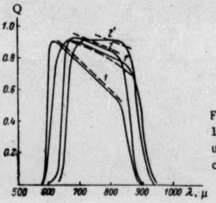

Fig. 4. The collection coefficient Q(λ). 1, 2) Q(λ) at 300°K (experimental values); the dashed curves refer to calculated Q(λ) values.

The dependence of the basic parameters of $Al_xGa_{1-x}As-GaAs$ converters on the illumination intensity has been studied in the interval (1-40) $\cdot 10^3$ W/m² at T = 300°K; a K-22 cinema projector lamp provided with lenses and neutral filters is used as the illuminating source. Converters having different initial parameters I_{ph}, I_0, and β are examined. As in the case of the measurements of the temperature dependence the initial parameters are determined from the forward branch of the voltage–current characteristic, i.e., from the branch which corresponds to the high-current region. The experimental dependences $I_{ph} = f(E)$, $I_{sh.c.} = f(E)$, and $P_{opt} = f(E)$ are shown in Fig. 5. Figure 5 includes, for comparison, the relations for a typical GaAs element. The measurements of the photocurrent are made in the range of high light fluxes while an inverse bias voltage is applied to the illuminated sample. This makes it possible to establish differences in the behavior of the measured short-circuit current $I_{sh.c.}$ and the photocurrent I_{ph}, which is independent of the series resistance of the units. A linear dependence of I_{ph} on the light flux is observed in all cases, but the slope of the dependence is usually much greater than for GaAs. At light fluxes corresponding to approximately 25 solar constants, a photocurrent density of ~600 mA · cm^{-2} is reached in some of the samples. With series resistances which are the same as in the case of GaAs elements, the deviations of $I_{sh.c}$ from the linear dependence are observed at much greater light fluxes. The flux value at which the deviations begin depends upon the current I_0. The optimum power also depends on the current I_0 at increasing light fluxes and is characterized by two sections: a linear section extending to fluxes of (10-20) $\cdot 10^3$ W/m² at various I_0, and a section on which the power depends upon the flux like $P \sim E^{1/2}$. A linear dependence $P_{opt} = f(E)$ of GaAs elements is usually observed only to (10-12) $\cdot 10^3$ W/m².

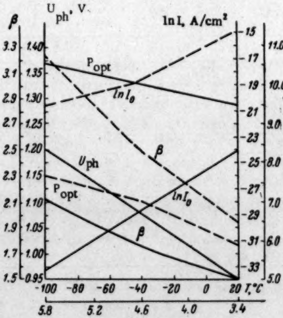

Fig. 3. Temperature dependences of the optimum power P_{opt}, the open-circuit voltage U_{ph}, the inverse saturation current I_0, and the parameter β at negative temperatures. The solid lines indicate P = *f*(T), U_{ph} = *f*(T), I_0 = *f*(T), and β = *f*(T) for $Al_xGa_{1-x}As-GaAs$ photoconverters; the dashed curves indicate P = *f*(T), U_{ph} = *f*(T), I_0 = *f*(T), and β = *f*(T) for GaAs photoconverters.

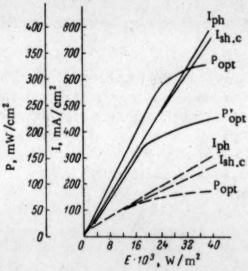

Fig. 5. Dependences of the photocurrent I_{ph}, the short-circuit current $I_{sh.c}$, and the optimum power P_{opt} upon the light flux. The solid curves refer to I_{ph} = *f*(E), $I_{sh.c}$ = *f*(E), and P_{opt} = *f*(E) for $Al_xGa_{1-x}As-GaAs$ photoconverters (P_{1opt} refers to photoconverters with $I_0 \approx 10^{-13}$ A/cm² and P_{2opt}, to photoconverters with $I_0 \approx 10^{-11}$ A/cm²); the dashed curves indicate I_{ph} = *f*(E), $I_{sh.c}$ = *f*(E), and P_{opt} = *f*(E) for GaAs photoconverters.

2. DISCUSSION OF RESULTS

The observed temperature and intensity dependences of the basic parameters of $Al_xGa_{1-x}As-GaAs$ converters result from two factors: an inverse current I_0, which is smaller than that of GaAs elements, and a higher integrated sensitivity, due to the integrated collection coefficient approaching the value unity.

The temperature dependence of the optimum power is

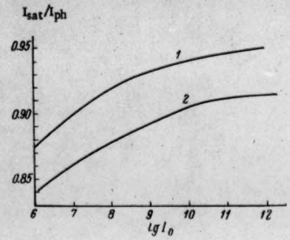

Fig. 6. Dependence of the ratio I_{sat}/I_{ph} upon $\log I_0$. 1) $R_{series} = 0$; $R_{series} = 16\Omega$.

of greatest interest as far as practical applications are concerned. The temperature dependence of the power is anomalous relative to that of the usual diffused GaAs elements at temperatures up to + 100°C and is associated with the low (less than 10^{-9} A/cm^2) inverse saturation current, which, in this temperature interval, is described by the equation

$$I_0 = Ce^{-\frac{E_g}{\beta kT}} \quad (\beta = 1.6). \tag{1}$$

and with a current which is almost equal to the photocurrent at the optimum point (Fig. 6). The increase in the inverse saturation current at increasing temperatures in the range of large inverse currents implies that the current increasingly deviates from the photocurrent at the optimum point. The latter determines the usual temperature dependence of the power of GaAs elements with a temperature gradient dP/PdT ~ 0.25%/deg C. Figure 1 shows the computed temperature dependence of the power of elements with realistic parameters. It is assumed in the calculations that the inverse saturation current is given by Eq. (1) and amounts to 10^{-13} A/cm^2 at 300°K. The temperature dependence of the photocurrent corresponds to the experimentally obtained dependence in Fig. 2. Good agreement between calculated and experimental values is observed in Fig. 1.

It has been shown[4] that the collection coefficient as a function of the wavelength can be calculated with the equation

$$Q = q\left\{\frac{1 - \exp(-\alpha l)}{1 + \alpha L}\right\}, \tag{2}$$

where α denotes the absorption coefficient, l the width of the depletion region in GaAs, and L the diffusion length of holes in the GaAs base.

Figure 4 depicts experimental values of the collection coefficients and collection coefficient figures calculated with Eq. (2) for the temperatures 300°K and 423°K. Good agreement between the calculated and experimental functions is obtained even when only the temperature dependence of the collection coefficient is taken into account (curves 1, 2, 1', and 2').

The temperature dependence of the photocurrent is strongly affected by the temperature dependence of the absorption coefficient, because when the temperature dependence of the absorption coefficient is taken into account good agreement between calculated and experimental collection coefficients as functions of the wavelength is obtained (Fig. 4). Two spectral dependences of the collection coefficient are characteristic of the units examined[4] (Fig. 4). Since the influence of the absorption coefficient on the spectral sensitivity is reduced in the case of high initial collection coefficient values, a unit with a "drop" of the spectral sensitivity in the long-wave part of the spectrum is characterized by a high temperature gradient of the photocurrent (γ ~ 0.2%/deg C, curve 1 of Fig. 4). This figure is twice that of conventional GaAs photoelements. When high temperature gradients of the photocurrent appear in combination with low inverse currents (I_0 ~ 10^{-13} A/cm^2), temperature stability of the power is obtained up to + 100°C. This corresponds to a temperature gradient of the power of ∂P/PdT ~ 0.08%/deg (Fig. 1).

At low temperatures the characteristic feature of $Al_xGa_{1-x}As$–GaAs converters is the absence of the inflection of the functions P(T) and U_{ph}(T) at a "critical temperature," which is typical[5] for Si and GaAs elements. The inflection is associated with a change in the mechanism of the current flow. The absence of this inflection in $Al_xGa_{1-x}As$–GaAs converters is attested by the parameter β, which is constant in the temperature interval under consideration.

The low inverse currents of the units, along with their high temperature stability, cause a peculiar behavior at high illumination fluxes. As has been shown in ref. 7, the light flux intensity at which the increase in the optimum power begins to slow down depends strongly upon the inverse saturation current I_0 and the series resistance R_{series} of the unit. The units examined had identical series resistance (~ 5 Ω) and similar photocurrents I_{ph}. The dependence of the optimum power upon the light flux is in this case determined by the inverse saturation current I_0. It follows from Fig. 5 that the deviation of the optimum power from the linear dependence begins at light fluxes of about (1.4–1.6) · 10^4 W/m^2 in the case of the elements with $I_0 = 10^{-12}$–10^{-13} A/cm^2 and at light fluxes of (1.3–1.4) · 10^4 W/m^2 in the case of units with $I_0 = 10^{-11}$ A/cm^2, i.e., the linear increase in optimum power continues to higher light fluxes than in the case of diffused GaAs units having inverse saturation currents[7] I = 10^{-9}–10^{-10} A/cm^2. The region of light fluxes at which the linear dependence of the power upon the light flux no longer exists is characterized by the function P(E) ~ $E^{1/2}$. This function results from the distributed series resistance. Our investigations have shown that the function P(E) ~ $E^{1/2}$ holds to light fluxes of 40 · 10^3 W/m^2 and a substantial saturation of the power produced by the light flux does not set in.

The high constant collection coefficients of the entire spectral interval imply a high integrated sensitivity K. Since I_{ph} = KE, an increased dependence of both the photocurrent and the optimum power upon the light flux is observed in the units examined. This, in turn, makes it possible to obtain a specific power P > 200 mW/m^2 at light fluxes E ~ 35 · 10^3 W/m^2.

---

[1] Zh. I. Alferov, V. M. Andreev, M. B. Kagan, I. I. Protasov, and V. G. Trofim, Fiz. Tekh. Poluprovodn., 4, 2378 (1970) [Sov. Phys.—Semicond.,

4, 2047 (1971)].

[2] J. M. Woodall and H. J. Hovel, Electronic Design, No. 12, 37 (1972).

[3] M. B. Kagan, A. P. Landsman, and T. L. Lyubachevskaya, Geliotekhnika, No. 2, 1968.

[4] V. M. Andreev, T. M. Golovner, M. B. Kagan, N. S. Koroleva, T. L. Lyubashevskaya, T. A. Nuller, and D. N. Tret'yakov, Fiz. Tekh. Poluprovodn., 7, 2289 (1973) [Sov. Phys.—Semicond., 7, 1525 (1974)].

[5] K. L. Kennerud, IEEE Trans. Aerospace and Electron. Syst., AES-3, No. 4, 586 (1967).

[6] M. B. Kagan, A. P. Landsman, and T. L. Lyubashevskaya, Kosmich. Issled. Akad. Nauk SSSR, 4 (1971).

[7] M. B. Kagan and T. L. Lyubashevskaya, Geliotekhnika, No. 2, 12 (1971).

Excitation of thermoelastic vibrations of a thin plate by a beam of fast charged particles

A. I. Kalinichenko and V. T. Lazurik-Él'tsufin

A. M. Gor'kii Khar'kov State University

(Submitted October 30, 1973; resubmitted February 21, 1974)
Zh. Tekh. Fiz., 44, 2235-2238 (October 1974)

The acoustic signal and the stress in a thin plate produced by a dense beam of fast charged particles which penetrates the plate have been calculated. Amplitudes for various particle distribution functions in the beam are presented. It is concluded that the acoustic signal can be used to determine the number density distribution in the beam.

1. When a beam of charged particles passes through a solid various acoustic oscillations are excited in the solid. One cause of the excitation is the superheating of the interaction zone caused by energy losses of the beam particles in the solid. In refs. 1 and 2 the thermoelastic stresses that arise in instantaneous[1] and gradual[2] heating of a free surface of a semiinfinite solid are investigated theoretically. The results can be used to find the thermoelastic response in a solid penetrated by a beam of particles when the depth of penetration into the solid is small in comparison with the characteristic thermal-conductivity length. Experiments based on the one-dimensional thermoelastic response of a solid to collision with a beam of low-energy electrons[3] show good agreement with the theory. The one-dimensional thermoelastic response of a solid when the depth of penetration cannot be neglected is studied experimentally and theoretically in refs. 4 and 5.

Recent experiments have been concerned with the excitation of acoustic vibrations in a thin plate by a beam of relativistic electrons[6] when the acoustic detector is fastened to the lateral face rather than the rear surface of the plate.[7] In this case the acoustic vibrations are diverging cylindrical waves. There is interest in the theoretical thermoelastic response in this case and a comparison of the calculation with experiment.

In the present work we consider fast particles [$h(dE/dx)_{\text{ion}} \ll E$, where h is the plate thickness, E is the energy of the beam particles, $(dE/dx)_{\text{ion}}$ are the ionization losses of a particle per unit path in the target material], thin plates ($h \ll t_0$, where t_0 is the radiation length of the target material), and dense beams.

2. We consider the acoustic signal from a cylindrical beam of charged particles whose current density j(r) depends only on the distance r to the beam axis. The ionization losses of fast charged particles of the beam lead to the generation (in the solid) of a volume thermoelastic force

$$\mathbf{F}_T(r,\ t) = -\Gamma \nabla P(r,\ t), \tag{1}$$

where Γ is the Grüneisen constant of the target material (we assume that Γ is independent of direction in the target material as is the case in polycrystalline media and in single crystals with cubic symmetry); P(r, t) is the density of the absorbed energy. Assuming that in a thin plate only the ionization losses are of basic importance, and all other forms of loss of charged particles (bremsstrahlung, Cerenkov radiation, transition radiation) can be neglected, we obtain the following expression for the density of absorbed energy:

$$P(r,\ t) = j(r)\left(\frac{dE}{dx}\right)_{\text{ion}}[t - (t - t_b)\,\theta(t - t_b)], \tag{2}$$

where t is the time measured from the beginning of the interaction of the beam with the solid plate:

$$\theta(t - t_b) = \begin{cases} 0, & t - t_b < 0, \\ 1, & t - t_b \geqslant 0, \end{cases}$$

t_b is the time that the beam acts. We assume that both the time that the beam acts t_b and the acoustic relaxation time between the beam and the plate $\tau_S = R/c_l$ are considerably smaller than the time for temperature $\tau_T = R^2/4a$ which, for real beams, is 0.01-0.1 sec. (Here R is the beam radius, c_l is the velocity of longitudinal sound in the target material, and a is the thermal-conductivity coefficient of the target material.) Thus, during the time of energy deposition and generation of the acoustic signal the temperature field in the target depends only on the density of the absorbed target material of energy

$$T(r,\ t) = \frac{P(r,\ t)}{C\rho}, \tag{3}$$

where C and ρ are the specific heat and density of the target material.

Taking account of the axial symmetry of the problem, we use the wave equation for longitudinal vibrations with a thermoelastic load on the right side[8]

$$\frac{\partial^2 u(r,\ t)}{\partial t^2} - c_l^2\left(\frac{\partial^2 u(r,\ t)}{\partial r^2} + \frac{1}{r}\frac{\partial u(r,\ t)}{\partial r} - \frac{u(r,\ t)}{r^2}\right) = \frac{F_T(r,\ t)}{\rho}, \tag{4}$$

where u(r, t) is the amplitude of the diverging cylindrical sound wave.

An exact solution for Eq. (4) can be obtained by the Laplace-transform method; in view of the cumbersomeness of this solution we do not present it here. In actual experiments, as a rule, the condition

$$R \ll r_0 \tag{5}$$

is satisfied, where r_0 is the distance from the beam axis to the observation point. When condition (5) is satisfied the solution of Eq. (4) is simplified considerably:

$$u(r_0,\ \tau) = \frac{\Gamma}{\pi\rho c_l^2 t_b\sqrt{2r_0}} \int\limits_0^{\min(2R,\ c_l\tau)} f(\xi)\,d\xi\,\Big[\sqrt{c_l\tau - \xi} - \sqrt{(c_l\tau - c_l t_b - \xi)\,\theta(c_l\tau - c_l t_b - \xi)}\Big], \tag{6}$$

where τ is the time measured from the time that the acoustic signal arrives at the observation point; ξ is the vari-

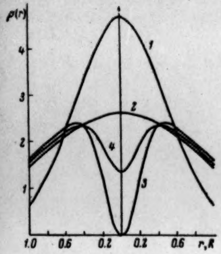

Fig. 1. Radial distribution functions for beam particles.

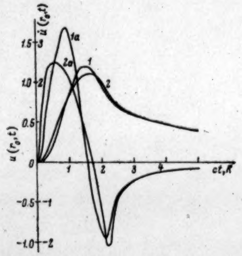

Fig. 2. Time dependence of acoustic amplitudes and stresses, for the case of a Gaussian particle distribution in the beam.

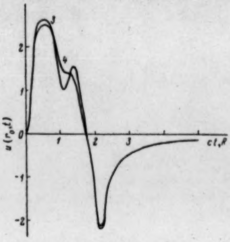

Fig. 3. Time dependence of acoustic stresses, for the case of a non-Gaussian particle distribution in the beam.

able of integration over the cross section of the beam; and $f(\xi)$ is the distribution of heat sources

$$f(\xi)=2\int\limits_{R-\xi}^{R}\frac{S(r)\,rdr}{\sqrt{r^2-(R-\xi)^2}}, \tag{7}$$

$S(r) = j(r)(dE/dx)_{ion}t_b$ is the source density.

3. By comparing the amplitudes of the acoustic signals calculated for various t_b, for $t_b < 10^{-7}$ sec and R = 1 cm we see that it is valid to assume that the energy is produced instantaneously. Then the expression for acoustic signal can be simplified further. We obtain

$$u(r_0,\ \tau)=\frac{\Gamma}{2\pi\rho c_l^2\sqrt{2r_0}}\int\limits_0^{\min(2R,\,c_l\tau)}\frac{f(\xi)\,d\xi}{\sqrt{c_l\tau-\xi}}. \tag{8}$$

Since the integral in Eq. (8) is a universal function of the variable $c_l\tau$, the acoustic signal in different materials reaches maximum for the same value of $c_l\tau$. Thus, the condition

$$c_l\tau_m = \text{const} \tag{9}$$

should be satisfied for different materials, where τ_m is the rise time of the acoustic signal. In different materials the ionization losses of a fast charged particle are usually proportional to the density of the material; thus the ratio of the amplitude in two different materials is

$$\frac{u_{\max}^{(1)}}{u_{\max}^{(2)}}=\frac{\Gamma_1}{\Gamma_2}\frac{c_{l_2}^2}{c_{l_1}^2}. \tag{10}$$

4. The distribution functions for the beam particles, normalized to unit flux are given in Fig. 1, and the corresponding acoustic signals are given in Figs. 2 and 3.

Figure 2 refers to the case of a Gaussian distribution of particles in the beam (curves 1 and 2 in Fig. 1); curves 1 and 2 correspond to acoustic displacements, curves 1a and 2a correspond to the stresses that are generated. Figure 3 shows the acoustic stresses for the case of particle distributions in the beam represented by curves 3 and 4 in Fig. 1.

Evidently, the shape of the acoustic signal can be used, in principle, to determine the distribution of particles in the beam. From this point of view, it is not favorable to measure the displacements of the material. Instead, the stresses that are generated in the material are measured. It follows from Fig. 2 that the stresses in the material are more sensitive to the distribution of particles in the beam than the acoustic displacement.

In conclusion we thank I. A. Akhiezer and V. D. Volovik for valuable discussion.

---

[1] V. I. Danilovskaya, Prikl. Matem. Mekhan., 14, 316 (1950).
[2] V. I. Danilovskaya, Prikl. Matem. Mekhan., 16, 341 (1952).
[3] R. M. White, J. Appl. Phys., 34, 2123 (1963).
[4] R. B. Oswald, Jr., F. B. McLean, D. R. Schallhorn, and L. D. Buxton, J. Appl. Phys., 42, 3463 (1971).
[5] F. C. Perry, Appl. Phys. Lett., 17, 408 (1970).
[6] I. A. Borshkovskii, V. D. Volovik, I. A. Grishaev, G. P. Dubovik, I. I. Zalyubovskii, and V. V. Petrenko, ZhETF Pis. Red., 13, 546 (1971) [JETP Lett., 13, 390 (1971)].
[7] E. V. Armenskii, V. K. Emel'yanov, V. M. Rybin, N. A. Nikolaev, and A. I. Tokarev, Prib. Tekh. Eksp., No. 2, 47 (1973).
[8] G. Parkus, Unsteady Temperature Stresses [in Russian], Fizmatgiz, Moscow (1963), p. Ch. 5, Sec. 8.

BLANK
PAGE

Diffraction of electromagnetic waves by a dielectric wedge

A. A. Aleksandrova and N. A. Khizhnyak

A. M. Gor'kii Khar'kov State University

(Submitted November 5, 1973)
Zh. Tekh. Fiz., 44, 2241-2249 (November 1974)

A rigorous solution for the problem of plane-wave scattering by a rectangular dielectric wedge is obtained with the help of Maxwell's equations in integral form. Solutions in the internal and external regions are obtained in the form of a combination of plane waves and a wave from the edge in the form of a Sommerfeld integral.

The diffraction of an arbitrarily incident plane electromagnetic wave by a dielectric wedge is analyzed in this paper. As is well known, the problem of wave diffraction by a metal wedge has been solved,[1,2] but generalization of this solution to the case of a dielectric wedge entails serious mathematical difficulties. These difficulties can be avoided if the integral form of Maxwell's equations is used.[3] Solution of the boundary-value problem using integral equations for the field is characterized by a number of features which are also discussed here.

The original integral field equations, which have an $e^{-i\omega t}$ dependence on time, have the form

$$\left.\begin{aligned}\mathbf{E}(\mathbf{r})&=\mathbf{E}_0(\mathbf{r})+\frac{1}{4\pi}(\operatorname{grad}\operatorname{div}+k^2)\int\limits_V(\varepsilon-1)\mathbf{E}(\mathbf{r}')f(|\mathbf{r}-\mathbf{r}'|)\,d\mathbf{r}\\&\quad+\frac{ik}{4\pi}\operatorname{curl}\int\limits_V(\mu-1)\mathbf{H}(\mathbf{r}')f(|\mathbf{r}-\mathbf{r}'|)\,d\mathbf{r}',\\\mathbf{H}(\mathbf{r})&=\mathbf{H}_0(\mathbf{r})+\frac{1}{4\pi}(\operatorname{grad}\operatorname{div}+k^2)\int\limits_V(\mu-1)\mathbf{H}(\mathbf{r}')f(|\mathbf{r}-\mathbf{r}'|)\,d\mathbf{r}'\\&\quad-\frac{ik}{4\pi}\operatorname{curl}\int\limits_V(\varepsilon-1)\mathbf{E}(\mathbf{r}')f(|\mathbf{r}-\mathbf{r}'|)\,d\mathbf{r},\\f(|\mathbf{r}-\mathbf{r}'|)&=\frac{e^{ik|\mathbf{r}-\mathbf{r}'|}}{|\mathbf{r}-\mathbf{r}'|},\end{aligned}\right\}\quad(1)$$

where $k = \omega/c$; ε and μ are the dielectric and magnetic constants of the medium; $\mathbf{E}_0$ and $\mathbf{H}_0$ are the fields in the incident wave; V is the volume of the scattering body.

The first feature of the solution of (1) is that the internal field in the medium is determined directly through the unperturbed field of the incident wave ($\mathbf{r} \in V$). The scattered field is determined through the known internal field by the same relations (1) for ($\mathbf{r} \ni V$).

The second feature is that a formal expression for the desired field in the medium is the sum of the fields of the unperturbed wave and of the waves formed by the integral terms.[3] In the performance of all integrations this term should yield a series of terms including a wave with a propagation constant coinciding with the propagation constant for the unperturbed wave. As a result of the "extinction" of the field of the unperturbed wave, the amplitudes of the fields of the penetrating waves are determined by these terms. In point of fact, this means there is no unperturbed incident wave inside the dielectric wedge. This condition is known formally in electrodynamics as the Oseen–Ewald "extinction principle," the universal nature of which has been demonstrated.[4]

We consider the specific problem of scattering of a plane electromagnetic wave

$$\left.\begin{aligned}\mathbf{E}_0(\mathbf{r})&=\mathbf{E}_0e^{i(k_{20}y+k_{30}z)},\\\mathbf{H}_0(\mathbf{r})&=\mathbf{H}_0e^{i(k_{20}y+k_{30}z)}\end{aligned}\right\}\quad(2)$$

by a rectangular dielectric wedge (y > 0, z > 0) with a permittivity ε (we assume the magnetic permeability is unity). We choose a polarization of the incident wave such that $\mathbf{E} = (E_x, 0, 0)$, and $\mathbf{H} = (0, H_y, H_z)$. We then have from Eq. (1) for $\mathbf{r} \in V$ the following fundamental integral equation for the determination of the internal fields:

$$E_x(\mathbf{r})=E_{0x}(\mathbf{r})+\frac{k^2(\varepsilon-1)}{4\pi}\int\limits_V E_x(\mathbf{r}')\frac{e^{ik|\mathbf{r}-\mathbf{r}'|}}{|\mathbf{r}-\mathbf{r}'|}\,d\mathbf{r},\quad(3)$$

for the magnetic fields

$$\left.\begin{aligned}H_y(\mathbf{r})&=H_{0y}(\mathbf{r})-\frac{ik(\varepsilon-1)}{4\pi}\frac{\partial}{\partial z}\int\limits_V E_x(\mathbf{r}')\frac{e^{ik|\mathbf{r}-\mathbf{r}'|}}{|\mathbf{r}-\mathbf{r}'|}\,d\mathbf{r}',\\H_z(\mathbf{r})&=H_{0z}(\mathbf{r})+\frac{ik(\varepsilon-1)}{4\pi}\frac{\partial}{\partial y}\int\limits_V E_x(\mathbf{r}')\frac{e^{ik|\mathbf{r}-\mathbf{r}'|}}{|\mathbf{r}-\mathbf{r}'|}\,d\mathbf{r}',\end{aligned}\right\}\quad(4)$$

where the region of integration V is one quadrant ($-\infty < x < \infty$, $y > 0$, $z > 0$; Fig. 1).

We seek a solution in the form of a superposition of plane refracted waves and an unknown wave from the edge

$$\begin{Bmatrix}E\\H\end{Bmatrix}=\sum_j\begin{Bmatrix}A_j\\B_j\end{Bmatrix}e^{i(k_{2j}y+k_{3j}z)}+\int\limits_\alpha\frac{e^{ity+isz}}{s}\begin{Bmatrix}f_E(t)\\f_H(t)\end{Bmatrix}dt,\quad(5)$$

where $k_{2j}^2 + k_{3j}^2 = \varepsilon k^2$; $s = \sqrt{\varepsilon k^2 - t^2}$; the contour α is defined below by the conditions of the problem; the subscript "j" determines the number of waves produced in the wedge because of diffraction at its faces. The wave from the edge is sought in the form of a Sommerfeld integral with unknown weight functions $f_{E,H}(t)$. To determine these functions we reduce the integral equation (3) to a well known singular integral equation of the first kind.

Before turning to specific calculations, we note there

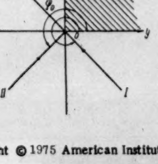

Fig. 1. Schematic diagram of incident ray. Ray I is a plane wave which illuminates one face of the wedge. Ray II is a plane wave which illuminates both faces of the wedge. The angle of incidence is measured from the plane z = 0.

can be one of two possible cases in the arbitrary incidence of a plane wave on the wedge: 1) A plane wave illuminates a single face of the wedge ($\pi/2 \leq \varphi_0 \leq \pi$ or $3\pi/2 \leq \varphi_0 \leq 2\pi$); 2) the plane wave illuminates both faces of the wedge simultaneously ($\pi \leq \varphi_0 \leq 3\pi/2$), where φ_0 is the angle of incidence of the wave measured from the plane $z = 0$. The calculations are somewhat different in these two cases and we discuss them separately.

Substituting Eq. (5) into Eq. (3) and noting that

$$\int_{-\infty}^{\infty} \frac{e^{ik|\mathbf{r}-\mathbf{r}'|}}{|\mathbf{r}-\mathbf{r}'|} dx' = \pi i H_0^{(1)}\left(k\sqrt{(y-y')^2+(z-z')^2}\right)$$
$$= \begin{cases} i \int\limits_{-\infty}^{\infty} \frac{\exp[i(\omega|y-y'|+v|z-z'|)]}{v} d\omega \quad \text{for} \quad \pi \leqslant \varphi_0 \leqslant 2\pi, \\ i \int\limits_{-\infty}^{\infty} \frac{\exp[i(v|y-y'|+\omega|z-z'|)]}{v} d\omega, \text{ for } \frac{\pi}{2} \leqslant \varphi_0 \leqslant \frac{3\pi}{2}, \end{cases} \tag{6}$$

where $v = \sqrt{k^2 - \omega^2}$, Im $v > 0$, we carry out the integration over y' and z'. In doing this we assume that the surrounding space is characterized by certain losses which ensure convergence of the integrals at infinity ($e^{ivy}|_{y \to \infty} \to 0$). In the integration over y' and z' the region of integration for each of the integrals is divided into two areas: $y' < y$ and $y' > y$ (correspondingly, $z' < z$ and $z' > z$) since the exponential in Eq. (6) contains the modulus of the differences of these quantities. As a result of the calculation we have

$$\int_V E(\mathbf{r}') \frac{e^{ik|\mathbf{r}-\mathbf{r}'|}}{|\mathbf{r}-\mathbf{r}'|} d\mathbf{r}' = S_1 + S_2 =$$
$$= i\sum_j A_j \left\{ 2\int_{-\infty}^{\infty} \frac{e^{i(\omega y + k_{3j}z)} d\omega}{(k_{2j}-\omega)(k_{3j}^2+\omega^2-k^2)} - \int_{-\infty}^{\infty} \frac{e^{i(\omega y + vz)} d\omega}{v(k_{3j}-v)(k_{2j}-\omega)} \right\}$$
$$+ i\int_a \frac{f(t)\,dt}{s} \int_{-\infty}^{\infty} d\omega$$
$$\times \left\{ \frac{2e^{i(\omega y + sz)}}{(t-\omega)[k^2(\varepsilon-1)+\omega^2-t^2]} - \frac{e^{i(\omega y + vz)}}{v(t-\omega)[\sqrt{\varepsilon k^2 - t^2} - \sqrt{k^2-\omega^2}]} \right\} \tag{7}$$
$$(\text{for } \pi \leqslant \varphi_0 \leqslant 2\pi).$$

For the subsequent discussion it is convenient to introduce the notation

$$\left.\begin{aligned} k_{2j}y + k_{3j}z &= \sqrt{\varepsilon}\, k\rho(\cos\varphi\cos\psi_j + \sin\varphi\sin\psi_j), \\ \omega y + vz &= k\rho(\cos\varphi\cos\xi + \sin\varphi\sin\xi),\ t = k\sqrt{\varepsilon}\cos\eta, \end{aligned}\right\} \tag{8}$$

where ψ_j is the angle of refraction of the waves; ξ is a new variable of integration; ρ and φ are the running coordinates of the point of observation. In this notation, the integrals S_1 and S_2 take the forms

$$S_1(\rho, \varphi) = -\frac{i}{k^2}\sum_j A_j \left[2\int_{F_1} \frac{\exp[ik\rho(\sqrt{\varepsilon}\sin\varphi_j\sin\psi + \cos\xi\cos\varphi)]\sin\xi\, d\xi}{(\sqrt{\varepsilon}\cos\psi_j - \cos\xi)(\varepsilon\sin^2\psi_j - \sin^2\xi)} \right.$$
$$\left. - \int_{F_2} \frac{\exp[ik\rho\cos(\xi-\varphi)]\, d\xi}{(\sqrt{\varepsilon}\cos\psi_j - \cos\xi)(\sqrt{\varepsilon}\sin\psi_j - \sin\xi)} \right], \tag{9}$$

$$S_2(\rho, \varphi) = 2i\int_{G_0} f(\eta)\, d\eta\, e^{i\sqrt{\varepsilon}\, k\rho\sin\eta\sin\varphi}$$
$$\times \int_{F_1} \frac{\exp[ik\rho\cos\xi\cos\varphi]\, d\xi}{k^2(\sqrt{\varepsilon}\cos\eta - \cos\xi)(\varepsilon\sin^2\eta - \sin^2\xi)}$$
$$- i\int_{G_0} f(\eta)\, d\eta \int_{F_2} \frac{\exp[ik\rho\cos(\xi-\varphi)]\, d\xi}{k^2(\sqrt{\varepsilon}\cos\eta - \cos\xi)(\sqrt{\varepsilon}\sin\eta - \sin\xi)}. \tag{10}$$

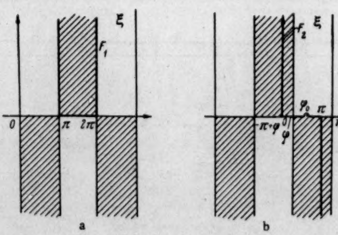

Fig. 2. Integration contours F_1 and F_2 in the plane of the complex variable ξ.

The integration contours F_1 and F_2 are shown in Figs. 2a and 2b. The shaded portions in the plane of the complex variable indicate regions for which Im $\cos\xi > 0$ (2a) and Im $\cos(\xi - \varphi) > 0$ (2b).

Each of the integrals in Eqs. (8) and (9) has singularities. Depending on the value of the angle ψ_j, the poles of the integrand will be located either inside or outside the shaded region. This result is in accordance with the fact that two cases are possible for arbitrary incidence of a plane wave on a dielectric wedge: only one face is illuminated and the first and second integrals in S_1 have the poles $\cos\xi_1 = \sqrt{\varepsilon}\cos\psi$, $\sin\xi_2 = \sqrt{\varepsilon}\sin\psi$ ($3\pi/2 \leq \varphi_0 \leq 2\pi$), or both faces of the wedge are illuminated and the second integral in S_1 has the poles $\cos\xi_{1,2} = \sqrt{\varepsilon}\begin{Bmatrix}\sin\psi_2 \\ \cos\psi_1\end{Bmatrix}$ and the first integral in S_1 has the poles $\cos\xi_1 = \sqrt{\varepsilon}\cos\psi_1$ and $\cos\xi_2 = \sqrt{\varepsilon}\sin\psi_2$. We consider the singularities in S_2 in similar fashion. Using the Cauchy theorem we calculate the corresponding integrals in Eqs. (9) and (10) separately for each of the possibilities. Furthermore, knowing the location of the poles, we deform the integration contour F_1 or F_2 into the contour $G\begin{pmatrix}-\pi/2 + i\infty \\ \pi/2 - i\infty\end{pmatrix}$, as a result of which we obtain the following:

$$S_1^{(1)} = \frac{2\pi A}{k^2}\left[\frac{2\exp[ik\rho\sqrt{\varepsilon}\cos(\varphi-\psi)]}{\varepsilon-1} \right.$$
$$\left. - \frac{\exp[ik(\sqrt{\varepsilon}\, y\cos\psi + \sqrt{1-\varepsilon\cos^2\psi}\, z]}{[\sqrt{\varepsilon}\sin\psi - \sqrt{1-\varepsilon\cos^2\psi}]\sqrt{1-\varepsilon\cos^2\psi}} \right]$$
$$+ i\int_G \frac{A\exp[ik\rho\cos(\varphi-\xi)]\, d\xi}{k^2(\sqrt{\varepsilon}\cos\psi - \cos\xi)(\sqrt{\varepsilon}\sin\psi - \sin\xi)},\quad \frac{3\pi}{2} \leqslant \varphi_0 \leqslant 2\pi, \tag{11}$$

$$S_1^{(2)} = \frac{2\pi}{k^2}\sum_{j=1}^{2} A_j \left[\frac{2\exp[ik\rho\sqrt{\varepsilon}\cos(\varphi-\psi_j)]}{\varepsilon-1} \right.$$
$$- \frac{\exp[ik(\sqrt{\varepsilon}\, y\cos\psi_j + z\sqrt{1-\varepsilon\cos^2\psi_j}]}{[\sqrt{\varepsilon}\sin\psi_j - \sqrt{1-\varepsilon\cos^2\psi_j}]\sqrt{1-\varepsilon\cos^2\psi_j}}$$
$$- \frac{\exp[ik(\sqrt{\varepsilon}\, z\sin\psi_j + y\sqrt{1-\varepsilon\sin^2\psi_j})]}{[\sqrt{\varepsilon}\cos\psi_j - \sqrt{1-\varepsilon\sin^2\psi_j}]\sqrt{1-\varepsilon\sin^2\psi_j}}$$
$$\left. + \frac{i}{2\pi}\int_G \frac{\exp[ik\rho\cos(\varphi-\xi)]\, d\xi}{(\sqrt{\varepsilon}\cos\psi_j - \cos\xi)(\sqrt{\varepsilon}\sin\psi_j - \sin\xi)} \right],\quad \pi \leqslant \varphi_0 \leqslant \frac{3\pi}{2}, \tag{12}$$

$$S_2^{(1,2)} = \frac{4\pi}{k^2(\varepsilon-1)}\int_{G_0} \exp[ik\rho\sqrt{\varepsilon}\cos(\eta-\varphi) f(\eta)\, d\eta\ -$$

$$-\frac{i}{k^2}\int_G \exp[ik\rho\cos(\xi-\varphi)\,d\xi\int_{G_0}\frac{f(\eta)\,d\eta}{(\sqrt{\varepsilon}\cos\eta-\cos\xi)(\sqrt{\varepsilon}\sin\eta-\sin\xi)},\tag{13}$$

where the contour G_0 is defined by the equation for the curve $\arccos(\cos\xi/\sqrt{\varepsilon})$, $\xi \in G$. In the last integral, the order of integration is interchanged in accordance with a corollary to the Poincaré–Bertrand formula.[5]

We consider the structure of the resultant expressions. The first term in $S_1^{(1,2)}$ represents a wave with a propagation constant equal to the propagation constant in the medium. The second term in $S_1^{(1)}$ also represents a plane wave and, in accordance with the extinction principle, this wave must have a propagation constant equal to the propagation constant of the wave in free space. This means that $k\sqrt{\varepsilon}\cos\psi = k\cos\varphi_0$, where φ_0 is the angle of incidence of the wave at the face $z = 0$. Hence

$$\cos\psi=\frac{\cos\varphi_0}{\sqrt{\varepsilon}}.\tag{14}$$

The second and third terms in $S_1^{(2)}$ represent two plane waves produced by the faces $z = 0$ and $y = 0$ respectively. Consequently, it is necessary to set

$$\sqrt{\varepsilon}\sin\psi_2=\sin\varphi_0,\tag{15}$$

for the first wave (from the face $y = 0$), which is the well-known law for wave refraction at the boundary of a dielectric, and to set

$$\sqrt{\varepsilon}\cos\psi_1=\cos\varphi_0.\tag{16}$$

for the second wave (from the face $z = 0$).

These relations do not contradict each other; if φ_0 is the angle of incidence of the wave at the face $y = 0$, this angle, measured from the plane $y = 0$, is $(\pi/2 - \varphi_0)$ at the face $z = 0$ (the relation given also holds for the angle of refraction), and Eq. (15) becomes Eq. (16).

Thus for the chosen polarization of the incident wave, only a single plane wave is propagated in the dielectric wedge and it is sufficient to determine only a single weight function $f(\eta)$ to determine the wave from the edge.

We now substitute the expressions obtained for the integral term (7) into the integral equation (3); in this case, terms with spatial dependence $\exp[ik\rho\sqrt{\varepsilon}\cos(\varphi-\psi)]$ cancel. The remaining exponential terms have the same phase velocity as the incident wave. These terms give zero when added to the field of the incident wave and hence we find the amplitudes of the plane waves in the medium for each of the possible cases are

$$A=\frac{2E_0\sin\varphi_0\cos\psi}{\sin(\varphi_0+\psi)},\quad \sqrt{\varepsilon}\sin\psi=\sqrt{\varepsilon-\cos^2\varphi_0}.\tag{17}$$

It is easy to verify that the resultant expression is a Fresnel equation for the corresponding electrodynamic problem when $3\pi/2 \le \varphi_0 \le 2\pi$,

$$A_1=\frac{2E_0\sin\varphi_0}{\sqrt{\varepsilon}\sin\psi_1+\sin\varphi_0}\tag{18}$$

$$\sqrt{\varepsilon}\cos\psi_2=\sqrt{\varepsilon-\sin^2\varphi_0},\quad \sqrt{\varepsilon}\sin\psi_1=\sqrt{\varepsilon-\cos^2\varphi_0},$$
$$A_2(\varphi_0)=A_1\left(\frac{\pi}{2}-\varphi_0\right)$$
$$\text{for}\quad \pi\leqslant\varphi_0\leqslant\frac{3\pi}{2},$$

where E_0 is the amplitude of the incident wave and φ_0 is the angle of incidence at the face $z = 0$. If the angle of incidence is such that $\pi/2 \le \varphi_0 \le \pi$, we find the corresponding expression for A from Eq. (17) by replacing φ_0 with $\pi/2 - \varphi_0$.

The remaining terms of the equation, which vary as $\int_G \exp[ik\rho\cos(\xi-\varphi)]L(\xi)d\xi$, form an equation which contains the desired function $f(\eta)$,

$$\int_G e^{ik\rho\cos(\xi-\varphi)}d\xi\left\{\frac{A}{(\sqrt{\varepsilon}\cos\psi-\cos\xi)(\sqrt{\varepsilon}\sin\psi-\sin\xi)}\right.$$
$$\left.-\int_{G_0}\frac{f(\eta)\,d\eta}{(\sqrt{\varepsilon}\cos\eta-\cos\xi)(\sqrt{\varepsilon}\sin\eta-\sin\xi)}\right\}=0.$$

This equation is clearly satisfied if

$$\frac{A}{(\sqrt{\varepsilon}\cos\psi-\cos\xi)(\sqrt{\varepsilon}\sin\psi-\sin\xi)}$$
$$=\int_{G_0}\frac{f(\eta)\,d\eta}{(\sqrt{\varepsilon}\cos\eta-\cos\xi)(\sqrt{\varepsilon}\sin\eta-\sin\xi)}.\tag{19}$$

Equation (19) is also the desired singular integral equation of the first kind for the function $f(\eta)$. Construction of a solution for this equation reduces to a Riemann boundary-value problem.[6]

We consider the generalized curvilinear Cauchy integral

$$U(z)=\frac{1}{2\pi i}\int_{G_0}\frac{f(\eta)\,d\eta}{Q(\eta,\ z)}.\tag{20}$$

The value of this integral depends significantly on the behavior of the function $Q(\eta, z)$. On some contour Γ in the plane of the complex variant η let

$$Q(\eta,\ z)=0,\ \text{but}\ Q'_\eta\neq 0,\ Q'_z\neq 0,\tag{21}$$

i.e., $z = \varphi(\eta)$ on this contour. Since η takes on all values in the integration over the contour G_0, we indicate its values on the contour Γ by $t = \varphi^{-1}(z)$. We indicate the region lying within Γ by D^+ and the region complementary to $D^+ + \Gamma$, including the point at infinity $z \to \infty$, by D^-. We divide the function $U(z)$ into a sum of functions analytic in D^+ (the function U^+) and in the region D^- (the function U^-). The generalized integral (20) is then given by

$$U^\pm(z)=\pm\frac{1}{2}\frac{f(z)}{Q'_t(t,\ z)}+\frac{1}{2\pi i}\int\frac{f(\eta)\,d\eta}{Q(\eta,\ z)},\tag{22}$$

which is similar to the Sokhotskii formula for a Cauchy integral; the solution of the integral equation (19) then reduces to the following Riemann boundary-value problem. It is required to find two functions U^+ and U^- which are respectively analytic in the regions D^+ and D^- and which satisfy the condition

$$U^+(z)=-U^-(z)+g(z),\tag{23}$$

on the contour Γ, where

$$g(z)=\frac{A}{(\sqrt{\varepsilon}\cos\psi-\cos z)(\sqrt{\varepsilon}\sin\psi-\sin z)}.$$

Then,

$$f(z)=Q'_t(t,\ z)[U^+(z)-U^-(z)].\tag{24}$$

In our case, the index of the integral equation is zero and therefore $U^+(z) = g^+(z)$ and $U^-(z) = g^-(z)$, which simplifies the problem considerably.

Since the function g(z) has isolated singularities in the form of simple poles in the plane of the complex variable z its partition into regular functions is easily performed. The value of the angle ψ is such that both poles of the function g(z) belong to the region D^-. Then

$$g^+(z) = 0, \tag{25}$$

$$g^-(z) = -g(z). \tag{26}$$

Calculating the quantity $Q'_t(t, z)$ on the contour Γ we have

$$f_1(\eta) = \frac{A\left(\varepsilon \sin\eta - \sqrt{1 - \varepsilon\cos^2\eta}\right)\varepsilon \sin\eta}{2\pi i\left(\cos\varphi_0 - \sqrt{\varepsilon}\cos\eta\right)\left(\sqrt{\varepsilon - \cos^2\varphi_0} - \sqrt{1 - \varepsilon\cos^2\eta}\right.} \tag{27}$$

in the first case if $3\pi/2 \le \varphi_0 \le 2\pi$, and

$$f_2(\eta) = \frac{1}{2\pi i}\left\{\frac{A_1\left(\varepsilon\cos\eta - \sqrt{1 - \varepsilon\sin^2\eta}\right)\varepsilon\cos\eta}{\left(\sin\varphi_0 - \sqrt{\varepsilon}\sin\eta\right)\left(\sqrt{\varepsilon - \sin^2\varphi_0} - \sqrt{1 - \varepsilon\sin^2\eta}\right)}\right.$$
$$+ \frac{A_2\left(\varepsilon\sin\eta - \sqrt{1 - \varepsilon\cos^2\eta}\right)\varepsilon\sin\eta}{\left(\cos\varphi_0 - \sqrt{\varepsilon}\cos\eta\right)\left(\sqrt{\varepsilon - \cos^2\varphi_0} - \sqrt{1 - \varepsilon\cos^2\eta}\right)} \tag{28}$$

in the second if $\pi \le \varphi_0 \le 3\pi/2$.

Thus one can represent the internal field in the dielectric wedge by the following expressions:

$$E_x(\mathbf{r}) = \frac{2E_{x0}\sin\varphi_0\cos\psi}{\sin(\varphi_0 + \psi)}\exp\left[ik\rho\left(\cos\varphi\cos\varphi_0 + \sin\varphi\sqrt{\varepsilon - \cos^2\varphi_0}\right)\right]$$
$$+ \int\limits_{G_0}\exp\left[ik\rho\sqrt{\varepsilon}\cos(\eta - \varphi)\right]f_1(\eta)\,d\eta, \quad \sqrt{\varepsilon}\cos\psi = \cos\varphi_0 \tag{29}$$

in the first case if $3\pi/2 \le \varphi_0 \le 2\pi$, and

$$E_x(\mathbf{r}) = A_1\exp\left[ik\rho\left(\sin\varphi_0\sin\varphi + \cos\varphi\sqrt{\varepsilon - \sin^2\varphi_0}\right)\right]$$
$$+ A_2\exp\left[ik\rho\left(\cos\varphi_0\cos\varphi + \sin\varphi\sqrt{\varepsilon - \cos^2\varphi_0}\right)\right]$$
$$+ \int\limits_{G_0} f_2(\eta)\exp\left[ik\rho\sqrt{\varepsilon}\cos(\eta - \varphi)\right]d\eta \quad \text{for} \quad \pi \leqslant \varphi_0 \leqslant \frac{3\pi}{2}. \tag{30}$$

The remaining components of the field, H_y and H_z, are found from the known E_x through Eq. (4).

One can now set up the scattered field from the known internal fields. The same relations (3) are used but points **r** are considered which are outside the boundaries of the dielectric wedge (**r** $\ni$ V) and the previously obtained expressions (29) and (30) for the internal fields are used in the integrals.

We consider the case where only the single face z = 0 is illuminated. Using the following representation for the Green's function:

$$H_0'\left(k\sqrt{d^2 + z^2}\right) = \frac{i}{\pi}\int\limits_{-\infty}^{\infty}\frac{\exp(ivd + i\omega z)}{v}\,d\omega \tag{31}$$

($v = \sqrt{k^2 - \omega^2}$, Im v > 0, d > 0), we investigate the scattered field in the three quadrants in accordance with the rules for integration of functions containing the modulus of the difference of two quantities. To determine the scattered field in the second quadrant $\pi < \varphi < \pi/2$, it is necessary to divide the region of integration over y' into two (y < y' and y > y'); in the third quadrant $\pi < \varphi < 3\pi/2$, y' < y and z' < z always; in the fourth quadrant $3\pi/2 < \varphi < 2$, it is necessary to divide the region of integration over z' into two (z' < z and z' > z).

As a result of the calculations, we have the three types of expressions

$$\text{a)}\ i\left\{\int\limits_{-\infty}^{\infty}\frac{2e^{ik_3 z - i\omega y}}{(k_3^2 - v^2)(k_{20} + \omega)} - \int\limits_{-\infty}^{\infty}\frac{e^{ivz - i\omega y}}{v(k_3 - v)(k_{20} + \omega)}\right.$$
$$- \int\limits_{G_0} f(\eta)\,d\eta\int\limits_{-\infty}^{\infty}\left[\frac{2e^{ik\sqrt{\varepsilon}\sin\eta z - i\omega y}}{(k^2\varepsilon\sin^2\eta - v^2)(k\sqrt{\varepsilon}\cos\eta + \omega)}\right.$$
$$\left.\left. - \frac{e^{ivz - i\omega y}}{v(k\sqrt{\varepsilon}\sin\eta - v)(k\sqrt{\varepsilon}\cos\eta + \omega)}\right]d\omega\right\}, \quad \frac{\pi}{2} \leqslant \varphi \leqslant \pi, \tag{32}$$

$$\text{b)}\ -i\left[\int\limits_{-\infty}^{\infty}\frac{e^{-i\omega y - ivz}d\omega}{v(k_3 + v)(k_{20} + \omega)}\right.$$
$$\left. - \int\limits_{G_0} f(\eta)\,d\eta\int\limits_{-\infty}^{\infty}\frac{e^{-i\omega y - ivz}d\omega}{v(k\sqrt{\varepsilon}\sin\eta + v)(k\sqrt{\varepsilon}\cos\eta + \omega)}\right], \quad \pi < \varphi < \frac{3\pi}{2}, \tag{33}$$

$$\text{c)}\ -i\left[\int\limits_{-\infty}^{\infty}\frac{e^{i\omega y - ivz}d\omega}{v(k_3 + v)(k_{20} - \omega)}\right.$$
$$\left. - \int\limits_{G_0} f(\eta)\,d\eta\int\limits_{-\infty}^{\infty}\frac{e^{i\omega y - ivz}d\omega}{v(k\sqrt{\varepsilon}\sin\eta + v)(k\sqrt{\varepsilon}\cos\eta - \omega)}\right], \quad \frac{3\pi}{2} < \varphi < 2\pi. \tag{34}$$

We carry out a detailed calculation for the third case only since the other calculations are similar. We make the change of variables

$$\omega = k\cos\xi, \quad v = k\sin\xi. \tag{35}$$

Then

$$I_3 = \frac{i}{k^2}\left[\int\limits_{F_2}\frac{e^{ik\rho\cos(\xi - \varphi')}d\xi}{\left(\sqrt{\varepsilon - \cos^2\varphi_0} + \sin\xi\right)(\cos\varphi_0 - \cos\xi)}\right.$$
$$\left. - \int\limits_{G_0} f(\eta)\,d\eta\int\limits_{F_2}\frac{e^{ik\rho\cos(\xi - \varphi')}d\xi}{\left(\sqrt{\varepsilon}\sin\eta + \sin\xi\right)\left(\sqrt{\varepsilon}\cos\eta + \cos\xi\right)}\right], \tag{36}$$

where φ' varies within the limits $(0, \pi/2)$ and $3\pi/2 < \varphi_0 < \pi$. The contour G_0 is the defined by the equation $\eta = \arccos(\cos\xi/\sqrt{\varepsilon})$, $\xi \in G$. The integration contour F_2 and the location of the singularities of the integrand in I_3 are shown in Fig. 2b.

Since $\varphi' < \varphi_0$, a reflected wave exists for all values of the angle φ_0. We deform the contour F_2 into the contour $G\begin{pmatrix}-\pi/2 + j\infty \\ \pi/2 - j\infty\end{pmatrix}$ and calculate the first integral in I_3 by means of the theorem of residues

$$\frac{2\pi e^{ik\rho\cos(\varphi + \varphi_0)}}{k^2\sin\varphi_0\left(\sqrt{\varepsilon - \cos^2\varphi_0} + \sin\varphi_0\right)}$$
$$+ \frac{i}{k^2}\int\limits_{G}\frac{e^{ik\rho\cos(\xi - \varphi')}d\xi}{\left(\sqrt{\varepsilon - \cos^2\varphi_0} + \sin\xi\right)(\cos\varphi_0 - \cos\xi)}. \tag{37}$$

In the second integral, we pick out the pole $\sin\xi_1 = -\sqrt{\varepsilon}\sin\eta$ (with subsequent deformation of the contour F_2 into G), which determines the wave from the edge in free space. The remaining integrals are brought to the form

$$i\int\limits_{G}\frac{e^{ik\rho\cos(\xi-\varphi)}d\xi}{k^2}\left[\frac{A_1}{\sqrt{\varepsilon}\,\sin\psi+\sin\xi)(\cos\varphi_0-\cos\xi)}\right.$$
$$\left.-\int\limits_{G_0}\frac{f(\eta)\,d\eta}{(\sqrt{\varepsilon}\,\cos\eta-\cos\xi)(\sqrt{\varepsilon}\,\sin\eta+\sin\xi)}\right], \qquad (38)$$

and since the function $f(\eta)$ satisfies the singular integral equation (19), this expression is identically zero.

Thus the scattered field in the region $3\pi/2 < \varphi < 2\pi$ is the superposition of a plane wave and the known boundary wave from the edge.

Finally, we have the following expressions for the field scattered from a dielectric wedge:

$$E_{\text{scat}}=E_{0z}$$
$$\times\begin{cases} e^{ik\rho\cos(\varphi-\varphi_0)}-\dfrac{(\varepsilon-1)\,e^{ik\rho\cos(\varphi+\varphi_0)}}{(\sqrt{\varepsilon-\cos^2\varphi_0}+\sin\varphi_0)^2}+P(\varphi,\varphi_0), & 3\pi-\varphi_0\leqslant\varphi\leqslant 2\pi,\\ e^{ik\rho\cos(\varphi-\varphi_0)}+P(\varphi,\varphi_0), & -\pi+\varphi_0\leqslant\varphi\leqslant 3\pi-\varphi_0,\\ P(\varphi,\varphi_0), & \dfrac{\pi}{2}\leqslant\varphi\leqslant\varphi_0-\pi, \end{cases} \qquad (39)$$

where

$$P(\varphi,\varphi_0)=-2\pi\int\limits_{G_1}\frac{f_1(\arcsin(\sqrt{\varepsilon}\sin t))\,e^{-ik\rho\cos(\varphi+t)}dt}{k^2(\cos t+\sqrt{\varepsilon-\sin^2 t})\sqrt{\varepsilon-\sin^2 t}}, \qquad (40)$$

the integration contour G_1 is defined by the equation for the curve $t = \arcsin(\sqrt{\varepsilon}\sin\eta)$, $\eta \in G_0$; the function $f_1(t)$ is given by Eq. (27).

We have not derived the expressions for the scattered field in the case of illumination of both faces of the wedge; these can be obtained by means of similar calculations.

Thus, using the integral equation makes it possible to obtain a complete solution for the diffraction of a plane electromagnetic wave by a dielectric wedge with the expression for the boundary wave from the edge of the wedge in the form of a definite integral. The value of this integral can be found for specific values of the wedge permittivity, particularly by numerical methods. In the general case, the integral which determines the boundary wave is not expressed through known functions but its value when $k\rho\sqrt{\varepsilon} \gg 1$ can be obtained either by the method of steepest descent or by the method presented in ref. 7.

We consider the integral

$$\int\limits_{G_0} e^{ik\rho\sqrt{\varepsilon}\cos(\eta-\varphi)}f(\eta)\,d\eta. \qquad (41)$$

By using the short-wave asymptotic expansion previously obtained,[7] we have

$$\frac{\exp\left[i\left(k\rho\sqrt{\varepsilon}+\frac{\pi}{4}\right)\right]\Gamma\left(\frac{1}{2}\right)}{(2k\rho\sqrt{\varepsilon})^{1/2}}f(\varphi)+O\left(\frac{1}{(k\rho\sqrt{\varepsilon})^{1/2}}\right), \qquad (42)$$

i.e., the boundary wave for $k\rho\sqrt{\varepsilon} \gg 1$ is described by a cylinder function.

---

[1] F. Frank and R. von Mises, Differential and Integral Equations of Mathematical Physics [Russian translation], Ch. XX, ONTI (1937).

[2] G. D. Malyuzhinets and A. A. Tuzhilin, Dokl. Akad. Nauk SSSR, 146, 1039 (1962) [Sov. Phys. – Dokl., 7, 879 (1963)].

[3] N. A. Khizhnyak, Zh. Tekh. Fiz., 28, 1592 (1958) [Sov. Phys. – Tech. Phys., 3, 1466 (1959)].

[4] N. A. Khizhnyak, Rept. 94, Proc. Radiophysics Faculty, Khar'kov State Univ., 2, 5 (1957).

[5] N. I. Muskhelishvili, Singular Integral Equations [in Russian], Izd. Nauka, Moscow (1968).

[6] F. D. Gakhov, Boundary-Value Problems [in Russian], Fizmatgiz, Moscow (1963).

[7] A. A. Tuzhilin, ZhVM i MF, 9, 1024 (1969).

Propagation of shock waves in inhomogeneous media

R. A. Glatman

Gipronikel' Design and Research Institute, Leningrad

(Submitted December 10, 1973; resubmitted March 29, 1974)
Zh. Tekh. Fiz., 44, 2250-2254 (November 1974)

A new model is proposed for an approximate solution of the problem of shock-wave propagation in an inhomogeneous medium which makes it possible to interpret the method developed by Whitham physically and to establish its region of applicability. General conditions are given for which use of the Whitham method gives good results. Particular cases of shock-wave motion in media with stationary inhomogeneities are studied in hydrodynamics and magnetohydrodynamics; the propagation of weak shock waves is analyzed.

An exact solution for the problem of shock-wave propagation in an inhomogeneous medium is only available for the few particular cases in which the process is self-similar;[1] therefore the investigation of the various aspects of this problem usually rests on the approximate methods developed by Chisnell[2] and Whitham.[3] Chisnell considered motion of a shock wave in a medium with a pressure p_0 = const and a variable density ρ_0 for hydrodynamics; he replaced the continuous density distribution by a stepped distribution and investigated the behavior of refraction and reflection of shock waves passing through a sequence of thin layers of different densities. Whitham, pointing out the limited group of problems to which this method is applicable (with $p_0 \neq$ const the physical picture of the process[2] becomes unclear because the layer can not be in equilibrium), proposed another method in which simplicity is combined with near universality; in particular, this new method has been used by Whitham in both hydrodynamics and in magnetohydrodynamics. To determine the velocity D of the shock wave in this method, the supplementary condition

$$dp + \rho c dv = 0, \tag{1}$$

is used behind the shock front, where v is the gas velocity and c is the velocity of sound; this condition expresses the conservability of the Riemann invariant along the characteristic C_+. In this approach, however, there is no a priori physical interpretation whatever of the prescribed assumption (1) and, as pointed out by the author himself,[3] it is unclear to what extent the unexpected accuracy of the results in certain cases must be attributed to chance.

In the present paper, a special mode of the process is proposed on the basis of which the possibility of using Eq. (1) is justified; this model has a clear physical significance and makes it possible to determine in which cases the use of the Whitham method for solving the problem of shock-wave propagation in inhomogeneous media yields good results. We also present calculated results for limiting cases of weak shock waves in hydrodynamics and in magnetohydrodynamics (the magnetic field is perpendicular to the direction of wave propagation) for a stationary state of an unperturbed gas where one can count on good agreement of approximate data with the true values. In addition to a detailed analysis of these cases, relations are also obtained for the determination of the velocity of a shock wave of arbitrary intensity in a medium with a transverse magnetic field and stationary distribution of parameters.

During the motion of the shock front the values of the parameters q_i change; the magnitudes of these changes at the leading edge of the shock front during a small time interval δt can be written in the form

$$\delta q_{0i} = \left(\frac{dq_{0i}}{dt}\right)_{x=X(t)+0} \delta t = \left(\frac{\partial q_{0i}}{\partial t} + D\frac{\partial q_{0i}}{\partial x}\right)_{x=X(t)+0} \delta t, \tag{2}$$

where X(t) is the coordinate of the shock front in the laboratory system, with the x axis being in the direction of shock-wave motion. The actual picture of the process will be replaced by the following scheme: Starting at the time $t = t^*$, let a shock wave be propagated in a homogeneous medium with the parameters $q_{0i}(X(t^*), t^*)$ at a velocity $D = (dX/dt)_{t=t^*}$; at time $t^* + \delta t$, there is incident on the shock front a set of small perturbations (acoustic and entropy waves in ordinary hydrodynamics, fast and slow magnetoacoustic, Alfvén, and entropy waves in magnetohydrodynamics) which bring about parameter perturbations δq_{0i}. This gives rise to a perturbation δD in the velocity of the shock front. By letting the value of the interval δt go to zero one can approximate the true picture of the continuous variation of the parameters ahead of the shock front. Thus, a given inhomogeneity of a medium is specifically simulated by means of sets of small perturbations transmitted sufficiently often to the shock front (the means for this "transmission" plays no part).

If the perturbations arriving at the shock front are assigned specifically to reproduce a set of parameter variations δq_{0i}, the number and direction of the outgoing small perturbations for the evolving shock waves are rigorously determined. This makes it possible to use additional relations between the magnitudes of the parameter variations behind the shock front. For example, in hydrodynamics an acoustic wave and an entropy wave will be propagated behind the shock front; consequently one can write an additional relation between the velocity variation δv and the pressure variation δp behind the shock front: $\delta v = -\delta p/\rho c$ (the acoustic wave is propagated in a direction opposite to that of the x axis). This condition also leads to Eq. (1). Since the subsequent solution reduces to variation of the relations at the discontinuity (as done previously[4]) and the determination of the quantity δD from the resultant system, the quantitative aspect of this method is not different, in principle, from the method previously proposed.[3] One should also note that the representation of the parameters in the unperturbed gas in the form of piecewise constant functions used here is similar to what has been done before,[2] but now it plays a more formal role and does not limit the region of applicability of the method so significantly.

The basic limitations of this formulation of the problem are associated with the fact the parameter variations given by Eq. (2) must, in fact, not be propagated with velocities $v_0 + c_{0j}$ ($c_{0j} \gtrless 0$ is the velocity of the small perturbations transmitted to the shock front with the direction of propagation taken into account) but must be stationary with respect to the coordinate system. However, when the inequality

$$D \gg |v_0 + c_{0j}|, \tag{3}$$

is satisfied for all c_{0j}, the indicated deficiency in the formulation should not have a significant effect since the artificially created conditions under which the shock wave is propagated will approximate the true conditions. Thus, the use of this method yields results which are more accurate, the more significantly the velocity of the shock wave exceeds the velocity of each of the small perturbations in the set required to reproduce the necessary parameter variations in the gas ahead of the shock front.

The results obtained with this method for several specific problems are given below. The limiting case of a weak shock wave in hydrodynamics is not considered in refs. 2 and 3. Nevertheless, the Whitham method can give good results over the entire range of shock wave intensities for the case mentioned where $v_0 = 0$, $p_0 = \text{const}$, and ρ_0 is an arbitrary function of x since the density perturbation is only transmitted by the entropy wave and $v_0 + c_e = 0$. An expression for the velocity of a weak shock wave ($v_0 = 0$, $p_0 = \text{const}$) can be obtained in explicit form if D is represented as

$$D(t) = (c_0)_{x=X(t)}[1 + \zeta(t)], \quad \zeta \ll 1$$

[$c_0 = \sqrt{\gamma p_0/\rho_0(x)}$, γ is the ratio of the heat capacities] and X(t) is then used as the independent variable. We then have

$$\zeta = \tilde{\zeta}\left[\frac{\rho_0(X)}{\tilde{\rho}_0}\right]^{1/4}, \tag{4}$$

$$D - c_0 \sim \left[\frac{\rho_0(X)}{\tilde{\rho}_0}\right]^{-1/4}, \tag{5}$$

where $\tilde{\zeta}$ and $\tilde{\rho}_0$ are values of the corresponding quantities at t = 0, X = X(0). One should note that the exponent in Eqs. (4) and (5) does not depend on γ in contrast to the strong shock wave case already investigated.[3]

The analogous case of a stationary inhomogeneity can also be considered in magnetohydrodynamics, where the total pressure in the unperturbed gas

$$p_0 + \frac{H_0^2}{8\pi} = A = \text{const}, \tag{6}$$

is conserved in a medium with a transverse magnetic field H ($H = H_y$) and $v_0 = 0$. Arbitrary perturbations of density and also perturbations in pressure and magnetic field, which are related through Eq. (6), correspond to a stationary hybrid wave relative to the gas[5] which is a combination of an entropy wave and a degenerate (for $H_x = 0$) slow magnetoacoustic wave. In such a hybrid wave

$$\delta v_x = 0; \quad \delta H = -\frac{4\pi}{H}\delta p; \quad \delta w = \frac{\gamma}{\rho(\gamma-1)}\left(\delta p - \frac{p}{\rho}\delta\rho\right)$$

(w is enthalpy), and δp, $\delta\rho$, and δv_y are arbitrary functions of x. A fast magnetoacoustic wave and a hybrid wave will be propagated behind the shock front. Finally, the velocity of a shock wave of arbitrary intensity can be found from the equation,

$$\frac{dD}{dX} = \frac{D}{\eta}\,\frac{D\left(\frac{c_+}{\gamma-1} - \frac{1}{2}D\frac{\eta-1}{\eta}\right)\frac{d\rho_0(X)}{dX} + \frac{2-\gamma}{\gamma-1}\eta\frac{dp_0(X)}{dX}}{\frac{1}{2}\rho_0 D^2\frac{\eta-1}{\eta^2} - \frac{1}{\gamma-1}\rho_0 D\frac{1}{\eta}(c_+ + D) - \frac{2-\gamma}{\gamma-1}\frac{H_0^2}{8\pi}(\eta-1)}, \tag{7}$$

where

$$c_+ = \left\{c_{0+}^2 + (\eta-1)\left[\frac{\gamma-1}{2}D^2\frac{1}{\eta^2}(\eta+1) + (2-\gamma)\frac{H_0^2}{4\pi\rho_0}\right]\right\}^{1/2}.$$

The quantity $\eta = \rho/\rho_0$ is determined from the condition

$$\frac{2-\gamma}{\gamma-1}\frac{H_0^2}{8\pi\rho_0}\eta^2 + \eta\left(\frac{\gamma}{\gamma-1}\frac{p_0}{\rho_0} + \frac{\gamma}{\gamma-1}\frac{H_0^2}{8\pi\rho_0} + \frac{1}{2}D^2\right) - \frac{\gamma+1}{2(\gamma-1)}D^2 = 0. \tag{8}$$

Here, $c_{0+} = \sqrt{c_0^2 + H_0^2/(4\pi\rho_0)}$ is the velocity of the fast magnetoacoustic wave in the unperturbed gas. For a strong shock wave and $p/p_0 \gg H_0^2/8\pi p_0$, the result remains the the same as in ordinary hydrodynamics;[3] as follows from the inequality (3), this result possesses great universality and is not only applicable to a medium with stationary nonuniformity. A simpler relationship can also be obtained for a weak shock wave when the velocity D is represented in the form

$$D(X) = c_{0+}(X)[1 + \xi(X)], \quad \xi \ll 1.$$

In this case,

$$\eta = 1 + \frac{2c_{0+}^2}{\frac{\gamma+1}{2}c_0^2 + \frac{3H_0^2}{8\pi\rho_0}}\xi,$$

$$\xi = \tilde{\xi}\left[\frac{\rho_0(X)}{\tilde{\rho}_0}\right]^{1/4}\frac{\frac{6A}{(2-\gamma)(\gamma+3)} - p_0(X)}{\frac{6A}{(2-\gamma)(\gamma+3)} - \tilde{p}_0}\left[\frac{\frac{2A}{2-\gamma} - p_0(X)}{\frac{2A}{2-\gamma} - \tilde{p}_0}\right]^{-7/4}, \tag{9}$$

$$D - c_{0+} \sim [\rho_0(X)]^{-1/4}\left[\frac{6A}{(2-\gamma)(\gamma+3)} - p_0(X)\right]\left[\frac{2A}{2-\gamma} - p_0(X)\right]^{-5/4}, \quad \gamma < 2 \tag{10}$$

($\tilde{\xi}$, $\tilde{\rho}_0$, and $\tilde{p}_0$, as before, are initial values of the corresponding quantities). Equations (9) and (10) are valid for $\gamma < 2$; for $\gamma = 2$, the same relation is obtained as in the absence of a magnetic field [this is completely reasonable since the expressions in ordinary hydrodynamics and magnetohydrodynamics agree for a transverse magnetic field and $\gamma = 2$ except for the replacement of p by $p + H_0^2/8\pi$ (ref. 6)].

It is easy to verify that $(\partial/\partial p_0)(D - c_{0+}) < 0$ always, i.e., with an increase in the fraction of the hydrodynamic pressure p_0 in a constant total pressure A, the difference $D - c_{0+}$ decreases as does the quantity c_{0+} itself $[\partial c_{0+}/\partial p_0 \sim -(2A/(2-\gamma) - p_0)^{1/2} < 0]$. The nature of the dependence of $D - c_{0+}$ on $\rho_0(X)$ remains the same as with no magnetic field. When derivatives $\rho_0' = d\rho_0/dX$ and $p_0' = dp_0/dX$ have opposite signs, there are special regions of parameter values where the propagation of the magnetoacoustic and shock waves is different. The conditions $d(D - c_{0+})/dX < 0$ and $dc_{0+}/dX < 0$ are respectively satisfied when

$$p_0' + K_1\rho_0' > 0 \quad \text{и} \quad p_0' + K_2\rho_0' > 0,$$

where

$$K_1 = \frac{\left[\frac{6A}{(2-\gamma)(\gamma+3)} - p_0\right]\left(\frac{2A}{2-\gamma} - p_0\right)}{\rho_0\left[p_0 + \frac{2A(4\gamma-3)}{(2-\gamma)(\gamma+3)}\right]}; \quad K_2 = \frac{\frac{2A}{2-\gamma} - p_0}{\rho_0}.$$

Therefore, we have the following two possibilities.

1) $K_1 < K_2$. This corresponds to the inequality

$$\frac{p_0}{A} > \frac{2(3-2\gamma)}{(2-\gamma)(\gamma+3)}, \tag{11}$$

which is always satisfied when $\gamma > 3/2$ or when $p_0 > A/2$ (if $1 < \gamma < 2$). In this case, the magnetoacoustic wave loses velocity more rapidly than a weak shock wave in the region $K_1 < |p'_0/\rho'_0| < K_2$ when $\rho'_0 > 0$ and $p'_0 < 0$. Thus the weak shock wave will not be damped although its velocity also decreases. If $\rho'_0 < 0$ and $p'_0 > 0$, the shock wave is accelerated more weakly in this region than the fast magnetoacoustic wave and consequently is damped.

2) $K_1 > K_2$. This condition occurs when the inequality which is the reverse of (11) is satisfied, i.e., when $\gamma < 3/2$ and when the p_0 fraction of the total pressure A is sufficiently small. The region of permissible ratios between p_0 and A is more extensive for smaller γ and the inequality takes the form $p_0 < A/2$ when $\gamma = 1$. Then both waves are accelerated in the region $K_2 < |p'_0/\rho'_0| < K_1$ when $\rho'_0 > 0$ and $p'_0 < 0$, but the difference $D - c_{0+}$ decreases; deceleration of both waves occurs when $\rho'_0 < D$ and $p'_0 > 0$ but $D - c_{0+}$ increases.

For a strong magnetic field $H_0^2/(8\pi) \gg p_0$, the relation (10) takes the form

$$D - c_{0+} \sim \rho_0^{-1/4} H_0^{-1/2},$$

and in the opposite case of a weak field

$$D - c_{0+} \sim \rho_0^{-1/4} p_0^{-1/4}.$$

It is impossible to compare the results obtained directly with known accurate solutions for certain particular cases of inhomogeneity because such solutions were based on relations which were only satisfied for a strong shock wave.[1] Therefore a comparison of results obtained by the Whitham method with precise results is only possible for the case of a strong shock wave; the agreement is good in many cases[7] as also follows from the general conditions established on the basis of the physical model of the process proposed here.

Finally, if the inhomogeneity of the medium is merely a result of small oscillations of the magnetic field intensity about the x, y plane, i.e., $H_{z0} = H_{z0}(x, t)$, $H_{z0}^2 \ll H_0^2$ (H_{x0}, H_{y0}, p_0, and $\rho_0 = \text{const}$, $v_{x0} = v_{y0} = 0$), which produces oscillations of the z component of the velocity in accordance with the relation $v_{z0} = H_{z0}/\sqrt{4\pi\rho_0}$, the corresponding set of small perturbations will consist only of Alfvén waves. Since the interaction of a shock wave with an Alfvén wave does not lead to perturbation of the shock-front velocity,[6] oscillations of H_{z0} do not create variation in the propagation velocity of a shock wave for $D \gg c_{0A} = H_{x0}/\sqrt{4\pi\rho_0}$.

---

[1] Ya. B. Zel'dovich and Yu. P. Raizer, Physics of Shock Waves and High-Temperature Hydrodynamic Phenomena [in Russian], Fizmatgiz, Moscow (1963).

[2] R. F. Chisnell, Proc. R. Soc. A, 232, 350 (1955).

[3] G. B. Whitham, J. Fluid, Mech., 4, 337 (1958).

[4] L. D. Landau and E. M. Lifshitz, Mechanics of Continuous Media [in Russian], GITTL, Moscow (1953).

[5] R. A. Glatman, Zh. Tekh. Fiz., 43, 2115 (1973) [Sov. Phys. – Tech. Phys., 18, 1329 (1974)].

[6] A. G. Kulikovskii and G. A. Lyubimov, Magnetohydrodynamics [in Russian], Fizmatgiz, Moscow (1962).

[7] A. Sakurai, Commun. Pure and Appl. Math., 13, 353 (1960).

Ponderomotive forces on a rotating conducting sphere in a time-varying inhomogeneous magnetic field

R. V. Lin'kov and Yu. M. Urman

Scientific Research Institute for Applied Mathematics and Cybernetics, Gor'kii

(Submitted September 11, 1973)

Zh. Tekh. Fiz., 44, 2255-2264 (November 1974)

The forces and torques arising from the rotation of a conducting sphere in a time-varying, inhomogeneous magnetic field are calculated. The angular and frequency dependences of these forces and torques are investigated. It is shown that the signs of the components of the torques and force can change in a time-varying field; that in particular an accelerating torque can be produced. The effect of the magnetic permeability on the forces and torques is analyzed.

The development of instruments employing the contactless suspension of a rotor in a magnetic field has produced great interest in the ponderomotive interaction between the rotor and the supporting field.

The present authors have considered the forces and torques which arise when a conducting magnetic sphere rotates in a constant inhomogeneous magnetic field.[1] It is of interest to treat the analogous problem for a time-varying field.

The rotation of a conductor in a time-varying field leads to a series of new effects; one of these, the possibility of an accelerating torque, has already been pointed out in ref. 2. However, the torques were only found for a conducting nonmagnetic sphere in a homogeneous field and the frequency dependence was studied only for a decelerating torque.

In this paper we consider the rotation of a conducting magnetic ($\mu \neq 1$) sphere in an inhomogeneous field so that both torques and forces can be determined. For certain values of the parameters the frequency characteristics of the torques and forces change sign; under certain conditions the supporting force can, in fact, undergo two changes of sign.

The results obtained here can be considered as a generalization of earlier work[1-6] on the ponderomotive interaction between a conducting sphere and a magnetic field.

DETERMINATION OF THE MAGNETIC FIELD OUTSIDE AND INSIDE THE ROTATING SPHERE AND CALCULATION OF THE FORCES AND TORQUES

Suppose that a sphere of radius R with conductivity σ and magnetic permeability μ rotates in an external inhomogeneous magnetic field which varies periodically at frequency Ω. We assume that the external field has axial symmetry, that the center of the sphere lies on the symmetry axis, and that the sphere rotates with constant angular velocity ω at an angle α to the axis of the field. We calculate the fields under the assumption that the conditions for stationarity are satisfied.

As in ref. 1, we introduce two fixed rectangular coordinate systems oxyz and ox'y'z', which are related to the rotation axis of the sphere (oz) and to the field sources (the field axis is oz'); the origin of the systems lies at the center of the sphere, the oy and oy' axes are coincident, and the angle $\angle zoz' = \alpha$. We also use the related spherical coordinate systems r, θ', φ' and r, θ, φ with polar axes oz' and oz.

The field of the external sources is given by a scalar potential in the system OX'Y'Z:

$$U_0 = \sum_{n=1}^{\infty} \sqrt{\frac{4\pi}{2n+1}}\, a_n r^n Y_{n,0}(\theta') \cos \Omega t; \tag{1}$$

the a_n are coefficients which depend on the geometry of the sources and the distance to them and on the currents involved, and $Y_{n,m}$ is the normalized spherical function.

It can be shown[1] that the field $\mathbf{H}^i$ inside the sphere in the coordinate system related to the axis of rotation can be described by the equations

$$\left.\begin{aligned} \Delta \mathbf{H}^i &= \frac{4\pi\mu\sigma}{c^2}\left(\omega \frac{\partial \mathbf{H}}{\partial \varphi} + \frac{\partial \mathbf{H}}{\partial t}\right), \\ \operatorname{div} \mathbf{H}^i &= 0. \end{aligned}\right\} \tag{2}$$

The field outside the sphere $\mathbf{H}^e$ satisfies

$$\Delta \mathbf{H}^e = 0, \ \operatorname{div} \mathbf{H}^e = 0. \tag{3}$$

The solution of (2) is of the form

$$\mathbf{H}^i = \operatorname{curl} \hat{L} \Phi (r, \theta, \varphi), \tag{4}$$

where $\hat{L} = -i[\mathbf{r}\nabla]$, and the function Φ satisfies the scalar equation

$$\Delta \Phi + k_m^2 \Phi = 0, \tag{5}$$

and

$$k_m^2 = -i\, \frac{4\pi\mu\sigma}{c^2} (m\omega + \Omega). \tag{6}$$

The field outside the sphere has the solutions

$$\mathbf{H}^e = \operatorname{curl} \hat{L} \psi (r, \theta, \varphi), \tag{7}$$

where ψ satisfies the scalar equation

$$\Delta \psi = 0. \tag{8}$$

Since the general solutions of the Helmholtz and Laplace scalar equations are well known, the problem of determining the field reduces to vector operations with scalar functions.

The general solution of (5) which has no singularity at the origin is of the form

$$\Phi = \sum_{n,m} A_{n,m} j_n (k_m r)\, Y_{n,m}(\theta, \varphi)\, e^{i\Omega t}, \tag{9}$$

and the solution of (8) which is regular at infinity is

$$\phi=\sum_{n,m} B_{nm} r^{-(n+1)} Y_{n,m}(\theta, \varphi) e^{i\Omega t}. \tag{10}$$

Here, $j_n = \sqrt{\pi/2kr} J_{n+1/2}$ is the spherical Bessel function. The coefficients A_{nm} and B_{nm} are determined from the boundary conditions at the surface of the sphere r = R:

$$H_r^0 + H_r^e = \mu H_r^i, \; H_\tau^0 + H_\tau^e = H_\tau^i. \tag{11}$$

In order to satisfy the boundary conditions the field from the external sources (1) must be transformed to the coordinate system based on the axis rotation. If we carry out this transformation and then satisfy (11), we get the following values for the coefficients:

$$A_{nm} = i\sqrt{\frac{4\pi}{2n+1}} \frac{R^{n-1}(2n+1) b_{nm}}{(n+1)\left[\frac{\partial j_n(k_m r)}{\partial r} + (1+n\mu)\frac{j_n(k_m r)}{r}\right]_{r=R}}, \tag{12}$$

$$B_{n,m} = i\sqrt{\frac{4\pi}{2n+1}} \frac{R^{2n+1}}{n+1} b_{nm}\left[\frac{\mu(2n+1) j_n(k_m r)}{R\left[\frac{\partial j_n(k_m r)}{\partial r} + (1+n\mu)\frac{j_n(k_m r)}{r}\right]_{r=R}} - 1\right], \tag{13}$$

where

$$\left.\begin{aligned} b_{nm} &= a_n \sqrt{\frac{(n-m)!}{(n+m)!}} P_n^m(\cos\alpha), \\ b_{nm} &= (-1)^m b_{n,-m}. \end{aligned}\right\} \tag{14}$$

The forces and torques are found by means of the Maxwell stress tensor. The average values over the period of the time-varying field are defined by the following integrals:

$$\left.\begin{aligned} \mathbf{F} &= \frac{1}{8\pi}\operatorname{Re}\oint_s \left(\mathbf{H}^* H_r - \frac{1}{2}|H|^2 \mathbf{e}_r\right) ds, \\ \mathbf{M} &= \frac{1}{8\pi}\operatorname{Re}\oint_s [\mathbf{r}\mathbf{H}^*] H_r ds. \end{aligned}\right\} \tag{15}$$

The evaluation of these integrals is carried out by the same method as in ref. 1. In cyclic projections the forces and torques have the form

$$M_\nu = -\frac{i}{4}\mu \sum_{n=1}^{\infty}\sum_{m=0}^{n} \sqrt{\frac{n}{n+1}} \frac{n(2n+1)^2}{n+1+n\mu} R^{2n+1} \times b_{nm} b^*_{n,m+\nu} \begin{bmatrix} n & 1 & n \\ m & \nu & m+\nu \end{bmatrix} \{Q_{nm} - Q^*_{n,m+\nu}\}, \tag{16}$$

$$F_\nu = \frac{1}{4}\sum_{n=1}^{\infty}\sum_{m=-n}^{n} R^{2n+1} n \sqrt{\frac{2n+1}{n+1}} b_{nm} b^*_{n+1,m+\nu} \times \begin{bmatrix} n & 1 & n+1 \\ m & \nu & m+\nu \end{bmatrix} \left\{2\frac{(\mu-1)(n+1)}{n+1+n\mu} + \frac{\mu(2n+1)^2}{n+1+n\mu} Q_{nm}\right\}, \tag{17}$$

where

$$\left.\begin{aligned} Q_{nm} &= \frac{\chi_n(k_m^+ R)}{n+1+n\mu+n(\mu-1)\chi_n(k_m^+ R)} \\ &+ \frac{\chi_n(k_m^- R)}{n+1+n\mu+n(\mu-1)\chi_n(k_m^- R)}, \\ \chi_n &= \frac{j_{n+1}(k_m R)}{j_{n-1}(k_m R)}; \; k_m^\pm = \frac{1-i}{c}\sqrt{2\pi\mu\sigma(m\omega \pm \Omega)}, \end{aligned}\right\} \tag{18}$$

ν is the cyclic coordinate index, which takes the three values $\nu = -1, 0, 1$, $[F_0 = F_z, F_1 = -(1/\sqrt{2})(F_x + iF_y), F_{-1} = (1/\sqrt{2})(F_x - iF_y)]$, and the coefficient in square brackets is the Clebsch–Gordan coefficient.

Although the forces and torques have been evaluated for an axially symmetric external field, Eqs. (16) and (17) are valid for a field of arbitrary configuration if the b_{nm} are interpreted simply as the expansion coefficients of the external field in the coordinate system related to the axis of rotation.

The force equation (17) is best written in the system of coordinates related to the field axis as this makes the description of the behavior of the sphere most convenient and physically obvious (as in the case of magnetic, axially symmetric suspension, for example).

Transferring from cyclic to Cartesian coordinates and symmetrizing only over positive indices m in the OX'Y'Z' system we get

$$\begin{aligned} \mathbf{F}' &= \mathbf{e}_{z'}\frac{\mu-1}{2}\sum_{n=1}^{\infty}\frac{n(n+1)R^{2n+1}}{2n+1+n(\mu-1)} a_n a_{n+1} \\ &+ \mathbf{e}_{z'}\frac{\mu}{4}\sum_{n=1}^{\infty}\frac{n(n+1)(2n+1)^2}{(2n+1)+n(\mu-1)} R^{2n+1} a_n a_{n+1} \operatorname{Re} Q_{n0} \\ &+ \frac{\mu}{2}\sum_{n=1}^{\infty}\frac{n(2n+1)^2}{2n+1+n(\mu-1)} R^{2n+1} a_n a_{n+1} \sum_{m=1}^{n}\frac{(n-m)!}{(n+m)!} \\ &\times \Big\{\Big\langle \mathbf{e}_{z'}[P_n^m(\cos\alpha)]^2 + \mathbf{e}_{x'}\frac{1}{n+1} P_n^m(\cos\alpha)\big[m \operatorname{ctg}\alpha\, P_n^m(\cos\alpha) \\ &- 2P_n^{m+1}(\cos\alpha)\big]\Big\rangle \operatorname{Re}(Q_{nm} - Q_{n0}) + \mathbf{e}_y\frac{1}{n+1}\frac{2m}{\sin\alpha} \\ &\times [P_n^m(\cos\alpha)]^2 \operatorname{Im} Q_{nm}\Big\}. \end{aligned} \tag{19}$$

The first term in this equation describes the static force and the second term describes the force which arises in a time-varying field as a result of the conductivity of the sphere. The last term is related to the force due to the rotation.

We write the torques of the forces as projections on the Cartesian axes OXYZ

$$\begin{aligned} \mathbf{M} &= -\frac{\mu}{4}\sum_{n=1}^{\infty}\frac{n(2n+1)^2 R^{2n+1}}{(n+1)[2n+1+n(\mu-1)]} a_n^2 \sum_{m=0}^{n}\frac{(n-m)!}{(n+m)!} \\ &\times \{P_n^m(\cos\alpha) P_n^{m+1}(\cos\alpha)[\mathbf{e}_x \operatorname{Im}(Q_{n,m+1} + Q_{nm}) \\ &+ \mathbf{e}_y \operatorname{Re}(Q_{n,m+1} - Q_{nm})] + \mathbf{e}_z 2m [P_n^m(\cos\alpha)]^2 \operatorname{Im} Q_{nm}\}. \end{aligned} \tag{20}$$

It can be seen from (19) and (20) that the forces and torques have been derived in the form of series, each term of which is the product of amplitude (depending on a_n, n, m), angular [depending on $P_n^m(\cos\alpha)$], and frequency [depending on $\chi_n(\Omega, \omega)$] parts. The factors in (19) and (20) which depend on frequency are the most interesting and are considered in detail.

ANALYSIS OF THE FREQUENCY CHARACTERISTICS

1. The frequency characteristics of the forces and torques are defined by the function $\chi(\Omega, \omega)$ when $\mu = 1$, or by the rational function $N_n = (2n + 1)\varkappa_n/[2n + 1 +$

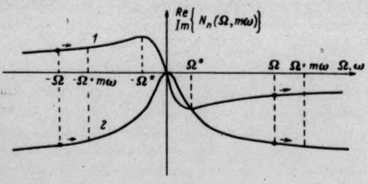

Fig. 1. The frequency variation with ω for fixed Ω. 1) Im $N_n(\Omega, m\omega$; 2) Re $N_n(\Omega, m\omega)$.

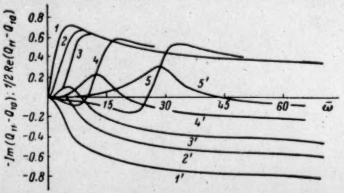

Fig. 2. Frequency characteristics of the torques in a homogeneous field and of the forces in the field of the first and second harmonics with $\mu = 1$ Im (1-5), Re (1'-5'); $\bar\Omega$: 1) 0; 2) 3.75; 3) 5.75; 4) 12.5; 5) 27.5.

$n(\mu-1)+n(\mu-1)\chi_n]$ when $\mu \neq 1$. The variation of the real and imaginary parts of $\chi_n(\omega)$ with the dimensionless frequency $\bar\omega = \omega(2\pi\mu\sigma R^2/c^2)$ is shown in Figs. 1-3 (curves 1 and 1').

For $\bar\omega > 0$ the real part is a monotonic function which decreases from 0 to −1, which is the asymptote for $\bar\omega \to \infty$ for Re χ_n of any index number.

The imaginary part is equal to zero at $\bar\omega = 0$, has a single minimum (for $\bar\omega > 0$), and tends to zero as $\bar\omega \to \infty$ (for all n). The qualitative form of the $N_n(\bar\omega)$ curves is similar to those of $\chi_n(\bar\omega)$, but the frequency scale is extended roughly by a factor of μ ($\mu \gg 1$).

The way that χ_n and N_n vary with ω, n, and μ can be seen in the Appendix, in which we derive a finite expression for χ_n in power and trigonometric functions, the asymptotic behavior of χ_n and N_n at small and large values of the argument, the position of the minimum in the real part for χ_n with n up to 10, the value at the minimum of $\left.\begin{matrix}\text{Re}\\ \text{Im}\end{matrix}\right\}\chi_n$, etc.

2. It follows from (16) and (17) that the equations for the forces and torques acting on a rotating sphere in a time-varying field can be obtained from the corresponding equations for a constant field,[1] if the frequency part is replaced by two terms with arguments expressed in terms of Bessel functions $[(1-i)/c]R\sqrt{2\pi\mu\sigma(m\omega\pm\Omega)}$.

The frequency function $Q_{nm}(\omega, \Omega)$ can be constructed from a knowledge of $N_n(\Omega, 0)$ given over the entire Ω axis. Since the argument of Q_{mn} depends on $m\omega \pm \Omega$, the construction of $Q_{nm}(\omega, \Omega)$ for fixed Ω reduces to the summation of two curves with the frequencies ωm measured in the positive direction from $+\Omega$ and $-\Omega$. The process is shown schematically in Fig. 1.

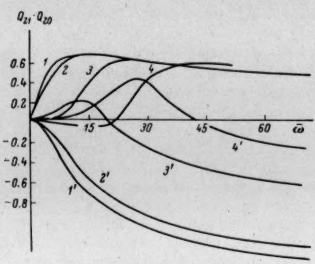

Fig. 3. Frequency characteristics of the torques in the field of the second harmonic a_2 and of the forces in the fields a_2 and a_3 with $\mu = 1$. Im (1-4), Re (1'-4'). $\bar\Omega$: 1) 0; 2) 3.75; 3) 13.75; 4) 27.5.

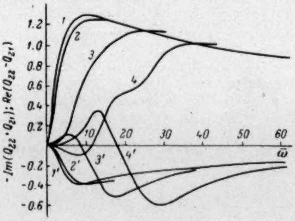

Fig. 4. Frequency characteristics of the torques in a field a_2 with $\mu = 1$. Im (1-4), Re (1'-4'); $\bar\Omega$: 1) 0; 2) 3.75; 3) 13.75; 4) 27.5.

We now consider the nature of the frequency variations $Q_{nm}(\bar\omega)$ for various external field frequencies $\bar\Omega$. For the curves described by the imaginary part, the critical value of the external field frequency is $\bar\Omega^*$, at which Im $N_n(\bar\Omega^*, 0)$ reaches its minimum. For $\bar\Omega < \bar\Omega^*$ the initial slope of the $Q_{nm}(\bar\omega)$ curve decreases and the minimum is shifted towards the right. An additional maximum appears when $\bar\Omega > \bar\Omega^*$ and the single-peaked curve for $\bar\omega > 0$, $0 \le \bar\Omega \le \bar\Omega^*$ is replaced by a double-peaked curve when $\bar\omega > 0$, $\bar\Omega > \bar\Omega^*$. If the frequency of the external field is high ($\bar\Omega \gg \bar\Omega^*$), the maximum is reached when $\bar\omega m \simeq \bar\Omega - \bar\Omega^*$, being equal to Im $[N_n(\bar\Omega^*) + N_n(2\bar\Omega - \bar\Omega^*)]$ and the minimum is reached when $\bar\omega m \simeq \bar\Omega + \bar\Omega^*$, being equal to Im $[N_n(\bar\Omega^*) + N_n(2\bar\Omega + \bar\Omega^*)]$. Thus the region where the frequency characteristics change most is the interval $\bar\Omega - \bar\Omega^* \le m\omega \le \bar\Omega + \bar\Omega^*$.

The frequency variation described by the real part has a critical frequency $\bar\Omega_1$ (turning point), which is somewhat smaller than $\bar\Omega^*$. For $\bar\Omega < \bar\Omega_1$ and $\bar\omega > 0$ the curve remains monotonic but for $\bar\Omega > \bar\Omega_1$ a maximum appears. At high frequencies $\bar\Omega \gg \bar\Omega_1$ (or $\bar\Omega^*$) the maximum occurs at $m\bar\omega = \bar\Omega$ and its value is Re $N_n 2\bar\Omega$. Re $Q_{nm}(\bar\omega)$ is an even function and Im $Q_{nm}(\bar\omega)$ is an odd function. Thus at small values of $\bar\omega$ the characteristics described by the real and imaginary parts begin with quadratic and linear terms respectively (except for special values of $\bar\Omega$).

These points are illustrated in Fig. 2, which shows the variation of $\left.\begin{matrix}\text{Re}\\ \text{Im}\end{matrix}\right\}[Q_{11} - Q_{10}]$ with $\bar\omega$ at various external field frequencies.

3. It is well known that no torques act on an isotropic nonrotating sphere. This can easily be seen from (20) by putting $\omega = 0$ and making use of the fact that $\mathrm{Im}\,N_n$ is an odd function and $\mathrm{Re}\,N_n$ an even function of Ω. If the sphere begins to rotate then torques M_x, $M_z \sim \omega$, and $M_y \sim \omega^2$ arise. For sufficiently high external field frequencies, ($\bar{\Omega} > \bar{\Omega}^*$) all the components of the torques in the initial frequency region for $\bar{\omega}$ have the opposite sign to the torques in a static field. This means that instead of deceleration and alignment of the rotation axis with the field axis which are observed in a constant field, the sphere accelerates to a stationary speed and its axis moves away from the field axis. The reverse precession about the field axis is replaced by direct precession.

At a high frequency $\bar{\Omega} \gg \bar{\Omega}^*$, the torque M_y grows very slowly in the initial frequency region and its asymptotic value as $\bar{\omega} \to \infty (m = 0)$ decreases from 2 in the case of a static field to $2\,[1 - |\mathrm{Re}\,N_n(\Omega)|\,]$ for a time-varying field. This last value decreases with increasing $\bar{\Omega}$ and tends to zero as $\bar{\Omega} \to \infty$.

The frequency parts of the torques for the first and second harmonic fields are shown in Figs. 2-4.

In the simplest case (homogeneous field) only one term remains in the series (20). If we substitute into (20) the explicit expression

$$\chi_1 = \frac{1}{z^2}(3 - z^2 - 3\,\mathrm{tg}\,z) = -1 + \frac{3}{2\varkappa}\frac{\mathrm{sh}\,3\varkappa - \sin 2\varkappa}{\mathrm{ch}\,2\varkappa - \cos 2\varkappa}$$
$$+ i\left[\frac{3}{2\varkappa^2} - \frac{3}{2\varkappa}\frac{\mathrm{sh}\,2\varkappa + \sin 2\varkappa}{\mathrm{ch}\,2\varkappa - \cos 2\varkappa}\right]$$

with $z = (R/c)(1 - i)\sqrt{2\pi\mu\sigma(\omega + \Omega)} = (1 - i)\varkappa$ and put $\mu = 1$, $\Omega = 0$, $a_1 = H$, we get values of the torques which coincide with those calculated in refs. 5 and 6; for $\Omega \neq 0$ the results agree with those in ref. 2.

The calculations show that the speeding up of the sphere in a uniform field occurs if the external field frequency $\Omega > \Omega^* = (c\varkappa^*)^2/R^2 2\pi\mu\sigma$, where $\varkappa^* = 2.409$ for $\mu = 1$ and $\varkappa^* = (\mu - 1)/\sqrt{2}$ for $\mu \gg 1$. With a copper sphere of radius 1 cm, for example, $f = \Omega^*/2\pi = 250$ Hz and with an iron sphere ($\mu = 200$), $f = 4.4$ kHz.

4. In an axially symmetric field with $\omega = \Omega = 0$ there is a single component of static force $F_{z'}$. If the field is time-varying ($\Omega \neq 0$) but the sphere does not rotate, then only $F_{z'}$ is nonzero as before, but it now contains a term with sign opposite to that of the static part ($\mu > 1$). At some frequency the ferromagnetic and diamagnetic parts become equal to each other and the force vanishes. The force is diamagnetic above this frequency.

At very high frequencies ($\Omega \to \infty$) $\lim\limits_{\Omega \to \infty} F_{z'}(\Omega, \mu, \omega = 0) = F_{z'}(\mu = 0)$ whatever the value of μ ($\mu < \infty$). A magnitude of 0.6-0.7 of the limiting value is reached quite rapidly as the frequency goes up, but thereafter the limit is approached quite slowly.

The limiting value of the lifting force developed by a loop of wire carrying a current is derived in ref. 3. This value can be obtained from (19) by putting $\mu = 1$, $\mathrm{Re}\,\chi_n(\infty) = -1$, $\cos\alpha = 1$, and

$$a_n = \frac{2\pi I r_l}{cb}\,\frac{P_n^1(\cos\beta)}{n}\,\frac{1}{b^n}$$

(where I is the current in the loop, b is the distance from the center of the sphere to the loop, and r_l is the radius of the loop).

If the sphere begins to rotate at an angle to the field then the frequency variation of the component $F_{z'}$ is changed and force components $F_{x'}$ and $F_{y'}$ appear. When $\bar{\Omega} \gg \bar{\Omega}^*$ the absolute value of the force $F_{z'}$ has a minimum at the frequency $m\bar{\omega} = \bar{\Omega}$ and retains its sign if $\mu \leq 1$. If, however, $\mu \gg 1$, then $F_{z'}$ (apart from the constant components) is similar to that of M_z. The characteristics of the forces Q_{nm} in the field of the first three harmonics for $\mu = 1$ are shown in Figs. 2 and 3.

As an example, we consider in somewhat more detail a very simple case: The force in the field of the first two harmonics (a_1 and a_2) is

$$\mathbf{F}' = \frac{a_1 a_2}{2}R^3\left\{\left\langle 2\frac{\mu - 1}{\mu + 2} + \frac{9\mu}{\mu + 2}\mathrm{Re}\,Q_{10}\right\rangle \mathbf{e}_{z'}\right.$$
$$+ \frac{9}{2}\frac{\mu}{\mu + 2}\left[\left(\mathbf{e}_{z'}\sin^2\alpha + \mathbf{e}_{x'}\frac{1}{4}\sin 2\alpha\right)\right.$$
$$\left.\left.\times\,\mathrm{Re}\,(Q_{11} - Q_{10}) + \mathbf{e}_{y} + \sin\alpha\,\mathrm{Im}\,Q_{11}\right]\right\}.$$

An analysis of this equation shows that for a nonrotating sphere the ferromagnetic and diamagnetic parts of the forces become equal at a frequency Ω_0 defined by the expression

$$\varkappa(\Omega_0) = \frac{R}{c}\sqrt{2\pi\sigma\mu\Omega_0} \approx \mu\frac{16(\mu - 1)(2\mu + 1)}{25\mu^2 - 12\mu - 16}\ (\mu \geqslant 3). \qquad (21)$$

At the same frequency $F_{z'}$ also vanishes in a constant field if the sphere rotates at an angle of $\alpha = 90°$.

An interesting effect occurs if (with $\mu \gg 1$) the frequency of the external field $\Omega > \Omega_0$ is chosen so that when $\omega = 0$, $F_{z'}(0, \Omega)$ is diamagnetic. Then as the sphere accelerates the force $F_{z'}$ decreases and over some frequency interval in the neighborhood of $\omega \approx \Omega$ the diamagnetic force becomes a ferromagnetic force (Fig. 5). This effect occurs if $\mu > 4$ and $\alpha > (2/3)\,[(\mu + 2)/\mu]$. The frequency Ω_0 is the minimum one for $\alpha = 90°$ and is defined by (21); with $\alpha = \arcsin\sqrt{(2/3)[\mu + 2)/\mu]}$, $\Omega_0 \to \infty$.

If $\mu \leq 1$, no change occurs in the sign of the lifting force $F_{z'}(\omega)$ but the absolute value drops sharply at $\omega =$

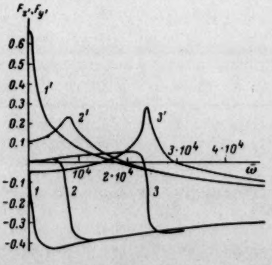

Fig. 5. Frequency variation of the forces $F_{y'}(\omega)$ (1-3) and $F_{z'}(\omega)$ (1'-3') in the field of the two harmonics a_1 and a_2 with $\mu = 100$ and $\alpha = 90°$. $\bar{\Omega}$: 1) 0; 2) $8\cdot10^3$; 3) $2.4\cdot10^4$.

Ω and can reach 0.5 of $F_{z'}(\omega = 0)$ at $\alpha = 90°$. Such a decrease in the lifting force can in principle lead to instability in the suspension of a conducting sphere in a time-varying field.

The forces $F_{x'}$ and $F_{y'}$ arise only when the sphere rotates. It is shown in ref. 4 that $F_{y'}$ leads to a loss of stability in the magnetic support of a conducting sphere in a constant field. This kind of instability remains in a time-varying field but only at the single point $\omega = \omega_{\text{synch}}$ does $F_{y'}$ fall. The force $F_{x'}$ does not seriously affect the stability of magnetic suspension if the static rigidity is sufficiently high. It produces a shift in the equilibrium state from the field axis towards the direction of slope of the rotation axis in the initial ω frequency region if $\Omega > \Omega^*$, and in the opposite direction when $\omega \to \infty$ (or if $\Omega = 0$ at any $\omega \neq 0$).

5. Thus the frequency characteristics of the forces and torques acting on a rotating sphere in a time-varying magnetic field are quite different from the case of a static field. If the frequency of the external field is greater than Ω^*, then in the initial ω regions the components M, $F_{x'}$, and $F_{y'}$ have the opposite sign to the static field case. The frequency curves of these components pass through zero and $F_{z'}$ can in fact pass through twice (if $\mu \gg 1$, $\alpha = 90°$, $\Omega > \Omega_0$). The characteristics of the components $F_{z'}$, $F_{x'}$, and M_y, which are monotonic in a static field, pass through a maximum at $m\omega \approx \Omega$ (for $\Omega \gg \Omega^*$) for a time-varying field and have a smaller asymptotic value as $\omega \to \infty$. The frequency characteristics of $F_{y'}$, M_z, and M_x, which are single-peaked in a static field, have a maximum and a minimum in a time-varying field.

6. The angular dependence of the forces and torques in (19) and (20) is defined by the adjoint Legendre polynomials. For arbitrary values of the frequencies Ω and ω and of the harmonic amplitudes a_n, the angular dependence can take many different forms. However, some general relationships can be discerned: 1) The components $F_{z'}$ and M_z have the factor $\sin^2\alpha$ since P_n^m has the factor $\sin^m\alpha$; 2) for the same reason $F_{y'} \sim (P_n^m)^2/\sin\alpha$ has the factor $\sin\alpha$; 3) $F_{x'}$, M_x, and M_y have the factor $\sin\alpha\cos\alpha$, since $P_n^m(\cos\alpha)$ $(m \neq 0)$ with an odd sum n + m is proportional to $\sin\alpha\cos\alpha$, and the product $P_n^m P_n^{m+1}$ always satisfies this condition.

Using (19) and (20) we get an expansion over small angles for the cases $\alpha \ll 1$ and $\pi/2 - \alpha \ll 1$, which are important in practice. In this case only 1-2 terms over the index m remain in the sums and the equations are simplified.

APPENDIX

The function $\chi_n(z) = j_{n+1}(z)/j_{n-1}(z)$ can be expressed in terms of trigonometric and power functions by the use of the representation[7]

$$j_n(z) = \frac{1}{z}\left\{\sin\left(z - \frac{\pi n}{2}\right)\sum_{p=0}^{\leqslant \frac{n}{2}}(-1)^p \frac{(n+2p)!}{(2p)!\,(n-2p)!}(2z)^{-2p}\right.$$
$$\left.+\cos\left(z - \frac{\pi n}{2}\right)\sum_{p=0}^{\leqslant \frac{n-1}{2}}(-1)^p \frac{(n+2p+1)!}{(2p+1)!\,(n-2p-1)!}(2z)^{-2p}\right\}. \quad \text{(A.1)}$$

For a sufficiently large value of the argument $z = (1 - i)\varkappa$, $\varkappa \gg 1$, χ_n can be represented as the ratio of polynomials with complex coefficients by means of the relationship

$$\operatorname{tg}\left[(1 - i)\varkappa - \frac{n-1}{2}\pi\right] \approx -i \quad (\varkappa \gg 1).$$

The asymptotic behavior of χ_n for large values of the argument can be found from (1) by retaining the two leading terms ($\sim 1/z$ and $1/z^2$):

$$\chi_n[(1 - i)\varkappa] = -1 + \frac{2n+1}{2\varkappa} - i\,\frac{2n+1}{2\varkappa}\left(\varkappa^2 \gg \frac{n^2}{2}\right). \quad \text{(A.2)}$$

For small values of the argument it is convenient to make use of the Bessel function representation[7]

$$j_n(z) = z^n \sum_{p=0}^{\infty} \frac{(-1)^p z^{2p}}{2^p p!\,[2(n+p)+1]!!}. \quad \text{(A.3)}$$

If we limit ourselves to two terms in (3), we get

$$\chi_n[(1 - i)\varkappa] = \frac{2}{(2n+1)(2n+3)}$$
$$\times\left[-\frac{4\varkappa^4}{(2n+1)(2n+5)} - i\varkappa^2\right](\varkappa^2 \ll 2n+1). \quad \text{(A.4)}$$

A characteristic point of the function $\chi_n[(1 - i)\varkappa]$ is the minimum of the real part. Table 1 gives the values of $\varkappa_{\max} = \varkappa^*$ and the magnitudes $\left.\begin{matrix}\text{Re}\\ \text{Im}\end{matrix}\right\}\chi_n[(1 - i)\varkappa^*]$ for functions of the first ten values of n.

The frequency-dependent function for $\mu \neq 1$ is

$$N_n = \frac{(2n+1)\chi_n(z)}{2n+1+n(\mu-1)+n(\mu-1)\chi_n(z)}.$$

The asymptotic variations for this are obtained in the same way as for χ_n and have the form

$$N_n[(1 - i)\varkappa] = \frac{1}{[(2n+1)+n(\mu-1)]^2}\left\{-\frac{4\varkappa^4[n(\mu-1)+2(2n+3)]}{(2n+3)^2(2n+5)}\right.$$
$$\left.-i\,\frac{2\varkappa^2}{2n+3}[2n+1+n(\mu-1)]\right\}, \quad \varkappa \ll \mu n,$$

$$N_n[(1 - i)\varkappa] = -1 + \frac{2n+1+n(\mu-1)}{2\varkappa}$$
$$-i\,\frac{2n+1+n(\mu-1)}{2\varkappa}, \quad \varkappa \gg \mu n.$$

TABLE 1

	Function number n									
	1	2	3	4	5	6	7	8	9	10
$\varkappa^*$	2.409	3.719	5.111	6.538	7.960	9.395	10.825	12.259	13.715	15.15
$-\text{Im}\chi_n$	0.355146	0.332728	0.322635	0.31724	0.313955	0.311738	0.310140	0.308933	0.307992	0.307242
$-\text{Re}\chi_n$	0.3660	0.3594	0.3623	0.3667	0.3687	0.3710	0.3721	0.3736	0.3752	0.3759

One case of interest is when the frequency is such that the expansion (4) is satisfied and μ is high ($\mu \gg n$). Then

$$N_n[(1-i)\varkappa]$$

$$= \frac{-1 + \frac{2n+1-n(\mu-1)}{2\varkappa} + \frac{(2n+1)n(\mu-1)}{2\varkappa^2} - i\frac{(2n+1)+n(\mu-1)}{2\varkappa}}{1 + \frac{n(\mu-1)}{\varkappa} + 2\frac{n^2(\mu-1)^2}{\varkappa^2}}$$

and the minimum of the imaginary part occurs at $\varkappa = n(\mu - 1)/\sqrt{2}$. The values of $\left.\begin{matrix}\mathrm{Re}\\ \mathrm{Im}\end{matrix}\right\} N_n$ at this point are respectively

$$\frac{1}{2}\left[-1 + \frac{2n+1}{n(\mu-1)}\right] \simeq -0.5, \quad \frac{1}{2(1+\sqrt{2})}\left[1 + \frac{2n+1}{n(\mu-1)}\right] \simeq 0.207.$$

We can conclude from the asymptotic behavior of the functions χ_n and N_n and from the position of $\max \mathrm{Im}\frac{\chi_n}{N_n}$ that the scale of the functions χ_n of $\varkappa$ varies approximately proportional to the number n and of N_n proportional to μn.

---

[1] R. V. Lin'kov and Yu. M. Urman, Zh. Tekh. Fiz., 43, 2472 (1973) [Sov. Phys. – Tech. Phys., 18, 1557 (1974)].

[2] A. F. Hayes, IEEE Trans. Aerospace and Navigation Electronics, ANE-11, 122 (1964).

[3] A. A. Fomin, Zh. Tekh. Fiz., 33, 1021 (1963) [Sov. Phys. – Tech. Phys., 8, 763 (1964)].

[4] V. V. Vladimirskii and S. M. Kalebin, Prib. Tekh. Eksp., No. 2, 41 (1959).

[5] L. D. Landau and E. M. Lifshitz, Electrodynamics of Continuous Media, Pergamon Press, Oxford–New York (1960).

[6] B. P. Halverson and H. Cohen, IEEE Trans. Aerospace and Navigation Electronics, ANE-11, 118 (1964).

[7] H. Bateman and A. Erdelyi, Higher Transcendental Functions, McGraw-Hill, New York (1955).

Electromagnetic levitation of a liquid metal droplet with strong skin effect (surface shape and internal pressure)

A. N. Tverdokhlebov and A. L. Shuster

(Submitted October 9, 1973; resubmitted March 13, 1974)
Zh. Tekh. Fiz., 44, 2265-2271 (November 1974)

The shape of a liquid metal droplet levitated in a stationary electromagnetic field is analyzed. The structure inside the drop and the first correction for the deviation from a spherical shape are found for a large surface tension σ and strong skin effect. These are expressed in terms of integrals of the magnetic field without a droplet. An upper bound is obtained for the power W which can be dissipated in a droplet equivalent to a sphere of radius a: $W < 8\pi\sigma a^2\omega$ (ω is the frequency).

1. INTRODUCTION

In various technological problems, e.g., melting of metals and alloys without a crucible,[1] the molten metal is levitated in a quasispherical shape and is heated by an electromagnetic field. The power introduced into the metal increases with decreasing skin-depth; therefore high-frequency electromagnetic fields are normally used, the frequency being such that the skin depth is much smaller than the characteristic size of the molten metal.

In this note we find the pressure inside a suspended metal droplet in an external stationary magnetic field (and gravity field) and the deviation from sphericity for the case of a strong skin effect and large surface-tension σ (for small deviations from sphericity). The desired quantities are expressed in terms of integrals of the squares of the fields with no droplet.

The calculations are based on the equation

$$\operatorname{div}\left\{\frac{\operatorname{grad} F}{|\operatorname{grad} F|}\right\} + F(\mathbf{r}) = \frac{1}{\sigma}\Psi(F,\ \mathbf{r}), \tag{1.1}$$

obtained in Sec. 2; the solution $F(\mathbf{r})$ defines a family of surfaces $F(\mathbf{r}) = \text{const}$, which includes the desired surface of the drop. The expression $\Psi(F,\ \mathbf{r})$ on the right side of (1.1) is the pressure difference $p(\mathbf{r}_0) - p(\mathbf{r})$, where $p(\mathbf{r})$ is the pressure created by external forces at the point $\mathbf{r}$ on one surface of the family $F(\mathbf{r}) = \text{const}$ (passing through $\mathbf{r}$), while $p(\mathbf{r}_0)$ is the pressure at some fixed point inside the droplet. The initial data, e.g., the total volume of the liquid droplet, make it possible to isolate the desired surface from the family $\varkappa(\mathbf{r}) = \text{const}$. The value of the constant is $p(\mathbf{r}_0)/\sigma$, so that $F(\mathbf{r})$ simultaneously determines both the surface shape and the pressure inside the droplet.

As $\sigma \to \infty$ the solution of (1.1) becomes the function $F_0(\mathbf{r}) = 2/|\mathbf{r} - \mathbf{R}|$, where $\mathbf{R}$ is an arbitrary vector. In Sec. 3 we obtain linear equation (3.2) for the first correction ($1/\sigma$) to $F_0(\mathbf{r})$. On the basis of this linear equation we find explicit expressions in Secs. 4 and 5 for the pressure at the center of gravity of the surface and for the extent to which its shape differs from a sphere [see (4.7) and (5.7)]. The desired quantities are expressed in terms of integrals of the squares of the field H as specified with no drop. The results are evaluated in Sec. 6.

2. EQUATION OF THE SURFACE

In static equilibrium we have the following pressure equation on the curved surface of a liquid with surface tension σ:

$$2\sigma\varkappa(\mathbf{r}) + p(\mathbf{r}) + p_{\text{ext}} = 0, \tag{2.1}$$

where $x(\mathbf{r})$ is the average curvature of the surface at $\mathbf{r}$, defined as the half-sum of the curvatures of any two mutually perpendicular cross sections, $p(\mathbf{r})$ is the pressure due to external forces (ponderomotive and gravitational) at the given point of the surface, and p_{ext} is the external pressure (atmospheric), which, without loss of generality, can be taken equal to zero. (Otherwise we can simply add the external pressure to the desired pressure within the droplet.)

The field of normals $\mathbf{n}$ to the family of surfaces $F(\mathbf{r}) = \text{const}$ is expressed in terms of the function $F(\mathbf{r})$:

$$\mathbf{n} = \frac{\operatorname{grad} F}{|\operatorname{grad} F|}, \tag{2.2}$$

while the average curvature $\varkappa(\mathbf{r})$ of a given family of surfaces is given by the following expression:[4]

$$2\varkappa(\mathbf{r}) = \operatorname{div}\mathbf{n} = \nabla\left\{\frac{\nabla F}{|\nabla F|}\right\}. \tag{2.3}$$

Isolating the pressure at some fixed interior point $\mathbf{r}_0$ from $p(\mathbf{r})$, we can rewrite (2.1) in the form

$$\sigma\left\{\nabla\left\{\frac{\nabla F}{|\nabla F|}\right\}\right\}_{\mathbf{r}\in S} + p(\mathbf{r}_0) = \{p(\mathbf{r}_0) - p(\mathbf{r})\}_{\mathbf{r}\in S}, \tag{2.4}$$

where S is the unknown surface.

The equations $F(\mathbf{r}) = C_0$ and $f(F(\mathbf{r})) = f(C_0)$ define the same surface provided that $df/dz|_{z=C_0} \neq 0$. Using this ambiguity and choosing $F(\mathbf{r})$ to be such that its value on the surface is $p(\mathbf{r}_0)/\sigma$, we obtain

$$\left\{\nabla\left\{\frac{\nabla F}{|\nabla F|}\right\} + F\right\}_{\mathbf{r}\in S} = \frac{1}{\sigma}\{\Psi(F(\mathbf{r}),\ \mathbf{r})\}_{\mathbf{r}\in S}. \tag{2.5}$$

The expression $\Psi(F(\mathbf{r}),\ \mathbf{r}) = p(\mathbf{r}_0) - p(\mathbf{r})$ is a functional of $F(\mathbf{r})$ and a function of $\mathbf{r}$ [see the clarifications to (1.1) in Sec. 1]. Once we have removed the condition $\mathbf{r} \in S$, we obtain the final equation (1.1).

The initial conditions, e.g., the total volume of the liquid V, make it possible to isolate the desired surfaces from the family of surfaces defined by $F(\mathbf{r})$. The value of $F(\mathbf{r})$ itself on this surface yields the pressure at the chosen point $\mathbf{r}_0$ (or, more precisely, the drop between the pressure at this point and the external pressure p_{ext}).

We note that

$$\oint_{F=\mathrm{const}} dS_\mu \Psi(F(\mathbf{r}),\ \mathbf{r}) = 0. \tag{2.6}$$

Physically this means that the metal droplet is at a point in space at which the resultant of the external forces is zero. Equation (1.1) satisfies this condition; indeed,

$$\oint_S dS_\mu F(\mathbf{r}) = \left(\frac{p_0}{\sigma}\right)\oint_S dS_\mu = 0,$$

and to prove that $\oint 2\sigma\varkappa dS_\mu$ is equal to zero we use expression (2.3). Assuming that the field of normals (2.2) satisfies the condition of being twice differentiable, we obtain

$$\sigma\oint_S dS_\mu 2\varkappa = \sigma\oint_S dS_\mu \nabla_\nu n_\nu = \sigma\int_V dV\nabla_\mu\nabla_\nu n_\nu = \sigma\int dV\nabla_\nu\nabla_\mu n_\nu$$
$$= \sigma\oint_S dS_\nu\nabla_\mu n_\nu = \sigma\oint dS n_\nu\nabla_\mu n_\nu = 0.$$

In the last integral, the integrand is identically zero, since $n_\nu\nabla_\mu n_\nu = 1/2\nabla_\mu(n_\nu^2) \equiv 0$, $\mathbf{n}^2 \equiv 1$.

3. SOLUTION OF (1.1) TO FIRST ORDER IN $(1/\sigma)$

Setting $(1/\sigma) = 0$ in (1.1), we obtain the zero-order equation

$$\nabla\left\{\frac{\nabla_0 F}{|\nabla F_0|}\right\} + F_0 = 0.$$

The solution is the function $F_0 = 2/|\mathbf{r}-\mathbf{R}_0|$, where $\mathbf{R}_0$ is determined from Eq. (2.6) with $F = F_0$. The surface $F_0(\mathbf{r}, \mathbf{R}_0) = \mathrm{const}$ is a sphere whose center is at $\mathbf{R}_0$. We will seek the first approximation in the form

$$F_1(\mathbf{r}) = \frac{2\left[1 + \frac{1}{\sigma}u(\mathbf{r})\right]}{|\mathbf{r}-\mathbf{R}_1|}. \tag{3.1}$$

We introduce the notation $\mathbf{r}-\mathbf{R}_1 = \rho\mathbf{n}(\mathbf{n}^2 = 1)$ and substitute $F_1(\mathbf{r})$ into (1.1). Retaining terms of order $(1/\sigma)$, we obtain the following linear equation for the function $u(\mathbf{r}) = u(\mathbf{R}_1 + \rho\mathbf{n})$:

$$(2 + \Delta_{\theta\varphi})u = \rho\Psi(F_0(\mathbf{r},\ \mathbf{R}_1),\ \mathbf{R}_1 + \rho\mathbf{n}), \tag{3.2}$$

where $\Delta_{\theta\varphi}$ is the angular part of the Laplacian Δ in the spherical coordinates specified by the vector $\rho\mathbf{n}$.

Before solving (3.2) let us consider the properties of the surface S defined by the equation $F_1(\mathbf{r}, \mathbf{R}_1) = \mathrm{const}$. The radius vector that describes this surface to order $1/\sigma$ is defined by the equation

$$\mathbf{r}_S = \mathbf{R}_1 + C\mathbf{n}\left[1 + \frac{1}{\sigma}u(\mathbf{R}_1 + C\mathbf{n})\right], \tag{3.3}$$

where C is a constant. We take $\mathbf{R}_1$ to be the center of gravity of the surface [i.e., $\oint_S dS(\mathbf{R}_1 - \mathbf{r}_S) = 0$], and we choose C to be such that the volume bounded by S is equal to that of a sphere of a radius a. This requirement imposes the following conditions on u:

$$\langle\mathbf{n}u\rangle = 0, \tag{3.4}$$

$$C = a\left(1 - \frac{1}{\sigma}\langle u\rangle\right) \tag{3.5}$$

[we use the notation $\langle f(\mathbf{r})\rangle = (1/4\pi)\int d\Omega_{\mathbf{n}} f(\mathbf{R}_1 + a\mathbf{n})$]. Allowing for these conditions, and taking the coordinate origin at $\mathbf{R}_1$, we can rewrite (3.3) as

$$\mathbf{r}_S = a\mathbf{n}\left(1 + \frac{1}{\sigma}[u(a\mathbf{n}) - \langle u\rangle]\right). \tag{3.6}$$

Correspondingly, Eq. (3.2) becomes an equation in $u(a\mathbf{n})$:

$$(2 + \Delta_{\theta\varphi})u(a\mathbf{n}) = a\Psi\left(\frac{2}{|\mathbf{r}|},\ a\mathbf{n}\right). \tag{3.7}$$

Here, we have allowed for the fact that $\mathbf{R}_1$ differs from $\mathbf{R}_0$, obtained from (2.6) in the zeroth approximation by a quantity of order $(1/\sigma)$; hence, in substituting into Ψ this difference should be neglected in the approximation in question. We expand $u(a\mathbf{n})$ and Ψ in spherical harmonics $J_m(\mathbf{n})$:

$$u(a\mathbf{n}) = \sum_m u_m J_m(\mathbf{n}),\quad \Psi = \sum_m \Psi_m J_m(\mathbf{n}),$$
$$\langle J_m J_l\rangle = \delta_{ml},\quad \Delta_{\theta\varphi}J_m = -m(m+1)J_m.$$

Then Eq. (3.7) becomes the system

$$\left.\begin{aligned} &[2 - m(m+1)]u_m = a\Psi_m \\ \text{or}\quad &u_m = -\frac{a\Psi_m}{(m-1)(m+2)},\quad m \neq 1. \end{aligned}\right\} \tag{3.8}$$

The indeterminacy for m = 1 is resolved by choosing the center of gravity of the surface as the coordinate origin ($u_1 = 0$) and by (2.6), which yields $\Psi_1 = 0$ in this approximation. Since the pressure of the force of gravity is $\lambda(\mathbf{g}\mathbf{r})$, λ being the density of the metal and g the acceleration of gravity, it makes a contribution only to Ψ_1 and hence [besides the definition of the equilibrium position from condition (2.6)] it does not appear more explicitly in the definition of the shape of the surface in the first approximation in $(1/\sigma)$.

4. DETERMINATION OF THE PRESSURE AT THE CENTER OF THE DROP

In accordance with Sec. 2, the pressure p_0 at the center of gravity of the drop is $\sigma F(\mathbf{r})|_{\mathbf{r}\in S}$. In the first approximation in $(1/\sigma)$ we have

$$p_0=\frac{2\sigma}{a}\left(1+\frac{1}{\sigma}\langle u\rangle\right); \tag{4.1}$$

from (3.8) we have

$$\langle u\rangle\equiv u_0=\frac{a}{2}\Psi_0\equiv\frac{a}{2}\langle p_{\text{magn}}\rangle, \tag{4.2}$$

where p_{magn} is the pressure of magnetic ponderomotive forces on a sphere of radius a. The pressure of gravity does not appear explicitly in the computations in this approximation, as noted at the end of the preceding section.

When there is a pronounced skin effect the surface pressure of the magnetic forces is[2]

$$p_{\text{magn}}=\frac{1}{8\pi}\mathscr{H}^2, \tag{4.3}$$

where $\mathscr{H}$ is the effective (not the amplitude) value of the exact field on the surface of the sphere. Inside the sphere the current density $\mathbf{j}(\mathbf{r})$ is $(1/4\pi)[\nabla\mathscr{H}]$. Because the field attenuates exponentially as we go into the interior of the sphere, we can make the substitution $\nabla = ik\mathbf{n}[k=(1+i)/\delta$; $\delta=(2\pi\omega\tau)^{-1}$; ω is the field frequency; and τ is the conductance of the metal, following the notation in ref. 3]. Then we have

$$p_{\text{magn}}=\pi\delta^2(\mathbf{j}\mathbf{j}^*).$$

On the surface of the sphere the quantity $\mathbf{j}(a\mathbf{n})$ can be determined from the expression [see Eq. (2.9) in ref. 3]

$$\mathbf{j}(a\mathbf{n})=-\frac{ik}{4\pi a}\frac{1}{a}\int_0^a dr\left(2r\frac{d}{dr}+1\right)[\mathbf{r}\mathbf{H}(\mathbf{r})], \tag{4.4}$$

where $\mathbf{H}(\mathbf{r})$ is the field with no sphere, for which we use the representation in terms of the scalar potential

$$\varphi=\sum_m A_m\left(\frac{r}{a}\right)^m J_m(\mathbf{n}),\quad -\nabla\varphi=\mathbf{H}.$$

Substituting (4.4) into (4.3), we obtain

$$\begin{aligned} p_{\text{magn}}&=\frac{1}{8\pi}\hat{G}_0\left(\frac{a}{r_1}\right)\hat{G}_0\left(\frac{a}{r_2}\right)\left(\frac{r_1}{a}\right)\left(\frac{r_2}{a}\right)\\ &\times[\nabla\varphi(r_1\mathbf{n})\nabla\varphi(r_2\mathbf{n})-(\mathbf{n}\nabla)\varphi(r_1\mathbf{n})(\mathbf{n}\nabla)\varphi(r_2\mathbf{n})], \end{aligned} \tag{4.5}$$

where

$$\hat{G}_0\left(\frac{r}{\rho}\right)f(\rho)=\left(2r\frac{d}{dr}+1\right)\frac{1}{r}\int_0^r d\rho f(\rho),$$

as in ref 3.

Evaluation of the integral $\langle p_{\text{magn}}\rangle$, which is similar to ref. 3 (see Sec. 5 in ref. 3, "Computation of the power"), leads to the following expression for $\langle u\rangle$ from (4.2):

$$\langle u\rangle=\frac{a}{8\pi}\left\{\langle\mathbf{H}^2\rangle-\frac{1}{4\pi a^3}\int_{|\mathbf{r}|<a}dV\left(\frac{r}{a}\right)\mathbf{H}^2(\mathbf{r})\right\}. \tag{4.6}$$

Substituting (4.6) into (4.1) yields an expression for the pressure p_0 at the center in terms of integrals of the squares of the fields with no droplet:

$$p_0=\frac{2\sigma}{a}+\frac{1}{4\pi}\left[\langle\mathbf{H}^2\rangle-\frac{1}{4\pi a^3}\int_{|\mathbf{r}|<a}dV\left(\frac{r}{a}\right)\mathbf{H}^2(\mathbf{r})\right]. \tag{4.7}$$

5. DEVIATION FROM SPHERICITY (FIRST CORRECTION)

We write the second harmonic of the expansion of $u(a\mathbf{n})$ in the form

$$u_2J_2(\mathbf{n})=(u_2)_{\alpha\beta}\left(n_\alpha n_\beta-\frac{1}{3}\delta_{\alpha\beta}\right),\quad (u_2)_{\alpha\alpha}=0.$$

Taking account of the second harmonic leads to an elliptical shape. With m = 2 Eq. (3.8) yields

$$(u_2)_{\alpha\beta}=-\frac{15a}{8}\left\langle\left(n_\alpha n_\beta-\frac{1}{3}\delta_{\alpha\beta}\right)\Psi\right\rangle. \tag{5.1}$$

In computing $(u_2)_{\alpha\beta}$ we omit terms proportional to $\delta_{\alpha\beta}$, since these do not appear in $(u_2)_{\alpha\beta}[n_\alpha n_\beta-(1/3)\delta_{\alpha\beta}]$. Substituting p_{magn} from (4.5) in place of Ψ in (5.1) and proceeding as shown in the appendix to [3], we obtain

$$\begin{aligned}(u_2)_{\alpha\beta}=\frac{15a}{32\pi}\Bigg\{&\sum_{m=0}^{\infty}\left[1+\frac{3}{(m+2)^2}+\frac{18}{2m+5}-\frac{11}{m+2}\right]\frac{(a^2\Delta)^m}{(2m+1)!}\left(\frac{\partial\varphi}{\partial x_\alpha}\frac{\partial\varphi}{\partial x_\beta}\right)\\ &+a^2\sum_{m=0}^{\infty}\left[\frac{1}{m+2}-\frac{2}{2m+5}\right]\frac{(a^2\Delta)^m}{(2m+1)!}\left(\frac{\partial\varphi}{\partial x_\mu}\frac{\partial^3\varphi}{\partial x_\mu\partial x_\alpha\partial x_\beta}\right)\Bigg\}_{\mathbf{r}=0}+\delta_{\alpha\beta}(\ldots).\end{aligned} \tag{5.2}$$

We use the following equations:

$$\left\{\sum_{m=0}^{\infty}\frac{(a^2\Delta)^m}{(2m+1)!}f(\mathbf{r})\right\}_{\mathbf{r}=0}=\langle f(\mathbf{r})\rangle\equiv\frac{1}{4\pi a^2}\oint_{|\mathbf{r}|=a}dS f(\mathbf{r}), \tag{5.3}$$

$$\left\{\sum_{m=0}^{\infty}\frac{1}{(m+q)}\frac{(a^2\Delta)^m}{(2m+1)!}f(\mathbf{r})\right\}_{\mathbf{r}=0}=\frac{1}{2\pi a^3}\int_{|\mathbf{r}|<a}dV\left(\frac{r}{a}\right)^{2q-3}f(\mathbf{r}), \tag{5.4}$$

$$\left\{\sum_{m=0}^{\infty}\frac{1}{(m+q)^2}\frac{(a^2\Delta)^m}{(2m+1)!}f(\mathbf{r})\right\}_{\mathbf{r}=0}=\frac{1}{\pi a^3}\int_{|\mathbf{r}|<a}dV\left(\frac{r}{a}\right)^{2q-3}\ln\left(\frac{a}{r}\right)f(\mathbf{r}). \tag{5.5}$$

Equations (5.4) and (5.5) can be obtained by expanding $f(\mathbf{r})$ in a Fourier integral, while (5.3) is obtained by going to the limit in (5.4) [we multiply both sides of (5.4) by q and and take the limit as q → ∞ on both sides].

Using (5.3)-(5.5) we write (5.2) in the form ($H_\mu = -\partial\varphi/\partial x_\mu$)

$$\begin{aligned}(u_2)_{\alpha\beta}=\frac{15a}{32\pi}\Bigg\{&\langle H_\alpha H_\beta\rangle+\frac{1}{2\pi a^3}\int_{|\mathbf{r}|<a}dV H_\alpha H_\beta\left[6\left(\frac{r}{a}\right)\ln\left(\frac{a}{r}\right)+9\left(\frac{r}{a}\right)^2\right.\\ &\left.-11\left(\frac{r}{a}\right)\right]-\frac{1}{2\pi a}\int_{|\mathbf{r}|<a}dV\left(H_\mu\frac{\partial^2 H_\mu}{\partial x_\alpha\partial x_\beta}\right)\left[\left(\frac{r}{a}\right)-\left(\frac{r}{a}\right)^2\right]\Bigg\}.\end{aligned} \tag{5.6}$$

Using the identity

$$\int\limits_{|\mathbf{r}|<a} dV f(r) H_\mu \frac{\partial^2 H_\mu}{\partial x_\alpha \partial x_\beta} = f(a) \oint\limits_{|\mathbf{r}|=a} dS_\mu H_\mu \frac{\partial H_\alpha}{\partial x_\beta} - \int\limits_{|\mathbf{r}|<a} dV \frac{df(r)}{dr} (\mathbf{nH}) \frac{\partial H_\alpha}{\partial x_\beta},$$

we obtain the final expression for the first correction for the deviation from sphericity:

$$(u_2)_{\alpha\beta} = \frac{15a}{32\pi} \left\{ \frac{1}{4\pi a^2} \oint\limits_{|\mathbf{r}|=a} dS H_\alpha H_\beta + \frac{1}{2\pi a^3} \int\limits_{|\mathbf{r}|<a} dV H_\alpha H_\beta \left[6\left(\frac{r}{a}\right) \ln\left(\frac{a}{r}\right) + 9\left(\frac{r}{a}\right)^2 - 11\left(\frac{r}{a}\right) \right] - \frac{1}{2\pi a^2} \int\limits_{|\mathbf{r}|<a} dV (\mathbf{nH}) \frac{\partial H_\alpha}{\partial x_\beta} \left[1 - 2\left(\frac{r}{a}\right) \right] \right\}. \quad (5.7)$$

6. REMARKS

1. We can obtain an explicit expression for the solution of Eq. (3.7) without expanding in spherical harmonics. We write $\Psi(2/|\mathbf{r}|, a\mathbf{n}) \equiv \Psi(a\mathbf{n})$ from (3.7) as the boundary value of a function $\psi(r\mathbf{n})$ that is harmonic within the sphere:

$$\psi(r\mathbf{n}) = \sum_m \left(\frac{r}{a}\right)^m \Psi_m J_m(\mathbf{n}).$$

Then the denominator $1/(m-1)(m+2)$ from (3.8) can be replaced by integration with respect to r from zero to a:

$$u(a\mathbf{n}) = -\frac{a}{3} \int\limits_0^a d\left(\frac{r}{a}\right) \left[\left(\frac{a}{r}\right)^2 - \left(\frac{r}{a}\right) \right] \psi(r\mathbf{n}). \quad (6.1)$$

Solving the Dirichlet problem for $\psi(r\mathbf{n})$ by means of the Green's function for a sphere, we obtain

$$\psi(r\mathbf{n}) = \frac{a}{4\pi} \int d\Omega_\nu \frac{r^2 - a^2}{[r^2 + a^2 - 2ar(\mathbf{n\nu})]^{3/2}} \Psi(a\boldsymbol{\nu}).$$

Thus we obtain the following representation for $u(a\mathbf{n})$:

$$u(a\mathbf{n}) = u_0 - \frac{a}{3} \int\limits_0^a d\left(\frac{r}{a}\right) \left[\left(\frac{a}{r}\right)^2 - \left(\frac{r}{a}\right) \right] \left[\psi(r\mathbf{n}) - \psi(0) - r \left.\frac{\partial\psi}{\partial r}\right|_{r=0} \right].$$

The integral in (6.1) has a singularity of order $(1/r)^2$ at zero. For this reason there is a double subtraction at zero in the above integral [$u_1 = 0$ in view of (2.6)]. Finally we write $u(a\mathbf{n})$ in the form

$$u(a\mathbf{n}) = u_0 - \frac{a}{4\pi} \int d\Omega_\nu \gamma((\mathbf{n\nu})) p_{\text{magn}}(a\boldsymbol{\nu}), \quad (6.2)$$

where

$$\gamma(z) = \frac{1}{3} \int\limits_0^1 dx \left(\frac{1 - x^3}{x^2}\right) \left(1 + 3xz - \frac{1 - x^2}{[x^2 + 1 - 2xz]^{3/2}}\right) = \frac{1}{3} \left[\frac{3}{2} + 5z - 3z \ln \frac{2}{1 - z} \right].$$

2. Equation (4.7) for the pressure at the center of gravity of the surface can be written in the following form, allowing for the results of ref. 3 [see Sec. 5, Eq. (5.2) in ref. 3]:

$$p_0 = \frac{2\sigma}{a} + \frac{1}{4\pi\omega a^2\delta} W,$$

where W is the power dissipated in the sphere. Because the sphere is closed and simply connected, there should be (at least two) points on the surface at which the current density is zero. At such points the pressure of ponderomotive forces is also zero and the internal pressure of the liquid is confined only by surface-tension forces. The radius of the average curvature $R_{\min}$ at this point (which obviously will be at a minimum at such point) is determined from the expression (gravity is neglected)

$$\frac{2\sigma}{R_{\min}} = \frac{2\sigma}{a} + \frac{1}{4\pi a^2\omega\delta} W. \quad (6.3)$$

From (6.3) we can obtain an upper bound for the power dissipated in a suspended liquid drop. The radius of mean curvature cannot be less than the skin depth δ, so that

$$\frac{2\sigma}{a} + \frac{1}{4\pi a^2\omega\delta} W < \frac{2\sigma}{\delta}.$$

Allowing for the fact that $a \gg \delta$, we obtain

$$W < 8\pi\sigma a^2\omega. \quad (6.4)$$

Taking account of the force of gravity introduces a slight correction in the form of the factor $(1 - \lambda gh\delta/\sigma)$, where h is the vertical distance between the center of the droplet and the point at which the current density is zero.

The authors thank M. L. Levin for comments.

---

[1] I. M. Kirko, Liquid Metal in Electromagnetic Fields [in Russian], Énergiya, Moscow–Leningrad (1964).

[2] L. Landau and M. Lifshitz, Electrodynamics of Continuous Media, Addison-Wesley (1960), Chap. 6, Sec. 41.

[3] A. N. Tverdokhlebov and A. L. Shuster, Zh. Tekh. Fiz., 42, 1777 (1972) [Sov. Phys.–Tech. Phys., 17, 1427 (1973)].

[4] H. Lamb, Hydrodynamics, Dover (1932).

Fifth-order spherical aberration in focusing and correcting quadrupole–octupole systems

Ya. G. Lyubchik and T. Ya. Fishkova

A. F. Ioffe Physicotechnical Institute, Academy of Sciences of the USSR, Leningrad

(Submitted November 19, 1973)
Zh. Tekh. Fiz., 44, 2272-2279 (November 1974)

The third-order spherical aberration is treated in systems of quadrupole–octupole (Q–O) lenses used as a focusing system or as a correction system (with an axisymmetric lens) in the negative spherical aberration mode. Expressions are obtained for the fifth-order spherical aberration of a system consisting of an arbitrary number of Q–O lenses. A computer is used to design specific Q–O systems; on this basis the possible gain in resolution and current is evaluated for a number of existing scanning electron microscopes and microanalyzers. A new electrostatic lens is proposed that makes it possible to adjust third- and fifth-order spherical aberrations simultaneously with respect to magnitude and sign.

The interest in elements with multiple symmetry is primarily related to the possibility of compensating various aberrations in electron-optical systems. Of particular importance are quadrupole and octupole lenses, since such systems can correct for one of the major aberrations that limits the resolving power of electron-optical devices, namely spherical aberration.

Analysis of studies along these lines, e.g., refs. 1-3, shows that the difficulties are associated primarily with the cumbersomeness of correcting systems, and with the complexity of making the separate elements to precise tolerances and aligning them with respect to each other. The design problems for electrostatic lenses have recently been overcome in a combined five-element quadrupole–octupole (Q–O) element,[4] and new methods of aligning quadrupole systems have been developed.[5]

A more fundamental question is that of using quadrupole–octupole systems for correcting spherical aberration. Estimates given in ref. 6 for a complex electron-optical system (objective of a transmission electron microscope consisting of seven 12-pole electromagnetic lenses) show that when first-order chromatic aberration and third-order spherical aberration are corrected simultaneously it is possible to obtain a resolving power of 0.5 Å at an energy of 60 keV. The effectiveness of partial correction for an elementary system consisting of an axisymmetric lens and an octupole is evaluated in ref. 7. This system is intended for the condenser of an x-ray microanalyzer and can yield a current gain of 2-2.5.

Experience with nonaxisymmetrical lenses shows that it is best to use correction elements consisting of two or three (but not more than four) combined Q–O lenses of simplified design. A system of two such lenses can provide stigmatic focusing and simultaneously correct for spherical aberration of the width of a linear image, a fact which is of importance in spectrometers[8] and certain types of electron-beam devices.[9] In microprobe systems (scanning electron microscopes, x-ray microanalyzers, cathode-ray tubes) it is necessary to have three (or four) Q–O lenses, which can yield similar or equal linear magnification factors and zero or negative spherical aberration in all directions.

Complex systems of five to seven lenses in which each lens has eight to 12 electrodes are not feasible in practice, while one Q–O lens generally does not yield the desired effect.

The aim of the present paper is to consider fifth-order spherical aberration for systems consisting of an arbitrary number of quadrupole–octupole lenses. On this basis we determine the gain from correcting for third-order spherical aberration for various probe devices.

In ref. 10 we obtained expressions for the fifth-order spherical aberration coefficients in the central planes of an individual quadrupole–octupole lens for a point (aberration-free) source C_5. For each lens in the system, beginning with the second, the source can no longer be regarded as aberration-free, since fifth-order aberration will be contributed to by the third-order aberrations of the preceding part of the system. Let us determine the contribution.

The additional broadening of a Gaussian image as a result of third-order geometrical aberrations in the preceding system in the central planes of a Q–O lens can be written

$$\left.\begin{aligned}\Delta^0 x(z_i) &= M_x(c_{5-3,x}+c^*_{5-3,x})\,x_0'^5,\\ \Delta^0 y(z_i) &= M_y(c_{5-3,y}+c^*_{5-3,y})\,y_0'^5,\end{aligned}\right\}\qquad(1)$$

where M is the linear magnification factor of the lens; x_0' and y_0' are the slopes of the trajectories at the lens input. The asterisk everywhere denotes quantities referring to the octupole. The quantity c_{5-3} can be expressed in terms of the third-order coefficient

$$c_{5-3}+c^*_{5-3}=A(b+b^*)+3G(p+p^*).\qquad(2)$$

Here, p is the aberration coefficient in the corresponding principal plane for the cube of the angle (spherical aberration), while b are the aberration coefficients in the central planes for the square of the angle and the first power of the distance.[11] The constants A (associated with the broadening of the image because of third-order aberrations) and G (associated with the change of the angle of inclination of the third-order trajectory) depend on the aberrations of the system that the given lens represents as follows:

$$\left.\begin{aligned}A^n &= \mathscr{M}_n(P_n+P^*_n),\\ G_n &= \frac{1}{2}(1-\mathscr{M}^2_n)-\frac{\mathscr{M}^3_n}{F_n}(P_n+P^*_n)-\frac{1}{3}\mathscr{M}^2_n(B_n+B^*_n),\end{aligned}\right\}\qquad(3)$$

n is the number of lenses in the preceding system; $\mathscr{M}_n$ and F_n are the magnification and focal length of the system, expressed in terms of the magnifications M_i and focal length f_i of the individual lenses as follows:

$$\mathcal{M}_n = \prod_{i=1}^{n} M_i, \tag{4}$$

$$F_n = \frac{\mathcal{M}_n}{\sum_{i=1}^{n} \mathcal{M}_i \mathcal{M}_{i-1} f_i^{-1}}, \tag{5}$$

P_n is the spherical aberration coefficient, and B_n is the aberration coefficient to the term containing the square of the angle and the first power of the distance for the entire preceding system:[11]

$$P_n + P_n^* = \sum_{i=1}^{n} \frac{(p_i + p_i^*)}{\mathcal{M}_{i-1}^3}, \tag{6}$$

$$B_n + B_n^* = \sum_{i=1}^{n} \frac{(b_i + b_i^*)}{\mathcal{M}_{i-1}^3} - 3 \sum_{i=2}^{n} \frac{(p_i + p_i^*)}{(\mathcal{M}_{i-1}^3 F_{i-1})}. \tag{7}$$

The parameters of each lens are substituted into the expressions (2) and (4)-(7) taking into account whether they converge or diverge in the central plane of the system under consideration.

Using Eqs. (10)-(13) of ref. 10 for c_5, allowing for the corrections for nonzero inputs, we can determine the fifth-order spherical aberration for one quadrupole or quadrupole–octupole lens that is arbitrarily positioned in the system.

We will find the spherical aberration in the plane of the Gaussian image for a system consisting of k successive lenses:

$$\Delta_k = \Delta_k^{(3)} + \Delta_k^{(5)} + \ldots = \mathcal{M}_k [C_3 \alpha_0^3 + C_5 \alpha_0^5 + \ldots], \tag{8}$$

where

$$C_3 = P_k + P_k^*, \tag{9}$$

$$C_5 = \sum_{i=1}^{k} \frac{c_{5i}}{\mathcal{M}_{i-1}^5} + \sum_{i=2}^{k} \Big\{ (P_{i-1} + P_{i-1}^*) \Big[(B_i + B_i^*) + \frac{3}{2} (1 - \mathcal{M}_{i-1}^{-2}) \Big] - (P_i + P_i^*) \Big[(B_{i-1} + B_{i-1}^*) + \frac{3}{2} (1 - \mathcal{M}_{i-1}^{-2}) \Big] \Big\}, \tag{10}$$

α_0 being the slope of the extreme trajectory of the beam at the system input. The second sum in (10) determines the contribution to the fifth order from the trajectory perturbations resulting from third-order geometrical aberrations. It is proportional to the product of two third-order aberration coefficients. In a correction mode this contribution increases sharply as a result of the octupole component, this being larger, the larger the negative value of the third-order coefficient created by the correction element. We should expect, therefore, that it is this term which will yield the major contribution to the residual fifth-order spherical aberration (see ref. 7).

Let us consider a specific system consisting of combined electrostatic quadrupole–octupole lenses. It can function independently as a focusing system or in conjunction with an axisymmetrical lens in a negative spherical aberration mode. To achieve high resolving power it is best to use the correction element in front of an axisymmetric lens in a reduction mode.

The typical probe geometry for a quadrupole–octupole system consisting of four successive lenses is as follows: effective length of all lenses the same and equal to L = 2 cm, distances between edges of fields s = 3 cm, distance from crossover to system input a = 10 cm, distance from system output to image (working portion) g = 3 cm.

This system can be used either as a quadruplet [analog of an axisymmetrical lens (ref. 12)] or as a triplet (charged-particle trajectories are shown in Fig. 1).

Figure 2 shows triplet parameters as determined on a computer using the FAS-48 program:[13] excitation of quadrupole lenses β (curves 1-3), magnification in the CDC plane (curve 7) and third-order spherical aberration coefficient (curves 4-6) as functions of the magnification ratio in two characteristic planes.

On the basis of these calculations we choose the optimum modes of triplet operation. The first-order requirements mean in effect that the magnifications in two mutually perpendicular planes differ by a factor of not more than 2. It is also desirable that the excitations of two out of the three lenses be roughly the same. The correction element should have small octupole excitations and also low residual aberration values (Fig. 3). In accordance with the above requirements, we select two modes (I, II), shown in Figs. 2 and 3. The first-order trajectories for the optimum modes in question are shown in Fig. 1 (curves 2,3).

For the quadruplet (curve 1 in Fig. 1) we obtain the following results: excitation of first and fourth lenses

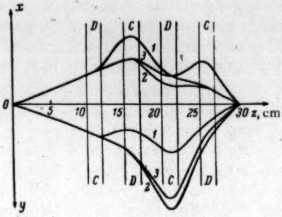

Fig. 1. Projections of electron-beam trajectories in two optimum triplet and quadruplet modes. 1) quadruplet, $\mathcal{M} = -0.6985$; 2) triplet, $\mathcal{M}_{CDC} = -0.751$, $\mathcal{M}_{DCD} = -0.372$; 3) triplet $\mathcal{M}_{CDC} = -0.266$, $\mathcal{M}_{DCD} = -0.498$.

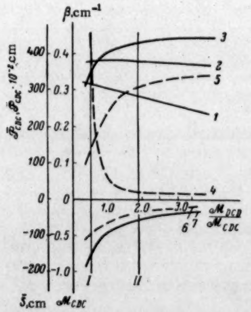

Fig. 2. First- and third-order electron-optical parameters of triplet: 1, 2, 3) excitation of first, second, and third lens respectively; 4) coefficient of spherical aberration $\bar{P}_{CDC}$ (in xoz plane); 5) $\bar{P}_{DCD}$ (in yoz plane); 6) third spherical aberration coefficient $\bar{S}$; 7) magnification in CDC plane.

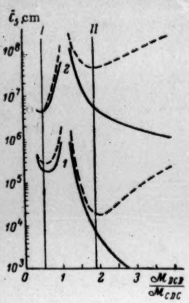

Fig. 3. Fifth-order spherical aberration coefficients of triplet C_5 for $C_3 = 0$ (curves 1) and $C_3 = -10^3$ cm (curves 2). The solid lines refer to the xoz plane, while the dashed lines refer to the yoz plane.

$\beta_{1,4} = 0.2715$ cm^{-1}, of second and third lenses $\beta_{2,3} = 0.3602$ cm^{-1}; magnification $\mathscr{M} = -0.6985$; aberration coefficients $\bar{P}_{CDCD} = 0.702 \cdot 10^3$ cm, $\bar{P}_{DCDC} = 2.554 \cdot 10^3$ cm, $\bar{S} = -0.225 \cdot 10^3$ cm. The aberration coefficients are adjusted to the state of the image of the system, so that $\bar{P} = P\mathscr{M}^4$.

Figure 3 shows the fifth-order spherical aberration coefficient for third-order spherical aberration corrected to zero and the negative value $\bar{C}_3 = -10^3$. Calculations are made on a computer using Eq. (10) in the "short-lens" approximation. The figure shows results for quadrupole fields without the sixth harmonic in the radial expansion of the potential ($K_6 = 0$). The role of nonlinear terms ($K_6 \neq 0$) will be discussed below. In addition, the calculations assume that the drop in the quadrupole field along the longitudinal axis is linear.

We should note that, according to the data of ref. 14, the difference between the fifth-order coefficients as measured on a model of a probe system and the computed values does not exceed a factor of 2-3.

For comparison we compute the fifth-order coefficients in certain modes (for $\bar{C}_3 = 0$), using the third-order coefficients appearing in c_{5-3} as found in the rectangular-field-model approximation. The discrepancy in using the two models is not great. This is due to the fact that the trajectories do not intersect the axis of the system and the assumption that a trajectory is constant within the limits of the lens field is met satisfactorily.

Our calculations indicate that the contribution to the total fifth-order aberration from the intrinsic coefficient of each lens $c_{5,i}$ is smaller by one to two orders of magnitude than the contribution from trajectory perturbation as a result of third-order geometrical aberrations, and the proportion decreases with increasing negative values of $\bar{C}_3$.

We will study in greater detail the effectiveness of correcting for third-order spherical aberration by using correction elements based on triplets in modes I and II and on the quadruplet analog of an axisymmetrical lens. For the range of variation of $\bar{C}_3 = 0\text{-}10^5$ cm created by the correction element we compute the fifth-order aberration coefficients of a quadrupole–octupole system, these being given in Fig. 4. For small $\bar{C}_3$ these coefficients are virtually constant; then they begin to increase and the dependence becomes quadratic for large negative $\bar{C}_3$.

In choosing the mode of a spherical-aberration correction element, we must allow for the residual spherical aberration (primarily fifth-order) of both the correction element and the lens being corrected. We compute the third- and fifth-order spherical aberration coefficient of a magnetic axisymmetrical lens. The lens that we have studied has a channel radius R equal to 1.25 the length of the nonmagnetic gap. The results are obtained by computer-implemented numerical methods using a program which N. I. Maleeva and L. A. Pavlova helped to write. Figure 5 shows the longitudinal spherical aberration coefficients, as adjusted to the image space, as functions of the size of the working segment g for fixed linear magnification M = −0.1. The third-order coefficients are in good agreement with the values in ref. 15. The fifth-order coefficients depend more sensitively on g, and there is a region with small working segments where $\bar{C}_5 < \bar{C}_3$. When the correction element is included the residual coefficients $\bar{C}_5^0$ differ sharply from $\bar{C}_5$ (the sign changes). For other electron-optical magnifications the nature of the above dependences remains the same.

On the basis of the fifth-order results we can evaluate the gain in resolving power and probe currents for spe-

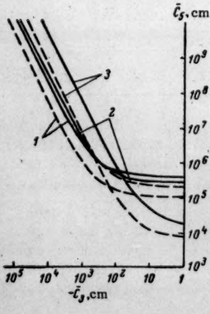

Fig. 4. Relationship between the third- and fifth-order spherical aberration coefficients in quadrupole–octupole systems. The solid curves refer to the yoz plane, while the dashed curves refer to the xoz plane. Notation is the same as in Fig. 1.

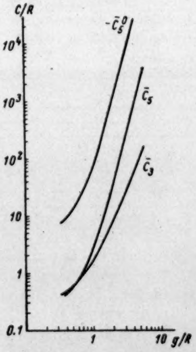

Fig. 5. Spherical aberration coefficients of a magnetic axisymmetric lens as a function of the size of the working segment.

TABLE 1

	Device	d	Φ, kV	I, A	ρ, A/(cm$^2\cdot$sr)	$\bar{C}_3$, cm	η	$(d_3/d_5)^{**}$	d_3/d_5	$(I_5/I_3)^{**}$	I_5/I_3
Scanning microscopes	Descr. in[17]	5 Å	25	10^{-11}	$2.5\cdot10^7$	0.03	0.15	4.0	3.0	32	16
	Stereoscan [18]	50	30	10^{-12}	$6\cdot10^4$	1	0.03	4.9	2.8	44	12
	Descr. in [19]	30	23	10^{-12}	$5.6\cdot10^5$	1.8	0.02	5.5	2.9	59	13
	HSM-2	100	40	10^{-13}	10^5	7.6	0.01	6.4	3.1	63	10
	Descr. in [20]	200	20	10^{-11}	$4\cdot10^4$	2	0.02	4.7	2.3	37	7.0
	jSM-2	250	25	10^{-11}	$5\cdot10^4$	1	0.03	4.5	2.5	29	7.5
Microanalyzers	Instrument of [21]	0.1 μ	30	10^{-9}	$6\cdot10^4$	3	0.02	4.3	2.0	29	5.0
	RÉMN [22]	0.5	5	$5\cdot10^{-9}$	10^4	2	0.02	3.6	1.7	17	2.9
	MAP-2	1.5	50	10^{-8}	10^5	5	0.01	3.4	1.5	16	2.4

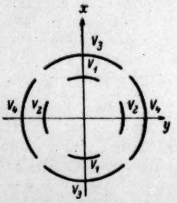

Fig. 6. Electrostatic quadrupole lens with adjustable spherical aberrations: $V_1 = V+u-v$, $V_2 = -V+u+v$, $V_3 = -u+v$, $V_4 = -u-v \pm V$ is the focusing potential, ±u and ±v are the correcting potentials.

cific devices. Assume that the probe diameter d in the plane of minimum cross section is given by the expression

$$d=\sqrt{d_g^2+d_s^2+d_d^2}, \tag{11}$$

where d_G is the diameter of the Gaussian image, d_s is the spreading due to spherical aberration, and d_d is the diameter of the diffraction-scattering circle.

For optimum aperture and reduction coefficients, the gain in probe size resulting from the correction of third-order spherical aberration for any nonzero $\bar{C}_5$ and constant probe current can be written as[16]

$$\frac{d_3}{d_5}=0.95\left[\frac{\bar{C}_3^2}{\frac{4I}{(\pi^2\rho)}+(1.22\lambda)^2}\right]^{1/24}\left(\frac{\bar{C}_3}{\bar{C}_5}\right)^{1/6}=\left(\frac{d_3}{d_5}\right)^{**}\eta^{1/6}. \tag{12}$$

Here d_3 is the probe diameter before correction, while d_5 is after correction; I is the probe current; ρ is the beam intensity; λ is the electron wavelength; $\eta = \bar{C}_3/\bar{C}_5$.

If the probe diameter is left unchanged, the current gain can be expressed as follows:

$$\frac{I_5}{I_3}=0.92\left(\frac{\bar{C}_3}{d}\right)^{4/15}f\left(\frac{\lambda}{d}\right)\left(\frac{\bar{C}_3}{\bar{C}_5}\right)^{2/5}=\left(\frac{I_5}{I_3}\right)^{**}\eta^{2/5}. \tag{13}$$

If $\lambda \ll d$, then we have $f(\lambda/d) \simeq 1$ in (13).

On the basis of (12) and (13) we evaluate the gain from correction for a number of existing scanning microscopes[17-20] and microanalyzers.[21,22] The results are shown in Table 1. The quantities $(d_3/d_5)^{**}$ and $(I_5/I_3)^{**}$ denote the gain in probe size and current for the case in which the third- and fifth-order aberration coefficients are roughly equal ($\eta \simeq 1$).

In computing η, we take only the residual correction-element aberrations as $\bar{C}_5$. Since no such data are available for the axisymmetric lenses used in the devices we have considered, it is assumed that they do not increase $\tilde{C}_5$. But the sign of $\tilde{C}_5$ for the magnetic axisymmetric lens that we have investigated (Fig. 5) – which is the reverse of that of $\bar{C}_5$ – permits us to hope that the gain from correction will increase. Moreover, an increase in resolving-power or current gain is possible when there is some overcorrection and partial compensation of the residual aberration by small negative values of the third-order coefficient.[23] In practice this mode is provided for automatically if the correction mode is chosen from the criterion of minimum probe size.

To further enhance the resolving power it is desirable to compensate for (or reduce) fifth-order spherical aberration. This is possible, for example, by appropriate choice of the shape of the electrodes of the quadrupole lens.[10,24] Because of the fixed harmonic in the expansion of the potential we find additional terms contributing to the fifth order; their value may be chosen so as to compensate for the remaining terms. In a five-electrode lens, this is accomplished technically by choice of the angle between electrodes. This procedure is not very effective, since it is adequate for only some single mode, and it is hardly feasible to vary lens geometry in the process of operation.

Simultaneous compensation of third- and fifth-order spherical aberration can be achieved by a new lens with aberrations that are electrically adjustable in magnitude and sign.[25] Electrostatic lenses of this type are formed by four inner electrodes arranged symmetrically with respect to mutually perpendicular planes xoz and yoz, and four external electrodes that surround them and are symmetric to the same planes (Fig. 6). The electrode shape can be arbitrary, but the symmetry conditions mentioned should be maintained.

Systems of such lenses can operate independently as focusing systems, and, moreover, can correct geometrical aberrations up to the fifth order inclusive of other electron-optical systems.

In conclusion we should note that, while technically difficult, quadrupole–octupole corrections make it possible to obtain a perceptible gain in microprobe devices. For charged-particle spectrometers, CRT's, and other electron-optical devices, the question merits further study.

---

[1] R. Seeliger, Optik, 5, 490 (1949), G. D. Archard, Proc. Phys. Soc., B68, 156 (1955); B. Von Bastian, K. Spengler, and D. Typke, Optik, 33, 591 (1971).

[2] D. Dhuicq and P. A. Möller, Proc. Seventh Intern. Congr. Electr. Microsc., Grenoble, 2, 45 (1970).

[3] M. G. R. Thomson, Optik, 34, 528 (1972).

[4] L. A. Baranova, T. Ya. Fishkova, and S. Ya. Yavor, Radiotekh. Elektron., 13, 2105 (1968).

[5] B. É. Bonshtedt and M. G. Markovich, Beam Focusing and Deflection in Electron-Beam Devices [in Russian], Izd. Sov. Radio, Moscow (1967), p. 111; Ya. G. Lyubchik, Author's Certificate No. 368675, Byull. Isobret., No. 9 (1973); H. D. Bauer, Optik, 23, 596 (1965/66).

[6] H. Rose, Optik, 33, 285 (1971).

[7] G. V. Der-Shvarts and A. N. Ignat'ev, Proceedings of Fourth All-Union Seminar on Methods of Solving Electron-Optical Problems [in Russian], Novosibirsk (1971).

[8] E. V. Shpak, S. Ya. Yavor, and Ya. G. Lyubchik. Nucl. Instrum. Meth., 64, 97 (1968).

[9] B. G. Podlaskin and V. V. Sumachev, Zh. Tekh. Fiz., 38, 1169 (1968) [Sov. Phys.-Tech. Phys., 13, 966 (1969)].

[10] Ya. G. Lyubchik, L. P. Ovsyannikova, and T. Ya. Fishkova, Zh. Tekh. Fiz., 41, 2175 (1971) [Sov. Phys.—Tech. Phys., 16, 1724 (1972)].

[11] S. Ya. Yavor, L. P. Ovsyannikova, and L. A. Baranova, Nucl. Instrum. Meth., 99, 103 (1972).

[12] S. Ya. Yavor, Focusing of Charged Particles by Quadrupole Lenses [in Russian], Atomizdat, Moscow (1968), p. 100.

[13] Ya. G. Lyubchik, Preprint FTI-354, Leningrad (1971).

[14] Ya. G. Lyubchik, Proceedings of Fourth All-Union Seminar on Methods of Solving Electron-Optical Problems [in Russian], Novosibirsk (1971).

[15] G. V. Der-Shvarts and I. S. Makarova, Radiotekh. Elektron., 11, 89 (1966); 12, 168 (1967); Ya. G. Lyubchik and A. V. Mokhnatkin, Radiotekh. Elektron., 17, 2234 (1972); W. Kamminga, J. L. Verster, and J. C. Francken, Optik, 28, 442 (1968/69).

[16] S. Ya. Yavor, V. N. Vertsner, Ya. G. Lyubchik, A. V. Mokhnatkin, and Yu. V. Chentsov, Proc. Fifth Europ. Congr. Electr. Microsc., Manchester (1972), p. 92.

[17] A. V. Crewe, Quarterly Rev. Biophys., 3, 137 (1970).

[18] R. F. W. Pease and W. C. Nixon, J. Sci. Instr., 42, 81 (1965).

[19] A. N. Broers, Rev. Sci. Instr., 40, 1040 (1969).

[20] V. N. Vertsner, V. M. Krygin, and Yu. V. Chentsov, Opt.-Mekh. Prom., No. 1, 38 (1971).

[21] P. Duncumb, Proc. Fifth Intern. Conf. Electr. Microsc., 1, KK-4, Philadelphia (1962).

[22] Yu. V. Chentsov, G. D. Kisel', V. M. Krygin, and V. N. Keis, Opt.-Mekh. Prom., No. 5, 59 (1968).

[23] O. Scherzer, J. Appl. Phys., 20, 20 (1949).

[24] L. P. Ovsyannikova and S. Ya. Yavor, Zh. Tekh. Fiz., 41, 1023 (1971) [Sov. Phys.—Tech. Phys., 16, 803 (1971)].

[25] T. Ya. Fishkova and Ya. G. Lyubchik, Author's Certificate No. 408393, Byull. Izobret., No. 47 (1973).

Mechanism for plasma loss from a magnetic trap

V. I. Volosov

Institute of Nuclear Physics, Siberian Branch,
Academy of Sciences of the USSR, Novosibirsk

(Submitted March 18, 1974)
Zh. Tekh. Fiz., 44, 2280-2285 (November 1974)

The interaction between plasma particles in a magnetic well with helical magnetic field lines (for example, in a stellarator) and the electric field due to a low-frequency (drift) instability is considered. It is shown that even when the amplitude of the electrostatic oscillations is small, $\varphi < kT_e/e$, the radial displacement of the particles (ions and trapped electrons) can be larger than the displacement computed from the neoclassical theory. When $\varphi \approx kT_e/e$ the radial displacement of the particles is equal to the plasma dimension. The loss rate is determined by the time $\tau_p \approx \gamma^{-1}$. For the collisionless drift mode it follows that $\tau_p \approx k\tau_{\text{Bohm}}$, where τ_{Bohm} is the Bohm time. For most stellarator experiments k ~ 1-10; this quantity depends on both the magnetic parameters (average shear $\bar{\theta}$ and ε) and the plasma parameters (T_i/T_e and m_i/m_e). The present estimates are compared with experiment.

1. It is well known that in the classical approximation plasma loss from a closed magnetic well depends significantly on the presence of trapped particles in the plasma, i.e., particles whose longitudinal motion is localized in bounded regions of the magnetic field. The radial displacement of these particles is much larger than the Larmor radius and plasma loss from the traps across the magnetic field is largely due to these particles (so-called neoclassical diffusion[1,2]).

However, the presence of trapped particles can also have a considerable influence on plasma loss in the presence of low-frequency instabilities if the frequency ω is smaller than the characteristic frequency of trapped electrons in the local well Ω_e and if the ion thermal velocity v_{Ti} is smaller than the longitudinal phase velocity ω/k_z. These conditions are usually satisfied by drift oscillations – the most widely encountered low-frequency instabilities.[3,4]

2. Consider the radial displacement (drift) of individual plasma particles in the field of the drift wave Δr_j. Since the longitudinal phase velocity of the wave ω/k_z satisfies the condition

$$v_{Ti} \ll \frac{\omega}{k_z \ll v_{Te}}, \tag{1}$$

the ion longitudinal velocity can be neglected in estimating Δr_i (here, Δr_i is the ion radial drift and Δr_e is the same for the electrons). Assuming that the wavelength in the radial direction (or the correlation length of the oscillations l in this direction for $l < k_r^{-1}$) is larger than or of the order of Δr_i (this assumption is valid, for example, in stellarator experiments; see refs. 5 and 6), for monochromatic oscillations with $\omega = \omega_e \equiv cT_e k_{ye}/eHa_n$ we have

$$\Delta r_i = \int_0^{\pi/\omega} v_{\text{dr}}\, dt = \alpha a_n; \quad v_{\text{dr}} = c\frac{E_\varphi(t)}{H_z}, \tag{2}$$

where a_n is the characteristic plasma inhomogeneity scale length – $(\partial \ln n/\partial r)^{-1}$; $\alpha = e\varphi/T_e$, where φ is the potential associated with the wave.

For a spectrum that can be represented as a sum of Fourier components, the displacement $\Delta r_i(t)$ is

$$\Delta r_i(t) = a_n \sum_q \alpha_q \left(\frac{k_{yq}}{k_{ye}}\right)\left(\frac{\omega_e}{\omega_q}\right) \int_0^t \sin(\omega_q t + \psi_q)\, d\omega_q t.$$

The maximum value of Δr_i in this case (for appropriate values of ψ_q) is

$$\Delta r_i = a_n \sum_q \alpha_q \left(\frac{k_{yq}}{k_{ye}}\right)\left(\frac{\omega_e}{\omega_q}\right), \tag{3}$$

where q is the harmonic number; $\alpha_q = e\varphi_q/T_e$; φ_q is the amplitude of the q-th harmonic. If the lowest oscillation frequency ω_1 is much smaller than ω_e (and $k_{y1} \approx k_{ye}$) the particle displacement in the field of such a wave is larger than the transverse plasma dimensions (i.e., $\Delta r_i > a_n$) even when $e\varphi_1/T_e \ll 1$ (this is equivalent to $\Delta n_1/n \ll 1$, where n is the plasma density and Δn_1 is the fluctuation).[1)]

Since $v_{Te} \gg \omega/k_z$ a similar estimate for untrapped electrons gives

$$\Delta r_e \simeq \alpha a_n \left(\frac{\omega}{k_z v_{Te}}\right) \ll a_n. \tag{4}$$

Several properties of the motion of the trapped electrons are taken into account in calculating Δr_e. Let the longitudinal drift wavelength k_z^{-1} be larger than the longitudinal dimension of localization of the trapped electrons z_e, and thus $\Omega_e \gg \omega_e$; let k_y^{-1} be larger than electron displacement in the y direction in one oscillation period, and let $k_r^{-1} \geq \Delta r_e$ or $l \geq \Delta r_e$ for $l < k_r^{-1}$ (these assumptions have also been confirmed experimentally; see refs. 5-7). The calculation of Δr_e is carried out for the time period ω^{-1} so that the phase velocity of the wave ω/k_z should not be compared with the instantaneous velocity $v_{\parallel e}$, but with the average value of $v_{\parallel e}$ for time $\sim \omega^{-1}$ (it is denoted by $\bar{v}^{\omega}_{\parallel e}$. The distribution function $f(\bar{v}^{\omega}_{\parallel e})$ is given in Fig. 1. For the trapped electrons the average value of $\bar{v}^{\omega}_{\parallel e}$ is the same order of magnitude as $z_e(\omega + \nu_e)$, where ν_e is the effective collision frequency (below $\nu_e \leq \omega$). With these assumptions Δr_e for the trapped electrons is determined by (2).

The fraction of trapped electrons is $\sqrt{\varepsilon_1}$ ($\varepsilon_1 \equiv \Delta H/H$ is the ratio of the periodic magnetic field to the constant field along the line of force and usually ranges from 0.1 to 0.5, i.e., it is fairly large). Note also that the profile of the magnetic surfaces in magnetic wells like the stellarator type is usually not the same as the linear profile. Therefore, the azimuthal electric field (and thus the particle drift velocity) is nonzero in the neighborhood of the separatrix; thus, the plasma particles can be lost to the

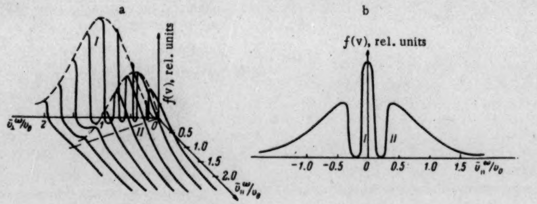

Fig. 1. Shape of the functions $f(\bar{v}_{\parallel e}^{\omega}, v_{\perp} = \text{const})$ (a) and $f(\bar{v}_{\parallel e}^{\omega}, \bar{v}_{\perp e}^{\omega})$ (b) at the point where the magnetic field is a minimum along the line of force. I) Region of trapped electrons; II) of untrapped electrons.

chamber wall due to radial drift.

For a high oscillation amplitude the fraction of electrons trapped by the electric field of the wave increases. However, the radial displacement of these particles in the wave field is small. The average value of Δr_e in one period of particle oscillation in the wave is zero; when $\alpha \approx 1$ the frequency is much larger than ω_e. In this case an estimate of the maximum Δr_e gives a value close to (4):

$$\Delta r_e \simeq 2\sqrt{\alpha}\, a_n \left(\frac{\omega}{k_z v_{Te}}\right)\left(\frac{z_0}{\lambda_z}\right), \tag{5}$$

where z_0/λ_z is the ratio of the particle localization dimension in the wave to the wavelength ($z_0/\lambda_z < 1$).

Thus, the maximum value of Δr_e is associated with electrons trapped in the troughs of the external magnetic field [see (2), (4), and (5)].

3. The expressions obtained above are now compared to the radial displacement of trapped electrons in closed magnetic wells given by neoclassical diffusion theory. When $\varepsilon_t \gg \varepsilon_h$ the maximum deviation of the trapped particles[8,9] is

$$\Delta r \simeq \left(\frac{\rho_{wj}}{\iota}\right)\left(\frac{R}{r_0}\right)^{1/2}, \tag{6}$$

where ι is the rotational transform.

In the opposite limit, $\varepsilon_t/\varepsilon_h \ll 1$, the radial deviation is determined by the precession of trapped particles in a banana orbit in the bounded region of the line of force:[1]

$$\sqrt{\frac{\varepsilon_t}{\varepsilon_h}}\, r_0 \geqslant \Delta r \geqslant \frac{2\varepsilon_t}{3\varepsilon_h} r_0. \tag{7}$$

Here, r_0 is the average radius of the magnetic surface. The majority of trapped particles suffer displacements close to the minimum value.

It follows from the estimates above that the radial displacement in the drift-wave field can be larger than or of the order of Δr in the neoclassical theory. Therefore, in calculating particle lifetimes in a plasma both of these processes must be taken into account. Obviously, the first process predominates when $\alpha \gg (\rho_{wj}/\iota a_n)(R/r_0)^{1/2}$ for $\varepsilon_t \gg \varepsilon_h$ or $\alpha \gg \varepsilon_t/\varepsilon_h$ for $\varepsilon_t \ll \varepsilon_h$.

4. We now estimate the plasma lifetime time when Δr is comparable to the transverse plasma dimensions (i.e., $\alpha \simeq 1$ for $\omega \simeq \omega_e$).

The growth rate of the radial motion is determined by the growth rate γ of the corresponding low-frequency instability. If the radial oscillation extends over the entire plasma the number of particles ΔN lost to the wall in one period is

$$\Delta N \simeq N \frac{\gamma}{\omega}, \tag{8}$$

which gives the decay time

$$\tau_p \simeq \gamma^{-1}. \tag{9}$$

Here, γ is the growth rate averaged over the volume. If only some of the particles (for example only the trapped electrons) participate in the radial oscillations and the fraction of trapped electrons is $\sqrt{\varepsilon_1}$ then

$$\tau_p \simeq (\gamma \sqrt{\varepsilon_1})^{-1}. \tag{9'}$$

The loss of plasma from the magnetic well in the case considered above is due to the flow of particles to the chamber wall, an anomalous "pumpout" effect.

In the case considered above the plasma decay time τ_p due to the instability is much smaller than the classical decay time of both the electron τ_e and ion τ_i components. When $\tau_e < \tau_p < \tau_i$ or when $\tau_i < \tau_p < \tau_e$ the nature of the plasma loss is somewhat different. In the first case ($\tau_e < \tau_p$) the plasma confinement time is determined by the ion confinement time, i.e., $\tau_p \simeq \gamma^{-1}$. If τ_e is determined by the loss of trapped particles, the plasma flow is in the direction of the separatrix angles. When $\tau_i < \tau_p$, the plasma decay time is determined by the trapped-electron confinement, i.e., $\tau_p \simeq \gamma^{-1}\varepsilon_1^{-1/2}$.

A somewhat more general approach to the problem is also possible. We can assume that the nonlinear mechanism that saturates the growth of the amplitude of low-frequency oscillations is the loss to the wall of a certain number of plasma particles due to a high amplitude of the radial oscillations $\tilde{n}$ ($\tilde{n}$ is the particle density when the amplitude of the radial oscillations becomes larger than some thereshold value Δr_0).

Due to the positive growth rate, the value of $\tilde{n}$ (and thus the amplitude of the electrostatic oscillations) increases with time; on the other hand the loss of plasma component to the wall reduces the trapped fraction and thus reduces the amplitude of the oscillations. Balancing these two processes we find

$$\frac{\partial n}{\partial t} = \delta n \gamma - \frac{n}{\tau_p} = 0 \qquad (10)$$

($\delta \leq 1$ is a factor that depends on the geometry and the parameters), from which (9) or (9') follows. This estimate is also valid when the condition $\alpha \simeq 1$ (or $\Delta r \simeq a$) is not satisfied.

5. As an example, we consider the particular case of the collisionless drift instability. We assume that $T_e > T_i$. This condition holds in the majority of experiments with closed traps. If the conditions $v_{Ti} \ll \omega/k_z \ll v_{Te}$, $\nu_e < k_z v_{Te}$, $s \equiv k_\perp^2 \rho_i^2/2 < 1$ are satisfied, the dispersion relation[10] is

$$\frac{k_\perp^2 T_e}{m_i \Omega_{0i}^2} + 1 + \frac{\omega_*}{\omega} - \left(\frac{k_z c_s}{\omega}\right)^2 + \frac{i\sqrt{\pi}}{k_z v_{Te}}(\omega - \omega_*) = 0. \qquad (11)$$

When $\omega/k_z \gg c_s$ or $\rho_i^* k_\perp / a k_z \gg 1$ [$\rho_i^* = \rho_e (m_i/m_e)^{1/2}$], the term $(k_z c_s/\omega)^2$ can be dropped. The solution of (11) for $\mathrm{Re}\,\omega \gg |\mathrm{Im}\,\omega|$ is

$$\mathrm{Re}\,\omega \simeq \frac{\omega_*}{1+b}; \quad \gamma \equiv \mathrm{Im}\,\omega = \sqrt{\pi}\frac{(\mathrm{Re}\,\omega)^2}{k_z v_{Te}}\frac{b}{1+b}, \qquad (12)$$

where $b = sT_e/T_i = k_\perp^2 \rho_i^{*2}/2$. When $a_n \gg \rho_i$ waves with $b \simeq 1.0$ have the maximum growth rate; an increasing ion collision frequency reduces the growth rate[11,12] and the maximum of $\gamma(k_\perp; \rho_i^*)$ is shifted towards longer wavelengths. In the opposite limit $a_n \ll \rho_i$ the maximum growth rate holds for waves with $k_\perp \simeq a^{-1}$. The longitudinal wavelength is determined by the relation

$$k_z = k_{z0} + k_y \bar{\theta}' x_1$$

or, for $k_{z0} \ll k_z$,

$$k_z \simeq k_y \bar{\theta}' x_1,$$

where $\bar{\theta}'$ is the average value of $\partial\theta/\partial r \simeq \theta(r)/r$ in the region of developed oscillations; θ is the shear (here $\theta = r^2 \partial[H_\varphi / r^2 H_z]/\partial r$). Using (9) and (12) and assuming that $x_1 \simeq r \simeq a$ we find the decay time

$$\tau_p \simeq \left(\frac{eH}{cT}\right)^2 \frac{a_n^2 \bar{\theta} v_{Te}}{k_y} \frac{(1+b)^2}{\sqrt{\pi}\, b}. \qquad (13)$$

We assume that the characteristic scale length and the radius of the plasma are related by $a_n = a/2.4$. For the case $\rho_i^* \ll a$ (i.e., $b \simeq 1.0$, $k_\perp \simeq \rho_i^{*-1}$) we find from (13)

$$\tau_p = A\bar{\theta}\left(\frac{m_i}{m_e}\right)^{1/2} \tau_{\mathrm{Bohm}}, \qquad (14)$$

where $\tau_{\mathrm{Bohm}} = a_n^2 (cT/16eH)^{-1}$ is the Bohm time; $\bar{\theta}$ is the mean shear; A is a constant, $A \simeq 1$ ($A \simeq 0.4/\sqrt{\varepsilon_1}$, where $\sqrt{\varepsilon_1}$ is the fraction of trapped electrons). In the opposite limit $\rho_i^* \geq a$ (i.e., $k_\varphi \simeq Ma$, where M is the mode number):

$$\tau_p \simeq A\bar{\theta}\left(\frac{m_i}{m_e}\right)^{1/2} \tau_{\mathrm{Bohm}} \left(\frac{a}{\rho_i^*}\right) \frac{(1+b)^3}{3.8M\sqrt{\pi}\, b}. \qquad (15)$$

One can obtain estimates for τ_p similar to those given above for an arbitrary ratio of T_e to T_i (assuming that $\rho_i^* \ll a$). For the cases $T_e = T_i$ and $T_e < T_i$ the maximum growth rate holds for $s \simeq 1.0$; the value of τ_p is determined by (14), where $A \simeq 0.5/\sqrt{\varepsilon_1}$ for $T_e = T_i$ and $A \simeq 0.3(T_e/T_i)^{1/2}/\sqrt{\varepsilon_1}$ for $T_e < T_i$. Obviously, these estimates are only valid when the drift wave is unstable [for example, see ref. 13, Eq. (57), and ref. 14].

Comparison of the above expressions with experiment (primarily involving stellarators) requires that the value of $\bar{\theta}$ be known. In most of the published papers, however, the maximum shear is given, i.e., the value of $\bar{\theta}$ on the last complete magnetic surface. In the general case a unique correspondence does not hold between $\theta_{\max}$ and $\bar{\theta}$. The value of $\theta_{\max}$ depends primarily on the quality of the helical windings, the amplitude of the different magnetic field disturbances, and the stellarator geometry, while $\bar{\theta}$ is determined only by the mean radius and the amplitude of the fundamental helical magnetic field harmonic, being independent of the above parameters of the magnetic system. We can obtain an estimate by assuming that $\bar{\theta}$ is the same order of magnitude as the shear in the region of the maximum drift oscillations $\bar{\theta} = \theta(\bar{r})$ (we assume that $\bar{r} = 0.7 - 0.8\, r_{\mathrm{sep}}$, where r_{sep} is the radius of the separatrix). In the center regions (i.e., $r/r_{\mathrm{sep}} < 0.9$–0.85) the shear is determined only by the fundamental magnetic field harmonic: $\theta(r) = 0.33\,(r/r_{\mathrm{sep}})^3 F(\beta_{\mathrm{sep}})$ for $n = 3$ and $\theta(r) = 0.26\,(r/r_{\mathrm{sep}})^3 F(\beta_{\mathrm{sep}})$ for $n = 2$, where $0.5 < F(\beta_{\mathrm{sep}}) < 1$ for $8° < \beta_{\mathrm{sep}} < 45°$ ($n = 3$) and $25° < \beta_{\mathrm{sep}} < 60°$ ($n = 2$); β_{sep} is the angle of incidence of the edge of the separatrix to the axis of the torus.[15] For most modern stellarators with an optimum separatrix dimension, $F \simeq 0.5$-1.0 and thus $\bar{\theta} \simeq 0.05$-0.1. Taking this estimate into account we find from (14)

$$\tau_p = A_1\left(\frac{m_i}{m_{\mathrm{pr}}}\right)^{1/2} \tau_{\mathrm{Bohm}}, \qquad (16)$$

where A_1 is a constant ($A_1 = 2A$ to $4A$), m_i is the plasma ion mass, and m_{pr} is the proton mass.

The dependence of plasma lifetime on temperature and magnetic field given above (proportional to the Bohm dependence) has been observed in many experiments both with stellarators[16–19] and with other types of closed systems.[20,21] Within the spread of the experimental points and the accuracy of the estimate of A_1, the absolute values of τ_p obtained from experiment and calculated from (16) also coincide (in many cases). In a number of cases the dependence of τ_p on the shear (or the rotational transform) and the ion mass agrees with (14) and (16) [see refs. 16 and 22].

However, to establish a unique relation between the above mechanism for radial displacement of a plasma and experiment requires detailed information on the radial plasma losses produced by the fluctuation fields and their spatial distribution. At the present time, such measurements have been performed only for a cold plasma. As a rule, they indicate a good agreement with the loss mechanism considered above.[5–7,23]

Thus, in the presence of low-frequency oscillations the mechanism considered above can determine the rate of loss of plasma and not only for closed systems, but for any system with trapped electrons.

In conclusion, the author thanks S. S. Moiseev, V. N. Bocharov, and Yu. N. Yudin.

---

*Publishers note: Reference 14 is missing in the Russian original.

1) It is assumed here that ν_i, the effective frequency of ion collisions, is small compared to ω (in the latter case to ω_1).

---

[1] A. A. Galeev and R. Z. Sagdeev, in: Reviews of Plasma Physics [in Russian], No. 7, Atomizdat, Moscow (1973), p. 205.

[2] A. A. Galeev, R. Z. Sagdeev, and G. P. Fyurs, Prikl. Mekh. Tekh. Fiz., No. 6, 3 (1968).

[3] A. A. Galeev, S. S. Moiseev, and R. Z. Sagdeev, At. Energ., 15, 451 (1973).

[4] A. B. Mikhailovskii, Theory of Plasma Instabilities, Vol. 2, Consultants Bureau, New York (1973), Chap. 3.

[5] K. Bol and R. A. Ellis, Report MATT-580, Princeton (1968).

[6] V. N. Bocharov, V. I. Volosov, A. V. Komin, V. M. Panasyuk, and Yu. N. Yudin, in: Proceedings of the Fourth Intern. Conf. on Plasma Physics and Controlled Thermonuclear Fusion, Madison, 1971 (IAEA, Vienna, 1971).

[7] V. I. Volosov, and Yu. N. Yudin, in: Proc. of the Fifth European Conference on Plasma Physics and Controlled Thermonuclear Fusion, Vol. 1, Grenoble (1972), p. 79.

[8] H. L. Berk and A. A. Galeev, Phys. Fluids, 10, 441 (1967).

[9] B. B. Kadomtsev and O. P. Pogutse, Zh. Eksp. Teor. Fiz., 51, 1734 (1966) [Sov. Phys.–JETP, 24, 1172 (1967)].

[10] B. B. Kadomtsev, in: Reviews of Plasma Physics, Vol. 4, Consultants Bureau, New York (1966).

[11] A. B. Mikhailovskii and O. P. Pogutse, Dokl. Akad. Nauk SSSR, 156, 64 (1964) [Sov. Phys.–Dokl., 9, 379 (1964)].

[12] A. A. Rukhadze and V. P. Silin, Usp. Fiz. Nauk, 82, 499 (1964) [Sov. Phys.–Usp., 7, 209 (1964)].

[13] Y. Nishida, T. Dodo, T. Kuroda, and G. Horikoshi, Report IPPJ-166, Nagoya Univ. (1973).

[15] V. I. Volosov and A. V. Komin, Report Inst. Yad. Fiz. Sib. Otdel. Akad. Nauk SSSR, No. 8, Novosibirsk (1970).

[16] D. Grove, E. Meservey, W. Stodiek, and K. M. Young, in: Proc. of the Third Intern. Conf. on Plasma Physics and Controlled Thermonuclear Fusion, Novosibirsk, 1968 (IAEA, Vienna, 1969), Vol. 1, p. 479.

[17] K. Miamoto and A. Mokhri, in: Proc. of the Fourth Intern. Conf. on Plasma Physics and Controlled Thermonuclear Fusion, Madison, 1971 (IAEA, Vienna, 1971), Vol. 3, p. 93.

[18] L. M. Kovrizhnykh, in: Proc. of the Fifth European Conference on Plasma Physics and Controlled Thermonuclear Fusion, Vol. 2, Grenoble (1972), p. 147.

[19] R. A. Ellis and D. Eckhartt, Report IPP/2/85, Munich (1970).

[20] B. B. Kadomtsev, in: Proc. of the Sixth European Conf. on Plasma Physics and Controlled Thermonuclear Fusion, Vol. 2, Moscow (1973).

[21] S. Yoshikawa, Nucl. Fusion, 13, 433 (1973).

[22] R. A. Ellis and H. P. Eubank, Phys. Fluids, 2, 1109 (1968).

[23] K. M. Young, Phys. Fluids, 10, 213 (1967).

Measurement of ion density by the dispersion relation for an ion-beam plasma

M. D. Gabovich, L. P. Katsubo, and I. A. Soloshenko

Physics Institute, Academy of Sciences of the USSR, Kiev

(Submitted January 30, 1974)
Zh. Tekh. Fiz., 44, 2286-2289 (November 1974)

An experimental study has been made of the dispersion properties of transverse ion modes excited by a fast ion beam which also ionizes the background gas. In accordance with theory, for $k^2d_e^2 \ll 1$ (d_e is the electron Debye radius) the frequency $\omega_k = kc_s$, where c_s is the ion acoustic velocity; in the opposite limit ($k^2d_e^2 \gg 1$), $\omega_k \approx \omega_{pi}$, where ω_{pi} is the ion plasma frequency. The ion plasma modes have the growth rate ($\omega \approx \omega pi$). This result, and the fact that the oscillations are localized, ($k^2d_e^2 \gg 1$), means that the radial density profiles of the slow ions can be measured.

In the transport of intense ion beams the space charge is usually neutralized by charges produced in the ionization of the residual gas in the beam. The degree of neutralization of the beam, the phase volume, and the specific power are then determined by the properties of the plasma which is formed. It is therefore important to know the parameters of this plasma. The use of the probe method is complicated in an ion-beam plasma because of the presence of the beam itself and because of the low density. The low density also hinders the use of the resonator method. In this note we consider the possibility of measuring the ion density using waves excited in the system.

The ion dispersion equation in a nonisothermal plasma ($T_i \ll T_e$) penetrated by a monoenergetic beam of ions with velocity v_0 is[1,4]

$$1+\frac{1}{k^2d_e^2}-\frac{\omega_{pi}^2}{\omega^2}+\frac{\omega_{bi}^2}{(\omega-k_zv_0)^2}=0, \tag{1}$$

where T_e and T_i are the electron and ion temperatures respectively in the plasma, ω_{pi} and ω_{bi} are the ion plasma frequencies in the plasma and the beam, d_e is the electron Debye radius. It follows from (1) that the maximum growth rate $\gamma = (\sqrt{3}/2^{4/3})\alpha^{1/3}\omega_k(\alpha = \omega_{bi}^2/\omega_{pi}^2)$ obtains for

$$\omega_k^2 \approx \frac{\omega_{pi}^2}{1+\frac{1}{k^2d_e^2}} \approx k_z^2v_0^2. \tag{2}$$

When $k^2d_e^2 \ll 1$ the frequency $\omega_k = kc_s$, where $c_s = (T_e/m_i)^{1/2}$ is the ion acoustic velocity; in the opposite limit ($k^2d_e^2 \gg 1$), $\omega_k \approx \omega_{pi}$. The growth rate peaks when $\omega_k \approx \omega_{pi}$. This result, and the fact that the ion plasma oscillations are localized ($k^2d_e^2 \gg 1$), mean that it is possible to determine the local density of the plasma ions. It must be noted, however, that for a high value of T_i the maximum amplitude can shift towards lower frequencies as a result of the severe attenuation near ω_{pi}. For this reason it is necessary to make an experimental check that the maximum amplitude coincides with the ion plasma frequency.

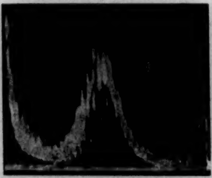

Fig. 1. Spectrum. $\dot{H}_2^+$ ion beam with energy eU_0 = 30 keV and current I_i = 15 mA passes through argon at a pressure of p = $5 \cdot 10^{-5}$ mm Hg. The calibration marks correspond to 0 and 750 kHz.

The experiments are carried out on the apparatus which has been described in detail in refs. 2-4. An H_2 ion beam with current I_i = 40 mA, energy eU_0 = 40 keV, and density $n_b \sim 10^7$ cm^{-3} passes through a chamber of length L = 500 cm to a grounded target. The pressure of the neutral gas is varied over the range p = $5 \cdot 10^{-6}$ - $1 \cdot 10^{-3}$ mm Hg. The waves excited in the system are recorded by means of insulated probes which can be moved in the radial direction.[4] The radial distribution of the static potential is measured by means of hot probes.

Ion oscillations are only excited when the pressure reaches a certain value[4] which depends on the type of gas. Figure 1 shows a typical spectrum. Measurements of the wave number as a function of frequency show that the maximum amplitude coincides with the ion plasma frequency. For the purpose of these measurements the beam is modulated by means of an external generator with a signal which is fed to a modulating probe at the entrance to the chamber. Since $v_0 \gg c_s$ and $k \gg k_z$, the wave number can be calculated by measuring the variation of the phase of the oscillations with distance along a radius by means of a recording probe.

Figure 2a shows the dispersion relationships obtained at various pressures. The dashed straight lines correspond to the oscillation frequency at which the amplitude is a maximum. In accordance with (2) the frequency increases linearly with k at long wavelengths; the phase velocity under these conditions $\omega/k \approx 3.2 \cdot 10^5$ cm/sec, in agreement with the value for the ion acoustic velocity $c_s \approx 2.5 \cdot 10^5$ cm/sec calculated for T_e = 2 eV. (The value of T_e for air has been measured experimentally.[3]

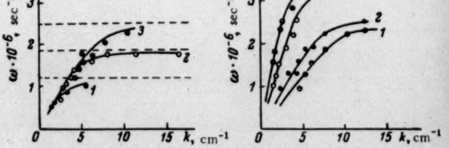

Fig. 2. Dispersion relationships for ion oscillations. a) Air, p(mm Hg): 1) $3 \cdot 10^{-5}$; 2) $5 \cdot 10^{-5}$; 3) $8 \cdot 10^{-5}$. b: 1) Krypton, p = $4 \cdot 10^{-5}$; 2) air, p = $6 \cdot 10^{-5}$; 3) helium, p = $2 \cdot 10^{-4}$; 4) hydrogen, p = $2 \cdot 10^{-4}$. Ion beam current I_i = 15 mA, energy eU_0 = 25 keV.

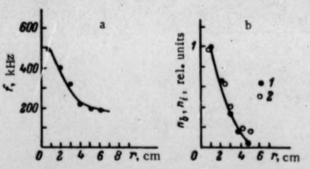

Fig. 3. a) Dependence of the frequency of the excited oscillations on the radius; b) radial distribution of beam current density (1) and density of slow ions (2). A beam of H_2^+ ions with I_i = 15 mA, energy eU_0 = 25 keV passes through air at a pressure of $p = 6 \cdot 10^{-5}$ mm Hg.

The measurements carried out on other gases (Fig. 2b) are also in agreement with theory. The phase velocities at long wavelengths for hydrogen, helium, and krypton are $9.3 \cdot 10^5$, $6.3 \cdot 10^5$, and $2.2 \cdot 10^5$ cm/sec respectively and these agree in order of magnitude with the corresponding ion acoustic velocities for T_e = 2 eV.

It can be seen from Fig. 2a that as the modulation frequency approaches the frequency corresponding to the maximum amplitude the wavelength tends to zero. We conclude that the maximum amplitude is observed at a frequency equal to the ion plasma frequency; therefore measurements of these frequencies can be used to calculate the density of slow ions.

Figure 3a shows the variation of the frequency of the spontaneously excited oscillations with maximum amplitude with distance along a radius; Fig. 3b gives the density profile of slow ions obtained from the data in Fig. 3a. For comparison the radial density profile of the beam particles is also given.

Figure 4 shows how the ratio of the slow-ion density n_i to the beam density n_b varies with pressure at the center of the beam for various gases (the beam parameters remaining constant).

The experimentally measured values of n_i are in qualitative agreement with the values calculated from a solution of the slow-ion continuity equation

$$n_i(r) = \int\limits_0^r \frac{n_b(r)\, v_0 n_a \sigma_i 2\pi x\, dx}{2\pi r \left(\frac{2e}{m_i}\right)^{1/2} \sqrt{\varphi(x) - \varphi(r)}}, \tag{3}$$

where n_a is the density of gas molecules and σ_i is the cross section for the formation of slow ions. If we assume that $n_b(z) = n_0(1 - r^2/r_0^2)$, and $\varphi = \varphi_0(1 - r^2/r_0^2)$, we can integrate (3) to get

$$\frac{n_i(r)}{n_b(r)} = \frac{n_a \sigma_i r_0 v_0}{\sqrt{2 \frac{e}{m_i} \Delta\varphi}} \frac{1 - \frac{2}{3}\frac{r^2}{r_0^2}}{1 - \frac{r^2}{r_0^2}}, \tag{4}$$

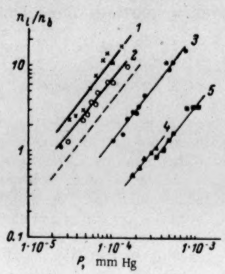

Fig. 4. Variation of the slow ion density with pressure. An H_2^+ ion beam with I_i = 15 mA and energy eU_0 = 25 keV passes through argon (1), air (2), neon (3), hydrogen (4), and helium (5).

where $\Delta\varphi$ is the radial drop in potential in the beam. The variation of $\Delta\varphi$ with the pressure of air has been measured experimentally. Substituting into (4) the values r_0 = 3 cm, $\sigma_i = 2 \cdot 10^{-15}$ cm², and the experimental values of $\Delta\varphi$, we can calculate the variation of n_i/n_b with pressure at r = 0. The results are shown in Fig. 4 by the dashed line. The calculated and experimental lines have the same slope and give nearly the same values of n_i/n_b. (The fact that n_i does not increase in proportion to the pressure is due to the reduction in $\Delta\varphi$ and the reduction in the velocity of the slow ions away from the beam region as the pressure increases.) The fact that the slow ion density at a given pressure is greater for gases with a high production cross section is also in agreement with the calculations. For argon and air, n_i/n_b exceeds unity when $p > 2 \cdot 10^{-5}$ mm Hg; for hydrogen and helium, n_i becomes significant only when $p > 1 \cdot 10^{-4}$ mm Hg.

Thus we have obtained experimental dispersion relationships for ion oscillations excited in a plasma by a fast ion beam. It has been shown that under the given experimental conditions the maximum amplitude corresponds to the ion plasma frequency. This means the radial distribution of slow ions in the ion-beam plasma can be measured.

We note in conclusion that the method we have described can be used for the diagnostics of an independently created nonisothermal plasma in a magnetic field.[5]

---

[1] A. B. Mikhailovskii, Theory of Plasma Instabilities, Consultants Bureau, New York (1973).

[2] M. D. Gabovich and I. A. Soloshenko, Zh. Tekh. Fiz., 41, 1627 (1971) [Sov. Phys. – Tech. Phys., 16, 1281 (1972)].

[3] M. D. Gabovich, I. A. Soloshenko, and L. S. Soloshenko, Zh. Eksp. Teor. Fiz., 62, 1369 (1972) [Sov. Phys. – JETP, 35, 721 (1972)].

[4] M. D. Gabovich, I. A. Soloshenko, and A. A. Goncharov, Zh. Tekh. Fiz., 43, 2292 (1973) [Sov. Phys. – Tech. Phys., 18, 1450 (1974)].

[5] M. D. Gabovich, A. A. Goncharov, V. Ya. Poritskii, and I. M. Protsenko, Zh. Eksp. Teor. Fiz., 64, 1291 (1973) [Sov. Phys. – JETP, 37, 655 (1973)].

Axially symmetric neutralized electron beam

G. N. Vyalov, V. N. Evteev, Yu. M. Zolotaikin, and K. N. Ul'yanov

(Submitted October 12, 1973)
Zh. Tekh. Fiz., 44, 2290-2295 (November 1974)

The laminar approximation is frequently used to estimate the shape of a neutralized cold electron beam. It is based on the assumption that the electron trajectories do not intersect. For example, the laminar approximation has been used[1] to calculate the shape of an axially symmetric beam with parallel initial velocities and uniform initial density along the transverse coordinate. The assumption of a constant longitudinal velocity for the electrons in the beam has been used in addition to the assumption about the laminar state.[1] The calculations lead to a longitudinally periodic beam structure, in which the transverse profile of the beam is described by the error function.

The problem dealt with in this paper is the evaluation of the limits of applicability of the laminar approximation and the calculation of the shape of a neutralized cold beam.

I. LAMINAR MODEL

It is useful to analyze the laminar approximation without any assumption as to the constancy of the longitudinal velocity. Since the electron trajectories do not intersect, each trajectory with an initial transverse coordinate r_0 defines a region within which a constant electron current $I(r_0)$ flows. This trajectory is determined by the equations of motion (for the axially symmetric case)

$$m\ddot{r} = -\frac{e}{c}\dot{z}H_0, \qquad (1)$$

$$m\ddot{z} = \frac{e}{c}\dot{r}H_0, \qquad (2)$$

$H_0 = 2I(r_0)/cr$ along the trajectory,

$$I(r_0) = I\frac{r_0^2}{a^2} \qquad (3)$$

(the Gaussian system of units is used and the dots indicate differentiation with respect to time). Here, I is the total current and a is the initial radius of the beam. We have

$$\ddot{\eta} = \frac{\alpha\eta_0^2\dot{\xi}}{\eta}, \qquad (1')$$

$$\ddot{\xi} = \frac{\alpha\eta_0^2\dot{\eta}}{\eta}. \qquad (2')$$

Here, we have used the dimensionless variables

$$\eta = \frac{r}{a};\quad \xi = \frac{z}{a};\quad \tau = \frac{vt}{a}, \qquad (4)$$

$$\alpha = \frac{2I}{\beta I_0\gamma};\quad I_0 = \frac{m_0c^3}{|e|} \approx 17\ \text{kA}. \qquad (5)$$

The dots in Eqs. (1') and (2') indicate differentiation with respect to τ. The first integral of Eq. (2') yields

$$\dot{\xi} = \alpha\eta_0^2\ln\frac{\eta}{\eta_0} + 1. \qquad (6)$$

Using the condition for the conservation of total velocity,

$$\dot{\xi}^2 + \dot{\eta}^2 = 1 \qquad (7)$$

together with Eq. (6), we obtain

$$\dot{\eta} = -\sqrt{-\alpha\eta_0^2\ln\frac{\eta}{\eta_0}\left(2 + \alpha\eta_0^2\ln\frac{\eta}{\eta_0}\right)}. \qquad (8)$$

The shape of the trajectory is determined by

$$\frac{d\xi}{d\eta} = -\frac{1 + \alpha\eta_0^2\ln\frac{\eta}{\eta_0}}{\sqrt{-\alpha\eta_0^2\ln\frac{\eta}{\eta_0}\left(2 + \alpha\eta_0^2\ln\frac{\eta_0}{\eta}\right)}}$$

or

$$\xi = \int_{\eta}^{\eta_0}\frac{\left(1 + \alpha\eta_0^2\ln\frac{\eta}{\eta_0}\right)d\eta}{\sqrt{-\alpha\eta_0^2\ln\frac{\eta}{\eta_0}\left(2 + \alpha\eta_0^2\ln\frac{\eta}{\eta_0}\right)}}. \qquad (9)$$

The condition

$$\left|\alpha\eta_0^2\ln\frac{\eta}{\eta_0}\right| \ll 1 \qquad (10)$$

corresponds to the assumption of constant longitudinal velocity. We then have

$$\xi = \sqrt{\frac{2}{\alpha}}\int_0^{\sqrt{\ln(\eta/\eta_0)}} e^{-x^2}dx = \sqrt{\frac{\pi}{2\alpha}}\,\Phi\left(\sqrt{\ln\frac{\eta_0}{\eta}}\right), \qquad (11)$$

where $x^2 = \ln\eta/\eta_0$. Under the condition (10), there is a focus according to Eq. (11), i.e., all trajectories intersect at the point $\eta = 0$, $\xi = \sqrt{\pi/2\alpha}$.

Equation (9) indicates that such a focus does not exist under the approximation of a laminar state. Moreover, the longitudinal velocity vanishes and the electron velocity is reversed according to Eq. (6) when $\eta = \eta_0 e^{-1/\alpha\eta_0^2}$. According to Eq. (8), the trajectory does not reach the axis ($\eta = 0$). At the point $\eta = \eta_0 e^{-1/2\alpha\eta_0^2}$ the transverse velocity goes to zero and the electron begins to move away from the axis. The electron trajectory forms a sequence of loops, i.e., it crosses itself. In addition, different trajectories cross each other. This result contradicts the original assumption about the laminar nature of the electron flow, i.e., the absence of trajectory crossings.

There are at least two possibilities: 1) as a result of trajectory intersection the sign of the longitudinal velocity is unchanged and the trajectories intersect the beam axis; 2) the sign of the longitudinal velocity changes, the trajectories are reversed, and this model has no region of applicability. Assuming that there is a region of applicability for the model, we estimate its limits of applicability. Trajectories cross if (10) is violated. This condition breaks down primarily for the limiting trajectory for which η_0 is a maximum (equal to unity). The trajectory intersection condition can be written in the form

$$\frac{\partial\eta(\xi,\ \eta_0)}{\partial\eta_0}=0. \tag{12}$$

Differentiating both parts of Eq. (9) with respect to η_0 for $\eta_0 = 1$, we have

$$\frac{(1-\alpha x^2)}{\sqrt{2-\alpha x^2}}e^{-x^2}=2\alpha x\int_0^x\frac{3-\alpha x^2}{(2-\alpha x^2)^{3/2}}x^2e^{-x^2}dx. \tag{13}$$

Equation (13) determines the transverse coordinate of the limiting trajectory at which the first intersection occurs. For $\alpha \ll 1$, we have approximately

$$e^{-x_n^2}\approx 3\alpha x_n\int_0^{x_n}x^2e^{-x^2}dx \tag{13'}$$

or

$$\alpha=\frac{4}{3\sqrt{\pi}}\frac{e^{-x_n^2}}{x_n}=\frac{4}{3\sqrt{\pi}}\frac{\eta_n}{\sqrt{\ln\frac{1}{\eta_n}}}, \tag{14}$$

i.e., $\eta_n \ll 1$ when $\alpha \ll 1$.

Thus for small α there is a reasonably large region for which a laminar treatment holds ($\zeta_0 = \sqrt{\pi/2\alpha}$). When $\alpha \ll 1$ deviations from the laminar state begin near the focus.

II. NUMERICAL CALCULATION OF ELECTRON BEAM SHAPE

It is necessary to introduce trajectory crossing in order to determine the conditions for beam propagation and to calculate beam shape beyond the first focus. There is as yet no analytic solution of the problem with trajectory intersection. We have carried out a numerical solution of this problem which confirms the importance of including trajectory intersections near and beyond the focus.

In the general case with trajectory intersection, the electron trajectories are described by Eqs. (1)-(3), where one should understand the current $I(r_0)$ in Eq. (3) to be the quantity

$$I(r_0)=If(\eta_0,\ \xi)\eta_0^2. \tag{15}$$

The function

$$f(\eta_0,\ \xi)=2\int_0^1\Theta[\eta(\xi,\ \eta_0)-\eta(\xi,\ \eta_0')]\eta_0'd\eta_0' \tag{16}$$

takes account of the possibility of trajectory intersection,

$$\Theta(x)=\begin{cases}1 & \text{for } x>0,\\ 0 & \text{for } x<0.\end{cases}$$

This means that at each point ξ, η of a trajectory with an initial parameter value $\eta = \eta_0$, there the electron sees a magnetic field to which all trajectories located closer to the axis of the beam make a contribution, i.e., trajectories satisfying the condition $\eta(\xi, \eta'_0) < \eta(\xi, \eta_0)$. Using the conservation of total velocity, we can transform to the independent variable ξ; differentiation with respect to this variable is denoted by primes. In this case the trajectories are given by the infinite system of equations

$$\eta''(\eta_0,\ \xi)=-\alpha f(\eta_0,\ \xi)\frac{(1+\eta'^2)^{3/2}}{\eta(\eta_0,\ \xi)} \tag{17}$$

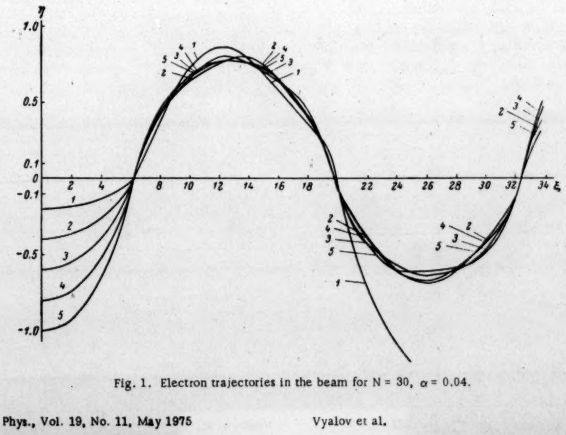

Fig. 1. Electron trajectories in the beam for N = 30, α = 0.04.

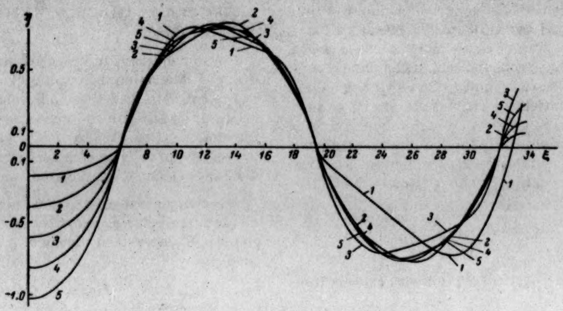

Fig. 2. Electron trajectories in the beam for N = 10, α = 0.04.

(η_0 varies continuously from 0 to 1). In a numerical solution the infinite system (17) is replaced by a system containing a finite number of equations. To accomplish this the cylindrical beam is divided into N concentric layers corresponding to division of the initial radius into N equal parts. Each layer is described by an equivalent trajectory with an initial parameter $\eta_{0i} = i/N$, i = 1, 2, ... , N. The initial system of N equations has the form

$$\left.\begin{aligned} \eta_i''(\xi) &= \frac{-\alpha f_i(\xi)\,(1+\eta_i'^2)^{3/2}}{\eta_i(\xi)}, \\ f_i(\xi) &= \sum_{j=1}^{N} \Theta(\eta_i-\eta_j)(\eta_{0j}^2-\eta_{0j-1}^2)\ (i=1,\ 2\ldots N) \end{aligned}\right\} \qquad (18)$$

and is integrated under the initial conditions $\eta_{0i} = i/N$ (i = 1, 2, ... , N). The numerical calculation of equivalent trajectories for α = 0.04 has been carried out on the Minsk-22 and BÉSM-6 computers. In addition, calculations for α = 0.5 and N = 20, 30, and 50 have been performed on the BÉSM-6 computer. However, calculations of the versions with N = 30 and 50 require a large amount of machine time and are not performed on the Minsk-22 computer. All these calculations give qualitatively identical results. The calculations for N = 10 and N = 20 are carried out over the range of ξ from 0 to 34 with all trajectories crossing the beam axis three times. The calculation for N = 50 is carried out to ξ = 6.6 to evaluate the effect of the number of equivalent trajectories (method of subdivision) on the accuracy of the calculation. In the region of laminar motion the corresponding trajectories calculated for different N agree within the accuracy of the calculations; in the region of trajectory intersection, the difference between corresponding trajectories (for example, the 24th in the case of N = 30 and the 40th in the case of N = 50) is insignificant. The maximum disagreement at the point ξ = 6.6 does not exceed 0.001. Thus a subdivision with N = 30 (Fig. 1) gives reasonably accurate results. The 6th, 12th, 18th, 24th, and 30th trajectories corresponding to N = 30 are sketched in Fig. 1. For comparison, Fig. 2 shows the corresponding trajectories for N = 10.

First, the results of the numerical calculation confirm the existence of an extended region of applicability for the laminar approximation up to the neighborhood of the first node.

Second, they confirm the importance of including trajectory intersections in the neighborhood of the first node and beyond it. A diagram of the trajectory intersections at the first node is shown in Fig. 3.

Third, the numerical calculation of the structure of the initially neutralized uniform beam reveals bunching of such a beam into a clearly expressed shell structure immediately beyond the first node (Figs. 1, 2). This struc-

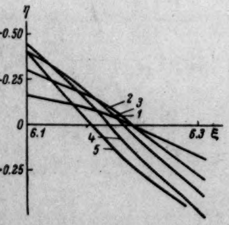

Fig. 3. Electron trajectories in the neighborhood of the first node for N = 30, α = 0.04.

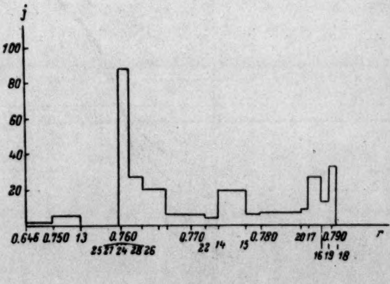

Fig. 4. Radial distribution of current density at the section ξ = 12 for N = 30, α = 0.04.

ture is maintained subsequently. The current density distributions in the two sections at $\xi = 12$ and $\xi = 26$ are shown in Figs. 4 and 5 and are of a semiquantitative nature. The structure of the shells has not been studied in detail.

Fourth, the beam has a longitudinally periodic spatial structure with the location of the nodes ("foci") being estimated sufficiently accurately by the laminar approximation.

Fifth, a reduction in the maximum transverse dimension of the beam is observed; the maximum dimension of the beam between the first and second nodes is about 0.8 times the initial dimension and about 0.7 times between the second and third nodes. The "escape" of individual trajectories, for example the trajectory numbered 1 in Fig. 1, does not change this conclusion since a comparatively small portion of the current is involved. In addition, it is impossible to consider that type of trajectory to have been established with sufficient accuracy. Its appearance is possibly associated with an error arising out of the finite number of subdivisions. For example, such an escape is not noted in the case N = 10. The question of the existence of "escape" trajectories has not been studied in detail.

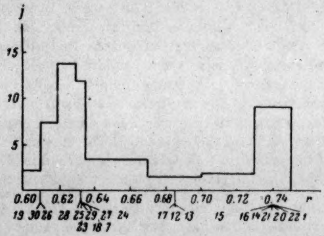

Fig. 5. Radial distribution of current density at the section $\xi = 26$ for N = 30, $\alpha = 0.04$.

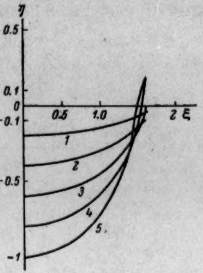

Fig. 6. Electron trajectories in the beam up to the first node for N = 30, $\alpha = 0.5$.

Results of the calculation for $\alpha = 0.5$ are shown in Fig. 6. It is clear that the first focus is located at $\xi = 1.5$ in accordance with the approximate theory.

---

[1] D. A. Dunn and A. S. Halsted, Proc. El. Las. Beam Symp., March 31-April 2, 1965, ed. by A. B. El Kareh.

Plasma synthesis by injection of an electron beam through an ion source

V. F. Virko, M. D. Gabovich, G. S. Kirichenko, and O. K. Nazarenko

Institute of Physics, Academy of Sciences of the Ukrainian SSR, Kiev

(Submitted October 2, 1973)
Zh. Tekh. Fiz., 44, 2296-2301 (November 1974)

A method is described for producing a plasma by injecting electrons through an ion source. Certain properties of the resulting plasma and its sensitivity to an external transverse magnetic field are studied.

INTRODUCTION

The production of neutral ion beams is an important and complicated physical and technical problem which has not yet been fully resolved. When the beam is to be used in a high vacuum the neutralization of the space charge, or of the space charge and the beam current, is usually achieved by means of a cold plasma.[3,4]

Without going into an analysis of the results which have been achieved so far, we wish to point out another method for neutralizing an ion beam; this involves the axial injection of electrons through the ion source. This system has been studied previously,[5,6] but no information has been reported on the properties of the neutralized ion beams.

In this paper[1] we describe a method for neutralizing an ion beam by means of electron injection through the ion source, and we report on the resulting plasma, in particular, on its sensitivity to a weak transverse magnetic field.

1. EXPERIMENTAL APPARATUS

The experimental apparatus (Fig. 1) consists of an ion source with a focusing system, an electron gun, and a vacuum chamber for studying the properties of the plasma. As a rule, a plasmatron ion source is used. The cathode of the source is moved in order to reduce the magnetic field at the axis of the system. The axisymmetric focusing system, which has a single lens, is used to extract, accelerate, and shape the ion beam. The electron gun, which consists of a planar hot cathode, a control electrode, an anode containing an aperture, and a magnetic lens, is used to shape a sharply focused electron beam and to guide it into the ion source along the axis of the system. The potential profile in the system and the elements of the high-voltage insulating and the pumping system are shown in Fig. 1. The electron beam passes through the ion source, the gap accelerating the ions (the gap retards electrons), and a single lens and moves into the region in which the ion beam propagates freely.

The ion–electron beam propagates in an evacuated cylindrical tube 10 cm in diameter and ~1 m long. Electrostatic probes are used to study the properties of the plasma. The ion-beam current and the spatial profile of the beam current density are determined by electrodes of a refractory material, whose temperature is controlled by thermocouples. The preliminary calibration of these power meters is carried out with the electron beam. The static distribution of the potential in the plasma with respect to the grounded tube is determined within a few hundredths of an electron volt by means of hot probes.

A homogeneous transverse magnetic field, H = 0-60 Oe, is produced in the evacuated tube by means of external conductors in which the current flows in the direction of the neutralized ion beam.

This apparatus is suitable for measurements under the following conditions: beam currents of 2, 1, and 0.5 mA at an energy of $\mathcal{E}$ = 15-20 keV for hydrogen, helium, and argon ions, respectively; electron injection current of 0-10 mA; a pressure of $(1\text{-}2)\cdot 10^{-5}$ torr in the drift tube.

2. NEUTRALIZATION OF THE ION BEAM BY INJECTED ELECTRONS; PLASMA PRODUCTION

The ion beam, moving in high vacuum, expands under the influence of its own space charge. The parameter governing the degree of neutralization of the beam by charges

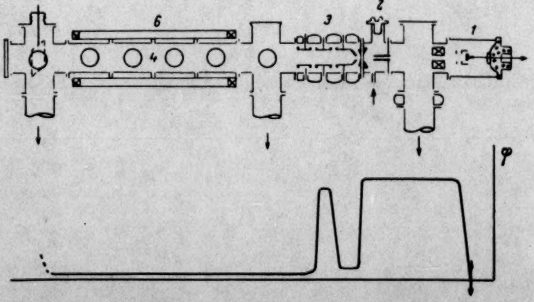

Fig. 1. The experimental apparatus. 1) Electron gun; 2) ion source; 3) electrostatic lens; 4) drift tube; 5) target; 6) conductors that produce the transverse magnetic field.

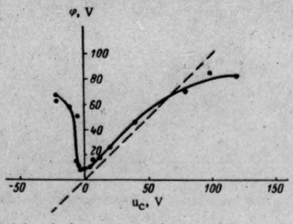

Fig. 2. Potential at the beam axis as a function of the potential of the electron-gun cathode.

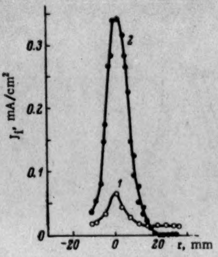

Fig. 4. Radial distributions of the current density of an ion beam which is not neutralized (1) and which is neutralized (2) by electrons. Ar$^+$, ε = 15 keV, $I_i \sim 0.5$ mA.

of the opposite sign is the potential associated with the net charge. The experiments show that the introduction of slow electrons into the ion beam by longitudinal injection through the ion source can reduce significantly the electric fields in the beam due to the ion space charge. The velocity of the injected electrons in this neutralization method is governed by the potential difference between the beam and the cathode of the electron gun, i.e., the average electron flow velocity is essentially a self-consistent parameter. Figure 2 illustrates the establishment of the self-consistent potential in the beam. Here, the ordinate shows the potential at the beam axis, while the abscissa shows the potential of the electron emitter with respect to the drift tube. In the absence of an ion beam electrons can enter the drift region only for negative values of u_c. When there is an ion beam the ion space charge makes it possible for electrons to move into the system even at a positive cathode potential. The ion space charge is neutralized at the level of the average beam potential $\varphi \gtrsim u_c$ (dashed line in Fig. 2). The average energy of the neutralizing electrons is then governed by the distance between the solid curve and the dashed line in Fig. 2. When $u_c < 0$ the neutralizing effect of the electrons falls off sharply with increasing electron energy, leading to the establishment of the relatively high potential of the unneutralized ion beam.

The neutralization of the positive space charge by slow electrons essentially eliminates the electric field along the path of the ions. Figure 3 shows the potential profiles along the axis of the system for unneutralized (1) and neutralized (2) ion beams. These measurements are carried out in the part of the drift tube immediately adjacent to the focusing system (curve 3 shows the measured potential profile of the single lens in the drift region in the absence of beams). The introduction of electrons into the ion beam essentially removes the electric field about the axis over the entire drift region – from the target, which bounds this region, to the focusing region. The resulting plasma consists of beam ions which are at a high energy and electrons whose energy is governed by the self-consistent residual potential. It should be noted that under typical experimental conditions the Debye shielding radius (0.1–0.2 cm) is much shorter than the transverse dimension of the plasma column (the effective diameter is ~1.5 cm).

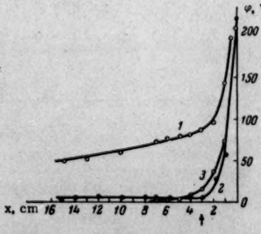

Fig. 3. Longitudinal potential profiles in the system. 1) Ion beam without neutralization, He$^+$, ε = 15 keV, $I_i \sim 1.5$ mA; 2) the same, with neutralization by electrons; 3) potential profile in the absence of ions and electrons. The arrow shows the edge of the last electrode of the focusing system.

The reduction in the positive potential in the beam due to the injection of electrons and the reduction in the associated radial electric field lead to a significant reduction of the spatial expansion of the ion beam. Figure 4 shows radial profiles of the ion-current density in the beam, obtained at a distance of 1 m from the source with (2) and without (1) the neutralizing electrons. The initial diameter and the electrical properties of the beam are the same in the two cases. We see that most of the beam current is distributed homogeneously in the entire cross section of the drift tube. The neutralized beam is concentrated in a narrow axial region.

The experiments show that in the case of longitudinal electron injection into the ion beam, where there is optimum neutralization of the space charge, there is also neutralization of the beam current in irradiation of an insulated target.

Accordingly, the introduction of electrons into the ion beam by longitudinal injection through the ion source can result in an effective neutralization of an ion beam moving in high vacuum. There is a reduction of the electric fields

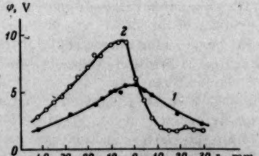

Fig. 5. Radial potential profiles in the beam in the absence (1) and presence (2) of a transverse magnetic field. He$^+$, ε = 16 keV, $I_i \sim 1$ mA.

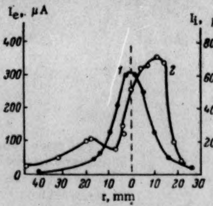

Fig. 6

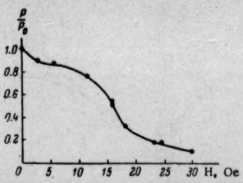

Fig. 7. Relative decrease in the beam power evolved at the target with increasing intensity of transverse magnetic field.

associated with the ion space charge and a corresponding decrease in the expansion of the ion beam in its motion. It is interesting to compare the self-consistent residual potential drop in the plasma produced in this manner with an estimate of this potential drop taking account of the thermal spread of the electron velocities.[2] The minimum potential drop in a beam with an ion current I_i, an ion velocity v_i, and the neutralizing-electron temperature is calculated to be

$$\Delta\varphi = \left(\frac{2I_i}{v_i}\frac{T_e}{e}\right)^{1/2}.$$

Under typical experimental conditions, i.e., at $I_{He+} = 1$ mA and E_i = keV, this value is a few volts, in order-of-magnitude agreement with the measured value of the potential drop in the beam.

3. EFFECT OF A TRANSVERSE MAGNETIC FIELD ON THE MOTION OF THE RESULTING BEAM

When ion–electron beams are used to process solids[7] magnetic fringing fields can exist near the object being processed. In this connection it is worthwhile to study the stability of such intense beams with respect to a transverse magnetic field, i.e., to determine how the motion of such beams is affected by such a field. We also note that an ion–electron plasma can serve as a model for continuous-operation study of the polarization which results from the influence of magnetic fields on the plasmas used for injecting fast particles into traps.[8]

Even in a relatively weak transverse magnetic field, as the neutralized ion beam propagates, the Lorentz force $F_\pm = e[v_\pm H]/c$ leads to charge separation and to the appearance of an electric field in the beam region. This polarization is demonstrated in Fig. 5, which shows the potential profile in the beam in the direction perpendicular to the external magnetic field (H = 6 Oe, curve 2). Curve 1 shows the potential profile in the absence of a magnetic field. The intensity of the polarization field agrees with the calculated value. Figure 6 shows the corresponding profiles of the ion (1) and electron (2) probe currents in the beam in the magnetic field; these profiles confirm the spatial separation of the charges of different sign. The slight additional peak in the electron profile (at the left in Fig. 6) is due to a reverse flow of electrons from the beam-irradiated target. Because of the polarization electric field, most of the fast ions in the beam move in the drift region without being deflected in the relatively weak magnetic field. The existence of a transverse magnetic field along the path of the neutralized ion beam hinders the motion of the injected electrons from the source to the target. In particular, at a certain field (~5 Oe in these experiments), the neutralization of the ion current at the insulated (floating) target is disrupted, so that this target is charged by the fast beam ions, and there is a corresponding reduction in the power evolved at the target. Figure 7 demonstrates the relative decrease in the beam power at the insulated target with increasing intensity of the transverse magnetic field in the drift region (the initial beam power is $P_0 \sim 15$ W). The region in which the ion motion is essentially unperturbed by the polarization field corresponds to magnetic fields H < 10-15 Oe.

CONCLUSION

We have reported here a method for producing a plasma by electron injection through the ion source. The apparatus is characterized by its small size and simplicity of operation as compared with other methods for producing ion–electron beams.[7,9]

The information found regarding the degree of neutralization of the ion–electron beam, in particular, the information found on the minimum potential drop in the beam, agrees with the model for a generated plasma incorporating the equality of the total ion and electron charges and incorporating the existence of an electron atmosphere outside the ion core.[2]

We have reported the first experimental study of the effect of a transverse magnetic field on the transport of the generated plasma, consisting of ions and electrons moving at approximately equal velocities.

[1)] This work was carried out in the Institute of Physics, Academy of Sciences of the Ukrainian SSR, in 1968-1969.

---

[1] Collection: Electrostatic Rocket Engines [Russian translation, ed. Yu. A. Ryzhov], Izd. Mir, Moscow (1964).
[2] M. D. Gabovich, I. A. Soloshenko, and A. A. Ovcharenko, Ukr. Fiz. Zh., 16, 813 (1971).
[3] N. F. Balaev and R. N. Kuz'min, Zh. Tekh. Fiz., 40, 1537 (1970) [Sov. Phys. – Tech. Phys., 15, 1187 (1971)].
[4] O. V. Gavrilov, A. S. Myasnikov, G. G. Zhdan, G. S. Orlov, and M. V. Strokin, Kosmich. Issled., 11, 140 (1973).
[5] I. S. Luce, Plasma Phys. and Therm. Research, 2, 120 (1963).
[6] V. V. Kuznetsov and N. N. Semashko, Zh. Tekh. Fiz., 42, 2609 (1972) [Sov. Phys. – Tech. Phys., 17, 2027 (1973)].
[7] B. I. Verkin, A. M. Markus, V. S. Suslo, and N. A. Tsurikov, in: Radiation Physics of Nonmetallic Crystals [in Russian], Izd. Naukova Dumka, Kiev (1967), p. 437.
[8] I. N. Golovin, K. B. Kartashev, V. I. Pistunovich, V. V. Platonov, V. D. Pyutov, and E. A. Filimonova, Plasma Physics and Controlled Nuclear Fusion Research, Vol. 2, IAEA, Vienna (1971), p. 679.
[9] P. S. Markin, A. A. Tsishkalo, F. P. Sapin, and E. I. Anpilogov, Prib. Tekh. Eksp., No. 2 (1973).

Measurement of plasma electron temperature with a sinusoidal probe potential

B. I. Kanaev, V. V. Piterskii, and E. E. Yushmanov

(Submitted November 19, 1973; resubmitted March 11, 1974)
Zh. Tekh. Fiz., 44, 2302-2306 (November 1974)

A method for measuring the electron temperature which does not require the recording of the voltage–current characteristics is described. The method exploits the rectifying properties of the probe; these cause a shift of the floating potential of the probe when an rf voltage is applied to it. The output signal from the probe reflects the electron temperature directly, so that this temperature can be monitored continuously during one-shot processes. Another advantage of this method is its insensitivity to changes in plasma properties other than T_e. In most cases a magnetic field does not hinder measurements. The method has been used successfully in experiments on the confinement of hot plasmas in magnetic traps.

INTRODUCTION

In certain cases the classical Langmuir-probe method for measuring the plasma electron temperature from the slope of a semilogarithmic plot of the electron current collected by the probe is inconvenient. Let us assume, for example, that we are to follow the behavior of T_e during a transient one-shot process. The usual procedure might involve repeating the process many times in order to obtain a family of probe-current curves as a function of the time for various values of the probe potential. This family of curves would then be used to construct the voltage–current probe characteristics at various times: The electron components of the current are then found from the characteristics and plotted on a logarithmic scale; the slopes of the resulting lines yield the values of $T_e(t)$. This method obviously suffers from the disadvantage that both the measurements (involving repetitions of the process) and the subsequent calculations are laborious. A further disadvantage arises if the process in question is not perfectly reproducible from shot to shot, e.g., if systematic changes in properties such as the plasma density and potential or the component temperatures are subject to random fluctuations due to an instability, turbulence, etc. These fluctuations cause a "jitter" in the probe-current curves, which can make it impossible to plot the voltage–current characteristics. In any case, the result (if it is found) reflects only the average behavior of T_e over many repetitions, and the details of the individual processes are lost.

Ideally, we would like a method free of all these disadvantages. Specifically, this ideal method would a) make it possible to obtain all the information about the behavior of T_e during a single shot, b) be insensitive to changes in any of the plasma properties (the potential, the density, or T_i) other than T_e, and c) allow the information to be displayed in a form not requiring a complicated analysis, i.e., in terms of a quantity related to T_e in some simple manner.

Below we discuss a method which satisfies these requirements in many cases. It incorporates no concepts other than those of the Langmuir method, differing from the latter only in its use of rapid, automatic measurements of the characteristic constant $1/T_e$ of the exponential function describing the electron current collected by the probe.

THE MEASUREMENT PRINCIPLE

This method exploits the well-known rectifying properties of probe–plasma contacts which result from the nonlinearity of the voltage–current characteristic of the probe. As a result of this rectification process an alternating voltage fed to a probe which is floating (in terms of direct current) causes a shift of the average floating potential; this shift is related to T_e.

In particular, let us consider the circuit in Fig. 1. Let us assume for the moment that the plasma is in a steady state. We also assume that the output impedance of the oscillator and the isolation capacitor C is small in comparison with the resistance of the probe–plasma contact, so that all the rf voltage is fed to the probe and this voltage retains its sinusoidal shape. Since the probe is in a dc open circuit its potential is equal to the floating potential V_{fl} when the oscillator is off. When the oscillator is on how does the constant component of the probe potential respond?

It has been shown many times (see the review in ref. 1) that when a sinusoidal voltage of amplitude u is fed to a probe at some potential the average electron current collected by the probe increases by a factor $I_0(u/T_e)$, where $I_0(x)$ is the Bessel function of imaginary argument (and T_e is expressed in potential units). This statement holds if the probe characteristic has an exponential shape, as it does if the electrons have a Maxwell distribution and if the probe sheath is thin in comparison with the probe dimensions. This result means that when the oscillations are introduced the average characteristic simply shifts to the left by an amount $\Delta V = T_e \ln I_0(u/T_e)$ in the region in which this characteristic remains exponential. Obviously, the intersection of the characteristic with the abscissa, i.e., the floating potential, shifts by the same amount. The equation given above for ΔV has been verified experimentally,[2] with corrections made for the slope of the ion branch of the characteristic. It has also been suggested[2] that it might be possible to measure T_e on the basis of ΔV, although this possibility was not analyzed.

According to this equation, then, we can get information about T_e from the shift in the floating potential, ΔV. The most convenient case is that of moderate amplitudes of the superimposed alternating voltage, for which $u \leqslant T_e$. Expanding ΔV in a series

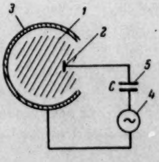

Fig. 1. "Oscillating-voltage" probe for measuring T_e. 1) Plasma; 2) probe; 3) reference electrode; 4) rf oscillator; 5) isolation capacitor.

$$\Delta V = -u\left[\frac{1}{4}\frac{u}{T_e} - \frac{1}{64}\left(\frac{u}{T_e}\right)^3 + \ldots\right],$$

we see that at moderate amplitudes we can assume $\Delta V = (-1/4)u^2/T_e$. At large amplitudes, $u \gg T_e$, on the other hand, we lose the relationship between ΔV and T_e because $\Delta V \to u$.

We note that measurements of ΔV to determine the electron temperature have the desirable features listed above: These measurements are not affected by plasma properties other than T_e, and the measured results are related to T_e in a simple manner, so that the ΔV signal can be read off in terms of T_e in the course of the experiments.

Furthermore, this method of determining T_e from the shift in the floating potential can also be used in the presence of a magnetic field: In the floating-potential region, i.e., at electron currents small in comparison with the saturation electron current, the characteristic is usually exponential.

MEASUREMENT METHOD

In order to measure $\Delta V(t)$ during a single rapid process we must evidently make a continuous comparison of the floating potentials with and without the rf signal. One of the major difficulties here is that the small signal $\Delta V(t)$ (which is much smaller than T_e) appears in a sum with the large signal $V_{fl}(t)$ (which is usually larger than T_e), so that we must find some highly accurate method for separating the two signals. One simple method for doing this is based on the use of two identical probes placed close together, one an "oscillating-voltage" (i.e., connected in the circuit of Fig. 1) and the other simply floating. The probes are connected to the inputs of a well-balanced differential amplifier; there should of course be high resistances in the input circuits to avoid disrupting the condition that the probes be floating in terms of direct current. The resulting differential signal is the signal $\Delta V(t)$.

However, the use of this method can be limited: At a low level of the signal $\Delta V(t)$ a difference may appear between the floating potentials of the two probes because of the unavoidable spatial separation. This difference is superimposed on the desired signal as a type of noise. It is possible that this noise may not be perfectly reproducible in shape and level from shot to shot, so that we would again be faced with the need for a statistical averaging and would lose our capability of studying each separate instance of the process in question.

In principle, this problem can be overcome by using a different method, involving only a single probe, which is fed an amplitude-modulated rf voltage with a modulation frequency much higher than the frequencies characteristic of the process under study. If the modulation is described by $u(t) = u_0 \sin \Omega t$ (a mixture of two high frequencies at the same amplitude), the signal $\Delta V(t)$ also oscillates sinusoidally at frequency $F = \Omega/\pi$. Using a resonant filter to extract this signal, we can eliminate the signal $V_{fl}(t)$.

Figure 2 shows the measurement circuit. The rf oscillator produces an alternating voltage at two frequencies. Comparison with the circuit in Fig. 1 shows that we have now added a measuring circuit consisting of the high resistance R and a filter passing frequency F and a circuit for measuring and monitoring the rf signal, which consists of elements C_1, R_1, and ρ (the characteristic impedance of the cable). The measured signal is sinusoidal at frequency F, and the peak-to-peak amplitude of the oscillations, $\Delta V(t)$, is related to the electron temperature by $\Delta V(t) = u_0^2/4T_e(t)$.

CHOICE OF PARAMETERS

In choosing the parameters for this circuit we must observe several quantitative conditions. An important role is played by the quantity R_{fl}, the dynamic resistance of the probe–plasma contact, when the probe potential is near the floating potential. If the probe current I is exponential we can write

$$R_{fl} \equiv \left(\frac{\partial I}{\partial V}\right)^{-1}_{V=V_{fl}} = \frac{T_e}{I_i},$$

where I_i is the saturation ion current. We first need some idea of the numerical value of R_{fl}.

As we mentioned above, to avoid superimposing the rf voltage on the probe we must use an rf oscillator and a capacitance C whose resultant impedance (including the impedance of the associated leads) is several times lower than R_{fl}. Another circuit parameter which affects R_{fl} is the resistance R in the measuring circuit. To satisfy the floating condition we require $R \gg R_{fl}$.

The choice of modulation frequency F is also governed significantly by R_{fl}. On the one hand, we cannot use a frequency F which is too high, since we must avoid superimposing the measured signal on the capacitance C_{tot} connected to the probe. This capacitance is governed primarily by the capacitance C and the parasitic capacitance between the probe and ground; it is also governed by the probe–plasma capacitance and by C_1. Since the output resistance of the equivalent generator of the measured signal is the same quantity, R_{fl}, the condition which must be met to avoid interference is $F \ll (2\pi R_{fl} C_{tot})^{-1}$. On the other hand, it is not desirable to use too small a value of F because the time resolution can be degraded (the resolving time is $\tau_{rslv} \approx Q/\pi F$, where Q is the quality factor of the filter) and because the interfering low-frequency signal $V_{fl}(t)$ would not be adequately filtered [the noise level is $\approx V_{fl}(2\pi F\tau Q)^{-1}$,

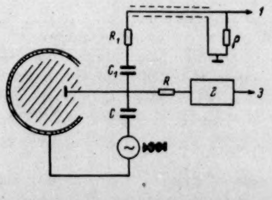

Fig. 2. Circuit for measurements with a modulated rf signal. 1) rf monitor; 2) filter; 3) measurement of $\Delta V(t)$.

where τ is the characteristic time for the changes in V_{fl}]. We must thus choose a value for F to satisfy all three of these conditions as well as possible. Finding such a value is easier, the smaller R_{fl}; in this connection we recall that R_{fl} is governed by the properties of the probe itself as well as by the plasma properties.

There is a lower limit on the carrier frequency f set by the obvious requirement $f \gg F$; generally speaking, the upper limit is fixed by the inertia of the plasma sheath near the probe, but this limit evidently lies near the electron plasma frequency, i.e., is usually quite remote. Thus the choice of f is governed primarily by practical considerations, e.g., the convenience in feeding the rf voltage from the oscillator to the probe, etc.

EXPERIMENTAL TESTS

We have used this method based on a modulated rf signal to monitor the electron temperature during the decay of a hot-ion hydrogen plasma in a mirror system. The decay, i.e., the loss of plasma from the trap occurs over a time scale of the order of 100-200 μsec; during the decay all the plasma properties — the density, the ion and electron temperatures, and the potential — undergo large changes. The local values of the density and the potential fluctuate because of the ion cyclotron instability characteristic of this confinement method. The plasma density at the beginning of decay is $\leqslant 10^{11}$ cm^{-3} near the probe; the ion and electron temperatures are about 100 and 5 eV, respectively. The magnetic field is 5 kOe.

We measure T_e at a carrier frequency of 10-15 MHz and at a modulation frequency of 100 kHz. The probe tip has an area of 5 mm^2. Figure 3 shows a typical $\Delta V(t)$ signal (oscillogram b). The behavior of the signal implies an increase in the electron temperature from 5 to ≈ 25 eV. This increase follows an intensification of the induced instability of the rf oscillations (oscillogram a), implying energy transfer from ions to electrons via the instability.

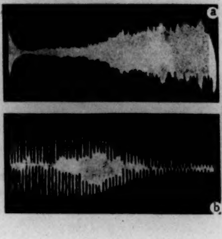

Fig. 3. a) Signal of the rf plasma noise due to the onset of instability; b) the signal $\Delta V(t)$, reflecting the increase in the electron temperature.

We have also studied the behavior of the electron temperature in this experiment, to the extent possible, by a method involving a recording of characteristics like those described earlier in this paper. As a further check we measure the energy spectrum of the plasma electrons escaping from the trap through the magnetic mirrors, by the cutoff method. The results found by both of these methods agree with the results found by the oscillating-voltage method.

---

[1] F. F. Chen, in: Plasma Diagnostic Techniques (ed. R. H. Huddlestone and S. L. Leonard), Academic Press, New York (1965).

[2] V. A. Godyak, A. N. Ivanov, and A. A. Kuzovnikov, Zh. Tekh. Fiz., 37, 1063 (1967) [Sov. Phys. – Tech. Phys., 12, 766 (1967)].

Atomic density in the low-voltage arc in a cesium diode

F. G. Baksht, A. A. Kostin, Yu. L. Serov, and I. P. Yavor

A. F. Ioffe Physicotechnical Institute, Academy of Sciences of the USSR, Leningrad

(Submitted October 9, 1973)
Zh. Tekh. Fiz., 44, 2307-2310 (November 1974)

The calculated and experimental distributions of the cesium density are compared in the low-voltage arc of a planar cesium diode. The measurements are carried out by an interferometer method. The calculations are based on the measured distributions of the electron density and temperature in the arc. The calculated results agree with the experimental results. As the current is increased the atomic density in the arc decreases, because of heating of the ion–atom component and because of the reduction in the atomic pressure due to the increased electron–ion pressure. The heat carried to the electrodes by atoms is estimated. It is possible to determine the thermal conductivity of the cesium vapor by comparing the calculated and measured temperature distributions of the atoms.

Study of the distributions of the macroscopic properties of a hot-cathode gas discharge in cesium vapor is of considerable importance in determining the processes that occur in the discharge. These distributions have received much study over the years because of the practical application of thermionic converters. Accurate spectroscopic and probe methods are available for determining the electron density n and temperature T_e, but the density of neutral Cs atoms is usually determined indirectly and with large error. The use of interferometer methods – the hook method[1] and the superposition of interference patterns[2] – yields a direct determination of the atomic density and points to several conclusions regarding the interactions between the plasma components.

We describe here a study of the distribution of the cesium-atom density in the gap of a planar diode as a function of the current through the diode and the Cs vapor pressure. The atomic density determined experimentally by an interferometer method is compared with the calculated density. The calculations are based on the experimental distributions of the electron temperature and density over the gap.

The experimental apparatus contains a two-beam interferometer and a spectrograph. A planar cesium diode with molybdenum electrodes and an adjustable gap d is located in one arm of the interferometer. The interference fringes are localized in the central part of the diode gap by adjustment of the interferometer to permit a determination of the distribution of atoms over the gap. A spatial resolution of about 0.1 mm is achieved. The observations are carried out near the resonant absorption line of cesium, λ = 8521 Å. Some of the details are discussed in refs. 3 and 4.

The electron temperature T_e is determined from the recombination rate of the 6P continuum on the basis of the recombination cross section from ref. 5: $\sigma(v) = 3.74 \cdot 10^{-6} v^{-2} \cdot \mathrm{cm}^2$, where v is the electron velocity. The electron density n is determined from the Stark broadening of the lines of the fundamental series and the results of ref. 6. Typical experimental distributions of the electron density n(x) and temperature $T_e(x)$ are shown in Fig. 1. We note that the displacement of the interference pattern by the electron component of the plasma is negligible, being less than 10^{-2} of a fringe.

The increase in the electron density and temperature which occur as the diode current j is increased are accompanied by a heating of the atoms and a reduction of their neutral density n_a. The decrease in the atomic density due to increased current is indicated by $\gamma = n_{aa}/n_{afr}$, where n_{aa} is the atomic density in the arc, and n_{afr} is the atomic density in the free-run mode. The calculated and experimental values of $\gamma(x)$ are compared in Fig. 2 for various points of the gap. Figure 3 shows the quantity $1 - \gamma(d/2)$, calculated and measured at the center of the gap, as a function of the gap width d.

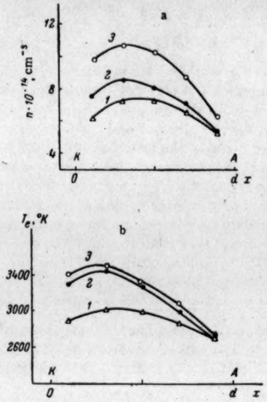

Fig. 1. a) Experimental electron density distributions; b) experimental electron temperature distributions over the gap for various arc currents. p = 7.1 torr, T_k = 1400°K, T_a = 750°K, d = 1.6 mm. j(A/cm²): 1) 10; 2) 15; 3) 20.

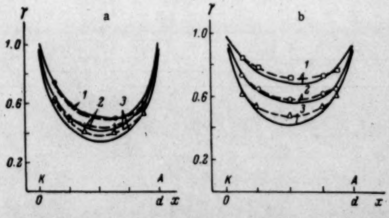

Fig. 2. Comparison of experimental and calculated values of $\gamma(x) = n_{aa}(x)/n_{afr}(x)$ for various arc currents. T_k = 1400°K, T_a = 750°K, d = 1.6 mm. a) p = 7.1 torr; b) 3 torr. 1) j = 10 A/cm²; 2) 15 A/cm²; 3) 20 A/cm². Solid curves–calculated; dashed–experimental.

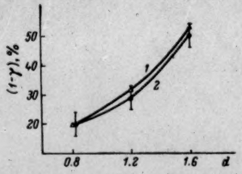

Fig. 3. Comparison of the calculated and experimental values of 1 − γ for various gap widths. j = 20 A/cm², p = 3 torr, T_k = 1400°K, T_a = 750°K. 1) Calculated; 2) experimental.

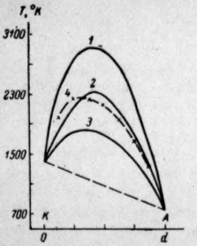

Fig. 4. Comparison of the values of T(x) calculated for various values of the thermal conductivity $\varkappa_a$ with the experimental values. $\varkappa_a$ (W/cm · deg): 1) $5 \cdot 10^{-7}\sqrt{T}$ (ref. 12); 2) $1.65 \cdot 10^{-6}\sqrt{T}$ (ref. 10); 3) $5 \cdot 10^{6}\sqrt{T}$ (ref. 11); 4) experimental results for j = 15 A/cm² and p = 7.1 torr.

The calculation of the atomic density $n_a(x)$ and temperature T(x) involves a numerical solution of the system of equations[7]

$$\frac{d}{dx}\left[(\varkappa_i+\tilde{\varkappa}_a)\frac{dT}{dx}\right]=\Delta Q_{ei}+\Delta Q_{ea}, \qquad (1)$$

$$p=n_a kT+nk(T_e+T). \qquad (2)$$

Here, $\varkappa_i = 3.9nk^2T(\tau_i/M)$ is the ion thermal conductivity, $\Delta Q_{ei} = (3m/M)(n/\tau_e)k(T_e - T)$ is the energy transferred from electrons to ions in collisions,[8] $\Delta Q_{ea} = (4m/M) \cdot (n\bar{v}_e/l_0)\,k(T_e - T)$ is the energy transferred from electrons to atoms in collisions $\tilde{\varkappa}_a = \varkappa_a[(nQ_{ai}/n_a Q_{aa}) + 1]^{-1}$ is the thermal conductivity of the atoms, with atom − ion collisions taken into account,[9] and $\varkappa_a$ is the thermal conductivity of cesium vapor.1) Equation (1) is solved under the boundary conditions T(o) = T_k, and T(d) = T_a, where T_k and T_a are the cathode and anode temperatures.

The calculated results, shown in Figs. 2 and 3, agree with the measured distributions of the atomic density in the gap, implying that the decrease in the atomic density in a low-voltage arc at higher currents is, in fact, due to the heating of the ion−atom component in the discharge and to the decrease in the atomic pressure, which itself is due to the increase in the electron−ion pressure $nk(T_e + T)$ (in a weakly ionized plasma, however, this latter factor is relatively unimportant).

By independently measuring n, T_e, and n_a and then determining T(x) from Eq. (1) we can, in principle, find

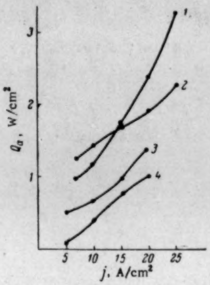

Fig. 5. Heat fluxes to the electrodes calculated from the measured distributions $T_e(x)$ and n(x) for various arc currents. 1,4) Heat flux to the cathode; 1) p = 7.1 torr; 4) 3 torr; 2, 3) heat flux to the anode; 2) 7.1 torr; 3) 3 torr. T_k = 1400°K, T_a = 750°K, d = 1.6 mm.

the thermal conductivity of the cesium vapor, $\varkappa_a$. We vary the quantity $\varkappa_a$ in (1) for best agreement between the calculated and experimental results. We use the values of $\varkappa_a$ from refs. 10-14 in comparing the calculated and experimental results. The best agreement is found when the results on $\varkappa_a$ from ref. 10 are used: $\varkappa_a = 1.65 \cdot 10^{-6}\sqrt{T}$ W/cm · deg (Fig. 4). Using this value of $\varkappa_a$ we find the results shown in Figs. 2 and 3. The intensified heating of ions and atoms which occurs as the current through the diode is increased is accompanied by an increase in the heat transfer from the heavy component to the electrodes. This heat flux can make an appreciable contribution to the total energy transfer from the plasma to the electrodes. The effect is illustrated in Fig. 5 by the functional dependence Q_a(j), where Q_a is the heat flux from atoms to the electrode.

---

1)A small term on the right-hand side of (1) describing the heating of ions in the electric field is neglected.

---

[1] D. S. Rozhdestvenskii, Papers on Anomalous Dispersion in Metal Vapor [in Russian], Izd. Akad. Nauk SSSR, Moscow (1951).

[2] A. M. Shukhtin, in: Spectroscopy of Gas-Discharge Plasmas [in Russian], Izd. Nauka, Moscow (1970), p. 110.

[3] I. P. Yavor and Yu. L. Serov, Phys. Lett., 39A, 109 (1972).

[4] Yu. L. Serov and I. P. Yavor, 11th Intern. Conf. on Phenomena in Ionized Gases, Prague, 1973.

[5] L. Agnew and C. Summers, Proc. of the Seventh Intern. Conf. on Phenomena in Ionized Gases, Beograd, 1965.

[6] H. Griem, Phys. Rev., 128, 515 (1962).

[7] F. G. Baksht, I. L. Korobova, and B. Ya. Moizhes, Zh. Tekh. Fiz., 41, 387 (1971) [Sov. Phys. – Tech. Phys., 16, 292 (1971)].

[8] S. I. Braginskii, in: Reviews of Plasma Physics, Vol. 1, Consultants Bureau, New York (1965).

[9] B. Ya. Moizhes and G. E. Pikus (eds.), Thermionic Converters and Low-Temperature Plasmas [in Russian], Izd. Nauka, Moscow (1973).

[10] S. Kitrilakis and M. Miker, in: Thermionic Energy Conversion [Russian translation], Atomizdat, Moscow (1964), p. 45.

[11] R. J. Zollweg, Proceedings of the Round Table Discussions on Thermionic Processes and Materials, PIC-ELETI 3/2, Appendix I-1, March 20, 1961.

[12] "First quarterly report for the thermionic emitter materials research program," TEE-4015-1, Thermo Electron Engineering Corp. (1961).

[13] L. P. Zarkova and B. I. Stefanov, Report to the International Symposium on the Properties and Uses of Low-Temperature Plasmas, 20th Intern. Congress on Theoretical and Applied Chemistry, Moscow, 1965.

[14] N. B. Vargaftik and V. V. Kerzhentsev, Teplofiz. Vys. Temp., 10, 59 (1972).

Free expansion of plasma jets

P. A. Demchenko, L. I. Krupnik, and E. S. Lyangner*

(Submitted December 29, 1972)
Zh. Tekh. Fiz., 44, 2311-2316 (November 1974)

An experimental study is reported of the free expansion in vacuum of plasma jets with densities $n \sim 10^{14}$ cm^{-3} and velocities $v \sim (0.5\text{-}1) \cdot 10^7$ cm/sec. The radial distribution of the density and the density distribution along the flow axis are studied. The electron temperature is measured. The results are compared with existing theoretical models for the expansion of plasmas and molecular fluxes. The possibility of finding the ion temperature is discussed.

INTRODUCTION

Several papers have been published on the expansion of plasmas in vacuum.[1-7] As a rule, the theoretical models deal with semiinfinite plasmas whose ions are initially at rest, for which the expansion occurs as a result of a finite electron temperature T_e.

Under actual conditions, however, the plasma is always bounded and the ion temperature is finite. Even if the ions are not in thermodynamic equilibrium there is always a finite ion velocity distribution.

In working with plasma jets generated by electrodynamic accelerators it is frequently necessary to calculate the density distributions in freely expanding jets. In particular, problems of this type arise in the transport of plasma jets, in the production of ion beams from plasmas in a determination of plasma properties,[8] and in other cases. Examination of the expansion mechanism and its sensitivity to a finite ion temperature thus becomes an important question.

In this work we study the expansion of moving plasma jets in vacuum in the absence of an external magnetic field. The experiments are carried out over ranges of initial densities n_0 and initial jet radii r_0 which satisfy the condition $r_0 \ll \lambda$, where $\lambda = 2E^2/\pi e^4 n_0 \ln\Lambda$ is the Coulomb mean free path.

EXPERIMENTAL PROCEDURE AND RESULTS

Figure 1 shows the experimental arrangement. A flow of hydrogen plasma is produced by conical electrode-type injector 1 with pulsed gas injection.[10,11] A plasma jet cut off sharply in the radial direction is isolated from the original flow, which fills the entire cross section of plasma guide 2, by conical limiter 3. The conical profile of the limiter is chosen to suppress the hydrodynamic effects which arise as the plasma strikes the barrier. We have studied the expansion of jets in vacuum chamber 5, 45 cm in diameter, varying the initial jet radius r_0 from 2.5 to 10 mm.

The radial distribution of the density is measured at various distances from the limiter by double probes.[12] For this purpose there are several probes, one of which (4) is moved along the axis of the moving jet; the others are moved in the radial direction, at several distances from the plane of the limiter. The double probes can also measure the electron temperature in the expanding plasma and the flow velocity.

The absolute densities of the charged and neutral particles are determined by probing the plasma with beams of fast hydrogen atoms and ions.[11,13]

Figure 2 shows the time evolution of the density at the axis, at a point 9 cm from the limiter; trace a is an oscillogram of the saturation ion current collected by the probe, while trace b is an oscillogram of the intensity of the diagnostic atomic beam.

We can explain this difference in the divergence behavior at a given electron temperature by assuming that the ion temperature does not remain constant along the jet. If the ions are not in thermodynamic equilibrium the radial dispersion in the ion velocity should be greater for the first density maximum than for the second. Since the plasma formation has finite dimensions along the axis of the jet, we should also observe a spreading along the longitudinal axis The experimental results show that for a given longitudinal dimension the longitudinal expansion is not important over the time interval studied here (or, correspondingly, over the distances traversed by the jets). We can therefore assume the expansion to be purely axisymmetric.

Let us compare the expansion of the plasma jet having the properties given above with the expansion of a jet of neutrals. For collisionless expansion into vacuum of an initially cylindrical cloud of neutrals of mass M and temperature T we can write the following equation for the functional dependence of the density of atoms at the axis on time t (ref. 14):

$$n = n_0\left(1 - e^{-\alpha r_0^2/t^2}\right),$$

where $\alpha = M/2kT$, r_0 is the initial cloud radius, and n_0 is the initial density. Generalizing this equation to the case of motion along the longitudinal axis at a velocity v_0, we

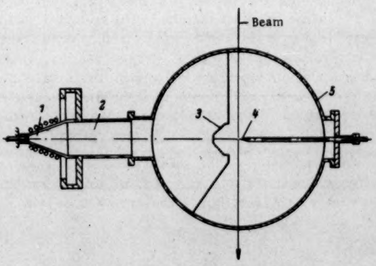

Fig. 1. The experimental arrangement.

find the density of atoms at the jet axis as a function of the distance which has been traversed, x:

$$n = n_0(1 - e^{-\beta/z^2}), \tag{1}$$

where $z = x/r_0$ and $\beta = Mv_0^2/2kT = E_0/kT$. Here E_0 is the energy associated with the directed motion of the particles. At large distances, $z \gg 1$, we can expand the exponential function in Eq. (1) in powers of z. We assume hydrogen atoms H_1^0 at an energy of 16 keV. It follows from the oscillograms shown here that the plasma jet is characterized by three regions of high density; these regions appear some 12-15 μsec apart. The directed velocities of the density maxima are $v_1 = 8.1 \cdot 10^6$, $v_2 = 5.2 \cdot 10^6$, and $v_3 = 3.3 \cdot 10^6$ cm/sec, respectively, and do not vary as the jet moves. The densities measured at the corresponding maxima at the jet axis at the position of the limiter are $(n_0)_1 = 1.5 \cdot 10^{14}$, $(n_0)_2 = 3.6 \cdot 10^{14}$, and $(n_0)_3 = 2.3 \cdot 10^{14}$ cm^{-3}. The electron temperature measured in the plane of the limiter is approximately the same for all three maxima at $T_e = 5$ eV.

The results on the jet divergence discussed below refer primarily to the first and the second density maxima, since important differences are found in the nature of their divergence.

Figure 3a shows the plasma density at the jet axis during the motion of the jet for the first (I) and second (II) density maxima. The distance along the motion axis is measured from the limiter and divided by the initial radius r_0 (radius of the aperture in the limiter). The densities are normalized to the density at the center of the aperture in the limiter, n_0.

The behavior of these curves remains the same as r_0 is changed from 2.5 to 10 mm. It follows from this figure that the divergence of the various parts of the jet are different; in particular, the part of the jet corresponding to the first density maximum expands more than the part of the jet corresponding to the second maximum.

While the plasma density at the axis of the jet varies by two orders of magnitude the electron temperature decreases from 5 to 3 eV, so that the density at the axis of the jet falls off in proportion to $1/z^2$, i.e., we have $n \approx n_0E_0/kTz^2$.

Accordingly, in the case of the jet of neutrals the functional dependence of $\ln(1 - n/n_0)$ on $1/z^2$ must be described by a straight line whose slope with respect to the $1/z^2$ axis is given by E_0/kT.

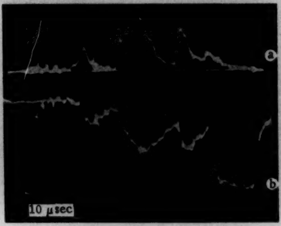

Fig. 2

Figure 3b shows the corresponding functional dependence for the plasma jet. We also observe a linear functional dependence in this case. From the slopes of the analogous lines and the known velocity of the directed motion of the particles we determine the values of the parameter kT for the three density maxima: $(kT)_1 = 5.3$, $(kT)_2 = 0.5$, and $(kT)_3 = 0.35$ eV.

It should be noted that we compare this parameter with the electron temperature only at the first maximum of the plasma flow; in subsequent regions it is an order of magnitude below the experimental value of the electron temperature. If we identify the parameter kT with the ion temperature we conclude that the expansion of the dense plasma jet in vacuum is governed solely by the initial spread in the ion velocity.

Having determined the ion temperature of the plasma jet in this manner we can calculate the radial distribution of the particle density at various distances from the limiter and compare the calculated curves with the experimental curves.

The curves in Fig. 4a correspond to the first (I) and second (II) density in the jet and are obtained for $x/r_0 = 9$. The solid curves show the calculated results; the points are experimental.

The theoretical curves are obtained through a generalization of the calculations of ref. 5 to the case of a moving jet. These curves are described by

$$\frac{n(\rho, z)}{n(0, z)} = \frac{2Ae^{-A\rho^2}}{1 - e^{-A}} \int_0^1 e^{-A\rho^2} I_0(2A\rho\tau)\tau d\tau,$$

where $\rho = r/r_0$; $z = x/r_0$; $A = (E_0/kT)/(x/r_0)^2$; and I_0 is the modified Bessel function. In this case we observe good agreement between the calculated and experimental results over a certain density range [$n(0, z) \sim 10^{14}$-10^{13} cm^{-3}]. Differences appear at radii for which the density

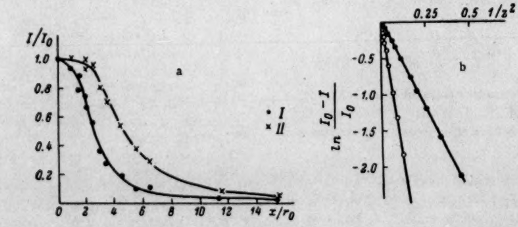

Fig. 3

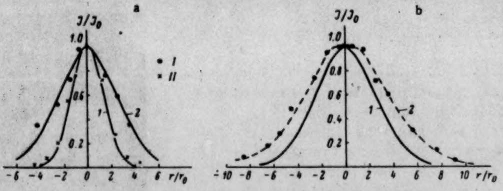

Fig. 4. Radial profile of the ion component in the plasma jet.

becomes significantly lower than the density at the axis, $n(\rho, z)/n(0, z) < 10^{-2}$.

Far from the limiter we observe an important difference between the divergence of the plasma jet and that of a flow of neutrals with similar properties. Figure 4b shows the radial profiles of the charged-particle density for the second maximum, obtained for $x/r_0 = 19$. The two curves show the calculated (1) and experimental (2) functional relations. In this case the divergence of the plasma jet is much more pronounced than that of the neutral flow for the same values of the parameter kT.

The electron pressure, which is only significant at the boundary of the jet for high densities (Fig. 4a), evidently has a significant effect on the nature of the plasma divergence in vacuum at lower plasma densities [$n(0, z) \sim 10^{12}$–10^{11} cm^{-3}; Fig. 4b].

The electron gas reaches a thermodynamic equilibrium over the characteristic times (the voltage–current characteristic implies a Maxwellian electron distribution).

An attempt to detect a concentric layer expanding at three times the ion sound velocity, $(kT_e/M_i)^{1/2}$, in accordance with the results of ref. 2, does not yield a definite result, perhaps because the probe measurements at the boundary of the jet are hindered by the intense fluctuations in the density. These fluctuations lead to a modulation of the probe current at 1-2 MHz.

CONCLUSION

These experiments are carried out in connection with the generally accepted model[16] for the free expansion of plasma in vacuum, according to which a thermal expansion due to an initial spread in the velocities (both ions and electrons) is superimposed on the macroscopic motion of the jet. We also assume that the thermal expansion in vacuum of plasma jets is similar to that of molecular beams, except that the sound velocity in the gas, which is characteristic of the expansion of beams, is associated with the acoustic velocity in the plasma:[17]

$$v_s = \sqrt{\frac{\gamma_i kT_i + \gamma_e kT_e}{M_i}},$$

where T_i and T_e are the ion and electron temperatures, γ_i and γ_e are the ratios of specific heats for the ion and electrons, M_i is the ion mass, and k is the Boltzmann constant.

Accordingly, the plasma expansion is characterized by the parameter $kT = k(T_i + T_e)$, which is a function of both the ion and electron temperatures. If neither component is in thermodynamic equilibrium we can treat this quantity as an average energy governed by the spread in particle velocities.

These experiments on the free expansion in vacuum of plasma jets carried out under approximately collisionless conditions at densities $0.5 \cdot 10^{15}$ cm^{-3} $\leq n_i \leq 1 \cdot 10^{12}$ cm^{-3} and a comparison of these results with those calculated for the case of free molecular expansion have revealed two important differences from the model described above.

The expansion of the plasma jet is governed primarily by the ion temperature, even when the electron temperature is an order of magnitude higher than the ion temperature.

The free expansion of plasma jets in vacuum is analogous to the expansion of a collisionless molecular flow (under the condition $\lambda \geq r_0$) up to the point at which the divergence of the jet causes the density to fall off by two orders of magnitude, $n/n_0 \geqslant 10^{-2}$. At a divergence $n/n_0 < 10^{-2}$ there is a significant difference between the experimental and calculated data.

In conclusion the authors thank B. A. Shevchuk for the computer calculations, and A. A. Kalmykov for useful discussion.

*Institute of Nuclear Research, Warsaw.

---

[1] A. V. Gurevich, L. V. Pariiskaya, and L. P. Pitaevskii, Zh. Eksp. Teor. Fiz., 49, 647 (1965) [Sov. Phys. – JETP, 22, 449 (1966)].
[2] M. Widner, J. Alexeff, and W. D. Jones, Phys. Fluids, 14, No. 3, 795 (1971).
[3] P. Montgomery, Phys. Rev. Lett., 19, 1465 (1967).
[4] H. W. Hendel and T. T. Reboul, Phys. Fluids, 5, 360 (1962).
[5] R. J. Mason, Phys. Fluids, 13, 1042 (1970).
[6] A. A. Plyutto, V. N. Ryzhkov, and A. T. Kapin Zh. Eksp. Teor. Fiz., 47, 494 (1964) [Sov. Phys. – JETP, 20, 328 (1965)].
[7] P. F. Little, J. Nucl. Energy, Part C, 4, 15 (1962).
[8] C. S. Leffel, J. Appl. Phys., 41, 9 (1970).
[9] B. A. Trubnikov, in: Reviews of Plasma Physics, Vol. 1, Consultants Bureau, New York (1965).
[10] Yu. S. Azovskii, I. T. Guzhovskii, and B. G. Safronov, Zh. Tekh. Fiz., 34, 841 (1964) [Sov. Phys. – Tech. Phys., 9, 641 (1964)].
[11] L. I. Krupnik, N. G. Shulika, and P. A. Demchenko, Zh. Tekh. Fiz., 35, 711 (1965) [Sov. Phys. – Tech. Phys., 10, 556 (1965)].
[12] E. O. Johns and L. Malter, Phys. Rev., 80, 58 (1950).
[13] L. I. Krupnik, N. G. Shulika, and P. A. Demchenko, in: Plasma Physics [in Russian], Naukova Dumka, Kiev (1965).
[14] P. Molmud, Phys. Fluids, 3, 362 (1960).
[15] O. V. Kozlov, Electric Probes in Plasmas [in Russian], Atomizdat, Moscow (1969).
[16] Yu. S. Azovskii, I. T. Guzhovskii, Yu. P. Mazalov, and V. M. Pispryak, Zh. Tekh. Fiz., 35, 643 (1965) [Sov. Phys. – Tech. Phys., 10, 505 (1965)].
[17] V. D. Shafranov, in: Reviews of Plasma Physics, Vol. 3, Consultants Bureau, New York (1967).

Laser-initiated vacuum discharge

V. P. Kovalenko, A. A. Makarevich,

V. A. Rodichkin, and A. M. Timonin

(Submitted August 15, 1973; resubmitted December 13, 1973)
Zh. Tekh. Fiz., 44, 2317-2321 (November 1974)

The amplitude and time characteristics of a vacuum discharge (initial pressure $p = 2 \cdot 10^{-6}$ torr) are studied in a two-electrode gap; the discharge is driven by the light pulse from a 15 MW ruby laser, which is focused on one of the electrodes. As the laser-produced plasma expands across the gap, a current flows due to the emission of charged particles from the plasma and changes caused in the strength and configuration of the electric field in the gap by the laser plasma. The maximum current across the gap and the time required for the current to reach its maximum value are functions of the gap voltage (U_0 = 5-50 kV) and the capacitance (C_0 = 1100-4400 pF).

Electrical discharges in vacuum are used for switching high pulsed currents, for producing plasmas, and for generating bursts of x radiation. One common method for initiating a vacuum discharge involves the use of the auxiliary spark produced between one of the main electrodes and the ignition electrode when an ignition-voltage pulse is fed to the latter electrode. Laser ignition seems promising as a method for initiating electrical discharges in general and vacuum discharges in particular. Guenther and Bettis[1] reported a study of laser-ignited arc switches with various dielectrics, including vacuum. The delay of the vacuum breakdown is of the order of 10^{-6} sec, while the rise time of the current ranges from 10^{-7} sec for a positive target electrode to $\sim 10^{-6}$ for a negative target electrode.

We report here a study of vacuum discharges initiated by laser radiation. We have obtained new data on the operation of laser-ignited vacuum arc switches. In particular, we have obtained breakdown delay times below 10^{-8}-10^{-7} sec. We observe a stepped switching of the current, a functional dependence of the current amplitude on the amount of energy, and certain other features.

1. EXPERIMENTAL CIRCUIT AND PROCEDURE

Figure 1 shows the schematic circuit of the apparatus used to study laser-ignited vacuum discharges.

The vacuum chamber, evacuated by a diffusion pump to a pressure of $p \sim 10^{-6}$ torr, holds the target M, the collector K, and the Faraday cup C. The distance between the target and the collector is 10 mm. Radiation from a ruby laser L at a power of 15 MW and a pulse length of ~20 nsec is focused on the target by lens FL, which has a focal length of 210 mm. The laser power and energy are monitored by a calorimeter Ca and an FÉK-15 photocell.

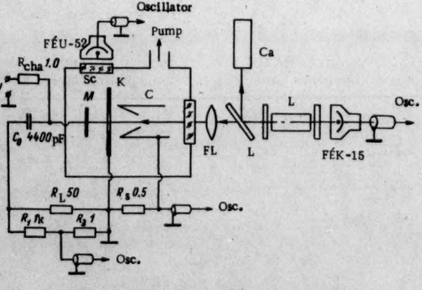

Fig. 1. Circuit used to study vacuum discharges.

The voltage from a high-voltage, low-inductance disk capacitor (C_0 = 1100-4400 pF) charged through charging resistance R_{cha} = 1 MΩ to a voltage of U_0 = 1-50 kV is applied across the discharge gap formed by the target and the collector. Connected in series with the capacitor is a load resistance R_L = 50 Ω, which limits the breakdown current.

The discharge current is measured by resistive divider $R_1 - R_2$ from the voltage drop across the load resistance. The current to the Faraday cup is measured by low-inductance shunt R_s = 0.5 Ω. In addition to measuring the current, we use an oscilloscope to study the x rays produced in the vacuum breakdown. The x radiation is detected by plastic scintillator Sc and an FÉU-52 photomultiplier.

All the oscilloscope measurements are carried out with S1-11 oscilloscopes, triggered by the signal from the photocell that detects the laser pulse.

2. EXPERIMENTAL RESULTS

Figure 2 shows an oscillogram of the voltage across the load resistance, recorded with a negative target electrode at a residual pressure of $p = 2 \cdot 10^{-6}$ torr. The current in the gap lags behind the beginning of the laser pulse by less than 12-15 nsec, regardless of the magnitude of the applied voltage, U_0 = 5-50 kV. During the first 50-60 nsec with a negative target the current across the gap remains essentially constant; then it increases to its maximum value in ~40 nsec. Thereafter it decays exponen-

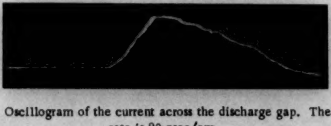

Fig. 2. Oscillogram of the current across the discharge gap. The sweep rate is 20 nsec/cm.

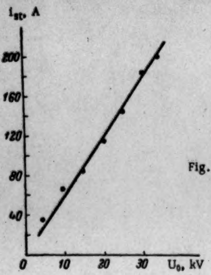

Fig. 3. Current step as a function of the applied voltage.

tially. The behavior of the current is similar when the target electrode is positive; in this case the lag time of the current is generally 2-3 nsec less and the current step has a clearly defined maximum. The size of the initial step is essentially the same for both polarities of the target electrode, being a linear function of the applied voltage (Fig. 3).

During the step a current pulse I_C is observed at the Faraday cup. With a negative target (see the data below) this current is more than an order of magnitude higher for the opposite polarity.

When the target is negative we observe an x-ray burst which is similar in shape and duration to the current pulse at the Faraday cup. Figure 4 shows an oscillogram of the current pulse at the Faraday cup. We see that the current at the Faraday cup increases smoothly, reaching a maximum at the end of the step; then it decays comparatively rapidly, vanishing when the current in the gap reaches its maximum.

The magnitude of the maximum current in the gap is a function of both the voltage applied to the gap and the discharge capacitance. Figure 5 illustrates the functional dependence of the gap current on the voltage for three capacitances. The time t_m between the beginning of the discharge and the current maximum is a function of the charge on the capacitor for a positive target.

U_0, kV	10	15	20	25	30	35	40
I_C, A	4.1	7.4	13.2	21.5	25.6	49.5	56

Figure 6 shows t_m as a function of the applied voltage for a capacitance of $C_0 = 4400$ pF.

Variation of the interelectrode distance d over the range 5-20 mm causes no significant change in the processes occurring in the discharge gap. Furthermore, we find that the gas pressure in the gap has no effect when $p \leqslant 2 \cdot 10^{-3}$ torr. At $p \geqslant 2 \cdot 10^{-3}$ torr the processes in the gap change: When the laser beam strikes the target a discharge occurs in the residual gas, and the current in the circuit varies as it does during the breakdown of the gas-filled gap.[2]

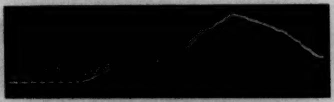

Fig. 4. Oscillogram of the current to the Faraday cup. The sweep rate is 10 nsec/cm.

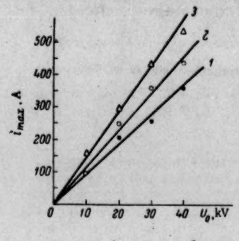

Fig. 5. Maximum current across the gap as a function of the applied voltage. C_0 (pF): 1) 1100; 2) 2200; 3) 4400.

Reducing the laser power leads to a reduction in the current and an increase in the length of the current pulse at the Faraday cup and of the x-ray burst. The integrated characteristics of these pulses (the charge and dose) remain approximately constant, regardless of the laser power.

3. DISCUSSION OF RESULTS

When a metal target is struck by focused laser radiation a laser plasma is formed and expands at a velocity $\sim 10^7$ cm/sec (ref. 3); this plasma apparently emits charged particles and changes the strength and configuration of the electric field in the gap. Accordingly, the current in the gap before breakdown (before the end of the step) must be governed by the current of the emitted charged particles, I_e, and the bias current I_c.

The emission current density is governed by the familiar "three-halves" law, which can be approximated in the following manner for the present case:

$$j_e = A\frac{\varepsilon_0}{9\pi}\sqrt{\frac{2e}{m}}\frac{U^{3/2}}{\left(d - \int\limits_0^t v\,dt\right)^2},$$

where A takes account of the gap form factor, ε_0 is the dielectric constant, e and m are the charge and mass of the particle, and v is the velocity of the emitting boundary of the plasma.

The current at the Faraday cup and estimates from Eq. (1) show that the emission component of the electron

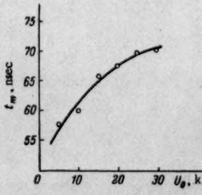

Fig. 6. Time required for the current to reach its maximum value as a function of the voltage on the capacitor.

current does not play an important role during the first ~20 nsec after the formation of the plasma (the time resolution of the measuring circuit is ~8 nsec). The emission component of the current of positive ions (with the target at positive polarity) can be neglected while the plasma expands to the opposite electrode. Accordingly, at least during the initial stage of the plasma expansion, the step in the voltage across the load can be caused only by the bias current (the inductance of the discharge circuit is less than 50 nH). This bias current is due to the change in configuration of the electric field in the gap under the influence of the laser plasma, the changes in the dielectric properties of the evacuated gap due to its filling by plasma and vapor, and the ejection into the gap of molten charged particles of macroscopic size.

Since the plasma velocity falls off during the expansion and while the plasma dimensions become comparable to the length of the gap, the bias current must fall off as a function of the time and the emission current must increase. As a result, with the target electrode at a negative polarity the total current across the gap remains essentially constant throughout the step. With the target at a positive polarity the emission component of the current is low, and the total current across the gap falls off toward the end of a step, then increasing to a maximum.

The functional dependence on the initial capacitor charge of the current and the time required to reach its maximum value is governed by two competing processes: On the one hand, the current increase after the step is due to a decrease in the resistance of the gap; on the other hand, the residual voltage on the capacitor at time t_m depends on the value of C_0. If we assume that the conductivity of the gap is a linear function of the charge which has flowed across the gap, we can write the following equation for t_m:

$$U_0 - I_m R_L - \frac{2}{C_0}\int_0^{t_m} i\,dt = 0, \tag{2}$$

where I_m is the maximum current.

Since the functional dependence of the current on the time is described by $i \sim t^n$ ($n > 0$) while the current increases, we can write the following relation for t_m:

$$t_m^{n+1} \sim n\left(1 - \frac{I_m R_L}{U_0}\right)\frac{C_0 U_0}{2}. \tag{3}$$

We see from (3) that the time required for the current to reach its maximum value is a function of the initial charge on the capacitor. The fact that this functional dependence is not observed when the target is at the negative polarity can be attributed to the fact that a large electron charge, which "conditions" the discharge channel, flows across the gap during the current step. Evidence for this conclusion comes, in particular, from the fact that the total charge which flows across the gap before the current maximum remains essentially constant as the radiation power is reduced.

Accordingly, we can conclude from these results that a laser-initiated vacuum discharge occurs as a result of the short-circuiting of the discharge gap by the expanding laser plasma. Before the gap is short-circuited the plasma is a source of an intense flux of accelerated charged particles, particularly electrons, which can be used to generate intense bursts of relatively soft x rays for nanosecond periods.

In conclusion the authors thank L. V. Dubovoi for critical comments and discussion.

---

[1] A. H. Guenther and J. R. Bettis, Proc. IEEE, 59, 689 (1971).

[2] A. I. Babalin, B. I. Petrov, V. A. Rodichkin, and A. M. Timonin, Zh. Tekh. Fiz., 40, 1718 (1970) [Sov. Phys. – Tech. Phys., 15, 1335 (1971)].

[3] N. G. Basov, V. A. Boiko, V. A. Dement'ev, O. N. Krokhin, and G. V. Sklizkov, Zh. Eksp. Teor. Fiz., 51, 989 (1956) [Sov. Phys. – JETP, 24, 659 (1967)].

Effects due to streamer shape

É. D. Lozanskii and D. B. Pontekorvo

Joint Institute for Nuclear Research, Dubna

(Submitted November 20, 1973; resubmitted March 18, 1974)
Zh. Tekh. Fiz., 44, 2322-2325 (November 1974)

A model of streamer development is proposed. The difference between the shape of the streamer surface and an ellipsoid of revolution is taken into account. Calculations based on the model agree with the experimental data.

The increasing number of papers devoted to experimental investigations of the development of discharges in streamer chambers makes it interesting to compare the existing theoretical results with the data of the latest experiments. A theory of streamer propagation is developed in refs. 1 and 2. The models discussed in these papers are represented mathematically in the form of a Laplace equation for the potential generated by the streamer in the surrounding space:

$$\Delta\Phi(\rho,\ z,\ t)=0. \tag{1}$$

Here, ρ and z are cylindrical coordinates, the z axis is in the direction of the applied field E_0, and t is the time. The potential of an ideally conducting sphere in a uniform field E_0 is taken to be the initial condition for Eq. (1):

$$\Phi(\rho,\ z,\ 0)=-E_0 z\left(1-\frac{r_0^3}{(z^2+\rho^2)^{3/2}}\right). \tag{2}$$

Here, r_0 is the initial radius of the avalanche, which is determined by electron diffusion and mobility at the point at which the avalanche changes into a streamer. The velocity of the equipotential surface $\Phi = 0$ is determined by the electron velocity in the resulting field near this surface, i.e.,

$$v=|k\nabla\Phi|, \tag{3}$$

where k is the electron mobility.

It is shown in ref. 2 that near the ends of a streamer its surface is essentially the same as the surface of an ellipsoid of revolution; accordingly the true shape of the streamer, i.e., the equipotential $\Phi = 0$ is replaced by an ellipsoid of revolution.

To compare theory with experiment, however, requires that the theory developed in refs. 1 and 2 be refined It follows from (2) that when z = 0 the field is equal to zero; thus, all the points of this plane on the streamer surface remain fixed. It is easy to see that this leads to the formation of a "neck" and, thus, to a difference between the streamer shape and an ellipsoid of revolution.

Model of streamer propagation with the effect of the "neck" taken into account. The effect of the neck on streamer development can be considered if the following function is taken as the solution of Eq. (1):

$$\Phi=-E_0 z\left[1+\frac{p r_0^3}{(z^2+\rho^2)^{3/2}}-(1+p)\frac{\ln\frac{\sqrt{(f-z)^2+\rho^2}+f-z}{\sqrt{(f+z)^2+\rho^2}-f-z}+\frac{\sqrt{(f-z)^2+\rho^2}-\sqrt{(f+z)^2+\rho^2}}{z}}{\ln\frac{\sqrt{f^2+r_0^2}+f}{\sqrt{f^2+r_0^2}-f}-\frac{2f}{\sqrt{f^2+r_0^2}}}\right]. \tag{4}$$

Here,

$$p=\frac{\ln\frac{\sqrt{r_0^2+f^2}+f}{\sqrt{r_0^2+f^2}-f}-\ln\frac{a+f}{a-f}-\frac{2f}{\sqrt{r_0^2+f^2}}-\frac{2f}{a}}{\ln\frac{a+f}{a-f}-\frac{2f}{a}-\frac{r_0^3}{a^3}\left(\ln\frac{\sqrt{r_0^2+f^2}+f}{\sqrt{r_0^2+f^2}-f}-\frac{2f}{\sqrt{r_0^2+f^2}}\right)}. \tag{5}$$

The selection of Φ in the form of (4) is due to the following considerations. If we set p = 0, the rest of expression (4) gives the equipotential $\Phi = 0$ in the form of the surface of an ellipsoid of revolution with f as the distance between foci and major semiaxis a. If we set $a = r_0$, which is valid at the initial time, it then follows from (5) that p = −1 and (4) then gives the equipotential $\Phi = 0$ in the form of a sphere of radius r_0. Finally, when z = 0, $\rho = r_0$ the resulting field is

$$E=\sqrt{E_z^2+E_\rho^2}=\sqrt{\left(\frac{\partial\Phi}{\partial z}\right)^2+\left(\frac{\partial\Phi}{\partial\rho}\right)^2}=0, \tag{6}$$

which ensures that a neck is formed. The following two relations, which are independent of the model, are given in ref. 2 for the radius of curvature R of the streamer surface near its ends:

$$R=\frac{2\Phi'}{\Phi''}, \tag{7}$$

$$\frac{dR}{da}=2\left(\frac{\Phi'\Phi'''}{\Phi''^2}-2\right), \tag{8}$$

where Φ', Φ'', and Φ''' are values corresponding to the first, second, and third derivatives of the potential with respect to z at the point $z = a$, $\rho = 0$, i.e., at the end of the streamer. Finding the values of these derivatives from (4) and substituting into (7) and (8), we obtain (more detailed calculations are given in ref. 3)

$$R=-\frac{a^2-f^2}{a}\frac{1-\frac{r_0^3}{a^3}-\frac{3}{2}\frac{r_0^3(a^2-f^2)}{a^2f^3}A}{1-\frac{r_0^3}{a^3}-\frac{3}{2}\frac{r_0^3(a^2-f^2)^2}{a^4f^3}A}, \tag{9}$$

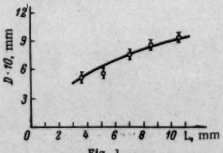

Fig. 1

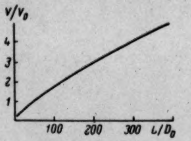

Fig. 2

$$\frac{dR}{da} = -6\frac{(a^2-f^2)r_0^3 f\left(1-\frac{r_0^3}{a^3}\right)A}{\left[1-\frac{r_0^3}{a^3}-\frac{3}{2}\frac{(a^2-f^2)^2 r_0^3}{a^4 f^3}A\right]^2 a^6}, \tag{10}$$

where

$$A = \ln\frac{\sqrt{f^2+r_0^2}+f}{\sqrt{f^2+r_0^2}-f} - \frac{2f}{\sqrt{f^2+r_0^2}} - \ln\frac{a+f}{a-f} + \frac{2f}{a}.$$

For $f \ll r_0$, i.e., $a \to r_0$, from (10) we find

$$\frac{dR}{da} \sim \left(1-\frac{r_0^3}{a^3}\right),$$

i.e., it is close to zero. As a increases dR/da goes to zero rapidly. Consequently, one can assume in the first approximation that as the streamer develops dR/da remains equal to zero, i.e., R = const; thus, as follows from (9) and (10),

$$|R| = r_0. \tag{11}$$

Using (9) to express f in terms of a and r_0 and substituting this value into the expression for $\Phi'(a)$ we find the relation $v = |k\Phi'|$. Since the streamer velocity is

Using (9) to express f in terms of a and r_0 and substituting this value into the expression for Φ' we find the relation $\Phi'(a)$. Since the streamer velocity is $v = |k\Phi'|$ we can find the dependence of the streamer velocity on its length.

It is also interesting to consider what shape the streamer surface will assume during its development. For this purpose the value of f obtained from (9) is substituted into (5). Then the function obtained, $p(a)$, is substituted into (4); for a definite value of a, after equating (4) to zero, we obtain the relation $z(\rho)$, i.e., the equation of the surface.

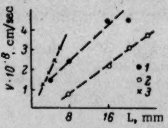

Fig. 3. Streamer propagation velocity as a function of length for different fields.

By selecting the maximum value of ρ for each a and considering this value to be the effective half-width of the streamer, we can also find the dependence of the half-width of the streamer on its length.

Figure 1 gives the maximum width of the streamer as a function of its length L, where $L = 2a$. The experimental results (points) obtained by Davidenko et al.[4] are also given in Fig. 1. In Fig. 2, the streamer propagation velocity is given as a function of length in the dimensionless parameters V/V_0 and L/D_0, where $D_0 = 2r_0$ and $V_0 = kE_0$. The calculations are performed on a CDC-1604A computer. Figure 3 gives the experimental results of Davidenko et al.[5] (1 – 16, 2 – 10.4 kV/cm) and Rudenko and Smetanin[6] (3 – 16.7 kV/cm).

It can be seen from Figs. 1-3 that good qualitative agreement exists between the theory and the experimental data. A quantitative comparison with experiment is difficult at the present time because of the absence of reliable data on the value of r_0, which is only known in order-of-magnitude terms.

In conclusion, the authors thank O. B. Firsov, M. M. Kulyukin, I. V. Falomkin, and Yu. A. Shcherbakov for useful discussion.

---

[1] É. D. Lozanskii and O. B. Firsov, Zh. Eksp. Teor. Fiz., 56, 670 (1969) [Sov. Phys.—JETP, 29, 367 (1969)].

[2] É. D. Lozanskii (Lozansky) and O. B. Firsov, J. Phys. D, 6, 976 (1973).

[3] É. D. Lozanskii and D. B. Pontekorvo, Preprint, Ob. Inst. Yad. Issled. (1973).

[4] V. A. Davidenko, B. A. Dolgoshein, and S. V. Somov, Zh. Eksp. Teor. Fiz., 55, 435 (1968) [Sov. Phys.—JETP, 28, 227 (1969)].

[5] V. A. Davidenko, B. A. Dolgoshein, and A. V. Somov, Nucl. Instrum. Meth., 75, 277 (1969).

[6] N. S. Rudenko and V. I. Smetanin, Zh. Eksp. Teor. Fiz., 61, 146 (1971) [Sov. Phys.—JETP, 34, 76 (1972)].

Electrical breakdown of vacuum gaps under superhigh voltage pulses

I. I. Kalyatskii, G. M. Kassirov, and G. V. Smirnov
S. M. Kirov Tomsk Polytechnical Institute

(Submitted November 12, 1973; resubmitted April 2, 1974)
Zh. Tekh. Fiz., 44, 2326-2328 (November 1974)

Experimental results are reported for electrical breakdown of centimeter vacuum gaps under superhigh voltage pulses. At distances up to 15 cm the breakdown field across the cathode is virtually constant, and the processes leading to the breakdown occur in short time intervals. In the microsecond time range the breakdown voltage is independent of the pressure and species of the residual gas.

The inadequate data on electrical breakdown of large vacuum gaps and the remarkable differences in the breakdown properties at superhigh voltages[1-4] have stimulated experimental investigations into voltages higher than 1 mV. For this purpose we have constructed a vacuum apparatus with a maximum pulsed working voltage of 2 mV. In the first stage of the investigation we study the electrical strength of the vacuum insulation in large gaps subjected to voltage pulses as a function of electrode separation and residual gas pressure. The experiments are performed in a steel vacuum chamber with superhigh voltage pulses provided by a GIN-3MV generator with a capacitance of 7200 pF. The voltage and current pulses are recorded on a dual beam OK-17M oscilloscope, and all the experiments employ aluminum electrodes. The cathode is a sphere 150 mm in diameter. The anode is a disk 200 mm in diameter. The working vacuum in the apparatus is $1\text{-}2\cdot 10^{-5}$ torr. The electrode separation is varied by means of a Wilson seal and is measured to within 0.05 mm.

Before the dependence of the breakdown voltage on the gap width is measured the electrodes are subjected to repeated preliminary breakdowns, which result in an increase and stabilization of the breakdown voltage. To estimate the effect of the resistance of the discharge circuit on the gap aging process, aging curves are plotted for three sharply differing resistances of the discharge circuit (Fig. 1). It can be seen from this figure that at all three resistances the breakdown voltage increases with the number of preliminary discharges. Since the width of the leading edge of the voltage pulse, and thus the time that the voltage acts on the vacuum gap, increases as the resistance of the discharge gap increases, the breakdown voltage is higher for small resistances than for large resistances. Since the resistance does not have a significant effect on the aging process, all the subsequent experiments are carried out for the smallest resistance, and the leading edge of the voltage pulse is then 0.5 μsec. The breakdown voltage is measured after 200-300 preliminary pulses. The curve is plotted from 20 oscilloscope traces of the breakdown for each electrode separation. The curve is plotted three times – for a change in the separation from a maximum to a minimum and vice versa.

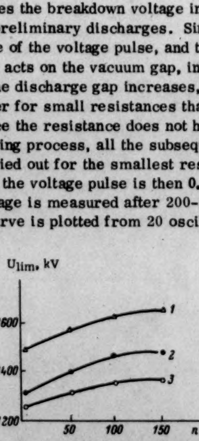

Fig. 1. Aging curves of vacuum gaps 90 mm wide with aluminum electrodes. 1) 50 Ω; 2) 4 kΩ; 3) 30 kΩ.

The curve in Fig. 2 shows the effect of electrode separation on breakdown voltage for breakdown at the leading edge of the voltage pulse. As can be seen from this figure, the breakdown voltage increases more slowly than the electrode separation. However, as a result of the increase in field inhomogeneity due to the increase in the electrode separation, the field voltage across the cathode, calculated from the well-known equation for a sphere-plane system:

$$E_{\text{lim}} = 0.9\frac{U_{\text{lim}}}{d}\left(\frac{r+d}{r}\right),$$

where E_{lim} is the field at the cathode, U_{lim} is the breakdown voltage, r is the radius of the sphere, and d is the electrode separation, varies by a small amount from 408 kV/cm for a 10 mm gap to 361 kV/cm for a 150 mm gap, i.e., it is virtually constant. Analytically the curve of breakdown voltage vs electrode separation is described by

$$U_{\text{lim}} = 400d^{0.61},$$

where U_{lim} is the breakdown voltage (kV), and d is the electrode separation (cm).

To estimate the possible coefficients of the pulse for a breakdown of large gaps the breakdown voltage is measured in 100 μsec pulses. This breakdown voltage is conventionally taken to be "static." The pulse coefficient for an 8 cm gap is of the order of 3.

Our experiments on the breakdown of centimeter vacuum gaps for different residual gas pressures indicate that the well-defined dependence of the breakdown voltage on the pressure for a constant voltage does not occur for a pulsed voltage in the microsecond range. The corresponding experimental results for 40 and 90 mm gaps are shown in Fig. 3 (curves 1 and 2). The dependence of breakdown voltage on the gas species is also absent. It should be noted that as for small gaps with pressures of 10^{-3}-10^{-2} torr the spread of breakdown voltages increases. Evidently, the processes leading to an increase in the

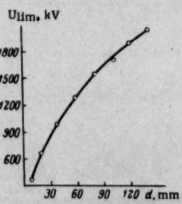

Fig. 2. Breakdown voltage as a function of gap width.

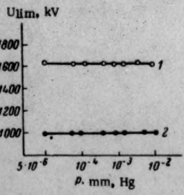

Fig. 3. Dependence of breakdown voltage on residual gas pressure in gaps of different width. 1) 90 mm; 2) 40 mm.

electrical strength of vacuum insulation of large gaps under static voltages at pressures of 10^{-3}-10^{-4} torr do not occur for pulsed voltages.

Thus, our investigation of the breakdown voltage of centimeter vacuum gaps under microsecond pulses leads to the following conclusions:

1. Under vacuum breakdown of centimeter gaps the breakdown field remains virtually unchanged as the gap width increases.

2. The well known dependence of the breakdown voltage of centimeter gaps on gas pressure for a constant voltage does not operate for microsecond pulses.

3. A reduction in the width of the pulse acting on an 8 cm vacuum gap from 100 to 0.5 μsec leads to a threefold increase in the breakdown voltage.

---

[1] V. R. Ergakov, I. I. Kryuchkov, and Yu. V. Trebukhovskii, Preprint, Inst. Teor. Eksp. Fiz., No. 265, Moscow (1964).

[2] F. Rohrbach, Preprint, CERN, No. 64-50 (1964).

[3] V. R. Ergakov, I. I. Kryuchkov, and Yu. V. Trebukhovskii, Prib. Tekh. Eksp., No. 6 (1971).

[4] P. Coet, Preprint, MPS/Int, 88-22 (1968).

Volt–ampere characteristic of the low-voltage arc.
I. Recombination model

P. P. Shcherbinin

(Submitted March 26, 1973; resubmitted October 12, 1973)
Zh. Tekh. Fiz., 44, 2329-2339 (November 1974)

The parameter dependence of the volt–ampere characteristic is given with recombination and Coulomb scattering included; the derived expressions can be used for rapid analysis. The dependence of the characteristic on gap width is given as an illustration.

Baksht, Moizhes, and others (e.g., refs. 1, 2) have given a general theory of ionization and recombination processes in the plasma in a thermionic converter (TC) and have given solutions of the transfer equations. A number of other workers have studied qualitatively the specific effects on the volt–ampere characteristic due to specific phenomena. For example, volume ionization is considered in ref. 3, surface and volume ionization in ref. 4, volume ionization and Coulomb scattering in ref. 5, the Schottky effect in ref. 6, and the possibility of formation of a virtual cathode in refs. 5-7. In the present paper we analyze a model which takes account of surface and volume ionization, recombination, Coulomb scattering, and the Schottky effect. These are the most important physical phenomena that occur in the gap.

The only basic phenomenon that is not allowed for is the finite thermal conductivity of the electrons. At low pressures,[8] and at high voltages and high pressures,[9] the electron temperature can be assumed to be constant. In other cases the electron temperature can vary by some tens of percent along the gap.[1] If the electron temperature is not constant the generation rate is a function of the coordinate. As a result, in the model with $T_e(x)$ = const = T_e (T_e being understood as the mean electron temperature over the gap) the theoretical density profile will differ qualitatively from the experimental profile. But since the volt–ampere characteristic is defined by the integrated characteristic of the plasma[8,10] we expect that the model density profile will only introduce quantitative differences.

PLOTTING THE VOLT–AMPERE CHARACTERISTIC

To plot the characteristic we must obtain expressions for the potential jump $\varphi_{1,2}$ near the electrodes and the potential drop in the plasma $\delta\varphi$, which determine the voltage V across the gap (the subscript 1 refers to the cathode, 2 to the anode, $\varphi_1 > 0$, $\varphi_2 < 0$):

$$V = \varphi_1 + \delta\varphi + \varphi_2. \tag{1}$$

The jumps near the electrode can be determined from the boundary conditions for the particle and energy fluxes (we take these conditions in elementary form: $1/2$ for ions, $1/4$ for electrons[11]). But the number of unknown parameters in the boundary conditions ($\varphi_{1,2}$, $\delta\varphi$, $n_{1,2}$, the plasma density, V, $J_{1,2}$, the electron flux $J_{i\,1,2}$, the ion flux, and $Q_{1,2}$, the total energy flux of the electrons) is 12, while the number of boundary conditions is six. To close the system of equations we must find a link between the plasma parameters at the cathode and the anode, i.e., we must solve the system describing the plasma in the TC gap.

This system has the following form[5,12] ($0 \le x \le d$):

$$\frac{eJ_e}{\mu_{ea}} + \frac{e(J_e - J_i)}{\mu_{ei}} = -\Theta_e n' + en\varphi', \tag{2}$$

$$-\frac{eJ_i}{\mu_{ia}} - \frac{e(J_i - J_e)}{\mu_{ei}} = \Theta_i n' + en\varphi', \tag{3}$$

$$J'_e = J'_i = \alpha n\left(1 - \frac{n^2}{n_p^2}\right), \tag{4}$$

$$-Q' = (E_i + e\varphi)\, J'_e. \tag{5}$$

Here, E_i is the ionization energy; n_p is the plasma equilibrium density; $\Theta_{e,i} = kT_{e,i}$; the coefficients $\mu_{ea} = a_0/n_a$, $\mu_{ia} = c_0/n_a$, $\mu_{ei} = b_0/n$ are defined in refs. 5, 12, and 13; is n_a is the neutral density. Equation (4), as can be seen from ref. 14, is a qualitatively accurate description of the ionization and recombination process in the plasma; $\alpha = v_e n_a \sigma$; we use the expression given in ref. 14 for σ.

From (2), (3) we obtain [$\Lambda = \mu_{ia}/\mu_{ea}$, $D_a = (1 + \lambda)D_i$, $\lambda = \theta_e/\theta_a$, $\theta_i = \theta_a$].

$$J_i = -\Lambda J_e - D_a n' \tag{6}$$

and the equation for determining the density

$$n'' + \gamma^2 n\left(1 - \frac{n^2}{n_p^2}\right) = 0, \quad \gamma^2 = \frac{1 + \Lambda}{D_a}\alpha. \tag{7}$$

The fact that n_a depends on x is not taken into account, since $n \ll n_a$ at thermodynamic equilibrium; and as the discharge develops further the plasma density is determined by the expression $n \simeq n_p$.

From (7) we find

$$n'^2 = \frac{\gamma^2}{2n_p^2}(n_3^2 - n^2)(2n_p^2 - n_3^2 - n^2), \tag{8}$$

where n_3 is the maximum density in the gap; $n_3 < n_p$, and it follows from (8) that n(x) can reach the value n_p only in an infinitely long gap (for $n_{1,2} \neq n_p$).

The plasma density is ($z = n/n_3$, $y = n/n_p$, sn(x) is the elliptic sine[15])

$$z(x) = \operatorname{sn}(F\gamma x + \beta), \quad F = \sqrt{1 + \frac{y_3^2}{2}}. \tag{9}$$

Here, y_3 and β are integration constants and are determined from the boundary conditions for Eq. (7):

$$z_1 = \operatorname{sn}\beta, \tag{10}$$

$$z_2 = \operatorname{sn}(F\gamma d + \beta). \tag{11}$$

The resultant density profile makes it possible to determine the relationship between the plasma parameters between the cathode and the anode. Substituting (8) into (6), we obtain

$$J_{i2} - J_{i1} = J_{e2} - J_{e1} = \frac{D_a\gamma n_3}{\sqrt{2}\,(1 + \Lambda)}(K_1 + K_2),$$

$$K_{1,2} = [(1 - z_{1,2}^2)(2 - y_3^2 - y_{1,2}^2)]^{1/2}. \tag{12}$$

From (6), (8), and the boundary conditions for the ion flux we obtain a system of three equations for the three unknowns $n_{1,2,3}$ ($\psi_{1,2} = |e\varphi_{1,2}|/\Theta_e$; eJ_C is the Saha current):

$$z_1 = 2\frac{J_C e^{-\lambda\psi_1} + \Lambda J_{e1}}{n_3 v_i} + aK_1, \tag{13}$$

$$z_2 = -2\Lambda\frac{J_{e2}}{n_3 v_i} + aK_2, \tag{14}$$

$$F^{-1}(z,\ k) = \sqrt{(1 - z^2)(1 - k^2 z^2)},\quad k^2 = \frac{y_3^2}{2 - y_3^2},\quad a = \frac{\sqrt{2}\gamma D_a}{v_i},$$

$$F\gamma d = \int\limits_{z_1}^{1} dz F(z,\ k) + \int\limits_{z_2}^{1} F(z,\ k). \tag{15}$$

From (2), using (8), we can determine the voltage drop in the gap $\delta\psi = e\delta\varphi/\Theta_e$; F_R is the Richardson current (A/cm^2), D is the gap length (cm); $t_i = T_i/(10^3\,°K)$; eJ_R is the Richardson current; Λ_E is the Coulomb logarithm,

$$\delta\psi = \delta\psi_1 + \delta\psi_2 + \ln\frac{z_2}{z_1}, \tag{16}$$

$$\delta\psi_1 = \frac{J_{e2}}{D_e n_3 \gamma F}\ln F_1,\quad F_1 = \frac{\sqrt{1 - z_2^2 k^2} + \sqrt{1 - z_2^2}}{\sqrt{1 - z_1^2 k^2} - \sqrt{1 - z_1^2}}\frac{z_1}{z_2}, \tag{17}$$

$$\delta\psi_2 = c_5\frac{J_e - J_i}{J_R},\quad c_5 = \frac{edJ_R}{b_0\Theta_e} \simeq \frac{2.5\Lambda_e F_R D}{(\lambda t_i)^{3/2}}. \tag{18}$$

Here, $\delta\psi_1$ results from electron scattering on atoms (ohmic resistance of the plasma), while $\delta\psi_2$ results from scattering on ions (Coulomb scattering); $D_{e,i} = l_{e,i} v_{e,i}/3$; $l_e = 3l_i$. In integrating the term with J_e in (2), the quantity J_e is removed from the integral sign for $J_e = J_{e2}$; thus the expression for $\delta\psi_1$ is too high.

From (5) and the boundary conditions[11] for Q we obtain an equation which determines the energy balance in the gap ($U = eV/\Theta_e$),

$$J_{e2}U = 2\left(1 - \frac{1}{\lambda}\right)J_{em} + \left(\frac{S_3}{\lambda} + \bar{\psi} + 2\right)(J_{e2} - J_{e1}), \tag{19}$$

$$\psi_1 = \ln\frac{n_1 v_e}{4}\frac{1}{J_{em} - J_{e1}},\quad \psi_2 = \ln\frac{n_2 v_e}{4J_{e2}}, \tag{20}$$

$$V = \frac{\Theta_e}{e}\left(\ln\frac{J_{e2}}{J_{em} - J_{e1}} + \delta\psi_1 + \delta\psi_2\right). \tag{21}$$

Here, $\bar{\psi} \simeq \psi_1$ is the value of $e\varphi/\Theta_e$ at some median point of the gap; $s_3 = E_i/\Theta_i$; the term equal to two in (19) appears because J_{e2} differs from J_{e1} in $Q_{1,2}$; J_{em} is the electron emission flux.

$$J_{i2} - J_{i1} = \frac{n_1 + n_2}{2}v_i - J_C e^{-\lambda\psi_1}; \tag{22}$$

and setting $\bar{\psi} - \psi_1 - \delta\psi \simeq 0$, we find that (19) is replaced by

$$J_{e1}U = 2\left(1 - \frac{1}{\lambda}\right)J_{em} + \left(\frac{s_3}{\lambda} + 2 + \psi_2\right)\left(n_1 + n_2 - \frac{2}{v_i}J_C e^{-\lambda\psi_1}\right)\frac{v_i}{2}. \tag{23}$$

The boundary conditions for $Q_{1,2}$ used in deriving (23) are derived under the assumption that the beam of emission electrons is thermalized immediately at the cathode; this occurs at both low[8] and high[9] pressures.

We should note that the right side of (23) has the same form for any plasma density profile. Without volume ionization the losses due to this phenomenon are small and $n_1 + n_2 - 2J_C e^{-\lambda\psi_1}/v_i \to 0$. Equations (12) and (23) make it possible to determine V as a function of the total current $e(J_e - J_i) = eJ$. As can be seen from (12)-(23), Coulomb scattering only introduces additional losses – the term[5] $\delta\psi_2$ in V.

Above we have taken account of divergence of the electron current. The corresponding corrections in the expression for γ^2 and $J_{1,2,3}$ are of order λ [therefore J_{e2} can be replaced by J_{e1} in (14)]. Allowing for the fact that $J_e' \neq 0$ only in ψ_2 introduces a major contribution: From (22) for $n_{1,2}/2 \gg J_C e^{-\lambda\psi_1}/v_i$, $n_1 \sim n_2 \gg J_{em}/v_e$ we obtain $J_{e2} \simeq n_1 v_i$ and

$$\psi_2 \to \ln\frac{v_e}{4v_i},\quad n \to \infty, \tag{24}$$

whereas for $J_{e2} = J_{e1} < J_{em}$, $n_1 \simeq n_2$, bounded J_{em}, and $n_1 \to \infty$ (the model in ref. 4) we have $\psi_2 \to \infty$. From (13) and (14) we obtain

$$\frac{n_1 + n_2}{2}v_i = J_C e^{-\lambda\psi_1} + \frac{D_a\gamma n_3}{\sqrt{2}}(K_1 + K_2). \tag{25}$$

The left side of (25) is the ion flux leaving the gap, while the right side is the sum of ion fluxes arriving at the gap and generated in the gap. Analysis shows that balance of the ion fluxes [the left and right sides are equal in (25)] does not occur for any arbitrarily specified value of Θ_e. For example, in the absence of recombination Θ_e cannot be greater than the quantity Θ_{e0} defined by the equation [a consequence[3-5,16] of (25), where $s = \sin\gamma d$, $c = \cos\gamma d$]

$$\frac{n_1 + n_2}{2}v_i = (1 - c)\gamma D_a\frac{n_1 + n_2}{s} + J_C e^{-\lambda\psi_1} \tag{26}$$

for $J_C = 0$. If $\Theta_e > \Theta_{e0}$, more ions are generated in the gap than go to the electrodes. Recombination limits the regeneration rates and therefore we expect that Eqs. (13)-(15) will also have solutions for $\Theta_e > \Theta_{e0}$.

To take account of the Schottky effect, we need only add the expression[16,17] for J_{em} to the above equations.

VOLT–AMPERE CHARACTERISTIC WITHOUT RECOMBINATION

The case in which the Schottky effect is small and there is no Coulomb interaction and $J_e' = 0$ is considered in ref. 4 (the boundary conditions for ions are taken with $1/4$ in ref. 4), it is shown that surface ionization leads to Θ_e being a function of J [this conclusion can be readily obtained from (26)]. However, near $J_e \simeq J_{em}$ ($J_e > 0.5\,J_{em}$) $\Theta_e \simeq$ const, while[16] $n_1 \simeq n_2$. The same is valid (as can readily be shown) for the case under consideration (Schottky effect and Coulomb scattering $J_e' \neq 0$). When $d//l_i \gg 1$, Eq. (26) for Θ_{e0}, which can conveniently be written in the form $M = 0$ [$M = c + B - 1$, $B = sv_i/(2D_a\gamma)$], reduces to the expression[3,5] $\gamma d = \pi = \varepsilon_1$, $\varepsilon_1 = 4D_a\gamma/v_i$.

The plasma density at the maximum n_3 is related to $n_{1,2}$ by an expression that is a consequence[4] of (15),

$$sn_3 = \sqrt{n_1^2 + n_2^2 - 2n_1 n_2 c}. \tag{27}$$

In the $M = 0$ approximation we obtain $z_1^2 = 2a^2/(1 + a^2) =$ const, and from (27) for $d/l_i \gg 0$ we find ($n_1 = n_2$).

$$n_1 = \frac{1}{2}\varepsilon_1 n_3. \tag{28}$$

For small current $J_e \nless 0.5\,J_{em}$, if we disregard the possibility of formation of a virtual cathode[5-7] and surface ionization,[4] the voltage begins to increase with decreasing current. Allowance for surface ionization and the possibility of a virtual cathode markedly narrows (in terms of parameter values) the region of formation of the drooping part of the volt–ampere characteristic.[4,7] For $J \gtrsim 0.5\, J_{em}$ the voltage increases monotonically with the current, while $n(x) \to \infty$.

ALLOWANCE FOR RECOMBINATION

The size of the electrode region L in which the plasma is not in equilibrium is defined by an expression obtained in refs. 1 and 2 (p is the pressure in mm Hg),

$$\frac{L}{d} \equiv \frac{1}{\gamma d} = \frac{1}{pD} 10^{-5+\frac{8.1}{\lambda l_i}}.$$

In the model without recombination, taking M = 0 for $d \simeq l_i$ we obtain L > d; for $d \gg l_i$ $\gamma d \simeq \pi$. Here, γ increases with Θ_e, equilibrium is established at the center of the gap, and the nonequilibrium regions are restricted to the electrode regions.

Let us first consider the case in which the recombination is small: $y_3 \ll 1$. From (8) we obtain

$$F\gamma x = \int_{z_1}^{z} dz' F(z', k). \tag{29}$$

We expand the integrand in powers of $k^2 \ll 1$; retaining the first two term we obtain [the upper sign for $0 < x < x_3$, the lower for $x_3 < x < d$, $n(x_3) = n_3$]

$$z(x) = \sin\left[\gamma_1 x + \beta \pm \frac{k^2}{4+k^2}\left(z\sqrt{1-z^2} \mp z_1\sqrt{1-z_1^2}\right)\right],$$

$$\gamma_1 = \gamma \frac{F}{\varepsilon_5}, \quad \varepsilon_5 = 1 + \frac{k^2}{4}. \tag{30}$$

The third term in brackets in (30) is of order (y_3^2) and can be neglected. Then $z(x) = \sin(\gamma x + \beta)$, and all the results of ref. 4 hold provided that we replace γ by γ_1. Here, Eq. (27) will be a transcendental equation in n_3.

When $z_{1,2} \ll 1$, (30) is a fairly good approximation all the way to $k^2 \le 0.95$ [this follows from comparing the exact value of (15) (with $z_{1,2} = 0$)] and its expansion in powers of k^2]. This result follows because the contribution to recombination is determined by an integral of $J_e' \sim 1 - n^2/n_p^2$.

Let us investigate the case $1-k^2 \ll 1$ ($k^2 > 0.95$), $z_{1,2} \in [0, 1)$ further. We assume that the terms with $J_{e1,2}$, J_C in (13) and (14) can be omitted because they are small (developed arc). In this case $y_1 = y_2$, and we obtain the following expression for y_1 from (13) (which can also be used for $k^2 < 0.95$, $y_1 = y_2$)

$$y_1^2 = 1 + \frac{1}{2a^2} - \sqrt{\left(1 + \frac{1}{2a^2}\right)^2 - y_3^2(2 - y_3^2)}. \tag{31}$$

We make the following estimates, using the fact that $\int_0^z dz' F(z', k) < \int_0^{z_1} dz' F(z', 1) \equiv \ln[(1 + z_1)/(1 - z_1)]/2$:

$$\int_{z_1}^{1} dz' F(z', k) + \int_{z_2}^{1} dz' F(z', k)$$

$$\leqslant \int_0^1 dz' F(z', k) - \ln b, \quad b^2 = \frac{(1+z_1)(1+z_2)}{(1-z_1)(1-z_2)}. \tag{32}$$

When $z_{1,2} \ll 1$ the second term in (32) is small ($b \simeq 1 + 2z_1$), and (15) is replaced by K(k), an elliptic integral of the second kind:

$$F\gamma d = 2K(k). \tag{33}$$

We note that Eqs. (31) and (32) have a solution for all $\lambda \in [1, \infty)$; in the case in question, therefore, ion balance does not impose constraints upon the growth of λ. When $1-k \ll 1$ we have[18] $k(j) \simeq \ln(4/\sqrt{1-k^2})$. This expression for K(k) can be used for all $k \in [0, 1)$; when $k^2 \to 1$ it coincides with the exact expression, and when k = 0 it differs by less than 15%. From (15) and (32) we obtain

$$\gamma d = \frac{1}{F} \ln \frac{16}{(1-k^2)\, b}. \tag{34}$$

Thus Eqs. (31) and (34) determine the quantities $y_{1,3}$. For $k^2 > 0.95$, y_3 is almost equal to unity, and only in (17) is this difference substantial ($\delta\psi_1$ diverges if we formally set $z_1 = z_2$, $k^2 = 1$). Expanding F_1 in (17) in the neighborhood of $z_1 = 0$ ($a^2 \gg 1$, see (31); $F_1 \simeq 4/[(1-k^2) z_1^2]$), and then in the neighborhood of $z_1^2 = 1$ ($a^2 \gg 1$, $z_1 = 1 - 1/a$), and using (34), we obtain an approximation for $\delta\psi_1$:

$$\delta\psi_1 = \frac{J_{e2}(d + d_1)}{D_e n_3}, \quad d_1 = \frac{1}{\gamma F} \ln \frac{b}{(4 + 2a) z_1^2}, \tag{35}$$

which, for $a^2 \ll 1$ and $a^2 \gg 1$ [and also as $k^2 \to 0$, γd being determined from (34) in this case], goes over the exact expressions.

Equations (31) and (34) together with (21) and (23) [the term with J_C being dropped in (23)] describe the volt–ampere characteristics; they hold for all $k \in [0.1)$. If Θ_e is taken as a parameter the numerical solution of these equations presents no problems. Indeed, if Θ_e is known the equations separate into Eqs. (31) and (34) in $y_{1,3}$ and Eqs. (21) and (23) in V and J_{e1}. Finding $y_{1,3}$ and substituting V from (21) into (23) we can obtain a simple expression for J_{e1}.

As z_1 approaches unity, we obtain $z_1^2 = 1 - 1/a$, $b = 2a$ from (31) (for $y_3 = 1$), and d_1 vanishes ($2a \gg 4$):

$$\delta\psi_1 = \frac{J_{e2} d}{D_e n_3}. \tag{36}$$

Equation (36) can also be obtained directly from (2) when $n(x) \equiv n_3$.

When $y_{1,2,3} \simeq 1$ the plasma in the gap is in equilibrium, and therefore the relationship between the plasma densities at the cathode and anode is trivial, since $n_1 = n_2 = n_3 = n_p$, and the need for considering (13)-(15) is obviated. It is also easy to obtain (36). This case is equivalent to the total equilibrium model in ref. 1.

SIMPLIFIED EXPRESSIONS FOR THE VOLT–AMPERE CHARACTERISTIC

When surface ionization is unimportant we can obtain simple expressions (where we assume that $J_{e1} = J_{e2} = J$, the difference between J_{e1} and J_{e2} being small). In this region, Eqs. (21) and (23), which describe the basic processes in the plasma, assume the following form [$n_1 = n_2$, $b = (1 + z_1)/(1 - z_1)$]:

$$V = \frac{\Theta_e}{e}\left[\ln \frac{J}{J_{em} - J} + \frac{J(d + d_1)}{D_e n_3} + \delta\psi_2\right], \tag{37}$$

$$VJ=\frac{\Theta_e}{e}[a_5J_{\text{em}}+a_3v_in_1],\quad a_3=\frac{\varepsilon_3}{\lambda}+2,\ a_5=2\left(1-\frac{1}{\lambda}\right). \tag{38}$$

To close (37) and (38), it remains only to give the relationship between the density at the maximum n_3 and the density at the electrode n_1, and to find Θ_e; this is done by using (31) and (34) (for arbitrary $y_{1,3}$).

Let us first consider the case $k^2 \ll 1$. Replacing γ by γ_1 in $M(\lambda)$ and in (27), we obtain

$$\gamma_1 d \simeq \pi,\quad \gamma d=\frac{\varepsilon_5\pi}{F}, \tag{39}$$

$$n_1 \simeq \frac{F}{\varepsilon_5}\frac{\varepsilon_1}{2}n_3 \equiv \frac{2\pi D_a}{v_i d}n_3, \tag{40}$$

where Eq. (39) is the analog of (13), and (14), while Eq. (40) is the analog of (15). Expression (39) implies that Θ_e varies slightly with increasing y_3 (by about 0.1 Θ_e for $J_3 = 1$), while (40) indicates that the ratio n_1/n_3 does not change and is the same as (28) (there is no recombination).

We obtain expressions for $\delta\psi_1$ by setting k = 0 (17) and replacing γ by γ_1. If we obtain an expression for $\delta\psi_1$ from (35) we should not retain the term with k^2 in F and use (40); if the term with k^2 is kept in F we obtain the expression $z_1 = z_{1a} + z_{11}k^2$ from (31) in place of (40) (the subscript *a* indicates that the value is defined without recombination). From (37), (38), and (40) we obtain the expression $[b \simeq 1,\ 4+2a \simeq 4,\ d+d_1 \simeq d_0 \equiv 2d\ln[\nu_i d/(\pi D_a)]/\pi]$

$$V=\frac{\Theta_e}{e}\left[\ln\frac{J}{J_{\text{em}}-J}+a_2\left(\frac{eV}{\Theta_e}-\frac{a_5J_{\text{em}}}{J}\right)^{-1}+\delta\psi_2\right],\quad a_2=\frac{2a_3d_0D_a\pi}{dD_e}, \tag{41}$$

which is the same in form (if we omit $\delta\psi_2$) as the volt–ampere characteristic without recombination,[16] but now $\Theta_e \neq$ const. The next approximation can be obtained by allowing for z_{1a} in z_1. When $z_1 \ll 1$ the approximation holds all the way to $k^2 \leq 0.95$; it then follows that recombination has virtually no effect on the characteristic in its initial stage of development ($z_3 \to 1$). If, however, z_1 is not small, if $z_3 \simeq 1$ there will be substantial recombination over the entire gap and we must use a more exact approximation for the characteristic.

From (38) and (41) we find $n_1 = n_1(J)$, and hence $n_3(i = J/J_R)$:

$$n_1=\frac{10^{13}}{2.9}\lambda\sqrt{t_i}\varepsilon_2F_R,$$

$$\varepsilon_2=\sqrt{4i^2a_2+(a_1+i\delta\psi_2)^2}+a_1+i\delta\psi_2, \tag{42}$$

$$a_1=i\ln\frac{J}{J_{\text{em}}-J}-2\left(1-\frac{1}{\lambda}\right)\frac{J_{\text{em}}}{J_R}.$$

Setting $\Theta_e = \Theta_{e0}$ and comparing the results with $n_p(\Theta_{e0})$, we can readily determine how close $n_{1,3}$ is to the equilibrium value for a given J.

When $k^2 > 0.95$ the approximation above is no longer effective. Since $y_3 \simeq 1$, when $k^2 > 0.95$, by setting $y_3 = 1$, we replace (34) by

$$n_3=n_p\equiv\left(n_aN_ee^{-\frac{E_i}{\Theta_e}}\right)^{1/2}, \tag{43}$$

(N_e is the density of electron states), which makes it possible to express γ, a quantity which depends exponentially on Θ_e, in terms of n_3, $[\gamma \sim \sigma^{1/2} \sim e^{-E_0/2\Theta_e}$, $E_0 = 3.21$ eV, (ref. 14), $\omega_1 = E_0/E_i]$:

$$n_3^2=n_aN_e\left(\frac{\gamma}{\gamma_2}\right)^{2/\omega_1},\quad \gamma_2=\gamma e^{\frac{E_0}{2\Theta_e}}. \tag{44}$$

As a result, only an algebraic dependence of the terms on Θ_e remains in all equations except for (43). Since Θ_e varies slowly, Eq. (43) can be omitted, in a first approximation by setting $\Theta_e = \Theta_{e0}$ in the remaining one.

As already noted, however, the solution of the complete system of equations does not present difficulties when Θ_e is taken as a parameter, the more so because when $y_3 = 1$ (43) and $[a = n_3^{\omega_1}/A$, $A = v_i(n_a N_e)^{\omega_1/2}/\sqrt{2}D_a\gamma_2$, $x = 1/a]$:

$$z_1=\sqrt{1+\frac{x^2}{4}}-\frac{x}{2}, \tag{45}$$

this being a consequence of (31) for $y_3 = 1$, determines $n_{1,3}$ directly.

It follows from the above expressions that the effect of recombination of $\delta\psi_1$ is marked if $\delta\psi_1 \gg \delta\psi_{1a}$:

$$\frac{1}{n_3}\left(1+\frac{d_1}{d}\right)\gg\frac{1}{n_{3a}}\frac{2}{\pi}\ln\frac{1}{z_{1a}}, \tag{46}$$

where n_{3a} is determined from (28) and (42). The quantity d_1 characterizes the degree of recombination. When $z_1 \simeq z_{1a}$ recombination is important only in the center of the gap ($y_3 \to 1$, γ of order π/d, and $d + d_1 \simeq d_0$). When $z_1 \gg z_{1a}$ recombination is important over the entire gap, and $d_1 \gg d$, when $a \ll 1$, we obtain from (45):

$$z_1=a(\gamma)\ll 1. \tag{47}$$

We note that (47) is the same as (40) to within 4/5 ($k^2 = 1$). From (47) we find ($\omega = E_i/(E_0 + E_i)$).

$$n_3=(An_1)^{\omega}, \tag{48}$$

and the volt–ampere characteristic is defined by the following equation ($b \simeq 1$, $4 + 2a \simeq 4$, $z_1 = n_1^{1-\omega}/A^{\omega}$):

$$V=\frac{\Theta_e}{e}\left\{\ln\frac{J}{J_{\text{em}}-J}+\frac{J}{D_e(An_1)^{\omega}}\left[d+\frac{4D_a(An_1)^{\omega}}{n_1v_i}\ln\frac{A^{\omega}}{n_1^{1-\omega}}+\delta\psi_2\right]\right\}. \tag{49}$$

When d_1 is small and can be omitted, we can readily determine n_3 from (37). Finding $n_1 = n_1(n_3)$ from (45) and substituting it into (38) with n_3 from (37), we obtain

$$UJ=a_5J_{\text{em}}+a_3v_in_3\left[\sqrt{1+\frac{A^2}{4}\frac{1}{n_3^{2\omega_1}}}-\frac{A}{2}\frac{1}{n_3^{\omega_1}}\right]. \tag{50}$$

The quantity ω is close to 1/2. Using this fact and setting $E_0 = E_i$, we find from (45)

$$n_3=\sqrt{An_1+n_1^2}. \tag{51}$$

In the limiting case $y_1 \simeq 1$

$$n_1=n_3=n_p(\Theta_e), \tag{52}$$

and (37) assumes the form

$$V=\frac{\Theta_e}{e}\left[\ln\frac{J}{J_{\text{em}}-J}+a_{21}\left(\frac{eV}{\Theta_e}-\frac{a_5J_{\text{em}}}{J}\right)^{-1}+\delta\psi_2\right],\quad a_{21}=\frac{a_3v_id}{D_e}, \tag{53}$$

which differs from the volt–ampere characteristic (41) without recombination by the coefficient a_{21} (which defines the relation between n_3 and n_1), this being larger than a_2 by roughly a factor of d/l_i. Equation (53) together with (38) and n_1 from (52) define the volt–ampere characteristic. These expressions imply expression (42) for the density, in which a_2 should be replaced by a_{21}.

In view of our approximations, when $y_3 \rightarrow 0$ Eq. (31) does not lead to the equation $M = 0$ for Θ_{e0}, but to the equation $\gamma d = \ln [16(1-z_1)/(1+z_1)]$, where z_1 is determined from (34) and is the same as its exact limiting value $z_1^2 = 2a^2/(1+2a^2)$. The quantity $\Theta_e = \Theta_{e1}$, which is a solution of these two equations, differs very little from Θ_{e0}; thus, when $d/l_1 = 2, 10, 100$ we obtain $\Theta_{e1} = 1.866, 1.657, 1.278$ and $\Theta_{e0} = 1.849, 1.699, 1.297$, respectively. Thus, approximation (31) is a qualitatively correct description of the way in which Θ_e changes with increasing y_3 and yields quantitative values that are close to the exact values.

Equations (43)-(53) for the characteristic (in which Θ_e should obviously be compared to Θ_{e1} and not Θ_{e0}) have a solution for all $J \in (0, J_{em})$, small currents corresponding to $\Theta_e < \Theta_{e1}$. We note that the solutions of (43)-(53) become meaningless for $\Theta_e \simeq \Theta_{e1}$ (and the more so for $\Theta_e < \Theta_{e1}$), and Eqs. (31) and (34) must be used instead. To describe the region of the characteristic with $\Theta_e < \Theta_{e1}$ we must take account of surface ionization [Eqs. (13) and (14)].

Figure 1 shows the volt–ampere characteristic in various approximations ($J_{em} = J_R$, $p = 4$ mm Hg, $J_R = 20$ A/cm², $d = 0.05$ cm, $T_k = 1800$°K). Curve 1 is plotted without recombination and Coulomb scattering [Eqs. (28), (37), (38), $\Theta_e = \Theta_{e1}$]; curve 2 from (37), (38), (43), (51) with $\delta\psi_2 = 0$ (without Coulomb scattering); curve 3 from (38), (49) with $\Theta_e = \Theta_{e1}$, $\delta\psi_2 = 0$; and curve 4 from (38), (43), (48), (49), $\delta\psi = 0$. Calculations using (37), (38), (44), (45), $\delta\psi_2 = 0$ coincide with this curve; $\Theta_e > \Theta_{e1}$ at all points of curve 4. Curve 9 is computed from (31), (34), (37), (38), $\delta\psi_2 = 0$; for this curve we also give the following functions: 10) $\lambda = \lambda(J)$, 11) $y_1 - y_1(J)$, 12) $y_3 = y_3(J)$. The shift in curve 9 relative to curve 4 toward curve 1 is due to the fact that y_3 is different from unity. Thus approximations with $\Theta_e(J) =$ const and (51) are unsatisfactory.

The voltage drop resulting from Coulomb scattering can be either much less than or much greater than $\delta\psi_1$. The case $\delta\psi_2 \gg \delta\psi_1$ is illustrated by curve 5 in Fig. 1, which is constructed from (31), (34), (37), (38) allowing for $\delta\psi_2$, and curves 6) $\lambda = \lambda(J)$, 7) $y_1 = y_2(J)$, 8) $y_3 = y_3(J)$. As indicated by (42), Coulomb scattering (for the same current value) leads to an increase in recombination (an increase in λ, y_1, y_3), and this is confirmed by curves 6-8 and 10-12.

Reference 19 gives equations analogous to (9), (13), and (14); in place of y_1 the author introduces d_e, the extrapolated length, this being equivalent to the use of inhomogeneous boundary conditions. The inequality $\Delta d_e/d \ll 1$ is the same as $y_1 = a \ll 1$; unlike this purpose here, however, the object in ref. 19 is to determine the optimum parameters.

QUALITATIVE FEATURES OF VOLT–AMPERE CHARACTERISTICS

Equations (37) and (38) are conveniently written in a form that is invariant to recombination. Let us follow the development of the plasma (increase in density and temperature) in the gap. From (37) we have that $V \rightarrow \infty$ as $J \rightarrow J_{em}$, which results in an unbounded increase in the left side of (38); the right side (for bonded J_{em}) can increase if n_1 and λ increase. In going to the arc mode, at first the applied energy JV (if we take the contact potential difference as the external source) is spent in heating the plasma from $\Theta_e \simeq \Theta_l$ to $\Theta_e \simeq \Theta_{e0}$; the term $a_5 J_{em}$ in (38) increases, and the term with n_1 is small,[4] since volume ionization is weak as a result of the low electron temperature.[4] When a temperature $\Theta_e \simeq \Theta_{e0}$ is reached, intensive volume ionization begins, the applied energy is spent in creating the plasma in the gap [n_1 in (38) increases, while $a_5 J_{em}$ is small], and the electron temperature remains virtually the same. As n_3 approaches $n_p(\Theta_{e0})$, recombination starts to come into play, and the increase in the plasma density is retarded. The applied energy is spent more on further heating of the plasma. Now Θ_e again begins to increase and equilibrium obtains.

The parameter pd in (31) and (34) is involved only in (34) and has almost no influence on z_1 for $y_3 \simeq 1$, as can be seen from (31). The degree of ionization, on the other hand, depends on p. At low pressures and with increasing Θ_e, therefore, the density n_p approaches n_a even for $z_1 \ll 1$ and the degree of ionization approaches unity at the center of the gap.

Since recombination increases Θ_e and retards the growth of n_3, it follows from (37) that the characteristic shifts to the right when recombination is allowed for. In the $\Theta_e(J_e) =$ const approximation it is easy to show that dJ/dV decreases when recombination is allowed for. As a result, the increase in the characteristic is more shallow, and the point of transition to the segment with $dJ/dV < 0$ (if it exists) occurs farther down (curves 1, 5, and 9 in Fig. 1).

Recombination alters the function $V = V(d)$, $J =$ const. Recombination is weak for small d, and from $\gamma d = \pi$ we obtain

$$\lambda \simeq \lambda_0 = \frac{E_0}{2} \frac{1}{\ln(100 b_2 l_i/d)}, \quad b_3 = \left(\frac{1.5\sqrt{\lambda}}{1+\lambda}\right)^{1/3}. \tag{54}$$

The decrease in Θ_e with increasing d here is the result of the same factors as the decrease in Θ_e in a positive glow-discharge column[20] with increasing tube radius. Thus, as is seem from (37), the characteristic shifts to the left ($V \sim \Theta_e$), and $d + d_1 \simeq d_0$

Recombination is more important for large d, and

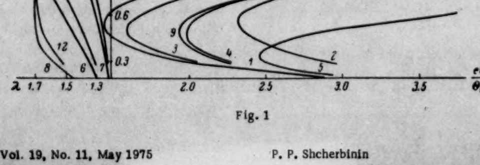

Fig. 1

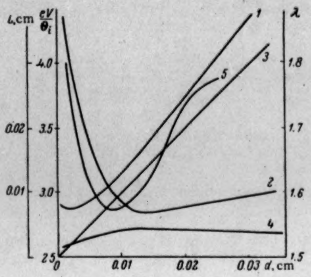

Fig. 2

near equilibrium we have $d_1 \ll d$, $n_1 \simeq n_3$. A strong dependence on d appears in $\delta\psi_1$, and this causes the characteristic to shift to the right ($d_1 \ll d$). For $\delta\psi_2 \gg \delta\psi_1$, Coulomb scattering leads to a similar result. Near equilibrium, we can use (42) in place of (54) for λ, with a_{21} instead of a_2; this implies that for the case of equilibrium, λ increases with d. Thus with increasing d the electron temperature first drops, and then begins to increase (curve 2 in Fig. 2).

Curve 1 in Fig. 2 shows V = V (d) as found for the parameters indicated in ref. 21, and $J/J_R = 0.8$ from (31), (34), (37), (38); the basic contribution to $\delta\psi$ in this case comes from $\delta\psi_2$. Curve 5 shows the experimental V = V (d) dependence (ref. 21, Fig. 3); curves 1 and 5 are combined with respect to voltage). Curves 2) λ = λ (d), 3) L = d, 4) L = L(d) illustrate the process of formation of a positive column in the gap (regions with a plasma in equilibrium[14,21,22]). In Fig. 2 we have p = 4 mm Hg, J_R = 20 A/cm², T_k = 1800°K.

CONCLUSIONS

1. The model we have considered with infinite electron thermal conductivity [$T_e(x)$ = const] makes it possible to establish the effects of the various physical phenomena, such as recombination and Coulomb scattering on the volt–ampere characteristic. But certain model-related results appear here, namely the symmetric distribution of the plasma density n(x) and the absence of a region in which recombination predominates [everywhere we have $n(x) < n_p$; in the model with $T_e(x)$ = const we have $n(x) > n_p(x)$ near the anode[14]].

2. Recombination and Coulomb scattering shift the characteristic to the right.

3. Coulomb scattering results in an increase in recombination.

4. Electron temperature increases with current, the value being determined, by surface ionization (and radiation),[4] in the transition to the arc mode and by recombination and Coulomb scattering in the arc mode.

5. The appearance of an optimum voltage as the gap is increased[21] results from the development of recombination and Coulomb scattering.

6. Expressions have been obtained that make it possible to determine $T_e(J)$ and the contribution from recombination and Coulomb scattering to the characteristic in various approximations. The most satisfactory results are provided by expressions (31), (34), (37), and (38), which hold with good accuracy for an arbitrary degree of recombination.

---

[1] B. Ya. Moizhes and F. G. Baksht, Zh. Tekh. Fiz., 38, 724 (1968) [Sov. Phys. – Tech. Phys., 13, 540 (1968)].

[2] F. G. Baksht, I. L. Korobova, and B. Ya. Moizhes, Zh. Tekh. Fiz., 39, 408 (1969) [Sov. Phys. – Tech. Phys., 14, 300 (1969)].

[3] I. P. Stakhanov and I. I. Kasikov, Zh. Tekh. Fiz., 39, 1496 (1969) [Sov. Phys. – Tech. Phys., 14, 1122 (1970)].

[4] P. P. Shcherbinin, Third Intern. Conf. Therm. El. Power Gen., Jülich, FRG (1972).

[5] L. Hansen, Second Intern. Conf. Therm. El. Power Gen., Stresa, Italy (1968).

[6] I. P. Stakhanov and P. P. Shcherbinin, Zh. Tekh. Fiz., 42, 349 (1972) [Sov. Phys. – Tech. Phys., 17, 278 (1972)].

[7] C. Warner. Therm. Conv. Spec. Conf. Framingham (1968).

[8] G. A. Dyuzhev, B. Ya. Moizhes, E. A. Startsev, and V. G. Yur'ev, Zh. Tekh. Fiz., 41, 2393 (1971) [Sov. Phys. – Tech. Phys., 16, 1900 (1972)].

[9] G. A. Dyuzhev, V. B. Kaplan, B. Ya. Moizhes, and V. G. Yur'ev, Zh. Tekh. Fiz., 41, 453 (1971) [Sov. Phys. – Tech. Phys., 16, 350 (1971)].

[10] D. Wilkins and E. Gyftopoulos, J. Appl. Phys., 37, 7, 2888 (1966).

[11] I. P. Stakhanov, A. S. Stepanov, V. P. Pashchenko, and Yu. K. Gus'kov, Thermionic Plasma Energy Conversion [in Russian], Atomizdat, Moscow (1968).

[12] S. I. Braginskii, in: Thermionic Energy Conversion [in Russian], Atomizdat, Moscow (1965).

[13] D. Wilkins and E. Gyftopoulos, J. Appl. Phys., 37, 9, 3533 (1966).

[14] F. G. Baksht, I. L. Korobova, and B. Ya. Moizhes, Zh. Tekh. Fiz., 41, 387 (1971) [Sov. Phys. – Tech. Phys., 16, 292 (1971)].

[15] D. Wilkins, J. Appl. Phys., 39, 5, 2452 (1968).

[16] V. A. Zherebtsov and I. P. Stakhanov, Zh. Tekh. Fiz., 41, 1974 (1971) [Sov. Phys. – Tech. Phys., 16, 1560 (1972)].

[17] P. P. Shcherbinin, Zh. Tekh. Fiz., 42, 2379 (1972).

[18] E. Jahnke, F. Emde, and F. Lösch, Special Functions [Russian translation], Izd. Nauka, Moscow (1964).

[19] A. P. Loshkarev, Zh. Tekh. Fiz., 42, 2127 (1972) [Sov. Phys. – Tech. Phys., 17, 1684 (1973)].

[20] A. von Engel, Ionized Gases, Oxford Univ. Press (1965).

[21] A. Campbell and A. Jensen, in: Thermionic Energy Conversion [Russian translation], Atomizdat, Moscow (1971).

[22] F. G. Baksht, G. A. Dyuzhev, I. L. Korobova, V. B. Kaplan, A. M. Martsinovskii, B. Ya. Moizhes, G. A. Shakhnazarova, and V. G. Yur'ev, Zh. Tekh. Fiz., 38, 1075 (1968).

Gasdynamic model of the spark discharge

Yu. K. Bobrov

Kiev Polytechnic Institute

(Submitted March 30, 1972; resubmitted April 8, 1974)

Zh. Tekh. Fiz., 44, 2340-2347 (November 1974)

Spectroscopic investigations of the temperature and density characteristics of the plasma in a pulsed arc in air are described. Concepts of gasdynamic processes during detonation and deflagration of the fuel gases together with the physical conditions at the boundary of the discharge are used to interpret the experimental data. The boundary of the spark channel is treated as the front of a cylindrical ionization wave, whose velocity is determined by radiant heating of the cold gas.

Studies of spark discharges in gases[1-15] have provided the basic theoretical mode for the electrical and physical processes which occur in gas discharge gaps. It has been experimentally established that shock waves are initiated by the discharge in free gaseous atmospheres. These serve as a basis for the development of a gasdynamic theory of the spark.[8,9] The mechanism by which the high-temperature spark channel expands can be described by a model with nonequilibrium[12] or equilibrium[13,15] thermal waves. A series of self-similar solutions for the motion of the gas in expansion of a cylindrical piston[8,9,12] indicates agreement between experiment and theory for the temperature and expansion velocity of the spark channel. Continuity of the gas velocity and pressure at the channel boundary is taken as the boundary condition for these solutions. Under certain experimental conditions[13,14] a pressure jump is observed at the boundary of the channel; this has an important role in the gasdynamics of the spark discharge. The present work discusses the basic results of earlier investigations of the physical properties in a pulsed arc channel in air.[13,14] In the analysis of these results we use concepts from an earlier theory of detonation and deflagration of fuel gases.[16-18] As Raizer[19] has shown in a series of papers, some processes in the propagation of electrical and optical discharges can be regarded as direct analogs of the detonation and deflagration regimes of fuel gases.

In refs. 13 and 14 spectroscopic investigations of the temperature and density characteristics of a pulsed arc channel in air are performed in a discharge gap up to 50 cm long with discharge currents of 10 to 50 kA and a current rise time τ_M = 13-22 μsec. By mirror scanning of the stigmatic image of the pulsed arc channel in the plane of the input slit of an ISP-51 spectrograph (focal length f = 270 mm), with an exposure time of t_e = 1 μsec, spectrograms of the emission from the discharge channel are obtained at various values of the discharge current. The spectrograms yield the spatial and temporal characteristics of the channel. The experimental apparatus and technique for determining the temperature and density of the electrons are described in detail in refs. 10, 13, and 14.

The temperature is determined from the relative intensities of the nitrogen lines N II 504.5 nm, N II 517.9 nm, N II 549.5 nm, and N II 553.5 nm, which have previously been used for this purpose in ref. 7. This temperature coincides with that of the heavy particles in the plasma. The electron–ion relaxation time, τ_{ei}, for the plasma in the discharge channel with electron temperature $T_e = 4 \cdot 10^4$ °K, ion density $N_i \sim 10^{17}$ cm^{-3}, charge $z_i \approx 2$, and atomic weight A = 16 (oxygen) is[20]

$$\tau_{ei} = \frac{250 A T_e^{3/2}}{N_i z_i^2 \ln \lambda} \sim 10^{-7} \text{ sec}$$

($\ln \lambda = 5$ is the Coulomb logarithm), which is two orders of magnitude smaller than the characteristic time for the discharge current, $\tau_p = 10^{-5}$ sec.

The electron density is determined from the half-widths of Stark profiles (Hα, Hβ) of hydrogen fed into the discharge gap as a small impurity; the nitrogen lines (N II 453 nm, N II 442.7 nm) are also used. The parameters for Stark broadening of these lines are given in ref. 21. The absolute values of the electron density obtained from broadening of the nitrogen and Hβ lines are in satisfactory agreement. The time dependence of the electron density in the discharge channel is constructed from the data on broadening of nitrogen lines since these are available for the entire time interval of interest. The intensities and half-widths of the spectral lines are determined from the contours of the corresponding spectral lines obtained after conversion of the observed intensities into local values for an optically thin cylindrical radiator (Abel inversion).[21]

Some of the resulting radial and temporal properties of the pulsed arc channel in air are shown in Figs. 1 and 2. A characteristic of the radial temperature profile is the flat central part and the sharp decrease in temperature at the boundary of the channel (Fig. 1). The channel boundary is defined by the emission of nitrogen lines whose excitation temperature is high. In the time interval studied here (Fig. 2) the temperature on axis decreases monotonically from $T = 4.5 \cdot 10^4$ °K (t = 1 μsec) to $T = 3 \cdot 10^4$ °K (t = 18 μsec). According to line-broadening data on Hα from the sheath surrounding the channel, the electron density is continuous at the channel boundary (Fig. 1). An increase in the electron density with time is observed as

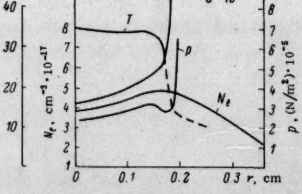

Fig. 1. Radial distributions of electron density (N_e), relative density ($\delta = \rho/\rho_H$), kinetic pressure (p), and temperature (T) of the air in a spark channel with a discharge gap of length 50 cm at t = 5 μsec with a current amplitude I_M = 13 kA and a current rise time to maximum of τ_M = 19 μsec. $\rho_H = 1.29 \cdot 10^{-3}$ g/cm³ is the normal pressure of air.

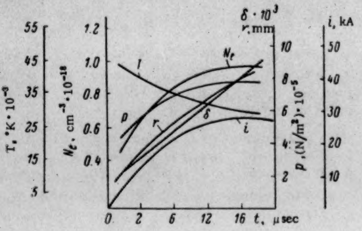

Fig. 2. Time variation of temperature (T), relative density (δ), kinetic pressure (p) of the air, and electron density (N_e) in a spark channel with a discharge gap of length 50 cm and current i. r is the radius of the spark channel.

current varies from zero to its maximum value and the temperature decreases (Fig. 2).

The rate of the relatively slow process of establishment of equilibrium ionization in the plasma can be estimated from the relaxation times for ionization of atoms from the ground state by electron impact (τ_e) and by photoionization (τ_ν). According to ref. 20, $\tau_e = (\alpha_e N_a)^{-1}$, where N_a is the density of atoms, and α_e is the rate constant for electron impact ionization, given by $\alpha_e = \sigma_e \bar{v}_e (I/T_e + 2) \exp(-I/T_e)$. Here, $\sigma_e = CT_e$ is the mean value of the effective cross section for ionization by electron impact (the constant $C \sim 10^{-17}$ cm^2/eV), I is the ionization potential of the atom, T_e is the electron temperature, and $\bar{v}_e = 6.71 \cdot 10^7 T_e^{1/2}$ is the mean thermal velocity of the electrons. From interferometer measurements,[5] we find $N_a \sim 10^{16}$ cm^{-3} in the spark channel, which for I = 14.6 eV (nitrogen) and $T_e = 4$ eV gives $\sigma_e \approx 4 \cdot 10^{17}$ cm^2, $\bar{v}_e = 1.34 \cdot 10^8$ cm/sec, $\alpha_e = 1.05 \cdot 10^{-10}$ cm^3/sec, and $\tau_e = 10^{-6}$ sec. The photoionization relaxation time τ_ν is given by $\tau_\nu (N_e)/\alpha_\nu N_a$, with $\alpha_\nu = 8.68 \cdot 10^6$ sec^{-1}, which for the same conditions, an equilibrium electron density $(N_e) \sim 10^{17}$ cm^{-3}, and an effective photoionization cross section $\sigma_\nu = 7.5 \cdot 10^{-18}$ cm^2, gives $\alpha_\nu = 8.68 \cdot 10^6$ sec^{-1} and $\tau_\nu \approx 10^{-6}$ sec. Thus, the time required to establish ionization equilibrium in this discharge channel is an order of magnitude less than the characteristic time for changes in the discharge current ($\tau_e \sim \tau_\nu < \tau_p$) and the experimentally measured[14] electron densities are nearly in equilibrium. Thus, the measured electron temperature and density can be used in determining the density and kinetic pressure of the gas in the channel from calculations of the equilibrium composition of an air plasma. In addition to providing estimates of the absolute values of the density and kinetic pressure of the gas, this approach demonstrates the tendency of these quantities to change in time and at the boundary of the channel. Thus, in moving from the channel to the sheath [whose temperature is tentatively equal to the temperature of maximum excitation of the Hα line ($T_0 = 1.5 \cdot 10^4$ °K) and whose particle density $N_a \sim 10^{18}$ cm^{-3}], the electron density measured in the sheath can be less than the equilibrium value since $\tau_{e,\nu} \sim 10^{-5}$ sec. In this case the possibility remains of explaining the direction of change in the density and gas pressure at the channel boundary, in addition to a jump in gas density,[5] there is a pressure jump from a lower value of the pressure in the channel (while the gas density in the channel increases in time). The possible existence of this kind of pressure jump and of this time dependence for the gas and electron densities must be explained on the basis of the general propositions of gasdynamics and appropriate numerical estimates.

We now consider possible reasons for the experimentally observed expansion of the spark channel in time. Expansion of the discharge at a boundary with cold air layers is possible if the electrical conductivity attained in these boundary layers is high during heating and ionization (comparable with the electrical conductivity of the plasma in the channel). From theoretical and experimental data,[22] the electrical conductivity σ of an air plasma increases sharply with temperature for $T = 0.4$–$1.2 \cdot 10^4$ °K and reaches some sort of saturation for $T_I \ge 1.5 \cdot 10^4$ °K, for which it is possible to use the approximation $\sigma(T_I) \approx \sigma(T)$. Up to the ionization temperature[19] T_I, heating the layers of air adjacent to the spark channel will cause propagation of the current zone with the release of Joule heat into the layer and heating of the gas up to the channel temperature. Regardless of the specific mechanism for initial heating of the air up to T_I, the subsequent heating is due to the Joule heating by the discharge current, since the effectiveness of the initial heating mechanism is reduced sharply. It is evident that the rate of expansion of the channel must be considered on the basis of the initial mechanism for heating of the gas to T_I; however, the magnitude of the Joule energy in the channel can affect this process.

Shock heating of the gas at maximum front velocities of $D_s = 2$–5 km/sec yields low temperatures at the front, $T_s = 2$–$7 \cdot 10^3$ °K $< T_I$. Thus the boundary of the spark channel, which moves at the indicated velocities, cannot be a shock front. This is certainly the case for the subsequent stages, in which the expansion velocity of the spark channel is smaller than the sound speed in the sheath surrounding the channel, where the gas temperature is between 1 and $1.5 \cdot 10^4$ °K.

The heating of the air to T_I can be due to the absorption of radiation from the channel itself as in the propagation of equilibrium and nonequilibrium thermal waves.[20] The release of Joule energy in the channel during expansion leads to conditions differing from those usually considered for thermal waves produced by the instantaneous release of energy at an initial time.

In the initial stages of the discharge, when the shock front has not yet separated from the channel and the latter is expanding into a region of cold and motionless air, the plasma density in the channel is determined by the density of the air swept up by it. The plasma radiates approximately as a blackbody at temperatures T = 4–5 eV as indicated by the high continuum levels in the emission in the earliest states. It is known that cold air at normal density completely absorbs radiation at $\lambda = 186$ nm or less in molecular levels. For a channel temperature T of 4–5 eV the maximum spectral density of the radiated energy occurs at $\lambda_M = 62$–50 nm. That is, the radiation from the channel is absorbed, for the most part, by the cold layers of air at the channel boundary, heating them. Depending on how much the gas has been heated, the mechanism by which light is absorbed changes, so that after complete molecular dissociation the basic absorption mechanism is the absorption of photons by atoms in the ground state or in low excited states. Absorption of photons is also the principal mechanism for heating the air in the subsequent stages of the spark, when the shock front has separated from the channel boundary. In this case the channel is in the rear of the shock wave, the density of gas in the channel is small, and the emission is characteristic of an optically thin medium. The width of the radiative heating zone in both cases may be estimated from the absorption coefficient $\varkappa_\nu = 1/l_\nu \sim 1/\Delta r$ for photons with an energy, $h\nu$, equal to the ionization energy, I, of air[20]

$$\varkappa_\nu = 0.96 \cdot 10^{-7} \frac{N z^{*2}}{T^2} \frac{2x_1}{x^3} \text{ cm}^{-1},$$

where $x_1 = I/kT$, $x = h\nu/kT$, and $z^* \approx 4$ is the effective charge of the "atomic residue" according to Unsöld. For sheath conditions $T = 1.2 \cdot 10^4$°K, $N_0 = 5 \cdot 10^{18}$ cm^{-3}, and $x_1 = x = 10$ we obtain a value for the photon mean free path $l_\nu = 1/\varkappa_\nu = 0.59 \cdot 10^{-2}$ cm. This value of l_ν is approximately two orders of magnitude smaller than the radius of the spark channel, so that the channel boundary can be regarded as a thin absorbing and ionizing layer. The heated layer is optically dense in the initial stages and transparent in the subsequent stages.

The electron thermal conductivity can play a significant role in the region of large temperature gradients at the channel boundary. The thickness of the electron relaxation layer in the channel sheath is determined by the magnitude of the electron mean free path $l_e = \tau_{ei} \bar{v}_e = 0.67 \cdot 10^{-2}$ cm ($\tau_{ei} = 10^{-10}$ sec, $\bar{v}_e = 6.7 \cdot 10^7$ cm/sec). Thus, the electron thermal flux is absorbed at the channel boundary in a layer of thickness $\Delta r \sim l_\nu \sim l_e \sim 0.6 \cdot 10^{-2}$ cm. That is, there is simultaneous radiative and thermal conduction heating of a single layer of gas at the channel boundary.

Under these conditions the heating zone is displaced to new layers of cold gas. This situation can be regarded as wave motion of a thin heating and ionization front, or an ionization wave.

The speed of the front of the ionization wave can be estimated from energy balance. A cylindrical channel of unit length and radius r at time t radiates energy

$$Q_\Sigma = \int S d\Sigma = \sigma_0 T^4 2\pi r dt,$$

$$Q_V = \int J dV = \frac{4\sigma_0 T^4}{l_1} \pi r^2 dt$$

in time dt. Here, Q_Σ is the energy of the blackbody emission of the spark channel in the initial stages of its development; $S = \sigma_0 T^4$ is the radiation flux from the side surface, $\Sigma = 2\pi r$, of the channel, emitted as from a blackbody with a plane radial temperature profile at T; Q_V is the energy of the transparent volume radiation from the spark channel in subsequent stages of its development; $J = 4\sigma_0 T^4/l_1$ is the integrated emissivity per unit volume of the channel for transparent radiation with a Planck mean free path l_1; and $\sigma_0 = 5.67 \cdot 10^{-12}$ J/cm^2 · sec · (deg K)^4 is the Stefan–Boltzmann constant. The electron thermal conduction energy is given by

$$Q_e = \int S_e d\Sigma = -\varkappa_e \frac{dT}{dr} 2\pi r dt,$$

where the effective coefficient of electron thermal conductivity is[20] $\varkappa_e = \xi\, 1.93 \cdot 10^{-5} T^{5/2}/(z \ln \lambda) \approx 4 \cdot 10^5$ erg/sec · cm · (deg K) for channel conditions $T = 4–5 \cdot 10^4$ °K, $Z = 2$, $\ln \lambda = 5\xi (Z = 2) = 1.5$.

The internal energy of a gas layer heated to a temperature T_I is given by $Q_n = 2\pi r dr N\varepsilon(T_I)$, where $\varepsilon = 8.3(T/10^4)^{1.5\delta^{-0.12}}$ eV/atm is the specific internal energy of air at temperature T and relative density $\delta = N/N_L$ (where $N_L = 2.69 \cdot 10^{19}$ cm^{-3} is the Loschmidt number).

In the initial stage of expansion of the spark channel into the region of cold motionless air the equality $Q_\Sigma + Q_e = Q_I$ must hold; therefore

$$D_{\Sigma,e} = \frac{dr}{dt} = \frac{\sigma_0 T^4 - \chi_e \frac{dT}{dr}}{N\varepsilon(T_I)}.$$

The rate of expansion of the spark channel in the initial stages $D_{\Sigma,e}$ for $T = (4–5) \cdot 10^4$ °K, $N = 2N_L = 5.38 \cdot 10^{19}$ cm^{-3}, $T_I = 1.5 \cdot 10^4$°K, $\varepsilon(T_I) = 15$ eV/atm, and $-\varkappa_e dT/dr \sim \varkappa_e T/\Delta r = (1.3–1.7) \cdot 10^{12}$ erg/sec · cm^2, is given by $D_{\Sigma,e} = 1.14–2.77$ km/sec, for which the role of electron thermal conductivity in this regime is negligibly small. These values of $D_{\Sigma,e}$ correspond to the experimentally observed rates of expansion of a spark channel.[1–6]

At later times, the equality $Q_V + Q_e = Q_I - Q_0$ holds within the hot sheath at temperature T_0. It is then possible to estimate the velocity of propagation of the ionization wave for nonequilibrium emission from the channel by

$$D_{V,e} = \frac{dr}{dt} = \frac{\frac{2r}{l_1}\sigma_0 T^4 - \varkappa_e \frac{dT}{dr}}{N_0[\varepsilon(T_I) - \varepsilon(T_0)]}.$$

In the completely ionized gas of the spark channel absorption of light is due to bound–free and free–free transitions and the Planck mean free path of the radiation is given by[20]

$$l_1 = \frac{1.1 \cdot 10^{23} T^{7/2}}{N^2 \bar{m} (\bar{m} + 1)^2 \bar{x}_1} \text{ cm}.$$

For the channel conditions (Figs. 1 and 2) given by temperature $T = 3.5 \cdot 10^4$°K, ion density $N = 5 \cdot 10^{17}$ cm^{-3}, mean ion charge $\bar{m} = 1.9$, and relative ionization potential $\bar{x}_1 = \bar{I}/kT = 9.3$, this equation yields $l_1 = 200$ cm. Taking $T_0 = 1.2 \cdot 10^4$°K, $[\varepsilon(T_I) - \varepsilon(T_0)] = 3$ eV/atm, $N_0 = 5 \cdot 10^{18}$ cm^{-3}, and $\varkappa_e dT/dr \sim \varkappa_e (T - T_0)/\Delta r = 7.68 \cdot 10^{11}$ erg/sec · cm^2, for example, at time t = 5 μsec, r = 0.4 cm (Fig. 2), we obtain $D_{V,e} = D_V + D_e = 100 + 320 = 420$ m/sec. Here the significance of the electron thermal conductivity is already shown, as it contributes the basic portion, $D_e/D_{V,e} = 76\%$, of the ionization wavefront velocity. From Fig. 2, at t = 5 μsec we have dr/dt = 474 m/sec, which is close to the value obtained here, $D_{V,e} = 420$ m/sec. It should be noted that the mass velocity of the gas in the channel and the sheath is nearly zero since the speed of sound in the channel c and in the sheath c_0 greatly exceed the expansion velocity. Under these conditions all the gasdynamic parameters of the channel and sheath rapidly reach equilibrium. The mass velocity is zero since it is zero at the axis of the channel by symmetry considerations.

The energies of the absorbed radiation, q_V, of the electron thermal conductivity, q_e, and of the Joule heating, q_h, due to the longitudinal discharge current i are released in the front of the ionization wave. For the present example at t = 5 μsec (Fig. 2), these energies are given by

$$q_V = \sigma_0 T^4 \frac{2r}{l_1} \frac{1}{D_{V,e}} = 0.58 \ \mathrm{J/cm^3},$$

$$q_e = \varkappa_e \frac{T - T_0}{\Delta r} \frac{1}{D_{V,e}} = 1.83 \ \mathrm{J/cm^3},$$

$$q_h = \left(\frac{i}{\pi r^2}\right)^2 \eta \frac{\Delta r}{D_{V,e}} = 2.54 \ \mathrm{J/cm^3},$$

where[22] $\eta = 0.02 \ \Omega \cdot \mathrm{cm}$ at $T_1 = 1.5 \cdot 10^4$ °K. The total energy q_{0V} dissipated in the front is equal to $q_{0V} = q_V + q_e + q_h = 4.95 \ \mathrm{J/cm^3}$. A calculation of the energy per unit mass of a heated layer with a mean density $\sim 0.01 \rho_H = 1.3 \cdot 10^{-5} \ \mathrm{g/cm^3}$ gives $q_0 = 3.81 \cdot 10^5$ J/g. When the ionization wave front is propagating, gas particles from the sheath pass through the front into the channel region as they are heated and the energy q_0 must be taken into account in the equation of energy conservation at the front. The usual equations of mass, momentum, and energy conservation for the front of an ionization wave can be written in the form

$$\rho_0 u_0 = \rho u, \quad p_0 + \rho_0 u_0^2 = p + \rho u^2, \quad i_0^* + \frac{u_0^2}{2} + q_0 = i^* + \frac{u^2}{2},$$

$$\rho = \frac{1}{V}, \quad i^* = \varepsilon + pV.$$

In the general case these equations do not assume any particular physical mechanism by which energy is released in the discontinuity. They are used to analyze the detonation and deflagration regimes of fuel gases;[16–18] to a certain degree, the similar features of these regimes and the gasdynamic processes in the spark discharge must be determined by them. The difference lies in the fact that, first, the chemical reaction of combustion occurs only in a thin reaction layer and energy is not released in the region of burned-up gas, and, second, the chemical energy is a constant for a given fuel gas. In the case of a spark, the Joule energy continues to be released in the heated gas even after the ionization wave front passes it. Hence, the amount of energy released in the channel varies in time.

In the coordinate system fixed in the motionless gas in the channel and in the sheath ahead of the front, we have

$$D = V_0 \sqrt{\frac{p - p_0}{V_0 - V}}, \quad \frac{pV}{\gamma - 1} - \frac{p_0 V_0}{\gamma_0 - 1} - q_0 = \frac{p + p_0}{2}(V_0 - V),$$

Since $\gamma p/V = (p - p_0)/(V_0 - V)$ along the tangent to the Hugoniot adiabatic we obtain conditions for the transition of the gas particles to the Jouguet point from an initial state (0) in the sheath:[18]

$$p - p_0 = \frac{\rho_0 D^2}{\gamma + 1}\left(1 - \frac{\gamma}{\gamma_0} \frac{c_0^2}{D^2}\right),$$

$$V_0 - V = \frac{V_0}{\gamma + 1}\left(1 - \frac{\gamma}{\gamma_0} \frac{c_0^2}{D^2}\right),$$

$$\frac{D}{c_0} = \sqrt{\frac{\gamma^2 - 1}{2} \frac{q_0}{c_0^2} + 1} \pm \sqrt{\frac{\gamma^2 - 1}{2} \frac{q_0}{c_0^2}}.$$

From the last of these equations with a negative sign (corresponding to propagation of a slow ionization front at subsonic speed), written with the adiabatic index $\gamma = \gamma_0$, with $c_0 = 3$ km/sec, $\gamma = 1.2$, and $q_0 = 3.81 \cdot 10^5$ J/g we have $D \approx 450$ m/sec. The pressure difference and ratio of the specific volumes of gas on both sides of the discontinuity (for $\rho_0 = 1.3 \cdot 10^{-4} \ \mathrm{g/cm^3}$) are $p - p_0 \approx -5.2$ bar, and $V/V_0 = 20.7$.

Thus, with the use of the mechanism proposed here, including the values of the parameters, the experimentally observed radial profiles of pressure and gas density in the discharge channel (Fig. 1) are reasonable. The front of the slow ionization wave is similar to a deflagration front with its associated pressure drop. As is known,[16] in this case the ionization front (boundary of the spark channel) can be regarded as a moving permeable piston. The channel boundary emits pressure waves in the sheath by means of which energy is transferred from the channel into the shock-wave region. This explains how the shock front is accelerated as the expansion velocity of the spark channel increases. The velocity of the gas at the slow ionization front is directed toward the front. The wave front encounters gas at a higher pressure, which leads to an increase in the gas pressure in the spark channel. Due to the growth in gas density with time the electron density in the channel increases (Fig. 2) although the temperature and degree of ionization of the plasma decrease.

Therefore, the ideas developed here on the mechanism for expansion of a spark channel as the propagation of an ionization wave, taking account of the Joule energy and considering the boundary conditions at the channel boundary to be analogous to those at a combustion front in fuel gases, provide a good explanation of the experimental results.

The author thanks A. A. Rukhadze, I. S. Marshak, and A. F. Aleksandrov for discussion and Yu. P. Raizer for helpful comments.

---

[1] I. S. Abramson and I. S. Marshak, Zh. Tekh. Fiz., 12, 632 (1942).

[2] I. S. Abramson, N. M. Gegechkori, S. I. Drabkina, and S. L. Mandel'shtam, Zh. Eksp. Teor. Fiz., 17, 862 (1947).

[3] I. S. Abramson and N. M. Gegechkori, Zh. Eksp. Teor. Fiz., 21, 484 (1951).

[4] N. M. Gegechkori, Zh. Tekh. Fiz., 21, 493 (1951).

[5] G. G. Dolgov and S. L. Mandel'shtam, Zh. Eksp. Teor. Fiz., 24, 691 (1953).

[6] M. P. Vanyukov, V. I. Isaenko, and L. D. Khazov, Zh. Tekh. Fiz., 25, 1248 (1955).

[7] S. L. Mandel'shtam and N. K. Shukhodrev, Zh. Eksp. Teor. Fiz., 24, 701 (1953).

[8] S. I. Drabkina, Zh. Eksp. Teor. Fiz., 21, 473 (1951).

[9] S. I. Braginskii, Zh. Eksp. Teor. Fiz., 34, 1548 (1958) [Sov. Phys. – JETP, 7, No. 5 (1958)].

[10] I. K. Fedchenko, N. I. Fal'kovskii, and Yu. K. Bobrov, Izv. VUZOV, Energetika, No. 1 (1967).

[11] N. G. Basov, B. L. Borovich, V. S. Zuev, V. B. Rozanov, and Yu. Yu. Stoilov, Zh. Tekh. Fiz., 40, 516 (1970) [Sov. Phys. – Tech. Phys., 15, 399 (1970)].

[12] N. G. Basov, B. L. Borovich, V. S. Zuev, V. B. Rozanov, and Yu. Yu. Stoilov, Zh. Tekh. Fiz., 40, 805 (1970) [Sov. Phys. – Tech. Phys., 15, 624 (1970)].

[13] I. K. Fedchenko and Yu. K. Bobrov, Elektrichestvo, No. 5 (1971).

[14] I. K. Fedchenko and Yu. K. Bobrov, in: Electrical Networks and Systems [in Russian], No. 8, L'vov (1971).

[15] I. K. Fedchenko and Yu. K. Bobrov, Izv. VUZOV, Energetika, No. 12 (1971).

[16] Ya. B. Zel'dovich, Theory of Combustion and Detonation in Gases [in Russian], Izd. AN SSSR, Moscow – Leningrad (1944).

[17] Ya. B. Zel'dovich and A. S. Kompaneets, Theory of Detonation [in Russian], GITTL, Moscow (1955).

[18] K. P. Stanyukovich, Nonstationary Motion of Continuous Media [in Russian], Nauka, Moscow (1971).

[19] Yu. P. Raizer, Usp. Fiz. Nauk, **108**, 429 (1972) [Sov. Phys. – Usp., **15**, 688 (1973)].

[20] Ya. B. Zel'dovich and Yu. P. Raizer, Physics of Shock Waves and High-Temperature Hydrodynamic Phenomena [in Russian], Nauka, Moscow (1966).

[21] H. Griem, Plasma Spectroscopy, McGraw-Hill, New York (1950).

[22] L. S. Polak, ed., Summaries of Low-Temperature Plasma Physics and Chemistry [in Russian], Nauka, Moscow (1971).

Development of an inhibited glow discharge

Yu. A. Bystrov, S. A. Ivanov, and Yu. F. Radchenko

V. I. Ulyanov-Lenin Electrotechnical Institute, Leningrad

(Submitted December 10, 1973)
Zh. Tekh. Fiz., 44, 2348-2351 (November 1974)

The effect of the anode material on the development time of an inhibited glow discharge is investigated. It is shown that the dependence of the formation time on the nature of the anode material is due to ultrasoft x rays produced by fast-electron bombardment of the anode.

The nature of electron emission from the cathode in a glow discharge, in particular in an anomalous glow discharge, has been discussed. Some authors attribute the existence of anomalous discharges to the increased contribution by charge exchange to ion motion which produces fast atoms and molecules capable of increasing the coefficient[1] γ. Others consider the increase in electron emission from the cathode as due to enhancement of the ion flux from the region of negative glow[2,3] and the subsequent "potential" or "kinetic" ejection of ions. In each case, one mechanism or the other will predominate depending on the specific conditions. In particular, some authors[4,5] consider the basic mechanism for anomalous glow discharges to be photoemission induced by photons emitted by the discharge.

In considering the contribution of the photoeffect to confinement of the discharge, usually only ultraviolet radiation from the cathode dark space and the negative glow are considered.[6] This approach is valid for anomalous and normal glow discharges when the electrode separation is larger than the length of the normal cathode drop. In an inhibited glow discharge the negative glow is partially or completely absent and the anode is in the region of the cathode potential drop. Therefore, ion and ultraviolet fluxes incident on the cathode from the negative glow are negligible in this case.

But the fact that the primary electrons strike the anode at high velocities in an inhibited discharge indicates the existence of another mechanism for electron emission from the cathode. We refer to photoemission induced by ultraviolet and x radiation resulting from electron bombardment of the anode at energies of tens and hundreds of electron volts, which occurs in an inhibited glow discharge.[7]

Soft x-ray bremsstrahlung arises with a continuous spectrum that overlaps the vacuum ultraviolet when electrons of the above energies are retarded at the surface of the anode. Furthermore, characteristic x-ray radiation can be exicited in the atoms of the anode material. Since the quantum yield of different metals attains large values in the vacuum ultraviolet[8,9] and has a relatively large value at the edge of the x-ray region,[10] in spite of the low intensity of the radiation from the anode, fairly high photoemission from the cathode can be expected for an inhibited glow discharge. The ignition time of the discharge, in particular the development time t_d, is determined by secondary processes at the cathode. Since the x-ray photoemission current of metals has a complex dependence on the nature of the anode material,[11,12] t_d depends on the nature of the anode material for an inhibited glow discharge. Therefore, by measuring the length of the formation stage of discharges in tubes with anodes of different materials and comparing it to the x-ray photoemissivity of a cathode with the same material as the anode, the above assumptions can be checked. In other words, a definite relationship must exist between the curves $t_d = f(z)$ and $I_{ph} = F(z)$, where t_d is the development time of the discharge, z is the atomic number of the anode material, and I_{ph} is the x-ray photocurrent from the cathode. Smaller t_d values correspond to larger photocurrent densities. The curve $I_{ph} = F(z)$ can be obtained from an independent experiment, for example using the technique described in ref. 12.

Special investigations are required to explain the nature of the dependence of t_d on z. For example, it is important to ensure that after the anode is replaced all the other experimental conditions are the same. The voltage applied to the gap is of special importance. On the one hand, it should be high enough to increase the x-radiation intensity and exclude the statistical delay time of the discharge; on the other, it should not be so strong that the development time is reduced and the experimental error increased.

The existing methods of estimating the contribution of the photoeffect consist of measuring the photocurrent from a target which is usually fabricated from the same material as the cathode. In some cases; this involves placing extended electrodes in the gap and subjecting them to an applied transverse field; in others, the discharge gap is

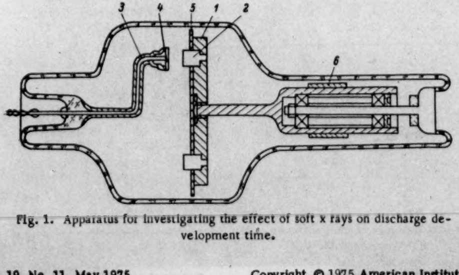

Fig. 1. Apparatus for investigating the effect of soft x rays on discharge development time.

separated from the target by a vacuum barrier, for example of lithium fluoride,[13,14] that transmits ultraviolet radiation. Theoretically, such methods do not permit ultrasoft x rays to be detected in the discharge.

The apparatus in Fig. 1, which is used to investigate the effect of ultrasoft x rays on the formation time t_d of an inhibited discharge, allows the anode to be replaced without destroying the vacuum or the gap geometry. The electrode of the device rotates on ball bearings, and on the holder 1 are mounted anodes 2 of different materials: graphite, titanium, molybdenum, and tungsten. The nickel cathode 4 is displaced with respect to the axis of rotation of the anode assembly and is 5 mm from the anode. The anodes are replaced by rotating the holder with a permanent magnet 6. To avoid arcing of the discharge along the "long path" the inputs of the cathode mount are covered with a special vacuum cement 3, and the holder surface is covered by a mica sheet 5. The apparatus is filled with spectrally pure neon and argon to a pressure of 0.1-1.0 torr. Thus, in tubes with this design almost completely identical test conditions are maintained after the anode is replaced.

The discharge tube is connected to a pulsed generator which supplies 50-100 μsec square current pulses with a leading edge of not more than 20 nsec. To decrease the statistical delay time the output voltage of the generator is maintained at 30-40% above the discharge initiation voltage.

The formation time t_d is measured as the period from the instant the anode current appears to the instant that the leading edge of the current pulse is formed. The shape and amplitude of the current pulse are measured using a noninductive coaxial shunt. The discharge voltage is measured simultaneously.

Figure 2 shows the dependence of the formation time t_d/t_a of the discharge in the gas gap with a nickel cathode on the atomic number z of the anode material for different gap voltages and it also shows the dependence of the x-ray photocurrent I_{ph}/I_a of a nickel cathode[11] on z.

Comparison of the curves $t_d/I_a = f(z)$ and $I_{ph}/I_a = F(z)$ indicates that there is a close relationship between them: Smaller formation times correspond to larger x-ray photocurrents from the cathode.

Actually, the formation time determined from the Schade method,[15] but including the effect on its duration of γ_ν processes due to soft x rays from the anode, is

$$t_d = \frac{\tau_i \mu}{\mu + \gamma_\nu \exp(\alpha d) - 1} \ln \frac{1 + \frac{i(t_d)}{i_0}[\mu + \gamma_\nu \exp(\alpha d) - 1]}{\mu}. \quad (1)$$

Here, $\mu = \gamma_p[\exp(\alpha d) - 1]$; γ_p is the coefficient of secondary emission due to ion bombardment; τ_i is the ion transit time; $i(t_d) = (E_a - U_a)/R_v$; α is the electron-impact ionization coefficient; γ'_ν is a coefficient characterizing photoemission due to ultrasoft x rays; $\gamma_\nu = \gamma'_\nu G\beta$ is a reduced coefficient characterizing the photoemission; G is a geometrical factor; β characterizes the radiation output for one electron interacting with the anode.

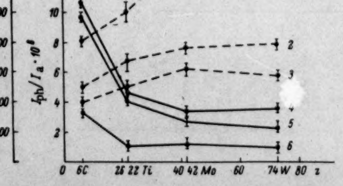

Fig. 2. Curves $t_d/I_a = f(z)$ and $I_{ph}/I_a = F(z)$. Solid lines are for the formation time, and the dashed lines are for the photocurrent. Cathode material is Ni. 1, 4) $U_a = 300$; 2) 200; 3) 100; 5) 320; 6) 340 V.

It can be seen that if ultrasoft x rays are absent from the discharge, this equation has the form of the well known Schade equation[15] obtained with only γ_p processes taken into account. In this case the duration of the formation stage is a maximum.

With other conditions equal, γ_ν is determined only by the anode material. The lack of data in the literature on β which characterizes the radiation output for the interaction between one electron and the anode makes a quantitative analysis of the equation difficult. Even a purely qualitative analysis, however, indicates the possibility of decreasing t_d by selecting the appropriate anode material.

It follows from the experimental curves $t_d/I_a = f(z)$ given above that the relative formation time t_d/I_a for a tungsten anode (z = 74) is four to five times smaller than for a graphite anode (z = 6). However, the relative photocurrent for a tungsten target is 1.5-2 times larger than for a graphite target. Thus, one can conclude that under certain conditions, and especially in an inhibited discharge, ultrasoft x rays can have a considerable effect.

Ultrasoft x rays not only affect the formation time t_d but also the statistical delay time of initiation of an inhibited discharge; this effect can be even stronger since in this stage the predischarge current is a purely electron current. The presence of x rays can considerably accelerate the appearance of a "successful" electron in the discharge gap. A final solution of this problem will be possible only after a careful experimental investigation.

---

[1] H. Neu, Z. Phys., 155, 77 (1959).

[2] V. L. Granovskii, Electric Current in a Gas [in Russian], GITTL, Moscow–Leningrad (1952).

[3] H. Neu, Z. Phys., 154, 423 (1959).

[4] P. N. Chistyakov, Zh. Tekh. Fiz., 40, 303 (1970) [Sov. Phys. – Tech. Phys., 15, 220 (1970)].

[5] E. Badareu, I. Popescu, and I. Iova, Ann. Phys., 5, 308 (1960).

[6] J. R. Acton and J. D. Swift, Cold Cathode Discharge Tubes, Academic Press, New York (1963).

[7] A. von Engel and M. Steinbeck, Physics and Methods of Electrical Discharges in Gases [Russian translation], Vol. 2, ONTI, Moscow (1936).

[8] H. E. Hinterreger, Phys. Rev., 96, 538 (1956).

[9] W. C. Walker, O. P. Rustgi, and C. L. Weissler, J. Opt. Soc. Am., 49, 471 (1959).

[10] A. N. Rumsh, A. P. Lukirskii, and V. N. Shchemelev, Dokl. Akad. Nauk SSR, 135, 55 (1960) [Sov. Phys.–Dokl., 5, 1231 (1961)].

[11] S. A. Ivanov, Izv. Leningr. Elektrotekh. Inst., No. 126, 84 (1972).

[12] S. A. Ivanov, N. I. Komyak, F. N. Kharadzha, and F. F. Chigak, Apparatus and Methods for X-Ray Analysis [in Russian], No. 2, Mashinostroenie, Leningrad (1967), p. 170.

[13] H. Costa, Z. Phys., 113, 531 (1935).

[14] B. N. Klyarfel'd and B. I. Moskalev, Zh. Tekh. Fiz., 39, 1066 (1969) [Sov. Phys. – Tech. Phys., 14, 800 (1969)].

[15] R. Schade, Z. Phys., 104, 487 (1937).

Resistance and inductance of a gas arc

S. I. Barannik, S. B. Vasserman, and A. N. Lukin

Institute of Nuclear Physics, Siberian Branch, Academy of Sciences of the USSR, Novosibirsk

(Submitted May 30, 1973; resubmitted April 2, 1974)
Zh. Tekh. Fiz., 44, 2352-2359 (November 1974)

The resistance and inductance of arc channels (40 cm long) in air, SF_6, and mixtures of SF_6 with nitrogen have been measured at pressures up to 12 atm and at voltages up to 5 MV. The discharge is ignited by a trigatron. The experimental procedure and results are reported. The results are used to calculate the constants in the functional dependences obtained from the Braginskii theory. These functional dependences relate the radius of the arc channel and its resistance to the arc current as a function of the time. The electrical properties of the arc channel are studied in connection with the development of sources for high-power pulses of relativistic electron beams in the nanosecond range; in these the characteristics of the high-voltage switch influence the properties of the electron beam (the shape and length of a current pulse, the maximum energy and energy spectrum of the electrons, and the total energy per pulse).

EXPERIMENTAL PROCEDURE AND RESULTS

The experiments are carried out with an RIUS-5 source of relativistic electron beams in the nanosecond range.[1] The arc channel is part of the discharge circuit of the source, which also includes the high-voltage electrode (conductor), the electrode of the accelerating tube with the cathode, and an evacuated accelerating gap.

On the basis of the geometric dimensions of the elements and of the system and the experimental rates of change of the currents and voltages we can treat the discharge circuit as a lumped-parameter circuit. The equivalent circuit is shown in Fig. 1 and is described by

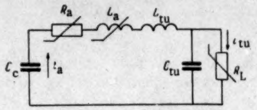

Fig. 1. Discharge circuit.

$$U_c = \left[R_a(t) + \frac{dL_a(t)}{dt}\right] i_a + L(t)\frac{di_a}{dt} + U_{tu}, \tag{1}$$

$$i_a = C_{tu}\frac{dU_{tu}}{dt} + i_{tu}, \tag{2}$$

$$U_c = U_{c0} - \frac{1}{C_c}\int_0^t i_a(\tau)\,d\tau, \tag{3}$$

$$L(t) = L_a(t) + L_{tu}, \tag{4}$$

$$i_{tu} = \frac{U_{tu}}{R_L}, \tag{5}$$

where i_a is the current in the arc channel, i_{tu} is the current in the load (the tube), U_{tu} is the voltage on the tube electrode, U_c is the voltage on the conductor, C_c is the capacitance between the conductor and the vessel, $L_a(t)$ is the inductance of the arc channel, $R_a(t)$ is the resis-

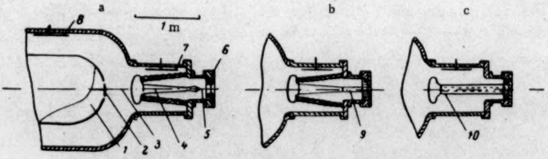

Fig. 2. Construction of the apparatus. 1) High-voltage electrode (conductor); 2) ignition electrode; 3) gas-filled discharge gap; 4) tube electrode with cathode; 5) vacuum accelerating gap; 6) Rogowski loop; 7,8) capacitive pickups; 9) shorting electrode; 10) water-filled resistor.

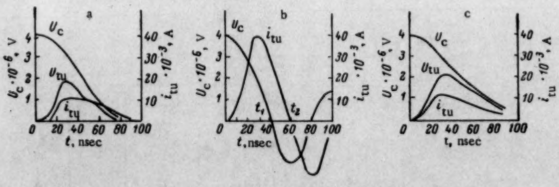

Fig. 3. Characteristic current and voltage oscillograms. a) Working regime; b) short-circuited regime; c) regime of a constant load resistance.

tance of the arc channel, L_{tu} is the inductance of the tube cathode, C_{tu} is the capacitance between the tube electrode and ground, and R_a is the load resistance of the source.

Figure 2a shows the construction of the part of the source that forms the discharge circuit. Using the oscillograms of the conductor and tube voltages and of the tube current along with Eqs. (1)-(5), we can determine R_a and L_a at certain times, and we can determine the average values of these properties over selected time intervals. Analyzing the current and voltage oscillograms, we can find the arc resistance as a function of the time. The voltages on the conductor and tube are measured by capacitive pickups, while the tube current is measured by a Rogowski loop;[2] the signals are displayed on an OK-19M oscilloscope. Figure 2 shows the pickups. We studied three regimes: a) the working regime of the accelerator (in general, with $R_L \neq$ const; Fig. 2a); b) the regime in which the accelerating gap is short-circuited ($R_L = 0$; Fig. 2b); and c) a regime in which the accelerating tube is replaced by its water equivalent (R_L = const; Fig. 2c). In the latter case we vary the concentration of KCl in water, using a vinyl plastic tube.

Figure 3 shows typical oscillograms for all three regimes. The arc resistance at time t_1 ($di_a/dt = 0$) is, according to Eq. (1),

$$R_a + \frac{dL_a}{dt} = \frac{U_c - U_{tu}}{i_a}.$$

Since the discharge current is not measured directly in regimes "a" and "b" it is determined from the curve for the voltage [$i_a = C_c(dU_c/dt)$] and compared with (2). We see from the experimental data below that dL_a/dt does not exceed 5% of R_a and it is neglected in the calculations.

More information on the arc resistance is obtained in experiments in the short-circuit regime ($R_a = 0$). From energy conservation we can evaluate the equivalent resistance of the arc channel, R_a, during the first, second, etc., current half-cycles in the following manner: The difference between the energies stored in capacitance C_c at zero times and t_2 is determined by the energy loss in the arc channel (i.e., the energy dissipated in R_a) for the first (1) current half-cycle:

$$W_{R_a I} = \frac{C_c U_{ca}^2}{2} - \frac{C_c U_{c1}^2}{2} = \int_0^{t_2} i_a^2 R_a \, dt.$$

Then we can define a resistance which is equivalent in terms of the loss over the time interval under consideration:

$$R_{a\,\mathrm{equ}} = \frac{W_{R_a I}}{\int_0^{t_2} i_a^2 \, dt}.$$

Similarly, we can find the equivalent (in terms of loss) arc resistance during the second half-period. The inductance of the arc channel is determined from the oscillation period in the experiments in the short-circuit regime. From the equation

$$\frac{T}{2} = \frac{\pi}{\sqrt{\frac{1}{L_{\mathrm{equ}} C_c} - \frac{R_{a\,\mathrm{equ}}^2}{4 L_{\mathrm{equ}}^2}}}$$

and the known values of T/2, C_c and $R_{a\,\mathrm{equ}}$, we can calculate the equivalent circuit inductance $L_{\mathrm{equ}} = L_{a\,\mathrm{equ}} + L_{tu}$ over the half-period under consideration. The instantaneous values of the inductance at points for which $i_a = 0$ (the short-circuit regime) are found from Eq. (1):

$$L(t_2) = \frac{U_c}{\frac{di_a}{dt}}.$$

The values of R_a and L_a at certain times and the equivalent values over a half-period $R_{a\,\mathrm{equ}}$ and $L_{a\,\mathrm{equ}}$, obtained in the experiments in the short-circuit regime, are shown in Table 1. Table 2 shows the values of R_a obtained in the working regime and in the regime with R_L = const. All the experiments in these regimes are carried out at a gas pressure of 12 atm; the voltages and currents are

TABLE 1. Short-Circuited Load

Gas	Pressure, atm	U_{C0}, MV	$I_{a\,\max}$, kA	$R_a(t_1)$, Ω	$L_a(t_2)$, μH	First half-period		Second half-period	
						$R_{a\,\mathrm{equ}}$, Ω	$L_{a\,\mathrm{equ}}$, μH	$R_{a\,\mathrm{equ}}$, Ω	$L_{a\,\mathrm{equ}}$, μH
Air	12	1.0	6.3	77	0.56	73	0.57	40	0.56
Air	6	0.9	5.6	80	0.56	75	0.57	42	0.56
SF_6	3	1.4	7.0	80	0.56	71	0.57	35	0.56
1 : 9 mixture of $SF_6 + N_2$	12	4.0	40	32	0.52	30	0.54	13	0.51
1 : 1 mixture of $SF_6 + N_2$	12	3.5	30	39	0.53	37	0.55	16	0.52

Note: Three to five experiments are carried out for each gas; in general, the scatter in the results does not exceed ± 15%. This table shows the average values.

TABLE 2

Regime		L_{tu}, μH	C_{tu}, pF	SF_6:N_2	U_{C0}, MV	$i_{a\,\max}$, kA	$R_a(t_1)$, Ω
Working		0.55	44	1 : 9	4.0	14	70
				1 : 1	4.7	16	60
R_L = const	R_L = 180 Ω	0.28	40	1 : 1	4.7	17	57
	R_L = 120 Ω					20	53
	R_L = 60 Ω					23	50

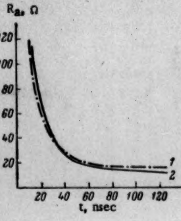

Fig. 4. Arc resistance as a function of the time in one regime. 1) Result of an analysis of the oscillograms; 2) calculated from Eq. (10).

measured within 10%. In all experiments the discharge gap is 40 cm long. The capacitance of the conductor is 220 pF, and the inductance of the tube electrode in the short-circuited regime is 0.58 μH. The values of U_{C0} obtained from the various experiments lie in the range 0.4-0.9 of the self-breakdown voltage of the gas-filled gap.

Because of the small difference between the values of $L_{a\,equ}$ in the first and second half-periods in the short-circuit regime, which can be attributed to the weak functional dependence of the inductance on the channel diameter, we can neglect the functional dependence of the inductance on the time in many calculations. Assuming L_a = const, we can find the functional dependence of the arc resistance on the time by a graphical solution of Eq. (1) based on the current and voltage oscillograms. Figure 4 shows the results calculated for the $R_L = 0$ case in a 1 : 1 mixture of SF_6 and N_2 at a pressure of 12 atm and at U_{C0} = 2.5 MV. Similar curves can be constructed for the other experiments.

DISCUSSION OF RESULTS

The Braginskii theory[3] is apparently the most complete of the known theories for the arc channel. Integrating the basic differential equation for the model of the channel adopted in this theory

$$2\pi^2\rho_0 a_a^3 \dot{a}_a^3 \xi = \frac{i_a^2}{\sigma}$$

we find the functional dependence of the channel radius on the time, which involves the time t_0 at which the channel is formed:

$$a_a(t) = \left[\left(\frac{4}{\rho_0\pi^2}\right)^{1/3} \int_{t_0}^{t} \left(\frac{i_a^2(\tau)}{\sigma\xi}\right)^{1/3} d\tau + a_a^2(t_0)\right]^{1/2}, \qquad (6)$$

where ρ_0 is the density of the gas in which the discharge occurs, σ is the electrical conductivity of the plasma in the channel,

$$\xi = K_e\left[1 + (\gamma - 1)^{-1}\frac{1}{2\dot{a}_a^2}\frac{d^2 a_a^2}{dt^2}\right], \qquad (7)$$

$K_e = 2/(\gamma + 1)$ is the expansion coefficient, and γ is the effective ratio of specific heats.[4]

In applying this theory to the geometric and electrical properties of the arc channel we are assuming that the channel is a straight cylinder and that the temperature, pressure, and density of the gas in the channel are constant over a cross section. We did not record the geometric characteristics of the channel in our experiments, but data from the literature for long channels (see, e.g., ref. 5) show that under conditions like ours an arc channel is usually neither homogeneous nor straight. However, in the experiments described here, involving the use of the RIUS-5 apparatus, the current and voltage oscillograms obtained under identical conditions are essentially the same for many of the measurements. For our purposes we can then assume that the electrical properties of the arc channel are stable, so that it is legitimate to replace the actual channel geometry by an equivalent geometry.

In order to use the Braginskii theory we must ensure that the condition $P_m/P_g \ll 1$ is satisfied, where P_m and P_g are the magnetic pressure on the channel and the gas-kinetic pressure in the channel, respectively.

According to ref. 6, we have

$$\frac{P_m}{P_g} = 1.4\left(\frac{\rho_A}{\rho_0}\right)\left(\frac{i_a}{\dot{a}_a a_a}\right)^2. \qquad (8)$$

Here, ρ_v is the density of air at normal conditions. To evaluate the ratio P_m/P_g for the regime with the maximum current i_a, i.e., for the experiments in the short-circuit regime, we can use the values U_{C0} = 4 MV, $i_a(t_1)$ = 40 kA, $\rho_v/\rho_0 \approx 0.08$, $a_a(t_1) \approx 4 \cdot 10^{-2}$ cm, and $\dot{a}_a(t_1) \approx 10^6$ cm/sec [a_a and $\dot{a}_a$ are obtained from Eq. (9)]. As a result we find $P_m/P_g \approx 0.1$.

As shown in the Appendix, at the plasma temperatures prevailing in the arc channel the quantities σ and ξ [(7)] which appear in Eq. (6) can be assumed to be independent of the time and can be taken through the integral sign.

The literature reveals no data on the initial radius of the arc channel [$a_a(t_0)$] in long gaps, so we replace Eq. (6) for $a_a(t)$ by an approximate equation, from which $a_a(t_0)$ is omitted:

$$a_a(t) \approx K_1\rho_0^{-1/6}\left[\int_{t_0}^{t} i_a^{1/3}(\tau)\, d\tau\right], \qquad (9)$$

where $K_1 \approx (4/\pi^2\sigma\xi)^{1/6}$. This quantity is determined experimentally for each gas and for each pressure from the value of L_a at time t_2 (Table 3).

In evaluating the integral in Eq. (9), we choose t_0 to be the time at which the current pulse begins on the oscillogram. It is apparently possible to determine more rigorously the time at which the channel formation ends,[7,8] but this procedure is of no particular interest since no changes occur in systems of this type which are significant from the standpoint of energy transfer over the time required for the formation of the channel. Below we replace t_0 in the equations by t = 0.

Because of our assumptions and the method used to determine the coefficient K_1 from the value of the inductance, which is related logarithmically to the channel radius, the error involved in the determination of a_a from (9) is very large. However, for our purposes – to calcu-

TABLE 3

Gas	Pressure, atm	l_a, cm	K_1, $2^{1/6}$ $cm^{1/2}/A^{1/3}\cdot sec^{1/2}$	10^5K_2, $\Omega^{2/3}\cdot sec/2^{1/3}$
SF_6	3	40	4.6	7.5
1 : 1 mixture of SF_6+N_2	12	40	4.9	6.4
1 : 9 mixture of SF_6+N_2	12	40	4.9	6.5
Ar	12	40	4.7	7.2
Ar	6	40	4.6	7.6
Ar*	1	0.8	4.9	6.5

*The last row of this table shows the coefficients obtained through an analysis of the data in ref. 6 for an air-filled gap 0.8 cm long.

late the inductance of the arc channel (except in the initial period) – this circumstance is unimportant.

The resistance of the arc channel is

$$R_a(t)=\frac{l_a}{\sigma\pi a_a^2}\approx\frac{K_2\rho_0^{1/3}}{\int\limits_0^t i^{2/3}(\tau)\,d\tau}, \tag{10}$$

where l_a is the length of the discharge gap, and Q_2 is a coefficient which is determined experimentally for each type of gas and each pressure from the resistance of the arc channel at time t_1 (Table 3). The coefficients K_2 and K_1 are related by $K_2 = 1/\sigma\pi K_1^2$.

Figure 4 shows the functional dependence $R_a(t)$ calculated from Eq. (10). Comparison with the curve constructed from the oscillograms reveals completely satisfactory agreement; the discrepancy between the curves in the early stages occurs apparently because Eq. (9) gives an underestimate of the channel radius in these stages. To estimate the initial channel radius from Eq. (6), which would lead to coincidence of the two curves at time[1] $t_0 \approx$ 10 nsec (with coincidence at time t_1 also), we assume that at time t_0 the plasma conductivity reaches a quasistable value of about 200 $\Omega^{-1}\cdot cm^{-1}$ (Appendix); we find $a_a(t_0) \approx$ 0.25 mm. This result is consistent with the known results. The quantity $a_a(t_0)$ has been measured previously[8] for short air-filled gaps (pd = 600 torr · cm) and found to be 0.1-0.12 mm for those particular conditions.

We see from Table 3 that the coefficients K_1 and K_2 are essentially independent of the nature and pressure of the gas. The apparent explanation is that the electrical conductivities of different highly ionized gases are essentially the same at identical electron temperatures.[9] The curves in Fig. 6 (see the Appendix) offer further support for this conclusion.

Accordingly, in calculating the electrical properties of high-voltage, gas-filled arc switches we can use the approximate functional dependences of the radius and resistance of the arc channel on the time given above, with average values of the common constants for the cases considered (Table 3):

$$a_a(t)\approx 4.8\rho_0^{-1/6}\left[\int\limits_0^t i_a^{2/3}(\tau)\,d\tau\right]^{1/2}\ \text{cm}, \tag{11}$$

$$R_a(t)\approx l_a\frac{7\cdot 10^{-5}\rho_0^{1/3}}{\int\limits_0^t i_a^{2/3}(\tau)\,d\tau}\ \Omega, \tag{12}$$

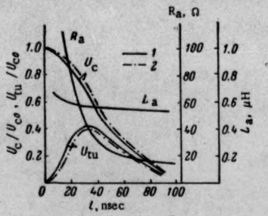

Fig. 5. Calculated (1) and experimental (2) curves for the voltage on the high-voltage electrode and the tube in the regime with R_L = 120 Ω. The calculated $R_a(t)$ and $L_a(t)$ curves are also shown.

where ρ_0 is the gas density in the arc switch (grams per cubic centimeter), l_a is the length of the discharge gap (centimeters), i_a is in amperes, and t is in seconds.

Using Eqs. (11) and (12) we can compare different types of switches (differing in the nature and pressure of the gas). In particular, we see that for a given gas the resistance of the arc channel falls off with increasing pressure according to $\sim 1/P^{2/3}$ ($l_a \sim 1/p$). We also see that the use of multichannel switches, which significantly reduce the inductance (or characteristic impedance) of a commutator, leads to a relatively slight reduction in the resistance (for a given current). With N channels we would have $R_a(N) = (1/N^{2/3})R_a$ (1).

The use of these equations facilitates calculations of the amplitudes and lengths of current and voltage pulses in nanosecond-range sources of relativistic electron beams involving gas-filled arc switches. Our calculations for the regime with R_L = const leads to good agreement with the experiment results (Fig. 5).

APPENDIX

Analysis[3,10] of Eq. (7) for the parameter ξ has shown it can be assumed to be independent of the time. This conclusion follows from the established fact[10-13] that the expansion of the visible part of the channel during the stage of intense energy evolution in the channel can be described approximately by the power law $a_a \approx At^n$ (where A and n are constants). Substituting the latter relation into (7), we find

$$\xi=\frac{2}{\gamma+1}\left[1+\frac{2n-1}{n(\gamma-1)}\right]. \tag{A.1}$$

At temperatures $10^4 < T < 3\cdot 10^4$°K and at relative gas densities $10^{-4} < \rho/\rho_0 < 10$, the value of γ for air is found to be 1.22 in ref. 4.

The effective value of the ratio of specific heats for SF_6 can be determined from the experimental values of the enthalpy of an SF_6 plasma, obtained in ref. 11 at temperatures from 10,000 to 45,000°K and at unperturbed-gas pressures from 1 to 16 atm. Over this temperature range and over the range of relative gas densities $10^{-3} < \rho/\rho_0 < 10^0$, the value is γ = 1.17. On the basis of the slight difference between γ for air and SF_6 we would expect that the values of the parameter ξ for these gases would also differ only slightly.

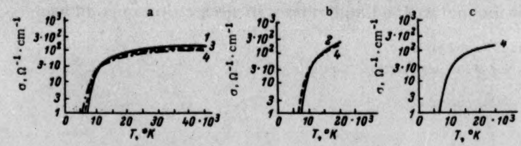

Fig. 6. Pressure (atm): 1) 16; 2) 10; 3) 4; 4) 1.

The values of the conductivity σ are calculated in refs. 11, 14, and 15 for SF_6, air, and nitrogen plasmas as a function of the temperature for various pressures of the unperturbed gases; the results are shown in Fig. 6, a–c, respectively. We see that the conductivity is a weak function of the pressure and that the values of σ are approximately the same for the different gases. At $T \geqslant 2$ eV the conductivity changes only slightly and can be assumed essentially constant. According to the data of ref. 16, the plasma temperature in the channel lies in the range 3.6–5.3 eV for a relatively low rate of energy evolution in the channel but for a total energy per unit length which is approximately equal to that in our experiments. The value of σ is also assumed to be constant over the first current half-period in ref. 6. According to the arguments of ref. 7, a rapid change in the value of σ in the channel ($T < 2$ eV) occurs during channel formation.

---

1) According to ref. 8, the time t_0 is the time at which the derivative of the current in the channel reaches its maximum value.

[1] E. A. Abramyan, S. B. Vasserman, V. M. Dolgushin, L. A. Morkin, O. P. Pecherskii and V. A. Tsukerman, Dokl. Akad. Nauk SSSR, 192, 76 (1970) [Sov. Phys. – Dokl., 15, 490 (1970)].

[2] S. B. Vasserman, Prib. Tekh. Eksp., No. 2, 99 (1972).

[3] S. I. Braginskii, Zh. Eksp. Teor. Fiz., 34, 1458 (1958) [Sov. Phys. – JETP, 7, 1068 (1958)].

[4] S. I. Drabkina, Zh. Eksp. Teor. Fiz., 21, 473 (1951).

[5] J. J. Moriarty, H. I. Milde, J. R. Bettis, and A. H. Guenther, Rev. Sci. Instrum., 42, No. 12, 1767 (1971).

[6] S. I. Andreev and B. I. Orlov, Zh. Tekh. Fiz., 35, 1411 (1965) [Sov. Phys. – Tech. Phys., 10, 1097 (1966)].

[7] S. I. Andreev and M. P. Vanyukov, Zh. Tekh. Fiz., 31, 961 (1961) [Sov. Phys. – Tech. Phys., 6, 700 (1962)].

[8] S. I. Andreev and B. M. Sokolov, Zh. Tekh. Fiz., 35, 1295 (1965) [Sov. Phys. – Tech. Phys., 10, 1003 (1966)].

[9] V. L. Granovskii, Electric Currents in Gases [in Russian], Izd. Nauka, Moscow (1971), p. 116.

[10] S. I. Andreev, M. P. Vanyukov, and A. B. Komolov, Zh. Tekh. Fiz., 32, 57 (1962) [Sov. Phys.–Tech. Phys., 7, 37 (1962)].

[11] L. S. Frost and R. W. Liebermann, Proc. IEEE, 59, No. 4, 475 (1971).

[12] J. B. Higham and J. M. Meek, Proc. Phys. Soc., B63, 649 (1950).

[13] B. A. Demidov, Yu. A. Skachkov, and S. D. Fanchenko, Zh. Eksp. Teor. Fiz., 40, 385 (1961) [Sov. Phys. – JETP, 13, 263 (1961)].

[14] P. P. Kulik and N. V. Ermokhin, in: Proceedings of the All-Union Conference on the Thermophysical Properties of Substances at High Temperatures, Novosibirsk, July 25-30, 1966 [in Russian], Vol. 2, Izd. Standartov, Moscow (1969).

[15] W. Finkelburg and H. Maecker, Handbuch der Physik, Vol. 22, Berlin–Göttingen–Heidelberg (1956), p. 352.

[16] V. F. Egorova, V. I. Isaenko, A. A. Mak, and A. I. Sadykova, Zh. Tekh. Fiz., 32, 339 (1962) [Sov. Phys. – Tech. Phys., 7, 242 (1962)].

Electrical explosion of the metastable liquid phases of zinc, cadmium, and lead

M. M. Martynyuk and I. Karimkhodzhaev

Patrice Lumumba Friendship of Nations University, Moscow

(Submitted June 1, 1973)
Zh. Tekh. Fiz., 44, 2360-2366 (November 1974)

The relative resistances of Zn, Cd, and Pb are measured by a pulsed oscilloscope method as functions of molar enthalpy in the electrical explosion of conductors caused by current pulses 15-25 μsec. The enthalpy of the liquid phase at the initial point of the explosion for all three metals is much higher than its value at the normal boiling point because the liquid becomes metastable. This behavior shows that the electrical explosion of a conductor is accompanied by an explosive transition of the metastable liquid-metal phase into a stable state. The critical parameters of Zn, Cd, and Pb are evaluated from the experimental data on the basis of the theory developed previously by Martynyuk for exploding wires.

Martynyuk[1] used the thermodynamics and kinetics of evaporation and boiling to show that the initial point of the electrical explosion of a conductor, T_3 (T is the temperature), for a specified duration of the heating of the liquid phase, τ, must lie in the neighborhood of the cusp point T_c, which is the thermodynamic-stability boundary of the liquid phase in the case of a continuous change.[2] These points are approximately equal ($T_3 \approx T_c$) only if τ satisfies the conditions

$$\tau_1 > \tau \gg \tau_2, \tag{1}$$

where τ_1 is the maximum period of liquid-phase heating over which the effect of heterogeneous vapor nuclei and the effect of MHD instabilities of the liquid sample can be neglected; τ_2 is the time required for the establishment of steady-state homogeneous formation of vapor nuclei in a superheated liquid metal (according to theoretical estimates, $\tau_2 = 10^{-7}$-10^{-8} sec). Accordingly, when (1) holds the point T_3 has a definite thermodynamic meaning, and a determination of this point can yield valuable information about the high-temperature properties of the metal in question.

Working on the basis of arguments of this type regarding the nature of exploding wires, we have carried out oscilloscope measurements of the electrical resistance and enthalpy of the liquid phases of Zn, Cd, and Pb in the states preceding explosion. The basic purpose of this study is to demonstrate experimentally the possibility of superheating a liquid metal above its boiling point under pulsed-heating conditions and to evaluate the temperature T_3 at the initial point of the explosion. We choose these particle metals because the literature reveals data on the resistivity[3,4] and the enthalpy[5] of Zn and Cd up to temperatures exceeding the normal boiling point T_{nb}, so that we were able to compare the results obtained in pulsed and ordinary measurements. The same comparison is possible for Pb, which has a relatively low value of T_{nb}.

1. EXPERIMENTAL PROCEDURE AND RESULTS

For a current pulse 200-400 μsec long the destruction of the sample begins immediately after melting, after a weak penetration into the liquid region.[6] For our experiments we assemble a pulsed apparatus with which we are able to reduce the pulse length by a factor of more than 10. The apparatus is described in ref. 7. The apparatus operates on the basis of an aperiodic discharge of a pulsed capacitor (200 μF) charged to 3 kV; it discharges through a wire sample held on the axis of a cylindrical copper chamber. The discharge is initiated by arc switching (with a trigatron). A nondistorting cylindrical current shunt[6] with a constantan resistance of (5-20) · 10^{-3} Ω is used to detect the current. A capacitive–resistive voltage divider is used to record the voltage oscillograms. This divider has several advantages[8] over simple resistive or simple capacitive dividers; it is capable of maintaining a constant division factor above 10 MHz and also transmits voltage pulses with rise times shorter than 0.1 μsec without any significant distortion.

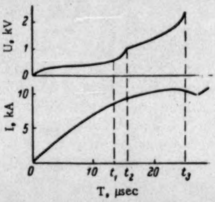

Fig. 1. Current and voltage oscillograms for lead, obtained in explosion in air.

Using the oscillograms of the current I and the voltage U and the equations of ref. 6, we calculate the resistance of the metal R/R_0 as a function of its molar enthalpy $H = H_T - H_{298}$ (R_0 is the initial resistance of the sample at 298°K) on a Minsk-22 computer. The rms error in the determination of R/R_0 is ± 5% (six experiments) and the corresponding error in the determination of H is ± 7%. The details of the oscilloscope study, the calibration, and the analysis of the oscillograms are given in ref. 6, along with a description of the effects of various factors on the results of the pulsed measurements of R/R_0 and H.

The Zn samples are 99.98% pure, the Cd samples are 99.99% pure, and the Pb samples are 99.999% pure; the diameter of the wire samples is 0.5 mm in the case of Zn and Cd or 0.86 mm in the case of Pb, and the samples are about 62 mm long. The wires are exploded in air, and additional experiments are carried out in water for the case of Zn and Cd. Figure 1 shows current and voltage oscillograms for Pb; the oscillograms for Zn and Cd are similar. On the voltage oscillogram we observe the beginning t_1 and end t_2 of the melting of the sample as well as the beginning of the explosion t_3; beyond this point the beam moves so rapidly that it leaves essentially no trace on the film.

Figure 2, a-c, shows $(R/R_0)(H)$ curves averaged over the data of six experiments for each metal. On these curves we see the points corresponding to the beginning

TABLE 1. Relative Resistance and Enthalpy of Zn, Cd, and Pb at the Beginning (R_1/R_0, H_1) and End (R_2/R_0, H_2) of Melting as Well as at the Beginning of the Electrical Explosion (R_3/R_0, H_3)

Metal	t, μsec		ρ_0, μΩ·cm	$\frac{R_1}{R_0}$	$\frac{R_2}{R_0}$	$\frac{R_3}{R_0}$	$H = H_t - H_{298}$, kJ/mole		
	t_2	τ					H_1	H_2	H_3
Zn	14.5	3.5	6.23	2.60	4.55	7.70	12.0	18.8	69.6
	16.0	4.6	6.23	2.60	4.45	7.65	12.0	19.6	74.0
				2.68 [3]	6.00 [3]		10.8 [5]	18.2 [5]	
Cd	13.5	4.1	7.84	2.10	3.20	7.5	8.6	14.0	63.0
	15.0	3.7	7.84	2.10	3.20	7.5	8.6	15.0	66.0
				2.18 [3]	4.30 [3]		8.2 [5]	14.3 [5]	
Pb	25.0	9.0	21.7	2.45	4.45	10.3	9.3	14.2	104
				2.26 [3]	4.37 [3]		8.5 [5]	13.2 [5]	

Note: Here ρ_0 and R_0 are referred to 298°K; t_3 is the time required for heating to the beginning of the explosion; τ is the time over which the liquid phase is heated. For each metal the data in the first row correspond to explosions in air, the data in the second row correspond to explosions in water, and the data in the third row are for slow heating as given in the literature.

1 and end 2 of melting and the beginning of the electrical explosion, 3; here, nb is the normal boiling point of the metal.[5] Table 1 shows the values of R/R_0 and H obtained for these points.

Comparison of these results with the slow-heating results in the literature[3-5] shows the following:

1) The values of R_1/R_0, H_1, H_2, and $H_2 - H_1$ for Zn, Cd, and Pb agree with the results in the literature within the experimental errors.[1)]

2) The shape of the $(R/R_0)(H)$ curves for liquid Zn and Cd agrees with the shape of the $(R/R_0)(T)$ curves obtained in ref. 4. After melting the value of R/R_0 for Cd remains constant over a broad temperature range; that for Zn falls off with increasing T. At high temperatures, the value of R/R_0 begins to increase for liquid Zn and Cd. The increase in R/R_0 for liquid Zn and Cd is observed in our experiments at temperatures higher than in ref. 4.

3) The value of R_2/R_0 for Pb agrees with the data of ref. 3, but in the case of Zn and Cd it is lower than the data of refs. 3 and 4 by about 25%, larger than the experimental errors of the present measurements. We attribute this discrepancy in R_2/R_0 to the magnetic pressure caused by the pinch effect. The value of this pressure[6] averaged over the cross section for the Zn and Cd samples is less than 220 bar; for the Pb samples it is less than 80 bar.

4) For all three metals the enthalpy at the beginning of the electrical explosion, H_3, is much higher than the enthalpy of the liquid phase at the normal boiling point T_{nb}, H_{nb} (ref. 5); if the heating rate is high enough the liquid phase exists over a larger range (Fig. 2, a–c). This increase can be described by the ratio $\gamma = (H_3 - H_2)/(H_{nb} - H_2)$. For explosions in air the values of γ for Zn, Cd, and Pb are 3.4, 3.6, and 2.2, respectively. (According to ref. 5, the values of H_{nb} for Zn, Cd, and Pb are 33.6, 27.6, and 54.6 kJ/mole, respectively.) In the explosions of Zn and Cd in water we observed slight increases in H_2 and H_3 (Fig. 2, a and b).

2. DISCUSSION OF RESULTS

Let us consider the factors which could lead to values of H_3 higher than H_{nb} under these experimental conditions. The difference between these values cannot be attributed to thermal loss resulting from heat transfer between the sample and the surrounding air or between the sample and the massive copper clamps; solution of the corresponding heat-conduction equations[6] and a consideration of the radiation of the metal show that this loss is less than 0.5% of H. In our experiments the sample cannot be ruptured before time t_3, and the associated appearance of local arcs, whose maintenance requires additional expenditure of heat, cannot occur. Any changes of this type would be reflected on the voltage oscillogram by a sharp increase in the resistance of the sample. It can also be argued that H_3 is larger than H_{nb} because the boiling temperature of the liquid metal is raised by the pressure exerted on the surface of the conductor during the pulsed heating, but the

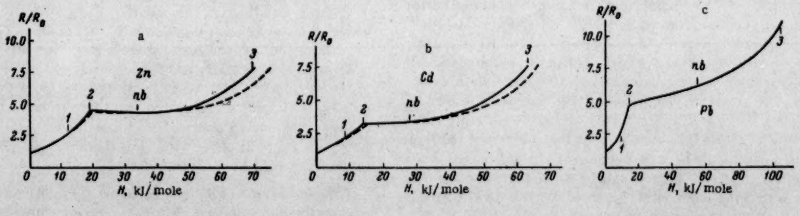

Fig. 2. Relative electrical resistance of zinc (a), cadmium (b), and lead (c) as a function of the molar enthalpy in pulsed heating. Solid curves show heating in air; dashed curves, in water.

conclusions reached below show that this is not the case.

The boiling of a thin film near the surface of a sample of radius r_0 cannot be affected by the magnetic pressure p_m, since this pressure is nonvanishing only in the interior of the sample; as $r \rightarrow r_0$, we would have $p_m \rightarrow 0$ (ref. 6). Vapor nuclei can form in a surface film;[2] the average magnetic pressure for Zn and Cd is less than 4.5 bar, and that for Pb is less than 1.5 bar, so that there can be only a slight displacement of the boiling point of the metal. The pressure due to the inertial forces during the radial thermal expansion of the sample would have a similar effect. Simple calculations show that p_{in} is much lower than p_m.

When a liquid sample is subject to pulsed heating in atmospheric air the surface of the sample is subject to the atmospheric pressure p_{at} as well as the pressure produced by the reaction of the flow of metal vapor evaporated from the metal surface; at any temperature T this latter pressure is $(2\alpha/\pi)p_b$, where p_b is the saturation vapor pressure at this temperature and α is the evaporation coefficient.[1] For a clean metal surface we have $\alpha = 1$, but for the contaminated surfaces of our experiments we have $\alpha \ll 1$ (ref. 9), so that this pressure can be neglected. Accordingly, the pulsed heating of a thin metal film near the surface of the sample in the experiments in air can be assumed to be approximately isobaric when $p = p_{at}$.

It has been shown[1] that at $p < p_k$ (where p_k is the critical pressure) a rapid heating of a liquid metal must be accompanied by a superheating of this metal above the boiling point, so that we can assume that the time t_3 determined on the voltage oscillogram and the corresponding value H_3 refer to the explosive boiling of a thin film of superheated liquid metal lying near the surface of the sample as the cusp point (T_c, H_c) is approached at $p_c \approx 1$ atm. An objection can be raised against this conclusion, however: A constrictive MHD instability can arise in a liquid sample during Joule heating (in ref. 10 the time constant for this instability is shown to be about 0.1 μsec for Pb). In this case the explosive boiling of the metal does not begin throughout the entire volume of the sample, but only at points at which the cusp point has been previously reached. It is understandable that the instabilities lead to a situation in which the value of H_3 determined from the oscillograms is lower than H_c, since H_3 is obtained by averaging over the entire volume of the sample. However, the large values of γ found in these experiments indicate that if it occurs at all the constrictive instability develops as the metal approaches T_c.

Evidence that the beginning of the electrical explosion, H_3, is near the cusp point, and not near the phase-equilibrium curve, comes from experiments involving explosions of Zn and Cd in water: The values found for H_3 in these experiments are not much higher than the value obtained for explosions in air (Fig. 2, a and b). In the state preceding the electrical explosion of the sample in water a thin sheath of water vapor forms around the sample and exerts a considerable pressure on the surface of the liquid metal; however, this pressure does not significantly displace the point H_3. This result is consistent with the conclusion that the cusp point T_c, in contrast with the boiling point, is a slight function of the pressure p_c (refs. 1, 2). As the voltage on the capacitor is changed by 20-30% the value of H_3 for these metals remains essentially constant.

TABLE 2. Melting Temperature T_2 and Specific Heat C_2 of the Liquid Phase near T_2, Normal Boiling Point T_{nb}, the Temperature at the Beginning of the Electrical Explosion T_3, and the Critical Parameters T_k and P_k for Zinc, Cadmium, and Lead

Metal	T_2[5], °K	C_2[5], J/(mole·°K)	T_{nb}[5], °K	T_3, °K	T_k, °K	P_k, atm
Zn	692.7	31.38	1184	2333	2590	740
Cd	594.0	29.71	1040	2230	2480	980
Pb	600.6	30.63	2016	3570	3970	160

That the MHD instabilities have no appreciable effect on the value of H_3 found for Cd has been confirmed in subsequent experiments involving the electrical explosion of this metal in a plastic medium (Teflon) under a pressure p up to 6 kbar at a current pulse length of about 100 μsec. At $p > 1$ kbar the instability is completely suppressed and H_3 is a weak function of p; the function $H_3(p)$ is approximately linear. Extrapolation of this functional dependence to $p = 0$ yields $H_3 = 64$ kJ/mole, in good agreement with the values shown in Table 1 for the experiments in air.

A calculation of the cusp point in the coordinates p−T for Cs on the basis of the Furth equation[1] has shown that this point is described accurately by

$$\frac{p_c}{p_k} = \frac{10T_c}{T_k} - 9 \tag{2}$$

(here the subscript "c" refers to the cusp point, while the subscript "k" refers to the critical parameters); this equation agrees with the equation of the cusp point for several organic liquids determined experimentally by various methods, including a pulsed-heating method.[2] On the basis of this agreement we can assume that thermodynamic similarity holds satisfactorily for the cusp points of liquids differing in their physical properties. Assuming that $p_c = p_{at} \ll p_k$ for our experiments in air, we find from (2) that

$$T_k = \frac{10T_c}{9} \approx \frac{10T_3}{9}. \tag{3}$$

We can evaluate T_3 from the specific heat of the liquid metal, C_2, near the melting point T_2 and from the data obtained on H_2 and H_3. Then we can write the critical temperature as

$$T_k = \frac{10}{9}\left[T_2 + \frac{H_3 - H_2}{C_2}\right]. \tag{4}$$

Some justification for equating C_2 in (4) to the average value of C_p over the range from T_2 to T_3 comes from the circumstance that for liquid metals the value of C_p generally falls off initially and then increases with increasing T; as we approach T_c we evidentally have $C_p > C_2$. The values of T_3 and T_k calculated from (4) on the basis of the values of H_2 and H_3 obtained for explosions in air are shown in Table 2, along with the values of T_2, C_2, and T_{nb} taken from ref. 5 for these metals.

These values of T_k are apparently slightly underestimated, for two reasons: First, because of the possible onset of MHD instabilities H_3 can be slightly lower than H_c at $p = 1$ atm. Second, since the internal layers of the metal in a sample are compressed by the magnetic pressure, we should not substitute in Eq. (4) the value of C_2 which is generally measured in vacuum, but a slightly lower value (as the value of p increases for liquids, the value of C_p is known to decrease). However, this factor cannot presently be taken into account in the absence of data on the influence of p on C_p for Zn, Cd, and Pb in the liquid state. We can nevertheless assume that this effect does not exceed the error in the determination of H_3 in our experiments.

We can use these values of T_k to evaluate the critical pressure p_k for Zn, Cd, and Pb by extrapolating data (given in ref. 5 for pressures up to p = 1 atm) on the functional dependence of the saturation vapor pressure of these metals on the temperature. We plot this functional dependence in the coordinates log p vs 1/T and extrapolate linearly to $T = T_k$. Table 2 shows the values found in this manner for p_k for Zn, Cd, and Pb; for all three metals the values are much higher than the corresponding maximum values of the magnetic pressure at the axis of the sample. This circumstance again demonstrates that a superheated, metastable, liquid-metal phase existed under our experimental conditions. When this method for determining p_k is applied to Cs and Hg the values are approximately equal to those found in direct measurements.[11]

After the beginning of the electrical explosion the supply of energy to the conductor is essentially cut off because of the rapid increase in the resistance of the conductor. As the cusp point is approached this increase is due to the rapid growth of fluctuations in the superheated liquid metal, which lead to a localization of conduction electrons and to the conversion of the metal into a nonmetal.[1] The free energy of the superheated liquid-metal phase near the cusp point is much higher than the energy of its saturated vapor, so that the conversion of this liquid into vapor is of an explosive nature (a phase explosion) and occurs due to the excess enthalpy of the superheated liquid metal, $H_3 - H_{nb}$, which can be called the "energy release" during a phase explosion. For experiments in air (Table 1) the values of $H_3 - H_{nb}$ for Zn, Cd, and Pb are, respectively, 0.55, 0.31, and 0.24 kJ/g or, per unit of the original volume, 3.9, 2.7, and 2.7 kJ/cm^3. If the final state of the two-phase system which arises after the explosion without external supply of energy is associated with the normal boiling point of the metal, we conclude that the ratio $x = (H_3 - H_{nb})/\lambda$ (where λ is the heat of vaporization at this point) is equal to the fraction of evaporated metal. For explosions in air, according to the values found for H_3, we have x = 0.31 for Zn, 0.35 for Cd, and 0.31 for Pb.

---

1) Martynyuk and Gerrero[6] show that at a heating rate of about 10^6 deg K/sec the points H_1 and H_2 lie about 40°K above the normal melting point in the case of Pb; this result has been confirmed in subsequent experiments by Martynyuk and Tsapkov. There was also apparently a superheating of the solid phase of Pb in these experiments, but this superheating does not exceed the error in the determination of H.

[1] M. M. Martynyuk, Zh. Tekh. Fiz., 44, 1262 (1974) [Sov. Phys. – Tech. Phys., 19, 793 (1974)].

[2] V. P. Skripov, Metastable Liquids [in Russian], Izd. Nauka, Moscow (1972).

[3] N. E. Cusack, Rep. Progr. Physics, 26, 361 (1963).

[4] A. R. Regel', Zh. Tekh. Fiz., 28, 521 (1958) [Sov. Phys. – Tech. Phys., 3, 489 (1958)].

[5] R. Hultgren, R. L. Orr, P. D. Anderson, and K. K. Kelley, Selected Values of Thermodynamic Properties of Metals and Alloys, Wiley, New York (1963).

[6] M. M. Martynyuk and G. É. Gerrero, Zh. Tekh. Fiz., 42, 187 (1972) [Sov. Phys. – Tech. Phys., 17, 148 (1972)].

[7] M. M. Martynyuk and I. Karimkhodzhaev, Dokl. Akad. Nauk TadzhSSR, 14, No. 8, 14 (1971).

[8] Ya. S. Itskhoki, Pulse Techniques [in Russian], Izd. Radio, Moscow (1968).

[9] M. Knudsen, Ann. Physik, 4-te Folge, 29, 179 (1911); 34, 593 (1911).

[10] K. B. Abramova, V. P. Valitskii, Yu. V. Vandakurov, N. A. Zlatin, and B. P. Peregud, Dokl. Akad. Nauk SSSR, 167, 778 (1966) [Sov. Phys. – Dokl., 11, 301 (1966)].

[11] R. G. Ross and D. A. Greenwood, Progr. Mater. Sci., 14, 173 (1969).

Resistance and enthalpy of refractory exploding wires

M. M. Martynyuk, I. Karimkhodzhaev, and V. I. Tsapkov
Patrice Lumumba Friendship of Nations University, Moscow

(Submitted June 7, 1973)
Zh. Tekh. Fiz., 44, 2367-2373 (November 1974)

A pulsed oscilloscope method has been used to measure the relative electrical resistance R/R_0 as a function of the enthalpy H for Zr, Hf, Nb, Mo, W, and Pt as the wire samples are heated by current pulses with t_3 = 400-500 and 30-35 μsec. In the prolonged heating the samples are ruptured immediately after melting; with a briefer heating, there is a deeper penetration into the liquid-state region, up to temperatures far above the normal boiling point of the metal. The values of R/R_0 and H for the solid and liquid phases of these metals are measred at the boiling point and at the temperature corresponding to the beginning of the electrical explosion, T_3; in pulsed heating in water at t_3 = 30-35 μsec, the values of R/R_0 for Zr, Hf, Nb, and Mo remain essentially constant in the liquid-state region up to T_3. The temperature T_3, which is identified as being approximately equal to the critical temperature, is evaluated. In pulsed heating in air there is a dip in the value of R/R_0 for the liquid state of all these metals; this behavior is attributed to discharge shunting the sample.

The electrical resistance R/R_0 (where R_0 is the resistance of the sample at T = 298°K) and the enthalpy $H = H_T - H_{298}$ of the refractory d-transition metals have not been studied adequately at high temperatures.[1,2] For many of these metals the value of H has been measured only up to $T < T_{me}$ (where T_{me} is the melting point), and the heat of melting is not known; the information which has been reported requires verification. There is little information available about the physical properties of the d-transition metals in the liquid state. This situation results from the difficulty of carrying out high-temperature studies of metal properties by classical methods, which generally involve slow heating.

We report here measurements of R/R_0 and H for Zr, Hf, Nb, Mo, W, and Pt by a method involving the heating of a wire sample by a powerful current pulse and simultaneous oscilloscope study of the current and voltage in the sample; the R/R_0 (H) functional dependences are calculated from the oscillograms.[3] When a liquid metal is subjected to pulsed heating at a sufficiently high rate the metal undergoes a transition to its metastable state; then there is an explosive transition to the gaseous state[4,5] (an electrical explosion), so that we measure R/R_0 and H not only in the regions of the stable states of these metals, but also in the states preceding their electrical explosion. Measurements of this type are extremely important for studying the nature of this phenomenon.

1. EXPERIMENTAL PROCEDURE AND RESULTS

The measurements are carried out on two types of pulsed experimental devices. In arrangement No. 1, current pulses of 0.7-4 kA, approximately rectangular, are produced by an artificial line with a characteristic impedance of 0.4 Ω. This line is charged to 3 kV. The voltage across the sample does not exceed 350 V. The current pulses are detected by a nondistorting cylindrical shunt of constantan foil as suggested by Park.[6] Otherwise, the apparatus is the same as in ref. 3. The rms error in the measurements, averaged over the data of six experiments, is ± 2% for R/R_0 and ± 3% for H.

Arrangement No. 2 uses the aperiodic discharge of a capacitor charged to a voltage of 3 kV; the circuit is described in ref. 5. In this case the length of the pulses before the beginning of the electrical explosion, t_3, is 30-35 μsec; the samples are heated in the liquid state for τ = 10-15 μsec; and the maximum current reaches 10 kA. The rms error in the determination of R/R_0 with this arrangement is ±5%, and that for H is ±7%.

The samples are made from 99.76% pure Zr, 99.0% pure Hf, 99.94% pure Nb, 99.96% pure Mo, 99.9% pure W, and 99.93% pure Pt. The diameter of the Hf samples is 0.74 mm, and that for the other metals is about 0.5 mm; the samples range in length from 33 to 84 mm. The experiments with arrangement No. 1 are carried out only in air, while those with arrangement No. 2 are carried out in both air and water, since the shunting discharge is observed to have a significant effect on the experimental results for the experiments in air at high temperatures.

Figure 1 illustrates the results with oscillograms of the current I and the voltage U for the case W; Fig. 2,

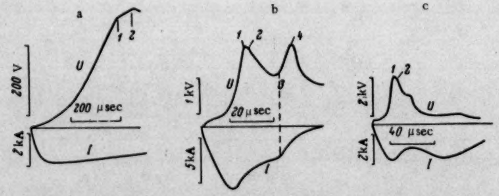

Fig. 1. Oscillograms of the current I through the sample and the voltage U for W samples. a) Arrangement No. 1 in air; b) arrangement No. 2 in water; c) the same, in air. 1) Beginning of melting; 2) end of melting; 3) beginning of electrical explosion; 4) "peak" in the voltage across the sample.

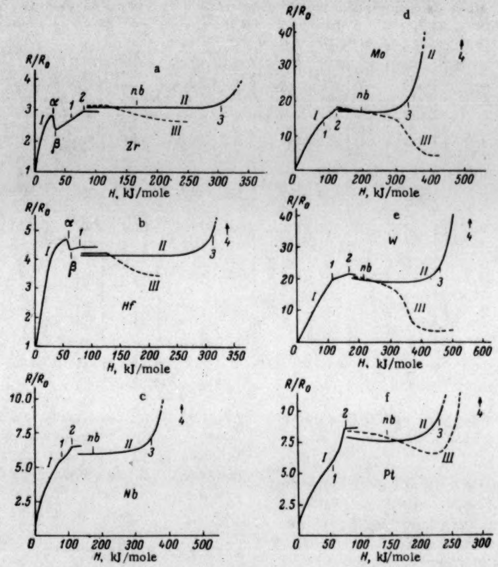

Fig. 2. Relative resistance of Zr, Hf, Nb, Mo, W, and Pt as a function of the enthalpy. I) Arrangement No. 1 in air; II) arrangement No. 2 in water; III) the same, in air. 1) Beginning of melting; 2) end of melting; 3) beginning of electrical explosion; 4) "peak" in the voltage across the sample. The beginning α and end β of the polymorphic transitions are indicated for Zr and Hf.

a-f, shows the functional dependence (R/R_0) (H) calculated from the oscillograms for the various metals studied. On the voltage oscillograms and the (R/R_0) (H) curves we mark the points of slope change, corresponding to the beginning (t_1, R_1/R_0, H_1) and end (t_2, R_2/R_0, H_2) of the melting of the sample. For Zr and Hf in the solid state we also mark the beginning (t_α, R_α/R_0, H_α) and end (t_β, R_β/R_0, H_β) of the polymorphic $\alpha-\beta$ transition, which is accompanied by a conversion of the hcp crystal structure into a bcc structure.

In the experiments with arrangement No. 1 the samples are ruptured immediately after melting; the beginning of rupture is identified with the rapid change on the oscillogram of U. In the experiments with arrangement No. 2 in water we determine the beginning of the electrical explosion, t_3; beyond this point the current falls off sharply, and the voltage across the sample increases to its "peak" value at t_4 (Fig. 1). On the (R/R_0) (H) curves (curves II in Fig. 2, a-f), after the beginning of the explosion (R_3/R_0, H_3) we observe a rapid increase in R/R_0. The values of H_3 at this point, in contrast with the values H_4 at the voltage peak, are reproducible well from experiment to experiment for a given metal. We believe that the explosive destruction of the sample begins at t_3, but the oscillograms are continuous up to t_4 because of the discharge through the explosion products.

In the experiments carried out with arrangement No. 2 in air we observe a decrease in R/R_0 in the liquid-state region (Fig. 2, a-f), apparently due to the development of a surface discharge shunting the liquid sample. In this case the points t_3 and t_4 are not found from the oscillograms (Fig. 1).

Each of the curves shown in Fig. 2, a-f, is obtained by averaging the experimental data for six experiments; computer analysis of the oscillograms for each curve yields 250-300 points. The results found with arrangement No. 2 are shown in Fig. 2, a-f, only for the liquid-state region (curves II and III). In the case of pulse heating in water for Zr, Hf, Nb, and Mo (curves II in Fig. 2, a-e), there are no changes of any kind in the value of R/R_0 during the heating over a broad temperature range in the liquid state. For the solid state and for the melting region we show the experimental data obtained with arrangement No. 1 (curves I); these data are more accurate than those obtained with arrangement No. 2. The results found with the two experimental arrangements agree within the error corresponding to arrangement No. 2 over the ranges where the experiments overlap.

Within the experimental error we observe a tendency toward a decrease in the resistance of the liquid metal in the results found with arrangement No. 2 (curves I and II in Fig. 2, b-f); this decrease can be attributed to the higher magnetic pressure in the experiments carried out with this arrangement. The value of this pressure, averaged over

TABLE 1. Relative Resistance and Enthalpy of the Solid Phase (R_1/R_0, H_1) and Liquid Phase (R_2/R_0, H_2) of Zr, Hf, Nb, Mo, W, and Pt at the Melting Point and in the Liquid Phase at the Beginning of the Electrical Explosion (R_3/R_0, H_3)

Metal	μΩ·cm	$\frac{R_1}{R_0}$	$\frac{R_2}{R_0}$	$\frac{R_2}{R_1}$	$\frac{R_3}{R_0}$	H, kJ/mole			
						H_1	H_2	H_2-H_1	H_3
Zr	47.9	2.69	2.95	1.10	3.35	60.0	81.5	21.5 21.2 [8]	310
Hf	35.3	4.42	4.42	1.00	4.99	78.0	—	—	312
Nb	15.8	5.50	6.50	1.18	7.20	76.0 72.8 [1]	109.0	33.0	348
Mo	5.54	14.5	17.5	1.21 1.18 [10]	20.5	85.0 85.0 [1]	123.0	38.0 36.6 [9]	336
W	5.90	19.5	21.2	1.09 1.08 [10]	23.9	112.5	167.0	54.5 55.2 [10]	460
Pt	10.9	5.70	8.50	1.49 1.48 [10]	9.36	55.0 52.9 [7]	77.0 74.2 [7]	22.0 21.3 [7]	230

Note: Here ρ_0 is the resistivity at T = 298°K. The upper row for each metal shows the data of the present work.

the cross-section of the sample,[3] is no higher than 40 bar for arrangement No. 1 and no higher than 250 bar for arrangement No. 2.

Table 1 shows the values of R/R_0 and H found for the beginning (R_1/R_0, H_1) and end (R_2/R_0, H_2) of melting with arrangement No. 1, along with the values (R_3/R_0, H_3) corresponding to the beginning of the electrical explosion, obtained from the experiments in water with arrangement No. 2. The values R_1/R_0, H_1 and H_2 for Zr, Mo, and Pt agree with the results of experiments carried out by ordinary methods,[1,2,7-9] so that we have grounds for assuming that under these experimental conditions no significant shift of the melting point of these metals is observed and that the values obtained for these quantities are approximately equal to the equilibrium values. Our data on R_2/R_1 for Pt, Mo, and W and on the heat of melting H_2-H_1 for W agree with the results of pulsed measurements carried out by Lebedev et al.;[10] for Pt and Mo the values of H_2-H_1 from ref. 10 are slightly higher than our values.

Comparison of H_3 with the enthalpy H_{nb} corresponding to the normal boiling point of the liquid metal, T_{nb}, which is estimated in ref. 1, shows that $H_3 > H_{nb}$ for all the metals studied, i.e., for a prolonged heating of the liquid phase, for 10-15 μsec, corresponding to a heating rate of $5 \cdot 10^8$ deg/sec, we observe a significant elongation of the enthalpy range corresponding to the existence of the liquid phase (Fig. 2, a-f).

In additional to determining the data shown in Table 1 for Zr and Hf, we determine the values of R/R_0 and H corresponding to the beginning (R_α/R_0, H_α) and end (R_β/R_0, H_β) of the polymorphic transition. For Zr we find $H_\alpha = 30.5$, $H_\beta = 35.0$, and $H_\beta - H_\alpha = 4.5$ kJ/mole and $R_\alpha/R_0 = 2.82$, $R_\beta/R_0 = 2.36$, and $R_\beta/R_\alpha = 0.836$. For Hf we find $H_\alpha = 58.2$, $H_\beta = 63.4$, and $H_\beta - H_\alpha = 5.2$ kJ/mole and $R_\alpha/R_0 = 4.68$, $R_\beta/R_0 = 4.32$, and $R_\beta/R_\alpha = 0.923$. Comparison with data from the literature[1,11] on Zr, obtained in slow heating, shows that our values of H_α and H_β are higher by $\Delta H_{\alpha\beta} = 5.65$ kJ/mole, while the heat of the polymorphic transition, $H_\beta - H_\alpha$, agrees with the data of refs. 1 and 11. The discrepancy can be attributed to a superheating of the α phase above the phase-equilibrium temperature $T_{\alpha\beta}$. According to the value of $\Delta H_{\alpha\beta}$ and the specific heat of the α phase near $T_{\alpha\beta}$, this superheating is about $T_\alpha - T_{\alpha\beta} = 160$°K (the heating rate is about 10^7 deg/sec). Although we know of no other data for Hf, we would expect its behavior in the region of the α−β transition during pulsed heating to be analogous to that of Zr.

2. DISCUSSION OF RESULTS

Resistance of the liquid d-transition metals. Let us examine the change in the resistivity ρ of the liquid-transition metals during heating on the basis of the data (curves II in Fig. 2, a-f). We use the natural assumption, which has been confirmed experimentally,[14] that in our experiments the thermal expansion of the sample in the solid state occurs in both the radial and axial directions, while that during melting and during the liquid of the heating occurs in the radial direction. Then using the standard equation $R = \rho l/s$, we find the relation between ρ and R/R_0 for the liquid metal to be

$$\rho = \rho_0 \frac{1+2\gamma}{1+\gamma} \frac{R}{R_0} \left(1 + \frac{\Delta V_{me}}{V_1} + \frac{\Delta V_L}{V_1}\right). \tag{1}$$

where $\gamma = \Delta l_1/l_0$ is the relative elongation of the sample during its heating from $T_0 = 298$°K to $T = T_1 = T_2 = T_{me}$, $\Delta V_{me}/V_1$ is the relative change in the volume of the sample during its melting, $\Delta V_{em}/V_1$ is the relative change in the volume of the liquid metal as it is heated from T_2 to T, and ρ_0 refers to $T_0 = 298$°K. It follows from Eq. (1) that over the range in which R/R_0 is constant the value of ρ is governed solely by the thermal expansion of the metal

TABLE 2. Melting Point T_2, Normal Boiling Point T_{nb}, and Critical Parameters T_k and p_k for Zr, Nb, Mo, W, and Pt

Metal	T_2 [1], °K	T_{nb} [1], °K	$T_3 = T_k$ °K	p_k, atm
Zr	2125	4688	8950	1480
Hf	2500	—	—	—
Nb	2740	5007	9880	3240
Mo	2890	4924	7990	270
W	3650	5890	11880	6030
Pt	2043	4097	6450	250

$\Delta V_{em}/V_1$, and that the temperature coefficient of the resistance, $\alpha = d\rho/(\rho_0 dT)$, is directly proportional to the bulk expansion coefficient $\beta \doteq dV_{em}/(V_1 dT)$:

$$\alpha = \frac{1+2\gamma}{1+\gamma}\frac{R}{R_0}\beta. \tag{2}$$

This behavior is observed over a broad temperature range, about 5000°K, for Zr, Hf, Mo, and Nb (Fig. 2, a–e). There are apparently two possible explanations for this effect: (1) The scattering cross-section for conduction electrons for these metals does not change as a function of T in the liquid state of these metals, and ρ is governed solely by the number of atoms per unit volume; (2) the scattering cross-section varies as a function of T, so that there should be a change in ρ. However, some other process, e.g., a change in the concentration of conduction electrons occurs simultaneously in the metal and acts to offset this change in the scattering cross-section. The behavior of the liquid d-transition metals described by Eq. (2) must be taken into account in theories for their electrical conductivity.

Estimate of the critical parameters. We turn now to the possibility of estimating the critical temperature T_k and the critical pressure p_k for these metals on the basis of the experimental data obtained here for H_2 and H_3. Martynyuk[4] specifies conditions under which the beginning of the electrical explosion, T_3, lies near the cusp point T_c, at which the liquid phase becomes thermodynamically unstable. At the cusp points the average kinetic energy corresponding to the thermal motion of atoms is so large that these atoms can overcome the attractive forces acting between atoms in the condensed state. Experimental data on the cusp points for several organic liquids,[12] plotted as p/p_k vs T/T_k (where p is the pressure), can be approximated by

$$\frac{p_c}{p_k} = \frac{10T_c}{T_k} - 9, \tag{3}$$

which ends at the critical point. The continuation of the cusp and of the phase-equilibrium curve beyond the critical point is the transcritical-transition curve.[13] Thermodynamic-similarity conditions are satisfied for the cusps of various liquids,[4] so that we can apparently apply Eq. (3) to liquid metals. For electrical explosions in air we have $p_c = p_{at} = 1$ atm $\ll p_k$ and thus, according to (3), $T_k = (10/9)T_c \approx (10/9)T_3$. For electrical explosions in water, the sample is surrounded by a thin film of dense water vapor, which exerts a significant but unknown pressure on the surface of the sample. However, since, according to (3), T_c is a weak function of p, we do not make a large error in our estimate of T_k in this case if we assume that we have $p = p_c = p_k$ at the beginning of the electrical explosion; then from (3) we find $T_k = T_c = T_3$. We can estimate T_3 from the data on $H_3 - H_2$ and from data in the literature[1,7] on the specific heat of the liquid metal, C_2, near the melting point, T_2; we thus write

$$T_k \approx T_3 = T_2 + \frac{H_3 - H_2}{C_2}. \tag{4}$$

The values found for T_k in this manner are shown for the various metals in Table 2.

To estimate the critical pressures for these metals we used data on the saturation vapor pressure as a function of the temperature, given in ref. 1 for pressures up to p = 1 atm. These data are plotted as log p vs 1/T and extrapolated linearly to the values which we have found for T_k. The results of these estimates of p_k are shown in Table 2. Our calculations show that the highest critical parameters are those of tungsten, for which we find $T_k = 1.2 \cdot 10^4$°K and $p_k = 6$ kbar.

---

[1] R. Hultgren, R. L. Orr, R. D. Anderson, and K. K. Keley, Selected Values of Thermodynamic Properties of Metals and Alloys, Wiley, New York (1963).

[2] Y. S. Touloukian (ed.), Thermophysical Properties of High Temperature Solid Materials, Macmillan, New York (1967).

[3] M. M. Martynyuk and G. E. Gerrero. Zh. Tekh. Fiz., 42, 187 (1972) [Sov. Phys. – Tech. Phys., 17, 148 (1972)].

[4] M. M. Martynyuk, Zh. Tekh. Fiz., 44, 1262 (1974) [Sov. Phys. – Tech. Phys., 19, 793 (1974)].

[5] M. M. Martynyuk and I. Karimkhodzhaev, Dokl. Akad. Nauk TadzhSSR, 14, No. 8, 14 (1971).

[6] J. H. Park, J. Res. National Bureau of Standards, 39, No. 3, 191 (1947).

[7] O. Vollmer, Die Speciefische Warme von Rhodium, Palladium und Platin in Bereich hoher Temperaturen, Köln (1971).

[8] V. P. Elyutin, M. A. Maurakh, and G. M. Sverdlov, Izv. VUZOV Tsvetnaya Metallurgiya, No. 2, 87 (1967).

[9] B. Ya. Berezin, V. Ya. Chekhovskoi, and A. E. Sheindlin, High Temperature-High Pressure, 3, No. 3, 287 (1971).

[10] S. V. Lebedev, A. I. Savvatimskii, and Yu. B. Smirnov, Teplofiz. Vys. Temp., 9, 635 (1971).

[11] O. Vollmer, M. Braun, and R. Kohlhaas, Z. Naturforsch., 22a, 833 (1967).

[12] V. P. Skripov, Metastable Liquids [in Russian], Izd. Nauka, Moscow (1972).

[13] M. M. Martynyuk and N. F. Ganzhela, Izv. VUZ. Fiz., No. 3, 30 (1970).

[14] V. M. Kul'gavchuk and G. A. Novoskol'tseva, Zh. Tekh. Fiz., 36, 549 (1966) [Sov. Phys. – Tech. Phys., 11, 406 (1966)].

Electronics

Ion-optical system for shaping high-current ion beams

S. D. Grishin, V. F. Kuzovlev, R. V. Orlov, and S. N. Ogorodnikov

(Submitted November 26, 1973)
Zh. Tekh. Fiz., 44, 2374-2377 (November 1974)

A description is given of an ion-optical system capable of shaping high-current hydrogen-ion beams (up to 100 A). Its characteristics are discussed.

At the present time there is a need for high-current ion beams of high average density.[1] A beam of Cs ions with a current of 15.7 A and an average density < 1 mA/cm^2 has been shaped by using an ion-optical slit system.[2] It turns out to be difficult to increase the density because of the severe misalignment of the electrodes caused by thermal distortion. For this reason, an ion-optical slit system cannot be used to shape beams of heavy ions such as Hg, Bi, Pb, etc., with a current of tens of amperes and densities of a few tens of mA/cm^2.

We present here the characteristics of an ion-optical system capable of shaping a high-current beam of heavy ions (20-30 A) with an average density of 25-30 mA/cm^2.

2. The construction of the ion-optical system is shown in Fig. 1. The shaping 1, accelerating 2, and decelerating electrodes 3, are each formed of a flat grid of metal rods fastened at their ends to quartz supports 4, 5, 6. The rods of the accelerating and decelerating electrodes are fastened to their quartz supports with metal clips 7 so arranged that as they heat up they can stretch. This avoids mechanical stresses in the quartz and ensures electrical contact between the electrode rods and the potential source. The grooves in the quartz supports are 20-40 mm long and serve to fasten the electrodes and as high-voltage insulation. The shaping electrode is fastened and adjusted by tightening holder 4 by screws 8 to the front cover of the discharge chamber 9, and by screws 10 through the springs to the surface of the adjusting plate 11. Thus, the electrode rods are in direct contact with the discharge chamber 9. The accelerating and decelerating electrodes are fastened and adjusted in the same way as the shaping electrode except that the ends of their quartz supports are clamped to the cover of the discharge chamber through appropriate bushings 12 or 13, ensuring a gap between the electrodes. Since the grooves in the quartz supports are cut simultaneously, their clamping by screws 10 to one adjusting plate ensures reliable adjustment of the electrodes (alignment of slits). The decelerating and accelerating electrodes are made of tungsten rods 2 mm in diameter, and in three variants of the system the shaping electrodes are made of 2, 1, and 0.5 mm diameter rods on a 4 mm pitch. The 1 and 0.5 mm diameter rods are fastened with individual springs. The accelerating gap, i.e., the distance between the shaping and accelerating electrodes, is 2 mm in the first variant and 2.5 mm in the second and third. The maximum useful length of the rods which can be utilized by the beam is 150 mm. The width of the electrodes measured across the rods, or the useful length of the quartz supports, is also 150 mm, and is determined by the dimensions of the ion source. Thus the maximum cross sectional area of the beam can be 225 cm^2.

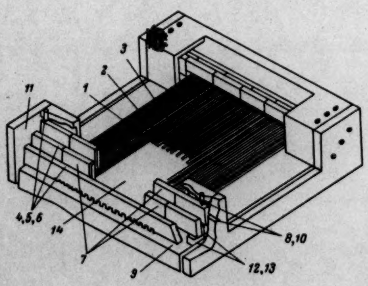

Fig. 1. Ion-optical system.

3. The characteristics of the ion-optical system developed have been investigated together with those of a Bi plasma ion source.

In the shaping of an ion beam from a solid emitter the focusing can be characterized by the dimensionless parameter

$$\gamma=\sqrt{\frac{2e}{\mu}}\frac{U^{3/2}}{d_0^2 j}, \qquad (1)$$

which is a similarity parameter that defines the shape of the beam. Here, U is the accelerating potential, d_0 is the width of the accelerating gap, j is the local beam current density, and e and μ are respectively the charge and mass of the ion. In shaping a beam from the plasma the parameter γ defined by (1) cannot generally be considered a similarity parameter since the emitting surface changes its position and shape with the plasma parameters in the ion source, e.g., the electron temperature. However, with certain restrictions γ can be regarded as a similarity parameter in this case.[3] A theoretical consideration shows that these restrictions reduce to the condition

$$U \geqslant 1.5\cdot 10^3 T_{e\,\max}, \qquad (2)$$

where $T_{e\max}$ is the maximum temperature of the plasma electrons in volts. The validity of condition (2) has been confirmed experimentally.

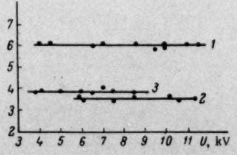

Fig. 2. γ_0 as a function of the accelerating potential.

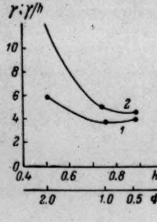

Fig. 3. γ_0 and γ_0/h as functions of the geometrical transmittance of the shaping electrode h.

The experiments are performed with an ion source in which T_e is maintained at 2-3 V. Then condition (2) gives a design value U = 3-4.5 kV.

Curves 1, 2, and 3 of Fig. 2 show the optimum value of γ_0 (best focusing, minimum angle of divergence of the beam) as a function of the accelerating potential for three variants of the ion-optical system. In this case the current density is not constant. The curves show that for the ion-optical systems under consideration γ_0 hardly changes as U varies from 4.5 to 14 kV, which is in good agreement with the calculated value of U, and indicates the validity of the similarity relation.

Thus, under our conditions for $U \geq 4.5$ kV the extraction of a beam from the plasma is described by the similarity relation (1), valid for beams formed from solid emitters, and γ can, in practice, be considered a similarity parameter. In this case knowing γ_0 makes it possible to determine the optimum value of the accelerating potential for specified densities, and to calculate the optimum parameters of geometrically similar structures for any working materials. A second parameter characterizing the ion-optical system is the geometrical transmittance of the shaping electrode:

$$h=\frac{a-\Phi}{a}, \qquad (3)$$

where Φ is the diameter of an electrode rod, and a is the pitch, in our case 4 mm.

Curve 1 of Fig. 3 shows γ_0 as a function of h. It is clear from this curve that as h increases (the diameter decreases) γ_0 at first decreases, reaches a minimum, and then increases. When γ_0 is a minimum the local density of the ion beam is a maximum. According to Eqs. (1) and (3) the reciprocal of γ_0/h characterizes the average current density of the beam or the total beam current. Curve 2 of Fig. 3 shows γ_0/h as a function of h. γ_0/h varies more rapidly than γ_0, but its minimum is smoothed. Beginning with h = 0.75, as h increases γ_0/h varies slowly and reaches a value of about 4.2. According to curve 1, if the local current density (emission density) is doubled, the average beam current density and the total beam current are tripled as h increases from 0.5 to 0.75.

Experiments show that in the forming of a beam from the plasma an increase in the accelerating potential increases the beam current in spite of the fact that the parameters of the plasma in the ion source and the flow through the optical system remain unchanged. The current increases because the plasma density on the boundary (on the meniscus) from which the acceleration of the ions occurs increases with the deepening of the meniscus in the slit of the shaping electrode with an increase in the accelerating potential. The plasma density at the meniscus is determined, on the one hand, by the entrance of ions from the source into the slit of the shaping electrode, and, on the other, by the neutralization of a part of the entering ions at the lateral walls of the slit of the shaping electrode adjoining the plasma and the subsequent emergence from the ion-optical system of part of the neutrals formed.

Figure 4 shows the ratio of the beam current $J(\gamma)$ for arbitrary focusing to the beam current $J(\gamma_0)$ for optimum focusing as a function of γ/γ_0 (proportional to $U^{3/2}$) for constant parameters of the plasma in the ion source. Curves 1 and 2 are for shaping electrodes 2 and 0.5 mm in diameter having geometric transmittances of 0.5 and 0.875 respectively. Figure 4 shows that the beam current increases as γ increases (as U increases), which agrees with the above point of view. The rate of increase of the current decreases with decreasing diameter of the electrode rods (curves 1, 2), which is accounted for by the decrease in the relative thickness of the electrode and the relative area of neutralization of the ions, which is proportional to the ratio of the diameter of a rod to the grid pitch. From this point of view the optimum shaping electrode is made of thin films. Curve 3 in Fig. 4 characterizes the variation of the beam current for a shaping electrode having a transmittance h = 0.5 made of square rods. The fact that curve 3 is steeper than curve 1 (h = 0.5) indicates the relatively larger yield of neutrals from a given ion-optical system for the same discharge and is explained by the fact that for curve 1 the surface of neutralization of plasma ions is largely changed in the discharge chamber. Also from this point of view the optical system with a shaping electrode made of foil is optimum because of the relatively small yield of neutrals.

Thus the beam current is a maximum for minimum γ_0 and a shaping electrode with a transmittance $h \approx 0.75$ and a thickness small in comparison with the slit size (ribbon electrode), all other conditions remaining the same.

4. The experimental investigations of the device have been carried out over several years and show that it is reliable. It has been subject to extended use and the electrodes have remained in good adjustment under all operating conditions. This ion-optical system has been used to

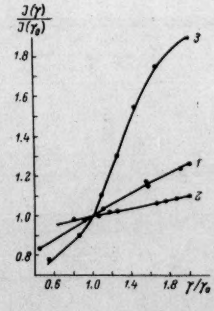

Fig. 4. Relative beam current as a function of γ/γ_0.

shape a 2.0 A beam of Bi ions ~100 cm^2 in cross section, limited by the dimensions of the ion source.

Our results are used to produce an ion-optical system for shaping ion beams with currents of tens of amperes (20-30 A for heavy ions) with a cross sectional area of 10^3 cm^2. In addition the results described here can be used to develop ion-optical systems capable of shaping hydrogen ion beams with currents up to 100 A and average densities of hundreds of mA/cm^2.

---

[1] N. N. Semashko, Proc. of the Second All-Union Conference on Plasma Accelerators [in Russian], Minsk (1973), p. 186.

[2] S. Nakanishi, J. Spacecraft and Rockets, 5, 801 (1968).

[3] V. I. Raiko, Zh. Tekh. Fiz., 33, 244 (1963) [Sov. Phys. – Tech. Phys., 8, 175 (1963)].

Elimination of carbon impurities from platinum by heating in an oxygen atmosphere

L. P. Rekova, V. V. Mozgin, L. N. Zvyagintseva, V. N. Bondarenko, and Ya. M. Fogel'

Physicotechnical Institute,
Academy of Sciences of the Ukrainian SSR, Khar'kov

(Submitted July 4, 1973; resubmitted December 14, 1973)
Zh. Tekh. Fiz., 44, 2378-2382 (November 1974)

Secondary ion–ion emission is used to investigate the process by which platinum is cleansed of carbon impurities when it is heated in an oxygen atmosphere. The carbon contamination of the surface of platinum affects the way in which oxygen acts on the thermal emission current of alkali-metal ions.

INTRODUCTION

Contamination of metal surfaces by carbon atoms markedly affects processes that take place on these surfaces.[1-6] Carbon can be eliminated from these surfaces by heating in a rarefied-gas atmosphere whose molecules form chemical compounds with carbon that can be readily desorbed from the metal surface.[6,7]

In our study the cleansing of heated platinum in an oxygen atmosphere is studied by the method of secondary ion–ion emission.[8] These results, as well as those of certain experiments that establish the effect of a carbon coating on the behavior of the thermal emission current of Na^+ and K^+ ions when oxygen acts on platinum,1) comprise the principal focus of our study.

APPARATUS AND MEASUREMENT PROCEDURE

To investigate cleansing of volume impurities from metals, we set up the mass-spectrometer device shown in Fig. 1. In designing it, we have provided for monitoring the coating of the metal surface by impurity particles using the emission current of secondary ions. Secondary ions are ejected from the surface of the metal under study by bombarding the target with Kr^+ ions at an energy of 4 keV and current density of $5 \cdot 10^{-6}$ A/cm^2. To create the beam of Kr^+ ions we use the gas ion source of the MI-1305 (1) mass spectrometer, into which krypton is admitted at a pressure of $4 \cdot 10^{-5}$ mm Hg. To reduce the krypton pressure in chamber 2, where the target 3 is located, the ion source is isolated from the chamber by a system of three slits 4.

Secondary ions ejected from the target surface are formed into a 2 keV beam by using a four-electrode electrostatic lens 5. By appropriate choice of the electrode potentials of the lens the beam of secondary ions is focused onto the input slit 6 of magnetic mass spectrometer 7. The secondary ions thus separated according to mass-to-charge ratio are incident on the first diode of secondary electron multiplier 8. The output current of the multiplier is amplified by a U1-2 dc amplifier. The sensitivity of the secondary ion detection device is $\sim 1 \cdot 10^{-17}$ A/div.

For an additional check on the cleansing process on the basis of the flux of impurity particles or molecular compounds evaporated from the surface, the device is furnished with Pierce electron gun 9. The electron gun is attached to the wall of the first electrode of the ion lens and creates a plane electron beam at a current of ~300 mA and an energy of 300 eV that passes the target surface at a distance of 3 mm. Particles evaporated from the target surface are ionized by the electrons, and the resultant ions are formed into a beam, analyzed, and detected by the same devices used for secondary ions. When

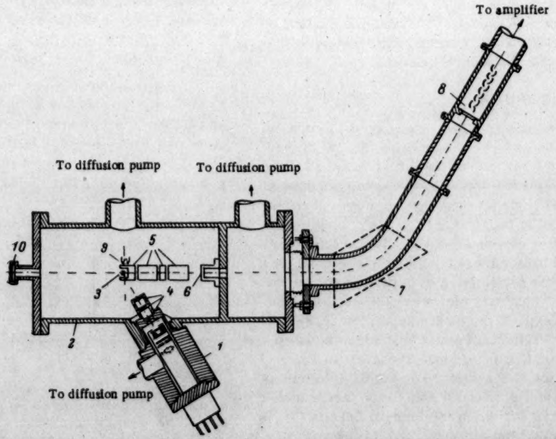

Fig. 1. Cross section of experimental arrangement.

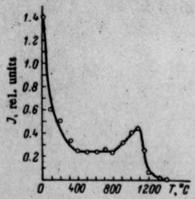

Fig. 2. J(T) for secondary C_2^- ions, for a platinum strip in residual-gas atmosphere.

the ion and electron guns are switched off we observe emission of some impurity particles that are readily ionized in the process of surface ionization (thermionic emission of the alkali metals Mg, Ca, Al, Ba).

The vacuum in the device is created by three DRN-50 mercury diffusion pumps which pump the target chamber, the mass spectrometer, and the ion gun. A carbon adsorption pump is used as a forepump. Mercury vapor is frozen out by three liquid-nitrogen-cooled traps. The limiting pressure in the target chamber is $2 \cdot 10^{-6}$ mm Hg.

Strips with dimensions 35 × 6 × 0.05 mm fabricated from commercially pure platinum (99.93%) are used as targets. These are heated by alternating current. The temperature of the strips in the 900-1400°C interval is measured by an optical pyrometer through quartz window 10. The temperature over the entire interval investigated, 20-1400°C, is measured by a Pt−PtRh thermocouple.

After boiling in alkali and then in distilled water, the platinum strips are inserted into the target chamber. The experiments are performed after the strips are vacuum-annealed at 1300°C for several hours.

In accordance with the data of refs. 5-7, it is established through preliminary experiments that the degree to which the surface of the strip is covered by particles of free carbon can be characterized by the emission current of secondary C^- and C_2^- ions. The basic data on cleansing of platinum from carbon impurities are obtained by investigating the functions J(t) and J(T) (J being the current of the beam of secondary C^- or C_2^- ions, t the isothermic annealing time, and T the strip temperature).

EXPERIMENTAL RESULTS

We first investigate J(T) for secondary C_2^- ions when the strip is in a residual-gas atmosphere (Fig. 2). The sharp drop in the C_2^- current on the initial segment of the curve results from desorption of hydrocarbon molecules from the surface of the strip. The behavior of $J_{C_2^-}(T)$ above 400°C results from the fact that, as the strip temperature increases, the flux of carbon atoms that diffuse from within the strip to its surface increases, on the one hand, and, on the other, the rate of oxidation of carbon on the surface by oxygen in the residual gas increases. These two factors can evidently explain the maximum on the $J_{C_2^-}(T)$ curve in the 1100°C region. We note that when the strip is heated above 1400°C it is no longer possible to detect carbon contamination of the surface on the basis of emission of C_2^- ions. This is evidently due to the fact that the rate of elimination of carbon in the form of CO and CO_2 is high at these elevated temperatures, and this results in a carbon coating that is so small that it can no longer be detected from C_2^- emission.

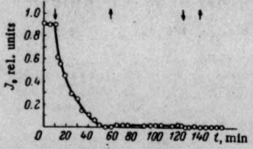

Fig. 3. J(t) for secondary C^- ions; platinum strips in oxygen atmosphere; strip temperature 1200°C. Downward arrows denote admission of oxygen upward arrows indicate oxygen valve shut off.

Experiments involving annealing of platinum strips in an oxygen atmosphere yield markedly different results. The annealing is performed at 1200°C, when the rate of carbon oxidation is fairly high (curve on Fig. 2), and with an oxygen pressure of $1.5 \cdot 10^{-5}$ mm Hg. The $I_{C^-}(T)$ curve characterizing this experiment is shown in Fig. 3. As can be seen from this figure, the C^- ion current drops monotonically immediately after the oxygen is admitted into the chamber; after about 50 min it becomes so small that it cannot be measured. Evacuation of oxygen from the chamber results in the appearance of a small C^- ion current which disappears when oxygen is again admitted, and does not return when oxygen is again pumped out.[2)] When the strip is cooled to room temperature, emission of secondary C^- and C_2^- ions is not observed. From this we can conclude the following: 1) The partial pressure of hydrocarbon vapor in the target chamber is small; 2) annealing the strips in an oxygen atmosphere results in virtually complete elimination of carbon contamination from the surface.

It was pointed out in the introduction that carbon contamination of metal surfaces affects the processes that occur on these surfaces. In this study we observe the effect of carbon contamination of platinum surfaces on the way in which oxygen affects the thermal emission current of alkali-metal ions.[9,10] This can be judged by considering Fig. 4, from which we see the variation in thermal emission current of K^+ ions when oxygen is admitted into a chamber containing a heated platinum strip.

The presence of carbon on the surface of a strip at 1100°C is established from the emission of secondary C^- and C_2^- ions. Admission of oxygen at $1 \cdot 10^{-5}$ mm Hg results in a rapid increase in the K^+ current, which then promptly begins to drop off and reaches a constant value in about an hour. After the oxygen is evacuated, we mea-

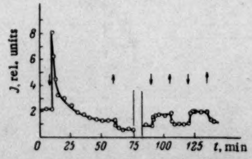

Fig. 4. J(t) for thermal emission current of K^+ ions; platinum emitter temperature 1100°C; downward arrows denote admission of oxygen, upward arrows indicate oxygen valve shut off. Emission currents of secondary C^- and C_2^- ions are measured during the time interval indicated by the discontinuity.

sure the emission currents for C^- and C_2^-. It turns out that these currents are so small they cannot be measured, indicating that the platinum surface has been cleansed of carbon contamination. Admission of oxygen a second time, after the platinum surface is already cleansed, also causes the K^+ current to increase, but the behavior of this current in time differs markedly from what was observed in the first instance. The sharp spike in the K^+ current which is observed when oxygen acts on a carbon-contaminated platinum surface is absent when the surface has already been cleansed. This has been repeated with many platinum strips and, without exception, all cases yield the same qualitative results.

We have also conducted experiments in reverse order on the effect of oxygen on the thermal emission current of K^+ from platinum emitters contaminated by carbon and emitters that had been cleansed of it. First the platinum strip is cleansed, as indicated above, of carbon impurities, and then we observe the behavior of the K^+ current when oxygen is admitted and evacuated. The behavior of this current is the same as in the case of carbon-cleansed platinum (right side of Fig. 4). If we now admit benzene vapor into the emitter chamber after oxygen has been evacuated, pyrolysis of benzene molecules on the heated surface causes a carbon coating to appear there. The presence of this coating is established from the appearance of an emission current of secondary C^- and C_2^- ions. After evacuation of bezene vapor and admission of oxygen, we observe the spikes in the K^+ thermal emission current that are typical of carbon-contaminated platinum.

In conclusion, we can express some preliminary considerations regarding the spike in the K^+ thermal emission current when oxygen acts on a carbon-contaminated platinum strip. As is shown in refs. 9 and 11, the influence of gases on the thermal emission current of alkali-metal ions involves volume impurities of alkali metals that arrive at the surface of the emitter under study through dislocation. Diffusion of carbon atoms onto the emitter surface can also take place through dislocation, but, in view of its low vaporizability, carbon that has diffused from within the emitter can collect near the point where the dislocations emerge onto the surface and thus block the evaporation of alkali-metal ions to some extent. When oxygen is admitted into the emitter chamber, the carbon that has collected around these points is eliminated, and this causes the spike in the alkali-metal ion current. When platinum surfaces are contaminated by pyrolysis of benzene molecules, the carbon may be preferentially deposited around the dislocation points, as is the case, e.g., in the formation of oxide centers when nickel is oxidized.[12] Elimination of this carbon when oxygen is allowed to act on a heated platinum strip can also result in the spike in the K^+ current, and this is in fact observed.

---

[1] Data on this effect are to be found in refs. 9 and 10.

[2] It is possible that a small diffusion flux of carbon atoms onto the surface of the strip still exists in this stage, but the resultant contamination of the surface by carbon is eliminated because oxygen in the residual gas oxidizes the carbon.

---

[1] É. Ya. Zandberg, A. Ya. Tontegode, and F. K. Yusifov, Zh. Tekh. Fiz., 41, 2420 (1971) [Sov. Phys.-Tech. Phys., 16, 1920 (1972)].

[2] É. Ya. Zandberg and A. Ya. Tontegode, Zh. Tekh. Fiz., 38, 737 (1968) [Sov. Phys.-Tech. Phys., 13, 550 (1968)].

[3] D. J. Fabian and A. J. B. Robertson, Proc. R. Soc. A, 235, 1 (1956).

[4] L. O. Apel'baum and M. I. Temkin, Zh. Fiz. Khim., 33, 2697 (1959).

[5] Ya. M. Fogel', B. T. Nadykto, V. F. Rybalko, R. P. Slabospitskii, I. E. Korobchanskaya, and V. I. Shvachko, Kinet. Katal., 5, 154 (1964).

[6] V. Ya. Kolot, V. I. Tatus', V. F. Rybalko, and Ya. M. Fogel', Ukr. Fiz. Zh., 15, 278 (1970).

[7] V. Ya. Kolot, V. I. Tatus', V. V. Vodolazhchenko, V. F. Rybalko, A. E. Grodshtein, N. D. Kirsanov, and Ya. M. Fogel', Zh. Tekh. Fiz., 42, 144 (1972) [Sov. Phys.-Tech. Phys., 17, 111 (1972)].

[8] Ya. M. Fogel, Int. J. Mass Spectrom. Ion. Phys., 9, 109 (1972).

[9] L. P. Rekova and Ya. M. Fogel', Zh. Tekh. Fiz., 38, 1980 (1968) [Sov. Phys.-Tech. Phys., 13, 1588 (1969)].

[10] L. P. Rekova and Ya. M. Fogel', Metallofizika, 29, 63 (1970).

[11] L. P. Rekova, Ya. M. Fogel', and L. V. Nesterov, Fiz. Tverd. Tela, 11, 1891 (1969) [Sov. Phys.-Solid State, 11, 1524 (1970)].

[12] L. P. Rekova, V. V. Mozgin, O. V. Kisel', and Ya. M. Fogel', Fiz. Tverd. Tela, 14, 2265 (1972) [Sov. Phys.-Solid State, 14, 1961 (1973)].

Radiation yield of ions in liquid dielectrics as a function of temperature and radiation energy

V. I. Ivanov, E. D. Kleshchenko, Yu. P. Sukhanovskii, and V. V. Frolov

Moscow Engineering Physics Institute

(Submitted July 16, 1973; resubmitted February 27, 1974)
Zh. Tekh. Fiz., 44, 2383-2387 (November 1974)

The Onsager theory is used to obtain the ion radiation yield G as a function of E the energy of the ionizing radiation and the temperature T in analytic form: $G(E, T) = aT \exp[-b(E)/T]$, where $b(E) = c_1[c_2E - \sqrt{c_2E}]^{-1}$; a, c_1, and c_2 are constants. The radiation yield of ions in hexane at T = 217-333°K is measured. The theoretical and experimental functions $G = G(T)$ are in satisfactory agreement, while the temperature dependence of the slope of the volt–ampere characteristic confirms the hypothesis.

INTRODUCTION

There have been many investigations of conduction in liquid dielectrics,[1–4] but as yet there is no unified opinion about the conduction mechanism in such media. In our view, the soundest theory is that developed by Onsager,[5] which takes account of initial or preferential recombination. According to this theory, an electron liberated by ionization can recombine with the parent ion through Coulomb attraction. The probability φ_0 that the electron will avoid such recombination, according to Onsager, is given by the expression

$$\varphi_0 = \exp\left[-\frac{r_k}{r}\right], \tag{1}$$

where r is the distance between the electron and the parent ion at thermalization, r_k is found from the expression $e^2/\omega r_k = kT$, e is the charge of the electron, ω is the permittivity, k is Boltzmann's constant, and T is the temperature of the medium.

A similar process occurs in gases as well, but since the distance r is large, initial recombination is not a factor in gases. Electrons which avoid initial recombination form negative ions which diffuse from the formation site into the liquid and are involved in volume recombination, as in gases.

Jahns and Jacobi[6] use this fact to derive the equation for the volt–ampere characteristic of an ionization chamber filled with a liquid dielectric. They set r = const and determine this parameter from the condition that the experimental and theoretical volt–ampere characteristics should agree. Other authors[1–7] also use parameters which are determined on the basis of such comparisons, a procedure which is not entirely correct.[8]

1. THEORETICAL

In this study we propose an explanation for certain phenomena that occur in liquid dielectrics on the basis of Onsager's theory,[5] using only parameters which can be determined independently.

We take $r = r(E_e)$ in (1), where E_e is the energy of an electron that has been liberated by ionization (the energy of a secondary electron). The probability that the electron will avoid initial recombination, as averaged over the spectrum of secondary electrons, is

$$\bar{\varphi}_0 = \frac{\int\limits_{E_e} n(E_e)\exp\left[-\frac{r_k}{r(E_e)}\right]dE_e}{\int\limits_{E_e} n(E_e)\,dE_e}, \tag{2}$$

where $n(E_e)dE_e = N\sigma(E, E_e)dE_e$ in (1), is the number of secondary electrons whose energy lies in the interval E_e–$E_e + dE_e$, generated by one ionizing particle with energy E; N is the number of molecules per unit volume of liquid and $\sigma(E, E_e)$ is the differential ionization cross section.

The basic difficulties in computing $\bar{\varphi}_0$ are associated with the determination of $r = r(E_e)$. In the $E_e > 10$ keV region we have $r(E_e) \gg r_k$ and $\exp[-r_k/r(E_e)]$ is equal to unity. In this case the exact form of $r(E_e)$ is unimportant. For $E_e = 0.3$–10 keV the function can be described by a relation of the form[9]

$$r = \eta E_e, \tag{3}$$

where η = const. For $E_e \le 0.3$ keV, however, where the form of the function is important since $r(E_e) \le r_k$, we must employ various types of extrapolations[9,10] because of the lack of experimental and theoretical data. To obtain an expression for $\bar{\varphi}_0$ in a form that is convenient for analysis we extrapolate $r(E_e)$ using function (3) for $E_e = 0$.

In conformity with the expression for the differential ionization cross section obtained by Garcia,[11] the numerator and denominator in (2) can be written as the sum of four terms, each of which has the following form: For the numerator $I_i = \int\limits_{\Delta E_e^i} N\sigma_i(E, E_e)\exp[-r_k/r(E_e)]dE_e$ and for the denominator $J_i = \int\limits_{\Delta E_e^i} N\sigma_i(E, E_e)dE_e$, where ΔE_e^i is the interval of secondary-electron energy in which the ionization cross section is determined by the function $\sigma_i(E, E_e)$. Equation (2) becomes simplest when the ionizing particle is an electron. In this case all the terms except the first are zero. We can also show that for protons with $E_p > 0.5$ MeV that $I_1/I_2 < 5 \cdot 10^{-2}$ and $J_1/J_2 < 10^{-2}$. Substituting the value of r from (3) into (2) and using the expression for the ionization cross section from ref. 11 for $\bar{\varphi}_0$, we obtain

$$\bar{\varphi}_0 = aT \exp\left[-\frac{b(E)}{T}\right], \tag{4}$$

where $a = 7\omega k/5e^2$, $b(E) = e^2[4\eta u\omega k(\lambda E/u - \sqrt{\lambda E/u})]^{-1}$, λ is the ratio of the electron mass m_e to that of the ionizing particle m, u is the binding energy of the electron in the molecule.

In integrating we use the change of variable

$$x = \left[1 + \frac{1}{4}\left(\frac{\lambda E}{u} - \sqrt{\frac{\lambda E}{u}}\right)\right]\frac{r_k}{\eta u}$$

and the expression

$$Ei(-x) = -\frac{e^{-x}}{x}\left(1 - \frac{1}{x}\right),$$

which is valid[12] for $x > 2$.

Strictly speaking, in computing $\bar{\varphi}_0$ we should allow for δ electrons of subsequent generations, and this makes the computations much more difficult. The nature of the dependence of $\bar{\varphi}_0$ on E and T remains virtually unchanged in this case.

In an external electric field $\mathcal{E}$ the probability that an electron will avoid initial recombination increases[5] in accordance with the expression

$$\varphi(\mathcal{E}, E, T) = \varphi_0(E, T)\left(1 + \frac{\mathcal{E}e^3}{2\omega k^2 T^2}\right). \tag{5}$$

Following Jahns and Jacobi,[6] for fields in which diffusion and volume recombination are negligible ($\mathcal{E} > 1$-2 kV/cm), we can obtain the equation of the volt–ampere characteristic of an ionization chamber field with liquid dielectrics in the form

$$i(\mathcal{E}, E, T) = \frac{ePV}{w}\varphi(\mathcal{E}, E, T), \tag{6}$$

where i is the ionization current through the chamber, P is the dose rate, V is the sensitized volume of the chamber, and w is the energy of formation of a pair of ions for the type of vapor involved.

The probability $\bar{\varphi}$ that an electron will avoid initial recombination (or the proportion of electrons that result in the ionization current through the chamber) is analogous to the efficiency of ion collection in gas chambers. Unlike gases, in fluids we have $\varphi \ll 1$ and this increases with the field up to field strengths corresponding to electrical breakdown.

In radiation chemistry and radiobiology it is of practical importance to know the ion radiation yield G, this being related to the efficiency of ion collection $\bar{\varphi}$ by the simple expression

$$G(\mathcal{E}, E, T) = \frac{100}{w}\varphi(\mathcal{E}, E, T). \tag{7}$$

The radiation yield can be determined directly from the volt–ampere characteristic.

Figure 1 shows G = G(O, E = const, T) as computed from (4) and (7) for electron-ionized hexane. For small b(E) in (4) the temperature dependence of the radiation yield can be written in the form

$$G(T) = A(T - T_0), \tag{8}$$

where A is a dimensional constant and T_0 = const, which is in qualitative agreement with the measurement results.

Figure 2 shows G = G(O, E, T = const) as determined from (4) and (7). A comparison of G = G(E) with the experimental data is valid only if we allow for the energy variation of the ionizing particle along the track, this being determined by the specific experimental conditions. The results in Fig. 2 are obtained for the case of complete electron absorption in hexane. We should note that since the energy appears in (4) in the form of the dimensionless parameter $\lambda E/u$, the results given in Figs. 1 and 2 are valid for any charged particles.

The authors are unaware of systematic data on the function G = G(E); scattered reports of conduction measurements for liquid paraffins acted on by radiation at various energy levels are unsuited for comparisons with one another and with theory because of the absence of a complete description of the specific experimental conditions.

2. EXPERIMENTAL

We have investigated experimentally the conductivity of liquid dielectrics at various temperatures. We use a plane-parallel ionization chamber, whose design is such that we can measure the distance between electrodes from 0 to 20 mm to within 0.05 mm. The body of the chamber is 60 mm in diameter and 3 mm thick and is fabricated from polyethylene of a tissue-like composition. The diameter of the collecting electrode, which is coaxial with the body, is 20 mm. The chamber is filled with spectroscopically pure hexane and is maintained in a 20 kV/cm electric field for 48 h before the measurement. The conductivity of hexane that has been prepared in this fashion is $5 \cdot 10^{-8}\ \Omega^{-1} \cdot \text{cm}^{-1}$.

Co^{60} sources of varying radioactivity are used to irradiate the hexane. The dose rate at the point at which the hexane chamber is located is measured by a spherical tissue-equivalent ionization chamber filled with propane.[13]

Figure 1 shows the experimentally determined ion radiation yield as a function of temperature (curve 3). Comparison with curves 1 and 2 indicates that the experi-

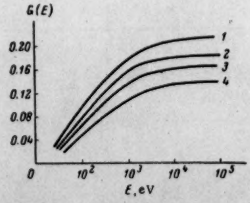

Fig. 1. Radiation yield of ions for hexane irradiated by electrons. Theoretical: 1) E = 0.1 MeV; 2) E = 1 keV; experimental: 3) Co^{60}.

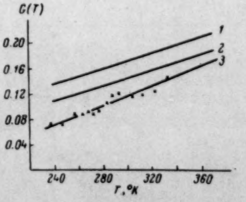

Fig. 2. Radiation yield of ions in hexane as a function of primary electron energy. T(°K): 1) 370; 2) 330; 3) 298; 4) 237.

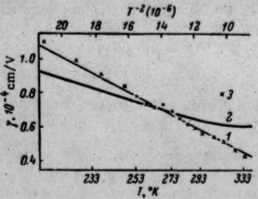

Fig. 3. Temperature dependence of the slope of the volt−ampere characteristic: 1) using Onsager's calculations;[5] 2) using Adamczewski's calculations;[1] 3) experimental.

mental and theoretical values of G = G(T) agree qualitatively. The difference in slope of 1, 2, and 3 is evidently due to errors in extrapolating $r(E_e)$ from (3) to low secondary-electron energies. There is reason to assume[14] that for $E_e > 20$ eV $r(E_e)$ is greater than the expression employed in calculations would imply. Despite the fact that curves 1 and 2 are computed for monoenergetic electrons, a fact which makes comparison with the resultant experimental data not entirely correct, we can assume that Eqs. (4) and (8) basically describe the behavior of G = G(T) accurately.

The efficiency of ion collection, which is also determined by curve 3, is in agreement with the earlier value[15] and with that obtained by Januszaitis[16] using another procedure, within the limits of experimental error (≃ 20%).

Figure 3 shows the slope γ of the linear portion of the volt−ampere characteristic as a function of temperature. It has been shown earlier[8,17] that the behavior of $\gamma = \gamma(T)$ can offer evidence in favor of one of the three hypotheses regarding the conduction mechanism in liquid dielectrics.[1,5,7] It can be seen from Fig. 3 that the experimental values of $\gamma(T)$ fit a straight line in (γ, T^{-2}), a fact which agrees with Onsager's theory[5] [see Eqs. (5) and (6)]. For comparison we also show curve 2 (Adamczewski's data[1]). The error in determining $\gamma(T)$ does not exceed 10%.

The authors thank Yu. V. Semenov for help with the tissue-equivalent ionization chamber.

---

[1] I. Adamczewski, Les Phénomes d'Ionization et de Conductivité des Dielectriques Liquides, Masson, Paris (1968).

[2] M. Ladu and M. Peelliccioni, Nucl. Instr. and Meth., 39, 339 (1966).

[3] D. Blanc, J. Mathieu, L. Torres, and P. Vermande, Onde. Elec., 457, 456 (1965).

[4] A. Hummel and A. O. Allen, J. Chem. Phys., 46, 1602 (1967).

[5] L. Onsager, Phys. Rev., 54, 554 (1938).

[6] A. Jahns and W. Jacobi, Zeits. für Naturforsch., 21a, 1400 (1965).

[7] J. Mathieu, Deuxieme these, Universite de Toulouse (1968).

[8] V. I. Ivanov, E. D. Kleshchenko, and V. V. Frolov, Advances in Physical and Biological Radiation Detectors, IAEA, Vienna (1971), p. 391.

[9] E. J. Kobetich and R. Katz, Phys. Rev., 170, 391 (1968).

[10] G. R. Fayadh and J. M. Fayadh, J. Chem. Phys., 43, 86 (1965).

[11] J. D. Garcia, Phys. Rev., 177, 223 (1969).

[12] E. Jahnke, F. Emde, and F. Losch, Tables of Functions [Russian translation], Izd. Nauka, Moscow (1968), p. 63.

[13] I. M. Dmitrievskii, Yu. V. Semenov, and V. V. Frolov, in: Problems of Dosimetry and Radiation Shielding [in Russian], No. 12, 46 (1971).

[14] J. W. Baum, S. L. Stone, and A. V. Kuchner, First Symposium on Microdosimetry, Italy, ed. H. Ebert (1967).

[15] V. I. Ivanov, E. D. Kleshchenko, V. A. Mashchenko, and V. V. Frolov, in: Problems of Dosimetry and Radiation Shielding, [in Russian], No. 11, 86 (1970).

[16] A. Januszaitis, Acta Phys. Polon., 24, 809 (1969).

[17] V. I. Ivanov, E. D. Kleshchenko, and V. V. Frolov, in: Problems of Dosimetry and Radiation Shielding [in Russian], No. 11, 92 (1970).

Steady-state electron density in photoionization of aerosol particles

G. V. Karachevtsev and A. A. Fridman

Moscow Dolgoprudnyi Physicotechnical Institute

(Submitted May 7, 1973; resubmitted November 6, 1973)
Zh. Tekh. Fiz., 44, 2388-2392 (November 1974)

Equations are derived for the steady-state density of electrons generated by photon interaction with aerosol particles. It is assumed that the aerosol particles are of the same size. It is assumed that the photoionization cross sections of the aerosol particles and the electron sticking cross sections to particles are independent of the particle charge in the range from the critical negative charge, for which the work function is equal to the photon energy. A transcendental equation is derived for the electron density in the case of ionization by monochromatic light. Approximate expressions are derived for the limiting cases of high and low light intensities. A curve convenient for numerical calculations is given. Ionization by continuum radiation is also considered. An approximate expression is derived for the electron density for an exponential photon energy. The relaxation time is estimated for low steady-state electron densities.

Consider a gas containing aerosol particles with density n. The aerosol particles are spherical and their particle radius is r. We calculate the steady-state electron density n_e due to photoionization. The upper limit of the charge of the aerosol particles n_+e is determined by the fact that the work function increases for each subsequent electron: $\varphi_m = \varphi_0 + me^2/r$, where me is the particle charge before ionization. The lower limit of the particle charge $n_-e(n_- <$ 0 is defined by zero work function for emission from a particle. It is evident that

$$n_+ = \frac{(E-\varphi_0)r}{e^2}, \tag{1}$$

$$n_- = -\frac{r\varphi_0}{e^2}. \tag{2}$$

Here, E is the photon energy.

For conductors φ_0, the work function of the first electron, is determined[1] by A_0 the work function for a flat surface and by the radius of the aerosol particle. We consider the cases of ionization by monochromatic and by continuum radiation separately.

1. MONOCHROMATIC RADIATION

We write the equations for the densities of aerosol particles with different charges neglecting the coalescence of particles:

$$\left.\begin{aligned}
\frac{dn_{n_-}}{dt} &= -\gamma p n_{n_-} + \alpha n_e n_{n_-+1},\\
\frac{dn_{n_-+1}}{dt} &= \gamma p n_{n_-} - \alpha n_e n_{n_-+1} - \gamma p n_{n_-+1} + \alpha n_e n_{n_-+2},\\
\frac{dn_i}{dt} &= \gamma p n_{i-1} - \alpha n_e n_i - \gamma p n_i + \alpha n_e n_{i+1},\\
&\cdots\cdots\cdots\cdots\cdots\cdots\\
\frac{dn_{n_+-1}}{dt} &= \gamma p n_{n_+-2} - \alpha n_e n_{n_+-1} - \gamma p n_{n_+-1} + \alpha n_e n_{n_+},\\
\frac{dn_{n_+}}{dt} &= \gamma p n_{n_+-1} - \alpha n_e n_{n_+}.
\end{aligned}\right\} \tag{3}$$

Here, $\alpha \simeq v_e\sigma$ is the sticking coefficient for an electron with the mean velocity v_e and a particle with the cross section σ, γ is the photoionization cross section of the particle, which is assumed to be independent of the charge in the range $(n_- - n_+)$, and n_i is the density of particles with the charge ie.

Consider (3) under steady-state conditions $dn_i/dt = 0$ for any i. By adding the first equation in (3) to the second and adding the sum to the third, etc., we obtain a stationarity relationship for $i = n_-, \ldots, n_+ - 1$:

$$\alpha n_e n_{i+1} = \gamma n_i p. \tag{4}$$

We use the notation

$$q = \frac{n_{i+1}}{n_i} = \frac{\gamma p}{\alpha n_e}. \tag{5}$$

Then, from the electrical neutrality of the system and the mass balance, we find

$$\frac{n_e}{n} = \frac{\sum\limits_{k=n_-}^{n_+} k n_k}{\sum\limits_{k=n_-}^{n_+} n_k} \simeq \frac{\int\limits_{n_-}^{n_+} x q^x dx}{\int\limits_{n_-}^{n_+} q^x dx}.$$

Integration yields

$$\frac{n_e}{n} = \frac{n_+ q^{n_+} - n_- q^{n_-}}{q^{n_+} - q^{n_-}} - \frac{1}{\ln q}. \tag{6}$$

The problem of calculating n_e as a function of A_0, r, E, n, and p is solved by Eq. (6). In general, this dependence cannot be expressed in explicit form. Let us analyze the cases in which $n_e = f(A_0, r, E, n, p)$ can be expressed in simple explicit form.

1) Let $q \gg 1$. This means that $p \gg \alpha n_e/\gamma$. Equation (6) is then simplified:

$$\frac{n_e}{n} \simeq \frac{n_+ q^{n_+}}{q^{n_+}} = n_+. \tag{7}$$

Hence, the condition $q \gg 1$ means that

$$p \gg \frac{\alpha n n_+}{\gamma}. \tag{8}$$

2) We now reduce the flux p. Since $p \gg \alpha n n_+/\gamma$, n_e is independent of p. Consider Eq. (6). We note that its two terms vary in different ways when g is reduced ($q >$ 1): The first term remains virtually unchanged (for large values of n_+ and n_-), while the second increases in constant fashion. The value of n_e decreases and depends on p. The value of $q = \gamma p/\alpha n_e$ decreases at a lower rate for smaller p, and, for small p,

$$p \ll \frac{\alpha n}{\gamma} \tag{9}$$

the density n_e is low, $n_e/n \ll 1$, while q assumes the limiting value q_1, which is close to unity and is determined by Eq. (6) under the assumption that $n_e/n = 0$. If (9) is satisfied,

$$n_e = \frac{\gamma p}{\alpha q_1}, \tag{10}$$

where q_1 is determined by

$$\frac{n_+ q_1^{n_+} - n_- q_1^{n_-}}{q_1^{n_+} - q_1^{n_-}} = \frac{1}{\ln q_1}. \tag{11}$$

It can be shown that (11) has the following approximate solution:

$$q_1 = \begin{cases} e^{1/n_+} \text{ for } \delta \gg 1, \\ e^{1/n_-} \text{ for } \delta \ll 1, \\ \text{close to unity for } \delta \simeq 1. \end{cases} \tag{12}$$

Here, $\delta = |n_-/n_+|$. It is evident from (12) that q_1 is always close to unity. Consequently, the approximate solution of the basic equation (6) is

$$n_e = \frac{\gamma p}{\alpha} \text{ for } p \ll \frac{\alpha n}{\gamma}. \tag{13}$$

The curves of constant values of n_e, plotted by means of Eqs. (7), (8), and (13), are shown in Fig. 1 in a plot of log p vs log (nn_+). Estimates of the errors in (7), (8) and (13) with respect to the more accurate equation

$$\frac{n_e}{n} = n_+ - \frac{1}{\ln q} \tag{14}$$

are given in the figure.

If $p \gg \alpha n n_+/\gamma$ and $\eta = \Delta n_e/n_e$ is the relative error in measuring n_e, then

$$p = \frac{\alpha}{\gamma} n n_+ e^{1/\eta n_+}. \tag{15}$$

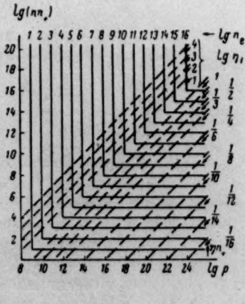

Fig. 1

For $p \ll \alpha n/\gamma$,

$$p = \frac{\alpha}{\gamma} \eta_1 n n_+, \tag{16}$$

where $\eta_1 = \Delta n_e/2.3 n_e \log n_e$ is the relative error in the measurement of log n_e. The results of calculations based on expressions (7), (8), (13), (15), and (16) for $\alpha/\gamma = 10^{-8}$ cm/sec are given in Fig. 1 as the dependences of log n_e, log η_1, and ηn_+ on log p and log (nn_+). The value of n_e is constant along the solid curves, while the approximation error is constant along the dashed curves.

II. IONIZATION BY CONTINUUM RADIATION

The basic stationarity equation (4) is

$$\gamma p_i n_i = \alpha n_e n_{i+1}, \tag{17}$$

where p_i is the flux density of photons with an energy sufficient for the (i + 1)-th ionization. We introduce the notation $\xi_i = p_i/p_0$. Then, from (17)

$$\left.\begin{aligned} n_1 &= n_0 \left(\frac{\gamma p_0}{\alpha n_e}\right) \xi_0, \\ n_2 &= n_1 \left(\frac{\gamma p_0}{\alpha n_e}\right) \xi_1 = n_0 \left(\frac{\gamma p_0}{\alpha n_e}\right)^2 \xi_0 \xi_1, \\ &\cdots\cdots\cdots\cdots\cdots \\ n_k &= n_0 \left(\frac{\gamma p_0}{\alpha n_0}\right)^k \prod_{i=0}^{k-1} \xi_i. \end{aligned}\right\} \tag{18}$$

Relationships (18) hold also for k < 0; in this, $\prod_{i=0}^{k} \xi_i$ is to be considered as $\prod_{i=0}^{-k} (1/\xi_{-i})$. By taking account of the electrical neutrality of the system and the mass balance, we obtain a generalization of Eq. (6):

$$\frac{n_e}{n} = \frac{\sum\limits_{k=n_-}^{\infty} k n_k}{\sum\limits_{k=n_-}^{\infty} n_k} = \frac{\sum\limits_{k=n_-}^{\infty} k q_0^k \prod\limits_{i=0}^{k-1} \xi_i}{\sum\limits_{k=n_-}^{\infty} q_0^k \prod\limits_{i=0}^{k-1} \xi_i}. \tag{19}$$

Here, $q_0 = \gamma p_0/\alpha n_e$. Determination of n_e by means of expression (19) is complicated for an arbitrary photon energy distribution, i.e., for arbitrary values of ξ_i. The problem is much simpler if $p(E) = pe^{-\delta E}$, which is fairly accurate in the tail of thermal radiation.

We determine p_0 and ξ_i for this case:

$$p_0 = \int_{\varphi_0}^{\infty} p(E)\,dE = \frac{p}{\delta} e^{-\delta \varphi_0}, \tag{20}$$

$$\xi_i = \frac{p_i}{p_0} = \frac{\int_{\varphi_i}^{\infty} p(E)\,dE}{\int_{\varphi_0}^{\infty} p(E)\,dE} = e^{-\delta i \frac{e^2}{r}}. \tag{21}$$

Then,

$$\prod_{i=0}^{k-1} \xi_i = e^{-\frac{\delta e^2}{r} \frac{k(k-1)}{2}}.$$

We write $\delta e^2/r = \lambda$ and substitute in (19), assuming that $n_- \to -\infty$ for the sake of simplicity. Then,

$$\frac{n_e}{n} = \frac{\sum\limits_{-\infty}^{\infty} k q_0^k e^{-\lambda \frac{k(k-1)}{2}}}{\sum\limits_{-\infty}^{\infty} q_0^k e^{-\lambda \frac{k(k-1)}{2}}}. \tag{22}$$

The problem of solving (22) is identical mathematically to the problem of thermal ionization of aerosol particles.[2] The solution is

$$\frac{n_e}{n} = y + \frac{\rho}{2\pi}\frac{d}{dy}\theta_3(y,\ \rho), \tag{23}$$

where $\theta_3(y, \rho)$ is an elliptic θ function, and $y = (1/\lambda)\ln q_0 + 1/2$, $\rho = 2\pi/\lambda$. For $\rho \gg 1$, we obtain the equation

$$\frac{n_e}{n} = \frac{1}{\lambda}\ln q_0 + \frac{1}{2}, \tag{24}$$

while, for $\rho \ll 1$,

$$\frac{n_e}{n} \simeq \frac{q_0}{1+q_0}. \tag{25}$$

It should be noted that, if $p(E)$ is not an exponential, but decreases sharply with E for $E \to \infty$, we can determine n_e by means of (19), retaining a finite number of terms, depending on the required accuracy.

III. ESTABLISHMENT OF THE STEADY STATE

In considering the establishment of the steady state, it is necessary to solve the system of kinetic equations for the densities of electrons and aerosol particles. For instance, in order to solve this problem for the case of monochromatic radiation it is necessary to solve system (3) by observing the condition of electrical neutrality of the system as a whole.

Even if stated in this way, this problem involves mathematical difficulties and requires numerical methods. The solution can be obtained in explicit form for $p \ll \alpha n/\gamma$, since $q \simeq 1$ in this case and $n_{n+} \ll n$ and $n_{n-} \ll n$. Then, the equation assumes the following form:

$$\frac{dn_e}{dt} = \gamma p n - \alpha n_e n. \tag{26}$$

It follows from this equation that

$$n_e(t) = \frac{\gamma p}{\alpha}\left(1 - e^{-\alpha n t}\right) \tag{27}$$

and the characteristic time for the establishment of steady-state conditions is

$$\tau = \frac{1}{\alpha n}. \tag{28}$$

Numerical estimates based on (28) for $n = 10^7$ cm^{-3} and $\alpha = 10^{-5}$ cm^3/sec yield $\tau = 10^{-2}$ sec.

---

[1] A. P. Maksimenko and V. I. Tverdokhlebov, Izv. VUZOV, Fizika, No. 1, 84 (1964).

[2] Yu. S. Sayasov, Dokl. Akad. Nauk SSSR, 122, 848 (1958).

General

Surface evaporation of a solid transparent dielectric under the action of laser radiation

A. M. Bonch - Bruevich, Ya. A. Imas, A. A. Kovalev, P. S. Kondratenko, and B. I. Makshantsev

(Submitted December 28, 1973)
Zh. Tekh. Fiz., 44, 2393-2397 (November 1974)

A method is suggested for the solution of the problem of self-similar surface evaporation of a solid transparent dielectric under the action of laser radiation. Simple equations are derived for the quantities which characterize the absorption wave front of the laser radiation. Expressions are obtained for the temperature of the surface and its evaporation rate.

INTRODUCTION

As shown in refs. 1 and 2 microinclusions absorbing laser radiation can, under certain conditions, lead to the onset of a thermal ionization avalanche in the basic material. The local temperature of the material then reaches values of $T \sim 10^{4\circ}$. If such a microinclusion lies close to the surface of a transparent dielectric, the ionization avalanche can reach the surface; as a result, the corresponding section of the latter will start to evaporate. Thus, there arises the problem of the evaporation rate and the corresponding surface temperature. This problem has been studied in the case of a metal surface.[3] The situation which exists in transparent dielectrics is, broadly speaking, substantially different from that in a metal, and requires special consideration.

It should be noted that at temperatures $T \sim 10^{4\circ}$ the local electron density n_e is already so high that further ionization of the material proceeds by electron impact.[4] Since the response time of the local temperature for values of the parameters of the problem considered below is much larger than the characteristic ionization and recombination times, the electron density will be determined solely by the temperature, i.e., $n_e = n_e(T)$. For $T \lessdot 10^{4\circ}$ the plasma can, at least qualitatively, be considered as ideal; therefore, the quantity $n_e(T)$ can be estimated from the Saha equation. As the ionization potential J is much larger than the temperature, we shall, for the sake of simplicity, retain for all values only the exponential temperature dependence, i.e, $\exp(-I/T)$, where $I = J/2$. Let us note that we are only interested in the range where the temperature is much larger than the initial temperature of the material. The latter can, therefore, be taken as zero.

It follows from the foregoing that the temperature $T(\mathbf{r}, t)$ is given by the thermal conductivity equation, the heat source $g(T, |\mathbf{E}|^2)$ of which is a function of the electric field E. The latter is determined by the corresponding Maxwell equation. The system of equations has the form

$$\frac{\partial T}{\partial t} = \chi \Delta T + g(T, |\mathbf{E}|^2), \tag{1}$$

$$\Delta \mathbf{E} + \left(\frac{\omega}{c}\right)^2 \varepsilon(T) \mathbf{E} = 0. \tag{2}$$

Here, χ is the thermal conductivity, $g(T, |\mathbf{E}|^2) = (\omega/8\pi c)\, \mathrm{Im}\,\varepsilon(T)\, |\mathbf{E}|^2$, ω is the frequency of the laser radiation, c is the velocity of light, $\tilde{c}$ is the thermal capacity of a unit volume of the dielectric, $\varepsilon(T)$ is the complex dielectric constant, which, in the collision-time approximation, can be written in the form

$$\varepsilon(T) = 1 - \frac{\tilde{\omega}^2 e^{-I/T}}{\omega^2 + \nu^2}\left(1 - \frac{i\nu}{\omega}\right), \tag{3}$$

where $\tilde{\omega} e^{-I/2T}$ is the electron plasma frequency, and ν is the electron collision frequency.

Equation (2) for the electrical field E takes account of the fact that the wave period is considerably shorter than the characteristic times of heat propagation.

The system of equations (1), (2) describes the motion of the volatile surface. We shall consider such times when the width of the temperature front near the surface is much smaller than its radius of curvature. If, therefore, we are interested in the surface, the problem can, at least qualitatively, be considered as one-dimensional. It should be noted that since the heat source function $g(T)$, $|\mathbf{E}|^2$ is proportional to $\exp(-I/T)$, the problem under consideration resembles the problem of the heat propagation of a flame.[5,6]

GENERAL RELATIONS

As in refs. 5 and 6 we seek a solution of the system (1), (2) which depends only on the combination of variables $\xi = x - vt$, where the positive direction of the x axis coincides with the light propagation direction, while the point $\xi = 0$ is taken as the origin, at which the heat source function $g(\xi)$ is maximum. Below, we examine the stability of such a solution.

It is necessary to add to the system of equations (1), (2) the boundary conditions

$$\left.\begin{aligned} T_1' &= \frac{\Lambda v}{\chi}, \\ T(\xi = +\infty) &= 0, \end{aligned}\right\} \tag{4}$$

where

$$T_1' = \left.\frac{dT(\xi)}{d\xi}\right|_{\xi=-\xi_0},$$

$T_1 = T(\xi)|_{\xi=-\xi_0}$; ξ_0 is the distance of the surface boundary from the point $\xi = 0$, Λ is the evaporation heat, expressed in degrees,

$$v = s e^{-\Lambda/T_1}, \tag{5}$$

s is the order of magnitude of the sound velocity. The electrical field of the wave is given by

$$\left.\begin{aligned} \mathbf{E}(-\xi_0 - 0) &= \mathbf{E}(-\xi_0 + 0), \\ \left.\frac{d\mathbf{E}}{d\xi}\right|_{\xi=-\xi_0-0} &= \left.\frac{d\mathbf{E}}{d\xi}\right|_{\xi=-\xi_0+0}, \end{aligned}\right\} \tag{6}$$

the incident plane wave at $\xi < -\xi_0$ being given by the flux density q of the laser radiation.

Let us remark that the boundary conditions formulated above correspond, as in ref. 3, to the neglect of the effect of the evaporated material on the evaporation process.

In accordance with the foregoing, we have

$$\frac{I}{T_0} \gg 1, \tag{7}$$

where $T_0 = T|_{\xi=0}$. In addition, we shall assume, and this is supported by the results that the temperature can be written in the form

$$T(\xi) = T_0 + T'_0 \xi, \tag{8}$$

where $T'_0 = (dT/d\xi)_{\xi=0}$ for all values of the variable ξ satisfying the following inequality

$$\left.\begin{aligned} &\frac{T_0}{I}\beta|\xi| \ll 1, \\ &\beta = \frac{I}{T_0^2}T'_0, \quad -\xi_0 \leqslant \xi \leqslant \xi_+, \text{ where } \xi_+ > 0, \end{aligned}\right\} \tag{9}$$

$$g(\xi_+) \ll g(0). \tag{10}$$

We then have $\exp(-I/T) \simeq \exp(-I/T_0)e^{\beta\xi}$. When Eq. (2) is solved taking (5) in consideration, Eq. (1) takes the form

$$\chi\frac{d^2T}{d\xi^2} + v\frac{dT}{d\xi} + g(\xi) = 0, \tag{11}$$

where

$$g(\xi) = \frac{\frac{4\nu\alpha^2 q}{\varepsilon c} y^2 |K_{i\mu}(\eta y)|^2}{\left|K_{i\mu}(\eta y_1) - i\frac{y_1}{\mu}\frac{d}{dy_1}K_{i\mu}(\eta y_1)\right|^2},$$
$$\alpha^2 = \frac{\tilde{\omega}^2 e^{-I/T_0}}{\omega^2 + \nu^2}, \quad \mu = \frac{2\omega}{\beta c}, \quad \eta = \mu\alpha\sqrt{1 - i\frac{\nu}{\omega}}, \quad y = e^{\beta\xi/2},$$

$y_1 = y|_{\xi=-\xi_0}$; $K_{i\mu}(\eta y)$ is the Bessel function of imaginary index. We shall subsequently assume the validity of the inequality

$$\frac{\nu}{\omega} \ll 1. \tag{12}$$

The extremum condition of $g(\xi)$ at the point $\xi = 0$ leads to

$$|K_{i\mu}(\eta)| + \eta\frac{\partial|K_{i\mu}(\eta)|}{\partial\eta} = 0. \tag{13}$$

Integrating Eq. (11) in the interval from $\xi = -\xi_0$ to $\xi = +\infty$ taking (4) into consideration, we obtain

$$v(\Lambda + T_1) = \frac{\varkappa q}{\tilde{c}}, \tag{14}$$

where $\varkappa = (\tilde{c}/q)\int_{-\xi_0}^{\infty} d\xi\, g(\xi)$ is the absorption coefficient of light.

On account of Eq. (8), we have

$$T'_1 = T'_0, \tag{15}$$

$$T_1 = T_0 - T'_0\xi_0. \tag{16}$$

Equations (4), (5), (13)-(16) constitute a closed system of equations for the determination of the unknown quantities T_1, T'_1, T_0, T'_0, v, and ξ_0. It is thereby easy by means of (11), to find the temperature profile $T(\xi)$, the electron density $n_e(\xi)$, etc. Let us emphasize that the system of equations mentioned is only valid when the inequalities (7)-(10) are fulfilled.

Two limiting cases are of real interest, one of which corresponds to the classical electromagnetic field, while the other to the presence of strong reflection from the absorption wave front.

The quasiclassical limit corresponds to the inequalities $\mu \gg 1$ and $\alpha|\sqrt{1 - i\nu/\omega}| \simeq \alpha < 1$, which are satisfied at small values of q. Therefore, when the expression for the function $g(\xi)$ is taken into account, we find that the quantity ν in Eq. (15) is equal to unity. The corresponding equations for the quantities T_1 and v will be analogous to the equations for these quantities in the problem of the evaporation of a metal surface.[3] Consequently, a detailed discussion of this situation is not necessary. We shall present only the expressions for v and T_1 valid for small values of the ratio T_1/λ

$$\left.\begin{aligned} &v \simeq \frac{q}{\Lambda\tilde{c}}, \\ &T \simeq \frac{\Lambda}{\ln\left(\frac{\tilde{q}_0}{q}\right)}, \end{aligned}\right\} \tag{17}$$

where $\tilde{q}_0 = s\Lambda\tilde{c}$.

The case of strong reflection requires special examination.

STRONG REFLECTION

The situation in which strong light reflection from the absorption wave front occurs corresponds to the inequalities

$$\left.\begin{aligned} &\mu^2 \ll 1, \\ &\alpha^2 \gg 1. \end{aligned}\right\} \tag{18}$$

Below, it will be important for us to be able, because of the first of the inequalities in (18), to retain the first terms in the series expansion of the function $K_{i\mu}(\mu\alpha\sqrt{1 - i\nu/\omega}\cdot e^{\beta\xi/2})$ for $\xi \neq 0$. Taking this fact as well as inequality (12) into consideration the absorption coefficient $\varkappa$ in Eq. (14) is given by $\varkappa = 2\mu\nu/\omega$. Bearing in mind the expression for the quantity μ as well as relations (15), (16), we have

$$\varkappa = \frac{4\nu T_1^2}{IcT'_1}(1 + x)^2, \tag{19}$$

where $x = T'_1\xi_0/T_1$.

Because of inequality (9), the quantity x is small enough in comparison with unity, so that, if we are not interested in ξ_0, we can in the first approximation, set x = 0 in Eq. (13). In principle, the quantity x can be determined in the following way. It follows from Eq. (13) that $\mu\alpha = 2e^{-1-c}$, where $c \simeq 0.58$ is Euler's constant. Hence, taking relations (15), (16) and the expression for α into consideration, we obtain the equation

$$\frac{\tilde{\omega}}{c}\frac{T_1^2}{IT_1'}(1+x)^2\exp\left(-\frac{I}{2T_1(1+x)}+1+C\right)=1. \tag{20}$$

Setting x = 0 in Eq. (19) and substituting the expression for the coefficient $\varkappa$ in Eq. (14), we find, after solving it jointly with Eqs. (4), (5),

$$T_1=\frac{\Lambda}{\ln\sqrt{\frac{q_0}{q}}+\ln\ln\sqrt{\frac{q_0}{q}}}, \tag{21}$$

$$v=\frac{2s\sqrt{\frac{q}{q_0}}}{\ln\frac{q_0}{q}}, \tag{22}$$

where

$$q_0=\frac{Is^2c\tilde{c}}{4\varkappa\nu}.$$

Let us recall that the intensity interval of the laser radiation flux for which Eqs. (21), (22) are valid is determined by the inequalities (7), (9), (10), (18).

We shall evaluate from Eqs. (21), (22) the characteristic values of the temperature T_1 and the velocity v. Assuming $I \simeq 4\cdot 10^{4\circ}$, s $\sim 10^5$ cm/sec, $\tilde{c} \sim 1$ J/cm^3/deg, $\varkappa \sim 10^{-2}$ cm^2/sec, $\nu \sim 10^{14}$ sec^{-1}, $\lambda = 3\cdot 10^{4\circ}$, we obtain for q $\sim 10^8$ W/cm^2, $T_1 \approx 8\cdot 10^{3\circ}$, v = 10^2 cm/sec, which agrees with the experimental data of ref. 7.

In conclusion, let us note that the stability of the solution obtained above must be investigated. For this purpose, as usual, a small perturbation must be added to the solution found above for the system (1), (2), i.e.,

$$T(\xi,t)=T(\xi)+\tilde{T}(\xi)e^{-pt},\quad \mathbf{E}(\xi,t)=\bar{\mathbf{E}}(\xi)+\tilde{E}(\xi)e^{-pt}.$$

The problem of stability is then reduced to the finding of a range of the problem parameters where the system (1), (2), linearized with respect to $\tilde{T}(\xi)$, $\tilde{E}(\xi)$, has no eigenvalues of p the real part of which is negative. As a result of the elimination of $\tilde{E}(\xi)$ from the system of equations we obtain, substituting $\tilde{T}(\xi) = e^{(-v/2\varkappa)\xi}\psi(\xi)$, an equation of the Schrödinger type with a nonlocal non-Hermitian potential and with the corresponding boundary condition at $\xi = -\xi_0$ for the logarithmic derivative of the "wave function" $\psi(\xi)$. It turns out that this equation corresponds to the case of a shallow potential well. Without showing the rather cumbersome calculations, let us note that the characteristics of the boundary conditions lead to the absence of bound states. Thereby, there are no eigenvalues of p with Rep < 0, i.e., within the framework of the assumptions made in the examination of the problem, the question of stability is solved favorably.

The authors wish to express their appreciation to S. I. Anisimov and I. P. Perstnev for helpful discussion.

---

[1] S. I. Anisimov and B. I. Makshantsev, Fiz. Tverd. Tela, 15, 1090 (1973) [Sov. Phys. – Solid State, 15, 743 (1973)].

[2] B. I. Makshantsev, P. S. Kondratenko, and G. M. Gandel'man, Fiz. Tverd. Tela, (in press).

[3] S. I. Anisimov, Ya. A. Imas, G. S. Romanov, and Yu. V. Khodyko, The Action of Highpower Radiation on Metals [in Russian], Izd. Nauk, (1970).

[4] Ya. B. Zel'dovich and Yu. P. Raizer, The Physics of Shock Waves and High Temperature Hydrodynamic Phenomena, Academic Press, New York (1968).

[5] Ya. B. Zel'dovich and D. A. Frank-Kamenetskii, Dokl. Akad. Nauk, SSSR, 19, 693 (1938).

[6] D. A. Frank-Kamenetskii, Diffusion and Thermal Transport in Chemical Kinetics [in Russian], Izd. Nauka, (1967), p. 307.

[7] L. V. Aleshin, A. M. Bonch-Bruevich, Ya. A. Imas, V. L. Komolov, and V. S. Saledinov, Zh. Tekh. Fiz., 41, 820 (1971) [Sov. Phys. – Tech. Phys., 16, 642 (1971)].

Interaction of intense laser radiation with solid targets

L. V. Dubovoi, V. D. Dyatlov, V. I. Kryzhanovskii, A. A. Mak, R. N. Medvedev, A. N. Popytaev, V. A. Serebryakov, V. N. Sizov, and A. D. Starikov
D. V. Efremov Scientific Research Institute of Electrophysical Apparatus, Leningrad
(Submitted October 15, 1973)
Zh. Tekh. Fiz., 44, 2398-2403 (November 1974)

The interaction of intense laser radiation with solid targets of lithium deuteride has been investigated. A neutron yield of $6 \cdot 10^5$ neutrons per pulse is recorded. The reflection coefficient is measured and the second harmonic is detected in the reflected radiation. The results indicate the intrinsically nonlinear character of the interaction.

Progress in the construction of lasers has made it possible to concentrate large energies in small volumes for short times. This opens the way to the utilization of ultrahigh-power sources of light radiation and the investigation of controlled thermonuclear fusion. However, the interaction process of high-intensity radiation with solid targets has not yet been studied well enough. This is due, in particular, to the complexity of the phenomena. It is, therefore, of obvious interest to carry out investigations which clarify the relative role and influence in these processes of both the plasma parameters and the radiation in the simplest cases. Thus, for instance, using short radiation pulses, it is possible to reduce the effect of the material disintegration on the target parameters in question. The regime in which the material disintegration can be neglected is realized[1] during the time interval

$$t \leqslant 8 \cdot 10^{-25} I_{in}, \tag{1}$$

which for $I_{in} \sim 10^{15}$ W/cm² gives $t \leq 8 \cdot 10^{-10}$ sec, if the target material is lithium deuteride. The shape of the radiation pulse is also an important parameter.

It is known that the main pulse is preceded by some background level E_p, which can contain an energy sufficient for the evaporation of an appreciable quantity of material. The vapor cloud thus formed will affect the subsequent interaction between the radiation and the plasma. It is necessary to lower the background level E_p to a level E_c, which will not, under the experimental conditions, affect the state of the target:

$$E_p < E_c. \tag{2}$$

The measurement of the number of neutrons produced per flash allows an evaluation of the ion energy contribution. Since, however, nonthermonuclear neutron generation is possible,[2] the measurable yield cannot be unambiguously associated with the ion temperature. Assuming that during the time τ a Maxwellian ion velocity distribution is established, a calculation has been carried out[3] for short pulses of duration

$$t \ll \tau = 3 \cdot 10^{10} \frac{Q^{1/3}}{n_m}, \tag{3}$$

according to which the number of neutrons is determined by the magnitude of the energy Q(J/cm²) absorbed by the target:

$$N_{d-d} = 2.5 \cdot 10^{18} \left(\frac{n}{n_m}\right)^2 Q^{11/18} \exp\left\{-\left(\frac{10^{17}}{Q}\right)^{1/9}\right\}. \tag{4}$$

Here, n is the ion density in the interaction region, n_m is the density of target atoms, and N_{d-d} is the number of electrons emitted from 1 cm² of the illuminated surface of deuterated ice.

The electron temperature in a target illuminated by a short pulse[1] is related to the light intensity by

$$T_e \sim I_{in}^{\alpha},$$

where $4/9 < \alpha < 2/3$, and depends on the hydrodynamics of the corona disintegration. The measurement of the electron temperature and the reflection coefficient of light from the target plasma makes it possible to clarify the character of the interaction of radiation with the target material. Thus, when this interaction has a classical character, i.e., when the absorption is due to bremsstrahlung, the absorption coefficient[4] is given by the expression

$$K = \frac{\omega_p^2}{[c\omega\tau_{ei}(\omega^2 - \omega_p^2)^{1/2}]}, \tag{5}$$

where c is the velocity of light in vacuum, ω is the frequency of the incident radiation, and $\omega_p = (4\pi n_e e^2/m)^{1/2}$ is the plasma frequency.

Hence, it follows that as the intensity is increased, and consequently the temperature, the absorption must decrease. If, however, the character of the interaction is determined by a nonlinear process (for example ref. 5), the effective electron collision frequency can exceed the Coulomb frequency by one order of magnitude and, since it grows with intensity, it leads to an increased absorption. When the character of the interaction is nonlinear, intense harmonics of the radiation: 2ω, $3\omega/2$, $\omega/2$, where ω is the frequency of the pumping wave, may also appear.[6]

We have carried out experiments on the heating of

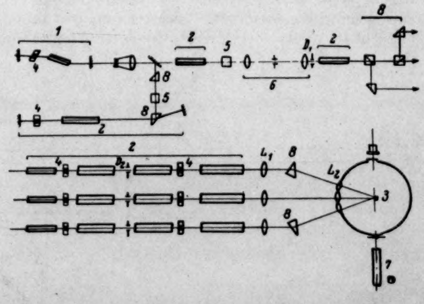

Fig. 1. Diagram of the experimental arrangement. 1) Master oscillator; 2) amplifier stages; 3) target; 4) passive switches; 5) Pockels switches; 6) lens selector; 7) aligning He–Ne laser; 8) rotating prisms; L_1, L_2) focusing lenses; D_1, D_2) collimating slits.

LiD plasma by means of a neodynium-glass laser with an output aperture of 60 mm, which makes it possible to satisfy conditions (1), (2). A diagram of the experimental arrangement is shown in Fig. 1. Working with three light channels, the single pulse energy can attain 1000 J. In the given series of experiments, carried out with the use of a single channel, the maximum energy does not exceed 120 J. This is the case because in carrying out these experiments special attention is paid to increasing the contrast of the laser pulse. The magnitude of the contrast, i.e., the ratio of the energy in the main pulse and the background energy, reaching values of > 10^4, is provided by two Pockels cells 5 and three liquid passive Q switches 4. The use of switches reduces, naturally, the magnitude of the maximum energy. It also, however, permits a substantial reduction of the quantity of material being evaporated from the target by the background radiation. The system of optical decoupling makes it possible to ensure laser operation under conditions in which the background energy at the target surface does not exceed 10 mJ. Figure 2 gives an idea of the effect of the magnitude of background energy on the evaporation of the target.

The angular divergence of the main radiation pulse is $\psi = 10^{-3}$ rad. A focusing lens with an aperture of 90 mm and focal distance of 235 mm ensures a focal spot size of

$$a = \psi f \cong 230\ \mu. \tag{6}$$

When the length of the pulse is $t = 9 \cdot 10^{-11}$ sec, the intensity of the laser light flux at the target surface $I_{in} = 10^{15}$ W/cm^2.

The target being illuminated is in a vacuum of $p = 10^{-5}$ torr and can, by means of a special mechanism, be displaced in the focal plane and along the optical axis with an accuracy of $\sim 5\ \mu$. An auxiliary He–Ne laser is used with a set of slits and focusing lenses.

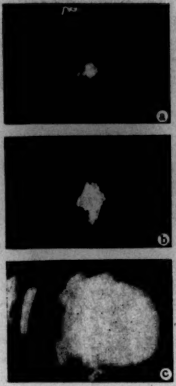

Fig. 2. Evaporation of the material of a LiD target by background radiation. The radiation is incident from the right side of the target, its duration is 100 μsec. The background energy (in mJ) is a) 10; b) 30; c) 100. The scale is 2 : 1. Photographed in white light.

Fig. 3. Oscillogram of the pulse from the x-ray radiation detector (a) and from the neutron detector (b). The pulse delays are not synchronized. The sweep duration is 250 nsec.

The neutron yield is measured by means of an activation unit with indium tracer, the sensitivity of which (at the existing background level) permits the measurement of 10^4 neutrons emitted in an angle of 4π. In addition, a plastic scintillator of 80 × 80 mm with an FÉU-110 M unit is used, recording separate neutrons. When the scintillator is placed at a distance of 30 cm from the target each count corresponds of 10^3 neutrons emitted in an angle of 4π. In the experiments, the electron temperature is measured by means of a method according to which a set of Al foils are placed in front of the scintillators. These are connected with an ÉLU photomultiplier through flexible lightguides of various lengths, constituting a light delay. A characteristic signal from an x-ray "thermometer" is shown in Fig. 3. Also shown is a pulse due to the incidence of a neutron on a scintillator. The electron temperature, determined by the measurement of the fraction of absorbed radiation in foils of different thicknesses,

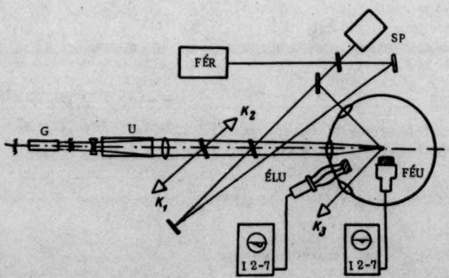

Fig. 4. Arrangement of the diagnostic apparatus.

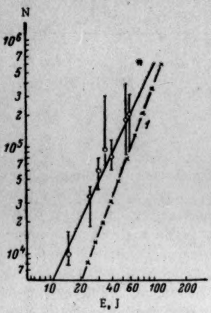

Fig. 5. Dependence of the neutron yield on the energy input to the target. The asterisk denotes the maximum yield of $6 \cdot 10^5$ n/4π. Curve 1 shows the results of calculation according to expression (4) for LiD.

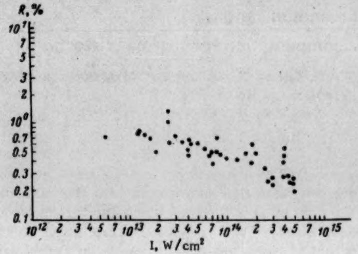

Fig. 6. Dependence of reflectivity $R = E_2/E_{in}$ on the intensity of light incident on the target.

is 1-2 keV. The estimate of the total energy of the x-ray radiation, taking into account the conversion efficiency of the scintillators, the quantum yield of the ÉLU photocathode, the transmission of the optical filters and the lightguide, gives a magnitude of 100 mJ. These figures agree satisfactorily with theoretical models of heating matter by short light pulses. The energy incident on the target, the backward reflected energy, and that scattered at an angle of 135° are measured by the calorimeters K_1, K_2, and K_3, respectively (Fig. 4). Simultaneously, the time development of the incident and reflected light intensity was recorded by means of the photoelectronic detector unit FÉR. The spectral composition of the scattered radiation was recorded by the spectrograph SP with a dispersion of 30 Å/mm. The disposition of the diagnostic apparatus is shown on Fig. 4.

In experiments with solid crystalline targets of lithium deuteride, a neutron yield attaining $6 \cdot 10^5$ neutrons in an angle of 4π is recorded. As a rule, the neutron yield is largest when the focal plane of the focusing lenses coincides with the target surface.

The dependence of the neutron yield on the magnitude of the absorbed energy is presented in Fig. 5. Expression (4) gives a somewhat lower value for the neutron yield. Since $t \sim \tau$, the agreement can be reckoned as satisfactory. As the input energy is increased, the "zero-time" condition (3) is more accurately satisfied and the difference between the experimentally obtained values and theoretical predictions decreases. The scatter in neutron yield is due mainly to the variation in the state of target surfaces. The variation can arise both because of isotope exchange and because of chemical processes.

The experimentally determined dependence of the reflectivity

$$R = \frac{E_r}{E_{in}} \qquad (7)$$

on the intensity I_{in} of the light incident on the target is shown in Fig. 6 (E_r is the light energy reflected into the aperture of the focusing lenses). A similar dependence is found[8] in similar experiments in which deuterated polyethylene is illuminated. The characteristic feature of this dependence is the reduction of the reflection coefficient with increasing I_{in}, which may indicate the presence of nonlinear absorption by the target material. This is supported by the detection in the experiments of a noticeable amplitude of the second harmonic of the incident radiation, with maximum intensity recorded at an angle of 162°. No second harmonic can be detected at an angle of 135° to the incident radiation. However, at this angle a large number of spectral lines of lithium, deuterium, and impurities is recorded, the brightest of which is a Li II line corresponding to the transition $2s^3S-2p^3P^0$ with λ = 5484.7 Å. The total energy radiated by the plasma at an angle of 135° into the aperture of the collecting lenses, equal to the aperture of the focusing lenses (0.12 sr), constitutes 10^{-4} of the laser-pulse energy. This magnitude agrees satisfactorily, within the limits of accuracy, with the energy radiated by a plasma having a temperature of ~1 keV.

In conclusion, it should be noted that the small reflection coefficient measured in the experiments can be due to the large contrast of the laser radiation and its short duration, which ensures that the main pulse interacts with a practically stationary target, reduces the contribution of the corona region, and leads to and increase of the effectiveness of nonlinear absorption processes. The relatively high neutron yield also supports the conclusion about the strong influence of the laser-radiation parameters on the character of the interaction. Consequently, it may be assumed that in experiments with an easily evaporable target (deuterated ice), considerably higher contrast is required in order to obtain similar results.

The authors wish to thank V. B. Ivanov for assistance in carrying out the experiments.

---

[1] A. Caruso, Laser Interaction and Related Plasma Phenomena, Vol. 1, Plenum Press, New York (1971), p. 289.

[2] R. Siegel, E. Eidmann, and H. Buchl, Preprint IPPIV/28 Munich (1971).

[3] A. I. Plis, E. L. Tyurin, and V. A. Shcheglov, Zh. Tekh. Fiz., 42, 2568 (1972) [Sov. Phys. – Tech. Phys., 17, 1995 (1973)].

[4] L. Spitzer, Jr., The Physics of Fully Ionized Gases, Wiley, New York (1962).

[5] V. V. Pustovalov and V. P. Silin, Zh. Eksp. Teor. Fiz., 65, 195 (1973) [Sov. Phys. – JETP, 38, 96 (1974)].

[6] J. L. Bobin, M. Decroisette, B. Meyer, and Y. Vitel, Phys. Rev. Lett., 30, 595 (1973).

[7] M. P. Vanyukov, V. I. Kryzhanovskii, V. A. Serebryakov, V. N. Sizov, and A. D. Starikov, Opt. Mekh. Promyshlennost', No. 12, 32 (1972).

[8] A. A. Rupasov, G. V. Sklizkov, V. P. Tsapenko, and A. S. Shikanov, Preprint Fiz. Inst. Akad. Nauk, No. 53 (1973).

Laser compensation for thermal distortion in optical pumping

V. K. Zaitsev, V. A. Il'inskii, A. M. Marugin, and V. M. Ovchinnikov

(Submitted January 24, 1974)
Zh. Tekh. Fiz., 44, 2404-2405 (November 1974)

References 1-5 investigate phenomena associated with the nonuniformity of optical pumping in an active element that result in distortion of the wave front and birefringence. A number of studies$^{1-4,6-10}$ propose various procedures for eliminating or compensating for distortion resulting from the nonuniform temperature distribution associated with optical pumping.

In this paper we investigate a procedure that makes it possible to substantially reduce birefringence and distortion of the wave front by eliminating the temperature nonuniformity induced in the active element by optical pumping. A compensating temperature field is produced in the element, i.e., a field whose gradient is roughly equal but opposite to that caused by the optical pumping.

Reference 11 proposes heating of the active element by open-circuit optical pumping pulses for this purpose.

In our case the compensating temperature field is created by alternately pumping "cold" and "hot" water through the chamber containing the active element. During the experiment we measure the angle of divergence of a probe beam passed through the element. Figure 1 shows the experimental arrangement. The angle of divergence is determined from the diameter of the slit (at the 0.1 maximum amplitude level) that forms in the focal plane of lens 7. Photomultiplier 11 measures the delay time of the probe pulse relative to the pumping pulse of the element. Active element 3, fabricated from GLS-1 glass with dimensions Ø 30 × 280 mm is placed in cooling chamber 4 (volume about 1.2 l) together with four symmetrically arranged IFP-8000 pump lamps. The width of the pump pulse (at the 0.1 maximum intensity level) is 2000 μsec. A ruby laser with selection of transverse modes makes it possible to obtain a probe pulse 30 nsec wide at an energy $W_{\text{gener}} = 0.2$ J and divergence angle $\theta_{0.1}^{\text{gener}} = 2' \, 30''$. The divergence angle of the probe beam $\theta_{0.1}^{\text{probe}}$ is 1' on the other side of the × 2.5 telescope. The focal length of lens 7 is 1600 mm. The spot in the focal plane of the lens is photographed on KN-1 film.

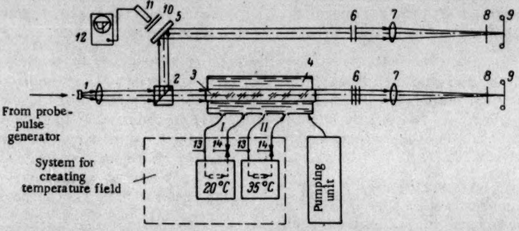
11
10
5
12
6
7
8
9
1
2
3
4
6
7
8
9
From probe-pulse generator
I
II
13
14
13
14
System for creating temperature field
20°C
35°C
Pumping unit

Fig. 1. Diagram of experimental apparatus. 1) Telescope; 2) light-splitting cube; 3) active element under investigation; 4) cooling chamber; 5) rotating plate; 6) neutral density light filters; 7) long-focus lens; 8) red filter; 9) camera; 10) light filters; 11) photomultiplier; 12) oscilloscope; 13) thermometer; 14) valve; I indicates the "cold-water" system, II the "hot-water" system.

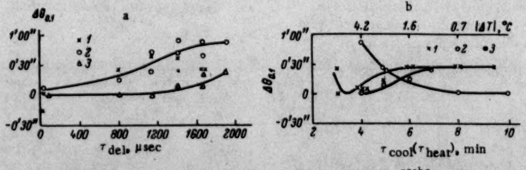

Fig. 2. Change in angle of divergence of probe beam $\Delta\theta_{0.1} = \theta_{0.1} - \theta_{0.1}^{\text{probe}}$ after passing through a passive element with nonuniform temperature: a) without thermal compensation depending on the delay time of the probe pulse; W_{pump}, kJ, as follows: 1) 26, 2) 17, 3) 11; b) with preliminary creation of nonuniform temperature field depending on the cooling (or heating) time τ_{cool} (τ_{heat}); curve 3 is for temperature gradient in same direction as that induced by pumping, no pump; curves 1 and 2 are for the temperature gradient directed opposite to that induced by pumping, pumping 26 and 17 kJ. $\Delta T = T_c - T_s$ is the temperature difference between the center and surface of the active element as computed from the cooling (or heating) time.

The system for creating the temperature field consists of two parallel water systems. The temperature in cold-water system I is maintained at 20°C by the stabilizer of a GOS-1001 device, while the temperature in system II is maintained at 35°C. The pumping rate in both systems is 8 liter/min. Since the center of the active element is heated less than the peripheral layers with optical pumping, the active element is first heated for around 20 min by system II, then cooled by system I, after which the pumping lamps are switched on. The cooling time for the specific experimental conditions is calculated or selected experimentally. Figure 2a shows the change in the angle of divergence of the probe beam passing through the active element as a function of the delay time relative to the beginning of optical pumping (W_{pump} being the pumping energy stored in the capacitors).

Figure 2b shows the change in angle when a temperature field, nonuniform over the cross section, is artificially created in advance. Compensation is selected for the time of maximum population inversion for a probe-pulse delay time $\tau_{\text{probe}} = 1100$ μsec relative to the beginning of the pump pulse for two different pump levels.

The results in Figs. 1 and 2 indicate that temperature compensation of the change in angle of divergence resulting from optical pumping is possible.

In conclusion, we note that our procedure for compensating for temperature nonuniformities in an active element is basically suitable for modes of operation with a low repetition frequency with pulse lengths short compared to the pump on-time.

---

[1] F. V. Quelly, Appl. Opt., 5, 633 (1966).

[2] Yu. A. Anan'ev, Usp. Fiz. Nauk, 103, 705 (1971) [Sov. Phys. – Usp., 14, 197 (1971)].

[3] E. M. Dianov and A. M. Prokhorov, Dokl. Akad. Nauk SSSR, 192, 531 (1970) [Sov. Phys. – Dokl., 15, 481 (1970)].

[4] E. P. Readel and G. D. Boldwin, J. Appl. Phys., 38, 2720 (1967)].

[5] B. R. Belostotskii, Yu. V. Lyubavskii, and V. M. Ovchinnikov, Fundamentals of Laser Techniques [in Russian], Izd. Sov. Radio, Moscow (1972).

[6] W. R. Hook, US Patent No. 3564454, class 331-94.5 (1971).

[7] H. V. Winston, US Patent No. 3577098, class 331-94.5 (1971).

[8] Kiyo Tomiyasu, US Patent No. 3569860, class 331-94.5 (1971).

[9] Kiyo Tomiyasu, US Patent No. 3665335, class 331-94.5 (1972).

[10] W. Koechner, US Patent No. 3662881, class 331-94.5 (1970).

[11] M. K. Chun and J. T. Bischoff, IEEE J. Quant. Electron., QE-7, 200 (1971).

Theory of nonequilibrium shock waves

R. A. Glatman and I. V. Ioffe

A. F. Ioffe Physicotechnical Institute,
Academy of Sciences of the USSR, Leningrad
(Submitted February 18, 1974)
Zh. Tekh. Fiz., 44, 2405-2407 (November 1974)

The propagation of a shock wave is treated in a binary mixture of monatomic gases in which the mean velocities of the component molecules are not the same. Under certain conditions rarefaction shock waves can exist. If the difference between the mean molecular velocities for the lighter and heavier components is directed against the motion of the front, compression shock waves can only occur at high strength.

The propagation of a shock wave in a binary gas mixture has been studied by Cowling[1] for the case in which the mean velocities of the molecules of the two components are everywhere the same except for the region of the shock front. It turns out that the effect of diffusion in the front can be important. If the mean molecular velocities differ in the unperturbed gas ahead of the front, we can expect even more serious discrepancies relative to the analogous process in a single-component medium.

We consider a mixture of monatomic gases $\gamma_1 = \gamma_2 = 5/3$ (γ being the ratio of the heat capacities, the subscripts 1 and 2 referring to the components with larger and smaller molecular mass respectively, $m_1 > m_2$). It is also assumed that the front does not create additional ionization, dissociation, etc., and that the number of molecules of each component remains unchanged across the front. Hence the proportion of molecules of the first component in the overall number

$$f = \frac{n_1}{n}$$

(n_1 and n being the number of molecules of the first component and the total number of molecules per unit volume ahead of the front respectively) remains constant everywhere except for the region of the front itself.

We introduce a moving coordinate system associated with the front whose x axis is directed from the unperturbed gas toward the gas beyond the discontinuity. At the discontinuity we have[1]

$$\rho u = \rho' u'; \quad \rho_i u_i = \rho_i' u_i' \quad (i = 1,\ 2), \tag{1}$$

$$p + \rho u^2 = p' + \rho' u'^2, \tag{2}$$

$$\frac{5}{2} p\,[f u_1 + (1-f)\,u_2] + \frac{1}{2}\rho u^3 = \frac{5}{2} p'\,[f u_1' + (1-f)\,u_2'] + \frac{1}{2}\rho' u'^3, \tag{3}$$

where ρ, ρ', u, u', and p, p' are the density of the mixture, the mean-mass velocity, and the pressure ahead of and behind the front. The difference of the mean velocities in (3) of the light and heavy components ahead of the front is

$$v_0 = u_2 - u_1 \neq 0.$$

We note that

$$\frac{\rho_1}{\rho} = \frac{m_1 n_1}{m_1 n_1 + m_2 n_2} = \frac{m_1 f}{m_1 f + m_2 (1-f)} = \text{const} = \frac{\rho_1'}{\rho'}, \tag{4}$$

and, allowing for (1),

$$\frac{u_1}{u} = \frac{u_1'}{u'}; \quad \frac{u_2}{u} = \frac{u_2'}{u'}. \tag{5}$$

Introducing

$$z = \frac{p}{\rho u^2},$$

and transforming (1)-(5), we obtain

$$5\varkappa\sqrt{z} = \frac{4z\varepsilon + z - 3}{1 - z\varepsilon}. \tag{6}$$

Here

$$\varkappa = v_0 \sqrt{\frac{\rho}{p}}\left(\frac{\rho_1}{\rho} - f\right); \quad \varepsilon = \frac{p'}{p}.$$

Equations (1) and (2) imply that

$$\frac{\rho}{\rho'} = 1 - z(\varepsilon - 1). \tag{7}$$

Equation (6) can be analyzed graphically. It turns out that three points of intersection of the curves $\varphi_1(z) = 5\varkappa\sqrt{z}$ and $\varphi_2(z) = (4z\varepsilon + z - 3)/(1 - z\varepsilon)$ are possible:

for $\varkappa \geq 0$

$$z = X, \quad \frac{3}{4\varepsilon + 1} \leqslant X < \frac{1}{\varepsilon},$$

for $\varkappa < 0$

$$z = \tilde{X}_1 < \frac{3}{4\varepsilon + 1}, \quad z = \tilde{X}_2 > \frac{1}{\varepsilon}.$$

Since

$$\frac{\rho_1}{\rho} - f = \frac{(m_1 - m_2)\,f\,(1-f)}{m_1 f + m_2 (1-f)} > 0,$$

the sign of $\varkappa$ is the same as that of v_0.

The criterion for the process to be possible can be taken, as before, to be the sign of the entropy difference on both sides of the front if the external forces there are independent of the molecular velocity:[2]

$$S' - S = C \ln I, \quad I = \frac{\rho}{\rho'}\varepsilon^{3/5} \tag{8}$$

($C = \text{const} > 0$). To investigate the behavior of (8), it is convenient to compute the derivative of the entropy difference at $\varepsilon = 1$ (here $z = z_0$):

$$\frac{d}{d\varepsilon}(S' - S) = \frac{C}{I}\frac{dI}{d\varepsilon} = \frac{C}{I}\left(\frac{3}{5} - z_0\right).$$

For $\varkappa = 0$ the derivative vanishes; for $\varkappa < 0$ and $z = \tilde{X}_1$ it is positive and for a weak compression shock wave ($\varepsilon > 1$, $\varepsilon - 1 \ll 1$) the entropy difference is positive (since

$S' - S$ for $\varepsilon = 1$). For $\varkappa > 0$, $z_0 > 3/5$, and for $|\varepsilon - 1| \ll 1$ the difference $S' - S$ is negative (if a compression wave is involved). Consequently for $\varkappa > 0$ a weak compression shock wave is impossible but there is no energy prohibition on the existence of a weak rarefaction shock. By (6) in the limiting cases of strong compression and rarefaction shock waves (such solutions can readily be obtained in the form of series in $1/\sqrt{\varepsilon}$ and ε respectively) we can show that for both possible solutions ($z = X, \tilde{X}_1$) there exists a strong compression shock wave, while a strong rarefaction shock wave ($\varepsilon \to 0$) cannot occur.

Thus, for $\varkappa > 0$ (when the molecules of the light component move on average toward the front of the shock wave relative to the behavier molecules) only a fairly strong compression shock wave can exist; moreover, there is no energy prohibition on the existence of rarefaction shock waves of sufficiently low intensity.

Two types of shock waves are possible for $\varkappa < 0$. For one of these ($z = \tilde{X}_1$) only compression shock waves can occur (but at any intensity – as for $\varkappa = 0$). The other root ($z = \tilde{X}_2$) corresponds for $\varkappa = 0$ to an entropy wave (as graphic analysis indicates, as $\varkappa \to 0$, $\tilde{X}_2 \to \infty$, and $u \to 0$); the condition $S' - S > 0$ holds for it, it turns out, for any $\varepsilon < 1$.

---

[1] T. Cowling, Phil. Mag., 33, 61 (1942).

[2] S. Chapman and T. Cowling, The Mathematical Theory of Nonuniform Gases, Cambridge Univ. Press (1952).

Radio-frequency absorption in a plasma confined by rf plugs

K. S. Golovanivskii, V. D. Dougar-Jabon, and L. A. Pokhmel'nykh

Patrice Lumumba Friendship of Nations University, Moscow

(Submitted February 15, 1973; resubmitted September 21, 1973)
Zh. Tekh. Fiz., 44, 2407-2410 (November 1974)

The absorption of radio-frequency energy is investigated in a plasma with energetic ions which is confined by radio-frequency plugs operated at the electron cyclotron resonance (ECR). With a magnetic field gradient of 10-40 G/cm in the ECR region and with longitudinal ion energies of 1 keV the plasma reflection is essentially elastic.

1. The possibility of confining a plasma by an RF "plug" in a mirror device was first pointed out by Consoli,[1] who used a single-particle model with tensor mass. Experiments have confirmed this possibility,[2,3] but the question of the energy exchange between the plasma and the high-frequency field and the final energy balance in this combination of fields remains unresolved. In general, when a plasma is reflected from a barrier the plasma can be heated by absorbing energy from the high-frequency field. It is of interest to determine the minimum amount of high-frequency power which must be introduced into the plasma to ensure that it will be reflected for a given profile of the mirror magnetic field.

The high-frequency energy dissipated in the plasma in the process of reflection of the beam characterizes the adiabaticity of the barrier. In passing through the resonance zone each electron accumulates some transverse energy $W_{e\perp}$, which in the mirror magnetic field, stops ions with longitudinal energy $W_{i\parallel}$ by the ambipolar mechanism. The local value of the mirror ratio R^* in the plane of the turning point with respect to the resonance plane is B/B_{res}. Using the expresion[4]

$$W_{e\perp}=\frac{W_{i\parallel}}{R^*-1}, \tag{1}$$

we obtain the high-frequency power absorbed by the plasma flux in one pass through the resonance zone:

$$P_1=\frac{J_i W_{i\parallel}}{q(R^*-1)}, \tag{2}$$

where J_i is the flux of plasma ions and q is the ion charge. When the reflected plasma passes back through the ECR zone the energy exchange between the plasma and the field is characterized by the power P_2, which is positive if the energy goes from the plasma to the field or negative if energy is transferred in the reverse direction. The total reflection energy balance will be characterized by the power P taken by the plasma from the high-frequency field:

$$P=P_1+P_2. \tag{3}$$

We introduce the recovery factor

$$\eta=-\frac{P_2}{P_1}=1-\frac{P}{P_1}, \tag{4}$$

which characterizes the energy recovered from the plasma or introduced into it in repeat passage through the resonance zone. Using (2), we have for η

$$\eta=1-\frac{Pq(R^*-1)}{J_i W_{i\parallel}}. \tag{5}$$

Since the second term on the right side of (5) is always positive, the maximum value of η is unity, corresponding to total recovery of high-frequency energy and, thus, elastic reflection of the plasma flux from the barrier. When $0 < \eta < 1$ the recovery is partial, in which case the plasma does not completely give up in the reverse pass the energy that is acquired in the first pass. The case $\eta < 0$ corresponds to additional absorption of energy by the plasma in passing back through the resonance zone.

2. Our experiments employ the apparatus shown schematically in Fig. 1. A Penning plasma source 1 yields a stationary argon plasma flux with density in the range $5\cdot10^7$-$5\cdot10^8$ cm^{-3}, longitudinal ion energy $W_{i\parallel}=0.3$-1.6 keV, and electron thermal energy 20-40 eV, depending on the mode in which the source operates. The flux moves, along a glass tube 5 cm in diameter. The residual gas pressure in the system does not exceed $1\cdot10^{-5}$ torr with dynamic pumping with gas leaked continuously into the source. Coil 2 creates a magnetic mirror that is axisymmetric with the beam; the profile is shown in Fig. 1. A high-frequency TE_{111} field with electric vector perpendicular to the direction of motion of the plasma flux is excited in cylindrical cavity resonator 3. The resonator is driven by generator 4 at 2375 MHz, the peak generator power being 10 W. The magnetic field in the center plane of the resonator is kept equal to the ECR resonance value of 850 G; the gradient in the neighborhood of this plane varies over the range 10-40 G/cm. The ion flux J_i, the longitudinal energy $W_{i\parallel}$, and the turning point of the plasma flux are found by using a movable five-grid charged-particle energy analyzer 5. In the experiments, the turning point is 5-6 cm from the resonance plane. From this we can readily determine the local mirror ratio R*.

The absolute value of the high-frequency loss in the plasma is given by

$$P=P_0\left(1-\frac{E^2}{E_0^2}\right), \tag{6}$$

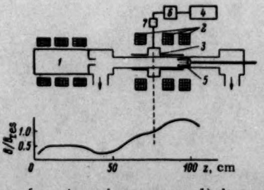

Fig. 1. Diagram of experimental arrangement: 1) plasma source; 2) dc coils; 3) resonator; 4) high-frequency generator; 5) movable analyzer; 6) attenuator; 7) ferrite isolator.

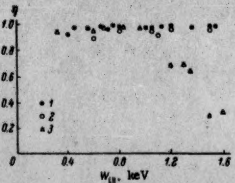

Fig. 2. Recovery factor as a function of the longitudinal ion energy for various magnetic-field gradients dB/dz in the ECR zone.

where E_0 and E are the electric component of the field in the empty resonator and with plasma; P_0 is the power loss in the empty resonator, this being determined by customary methods. This equation holds for $E^2/E_0^2 \simeq Q/Q_0$, which is the case in this experiment. Here, Q_0 and Q are the quality factors of the empty resonator and the resonator with plasma. The absolute value of E is determined by using a calibrated detector.

3. Figure 2 shows the experimental results obtained for all three longitudinal magnetic-field gradients in the resonance region (10, 32, and 40 G/cm; points 1, 2, and 3, respectively). Experimental data for the gradients are not given in the 10–32 G/cm range since the results are identical to the case of 10 and 32 G/cm over the entire $W_{i\parallel}$ range we have investigated.

As can be seen from Fig. 2, for all gradients below 32 G/cm we have total recovery of the transverse electron energy in the range of longitudinal ion energies 0.4–1.6 keV. Consequently, under these conditions the plasma flux is reflected with low energy loss. As the field gradient increases to 40 G/cm effective recovery is observed at energies $W_{i\parallel} \nless 1.0$ keV. For $W_{i\parallel} > 1.0$ keV we observe a sharp decrease in the recovery level, all the way to $\eta = 0.3$ for $W_{i\parallel} = 1.6$ keV, in which case the electrons maintain about 70% of the recovered energy in passing back through the ECR zone.

4. The total energy for recovery for appropriate field gradients is a result of the double resonance interaction between the electrons and the high-frequency field; this is associated with the ambipolar coupling between the ions and electrons beyond the resonance plane. If the electrons and ions are not coupled in the ECR zone the model proposed in ref. 5 is valid; in this model the electrons are reflected directly in the ECR plane and the interaction between the electrons and the field is a single-pass process so that energy recovery is impossible. But the present results indicate that recovery occurs and the plasma particles penetrate beyond the resonance plane by distances that are much greater than the distances traversed in a Larmor period. The existence of a broad range of field gradients for which elastic reflection occurs indicates that an automatic phase-focusing mechanism exists for particles when they pass back through the resonance plane. This self-focusing could result from the relativistic change in electron mass, as shown in ref. 6. According to ref. 6, phase self-focusing and energy recovery occur when the electrons pass back through the ECR zone:

$$\frac{dB}{dz} < 4.7 \cdot 10^{-7} \mu \frac{E^2}{W_{i\parallel}} B_{\text{res}} |z - z_0| \tag{7}$$

in this region, where z_0 is the classical ECR point; z is the coordinate along the axis (in cm), dB/dz is the magnetic field gradient at z, μ is the ion mass number; E is the high-frequency field in the zone (in V/cm), $W_{i\parallel}$ is the longitudinal ion energy (in keV), and B_{res} is the magnetic field corresponding to classical ECR (in G).

According to the experimental data, energy recovery occurs when the magnetic-field gradients in the ECR zone are small; as dB/dz increases, recovery occurs for smaller $W_{i\parallel}$ values. These facts are in qualitative agreement with (7). To compare (7) quantitatively with experimental results we must have experimental data on dB/dz as a function of z within the resonance zone, i.e., over a length of a few millimeters. It does not seem possible to make such measurements, and therefore the theoretical and experimental results can only be compared roughly, using parameter values that are averaged over the ECR zone. Taking the average value of dB/dz = 40 G/cm, the width of the resonance zone $d = |z - z_0|$, using the experimental parameters $\mu = 40$, $B_{\text{res}} = 850$ G, E = 70 V/cm, and assuming that the limiting ion energy for phase self-focusing is $W_{i\parallel} = 1$ keV, we find from (7) that d = 0.5 cm. The magnetic field varies by about 2% of B_{res} for this length, and therefore for ECR to occur in this zone the relativistic change in mass on d should also be about 2% i.e., the transverse electron energy starting the second pass reflection should be $W_{e\perp} \simeq 0.02 \cdot mc^2 = 10$ keV. According to (1), this value of $W_{e\perp}$ will stop ions for $R^* = 1.1$, this being of the same order as the experimentally measured value of $R^* = 1.3$ for this case. Thus criterion (7) agrees roughly with the experimental results, and we can explain the observed effect of quasiadiabatic plasma reflection from a magnetic mirror with local ECR by a phase self-focusing effect, associated with the relativistic change in electron mass.

---

[1] T. Consoli, Phys. Lett., 7, 254 (1963); T. Consoli and R. Hall, Nucl. Fusion, 3, 237 (1963).

[2] R. Bardet, T. Consoli, and R. Geller, Nucl. Fusion, 4, 48 (1964).

[3] K. S. Golovanivskii (Golovanivsky) and V. D. Dougar-Jabon, Phys. Lett., 34A, 222 (1971).

[4] K. S. Golovanskii (Golovansky) and L. A. Pokhmel'nykh (Pokhmelnykh), Fifth European Conf. on Controlled Fusion and Plasma Physics, Grenoble (1972).

[5] A. D. Piliya and R. Ya. Frenkel', Zh. Tekh. Fiz., 34, 1752 (1964) [Sov. Phys.—Tech. Phys., 9, 1356 (1965)].

[6] K. S. Golovanivskii (Golovanivsky), Phys. Lett., 44A, 3 (1973).

Motion of stable aerosol particles

O. A. Barsegyan and Yu. I. Yalamov

Kalinin State University

(Submitted July 9, 1973; submitted January 22, 1974)
Zh. Tekh. Fiz., 44, 2410-2412 (November 1974)

The velocity of stable (nonvolatile) aerosol particles is compared with that of drops that increase in size or vaporize. When a phase transition occurs the material in the drop becomes one of the components of a binary gas mixture; the aggregate of drops and aerosol particles in such a mixture is considered. The derivation of the expression for aerosol-particle speed is based on the theory of thermophoresis and diffusophoresis in binary gas mixtures, as elaborated in earlier studies by Yalamov and coworkers. This study takes account of the radial components (relative to the drop) of the center of inertia for a binary gas system consisting of two parts that are proportional to the concentration and temperature gradients respectively. The time required to cleanse a given volume of dust aerosols can be estimated from the results.

Aerosol particles suspended in gases acquire a directed motion when the components of the gas mixture are subject to a concentration field or temperature gradient. The theory of this motion (thermophoresis and diffusophoresis) is elaborated most rigorously in refs. 1 and 2 for stable aerosol particles. The present paper is concerned primarily with computing the velocity of stable aerosol particles toward increasing or vaporizing drops that are capable (as a result of phase transition of the drop material) of changing into one of the components of the binary gas mixture in which the entire system of drops and aerosol particles is suspended. By determining the concentrations and temperatures near the drop, when there is a decrease in these quantities on the surface of the drop and within the gas mixture, we obtain the radial components of the concentration gradients of the mixture component undergoing phase transition on the surface of a particle, and the temperature gradient:

$$(\nabla C_1)_r = (C_{1\infty} - C_{10}) \frac{R_0}{r^2}, \tag{1}$$

$$(\nabla T)_r = (T_\infty - T_0) \frac{R_0}{r^2}, \tag{2}$$

where C_1 is the relative concentration in the volume of gas that evaporates (or condenses) on a drop, $C_{1\infty}$ and C_{10} are the concentrations at a great distance from the drop and on its surface respectively, T is the gas temperature, T_∞ and T_0 are the temperature at a great distance from the drop and on its surface, R_0 is the drop radius, and r is the distance from the center of the drop to a point within the volume of gas ($r > R$).

Knowing the concentration and temperature gradients ∇C_1 and ∇T and allowing for the Stefan transfer velocity of the center of inertia of a binary gas mixture from ref. 3 and the rates of thermophoresis and diffusophoresis of nonvolatile aerosol particles in binary gas mixtures,[4,5] we can obtain the following expression for the radial velocity of the aerosol particles relative to the drop:

$$u_r = -(\gamma_1 + \gamma_2) \frac{R_0}{r_2}, \tag{3}$$

$$\gamma_1 = \frac{2\left(K_{Tsl}\eta_0 + K_{TD}^{(sl)} T_0\rho_0\right)\varkappa_e (T_\infty - T_0)}{(\varkappa_i + 2\varkappa_e)\, T_0\rho_0}, \tag{4}$$

$$\gamma_2 = \left(K_{sl} + \frac{n_0^2 m_1}{n_2\rho_0}\right) D_{12} (C_{1\infty} - C_{10}). \tag{5}$$

We have employed the following notation in (4) and (5): η_0 and ρ_0 are the average viscosity and density of the gas mixture, $\varkappa_e$ and $\varkappa_i$ are the thermal conductivities of the gas mixture and particle, m_1 is the molecular mass for the mixture component with relative concentration C_1, $K_{Tsl}K_{TD}^{(sl)}$ are the thermal and thermal-diffusion slipping coefficients respectively, K_{sl} is the diffusion slipping coefficient, D_{12} is the mutual diffusion coefficient for the mixture component, $n_0 = n_{01} + n_{02}$ is the total number of gas molecules per unit volume as $r \to \infty$, and n_{01} and n_{02} are for the first and second components taken separately.

Equation (3), with (4) and (5), is written under the assumption that λ, the mean free path of the gas molecules, is much smaller than the radius R of the gas particles.

Furthermore, it is assumed that n_{01} is comparable to n_{02}, i.e., the numerical concentration of molecules of the first component, which undergoes phase transition on the particle surface, is not small as compared to the numerical concentration of the carrier-gas molecules. In terms of the relative concentrations, this condition is

$$C_{10} = \frac{n_{01}}{n_0} \sim C_{20} = \frac{n_{02}}{n_0}.$$

Equation (3) can be refined by allowing for thermal-diffusion transport of the center of inertia of a binary mixture in a temperature-gradient field. Like thermal-diffusion slipping, which is proportional to $K_{TD}^{(sl)}$ in (4), this effect is important for comparable concentrations n_{01} and n_{02}. It can be shown that the velocity of thermal-diffusion transport of the center of inertia is

$$v_{\mathrm{ci}}^{(TD)} = -\frac{n_0 D_{12}}{\rho_0} (m_1 - m_2) K_{TD} \frac{\nabla T}{T_0}, \tag{6}$$

where m_2 is the molecular mass for the carrier gas and K_{TD} is the coefficient of the volume thermal diffusion (see, e.g., ref. 6). Substituting (2) into (6), we obtain

$$v_{r,(\mathrm{ci})}^{(TD)} = -\frac{n_0 D_{12}}{\rho_0 T_0} (m_1 - m_2)(T_\infty - T_0) K_{TD} \frac{R}{r^2}. \tag{7}$$

Finally, from (3)-(5) and (7) we obtain

$$u_r = -\frac{2\left(K_{Tsl}\eta_0 + K_{TD}^{(sl)} T_0\rho_0\right)\varkappa_e}{T_0\rho_0(\varkappa_i + 2\varkappa_e)} (T_\infty - T_0)\frac{R}{r^2} - \frac{n_0 D_{12}}{\rho_0 T_0}(m_1 - m_2)(T_\infty - T_0) \times K_{TD}\frac{R}{r^2} - \left(K_{sl} + \frac{n_0^2 m_1}{n_{20}\rho_0}\right) D_{12} (C_{1\infty} - C_{10}) \frac{R}{r^2}. \tag{8}$$

The relative value of the terms obtained in (8), the sign of the velocity, and the cleansing time (for aerosol particles attracted to drops) of a given volume (cleansing of dust aerosols) can be computed from (8) for specific systems.

The authors are grateful to V. S. Galoyan for comments.

---

[1] Yu. I. Yalamov and I. N. Ivchenko, Zh. Fiz. Khim., 45, 577 (1971).

[2] Yu. I. Yalamov and B. A. Obukhov, Zh. Tekh. Fiz., 42, 1064 (1972) [Sov. Phys.– Tech. Phys., 17, 844 (1972)].

[3] Yu. I. Yalamov, Doctoral dissertation, Institute of Physical Chemistry, Academy of Sciences of the USSR, Moscow (1968).

[4] Yu. I. Yalamov, O. A. Barsegyan, V. S. Galoyan, and B. V. Deryagin, Dokl. Akad. Nauk SSSR, 216, No. 2 (1974).

[5] Yu. I. Yalamov, O. A. Barsegyan, and V. S. Galoyan, Zh. Fiz. Khim. VINITI deposition No. 6328-73, June 21, 1973.

[6] S. Chapman and T. Cowling, Mathematical Theory of Nonuniform Gases, Cambridge Univ. Press (1952).

Motion of charged particles in a nonneutral plasma

E. N. Agafonova and L. I. Grechikhin

(Submitted March 6, 1973; resubmitted October 16, 1973)
Zh. Tekh. Fiz., 44, 2412-2414 (November 1974)

We analyze the nonlinear oscillations of a charged particle in the field of a nonneutral plasma. This is done by first finding the electric field equivalent to that of a stack of plates each with a charge density which varies linearly in a given direction. The equations for the nonlinear oscillations are integrated by methods due to Newcomb and Lindstedt. It is found that the charged particle oscillates in the field with a period which depends on the charge and mass of the particle and on the maximum density of the uncompensated charge, its dimensions, and the conditions of formation.

Regions with uncompensated electric charge can form in a plasma in an electric or a magnetic field. These can be regions near the electrodes in electric discharges or in thermionic converters. Regions with an uncompensated electric charge can be formed in a plasma moving at right angles to a magnetic field as a result of the Hall effect. We consider the behavior of charged particles in a plasma with an uncompensated electric charge. In such a plasma the oscillatory phenomena can have an effect on the operation of various plasma power devices. We consider the oscillations of charged particles in a plasma with an uncompensated electric charge of the opposite sign.

In the first approximation the distribution of uncompensated charge can be described by the linear relation

$$n=n_0(1-c|x|), \tag{1}$$

where n_0 is the maximum value of the uncompensated charge density, n is the charge density at a distance x from the position of the maximum, and c is a constant depending on how the uncompensated charge is formed.

We use Gauss' theorem to calculate the intensity of the electric field E produced by the charge distribution (1). We represent the field as the sum of the fields of a stack of plates each of thickness dx and carrying a surface density of uncompensated charge $d\sigma = n dx = n_0(1-c|x|)dx$, which decreases from the center to the edges. The total charge of a stack of thickness 2x is $Q = S_0\int_{-x}^{x} d\sigma$. Here, S_0 is the area of a plate and x is the distance from the center of the stack to the points with coordinates x and −x. The electric field is

$$E=\frac{n_0 x}{\varepsilon}-\frac{n_0 c x^2}{\varepsilon}. \tag{2}$$

A charged particle in this field experiences a force, and its equation of motion is

$$m\ddot{x}=-\alpha x+\alpha_1 x^2, \tag{3}$$

where $\alpha = en_0/\varepsilon$, $\alpha_1 = en_0c/\varepsilon = \alpha c$. Equation (3) describes nonlinear oscillations. It can be put in a simpler form by the change of variables

$$t=\sqrt{\frac{m}{\alpha}}\,\tau. \tag{4}$$

Then (3) becomes

$$\frac{d^2x}{d\tau^2}+x=cx^2. \tag{5}$$

To determine the limits of variation of x we use the conservation of energy:

$$\left(\frac{dx}{d\tau}\right)^2+x^2=V_0^2+\frac{2}{3}cx^3, \tag{6}$$

where V_0 denotes the generalized velocity at x = 0. By setting $dx/d\tau = 0$ in (6) we find the equation for the limiting positions

$$x^2=V_0^2+\frac{2}{3}cx^3. \tag{7}$$

We solve Eq. (7) for x by expanding x in a power series in V_0 with undetermined coefficients and substituting into (7). This gives the upper and lower limits for x:

$$\left.\begin{aligned} x_1&=V_0+\frac{1}{3}cV_0^2+\frac{5}{18}c^2V_0^3+\ldots,\\ x_2&=-V_0+\frac{1}{3}cV_0^2-\frac{5}{18}c^2V_0^3+\ldots.\end{aligned}\right\} \tag{8}$$

We specify the initial conditions in the form

$$\tau=0,\quad x=x_1,\quad \frac{dx}{d\tau}=0. \tag{9}$$

In order to ensure a finite solution we replace τ by η, as in ref. 1:

$$\tau=\frac{\eta}{\sqrt{1+\mu}}, \tag{10}$$

$$t=\eta\sqrt{\frac{m}{\alpha(1+\mu)}}. \tag{11}$$

We seek the solution of Eq. (5) in the form of a power series in x_1 (or x_2), i.e.,

$$\left.\begin{aligned} x&=x_1y_1(\eta)+x_1^2y_2(\eta)+x_1^3y_3(\eta)+\ldots,\\ \mu&=\mu_1x_1+\mu_2x_1^2+\mu_3x_1^3+\ldots.\end{aligned}\right\} \tag{12}$$

By substituting (12) into (5) and comparing coefficients of the same powers of x_1 we obtain the equations

$$\left.\begin{aligned} \ddot{y}_1+y_1&=0,\\ \ddot{y}_2+y_2&=-\mu_1\ddot{y}_1+cy_1^2,\\ \ddot{y}_3+y_3&=-\mu_2\ddot{y}_1-\mu_1\ddot{y}_2+2cy_1y_2,\\ \ldots&\ldots\ldots\end{aligned}\right\} \tag{13}$$

We solve these equations in sequence, arranging the coefficients μ_i so that the solutions do not increase without bound with time. Limiting ourselves to the first three terms in expansion (12) we obtain

$$\begin{aligned} x=\frac{c}{2}x_1^2-\frac{c^2}{3}x_1^3+\ldots+\left(x_1-\frac{c}{3}x_1^2+\frac{29}{144}c^2x_1^3+\ldots\right)\cos\eta_1\\ +\left(-\frac{c}{6}x_1^2-\frac{c^2}{9}x_1^3+\ldots\right)\cos 2\eta+\frac{c^2}{48}x_1^3\cos 3\eta+\ldots,\end{aligned} \tag{14}$$

where

$$\eta=t\sqrt{\frac{\alpha}{m}(1+\mu)}=t\sqrt{\frac{\alpha}{m}\left(1-\frac{5}{6}c^2x_1^2+\ldots\right)}. \tag{15}$$

The period of series (14) for x is 2π. If we return to the characteristic time scale t the period of the series is

$$T = 2\pi \sqrt{\frac{m}{a(1+\mu)}} \simeq 2\pi \sqrt{\frac{m}{a}} \left(1 - \frac{5}{6} c^2 x_1^2\right)^{-1/2}. \qquad (16)$$

Neglecting higher-order terms (16) can be written in the form

$$T = 2\pi \sqrt{\frac{m}{a}} \left(1 + \frac{5}{12} c^2 x_1^2\right) = 2\pi \sqrt{\frac{m\varepsilon}{en_0}} \left(1 + \frac{5}{12} c^2 x_1^2\right). \qquad (17)$$

Thus a charged particle moving in the field of an uncompensated charge distribution of the opposite sign oscillates with a period which depends on the mass and charge of the particle and on the parameters of the field of the uncompensated charge -- the maximum density of the uncompensated charge n_0, the conditions of formation of the uncompensated charge, and its dimensions.

---

[1] W. Hort, Technische Schwingungslehre, Berlin (1922).

Initial stage of a high-current discharge in air

A. F. Aleksandrov, V. V. Perebeinos, A. T. Savichev, and I. B. Timofeev
M. V. Lomonosov State University, Moscow

(Submitted July 31, 1973; resubmitted February 27, 1974)
Zh. Tekh. Fiz., 44, 2414-2415 (November 1974)

The present work investigates the initial stage of a discharge in air created by an exploding wire. The initial stage of rupture, whose development depends on the rate of rise of the current, determines the subsequent development of the discharge and the validity of the self-similar description.

Reference 1 is an investigation of the dynamics and radiation of high-current discharges in air. Experimental results are compared with those given by the self-similar model and numerical calculations.

For a linear rate of rise of the current, I = Ft, the plasma parameters in the discharge[1,2] depend on the initial conditions; more specifically, they depend on the rate of rise $F = I_0 2\pi/T$, where I_0 is the maximum current and T is the period. The physical picture of the discharge presupposes that there is a shock wave that propagates through the unperturbed gas immediately ahead of the edge of the thermal zone $R_{sw} = \lambda R_{tz}$ (where R_{sw} and R_{tz} are the radii of the shock front and the current zone, while $\lambda = 1.1$); the shock wave carries off a constant proportion of the energy introduced into the discharge channel[3] $E_{sw} = 0.2\ E_{tz}$. Here, $E_{tz} = Q - W - E_{sw}$, Q being the energy contained in the discharge and W the energy radiated in the transparency band of air ($\lambda > 1860$ Å).

At high rates of energy input into the discharge ($F > 10^{10}$ A/sec) we observe satisfactory agreement between the theory and the experimental data; as F decreases the discrepancy between theory and experiment increases. This result is evidently to be associated with processes that occur in the initial stage of the discharge.

The numerical solution of the magnetohydrodynamic equations on a computer is also extremely sensitive to the choice of initial conditions. Hence we give results pertaining to the initial stage of a high-current discharge in air, 40 cm long. Our experiments employ the apparatus described in ref. 1. The current period is $T \simeq 70$ μsec. Wires of varying diameter and of different materials (nichrome, aluminum, iron, tungsten, and molybdenum) are used with various initial conditions (the injected energy $Q' = Q/l$ per unit discharge length over the first half-period of the discharge current varies from 0.125 to 1.6 kJ/cm, to variation in F from $1.5 \cdot 10^9$ to $1.6 \cdot 10^{10}$ A/sec).

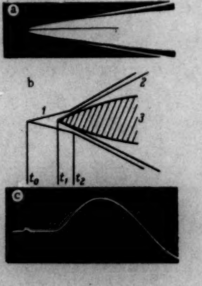

Fig. 1

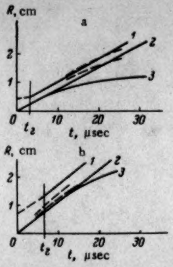

Fig. 2

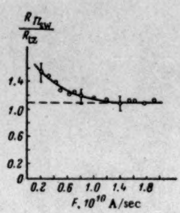

Fig. 3

Figure 1a (rupture of aluminum wire 0.3 mm in diameter, $CU^2/2l = 0.72$ kJ/cm, $F = 7 \cdot 10^9$ A/sec) gives a typical slit luminescence scan of the discharge channel with time. The basic details which can be seen in the photograph are shown schematically in Fig. 1b (1 being the front of I_{sw}, 2 the front of II_{sw}, and 3 the current zone), while Fig. 1c gives an oscillogram of the discharge current. We can readily discern all three characteristic phases of the discharge: the first current pulse (at time t_0), then the pause, and secondary breakdown of the discharge channel ($t_0 - t_1$). It can be seen from Fig. 1 that the first shock wave (1) appears at time t_0, corresponding to the first current pulse; this is evidently associated with the rapid phase transition in the wire. Some time later there is a secondary breakdown (t_1), resulting in the appearance and broadening of the thermal zone. As it expands, the thermal zone generates a second shock wave (II), which propagates immediately ahead of the thermal zone of the discharge. The first shock wave arising at t_0 has low velocity and weak luminescence. A few microseconds after the formation of the thermal zone, the luminescence and rate of propagation of shock wave I increase, this probably being due to its interaction with shock wave II and the radiation of the thermal zone. Then (at t_2) shock wave II breaks away from the current channel; for these experimental conditions shock wave II never overtakes the first wave. In most cases we observe a few post-breakdown shock waves corresponding to the formation of streamer channels.

Figure 2 shows the radii of the fronts of shock waves I and II and the current zone of the discharge channel (curves 1, 2, and 3 respectively), these being obtained by processing the raw data, for the rupture of a thin aluminum wire (0.1 mm in diameter) and various values of the energy per unit discharge length [$Q' = 0.2$ kJ/cm, $F = 2.5 \cdot 10^9$ A/sec (*a*) and $Q' = 1.2$ kJ/cm, $F = 1.3 \cdot 10^{10}$ A/sec (b)]. The dashed curves correspond to calculations using self-similar theory. It can be seen from Fig. 2 that for small F (low rate of energy input) there is a considerable discrepancy between the experimental data and the self-similar calculations (up to a factor of 2), whereas for large F (Fig. 2b) the agreement is good.

Figure 3 shows the ratio of the radius of the front of shock wave II to the radius of the thermal zone $\lambda = R_{sw}/R_{tz}$ as a function of F. The dashed line corresponds to calculations using self-similar theory. It can be seen from Fig. 3 that for small F the experimental data differ markedly from self-similar theory; for large F they are virtually the same. As implied by the above results, this is associated with the fact that the self-similar theory does not take account of events at the beginning of the process — the phase transition and subsequent breakdown of the gap, the duration and features of these processes, the appearance of shock wave I, and its interaction with the current zone of the discharge channel.

---

[1] A. F. Aleksandrov, V. V. Zosimov, S. P. Kurdyumov, Yu. P. Popov, A. A. Rukhadze, and I. B. Timofeev, Zh. Eksp. Teor. Fiz., 61, 1841 (1971)[Sov. Phys. – JETP, 34, 979 (1972)].

[2] A. F. Aleksandrov, V. V. Zosimova, A. A. Rukhadze, V. I. Savoskin, and I. B. Timofeev, Krat. Soobshch. Fiz., No. 8, 72 (1970).

[3] V. B. Rozanov and A. A. Rukhadze, Survey Paper presented to Ninth Intern. Conf. on Phenomena in Ionized Gases, Bucharest (1969).

Electron energy distribution in a constricted, low-pressure hydrogen discharge

M. A. Abroyan, Yu. M. Kagan, N. B. Kolokolov, and B. P. Lavrov

A. A. Zhdanov Leningrad State University

(Submitted February 22, 1974)
Zh. Tekh. Fiz., 44, 2416-2417 (November 1974)

The distribution function is measured in a constricted arc discharge in hydrogen. The probe-current modulation method is used. The measurements are carried out in the pressure range 0.02-0.2 torr at discharge currents up to 0.55 A. The distribution of fast electrons is found to be strongly non-Maxwellian; this feature must be taken into account in computing direct dissociation, excitation, and ionization from atomic and molecular states. A qualitative description of the formation of the distribution function is given .

Constricted arc discharges at low pressures are used[1] widely.

In the available studies of this discharge[2-4] the electron energy distribution function $f(\varepsilon)$ is assumed to be Maxwellian. This assumption is unjustified. Since theoretical calculation of the distribution function entails substantial difficulties under these circumstances, it becomes particularly important to make a direct experimental determination of $f(\varepsilon)$.

In this paper we study a hot-cathode arc discharge in hydrogen, constricted by the effect of a cone-shaped electrode between the cathode and the anode.[5] A double space-charge sheath forms at the point at which the discharge gap contracts.[1] Our investigations pertain to the pressure range 0.02-0.2 torr and current range 0.1-0.55 A with the intermediate electrode at floating potential.

We introduce a movable electric probe of molybdenum wire 0.035 mm in diameter sheathed in a quartz capillary into the region between the intermediate electrode and the anode. The length of the uninsulated part is 1.0 mm. In measuring the energy distribution function of the electrons in the plasma near the anode we used the procedure based on probe-current modulation.[6] We calibrate the measurement system so as to be able to obtain $f(\varepsilon)$ in absolute value.[7] The electron density n is found by integrating the distribution function.

Figure 1 shows the $f(\varepsilon)$ obtained at the axis 4 mm from the anode. The axial variation in the energy distribution function of the electrons is illustrated by Table 1. This table gives the electron density n, the average distribution energy $\bar{\varepsilon}$, the relative number of electrons whose energy exceeds the value required for effective hydrogen dissociation (9 eV), and the relative number of electrons making up a pronounced group in the high-energy region. The measurements are performed at various distances l from the anode. For comparison, the table includes the same quantities with a Maxwellian distribution. The distribution of slow electrons ($\varepsilon \leq 5$ eV) in our experiments is quasiequilibrium with a temperature that is determined by taking the logarithm of the second derivative of the probe current with respect to the potential in this energy region. The temperature as determined in this manner is 1 eV at a distance of 4 mm from the anode. It is clear from Fig. 1 and Table 1 that $f(\varepsilon)$ is markedly a nonequilibrium function.

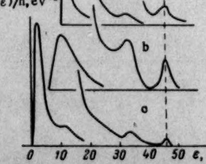

Fig. 1. Energy distribution function of electrons: p (in torr) and i (in A) as follows: a) 0.1, 0.4; b) 0.1, 0.2; c) 0.2, 0.2.

TABLE 1. Axial Variation in the Energy Distribution Function of Electrons for p = 0.1 torr, i = 0.4 A

		n, 10^{11}cm^{-3}	$\bar{E}$, eV	$\frac{\Delta n_\varepsilon > 9 \text{ eV}}{n}$	$\frac{\Delta n_\varepsilon > 32.5 \text{ eV}}{n}$
l, mm	6.5	7.0	5.2	0.16	0.004
	5.0	5.4	4.6	0.14	0.003
	4.0	3.4	3.8	0.12	0.002
Maxwellian distribution, ε = 3.8 eV		—	3.8	$7 \cdot 10^{-2}$	$1 \cdot 10^{-5}$
Maxwellian distribution, kT = 1 eV		—	1.5	$4 \cdot 10^{-4}$	$5 \cdot 10^{-14}$

Our results can be interpreted qualitatively as follows: A group of electrons that accelerate in the field of the double sheath relax with respect to energy through inelastic collisions with atoms and molecules of the gas. The maximum in the high-energy region comes from electrons that experience only elastic collisions on their path to the probe. When the discharge conditions change the position of this maximum varies in accordance with the change in the potential drop in the sheath but the configuration of the maxima and the form of the distribution function in the high-energy region remain the same.

Thus, in a constricted arc discharge the electron energy distribution function is markedly different from the equilibrium distribution; this must be taken into account in computing direct dissociations, excitation, and ionization from atomic and molecular states.

---

[1] M. D. Gabovich, Physics and Engineering of Plasma Ion Sources [in Russian], Atomizdat, Moscow (1972).

[2] A. Singh and J. E. Rowe, J. Appl. Phys., 36, 3535 (1965).

[3] M. Watanabe and T. Suita, Japan. J. Appl. Phys., 6, 758 (1967).

[4] C. Lejeune, Proc. 10th ICPIG, Contr. Papers Oxford (1971), p. 218.

[5] M. A. Abroyan, Yu. M. Kagan, N. B. Kolokolov, and B. P. Lavrov, Opt. Spektrosk., 36, 644 (1974).

[6] Yu. M. Kagan, in: Spectroscopy of Gas-Discharge Plasmas [in Russian], Izd. Nauka, Leningrad (1969), p. 201.

[7] Yu. M. Kagan and N. K. Mitrofanov, Zh. Tekh. Fiz., 41, 2065 (1971)[Sov. Phys.—Tech. Phys., 16, 1636 (1972)].

Spectral narrowing of a single-mode beam oscillator

V. A. Buts and V. I. Kurilko

Physicotechnical Institute, Academy of Sciences of the Ukrainian SSR, Khar'kov

(Submitted March 18, 1974)
Zh. Tekh. Fiz., 44, 2417-2419 (November 1974)

The correlational characteristics of the signals of a single-mode beam generator resulting from fluctuations in the beam distribution function (at the input to the interaction regions) are studied. The intensity of the fluctuations depends on the stationary signal level. It is also shown that preliminary modulation of the beam at the system input, at the frequency of the generated signal, causes a marked reduction in spectral width.

The possibilities for practical utilization of high-frequency signals excited through collective interaction between beams of charged particles and plasmas[1,2] and vacuum waveguide (resonance) systems[3,4] depend markedly on the degree to which the signals are monochromatic. In this connection, ref. 1 poses the problem of controlling the spectra and intensity of beam instabilities, and proposes methods for solving this problem (see also ref. 2). This paper will consider the theory of controlling the spectrum of a single-mode beam generator. The spectral shape for nonequilibrium systems with lumped parameters has been studied in the approximation of known sources of fluctuation perturbations.[5] When the problem can be reduced to a system of exact differential equations, this approach can be generalized to self-oscillatory systems with distributed parameters, e.g., multimode lasers.[6] Below we consider the spectral shape of a single-mode beam generator with distributed wave attenuation in the interaction region; the self-excitation of this type of generator is investigated in refs. 7, 8.

Assume we are given a slow-wave resonator in which the beam excites a field

$$E_z = E(t)\,\Phi_m(r)\sin k_m z\cos(\omega_m t-\varphi)\ (\Phi_m(0)=1;$$
$$k_m = 2/L\,\pi(m+1/2);\ |z|\leqslant L/2).$$

If the average beam velocity V_0 is close to the phase velocity of the wave $V_m \equiv \omega_m/k_m$ and the transit time for the beam particles through the resonator $T_p \equiv L/V_0$ is small as compared to that of the amplitude and phase of the field in the resonator $T_f (T_p \ll T_f)$, these quantities are given by the equations

$$\left.\begin{array}{c} \dfrac{dR}{d\theta} = \langle \overset{\bullet}{S}(R,\psi\, q_0)\,F(q_0)\rangle; \\[2ex] R\dfrac{d\varphi}{d\theta} = \langle C(R,\ \varphi,\ q_0)\,F(q_0)\rangle;\quad R\equiv\dfrac{|e|\,Ek_m}{m_0\omega_m^2}, \\[2ex] C(R,\ \varphi,\ q_0)+iS(R,\ \varphi,\ q_0) \\[1ex] \equiv\displaystyle\int\limits_{\tau_0}^{\tau_f} d\tau\exp\{i[\Delta(\tau,\ q_0)+\varphi-\vartheta_0]\};\quad \vartheta_0\equiv\omega_m t_0, \\[2ex] \langle U(q_0)\rangle\equiv\displaystyle\int\limits_{\theta-\pi}^{\theta+\pi} d\vartheta_0\int dv_0 2\pi r_0 dr_0 U(q_0);\ \theta\equiv\omega_m t;\ q_0\equiv(\vartheta_0,\ v_0,\ r_0). \end{array}\right\}\quad(1)$$

Here $F(q_0)$ is the distribution function for beam particles at the resonator input $(z=-L/2)$ with respect to the entrance time ϑ_0, the initial velocities v_0, and radius r_0, the dependences on the Lagrangian time τ of the deviations $\Delta\equiv k_m Z_l-\tau$ in the particle trajectories $Z_l(\tau,\ q_0)$ from the straight line $k_m Z_l = \tau-\tau_0$ and the instant these particles leave the resonator $\tau_f(q_0)$ are given by the equations of the characteristic

$$\dot\Delta = (\dot\Delta_0^2 + R[\cos(\Delta+\varphi-\vartheta_0)-\cos(\varphi-\vartheta_0)])^{1/2}\operatorname{sgn}\dot\Delta_0,$$

$$\tau_f(q_0)+\Delta[\tau_f(q_0);\ q_0] = \pi\left(m+\frac{1}{2}\right). \qquad (2)$$

Writing $F(q_0)$ as the sum of regular (F) and stochastic ($\mathcal{F}$) functions, we can reduce the study of the field dynamics in the resonator to the solution of coupled linear equations for the perturbations $\rho\equiv R-R_0$ and $\xi\equiv\varphi-\varphi_0$ of the amplitude and phase respectively that are induced by the fluctuation forces:[5,7,8]

$$\left.\begin{array}{c} \dfrac{d\rho}{d\theta} = a_{11}\rho + a_{12}\xi + g_\rho(\theta);\ R\dfrac{d\xi}{d\theta} = a_{21}\rho + a_{22}\xi + g_\xi(\theta). \\[2ex] a_{11}+ia_{12}\equiv\left(\dfrac{\partial}{\partial R}+i\dfrac{\partial}{\partial\varphi}\right)\langle SF\rangle;\ a_{21}+ia_{22}\equiv\left(\dfrac{\partial}{\partial R}+i\dfrac{\partial}{\partial\varphi}\right)\langle CF\rangle; \\[2ex] \langle CF\rangle = \langle SF\rangle = 0;\ g_\xi + ig_\rho \\[1ex] \equiv\displaystyle\int\limits_{\theta-\pi}^{\theta+\pi} a\vartheta_0\int dv_0 2\pi r_0 dr_0\mathcal{F}(q_0)\,[C(R_0,\ \psi_0\, q_0)+iS(R_0,\ \varphi_0,\ q_0)]. \end{array}\right\}\quad(3)$$

Using (3) to compute the perturbation correlation functions for the amplitude and phase, we obtain the correlation function of the field and the shape of the line excited by the beam in the resonator. When the beam is not modulated at the resonator input, $a_{12} = a_{22} = 0$, for δ-correlated functions $\overline{g_\rho(\theta)}$ and $g_\xi(\theta)$ this line is a resonant curve with width $\nu_- \equiv \overline{g_\xi^2}/2R_0^2 \ll 1$ and height $H_- \simeq \nu_-^{-1}$, rising above a pedestal of width $\nu_+ \equiv -a_{11} > 0$ and height $H_+ \equiv \overline{g_\rho^2}/R_0^2\nu_+ \ll 1$. Unlike the results in refs. 5, in this case the functions $\overline{g_\rho^2}$ and $\overline{g_\xi^2}$ depend on the amplitude and phase of the steady-state field, which, in particular, results in a change in the effective linewidth.[9]

The basic reason for line broadening in the case in question is diffusion of the mean-square phase of the field as a result of fluctuation forces. To stabilize this diffusion, and thus narrow the line, we must introduce restoring forces that depend on the phase of the field φ. When such forces are present, the fluctuation deviations of the phase attenuate exponentially in time, so that the line shape becomes a δ-shaped peak against the background of two pedestals, whose widths $\nu_\pm \ll 1$ and heights $H_\pm \equiv \overline{g^2}/2R_0^2\nu_\pm$, where $\nu_\pm$ are the characteristic numbers of the corresponding (3) homogeneous system of equations $(dU_\pm/d\theta = -\nu_\pm U_\pm)$.

For a beam generator, such phase stabilization can be provided by modulating the beam at the resonator input. For regular periodic modulation of the form

$$F(q_0)\equiv\left[\frac{1-h}{2\pi}+h\delta(\vartheta_0)\right]\delta(v_0-V_0)\,G(r_0);\ |\vartheta_0|\leqslant\pi;\ \langle F(q_0)\rangle = 1$$

spectral narrowing is observed when the condition $h > h_{cr}$ holds, where h_{cr} is determined from the equation $H_-(h_{cr}) = 1$:

$$h_{cr} \simeq \frac{\mathcal{E}_{\zeta}^{2}}{R_{0}^{2}} \quad \left(\nu_{-} \equiv -a_{22} + \frac{a_{21}a_{12}}{a_{11}} \sim h\right).$$

Physically, the basis of this method of controlling the spectra of self-oscillators is provided by the amplification effect for the induced interaction with the field of bunched beam particles. This bunching imposes the phase of the signal on the self-oscillator; deviations from this phase attenuate exponentially as a result of the corresponding frequency drift ($\sim a_{22}$) or change in field amplitude ($\sim a_{12}$).

Thus our examination shows that the intensity of the effective fluctuation forces in a beam generator depends on the steady-state signal amplitude, and the use of the method proposed in ref. 1 of controlling the spectrum by preliminary beam modulation makes it possible to markedly narrow the signal spectrum. Unlike ref. 10, which considers the dynamics of interaction of regular perturbations of finite amplitude in a plasma–beam system, in our study the spectrum of a beam generator in the steady-state mode is controlled by preliminary modulation of the beam at the system input, so as to suppress fluctuation broadening of the line through the use of negative feedback.

The authors are grateful to Ya. B. Fainberg and B. B. Kadomtsev for comments.

---

[1] Ya. B. Fainberg, Atom. Energ., 11, 313 (1961).
[2] Ya. B. Fainberg, A Survey of Phenomena in Ionized Gases, IAEA, Vienna (1968), p. 149.
[3] A. V. Gaponova, M. N. Petelin, and V. K. Yulpatov, Izv. VUZ Radiofizika, 10, 1414 (1967).
[4] L. L. Vainshtein and G. S. Solntsev, Lectures on Microwave Electronics [in Russian], Izd. Sov. Radio, Moscow (1973).
[5] A. N. Malakhov, Fluctuations in Self-Oscillating Systems [in Russian], Izd. Nauka, Moscow (1968).
[6] L. A. Vainshtein, High-Power Electronics [in Russian], No. 6 (1969).
[7] V. I. Kurilko, Zh. Eksp. Teor. Fiz., 57, 885 (1969) [Sov. Phys.–JETP, 30, 484 (1970)].
[8] V. I. Kurilko, A. P. Tolstoluzhskii, and Ya. B. Fainberg, Atom. Energ., 32, 137 (1972).
[9] G. M. Zaslavskii and B. V. Chirikov, Usp. Fiz. Nauk, 105, 3 (1971) [Sov. Phys.–Usp., 14, 549 (1972)].
[10] N. G. Matsiborko, I. N. Onishchenko, Ya. B. Fainberg, V. D. Shapiro, and V. I. Shevchenko, Zh. Eksp. Teor. Fiz., 63, 874 (1972) [Sov. Phys.–JETP, 36, 460 (1973)].

Stabilization of two-stream instabilities

V. A. Buts

Physicotechnical Institute, Academy of Sciences of the Ukrainian SSR, Khar'kov

(Submitted March 23, 1974)
Zh. Tekh. Fiz., 44, 2419-2420 (November 1974)

It is shown that two-stream instabilities can be stabilized by electromagnetic waves or by variation of the beam velocity.

It is well known that the strength of the two-stream instability is determined by the elementary emission mechanism and by the number of coherent particles.[1,2] Instabilities develop as follows. In the unperturbed beam spontaneous emission from individual particles is quenched by mutual interactions. A perturbation causes particle bunching. The field which arises as a result of coherent radiation of the particles in these bunches, allowing for coherence between bunches, increases the perturbation amplitude, which in turn increases the bunching, and so on. The growth rate is greater, the greater the emission of the beam particles and the greater the number of coherent particles. This picture not only provides a qualitative representation of the process but also yields quantitative results which are in good agreement with those obtained in calculations.[2-4] Moreover, the picture indicates that there are three parameters of system instability which can be used to control the instability. These parameters are the emission from an individual beam particle, the number of coherent particles in a bunch, and the number of coherent bunches. All possible stabilization mechanisms can be considered in terms of these three parameters. In this note we consider two simple and effective means of affecting two-stream instabilities.

1. Assume that an electromagnetic wave propagates in a system containing an electron beam. If the wave characteristics are such that it smears out bunches that result from the growing perturbations, even a weak wave might inhibit the instability. As an example, let us consider the effect of a wave on two-beam instability. In the reference system which moves with the phase velocity of the wave, assuming that the unperturbed velocities of the beam and plasma v_{0S} only vary in space, we obtain the following system for the electrostatic oscillations:

$$\Psi_s'' + \Psi_s\left[\frac{\omega_{ps}^2}{v_{0s}^2} - \frac{3}{4}\left(\frac{v_{0s}'}{v_{0s}}\right)^2 - \frac{3}{2}\frac{v_{0s}''}{v_{0s}}\right] = -\frac{\omega_{ps}^2}{v_{0s}^2}\Psi_{1-(1)^s}e^{(-1)^s\varphi}, \tag{1}$$

where

$$\Psi_s \equiv j_s \exp\left[\frac{1}{2}\int^x P_s dx_1\right]; \quad P_s \equiv -2\frac{i\omega}{v_{0s}} + 3\frac{v_{0s}'}{v_{0s}} \quad (s = 0;\ 1),$$

and $\varphi \equiv (1/2)\int^x (P_0 - P_1)dx_1$; j_S is the perturbation current.

Assume that the unperturbed velocities vary in accordance with $v_{0S} = v_S(1 - (2/3)\alpha_S \sin \varkappa x)$, $\alpha_S \ll 1$. If $\omega_{pS}/v_S\varkappa \sim 1$, then by applying an averaging procedure to (1) we obtain the following dispersion equation (in the laboratory system):

$$1 - \frac{\omega_p^2}{\omega^2} - \frac{1}{2}\frac{\varkappa^2\tilde{v}_p}{\omega^2} = \frac{\omega_b^2\left(\omega^2 - \frac{1}{2}\varkappa^2\tilde{v}_p^2\right)}{\omega^2\left(\omega^{*2} - \frac{1}{2}\varkappa^2\tilde{v}_b^2\right)}, \tag{2}$$

where $\tilde{v}_p$, $\tilde{v}_b$ are the variable plasma and beam velocities in the field of the external wave, $\omega^* \equiv \omega - kv$, and v is the beam velocity.

From (2) we find that the waves which grow in space satisfy the following condition:

$$\frac{1}{2}\varkappa^2\tilde{v}_b^2 < (kv)^2 < \omega_{pe}^2 \equiv \left(\omega_p^2 + \frac{1}{2}\varkappa^2\tilde{v}_p^2\right). \tag{3}$$

Only modes for which $\omega = \omega_{pe}$ and $kv \simeq (\omega_{pe} - (1/\sqrt{2})\varkappa\tilde{v}_b)$ are unstable in time. The growth rate is

$$\gamma = \frac{\omega_p\omega_b}{(2)^{3/4}\sqrt{\omega_{pe}\varkappa\tilde{v}_b}}. \tag{4}$$

These results imply that the convective instability is damped when $\varkappa\tilde{v}_b = \sqrt{2}\omega_{pe}$. Moreover, since the wavelength of the absolute instabilities rises sharply in this case ($\tilde{v}_b \gg \tilde{v}_p$), these can be quenched by the finite dimensions of the apparatus.

2. Accelerating or retarding the beam should disrupt the synchronism between the wave and the particle bunches (the number of coherent bunches will decrease); moreover, when the beam is accelerated in space the density decreases (the number of coherent particles decreases). Moreover, the conditions for the emission mechanism can change (emission may not occur at a specified frequency). This indicates the possibility of inhibiting instabilities by beam acceleration or retardation. As an example, let us consider the effect of acceleration on the Pierce instability. Assuming that the beam velocity depends on the coordinate as $v_0 = v(1 + \alpha z)$, in the WKB approximation we find

$$\omega = i\frac{v}{L}\frac{\pi n}{4}\left[\delta - \frac{3}{4}\alpha L\pi n\right] \quad (n = 1;\ 3;\ 5\ldots), \tag{5}$$

where L is the distance between electrodes. We can show (and we have been able to solve this problem rigorously) that a beam accelerated in a diode is stable, while one that is retarded in it is unstable. We can also show that a beam moving between two cylindrical surfaces with constant velocity is stable if it moves from the smaller one to the larger one, and unstable if the motion is the reverse. The anisotropy in all these cases is evidently the result of the change in the number of coherent particles in the bunches.

To confirm the possibility of cutting off instabilities by using acceleration, Izmailov has added to the glass tube of the apparatus described in ref. 5 a narrow electrode ($d \simeq 3$ cm), to which constant retarding and acceleration potentials are applied. It is found that an accelerating potential of 200 V cuts off all the instabilities described in ref. 5. Retarding potentials up to 1.5 kV have no effect. Certain other instabilities are also cut off; the details of the experiments are to be published in the future.

We should note that the use of external fields can result in the appearance of new instabilities. In many cases, however, the cutoff conditions for these oscillations can be satisfied or the growth rates are small.

The author is grateful to Ya. B. Fainberg and V. I. Kurilko for discussion.

---

[1] Ya. B. Fainberg, Atom. Energ., 11, 313 (1961).

[2] V. I. Kurilko, Dissertation, Khar'kov State University (1970).

[3] V. I. Kurilko, Dokl. Akad. Nauk SSSR, 208, 1059 (1973) [Sov. Phys.-Dokl., 18, 132 (1973)].

[4] V. A. Buts, Zh. Tekh. Fiz., 42, 710 (1972); 43, 456 (1973). [Sov. Phys.-Tech. Phys., 17, 559 (1972); 18, 293 (1973)].

[5] V. A. Buts and A. N. Izmailov, Zh. Tekh. Fiz., 43, 2006 (1973) [Sov. Phys.-Tech. Phys., 18, 1267 (1974)].

Acceleration of plasma electrons in strong electric fields

Z. A. Al'bikov, M. I. Ivanov, V. I. Kazacha, O. V. Kozlov, V. D. Rusanov, and S. S. Sobolev

(Submitted April 10, 1974)
Zh. Tekh. Fiz., 44, 2421-2423 (November 1974)

The present paper reports a study of the acceleration of plasma electrons in electric fields ($2 \cdot 10^2$ to 10^3 V/cm) with rise times of 10-15 nsec. Stefanovskii[1] and Skarsgard[2] show that in electric fields from 50 to 200 V/cm all the electrons of a previously produced plasma are initially freely accelerated; the acceleration then stops either because of the attenuation of the electron beam[5] or because of a loss of stability of equilibrium. At the same time papers on turbulent heating[3,4] report the acceleration of a small group of electrons; therefore it is of particular interest to find the conditions under which all the plasma electrons are accelerated. This can be expected to occur for a high rate of growth of the potential in the plasma. In addition the experimentally observed time of free acceleration of electrons, which is 50-100 nsec in ref. 5, leads one to hope that in a stronger electric field all the plasma electrons can be accelerated to relativistic energies in the initial stage of the process. This in turn should decrease the instability growth rate in the plasma during the passage of an electron beam, and thus increase the acceleration and plasma lifetime.

The experimental arrangement consists of a copper toroidal chamber with a minor diameter of 7 cm and a major diameter of 70 cm. The chamber walls are 3 mm thick. The chamber is divided along a major diameter (Fig. 1) and Teflon insulators are inserted in both gaps. The voltage from two capacitor banks is fed through spark-gap switches to the edges of the chamber through bus bars. Each bank consists of six 0.5 μF capacitors with a working potential of 25 kV. By firing the spark gaps the two banks are connected in series and a potential of 300 kV is applied to the circuit. A steady toroidal magnetic field H_0 up to 7 kG is produced by 24 coils uniformly spaced around the circumference of the chamber. Argon is fed in continuously and symmetrically from both sides of the chamber, which is pumped continuously. Preionization is produced by two loops inserted into the chamber through the pumping connections, which are driven with 20 kW from two high-frequency oscillators at 15 MHz. The chamber is first pumped to 10^{-6} mm Hg, and argon is then introduced to maintain the pressure at 10^{-4} mm Hg.

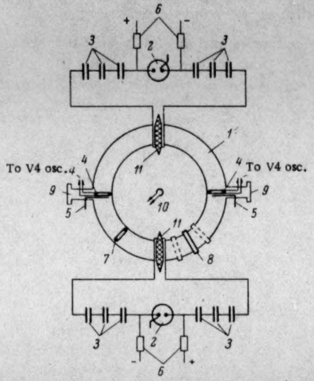

Fig. 1. General view of apparatus. 1) Copper chamber; 2) spark-gapswitch; 3) capacitor banks; 4) loop of high-frequency preionization oscillator; 5) gas admission tube; 6) capacitor bank charging resistor; 7) Rogowski loop; 8) one of 24 coils producing a steady magnetic field; 9) connection to evacuation system (grounded point of chamber); 10) loop for measuring circuit voltage; 11) dielectric gap in chamber.

The distribution of the density n_e of the preionization plasma in a cross section of the chamber and T_e are measured with a movable double Langmuir probe and are calculated by the usual equations. The quantity n_e is measured along a diameter of the plasma column with a two-channel 1.6 cm interferometer. The voltage across the circuit is measured with a loop at the center of the torus in the horizontal plane (resolving time 1 nsec). Because of the parasitic inductances of the capacitor banks and the busbars it is 15% smaller than the voltage across the charged capacitor banks. The plasma current is measured with a self-integrating Rogowski loop with a resolving time of 25-30 nsec located inside the chamber and encircling the plasma loop. The intensity and hardness of the x-ray spectrum are measured with four detectors and a plastic scintillator. The detectors have a resolving time of 7 nsec and a linear photomultiplier current up to 5 A.

The quantity n_e varies from $3 \cdot 10^{10}$ to 10^{11} cm^{-3}; for neutral atom densities of 10^{13} to $2 \cdot 10^{13}$ cm^{-3} this is 1%

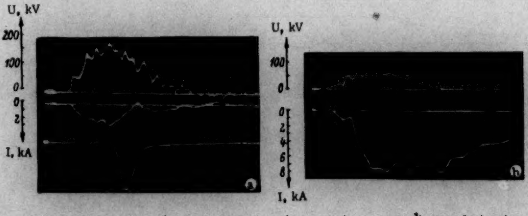

Fig. 2. Oscillograms of voltage, current, and x-ray pulse. n_e(cm^{-3}), U_{cir} (kV): a) $3 \cdot 10^{10}$, 150; b) 10^{11}, 50.

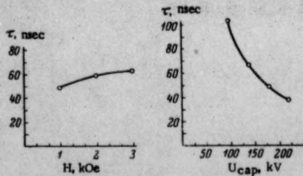

Fig. 3. Time of appearance of x-ray pulse relative to the voltage front across the circuit as a function of the toroidal magnetic field and the capacitor bank voltage.

ionization. The initial T_e is ~20 eV. The preionization plasma is collision-free.

The first experiments show that a current begins to flow in the plasma when the voltage is applied to the circuit; it reaches a value of about 3 kA in 50-100 nsec and then falls to zero, although the voltage across the circuit is still higher. Simultaneously with the fall of the current a pulse of hard x rays appears from the chamber wall, with its maximum coinciding with the drop in current (Fig. 2a, lower oscillogram). The current obtained in the experiment is equal to the expected value of the current of accelerated electrons under the assumption that all the plasma electrons are accelerated. The calculation is performed with the equation $J = en_eSc$, where S is the cross-sectional area and c is the velocity of light. As H_0 is increased the plasma current remains essentially unchanged, but becomes smoother and the interval between the voltage front and the maximum of the x-ray pulse increases slightly. The current also remains unchanged as the capacitor bank voltage is increased. Both these relations are shown in Fig. 3. The x-ray measurements using filters in all regimes show that the average energy of an x-ray photon is always between 200 and 250 keV, which corresponds to to an accelerated electron energy of about 500 keV. The smallest number of accelerated electrons is estimated independently from absolute measurements of the total energy of the accelerated electrons from the whole apparatus during a pulse. This is measured by placing x-ray detectors around the apparatus in such a way that the radiation from each part of the apparatus can fall on only one detector. We estimate the readings of calibrated detectors, introducing corrections for the spectral sensitivity of the detectors, and using the conversion coefficient for electrons on copper. Dividing this energy by 500 keV, the energy of one electron, we obtain the number of accelerated electrons. This number is 30% of the total number of plasma electrons. This result is clearly an underestimate since the calculation assumes that the electrons are incident normally on the wall, i.e., the wall is a thin target and the maximum of the x-ray directional diagram is along a major radius of the torus. But even these crude measurements show that most of the plasma electrons are accelerated, rather than a fraction of a percent as in refs. 2 and 3. The drop in current and the loss of accelerated electrons to the chamber wall require more detailed investigation. It is believed that the effect is related to the inhomogeneity of the magnetic field in the gaps. Under our experimental conditions the drop in current plays a positive role since it permits an estimate of the number of accelerated electrons from the intensity and hardness of the x rays; therefore we have not tried to prevent it. Further experiments show that by decreasing the circuit voltage and increasing the initial value of the density a mode of operation can be obtained with no fall of current. In this case the voltage and current oscillograms are of a different character (Fig. 2b). In this case there is no electron drift to the chamber wall; therefore no quantitative calculations can be made of the number of accelerated electrons from the x-ray intensity, which is three orders of magnitude smaller than in the case with the fall in current.

Thus, the current of about 3 kA observed in the plasma, the fact that the current and the integrated x-ray intensity are independent of the circuit voltage and the longitudinal magnetic field, and the absolute x-ray measurements lead us to the conclusion that most of the electrons are accelerated to energies of the order of 500 keV in the first 50-100 nsec. Problems of further acceleration and confinement of an electron beam require additional work.

---

[1] A. M. Stefanovskii, Yadernyi sintez, 5, 215 (1965).

[2] H. M. Skarsgard and P. Reinolds, CERN Symposium (1968).

[3] B. A. Demidov et al., Zh. Eksp. Teor. Fiz., 48, 454 (1965) [Sov. Phys. – JETP, 21, 302 (1965)]; Zh. Tekh. Fiz., 36, 1166 (1966) [Sov. Phys. – Tech. Phys., 11, 863 (1967)].

[4] I. A. Kovan, Fifth Intern. Conf. on Phenomena in Ionized Gases, Belgrade (1965).

[5] A. Hirose et al., Phys. Rev. Lett., 28, 1185 (1972).

Two modes of operation of an arc plasma source in an external magnetic field

A. G. Korsun and S. A. Meshcheryakov

(Submitted February 27, 1973)
Zh. Tekh. Fiz., 44, 2423-2425 (November 1974)

Two different modes of operation are found for a plasma source with an external axial magnetic field. In the "cathode" the predominant axial voltage drop occurs near the axis. In this case the source produces an electron flux which carries a high proportion of the discharge power. As the discharge current and working gas flow rate increase, a transition to an "anode" mode occurs, in which the voltage drop is concentrated in a sheath near the anode, where an ion flux is formed.

We have investigated a coaxial arc plasma source with an external magnetic field (Fig. 1), known in the literature as a source with a magnetoplasma arc[1] or an end-on Hall arc.[2] The molybdenum anode is funnel-shaped, its minimum diameter being 3.6 cm. The thermionic cathode is a disk of lanthanum hexaboride 2 cm in diameter heated to 1500-2000°K. The magnetic field is created by a solenoid. Iron disks at the output of the source shape magnetic lines of force (dashed lines in Fig. 1) so that three magnetic regions can be distinguished inside the source: lines intersecting the anode in the peripheral region, lines intersecting the cathode near the axis, and lines intersecting the insulators in the space between these two regions. The source power comes from a constant-voltage generator through a ballast resistor. The working gas, argon, is fed in through a slit between the anode and the insulator. The plasma source operates with the following parameters: : flowrate G, 10 mg/sec; current I, 30 A; voltage V, 500 volts; magnetic field B, 1000 G; power consumption W_h, 1 kW; pressure, 10^{-3} mm Hg.

We observe two different modes of operation of the source. At low discharge currents, a mode with a volt–ampere characteristic that rises steeply is found (Fig. 2). As the discharge current increases the ignition voltage drops abruptly and the volt–ampere characteristic rises slowly. The momentum of the plasma flow as measured by a pendulum is much lower in the first mode than in the second.

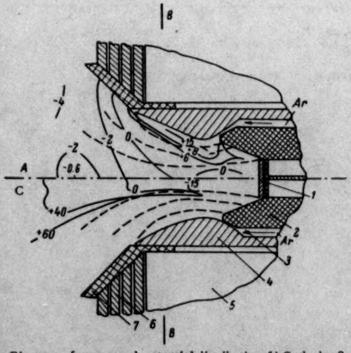

Fig. 1. Diagram of source and potential distribution. 1) Cathode; 2, 7) insulators; 3) gas feed channel; 4) anode; 5) solenoid; 6) iron disks. A represents the anode mode and C the cathode mode. In mode C: I = 2A, V = 160 volts, B = 250 G, W_h = 450 W, G < 0.1 mg/sec; in mode A: I = 18.5 A, V = 50 volts, B = 250 G, W_h = 650 W, G = 3.5 mg/sec.

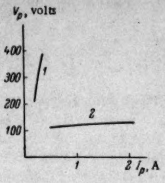

Fig. 2. Volt–ampere characteristics. 1) C mode, G = 0.3 mg/sec, W_h = 530 W, B = 250 G; 2) A mode, G = 0.3 mg/sec, W_h = 800 W, B = 250 G.

Investigation of the electrostatic potential distribution inside the source confirms that the two modes are qualitatively different. We measure the floating potential of the plasma by using a long cylindrical probe oriented along the flow axis. Since the electron temperature as estimated by the probe characteristic does not exceed a few electron volts, this potential is roughly the same as the space potential. The corresponding equipotential lines are shown in Fig. 1 by solid lines, below the axis for the first mode and above the axis for the second; the numbers next to the curves represent the potential.

The radial potential distribution is shown in Fig. 3. As can be seen from Figs. 2 and 3, in the first mode a potential jump, located approximately on those magnetic lines of force which intersect the edge of the anode, forms near the cathode. The length of the region in which the potential is close to the cathode potential is roughly the same as the anode length. This potential distribution is similar to the distribution in a Penning source when the density of neutrals is fairly high.[3] In both devices we observe a potential jump in the radial direction in the space between the cathode and anode (Fig. 3). A major difference in our source, however, is the large voltage drops along the axis (Fig. 1). A characteristic feature of this mode, therefore, is the formation of a plasma jet, whose potential is close to the anode potential and which carries a considerable amount of energy concentrated on the axis.[4]

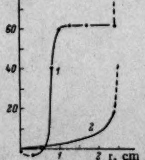

Fig. 3. Radial potential distribution in the cross-section B–B: 1) cathode mode; 2) anode mode.

Thermal measurements and probe measurements[5] using this source and similar ones show that a well-focused electron flux forms in the cathode region, and this flux transports up to 90% of the energy imparted to the discharge. Hence the first mode can be called a cathode mode. In the second mode the potential distribution is restructured so that most of the voltage drop is concentrated in an anode sheath about 0.5 cm thick. The marked increase in flow momentum in going from one mode to another is evidently associated with the formation and acceleration of ions near the anode in a sheath similar to that considered in ref. 6. Therefore the second mode can be called an anode mode. The potential of the plasma jet leaving the source is close to the cathode potential, and at elevated magnetic fields and cathode temperatures it reaches a value of −20 V relative to the cathode.

We have made oscillograms of the discharge voltage and current in the 10^3-10^6 Hz range. It turns out that the current fluctuations are small. This is evidently associated with the high generator inductance in the circuit. The amplitude of the voltage fluctuations increases sharply in going from the cathode to the anode mode, particularly in the 10^5-10^6 Hz range. In the cathode mode we observe regular oscillations; in the anode mode the fluctuations are random. For flowrates below 0.1 mg/sec, voltage fluctuations arise on the electrode in the anode mode such that air breakdown between the conductors occurs. The air gaps in question are greater than 1 cm; consequently the voltage fluctuations[7] are not less than 10 kV. This is evidently associated with the fact that the discharge gap periodically breaks a circuit containing a large inductance.

---

[1] R. Patric and A. Schneiderman, AIAAJ, 4, No. 2 (1966).

[2] A. A. Porotnikov, in: Plasma Accelerators [in Russian], Izd. Mashinostroenie, Moscow (1972).

[3] É. M. Reikhrudel', G. V. Smirnitskaya, and Nguen Hyu Thi, Zh. Tekh. Fiz., 39, 1052 (1969)[Sov. Phys.–Tech. Phys., 14, 789 (1969)].

[4] A. G. Korsun and S. A. Meshcheryakov, Reports to First All-Union Conference on Plasma Accelerators [in Russian], Moscow (1971).

[5] A. I. Bugrova, A. M. Bishaev, S. D. Grishin, and A. G. Korsun, in: Plasma Accelerators [in Russian], Izd. Mashinostroenie, Moscow (1972).

[6] A. V. Zharinov and Yu. S. Popov, Zh. Tekh. Fiz., 37, 294 (1967)[Sov. Phys.–Tech. Phys., 12, 208 (1967)].

[7] J. Mick and J. Craggs, Electrical Breakdown in Gases [Russian translation], IL, Moscow (1960).

Loss of neutralization for a stable neutralized ion beam

M. D. Gabovich
Institute of Physics,
Academy of Sciences of the Ukrainian SSR, Kiev
(Submitted November 14, 1973)
Zh. Tekh. Fiz., 44, 2425-2428 (November 1974)

The view is developed that the achievable degree of neutralization of an ion beam passing through a rarefied gas is associated with the transfer of energy to neutralizing electrons in Coulomb collisions with beam ions and in the excitation of electron plasma oscillations by the beam.

The passage of a beam of fast positive ions through a rarefied gas is accompanied by ionization; the resulting electrons neutralize the space charge of the beam to a certain degree. In studying this familiar phenomenon, two basic questions arise: the achievable degree of neutralization of a stable ion beam (i.e., a beam whose current fluctuations are small in the initial cross section or are characterized by frequencies that lie outside of some danger range) and the loss of neutralization of a neutral ion beam caused by current fluctuations. Whereas the second question has been studied satisfactorily,[1-4] the first is not resolved. We can cite the following considerations.

1. The spreading of a neutral ion beam is determined by the residual radial potential drop φ, which can be much smaller than the potential drop in an unneutralized beam $\varphi_+ = \pi e R^2 n_+$, where R is the beam radius and n_+ the density of beam ions. In a beam neutralized by electrons that are formed through gas ionization φ is frequently expressed by an expression like[3,5,6] $\varphi \approx (kT_e/e) \ln \xi$, T_e being an electron temperature that actually depends on φ. In practice, therefore, equations of this type cannot be used to calculate φ.

2. A beam of positive ions with space charge that is not fully neutralized is a self-consistent potential well of depth φ which traps the slowest-moving electrons. The overall number of electrons formed per cm^3 per sec is $\nu = \int_0^\infty f(\varepsilon)\, d\varepsilon = n_+ v_+ n_a \sigma_i$, where $f(\varepsilon)\, d\varepsilon$ is the number of electrons per cm^3 per sec formed in ionization whose energy is in the interval between ε and $\varepsilon + d\varepsilon$; v_+ is the velocity of the beam ions; and n_a and σ_i are the density of atoms on the beam path and the corresponding ionization cross section. The ratio of the number of electrons trapped by the well to the total number of those formed is $\beta = \int_0^{e\varphi} f(\varepsilon)\, d\varepsilon \Big/ \int_0^\infty f(\varepsilon)\, d\varepsilon$. When the potential well is rectangular the energy of each trapped electron $\leq e\varphi$, the energy of each (previously trapped) electron that leaves the well $\geq e\varphi$, and in the steady state a total of $\nu\beta$ electrons is lost from the well in time. Thus, when electrons cannot escape along the beam a steady state is impossible without an additional energy source. In the usual definition of φ, however,[6] the number of electrons trapped by the well and the number leaving are taken to be the same, without any indication of the need for an additional energy source and without the appropriate allowance for energy balance.

In this note we are evidently the first to point out that the ion beam itself can be the source of this additional energy. Coulomb collisions between beam ions and neutralizing electrons, as well as the excitation of electron plasma oscillations by the beam, cause the trapped electrons to obtain additional energy and leave the beam. Allowance for the interaction between the beam and the plasma permits us to compute the depth of the potential well that is set up.

To determine φ we use the energy balance equation for the electrons trapped by the well and those trapped earlier which leave it:

$$W + Q = \nu'(e\varphi + \varepsilon_T), \tag{1}$$

where $W = \int_0^{e\varphi} f(\varepsilon)\, \varepsilon d\varepsilon$ is the energy of the electrons trapped per cm^3 per sec; Q is the additional energy imparted to the ion beam by the electron gas per cm^3 per sec; $\bar{\varepsilon}_T$ is the mean kinetic energy of the electrons trapped earlier beyond the limits of the well. We would note that the conservation of the number of electrons is also taken into account in (1), since the number of electrons ν' that leave from 1 cm^3 per sec is taken to be equal to the number trapped per cm^3 per sec, $\nu\beta$.

Equation (1) can be put in the form

$$\varepsilon + \frac{Q}{\nu\beta} = e\varphi + \varepsilon_T, \tag{2}$$

where $\bar{\varepsilon}$ is the mean energy of the trapped electrons.

The distribution function of the electrons that are generated is fairly complicated.[7] For simplicity, we approximate $f(\varepsilon)$ by the expression $f(\varepsilon) \sim 1/(\varepsilon + \varepsilon_i)^2$, which can be obtained from the classical Thomson theory of ionization,[8] where $\varepsilon_i = e\varphi_i$, φ_i being the ionization potential. In this case

$$\varepsilon = \frac{W}{\nu\beta} = \frac{\int_0^{e\varphi} f(\varepsilon)\, \varepsilon d\varepsilon}{\int_0^\infty f(\varepsilon)\, d\varepsilon} \frac{1}{\beta} = \frac{\int_0^{e\varphi} f(\varepsilon)\, \varepsilon d\varepsilon}{\int_0^{e\varphi} f(\varepsilon)\, d\varepsilon} = e\varphi_i \left[\left(1 + \frac{\varphi_i}{\varphi}\right) \ln\left(1 + \frac{\varphi}{\varphi_i}\right) - 1\right]. \tag{3}$$

Then β is

$$\beta = \frac{\int_0^{e\varphi} f(\varepsilon)\, d\varepsilon}{\int_0^\infty f(\varepsilon)\, d\varepsilon} = \frac{\varphi}{\varphi + \varphi_i}. \tag{4}$$

If we neglect the excitation of electron plasma oscillations by the beam and use the available expression for fast-ion energy transfer to electrons,[9] we can obtain the following expression for Q:

$$Q = n_+ v_+ \frac{\partial\left(\frac{Mv_+^2}{2}\right)}{\partial z} = Mn_+ v_+ \frac{\partial v_+}{\partial t} = \frac{n_+ n_e e^4 \alpha}{m v_+}, \qquad (5)$$

where $\alpha = 4\pi \ln(1\ m^{3/2} v_+^3 / 1.78\pi^{1/2} n_e^{1/2} e^3)$; M is the ion mass.

The Poisson equation in conjuction with (2)-(5) yields φ. It is of greatest practical interest to determine φ for a well-neutralized beam, i.e., to determine the degree of neutralization. In this case we can use the neutrality condition

$$n_e + n_{ef} \approx n_+ + n_{+s}, \qquad (6)$$

where n_{ef} is the density of fast electrons not trapped by the well; n_{+m} is the density of slow ions formed by ionization and ejected by the field from the beam. The balance equation for the formation and loss of fast electrons implies the inequality $n_{ef} \ll n_+$. The analogous balance equation for slow ions leads to the relationship

$$n_{+s} = \frac{n_+ v_+ n_a \sigma_i' R}{2\bar{v}_{+s}}, \qquad (7)$$

where $\bar{v}_{+s}$ is the mean slow-ion velocity; σ_i' is the cross section of formation of slow ions.

In a well-neutralized ion beam, e.g., when $\varphi \ll \varphi_i$, we can obtain the desired expression for φ, neglecting $\bar{\varepsilon}_T$ in (2) and using (2)-(7):

$$\varphi = \alpha^{1/3} e \left(\frac{M}{m}\right)^{1/3} \left(\frac{\varphi_i}{\varphi_0}\right)^{1/3} \left(\frac{1}{n_a \sigma_i} + \frac{v_+ \sigma_i' R}{v_{+s} \sigma_i 2}\right)^{1/3} n_+^{1/3}, \qquad (8)$$

where $e\varphi_0$ is the energy of the beam ions.

Errors in determining φ are associated with inaccuracies in the approximation for $f(\varepsilon)$ and with the assumption $\bar{\varepsilon}_T \ll e\varphi$. As regards the latter, we can observe that even when $\bar{\varepsilon}_T \approx e\varphi$ (Maxwellian electron distribution in a shallow well) the error involved does not change the order of φ. It would seem that the greatest discrepancy between values of φ computed from (8) and the experimental values would occur when the beam excites intense electron plasma oscillations. In this case the energy is transferred to the electrons and facilitates their leaving the well. Here the maximum value of Q can be evaluated as follows:

$$Q_{\max} \approx \gamma_{\max} \frac{E_{\max}^2}{4\pi}. \qquad (9)$$

Here $\gamma_{\max} = (\sqrt{3}/2)\,\omega\,(m/2M)^{1/3}$ is the maximum growth rate for excitation of electron plasma oscillations by an ion beam, the ion and electron densities being equal;[10] ω is the plasma frequency; and $E_{\max} = k\tilde{\varphi}_{\max} = (\omega/v_+) \cdot mv_+^2/4e$ represents the maximum field, a quantity which is limited by electron trapping by the wave field.[11] Using (2)-(4), (6), and (9), we can obtain an expression for the potential well depth at maximum amplitude:

$$\varphi_{\max} \approx 0.46 \left(\frac{m}{M}\right)^{5/12} \frac{\varphi_0^{1/4} \varphi_i^{1/3} n_+^{1/6} e^{1/6}}{(n_a \sigma_i)^{1/3}}. \qquad (10)$$

Equations (8) and (10) pertain to the two limiting cases of no oscillation or maximum oscillation. A detailed experimental verification of these equations is a problem in itself; we note the following. At a gas pressure of 10^{-3} mm Hg, when the ion beam does not excite oscillations (because of the relatively large number of electron neutral collisions) the experimental value $\varphi = 1$ V is in good agreement with the value of 0.9 V as computed from (8) (with the following parameter values: $\varphi_i = 15$ V, $\varphi_0 = 25$ kV, $M = 3.2 \cdot 10^{-24}$ G, $n_+ = 10^8\ \text{cm}^{-3}$, $\bar{v}_{+s} = 3 \cdot 10^5$ cm/sec, $\sigma_i = 9 \cdot 10^{-16}\ \text{cm}^2$, $\sigma_i' = 1.6 \cdot 10^{-15}\ \text{cm}^2$). For the range of gas pressure $p = 10^{-4}$–10^{-5} mm Hg, when the amplitude of electron oscillations excited by the ion beam is a maximum (see ref. 10), the experimental values of φ, as expected, are substantially greater than those computed by (8), and are close to those computed by (10). The most convincing confirmation of the important role of the effect in question is the experimentally established correlation[12] between the amplitude of the oscillations excited by the ion beam and the electron heating, which is accompanied by an increase in φ.

Thus our comparison of φ with experimental data, as well as the results of an experimental study,[12] confirm the view that the loss of neutralization of an ion beam is due to energy transfer to neutralizing electrons through Coulomb collisions between these electrons and ions and through excitation of electron plasma oscillations by the beam.

The author is grateful to É. A. Pashitskii and I. A. Soloshenko for useful discussions.

---

[1] M. V. Nezlin and P. M. Morozov, Proc. of the Second Intern. Conf. on the Peaceful Uses of Atomic Energy: Papers by Soviet Scientists, Vol. 6 [in Russian] (1959), p. 117.

[2] M. V. Nezlin, Zh. Tekh. Fiz., 30, 168 (1960); Plasma Physics, 10, 337 (1968).

[3] A. V. Zharinov, ZhETF Pis. Red., 17, 508 (1973) [JETP Lett., 17, 366 (1973)].

[4] V. I. Raiko, Zh. Tekh. Fiz., 33, 244 (1963) [Sov. Phys. – Tech. Phys., 8, 175 (1963)].

[5] V. S. Anastasevich, Dokl. Akad. Nauk SSSR, 105, 442 (1955).

[6] J. Koch, R. H. V. Dawton, M. L. Smith, and W. Walcher, Electromagnetic Isotope Separators and Applications of Electromagnetically Enriched Isotopes, Interscience, New York (1958).

[7] G. N. Ogurtsov, Rev. Mod. Phys., 44, 1 (1972).

[8] V. L. Granovskii, Electrical Currents in Gases [in Russian], Vol. 1, GITTL, Moscow (1952).

[9] I. Shkarovsky, T. Johnston, and M. Baczinski, Kinetics of Plasma Particles [Russian translation], Atomizdat, Moscow (1969).

[10] M. D. Gabovich and I. A. Soloshenko, Zh. Tekh. Fiz., 41, 1627 (1971) [Sov. Phys. – Tech. Phys., 16, 1281 (1972)].

[11] M. D. Gabovich, I. A. Soloshenko, and L. S. Simonenko, Ukr. Fiz., Zh., 17, 1362 (1972); Zh. Eksp. Teor. Fiz., 62, 1369 (1972) [Sov. Phys. – JETP, 35, 725 (1972)].

[12] M. D. Gabovich and I. A. Soloshenko, Zh. Tekh. Fiz., 43, 1657 (1973) [Sov. Phys. – Tech. Phys., 18, 1044 (1974)].

Analysis of magnetic deflection systems

O. M. Vovk and O. Ya. Popov

(Submitted March 11, 1974)
Zh. Tekh. Fiz., 44, 11, 2428-2429 (November 1974)

The field analysis for the basic types of magnetic deflection systems can be reduced to the solution of integral Fredholm equations of the first kind[1] whose kernels are the functions

$$f_n^m(a,\ b)=\frac{1}{2\pi}\int_0^{2\pi}\frac{\cos m\varphi d\varphi}{(a+b\cos\varphi)^{n+1/2}},$$

where

$$a=r^2+R^2+(z-z')^2;\quad b=-2rR.$$

These can be expressed simply in terms of associated Legendre functions of half-integral argument:[2]

$$f_n^m(a,\ b)=(-1)^m c^{-(n+1/2)}\frac{\Gamma\left(n-m+\frac{1}{2}\right)}{\Gamma\left(n+\frac{1}{2}\right)}P_{n-1/2}^m(x), \tag{1}$$

where x = a/c; c = $\sqrt{a^2-b^2}$.

Representations of the Legendre function in terms of a hypergeometric series[3,4] are frequently used in computation of (1). The following recursion relation is known[5] for n = 0:

$$(2m+1)f^{m+1}+(2m-1)f^{m-1}=2m\left(\frac{u}{v}+\frac{v}{u}\right)f^m, \tag{2}$$

where

$$u=\frac{1}{2}\{\sqrt{(z-z')^2+(R+r)^2}+\sqrt{(z-z')^2+(R-r)^2}\},$$
$$v=\frac{1}{2}\{\sqrt{(z-z')^2+(R+r)^2}-\sqrt{(z-z')^2+(R-r)^2}\}.$$

The basic functions can be expressed in terms of complete elliptic integrals:

$$f^0=\frac{2}{\pi u}K\left(\frac{v}{u}\right),$$
$$f^1=\frac{2}{\pi v}\left[K\left(\frac{v}{u}\right)-E\left(\frac{v}{u}\right)\right].$$

Derivatives of $f_n^m(a,\ b)$ are expressed in terms of these same functions, but with n' = n + 1.

In problems in electron optics we frequently must determine the components of a magnetic field which are derivatives of a potential, i.e., it becomes necessary to make computations of $f_n^m(a,\ b)$ for n > 0.

We can derive the following recursion relations:

$$\left(n+\frac{1}{2}\right)\left(n+\frac{3}{2}\right)c^2f_{n+2}^m(a,\ b)=(n+1)(2n+1)xcf_{n+1}^m(a,\ b)-\left[\left(n+\frac{1}{2}\right)^2-m^2\right]f_n^m(a,\ b), \tag{3}$$

$$\left(n-m-\frac{3}{2}\right)f_n^{m+2}(a,\ b)=\frac{2(m+1)x}{\sqrt{x^2-1}}f_n^{m+1}(a,\ b)+\left(n+m+\frac{1}{2}\right)f_n^m(a,\ b), \tag{4}$$

$$\left(n-m-\frac{1}{2}\right)\sqrt{x^2-1}f_n^{m+1}(a,\ b)=\left(n+m+\frac{1}{2}\right)xf_n^m(a,\ b)-\left(n+\frac{1}{2}\right)cf_{n+1}^m(a,\ b), \tag{5}$$

$$\left(n+\frac{1}{2}\right)c\sqrt{x^2-1}f_{n+1}^{m+1}(a,\ b)=\left(n+m+\frac{1}{2}\right)f_n^m(a,\ b)-\left(n+\frac{1}{2}\right)cxf_{n+1}^m(a,\ b). \tag{6}$$

Recursion relations (3)-(6) are valid for all n and m, except for real |x| < 1, a situation which holds in virtually every case. The basis functions for these relations have the form

$$f_0^0(a,\ b)=\frac{2}{\pi(a-b)^{1/2}}K(k),$$
$$f_1^0(a,\ b)=\frac{2}{\pi(a-b)^{3/2}}\frac{1}{k'^2}E(k),$$

where K(k) and E(k) are complete elliptic integrals of the first and second kind respectively, while k and k' are respectively the modulus and complementary modulus of the elliptic integrals,

$$k'=\sqrt{1-k^2};\quad k^2=-\frac{2b}{a-b}.$$

By simple manipulation we can show that (2) is identical to (4) for n = 0.

The need for using the above recursion relations for $f_n^m(a,\ b)$ is dictated by the great expenditures of machine time that are involved when these functions are represented by a hypergeometric series.[4] When (3)-(6) are used the computation time can be reduced by a factor of 5.

---

[1] L. E. Tsyrlin, Zh. Tekh. Fiz., 34, 1293 (1964) [Sov. Phys. – Tech. Phys., 9, 999 (1965)].

[2] K. S. Gradshtein and I. M. Ryzhik, Tables of Integrals, Sums, Series, and Products [in Russian], Izd. Nauka, Moscow (1971)

[3] B. E. Bronshted and L. E. Tsyrlin, ÉT, series 4, No. 2 (1967).

[4] Tables of Associated Legendre Functions [Russian translation], No. 26, VTs AN SSSR (1965).

[5] P. L. Kapitsa, V. A. Fock, and L. A. Vainshtein, Zh. Tekh. Fiz., 29, 1188 (1959) [Sov. Phys. – Tech. Phys., 4, 1088 (1960)].

Nonlinear behavior of monochromatic surface waves excited by a beam

A. B. Kitsenko, I. M. Pankratov, and K. N. Stepanov

(Submitted December 21, 1973)
Zh. Tekh. Fiz., 44, 2430-2432 (November 1974)

The motion of a charged particle in the electric field of a monochromatic electrostatic surface wave of small but finite amplitude in an external magnetic field is analyzed by the method of averaging. The amplitude of a monochromatic surface wave excited by a monoenergetic low-density beam of particles is estimated in the saturation stage, in which the oscillation frequency of the trapped particles is of the same order as the linear growth rate.

The amplification of volume and surface waves becomes appreciable in the interaction of beams of charged particles with a plasma under laboratory conditions. The particles of the beam are trapped by the wave field in the nonlinear stage. The theory of the nonlinear stage of volume-wave amplification in an unconfined plasma has been developed for the cases of zero external magnetic field[1-3] and a finite external magnetic field.[4]

In this work we estimate the amplitude of a monochromatic potential surface wave propagating along the plane boundary of a plasma (dielectric, slow-wave) in the nonlinear stage.

To estimate the amplitude of the oscillations in the saturation regime it is necessary to consider the motion of a single particle of the beam in the constant magnetic field and the electric field of the monochromatic electrostatic surface wave of finite amplitude. We assume that wave potential is of the form

$$\varphi = \mathrm{Re}\,\varphi_0 e^{-\varkappa y + i(\mathbf{kr} - \omega t + \alpha)}. \tag{1}$$

The y axis is perpendicular to the plane along which the surface wave propagates (the interface between the two media) and the z axis is parallel to the external magnetic field $\mathbf{B}_0$, which is directed along the interface. The quantity $\varkappa$ has different forms, depending on the type of surface wave, the oscillation frequency ω, and the wave vector $\mathbf{k} = (k_x, 0, k_z)$. We assume for simplicity that the beam particles do not cross the boundary y = 0. Making the following change of variables in the equations of motion for the charged particle:

$$\left.\begin{aligned} v_x &= v_\perp \cos\theta, \quad v_y = v_\perp \sin\theta, \\ x &= \xi - \frac{v_\perp}{\omega_B}\sin\theta, \quad y = \eta + \frac{v_\perp}{\omega_B}\cos\theta \quad \left(\omega_B = \frac{eB_0}{mc}\right), \end{aligned}\right\} \tag{2}$$

where θ is the azimuthal angle in velocity space and ξ and η are the transverse coordinates of the guiding center, we obtain

$$\left.\begin{aligned} \frac{d\xi}{dt} &= \frac{e\varkappa\varphi_0}{m\omega_B} e^{-\varkappa\eta} \sum_l A_l(v_\perp)\cos(\Phi_l + \alpha), \\ \frac{d\eta}{dt} &= -\frac{ek_x\varphi_0}{m\omega_B} e^{-\varkappa\eta} \sum_l A_l(v_\perp)\sin(\Phi_l + \alpha), \\ \frac{dv_z}{dt} &= \frac{ek_z\varphi_0}{m} e^{-\varkappa\eta} \sum_l A_l(v_\perp)\sin(\Phi_l + \alpha), \\ \frac{dv_\perp}{dt} &= \frac{e\varphi_0}{m}\frac{\omega_B}{v_\perp} e^{-\varkappa\eta} \sum_l lA_l(v_\perp)\sin(\Phi_l + \alpha), \\ \frac{d\theta}{dt} &= -\omega_B - \frac{e\varphi_0}{m}\frac{\omega_B}{v_\perp} e^{-\varkappa\eta} \sum_l \frac{d}{dv_\perp} A_l(v_\perp)\cos(\Phi_l + \alpha). \end{aligned}\right\} \tag{3}$$

Here, $J_n(x)$ is a Bessel function, $I_n(x)$ is the Bessel function of an imaginary argument, and

$$\left.\begin{aligned} A_l(v_\perp) &= \sum_s (-1)^s I_s\left(\frac{\varkappa v_\perp}{\omega_B}\right) J_{l-s}\left(\frac{k_x v_\perp}{\omega_B}\right), \\ \Phi_l &= k_x\xi + k_z z - \omega t - l\theta. \end{aligned}\right\} \tag{4}$$

We assume that the wave amplitude is small:

$$c\frac{k\varphi_0}{B_0} \ll \frac{|\omega_B|}{k}, \quad c\frac{k_x\varphi_0}{B_0} \ll v_\perp, \quad c\frac{\varkappa\varphi_0}{B_0} \ll v_\perp. \tag{5}$$

Then the system (3) contains rapidly varying phase angles θ and $k_z z - \omega t$ and can be investigated by the method of averaging.[5]

We consider only resonance frequencies, for which

$$\omega - k_z v_z \approx n\omega_B \quad (n = 0, \pm 1, \ldots). \tag{6}$$

Averaging Eqs. (3), we obtain a system of first-approximation equations for the average variables $\bar{\xi}$, $\bar{\eta}$, $\bar{v}_z$, $\bar{v}_\perp$, $\bar{\theta}$ under resonance conditions (6):

$$\left.\begin{aligned} \frac{d\bar{\xi}}{dt} &= \frac{e\varkappa\varphi_0}{m\omega_B} e^{-\varkappa\bar{\eta}} A_n(\bar{v}_\perp)\cos(\bar{\Phi}_n + \alpha), \\ \frac{d\bar{\eta}}{dt} &= -\frac{ek_x\varphi_0}{m\omega_B} e^{-\varkappa\bar{\eta}} A_n(\bar{v}_\perp)\sin(\bar{\Phi}_n + \alpha), \\ \frac{d\bar{v}_z}{dt} &= \frac{ek_z\varphi_0}{m} e^{-\varkappa\bar{\eta}} A_n(\bar{v}_\perp)\sin(\bar{\Phi}_n + \alpha), \\ \frac{d\bar{v}_\perp}{dt} &= \frac{e\varphi_0}{m}\frac{\omega_B n}{\bar{v}_\perp} e^{-\varkappa\bar{\eta}} A_n(\bar{v}_\perp)\sin(\bar{\Phi}_n + \alpha), \\ \frac{d\bar{\theta}}{dt} &= -\omega_B - \frac{e\varphi_0}{m}\frac{\omega_B}{\bar{v}_\perp} e^{-\varkappa\bar{\eta}} \frac{d}{d\bar{v}_\perp} A_n(\bar{v}_\perp)\cos(\bar{\Phi}_n + \alpha). \end{aligned}\right\} \tag{7}$$

It is also convenient to introduce the following equation for the resonance phase $\bar{\Phi}_n$:

$$\frac{d\bar{\Phi}_n}{dt} = n\omega_B - \omega + k_z\bar{v}_z + \frac{e\varphi_0}{m} e^{-\varkappa\bar{\eta}}\left[\frac{\varkappa k_x}{\omega_B} A_n(\bar{v}_\perp) + \frac{n\omega_B}{\bar{v}_\perp}\frac{d}{d\bar{v}_\perp} A_n(\bar{v}_\perp)\right]\cos(\bar{\Phi}_n + \alpha). \tag{8}$$

For simplicity we drop the bar over the averages below. In the case of the Cerenkov resonance (n = 0) Eqs. (7) and (8) have integrals of the motion ($k_z \neq 0$)

$$v_\perp = C_1, \quad \eta + \frac{k_x}{k_z\omega_B} v_z = C_2, \tag{9}$$

$$\frac{e\varphi_0}{m} A_0(C_1)\cos(\Phi_0 + \alpha) = \left[C_3 - \frac{1}{2}\left(v_z - \frac{\omega}{k_z}\right)^2\right]\exp\left(\varkappa C_2 - \frac{\varkappa k_x}{\omega_B k_z} v_z\right). \tag{10}$$

In the case of cyclotron resonance (n = ± 1, ± 2, . . .) we obtain the following integrals from (7) and (8):

$$v_z - \frac{k_z}{2n\omega_B} v_\perp^2 = C_1, \quad \eta + \frac{k_x}{2n\omega_B^2} v_\perp^2 = C_2, \tag{11}$$

$$\frac{e\varphi_0}{m} A_n(v_\perp)\cos(\Phi_n + \alpha) = -\left[\frac{n\omega_B - \omega + k_z C_1}{n\omega_B}\frac{v_\perp^2}{2} + \frac{k_z^2}{(n\omega_B)^2}\frac{v_\perp^4}{8} + C_3\right]\exp\left(\varkappa C_2 - \frac{\varkappa k_x}{2n\omega_B^2} v_\perp^2\right). \tag{12}$$

The integrals (10) and (12) describe completely the motion of the charged particle in the phase planes (v_z, Φ_0) for n = 0 and $(v_\perp, \Phi_n)$ for n ≠ 0. It follows from (10) and (12) that the motion of the particle in the phase plane can be unlimited or bounded. In the latter case the particle is trapped by the wave field.

For example, in the case of a wave that propagates at an angle not too close to $\pi/2$ relative to the magnetic field the motion of the charged particles near centers whose coordinates Φ_n are given by the relation $\sin(\Phi_n + \alpha) = 0$ is described by the oscillation frequency

$$\left.\begin{aligned} \Omega_{tr}^2 &= \left|\frac{ek_z^2\varphi_0}{m} A_0(C_1)\right| \exp\left(-\varkappa C_2 + \frac{\varkappa k_x}{k_z^2}\frac{\omega}{\omega_B}\right) \quad (n = 0),\\ \Omega_{tr}^2 &= \left|\frac{ek_z^2\varphi_0}{m} A_n(v_{\perp 0})\right| \exp\left(-\varkappa C_2 + \frac{\varkappa k_x}{2n\omega_B^2} v_{\perp 0}^2\right) \quad (n \neq 0), \end{aligned}\right\} \tag{13}$$

where $v_{\perp 0}$ is the coordinate of the center in the $(v_\perp, \Phi_n)$ plane.

In the case $k_z \sim k_x$ the trapping domain with respect to the variable v_z for Cerenkov resonance is

$$\Delta v_z \sim \left|\frac{e\varphi_0}{m} A_0 \exp\left(-\varkappa C_2 + \frac{\varkappa k_x}{k_z^2}\frac{\omega}{\omega_B}\right)\right|^{1/2} \quad (n = 0),$$

and the trapping domain with respect to $v_\perp$ for cyclotron resonances (n ≠ 0) is

$$\Delta v_\perp \sim \left|\frac{e\varphi_0}{m} A_n \exp\left(-\varkappa C_2 + \frac{\varkappa k_x}{2n\omega_B^2} v_{\perp 0}^2\right)\right|^{1/2}.$$

The presence of the factors $\exp(-\varkappa C_2)$ in the expressions for Ω_{tr}^2, Δv_z, and $\Delta v_\perp$ is due to the fact that the typical particle "senses" the field in the domain $\Delta y \sim C_2$. If $k_z \ll k_x$ (n ≠ 0), the trapping domain with respect to $v_\perp$ grows larger, and the oscillation frequency of particles near the centers is lower than in the case $k_z \sim k_x$ (this situation is analogous to the case of particle motion in the field of a volume wave).

Let us assume that a charged-particle beam with a small thermal velocity spread moving parallel to B_0 with velocity v_{z0} has dimensions $\Delta y \lessdot \varkappa^{-1}$ in the y direction. If a surface wave is generated at the plasma–vacuum interface, the beam can be located inside the plasma near the surface or in the vacuum outside the plasma. In this case, under Cerenkov resonance conditions (n = 0) the linear growth rate $\gamma_L \sim (n_b/n_p)^{1/3}\omega$ for $k_z \sim k_x$, where $n_{p,b}$ are the respective densities of the plasma and beam. The same growth rate occurs for waves excited by a beam of oscillators (charged particles with the same Larmor radius and a uniform distribution with respect to the phase angles θ) for both Cerenkov and cyclotron resonances ($|n| \geq 1$) if the Larmor radius of the beam particles is too large ($|\varkappa| v_\perp / |\omega_B| \sim 1$, $k_x v_\perp / |\omega_B| \sim 1$, $v_\perp \sim v_{z0}$). The oscillation level is saturated when Ω_{tr} is of the same order as γ_L, i.e., when

$$E \sim k\varphi_0 \sim \sqrt{4\pi n_b m v_{z0}^2}\left(\frac{n_b}{n_p}\right)^{1/3}, \quad (k_z \sim k_x). \tag{14}$$

Expression (14) for the surface-wave amplitude in the saturation stage is of the same order of magnitude as the analogous expression for plasma volume waves.[4]

---

[1] I. N. Onishchenko, A. P. Linetskii, N. G. Matsiborko, V. D. Shapiro, and V. I. Shevchenko, ZhETF Pis. Red., 12, 407 (1970) [JETP Lett., 12, 281 (1970)].

[2] T. O'Neil, I. H. Winfrey, and J. H. Malmberg, Phys. Fluids, 14, 1204 (1971).

[3] N. G. Matsiborko, I. N. Onishchenko, V. D. Shapiro, and V. I. Shevchenko, Khar'kov Physicotechnical Institute Preprint 71-40 [in Russian], Khar'kov (1971); Plasma Phys., 14, 591 (1972).

[4] A. B. Kitsenko, I. M. Pankratov, and K. N. Stepanov, Zh. Eksp. Teor. Fiz., 66, 166 (1974) [Sov. Phys. – JETP, 39, 77 (1974)].

[5] N. N. Bogolyubov and Yu. A. Mitropol'skii, Asymptotic Methods in the Theory of Nonlinear Oscillations [in Russian], Fizmatgiz (1963), p. 296.

Electron lifetimes in atmosphere at high pressure

V. N. Kapinos, Yu. A. Medvedev, N. N. Morozov, and B. M. Stepanov
All-Union Scientific Research Institute of Optical and Physical Measurements, Moscow

(Submitted September 17, 1973)
Zh. Tekh. Fiz., 44, 2432-2433 (November 1974)

Electron lifetimes θ are measured by a waveguide method in an air afterglow plasma produced by a short pulse of relativistic electrons. For air pressures p from 50 to 600 torr we find $\theta \sim p^{-2}$.

Up to the present time direct measurements of electron lifetimes in air have been restricted to pressures p not exceeding[1,2] 160 torr because of the relatively low time resolution of the measurement procedure employed. In ref. 1, for example, the length of the pulse of ionizing radiation is $5\ \mu$sec, and in ref. 2 it is $1.5\ \mu$sec. This poor time resolution leads to appreciable errors in measurements at high pressures and, apparently, to a false interpretation of the measurements in ref. 1, where the observed deviation of the dependence of the two-particle attachment coefficient of electrons from a linear relation at pressures $p \geqslant 50$ torr is related to the Bloch and Bradbury mechanism.[3]

In view of the above situation we have measured electron lifetimes in an air afterglow plasma at pressures from 50 to 600 torr.

The experimental arrangement is similar to that shown in ref. 1. The H_{10} mode at 2.9 GHz is excited in a waveguide cell. To eliminate the effect of power at the characteristic frequency of the waveguide accelerator ($\sim$2.2 GHz), a reentrant cavity tuned to the microwave frequency is inserted in the waveguide cell. This eliminates the strong signal induced in the detector section by the bunched beam of electrons from the accelerator. A plasma is produced in the waveguide cell by a pulse of 8 MeV electrons of 40 nsec duration and a maximum pulse current of 2 A: The resolving time of the measurement is $\sim 10^{-8}$ sec; this permits direct measurements of electron lifetimes in air up to atmospheric pressure.

The electron lifetime θ is determined from a log–log plot of the ratio of the amplitudes of the signals from the detector with and without plasma in the waveguide. Figure 1 shows the electron lifetime θ as a function of the air pressure. The data show that $\theta \sim p^{-2}$ in the pressure range 50-600 torr.

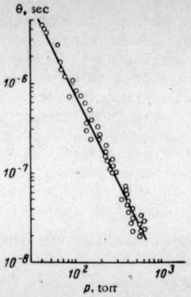

Fig. 1

The maximum experimental error is estimated to be 30% and decreases at lower pressures because of the improved resolving time.

The experimental value of the three-particle attachment coefficient $K = 2.8 \cdot 10^{-30}$ cm^6/sec is in satisfactory agreement with the results reported in refs. 2, 4-6.

---

[1] V. B. Brodskii and S. Z. Zagik, Zh. Tekh. Fiz., 36, 672(1966) [Sov. Phys.–Tech. Phys., 11, 498 (1966)].

[2] G. L. Kabanov, Yu. A. Medvedev, N. N. Morozov, D. Z. Neshkov, and B. M. Stepanov, Zh. Tekh. Fiz., 43, 1275 (1973) [Sov. Phys. – Tech. Phys., 18, 807 (1973)].

[3] N. E. Bradbury, Phys. Rev., 44, 883 (1933).

[4] L. M. Chanin, A. V. Phelps, and M. A. Biondi, Phys. Rev., 128, No. 1 (1962).

[5] J. L. Pack and A. V. Phelps, J. Chem. Phys., 44, 1870 (1966).

[6] V. A. Van Lint, E. G. Wikner, and D. L. Trueblood, Bull. Amer. Phys. Soc., Ser. II, 5, 122 (1960).

Low-frequency helical instability in a high-frequency electric field

V. S. Paverman and D. D. Tskhakaya

Tbilisi State University and Institute of Physics, Academy of Sciences of the Georgian SSR

(Submitted October 22, 1973; resubmitted January 21, 1974)
Zh. Tekh. Fiz., 44, pp. 2433-2436 (November 1974)

Low-frequency helical waves that propagate in an electron magnetoplasma in an external time-varying electric field are treated. These waves are unstable in a weak high-frequency field when certain decay conditions hold.

Of late there has been increased interest in problems of the interaction between an external high-frequency field and a plasma. One reason for this interest is the need for a detailed investigation of the phenomena that occur when electromagnetic waves propagate in the ionosphere and in plasmas in outer space. It has been shown in a number of studies[1] that a plasma becomes unstable to both electrostatic and electromagnetic modes in a high-frequency field. These instabilities, however, are due to wave motion of the plasma ions or the coupling of electron radiation to wave processes in the plasma.

In this paper we investigate the behavior of a pure electron plasma in a weak high-frequency electric field and a fixed magnetic field. The high-frequency field $\mathbf{E}_0(t)$ and the external magnetic field $\mathbf{H}_0$ are in the same direction $\mathbf{H}_0(0, 0, H_0)$. This means that an external transverse high-frequency wave propagates across $\mathbf{H}_0$. The wavelengths we consider are assumed to be much smaller than the length of the external high-frequency wave. As a result, the external high-frequency field can be written in the form $\mathbf{E}_0(t) = \mathbf{E}_0 \sin\omega_0 t$. Under these conditions, for external frequencies close to the electron plasma frequency even in weak high-frequency fields the plasma is unstable against low-frequency transverse modes (whistlers) that propagate along the magnetic field.

The equations are

$$\left.\begin{aligned} \operatorname{curl}\ \mathbf{E} &= -\frac{1}{c}\frac{\partial \mathbf{H}}{\partial t}, \\ \operatorname{curl}\ \mathbf{H} &= \frac{1}{c}\frac{\partial \mathbf{E}}{\partial t} + \frac{4\pi}{c} en\mathbf{V}, \\ \frac{d\mathbf{V}}{dt} &= \frac{e}{m}\mathbf{E} + \frac{e}{mc}[\mathbf{VH}], \\ \frac{\partial n}{\partial t} &+ \operatorname{div}(n\mathbf{V}) = 0. \end{aligned}\right\} \tag{1}$$

The behavior of the plasma in equilibrium is described by the equations

$$\frac{d\mathbf{V}_0}{dt} = \frac{e}{m}\mathbf{E}_0(t); \quad \frac{\partial n_0}{\partial t} = 0. \tag{2}$$

If we assume that the deviations from the unperturbed values $\mathbf{V}_0(t)$, $\mathbf{E}_0(t)$, n_0, and $\mathbf{H}_0$ are small, we can linearize system (1) and write the coordinate dependence of the nonequilibrium quantities in the form $e^{i\mathbf{kr}}$. We consider perturbations that propagate along the z axis. It is easy to show that the equations for the longitudinal and transverse waves separate in this case. The effect of the high-frequency field on the longitudinal waves appears only in the Doppler shift. For the transverse waves we have

$$\frac{d^2H_\pm(t)}{dt^2} + (\omega_L^2 + c^2k^2)H_\pm(t) \mp i\omega_H\omega_L^2 e^-(t)\, e^{\mp i\omega_H t}\int_{-\infty}^{t} e^+(t_1)H_\pm(t_1)\, e^{\pm i\omega_H t_1}dt_1, \tag{3}$$

where

$$H_\pm(t) = \frac{H_x(t) \pm iH_y(t)}{\sqrt{2}},$$

$$e^\pm(t) = \exp\left\{\pm ik\int_{-\infty}^{t} V_0(t_1)\,dt_1\right\} = \sum_{n=-\infty}^{\infty} J_n(a)\, e^{\pm in\omega_0 t},$$

$$\omega_L^2 = \frac{4\pi e^2 n_0}{m}; \quad \omega_H = \frac{eH_0}{mc}; \quad a = \frac{kV_0}{\omega_0},$$

and $J_n(x)$ is the Bessel function. Changing to Fourier components

$$H_\pm(\omega) = \int_{-\infty}^{\infty} H_\pm(t)\, e^{i\omega t}dt$$

and setting $a \ll 1$ (i.e., considering weak high-frequency fields), we obtain

$$\Psi_\pm(\omega)H_\pm(\omega) = a\,(A_\pm(\omega, \omega_0)H_\pm(\omega + \omega_0) - A_\pm(\omega, -\omega_0)H_\pm(\omega - \omega_0)), \tag{4}$$

where

$$A_\pm(\omega, \omega_0) = \pm\frac{\omega_0\omega_H\omega_L^2}{2(\omega \mp \omega_H)(\omega + \omega_0 \mp \omega_H)},$$

$$\Psi_\pm(\omega) = \omega^2 - c^2k^2 - \omega_L^2 \mp \frac{\omega_H\omega_L^2}{\omega \mp \omega_H}. \tag{5}$$

In the absence of an external electric field ($a = 0$), we obtain the familiar dispersion relations for a plasma in a constant magnetic field (see, e.g., ref. 2) from this equation. Each of the equations $\Psi_\pm(\omega) = 0$ describes the characteristic modes of a plasma with a given polarization and has three solutions, one of which is the low-frequency whistler; the other two are high-frequency modes.

First we consider Eq. (4) for H_+. Successively eliminating $H_+(\omega \pm \omega_0)$, $H_+(\omega \pm 2\omega_0)$, ..., we obtain the dispersion relation in the form of an infinite continued fraction,[3] which can be truncated for $a \ll 1$. We have

$$\Psi_+(\omega) = a^2\left\{\frac{A_+^2(\omega, \omega_0)}{\Psi_+(\omega + \omega_0) + O(a^2)} + \frac{A_+^2(\omega - \omega_0)}{\Psi_+(\omega - \omega_0) + O(a^2)}\right\}. \tag{6}$$

Here, $O(a^2)$ denotes terms of order a^2. We assume below that $\omega_0 \sim \omega_L \gg \omega_H$, ck. For $a = 0$ we choose the low-frequency solution of the dispersion equation $\Psi_+(\omega) = 0$:

$$\omega_1 = \frac{c^2k^2}{\omega_L^2}\omega_H\left(1 - \frac{c^2k^2}{\omega_L^2}\right).$$

We will seek a solution of (6) that is close to ω_1. Assume that $\omega = \omega_1 + i\gamma(|\gamma| \ll \omega_1)$ and $\omega_0 = \omega_2 + \omega_1 + \Delta$, where the detuning $|\Delta| \ll \omega_1$ and

$$\omega_2 \approx \omega_L \left\{1 + \frac{c^2k^2}{\omega_L^2} - \frac{\omega_H}{\omega_L} + \frac{1}{2}\frac{\omega_H^2}{\omega_L^2} + \frac{1}{2}\frac{c^2k^2}{\omega_L^2}\frac{\omega_H}{\omega_L}\right\}^{1/2} \tag{7}$$

is the high-frequency solution of the equation

$$\Psi_+(\omega_1 - \omega_0) = \Psi_+(-\omega_2) = 0.$$

Under these assumptions, the first term in brackets in (6) is small. The quantity γ is given by

$$\gamma = i\frac{\Delta}{2} \pm \frac{1}{2}\left\{\frac{a^2}{2}\omega_H\omega_L - \Delta^2\right\}^{1/2}. \tag{8}$$

The maximum growth rate is obtained for $\Delta = 0$:

$$\gamma_{\max} = \frac{kV_0}{2\sqrt{2}}\left(\frac{\omega_H}{\omega_L}\right)^{1/2}.$$

and the condition $|\gamma_{\max}| \ll \omega_1$ can be rewritten in the form

$$\frac{V_0^2}{c^2} \ll \frac{\omega_1}{\omega_L} \ll 1,$$

which indicates that an instability occurs for weak external fields. Similarly, from (4) we can obtain the growth rates for the H_- waves. Here the following condition should hold:

$$\omega_0 = \omega_2' - \omega_1' + \Delta', \quad |\Delta'| \ll |\omega_1'|, \tag{9}$$

where $\omega'_1 = -\omega_1$ and $\omega'_2 = \omega_2$ satisfy the equation

$$\Psi_-(\omega_0 + \omega_1') = \Psi_-(\omega_2') = 0.$$

Condition (9) implies that the expressions for the external frequency coincide when the H_+ and H_- modes are excited. This means that both waves can be excited simultaneously.

The physical picture of the instability can be represented as follows. When an electron moves in the field of the low-frequency helical wave under consideration it is acted on by a force $(e/c)\,[\mathbf{V}_0\mathbf{H}]$, where $\mathbf{V}_0$ is the electron velocity in the external high-frequency field and H is the magnetic component of one of the high-frequency circularly polarized waves. When the decay condition

$$\omega_0 - \omega_1 = \omega_2 \tag{10}$$

holds in the system associated with the moving electron, a constant force that accelerates the electron appears. This force results in the development of an instability in the low-frequency helical waves.

To determine the threshold value of the external high-frequency field we must take account of damping of the helical waves. In the limit of a cold completely ionized plasma the absorption is due basically to electron–ion collisions. Allowance for this mechanism leads to the appearance of the following additional term in (5):

$$\delta\Psi_\pm = i\nu\frac{\omega\omega_L^2}{(\omega \mp \omega_H)^2}.$$

Here, ν is the electron–ion collision frequency. For weakly damped low-frequency helical waves,[4] $\nu \ll \omega_H$.

Calculations similar to those above (allowing for the term $\delta\Psi_\pm$) for $\Delta = 0$ yield the following expression for the threshold value E_{thr}:

$$\frac{E_{\text{thr}}^2}{8\pi n_0 mc^2} = \frac{2\nu^2}{\omega_H\omega_L}.$$

Obviously, the results are valid if the wave-vector components $k_\parallel$ and $k_\perp$ (longitudinal and transverse with respect to the magnetic field) satisfy

$$k_\perp^2 \ll k_\parallel^2 \sim k^2.$$

Here, the pump field can be regarded as uniform only for

$$k_0^2 = \frac{(\omega_0^2 - \omega_L^2)}{c^2 \ll k_\perp^2 \ll k^2}.$$

Allowing for (10) and the definition of ω_2 in (7), the condition for the field of the pump wave to be uniform becomes

$$\left|k^2 - \frac{|\omega_H|\,\omega_L}{c^2}\right| \ll k^2.$$

It is obvious that this inequality can be satisfied.

---

[1] V. P. Silin, Usp. Fiz. Nauk, 108, 625 (1972) [Sov. Phys. – Usp., 15, 742 (1973)]; V. A. Buts, Zh. Tekh. Fiz., 42, 709 (1972) [Sov. Phys. – Tech. Phys., 17, 559 (1972)].

[2] V. D. Shafranov, Reviews of Plasma Physics, Vol. 3, Consultants Bureau, New York (1967).

[3] P. M. Morse and H. Feshbach, Methods of Theoretical Physics, McGraw-Hill (1953).

[4] V. L. Ginzburg and A. A. Rukhadze, Waves in Magnetoactive Plasmas [in Russian], Izd. Nauka, Moscow (1970).

Method for optical modulation of an electron beam

V. I. Sotnikov

Moscow Physicotechnical Institute

(Submitted February 11, 1974)
Zh. Tekh. Fiz., 44, 2436-2438 (November 1974)

It is proposed to modulate an electron beam by nonlinear transformation of an electromagnetic wave into a charge-density wave. Expressions are obtained for the modulation depth for a modified decay relation and the usual decay relation.

According to ref. 1, preliminary modulation of a relativistic beam at the plasma frequency results in a marked decrease in the relaxation length of the beams and makes collective relaxation in a D−T target possible. In considering modulation of a high-current relativistic beam at a resonant frequency corresponding to a high plasma density ($n > 10^{19}$), the most promising method involves the use of a high-power laser. In this paper we study one possible mechanism for optical modulation of an electron beam; this is based on the nonlinear transformation of an electromagnetic wave into a charge-density wave. This mechanism provides fairly good modulation depth $\Delta n/n = 10^{-2}$ even at laser powers $P \sim 3 \cdot 10^{12}$ W.

Consider an electromagnetic pump wave that propagates along a monochromatic relativistic electron beam moving along the z axis with velocity v_0; the electromagnetic wave decays into an electromagnetic wave and a plasma wave ($t_0 \to t_1 + l$). The nonlinearity which saturates the wave amplitude is associated with the feedback reaction of the pump wave on the perturbation. When the amplitude of the plasma wave is high enough the electron density in the beam is modulated.

We consider two cases.

1. In the first case, the instability growth rate $\nu \ll \omega_b \Gamma^{-3/2}$, where $\omega_b = \sqrt{4\pi e^2 n_0/m}$, n_0 is the electron density beam, and $\Gamma = (1 - v_0^2/c^2)^{-1/2}$. This corresponds to ordinary decay. In this case we have a system of equations that describes the decay of the electromagnetic pump wave $E_0(z, t)$ into an electromagnetic wave and a plasma wave $E_1(z, t)$ and $E_2(z, t)$, where

$$\left.\begin{aligned} &E_j(z, t) = E_j(t)\, e^{i(k_j z - \omega_j t + \alpha_j(t))} \quad j = 0, 1, 2, \\ &\frac{d}{dt}\left(E_0 e^{i\alpha_0}\right) = \frac{ek_2}{4m\omega_1\Gamma} E_1 E_2 e^{i(\alpha_1+\alpha_2)}, \\ &\frac{d}{dt}\left(E_1 e^{i\alpha_1}\right) = -\frac{ek_2}{4m\omega_0\Gamma} E_0 E_2 e^{i(\alpha_0-\alpha_2)}, \\ &\frac{d}{dt}\left(E_2 e^{i\alpha_2}\right) = -\frac{ek_2\omega_b}{4m\omega_0\omega_1\Gamma^{3/2}} E_0 E_1 e^{i(\alpha_0-\alpha_1)}. \end{aligned}\right\} \tag{1}$$

In deriving this system we assume that the following resonance conditions hold:

$$\omega_0 = \omega_1 + \omega_2; \quad k_0 = k_1 + k_2; \tag{2}$$

using these, we obtain

$$k_2 = \frac{\omega_b}{(c - v_0)\Gamma^{3/2}}. \tag{3}$$

In the specified pump-wave approximation, we obtain a linear growth rate:

$$\nu = \frac{ek_2\mathcal{E}_0}{4m\omega_0}\sqrt{\frac{\omega_b}{\omega_1\Gamma^{3/2}}}, \tag{4}$$

where $\mathcal{E}_0 = E_0(t = 0)$.

From the solutions[2] of nonlinear system (1), we can find the beam modulation depth:

$$\frac{\Delta n}{n_0} = \frac{ek_2\mathcal{E}_0}{m\omega_b^2}\sqrt{\frac{\omega_b}{\omega_0\Gamma^{3/2}}}. \tag{5}$$

Using (4) we find that decay occurs at pump-wave amplitudes

$$\mathcal{E}_0 < \mathcal{E}_0^* = \frac{4m\omega_0\Gamma^{3/4}}{ek_2}\sqrt{\omega_b\omega_1},$$

which corresponds to a laser power

$$P^* = \frac{4m^2 c\omega_0^2\omega_1\omega_b\Gamma^{3/2}}{\pi e^2 k_2^2}.$$

2. Now let us consider the case $\nu_{\text{mod}} \gg \omega_b \Gamma^{-3/2}$; this corresponds to "modified" decay and an aperiodic growth with time.[3] In this case the system describing the decay of the electromagnetic pump wave has the form

$$\frac{d}{dt}\left(E_0 e^{i\alpha_0}\right) = \frac{R(\omega_1 + k_2 v_0)}{2\delta^2} E_1 E_2 e^{i(\alpha_1+\alpha_2+\delta t)}, \tag{6}$$

$$\frac{d}{dt}\left(E_1 e^{i\alpha_1}\right) = -\frac{R(\omega_0 - k_2 v_0)}{2\delta^2} E_0 E_2 e^{i(\alpha_0-\alpha_2-\delta t)}, \tag{7}$$

$$\frac{d^2}{dt^2}\left(E_2 e^{i\alpha_2}\right) + \frac{\omega_b^2}{\Gamma^3} E_2 e^{i\alpha_2} = iRE_0 E_1 e^{i(\alpha_0-\alpha_1-\delta t)}, \tag{8}$$

where $\delta = \omega_0 - \omega_1 - k_2 v_0$, $R = e\omega_b^2 k_2/2m\omega_0\omega_1\Gamma^4$, the field of the plasma wave being specified in the form

$$E_2(z, t) = E_2(t)\, e^{i(k_2 z - k_2 v_0 t + \alpha_2(t))}.$$

In the specified-pump-wave approximation, setting $E_2 e^{i\alpha_2} \sim e^{i\varkappa t}$, we obtain the linear dispersion relation from (7) and (8); if we use dimensionless variables this becomes

$$(\varkappa + \Delta_1)(\varkappa^2 - B) = 1, \tag{9}$$

where

$$\Delta_1 = \frac{\delta}{\xi}, \quad B = \frac{\omega_b^2}{\xi^2\Gamma^3}, \quad \xi = (2\delta)^{-2/3} R^{2/3}\mathcal{E}_0^{2/3}(\omega_0 - k_2 v_0)^{1/3}.$$

As $B \to 0$, an instability develops for all $\Delta_1 < 3/2^{2/3}$. An analytic solution of the nonlinear problems can be obtained for $|\Delta_1| \gg 1$. The fact that

$$k_2=\frac{\Delta_1\xi}{c-v_0}<0 \qquad (10)$$

for $\Delta_1 < 0$ implies that the process occurs with a higher frequency ω_1. Since $|\Delta_1|\xi \gg \nu_{\text{mod}} \sim \xi/\sqrt{\Delta_1}$, (10) implies that k_2 increases compared to (3) and can correspond to wavelengths in the visible range. For $|\Delta_1| \gg 1$ the wave amplitude varies much more slowly than the phase. Allowing for this fact, we can obtain the following equation for the amplitude of the plasma wave (in dimensionless variables):

$$\left(\frac{du_2}{d\tau}\right)^2=\left(\frac{du_{20}}{d\tau}\right)^2+\sqrt{\frac{\Delta_1^2}{4}+u_2^2}-\sqrt{\frac{\Delta_1^2}{4}+u_{20}^2}-B\left(u_2^2-u_{20}^2\right), \qquad (11)$$

where

$$u_{20}=u_2(\tau=0);\quad \frac{du_{20}}{d\tau}=\left.\frac{du_2}{d\tau}\right|_{\tau=0};\quad \tau=\xi t,$$

$$E_2=\frac{2\beta^2\xi}{(\omega_1+k_2v_0)^{1/2}(\omega_0-k_2v_0)^{1/2}R}u_2.$$

Equation (11) has a periodic solution with period $\tau_0 = 2\pi/\sqrt{B} + \sqrt{\Delta_1}K(k)$, where K(k) is a complete elliptic integral of the first kind; $k = 1 - |a|/\Delta_1$; $a = u_{20}^2/\Delta_1 - [(du_{20}\cdot d\tau)^{-1}]^2$; u_2 varies from its minimum value $u_{2\min} = \sqrt{a\Delta_1}\cdot$ ($u_{2\min} = 0$ for $a < 0$) to its maximum value[4] $u_{2\max} = (1/B)$. The modulation depth is

$$\frac{\Delta n}{n_0}=\frac{k_2^2e^2\mathcal{E}_0^2}{2m^2\omega_0\omega_1\omega_2^2\Gamma}. \qquad (12)$$

For an amplitude

$$\mathcal{E}_0=\frac{2m\omega_1\Gamma^{1/2}}{k_2e}\sqrt{\omega_2\omega_0}\sim\mathcal{E}_0^*,$$

Eq. (5) becomes Eq. (12).

The author is grateful to V. D. Shapiro for proposing the topic and for guidance.

---

[1] V. D. Shapiro and Ya. (Ja.) B. Fainberg, Sixth European Conference on Controlled Fusion and Plasma Physics, Moscow, USSR (1973).

[2] N. Bloembergen, Nonlinear Optics, Benjamin (1965).

[3] A. A. Galeev and R. Z. Sagdeev, Nucl. Fusion, 13, 4 (1973).

[4] B. A. Al'terkop, A. S. Volokitin, V. D. Shapiro, and V. I. Shevchenko, ZhETF Pis. Red., 18, 46 (1973) [JETP Lett., 18, 24 (1973)].

Liquid metal droplet with high surface tension in an axially-symmetric electromagnetic field (strong skin effect)

A. N. Tverdokhlebov and A. L. Shuster

(Submitted February 4, 1974)
Zh. Tekh. Fiz., 44, 2438-2441 (November 1974)

The stable equilibrium, total potential energy, dissipated power, and aspherical corrections for the second and third terms of the Legendre polynomial expansion are obtained for a liquid-metal droplet with high surface tension suspended in an arbitrary axially-symmetric magnetic field. The expressions are obtained for the case of a strong skin effect.

In refs. 1 and 2 the generalized results are obtained for the potential energy, dissipated power, and shape of a liquid-metal droplet with a high surface tension σ in an arbitrary magnetic field, for the case of a strong skin effect.

In the experimental work, as, for instance, in vacuum melting,[3] kinetics of interaction between the gas flow and a levitating drop[4], axially-symmetric magnetic fields are of the most practical interest; these are produced by the coaxial currents. In this case simple expressions are obtained for the stability of a levitated metal droplet, its shape, etc. In the present work several relevant expressions are derived.

Conditions for a stable equilibrium position of a sphere. Let the magnetic field $\mathbf{H}(\mathbf{r})$ be produced by a system of n coaxial rings of radius R_k in which currents $\varepsilon_k I_k \exp(-i\omega t)$ flow, where $\varepsilon_k = \pm 1$, I_k is the effective value of the alternating current with frequency ω in the k-th ring; k = 1, 2, . . ., n. In the spherical system of coordinates (r, θ, φ) the nonzero component of the vector potential $\mathbf{A}(\mathbf{r})$ is given by [omitting the multiplier $\exp(-i\omega t)$]

$$A_\varphi = \sum_{l=1}^{\infty} \frac{1}{l(l+1)} r^l P_l^1(\cos\theta)\, \psi_l, \tag{1}$$

$$\psi_l = \sum_{k=1}^{n} \frac{2\pi}{c} \varepsilon_k I_k (R_k)^{-l} (\sin\alpha_k)^{l+1} P_l^1(\cos\alpha_k), \tag{2}$$

where $P_l^\mu(z)$ is the associated Legendre polynomial, while $2\alpha_k$ is the angle subtended by the diameter of the k-th ring at the origin.

In the zeroth approximation in $1/\sigma$, the drop is a sphere. The potential energy $U(\mathbf{r})$ of the sphere with radius a calculated according to expressions given in ref. 1 is

$$U(\mathbf{r}) = \frac{1}{4\pi} \int\limits_{|\mathbf{r}-\mathbf{r}'|<a} d^3r' \frac{|\mathbf{r}-\mathbf{r}'|}{a} \mathbf{H}^2(\mathbf{r}')$$

$$\equiv \frac{1}{2} a^3 \sum_{m=0}^{\infty} \frac{a^{2m}}{(m+2)(2m+1)!} \Delta^{(m)} \mathbf{H}^2(\mathbf{r}), \tag{3}$$

where a is the radius of the sphere of equivalent volume to the liquid-metal droplet, $\Delta^{(m)}$ is the Laplace operator taken m times, $\mathbf{H}(\mathbf{r})$ is the magnetic field in the absence of the sphere.

Let the center of the sphere be located at the origin. To obtain the necessary and sufficient conditions for a stable equilibrium of a sphere we expand the potential energy $U(\mathbf{r})$ in r about the origin to second order. Expression (3) for $U(\mathbf{r})$, with $\mathbf{H}$ from (1) and (2), gives

$$U(\mathbf{r}) - U(0) = \frac{1}{4} a^3 \sum_{m=1}^{\infty} a^{2m} \left\{ \frac{2}{m+1} \psi_m \psi_{m+1} (r\cos\theta) \right.$$
$$\left. + \left(\frac{m}{m+1} \psi_{m+1}^2 + \psi_m \psi_{m+2} \right) (r\cos\theta)^2 + \frac{1}{2} \left(\frac{m^2}{(m+1)^2} \psi_{m+1}^2 - \psi_m \psi_{m+2} \right) (r\sin\theta)^2 \right\}. \tag{4}$$

By considering the gravitational energy $U_g(\mathbf{r}) = (4/3)\pi a^3 d(\mathbf{g}\mathbf{r})$, where $\mathbf{g}$ is the gravitational acceleration and d is the specific weight, we obtain the necessary and sufficient conditions for stable equilibrium:

$$\frac{4}{3}\pi d = -\frac{1}{2} \sum_{m=1}^{\infty} \frac{1}{m+1} a^{2(m-1)} \psi_m \psi_{m+1}, \tag{5}$$

$$\left. \begin{aligned} &\sum_{m=1}^{\infty} a^{2(m-1)} \left[\frac{m}{m+1} \psi_{m+1}^2 + \psi_m \psi_{m+2} \right] > 0, \\ &\sum_{m=1}^{\infty} a^{2(m-1)} \left[\left(\frac{m}{m+1} \right)^2 \psi_{m+1}^2 - \psi_m \psi_{m+2} \right] > 0. \end{aligned} \right\} \tag{6}$$

To calculate the total potential energy according to Eq. (3) we reduce the expression for $\Delta^{(m)}\mathbf{H}^2(\mathbf{r})$, derived from (1) and (2), to

$$\Delta^{(m)}\mathbf{H}^2 = \sum_{l=0}^{\infty} (2l+1) P_l(\sin\theta) \sum_{l_1, l_2=1}^{\infty} r^{l_1+l_2-2-2m} \psi_{l_1} \psi_{l_2} b_{ll_1l_2}^m, \quad m = 0, 1, 2, \ldots, \tag{7}$$

where

$$b_{ll_1l_2}^m = \frac{1}{2l_1l_2} \frac{(L-l)!\,(2L+1)!\,(L-m-1)!}{(L-l-m-1)!\,L!\,(2L-2m-1)!} \begin{pmatrix} l & l_1 & l_2 \\ 0 & 0 & 0 \end{pmatrix}^2,$$
$$2L = l + l_1 + l_2,$$

$\begin{pmatrix} l & l_1 & l_2 \\ 0 & 0 & 0 \end{pmatrix}$ is the 3j Wigner symbol, identically equal to zero, when the triplet l, l_1, l_2 does not satisfy the triangle condition $|l_1 - l_2| \le l \le |l_1 + l_2|$ or when $l_1 + l_2 + l$ is an odd number. For all other cases

$$\begin{pmatrix} l & l_1 & l_2 \\ 0 & 0 & 0 \end{pmatrix} = (-1)^L \sqrt{\frac{(2L-2l_1)!\,(2L-2l_2)!\,(2L-2l)!}{(2L+1)!}}$$
$$\times \frac{L!}{(L-l_1)!\,(L-l_2)!\,(L-l)!}.$$

To derive the equation (7) the following relations are used:

$$P_{l_1}(\cos\theta) P_{l_2}(\cos\theta) = \sum_l (2l+1) \begin{pmatrix} l & l_1 & l_2 \\ 0 & 0 & 0 \end{pmatrix}^2 P_l(\cos\theta),$$

$$P_{l_1}^1(\cos\theta) P_{l_2}^1(\cos\theta) = \frac{1}{2} \sum_l (2l+1) [l_1(l_1+1) + l_2(l_2+1) - l(l+1)]$$
$$\times \begin{pmatrix} l & l_1 & l_2 \\ 0 & 0 & 0 \end{pmatrix}^2 P_l(\cos\theta).$$

Power dissipated in the sphere. To calculate the dissipated power W we use the equation (5.2) from ref. 1 in the first approximation in the skin depth δ:

$$W=\omega\delta\left\{\frac{1}{4\pi}\oint dS\mathbf{H}^2-\frac{1}{4\pi a}\int\limits_{r<a}d^3r\left(\frac{r}{a}\right)\mathbf{H}^2\right\}.$$

Using the same approach as in the preceding section, we obtain the following expansion for the case of an axially-symmetric field:

$$W=\frac{\omega\delta}{2}a^2\sum_{m=0}^{\infty}\frac{2m+3}{(m+1)(m+2)}a^{2m}\psi_{m+1}^2. \tag{8}$$

Corrections for the shape of a liquid metal drop. As follows from ref. 2, to the first order in $1/\sigma$ the shape of a drop is given by the equation

$$r=a\left(1+\frac{1}{\sigma}\sum_{l=2}^{\infty}u_l(\theta,\varphi)\right), \tag{9}$$

where u_l is determined from the equation ($l \geq 2$)

$$(1-l)(2+l)u_l=aG_l,$$

while G_l is the expansion in spherical harmonics of the surface pressure exerted by the magnetic forces p_{mag} on the sphere. The pressure p_{mag} is determined from the equation

$$p_{\text{mag}}=-\frac{1}{2}\pi\delta^2(\mathbf{j}\mathbf{j}^*),$$

where $\mathbf{j}$ is the surface current density on the sphere. The surface current density is calculated from Eq. (2.9) in ref. 1 in terms of the magnetic field $\mathbf{H}(\mathbf{r})$, as given in the absence of the sphere:

$$\mathbf{j}=\frac{1-i}{4\pi a\delta}\frac{1}{a}\int\limits_0^a dr\left(2r\frac{\partial}{\partial r}+1\right)[\mathbf{r}\mathbf{H}(\mathbf{r})].$$

In our case of axial symmetry with the magnetic field given by (1), (2), we have

$$j_\varphi=\frac{1-i}{4\pi a\delta}\sum_{l=1}^{\infty}\frac{2l+1}{l(l+1)}a^l\psi_l P_l^1(\cos\theta).$$

Expanding p_{mag} into Legendre polynomials, we obtain G_l:

$$G_l=\frac{1}{32\pi}(2l+1)P_l(\cos\theta)\sum_{l_1,l_2=1}^{\infty}\frac{(2l_1+1)(2l_2+1)}{l_1l_2(l_1+1)(l_2+1)}[l_1(l_1+1)$$
$$+l_2(l_2+1)-l(l+1)]\begin{pmatrix}l & l_1 & l_2\\ 0 & 0 & 0\end{pmatrix}^2 a^{l_1+l_2-2}\psi_{l_1}\psi_{l_2}.$$

We reduce the expressions for u_2 and u_3

$$u_2=-\frac{5}{64\pi}\sum_{m=1}^{\infty}\left\{\frac{(2m+1)(m^2+m-3)}{(2m+3)(m+1)m(2m-1)}a^{2m-1}\psi_m^2\right.$$
$$\left.+\frac{3}{2m+3}a^{2m+1}\psi_m\psi_{m+2}\right\},$$

$$u_3=-\frac{7}{32\pi}\sum_{m=1}^{\infty}\left\{\frac{3}{5}\frac{m^2+2m-5}{(2m+5)(m+1)(2m-1)}a^{2m}\psi_m\psi_{m+2}+\right.$$
$$\left.+\frac{m+2}{(2m+5)(2m+3)}a^{2m+2}\psi_m\psi_{m+3}\right\}.$$

The surface (9), for instance in the case of a "counter-current induction coil" (two rings with current phase shifted by 180°) gives the "pear-shaped" drop that is observed experimentally.

---

[1] A. N. Tverdokhlebov and A. L. Shuster, Zh. Tekh. Fiz., 42, 1777 (1972) [Sov. Phys. – Tech. Phys., 17, 1427 (1973)].

[2] A. N. Tverdokhlebov and A. L. Shuster, Zh. Tekh. Fiz., 44, 2265 (1974) [Sov. Phys. – Tech. Phys., 19, 1399 (1975)].

[3] A. A. Fogel', T. A. Sidorova, V. V. Smirnov, Z. A. Tuts, and I. V. Korkin, Izv. Akad. Nauk SSSR, No. 2, 139 (1968).

[4] G. W. Toop and F. D. Richardson, in: Symposium on Extractive Metallurgy, Inst. Mining and Metallurgy, Preprint 9 (April 1967).

[5] R. P. Zhizherin, Problems of Magnetic Hydrodynamics and Dynamics of Plasma [in Russian], Izd. Akad. Nauk LatvSSR, Riga (1959).

Solution of the Stefan problem

A. M. Tsybin

B. E. Vedenov All-Union Scientific Research Institute of Hydraulic Engineering, Leningrad

(Submitted January 18, 1974)
Zh. Tekh. Fiz., 44, 2441-2444 (November 1974)

It is shown that the solution of the Stefan problem can be constructed if the trajectory of the zero isotherm is known. The desired function is written as a series of harmonic functions.

Consider the following problem:

$$\frac{\partial U}{\partial \tau} = a\frac{\partial^2 U}{\partial x^2} \quad (0 < x < S(\tau)),$$
$$U(0, \tau) = f(\tau) < 0, \quad U(S(\tau), \tau) = 0, \quad S(0) = 0,$$
$$\lambda \frac{\partial U}{\partial x}(S(\tau), \tau) = A\frac{\partial S}{\partial \tau}.$$

We use the transformation introduced in ref. 1,

$$J(p, \tau) = \int_0^{S(\tau)} U(x, \tau)\,\mathrm{sh}\sqrt{p}\,x\,dx, \quad \mathrm{Re}\,p > 0. \tag{1}$$

Then, as shown there, we have

$$J(p, \tau) = \frac{aA}{\lambda\sqrt{p}} e^{ap\tau}\left[e^{-ap\tau}\,\mathrm{ch}\left(\sqrt{p}\,S(\tau)\right) - 1 + ap\int_0^{\tau} e^{-apz}\,\mathrm{ch}\left(\sqrt{p}\,S(z)\right)dz\right] + a\sqrt{p}\,e^{ap\tau}\int_0^{\tau} f(z)\,e^{-apz}dz, \tag{2}$$

where S(τ) satisfies the integral equation

$$\int_0^{\infty} \mathrm{ch}\left(\sqrt{p}\,S(z)\right)e^{-apz}dz = \frac{1}{ap} - \bar{f}(ap)\frac{\lambda}{Aa}, \tag{3}$$

where

$$\bar{f}(ap) = \int_0^{\infty} f(\tau)\,e^{-ap\tau}d\tau.$$

We will seek U(x, τ) in the form

$$U(x, \tau) = \sum_{k=1}^{\infty} a_k(\tau)\sin\frac{k\pi x}{S(\tau)}. \tag{4}$$

Substituting (4) into (1), we obtain

$$\sum_{k=1}^{\infty} \frac{k a_k(\tau)(-1)^{k+1}}{p + \frac{k^2\pi^2}{S^2(\tau)}} = \frac{J(p, \tau)\,S(\tau)}{\pi\,\mathrm{sh}\left(\sqrt{p}\,S(\tau)\right)}. \tag{5}$$

The left part of this expression is regular everywhere except for poles on the negative semiaxis:

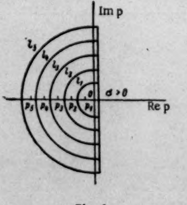

Fig. 1

$$p_k = -\frac{k^2\pi^2}{S^2(\tau)}, \text{ where } k = 1, 2, \ldots. \tag{6}$$

We integrate both sides of (5) successively over the contours $l_1, l_2, \ldots, l_k, \ldots$ (see Fig. 1). The contour l_k consists of the vertical line $\sigma > 0$, $\mathrm{Im}\,\sigma = 0$, a semicircle radius $[\pi^2/2S^2(\tau)](2k^2+2k+1)$, whose center is the coordinate origin, and the two horizontal lines $y = [\pm\pi^2/2S^2(\tau)](2k^2+2k+1)$. Then,

$$\left.\begin{aligned} a_1(\tau) &= \frac{S(\tau)}{2\pi^2 i}\int_{l_1}\frac{J(p, \tau)\,dp}{\mathrm{sh}\left(\sqrt{p}\,S(\tau)\right)}, \\ a_k(\tau) &= \frac{(-1)^{k+1}S(\tau)}{\pi k}\left[\frac{1}{2\pi i}\int_{l_k}\frac{J(p, \tau)\,dp}{\mathrm{sh}\left(\sqrt{p}\,S(\tau)\right)} - \frac{1}{2\pi i}\int_{l_{k-1}}\frac{J(p, \tau)\,dp}{\mathrm{sh}\left(\sqrt{p}\,S(\tau)\right)}\right] \quad (k = 2, 3, \ldots). \end{aligned}\right\} \tag{7}$$

From an analysis of the integrand

$$\frac{J(p, \tau)}{\mathrm{sh}\left(\sqrt{p}\,S(\tau)\right)} = \frac{aA\,\mathrm{ch}\left(\sqrt{p}\,S(\tau)\right)}{\lambda\sqrt{p}\,\mathrm{sh}\left(\sqrt{p}\,S(\tau)\right)} - \frac{aAe^{ap\tau}}{\lambda\sqrt{p}\,\mathrm{sh}\left(\sqrt{p}\,S(\tau)\right)} + \frac{a^2A}{\lambda}\frac{\sqrt{p}\,e^{ap\tau}\int_0^{\tau}e^{-apz}\,\mathrm{ch}\left(\sqrt{p}\,S(z)\right)dz}{\mathrm{sh}\left(\sqrt{p}\,S(\tau)\right)} + \frac{a\sqrt{p}\,e^{ap\tau}\int_0^{\tau}f(z)\,e^{-apz}dz}{\mathrm{sh}\left(\sqrt{p}\,S(\tau)\right)} \tag{8}$$

it is clear that the first two terms in (8) are regular everywhere except for the poles p = 0 and p = p_k (6). Therefore we have

$$a_k(\tau) = \frac{2(-1)^{k+1}aA}{\pi k\lambda}\left[1 + (-1)^{k+1}e^{-a\frac{k^2\pi^2}{S^2(\tau)}\tau}\right] + \frac{(-1)^{k+1}aS(\tau)}{\pi k}\left[\frac{1}{2\pi i}\int_{l_k}V(p, \tau)\,dp - \frac{1}{2\pi i}\int_{l_{k-1}}V(p, \tau)\,dp\right] \quad (k = 1, 2, \ldots), \tag{9}$$

where

$$V(p, \tau) = \frac{e^{ap\tau}\sqrt{p}}{\mathrm{sh}\left(\sqrt{p}\,S(\tau)\right)}\left[\frac{aA}{\lambda}\int_0^{\tau}e^{-apz}\,\mathrm{ch}\left(\sqrt{p}\,S(z)\right)dz + \int_0^{\tau}f(z)\,e^{-apz}dz\right]. \tag{10}$$

Thus, if S(τ) is determined from integral equation (3) and the coefficient $a_k(\tau)$ is computed from (9), we can construct a solution for the initial problem and write it in form of (4).

We will show that for $f(\tau) = N = \text{const} < 0$ the resultant solution becomes the familiar self-similar solution

$$W = N + \frac{A\beta}{2\lambda}\sqrt{\pi a}\,e^{\beta^2/4a}\,\mathrm{erf}\left(\frac{x}{2\sqrt{a\tau}}\right), \tag{11}$$

where β is determined from the solution of the transcendental equation

$$-\frac{2N\lambda}{A\sqrt{\pi a}} = e^{\beta^2/4a}\,\mathrm{erf}\left(\frac{\beta}{2\sqrt{a}}\right)\beta. \tag{12}$$

We have $S(\tau) = \beta\sqrt{\tau}$, in this case, where β [as follows from (3)] is given by the equation

$$\int_0^{\infty}\mathrm{ch}\left(\beta\sqrt{t}\right)e^{-at}dt = \frac{1}{a}\left(1 - \frac{\lambda N}{aA}\right). \tag{13}$$

Making the change of variable t = z^2 and using ref. 2, we obtain

$$\int_0^\infty \operatorname{ch}(\beta\sqrt{t})\, e^{-at}dt = 2\int_0^\infty \operatorname{ch}(\beta z)\, e^{-az^2}z\,dz = \frac{\beta}{2a}\sqrt{\frac{\pi}{a}}\, e^{\beta^2/4a}\operatorname{erf}\left(\frac{\beta}{2\sqrt{a}}\right) + \frac{1}{a},$$

i.e., β is exactly the same as in the self-similar solution. In this case the integrals in (9) can be readily evaluated and

$$a_k(\tau) = a_k = \frac{2Aa}{\lambda\pi k}\left[(-1)^{k+1} + e^{-a\frac{k^2\pi^2}{\beta^2}} + a e^{-a\frac{k^2\pi^2}{\beta^2}} \int_0^{\frac{k^2\pi^2}{\beta^2}} \cos\beta\sqrt{t}\, e^{at}dt\right] + \frac{2N}{\pi k}\left(1 - e^{-a\frac{k^2\pi^2}{\beta^2}}\right) = \text{const} \quad (k = 1, 2, 3, \ldots). \tag{14}$$

Again making the substitution t = z^2 and performing the necessary calculations, we find

$$a_k = \frac{2Aa\beta}{\lambda\pi k} e^{-a\frac{k^2\pi^2}{\beta^2}} \int_0^{\frac{k\pi}{\beta}} e^{az^2} \sin\beta z\,dz + \frac{2N}{\pi k}\left(1 - e^{-a\frac{k^2\pi^2}{\beta^2}}\right) \quad (k = 1, 2, 3, \ldots). \tag{15}$$

Expanding sin βz in a power series, we have

$$a_k = \frac{A\beta^2}{\lambda\pi k}\left(1 - e^{-a\frac{k^2\pi^2}{\beta^2}}\right)\sum_{i=0}^\infty \frac{\beta^{2i}\, i!}{a^i(2i+1)!} + \frac{2N}{\pi k}\left(1 - e^{-a\frac{k^2\pi^2}{\beta^2}}\right)$$

$$+ \frac{A\beta^2}{\lambda\pi k}\sum_{i=1}^\infty \frac{\left(\frac{a\pi^2}{\beta^2}\right)^i k^{2i}(-1)^i}{i!}\sum_{j=1}^\infty \frac{\left(\frac{\beta^2}{a}\right)^j j!}{(2j+1)!} \quad (k = 1, 2, 3, \ldots).$$

It can be shown that

$$\sqrt{\pi a}\, e^{\frac{\beta^2}{4a}} \operatorname{erf}\left(\frac{\beta}{2\sqrt{a}}\right) = \sum_{i=0}^\infty \frac{\beta^{2i+1}\, i!}{a^i(2i+1)!}. \tag{16}$$

This result is understandable if we represent erf as an integral and then integrate successively by parts, setting U = e^{-z^2} each time. Then, using (12), we obtain

$$a_k = \frac{A\beta^2}{\lambda\pi k}\sum_{i=1}^\infty \frac{(-1)^i k^{2i}\pi^{2i}}{i!}\left(\frac{a}{\beta^2}\right)^i \sum_{j=1}^\infty \frac{\left(\frac{\beta^2}{a}\right)^j j!}{(2j+1)!} \quad (k = 1, 2, \ldots). \tag{17}$$

On the other hand, if

$$b_k = \int_0^{\frac{x}{\beta\sqrt{\tau}}} W \sin\frac{k\pi x}{\beta\sqrt{\tau}}\, dx, \tag{18}$$

where W is given by (11), after a number of operations we can write

$$b_k = \frac{A\beta^2}{2\lambda\pi k} e^{\frac{\beta^2}{4a}} \sum_{i=1}^\infty \frac{(-1)^i k^{2i}\pi^{2i}}{(2i)!}\int_0^1 e^{-\frac{\beta^2 z^2}{4a}} z^{2i}dz \quad (k = 1, 2, \ldots). \tag{19}$$

Reasoning in exactly the same way as in deriving (16), we find that $b_k = a_k$ (k = 1, 2, ...), i.e., solution (9) does indeed become the familiar self-similar solution for $f(\tau)$ = N = const < 0.

---

[1] O. M. Chekmareva, Zh. Tekh. Fiz., 41, 1115 (1971) [Sov. Phys. – Tech. Phys., 16, 882 (1971)].

[2] I. S. Gradshtein and I. M. Ryzhik, Tables of Integrals, Sums, Series, and Products [in Russian], Izd. Nauka, Moscow (1971).

Stigmatic sectored magnetic analyzer for a multiple-beam mass spectrometer

G. Kh. Chedzhemov

I. Franko State University, L'vov

Zh. Tekh. Fiz., 44, 2444-2446 (November 1974)

A method of design is presented for a stigmatic analyzer for a multiple-beam mass spectrometer with a homogeneous sectored magnetic field and straight magnet edges. Relations that determine the variable parameters are derived. Attention is drawn to mass discrimination in the absence of stigmatic focusing.

The simultaneous focusing of ion beams in the horizontal and vertical plane makes it possible to increase the optical power and sensitivity of mass spectrometers. Stigmatic focusing in single-beam mass spectrometers has been considered in various papers,[1-6] but no attention has been paid to the problem of stigmatic focusing in multiple-beam mass spectrometers. It is desirable to carry out measurements of isotopic abundance in multiple-beam mass spectrometers, since the comparison of ion currents under stable conditions yields high accuracy. Conditions of stigmatic focusing in single beam mass spectrometers are well understood, but not directly applicable to multiple-beam devices. The introduction of two or more collectors with focusing only in the horizontal plane leads to different optical powers of the collectors, causes mass discrimination and possible errors in isotopic abundance ratios. This fact has not received attention until now. In this paper we describe the design of a sectored analyzer of a multiple-beam mass spectrometer with homogeneous magnetic field and straight edges, permitting the simultaneous stigmatic focusing of ion beams with different masses without beam scanning.

We express all distances in absolute units and label all parameters that depend on mass with an appropriate superscript i (i = 1, i = 2, etc. according to collector number), thus

$$l_{2H}^{i}=r^{i}\cos\varepsilon_2^{i}\,\frac{\sin\varphi^{i}+\dfrac{l_1\cos(\varphi^{i}-\varepsilon_1)}{r^{i}\cos\varepsilon_1}}{\dfrac{l_1\sin(\varphi^{i}-\varepsilon_1-\varepsilon_2^{i})}{r^{i}\cos\varepsilon_1}-\cos(\varphi^{i}-\varepsilon_2^{i})},\qquad(1)$$

$$l_{2V}^{i}=r^{i}\,\frac{\varphi^{i}+\dfrac{l_1}{r^{i}}(1-\varphi^{i}\,\mathrm{tg}\,\varepsilon_1)}{\dfrac{l_1}{r^{i}}[\mathrm{tg}\,\varepsilon_1+(1-\varphi^{i}\,\mathrm{tg}\,\varepsilon_1)\,\mathrm{tg}\,\varepsilon_2^{i}]-(1-\varphi^{i}\,\mathrm{tg}\,\varepsilon_2^{i})},\qquad(2)$$

where l^{i}_{2H} and l^{i}_{2V} are the distances between the point of emergence from the field and the image in the horizontal and vertical plane, r^{i} and φ^{i} are the radii and deflection angles of ion trajectories in the magnetic field, ε_1 and ε_2^{i} are the entry and exit angles of the beams, l_1 is the distance from the source to the point of entry into the magnetic field. Denoting by r'' the radius corresponding to ions of mass m'', all other radii are determined by

$$r^{i}=r''\sqrt{\frac{m^{i}}{m''}},\qquad(3)$$

as the accelerating voltage and magnetic field are common to all ions. If φ'' = 90°, all other angles φ^{i} can be easily determined from the relation

$$\varphi^{i}=90^{\circ}+\varepsilon_2^{i}-\varepsilon_2''.\qquad(4)$$

The angles ε_2^{i} can be found from

$$\varepsilon_2^{i}=\arcsin\frac{[(r''-r^{i})+r''\,\mathrm{tg}\,\varepsilon_2'']\cos\varepsilon_2''}{r^{i}}.\qquad(5)$$

Three independent variables (l_1, ε_1, ε''_2) remain in equations (1) and (2); the choice of these, subject to the condition

$$l_{2H}^{i}=l_{2V}^{i},\qquad(6)$$

TABLE 1. Parameters of Sectored Magnetic Analyzers

Analyzer No.	l_1, mm	ε_1	ε_2''	l^{i}_{2H}, mm/l^{i}_{2V}, mm		
				i = '	i = "	i = ‴
1	222	0°	38°38′	335.6 325.0	414.6 406.7	499.6 510.7
2	272	5°39′50″	38°58′25″	291.1 288.6	356.3 352.7	424.6 430.2
3	390	13°19′52″	38°38′25″	236.2 240.8	284.7 284.2	333.9 333.0
4	241	47°	−3°20′	281.5 237.5	296.1 296.2	310.1 370.2

continued

Analyzer No.	$\sum_{i='}^{i='''}(l^{i}_{2H}-l^{i}_{2V})$, mm	Dispersion coefficient	Magnification		Resolution with S_1 = 0.2 mm	Percentage ion efficiency
			plane H	plane V		
1	29.6	5.144*r*	2.30	0.81	220	55
2	11.7	4.581*r*	1.72	0.69	260	45
3	6.0	3.846*r*	1.05	0.54	330	31
4	104.2	2.549*r*	0.68	2.51	380	51

determines the required stigmatic analyzer of the multiple-beam mass spectrometer.

In particular, with $\varphi = 90°$ and $\varepsilon_2 = -45°$ the condition of stigmatic focusing simplifies as $\varepsilon'_2 = \varepsilon''_2 = \varepsilon'''_2 = \varepsilon$ and $\varphi' = \varphi'' = \varphi''' = \varphi$ and the beams entering the device are parallel. The equality of the angles ε_2^i and φ^i and the parallel entry of the beams is maintained for arbitrary ε_1 provided the straight line representing the continuation of the exit edge of the magnet passes through the point at which the ion beam enters the analyzer. The resolution is low in this case even with $\varphi = 180°$.

The choice of the independent variable parameters is accomplished with the aid of a MIR-1 computer by minimization of the sum of differences $\sum_{i='}^{i='''} (l^i_{2H} - l^i_{2V})$. Data pertaining to several versions of analyzers with r" = 180 mm and $\varphi'' = 90°$ computed for masses m' = 36, m" = 38, m''' = 40 are given in Table 1.

A comparative estimate of resolution (see refs. 2 and 5) and ion efficiency makes it possible to select analyzer No. 2 (see Table 1). The vertical crossovers of the ion beams in this analyzer are very close to the collector slits, which are located in accordance with horizontal focusing requirements.

Computations on a series of analyzers with minor variations of the independent variables have shown that tolerances in the manufacture of the analyzers are determined mainly by the condition of horizontal focusing, the latter being six times more stringent than the conditions of vertical focusing. In addition, if the linear dimensions are maintained to tenths of a millimeter, the angles should be satisfied to an accuracy of one minute.

The author thanks B. I. Smirnov for computations carried out on the MIR-1 computer.

---

[1] W. G. Cross, Rev. Sci. Instrum., 22, 717 (1951).

[2] H. Ewald and H. Hintenberger, Methoden u. Anwendungen der Massenspektroskopie, Verlag Chemie, Weinheim (1952).

[3] R. N. Gall', Zh. Tekh. Fiz., 32, 402 (1962) [Sov. Phys. – Tech. Phys., 7, 292 (1962)].

[4] H. Ezoe, Rev. Sci. Instrum., 38, 390 (1967).

[5] A. A. Sysoev and G. A. Samsonov, Theory and Design of Statistical Mass Analyzers [in Russian], Izd. IFI, Moscow (1972).

[6] B. B. Leporskii, É. I. Zaletskii, and V. N. Erokhin, Zh. Tekh. Fiz., 43, 871 (1973) [Sov. Phys. – Tech. Phys., 18, 552 (1973)].

Rotation of Poynting vector for ultralow-frequency ion waves in an inhomogeneous plasma

Ya. L. Al'pert and R. N. Kaufman

Institute of Terrestrial Magnetism, Ionosphere, and Radiowave Propagation, Academy of Sciences of the USSR

(Submitted October 23, 1973; resubmitted March 15, 1974)
Zh. Tekh. Fiz., 44, 2449-2453 (December 1974)

A theoretical study is made of the region in which the Poynting vector S of ultralow-frequency ion waves incident upon the planar boundary (xy plane) of a magnetoactive inhomogeneous plasma turns is rotated in the direction of the static magnetic field H_0. The frequency of the investigated waves varies in the range $0 < \omega \lesssim \omega_L$ (ω_L is the lower hybrid frequency). The solution is found in the quasilongitudinal approximation. The Poynting vector S is shown to turn rapidly at the plasma surface, the angle ψ between S and H_0 reaching the limiting value ψ_∞ ($z \to \infty$) at distances (z) of 20-30 km from the boundary. The dependence of ψ_∞ on frequency is investigated allowing for the collision frequency ν.

INTRODUCTION

In a previous paper[1] we have investigated the rotation of the Poynting vector in low-frequency electron (lf) waves ($\omega_L \ll \omega \lessdot \omega_H$ is the lower hybrid frequency, ω_H is the electron gyrofrequency, ω is the wave frequency) normally incident on the planar boundary of a one-dimensionally inhomogeneous magnetoactive plasma. The problem is solved in ref. 1 for two models of the inhomogeneous plasma [see (10) below] in the quasilongitudinal approximation ignoring the effect of ions, as is permissible for lf waves.

Allowing for the effect of ions greatly complicates the problem, especially in the case of superlow frequencies (slf): $\Omega_H < \omega \sim \omega_L$ (Ω_H is the gyrofrequency). Mathematically this is connected with the complexity of the expression for the refractive index n and of the corresponding differential equations, and physically with the fact that slf waves can propagate at any angle to the static magnetic field H_0. They are coupled by the external static magnetic field only under certain conditions. The solution of this problem for slf waves is undoubtedly of great interest, but the attendant mathematical difficulties have still to be overcome. However, in an analysis of the problem it is found that a rigorous solution allowing for the effect of the ions can be obtained for ultralow-frequency (ulf) waves (corresponding to the frequency range $0 < \omega \sim \Omega_H$) subject to certain conditions that are frequently met in practice, particularly in the near-earth plasma. In this work we present a solution of this problem. The equations obtained for n and the differential equations and their solutions are analogous to those obtained previously[1] for lf electron waves; accordingly, we omit here some of the mathematical details of the computations and refer the reader to ref. 1.

1. INITIAL EQUATIONS. FORMULATION OF THE PROBLEM AND ITS SOLUTION

We consider a magnetoactive plasma consisting of electrons and a single ion species which is inhomogeneous with respect to the coordinate z and upon the planar boundary (xy plane) of which there is normally incident a plane wave of frequency ω in the range

$$0 < \omega \ll \omega_L \simeq \sqrt{\omega_H \Omega_H}, \tag{1}$$

the time dependence being of the form $\exp\{i\omega t\}$. The vector external magnetic field H_0 lies in the yx plane and the vector $-H_0$ makes an acute angle θ with the wave vector of the incident wave $\mathbf{k}_0$, which is parallel to the positive z direction.

In the frequency range defined by (1) two waves can exist in the plasma. One of them is the ordinary wave, which is cut off at a frequency $\omega \simeq \Omega_H$; the other is the extraordinary wave. The latter propagates with small damping even when $\omega > \Omega_H$, and is cut off at frequency $\omega \simeq \omega_H$.

Let $\nu = \nu_{ei}$ be the frequency of electron–ion collisions; $\gamma_0 = m/M$ is the ratio of electron mass to ion mass; $\Omega_0^2 = (4\pi e^2/M)N(z)$ is the square of the ion plasma frequency; N(z) is the electron density. Then, (1) is satisfied and, in addition, if everywhere in the plasma

$$\alpha_0 = \omega\nu\gamma_0 \ll \Omega_0^2(z), \quad \Omega_H^2 \ll \Omega_0^2(z), \tag{2}$$

we obtain from the general equation for the refractive index (see ref. 2) the following comparatively simple expression for n^2:

$$n_\pm^2 = 1 + \frac{2\Omega_0^2}{2\Omega_H^2\cos^2\theta + \Omega_H^2\sin^2\theta + 2i\alpha_0 \pm \sqrt{\Omega_H^4\sin^4\theta + 4\omega^2\Omega_H^2\cos^2\theta}}, \tag{3}$$

where the plus and minus signs pertain respectively to the extraordinary and ordinary waves. It is readily seen that expression (3) is similar in structure to the well-known Appleton–Hartree equation for the refractive index of electron waves when the effect of the ions is ignored (see refs. 3 and 4). It is reasonable therefore to expect that the subsequent simplification and solution of the present problem in the frequency range (1) should lead mathematically to equations similar to those obtained previously[1] for lf electron waves at $\omega \gg \omega_L$.

Considering Eq. (3) in the quasilongitudinal approximation, the condition for which in the present case has the form

$$\left|\frac{\sin^2\theta}{\cos\theta}\right| \ll 2\frac{\omega}{\Omega_H}, \tag{4}$$

we find that

$$n_\pm^2 = \frac{\Omega_0^2}{\Omega_H\cos\theta(\Omega_H\cos\theta \pm \omega) + i\alpha_0}. \tag{5}$$

Equation (5) is similar in structure to the equation for n^2 in the case of lf electron waves [see Eq. (3) in ref. 1].

We note that the second of conditions (2) enables us to drop the unity from (3), which has in fact been done in Eq. (5).

The components of the electric field of the wave are denoted by E_x, E_y, E_z. Utilizing inequality (4), the expressions for the components of the tensor dielectric constant, and Maxwell's equations (see refs. 2-5), we obtain the following simple equations for the polarization of the electric field:

$$\rho_\pm = \frac{E_y}{E_x} = \pm i, \tag{6}$$

$$\frac{E_z}{E_x} = q_\pm \operatorname{tg}\theta, \tag{7}$$

where

$$q_\pm = -\frac{\Omega_H\left[a_0\omega + i\gamma_0\omega^2 + \rho_\pm\Omega_H\cos\theta\left(\omega^2 - \Omega_H^2 - ia_0\right)\right]}{\cos\theta\left[\left(\Omega_H^2 + ia_0\right)^2 - \omega^2\omega_H^2\right]}. \tag{8}$$

For the present case of normal incidence, the Maxwell equations yield two equations of the second order in E_x and E_y, the coefficients of which are expressed through the refractive index and the polarization ρ of the two normal waves in the plasma (Sec. 18.5 of ref. 4). For n^2 and ρ described by Eqs. (5) and (6) we eventually obtain the following wave equation:

$$\frac{d^2(E_x \pm iE_y)}{dz^2} + \frac{\omega^2}{c^2} n_\mp^2 (E_x \pm iE_y) = 0. \tag{9}$$

This equation reduces to a Whittaker equation if ν = const and if we use the height dependences of the electron density utilized in ref. 1 augmented by the addition of certain constant terms to secure fulfillment of the second of inequalities (2), i.e., if

$$\left.\begin{aligned} N(z) &= N_0 + N_1(1 + be^{-\alpha z})(1 - e^{-\alpha z}) \text{ for model ,} \\ N(z) &= N_0 + N_1(1 - e^{-\alpha z})^2 \text{ for model 2.} \end{aligned}\right\} \tag{10}$$

Denoting by $n_{\infty,\pm}$ the value of the refractive index at $z \to \infty$ (it corresponds to the value $N = N_\infty = N_0 + N_1$), we obtain the solution of Eq. (9) in the form

$$E_x \mp iE_y = \exp\left\{i\frac{\omega}{c}(n_{\infty,\pm})z\right\} f(z), \tag{11}$$

where

$$f(z) = \exp\{-a_\pm e^{-\alpha z}\}\,\Phi(\beta_\pm, \gamma_\pm, 2a_\pm e^{-\alpha z}). \tag{12}$$

Here $\Phi(\beta_\pm, \gamma_\pm, 2a_\pm e^{-\alpha z})$ is the degenerate hypergeometric function[6] with argument $2a_\pm e^{-\alpha z}$ and parameters $\beta_\pm$, $\gamma_\pm$, equal to

$$\beta_\pm = \frac{1}{2} - P_\pm - S_\pm, \quad \gamma_\pm = 1 - 2P_\pm,$$

where for model 1 we have

$$a_\pm = \alpha^{-1}\frac{\omega}{c}\sqrt{b}\,(n_\pm)_{N=N_1}; \quad P_\pm = i\alpha^{-1}\frac{\omega}{c} n_{\infty,\pm}; \quad S_\pm = \frac{1}{2}\frac{b-1}{b}a_\pm,$$

and for model 2

$$a_\pm = S_\pm = i\alpha^{-1}\frac{\omega}{c}(n_\pm)_{N=N_1}; \quad P_\pm = i\alpha^{-1}\frac{\omega}{c} n_{\infty,\pm}.$$

[Here $(n_\pm)_{N=N_1}$ is the value of the refractive index $n_\pm$ at $N = N_1$.]

Subsequent calculations similar to those made previously[1] lead to the following expression for the angle $\psi_\pm(z)$ between the wave vector $\mathbf{k}_0$ and the time-averaged Poynting vector $\mathbf{S}_\pm$:

$$\operatorname{tg}\psi_\pm(z) = -\frac{\operatorname{tg}\theta}{2}\,|q_\pm|\,\frac{|F(z)|}{\operatorname{Re}F(z)}, \tag{13}$$

where

$$F(z) = n_{\infty,\pm} - i\frac{c}{\omega}\frac{d}{dz}\ln f(z),$$

and $q_\pm$ is defined by Eq. (8). We note that in the limit $z \to \infty$ and $\nu = 0$, we have

$$\operatorname{tg}\psi_{\infty,\pm} \simeq -\frac{\operatorname{tg}\theta}{2}. \tag{14}$$

Expression (14) coincides with the expression for $\tan\psi$ determined from the general equation for $\tan\psi$ in a homogeneous medium:

$$\operatorname{tg}\psi = \frac{\sin\theta}{n}\,\frac{\partial n}{\partial(\cos\theta)}, \tag{15}$$

obtained in ref. 7 for $\nu = 0$. In the calculation of $\tan\psi$ from expression (15) it is necessary here when taking the derivative $\partial n/\partial(\cos\theta)$ to utilize Eq. (3) for the refractive index and then make recourse to the quasilongitudinal approximation.

It can be seen from (14) that in the quasilongitudinal approximation in a collisionless homogeneous plasma, the angles $\psi_{\infty,\pm}$ for both ulf waves coincide and do not depend on frequency. In the following section it will be shown how these angles for the two waves vary with frequency when allowance is made for the frequency of collisions ($\nu \neq 0$). The variation of the angles $\psi_\pm(z)$ with height z is also found.

2. RESULTS OF THE CALCULATIONS

In order to calculate the variation with height of the angle $\psi_\pm(z)$ between the Poynting vector $\mathbf{S}_\pm$ and the z axis through Eq. (3), the values of the degenerate hypergeometric function Φ appearing in the expression for $f(z)$ [see Eq. (12)] are computed on a BÉSM-6 high-speed computer as the sums of the corresponding series.[6] The numerical calculations are performed for model 2 for $N_1 = 10^4$ cm^{-3}, $N_0 = 10$ cm^{-3}, $\alpha = 0.03$ km^{-1}. The values of the remaining parameters are as follows: $\theta = 15°$; ion gyrofrequency $\Omega_H = 150$ Hz; frequency of collisions $\nu = 10^6$ sec^{-1}. For the ordinary wave the function $\psi_\pm(z)$ is calculated for ratios $\omega/\Omega_H = 0.5$, 0.73, 0.91, and 1.2. For the ordinary wave, as it cuts off at a frequency $\omega \simeq \Omega_H$, the function $\psi_\pm(z)$ is calculated only for the values $\omega/\Omega_H = 0.5$, 0.73, and 0.91. Conditions (1), (2), and (4) are well satisfied everywhere in the calculations.

The angles $\psi_{\infty,\pm}$ for $\nu \neq 0$ are calculated through the

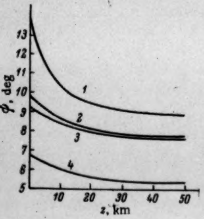

Fig. 1. Angle ψ between time-averaged Poynting vector S and z axis as function of z. 1,2) Ordinary wave (-), $\psi_{\infty -}$; 3,4) extraordinary wave (+); $\psi_{\infty +}$, 1,4) $\omega/\Omega_H = 0.92$; 2,3) 0.5.

equation

$$\operatorname{tg}\psi_{\infty,\pm} = -\frac{\operatorname{tg}\theta}{2}|q_\pm|\frac{|n_{\infty,\pm}|}{\operatorname{Re}(n_{\infty,\pm})}. \tag{16}$$

For both waves it turns out that $\psi(z)$ is at its greatest for z = 0 (Fig. 1) and is around (1.5-5)° greater than the corresponding values of ψ_∞ in the investigated frequency range. The function $\psi(z)$ decreases monotonically for increasing z, and is close to ψ_∞ at $z \approx 20$-30 km. This behavior of $\psi(z)$ is probably due to the fact that we have assumed a nonzero electron density at the boundary of the inhomogeneous medium (z = 0) in order to comply with conditions (2). For this reason it is not possible to trace, as was done in ref. 1 for lf electron waves, the way the angle $\psi(z)$ reaches the limiting value ψ_∞ by gradually increasing from the incident-wave value of $\psi = 0$, and the vector S gradually turns towards the vector $-H_0$. The maximum of $\psi(z)$ at z = 0 is probably due, as in ref. 1 for lf waves, to the effect of the quasilongitudinal approximation. In actual fact the direction of the Poynting vector of ulf waves very rapidly reaches the limiting value ψ_∞. In this range of frequencies the turning of the Poynting vector occurs in a narrower region than for lf waves, i.e., than at frequencies $\omega_L \ll \omega \lessapprox \omega_H$.

The dependence of the limiting values $\psi_{\infty,\pm}$ on frequency ω is calculated for both waves using (16); the results are presented in Fig. 2. It can be seen that as the wave frequency approaches the ion gyrofrequency Ω_H the ordinary-wave Poynting vector S moves closer and closer to the direction of the vector $-H_0$. For the extraordinary wave the angle ψ_∞ has a minimum near $\omega \simeq \Omega_H$ and then increases with increasing frequency to a limiting value: $\tan\psi_\infty \simeq -\tan\theta/2$ in a collisionless plasma ($\nu = 0$). The features of the function $\psi_\infty(\omega)$ manifest in Fig. 2 are in fact due to the effect of ν. For $\nu = 0$, $\tan\psi_\infty \approx -\tan\theta/2$ for both waves and is quite independent of frequency. The use of the quasilongitudinal approximation prevents us from tracing how ψ_∞ varies with decreasing frequency,

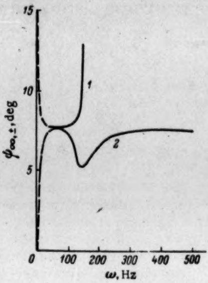

Fig. 2. Limiting value of angle ψ_∞ as function of angular frequency ω for ordinary (1) and extraordinary (2) waves.

when $\omega \to 0$. It was shown in a previous paper[8] that as $\omega \to 0$ for arbitrary θ and $\nu = 0$, then $\tan\psi_{\infty,+} \to 0$ and $\tan\psi_{\infty,-} \to -\tan\theta$ for the extraordinary and ordinary waves respectively.[1)] Approximation of the curves of $\psi_\infty(\omega)$ shown in Fig. 2 to these limiting values (the dashed curves) shows that the direction of the Poynting vector behaves in a more complex manner at frequencies $0 \lessapprox \omega \lessapprox \omega_L$ than for lf waves in the range $\omega_L \ll \omega \lessapprox \omega_H$, where $\psi_{\infty,+}$ increases monotonically with frequency. It should be noted that the approximation of $\psi_\infty(\omega)$ utilized in Fig. 2 for $\nu = 0$ is justified by the fact that the dependence of ψ_∞ on ν is determined by the parameter $\alpha_0 = \gamma_0\nu\omega$ [see Eq. (3), for example], while $\alpha_0 \to 0$ as $\omega \to 0$ and the effect of ν vanishes.

In conclusion we should like to thank G. N. Borisov, G. D. Komlev, and T. A. Londin for the numerical calculations.

[1)] The negative sign of the tan ψ for $\nu = 0$ means that the vector S lies between[8] the vectors $\mathbf{k}_0$ and $-\mathbf{H}_0$.

[1] Ya. L. Al'pert and R. N. Kaufman, Zh. Eksp. Teor. Fiz., 64, 1283 (1973) [Sov. Phys. – JETP, 37, 651 (1973)]; J. Atm. Terr. Phys., 35, 1843 (1973).
[2] Ya. L. Al'pert and D. S. Fligel', Propagation of Low-Frequency Electromagnetic Waves in the Terrestrial-Ionosphere Waveguide [in Russian], Izd. Nauka, Moscow (1967).
[3] J. A. Ratcliffe, The Magnetoionic Theory and Its Applications in the Ionosphere, Cambridge Univ. Press (1959).
[4] K. G. Budden, Radio Waves in the Ionosphere, Cambridge Univ. Press (1961).
[5] V. L. Ginzburg, The Propagation of Electromagnetic Waves in a Plasma [in Russian], Izd. Nauka, Moscow (1967).
[6] H. Bateman and A. Erdélyi, Higher Transcendental Functions [Russian translation], Izd. Nauka, Moscow (1967).
[7] Ya. L. Al'pert, Izv. AN SSSR, Ser. Fiz., 12, 241 (1948).
[8] Ya. L. Al'pert (Ja. L. Alpert), Space Sci. Rev., 6, 781 (1967).

Anomalous resistivity of a transverse plasma current at electron-cyclotron harmonics

V. I. Aref'ev and A. A. Chernov

Moscow Physicotechnical Institute

(Submitted July 26, 1973; resubmitted November 12, 1973)
Zh. Tekh. Fiz., 44, 2454-2466 (December 1974)

Microscopic instabilities of the transverse current at electron-cyclotron harmonics (Bernstein modes) are investigated in a plasma with hot ions $T_i > T_e$. It is shown that the main problem connected with instabilities at cyclotron harmonics, which make a large contribution to the anomalous resistivity of a plasma, for example in the leading edge of a shock wave, is to explain the nonlinear mechanism that saturates the oscillation energy. For the Bernstein modes a nonlinearity is associated with the electrons. Nonlinear damping is determined from the linear theory by using a collision integral that takes account of the similarity between the usual binary collisions and the collective scattering of electrons by microscopic turbulence. The effective electron-scattering frequencies are found from the stabilization condition for different spectra. It is shown that the collective friction force produced by the instabilities does not always stabilize them; for example, stabilization does not occur for current velocities that significantly exceed the ion thermal velocity. In this case a broad spectrum of current-dissipative instabilities develops, and the collective friction force favors the development of cyclotron instabilities. Some nonlinear mechanisms that stabilize the current-dissipative instabilities are investigated. Typical examples are the development of vortical instabilities in an electron gas and the appearance of anomalous viscosity.

In connection with anomalous resistivity in the leading edge of a collisionless shock wave,[1] a recent discussion has arisen in regard to instabilities of transverse plasma currents at electron-cyclotron harmonics[2,3] (Bernstein modes); these modes have wave vectors **k** that are essentially perpendicular to the magnetic field and frequencies that are multiples of the electron-cyclotron frequency $\sim n\omega_{He}$, n = 1, 2, 3, ... These instabilities can develop in the leading edge of a shock wave for a fairly large electron current velocity $u \gg (T_e/M)^{1/2}$ and the growth rates exceed the hybrid frequency $\omega_{e,i} = (\omega_{Hi}\,\omega_{He})^{1/2}$.

In contrast to the ion-acoustic instability, which has a comparatively low current-excitation threshold[4] and which can be excited in a plasma with hot electrons $T_e > T_i$, the instability at the cyclotron harmonics can be excited in a plasma with hot ions $T_i > T_e$. The main problem connected with instabilities at cyclotron harmonics, as is noted in ref. 2, is to explain the nonlinear mechanism that restricts the growth of the energy. Nonlinear electron effects can fill this role for the Bernstein modes.[2,3] This situation has also been examined in ref. 5 in connection with the electron-acoustic instability in a plasma with hot ions, which can be regarded as an instability at the zero cyclotron harmonic.

In the present paper, as an extension of refs. 2 and 3, we use linear theory to examine new current-dissipative instabilities at the electron-cyclotron harmonics; these have a comparatively low excitation threshold and high growth rate, and it will be shown that the excitation of these instabilities, which make a large contribution to the anomalous resistivity of a plasma, is related to the drift current and to collisional processes, for example binary (Coulomb) collisions, or to collective scattering of particles by fluctuations. Stabilization of the instability through the collective friction force between the electrons and ions is then analyzed in a self-consistent nonlinear theory. It will be shown that collisional process and the scattering of particles by the waves, which is accounted for by means of the collective friction force R_f, does not always lead to stabilization of current-dissipative instabilities. This is the case because the instabilities are explosive and, as is noted in refs. 2 and 3, are negative-energy waves. Therefore, a nonlinear theory for such instabilities based on the method of successive approximations in the small parameters—the ratio of the growth rate γ_k to the frequency ω_k, $\gamma_k/\omega_k < 1$—is an incorrect formulation of the problem. An approach which takes account of the similarity between the binary collisions and the collective scattering of particles by random oscillations is necessary. This approach to the nonlinear theory of the explosive instability is proposed in refs. 2 and 3.

In contrast to ref. 3, where the approach to the nonlinear saturation of the instability exploits the similarity between binary collisions and particle scattering by the oscillations in an unstable plasma with a constant effective collision frequency ν_f, in the present paper we use a collision integral from the quasilinear theory[4] to describe the dynamics of instabilities in a weakly turbulent plasma; the effective collision frequency ν_f is then not a constant, but varies during the relaxation of the instability.

1. FORMULATION OF THE PROBLEM AND SELECTION OF THE COLLISION INTEGRAL

The stability of a transverse plasma current will be considered in the same formulation as in refs. 2, 3, 5, and 6. We treat an unbounded homogeneous plasma in quasistationary electric $\mathbf{E}_0$ and magnetic $\mathbf{H}_0$ fields with a drift current

$$\mathbf{j} = -en_e\mathbf{u} = -en_e\frac{c}{H_0^2}[\mathbf{E}_0, \mathbf{H}_0], \tag{1}$$

where **u** is the electron current velocity. We assume throughout that the external electric field is in the direction of the y axis, the magnetic field is along the z axis, and the current velocity is along the x axis.

Two types of elastic scattering of electrons will be taken into account in considering collision processes: binary (Coulomb) collisions, which can be allowed for by employing the Landau collision integral, or in simplified form by analogy with ref. 7, and collective collisions of electrons which appear in an unstable plasma. It is noted in ref. 3 that both processes can be considered by using the same collision integral and introducing the effective collision frequency ν_f, which is assumed to be constant in ref. 3.

Actually, the value of ν_f can vary during the instability relaxation process. This effect can be taken into account in the self-consistent quasilinear theory.[4] A mode of this theory will be used in which the oscillation energy is near saturation. As noted in refs. 2 and 3, the basic process restricting the amplitudes of unstable oscillations is the nonlinear damping of oscillations by electrons. In this case the momentum lost by one particle species due to Cerenkov radiation produced by the oscillations is completely transferred to the other particle species by nonlinear processes, and the linear growth rate γ_k is equal to the nonlinear damping rate γ_{nonl} (see ref. 6 for example). It should be noted that one of the possible nonlinear processes responsible for stabilization of the explosive instability can be a change in the wave dispersion.[6]

Thus, we consider a mechanism for the stabilization of an explosive instability in the quasilinear theory, which takes account of the self-consistent anomalous resistivity. The kinetic equation that describes particle scattering by the oscillations is

$$\frac{\partial f_\alpha}{\partial t}+\mathbf{v}\frac{\partial f_\alpha}{\partial \mathbf{r}}+\frac{e_\alpha}{m_\alpha}\left(\mathbf{E}+\frac{1}{c}[\mathbf{vH}]\right)\frac{\partial f_\alpha}{\partial \mathbf{v}}=\mathrm{St}_{\alpha f}, \tag{2}$$

where $\mathrm{St}_{\alpha f}$ is the collision term, which, according to ref. 4, has the following more general form:

$$\left.\begin{aligned}\mathrm{St}_{\alpha f}&=\frac{\partial}{\partial v_i}\sum_k D_{ij}(\mathbf{k},W_k)\frac{\partial f_\alpha}{\partial v_j},\\ D_{ij}&=\frac{k_ik_j|\varphi_k|^2e_\alpha^2}{m_\alpha^2}\delta(\omega_k-\mathbf{kv}).\end{aligned}\right\} \tag{3}$$

Here, we only consider scattering by electrostatic oscillations. It can be seen from (3) that the diffusion coefficient D_{ij} depends both on the shape of the spectrum and on the energy of the unstable oscillations W_k. If the energy density is

$$W_k=\frac{k^2|\varphi_k|^2}{8\pi}\omega_k\frac{\partial\varepsilon}{\partial\omega_k},$$

we can write

$$\left(\frac{\partial}{\partial t}+\frac{\partial\omega_k}{\partial\mathbf{k}}\frac{\partial}{\partial\mathbf{r}}-\frac{\partial\omega_k}{\partial\mathbf{r}}\frac{\partial}{\partial\mathbf{k}}\right)\ln W_k=2\left(\gamma_k^{(i)}+\gamma_k^{(e)}\right), \tag{4}$$

where $\gamma_k^{(i)}$ and $\gamma_k^{(e)}$ are the ion and electron parts of the growth rate (damping rate) of the instability; these include both linear mechanisms for the instability – Cerenkov radiation-absorption by oscillating resonance particles – and nonlinear processes restricting the amplitudes of unstable oscillations. Saturation is described by

$$\gamma_k^{(i)}+\gamma_k^{(e)}=0.$$

The effect of stabilization by means of the collective friction force R_f acting on the electrons becomes clearer if, retaining (2), we employ a hydrodynamic description of the electron component with the aid of two equations: the continuity equation and the momentum balance equation:

$$\left.\begin{aligned}&\frac{\partial n_e}{\partial t}+\operatorname{div}(n_e\mathbf{v}_e)=0,\\ &mn_e\left(\frac{\partial\mathbf{v}_e}{\partial t}+(\mathbf{v}_e\nabla)\mathbf{v}_e\right)=-en_e\mathbf{E}-\frac{en_e}{c}[\mathbf{v}_e\mathbf{H}]-\mathbf{R}_f;\\ &\mathbf{R}_f=\sum_k\frac{\mathbf{k}}{\omega_k}\gamma W_k,\end{aligned}\right\} \tag{5}$$

where the collective friction force R_f is determined in the usual manner (see ref. 6, for example). In this notation the collective friction force will generally appear in the growth rate γ_k as an arbitrary function of the drift current $\gamma_k(\mathbf{u})$.

In the present paper, the approach to the stabilization problem and to the investigation of the nonlinear process restricting the oscillation amplitudes is based on perturbation theory for the self-consistent system of equations of type (4) and (5) and the supplementary equations for the ion component and the potential φ. Therefore, to find the variation in the collective friction force, which depends on the drift current and the other mean plasma parameters, for example in the form $\delta R_f = \delta u(\partial R_f/\partial u) + \delta n_e(\partial R_f/\partial n) + \ldots$, we introduce the following definition of the effective frequencies of elastic scattering of electrons by the oscillations:

$$\nu=\frac{1}{mn_eu}R_f,\quad \nu_f=\frac{1}{mn_e}\frac{\partial R_f}{\partial u}. \tag{6}$$

Using these effective frequencies we can, by analogy with (3), introduce the anomalous conductivity of the plasma:

$$\sigma_f=\frac{ne^2}{m\nu_f},\quad \sigma=\frac{ne^2}{m\nu}. \tag{7}$$

In the present paper, the method for finding the effective frequencies ν and ν_f, as in ref. 3, is based on the stability condition, i.e., $\gamma_k^{(i)} + \gamma_k^{(e)} = 0$. In contrast to ref. 3, however, it is important for us to find not only the maximum value of ν_f but also to establish its dependence on the drift current $\nu_f(u)$. This approach to the nonlinear processes, which is based on a self-consistent system of equations like (4) and (5), can be used, for example, for the electron-acoustic instability considered in ref. 6, which can arbitrarily be considered an instability at the zero cyclotron harmonic.

The hydrodynamic approximation is not applicable to an instability at electron-cyclotron harmonics; therefore, it is necessary to apply perturbation theory to a more general kinetic equation of type (2). For this reason, we simplify the collision integral by using the similarity between the usual binary collisions and the collective scattering of particles by oscillations. We consider only the approximation in which the following two laws are satisfied: the conservation of the number of particles and the conservation of momentum in the form of (5).

Also, we note the following property, well known in the quasilinear theory,[4] of the distribution function, which varies due to unstable oscillations. In the quasilinear relaxation, the derivative of the distribution function, and not the function itself, has the greatest variation. This property can be used to simplify the collision integral.

Consider a Maxwellian distribution function f_0 in the zeroth approximation. The interaction between the resonance particles and the random oscillations produced by the instability is described by a collisional term in the form of (3), which is taken in the most general form. Let the velocities of the resonance electrons, which are of the same order of magnitude as the phase velocity of the oscillations $v_{res} \simeq \omega/k$, be much smaller than their average thermal velocity $v_{res} \ll v_{Te}$. For the oscillations in question the phase velocities are of the same order of magnitude as the current velocity $\omega/k \simeq u$; therefore, the above-mentioned requirement reduces to the inequality $u \ll v_{Te}$. In this case, one can carry out expansion in powers of $(v - v_{res})/v_{Te}$ near the resonance velocities $v \simeq v_{res}$ which are related to the wave vectors **k** by the relation $\omega = \mathbf{kv}$; only the first two terms of the expansion are considered:

$$\mathrm{St}_{\alpha} f = C_1 + \mathbf{v}\mathbf{C}_2 + \ldots . \tag{8}$$

It is required that the two laws of conservation (number of particles and momentum) mentioned above follow from Eq. (2), with allowance for (8). In this case the coefficients in the expansion C_1 and C_2 can be selected by analogy with ref. 7, where the collisional term is represented as

$$\mathrm{St}_{\alpha f} = \left[\nu(f_e - \eta) - \nu_f \frac{m}{T_e}(\mathbf{vq}) f_0\right], \tag{9}$$

where we have used the notation

$$\eta = \frac{f_0}{n_0}\int f_e d\mathbf{v}, \quad \mathbf{q} = \frac{1}{n_0}\int \mathbf{v} f_e d\mathbf{v}, \tag{10}$$

f_e is the electron distribution function, and f_0 is its equilibrium value (Maxwellian distribution function).

A collisional integral in the form of (9) will be used below to investigate electrostatic instabilities of the drift current. The structure of this integral allows the contributions of the pair and collective collisions to be treated similarly. In the case of binary (Coulomb) collisions the effective elastic-scattering frequencies (6) are determined in the same manner. In collective scattering the dependence of the effective frequencies ν_f and ν on the drift current is important. Note that with this type of notation for the collision integral only perturbations with wavelengths larger than the electron Larmor radius $\lambda > \rho_{He}$ can be considered, and we will restrict ourselves to this approximation.

2. DISPERSION RELATION FOR ELECTROSTATIC OSCILLATIONS

The linearized kinetic equation for the electron component with a collision integral in the form of (9), which allows for the effect of collective friction, is

$$\frac{\partial f_e}{\partial t} + (\mathbf{v}\nabla) f_e - \frac{e}{m}\left(\mathbf{E}_0 + \frac{1}{c}[\mathbf{vH}_0]\right)\frac{\partial f_e}{\partial \mathbf{v}}$$
$$= \frac{e}{m}\left(\mathbf{E} + \frac{1}{c}[\mathbf{vH}]\right)\frac{\partial f_0}{\partial \mathbf{v}} - \left[\nu(f_e - \eta) - \nu_f \frac{m}{T_e}(\mathbf{vq}) f_0\right]. \tag{11}$$

Here, f_e is a small perturbation of the electron distribution function, **E** and **H** are small perturbations of the electric and magnetic fields, and e and m are the electron charge and mass.

Solving Eq. (4) by integration over the trajectories,[8] we obtain the expression for the tensor components

$$\varepsilon_{\alpha\beta} = \varepsilon_{\alpha\beta}^{(0)} + \varepsilon_{\alpha\beta}^{(1)}, \tag{12}$$

where $\varepsilon_{\alpha\beta}^{(0)}$ is the dielectric tensor for a collisionless current-carrying plasma, which is obtained, for example, in ref. 9; $\varepsilon_{\alpha\beta}^{(1)}$ are the collisional components of the tensor. We obtain the following expressions for $\varepsilon_{\alpha\rho}^{(1)}$:

$$\varepsilon_{\alpha\beta}^{(1)} = \frac{8\pi e n_0}{\omega}\sum_{n=-\infty}^{\infty}\left\{\begin{array}{l}\left(\frac{n\omega_{H_e}}{k_\perp} + u\right)\left(-i\frac{\sqrt{\pi}}{k_z v_{T_e}} W_n\right) I_n e^{-\mu} \\ -\frac{k_\perp T_e}{m\omega_{H_e}}\left(\frac{\sqrt{\pi}}{k_z v_{T_e}} W_n\right)(I_n - I_n')e^{-\mu} \\ -\frac{1}{k_z}\left[1 + i\sqrt{\pi}\, z_n W_n\right] I_n e^{-\mu}\end{array}\right\}$$
$$\times\left[\nu\eta^\beta + \nu_f \frac{m q_x^\beta}{T_e}\left(u + \frac{n\omega_{H_e}}{k_\perp}\right)\right]. \tag{13}$$

We introduce the notation

$$v_{T_\alpha} = \left(\frac{2T_\alpha}{m_\alpha}\right)^{1/2}, \quad \mu = \frac{k_\perp^2 \rho_{H_e}^2}{2}, \quad \rho_{H_e} = \frac{v_{T_e}}{\omega_{H_e}}, \quad \omega_{H_e} = \frac{eH_0}{mc},$$
$$z_{ne} = \frac{\tilde{\omega} - n\omega_{H_e} + i\nu}{k_z v_{T_e}}, \quad W_n(z_n) = e^{-z_n^2}\left(1 + \frac{2i}{\sqrt{\pi}}\int_0^{z_n} e^{t^2} dt\right),$$
$$\eta^\beta = \frac{\eta}{E_\beta}, \quad q_x^\beta = \frac{q_x}{E_\beta}, \quad \tilde{\omega} = \omega - \mathbf{ku},$$

$I_n(\mu)$ is the Bessel function of imaginary argument, and $\mathbf{k} = (k_\perp, 0, k_z)$. To obtain the dispersion relation describing the instabilities at cyclotron harmonics with collisional dissipation taken into account we use Eqs. (10), (12), and (13), in Maxwell's equation. As a result a homogeneous system of equations is obtained for the components of the field E_β. The dispersion relation is found from the condition for solving this system. It has the following form for the electrostatic oscillations:

$$\varepsilon = 1 + \frac{1}{k^2 d_i^2}\left[1 + i\sqrt{\pi}\, z_i W(z_i)\right]$$
$$+ \frac{1}{k^2 d_e^2}\sum_{n=-\infty}^{\infty} I_n e^{-\mu}\left[1 + i\sqrt{\pi}\frac{\tilde{\omega}}{k_z v_{T_e}} W_n(z_{ne})\right] + \varepsilon_e^{(1)} = 0,$$
$$d_\alpha^2 = \frac{v_{T\alpha}^2}{\omega_{p\alpha}^2}, \quad \omega_{p\alpha}^2 = \frac{4\pi n_0 e_\alpha^2}{m_\alpha}, \quad z_i = \frac{\omega}{k v_{T_i}}, \quad \alpha = e,\ i, \tag{14}$$

where the term $\varepsilon_e^{(1)}$ which is the collision contribution to the dispersion relation, has the form

$$\varepsilon_e^{(1)} = 2i\sum_{n=-\infty}^{\infty}\frac{\left(1 + i\sqrt{\pi}\frac{\omega}{k_z v_{T_e}} W_n\right) I_n e^{-\mu}}{\left[1 - \sum\limits_{n'=-\infty}^{\infty}\frac{4(\mathbf{ku} + n'\omega_{H_e})^2\sqrt{\pi}\,\nu_f}{k^2 v_{T_e}^2 k_z v_{T_e}} W_{n'} I_{n'} e^{-\mu}\right]}$$
$$\times\left\{\frac{\nu}{\omega}\left[1 + \frac{1}{k^2 d_i^2}\left(1 + i\sqrt{\pi}\, z_i W(z_i)\right)\right]\right.$$
$$\left. - \frac{2\nu_f(\mathbf{ku} + n\omega_{H_e})}{k^2 v_{T_e}^2}\frac{1}{k^2 d_e^2}\sum_{n'=-\infty}^{\infty}\left[\frac{i\sqrt{\pi}\,\tilde{\omega}}{k_z v_{T_e}} W_{n'} I_{n'} e^{-\mu}\frac{(n'\omega_{H_e} + \mathbf{ku})}{\omega} + \frac{\mathbf{ku}}{\omega}\right]\right\}. \tag{15}$$

3. DISSIPATIVE INSTABILITIES AT ELECTRON-CYCLOTRON HARMONICS $n\omega H_e$ FOR $\mu < 1$ AND $T_i > T_e$

We first consider pure transverse oscillations $k_z \equiv 0$.

Using (14) and (15) near the frequencies $\sim n\omega_{He}$ and $\tilde{\omega} \simeq n\omega_{He}$ for $\mu \leqslant 1$ we obtain the following dispersion relation:

$$\varepsilon = \left[1 + \frac{1}{k^2 d_i^2}\left(1 + i\sqrt{\pi}\, z_i W(z_i)\right)\right]\left[1 - 2i\,\frac{\nu}{\omega}\,\frac{(\mathbf{ku} + n\omega_{H_e})}{(\tilde{\omega} - n\omega_{H_e})}\, I_n e^{-\mu}\right] - \frac{I_n e^{-\mu} n\omega_{H_e}}{(\tilde{\omega} - n\omega_{H_e})\, k^2 d_e^2}\left[1 + \frac{4i\nu_f \tilde{\omega} I_n e^{-\mu} (\mathbf{ku} + n\omega_{H_e})^3}{k^2 v_{T_e}^2\, \omega n\omega_{H_e} (\omega - n\omega_{H_e})}\right] = 0. \quad (16)$$

Neglecting the ion motion and the collisions in (16), near the frequencies $\sim n\omega_{He}$ we have

$$\tilde{\omega}^* = n\omega_{H_e}\left[1 + I_n e^{-\mu}\frac{1}{1 + k^2 d_e^2}\right]. \quad (17)$$

The instability appears from the condition for the intersection of the branches, i.e., with inclusion of the ion motion for frequencies $\omega \ll |\mathbf{ku}|$. It is easy to be convinced of this by treating the ions as cold $\omega \gg kv_{T_i}$ in (16) and expanding in the small parameter $\omega/|\mathbf{ku}| \ll 1$.

In the zeroth approximation we have

$$\omega = i\,\frac{kv_s}{(1 + k^2 d_e^2)^{1/2}}\left(\frac{ku - n\omega_{H_e}}{\tilde{\omega}^* - ku}\right)^{1/2}, \quad v_s = \left(\frac{T_e}{M}\right)^{1/2}. \quad (18)$$

Here, $\mathbf{ku} = -ku$. The oscillations become unstable for

$$n\omega_{H_e} < ku < \tilde{\omega}^*.$$

The maximum growth rate can be found by taking account of the higher terms in the expansion in the small parameter $\omega/|\mathbf{ku}| \ll 1$. As a result we find the hydrodynamic cyclotron oscillations[3] with the maximum growth rates

$$\omega = \frac{1 + i\sqrt{3}}{2^{4/3}}\left(\frac{\omega_{pi}^2 I_n e^{-\mu} n\omega_{H_e}}{1 + k^2 d_e^2}\right)^{1/3}, \quad \frac{I_n e^{-\mu}}{(1 + k^2 d_e^2)} \ll 1. \quad (19)$$

It is evident that $\operatorname{Im}\omega < \omega_{He}$; otherwise, the cyclotron resonances are "smeared out" and the unstable oscillations have a continuous spectrum. Still considering the hydrodynamic instability, we examine the effect of collisions on the cyclotron instabilities. Using the initial dispersion relation (16), we consider those current velocities for which the expansion in the small parameters $\omega/|\mathbf{ku}| \ll 1$, $\nu_f/|\mathbf{ku}| \ll 1$ is valid. Then we obtain the spectrum of cyclotron oscillations (18) in the zeroth approximation. This relation essentially determines the values of the wave numbers **k** for which the growth rate of the hydrodynamic instability is a maximum. In the next approximation we find the equation describing the spectrum of the dissipative instabilities:

$$\omega = \frac{1 + i\sqrt{3}}{2^{4/3}}\left(\frac{\omega_{pi}^2 I_n e^{-\mu} n\omega_{H_e}}{1 + k^2 d_e^2}\right)^{1/3} \frac{\left[1 - \frac{2i\nu}{\omega}\,\frac{(n\omega_{H_e} - \mathbf{ku})\, k^2 d_e^2}{n\omega_{H_e}}\right]^{1/3}}{\left[1 + \frac{4i\nu_f \tilde{\omega}^* (n\omega_{H_e} - \mathbf{ku})^4 k^2 d_e^2}{k^2 v_{T_e}^2 \omega^2 (n\omega_{H_e})^2}\right]^{1/3}}. \quad (20)$$

It can be seen from this equation that the maximum growth rate has the same order of magnitude as for $\nu_f \equiv 0$ [Eq. (19)].

We will explain for the hydrodynamic instability how the inclusion of the collisions changes the limit of excitation of the cyclotron oscillations. For the clearest view of the expected result we simplify the problem by assuming that $I_n e^{-\mu} \ll 1$. Then, from (16)

$$\omega = i\,\frac{kv_s}{(1 + k^2 d_e^2)^{1/2}}\left\{\frac{ku - n\omega_{H_e}}{\omega^* - ku\left[1 + \frac{4i\nu_f n\omega_{H_e} (I_n e^{-\mu})^5}{\omega_{pi}^2}\left(\frac{u}{v_{T_e}}\right)^2\right]}\right\}. \quad (21)$$

From this it can be seen that the instability can be excited for two reasons. Either, as is already well known, for

$$n\omega_{H_e} < ku < \tilde{\omega}^*,$$

or, even if this condition is not satisfied, for $[(\nu_f n\omega_{He}) \cdot (\omega_{pi}^2)^{-1}] (I_n e^{-\mu})^5 < (v_{T_e}/u)^2$, i.e., for arbitrarily small current velocities only if the above condition for small $I_n e^{-\mu} \ll 1$ is satisfied. Thus, for the hydrodynamic instability the collisional dissipation removes the restriction on the current velocity threshold which is valid in the case of cold electrons.

We now consider kinetic instabilities in a plasma with hot ions $T_i < T_e$ for fairly long-wavelength perturbations $k\rho_{He} < 1$. We first consider transverse oscillations, assuming that $I_n e^{-\mu}(T_i/T_e) < 1$. Then from (16) for $\mathbf{ku} = -ku$ we find the following frequencies ω_k) and growth rates γ_k of the most unstable oscillations near the instability limit, i.e., when ($\gamma_k < \omega_k$):

$$\left.\begin{aligned} \omega_k &= \mathbf{k}(\mathbf{u}^* - \mathbf{u}), \\ u^* &= \frac{n\omega_{H_e}}{k}\left[1 + I_n e^{-\mu}\frac{T_i}{T_e}\right], \end{aligned}\right\} \quad (22)$$

$$\gamma_k = -\nu + \frac{1}{2}\, n\omega_{H_e}\left(\frac{T_i}{T_e}\right) I_n e^{-\mu}\left\{\sqrt{\pi}\, z_i \operatorname{Re} W(z_s) - \frac{4\nu_f (\mathbf{ku} - n\omega_{H_e})^3 \tilde{\omega} T_e}{k^2 v_{T_e}^2 \omega (n\omega_{H_e})^2 T_i}\right\},$$

$$z_i = \frac{u - u^*}{v_{T_i}}. \quad (23)$$

The oscillations are unstable for

$$\nu_f \leqslant \frac{\omega^2 (n\omega_{H_e})^2 k^2 v_{T_e}^2}{\tilde{\omega}(n\omega_{H_e} - \mathbf{ku})^3 kv_{T_i}}\left(\frac{T_i}{T_e}\right). \quad (24)$$

Maximizing the wavelengths of the most stable oscillations, i.e., using the conditions $k \simeq n\omega_{He}/u$, $I_n e^{-\mu}(T_i/T_e) < 1$, we obtain an estimate for the effective frequency of elastic scattering of electrons by oscillations of the given type, i.e., in complete agreement with the method proposed in ref. 2,

$$\nu_f \simeq n\omega_{e,i}\left(\frac{v_{T_e}}{u}\right)^3\left(I_n e^{-\mu}\frac{T_i}{T_e}\right)^{-3}. \quad (25)$$

We use this estimate to obtain the anomalous resistivity

$$\sigma_f = \frac{n_e e^2}{m\nu_f} \simeq \left(\frac{n_e e^2}{mn\omega_{e,i}}\right)\left(\frac{u}{v_{T_e}}\right)^3\left(I_n e^{-\mu}\frac{T_i}{T_e}\right)^3. \quad (26)$$

Note, however, that estimates (25) and (26) have a very restricted region of validity (this will be shown later). This is because, remembering the definitions of ν and ν_f in (6), it is necessary in perturbation theory to evaluate more precisely the dependence of ν and ν_f on the mean plasma parameters, for example on the current velocity.

We now investigate oblique modes $k_z/k \simeq (m/M)^{1/2}$. Thus, for example, when $k\rho_e < 1$ and $T_i > T_e$ at the zeroth cyclotron harmonic ($n = 0$), we use the dispersion relation (14) to obtain the branch of the electron-acoustic oscillations[6] with an extremely low excitation threshold $v_{T_i}\{(m/M)^{1/4}, (\nu_f/\omega_{e,i})^{1/4}\}$; the frequency ω_k and the growth rate γ_k are

$$\left.\begin{aligned} \omega_k &= \mathbf{ku} + k_z\left(\frac{T_i}{m}\right)^{1/2}\bar{a}, \quad \bar{a} = (1 + k_\perp^2\rho_e^2)^{-1/2},\\ \gamma_k &= -\frac{(k\rho_e)^2}{2}\nu_f - \frac{\sqrt{\pi}}{2}k_z\left(\frac{T_i}{m}\right)^{1/2}\bar{a}^3 z_i \operatorname{Re} W(z_i), \quad z_i = \frac{\omega}{kv_{T_i}}. \end{aligned}\right\} \quad (27)$$

These oscillations can be obtained in a simpler manner by using the system of hydrodynamic equations (5) for the electron component. In the electron-acoustic instability the contribution of nonlinear effects to stabilization is seen clearly. Damping can be due to nonlinear processes which, accordihg to Eq. (5) for the electron motion, can be formally taken into account by means of the effective elastic-scattering frequency (6)

$$\nu_f = \frac{1}{mn_e}\frac{\partial R_f}{\partial u}.$$

It will be shown below that this term can be negative, i.e., $\partial R_f/\partial u < 0$ and stabilization due to the collective friction force is impossible.

The effect of a finite k_z on the development of cyclotron instabilities can be described in the following manner. We assume that the current velocities are fairly large $u \gg v_s$. Assuming in the initial equations (14) and (15) that $|\tilde{\omega} - n\omega_{He}| \gg k_z v_{Te}$ for all numbers n except $n \neq n'$, for which $|\tilde{\omega} - n'\omega_{He}| \lessgtr k_z v_{Te}$, and assuming the ions to be cold $\omega \gg kv_{T_i}$ we have

$$\varepsilon = 1 - \frac{\omega_{pi}^2}{\omega^2} + \frac{1}{k^2 d_e^2}\left\{1 - e^{-\mu}I_0 + i\sqrt{\pi}\frac{\tilde{\omega}}{k_z v_{T_e}}e^{-\mu}I_{n'} + \frac{\frac{4\tilde{\omega}}{\omega}(I_{n'}e^{-\mu})^2\left(1 + i\sqrt{\pi}\frac{\omega}{k_z v_{T_e}}\right)\frac{\sqrt{\pi}\,\nu_f}{k_z v_{T_e}}\left(\frac{n'\omega_{H_e} + \mathbf{ku}}{kv_{T_e}}\right)^2}{\left[1 - 4\left(\frac{n'\omega_{H_e} + \mathbf{ku}}{kv_{T_e}}\right)^2\frac{\sqrt{\pi}\,\nu_f}{k_z v_{T_e}}I_{n'}e^{-\mu}\right]}\right\} = 0. \quad (28)$$

Here, we retain the negative term for the n'-th cyclotron harmonic, which is important for $|\tilde{\omega} - n'\omega_{He}| \leq k_z v_{Te}$. The other negative terms are exponentially small. Solving Eq. (28) for ω we obtain the following spectrum of unstable oscillations for $4\sqrt{\pi}(ku/k_z v_{Te})(\nu_f/n'\omega_{He})I_{n'}e^{-\mu} \ll 1$:

$$\omega = \omega_{e,i}\left\{1 + \frac{4n'\omega_{H_e}}{k_z v_{T_e}}\frac{(I_{n'}e^{-\mu})^2\sqrt{\pi}}{\mu}\left(\frac{\nu_f}{\omega_{e,i}}\right)\frac{(n'\omega_{H_e} + \mathbf{ku})^2}{k^2 v_{T_e}^2} + i\sqrt{\pi}\frac{n'\omega_{H_e}}{k_z v_{T_e}}\frac{e^{-\mu}I_{n'}}{\mu}\left[1 + \frac{I_{n'}e^{-\mu}\sqrt{\pi}\,\nu_f}{k_z v_{T_e}}\frac{(n'\omega_{H_e} + \mathbf{ku})^2}{k^2 v_{T_e}^2}\right]\right\}^{-1/2}. \quad (29)$$

This spectrum of dissipative instabilities can be excited for

$$|\mathbf{k}| \simeq \frac{n'\omega_{H_e}}{|\mathbf{u}|}, \quad \frac{m}{M} \ll \frac{k_z}{k}\frac{v_s}{u} \ll \left(\frac{m}{M}\right)^{1/2},$$

and has a discrete structure. In any case collisions due to the friction force are favorable to the development of the spectrum of oblique oscillations obtained above. Consequently, stabilization by the collective friction force is impossible.

4. VORTICAL ELECTRON OSCILLATIONS AND THE ANOMALOUS VISCOSITY EFFECT

We now show the possibility of exciting an instability of vortical oscillations $|\operatorname{curl}\mathbf{E} \neq 0|$ in an incompressible electron fluid $\operatorname{div}\mathbf{v}_e = 0$ at frequencies near $\sim \omega_{He}$ in a plasma in which $\partial R_f/\partial u < 0$. We introduce the following notation for the velocity $\mathbf{v}_e$ and the vorticity $\mathbf{\Omega}$:

$$\mathbf{v}_e = -\frac{c}{4\pi en_0}\operatorname{curl}\mathbf{H}, \quad \mathbf{\Omega} = \operatorname{curl}\mathbf{v}_e = \frac{c}{4\pi en_0}\Delta\mathbf{H}. \quad (30)$$

Applying the curl operator to the equation of electron motion (5) and using a Fourier transform for the small perturbations, which are represented by $\sim H_\sim(y)\exp(-i\omega t + ikx)$, we find the differential equation that describes unstable flow of the incompressible electron fluid:

$$(\tilde{\omega} + i\nu_f)(H''_\sim - k^2H_\sim) + \left(\mathbf{k}\mathbf{u}'' - \frac{\omega}{a^2}\right)H_\sim = i\eta_f(H^{\mathrm{IV}}_\sim - 2k^2H''_\sim + k^4H_\sim). \quad (31)$$

Here, as has already been mentioned, ν_f is the effective frequency of elastic scattering (6), $a = c/\omega_{pe}$ and $H_\sim$ is the magnetic field amplitude in the vortical oscillations, which depend on the y coordinate.

The structure of (31) is similar to that of the equation for vortical oscillations of a conventional fluid. To provide eigensolutions for Eq. (31) a kinematic electron viscosity term η_f is added which does not have a theoretical value for the problem discussed below. We consider the spectrum of unstable oscillations in the semiclassical approximation $k(d\ln H_\sim\, dy)^{-1} \gg 1$. Applying the method of "semiclassical quantization" to Eq. (31) for the limiting case $k(c/\omega_{pe}) \gg 1$ and $k|d\ln H_0/dy|^{-1} \gg 1$ we find the following values for the frequencies ω_k and the growth rate γ_k

$$\left.\begin{aligned} \omega_k &= \tilde{\mathbf{k}}\mathbf{u} + \frac{\mathbf{k}\mathbf{u}''}{(k^2 + \bar{k}_y^2)},\\ \gamma_k &= -\nu_f - k^2\eta_f, \text{ where } \bar{k}_y^2 = \left(\frac{2\pi m}{\Delta y}\right)^2, \quad m = 1, 2, 3, \ldots \end{aligned}\right\} \quad (32)$$

As in the case of electron-acoustic oscillations (27), the frequencies have a dependence on the current velocity. The oscillation frequency is a maximum in the region of short wavelengths. The instability criterion for electron vortical oscillations has the simple form

$$\nu_f = \frac{1}{mn_0}\frac{\partial R_f}{\partial u} < 0 \quad (\eta_f \to 0),$$

i.e., a decreasing dependence of the friction force on the electron current velocity.

We use the hydrodynamic equations (5) to analyze the basic nonlinear effect resulting from the development of vortical electron oscillations. In the initial hydrodynamic equation (5) we average over the random phases of the vortical oscillations. As a result, a new term is added to the total momentum balance for the electron component

$$\Pi_{yx} = mn_0 \langle v_{x\sim} v^*_{y\sim} + \text{c.c.} \rangle,$$

which physically denotes the component of the viscous stress tensor giving the mean force in the direction of the current

$$R_x = -\frac{\partial \Pi_{yx}}{\partial y}.$$

To calculate this term we multiply the equation for the vortical oscillations (31) by the complex-conjugate amplitude $H^*_{\sim}$ and subtract the complex conjugate from the equality thus obtained. As a result, for the case $k|d \ln H/dy|^{-1} \gg 1$

$$\Pi_{yx} = -\sum_k 2\pi m n_0 |\mathbf{v}_{ky}|^2 \delta(\omega_k - \mathbf{k}\mathbf{u}) \frac{\partial u}{\partial y}, \qquad (33)$$

where

$$v_{ky} = -i \frac{kc}{4\pi e n_0} H_k.$$

The appearance of the δ function denotes a resonance mechanism for the interaction between segments of the electron velocity profile u(y) and the excited vortical oscillations, for which the phase velocity is $\omega/k = u(y)$. Thus, the macroscopic effect on the vortical oscillations consists of the appearance of a friction force for the electrons which is proportional to the second derivative of the current velocity $\sim (\partial/\partial y)\eta_f(\partial u/\partial y)$. In the physical sense, this force is similar to a viscous friction force due to a viscosity

$$\eta_f = \sum_k 2\pi m n_0 |v_{ky}|^2 \delta(\omega_k - \mathbf{k}\mathbf{u}), \qquad (34)$$

which is proportional to the amplitude of the vortical oscillations $\sim |v_{ky}|^2$. The anomalous electron viscosity, which contains an unknown term $|v_{ky}|^2$, can be found from the condition that viscous friction is the principal nonlinear effect stabilizing cyclotron instabilities of type (22). To determine the anomalous electron viscosity in an instability of type (22), for example, it is necessary to make the formal substitution

$$k_y^2 \eta_f = \nu_f. \qquad (35)$$

5. CONTRIBUTION OF THE COLLECTIVE FRICTION FORCE TO STABILIZATION OF CYCLOTRON INSTABILITIES

We will analyze the basic macroscopic effects resulting from the development of turbulence near cyclotron harmonics. One of the effects has been discussed above. A basic nonlinear effect produced by the electrostatic oscillations, as has already been noted, is the appearance of a collective friction force R_f which acts on the electrons. The momentum of cyclotron oscillations is transferred to electrons by nonlinear processes so that for Cerenkov radiation due to the oscillations in question the ions suffer the major loss of moment (negative energy waves).[2] At saturation of the oscillation amplitudes the momentum lost by the ions due to Cerenkov radiation produced by the oscillations is completely absorbed by the electrons by nonlinear processes. In this case the nonlinear damping rate $\gamma_H(W_k)$ which depends on the energy w_k is equal to the linear growth rate of the instability $\gamma_k(u)$. Therefore, at saturation the collective friction force acting on the electrons is

$$\mathbf{R}_f(u) = \sum_k \gamma_k(u) \mathbf{P}_k.$$

Here, P_k is some quasistationary momentum taken over the entire spectral interval of unstable waves k. According to this definition, we assume that the friction force depends on the current velocity through the instability growth rate $\gamma_k(u)$.

This dependence will be established as for the instability with a frequency spectrum (22). Since the short-wavelength perturbations are the most unstable

$$\bar{k} = \frac{n\omega_{He}}{u}\left[1 + I_n e^{-\mu} \frac{T_i}{T_e}\right],$$

the sum over k in the expression for the friction force can be replaced by a term with the most unstable value $\bar{k}$, when $\bar{k} \simeq n\omega_{He}/u$. Then we obtain a simple expression for the effective elastic-scattering frequency ν_f which is defined in (6),

$$\nu_f = \left(\frac{P_{\bar{k}}}{mn_e}\right) \frac{\partial \gamma_{\bar{k}}}{\partial u}. \qquad (36)$$

Substituting this expression into the equation for the growth rate (22), we obtain the differential equation for $\gamma_{\bar{k}}(u)$

$$\bar{u} \frac{\partial \gamma_{\bar{k}}}{\partial u} + \gamma_{\bar{k}} = \gamma_{\max} \left(\frac{u - u^*}{v_{Ti}}\right) \exp\left\{-\left(\frac{u - u^*}{v_{Ti}}\right)^2\right\}. \qquad (37)$$

Here we set

$$\bar{u} = \left(2 \frac{T_i}{T_e} I_n e^{-\mu} \frac{u}{v_{Te}}\right)^2 \frac{P_{\bar{k}}}{mn_e},$$

$$\gamma_{\max} = n\omega_{He} \frac{v_{Ti}}{u}\left[2 \ln\left(\frac{u}{v_{Ti}} \sqrt{\pi} \frac{T_i}{T_e} I_n e^{-\mu}\right)\right]^{1/2}.$$

The solution of this equation must satisfy the requirement that the growth rate γ_k vanish at the boundary of the instability

$$\gamma_{\bar{k}} = 0 \text{ for } u = u^*.$$

The solution of (37) has the form

$$\gamma_{\bar{k}}(u) = \gamma_{\max}\left\{\int_{u^*}^{u} \frac{du'}{\bar{u}} \left(\frac{u' - u^*}{v_{Ti}}\right) \exp\left[\frac{u' - u}{\bar{u}} - \left(\frac{u' - u^*}{v_{Ti}}\right)^2\right] - \frac{u}{v_{Ti}}\left[1 - \exp\left(\frac{u^* - u}{\bar{u}}\right)\right]\right\}.$$

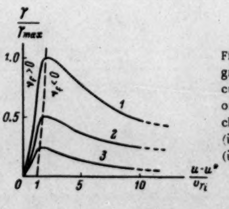

Fig. 1. Dependence of the nonlinear growth rate of the instability on the current velocity for different values of the free parameter $\bar{u}/v_{Ti}$, which characterizes the noise level. 1) $(\bar{u}/v_{Ti}) = 0$, 2) $0 < (\bar{u}/v_{Ti}) < 1$, 3) $(\bar{u}/v_{Ti}) > 1$.

It has the simplest form in the two limiting cases

$$\gamma_{\bar{k}} = \gamma_{\max} \begin{cases} \dfrac{u-u^*}{v_{Ti}} - \dfrac{\bar{u}}{v_{Ti}}\left(1 - e^{\frac{u^*-u}{\bar{u}}}\right) & \text{for } \dfrac{u-v^*}{v_{Ti}} < 1, \\ \dfrac{v_{Ti}}{u} e^{\frac{u^*-u}{\bar{u}} + \frac{v_{Ti}^2}{4\bar{u}^2}} & \text{for } \dfrac{u-u^*}{v_{Ti}} \gg 1. \end{cases} \tag{38}$$

Figure 1 illustrates the dependence of the nonlinear growth rate $\gamma_k^-(W)$ on the current velocity. It can be seen that beginning with current velocities $u > u^* + v_{Ti}$, $\gamma_k^-(u)$ falls off and ν_f becomes negative. Thus, for large current velocities $u > u^* + v_{Ti}$ the friction force has a decreasing dependence on u, and consequently the nonlinear effect of the friction force does not stabilize the instabilities in question. But when $\partial R_f/\partial u < 0$ a factor appears which excites vortical electron oscillations and a stabilizing effect of the electron viscosity type emerges. From the stability condition for an instability with a frequency spectrum (22), with allowance for (35), we find the anomalous electron viscosity

$$\eta_f \simeq \frac{\nu_f}{\bar{k}_\perp^2} \simeq \left(\frac{u^3}{n\omega_{He}}\right)\left(\frac{m}{M}\right)^{1/4}\left(\frac{v_{Te}}{u}\right)^3\left(I_n e^{-\mu}\frac{T_i}{T_e}\right)^{-3}. \tag{39}$$

Here we maximize the wavelengths of the most unstable electron-cyclotron oscillations, i.e., for $\bar{k}_\perp \simeq n\omega_{He}/u$. A similar result can be obtained for the electron-acoustic instability (27), i.e., it can be shown that the collective friction force produced by this instability also has a falling dependence on the current velocity for large current velocities $u \gg v_{Ti}$ and thus cannot stabilize the given instability.

CONCLUSIONS AND RESULTS

Thus, it has been shown that for a fairly large drift velocity u in a plasma with hot ions $T_i > T_e$, electron-cyclotron oscillations can be excited which have comparatively high growth rates $[\gamma_{\max} \simeq (m/M)^{1/4}\omega_{He}]$ and which make a large contribution to the anomalous resistivity of the plasma. An investigation of this process must consider nonlinear processes which restrict the unstable wave amplitudes and set up a quasistationary level of microscopic turbulence. A nonlinearity associated with the electrons plays such a role for electron-cyclotron oscillations (Bernstein modes). A model with a Landau collision integral has been proposed to provide a qualitative description of the basic nonlinear process: collective scattering of electrons by cyclotron oscillations excited by the instability and the stabilizing effect of the collective friction force.

The model is used in linear theory to establish a wide spectrum of current-dissipative instabilities at electron-cyclotron harmonics, which are excited, on one hand, by the flow of the drift current, and on the other by collisional processes including collective scattering of electrons by the oscillations. It has been shown that due to the collective friction force the stabilizing effect is possible only at low current velocities ($u < v_{Ti} + v_s$) near the instability limit (small supercriticality). For sufficiently large current velocities ($u > v_{Ti} + v_s$), however, long-wavelength oscillations ($\lambda > \rho_{He}$) are not stabilized by the collective friction force resulting from nonlinear scattering of electrons by the excited oscillations. Formally, this is the case because at high current velocities the collective friction force has a declining dependence on the drift current. Physically, this means that the momentum of the waves cannot be completely transferred to the electrons through the given nonlinear process. In this case part of the momentum can be carried out of the instability region and dissipated elsewhere. Secondly, the restriction on the unstable wave amplitude and the dissipation of the transferred momentum can also result from nonlinear scattering of electrons during the development of decay processes, for example the excitation of vortical electron oscillations. Assuming total absorption of the wave momentum, we have estimated the anomalous electron viscosity (39), which is a possible nonlinear process leading to stabilization of the cyclotron oscillations.

Finally, for a sufficiently high level of oscillations a change in wave dispersion can have a stabilizing effect (see ref. 6).

---

[1] R. Z. Sagdeev, in: Reviews of Plasma Physics, Vol. 4, Consultants Bureau, New York (1966).

[2] A. A. Galeev, D. G. Lominadze, A. D. Pataraya, R. Z. Sagdeev, and K. N. Stepanov, ZhETF Pis. Red., 15, 417 (1972) [JETP Lett., 15, 294 (1972)].

[3] D. G. Lominadze, Zh. Eksp. Teor. Fiz., 63, 1300 (1972) [Sov. Phys. – JETP, 36, 686 (1973)].

[4] A. A. Vedenov, in: Reviews of Plasma Physics, Vol. 3, Consultants Bureau, New York (1967).

[5] V. I. Aref'ev, Zh. Tekh. Fiz., 39, 1973 (1969) [Sov. Phys. – Tech. Phys., 14, 1487 (1970)].

[6] V. I. Aref'ev, Zh. Eksp. Teor. Fiz., 55, 679 (1968) [Sov. Phys. – JETP, 28, 354 (1969)].

[7] R. L. Bhatnagar, E. P. Cross, M. Krook, Phys. Rev., 94, 511 (1954).

[8] A. B. Mikhailovskii, in: Reviews of Plasma Physics, Vol. 3, Consultants Bureau, New York (1967).

[9] V. I. Aref'ev, Zh. Tekh. Fiz., 43, 1445 (1973) [Sov. Phys. – Tech. Phys., 18, 916 (1974)].

Anomalous ion heating in a parametrically unstable plasma

I. S. Baikov and V. P. Silin
P. N. Lebedev Institute of Physics, Academy of Sciences of the USSR, Moscow
(Submitted December 20, 1973)
Zh. Tekh. Fiz., 44. 2467-2475 (December 1974)

Anomalous ion heating is investigated in a plasma driven by an ac electric field with a frequency near the electron plasma frequency. The anomalous heating is due to the coupling between the external electric field and the plasma caused by ion-acoustic fluctuations; these grow exponentially in the parametric instability and are the cause of anomalous ion heating in a plasma with $T_e \lessdot T_i$ when strong absorption of the ion-acoustic oscillations occurs.

In recent years, the development of programs for thermonuclear research[1] and experiments in the ionosphere[2] has stimulated interest in investigations of the anomalous properties of a plasma that interacts with powerful electromagnetic radiation. Increasing attention has been paid to plasmas with $T_i \gtrsim T_e$ in which strong absorption of ion-acoustic oscillations occurs; this is of interest for problems of laser fusion since the plasma corona with hot ions $T_i \gtrsim T_e$ which is produced by the laser-material interaction can have a small reflection coefficient.[3] According to the linear theory, strong electromagnetic radiation produces oscillating two-stream and ion-acoustic decay instabilities in a plasma with $T_i \gtrsim T_e$ (see refs. 4 and 5). The phase velocities of the ion-acoustic perturbations lie near the ion thermal velocity. In this case the perturbations interact effectively with the bulk of the ions, which leads to an effective coupling between the external electric field and the plasma through the ion fluctuations.

Anomalous resistivity and heating of electrons in a highly nonisothermal plasma $T_e \gg T_i$ have been studied in several papers by numerical simulation.[6] These experiments have confirmed anomalous heating of electrons in such a plasma when the nonacoustic fluctuations saturate, and they indicate that an appreciable portion of the external-field energy is not expended in increasing the electron temperature, but in forming energy tails in the electron distribution function (fast particles). The ion distribution function retains its initial Maxwellian character although the temperature varies somewhat in time (but several orders of magnitude slower than the electron temperature). However, analytical relations have not yet been obtained for the variation in the ion temperature.

In the present paper we investigate the anomalous heating of ions in an isothermal plasma or for $T_i > T_e$. We use the quasilinear theory (see ref. 7) to describe the turbulent state resulting from the development of the parametric instability. In Sec. I, the linear theory of a parametric instability is discussed. Special attention is given to the case $T_i \gtrsim T_e$, which has not been discussed in detail in the literature. In Sec. II, the quasilinear theory is used to analyze the results of an investigation of anomalous heating of ions.

I. LINEAR THEORY

We consider a homogeneous plasma driven by an external electric field $E = E_0 \sin\omega_0 t$ with a frequency near the electron plasma frequency ω_{Le}. For fairly weak microwave fields, in which the electron oscillation amplitude in the electric field is small compared to the wavelength of the excited oscillation, we can obtain the following dispersion relation to describe the low-frequency parametric instabilities[4] ($\omega \ll \omega_{Le}$):

$$\frac{1}{\delta\varepsilon_i(\omega,\mathbf{k})} + \frac{1}{1+\delta\varepsilon_e(\omega,\mathbf{k})} = \frac{(\mathbf{k}\cdot\mathbf{r}_E)^2}{4} \times \left[\frac{\omega_{Le}^2}{\omega_{Le}^2 + 3k^2 v_{Te}^2 - (\omega+\omega_0)^2 - i\nu_e(\omega+\omega_0)} + \frac{\omega_{Le}^2}{\omega_{Le}^2 + 3k^2 v_{Te}^2 - (\omega-\omega_0)^2 - i\nu_e(\omega-\omega_0)^2}\right], \tag{1}$$

where $\delta\varepsilon_\alpha$ is the partial contribution of particles of species α to the low-frequency dielectric constant of the plasma $\varepsilon(\omega,\mathbf{k}) = 1 + \sum_{\alpha=e,i}\delta\varepsilon_\alpha$; r_E is the electron oscillation amplitude in the external field; the other notation is standard.

We are interested in the case of a collisionless plasma, in which the ion-acoustic frequency exceeds the particle collision frequency ($\nu_\alpha \ll \omega$). Considering long-wavelength oscillations $k^2 r_{D\alpha}^2 \ll 1$ where $r_{D\alpha}$ is the Debye radius for species α in the frequency range $\omega < |k| v_{Te}$ and the inequality $\omega_0 \sim \omega_{Le} \gg \omega$ we can reduce Eq. (1) to

$$\frac{T_e}{T_i}\left(1 - i\sqrt{\frac{\pi}{2}}\frac{\omega}{|k| v_{Te}}\right) + \frac{1}{1 - J_+\left(\frac{\omega}{|k| v_{Ti}}\right)} = -\frac{(\mathbf{k}\cdot\mathbf{r}_E)^2}{8k^2 r_{Di}^2}\frac{\omega_{Le}^2}{\omega_0}\left(\frac{1}{\omega+\delta+i\tilde{\gamma}} - \frac{1}{\omega-\delta+i\tilde{\gamma}}\right), \tag{2}$$

where

$$\tilde{\gamma} = \frac{\nu_e}{2}, \quad \delta = \omega_0 - \omega_{Le}\left(1 + \frac{3}{2}k^2 r_{De}^2\right) = \omega_0 - \omega_L(\mathbf{k}), \tag{3}$$

The expression (2) is a complex equation for determining the frequency and growth rate. Setting $\omega = \mathrm{Re}\,\omega + i\gamma$ and using ω for $\mathrm{Re}\,\omega$, for $\gamma < \omega$ we can write [the general case $\gamma \gtrsim \omega$, which corresponds to very large electric fields, usually requires a numerical solution of Eq. (2)]

$$\frac{1}{1 - J_+\left(\frac{\omega + i\gamma}{|k| v_{Ti}}\right)} = \frac{1}{1 - J_+(x)} + i\frac{\gamma}{|k| v_{Ti}}\frac{x^2 + (1-x^2)J_+(x)}{x[1 - J_+(x)]^2} + 0\left(\frac{\gamma^2}{k^2 v_{Ti}^2}\right),$$

where $x = \omega/|k| v_{Ti}$. Substituting this expansion into (2) and separating the real and imaginary parts, we obtain

$$\frac{T_e}{T_i}\left(1 + \sqrt{\frac{\pi}{2}}\frac{\gamma}{|k| v_{Te}}\right) + \frac{1 - \mathrm{Re}\,J_+}{(1 - \mathrm{Re}\,J_+)^2 + (\mathrm{Im}\,J_+)^2} - \frac{\gamma}{\omega}\mathrm{Im}\,J_+\frac{2x^2(1 - \mathrm{Re}\,J_+) + (1-x^2)[1 - (\mathrm{Re}\,J_+)^2 - (\mathrm{Im}\,J_+)^2]}{[(1 - \mathrm{Re}\,J_+)^2 + (\mathrm{Im}\,J_+)^2]^2} = -\frac{(\mathbf{k}\cdot\mathbf{r}_E)^2}{4k^2 r_{Di}^2}\frac{\omega_{Le}^2\delta}{\omega_0}\frac{\delta^2 - \omega^2 + (\gamma+\tilde{\gamma})^2}{[(\omega+\delta)^2 + (\gamma+\tilde{\gamma})^2][(\omega-\delta)^2 + (\gamma+\tilde{\gamma})^2]}. \tag{3a}$$

$$-\frac{T_e}{T_i}\sqrt{\frac{\pi}{2}}\frac{\omega}{|k|v_{Te}}+\frac{\mathrm{Im}\,J_+}{(1-\mathrm{Re}\,J_+)^2+(\mathrm{Im}\,J_+)^2}+\frac{\gamma}{\omega}\frac{[x^2+(1-x^2)\,\mathrm{Re}\,J_+]\,[(1-\mathrm{Re}\,J_+)^2-(\mathrm{Im}\,J_+)^2]-2\,(1-x^2)\,(\mathrm{Im}\,J_+)^2\,(1-\mathrm{Re}\,J_+)}{[(1-\mathrm{Re}\,J_+)^2+(\mathrm{Im}\,J_+)^2]^2}$$

$$=-\frac{(\mathbf{k}\cdot\mathbf{r}_E)^2}{4k^2r_{Di}^2}\frac{\omega_{Le}^2\delta}{\omega_0}\frac{2\omega\,(\gamma+\tilde{\gamma})}{[(\omega+\delta)^2+(\gamma+\tilde{\gamma})^2]\,[(\omega-\delta)^2+(\gamma+\tilde{\gamma})^2]}. \tag{3b}$$

If the pump field is close to the threshold value, the problem can be solved by successive approximations. This method gives a good description when the pump field does not produce a substantial shift in the frequencies of the characteristic plasma oscillations; this is known to be the case for moderate external fields. The growth rate can vary considerably due to the presence of the pump field. Thus, we find from (3a) in the zeroth approximation with respect to the pump field (small terms containing γ can be dropped)

$$\frac{\mathrm{Re}\,J_+(x)-1}{[1-\mathrm{Re}\,J_+(x)]^2+[\mathrm{Im}\,J_+(x)]^2}=\frac{T_e}{T_i}. \tag{4}$$

The solution of this equation is

$$\omega_1=x_0\,|k|\,v_{Ti}, \tag{5}$$

where x_0 is the root of Eq. (4), which depends only on the temperature ratio. The dependence of x_0 on $(T_e/T_i)^{1/2}$ is shown in Fig. 1. Note that the coefficient x_0 is almost constant in the region $T_i \gtrsim T_e$; in particular $x_0 = 1.3$ for $T_i \gg T_e$, $x_0 = 1.7$ for $T_e = T_i$, and $x_0 = (T_e/T_i)^{1/2}$ for $T_e \gg T_i$.

The frequency, with a correction for the external magnetic field, and the corresponding growth rate are determined by

$$\omega_1(\omega-\omega_1)=-\frac{(\mathbf{k}\cdot\mathbf{r}_E)^2}{4k^2r_{Di}^2}\frac{\omega_{Le}^2\delta\omega_1\,|k|\,v_{Ti}}{\omega_0c_1}$$

$$\times\frac{\delta^2-\omega^2+(\gamma+\tilde{\gamma})^2}{[(\omega+\delta)^2+(\gamma+\tilde{\gamma})^2]\,[(\omega-\delta)^2+(\gamma+\tilde{\gamma})^2]}, \tag{6}$$

$$\omega_1\left(\gamma+\frac{c_0}{c_1}|k|\,v_{Ti}\right)=-\frac{(\mathbf{k}\cdot\mathbf{r}_E)^2}{4k^2r_{Di}^2}\frac{\omega_{Le}^2\delta\omega_1\,|k|\,v_{Ti}}{\omega_0c_1}$$

$$\times\frac{2\omega\,(\gamma+\tilde{\gamma})}{[(\omega+\delta)^2+(\gamma+\tilde{\gamma})^2]\,[(\omega-\delta)^2+(\gamma+\tilde{\gamma})^2]}, \tag{7}$$

where

$$c_0=-\frac{T_e}{T_i}\sqrt{\frac{\pi}{2}}\frac{\omega_1}{|k|\,v_{Te}}+\frac{\mathrm{Im}\,J_+(x_0)}{[1-\mathrm{Re}\,J_+(x_0)]^2+[\mathrm{Im}\,J_+(x_0)]^2},$$

$$c_1=\frac{\partial}{\partial x}\left[\frac{1-\mathrm{Re}\,J_+}{1-\mathrm{Re}\,J_+)^2+(\mathrm{Im}\,J_+)^2}\right]_{x=x_0}=\frac{[x_0^2+(1-x_0^2)\,\mathrm{Re}\,J_+]\,[(1-\mathrm{Re}\,J_+)^2-(\mathrm{Im}\,J_+)^2]-2\,(1-x_0^2)\,(\mathrm{Im}\,J_+)^2\,(1-\mathrm{Re}\,J_+)}{x_0\,[(1-\mathrm{Re}\,J_+)^2+(\mathrm{Im}\,J_+)^2]^2}.$$

Note that the coefficients $c_1 \lesssim 0$ and $c_0 < 0$. In particular, $c_0 = -1.4$ and $c_1 = -1.53$ for $T_e \ll T_i$; for $T_e \gg T_i$ the coefficient $c_0 = (-T_e/T_i)\cdot[(\pi/2)(m/M)]^{1/2}$. It follows from (7) that the parametric decay instability ($\gamma > 0$) can exist only in the region $\delta > 0$. In the absence of an external pump field, the ion-acoustic damping is

$$\gamma_s=\frac{c_0}{c_1}|k|\,v_{Ti}. \tag{8}$$

By solving (6) and (7), we obtain the following expression for the growth rate of the parametrically unstable solution for pump fields slightly larger than the threshold value:

$$\gamma=\tilde{\gamma}\left[\frac{(\mathbf{k}\cdot\mathbf{r}_E)^2\,\omega_L(\mathbf{k})}{4\,|c_0|\,k^2r_{Di}^2\nu_e\left(1+\frac{\Delta^2}{\gamma_s^2}\right)}-1\right], \tag{9}$$

where the detuning $\Delta(\mathbf{k})$ is given by

$$\Delta=\delta-\omega_1=\omega_0-\omega_L(\mathbf{k})-\omega_1(\mathbf{k}). \tag{10}$$

Equation (9) can be written in the form

$$\gamma=\tilde{\gamma}\left[\frac{P\cos^2\theta}{1+\left(\frac{k-k_m}{\Delta k}\right)^2}-1\right], \tag{11}$$

where θ is the angle between the vectors k and $\mathbf{E}_0$; the wave number k_m is the root of $\Delta(\mathbf{k}) = 0$ and is equal to

$$3k_mr_{De}=-x_0\frac{v_{Ti}}{v_{Te}}+\left[\left(x_0\frac{v_{Ti}}{v_{Te}}\right)^2+6\left(\frac{\omega_0}{\omega_{Le}}-1\right)\right]^{1/2}, \tag{12}$$

the spread in the wave vectors Δk is

$$\Delta kr_{De}=\frac{c_0}{c_1}\frac{v_{Ti}}{v_{Te}}\left(3+\frac{v_{Ti}}{v_{Te}}\frac{x_0}{k_mr_{De}}\right)^{-1}, \tag{13}$$

and the supercriticality parameter P is

$$P(\mathbf{k})=\frac{r_E^2\omega_L(\mathbf{k})}{4\,|c_0|\,r_{Di}^2\nu_e}. \tag{14}$$

It can be seen from (12) and (13) that for typical plasma parameters $\Delta k \ll k_m \lesssim k_1$, where k_1 is the root of $\delta(k_1) = 0$ and is equal to

$$k_1r_{De}=\left[\frac{2}{3}\left(\frac{\omega_0}{\omega_{Le}}-1\right)\right]^{1/2}. \tag{15}$$

For example, in experiments in the ionosphere plasma,[8] where $T_e \sim T_i$, the spread in the wave vectors is $\Delta k \approx (k_D/3)(m/M)^{1/2}$. Here, $k_D = r_{De}^{-1}$ is the Debye wave vector, and k_mr_D varies from 0.1 to 0.3 depending on the frequency of the external pump.

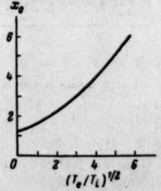

Fig. 1

II. NONLINEAR THEORY

We now consider the nonlinear theory for the instability discussed in the previous section. We are interested in how this parametric instability affects the ion distribution function. The equation for the evolution of the ion distribution in the turbulent state resulting from the imposition of an external hf field on the plasma can be written

$$\frac{\partial F(\mathbf{P},\, t)}{\partial t}=\frac{\partial}{\partial P_i}D_{ij}\frac{\partial F(\mathbf{P},\, t)}{\partial P_j}, \tag{16}$$

where the ion diffusion coefficient is

$$D_{ij}(\mathbf{P})=e^2\int\frac{d\mathbf{k}}{(2\pi)^3}k_ik_j\sum_{\mathrm{n}}|\varphi_0(\omega_{\mathrm{n}}(\mathbf{k}),\ \mathbf{k},\ t)|^2\{\pi\delta[\omega_{\mathrm{n}}(\mathbf{k})-\mathbf{k}\cdot\mathbf{v}]$$
$$-\gamma(\omega_{\mathrm{n}},\ \mathbf{k},\ t)\frac{\partial}{\partial\omega_{\mathrm{n}}}\left[\frac{P}{\omega_{\mathrm{n}}(\mathbf{k})-\mathbf{k}\cdot\mathbf{v}}\right]$$

and φ_0 is the potential of the perturbed longitudinal electric field in the plasma. The ion distribution function satisfying Eq. (16) will be sought in the form of a Maxwellian distribution with a time-dependent temperature

$$F=\frac{n}{[2\pi MT_i(t)]^{3/2}}\exp\left[-\frac{P^2}{2MT_i(t)}\right].$$

Substituting this expression into (16) and integrating over the velocities, we obtain

$$\frac{d}{dt}\left(\frac{3}{2}n_iT_i\right)=\frac{\omega_{Li}^2}{\sqrt{2\pi}}\int\frac{d\mathbf{k}}{(2\pi)^3}\frac{k^2}{4\pi}\sum_{\mathrm{n}}|\varphi_0|^2\int_{-\infty}^{\infty}dx\,x^2e^{-x^2/2}$$
$$\times\left[\pi\delta(\omega_{\mathrm{n}}-kv_{Ti}x)-\gamma\frac{\partial}{\partial\omega_{\mathrm{n}}}\left(\frac{1}{\omega_{\mathrm{n}}-kv_{Ti}x}\right)\right], \tag{17}$$

where x is the component, normalized to $v_{Ti}=(T_i/M)^{1/2}$, of the ion velocity along the vector **k**.

Below, we consider the resonant interaction, leaving only the term with the δ function in (17). This approximation is reasonable when the growth rate of the parametric instability does not exceed the rate at which ion waves are damped in the absence of a pump field.

In the resonance approximation we have the following equation for the ion temperature:

$$\frac{d}{dt}\left(\frac{3}{2}n_iT_i\right)=\sqrt{\frac{\pi}{2}}\,\omega_{Li}^2\int\frac{d\mathbf{k}}{(2\pi)^3}\frac{1}{4\pi}\sum_{\mathrm{n}}|\varphi_0|^2\frac{\omega_{\mathrm{n}}^2(\mathbf{k})}{kv_{Ti}^3}\exp\left(-\frac{\omega_{\mathrm{n}}^2}{2k^2v_{Ti}^2}\right). \tag{18}$$

The potential of the longitudinal field in the plasma is given by

$$\frac{d}{dt}\varphi_0(\omega_{\mathrm{n}},\ \mathbf{k},\ t)=\gamma(\omega_{\mathrm{n}},\ \mathbf{k},\ t)\varphi_0(\omega_{\mathrm{n}},\ \mathbf{k},\ t),$$

whose solution is written in the form

$$|\varphi_0(\mathbf{k},\ t)|^2=|\varphi_0(\mathbf{k},\ 0)|^2\exp\left[2\int_0^t\gamma(t')\,dt'\right]. \tag{19}$$

The initial value of the perturbation is determined by the thermal noise:

$$|\varphi_0(\mathbf{k},\ 0)|^2=\frac{4\pi}{k^2}(T_{e0}+T_{i0}). \tag{20}$$

The fact that the properties of the growing modes are independent of the small-scale properties of the ion distribution indicates the possibility of using in (19) the expression for γ obtained in the linear theory, but time-dependent through the macroscopic plasma parameters (the temperature). Substituting (19) and (20) and using the equations of the preceding section for ω and γ we write (18) as

$$\frac{d}{dt}(3n_iT_i)=(T_{e0}+T_{i0})\frac{\omega_{Li}^2}{\pi^{3/2}}\int_0^{k_D}kdk\frac{x_0^2}{v_{Ti}}e^{-x_0^2/2}$$
$$\times\int_0^1d\mu\exp\left[\nu_e\int_0^t\frac{P\mu^2dt'}{1+\left(\frac{k-k_m}{\Delta k}\right)^2}-\nu_et\right]. \tag{21}$$

The integral is

$$\int_0^1d\mu e^{\beta^2\mu^2}=f(\beta^2)e^{\beta^2}=\begin{cases}1+\frac{\beta^2}{3}+\dots & \text{for}\quad \beta^2\ll1,\\ \frac{1}{2\beta^2}e^{\beta^2}\left(1+\frac{1}{2\beta^2}+\dots\right) & \text{for}\quad \beta^2\gg1.\end{cases}$$

The function $f(\beta^2)$ will be approximated by the following simple expression:

$$f(\beta^2)\approx\frac{1}{1+2\beta^2}.$$

This approximation gives a good estimate for large and small values of the argument and is not very different from the true value for $\beta=1$. Then (21) reduces to

$$\frac{d}{dt}(n_iT_i)=(T_{e0}+T_{i0})\frac{\omega_{Li}^2}{3\pi\sqrt{2\pi}}\int_0^{k_D}kdk\frac{x_0^2}{v_{Ti}}e^{-x_0^2/2}f(\beta^2)\exp(\beta^2-\nu_et),$$

where

$$\beta^2=\nu_e\int_0^t\frac{Pdt'}{1+\left(\frac{k-k_m}{\Delta k}\right)^2}.$$

Since P has a fairly weak dependence on k, it can be neglected in the above equation. The dependence of $f(\beta^2)$ on k is of small importance compared to the dependence on k of the subintegrand contained in the exponent. This dependence on k in the exponent is very important since it determines the wave vector interval within which the initial thermal noise increases. Therefore, in calculating the integral over k, the function $f(\beta^2)$ can be assumed to be independent of k by setting $k=k_m$. Furthermore, we have

$$\beta^2\approx\frac{\nu_eP(t)\,t}{1+\left[\frac{k-k_m(t)}{\Delta k(t)}\right]^2}.$$

Then, the integration over k reduces to the calculation of the following integral:

$$\Psi(a,\ \Delta k,\ k_m,\ k_D)=\int_0^{k_D}kdk\exp\left[\frac{a}{1+\left(\frac{k-k_m}{\Delta k}\right)^2}\right]=\Psi_1+\Psi_2,$$

where

$$2\Psi_1=(\Delta k)^2\int_{-\frac{k_m}{\Delta k}}^{\frac{k_D-k_m}{\Delta k}}dx^2e^{\frac{a}{1+x^2}}=[(\Delta k)^2+(k_D-k_m)^2]\,e^{\frac{a(\Delta k)^2}{(\Delta k)^2+(k_D-k_m)^2}}$$

$$-[(\Delta k)^2+k_m^2]\,e^{\frac{a(\Delta k)^2}{(\Delta k)^2+k_m^2}}$$

$$+a(\Delta k)^2\left[Ei\left(\frac{a(\Delta k)^2}{(\Delta k)^2+k_m^2}\right)-Ei\left(\frac{a(\Delta k)^2}{(\Delta k)^2+(k_D-k_m)^2}\right)\right],$$

$$\Psi_2=\Delta k k_m\int\limits_{-\frac{k_m}{\Delta k}}^{\frac{k_D-k_m}{\Delta k}}dx e^{\frac{a}{1+x^2}}\approx k_m\left[k_D+\Delta k\sqrt{\frac{\pi}{a}}e^a\Phi(\sqrt{a})\right].$$

Here, Ei(x) is the exponential integral, and Φ is the error function. The second integral is estimated from an equation which gives a fairly good approximation if the limits of integration are on the order of unity. This is true in our case ($\Delta k \ll k_m < k_D$). Using the small value of Δk we obtain the following expression for Ψ:

$$\Psi\approx\frac{k_D^2}{2}+k_m\Delta k\left[\sqrt{\frac{\pi}{a}}e^a\Phi(\sqrt{a})-2\right]\quad\text{for}\quad 0<\Delta k\ll k_m<k_D.$$

As a result, the equation for the ion temperature becomes

$$\frac{dT_i}{dt}\approx(T_{e0}+T_{i0})\frac{x_0^2e^{-\frac{x_0^2}{2}}}{6\pi\sqrt{2\pi}}\frac{\omega_{Li}^2}{nv_{Ti}r_{De}^2}f(\nu_e Pt)e^{-\nu_e t}$$

$$\times\left\{1+2\frac{k_m(t)\Delta k(t)}{k_D^2}\left[\frac{\pi^{1/2}}{(\nu_e Pt)^{1/2}}\Phi\langle(\nu_e Pt)^{1/2}\rangle e^{\nu_e Pt}-2\right]\right\}. \tag{22}$$

The variation in the ion temperature depends on the characteristic parameter

$$\nu_e t_p=\frac{\nu_e}{\omega_{Li}}nr_{De}^3\left(\frac{T_{i0}}{T_{e0}}\right)^{1/2}\approx L\left(\frac{MT_{i0}}{mT_{e0}}\right)^{1/2}\gg 1,$$

where L is the Coulomb logarithm. In view of the large value of this parameter, marked temperature changes can be expected only for large times, when $\nu_e t \gg 1$. For such times we have

$$\frac{dT_i}{dt}\approx(T_{e0}+T_{i0})\frac{x_0^2}{6\pi}e^{-\frac{x_0^2}{2}}\frac{\omega_{Li}^2}{nv_{Ti}}\frac{k_m\Delta k}{(2\nu_e Pt)^{3/2}}e^{\nu_e(P-1)t}. \tag{23}$$

This equation describes the anomalous heating of ions due to the parametric instability and the exponential increase in the initial thermal noise in the region of wave vectors mentioned above. From this equation we obtain the following estimate of the characteristic time of change in the ion temperature due to the parametric instability:

$$t_T\sim\frac{1}{\nu_e(P_0-1)}\left[\frac{T_{e0}}{2T_{i0}}+8+\ln(\nu_e t_p)\right]. \tag{24}$$

It follows from this estimate that anomalous heating of ions due to the mechanism in question for the same initial supercriticality P_0 occurs much faster in a plasma with $T_{e0} \lesssim T_{i0}$ than in a strongly nonisothermal plasma with $T_{e0} \gg T_{i0}$, where the ion sound is weakly absorbed by the plasma.

Note that the case $T_{e0} \gg T_{i0}$ generally requires a more detailed analysis since we must allow for the time variation of the electron temperature, which in this limit has a significant effect on the properties of the exponential ion-acoustic fluctuations (the frequency and growth rate of the parametric instability in this limit are determined by the electron temperature).

It is also useful to point out that the ratio of the energy of the noise increasing exponentially in the initial stage to the total plasma energy at time t_T is approximately ν_e/ω_{Le}. This means that the rms electric-field fluctuation in the parametrically unstable plasma increases for a time t_T (or somewhat larger) almost to the pump-field amplitude. In this stage the fluctuations can be saturated by nonlinear effects related to interaction with the noise and scattering or beating by the ion fluctuations. If the parametric instability is not stabilized for such times due to some other processes (for example, heating of the plasma), and the ratio of noise to the total plasma energy remains constant, then

$$\frac{d}{dt}(nT_i)\sim\frac{\omega_{Li}}{k_m r_{Di}}W,$$

where W is the total noise energy. It follows that the characteristic time for a change in the ion temperature at saturation is proportional to ν_e^{-1} (it is assumed that the pump amplitude is slightly above threshold). However, these problems are beyond the scope of the present paper. Therefore, we will consider in more detail the initial stage of ion heating, when the noise level is not very large and nonlinear interaction with the noise can be neglected.

Taking the above into account, we consider the case $T_e \leq T_i$. The equation for the ion temperature is written

$$\frac{d\ln T_i}{d\tau}=\frac{c}{\tau^{3/2}}k_m\Delta k r_{De0}^2\exp\left[\tau\left(\frac{P_0T_{i0}}{T_i}-I\right)\right],\quad \tau\gg 1, \tag{25}$$

where

$$c=\frac{\omega_{Li}}{\nu_0}\frac{\left(1+\frac{T_{e0}}{T_{i0}}\right)x_0^2\exp\left(-\frac{x_0^2}{2}\right)}{12\pi\sqrt{2}nr_{Di0}r_{De0}^2}\approx\frac{1}{50\nu_0 t_p},$$

$\tau = t\nu_0$ is the dimensionless time, $I = \nu_e[T_e(t)]/\nu_0$, $\nu_0 = \nu_e(T_{e0})$, and the zero subscript denotes the initial value of the quantity. It can be seen from the equation that the time dependence of the right-hand side is determined primarily by the exponent.

If the variation in the electron temperature is neglected for time t_T, then $I(T_e) = 1$, and it follows from (25) that the ion temperature for fairly large times must reach a steady-state value due to stabilization of the ion-acoustic parametric instability by ion heating. As a result we find the maximum ion temperature which can be attained by the process in question while the electron temperature has not yet changed

$$(T_i)_{\max}=P_0T_{i0}. \tag{26}$$

In the case of small supercriticality $1 < P_0 \lesssim 2$ for $(P_0-1)\tau \gg 1$, when a marked increase in the fluctuations in the plasma is to be expected, the solution of (25) is written

$$\frac{T(\tau)}{T_{0i}}\approx 1+\frac{ck_m\Delta k r_{De0}^2}{(P_0-1)}\left(\frac{1}{\tau}+\frac{1}{\tau_{Ti}}\right)^{1/2}\exp\left[(P_0-1)\frac{\tau\tau_{Ti}}{\tau+\tau_{Ti}}\right]. \tag{27}$$

The characteristic time for a change in the ion temperature τ_{Ti} is determined by the stability condition (26) for large times $\tau \gg \tau_{Ti}$; as a result, we have

$$(P_0-1)^3\tau_{Ti}^{3/2}=ck_m\Delta k r_{De0}^2 \exp[\tau_{Ti}(P_0-1)]. \tag{28}$$

Note that the times for the characteristic change in the ion temperature obtained from (24) and (28) are of the same order of magnitude.

In the case of large supercriticality, $P_0 > 2$, Eqs. (27) and (28) still describe qualitatively the change in the ion temperature. In the initial stage the ion temperature increases exponentially, and for time τ_{Ti} the temperature increase is comparable to the initial value; then the temperature increases almost linearly ($\sim \tau/\tau_{Ti}$) and reaches a plateau fairly quickly.

In a realistic plasma with a parametric instability the electrons will also be heated after a time. This is apparent from Eq. (26). The situation is completely different for weakly and fully ionized plasmas. In a weakly ionized plasma the electron heating accelerates the stabilization process for the ion-acoustic parametric instability since $I_{\text{weak}}(T_e) = [T_e(t)/T_{e0}]^{1/2}$ increases as the electron temperature increases. The stabilization time is determined by the characteristic time of heating in a hf field of the lighter electrons, and not by the time for anomalous ion heating τ_{Ti} obtained above, although the latter is evidently a characteristic time for the change in ion temperature. The maximum ion temperature to which a relatively weak hf field (P_0 is small) heats ions in a weakly ionized plasma can be obtained from the following considerations. Since Eq. (25) is applicable when $T_i \gg T_e$ and the electrons are generally heated more rapidly than the ions, in the final analysis the electron temperature is comparable to the ion temperature (since P_0 is assumed not very large, the discontinuity in the initial values of the ion and electron temperatures should not be too large). Then the condition for reaching a plateau becomes

$$(T_i)_{\max} \sim \frac{4\pi e^2 n r_E^{4/3}}{\left[\frac{32}{3}\sqrt{2\pi}\,|c_0|\,a^2 N\right]^{2/3}} \approx \left[\frac{eE_0^2}{28\pi\,|c_0|\,n^{1/2}a^2 N}\right]^{2/3},$$

where a is the effective radius of the electron–neutral interaction ($a \sim 10^{-8}$ cm), n is the electron density, and N is the neutral density. It can be seen that the maximum attainable ion temperature in the anomalous heating process under consideration increases with the increase in the pump amplitude as $E_0^{4/3}$.

In a fully ionized plasma, heating of the electrons broadens the region with the ion-acoustic instability since $I_{\text{inst}}(T_e) = [T_{0e}/T_e(t)]^{3/2}$ declines as t increases. In view of the more rapid heating of the electrons, the parametric instability will obtain during the entire ion heating process; in this case the ion temperature will not reach a plateau. In the initial stage of the heating the characteristic time for a change in the ion temperature is determined, as before, by Eq. (24), and stabilization of the instability due to ion heating does not occur.

---

[1] N. G. Basov and O. N. Krokhin, Vestn. Akad. Nauk SSSR, 6, 55 (1970).

[2] F. W. Perkins and P. K. Kaw, J. Geophys. Res., 76, 282 (1971).

[3] R. Z. Sagdeev, Usp. Fiz. Nauk, 110, 437 (1973) [Sov. Phys. – Usp., 16, 557 (1974)].

[4] V. P. Silin, Parametric Effect of High-Power Radiation on a Plasma [in Russian], Nauka, Moscow (1973).

[5] I. S. Baikov and V. P. Silin, Zh. Tekh. Fiz., 43, 3 (1973) [Sov. Phys. – Tech. Phys., 18, 1 (1973)].

[6] W. L. Kruer and J. M. Dawson, Phys. Fluids, 15, 446 (1972).

[7] V. P. Silin, Zh. Eksp. Teor. Fiz., 57, 183 (1969) [Sov. Phys. – JETP, 30, 105 (1970)].

[8] D. F. DuBois, and M. V. Goldman, Phys. Fluids, 15, 919 (1972).

Transformation of nonlinear MHD waves

G. M. Zaslavskii, S. S. Moiseev, and V. V. Mukhin

Physicotechnical Institute, Academy of Sciences of the Ukrainian SSR, Khar'kov

(Submitted December 21, 1973)
Zh. Tekh. Fiz., 44, 2476-2482 (December 1974)

The transformation of a slow nonlinear acoustic wave into a fast acoustic wave in a slightly inhomogeneous plasma is analyzed. The transformation coefficient is calculated for the case in which the nonlinearity can be assumed slight.

INTRODUCTION

The existing theory for a wave transformation in an inhomogeneous medium (see, e.g., the reviews in refs. 1,2) is valid only for small amplitudes of the interacting waves. In this work we treat the transformation of weakly nonlinear stationary waves that propagate in a weakly inhomogeneous medium. Problems of this type are usually treated by various methods[3–6] in the adiabatic approximation, i.e., in the approximation that the deviation from conservation of the adiabatic invariant of the wave is exponentially small in the weakly inhomogeneous medium. Nevertheless, slight nonadiabatic corrections can be important if they alter the physical nature of the process. In this work we take account of nonadiabatic effects and the resulting transformation of essentially nonlinear waves. This method is analogous to that used in ref. 7 in a study of the reflection of nonlinear waves from a smooth inhomogeneity.

1. GENERAL STATEMENT OF THE PROBLEM

We briefly review the conditions for linear wave transformation. We assume that a medium supports two independent wavelike motions with dispersion relations $D_1(\omega, k) = 0$ and $D_2(\omega, k) = 0$, where ω is the frequency and k is the wave vector. When these waves are weakly coupled the wave motion is described by a new dispersion relation $D(\omega, k)$, which has two solutions; for weak coupling these are approximately equal to the solutions $k_1 = k_1(\omega)$ and $k_2 = k_2(\omega)$ of the original dispersion relations.

If the medium is inhomogeneous, the wave vectors are functions of the coordinate, and a linear wave transformation occurs because solutions "intersect" i.e., $k_1(\omega, x_0) = k_2(\omega, x_0)$. We have an analogous situation in the nonlinear case. The system of weakly coupled nonlinear equations describing nonlinear waves leads to the nonlinear dispersion relation $D(\omega, k, A)$, where $k \equiv \omega/u$, $u = u(A)$, is the velocity of the nonlinear wave, and A is a parameter which serves as a measure of the nonlinearity. Let us assume that this dispersion relation has the system of solutions $k_1 = k_1(\omega, A)$, $k_2 = k_2(\omega, A)$. In the case of weak coupling each of these solutions is approximately equal to the corresponding nonlinear uncoupled-wave solution. In an inhomogeneous medium we have $k_{1,2} = k_{1,2}(\omega, A(x), x)$, and there can be an intersection of the roots, i.e., regions in which two solution branches exist simultaneously. This leads to transformation of the nonlinear waves. If the transformation coefficient is small and if one of the waves, corresponding to the solution with wave vector k_2 vanishes at $x=-\infty$, while the wave corresponding to the first solution has a wave vector A_1 and an amplitude k_1, the transformation coefficient will obviously be a function of k_1 and A_1. The amplitude of the second wave (which results from the transformation) is determined by the transformation coefficient, and its wave vector is unambiguously governed by the properties of the medium and of the first wave in accordance with the nonlinear dispersion relation.

2. EQUATIONS FOR THE INTERACTION OF NONLINEAR MHD WAVES

Let us consider, for example, the interaction of nonlinear MHD waves, specifically, the fast and slow acoustic waves. We assume an inhomogeneous plasma in which the gradient of the inhomogeneity is along the oz axis; the plasma is in a fixed magnetic field $\mathbf{H}_0$, which makes a small angle ($\theta \ll 1$) with the oz axis and lies in the zy plane. We assume that MHD waves propagate parallel to the gradient of the inhomogeneity. Here the angle θ is the linear-coupling parameter: At small values of θ, the coupling is weak; for very small angles ($\theta \to 0$), on the other hand, the slow acoustic wave becomes the ion-acoustic wave, while the fast acoustic wave becomes the Alfvén wave. Accordingly, at small values of θ it is reasonable to incorporate the dispersion for the slow acoustic wave by analogy with the ion-acoustic wave.

The interaction of fast and slow acoustic waves has been analyzed thoroughly in the linear approximation.[8,9] The system of equations describing the MHD motion is

$$\left.\begin{aligned} m_i\left[\frac{\partial \mathbf{v}_i}{\partial t}+(\mathbf{v}_i\nabla)\mathbf{v}_i\right] &= e\mathbf{E}+\frac{e}{c}[\mathbf{v}_i\times\mathbf{B}],\\ m_e\left[\frac{\partial \mathbf{v}_e}{\partial t}+(\mathbf{v}_e\nabla)\mathbf{v}_e\right] &= -e\mathbf{E}-\frac{\nabla P_e}{N_e}-\frac{e}{c}[\mathbf{v}_e\times\mathbf{B}],\\ \frac{\partial N_{i,e}}{\partial t}+\operatorname{div}(N_{i,e}\mathbf{v}_{i,e}) &= 0;\ \operatorname{curl}\mathbf{B}=\frac{4\pi e}{c}(N_i\mathbf{v}_i-N_e\mathbf{v}_e),\\ \operatorname{div}\mathbf{E} &= 4\pi e(N_i-N_e);\ \operatorname{curl}\mathbf{E}=-\frac{1}{c}\frac{\partial\mathbf{B}}{\partial t};\quad \operatorname{div}\mathbf{B}=0. \end{aligned}\right\} \qquad (1)$$

We neglect the thermal motion of the ions. The plasma inhomogeneity is maintained by external conditions (e.g., an external gravitational field) and is assumed to be smooth, $[(1/N_0)/(\partial N_0/\partial z)]^{-1} \gg \lambda$, where λ is the characteristic wavelength. Neglecting the electron inertia in the longitudinal motion for the slow acoustic wave, to second order in the perturbation, we can write[10]

$$\frac{\partial^2 v_{zi}}{\partial t^2}+\frac{\partial^2}{\partial z\partial t}(v_{zi}^2)-c_s^2\frac{\partial^2 v_{zi}}{\partial z^2}-r_g^2c_s^2\frac{\partial^4 v_{zi}}{\partial z^4}=-\frac{1}{2}v_A^2\frac{\partial^2 h^2}{\partial z\partial t}-\sin\theta v_A^2\frac{\partial^2 h}{\partial z\partial t}, \qquad (2)$$

where $h = H_y/H_0$; $c_s^2 = T_e/M$; $r_g = (T_e/4\pi e^2N_0)^{1/2}$ is the Debye length, $v_A = H_0/\sqrt{4\pi m_e N_0}$ is the Alfvén velocity, and N_0 is the unperturbed density of the inhomogeneous plasma. The derivation of (2) is based on the assumption

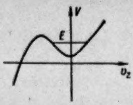

Fig. 1

that the dispersion is weak, so that the dispersion is incorporated only in the linear terms. In accordance with the discussion above, we now assume the angle θ to be small: $\theta \sim \sin\theta < 1$. In particular, we omit the nonlinear terms which are proportional to θ. For the fast acoustic waves we can write, to second order,

$$\left.\begin{aligned} &\frac{\partial h}{\partial t} = \cos\theta\frac{\partial v_{yt}}{\partial z} - \sin\theta\frac{\partial v_{zt}}{\partial z} - \frac{\partial}{\partial z}(hv_{zt}),\\ &\frac{\partial v_y}{\partial t} = v_A^2\cos\theta\frac{\partial h}{\partial z}\left(1 - \frac{\tilde{N}}{N_0}\right) - v_z\frac{\partial v_y}{\partial z},\\ &\frac{1}{N_0}\frac{\partial \tilde{N}}{\partial t} + \frac{1}{N_0}\frac{\partial}{\partial z}(\tilde{N}v_{zt}) + \frac{\partial v_{zt}}{\partial z} = 0. \end{aligned}\right\} \qquad (3)$$

In contrast with (2), the equation for the fast acoustic wave, (3) contains no nonlinear terms which refer to a wave of one type only. All the nonlinear terms in (3) are cross terms, because of the smallness of the angle θ. It should be noted that at very small angles θ the fast sound can have nonlinear "self-effect" terms only in third order in the perturbation;[11] these terms are not included in (3). Accordingly, in the absence of longitudinal motion, $v_z \simeq 0$, the fast acoustic wave (at $\theta \ll 1$) is a packet of noninteracting harmonics. An interaction among them is possible only in the presence of longitudinal motion (slow sound).

3. STEADY-STATE SOLUTIONS IN THE HOMOGENEOUS CASE

We first consider the interaction of waves in a homogeneous plasma, writing the solution as $\sim f(z - ut)$, where u is the velocity of the steady-state nonlinear wave. From (2) and (3) we find the energy integral:

$$\frac{1}{2}r_g^2(v_z')^2 + \frac{1}{2}\left(1 - \frac{u^2}{c_s^2}\right)v_z^2 + \frac{u}{3c_s^2}v_z^3 - \frac{uv_A^2}{2c_s^2}\sin^2\theta\, v_z$$
$$- \frac{uv_A}{2c_s^2}\frac{\left[\sin\theta\left(-u + \dfrac{v_A^2}{u}\cos^2\theta\right) + A\cos\theta\right]^2}{v_z - u + \dfrac{v_A^2\cos^2\theta}{u}} = E = \text{const}, \qquad (4)$$

which describes the family of possible trajectories in the phase plane, where A and E are the constants of integration. Equation (4) describes two coupled nonlinear waves. At small values of θ and of $u \gtrsim c_s$ and of $u \gtrsim v_A$ we obtain a wave which is approximately a slow or fast acoustic wave, respectively. We consider two limiting cases: a) $c_s \gg v_A$; b) $v_A \gg c_s$. In case a) we first assume $u \gtrsim c_s$; then the last term in (4) reduces to a constant increment, and the equation corresponds to the oscillation of a nonlinear oscillator describing a nonlinear slow acoustic wave. The potential is

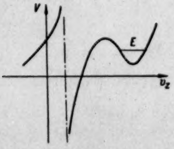

Fig. 2

$$V = \left(1 - \frac{u}{c_s}\right)v_z^2 + \frac{v_z^3}{3c_s} - \frac{v_A^2\sin\theta}{2c_s}v_z + \frac{v_A}{2c_s^2}[-u\sin\theta + A\cos\theta]^2,$$

and the potential well is shown in Fig. 1.

At $u \gtrsim v_A$ and at small values of θ, the last term in (4) becomes important. The structure of the potential well is different (Fig. 2), and the potential is

$$V = \frac{v_z^2}{2} + \frac{v_A}{3c_s^2}v_z^3 - \frac{v_A^3}{2c_s^2}\sin\theta\, v_z - \frac{v_A^2}{2c_s^2}\frac{[A\cos\theta - v_A\sin^2\theta]^2}{v_z - v_A\sin^2\theta}.$$

The solution in this case corresponds to fast sound.

In case b) the structure of the potential wells is slightly different. The structure can be easily determined by analyzing Eq. (4) for the cases $u \gtrsim v_A$ and $u \gtrsim c_s$.

Figure 3 shows the shape of the potential wells for the case $c_s \simeq v_A$. We see that both the nonlinear solutions, for slow and fast sound, exist simultaneously, and the waves propagate at the same velocity c_s. Accordingly, they interact strongly. Then even in the homogeneous case we see that as the ratio v_A/c_s changes from a very small value to a large value the structure of the solution changes. It is also easy to see that in an inhomogeneous plasma in the case $v_A \sim c_s$ we should find a new characteristic mode, i.e., there should be a transformation of one type of wave into another.

4. WAVE-TRANSFORMATION COEFFICIENT IN AN INHOMOGENEOUS PLASMA

We consider nonlinear waves which are periodic in time (with frequency ω) and which propagate in a weakly inhomogeneous plasma. To determine the coefficient of the transformation between these waves we expand (2) and (3) in a Fourier series, finding

$$\left.\begin{aligned} &\frac{d^2v_{zn}}{dz^2} + \frac{n^2\omega^2}{c_s^2}v_{zn} + r_g^2\frac{d^4v_{zn}}{dz^4} - \frac{i\omega_n}{c_s^2}\\ &\times\sum_{(k,\,m)}\frac{d}{dz}(v_{zm}v_{zk})\,\delta(n - k - m) = -\theta\frac{\omega^2n^2}{c_s^2}v_{ny},\\ &\frac{d^2v_{yn}}{dz^2} + \frac{\omega^2n^2(c_s^2 + \theta^2v_A^2)}{v_A^2c_s^2}v_{ny} = -\theta\frac{n^2\omega^2}{c_s^2}v_{zn}\\ &-\sum_{(k,\,m)}\frac{d^2}{dz^2}\left[\frac{1}{i\omega_k}\frac{dv_{yk}}{dz}v_{mz}\right]\delta(n - m - k), \end{aligned}\right\} \qquad (5)$$

where

$$v_{z,y} = \sum_n (v_{z,y;n}e^{i\omega_nt} + v^*_{z,y;n}e^{-i\omega_nt}).$$

In particular, for slow sound with N_0 = const and $\theta \ll 1$ (ref. 7), we have $v_{zn} = a_ne^{-ink_sz}$, where k_s is the wave vector of the first harmonic, and a_n is independent of z and t, being given by

$$a_n = \begin{cases} \text{const}, & n \leqslant N_*,\\ e^{-n/N_*}, & n \geqslant N_*, \end{cases}$$

where N∗, the number the harmonics whose amplitudes

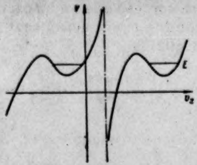

Fig. 3

are of the order of the first harmonic, is governed by the extent of the nonlinearity. In a weakly inhomogeneous plasma, we seek a solution of (5) in the form

$$\left.\begin{aligned} v_{zn}^{(\pm)} &= B_n^{(\pm)} \exp\left\{ \mp in \int^{z} k_s^{(\pm)}(z')\,dz' \right\}, \\ v_{yn}^{(\pm)} &= A_n^{(\pm)} \exp\left\{ \mp in \int^{z} k_A^{(\pm)}(z')\,dz' \right\}, \end{aligned}\right\} \quad (6)$$

where $u_{nz}^{(+)}$ and $v_{ny}^{(+)}$ are the harmonics of the incident wave $v_z^{(+)} = \sum_n v_{zn}^{(+)} e^{in\omega t}$ and $v_y^{(+)} = \sum_n v_{yn}^{(+)} e^{in\omega t}$, and $v_{n;\,y,z}^{(-)}$ are those of the reflected waves $v_{y,\,z}^{(-)} = \sum_n v_{z,y;\,n}^{(-)} e^{-in\omega t}$; k_s and k_A are the wave numbers of the slow and fast acoustic waves at the first harmonic.

Substituting (6) into (5), we see that in the first approximation $v_{nz}^{(+)}$ and $v_{ny}^{(+)}$ satisfy the equations

$$\left.\begin{aligned} \frac{d^2 v_{zn}}{dz^2} + n^2 k_s^2(z) v_{nz} &= -\alpha v_{yn}, \\ \frac{d^2 v_{yn}}{dz^2} + n^2 k_A^2(z) v_{ny} &= -\alpha v_{zn}, \end{aligned}\right\} \quad (7)$$

where $k_A(z)$ and $k_s(z)$ are functions of z and of the parameter, through $N_0(z)$; and where $\alpha \equiv \theta n^2 \omega^2 / c_s^2$. We assume for the moment that we are solving system (7) separately for each pair v_{zn} and v_{yn}, neglecting the interaction between harmonics. Then the process of finding the transformation coefficient for system (7) reduces to the linear case for each harmonic n, and the relationship between the amplitudes on different sides of the interaction region is[12]

$$\left.\begin{aligned} A'_n &= e^{-n\delta} A_n + \sqrt{1 - e^{-2n\delta}}\, B_n, \\ B'_n &= \sqrt{1 - e^{-2n\delta}}\, A_n - e^{-n\delta} B_n, \end{aligned}\right\} \quad (8)$$

where

$$\delta = -\frac{i}{4} \oint_{c} (k_A - k_s)\,dz'. \quad (9)$$

The integral is evaluated along a closed contour in the complex plane encompassing points at which $k_A^2(z) = k_s^2(z)$. Since $\delta \gg 1$, in a first approximation it is sufficient to consider a transformation effect of order $e^{-\delta}$, i.e., the transformation of the first harmonic, and to neglect the transformation of the higher harmonics. We have derived Eqs. (8) without taking account of the coupling between harmonics. Now we assume a weak coupling, due to the nonlinear terms, and we seek the solution in the form

$$v_{zn}^{(\pm)} = \left[\mp \frac{B_n^{(\pm)}(z)}{ik_s^{(\pm)}(z)\,n} + b_n^{(\pm)}(z) \right] e^{\mp in \int^{z} k_s^{\pm}(z')\,dz'},$$

$$v_{yn}^{(\pm)} = \left[\mp \frac{A_n^{(\pm)}(z)}{ik_A^{(\pm)}(z)\,n} + a_n^{(\pm)}(z) \right] e^{\mp in \int^{z} k_A^{\pm}(z')\,dz'}, \quad (10)$$

where $B_n^{(\pm)}$ and $A_n^{(\pm)}$ are slowly varying functions of z, and $b_n^{(\pm)}$ and $a_n^{(\pm)}$ are rapidly varying functions. Substituting (10) into system (5), and omitting the second derivatives of the slowly varying functions, we find

$$\frac{dB_n}{dz} = -i\,\frac{k_s n}{c_s}\, B_n A_0, \quad (11)$$

$$\frac{dA_n}{dz} = i\,\frac{k_A n}{c_s}\, A_n B_0 \quad (12)$$

where

$$\Delta k_s \simeq \frac{k_s}{c_s} A_0; \quad \Delta k_A \simeq \frac{k_A}{c_s} B_0.$$

That is, the phase corrections to the wave number due to the nonlinear terms are governed by the zeroth wave harmonics in the first approximation,[8] i.e.,

$$k_A(z) \simeq \frac{\omega}{v_A(z)(1 + \alpha_A)} \text{ and } k_s = \frac{\omega}{c_s(1 + \alpha_s)},$$

where α_s and α_A are given by (12) ($\alpha_s, \alpha_A \ll 1$). Since $\alpha_s, \alpha_A \ll 1$, we can neglect the functional dependences of these quantities on z. Then the analytic properties of k_A and k_s are independent of the wave amplitude and are determined as in the linear case.

Substituting the expressions for k_A and k_s into (9), we find

$$\delta = -\frac{i}{4} \oint (k_A - k_s)\,dz' \simeq \frac{\pi}{2} \theta^2 \frac{\omega L}{c_s(1 + \alpha_s)}. \quad (13)$$

We see from (13) that, generally speaking, the nonlinearity leads to a reduction of δ and thus an increase in the efficiency of the transformation between normal modes.[2] If, as x → −∞, we have

$$v_z(z - ut) = \sum_n B_n^{(+)} \exp\left\{ in \left[\omega t - \int^{z} k_s(z')\,dz' \right] \right\},$$

then as x → + ∞ we find

$$v_z(z - u_s t) = \sum_n B_n^{(+)} \exp\left\{ in \left[\omega t - \int^{z} k_s(z')\,dz' \right] \right\};$$

in addition, we find

$$v_y = B_1^{(+)} e^{-\delta} \sin\left[\omega t - \int^{z} k_A(z')\,dz' + \varphi \right],$$

where φ is the phase.

CONCLUSION

We have analyzed the effect of nonlinearity in the case in which there is a "super-barrier intersection of solutions" in the linear approximation.[2] Generally speaking, a nonlinear stationary wave is destroyed in the transformation, and a many-stream mode should arise.[8] These arguments are plausible since the phase and amplitude relations between the harmonics of a stationary wave are maintained very closely, and these relations can be violated in the transformation. In this problem, however, the higher harmonics of the resulting wave are exponentially small in comparison with the first harmonic, so that a single-stream mode is "generated" in the first approximation. On the other hand, we can cite at least two examples in which the flow is of a many-stream nature: first, reflection of a nonlinear stationary wave from a δ-shaped singularity[8] (in general, reflection and transformation at a sharp boundary should have the same properties); second, incidence of a nonlinear stationary wave on a region in which the refractive index for one of the harmonics has a singularity in the linear approximation.[13] In this case, despite the nonlinear dispersion relation, the first harmonic is effectively synchronized with other harmonics even in the linear approximation, so that there can be a "scattering" of the nonlinear stationary wave.[13] We note that in this case for the linear approximation the transformation in question is of an anomalous type.[2]

The authors thank N. S. Erokhin for useful discussion.

---

[1] V. E. Golant and A. D. Piliya, Usp. Fiz. Nauk, 104, 413 (1971) [Sov. Phys. – Usp., 14, 413 (1972)].

[2] N. S. Erokhin and S. S. Moiseev, Usp. Fiz. Nauk, 109, 225 (1973) [Sov. Phys. – Usp., 16, 64 (1973)].

[3] T. C. Luke, Proc. Roy. Soc. A, 292, 403 (1966).

[4] T. K. Moser, Averaging of Nonlinear Waves, Courant Inst. (1968).

[5] G. B. Whitham, Proc. Roy. Soc. A, 283, 268 (1965); J. Fluid. Mech., 22, 273 (1973).

[6] G. M. Zaslavskii, Dokl. Akad. Nauk SSSR, 192, 760 (1970) [Sov. Phys. – Dokl., 15, 542 (1970)].

[7] G. M. Zaslavskii, Zh. Eksp. Teor. Fiz., 62, 2129 (1972) [Sov. Phys. – JETP, 35, 1113 (1972)].

[8] S. S. Moiseev and V. R. Smilyanskii, Magnitnaya Gidrodinamika, No. 2, 23 (1965).

[9] A. S. Grebinskii, Zh. Tekh. Fiz., 39, 1166 (1969) [Sov. Phys. – Tech. Phys., 14, 877 (1970)].

[10] V. I. Karpman, Nonlinear Waves in Dispersive Media [in Russian], Izd. Nauka, Moscow (1973).

[11] A. Cavaliere and F. Engelmann, Nucl. Fusion, 7, 137 (1967).

[12] G. M. Zaslavskii, Lectures on the Applications of the WKBJ Method in Physics [in Russian], NGU, Novosibirsk (1965).

[13] N. S. Erokhin, V. I. Kurilko, M. B. Levin, M. G. Lyubarskii (Lyubarsky), N. G. Matsiborko, S. S. Moiseev, I. N. Onishenko, A. D. Tolstoluzhskii (Tolstoluzhsky), Ya. B. (Ja. B.) Fainberg, V. D. Shapiro, and V. I. Shevchenko, Proc. Fourth Intern. Conf. on Plasma Physics and Controlled Nuclear Fusion Research. Nuclear Fusion Supplement (1972), p. 135.

Two-stream flow in a thin plasma slab

A. V. Pashchenko and B. N. Rutkevich

(Submitted December 21, 1973)
Zh. Tekh. Fiz., 44, 2483-2488 (December 1974)

A general solution is found for the problem of two-stream hydrodynamic flow in a thin plasma slab in a strong longitudinal magnetic field. The solutions of problems with initial boundary conditions are classified, and the role of a simple wave in the general solution is indicated. The possible use of the simple-wave concept to describe the two-stream instability in a beam–plasma system is discussed.

INTRODUCTION

Various cases of two-stream flow in plasma have been treated in a long series of papers, beginning with refs. 1 and 2. In particular, there has been an analysis of the beam–plasma system, in which the beam electrons and the plasma execute certain types of motion against a fixed ion background. The electromagnetic fields which arise must be small for the analysis to hold.

In this work we find a general solution for the problem of two-stream hydrodynamic flow in a thin plasma slab. We determine the nature of the wave motion in the two-stream system for specified initial or boundary conditions. The results are obtained without the assumption that the field amplitudes are small, and the results can be extended to both electron–electron and electron–ion flow.

1. EQUATIONS OF A THIN PLASMA SLAB

The model of a thin plasma slab for the case of single-stream electron flow is described in detail in refs. 3, 7; we treat two-stream flows on the basis of this model.

We consider a slab of cold plasma of thickness of 2d, arranged symmetrically with respect to the x = 0 plane between two conducting planes at x = ± D, held at ground potential. We assume the system to be homogeneous in the y direction. Along the z axis is a magnetic field, which we assume to be so strong that we need take into account only the longitudinal motion of the particles.

Two-stream electron–electron flow in the slab is described by

$$\frac{\partial v_j}{\partial t}+v_j\frac{\partial v_j}{\partial z}=-\frac{e_j}{m_j}\frac{\partial \varphi}{\partial z}, \tag{1}$$

$$\frac{\partial n_j}{\partial t}+\frac{\partial (n_j v_j)}{\partial z}=0, \quad j=1,\ 2, \tag{2}$$

$$\frac{\partial^2 \varphi}{\partial x^2}+\frac{\partial^2 \varphi}{\partial z^2}=\begin{cases}-4\pi\sum\limits_{l=1}^{3} e_l n_l, & |x|<d,\\ 0, & d<|x|<D;\end{cases} \tag{3}$$

where the notation is standard. In Eq. (3), $e_1 = e_2 = -e$, $e_3 = e$, and $n_3 = n_0$ is the density of the ion background.

As in the single-stream case,[3,7] we find that, under the conditions d ≪ D ≪ L (where L is the scale length of the perturbation), the Poisson equation, Eq. (3), reduces to

$$\varphi=\begin{cases}4\pi\sum\limits_{l=1}^{3} e_l n_l\left(1-\frac{d}{2D}-\frac{x^2}{2dD}\right)dD, & |x|\leqslant d,\\ 4\pi\sum\limits_{l=1}^{3} e_l n_l\left(1-\frac{|x|}{D}\right)dD, & d\leqslant|x|\leqslant D.\end{cases}$$

Since d ≪ D, within the slab we can write, to order O(d/D),

$$\varphi=4\pi dD\sum_{l=1}^{3} e_l n_l. \tag{4}$$

Substituting (4) into (1), we find

$$\frac{\partial v_j}{\partial t}+v_j\frac{\partial v_j}{\partial z}+\lambda\sum_{l=1}^{2}\frac{\partial n_l}{\partial z}=0, \tag{5}$$

where

$$\lambda=\frac{4\pi e^2 dD}{m}.$$

2. GENERAL SOLUTION

Equations (2) and (5) give v_j and n_j as functions of z and t. We seek a solution of this system of equations by the method of characteristics.[4] In vector and matrix notation, we can write this system as

$$L_j[u]=a_{ij}\frac{\partial u^i}{\partial t}+b_{ij}\frac{\partial u^i}{\partial z}=0 \quad (j=1,\ 2,\ 3,\ 4), \tag{6}$$

where u is a vector having the components $u^1 = v_1$, $u^2 = v_2$, $u^3 = n_1$, $u^4 = n_2$; a_{ij} and b_{ij} are the elements of matrices A and B;

$$B=\begin{pmatrix} v_1 & 0 & \lambda & \lambda\\ 0 & v_2 & \lambda & \lambda\\ n_1 & 0 & v_1 & 0\\ 0 & n_2 & 0 & v_2\end{pmatrix}; \tag{7}$$

and A = E is the unit diagonal matrix. To find the characteristic curves of system (6), we must solve the equation

$$|B-\tau A|=0 \tag{8}$$

or, equivalently, the equation

$$\frac{\lambda n_1}{(v_1-\tau)^2}+\frac{\lambda n_2}{(v_2-\tau)^2}=1 \tag{9}$$

(which becomes the familiar dispersion relation in the linear limit) for τ. The characteristic curves are described by

$$\frac{dz}{dt}=\tau. \tag{10}$$

On these curves we solve the following system of linear homogeneous equations for the vector l, with components l_1, l_2, l_3, l_4:

$$l_j(b_{ij}-\tau a_{ij})=0, \quad j=1,\ 2,\ 3,\ 4.$$

We find

$$l_2=\frac{n_2(v_1-\tau)^2}{n_1(v_2-\tau)^2}l_1,\quad l_3=-\frac{v_1-\tau}{n_1}l_1,\quad l_4=-\frac{(v_1-\tau)^2}{n_1(v_2-\tau)}l_1. \quad (11)$$

Now using the linear combination $\sum_{j=1}^{4} l_j L_j[u]$, we can write the original system of equations in characteristic canonical form:

$$\left(\frac{\partial}{\partial t}+\tau_j\frac{\partial}{\partial z}\right)\left(\frac{\tau_j}{\lambda}-\frac{n_1}{v_1-\tau_j}-\frac{n_1}{v_2-\tau_j}\right)=0,\quad j=1,2,3,4. \quad (12)$$

The differentiation in (12) is carried out along the direction of the characteristic curve corresponding to the root τ_j. After integrating (12), we find a system of algebraic equations:

$$\frac{\tau_j}{\lambda}-\frac{n_1}{v_1-\tau_j}-\frac{n_2}{v_2-\tau_j}=F_j\left(t-\int_0^z\frac{dz}{\tau_j}\right),\quad j=1,2,3,4, \quad (13)$$

where F_j is some arbitrary function.

Equations (9) and (13), with specified F_j, give v_1, v_2, n_1, and n_2 as functions of t and z. The functions F_j are determined from system (13) if, at z = 0, we specify v_1, v_2, n_1, and n_2 as functions of the time or if these quantities are specified as functions of the coordinate at t = 0. Below we treat the first case in its general form.

3. PROBLEM WITH A BOUNDARY CONDITION

We assume that the u^j are specified as functions of the time at z = 0. Without any loss of generality we can assume

$$u^j(t_0)=c_{1j}+g_j(t_0)\,1(t_0), \quad (14)$$

where

$$1(s)=\begin{cases}1, & \operatorname{Re}s>0,\\ 0, & \operatorname{Re}s<0,\end{cases} \quad (15)$$

and c_{ij} is a constant, i.e., we are assuming that before time $t_0 = 0$ the variable component of u^j is zero. Then from (9) and (13) we find

$$F_j(t_0)=c_{2j}+f_j(t_0)\,1(t_0), \quad (16)$$

and system (13) becomes

$$\frac{\tau_j}{\lambda}-\frac{n_1}{v_1-\tau_j}-\frac{n_2}{v_2-\tau_j}=c_{2j}+f_j\left(t-\int_0^z\frac{z}{\tau_j}\right)1$$
$$\times\left(t-\int_0^z\frac{dz}{\tau_j}\right),\quad j=1,2,3,4. \quad (17)$$

To classify the solutions of this problem on the basis of (9) and (17), we write Eq. (9) as the system of equations

$$\left.\begin{aligned}y=\frac{\lambda n_1}{(v_1-\tau)^3}+\frac{\lambda n_2}{(v_2-\tau)^3},\\ y=1.\end{aligned}\right\} \quad (18)$$

The solution is shown qualitatively in Fig. 1 by the abscissas of the points A_1, A_2, A_3, and A_4. As long as the ordinate of point M satisfies $y_M < 1$, the roots τ_1, τ_2, τ_3, and τ_4 are real and different. They represent "phase" velocities of the waves propagating in the slab. Below we refer to the wave corresponding to τ_j as "wave j."

Waves 1 and 2 are "coupled" with stream 1, and waves 3 and 4 are coupled with stream 2. In the case $v_{10} = 0$, $v_{20} \neq 0$, the former are the "backward" and "forward" plasma waves, while the latter are "slow" and "fast" beam waves.

The ordinate of point N can be either larger than or smaller than unity, depending on the values of v_1, n_1, n_2, and v_2. If it is smaller than unity we have $\tau_1 > 0$, and we find that all the waves propagate in the same direction.

When $y_M = 1$ the quantities τ_2 and τ_3 are equal; when $y_M > 1$ they are complex. This corresponds to instability. The threshold for the instability is determined from

$$\left.\begin{aligned}y=1,\\ \frac{dy}{d\tau}=0,\end{aligned}\right\} \quad (19)$$

so that the condition relating the parameters at the boundary and in the instability region is

$$\lambda^{1/3}(n_1^{1/3}+n_2^{1/3})\geqslant(v_2-v_1)^{2/3}. \quad (20)$$

At the boundary we have

$$\tau_2=\tau_3=\alpha_0=v_2-[\lambda n_2(v_2-v_1)]^{1/3}=v_1-[\lambda n_1(v_1-v_2)]^{1/3}, \quad (21)$$

$$\tau_{1,4}=(v_1+v_2-\alpha_0)\left\{1\mp\left[1+\frac{\alpha_0(v_1+v_2)-3v_1v_2}{(v_1+v_2-\alpha_0)^2}\right]^{1/2}\right\}. \quad (22)$$

If $\tau_j = \alpha_j + i\beta_j$ in the instability region, then $\beta_j = 0$ at the boundary.

Let us find the "phase" velocities of waves 2 and 3 in the unstable case. We see from (17) that the phases are given by

$$t-\int_0^z\frac{dz}{\tau_j}=t-\int_0^z\frac{\alpha_j dz}{\alpha_j^2+\beta_j^2}+i\int_0^z\frac{\beta_j dz}{\alpha_j^2+\beta_j^2},$$

so that

$$v_p^{(j)}=z\left(\int_0^z\frac{\alpha_j dz}{\alpha_j^2+\beta_j^2}\right)^{-1}. \quad (23)$$

Since τ_2 and τ_3 are complex conjugates, we have $v_p^{(2)} = v_p^{(3)}$.

Because of the unit functions on the right-hand side of (17), we can classify the solutions of this problem. In accordance with the definition of the unit function, (15), we conclude that in the case $[t - z/v_p^{(j)}] < 0$ we are left with only the constant term on the right-hand side of (17). Since, on the other hand, the phase velocities of the waves are related by

$$v_p^{(1)}<v_p^{(2)}\leqslant v_p^{(3)}<v_p^{(4)},$$

we find that in the {z, t} plane there are four distinct regions of nonvanishing solutions ($v_p^{(2)} < v_p^{(3)}$, correspond-

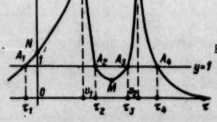

Fig. 1. Graphical solution of the characteristic equation.

ing to stability) or three such regions ($v_p^{(2)} = v_p^{(3)}$, corresponding to instability), and we can replace (17) for each by the equivalent system

$$\frac{\tau_i}{\lambda} - \frac{n_1}{v_1 - \tau_i} - \frac{n_2}{v_2 - \tau_i} = c_{2i}, \quad i = 0, 1, \ldots, k, \tag{24}$$

$$\frac{\tau_j}{\lambda} - \frac{n_1}{v_1 - \tau_j} - \frac{n_2}{v_2 - \tau_j} = c_{2j} + f_j\left(t - \int_0^z \frac{dz}{\tau_j}\right),$$

$$j = (k+1), \ldots, 4, \tag{25}$$

where $0 \leq k \leq 3$.

In the case k = 3 the solution of system (9), (24), and (25) is a simple wave. In fact, Eqs. (9) and (24), in correspondence with the theorem for the existence of implicit functions,[5] give any three quantities in the set n_1, n_2, v_1, v_2 as a function of the fourth. The Jacobian used in this existence theorem turns out to be nonvanishing in all cases in which we can speak of two streams ($n_2 \neq 0$, $v_1 \neq v_2$). Substituting the quantities determined in this manner into (25), we find an equation which gives the fourth quantity as a function of the coordinates and the time.

The simple wave describes the part of the propagation region of the fast wave of the second beam not yet reached by the slow wave of the same beam and, in the case $\tau_1 < 0$, the backward wave of the first beam. The simple wave delineates the region of a "common solution," on the one hand, and the unperturbed region on the other, in accordance with the theorem of ref. 6. The boundaries of the region occupied by the simple wave are described by the inequalities

$$v_p^{(3)} < \frac{z}{t} < v_p^{(4)} \tag{26}$$

($\tau_1 < 0$),

$$z < 0. \tag{26a}$$

In the case k = 0 we can, in principle, determine from system (9), (24) any two quantities as functions of the other two; system (25) then gives these remaining quantities as functions of the time and the coordinate. This solution describes the region in which the fast and slow waves of the second beam interact in the stable regime. If the parameters are such that both $\tau_1 < 0$ and $\tau_2 < 0$ (oppositely directed beams), the interaction of waves 1 and 2 is also covered in this case. The boundaries of the region are given by the inequalities

$$v_p^{(2)} < \frac{z}{t} < v_p^{(3)}, \tag{27}$$

and, in the case $\tau_1 < 0$, $\tau_2 < 0$, by the inequalities

$$0 < \frac{z}{t} < v_p^{(3)}, \tag{27a}$$

$$v_p^{(2)} < \frac{z}{t} < 0. \tag{27b}$$

The case k = 1 leads to three equations of system (25), which describe the region in which the second, third, and fourth waves interact. The boundaries of this region are given by

$$v_p^{(2)} > \frac{z}{t} > \begin{cases} v_p^{(1)}, & v_p^{(1)} > 0, \\ 0, & v_p^{(1)} > 0. \end{cases} \tag{28}$$

The solution with k = 0 holds only in the case $v_p^{(1)} > 0$ and describes the region in which all four waves interact ($0 < z/t < v_p^{(1)}$). The solutions match up in a natural manner at the boundary of the regions if we choose the $u^j(t_0)$ to be continuous functions satisfying $u^j(0) = 0$. This latter condition is a natural condition and does not restrict the generality of the discussion, if we exclude the propagation of discontinuities from this analysis.

In a study of the two-stream instability a case of particular interest is the case k = 1, which describes the region z > 0 in the beam–plasma system for large values of t. The region z < 0 is described by a simple wave here. The simple-wave concept has been used previously[3] to describe the two-stream instability in the k = 1 region; this procedure is valid only in a certain approximation. Let us examine the meaning of this approximation.

As mentioned earlier, in the case k = 1 the solution follows from a system of three equations like (25), while the simple wave is described by a single equation of this type. Accordingly, in two of the equations the f_j must be assumed equal to zero. Let us see whether there is a justification for this assumption.

We can treat the solution with k = 1 as the result of an interaction between unstable waves 2 and 3 propagating against the background of wave 4 and interacting with this background. Since one of the waves (2 or 3) decays while the second grows, at a sufficiently high amplitude of the growing wave the amplitudes of the other waves are negligible in comparison with the amplitude of the growing wave, so that we can neglect them. In this approximation an unstable growing wave delineates the region of unperturbed plasma and is described by a single equation like (25), i.e., it is in fact a simple wave.

We have thus found a general solution for the problem of electron–electron flow in a thin plasma slab. The entire solution can be easily generalized to the case of ion–electron flow.

The initial-condition problem can be solved in similar fashion; a fundamental difference in this case is that we can introduce unit functions over some interval of the z axis only if the functions f_j vanish on this interval. In general, on the other hand, the solution of the problem at any point z and at any time is the result of the interaction of all four waves and is described by a system of equations analogous to (9), (25) in the case k = 0.

---

[1] A. I. Akhiezer and Ya. B. Fainberg, Dokl. Akad. Nauk SSSR, 64, 555 (1949).
[2] D. Bohm and E. P. Gross, Phys. Rev., 75, 1864 (1949).
[3] B. N. Rutkevich, A. V. Pashchenko, V. D. Fedorchenko, and V. N. Muratov, Zh. Tekh. Fiz., 42, 493 (1972) [Sov. Phys. – Tech. Phys., 17, 391 (1972)].
[4] R. Courant, Partial Differential Equations [Russian translation], Izd. Mir, Moscow (1964), pp. 125, 422, 495.
[5] G. M. Fikhtengol'ts, Course in Differential and Integral Calculus [in Russian], Vol. I, Izd. Nauka, Moscow (1966), p. 455.
[6] G. Ya. Lyubarskii and R. V. Polovin, Plasma Physics and the Problems of Controlled Thermonuclear Fusion [in Russian], No. 1, Izd. Akad. Nauk UkrSSR, Kiev (1962), p. 79.
[7] A. V. Pashchenko and B. N. Rutkevich, Zh. Tekh. Fiz., 44, 1151 (1974) [Sov. Phys. – Tech. Phys., 19, 726 (1974)].

Energy balance in Tokamaks in the "plateau–banana" transition region

Yu. N. Dnestrovskii and D. P. Kostomarov

Physics Faculty, M. V. Lomonosov Moscow State University

(Submitted December 14, 1973)
Zh. Tekh. Fiz., 44, 2489-2492 (December 1974)

The transition to a collisionless regime at large currents in modern Tokamaks is investigated by numercial integration of the energy-balance equations. It is shown that the presence of cold neutrals can reduce significantly the plasma ion temperature and impede the transition from the plateau regime to the banana regime.

Theoretical investigations yield significantly different values and scaling of the thermal conductivity, χ_i, for different collision frequencies.[1-3] If the collision frequency is small, i.e.,

$$\tilde{\nu}=\frac{\nu_j}{\nu_B}=20\frac{Rn}{T_j^2}\left(\frac{R}{r}\right)^{3/2}\ll 1 \tag{1}$$

(this is the region of banana orbits for trapped particles; ν_B is the bounce frequency in the banana), then

$$\chi_j\sim\frac{a^2n}{H^2\sqrt{T_j}}, \tag{1a}$$

if

$$\tilde{\nu}_j\gg 1 \tag{2}$$

(plateau region), then

$$\chi_j\sim\frac{T_j^{3/2}q}{H^2}. \tag{2a}$$

Here, R is the major radius of the torus, n is the plasma density in 10^{13} cm^{-3}, T_j is the temperature of the j-th species in eV, and q is the safety factor with respect to MHD stability. At present a number of machines are operating in which the transformation from region (2) to region (1) is possible for the ions. Experimental confirmation of the existence of a banana region and of the scaling in Eq. (1a) will evidently be one of the basic goals of Tokamak research in the next few years. In addition, the complex dependence of all variables on the coordinates and the presence of a series of poorly controllable factors which increase losses (cold neutrals, impurities) require that detailed calculations be carried out in order to compare the results of theory with experiment. Some results of these kinds of calculations (without considering the effect of impurities) are presented in this note.

The following system of equations[4] is used to describe the energy balance:

$$\left.\begin{aligned}\frac{\partial T_i}{\partial t}&=\frac{1}{xn}\frac{\partial}{\partial x}\left(xn\chi_i\frac{\partial T_i}{\partial x}\right)+Q_{ei}-Q_{in},\\ \frac{\partial T_e}{\partial t}&=\frac{1}{xn}\frac{\partial}{\partial x}\left(xn7\gamma\chi_e\frac{\partial T_e}{\partial x}\right)-Q_{ei}-Q_{en}+Q_{\text{joul}},\\ \frac{\partial\mu}{\partial t}&=\frac{A}{x}\frac{\partial}{\partial x}\left[\frac{\gamma}{T_e^{3/2}}\frac{1}{x}\frac{\partial}{\partial x}(x^2\mu)\right].\end{aligned}\right\} \tag{3}$$

Here $x = r/a$, a is the semiminor axis of the torus, t is the time in msec, $\mu = 1/q = RH_\vartheta/rH$, H is the longitudinal magnetic field in kOe, $n = n_0(1 - 0.8x^2)$ $A = 6.1\cdot 10^3/a^2$, $Q_{ei} = Cn/T_e^{3/2}(T_e - T_i)$ is the Coulomb heat exchange between the electrons and ions, Q_{in} and Q_{en} are the thermal losses through the cold neutrals, $Q_{\text{joul}} = (B\gamma/nT_e^{3/2})\cdot[(1/x)(\partial/\partial x)(x^2\mu)]^2$ is the Joule heat, $C = 470/p$, $B = 2\cdot 10^7H^2/R^2$, p is the reduced mass of the plasma ions, γ is the anomalous resistance factor as compared with the classical value, and

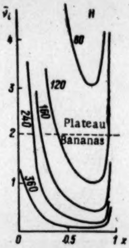

Fig. 1

$$\left.\begin{aligned}\chi_j&=300F_j\frac{nq^2}{a^2H^2\sqrt{T_j}}\left(\frac{R}{r}\right)^{3/2}J(\tilde{\nu}_j),\\ J(\nu)&=0.3\int_0^\infty\frac{e^{-z}z^2dz}{\sqrt{z+\nu^2}},\quad F_i=\sqrt{p},\quad F_e=5\left(\frac{m_e}{m_i}\right)^{1/2}.\end{aligned}\right\} \tag{4}$$

The model kinetic equation of refs. 5 and 6 is used to describe the neutrals in the plasma and to calculate Q_{in} and Q_{en}.

As an example the results of an energy balance calculation for the T-4 device,[7] with parameters R = 90 cm, a = 17 cm, n_0 = 5, and H = 40 kOe, are presented in the figures. Figures 1 and 2 refer to a hydrogen plasma without neutrals. Figure 1 shows the dependence of the ion collision frequency, ν_i, on the spatial coordinate for various plasma currents, I = 80, 120, 160, 240, and 360 kA. The dotted line separates regions (1) and (2). For currents I < 100 kA the curves lie within region (2). The current range 100 < I < 200 kA corresponds to a transition region. For I > 200 kA the major part of the plasma cross section is

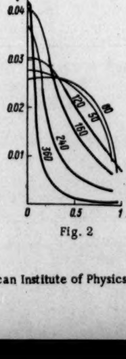

Fig. 2

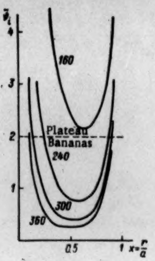

Fig. 3

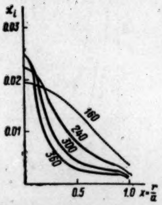

Fig. 4

in region (1) and only in the center of the plasma is $\tilde{\nu}_i$ large.

Figure 2 shows the dependence of the coefficients of ion thermal conductivity, χ_i (Eq. 4), on x for the same parameter ranges. The thick parts of the curves correspond to region (1). For small currents [region (2)] χ_i increases with current. In this case $T_i \sim I$, $\chi_i \sim I^{1/2}$ (Eq. 2a). In the transition to regime (1), χ_i begins to fall off rapidly as the current increases; however, this reduction is not uniform over the plasma cross section. For currents, $I \sim 150$ kA, χ_i is as large as before over the bulk of the plasma and only the peripheral region of the plasma forms a thermally insulating layer. In the transition region for the current, regime (1) still does not hold for the ring as a whole. For currents $I > 200$ kA the thickness of the thermally insulating shell becomes comparable to the plasma radius and the discharge goes over to region (1).

The presence of cold neutrals impedes the transition to a banana regime. Figures 3 and 4 show the analogous distributions of $\tilde{\nu}_i$ and χ_i with respect to radius for various currents for a reasonable vacuum value of the neutral density, $N = 5 \cdot 10^9$ cm^{-3}. It is clear that only at large currents, $I > 300$ kA, can we expect a transition into regime (1). Even larger currents are required for a deuterium plasma to enter the banana regime. Figure 5 shows the dependence of the maximum ion temperature, $T_{i\max}$, on the current for hydrogen (H) and deuterium (D) plasmas for the cases N = 0 and $5 \cdot 10^9$ cm^{-3} (curves 1 and 2, respectively). The behavior of the curves for N = 0 corresponds to the above noted features of the transition from regime (2) to regime (1). For a hydrogen plasma at $I < 120$ kA, $T_{i\max}$ shows a linear dependence on the current. Artsimovich's formula, $T_i \sim I^{1/3}$, for a density of $n_0 = 5$ applies poorly since the ratio $\delta = (T_e - T_i/T_e)$ is small (for a hydrogen plasma at I = 100 kA, $\delta \sim 0.2$). For currents, $I > 150$, kA $T_{i\max}$ increases more rapidly than linearly, which agrees with the estimate for regime (1): $T_i \sim 0.01\ (I^2/p^{3/2})\ (R/a)^{1/2}$.

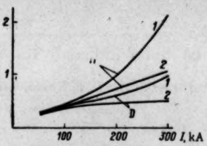

Fig. 5

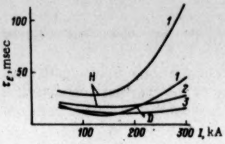

Fig. 6

For a neutral density $N \sim 5 \cdot 10^9$ cm^{-3} the linear behavior of $T_{i\max}$ as a function of the current, I is maintained up to $I \sim 300$ kA, and it is difficult to define the transition into the banana regime in terms of the ion temperature alone in this case.

The dependence of the energy lifetime, τ_E, on the current for the same discharge parameters is shown in Fig. 6. At low neutral densities experimental measurements in regime (1) are complicated by the large values of τ_E. For $I \sim 300$ kA, $\tau_E \sim 100$ msec, and in order to establish a stationary regime it is necessary to keep the current constant over 200-300 msec.

Thus, the transition to the banana regime is possible in T-4 devices; however, experimental confirmation of such a transition requires large currents ($I \sim 300$ kA), a high vacuum ($N \leqslant 10^9$ cm^{-3}), and a long discharge. We note that when the plasma density is increased and the torus radius is small the effect of the remaining gas on the energy balance decreases. In this case the transition to a banana regime may be easier.

The present work was done at the suggestion of the late Academician L. A. Artsimovich.

---

[1] A. A. Galeev and R. Z. Sagdeev, Zh. Eksp. Teor. Fiz., 53, 348 (1967) [Sov. Phys. – JETP, 26, 233 (1968)].

[2] L. M. Kovrizhnykh, Zh. Eksp. Teor. Fiz., 56, 877 (1969) [Sov. Phys. – JETP, 29, 475 (1968)].

[3] M. N. Rosenbluth, R. D. Hazeltine, and F. L. Hinton, Phys. Fluids, 15, 116 (1972).

[4] Yu. (Y.) N. Dnestrovskii, D. P. Kostomarov, and N. L. Pavlova, in: Fourth European Conf. on Thermonuclear Reactions and Plasma Physics, Rome (1970), p. 4.

[5] Yu. N. Dnestrovskii, D. P. Kostomarov, and N. L. Pavlova, Atom. Energ., 32, 301 (1972).

[6] Yu. (Y.) N. Dnestrovskii, D. P. Kostomarov, N. V. Karetkina, N. L. Pavlova, and A. M. Popov, in: Sixth European Conf. on Thermonuclear Reactions and Plasma Physics, Moscow (1973), p. 42.

[7] L. A. Artsimovich, V. A. Vershkov, A. V. Glukhov, E. P. Gorbunov, V. S. Zaveryaev, S. E. Lysenko, S. V. Mirnov, I. V. Semenov, and V. S. Strelkov, in: Plasma Physics and Controlled Nuclear Fusion Research, Vol. 1, Vienna, IAEA (1971), p. 443.

Anisotropic plasma heating near the lower hybrid frequency

V. M. Glagolev, V. V. Martynenko, and Yu. V. Skosyrev

(Submitted September 6, 1973; resubmitted March 23, 1974)
Zh. Tekh. Fiz., 44, 2493-2499 (December 1974)

The ion and electron energy components associated with the transverse and longitudinal motion with respect to a fixed magnetic field are measured in the heating of a plasma with a density of 10^{12} cm^{-3} at a frequency near the lower hybrid frequency. The transverse energy of the particles is determined with a multigrid probe which measures the currents parallel to the magnetic field. The method for finding the energy is based on the effect of the magnetic field at the probe on the voltage–current characteristics of the probe. The plasma is heated by the excitation of ordinary and extraordinary waves at the plasma surface by means of a coupling loop and the subsequent transformation of these waves into plasma waves. Measurements show that the average ion energy associated with the motion across the magnetic field is equal to the total transverse energy of the plasma found from the diamagnetic signal. Thus, the transverse energy of the ion component increases in the heating process. The average ion energy, measured from the spectrum of charge-exchange neutrals over the range 0.5-3 keV, is 250 eV, in good agreement with the results obtained by the method described above. The transverse electron energy is much lower than the transverse ion energy. It is found experimentally that both transverse and longitudinal ion heating occur in a homogeneous magnetic field.

INTRODUCTION

Recent theoretical[1,2] and experimental[3-5] work has shown that one of the most promising methods for increasing the energy of plasma ions is plasma heating at a frequency near the lower hybrid frequency. The ion heating results from Cerenkov absorption of energy from the plasma waves which appear in the linear transformation of electromagnetic waves or from nonlinear effects, e.g., parametric instabilities. Since a plasma wave propagates nearly perpendicularly to the magnetic field near the lower hybrid resonance, the transverse ion energy increases. The Cerenkov absorption of electromagnetic waves by magnetized electrons tends to build up the longitudinal electron energy.

It has been reported[6] that the plasma diamagnetism increases when the plasma is subjected to a high-frequency electric field. A study of the propagation conditions for electromagnetic waves near the lower hybrid resonance is reported in ref. 7. The observed retardation and strengthening of the electric field of the ordinary (type E) wave during heating verify the suggestion that the plasma heating is due to wave transformation. On the other hand, the relative number of ions which are heated, the ratio of the longitudinal and transverse ion energies, and whether the transverse electron energy increases during the heating are not resolved.

We report here measurements of the transverse ion and electron energy in plasma heating at a frequency near the lower hybrid frequency. The idea behind these measurements is that as the magnetic field at the multigrid probe changes, there are changes in the voltage–current characteristics of the probe, since the inhomogeneity of the magnetic field affects the motion of charged particles.

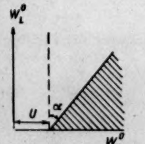

Fig. 1. Particles whose energies correspond to the hatched region strike the collector of the probe if the probe is in a relatively strong magnetic field.

A similar method for measuring the transverse ion energy is proposed in ref. 8, and a similar method for the transverse electron energy is proposed in ref. 9. The probe used in the present experiments is structurally similar to that of refs. 10 and 11. The probe has three grids and a collector; the particles enter through apertures with diameter smaller than the Debye length.

THEORY FOR THE MEASUREMENT METHOD

1. Probe in a relatively strong magnetic field. We denote by H_0 the magnetic field in the part of the plasma in which we are to determine the transverse energy of the particles, and we denote that near the probe by $(H_0 + \Delta H)$; here $\Delta H > 0$. If U is the retarding potential of the probe, the particles reach the collector when $W_\parallel^0 > W_\perp^0 \Delta H/H + U$, where $W_\parallel^0$ and $W_\perp^0$ are the longitudinal and transverse energies of the particle in the field H_0. The hatched region in Fig. 1 shows the energies of particles which reach the collector for the specified value of U; here $\tan\alpha = \Delta H/H_0$. The density of the current collected by the probe along the magnetic field is

$$j_\parallel = 2\pi \int\limits_{W_\perp=0}^{\infty} F_\perp(W_\perp)\,dW_\perp \int\limits_{U+W_\perp^0(\Delta H/H_0)}^{\infty} F_\parallel(W_\parallel)\,dW_\parallel,$$

where the distributions with respect to transverse energy, $F_\perp(W_\perp)$, and with respect to longitudinal energy, $F_\parallel(W_\parallel)$, are assumed to be Maxwellian:

$$F_\perp(W_\perp) = Ae^{-W_\perp/T_\perp};\quad F_\parallel = Be^{-W_\parallel/T_\parallel}.$$

When U = 0, ΔH = 0 the current density at the probe reaches a maximum:

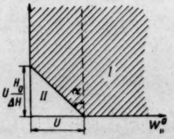

Fig. 2. The same as Fig. 1, for the case in which the probe is in a relatively weak magnetic field.

$$j_{\max}=2\pi\int_{\infty}^{\infty}F_{\perp}(W_{\perp})\,dW_{\perp}\int_{0}^{\infty}F_{\parallel}(W_{\parallel})\,dW_{\parallel}=2\pi ABT_{\parallel}T_{\perp}.$$

Then we have

$$\frac{j_{\parallel}}{j_{\max}}=\frac{1}{T_{\parallel}T_{\perp}}\int_{0}^{\infty}e^{-W_{\perp}/T_{\perp}}dW_{\perp}\int_{U+W_{\perp}(\Delta H/H_0)}^{\infty}e^{-\frac{W_{\parallel}}{T_{\parallel}}}dW_{\parallel},$$

and

$$\frac{j_{\parallel}}{j_{\max}}=e^{-U/T_{\parallel}}\frac{1}{1+\varkappa},\ \text{where}\ \ \varkappa=\frac{T_{\perp}}{T_{\parallel}}\frac{\Delta H}{H_0}.$$

Comparing this function with the function

$$j_{\parallel}=j_{\max}e^{-U/T_{\parallel}}$$

corresponding to a homogeneous magnetic field, we see that the nature of the functional dependence does not change when the field at the probe is strengthened, and the maximum current decreases.

2. Probe in a relatively weak magnetic field. If the magnetic field near the collector is weaker than that in the heating region, and if the retarding potential is zero, all the particles reach the collector, regardless of the field strength. If $U > W_{\perp}^{0}(\Delta H/H_0)$, the collector collects particles whose longitudinal energies satisfy

$$W_{\parallel}^{0}>U-W_{\perp}^{0}\frac{\Delta H}{H_0}.$$

If $W_{\perp}^{0}(\Delta H/H_0) > U$, all the particles reach the collector. Particles whose energies correspond to the hatched region in the plot of $W_{\parallel}^{0}$ vs $W_{\perp}^{0}$ in Fig. 2 reach the collector. We divide the first quadrant in Fig. 2 into two regions, I (the region in which particles do not reach the collector) and II (the region in which particles do reach the collector). The current drawn by the collector, which is due to particles in region I, is conveniently written $j_{\parallel}^{\mathrm{I}} = j_{\parallel}^{\mathrm{I+II}} - j_{\parallel}^{\mathrm{II}}$, where $j^{\mathrm{I+II}}$ is the total current which would be drawn by the collector if all the particles reached it, and $j_{\parallel}^{\mathrm{II}}$ is the current associated with the particles which are in fact prevented from reaching the collector by the retarding field:

$$j_{\parallel}^{I+II}=j_{\max}=2\pi\int_{0}^{\infty}F_{\perp}dW_{\perp}\int_{0}^{\infty}F_{\parallel}dW_{\parallel}=2\pi ABT_{\perp}T_{\parallel},$$

$$j_{\parallel}^{II}=2\pi\int_{0}^{U(H/\Delta H)}F_{\perp}dW_{\perp}^{0}\int_{W_{\parallel}=0}^{U-W_{\perp}^{0}(\Delta H/H_0)}F_{\parallel}dW_{\parallel}^{0}.$$

Assuming $F_{\perp}$ and $F_{\parallel}$ to be Maxwell distributions, as in subsection 1, we find

$$j_{\parallel}^{II}=2\pi ABT_{\parallel}\int_{0}^{U(H/\Delta H)}e^{-\frac{W_{\perp}}{T}}\left[1-e^{-\frac{U}{T_{\parallel}}+\frac{W_{\perp}^{0}}{T_{\parallel}}\frac{\Delta H}{H_0}}\right]dW_{\perp}^{0}.$$

Integrating, we find

$$j_{\parallel}^{II}=\frac{j_{\max}e^{-\frac{U}{T_{\parallel}}}}{1-\varkappa}\left(1-\varkappa e^{-\frac{U}{T_{\parallel}}\frac{1-\varkappa}{\varkappa}}\right),$$

$$j_{\parallel}^{II}=2\pi ABT_{\parallel}T_{\perp}\left\{1-\frac{e^{-\frac{U}{T_{\parallel}}}-\varkappa e^{-\frac{u}{T_{\parallel}\varkappa}}}{1-\varkappa}\right\}.$$

Let us examine some particular cases. (1) $\varkappa \ll 1$ as $\Delta H \to 0$; then $j_{\parallel}^{\mathrm{I}} = j_{\max}e^{-u/T_{\parallel}}$. (2) $\varkappa \gg 1$, $j_{\parallel}^{1} \simeq j_{\max}$ (regardless of the magnetic field, all the particles overcome the retarding potential U). (3) $\varkappa - 1 \to 0$, $j = j_{\max}e^{-u/T_{\parallel}}(1 + U/T_{\parallel})$, i.e., the collector current is rich in high-energy particles. (4) When U = 0 we have $j = j_{\max}$, regardless of the magnetic field, since all the particles reach the collector.

Accordingly, when the field is relatively weak near the probe and the particles have a Maxwellian energy distribution the collector current is rich in high-energy particles. This effect should be observed when $\varkappa \sim 1$. Since $\Delta H/H \lessdot 1$, the larger values of $\varkappa$ correspond to $T_{\perp}/T_{\parallel} \gtrdot 1$ (a pronounced anisotropy). A greater enrichment with energetic particles is found in the case $U/T_{\parallel} \gtrdot 1$. Figure 3 shows the calculated function $f(x)$ for various values of $\varkappa$, according to

$$f(x)=\frac{e^{-x}}{1-\varkappa}\left[1-\varkappa e^{-x\frac{(1-\varkappa)}{\varkappa}}\right].$$

A TEST OF THE METHOD

To test the method we use an electron beam in which the transverse and longitudinal energies can be regulated independently. The beam is produced by an electron gun having two close-space electrodes (a few Larmor radii apart): a hot cathode and anode with a small aperture, 1 mm in diameter. An external magnetic field of ~300 Oe is used for focusing. The gun is rotated around the axis perpendicular to the magnetic field in order to produce beams with different values of the ratio $v_{\perp}/v_{\parallel}$. The longitudinal beam energy is calculated from the longitudinal magnetic fields at which the beam is focused onto a screen covered with a phosphor, held a known distance from the gun. With the screen at an oblique angle with respect to the magnetic field the electron beam traces out an arc of a Larmor circle. By measuring the radius of this circle we find the transverse energy of the beam. The longitudinal and transverse beam energies found in this manner are compared with the values obtained from the voltage–current characteristics of the multigrid probe in magnetic fields which are weak and strong with respect to that at the gun. Figure 4 shows typical characteristics. This figure shows, on an arbitrary scale, the current drawn by the collector of the multigrid probe as a function of the retarding potential. The beam makes an angle of 20° with the magnetic field. Curve a is obtained in a homogeneous field, while curve b corresponds to a relative reduction of $\Delta H = 0.47H_0$ in the field at the probe position. From the retarding potential which causes the electron current to

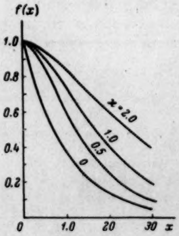

Fig. 3. The function $f(x) = e^{-x}(1-\varkappa)^{-1}[1-\varkappa e^{-x(1-\varkappa)/\varkappa}]$, which is representative of the current drawn by the probe as a function of the retarding potential.

drop to 0.5 of its maximum value (at the plateau), we find the transverse energy to be 30 eV. This result is consistent with the transverse energy corresponding to the angular position of the gun and determined from the measurements of the Larmor radius. The transverse beam energy $W_\perp^1$ in a homogeneous field is determined from

$$W_\perp^1 = (W_\parallel^1 - W_\parallel^2)\frac{H_0}{\Delta H},$$

where $W_\parallel^1$ (the longitudinal particle energy in field H_0) and $W_\parallel^2$ (the longitudinal energy of the particles in a field which is weaker than the homogeneous field by ΔH) are found from the retarding potential corresponding to a reduction by a factor of the current drawn by the collector of the multigrid probe. As the particles pass through the entrance apertures and the grids of the multigrid analyzer their energy distribution changes.[12] Experiments with electron beams show that the particle-detection efficiency decreases with increasing angle between the velocity of the particles and the magnetic field. The particle current drawn by the collector at an angle of 45° is several times smaller than that corresponding to an angle of 10°, for a given emission current. To reduce this error we use a procedure which exploits a difference between the characteristics of a probe in a homogeneous magnetic field from those of a probe in a highly inhomogeneous field. In a relatively weak field the transverse particle energy is converted into longitudinal energy in accordance with conservation of the magnetic moment, and the conditions for transmission through the grids of the probe are degraded. Then the particle distribution can be enriched by particles with large longitudinal velocities. In plasma experiments an additional source of systematic errors is the difference between the times required for particles with different energies to traverse the distance between the region in which the particles are produced and the region in which they are detected. To reduce this error we measure the current drawn by the collector of the probe at the time at which this current is a maximum. Taking these errors into account we conclude that the errors in the measurement of the transverse energy of particles by this method are ~10% in experiments with electron beams and ~20% in experiments with plasmas.

MEASUREMENT OF THE ANISOTROPY IN THE PLASMA HEATING

The experimental apparatus is shown schematically in Fig. 5; it is described in detail in ref. 6. The plasma 7, produced in a discharge on the surface of a hydrogen-saturated titanium disk 1, propagates along the lines of force of homogeneous magnetic field 2 and enters the heating region. The plasma is heated by coupling loop 3, which carries an rf current (f = 140 MHz). This coupling loop is part of a heating resonator formed by two-conductor line 4, connected to the rf oscillator. When coils 5 are activated a mirror field with a mirror ratio of 1.5 is produced in the heating region. It is shown in ref. 6 that when a plasma is heated in a mirror system the plasma energy increases to a value 1.5 to 2 times that of a plasma heated in a homogeneous field. Multigrid probe 6 is located behind the mirror coil, ~1.5 m from the heating region. The maximum magnetic field in the heating region is 3 kOe; a field of 2.2 kOe corresponds to the lower hybrid resonance of a dense plasma, i.e., to $\omega^2 = \omega_{He}\omega_{Hi}$, where $\omega = 2\pi f$, and ω_{He} and ω_{Hi} are the electron and ion gyrofrequencies. Because of the limited power supplying the magnetic-field coils we are not able to exceed a field of 1.8 kOe at the probe. The transverse energy of the particles is determined by comparing the characteristics of probes in magnetic fields of 1.7 kOe and 40 Oe. The transverse energy of the particles in the heating region, where the magnetic field is 3 kOe, is calculated from the transverse energy in a field of 1.7 kOe, with conservation of energy and the magnetic moment of the particles taken into account. As mentioned above, the total current in the fringing-field region is equal to the total current in the heating region. The current collected by the probe falls off in inverse proportion to the magnetic field; at a field of 40 Oe it is lower than the current in a field of 1.7 kOe by a factor of ~40. The difference is due to the spreading of the plasma along the lines of force of the weakened field. Since the calculated curves do not incorporate the changes in the current density in the fringing field, the probe characteristics in a field of 40 Oe are normalized so that the ion currents for a retarding potential of 100 V and the electron currents at zero potential coincide. A potential of 100 V is selected because it is near this potential that there is a break in the voltage–current characteristic due to the potential of the sheath which accelerates ions near the entrance grid of the probe.

Figure 6 shows the basic results of the measurements of the heating anisotropy. This figure shows, on an arbitrary scale, the ion current I_j and the electron current I_e drawn by the collector of the multigrid probe as a function of the potential on the retarding grid of the probe. The solid curves are experimental; curves 1 and 3 pertain to a field of 1.7 kOe, and curves 2 and 4 to a field of 40 Oe. Dashed curves a and b are calculated (they are of the same nature as the curves in Fig. 3). Curve a shows how the retarding potential affects the probe current corresponding to ions with a Maxwellian longitudinal-velocity distribution with $T_\parallel$ = 330 eV and $\varkappa$ = 0. Calculated curve b is the same, except that $\varkappa$ = 0.5. The experimental error is reduced through the use of a strong variation in the

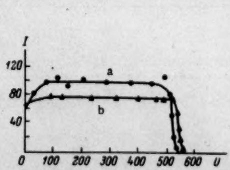

Fig. 4. Typical voltage–current characteristic for a multigrid probe used to check the measurement method.

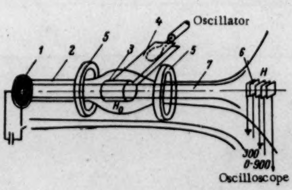

Fig. 5. The experimental apparatus.

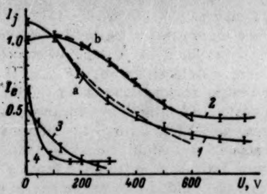

Fig. 6. Voltage–current characteristics for the ion current I_j and the electron current I_e from the heated plasma.

magnetic field ($\Delta H \simeq H$), since the differences between the experimental curves are more distinct in this case. On the other hand, since $\Delta H \simeq H$, then $\varkappa = T_\perp / T_\parallel$. The transverse ion temperature in the heating region in a magnetic field of 3 kOe is calculated to be $T^0_{\perp j} = 280$ eV with $T^0_{\parallel j} = 210$ eV under the assumption that the adiabatic invariant is conserved. Similar measurements carried out for heating in a homogeneous field reveal $T^0_{\perp j} = 150$ eV at $T^0_{\parallel j} = 250$ eV, i.e., $T_\perp / T_\parallel = 0.6$. These measurements show that the ions acquire longitudinal as well as transverse energy in the heating. The transverse energy of ions at the center of the mirror system found from measurements of the charge-exchange current is 300 eV, in agreement with measurements by the method described above. The ratio $(T^0_\perp + T^0_\parallel)/T^0_\perp = 1.75$ is comparable to the mirror ratio (1.5). Figure 6 shows, along with the ion-current characteristics, the electron current (arbitrary scale) drawn by the probe collector as a function of the retarding potential. The average electron energy calculated from curve 3, recorded in a field of 1.7 kOe, is 120 eV. Curve 4 is obtained with a magnetic field of 40 Oe at the probe; the average electron energy calculated from this curve is 40 eV. The decrease in the average electron energy in the fringing field is evidently due to the circumstance that the electrons are heated in the surface layer of the plasma.[6] The electron temperature is a minimum at the center of the plasma. In the fringing field the electrons striking the probe come from the central region and the average electron energy decreases. We can thus assume that the transverse energy of the electrons is low. This conclusion is supported by the argument[6] that the plasma diamagnetism is due to the ion component. We can summarize the experimental results as follows:

(1) The "transverse" ion temperature, determined from the charge-exchange spectrum at energies 0.5-3 keV, agrees with the temperature measured by the procedure of this paper.

(2) The average energy of the plasma ions is raised by heating.

(3) The ion energy spectrum becomes enriched with high-energy ions in comparison with a Maxwellian spectrum.

(4) The transverse plasma energy is concentrated in the ion component ($T_{\perp j} \gg T_{\perp e}$).

(5) $T_{\perp j} \simeq 1.5\, T_{\parallel j}$ for heating in a mirror field; $T_{\perp j} = 0.6\, T_{\parallel j} = 150$ eV for heating in a homogeneous field.

DISCUSSION OF RESULTS

The experimentally demonstrated low transverse electron energy can be explained under the assumption that for these experimental conditions, i.e., $\omega_{Hi} < \omega < \omega_{He}$, the electrons are magnetized and do not absorb energy in the propagation of the ordinary wave launched by the coupling loop. The observed "longitudinal" heating of the electrons can be attributed to a Cerenkov interaction due to oblique propagation with the wave. The electromagnetic wave is transformed into plasma waves, which propagate nearly perpendicularly to the magnetic field. When $\omega \gg \omega_{Hi}$ the magnetic field has little effect on the ion motion, so that the Cerenkov interaction should lead to a transverse heating of the ion component, as observed experimentally. However, this mechanism for the determination of the ion energies does not explain the observed longitudinal ion heating. Further experiments are necessary to clarify the heating mechanism.

In conclusion the authors thank N. A. Krivov for assistance in the experiments.

---

[1] V. M. Glagolev, Plasma Physics, Part I, 14, 301 (1972); Plasma Physics, Part II, 14, 315 (1972).

[2] A. V. Longinov and K. N. Stepanov, Preprint 72-1, Khar'kov Physicotechnical Institute (1972).

[3] Yu. V. Skosyrev, N. A. Krivov, and V. M. Glagolev, Report to the Sixth European Conference on Plasma Physics and the Problem of Controlled Thermonuclear Fusion, Moscow, 1973.

[4] V. F. Tarasenko, A. B. Kitsenko, V. I. Panchenko, and K. N. Stepanov, Zh. Tekh. Fiz., 42, 1996 (1972) [Sov. Phys. – Tech. Phys., 17, 1599 (1973)].

[5] Y. Terumichi and Y. Katagawa, J. Phys. Soc. Japan., 35, 1273 (1973).

[6] V. M. Glagolev, N. A. Krivov, and Yu. V. Skosyrev, Report to Fourth Intern. Conf. on Plasma Physics and Controlled Thermonuclear Research, Madison, 1971, p. 859.

[7] Yu. V. Skosyrev, N. A. Krivov, and V. M. Glagolev, Atom. Energ., 35, 260 (1973).

[8] R. G. Chambers, Preprint CLM-P295, Culham Laboratory (1971).

[9] N. Yamomota and Y. Hatta, Appl. Phys. Lett., 17, 512 (1970).

[10] E. A. Lobikov and A. I. Nastyukha, Zh. Tekh. Fiz., 32, 122 (1962).

[11] D. G. Bulyginskii, B. V. Galaktionov, K. A. Dolmatova, and V. A. Ovsynnikov, Zh. Tekh. Fiz., 33, 183 (1963) [Sov. Phys. – JETP, 8, 131 (1963)].

[12] V. I. Aref'ev, Zh. Eksp. Teor. Fiz., 55, 679 (1968) [Sov. Phys. – JETP, 28, 354 (1969)].

[13] A. I. Pyatak, V. L. Sizonenko, and K. N. Stepanov, Zh. Tekh. Fiz., 43, 475 (1973) [Sov. Phys. – Tech. Phys., 18, 304 (1973)].

Interaction of a hollow electron beam with a plasma

N. M. Zemlyanskii, A. K. Berezin, Ya. B. Fainberg, L. I. Bolotin, and S. S. Krivulya

(Submitted September 12, 1973; resubmitted March 4, 1974)
Zh. Tekh. Fiz., 44, 2500-2503 (December 1974)

An experimental study has been made of the intereaction of a high-current electron beam with a plasma in a longitudinal magnetic field. When the plasma density is lower than the beam density instabilities are excited by the Cerenkov effect.

Instabilities in a beam–plasma system can be caused by the anomalous and normal Doppler effects, and by the Cerenkov effect. When an electron beam interacts with a plasma whose density n_p is lower than the beam density n_b, instabilities are excited because of the anomalous Doppler effect.[1-3] The excitation conditions and frequency spectra are examined in ref. 3; the frequencies are

$$\omega_m = \frac{\pi v_0 m}{L(1+\alpha^{-1/2})}, \tag{1}$$

where $\alpha = n_p/n_b$; L is the interaction length; n = 1, 2, 3, ... ; and v_0 is the beam velocity.

It follows from (1) that a) harmonics are excited and b) the frequency is a linear function of the beam velocity. If $n_p > n_b$, instabilities are excited because of the Cerenkov effect. The instability condition is the equality of the beam velocity v_0 and the slow-wave phase velocity in a hollow plasma waveguide, v_h. In a strong magnetic field ($\omega < \omega_0 < \omega_{He}$) we can write this condition, by analogy with refs. 2 and 4, in the following form:

$$v_0 \simeq v_h = c\left[1 + \frac{(1+|\varepsilon_\parallel|)\lambda_p^2 c^2}{|\varepsilon_\parallel|\omega_0^2 a^2}\right]^{-1/2}, \tag{2}$$

where $|\varepsilon_\parallel| = [(\omega_0^2/\omega^2) - 1]$, c is the speed of light in vacuum, ω is the frequency, ω_{He} is the electron gyrofrequency, ω_p is the electron plasma frequency, a is the waveguide radius, and λ_p is a constant governed by the boundary conditions.[5] From this equation we can determine the critical plasma density n_p^* for the onset of the Cerenkov instability. If the beam electrons have a velocity $v_0 = 0.5c$ and if $\omega = 3 \cdot 10^9$ sec^{-1} we find $n_p^* = 6 \cdot 10^{10}$ cm^{-3}.

Figure 1 shows a block diagram of the experimental apparatus, described in ref. 6. The electron beam interacts with the plasma in a cylindrical chamber 7 cm in diameter and 100 cm long, in a homogeneous external magnetic field from 500 to 1200 G. Probes to detect the E_r and H_φ components of the electromagnetic field are located along the chamber. The plasma density is measured by the "open-resonator" method.[7]

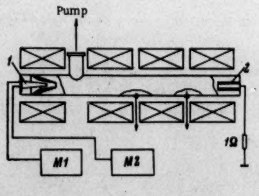

Fig. 1. The experimental apparatus.

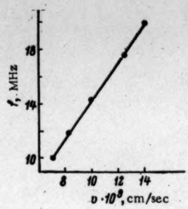

Fig. 2. Frequency of the oscillations as a function of the velocity of the beam electrons ($n_b > n_p$).

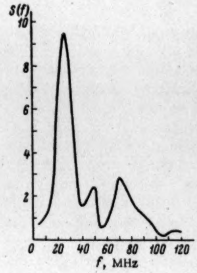

Fig. 3. Frequency spectrum $n_b > n_p$.

The electron beam is produced by magnetron gun 1, which produces a 100 A beam at a voltage of 100 kV. It has an annular cross section, an inside diameter of 2.5 cm, and an outside diameter of 3.5 cm. The gun is fed by two modulators; modulator M-1 produces a voltage pulse 120 μsec long, while M-2 produces a pulse 2.5 μsec long. The first current pulse (15 A and 20 keV) produces plasma as it passes through the working gas (hydrogen); the primary beam (100 A and 100 keV) interacts with this

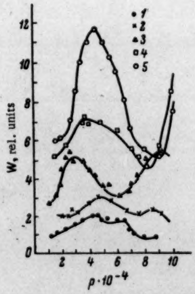

Fig. 4. Power of the instabilities as a function of the pressure p and beam power W ($n_b > n_p$). 1) 2.4; 2) 3.5; 3) 4.8; 4) 6.3; 5) 8 MW.

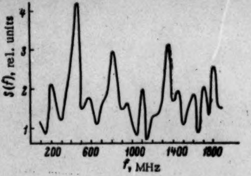

Fig. 5. Spectrum ($n_b > n_p$).

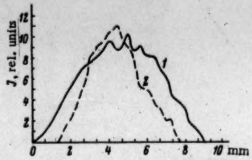

Fig. 6. Profile of the electron beam. 1) Before the interaction with the plasma; 2) after.

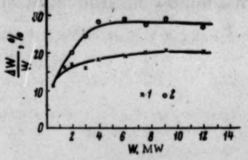

Fig. 7. Relative energy loss of the beam as a function of the beam power. 1) $n_p = 7 \cdot 10^{10}$; 2) $2 \cdot 10^{11}$ cm^{-3}.

plasma. The delay between the ignition and primary pulses can be adjusted from 0 to 2 msec, so that the interaction of the electron beam with plasmas of various densities can be studied. The energy lost by the beam as it passes through the plasma is measured by a thermal probe – a platinum foil 10 × 20 mm in area and 50 μ thick, located behind a radial slit cut in collector 2 in such a manner that about 1/10 of the beam electrons reach the foil. Because of this radial slit the electron current drawn by the thermal probe remains constant as the diameter of the current tube is changed. After the beam passes through the plasma its profile is recorded by x-ray photography, and the x-ray image is studied photometrically. The frequency spectra excited in the system are determined with a computer. In a beam–plasma interaction with $n_p < n_b$ the oscillations excited in the plasma are due to the anomalous Doppler effect, at the frequencies given in (1). Figure 2 shows the frequency as a function of the velocity of the beam electrons. Figure 3 shows a typical spectrum obtained with $v_0 = 1.5 \cdot 10^{10}$ cm/sec, $\alpha = 0.2$, and L = 100 cm. Figure 4 shows the power associated with these oscillations as a function of the gas pressure for various beam power levels. We see that the oscillation power increases with the beam power. In this case the efficiency of the beam–plasma interaction does not exceed 4%. As the beam passes through a plasma with density higher than n^*_p, an instability occurs as a result of the Cerenkov effect. The spectrum is much broader than that in the case $n_p < n_b$ and is shifted toward higher frequencies (Fig. 5). It follows from measurements of the beam profile that the beam narrows after passing through the plasma (Fig. 6). Figure 7 shows the relative energy loss of the beam as a function of the beam power for the case of the oscillations resulting from the Cerenkov effect. The interaction is most efficiency in a narrow pressure range (2.10^{-5}–$7 \cdot 10^{-5}$ torr). Similar results are reported in ref. 8.

Accordingly, in this study of the collective interaction of an intense hollow electron beam with a plasma we have found that the interaction is due to the anomalous Doppler effect in the case $n_p < n_b$. The corresponding efficiency is less than 4%. In the case $n_b < n_p$, the oscillations which are excited are due to the Cerenkov effect, and the efficiency reaches 28%.

---

[1] Ya. B. Fainberg, Atom. Energ., 11, 313 (1961).

[2] A. K. Berezin, Ya. B. Fainberg, L. I. Bolotin, G. P. Berezina, I. A. Bezyazychnyi (Bezÿazychnyi), V. I. Kurilko, V. D. Shapiro, V. P. Zeidlits, and I. Ulshmid, Plasma Physics and Controlled Nuclear Fusion Research, Vol. 2 (1969), p. 723.

[3] M. V. Nezlin, Zh. Eksp. Teor. Fiz., 50, 349 (1966) [Sov. Phys. – JETP, 23, 232 (1966)].

[4] A. S. Bogdankevich and A. A. Rukhadze, Usp. Fiz. Nauk, 103, 64 (1971) [sic]; 103, 609 (1971) [Sov. Phys. – Usp., 14, 163 (1971)].

[5] S. S. Kalmykova and V. I. Kurilko, in: Plasma Physics and Problems of Controlled Thermonuclear Fusion [in Russian], Vol. 4, Izd. Akad. Nauk UkrSSR, Kiev (1965), p. 68.

[6] S. S. Krivulya, A. K. Berezin, Ya. B. Fainberg, L. I. Bolotin, and N. M. Zemlyanskii, Proc. of the Ninth Intern. Conf. on Phenomena in Ionized Gases, Bucharest, 1970 [in Russian], p. 577.

[7] A. I. Anisimov, Zh. Tekh. Fiz., 35, 2042 (1965) [Sov. Phys. – Tech. Phys., 10, 1566 (1966)].

[8] N. I. Leont'ev, A. P. Timoshenko, and Yu. K. Udovichenko, Zh. Tekh. Fiz., 40, 942 (1970) [Sov. Phys. – Tech. Phys., 15, 728 (1970)].

Low-pressure self-maintained discharge with suppressed electron drift. I

V. K. Kalashnikov and Yu. V. Sanochkin

(Submitted January 8, 1973; resubmitted July 8, 1973)
Zh. Tekh. Fiz., 44, 2504-2511 (December 1974)

The structure of the anode sheath in a low-pressure, high-voltage discharge with a suppressed Hall current is analyzed in the diffusion approximation. "Weak effects," e.g., the functional dependence of the ionization coefficient on the electron energy, the inelastic energy loss, and the existence of an electron-depleted region, are shown to have a significant influence on the discharge characteristics. It is shown that the properties of the sheath are essentially independent of the choice of initial conditions (over certain ranges of these conditions).

Discharges in strong transverse magnetic fields with suppressed electron drift have been studied in Penning cells and straight or inverted magnetrons (see, e.g., refs. 1 and 2). The recently intensified interest in such discharges stems from their important applications in producing and accelerating intense ion beams.[3] Because of the low conductivity across the magnetic field, at pressures $p < 10^{-3}$ torr, the discharge current does not exceed a few milliamperes per square centimeter while the density of the Hall current is several orders of magnitude higher (by a factor of $\omega_e \tau_e$), for typical discharge voltages φ_0 at the kilovolt level. For typical magnetic fields $H \leqslant 1$ kOe the electron density is of the order of $n_e \leqslant 10^{10}$ cm^{-3} and is independent of the pressure. Under these conditions the discharge is highly inhomogeneous. A sheath of negative space charge forms near the anode; this consists of magnetized electrons and the thickness is of the order of the Larmor radius of electrons with energy $e\varphi_0$. The entire discharge voltage appears in the voltage drop across this sheath. A one-dimensional theory for the low-pressure anode sheath is derived in refs. 2, 4, and 5 (for a system homogeneous in the direction of the magnetic field and in the electron-drift direction). Several factors are not incorporated in this derivation, e.g., the calculations involved in an analysis of the structure of the sheath are simplified by neglecting the electron energy equation. The electrons at ~1 eV formed in each cross section of the sheath in the ionization of atoms acquire, as they move toward the anode, an energy sufficient to excite and ionize neutrals. It is therefore worthwhile to examine the effect of the inelastic electron energy loss on the discharge characteristics. Since the electron energies in the sheath span a broad range, it is also necessary to take account of the dependence of the ionization rate on the electron energy. In weak electric fields (the beginning of the sheath), where there is a flux of fast ions and the average electron energy is low, a possible contribution of ionization by ions must be taken into account. Finally, sensitivity of the discharge characteristics to the part of the sheath near the anode which is deficient in electrons (the electron-depleted region) is neglected in refs. 4 and 5. The finite size of the region must be taken into account in an analysis of electron heating. We show below that a small parameter can be associated with each of these effects, so that we refer to these effects as "weak effects" for brevity. The primary purpose in Part I of this work is to study systematically the influence of these weak effects on the discharge characteristics and to estimate the influence of each effect on the structure of the sheath.

We also take note of the following circumstance: Homogeneous boundary conditions on the electric field and the electron current ($E_0 = j_0 = 0$) are assumed at the beginning of the sheath in refs. 2, 4, and 5. Actually, in this case the quantities must assume certain finite values, which are governed by relations similar to the familiar Bohm criterion.[6] These relations make possible the formation of an anode sheath with monotonic distributions of the appropriate parameters so that the solutions in the sheath and in the plasma can be matched. In the present work the derivation of these criteria is not given and we restrict the study to the influence of changes in the boundary conditions, within certain allowed ranges, on the sheath structure.

In the second part of this paper we treat the influence of two-dimensional effects on the structure of the discharge, primarily the two-dimensional effect of the loss of electrons along the magnetic field to the cathodes. While the electron Larmor radius serves as the mean free path across the magnetic field, the motion of electrons along the magnetic field is collisionless in the pressure range under consideration. The fastest electrons overcome the potential barrier and escape to the walls; the corresponding leakage current can in fact become comparable to the discharge current. The two-dimensional nature of the model requires a specification of the geometry, the conditions at the walls bounding the system, and the conditions in the plasma adjacent to the sheath. We adopt a model for the discharge corresponding to an inverted magnetron or to a Hall-current accelerator with a short acceleration zone.[3] The problem of an ion beam propagating between equipotential electrodes, with the space charge balanced by ionization of residual gas, is solved. This problem is of some independent interest, but for our purposes we need the solution to establish certain approximate boundary conditions for the sheath.

STATEMENT OF THE PROBLEM

Instruments in which the electron drift is suppressed are axisymmetric. As in refs. 4 and 5 we treat the planar problem for simplicity; the x axis is across the sheath, the z axis is along the magnetic field, the Hall current is along the y axis, and the circuit is closed at infinity. The discharge chamber is bounded by the cathodes ($z = \pm h$) and the anode ($x = x_0$, $|z| \leq A < h$, $A \gg x_0$). The electron-depleted region is $x_{ed} < x < x_0$. Figure 1 gives an idea of the two-dimensional distribution of the potential $\Phi(x, z)$ in such a system. By definition, the voltage drop along z for a given x consists of the drop near the wall, $\Delta\varphi_{ed}(x)$, and the change in the core of the discharge, $\Delta\varphi \simeq [\delta(x)/e]W(x)$ [$W(x)$ is the average electron energy at cross section x, and $\delta(x) \leqslant 1$ is some function]. These potential drops satisfy

$$\varphi(x) + \Delta\varphi_0 = \frac{\delta(x)}{e} W(x) + \Delta\varphi_{ed}(x),$$

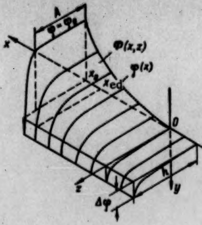

Fig. 1

where $\varphi(x)$ is the potential distribution in the $(z = 0)$ symmetry plane, and $\Delta\varphi_0$ is the total potential drop toward the wall in the initial cross section (Fig. 1).

We can partition the space along the x axis somewhat arbitrarily into three regions: a quasineutral plasma $(x \to -\infty)$, a transition region $(x < 0)$, and a sheath $(0 \le x \le x_0)$. Of course it is not possible to unambiguously define the boundary or the thickness of the sheath. Although the sheath boundary is at a potential extremely close to the plasma potential, the shielding of the plasma from the anode field is incomplete. This simplified approach is based on the fact that the field in the transition region is weak in comparison with that in the sheath, so that the changes in the potential over distances of the order of the sheath thickness are negligible. Accordingly, for $x < 0$ we can assume $\varphi(x) = \varphi_b = \text{const}$. We arbitrarily assume $\varphi_b = 0$, since we can always redetermine the reference point for the potential from the known solution if necessary. The field $E_0 = \varphi'(0)$ cannot be neglected, even though it is weak, since it determines j_0 and perhaps the initial electron energy W_0. Strictly speaking, with weak electric fields the sheath solution must be matched with the solution of the corresponding problem for the transition region. This procedure would help us define the sheath and the transition region and would permit an unambiguous determination of the boundary conditions at the sheath.

The problem is solved under the following assumptions: The electrons are magnetized, and the ions are not magnetized over distances $\sim x_0$ $(\rho_i \gg x_0 \gg \rho_e)$. Charge exchange, recombination, and secondary ionization are negligible, as are secondary processes at the walls. We assume discharge conditions such that

$$\frac{m\omega_e\nu_i}{4\pi e^2 n_n}\sqrt{\frac{e\varphi_0}{mv_n^2}\frac{\nu_i}{\nu_0}} < 1, \quad \beta = \sqrt{\frac{M}{2m}\frac{\nu_i\nu_0}{\omega_e^2}} \ll 1. \tag{1}$$

Here, ω_e is the electron gyrofrequency; $\nu_i = \langle\sigma_{ie}v_e\rangle n_n$ is the rate of ionization collisions of electrons; $\nu_0 = \langle\sigma_0 v_e\rangle n_n$ is the rate of electron collisions involving a loss of directed momentum; v_e, σ_{ei}, σ_0 are the electron thermal velocity and the corresponding cross sections; and n_n, v_n are the density and velocity of the neutrals. If the first of these inequalities holds we can neglect the "burn up" of neutrals in the sheath and assume[5] $n_n = \text{const}$. The second condition means that the density of the ion space charge in the sheath is negligible. When $\langle\sigma_{ie}v_e\rangle \simeq 10^{-7}$ cm^3/sec, $\nu_0/\nu_i \simeq 3$, and $v_n \simeq 3 \cdot 10^4$ cm/sec the first inequality holds for $H\sqrt{\varphi_0} < 10^6$ eV$^{1/2}$. With $H \simeq 10^3$ Oe the second condition holds for $n_n < 10^{12}$-10^{13} cm^{-3}.

To estimate the size of the region we note that the lifetime of en electron in the sheath is of order $\tau_e = \nu_0^{-1}$. In a time of order ω_e^{-1} electrons move without collisions from the cutoff region to the anode, i.e., the electron lifetime is shorter than that in the sheath by a factor $\omega_e\tau_e$. We can thus use the crude assumption that the electron density vanishes in the electron-depleted region. An electron whose velocity components in the plane $x = x_{ed}$ are v_x, v_y traverses the following distance to the turning point:

$$d = \frac{1}{\omega_e}\left[\frac{cE}{H} - v_y + \sqrt{v_x^2 + \left(\frac{cE}{H} - v_y\right)^2}\right].$$

Averaging this quantity over the electron distribution

$$f \sim \exp\left\{-\frac{m}{2W}\left[v_x^2 + \left(\frac{cE}{H} - v_y\right)^2\right]\right\},$$

we find

$$\bar{d} = \frac{1}{\omega_e}\sqrt{\frac{\pi}{2m}W}\ . \tag{2}$$

Accordingly, the size of the electron-depleted region, $x_0 - x_{ed}$, is equal to the electron Larmor radius in the plane x_{ed}, within a coefficient of order unity. In this region the average electric field is approximately homogeneous, and the electron energy and potential vary linearly with the coordinate x.

To describe the distributions of the unknown quantities over most of the sheath we use

$$\frac{\partial j_x}{\partial x} + \frac{\partial j_z}{\partial z} = \langle\sigma_{ie}v_e\rangle n_n n_e + \langle\sigma_{ii}v_i\rangle n_n n_1, \tag{3}$$

$$\frac{\partial q_x}{\partial x} + \frac{\partial q_z}{\partial z} = -ej_x E_x - ej_z E_z - \mathcal{E}_i\langle\sigma_{ie}v_e\rangle n_n n_e, \tag{4}$$

$$\frac{\partial E_x}{\partial x} + \frac{\partial E_z}{\partial z} = -4\pi e n_e \quad (\mathbf{E} = -\nabla\Phi), \tag{5}$$

$$j_x = b_\perp n_e \frac{\partial\Phi}{\partial x} \quad \left(b_\perp = \frac{e}{m\tau_e}\frac{1}{\omega_e^2}\right). \tag{6}$$

Here j_x, j_z, q_x, and q_z are the corresponding components of the electron current density and of the energy carried by electrons; n_1 is the density of the fast ions, which are efficient in causing ionization; σ_{ii} and v_i are the cross section for ionization collisions and the velocity of the ions; $b_\perp$ is the transverse electron mobility; and $\mathcal{E}_i$ is the "effective cost" of an ion. The second term on the right side of (3) can make an appreciable contribution only at the beginning of the sheath, where W_0 is small and where $\langle\sigma_{ie}v_e\rangle \to 0$. We deliberately overestimate its value, setting it equal to the constant $n_n\langle\sigma_{ii}v_i\rangle n_{10}$, where n_{10} is the density of fast ions in the initial cross section. Conflicting arguments have been advanced regarding the mechanism for the electron transport to the anode, so that this mechanism is in doubt; we work on the basis of refs. 1 and 7, where it was shown that classical transverse mobility is the predominant mechanism at low pressures. The function dependence of the ionization rate by electron impact on electron energy can be approximated by

$$\langle\sigma_{ie}v_e\rangle = \langle\sigma_{ie}v_e\rangle_0 \nu\left(\frac{W}{eV_i}\right), \tag{7}$$

where

$$\nu = -\frac{1}{0.57}\sqrt{\frac{eV_i}{W}}\,\mathrm{Ei}\left(-\frac{eV_i}{W}\right), \quad \langle\sigma_{ie}v_e\rangle_0 = \frac{1.14}{\sqrt{\pi}}\sqrt{\frac{2eV_i}{m}}\,\sigma_{i0},$$

V_i is the ionization potential, σ_{i0} is the characteristic cross section for the given material, and Ei(x) is the exponential integral function.[8] With $W \leqslant eV_i$ and $\nu \ll 1$, the maximum value $\nu \simeq 1$ is reached at $W \simeq (3\text{-}6)eV_i$. The energy expenditure per ionization event includes the inelastic and elastic loss and is governed by the conditions in the discharge. At an electron energy $\sim eV_i$ this quantity can reach hundreds of electron volts; as the energy drops to $\sim 10^3$ eV, it drops to 30-50 eV. For a qualitative treatment we assume $\mathcal{E}_i$ = const to be a few eV_i.

AVERAGING THE SYSTEM OF EQUATIONS

Below we use averages over z of the distributions of physical quantities in the core of the sheath for $|z| < a < A$:

$$\Phi(x) = \frac{1}{a}\int_0^a \Phi(x, z)\,dz.$$

It follows from symmetry considerations that everywhere, except near the cathodes, where all quantities are strong functions of z, we can approximate the distributions of the unknown quantities by expansions like

$$\left.\begin{aligned} \Phi(x, z) = \varphi(x) - \varphi_1(x)\frac{z^2}{h^2} - \ldots, \quad n_e = n_0(x) - n_1(x)\frac{z^2}{h^2} - \ldots, \\ j_z = j_1(x)\frac{z}{h} + \ldots, \quad q_z = q_1(x)\frac{z}{h} + \ldots \text{ etc.} \end{aligned}\right\} \tag{8}$$

As a rough first approximation we only consider terms which are linear or quadratic in z. We neglect the structure of the cathode regions, and we assume the thickness to be small in comparison with h. Then we can set $\varphi_1 \simeq [\delta(x)/e]W(x)$. The quantity $n_1(x)$ can be determined from the Boltzmann distribution

$$n_e(x, z) = n_0 \exp\left\{-\frac{e}{W(x)}[\varphi(x) - \Phi(x, z)]\right\}.$$

Integrating system (3)-(6) over z within the framework of approximation (8), we find the quasi-one-dimensional equations

$$\frac{d}{dx}J_x = \langle\sigma_{ie}v_e\rangle n_n\bar{n}_e + \langle\sigma_{ii}v_i\rangle n_n n_{10} - \frac{1}{h}j_1(x),$$

$$\frac{d}{dx}q_x = -e\overline{j_xE_x} - \frac{2}{3}\delta\frac{a^2}{h^2}\frac{W}{h}j_1 - \frac{1}{h}q_1(x) - \mathcal{E}_i\langle\sigma_{ie}v_e\rangle n_n\bar{n}_e,$$

$$\frac{d}{dx}E_x = -4\pi e\bar{n}_e - \frac{2\delta}{h^2}\frac{W}{e},$$

$$E_x = -\frac{d}{dx}\Phi, \quad E_z = \frac{\delta}{a}\frac{W}{e}\frac{a^2}{h^2},$$

$$J_x = b_\perp\overline{n_e\frac{\partial\Phi}{\partial x}}.$$

It can be shown that the following relations hold within 10%:

$$\overline{j_xE_x} \simeq J_xE_x, \quad \overline{n_e\frac{\partial\Phi}{\partial x}} \simeq \bar{n}_e\frac{d}{dx}\Phi.$$

We introduce the dimensionless quantities

$$s = \frac{x}{l^*}, \quad n = \frac{\bar{n}_e}{n^*}, \quad n_1 = \frac{n_{10}}{n^*}, \quad \theta = \frac{W}{e\varphi_0},$$

$$\eta = \frac{\Phi + \frac{\delta_0}{3}\frac{a^2}{h^2}\frac{W_0}{e}}{\varphi_0}, \quad \Delta\eta = \frac{\Delta\varphi_0}{\varphi_0}, \quad j = \frac{J_x}{j^*},$$

where

$$l^* = \sqrt{\frac{e\varphi_0}{m\omega_e^2}\frac{\nu_0}{\nu_{i0}}}, \quad n^* = \frac{m\omega_e^2}{4\pi e^2}\frac{\nu_{i0}}{\nu_0}, \quad j^* = \nu_{i0}n^*l^* \quad (\nu_{i0} = n_n\langle\sigma_{ie}v_e\rangle_0).$$

Assuming $\bar{\bar{q}}_z = W\bar{j}_x$ and using the Boltzmann approximation for the electron flux to the wall, we can write the system of equations for the averages in final form:

$$\frac{dj}{ds} = \nu(\theta)n + In_1 - \Lambda j_w, \tag{9}$$

$$j = n\frac{d\eta}{ds}, \tag{10}$$

$$\frac{d^2\eta}{ds^2} = n + 2\delta\Lambda^2\theta, \tag{11}$$

$$\frac{d}{ds}(j\theta) = j\frac{d\eta}{ds} - \Lambda\left(1 + \frac{2}{3}\delta\alpha^2\Lambda^2\right)\theta j_w - \mathcal{E}\nu(\theta)n, \tag{12}$$

$$j_w = Qn\sqrt{\theta}\exp\left(-\frac{\eta + \Delta\eta}{\theta}\right), \tag{13}$$

$$\nu(\theta) = -\frac{1}{0.57}\frac{1}{\sqrt{K\theta}}E_i\left(-\frac{1}{K\theta}\right). \tag{14}$$

Here we obtain

$$I = \frac{\langle\sigma_{ii}v_i\rangle}{\langle\sigma_{ie}v_e\rangle_0}, \quad \Lambda = \frac{l^*}{h}, \quad \alpha = \frac{a}{l^*}, \quad Q = \frac{\sqrt{2}}{4}\frac{\omega_e}{\sqrt{\nu_{i0}\nu_0}},$$

$$\mathcal{E} = \frac{\mathcal{E}_i}{e\varphi_0}, \quad K = \frac{\varphi_0}{V_i}.$$

The initial conditions are $s = 0$, $\eta = 0$, $d\eta/ds = E_0$, $j = j_0$, and $\theta = \theta_0$.

To determine the coordinate of the electron-depleted region, $s = s_{ed}$ we use

$$\eta(s_{ed}) + \frac{1}{3}\delta(s_{ed})\alpha^2\Lambda^2\theta(s_{ed}) = 1 - d(s_{ed})\left[\eta'(s_{ed}) + \frac{1}{3}\delta(s_{ed})\alpha^2\Lambda^2\theta'(s_{ed})\right],$$

where $d(x) = \bar{d}/l^*$.

ONE-DIMENSIONAL TREATMENT.

If we set $h = \infty\,(\Lambda = 0)$ in (9)-(12), we find that E_z, j_z, and q_z vanish, and we find the equations of the one-dimensional problem. We solve it, adding various physical effects in succession.

If we neglect the electron-depleted region and set $\nu(\theta) = 1$, and $I = 0$, we can write the solution of (9)-(12) as

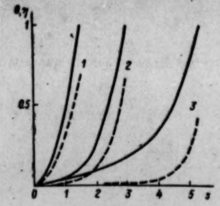

Fig. 2

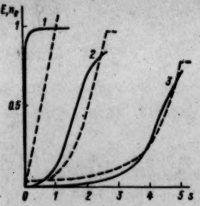

Fig. 3

$$
\left.\begin{aligned}
s&=(E-E_0)-(j_0-E_0)\ln\left(1+\frac{E-E_0}{j_0}\right),\\
\eta&=\frac{1}{2}(E^2-E_0^2)-(j_0-E_0)(E-E_0)\\
&\quad+(j_0-E_0)^2\ln\left(1+\frac{E-E_0}{j_0}\right),\\
\theta&=\frac{1}{E-E_0+j_0}\left[\theta_0 j_0+\frac{1}{3}(E^3-E_0^3)-\mathcal{E}(E-E_0)\right],\\
j&=j_0+(E-E_0).
\end{aligned}\right\}\qquad(15)
$$

In this case the increase in the electron energy in the sheath does not affect the sheath structure. When $\mathcal{E} > 0$ at the beginning of the sheath solution (15) yields $\theta < 0$, i.e., the problem of the effect of the energy loss on the electron heating is not well posed. The solution for the sheath, (15), is very nearly the same as the solution

$$\eta=\frac{1}{2}s^2,\quad j=E=s,\quad n=1\quad (s_0=\sqrt{2}),$$

obtained for homogeneous boundary conditions.[4] For example, as E_0 and j_0 are varied over broad ranges (10^{-4}–10^{-1}), the sheath thickness varies only slightly (s_0 = 1.29–1.77), the electron energy at the anode varies only slightly (from 0.66 to 0.69), and $n(s) \simeq 1$ everywhere except in a small neighborhood of the initial cross section. Typical $\eta(s)$ and $\theta(s)$ distributions according to (15) are shown in Fig. 2 (the solid curve and dashed curve 1, respectively). Figure 3 shows the corresponding functions n(s) and E(s), and Fig. 4 shows the j(s) and $j_i(s)$ distributions (the solid and dashed curves, respectively). As noted above, as $E_0 \to 0$ and $j_0 \to 0$, solution (15) goes over to the similar solution of ref. 4. The situation is different if we take weak effects into account; in this case solutions of the sheath type do not exist for E_0 and j_0 for homogeneous boundary conditions. This result is evident from the linear conditions for the growth of the electron density and energy:

$$n_0<\nu(\theta_0)+I\frac{n_1}{n_0},\quad E_0^2>(\mathcal{E}+\theta_0)\nu(\theta_0)+I\frac{n_1}{n_0}\theta_0\quad \left(n_0=\frac{j_0}{E_0}\right).$$

As is evident from the discussion below, a lower limit on n_0 (i.e., on j_0) can be estimated in accordance with our definitions of the sheath and the transition region:

$$\eta_b \leqslant 0.1,$$

where η_b is the potential in the region where the rapid increases in the field and in the electron density, current, and energy begin. A check shows that the solutions become meaningless if these conditions are violated (the check has been carried out for broad ranges of the boundary values: $n_0 = 5\cdot10^{-2}$–10^{-5}, $E_0 = 5\cdot10^{-2}$–10^{-4}, $\theta_0 \simeq 10^{-3}$–10^{-2}). As n_0 decreases, the distributions of the physical quantities become deformed in a certain specific manner: "Tails" form in the n, j, θ, and E profiles at the beginning of the sheath, where the values of the corresponding functions are on the order of the initial values, i.e., where the gradients along x are small, but where the greater part of the applied potential difference is nevertheless found. There are slow decreases in the basic properties of the sheath: $j_d = j(s_0) = j_i(0)$, $\theta_{ed} = \theta(s_{ed})$, $\theta_A = \theta(s_0)$, n_{ed}, and E_{ed}. Because of the lengthening of the tail, the formal thickness of the sheath, s_0, increases. (As $j_0 \to 0$, we have $s_0 \to \infty$, and the sheath-type solution disappears.) The conditions prevailing in the tail of the distributions are suitable for further rapid increases in the properties; these increases occur in a region ~ 2-3 units long. This region is naturally identified as the sheath proper. Accordingly, solutions displaying a large potential drop in the tails of the distributions should be treated as formal solutions resulting from an incorrect choice of initial conditions. Analysis of the solutions obtained by varying the boundary conditions over the allowed ranges shows that, within the error associated with this analysis, all properties of the sheath except the formal length s_0 remain constant.

If we take the functional dependence of the rate of ionization collisions of electrons on the electron energy into account [$\nu = \nu(\theta)$], we find that the electron heating in the sheath affects the sheath structure. In this case it is natural to expect decreases in the density, the electric field, and the discharge current. Curves 2 in Figs. 2-4 demonstrate the changes in the distributions of the corresponding quantities.

The energy losses which occur in electron collisions should lead to reductions in the average electron energy,

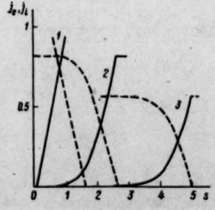

Fig. 4

and the ionization, and thus the density and currents. Curves 3 show the corresponding changes in the sheath structure. (Figures 2-4 show curves for $K = 63$, $\mathscr{E} = 0.05$, corresponding to $\varphi_0 = 1\,\text{kV}$, $\mathscr{E}_i \simeq 3\ \text{eV}_i$ for argon.) From the curves in Figs. 2-4 we see that the weak effects deform the distributions. The sheath thickness increases systematically by a factor of 2 or 3, while the profiles of the field, the potential, and the density become smoother. However, the actual thickness of the sheath, over which most of the increase in the field and electron energy, current, and density occurs, and where the ion beam is shaped, turns out to be some 2 or 3 units in all cases. In the one-dimensional theory the electron current drawn by the anode is always equal to the ion current at the beginning of the sheath (Fig. 4). The maximum electric field and currents fall off systematically by factors of 2 or more. The density attained changes relatively little (by about 30%). The energy loss strongly influences electron heating in the sheath. The energy of the electrons reaching the anode falls off by a factor of more than 1.5 (to about 0.4 unit). The cutoff region corresponds to the horizontal parts of the E(s) and j(s) distributions; although this region is relatively narrow, $s_0 - s_{ed} \simeq 0.2\text{–}0.3$ (about 10% of the effective sheath thickness), there is a voltage drop of about $(0.2\text{–}0.3)\varphi_0$ in it, and the electrons acquire in this region about half the energy brought to the anode. The quantity θ_{ed} is about 0.2, i.e., the electrons in the sheath have energies much lower than 1 unit. This circumstance offers some justification for the assumption that the term in Eq. (6) containing the gradient of the electron pressure is small.

As is shown in Part II of this work (the following paper), $n_1 \to 0$ as $h \to \infty$. To determine the effect on ionization by ions on the sheath structure we assume both $n_1 = 0$ and the limiting value $n_1 = n_0$ in the calculations ($I \nless 10^{-2}$). It turns out that ionization by fast ions, even if it is predominant at the beginning of the sheath $[\nu(\theta_0)n_0 \ll In_1]$, does not affect the characteristics of the sheath. The reason is that the increase in θ is accompanied by a very rapid increase in $\nu(\theta)$, and ionization by electrons becomes predominant.

In the one-dimensional formulation of the problem there are two dimensionless parameters, $\mathscr{E}$ and K, which are functions of φ_0 and the gas properties. Calculations show that an increase in $\mathscr{E}$ (or a decrease in K) is accompanied by monotonic decreases in the sheath properties θ_A, j_d, θ_{ed}, n_{ed}, and E_{ed}. We can thus extrapolate the available data to estimate the properties of the discharge for other values of K and $\mathscr{E}$.

In summary we can say that the weak effects, described by the small parameters ν, $\mathscr{E}$, and d/s_0, have a significant influence on the discharge characteristics.

Finally, we note that since the electron energy in the sheath is lower than $e\varphi_0$ by a factor of 4 or 5, while the effective thickness of the anode sheath is $L \simeq (2\text{–}3)\rho_e(\varphi_0)\sqrt{\nu_0/2\nu_{i0}}$, we conclude that the ratio of L to the average electron Larmor radius in the sheath, $\rho_e(\overline{W})$, is about 10. This circumstance justifies the diffusion approach.

---

[1] W. Knauer, J. Appl. Phys., 33, 2093 (1962).

[2] N. A. Kervalishvili and A. V. Zharinov, Zh. Tekh. Fiz., 35, 2194 (1965) [Sov. Phys. – Tech. Phys., 10, 1682 (1966)].

[3] S. D. Grishin, V. S. Erofeev, and A. V. Zharinov, in: Plasma Accelerators [in Russian], Izd. Mashinostroenie, Moscow (1973), p. 54; A. I. Morozov, in: Plasma Accelerators [in Russian], Izd. Mashinostroenie, Moscow (1973), pp. 5, 85.

[4] Yu. S. Popov, Zh. Tekh. Fiz., 37, 61 (1967) [sic]; 37, 118 (1967) [Sov. Phys. – Tech. Phys., 12, 81 (1967)].

[5] V. S. Erofeev, Yu. V. Sanochkin, and S. S. Filippov, Zh. Prikl. Mekh. Tekh. Fiz., No. 5 (1969).

[6] A. Guthrie and R. K. Wakerling (eds.), The Characteristics of Electrical Discharges in Magnetic Fields (1949), Ch. 3.

[7] W. Knauer and M. Lutz, Appl. Phys. Lett., 2, 109 (1963).

[8] N. N. Lebedev, Special Functions and Their Applications [in Russian], GIFML, Moscow–Leningrad (1963).

Low-pressure self-maintained discharge with suppressed electron drift. II

Yu. V. Sanochkin and V. K. Kalashnikov

(Submitted January 8, 1973; resubmitted July 8, 1973)
Zh. Tekh. Fiz., 44, 2512-2518 (December 1974)

The influence of two-dimensional effects on the discharge characteristics is analyzed for a Hall-current accelerator or an inverted magnetron. The properties of the plasma adjacent to the anode sheath, the electron density and average energy, the electric field, and the electron and ion currents in the anode sheath are found; the loss of electrons along the magnetic field to the cathodes is taken into account. A comparison is made with the results of the one-dimensional treatment. A study is made of the influence of the pressure on the discharge characteristics. The calculated results can be used to interpret experimental data.

In Part II of this work we report an approximate analysis of the influence of two-dimensional effects on the discharge characteristics, and we compare the theoretical results with experiment. The geometry of the discharge chamber, the physical conditions, and the statement of the problem are given in Part I of this work,[1] where we also derive "quasi-one-dimensional" equations for the system [Eqs. (9)-(14)], which describe the distributions of various parameters in the axial part of the discharge for finite values of h. The quantities n_1, $\Delta\eta$, and δ in these equations are not yet determined. There is an ion beam in the beginning of the sheath;[1] it is a natural procedure to determine the missing boundary conditions by solving the problem of a neutralized parallel ion beam propagating in a plasma adjacent to the anode sheath.

NEUTRALIZED ION BEAM PARALLEL TO EQUIPOTENTIAL SURFACES

We consider the region at the exit from the system ($x \to -\infty$) where the gradients with respect to x are small, and the ion beam moves in the x direction. If the electrons are still magnetized in this region they cannot neutralize the ion beam, even partially. However, the ion space charge must be neutralized. We assume that a parallel ion beam propagates between equipotential planes $z = \pm h$ and that the ion space charge is neutralized by ionization of the residual gas (there are no thermionic cathodes). The plasma in this region consists of the "primary" ions (which enter this region as ions) and "secondary" ions and electrons (which are formed in this region).

Neglecting the initial velocity of the secondary ions, we write their density as

$$n_2 = \int_0^z \frac{\langle\sigma_{ii}v_i\rangle n_n n_1 + \langle\sigma_{ie}v_e\rangle n_n n_0 e^{\frac{e\varphi}{T_e}}}{\sqrt{\frac{2e}{M}[\varphi(z') - \varphi(z)]}}\, dz'. \qquad (1)$$

Here, n_0 is the electron density at $z = 0$, and n_1 is the ion density in the beam. The potential distribution $\varphi(z)$ is determined from the Poisson equation:

$$\frac{d^2\varphi}{dz^2} = 4\pi e\left(n_0 e^{\frac{e\varphi}{T_e}} - n_1 - n_2\right). \qquad (2)$$

Assuming

$$\chi = -\frac{e\varphi}{T_e}\,(\chi \geqslant 0),\quad s_z = \frac{z}{l_z}\quad \left(l_z = \frac{\sqrt{\frac{2T_e}{M}}}{\langle\sigma_{ii}v_i\rangle n_n}\right),$$

$$N = \frac{n_1}{n_0},\quad G(T_e) = \frac{\langle\sigma_{ii}v_e\rangle}{\langle\sigma_{ei}v_i\rangle},$$

we can rewrite (2) in the dimensionless form

$$-\frac{\langle\sigma_{ii}v_i\rangle^2 n_n^2 M}{8\pi e^2 n_0}\frac{d^2\chi}{ds_z^2} = e^{-\chi} - N - \int_0^{s_z}\frac{N + Ge^{-\chi'}}{\sqrt{\chi' - \chi}}\, ds_z'. \qquad (3)$$

We see from (3) that the neutrality is violated only in regions near the walls with dimensions of the order of the Debye length. Assuming for simplicity that the density of primary ions N is constant over the beam cross section, we find the following result from the neutrality condition (by means of an Abel transformation):

$$(N + Ge^{-\chi})\frac{ds_z}{d\chi} = \frac{2}{\pi}\frac{d}{d\chi}[F(\sqrt{\chi}) - N\sqrt{\chi}], \qquad (4)$$

where $F(x) = e^{-x^2}\int_0^x e^{t^2}dt$ is the well known tabulated function.[2] We now introduce the variable $u = \sqrt{\chi}$; following ref. 3, we determine the potential drop in the plasma, $u_r = (-e\Delta\varphi_r/T_e)^{1/2}$, from the condition

$$\frac{ds_z}{du} = \frac{2}{\pi}\frac{F'(u) - N}{N + Ge^{-u^2}} = 0. \qquad (5)$$

We see from (5) that when $1 > N > 0$ the corresponding values of u_r lie in the range $0 < u_r < 0.92$, i.e., the potential drop in the neutral region does not exceed $0.92\,T_e$. Interestingly, the numerator in (5) contains the ratio of the density of electrons to that of primary ions, while the denominator contains the density of secondary ions. Accordingly, regardless of the mechanism by which the ions are produced in this region the potential drop in the plasma is governed solely by the ratio of the density of "background" ions to the total ion density. The potential distribution is given by

$$s_z = \frac{2}{\pi}\int_1^u \frac{1 - N - 2xF(x)}{N + Ge^{-x^2}}\, dx. \qquad (6)$$

Neglecting the Debye length compared with h, we find from (6)

$$\frac{\langle\sigma_{ii}v_i\rangle n_n}{\sqrt{\frac{2T_e}{M}}}h = s_h = \frac{2}{\pi}\int_0^{u_r}\frac{1 - N - 2xF(x)}{N + Ge^{-x^2}}\, dx. \qquad (7)$$

It follows from (5) and (7) that if T_e, n_n, h, and the velocity of the primary ion beam are specified, the quantities u_r and N are determined unambiguously. To find the total potential drop from the axis to the wall we use the steady-state equality of the fluxes of electrons and secondary ions to the wall:

$$n_0\sqrt{\frac{2T_e}{m}}\exp\left\{\frac{e(\Delta\varphi_r + \Delta\varphi_0)}{T_e}\right\} = \langle\sigma_{ii}v_i\rangle n_n n_1 h + \langle\sigma_{ie}v_e\rangle n_n n_0\int_0^h \exp\left(\frac{e\varphi}{T_e}\right) dz$$

or, in dimensionless form,

$$u_c^2+u_r^2=-\ln\left\{\sqrt{\frac{m}{M}}\left(s_hN+G\int\limits_0^{s_h}e^{-u^2(s)}ds\right)\right\}. \qquad (8)$$

Using Eqs. (5), (7), and (8) we can determine u_r, u_c, and N as functions of the type of gas, the pressure, the geometric dimension h, and the electron temperature T_e. It is convenient to replace s_b by the T_e-independent quantity $s_w = \sqrt{T}s_h$, where $T = T_e/eV_i$. Figure 1 shows illustrative functional dependences of N on s_w calculated from (5) and (7) for argon for various values of T [1) 0.5; 2) 0.3; 3) 0.5; 4) 0.125; 5) 0.2]. In the calculations we assume the primary ions to have an energy of 1 keV. Figure 2 shows the corresponding potential drops u_r^2 (dashed curves) and $u_r^2 + u_c^2$ as functions of s_w [1) 0.5; 2) 0.3; 3) 0.05; 4) 0.125; 5) 0.2]. Since the potential drop in the plasma u_r^2 is lower than T_e, the potential drop $u_r^2 + u_c^2$ is governed primarily by u_c^2. We see from Fig. 1 that N → 1 for all T as s_w decreases, i.e., the density of the secondary plasma becomes small. With h ~ 1 cm and $n_n \leq 10^{13}$ cm^{-3} we have $s_w \leq 10^{-2}$; for $T_e < 0.3eV_i$, according to the curves, N ≥ 0.8. An estimate for argon for $T_e \simeq 0.2eV_i$ yields $G(T_e) \simeq 0.9$, i.e., the ionization by ions is comparable to that by electrons. As T_e decreases, G increases exponentially, and when $T_e < 0.2eV_i$ the ionization by ions becomes predominant. As s_w increases N decreases, i.e., the density of the secondary plasma increases. This means, in particular, that the ionization by electrons becomes predominant, even if the electron temperature is low [$G(T_e) \ll 1$], as, e.g., the geometric dimension h increases. These results suggest the following procedure for finding the boundary values of $\Delta\eta$ and n_1 for various values of h, mentioned above. Specifying certain values of Λ, i.e., of s_w, we use the corresponding curves (Figs. 1 and 2) to determine (for a particular value of T) the values of $u_c^2 + u_r^2$ and N, which can then easily be converted to $\Delta\eta = \theta_0(u_r^2 + u_c^2)$ and $n_1 = Nn_0$. In particular, if the conditions are such that most of the ionization is due to ions, $IN \gg \nu(\theta_0)$, we find the initial potential drop to be given by $\Delta\eta/\theta_0 \simeq \ln \Lambda Q\sqrt{\theta_0}/IN$. The unknown function δ(s) introduced in ref. 1 can be assigned a boundary value δ(0) of u_r^2. As $s \to s_c$ we have δ → 0, so it is natural to assume δ(s) < 1. At Λ ≤ 0.1-0.2 the detailed nature of the function δ(s) is unimportant.

QUASI-ONE-DIMENSIONAL TREATMENT

According to the one-dimensional theory[1] the properties of the sheath are essentially independent of the choice of initial conditions, including n_0. Solution of the quasi-one-dimensional system of equations for finite h and for various initial conditions shows (as in the one-dimensional case) that variations in j_0 and E_0 at fixed n_0 lead to a negligible scatter in the discharge characteristics about their average value. However, the solutions are sensitive to the choice of n_0 – the more so, the higher Λ. If the quantities $j_i(0)$, θ_A, θ_c, E_c, and η_c remain essentially independent of n_0 then $j_d = j(s_0)$ and n_c falls off relatively slowly (logarithmically) with increasing n_0. We are thus led to the question of choosing n_0. At pressures which are not too low (p ~ 10^{-3}-10^{-5} torr) we can evidently approximate n_0 by

$$n_0\geqslant n_i(0)=\beta\int\limits_0^{s_c}\frac{\nu n+In_1}{\left(1+\Lambda^2 s\frac{\theta}{E}\right)\sqrt{\eta}}ds \quad \left(\beta=\sqrt{\frac{M}{2m}\frac{\nu_i\nu_0}{\omega_e^2}}\sim n_n\right), \qquad (9)$$

where $n_i(0)$ is the ion density in the initial cross section.

Taking the two-dimensional effects into account we find, in addition to K and $\mathscr{E}$, the dimensionless parameters $\Lambda \sim \sqrt{\varphi_0}/hH$, $Q \sim H/n_n$. It should be noted that the experiments on the discharges are carried out in devices which cannot be treated as one-dimensional: Using the quantity Λ as a measure of the importance of two-dimensional effects, we find its value to be 0.05-2, 0.2-0.5, 0.25, and 0.2 for the experimental conditions of refs. 4-7, respectively. Figures 3-5 show how the distributions of the quantities over the sheath vary with increasing Λ (parameters of the curve). Figure 3 shows typical η(s) and θ(s) distributions, Fig. 4 shows n(s) and E(s), and Fig. 5 shows j(s) and $j_i(s)$ (the solid and dashed curves, respectively). The coordinate s is measured from the anode on the curves, and the electron-depleted region corresponds to the horizontal parts of the E(s) and j(s) distributions. For convenience in comparing with the results of the one-dimensional treatment we use the same scaling and parameters (K = 63, $\mathscr{E}$ = 0.05, I = 10^{-2}, Q = $6.7\cdot10^3$, β = 10^{-2}, α = 5, and Λ = 0.25/h, corresponding to φ_0 = 1 kV, H = 1 kOe, and p = $5\cdot10^{-5}$ torr for argon).

It follows from these curves that with Λ → 0 we find the results of the one-dimensional treatment. As Λ increases, we find differences, which are particularly

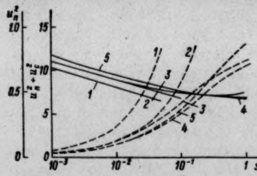

Fig. 2

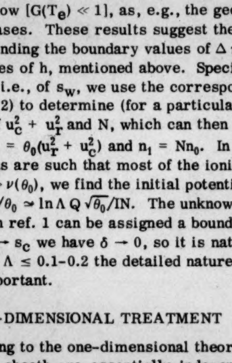

Fig. 1

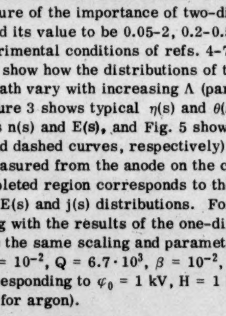

Fig. 3

marked in the distributions of the currents and the density of electrons. The loss of electrons along the magnetic field to the cathodes reduces the electron density and thus the number of ionization events caused by electrons and the electric field. Consequently, there is a certain decrease in the ion current at the exit of the system, but the loss of electrons has a particularly marked effect on the electric current which reaches the anode. As Λ is increased from 0 to 0.1 the ratio of this leakage current to the discharge current changes from 0 to 2. These values can be found from the curves in Fig. 5 and

$$\frac{\int_0^{x_0} j'_w dx}{A j_e(x_0)} = \frac{h}{A}\frac{j_i(0) - j_e(x_0)}{j_e(x_0)} > \frac{j_i - j_d}{j_d}.$$

Another interesting quantity is the ratio of the power evolved at the anode to that supplied to the discharge, which is equal to the average electron energy at the anode in units of $e\varphi_0$. As Λ increases this quantity decreases slightly. As Λ changes, the distributions become deformed in a relatively narrow region near the anode (Figs. 3-5). The length of the sheath and the nature of the distributions at the beginning of the sheath change negligibly. In the electron-depleted region, despite its comparatively small size, the electrons acquire roughly half the energy brought to the anode.

Let us examine the discharge characteristics as functions of the pressure. The density of neutrals governs the value of Q and, when condition (9) is used, the value of n_0. Analysis of the solutions shows that when the pressure is changed by two orders of magnitude the sheath characteristics j_l, j_d, E_c, n_c, and θ_A vary over 30%. Certain difficulties arise in interpreting the solutions obtained at very low pressures ($p < 10^{-5}$ torr). In this case the distributions of all the quantities display a tail, over which there is an increasing voltage drop ($\eta_b > 0.1$). Adjacent to this part of the sheath, which should be included in the transition region, is the sheath proper, in which the predominant changes occur in the physical properties. Using the substitution $\eta' = (\eta - \eta_b)/(1 - \eta_b)$, which takes account of the actual voltage drop over the sheath, we can compare the solutions for different pressures. There are also changes in the scale quantities l^*, j^*, and θ^*, which lead to correction factors of $(1 - \eta_b)^{-1/2}$ for j and s and of $(1 - \eta_b)^{-1}$ for θ. After this conversion we find that all these characteristics of the sheath and its actual thickness are approximately the same for the different pressures. Figure 6 shows some finer features of the sheath, which are governed by the nature of the distributions: the ion energy spectra $j_l(\eta')$ for various pressures and Λ = 0.1. The absence of ions at energies of 0.85-1.0 from the spectrum is due to the electron-depleted region. We see that the retardation characteristics agree over a broad range of pressures. If we plot the distributions over the sheath of the leakage current (corresponding to the electrons escaping along the magnetic field to the cathodes), we find that the curves do not agree as well as those in Fig. 6. The corresponding curves are asymmetric because of our simplified model of the electron-depleted region.

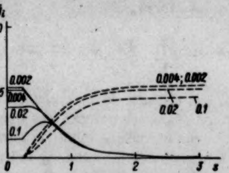

Fig. 5

DISCUSSION OF RESULTS AND COMPARISON WITH EXPERIMENT

Experimental study of low-pressure discharges with inhibited Hall current has led to the following conclusions. The discharge current increases with increasing voltage[6,8] and with increasing magnetic field[4] (this latter conclusion holds for an anode which is well-aligned along the magnetic field). The discharge current, the current corresponding to electrons being lost to the cathode, and the ion current are proportional to the pressure, while the Hall current is essentially independent of the pressure.[4-6] The effective thickness of the anode sheath increases with increasing discharge voltage and decreasing magnetic field and is independent of the pressure.[4] The distribution of the electron current to the cathode and the retardation curves for the ion current are independent of the pressure.[4,6] These results imply that the electron density and the potential distribution are also independent of the pressure. These discharge characteristics are also obtained theoretically; the solution leads to distributions corresponding to a sheath near the wall whose thickness is ~2-3 units of the quantity $l^* \sim \sqrt{\varphi_0}/H$ over broad ranges of the physical properties K, Q, Λ, and $\mathcal{E}$, independent of the initial conditions. The discharge current, the leakage current, and the ion current are expressed in units of $j^* \sim n_n H \sqrt{\varphi_0}$. The unit of measurement for the Hall current, $\omega\tau j^* \sim H^2 \sqrt{\varphi_0}$, is independent of the pressure. The density of the negative space charge is expressed in units of $n^* \sim H^2$. As noted above, the ion energy spectrum (Fig. 6) is only a weak function of the pressure. The values of the

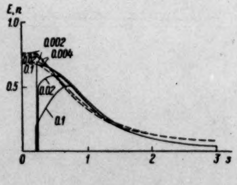

Fig. 4

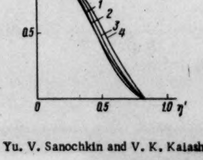

Fig. 6. 1) $p = 3 \cdot 10^{-4}$, 2) $5 \cdot 10^{-5}$; 3) $5 \cdot 10^{-6}$; 4) $5 \cdot 10^{-7}$ torr.

basic characteristics of the sheath, j_i, j_d, E_c, n_c, θ_A, and θ_c are approximately the same for various pressures. Accordingly, the basic functional dependences among the discharge properties are incorporated in the scales chosen for the physical quantities, l^*, j^*, and n^*, and the calculations reveal only the coefficients of the proportionalities between the corresponding quantities and their units of measurement for the various conditions.

Let us attempt a quantitative comparison of the calculated and experimental results for several situations. According to ref. 4, for $p = 3 \cdot 10^{-4}$ torr, $\varphi_0 = 1$ kV, and H = 1 kOe in an inverted magnetron having dimensions of h = 3.7 cm, A = 3.5 cm, and $r_A = 0.9$ cm the discharge current is about 7.5 mA for an adjusted anode, i.e., we would have $ej_d \simeq 0.19$ mA/cm². Under the specified conditions for argon, assuming $\nu_i/\nu_0 = 0.1$, we find $l^* = 0.24$ cm, $n^* = 10^{10}$ cm^{-3}, $\nu_i \simeq 1.5 \cdot 10^{-7} n_n$, $ej^* = 0.62$ mA/cm², $\Lambda \simeq 0.07$, K = 63, $Q = 1.24 \cdot 10^3$; $\beta = 5.5 \cdot 10^{-2}$. The values of j_d calculated for these parameter values lie in the range 0.22-0.40 for the reasonable range $\mathscr{E} = 0.035$ 0.055. The corresponding current density is $ej_d \simeq 0.14$-0.25 mA cm²; the calculated value agrees with experiment at $\mathscr{E} = 0.044$. The calculations also yield the following values of the other quantities: $\theta_A \simeq 0.46$-0.43, $\theta_c =$ 0.26-0.23, $n_c = 0.3$-0.5, $E_c = 0.75$-0.77, and $j_i \simeq 0.55$ ($ej_i \simeq 0.34$ mA/cm²). The ratio of the leakage current to the discharge current varies from 1.5 to 0.4; with $\mathscr{E} =$ 0.044, it is ~0.8.

A detailed study has been made[5] of the discharge conditions in argon for $p \simeq 2.7 \cdot 10^{-4}$ torr, $\varphi_0 = 4$ kV, and H = 1 kOe in an inverted magnetron having dimensions of A = 2.5 cm, h = 2.7 cm, and $r_A = 0.9$ cm. The measurements yielded the following values: a discharge current $I_d \simeq$ 11.5 mA ($ej_d \simeq 0.41$ mA/cm²), an ion current $I_i \simeq 18$ mA, and an electron leakage current $I_e \simeq 6.5$ mA (the corresponding ratios are $I_e/I_d \simeq 0.56$ and $I_e/I_i \simeq 0.37$). The energy evolved at the anode and cathode disks was measured calorimetrically, so that the value $\theta_A = 0.37$ could be determined. Knowing the ion energy spectrum[4] we can estimate the energy evolved by ions at the cathode and write the heat balance equation; from it we can estimate the parameter $\mathscr{E} \simeq 0.06$-0.08. For the specified conditions we have $l^* \simeq 0.5$ cm, $n^* \simeq 10^{10}$ cm^{-3}, $ej^* \simeq 1.1$ mA/cm², $\Lambda \simeq 0.19$, K = 252, $Q = 1.35 \cdot 10^3$, $\beta \simeq 5 \cdot 10^{-2}$, and $I \simeq 10^{-2}$. For the specified range of $\mathscr{E}$ the calculations yield $j_d =$ 0.16-0.38, $j_i = 0.55$-0.53, $\theta_A = 0.42$-0.38, $\theta_c = 0.23$-0.2, $n_c = 0.21$-0.49, and $E_c = 0.81$-0.82 (or, in dimensional form, $ej_d \simeq 0.18$-0.42 mA/cm²). The corresponding current ratios fall in the ranges $I_e/I_d \simeq 2.4$-0.4 and $I_e/I_i \simeq$ 0.70-0.29. At $\mathscr{E} = 0.075$ the calculated and experimental values agree: $ej_d \simeq 0.38$ mA/cm², $\theta_A \simeq 0.39$, $I_e/I_d \simeq 0.58$, and $I_e/I_i \simeq 0.37$. The correspondence between the experimental and calculated data is evidence that the diffusion theory can in fact be used to describe the discharge. The assumption that the electron transport to the anode is due primarily to binary collisions also seems to be justified.

It is interesting to note the strong functional dependences of the discharge current j_d and the density n_e in the sheath on $\mathscr{E}$. To obtain unambiguous results we must drop the assumption $\mathscr{E}_i =$ const and use reliable data on the "cost" of an ion.

At the same time we have learned that variations in $\mathscr{E}$ and the two-dimensional effects have little influence on such parameters as E_c, θ_A, θ_c, j_i and the effective sheath thickness, so that these parameters can be estimated on the basis of the one-dimensional theory. The discharge current and the electron density in the sheath, on the other hand, are strongly influenced by the two-dimensional effects. Our model for the escape of electrons along H is evidently extremely crude, as we see, e.g., from the circumstance that the calculations predict the leakage to be concentrated primarily in a region from 0.5 to 1.0 unit in size adjacent to the stripping region, while experimentally[4] the leakage current apparently reaches a maximum near the beginning of the sheath. Furthermore, the calculations predict a weak functional dependence of the distribution of this leakage current on the pressure. We can thus assert that the electrons in a low-pressure discharge with magnetized electrons do not have a purely Boltzmann distribution.

It is now established that the anode sheath is not in a steady state at these parameter values;[9,10] in particular, periodic pulses have been observed in the electron leakage current along with the constant component of this current. The frequency of these relaxation oscillations increases with increasing pressure.

In this work we have attempted to determine the steady-state characteristics; it seems reasonable to speak of a steady state as long as the fraction of the current associated with the pulses is small in comparison with the constant current, i.e., at a sufficiently low pressure.

In conclusion the authors thank V. S. Erofeev for useful discussions.

---

[1] V. K. Kalashnikov and Yu. V. Sanochkin, Zh. Tekh. Fiz., 44, 2504 (1974) [Sov. Phys. – Tech. Phys., 19, 1549 (1975)].

[2] N. N. Lebedev, Special Functions and Their Applications [in Russian], GIFML, Moscow–Leningrad (1963).

[3] L. Tonks and I. Langmuir, Phys. Rev., 34, 876 (1929).

[4] N. A. Kervalishvili and A. V. Zharinov. Zh. Tekh. Fiz., 35, 2194 (1965) [Sov. Phys. – Tech. Phys., 10, 1682 (1966)].

[5] J. P. Hobson and P. A. Redhead, Can. J. Phys., 36, 271 (1958).

[6] W. Knauer, J. Appl. Phys., 33, 2093 (1962).

[7] N. A. Kervalishvili, Zh. Tekh. Fiz., 38, 637 (1968) [Sov. Phys. – Tech. Phys., 13, 476 (1968)].

[8] R. Haefer, Acta Phys. Austriaca, 8, 213 (1954).

[9] N. A. Kervalishvili, Zh. Tekh. Fiz., 38, 770 (1968) [Sov. Phys. – Tech. Phys., 13, 580 (1968)].

[10] É. M. Barkhudarov, N. A. Kervalishvili, and V. P. Kortkhondzhiya, Zh. Tekh. Fiz., 42, 1904 (1972) [Sov. Phys. – Tech. Phys., 17, 1526 (1973)].

Formation of a plasma focus in a plasma erosion accelerator.
II. Energy characteristics of the dense plasma focus

N. P. Kozlov, L. V. Leskov, Yu. S. Protasov, and V. I. Khvesyuk
N. É. Bauman Moscow Higher Technical School
(Submitted April 18, 1972; resubmitted October 20, 1973)
Zh. Tekh. Fiz., 44, 2519-2522 (December 1974)

The integrated characteristics of the plasma focus in erosion plasma accelerators have been determined: the enthalpy and specific heat flux of the focus, the energy and light efficiencies, the utilization factor of the working medium, and the overall energy balance in the system. It is shown that these characteristics can be varied over broad ranges to suit a specific problem.

Under certain conditions, stable quasistationary, self-constricting plasma flows form beyond the end of pulsed electromagnetic plasma accelerators of the erosion type.[1-3] The flow velocity is $\sim 10^7$ cm/sec, the temperature is ~ 5 eV, and the particle density is $5 \cdot 10^{18}$ cm^{-3}.

The plasma properties attained in the plasma focus and the circumstance that these properties can be adjusted comparatively easily over wide ranges raise the hope that this type of plasma flow will find many applications.[4] In this connection it is worthwhile to study the integrated characteristics of the plasma focus – the energy and light efficiencies, the utilization factor of the working medium, etc.

We have previously reported[2] a study of the properties of the plasma in the focus; there we were concerned with determining the energy characteristics of the plasma focus in erosion plasma accelerators.

The local enthalpy of the compressed flow is given as a function of the time by

$$i^*(r,\ t) = n(r,\ t)\left[kT(r,\ t) + \frac{mV^2(r,\ t)}{2}\right], \tag{1}$$

where n(r, t) is the particle density, T(r, t) is the plasma temperature, V(r, t) is the average-mass velocity in the zone of maximum compression, m is the particle mass, r is the coordinate, t is the discharge time, and k is the Boltzmann constant.

The total enthalpy of the flow at the focus is

$$I^* = \frac{2\pi \int_t dt \int_{S(t)} i^*(r,\ t)\, r dr}{\int_t S(t)\, dt}, \tag{2}$$

where S(t) is the cross-sectional area at the region of maximum compression. The specific heat flux q is defined as the product of the enthalpy of the flow and the average-mass velocity,

$$q(r,\ t) = i^*(r,\ t)\, V(r,\ t), \tag{3}$$

while the total specific heat flux $\bar{q}$ is

$$\bar{q} = \frac{2\pi \int_t dt \int_{S(t)} i^*(r,\ t)\, V(r,\ t)\, r dr}{\int_t S(t)\, dt}. \tag{4}$$

We define the energy efficiency of the plasma focus as the ratio of the plasma energy at the focus to that stored in the capacitor bank:

$$\eta_{\text{en}} = \frac{\int_t dt \int_{S(t)} q(r,\ t)\, r dr}{W_0}, \tag{5}$$

where W_0 is the energy stored in the bank. The utilization factor of the working medium is

$$\varepsilon_{\text{wm}} = \frac{m \int_t dt \int_{S(t)} n(r,\ t)\, V(r,\ t)\, r dr}{\dot{m}}, \tag{6}$$

where the numerator is the amount of medium which passes through the focus during the discharge pulse, and $\dot{m}$ is the expenditure of working medium per pulse.

The light efficiency is defined as the ratio of the energy emitted over the range 50-20,000 Å to that stored in the capacitor bank. Measurements of the relative mass outflow and of the particle density at the surface of the dielectric in the discharge gap[5] and at the focus show that the degree of compression of the flow can be determined under the assumption of a polytropic process. As is shown in ref. 3, this is the case when the focus is formed under certain conditions. Thus,

$$\nu_{\text{co}} = \frac{\rho_{\max}}{\rho}\left[(\gamma - 1)\frac{C_{A0}^2}{C_{T0}^2}\right]^{1/\gamma-1}, \tag{7}$$

where

$$C_{A0}^2 = \frac{H_0^2}{4\pi\rho_0} \text{ and } C_{T0} = \gamma\frac{p_0}{\rho_0}$$

are the Alfvén and sound velocities, respectively, and γ is the ratio of the specific heats. Finally, the electrical efficiency of the system, which is a measure of how efficiently the energy stored in the capacitor bank is transferred to the discharge, is defined by

$$\eta_{\text{el}} = \frac{\int_t dt \int_t I(t)\, U(t)\, dt}{W_0}. \tag{8}$$

The energy characteristics of the plasma in the focus defined in this manner are shown in Table 1 as functions of the initial voltage on the capacitor bank, U_0. The M2-K accelerator is described in ref. 2, and the working medium is Fluoroplast-4 (Teflon) or copper.

The enthalpy and the specific heat fluxes increase rapidly as the energy supplied to the discharge is increased, and their values differ only slightly in accelerators differing in the geometry of the accelerating electrodes. These values are much higher at U_0 = 2 kV than at U_0 = 1 kV because of the markedly smaller size of the plasma in the case U_0 = 2 kV. The maximum heat fluxes, like the maximum degrees of compression, are obtained in accelerators whose electrodes have a "compressional" geometry. The degree of compression increases with the energy supplied to the discharge, amounting to ~ 100 at U_0 = 5 kV.

TABLE 1. Energy Characteristics of the Plasma Focus

Plasma forming material	U_0, kV	i^*, erg/cm^3	q, erg/sec·cm^2	η_{en} %	ε_{wm}, rel. units	ν_{co}, rel. units	η_{li} %	η_{el} %
Teflon	1	$5.7 \cdot 10^6$	$1.3 \cdot 10^{13}$	22	0.42	—	7.4	62
	2	$9.0 \cdot 10^8$	$2.7 \cdot 10^{15}$	54	0.59	38	5.2	78
	3	$3.1 \cdot 10^9$	$1.2 \cdot 10^{16}$	67	0.73	62	13.9	79
Copper	1	$4.2 \cdot 10^6$	$1.1 \cdot 10^{13}$	19	0.33	—	8.0	58
	2	$7.3 \cdot 10^8$	$1.8 \cdot 10^{15}$	51	0.58	45	18.4	74
	3	$8.9 \cdot 10^8$	$4 \cdot 10^{15}$	48	0.51	71	24.5	70

Its minimum values are found in end-type accelerators, i.e., the "two-step" compression due to processes in the interelectrode gap and in the external currents is more effective than the free pinching in the external currents. By shaping the electrodes in the appropriate manner it is possible to obtain a high flow velocity and to increase the kinetic component of the enthalpy [Eq. (1)], which is the predominant component.

It should be noted that the energy efficiency is reduced by 8-22% when the plasma is formed from a metal, because of the much more intense emission from the focus, the increased loss in the accelerator itself, and the removal of working medium in the form of droplets.

This high utilization factor of the working medium in erosion plasma accelerators (in comparison with gas-discharge plasma accelerators[6]) is evidently a characteristic feature of this type of accelerator.

As noted in ref. 2, the decrease in the light efficiency as the energy supplied to the discharge is raised to 1-2 kJ (i.e., the energy threshold for the formation of a focus) is due to sharply intensified reabsorption in focus. The energy of this emission increases ~45% in operation with a metal plasma (copper or aluminum), the nature of the emission spectrum changes (there is a sharp intensification of the continuum), and the light efficiency at $U_0 \doteq 3$ kV is 24.5%. From the standpoint of the light efficiency the best accelerator is the end-type accelerator working with a metal plasma. By choosing the working medium and discharge parameters properly one can achieve focused light pulses of any desired intensity and duration with any desired energy spectrum.

The overall energy balance consists of the components corresponding to the processes occurring in the accelerator and at the focus. The loss at the electrodes[7] is ~10-15% of the energy stored in the capacitor bank, essentially independent of the energy supplied to the discharge. The other losses in the accelerator – due to ablation of the dielectric, ionization, etc. – make up ~ 10% of the total energy balance. Thus the transfer of energy from the capacitors to the plasma focus can be very efficient in erosion accelerators with high electrical efficiency (up to ~0.94).

The properties of the plasma flow at the focus can be manipulated in order to achieve a high efficiency in the particular application, e.g., the production of a high-energy plasma flow for some plasma-chemistry process,[4] the production of a flow with a high working-medium utilization factor and a highly monoenergetic nature for use in hypersonic aerodynamics, or the production of focused light pulses for optical pumping of laser media. The particular plasma properties are achieved by choosing the appropriate accelerator geometry, working medium, and energy and dynamic characteristics of the discharge loop.

---

[1] A. A. Kalmykov, L. V. Leskov, and M. I. Pergament, in: Plasma Accelerators [in Russian], Izd. Mashinostroenie, Moscow (1973).

[2] N. P. Kozlov, L. V. Leskov, Yu. S. Protasov, and V. I. Khvesyuk, Zh. Tekh. Fiz., 43, 860 (1973) [Sov. Phys. – Tech. Phys., 18, 542 (1973)].

[3] Yu. M. Grishin, N. P. Kozlov, Yu. S. Protasov, and V. I. Khvesyuk, Zh. Tekh. Fiz., 43, 1496 (1973) [Sov. Phys. – Tech. Phys., 18, 948 (1974)].

[4] N. P. Kozlov, L. V. Leskov, Yu. S. Protasov, and V. I. Khvesyuk, First All-Union Symposium on Plasmochemistry [in Russian], Moscow (1971), p. 58.

[5] V. Ya. Gubarev, N. P. Kozlov, L. V. Leskov, and Yu. S. Protasov, Zh. Tekh. Fiz., 42, 826 (1972) [Sov. Phys. – Tech. Phys., 17, 650 (1972)].

[6] I. N. Burdonskii, A. I. Morozov, M. I. Pergament, and A. I. Yaroslavskii, in: Plasma Accelerators [in Russian], Izd. Mashinostroenie, Moscow (1973).

[7] V. Ya. Gubarev, N. P. Kozlov, Yu. S. Protasov, and V. I. Khvesyuk, Zh. Tekh. Fiz., 42, 1033 (1972) [Sov. Phys. – Tech. Phys., 17, 818 (1972)].

[8] V. Ya. Gubarev, N. P. Kozlov, L. V. Leskov, and Yu. S. Protasov, Report to the Sixth All-Union Conference on the Thermophysical Properties of Matter, Kiev, 1974.

Effect of rf ionization on Hall-current plasma accelerator

I. I. Demidenko, N. S. Lomino, A. I. Morozov, and V. G. Padalka

(Submitted December 12, 1973)
Zh. Tekh. Fiz., 44, 2523-2528 (December 1974)

The effect of auxiliary radio-frequency ionization of the gas near the anode on the properties of a Hall-current plasma accelerator are investigated. Displacement of the region in which the entering gas is ionized toward the anode by the rf fields leads to an increase in the ion energy in the plasma and to a reduction of the spatial divergence of the plasma jet.

Of the various injectors used in thermonuclear research the most common are ion sources and pulsed plasma accelerators. Potential plasma injectors operating continuously or quasicontinuously with ion currents of ~1-10 kA at an ion energy of 1-10 keV are promising sources of plasma for thermonuclear reactors. Since the medium remains neutral in the acceleration region the plasma accelerator is not subject to the space-charge limitations of an ordinary ion source.

An electric field can only exist in a cool, low-density plasma in the presence of a magnetic field and electron drift; the electric field is perpendicular to both H and $\mathbf{v}_e$ (ref. 1). The marked reduction in the transverse electron conductivity in a strong magnetic field makes it possible for a strong electric field to penetrate into the plasma; this penetration can be exploited in effective acceleration of the ions.

Hall-current accelerators can be divided into two groups on the basis of the transverse electronic conductivity: If this conductivity is due to binary Coulomb collisions, the corresponding Hall-current accelerators have a comparatively short accelerating gap, $\Lambda_E \sim \rho_e$. Accelerators of this type have a metal channel, containing the accelerating gap, and a system for ionizing the working medium. In accelerators of this type the beam of accelerated ions is highly monoenergetic, ion beams at energies up to 20-30 keV can be produced, and the beam divergence is small. However, the currents are relatively weak ($j_i \sim 10^{-1}$ A/cm^2), and strong magnetic and electric fields must be used.[2]

In Hall-current accelerators with an extended acceleration region the mechanisms responsible for the transverse electron conductivity are the more intense turbulent and wall mechanisms. These systems can produce extremely high ion current densities (1-3 A/cm^2) at an overall ion current ~1 kA, and the electric and magnetic fields are weak. However, the ion beams are decidedly not monoenergetic, and the angular divergence is large (up to ± 30°) (ref. 3). These properties are consequences of the relatively large size of the region in which the working medium is ionized; these effects make difficult the analysis of the possible use of such accelerators as injectors for thermonuclear devices.

One type of Hall-current accelerator with an extended acceleration zone is the two-lens accelerator. It has an axial accelerating channel with a "two-lens" radial magnetic field; the field is in opposite directions in the first and second lenses. The working gas entering the system is ionized in this channel, and the ions are accelerated by the electric field along the channel. The magnetic field serves two purposes: It "freezes" the electron component and focuses the ion beam.

The ion motion in the accelerating channel is analyzed in detail in ref. 4. The ions crossing the exit plane of the accelerators move along straight lines whose directions are governed by the relations among v_z, v_r, and v_φ, i.e., the longitudinal, radial, and azimuthal components of the ion velocity $\mathbf{v}_i$ at the exit plane. In general the shape of the ion beam leaving the accelerator can be described by a set of surfaces of revolution (single-sheet hyperboloids) which intersect the exit plane of the accelerator.

Since the plasma density in the accelerating channel is relatively low (~10^{11}-10^{12} cm^{-3}), the motion of an ion under the influence of the electric and magnetic fields can be assumed to be collisionless. If we neglect plasma noise and the azimuthal components of the magnetic and electric fields, we can estimate the ratio of the azimuthal component of the ion velocity to the magnitude of the total velocity at the exit plane on the basis of conservation of the azimuthal component of the generalized momentum:

$$P_\varphi = Mv_\varphi + \frac{e}{c}A_\varphi = \frac{e}{c}\frac{r^0}{r}A_\varphi^0, \qquad (1)$$

where A_φ, the only nonvanishing component of the magnetic vector potential, is related to the field components by

$$H_r = -\frac{\partial A_\varphi}{\partial z}; \quad H_z = \frac{\partial A_\varphi}{\partial r}, \qquad (2)$$

where A_φ^0 denotes the value of A_φ at the point at which an ion with radial coordinate r_0 is produced (we assume that the ion velocity is zero at this point). The total ion velocity can be estimated from energy conservation:

$$\frac{Mv^2}{2} + e\Phi = e\Phi_0, \qquad (3)$$

where Φ is the electric potential. Then we have

$$\frac{v_\varphi}{v} = \frac{v_\varphi}{v_z}\frac{1}{\sqrt{1+\left(\frac{v_r}{v_z}\right)^2+\left(\frac{v_\varphi}{v_z}\right)^2}} = \sqrt{\frac{e}{2M}}\,\frac{r^0A_\varphi^0 - rA_\varphi}{cr\sqrt{\Phi_0-\Phi}}. \qquad (4)$$

In the exit plane of a two-lens accelerator we have $A\varphi = \Phi = 0$ and

$$\frac{v_\varphi}{v} = \sqrt{\frac{e}{2M}}\,\frac{r^0A_\varphi^0}{cr\sqrt{\Phi_0}} = f(r^0,\ z^0), \qquad (5)$$

where r^0, z^0 are the coordinates of the point at which the ion is produced.

The ionization occurs over a long distance in the accelerating channel[5] (~10 cm), spanning essentially the entire length of the first lens. Measurements of the ion current lines in the accelerator channel have confirmed this conclusion. In certain cases the ionization region even extends into the second lens.[6] These effects tend to smear the energy spectrum of the accelerated ions at low energies and produce a pronounced divergence of the beam leaving the accelerator.

If we assume the ideal case of collisionless ion motion in an accelerator with two sections of equal radial magnetic flux, then the ions produced near the anode ($A_\varphi^0 = 0$) acquire an azimuthal velocity v_φ as they move through the first lens (the length of the lens is $L < \rho_i$, where ρ_i is the characteristic ion Larmor radius); when the ions intersect the magnetic flux of the second lens they lose this velocity. As a result, the flux of ions produced near the anode should have a low divergence and the maximum possible energy at the accelerator exit. In the other limiting case in which the ion is produced in the region between lenses ($A_\varphi^0 = A_{\varphi\max}^0$) the particle is accelerated to an intermediate energy and is deflected significantly after passing the maximum magnetic flux. Accordingly, the optimum acceleration of ions in a two-lens Hall-current accelerator would require the displacement of the ionization to the region near the anode; this displacement can be achieved by using correcting magnetic fields or by preliminary ionization of the working gas entering the accelerator.

Figure 1 shows the two-lens Hall-current accelerator studied here which uses rf ionization of the working gas. The inner, alundum wall of the accelerator is 8 cm in diameter, and the outer glass wall is 13.5 cm in diameter. The accelerator is 30 cm long. It is part of a vacuum chamber with a volume of 1 m^3; the cathode is made up of the exit flange of the accelerator and the walls of the evacuated volume. The power supply is a 350 μF capacitor bank, which is discharged through a line which produces a rectangular voltage pulse. For typical operating conditions the voltage on the accelerator is 1 kV (with a current ~1 kA and a pulse length of 750 μsec. The working gas (hydrogen) is admitted into the accelerator in quantities ~1 $cm^3 \cdot$ atm by means of an electrodynamic valve through an aperture in the anode. The initial pressure in the volume, before the gas is admitted, is $5 \cdot 10^{-6}$ torr. The radial magnetic field in the lenses is ~250 Oe, and the lenses are 10 cm apart (Fig. 2). The lens-shaped magnetic field provides magnetic and electrostatic focusing of the ion beam.[1,4]

The gas entering the system is ionized by a three-turn rf coil around the outer wall of the accelerator, between the anode and the first magnetic lens. The pulsed rf oscillator is a half-wave circuit using a GI-14B metal-ceramic triode; it operates at a frequency ~180 MHz with a pulse length ~600 μsec). Power is fed from the oscillator to the load by a conductive coupling; the power taken from the oscillator is ~100 kW. The unipolar voltage pulse at the oscillator is produced by the capacitor bank through the pulse-shaping line and a step-up transformer. Effective absorption of rf energy by the plasma is achieved by using the electron cyclotron resonance. Under the coil the longitudinal magnetic field H_z is 50 Oe at the mean radius of r = 5.4 cm, and the oscillator frequency is $\omega \simeq \omega_{He}$.

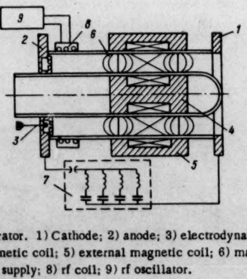

Fig. 1. Accelerator. 1) Cathode; 2) anode; 3) electrodynamic gas valve; 4) internal magnetic coil; 5) external magnetic coil; 6) magnetic lines of force; 7) power supply; 8) rf coil; 9) rf oscillator.

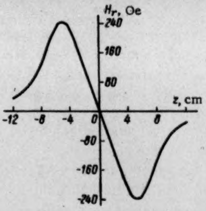

Fig. 2. Radial magnetic field H_r along the accelerator at r = 5.4 cm.

The voltage is fed to the accelerator 750 μsec after the electrodynamic gas valve is operated; the shape of the voltage pulse at the source is approximately rectangular (Fig. 3c), and the pulse height is ~1 kV. We do not study the spatial distribution of the hydrogen pressure in the system at the beginning of the discharge or the rate at which the hydrogen is supplied. The shape of the current pulse is different from the shape of the voltage pulse but similar to the time dependence of the plasma emission from the accelerator (Fig. 3b). The peak current is ~1 kA.

The energy spectra of the plasma ions and the angular divergence of the jet have been studied with and without the auxiliary rf ionization of the working gas. The rf oscillator is turned on 650 μsec after the inlet valve is operated (Fig. 3a shows the envelope of the rf pulse). The measurements show that this time delay is optimum in terms of the change in the plasma energy spectrum at the second maximum of the discharge current and the plasma emission (500 μsec after the beginning of the discharge in the source).

The plasma energy spectra are measured by a retarding-potential method with a wide-aperture multigrid

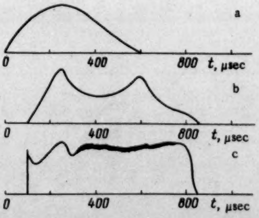

Fig. 3. Oscillograms of a) the envelope of the rf pulse; b) the plasma emission; c) the voltage across the accelerator.

probe,[3,7] which consists of four high-transmission, plane-parallel molybdenum grids in front of a (solid) ion collector. The first grid, connected to the housing of the probe, is at a floating potential, so that there is no current flow from the discharge through the probe housing. The second grid is at a negative potential ~100 V, to separate the plasma entering the probe into its ion and electron components. The third grid is used for the energy analysis of the ions, with a retarding potential (from 0 to 1 kV). The fourth (suppressor) grid shields the collector from the fields of the other grids and suppresses secondary electron emission from the collector; it is held at a negative potential of −100 V. The ion current drawn by the collector is displayed on an S1-29 oscilloscope. The probe is held 60 cm from the exit plane of the accelerator and can be moved in the radial direction ($\Delta r = \pm 45$ cm).

Figure 4 shows the ion current drawn by the collector as a function of the retarding potential with and without the auxiliary rf ionization of the hydrogen in the anode region of the accelerator. These measurements are carried out with the probe at the axis at a time $t = 500$ μsec after the beginning of the discharge (the second maximum in the ion flux). Turning on the rf ionizer does not affect the current drawn at a zero retarding potential (with respect to the housing of the probe), but the functional dependence of the ion current on the retarding potential is shifted toward higher retarding voltages. This behavior implies a shift in the energy spectrum of the accelerated ions toward higher energies because of the auxiliary rf ionization.

The average ion energy can be estimated from

$$\bar{\varepsilon}_{\parallel}=\frac{\int_0^{\infty}\varepsilon_{\parallel}g(\varepsilon_{\parallel})\,d\varepsilon_{\parallel}}{\int_0^{\infty}g(\varepsilon_{\parallel})\,d\varepsilon_{\parallel}}, \qquad (6)$$

where

$$g(\varepsilon_{\parallel})=\left.\frac{dJ_i}{d\varepsilon_{\parallel}}\right|_{\varepsilon_{\parallel}=eV_{\parallel}}.$$

The numerator of this fraction is proportional to the area bounded by the given curve and the coordinate axes, while the denominator is proportional to the ion current at $V_{\parallel} = 0$. Calculations show that in the absence of the rf ionization of the gas near the anode the average ion energy is $\bar{\varepsilon}_{\parallel} = 400$ eV; the ionizer increases this energy to 550 eV.

The ion energy spectra can be found by a graphical differentiation of the curves in Fig. 4, although the error of this procedure can be large. Figure 5 shows the results of a differentiation of the functional dependence of the ion current on the retarding potential with and without the rf ionization. In the absence of the auxiliary rf ionization the energy sepctrum has two peaks, at 150 and 600 eV, apparently due to ionization of the gas in both lenses, confirming the extension of the ionization region into the accelerating channel. The auxiliary rf ionization increases the height of the higher-energy peak and shifts it up to 700 eV. At the same time, the lower-energy peak falls to half its height and shifts to 250 eV. This behavior implies that the auxiliary rf ionization of the gas near the anode tends to increase the relative number of particles which traverse the entire potential difference and tends to reduce the relative number of accelerated particles which are produced near the exit plane of the accelerator in the vicinity of the second magnetic lens. Accordingly, the shift of the hydrogen-ionization region toward the anode increases the average energy of the ions in the plasma jet produced by the accelerator.

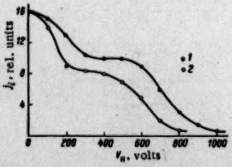

Fig. 4. Ion current drawn by the collector of the multigrid probe as a function of the retarding potential. 1) With; 2) without rf ionization of the hydrogen in the anode region of the accelerator.

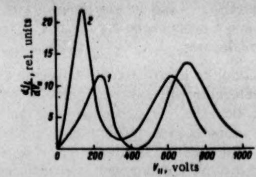

Fig. 5. Energy spectra of the plasma ions with (1) and without (2) rf ionization of the hydrogen in the anode region of the accelerator.

An increase in the average ion energy in the plasma jet should be accompanied by a contraction of the angular distribution of the ion velocities beyond the exit plane. In the ideal case in which an ion is produced in a region with $A_{\varphi}^{0} = 0$ and $\Phi_0 = \Phi_{0\max}$, the azimuthal velocity would be $v_{\varphi} = 0$, and we would have $v = v_{\max}$. We measure the spatial divergence of the plasma jet with the multigrid probe with a zero retarding potential in a plane parallel to the exit plane of the accelerator and 60 cm away from it. These measurements are carried out at the same time ($t = 500$ μsec) as the measurements of the ion energy spectra. The results are shown in Fig. 6. The angular divergence of the accelerated plasma in the case of no rf ionization is ± 35°; the rf ionizer contracts the ion spatial distribution to ± 25° and increase the signal level at the axis.

Accordingly, the properties of the plasma jet produced by a Hall-current accelerator with an extended acceleration region can be significantly improved by a more

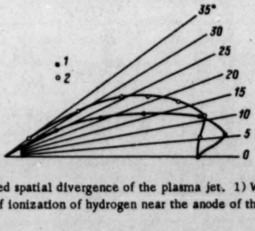

Fig. 6. Measured spatial divergence of the plasma jet. 1) With; 2) without the auxiliary rf ionization of hydrogen near the anode of the accelerator.

rationally planned ionization of the working gas. By displacing the region in which the gas entering the accelerator is ionized toward the anode, through the use of auxiliary rf fields, one can increase the energy of the plasma ions and reduce the angular divergence of the plasma jet.

---

[1] A. I. Morozov, Dokl. Akad. Nauk SSSR, 163, 1363 (1965) [Sov. Phys. – Dokl., 10, 775 (1966)].

[2] S. D. Grishin, V. S. Erofeev, and A. V. Zharinov, in: Plasma Accelerators [in Russian], Izd. Mashinostroenie, Moscow (1973), p. 54.

[3] I. P. Zubkov, A. Ya. Kislov, and A. I. Morozov, Zh. Tekh. Fiz., 41, 880 (1971) [Sov. Phys. – Tech. Phys., 16, 695 (1971)].

[4] S. V. Lebedev and A. I. Morozov, Zh. Tekh. Fiz., 37, 631 (1967) [Sov. Phys. – Tech. Phys., 12, 455 (1967)].

[5] I. P. Zubkov, A. Ya. Kislov, S. V. Lebedev, and A. I. Morozov, Zh. Tekh. Fiz., 41, 526 (1971) [Sov. Phys. – Tech. Phys., 16, 409 (1971)].

[6] H. C. Cole, Nucl. Fusion, 10, 269 (1970).

[7] M. V. Nezlin and A. M. Solntsev, Zh. Eksp. Teor. Fiz., 48, 1237 (1965) [Sov. Phys. – JETP, 21, 826 (1965)].

Analytic model for the arc regime and the thermionic converter

V. D. Bondarenko and A. I. Loshkarev

(Submitted November 5, 1973)
Zh. Tekh. Fiz., 44, 2529-2536 (December 1974)

Questions involved in the determination of absolute work functions for the cathode and anode from the experimental voltage–current characteristics for an arc are discussed. This diagnostic procedure is based on a matching of the quenching region on the theoretical characteristic, where a virtual cathode forms, with the corresponding region on the experimental characteristic. Simple analytic expressions for the theoretical dimensions of this region are derived. The changes in the electron temperature over the gap are taken into account in the approximation according to which all the ions generated in the volume are scattered to the cathode. Analysis of many experimental voltage–current characteristics by this method reveals a good agreement between the theoretical electrode work functions obtained and the results of independent measurements.

The diagnostics of the internal properties of thermionic converters (the cathode work function Φ_K, the anode work function Φ_A, etc.) on the basis of the voltage–current characteristics is an extremely important question, e.g., from the standpoint of interpreting lifetime tests. Essentially no work has been reported on the development of procedures for determining the emission properties of electrodes in the arc regime at high cesium vapor pressures, in which case there is no clearly defined break on the arc branch of the voltage–current characteristic at the transition from the region in which the potential in the cathode drop is distributed monotonically to the region with a virtual cathode. Even when there is a clearly defined break the current J at the break cannot be identified with the emission current J_{em}. As is shown below, the coefficient $t = J_{em}/J$ at this point takes on significantly different values for various gaps d and for various cesium pressures p_{Cs}. The method of ref. 1 determining emission properties of cathodes requires that the interelectrode gap be changed, but this is not always possible. For diagnostic purposes there are definite advantages in the use of analytic models, which can be used to trace the explicit functional dependence of the voltage–current characteristics on all the adjustment parameters, so that a closed system of algebraic equations can be found and used to determine several of the internal properties. The successful use of analytic models for diagnostics depends on a good matching of the theoretical and experimental voltage–current characteristics. In the familiar arc-regime model,[2,3] the effects of Coulomb scattering and volume recombination are neglected, but these processes can contribute significantly to the developed arc. These effects are incorporated in the analytic model of ref. 4. In both these models the assumption that the electron temperature T_e is constant over the gap leads to a symmetric density distribution over the gap, so that the same number of ions, S/2, where S is the total number of ions generated in the gap, is scattered to each electrode.

Actually, the maximum of the generation function is closer to the cathode than to the anode because the electron temperature is higher at the cathode, and most of the ions are scattered to the cathode.

It has been shown[4] that the voltage–balance equation

$$\Delta V = \frac{T_e}{e} \ln \frac{J}{J_{em}^{ef} - J} + J\,(R_{Cou} + R_n) \tag{1}$$

and the energy-balance equation for electrons,

$$e\Delta V J = J_{em}^{ef}(2T_e - 2T_K) + eSE_i^{ef} \tag{2}$$

retain the same form when there is a variation in the electron temperature, provided that the average electron temperature is used in these equations.

In these equations we have adopted the following notation: ΔV is the potential drop between the potential minimum at the cathode and the potential of the anode surface, $J_{em}^{ef} = J_{em}\exp(-e\Delta\varphi_{vir}/T_K)$ is the effective emission current in the presence of a virtual cathode having the effective work function, $\Phi_K^{ef} = \Phi_K + \Delta\varphi_{vir}$, $\Delta\varphi_{vir}$ is the additional potential jump, which retards the emitted electrons, $R_{Cou} = (4\sqrt{2\pi}/3)(m_e^{1/2}e^2T_e^{3/2})\Lambda d$ is the part of the plasma resistance due to Coulomb scattering and independent of the density profile in the gap, Λ is the average value of the Coulomb logarithm, $R_{Cou} = (8\sqrt{2}/3\sqrt{\pi}) \cdot (m_e^{1/2}/e^2)\sigma_{ea}T_e^{1/2}n_a \int_{x_K}^{x_A} dx/n$ is the part of the resistance due to scattering by neutrals, σ_{ea} is the cross section for scattering of electrons by neutrals, and $E_i^{ef} \approx 6$ eV is the effective energy expended on the formation of an electron–ion pair.[4]

The minimum average electron temperature in the arc can be determined from

$$\delta^2 \equiv 1.44 \cdot 10^{-12} \exp\left(-\frac{3.21}{T_e}\right) n_a v_{eT} \frac{d_E^2}{D_a} = \pi^2, \tag{3}$$

where n_a is the average density of atoms in the gap, v_{eT} is the mean electron thermal velocity, d_E is the extrapolated size of the interelectrode gap, and D_a is the average ambipolar diffusion coefficient.

It follows from the equation for R_n that this quantity is governed primarily by the density near the electrode. Since

$$S = \frac{1}{2} n_K v_{iTK} + \frac{1}{2} n_A v_{iTA},$$

where n_K (n_A) is the plasma density near the cathode (anode), and v_{iTK} (v_{iTA}) is the electron thermal velocity near the cathode (anode), we can write R_n approximately as

$$R_n = \frac{K_{RS}(S)}{eS}, \tag{4}$$

where $K_{RS}(S)$ is a slowly varying function of S, governed by the nature of the density profile in the gap.

The details of the density profile are important only near the electrodes, where n reaches its minimum values. Using a sinusoidal density profile after the model of ref. 3 to calculate K_{RS} we find

$$K^0_{RS} = 4\sqrt{2}\sqrt{\frac{m_e}{m_i}}\frac{\sigma_{ea}}{\sigma_{ia}}\sqrt{\frac{T_e}{T_i}}\left(\frac{T_i}{e}+\frac{T_e}{e}\right)\cos\pi\frac{\Delta d_E}{d_E}\ln\frac{1}{\operatorname{tg}\frac{\pi}{2}\frac{\Delta d_E}{d_E}}, \quad (5)$$

where $\Delta d_E = (1/2)(d_E - d)$ is the extrapolated increment. Calculations of K_{RS} for a density distribution described by an elliptic sine, as in the model of ref. 4, and calculations in the piecewise-linear approximation for the density profile, in which case the densities and their derivatives are equal at the edges of the gap (so that S is constant in all three cases), give approximately equal results. The scatter is comparable to the scatter in values of the ratio σ_{ea}/σ_{ia}.

Calculations show that, with the maximum of the generation function right at the cathode surface, we have, for a broad range of $\Delta d_E/d_E$,

$$K_{RS} \approx (2-3)K^0_{RS}. \quad (6)$$

System (1), (2), (4) can be used to construct a J^{ef}_{em} = const grid in the V−J plane for each value of δ.

A perturbation study of the stability of this grid shows that as δ is changed from its minimum value of π (corresponding to a weakly developed arc with negligible recombination) to $\delta = 15$ (a highly developed arc with an ionization equilibrium in a large part of the gap), and for K_{RS} or E_i^{ef} different from its actual value by a factor of 2, the maximum deformation of the J_{em} = const grid near the turning point is no more than $0.4\,T_K$ for the specified current. The error in the current on the gently sloping branches of this grid is extremely small (a few percent).

Accordingly, the J_{em} = const grid is stable with respect to the detailed structure of the model, specified by the quantities δ, K_{RS}, and E_i^{ef}; and the maximum deformation of this grid due to errors must not exceed 0.1 V. For the analysis below we therefore adopt the values $\delta = \pi$, $K_{RS} = 2k^0_{RS}$, $E_i^{ef} = 6$ eV, $\sigma_{ia} = 10^{-13}$ cm², $\sigma_{ea} = 2.5 \cdot 10^{-14}$ cm², $T_{i,a} = (1/2)(T_K + T_A)$, and $\Lambda = 5$.

In the arc-quenching region, where a virtual cathode is formed, the potential drop near the cathode, $\Delta\varphi_K$, measured from the potential minimum in the cathode sheath, is related to the parameters $t = J^{ef}_{em}/J$ and $\theta_K = T_{eK}/T_K$ by[5]

$$(t-1)\exp\left(\frac{e\Delta\varphi_K}{T_{eK}}\right) = \frac{\pi}{\sqrt{2}\,b_{iE}}\frac{\sigma_{ia}}{\sigma_{ea}}\left[\frac{1+\theta_K^{1/2}}{\theta_K^{1/2}}(t-1)+1\right]^2, \quad (7)$$

where $b_{iE} \approx 2$ is the ratio of the flux of ions scattered to the cathode to the random ion flux at the cathode.

Using the boundary condition on the electron current at the cathode,

$$J = J^{ef}_{em} - \frac{1}{4}n_K v_{eTK}\exp\left(-\frac{e\Delta\varphi_K}{T_{eK}}\right),$$

and the assumption that all the ions generated in the gap are scattered to the cathode, we conclude that

$$\frac{eS}{J} = \frac{\pi}{\sqrt{2}}\frac{\sigma_{ia}}{\sigma_{ea}}\frac{1}{\theta_K^{1/2}}\sqrt{\frac{m_e}{m_i}}\left[\frac{1+\theta_K^{1/2}}{\theta_K^{1/2}}(t-1)+1\right]^2. \quad (8)$$

Through a joint solution of Eqs. (1), (2), and (8) we find the following parametric functional dependences of the current voltage in the part of the voltage−current characteristics corresponding to quenching of the arc and the formation of a virtual cathode:

$$J_{vir}(t) = \frac{1}{R_{Cou}}\left\{\frac{2T_K}{e}t(\theta-1)+\frac{T_K}{e}\theta\ln(t-1) + \frac{E_i^{ef}}{e}A\left[\frac{1+\theta_K^{1/2}}{\theta_K^{1/2}}(t-1)+1\right]^2 - \frac{K_{RS}}{A}\left[\frac{1+\theta_K^{1/2}}{\theta_K^{1/2}}(t-1)+1\right]^{-2}\right\}, \quad (9)$$

$$V_{vir}(t) = \Phi_K^{ef} - \Phi_A - \frac{2T_K}{e}(\theta-1)t - \frac{E_i^{ef}}{e}A\left[\frac{1+\theta_K^{1/2}}{\theta_K^{1/2}}(t-1)+1\right]^2, \quad (10)$$

where

$$\theta = \frac{T_e}{T_K}, \quad A = \frac{\pi}{\sqrt{2}}\frac{\sigma_{ia}}{\sigma_{ea}}\frac{1}{\theta_K^{1/2}}\left(\frac{m_e}{m_i}\right)^{1/2},$$

and Φ_K^{ef} can be evaluated by means of the Richardson equation, from

$$J^{ef}_{em}(t) = tJ(t).$$

Equation (8) describes a weak functional dependence on the quantity Θ_K. Calculations carried out under the assumption $\theta_K = \theta$ and $\theta_K = 2\theta$ show that the quenching curve, i.e., the function $J_{Cou} = J_{Cou}(V_{Cou})$, remains essentially constant, while the values of the parameter t at the corresponding points of this curve differ by less than 20%. Thus, assuming $\theta_K > \theta$, we set $\theta_K = 2\theta$ in the calculations below.

The maximum value of Φ_K^{ef} can be estimated in the following manner: The plasma synthesized at the hot cathode has an equilibrium chemical potential $\mu_K(T_K, p_{Cs})$. For typical conditions ($T_K = 2000$°K, p_{Cs} = 1-10 torr) we have $\mu_K \approx 2.95$, and the optimum value is $\Phi_K \approx 2.7$-2.8 eV (ref. 4). Accordingly, under approximately optimum conditions the arc discharge in a thermionic converter is usually ignited from an undercompensated regime. The ion flux from the plasma toward the cathode resulting from volume ionization, which is much higher than the equilibrium random fluxes, reduces or totally eliminates the virtual cathode, and the equilibrium chemical potential μ_K can be used as an upper estimate of Φ_K^{ef}.

Then the characteristic regions of the voltage−current characteristics can be constructed in the following manner (Fig. 1). In region 1 we can assume that the characteristic coincides with the $J^{ef}_{em} = J_{em}$ line, determined from the cathode work function for the specified values of p_{Cs} and T_K at zero field. This assumption is valid for cathodes for which the work function is homogeneous over the surface. Taking account of the normal Schottky effect and the change in the coverage of the cathode surface with

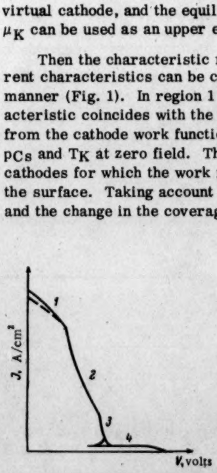

Fig. 1. General nature of the voltage−current characteristics of the thermionic converter.

a change in the degree of ionization of the plasma in the gap[6] leads us to the conclusion that J_{em}^{ef} will increase and the characteristics in region 1 will deviate from the J_{em}^{ef} = const line. Since these effects cancel out to a certain extent, this region can be constructed approximately from Eqs. (1) and (2) with fixed J_{em}^{ef}.

Equations (9) and (10) describe region 2. Since there is an upper limit on the virtual cathode, these equations apparently hold for currents $J > J_{\mu}$, where J_{μ} is the random electron current in the equilibrium plasma at temperature T_K. As the current is reduced further, two limiting cases can be reached. First, a diffusion region of the plasma, in which there is negligible volume ionization, can appear and expand.[7] Beyond this region is a layer in which there is a rapid potential jump, $\Delta\varphi$, within a Debye length. We note that, as follows from ref. 5, the total and oppositely directed electron flux Γ_e and ion flux Γ_i in this region are related by

$$\frac{\Gamma_e}{|\Gamma_i|}\sqrt{\frac{m_e}{m_i}} \approx \frac{1}{\theta^{1/2}}\frac{\sigma_{ia}}{\sigma_{ea}}\frac{\sqrt{2}\,\pi}{b_i^2}\exp\left(-\frac{2e\Delta\varphi}{T_{eK}}\right) \ll 1\ ;$$

i.e., the Langmuir equation for the double sheath, used in ref. 7, does not hold here.

The other possible limiting case can arise if the discharge is shunted. Nor do we rule out the possibility of a hybrid quenching mechanism, involving the contraction of the discharge and the simultaneous expansion of the diffusion region. It is difficult to treat such a two-dimensional system theoretically, since slight deviations of the electrodes from the isothermal, equipotential models can have strong effects. These effects are manifest in region 3 of the voltage–current characteristics.

Region 4 corresponds to a diffusion branch and negligible volume generation.

To compare these theoretical conclusions with experiment we use the most systematic experimental data available, that of refs. 8-13. Since the cathodes in these experiments are fabricated from gaseous tungsten, with a predominant orientation of the (110) faces, or are cut from tungsten single crystals, the patch effects (neglected in the theory) are minimized.

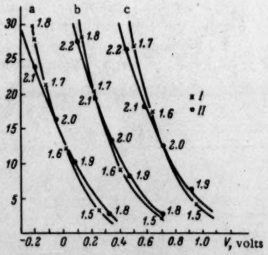

Fig. 2. Theoretical regions of arc quenching and the formation of a virtual cathode; variation of the parameter t along the quenching curve. a) T_K = 1600, b) 1800; c) 2000°K. T_A = 970°K, Φ_A = 1.8 eV. I) p_{Cs} = 0.70; II) 7 torr.

The theoretical regions of the characteristics constructed from Eqs. (9) and (10) are shown in Fig. 2. We see that even with a significant change in the pressure these regions are quite stable, due to the constancy of the anode work function assumed for the calculations (Φ_A = 1.8 eV). Furthermore, the parameter t is a strong function of the pressure at a specified current. The experimental characteristics of refs. 8-10 are influenced strongly by the cesium pressure; we can associate the changes in the characteristics with the significant changes which occur in the anode work function with increasing pressure. To determine Φ_A from the arc characteristics we bring the theoretical quenching regions (Fig. 2) into coincidence with the experimental regions (region 2 in Fig. 1). We observe good agreement between the theoretical and experimental regions over a broad current range, especially at high values of p_{Cs}. The values of Φ_A obtained in this manner are shown in Fig. 3 and Table 1. The good agreement between the values of Φ_A and the results of independent measurements by other methods[12-14] implies that the output voltages predicted by the theory are correct.

It should be noted that this model for the arc regime neglects inverse emission from the anode, and the anode potential drop is assumed to retard the electrons coming from the plasma.

At low cesium vapor pressures, and with a sufficiently hot anode, for which inverse emission becomes comparable to the current through the converter, there is an additional voltage loss

$$\Delta V_{inv} \approx \frac{T_e}{e}\ln\frac{J + J_{em,A}}{J}$$

where $J_{em,A}$ is the emission current from the anode. In this case the experimental treatment of the characteristics by the procedure described above should lead to a value of Φ_A larger than the actual value at low cesium pressures; we in fact observe this behavior in Fig. 3 (an estimate of ΔV_{inv} yields a value on the order of 0.05 V).

The tendency for an increase in Φ_A at high cesium pressures can be attributed to a reduction of the potential jump near the anode and even a change in the sign of this

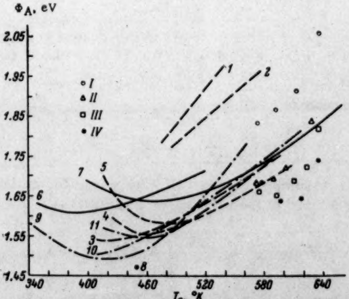

Fig. 3. Anode work function as a function of the cesium pressure and temperature, as determined by various methods.

TABLE 1

Designation in Fig. 3	T_A, °K	Material	Method	Reference
1	625	Polycrystalline molybdenum	Retarding field	[12]
2	675			
3	810	Polycrystalline molybdenum, polished	Inverse emission	[13]
4	860			
5	900			
6	673	Molybdenum sublimated onto a niobium substrate	Inverse emission	[11]
7	773			
8	673	Polycrystalline niobium, polished		[11], [13]
9	723			
10	810	Polycrystalline niobium, polished	Inverse emission	[14]
11	900			
I	673	Anode of molybdenum, sublimated niobium, $\Phi_0 = 4.78$ eV. Cathode of gaseous tungsten. $T_K = 1800$°K, $d = 0.25$ mm. Experimental data of ref. 8.	Proposed method	
II	773			
III	873			
IV	973			

jump, since there is a decrease in the ion current to the anode and a simultaneous increase in the current through the converter.

We note that, as shown in Fig. 3, it is incorrect to describe the experimental data on Φ near the minimum by a universal function of T_K/T_{Cs}. The minimum work function displays a strong temperature dependence, explaining the large scatter in the values of Φ_{min} plotted in Rasor coordinates.

The cathode work function is determined in the following manner: The beginning of the formation of the virtual cathode is identified with that point on the voltage–current characteristic at which the characteristic begins to deviate from the theoretical quenching regions as the current increases. The value of the parameter t at this point is chosen from the theoretical curve (Fig. 2). In this manner we treated about 200 characteristics spanning the following parameter ranges: $T_K = 1600$–2000°K, $p_{Cs} = 0.7$–10 torr, $d = 0.036$–1.0 mm, and $T_A = 673$–1073°K. As the gap is reduced in size we observe some decrease in the calculated value of J_{em}, which corresponds to an increase in Φ_K by no more than 0.03 eV. More pronounced differences are observed when Φ_A is plotted in Rasor coordinates and the cathode temperature is raised (Fig. 4). The designations are explained in Table 2. These differences can hardly be attributed solely to errors of the model used, since the parameter t would have to be increased to 3 or 4 in order to suppress the differentiation at a temperature of 2000°K. Nevertheless, the agreement between the emission properties of the cathode obtained by the various methods is quite good: All the data for a given cathode fall within a band 0.1 eV wide. In comparing the data in Fig. 4 it is necessary to take into account the fact that the emission determined from the measurements in the overneutralized regime (Fig. 4b) corresponds to the emission of spots of minimum work function in the cesium vapor in the presence of an extracting field at the surface. The proposed procedure (Fig. 4a) makes it possible to determine the emission when there is essentially no field at the cathode, when the virtual cathode begins to form above spots of maximum work function in the cesium vapor. We note that the emission is inhomogeneous even on single-crystal cathodes, as detailed studies have shown.

The functional dependence of the values of Φ_K on the cathode temperature and the gap size can be attributed partially to the variations in the density of cesium atoms over the gap. The formation of the equilibrium surface coverage of the electrode is governed primarily by atoms

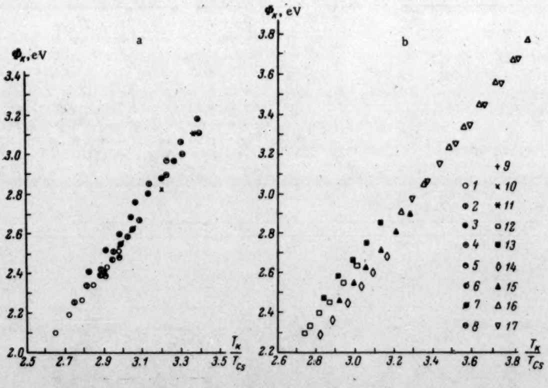

Fig. 4. Cathode work functions as a function of the parameter T_k/T_{Cs} as determined by various methods.

TABLE 2

T_K, °K	Gaseous oriented tungsten, Φ_0 = 4.98 eV			Gaseous oriented tungsten Φ_0 = 4.78 eV	(110) face of tungsten single crystal, Φ_0 = 5.14 eV	Gaseous oriented tungsten, Φ_0 = 4.87 eV
	Proposed method	method of ref. 1	Data of ref. 8	proposed method		acc. to saturation currents in the overcompensated regime[11]
1600	*1*	*5*	*9*	—	—	—
1700	*2*	*6*	—	*12*	*14*	*16*
1800	*3*	*7*	*10*	*13*	*15*	*17*
2000	*4*	*8*	*11*	—	—	—

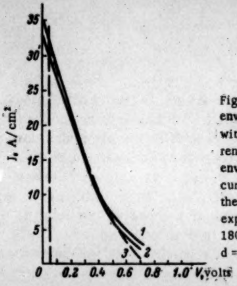

Fig. 5. Comparison of the theoretical envelope and the quenching curve with the experimental voltage–current characteristic. 1) Theoretical envelope of the characteristic; 2) curve corresponding to quenching and the formation of a virtual cathode; 3) experimental characteristic. T_K = 1800°K, T_A = 970°K, T_{Cs} = 636°K, d = 0.25 mm, Φ_A^{calc} = 1.8 eV.

in a sheath near the electrode having a thickness on the order of the atomic mean free path λ_a. If $d \approx \lambda_a$, the density of these atoms is governed by the electrode temperature for a fixed pressure in the cesium reservoir. In the case $d \gg \lambda_a$ the density is governed by half the sum of the cathode and anode temperatures. Accordingly, for small gaps and for identical cesium pressures, the cathode coverage will be higher and the anode coverage will be lower than for large gaps. Another factor leading to this dependence is the decrease in coverage due to the increase in the degree of ionization of the plasma near the cathode with increasing T_K. Nor do we rule out an effect of the temperature coefficient of the work function (in the Rasor coordinates). This dependence is also observed when the cathode work function is determined from the dynamic voltage–current characteristics.[15]

The curves corresponding to quenching and the formation of a virtual cathode at high currents lie near the envelopes bounding the characteristics.[4] According to our model the envelope can be calculated from

$$\frac{JR_{Cou}}{T_K} = 2t(\theta - 1) + \theta \ln (t - 1)$$

$$+ \frac{(E_i^{ef} K_{ks}^{0})^{1/2}}{T_K} \frac{[1 + 2t(\theta - 1)](t - 1) - [1 + t(\theta - 1)]}{\{[1 + 2t(\theta - 1)](t - 1)[1 + t(\theta - 1)]\}^{1/2}}, \tag{11}$$

which is easily found from (1) and (2) by setting $\partial(\Delta V) \cdot (\partial J_{em})^{-1} = 0$. Figure 5 compares the experimental voltage–current characteristics from refs. 8 and 9 with the envelope and the curve corresponding to quenching and the formation of a virtual cathode.

In conclusion the authors thank N. V. Kudryavtseva for assistance in the calculations.

---

[1] N. S. Rasor, Report at the International Conference on Thermionic Power Generation, London, 1965.

[2] I. P. Stakhanov and I. I. Kasikov, Zh. Tekh. Fiz., 39, 1496 (1969) [Sov. Phys. – Tech. Phys., 14, 1122 (1970)].

[3] I. P. Stakhanov (ed.), Physics of Thermionic Energy Conversion [in Russian], Atomizdat, Moscow (1973).

[4] A. I. Loshkarev, Zh. Tekh. Fiz., 42, 2127 (1972) [Sov. Phys. – Tech. Phys., 17, 1684 (1973)].

[5] A. I. Loshkarev, Zh. Tekh. Fiz., 44, 2109 (1974) [Sov. Phys. – Tech. Phys., 19, 000 1975)].

[6] F. G. Baksht, I. L. Korobova, and B. Ya. Moizhes, Zh. Tekh. Fiz., 41, 387 (1971) [Sov. Phys. – Tech. Phys., 16, 292 (1971)].

[7] Yu. Yu. Abramov and G. G. Gladush, Third Intern. Conf. on Thermionic Electrical Power Generation, Jülich, FRG, Rpt. H-126, 1972.

[8] D. Lieb and F. Rufeh, Thermo Electron Report TE4137-134-71, May, 1971.

[9] D. Lieb and F. Rufeh, IEEE Conference Rec. Thermionic Conversion Specialists. Ninth Annual Conference, Miami Beach, 1970, p. 474.

[10] D. Lieb, A. Donaker, and F. Rufeh, Report on 1969 Thermionic Conversion Spec. Conference, Carmel, California, 1969, p. 66.

[11] G. N. Hatsopoulos and F. Rufeh, Report on 1969 Thermionic Conversion Spec. Conference, Carmel, California, 1969, p. 1.

[12] F. Rufeh and D. Lieb, Report on 1969 Thermionic Conversion. Spec. Conference, Carmel, California, 1969, p. 237.

[13] F. Rufeh, B. Gunter, and D. Lieb, IEEE Conference Rec. Thermionic Conversion Spec. Ninth Annual Conference, Miami Beach, 1970, p. 233.

[14] R. J. McCandless and D. R. Wilkins, IEEE Conference Rec. Thermionic Conversion Spec. Ninth Annual Conference, Miami Beach, 1970, p. 277.

[15] N. S. Lidorenko, A. I. Loshkarev, and V. D. Bondarenko, Zh. Tekh. Fiz., 43, 1203 (1973) [Sov. Phys. – Tech. Phys., 18, 763 (1973)].

Dielectric breakdown of detonation products

V. L. Korol'kov, M. A. Mel'nikov, and A. P. Tsyplenko
Scientific-Research Institute of High Voltages, Tomsk

(Submitted October 15, 1973; resubmitted April 1, 1974)
Zh. Tekh. Fiz., 44, 2537-2538 (December 1974)

An experimental study has been made of the dielectric breakdown of the products of the detonation of PETN and RDX behind the detonation front. The measured breakdown voltages are of the same order as those for solid dielectrics.

Study of the dielectric breakdown of detonation products is inspired by the use of high explosives in electrical separation devices, in which the detonation products are located between the parts of the ruptured conductor and are subjected to a strong electric field. The dielectric strength of these detonation products thus strongly influences the separation process.

The high-voltage pulses are produced by a 100 kV pulse generator with a capacitance of 400 pF and a pulse front which rises at 0.8 mV/μsec [sic]. The test gap (with a "point–point" geometry) has an interelectrode separation of 0.5±0.03 mm. The jacket of the explosive charge is designed to prevent breakdown outside the test gap. The charge is 7 mm in diameter and has a density of 1.0 g/cm^3.

Figure 1 shows the electrical circuit for the apparatus. As the detonation front propagates through the charge it acutates an ionization gauge; the pulse generator and the oscilloscope are triggered. The distance between the test gap and the ionization gauge is varied so that the voltage pulse is fed to the test gap at various times after the shock front of the detonation wave passes the plane of the test gap. This range of times is 0-4 μsec, being limited by structural features of the separation devices used.

A pulsed x-ray photograph (exposure time 10^{-7} sec) is taken of the detonating charge in order to detect the position of the gap electrodes. The resulting photographs show that the electrodes remain coaxial for 4 μsec after the shock front passes the plane of the test gap, and the distance between the electrodes does not increase by more than 30%. This increase in interelectrode distance is determined for various times and taken into account in the analysis of the results. The conductivity of the detonation products is measured by an electrical-contact method like that of ref. 1.

Behind the detonation front the detonation products constitute a dense ionized gas with a high electrical conductivity which evidently is of major importance in determining the nature of the discharge. Measurements of the conductivity of the detonation products show that this conductivity reaches $10^{-1}\ \Omega^{-1}\cdot\text{cm}^{-1}$ behind the shock front; it then falls rapidly, reaching 10^{-4}-$10^{-5}\ \Omega^{-1}\cdot\text{cm}^{-1}$ after 2 to 3 μsec (the time reference is the time at which the shock front passes the test gap).

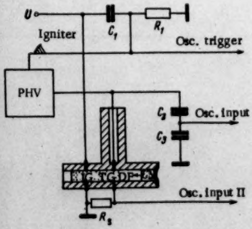

Fig. 1. Experimental apparatus.

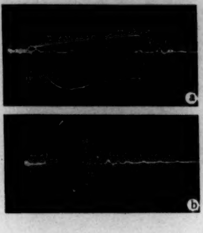

Fig. 2. Oscillograms of the discharge in the test gap. The pulse is triggered at: a) 0.7; b) 2.3 μsec. The time markers are 0.1 μsec apart.

Oscillograms of the gap voltage and current show that the breakdown involves a significant deformation of the voltage pulse over the interval 0-1.6 μsec: The height and front steepness of the pulse are lower than in the no-load case. Large prebreakdown currents are observed (Fig. 2a). This behavior results from the high conductivity of the test gap (10^{-1}-$10^{-3}\ \Omega^{-1}\cdot\text{cm}^{-1}$) and the limited power of the pulse generator.

The oscillograms of the gap breakdown are reminiscent of the breakdown of conducting liquids, for which the formation of the discharge channel occurs after some delay. This similarity probably results from the circumstance that the detonation products are essentially a liquid[1] in this interval (pressure ~ 10^4 kbar, temperature ~ $3\cdot10^{30}$ °K, density 0.8-0.5 g/cm^3).

The reduced temperature and pressure in the test gap which result from the use of an inert additive (10% talc) in the explosive charge lead to a reduced conductivity and to the loss of the conducting-liquid properties of the test gap; over the specified interval the breakdown occurs at the front of the nondeformed voltage wave.

The conductivity of the test gap becomes low (~ 10^{-4} $\Omega^{-1}\cdot\text{cm}^{-1}$) by 1.7-1.8 μsec, and the breakdown occurs at the

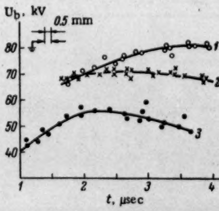

Fig. 3. Functional dependence of the dielectric strength of the test gap on time. 1) PETN; 2) RDX; 3) 90% PETN + 10% talc.

front of the pulse with a steepness governed solely by the generator parameters (Fig. 2b). We measure the dielectric strength of the gap in the interval 1.7-4 μsec; the functional dependence of this dielectric strength on time is shown in Fig. 3. We see that the breakdown voltage of the test gap is of the same order of magnitude as those for solid dielectrics. Complex, uncontrollable processes occur in the gap, and there are simultaneous changes in the pressure, the temperature, the electrical conductivity, and the density. It is difficult to separate the effects of these changes on the basis of the information available. The increase in the breakdown voltage at the beginning of the interval 1.7-4 μsec is due to a reduction of the electrical conductivity; then the pressure decrease becomes predominant, and the breakdown voltage decreases.

---

[1] R. Hajossy, Acta F. R. Natur Univ. Comen Phys., 12 (1971).

Anomalous high emission of a nonevaporating thermionic cathode in an arc

B. Ya. Moizhes and V. A. Nemchinskii

(Submitted December 28, 1973)
Zh. Tekh. Fiz., 44, 2539-2547 (December 1974)

Various factors that can increase the emission of a thermionic cathode in an arc are examined. The effect on the thermionic emission of fluctuations in the electric field at the cathode due to the discrete nature of the ion charge is calculated. Under conditions typical of high-pressure arcs ($j < 10^5$ A/cm², $E < 10^7$ V/cm), the number of additional electrons emitted by the cathode due to fluctuations in the electric field is much less than one per ion. Under these conditions the average electric field of all the ions increases the electron emission by more than one electron per ion. A rigorous resolution of the field of an individual ion from the average field avoids the divergences which usually arise in such calculations. The range of applicability of the classical description of thermionic emission is discussed, and the need for quantum-mechanical corrections for local decreases in the potential barrier at the surface is analyzed. It is shown that faces of working cathodes with relatively low work function evaporate less because of the intense emission cooling, so that the surface can acquire a faceted structure dominated by faces with the minimum work function. Then the effective work function of the cathode should decrease to this minimum value. Another possible reason for an increase in emission is the formation of a microscopic roughness on the cathode surface. This roughness arises because of the intense electronic cooling of protuberances.

INTRODUCTION

One of the most important questions in the physics of the arc discharge is the mechanism for the cathode emission. It is now generally agreed that in an arc with a tungsten cathode at a pressure of 0.1-1 atm the emission mechanism is thermionic, supplemented by the Schottky effect. Experimentally, however, thermionic cathodes sometimes display an anomalously high emission, which seems at odds with the concept of thermionic emission.[1] It has been suggested[2,3] that this anomalous emission could be due to the influence of fields of individual ions.

The emission current density is a strong function of E, the electric field at the cathode surface. In an arc this field is produced by the space charge due to the ions in the cathode sheath. The average field j_e is usually determined from the Mackoen equation, and the ion charge is assumed to be continuous. The field $\bar{E}$ is related to the average ion density n_i by $\bar{E} = 4\pi n_i d$, where d is the thickness of the space-charge sheath. Since the ion charges are actually discrete, however, the field E can be much higher than the average value $\bar{E}$ as an ion approaches the surface. Since the function $j_e(E)$ is very nonlinear in the region of the strong Schottky effect, the average emission density can be higher than that corresponding to a homogeneous charge distribution. We are thus concerned with calculating the influence of those fluctuations in the electric field at the cathode surface which result from the discrete nature of the ion charge.

Ecker and Muller[4] and Ecker[5] have carried out calculations for this effect in the case of field emission, finding a significant increase in the emission only at very strong fields (on the order of $5 \cdot 10^7$ V/cm).

Bauer[2] analyzed the influence of the individual-ion fields on thermionic emission, concluding that the effect could also be important at fields $\sim 10^6$ V/cm, typical of an arc. In these calculations, however, the field associated with an individual ion is in a sense added to the general space-charge field, so that the field of each ion is taken into account twice: in the average field and in the calculation of the individual field. Another shortcoming of these calculations[2] is that they incorporate only the field at the cathode and do not deal with the entire potential well produced by an ion at the cathode; in particular, the fact that the emission can be limited by a potential peak behind the ion, rather than at the cathode, is neglected. As a result, divergences appear in the calculations at small and large distances from the cathode; these divergences are eliminated by an arbitrary cutoff of the potential.

In the present work we calculate the influence of the individual ion fields on thermionic emission in a manner that avoids these shortcomings. We also discuss other effects which can intensify thermionic emission in an arc, e.g., the formation of a faceted structure at the cathode surface dominated by faces with the minimum work function, because of the instability of a smooth cathode surface.

INDIVIDUAL ION FIELDS

Singling out a particular ion in the cathode sheath, we want to find how many more electrons are emitted by the cathode because the field near this ion differs from the average field. We construct a coordinate system (Fig. 1) in which the ion moves along the z axis, and the cathode surface is the z = 0 plane.

The normal component of the field at the cathode surface at point (r, 0) produced by this ion and its image is

$$\Delta E = \frac{2ez_0}{(r^2 + z_0^2)^{3/2}}, \tag{1}$$

where z_0 is the coordinate of the ion and e is its charge. The resultant normal field component consists of the average field $\bar{E}$ produced by all the ions, and the field due to the ion in question, ΔE, minus the contribution of this ion to the average field, $\overline{\Delta E}$:

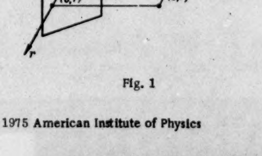

Fig. 1

$$E=\bar{E}+\Delta E-\overline{\Delta E}. \qquad (2)$$

The additional emission current due to the deviation of the local field from the average field is$^{1)}$

$$\Delta I_e=2\pi\int rdr\,[j_e(E)-j_e(\bar{E})]. \qquad (3)$$

To find the additional number of thermionic electrons emitted by the cathode (per ion), we integrate (3) over the time of the ion motion, and divide by the electron charge. Denoting the result by γ_T, we have

$$\gamma_T=\frac{1}{e}\int dt\Delta I_e=\frac{2\pi}{e}\int\frac{dz_0}{v}\int rdr\,[j_e(E)-j_e(\bar{E})], \qquad (4)$$

where v is the ion velocity. The total emission current can be expressed in terms of γ_T:

$$j_e=j_e(\bar{E})+\gamma_T j_i+\gamma j_i, \qquad (5)$$

where j_i is the ion current density and γ is the ordinary ion–electron emission yield, which is related to the transfer of the ion-neutralization energy to a single electron (the Auger effect), rather than to the emission of thermionic electrons.

We assume that the charge of the given ion is distributed over some surface of area S; then, $\overline{\Delta E} = 4\pi e/S$. We can show that the additional current in (4) due to $\overline{\Delta E}$ is independent of S: We can always choose S so large that $\overline{\Delta E} \ll \bar{E}$, so that

$$\Delta j=\frac{dj}{d\bar{E}}\overline{\Delta E}\ \text{and}\ \Delta I_e=2\pi\int rdr\frac{dj_e}{d\bar{E}}\overline{\Delta E}=S\frac{dj_e}{d\bar{E}}\frac{4\pi e}{S}=4\pi e\frac{dj_e}{d\bar{E}}.$$

The fact that this result is independent of S justifies our approach. We now write

$$\gamma_T=\frac{2\pi}{e}\int\frac{dz_0}{v}\left\{\int_0^\infty rdr\,[j_e(\bar{E}+\Delta E)-j_e(\bar{E})]-2e\frac{dj_e}{d\bar{E}}\right\}. \qquad (6)$$

Since we have not yet specified the nature of the function $j_e(E)$, we conclude that (6) holds for both field and thermionic emission as well as for the case in which the emission is governed by the entire profile of the potential barrier in the cathode sheath. In the case of thermionic emission we have

$$j_e(E)=j_e(0)\exp\frac{\sqrt{e^3E}}{T_k}, \qquad (7)$$

where T_k is the cathode temperature. The two integrals in (6) can be combined into a single integral; also, using (1), we can write

$$\gamma_T=\frac{2\pi}{e}\int_{z_L}^{z_U}\frac{dz_0}{v}\int_0^\infty rdr\left\{\exp\left(\frac{\sqrt{e^3(\bar{E}+\Delta E)}-\sqrt{e^3\bar{E}}}{T_k}\right)\right.$$
$$\left.-1-\frac{\Delta E}{T_k}\sqrt{\frac{e^3}{\bar{E}}}\right\}j_e(\bar{E}). \qquad (8)$$

We again emphasize the need to consider $\overline{\Delta E}$, which leads to the last term in the integrand in (8): Without it, the integral diverges at large distances (this divergence forced an arbitrary cutoff of the integral in refs. 2, 3 at $0.1n_i^{-1/3}$). Equation (8) does not diverge at large distances, and the integration can be extended to infinity ($z_b = \infty$).

However, the integral in (8) does diverge at small z_0, because of the unlimited decrease in the effective work function calculated from the Schottky equation as the ion approaches the cathode. The integral in (8) is usually cut off at the ion-neutralization distance at small z_0. Since the integrand in (8) increases rapidly at small z_0, a small error in z_L can significantly change γ_T. However, a more detailed analysis of the potential near the emitting surface shows that this cutoff is not necessary. As the ion approaches the surface a second potential-energy peak forms behind it, limiting the emission.[3]

In the presence of the ion the effective potential of the emitted electron consists of the potential produced by the average field, the potential of the interaction between the electron and its image, and the potential of the interaction between the ion and its image.$^{2)}$ The potential at (r, z) is (Fig. 1)

$$U(r,z)=-\frac{e}{4z}-\bar{E}z-\frac{e}{\sqrt{(z-z_0)^2+r^2}}+\frac{e}{\sqrt{(z+z_0)^2+r^2}}. \qquad (9)$$

The maximum potential determines the reduction of the work function; in the absence of the ion this maximum is $-\sqrt{e^3\bar{E}}$ (the Schottky correction). In the presence of the

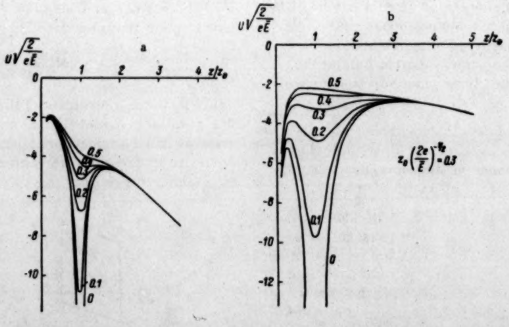

Fig. 2. Electron potential energy for the cases in which the ion is far from (a) and close to (b) the surface. a) $z_0(2e/\bar{E})^{-1/2} = 1$; b) 0.3. The curves are labeled with the values of $r - (2e/\bar{E})^{-1/2}$.

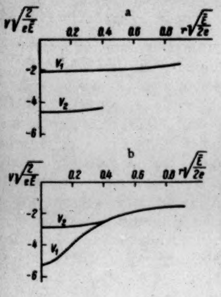

Fig. 3. Height of the front potential barrier V_1 and height of the rear barrier of V_2 as functions of the radius for the cases in which the ion is far from (a) and close to (b) the surface. a) $z_0(2e/\bar{E})^{1/2} = 1$; b) 0.3.

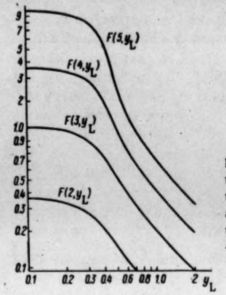

Fig. 4. Additional emission per ion as the ion moves from infinity to a distance y_L from the surface for various average electric fields [$F(\alpha, y_L)$ is taken from (11); $\alpha = \sqrt{e^3\bar{E}}/T_k$ = 2, 3, 4, 5].

ion the profile of the function U becomes more complicated. Figure 2 shows intersections of the U(r, z) surface with r = const planes; Fig. 2a corresponds to a large separation of the ion from the cathode, while Fig. 2b corresponds to a small separation. Figure 3 shows the height of the potential peak as a function of r. We see that there are two crests on the potential surface: in front of the ion and behind it. The corresponding maximum potentials at these crests are described by the $V_1(r)$ and $V_2(r)$ curves.

Accordingly, the effective cathode emission is governed not only by the field at the electrode but also by the entire profile of the potential energy of the emitted electron. In this connection we should write thermionic-emission equation (7) as

$$j_e = j_e(0)\exp\frac{\Delta\varphi(r)}{T_k}, \tag{7a}$$

where $\Delta\varphi = \max(V_1(r), V_2(r))$. Equation (8) should also be modified slightly:

$$\gamma_T = \frac{2\pi}{e}\int\limits_{z_L}^{z_U}\frac{dz_0}{v}\int\limits_0^\infty r\,dr\left\{\exp\left(\frac{\Delta\varphi - \sqrt{e^3E}}{T_k}\right) - 1 - \frac{\Delta E}{T_k}\sqrt{\frac{e^3}{E}}\right\} j_e(E). \tag{8a}$$

When the ion is far from the surface (Fig. 3a) the front potential barrier determines the emission. Since the ion is comparatively far from the cathode in this case, the field of the ion varies little between the cathode surface and the crest in the potential surface, so we can write $\Delta\varphi \simeq \sqrt{e^3(\bar{E} + \Delta E)}$. This approximation is valid as long as the front barrier is higher than the second. When the ion is close to the cathode the rear barrier is higher than the front barrier over part of the surface (Fig. 3b). In this case the problem of the emission of an electron from the cathode is complicated, and a classical approach must, generally speaking, deal with the various trajectories between the front and rear barriers. In our calculations we assume that an electron which has overcome the barrier is emitted if its energy is greater than the absolute minimum of barrier V_2. We see from Fig. 3 that the function $V_2(r)$ is weak, so that the overestimate resulting from this approximation is not serious.

Introducing the dimensionless quantities

$$y = \frac{z}{\sqrt{\frac{2e}{E}}},\quad \alpha = \frac{\sqrt{e^3E}}{T_k}, \tag{10}$$

we can express $\gamma_T(z_L)$ in terms of the dimensionless function $F(\alpha, y_L)$:

$$\gamma_T(y_L) = \frac{2\pi j_e(\bar{E})}{ev}\left(\frac{2e}{\bar{E}}\right)^{3/2} F(\alpha, y_L). \tag{11}$$

Figure 4 shows the calculated functions $F(\alpha, y_L)$ for various values of α; the values of $F(\alpha, 0)$ are shown in Table 1. We can use these data to determine the effect of the individual ion fields on the emission. For example, for argon ions and a tungsten cathode (work function of 4.5 eV), heated to T_k = 3500°K in a field of $E = 2.5 \cdot 10^6$ V/cm, and with a cathode drop of 10 V, we find $\alpha = 2$ and $j_s(\bar{E}) = 3.2 \cdot 10^3$ A/cm². Here the distance is measured in units of $\sqrt{2e/\bar{E}}$ = 34 Å. The neutralization distance for argon ions at tungsten is ~ 5 Å (ref. 7), so that we find an effective value $\gamma_T = \gamma_T(0.15)$. From Fig. 4 we see that we can accurately assume $\gamma_T(0.15) = \gamma_T(0)$, so that it is the lifting of the rear barrier, rather than the neutralization, which governs the decrease in the local emission of the cathode as the ion approaches it. We see from Table 1 that the value of γ_T for a singly charged ion is $3.6 \cdot 10^{-3}$, while that for a doubly charged ion is $\gamma_T = 1.6 \cdot 10^{-2}$. At a strong field of $E = 10^7$ V/cm we find $\gamma_1 = 2.9 \cdot 10^{-2}$ and $\gamma_2 = 0.27$, respectively.

These calculations show that the increase in γ due to the individual ion fields is usually slight; at the same time the value of γ under the influence of the average field $\bar{E}$ (the collective value γ_{coll} corresponding to the ion charge),

$$\gamma_{\text{coll}} = \frac{j_e}{j_i}[1 - \exp(-\alpha)],$$

is usually larger than unity, since $j_e/j_i > 1$ and $\alpha > 1$. The large value of γ_{coll} is evidently due to long-range Coulomb forces and the circumstance that the thickness of the space-charge sheath is much larger than the average distance between ions.

In these calculations we have distinguished the field of one ion from the background field due to a smearing of the charges of the other ions. We now have an a posteriori justification for this approach: The individual ion field should be distinguished at distances on the order of $(2e/\bar{E})^{1/2}$, and the probability of finding another ion this close to the ion in question is on the order of $n_i(2e/E)^{3/2}$, usually much less than unity.

To conclude this section we turn to the range of applicability of the classical approach to thermionic emission for the case in which there are local depressions of the potential barrier for electrons. In determining the emission from the cathode as the ion approaches the surface we assume that the electron can have any velocity parallel to the surface (v_x and v_y); in particular, this velocity can be zero. Turning to Figs. 2 and 3 now, we see that in the case of emission into the potential-energy saddle the electron will be localized in the xy plane. According to the uncertainty principle this localization means an uncertainty in the electron momentum. An electron moving into the plasma must thus have an additional energy; if this minumum additional energy is larger than or on the order of T_k, the electron emission must be much weaker than that predicted in the classical treatment.

To evaluate this minimum additional energy, we note that an electron whose energy exceeds the potential minimum is free to move in the z direction but is confined in a two-dimensional potential well in the x and y directions. If the size of this well (in the z direction) is much longer than the de Broglie wavelength of the electron, as it clearly is in our case, we conclude that a system of discrete energy levels associated with the x and y motion of the electron is formed in the well:

$$\mathcal{E}=\hbar\omega_0(n_x+n_y+1)+\frac{\hbar k_z^2}{2m};\quad n_x,\ n_y=0,\ 1,\ 2\ldots.$$

We see that the minimum electron energy related to the motion in the xy plane must be larger than $\hbar\omega_0$, where $\omega_0=\sqrt{(1/m)(\partial^2U/\partial r^2)}|_{r=0}$. For example, with $y_0=0.48$ (the separation of the ion from the surface at which the front and rear barriers are comparable in height) and $E=3\cdot10^6$ V/cm we find $\hbar\omega_0\simeq0.1$ eV. However, even at higher energies there must be a quantum-mechanical coefficient for reflection of the electron from the potential barrier.

Accordingly, in calculating the electron emission through local depressions of the potential barrier (corresponding to an ion at the surface, an adsorbed ion, a microscopic sharp point, etc.) we must incorporate quantum-mechanical corrections, whose calculation is an independent problem.

STABILITY OF VARIOUS FACES OF A CRYSTALLINE EMITTER

Since the anomalously high emission of a thermionic cathode cannot be explained on the basis of the individual ion fields, it is worthwhile to consider other mechanisms, which could intensify the cathode emission under the actual experimental conditions. Among these mechanisms we can cite the crystallographic orientation of the surface and the existence of a microscopic roughness, which leads to a concentration of the electric field near sharp protuberances.

The work function can vary considerably as a function of the crystallographic orientation of the surface, e.g., while the average work function of tungsten is 4.5 eV, there are faces whose work functions range from 4.2 to 5.1 eV (ref. 8). At high temperatures the migration of atoms over the surface leads to the growth of the faces having the minimum surface energy (cleavage planes), but during the operation of a cathode the faces having relatively low work functions will be cooled relatively intensely because of the thermionic emission, so that the evaporation from these faces will be reduced. The result should be a tendency for faces of minimum work function to grow, even if their surface energies are relatively high, and the effective emissivity of the cathode should increase.

To evaluate the local change in the cathode temperature corresponding to a change in the local work function we assume that the work function varies sinusoidally along the surface:

$$\varphi(x)=\bar{\varphi}+a_\varphi\cos kx\quad(a_\varphi\ll\bar{\varphi}).\tag{12}$$

Here the x axis is parallel to the cathode, and the z axis is normal to it. The cathode temperature satisfies the Laplace equation with the boundary condition

$$\varkappa\frac{\partial T_k}{\partial z}\Big|_{z=0}=q,\tag{13}$$

where $\varkappa$ is the thermal conductivity of the cathode, and q is the heat flux to its surface. We assume that q consists of the heat carried by ions to the cathode and the heat flux associated with the emission cooling:[9]

$$q=j_i(E_i+V_k+2T_p-\varphi)-j_e(\varphi+2T_k),\tag{14}$$

where E_i is the ionization potential of the plasma atoms, V_k is the cathode drop, and T_p is the plasma temperature. A change in the electron current along the surface leads to a variation in the emission cooling and thus to a change in the cathode temperature. The solution of the Laplace equation for the cathode temperature is

$$T_k(x,\ z)=\bar{T}+\frac{\overline{dT}}{dz}z+a_T\cos kxe^{kz},\tag{15}$$

where $\bar{T}$ is the average surface temperature and $\overline{dT}/dz$ is the average gradient due to the unperturbed heat flux $\bar{q}$. We write the distribution of the electron current as

$$j_e=\bar{j}_e+a_j\cos kx.\tag{16}$$

From the Richardson equation we have

$$a_j=\frac{\bar{j}_e}{\bar{T}}a_\varphi+\frac{\bar{j}_e\bar{\varphi}}{\bar{T}^2}a_T.\tag{17}$$

If the dimensions of the spots are smaller than the ionization length in the plasma, the ion current remains constant over the cathode surface; then from (13) and (14) we find

$$a_T=a_\varphi\frac{\frac{\bar{\varphi}\bar{j}_e}{\bar{T}}}{k\varkappa+\frac{\bar{\varphi}^2\bar{j}_e}{\bar{T}^2}}.\tag{18}$$

We see that those faces whose work functions are relatively high are in fact heated most. Let us estimate the effect of inhomogeneities of micron size, with $k=10^4\,\mathrm{cm}^{-1}$.

TABLE 1

α	$F_1(\alpha,0)$	$F_2(\alpha,0)$
1	$4.48\cdot10^{-2}$	0.14
2	0.36	1.58
3	1.29	7.61
4	3.65	32.9
5	9.97	166.9

Note: The number of additionally emitted electrons per singly charged ions, γ_1, and per doubly charged ion, $(2\pi/ev)j_e(\bar{E})(2e/\bar{E})^{3/2}F_{1,2}(\alpha,0)$; $\alpha=\sqrt{e^3\bar{E}}/T_k$.

With $\varkappa = 1$ W/cm · deg, $\alpha\varphi = 0.2$ eV, and $\bar{j}_e = 2 \cdot 10^4$ A/cm^2 we find $\alpha_T \cong 6$°K. Since the evaporation rate is a strong exponential function of the temperature, a difference of this magnitude in temperatures can lead to a rapid restructuring of the surface. Faces having the minimum work functions turn out to be stable. Accordingly, in evaluating the work function of an emitting cathode it is more accurate to use the minimum work function among the various faces rather than the average work function, i.e., for pure tungsten we should use $\alpha_\varphi = 4.2$–4.3 eV, which would lead to an emission intensification by a factor of 2 or 3 at a cathode working temperature of 3500°K.

A similar effect should occur on film cathodes, e.g., of tungsten containing Th or La additives. The faces for which the heat of adsorption is relatively high should be relatively stable. It should be kept in mind here that the work function of a film cathode can vary much more significantly than that for a pure emitter. The useful anisotropy effect vanishes in the formation of the liquid film, so that the work function should evidently increase upon melting.

STABILITY OF A FLAT EMITTING SURFACE

Another factor which could increase the effective emissivity of a cathode is a surface roughness, which would lead to a local intensification of the electric field. However, for such a roughness to actually exist, it would have to be stable. This stability could be achieved if the protuberances were relatively cool and evaporated less than depressions; otherwise the roughness on a working cathode would be reduced, and the cathode would become polished.

We can classify possible surface roughnesses into three groups from the standpoint of the thermal and electrical processes which occur on the cathode. For a roughness of the finest scale (for which the characteristic dimension is shorter than the thickness of the space-charge sheath, L_{sc}), the lines of force of the electric field can concentrate at sharp protuberances, and this concentration can result in an anomalous large Schottky effect. For a coarser roughness this concentration of lines of force does not occur; as long as the characteristic dimension of this roughness is shorter than the distance over which ions are generated (L_i; see ref. 9), the heat flux associated with the ions can be assumed to be homogeneous. Finally, for roughness of the coarsest nature ($k \ll L_i^{-1}$) the ion flux would no longer be homogeneous, and different parts of the surface would emit independently. Let us examine the first and second types of roughness, for which the ion flux is homogeneous and for which variations in the emission cooling lead to temperature variations.

The stability of a surface roughness can be affected by many factors other than the thermal processes associated with the evaporation and migration of atoms. For example, a flat surface is subjected to two balanced forces: the force exerted by the electric field on the charged cathode surface and the ion pressure. If the surface is curved (if there is a roughness) this equilibrium will be disrupted, and there may be a tendency for the roughness to become more pronounced. A competing process is the smoothing of the surface under the influence of surface-tension forces.

During evaporation, even if the surface is heated uniformly, the resultant evaporation rates at protuberances and depressions will be different, because an atom evaporated in a depression can revert to the condensed state there, while the probability of this reversion for an atom evaporated from a sharp protuberance is lower. Even if the evaporation occurs in a plasma-forming gas, rather than in vacuum, the diffusion of atoms evaporated from protuberances will still be easier than that of atoms evaporated from depressions. This effect (the geometric factor) tends to make a flat surface stable.

To illustrate these arguments we consider the stability of a surface roughness characterized by $L_{sc}^{-1} > k > L_i^{-1}$; in this case we can assume that the potential in the plasma satisfies the Laplace equation, so that

$$V(x,\ z) = Ez + \alpha_s \cos kx e^{-kz} \simeq Ez + \alpha_s (1 - kz) \cos kx. \quad (19)$$

At the cathode surface we have V = 0, so that the equation of the surface is

$$z(x) = -\frac{\alpha_s \cos kx}{E} = \alpha_z \cos kx. \quad (20)$$

The temperature distribution is given as before by Eq. (15). Because of the change in the surface temperature, there will be changes in the electron current [Eq. (17) with $\alpha_\varphi = 0$] and the heat flux to the cathode [Eq. (14)]. After some straightforward calculations we find

$$\alpha_T = \alpha_z \left\{ \frac{\overline{dT}}{dz} - \frac{\varphi J_e}{\varkappa + \frac{\varphi^2 J_e}{T^2}} \left[\frac{\varphi}{T^2} \frac{\overline{dT}}{dz} + \frac{k\sqrt{e^3 E}}{2T} \right] \right\}. \quad (21)$$

If the cathode conducts heat poorly, we have dT/dz → 0; in this limiting case we obtain

$$\alpha_T = -\alpha_z \frac{\varphi J_e}{\varkappa + \frac{J_e \varphi^2}{T^2}} \frac{k\sqrt{e^3 E}}{2T_k}. \quad (22)$$

We see that in the case of a coarse roughness the protuberances on the cathode can be cooler than the depressions. To evaluate α_T for $j_e = 10^4$ A/cm^2, $\varkappa = 1$ W/cm · deg, $T_k = 3500$°K, $\varphi = 4.5$ eV, and $\Delta\varphi_s = \sqrt{e^3 E} = 0.35$ eV, we adopt $1/k = \alpha_z = 5 \cdot 10^{-4}$ cm, finding $\alpha_T \simeq 10$°K.

It is difficult to evaluate the effects of various types of roughness on the thermionic emission of a cathode, especially since the shape of the roughness must be found from a self-consistent solution taking into account the heat fluxes, electrical currents, and evaporation of the cathode. Our purpose here has been to demonstrate that there are factors which lead to the development of, and prevent the smoothing of, a cathode surface.

---

1) In some cases the current cannot be written in terms of the field at the surface; instead, the entire curve for the potential energy of the emitted electron should be taken into account (see the text below).

2) Emeleus has shown recently[6] that the surface charge can be replaced by its mirror image down to small distances from a metal surface.

---

[1] A. M. Dorodnov, Teplofiz. Vys. Temp., 9, No. 3 (1971).
[2] A. Bauer, Beitr. Plasmaphys., 6, 281 (1966).
[3] A. M. Dorodnov, in: Accelerators [in Russian], Izd. Mashinostroenie, Moscow (1973).
[4] G. Ecker and K. G. Müller J. Appl. Phys., 30, 1466 (1959).
[5] G. Ecker, Ergeb. Exact. Naturwiss., 33 (1961).

[6] K. M. Emeleus, Phys. Rev., 154, 2318 (1972).
[7] P. Kisliuk, J. Appl. Phys., 30, 51 (1959).
[8] V. S. Fomenko, Emission Properties of Materials [in Russian], Izd. Naukova Dumka, Kiev (1970).
[9] B. Ya. Moizhes and V. A. Nemchinskii, Zh. Tekh. Fiz., 42, 1001 (1972); 43, 2309 (1973) [Sov. Phys. – Tech. Phys., 17, 793 (1972); 18, 1460 (1974)].

High-pressure hot-cathode arc without forced cooling

V. A. Nemchinskii

(Submitted December 28, 1973)
Zh. Tekh. Fiz., 44, 2548-2550 (December 1974)

The operation of a nonevaporating thermionic cathode in a high-pressure arc is analyzed for the case in which the cathode is cooled by radiation alone. Calculations are carried out for a tungsten cathode for two pressures of the gas (argon): 20 and 760 torr. The cathode potential drop under these conditions is relatively low (8-10 V). The range of possible current densities is governed by the gas pressure: At low pressures the range of possible current densities is comparatively narrow and the cathode is comparatively cool.

A large part of the electrical power of a high-current arc can be evolved near the cathode; much of this energy is transferred to the anode, which is thus heated intensely. Overwhelming and failure of the cathode are prevented by cooling, with either flowing water or gas. In several applications, however, effective external cooling is impossible, or it is desirable to minimize its use. In an effort to determine possible operating conditions for which forced cooling would not be necessary, we have calculated the parameters of this type of operation in a high-pressure arc in a neutral gas. Specific calculations have been carried out for an arc in argon at pressures of 20 torr and 1 atm with a tungsten cathode.

The equations used to describe the operation of the cathode are essentially the same as those used to calculate the parameters of the cathode spot in a high-current arc in refs. 1 and 2. The calculations are based on the energy-balance equation for the cathode. We assume that the cathode is heated by ion bombardment and by the inverse flux of hot plasma electrons reaching the cathode, and we assume that the cathode is cooled as a result of the particle emission and the natural electromagnetic radiation. Then the total heat flux to the cathode is

$$q=j_i(E_i+V_k+2T_p-\varphi)+j_e^{(\mathrm{inv})}(2T_p+\varphi) -j_e^{(\mathrm{em})}(\varphi+2T_k)-\varepsilon\sigma T_k^4\;, \tag{1}$$

where j_i and $j_e^{(\mathrm{inv})}$ are the ion flux and the flux of inverse electrons to the cathode, $j_e^{(\mathrm{em})}$ is the cathode emission current density, E_i is the ionization potential of the neutral gas, V_k is the cathode potential drop, φ is the cathode work function, T_k and T_p are the temperatures of the cathode and of the plasma near the cathode, respectively; σ is the Stefan–Boltzmann constant, and ε is the cathode emissivity (we assume $\varepsilon = 0.5$ for the calculations). Without forced cooling $q = 0$.

It is sometimes assumed that the emission of a thermionic cathode can be anomalously high because of fluctuations of the electric field at the cathode surface (due to the "effect of the individual ion fields"),[3,4] but calculations[5] have shown that this effect is negligible for ordinary operating conditions ($j_e \leqslant 10^5$ A/cm², $E \leqslant 10^7$ V/cm). We can thus assume that the emission is described by the Richardson equation with a correction for the Schottky effect (the field intensity at the cathode is taken from the Mackoen equation):

$$j_e^{(\mathrm{em})}=AT_k^2\exp\left(-\frac{\varphi}{T_k}\right), \tag{2}$$

$$\varphi=\varphi_0-\gamma V_k^{1/4}j_i^{1/4}, \tag{3}$$

where φ_0 is the cathode work function for the case of zero field at the cathode, and γ is the constant in the Mackoen equation.

The ion current is governed by the energy balance in the plasma near the cathode, which involves the energy carried to the plasma by the emitted electrons, that carried away from the plasma by ions and the inverse electron flux to the cathode, and that carried by electrons into the interior of the plasma:

$$j_e^{(\mathrm{em})}(V_k+2T_k)=j_i(E_i+2T_p)+j_e^{(\mathrm{inv})}(V_k+2T_p)+3.2jT_p. \tag{4}$$

The density of the total current to the cathode is

$$j=j_e^{(\mathrm{em})}-j_e^{(\mathrm{inv})}+j_i. \tag{5}$$

The temperature of the plasma near the cathode, T_p, is determined from the condition that the plasma must be heated to a temperature high enough to provide the necessary density of the ion current to the cathode:

$$j_i=\alpha qn(T_p)v_i. \tag{6}$$

Here, q is the ion charge, $n(T_p)$ is the (Saha) equilibrium charged-particle density corresponding to temperature T_p, and α is a numerical factor governed by the mechanism generating ions in the cathode sheath. Since T_p appears exponentially in $n(T_p)$, the temperature can be determined accurately from (6) without refining the value of α. Finally, the density of the inverse electron flux to the cathode is

$$j_e^{(\mathrm{inv})}\simeq\frac{1}{4}qn(T_p)v_e\exp\left(-\frac{V_k}{T_p}\right). \tag{7}$$

Using these seven equations we can determine the seven unknowns ($j_e^{(\mathrm{em})}$, j_i, $j_e^{(\mathrm{inv})}$, T_k, T_p, V_k, φ) as functions of the cathode current density j. We proceed in the follow-

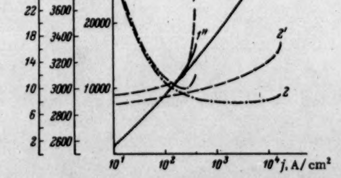

Fig. 1. The cathode fall V_k, the plasma temperature, and the cathode temperature of the tungsten cathode T_k, as functions of the current for various argon pressures. p (mm Hg): 1, 1', 1") 20; 2', 2") 760, for V_k, T_p, T_k respectively.

ing manner: After specifying an ion current j_i we determine T_p from (6). Then we select some value of V_k; we find $j_e^{(inv)}$ from (7) and j and $j_e^{(em)}$ from (4) and (5). Equation (3) then yields φ, and Eq. (2) yields T_k. Finally, we use Eq. (1) to determine how well the selected value of V_k corresponds to the selected value of j_i. By choosing V_k we ensure that Eq. (1) is also satisfied. We find the functional dependences of all quantities of interest on j_i or, equivalently, j.

Figure 1 shows the calculated results for two argon pressures (20 torr and 1 atm). We can draw certain conclusions from this figure.

1. Operation of the cathode without forced cooling requires a small cathode drop (8-10 V).

2. The voltage–current characteristic has rising and falling branches. Because of the strong exponential function $j_e^{(em)}(T_k)$, the cathode temperature varies relatively slowly along the characteristic. If the electron current density is low, the ion current density is corresponding low [Eq. (4)]. Accordingly, the ions must be accelerated by a high cathode barrier to heat the cathode to the necessary temperature. As the electron current density increases, so does j_i, and there is a corresponding drop in V_k. The plasma temperature increases to maintain the necessary ion current; the increase in the ion current with the plasma temperature continues until the plasma is completely ionized. With a further increase in the current the necessary increase in the heat flux is provided by an increase in V_k, until doubly charged ions appear in the plasma.

2. The possible cathode current densities are governed by the neutral gas pressure, because the plasma can provide only a limited ion current to the cathode. The magnitude of this current is governed by the gas pressure; at high pressures, the value of j_i can be high at a comparatively low plasma temperature, so that this operating regime spans a broad current range. At low pressures, on the other hand, the range of possible values of j is narrower.

---

[1] B. Ya. Moizhes and V. A. Nemchinskii, Zh. Tekh. Fiz., 42, 1001 (1972) [Sov. Phys. – Tech. Phys., 17, 793 (1972)].

[2] B. Ya. Moizhes and V. A. Nemchinskii, Zh. Tekh. Fiz., 43, 2309 (1973) [Sov. Phys. – Tech. Phys., 18, 1460 (1974)].

[3] A. Bauer, Beitr. Plasmaphys., 6, 281 (1966).

[4] A. M. Dorodnov, N. P. Kozlov, and Ya. A. Pomelov, Teplofiz. Vys. Temp., 9, No. 3 (1971).

[5] B. Ya. Moizhes and V. A. Nemchinskii, Zh. Tekh. Fiz., 44, 2539 (1974) [Sov. Phys. – Tech. Phys., 19, 1571 (1975)].

Hot probe measurements in a rarefied streaming plasma

E. M. Netsvetailov, L. V. Nosachev, and V. V. Skvortsov

(Submitted December 18, 1973)
Zh. Tekh. Fiz., 44, 2551-2558 (December 1974)

An experimental and theoretical investigation has been made of the error in the readings of a hot probe, as a function of the parameters of the surrounding medium and the emitter operating conditions. The case in which the probe current is electron space-charge-limited, the energy of directed motion of the ions is appreciably larger than the plasma potential, and the electron distribution in the plasma is Maxwellian is treated. The problem has been solved numerically in the one-dimensional case. From an analysis of the results an approximate equation is found for the potential barrier near the probe emitter surface. The results show that the thermionic electron component of the volt–ampere characteristic must have two asymptotes on a semilogarithmic scale. The point of intersection of the asymptotes gives the plasma potential with high accuracy. A method is described for constructing the potential field in a flow using a hot probe; it is based on a combination of the asymptote intersection method and the widely-used method for determining the potential of a plasma from the point of intersection of the characteristics of hot and cold probes. The combination method gives good accuracy with comparatively small effort.

A hot probe is widely used to determine the potential of a plasma at rest (refs. 1-3). There is information on the use of such probes in a rarefied streaming plasma (e.g., (refs. 4, 5). However, in the latter case the literature as yet has no results of a systematic investigation of the probe operation; no one has determined the dependence of probe error on the emitter temperature, its emission properties, and the parameters of the surrounding plasma.

The special feature of the hot probe is that it operates in a regime in which the current is limited by the electron space charge, i.e., there is a potential dip near the emitter surface.

This paper presents the results of a theoretical and experimental investigation of special features of the operation of a hot probe in the above application.

The hot probe is a spiral 1.0 mm in diameter, containing 10 turns of tungsten wire 0.089 mm in diameter, and is used with the circuit (Fig. 1) described in ref. 3. In this arrangement the probe cooling curve, observed on an oscilloscope, can be used to determine the point of divergence of the characteristics of the hot and cold probes. The probe is switched repetitively at a frequency of 20 Hz, by means of a relay, from the hot regime to the measurement regime, the spiral being heated by means of a dc current of 0.6–1.0 A. When the probe is switched to the measurement regime it has a certain potential, whose value is determined by means of a circuit consisting of a battery B and potentiometer R_p. Since there is no heating current in the measurement regime, the difference in potentials at the ends of the spiral is determined only by the voltage drop due to the emission current and the current of electrons and ions arriving from the plasma. In our experiments this quantity is of the order of 10^{-3} V, i.e., considerably less than the accuracy of measurement of the plasma potential.

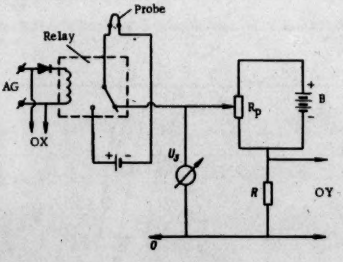

Fig. 1

The signal from the resistor R, proportional to the probe current, goes to the OY input of the oscilloscope. The horizontal sweep of the oscilloscope beam is generated by the audio generator AG, which feeds the relay winding.

If the probe potential is less than the plasma potential, the probe receives ions and the fastest electrons from the surrounding plasma, while the thermionic electrons leave the probe. In one cycle of measurement the thermionic emission current drops off as the probe cools. An oscillogram of this signal has the form 1 shown in Fig. 2. As the emitter potential approaches the plasma potential the electron current from the probe to the plasma decreases, and the signal on the oscilloscope screen takes the form 2 of Fig. 2.

For probe potentials appreciably greater than the plasma potential thermionic electrons cannot reach the probe, and the probe surface only receives electrons and ions from the plasma; the current does not change during the measurement cycle, so that the signal takes the form of the straight line 3, parallel to the horizontal axis. Thus, by varying the probe potential from values certainly less than the plasma potential and increasing, one can determine the time when the signal on the oscilloscope screen becomes rectangular. The probe potential corresponding to this time is taken initially to be the plasma potential.

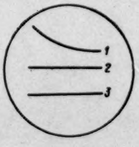

Fig. 2

Experiments are conducted in so-called synthesized plasma streams, which are created by neutralizing a stream of ions from an ion source with electrons emitted by a heated tungsten wire: The charged particle density is 10^{13} to 10^{14} m^{-3}, the ion energy is 100 eV, and the electron temperature is 1 eV. The working gas for the ion source is argon.

It is noted in the experiments that the hot probe gives increased values of the plasma potential in comparison with results obtained by means of a multielectrode probe (ref. 6), which is taken as a standard. As the emitter temperature increases the error in determining the potential increases. To find the cause of this phenomenon, the volt–ampere characteristics of the hot probe are measured for various heating currents I_h of the spiral (Fig. 3). As can be seen from the results, the shape of the characteristics does not depend on the emitter temperature, for large positive potentials on the hot probe relative to the plasma potential. However, as the spiral potential decreases, the curves begin to diverge in a fanwise manner. The greater the heating current, the earlier the curve deviates from the characteristic of the cold probe. This behavior of the characteristic can be explained by the effect of the initial velocities with which the electrons leave the probe: The higher the emitter temperature, the larger the initial velocity of these thermal electrons, and the higher the potential at which divergence of the characteristics of the hot and cold probes occurs.

The decrease in the slope of the volt–ampere characteristics when the probe potential is lower than that of the plasma is apparently due to the fact that at the emitter–plasma interface there is a potential dip associated with the current being limited by the electron space charge. Experiments and estimates of the present authors show that this effect cannot be explained by simple Richardson current limitation of the emitter.

The following fact is also noted: When the thermionic component of the volt–ampere characteristic of the heated probe is drawn on a semilogarithmic scale the curve has two asymptotes for large positive probe potentials and for large negative values (Fig. 4). The point of intersection of the asymptotes is a better approximation to the plasma potential as determined by the multielectrode probe than the potential determined from the point of divergences of the characteristics of the hot and cold probes.

To explain the experimental results a theoretical analysis is made of the distribution of potentials at the emitter surface. The problem is solved in the one-dimensional case. The potential distribution near the emitter surface has the form shown in Fig. 5. The X axis is directed along the normal to the emitter surface. For x = 0 the spatial potential U is equal to the surface potential U_x, and the potential has a minimum dV/dx = 0 in region 2. Region 3 corresponds to the region of neutralization $d^2V/dx^2 = 0$; the plasma potential V_n in this region has a finite value, but changes rather slowly, and one can take $(dV/dx)_3 = 0$ in the calculations.

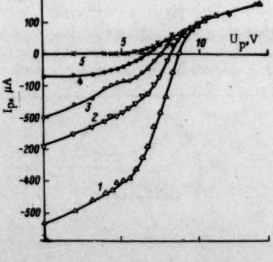

Fig. 3. I_h(A): 1) 1.0; 2) 0.9; 3) 0.8; 4) 0.7; 5) 0.

We assume, as is the case in the experimental conditions, that the energy of the ions in the stream is appreciably greater than the probe potential and that the ion density is constant, while the electron distribution function in the plasma is Maxwellian. The total current density of thermionic electrons is determined only by the temperature and the emission properties of the surface material.

The starting equation is the Poisson equation

$$\frac{d^2V}{dx^2} = 4\pi(\rho_+ - \rho_-), \tag{1}$$

where ρ_+ is the ion charge density and ρ_- is the electron charge density.

A similar problem has been solved in ref. 7 in an application concerning neutralization of an ion beam. But the authors do not take account of the electron current from the plasma to the emitter, and make the assumption, quite unacceptable for our case, that dV/dx = 0 on the emitter surface. For these reasons the results obtained in ref. 7 cannot be used to explain the effects arising when a hot probe is operated in a plasma stream.

We turn now to the solution of the problem. The density of thermionic electrons ρ_k in regions 2 and 3 can be found in the same way as for the space charge in a plane diode:

$$\rho_k = \frac{m}{kT_k}\int\limits_{\sqrt{eV/m}}^{\infty} j_k \exp\left(-\frac{mv^2}{2kT_k}\right) dv, \tag{2}$$

where T_k is the emitter temperature, v is the electron velocity, m is the electron mass, e is the electron charge,

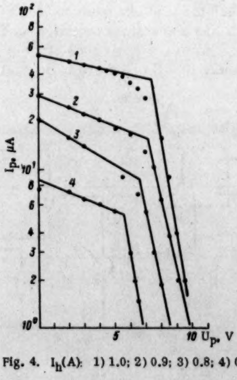

Fig. 4. I_h(A): 1) 1.0; 2) 0.9; 3) 0.8; 4) 0.7.

k is the Boltzmann constant, and j_k is the total emission current density as given by the Richardson law.

We express the ambient velocity v in terms of its initial value v_0:

$$\frac{mv^2}{2}=\frac{mv_0^2}{2}-(V_m+V_k)+V. \tag{3}$$

Substituting the value of v_0 obtained from Eq. (3) into Eq. (2), we can integrate over energy instead of velocity. Then, since

$$\frac{2}{\pi}\int_0^\infty \exp(-x^2)\,dx=1,$$

$$\frac{2}{\pi}\int_0^y \exp(-x^2)\,dx=P(y),$$

where P(y) is the probability integral, and $\eta = eV/kT_k$, $\mu = e(V_m-V_H)/kT_k$, we obtain a final expression for the density of electrons emitted by the probe:

$$\rho_k=\sqrt{\frac{\pi m}{2kT_k}}\,j_k\exp(\eta-\mu)(1-P\sqrt{\eta}). \tag{4}$$

The density of electrons coming from the plasma, ρ_a, in regions 2 and 3 can be written in the form

$$\rho_a=\frac{\pi m}{2kT_a}j_a\exp\left[(\eta-\nu)\frac{T_k}{T_a}\right]\left(1-P\sqrt{\eta\frac{T_k}{T_a}}\right), \tag{5}$$

where $\nu = eV_m/kT_k$; T_a is the electron temperature in the plasma, $j_a = evN$ is the density of the random electron current from the plasma to the probe, and N is the density of charged particles in the plasma.

We introduce the dimensionless variable $\xi = C(x-x_m)$, where x_m is the distance from the emitter to the section in which the potential reaches its minimum, and C is a scale constant, for example the Debye radius in the plasma.

In the variables η and ξ Eq. (1) takes the form

$$\frac{d^2\eta}{d\xi^2}=4\pi\frac{kT_k}{eC^2}\left[eN-j_k\frac{\pi m}{2kT_k}\exp\left[-\frac{e(V_m-V_k)}{kT_k}\right](1-P\sqrt{\eta})\right.$$
$$\left.-j_a\sqrt{\frac{\pi m}{2kT_a}}\exp\left(\eta\frac{T_k}{T_a}\right)\left(1-P\sqrt{\eta\frac{T_k}{T_a}}\right)\right], \tag{6}$$

and has the boundary conditions

$$\left.\begin{array}{l}\text{for } \xi=\xi_m,\ \eta=0,\ \frac{d\eta}{d\xi}=0,\\ \text{for } \xi=\xi_3,\ \eta=\mu,\ \frac{d\eta}{d\xi}=0,\ \frac{d^2\eta}{d\xi^2}=0.\end{array}\right\} \tag{7}$$

We integrate Eq. (6):

$$\frac{1}{2}\left(\frac{d\eta}{d\xi}\right)^2=2\pi\frac{kT_k}{eC^2}\left\{eN\eta-j_k\sqrt{\frac{\pi m}{2kT_k}}\exp\left[-\frac{e(V_m-V_k)}{kT_k}\right]\right.$$
$$\times\left(\exp\eta-\exp\eta P\sqrt{\eta}+\frac{2}{\sqrt{\pi}}\sqrt{\eta}-j_a\sqrt{\frac{\pi m}{2kT_a}}\frac{T_a}{T_k}\exp\left(-\nu\frac{T_k}{T_a}\right)\right.$$
$$\left.\times\exp\left(-\nu\frac{T_k}{T_a}\right)\left[\exp\left(\eta\frac{T_k}{T}\right)+\exp\left(\eta\frac{T_k}{T_a}\right)P\sqrt{\eta\frac{T_k}{T_a}}-\frac{2}{\sqrt{\pi}}\sqrt{\eta\frac{T_k}{T_a}}\right]\right\}-C_1. \tag{8}$$

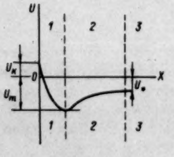

Fig. 5

Using the boundary conditions of Eq. (7) and introducing the notation

$$\beta=\frac{eU_k}{kT_k},\ T=\frac{T_a}{T_k},\ j=\frac{j_a}{j_k},\ \alpha=\frac{eN}{j_k\sqrt{\frac{\pi m}{2kT_k}}}=\frac{j}{\sqrt{T}},$$

we reduce Eqs. (6) and (8) to the form

$$\alpha-\exp(-\beta-\nu)\exp\mu(1-P\sqrt{\mu})$$
$$-2\alpha\exp\left(-\frac{\nu}{T}\right)\exp\left(\frac{\mu}{T}\right)\left(1+P\sqrt{\frac{\mu}{T}}\right)=0, \tag{9}$$

$$\alpha\mu-\exp(-\beta-\nu)\left(\exp\mu-\exp\mu P\sqrt{\mu}+\frac{2}{\sqrt{\pi}}\sqrt{\mu}-1\right)$$
$$-2\alpha T\exp\left(-\frac{\nu}{T}\right)\left(\exp\frac{\mu}{T}+\exp\frac{\mu}{T}P\sqrt{\frac{\mu}{T}}-\frac{2}{\sqrt{\pi}}\sqrt{\frac{\mu}{T}}-1\right)=0. \tag{10}$$

The results of numerical solution of the system of equations (9) and (10) are shown graphically in Fig. 6. By analyzing this system of equations and the result of numerical solution we can obtain an approximate equation

$$\Phi_{\min}=\nu+\beta=-1.2+2.3\lg\frac{1}{j}+1.4\lg T$$
$$+0.033T+4.71\cdot10^{-3}\beta+0.33\cdot10^{-3}\beta T$$
$$+\exp(0.11T+0.07\beta), \tag{11}$$

where $\Phi_{\min}$ is the dimensionless value of the potential dip.

In the range $-20 > \beta > -200$ the difference in values calculated using Eq. (11) for the data for numerical solution of the system of equations is less than a few tenths of a percent. For $\beta > -20$ the error increases and for values $\beta > 0$ the error can be 10% or more.

It can be seen from Eq. (11) and the curves of Fig. 6 that when $\beta < -50$ the potential dip varies in a linear manner with decreasing β. For large positive values of β the value of ν tends to zero, and the potential opposing electrons leaving the emitter surface tends to β. The electron current from the probe to the plasma is

$$I=I_0\exp(-\nu-\beta),$$

where I_0 is the total current from the emitter.

Then the thermoelectric component of the volt–ampere characteristic of the hot probe, drawn on a semilogarithmic scale, must have two asymptotes. One asymptote is due to the linear dependence of the depth of the potential barrier on the emitter potential, and the second is due to the fact that at large positive potentials $\nu \to 0$ and the current from the emitter becomes a function of β only.

Using these results we find the error in determining

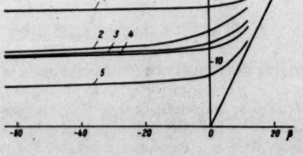

Fig. 6. j, T: 1) 10^{-8}, 3; 2) 10^{-5}, 10; 3) 10^{-5}, 5; 4) 10^{-5}, 3; 5) 10^{-3}, 3.

the plasma potential at the point of intersection of the asymptotes. We write the equation of the asymptotes in the coordinates $[\Phi_{\min}, \beta]$. For negative values of β we have

$$\Phi_{\min} = -1.2 + 2.3 \lg \frac{1}{j} + 1.4 \lg T$$
$$+ 0.033T + 4.71 \cdot 10^{-3}\beta + 0.33 \cdot 10^{-3}\beta T,$$

and for positive values of β,

$$\Phi_{\min} = \beta.$$

The point of intersection of the asymptotes is found by the simultaneous solution of the equations*

$$\beta = -1.2 + 2.3 \lg \frac{1}{j} + 1.4 \lg T + 0.033T$$
$$+ 4.71 \cdot 10^{-3}\beta + 0.33 \cdot 10^{-3}\beta T.$$

The last two terms on the right side of this expression can be neglected in comparison with β, and then the error in the probe readings is determined from the equation

$$\beta = -1.2 + 2.3 \lg \frac{1}{j} + 1.4 \lg T. \qquad (12)$$

From the results shown in Fig. 6 it can be seen that $\beta > 0$ in Eq. (12). We can find the ratio for which the current from the emitter will not be limited by the electron space charge. The latter case cannot be examined in the present form of the theory.

We now find the error in determining the plasma potential from the point of divergence of the characteristics of the hot and cold probe. For emitter potential values close to the point of divergence of the characteristics, the depth of the potential well at the emitter surface is zero. In this case the current density of electrons from the probe to the plasma is

$$j_{ek} = j_k \exp(-\beta). \qquad (13)$$

At the point of divergence of the characteristics we obtain

$$\frac{j_{ek}}{j_{ea} - j_i} \ll 1,$$

where j_{ek} is the current density of electrons from the probe to the plasma, j_{ea} is the current density of electrons from the plasma to the probe, and j_i is the current density of ions from the plasma to the probe.

For our estimates we assume that

$$\frac{j_{ek}}{j_{ea}} = 0.1. \qquad (14)$$

The quantity j_i can be neglected, since for probe potentials equal to and larger than the plasma potential $j_i \ll j_{ea}$. Substituting Eq. (13) into Eq. (14) and taking into account that $j = j_{ea}/j_k$, we find that

$$\beta = \ln 10 + \ln \frac{1}{j} = 2.3 + 2.3 \lg \frac{1}{j}.$$

Comparing the expression obtained for the error with Eq. (12), we see that the error in determining the plasma potential from the intersection point of the asymptotes gives greater accuracy than the method of determining the plasma potential from the point of divergence of the characteristics of the hot and cold probes.

The results obtained here are in qualitative agreement with experimental data. However, it follows from the theoretical analysis that the slope of the right asymptote of the volt–ampere characteristic of the hot probe must be numerically equal to 0.43e/kT, while its value is less by a factor of 2 or 3 as given by the experimental relations. To explain this discrepancy in the results we turn to Fig. 6. It is not difficult to see that the dependence of $\nu + \beta$ on β approaches the asymptote and in practice, in processing the experimental results beyond the right asymptote, a certain value of an approximate straight line is assumed for which the tangent of the slope is smaller than for the asymptote. In this case the point of intersection of the left asymptote and the straight-line approximation is closer to the true value of the plasma potential than the point of intersection of the asymptotes.

A quantitative comparison between the theoretical and experimental results has not been made because the emitter temperature is not constant along the length of the spiral, and it would be difficult to correct the measurement.

A defect of the above method is that it is laborious, since it entails a determination of the characteristics of the hot and cold probes, which is particularly complicated when one constructs the potential field for the space occupied by the plasma. Therefore we estimate the dependence of the error in determining the plasma potential from the point of divergence of the characteristics on the the properties of the emitter surface and the parameters of the surrounding plasma. It is clear that when the plasma potential is determined using a hot probe, a relation analogous to Eq. (14),

$$\frac{I_{ek}}{I_{ea}} = \frac{S_{\mathrm{em}} j_k}{S_{\mathrm{tot}} j_{ea}} = \frac{S_{\mathrm{em}}}{S_{\mathrm{tot}}} \frac{j_k \exp\left(-\frac{eU}{kT_k}\right)}{j_{ea}} \leqslant 0.1, \qquad (15)$$

must hold, where I_{ek} is the total ion current passing from the probe to the plasma, I_{ea} is the total current from the plasma to the probe, S_{em} is the area of the emitter surface, S_{tot} is the area of the effective probe surface; and V is the probe potential relative to the plasma, i.e., the value of the error of measurement. We find the value of j_{ea} from the equation

$$j_{ea} = \frac{1}{4} en \sqrt{\frac{8kT_a}{\pi em}}.$$

We transform Eq. (15) and find the error

$$U = \frac{kT_k}{e} \ln\left(10 \frac{j_k}{j_{ea}} \frac{S_{\mathrm{em}}}{S_{\mathrm{tot}}}\right). \qquad (16)$$

But we are interested in the variation of V when the probe is moved from point 1 with plasma parameters n_1 and T_{a1} to the point 2, where $n = n_2$ and $T = T_{a2}$:

$$\Delta U = \frac{kT_k}{e} \ln \frac{n_1 \sqrt{T_{a1}}}{n_2 \sqrt{T_{a2}}}. \qquad (17)$$

If the distribution function for electrons in the plasma is Maxwellian, then $T_{a1} = T_{a2}$. It follows from Eq. (17) that as the parameters of the surrounding plasma vary, the error varies over a narrow range; thus, in constructing the potential field for the flow we can use the heated probe, in the circuit shown in Fig. 1, and then introduce a correction for the whole potential field due to individual sections of the flow. This correction is found by comparing results obtained at one point in space from the point of intersection of the asymptotes and from the point of divergence of the characteristics.

---

*Publisher's note: Only one equation was given in the Russian original.

---

[1] N. A. Kaptsov, Physical Phenomena in a Plasma and in Rarefied Gases [in Russian], ONTI, Moscow–Leningrad (1937).

[2] E. E. Yushmanov, in: Plasma Physics and Problems of Controlled Thermonuclear Reactions, 4, 235, Izd. AN SSSR, Moscow (1958).

[3] N. D. Gabovich, O. A. Bartkovskii, and Z. P. Fedorus, Zh. Teor. Matem., 30, 345 (1960).

[4] D. F. Hall, R. F. Kemp, and I. M. Sellen, AIAA J., 2, 1032 (1964).

[5] S. D. Hester and A. A. Sonin, AIAA J., 8, 1090 (1970).

[6] V. V. Skvortsov, L. V. Nosachev, and E. M. Netsvetailov, Kosmich. Issled., 415 (1969).

[7] M. D. Gabovich, I. A. Soloshenko, and A. A. Ovcharenko, Ukr. Fiz. Zh., 16, 834 (1971).

[8] B. M. Tsarev, Design and Construction of Electron Tubes [in Russian], GÉI, Moscow–Leningrad (1961).

Wave excitation at half the gyrofrequency in counterstreaming electron beams

A. P. Timoshenko, D. V. Iremashvili, and Yu. K. Udovichenko

(Submitted January 21, 1974; resubmitted March 12, 1974)
Zh. Tekh. Fiz., 44, 2559-2562 (December 1974)

An experimental study has been made of the influence of the transverse and thermal electron velocities in counterstreaming beams on the excitation of oscillations at half the gyrofrequency and its harmonics. The injection current is 1.5 A, the energy of the beam electrons is 15 keV, and the magnetic field is 200-600 Oe. An increase in the transverse electron velocity leads to stronger oscillations, but this process is limited by collisionless damping due to the large spread in electron velocities.

A system of counterstreaming electron beams in a fixed, homogeneous, longitudinal magnetic field can support waves at half the gyrofrequency and its harmonics:[1,2] $n\omega_H/2(n = 1, 2, 3, \ldots)$. Waves exist at the harmonic frequencies only if there are waves at the fundamental frequency ($n = 1$).

Under certain conditions, such waves cannot be excited in counterstreaming beams because of collisionless damping.[3,4] These conditions can be derived from

$$\frac{\lambda_1}{\lambda_D}=\frac{\frac{\omega_b}{\frac{\omega_H}{2}}}{}\frac{v_z}{v_T}, \qquad (1)$$

where $\lambda_1 \doteq 4\pi v_z/\omega_H$ is the wavelength of the standing wave at the fundamental frequency, $\lambda_D = 2\pi v_T/\omega_b$ is the Debye length in the beam, ω_b is the electron plasma frequency in the beam, v_z is the longitudinal electron velocity in the beam, and v_T is the thermal velocity, which we identify with the spread of electron velocities in the beam. When the wavelength of the driven wave, λ_1, becomes comparable to the Debye length λ_D, the damping predominates over growth, so there is no instability. Experimentally this situation has been observed[4] at $\lambda_1/\lambda_D < 5$. We see from Eq. (1) that a lower limit on the excitation of waves in counterstreaming beams is set by the beam density ($\omega_{bcr} \sim \omega_H$), while an upper limit is set by the magnetic field ($\omega_{Hcr} \sim \omega_b$), for a fixed value of the parameter v_T/v_z for the injected beams. These limits have been studied experimentally for a system with a homogeneous magnetic field in the absence of a transverse velocity of the beam electrons[4] ($v_\perp = 0$).

It follows from the theory of ref. 5 that the growth rate increases if the electrons in the beam have a transverse velocity ($v_\perp \neq 0$). As a rule, such beams also have large values of v_T, which must significantly restrict the excitation of waves because of collisionless damping. For beams with a nonvanishing transverse electron velocity ($v_\perp \neq 0$), Eq. (1) remains valid for the longitudinal component v_z.

The excitation of waves at half the gyrofrequency in counterstreaming high-current beams has also been observed[6] in a system with an inhomogeneous magnetic field and $v_\perp \neq 0$, but no definite conclusions were drawn about the influence of $v_\perp$ on the wave excitation.

We report here a study of the conditions for the excitation of waves at half the gyrofrequency when electrons having a large velocity spread v_T and a large transverse velocity component $v_\perp$ are injected into the system. We find how the parameters v_T/v_z and $v_\perp/v_z$ affect the damping and growth of the high-frequency waves. We find the beam parameters for which it is possible to obtain a significant increase in the wave intensity because of $v_\perp$.

The experimental apparatus is described in ref. 6. Most of these experiments are carried out with an unshielded electron gun, which is located, along with a working chamber up to 40 cm long, in a fixed, homogeneous, longitudinal magnetic field H = 200–600 Oe. The injected beam current is 1.5 A, the electron energy is 15 keV, and the current pulse is 10–40 μsec long. The beam diameter at the entrance to the working chamber is 1 cm. The residual pressure in the system is $5 \cdot 10^{-6}$ torr. The counterstreaming beams are obtained upon the reflection into the chamber of an electron beam from an electrode held at the negative potential of the gun cathode. In measurements of the injected current the reflection electrode is used as a collector. The longitudinal distribution of the beam electrons is measured with a multigrid analyzer; the analyzer is moved across an aperture 0.03 cm in diameter in the collector, which can be moved to various beam radii. The currents in the collector circuit and in the circuit of the gun cathode are measured by a Rogowski loop. The high-frequency waves are detected by coaxial probes and then displayed on an oscilloscope.

Electron beams with $v_\perp \neq 0$ can be produced by injecting the beams through an increasing magnetic field. As a rule, hot beams result.[7] In our experiments, in a system with a homogeneous magnetic field, such beams are produced by injection through a transverse magnetic field of 100 Oe over a distance ~ 4 cm at the entrance to the chamber. The transverse magnetic field is produced by two magnetic coils arranged symmetrically with respect to the axis of the solenoid.

The excitation of high-frequency waves in counterstreaming beams is studied in ref. 6 under conditions such that the transverse electron velocity in the beam is comparable to the longitudinal component ($v_\perp \sim v_z$). A large transverse component $v_\perp$, as determined from the pulsations, is obtained by injecting the beam into the interaction chamber through a growing axisymmetric magnetic field. In such a beam we would expect pronounced changes in the parameters $v_\perp/v_z$ and v_T/v_z along a diameter. In fact, as the experiments show, the beam has complex characteristics over a cross section. As an example, Fig. 1 shows the beam energy spectra along the radius of the working chamber, r, at the maximum of the pulsations. We see from this figure that the velocity v_z falls off with increasing r, as does the current density, while v_T/v_z increases (curves 1-4). Because of energy conservation, there is an increase in the transverse velocity of the beam electrons: $v_\perp^2 = v_0^2 - v_z^2 (v_0 = \sqrt{2eU/m}$, e and m are the electron charge

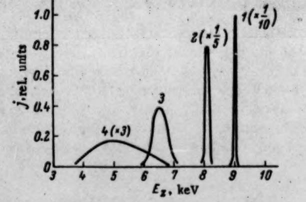

Fig. 1. Energy spectra of the beam electrons at various radii. E_0 = 9 keV, I = 0.6 A, H = 500 Oe. 1) r = 0; 2) 0.2; 3) 0.45; 4) 0.75 cm.

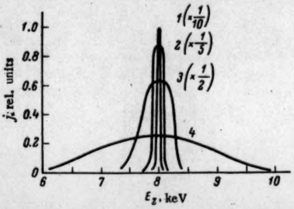

Fig. 2. Energy spectrum of the beam electrons. I = 0.4 A, H = 300 Oe. 1) E_0 = 8; 2) 8.4; 3) 8.8; 4) 10.6 keV.

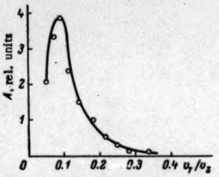

Fig. 3. Wave amplitude as a function of v_T/v_z (an increase in v_T/v_z is accompanied by an increase in $v_\perp/v_z$). The values of the parameters are the same as for Fig. 2.

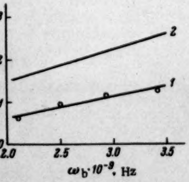

Fig. 4. The critical value of v_T/v_z as a function of ω_b. The values of the parameters are the same as for Fig. 2.

and mass, and U is the accelerating voltage). According to Eq. (1), when $\lambda_1/\lambda_0 \geq 5$, those beam electrons for which $v_T \leqslant 0.14\ v_z$ can contribute to the wave growth. Curve 2 corresponds to beam electrons with $v_\perp = 0.3\ v_z$ and $v_T = 0.08\ v_z$, for which there should be growth in the interaction of counterstreaming electron beams of this type.[5] The beam electrons (curve 3) have $v_T = 0.22\ v_z$, and they should not contribute to the wave intensity, despite the large value $v_\perp \simeq 0.6\ v_z$. The peripheral part of the beam (curve 4), on the other hand, exhibits a large transverse velocity ($v_\perp \simeq v_z$) but a low current density and a large value of v_T($v_T = 0.43\ v_z$), so that these electrons cannot drive instabilities.

When we take collisionless damping into account, we see that the velocity $v_\perp$ can affect the wave excitation in this system only near the central part of the beam. The important factor is that the variation in $v_\perp$ over the beam cross section be accompanied by a variation in v_z. As a result, the condition for optimum excitation (the condition that the length of the working chamber be equivalent to an integral number of half-waves of the fundamental mode) does not hold for all "layers" of electrons over the beam cross section. It is a complicated matter to analyze the effect of $v_\perp$ on the wave intensity in such a system, so we carry out an experiment in which the electrons acquire a transverse velocity $v_\perp$ while v_T is held constant over the beam cross section.

In the system with the homogeneous longitudinal magnetic field the beam is essentially monoenergetic over the cross sections. When a transverse magnetic field is imposed, the beam as a whole acquires a transverse velocity $v_\perp$, and the distribution over the cross section changes slightly. Figure 2 shows longitudinal electron energy spectra of the beam injected into the system for a fixed velocity component v_z, corresponding to a longitudinal energy of E_z = 8 keV and to an increase in the initial electron energy E_0 with increasing $v_\perp$ (curves 2-4). Curve 1 shows the monoenergetic (cold) beam. Curve 2 shows a beam with $v_T = 0.11\ v_z$ and $v_\perp = 0.25\ v_z$. Here, the amplitude at the fundamental frequency has approximately doubled. The increase in the wave intensity with increasing $v_\perp$ agrees with the theory of ref. 5. Curves 3 and 4 show hot beams with v_T/v_z equal to 0.2, 0.4 and with v_T/v_z equal to 0.35, 0.6, respectively. As v_T increases the beam diameter increases. For curve 2 the beam diameter is nearly the same. For curve 3 the increase is about 20-25%, while for curve 4 it reaches 50%. Despite the significant increase in $v_\perp$ for the beams with the distribution functions described by curves 3 and 4, we observe a pronounced damping of the high-frequency waves; this can be attributed to the collisionless damping resulting from the increase in ($\lambda_1/\lambda_D < 5$). The damping of the waves for curves 3 and 4 is 15 and 30 dB. Figure 3 shows the change in the amplitude of the high-frequency waves under the experimental conditions corresponding to Fig. 2. The damping at harmonics of half the gyrofrequency becomes apparent at values of v_T lower than that at which the damping at the fundamental frequency becomes apparent.

We note that in practice it is difficult to produce beams with a high transverse electron velocity ($v_\perp \sim v_z$) with $v_T/v_z \leq 0.1$. An increase in the transverse magnetic field to 100 Oe leads, because of the fringing fields and the inhomogeneity of the distribution with respect to the coil diameter, to an appreciable increase in the beam diameter (or a reduction in the beam density) and to a significant increase in the parameter v_T/v_z.

Figure 4 shows the critical value of the parameter v_T/v_z as a function of the beam plasma frequency (line 1) at which the waves begin to be damped. We see from this figure that the experimental functional dependence differs significantly from the theoretical functional dependence (line 2) for the case $\lambda_1/\lambda_D = 5$. The quantitative discrepancy can be attributed to the circumstance that the distribution of the oscillating beam electrons is stretched out significantly during the growth of the high-frequency waves.[8]

The results shown in Figs. 2-4 are obtained in the case v_z = const, corresponding to optimum excitation of high-frequency waves in the system.

On the basis of an analysis of these results we can assert that electron beams can be used in a system of counterstreaming beams to excite waves at frequencies $n\omega_H/2$ with a velocity spread $v_T > 0.1\ v_z$ with an increase in the beam density for a fixed magnetic field. We can thus also use beams having large values of $v_\perp$ to produce more intense high-frequency waves. On the other hand, as the current decreases it is necessary to have beams which are monoenergetic. This latter requirement is apparently responsible for the fact that waves at frequencies $n\omega_H/2$ are not observed[9] in a system of counterstreaming beams involving low-current beams in the case in which the electron beam is in an inhomogeneous magnetic field.

Accordingly, we have shown experimentally that an increase in the transverse electron velocity of the beam injected into a system of counterstreaming beams, $v_\perp$, leads to a growth of the waves at half the gyrofrequency and at its harmonics. However, an increase in $v_\perp$ is accompanied by an increase in v_T. At a certain value of v_T the wave amplitude becomes limited by collisionless damping.

---

[1] C. Etivant and M. Perulli, EUR-CEA-FC-191, 1962.

[2] J. Olivain, Rapport CEA-R-3075, Fontenay aux Rouses, 1966.

[3] C. Etivant and M. Perulli, Sixth Intern. Conf. on Ionization Phenomena in Gases, Paris, 1963.

[4] D. Handel and G. Müller, Plasma Physics and Controlled Nuclear Fusion Research, Vienna, Vol. 2 (1969).

[5] V. Kopecky and J. Preinhaelter, Czech. J. Physics, B22, 58 (1972).

[6] D. V. Iremashvili, A. P. Timoshenko, and Yu. K. Udovichenko, Zh. Tekh. Fiz., 43, 550 (1973) [Sov. Phys. – Tech. Phys., 18, 348 (1973)].

[7] M. Seidl and P. Sunka, Nucl. Fusion, 7, No. 4, 237 (1967).

[8] M. Murakamy and L. M. Lidsky, Phys. Rev. Lett., 24, 297 (1970).

[9] G. Müller and G. Landaner, Eighth Intern. Conf. on Ionization Phenomena in Gases, Vienna, 1967.

Mass spectrum of secondary ions ejected from the surface of a single crystal of gallium arsenide by argon ions

A. G. Koval', V. V. Bobkov, Yu. A. Klimovskii, S. S. Strel'chenko, V. V. Shubina, V. V. Lebedev, and Ya. M. Fogel'

A. M. Gor'kii Khar'kov State University

(Submitted December 19, 1973; resubmitted April 26, 1974)
Zh. Tekh. Fiz., 44, 2563-2567 (December 1974)

The mass spectrum of charged and neutral particles ejected from the surface of single-crystal films of gallium arsenide by Ar^+ ions is studied. The charged particles include ions of the elements of the gallium arsenide lattice and complex ions like Ga_mAs_n. In addition, ions of molecules of surface compounds of lattice elements with residual gas molecules are found. The composition of the ejected neutrals is significantly different from that of the secondary ions.

The construction of almost all present-day semiconductor devices requires the synthesis of compounds of the $A^{III}B^{V}$ groups in the form of homo- or heteroepitaxial layers with various dopings.[1]

Up to the present time the methods used to investigate the processes of formation and growth of epitaxial layers and their doping do not give information on the initial stages of these processes. The method of secondary ion–ion emission (SIIE)[2,3] can be used to study the initial stages of the formation of thin films[4-6] and the distribution of impurities over the thickness of a thin layer of material.[3-7]

It is advantageous to use the SIIE method to study the important semiconductor compound gallium arsenide (GaAs). We present the results of a study of the mass spectrum of secondary ions formed in the surface bombardment of single crystals of gallium arsenide by argon ions. This information is necessary for more detailed information.

This work is performed on a mass spectrometer built from a modified MI-1305 mass spectrometer. The construction and characteristics of this instrument are described in refs. 8 and 9. A GaAs target is bombarded with a beam of 2 keV Ar^+ ions at a current density of 0.6 $\mu A/cm^2$. The pressure of the residual gas in the target chamber is 10^{-6} torr. The targets are single crystals or single-crystal epitaxial layers of GaAs 30–100 μ thick grown on oriented GaAs substrated by the method described in ref. 10 and doped with tin or tellurium to a level of $\sim 10^{18}$ cm^{-3}.

The mass spectra of secondary ions obtained from thick single crystals and from epitaxial films are identical both in structure and in the relative intensities of the mass lines, within the limits of experimental error. Most of the mass lines correspond either to secondary ions of target particles or various complexes of these, or to secondary ions of compounds of target particles or complexes of them with particles of the residual gases. In addition the mass spectra contain the usual secondary ions produced from molecules of the residual gases adsorbed on the target surface, and secondary ions from the bulk contamination of the target material (Na^+, Al^+, Si^+, K^+).

Table 1 shows the secondary ions ejected by Ar^+ ions from the (100) face of an epitaxial film of GaAs at 700°K. The intensities of the beams of secondary ions are summed over all isotopes. The relative intensities of the beams of ions of gallium isotopes and ions of various of its com-

TABLE 1

m, amu	Interpretation	Intensity, rel. units	m, amu	Interpretation	Intensity, rel. units
12	C^+	5	92, 94	$GaNa^+$	20
13	CH^+	10	138, 140, 142	Ga_2^+	25300
14	CH_2^+	43	144, 146	$GaAs^+$	429*
15	CH_3^+	99	150	As_2^+	54*
16	CH_4^+, O^+	3	154, 156, 158	Ga_2O^+	267*
17	OH^+	2	155, 157, 159	Ga_2OH^+ (1782)	124*
18	H_2O^+	4	160, 162	$GaAsO^+$	17*
23	Na^+	656	166	As_2O^+	24
24–26	Mg^+, X_n^+	51	207–213	Ga_3^+	339
27	Al^+	144	213–217	Ga_2As^+	422
28–30	Si^+, X_n^+	278	219, 221	$GaAs_2^+$	66
39.41	K^+	5944	223–229	Ga_3O^+, As_3^+	407
40	Ar^+, Ca^+	12800	239–245	$Ga_3O_2^+$	53
69.71	Ga^+	227000	282–288	Ga_3As^+	141
75	As^+	340*	288–292	$Ga_2As_2^+$	33
86.88	$GaOH^+$	(1680)7	351–359	Ga_4As^+	97
91	AsO^+	18			

Note: The X_n^+ are ions of unknown origin; the asterisk denotes a peak poorly resolved from neighboring peaks; the numbers in parentheses give the intensity at room temperature.

TABLE 2

m, amu	Interpretation	Intensity, rel. units
75	As	190
144, 146	Ga As	12
150	As_2	358
225	As_3	28
300	As_4	180

pounds correspond to the values calculated from tabulated data on the abundance of gallium isotopes by better than ±5%, which is within the limits of experimental error.

Table 1 shows that the intensities of the mass lines corresponding to various secondary ions vary over wide limits. The intensity of the line corresponding to the arsenic ion As^+, in contrast with the results reported in ref. 11, is more than two orders of magnitude smaller than the intensities of the lines for Ga ions.

It is worth noting that the mass spectra show lines corresponding to ions of complex compounds of gallium and arsenic atoms like $Ga_mAs_n^+$. While cluster forms of arsenic particles As_n^+ are also observed in thermal evaporation,[12] particles of the form Ga_mAs_n have so far been assumed to be unstable.[13] The lifetimes of Ga_m^+ and $Ga_mAs_n^+$ particles estimated from their energies and ranges from the target to the secondary ion detector are at least $2 \cdot 10^{-5}$ sec.

In addition to the mass spectrum of secondary ions our investigation includes a study of the mass spectrum of neutral particles ejected from the surface of GaAs by primary Ar^+ ions and then ionized by a beam of electrons. The structure of the mass spectrum of neutrals obtained in this way is shown in Table 2. The table shows that the neutrals ejected from the surface of gallium arsenide are mainly atomic and cluster forms of neutral arsenic particles: As, As_2, As_3, and As_4. No gallium atoms or molecules are found in the mass spectrum of neutrals.

A comparison of Tables 1 and 2 shows that the composition of atomized neutrals differs radically from the composition of the ejected ions, and is closer to the composition of particles evaporated by heating gallium arsenide. Possible reasons for this difference are given in ref. 14.

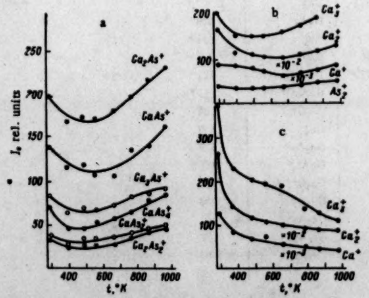

Fig. 1. J (T) for beams of secondary ions Ga_m^+, $Ga_mAs_n^+$, As_2^+. a, b) (100) face; c) (111) face.

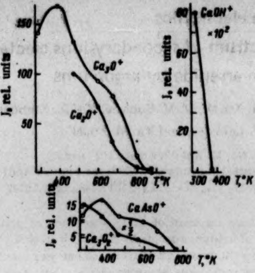

Fig. 2. J (T) for beams of secondary ions of oxides and hydroxides, (100) face.

The intensities of the beams of secondary ions J listed in Table 1 are found as functions of the target temperature T. Below, these relations are denoted by J(T).

Figure 1 shows the intensities of beams of ions of the first group, which includes ions of target elements and their various complexes, and varies slowly with temperature in the 300–1000°K range. Only for the ions Ga^+, Ga_2^+, and Ga_3^+ ejected from the (111) face of a single crystal of GaAs is there a significant decrease in intensity with rising target temperature. At the same time Figs. 2 and 3 show a rapid variation of intensity with target temperature for secondary ions of various compounds of target particles and their complexes with particles of the residual gases (ions of the second group). The decrease in intensity for ions of gallium hydroxides ($GaOH^+$, Ga_2OH^+) with an increase in target temperature is much more rapid than for ions of gallium oxide or an ion of the complex compound $GaAsO^+$.

The difference in the character of the J(T) curves for secondary ions of the first and second groups enables us to state with considerable confidence that ions of the first group are ejected mainly from the GaAs crystal lattice, while precursors of ions of the second group are molecules of chemical compounds of lattice particles with particles adsorbed on its surface.

A comparison of Figs. 2 and 3 shows that the J(T) curves for the (111) and (100) faces of a GaAs single crys-

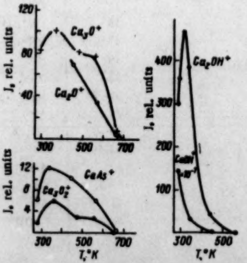

Fig. 3. J (T) for beams of secondary ions of oxides and hydroxides, (111) face.

tal behave somewhat differently. This may be a consequence of the difference in adsorbing power and chemical activity of these faces.

The currents of secondary ions of the first and second groups are also found as functions of the primary ion current J_0.

Over the whole range of primary beam currents studied the relation $J = f(J_0)$ is found to be linear for ions of the first group, which indicates a bulk origin of these ions. At the same time the curve of $J = f(J_0)$ for ions of the second group shows saturation, which is characteristic of ions ejected from surface compounds.[15]

It is interesting to note that there is a definite correlation between the mass spectrum of particles ejected by a beam of Ar^+ ions from the surface of a GaAs single crystal and its crystal lattice.

It is known that the GaAs crystal lattice consists of body-centered tetrahedrons of Ga_4As and $GaAs_4$. At the same time if no account is taken of ions of sorbed particles and bulk impurities in gallium arsenide the mass spectrum of ejected particles contains mainly ions of fragments of unit cells of the Ga_4As lattice and ions of compounds of these fragments with sorbed particles (Tables 1 and 2). By examining the mass spectra of particles ejected from semiconductor compounds having different types of crystal lattices we hope to obtain information on the mechanism of the breaking of bonds in a unit cell of a crystal lattice by the transfer of momentum to some particle of this lattice from a cascade of atomic collisions arising from the penetration of a primary ion into the depth of the lattice.

An important practical conclusion of these results is that in an ordinary vacuum (~ 10^{-6} torr) at a temperature of the order of 900°K it is possible to clean a GaAs crystal surface of molecules of surface chemical compounds of lattice atoms with particles adsorbed on its surface.

The authors thank their co-workers of the V. M. Kozlov Laboratory of Ionic Processes for their help.

---

[1] V. I. Chernyaev, Electronic Engineering Reviews, Data [in Russian], Elektronika, Moscow (1970).

[2] Ya. M. Fogel', Usp. Fiz. Nauk, 91, 75 (1967) [Sov. Phys. – Usp., 10, 17 (1967)]; J. Mass. Spectr. and Ion. Phys., 9, 109 (1972).

[3] A. Benninghoven, Z. Phys., 230, 403 (1970).

[4] A. D. Abramenkov, V. M. Azhazha, Ya. M. Fogel', and V. I. Shvachko, Fiz. Met. Metalloved., 29, 519 (1970).

[5] A. D. Abramenkov, Ya. M. Fogel', V. V. Slezov, L. V. Tanatarov, and O. P. Ledenev, Fiz. Met. Metalloved., 30, 1310 (1970).

[6] A. D. Abramenkov, A. L. Seryugin, V. V. Dyatlova, Ya. M. Fogel', and G. F. Potebnya, Fiz. Met. Metalloved., 33, 853 (1972).

[7] V. M. Pistryak, A. K. Gnap, V. F. Kozlov, R. I. Garber, and A. I. Fedorenko, Fiz. Tverd. Tela, 12, 1281 (1970) [Sov. Phys. – Solid State, 12, 1005 (1970)].

[8] A. G. Koval', A. I. Lysaya, V. V. Bobkov, A. A. Rivlin, Ya. M. Fogel', and O. A. Lunev, Zashchita Metal., 8, 152 (1972).

[9] V. V. Bobkov, Yu. A. Klimovskii, A. G. Koval', and Ya. M. Fogel', in: Diffused Junction in a Vacuum [in Russian], Moscow (1973), p. 155.

[10] V. V. Lebedev, A. A. Matyash, S. S. Strel'chenko, V. V. Shubina, V. I. Maior, A. A. Potepalova, and Yu. G. Nadtochnyi, in: Proc. First All-Union Symp. on Semiconductor Devices, Part II [in Russian], Moscow (1970), p. 158.

[11] R. E. Honig, Advances in Mass Spectrometry, Vol. 2, Pergamon, New York (1963), p. 25.

[12] J. Drowart and P. Goldfinger, J. Chem. Phys., 55, 721 (1958).

[13] P. Goldfinger, in: Semiconductor Compounds, 682 [in Russian], Metallurgiya, Moscow (1967).

[14] A. G. Koval', G. I. Vyagin, V. V. Bobkov, Yu. A. Klimovskii, S. S. Strel'chenko, and Ya. M. Fogel', Zh. Tekh. Fiz., 43, 1753 (1973) [Sov. Phys. – Tech. Phys., 18, 1105 (1974)].

[15] V. F. Kozlov, V. M. Pistryak, and Ya. M. Fogel', Fiz. Tverd. Tela, 10, 3713 (1968) [Sov. Phys. – Solid State, 10, 2952 (1969)].

Coherent Compton effect in crystals

V. A. Bushuev and R. N. Kuz'min
Department of Physics, M. V. Lomonosov Moscow State University
(Submitted December 10, 1973; resubmitted April 8, 1974)
Zh. Tekh. Fiz., 44, 2568-2571 (December 1974)

The effect of the dynamic interaction of scattered waves on the frequency and angular distribution of the scattered radiation is discussed using the Compton effect in ideal crystals as an example. It is shown that the presence of a perfect crystal lattice leads to the appearance of lines of the spatially coherent Compton effect superimposed on the ordinary incoherent Compton scattering background. The shapes and intensities of these lines are found by taking account of the absorption of the incident and scattered radiation.

The effect of a crystal lattice on the effectiveness of inelastic scattering of x rays appears in the change of shape and width of the Compton[1-3] and plasmon[4] scattering lines in comparison with scattering in a free-electron gas, in the appearance of the nonlinear Bragg condition of synchronism in parametric scattering,[5] and in the possibility of a mixture of x rays with the short-wavelength components of a field of optical frequency.[6]

In the present paper we point out another aspect of inelastic scattering related to the presence of a perfect crystal structure. Since the frequency of the scattered radiation (signal) depends on the scattering angle, it is easy to explain the directions in which the usual Bragg–Wolf conditions will be satisfied for the signal waves in the medium. Because of the dynamic exchange between the spatially coupled modes $q(\omega)$ and $q + H$, where H are the appropriate reciprocal lattice vectors, there must be a redistribution of energy in these modes, and radiation of frequency ω can be observed in new directions previously forbidden by the laws of conservation of energy and momentum. Now part of the momentum H will be taken up by the lattice itself. Thus this is interference of inelastically scattered waves as a consequence of spatial (lattice) coherence.

For simplicity we limit ourselves to a consideration of dynamic effects in Compton scattering. Suppose a monochromatic wave (pump) $e_1E_1\exp(ik_1r - i\omega t) + \text{c.c.}$ is incident on a crystal slab of thickness l, where the angle φ between k_1 and the plane perpendicular to H is different from the Bragg angle. The scattered radiation is observed in the far zone in the direction $\varkappa$ ($\varkappa = \omega/c$).

By generalizing the method developed in ref. 7 the differential scattering cross section in the two-wave approximation with respect to the signal can be obtained in the form

$$\sigma(\omega, \vartheta_0) = \sum_{m=1}^{2}\sum_{\mu=1}^{2} v_{m\mu}\,[D_{m\mu}^{(0)}(\mathbf{e}_{m0}\mathbf{e}_1)^2\sigma^{(0)}(\omega, \vartheta_0) + D_{m\mu}^{(H)}(\mathbf{e}_{mh}\mathbf{e}_1)^2\sigma^{(0)}(\omega, \vartheta_h)]\left[\sum_{m=1}^{2}(\mathbf{e}_{m0}\mathbf{e}_1)^2\right]^{-1}. \tag{1}$$

Here, $\sigma^{(0)}(\omega, \vartheta)$ is the Compton scattering cross section neglecting dynamic exchange and the absorption of the signal and pump; ϑ_0 and ϑ_h are the angles between k_1 and $\varkappa$ and between k_1 and $\varkappa + H$ respectively. For simplicity only those terms which make the main contribution to the scattered intensity are retained in (1). The coefficients $D_{m\mu}$ describe the effectiveness of the dynamic interaction.

$$D_{m\mu}^{(0)} = \frac{|p_m \pm \sqrt{p_m^2+1}|^2}{4(p_m^2+1)}, \quad D_{m\mu}^{(H)} = \frac{\gamma_0}{4\gamma_h(p_m^2+1)}, \tag{2}$$

$$\left.\begin{aligned} p_m = -\frac{\Delta\omega \sin^2\delta}{2\pi\omega|\alpha_m|}\sqrt{\frac{\gamma_0}{\gamma_H}}, \quad \sin\delta = \frac{H}{2\varkappa}, \\ \gamma_0 = \sin\rho\sin(\chi+\delta), \quad \gamma_h = \sin\rho\sin(\chi-\delta), \end{aligned}\right\} \tag{3}$$

where the parameter p_m characterizes the deviation of the signal frequency $\omega = \omega_B + \Delta\omega$ from the Bragg frequency ω_B found[1)] from $H = 2(\omega_B/c)\sin u$, where $(\pi/2 + u)$ is the angle between the vectors $\varkappa$ and H which define the so-called plane of linear scattering or the dynamic plane. Equations (2) and (3) are obtained under the assumption that $\gamma_h > 0$ (Laue case). Here, ρ is the acute angle between the dynamic plane and the crystal surface, χ is the angle between the normal to H, lying in the dynamic plane, and its line of intersection with the crystal surface. The upper and lower signs in (2) refer respectively to the centers of propagation $\mu = 1$ and 2. The unit vectors of the signal waves e_{m0} and e_{mh} are perpendicular to the dynamic plane for $m = 1$, and parallel to it for $m = 2$. The dynamic coupling coefficient is $\alpha_m \equiv \alpha^{(H)}(\omega q)(e_{m0}\hat{\pi}_q e_{mh})$, where $\alpha^{(H)}$ is the part of the linear polarizability which is nondiagonal in H, and is proportional to the structure factor corresponding to H, $\hat{\pi}_q$ is the operator which projects onto the plane perpendicular to q, and the medium is assumed isotropic.

The dimensionless quantity $v_{m\mu}$ characterizes the effect of absorption of the pump and signal on the effective scattering volume

$$v_{m\mu} = \frac{e^{-y_{m\mu}} - e^{-y_1}}{y_1 - y_{m\mu}}, \quad v_{m\mu}(|p| \gg 1) = \frac{e^{-y} - e^{-y_1}}{y_1 - y} \equiv v. \tag{4}$$

Here $y_1 = \beta l/\cos(k_1 \cdot n)$, $y = \beta l/\cos(\varkappa \cdot n)$, β is the linear absorption coefficient at the pump frequency, n is the normal to the crystal surface, and $y_{m\mu}(p) = \sigma_{m\mu}l$, where $\sigma_{m\mu}(p_m)$ is the absorption coefficient in the Laue case, given in ref. 9 for example. The absorption coefficient $\sigma_{m\mu}$ has resonances and can be very different for centers 1 and 2 (the Bormann effect). In a transparent medium ($\beta l \ll 1$) $v_{m\mu} = 1$, but it should be remembered that the thickness l has a lower bound ($l \gg 10^{-3}$ cm) which is determined by the limits of applicability of the dynamic theory.

The quantities u and ϑ_- must now be expressed in terms of ϑ_0. If the direction of $\varkappa$ is characterized by the polar angle ψ with respect to the equatorial plane perpendicular to the $(k_1 \cdot H)$ plane, and the azimuthal angle Φ measured from the direction of k_1 in the equatorial plane, it is easy to show that $\cos\vartheta_0 = \cos\psi\cos\Phi$,

$$\sin u = \sin\psi\cos\varphi - \cos\psi\sin\varphi\cos\Phi,$$
$$\cos\vartheta_h = \sin\psi\sin 2\varphi + \cos\psi\cos 2\varphi\cos\Phi.$$

For $|p_m| \gg 1$ the effects of the dynamic interaction can be neglected, and according to (1) and (2) we obtain the usual single-wave approximation result: $\sigma(\omega,\vartheta_0) = v\sigma^{(0)}(\omega,\vartheta_0)$.

The shape of the Compton line becomes distorted as $|p_m|$ decreases. Depending on the values of the parameters φ, γ_0/γ_h and $\Delta\omega_e$ – the effective width of the $\sigma^{(0)}$ cross section – a dip or a spike is superimposed on the ordinary shape of the Compton line at the frequency $\omega_0(\vartheta_0)$. This increment has a Lorentz shape with a width $\Delta\omega_L = (2\pi\omega|\alpha_m|/\sin^2\delta)\sqrt{\gamma_h/\gamma_0}$ which is two or three orders of magnitude narrower then the $\sigma^{(0)}$ line. In the x-ray region $|\alpha_m| \sim 10^{-4}$-10^{-6}. At the present time such narrow increments apparently cannot be observed in the spectral distribution, although their amplitudes are of the order of $\frac{1}{2}\sigma^{(0)}(\omega_B, \vartheta_0)$.

It follows from (1)-(3) that a coherent inelastic scattering line should be observed in the integrated distribution of $\sigma(\vartheta_0)$ against an almost uniformly incoherent Compton background. This phenomenon is the spatially-coherent Compton effect. According to (1) the condition for maximum dynamic exchange

$$\omega_B(\psi, \Phi) = \omega_{cs} = \omega_1\left(1 - 2\frac{\hbar\omega_1}{mc^2}\sin^2\frac{\vartheta_0}{2}\right) \tag{5}$$

determines the spatial position of the coherent Compton lines. For $\hbar\omega_1/mc^2 \ll 1$ Eq. (5) is the equation of a slightly deformed cone with its axis along **H**.

The coherent Compton effect line has an angular fine structure since there is an excess or deficiency of radiation in the $\varkappa$ direction. Its angular spectrum for $\varphi \neq 0$ consists of two narrow closely spaced lines, one of which is brighter than the background and the other dimmer. For $\psi > \varphi$ the dimmer line should lie closer to the direction of $\mathbf{k}_1$. The angular shape of each individual line repeats the frequency shape with a width of the order of $\Delta\omega_e/\omega_1$. For $v_{m\mu} = 1$ the contrast, i.e., the absolute value of the intensity over background at the center of the line, is estimated as a fraction to a few percent for light materials such as Be, C, or LiF. For crude estimates the contrast can be taken equal to $(\pi/2)(\Delta\omega_L/\Delta\omega_e)$. It should be noted, however, that if absorption is taken into account the contrast can become many times larger. Since $v_{m\mu}(p_m = 0) > v$, in the region of anomalous transmission, in an overall decrease in scattered intensity the background is depressed more strongly. Thus for $y \approx y_1 = 5$, $y(p_m = 0) \approx 0.05y$, from (4) $v_m(0) = 0.15$, and the ratio of effective volumes is ~20.

For small angles $\vartheta_{0,h}$ the main contribution to inelastic scattering is made by Raman scattering from collective fluctuations of electron density – plasmons. If $|\sin\varphi| - \sin\delta < 2\sin\vartheta_c$, where ϑ_c is the critical angle determining Landau damping for plasmons,[4] coherent (lattice) Raman scattering can occur from plasmons. Expressions for the cross sections for Compton and plasmon scattering $\sigma^{(0)}$ in a degenerate electron gas in a metal are given in ref. 7, for example.

The Bragg case ($\gamma_h < 0$) does not appear to be of great interest; because of the primary extinction the effective volume for scattering into a coherent Compton line is decreased by several orders of magnitude and only a thin boundary layer contributes.

The observation of the coherent Compton effect described in the present paper requires perfect single crystals, preferably large enough to suppress incoherent Compton scattering. A number of papers have reported the observation of slightly curved lines with a fine structure in the angular spectrum of the scattering of a slightly divergent beam of monochromatic radiation in diamond single crystals[10,11] and in LiF crystals previously bombarded with neutrons or deformed by compression.[12] On the basis of geometrical considerations these interference lines are explained by the presence of Compton scattering. Since the crystals used have a very pronounced mosaic structure the intensity of the Compton interference lines should be described within the framework of kinematics and not by the dynamic theory of the scattering of x rays, while their geometric position,[2] as for ideal crystals, is determined by the neutral condition (5).

Elastic scattering in mosaic crystals is generally more effective than in ideal crystals,[8] and apparently for just this reason the coherent Compton lines were not observed in scattering in perfect diamond crystals,[11] and became observable in LiF only after directional deterioration of the crystal structure. Therefore it is of interest to perform a special experiment to observe the coherent Compton effect in perfect crystals of such materials as germanium or silicon which exhibit a strong anomalous transmission.

For example, suppose a silicon single crystal is oriented in such a way that the reciprocal lattice vector H(220) is parallel to the axis of a cylindrical chamber and the crystal faces, and the Mo Kα pump is incident perpendicular to H($\gamma_0 = \gamma_h$, $\varphi = 0$). In this case an x-ray photograph should show a pair of dim lines symmetrically located with respect to the straight line $\psi = 0$ at a distance $\psi \geq \psi_0 = 10°40'$, where $\Delta\psi\,(\Phi_0 = 170°) = 43'$. If the scattering angle is such that $k_2 = 2k_1\sin\vartheta_0/2 = 2k_F$ ($k_F = 1.8$ A^{-1} is the Fermi wave vector in the free-electron model with a density equal to the density of the valence electrons in silicon[3]) $\Delta\omega_e = 56$ eV, $\Delta\omega_L = 3.1$ eV, and according to (1) and (4) for k_2 a crystal of length $l = 2$ mm ($\beta = 15.4$ cm^{-1}, $\beta_{anom} = 0.04\beta$) the contrast at the center of Compton scattered lines at points on an x-ray photograph with coordinates $\psi = \pm 10°41'$ and $\Phi = \pm 20°50'$ should amount to 50% for an angular half-width of the lines $\Delta\psi_{1/2} = (\Delta\omega_e/\omega_1)\tan\psi = 2.3'$.

The authors are indebted to D. N. Klyshko for helpful discussion and to E. V. Kolontsova and I. V. Telegina for information regarding their experiments.

---

[1] We recall that in the usual dynamic theory, where the frequency of the waves is specified, the deviation parameter is the difference between the scattering angle and the Bragg direction.[8] In experiments on inelastic scattering the viewing angle is generally fixed. Therefore we are developing a variant of the dynamic theory with a frequency difference.

[2] If the angle $\varphi = 0$, then for a change $\Delta\psi$ in the polar angle ψ as Φ increases from 0 to Φ_0 it follows from (3) that $\Delta\psi = (\hbar\omega_1/mc^2)\sin\psi_0(1-\cos\Phi_0)$, where ψ_0 is the scattering angle at $\Phi = 0$. The fact that $\Delta\psi$ is positive indicates that the interference lines should be bent upward slightly from the line $\psi = \psi_0$. In the scattering of Mo Kα in LiF [reflection (220), $\psi_0 = 10°$] for $\Phi_0 = 170°$ we have $\Delta\psi = 40.5°$, which is in good agreement with the experimental result.[12]

3) Calculations[13] show that for sufficiently large transfer of momentum k_2 and energy $(\omega_1 - \omega_{C3})$ the difference in effective widths $\Delta\omega_e$ in semiconductors and metals with the same electron density can be neglected.

---

[1] B. I. Lundqvist and C. Lyden, Phys. Rev., B4, 3360 (1971).

[2] P. Eisenberger, L. Lam, P. M. Platzman, and P. Schmidt, Phys. Rev., B6, 3671 (1972).

[3] O. Terasaki, T. Fukamachi, S. Hosoya, and D. Watanabe, Phys. Lett., 43A, 123 (1973).

[4] P. Eisenberger, P. M. Pltazman, and K. C. Pandy, Phys. Rev. Lett., 31, 311 (1973).

[5] I. Freund and B. F. Levine, Phys. Rev. Lett., 23, 854 (1969).

[6] J. F. Woo and S. S. Jha, Phys. Rev., B6, 4081 (1972).

[7] V. A. Bushuev and D. N. Klyshko, Zh. Tekh. Fiz., 43, 2255 (1973) [Sov. Phys. – Tech. Phys., 18, 1427 (1974)].

[8] R. James, The Optical Principles of the Diffraction of X Rays, Bell, London (1948).

[9] R. W. James, Solid State Phys., 15, 55 (1963).

[10] H. J. Grenville-Wells, Nature, 168, 4268, 291 (1951).

[11] N. Norman, Acta Crystallogr., 11, 1 (1958).

[12] I. V. Telegina and E. V. Kolontsova, Kristallografiya, 14, 707 (1968) [Sov. Phys. – Crystallogr., 14, 603 (1970)].

[13] J. F. Walter and M. L. Cohen, Phys. Rev., B5, 3101 (1972).

Transformation of light beams by dynamic correctors using three-dimensional displacement phase holograms

V. G. Sidorovich and D. I. Stasel'ko

(Submitted June 11, 1974)
Zh. Tekh. Fiz., 44, 2572-2579 (December 1974)

The transformation of a beam consisting of several plane waves into a single plane wave is studied in an analysis of the nonlinear wave equation in the approximation of slowly varying amplitudes. The conditions under which essentially complete transformation is achieved are determined. The possibility of achieving these conditions in practice is examined.

Studies of the transformation of light beams by three-dimensional dynamic holograms are of considerable interest in connection with the use of such holograms to control the spatial and temporal characteristics of coherent radiation sources, one aspect of which is to correct the shape of nonstationary wave fronts. Experimental study of the simplest transformation case, in which two monochromatic plane waves at identical frequencies propagate in a three-dimensional dynamic phase hologram, has shown that a significant fraction of the energy of one wave can be transferred to the other wave when the hologram is displaced with respect to the sinusoidal interference pattern which forms it.[1] Theory for this situation has shown that a three-dimensional dynamic, displacement phase hologram can provide essentially complete energy transfer from one of the incoming waves to the other, regardless of the ratio of the corresponding wave intensities at the boundary.[2] In particular, this property makes it possible to stabilize the propagation direction of intense light beams. The transformation of light beams whose wave fronts have an arbitrary shape and which differ in frequency is of more practical interest. The recording and reconstruction of dynamic holograms by beams differing in frequency are analyzed in ref. 3 for arbitrary properties of the recording media; it is shown that the traveling dielectric-constant waves produced in such dynamic holograms are capable of transforming a plane reference wave into a wave of arbitrary shape. However, that analysis[3] is based on the assumption that the object and reference waves propagating in the hologram have constant amplitudes, so that the efficiency of this transformation could not be determined. Furthermore, no account is taken of the transformation of an object wave of arbitrary shape into a plane wave – a process which is important in connection with the problem of correcting wave fronts. In the present work we analyze the possible use of dynamic holograms recorded by beams of different frequency in cubic nonlinear media with inertial nonlinearity mechanisms to correct wave fronts. We find that the three-dimensional dynamic phase holograms recorded in such media are capable of transforming a beam consisting of several plane waves into a plane wave at a different frequency with essentially no energy loss. We derive the conditions under which this transformation is possible.

1. We choose a cubic nonlinear medium with inertial nonlinearity mechanisms as the material for recording the dynamic holograms on the basis of the following considerations: As beams at different frequencies propagate in such a medium, the phase lattices are displaced with respect to the sinusoidal interference patterns that shape them. This displacement is necessary for a high radiation-transformation efficiency.[4-7] There are many such nonlinear media, since significant changes in the dielectric constant due to such phenomena as electrostriction, heating, and the orientation of anisotropic molecules in optical-frequency fields occur under the influence of intense light beams in essentially any slightly absorbing medium. Also taking account of the possibility of recording dynamic holograms in large volumes (especially when liquid and gaseous nonlinear media are used) and the possibility of achieving short times for the establishment of the phase lattices (as short as 10^{-10}-10^{-13} sec), we see that these media have the necessary characteristics for practical use in dynamic holography. Among the processes leading to changes in the dielectric constant of cubic nonlinear media under the influence of light are vibrational processes (e.g., acoustic vibrations of the medium caused by electrostriction or vibrations of atoms in molecules excited by light). A distinctive feature of these processes is the resonant nature of the changes which they cause in the dielectric constant: When the difference between the frequencies of the interfering beams, Ω, is equal to the resonant frequency Ω_R, the amplitude of the phase lattice produced by the traveling interference patterns becomes a factor of $\Omega R/\Delta\Omega$ higher than the amplitude of the phase lattice formed by the beams of identical frequency (here $\Delta\Omega$ is the width of the resonance line of the oscillations), and the traveling lattice lags behind the interference pattern which forms it by one fourth of a period.[5,6] It becomes clear in the discussion below that the circumstance that the modulation of a traveling lattice becomes higher than that of a fixed lattice is extremely important for correction of wave fronts.

2. To analyze the correction of wave fronts by displacement dynamic phase holograms recorded in inertial cubic nonlinear media we state the problem as follows: We assume that the correcting beam – a plane wave of amplitude $c_1(0)$ – and the beam to be corrected [which consists of several plane waves propagating at small angles with respect to each other, e.g., two waves of amplitudes $c_2(0)$ and $c_3(0)$] are incident on the boundary of a transparent cubic nonlinear medium. The waves of the beam being corrected have the same frequency ω, while the frequency of the plane correcting wave is $\omega-\Omega (\Omega > 0)$. When the difference between the beam frequencies is of this sign, energy is transferred from the waves of the beam being corrected to the plane wave for the cases of most of the mechanisms which lead to a cubic nonlinearity of a medium.[8] We also restrict the discussion to the case $\Omega \ll \omega$, so that we can neglect dispersion of the medium. Figure 1 shows the geometry of the problem. The X and Y axes are

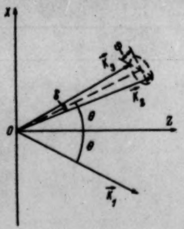

Fig. 1. Vector diagram of waves propagating in a dynamic hologram.

parallel to the surface of the medium, while the Z axis is normal to this surface. We assume that the wave vector of the correcting wave $\mathbf{k}_1$ and the bisector of the angle between the wave vectors $\mathbf{k}_2$ and $\mathbf{k}_3$ corresponding to the waves in the beam being corrected lie in the XoZ plane, making angles of $\pm\theta$ with the z axis. Here, φ is the angle between the XoZ plane and the plane containing $\mathbf{k}_2$ and $\mathbf{k}_3$, and δ is the angle between $\mathbf{k}_2$ and $\mathbf{k}_3$ ($\delta \ll 1$). Assuming that all the waves are polarized in the YoZ plane, we describe the light propagation in the medium by a nonlinear equation for that component E of the electric field **E** which is perpendicular to the plane of incidence:$^{1)}$

$$\nabla^2 E - \frac{1}{c^2}\frac{\partial^2}{\partial t^2}(\varepsilon(E)E) = 0, \qquad (1)$$

where c is the speed of light in vacuum, and $\varepsilon(E) = \varepsilon_0 + \Delta\varepsilon(E)$ is the dielectric constant of the medium,$^{2)}$ and

$$|\Delta\varepsilon(E)| \ll \varepsilon_0. \qquad (2)$$

3. The transformation of light beams by a dynamic hologram in this case can be described in the following manner: The interference of the second and third waves at identical frequencies in the nonlinear medium produces a fixed phase lattice P_{23}, which coincides in position with the interference pattern of these waves. The interference of the first wave with the second and of the first wave with the third leads to the formation of traveling lattices P_{12} and P_{13}, displaced with respect to the corresponding interference patterns by some fraction of a period. Scattering of the incident waves by the lattices formed in the medium leads to a change in the complex amplitudes of these waves and to the appearance of new waves.

We first consider the case in which the amplitudes of the waves arising in the hologram are negligibly small in comparison with the amplitudes of the waves propagating in the directions of the initial waves and having their frequencies; in this case we achieve the maximum efficiency for the transformation of the beam being corrected into an undistorted plane wave. We thus write solution (1) as

$$E(x, y, z, t) = \sum_{j=1}^{3} c_j(z)\, e^{i(\mathbf{k}_j\mathbf{r} - \omega_j t)}, \qquad (3)$$

where $c_j(z)$ are the amplitudes of the plane waves propagating in the hologram, $\mathbf{k}_j = (k_{jx}, k_{jy}, k_{jz})$; $\mathbf{r} = (x, y, z)$; $\omega_1 = \omega - \Omega$; and $\omega_{2,3} = \omega$. Using (3) and the displacements mentioned above between the traveling interference patterns and the corresponding lattices, we write the nonlinear increment to the dielectric constant of the medium, $\Delta\varepsilon(E)$, as

$$\Delta\varepsilon(E) = \alpha J_\Sigma + [(\beta'' - i\beta')\, c_1 c_2^* e^{i[(\mathbf{k}_1 - \mathbf{k}_2)\mathbf{r} + \Omega t]}$$
$$+ (\beta'' - i\beta')\, c_1 c_3^* e^{i[(\mathbf{k}_1 - \mathbf{k}_3)\mathbf{r} + \Omega t]} + \alpha c_2 c_3^* e^{i(\mathbf{k}_2 - \mathbf{k}_3)\mathbf{r}} + \text{c.c.}], \qquad (4)$$

where

$$J_\Sigma = |c_1(z)|^2 + |c_2(z)|^2 + |c_3(z)|^2 = |c_1(0)|^2 + |c_2(0)|^2 + |c_3(0)^2|$$

is the resultant intensity of the waves propagating in the hologram, α is the nonlinearity coefficient corresponding to the fixed lattice, and β'' and β' are the nonlinearity coefficients corresponding to the undisplaced component of the traveling lattices and the component which is displaced by one fourth of a period.$^{3)}$ Equations for the nonlinearity coefficients α, β', and β'' are given in ref. 5.

Substituting (3) and (4) into (1) and neglecting terms containing second derivatives of $c_j(z)$, we find a system of nonlinear differential equations for $c_j(z)$:

$$\left.\begin{aligned}
\frac{dc_1}{dz} &= iD_1\alpha J_\Sigma c_1 + D_1(\beta' + i\beta'')\, c_1(|c_2|^2 + |c_3|^2),\\
\frac{dc_2}{dz} &= iD_2\alpha J_\Sigma c_2 + D_2 c_2[i(\alpha + \beta'')|c_3|^2 - \beta'|c_1|^2],\\
\frac{dc_3}{dz} &= iD_3\alpha J_\Sigma c_3 + D_3 c_3[i(\alpha + \beta'')|c_2|^2 - \beta'|c_1|^2],
\end{aligned}\right\} \qquad (6)$$

where $D_i = k_{0i}^2/2k_{iz}$, and k_{0i} is the wave number of wave i. Turning to the intensities of the plane waves propagating in the dynamic hologram, $J_1(z)$, $J_2(z)$, and $J_3(z)$, we write equations for these intensities in integral form:

$$\left.\begin{aligned}
\frac{J_1(z)}{J_1(0)} &= e^{2D\beta'\int_0^z [J_2(z') + J_3(z')]\,dz'},\\
\frac{J_{2,3}(z)}{J_{2,3}(0)} &= e^{-2D\beta'\int_0^z J_1(z')\,dz'}
\end{aligned}\right\} \qquad (7)$$

(here we have used the approximation $D_1 \simeq D_2 \simeq D_3 \simeq D$, which holds for $\delta \ll 1$ and $\Omega \ll \omega$). Using the integral in (5) to solve system (7), we find

$$\left.\begin{aligned}
J_1(z) &= \frac{J_\Sigma J_1(0)}{J_1(0) + S(0)\, e^{-2D\beta' J_\Sigma z}},\\
J_{2,3}(z) &= \frac{J_\Sigma J_{2,3}(0)}{S(0) + J_1(0)\, e^{2D\beta' J_\Sigma z}},
\end{aligned}\right\} \qquad (8)$$

where $S(0) = J_2(0) + J_3(0)$.

It follows from (8) that at large values of z we have $J_1(z) \simeq J_\Sigma$, i.e., if the additional waves which are produced in the hologram are neglected, we can transform the beam being corrected into an undistorted plane wave with essentially no energy loss.

4. We turn now to the range of applicability of this analysis, and find the conditions under which the amplitudes of the additional waves are small. On the basis of their formation mechanisms we can classify the additional waves into four groups: (1) waves which arise in the scattering of each of the plane waves of the beam being corrected by the traveling lattice which is formed without the participation of the given plane wave (the scattering of the second wave by lattice P_{13} and of the third wave by lattice P_{12}); (2) the waves of the same direction and frequency which appear in the scattering of the first wave by lattice P_{23}; (3) the higher orders of diffraction of the original waves by the lattices P_{12} and P_{13}; and (4) the higher orders of diffraction of the second and third waves by lattice P_{23}.

The propagation directions of the waves of the first and second types make angles with respect to the correcting wave which are approximately equal to the angles between the plane waves in the beam being corrected. Accordingly, if the amplitudes of these waves are comparable to the amplitude of the correcting wave, $c_1(z)$, the divergence of the radiation transformed by the dynamic hologram can be at least as large as the divergence of the beam being corrected.

To derive the condition under which the amplitudes of the additional waves of the first two types are small in comparison with amplitude $c_1(z)$, we write the solution of (1), writing one of these waves in the form

$$E(x,\ y,\ z,\ t)=\sum_{j=1}^{3} c_j(z)\,e^{i(\mathbf{k}_j\mathbf{r}-\omega_j t)}+E', \qquad (9)$$

where $E' = c'(z)e^{i(\mathbf{k}'\mathbf{r}-\omega' t)}$ is the projection of the electric field of the wave in question onto the Y axis, $c'(z)$ is a quantity which is equal in modulus to the amplitude of the additional wave in question, $\mathbf{k}' = \mathbf{k}_1 - \mathbf{k}_2' + \mathbf{k}_3$ is the wave vector of the polarization wave which excites it, and $\omega' = \omega - \Omega$. Assuming $|E|' \ll |c_i|$ and using Eq. (4) for $\Delta\varepsilon(E)$, after substituting (4) and (9) into (1) we find an equation for $c'(z)$:

$$\frac{dc'}{dz}-i\frac{A}{2k'_z}c'=i\alpha J_\Sigma\frac{k_{01}^2}{2k'_z}c'+i(\alpha+\beta'')\frac{k_{01}^2}{2k'_z}c_1c_2^*c_3+\beta'\frac{k_{01}^2}{2k'_z}c_1c_2^*c_3, \qquad (10)$$

where $A = k_{01}^2 - (k_x'^2 + k_y'^2 + k_z'^2)$; k'_x, k'_y, k'_z are the projections of $\mathbf{k}'$ on the coordinate axes; and $A/2k'_z$ is the modulus of the vector difference between the phase velocities of the given additional wave and the polarization wave which excites it. Substituting the equations found for $c_i(z)$ by converting (6) to "total-differential" form into the right-hand side of Eq. (10), and neglecting the quantity $(D_1 - D_2 + D_3 - D')\alpha J_\Sigma$ $(D' = k_{01}^2/2k'_z)$ in comparison with $A/2k'_z$, we rewrite (10) as

$$\frac{d}{dz}\left[c'e^{-i\left(\frac{A}{2k'_z}+\alpha J_\Sigma\frac{k_{01}^2}{2k'_z}\right)z}\right]=[\beta'+i(\alpha+\beta'')]\,DC_1(0)\,c_2(0)\,c_3(0)$$

$$\times e^{D\beta'\int_0^z[|c_2(z')|^2+|c_3(z')|^2-2|c_1(z')|^2]dz'}\,e^{-i\frac{A}{2k'_z}z}. \qquad (11)$$

The ratio of the moduli of the amplitudes of the additional wave in question and of the first wave,

$$\left|\frac{c'(z)}{c_1(z)}\right|=\left|\frac{[\beta'+i(\alpha+\beta'')Dc_1(0)c_2(0)c_3(0)\int_0^z e^{D\beta'\int_0^{z'}[|c_2(z'')|^2+|c_3(z'')|^2-2|c_1(z'')|^2]dz''}\,e^{-i\frac{A}{2k'_z}z'}\,dz'}{c_1(0)\,e^{D\beta'\int_0^z[|c_2(z'')|^2+|c_3(z'')|^2]dz''}}\right|, \qquad (12)$$

obtained with the help of (6) and (11), becomes small if the second exponential term in the integral over z' oscillates rapidly in comparison with the first term. Under this condition this integral can be calculated by the method of stationary phase:

$$\left|\frac{c'(z)}{c_1(z)}\right|\simeq\left|\frac{[\beta'+i(\alpha+\beta'')Dc_2(0)\,c_3(0)\left(e^{D\beta'\int_0^z[|c_2(z')|^2+|c_3(z')|^2-2|c_1(z')|^2]dz'}\,e^{-i\frac{A}{2k'_z}z}-1\right)}{\frac{A}{2k'_z}e^{D\beta'\int_0^z[|c_2(z')|^2+|c_3(z')|^2]dz'}}\right|<2\left|\frac{[\beta'+i(\alpha+\beta'')Dc_2(0)\,c_3(0)}{\frac{A}{2k'_z}}\right|<\frac{\sqrt{(\Delta\varepsilon_{\alpha+\beta''})^2+(\Delta\varepsilon_{\beta'})^2}\,k_{01}^2}{A}, \qquad (13)$$

where $\Delta\varepsilon_{\alpha+\beta''} = (\alpha + \beta'')J_\Sigma$ and $\Delta\varepsilon_{\beta'} = \beta' J_\Sigma$. Using (13), we can write the condition under which the additional waves of the first two types are suppressed, $|c'(z)/c_1(z)| \ll 1$, in the form[4])

$$\frac{\sqrt{(\Delta\varepsilon_{\alpha+\beta''})^2+(\Delta\varepsilon_{\beta'})^2}}{4\sin\delta\sin 2\theta\cos\varphi+2\sin^2\delta}\ll 1. \qquad (14)$$

It follows from (14) that the condition for the suppression of these additional waves is governed strongly by the orientation of the plane containing $\mathbf{k}_2$ or $\mathbf{k}_3$ with respect to the XoZ plane. This dependence is illustrated by Fig. 2, which shows the values of the angle δ which satisfy the equation $[((\Delta\varepsilon_{\alpha+\beta''})^2+(\Delta\varepsilon_{\beta'})^2/(4\sin\delta\,\sin 2\theta\cos\varphi+2\sin^2\delta))]^{1/2} = 0.1$ for various values of the angle φ between these planes (when this equation holds, the intensity of the additional wave in question does not exceed 1% of that of the correcting wave). We see that the lower limit on the values of the angle δ, at which the additional waves of the first two types have small amplitudes, is vastly more stringent in the case $\varphi = 90°$ than in the case $\varphi = 0$.

The waves of the third type propagate at large angles with respect to the correcting wave, so that their influence is primarily one of reducing the efficiency with which the beam being corrected is transformed into a plane wave. The amplitudes of these waves are small if the lattices P_{12} and P_{13} are three-dimensional:

$$\frac{\Delta\varepsilon\sqrt{\beta'^2+\beta''^2}}{2\sin^2 2\theta}\ll 1, \qquad (15)$$

a condition which is analogous to condition (20) in ref. 2. We note that the satisfaction of condition (14) implies the satisfaction of condition (15) when $\delta \ll \theta$.

Waves of the fourth type can grow as a result of the decomposition of the beam being corrected into several thin filaments,[9,10] which prevent the transformation of the given beam into a plane wave. The effect of the self-focusing of the beam being corrected can be reduced by increasing the angle δ to a value satisfying the condition that the lattice P_{23} be three-dimensional:

$$\frac{\Delta\varepsilon\alpha}{2\sin^2\delta}\ll 1. \qquad (16)$$

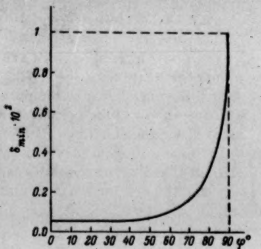

Fig. 2. Angular selectivity of a dynamic hologram as a function of the angle φ, the angle through which the plane of the wave vectors of the beam being corrected is rotated with respect to the incidence plane, XoZ, in the case $\sqrt{(\Delta\varepsilon_{\alpha+\beta''})^2+(\Delta\varepsilon_{\beta'})^2} = 10^{-4}$, $\theta = 0.1$ rad.

Another method for suppressing the self-focusing, which does not involve restriction (16) on the angle δ, is to terminate the transformation into a plane wave by the traveling lattices before the higher diffraction orders at the lattice P_{23} reach an appreciable level. An estimate of the necessary ratio β'/α for a specified ratio of the intensities of the beam being corrected and of the plane wave at the boundary, $S(0)/J_1(0)$, yields

$$\frac{\beta'}{\alpha} > \ln\frac{S(0)}{J_1(0)}. \tag{17}$$

Condition (17) can be achieved in practice, for example, through the use of resonant scattering of light by traveling acoustic waves produced by electrostriction. In this case β' is usually 20-50 times larger than α (ref. 11), and condition (17) holds at values of $S(0)/J_1(0)$ up to $\sim 10^3$. In this case the resonance condition is $\Omega_R(\Lambda) = 2\pi v_{so}/\Lambda$, where v_{so} is the sound velocity in the medium and Λ is the period of the interference pattern of the two plane waves; this condition can hold exactly only for one of the lattices formed as a result of the interference of the plane wave of the beam being corrected and the correcting wave. Since this condition does not hold for the other lattice, the modulation depth of the dielectric constant in this lattice is reduced. There is a corresponding reduction in the efficiency with which that wave being corrected is transformed into the correcting wave. To suppress this effect we must set an upper limit on the angle between the plane waves in the correcting beam: $\delta_{\max} = \Delta\Omega/v_{so}k_0$ where $\Delta\Omega$ is the width of the Brillouin line,[11] and k_0 is the average wave number of the interfering waves. The ratio of this quantity to the angle $\delta_{\min}$, defined by (14), is a measure of the number of plane waves which can be transformed into a plane wave without loss of energy. An estimate of this ratio for a medium with parameters $\Delta\varepsilon_{\beta'} \sim 10^{-5}$ ($\Delta\varepsilon_{\beta'} \gg \Delta\varepsilon_{\alpha+\beta''}$) and $\Omega_R/\Delta\Omega \simeq 20$, characteristic of organic liquids with an electrorestrictive nonlinearity mechanism, and $2\theta = 0.2$ in the case $\varphi = 90°$ yields a value $\delta_{\max}/\delta_{\min} \simeq 40$ and, in the case $\varphi = 0$, a value $\delta_{\max}/\delta_{\min} \sim 2$.

5. It has been shown above that if inequality (17) holds the beam being corrected must have parameters satisfying condition (14) if this beam is to be completely transformed into a plane wave. In practice, however, this condition may not always hold, so that it is worthwhile to analyze the correction possibilities in the opposite limiting case:

$$\frac{\sqrt{(\Delta\varepsilon_{\alpha+\beta''})^2+(\Delta\varepsilon_{\beta'})^2}}{4\sin\delta\sin 2\theta\cos\varphi+2\sin^2\delta} \gg 1. \tag{18}$$

For this analysis we partition the cross section of the beam being corrected into several small regions, within each of which we can assume the beam intensity to be essentially constant and the wave front to be planar. Using condition (18) we can treat the transformation of the beam being corrected into a plane wave independently within each of these small regions, using the procedure of ref. 2. In general, this independence of the transformation processes in the different regions leads to a modulation of the intensity over the cross section and to a distortion of the front. This distortion is not important when (17) holds, since the difference between the phase advances in different regions of the transformed wave is small [it must be kept in mind that in this case the satisfaction of condition (17) corresponds to an essentially complete transformation of the beam being corrected only in those regions where its intensity is a maximum]. The intensity modulation in the cross section of the transformed wave leads to the appearance of waves propagating at angles with respect to the original direction of the correcting wave. In a first approximation the energy expended on these waves can be estimated on the basis of the theory of static plane amplitude holograms.[12] A more rigorous calculation incorporating the functional dependence of the transformation efficiency of the beam being corrected on its intensity in the corresponding part of the cross section shows that the total energy of the waves propagating in directions different from that of the correcting wave does not exceed 20% if the hologram thickness corresponds to complete transformation of the beam in regions of maximum intensity.

Accordingly, the use of media with resonant nonlinearity mechanisms in dynamic correctors in the case in which condition (14) does not hold at least eliminates the distortions of the shape of the wave front, so that the divergence of the wave transformed by the corrector can be reduced to nearly diffraction value.

In conclusion we should point out that the general features of this analysis of holographic correctors using media with resonant nonlinearity mechanisms can apparently be extended to the case in which lithium niobate crystals are used as the medium for recording the dynamic holograms. According to the data of refs. 1 and 13, the modulation depth of the dielectric constant, $\Delta\varepsilon_\chi$, produced in such a medium for a certain exposure time for beams making an angle χ increases with increasing χ. Accordingly, if we use a large angle θ we can satisfy the inequality $\Delta\varepsilon_\theta/\Delta\varepsilon_\delta \simeq \sin 2\theta/\sin\delta > \ln S(0)/J_1(0)$, which is equivalent to (17).

The authors thank Yu. N. Denisyuk for useful discussion.

---

1) In Eq. (1) we have neglected a second-order term in δ, which is the projection of the vector $[\mathbf{E}\ \mathrm{grad}\ (\ln\varepsilon)]$ on the oY axis.

2) We assume below that $\varepsilon_0 = 1$, so that we can neglect reflection and refraction of light at the boundary of the medium.

3) These coefficients are related to the phase shift between the traveling interference patterns and the lattice they produce, ψ, by $\tan\psi = \beta'/\beta''$.

[4] Inequality (14) can also be interpreted as the condition for selectivity of the dynamic hologram with respect to all the waves incident on it.

---

[1] D. L. Staebler and J. J. Amodei, J. Appl. Phys., 43, 1042 (1972).

[2] D. I. Stasel'ko and V. G. Sidorovich, Zh. Tekh. Phys., 44, 580 (1974) [Sov. Phys. – Tech. Phys., 19, 361 (1974)].

[3] Yu. N. Denisyuk, Zh. Tekh. Fiz., 44, 131 (1974) [Sov. Phys. – Tech. Phys., 19, 77 (1974)].

[4] N. Bloembergen and V. Shen, Phys. Rev., 133A, 37 (1964).

[5] R. G. Harrison, R. V. Key, and I. V. Little, Proc. Roy. Soc. Lond., A334, 193 (1973).

[6] V. S. Starunov and I. L. Fabelinskii, Usp. Fiz. Nauk, 98, 441 (1969) [Sov. Phys. – Usp., 12, 463 (1970)].

[7] E. Garmire, F. Pandarese, and C. H. Townes, Phys. Rev. Lett., 11, 160 (1963).

[8] B. Ya. Zel'dovich and I. I. Sobel'man, Usp. Fiz. Nauk, 101, 3 (1970) [Sov. Phys. – Usp., 13, 307 (1971)].

[9] R. Y. Chiao, P. L. Kelley, and E. Garmire, Phys. Rev. Lett., 17, 1158 (1966).

[10] A. J. Campillo, S. L. Shapiro, and B. R. Suydam, Appl. Phys. Lett., 23, 628 (1973).

[11] I. L. Fabelinskii, Molecular Scattering of Light [in Russian], Izd. Nauka, Moscow (1965), p. 314.

[12] R. Collier, C. Burqhart, and L. Lin, Optical Holography [Russian translation], Izd. Mir, Moscow (1973), p. 256.

[13] S. G. Odulov and M. S. Soskin, Proceedings of the Fifth All-Union School on Holography [in Russian], Leningrad (1973), p. 535.

Electroluminescence spectra of the red luminescent diodes $p\text{-}Al_xGa_{1-x}As-n\text{-}Al_yGa_{1-y}As$ $(y > x)$

V. M. Busov, D. Z. Garbuzov, A. T. Gorelenok, and D. S. Kop'ev

A. F. Ioffe Physicotechnical Institute, Leningrad

(Submitted December 7, 1973)
Zh. Tekh. Fiz., 44, 2580-2584 (December 1974)

Red heterostructure luminescent diodes consisting of $Al_xGa_{1-x}As$ solid solutions with a zinc-doped active region have been studied. The electroluminescence spectra are studied as a function of the impurity concentration and as a function of the aluminum concentration in the active region. It has been found that injected electrons traversè the entire active region into the p-GaAs substrate if the active region is thin.

Preliminary results of a study of the properties of the heterostructure luminescent diodes $p\text{-}Al_xGa_{1-x}As-n\text{-}Al_yGa_{1-y}As$ $(y > x)$ are reported in refs. 1 and 2. As suggested in ref. 3, the use of zinc-doped p-type $Al_xGa_{1-x}As$ solid solutions as the active regions of these diodes makes it possible to produce injection light sources emitting efficiently at 300°K in the red region up to $\lambda \simeq 6400$ Å.

We reported here a more detailed study of the electroluminescence spectra of these diodes. The synthesis procedure and conditions are similar to those described in ref. 2. The heterostructure luminescent diodes are produced by liquid epitaxy in which the substrate is zinc-doped p-GaAs. The radiation is observed in the direction normal to the plane of the p − n junction through a $n\text{-}Al_yGa_{1-y}As$ wide-band emitter. The diode area is about 0.5 mm^2.

At 300°K these samples display an external quantum efficiency at $\lambda = 6900$ Å of 1-1.5%; that at $\lambda = 6700$ Å is 0.4-0.5%; and that at $\lambda = 6500\text{-}6400$ Å is 0.1-0.2%.

The electroluminescence spectra are recorded by a standard synthronous-detection procedure. The radiation is detected by an FÉU-62 photomultiplier or a germanium photodiode. The measurements are carried out over the temperature range 77-300°K.

We turn first to the nature of the electroluminescence spectra of these diodes as a function of the doping level of the p-type and n-type regions. The acceptor and donor concentrations (N_A and N_D, respectively) for some of these samples are shown in Table 1. The acceptor (zinc) concentration in the n-type region is lower than the donor (tellurium) concentration in the n-type region for all the diodes, and the value of N_A can be determined from the voltage−capacitance measurements. The donor concentration in the n-type region is determined from data in the literature on the tellurium segregation coefficient for the case in which solid solutions are doped during growth by the liquid method.[4] The Al concentration in the active region and that in the wide-band emitter are determined by microscopic x-ray spectral analysis.

TABLE 1

Sample	N_D (Fe)	N_A (Zn)	hν, eV; $T = 300°$ K
92 P 2	$2 \cdot 10^{17}$	$2 \cdot 10^{16}$	1.816
88 P 2	$2 \cdot 10^{17}$	$2 \cdot 10^{16}$	1.810
N 28	10^{18}	$4 \cdot 10^{17}$	1.874
145 P 2	$5 \cdot 10^{18}$	$1.7 \cdot 10^{17}$	1.865
148 P 1	$2 \cdot 10^{18}$	$1.4 \cdot 10^{17}$	1.856
153 P 2	$2 \cdot 10^{18}$	$4.6 \cdot 10^{17}$	1.920
144 P 2	$5 \cdot 10^{17}$	$1.2 \cdot 10^{17}$	1.928

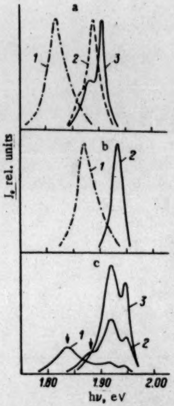

Fig. 1. Electroluminescence spectra of heterostructure luminescent diodes having various doping levels for the p-type and n-type regions. a: 92P2 structure. 1) T = 300; 3) 155; 3) 85°K. b: N28 structure. 1) T = 300; 2) 77°K. c: 145P2 structure. 1) $j = 3 \cdot 10^{-2}$; 2) 0.7; 3) $1.5 \cdot 10^2$ A/cm^2, T = 77°K. The arrows show the emission band due to diagonal tunneling.

Let us consider the structures with weakly doped p-type and n-type regions (samples 92P2 and 88P2; Table 1). The red spectrum of such structures at 77°K (Fig. 1a, curve 3) has the shape characteristic of weakly doped p-GaAs samples[5] and $p\text{-}Al_xGa_{1-x}As$ samples.[6,7] The short-wavelength emission band in this case is apparently of an excitonic nature, and the long-wavelength band 25 MeV away from it is due to transitions between the conduction band and acceptor level of zinc.[7] According to data obtained earlier in a study of the photoluminescence spectra of zinc-doped $Al_xGa_{1-x}As$ samples,[6] the energy gap between the exciton and "zinc" emission bands in the electroluminescence spectra of heterostructure luminescent diodes is not governed by the Al concentration in the active region for direct compositions of the solid solutions. As the excitation level is raised, the intensity of the short-wavelength band increases more rapidly. Increasing the temperature from 77 to 300°K leads to a continuous decrease in the relative intensity of the longer-wavelength zinc band (Fig. 1a, curves 1-3). At the same time, the short-wavelength band broadens and becomes asymmetric. The extended short-wavelength decay of this band at 300°K (curve 1 in Fig. 1a) implies that free electron−hole pairs participate in the recombination.[5,8] The characteristic radiative-transition times in these diodes at 300°K are about 50 nsec (ref. 2).

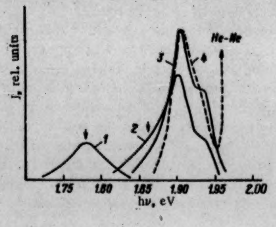

Fig. 2. Electroluminescence and photoluminescence spectra of the 148P1 structure with heavily doped p-type and n-type regions. 1-3) Electroluminescence spectrum. j (A/cm²): 1) 10^{-2}; 2) 20; 3) 120; 4) photoluminescence spectrum, T = 77°K. The arrows show the emission band due to diagonal tunneling.

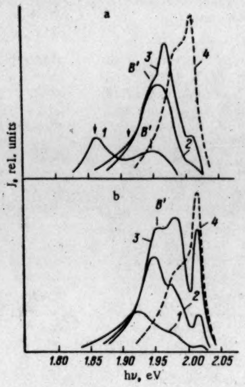

Fig. 3. Electroluminescence spectra of heterostructure luminescence diodes having a high Al−As concentration in the active region. a: 153P2 structure. 1) $j = 7 \cdot 10^{-2}$; 2) 20; 3) 80; 4) $2 \cdot 10^3$ A/cm² (pulsed excitation). b: 144P2 structure. 1) $j = 4 \cdot 10^{-2}$; 2) 10; 3) 120; 4) $1.6 \cdot 10^3$ A/cm² (pulsed excitation), T = 77°K. The arrows show the emission band due to diagonal tunneling.

As the zinc concentration in the active region is increased (sample N28; Table 1), the longer-wavelength band, due to transitions to acceptor levels becomes predominant in the emission spectrum of the diodes at 77°K (Fig. 1b, curve 2). Furthermore, as expected, the radiative-transition times at 300°K decrease to 10-15 nsec.

Increasing the tellurium concentration in the n-type region of the diodes (samples 148P1 and 145P2; Table 1) leads to the appearance in the electroluminescence spectra at 77°K of a broad long-wavelength emission band in addition to the edge bands. As the voltage applied to the diode is increased, the position of this band shifts in the short-wavelength direction (Fig. 1c, curves 1 and 2, and Fig. 2, curves 1 and 2). To determine the nature of this band we have studied the photoluminescence spectra of the active region of the corresponding structures when they are excited by a He−Ne laser on the side of the wide-band n-type emitter. Although the excitation level in the photoluminescence is chosen to be low, the long-wavelength emission band is not found in the photoluminescence spectrum (Fig. 2, curve 4). This result implies that the moving long-wavelength band in the electroluminescence spectra of the diodes is due to diagonal tunneling analogous to that which occurs in heavily doped p−n GaAs junctions[9-11] and GaAs−$Al_xGa_{1-x}As$ heterojunctions.[10,11]

These electroluminescence spectra are typical of heterostructure luminescent diodes in which the Al−As concentration in the active region is lower than 32%. As the Al concentration in the active region is increased, and the transition compositions are approached ($X_n = 0.37$; ref. 3), the nature of the electroluminescence spectra changes. At low and medium current densities the predominant feature in the electroluminescence spectrum of these samples at 77°K is the broad B' band (Fig. 3, a and b, curves 1 and 2).

The maximum of this band shifts considerably in the short-wavelength direction as the excitation level is raised; in contrast with the emission band considered above (due to diagonal tunneling), the rate at which the maximum of the B' band shifts is much lower, and its position does not correspond to the magnitude of the applied voltage. The B' band is observed in the electroluminescence spectra even at bias values considerably higher than the voltage corresponding to the height of the barrier at the heterojunction. The narrow edge emission bands characteristic of luminescent diodes with a narrower band-active region (Fig. 3, a and b, curves 3 and 4) are found in the electroluminescence spectra of these structures only at high current densities. Comparison of Figs. 3a and 3b shows that the energetic separation of B' and the edge bands increases with increasing aluminum concentration in the active region of the diodes.

The electroluminescence spectra in Fig. 3 are generally analogous to the photoluminescence spectra of solid $Al_xGa_{1-x}As$ solutions having the corresponding compositions.[12] Here, the B band is evidently due to indirect transitions between acceptor states and donor levels corresponding to the minimum X_1, which lie at a lower energy than the minimum[12] Γ_1. Increasing the aluminum concentration leads to a further displacement of this indirect donor level with respect to the direct minimum of the conduction band, causing the observed increase in the separation of B' and the edge emission bands, which are still due to direct transitions. With a further increase in the AlAs concentration in the active region the edge transitions also undergo a change in nature, becoming indirect.

Up to this point we have only considered the short-wavelength part of the emission spectra, due to recombination in the active region of the diodes. However, in addition to the short-wavelength bands, the emission spectra of all the diodes contain long-wavelength bands whose shape and position correspond to radiative transitions in the p-GaAs substrate. For samples with a thick active region (d = 20-25 μ) the intensity of the long-wavelength "gallium arsenide" band is no more than 5% of the intensity of the red band at 300°K, and the ratio of the intensities of these bands is independent of the current density over the range 10-10^4 A/cm². The long-wavelength band in this case is evidently due to optical excitation of the p-GaAs substrate by the short-wavelength emission band.

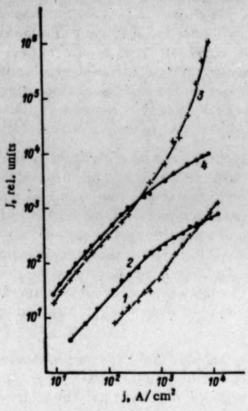

Fig. 4. Intensities of the short-wavelength and long-wavelength emission bands as a function of the current density for the N28 structure (the active region is d = 7 μ thick). 1, 3) Long-wavelength band at 300 and 77°K, respectively; 2, 4) short-wavelength band at 300 and 77°K, respectively.

For samples with a thin active region (d ≃ 4-7 μ) the relative intensity of the gallium arsenide band, even at low current densities, is much higher than that for structures with a thick active region. As the current density is increased we generally observe a faster-than-linear increase in the intensity of the long-wavelength band (Fig. 4, curve 1); at the same time, the increase in the intensity of the red band slows (Fig. 4, curve 2). As the temperature is reduced to 77°K these effects are displayed even more clearly (Fig. 4, curves 3 and 4). The intensity ratio of the red and long-wavelength bands changes at current densities lower than at 300°K, and the intensification of the gallium arsenide band is accompanied by a transition to stimulated emission.[1)] The observed intensification of the gallium arsenide accompanying an increase in the current density in the structures having thin active regions is evidently due to the complete traversal of the active region by the injected electrons, which reach the p-GaAs substrate.

The increase in the effective length of the diffusion-drift displacement for the minority carriers (electrons) as the current density is increased is apparently due to a strengthening of the electric field in the active region. On the one hand, a temperature reduction from 300 to 77°K strengthens the electric field because of the reduction in the free-hole concentration in the active region; on the other hand, it increases the electron mobility. These effects are probably responsible for the observed increase in the flow of carriers across the active region as the temperature is reduced from 300 to 77°K.

In conclusion the authors thank V. M. Tuchkevich and Zh. I. Alferov for their interest, and T. B. Godlinnik for a microscopic x-ray spectral analysis.

[1)] The ratio of the red and gallium arsenide bands was studied in diodes having solid contacts, with the emission observed parallel to the plane of the p–n junction. The spectral sensitivity of the pickup is taken into account in plotting the curves.

---

[1] Zh. I. Alferov, R. I. Chikovani, R. A. Charmakadze, G. M. Mirianashvili, N. K. Zosimov, and N. A. Grigoryan, Fiz. Tekh. Poluprovodn., 6, 2289 (1972) [Sov. Phys. – Semicond., 6, 1930 (1973)].
[2] Zh. I. Alferov, D. Z. Garbuzov, A. T. Gorelenok, B. V. Pushn[illegible], and M. K. Trukan, Fiz. Tekh. Poluprovodn., 7, 1457 (1973) [Sov. Phys. – Semicond., 7, 1000 (1974)].
[3] Zh. I. Alferov, V. I. Amosov, D. Z. Garbuzov, Yu. V. Zhilyaev, S. G. Konnikov, P. S. Kop'ev, and V. G. Trofim, Fiz. Tekh. Poluprovodn., 6, 1879 (1972) [Sov. Phys. – Semicond., 6, 1620 (1973)].
[4] K. Sugiyama and T. Kawakami, Jap. J. Appl. Phys., 10, 1007 (1971).
[5] E. W. Williams and E. R. A. Chapman, J. Appl. Phys., 38, 2547 (1967).
[6] Zh. I. Alferov, D. Z. Garbuzov, V. I. Kolyshkin, O. A. Ninua, and V. G. Trofim, Fiz. Tekh. Poluprovodn., 5, 1405 (1971) [Sov. Phys. – Semicond., 5, 1232 (1972)].
[7] D. Z. Garbuzov, A. I. Ekimov, P. S. Kop'ev, and V. I. Safarov, Fiz. Tekh. Poluprovodn., 6, 1749 (1972) [Sov. Phys. – Semicond., 6, 1507 (1973)].
[8] B. V. Tsarenkov, Ya. G. Akperov, A. N. Imenkov, and Yu. P. Yakovlev, Fiz. Tekh. Poluprovodn., 6, 677 (1972) [Sov. Phys. – Semicond., 6, 584 (1972)].
[9] J. I. Pankove, Phys. Rev. Lett., 9, 283 (1962).
[10] Zh. I. Alferov, D. Z. Garbuzov, E. P. Morozov, and E. L. Portnoi, Fiz. Tekh. Poluprovodn., 3, 1054 (1969) [Sov. Phys. – Semicond., 3, 885 (1970)].
[11] Zh. I. Alferov, D. Z. Garbuzov, P. S. Kop'ev (Kop'yov), and E. L. Portnoi, Proc. 10th Intern. Conf. on the Physics of Semiconductors, Cambridge, Mass. (1970), p. 478.
[12] Zh. I. Alferov, D. A. Garbuzov, O. A. Ninua, and V. G. Trofim, Fiz. Tekh. Poluprovodn., 5, 1116 (1971) [Sov. Phys. – Semicond., 5, 982 (1971)].

Gas temperature in the positive column of a medium-β helium discharge

Yu. M. Kagan and K. K. Paskalev
A. A. Zhdanov Leningrad State University

(Submitted July 23, 1973)
Zh. Tekh. Fiz., 44, 2585-2588 (December 1974)

We compare various approximate methods for calculating the radial distribution and the values of atomic temperatures on the axis in the positive column in helium at medium pressures.

1. In a previous paper we described a method for determining the parameters of a positive column discharge in helium at medium pressures using measurements of the continuum radiation arising from deceleration of electrons by atoms.[1] The expression was used for spectral radiative power per unit volume:

$$\varepsilon_\omega = 4\cdot 10^{-28}\, n\frac{p}{T}T_e e^{-\frac{\hbar\omega}{kT_e}}\int_0^\infty\left[x^{3/2}+\left(x+\frac{\hbar\omega}{kT_e}\right)^{3/2}\right]e^{-x}dx. \tag{1}$$

It follows from Eq. (1) that by measuring the ratio of the continuum intensities at two different frequencies we can determine the electron temperature T_e directly.

To determine the electron density n from the absolute intensity of the continuum at frequency ω we must know the "hot pressure" p and the gas temperature T.

When one can assume that the electrons lose their energy mainly in elastic collisions with the atoms, the relation

$$kT_e = \frac{1}{3}\frac{M}{m^2}\left(\frac{eET}{p\nu_0}\right)^2 \tag{2}$$

holds, where the collision frequency (independent of the electron velocity for helium) is

$$\nu = \nu_0\frac{p}{T};\quad \nu_0 = 6.3\cdot 10^{11}. \tag{2a}$$

Then Eq. (1) can easily be converted to the form

$$\varepsilon_\omega = 1.4\cdot 10^{-26}\, nEF(\tilde{T}_e), \tag{3}$$

where $\tilde{T}_e = T_e\cdot 10^{-4}$°K,

$$F(\tilde{T}_e) = \sqrt{\tilde{T}_e}\, e^{-\frac{\hbar\omega}{kT_e}}\int_0^\infty\left[x^{3/2}+\left(x+\frac{\hbar\omega}{kT_e}\right)^{3/2}\right]e^{-x}dx. \tag{3a}$$

For our wavelengths λ = 7800 Å in the range of $\tilde{T}_e$ from 1 to 3.5 we can assume that

$$F(\tilde{T}_e) \simeq 1.14\tilde{T}_e. \tag{3b}$$

From Eq. (3), knowing E and T_e, we can easily determine n, without measuring the values of p and T. The above method can also be used to determine the radial distribution of n and T_e. In accordance with experiment, we assume that the longitudinal field E does not vary over the radius.

2. In some cases we are interested in the radial variation of the atomic temperature. If we neglect the electron thermal conductivity and assume the electron distribution to be Maxwellian, for medium pressures the heat conduction equation takes the form

$$-\frac{1}{\rho}\frac{d}{d\rho}\left[\rho\varkappa_0\sqrt{T}\frac{dT}{d\rho}\right] = 2\frac{m}{M}\langle\varepsilon\nu\rangle n = 3\frac{m}{M}k\nu_0 T_e\frac{pn}{T}. \tag{4}$$

To solve this equation one must know the radial variation of T_e and pn/T. These can bedetermined from Eq. (1) by measuring the radial variation of the absolute intensity at a single wavelength and the ratio of intensities at two wavelengths. However, it is difficult to measure the radial variation of the intensity ratio with sufficient accuracy. The problem is simplified when Eq. (2) holds. Then, by introducing the variable $x = \rho/R$, we can rewrite Eq. (4) in the form

$$-\frac{1}{x}\frac{d}{dx}\left[x\frac{d}{dx}T^{3/2}\right] = An(x)T(x), \tag{5}$$

$$A = \frac{3}{2\varkappa_0}\frac{e^2}{m\nu_0}\left(\frac{E}{p}\right)^2 pR^2,$$

where $\varkappa_0 = 10^3$. The boundary condition for Eq. (5) has the form $dT/dx = 0$ for $x = 0T(0) = T_0$.

The solution of Eq. (5) will be

$$T^{3/2}(x) - T^{3/2}(1) = A\int_x^1\frac{dy}{y}\int_0^y n(z)T(z)z\,dz, \tag{6}$$

where T(1) is the temperature at the wall. If in the zero-order approximation we substitute

$$n(x)T(x) = n_0T_0, \tag{7}$$

for the integrand, we obtain

$$T^{3/2}(x) - T^{3/2}(1) = \frac{1}{4}An_0T_0(1-x^2). \tag{8}$$

The temperature on the axis is

$$T_0^{3/2} - T^{3/2}(1) = \frac{1}{4}An_0T_0. \tag{9}$$

The temperature T(x) falls off in the radial direction, as does the electron density n(x). Therefore we consider an approximation of the form

$$n(x)T(x) = n_0T_0(1-x^2)^2. \tag{10}$$

Then

$$T^{3/2}(x) - T^{3/2}(1) = \frac{1}{12}An_0T_0\left(\frac{11}{6} - 3x^2 + \frac{3}{2}x^4 - \frac{1}{3}x^6\right), \tag{11}$$

$$T_0^{3/2} - T^{3/2}(1) = \frac{11}{72}An_0T_0. \tag{12}$$

More accurately, we can relate the quantities n(x)T(x) with the experimentally measured behavior of the continuum intensity at a single wavelength. From Eqs. (2), (3), and (3b), we obtain

$$\frac{\varepsilon(x)}{\varepsilon_0} = \frac{n(x)T^2(x)}{n_0T_0^2}, \tag{13}$$

where ε_0 is the value of the continuum intensity on the axis.

TABLE 1. Values of Atomic Temperatures on the Column Axis, in Units of 10^{-2} °K, Obtained by the Various Approximations

i/R, mA/cm	Form of approximation	pR, torr·cm: 20		40		60		80	
		R, cm: 1.0	2.8	1.0	2.8	1.0	2.8	1.0	2.8
25	(7)	3.8	3.5	4.2	4.0	4.6	4.3	4.8	4.7
	(10)	4.0	3.8	4.5	4.4	5.1	4.9	5.4	5.4
	(15)	3.8	3.6	4.3	4.5	4.9	4.7	5.1	5.1
50	(7)	4.0	3.8	4.7	4.7	5.3	5.0	5.7	5.8
	(10)	4.4	4.3	5.3	5.5	6.1	6.1	6.7	7.0
	(15)	4.3	4.1	5.0	5.2	5.5	5.6	6.3	6.0
100	(7)	4.5	4.9	5.5	5.1	6.4	6.4	6.9	7.1
	(10)	5.1	5.7	6.4	7.1	7.1	8.0	8.4	9.0
	(15)	4.9	5.3	6.0	6.0	6.7	7.2	7.7	8.3
200	(7)	5.5	5.8	6.8	7.2	7.7	8.1	8.7	9.1
	(10)	6.5	7.1	8.2	9.0	9.7	10.0	11.1	12
	(15)	6.1	6.5	7.5	8.2	8.7	9.3	9.9	10

It follows from Eq. (6) that

$$T^{3/2}(x) - T^{3/2}(1) = A n_0 T_0^2 \int_x^1 \frac{dy}{y} \int_0^y \frac{\frac{\varepsilon(z)}{\varepsilon_0}}{T(z)} z\,dz. \tag{14}$$

For T(2) in the integrand we adopt the approximation, close to the approximations of Eqs. (8) or (11),

$$T(z) = (T_0 - T_R)(1 - z^2) + T_R, \tag{15}$$

where $T_R \equiv T(1)$.

In the range of values of pR from 20 to 80 torr · cm and of values of i/R from 25 to 200 mA/cm, for tubes of radius from 1 to 3 cm, the experimental variation of the continuum intensities over the radius can be described by an approximation of the form

$$\frac{\varepsilon(z)}{\varepsilon_0} = 1 - z. \tag{15a}$$

with sufficient accuracy [if we take into account that this quantity appears in the integrand of Eq. (14)].

Then Eq. (14) can be written in the form

$$T^{3/2}(x) - T^{3/2}(1) = A n_0 T_0 (1 + \beta) \int_x^1 \frac{dy}{y} \int_0^y \frac{1 - z}{1 + \beta - z^2} z\,dz, \tag{16}$$

where $\beta = T_R/(T_0 - T_R)$. In the further calculation it is more convenient to rewrite Eq. (16) in the equivalent form

$$T_0^{3/2} - T^{3/2}(x) = A n_0 T_0 (1 + \beta) \int_0^x \frac{dy}{y} \int_0^y \frac{1 - z}{1 + \beta - z^2} z\,dz.$$

The double integral can be expressed in terms of the Riemann Zeta function. Tables of this function are given in ref. 2:

$$\zeta(1, 2 \mid z) = -\int_0^z \frac{\ln|1 - t|}{t} dt,$$

$$T_0^{3/2} - T^{3/2}(x) = A n_0 T_0 (1 + \beta) \frac{1}{2}\left[2x - (\sqrt{1+\beta} - 1)\zeta\left(1, 2 \left| \frac{x}{\sqrt{1+\beta}}\right.\right) + (\sqrt{1+\beta} + 1)\zeta\left(1, 2 \left| \frac{-x}{\sqrt{1+\beta}}\right.\right)\right]. \tag{17}$$

$$T_0^{3/2} - T_R^{3/2} = A n_0 T_0 (1 + \beta) \frac{1}{2}\left[2 - (\sqrt{1+\beta} - 1)\zeta\left(1, 2 \left| \frac{1}{\sqrt{1+\beta}}\right.\right) + (\sqrt{1+\beta} + 1)\zeta\left(1, 2 \left| \frac{-1}{\sqrt{1+\beta}}\right.\right)\right]. \tag{18}$$

To find the radial behavior of the temperature from Eqs. (8), (11), and (17), we must know the quantities E, p, and n_0. In order to eliminate n_0 it is convenient to use an expression for the total current through the tube

$$i = 2\pi e E \int_0^R b_e n(\rho) \rho\, d\rho = B \int_0^1 n(x) T(x) x\,dx, \tag{19}$$

where

$$B = 2\pi \frac{e^2}{m v_0} \frac{E}{p} R^2.$$

The electron mobility is

$$b_e = \frac{e}{m v} = \frac{e}{m v_0} \frac{T}{p}.$$

Using the approximation of Eq. (7), we obtain

$$i = \frac{1}{2} n_0 T_0 B. \tag{20}$$

Using the approximation of Eq. (10), we obtain

$$i = \frac{1}{6} n_0 T_0 B. \tag{21}$$

Using the approximations of Eqs. (15) and (15a), we obtain

$$i = \frac{1}{2} B n_0 T_0 (1 + \beta)\left[2 + (\sqrt{1+\beta} - 1)\ln\left(1 - \frac{1}{\sqrt{1+\beta}}\right) - (\sqrt{1+\beta} + 1)\ln\left(1 + \frac{1}{\sqrt{1+\beta}}\right)\right]. \tag{22}$$

Using the corresponding expressions for the temperature on the axis and for the current, for the approximation of Eq. (7) we obtain

$$T_0^{3/2} - T_R^{3/2} = \frac{1}{2} \frac{A}{B} i = 1.19 \frac{i}{R} E R, \tag{23}$$

$$T_0^{3/2} - T_R^{3/2} = \frac{11}{12} \frac{A}{B} i = 2.18 \frac{i}{R} E R \tag{24}$$

for the approximation of Eq. (10), and

$$T_0^{3/2} - T_R^{3/2} = 2.29 I(\beta) \frac{i}{R} E R \tag{25}$$

for the approximation of Eqs. (15) and (15a).

In Eqs. (23)-(25) the current i is expressed in milliamperes and the field E in volts per centimeter,

$$I(\beta)=\frac{2-(\sqrt{1+\beta}-1)\zeta\left(1,2\left|\frac{1}{\sqrt{1+\beta}}\right.\right)+(\sqrt{1+\beta}+1)\zeta\left(1,2\left|\frac{-1}{\sqrt{1+\beta}}\right.\right)}{2+(\sqrt{1+\beta}-1)\ln\left(1-\frac{1}{\sqrt{1+\beta}}\right)-(\sqrt{1+\beta}+1)\ln\left(1+\frac{1}{\sqrt{1+\beta}}\right)}. \quad (26)$$

Table 1 shows calculated values of temperatures on the axis for these approximations. It can be seen from the table that the different approximations give temperature values on the axis which are about the same: The table shows that the similarities hold approximately.

---

[1] Yu. M. Kagan and K. K. Paskalev, Opt. Spektrosk., 37, No. 2 (1974).
[2] K. Mitchel, Phil. Mag., 40, 351 (1949).

Temperature and electron density in the positive column of a medium-pressure helium discharge.

Yu. M. Kagan and K. K. Paskalev

A. A. Zhdanov Leningrad State University

(Submitted July 23, 1973)
Zh. Tekh. Fiz. 44, 2588-2591 (December 1974)

We have calculated the electron temperature in the positive column of a discharge in helium at medium pressures taking account of inelastic losses; electron density on the axis is also determined.

It is conventional to assume that in the medium pressure region in helium electrons lose energy by elastic collisions with atoms. This leads to the relation

$$kT_e^0 = \frac{1}{3}\frac{M}{m^2}\left(\frac{eET}{p\nu_0}\right)^2, \tag{1}$$

where E is the field; T is the gas temperature; p is the pressure in the hot tube; ν is the collision frequency (independent of the velocity for helium), $\nu = \nu_0 (p/T)$; $\nu_0 = 6.3 \cdot 10^{11}$.

In the derivation of Eq. (1), the energy distribution of slow electrons is assumed to be a Maxwellian, as is valid for helium.

Table 1 compares the electron temperatures measured on the axis in a tube of radius R = 2.8 cm, by the method described in ref. 1, with temperatures calculated from Eq. (1). It can be seen that there is a divergence, particularly for small pressures and large currents. This divergence is associated with the fact that the values of E/p for helium are large and one should analyze the effect of inelastic losses. In the general case, with the electron thermal conductivity neglected, the electron energy balance has the form

$$eb_e E^2 - 2\frac{m}{M}\langle\nu\varepsilon\rangle - \frac{\alpha}{n} eV_1 = 0, \tag{2}$$

where b_e is the electron mobility; α is the total number of inelastic collisions; V_1 is the excitation potential of the first excited level; and n is the electron density.

For helium we have

$$2\frac{m}{M}\langle\nu\varepsilon\rangle = 3\frac{m}{M}kT_e\nu.$$

Introducing the notation $T^* = eV_1/k$, we obtain

$$T_e = T_e^0 - \frac{\alpha}{3\frac{m}{M}\nu n}T^*. \tag{3}$$

We take the expression for α from ref. 2

$$\alpha = \frac{4}{\sqrt{\pi}} n\nu_{ee}\left(1 + \gamma_2 u_1^{5/2}\right) e^{-\eta(u_1)}, \tag{4}$$

where

$$u_1 = \frac{eV_1}{kT_e} = \frac{T^*}{T_e},\quad \gamma_2 = \frac{m}{M}\frac{\nu}{\nu_{ee}},$$

and ν_{ee} is the frequency of electron–electron collisions,

$$\nu_{ee} = \frac{4\pi e^4 n}{m^2\left(\frac{2kT_e}{m}\right)^{3/2}}\ln\Lambda = \nu_{ee}^0\frac{n}{T_e^{3/2}},$$

$$\eta(u_1) = \int_0^{u_1}\frac{1 + \gamma_2 u^{5/2}}{1 + \gamma_2 u^{5/2}}\,du,\quad \gamma_1 = \frac{1}{6}\left[\frac{eE\lambda(T_e)}{kT_e}\right]^2\frac{\nu}{\nu_{ee}}.$$

We introduce the notation

$$\gamma_0 = \frac{m}{M}\frac{\nu_0}{\nu_{ee}^0},\quad x = \frac{nT}{p},\quad x_0 = \gamma_0 (T^*)^{5/2}.$$

The integral $\eta(u_1)$ becomes

$$\eta(u_1) = \frac{T^*}{T_e^0}\left\{1 + \frac{2}{3}\frac{x}{x_0}\left(1 - \frac{T_e}{T_e^0}\right)F(A)\right\}, \tag{5}$$

$$F(A) = -A\left\{\frac{1}{2}\ln\frac{(1+A)^2}{1+A^2A} - \sqrt{3}\,\mathrm{arc\,tg}\,\frac{2A-1}{\sqrt{3}} + \sqrt{3}\,\mathrm{arc\,tg}\,\frac{1}{\sqrt{3}}\right\}, \tag{6}$$

$$A = \left(\frac{x}{x_0}\frac{T^*}{T_e^0}\right)^{-1/3}. \tag{7}$$

Finally, we obtain

$$\left(\frac{\alpha}{3\frac{m}{M}\nu n_e} = \frac{1}{3\sqrt{\pi}}\frac{T^*}{T_e}\right)^{2/3}\left(1 + \frac{x}{x_0}\right)e^{-\eta(u_1)} \equiv \Phi(x, T_e^0, T_e), \tag{8}$$

TABLE 1. Values of Electron Temperature, Calculated without (T_e^0) and with (T_e). Allowing for Inelastic Loss and as Determined from Continuum Measurements

i/R	Method of temp. determ.	pR: 10	15	20	40	60	80
25	T_e^0	4.8	3.7	3.3	3.2	3.5	3.5
	T_e	2.9	3.0	2.9	2.9	2.9	2.9
	Continuum	3.7	3.3	3.0	2.0	2.3	2.5
50	T_e^0	5.8	4.5	3.7	4.2	3.9	2.8
	T_e	3.2	3.2	3.0	3.0	3.1	2.8
	Continuum	4.5	4.0	3.2	2.5	2.5	2.5
100	T_e^0	7.5	6.6	5.0	4.2	4.1	4.1
	T_e	3.5	3.4	2.9	3.1	3.1	3.0
	Continuum	3.6	3.6	2.8	2.1	2.5	2.0
200	T_e^0	7.6	6.7	4.2	4.3	4.5	3.5
	T_e	3.6	3.6	3.3	3.3	3.2	3.1
	Continuum	2.5	2.4	2.5	2.5	2.2	2.2

TABLE 2. Comparison of Values of n_0, Measured in the Continuum, with Those Determined from the Current

i/R, mA/cm	Method of density determ.	pR, torr·cm 20		40		60		80	
		R, cm 1	2.8	1	2.8	1	2.8	1	2.8
25	Continuum	3.1	2.0	1.7	1.5	1.5	2.2	1.4	2.1
	Current	1.2	1.0	10	1.1	0.9	0.9	1.0	1.0
50	Continuum	6.0	5.0	5.0	3.5	4.0	3.0	3.4	3.2
	Current	2.1	1.9	2.2	1.7	2.0	1.7	1.7	2.0
100	Continuum	14	12	15	11	9.0	8.5	6.5	8.5
	Current	7.5	5.0	7.0	7.0	6.0	5.5	5.0	6.0
200	Continuum	29	24	24	23	21	25	14	27
	Current	13	12	19	16	13	20	10	25

and Eq. (2) takes the form

$$T_e^0 - T_e = \Phi(x, T_e^0, T_e)\, T^*. \tag{9}$$

Equation (9) can be used to calculate the electron temperature T_e. Here, x and T_e^0 play the role of parameters which are determined by the values of E, T, p, and n. The quantities E and p can be measured, and the values of T can be calculated by methods described in ref. 3. The different approximations give values of T which are close. To calculate the density on the axis we can use Eq. (19) of ref. 3:

$$i = B \int_0^1 n(x)\, T(x)\, x\, dx,$$

$$B = 2\pi \frac{e^2}{m v_0} \frac{E}{p} R^2. \tag{10}$$

The approximations given there for the functions n(x) and T(x) are not sufficiently accurate for the case of large currents, when there is quite a steep fall in the continuum intensity. Therefore, we adopt a more accurate approximation for the continuum intensity:

$$\frac{\varepsilon(x)}{\varepsilon(0)} = (1 - x^2)\, e^{-\alpha' x^2}, \tag{11}$$

where the parameter α' is chosen in each specific case.

For T(x) we use the approximation given in ref. 3,

$$T(x) = (T_0 - T_R)\,[1 - x^2 + \beta], \tag{12}$$

where

$$\beta = \frac{T_R}{T_0 - T_R}.$$

By means of these approximations and a relation connecting the behavior of the derivative of n(x)T(x) and that of the continuum (ref. 3)

$$n(x)\, T(x) = n_0 T_0^2 \frac{\frac{\varepsilon(x)}{\varepsilon_0}}{T(x)}$$

we finally obtain an expression for the reduced electron density on the axis:

$$\tilde{n}_0 R = 7.1 \frac{\frac{i}{R}}{\frac{E}{p} T_0 \varphi(\alpha', \beta)}, \tag{13}$$

where $\tilde{n}_0 = n_0 \cdot 10^{-11}$, i/R is in mA/cm, E/p is in cm·torr.

For $\varphi(\alpha', \beta)$ we have

$$\varphi(\alpha', \beta) = (1 + \beta)\left\{\frac{1 - e^{-\alpha'}}{\alpha'} - \beta e^{-\alpha'(1+\beta)}\,[E_i(\alpha'(1 + \beta)) - E_i(\alpha', \beta)]\right\}. \tag{14}$$

By means of Eq. (11) we can perform the calculation for all pressures with i/R = 100 and 200. For the values i/R = 25 and 50 we use Eq. (15) of ref. 3.

The results of the calculation are shown in Table 2. Table 2 also shows results of measurements of electron density on the axis, measured by the continuum method described in ref. 1. The agreement is satisfactory.

Using the values of n_0 obtained, and Eq. (9), we can calculate the electron temperature T_e on the axis, allowing for inelastic collisions. For values of pR equal to 10 and 15, we insert the electron density measured in the continuum into Eq. (9) [Eq. (1) of ref. 3].

The calculated values of T_e, allowing for inelastic losses, are given in Table 1. It can be seen that in many cases they do not differ appreciably from the values of T_e^0, and are close to the experimental values.

---

[1] Yu. M. Kagan and K. K. Paskalev, Opt. Spektrosk., 37, No. 2 (1974).

[2] R. I. Lyagushchenko, Zh. Tekh. Fiz., 42, 1130 (1972) [Sov. Phys. – Tech. Phys., 17, 901 (1972)].

[3] Yu. M. Kagan and K. K. Paskalev, Zh. Tekh. Fiz., 44, 2585 (1974) [Sov. Phys. – Tech. Phys., 19, 1601 (1975)].

Direct current in a metal–selenium–metal structure bounded by an rf plasma

A. D. Andreev and S. I. Lubinskii

V. I. Lenin Belorussian State University, Minsk

(Submitted July 6, 1973; resubmitted January 30, 1974)
Zh. Tekh. Fiz., 44, 2591-2594 (December 1974)

The direct component of the current which arises in an Al–Se–Al structure under the influence of the plasma of an rf gas discharge has been measured. This current appears because of rectification at the plasma–selenium contact and because of the penetration of plasma electrons into the selenium film due to the field near the contact and thermal diffusion. The current increases with increasing density of the charged particles in the plasma. The influence of the potential of the control grid on the induced current has been studied.

We report here a study of the direct component of the electric current which arises in a metal–selenium–metal structure subjected to an rf plasma. In contrast with the case of a rectifying circuit using a gas-discharge gap between the working electrodes,[1] the plate of amorphous selenium (on which a metal electrode has been deposited) is in immediate contact with the plasma and is at a floating potential, which is governed by the power supplied to the plasma and the density and temperature of the charged particles in the plasma. In this arrangement it is possible to use a control grid[2] mounted in the discharge region near the surface of the film in order to study the contact layer.

Figure 1 shows the apparatus. An rf discharge is excited in chamber 6, made of molybdenum glass, 150 × 30 mm in size, and subjected to continuous evacuation. The air pressure in the chamber is adjusted by a needle inleakage value to a value of 0.02-10 torr. Metal grid 4, mounted near the Se film, ~ 1 mm from the surface of this film, reduces the effective contact area with the plasma. The film of amorphous selenium 2, having a thickness of ~ 60 μ and a dark resistivity of up to 10^{11} $\Omega \cdot$cm, is deposited by evaporation in vacuum on an aluminum substrate 1, previously coated with bismuth. On top of this selenium film is an aluminum electrode 3, a band 0.8 cm^2 in area, deposited by thermal evaporation in vacuum at a pressure of $5 \cdot 10^{-5}$ torr. The contact area between the rf plasma and the surface of the selenium film is $3 \cdot 10^{-4}$ m^2. Outer electrodes 8 are connected to the output terminals of an oscillator. The oscillator, which operates with pulsed excitation and has a resonant frequency of 400 kHz, uses a GMI-83 vacuum tube. The plate circuit of the oscillator consists of a coil itself consisting of 470 turns of wire 0.7 mm in diameter, mounted tightly on a textolite mount 70 mm in diameter. When the tube of the oscillator is triggered by a positive rectangular pulse rising at a rate of $5 \cdot 10^9$ V/sec, oscillations are excited in the circuit; they decay to 0.1 of their initial amplitude over $5 \cdot 10^{-5}$ sec. The trigger pulses are fed to the control grid of the tube of the oscillator from a pulsed amplifier using a GU-29 tube.[3]

The density and temperature of the charged particles in the plasma are measured with a double electrical probe consisting of two molybdenum wires 5, 0.5 mm in diameter, soldered to the chamber wall. A part of the probes, equal to 12 mm, extends into the plasma; the two wires are 12 mm apart. To suppress the rf interference, the probes are shorted by an 82 pF capacitor (chosen empirically), and each is connected to the measuring circuit through a single-layer coil having an inductance of 50 μH, wound on a cardboard frame. The density is determined on the basis of the average mass of the primary components of air through measurement of the voltage–current characteristics.[3] Table 1 shows the electron temperatures and densities corresponding to various amplitudes of the applied voltage and various pressures in the discharge chamber.

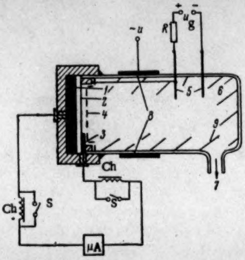

Fig. 1. The experimental apparatus. 1) Aluminum substrate; 2) film of amorphous selenium; 3) measuring electrode; 4) metal grid; 5) probes; 6) gas-discharge chamber; 7) pump; 8) metal electrodes for exciting the plasma; 9) plasma; R) limiting resistance (15 kΩ).

The capacitive method used here to excite the plasma cannot produce a charged-particle density and emission homogeneous throughout the volume in the specified pressure range. As a rule the emission is brighter and the plasma is denser near the electrodes connected to the measuring instruments, particularly at relatively high pressures or in places where the capacitive coupling with the mass is most pronounced. The scatter in the values of the electron temperature could be due to an instability of this type.

Figure 2 shows the induced voltage and the current flowing in the closed circuit of electrodes 1 and 3 (Fig. 1) as functions of the pressure in the chamber for various amplitudes of the rf voltage used to excite the plasma. We see from this figure that the current and voltage increase with increasing pressure and with increasing rf voltage. For the first 10-15 sec after the switch is closed the current in the circuit decays; then it reaches a steady value. The current decay could be due to the capture of charge

TABLE 1

	P, torr			U, kV
	0.05	0.08	0.2	
T_e, eV	6.3	11.2	6.3	5.0
	9.2	7.8	6.6	5.5
	7.8	7.4	9.5	6.0
n, cm^{-3}	$3.8 \cdot 10^{10}$	$6.3 \cdot 10^{10}$	$1.1 \cdot 10^{11}$	5.0
	$5.3 \cdot 10^{10}$	$9.2 \cdot 10^{10}$	$1.2 \cdot 10^{11}$	5.5
	$6.1 \cdot 10^{10}$	$1.1 \cdot 10^{11}$	$1.3 \cdot 10^{11}$	6.0

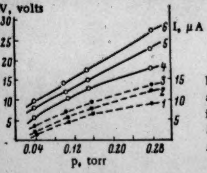

Fig. 2. Induced current (1-3) and voltage (4-6) as functions of the pressure in the chamber at amplitudes of 5.0, 5.5, and 6.0 kV, respectively, of the applied voltage.

carriers at traps in the semiconducting film.[4]

The sample is positioned with respect to the chamber in such a manner that it is at a floating potential, which arises because of the influence of only the part of the rf voltage due to the additional capacitive coupling of the oscillator output and the mass through the plasma and the substrate. Since the plasma–selenium–aluminum combination is a rectifying system,[5] a constant voltage component appears across the selenium film. Since the mobility of the plasma electrons is much higher than that of the ions, and the total current to the surface of the film must vanish over a cycle, we conclude that this surface becomes negatively charged.

This negative charge is a reservoir which can furnish electrons to the interior of the semiconducting film. During thermal diffusion, and under the influence of the alternating electric field, there can be a redistribution of the electron density from the surface to the substrate. The positive plasma ions, which have a higher mass and a lower penetrating ability than do the electrons, are retained at the surface. At a given power of the rf field, which is fed partially into the substrate, a potential difference is maintained between the substrate and the surface of the semiconductor. This potential difference produces a current in the closed circuit of electrode 3; the current consists of this current and the current component due to the rectification at the plasma–selenium junction. When the selenium surface is separated from the plasma by a transparent dielectric film and a grounded grid 4, there is no current in the circuit, and there is no voltage on electrodes 3 and 1.

Figure 3 shows the current and voltage arising in the metal–selenium–metal structure as a function of the voltage applied to metal grid 4. We see from this figure that the current and voltage both increase as the positive bias on this grid is increased in magnitude. As the positive bias on this grid is increased, plasma electrons are attracted to this grid, and an increasing number of these electrons penetrate into the selenium, increasing the induced current and voltage. As a negative bias on this grid is increased, a field is produced in the contact region which prevents electrons from reaching the selenium, and only some of the fast electrons turn out to be capable of penetrating into the film; an increasing number of ions strike the grid, and the ion component of the current increases. The voltage changes correlate with the current changes. The more rapid decay of curve 2 can be attributed to a weakening of the rectifying effect of the plasma–selenium junction as the grid is made negative. Measurements of the voltage–current characteristics show that there is essentially no rectification when the grid is held at −100 V.

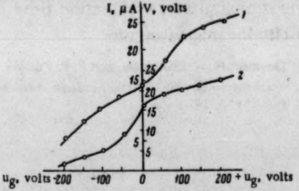

Fig. 3. Induced current (1) and voltage (2) as functions of the grid voltage.

On the basis of these experimental results and their qualitative analysis we can assume that the constant voltage and the direct component of the electric current which arise in the closed circuit containing the contact between an amorphous selenium film and an rf plasma can be due partially to the penetration of electrons into the selenium as a result of their thermal motion and under the influence of the alternating electric field; they can also be due partially to the rectification at the plasma–selenium contact. It can be suggested that in rf deposition during the film growth the impurity ions present in the film collect either at the surface of the film or at the substrate under the influence of the voltage, and the injected plasma electrons are either captured by neutral centers, producing a negative space charge, or neutralized positively charged centers, reducing their density in the film.

---

[1] A. D. Andreev, Zh. Tekh. Fiz., 41, 1744 (1971) [Sov. Phys. – Tech. Phys., 16, 1374 (1972)].

[2] A. D. Andreev, I. G. Nekrashevich, and V. I. Popko, Izv. Akad. Nauk Belorussian SSR, Ser.

[3] A. D. Andreev and Yu. N. Lobanov, Zh. Tekh. Fiz., 34, 1863 (1964) [Sov. Phys. – Tech. Phys., 9, 1437 (1965)].

[4] M. A. Lampert and P. Mark, Current Injection in Solids, Academic Press, New York (1970).

[5] Ch'ang Kim Loi and A. D. Andreev, Zh. Tekh. Fiz., 40, 647 (1970) [Sov. Phys. – Tech. Phys., 15, 500 (1970)].

Measurement of transverse relaxation time T_2 of optically oriented He^4 with an oscillator magnetometer

N. A. Dovator, R. A. Zhitnikov, and P. P. Kuleshov

A. F. Ioffe Physicotechnical Institute, Academy of Sciences of the USSR, Leningrad

(Submitted April 3, 1974)
Zh. Tekh. Fiz., 44, 2594-2595 (December 1974)

The dependence of the frequency of a self-excited oscillator magnetometer on the phase shift in the feedback loop is used to measure the transverse relaxation time T_2 of optically oriented He^4 atoms and to investigate the phase characteristics of the absorption chamber. The measured value of T_2 extrapolated to zero intensity of the pumping light is 0.2 msec for an absorption chamber at 0.2 torr. The frequency dependence of the absorption-chamber phase shift is given.

A method for measuring the transverse relaxation time of optically oriented atoms has been described by Kubo,[1] who has also investigated the phase characteristics of the absorption chamber directly in a cesium-oscillator magnetometer arrangement.

In the present paper a similar method is used to investigate the phase characteristics and to measure the transverse relaxation time T_2 of metastable He^4 atoms in a helium oscillator magnetometer apparatus.

The oscillation frequency ω is given by the equation[2]

$$\varphi(\omega) + \operatorname{arc\,ctg} \Delta\omega S_2 = 0, \qquad (1)$$

where $\varphi(\omega)$ is the phase–frequency characteristic of the feedback loop, $\Delta\omega = \omega - \omega_0$ is the deviation of the oscillation frequency from the Larmor frequency, $1/S_2 = 1/T_2 + 1/T_p$ is the effective transverse relaxation rate ($1/T_p$ is the optical pumping rate, which is proportional to the intensity I).

The phase–frequency characteristic of the feedback loop of the magnetometer can be represented as a linear function of frequency when the deviation of the oscillation frequency from the Larmor frequency lies within the width of the absorption line:

$$\varphi(\omega) = -90^\circ - k\Delta\omega + \Delta\Phi, \qquad (2)$$

where k is the slope of the phase–frequency characteristic of the feedback loop ($k > 0$); and $\Delta\Phi$ is an additional phase shift in the feedback circuit.

Inserting (2) into (1) gives

$$\operatorname{arc\,ctg} \Delta\omega S_2 = 90^\circ - \Delta\Phi + k\Delta\omega, \qquad (3)$$

$$S_2 = \frac{\operatorname{tg}(\Delta\Phi - k\Delta\omega)}{\Delta\omega}. \qquad (4)$$

The coefficient k is usually known, so that by prescribing $\Delta\Phi$ and measuring the frequency deviation $\Delta\omega$ it is possible to calculate S_2. Extrapolating $1/S_2$ to zero intensity gives the inverse relaxation time $1/T_2$.

The phase shift is tuned to a value corresponding to the center of the magnetic resonance line through the minimum of the S_z signal in an oscillator helium magnetometer with automatic phase lock with a sampling servo system.[3] A calibrated SLPZ-0.5 μsec delay line is used for the tuning and for the introduction of a prescribed phase shift. The phase modulation is switched off after tuning to the center of the magnetic resonance line in order to eliminate modulation broadening of the absorption line. A digital frequency meter is used to measure the deviation of the oscillation frequency as a function of the additional phase shift $\Delta\Phi$. The total error in S_2 measured in this manner is 6%.

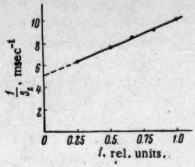

Fig. 1. Plot of $1/S_2$ vs light intensity I.

The absorption chamber of the helium magnetometer consists of a cylinder of diameter 50 mm and length 70 mm filled with spectrally pure He^4 at a pressure of 0.2 torr. The intensity of the discharge in the chamber corresponds to 40% absorption of the pumping light ($\Delta I/I = 40\%$).

Figure 1 shows a plot of $1/S_2$ measured for various intensities of the pumping light. Extrapolation of $1/S_2$ to zero light intensity gives the transverse relaxation time T_2. For the given conditions the value obtained is 0.2 msec, which coincides with the value of T_2 obtained by measuring the linewidth of the S_x signal with subsequent extrapolation to zero light intensity and resonance magnetic field amplitude.

In the determination of T_2 allowance must be made for the effect of inhomogeneity of the magnetic field in the volume of the absorption chamber. In our case this inhomogeneity is 12 γ/cm. An estimate made using Cagnac's formulas[4] shows that the effect is negligible here.

It can be seen from Eq. (3) that the method described above can also be used to measure the phase characteristic of the absorption chamber. This characteristic is shown in Fig. 2 for a chamber with a pressure P = 0.2 torr at an absorption of the pumping light $\Delta I/I = 40\%$. (I = 1

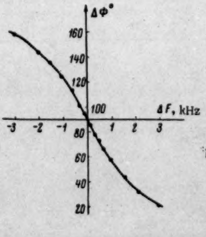

Fig. 2. Phase characteristic of absorption chamber.

in Fig. 1).

Within the limits of measurement error the phase shift of the absorption chamber is observed to be independent of the amplitude of the rf field for increases of the latter such that saturation had still not set in. This agrees with the theory of Bell and Bloom.[5]

---

[1] T. Kubo, Japan. J. Appl. Phys., 9, 1521 (1970).

[2] L. N. Novikov, Geofizicheskaya Apparatura, No. 36 (1968).

[3] N. A. Dovator, R. A. Zhitnikov, and P. P. Kuleshov, Geofizicheskaya Apparatura, No. 56 (1974).

[4] B. Cagnac, Ann. de Phys., 6, 467 (1961).

[5] W. Bell and A. Bloom, Phys. Rev., 107, 1559 (1957).

Current-convective instability in a three-component plasma

E. Z. Meilikhov

(Submitted April 11, 1974)
Zh. Tekh. Fiz., 44, 2595-2597 (December 1974)

The current-convective instability of a three-component plasma in the positive column of a discharge in a magnetic field is investigated using the semiclassical approximation. Properties related to the existence of two instability modes are noted. The calculations agree qualitatively with experiments in Ne + H_2 gas mixtures.

The Kadomtsev–Nedospasov[1] current-convective instability in a weakly ionized plasma with different ion species has several properties. In the present paper, the qualitative theory of this instability is considered and is used to analyze recent experimental results.[2]

The dispersion relation for the current-convective instability in a gas-discharge plasma with two ion species is obtained in the semiclassical approximation. Expressions for the perturbation of the ion and electron densities n'_1, n'_2, and n'_e are easily obtained (see ref. 3 for example) from the equations of motion. Assuming the electrons to be magnetized by an external magnetic field H_{0z} and nonmagnetized ions, we obtain

$$n'_{1,2} = -\varphi' n_{1,2} \frac{k^2 - i\varkappa k_x}{-\frac{i\omega}{\mu_{1,2}} + k^2 \frac{k_0 T_{1,2}}{e} + i\,(k_z E_{0z} + k_x E_{0x})}, \tag{1}$$

$$n'_e = \varphi' n_e \frac{\frac{k_z^2 + k_\perp^2}{\gamma_e^2} + \frac{i\varkappa k_y}{\gamma_e}}{-\frac{i\omega}{\mu_e} + \frac{k_0 T_e}{e}\left(\frac{k_z^2 + k_\perp^2}{\gamma_e^2}\right) - i\left(\frac{k_z E_{0z} - k_y E_{0x}}{\gamma_e}\right)}. \tag{2}$$

Here, φ' is the perturbation of the potential $n_{1,2,e}$, are the densities of ions of the first and second species and of electrons, respectively ($n_e = n_1 + n_2$); $\mu_{1,2,e}$ are their mobilities; ω and k are the frequency and wave vector; T_e and $T_{1,2}$ are the change temperatures; $\gamma_{1,2,e} = (1/c)\cdot\mu_{1,2,e} H_{0z}$ are parameters characterizing the degree of charge magnetization ($\gamma_e \gg 1$, $\gamma_{1,2} \ll 1$); $\varkappa = \nabla_x n_{1,2,e}$ is the parameter in the semiclassical approximation and characterizes the transverse inhomogeneity of the plasma density (or order $\varkappa \sim 1/a$, where a is the transverse dimension of the plasma column); k_0 is the Boltzmann constant; and E_{0z} and E_{0x} are, respectively, the longitudinal electric field and the transverse ambipolar field, which can be written

$$E_{0x} = -\frac{k_0 T_e}{e} \varkappa \frac{\frac{n_e \mu_e}{\gamma_e^2} - \frac{n_1 \mu_1 T_1}{T_e} - \frac{n_2 \mu_2 T_2}{T_e}}{\frac{n_e \mu_e}{\gamma_e^2} + n_1 \mu_1 + n_2 \mu_2}. \tag{3}$$

The dispersion relation is obtained assuming neutrality $n'_e = n'_1 + n'_2$ by substituting (3) into (1) and (2) and assuming the usually well-satisfied conditions $T_{1,2} \ll T_e$, $k_\perp^2 \gg k_z^2 \gamma_e^2$ (or $L^2 \gg \gamma_e^2 a^2$, where L is the length of the plasma column). We then obtain

$$\begin{aligned} n_1 &\left(\frac{\omega}{\mu_2} + \frac{k_0 T_e}{e} k_x \varkappa - k_z E_{0z}\right)\left[\left(\frac{\omega}{\mu_1} + \frac{k_0 T_e}{e} k_x \varkappa\right)\left(\frac{k_x \varkappa}{\gamma_e} - i\frac{k_\perp^2}{\gamma_e^2}\right)\right. \\ &\quad - \left(\frac{\omega}{\mu_e} + k_z E_{0z} - \frac{k_0 T_e}{e}\frac{k_x \varkappa}{\gamma_e}\right) \\ &\left.\times (k_x \varkappa - ik^2)\right] + n_2\left(\frac{\omega}{\mu_1} + \frac{k_0 T_e}{e} k_x \varkappa - k_z E_{0z}\right)\left[\left(\frac{\omega}{\mu_2} + \frac{k_0 T_e}{e} k_x \varkappa\right)\left(\frac{k_x \varkappa}{\gamma_e} - i\frac{k_\perp^2}{\gamma_e^2}\right)\right. \\ &\quad \left. - \left(\frac{\omega}{\mu_e} + k_z E_{0z} - \frac{k_0 T_e}{e}\frac{k_x \varkappa}{\gamma_e}\right)(k_x \varkappa - ik^2)\right] = 0. \end{aligned} \tag{4}$$

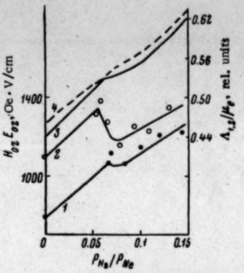

Fig. 1

To determine the threshold values of the frequency and the magnetic field we separate the real and imaginary parts of the dispersion relation (4). Introducing the dimensionless variables

$$\Omega = \frac{\omega}{\mu_e k_x \varkappa \frac{k_0 T_e}{e}}, \quad \Lambda = E_{0z} H_{0z} \frac{k_z \mu_e}{c k_x \varkappa \frac{k_0 T_e}{e}},$$

we obtain

$$\frac{\Omega\,(\gamma_e + \beta_1/\gamma_e) + \Lambda - 1}{\beta_1 \Omega + 1 - \Lambda/\gamma_e} + \alpha \frac{\Omega\,(\gamma_e + \beta_2/\gamma_e) + \Lambda - 1}{\beta_2 \Omega + 1 - \Lambda/\gamma_e} = 0, \tag{5a}$$

$$\frac{\Omega\,(\beta_1 - \gamma_e) - \Lambda + 2}{\beta_1 \Omega + 1 - \Lambda/\gamma_e} + \alpha \frac{\Omega\,(\beta_2 - \gamma_e) - \Lambda + 2}{\beta_2 \Omega + 1 - \Lambda/\gamma_e} = 0, \tag{5b}$$

where $\beta_{1,2} = \mu_e/\mu_{1,2}$; $\alpha = n_2/n_1$. The system of equations (5a) and (5b) has two solutions, which correspond to the two branches of current-convective instability in a plasma with two ion species

$$\Omega_{1,2} \simeq -\frac{1}{\beta_{1,2}}, \quad \Lambda_{1,2} = 1 + \frac{1}{\gamma_e} - \gamma_e \Omega_{1,2} \simeq 1 + \frac{1}{\gamma_e} + \frac{\gamma_e}{\beta_{1,2}}. \tag{6}$$

Since the charge mobilities $\mu_{1,2,e}$ (and thus the values of the parameters γ_e, $\beta_{1,2}$) depend essentially on the composition of the gas mixture (determined by the ratio of the neutral particles of different species), the oscillation frequencies and the values of the threshold field ($\Omega_{1,2}$ and $\Lambda_{1,2}$) also vary when the composition changes. For a certain ratio between the densities of the neutral plasma components, oscillations appear which correspond to one of the oscillation branches, namely, that branch corresponding to the term, either Λ_1 or Λ_2, having the smallest value. For some cases a change in the plasma composition leads to one oscillation branch replacing the other (formally, this means a change from $\Lambda_1 > \Lambda_2$ to $\Lambda_1 < \Lambda_2$, or vice versa) which, in turn, leads to peculiarities in the dependences of the instability frequency and the threshold magnetic field on the plasma composition.

Figure 1 (curves 1 and 2) gives the products of the threshold fields $E_{0z}H_{0z}$ (for the current-convective instability in Ne + H_2 mixtures) obtained from analysis of the experimental data of ref. 2. The partial pressure of Ne is 1) 0.3 and 2) 0.46 mm Hg. Note the features occurring for a certain value of ratio of Ne and H_2 partial pressures: $p_{H_2}/p_{Ne} = 0.06$. Evidently this is the phenomenon, noted above, where one branch replaces the other.

To check this hypothesis we obtain qualitative estimates using (6) and numerical values of charge mobilities in an Ne + H_2 plasma. Using the relation for mobility in a gas mixture:[4] $1/\mu_{1,2,e} = p_{Ne}/\mu_{1,2,e}^{(Ne)} + p_{H_2}/\mu_{1,2,e}^{(H_2)}$ [$\mu_{1,2,e}^{(Ne)}$ and $\mu_{1,2,e}^{(H_2)}$ are, respectively the charge mobilities in Ne and H_2 for a pressure p = 1 mm Hg], we can write the following expressions for γ_e, β_1, β_2:

$$\gamma_e = \frac{1}{c} H_{0z} \frac{\mu_e^{(Ne)}}{1 + \left[\frac{\mu_e^{(Ne)}}{\mu_e^{(H_2)}}\right]\left(\frac{p_{H_2}}{p_{Ne}}\right)}, \tag{7}$$

$$\beta_1 = \frac{\mu_e^{(Ne)}}{\mu_{Ne^+}^{(Ne)}} \frac{1 + \left[\frac{\mu_{Ne^+}^{(Ne)}}{\mu_{Ne^+}^{(H_2)}}\right]\left(\frac{p_{H_2}}{p_{Ne}}\right)}{1 + \left[\frac{\mu_e^{(Ne)}}{\mu_e^{(H_2)}}\right]\left(\frac{p_{H_2}}{p_{Ne}}\right)}, \tag{8}$$

$$\beta_2 = \frac{\mu_e^{(Ne)}}{\mu_{H_2^+}^{(Ne)}} \frac{1 + \left[\frac{\mu_{H_2^+}^{(Ne)}}{\mu_{H_2^+}^{(H_2)}}\right]\left(\frac{p_{H_2}}{p_{Ne}}\right)}{1 + \left[\frac{\mu_e^{(Ne)}}{\mu_e^{(H_2)}}\right]\left(\frac{p_{H_2}}{p_{Ne}}\right)}. \tag{9}$$

Using experimental values of the threshold magnetic field[2] and taking for the mobilities and their ratios:[4] $\mu_e^{(Ne)}/p_{Ne} = 1.2 \cdot 10^6$ cm^2/V · sec · torr, $\mu_e^{(Ne)}/\mu_e^{(H_2)} = 3$, $\mu_e^{(Ne)}/\mu_{Ne^+}^{(Ne)} = 3 \cdot 10^2$, $\mu_e^{(Ne)}/\mu_{H_+^2}^{(Ne)} = 2 \cdot 10^2$, $\mu_{Ne^+}^{(Ne)}/\mu_{Ne}^{H_2} = 1$, $\mu_{H_2^+}^{(Ne)}/\mu_{H_2^+}^{(H_2)} = 10$ we plot from (6)-(9) the curves of the ratio $\Lambda_{1,2}/\mu_e \sim E_{0z}H_{0z}$ vs the gas mixture. This is shown in the figure by curves 3 and 4 for $p_{Ne} = 0.46$ mm Hg, and the solid line is composed of the three parts of curves 3 and 4 corresponding to the smallest value of $E_{0z}H_{0z}$. It can be seen that for $p_{H_2}/p_{Ne} \simeq 0.06$ there is a characteristic point on the solid line corresponding to a change in the oscillation branches. The general nature of this characteristic point is similar to those of the experimental curves 1 and 2. Allowing for the roughness of the computational scheme, we can consider the theory to be in qualitative agreement with experiment.

In conclusion, we note that a detailed explanation of the phenomenon evidently requires that the nonlinear interaction between the two modes be taken into account when their thresholds and frequencies coincide.

The author thanks V. V. Parail for discussion.

---

[1] V. V. Kadomtsev and A. V. Nedospasov, J. Nucl. Energy, C1, 230 (1960).

[2] A. V. Nedospasov, K. I. Efendiev, and G. I. Garibov, Teplofiz. Vys. Temp., 9, 22 (1971).

[3] E. Z. Meilikhov, Fiz. Tekh. Poluprovodn., 4, 237 (1970) [Sov. Phys. – Semicond., 4, 191 (1970)].

[4] S. C. Brown, Basic Data of Plasma Physics, MIT Press, Cambridge, Mass. (1959).

Effect of a magnetic field on spontaneous mode-locking in a He–Ne laser ($\Lambda = 0.63\,\mu$)

V. Yu. Petrun'kin, V. M. Nikolaev, O. I. Kotov, and B. V. L'vov

M. I. Kalinin Polytechnical Institute, Leningrad

(Submitted January 10, 1974)
Zh. Tekh. Fiz., 44, 2598-2600 (December 1974)

The effect of an axial magnetic field on the coupling of the longitudinal modes in a gas laser is investigated experimentally. For magnetic field values at which splitting occurs between the σ components of the gain curve (the gain is equal to the basic separation modes or is a multiple of an odd number of these separations) the laser operates in a stable self-locking type II mode. It is shown that the width of the resonant spontaneous locking region depends on the cavity geometry and the magnitude of the excitation.

The present paper is an investigation of the coupling of the axial modes in a gas laser ($\lambda = 0.63\,\mu$) in a constant axial magnetic field. The magnitude of the coupling essentially determines the different laser operating modes: the free-running mode and the spontaneous locking mode (the pulsed mode). A stable mode must be attained for successful application of lasers to various problems.

Spontaneous locking of modes can be obtained in a gas laser by various methods: placing a modulator inside the optical cavity,[1] scanning by one of the mirrors,[2] choosing a definite operating mode, and spontaneous locking.[3] We will consider stable modes obtained by spontaneous locking of a gas laser.

The effect of a magnetic field on spontaneous mode-locking is noted in refs. 4 and 5. References 6 and 7 reported resonance values of the magnetic field at which dips are observed in the curve of output power vs magnetic field. In ref. 8, variations in the optical spectrum are observed for a resonance magnetic-field value at which the splitting of the σ components of the neon gain profile is equal to the separation between longitudinal modes.

The behavior of a gas laser in a constant magnetic field has been theoretically analyzed in general form in ref. 9. Many papers have considered spontaneous locking of laser modes in zero magnetic field, for example refs. 10 and 11. A rigorous theoretical examination of spontaneous locking of longitudinal modes of a gas laser in an axial magnetic field encounters serious mathematical difficulties. Therefore, an experimental investigation of this mode is of interest.

Tubes with Brewster windows are employed in the experiment. An iris is placed inside the cavity to select the transverse modes. All the results discussed below refer to the basic transverse mode. The intermode beat spectrum is investigated using a C4-5 spectrum analyzer, a wide-band U3-11 amplifier, and an FÉU-36 photomultiplier. The optical spectrum of the output radiation is observed on a Fabry–Perot scanning interferometer with an internal iris. To retune the mode spectrum with respect to the center of the atomic line one of the cavity mirrors is attached to a piezoceramic element. We consider (except for special cases) an He–Ne laser with an optical cavity $L = 1.5^{\mathrm{m}}$ long, a discharge gap $l_1 = 88$ cm, and a tube with an internal diameter $d = 5$ mm which is filled with a natural mixture of neon isotopes at 1.1 mm Hg and located in the center of the cavity. The axial magnetic field is produced by a solenoid $l_2 = 70$ cm in length, with an internal diameter of 8 cm. The investigation of the coupling resonances of longitudinal modes in the magnetic field is carried out by measuring the different parameters of the laser output radiation: intermode beat spectrum, optical mode spectrum, and the constant and variable components of the output radiation. The onset of the spontaneous locking mode is characterized by stabilization of the optical modes, narrowing of the intermode beat spectrum, a substantial decrease in the radiation noise, and the appearance of high-frequency fluctuations.

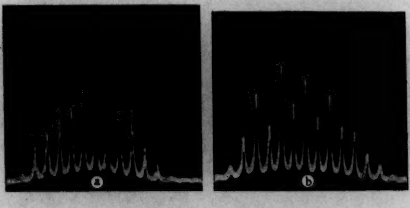

Fig. 1. Laser optical spectra. a) Free-running mode; 2) resonant self-mode-locking.

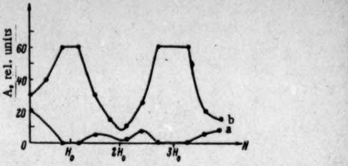

Fig. 2. Amplitude of the components of the intermode beat spectrum vs magnetic field. a) Beats at frequency c/2L; b) at 2c/2L.

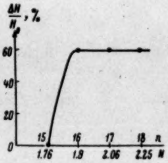

Fig. 3. Width of the resonant self-locking region vs relative excitation. n is the number of excited modes.

Under the experimental conditions the free-running mode of the gas laser is observed with zero magnetic field and maximum pumping. The optical mode amplitudes vary randomly (Fig. 1a), the components of the intermode beat spectrum have a small amplitude (Fig. 2), and strong low-frequency noise is observed in the output radiation. That is, only weak coupling occurs between the modes and they lase independently of each other.

If all the laser parameters remain unchanged, and the axial magnetic field is increased until it reaches the value at which splitting of the σ components of the gain curve is equal to the separation between the longitudinal modes ($H = H_0 = \Delta/2\mu g$, where $\Delta = c/2L$, μ is the Bohr magneton, g is the g factor, and c is the velocity of light), a significant change occurs: The free-running mode is replaced by spontaneous locking. The amplitudes of the modes are stabilized and assume a characteristic form – a regular alternation of modes with small and high amplitudes (Fig. 1b). The component of the intermode beat spectrum at $f_0 = c/2L = 100$ MHz falls off considerably in amplitude (to the noise level of the hf channel), and the component of the spectrum at $f_1 = 2c/2L = 200$ MHz increases greatly (Fig. 2); low-frequency noise is reduced in the output radiation and pulses appear with a repetition frequency $f_1 = 200$ MHz. These features are characteristic of the so-called type-II spontaneous locking.[12] When the modes are detuned with respect to the center of the atomic line, the envelope of the optical spectrum does not change its position and shape (comb), and the modes change their amplitudes smoothly.

Similar phenomena have been observed for magnetic field values $H = (2k + 1)H_0$, where $k = 1, 2, 3 \ldots$ (Fig. 2). No signs of spontaneous locking are observed for H values that are multiples of $2H_0$ when the experimental methods described above are used. Note that dips are formed in the curve of the output power vs magnetic field for all H values that are multiples[6,7] of H_0. The maximum splitting of the σ components of the gain curve at which resonant spontaneous locking is observed is determined by the amount the gain exceeds the losses in the laser – the relative excitation. In our case $H_{max} = 9H_0$.

Spontaneous mode-locking is observed for a range of magnetic fields near $(2k + 1)H_0$. For a given cavity geometry the width of this region depends essentially on the amount by which the gain exceeds the loss. In the experiment the relative excitation is varied by means of the iris or the current in the gas-discharge tube. The width of the spontaneous locking region has a tendency to saturate when the relative excitation is increased (Fig. 3). The maximum width of the region obtained in the experiments is ~ 60% of H_0.

A second factor having a considerable effect on spontaneous locking of longitudinal laser modes in a magnetic field is the cavity geometry, i.e., the dimensions, the ratio of the length of the active medium to the length of the cavity, and the position of the active medium in the cavity. Theoretically, all these parameters are taken into account in the calculation of the Fourier components[9] of the excitation density N_2, N_4, and N_6. The effect of cavity geometry on the width of the spontaneous locking region can be seen more clearly for an equal-isotope composition (50% Ne^{20} and 50% Ne^{22}) and a short tube ($l_1 = 37$ cm). The optimum conditions for obtaining stable resonant spontaneous mode-locking type-II operation are $N_2 = 0$ and $|N_4| = \max$ for $n_4 < 0$.

Obtaining stable spontaneous mode-locking operation of gas lasers in a magnetic field widens the possibilities of using spontaneous locking lasers for practical problems.

---

[1] P. W. Smith, TIIER, 58, 9, 49 (1970).
[2] W. C. Henneberger and H. J. Schulte, J. Appl. Phys., 37, 2189 (1966).
[3] T. Uchida and A. Ueki, IEEE J. Quantum Electron., QE-3, 17 (1967).
[4] D. M. Thymian and J. A. Carruthers, IEEE J. Quantum Electron., QE-5, 83 (1969).
[5] R. A. Paananen, H. Statz, and C. L. Tang, Proc. IEEE, 51, 63 (1963).
[6] G. Herman and A. Scharman, Z. Phys., 208, 367 (1968).
[7] P. Brun, A. LeFloch, and J. P. Tache, C. R. Acad. Sci., 266, B189 (1968).
[8] A. Shimauchi, T. Ishikawa, and Y. Hishiyama, Sci. Light, 19, 14 (1970).
[9] M. Sargent and W. Lamb, Phys. Rev., 164, 436 (1967).
[10] P. W. Smith, IEEE J. Quantum Electron., QE-3, 627 (1967).
[11] S. G. Zeiger, Opt. Spektrosk., 34, 133 (1973).
[12] F. R. Nash, IEEE J. Quantum Electron., QE-3, 189 (1967).

Exact solutions of the nonlinear electrodynamic equations

N. G. Puchkova and A. F. Kulish

Kiev Institute of Civil Aviation Engineers

(Submitted January 28, 1974)
Zh. Tekh. Fiz., 44, 2600-2602 (December 1974)

The electrodynamic problem is investigated for the case in which the permeability and permittivity are specified as products of two power functions of the electric and magnetic fields. Two classes of exact solutions characterizing inverse electrodynamic boundary-value problems are found for the nonlinear one-dimensional, nonstationary Maxwell equations.

Two exact solutions have been found for the nonlinear one-dimensional nonstationary system of electrodynamic equations when the permeability and permittivity can be represented as products of two power functions of the electric and magnetic fields. Both solutions make it possible to analyze the inverse boundary-value problems for an inhomogeneous plate with an initial distribution of E_0 and H_0 in the form of specified functions of the coordinate. On one boundary of the plate ($x = 0$) E and H vary as a function of the time according to definite laws. Each solution contains three arbitrary constants, which can be used to approximate the coordinate inhomogeneity for a real plate.

Kolesnikov[1] has investigated the case in which the nonlinear electrodynamic problem can be reduced to a linear problem by an inversion method. One of the present authors[2] has expanded the class of media to which that method is applicable.

Unlike refs. 1 and 2, we assume that the permeability μ and permittivity ε are given or determined experimentally as functions

$$\varepsilon=\varepsilon_0 H^p E^{q-1};\quad \mu=\mu_0 H^{p-1}E^q \tag{1}$$

Here, H and E are the dimensionless magnetic and electric fields, μ_0 and ε_0 are fixed constants of the appropriate dimensions, and p and q are arbitrary numbers.

We write the nonstationary Maxwell equations for the one-dimensional case:[3]

$$\frac{\partial D}{\partial t}=-\frac{\partial H}{\partial x};\ \frac{\partial B}{\partial t}=-\frac{\partial E}{\partial x}. \tag{2}$$

Here, D is the electric induction $D = \varepsilon E$, and B is the magnetic induction $B = \mu H$.

Using Eqs. (1), we find that the system (2) assumes the form

$$\varepsilon_0\frac{\partial}{\partial t}H^pE^q=-\frac{\partial H}{\partial x};\ \mu_0\frac{\partial}{\partial t}H^pE^q=-\frac{\partial E}{\partial x}. \tag{3}$$

Accordingly,

$$\frac{\partial}{\partial t}H^pE^q=-\frac{1}{\varepsilon_0}\frac{\partial H}{\partial x}=-\frac{1}{\mu_0}\frac{\partial E}{\partial x}.$$

Consequently,

$$H=\frac{\varepsilon_0}{\mu_0}E+A(t), \tag{4}$$

where A(t) is an arbitrary integration function.

We therefore replace system (3) by the single equation

$$\left(\frac{\varepsilon_0}{\mu_0}E+A\right)^{p-1}E^{q-1}\left\{\left[(p+q)\frac{\varepsilon_0}{\mu_0}E+qA\right]\frac{\partial E}{\partial t}+pEA'\right\}=-\frac{1}{\mu_0}\frac{\partial E}{\partial x}. \tag{5}$$

We have thus reduced the problem to the solution of the nonlinear first-order partial differential equation (5). As an example we consider the simplest case, in which $p = q = 1$, i.e., the permittivity depends linearly on the magnetic field only, $\varepsilon = \varepsilon_0 H$, and the permeability depends linearly on the electric field, $\mu = \mu_0 E$. In this case Eq. (5) is simplified:

$$\left[\frac{2\varepsilon_0}{\mu_0}E(x,t)+A(t)\right]\frac{\partial E}{\partial t}+A'(t)E(x,t)=-\frac{1}{\mu_0}\frac{\partial E}{\partial x}. \tag{6}$$

We seek a solution of the nonlinear equation (6) in the form

$$E(x,t)=a_0(t)z+a_1(t);\quad (z=x+t). \tag{7}$$

We insert the corresponding deviations from (7) into Eq. (6):

$$\frac{2\varepsilon_0}{\mu_0}a_0a_0'z^2+\left[\left(\frac{2\varepsilon_0}{\mu_0}a_1+A\right)a_0'+\frac{2\varepsilon_0}{\mu_0}(a_0^2+a_0a_1')+a_0A'\right]z$$
$$+\left[\frac{2\varepsilon_0}{\mu_0}(a_1'+a_0)+A'\right]a_1+A(a_1'+a_0)=-\frac{a_0}{\mu_0}.$$

We equate the coefficients of like powers of z. We then obtain the equations

$$\left.\begin{aligned}a_0&=\alpha=\text{const},\\ a_1'+a_0&=-\frac{\mu_0}{2\varepsilon_0}A',\\ \frac{\mu_0}{2\varepsilon_0}AA'&=\frac{a_0}{\mu_0}.\end{aligned}\right\} \tag{8}$$

From the latter we find

$$A=\frac{2}{\mu_0}\sqrt{\alpha\varepsilon_0(t+b)};\quad a_1=-\alpha t-\frac{\mu_0}{2\varepsilon_0}A+a \tag{9}$$

(α, *a*, and b are arbitrary constants of integration).

Equations (4), (7), and (9) allow us to write the following equations, which satisfy (3):

$$\left.\begin{aligned}E&=a+\alpha x-\sqrt{\frac{\alpha}{\varepsilon_0}(t+b)},\\ H&=\frac{\varepsilon_0}{\mu_0}\left[a+\alpha x+\sqrt{\frac{\alpha}{\varepsilon_0}(t+b)}\right].\end{aligned}\right\}$$

These equations characterize the inverse boundary-value problem for an inhomogeneous plate when the electric and magnetic field distributions at the initial time $t = 0$ are given as linear functions of the coordinate x:

$$E_0=a-\sqrt{\frac{\alpha b}{\varepsilon_0}}+\alpha x,$$

$$H_0=\frac{\varepsilon_0}{\mu_0}\left(a+\sqrt{\frac{\alpha b}{\varepsilon_0}}+\alpha x\right)$$

($0 \le x \le l$, where l is the plate thickness). The constants *a*, α, and b are usually known.

On one boundary of the plate (say, $x = 0$) the corresponding fields vary with time according to a special law [Eq. (10) for $x = 0$].

Next we examine the case in which $A(t) = 0$. Equation (5) assumes the form

$$(p+q)\frac{\varepsilon_0^p}{\mu_0^{p-1}}E^{p+q-1}\frac{\partial E}{\partial t}=-\frac{\partial E}{\partial x}. \tag{11}$$

We subject this equation to the separation of variables:

$$E(x, t) = X(x)\,T(t)$$

and obtain the solution

$$T(t) = \left[\frac{p+q-1}{\mu_0(p+q)}\left(\frac{\mu_0}{\varepsilon_0}\right)^p (c_1 - \lambda^2 t)\right]^{\frac{1}{p+q-1}},$$

$$X(x) = \left[-\frac{1}{(p+q-1)(c_2+\lambda^2 x)}\right]^{\frac{1}{p+q-1}}.$$

Consequently,

$$\left.\begin{aligned} E &= \left[\frac{1}{\mu_0(p+q)}\left(\frac{\mu_0}{\varepsilon_0}\right)^p \frac{\lambda^2 t - c_1}{c_2+\lambda^2 x}\right]^{\frac{1}{p+q-1}}, \\ H &= \frac{\varepsilon_0}{\mu_0} E. \end{aligned}\right\} \qquad (12)$$

Here, λ^2 is the separation constant for the variables, and c_1 and c_2 are arbitrary constants of integration.

It is impossible to derive (10) from these equations for $p = q = 1$ in a more specialized case ($A = 0$). This is a feature of the solutions of the nonlinear equations.

Equations (12) can also be interpreted as the solution of the inverse boundary-value problem for an inhomogeneous plate with complex initial distributions of E_0 and H_0 [Eqs. (12) for $t = 0$] and with E and H varying as a function of the time on the boundary $x = 0$. The constants c_1, c_2, and λ can be used to approximate a real inhomogeneity along the coordinate x for a given plate, for example, by analogy with the procedure in gasdynamics[4] (see also Puchkova[5]).

It is readily verified by the direct substitution of (9) and (4) into (12) that these functions satisfy the system of equations (3). The solutions (10) and (12) are not found in the literature. They can be used to check the numerical methods used in nonlinear electrodynamic problems.

---

[1] P. M. Kolesnikov, Introduction to Nonlinear Electrodynamics [in Russian], Izd. Nauka i Tekhnika, Minsk (1971).

[2] N. G. Puchkova, Zh. Tekh. Fiz., 39, 1372 (1969) [Sov. Phys. – Tech. Phys., 14, 1034 (1970)].

[3] I. G. Kataev, Electromagnetic Shock Waves [in Russian], Izd. Sov. Radio, Moscow (1963).

[4] G. A. Dombrovskii, Adiabatic Approximation Method in the Theory of Plane Gas Flows [in Russian], Izd. Nauka, Moscow (1964).

[5] N. G. Puchkova, Zh. Tekh. Fiz., 41, 857 (1971) [Sov. Phys. – Tech. Phys., 16, 678 (1971)].

Streamer propagation after the voltage termination in a streamer chamber

N. S. Rudenko and V. I. Smetanin

Scientific-Research Institute of Nuclear Physics, Electronics, and Automation, Tomsk

(Submitted June 18, 1973; resubmitted April 5, 1974)
Zh. Tekh. Fiz., 44, 2602-2604 (December 1974)

Streamers are observed to propagate stably in the direction of the electric field after the voltage in a streamer chamber is cut off. An electron-optical method has been used to study the influence of the initial conditions on this "self-propagation" of the streamers.

While working with streamer chambers we have noted a certain discrepancy between the lengths of the streamers observed visually in the streamer chamber and those photographed at corresponding times by means of an electron-optical image converter.[1] In an effort to find the reason for this discrepancy we have studied the processes which occur after the voltage is cut off in the chamber. Figure 1 is a schematic diagram of the experimental apparatus. The operation of the apparatus is described in detail in ref. 2. The apparatus used in the present experiments differs from that described in ref. 2 in that a cutoff switch 4 is installed in an effort to study the processes which occur in the chamber after the voltage is removed from the chamber electrodes. The time at which this switch operates can be accurately adjusted by changing the electrical length of the delay line for the ignition pulse, L_4. Line L_8 is not used in these experiments. The cutoff switch, which operates in a neon atmosphere ($P = 1$–5 atm), provides a stability of ±0.5 nsec in the length of the pulse applied to the chamber over a broad range of pulse lengths. The pulse length (the cutoff time) is chosen so that the streamer stage of the discharge is observed in the chamber at the given electric field.

Using this electron-optics system we photograph the traces in the chamber at various times after the chamber voltage is cut off. The voltage pulse in the chamber displays no oscillations after cutoff because of the damping effect of the resistance of the arc in the neon-filled switch (Fig. 2).

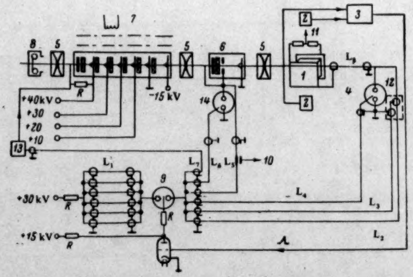

Fig. 1. Schematic diagram of the experimental apparatus. 1) Streamer chamber; 2) scintillators with photomultiplier; 3) coincidence circuit; 4) cutoff switch of the chamber; 5) objective lenses; 6) ZIM-2 high-speed electron-optical shutter; 7) UM-95 light intensifier; 8) camera; 9) switch for the nanosecond-pulse shaper; 10) capacitive voltage divider for observing the exposure pulse; 11) active divider for the voltage on the chamber electrodes; 12) connector; 13) device producing microsecond pulses of +50 kV to supply the fifth stage of the UM-95; 14) cutoff switch of the shutter; L_1) shaping lines; L_2-L_8) transmission lines.

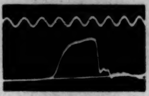

Fig. 2. Voltage pulse across the chamber. The calibration frequency is 100 MHz.

In monitoring the streamer traces in the chamber after the voltage cutoff we observe self-propagation of the streamers: After the voltage cutoff the streamers continue to propagate toward the electrodes of the chamber without any significant expansion for a considerable time, and the shape of the streamers is the same as that shown on the photographs in ref. 2. Figure 3 shows distributions of the average streamer length at various times after the voltage cutoff for an electric field of 14.5 kV/cm. The pulse applied to the chamber is 30 nsec long. The numbers above the peaks in these distributions show the exposure time with respect to the time at which the voltage is applied to the chamber electrodes. The separation of the peaks in Fig. 3 implies that the streamers propagate after the voltage is cut off and that the streamers exist for a considerable time. The streamers continue to propagate at an average velocity ~ $6 \cdot 10^7$ cm/sec. The propagation velocity of the streamers at the end of the development interval is ~ 10^7 cm/sec. After the voltage is cut off and the streamers propagate the average streamer brightness increases to a maximum and then decreases to the sensitivity threshold of the apparatus (Fig. 4). The peaks on the curves in Fig. 4 coincide, within the experimental error, with the end of the streamer-development interval. The distance which the streamers traverse after the voltage cutoff is governed by both the initial electric field in

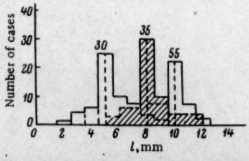

Fig. 3. Distribution of the length of the streamers on the trace at various times.

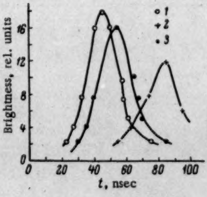

Fig. 4. Change in the brightness of the trace in the chamber after the voltage cutoff. 1) $E_0 = 16$; 2) 8.6; 3) 14.5 kV/cm.

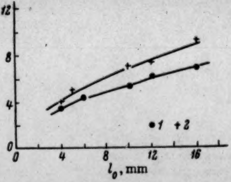

Fig. 5. Self-propagation length of the streamers as a function of the voltage and the initial length. 1) E_0 = 10.4; 2) 16 kV/cm.

the chamber and the length which the streamers acquire before the voltage cutoff (Fig. 5); the effect of the length of the streamers at the cutoff time is much stronger.

We will not discuss these results here, since we have submitted for publication a paper including a detailed discussion of the mechanism for streamer development in neon, including an explanation of the self-propagation of streamers after the voltage cutoff.[1)]

In conclusion we note that this self-propagation of the streamers does not have any significant effect on the working characteristics of streamer chambers,[1] since this effect displaces the streamer-regime working region toward shorter times by only 1-1.5 nsec at fields 10-20 kV/cm.

[1)] This paper has been submitted to Zhurnal Eksperimental'noi i Teoreticheskoi Fiziki [Soviet Physics – JETP].

[1] N. S. Rudenko and V. I. Smetanin, Prib. Tekh. Eksp., No. 6, 39 (1972).
[2] N. S. Rudenko and V. I. Smetanin, Zh. Eksp. Teor. Fiz., 61, No. 1, 146 (1971) [Sov. Phys. – JETP, 34, 76 (1972)].

Electron-optical properties of postdeflection quadrupole lenses

T. Ya. Fishkova

A. F. Ioffe Physicotechnical Institute, Academy of Sciences of the USSR, Leningrad

(Submitted March 29, 1974)
Zh. Tekh. Fiz., 44, 2604-2606 (December 1974)

In an analysis of the electron-optical properties of a quadrupole−octupole lens which receives a previously deflected beam, equations are found for the paraxial trajectory and for the third-order spherical abberation. The aberration coefficients for the deflected beam are expressed in terms of the wide-field geometric-aberration coefficients of the undeflected beam.

Quadrupole lenses are known to be capable of amplifying deflections.[1,2] This property is exploited in several electron-beam devices, in which quadrupole systems replace axisymmetric focusing lenses.[3-5] Certain quadrupole lenses are located beyond deflecting systems, so that the axial trajectory of the beam becomes curvilinear in these systems. It is reasonable that the resolution of the instrument at the edge of the raster will be governed not only by the intrinsic aberrations of the deflecting systems, but also by the aberrations of the postdeflection quadrupole lenses.

Figure 1 shows the trajectory of the charged-particle beam for the case of ideal deflection (in which the deflection angle is the same for all beam trajectories) in the presence of focusing (F) and defocusing (D) postdeflection quadrupole lenses. It is easy to show: first, the vertex angles x'_0 and y'_0 for the deflected and undeflected beams are different; second, the deflected trajectories intersect each other on a line passing through the point determining the position of the real or imaginary image (this point is adopted as the origin, z = 0); third, for small vertex angles (x'_0 and y'_0) and small deflection angles (ξ_0 and φ'_0) the initial conditions at the entrance of the quadrupole lens in the converging (xoz) and diverging (yoz) planes can be written as

$$\left.\begin{aligned} x_{en} &= x_0 + x'_0 a_F + \xi'_0\lambda_F, \quad x'_{en} = x'_0 + \xi'_0, \\ y_{en} &= y_0 + y'_0 a_D + \varphi'_0\lambda_D, \quad y'_{en} = y'_0 + \varphi'_0, \end{aligned}\right\} \tag{1}$$

where x_0 and y_0 are the dimensions of the object in the $z^* = 0$ plane.

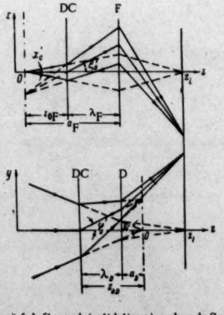

Fig. 1. Trajectories of deflected (solid lines) and undeflected (dashed lines) beams in the converging (xoz) and diverging (yoz) planes of the quadrupole lens. DC) Deflection centers; F and D) principal planes of the lens; O) real or imaginary source; z_i) Gaussian image.

To find the first-order trajectory of the deflected beam in the quadrupole lens we consider (as below) only the converging plane, since we can transform to the diverging plane by simply replacing x by y and y by x (x ⇌ y) and interchanging the deflection angles, $\xi'_0 \rightleftharpoons \varphi'_0$, and the indices F ⇌ D.

We seek a solution of the paraxial equation of the charged-particle trajectory in the quadrupole lens, $x'' + \beta^2 f(z)x = 0$, in the form

$$x_p = x'_0 x_\alpha + x_0 x_\beta + \xi'_0 x_\gamma \tag{2}$$

with the following initial conditions at the entrance to the lens, which satisfy Eq. (1):

$$\left.\begin{aligned} x_\alpha(\text{en}) &= a_F, \quad x_\beta(\text{en}) = 1, \quad x_\gamma(\text{en}) = \lambda_F \\ x'_\alpha(\text{en}) &= 1, \quad x'_\beta(\text{en}) = 0, \quad x'_\gamma(\text{en}) = 1. \end{aligned}\right\} \tag{3}$$

Expressing x_γ in terms of the linearly independent solutions x_α and x_β, we find

$$x_\gamma = x_\alpha + (\lambda_F - a_F)\, x_\beta. \tag{4}$$

For convenience we introduce the quantity z_0 − the distance from the source to the deflection center (Fig. 1). Finally, substituting (4) into (2), we find

$$x_p = (x'_0 + \xi'_0)\, x_\alpha + (x_0 + z_{0_F}\xi'_0)\, x_\beta. \tag{5}$$

To find the third-order aberrations we use successive approximations. It is interesting to consider an octupole lens along with the quadrupole lens; an octupole lens is capable of correcting geometric aberrations.

We substitute the paraxial solution (5) for a point source ($x_0 = y_0 = 0$) into the right-hand side of the equation for the charged-particle trajectory in a quadrupole−octupole lens,[6] taking terms of third order into account. Then we use the familiar equation (see, e.g., ref. 7) for the aberrational divergence in the plane of the Gaussian image, z_i, to find the third-order spherical aberration of a postdeflection quadrupole−octupole lens, Δx_{pd}, in quadrature form.

We write the following relationship between Δx_{pd} and the aberration coefficients:

$$\begin{aligned} \Delta x_{pd} = M_F\,[&(B_1 x'^3_0 + B_2 x'_0 y'^2_0) + A_3 x'^2_0\xi'_0 + A_4 y'^2_0\xi'_0 + A_5 x'_0 y'_0\varphi'_0 \\ &+ A_6 x'_0\xi'^2_0 + A_7 x'_0\varphi'^2_0 + A_8 y'_0\xi'_0\varphi'_0 + A_9\xi'^3_0 + A_{10}\xi'_0\varphi'^2_0]. \end{aligned} \tag{6}$$

The coefficients B_1 and B_2 determine the spherical aberration of the undeflected beam; the coefficients A_3, A_4, . . . , A_{10} determine the additional contribution due to the predeflection.

Comparison of our equations for the coefficients A_j

with the coefficients corresponding to the third-order geometric aberrations of a quadrupole field, B_l, given in ref. 8, with the corresponding modifications due to the octupole lens,[9] gives the relationships among these coefficients:

$$\left.\begin{array}{c} A_3=3B_1+z_{0F}B_3,\quad A_4=B_2+z_{0F}B_4,\quad A_5=2B_2+z_{0D}B_5,\\ A_6=3B_1+2z_{0F}B_3+z_{0F}^2B_6,\quad A_7=B_2+z_{0D}B_5+z_{0D}^2B_7,\\ A_8=2B_2+2z_{0F}B_4+z_{0D}B_5+z_{0F}z_{0D}B_8,\\ A_9=B_1+z_{0F}B_3+z_{0F}^2B_6+z_{0F}^3B_9,\\ A_{10}=B_2+z_{0F}B_4+z_{0D}B_5+z_{0D}^2B_7+z_{0F}z_{0D}B_8+z_{0F}z_{0D}^2B_{10}. \end{array}\right\} \quad (7)$$

Substituting (7) into (6), we find

$$\begin{gathered} \Delta x_{\mathrm{pd}}=M_{\mathrm{F}}[B_1(x_0'+\xi_0')^3+B_2(x_0'+\xi_0')(y_0'+\varphi_0')^2+B_3(z_{0F}\xi_0')(x_0'+\xi_0')^2\\ +B_4(z_{0F}\xi_0')(y_0'+\varphi_0')^2+B_5(z_{0D}\varphi_0')(x_0'+\xi_0')(y_0'+\varphi_0')+B_6(z_{0F}\xi_0')^2(x_0'+\xi_0')\\ +B_7(z_{0D}\varphi_0')^2(x_0'+\xi_0')+B_8(z_{0F}\xi_0')(z_{0D}\varphi_0')(y_0'+\varphi_0')+B_9(z_{0F}\xi_0')^3\\ +B_{10}(z_{0F}\xi_0')(z_{0D}\varphi_0')^2]. \end{gathered} \quad (8)$$

Accordingly, the aberrational divergence caused by the postdeflection quadrupole–octupole lens can be expressed in terms of the wide-field geometric-aberration coefficients.[8,9] The quantities ξ' and φ_0' are associated with the predeflection, while the products $z_{0F}\xi_0'$ and $z_{0D}\varphi_0'$ give the distances from the longitudinal axis to the intersection of the trajectories of the deflected beam in the planes determining the source position.

In the thin-lens approximation the geometric-aberration coefficients are related and are written analytically in terms of the spherical-abberation coefficients.[8,9] Taking this circumstance into account we can simplify (8):

$$\Delta x_{\mathrm{pd}}=M_{\mathrm{F}}\left[B_1\left(x_0'+\frac{\lambda_{\mathrm{F}}}{a_{\mathrm{F}}}\xi_0'\right)^3+B_2\left(x_0'+\frac{\lambda_{\mathrm{F}}}{a_{\mathrm{F}}}\xi_0'\right)\left(y_0'+\frac{\lambda_{\mathrm{D}}}{a_{\mathrm{D}}}\varphi_0'\right)^2\right]. \quad (9)$$

The conditions for correcting the abberations of a postdeflection quadrupole lens by means of an octupole lens are the same as the conditions for correcting the wide-field aberration coefficients.[9] In the thin-lens approximation these conditions reduce to the condition for correcting spherical aberration for an undeflected beam.

---

[1] M. G. Markovich and I. I. Tsukkerman, Tekhnika Kino i Televideniya, No. 6, 54 (1963).

[2] K. E. Johnson, REE, 28, No. 2, 115 (1964).

[3] V. P. Kartashev, V. I. Kotov, and B. A. Utochkin, Trudy IFVE, SEF, 67-11 (1967).

[4] T. Ya. Fishkova, V. A. Shkunov, B. N. Bandik, and Ya. G. Lyubchik, Radiotekh. Elektron., 18, 2213 (1973).

[5] A. Martin, Electr. Electronique Moderne, 25-29 (March 1972).

[6] Ya. G. Lyubchik, L. P. Ovsyannikova, and T. Ya. Fishkova, Zh. Tekh. Fiz., 41, 2175 (1971) [Sov. Phys. – Tech. Phys., 16, 1724 (1972)].

[7] S. Ya. Yavor, Focusing of Charged Particles by Quadrupole Lenses [in Russian], Atomizdat, Moscow (1968), p. 124.

[8] L. P. Ovsyannikova and S. Ya. Yavor, Zh. Tekh. Fiz., 35, 940 (1965) [Sov. Phys. – Tech. Phys., 10, 723 (1965)].

[9] L. A. Baranova, L. P. Ovsyannikova, and S. Ya. Yavor, Zh. Tekh. Fiz., 41, 1323 (1971) [Sov. Phys. – Tech. Phys., 16, 1040 (1971)].

Frequency locking in a 3.39μ laser

E. Yu. Andreeva, S. N. Gulyaev, and D. K. Terekhin

M. I. Kalinin Leningrad Polytechnical Institute

(Submitted October 20, 1973)
Zh. Tekh. Fiz., 44, 2607-2609 (December 1974)

An experimental investigation of the synchronization of a laser with linear polarization is described for two cases: 1) the polarization of the laser radiation is linear and orthogonal to the polarization of the input signal, and 2) the laser radiation is circularly polarized. It is shown that the interaction of the radiation with different polarization leads to frequency locking. When the input signal interacts with a laser that exhibits frequency splitting, locking occurs only when the amplitude of the input signal exceeds a certain threshold value.

One of the phenomena which occur in a laser acted upon by an external signal is locking, or synchronization of its frequency when the frequency of the input signal is close to the laser frequency. It follows from theoretical papers[1-3] devoted to this question that in a single-frequency laser the locking band $\Delta\nu_l$ is proportional to the ratio E_{in}/E_c (E_{in} is the amplitude of the input signal, and E_c is the field in the resonator with no input signal). For example, in ref. 3, in the weak-field approximation, the following expression is obtained for the locking band:

$$\Delta\nu_3 = \frac{1}{2\pi}\frac{C\sqrt{T}}{L\sqrt{\varepsilon}}|E_{in}|\sqrt{\frac{\beta}{\alpha}}, \tag{1}$$

where C is the velocity of light, T is the transmittance of the mirrors, L is the length of the active medium, ε is the dielectric constant, and $\sqrt{\beta/\alpha}$, according to ref. 4, defines the value of $1/E_c$. It is assumed that $E_{in} \ll E_c$, and the polarizations of the input and natural radiation are the same. Experimental data for the locking band in a 0.63 μ Brewster laser, obtained in ref. 5, are in qualitative agreement with theory. It is of interest to consider the interaction between two signals with different polarizations, and the possibility of obtaining frequency locking in this case.

In this paper we describe experimental results on the synchronization of the frequency of a laser with linear polarization for two cases.

The experiment is carried out on the 3.39 μ line of neon. A block diagram is shown in Fig. 1. Lasers Nos. 1 and 2 have semiconfocal resonators with mirror transmittances $T_1 = 12$ and $T_2 = 58\%$, and a length L = 30 cm. The spacing between axial modes is 500 MHz. The transverse modes are selected by irises located inside the resonators. The resonator frequency can be scanned using a piezoceramic element. To increase the frequency stability the resonator flanges are tightened with Invar rods, and the arrangement is mounted on a massive plate. The amplifying tubes of lasers Nos. 1 and 2 with lengths $l_1 = 21$ and $l_2 = 10.5$ cm respectively and diameter d = 0.3 cm are sealed with windows perpendicular to their axes. The tube of laser No. 2 is located in a solenoid. The linear polarization of the radiation from laser No. 1 is defined using a quartz plate placed in the resonator at a certain angle. Laser No. 2 generates radiation with circular polarization in an axial magnetic field. In zero field the introduction of the quartz plate into the resonator at a certain angle makes the polarization orthogonal to the polarization of the input signal. Frequency locking of laser No. 2 by the radiation of laser No. 1 is observed as follows: In zero field the axis of the polarizer coincides with the direction of polarization of the characteristic oscillation of the laser. The frequency of resonator No. 2 is scanned, and the frequency of the input signal is maintained constant. On the screen of the oscilloscope we observe the line shape of the emission of laser No. 2 with a dip in the frequency region close to the frequency of the input signal (Fig. 2). The presence of the dip indicates coincidence between the azimuths of the polarizations of the natural radiation and the input signal, i.e., over a certain frequency range "polarization" locking occurs. From the width of this region one can judge the value of the locking band. The frequency interval between the resonator axial modes serves as the reference for determining the locking band. All the measurements are made with the frequency of the input signal tuned to the center of the gain line. Figure 3 shows the relation between the polarization locking band thus obtained $\Delta\nu_{pl}$ and the amplitude of the input signal E_{in} for different levels of the natural emission E_c. The value of the polarization locking range increases linearly with E_{in}. An increase in the level of the natural emission leads to a narrowing of the locking band. The results obtained agree qualitatively with the results given by Eq. (1). This enables us to suggest that the phenomenon of locking with orthogonally polarized modes is subject to the same laws as those considered in ref. 5, in considering the same polarization. A difference can occur in the region of low input signals, where more detailed investigations are required, particularly for a different value of the resonator anisotropy.

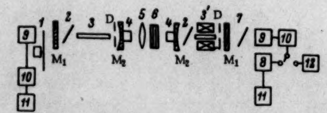

Fig. 1. Block diagram of the experimental arrangement. 1) Mechanical chopper; 2) quartz plate; 3) laser No. 1; 3') laser No. 2; 4) piezoceramic; 5) matching quartz lens; 6) optical wedge; 7) polarizer; 8) detecting circuit; 9) photoreceiver; 10) amplifier; 11) oscilloscope; 12) S4-8 spectrum analyzer; M$_1$ and M$_2$ are mirrors, and D is a diaphragm.

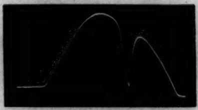

Fig. 2. Oscillogram of the emission line shape when an external signal is present.

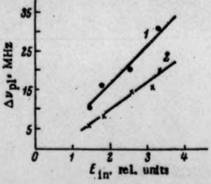

Fig. 3. Width of the polarization locking band as a function of the amplitude of the input signal $\Delta\nu_{pl}(E_{in})$. 1) $E_c = 5.8$; 2) $E_c = 8.6$ relative units.

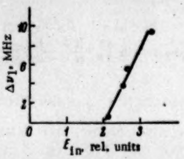

Fig. 4. Locking bandwidth as a function of the amplitude of the input signal when linearly and circularly polarized radiation interacts. $\Omega = 1.3$ MHz, $E_c = 15$ relative units.

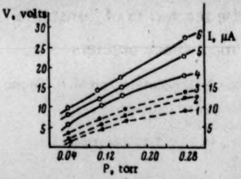

Fig. 5. Maximum splitting as a function of the amplitude of the input signal and the field of the natural oscillations. 1) $\Omega_M(E_{in})$, $E_c = 8.2$ relative units; 2) $\Omega_M(E_c)$, $E_{in} = 3.3$ relative units.

It should be noted that in this experiment the anisotropy of the resonator, set by the quartz plate, is fairly weak (the radiation is circularly polarized in a field H ~ 2 Oe). No polarization locking is observed for a tube with Brewster windows.

We will now consider the interaction between linearly and circularly polarized radiation. When an axial magnetic field is switched on, two circular frequencies appear in the radiation of laser No. 2, corresponding to σ^+ and σ^- polarization modes. The signal, proportional to the amplitude of the low-frequency beat between them, can be separated using a detection circuit placed in the photoreceiver circuit. The value of the splitting of the σ modes Ω is found from the beat frequency using an S4-8 spectrum analyzer. When scanning the frequency of resonator No. 2, one obtains on the screen of the oscilloscope the dependence of the beat amplitude on the detuning, similar to that shown in Fig. 2. The dip in the beat signal envelope is due to frequency locking in laser No. 2. The frequency locking is also recorded on the screen of the spectrum analyzer from the disappearance of the low-frequency beats.

The disappearance of the beat signal between the σ modes of laser No. 2 indicates that over a certain frequency range locking occurs between two circularly polarized oscillations and linearly polarization radiation. In this case the locking band should depend not only on the ratio E_{in}/E_c, but also on the frequency splitting between the σ modes Ω. The maximum splitting Ω_M for which locking occurs will be determined by the levels of E_{in} and E_c. Figure 4 shows $\Delta\nu_l$ as a function of E_{in} for constant Ω. The width of the locking band increases linearly as the amplitude of the input signal E_{in} increases, as in the theory of the interaction of two oscillations. The pronounced threshold of the dependence of $\Delta\nu_l$ on E_{in} is due to frequency splitting of the field E_c. Figure 5 shows the threshold characteristics of $\Omega_M(E_c)$ for E_{in} = const, and $\Omega_M(E_{in})$ for E_c = const. As can be seen from this figure Ω_M is proportional to the amplitude of the input signal and inversely proportional to the amplitude of the field of the natural oscillations. These relations can be written in the following approximate form:

$$\Delta\nu_1 \sim A\frac{E_{in}}{E_c} - B(\Omega). \tag{2}$$

The thereshold conditions correspond to the case $\Delta\nu_l \to 0$, when there is no locking.

Hence, the experimental results obtained in this investigation show that the interaction between radiation with different polarizations leads to frequency locking. The synchronization band depends linearly on the amplitude of the input signal. When the input signal interacts with radiation which is split in frequency, locking only occurs when E_{in} exceeds a certain threshold value.

The authors thank S. A. Fridrikhov for useful discussions.

---

[1] R. V. Khokhlov, Radiotekh. Elektron., 3, 566 (1958).
[2] C. L. Tang and H. Statz, J. Appl. Phys., 38, 323 (1967).
[3] R. F. Boikova, Candidate's Dissertation, LGU (1969).
[4] W. E. Lamb, Phys. Rev., 134, 1430 (1964).
[5] H. Stover and W. Steier, Appl. Phys. Lett., 8, 91 (1966).

Efficiency of the scattering of "unstable" charged particles in quadrupole mass spectrometers

E. P. Sheretov, B. I. Kolotilin, and M. P. Safonov

Ryazan' Radiotechnical Institute

(Submitted July 9, 1973)
Zh. Tekh. Fiz., 44, 2609-2613 (December 1974)

The scattering of "unstable" charged particles in a quadrupole mass spectrometer is discussed. Equations are derived for the rate at which the unstable particles leave the analyzer. The relations are found by the method of characteristic solutions of the Hill equation. The accuracy of the resulting relations and the phase characteristics of the scattering are discussed.

One of the important parameters involved in the design of the selector for quadrupole mass spectrometers is the time required to sort the charged particles. Unfortunately, the literature reveals extremely little on this important parameter of analyzers, which governs the size and sensitivity of the selector.[1-3]

In this work we use characteristic solutions of the Hill equation to derive relations required for calculating the efficiency at which unstable charged particles are scattered.[4,5]

We write the Hill equation as[5]

$$\ddot{R} + R\psi(t) = 0, \tag{1}$$

where $\psi(t)$ is a periodic function of the time with period of π or 2π.

With Eq. (1) we can associate two functions (two characteristic solutions) in the region of unstable solutions:[5]

$$R_{02}(n\pi) = A_3 \operatorname{ch} \beta_{02} n\pi + A_4 \operatorname{sh} \beta_{02} n\pi, \tag{2}$$

$$R_{03}(n\pi) = \cos n\pi \, [A_5 \operatorname{ch} \beta_{03} n\pi + A_6 \operatorname{sh} \beta_{03} n\pi]. \tag{3}$$

Characteristic solutions (2) and (3) agree with the general solution of Eq. (1) at times differing from each other by the period of the function $\psi(t)$ or by a time which is a multiple of this period[5] if the constants A_3, A_4, A_5, and A_6 are chosen correctly. Writing two independent particular solutions of Eq. (1) as[6]

$$R_{11}(t) = e^{\mu t} \sum_{-\infty}^{+\infty} C_{2r} e^{j2rt}; \quad R_{12}(t) - e^{-\mu t} \sum_{-\infty}^{+\infty} C_{2r} e^{-j2rt} \tag{4}$$

or

$$R_{21}(t) = e^{\mu t} \sum_{-\infty}^{+\infty} C_{(2r+1)} e^{j(2r+1)t}; \quad R_{22}(t) = e^{-\mu t} \sum_{-\infty}^{+\infty} C_{(2r+1)} e^{-j(2r+1)t}, \tag{5}$$

and following the procedure of ref. 5, we find

$$\beta_{02} = \mu; \quad \beta_{03} = 2\mu. \tag{6}$$

Let us compare characteristic solutions (2) and (3) with the general solution of Eq. (1) at time t_1. If we adopt the general solution in its standard form,[6] we find, e.g., for Eq. (2),

$$R_{02}(n\pi) = 2(AB)^{1/2} [R_{11}(t_1) R_{12}(t_1)]^{1/2} \times \operatorname{ch}\left[\mu\pi n + \operatorname{Arth} \frac{AR_{11}(t_1) - BR_{12}(t_1)}{AR_{11}(t_1) + BR_{12}(t_1)}\right]. \tag{7}$$

Here, A and B are the constants which appear in the general solution of Eq. (1). Now it is easy to show that the condition that the characteristic solution (7) be of an extremal nature corresponds to the equation

$$[\dot{R}_{11}(t_{10}) R_{12}(t_{10}) + R_{11}(t_{10}) \dot{R}_{12}(t_{10})] + \gamma_0 \operatorname{th}\left[\mu\pi n + \operatorname{Arth} \frac{AR_{11}(t_{10}) - BR_{12}(t_{10})}{AR_{11}(t_{10}) + BR_{12}(t_{10})}\right] = 0. \tag{8}$$

In Eq. (8), the quantity γ_0 is the Wronskian for Eq. (1).

If the working point of the particle under consideration is near the boundary of the region of stability on the stability diagram – the typical situation in the design of quadrupole mass spectrometers – then we have $\gamma_0 \to 0$, and condition (8) simplifies, becoming

$$\dot{R}_{11}(t_{10}) R_{12}(t_{10}) + R_{11}(t_{10}) \dot{R}_{12}(t_{10}) = 0. \tag{9}$$

Using (4) and (5), we can show that in this case

$$t_1 = t_{10} = \pi \quad \text{or} \quad \frac{\pi}{2}. \tag{10}$$

In calculating the extremal characteristic solutions for particles whose working points lie well within the instability region of the stability diagram, we find a refined value for the comparison time t_1:

$$t_1 = t_{10} + \Delta t_1, \tag{11}$$

where, in a first approximation, Δt_1 can be determined from

$$\Delta t_1 = (\pm 1) \frac{\gamma_0}{\left.\frac{d^2}{dt^2} [R_{11}(t) R_{12}(t)]\right|_{t=t_{10}}}. \tag{12}$$

These equations are general in nature. At present, sinusoidal signals are used in most cases to feed the selectors in quadrupole mass spectrometry.[7-9] When the analyzers are fed a sinusoidal signal, the motion of the charged particles in the selector volume is described by a system of Mathieu differential equations, which are a particular case of the Hill equation. Accordingly, we turn now to the application of the relations above to the Mathieu equation. In this case it is more convenient to write the two pairs of independent particular solutions as[6]

$$\left.\begin{aligned} R_{11} &= e^{\mu t} \sum_{-\infty}^{+\infty} [C_{u2r} \cos 2rt + C_{v2r} \sin 2rt], \\ R_{12} &= e^{-\mu t} \sum_{-\infty}^{+\infty} [C_{u2r} \cos 2rt - C_{v2r} \sin 2rt], \end{aligned}\right\} \tag{13}$$

$$\left.\begin{aligned} R_{21} &= e^{\mu t} \sum_{-\infty}^{+\infty} [C_{u(2r+1)} \cos (2r+1) t + C_{v(2r+1)} \sin (2r+1) t], \\ R_{22} &= e^{-\mu t} \sum_{-\infty}^{+\infty} [C_{u(2r+1)} \cos (2r+1) t - C_{v(2r+1)} \sin (2r+1) t]. \end{aligned}\right\} \tag{14}$$

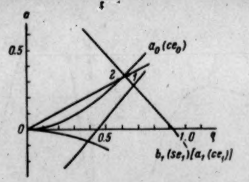

Fig. 1

The first pair of solutions, (13), is more convenient to use in the case in which the working point of the particle lies below the a_0 curve on the stability diagram; the pair in (14) is more convenient if the working point lies above the curve b_1 (se_1) or a_1 (ce_1) (Fig. 1). Now it is easy to show that Eq. (7) can be written as follows for the first pair of solutions, (13):

$$R_{02}(n\pi)=\nu_0\Bigg\{R_0\Bigg[\operatorname{ch}\mu n\pi\sum_{-\infty}^{+\infty}(\mu C_{\alpha 2r}+C_{\nu 2r}2r)\cos 2r\xi + \operatorname{sh}\mu n\pi\sum_{-\infty}^{+\infty}(C_{\alpha 2r}2r-\mu C_{\nu 2r})\sin 2r\xi\Bigg]+\dot{R}_0\Bigg[\operatorname{ch}\mu n\pi\sum_{-\infty}^{+\infty}C_{\nu 2r}\sin 2r\xi + \operatorname{sh}\mu n\pi\sum_{-\infty}^{+\infty}C_{\alpha 2r}\cos 2r\xi\Bigg]\Bigg\}. \tag{15}$$

Here ν_0 can take on two values:

$$\left.\begin{aligned}\nu_{01}&=\frac{\sum\limits_{-\infty}^{+\infty}C_{\alpha 2r}(-1)^r}{\sum\limits_{-\infty}^{+\infty}(\mu C_{\alpha 2r}+C_{\nu 2r}2r)\sum\limits_{-\infty}^{+\infty}C_{\alpha 2r}}\\ &\text{or}\\ \nu_{02}&=\frac{1}{\sum\limits_{-\infty}^{+\infty}(\mu C_{\alpha 2r}+C_{\nu 2r}2r)},\end{aligned}\right\} \tag{16}$$

where ξ is the initial phase of the high-frequency signal, and R_0 and $\dot{R}_0$ are the initial coordinate and velocity of the particle.

In calculating the characteristic solutions from (15) in order to determine the maximum deviation of the particle from the origin for a specified value of n, it is necessary to use (16) to determine the maximum value for ν_0.

For the second pair of particular solutions, (14), it is more convenient to use (3); in this case we find the two characteristic solutions

$$R_{031}(n\pi)=\frac{1}{\sum\limits_{-\infty}^{+\infty}[\mu C_{\alpha(2r+1)}+C_{\nu(2r+1)}(2r+1)]}\times\Bigg\{R_0\Bigg[\operatorname{ch}2\mu\pi n\sum_{-\infty}^{+\infty}[\mu C_{\alpha(2r+1)}+C_{\nu(2r+1)}(2r+1)]\cos(2r+1)\xi + \operatorname{sh}2\mu\pi n\sum_{-\infty}^{+\infty}[C_{\alpha(2r+1)}(2r+1)-\mu C_{\nu(2r+1)}]\sin(2r+1)\xi\Bigg] + \dot{R}_0\Bigg[\operatorname{ch}2\mu\pi n\sum_{-\infty}^{+\infty}C_{\nu(2r+1)}\sin(2r+1)\xi + \operatorname{sh}2\mu\pi n\sum_{-\infty}^{+\infty}C_{\alpha(2r+1)}\cos(2r+1)\xi\Bigg]\Bigg\}, \tag{17}$$

$$R_{032}(n\pi)=\frac{\sum\limits_{-\infty}^{+\infty}C_{\nu(2r+1)}(-1)^r}{\sum\limits_{-\infty}^{+\infty}C_{\alpha(2r+1)}\sum\limits_{-\infty}^{+\infty}[\mu C_{\alpha(2r+1)}+C_{\nu(2r+1)}(2r+1)]}\times\Bigg\{R_0\Bigg[\operatorname{ch}2\mu\pi n\sum_{-\infty}^{+\infty}[C_{\alpha(2r+1)}(2r+1)-\mu C_{\nu(2r+1)}]\sin(2r+1)\xi\Bigg] + \operatorname{sh}2\mu\pi n\sum_{-\infty}^{+\infty}[\mu C_{\alpha(2r+1)}+C_{\nu(2r+1)}(2r+1)]\cos(2r+1)\xi] + \dot{R}_0\Bigg[\operatorname{ch}2\mu\pi n\sum_{-\infty}^{+\infty}C_{\alpha(2r+1)}\cos(2r+1)\xi - \operatorname{sh}2\mu\pi n\sum_{-\infty}^{+\infty}C_{\nu(2r+1)}\sin(2r+1)\xi\Bigg]\Bigg\}. \tag{18}$$

Here, as for R_{02}, we are to choose from (17) and (18) the equation which provides the maximum value of $R_{03}(n\pi)$ for the specified value of n. Figure 2 shows the functional dependences (solid curves) of the r and z coordinates of the particles on the time for the case $a_r = 0.333840$, $q_r = 0.6240$, $R_0 = 1$, $\dot{R}_0 = 0$, $a_z = 0.323038$, $q_z = 0.6000$, $z_0 = 1$, $\dot{z}_0 = 0$, and $\xi = 0$.

The working points of the particles are denoted by 1 and 2, respectively, in Fig. 1. As we see from this figure, these working points lie near the boundaries of the overall stability diagram for a three-dimensional quadrupole mass spectrometer. The dashed curves in Fig. 2 show the corresponding characteristic solutions, calculated from Eqs. (15), (17), and (18). We see from Fig. 2 that there is a good agreement between the extremal excursions of particles from the origin calculated from the characteristic solutions and the actual values.

Figure 3 shows the r and z excursions of unstable particles for a specified value of n as functions of the phase at which the particles enter the high-frequency field, ξ. These functional dependences were calculated from the characteristic solutions given above. Interestingly, these phase functions have a form reminescent of the corresponding functions for the amplitudes of the r and z oscillations of stable particles, given in ref. 5. From this similarity we draw the important conclusion that the maximum sorting time, i.e., the maximum scattering time for the unstable ions, is required when the charged particles enter the selector in a favorable phase (corresponding to the lowest oscillation amplitude of stable particles). For a quadrupole mass filter, e.g., in which there is 100% trans-

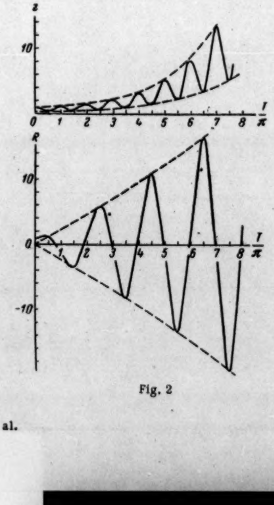

Fig. 2

mission of the ions, this circumstance should lead to the appearance of a functional dependence of the resolution on the time, since the efficiency with which unstable particles entering the selector at a phase of $\pi/4$ are scattered is much higher than that corresponding to a phase of 0 or, especially, $\pi/2$. In this connection we would expect a significant increase in the resolution of a mass filter if we were to modulate the velocity of the ions entering the selector in accordance with the phase of the high-frequency potential fed to the system.

As was mentioned above, the accuracy of Eqs. (15), (17), and (18) is governed by the value of the Wronskian γ_0. As the working point of the particle moves away from the boundary of the stability region the value of δ_0 changes for these particular solutions, and there is a corresponding change in the accuracy of these equations.

As we mentioned above, in calculating the extremal characteristic solutions we can improve the accuracy by refining the comparison time Δt_1. For example, when we use Eqs. (14), we find that Eq. (12) becomes

$$\Delta t_1=(\pm 1)\frac{\sum\limits_{-\infty}^{+\infty} C_{u(2r+1)} \sum\limits_{-\infty}^{+\infty} [\mu C_{u(2r+1)} + C_{v(2r+1)}(2r+1)]}{\sum\limits_{-\infty}^{+\infty} C_{u(2r+1)}(2r+1)^2 \sum\limits_{-\infty}^{+\infty} C_{u(2r+1)} + \sum\limits_{-\infty}^{+\infty} 2C_{v(2r+1)}(2r+1)}$$

or

$$\Delta t_1=(\pm 1)\cdot$$

$$\times\frac{\sum\limits_{-\infty}^{+\infty} C_{u(2r+1)} \sum\limits_{-\infty}^{+\infty} [\mu C_{u(2r+1)} + C_{v(2r+1)}(2r+1)]}{\sum\limits_{-\infty}^{+\infty} C_{v(2r+1)}(-1)^r \sum\limits_{-\infty}^{+\infty} C_{v(2r+1)}(2r+1)^2(-1)^r + \sum\limits_{-\infty}^{+\infty} 2C_{u(2r+1)}(2r+1)(-1)^r}.$$

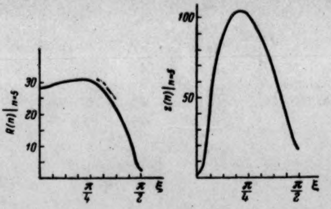

Fig. 3

Our calculations show that it is worthwhile to use these refined equations for Δt_1 only for points lying well within the unstable regions. For regions lying near the boundaries of the stability regions (which are the most important from the standpoint of the design of analyzers having a high resolution) the accuracy provided by Eqs. (15), (17), and (18) is completely adequate.

---

[1] W. Paul, H. P. Reinhard, and U. von Zahn, Z. Phys., 152, 143 (1958).
[2] G. I. Slobodenyuk, Zh. Tekh. Fiz., 37, 964 (1967) [Sov. Phys. – Tech. Phys., 12, 693 (1967)].
[3] É. I. Sheretov, V. A. Zenkin, and V. F. Samodurov, Zh. Tekh. Fiz., 43, 410 (1973) [Sov. Phys. – Tech. Phys., 18, 262 (1973)].
[4] É. P. Sheretov and V. I. Terent'ev, Zh. Tekh. Fiz., 42, 953 (1972) [Sov. Phys. – Tech. Phys., 17, 755 (1972)].
[5] É. P. Sheretov and B. I. Kolotilin, Zh. Tekh. Fiz., 42, 1931 (1972) [Sov. Phys. – Tech. Phys., 17, 1574 (1973)].
[6] N. W. M'Lachlan, Theory and Applications of Mathieu Functions, Oxford Univ. Press, London (1947).
[7] A. É. Rafal'son, Zh. Tekh. Fiz., 35, 3 (1965) [Sov. Phys. – Tech. Phys., 10, 1 (1965)].
[8] É. P. Sheretov, V. A. Zenkin, and O. I. Boligatov, Prib. Tekh. Eksp., No. 1, 1966 (1971).
[9] N. N. Bagrov, A. G. Furmanskii, and A. A. Guslyakov, Prib. Tekh. Eksp., No. 4, 136 (1969).

Reflection of a high-current relativistic electron beam from a conducting surface

A. N. Didenko, A. I. Ryabchikov, V. A. Tuzov, and Yu. P. Usov

Scientific-Research Institute of Nuclear Physics, Electronics, and Automation, Tomsk

(Submitted January 7, 1974; resubmitted April 24, 1974)
Zh. Tekh. Fiz., 44, 2613-2615 (December 1974)

Experiments are reported on the reflection of a high-current beam of relativistic electrons from a conducting surface at an air pressure sufficient for self-focusing of the beam. The reflection occurs with a low loss at a pressure of 0.09 torr and at reflection angles up to 30°. The experiments are carried out at electron energies of 0.6 and 1.0 MeV.

We report here an experimental study of the reflection of a high-current electron beam from a conducting surface at an air pressure sufficient to provide self-focusing of the beam. The experiments are carried out on the Tonus accelerator, which consists of an Arkad'ev–Marx generator with a stored energy of 27 kJ and a maximum output voltage of 2.2 MV, a double shaping line with an output impedance of 24 Ω, and a cold-cathode electron gun.[1]

Figure 1 shows the experimental arrangement. Electron beam 1, from the cathode of the accelerator 2, passes through a titanium foil 3, which is 50 μ thick, and which serves as the anode of the electron gun, into drift chamber 4. The dimensions of this chamber are 500 × 500 × 200 mm. The electron energy is varied from 0.6 to 1.0 MeV in the experiments. At high energies the chamber dimensions are inadequate because the chamber walls affect the reflection. The beam current is measured by Faraday cup 5 with a low-inductance foil shunt having a resistance of $6 \cdot 10^{-3}$ Ω. In the experiments the beam current coming from the accelerator is monitored by reverse-current shunt 6, and the electron energy is monitored by capacitive voltage divider 7. Reflecting plate 8, made of sheet copper 1 mm thick, is mounted on two movable shafts 9, which permit the position of the plate in the drift region to be changed without disrupting the vacuum. The reflecting plate is connected electrically to the drift chamber. In the measurement of the reflected-beam current the Faraday cup is mounted on arc 10, so that the beam reflected from the plate at some angle strikes the cup after traveling a constant distance in the drift chamber (500 mm). The upper wall of the chamber is Plexiglas; its inner side is covered with a metal grid, through which the beam is photographed and monitored by a television system.

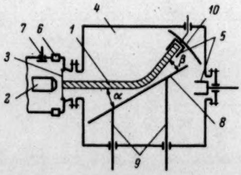

Fig. 1. Experimental arrangement.

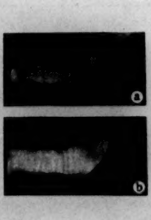

Fig. 2. Air glow as the electron beam passes through the drift chamber near the conducting plate. a) 0.6 MeV, 15 kA, α = 38°, β = 8°; b) 1.0 MeV, 25 kA, α_{cr} = 48°.

TABLE 1

α	β
5°	17°
10	16
15	15
20	13
25	12
30	10

TABLE 2

p, torr	d, mm					
	25	50	65	80	95	110
0.09	15	12	10	7.5	5	2.5
1.2	12	10.5	8	5	3.5	1

Figure 2 shows photographs of the beam in the drift chamber. Table 1 shows the angles of incidence α and the corresponding reflection angles β for an air pressure of 0.09 torr, at which we observe the minimum loss in the beam transport. The electron energy is 0.6 MeV, and the current is 15 kA. The functional dependence of β on α shown in Table 1 arises because as the position of the reflecting plate is changed there is a change in the initial distance from the beam axis to the conducting surface along with a change in the angle α. The photograph in ref. 2 of a beam reflected from a conducting surface, with $\alpha \approx \beta$, is the only published experimental result on the reflection of a high-current relativistic electron beam. The angles α and β are equal only for a certain angle of incidence (in our case, α = 15°); in general we have $\alpha \neq \beta$.

Table 2 shows β as a function of the distance between the beam axis and the reflecting plate in the case α = 0°, the distance d. In a time equal to the skin time the beam motion is parallel to the reflecting plate for a distance L without interacting with it. In our experiments, L is varied from 5 to 20 cm. The experimental results show that the interaction of the beam with the conducting surface is weaker than follows from the theoretical model of ref. 3. Measurements of the beam current as a function of the air pressure in the drift chamber show that the current varies only slightly as α is varied from 0 to 30°. Only at α near α_{cr} do we observe a rapid decrease in the current. The critical angle α_{cr}, at which the beam loss occurs

(Fig. 2b), is governed by the air pressure, changing from 40 to 48° as the pressure is reduced from 2 to 0.04 torr. At energies of 0.6 and 1 MeV (Fig. 2, a and b) and at a pressure of 0.09 torr we observe the unusual beam-structure features – bright spikes moving at acute angles with respect to the basic beam – which were first observed in ref. 4 at an electron energy of 300 keV. It should be emphasized that these spikes are not associated with loss of electrons from the beam channel, as in ref. 5. When the beam displays this structure we observe minimum values of the current; this structure is retained at small values of α. Figure 2a shows a photograph of the beam taken in the case in which the spikes disappear upon the reflection of the beam.

These results are important not only in connection with the physics involved, but also in connection with the development of methods for controlling the trajectories of high-current relativistic electron beams in injection, transport, and the shaping of closed configurations without the external electromagnetic fields.

---

[1] I. Z. Gleizer, A. N. Didenko, L. P. Dronova, A. G. Zherlitsyn, G. I. Kotlyarevskii, B. V. Okulov, V. S. Pak, G. E. Remnev, N. S. Rudenko, V. A. Tuzov, V. I. Smetanin, Yu. P. Usov, and A. A. Shatanov, At. Energ., 36, No. 5, 378-382 (1974).

[2] W. Link, Trans. IEEE, NO S-14, No. 3, 77 (1967).

[3] K. V. Khodataev, At. Energ., 32, 379 (1972).

[4] A. A. Kolomenskii, V. M. Likhachev, I. V. Sinil'shchikova, and O. A. Smit, ZhETF Pis. Red., 18, 153 (1973) [JETP Lett., 18, 89 (1973)].

[5] K. V. Khodataev, ZhETF Pis. Red., 18, 184 (1973) [JETP Lett., 18, 107 (1973)].

Thermal diffusion in a mixture of cesium vapor and helium

E. S. Bekmukhambetov and V. A. Donov

Institute of Nuclear Physics, Academy of Sciences of the Kazakh SSR, Alma-Ata

(Submitted November 9, 1973)
Zh. Tekh. Fiz., 44, 2615-2617 (December 1974)

The thermal-diffusion ratio in a mixture of cesium vapor and helium has been determined experimentally. It is compared with the value calculated on the basis of the Lennard–Jones model.

Study of thermal diffusion in mixtures of gases with cesium vapor is important for an understanding of transport processes in the cesium thermionic converter. We report on measurements of the thermal diffusion for a mixture of cesium vapor and helium over the temperature range 400-800°K.

Important technical difficulties arise in an experimental determination of the thermal-diffusion ratio k_T or the thermal-diffusion constant α_T in mixtures of gases with cesium vapor when conventional methods are used. Accordingly, we use an atomic-absorption method for these measurements, as discussed in ref. 1.

The lower chamber of the two-chamber apparatus contains metallic cesium; the upper chamber is an optical cell whose volume is much smaller than that of the lower chamber. The change in the concentration of cesium vapor due to thermal diffusion is determined from the change in the optical density. The optical cell is illuminated by the beam from a high-frequency cesium lamp. The measurements are carried out at the cesium line at 455.5 nm by the linear-absorption method.[2]

The idea behind these measurements is as follows: If the temperature maintained in the upper chamber, T_1, is higher than that of the lower chamber, T_2, the cesium vapor becomes distributed in the two chambers according to the ratio $n_1T_1 = n_2T_2$, where n_1 and n_2 are the concentrations of cesium vapor in the upper and lower chambers, respectively. When a foreign gas is admitted into the volume, this ratio changes as a result of thermal diffusion. If, in the absence of this additional component, the concentration of cesium vapor in the optical cell corresponds to an optical density D_0, and if this density changes to D when the foreign gas is admitted, we conclude that the separation in this case is $(1 - \eta)c_1$, where $\eta = D/D_0$ and c_1 is the relative fraction of cesium vapor. Accordingly, knowing the optical density D for a given relative concentration c_1 we can use the equation

$$(1-\eta)\,c_1 = k_T \ln\frac{T_1}{T_2} \qquad (1)$$

to determine the thermal-diffusion ratio k_T for various concentrations of the cesium vapor and the foreign gas.

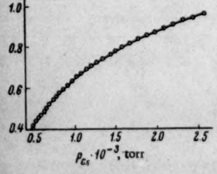

Fig. 1. Optical density as a function of the concentration of cesium vapor.

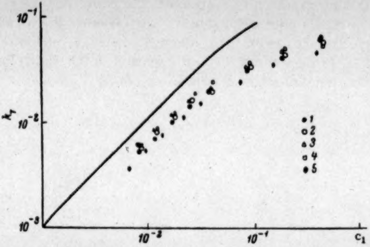

Fig. 2. Thermal-diffusion ratio for a cesium–helium mixture as a function of the relative concentration of cesium vapor. 1) 402-533; 2) 402-596; 3) 401-726; 4) 402-804; 5) 397-873°K.

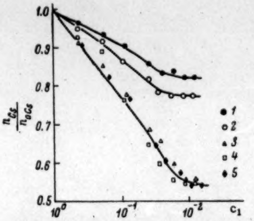

Fig. 3. Relative change in the concentration of cesium vapor due to thermal diffusion as a function of the relative amount of cesium in the mixture. 1) 402-533; 2) 402-596; 3) 401-726; 4) 402-804; 5) 397-873°K.

Equation (1) holds if the optical density of the vapor varies linearly with the concentration. In our measurements, based on the 455.5 nm cesium line, this linearity breaks down, so we use in η the values of the vapor concentrations corresponding to the given optical densities from the experimental functional dependence of D on the concentration n (Fig. 1).

We measure the ratio D/D_0 with added helium for five different temperature gradients. The error in the determination of η is less than 3%. The values of k_T determined from Eq. (1) are shown in Fig. 2 for concentrations $c_1 = 0.4$-0.008.

The curve in this figure is the functional dependence of k_T on the concentration ratio for temperatures 400-1000°K calculated on the basis of the Lennard–Jones model.[3] For these calculations we use[4] the geometric collision parameter $\sigma_{12} = 3.39$ Å and well depth $\varepsilon_{12}/k = 40.8$°K. The calculations show that k_T is a weak function of the temperature, so we have drawn only a single curve. For the temperature range 397-873°K the experimental values of k_T are slightly lower than for narrower temperature ranges. This circumstance should apparently be attributed to an error in the integral form of the equation for the steady state for broad temperature ranges.

Figure 3 shows the relative change in the cesium vapor concentration as a function of its relative concentration in the mixture. We see from this figure that the maximum change in the cesium vapor concentration occurs when there is relatively little of it in the mixture. As the helium concentration is increased, the ratio n^{Gs}/n_{0Gs} tends toward a constant value for each temperature range. A single line is drawn for the ranges 401-726, 402-804, and 387-873°K, since a further increase in the range has essentially no effect on the ratio n_{Gs}/n_{0Gs}.

This measurement procedure gives us a clear idea of the behavior of the cesium vapor concentration in the interelectrode gap of a thermionic converter in the presence of another gaseous component.

---

[1] E. S. Bekmukhambetov and V. A. Donov, Izv. Akad. Nauk KazSSR, Ser. Fiz.-Matem., No. 2 (1972).

[2] B. V. L'vov, Atomic Absorption Analysis [in Russian], Izd. Nauka, Moscow (1966).

[3] K. M. Aref'ev, I. I. Paleev, V. M. Borishanskii, B. M. Khomchenkov, and N. I. Ivashchenko, Inzh.-Fiz. Zh., 11, No. 6 (1966).

[4] L. B. Robinson, in: Thermionic Energy Conversion [Russian translation], Atomizdat, Moscow (1964).

Parametric excitation of helicon waves in a plasma by modulated radio frequency waves

V. S. Paverman and D. D. Tskhakaya

Institute of Physics, Academy of Sciences of the Georgian SSR, Tbilisi

(Submitted February 8, 1974)
Zh. Tekh. Fiz., 44, 2617-2620 (December 1974)

The excitation of helicon waves is studied in a magnetoactive plasma in an external weakly modulated high-frequency electric field. The characteristic frequencies of such a system are shown to depend on the amplitude of the external field. Parametric resonance phenomena appear at certain modulation frequencies and the characteristic helicon waves are excited. The growth rate and the threshold amplitude of the external field are determined.

In the present paper we consider helicon waves in a magnetoactive electron plasma in a transverse high-frequency wave with a weakly modulated amplitude. If the carrier frequency of the external wave is much greater than the characteristic frequencies of the plasma, the spectrum of the oscillations depends on the amplitude of the carrier wave. It is well known that the phenomenon of parametric resonance can occur if a parameter characterizing an oscillatory system is varied at a characteristic frequency, and the amplitude of the parametric oscillation increases exponentially. Accordingly, by amplitude modulating the pump wave at an appropriate frequency, it is possible to excite parametrically the natural helicon waves of a magnetoactive plasma.

A similar problem for an isotropic plasma has been considered by Aliev and Zyunder[1] who investigated the parametric excitation of electrostatic waves by a modulated microwave field.

The wavelength of the helicon waves considered in the present paper is assumed to be much smaller than the wavelength of the external wave. The external high-frequency field $E_0(t)$ can thus be represented in the form

$$\mathbf{E}_0(t) = \mathbf{E}_0 \sin \Omega t + \mathbf{E} \sin(\Omega + \Delta\Omega)t + \mathbf{E} \sin(\Omega - \Delta\Omega)t, \tag{1}$$

where E_0, E and the constant magnetic field H_0 (O, O, H_0) are all in the same direction. The carrier frequency Ω is of the order of the electron plasma frequency and is much greater than $\Delta\Omega$, the frequency at which the amplitude of the external high-frequency wave is modulated. The depth of modulation is to be assumed small, i.e., $E \ll E_0$.

The set of equations describing the behavior of an electron plasma in an alternating electric field and a constant magnetic field has the form

$$\left.\begin{aligned} \operatorname{curl} \mathbf{E} &= -\frac{1}{c}\frac{\partial \mathbf{H}}{\partial t}, \\ \operatorname{curl} \mathbf{H} &= \frac{1}{c}\frac{\partial \mathbf{E}}{\partial t} + \frac{4\pi}{c} en\mathbf{V}, \\ \frac{d\mathbf{V}}{dt} &= \frac{e}{m}\mathbf{E} + \frac{e}{mc}[\mathbf{VH}], \\ \frac{\partial n}{\partial t} &+ \operatorname{div}(n\mathbf{V}) = 0. \end{aligned}\right| \tag{2}$$

The equilibrium state is described by the equations

$$\frac{d\mathbf{V}_0(t)}{dt} = \frac{e}{m}\mathbf{E}_0(t); \quad \frac{\partial n_0}{\partial t} = 0. \tag{3}$$

Assuming that the deviations from the unperturbed values of $V_0(t)$, $E_0(t)$, n_0, and H_0 are small, we linearize (2) and write the coordinate dependence of the nonequilibrium quantities as exp(ikr). We consider perturbations propagating along the z axis. It is readily shown that the equations for the longitudinal and transverse waves decouple in this case. The effect of the high-frequency field on the longitudinal waves shows up only as a Doppler shift. For the transverse waves, however, we have

$$\frac{d^2H_\pm(t)}{dt^2} + (\omega_L^2 + c^2k^2)H_\pm(t) \mp i\omega_H\omega_L^2 e^-(t)\, e^{\pm i\omega_H t}\int_{-\infty}^{t} e^+(t_1) H_\pm(t_1)\, e^{\pm i\omega_H t_1} dt_1,$$

$$\left.\begin{aligned} H_\pm(t) &= \frac{H_x(t) \pm iH_y(t)}{\sqrt{2}}, \\ \omega_L^2 = \frac{4\pi e^2 n_0}{m};\quad \omega_H &= \frac{eH_0}{mc};\quad a_0 = \frac{ekE_0}{m\Omega^2};\quad a = \frac{ekE}{m\Omega^2}, \\ e^\pm(t) &= \exp\left\{\pm ik\int_{-\infty}^{t} V_0(t_1)\,dt_1\right\} \\ &= \sum_{n,m,l} J_n(a_0) J_m(a) J_l(a)\, e^{\pm i(m+n+l)\Omega t \pm i(m-l)\Delta\Omega t} \end{aligned}\right\} \tag{5}$$

and $J_n(x)$ is the Bessel function. The condition $\Delta\Omega \ll \Omega$ is used in (5).

We solve Eq. (4) for H_+. By (4) the transition from clockwise helicon waves H_+ to counterclockwise H_- can be effected through the substitution $\omega_H \to -\omega_H$. In what follows we assume everywhere that $a \ll 1$. Retaining first-order terms in a, we obtain the Fourier components $H_p(\omega)$:

$$H_p(\omega) = \int_{-\infty}^{\infty} H_+(t)\, e^{i(\omega + p\Omega)t} dt$$

which are given by the equation

$$\begin{aligned} \{\omega_L^2 + c^2k^2 - (\omega + p\Omega)^2\} H_p(\omega) + \omega_H\omega_L^2 \sum_{n,m} \frac{J_n(a_0) J_m(a_0)}{\omega - \omega_H + (l-n)\Omega} H_{p-n+m}(\omega) \\ = a\omega_H\omega_L^2 \sum_{n,m}\left\{\frac{J_n(a_0) J'_m(a_0)}{\omega_H - \omega - (p-n)\Omega} + \frac{J_m(a_0) J'_n(a_0)}{\omega_H - \omega - \Delta\Omega - (p-n)\Omega}\right\} \\ \times H_{p-n+m}(\omega + \Delta\Omega) + (\Delta\Omega \to -\Delta\Omega). \end{aligned} \tag{6}$$

Here, $J'_n(a_0) = (\partial/\partial a_0)\, J_n(a_0)$, and the second term on the right side of Eq. (6) ($\Delta\Omega \to -\Delta\Omega$) is obtained from the first by replacing $\Delta\Omega$ by $-\Delta\Omega$. Below we restrict the discussion to plasma waves with frequency ω such that

$$|\omega - \omega_l| \ll \Omega.$$

The presence of the small parameter a leads to an equation for $H_0(\omega)$. With p = 0 Eq. (6) contains summations of the form

$$\sum_n J_n(a_0) H_n(\omega) \text{ and } \sum_n J'_n(a_0) H_n(\omega).$$

These summations can be found from the same equation (6) for $p \neq 0$ by multiplying it by $J_p(a_0)$, $J'_p(a_0)$ and then summing over p. Applying the method of successive approximations and retaining terms of first order in a, we obtain the following equation for $H_0(\omega)$:

$$\mathcal{E}(a_0, \omega) H_0(\omega) = \frac{a}{2} \omega_0^2 (a_0, \omega) \frac{\partial}{\partial a_0} \left\{ \frac{\mathcal{E}(a_0, \omega) + \mathcal{E}(a_0, \omega + \Delta\Omega)}{\omega_0 (a_0, \omega)} \right\}$$
$$\times \frac{H_0(\omega + \Delta\Omega)}{\mathcal{E}(a_0, \omega + \Delta\Omega) - \omega_0(a_0, \omega + \Delta\Omega)} + (\Delta\Omega \rightarrow -\Delta\Omega). \tag{7}$$

Here

$$\left.\begin{aligned} \mathcal{E}(a_0, \omega) &= \omega - \omega_H + \sum_n \omega_n (a_0, \omega), \\ \omega_n (a_0, \omega) &= \frac{\omega_H \omega_L^2 J_n^2 (a_0)}{\omega_L^2 + c^2k^2 - (\omega + n\Omega)^2}. \end{aligned}\right\} \tag{8}$$

From Eq. (7), by successive elimination of $H_0(\omega \pm \Delta\Omega)$, $H_0(\omega \pm 2\Delta\Omega)$ etc., on, we can obtain a dispersion relation in the form of an infinite continued fraction.[2] We use the smallness of the parameter a to terminate this fraction; to terms of order a^2 the dispersion relation is

$$\mathcal{E}(a_0, \omega) = a^2 \frac{A(a_0, \omega, \Delta\Omega)}{\mathcal{E}(a_0, \omega) + \Delta\Omega - \omega_0(a_0) + 0(a^2)} + (\Delta\Omega \rightarrow -\Delta\Omega), \tag{9}$$

$$A(a_0, \omega, \Delta\Omega) = \frac{\left\{ \omega_0(a_0) \sum_n \frac{\partial \omega_n(a_0)}{\partial a_0} \left[\mathcal{E}(a_0, \omega) + \frac{\Delta\Omega}{2} \right] \frac{\partial \omega_0(a_0)}{\partial a_0} \right\}^2}{\left(\mathcal{E}(a_0, \omega) - \omega_0(a_0)\right) \left(\mathcal{E}(a_0, \omega) + \Delta\Omega\right)} \tag{10}$$

where $O(a^2)$ denotes terms of order a^2. The derivation of Eq. (9) utilizes the inequality

$$\omega \ll \omega_L. \tag{11}$$

Only if (11) holds can one regard ω_n, defined by expression (8), as independent of ω. For $c^2k^2 \ll \omega_L^2$ this assertion is valid if $c^2k^2 \gg \omega^2$ (it should be remembered that $a_0 \approx (ck/\omega_L)v_0/c$, where $V_0 = eE_0/m\Omega^2 \ll c$). With $a = 0$ we obtain the following solution to the dispersion equation $\mathcal{E}(a_0, \omega^*) = 0$;

$$\omega^* = \omega_H \left\{ 1 - \sum_n \frac{\omega_L^2 J_n^2 (a_0)}{\omega_L^2 + c^2k^2 - n^2\Omega^2} \right\}. \tag{12}$$

The summation in (12) is tabulated in ref. 3.

We seek a solution of Eq. (9) close to ω^*. Let

$$\omega = \omega^* + i\gamma \, (|\gamma| \ll \omega^*); \quad \Delta\Omega = \omega_0(a_0) + \Delta, \tag{13}$$

where the detuning $|\Delta| \ll \omega_0(a_0)$. Under these assumptions the second term on the right side of Eq. (9) is small. We then obtain the growth rate γ:

$$\gamma = \frac{i\Delta}{2} \pm \sqrt{\frac{a^2}{4} \left\{ 2 \sum_n \frac{\partial \omega_n (a_0)}{\partial a_0} - \frac{\partial \omega_0 (a_0)}{\partial a_0} \right\}^2 - \frac{\Delta^2}{4}}. \tag{14}$$

The growth rate is at a maximum when $\Delta = 0$. Recalling the definition of $\omega_n(a_0)$, we find that

$$\gamma_{\max} = \frac{a}{2} \left| \omega_H \sum_n \frac{\omega_L^2}{\omega_L^2 + c^2k^2 - n^2\Omega^2} \frac{\partial}{\partial a_0} \left(2J_n^2(a_0) - \delta_{n0} J_0^2(a_0)\right) \right|, \tag{15}$$

where δ_{n0} is the Kronecker delta.

When $c^2k^2 \lesssim \omega_L^2$ $(a_0 \ll 1)$, we obtain the following expressions for the frequency and the maximum growth rate:

$$\omega^* = \frac{c^2k^2 \omega_H}{\omega_L^2 + c^2k^2}, \tag{16}$$

$$\gamma_{\max} \approx a a_0 \frac{\omega_L^2}{c^2k^2} \left(\frac{1}{2} + \frac{\omega_L^2}{c^2k^2} \right)^2 \omega^*. \tag{17}$$

In order to determine the threshold value of the amplitude of the pump wave at which the instability occurs, it is necessary to take account of dissipative processes. In the cold-plasma limit absorption is determined primarily by particle collisions. In all expressions cited above collisions can be taken into account by making the formal substitution

$$\omega_H \rightarrow \omega_H - i\nu \quad (\nu \ll \omega_H).$$

Here, ν for a fully ionized plasma is the frequency of electron–ion collisions; in the case of a weakly ionized plasma ν is the frequency of electron–neutral collisions.[4]

When $c^2k^2 \lesssim \omega_L^2$, expressions (16) and (17) are valid and we find the threshold amplitude for a nonmonochromatic pump wave

$$\left(\frac{EE_0}{4\pi m n_0 c} \right)_{\text{th}} = 2 \frac{\nu}{\omega_H} \frac{kc \sqrt{\omega_L^2 + c^2k^2}}{2\omega_L^2 + c^2k^2}.$$

We note in conclusion that a corresponding expression for the growth rate can be obtained without imposing condition (11) by starting from Eq. (7) and following a presentation analogous to the above. For example, for $c^2k^2 \gg \omega_L^2$ but $a_0^2 \ll 1$ the frequency $\omega \approx \omega_H$ and can be of the order of ω_L, while the modulation frequency, by (13) and (8), is

$$\Delta\Omega = \frac{\omega_H \omega_L^2}{c^2k^2}$$

and is much smaller than Ω. However, the equations for the determination of the frequency of the natural oscillations and the modulation frequency

$$\mathcal{E}(a_0, \omega^*) = 0 \text{ and } \mathcal{E}(a_0, \omega^* + \Delta\Omega) = \omega_0(a_0, \omega^* + \Delta\Omega)$$

are transcendental in the general case and do not yield analytic expressions for ω^* and $\Delta\Omega$.

---

[1] Yu. M. Aliev and D. Zyunder, Zh. Eksp. Teor. Fiz., 61, 1057 (1971) [Sov. Phys. – JETP, 34, 564 (1972)].

[2] P. M. Morse and H. Feshbach, Methods of Theoretical Physics, McGraw-Hill, New York (1953).

[3] V. P. Silin, Parametric Effect of High-Power Radiation on a Plasma [in Russian], Izd. Nauka, Moscow (1973).

[4] V. L. Ginzburg and A. A. Rukhadze, Waves in a Magnetoactive Plasma [in Russian], Izd. Nauka, Moscow (1970).

Electrical strength of nitrogen and hyrodgen at high pressures

É. A. Avilov and N. V. Belkin

(Submitted June 3, 1973)
Zh. Tekh. Fiz., 44, 2620-2621 (December 1974)

The dependence of the static and pulsed breakdown voltages on pd is investigated in nitrogen and hydrogen in the pressure range 10-90 atm for two-electrode gaps with width up to 1 mm, in homogeneous and inhomogeneous fields. It is shown that the static breakdown voltage is lowered considerably as the field inhomogeneity near the cathode is increased; at lower pressures the breakdown voltage deviates from the linear dependence. When the static voltage is replaced by pulses, the breakdown voltage increases, whereas the departure from Paschen's law appears at higher values of pd. This makes it possible to obtain appreciable overvoltages. For the knife-edge–plane gap the pulse factor is 6.5 in hydrogen at pd ~ 3-6 atm • cm.

Gas-filled, high-pressure discharge tubes have recently become popular in various physical investigations and in the technology of short, high-voltage pulses. Such devices are used for the formation of nanosecond voltage pulses in portable pulsed x-ray generators,[1,2] for laser pumping, for pulsed high-power accelerators, and in other physical apparatus. To reduce inductive losses, the discharge tubes operate at pressures of 50 kg/cm^2 or higher. It is of considerable practical and scientific interest to examine the pulse factor (the ratio of the pulsed to static breakdown voltage) at high pressures and for various electric fields in the interelectrode gap.

In the present work, two-electrode gaps are used; these are plane-parallel electrodes 18 mm in diameter with rounded edges.[3] Knife-edge–plane gaps are also used. In the latter case the edge of a tungsten foil 50 μ thick rolled into a cylinder 8 mm in diameter and 5 mm high serves as cathode. The static breakdown voltage is measured by C-96 and C-100 kilovoltmeters, while the pulses are measured by a C1-26 oscilloscope by means of a capacitive voltage divider connected in parallel with the gap. The rate of rise of the pulse voltage is 100 kV/μsec. The breakdown of the spark gap always takes place on the leading edge of the pulse. The measurements are taken after 100 conditioning switching operations.

Breakdown voltages are measured for a gap width of 0.7-0.9 mm in nitrogen (Fig. 1a) and hydrogen (Fig. 1b). The experimental points are averaged over 30-40 values of the breakdown voltage. The working pressure varies from 10 to 90 atm. Curves 1, 3, 5, of Figs. 1 and 2 correspond to static breakdown voltages. Curves 2, 4, 6 represent pulsed voltages. The electrical strength is obtained for gaps with a smooth cathode (curves 5, 6). When the field inhomogeneity at the cathode is increased, the breakdown voltage diminishes. Gaps with an edge cathode (curves 1, 2) have the lowest electric field; curves 3, 4 correspond to a "ribbed" cathode.[4] When the static voltages are replaced by pulses, the breakdown voltage always increases, independently of the shape of the cathode, while the departure from Paschen's law begins at higher values of pd. For example, for pulsed voltages in nitrogen, the departure from the linear law has not been observed at all (curves 2, 4, 6 on Fig. 1). Thus, in all cases, the pulse factor is larger than unity. Figure 2 shows the dependence of the pulse factor on pd in nitrogen and hydrogen. The value is computed from the data of Fig. 1, a and b. It is seen from Fig. 2 that in nitrogen and hydrogen, in the pressure range of 10-90 atm, the pulse factor for gaps with a smooth cathode does not exceed 1.5, which agrees with the literature.[4] For gaps with an extremely inhomogeneous field of the knife-edge–plane type, the pulse factor attains 6.5.

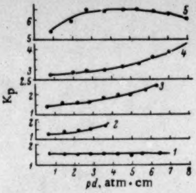

Fig. 2. Dependence of the pulse factor (K_p) on pd, in nitrogen and hydrogen; 1) nitrogen, hydrogen, smooth cathode; 2) nitrogen, "ribbed" cathode; 3) hydrogen "ribbed" cathode; 4) nitrogen, edged cathode; 5) hydrogen, edged cathode.

In this work the high value of the pulse factor is obtained as a result of the substantial lowering of the static breakdown voltage. The low static breakdown voltage can be explained by the action of the prebreakdown currents, which give rise to ionization and the formation of space charge in the gap. The lowest electrical strength appears in the knife-edge–plane gap. For an interelectrode gap of 0.9 mm and static voltage of 60 kV, the prebreakdown cur-

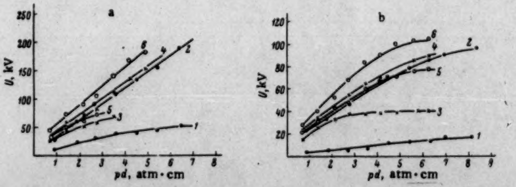

Fig. 1. Dependence of the static and pulsed breakdown voltage on the product of pressure and gap width, in nitrogen (a), hydrogen (b).

rent reaches 450 μA. When pulsed voltages are used the influence of the prebreakdown currents is reduced. Therefore, a higher voltage is required to complete the discharge processes in a short time. The detailed influence of the prebreakdown current on the breakdown voltages of gases at high pressures is considered in ref. 4.

[1] V. A. Tsukerman, Vestnik Akad. Nauk SSSR, 11, 18 (1971).

[2] N. V. Belkin, N. I. Komyak, E. A. Peliks, and V. A. Tsukerman, Prib. Tekh. Eksp., No. 2, 194 (1972).

[3] N. V. Belkin and É. A. Avilov, Zh. Tekh. Fiz., 41, 2167 (1971) [Sov. Phys. – Tech. Phys., 16, 1717 (1972)].

[4] A. H. Cookson, Proc. IEEE, 117, No. 1, 269 (1970).

Coherent phase oscillations of electrons in a synchrotron

M. M. Nikitin
Scientific-Research Institute of Nuclear Physics, Electronics, and Automation, Tomsk

(Submitted April 2, 1973; resubmitted October 19, 1973)
Zh. Tekh. Fiz., 44, 2622-2623 (December 1974)

An experimental study is reported of coherent phase oscillations of the center of gravity of an electron beam in a synchrotron. Differences in the interaction of the accelerated bunches with the accelerating system are indicated. Low-frequency relaxation of the bunches is observed. The particle loss caused by the beam oscillations can be eliminated by adjusting the frequencies of the resonator and the rf source.

Coherent oscillations of a beam have previously been observed and studied in storage systems.[1] Oscillations of the beam in the 1.5 GeV synchrotron of the Scientific-Research Institute of Nuclear Physics are observed in the interaction of the electron beam with the accelerating resonator itself at a beam current ~ 20 mA. The shunt resistance of the resonator is 37.5 kΩ, and its Q is 1500 (ref. 2).

The frequency and the changes in the amplitude of the oscillations of the center of gravity of the beam are studied from the synchrotron emission of the electrons; the simple apparatus used for this purpose has an optical filter of inhomogeneous optical density and a photomultiplier; it operates at frequencies up to hundreds of megahertz.[3]

On the oscillogram of the accelerated electron current taken during the acceleration cycle shown in Fig. 1a we see the overall nature of the growth and decay of the radial phase oscillations of the beam. The center of gravity of the bunches is excited at electron energies between 250 and 350 MeV.

The oscillations grow for several milliseconds and lead to a loss of the stored electrons; then the oscillations are quenched. There is an interesting low-frequency relaxation of the natural phase oscillations of the bunches (Fig. 1, b–d). The frequency of this low-frequency relaxation oscillation is proportional to the current of accelerated electrons and is governed by the properties of the accelerating system.

The mechanism for this relaxation is apparently similar to that described in ref. 1. A bunch splits into two parts: One part oscillates at a high amplitude, while the other oscillates at an extremely low amplitude. If the current of the oscillating part is not sufficient to maintain the natural oscillations, these oscillations cease. The bunch comes together again, leading to a repeated growth of the oscillations. This mechanism is illustrated by the oscillogram in Fig. 1d. In most cases the bunch comes together before the natural oscillations of the rapidly oscillating group of electrons are cut off completely.

The experimental frequencies of the coherent phase oscillations for electrons at 300 MeV ($t/T_c = 0.15$) (the energy at which the observations were made) agree with the theoretical value of 79 kHz.

Using an FÉU-30 photomultiplier with a time resolution ~ 2 nsec (the azimuthal dimension of a bunch at ~ 15 nsec), we are able to observe the interaction of the accelerating resonator with each separate bunch simultaneously. For this purpose we used a stepped optical filter, aligned precisely at the center of the beam and transmitting light from only one half of the beam (in the radial direction). It turns out that each of the four bunches in the synchrotron at a given time interacts with the accelerating system in a distinct manner. The differences apparently result from the nonidentical filling of the four separatrices with electrons, the independence of the interactions of the individual bunches with the resonator (when the center of gravity on one bunch reaches its maximum oscillation amplitude, another bunch splits into two parts), and the fact that the coordinates of a given bunch in the cross section of the vacuum chamber can differ slightly from those of other bunches.

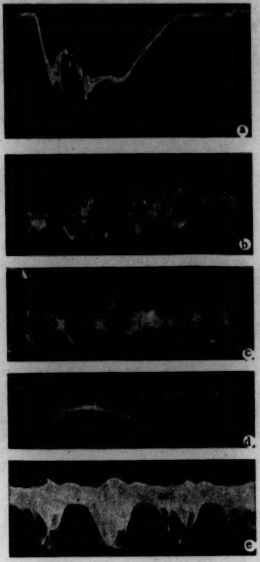

Fig. 1. Oscillograms of the coherent radial phase oscillations of the electrons in the synchrotron. Horizontal scale (msec/div): a) 10; b) 1; c) 0.5; d) 10^{-2}; e) 10^{-3}.

Our experiments showed that the beam oscillations occur primarily on the "unfavorable" slope of the resonance curve of the resonator, i.e., when the resonant frequency of the resonator is higher than the frequency of the rf power source. The natural beam oscillations can also arise on the other slope of the resonance curve, but only if the current of accelerated electrons is several times higher.

Since the accelerator operates unstably under these conditions, we are not able to carry out a detailed study of this case.

Study of the resonance curve of the accelerating resonator shows that there are no parasitic resonances at up to the fourth harmonic of the acceleration frequency. Presumably the bunches also interact with elements of the vacuum chamber and the straight sections of the synchrotron. We have been able to eliminate the particle loss due to natural beam oscillations by tuning the resonator below the frequency of the rf power source, within the range corresponding to nominal conditions for capture of electrons in the acceleration mode.

The author thanks A. N. Didenko for his interest in this work.

---

[1] V. L. Auslender, M. M. Karliner, B. A. Lazarenko, S. G. Popov, I. K. Sedlyarov, A. N. Skrinskii, and I. A. Shekhtman, At. Energ., 22, 194 (1967).

[2] A. A. Vorob'ev, L. P. Chuchalin, A. G. Vlasov, V. N. Kuz'min, G. A. Sipailov, B. A. Solntsev, G. P. Fomenko, and P. M. Shchanin, The 1.5-GeV Synchrotron of the Tomsk Polytechnical Institute [in Russian], Atomizdat, Moscow (1968).

[3] V. A. Vizir' and M. M. Nikitin, Prib. Tekh. Eksp., No. 5, 37 (1971).

Neutral particles from the interaction of laser radiation with a solid target

Yu. A. Bykovskii, N. M. Vasil'ev, I. D. Laptev, and V. N. Nevolin

(Submitted July 23, 1973)
Zh. Tekh. Fiz., 44, 2623-2624 (December 1974)

The characteristics of neutral hydrogen and deuterium atoms formed in the interaction of a single laser pulse with solid targets of zirconium hydride and deuteride are studied. The total number of neutral hydrogen and deuterium atoms is estimated.

Up to the present time investigations of a laser plasma by mass-spectrometer methods have been confined to a study of the ion component. Such important characteristics as the energy and spatial distributions of the ions have been obtained for various flux densities of the laser radiation and for various materials.[1,2] From these studies certain conclusions can be drawn about the processes taking place in a dense high-temperature laser plasma. At the same time the study of the neutrals formed in the interaction of laser radiation with a solid target has not received adequate attention. In our opinion the determination of the velocities, energies, and numbers of these neutrals enables us to draw conclusions about their origin and to supplement the picture of the processes going on in a laser plasma.

Such investigations can also have practical value. Up to the present time mass-spectrometer methods of gas analysis with laser probing of the specimens under study have operated with the lasers in the free running mode.[3] For this reason the amount of material evaporated varies greatly from burst to burst and the results are not reproducible. In the interaction of a giant pulse of radiation the amount of material evaporated depends on the radiation flux density and not on the properties of the irradiated solid. Thus the use of giant pulses for probing specimens significantly increases the reproducibility of the mass-spectrometer analysis of gases.

The neutrals are studied with an MSX-3A time-of-flight mass spectrometer. The ejection pulse of the ion source is delayed relative to the laser pulse up to 2000 μsec. With this experimental arrangement for a single triggering the time of arrival of the neutrals in the mass spectrometer ion source can be determined and their velocity, mass, and energy can be measured. The distance between the irradiated solid and the ion source of the mass spectrometer is ~ 33 cm. The Nd : glass laser has the following parameters: energy per pulse ~ 1 J, $\tau \approx 20$ nsec. The targets are zirconium hydride and deuteride. The radius of the focal spot is $\sim 200\ \mu$. The experiments are performed in a vacuum of $5 \cdot 10^{-6}$ torr.

The results of the experiments with neutral hydrogen atoms formed in the interaction of the laser radiation with the target of zirconium hydride are shown in Fig. 1. The energy of the ionizing electrons in the mass spectrometer source is 50 eV, which corresponds to the maximum of the effective ionization cross section of a hydrogen atom.[4]

The velocity distribution of hydrogen atoms is regular and its maximum corresponds to a velocity of $\sim 3.5 \cdot 10^6$ cm/sec (~ 6.4 eV). The error in determining the amplitude is ± 10%. The distribution of deuterium atoms is similar in character.

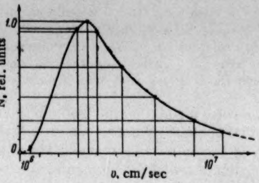

Fig. 1. Velocity distribution of neutral hydrogen atoms.

Using the parameters of our experiment the temperature of the hydrogen plasma formed in the interaction of the laser radiation with the target is estimated with the equations of ref. 5 as ~ 5.6 eV.

The number of detected neutral atoms of hydrogen and deuterium is estimated by admitting helium into the analytic volume through a flow regulator at a rate of $\sim 4.2 \cdot 10^{-5}$ liter/μsec. In doing this the specific form of the dependence of the total effective ionization cross sections of H, D, and He atoms is taken into account. The measured number of hydrogen and deuterium atoms formed by the action of the laser radiation on zirconium hydride and deuteride is $\sim 10^{16}$. This value is in good agreement with the total number of atoms evaporated by laser radiation with our experimental parameters interacting with a solid target.

Our results appear to indicate that the detected neutral hydrogen and deuterium atoms result from recombinations.

Thus a laser plasma can serve as an intense source of high-energy neutrals which can be used to study atomic collision processes.

---

[1] Yu. A. Bykovskii, N. M. Vasil'ev, N. N. Degtyarenko, V. F. Elesin, I. D. Laptev, and V. N. Nevolin, ZhETF Pis. Red., 15, 308 (1972) [JETP Lett., 15, 217 (1972)].

[2] Yu. A. Bykovskii, M. F. Gryukanov, N. N. Degtyarenko, V. G. Degtyarev, V. F. Elesin, I. D. Laptev, and V. N. Nevolin, ZhETF Pis. Red., 14, 238 (1971) [JETP Lett., 14, 157 (1971)].

[3] G. F. Ivanovskii, L. M. Blyumkin, S. V. Varnakov, and L. P. Lisovskii, Zav. Lab., 34, 10, 1263 (1968).

[4] J. Hasted, Physics of Atom Collisions, Butterworths, Washington (1964).

[5] V. A. Boiko, O. N. Krokhin, and G. V. Sklizkov, Preprint FIAN, No. 121 (1972).

Certain integral relations in the kinetic theory of gases

S. P. Bakanov

Institute of the Problems of Mechanics, Academy of Sciences of the USSR, Moscow

(Submitted November 19, 1973; resubmitted April 9, 1974)
Zh. Tekh. Fiz., 44, 2625-2529 (December 1974)

In solving a number of problems in the kinetic theory of gases by the moment method it is necessary to evaluate certain moments of the Boltzmann collision integral, a task which many authors regard as the most laborious part of solving the problems. A systematic method for evaluating these moments directly was developed by Uhlenbeck and Wang Chang;[1] in principle this enables one to solve a broad class of kinetic theory problems. The practical application of this method,[1] however, requires very laborious calculations and offers no way of checking the results. The authors[1] themselves have made mistakes in evaluating certain moments. Most important, in a number of cases the use of these moments leads to results which exceed the accuracy of the theory and to the prediction of nonphysical effects.

It is shown in refs. 2 and 3 on the basis of physical considerations that certain relations can be established among the moments of the collision integral. These relations simplify the calculation of the moments, determine the correctness of published calculations, and ensure that the solution corresponds to physical reality.

Without calculating these directly[1] we present another method of evaluating certain moments of the collision integral which has the same three attributes as the relations mentioned above.

1. We consider the Boltzmann equation in the Chapman–Enskog form[4]

$$f^{(0)}\left[\left(c^2-\frac{5}{2}\right)c_i\frac{\partial \ln T}{\partial r_i}+2\left(c_ic_j-\frac{1}{3}\delta_{ij}c^2\right)\frac{\partial c_{0i}}{\partial r_j}\right]=n^2I(\varphi).$$

This equation has a solution of the form

$$\varphi=-\frac{1}{n}\left[A_i\frac{\partial \ln T}{\partial r_i}+B_{ij}\frac{\partial c_{0i}}{\partial r_j}\right], \tag{1}$$

where

$$A_i=\sum_{r=1}^{\infty}a_2a_i^{(r)}=\sum_{r=1}^{\infty}a_2S_{\frac{3}{2}}^{(r)}(c^2)\,c_i, \tag{2'}$$

$$B_{ij}=\sum_{r=0}^{\infty}b_{r+1}b_{ij}^{(r)}=\sum_{r=0}^{\infty}b_{r+1}S_{\frac{5}{2}}^{(r)}(c^2)\,(c_ic_j-\delta_{ij}c^2), \tag{2''}$$

where a_r and b_{r+1} are quantities that depend on the nature of the molecular interaction. Within the framework of a theory which is linear in the derivatives $\partial T/\partial r$ and $\partial c_{0i}\cdot\partial r_j^{-1}$ the method of successive approximations consists of taking account of one, two, etc. terms in expansion (2) in Laguerre–Sonine polynomials. For any model of the molecular interaction, in the single-polynomial approximation solution (1) has the form

$$\varphi=-\frac{1}{n}\left[a_1\left(\frac{5}{2}-c^2\right)c_i\frac{\partial \ln T}{\partial r_i}+b_1\left(c_ic_j-\frac{1}{3}\delta_{ij}c^2\right)\frac{\partial c_{0i}}{\partial r_j}\right], \tag{3}$$

where the coefficients a_1 and b_1 are connected by the relation

$$-4a_1=3b_1. \tag{4}$$

In applications the specification of a molecular interaction leads to the calculation of a_1 and b_1. Thus, for the hard sphere model

$$b_1=\frac{5}{4}\sqrt{\pi}\lambda, \tag{5}$$

λ is the mean free path of the molecules; for Maxwellian molcules

$$b_1=\frac{4}{3}\left(\frac{m}{2k}\right)^{1/2}\frac{1}{\pi A_2(5)},\quad A_2(5)=0.436.$$

We consider the two-dimensional isothermal shear flow of a gas along the z axis ($\partial T/\partial r_i = 0$). Taking account of (3) we write the Boltzmann equation as

$$2c_xc_z=b_1I(c_xc_z).$$

We take the c_x sign $c_{x1}c_xc_{z1}c_zc^2$ sign c_x, and c_xc^2 sign c_x moments[1)] of this equation. On the right-hand side we obtain the moments of the collision integral which we seek:

$$\left.\begin{aligned}I_2&=[c_xc_{z1}c_z\operatorname{sign}c_x],\\ I_3&=[c_xc_{z_1}c_xc_z],\\ I_6&=[c_xc_{z_1}c_x^2c_z\operatorname{sign}c_x],\\ I_{15}&=[c_xc_{z_1}c_zc^2\operatorname{sign}c_x].\end{aligned}\right\} \tag{6}$$

The integrals on the left-hand side can be evaluated by elementary methods. As a result we have

$$\left.\begin{aligned}I_2&=-\frac{\pi}{b_1},\\ I_3&=-\frac{\frac{\pi\sqrt{\pi}}{2}}{b_1},\\ I_6&=-\frac{\pi}{b_1},\\ I_{15}&=-\frac{3\pi}{b_1}.\end{aligned}\right\} \tag{7}$$

We now consider the state of the gas when there is a temperature gradient

$$\frac{\partial T}{\partial r_i}=\frac{\partial T}{\partial z},\quad \frac{\partial c_{0i}}{\partial r_j}=0.$$

We have

$$\left(\frac{5}{2}-c^2\right)c_z=a_1I\left[\left(\frac{5}{2}-c^2\right)c_z\right].$$

We take the c_xc_z sign $c_{x1}c_z(5/2-c^2)$ moments. A simple calculation gives

$$\left.\begin{aligned}I_{11}&=\left[\left(\frac{5}{2}-c^2\right)c_{z_1}c_xc_z\operatorname{sign}c_x\right]=-\frac{\pi}{4a_1},\\ I_{13}&=\left[\left(\frac{5}{2}-c^2\right)c_{z_1}\left(\frac{5}{2}-c^2\right)c_z\right]=\frac{5\pi\sqrt{\pi}}{4a_1}.\end{aligned}\right\} \tag{8}$$

A comparison of Eqs. (7) and (8), taking account of

(4), shows that the following relations hold among the moments of the collision integral, independently of the assumed molecular interaction model:

$$\left.\begin{aligned} I_2 = I_8 = \frac{2}{\sqrt{\pi}} I_3, \\ I_{15} = 3I_2, \\ I_{11} = -\frac{1}{5\sqrt{\pi}} I_{13} = -\frac{1}{3} I_2. \end{aligned}\right\} \quad (9)$$

The moment

$$I_{12} = \left[c_z c_{z_1}, \left(\frac{5}{2} - c^2\right) c_z \operatorname{sign} c_x\right]$$

is also encountered in applications. It is easy to see that it satisfies the equality

$$I_{12} = -\frac{1}{2} I_2. \quad (10)$$

Equations (9) and (10) are a consequence of the single-polynomial approximation in expansion (1), which is satisfied with various degrees of accuracy for various molecular interaction models; for Maxwellian molecules it is satisfied exactly. It should be noted that the method of half-range expansions proposed by Yvon[5] and developed in the kinetic theory of gases by Gross, Jackson, and Ziering,[6] does not really fall outside the limits of the single-polynomial expansion. In higher approximations the method is unjustifiably complicated and no publications of such work are known to the author. Therefore in solving boundary-value problems by the Gross, Jackson, and Ziering (GJZ) method the failure to satisfy Eqs. (9) and (10) must be considered an excess of accuracy (cf. refs. 2, 3, 7, 8).

Thus the values of certain moments of the linearized Boltzmann collision integral can be established without a direct rather cumbersome calculation. These values are exact for Maxwellian molecules. For other molecules the accuracy depends on the limits of applicability of the single-polynomial approximation in the expansion by the Chapman–Enskog method. It should be emphasized, however, that in a number of cases the more accurate values used in numerous publications lead to the prediction of effects which really do not exist. As a rule this is a result of simply exceeding the accuracy of the theory.

Let us point out, finally, that the scheme we have described satisfies the following physical requirement:[2] In solving kinetic theory boundary-value problems the correct limiting transition is ensured in the body of the gas far from the walls.

2. By using Eqs. (9) and (10) we can simplify considerably the procedure for solving kinetic theory boundary-value problems by the GJZ method. We demonstrate the practical realization of the proposed procedure by the example of a Couette flow.

We consider the symmetric Couette problem. The distance between the plates is 2L. The upper plate moves along the z axis with a velocity −u/2, and the lower plate with a velocity + u/2. The x axis is normal to the plates.

The linearized Boltzmann equation has the form

$$c_x \frac{\partial \varphi}{\partial x} = I(\varphi). \quad (11)$$

We seek a solution in the form

$$\varphi^{\pm} = c_z (a_0^{\pm} + a_1^{\pm} c_x).$$

Taking the $c_z(1 \pm \operatorname{sign} c_x)$ and $c_x c_z(1 \pm \operatorname{sign} c_x)$ moments of Eq. (11) we obtain a system of linear differential equations for the expansion coefficients $a_i^{\pm}(x)$:

$$\left.\begin{aligned} \pi \frac{\partial}{\partial x}\left(\pm a_0^{\pm} + \frac{\sqrt{\pi}}{2} a_1^{\pm}\right) = \pm (a_0^+ - a_0^-) I_1 \pm (a_1^+ + a_1^-) I_2, \\ \pi \frac{\partial}{\partial x}\left(a_0^{\pm} \frac{\sqrt{\pi}}{2} \pm a_1^{\pm}\right) = (a_0^+ - a_0^-) I_2 + (a_1^+ + a_1^-) I_3 \pm (a_1^+ - a_1^-) I_4. \end{aligned}\right\} \quad (12)$$

The notation is standard (cf., e.g., ref. 2). Adding and subtracting pairs of Eqs. (12) and introducing the notation

$$a_0^+ + a_0^- = x_1, \quad a_1^+ + a_1^- = x_3,$$
$$a_0^+ + a_0^- = x_2, \quad a_1^+ - a_1^- = x_4,$$

we obtain

$$\left.\begin{aligned} \frac{\partial}{\partial x}\left(x_2 + \frac{\sqrt{\pi}}{2} x_3\right) = 0, \\ \frac{\pi}{2} \frac{\partial}{\partial x}\left(x_1 + \frac{\sqrt{\pi}}{2} x_4\right) = I_1 x_2 + I_2 x_3, \\ \frac{\pi\sqrt{\pi}}{4} \frac{\partial}{\partial x}\left(x_1 + \frac{2}{\sqrt{\pi}} x_4\right) = I_2 x_2 + I_3 x_3, \\ \frac{\pi\sqrt{\pi}}{4} \frac{\partial}{\partial x}\left(x_2 + \frac{2}{\sqrt{\pi}} x_3\right) = I_4 x_4, \end{aligned}\right\} \quad (13)$$

where the first of Eqs. (13) expresses the obvious law of the constancy of stress in the space between the plates.

By using (9) system (13) is reduced to a set of two differential equations:

$$\left.\begin{aligned} \frac{\partial}{\partial x} x_4 - a_{31} x_3 = -a_{31} \frac{2}{\sqrt{\pi}} A, \\ \frac{\partial}{\partial x} x_3 = a_{11} x_4; \end{aligned}\right\} \quad (14)$$

the other two can be integrated at once:

$$\left.\begin{aligned} x_2 + \frac{\sqrt{\pi}}{2} x_3 = A, \\ x_1 + \frac{2}{\sqrt{\pi}} x_4 = \frac{4}{\pi\sqrt{\pi}} I_2 A x + B. \end{aligned}\right\} \quad (15)$$

Here, we have introduced the notation

$$a_{11} = -\frac{8}{\pi(\pi - 4)} I_4 \quad a_{31} = -\frac{4\sqrt{\pi}}{\pi(\pi - 4)}\left(I_2 - \frac{\sqrt{\pi}}{2} I_1\right).$$

Finally by making the substitution $x_3^* = x_3 - (2/\sqrt{\pi})A$ we obtain

$$\left.\begin{aligned} \frac{\partial x_4}{\partial x} - a_{31} x_3^* = 0, \\ \frac{\partial x_3^*}{\partial x} - a_{11} x_4 = 0, \end{aligned}\right\} \quad (16)$$

i.e.,

$$x_3^* = \beta_{11} e^{\alpha x} + \beta_{12} e^{-\alpha x},$$
$$x_4 = \beta_{21} e^{\alpha x} + \beta_{22} e^{-\alpha x},$$

where

$$a = -\frac{4}{\pi(\pi-4)}\sqrt{2\sqrt{\pi}\, I_4\left(\frac{\sqrt{\pi}}{2} I_1 - I_2\right)}.$$

Substitution of the particular solution into one of Eqs. (16) gives

$$\beta_{21} = -\frac{a_{31}}{a}\beta_{11}.$$

Using the symmetry conditions

$$a_0^+(x) = -a_0^-(-x),$$
$$a_1^+(x) = a_1^-(-x)$$

and the boundary conditions

$$a_0^-(L) = -\varepsilon u_0 + (1-\varepsilon)\, a_0^+(L),$$
$$a_1^-(L) = -(1-\varepsilon)\, a_1^+(L),$$

we obtain B = 0, $\beta_{11} = \beta_{12}$, $\beta_{21} = -\beta_{22}$,

$$x_3^*(x) = 2\beta_{11}\,\mathrm{ch}\, ax,$$

$$x_4(x) = -2\frac{a_{31}}{a}\beta_{11}\,\mathrm{sh}\, ax,$$

$$x_2(L) = \frac{\varepsilon}{2-\varepsilon}\left[x_1(L) + 2u_0\right],$$

$$x_3^*(L) + \frac{2}{\sqrt{\pi}}A = \frac{\varepsilon}{2-\varepsilon}x_4(L).$$

From the last two equations we find the constants

$$\beta_{11} = -\frac{2}{\sqrt{\pi}}\frac{\varepsilon}{2-\varepsilon}\frac{u_0}{D},$$

$$A = \frac{2}{\sqrt{\pi}}\frac{\varepsilon}{2-\varepsilon}\frac{u_0}{D}\left(\mathrm{ch}\, aL + \frac{\varepsilon}{2-\varepsilon}\frac{a_{31}}{a}\,\mathrm{sh}\, aL\right),$$

where

$$D = -\frac{\varepsilon}{2-\varepsilon}\frac{4I_2L}{\pi^3}\left(\mathrm{ch}\, aL + \frac{\varepsilon}{2-\varepsilon}\frac{a_{31}}{a}\,\mathrm{sh}\, aL\right) + \frac{1}{\sqrt{\pi}}\left(\mathrm{ch}\, aL + \frac{\varepsilon}{2-\varepsilon}\frac{a_{31}}{a}\frac{4}{\pi}\,\mathrm{sh}\, aL\right),$$

$u_0 = u(m/2kT)^{1/2}$ is the dimensionless relative velocity of the plates. Finally the rate of flow of the gas is given by

$$q_x(x) = \frac{1}{8}\sqrt{\frac{8kT}{\pi m}}\left(\sqrt{\pi}x_1 + x_4\right)$$
$$= \frac{1}{2\pi}\sqrt{\frac{8kT}{\pi m}}\frac{\varepsilon}{2-\varepsilon}\frac{u_0}{D}\left[\frac{2I_2x}{\sqrt{\pi}}\left(\mathrm{ch}\, aL + \frac{\varepsilon}{2-\varepsilon}\frac{a_{31}}{a}\,\mathrm{sh}\, aL\right) - \frac{a_{31}}{a}\,\mathrm{sh}\, aL\right],$$

which agrees with the result obtained in ref. 3.

The author thanks V. V. Struminskii for helpful comments.

[1)] By the A(c) moment of the function $\Phi(c)$ we mean the integral $\int A(c)\,\Phi(c)\, e^{-c^2} d^3c$ over all values of the velocities.

[1] G. E. Uhlenbeck and C. S. Wang Chang, Transport Phenomena in Very Dilute Gases, Univ. of Michigan, Ann Arbor (1949).
[2] S. P. Bakanov and B. V. Deryagin, Dokl. Akad. Nauk SSSR, 139, 71 (1961) [Sov. Phys. – Dokl., 6, 588 (1962)].
[3] S. P. Bakanov and B. M. Markeev, Preprint IPM No. 29 (1973).
[4] S. Chapman and T. Cowling, The Mathematical Theory of Nonuniform Gases, Cambridge Univ. (1970).
[5] V. Kourganoff and W. Busbridge, Basic Methods in Transfer Problems, Dover, New York (1963).
[6] E. P. Gross, E. A. Jackson, and S. Ziering, Ann. Phys., 1, 141 (1957).
[7] S. Ziering, AIAA J., 1, 661 (1963).
[8] C. Cercignani, Nuovo Cimento, 27, 1240 (1963).

Connection of magnetic lines of force in a neutral layer

A. T. Altyntsev and V. I. Krasov

Institute of Terrestrial Magnetism, the Ionosphere, and Radio-Wave Propagation,
Siberian Branch, Academy of Sciences of the USSR

(Submitted October 22, 1973)
Zh. Tekh. Fiz., 44, 2629-2631 (December 1974)

The neutral layer in a collisionless plasma is shown experimentally to be unstable against the connection of magnetic lines of force. The characteristic time of the process is consistent with the development of the collisionless tearing mode.

The structure of magnetic force lines in a neutral plasma layer is important in connection with a number of astrophysical phenomena, e.g., solar flares, the interaction of the solar wind with the magnetosphere, the geomagnetic tail of the earth. The same problem is encountered in plasma confinement in the belt-pinch or the tokamak.[1,2]

We present below the results of direct measurements of the vector magnetic field in a collisionless neutral layer. The experiment is performed in the UN-Phoenix device[3,4] (Fig. 1). A hydrogen plasma ($n_0 = 10^{12}$–10^{14} cm^{-3}, T_0 = 1-5 eV) in a cylindrical glass chamber (l = 100 cm, ϕ = 16 cm) is located in a quasistationary homogeneous magnetic field ($H_0 = 10^2$–10^3 Oe, τ = 1500 μsec) directed along the axis of the system and is compressed by a cylindrical magnetic piston $H^{\sim}$ produced by means of a shock loop 30 cm long. The field of the piston increases sinusoidally ($H^{\sim}_{\max}$ = 1300 Oe, τ = 1.3 μsec) and is opposite to H_0. The initial parameters of the plasma, its density and temperature, are monitored by means of a triple Langmuir probe.

The disturbance of the magnetic field in the plasma accompanying the compression of the latter is recorded by magnetic probes (3 mm diameter). Figure 2 shows the axial magnetic field distribution H_z at times after the start of the process. In the initial stage, when $|H^{\sim}| \leqslant |H_0|$, a rarefaction wave propagates into the plasma. Compression of the plasma occurs when $|H^{\sim}| > |H_0|$, at which point a neutral layer is found; it consists of a cylindrical current layer within which the magnetic field H_z changes sign. When the value of the magnetic piston becomes greater than $2H_0$ a compression shock is formed in front of the neutral layer.[4]

Measurements show that the neutral layer tends towards a state in which the magnetic pressures on the boundaries of the layer are equal, the radial dimension of the layer amounting to (6-10)c/ω_0 for the entire range of initial plasma densities (ω_0 is the electron plasma frequency, c is the velocity of light). The measurements, made with local magnetic probes described in ref. 5, show that the electron temperature T_e in front of the neutral layer reaches 20-40 eV. This temperature is achieved by the dissipation of the energy of the azimuthal current in the anomalous resistance of the plasma in the rarefaction wave[3] and, in the succeeding stage, in the shock wave.[4,5] The Coulomb mean free path for $T_e \geqslant$ 20 eV is greater than the diameter of the plasma volume, so that the plasma can be regarded as collisionless as far as the processes occurring in the layer are concerned.

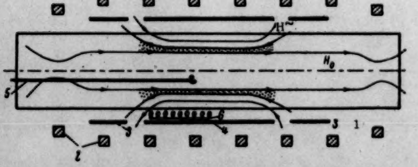

Fig. 1. Schematic diagram of UN-Phoenix device. 1) Vacuum volume; 2) mirror winding generating magnetic field H_0 of mirror configuration; 3) preionization loops; 4) shock loop; 5) magnetic probe in plasma; 6) system of external balanced probes.

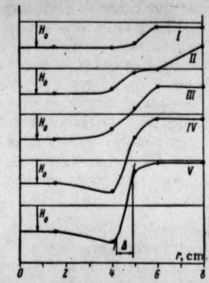

Fig. 2. Formation of neutral layer in plasma. H_0 = 430 Oe, $n_0 = 10^{13}$ cm^{-3}, t (nsec): I) 50; II) 150; III) 250; IV) 350; V) 450.

The axial structure of the magnetic field is investigated using a system of magnetic probes parallel to the axis of the plasma volume and 4 cm from it. The probes

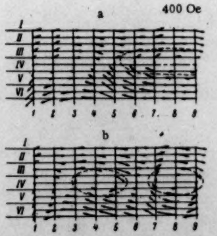

Fig. 3. Axial structure of magnetic field at different times. The origin is taken to be the time at which the region with H_z = 0 passes the probes. Numerals 1-9 denote the positions of the magnetic probes. The first probe is located at the edge of the shock loop. a) H_0 = 300 Oe, $n_0 = 1.8 \cdot 10^{12}$ cm^{-3}, layer velocity $u \doteq 3.3 \cdot 10^7$ cm/sec; b) H_0 = 300 Oe, $n_0 = 2.4 \cdot 10^{13}$ cm^{-3}, u = $1.3 \cdot 10^7$ cm/sec. Time t (nsec): I) –100; II) –60; III) –20; IV) 20; V) 60; VI) 100.

are spaced 2 cm from each other. The radial H_r and axial H_z components at each point are recorded. It is found that in the vicinity of the neutral layer, where $H_z = 0$, a radial field H_r appears which reaches a value of $(0.2\text{–}0.3) \cdot H_b$ (where H_b is the magnetic field at the boundary of the current layer). The behavior of the vector magnetic field as the neutral layer passes the probes is shown in Fig. 3 for two different plasma densities. The structure of the layer is symmetric about the midplane of the shock loop; accordingly, we show in Fig. 3 only the region from the edge of the shock loop to its midplane. The variation in magnitude and direction of the vector magnetic field along the layer can be regarded as being due to the connection of lines of force, which leads to the disintegration of the neutral layer into ring currents. Regions with these currents are indicated in Fig. 3 by the dashed lines. The number, dimensions, and relative location of these ring currents within the layer depend on the initial parameters of the plasma. Thus, a decrease in the initial density n_0 is accompanied by an increase in the width of the layer Δ and by an increase in the axial dimension of the regions with ring currents.

The initial stage of the process is studied using balanced magnetic H_z probes (similar to those used by Green[6]) located outside the plasma volume. It is found with the aid of these probes that the initially monotonic axial magnetic field at the boundary of the plasma volume exhibits a spatial modulation after the appearance of the neutral layer, the amplitude of these modulations reaching $\sim 0.1H^{\sim}$. The growth time of these oscillations $\tau = 30\text{–}50$ nsec. As the appearance of this modulation is associated with the formation of the neutral layer and as the spatial location of the maxima correlates with the position of the above-described current rings, it is reasonable to relate the modulation with the connection of lines of force in the plasma.

Our experimental data are consistent with the results of theoretical calculations on the tearing instability, which show that the lines can link up because of the violation of trapping within the layer due to the finite conductivity of the plasma or the finite Larmor radius of the particles.

The growth rate γ_r of the resistive tearing instability has been obtained by Furth et al.[7] An estimate of the conductivity σ in the neutral layer from the time delay of the signals from a local diamagnetic probe by the method described in ref. 5 gives a value $\sigma \sim 10^{13}$ sec^{-1}. Then $\gamma_r \lesssim 1/\tau$. We note that σ is much smaller than the Coulomb conductivity, which indicates its anomalous nature.

The growth rate of the collisionless tearing instability is obtained by Laval et al.[8] For our conditions, taking for T_e the estimate $T_e \simeq H_b^2/8\pi n$ (which is supported by the readings of local diamagnetic probes) we find that $1/\gamma \lesssim 5$ nsec. Accordingly, $\tau \sim 10/\gamma$, which makes the collisionless tearing instability the more likely mechanism.

In conclusion we should like to thank R. Z. Sagdeev for suggesting the problem, and R. Kh. Kurtmullaev and A. M. Fridman for their interest.

---

[1] A. G. Es'kov, O. A. Zolotovskii (Zolotovsky), R. Kh. Kurtmullaev, Ya. N. Laukhin (Lauhin), A. I. Malyutin, A. I. Markin, and V. N. Semenov, The Sixth European Conf. on Controlled Fusion and Plasma Physics, Vol. 1, Moscow (1973), p. 599.

[2] J. E. Crow, J. Killen, and D. C. Robinson, The Sixth European Conf. on Controlled Fusion and Plasma Physics, Vol. 1, Moscow (1973), p. 269.

[3] A. T. Altyntsev, N. A. Koshilev, V. I. Krasov, V. L. Masalov, O. G. Parfenov, and A. A. Shishko, ZhETF Pis. Red., 18, 397 (1973) [JETP Lett., 18, 233 (1973)].

[4] R. Kh. Kurtmullaev, Doctoral Dissertation [in Russian], Novosibirsk (1969).

[5] R. Kh. Kurtmullaev, V. I. Pil'skii, and V. I. Semenov, Zh. Tekh. Fiz., 40, 1044 (1970) [Sov. Phys. – Tech. Phys., 15, 804 (1970)].

[6] T. S. Green, Nucl. Fusion, 3, 57 (1963).

[7] H. P. Furth, J. Killen, and M. N. Rosenbluth, Phys. Fluids, 6, No. 4, 459 (1963).

[8] G. Laval, R. Pellat, and V. Vuillemin, Proc. Conf. on Plasma Physics and Controlled Nuclear Fusion, Culham, 1965; II, IAEA, Vienna (1966), paper CN-21/71.

Correction to the paper "Resonant properties of a pulsating dielectric sphere"

A. G. Nerukh and N. A. Khizhnyak

A. M. Gor'kii Khar'kov State University

(Submitted April 22, 1974)
Zh. Tekh. Fiz., 44, 2632 (December 1974)

A further analysis of the results obtained in ref. 1 reveals that we have made an error: A surface integral was unjustifiably omitted from integral equation (10). When this surface integral is taken into account the original integral equation becomes

$$
\begin{aligned}
\mathbf{E} = {}& \mathbf{E}_0 + \frac{\varepsilon-1}{4\pi}\left(\operatorname{grad}\operatorname{div} - \frac{1}{c^2}\frac{\partial^2}{\partial t^2}\right)\frac{\partial^2}{\partial t^2} \\
& \times\Bigg[\int\limits_{-\infty}^{\infty} dt' \int\limits_{V(t')} \frac{\tau-\frac{1}{c}R}{R}\, h \Bigg\{\mathbf{E} - c\mathbf{E}\int\limits_{-\infty}^{t'} \nabla\beta\, dt'' \\
& - c\left[\operatorname{curl}\beta \int\limits_{-\infty}^{t'} \mathbf{E}\,dt\right] - c\nabla\beta \int\limits_{-\infty}^{t'} \mathbf{E}\,dt'' + 2c\left(\int\limits_{-\infty}^{t'} \mathbf{E}\,dt''\nabla\right)\beta\Bigg\} d\mathbf{r}' \\
& - \operatorname{grad}\int\limits_{-\infty}^{\infty} dt' \int\limits_{V(t')} \frac{\tau-\frac{1}{c}R}{R}\, hc\beta \int\limits_{-\infty}^{t'} \mathbf{E}\,dt''\,d\mathbf{r}' \\
& + \operatorname{curl}\int\limits_{-\infty}^{\infty} dt' \int\limits_{V(t')} \frac{\tau-\frac{1}{c}R}{R}\, h \Bigg\{\left[c\beta \int\limits_{-\infty}^{t'} \mathbf{E}\,dt''\right] \\
& + c\int\limits_{-\infty}^{t'} [\beta\mathbf{E}]\,dt''\Bigg\} d\mathbf{r}''\Bigg] - \frac{\varepsilon-1}{4\pi}\left(\operatorname{grad}\operatorname{div} - \frac{1}{c^2}\frac{\partial^2}{\partial t^2}\right)\frac{\partial^2}{\partial t^2} \\
& \times \int\limits_{-\infty}^{\infty} dt' \int\limits_{S(t')} \frac{\tau-\frac{1}{c}R}{R}\, h \Bigg\{\left(c\beta\int\limits_{-\infty}^{t'} \mathbf{E}\,dt''\right)\mathbf{n} + \left[\left[\int\limits_{-\infty}^{t'} \mathbf{E}\,dt\,c\beta\right]\mathbf{n}\right]\Bigg\} ds. \qquad (10)
\end{aligned}
$$

All of the equations which follow from Eq. (10) must be corrected accordingly. In particular, the internal field in the case of the scattering of a wave by a sphere of variable radius in the quasistatic case is described by a revision of Eq. (13):

$$
\mathbf{E} = \left[\frac{\varepsilon+2}{3} - (\varepsilon-1)\,\xi(t)\right]^{-1}\mathbf{E}_0(t). \qquad (13)
$$

The resonant properties of the pulsating sphere are manifested in the behavior of the field amplitude averaged over a period. However, the resonant increase in the amplitude of the internal field obtained in the quasistatic approximation in ref. 1 does not occur.

---

[1] A. G. Narukh and N. A. Khizhnyak, Zh. Tekh. Fiz., 44, 257 (1974) [Sov. Phys. – Tech. Phys., 19, 166 (1974)].